ISES SWC 2017

SOLAR WORLD CONGRESS
29 OCT – 02 NOV, 2017
ABU DHABI, UAE

International Conference
on Solar Heating and Cooling
for Buildings and Industry

SHC CONFERENCE 2017
29 OCT - 02 NOV
ABU DHABI, UAE

ISES Solar World Congress 2017

IEA SHC International Conference on Solar Heating and Cooling for Buildings and Industry 2017

Proceedings

Conference of

ISES International Solar Energy Society

SHC SOLAR HEATING & COOLING PROGRAMME INTERNATIONAL ENERGY AGENCY

Hosted by

Masdar INSTITUTE
A Part of Khalifa University of Science and Technology

Online management

projects in solar energy

Proceedings of the ISES Solar World Conference 2017 and the IEA SHC Solar Heating and Cooling Conference for Buildings and Industry 2017

Edited by
Dr. Manuel Romero, Co-Chair of Technical Program Committee
Dr . Daniel Mugnier, Co-Chair of Technical Program Committee

Dr. David Renné, Co-Chair of International Organizing Committee
Mr. Ken Guthrie, Co-Chair of International Organizing Committee
Dr. Steven Griffiths, Co-Chair of International Organizing Committee

International Solar Energy Society
Wiesentalstr 50
79115 Freiburg
Germany

Tel + 49 761 45906 – 0
Fax + 49 761 45906 – 99
Email hq@ises.org
http://www.ises.org

ISBN 978-3-981 465 9-7-6

Produced by
International Solar Energy Society

Notice

The International Solar Energy Society, the International Energy Agency's Solar Heating and Cooling Programme nor any one of the hosts, supporters or sponsors of the ISES Solar World Congress 2017 / IEA SHC Solar Heating and Cooling Conference for Buildings and Industry 2017, makes any warranty, express or implied, or accepts legal liability or responsibility for the accuracy, completeness or usefulness of any information, apparatus, product or process disclosed, or represents that its use would not infringe privately on rights of others. The contents of articles express the opinion of the authors and are not necessarily endorsed by the International Solar Energy Society, the International Energy Agency's Solar Heating and Cooling Programme or by any of the hosts, supporters or sponsors of the joint conference. The International Solar Energy Society and the International Energy Agency's Solar Heating and Cooling Programme do not necessarily condone the politics, political affiliation and opinions of the authors or their sponsors.

Disclaimer

We cannot assume any liability for the content of external pages. The operators of those linked pages are solely responsible for their content. We make every reasonable effort to ensure that the content of this web site is kept up to date, and that it is accurate and complete. Nevertheless, the possibility of errors cannot be entirely ruled out. We do not give any warranty regarding the timeliness, accuracy or completeness of material published on this web site, and disclaim all liability for (material or non-material) loss or damage incurred by third parties arising from the use of content obtained from the web site.

Monday, October 30 2017

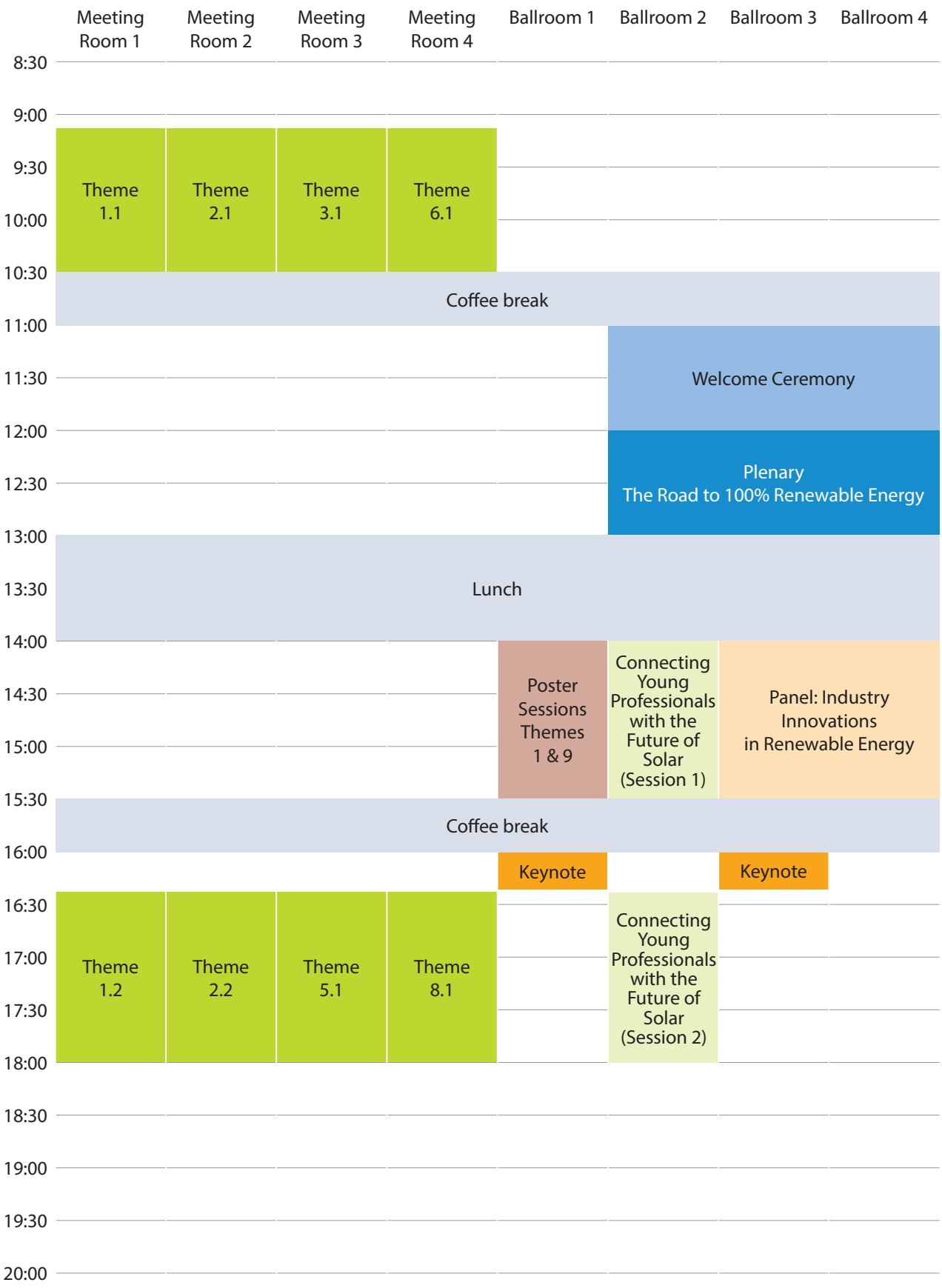

Tuesday, October 31 2017

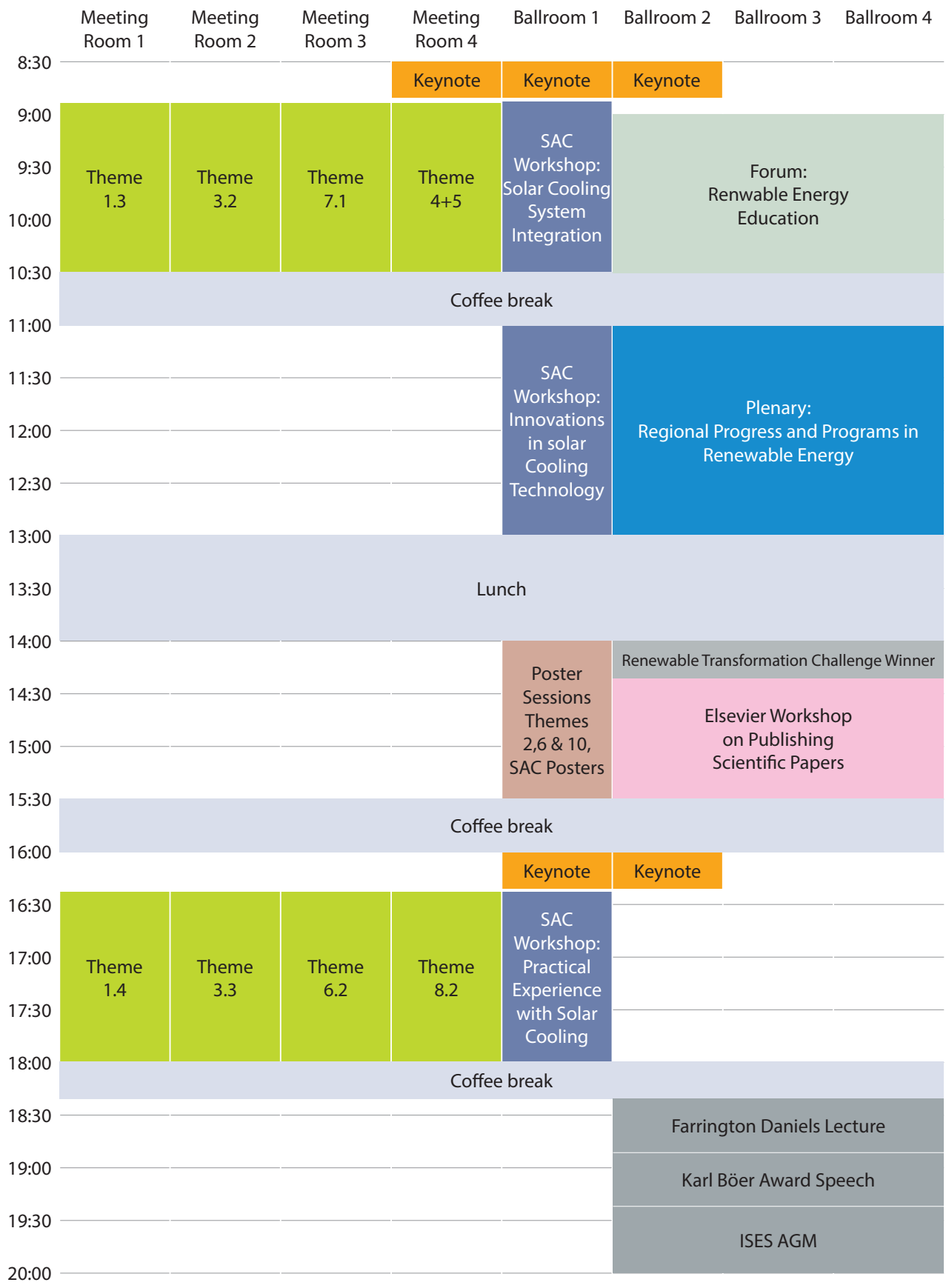

Wednesday, November 01 2017

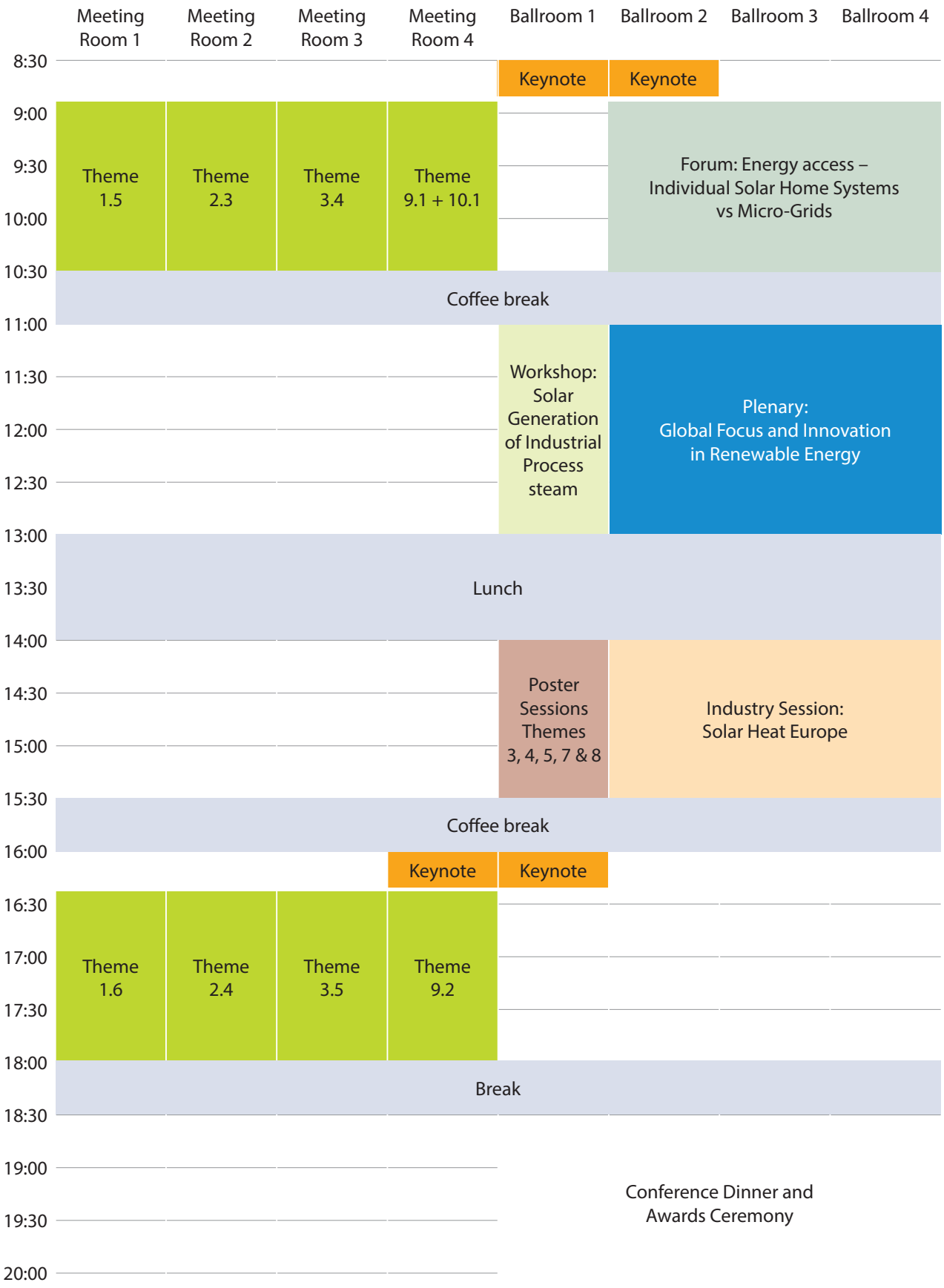

Thursday, November 02 2017

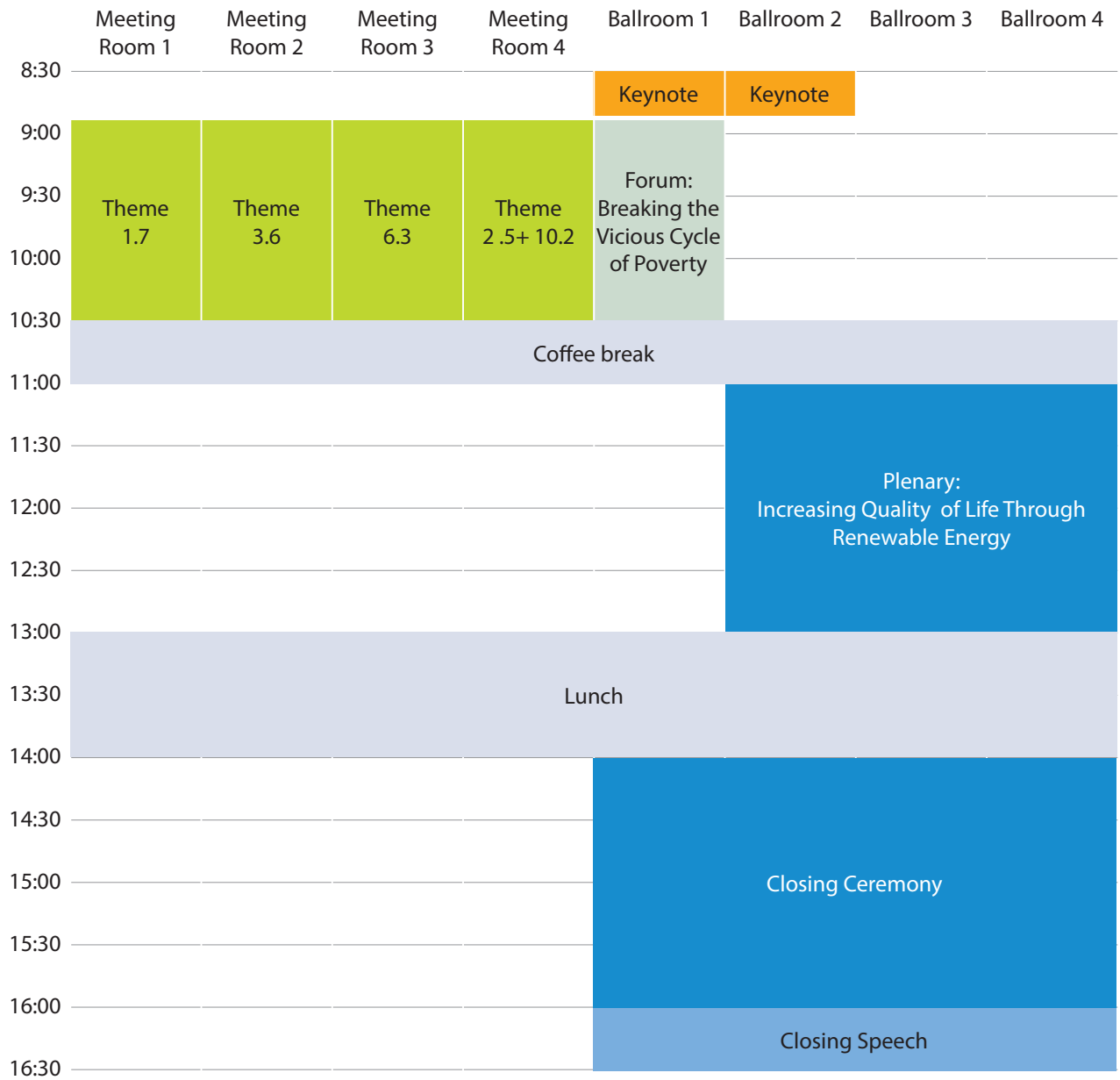

Masdar Institute of Science and Technology, part of the Khalifa University of Science and Technology

The Masdar Institute of Science and Technology (MI) is the local host of the joint International Solar Energy Society (ISES) Solar World Congress 2017 and International Energy Agency (IEA) Solar Heating and Cooling Programme's 2017 Conference on Heating and Cooling for Buildings and Energy. The Institute was established in 2007 in Abu Dhabi, in collaboration with the Massachusetts Institute of Technology (MIT), as an independent non-profit graduate level research university focused on advanced energy and sustainable technology. The Institute has served to develop the intellectual and human capital of relevance to the UAE's knowledge economy transformation through its high quality academics and research of relevance to local, regional and global needs.

Over the years MI has evolved an academic and research platform that articulates its mission and vision according to critical energy and sustainability challenges. It integrates theory and practice to incubate a culture of innovation and entrepreneurship to develop the critical thinkers and leaders of tomorrow. In this way the Institute has sought to be a leading renewable energy and clean technology player by providing a test bed for the world to develop commercially viable and sustainable energy solutions, engaging in research and development collaboration with the four corporate arms of its allied Masdar group and the UAE as a whole. It has maintained a particular focus on the research and development of renewable energy and related technologies, launching the Masdar Institute Solar Platform as part of the broader Masdar Solar Hub that additionally includes a Solar and Device Testing (SDT) Laboratory and a Solar Panel Testing Lab. This is just one example among many of the research facilities developed at the Institute to research, develop and test technologies, systems and prototypes for renewable energy applications.

In February 2017 MI merged with the Khalifa University of Science, Technology and Research (KUSTAR), and the Petroleum Institute (PI) to produce the new Khalifa University of Science and Technology, which is designed to serve as a world-class, research-intensive institution that develops world leaders and critical thinkers in science and engineering.

The resulting university endeavors to be a catalyst to the growth of Abu Dhabi and the UAE's rapidly developing knowledge economy as an education destination of choice and a global leader among research intensive universities. Bringing three excellent universities under a single umbrella intends to provide enhanced efficiency, interdisciplinary innovation, access to greater research facilities, and strengthened support for faculty, staff and students. It will also provide the UAE's youth with a single world-class university with the capability to take them from undergraduate to graduate education in advanced disciplines of great value to the country and region.

Today the Khalifa University of Science and Technology is home to the most advanced research facilities in the country and some of the brightest minds in the world. Its faculty include some the region's leading experts in clean and renewable energy, hydrocarbon exploration and production, water and environment, healthcare, aerospace, supply chain and logistics, advanced materials and manufacturing, robotics, artificial intelligence and data science, information communication technologies (ICT) and security. They work collaboratively across the university's many research centers in pursuit of scientific and technical advancement in sectors targeted for the UAE's high-tech knowledge economy. With its expansive academic programs, research centers, faculty, and interdisciplinary scope, the Khalifa University of Science and Technology will be able to improve the UAE's ability to meet the needs for the future.

جامعة خليفة للعلوم والتكنولوجيا
KHALIFA UNIVERSITY OF SCIENCE AND TECHNOLOGY

جامعة خليفة
KHALIFA UNIVERSITY

THE PETROLEUM INSTITUTE

Masdar INSTITUTE معهد مصدر

A Part of Khalifa University of Science and Technology

Masdar City

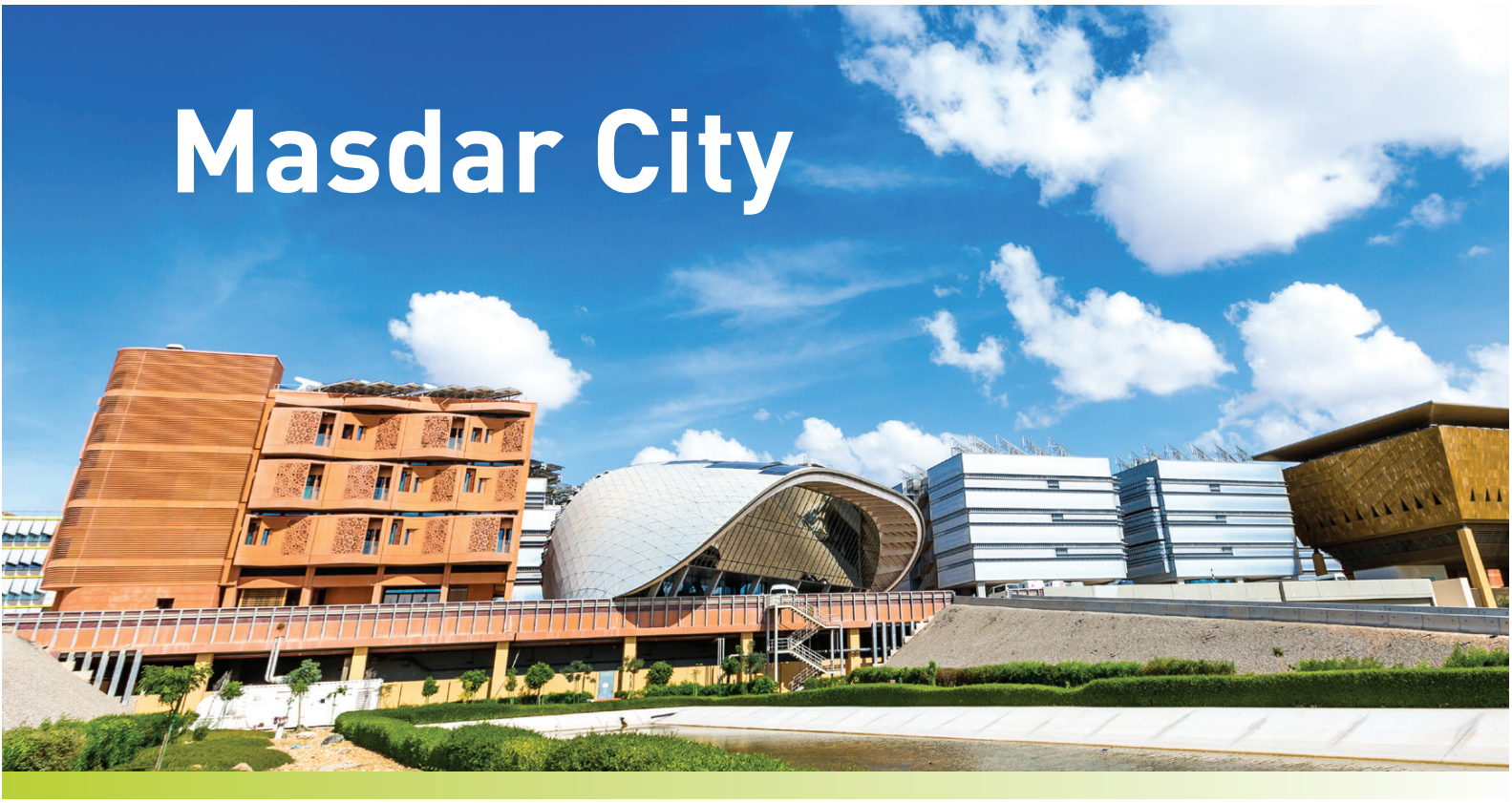

Sustainable Inside and Out

With more energy-efficient buildings in a single district than any other development in the region, Masdar City features both passive and active energy and water saving features that ensure all buildings are certified to at least 3 Pearls (equivalent to LEED Gold) under the Estidama programme, Abu Dhabi's sustainable building, villa and community rating system designed for the specific needs of the UAE climate. In fact, Estidama was incubated in Masdar City.

Master Plan

The city's master plan integrates office, residential, educational, leisure and retail in a way that maximises walkability and facilitates the use of public transportation, including personal rapid transit and group rapid transit systems. Ultimately, up to 50,000 people will live in Masdar City, while up to 40,000 will work and study there. The master plan's orientation of the city and its highdensity design help to optimise shading and capture prevailing winds, producing naturally cooler outdoor public spaces, while also reducing indoor cooling requirements. Buildings are constructed using low-carbon cement, recycled aluminium and sustainably sourced wood, while energy-efficient buildings mean Masdar City consumes 40% less energy and water than other developments in the UAE of a comparable size.

In addition, the city is powered in part by clean energy generated from an on-site 10MW solar power plant and a 1MW solar rooftop system. With such a commitment to urban sustainability, Masdar City represents a unique living laboratory for industry and academia to study how cities use, conserve and share resources, and for product developers to evaluate technologies in a real-world setting.

The city also offers a range of investment opportunities to purchase or lease land plots to develop projects designed to enhance mixed-use community living. Some of these investment opportunities include apartments, office buildings, schools, retail outlets, light industrial facilities, research and development initiatives, and hotels.

www.masdarcity.ae

@masdar
masdar.ae
MasdarVideo
@masdar

Masdar CITY

International Solar Energy Society

I would like to welcome all of you to the International Solar Energy Society (ISES) Solar World Congress (SWC) 2017 and the International Energy Agency Solar Heating and Cooling Programme's 2017 Conference on Heating and Cooling for Buildings and Energy. The Masdar Institute is serving as the local host of this joint conference, taking place here in the dynamic city of Abu Dhabi, United Arab Emirates on 29 October – 2 November 2017.

As with previous ISES SWCs, this joint conference will continue a long tradition of connecting the renewable energy research and academic community with decision makers, financiers, and practitioners. You will find a rich opportunity to network with researchers, solar practitioners, decision makers and financiers to learn more about best practices and the future opportunities for all solar technologies.. The joint conference program includes a variety of events, such as parallel technical oral and poster sessions that provide the latest renewable energy research results, keynote speeches discussing specific technologies, unique workshops and side events addressing critical cross-cutting topics, and a line-up of world-renowned experts at the plenary sessions. All of these events demonstrate how we are heading towards 100% renewable energy for meeting all of our end-use energy requirements, encompassing the power, heating, and transportation sectors. In addition, networking and social events, and technical tours have been designed to enhance your career and business development opportunities.

ISES is committed to achieving the vision of 100% renewable energy for all, used efficiently and wisely. This vision is particularly critical as the world addresses the challenges of mitigating climate change under the initiatives agreed to in the Paris Agreement signed in 2015.

Nevertheless, a transformation of our energy system is already occurring due to the strong public demand and to the efforts of grassroot activists as well as regional and national governments for creating a carbon-free energy system. This joint conference will address the key ingredients of this transformation: technology innovation, financial opportunities, policy developments, and, most important, community and grass-roots actions that are leading to case studies and best practices that already are leading towards achieving a 100% renewable energy system in cities and regions. Nevertheless, many challenges remain, and the joint conference will bring to the forefront a dialogue among diverse experts to discuss and formulate actions to meet these challenges.

I wish you all a very successful and inspiring conference experience.

Dr. David Renné, President
International Solar Energy Society

IEA Solar Heating and Cooling Programme

On behalf of the IEA Solar Heating & Cooling Programme, welcome to the 5th International Conference on Solar Heating and Cooling for Buildings and Industry (SHC 2017). For this conference, we are fortunate to be holding it together with the ISES Solar World Congress 2017. The joint conference is certain to reach a wider network of participants interested in exploring technical, industrial and policy synergies relevant to renewable energy deployment.

This year's conference is taking place in the United Arab Emirates and recognizes the leadership of the joint conference host, Masdar Institute, in the journey from fossil fuels to renewables.

Since 1977, the IEA Solar Heating & Cooling Programme has conducted international collaborative research to expand the use of solar energy for buildings and industry. Our global network of 21 countries and 6 international organizations has completed more than 45 research and dissemination projects. The current 10 research projects include approximately 600 participants, of which more than 25% are from industry.

With ISES and Masdar Institute, the IEA SHC Programme has strong partners and SHC 2017 will once again serve as a platform to build understanding, collaboration and strong cooperation between research and industry.

SHC 2017 is sure to inspire you as you participate in the conference sessions and discussions and learn firsthand about the developments in the Middle East. It is the goal of SHC 2017 to have you leave ready to help deploy solar thermal technologies to become an increasingly significant contributor to a sustainable and renewable energy future.

I am looking forward to meeting, discussing and learning with you at this joint conference.

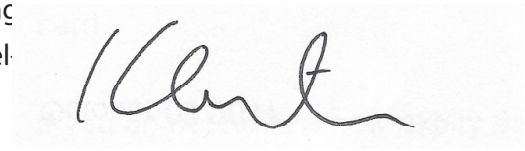

Ken Guthrie, Chair
IEA Solar Heating and Cooling Programme

Khalifa University of Science and Technology

It is with great pleasure that I welcome you to the joint International Solar Energy Society (ISES) Solar World Congress 2017 and International Energy Agency (IEA) Solar Heating and Cooling Programme's 2017 Conference on Heating and Cooling for Buildings and Energy. The theme of the joint event, "innovation for the renewable energy transformation", is perfectly aligned with the research and educational ambitions of the Masdar Institute of Science and Technology, which is this year's conference host and also now part of the new Khalifa University of Science and Technology.

The United Arab Emirates (UAE) is uniquely positioned to serve as the host country for this key event. The UAE Energy Strategy 2050 was launched in 2017 with the ambition to increase the contribution of renewable energy in the country's energy mix to 44 percent by 2050 while simultaneously slashing the country's carbon footprint from power generation by 70 percent in the same timeframe. Solar energy will be the primary form of renewable energy within this strategy and the UAE's commitment to solar has been visible through action, starting with establishment of the Masdar Initiative in 2006. More recently, the 100MW Shams 1 concentrated solar power plant in Abu Dhabi began operations in 2013 and the first three phases of the Mohammed bin Rashid Al Maktoum (MBR) Solar Park, which will ultimately have 5,000MW of solar energy capacity by 2030, were tendered and awarded between 2013 and 2016. In 2017, a 1,170MW solar PV power plant was tendered and awarded for development in Abu Dhabi and a 700MW Concentrated Solar Power (CSP) plant with storage was tendered and awarded for development in Dubai. This CSP power plant, which when operational will deliver electricity at a record low price for this technology of 7.3 US cents per kilowatt hour (kWh), will be part of the fourth phase of the MBR Solar Park.

In addition to these notable achievements, the global headquarters of the International Renewable Energy Agency (IRENA) is hosted in Abu Dhabi's Masdar City. The hosting of IRENA in Abu Dhabi is a reflection of the UAE's commitment to expanding access to sustainable, clean energy both domestically and internationally.

Strategically located at the crossroads of the world, Abu Dhabi is a perfect meeting place to bring together global energy experts. As the host of the annual Abu Dhabi Sustainability Week (ADSW) and the 2016 SolarPACES conference, Abu Dhabi will undoubtedly support this joint event in meeting with similar success and provide participants with the ideal setting to engage in networking, partnership development and exchange of ideas. I wish you a successful and enjoyable conference.

Dr. Steven Griffiths
Interim Executive Vice President for Research

International organizing committee

Chairs:

Dr. David Renné	International Solar Energy Society, USA
Mr. Ken Guthrie	IEA Solar Heating and Cooling Programme, Australia
Dr. Steven Griffiths	Khalifa University of Science and Technology, UAE

Members:

Ms. Joanna Costello	International Solar Energy Society, Germany
Ms. Beatrix Feuerbach	PSE, Germany
Dr. Hosni Ghedira	Khalifa University of Science and Technology, UAE
Ms. Jennifer McIntosh	International Solar Energy Society, Germany
Mr. Steve Meyers	International Solar Energy Society, USA
Dr. Daniel Mugnier	TECSOL, France
Ms. Pamela Murphy	IEA Solar Heating and Cooling Programme, USA
Dr. Manuel Romero	IMDEA Energía, Spain
Prof. Eicke Weber	International Solar Energy Society, Germany

Technical program committee

Chairs:

Dr. Daniel Mugnier	TECSOL, France
Dr. Manuel Romero	IMDEA Energía, Spain

Theme chairs:

• Chair theme 1:	M.Sc. Jan Erik Nielsen	Planenergi, Denmark
• Chair theme 2:	Mrs. Ing. Sabine Putz	SOLID, Austria
• Chair theme 3:	Dr. Manuel Romero	IMDEA Energía, Spain
• Chair theme 4:	Prof. Rodrigo Palma-Behnke	SERC, Chile
• Chair theme 5:	Mr. Geoff Stapleton	GSES, Australia
• Chair theme 6:	Prof. Maria Wall	Lund University, Sweden
• Chair theme 7:	Dr. Paulette Middleton	Panorama Pathways, USA
• Chair theme 8:	Dr. Philippe Blanc	MINES ParisTech, France
• Chair theme 9:	Prof. Bülent Yesilata	Harran University, Turkey
• Chair theme 10:	Prof. Hassan A. Arafat	Khalifa University of Science and Technology, UAE

Members:

Samuel Abreu, Instituto Federal de Santa Catarina, Brazil
Peter Adelmann, University of Applied Science Ulm, Germany
Afshin Afshari, Khalifa University of Science and Technology, UAE
Betsy Agar, Simon Fraser University, Canada
Aliakbar Akbarzadeh, RMIT University, Australia
Saif Al Mheir, Khalifa University of Science and Technology, UAE
Ameena Al-Sumaiti, Khalifa University of Science and Technology, UAE
Mohamed Ibrahim Hassan Ali, Khalifa University of Science and Technology, UAE
Ibraheem Almansouri, Khalifa University of Science and Technology, UAE
Hassan Arafat, Khalifa University of Science and Technology, UAE
Camilo Arancibia-Bulnes, UNAM, Mexico
Elie Azar, Khalifa University of Science and Technology, UAE
Fengwu Bai, IEE-Academy of Sciences, China
Dan Bauer, DLR, Germany
Liliana Beltran, Texas A&M University, USA
Nurettin Besli , Harran University, Turkey
Philippe Blanc , MINES ParisTech, France
Dwipen Boruah, GSE, India
Alessio Bosio, University of Parma, Italy
Lex Bosselaar, Netherlands Enterprise Agency, The Netherlands
Ruslan Botpaev, University of Kassel, Germany
François Boudéhenn, CEA, France
Christoph Brunner, AEE INTEC, Austria
Husamettin Bulut, Harran University, Turkey
Luisa Cabeza, University of Lleida, Spain
Nicolas Calvet, Khalifa University of Science and Technology, UAE
Maria Joao Carvalho, LNEG, Portugal
Manuel Castro, UNED, Spain
Laltu Chandra, IIT Jodhpur, India
Manuel Collares Pereira, University Evora, Portugal
Marcelo Cortés, University Antofagasta, Chile
Yanjun Dai, Jiao Tong University, China
Henrik Davidsson, Lund University, Sweden
Piero de Bonis, EU Commission, Belgium
Pierre Delmas, New Heat, France
Harald Drück, ITW, Germany
Jiangtao Du, Liverpool John Moores University, United Kingdom
Andreas Eckmanns, Federal Office of Energy, Switzerland
Yehia Eissa, Khalifa University of Science and Technology, UAE
Ricardo Enriquez Miranda, CIEMAT, Spain
Michael Epstein, Weizmann Institute, Israel
Janhua Fan, Technical University of Denmark, Denmark
Roberto Fedrizzi, EURAC Research, Italy
David Ferrari, Sustainability Victoria, Australia
Stephan Fischer, ITW, Germany
Daniela Fontani, CNR, Italy
Francesco Frontini, SUPSI, Switzerland
Simon Furbo, DTU, Denmark
Simon Gamble, Hydro Tasmania, Australia
Martin Gastón, CENER, SPAIN
Norbert Geuder, CSP Services GmbH, Germany
Imen Gherboudj, Khalifa University of Science and Technology, UAE
Markus Goelles, Bioenergy2020, Austria
José González-Aguilar, IMDEA Energia, Spain
Adel Gougam, Khalifa University of Science and Technology, UAE
Ian Grant, Bureau of Meteorology, Australia
Christian Gueymard, Solar Consulting Services, USA
Ken Guthrie, Sustainable Energy Transformation Pty Ltd, Australia
Caroline Hachem-Vermette, University of Calgary, Canada

Jean-Christoph Hadorn, Solar Energy & Strategies, Switzerland
Andreas Häberle, SPF Institute for Solar Technology, Switzerland
Andreas Hauer, ZAE-Bayern, Germany
James Hazelton, Macquarie University, Australia
Tao He, China Academy of Building Research, China
Zinian He, Beijing Solar Energy Research Institute, China
Detlev Heinemann, Carl von Ossietzky University Oldenburg, Germany
Dieter Holm, Soltrain, South Africa
Mohamed Ibrahim Hassan Ali, Khalifa University of Science and Technology, UAE
Pierre Ineichen, University of Geneva, Switzerland
Uli Jakob, Greenchiller, Germany
Qingtai Jiao, Sunrain, China
Erik Johansson, Lund University, Sweden
Mustapha Jouiad, Khalifa University of Science and Technology, UAE
Paul Kaaijk, ADEME, France
Jouri Kanters, Lund University, Sweden
Henner Kerskes, University of Stuttgart, Germany
Elisabeth Kjellsson, Lund University, Sweden
Jan Kleissl, University of California at San Diego (UCSD), USA
Christian Kok Nielsen, MOE, Denmark
Vlad Kostylev, Green Power Labs, Canada
Wolfgang Kramer, Fraunhofer ISE, Germany
Philippe Lauret, Laboratoire PIMENT/ Université Réunion, France
Ana Lázaro Unizar, University of Zaragoza, Spain
Antonio Lecuona, UC3M, Spain
Carmel Lindkvist, NTNU, Norway
Gabriele Lobaccaro, NTNU, Norway
Roberto Lollini, EURAC Research, Italy
Yoann Louvet, University of Kassel, Germany
Salvador Luque, IMDEA Energia, Spain
Thomas Mach, Technische Universität Graz, Austria
David Mathieum Laboratoire PIMENT/ Université Réunion, France
Yasuhiro Matsumoto, CINVESTAV, Mexico
Steven Meyers, University of Kassel, Germany
Adriano Moehlecke, PUCRS, Brazil
Andreu Moià, University Balearic Islands, Spain
Graham Morrison, University of New South Wales, Australia
Charles Muchunku, KEREA, Kenya
Michael Müller, Steca Elektronik, Germany
Daniel Mugnier, TECSOL, France
Ammar Nayfeh, Khalifa University of Science and Technology, UAE
Les Nelson, IAPMO, USA
Jan Erik Nielsen, Planenergi, Denmark
Monica Oliphant, Monica Oliphant Research, Australia
Gustaf Olsson, Lund University, Sweden
Jeremy Osborne, EnergyAE, Australia
Philippe Papillon, CEA, France
Cedric Paulus, CEA – INES, France
Bengt Perers, DTU, Denmark
Manuel Pérez, Universidad de Almeria, Spain
Kaj Pischow, SAVOSOLAR, Finland
Jesús Polo, CIEMAT, Spain
David Pozo Vazquez, University of Jaén, Spain
Milan Prodanovic, IMDEA Energía, Spain
Giovanni Puglisi, ENEA, Italy
Sabine Putz, S.O.L.I.D., Austria
Lourdes Ramírez, CIEMAT, Spain
Atul Raturi, University of the South Pacific, Fiji
Jan Remund, Meteotest, Switzerland
David Renné, Senior Consultant, Clean Power Research, USA
Wilfrido Rivera Gomez-Franco, National University of Mexico, Mexico
Roberto Román, Universidad de Chile, Chile
Manuel Romero, IMDEA Energia, Spain
Celestino Ruiv, University of Algarve, Portugal

Jose Antonio Ruiz Arias, University of Jaen, Spain
Hu Runqing, NDRC, China
Wasim Saman, University of South Australia, Australia
Mohamed Sassi, Khalifa University of Science and Technology, UAE
Marion Schroedter-Homscheidt, German Aerospace Center (DLR), Germany
Luis Serra, University of Zaragoza, Spain
Sulaiman Shaari, Universiti Teknologi MARA, Malaysia
Manuel Silva, University of Sevilla, Spain
Ted Soubdhan, University of the Antilles, France
Alistair Sproul, University of New South Wales, Australia
Geoff Stapleton, GSES, Australia
Wolfgang Streicher, Universität Innsbruck, Austria
João Tavares Pinho, Universidade Federal do Pará, Brazil
Costas Travasaros, Primelasertech, Greece
I-Tsung Tsai, Khalifa University of Science and Technology, UAE
Klaus Vajen, University Kassel, Germany
Loreto Valenzuela CIEMAT, Spain
Xavier Vallvé, TTA, Spain
Nieves Vela, CIEMAT, Spain
Lucien Wald, Mines ParisTech, France
Maria Wall, Lund University, Sweden
Petter Wallentén, Lund University, Sweden
Wilfred Walsh, Solar Energy Research Institute of Singapore, Singapore
Ruzhu Wang, Shanghai Jiao Tong University, China
Werner Weiss, AEE INTEC, Austria
Stephen White, CSIRO, Australia
Stefan Wilbert, German Aerospace Center (DLR), Germany
Alex Zahnd, RIDS, Nepal
Luis F. Zarzalejo, CIEMAT, Spain
TieJun Zhang, Khalifa University of Science and Technology, Institute UAE

Local organizing committee

Chairs:

Dr. Hosni Ghedira	Khalifa University of Science and Technology (Chair)
Dr. Nicolas Calvet	Khalifa University of Science and Technology (Co-Chair)

Members:

• Dr. Yehia Eissa	Khalifa University of Science and Technology
• Dr. Imen Gherboudj	Khalifa University of Science and Technology
• Dr. Maryam Al Shehhi	Khalifa University of Science and Technology
• Dr. Naseema Beegum	Khalifa University of Science and Technology
• Dr. Haifa Ben Romdhane	Khalifa University of Science and Technology
• Dr. Mustapha Jouiad	Khalifa University of Science and Technology
• Ms. Muniba Abdul Aziz	Khalifa University of Science and Technology
• Ms. Liny Mohammed	Khalifa University of Science and Technology
• Mr. Zaid Kokh	Khalifa University of Science and Technology
• Mr. Arttu Tuomiranta	Khalifa University of Science and Technology
• Mr. Pierre Vernier	Khalifa University of Science and Technology

Sponsors

Platinum sponsor

Gold sponsor

Silver sponsors

Standard sponsors

Supporters

Supporting partners

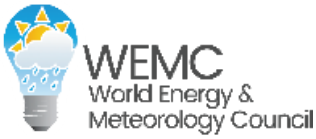

Media partners

Scientific Program

Active Demand-side Management

Clean Transportation Technologies and Strategies

Community Micro Power and Hybrid Systems

Concentrating Solar Power Technologies

Daylighting

District Heating

Domestic Solar Water Heating

Education and Workforce Development

Energy Storage in Buildings

Grid Integration of Variable Renewable Energy Systems

Integrating Desalination with Thermal and Electrical Systems

Integrating Renewable Technologies into Buildings

Low to Medium Temperature Thermal Storage

Medium/High Temperature Thermal Storage for Electricity Production with CSP Systems

Net Zero Energy Buildings

Off-Grid Energy Supply

Other Innovative Components and Systems

PVT Systems

Performance Measurement, Durability and Reliability

Photovoltaics

Renewable Resource Assessment and Applications

Resource Forecasting

Resource Measurement and Instrumentation

Solar Cooking and Clean Cook Stoves

Solar Detoxification of Water

Solar Heat for Industrial and Agricultural Processes

Solar Ponds

Solar Refrigeration and Solar Air Conditioning

Solar Space Heating and Hybrid Applications

Solar Supported Agriculture in Desert Regions

Solar Thermal Collectors

Solar Thermal Desalination Technology

Solar and Heat Pump Systems

Strategies, Policies, and Case Studies for Renewable Heat and Electricity

Sustainable Building Materials and Components

Testing, Standards, and Certification for Solar Thermal Technologies

Urban and Regional Planning to Maximize Renewable Energy

Wind Energy, Ocean Energy, Hydro and Other Direct Conversion Renewables

Active Demand-side Management

Price-based demand side management (DSM) coupled with cold thermal energy storage (TES) and solar PV for peak-load reduction

Mohammad Saffari[1], Alvaro de Gracia[2], Cèsar Fernández[1], Martin Belusko[3], Dieter Boer[2], Luisa F. Cabeza[1]*

[1]GREiA Research Group, INSPIRES Research Centre, Universitat de Lleida, Lleida, Spain

[2]Departament d'Enginyeria Mecànica, Universitat Rovira i Virgili, Tarragona, Spain

[3]Barbara Hardy Institute, University of South Australia, Mawson Lakes Boulevard, Mawson Lakes, South Australia, Australia

*Corresponding author: lcabeza@diei.udl.cat

Abstract

Peak electricity demand has become a global concern. It causes grid transmission constraints and congestion, and also increases the cost of electricity for all users, specifically industrial consumers with high peak demands. Time-of-use demand side management coupled with thermal energy storage and off-grid solar PV can be an alternative to increase the flexibility and security of the whole energy system. The aim of the current paper is to study the potential of implementing time-of-use demand side management coupled with thermal energy storage and solar PV technologies using optimization techniques for shifting electricity peak loads of cooling processes in an industrial unit. It was found that considerable reductions can be achieved in electricity power demands in different tariff periods using optimization-based demand side management (DSM) together with thermal energy storage and off-grid solar PV. In addition, it was seen that coupling cold thermal energy storage and solar photovoltaic technologies is more energy-beneficial than using them separately.

Keywords: Thermal energy storage, solar PV, time-of-use DSM, optimization, peak-load shifting.

1. Introduction

In developed nations electricity plays an important role to economic growth. A considerable rise in electricity demand can be seen in all end-use sectors, and further on, the share of electricity is steadily increasing in all sectors (IEA, 2016). In addition, increasing wealth in developing nations are likely to lead to bigger demand for energy services using electricity, such as cooling and refrigeration. The industry sector is one of the major energy-consuming sectors in the world with about one third of total final energy consumption and almost 40% of total energy-related CO_2 emissions. Reducing these hazardous emissions due to high non-renewable generations is an important issue in the global climate system. For this reason, many governments in the world are exploring alternatives to slow down the global warming by enforcing new rules and regulations for different sectors.

Peak electricity demand is a global policy concern which creates transmission constraints and congestion, and raises the cost of electricity for all end-users (Strengers, 2012). In addition, a considerable investment is required to upgrade electricity distribution and transmission infrastructure, plants and build non-renewable power generation to provide power during peak-demand periods (Strengers, 2012). For this reason, commonly service suppliers charge a higher price for services at peak-time than for off-peak time to compensate for the costly electricity generation at peak hours (Kim et al., 2016). So that, reducing some of this peak demand would benefit the whole energy system (Faruqui et al., 2007).

Solar PV is becoming an important technology in the world energy market for electricity generation, and it has proven its capability to reduce energy costs and hazardous energy-related emissions over time and this is projected to continue. However, in systems with high shares of PV generation, variability and uncertainty in electricity generation within the system may occur because of weather conditions. To overcome this uncertainty energy storage could be a solution to match energy supply and demand. As an example, battery storage technologies could be used to store generated electricity by solar PV, however, currently large-scale electricity storage technology is expensive and needs further technology development (Hameer and van Niekerk, 2015), as a result, electricity storage has limited potential and the generated electricity has to be consumed instantly

doi:10.18086/swc.2017.01.01 Available at http://proceedings.ises.org

(Faruqui et al., 2010).

Demand side management (DSM) is a proactive way to increase the energy efficiency among customers in the long-term (Barbato and Capone, 2014), and can reduce both the electricity peak power demand (kW) and the electricity consumption (kWh) (Warren, 2014; Zhou and Yang, 2015). Among DSM methods techniques load shifting is the most effective load management technique (Esther and Kumar, 2016) which can enhance the demand flexibility without compromising the stability and continuity of the process and, furthermore, a highlighted feature of DSM is that it can be 100% efficient, since no energy conversion to and from an intermediate storable form is required (Lund et al., 2015). However, in order to shift loads from high-demanding hours (on-peak hours) to low-demanding hours (off-peak hours), specifically for industrial and commercial units with considerably high power demand profiles due to their industrial processes, high-capacity energy storage is an essential component to provide an effective and continuous load shifting.

A considerable number of studies have been devoted to investigate the benefits of thermal energy storage (TES) for renewable energies applications and system integration. As an example, Alva et al. (Alva et al., 2017) extensively reviewed the application of TES materials and systems for solar energy applications. Additionally, Li and Zheng (Li and Zheng, 2016) studied different methods of TES system integration for building and industry applications. However, the application of cold storage systems has been broadly developed in the power generation sector, the building sector, and the industrial sector because of their high potential of cooling load shifting (Oró et al., 2012), and decreasing greenhouse gas emissions (de Sisternes et al., 2016). For this reason, there is growing interest in using DSM techniques together with TES, battery storage, and solar PV technologies for industrial and commercial sectors. However, there has been little discussion about coupling DSM together with solar PV and cold TES technologies to reduce peak loads in the industry sector and enhancing the overall performance of the energy system through interconnection of these technologies (Arteconi et al., 2017). Therefore, further research and technology advancement are required for electric load management to address the potential peak load shifting and energy savings considering the new time-of-use tariff structure and elevated electricity prices, high surplus demand charges, and variable solar PV share and its uncertainties in the energy system (Arteconi et al., 2012).

The objective of the current study is to address the potential for applying optimization-based time-of-use DSM in the industry sector to reduce peak electricity demands and eventually to decrease the annual electricity bill. Particularly of interest are, on one hand, to reduce contracted power demands and to shift electrical chiller peak loads from high-price times (on-peak hours) to low-price times (off-peak hours), by taking advantage of cold TES (sensible systems, ice or phase change materials) and off-grid solar PV; and on the other hand, to determine the optimum combinations of contracted power at different tariff periods by integrating TES and solar PV technologies with different capacities, and considering the solar PV variations and surplus charges of power demand.

2. Methodology

2.1. Case study

To give an estimation of the annual energy bill for an industrial consumer, it was assumed that for running its industrial processes, a conventional energy system with no demand management facilities, neither solar PV nor TES system is used. So that, the industrial consumer directly uses the electricity from the grid to run its processes whenever it is required and without considering the on-peak, mid-peak and off-peak demand and energy tariff periods (Figure 1a). The industrial processes take place from 8:00 to 17:00 all days except Saturdays and Sundays, requiring 450 kW of electric demand for cooling processes. To calculate the electricity consumption, the Spanish electricity tariff structure (6.1A time-of-use tariff structure) (Real Decreto 1164/2001, 2016) has been used. The tariff structure is divided into six different tariff periods, and consumers pay through the bill the energy cost and the demand cost. Further explanations of the above-mentioned tariff structure are provided in Section 2.4.1. Assuming that for all tariff periods the reference industrial unit contracts 450 kW power demand with 100% of load factor, the annual electricity bill for operational hours can be calculated using eq. 1:

$$Elec_{tot} = (E_p + E_e) + \left[(E_p + E_e) \times \text{VAT}\right] \quad \text{(eq. 1)}$$

$$E_p = \sum_{i=1}^{i=6}\left(P_{demand_i} \times CP_{p_{demand_i}}\right) \quad \text{(eq. 2)}$$

$$E_e = \sum_{i=1}^{i=6}\left(P_{energy_i} \times CE_{p_{energy_i}} \times h\right) \quad \text{(eq. 3)}$$

where $Elec_{tot}$ is annual electricity cost, E_p is power demand cost, E_e is energy consumption, VAT stands for value added taxes; P_{demand_i} stands for power contracted in different tariff periods; P_{energy_i} stands for consumed energy in different tariff periods; CP and CE are cost of power in kilowatt (kW) and cost of energy in kilowatt-hour (kWh), respectively, for period I, as explained in details in Section 2.4.1.

Three different optimization scenarios were considered to optimally analyze the possibility of shifting on-peak loads from daytime to nighttime by adopting DSM system on the basis of time-of-use tariffs and compare them with the reference model (Figure 1a):

- Scenario 1. time-of-use tariff DSM coupled with only cold TES system (Figure 1b).
- Scenario 2. time-of-use tariff DSM coupled with only off-grid solar PV (Figure 1c).
- Scenario 3. time-of-use tariff DSM coupled with both cold TES and off-grid solar PV systems (Figure 1d).

In Scenario 1 (Figure 1b), the cold TES tank has to be charged at nighttime during off-peak period and be discharged during day especially at on-peak period or the most expensive hours of the electricity tariff. In Scenario 2 (Figure 1c), the feasibility of reducing the energy costs by applying off-grid solar PV has been assessed. In the current study the off-grid solar PV was considered because in the selected tariff structure there is insufficient incentive for grid-connected solar PV system. Eventually, in Scenario 3 (Figure 1d) the possible economic benefits by coupling both cold TES and off-grid solar PV have been investigated. In addition, in should be noted that in the present study the costs of equipment and payback period as well as its environmental impact are not taken into account and might be covered in future studies. Figure 1 illustrates a scheme of the optimization scenarios.

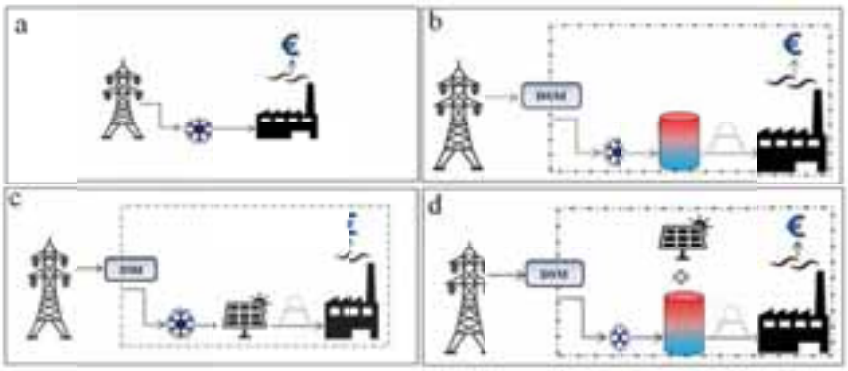

Figure 1. Schematic view of the methodology.

2.2. Simulation of PV module

The electricity generation by solar PV, was simulated using TRNSYS v17 (Klein, 2010). This software has an extensive library of components in which appropriate models could be selected for simulating thermal and electrical energy systems. The potential electricity generation from PV modules can be calculated using Type 94a which models the electrical performance of a photovoltaic array and could be used in simulations involving electrical storage batteries, direct load coupling, and utility grid connections. It applies equations for an empirical equivalent circuit model to predict the current-voltage characteristics of a single module. This circuit consists of a DC current source, diode, and either one or two resistors. The strength of the current source is dependent on solar radiation, and the IV characteristics of the diode are temperature-dependent (TRNSYS 17, 2016). Sunrise SR-M762315-B solar PV (Sunrise, 2016) technical data as shown in Table 1 was introduced to Type 94a and four different nominal power of 25 kWp, 50 kWp, 80 kWp, and 100 kWp were considered. Further on, an array slope of 40º and azimuth of 180º were taken into account. Simulations were performed using time steps of 15 minutes for fifteen consecutive years (1991-2005) using historical solar radiation data of Denver derived from National Renewable Energy Laboratory (NREL) weather data base (National Renewable Energy Laboratory, 2007). Denver, Colorado is dominated by BSk climate classification according to Köppen

Geiger classification and could be representative of climate condition of Lleida province, Spain.

2.3. Thermal energy storage model

A cold thermal storage was integrated into the system with the aim of shifting the electric demand (kW) and the energy consumption (kWh) from on-peak and mid-peak to off-peak hours. The storage model and corresponding charging/discharging modes are similar to the method presented by Ihm et al. (Ihm et al., 2004). The storage capacity can be characterized by a charge/discharge rate as shown in eq. 4. In addition, to convert thermal load to electrical load an average coefficient of performance (COP) of 3 was considered. Then, the electrical acquired energy could be calculated using eq. 5.

Table 1. Sunrise SR-M672315 module specifications (Sunrise, 2016).

Maximum power [W]	315
Module area [m^2]	1.94
Tolerance [%]	0~+3
Open circuit voltage (V_{oc}) [V]	45.42
Short circuit current (I_{sc}) [A]	9.24
Maximum power voltage (V_m) [V]	36.69
Maximum power current (I_m) [A]	8.59
Module efficiency [%]	16.20
Solar cell efficiency [%]	18.85
Cell type [mm]	156x156 (Mono-Crystalline Silicon)
Number of cells [P_{cs}]	72 (6x12)
Maximum system voltage [V]	DC1000
Temperature coefficient of Voc [%/°C]	-0.35
Temperature coefficient of Ise [%/°C]	0.05
Temperature coefficient of Pm [%/°C]	-0.45
Operating temperature [°C]	-40 to 85
Nominal operating cell temperature (NOCT) [°C]	45±2
Maximum series fuse [A]	15
Wind bearing [Pa]	2400
Pressure bearing [Pa]	5400
Standard Test Conditions (STC):1000W/m^2 AM=1.5 25 ºC	

$$\dot{Q}_{storage} = x \frac{SL}{\Delta t} \quad \text{(eq. 4)}$$

$$COP_{ave} = \frac{SL}{Elec_{ac}} \quad \text{(eq. 5)}$$

$$f(x) = \begin{cases} inactive\ mode, & x = 0 \\ charging\ mode, & x > 0 \\ discharging\ mode, & x < 0 \end{cases}$$

where $\dot{Q}_{storage}$ is the TES charge (+)/discharge (−) rate (kW), SL is the cold TES capacity (kWh), x the charge/discharge rate (fraction), Δt the simulation time step (15 minutes), COP_{ave} the average thermal to electrical load conversion COP, $Elec_{acq}$ the acquired electric energy (kWh).

The design is based on three operation schedules over the continuity of charge/discharge rates:

- Inactive mode: when the TES system is not working, for instance at the weekends, the charge/discharge

rate is set to zero in a sub-hourly schedule defined specifically for the TES operation.

- Charging mode: the dedicated TES chiller integrated in the TES module produces cold at the charging rate, *x*, during off-peak hours (the cheapest period) with the maximum charging rate of 375 kW.
- Discharging mode: in this stage the TES system supplies cooling at different capacities to meet the cooling demand during on-peak and mid-peak hours (avoiding or reducing compressor operation). In the present study, the economic impact due to the use of various TES capacities (75-9000 kWh) on the final electricity bill will be analyzed.

The steady-state storage model does not take into account the external weather conditions such as dry bulb temperature, humidity, etc. Moreover, charging and discharging efficiencies were kept a constant value of 100% throughout time steps.

2.4. Time-of-use tariff structure

2.4.1. The electricity bill

In many countries the electricity bill consists of an energy charge, peak demand charge, and taxes. In Spain, taxes are significant and include an electricity tax of 5.1% and a value-added tax (VAT) of 21%. Depending on which demand category the consumer fits in, it determines how many charge categories are applied to the contract. The industry sector has 6.1A demand category which is classified in periods P1 to P6. In each charge category a peak and energy charge is applied. Further on, for this demand category incentives are applied. Figure 2 shows the hourly and monthly periods during which each tariff structure is applied. PX refers to the tariff price profile consisting of an on-peak, mid-peak and off-peak price and P6 refers to all prices at off-peak rates. The tariff consists of both an energy price and a demand price per period as shown in Table 2.

Month/Hour	0	1	2	3	4	5	6	7	8	9	10	11	12	13	14	15	16	17	18	19	20	21	22	23
January	P6	P6	P6	P6	P6	P6	P6	P6	P2	P2	P1	P1	P1	P2	P2	P2	P2	P2	P1	P1	P1	P2	P2	P2
February	P6	P6	P6	P6	P6	P6	P6	P6	P2	P2	P1	P1	P1	P2	P2	P2	P2	P2	P1	P1	P1	P2	P2	P2
March	P6	P6	P6	P6	P6	P6	P6	P6	P4	P4	P4	P4	P4	P4	P4	P3	P3	P3	P3	P3	P3	P3	P4	P4
April	P6	P6	P6	P6	P6	P6	P6	P6	P5	P5	P5	P5	P5	P5	P5	P5	P5	P5	P5	P5	P5	P5	P5	P5
May	P6	P6	P6	P6	P6	P6	P6	P6	P5	P5	P5	P5	P5	P5	P5	P5	P5	P5	P5	P5	P5	P5	P5	P5
1-15 June	P6	P6	P6	P6	P6	P6	P6	P6	P4	P3	P3	P3	P3	P3	P3	P4	P4	P4	P4	P4	P4	P4	P4	P4
16-30 June	P6	P6	P6	P6	P6	P6	P6	P6	P2	P2	P2	P1	P1	P1	P1	P1	P1	P1	P1	P2	P2	P2	P2	P2
July	P6	P6	P6	P6	P6	P6	P6	P6	P2	P2	P2	P1	P1	P1	P1	P1	P1	P1	P1	P2	P2	P2	P2	P2
August	P6	P6	P6	P6	P6	P6	P6	P6	P6	P6	P6	P6	P6	P6	P6	P6	P6	P6	P6	P6	P6	P6	P6	P6
September	P6	P6	P6	P6	P6	P6	P6	P6	P4	P3	P3	P3	P3	P3	P3	P4	P4	P4	P4	P4	P4	P4	P4	P4
October	P6	P6	P6	P6	P6	P6	P6	P6	P5	P5	P5	P5	P5	P5	P5	P5	P5	P5	P5	P5	P5	P5	P5	P5
November	P6	P6	P6	P6	P6	P6	P6	P6	P4	P4	P4	P4	P4	P4	P4	P3	P3	P3	P3	P3	P3	P3	P4	P4
December	P6	P6	P6	P6	P6	P6	P6	P6	P2	P2	P1	P1	P1	P2	P2	P2	P2	P2	P1	P1	P1	P2	P2	P2

Figure 2. Incentive time-of-use electricity tariff structure.

Table 2. Incentive time-of-use electricity prices [59].

	P1	P2	P3	P4	P5	P6	---	---
Power	39.139	19.586	14.334	14.334	14.334	6.540	€/kW/ year	Regulated price
Energy	0.120	0.096	0.092	0.074	0.0708	0.065	€/kWh	Standard free price

2.4.2. Charges due to power excess (surplus charges)

In case that an industrial consumer requires more demand that it has contracted in each determined time interval (for some minutes or even hours), a penalization due to power excess is charged to the bill. This penalization is calculated according to the power contracted in each tariff period and, if applied, depending on each tariff period, the actual demanded power rates are metered using electricity metering equipment. The billing of the excesses of power for the 6.1 tariffs is calculated according to the formula established in Royal Decree 1164/2001 (Real Decreto 1164/2001, 2016) (eq. 6 and eq. 7), and it is measured every 15 minutes:

$$F_{ep} = \sum_{i=1}^{i=6} K_i \times 1.4064 \times A_{ei} \qquad \text{(eq. 6)}$$

where F_{ep} stands for charges in € and A_{ei} is a factor that weights excess of demand depending on the period, K_i is

the coefficient that takes the values depending on the tariff period *i* as shown in Table 3, A_{ei} is calculated according to the following conditional equation:

$$A_{ei} = \begin{cases} 0, & P_{dj} <= P_{ci} \\ \sqrt{\sum_{j=1}^{j=6} (P_{dj} - P_{ci})^2}, & P_{dj} > P_{ci} \end{cases} \quad \text{(eq. 7)}$$

where P_{dj} is demanded power in each quarter of hour which is excessed (higher than P_{ci}), P_{ci} is contracted power in each period and in the considered period.

Table 3. K_i coefficients according to the tariff periods.

Period (i)	1	2	3	4	5	6
K_i	1	0.5	0.37	0.37	0.37	0.17

These powers are expressed in kW and the excesses of power are billed monthly. For tariffs 6.1 at every breach is charged a penalty i.e. every 15 minute breach. Thus, it means that if the user demands over the contracted power during one hour, the penalty is charged four times. However, there is an optimum contracting demand that reduces the energy cost taking into account the penalties. The application of optimized DSM together with TES and PV can optimally find the contracting demands in each period and can improve the overall performance of the energy system.

2.5. Optimization

It could be understood that for given electricity consumption requirements, an optimization problem can be derived based on the power contracting plan, i.e. how much power is contracted for each one of the 6 period tariffs. The optimization problem results deterministic when no PV production is considered. Otherwise, PV uncertainty will lead to stochastic optimization. In both cases, constraint integer programming (CIP) was used as a novel paradigm that integrates constraint programming, mixed-integer programming (MIP), and satisfiability modeling and solving techniques in order to model and solve this problem (Achterberg, 2008; "SCIP Optimization Suite," 2017). Without PV generation, the system may be described as sets, parameters and functions as follows:

$P = \{P_1 .. P_6\}$, is the set of tariff periods; $CE_i, i \in \{1..6\}$ is the cost of energy consumption during period P_i according to Table 2 in €/kWh; $K_i, i \in \{1..6\}$ is the coefficient as defined in Table 3; *SL* is the cold TES storage capacity in kWh; *H, D* and *M* are the set of hours, days and months respectively; *T=H*D*M* is the set of hour periods in a year; $Period: T \rightarrow P$, is a function that maps an hour period to its corresponding tariff as corresponding to Figure 2; $C_i, i \in H$, is the required energy during an hour as shown in eq. 8:

$$C_i = \begin{cases} 450kW \cdot h, & i \in 8..17 \\ 0, & otherwise \end{cases} \quad \text{(eq. 8)}$$

Therefore, the cost of contracting power (*CP*), and the cost of consumed energy can be expressed as eq. 9 and eq. 10, respectively:

$$CP = \sum_{i=1..6} CP_i \cdot PC_i \quad \text{(eq. 9)}$$

Subjected to these constraints: $CP_6 \geq CP_5 \geq CP_4 \geq CP_3 \geq CP_2 \geq CP_1$

$$CE = \sum_{t \in T} S_t \cdot CE_{Period(t)} + K_{Period(t)} \cdot 1.4064 \cdot f\left(S_t - PC_{Period(t)}\right) \quad \text{(eq. 10)}$$

Subjected to the surplus charge constraint of $f(x)$ that is applicable when supplied energy from grid at time *t* is higher than the contracted power in period *i* (PC_i) as shown in eq. 11:

$$f(x) = \begin{cases} x, & x > 0 \\ 0, & x \leq 0 \end{cases} \quad \text{(eq. 11)}$$

where $PC_i \in R, i \in 1..6$, is the contracted power for tariff P_i; $S_t \in R, t \in T$, is the supplied energy from the grid in time *t.* When suitable, one can also denote S_t as $S_{h,d,m}$.

Finally, the following assumptions have been made: 1. The TES operation hours is between 00:00 to 07:00. This is an obvious optimal assumption since it is the off-peak period and no demand exists. 2. The stored energy can only be consumed during the same day. The objective is to find an optimum assignment of $PC_i \in R, i \in$

1..6, that minimizes CP+CE, which could be written as eq. 12, subject to constraint shown in eq. 13:

$$\min_{PC_i}(CP + CE) \quad \text{(eq. 12)}$$

$$SL > \sum_{h=0}^{7} S_{h,d,m} > \sum_{h=8}^{17} C_h - S_{h,d,m}, \forall (d,m) \in D * M \quad \text{(eq. 13)}$$

For example, for each day, the stored energy must not surpass the storage limit and must supply the eventual lack of obtained energy from the grid. In order to reduce the number of variables, symmetries may be considered. As energy requirements are invariant from day to day (C_i), the number of variables can be drastically reduced. More specifically, $S_i$can be indexed in *H*M* instead of *T*. We encoded and solved eq. 12 and eq. 13 with SCIP version 3.2.0 [64] in a 1.9 GHz processor. The problem results in 581 variables and 484 constraints, being solved in less than 2 seconds.

However, when solar PV production is considered, it can be taken into account as a multivariate random variable $PV_y = (pv_{1,y}..pv_{|T|,y})$, being $pv_{i,y}$ the PV production at hour $i \in T$in year *y*. Then, for a given year *y*, the eq. 14 could be written as:

$$SL > \sum_{h=0}^{7} S_{h,d,m} > \sum_{h=8}^{17} C_h - S_{h,d,m} - pv_{h,d,m,y}, \forall (d,m) \in D * M \quad \text{(eq. 14)}$$

When PV production is available over a set *Y* of years, we compute the expected optimization using the cost function presented in eq. 15:

$$E\left[\min_{PC_i}(CP + CE)\right] = \frac{1}{|Y|}\sum \min_{PC_i}(CP + CE) \quad \text{(eq. 15)}$$

subject to constraint as stated in eq. 14. Under this scenario, symmetry reduction as previously stated is no longer feasible and each year optimization problem results in 16469 variables and 16846 constraints, with a resolution time from 5 to 25 minutes depending on SL value.

3. Results

3.1. Economic benefits of optimized DSM with cold TES (Scenario 1)

In this section, the economic benefits due to the use of optimization-based DSM with only cold TES are presented. Figure 3 shows that the amounts of economic savings increase linearly with the increase of TES capacity. From Figure 3 it is apparent that with the increase of storage capacity the annual economic savings increase correspondingly from 418 € (below 1%) per year, in case of 75 kWh capacity of TES, to 53670 € per year (about 30%), in case of 3000 kWh TES. For example, adding 1500 kWh of TES can lead to about 8945 € per year cost savings, and when the storage capacity increases to 6000 kWh these savings rise to 3578 € per year.

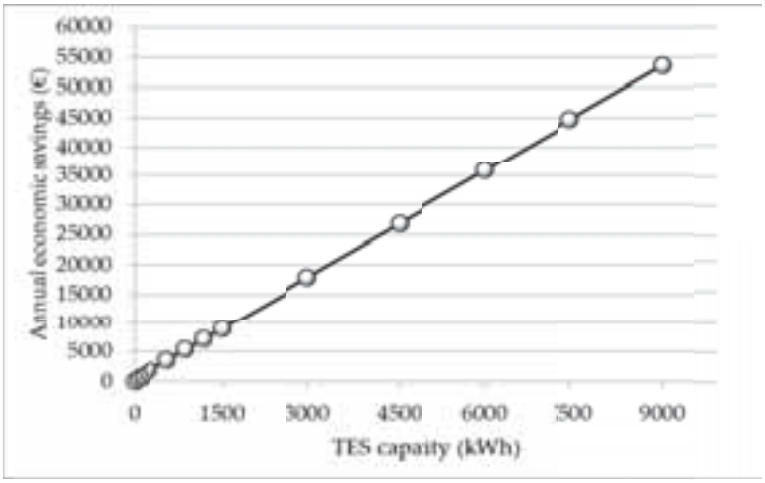

Figure 3. Economic benefits by using DSM and cold TES.

3.2. Economic benefits of optimized DSM with solar PV (Scenario 2)

In this section, the economic benefits due to the use of optimization-based DSM with off-grid solar PV system are presented and the results are shown in Figure 4. Off-grid solar PV yields economic benefits ranging from 4200 € to 16900 € in Denver.

It can be seen that adding 50 kW of off-grid solar PV could achieve annual cost savings of 8465 € in Denver. Compared to TES, lower savings could be achieved using off-grid solar PV. Actually, due to variable PV generation, the electric power demand contract cannot be decreased considerably, since in occasions of poor electricity generation from PV surplus penalties may apply to the electricity bill. However, solar PV can yield to substantial savings when there is enough solar radiation to produce electricity and reduce the real-time energy needs.

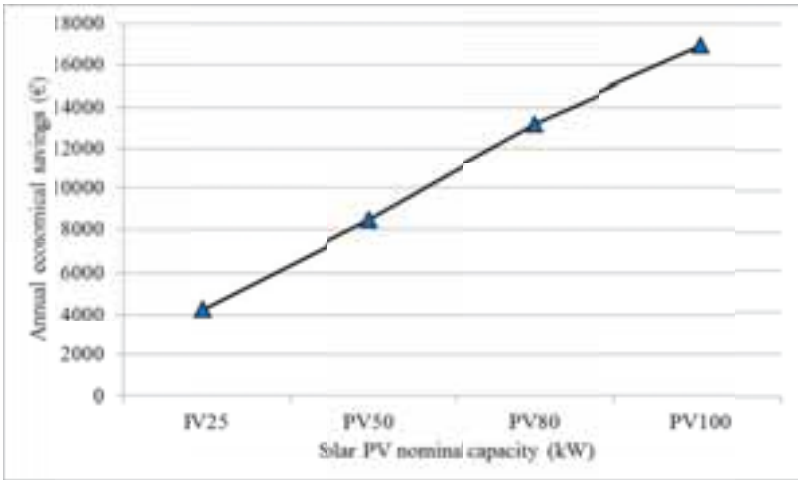

Figure 4. Economic benefits by using DSM and off-grid solar PV.

3.3. Economic benefits of optimized DSM coupled with cold TES and solar PV (Scenario 3)

In this section, the economic benefits due to the use of optimization-based DSM with cold TES coupled with off-grid solar PV system for an industrial consumer have been presented (Figure 5). In general, it can be seen that the annual cost savings have a linear correlation with TES capacity and solar PV nominal capacity. With the increase of TES and PV capacities the annual economic savings increase correspondingly.

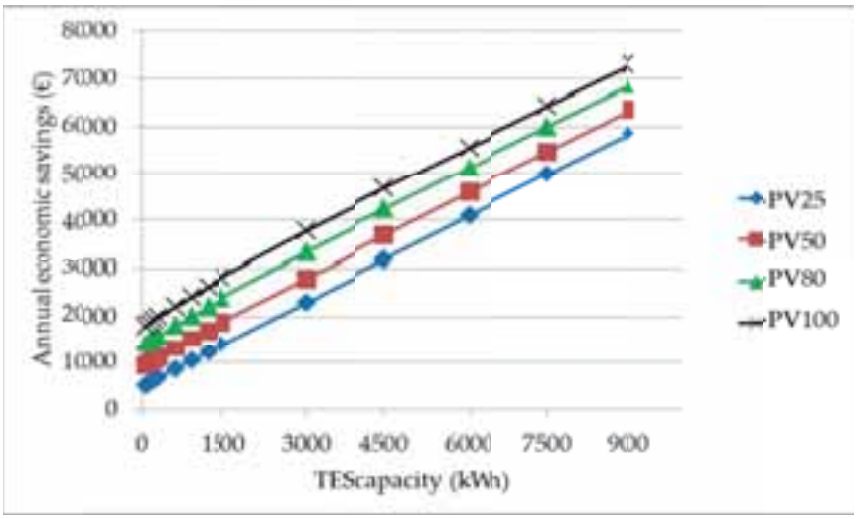

Figure 5. Economic benefits by using DSM coupled with cold TES and solar PV, Denver.

An interesting and very important issue that can be obtained from the results presented in this section is that when TES and PV technologies coupled together higher reductions in power contract demands could be achieved. Accordingly, coupling PV and cold TES together with an optimized DSM led to higher annual electricity cost reductions both for demand and energy terms. Further on, the authors would like to mention that important annual demand cost savings were achieved thanks to the application of TES, nevertheless, it was not

limited to only the demand term, but also, considerable cost savings can be observed for the energy term which mainly comes from renewable solar PV generation.

3.4. Improvements by coupling cold TES and solar PV technologies

An important issue that should be discussed herein is how the combination of solar PV and short-time cold TES technologies coupled to an appropriate time-of-use DSM can shift peak demands and reduce energy consumption and eventually improve the whole energy system. To find economic benefits due to interconnection of these two technologies, annual cost savings due to integration of only cold TES (Scenario 1) and only off-grid solar PV (Scenario 2) should be summed; and then, subtracted from annual cost savings due to coupling cold TES with solar PV (Scenario 3). Actually, these cost savings demonstrate how the interconnection of two renewable technologies together with an optimized DSM, can be energy-beneficial compared to when they are used individually.

The results presented in Figure 6 show the annual cost saving improvement ratios in Denver. In fact, when the solar PV share of the system is smaller, lower storage capacity is needed to provide the continuity and smoothness of supply in the system. The warm color area in the color map highlights the maximum improvement that could be achieved by coupling cold TES and solar PV technologies together. In general, by the increase of solar PV share higher short-term TES is required. In other words, the higher the dependency of energy system on the solar PV, the higher the storage is needed to ensure the security of electricity supply of the system without intermittency and hence avoid possible penalties.

For instance, in case of using 1500 kWh of TES a total annual savings of 8945 € could be achieved. On the other hand, when only off-grid solar PV of 50 kW is considered savings of 8465 could be achieved in Denver. On the other hand, when TES and solar PV technologies are coupled together these savings increase to 18803 €, which is about 7% higher than the sum of benefits achieved by using them separately (Figure 6).

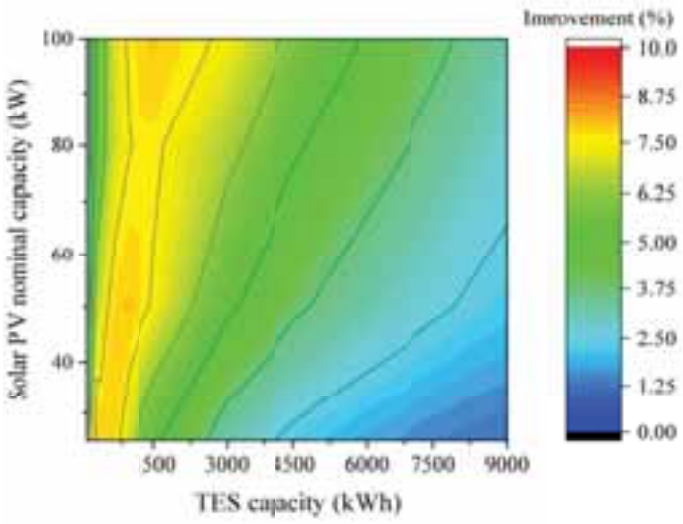

Figure 6. Annual electricity saving improvement by coupling cold TES and solar PV technologies, Denver.

4. Conclusions

In the present study, an optimization-based time-of-use DSM combined with short-term cold TES and off-grid solar PV technologies is used to shift on-peak electricity demand of an industrial consumer. Using numerical optimization and simulation it was found that both cold TES and off-grid solar PV coupled with an appropriate tariff structure can lead to annual electricity cost savings. However, savings attributed to the integration of cold TES are generally higher than those achieved by only off-grid solar PV. In addition, solar PV without storage can reduce the energy term but not significantly the power term of the energy bill. However, it should be highlighted that when cold TES and solar PV are coupled together, further economic benefits could be achieved in comparison with using these two technologies independently.

5. Acknowledgments

The work partially funded by the Spanish government (ENE2015-64117-C5-1-R (MINECO/FEDER), ENE2015-64117-C5-3-R (MINECO/FEDER), and TIN2015-71799-C2-2-P). The authors would like to thank the Catalan Government for the quality accreditation given to their research group (2014 SGR 123). This project has received funding from the European Union's Horizon 2020 research and innovation programme under grant agreement No 657466 (INPATH-TES). Alvaro de Gracia would like to thank Ministerio de Economia y Competitividad de España for Grant Juan de la Cierva, FJCI-2014-19940.

6. References

Achterberg, T., 2008. PhD thesis - Constraint Integer Programming. Universität Berlin.

Alva, G., Liu, L., Huang, X., Fang, G., 2017. Thermal energy storage materials and systems for solar energy applications. Renew. Sustain. Energy Rev. 68, 693–706.

Arteconi, A., Ciarrocchi, E., Pan, Q., Carducci, F., Comodi, G., Polonara, F., Wang, R., 2017. Thermal energy storage coupled with PV panels for demand side management of industrial building cooling loads. Appl. Energy 185, 1984–1993.

Arteconi, A., Hewitt, N.J., Polonara, F., 2012. State of the art of thermal storage for demand-side management. Appl. Energy 93, 371–389.

Barbato, A., Capone, A., 2014. Optimization Models and Methods for Demand-Side Management of Residential Users: A Survey. Energies 7, 5787–5824.

de Sisternes, F.J., Jenkins, J.D., Botterud, A., 2016. The value of energy storage in decarbonizing the electricity sector. Appl. Energy 175, 368–379.

Esther, B.P., Kumar, K.S., 2016. A survey on residential Demand Side Management architecture, approaches, optimization models and methods. Renew. Sustain. Energy Rev. 59, 342–351.

Faruqui, A., Harris, D., Hledik, R., 2010. Unlocking the €53 billion savings from smart meters in the EU: How increasing the adoption of dynamic tariffs could make or break the EU's smart grid investment. Energy Policy 38, 6222–6231.

Faruqui, A., Hledik, R., Newell, S., Pfeifenberger, H., 2007. The Power of 5 Percent. Electr. J. 20, 68–77.

Hameer, S., van Niekerk, J.L., 2015. A review of large-scale electrical energy storage. Int. J. Energy Res. 39, 1179–1195.

IEA, 2016. World Energy Outlook 2016. Iae.

Ihm, P., Krarti, M., Henze, G.P., 2004. Development of a thermal energy storage model for EnergyPlus. Energy Build. 36, 807–814.

Kim, J.-Y., Lee, M.H., Berg, N., 2016. Peak-load pricing in duopoly. Econ. Model. 57, 47–54.

Klein, S.A., 2010. TRNSYS 17: A Transient System Simulation Program, Solar Energy Laboratory, University of Wisconsin, Madison, USA.

Li, G., Zheng, X., 2016. Thermal energy storage system integration forms for a sustainable future. Renew. Sustain. Energy Rev. 62, 736–757.

Lund, P.D., Lindgren, J., Mikkola, J., Salpakari, J., 2015. Review of energy system flexibility measures to enable high levels of variable renewable electricity. Renew. Sustain. Energy Rev. 45, 785–807.

National Renewable Energy Laboratory, 2007. National Solar Radiation Database 1991 – 2005 Update : User's Manual. Task No. PVA7.6102 472.

Oró, E., de Gracia, A., Castell, A., Farid, M.M., Cabeza, L.F., 2012. Review on phase change materials (PCMs) for cold thermal energy storage applications. Appl. Energy.

Real Decreto 1164/2001, 2016. Real Decreto 1164/2001, de 26 de octubre, por el que se establecen tarifas de

acceso a las redes de transporte y distribución de energía eléctrica.(Royal Decree 1164/2001, 2016. Royal Decree 1164/2001, of 26 of October, by that there are established tariffs of access to the networks of transport and distribution of electric power) [WWW Document]. URL https://www.boe.es/diario_boe/txt.php?id=BOE-A-2001-20850 (accessed 7.24.16).

SCIP Optimization Suite [WWW Document], 2017. URL http://scip.zib.de (accessed 1.1.17).

Strengers, Y., 2012. Peak electricity demand and social practice theories: Reframing the role of change agents in the energy sector. Energy Policy 44, 226–234.

Sunrise, 2016. Monocrystalline Modules-Sunrise SOLARTECH (Solar Panel, Solar Module) [WWW Document]. URL http://www.srsolartech.cn/html/Monocrystalline_Modules/32.html (accessed 7.13.16).

TRNSYS 17, 2016. TRNSYS 17–Standard Component Library Overview, Volume 3 [WWW Document]. URL www.trnsys.com/assets/docs/03-ComponentLibraryOverview.pdf (accessed 7.14.16).

Warren, P., 2014. A review of demand-side management policy in the UK. Renew. Sustain. Energy Rev. 29, 941–951.

Zhou, K., Yang, S., 2015. Demand side management in China: The context of China's power industry reform. Renew. Sustain. Energy Rev. 47, 954–965.

Investigating Smart Grid Approaches for optimal Integration of PV Distributed Energy Resources in Dubai

Moustafa A. M. Shahin[1], Evangelia Topriska[1], Michael Gormley[2]

[1] EGIS, Heriot Watt University, Dubai, UAE
[2] EGIS, Heriot Watt University, Edinburgh, UK

Abstract

The rapid deployment of grid-connected roof-top photovoltaic systems in Dubai, as part of "Shams Dubai" initiatives and the anticipated high penetration of distributed PV generation have both raised several challenges and urged the need to study the technical solutions to address higher PV penetration levels. The intermittent nature of PV distributed generation could adversely impact the voltage profile and stability of distribution feeders throughout the daily load cycle resulting in voltage fluctuations and flicker that violate the established utility guidelines for voltage regulations. Moreover, the existing distribution networks were not designed to operate with intermittent sources of generation at medium or low voltage levels.

This paper discusses several smart grid strategies for Distributed Energy Resources (DER) integration including advanced control of smart inverters, automated demand response, and technical and regulation enhancement for DER integration to improve the PV hosting capacity of distribution feeders and enable wider deployments of roof-top PV systems, thus achieving successful renewable transformation of the existing power systems. A survey was conducted to investigate the existing solar PV projects in Dubai and identify the key challenges of the existing interconnection standards. The initial survey results and recommendations for PV integration strategy and grid interconnection regulations enhancement are presented.

Keywords: Grid-connected PV integration, DER integration, smart grid strategy, Shams Dubai, advance inverter management, DER interconnection regulations.

1. Introduction

In the UAE, the use of clean energy sources and low-carbon electrification are receiving increasing attention with the clean energy target set to increase to 24% by 2021 compared to about 1% toady. As part of the UAE's commitment to the Paris Climate Agreement, the clean energy strategy 2050 emphasised on diversifying the energy mix with more focus on clean energy shares. 25% of Dubai's total energy by 2030 and 75% by 2050 is predicted to come from renewable energy sources in order to transform Dubai into a global centre of clean energy with the smallest carbon footprint in the world (Dubai Carbon, 2017).

Shams Dubai programme was launched in 2015 to encourage household and building owners to install PV panels to generate electricity to feed their own loads and export the surplus to the utility grid. In two years, Four hundred and thirty five buildings have already installed photovoltaic panels on their roofs and generated a total capacity of 15.6 Megawatts (Gulf News, 2017).

The existing energy policy and grid standard of renewable distributed energy resources (DER) interconnection in Shams Dubai regulations imposed some restrictions to limit the capacity of distributed PV connections compared to the total connected loads of the customer in order to avoid the well-known concerns of integrating high PV penetration into distribution feeders (DWEA Shams Dubai, 2015 & 2016). However, those restrictions could limit larger PV deployments and hinder the achievement of the strategic targets of Shams Dubai initiatives to increase Dubai's share from clean energy sources to 75% by 2050. Smart grid technologies provide a more viable solution to address DER integration challenges at high PV penetration levels without limiting PV grid-connected capacity.

doi:10.18086/swc.2017.01.02 Available at http://proceedings.ises.org

2. Integration Strategies for PV distributed generation

Electric utilities around the world are seeking to develop strategies to increase resilient integration of DER integration while maintaining the grid performance. The IRENA study on PV integration emphasised on the importance on developing integrated strategy that covers technical, regulatory and economic aspects in order to tackle PV integration challenges successfully. The common theme of all implemented measures was to introduce additional flexibility into the existing power systems to accomdate renwable distibution genersation at different voltage levels (IRENA, 2017).

A study by the IEA's photovoltaic power systems programme on urban photovoltaic electricity policies concluded that GC-PV can be the solution to growing demand in the dense urban environment. In the perspective of a large photovoltaic deployment, it is quite important to have upfront good integration policies to assure that GC-PV is deployed with the maximum benefit to the community while reducing actual installation barriers associated with grid codes and permits. (IEA PVPS, 2009 & 2016). Sweco et al. investigated DER integration strategy in order to provide flexibility to the distribution power system and highlighted that the technologies needed for DER integration are available; the key challenge is to adjust to the regulatory framework and DER interconnection policy to make the market ready (Sweco et al., 2015). A survey was conducted by the authoers to investigate the strategies that provide flexibility measures for DER integration in which smart grid experts were asked about the following smart grid stregies as shown in Figure 1.

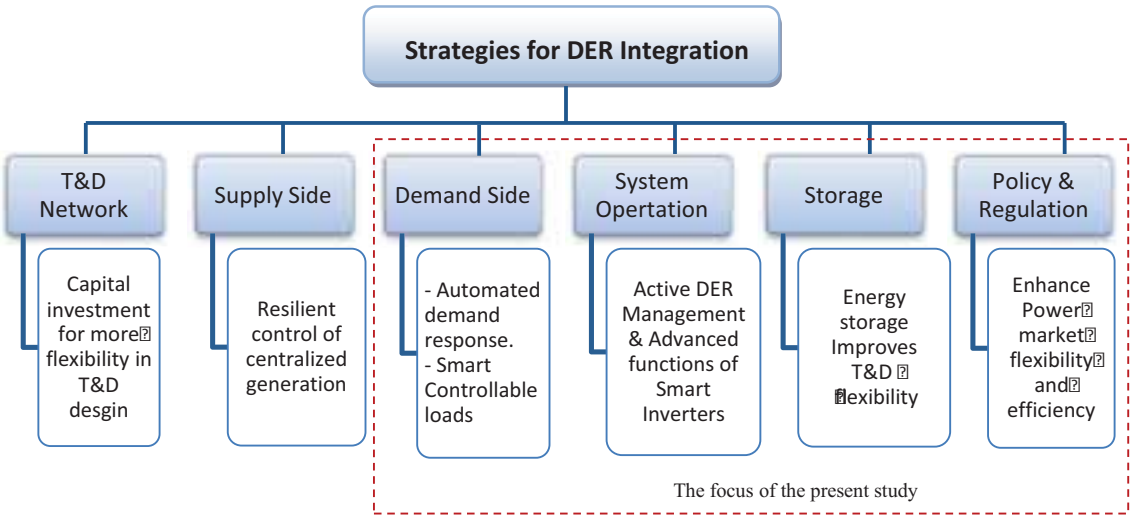

Figure 1: Smart Grid Strategies to improve the flexibility of the grid systems and DER Integration

Supply side and T&D networks integration strategies often require large capital investments are not considered for low and meduim DER penetration levels. This paper focuses on DER integration strategy based on advanced control of smart inverters, and policy/regulations enhacement to cope with the technology advancement. The majority of respondents (72%) viewed that advanced inverter functions offer a cost-effective solution to address the challenges of DER integration. Fifty eight perecent (58%) of the respondents considered that energy storage are not currently economical for grid-connected PV systems specially in Dubai and the gulf region.

2.1 PV Hosting Capacity of Distribution Feeders:

The concept of PV hosting capacity is well established in the literature and can be defined as the maximum limit on the amount of photovoltaic generation that can be integrated into a distribution feeder with no violation of grid operational conditions. (Whitaker et al. 2008; Reno et al. 2013; Dubey, Santoso, and Maitra 2015 ; Obi & Bass 2016; Palmintier et al. 2016a; Pecenak, Kleissl and Disfani, 2017)

The term photovoltaic penetration (PV_{pen}) could be defined as the ratio of the installed PV power to the peak load of a feeder (Pecenak, Kleissl and Disfani, 2017). Instantaneous PV_{pen} at a given time (t) can be obtained as:

$$PV_{pen}(t) = \frac{PV_{ins}(t)}{Load(t)} \text{(Eq 1)}$$

Where P_V is the photovoltaic installed power. Percentage penetration level % PV_{pen} for a given feeder configuration can be approximated as given in Eq2 below.

$$\%PV_{pen} = \frac{P_{V(Peak)}}{Load_{(peak)}} \text{x } 100 \text{(Eq 2)}$$

Many simulation studies and demonstration projects concluded that the integration strategy of PV distributed generation is dependent on the PV penetration level and location of PV system. EPRI research projects for several GC-PV case studies prove that PV penetration levels below 15% did not demonstrate integration issue. The voltage regulation issues due to distributed PV generation and the impact of PV location on the voltage profile of distribution feeders are illustrated in Figure 2 below.

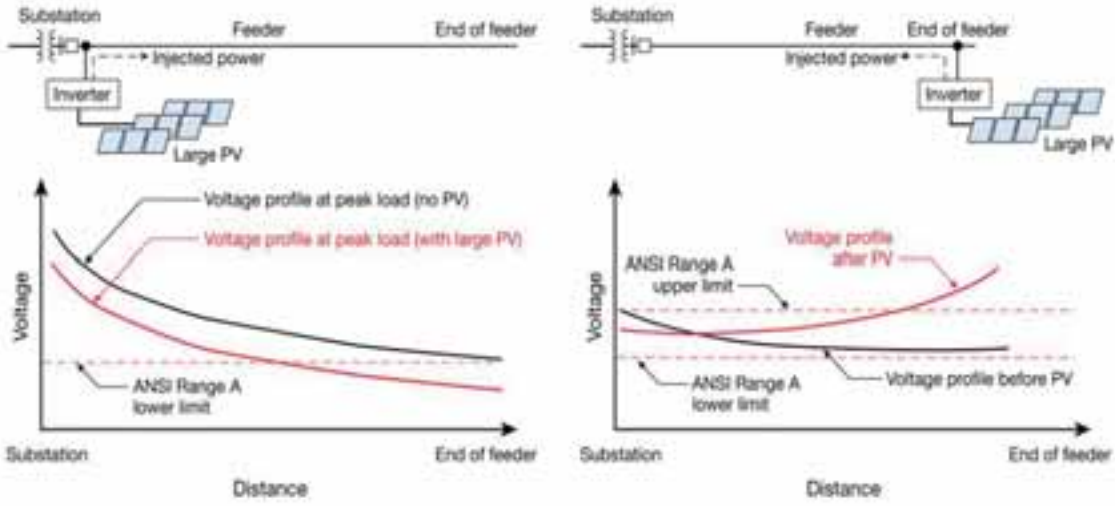

Figure 2 Voltage profile due to distributed PV generation. Figure 2.4a for GC-PV system at feeder's head while figure 2.4b shows CG-PV system at the end of the feeder (EPRI, 2013).

The analysis of many simulation studies of PV penetration on distribution feeders with EPRI's PV hosting capacity model concluded strong correlation with voltage regulators and feeder characteristics. Other significant factors include the location of point of connection (POC) of PV generators. On the other hand, EPRI's analysis concluded no significant correlation between hosting capacity and the peak load of the distribution feeder (EPRI, 2013). Figure 3 shows the hosting capacity in terms of voltage violations with the increasing penetration level of grid connected photovoltaic (GC-PV).

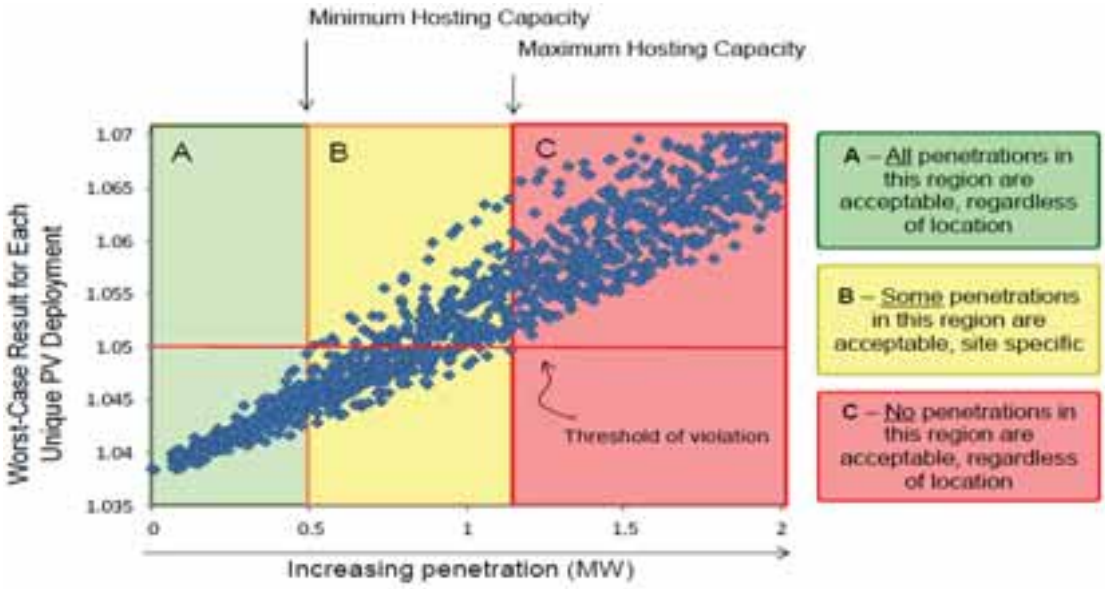

Figure 3: The voltage limit violation with the increasing penetration of GC-PV (EPRI, 2013)

The feeder's voltage profile issue due to PV DER integration can be explained in the view of the highly simplistic two bus feeder model shown in Figure 4. The voltage at substation bus is assumed to be constant as the nominal voltage with a magnitude of 1 per unit (p.u).

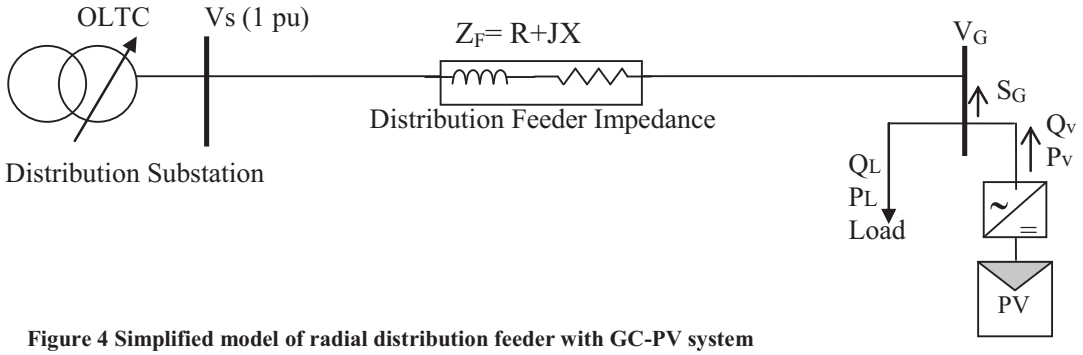

Figure 4 Simplified model of radial distribution feeder with GC-PV system

The voltage difference between substation bus (S) and distributed generation bus (G) is defined as:

$\Delta V = Vs - V_G = I \times Z_F = .(R+jX)$ (Eq. 3)

Where I is the current flowing from the DG-PV source (I) Ignoring the wiring power losses can be found using:

$I = \frac{S_G}{V_G}$ (Eq. 4)

The total apparent power S_G injected to the grid at the DER bus S_G can be calculated in terms of active power (P) and reactive power (Q) as:

$S_G = (Pv - P_L) + j(Qv - Q_L) = P + jQ$ (Eq. 5)

And the absolute value is $|S_G| = \sqrt{P^2 + Q^2}$ (Eq. 6)

Where Pv and Qv represent the active and reactive powers generated by the PV inverter respectively; and P_L and Q_L represent the active and reactive power consumed by the load respectively.

The power factor (PF) by definition is the ratio of the real power to the apparent power in the circuit:

$$PF = \frac{P}{S_G} = \frac{P}{\sqrt{P^2+Q^2}} \cong \frac{I^2 R}{I^2\sqrt{R^2+X^2}} \cong \frac{R}{\sqrt{R^2+X^2}} \quad \text{(Eq. 7)}$$

The current (I) flowing from the GC-PV to the DER bus. Ignoring the wiring loss through the can be found using:

$$I = \frac{P+jQ}{V_G} \quad \text{(Eq. 8)}$$

Combining (2. 3) and (2.8), hence: $\Delta V \cong \frac{P.R+QX}{V_n}$ (Eq. 9)

The overvoltage caused due to distributed generation depends on the variables in equation (9). V_n is the nominal grid voltage as set by the distribution utility and could not be controlled. Different methods have been developed to increase the PV hosting capacity focus on controlling one or more variables of the equation 2.9 numerator. For instance, Inverter volt/var controls reactive & power power (P, Q); while feeder reinforcement aims to control X/R values.

2.2 *Advanced Inverter Functions for improving PV hosting capacity:*

Current grid-connected PV systems use advanced inverters that become smart enough to operate autonomously according to pre-established software settings and with the addition of communications capabilities, DER systems can be directly monitored and controlled by utilities to modify or override their autonomous operations. DER systems can receive remote emergency commands, demand response pricing signals or schedules of modes/ commands to cause the inverters to change their electrical characteristics such as voltage levels, energy production rate, and active or reactive power outputs according to daily, weekly, or seasonal timeframes so long as they operate within the standard requirements of the interconnection regulations of the grid (see Table1) .

Smith et al. investigated inverter volt/var control through simulation study and concluded that the effectiveness of inverter based control for PV integration into the distribution system. Similarly, several simulation studies concluded that volt/var management is an effective strategy for distribution voltage regulations however, feeder characteristics shall be taken in conciderations (smith et al. 2011; Rizy et al 2011; Schauder and Mather 2014; Kim et al., 2016; Leite et al 2016).Alobeidli and Moursi compared different coordinated volt/var control strategies using conventional methods like OLTC and inverter-based control. They reported that inverter-based strategy is proven to be an efficient strategy for DER integration to improve feeder voltage profile and maximize reactive power reserve up to 80% (Alobeidli & Moursi, 2014).Rylander et al. and others analysed the potential performance benefits of advanced inverter control on different distribution feeders. The advanced volt/var function of the inverters improved PV hosting capacity between 43% and 133% (Rylander et al. 2016; Seuss et al. 2015)

Table 1: Advanced inverter functions to support DER integration (EPRI 2012; Rylander et al. 2016; Casey et al. 2010; Bower et al. 2012)

Classification	**Inverter Functions**	**Associated Standards**
Autonomous Functions: • *Behavior controlled by inverter's pre-configured operating parameters (defined during system commissioning).* • *Parameters can be re-configured, activated or deactivated at later date through on-site changes or remotely.* • *No communication capability is required.*	Low- / High-voltage ride-through	IEEE 1547a-2014
	Low- / High-frequency ride-through	
	Volt-var control (dynamic reactive power injection)	
	soft-reconnect	
	Ramp-rate controls	
	Fixed power factor	
Non-Autonomous Functions:	Remote connect/disconnect command to DER	

• *Direct control of inverter behavior from remote operator commands or feedback, based on conditions at the point of connection (POC)* • *Communication architecture and remote control infrastructure are required.*	system	IEEE smart inverter working group (SIWG) proposed Functionalities
	Set /Limit real power	
	Respond to real power pricing signals	
	Update/overwrite autonomous functions (volt-var curves, fixed power factor, voltage ride-through, frequency ride-through, ramp rate)	
	Provide black-start capability	
	Provide spinning reserves	
	Event/history logging	
	Status reporting	

Palmintier et al. investigated several active and reactive (volt/var) power management strategies of PV integration at different penetration levels. This could be achieved typically through controlling on-load tap changers of transformers, capacitor banks and line regulators. A techno-economic assessment of different volt/var strategies to enhance PV hosting capacity concluded that on-load tap changers of distribution transformer could be effective can prove only when PV penetration level exceeds beyond 75% (Palmintier et al. 2016a). For lower penetration levels (typically between 15% to 75%), PV inverter's reactive power support and active power control have been demonstrated in several studies to mitigate voltage regulation and power quality issues that could occur due to large PV deployment in the distribution grid (Palmintier et al. 2016b ; Wang et al. 2014).

Further, Hashemi, Ostergaard, and Yang suggested that advanced inverter control is a cost-effective solution to control active/ reactive power through the output curtailment functionality of advanced PV inverters and could therefore decrease the required storage capacity for grid balancing (Hashemi, Ostergaard, and Yang 2013)

3. Data Collection

3.1 DER Integration Survey:

A survey was conducted to investigate the existing solar PV projects in Dubai and identify the key challenges of the existing interconnection regulation of distributed energy resources (DER) related to advanced inverter management. The survey was circulated to participants represent Shams Dubai's experts from utility industry, PV inverter manufacturers; enrolled consultants and contractors in Shams Dubai programme as provided on DEWA website (DEWA Shams Dubai, 2017). The initial results of the survey revealed that advance remote management of DER system of smart PV inverter could be achieved through below list of advanced inverter functions ranked based on the feedback of the participants as shown in Figure 5. Remote configuration of inverter's power factor and real time volt/var management of smart inverter are among the most important capabilities to improve PV hosting capacity of distribution feeders.

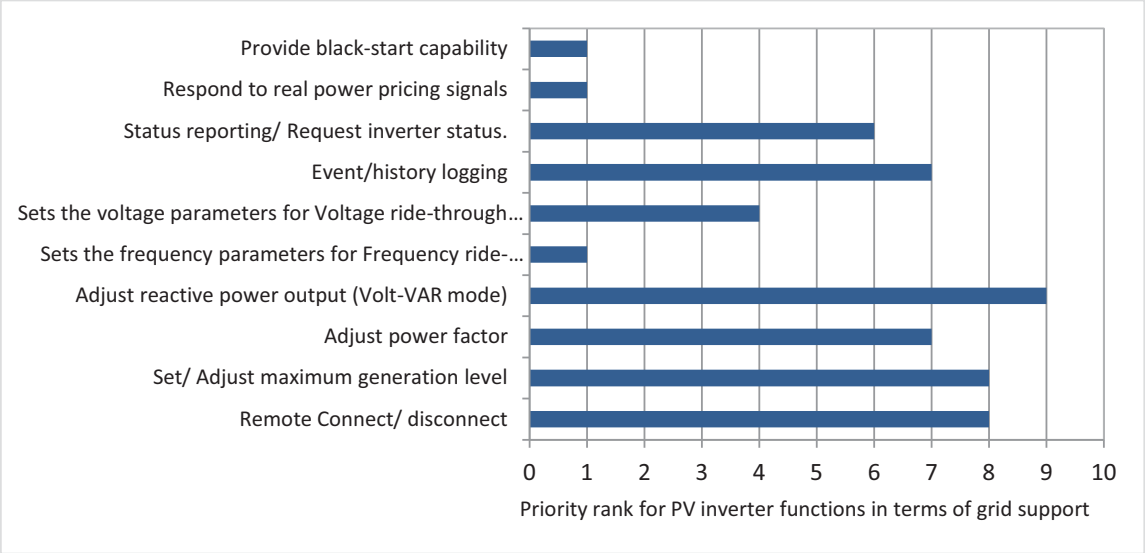

Fig 5: The key inverter's functions that could be remotely controlled/ re-configured for smooth DER integration.

The survey results also revealed that that some integration and interconnection regulation challenges shall be addressed to enable wider deployment of roof-top solar PV as shown in Figure6. The following challenges were identified:

- The interconnection standard is lagging behind the technological advances of smart inverters. The grid codes in Dubai did not cover some inverter's supporting functions like dynamic reactive power support during low voltage ride through (LVRT), hybrid inverter, inverter's volt/var and volt/watt modes.
- PV storage is not covered by the regulations.
- Dubai grid codes imposed restrictions to limit the maximum capacity of PV connections based on total connected Loads.
- Unclear guidelines about technical/ communications Architecture for of PV inverters remote monitoring & control by the utility through IEC61850.
- Lack of compensation mechanisms for DER aggressors (energy retailers) or ancillary service providers. The current grid codes did not support feed-in tariff or compensation scheme for energy service provides.

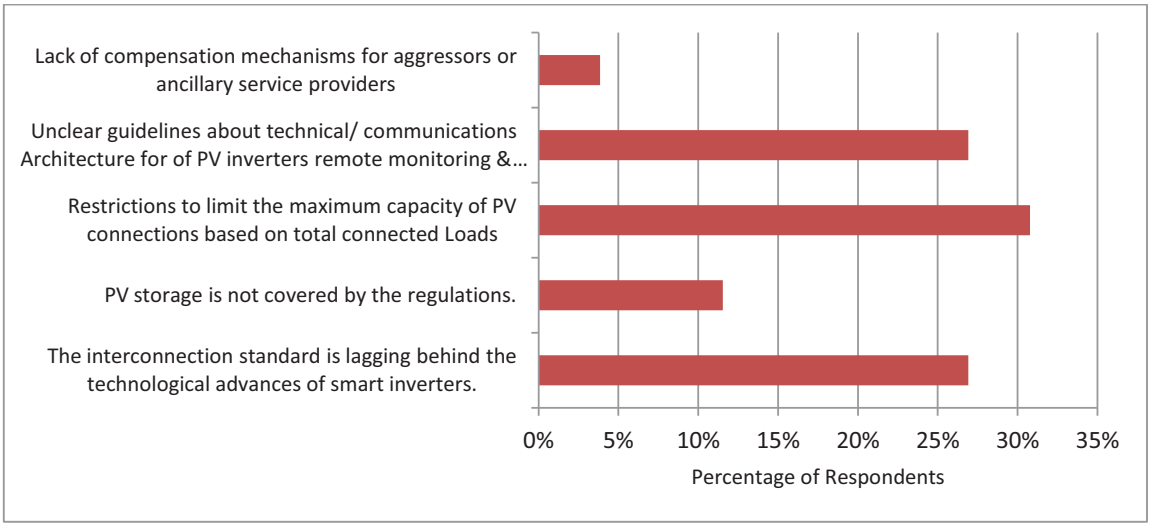

Fig 6: The key challenges you are facing with the existing PV interconnection Regulations and Standards.

3.2 Model Development:

The test system includes PV plant connected to 11KV (9 bus) distribution Feeder, Capacitor bank and OLTC substation transformer (see figure 7) include the flowing sub-systems:

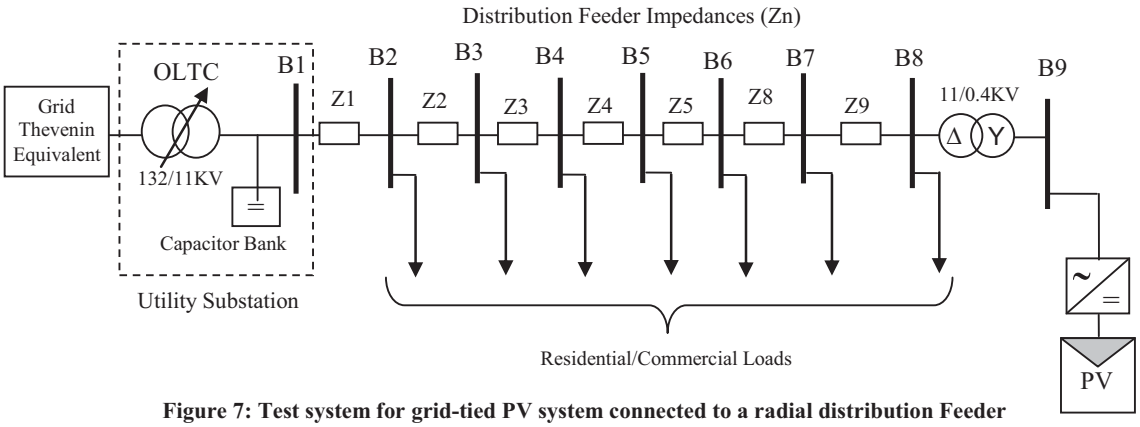

Figure 7: Test system for grid-tied PV system connected to a radial distribution Feeder

In order to examine the impact of inverter's volt/var control and other advance functions for remote monitor/ control, transient analysis for PV power fluctuation during irradiance dip or sundden PV system's failure at different penetration levels. The voltage source converter (VSC) in modern inverters can be controlled using digital signal processing (DSP) and microcontroller to compute the slope (dP/dV or dP/dI) of the PV power curve and feed it back to VSC control to drive it to zero (Sumathi, Ashok, & Surekha, 2015). Block diagram of smart inverter mamangemt through remote terminl unit (RTU) and demand response commands from Distributed Energy Resources management system (DERMS) as shown in figure 8.

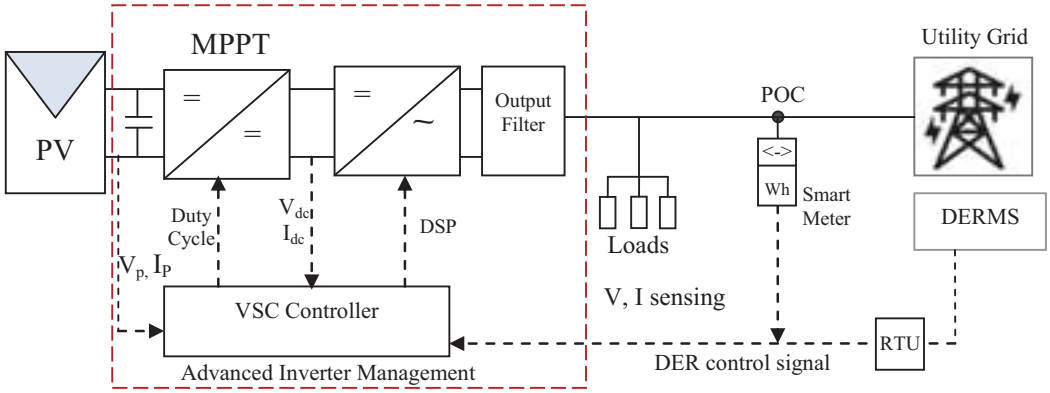

Figure 8 Smart Grid Approach for DER integration through advanced Inverter management and DERMS.

MATLAB/SIMULINK model reflecting grid-tied PV system is developed using Simscape power system components. A screenshot of the preliminary model is given in figure 9. The main components of grid-connected PV system connected to the model are:

(1) PV arrays comprises of SunPower SPR-315E modules. A photovoltaic module is commonly represented by an electrical equivalent one-diode four parameter model (Rekioua & Matagne, 2012). .

(2) DC/DC boost converter connected to each PV array controlled by a Maximum Power Point Tracker (MPPT) using P&O "Perturb and observe" algorithm to control PV array voltage in order reach the maximum power output.

(3) , (4) DC/AC Voltage Source Converter (VSC) control and a coupling 3-ph transformer to connect the converter to the distribution feeder.

(5) , (6) The grid model consists of typical 11kV distribution feeders and 132kV equivalent transmission system (DEWA Design guidelines, 2015).

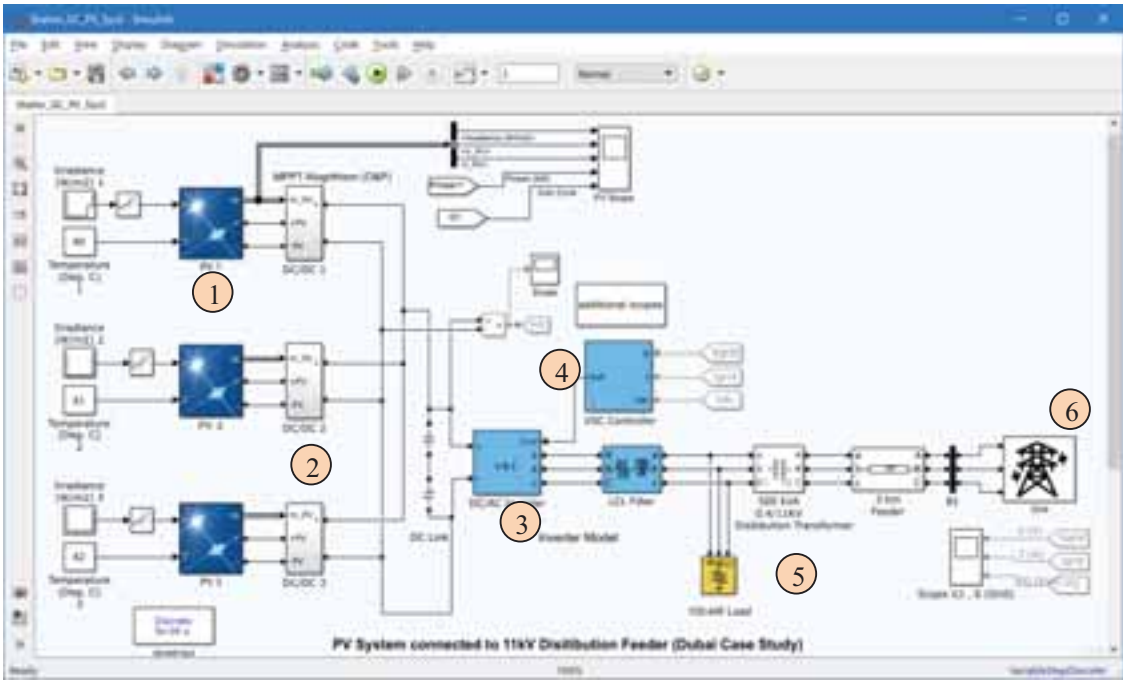

Figure 9: MATLAB/SIMULINK Model for GC-PV system connected to 11KV distribution feeder

4. Conclusion

In conclusion, it has been proven in the literature that advanced smart inverter functions and dynamic volt/var control are cost-effective strategies to improve PV hosting capacity of distribution feeders and help to mitigate adverse voltage impact compared to the conventional voltage regulation methods through OLTC which are more costly and have a slower response compared to smart inverters. However several simulation studies concluded that specific methods based on distribution network design and feeder's characteristics (mainly X/R ratio) should be developed to define the optimal inverter settings and functions for DER integration.Interconnection regulations need to be developed to cope with technolgoy advancesof the modern DER system rather than imposing limitation on the maximum PV power generation and the annual connection capacity to avoid the challenges of intermittent uncontrolled distributed generation. Based on the initial results of DER integrationsurvey, the following are key recommendations for further enhancement of DER interconnection regulations:

- The interconnection standard is lagging behind the technological advances of smart inverters. Advanced solar inverter features like advanced inverter's volt/var management need to be investigated and supported by the regulations.
- Hybrid inverters with PV storage shall be supported for feed-in tariff.
- Clear guidelines about communications protocols and technical architecture to be developed for utility's remote management of PV inverters.
- The proposed volt/var control settings (as recommend by IEEE P1547 working group) to be used as default inverter settings with most distribution feeders.
- Multiple volt/var profiles of smart inverters should be scheduled based on seasonal load profile to optimize the voltage profile of distribution feeders.
- Compensation mechanisms for ancillary service include volt/var control through smart inverters.

For future work, the dynamic volt-var control capability will be incorporated into inverter model and applied to an actual distribution feeder model in Dubai to investigate the impact on the chosen performance objective of the distribution network. Other DER management capabilities will be explored, such as scheduling multiple volt/var profiles for a residential PV systems based on seasonal load profiles for typical residential buildings.

5. References

- Alobeidli K., Moursi M.S. (2014) Novel coordinated secondary voltage control strategy for efficient utilisation of distributed generations. IET Renewable Power Generation 2014, Vol8, Issue5, pp. 569-579.
- Bower w., Sigifredo Gonzalez, Abbas Akhil, Scott Kuszmaul, et al. (2012)Solar Energy Grid Integration Systems: Final Report of the Florida Solar Energy Center Team. Sandia National Laboratories SAND2012-1395
- Casey, Leo F. ; Schauder, Colin ; Cleary, James ; Ropp, Michael (2010) Advanced inverters facilitate high penetration of renewable generation on medium voltage feeders - impact and benefits for the utility. IEEE Conference on Innovative Technologies for an Efficient and Reliable Electricity Supply, Sept. 2010, pp.86-93
- Denholm, Matthew O'Connell, Gregory Brinkman, and Jennie Jorgenson (2015) Overgeneration from Solar Energy in California: A Field Guide to the Duck Chart. National Renewable Energy Laboratory NREL/TP-6A20-65023 http://www.nrel.gov/docs/fy16osti/65023.pdf.
- DEWA Shams Dubai (2017) List of companies enrolled with DEWA as "Electrical & DRRG Solar PV" Consultant and Contractors for the Shams Dubai program. Available at: https://www.dewa.gov.ae/images/smartinitiatives/Shams_Dubai_Consultants_and_Contractor_list.pdf
- DEWA SHAMS DUBAI 2015. - Connection conditions for generators of electricity from solar energy Version 1.1 . https://www.dewa.gov.ae/images/smartinitiatives/DEWA_DRRG_Connection_conditions.pdf
- DEWA Shams Dubai. 2016. Standard for Distributed Renewable Resources Generation connected to the distribution network Version 2.0 Dubai Electricity & Water Authority. https://www.dewa.gov.ae/images/smartforms/DEWA_Standards_for_Distributed_Renewable_Resources_Generators.pdf
- Dubai Carbon Centre of Excellence. The state of green economy report 2017 [Online]. Available at: http://dcce.ae/state-of-green-economy-report-2017/[Accessed: 23 February 2017].
- EPRI. 2012. "Stochastic Analysis to Determine Feeder Hosting Capacity for Distributed Solar PV." 1026640. California: Electric Power Research Institute (EPRI).
- EPRI. 2013. "Modeling High-Penetration PV for Distribution Interconnection Studies." 3002002271. California: Electric Power Research Institute (EPRI).
- GulfNews (2017) Shams Dubai achieving impressive results with clean energy plan becoming more critical by the year, this initiative is already quite a pace-setter. Published: August 25, 2017 Available at: http://gulfnews.com/opinion/editorials/shams-dubai-achieving-impressive-results-1.2079948
- Hashemi, S., J. Ostergaard, and G. Yang. 2013. "Effect of Reactive Power Management of PV Inverters on Need for Energy Storage." In Photovoltaic Specialists Conference (PVSC), 2013 IEEE 39th, 2304–8. Tampa Bay, FL. doi:10.1109/PVSC.2013.6744938.
- IEA PVPS (2009) Urban Photovoltaic Electricity Policies. Report IEA-PVPS T10-07:2009 http://www.iea-pvps-task10.org/IMG/pdf/rep10_07.pdf
- IEA PVPS (2016) Trends in photovoltaic applications. International Energy Agency Report PVPS T1-30:2016 http://iea-pvps.org/fileadmin/dam/public/report/statistics/IEA-PVPS_RA2016-web.pdf

- IRENA 2017, REthinking Energy: Accelerating the global energy transformation.. The International Renewable Energy Agency, Abu Dhabi.

- Kim, Ys ; Kim, Gh ; Lee, JD ; Cho, C (2016) New Requirements of the Voltage/VAR Function for Smart Inverter in Distributed Generation Control. Energies, 2016 Nov, Vol.9(11(

- Leite, L. ; Boaventura, W. ; Errico, L. ; Cardoso, E. ; Dutra, R. ; Lopes, B. (2016) Integrated voltage regulation in distribution grids with photovoltaic distribution generation assisted by telecommunication infrastructure. Electric Power Systems Research, July 2016, Vol.136, pp.110-124

- Obi, M., & Bass, R. (2016). Trends and challenges of grid-connected photovoltaic systems – A review. Renewable and Sustainable Energy Reviews, 58, 1082-1094. doi:10.1016/j.rser.2015.12.289

- Palmintier B., Julieta Giraldez, Kenny Gruchalla, Peter Gotseff, Adarsh Nagarajan, Tom Harris, Bruce Bugbee, and Murali Baggu (2016b) Feeder Voltage Regulation with High-Penetration PV Using Advanced Inverters and a Distribution Management System; National Renewable Energy Laboratory. NREL/TP-5D00-65551 http://www.nrel.gov/docs/fy17osti/65551.pdf

- Palmintier B., Robert Broderick, Barry Mather, Michael Coddington, Kyri Baker, Fei Ding, Matthew Reno, Matthew Lave, and Ashwini Bharatkumar. (2016a) On the Path to SunShot: Emerging Issues and Challenges in Integrating Solar with the Distribution System. Golden, CO: National Renewable Energy Laboratory. NREL/TP-5D00-65331. http://www.nrel.gov/docs/fy16osti/65331.pdf

- Rekioua, D., & Matagne, E. (2012). Optimization of photovoltaic power systems: Modelization, simulation and control. London: Springer.

- Reno M. J., R. J. Broderick, and S. Grijalva, "Smart Inverter Capabilities for Mitigating Over-Voltage on Distribution Systems with High Penetrations of PV," in IEEE Photovoltaic Specialists Conference, Tampa, FL, 2013.

- Rizy, D. Tom ; Xu, Yan ; Li, Huijuan ; Li, Fangxing ; Irminger, Phil (2011) Volt/Var control using inverter-based distributed energy resources. IEEE Power and Energy Society General Meeting, July 2011, pp.1-8

- Rylander M. , Matthew J. Reno , Jimmy E. Quiroz , Fei Ding , Huijuan Li , Robert J. Broderick, Barry Mather, and Jeff Smith (2016) Methods to Determine Recommended Feeder-Wide Advanced Inverter Settings for Improving Distribution System Performance. USA. SANDIA http://energy.sandia.gov/wp-content/uploads/dlm_uploads/2016/06/SAND2016-4864C_PVSC-CSI4_MethodsAdvancedInverterSettings.pdf

- Samadi, A., R. Eriksson, L. Söder, B.G. Rawn, and J.C. Boemer. 2014. “Coordinated Active Power-Dependent Voltage Regulation in Distribution Grids with PV Systems.” IEEE Transactions on Power Delivery 29 (3): 1454–64. doi:10.1109/TPWRD.2014.2298614.

- Sandia National Laboratories (2012) Solar Energy Grid Integration Systems, Final Report SAND2012-1395, New Mexico USA.

- Schauder C. and B. Mather (2014) Advanced Inverter Technology for High Penetration Levels of PV Generation in Distribution Systems. National Renewable Energy Laboratory (NREL) technical report NREL/SR-5D00-60737 March 2014.

- Seal et al. (2012) Advanced Power System Management Functions and Information Exchanges for Inverter-based DER Devices, Modelled in IEC 61850-90-7 EPRI.

- Seuss, J. Reno, R. J. Broderick, and S. Grijalv (2015) "Improving Distribution Network PV Hosting Capacity via Smart Inverter Reactive Power Support," in IEEE PES General Meeting, Denver, USA.
- Smith J., B. Seal, W. Sunderman, and R. Dugan, "Simulation of Solar Generation with Advanced Volt-Var Control," in 21st International Conference on Electricity Distribution, CIRED, Frankfurt, Germany, 2011.
- Sweco et al (2015) Study on the Effective Integration of Distributed Energy Resources for Providing Flexibility to the Electricity System.

Clean Transportation Technologies and Strategies

Potential of Energy Storage and Rapid Charge System Using Electric Double Layer Capacitors for the Solar Right Rail

Takaki Kameya[1, 2], Hiroshi Takami[3], Jamal Uddin[4], William Ghann[4], Genji Suzuki[5] and Hidetoshi Katsuma[6]

[1] Kumamoto University, Kumamoto (Japan)

2 Tama Art University, Hachioji, Tokyo (Japan)

[3] Shibaura Institute of Technology, Tokyo (Japan)

[4] Coppin State University, Baltimore, Maryland (USA)

[5] Tokyo Denki University, Hatoyama, Saitama (Japan)

[6] Shonan Research Center for LRT, Hiratsuka, Kanagawa (Japan)

Abstract

Air pollution caused by exhaust gas, increasing carbon dioxide by burning fossil fuels, and the risk of drain on fossil fuels are the major problems of fossil fuels. In addition, low self-sufficiency rate of fossil fuels is also a large problem in Japan. 84.6% of electricity is generated by fossil fuels in Japan, so electrification such as electric vehicle does not mean breakaway from fossil fuels. Electricity should be generated by clean energy such as renewable energy in order to settle the problems of fossil fuels. A light rail system which runs on 100% renewable energy named the "Solar Light Rail" is proposed by authors. Experiments using a prototype model are carried out to demonstrate availability of the rechargeable power supply method using electric double layer capacitors. Two types of experiments are reported in this paper. From the experiment combination of PV and biomass, it was confirmed that clean stable energy is effective for this system under the bad condition for PV. In the experiments using PV, experimental condition is changed from passed experiments and energy consumption per run is decreased. Low energy consumption brings about running for longer time after sunset. The handmade equipment can be more efficient, and better result is expected by improvement.

Keywords: transportation, renewable energy, biomass, electric double layer capacitor

1. Introduction

In Japan, hybrid vehicles (HV) and electric vehicles (EV) are spreading. Fig. 1 shows the number and the rate of HV and EV, reported by the statistics of Automobile Inspection & Registration Information Association in Japan. The rate of HV and EV is only 7% for all automobiles in March 2016. However, the number and the rate of those vehicles are increasing every year.

The consumption of fossil fuels is one of the biggest causes of the environmental problem such as increasing in carbon dioxide and air pollution by the exhaust gas. The drain on fossil fuel is also a major issue. Furthermore, the self-sufficiency ratio of fossil fuels in Japan is extremely low. The self-sufficiency rate in 2015 of oil was 0.3%, that of natural gas was 2.5%, and that of coal was less than 0.1%. The excessive dependence on fossil fuels is undesirable for stable energy supply.

If all automobiles are replaced to EV, will the environmental problem by fossil fuels in the field of transportation be settled? Fig. 2 shows the power energy source of Japan in 2015. 84.6% of electricity is made from fossil fuels. It is reported that using electricity means consuming fossil fuels. The problem of fossil fuels will not be solved by only electrification. In order to settle the problem, all electricity must be made without fossil fuels, and should be generated by renewable energy.

doi:10.18086/swc.2017.02.01 Available at http://proceedings.ises.org

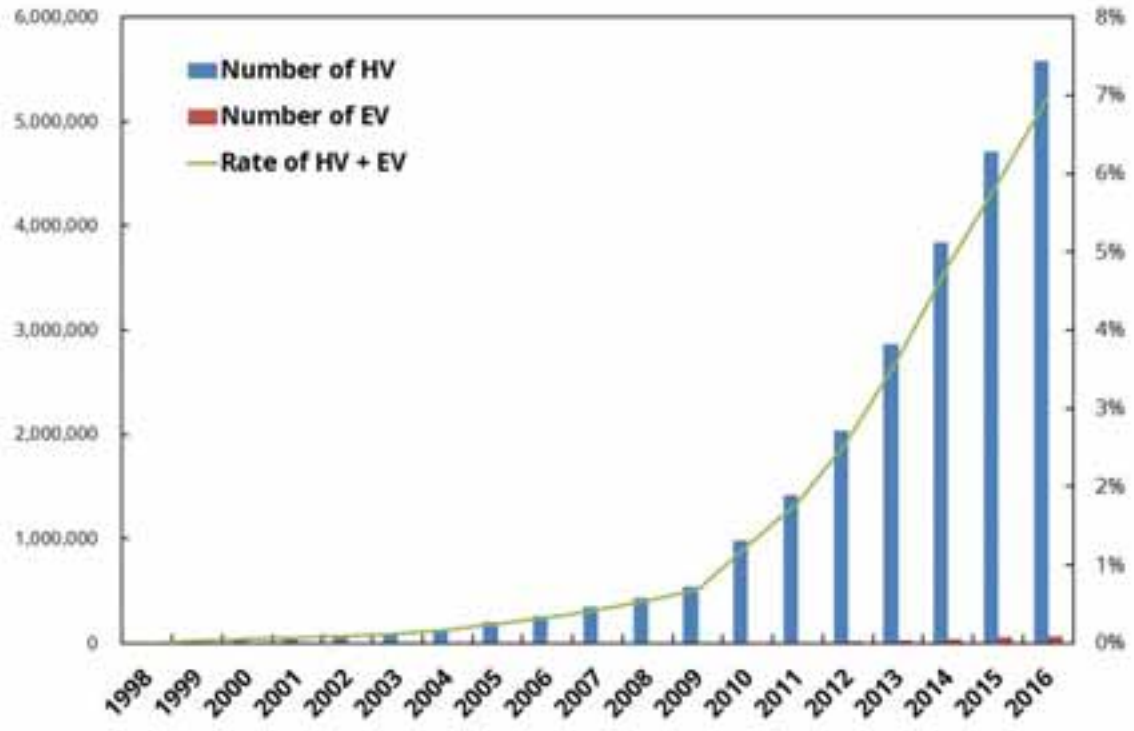

Fig. 1: The number and the rate of hybrid vehicle (HV) and electric vehicle (EV) in Japan

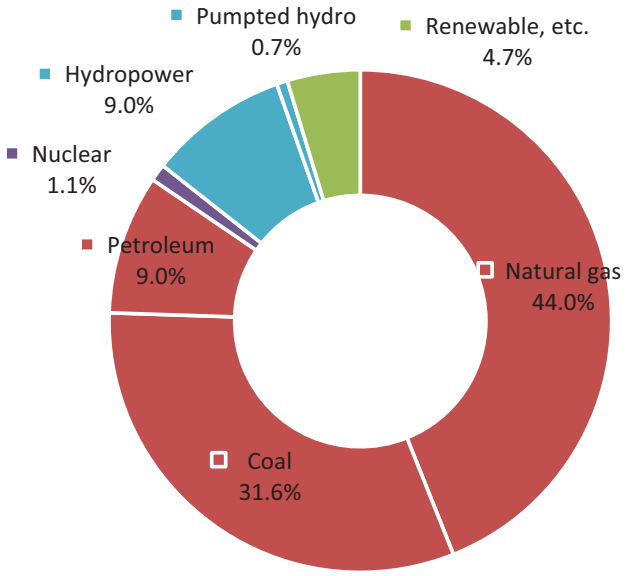

Fig. 2: Power energy source of Japan in 2015

1.1 The Solar Light Rail

A light rail is also known as a tram and a streetcar. A light rail which runs on 100% renewable energy such as solar, wind and micro hydro power generation is proposed by authors, and this light rail system is named the "Solar Light Rail".

The HIT solar panel produced by Panasonic is known as high efficiency silicon PV module. The energy conversion efficiency of this module is 19.7%, and the efficiency of thermal power generation with natural gas is 40%. Since the rolling resistance of iron wheels is lower than that of rubber tires, rail transport system is suitable for renewable energy.

A light rail is suitable transport system for the movement in the town. It is easy to ride without stairs like

subways and easy to across the rail without railroad crossing. Moreover, it is easy to know the name of street since rail trucks are installed on the road. For shifts from car-based town planning to people-based town planning, a light rail is reviewed in Europe and the United States.

It is easy to think of spreading solar panels all over the roof of the railcar to supply electricity like a solar car. However, the railcar cannot run in rainy days and during the night. In addition, it is hard to use wind turbines and water wheels in this method.

In conventional light rail system, most of electricity is supplied from thermal power plants to the railcar through the electric wire. Replacing thermal power plants to renewable energy power plants is also dreamed up. Even in this method, the railcar cannot run when the renewable energy power plants do not work such as a night without wind. Moreover, the power transmission loss cannot be neglected. The rate of transmission loss in Japan is 5.6%. Assuming 5.6% of loss is not a wise policy for renewable energy.

The first tram in Japan opened in 1895 in Kyoto. The railcars ran on electricity by hydro power generation at Lake Biwa. A light rail in Calgary, Canada runs on wind power generation. Several light rail systems already run on renewable energy. However, location requirements are limited to come true.

The power supply method, which is feasible in almost any location, to have a light rail run on renewable energy is shown in Fig. 3.

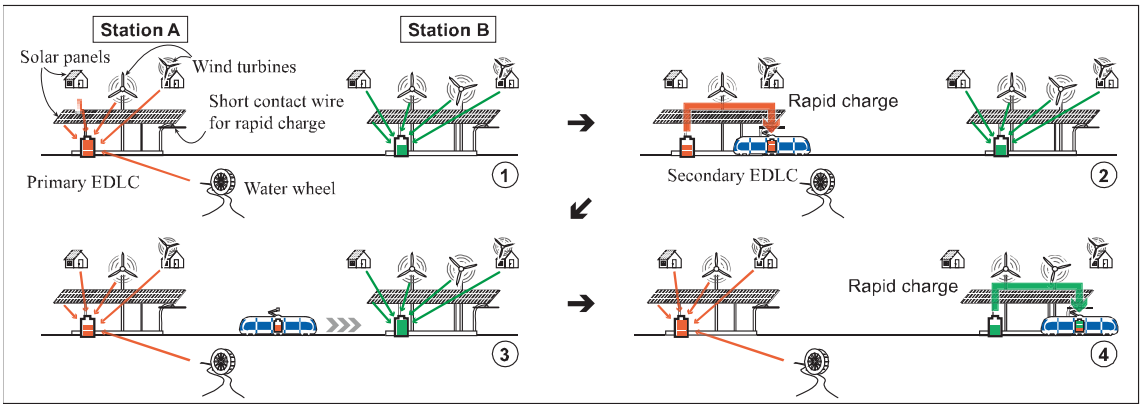

Fig. 3: Power supply method of the Solar Light Rail

1) Solar panels are mounted on the roof of the platform and around the station. Wind turbines are built around the station. Straight blade vertical axis wind turbines are suitable for this system, since their wind turbine noise is less than that of horizontal axis wind turbines. If there is a river or a water channel, micro hydro, not requiring a dam, should be used. An energy storage device is installed at the station, and this device is always charged from solar panels, wind turbines and water wheels. There is a short contact wire for rapid charge at the station.

2) Another energy storage device is also mounted on the railcar. When the railcar stops at the station, the energy storage device mounted on the railcar is charged rapidly from the energy storage device installed at the station through the short contact wire and a pantograph on the railcar.

3) The railcar runs to the next station by charged electricity.

4) There are same power generation system and an energy storage device at the next station, and rapid charge is carried out when the railcar stops at the next station. The railcar is operated by continuing this cycle.

Electric double layer capacitors (EDLCs) are suitable for the energy storage device of this system. In this system, energy storage devices repeat charge and discharge. The lifetime of EDLC is longer than that of batteries. High electric current is able to be put into and out from EDLC, and it makes rapid charge during railcar stopping. It becomes an advantage for this system that heavy metals are not included in EDLC. The capacitance of EDLC is lower than that of batteries. However, usually distance between stations of a light rail is shorter than that of railways, and charged electricity for an energy storage device mounted on the railcar should have quantity necessary to arrive at the next station. Therefore, low capacitance will not be a disadvantage in this system. In this system, an EDLC unit installed at the station is called the “primary EDLC”, and an EDLC unit mounted on the railcar is called the “secondary EDLC”.

According to the test outcome by the Railway Technical Research Institute of Japan, their hybrid light rail vehicle named “Hi-tram” consumes 8.9 MJ of electricity per kilometers at the maximum air conditioning load. If the interval between stations is 500 m for the assuming Solar Light Rail line, 4.5 MJ of electricity is required to reach the next station. When the voltage of secondary EDLC is 1500 V, the required capacitance of 4 F is calculated with eq. 1. The required time for rapid charge is calculated with eq. 2. It takes 6 seconds when this EDLC unit is charged at 1000 A.

$$W = \frac{1}{2}CV^2 \quad [\mathrm{J}] \qquad \text{(eq. 1)}$$

$$Q = CV = It \quad [\mathrm{C}] \qquad \text{(eq. 2)}$$

If railcars arrive and depart every 10 minutes in this assumed line, 15 kWh of electricity is required for every hour at a station. If this line works from 6:00 to 24:00 every day, the required electric power at a station is 270 kWh for one day, and 98,550 kWh for one year. If 98,550 kWh of electricity is supplied by renewable energy, the Solar Light Rail is feasible in the calculation.

1.2 Experiments using a prototype model

Demonstration experiments using solar panels and a handmade small scale prototype model were already carried out. From conventional experiments carried out under disadvantage condition for photovoltaic such as in winter or in cloudy day, it was confirmed that the proposed power supply system functions effectively in the daytime. The maximum voltage of the conventional primary EDLC was lower than the open circuit voltage of solar panel. Electricity had to be consumed to keep lower voltage, and electricity was not stored for after sunset. So the railcar could continue running for only one hour after sunset in passed experiments.

The experimental equipment was renewed this time. The gauge of rail is widened to 15 inches (381 mm) from 5 inches (127 mm). The voltage of the solar panel and the breakdown voltage of EDLCs rose.

Biomass is also a clean energy. Electricity is generated without an influence of climatic condition by biomass. In this paper, two types of experiments are reported. One is an experiment with combination of PV and biomass, and the other is an experiment with new equipment and new experimental condition.

2. Experimental equipment

Fig. 4 shows the schematic diagram of the experimental equipment.

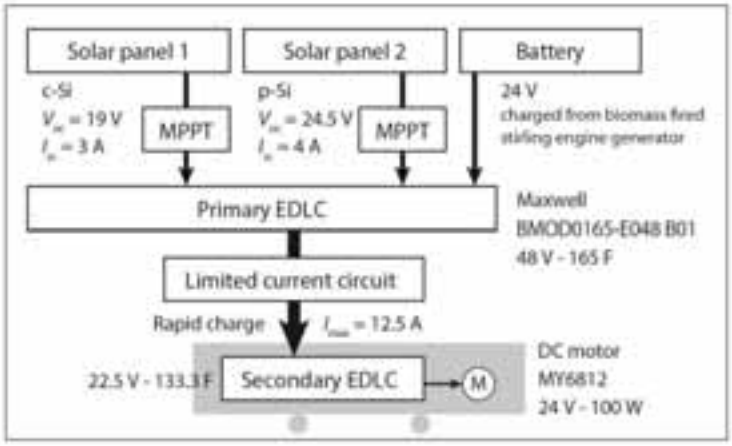

Fig. 4: The schematic diagram of experimental equipment

2.1 Solar panels

Two solar panels are used in the experiments. One is a mono-crystalline silicon panel made by ARCO Solar, Inc. 11 circular cells are wired in series, and three sets of wired cells are connected in parallel. Although this solar panel has been used more than 20 years, open circuit voltage of 19 V and short circuit current of 3A are

still measured in preliminary experiments. This solar panel is called as “solar panel 1” in this paper.

The other is a handmade solar panel using 56 poly-crystalline silicon solar cells made by Suntech Power Co. Measured open circuit voltage for one cell is 1.75 V, and short circuit current is 1 A. 14 rectangular cells are wired in series, and four sets of wired cells are connected in parallel. Open circuit voltage of 24.5 V and short circuit current of 4 A is expected this panel. This solar panel is called as “Solar Panel 2” in this paper.

These two solar panels are connected to the primary EDLC through the maximum power point trackers.

2.2 EDLC units

An EDLC unit model BMOD0165-E048 manufactured by Maxwell Technologies, Inc. is used for the primary EDLC. The capacitance is 165 F and maximum voltage is 48 V.

The secondary EDLC is fabricated with cylindrical EDLC cells. The capacitance for one cell is 600 F and maximum voltage is 2.5 V. 9 cells are wired in series, and two sets of wired cells are connected in parallel. The secondary EDLC becomes the capacitance of 133.3 F and the maximum voltage of 22.5 V. A resistor of 3.3 kΩ is wired in parallel for each EDLC cell as a voltage balancing resistor.

2.3 A limited current circuit

An excessive electric current flows when the primary EDLC is connected to the secondary EDLC directly. A limited current circuit is installed between the primary EDLC and the secondary EDLC during the rapid charge for safety. A small limited current circuit of 1.25 A is made with a three terminal regulator of LM317T, and the 12.5 A of limited current circuit for this system is made with connecting 10 small circuits in parallel.

2.4 A railcar and rail trucks

A 15 inches (381 mm) gauge four-wheel car is fabricated with four independent wheels. Driving force from the 100 W DC motor is decelerated at 22.25:1 and is transferred to the left rear wheel through the chain. The structure of a power controller is simple enough. The base current of the transistor is controlled by the variable resistor. The speed of the railcar depends on voltage of the secondary EDLC and the base current of the transistor.

Rail trucks are not made with rails for railways. A 1.8 m of iron angle bar is used for rail trucks. Total extension of the straight rail truck becomes 14.4 m.

2.5 Stirling engine generation system

Fig. 5 shows the schematic diagram of a biomass fired Stirling engine generation system. Biomass pellets are stored in the pellet hopper, and fed into the furnace automatically by pellet feeder. The Stirling engine works with combustion heat of biomass pellet and cold water. 1 kW of AC generator is connected to the Stirling engine, and electric power is supplied to load. Rated voltage of this system is DC 60 V, and five car batteries are installed for load balancing. Two of these batteries are used for charging to the primary EDLC.

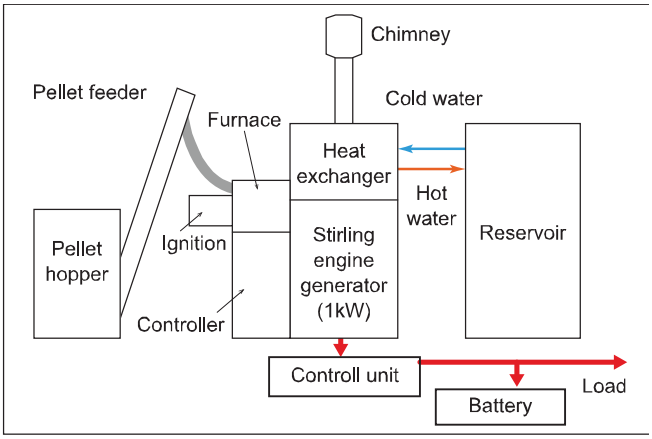

Fig. 5: The schematic diagram of biomass fired Stirling engine generation system

3. Experiment 1: Combination of PV and biomass

The experiment using a biomass Stirling engine generator was carried out during the science workshop for

children held on 10th October 2016 at Tokyo Tower (Tokyo, Japan). The event started at 10:00 and closed at 18:00. Many children visited our booth and enjoyed to riding the railcar one round trip on the 14.4 m of straight rail truck.

Fig. 6 shows the voltage transition of the solar panel 2, the primary EDLC and the secondary EDLC recorded with a data acquisition system IOtech Personnel Daq/55. The voltage of the solar panel 2 and the primary EDLC was recorded continuously since the solar panel 2 and the primary EDLC was always connected to the data acquisition system. However, the voltage of the secondary EDLC was recorded with break since the secondary EDLC was connected to the data acquisition system only during the rapid charges.

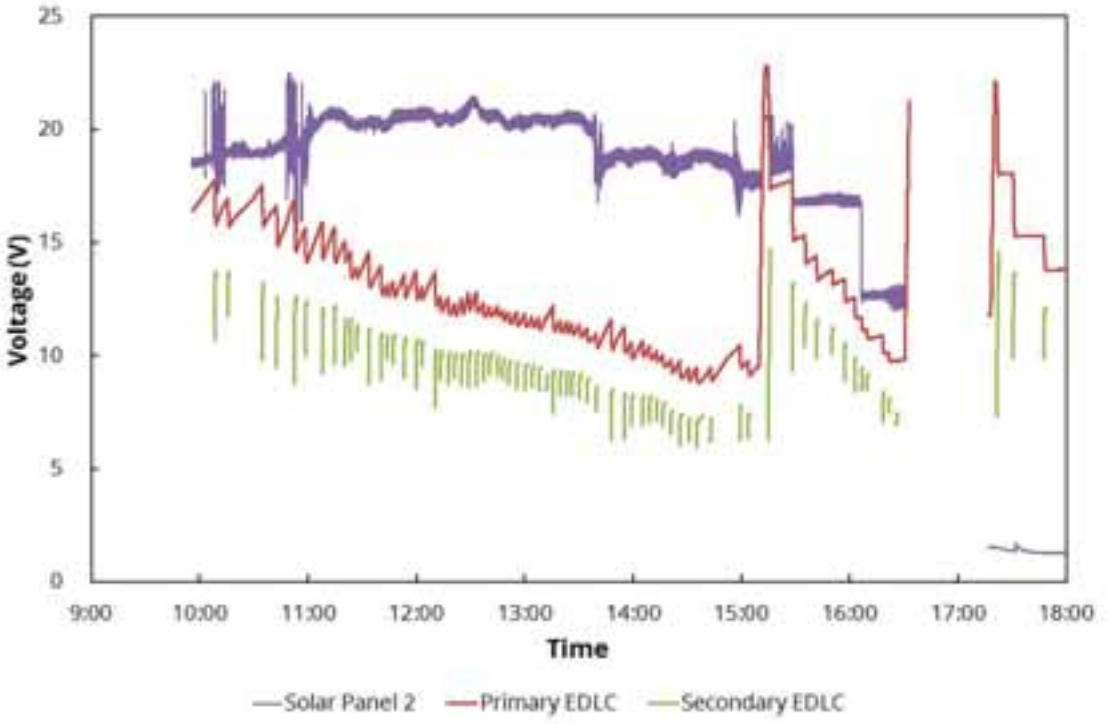

Fig. 6: Voltage transition of solar panel 2, primary EDLC and secondary EDLC under the experiment held on 10th October 2016

It was overcast from early morning. The voltage of the primary EDLC barely reached to 17 V at the beginning of the event. The railcar continued running without rest and the voltage of the primary EDLC dropped every time rapid charge was carried out. The railcar hardly moved around 15:00 since the voltage of the secondary EDLC also dropped, so a charging from the battery which was charged by the biomass fired Stirling engine generation system was carried out at 15:10. The voltage of primary EDLC rose to 22.8 V from 9.6 V. After that charging from battery was carried out at 16:30 and 17:18, and the railcar could continue running until the end of the event. The voltage was not recorded from 16:33 to 17:17 because of trouble of the laptop for data recording.

In this experiment, the railcar ran without the rest during overcast day. Even in harsh condition for photovoltaic, the railcar could continue running by charging from battery which is charged by the biomass fired Stirling engine generation system. It was confirmed that combination of clean energy such as biomass is effective to supply electricity stably for the Solar Light Rail. For practical use, the clean and stable generation system should be installed at main stations and stations which are located at a disadvantage to photovoltaic.

4. Experiment 2: Change of experimental condition

The experiment using new equipment without biomass stirling engine generation system was carried out on 1st November 2016 at Hachioji Campus of Tama Art University (Tokyo, Japan). The voltage of the solar panel 2 rose to 24.5 V from 17.5 V. The maximum voltage of the primary EDLC rose to 48 V from 17.5 V, and that of the secondary EDLC rose to 22.5 V from 15.0 V. Since the voltage of the primary EDLC became higher than the voltage of solar panels, it was not necessary to worry about overcharge of the primary EDLC.

The experimental condition is also changed. In conventional experiment, the railcar went forward and back 3 to 5 times on the 9 m of straight rail after rapid charge. In this experiment, the railcar went forward and back 1

time on the 14.4 m of straight rail. Running distance was decreased from 90 m to 28.8 m for each run. The time for rapid charge was fixed to 2 minutes.

The rail truck was laid on the corridor of the building and solar panels were put on the balcony facing south west. The sunrise was 6:03 and sunset was 16:46. It was rainy in the morning and became overcast in the afternoon. Fig. 7 shows the voltage transition of the solar panel 2, the primary EDLC and the secondary EDLC under the experiment. The voltage of the primary EDLC reached to 16 V at 10:55, and the first rapid charge was carried out at 11:00. The second rapid charge was carried out at 11:30, and interval of rapid charge was fixed to 15 minutes from the third rapid charge. The voltage of the solar panel 2 became lower than that of the primary EDLC at 15:38 since the sun disappeared behind a building.

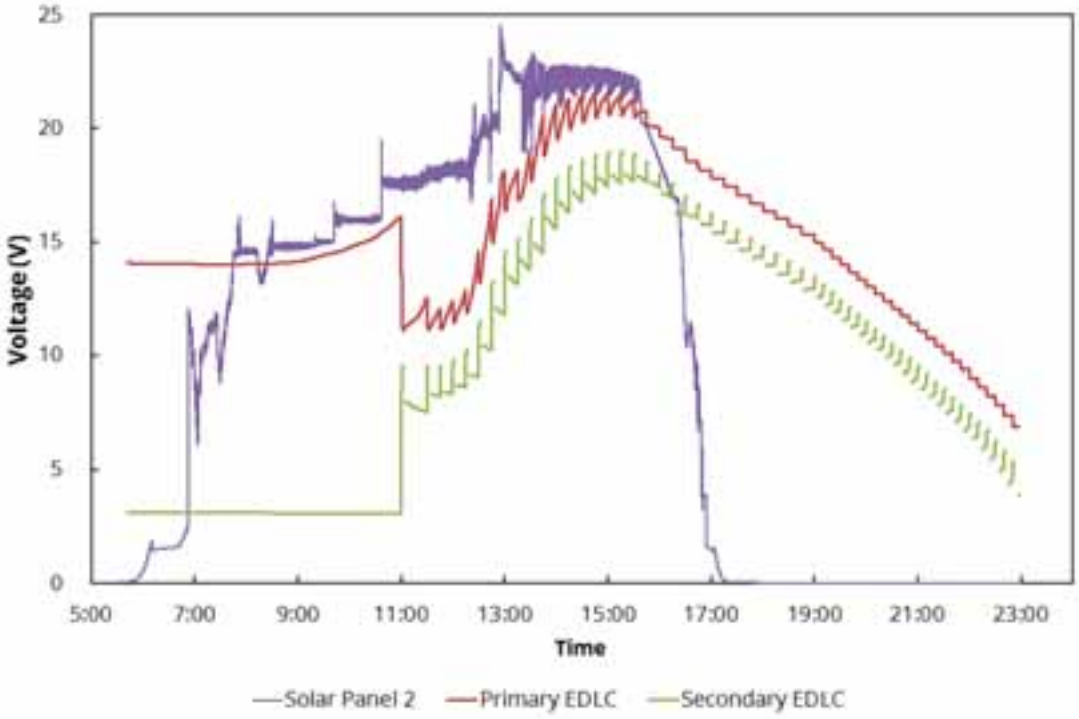

Fig. 7: Voltage transition of solar panel 2, primary EDLC and secondary EDLC under the experiment held on 1st November 2016

Finally, the railcar stopped at 22:56 and the final rapid charge was carried out at 22:50. The railcar continued running for 6 hours after sunset. Interval of rapid charge was shortened from 15 minutes to 10 minutes after 19:00. The final rapid charge would be carried out at 24:45 if the interval was not changed.

In the conventional experiments, the voltage of the secondary EDLC fell about 2.8 V in average after run. The capacitance of the secondary EDLC was 100 F, so the railcar consumed 280 C of electric charge per run. In this experiment, the voltage of the secondary EDLC fell about 1.0 V in average. The capacitance of the secondary EDLC was 133.3 F, so the railcar consumed 133.3 C of electric charge per run. 68% of shortening of distance per run caused 47.6% of decrease in energy consumption. Lower energy consumption brought about running longer time after sunset. This handmade equipment, such as rail trucks, a power controller, a power transmission system and electric circuits, can be more efficient. Better result is expected from improvement of equipment.

5. Conclusion

In this paper, a power supply method for a light rail which runs on 100% renewable energy is proposed. Two types of experiments using a prototype model were reported. In the experiment combination of PV and biomass, the railcar continued running by electricity which was brought from biomass under poor surroundings for PV. It was cleared that combination of clean stable energy is effective for the proposed system. The clean energy generation system should be installed at main stations to support power generation by unstable renewable energy.

In the experiment using only PV, railcar could continue running for 6 hours after sunset by 47.6% of reducing

energy consumption per run. It was confirmed that low energy consumption brings about running for long time after sunset. The handmade equipment could be more efficient, so better result is expected by improvement of equipment.

References

Agency for Natural Resources and Energy of Japan, FY2016 Annual Report on Energy (Energy White Paper 2017).

Fujii, O., 2004. Solar Train-Hybrid Truck System, Technical Report of Kurume Institute of Technology, 27, 39–47.

Kameya, T., Uddin, J., Suzuki, G., Katsuma, H., 2014. An energy storage and rapid charge system using EDLC for the Solar Light Rail. Computers in Railways XIV. 779–790, doi: 10.2495/CR140651.

Kameya, T., Uddin, J., Kezuka, H., Suzuki, G., Katsuma, H., 2013. Demonstration Experiment for Energy Storage and Rapid Charge System for the Solar Light Rail. Energy Procedia. 57, 906–915, doi: 10.1016/j.egypro.2014.10.300.

Kameya, T., Kezuka, H., Suzuki, G., Katsuma, H., 2012. The Solar Light Rail. Proceedings of World Renewable Energy Forum 2012. 2, 1047–1053.

Ogasa, M., 2010. LRT technology up to date 1. Rolling Stock & Technology. 16, 18–23.

Okamura, M., 2005. Electric Double Layer Capacitor and Charging System, third ed. Nikkan Kogyo Shimbun, Tokyo, Japan.

Sagara, K., Nomoto, K., Sasahara, Y., Seki, K., 2003. An application of straight blade non-articulated vertical axis wind turbine generation systems. Wind Energy. 27, 16–19.

Seki, K., 2001. Study of Straight Wing Non-Articulated Vertical Axis Wind Turbine System and Its Starting Characteristics, Wind Energy, 25, 52–55.

Syed Husain Imran Jaffery, Mushtaq Khan, Liaqat Ali, Hassan Abbas Khan, Riaz Ahmad Mufti, Ashfaq Khan, Nawar Khan, Syed M. Jaffery, 2014. The potential of solar powered transportation and the case for solar powered railway in Pakistan, Renewable and Sustainable Energy Reviews, 39, 270–276.

Taguchi, T., Ogasa, M., 2012. An Estimation Method of SOC of Lithium-ion Battery for Contact-wire and Battery Hybrid Electric Railway Vehicle, RTRI Report, 26, 35–40.

Takami, H., Shibazaki, M., Takamizawa, T., Tsuda, K., Hanano, N., 2014. Prototype Control System for Generation of Electricity by 1kW Stirling Engine, The Symposium on Stirling Cycle, 53–56.

Car ownership trend in Japan, Automobile Inspection & Registration Information Association, https://www.airia.orexuMmJRG.jp/publish/statistics/trend.html (last accessed 2017-10-12).

National Astronomical Observatory of Japan, Sunrise/Sunset Tokyo (Tokyo), http://eco.mtk.nao.exuMmJRGac.jp/koyomi/dni/2016/s1311.html.en (last accessed 2018-04-29).

Community Micro Power and Hybrid Systems

Integration of autonomous renewable energy generation systems with different topologies in a smart grid cluster to enhance performance in usual operational situations

Alex Renan Arrifano Manito[1], Kaue Novaes[1], André Ricardo Mocelin[1], Teddy Arturo Flores[1] Melendez, João Tavares Pinho[2] and Roberto Zilles[1]

[1] Instituto de Energia e Ambiente/Universidade de São Paulo, São Paulo (Brazil)

[2] Grupo de Estudos e Desenvolvimento de Alternativas Energéticas/Universidade Federal do Pará, Belém (Brazil)

Abstract

Renewable Energy Systems (RES) using resources found in loco might be an attractive solution to address the needs for electrification in many communities that are unlikely to be supplied by the interconnected grid. Though the design of isolated systems using intermittent renewable sources is discussed extensively, little attention has been given to the integration of autonomous RES for joint operation. The integration allows increased flexibility and modularity, which are important characteristics to improve the overall robustness of the system and tackle unpredicted adversities. This paper presents evaluations and conclusions about Autonomous Renewable Energy Generation Systems (AREGS) integration. The methodology is based on tests on a set of four AREGS operating integrated in a cluster in the Laboratório de Sistemas Fotovoltaicos (LSF) of the Universidade de São Paulo, Brazil, which allows the evaluation of several topologies and different operational scenarios; and also computer simulations for the extension and extrapolation of the evaluated scenarios.

Keywords: Autonomous Renewable Energy Generation Systems, energy management, distributed generation, control strategies.

1. Introduction

Renewable Energy Systems (RES) using local resources might be an attractive solution to address the needs for electrification with fewer environmental impacts, cost and maintenance, especially in the case of remote areas where the grid is not available. These kinds of systems are particularly interesting for countries like Brazil, with many communities that are unlikely to be supplied by the interconnected grid, and for which the only option is the use of isolated generation systems.

RES can use a large amount of primary resources available on site, presenting an advantage when compared to the use of generators operating with fossil fuels. However, the availability of these primary resources is not assured at any given moment, due to their flow-nature rather than stock-nature, which may directly influence the reliability of the system. Moreover, the design of the generation system faces many uncertainties not restricted to the supply side. On many occasions, the demand and the consumption pass through an adjustment phase, since these communities have a considerable amount of pent-up demand and even new consumers with the arrival of new settlers, especially in the early stages of electrification.

This requires the search for solutions to fit the problem in the beginning, while allowing flexibility and modularity to tackle the problem in the face of uncertainty and adversities. Modularity plays an important role for it allows a quick response to changes in the demand that would otherwise represent major modifications to the pre-existing generation system. In this sense, the integration of Autonomous Renewable Energy Generation Systems (AREGS) into a cluster may present a suitable manner to address the risks involved, and even to obtain higher levels of reliability and efficiency than those obtained by a single generation system.

doi:10.18086/swc.2017.03.01 Available at http://proceedings.ises.org

The integration of AREGS is desirable, not only due to the increased flexibility, but also from the point of view of the match between demand and primary resources. In some moments, a single AREGS may underuse its primary resource(s) for there is not enough demand and/or storage capacity left, and in other moments the available energy is not enough to meet the demand. Moreover, in order for a single AREGS to meet the demand at all times, it needs a generation/storage capacity to supply load peaks that seldom occur, increasing the already high initial investments of this kind of system. The integration of generation and storage units into a cluster allows dispatch flexibility between the systems, increases the value of the produced energy, contributes to power quality, and results in an overall more robust power system.

However, the application of such topologies has yet to overcome difficulties and barriers, so that all benefits can be appreciated. It is important to mention that the control of such topologies is more complicated, even if distributed control strategies and multi-agent strategies are applied. The grid forming inverters need a way to coordinate their operation to manage the energy exchange between AREGSs and the operation of all components in a seamless manner. Furthermore, the coordination between the agents involved needs to go beyond the technical level. Economic and even regulatory barriers also need to be overcome, since they may influence several stakeholders from the different integrated areas.

This new operating philosophy for AREGS lacks proof of its efficiency, effectiveness and reliability, both under normal and anomalous conditions, what increases the risks associated with operation and, consequently, decreases the interest in investing in such solutions. There are still questions to be answered on how to deal with the specificities and the operational aspects involved with these kinds of systems, which are critical to the long-term sustainability of the system's operation. In the literature, the design of isolated systems using intermittent renewable sources is discussed extensively, using a variety of techniques and optimization algorithms and works such as Lidula and Rajapakse (2011), Ustun et al. (2011), and Soshinskaya et al. (2014) present several examples of micro-grids installed around the world. However, only recently attention has been given to the integration of AREGS into a cluster for joint operation. For instance, Azaza and Wallin (2017) present and approach for optimizing a multi-micro-grid system using particle swarm. Koraz and Gabbar (2017) present a risk analysis for interconnected micro energy grids. Irfan et al. (2017) present a work on the opportunities and challenges concerning the micro-grid concept. Vasiljevska et al. (2013) present a work on the functionalities under a micro-grid concept.

This paper presents evaluations and conclusions about AREGS integration. The methodology is based on tests on a set of four AREGS operating integrated in a cluster in the Laboratório de Sistemas Fotovoltaicos (LSF) of the Universidade de São Paulo, Brazil, which allows the evaluation of several topologies and different operational scenarios; and also computer simulations for the extension and extrapolation of the evaluated scenarios. The conclusions drawn from the methodology may be used as guidelines for integrated AREGS operation, and even help in the development of proper regulation for this kind of operation.

2. Sizing of AREGS

The sizing of AREGS, as commented earlier, is extensively addressed in the literature and must often meet conflicting criteria such as reliability and cost to name a few, making an optimized solution a non-trivial problem. Usually the generation system needs to meet some quality criteria while minimizing costs, though other optimization variables are sometimes used as well. For instance, Fig. 1 exemplifies part of the solution space as a function of the Loss of Load probability (LLP) for a simulation considering a photovoltaic system with storage. The LLP (eq. 1) expresses the proportion of the energy not supplied in relation to the total energy needed by the system during a time period and it is often used as a measure of the reliability of the system.

$$LLP = \frac{\int_{t1}^{t2} P_{not\ supplied} dt}{\int_{t1}^{t2} P_{demanded} dt} \qquad \text{(eq. 1)}$$

Alex Renan Arrifano Manito

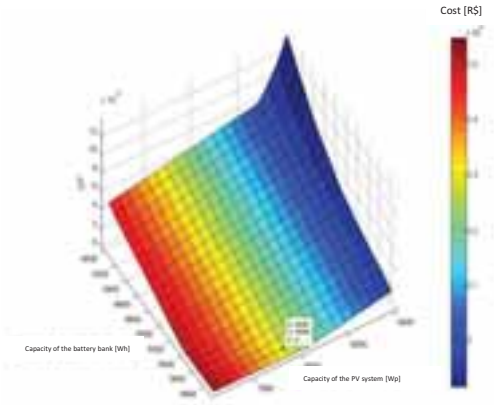

Fig. 1: LLP and cost as a function of the photovoltaic generator and storage capacity.

Fig. 1 shows that the same value for the reliability criteria (in this case the LLP) can be achieved by different configurations of the generator-storage pair with different costs. From the figure, it can also be inferred that the LLP does not present a linear characteristic of decrease, but rather one of saturation, with incremental increases of the capacity of the intermittent source or storage. In the case of the example given in Fig. 1, increasing the rated power of the photovoltaic generator becomes irrelevant past a certain value for a given capacity of the battery bank. The same behavior arises when increasing the capacity of the battery bank while keeping the rated power of the PV generator constant.

Consequently, the amount of generation and storage capacity are not decoupled and need to be proper matched to each other and to the load, otherwise the benefit of an additional investment in the capacity of one component may tend to zero. This is especially true when considering high penetration of non-dispatchable sources, which leads to the question of how to proper tune the generation-storage-load set in rural electrification projects and how to predict the evolution of the communities´ needs over the period of the project.

Optimization in the sizing of AREGS is important to maximize benefits of this approach while avoiding the waste of resources. However, optimization, though desirable, requires a reasonable amount of information for making suitable assumptions and decisions for the case at hand. Such information, on many occasions, are not available in rural electrification projects and some of it, such as the evolution of the demand curve over time, are hard to estimate.

Due to the nature of primary resources like solar or wind and to the limited capacity of energy storage, isolated system relying on them, on many occasions, need to underuse their capacity on certain periods and overuse it on others. This occurs due to the variation of the primary resource availability throughout a year and also to its match with the demand to be supplied. This may lead to situations in which the system generates considerably more energy than needed in a time period and yet the Loss of Load Probability (LLP) of the system is not zero.

This scenario of uncertainty leads to the conclusion that being able to respond to unforeseen situations is just as import as a proper sizing in the beginning. This implies that the generation and distribution system should be designed with a level of flexibility in order to avoid the impossibility of an eventual expansion. In a scenario of integrated AREGS, the energy which is not used or stored could be dispatched to nearby systems and increase the robustness and the reliability of all the systems involved due to the increased flexibility in the operation. Moreover, it can add modularity to the systems, since increases in the load peak can be met gradually without having to exchange the grid forming inverters to supply for peak demands that seldom occur. This decreases some of the risks involved with sizing of the system for rural electrification projects by giving more flexibility for the solution to be tailored to fit new scenarios during the operation phase. Clusters of AREGS would be more robust and would have a way to share infrastructure. Moreover, the expansion could be more suited to address new emerging situations.

3. Simulation of a stand-alone AREGS

In order to illustrate and evaluate how an AREGS composed of a photovoltaic generator with storage could benefit

Alex Renan Arrifano Manito

from integration with other systems, a scenario was simulated by numerically calculating the energy flow at each time step. The scenario considered a real consumer's load curve (CLC1) of an isolated community. Fig. 2 presents two different forms of observing the load curve. From these figures it is possible to observe that CLC1 presents a high load factor, with a demand close to the peak during most of the day. CLC1 spends 16 % of the time above 90 % loading and 54 % percent of the time with a loading above 75 %. However, when considering rural electrification, due to the relatively small number of households in isolated communities, the characteristic of the load may vary greatly and the demand curve is more sensible to demand increases that are hard to account for and would render the generation system unsuitable to meet the demand.

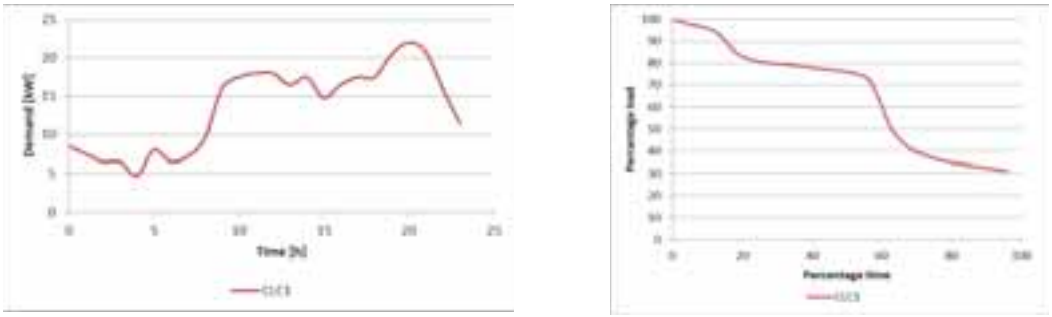

(a) (b)

Fig. 2: Isolated community load curve. (a) Average load curve over day time. (b) Percentage load versus percentage time.

The photovoltaic system was sized considering a location in the state of São Paulo, Brazil. Fig. 3 presents the monthly average irradiation and temperature. Since the system is isolated, a value of three peak sun-hours was considered, even though the annual average is 3.95. This was done to guaranty the supply in the month of least primary resource availability.

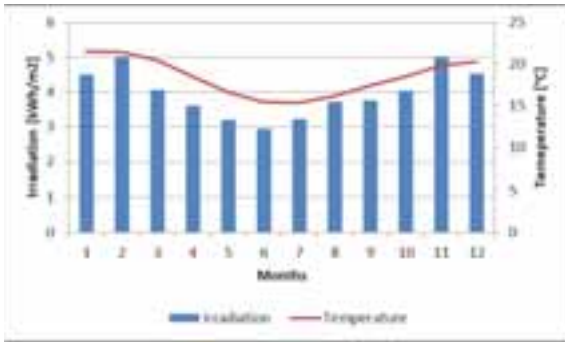

Fig. 3: Irradiation and temperature for the considered location.

The autonomy of the system was set as 2.4 days, which is higher than the minimum of two days recommended by the normative resolution RN 493/2012 (Aneel, 2012). This was done to oversize the battery bank to have a safe margin to unexpected situations. The depth of discharge for the sizing of the batteries was 60 %, which is a typical value for deep-cycle batteries. The round trip efficiency of the battery was considered as 95 %. Tab. 1 presents the values considered for the generator and storage to supply CLC1.

Tab. 1: Generation and storage capacity for CLC1.

Component	CLC1
Generator [kWp]	108.5
Storage [kWh]	1,302

Numerical simulations of the interactions between load, demand, and storage to supply the CLC1 are depicted in

Fig. 4, Fig. 5, and Fig.6. Throughout the year the state of charge profile of the battery varies greatly due to the variability in the primary resource and the amount of generation installed capacity. The system is underused during most of the year, what can be seen by the excess profile (green line), and during the month of June the system is constantly overusing the capacity of the storage. This behavior can be observed in Fig. 5 and Fig.6, which are zoomed in areas (respectively A and B) from the annual profile depicted in Fig. 4.

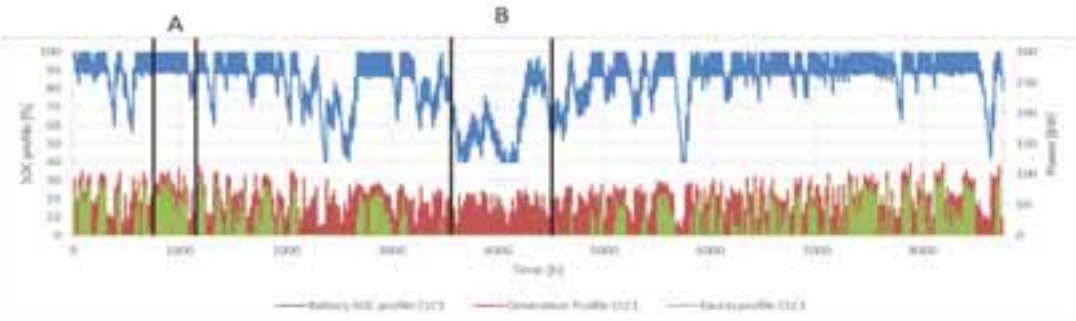

Fig. 4: Interactions between generation and storage to supply CLC1.

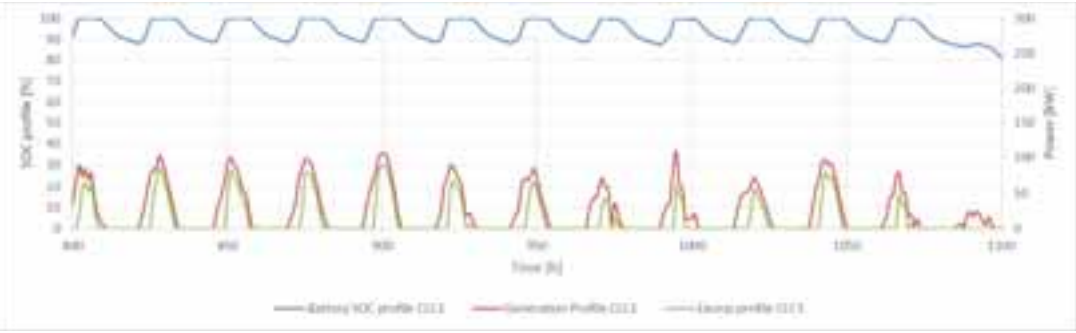

Fig. 5: Interactions between generation and storage to supply CLC1 (from hour 800 to hour 1,100).

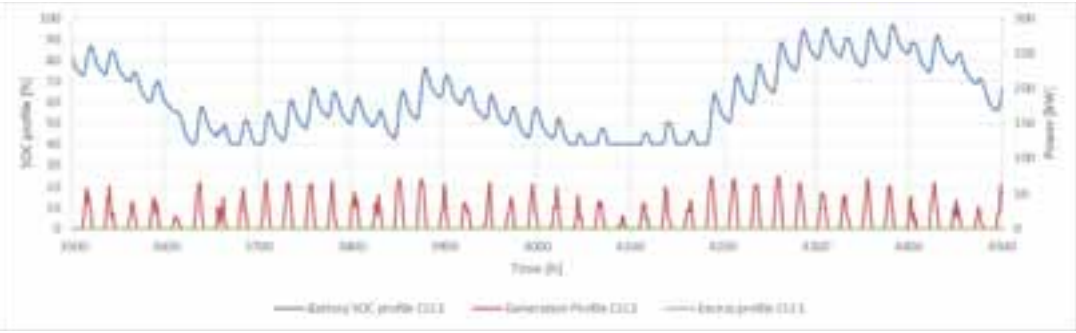

Fig. 6: Interactions between generation and storage to supply CLC1 (from hour 3,500 to hour 4,500).

In the beginning of the year part of the generated energy is not used and is thus wasted. Though the generation system would be able to supply an increasing demand in such months, during the months of low availability, the system would not be able to supply the demand. In this simulation, the LLP of the system was estimated as 1 %, which is an acceptable value. However, the system has little robustness to deal with demand increases.

In order to tackle this problem some alternatives can be used, namely over-dimensioning the system from the start, the use of solar home systems (SHS) to address variations in the predicted demand, the use a dispatchable source, such as a diesel generator or the integration of AREGS.

Over-dimensioning the generation system has the problem of increasing the initial investment, which is already an issue for AREGS, for an infrastructure that may or may not be used. This approach has also the drawback of assuming how the demand will increase over time, which may turn out not to be true and renders the additional investment not suitable or misused.

Alex Renan Arrifano Manito

The use of SHS to account for the additional load may be an option to tackle small loads or when due to some impossibility the AREGS cannot be extended to the new consumer. However, the new system stays isolated from the rest and it is usually less robust since it does not share infrastructure.

A dispatchable source, such as a diesel generator, is desirable in AREGs to supply for periods of low availability of primary resources and reduce the risks associated with intermittent sources like photovoltaics, for instance. However, the option with diesel to tackle demand increases would increase the operational costs of the system and its sensibility to fuel transportation logistics and price. Fig. 7 presents the increase in the hours of operation of the diesel, due to increases in the demand of CLC1. In the simulation, the diesel would supply the power that could not be met by the renewable generation and/or the battery.

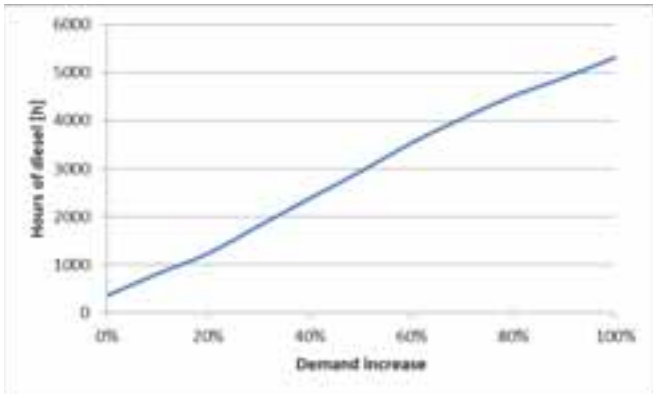

Fig. 7: Interactions between generation and storage to supply CLC1 (from hour 3,500 to hour 4,500).

Though the additional use of the diesel generator could be an option for a short term period, in the long run the operational costs would increase considerably and, as mentioned before, the service would be much more dependable on the fuel supply.

In the case of integrated systems, the additional AREGS could share infrastructure with the existing AREGS. The generation system of the additional AREGS could be smaller than the one that would be needed, if the new AREGS were isolated, due to the capacity of sharing the resources. It is important to mention that the use of one approach does not necessarily exclude the other. An optimized solution can be found by mixing the approaches, depending on the case.

4. Experimental setup and tests

The infrastructure of LSF is composed of four AREGS, each with its respective loads, storage, distributed generation, and grid forming inverters. The whole facility can operate in two main ways. Either the four AREGS are connected to a point of common coupling (PCC), where a diesel generator and the main grid can also be connected, or it can operate as a two levels hierarchy, where AREGS 2, 3, and 4 are connected to the load side of AREGS 1. Moreover, two standby circuits were introduced to allow the connection of temporary components like loads or distributed generation.

AREGS 1 is composed of three SMA Sunny Island inverters of 5 kVA each, forming a three-phase system, a 23.5 kWh battery bank and PV generators connected in the AC as well as in the DC bus with overall installed capacity of 6.71 kWp. AREGS 2 is composed of three Studer Xtender inverters of 6 kVA each, forming a three-phase system, a 19.2 kWh battery bank, and a 2.8 kWp PV generator. AREGS 3 is a single-phase system composed of a 5 kVA SMA Sunny Island inverter, a 9.6 kWh battery bank, and a 1.28 kWp PV generator. AREGS 4 is a single-phase system composed of a 4 kVA Schneider inverter, a 4.8 kWh battery bank, and a 0.4 Wp PV generator. Aside from the AREGSs there is also a 40 kVA diesel generator, which may be connected to all systems. Fig. 8 presents a schematic of the facility implemented at LSF and Fig. 9 presents some of the equipment installed in the laboratory.

Alex Renan Arrifano Manito

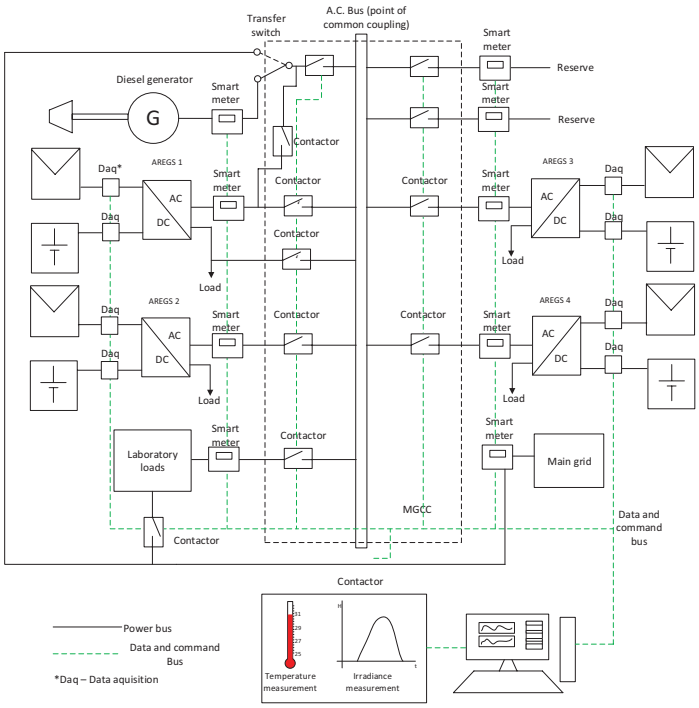

Fig.8: Infrastructure implemented at LSF.

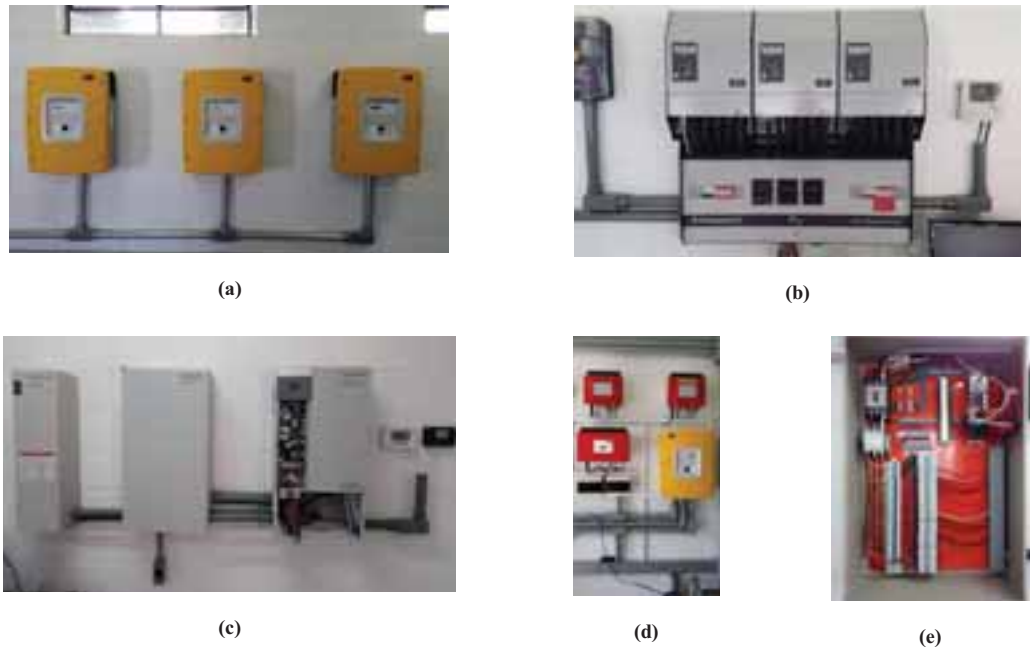

(a) **(b)** **(c)** **(d)** **(e)**

Fig. 9: AREGS installed in the LSF of the University of São Paulo, Brazil. (a) SMA three-phase system. (b) Studer three-phase system. (c) Schneider single-phase system. (d) SMA single-phase system. (e) Micro-grid Central Controller.

The facility was designed to enable a high level of flexibility and scalability, which permits to reproduce many real cases in the operation of the whole system, and considers the benefits and drawbacks of many topologies, including different levels of non-dispatchable renewable energy penetration and storage capacity.

Two conditions of multi-micro-grid operation with the interconnection of AREGS were tested. Fig. 10 presents the two conditions tested in the facility. In the condition presented in Fig. 10a (non-cascaded topology), all

AREGS are connected to a dispatchable source (in this case the diesel generator). In this situation, energy exchange between AREGS, though theoretically possible, needs a fine tuning, to avoid the attempt to inject energy in the diesel generator, which could damage it. This topology is more suitable when the dispatchable source is the grid for the parametrization of the AREGS is independent from one to the other. However, this is not the case for most rural electrification projects. This case is more suitable for micro-grids in the urban environment, where each could just feed the excess into the grid.

For rural electrification projects, the situation depicted in Fig. 10b (cascaded topology) is more suitable. In this situation there are two levels of AREGS. The first level (in this case formed by AREGS 1) creates a situation for the other systems that would resemble connecting them to the conventional grid. AREGS 2, 3 and 4 are connected to the load side of AREGS 1 and are able to inject the excess of energy in the battery of AREGS 1 or this excess could be used to support the loads in AREGS 1, which include the other AREGS.

The diesel would be explicitly controlled by AREGS 1. However, the other AREGS would also have an implicit control over the diesel generator, since for AREGS 1 they are loads which can cause AREGS 1 to trigger the diesel generator. In this situation, attention has to be given to the parametrization of all the AREGS as a whole to avoid undesirable disconnections between systems or the waste of potential to dispatch the excess energy.

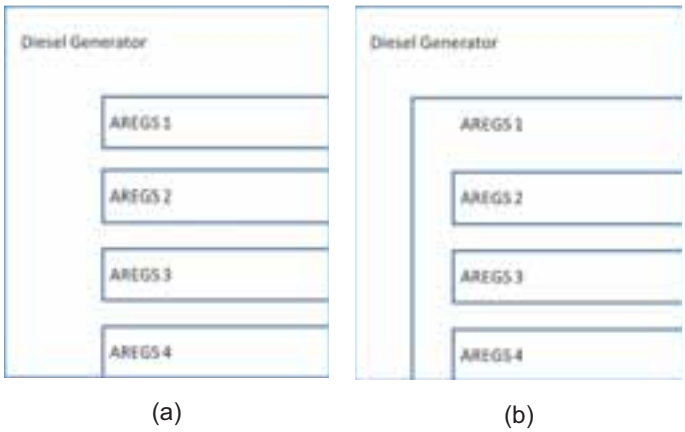

Fig.10: Tested topologies. (a) AREGS connected to a PCC. (b) Two-level AREGS set.

4.1 Experimental setup

In order to compare the two evaluated topologies (non-cascaded topology and cascaded topology), test were carried out. The tests sought to evaluate three scenarios (Case 1, Case 2 and Case 3). For Case 1, the AREGS were assembled in a non-cascaded topology. For Case 2 and Case 3, the AREGS were connected to operate as a cascaded system.

In Case 2 a 2.1 kW distributed generation was connected to the output side of AREGS 3 and the AREGS were parametrized to connect to one another. In Case 3, a 1 kW distributed generation was connected to the output side of AREGS 3. Although the system's topology remained the same as presented for Case 2, the AREGS were not properly parametrized to allow the injection of power from one AREGS to the other. This was done to emphasize the need for the proper parametrization of all the AREGS, considering the cascaded system as a whole.

Further details from the setup used in the tests for Case 2 and Case 3 are presented in Fig 11. For the purpose of the tests, the distributed generation of AREGS 3 was emulated by the output of a grid-tie inverter connected to a PV emulator at the load side of AREGS 3. This would provide a somewhat controlled environment for the experiments. AREGS 3 was then connected to the load side of AREGS 1.

Alex Renan Arrifano Manito

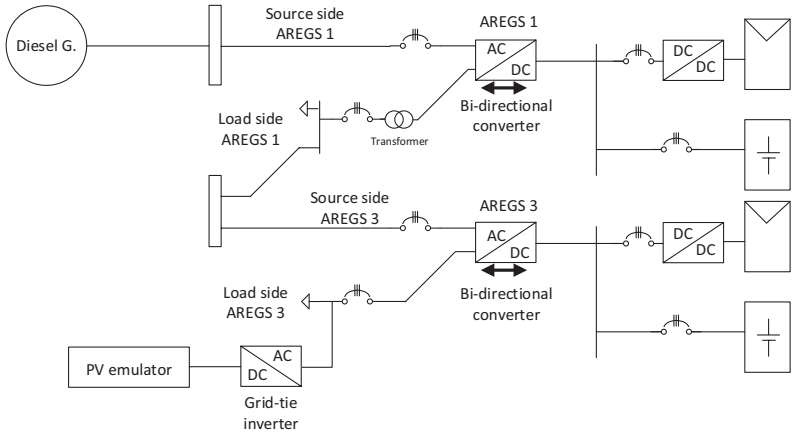

Fig. 11: Experimental setup for Case 2 and Case 3.

4.2 Experimental results

All the results are shown in per unit values and the bases of the system are presented in Tab. 2.

Tab. 2 Bases of the test systems.

Active Power (Pac)	Reactive Power	State of charge (SoC)	Voltage	Frequency	Irradiation
5 kW	5 kvar	100	220 V	60 Hz	1000 W/m^2

When all the AREGS are connected in a non-cascaded topology, the injection of power back to the external source is undesirable, in the case of standalone systems, since it could damage the source (usually a Diesel generator). In such situations the reverse power is usually blocked by the grid forming inverter, which should disconnect from the external source if a small amount of reverse power is measured. Fig. 12 presents the operation of AREGS 1 when all the AREGS have the same external source (a Diesel generator). The distributed generation (PV generator) from AREGS 1 injects power into its battery (consider negative values as power being fed to the battery) until the battery is full. Though there is still primary resource for the PV generator, the frequency is used as a way to limit the injection of power by the distributed generation since the power surplus cannot be used. In this situation, the only benefit is that all the AREGS can share the same external source, but the energy exchange from one to the other would not be possible due to safety reasons, which in turn, diminishes the benefits of interconnection.

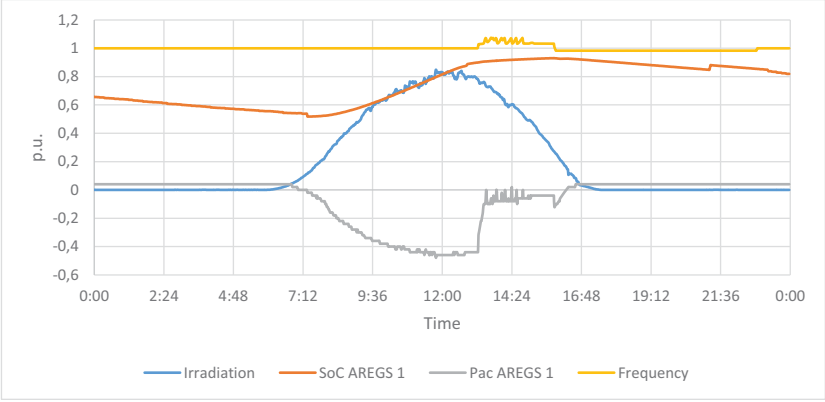

Fig. 12 – AREGS 1 operation when all the AREGS connect to the same source.

In the Case 2, the distributed generation from AREGS 3 charges the battery of AREGS 1, as shown in Fig. 13. Some of the power, however, is still injected into the battery of AREGS 3 until the battery is completely charged.

Alex Renan Arrifano Manito

A drop in the injection of active power occurred due to the supply of reactive power into the PCC as shown in Fig. 14. The reactive power was being injected due to the use of a transformer to connect AREGS 1 to the PCC, causing the grid-tie inverter to change its operation point to supply also reactive power.

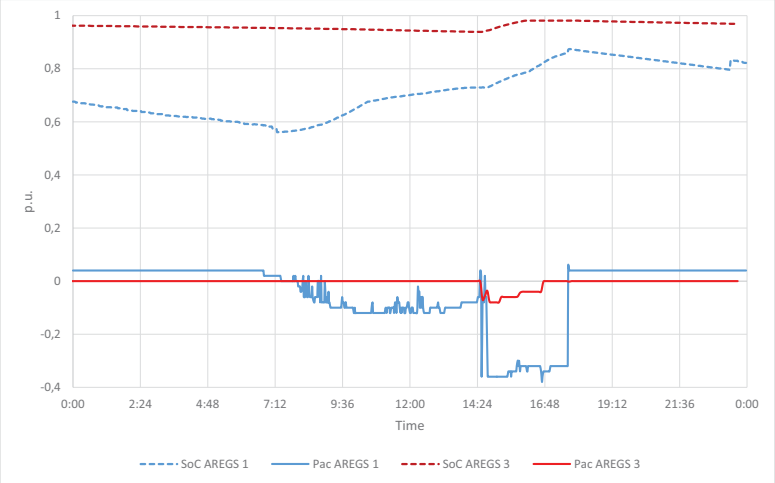

Fig. 13: Power exchange between AREGS (Case 2).

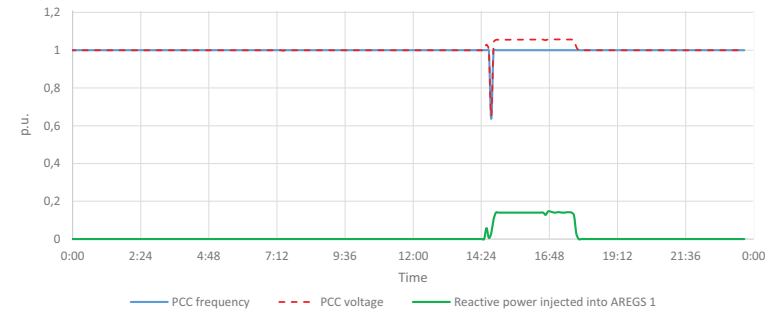

Fig. 14: Frequency, voltage and reactive power profile for Case 2.

During this period, there was no noticeable frequency deviation, however, there was a voltage rise at the PCC of 6%. This points to the fact that though some of the power may be injected into the other AREGS, there could be a deterioration in power quality at the PCC due to excess generation, similar to what happens in a conventional distribution grid with high distributed generation penetration if proper measures, such as power limitation, are not implemented to account for the moments when power quality deterioration occurs.

As stated before, the battery from AREGS 1 provides a security layer that would prevent any of the other AREGS from injecting into the diesel generator. Had the AREGS been assembled having a common coupling point with the Diesel generator (non-cascaded topology) and no measures were taken to block reverse power, such operation wound represent a risk in the case of an isolated power system, since the AREGS could perceive the Diesel generator as a load, especially when the Diesel generator powers off. During the period in which the rotor is decelerating the control of the AREGS could perceive a frequency drop try to inject power into the diesel generator.

In Fig. 15 it is shown that the proper parametrization of all AREGS connected to the cascaded micro-grid should be considered as a whole, otherwise the benefits of such topology can be hampered. In the situation depicted in Fig 15 (Case 3) though there is an excess in power in AREGS 3, it does not inject power into AREGS 1. Instead it limits the power injected into its own battery by causing a frequency rise at the point where the grid-tie inverter is connected. The limitation in the injected power and the frequency rise can be observed in Fig. 15 and Fig. 16 respectively. In this situation there is no noticeable voltage rise at the coupling point with the grid-tie inverter since the voltage at the output of the bi-directional inverter from AREGS 3 is the reference of the system, the

same does not occur in the Case 1. Fig. 17 presents qualitatively how the voltage behave in Case 2 and Case 3.

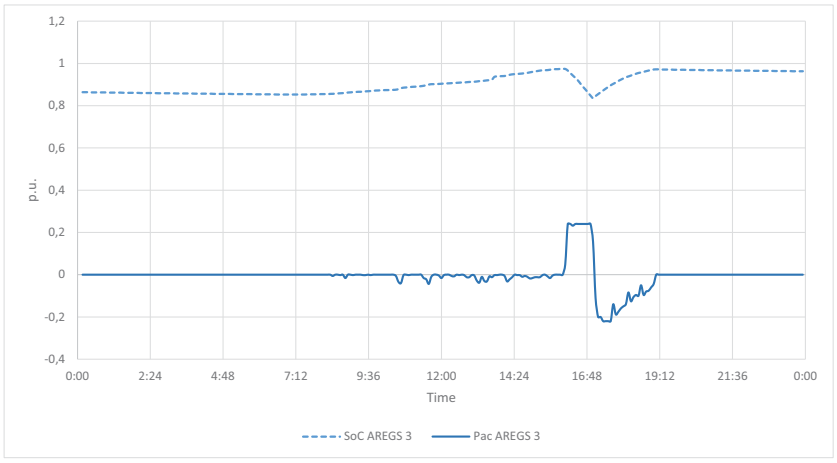

Fig. 15 – Power limitation due to AREGS 2 not connecting to AREGS 1 (Case 3).

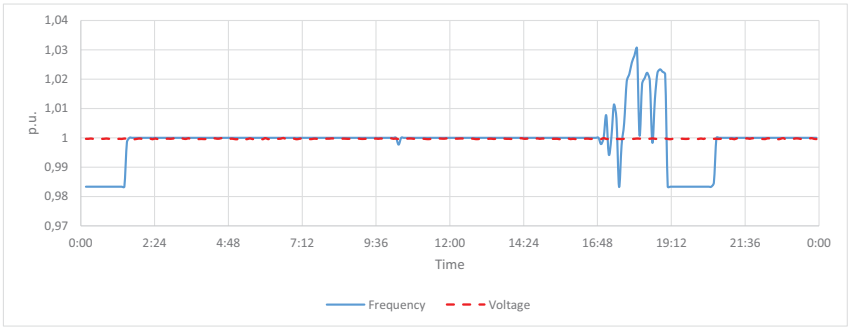

Fig. 16 – Frequency and voltage profile for Case 3.

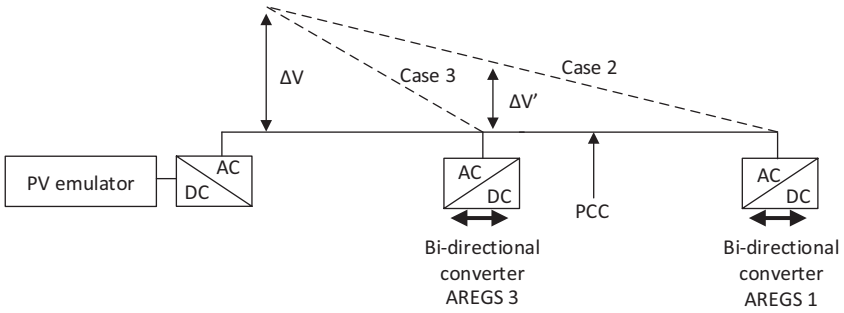

Fig. 17 – Voltage profile for the cascaded tested topologies.

5. Conclusions

Recently, attention is being given to the interconnection of micro-grids in multi-micro-grid topology. This is attributed to the new features that are being introduced in grid-forming inverters and that allow new topologies for the operation of micro-grids.

The ability to interconnect micro-grids and even stack them in a hierarchy improves the sustainability and robustness of the system as a whole, especially in rural electrification projects, where due to all the uncertainties regarding the demand and the evolution of the demand over the years of the project need to be robust and flexible to respond to changes. Consequently, the generation and distribution system should be designed with a level of

flexibility in order to avoid the impossibility of an eventual expansion.

During the tests, the use of a two-level set of AREGS was found to be a suitable topology to attribute modularity and scalability to the rural electrification solution. However, attention has to be given to the proper parametrization of the cascaded system as a whole and to the effects that the connection would produce at the PCC. It is emphasized that usually, standalone systems like the ones evaluated in this paper constitute relatively weak grids, and, therefore, more susceptible to power quality issues like voltage rise. In the case presented in the tests, voltage at the PCC could be a control signal for power limitation from the distributed generation if the voltage falls out of acceptable values.

The integrated AREGS can improve the management of energy and add modularity to deal with unpredicted situation. In order to study these problems the Laboratory of Photovoltaic Systems of the University of São Paulo implemented a test facility using the four available AREGS to form a smart micro-grid, which is being used both for research and capacity building.

6. References

Aneel, Agência Nacional de Energia Elétrica. Resolução normativa Nº 493. 2012. Available at: http://www2.aneel.gov.br/cedoc/ren2012493.pdf. Accessed in 02/10/2017.

Azaza, M., Wallin, F. Multi objective particle swarm optimization of hybrid micro-grid system: A case study in Sweden. Energy, 123 (2017), pp 108-118. DOI: 10.1016/j.energy.2017.01.149

Irfan, M., Iqdal, J., Iqdal, A., Iqbal Z., Riaz, R. A. Opportunities and challenges in the control of smart grids. Renewable and Sustainable Energy Reviews, 71 (2017), pp 652-674, DOI: 10.1016/j.rser.2016.12.

Koraz, Y., Gabbar, A. Risk analysis and self-healing approach for resilient interconnected micro energy grids. Sustainable Cities and Society, 32 (2017), pp 638-653. DOI: 10.1016/j.scs.2017.05.010

Lidula, N. W. A., Rajapakse, A. D. Microgrids research: A review of experimental microgrids and test systems. Renewable and Sustainable Energy Reviews, 15 (2011), pp 186-202. DOI: 10.1016/j.rser.2010.09.041

Soshinskaya, M., Crijns-Graus, W. H. J., Guerrero, J. M., Vasquez, J. C. Microgrids: Experiences barriers and success factors. Renewable and Sustainable Energy Reviews, 40 (2014), pp 659-672. DOI: 10.1016/j.rser.2014.07.198

Ustun, T. S., Ozansoy, C., Zayegh, A. Recent development in microgrids and example cases around the world – A review. Renewable and Sustainable Energy Reviews, 15 (2011), pp 4030-4041. DOI: 10.1016/j.rser.2011.07.033

Vasiljevska, J., Peça Lopes, J. A. Matos, M. A., Integrated micro-generation, load and energy storage control functionality under the micro-grid concept. Electric Power System Research, 95 (2013), 292-301. DOI: 10.1016/j.epsr.2012.09.014

Methodological Approach of Performance Evaluation for Using Pump as Micro Hydro-turbine

Ombeni J. Mdee [1]*, Cuthbert Z. Kimambo[1], Torbjorn K. Nielsen[2] and Joseph Kihedu[1]

[1]Department of Mechanical and Industrial Engineering, University of Dar es Salaam

P. O. Box 35091, Dar es Salaam, Tanzania.

[2]Department of Energy and Process Engineering, Norwegian University of Science

and Technology, NO-7491 Trondheim, Norway.

*Correspondence: ombenijohn@gmail.com; Tel.: +255-764-603-505

Abstract

The pumps work differently in terms of performance characteristics when operated in reverse mode to generate mechanical rotational energy driven by the water energy. The performance characteristics related to head, flow rate, specific speed and efficiency have been predicted differently from available conversion methods. Also, the procedure of selecting pump as hydro-turbine varies from different conversion methods. This article presents the methodological approach of evaluating the pump as hydro-turbine related to selection procedures, performance characteristics and challenges.

Keywords: Challenges, pump as hydro-turbine, performance characteristics, selection procedures.

1. Introduction

The micro or small hydropower is very potential for electricity generation in the remote areas of Africa continent, especially in the sub-Saharan African regions (Kaunda et al, 2012). The communities need a simple design, ease manufacturing and affordable technology that will sustain extreme local conditions, inexpensive and low maintenance cost for electricity generation (Mbabazi and Leary, 2010). Locally manufactured of hydro-turbine in a developing country will enable the costs per unit of energy output to be lower than the use of small diesel or petrol generators, solar PV systems or wind turbines (Williams and Simpson, 2008).

The selection of hydro-turbine depends on the site characteristics i.e, head and flow rate. Micro hydropower schemes can use the standardized equipment, low-cost approaches and off-the-shelf equipment (Patel et al, 2015). But, the main problem is to get a proper hydro-turbine within the remote market areas (Suarda et al, 2006). The equipment like pump that is used in water pumping for domestic and industrial use, irrigation, livestock and sewage systems in the off-grid remote areas are used as hydro-turbine for micro hydropower (Muttalli et al, 2014; Popescu et al, 2013). The off-the-shelf pump still limited to the less than 100 kW (Garay, 1990).

This article presents the methodological approach of getting the off-the-shelf Pump as Hydro-turbine (PAT) for potential micro hydropower. The selection procedures help to find the possible pump that fits the specific hydropower site. Through testing by using numerical analysis i.e., Computational Fluids Dynamics (CFD) or test rig in the laboratory is possible to get the PAT performance characteristics include head, flow rate, power delivered, efficiency and losses. Also, the conversion methods used to convert the pump performance characteristics to PAT characteristics. Therefore, the main objective of this article is to review the procedures of selecting the off-the-shelf pump, performance characteristics and challenges of using pump as turbine for hydropower schemes development.

doi:10.18086/swc.2017.03.02 Available at http://proceedings.ises.org

1.1. Pump as Hydro-turbine Application

The principle operation of pump is depending on the centrifugal force, cross-sectional area and fluid velocity. The main parts of pump are presented in Fig. 1 (a). The centrifugal force exerted on the water by the rotating impeller, moves the water away from the suction eye and out along the impeller vanes to their extreme tip where the liquid is then forced against the inside walls of the increasing cross-sectional area between impeller with blades and casing to convert kinetic energy of the water into pressure energy at the discharge part. For PAT as presented in Fig. 1(b), water pressure inflow at the discharge part and strike the impeller with blades to generate mechanical rotation connected to the shaft and rotate in the opposite direction of pump rotational speed. Motor or generator connected to the shaft for electricity generation.

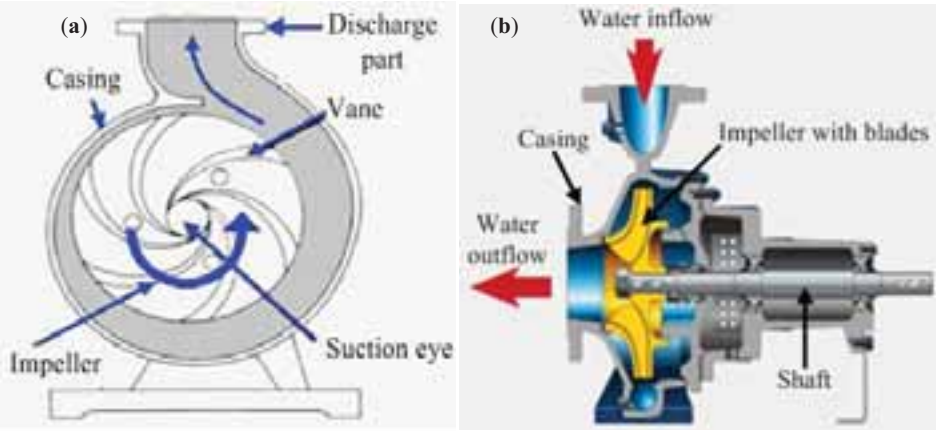

Fig. 1: Principle operation of pump. (a) sectional view of pump showing main parts (Chaurette, 2005). (b) sectional view of pump in reverse mode showing the direction of water flow and shaft connected to impeller (Orchard, 2009)

2. Methodological Approach

The methodological approach of selecting PAT is based on the methods used to convert pump performance characteristics related to head, flow rate, power and efficiency to the PAT characteristics (Fig. 2). The detail descriptions of the methodological approach is presented in the next sub-sessions.

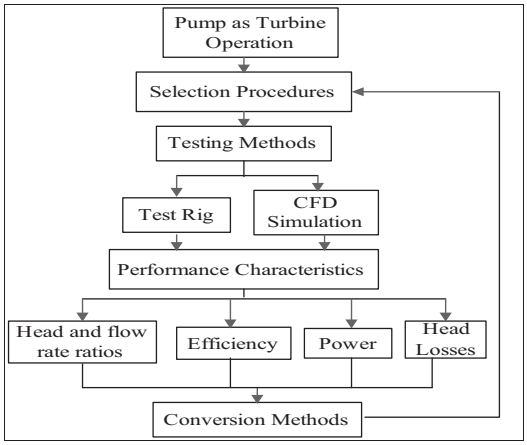

Fig. 2: Methodological approach of pump as turbine application

2.1 Selection Procedures

The selection procedures are based on the geometric shape of the pump controlled by calculating the specific speed. The procedures are as follows:

i. To calculate the hydro-turbine specific speed (n_{st}) related to head and flow rate for given hydropower site at a given rotational speed.

ii. To collect the pump datasheet that consists of head, flow rate, rotational speed, horse power and efficiency and used to calculate the specific speed (n_{sp}).

iii. To calculate the specific speed of PAT by using the conversion equations from Tan and Engeda (2016), Yang et al (2012), Singh and Nestmann (2011) and Chapallaz et al (1992). When the four conversion equations are compared to each other, indicated to have the fit-line of squared R of 0.944 as presented in Fig. 3. This step used to control the geometric shape of the pump related to hydro-turbine head and flow rate.

iv. Then, calculated PAT specific speed should be about equal to step (i) to select the pump related to the pump datasheet information.

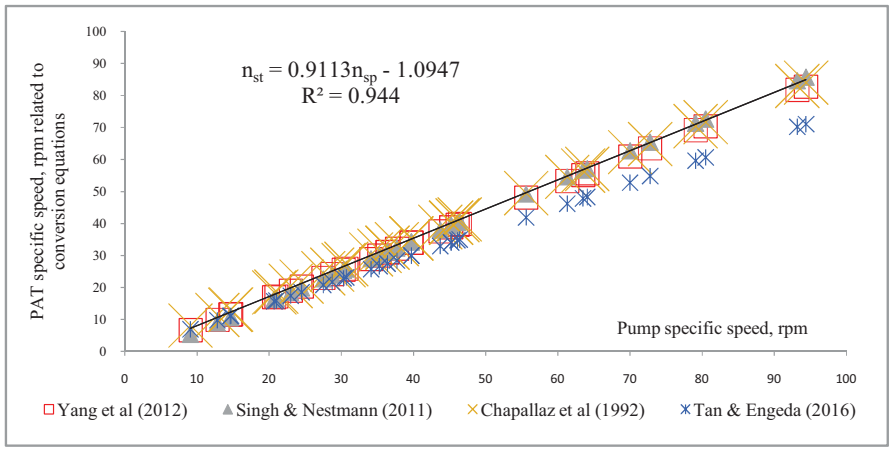

Fig. 3: Variation of PAT specific speed from various empirical equations

v. To regulate the rotation speed of pump as turbine by using modified affinity laws described in Carravetta et al (2014) or unmodified affinity laws described in Chapallaz et al (1992). Williams (1995) also regulated the head and flow rate ratios by using the efficiency and rotational speed.

2.2 Testing Methods

The PAT is tested by using a test rig or/and numerical analysis based on CFD simulation. The test rig simulates the site conditions and results can be very useful for predicting the real situation in the potential hydropower site. Krivichenko (1994) indicated the test rig can measure the PAT performance characteristics and cavitation effect. But, the use of CFD simulation helps to investigate the internal losses and flow patterns in the impeller

with blades, draft tube and casing which could not be measured experimentally (Nigussie and Dribssa, 2015; Agarwal, 2012).

2.3 Performance Characteristics

Pump performance characteristics for reverse mode is not declared from the off-the-shelf pump datasheet provided by the pump manufacturer (Buono et al, 2015). But, pump operated in reverse direction indicated to change their performance characteristics include head, flow rate, efficiency and specific speed. The PAT performance characteristics are still very complex to find a relationship to cover all pumps performance characteristics given in the datasheet (Baburaj et al, 2013). Fortunately, Nautiyal et al (2011) indicated the running of pump in reverse mode works without technical complications. The most common performance characteristics are presented below:

2.3.1 Head and flow rate

The ratios of head and flow rate for pump operating in reverse and pump modes is greater than 1. The conversion equations use slope/gradients method to correlate head and flow rate from optimum condition. More than twenty conversion equations are found in Bogdanovic-Jovanovic et al (2014); Nautiyal and Kumar (2011); Teuteberg (2010); Derakhshan and Nourbakhsh (2008); Singh (2005); Alatorre-Frenk (1994) and Williams (1994). The ratios of pump head and flow rate are calculated separately for most existing conversion methods. The head obtained in reverse mode is divided by pump head to get the head ratio and flow rate obtained in reverse mode is divided by pump flow rate to get flow rate ratio. The correlation of head and flow rate ratios related to specific speed for twenty eight (28) experimental data, separately collected from Tan and Engeda (2016), Singh (2005), Qian et al (2016), Fernández et al (2004), Derakhshan and Nourbakhsh (2008), Couzinet (2013) and Barbarelli et al (2017) as presented in Fig.4. The squared R is greater than 0.7.

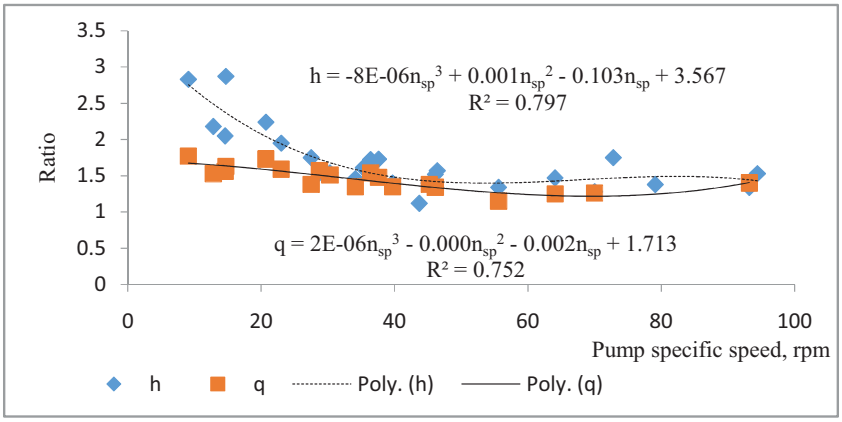

Fig. 4. Correlation of head and flow rate ratios versus specific speed

2.3.2 Power

The PAT power is the ratio of pump horsepower and its efficiency (Ventrone and Navarro, 1982). The efficiency data is collected from pump datasheet (Pedrollo, 2016). Alternatively, PAT power is estimated by using Equation (1) given the PAT efficiency conversion equations collected from Bogdanovic-Jovanovic (2014), Chapallaz et al (1992) and Williams (1994). Fig. 5 presents the variation of PAT power against standard pump rated power. The method is more suitable during the desk work studies. H, Q, g, η, ρ and P present the head, flow rate, acceleration due to gravity, efficiency, density of water and power. Subscripts t presents turbine mode.

$$P_t = \rho * g * H_t * Q_t * \eta_t \qquad \text{(eq. 1)}$$

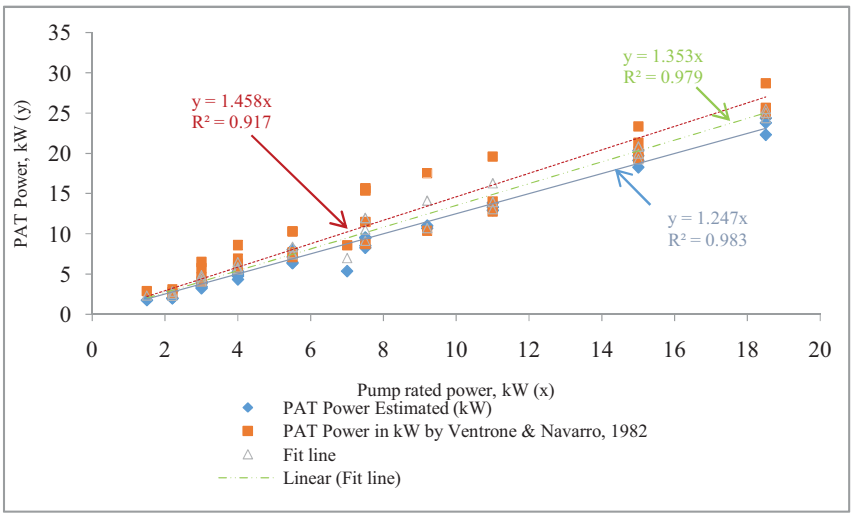

Fig. 5. Comparison of the PAT power with pump horsepower

2.3.3 Efficiency

The PAT efficiency tested from different research works for a range of the off-the-shelf pump (14.6 to 93.2rpm) is presented in Fig. 6. The efficiency-curves were digitized by using a Getdata software (GetData, 2017). Steller et al (2008) presented the overall efficiency of PAT against the percentage of flow rate. Tan and Engeda (2016) indicated the pump specific speed of 30.7, 43.7, 63.5 and 80.5 rpm operated with flow rate coefficient of less than 0.08 with constant flow rate coefficient. But, Singh (2005) indicated the pump specific speed range from 35, 36.4, 39.4, 45.2 and 46.2 rpm operated with flow rate coefficient less than 0.4 with percentage flow rate coefficient of less than 25 %; 61.3 and 79.1rpm operated with flow rate coefficient from 0.25 to 0.75. The flow rate coefficient variations do not affect the efficiency of the PAT. But, pump with low efficiency when operated in reverse mode has also a low efficiency. Also, the pump with higher specific speed delivered the highest efficiency and allowing the larger variation of flow rate coefficient compared to the low specific speed PAT. The overall-PAT efficiency is less than 86 %.

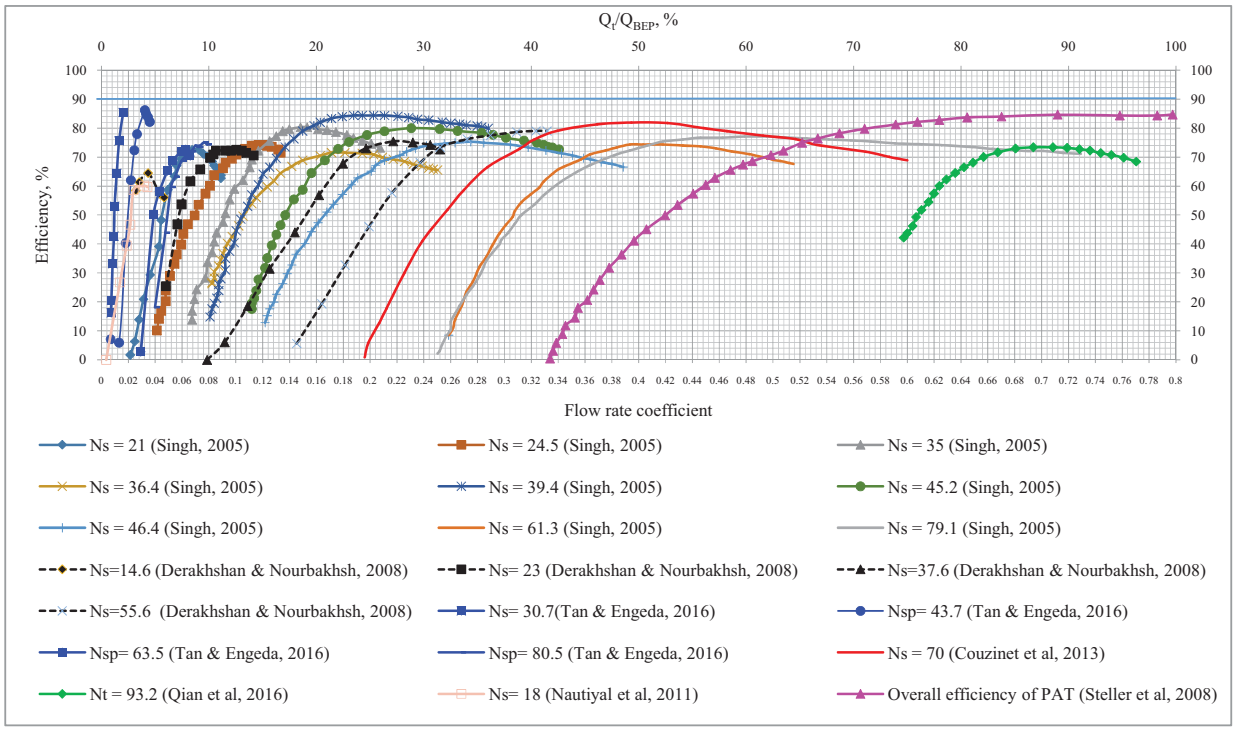

Fig. 6: Overall operating efficiencies for PAT from pump specific speed range from 14.6 to 93.2 rpm

2.4. Head losses

The difference of hydraulic pressure between the intake/forbay to the hydropower plant over the product of density and acceleration due to gravity presents the gross head. The head loss lower the available gross head that decreases the net head available to strike the impeller with blades. The head losses in the penstock, casing, impeller with blades and draft tube are discussed below.

2.4.1 Penstock

Water flowing through a penstock or canal encounters head losses due to friction and fittings (including elbow, tees, etc.). The head losses in the penstock are calculated by using friction loss tables, curves or a nomograph provided from the penstock/pipe manufacturer (Moran, 2016). For instance, 20 % increase in penstock diameter leads to a 60 % decrease in head losses (Gatte and Kadhim, 2012). Fernandez et al (2002) indicated that friction losses is reduced by increasing the diameter and/or reducing the equivalent length of the pump suction side. Alternatively, head loss estimated by using Equation (2) (Williams, 1995). Q_m is the pump flow rate given by the manufacturer based on the penstock diameter. L is the penstock length.

$$H_l(\%) = \frac{L}{H_t} * \left(\frac{Q_t}{Q_m}\right)^2 \qquad \text{(eq.2)}$$

Also, the Darcy-Weisbach equation used to calculate the head loss (Penche, 2004). Different penstock materials are based on the roughness height of commercial pipes for a given diameter and the Reynolds number obtained by using the Moody chart to interpolate the value of the friction factor (Moody, 1944). The roughness of commercial pipes is described in White (2011). Fig. 7 presents the variation of head loss against flow rate for 100 feet of PVC class 160 plastic pipe with a diameter less than 152.4 mm or 6 inches (Pipeline, 2017). Head loss reduces the available gross head as well as the expected power generation, but Penche and de Minas (1998) indicated that a power loss of 4 % is usually acceptable.

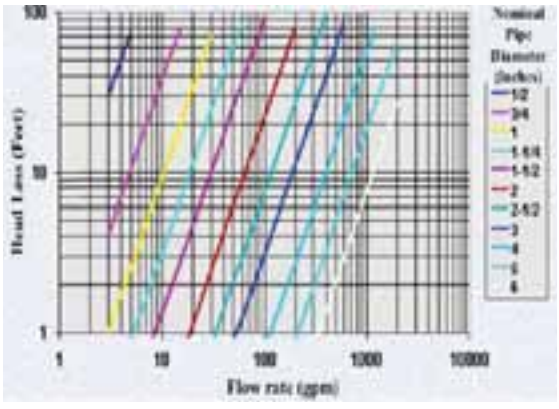

Fig. 7: Relationship of head loss versus flow rate (Pipeline, 2017).

2.4.2 Hydropower system

Water flow in the PAT from the inlet to strike the impeller with blades surrounding with casing is an exit at the outlet pipe connected to the draft tube. The most common micro hydropower head loss installed with PAT based on the rule of thumb and experimental data are presented in Table 1. Head loss varies from 5 to 33 % of the total penstock length and mostly are occurred for small and micro hydropower system (Williams, 1995). It is still indicated the head loss in the impeller with blades is higher compared to the draft tube and casing (Rawal and Kshirsagar, 2007).

Table 1: Percentage of head loss from PAT hydropower system

Head loss as percentage of total penstock length (%)	Applied condition	Source
5-25	Rule of thumb	Klingeman and Wheeler (1982)
10-20		Williams (1995)
10-15		Canyonhydro (2017)
10		Renewables First (2017)
12.2	Installed PAT	Smith and Ranjitkar (2000)
13.2	Installed PAT	Arriaga (2010)
< 33 for small systems	Rule of thumb	Gatte and Kadhim (2012)

3. Challenges of Using Pump as Hydro-turbine

The different challenges and description for PAT application in hydropower schemes are presented in Table 2.

Table 2. List of challenges and description for pump as hydro-turbine

Challenges	Description	Sources
Flow rate leakage	Leaking back of fluid from the high pressure side to the low pressure side that tends to lower the performance	Chapallaz et al (1992)
Range of flow rate	Particular pump can operate as much less that for a conventional turbine	Popescu et al (2003); Williams (1995)
Major design changes	Changing are based on the bearings design and checking the seals, stress and threaded of shaft	Chapallaz et al (1992)
Material types	i. Built-with carbon-impregnated nylon without many hard particles, broze or cast iron and eye-clearance fit the suction inlet ii. It also the shaft material should not easily scratched by knife	Williams (1995)
Head and flow rate	Pump operates at higher head and flow rates values in water turbine mode at the same rotational speed	Popescu et al (2003); Nautiyal et al (2011)
Efficiency	Efficiency of PAT is usually lower than that of conventional turbines	Patel et al (2015); Motwania et al (2013); Nautiyal et al (2011)

Torque	Reduction of rotation speed can lower the torque	Dribssa et al (2015)
Conversion equations	The performance characteristics related to head, flow rate, power, specific speed and efficiency are predicted differently from one pair to another by ±20 %	Williams (1995)
Runaway	Characteristic of runaway in PAT is more dangerous and essentially associated with increase of operating head compared to the actual operating head when is in load condition	Singh (2005)
Pump datasheet	Lacking of performance datasheet as the major limitation of using PAT	Buono et al (2015); Agarwal (2012)
Fixed geometric shape	PATs are very sensitive towards changing of head and flow rate within the fixed geometric shape i.e impeller and casing results to poor part-load performance	Ramos and Borga (2000); Singh (2005)
Constant flow rate	The construction of reservoir for PAT as small system is not a good option	Williams (1996)

4. Conclusions

This methodological approach helps to increase the awareness of harnessing the potential micro hydropower in off-grid remote areas by using off-the-shelf pump. The performance characteristics of pump that are changed when operated as turbine include head, flow rate, power, specific speed and efficiency. This article discusses the selection procedures, performance characteristics and challenges of using off-the-shelf pump. PAT efficiency indicates to have the maximum efficiency of about 86 % against the flow rate coefficient based on the twenty (20) collected tested characteristics for pumps specific speed range from 14.6 to 93.2 rpm and flow rate coefficient greater than 0 to 0.8. It also indicates the efficiency is constant when the percentage for flow rate coefficient variation is less than 25 %. Furthermore, this paper presents the main challenges of using PAT include the low range of flow rate, replacement of bearing, fixed the geometric shape, reduced of torque and lack of pump datasheet.

5. Acknowledgments

This paper is part of ongoing PhD study and supported by NORAD under Energy and Petroleum (EnPe) Program at the University of Dar es Salaam, Tanzania and Norwegian University of Science and Technology, Trondheim, Norway.

6. References

Agarwal, T., 2012. Review of pump as turbine (PAT) for micro-hydropower. Int. J. Emerg. Technol. Adv. Eng. 2(11), pp. 163-169.

Alatorre-Frenk, C., 1994. Cost minimisation in micro hydro systems using pumps-as-turbines, Coventry, United Kingdom. PhD Thesis, University of Warwick, Faculty of Sciences, Department of Engineering.

Arriaga, M., 2010. Pump as turbine - a Pico hydro alternative in Lao People's. Renew Energ. 35, pp. 1109-1115.

Baburaj, E., Sivaprakasam, R., Manikandan, C., Sudha, K., 2013. CFD analysis of pump as turbine for micro-hydro schemes. Int. J. Innov. Res. Sci. Eng. Technol. 2(3), pp. 590-594.

Barbarelli, S., Amelio, M., Florio, G., 2017. Experimental activity at test rig validating correlations to select pumps running as turbines in microhydro Plants, Energy Conversion and Management. http://dx.doi.org/10. 1016/j.enconman.2017.03.013, (2017).

Bogdanovic-Jovanovic, J. B., Milenkovic, D. R., Svrkota, D. M., Bogdanovic, B., Spasic, Z. T., 2014. Pumps used as turbines: power recovery, energy efficiency, CFD analysis. Thermal Science. 18(3), pp. 1029-1040.

Buono, D., Frosina, E., Mazzone, A., Cesaro, U., Senatore, A., 2015. Study of a pump as turbine for a hydraulic urban network using a tridimensional CFD modeling methodology. Energy Procedia. 82, pp. 201-208.

Canyonhydro, Guide to Hydropower. Available at: http://canyonhydro.com/resources.html[29/March/2017]

Carravetta, A., Conte, M. C., Fecarotta, O., Ramos, H. M., 2014. Evaluation of PAT performances by modified affinity law. Procedia Engineering. 89, pp. 581-587.

Chapallaz, J. M., Eichenberger, P., Fischer, G., 1992. Manual on pumps used as turbines. Vieweg, Braunschweig: Printed in the Federal Republic of Germany by Lengericher Handelsdruckerei, Lengerich.

Chaurette, J., 2005. Fluid Design:Centrifugal pump systems. Montreal, Quebec, Canada: Fluide Design Inc..

Derakhshan, S., Nourbakhsh, A., 2008. Theoretical, numerical and experimental investigation of centrifugal pumps in reverse operation. Exp. Therm. Fluid Sci. 32, pp. 1620–1627.

Dribssa, E., Nigussie, T., Tsegaye, B., 2015. Performance analysis of centrifugal pump operating as turbine for identified micro/Pico hydro site of Ethiopia. Int. J. Eng. Res. Gen. Sci. 3(3), pp. 6-19.

Fernández, J., Blanco, E., Parrondo, J., Stickland M.T., Scanlon, T.J,. 2004. Performance of a centrifugal pump running in inverse mode, Proc. Inst. Mech. Eng. J. Power and Energy.

Fernandez, K., Pysdrowski, B., Schiller, D. W., Smith, M. B., 2002. Understand the basics of centrifugal pump operation. pp. 52-56.

Garay, P. N., 1990. Using pumps as hydroturbines. Hydro Review, pp. 52-61.

Gatte, M. T., Kadhim, R. A., 2012. Hydro power. Open Access Publisher, INTECH, pp. 95-124.

GetData Graph Digitizer. Available at: http://getdata-graph-digitizer.com/download.php [23/Feb/2017]

Kaunda, C. S., Kimambo, C. Z., Nielsen, T. K., 2012. Potential of small-scale hydropower for electricity generation in Sub-saharan Africa: review article. ISRW: Renew Energ. pp. 1-15.

Klingeman, P. C., Wheeler, G., 1982. Micro-Hydropower: Oregon Development Guide. Oregon State University.

Krivichenko, G., 1994. Hydraulic Machines: Turbines and Pumps. USA: Lewis, Boca Raton, Fla.

Mbabazi, S., Leary, J., 2010. Analysis and design of electronic load controllers for micro-hydro systems in the developing world. University of Sheffield, E-Futures, p. 12.

Moody, L. F., 1944. Friction factors for pipe flow. Trans. ASME, 18 07, 66, pp. 671-678.

Moran, S., 2016. Pump sizing: bridging the gap between theory and practice. 38-44.

Motwania, K. H., Jain, S. V., Patel, R. N., 2013. Cost analysis of pump as turbine for Pico hydropower plants – a case study. Procedia Engineering: NUiCONE 2012, 51, pp. 721-726.

Muttalli, R. S., Agrawal, S., Warudkar, H., 2014. CFD simulation of centrifugal pump impeller using ANSYS-CFX. Int. J. Innov. Res. Sci. Eng. Technol. 3(8), pp. 15553-15561.

Nautiyal, H., Varun, Kumar, A., Yadav, S., 2011. Experimental investigation of centrifugal pump working as turbine for small hydropower systems. Energ Sci. Technol. 1(1), pp. 79-86.

Nigussie, T., Dribssa, E., 2015. Design and CFD analysis of centrifugal pump. Int. J. Eng. Res. Gen. Sci. 3(3), pp. 668-677.

Orchard, B., 2009. Pumps as turbines in the water industry. Available at: http://www.worldpumps.com/view/5086/pumps-as-turbines-in-the-water-industry/ [22/Feb/2017].

Patel, J. B., Mevada, R. N., Sardana, D., Rajput, V. P., 2015. Experimental and numerical investigation of centrifugal pump performance in reverse mode. Int. J. Adv. Technol. Eng. Sci. 3(1), pp. 1066-1072.

PEDROLLO, 2016. Standardized Centrifugal Pumps (EN 733-DIN 24255). Available at: http://www.pedrollo.co.uk/pdf/F%20Series.pdf [1/March/2016].

Penche, C., 2004. European Small Hydropower Association. Guide on how to develop a small hydropower plant. European Renewable Energy Council.

Penche, C., de Minas, I., 1998. Layman's guideBook: On how to develop a small hydro site. European Small Hydropower Association.

Pipelines. Available at: http://www.nooutage.com/hydroele.htm [7/Feb/2017].

Popescu, D., Duinea, A., Rusinaru, D., 2003. Study of centrifugal pump operating as turbine in small hydropower plants. Recent Researches in Electric Power and Energy Systems. pp. 285-288.

Ramos, H. M., Borga, A., 2000. Pumps yielding power. Dam Engineering, Water Power and Dam Construction, pp. 197-217.

Rawal, S., Kshirsagar, J. T., 2007. Numerical simulation on a pump operating in a turbine mode. pp. 21-27.

Renewables First. Available at: http://www.renewablesfirst.co.uk/hydropower/hydropower-learning-centre /how-much-power-could-i-generate-from-a-hydro-turbine/[29/March/2017].

Singh, P., 2005. Optimization of internal hydraulics and of system design for pumps as turbines with field implementation and evaluation, Karlsruhe: Ph.D Dissertation, University of Karlsruhe.

Singh, P., Nestmann, F., 2011. A consolidated model for the turbine operation of centrifugal pumps. J. Eng. Gas Turb. Power. 133, pp. 1-9.

Smith, P., Ranjitkar, G., 2000. Nepal case study-part one: installation and performance of the Pico power pack, Nottingham, UK: The Nottingham Trent University.

Steller, J., Adamkowski, A., Stankiewicz, Z., Lojek, A., Rduch, J., Zarzycki, M., 2008. Pumps as turbines for hydraulic energy recovery and small hydropower purposes in Poland. Poland.

Suarda, M., Suamadwipa, N., Adnyana, W. B., 2006. Experimental work on modification of impeller tips of a centrifugal pump as a turbine. Bangkok, Thailand, Department of Mechanical Engineering, Udayana University, Bali, Indonesia , pp. 1-5.

Tan, X., Engeda, A., 2016. Performance of centrifugal pumps running in reverse as turbine: Part II - systematic specific speed and specific diameter based performance prediction. Renew Energ. 99, pp. 188-197.

Teuteberg, B. H., 2010. Design of a pump-as-turbine micro hydro system for an Abalone Farm, Department of Mechanical and Mechatronic Engineering, Stellenbosch University: Final Report for Mechanical Project 878.

Ventrone, G., Navarro, G., 1982. Use of water power on a small scale. The Pump as Turbine Electricity, 59(3), pp. 101-107.

White, F. M., 2011. Fluid Mechanics. 7th ed. New York: McGraw-Hill.

Williams, A., 1995. Pumps as Turbines: A User's Guide. London: Intermediate Technology Publications.

Williams, A. A., 1994. The turbine performance of centrifugal pumps: a comparison of prediction methods. Proc. Inst. Mech. Eng. Part A. J Power and Energy. 208, pp. 59-66.

Williams, A. A., 1996. Pumps as turbines for low cost micro hydro power. Renew Energ. 9(1-4), pp. 1227-1234.

Williams, A. A., Simpson, R., 2008. Pico hydro – reducing technical risks for rural electrification. ISESCO Science and Technology Vision, 4(6), pp. 60-66.

Yang, S. S., Derakhshan, S., Kong, F. Y., 2012. Theoretical, numerical and experimental prediction of pump as turbine performance. Renew Energ. 48, pp. 507-513.

Concentrating Solar Power Technologies

Comparative analysis of energy demand and CO_2 emissions of residential buildings

Julià Coma[1], José Miguel Maldonado[2], Alvaro de Gracia[3], Toni Gimbernat[4], Teresa Botargues[5], Luisa F. Cabeza[2,*]

[1] Departament de Tecnologia de l'Arquitectura, Universitat Politècnica de Catalunya, Av. Dr. Marañón 44-50, Barcelona, (Spain).

[2] GREiA Research Group, INSPIRES Research Centre, Universitat de Lleida, Pere de Cabrera s/n, 25001, Lleida, (Spain).

[3] Departament d'Enginyeria Mecànica, Universitat Rovira i Virgili, Av. Paisos Catalans 26, 43007 Tarragona (Spain).

[4] SINAGRO ENGINYERIA S.L.P, Av. Estudi General 7, Altell 5, 25001, Lleida (Spain).

[5] USER FEEDBACK PROGRAM SL, Sant Jaume Apòstol 8, 25126, Almenar (Spain).

Abstract

Rapid expansion of solar thermal energy for increasing energy efficiency of buildings has been adopted in short/medium and long-term energy strategies of EU countries. Within this context, the overall objective of this work is to develop an innovative high performance and cost effective hybrid solar heat and power system. The initial application is to be implemented in individual dwellings and small business residential buildings for on-site electricity and heat generation using solar thermal energy. It is estimated that the proposed technology will deliver 60% of domestic energy requirements and provide 20% reduction in energy costs and greenhouse gas emissions compared to the best existing low carbon energy technologies. The aim of this study consists in performing a comparative analysis of the different building typologies, which can host this technology, and their energy demands for heating and domestic hot water, as well as their CO_2 emissions.

Keywords: Solar thermal energy, Micro-organic Rankine cycle, Phase change materials, Energy savings, Building energy demand, Residential building typology.

1. Introduction

In Europe the building sector represents 41% of the final energy consumption and the 40% of the total GHG emissions of end-use sectors (Directive 2010/31/EU). The Renewable Heat Incentive and similar schemes, which are deployed across a number of EU countries (e.g. UK, Germany, France, Italy, Spain), encourage uptake of renewable heat technologies to support the ambition of 12% of heating coming from renewable sources by 2020.

The present work is part of the Innova MicroSolar project, which is funded within the framework research and innovation programme Horizon 2020. The overall objective of this project is to develop an innovative high performance, cost effective and solar high durability 2-kW_{el}/18-kW_{th} heat and power system for on-site heat and power supply to individual dwellings and small business residential buildings using solar thermal energy. The proposed technology will be built around a small scale solar concentrating collectors which supply thermal energy to power the small high performance organic Rankine cycle (ORC) turbine with 2-kW_{el} output. To control the energy input and output, a thermal energy storage unit with phase change materials (PCM) will be designed. The system will provide 60% of the required building energy and reduce 20% the energy costs and greenhouse gas (GHG) emissions compared to the best existing low carbon energy technologies.

Figure 1 shows the preliminary scheme design of the system that mainly consists of the following parts:

- Concentrating solar collectors (CSP): The CSP system is based on linear Fresnel mirrors which are considerably easier and cheaper to manufacture than their parabolic equals. The system incorporates a sun tracking mechanism and can supply heat transfer fluid (HTF) flow at 295ºC.

doi:10.18086/swc.2017.04.01 Available at http://proceedings.ises.org

- PCM thermal energy storage: the storage block has two different main components, the PCM tank and the enhanced heat sink, which are connected by heat pipes. The novelties of this unit are the PCM compound with the tuned melting temperature for heat storage, and the reversible heat pipes capable of transferring heat at the required high heating rate in both directions.
- Micro-organic Rankine cycle plant: micro-ORC technology is equipped with a high speed permanent magnet AC alternator able to supply 2.3 kW_{el}.

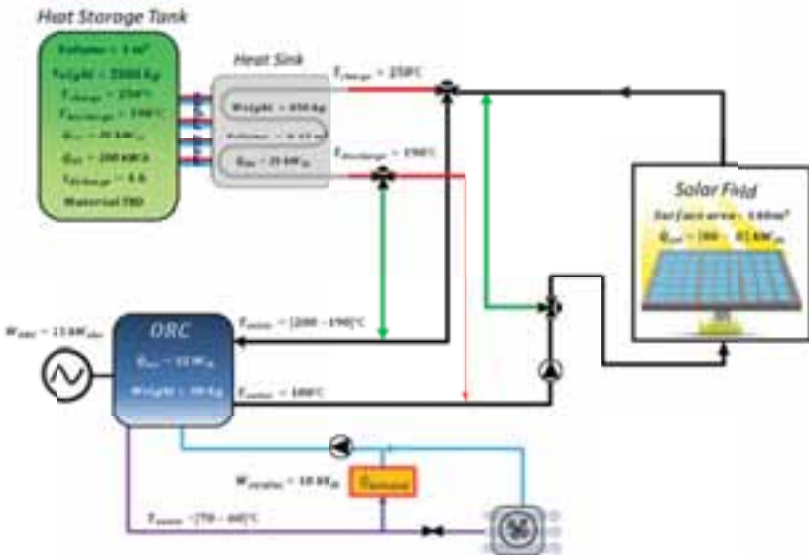

Fig. 1: Innova MicroSolar system diagram

The aim of this study consists in providing information on types of domestic residential buildings for Spain, Italy, UK, France, and Germany. This information will include specification of details on their architecture, building envelope, range of dimensions of living space, their insulation properties, hydronic domestic hot water (DHW), and space heating systems, seasonal and annual energy demands for DHW, heating, and electricity. This information will be used as input data to define and adapt the final design of the system, which will include different building typologies, climate conditions, and energy demand among other technical requirements.

2. Comparative evaluation of building typology, energy demand and CO_2 emissions

From the literature review, projects funded by the IEE agency such as DATAMINE, TABULA, and EPISCOPE (episcope.eu/iee-project) have previously studied the energy performance of the EU building stock by using the energy performance certificates and the different building typology approaches based on the DATAMINE structure and previous experiences of typological classifications used in European countries. The main outcome of these projects was an interactive database named TABULA WebTool created to share valuable information with the scientific community and building experts from European countries.

After performing a comprehensive analysis of these consecutive EU projects (2006-2016) a standardized building classification was identified. In addition, the energy demand for heating and DHW and the related CO_2 emissions sorted by building typology, age classes, and different climatic conditions were compared. Table 1 shows the classification that divides the EU building stock into four general typologies: single family house (SFH), terraced house (TH), multifamily house (MFH) and apartment block (AB). Since databases present different age classes by country (six in Spain, 12 in Germany, ten in France, eight in Italy, and eight in UK), an overall building classification grouped into three different age classes, from 1970 to 1985, from 1986 to 2000, and from 2001 to 2016 was used to unify and compare all the countries within the same age bands. Also, the climatic conditions inside a country were divided into three different classes: hot, temperate, and cold,

representing the hottest, the average, and the coldest climatic conditions of a country, respectively.

Tab. 1: Example of standardized building classification for Germany from 2001 to 2016 divided in four typologies by TABULA

Single family house (SFH)	Terraced house (TH)	Multifamily house (MFH)	Apartment block (AB)
			

3. Results

Up to 14 different climatic conditions have been analysed and treated for the different analysed countries (Spain, France, Italy, UK, Germany, and Sweden). However, due to the huge variation on climatic conditions across Europe, the scope of this study is focused only on the representative temperate climatic conditions of the countries in Table 2. The results are organized according to the main outcomes from the aforementioned findings divided in energy demand for heating and DHW and the derived CO_2 emissions.

Tab. 2: Temperate climates of the analysed countries

Country	Spain	Italy	France	Germany	U.K	Sweden
Climate	Atlantic	Middle	H2	Kassel	England	Zone 2

3.1. Annual energy demand for heating and DHW

Figure 2 shows the energy consumption for heating and DHW in temperate climatic conditions by country. As it was expected, the energy demand is lower in apartment blocks in comparison to single family houses and terraced houses for all the EU countries analysed. These results emphasize the importance of the building shape that presents higher compactness (lower form factor between the building surfaces in contact with the non-heated areas and total air volume of the building) in apartment blocks and multifamily houses, so requiring less energy for heating. Additionally, many variations in terms of energy demands for heating and DHW were observed for the same building typology when countries and building construction periods were compared for temperate regions.

Figure 2 also highlights the reduction of the energy demand of buildings over time, for each type of building. Since poor construction systems and low insulation levels were common in old building typologies (1970-1985), European energy policies towards more efficient buildings had a direct impact on reducing the energy demand of buildings. For instance, nowadays newest types of buildings in Spain (2001-2016) consume around 50 % less energy for heating and DHW compared to old building typologies (1970-1985). Similar energy trends were observed in Italy, UK, France, and Germany, but not in Sweden where higher insulation levels were implemented before the considered period in this study.

Regarding to examples of different thermal transmittance coefficient of buildings envelopes, the walls of a single family house in Germany (1986-2000) has 0.35 $W/m^2 \cdot K$ while in Spain the same building characteristics and period shows the double (0.60 $W/m^2 \cdot K$). However, as shown in Figure 2, for the specific construction period of 1986-2000 the German single family house consumes 190 $kWh/m^2 \cdot year$ for heating and DHW in temperate climatic conditions while in Spain the same building typology requires only 60 $kWh/m^2 \cdot year$. As expected, northern countries such as Sweden, UK, and Germany show higher energy demands for heating purposes than southern countries such as Spain and Italy, even using higher insulation levels on building skins. That fact highlights the relevant impact of the climatic conditions in the final energy consumption of a building.

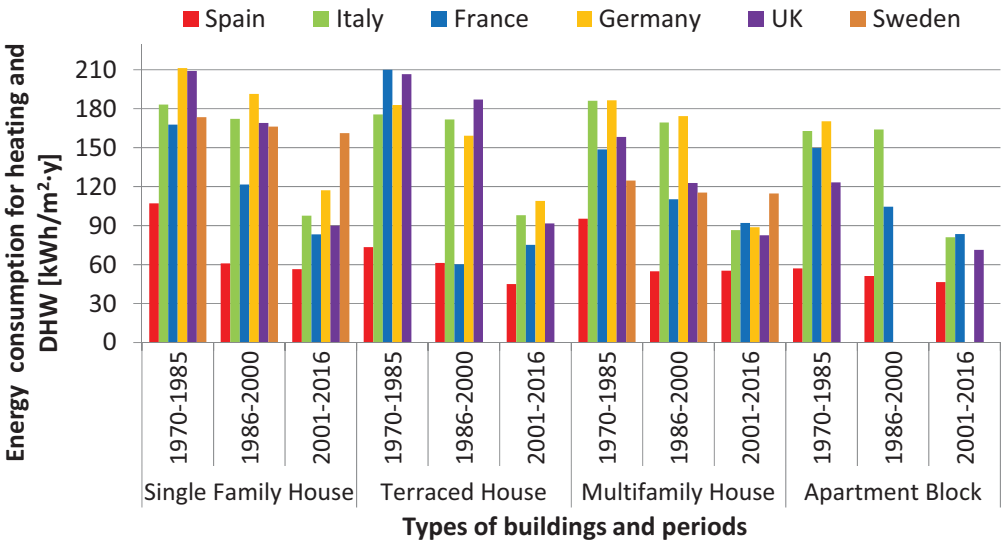

Fig. 2: Energy consumption for heating and domestic hot water in temperate climatic conditions by country

In southern countries such Spain, Italy, and some regions of France, in which Mediterranean climatic conditions are hot, the domestic hot water can account for more than a half of the total energy consumption of a building. As an example, a single family house in Spain (1986-2000) accounted for 41.8 kWh/m^2·y of consumed energy to cover heating and DHW demand (Figure 2) and 20.2 kWh/m^2·y come only from DHW requirements. However, in the opposite site, northern countries such as Germany or Sweden have higher rates in terms of energy consumption for heating in comparison to the energy consumption for DHW. For a similar case scenario in Germany, the calculated delivered energy for heating & DHW of a single family house, from 1986 to 2000, was 188.5 kWh/m^2·y while only 21.1 kWh/m^2·y were for DHW requirements.

These results highlight the wide application potential of new and innovative technologies such as the micro solar heat and power system in different countries and different building typologies.

3.2. Annual CO2 emissions

The expected trends in reducing the CO_2 emissions in all studied countries can be seen in Figure 3. All the building typologies show a reduction of the CO_2 emissions throughout the years, being the newest period (2001-2016) the lowest emissions. These results could be directly related to the reduction in the energy demand for heating purposes. However, Figure 3 shows that in UK, multifamily houses have a higher CO_2 emissions levels despite the fact that their energy consumption is lower than other building typologies. That difference is due to the heating technology considered on TABULA WebTool. Terrace houses supply the heating by condensing boilers while multifamily houses (from 1970 to 2000) use electrical heaters; and the CO_2 emissions per electrical kilowatt in UK is high because of the energy mix. For that reason, the Innova MicroSolar project can achieve its energy savings goal but depending on the current technology installed it may not fulfil the CO_2 emissions required. For instance, multifamily houses located in UK which were built from 1970 to 1985 emit 0.58 CO_2 kg/kW, these emissions go down to 0.28 CO_2 kg/kW in multifamily houses built from 2001 to 2016 due to the implementation of condensing boilers to provide the heat & DHW demand.

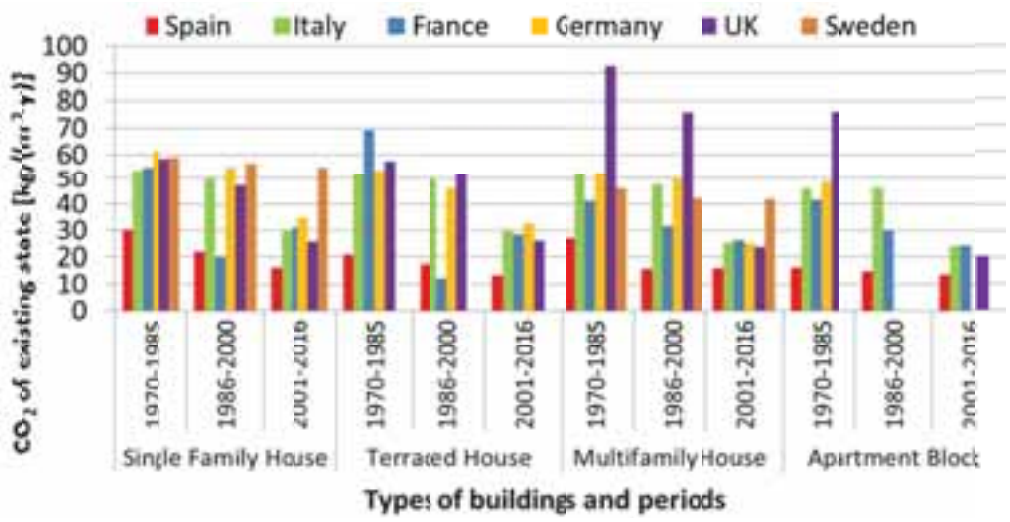

Fig. 3: CO_2 emissions in temperate climatic conditions

4. Conclusions

After performing an estimation of the energy demand for the most common domestic residential buildings in different European countries, the following are the main outcomes of this study:

- The energy policies proposed in many European countries towards more sustainable buildings are being a direct impact in reducing the energy demand in buildings.
- After a literature review, four main typologies of domestic residential buildings have detected for the aforementioned European countries: single family house (SFH), terraced house (TH), multifamily house (MFH) and apartment block (AB).
- The DHW demand of a building is mainly related to the human behaviour and the performance of the system while the heating demand is mainly attributed to the climatic conditions and the building insulation level.
- The estimated range of the energy consumption for heating and DHW was from 46.5 kWh/m^2·y for new apartment blocks in a temperate Spanish climate to 210 kWh/m^2·y for old French terraced house (1970-1985) in the same climatic conditions.
- The CO_2 emissions savings are related with the energy savings. However, the CO_2 emissions saved by the project depend on the current technology installed to supply the heat & DHW demand.

5. Acknowledgements

This study has received funding from European Union's Horizon 2020 research and innovation programme under grant agreement Nº723596 (Innova MicroSolar) and Nº 657466 (INPATH-TES). The work is partially funded by the Spanish government ENE2015-64117-C5-1-R (MINECO/FEDER) and ENE2015-64117-C5-3-R (MINECO/FEDER). GREA is certified agent TECNIO in the category of technology developers from the Government of Catalonia. The authors would like to thank the Catalan Government for the quality accreditation given to their research group (2014 SGR 123). Alvaro de Gracia would like to thank Ministerio de Economía y Competitividad de España for Grant Juan de la Cierva, FJCI-2014-19940.

6. References

Consecutive Projects co-funded by the Intelligent Energy Europe Programme (IEE). Available from: http://episcope.eu/iee-project/overview/ (October 2017).

Directive 2010/31/EU of the European parliament and of the council of 19 May 2010 on the energy performance of buildings. Available from: http://www.epbd-ca.eu (October 2017).

Horizon 2020, The EU Framework Programme for Research and Innovation. Available from: http://ec.europa.eu/programmes/horizon2020/en/ (October 2017).

TABULA WebTool. Available from: www.webtool.building-typology.eu (October 2017)

Key Aspects of a Novel Undulated Receiver for Parabolic Trough Collectors

Yassine Demagh[1] and Ahmed A. Hachicha[2]

[1] Laboratoire d'Etude des Systèmes Energétiques Industriels (LESEI), Université de Batna 2, Algérie.

[2] Sustainable and Renewable Energy Engineering, University of Sharjah, United Arab Emirates

Abstract

This study proposes the replacement of the conventional straight absorber by the newly designed longitudinally undulated. Numerical results revealed that the new absorber could dethrone the former for several reasons: Among others, it allows a more homogeneous distribution of concentrated solar radiations on its outer surface (Monte Carlo Ray Tracking results); unlike other techniques which improve the inner heat transfer by increasing simultaneously the load of the absorber and the pressure drop within it, the proposed curved absorber is going to generate in a natural way, without any additional mechanical components, vortices within the main streaming which allowed to increase the heat transfer coefficient of about 63 % with an increase of the pressure drop penalty of about 60 %. On the other hand, it allows a drastic reduction of the size of the solar collector field. All these facts lead to decreasing the wall temperature gradient bellow 40 K. Results are obtained for the Syltherm 800 Reynolds number range 2.5×10^4 to 12.3×10^4 and a fluid inlet temperature of 450 K.

Keywords: Parabolic trough collector (PTC), size reduction, undulated pipe, heat transfer enhancement.

1. Introduction

Parabolic trough collectors (PTCs) are the most promising technology for electricity generation and process heating application. The main option to drive the cost of PTC technology down is to reduce the size of the solar field (Price et al. 2002). One of the ways to achieve this goal is the improvement of the thermal performances of the solar absorber by passive techniques by adding additional mechanical components to the absorber pipe (Ghadirijafarbeigloo et al., 2014, Mwesigye et al., 2014); nevertheless, these techniques produce a significant pressure drops penalty. On the other hand, since the work of (Demagh et al., 2015), the heat transfer improvement should be achieved without any additional mechanical parts. In the present study, 3D steady-turbulent simulations are carried out to investigate the scenario where the conventional straight absorber is replaced by the novel undulated absorber (Fig. 1(a)) proposed by (Demagh et al., 2015) and highlight its thermal performances enhancement and effects on the solar collector sizes.

Fig. 1: (a) The novel undulated PTC receiver. (b) A PTC module with the novel undulated absorber.

doi:10.18086/swc.2017.04.02 Available at http://proceedings.ises.org

2. The numerical modelling and results

Fig. 1(b) shows the novel absorber mounted on a PTC module; its main characteristics schematized in Fig. 2 are summarized in Tab. 1.

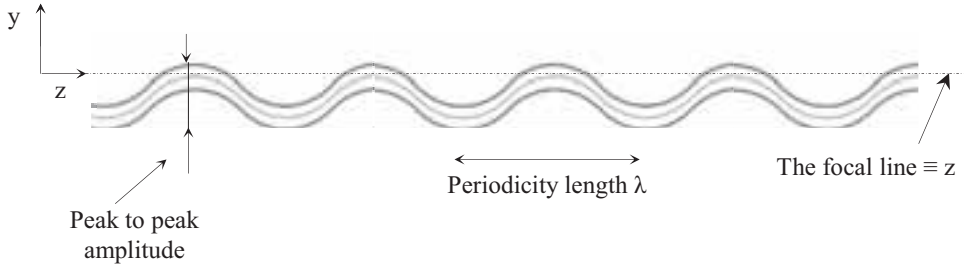

Fig. 2: Main characteristics of the undulated absorber.

Tab. 1: Absorber pipe c haracteristics.

Description	
Outer pipe diameter	0.070 m
Inner pipe diameter	0.066 m
Total length assumed in this study	0.975 m
Periodicity length	0.195 m
Peak to peak amplitude	0.020 m

The periodicity length is not the critical point, but the amplitude is (Demagh et al., 2015). The smaller the length, the more the transfer is efficient. For actual technical considerations of manufacturing, the selected periodicity length of 195 mm could be easy to achieve on a stainless steel pipe with inner/outer diameters of 66/70 mm.

2.1. Modelling and grid independence tests

(Di Piazza and Ciofalo, 2010) compared numerical results (the friction factor and Nusselt number) of different turbulence models with experimental data of curved pipes. The authors concluded that the SST k–ω eddy-diffusivity model gives the best agreement, but requires several computational grid nodes compared to k–ε model. Thus, by means of the CFD code (FLUENT 6.3), the k–ω based (SST) model was adopted to give accurate predictions of the onset and the amount of secondary flow, produced as a result of the curved shape.

The pipe absorber was meshed using tetrahedral elements with a structured mesh into the wall and an unstructured (tetra/mixed) non-uniform grids within the fluid medium, as shown in Fig. 3. During the meshing process, additional nodes are placed inside the viscous sub-layer to ensure the satisfaction of the $y^+ < 1$ requirement at the first grid point close to the wall.

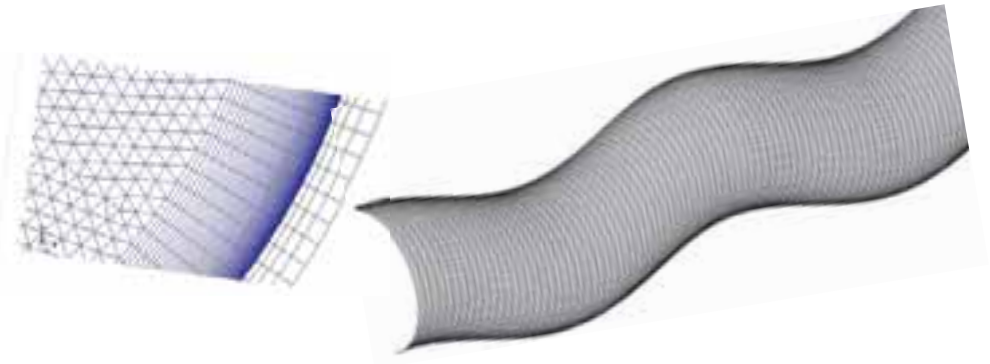

Fig. 3: The meshing generated by GAMBIT.

The grid independence was conducted in the analysis by adopting different grid sizes, and a sample of these tests is summarised in Table 2. The solution is considered mesh independent when the variations of the predicted mean heat transfer coefficient (h) and pressure drop (ΔP) are less than 1.5%. It is found that results for the global grid of 2,910,119 cells is not affected by the refinement and is therefore used in the present study.

Table 2- Grid independence test.

Global grid	% change of ΔP	% change of h
2,300,000	//	//
2,437,600	-1.6%	-0.45
2,910,119	-4.4%	2.4
3,256,400	1.5%	0.55

2.2. Results and interpretation

The Monte Carlo Ray Tracing method (MCRT) provided the non-uniform two-dimensional (2D) of the heat flux density distribution ($\boldsymbol{q}$) on the outer surface of PTC straight absorbers (He et al., 2011). The direct normal irradiance equals $933.7 W/m^2$; the parabolic trough rim angle used was 70°, aperture width 5 m and focal length 1.84 m. By means of the free code-source Tonatiuh, exploiting its validated results (Blanco et al., 2009), the reconstituted 3D heat flux density distribution on the outer wall of the undulated PTC absorber pipe as established by (Demagh et al., 2015) is shown in Fig. 4. With regard to the focal line (Fig. 2), the y-location of cross-section centres changes periodically along the undulated absorber, which is at the origin of the 3D nature of the ($\boldsymbol{q}$) relating to the 2D nature of the conventional straight absorber where the y-location of the cross-section centres remain unchanged (He et al., 2011).

Using the built-in curve fitting functions in Microsoft Excel, a UDF was written and compiled under Fluent GUI to set up the thermal boundary condition on the outer absorber pipe surface. The Heat transfer fluid (HTF) was the Syltherm 800 and its proprieties were considered as a temperature-depending.

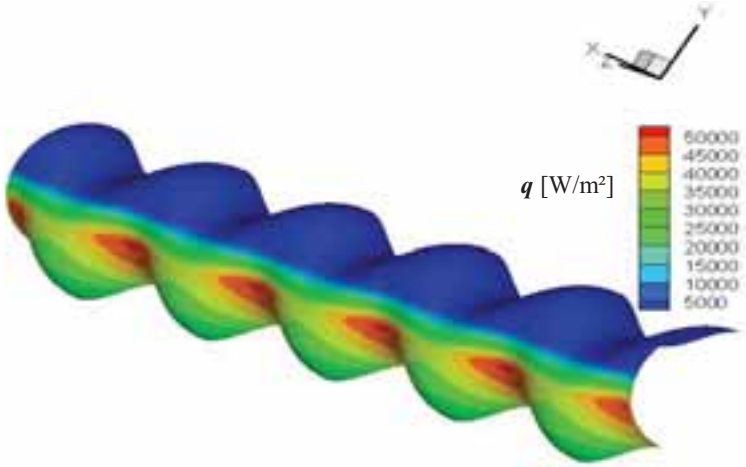

Fig. 4: Contours of the heat flux density distribution q [W/m²] on the outer face of the undulated absorber for a direct solar irradiance of 933.7 W/m² (Demagh et al., 2015).

The numerical results for the average heat transfer coefficient and the pressure drop obtained with Syltherm 800 flowing through the undulated PTC absorber are reported in Fig. 5 for $T_{in} = 450\,K$ and the Reynolds number range 2.5×10^4 to 12.3×10^4. It is evident that the heat transfer coefficients of the undulated absorber are larger than that of the conventional straight absorber obtained by Gnielinski's correlation (Incropera et al., 2007), about a 63% increase.

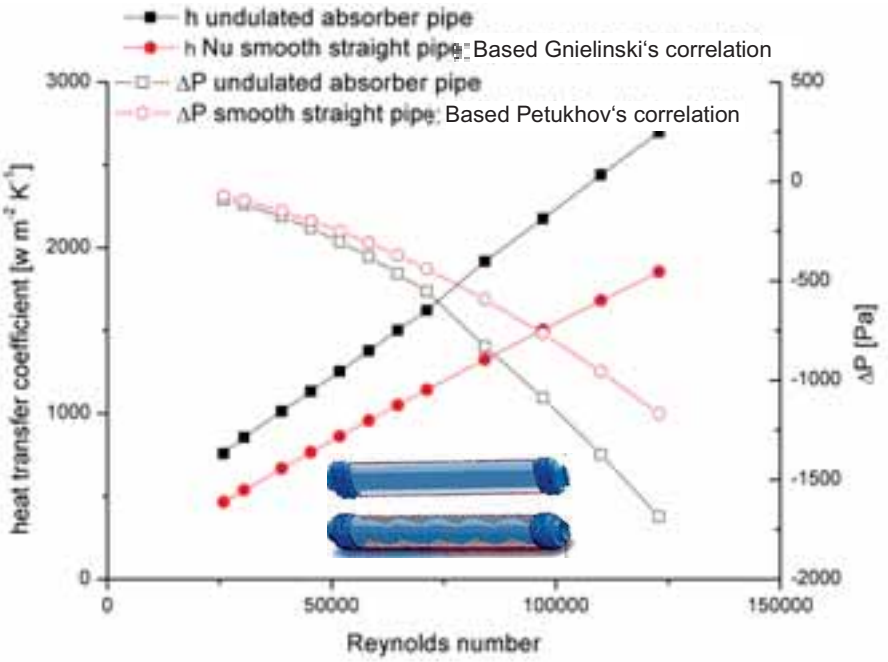

Fig. 5: The convective coefficients and pressure drops vs. Reynolds number. Correlation from (Incropera et al., 2007)

Also, as expected, the enhancement of the heat transfer is accompanied by an increasing of the fluid pressure drops, about 60 %. The better the distribution of $\boldsymbol{q}$ and the enhancement heat transfer cause the reduction of the circumferential temperature gradient ΔT bellow 40 K, as shown in Fig. 6.

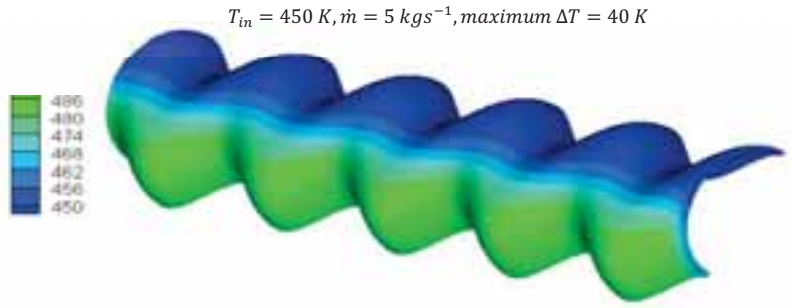

Fig. 6: Contour of the circumferential temperature gradient ΔT.

It is well known that curved configurations induce a secondary flow within it due to the centrifugal force, generated by curvatures of the pipe, as the fluid flows. The secondary streaming significantly enhances the heat transfer rate, causing a better mixture of fluid by the disturbance of the boundary layer. Vortices are identified in the bends, as shown in Fig. 7, where the y-velocity colours are synonymous of the intensification of vortices. Outside the bend-planes, the vortices are absent. On the other hand, compared to the conventional straight pipe absorber, the increase of the straight length of the undulated pipe absorber is insignificant, about 2.547 % for a peak amplitude of 10 mm (in this study), and the increase of the geometric concentration ratio will be the same. Thus, the improvement of heat transfer is mainly due to the existence of secondary flows rather than the increase of the heat exchange surface.

Fig. 8 shows the longitudinal change of the local Nusselt number along the second, third and fourth period for an inlet HTF temperature of $450K$ at Reynolds numbers of $\mathrm{Re} = 64740$, corresponding to an HTF mass flow rate of $5\ kg \cdot s^{-1}$.

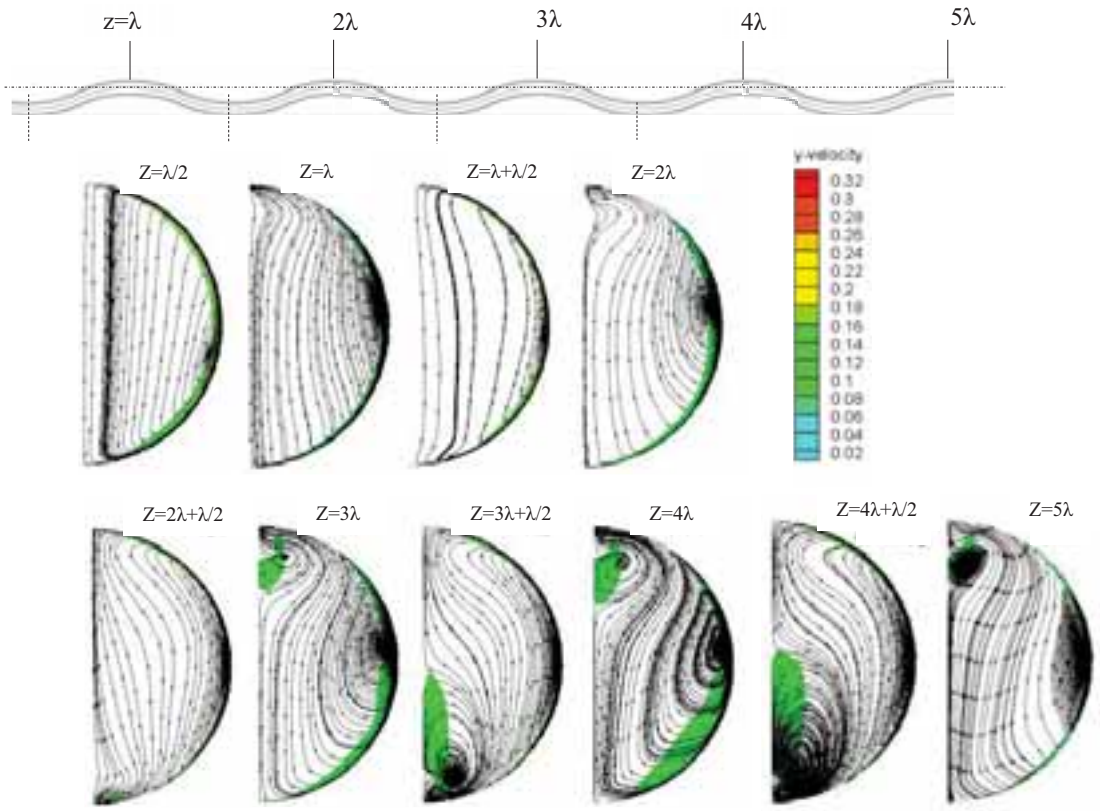

Fig. 6: The Secondary flow configuration. Colours refer to y-velocity magnitude [m/s].

The curve possesses a sinusoidal shape, the local Nusselt number increases up to a location at midway between the uppermost and bottommost bends. From this location, it starts decreasing, exceeding the bottommost bend, up to next midway location of the next periodic segment and increases again, and so on periodically along the entire length of the absorber.

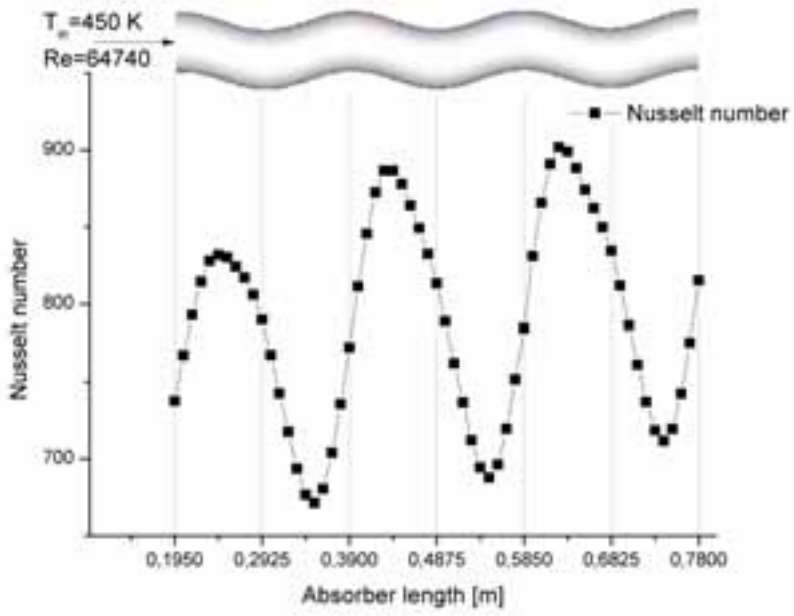

Fig. 8: Change of the local Nusselt number along the absorber length.

All rising branches of the curve occur on the upper half of the absorber pipe where the heat flux density distribution and wall temperature are moderate, see Figs 4 and 6. The HTF temperature will approximates the wall temperature, which it is not heated by the concentrated solar radiation and the local Nusselt number increases. On the other half of the absorber pipe, it's quite the opposite phenomenon, the Nusselt number decreases given that the temperature gap between the HTF and wall increases due to the concentrated solar radiation on this half (Fig. 4) heating the wall of the tube (see Fig. 6). It should be emphasized here that the local Nusselt number seems to respond to the heat flux density distribution to the flow dynamics (acceleration or deceleration in various branches or even the vortex in bends). The general trend of the local Nusselt number is increasing due to the mixture of fluid with each pass through the bends where the vortices occur.

3. Conclusion

For the range of Reynolds numbers, the inlet HTF temperatures and the geometrical parameters considered, it is established that the heat transfer rate may be increased by up to 63% compared with a straight pipe, while the pressure drop increased by less than 60%; the secondary streaming (reversed flow) contribute considerably to the overall heat transfer enhancement. The circumferential temperature difference of the absorber was decreased below 40 K for almost all the range of the mass flow rates and will significantly reduce the thermal stress on the absorber pipe. The local Nusselt number possesses a sinusoidal shape along the pipe absorber, and seems to respond to the heat flux density distribution to the flow dynamics (acceleration or deceleration in various branches or even the vortex in bends). With the 2.547 % increase of the straight length of the pipe absorber, the improvement of heat transfer is mainly due to the existence of secondary flows rather than the increase of the heat exchange surface. The final conclusion is that to achieve the same HTF temperature rise that the conventional straight absorber the length of the undulated absorber would be reduced due to the improvement in the heat transfer rate.

4. References

Blanco, M.J., Mutuberria, A., Garcia, P., Gastesi, R., Martin V., 2009. Preliminary validation of Tonatiuh. SOLARPACES Symposium, Berlin, Germany.

Demagh, Y., Bordja, I., Kabar Y., Benmoussa H., 2015. A design method of an S-curved parabolic trough collector absorber with a three dimensional heat flux density distribution. Sol Energy 122, 873–884.

Di Piazza, I., Ciofalo, M., 2010. Numerical prediction of turbulent flow and heat transfer in helically coiled pipes. Int. J. Therm. Sci. 49, 653–663.

Ghadirijafarbeigloo, S., Zamzamian, A.H., Yaghoubi, M., 2014. 3-D numerical simulation of heat transfer and turbulent flow in a receiver tube of solar parabolic trough concentrator with louvered twisted-tape inserts. Energy Proc. 49, 373–380.

He, Y.L., Xiao, J., Cheng, Z.D., Tao, Y.B., 2011. A MCRT and FVM coupled simulation method for energy conversion process in parabolic trough solar collector, Renew Energy 36, 976–985.

Incropera, F.P., Dewitt, D.P., Bergman, T.L., Lavine, A.S., 2007. Fundamentals of Heat and Mass Transfer. Sixth edition, J. Wiley & Sons.

Mwesigye, A., Bello-Ochende, T., Meyer, J.P., 2014. Heat transfer and thermodynamic performance of a parabolic trough receiver with centrally placed perforated plate inserts. Applied Energy 136, 989–1003.

Price H., Lüpfert E., Kearney D., Zarza E., Cohen G., Gee R., Mahoney R., 2002. Advances in parabolic trough solar power technology. J. Sol. Energy Eng. 124, 109–125.

The Novel Undulated Parabolic Trough Receiver: Performance Enhancement, Reduction in the Size and Cost of the Collector Fields

Yassine Demagh[1,2], Yassine Kabar[2] and El Wardi Bitam[3]

[1] Laboratoire d'Etude des Systèmes Energétiques Industriels (LESEI), Université de Batna 2, Algerie.

[2] Laboratoire d'Energétique Appliquée et Matériaux (LEAM), Université de Jijel, Algerie

[3] Faculté des Sciences, Département de Physique, Université Batna 1, Algerie

Abstract

One of the main options to drive the cost of parabolic trough collectors (PTCs) technology down is to reduce the size of the solar field. This work proposes a novel receiver longitudinally undulated as a replacement for the conventional straight tube and investigates the effects on the size of absorbers, PTC modules and entire solar field. For this purpose, the developed method based on the similitude analysis should provide tools for drawing a comparison between the various designs of the absorber and should give useful measures of the scenario of their commissioning. Undulated absorber in service and without added supplementary mechanical components; the size of a solar collector field should reduce about ~29.5% consequence of the reduced size of the solar collector module and the absorber. The increase of the pressure drops through the novel absorber pipe should be re-balanced by the reduction in its size.

Keywords: Parabolic trough, undulated receiver, similitude analysis, size reduction of the solar field.

1. Introduction

The PTC large scale technology has proved its capacity to produce power with the lower cost as possible. PTC plants consist mainly of four loops, a large solar collector field, a steam generation system, a turbine/generator cycle and an optional thermal storage. One of the main options to drive the cost of PTC technology down is to reduce the size of the solar field (Price et al. 2002). The first way of reaching this purpose is to increase the parabolic mirrors reflectance and/or the absorber absorptance of the direct solar irradiance. The latter can be achieved through adding a secondary non-imaging reflector on the receiver (McIntire, 1980, Gee et al. 2002).

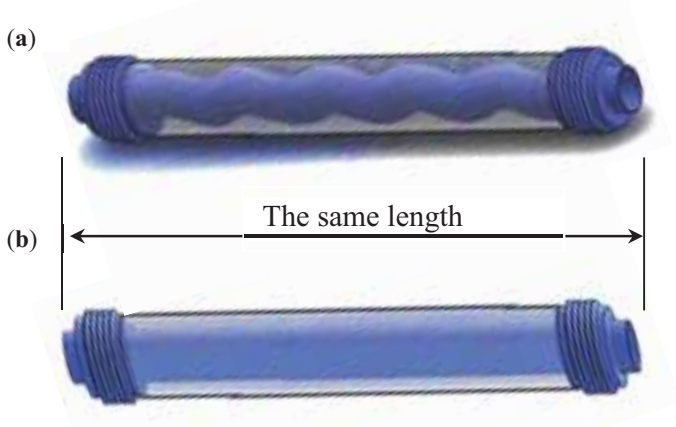

Fig. 1: (a) The novel PTC undulated absorber. (b) The conventional PTC absorber.

The second way is to improve thermal performances with a minimum pressure loss penalty as possible, which cannot be achieved by the passive techniques that add supplementary mechanical components to the absorber,

doi:10.18086/swc.2017.04.03 Available at http://proceedings.ises.org

the increase of the pressure losses is too important and the cost rise dramatically. In 2015, (Demagh et al. , 2015) introduce the possible use of longitudinal curved receiver in PTCs. The novel design (Fig. 1(a)) allows better characteristics of the outer heat flux due to its 3D distribution, with regard to the 2D nature of the conventional straight one (Fig. 1(b)). The focus of this study is to set up a general-purpose methodology to quantify effects of any heat exchanger enhancement technique on the reduction in the size of devices. The particular case of the newly designed undulated PTC absorber pipe will be the subject evaluation of the method.

2. Similitude analysis

It would be very interesting to be able to quantify the advantages of the heat transfer improvement on the reduction in the size of such exchangers. In a general-purpose, the methodology leads to develop expressions that could set up a comparison between two different pipe exchangers. Assuming steady-state conditions, the mean heat flow rate $\dot{Q}$ throughout the pipe can be defined as,

$$\dot{Q} = \rho \bar{c} u_{in} \left(\pi D_i^2 / 4 \right) \left(\bar{T}_{out} - \bar{T}_{in} \right) = h \left(\pi D_i L \right) \left(\bar{T}_w - \bar{T}_m \right) \quad \text{(eq. 1)}$$

u_{in}, ρ and $\bar{c}$ being the convective heat transfer fluid (HTF) inlet velocity, density and specific heat at the HTF mean temperature $\bar{T}_m$, respectively. D_i, h and L being the inner diameter, inner heat transfer coefficient and equivalent length, respectively. $\bar{T}_{in}$ and $\bar{T}_{out}$ being the inlet and outlet HTF bulk temperatures, respectively.

The ratio of equations resulting from the expression (1) when it is applied to a first configuration (subscript 1) and to a second configuration (subscript 2) leads to, after the rearrangement,

$$\left(\frac{L_1}{L_2} \right) = \frac{St_2}{St_1} \frac{\left(\bar{T}_{out} - \bar{T}_{in} \right)_1}{\left(\bar{T}_{out} - \bar{T}_{in} \right)_2} \frac{\left(\bar{T}_w - \bar{T}_m \right)_2}{\left(\bar{T}_w - \bar{T}_m \right)_1} \frac{(D_i)_1}{(D_i)_2} \quad \text{(eq. 2)}$$

$St = h / \rho u_{in} \bar{c}$ being the Stanton number. This result is extremely useful; it suggests that the comparison between the heat exchange rates of various exchangers may be modelled by an equality that introduces dimensionless groups which quantifying the dynamic and thermal behaviour

2.1. The novel undulated absorber: Thermal enhancement

3D steady-turbulent simulations are carried out to predict the flow fields using the CFD code (FLUENT 6.3). The k–ω based Shear-Stress-Transport (SST) model was used in the simulations. Exploiting the established 3D heat flux density distribution on the outer wall of the undulated PTC absorber pipe (Fig. 1(a)) (Demagh et al., 2015), a UDF was established and compiled in the commercial code Fluent. Numerical results for the turbulent heat transfer coefficient and the pressure drop obtained with Syltherm 800 flowing through the undulated PTC absorber are reported in Fig. 2. It is obvious that the average heat transfer coefficient of the undulated absorber is greater than that of the conventional straight absorber obtained by Gnielinski's correlation (Incropera et al., 2007), up to 63% increase, in addition to an increasing of the pressure drops, less than 60%.

2.2. The novel undulated absorber: Dimensional analysis and size reduction

- Without any enhancements, assuming the same pipe diameters and the similar operating conditions, it follows from expressions (2) that $L_2 / L_1 = 1$.
- In the particular case of this study, exchangers would be the conventional PTC straight absorber pipe and the novel undulated PTC absorber, respectively subscript 1 and 2, with the same inner diameter. To reach the similar rise of the HTF temperature (i.e. $\left(\bar{T}_{out} - \bar{T}_{in} \right)_2 = \left(\bar{T}_{out} - \bar{T}_{in} \right)_1$), when it is assumed the similar HTF inlet temperature (i.e., the similar HTF properties), the $\left(\bar{T}_w - \bar{T}_m \right)_1 = \left(\bar{T}_w - \bar{T}_m \right)_2$, the same flow regime (i.e., $\left(u_{in} D_i \right)_2 = \left(u_{in} D_i \right)_1$) and since $h_2 \geq h_1$, equation (2) becomes $L_1 / L_2 = h_2 / h_1 \geq 1$. Taking into account the results of Fig. 2, the trend of the equation (2) while varying the flow regime is

shown in Fig. 3. Until $\mathrm{Re} = 71000$ the trend is decreasing from $L_1/L_2 \cong 1.63$ to $\cong 1.41$; from this location it increases a little and becomes relatively flat, about $\cong 1.45$. To achieve the same HTF temperature increase of the classic straight absorber, the equivalent length of the novel absorber will be significantly reduced, consequence of the heat transfer improvement. With a mean equivalent length of $L_2 = L_1/1.63$, the area size of the solar collector field should reduce about $\cong 0.39\ \%$, consequence of the reduction in the size of solar PTC units. It is clear that the cost will be lower.

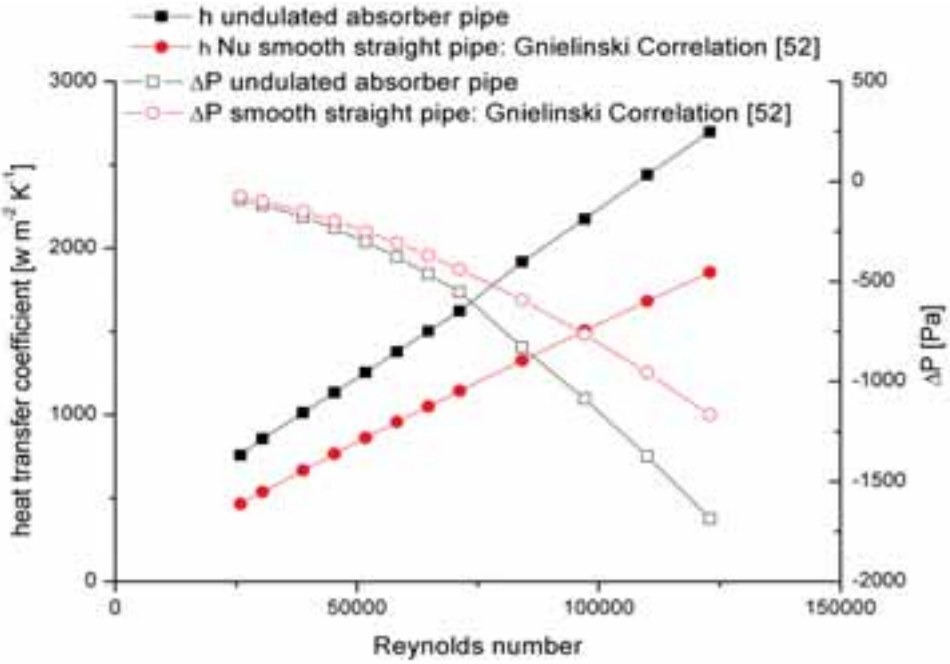

Fig. 2: The convective heat transfer coefficient and the pressure drops through the undulated pipe against Re, for $\bar{T}_m = 450\ \mathrm{K}$. Correlations refer to (Incropera et al., 2007)

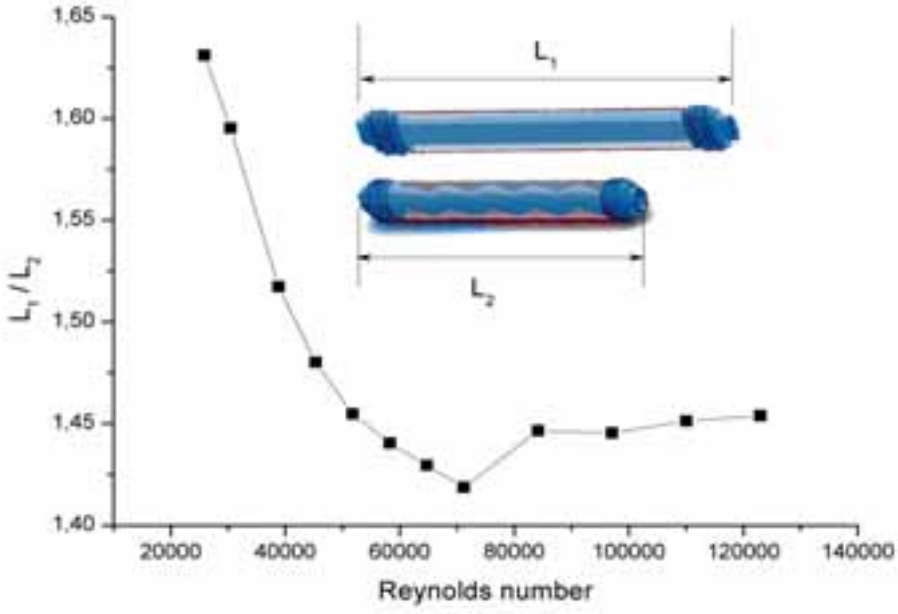

Fig. 3: The reduction in the size of the newly designed undulated PTC absorber

- Taking into account the reduction in the size of the novel absorber (with the length L_2), the pressure drop penalty $\Delta P|_{L1}$, shown in Fig. 2, for the length L_1, should be reconsidered as $\Delta P|_{L2} = \Delta P|_{L1} \cdot (L_2 / L_1)$, and decreases as shown in Fig. 4.

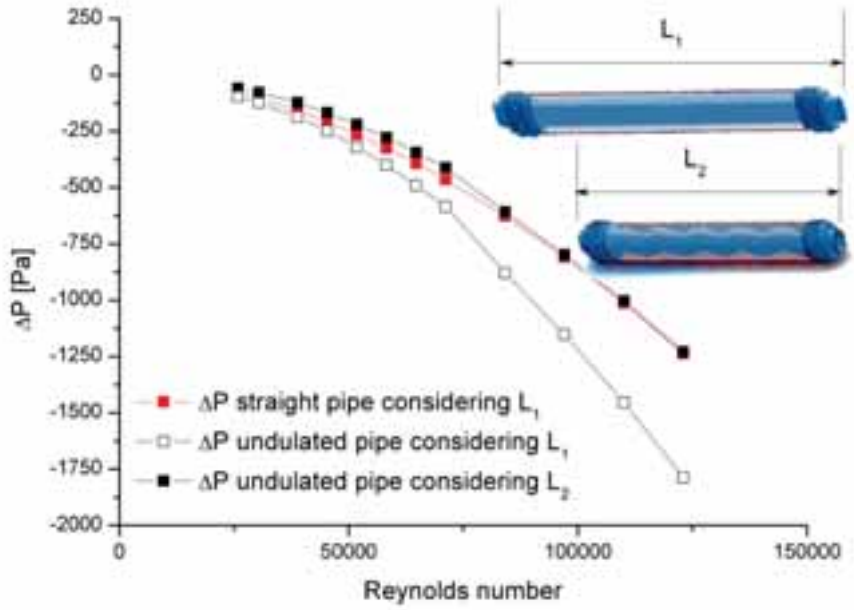

Fig. 4: The re-balancing of the pressure drops.

3. Conclusion

Following a similitude analysis developed in this study, the sizes of the absorber, solar collector modules and solar collector field should reduce about $\simeq 0.39\%$ by using of the novel undulated absorber. The increase of the pressure drop penalty of the novel solar absorber pipe is shown to be re-balanced by the reduction in its length. The manufacturing cost diminishes and the know-how remains unchanged with regard to the conventional absorbers, while the performance increases; the (performance/cost) ratio should be higher, what reduces drastically the kWh cost of the solar power.

4. References

Demagh, Y., Bordja, I., Kabar Y., Benmoussa H., 2015. A design method of an S-curved parabolic trough collector absorber with a three dimensional heat flux density distribution. Sol Energy 122, 873–884.

Gee R., Cohen G., Winston R., 2002. A Nonimaging Receiver for Parabolic Trough Concentrating Collectors, Proceedings of the ASME Solar 2002: International Solar Energy Conference (SED2002).

Incropera, F.P., Dewitt, D.P., Bergman, T.L., Lavine, A.S., 2007. Fundamentals of Heat and Mass Transfer. Sixth edition, J. Wiley & Sons.

McIntire W.R., 1980. Secondary concentration for linear focusing systems: a novel approach. Appl. Opt. 19, 3036–3037.

Price H., Lüpfert E., Kearney D., Zarza E., Cohen G., Gee R., Mahoney R., 2002. Advances in parabolic trough solar power technology. J. Sol. Energy Eng. 124, 109–125.

Long-Term Variability of Aerosol Optical Depth, Dust Episodes, and Direct Normal Irradiance over Kuwait for CSP Applications

Christian A. Gueymard[1], Majed Al-Rasheedi[2], Alaa Ismail[2] and Tahani Hussain[2]

[1] Solar Consulting Services, Colebrook, NH (USA)

[2] Kuwait Institute for Scientific Research, Shuwaikh (Kuwait)

Abstract

Two sources of aerosol data (from ground-based sunphotometry and long-term reanalysis), as well as irradiance data (from ground-based radiometric measurements) are investigated here. The daily, seasonal and interannual variability of aerosol optical depth is evaluated over Kuwait. Based on the MERRA-2 reanalysis, long-term aerosol trends are also established over the period 1980–2016, showing a slight increase in aerosol optical depth (AOD) since about 2000. This is conducive to a concomitant decrease in the direct normal irradiance (DNI) resource of ≈2% per decade, which can affect concentrating solar power (CSP) projects over the long-term. When compared with sunphotometer data from two AERONET stations located at a distance of only 90 km, but in somewhat differing environments, shortcomings are found in the aerosol data from the MERRA-2 reanalysis. Both bias and scatter are found in the hourly and daily AOD data, as well as occasional mismatch in the prediction of the more-or-less frequent AOD spikes caused by dust storm episodes. The use of MERRA-2 aerosol data for the prediction of clear-sky DNI with a high-performance irradiance model results in underestimation (of ≈13% on average) and substantial scatter on a 1-min basis, based on a comparison with co-located, high-quality DNI data.

Keywords: Aerosol optical depth (AOD), direct normal irradiance (DNI), CSP, dust storms, MERRA2.

1. Introduction

Many large solar projects involving various kinds of Concentrating Solar Power (CSP) technologies are being built in regions such as the Middle East. These arid or desert regions benefit from a low overall cloudiness, and thus overall high solar resource, but are also impacted by significant background aerosol loads and somewhat frequent dust episodes. These can be detrimental to the operation and yield of CSP plants for various reasons: (i) Intense atmospheric attenuation, leading to significant loss in incident direct normal irradiance (DNI); (ii) Increased slant atmospheric attenuation between mirrors and central receiver of solar tower power plants; (iii) Concomitant strong winds that may force an emergency shutdown of the plant; and (iv) Extreme dust soiling on concentrators or mirrors. The present study focuses on the first topic. A related study (López et al., 2017) explores the second one.

Ideally, dust storm episodes should be forecasted a few days early so that the plant and electric utility operators can take all necessary measures to prepare the plant and the electric grid for any potential disruption. Research has now started toward the development of an integrated forecasting system to help the development of CSP and other renewable energy technologies in Kuwait, where significant solar power is being built or projected. Solar forecasts need to focus on both clouds and dust episodes at various time scales.

Before construction, the solar resource needs to be well established in terms of both magnitude and temporal variability. Under arid conditions, DNI's variability directly depends on that in aerosol optical depth (AOD), as discussed elsewhere (Gueymard, 2012b; Polo et al., 2016). DNI also depends on the quantity of atmospheric water vapor, measured in the form of precipitable water (PW), albeit to a much lesser extent than AOD (Gueymard, 2014). More generally, the quality of the AOD data is a major factor that directly affects the accuracy of derived DNI predictions using current modeling techniques (Cebecauer et al., 2011), which in turn can negatively impact the bankability of the solar resource data used by the solar industry (Gueymard, 2011).

doi:10.18086/swc.2017.04.04 Available at http://proceedings.ises.org

Multi-site measurements conducted over Kuwait during the last five years have confirmed that DNI's solar resource is indeed highly variable on a daily and seasonal basis (Al-Rasheedi et al., 2014). This is particularly true during summer when the potential for solar electricity generation reaches its peak, thanks to virtually permanent cloud-free conditions during longer days and high-sun conditions. Until now, the specific link between the magnitude and variability of DNI and of its AOD counterpart had not been precisely defined over Kuwait. In the present contribution, various sources of DNI and AOD data are used to establish (i) the long-term variability in both quantities over Kuwait; (ii) the modeled effects of high-AOD conditions on DNI; and (iii) possible long-term trends in those two quantities.

2. Data sources

The present analysis focuses on both modeled and observed aerosol data, and on observed solar irradiance data. NASA's MERRA-2 reanalysis model provides historical estimates of the hourly AOD at 550 nm (hereafter, AOD550), Ångström exponent (AEX), and total scattering AOD (SAOD) since 1980, among many other atmospheric variables (such as PW), at a spatial resolution of 0.5x0.625°. Although this resolution is relatively coarse, it is not a serious limitation here because of the absence of strong topographic features over Kuwait. Moreover, MERRA-2's consistent evaluation of AOD550, SAOD, and AEX at hourly resolution over more than three decades is a highly desirable feature, which is unique among all reanalysis models currently available.

In parallel, shorter-term ground observations of spectral AOD and AEX from two AERONET sunphotometric stations are also available. The older one is located at the Kuwait University campus in the coastal urban area of the capital, Kuwait City, and has reported Level-2 (L2) data for 2006–2010 and Level-1.5 (L1.5) since 2006, albeit with many long data breaks in both datasets. The newer station is located in the Shagaya solar park, where PV, CSP and wind installations already exist. Shagaya is located 90 km to the west from the capital, in a remote and drier desert area. This AERONET station was commissioned in August 2015, after its installation alongside the existing radiometric station (whose data are also used in this study, see below). Thus far, this station has provided L2 aerosol data for the period August 2015 to July 2016, as well as L1.5 data since February 2017.

The L1.5 data record is much longer than the L2 record at both sites. It is therefore worthwhile to examine the difference in AOD when retrieved with version 2 (V2) of the algorithm applied to L2 data (V2L2) relative to the more elaborate version 3 applied to L1.5 data (V3L1.5). Based on 5000 instantaneous data points at Kuwait University, the distribution of differences shown in Fig. 1 reveals that all older AOD values (from V2L2) are slightly larger than those produced by the newer algorithm. Nevertheless, the difference virtually never exceeds 0.01, which is the typical uncertainty of AOD at that wavelength (Holben et al., 1998). This agreement is remarkable, which confirms information found on AERONET's website (https://aeronet.gsfc.nasa.gov/new_web/Documents/AERONET_V3_AOD.pdf) to the effect that V3L1.5 offers similar results to V2L2. Since V3L1.5 has a more complete historical record than V2L2, the former is exclusively used here in all what follows.

In any case, these observation periods, being relatively short, cannot be used for a long-term analysis of variability or trend, but can still be helpful to validate other sources of aerosol data (such as MERRA-2) and to provide the necessary inputs for short-term irradiance predictions with radiative-transfer models. These applications are discussed below.

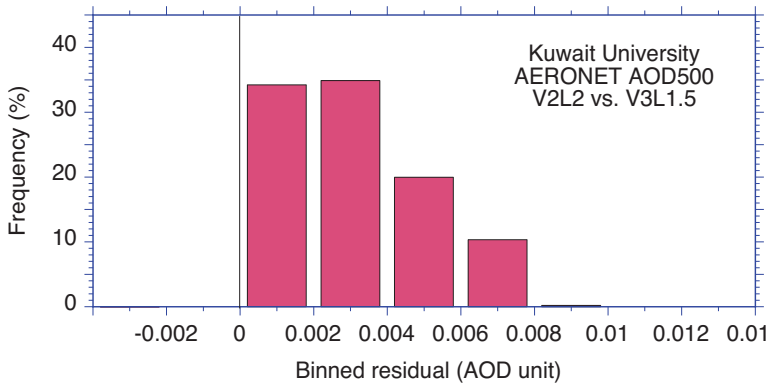

Fig. 1: Binned frequencies of difference between AOD at 500 nm retrieved from AERONET's V2L2 vs. V3L1.5 algorithms at Kuwait University.

The Shagaya sunphotometer is collocated with a well-maintained radiometric station. It monitors all irradiance components (including DNI) with both thermopile and photodiode instruments, thus providing redundancy. Details on the instrumentation, data quality control, early results, and comparisons between measured and satellite-derived modeled data were provided in a previous report (Al-Rasheedi et al., 2014). The Shagaya station has provided high-quality irradiance data since September 2012. Another radiometric station, Kabed, also provides redundant observations of DNI. The DNI resource of Kabed is similar to that of Shagaya, due to the short distance between them (≈65 km), so will not be discussed further here.

3. Results

3.1 Aerosol optical depth: MERRA-2 vs. AERONET

It is desirable to compare the AOD550 data predicted by MERRA-2 to those observed at AERONET stations. This constitutes the conventional way of validating modeled AOD data, and is also important in the context of discriminating high-AOD periods caused by dust storms of various strengths, or evaluating the historical frequency and seasonal variability of such events. This kind of study also prepares for the longer-term goal of qualifying the suitability of NASA's GEOS-5 research forecasting model (from which MERRA-2 is derived) to correctly forecast future dust-storm events over Kuwait.

A first comparison is done for daily-mean AOD data. Since AOD550 is not observed directly by AERONET sunphotometers, it is calculated here from Ångström's law using AOD at 500 nm and AEX evaluated between 440 and 870 nm. The daily-mean AOD550 is then obtained for all days that produce at least 3 instantaneous measurements (per standard AERONET procedures). This removes only a limited number of days (or periods during any day) since cloudiness is generally low or absent, particularly in summer. Observations, however, are only done for a sun zenith angle lower than 82°. To make things as comparable as possible, the MERRA-2 daily means are thus calculated for all hours for which the mid point corresponds to a zenith angle less than 80°.

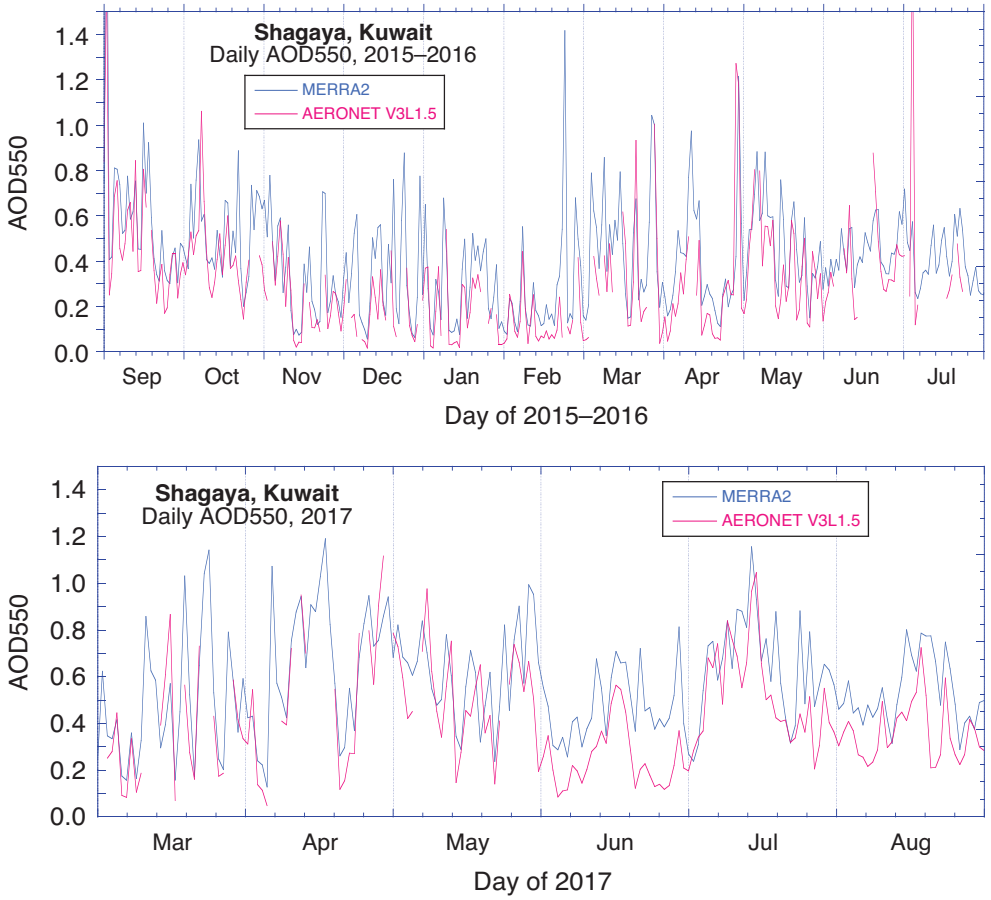

Fig. 2: Time series of daily AOD550 from both modeling by the MERRA-2 reanalysis and ground observations at the Shagaya AERONET station during 9/2015–7/2016 (top) and 3/2017–8/2017 (bottom).

Figure 2 shows the time series of daily-mean AOD550 obtained from MERRA2 and the Shagaya AERONET station during the 12-month period when the latter was operational before it was sent back for repair and calibration, and also for a more recent 6-month period of 2017. The MERRA-2 and AERONET sources of data show similar high daily and seasonal variability, with however occasional differences in magnitude or phase. It is clear that MERRA-2 tends to predict higher AOD than the ground observations. This is confirmed in Fig. 3a, which compares the *hourly* AOD550 data from MERRA2 and the corresponding *instantaneous* data from AERONET's V3L1.5. An additional characteristic is that MERRA2's overestimation is accompanied by significant scatter. A similar scatterplot appears in Fig. 3b, but for AEX. It shows large scatter too, but also a lack of similitude, due to generally too low predictions at high AEX. Figure 4 shows the frequency distributions of the differences between MERRA-2 estimates of AOD550 or AEX and matching AERONET observations. Interestingly, the two distributions of MERRA-2 deviations are skewed in opposite ways. The mean and median errors are ≈0.1 for AOD550. Hence, it can be expected that DNI simulations based on MERRA-2 AOD data should be too low by ≈10%.

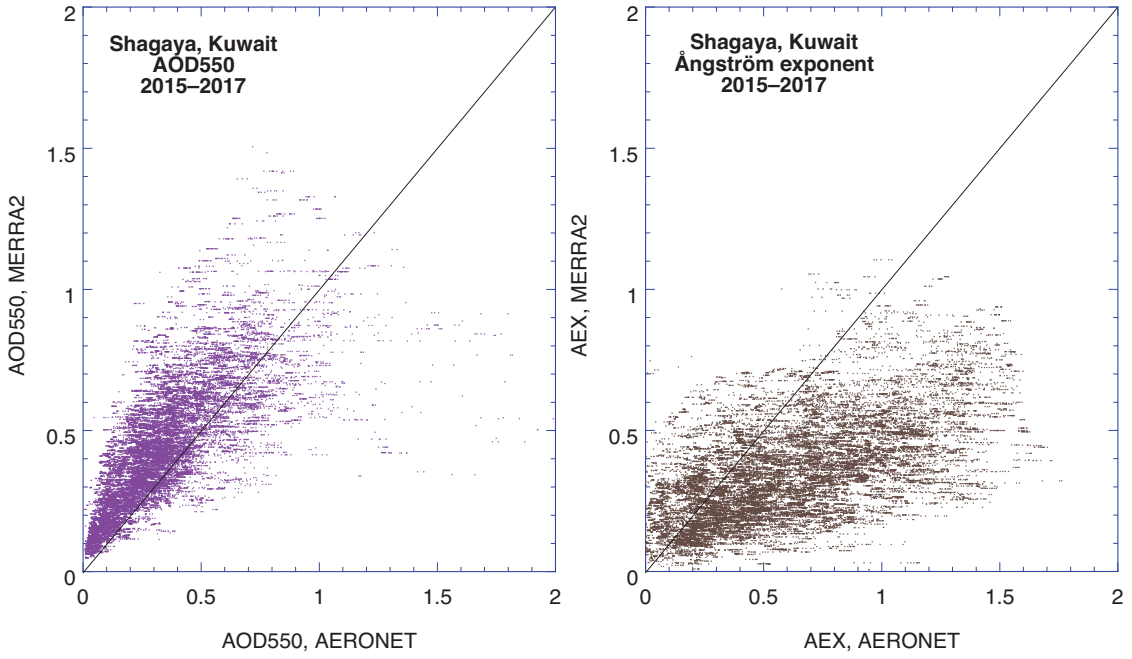

Fig. 3: Scatterplots of AOD550 (left) and AEX (right) comparing MERRA-2's predictions to ground observations from the Shagaya AERONET station.

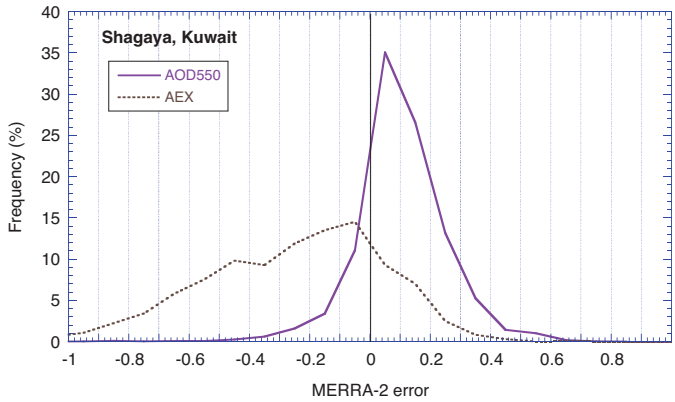

Fig. 4: Frequency distributions of MERRA-2's errors in AOD550 and AEX (compared to AERONET reference data) at Shagaya.

The difference between the predicted and observed AOD550 is reflected in their temporal frequency distribution over the period of record, as illustrated in Fig. 5. It is found that the daily AOD550 frequency distribution obtained from MERRA-2 better match that of AERONET at Kuwait University than at Shagaya. This can be ex-

plained, at least in part, by a statistical artifact caused by the lower number of days in the latter case. It is also possible that the variability of the aerosol loading is more difficult to predict in a pure desert environment such as Shagaya's, or that the (older) Kuwait University data points are assimilated into the GEOS-5 forecasting model, which would improve the aerosol modeling there.

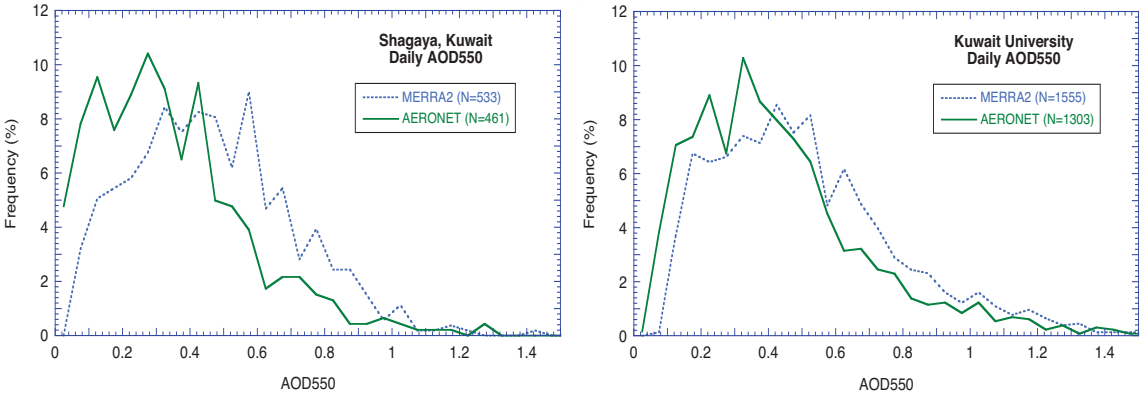

Fig. 5: Frequency distribution of daily AOD550 from MERRA-2 and AERONET for Shagaya (left) and Kuwait University (right). N is the number of days. Periods with 7 or more consecutive days of missing AERONET data were eliminated from the analysis.

Figure 5 also suggests that very hazy days (AOD550 > 0.6) are more frequent in Kuwait City than over Shagaya. For instance, the probability of days with a mean AOD550 higher than 1.0 is ≈2% at Shagaya and ≈5% in Kuwait City, based on AERONET data. At Shagaya, the maximum daily-mean AOD550 of 1.86 was observed on 2016-07-04 according to the 461-day record of AERONET V3L1.5 until end of 8/2017. In comparison, the daily mean for that day was much lower (1.17) at Kuwait University. At the latter site, the record maximum daily-mean value (2.39) was reached on 2017-04-29, while Shagaya simultaneously experienced only less than half of that value (1.06). These differences in peak AOD values and frequency distribution are remarkable, considering the relatively short distance between the two locations. Spatial variability in AOD is thus to be considered in addition to its temporal variability, which will require further study.

3.2 Aerosol optical depth: Historical time series

Based on MERRA2's 1980–2016 time series, the annual average AOD550 remained in the range 0.35–0.50 during that period, with significant interannual variability and possible decadal cycles (Fig. 6). Linear trends are evaluated separately over two distinct periods of similar duration: 1980–1996 and 1997–2016. The former is considered less certain than the latter because of the lack of satellite or AERONET data to constrain the aerosol transport model before 1997. The two last decades experienced an increasing trend in AOD, at the rate of 0.0024 AOD unit per year. This in turn translates into a likely decrease in the DNI resource of ≈2% per decade, based on the analysis of Gueymard (2012b). This positive trend in AOD is consistent with results from Hsu et al. (2012), which were based on AERONET and satellite data, and with the solar radiation dimming experimentally observed over Iran (Jahani et al., 2017; Rahimzadeh et al., 2015). Since a negative trend in DNI is likely to have a notable impact on the performance of CSP plants (many of which being built or planned in the region), more studies will be needed to better quantify this trend, and delineate its geographical extent.

Still using the whole 37-year MERRA-2 dataset currently available, the frequency distribution of AOD550 at Shagaya is shown in Fig. 7. Results are displayed for three important time scales: Hourly, daily, and monthly. The hourly and daily results are remarkably similar, much smoother than the short-term daily distribution in Fig. 5 (as could be expected, considering the much longer period), and show the characteristics of the anticipated log-normal distribution (Ruiz-Arias et al., 2016a). The monthly frequency distribution is substantially different in shape, which results in a lower median than the two other distributions. This statistical feature, in turn, has consequence on the modeling of DNI, and, ultimately, on the bankability of the DNI resource for CSP applications if monthly-mean AOD data are used as input of solar radiation models (Ruiz-Arias et al., 2016b, 2016c).

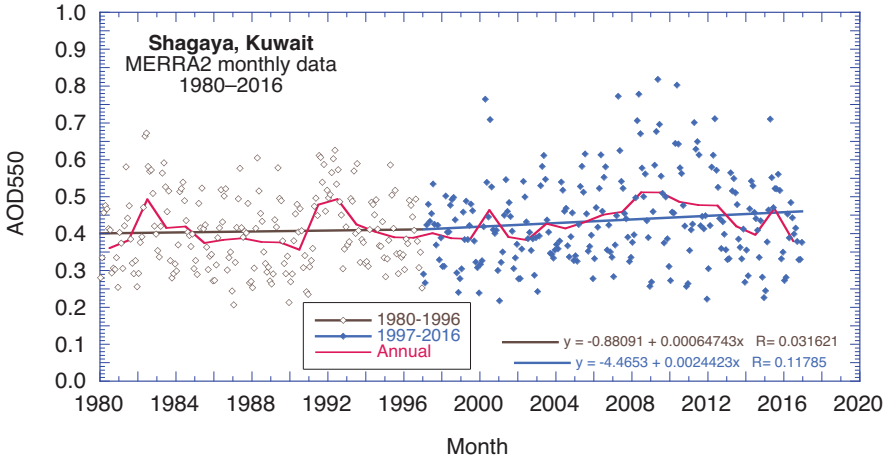

Fig. 6: Time series and trends of mean monthly and annual MERRA2's AOD550 separated into two periods.

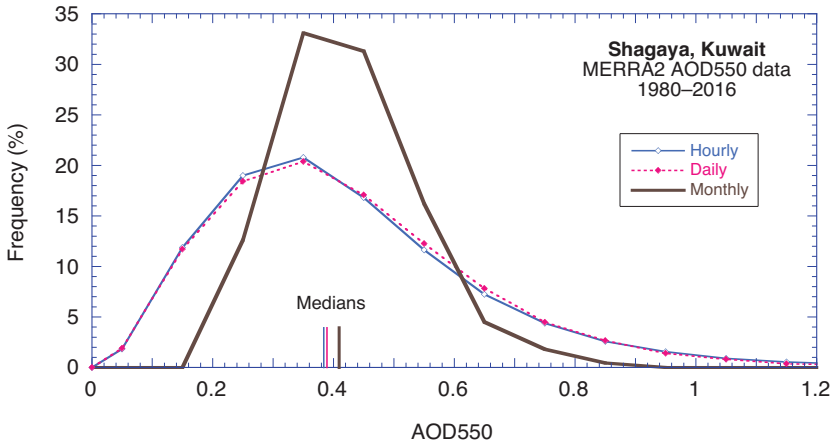

Fig. 7: Hourly, daily, and monthly frequency distributions of MERRA2's AOD550 over the period 1980–2016.

Figure 8 compares the daily variability in MERRA-2's AOD550 and in the measured DNI at Shagaya during summer 2015. Such a period being virtually cloudless (except in early May), the temporal variability in DNI is expected to be essentially due to that in AOD. Nevertheless, the two signals are not exactly in phase due to the shortcomings in the MERRA-2 AOD data discussed above. The daily-integrated DNI reached its maximum of ≈10 kWh/m^2 during a few days only, when the AOD was relatively low for the season at that location. Conversely, the strong aerosol-induced extinction makes DNI reach only 4–5 kWh/m^2 during high-AOD days.

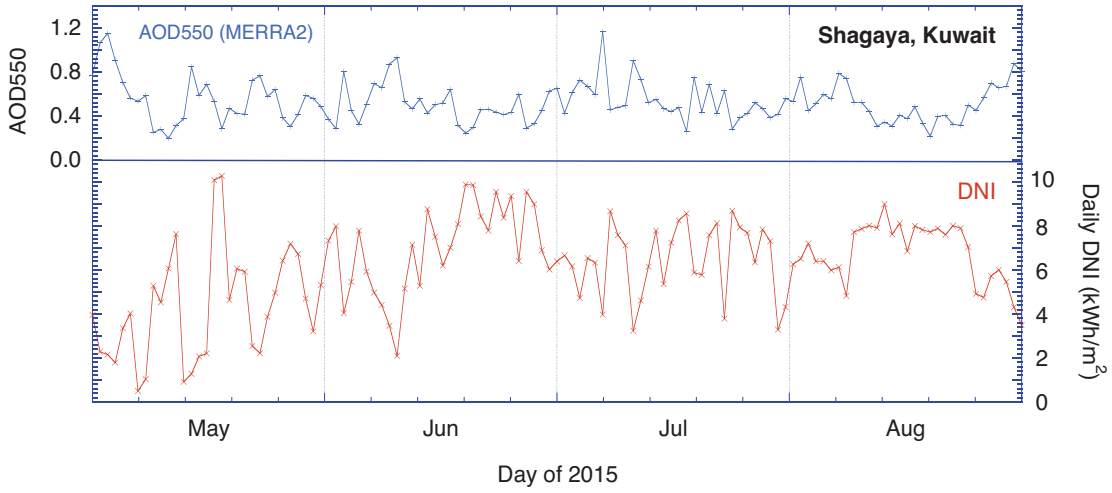

Fig. 8: Daily variability in MERRA2 AOD (top) and in DNI measured at Shagaya (bottom) during summer 2015.

3.3 Direct normal irradiance prediction

Solar irradiance is sensitive to the amount and optical characteristics of aerosols at any instant. This is most particularly true for DNI, which decreases substantially when AOD increases (e.g., Gueymard, 2005, 2012b). This also means that potential errors in AOD data used as input to a radiative transfer model necessarily result in errors (of opposite sign) in DNI. This, in turn, is important for the simulation of the power production of CSP systems before construction, since typically no long-term local DNI observations are then available. CSP systems are strongly non-linear, which makes their energy output sensitive to the quality and representativeness of the DNI resource data. The latter is actually the major source of uncertainty in the modeling of CSP plants (Ho et al., 2011). Even the use of conventional hourly Typical Meteorological Years (TMYs) may result in seasonal and annual errors (Polo et al., 2017). Simulations performed by Hirsch et al. (2010) showed that non-linearity impacts can be avoided, but this requires that calculations be done at high temporal resolution, with irradiance data time steps in the order of 1–10 minutes, which is highly demanding.

Evaluating clear-sky DNI can be done accurately if collocated instruments (e.g., sunphotometers) provide the most important aerosol and water vapor inputs at the required high temporal resolution (Gueymard, 2012a; Gueymard and Ruiz-Arias, 2015). The specialized stations reporting such data are still very scarce, which constitutes a serious limitation. Other sources of aerosol data do exist and are more readily available on a global scale (e.g., on a gridded basis), but their lower quality typically results in substantially biased or distorted DNI time series (Polo and Estalayo, 2015).

In this context, it is important to evaluate whether the MERRA-2 reanalysis data can provide accurate DNI estimates over Kuwait at sub-hourly resolution. To that effect, the latest version of the high-performance REST2 model (Gueymard, 2008) is used to simulate DNI at Shagaya. The best possible modeling of DNI is obtained when using observations of the main inputs (AOD550, AEX and PW) from AERONET V3L1.5. Secondary inputs (hourly ozone amount and station pressure) are obtained from MERRA-2. The (low) columnar amount of nitrogen dioxide is provided by spaceborne observations from the Ozone Monitoring Instrument (OMI) radiometer. The observational DNI dataset comes from a thermopile pyrheliometer and a silicon-based rotating shadowband irradiometer (RSI) that are installed side-by-side at Shagaya. The pyrheliometer observations are used preferably, but are replaced by RSI data in case of tracker malfunction or data not passing the tests of an elaborate quality control procedure, itself based on the method described by (Long and Shi, 2008). A related study has shown that the DNI observations from RSI and thermopile are in close agreement (Al-Rasheedi et al., 2017).

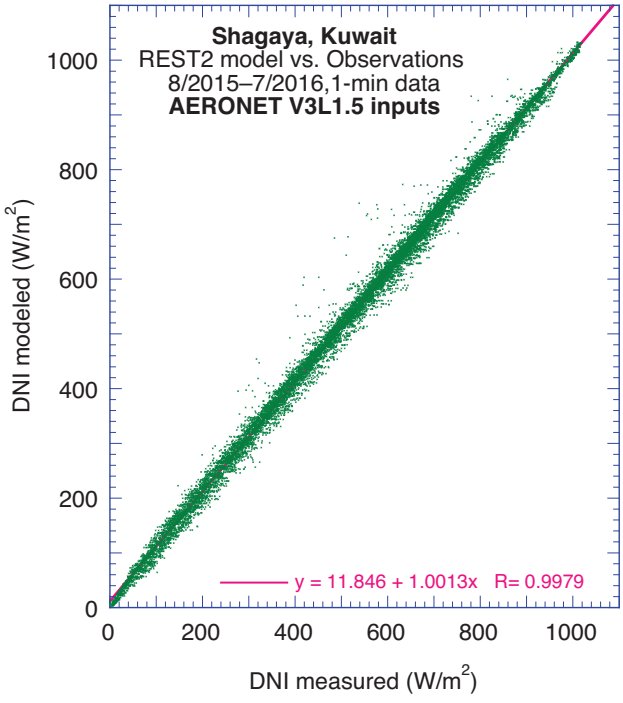

Fig. 9: Scatterplot of REST2-predicted DNI vs. ground observations using aerosol and water vapor input data from AERONET V3L1.5.

Figure 9 shows a scatterplot of the AERONET-based modeled DNI in comparison with its measured counterpart. As expected, the match is excellent, with only a few outliers caused by the passage of clouds during the irradiance observation. (Irradiance is integrated over a 1-min period, whereas AERONET observations are instantaneous, and are allowed to be as much as one minute away from the center of the 1-min period.) In comparison, this simulation is repeated with the main inputs (AOD550, AEX and PW) alternatively provided by MERRA-2 for the matching hour. The comparison of the modeled DNI thus obtained with the same measured data as in Fig. 9 shows a strong underestimation of DNI (≈13% on average) and large scatter (Fig. 10). These results can be directly traced back to the large bias and scatter in AOD (and possibly AEX) shown in Figs. 3 and 4. The difficulties of using the MERRA-2 reanalysis to simulate DNI corroborate previous findings (Polo and Estalayo, 2015), even though those were obtained with a different reanalysis model.

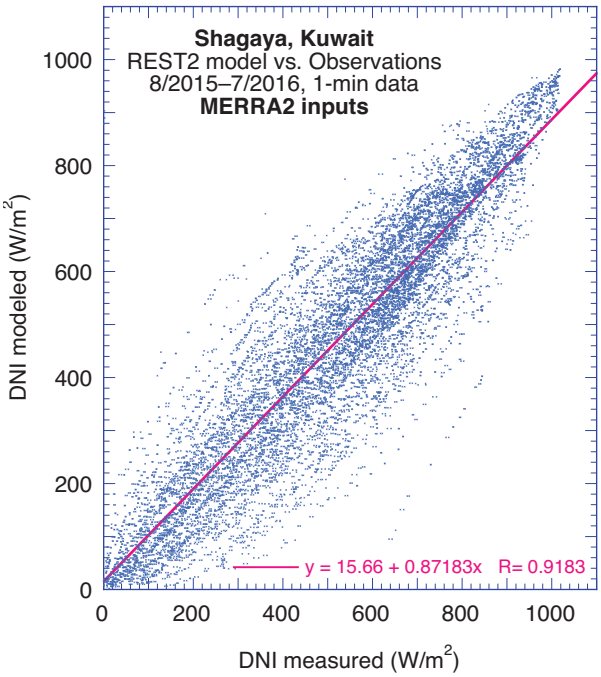

Fig. 10: Scatterplot of REST2-predicted DNI vs. ground observations using aerosol and water vapor input data from MERRA-2.

4. Conclusion

This investigation brings new information on the temporal variability in aerosol optical depth (AOD) and direct normal irradiance (DNI) under the arid conditions of Kuwait. Using data from two AERONET stations and from the MERRA-2 reanalysis, it is found that AOD is highly variable on a daily basis, and can reach very high values during any season, due to the incidence of dust storms. Some spatial variability is also apparent, even over relatively short distances. This significantly impacts the DNI solar resource in particular, and may limit the performance of CSP installations. Further investigation is needed to better characterize the spatio-temporal variability in AOD over Kuwait.

The MERRA-2 reanalysis predictions show a slight positive trend in AOD during the last two decades, signaling that a concomitant downward trend in DNI was likely. A continuation of this trend is possible in the near future, which would impact CSP projects in the region. The long-term MERRA-2 historical data has great value for, such trend analyses, but is found not accurate enough for the unbiased DNI resource evaluation required for the computerized simulation of CSP systems at high temporal resolution. Clear-sky modeled DNI predictions using MERRA-2 aerosol and water vapor data as inputs to a high-performance solar irradiance model are found noisy and too low by ≈13% on average, in comparison with actual high-quality irradiance observations with a 1-min time step.

Although the MERRA-2 aerosol transport-modeling module is still far from perfect, its main features (long time series at hourly frequency) are still unique among all other reanalysis models currently available. It is suggested that further research be carried out to compare the historical estimates of AOD from MERRA-2 or the forecasts

from its parent model, GEOS-5, to those from other similar sources, in an effort to evaluate and improve the uncertainty of modeled DNI over arid areas.

Acknowledgements

The authors thank the Kuwait Foundation for the Advancement of Sciences (KFAS) for its financial support, as well as Dr. Hala Khalid Al-Jassar, Principal Investigator, and her staff for establishing and maintaining the Kuwait University AERONET station used in this investigation. The first author is also grateful for the financial support provided by the Spanish Project "PRESOL" ENE2014-59454-C3-2-R, which is funded by the Ministerio de Economía y Competitividad and co-financed by the European Regional Development Fund (FEDER).

5. References

Al-Rasheedi, M., Gueymard, C.A., Ismail, A., Al-Hajraf, S., 2014. Solar Resource Assessment over Kuwait: Validation of Satellite-derived Data and Reanalysis Modeling. Proc. EuroSun 2014, Aix-les-Bains, France, International Solar Energy Soc.

Al-Rasheedi, M., Gueymard, C.A., Ismail, A., Hussain, T., 2017. Comparison of Two Sensor Technologies for Solar Irradiance Measurement in a Desert Environment. Proc. Solar World Congress, Abu Dhabi, UAE, International Solar Energy Soc.

Cebecauer, T., Suri, M., Gueymard, C.A., 2011. Uncertainty sources in satellite-derived direct normal irradiance: how can prediction accuracy be improved globally? Proc. SolarPACES Conf., Granada, Spain.

Gueymard, C.A., 2005. Importance of atmospheric turbidity and associated uncertainties in solar radiation and luminous efficacy modelling. Energy 30, 1603-1621.

Gueymard, C.A., 2008. REST2: High-performance solar radiation model for cloudless-sky irradiance, illuminance, and photosynthetically active radiation – Validation with a benchmark dataset. Solar Energy 82, 272-285.

Gueymard, C.A., 2011. Uncertainties in Modeled Direct Irradiance Around the Sahara as Affected by Aerosols: Are Current Datasets of Bankable Quality? J. Sol. Energ-T. ASME 133, 031024-031013, 10.1115/1.4004386.

Gueymard, C.A., 2012a. Clear-sky irradiance predictions for solar resource mapping and large-scale applications: Improved validation methodology and detailed performance analysis of 18 broadband radiative models. Solar Energy 86, 2145-2169.

Gueymard, C.A., 2012b. Temporal variability in direct and global irradiance at various time scales as affected by aerosols. Solar Energy 86, 3544-2553.

Gueymard, C.A., 2014. Impact of on-site atmospheric water vapor estimation methods on the accuracy of local solar irradiance predictions. Solar Energy 101, 74-82.

Gueymard, C.A., Ruiz-Arias, J.A., 2015. Validation of direct normal irradiance predictions under arid conditions: A review of radiative models and their turbidity-dependent performance. Renew. Sust. Energy Rev. 45, 379-396.

Hirsch, T., Schenk, H., Schmidt, N., Meyer, R., 2010. Dynamics of oil-based parabolic trough plants—Impact of transient behaviour on energy yields. Proc. SolarPACES Conf., Perpignan, France.

Ho, C.K., Khalsa, S.S., Kolb, G.J., 2011. Methods for probabilistic modeling of concentrating solar power plants. Solar Energy 85, 669-675.

Holben, B.N., Eck, T.F., Slutsker, I., Tanré, D., Buis, J.P., Setzer, A., Vermote, E., Reagan, J.A., Kaufman, Y.J., Nakajima, T., Lavenu, F., Jankowiak, I., Smirnov, A., 1998. AERONET—A Federated Instrument Network and Data Archive for Aerosol Characterization. Remote Sensing of Environment 66, 1-16.

Hsu, N.C., Gautam, R., Sayer, A.M., Bettenhausen, C., Li, C., Jeong, M.J., Tsay, S.C., Holben, B.N., 2012. Global and regional trends of aerosol optical depth over land and ocean using SeaWiFS measurements from 1997 to 2010. Atmos. Chem. Phys. 12, 8037-8053, 10.5194/acp-12-8037-2012.

Jahani, B., Dinpashoh, Y., Wild, M., 2017. Dimming in Iran since the 2000s and the potential underlying causes. International Journal of Climatology, 10.1002/joc.5265.

Long, C.N., Shi, Y., 2008. An Automated Quality Assessment and Control Algorithm for Surface Radiation Measurements. The Open Atmospheric Science Journal 2, 23-37.

Polo, J., Estalayo, G., 2015. Impact of atmospheric aerosol loads on Concentrating Solar Power production in arid-desert sites. Solar Energy 115, 621-631.

Polo, J., Fernandez-Peruchena, C., Gaston, M., 2017. Analysis on the long-term relationship between DNI and CSP yield production for different technologies. Solar Energy 155, 1121-1129.

Polo, J., Télez, F.M., Tapia, C., 2016. Comparative analysis of long-term solar resource and CSP production for bankability. Renewable Energy 90, 38-45.

Rahimzadeh, F., Sanchez-Lorenzo, A., Hamedi, M., Kruk, M.C., Wild, M., 2015. New evidence on the dimming/brightening phenomenon and decreasing diurnal temperature range in Iran (1961–2009). International Journal of Climatology 35, 2065-2079, 10.1002/joc.4107.

Ruiz-Arias, J.A., Gueymard, C.A., Quesada-Ruiz, S., Santos-Alamillos, F.J., Pozo-Vazquez, D., 2016a. Bias induced by the AOD representation time scale in long-term solar radiation calculations. Part 1: Sensitivity of the AOD distribution to the representation time scale. Solar Energy 137, 608-620.

Ruiz-Arias, J.A., Gueymard, C.A., Santos-Alamillos, F.J., Pozo-Vazquez, D., 2016b. Worldwide impact of aerosol's time scale on the predicted long-term concentrating solar power potential. Nature Scientific Reports 6, 30546, doi:10.1038/srep30546.

Ruiz-Arias, J.A., Gueymard, C.A., Santos-Alamillos, F.J., Quesada-Ruiz, S., Pozo-Vazquez, D., 2016c. Bias induced by the AOD representation time scale in long-term solar radiation calculations. Part 2: Impact on long-term solar irradiance predictions. Solar Energy 135, 625-632.

An Organic Rankine Cycle as Technology for Smaller Concentrated Solar Powered Systems

Louis Karsten[1], Dr Jaap Hoffmann[2] and Prof Frank Dinter[3]

[1, 2,] Solar Thermal Energy Research Group (STERG), Stellenbosch University, (South Africa)

[3] Fraunhofer Institute, (Chile)

Abstract

This paper analyses and simulates an organic Rankine cycle (ORC) specifically for smaller concentrated solar powered (CSP) systems to produce solar thermal electricity (STE) in the range from 500 kW to 5 MW. The plant efficiency is optimized with the evaporating and condensing temperatures as optimizing variables. A thorough process for selecting the working fluid is presented to help the designer with this monumental task. After considering various aspects n-Pentane is chosen as working fluid for the ORC. It is also the only organic working fluid that has been successfully used in conjunction with CSP on the scale from 500kW to 5MW. The power block is simulated by modelling each component and combining them to form a complete simulation model. The results of the simulation is document and a plant efficiency of about 14.2% is achieved across the power range. The output if the ORC simulation is then compared to a steam Rankine cycle under the same operating conditions and the ORC proved to be more efficient for a power output up to 3000kW.

Keywords: Organic Rankine Cycle (ORC), concentrated solar power (CSP)

1. Introduction

Even though steam Rankine cycles are more commonly used, the usage of organic fluids as working fluid is not a new concept. In 1826, Thomas Howard patented the first concept of an engine using ether as a working fluid (Casati, 2014), and the first operational solar ORC was built by Frank Shuman in Philadelphia USA in 1907 and was rated at 2.5 kW thermal output. With the 100 m^2 collector area, direct vapour of Ether at 115°C was used to drive an irrigation pump (Shuman, 1907). Currently ORC technology is used in a variety of industries mostly because of the modularity and versatility of the technology. Industries developed around the heat sources used for the ORC where the largest by far is the geothermal energy (76.5%), secondly the heat recovery industry (12.7%), thirdly the biomass industry (10.7%) whilst the solar industry only accounts for 0.1% of the total ORC industry (Tartiere, 2016).

Various micro-scale (1 kW – 10 kW) solar ORC test facilities exist and are well documented in literature but the lack of optimized technology in the ORC solar scale up to 5 MW, leads to industry lacking confidence in this technology. A resurgence of interest in the research and development of ORC as a viable small-scale solution for electrical production has developed after the successful completion of the 1 MW APS Saguaro PT plant in Arizona, USA in 2006. The plant has 10 340 m^2 of PT collectors using thermal oil at 300°C as heat transfer fluid in the solar field. The ORC module uses n-pentane as working fluid with a 1 MW_e turbine supplied by ORMAT. A major increase in efficiency was seen with an overall solar to electrical efficiency of 12.1% at design point. To date this is still the largest operating solar ORC plant in the world and a pioneer in solar ORC as it proved the simplicity of an ORC compared to that of a conventional steam Rankine cycle and this plant even allows for unattended operation. All of which are important factors in the economic considerations and commercial acceptance of this technology (Canada et al., 2005), (Quoilin et al., 2013).

CSP plants operating with traditional steam Rankine cycles tend to become unfeasible in the small scale power range (<5 MW) and ORC's might be able to fill that gap. For lower temperature thermodynamic cycles, the ORC have advantages over the steam Rankine cycle. The most promising advantage of ORC's is that less and cheaper components are needed due to lower temperatures and cycle simplicity. Another technical advantage is that typical working fluids used in ORC cycles have higher molecular weight than water which leads to the fact that a higher mass flow rate can be achieved with an ORC for the same size of turbine. This can lead to higher turbine work output with less turbine losses (Drescher & Bruggemann, 2007). This is a major advantage seeing that the turbine is a key component in an ORC having the largest effect on cycle efficiency.

doi:10.18086/swc.2017.04.05 Available at http://proceedings.ises.org

The benefits of successfully deploying small-scale CSP goes far beyond just the climate and environmental benefits. In South Africa the mining, construction, the auto and metals and engineering sectors contribute about 20% of South Africa's gross domestic product, hence it is important to sustain these industries (SEIFSA, 2016). The ORC technology might form part of the energy solutions to these industries once an optimised small-scale CSP technology is proven hence the proposed future output of electricity generating Rankine cycle plants are shown in figure 1.

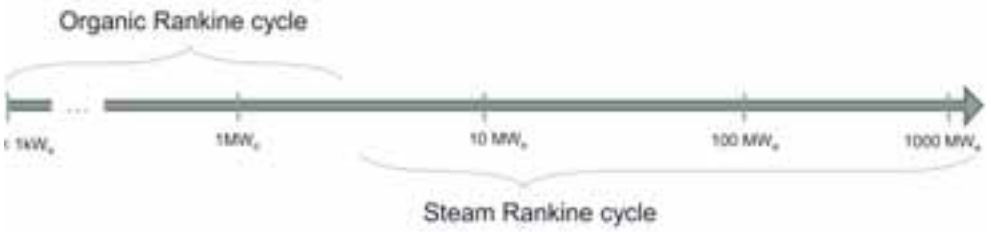

Figure 1: Proposed Thermal range of Rankine Cycles, adapted from (Dickes, 2016)

In this paper a Techno-thermodynamic design optimization is presented for an ORC using CSP as heat source across the gross electrical power output of 500 kW – 5 MW using the MATLAB environment. A specific focus is put on the working fluid selection whilst the paper elaborates on the methodology behind the design optimization, a technical analysis of the plant and components are presented and where after the design optimization results are discussed and conclusions are drawn on the feasibility of such a plant. The exact same simulation is run for a steam Rankine cycle to determine which is better suited for the current conditions.

2. Methodology

A holistic approach is taken on the power plant and its functional units namely the solar field, storage and power block. The main reasons for including storage is to prolong the operating hours of power plant and to eliminate spikes in the ORC caused by solar variations. A technological analysis is done in section 4 in order to model the whole plant consisting out of the various components in each functioning unit. By modelling each component a complete cycle simulation is achieved. For the solar field evacuated tube parabolic trough collectors are considered and Therminol 66 is used as heat transfer fluid. Therminol 66 has been developed especially for solar ORC applications by Eastman Chemicals in Italy. A Thermocline energy storage system will be incorporated in the solar field to balance out the solar variations. Regarding the power block components, it proved to be best to use an axial flow turbine for the wanted power range of 500 kW to 5 MW. A multistage centrifugal pump are commonly used in ORC's and is chosen for the current application (Macchi & Astolfi, 2017). A Plate type heat exchanger is taken for the evaporator due to their compactness and high heat transfer area. The lack of water resources in areas where CSP is implemented necessitates the use of an air cooled condenser. The final proposed ORC power plant that is used for the simulation is shown in figure 2 with the ORC T-S diagram produced by the simulation in figure 3.

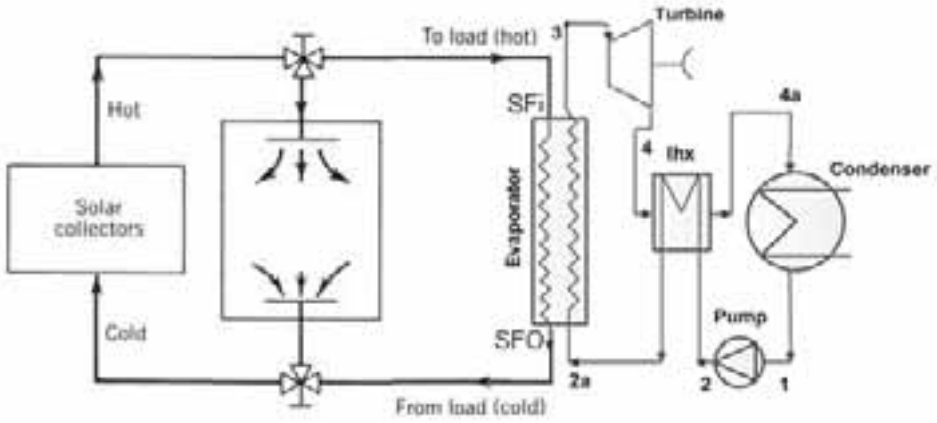

Figure 2: Final plant schematic, adapted form (Stine & Michael, 2001), (Li, G. 2016)

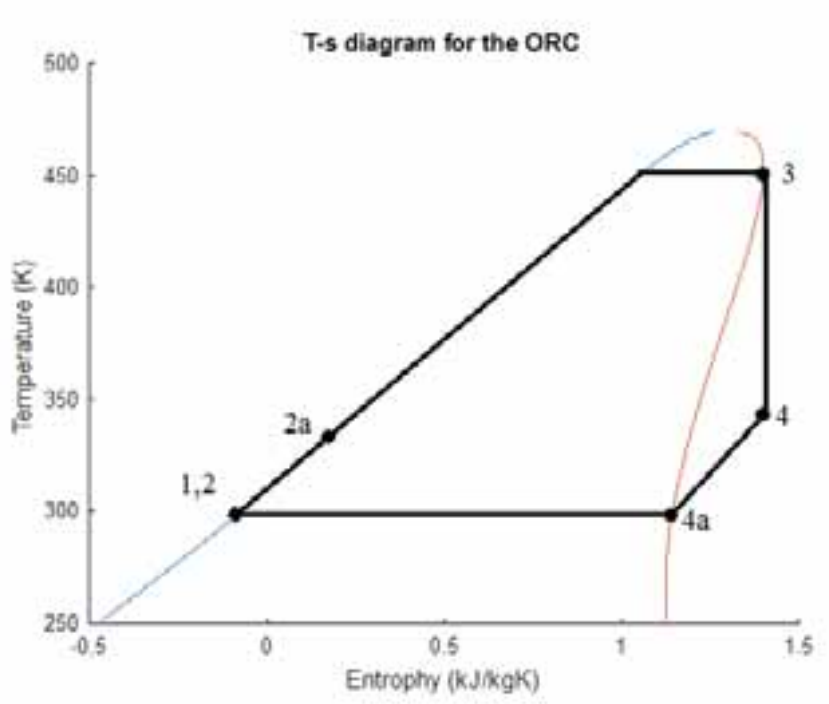

Figure 3: T-S diagram for the simulated ORC plant

A techno-thermodynamic optimization is conducted on the power plant where the total plant efficiency is used as objective function and defined as the ratio between the net power output and the maximum received thermal heat:

$$\eta_{plant} = \frac{W_{net}}{Q_{in}} \quad \text{(eq. 1)}$$

The independent decision variables that are used as optimizing variables are the condensing and evaporating temperatures. The optimization constraints are due to the working fluid property constraints. Looking at a subcritical cycle, the chosen working fluid's critical temperature is 470K which serves as the upper limit for the cycle evaporating temperature. The maximum condensing temperature is constraint at the boiling temperature at the condensing pressure. Due to the air-cooled condenser the minimum temperature to which the working fluid can be cooled down to during condensation is limited. The incorporation of a recuperator or also referred to as an internal heat exchanger as depicted in figures 2 and 3, enables the working fluid to be cooled down to a lower temperature as the working fluid now enter the condenser at a much lower temperature. A design choice is made for the lower limit of condensation temperature and it is set at 7°C above the average ambient temperature of 20°C to compensate for condenser ineffectiveness.

For each iteration of condensing and evaporating temperatures, all model equations are solved sequentially and with the black-box optimization approach the most efficient plant design with the corresponding temperatures, is determined. The flow chart of the calculation procedure is shown in figure 4:

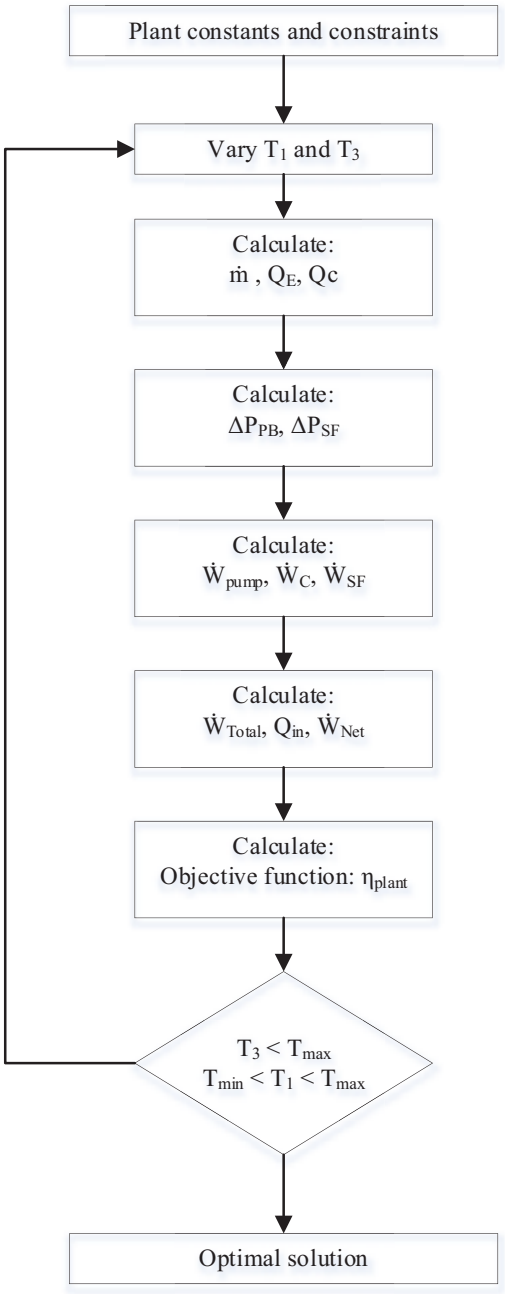

Figure 4: Simulation flow diagram

3. Choice of working fluids

The theory for an ORC is the same as to steam Rankine cycle with only the working fluid properties differing. The selection of the working fluid not only affects the efficiency of the system but also the design and sizes of the system components, stability, safety and environmental concerns and ultimately the cost of the system (Bao & Zhao, 2013). Hence, it is a very important degree of freedom for any ORC design process. Bao and Zhao continues by saying that the selection of an ORC working fluid is more complex than other thermodynamic cycles mainly due to two reasons:

- The heat type sources for ORC varies widely from 80 ^{0}C to 500 ^{0}C
- Excluding a few organic fluids whose critical temperatures are too high or too low, hundreds of fluids are available for usage including hydrocarbons, aromatic hydrocarbons, perfluorocarbons, alcohols, CFS's, siloxanes, ethers etc.

Due to the working fluid selection being so important, many researchers have carried on the fluid screening method and this method is by far the most used method for working fluid selection in scientific literature (Bao & Zhao, 2013). The method consists of building a steady state simulation model of the proposed ORC plant and run it with different working fluids to determine the most effective fluid for the current application.

Another fluid selection guideline has been developed by (Macchi & Astolfi, 2017) to help ORC designers with this monumental task of screening hundreds of working fluids. The number of applicable fluids can be drastically decreased by considering and comparing different fluids. The obvious requirements a fluid must meet is the fluid should be:

- *Commercially available at a reasonable cost*: with the intended MW range of the proposed system, a large fluid inventory is needed and the fluid cost can mount up to a significant portion of the total plant cost.
- *Non-flammable*: Hydrocarbons are flammable working fluids.
- *Nontoxic:* ammonia is toxic but is still sometimes adopted.
- *Compatible with materials*: the working fluid must be compatible with the lubricating oils, elastomers, metals etc.
- *Environmental benign*: the two main indexes that account for fluid acceptance is the Ozone Depletion Potential (ODP) and the Global Warming Potential (GWP).

Macchi & Astolfi continues to say that it is practically impossible to fulfil all these requirements with a working fluid that is suitable for ORC applications hence ORC manufacturers must overlook some of the qualities listed above but they are still aimed for. The second list of considerations in selection a suitable working fluid regards the thermodynamic considerations. The thermodynamic and physical properties of working fluids are what differentiate working fluids the most. The relationship between working fluid properties and thermodynamic cycle performance are discussed below:

- *Thermal stability:* The thermal stability of the fluid used can limit the temperature of the heat source as fluids can chemically brake down at certain temperatures hence a high thermal stability is desired.
- *Vaporization latent heat:* In terms of work output it has been found that for the same defined temperatures, a larger unit work output is produced with working fluids with a higher vaporization latent heat (Chen et al., 2010).
- *Density:* Bao and Zhao states that a high vapour density is of key importance especially for working fluids with a low condensing pressure. A low density leads to higher volume flow rates which in turn lead to larger pressure drops in the heat exchangers and the bigger turbine sizes.
- *Specific heat:* There is no direct recorded effect of specific heat and total system power output.
- *Critical temperature:* High critical temperature has a beneficial effect on cycle performance but has the adverse effect of lower vapour densities which has a benign effect on cycle performance.
- *Boiling temperature:* When comparing fluids of the same family a higher boiling temperature leads to an increase in cycle efficiency but it is by no means an absolute criteria.
- *Freezing temperature:* It serves as a constraint but has no effect on cycle efficiency.
- *Molecular weight:* Bao and Zhao concluded that high molecular weight has a positive impact on turbine efficiency but it must be noted that fluids with a high critical pressure and high molecular weight require higher heat transfer area which increases the total plant cost.
- *Molecular complexity:* A direct link between molecular complexity and cycle performance is not possible as most properties are affected by the molecular complexity and different properties have different effects on cycle performance.
- *Viscosity:* In order to maintain low friction losses in the pipes and heat exchangers, low viscosity is desired in both the liquid and vapour phase (Bao & Zhao, 2013).

- *Conductivity:* In order to obtain a high heat transfer coefficient in the heat exchangers, a high conductivity is required (Bao & Zhao, 2013).

In the case of varying heat source temperatures, it can be more advantageous to use mixtures of working fluids rather than pure working fluids. In such a system heat is supplied to or rejected at variable temperature but at constant pressure because the boiling temperature varies during phase change and the binary mixture evaporates over a large range of temperatures (Bao & Zhao, 2013). The storage incorporated in this analysis allows the heat addition to the power block at constant temperature and only pure working fluids are considered henceforward.

Working fluids are also categorised according to their saturation curve and the categorisation disregarded the structural point of view and type of atoms. When looking at the latter two, the possible ORC working fluids can be categorised in seven main classes and Bao and Zhao pointed out typical characteristics of each after screening the fluids over a range of applications:

1. Hydrocarbons including linear (n-butane, n-pentane), branched (Isobutane, Isopentane) and aromatic hydrocarbons (Toluene, Benzene)
    - Flammability issues
    - Desirable thermodynamic properties
2. Perfluorocarbons
    - Thermodynamically undesirable
    - Extremely inert and stable
    - Extreme molecular complexity
3. Siloxanes
    - Mostly used as mixtures rather than pure fluids
    - Isobaric condensation and evaporation are not isothermal and exhibit a certain glide
4. Partially flouro-substituted straight chain hydrocarbons
    - Several zero ODP fluids exists which are of interest
5. Ethers and fluorinated ether
    - Thermodynamically undesirable
    - Flammability and toxicity issues
6. Alcohols
    - Thermodynamically undesirable
    - Soluble in water
    - Flammability issues
7. Inorganics
    - Operational problems
    - Small environmental impact
    - Inexpensive

Even though the screening process covers a large number of fluids, only a few fluids are actually used in commercial plants. Hydrocarbons are the fluids with the most desirable thermodynamic properties and the flammability issues are often carefully managed in practice by restricting the operating conditions. One of the

hydrocarbon fluids, namely n-pentane, is the working fluid that is used in the 1 MW APS Saguaro PT plant in Arizona. According to Bao and Zhao no other working fluid has been used for commercial solar power plants (>500 kW) before 2013 and no new information has been published according to the author's knowledge since then. This serves as a very strong argument for the acceptance of n-Pentane as working fluid. The screening process further concluded that R134a and R245fa are also possibilities for a solar application and these fluids have been used as working fluids on micro scale (<10 kW) solar applications. Table 1 gives a summary of how n-pentane relates to the selection criteria when compared with R134a and R245fa:

Table 1: n-Pentane regarding the selection considerations

Initial selection	Availability and cost	Locally and affordably available.
	Non-flammable	NFPA 704 rating: 4; readily dispersed in air and will burn readily (Chemistry Reference, 2017).
	Non-toxic	NFPA 704 rating: 1; can cause human irritation (Chemistry Reference, 2017) .
	Compatible with materials	Compatible with all materials
	Environmental benign	Quickly evaporates and biodegrades in soil (National Refrigerants Inc., 2015)
Selection according to thermodynamic properties, (all properties are evaluated at 25°C)	Thermal stability	NFPA 704 rating: 0; very stable
	Vaporization latent heat	n-Pentane: 365 kJ/Kg R134a: 178 kJ/Kg R245fa: 197 kJ/Kg
	Density	n-Pentane: 620 kg/m^3 R134a: 1210 kg/m^3 R245fa:1339 kg/m^3
	Critical temperature	n-Pentane: 197°C R134a: 122°C R245fa: 154°C
	Molecular weight	n-Pentane: 72 R134a: 102 R245fa: 134
	Viscosity	n-Pentane: 0.217 mPa.s R134a: 12.06 mPa.s R245fa: 402.7 mPa.s
	Conductivity	n-Pentane: 0.1112 W/mK R134a: 0.013 W/mK R245fa: 0.0125 W/mK

From table 1 it can be seen that n-Pentane is the best option regarding the vaporization latent heat, viscosity and conductivity. The beneficial higher critical temperature of n-Pentane and the adverse effect thereof can be seen with the lower density. The much higher conductivity of n-Pentane caries a lot of weight as the total heat transfer area is greatly reduced resulting in smaller heat exchangers. Heat exchangers are large contributors to the total power plant cost hence smaller heat exchangers are desired. As a result n-Pentane is the best option for working fluid considering the preceding criteria hence n-Pentane is the working fluid of choice for this analysis.

4. Technical analysis

The numerical calculations were carried out for the gross power output range of 500 kW – 5 MW. Following the procedure of figure 4, the fluid properties at each state point as depicted in figures 2 and 3, are retrieved using compressed liquid, saturated liquid, saturated vapor and superheated vapor property tables for n-Pentane, (NIST, 2017). The heat and mass balance across the devices are used and the procedure follows:

The mass flow rate of the working fluid in the power block is given by:

$$\dot{m}_{PB} = \frac{W_{gross}}{(h_3 - h_4)\eta_T \eta_{gen}} \quad \text{(eq. 2)}$$

The heat supplied to the evaporator and the heat rejected by the condenser is given by:

$$Q_{PB,E} = \dot{m}_{PB}(h_3 - h_{2a}) \quad \text{(eq. 3)}$$

$$Q_{PB,C} = \dot{m}_{PB}(h_{4a} - h_1) \quad \text{(eq. 4)}$$

To calculate the pumping power of the power block pump, the pressure drops in the turbine, condenser and evaporator needs to be accounted for. They are calculated as such:

The pressure increase over the pump to overcome the turbine losses can be calculated by:

$$\Delta P_T = P_2 - P_1 \quad \text{(eq. 5)}$$

The total heat transfer area of the evaporator is given by:

$$A_e = \frac{Q_{PBe}}{U_e \Delta T_{m,E}} \quad \text{(eq. 6)}$$

Where the log mean temperature difference over the evaporator is defined as:

$$\Delta T_{m,E} = \frac{(T_{SFi} - T_3) - (T_{SFo} - T_2)}{\ln\left(\frac{T_{SFi} - T_3}{T_{SFo} - T_2}\right)} \quad \text{(eq. 7)}$$

The size of the evaporator is then determined by determining the number of plates to the upper integer:

$$n_E = \frac{A_E}{w_E \times l_E} \quad \text{(eq. 8)}$$

Due to the phase change in the evaporator the pressure drop across the core part of the evaporator can be a tedious procedure to calculate. By taking the pressure drop equation for single phase flow and incorporating the two phase flow effect in the multiplication factor ϑ^2, a satisfying result can be obtained with this equation (Shah & Sekulić, 2003):

$$\Delta P_{core,E} = \left(\frac{dp}{dz}\right) = f_E \left(\frac{4}{D_{h,}}\right)\left(\frac{G^2}{2\rho_E}\right)\vartheta^2 \quad \text{(eq. 9)}$$

Where:

$$\vartheta^2 = (1-x)^2 + x^2 \frac{\rho_l}{\rho_g}\frac{f_g}{f_l} + \frac{3.24(x^{0.78}(1-x)^{0.24})\left(\left(\frac{\rho_l}{\rho_g}\right)^{0.91}\left(\frac{\mu_g}{\mu_l}\right)^{0.19}\left(1-\frac{\mu_g}{\mu_l}\right)^{0.7}\right)}{\left(\frac{G^2}{gD_h\rho_{avg}}\right)^{0.045}\left(\frac{G^2 D_h}{\rho_{avg}}\right)^{0.035}} \quad \text{(eq. 10)}$$

The pressure losses due to the intake and outlet manifolds are evaluated by the following equation (Shah & Sekulić, 2003):

$$\Delta P_{M,E} = \frac{1{,}5 G_E^2 n_{p,E}}{2\rho_2} \quad \text{(eq. 11)}$$

The total pressure loss over the evaporator for the working fluid side is then after neglecting the gravitational effects due to fact that the tubes are horizontal:

$$\Delta P_E = \Delta P_{core,E} + \Delta P_{M,E} \quad \text{(eq. 12)}$$

The total pressure loss over the condenser, ΔP_c , is evaluated exactly the same way as that for the evaporator taking note that the geometrical features of the air-cooled condenser differs.

The work required for the power block pump is then:

$$W_{PB,pump} = \dot{V}(\Delta P_T + \Delta P_E + \Delta P_c) \quad \text{(eq. 13)}$$

To avoid the integrate and iterative design process of an air-cooled condenser in the scope of cycle optimization such as this, a general relationship between the work required by the air-cooled condenser fan and the turbine power output where (O'Donovan, 2013):

$$W_{c,F} = 0.02 \times W_{gross} \quad \text{(eq. 14)}$$

This relationship was confirmed by taking a typical air-cooled condenser fan that is used in a similar application with similar heat rejection requirements than the 5 MW case. The fan curve was available and by submitting the data in the power block simulation a relationship of about 4% was calculated between fan work and turbine power output. The relationship will be used with the more conservative relationship of 4% and by using a relationship the simulation can be used in a modular way across the power output range.

The next step is to calculate the work required by the solar field pump. After calculating the mass flow rate in the solar field with the following equation, the pressure drop in the evaporator, $\Delta P_{SF,e}$ can be calculated as in the case of the evaporator working fluid side.

$$\dot{m}_{SF} = \frac{Q_{PB,E}}{Cp_{SF}(T_{SFi} - T_{SFo})} \quad \text{(eq. 15)}$$

Neglecting minor losses, the frictional pressure drop of the rest of the solar field can be calculated with the following:

$$\Delta P_{SF,fr} = f \frac{L}{D_{SF,p}} \frac{\rho V_{SF}^2}{2} \quad \text{(eq. 16)}$$

The total pressure drop and maximum required work (during day time) of the solar field pump is given below:

$$\Delta P_{SF} = \Delta P_{SF,e} + \Delta P_{SF,fr} \quad \text{(eq. 17)}$$

$$W_{SF,pump} = \dot{V}_{SF}(\Delta P_{SF}) \quad \text{(eq. 18)}$$

The net power output of the plant is then calculated as given below:

$$W_{Net} = W_{gross} - (W_{PB,pump} + W_{C,F} + W_{SF,pump}) \quad \text{(eq. 19)}$$

Following the objective function can be calculated as described previously given that:

$$Q_{in} = \frac{Q_{PB,E}}{\eta_{trough}} \quad \text{(eq. 20)}$$

5. Results and discussion

A techno-thermodynamic optimization was set up for a solar ORC plant where the plant efficiency was used as the objective function. For the 1 MW gross power output case, the power plant reached an optimal objective function at a condensing temperature, T_C = 300K and evaporating temperature T_E = 450K. These values fall within the constraints set by the simulation which necessitated the evaporating temperature below the critical temperature of 470K of n-Pentane, and keeping the condenser outlet temperature above an ambient temperature of 298K. The evaporating pressure reached a value of 2.45 MPa and the condensing pressure reached a value of 67 kPa. The exact same simulation was run under the same conditions for steam Rankine cycle for comparison sake. The resulting plant efficiencies from the objective function for the whole simulated power range can be seen in table 2:

Table 2: Resulting optimized plant efficiencies with net power output

Turbine power output (kW)	Net ORC plant power output (kW)	Optimized ORC plant efficiency (%)	Optimized steam plant efficiency (%)
500	458	14.26	11.10
1000	916	14.26	11.82
2000	1 831	14.25	13.77
3000	2762	14.25	14.17
4000	3660	14.24	14.76
5000	4598	14.24	15.75

As can be seen from table 2, the ORC performs much better at the lower temperature range. The main reason is that steam turbines are very inefficient at low power outputs leading to the whole cycle efficiency being lower. As the turbine output increases above 4000kW, it can be concluded that a steam Rankine cycle would be a better choice. Furthermore the ORC turbine efficiencies remain relatively constant for different power outputs, hence the whole plant efficiency remains more or less constant with change in power output. The turbine and working fluid has the largest effect of all the components on the cycle efficiency. Typically the average temperature at which heat is added in the evaporator must be increased and the average temperature at which heat is being rejected in the condenser needs to be decreased in order to increase cycle efficiency. The first mentioned is directly linked to the turbine inlet temperature and the effect of the turbine inlet temperature on cycle efficiency can be seen in figure 5.

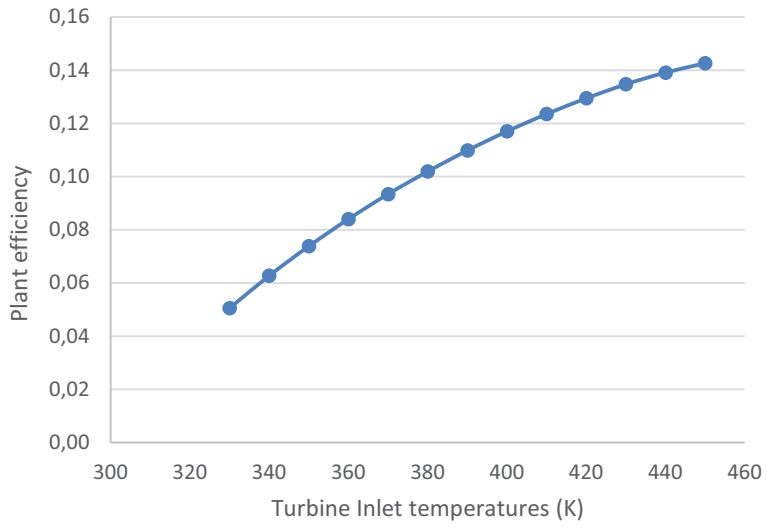

Figure 5: The influence of turbine Inlet temperature on plant efficiency for the 1 MW case

6. Conclusion

The paper optimized an ORC coupled with CSP and obtained a plant efficiency of about 14.2% across the power range of 500 kW – 5 MW. The efficiency correlates with an existing plant. The simulated plant operated at a maximum temperature and pressure of 450K and 2.45 MPa respectively. This is significantly lower than that of traditional Rankine cycles resulting in components needing to have less resilience. This in effect has a

great decreasing effect on plant cost and if accurate cost relations can be found one can conclude on the economical competiveness of an ORC. When the steam Rankine cycle was simulated under the same conditions and temperatures than the ORC, the ORC proved to be more efficient up to 3000kW power output. However the lack of optimized technology in the solar ORC field leads to industry not widely accepting the technology as a feasible solution yet but this paper concludes that further research in this topic is justified and that the solar ORC technology is deemed to reach maturity in the future.

7. References

Bao, J., & Zhao, L. (2013). A review of working fluid and expander selections for organic Rankine cycle. Renewable and Sustainable Energy Reviews, 24, 325–342

Canada, S., Brosseau, D., Kolb, G., Moore, L., Cable, R., & Price, H. (2005). Status of APS 1-Mwe Parabolic Trough Project, Size: 5 pp. Retrieved from www.osti.gov/servlets/purl/882807-d8b9mN

Casati, E. I. M. (2014). New Concepts for Organic Rankine Cycle Power Systems. Energy *Procedia*. Delft University of Technology. https://doi.org/10.1016/j.egypro.2014.10.220

Chen, H., Goswami, D. Y., & Stefanakos, E. K. (2010). A review of thermodynamic cycles and working fluids for the conversion of low-grade heat. Renewable and Sustainable Energy Reviews, 14(9), 3059–3067

Dickes, R. (2016). Solar-based ORC power systems. In *ORC-Plus Workshop*

Drescher, U. & Bruggemann, D., 2007. Fluid selection for the Organic Rankine Cycle (ORC) in biomass power and heat plants. *Applied Thermal Engineering,* Volume 27, pp. 223-228.

SEIFSA, 2016. High electricity price increase will have a crippling effect of the already embattled metals and engineering sector, s.l.: s.n.

Shah, R. K. (Ramesh K. ., & Sekulić, D. P. (2003). Fundamentals of heat exchanger design. John Wiley & Sons

Shuman, F., 1907. The Direct Acting Solar Engine: the Prime Mover of the Immediate Future. s.l.:s.n.

Tartiere, T. (2016). Analysis of the Organic Rankine Cycle market. Retrieved November 9, 2016, from http://orc-world-map.org/analysis.html

Quoilin, S., Broek, M. Van Den, Declaye, S., Dewallef, P., & Lemort, V. (2013). Techno-economic survey of organic rankine cycle (ORC) systems. *Renewable and Sustainable Energy Reviews*, *22*, 168–186

8. Appendix: Nomenclature

Symbol	Quantity	Unit
A	Area	m^2
Cp	Specific heat	J kg^{-1} K^{-1}
D_h	Hydraulic diameter	m
f	Friction factor	
g	Gravity	m s^{-2}
G	Mass velocity	kg m^{-2} s^{-1}
l	Length	m
$\dot{m}$	Mass flow rate	kg s^{-1}
n	Number of plates	
P	Pressure	kPa
S	Entropy	kJ kg^{-1} K^{-1}
T	Temperature	K
U	Overall heat transfer coefficient	W m^{-2} K^{-1}
V	Volume flow rate	m^3s
w	Width	m
W	Power	W

Greek symbol	Definition	Unit
η	Efficiency	
μ	Viscosity	Pa.s
ρ	Density	kg m^{-3}

Subscript	Definition
C	Condenser
E	Evaporator
F	Fan
fr	Friction
gen	Generator
l	Liquid
M	Manifolds
m	Log mean
PB	Power Block
SF	Solar Field
SFi	Evaporator in
SFo	Evaporator out
T	Turbine
v	Vapour
1,2,2a,3,4,4a	State Points

Assessment of Liquid Metals as Heat Transfer Fluid for Parabolic Trough Solar Collector

Krishna Chaitanya Nvv[1], Ravi Kumar K[2]

[1] Student, University of Petroleum and Energy Studies, Dehradun (India)

[2] Assistant Professor, Centre for Energy Studies, Indian Institute of Technology Delhi, New Delhi (India)

Abstract

In this article, heat transfer characteristics of various heat transfer fluids (HTF's) such as water, therminol oil, molten salt and liquid metals are studied for parabolic trough solar collector. A three dimensional (3-D) numerical simulation of absorber for parabolic trough solar collector is carried out using commercial computational fluid dynamics software Fluent 16.0. The numerical model is solved based on K-ε turbulent model with standard wall function. The influence of thermo-physical properties of HTF's on heat transfer rate from the absorber wall surface to the fluid is studied for various mass flow rates ranging from 0.5 kg/s to 1.5 kg/s insteps of 0.25 kg/s. The analysis is carried out for both uniform and non-uniform heat flux at the absorber wall surface. For both uniform and non-uniform heat flux configuration, liquid sodium offers better heat transfer characteristics among all the heat transfer fluids. Among all the heat transfer fluids, liquid sodium offers less temperature gradient (8.58 K) and therminol oil offers high temperature gradient (42.74 K) around the circumference of the absorber for the mass flow rate of 1 kg/s. Hence, liquid sodium offers significant benefits in terms of performance enhancement compared to other heat transfer fluids.

Key Words: Parabolic trough solar collector, Receiver, Variable heat flux, Heat transfer fluid, Liquid sodium

1. Introduction

A concentrated solar thermal collector concentrates solar radiation on the receiver that converts solar radiation in to useful high temperature heat. There are four concentrated solar thermal power (CSTP) technologies namely linear Fresnel reflector (LFR), parabolic trough collector (PTC), power tower (PT) and parabolic dish collector (PDC) that have reached reasonably high state of maturity. Globally ~ 4.8 GW CSTP plants are in operation and ~1.6 GW capacity of power plants are under construction as on March 2017 (NREL, 2017). Among the CSTP technologies, PTC is most proven technology and commercially available for power generation with potential of high dispatchability. The parabolic trough collector consists of parabolic shaped concentrator, receiver and supporting structure. Receiver is the most important component of the CSTP system. The PTC receiver consists of an absorber tube surrounded by glass envelope with annulus space evacuated. Heat transfer fluid is circulated through the receiver to collect the heat from the receiver. Typically organic or synthetic oils are used as a heat transfer fluid (HTF) in the PTC system. Synthetic oil has poor heat transfer characteristics and it has limitation of maximum operating temperature (< 400^{o}C). Design of receiver and heat losses from the receiver plays an important role on the performance of PTC. Heat losses from the receiver is the function of absorber temperature, ambient temperature, absorber type, wind velocity, etc. The temperature of the absorber may be reduced by increasing the heat transfer rate between inner wall surface of the absorber to the fluid.

There are few studies exist on enhancement of heat transfer rate from the absorber wall surface to the fluid. Almanza et al., (1997) conducted the experiments to study the deflection of absorber tubes due to temperature gradient in circumferential direction for direct steam generation in parabolic collector. Odeh et al., (1998) studied the performance of parabolic trough solar collector with synthetic oil and water as HTF. Kumar and Reddy (2009, 2012) studied the porous disc receiver for parabolic trough collector with therminol-55 and water as HTF and developed the empirical correlations for Nusselt number and friction factor. Cheng et al., (2010) performed the coupled flux distribution and heat transfer model for parabolic trough solar collector to analyze the heat distribution in the receiver. In recent days, liquid metals gaining much attention for CSTP applications as HTF. Boerema et al. (2012) studied liquid sodium and Hitec (a ternary molten salt 53% KNO_3 + 40% $NaNO_2$ + 7%

doi:10.18086/swc.2017.04.06 Available at http://proceedings.ises.org

$NaNO_3$) as heat transfer fluids and reported that both fluids are alternative for molten salts in PT systems for power generation. Kotze et al. (2012) compares the strengths and limitations of various HTF's for CSTP applications and proposed NaK may be the primary HTF for performance improvement. Pacioa et al. (2013) proposed liquid metals such as liquid sodium and lead-bismuth eutectic as efficient heat transfer fluids for PT systems. The recent development in HTF's for low, medium and high temperature solar thermal systems has been reviewed by Srivastva et al. (2015). Overall, liquid metals gaining momentum for CSTP applications to improve the performance of the receiver. In this paper, heat transfer ability of various HTF's and temperature gradient around the circumference of the absorber tubes are explored. The characteristics of HTF's such as stability at higher temperature, decomposition due to continuous heating and cooling, corrosion issues will be studied in future as continuation of this work.

2. Modeling of Absorber for Parabolic Trough Solar Collector

A 3-D numerical modeling is carried out to investigate the heat transfer rate from the absorber wall inner surface to the various working fluids such as water, therminol oil, molten salt, liquid sodium and eutectic NaK (77.8 % potassium and 22.2 % sodium by weight). The eutectic NaK hereafter referred as NaK78. The thermo-physical properties of various heat transfer fluids are given in Table 1. The schematic of absorber of parabolic trough solar collector is shown in Figure 1. The absorber of 4 m length is considered for the analysis with internal and external diameter of 66 mm and 70 mm respectively. The mass flow inlet and pressure outlet boundary condition is considered. The analysis is carried out for various mass flow rate ranging from 0.5 kg/s to 1.5 kg/s insteps on 0.25 kg/s. Constant and variable heat flux boundary conditions are considered for the analysis. For constant heat flux boundary condition, the absorber wall is subjected to 21000W/m^2 and for variable heat flux boundary conditions, the flux profile is given in Figure 2 (Khanna and Sharma, 2016).

Tab. 1: Thermo-physical properties of various heat transfer fluids (Kotze, 2012)

S. No.	Heat Transfer Fluid	Density (kg/m^3)	Specific Heat (kJ/kg K)	Thermal Conductivity (W/m K)
1	Water	995.7	4.178	0.60
2	Therminol Oil	1056	2.5	0.09
3	Molten salt	1794	1.21	0.55
4	Liquid Sodium	820	1.25	119.3
5	NaK78	749	0.94	26.2

Fig. 1 Schematic of absorber of a parabolic trough solar collector

The governing equations for steady, incompressible, forced convection in the absorber are given as (FLUENT, 2016):

Continuity equation:

$$\nabla \vec{V} = 0 \qquad \text{(eq. 1)}$$

Momentum equation:

$$\vec{V}\nabla\left(\vec{V}\right) = -\frac{\nabla P}{\rho} + \left(\frac{\mu + \mu_t}{\rho}\right)\nabla^2\left(\vec{V} + \vec{V}^T\right) + \overrightarrow{F_B} \qquad \text{(eq. 2)}$$

Energy equation:

$$\rho C_p \nabla\left(\vec{V}T\right) = \lambda \nabla^2 T \qquad \text{(eq.3)}$$

A steady state, 3-D model with incompressible and turbulent flow is solved using K- ε turbulent model. Reynolds Averaged Navier Stokes (RANS) model is used to solve the momentum equation with turbulent stresses. The RANS equations for incompressible flow is:

$$\frac{\partial}{\partial x_j}\overline{(u_i u_j)} = -\frac{1}{\rho_f}\frac{\partial \bar{p}}{\partial x_j} + \frac{\partial}{\partial x_j}\left[\vartheta_{eddy}\left(\frac{\partial u_i}{\partial x_j} + \frac{\partial u_j}{\partial x_i}\right)\right] \quad \text{(eq. 3)}$$

where, $\vartheta_{eddy} = C_\mu \frac{k^2}{\varepsilon}, C_\mu = 0.0845, k = 0.71\varepsilon^{2/3}L^{2/3}$

k and ε are the values of turbulent kinetic energy and turbulent dissipation rate.

The heat transfer coefficient from the absorber tube to the fluid may be given as:

$$h_f = \frac{q^{"}}{T_w - T_{ref}} \quad \text{(eq. 4)}$$

Where, $q^{"}$ is heat flux, T_w is the wall temperature and T_{ref} is reference temperature.

3. Boundary Conditions for Receiver

The following boundary conditions are applied for modeling of the absorber of the parabolic trough solar collector:

a) Inlet boundary condition

Mass flow inlet boundary condition is used at the absorber inlet with different temperature depends on the working fluid.

$$u = u_{in}; T_f = T_{in} \; at \; L = 0$$

$$0 \le r \le \frac{d_i}{2}, \; -180^o \le \theta \le 180^o \quad \text{(eq. 5)}$$

Since the melting temperature of molten salt and liquid metals are higher than the ambient temperature, the inlet temperature for various HTF's are considered as 300 K for water, therminol oil and NaK 78, 371 K for liquid sodium and 498 K for molten salt.

b) Wall boundary condition
Absorber inner wall:

No slip boundary condition is given to the inner and outer side of the wall.

$$u = 0 \; at \; 0 \le L \le 4, \; r = \frac{d_i}{2}, \; -180^o \le \theta \le 180^o \quad \text{(eq. 6)}$$

Absorber outer wall is subjected to heat flux boundary condition. Two boundary conditions are applied to study the performance of the absorber (a) Uniform (constant) heat flux boundary condition: the absorber wall is subjected to uniform heat flux of 21000W/m^2 and (b) Non-Uniform heat flux boundary conditions: the heat flux profile applied on the absorber wall surface is given in Figure 2 (Khanna and Sharma, 2016). In figure 2, zero degree corresponds to bottom of the absorber tube and ± 180^o corresponds to top of the absorber.

c) Pressure outlet boundary condition is employed across the outlet of the receiver.

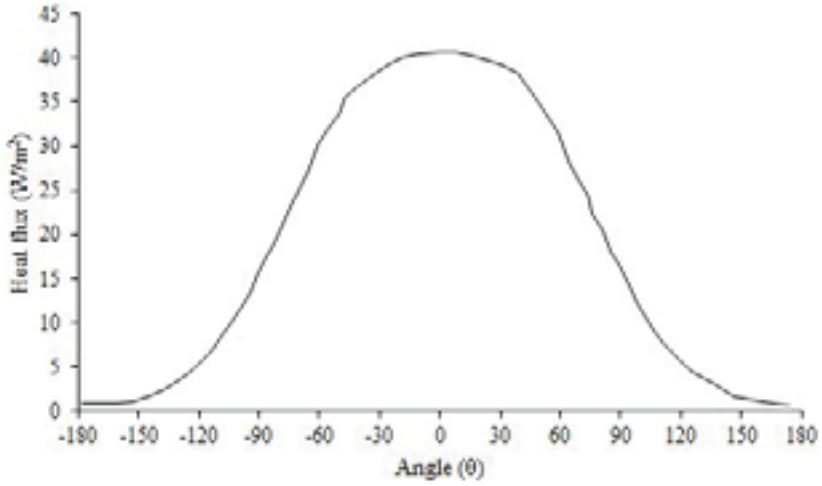

Fig. 2: Heat flux profile applied on the absorber surface (Khanna and Sharma, 2016)

4. Numerical Procedure

The governing equations are solved by finite volume method using CFD commercial software ANSYS Fluent 16.0 with segregated implicit solver and first order formulation (FLUENT, 2016). The first order discretization technique is used in pressure based solver. The velocity and pressure coupling is done by using SIMPLE algorithm. A convergence criteria of 10^{-3} is applied for velocity and momentum equations and 10^{-7} is applied for energy equation. The computational model is created in ANSYS 16.0 geometry module. The model is discretized into quadrilateral elements using ANSYS meshing module. Grid independence study is carried out and the number of mesh element is identified as 688539 cells. The variation of results are insignificant beyond the above mentioned element size. The geometric parameters of the absorber consists of a cylindrical tube with 4 m length having an inner diameter of 0.066 m and an outer diameter of 0.07 m. The computational domain consists of two zones such as solid and fluid. The wall is a solid zone where uniform and non-uniform heat flux is applied in two separate cases as discussed earlier. The fluid zone is the heat transfer fluid flowing the through the cylinder from inlet to outlet.

5. Validation

The model is validated by comparing the Nusselt number of present numerical model with Dittus-Boelter correlation. The result shows that the present model deviates from Dittus-Boelter correlation is around 9%.

The Dittus-Boelter equation is given as:

$$Nu = 0.023 Re^{0.8} Pr^{0.4} \qquad \text{(eq. 7)}$$

for $Re \geq 10,000$ *and* $0.7 \leq Pr \leq 160$

6. Results and Discussion

The numerical simulation of the absorber of a parabolic trough solar collector is carried out to analysis the influence of thermo-physical properties of various HTF's on heat transfer rate from absorber inner wall surface to the fluid with different mass flow rates. The HTF's mass flow rate varies from 0.5 kg/s to 1.5 kg/s insteps of 0.25 kg/s. In first case, simulations are carried out for the constant heat flux boundary condition to compare the heat transfer coefficients and temperature difference (ΔT) between the absorber wall surface and mean fluid temperature. The heat transfer coefficient increases with mass flow rate for all the HTF's. As shown in Figure 3 that the maximum heat transfer coefficient as 1268 W/m^{2}K at 1.5 kg/s is achieved for liquid sodium. For mass flow rate of 1 kg/s, the minimum ΔT is observed for liquid sodium as 1.38 K and maximum ΔT is observed for therminol oil as 31 K (Figure 4). It shows clearly that thermal conductivity of the HTF plays an important role in

heat transfer from absorber wall to the fluid. Also, it helps to reduce the absorber wall temperature that results in reduced heat losses from the absorber.

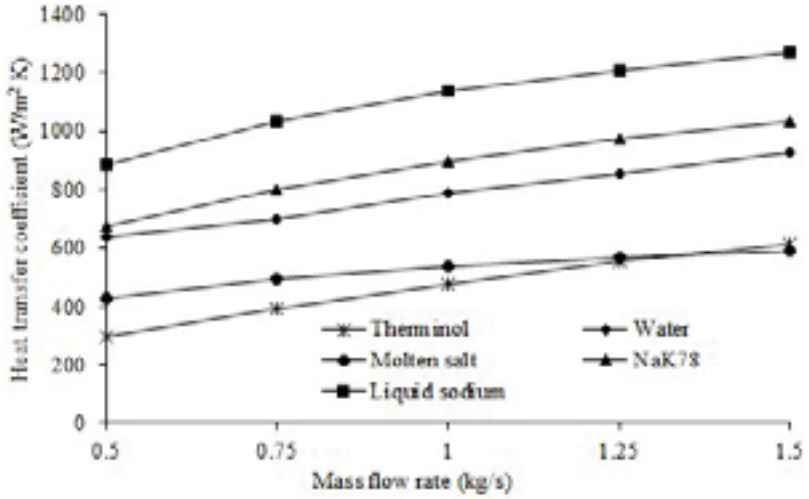

Fig. 3: Heat transfer coefficient for the absorber tube of parabolic trough solar collector for various HTF's with uniform heat flux boundary condition

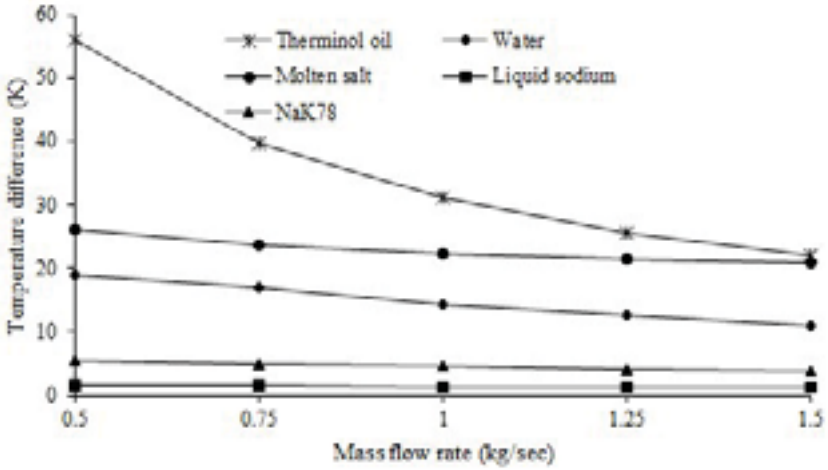

Fig. 4: Temperature difference between the absorber wall surafce and mean fluid temperature for various HTF's with uniform heat flux boundary condition

In second case, non-uniform heat flux boundary condition is applied around the absorber circumference to evaluate the heat transfer coefficient from wall to the fluid, temperature difference between the absorber inner wall surface to the mean fluid temperature and variation of temperature around the absorber circumference. Figure 5 shows that the surface heat transfer coefficient increases with flow rate. For 1.5 kg/s of mass flow rate, the maximum heat transfer coefficient of 1100 W/m^2 K is observed for liquid sodium and minimum of 600 W/m^2 K is observed for therminol oil. It is observed that the temperature difference between the inner wall surface to the mean fluid temperature (ΔT) is gradually decreases with increase in mass flow rate. Among all the HTF's, the maximum and minimum temperature difference occurs for therminol oil and liquid sodium respectively for the given mass flow rate.

Temperature of the absorber around the circumference for 0.5 kg/s and 1.5 kg/s is shown in Figure 7 and 8 respectively. Since the inlet temperature of liquid sodium and molten salt is higher than the other HTF's, the

absorber wall temperature also higher for liquid sodium and molten salt. At bottom of the absorber wall is subjected to higher heat flux (figure 2) and it decreases around the circumference while moving to top of the absorber. For most of the HTF's, higher wall temperature is observed at bottom of the absorber tube (0^o). Absorber wall temperature around the circumference is almost constant for liquid sodium. The temperature difference around the circumference of the wall in descending is observed as therminol oil followed by molten salt, water, NaK78 and liquid sodium for the given mass flow rate (Table 2).

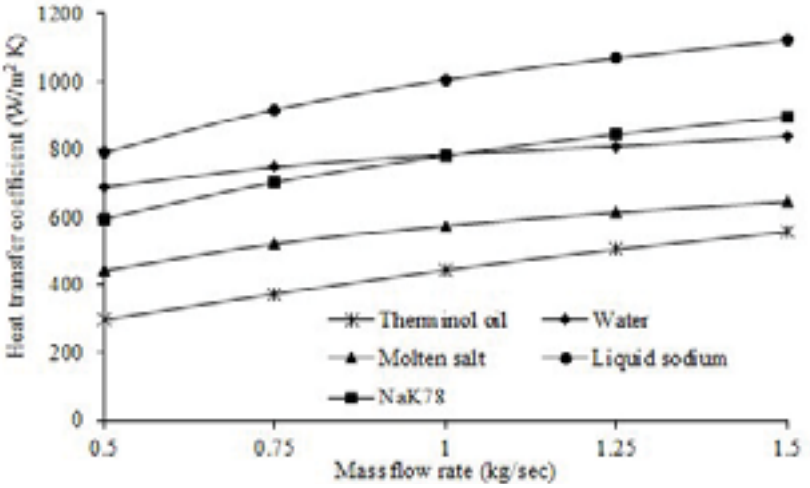

Fig. 5: Heat transfer coefficient for the absorber of PTC with non-uniform heat flux boundary condition

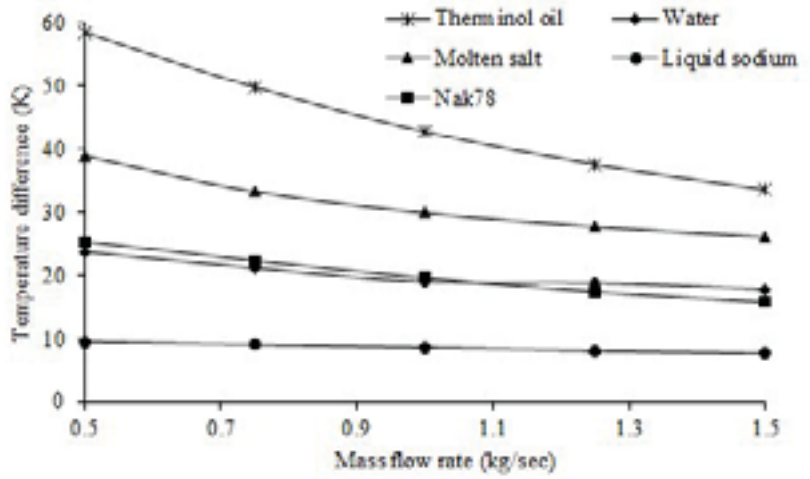

Fig. 6: Temperature difference between absorber wall and mean fluid temperature for various HTF's with non-uniform heat flux boundary condition

The temperature difference around the circumference of the absorber wall is maximum for lower mass flow rate and decreases with increase in mass flow rate. The temperature difference around the circumference is maximum for therminol oil at 0.5 kg/s of mass flow rate and minimum for liquid sodium at 1.5 kg/s. Higher the temperature difference results in thermal stress in the absorber wall. It leads to deflection of the absorber, results in poor optical efficiency. Hence, it is clear that thermo-physical properties of HTF's play an important role in performance of the receiver.

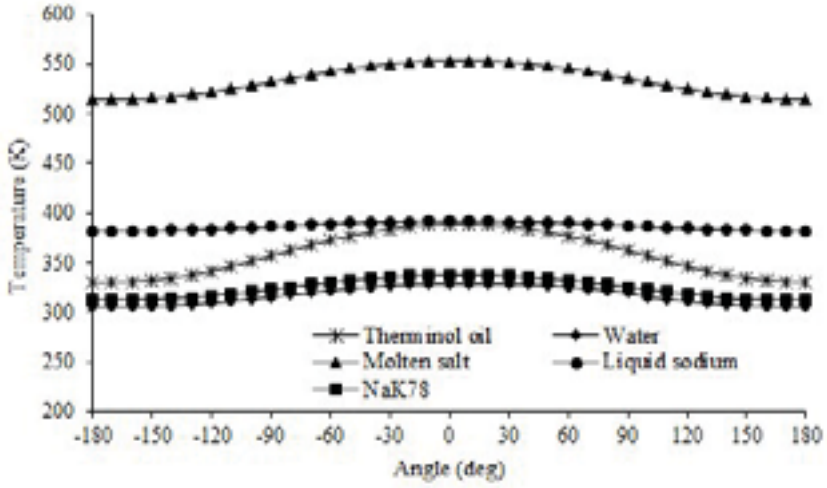

Fig. 7: Temperature of the absorber tube around the circumference for mass flow rate of 0.5 kg/s

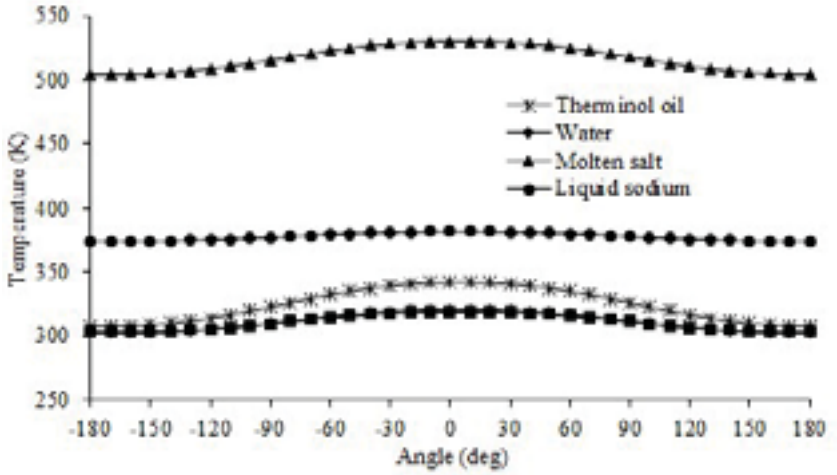

Fig. 8: Temperature of the absorber tube around the circumference for mass flow rate of 1.5 kg/s

Tab. 2: Temperature difference around the absorber circumference for different working fluids

Heat Transfer Fluids	**Temperature (K)**				
Mass flow rate (kg/s)	**0.5**	**0.75**	**1**	**1.25**	**1.5**
Therminol oil	58.45	49.79	42.74	37.56	33.59
Water	23.67	21.12	18.94	18.8	17.79
Molten salt	38.89	33.22	29.84	27.68	26.09
Liquid sodium	9.49	9.01	8.58	8.09	7.65
Nak78	25.37	22.27	19.55	17.4	15.8

The temperature contours along the length for therminol oil, water and Nak78 are sown in Fig.9 at 0.5 kg/s. The temperature increases gradually along the length from inlet temperature of 300 K. Temperature contours of molten salt and liquid sodium is shown in Figure 10 and 11 respectively.

Fig. 9: Temperature contours for (a) Therminol, (b) Water, (c) NaK78 at 0.5 kg/sec mass flow rate with non-uniform heat flux

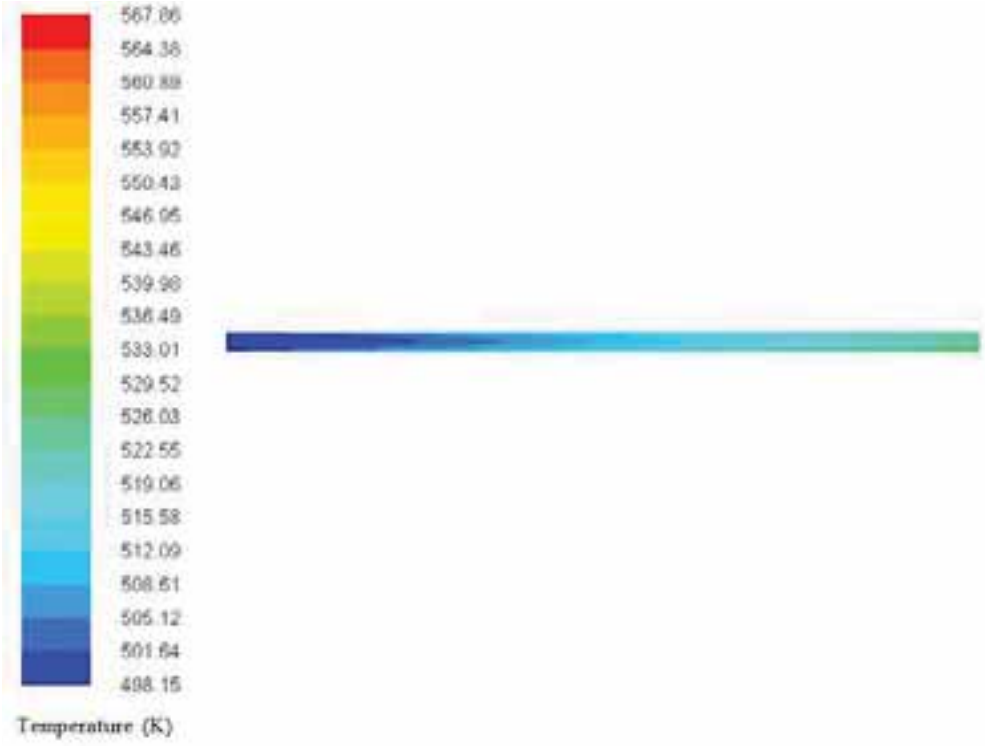

Fig. 10: Temperature contours for molten salt at 0.5 kg/sec mass flow rate with non-uniform heat flux

The temperature contours at the outlet of the absorber tube for therminol oil, water and NaK78 are shown in Figure 12. NaK78 achieves higher outlet temperature due to low specific heat and higher thermal conductivity. The temperature at outlet of absorber tube for various HTF's such as therminol oil, water and NaK78 at 0.5 kg/s are found as 314.3 K, 308.57 K and 337.3 K respectively. Figure 13 and 14 shows the temperature contours at the outlet of absorber for molten salt and liquid sodium respectively. The outlet temperature of the molten salt and liquid sodium is calculated as 527.6 K and 398.8 K respectively for 0.5 kg/s.

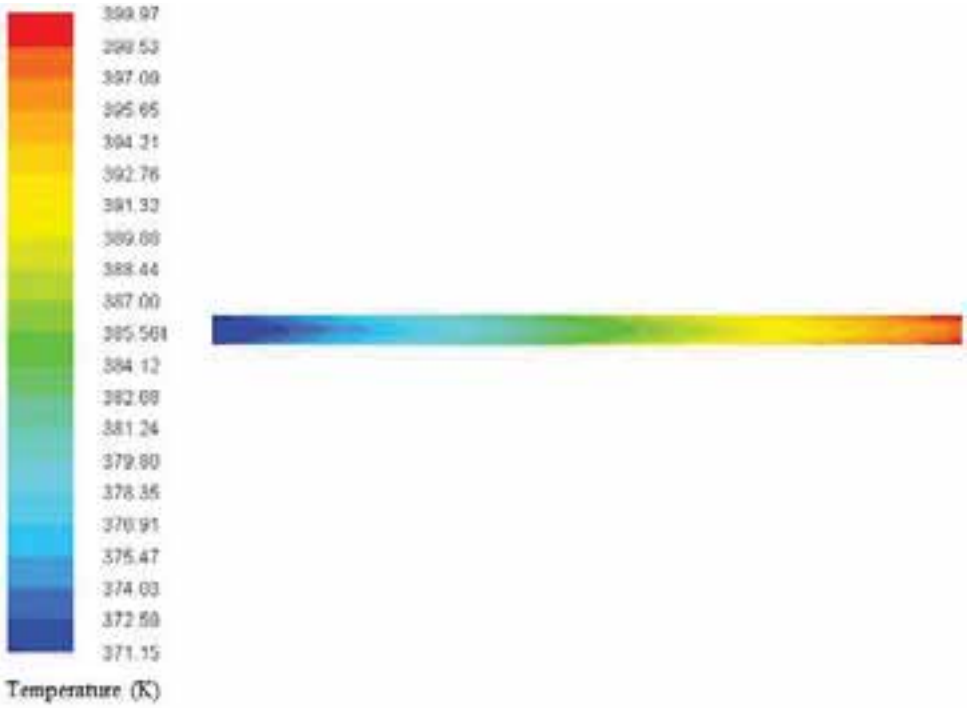

Fig. 11: Temperature contours for liquid sodium at 0.5 kg/sec mass flow rate with non-uniform heat flux

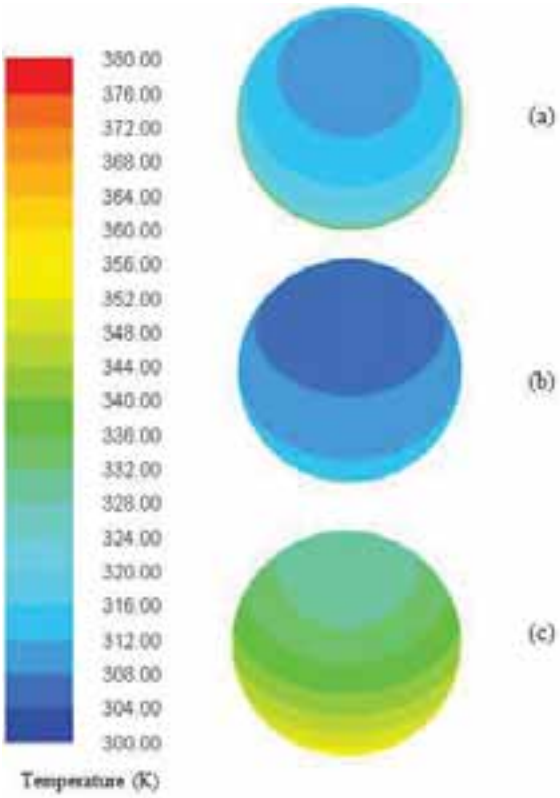

Fig. 12: Temperature contours at outlet of the absorber for (a) Therminol oil (b) water and (c) NaK78 at 0.5 kg/s with non-uniform heat flux distribution

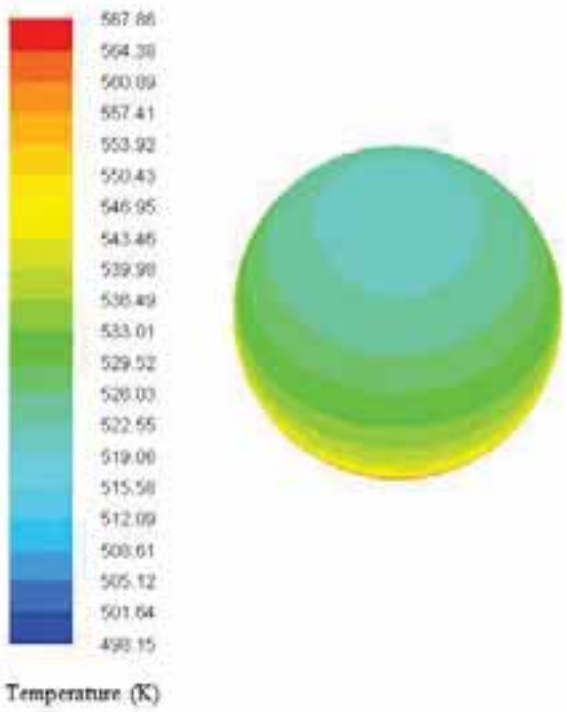

Fig. 13: Temperature contour at outlet of the absorber for molten salt at mass flow rate of 0.5 kg/s

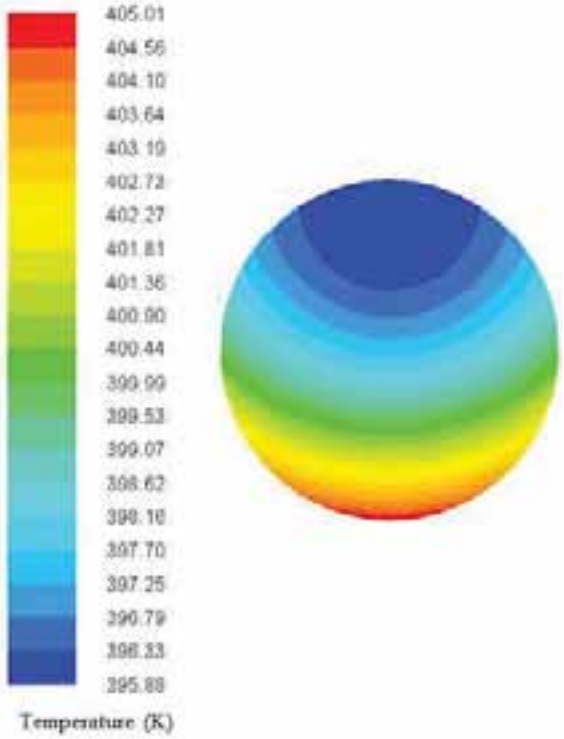

Fig.14: Temperature contour at outlet of the absorber for liquid sodium at mass flow rate of 0.5 kg/s

Based on the analysis, it is found that liquid sodium and NaK78 offers less temperature difference around the circumference of the absorber as well as temperature difference between the inner wall of the absorber to the mean temperature of the fluid as compared to other heat transfer fluids. Since melting temperature of the liquid sodium (97.82^{o}C) is higher than the ambient, it requires either option for draining of liquid sodium from the receiver or trace heating during plant startup. It increases plant operating cost which is not desirable. The melting point of NaK78 is12.6^{o}C which is less than the ambient temperature for most of the climatic conditions. It is desirable to use Nak78 as heat transfer fluid for parabolic trough solar collector to improve the performance of the absorber significantly.

7. Conclusions

The numerical simulation of absorber for a parabolic trough solar collector has been carried out for different HTF's and observed that the liquid sodium and NaK78 performs better than other HTF's due to its high thermal conductivity. It also reduces the temperature gradient between the absorber wall surface to the mean fluid temperature as well as around the absorber circumference. Hence it helps to reduce the heat losses from the absorber of the parabolic trough solar collector. By reducing the circumferential temperature difference, thermal stress in the absorber tube can be minimized which results in no / minimum deflection of the absorber in turn it improves the intercept factor / optical efficiency of the parabolic trough solar collector. Overall, using liquid metal as heat transfer fluid improves the overall performance of the parabolic trough solar collector. Since liquid sodium and NaK78 violently reacts with water and air, special precautions should be taken care to avoid the safety related issues.

8. References

Almanza, R., Lentz, A., Jimenez, G., 1997. Receiver behavior in direct steam generation with parabolic troughs. Sol Energy, 61(4), 275-278.

Boerema, N., Morrison, G., Taylor, R., Rosengarten, G., 2012. Liquid sodium versus Hitec as a heat transfer fluid in solar thermal central receiver systems. Solar Energy, 86, 2293–2305.

Cheng, Z. D., He, Y. L., Xiao, J., Tao, Y. B., Xu, R. J., 2010. Three-dimensional numerical study of heat transfer characteristics in the receiver tube of parabolic through solar collector. Int. Communications in Heat and Mass Transfer, 37, 782-787.

FLUENT, 2016. ANSYS Fluent theory guide, ANSYS, Inc. Canonsburg, PA 15317.

Khanna, S., Sharma, V., 2016. Explicit analytical expression for solar flux distribution on an undeflected absorber tube of parabolic trough concentrator considering sun-shape and optical errors, J. of Solar Energy Engineering, 138, 1-10.

Kotze, J. P., Backstrom, T. W. V., Erens, P. J., 2012. NaK as a primary heat transfer fluid in thermal solar power installations, 1st Southern African Solar Energy Conference (SASEC), 1-9.

Kumar, K. R., Reddy, K. S., 2009. Thermal analysis of solar parabolic trough with porous disc receiver, Applied energy, 86, 1804-1812.

Kumar, K. R., Reddy, K. S., 2012. Effect of porous disc receiver configurations on performance of solar parabolic trough concentrator, Heat Mass Transfer, 48, 555-571.

NREL (National Renewable Energy Laboratory), (2017). Accessed on 6th January 2017, from Concentrating Solar Power Projects by Project Name: https://www.nrel.gov/csp/solarpaces/by_project.cfm

Odeh, S. D., Morrison, G. L., Behnia, M., 1998. Modelling of parabolic trough direct steam generation solar collectors, Solar Energy, 395-406.

Pacio, J., Fritsch, A., Singer, C., Uhlig, R., 2014. Liquid metals as efficient coolants for high-intensity point-focus receivers: implications to the design and performance of next generation CSP systems, Energy Procedia, 49; 647-655.

Srivastva, U., Malhotra, R. K., Kaushik, S. C., 2015. Recent developments in heat transfer fluids used for solar thermal energy applications, Fundam. Renewable Energy Appl., 5(6), 1-11.

9. Nomenclature

C_p	Specific heat (J/kg K)
d_i	Inner diameter (m)
d_o	Outer diameter (m)
h_f	Heat transfer coefficient (W/m^2 K)
k	Turbulent kinetic energy (m^2/s^2)
L	Length of cylinder (m)
Pr	Prandtl number
q	Heat flux (W/m^2)
r	Radius (m)
Re	Reynolds number
T	Temperature (K)
T_{in}	Inlet temperature (K)
T_{ref}	Reference temperature (K)
T_w	Wall temperature (K)
u_{in}	Inlet velocity (m/s)
u_i, u_j	Velocity (m/s)
θ	Angle (deg)
ρ	Density (kg/m^3)
μ	Dynamic viscosity (N s/m^2)
ε	Turbulent dissipation rate (m^2/s^3)

Ni-Co CO-Modified Anodized Spectrally Selective Coatings With Enhanced Corrosion and Thermal Stability

Rajesh Kumar[1#], and Ambesh Dixit[1$]

[1]Department of Physics & Center for Solar Energy, Indian Institute of Technology Jodhpur, Rajasthan, India-342011.

[$]ambesh@iitj.ac.in

Abstract

Ni-Co/Nanoporous Al_2O_3/Aluminum spectrally selective structures are grown using electrochemical anodization of alumina, followed by electrochemical pigmentation of Ni and Co metallic particles simultaneously. The pigmentation of Ni and Co particles into nanoporous anodized alumina (AA) is achieved using the reduction of metal ions in the aqueous electrolyte. The measured absorptivity and emittance are ~ 0.90 ± 0.05 and 0.14 ± 0.04, respectively. These structures are subjected to the ten identical thermal cycling upto 300 °C in inert N_2 and air ambient conditions. The optical performance suggests that absorptivity is nearly same with slight enhancement in the emittance values as compared to the structure without any heat treatment. The accelerated corrosion studies suggest that Ni-Co co-pigmented AA structures are relatively corrosion robust as compared to that of the AA structure.

Keywords: Corrosion, spectrally selective coatings, emittance, absorptance,

Introduction

The energy crisis during 1970-1980 implied the consequences of fossil fuel depletion, greenhouse gases and subsequently the climate change and obligated to look for alternate energy resources. Thus, renewable energy sources are gaining attention continuously and their fractions are increasing slowly. Solar energy is one of the most abundant environmentally safe renewable energy resources. The simplest and direct method of harnessing solar energy is the solar thermal conversion, where thermal energy can be utilized for possible applications later or simultaneously including power generation. The spectrally selective solar absorbers are used to convert the incident solar radiation into thermal energy by employing on receiver tube of the solar collector, which is integrated into a solar thermal systems and sub-systems for different applications including solar thermal power plants [Granqvist 1991, Behar et al. 2013]. Solar collectors can be classified into two category in general: (i) non-concentrating and (ii) concentrating. The concentration ratio for nonconcentrating solar collector is one, which is greater than one (> 1) for concentrating collectors. Non-concentrating collector such as flat plate collectors and evacuated tube collectors are mainly used for relatively lower temperatures based applications including solar hot water and drying of agricultural products, whereas concentrating collectors are used for high-temperature application such as solar thermal power and industrial applications. The initial spectrally selective coatings are mostly electrodeposited black chrome, black nickel, Nis-ZnS composites and were integrated successfully in flat plate collectors. These coatings are useful for moderate temperature applications under vacuum/inert or corrosion free ambients. The performance of a solar absorber depends on optical properties of absorber surface, employed to intercept the incoming solar radiation. For an effective solar energy collection, the spectral selective coatings are used, which are capable of absorbing the maximum of solar spectrum without emitting large thermal radiations. Thus, spectrally selective absorbers should exhibit high absorptance ≥0.95 in the solar spectral range 0.3 - 2.5 μm and low thermal emittance ≤ 0.05 in the infrared spectral range 2.5-25 μm [Barshilia et al. 2006]. Ideally, a spectral selective coating (SSC) should have low reflectance (ρ) ~ 0 for wavelengths (λ) ≤ 2.5 μm and high reflectance ~1 for $\lambda \geq$ 2.5 μm. The cutoff wavelength may be higher or lower as the wavelength distribution of radiation emitted by a black body depends on the temeperature [Duffie 1980]. Concentrated solar thermal power systems(CSP) operate at high temperature (≥ 400 °C). For such application, SSCs should be chemically and thermally stable in the working environment under elevated temperature and thus, high thermal and structural stabilities are essential for both the combined and individual layers of the coating structures [Kennedy 2005]. The SSC performance may degrade at high-temperature not only because of oxidation in a residual environment in a vacuum or in air ambient but also

doi:10.18086/swc.2017.04.07 Available at http://proceedings.ises.org

due to the thermal cycling, causing periodic thermal stresses. In addition, this may also cause interlayer diffusion and chemical reactions, leading to the poor interlayer adhesion and thus deteriorating the solar performance. The chemical reactions, especially in open ambient and moist conditions, may corrode and thus damage the coating structure. Further, the challenge is to keep the emiittance (ε) low at high temperatures as the thermal radiative losses are proportional to the fourth power of the temperature in conjunction with high absorptance. Thus, there is a tradeoff between emittance and absorptance as these are mutually exclusive properties for SSCs [Kennedy 2002].

Among numerous SSCs, **cer**amic-**met**al (**cermet**) based spectrally selective absorber structures are extensively investigated and are still extensively under consideration due to their potential for solar thermal applications. Their high solar absorptance, low IR emittance and good thermal stability for mid and high temperature range make them very attractive for concentrated solar power applications [Cao et al. 2014]. The coating thickness and metal volume fraction in the ceramic matrix as well as particle size, shape and orientation can affect the spectral selectivity. For example, thicker cermet structures with smaller particle size are desired for high solar absorptance, whereas with increased thickness leads to the higher thermal emittance. Electrodeposited black chrome coatings are widely studied and used for solar hot water applications [Niklasson and Granqvist 1983, Craighead et al. 1981]. However, these are not very useful for high-temperature applications. Alumina (Al_2O_3) based cermet coating exhibit desired optical properties and thermal stabilities, showing relatively better solar thermal performance with enhanced thermal stability.The metal pigmented dielectric nanoporous structures such as anodized alumina may provide suitable cermet type spectrally selective absorber structures [Graqvist and Hunderi 1979]. The porous alumina layers with inclusion of transition metals like Fe, Co, Ni, Cu, Au, Ag, Mo, Cr, and W are widely studied [Galione et al. 2010,Salmi et al. 2000, Wackelgard 1996] for solar absorbers showing a high solar absorptance (α) of 0.93 and low thermal emittances (ε) ranging 0.04– 0.10 [Andersson et al. 1980]. In addition to the solar absorbers, metal pigmented anodized alumina is also used in nanostructured electronic devices [Sellmyer et al. 2001, Paulus et al. 2001].

Various physical and chemical deposition techniques are employed for synthesizing cermet structutre [Kennedy 2002].Among them electrochemical deposition is promising because of its easy synthesis process and the scalability for depositing coating structures on desired surfaces. This also provides the good control on synthesis parameters such as current density, electrolyte concentration, deposition time or combination of these as well to realize the optimized coating structures for possible applications. Thus, relatively good quality spectrally selective structures can be realized using electrodeposition with optimal solar thermal properties. The double anodization process is proposed by Masuda and Fukada [Masuda and Fukuda 1995] to obtain the ordered pore arrays and pores with straight side walls. The ordered pore arrays are useful when the porous alumina is used as a template, for example, in the electrodeposition of metallic or semiconducting nano-particles, wires and nanorods to achieve the metal-alumina composite matrix structure and also the specific structures for electronic device applications [Gerein and Haber 2005, Shin et al. 2009]. However, the requirement of straight pores is not so stringent for spectrally selective cermet coating structures and single step anodization process is used is followed to generate the porous alumina structure [Graqvist and Hunderi 1979, Salmi et al. 2000, Andersson et al. 1980, Cuevas et al. 2014]. These structures are obtained by anodizing aluminum in dilute phosphoric acid and electrolytically colored using nickel pigmentation. However, the stability of such structure is limited upto 250-300°C. Nahar et al and Cuevas et al also used cobalt pigmentation instead of nickel because of stronger oxidation resistance as compared to nickel [Cuevas et al. 2014, Nahar et al. 1986]. There are studies on Ni pigmented AA and Co pigmented AA spectrally selective coating structures as mentioned in Table 1 [Cuevas et al. 2014, Nahar et al. 1986, Niklasson and Granqvist 1984, Nahar et al. 1989]. However, very few studies are available on simultaneous Ni-Co pigmentation of anodized alumina for solar thermal applications in conjunction with their thermal and corrosion stabilities.

This work reports the development of Ni-Co/Nanoporous Al_2O_3/Aluminum structures. These structures are synthesized electrochemically. The anodization process has been optimized to get the desired pore size (~ 50 nm), followed by Ni and Co co-pigmentation into the nanoporous alumina structures. The detailed structural, microstructural and optical studies will be discussed in conjunction with their thermal and corrosion stabilities. The theoretical estimations are carried out to understand the impact of the metal fraction in a dielectric matrix on optical properties.

Table 1. Ni, Co pigmented anodized alumina as SSCs and their optical properties.

SSCs stucture	Absorptance	Emittance	Thermal stability	Corrosion Resistance	References
$Ni/Al_2O_3/Al$	0.93 - 0.96	0.01 - 0.20	300 °C (Air)	-	Kennedy 2002
$Co/Al_2O_3/Al$	0.92	0.28	400 °C (Air)	-	Niklasson and Granqvist 1984, Nahar et al. 1989
$Co/Al_2O_3/Al$	0.92	0.16	-	-	Cuevas et al. 2014

2.Experimental detail

The development of Ni-Co co-pigmented anodized alumina as the spectral selective coatings involve the three successive steps: (i) pre-treatment of substrate surface, (ii) electrochemical anodization for porous alumina structure and (iii) electrochemical co-pigmentation of nickel-cobalt in anodized alumina. The process is explained schematically in Fig 1. The pretreated degreased 80 mm × 40 mm × 1 mm aluminum 'Al' sheets are used as working electrodes and a 7 mm x 10 mm x 3 mm graphite plate as the counter electrode [Bostrom et al. 2003, Green et al. 2007]. The anodization is carried out at constant voltage 15 V_{DC} for about 15 minutes at room temperature (~ 25℃) in 2M phosphoric acid electrolyte solution. This led to the porous aluminum oxide structure with 50 ± 10 nm diameter pores. Further, aqueous electrolytic bath, containing 0.11M $CoSO_4$, 0.11 M $NiSO_4$, 0.2 M H_3BO_3 and 0.1 M ascorbic acid, is used for co-electrodeposition of Ni-Co metallic nanoparticulates inside the porous alumina structure. This is achieved under AC electrodeposition conditions at ~10 V_{AC} (frequency ~50 Hz) for 10 minutes [Foyet et al. 2008]. The solar thermal properties of these structures are investigated using UV-Vis and IR spectroscopic measurements. The accelerated corrosion tests are carried out in 3.5 wt% NaCl electrolyte solution at room temperature. The thermal treatments are carried out under ambient and inert N_2 gas environments. The microstructural and surface properties are investigated using Carl Zeiss EVO 18 especial edition scanning electron microscope (SEM). The elemental compositions are measured using the energy dispersive X-ray (EDX) instrument (OXFORD make); equipped with SEM system. The optical reflectance is measured using UV–Vis-NIR spectrophotometer (Carry 5000) in 0.2-25 μm wavelength range to understand the spectral response. These reflectance measurements are used to calculate the room temperature solar absorptance α(λ) in 0.2 - 2.5 μm wavelength range and thermal emittance ε(λ) in 2.5-25 μm respectively.

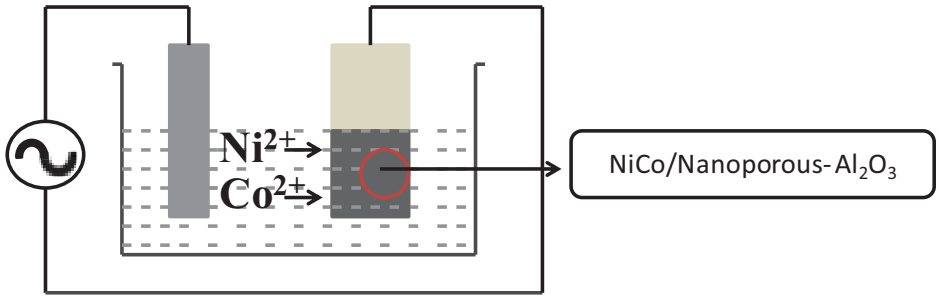

Fig.1: The schematic diagram explaining electrodeposition setup for Ni-Co pigmentation into the nanoporous Al_2O_3 structure.

3. Results and discussion

The SEM micrographs are shown in Fig. 2 (a) and 2(b) for anodized alumina and Ni-Co co-electrodeposited anodized alumina, respectively. The respective schematic structures are shown as the insets. The pore size of the anodized alumina is estimated using higher magnification image of anodized alumina, as shown in inset, in Fig. 3 (a)). We observed pore size ~ 40 ± 10 nm. For elemental composition determination, EDX measurement was performed and estimated results are shown as the insets in respective figures. The introduction of Ni and Co can be observed in anodized alumina structures, as shown in Fig. 2 (b). In spite of equimolar ratios for Ni and Co precursors, the electrodeposition of Co is preferred and larger Co fraction is deposited as compared to that of Ni in these Ni-Co co-pigmented anodized alumina structures.

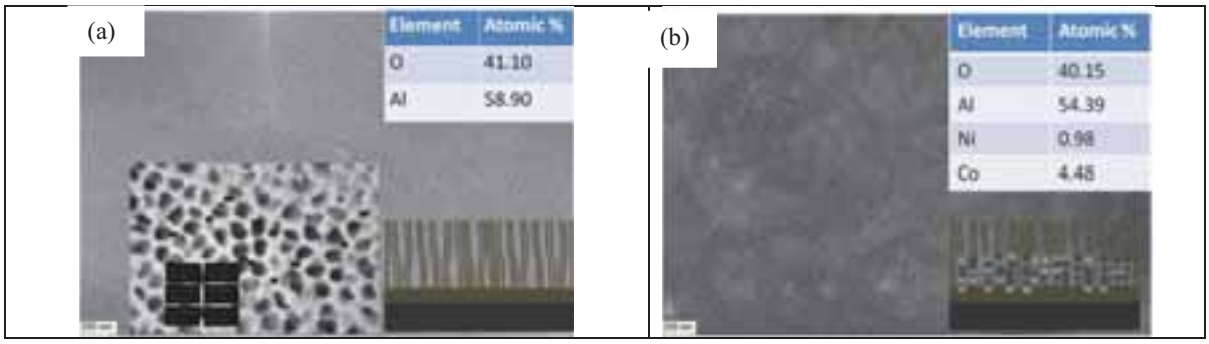

Fig. 2: SEM micrograph of the anodized alumina (a) and Ni-Co co-electrodeposition in anodized alumina (b)

The representative UV-Vis-NIR reflectance measurement is shown in Fig 3(a) for Ni-Co/Nanoporous Al_2O_3/Aluminum spectrally selective coatings ~ 0.2 – 25 μm wavelength range. The effective medium approach is used to simulate the reflectance for these structures [Niklasson et al. 2007] and is shown in Fig 3(a) in conjunction with experimentally measured reflectance. The materials parameters such as dielectric and optical constants are borrowed from references [Andersson et al. 1980, Palik 1998]. The metallic fraction is varied to achieve the best fit for the experimentally recorded reflectance, as shown in Fig. 3(a).

The simulated reflectance trend is similar to the experimentally measured reflectance and is in good agreement towards higher wavelength region. However, the simulated and measured reflectances are not showing good agreements and the difference is attributed to ignorance of the surface irregularities and lack of reliable materials parameters in the desired wavelength regions. The measured absorptance and emittance values are 0.95 and 0.14, respectively for the pristine spectrally selective structures. The measured absorptance is in close agreement with the simulated absorptance whereas the emittance value is slightly higher as compared that of the simulated emittance for optimal 25% metallic fraction in anodized alumina ceramic matrix. Further, these coating structures are thermally heat-treated at 300°C for 50 hours and respective reflectance results are summarized in Fig. 3(b) & (c). The emissivity value increased from 0.14 for as prepared structure to 0.20 and 0.22 for thermally treated structures in inert N_2 and air ambient conditions, suggesting that these structures are relatively thermally stable with a small increase in their emissivity values.

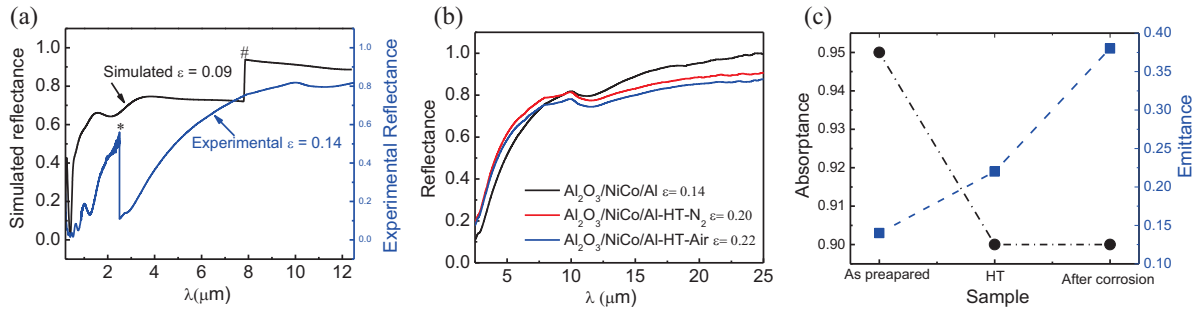

Fig. 3: Reflectance curves for (a) pristine Ni-Co/Nanoporous Al_2O_3/Aluminum coating, experimentally measured one with blue color and simulated one with black color (* glitch at 2.5 μm is the instrumental error, while changing the wavelength range near NIR region and # glitch in data taken from references at 7.8 μm); (b) high temperature (HT) thermally treated Ni-Co/Nanoporous Al_2O_3/Aluminum coatings, with respective emissivity values and (c) absorptance and emittance for as prepared, HT and after corrosion treatment of Ni-Co pigmented Ni-Co/Nanoporous Al_2O_3/Aluminum coatings.

For corrosion studies, potentiodynamic polarization measurements are carried out in 3.5 wt% NaCl electrolyte solutions for anodized alumina and fabricated SSCs structure at room temperature. The corrosion experiments were performed using Autolab (Metrohm) workstation in three electrode configuration, where platinum is used as counter electrode, Ag/AgCl as reference electrode and sample as working electrode. In both the corrosion measurements, sample was immersed in 3.5% NaCl solution for half an hour to establish open circuit potential (OCP). The OCP for anodized alumina was ~0.56 mV and -0.65 for fabricated SSC sample. So, measurement were performed in -1.5mV to 0 to cover the OCP range. The measured voltage versus logarithmic of current measurement is summarized as Tafel plots in Fig. 4(a). The respective corrosion parameters are calculated using Nova software, provided with Autolab (Metrohm) workstation and are summarized in Table 1. The polarization

resistance is measured using Stern-Geary relation, $R_p = \frac{b_c \times b_a}{2.3 \times i_{corr}\,(b_c + b_a)} (K\Omega cm^2)$, where b_a and b_c are anodic and cathodic curve slope. The corrosion current (i_{corr}) is lower ~0.182μA cm^{-2} for Ni-Co/Nanoporous Al_2O_3/Aluminum structure as compared to that of ~ 0.936μA cm^{-2} for anodized alumina at a scan rate of 10 mVs^{-1}, suggesting that corrosion resistance has increased for pigmented structure. The corrosion potential and polarization resistance (R_p) also showed higher values for fabricated SSCs with respect to that of anodized alumina. The corrosion rate after metal pigmentation is observed much lower as compared to that of anodized alumina. These results suggest that the Ni-Co/Nanoporous Al_2O_3/Aluminum structure is better corrosion resistant with respect to the anodized alumina. This is desirable for a SSC structure for longer lifetime in open environmental condition. After corrosion measurement, the optical characterization was performed to estimate the absorptance and thermal emittance. The observed absorptance of these corrosion treated samples remains nearly unaffected, whereas the emittance values showed enhancement upto 0.38 as shown in Fig. 4(b). This is mainly attributed to the increased surface roughness due to microstructure evolution, introduced during the accelerated corrosion testing.

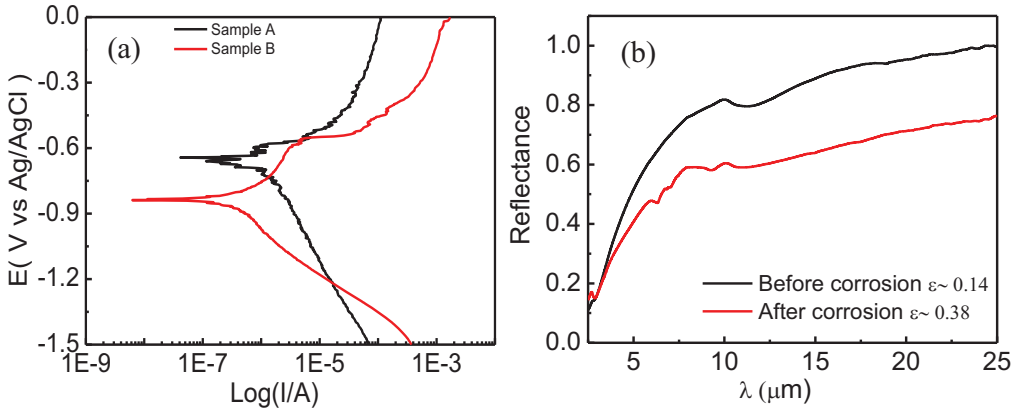

Fig. 4: (a) Potentiodynamic polarization curves and (b) respective reflectance curves for anodized alumina (black) and Ni-Co/Nanoporous Al_2O_3/Aluminum SSCs (red).

Table 2.The estimated corrosion parameter of anodized Al and Ni-Co/Nanoporous Al_2O_3/Aluminum SSCs

Sample	**E_{corr} (V)**	**i_{corr} (μA/ cm^{-2})**	**R_p (KΩ)**	**C. Rate (mm/y)**	**b_a (V/dec)**	**b_c (V/dec)**
Sample A	-0.6589	0.936	40.66	0.0108	0.100	0.359
Sample B	-0.837	0.182	135.03	0.0021	0.049	0.050

4. Conclusion

We demonstrated successful deposition of Ni-Co/Nanoporous Al_2O_3/Aluminum SSCs using simple electrodeposition process. These structures showed optimal absorptivity ~ 0.95 and emissivity ~ 0.14. Further, these structures showed enhanced thermal resistance without degrading their optical properties significantly. The corrosion studies suggest that Ni-Co co-pigmented SSCs structures are relatively corrosion resistant as compared to that of the bare anodized alumina substrate. The observed absorptance is nearly unaffected whereas the emittance values enhanced to ~ 0.38 for corrosion treated SSC structures. Thus Ni-Co co-pigmentation in anodized alumina structures may provide a thermally stable and corrosion resistant spectrally selective structure.

5. Acknowledgement

Authors acknowledge Ministry of New and Renewable Energy (MNRE), Gov. of India through project number XXX for carrying out this work.

6. References

Andersson, Å., Hunderi, O. and Granqvist, C.G., 1980. Nickel pigmented anodic aluminum oxide for selective absorption of solar energy. Journal of Applied Physics, 51(1), pp.754-764.

Barshilia, H.C., Selvakumar, N., Rajam, K.S., Sridhara Rao, D.V., Muraleedharan, K. and Biswas, A., 2006. Ti Al N⁄ Ti Al ON⁄ Si 3 N 4 tandem absorber for high temperature solar selective applications. Applied physics letters, 89(19), p.191909.

Behar, O., Khellaf, A. and Mohammedi, K., 2013. A review of studies on central receiver solar thermal power plants. Renewable and sustainable energy reviews, 23, pp.12-39.

Craighead, H.G., Howard, R.E., Sweeney, J.E. and Buhrman, R.A., 1981. Graded-index Pt-Al2O3 composite solar absorbers. Applied Physics Letters, 39(1), pp.29-31.

Cuevas, A., Martínez, L., Romero, R., Dalchiele, E.A., Marotti, R., Leinen, D., Ramos-Barrado, J.R. and Martin, F., 2014. Electrochemically grown cobalt-alumina composite layer for solar thermal selective absorbers. Solar Energy Materials and Solar Cells, 130, pp.380-386.

Cao, F., McEnaney, K., Chen, G. and Ren, Z., 2014. A review of cermet-based spectrally selective solar absorbers. Energy & Environmental Science, 7(5), pp.1615-1627.

Duffie, J.A. and Beckman, W.A., 1980. Solar engineering of thermal processes.

Foyet, A., Hauser, A. and Schäfer, W., 2008. Double template electrochemical deposition and characterization of NiCo and NiCu alloys nanoparticles and nano films. Journal of Solid State Electrochemistry, 12(1), pp.47-55.

Granqvist, C.G. and Hunderi, O., 1979. Selective absorption of solar energy in ultrafine metal particles: Model calculations. Journal of Applied Physics, 50(2), pp.1058-1065.

Granqvist, C.G., 1991. Solar energy materials. Applied Physics A, 52(2), pp.83-93.

Gerein, N.J. and Haber, J.A., 2005. Effect of ac electrodeposition conditions on the growth of high aspect ratio copper nanowires in porous aluminum oxide templates. The Journal of Physical Chemistry B, 109(37), pp.17372-17385.

Green, S., Badan, J.A., Gilles, M., Cortes, A., Riveros, G., Ramirez, D., Gómez, H., Quagliata, E., Dalchiele, E.A. and Marotti, R.E., 2007. Optical properties of nanoporous Al2O3 obtained by aluminium anodization. physica status solidi (c), 4(2), pp.618-621.

Galione, P.A., Baroni, A.L., Ramos-Barrado, J.R., Leinen, D., Martín, F., Marotti, R.E. and Dalchiele, E.A., 2010. Origin of solar thermal selectivity and interference effects in nickel–alumina nanostructured films. Surface and Coatings Technology, 204(14), pp.2197-2201..

Hutchins, M.G., 1983. Selective thin film coatings for the conversion of solar radiation. Surface technology, 20(4), pp.301-320.

http://rredc.nrel.gov/solar/spectra/am1.5/astmg173/ astmg173.html

Kumar, S.N., Malhotra, L.K. and Chopra, K.L., 1983. Nickel pigmented anodized aluminium as solar selective absorbers. Solar energy materials, 7(4), pp.439-452.

Kennedy, C.E., 2002. Review of mid-to high-temperature solar selective absorber materials (No. NREL/TP-520-31267). National Renewable Energy Lab., Golden, CO.(US).

Kennedy,C. E., Price , H., 2005, Progress in development of high-temperature solar selective coating, International Solar Energy Conference, ISEC 2005-76039, Orlando, USA, 2005.

Maxwel-Garnett, J.C., 1904. Colours in metal glasses and in metal films. Philos. Trans. R. Soc. London, 203, pp.385-420.

Masuda, H. and Fukuda, K., 1995. Ordered metal nanohole arrays made by a two-step replication of honeycomb structures of anodic alumina. science, 268(5216), p.1466.

Niklasson, G.A., Granqvist, C.G. and Hunderi, O., 1981. Effective medium models for the optical properties of inhomogeneous materials. Applied Optics, 20(1), pp.26-30.

Niklasson, G.A. and Granqvist, C.G., 1983. Solar absorptance and thermal emittance of coevaporated Co-Al2O3 cermet films. Solar Energy Materials, 7(4), pp.501-510.

Niklasson, G.A. and Granqvist, C.G., 1984. Optical properties and solar selectivity of coevaporated Co-Al2O3 composite films. Journal of applied physics, 55(9), pp.3382-3410.

Nahar, N.M., Mo, G.H. and Ignatiev, A., 1986. A spectrally selective high temperature stable Al_2O_3 Co solar absorber coating. Solar energy materials, 14(2), pp.129-141.

Nahar, N.M., Mo, G.H. and Ignatiev, A., 1989. Development of an Al2O3-Co selective absorber for solar collectors. Thin Solid Films, 172(1), pp.19-25.

Palik, E.D. ed., 1998. Handbook of optical constants of solids (Vol. 3). Academic press.

Paulus, P.M., Luis, F., Kröll, M., Schmid, G. and De Jongh, L.J., 2001. Low-temperature study of the magnetization reversal and magnetic anisotropy of Fe, Ni, and Co nanowires. Journal of Magnetism and Magnetic Materials, 224(2), pp.180-196.

Salmi, J., Bonino, J.P. and Bes, R.S., 2000. Nickel pigmented anodized aluminium as solar selective absorbers. Journal of materials science, 35(6), pp.1347-1351.

Sellmyer, D.J., Zheng, M. and Skomski, R., 2001. Magnetism of Fe, Co and Ni nanowires in self-assembled arrays. Journal of Physics: Condensed Matter, 13(25), p.R433.

Shin, H.S., Song, J.Y. and Yu, J., 2009. Template-assisted electrochemical synthesis of cuprous oxide nanowires. Materials Letters, 63(3), pp.397-399.

Tesfamichael, T., 2000. Characterization of selective solar absorbers: Experimental and theoretical modeling (Doctoral dissertation, Acta Universitatis Upsaliensis).

Tabor, H., 1961. Solar collectors, selective surfaces, and heat engines. Proceedings of the National Academy of Sciences, 47(8), pp.1271-1278.

Wäckelgård, E., 1996. A study of the optical properties of nickel-pigmented anodic alumina in the infrared region. Journal of Physics: Condensed Matter, 8(27), p.5125.

Thermal Stress Analysis of Parabolic Trough Receivers with Concentrated Solar Radiation

Dongqiang Lei[1,2,3,4] Xuqiang Fu[5] Yucong Ren[1,2,3] Zhifeng Wang[1,2,3,4]

[1]Key Laboratory of Solar Thermal Energy and Photovoltaic System, Institute of Electrical Engineering, Chinese Academy of Sciences;

No.6 Beiertiao, Zhongguancun, Beijing, China, 100190.

[2]Beijing Engineering Research Center of Solar Thermal Power;

No.6 Beiertiao, Zhongguancun, Beijing, China, 100190.

[3]University of Chinese Academy of Sciences;

No.19 (A) Yuquan Rd, Shijingshan District, Beijing, P.R.China 100049

[4]China National Solar Thermal Energy Alliance;

No.6 Beiertiao, Zhongguancun, Beijing, China, 100190.

[5]Hebei University of Technology, Xiping Road No. 5340, Beichen District, Tianjin, China,300130.

Abstract

The failure of receiver tube is the primary ongoing issue in the parabolic trough power system. In this study, the stress field of the receiver is studied by numerical simulation and the field measurements. The three-dimensional numerical simulation on the whole receiver is conducted firstly by combining the Monte-Carlo Ray Tracing method and the Finite Volume Method. The temperature, the heat loss and the expansion length of the receiver were tested on a heat loss test bench. The simulated concentrated heat flux on the absorber tube and the glass envelope have good agreement with Jeter's results. The temperature field of the entire receiver then was used to analyze the thermal stress and the deformation of the receiver. Finally, the effects of the DNI, the fluid temperature and flow rate on the temperature gradients and the thermal stress fields of the whole receiver were studied. The absorber tube bending and glass to metal seals failure were also analyzed. The Von-Misses stress and allowable strain of 316L stainless steel were used to analyze the deformation and the fatigue failure of the receiver.

Keywords: parabolic trough receiver, thermal stress, DNI, temperature distribution

1. Introduction

Solar thermal electricity generation is one of the feasible renewable technologies to reduce the consumption of conventional fossil fuels and CO_2 emissions. At present, large-scale solar thermal electricity generation mainly has four types of systems: parabolic trough, solar tower, solar dish and linear Fresnel, among them parabolic trough technology is the most proven and widespread solar thermal power technology today.

In a parabolic trough system, the mirrors concentrate the sun rays on the receivers. The heat transfer fluid (HTF) passes through the receivers and transfers heat from the receiver tubes to a heat exchanger in a power station. The receiver is one of the most important elements in the system for converting the solar energy into thermal energy of HTF. The parabolic trough receiver consists of an absorber tube with a selective coating and a glass envelope surrounding the absorber tube to form a vacuum annular space between the glass envelope and the absorber tube. A glass to metal sealing element is arranged on each free end of the glass envelope, wherein the central absorber tube and the glass to metal sealing element are connected with each other by means of bellows, as shown in Fig. 1 (Price et al. 2002). In order to decrease the sealing residual stress, a thermal coefficient matched material combination that composed of the Kovar alloy and the 5.0 borosilicate glass was applied in the receiver studied in this paper (Lei et al. 2012).

doi:10.18086/swc.2017.04.08 Available at http://proceedings.ises.org

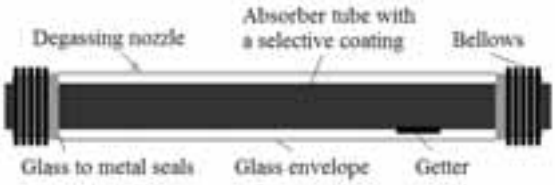

Fig.1 Typical parabolic trough receiver

The receiver's structural reliability has a significant influence on the safety and economic operation of the parabolic trough system (Cheng et. 2010, Glenn, 2012). Data from existing commercial parabolic trough power stations show that receiver failure is the primary ongoing issue. The first nine solar energy generation system plants (SEGS) have experienced very high receiver failure (about 5.5% per year) in the first few years (Price, 2002,). The most recent data for SEGS pants indicated that receiver failures had decreased to 3.4% of the total field receivers per year, which still seems unacceptably high. These failures involved vacuum loss, glass envelope breakage and degradation of the coating. Of these failures, 55% were reported to involve broken glass and 29% involved loss of vacuum, in most cases due to the failure of glass to metal seals, but also due to bowing tubes (Mills, 2004). The receivers themselves represent 30% of the solar field material cost and would require additional labor to replace (Charles, 2010).

In order to investigate the failure mechanisms, some researchers have focused on the temperature gradients and stress fields on the absorber tube due to the non-uniform heat flux (Cheng et al. 2010; Wu et al. 2014b; Abedini et al. 2015). The literature survey shows that most of their models mentioned above ignored the end parts of the receiver (without bellows and glass to metal sealing element). There are few researchers to study the detailed heat transfer and thermal stress of whole receiver under non-uniform concentrated solar heat flux in a parabolic trough system. They did not consider the temperature and stress distribution of the bellows and the glass to metal seals which could result in the glass envelope breakage or vacuum loss. Especially, their models ignored the effect of the bellows and glass envelope on the temperature and stress distribution of the absorber tube. Actually, the bellows and glass envelope will also affect or constrain the axial expansion of the absorber tube.

In this paper, the stress distribution of the whole receiver is further studied by numerical simulation and the experimental measurements. The three-dimensional numerical simulation on the whole receiver is conducted firstly by combining the MCRT method and the FVM. The non-uniform concentrated heat flux on the absorber tube and the glass envelope was obtained through the coordinate transformations (CT) and Monte-Carlo ray tracing (MCRT) method. The heat flux verified by comparing with Jeter's results was used as a boundary condition of the coupled heat transfer modeling. The processes of fluid dynamics and coupled heat transfer of the receiver was analyzed by FVM. Then the temperature, the heat loss and the expansion length of the receiver were tested on a heat loss test stand. After validation, the temperature field of the entire receiver was used to analyze the thermal stress and the deformation of the receiver. Finally, the effects of the DNI, the fluid temperature and flow rate on the temperature gradients and the thermal stress fields of the whole receiver were studied. The absorber tube bending and glass to metal seals failure were also analyzed. The Von-Misses stress and allowable strain of 316L stainless steel were used to analyze the deformation and the fatigue failure of the receiver.

2. Methodology

There are three steps for the methodology in this study. Firstly, the solar energy flux distribution on the selective coating and glass envelope is calculated and validated. Secondly, three dimensional temperature distribution of the whole parabolic trough receiver tube is analyzed based on the previous step as a boundary condition. At the third step, the temperature distribution data are used to calculate the thermal stress and deformation of the receiver tube.

2.1. Simulation of solar energy flux distribution

The coordinate transformations (CT) and Monte-Carlo ray tracing (MCRT) method were combined to simulate the solar energy flux distribution on the receiver tube. In the simulation process, non-parallelism of solar rays with a 9.3mrad optics cone, rim angle, transmittance of the glass tube, absorptance of the coating, reflectance of the glass tube and reflectance of the parabolic trough mirror were considered (Zhao et al. 2015). The detail calculating process was presented in the Ref. Zhao et al. 2015. The heat distributions on the selective coating and the glass tube were calculated under the same parameters as Jeter's (Jeter, 1986). The simulation results in this paper show that the heat flux distribution has a very good agreement with Jeter's results as shown in Fig.2. The heat flux on the absorber tube is low near angle of 0° due to the radiation shadow of the absorber, and then increases very fast up to

the maximum value. After that, the heat flux decreases down rapidly with the angel and then it keeps the minimum value due to the one sun radiation. The heat flux distributions on absorber tube and glass envelope were treated as the heat flux boundary for the heat transfer simulation model.

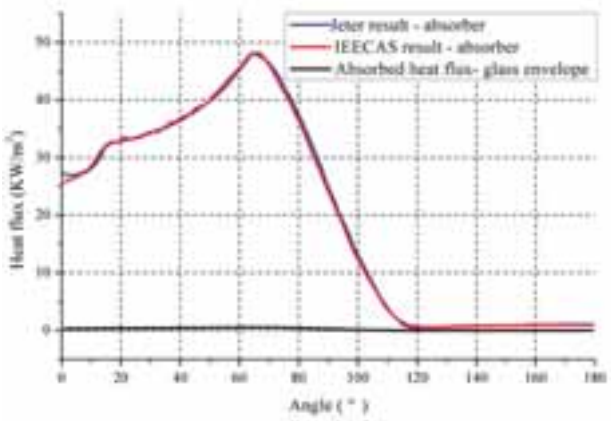

Fig. 2 Simulated heat flux distribution result compared with Jeter's result

2.2. Simulation of temperature distribution

In typical parabolic trough solar system, the solar radiation is reflected and concentrated on the glass envelope, and then it transmits the glass envelope and finally arrives on the coating of the absorber tube. The coating converts the solar energy into the heat energy, and then the heat energy is conducted to the absorber inner surface. The heat transfer fluid (HTF) passes through the absorber tube then obtains the heat energy by convection. Meanwhile, a part of heat energy (heat loss) passes through the glass thickness and by radiation and convection to the environment from the outer surface of the glass envelope.

2.2.1 Assumptions in the simulation

A three-dimensional computational fluid dynamics and heat transfer simulation of whole receiver was established. Fig. 3 shows the three dimensional mesh of the receiver tube used in this study. All of the meshes were generated with O-grid method by Ansys ICEM. After performing a grid independent, the study based on the variation of frictional pressure drop and temperature increase within the absorber tube, a grid of 3,000,000 cells was chosen for the simulation of the temperature and the stress distribution.

In order to investigate the temperature gradient in the glass-to-metal seals and the bellows, finer grids were generated near the glass-to-metal seals where large temperature gradient exists.

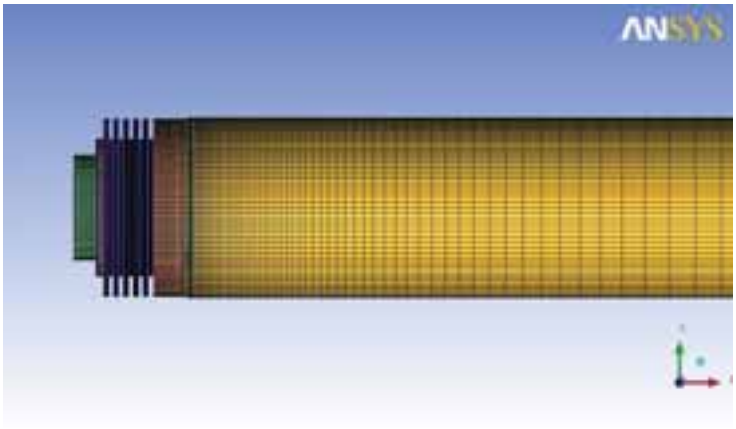

Fig. 3 Three-dimensional mesh of the receiver tube

The three dimensional heat transfer problem was solved using FVM model. Some assumptions in the simulation are listed as follow:

1) The vacuum level between the absorber tube and the glass envelope is so good that the convection can be ignored.

2) The fluid flow is in steady state conditions. The calculated Reynolds number ($Re=\rho ud/\mu$) of HTF flow in the absorber tube is much higher than 2300, and the flow is turbulent. Therefore, standard k-ε model, a turbulence model, was used in this study.

2.2.2 The governing equations

The governing equations include continuity equation, momentum equation, energy equation and standard k-ε two-equation turbulence model equation.

Continuity equation:

$$\frac{\partial}{\partial X_i}(\rho u_i) = 0 \qquad \text{(eq.1)}$$

Momentum equation:

$$\frac{\partial p}{\partial x_i} = \rho g_i + \frac{\partial}{\partial x_j}[(\mu+\mu_t)(\frac{\partial u_i}{\partial x_j}+\frac{\partial u_j}{\partial x_i}) - \frac{2}{3}(\mu+\mu_t)\frac{\partial u_l}{\partial x_l}\delta_{ij}] - \frac{\partial}{\partial x_i}(\rho u_i u_j) \qquad \text{(eq.2)}$$

Energy equation:

$$\frac{\partial}{\partial x_i}(\rho c_p u_i T) = -\lambda\frac{\partial T}{\partial x_i} \qquad \text{(eq.3)}$$

κ equation:

$$\frac{\partial(\rho u_i \kappa)}{\partial x_i} = G_k - \rho\varepsilon + \frac{\partial}{\partial x_i}[(\mu+\frac{\mu_t}{\sigma_k})\frac{\partial \kappa}{\partial x_i}] \qquad \text{(eq.4)}$$

ε equation:

$$\frac{\partial(\rho u_i \varepsilon)}{\partial x_i} = C_1 G_k\frac{\varepsilon}{\kappa} - C_2\rho\frac{\varepsilon^2}{\kappa} + \frac{\partial}{\partial x_i}[(\mu+\frac{\mu_t}{\sigma_\varepsilon})\frac{\partial \varepsilon}{\partial x_i}] \qquad \text{(eq.5)}$$

With

$$\mu_t = C_\mu\rho\frac{\kappa^2}{\varepsilon}, \quad G_k = \mu_t\frac{\partial u_i}{\partial x_j}(\frac{\partial u_i}{\partial x_j}+\frac{\partial u_j}{\partial x_i}) \qquad \text{(eq.6)}$$

The model constants $C_1, C_2, C_\mu, \sigma_\kappa, \sigma_\varepsilon$ have the following default values:

$$C_1 = 1.44, C_2 = 1.92, C_\mu = 0.09, \sigma_K = 1, \sigma_\varepsilon = 1.3$$

2.2.3 Boundary conditions

(1) The following boundary conditions are applied to the inlet and outlet:

Inlet: $u_x = u_{in}, u_y = u_z = 0, T = T_{in}$

$\kappa_{in} = 0.005u_x^2, \varepsilon_{in} = c_\mu \cdot \rho(T)\cdot\kappa_{in}^2/\mu_t$, where $c_\mu = 0.09, \mu_t = 100$

Outlet: fully-developed conditions.

(2) The selective coating is defined as a wall with the heat flux distribution calculated by the CT and MCRT Method.

(3) Surface-to-surface (S2S) radiation model is used between the selective coating and inner surfaces of the glass envelope, the Kovar rings and the bellows. The participating surfaces were assumed to be gray and diffuse.

(4) The outer surface of the glass envelope was defined with the equivalent coefficient of convective heat transfer for convection and radiation.

2.3. Simulation of thermal stress

The ANSYS software was used in the thermal stress analysis. Except the temperature distribution data of HTF, the temperature distribution data of the receiver obtained in the CFD analysis were imported into the nodes of thermal-stress analysis model with the same grids as the temperature analysis model. According to the materials used in the receiver, thermo-elastic equations of hollow cylinder were solved by using finite element analysis (FEA) with the aim of calculating thermal stress field and deformation for the receiver in this study.

In the parabolic trough collectors, the receiver tubes of the triples are generally straight and the mounting arms can compensate the axial heat expansion of the absorber tubes. In the study, one end of the absorber tube was fixed in X axial direction however the other end was allowed to move along the X axis freely and rotate around the X axis freely. The gravity of the receiver tube was considered and its direction was assumed the negative Z axial direction.

In the parabolic trough receiver, although the bellows are used to compensate the axial and radial expansion differences between the glass envelope and the absorber tube, the bellows are mainly subject to the axial force and affect the deformation of the absorber tube in actual operation. Therefore, the bellows axial stiffness was considered and input into the Ansys software.

In this study, the analysis of thermal stress field considers the combined effects of temperature gradients, support constraints, internal constraints and gravity. According to the Von-Mises theory, the equivalent stress equation is expressed as follows:

$$\sigma_{eff} = \sqrt{\sigma_x^2 + \sigma_y^2 + \sigma_z^2 - (\sigma_x\sigma_y + \sigma_x\sigma_z + \sigma_z\sigma_y)} \quad \text{(eq.7)}$$

The Von-Misses stress and allowable strain of 316L stainless steel were used to analyzed the deformation and the failure of the receiver

3. Experimental system description

A heat loss test stand was built in Institute of Electrical Engineering, Chinese Academy of Sciences (IEECAS). This test bench was used to test the temperature of the glass envelope and the heat loss of the receiver. In order to get the real thermal emittance of the coating, the heat losses depended on temperature were used to calculate the thermal emittance (Lei et al. 2013).

Fig. 3 Receiver heat loss test stand at IEECAS

4. Results and discussion

4.1. Validations of numerical simulation results

4.1.1 Comparison between FVM model and experiment

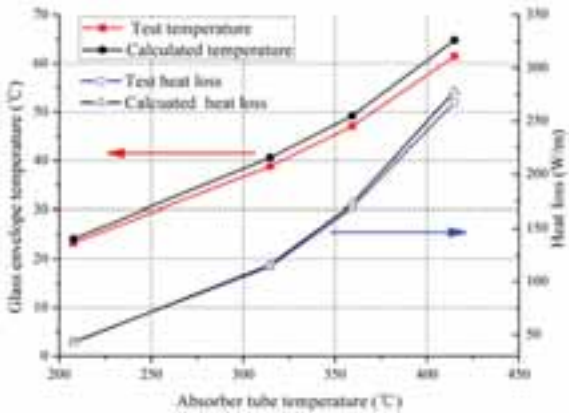

Fig. 4 Compared results between the test and the simulation

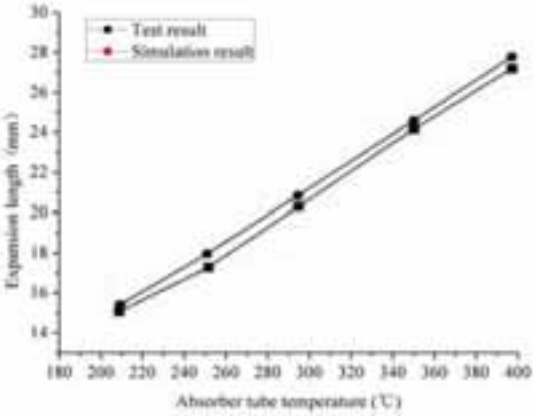

Fig. 5 Simulated result compared with test result

The FVM model generally can be validated by comparing the heat loss test results (Wu et al. 2014a; Chenget al. 2010). A heat loss test bench of the receiver was built in IEECAS in 2012. The heat loss test method, procedure, test conditions and results were described in Ref.12 in detail. In this paper, the same test conditions as the Ref.12 were used to calculate the temperature and the heat loss of the receiver. In the simulation, the inner surface temperature of the absorber tube was assumed to be constant, and no HTF was in the absorber tube. The average temperature of the glass envelope was calculated by the same method in the heat loss test. The heat loss was obtained by calculating the heat flux from the inner surface of the absorber tube in the simulation. Fig. 4 shows the compared results between the test and the simulation. The heat loss difference between the simulation results and the test results were between 1.6 and 10.3W/m with a relative error range of 1.4%-3.8%. The calculated glass envelope temperature had a maximum 5.4% relative error with the test results. Considering the uncertainty associated in both simulation and test, the agreement is very good. The uncertainty in the simulation contains the uncertainty of the equivalent convective heat transfer coefficient used between the glass envelope and the ambient and the thermal emittance of the coating. Especially, the thermal emittance of the coating is a very important parameter for the simulation and can remarkably affect the simulated results. If the thermal emittance increases only 1%, the heat loss will increase about 10%. Therefore, the thermal emittance of the coating should be tested at different temperature because it is temperature-dependent. In this paper, the thermal emittance of the coating has been tested in IEECAS heat loss test bench. Therefore, the numerical simulation methodology is valid in this study.

4.1.2 Comparison between FEA model and experiment

The validation of FEA model with real field test results is very difficult because the complicated external environment, such as the real concentrated heat flux, the changeable wind speed, the installation error, the end support condition of the receiver and the mirror shape error. In addition, the internal mechanical stress and residual stress on the receiver tube also affect the test results.

Fig. 5 indicates the expansion length curves of the absorber tube with temperature. The expansion length of the absorber tube was tested when the heat loss test was carried out. It shows that the simulation results agree with the test results very well. The maximum HTF temperature is generally less than 400℃ in parabolic trough system, the material of the absorber tube is within the elastic range. Therefore, if the two end supports do not constrain the axial expansion of the absorber tube, the stress is caused only by temperature and is linear functional relation with the thermal strain in the absorber tube. The FEA methodology is valid and reliable for the stress analysis on the absorber tube.

4.2. Temperature distribution of receiver tube

In order to calculate thermal stress field, the temperature distributions of the whole receiver and the key components were shown in Fig.6.

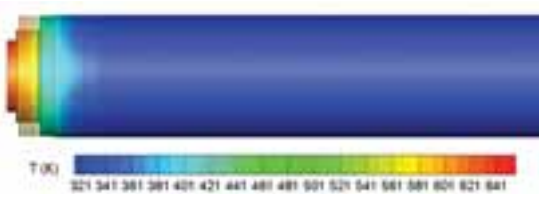

Fig.6 Temperature distributions of the whole receiver tube and the key components

In Fig. 6, DNI is 1000W/m^2. HTF inlet temperature is 350℃ and the flow rate is 2 m/s which is a typical condition in system operation. Fig.10 a) shows the temperature distribution on the out surface of the whole receiver tube. The temperature varies considerably at the end of the receiver tube, which decreases from 641K to 321K from the end of the absorber to the middle of the glass envelope. Therefore, the receiver is subject to very large temperature gradients in operation. In order to obtain the temperature information of the key components in detail, Fig. 6 clearly exhibits the temperature distribution of the absorber tube, the Kovar ring and the bellows. It shows that the temperature distribution is very nonuniform along both the axial and the circumferential direction of the absorber tube. The larger temperature gradient occurred on the end part of the absorber tube due to the shield of the bellows and the glass to metal sealing element. This nonuniform temperature along the axial direction of the absorber tube can also cause thermal stress and the deformation of the absorber tube. Therefore, it is not reasonable to ignore the bellows and the glass metal sealing elements when the temperature and stress are simulated for the receiver. The temperature distribution of cross section of the absorber tube and HTF is symmetrical approximately, which is very similar to the heat flux distribution on the surface (see Fig. 2). This temperature difference creates variable expansion and nonuniform deformation of the absorber tube. The above temperature data are very important and helpful for the structure design, optimization and the reliable operation of the receiver.

4.3. Stress distribution and deformation of receiver tube

The temperature information was further used to analyze the thermal stress distribution on the whole receiver tube. Fig. 7 shows the stress distributions on the absorber tube, the glass envelope, the bellows and the Kovar ring. The stress distribution on the absorber tube is nonuniform and similar to the temperature distribution and the heat flux distribution. The maximum equivalent tensile stress is a bout 34MPa at the place of the maximum heat flux density. It also shows that the absorber tube has a little deflection of 4.2mm, as shown in Fig 7 a). In the field test, although the absorber bending has been seen, the deflections of the absorber tubes are no any rule when HTF velocity is higher than 1m/s. When HTF velocity is lower than 1m/s, the absorber tube can easily bend and the bending generally is permanent. The absorber tube bending can cause part of solar radiation out of the absorber tube and decreases the thermal efficiency of the collector.

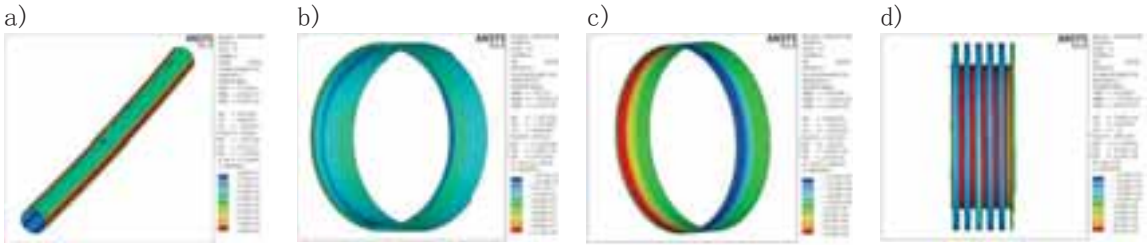

Fig. 7 stress distributions on the absorber tube, the glass envelope, the bellows and the Kovar ring

Fig. 7 b) and c) illustrate the axial stress distribution on the end of glass envelope and the Kovar ring. The two figures present that the bigger stress concentration occurs at the junction between the Kovar ring and the glass envelope. The maximum tensile stress of 11MPa locates at the end of the glass envelope. The reason may be that the expansion difference between the absorber tube and the glass envelope causes the tensile force on the end of the glass envelope, and the expansion difference between the Kovar ring and the glass also causes the tensile stress on the end of the glass envelope. If the coefficient of thermal expansion (CTE) of the Kovar ring is much bigger than CTE of the glass envelope, the larger tensile stress may exceed the tensile strength of the glass and cause the glass break. Therefore, the difference of CTEs between the glass and the metal is an important factor affecting the magnitude of stress.

The stress distributions on the bellows are also very nonuniform, as shown in Fig.7 d). The maximum axial stress is at the third trough of the bellows. The bellows are subject to the larger axial stress due to the expansion difference between the glass envelope and the absorber tube. While the maximum equivalent stress of 757 MPa is at the wield

junction between the bellows and the Kovar ring, which the magnitude may be too big. The authors contribute the large equivalent stress to the difference of CTEs between the Kovar ring and the bellows, and the unsuitable elastic modulus or axial stiffness used in simulation. Because the thickness of the bellows is generally 0.2-0.3mm and the bellows cyclically expand and compress every day, the bellows with large stress are easy to fatigue or crack, and then lead to the vacuum failure of the receiver. Therefore, the bellows, as the key component, should have enough fatigue strength and be protected from any concentrated solar radiation.

5. Conclusions

In this study, the distributions of the temperature and the stress were studied by numerical simulation and the experimental measurements. The three-dimensional numerical simulation on the whole receiver was conducted successfully by combining the MCRT method, the FVM and the FEA. The distributions of the temperature and the stress were analyzed for the whole receiver including the bellows, the Kovar ring, the glass envelope and the absorber tube in detail. After validating the numerical model, the effects of the fluid temperature and flow rate on the temperature gradients and the thermal stress fields of the whole receiver were studied. The results show that：

1） Thermal emittance of the coating should be tested at different temperature because it is a very important parameter in the simulation and can remarkably affect the simulated temperature results.

2） The stress distribution is nonuniform along both the axial and the circumferential direction on the absorber tube, which is similar to the temperature distribution and the solar flux distribution.

3） The bigger stress concentration occurs at the junction between the Kovar ring and the glass envelope. The difference of CTEs between the glass and the metal is an important factor affecting the magnitude of stress.

4） The bellows are subject to the larger axial stress due to the expansion difference between the glass envelope and the absorber tube.

6. Acknowledgements

The authors thank Ph. D Zhiyong Wu for his technical assistance of CFD software. This study was supported by the National Nature Science Foundation of China (Grant No. 51476165).

7. References

Abedini-Sanigy, M. H., et al. (2015). Thermal Stress Analysis of Absorber Tube for a Parabolic Collector under Quasi-Steady State Condition. Energy Procedia 69(0): 3-13.

Charles MM, Craig T, Glatzmaier G, 2010. Line-Focus Solar Power Plant Cost Reduction Plan, National Renewable Energy Laboratory NREL/TP-5500-48175.

Cheng ZD, He YL, Xiao J, Tao YB, 2010. Three-dimensional numerical study of heat transfer characteristics in the receiver tube of parabolic trough solar collector, International Communications in Heat and Mass Transfer, 37 (2010) 782–787

Glenn KW, Ho CK, 2012. Impact of Aperture Size, Receiver Diameter, and Loop Length on Parabolic Trough Performance with Consideration of Heat Loss, Pumping Parasitics, and Optics for a Typical Meteorological Year. SolarPACES 2012, Marrakech, Morocco, September 11-14.

Jeter SM, 1986. Calculation of the concentrated flux density distribution in parabolic trough collectors by a semifinite formulation, solar energy vol. 37, no. 5, pp. 335-345.

Lei, D. Q., et al. (2010). The calculation and analysis of glass-to-metal sealing stress in solar absorber tube. Renewable Energy 35(2): 405-411.

Lei, D., et al. (2012). Experimental study of glass to metal seals for parabolic trough receivers. Renewable Energy 48(0): 85-91.

Lei, D., et al. (2013). An experimental study of thermal characterization of parabolic trough receivers. Energy Conversion and Management 69(0): 107-115.

Mills, D. (2004). Advances in solar thermal electricity technology. Solar Energy 76(1-3): 19-31.

Price, H., et al. (2002). Advances in Parabolic Trough Solar Power Technology. Journal of Solar Energy

Engineering 124(2): 109-125.

Wu, Z., et al. (2014a). Structural reliability analysis of parabolic trough receivers. Applied Energy 123(0): 232-241.

Wu, Z., et al. (2014b). Three-dimensional numerical study of heat transfer characteristics of parabolic trough receiver. Applied Energy 113: 902-911.

Zhao, D., et al. (2015). The Simulation Model of Flux Density Distribution on an Absorber Tube. Energy Procedia 69: 250-258.

Exergy cost decomposition and comparison of integrating seawater desalination plant, refrigeration plant, process heat plant in a concentrated solar power plant

Roberto Leiva-Illanes[1,2,a)], Rodrigo Escobar[1], José M. Cardemil[3], Diego-César Alarcón-Padilla[4], Javier Uche[5], Amaya Martínez[5]

[1] Escuela de Ingeniería, Pontificia Universidad Católica de Chile, Santiago (Chile)

[2] Departamento de Mecánica, Universidad Técnica Federico Santa María, Viña del Mar (Chile)

[3] Departamento de Ingeniería Mecánica. Universidad de Chile, Santiago (Chile)

[4] CIEMAT-Plataforma Solar de Almería, Almería (Spain)

[5] Departamento de Ingeniería Mecánica, Instituto CIRCE, Universidad de Zaragoza, Zaragoza (Spain)

[a)] Corresponding author: roberto.leiva@usm.cl, rleivaillanes@puc.cl

Abstract

A thermoeconomic analysis of a solar polygeneration plant for the joint production of electricity, fresh water, cooling, and process heat is carried out, in order to analyze in depth the process of exergy cost formation and comparing with standalone systems. The solar polygeneration plant consists of a concentrated solar power as prime mover, and a multi-effect desalination, a refrigeration absorption, and a process heat plants. Results show that the main components that contribute to the costs formation are: solar collectors, evaporator, re-heater, economizer, turbine, and super-heater. Also, a solar polygeneration plant is more cost effective than stand-alone systems, which produces the lower unit exergy cost of electricity, water, cooling and heat.

Keywords: polygeneration, symbolic thermoeconomic, exergy cost theory, concentrated solar power, multi-effect distillation, refrigeration.

1. Introduction

Polygeneration is the integration of multiple utility outputs with one or more inputs for better performance. The better performance may be assessed from different aspects, such as, thermodynamic, economic, environmental, and social, in which the main advantages are in terms of the improvement of energy efficiency and cost-effectiveness, use of alternative fuels and energy carriers, and reduction of emissions. Its advantages make polygeneration competitive technologies [1]. In a topping cycle polygeneration system [2], fuel is used in the prime mover, typically in a power cycle such as Rankine, Brayton or Diesel cycles, that generates electricity, and the prime mover's hot exhaust is used to supply thermal energy to other technologies driven by heat, like thermal distillation, process heat (industrial heating, production of synthetic fuels, and other), and absorption cooling. The concentrated solar power (CSP) as a prime mover is an interesting alternative to analyze the operation of a polygeneration scheme since it produces electricity fueled by solar energy, and could be helped by a thermal energy storage or the hybridization with a fossil fuel or a biofuel. This allows continuous operation, with a capacity factor similar to a conventional plant to better match supply with demand, and additionally, rejects thermal energy from the power cycle that it is feasible to couple it with technologies driven by thermal energy. In order to evaluate the integration in a polygeneration scheme there are several methods [1], [3], [4], however the thermoeconomic (or exergoeconomic) method [5] is recommended because provides compact matrix-based formulation for the detailed analysis of complex systems such as polygeneration systems, where the Second Law of Thermodynamics provides its physical roots [6]. Exergy indicates the maximum work that a flow or a system might produce while interacting with the environment, and it is very useful for the analysis of this system because it allows measuring in the same physical unit resources of very different nature, for instance electricity, energy, water, cooling, heat, resources, and waste. The exergy cost of mass and/or energy flow represents the units of exergy used to produce it, i.e. the exergy cost of a flow is the amount of resources expressed in exergy consumed for producing this flow [7]. The unit exergy cost allows analyzing and identifying integrations because it is possible to determine the potential for resources savings. Exergy cost is a conservative magnitude that increases in every process according to the irreversibility involved in that process. So, in an integrated process, it is interesting to study in depth how exergy costs are being formed, therefore the process of cost formation

doi:10.18086/swc.2017.04.09 Available at http://proceedings.ises.org

provides vital information for the designer and evaluator that allows a better design and performance analysis, respectively.

CSP could be integrated into polygeneration schemes [8] and different studies have focused mainly on the final cost of each product [9]–[12]. However, such those studies do not consider the evaluation of the process of exergy cost formation and the decomposition of each cost. For the reasons mentioned above, a solar polygeneration system is analyzed by applying the symbolic exergoeconomic method to study the process of exergy cost formation and to determine the main components that contribute to the cost formation of each product, so that find out new opportunities for savings. The solar polygeneration scheme considered in this work is composed of a concentrated solar power, a multi-effect desalination plant, a single-effect refrigeration absorption module, and a process heat module.

2. Methodology

The methodology consists first of the modeling of a solar polygeneration plant and stand-alone plants. Secondly symbolic exergoeconomic methodology [6], [13], [14], which is a technique based on the exergy cost theory [15], was then applied.

The solar polygeneration plant is depicted in Figure 1, this consists of a concentrated solar power [16], [17] type parabolic trough with thermal energy storage (TES) and backup system (BS), a multi-effect desalination (MED) plant [18], a single-effect refrigeration absorption (REF) plant [19], and a process heat (PH) module. The configuration and validation of the solar polygeneration plant and the stand-alone systems are described as Poly 1 and stand-alone plants in a previous study of the authors [11].

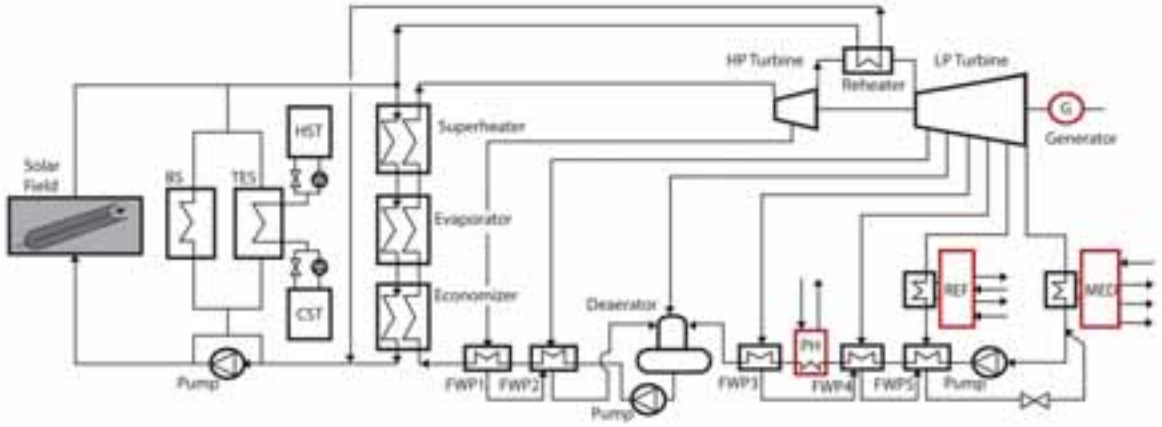

Fig.1. Configuration solar polygeneration plant. CST: cold storage tank, FWP: feed water preheater, G: generator, HP: high pressure, HST: hot storage tank, LP: low pressure.

The main characteristics of those plants are shown in the Table 1.

Tab. 1: Main characteristics of the polygeneration plant and the stand-alone plants.

Property	Polygeneration	Stand-alone
CSP		
TES, storage fluid	Two tank, molten salt	
Tank temperature (cold/hot), °C	292 / 386	
Full load hours of TES, h	12	
Parabolic trough collector model	EuroTrough	
Absorber tube	Schott PTR-70	
Heat transfer fluid	DowTherm A	
Collector optical efficiency, %	72.073	
Irradiance at design day, W/m^2	1 010	
Solar Field inlet temperature (inlet/outlet), °C	293 / 393	
Aperture area, m^2	616 650	510 520

Solar Multiple	2.56	
BS efficiency	90 %	
Capacity factor	96 %	
Gross power production, MW_e	55.0	
HP turbine inlet pressure, bar	100.0	
LP turbine back pressure, bar	0.37	0.06
MED		
Feed seawater intake temperature, °C	25	
Feed seawater intake salinity, kg/kg	0.042	
Feed seawater after down condenser temperature, °C	35	
Maximum salinity in each effect, kg/kg	0.072	
Top brine temperature, °C	65	
Gained Output Ratio, kg/kg	9.07	
Fresh water production, m^3/day	37 168	
Concentration factor	1.7	
Specific heat consumption, kJ/kg	245.2	
Specific electricity consumption, kWh/m^3	1.5	
REF (single stage absorption chiller)		
Cooling capacity, MW_{th}	5	
Chilled water temperature (inlet/outlet), °C	10 / 6	
Cooling water temperature (inlet /outlet), °C	25 / 35	
Inlet temperature desorber, °C	108.49	
Coefficient of Performance (COP)	0.70	
PH (countercurrent heat exchanger)		
Process heat capacity, MW_{th}	7	
Heat exchanger temperature (inlet/outlet), °C	63 / 90	

The solar systems were simulated at the design point by considering an hourly meteorological year [20]. The software IPSEpro [21] and MATLAB were used for the simulation of the different systems. The exergoeconomic evaluation was conducted using MATLAB, and the ExIO module [22] as a complement of the Microsoft Excel.

The exergy cost theory (ECT) provides a general criterion that enables to assess the efficiency of energy systems and rationally explains the process of cost formation of products. Thus, it is a cost accounting methodology that propose methods to determine the number of resources required for getting a product. As a numerical technique, cost values could be assessed. And with the help of the symbolic exergoeconomic method, the causes of the cost formation process can be easily obtained by using matrix algebra. The ECT requires that the system be described by a physical structure and a productive structure, the last structure is built according to the purpose of each component, and shows the origin of the resources of each component and its product. Each plant has only one physical structure to describe the physical relations between the process units, but various productive structures can be defined depending on the fuel and product definitions as well as the disaggregation level selected. The disaggregation level is interpreted as the degree of accuracy of the analysis. Each subsystem can be a part of an equipment, an equipment, or a group of equipment. The productive diagram is a graphic representation of the thermoeconomic model of the plant, in which the inputs of a component are its resources, and the outputs of a component are its products. This structure is composed of n components connected by flows characterized by its exergy. Each component consumes resources from other components or from an environment (those resources are named Fuel), to produce useful effects for other components or for the environment (those useful effects are named Product). Fuel (F) is partially transformed into product (P) and partially destroyed as irreversibility (I). A flow from component i to component j is represented by the exergy flow, then, the Fuel and Product is defined as

$$F_i = P_i + I_i = \sum_{j=0}^{n} E_{ji} \quad \text{(eq. 1)}$$

$$P_i = F_i - I_i = \sum_{j=0}^{n} E_{ij} \quad \text{(eq. 2)}$$

where E_{ij} is the exergy flow, the subscripts i and j are generic components.

The fuel-product presentation is the adjacency matrix of the productive graph, that allows getting all flows within the productive structure, and is based on distribution coefficients y_{ij} which indicate the proportion of the production of the j-th component used as resource for the i-th component: it shows how the product of a component is distributed among the other components and the environment.

$$y_{ij} = \frac{E_{ij}}{P_j} \quad \text{(eq. 3)}$$

Expressing the Equation 1 as function of y_{ij}, it yields:

$$F_i = E_{0i} + \sum_{j=1}^{n} E_{ji} = E_{0i} + \sum_{j=1}^{n} y_{ij} \cdot P_j \quad \text{(eq. 4)}$$

The previous equation in matrix notation is:

$$\boldsymbol{F} = \boldsymbol{F}_e + \langle \boldsymbol{FP} \rangle \cdot \boldsymbol{P} \quad \text{(eq. 5)}$$

where $\boldsymbol{F}$ and $\boldsymbol{P}$ are vectors of all fuels and products, $\boldsymbol{F}_e$ is the vector of external resources, and $\langle \boldsymbol{FP} \rangle$ is a matrix composed of elements y_{ij}.

Similarly, with the same procedure, it is obtained:

$$\boldsymbol{P} = (\boldsymbol{K}_D - \langle \boldsymbol{FP} \rangle)^{-1} \cdot \boldsymbol{F}_e \quad \text{(eq. 6)}$$

where $\boldsymbol{K}_D$ is a diagonal matrix containing the unit exergy consumptions of all components (k_i), defined as

$$k_i = \frac{1}{\psi_i} = \frac{F_i}{P_i} \quad \text{(eq. 7)}$$

where ψ_i is the exergy efficiency.

Equation 6 allows to calculate the products of all components starting from the external resources consumed by the plant ($\boldsymbol{F}_e$) and using the parameters that define the components (unit exergy consumptions and distribution coefficients).

The thermoeconomic analysis of energy systems, such as a polygeneration plant, has productive and dissipative components. The productive components provide functional products, fuel (resources) to other processes, and residues and waste disposals. Likewise, the dissipative components are required to reduce or eliminate the environment impact of residues and waste, to maintain the operation conditions of the system, and to improve the efficiency of the system.

According to the cost model, the exergy cost of the product is defined as

$$C_{P,i} = C_{F,i} + C_{R,i} \quad \text{(eq. 8)}$$

where C is the exergy cost, and the subscripts P, F, and R mean product, fuel, and residues, respectively.

The costs of the external resources are known values as

$$C_{e,i} = E_{0i} \quad \text{(eq. 9)}$$

and the cost of each flow making up the product is proportional to its exergy

$$C_{ij} = c_{P,i} \cdot E_{ij} \quad \text{(eq. 10)}$$

where $c_{P,i}$ is the unit exergy cost of the product of i-th component.

The exergy cost of residues allocated to each productive unit is

$$C_{R,i} = \sum_{r \epsilon V_D} C_{ri} = \sum_{r \epsilon V_D} \beta_{ir} \cdot C_{P,r} \quad \text{(eq. 11)}$$

where C_{ri} is the exergy cost of the residues dissipated in the r-th component that has been generated by the i-th productive component, β_{ir} is the residue cost distribution ratio, V_D is the set of the dissipative system components. The residue cost distribution ratios represent the portion of the cost of the residue dissipated in the r-th component which has been generated in the i-th productive component.

The exergy cost of the product is decomposed into two parts

$$\boldsymbol{C}_P = (\boldsymbol{C}_e + \boldsymbol{C}_R) \cdot (\boldsymbol{U}_D - \langle \boldsymbol{FP} \rangle)^{-1} = \boldsymbol{C}_P^e + \boldsymbol{C}_P^r \quad \text{(eq. 12)}$$

where $\boldsymbol{C}_P^e$ is the exergy cost due to irreversibilities of the components, $\boldsymbol{C}_P^r$ is the exergy cost due to the residues allocation, and $\boldsymbol{U}_D$ is the identity matrix.

In the same form, the unit exergy cost of the product is decomposed into two parts

$$c_p = c_P^e + c_P^r \quad \text{(eq. 13)}$$

where c_P^e is the unit production cost due to irreversibilities of the components, c_P^r is the unit production cost due to the residues, they are calculated by

$$c_P^e = (\boldsymbol{U}_D - \langle \boldsymbol{FP} \rangle)^{-1} \cdot \boldsymbol{c}_e \quad \text{(eq. 14)}$$

$$c_P^r = (\boldsymbol{U}_D - \langle \boldsymbol{FP} \rangle)^{-1} \cdot \boldsymbol{c}_R \quad \text{(eq. 15)}$$

where $\boldsymbol{c}_e$ is the unit exergy cost of the external resources, $\boldsymbol{c}_R$ is the unit exergy cost of the residues.

In summary, the process to assess the cost of the flow streams and processes in a polygeneration plant helps to understand the process of cost formation, from the input resources to the final products.

Note that in this analysis different levels of disaggregation were taken: in the case of the CSP plant, is considered at the level of components, but in the case of the systems to provide the other products, there are considered at the level of a unique subsystem. Finally, nominal conditions of both alternatives have been used estimates this exergy cost analysis.

3. Results and discussion

3.1. Stand-alone plants

The results about the costs decomposition for the stand-alone CSP plant are depicted in Figure 2 and shows how the unit cost of product is obtained as the sum of the irreversibility contributions of the other devices which are preceeding this product. The main components that contribute to the costs formation of electricity cost (in the generator), in descending order of importance, are: solar collectors, evaporator, condenser, reheater, low-pressure turbine, economizer, and superheater. In the solar collectors is produced the most significant exergy destruction, that it is attributable to the irreversibilities associated with the large temperature difference between the sun and the heat transfer fluid. Furthermore, it can be seen that this exergy cost is charged to the rest of components according to a topping cycle scheme. On the other hand, the condenser is a dissipative component, that is allocated to all productive units. It interacts with other components, in the sense is that the device allowing to close a thermodynamic power cycle. As its operating temperature is quite low, from the point of view of the Second-Law of Thermodynamic, its contribution to exergy costs is not so high, being the steam generator (or solar collectors in this case) the main inefficient components.

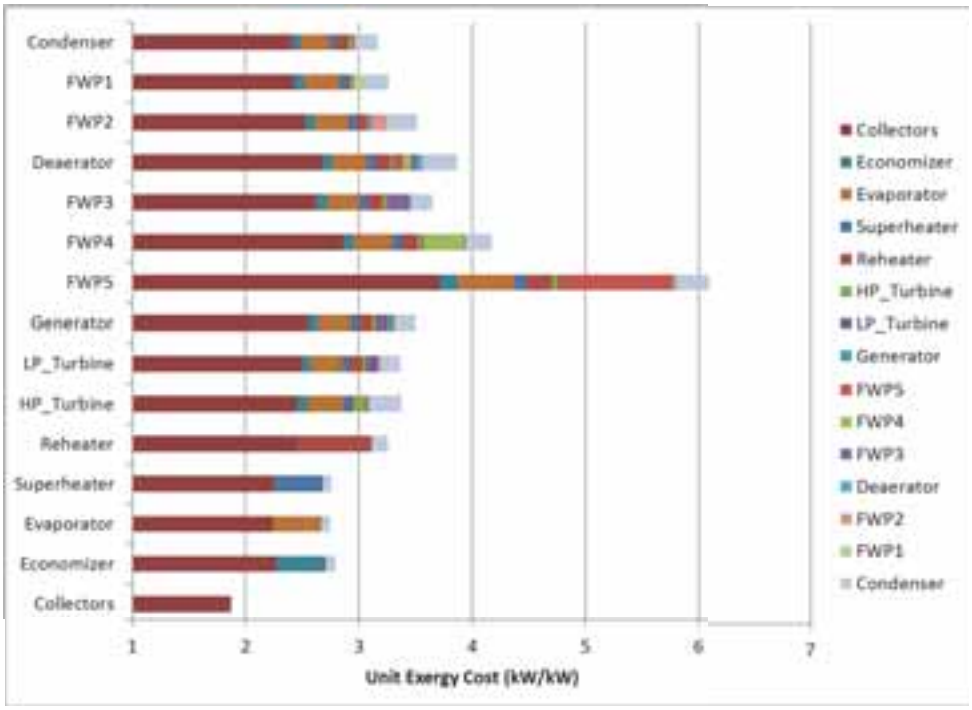

Fig. 2: Cost decomposition in stand-alone CSP plant.

In the case of other stand-alone plants, the main contribution in the cost of each product comes from the boiler, being the higher heat source and then having the higher exergy destruction. Note that since both the MED plant and the REF plant include a dissipative component to operate, they participate in the costs formation. Figures 3, 4 and 5 show the costs decomposition in the other stand-alone plants. In the case of the PH major exergy costs comes from the boiler and a residual additional cost comes from the heat exchanger to accommodate the heat supply.

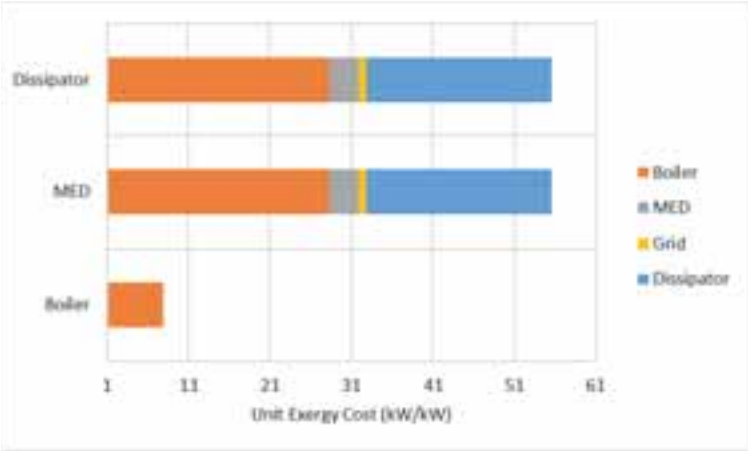

Fig. 3: Cost decomposition in stand-alone MED plant.

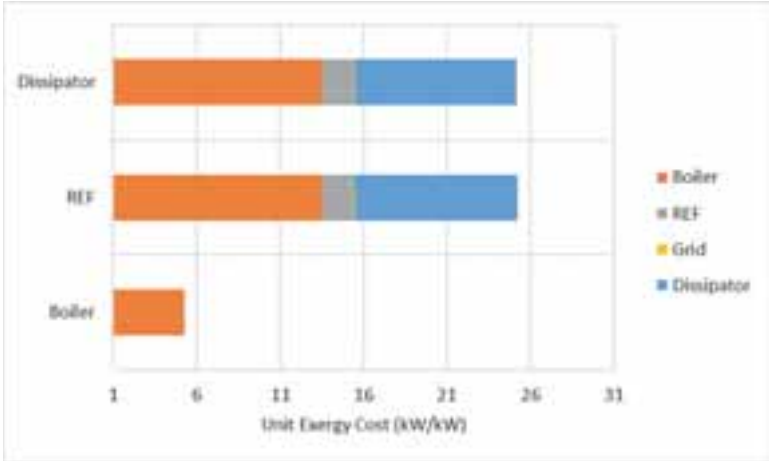

Fig. 4: Cost decomposition in stand-alone REF plant.

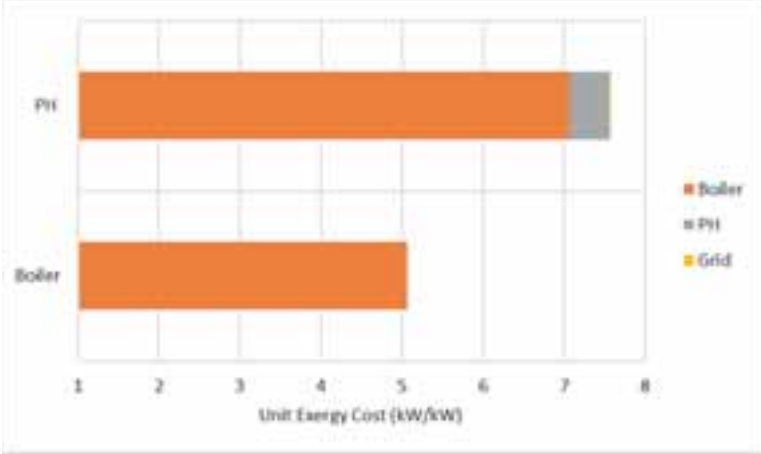

Fig. 5: Cost decomposition in stand-alone PH plant.

3.2. Polygeneration plant

The costs decomposition in the solar polygeneration plant is depicted in Figure 6. The products such as electricity, fresh water, cooling, and head are produced in Generator, MED, REF and PH, respectively. The main components that contribute to the costs formation of electricity are: solar collectors, evaporator, reheater, economizer, low-pressure turbine, and superheater. In the case of water, these components are: MED's dissipative, solar collectors, MED, evaporator, reheater, economizer, and superheater. In the case of cooling, the devices are: REF's dissipative, solar collectors, REF, evaporator, reheater, economizer, and superheater. Finally, in the case of process heat, they are: solar collectors, PH, evaporator, reheater, feed water preheater (FWP4), economizer, and superheater. In order to reduce the costs of products, it is necessary to first consider these components in an in-depth process of analysis and optimization.

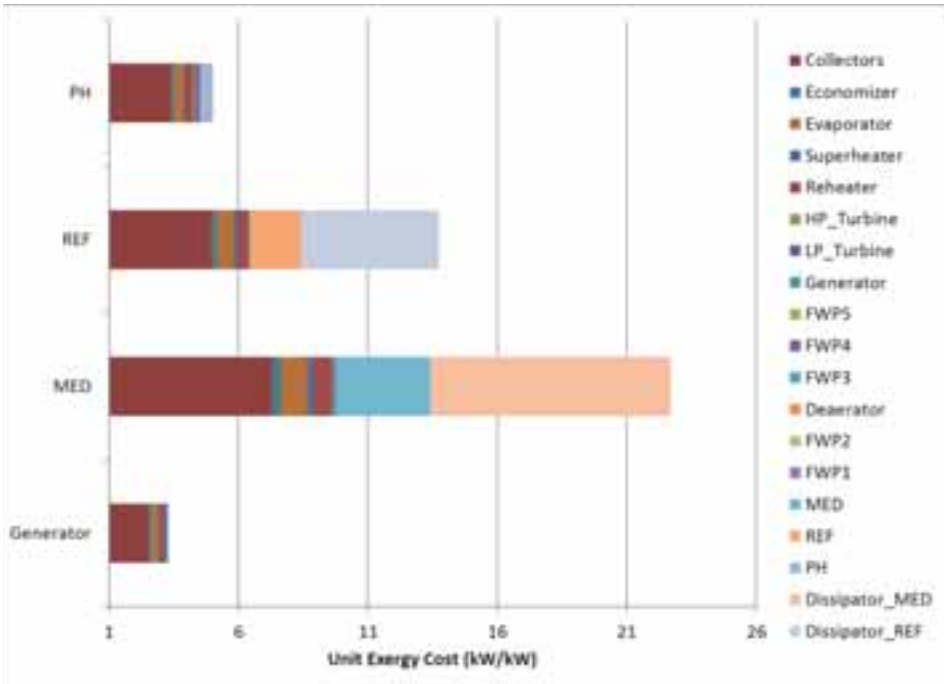

Fig. 6: Cost decomposition in polygeneration plant.

3.3. Comparison between polygeneration plant and stand-alone systems

Regarding the comparison between polygeneration plant and standalone systems, the results are presented in Figure 7. According to these results, a solar polygeneration plant is more cost-effective than stand-alone systems, since a lower unit exergy costs of electricity, water, cooling and process heat has found with respect to the stand-alone scheme. Remember that the unit exergy cost represents the amount of exergy required to get a unit of exergy of the product, i.e. the resources required to carry out the production. For instance, a unit of exergy cost of electricity of 3.3 kW means that 3.3 kW of exergy of resources is needed for producing 1 kW of electricity. The unit exergy cost is possible to express in USD/kWh also, but in this case, is necessary to consider the investment and operation costs. Anyway, this analysis was already done in a previous study conducted by the authors [11].

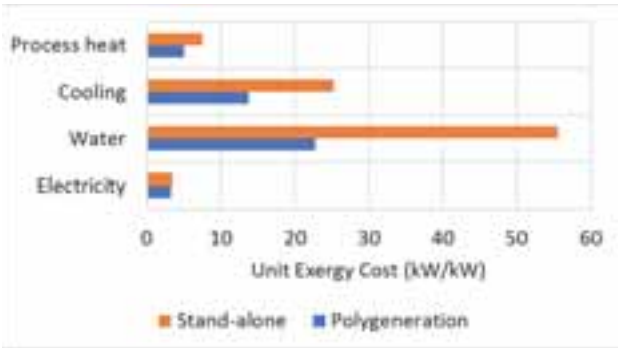

Fig. 7: Unit exergy cost of each product.

4. Conclusions

The exergy cost theory was applied to a solar polygeneration plant and stand-alone plant to analyze the process of exergy cost formation in this complex and integrated scheme, as it is a solar polygeneration plant using a concentrated solar power as prime mover, a multi-effect desalination, a refrigeration absorption, and a process heat plants. The solar polygeneration plant was simulated in a location with high direct normal irradiations.

Symbolic thermoeconomic provides a method to decompose the production costs into the contributions of the components irreversibilities and residues cost, thus it determines the cost formation process in a solar polygeneration scheme. This method delivers information that is crucial to the design and optimization process of those complex schemes.

Results show that the main components that contribute to the costs formation of electricity in a solar polygeneration plant are: solar collectors, evaporator, reheater, economizer, low-pressure turbine, and superheater. In the case of stand-alone CSP plant is similar, but includes the condenser, the order is: solar collectors, evaporator, condenser, reheater, low-pressure turbine, economizer, and superheater. On the other hand, the main components that contribute to the costs formation of water are: MED's dissipative, solar collectors, MED, evaporator, reheater, economizer, and superheater. In the cooling are: REF's dissipative, solar collectors, REF, evaporator, reheater, economizer, and superheater. Finally, in the process heat are: solar collectors, PH, evaporator, reheater, feed water preheater (FWP4), economizer, and superheater. To sum up, it is noted that ECT allows finding some interactions between different plant components that are not necessarily very close one from the other.

The analysis shows that the integrated solar polygeneration plant is more cost-effective than stand-alone systems since it produces the lower unit exergy cost of electricity, water, cooling and heat.

Nevertheless, the ECT applied here should be enlarged in future studies to different configurations of solar multi-generation plants (cogeneration, trigeneration, and polygeneration schemes) through different coupling points in a concentrated solar power plant. Also, it might be considered other alternative technologies to provide desalted water and cooling.

Acknowledgments

This research work was funded by CONICYT-PCHA/Doctorado_Nacional/año2013-folio21130634 and the project Fondecyt Nº 1130621.

References

[1] L. M. Serra, M.-A. Lozano, J. Ramos, A. V. Ensinas, and S. a. Nebra, "Polygeneration and efficient use of natural resources," *Energy*, vol. 34, no. 5, pp. 575–586, May 2009.

[2] H. Al Moussawi, F. Fardoun, and H. Louahlia-Gualous, "Review of tri-generation technologies: Design evaluation, optimization, decision-making, and selection approach," *Energy Convers. Manag.*, vol. 120, pp. 157–196, 2016.

[3] A. Nuorkivi, "Allocation of Fuel Energy and Emissions to Heat and Power in CHP," *Energy-AN Consulting*, 2010. [Online]. Available: http://era17.fi/wp-content/uploads/2012/02/Report-Nordic-CHP-Allocation_Energy-AN-Consulting_2010-9-7.pdf. [Accessed: 24-Aug-2017].

[4] A. Bejan, G. Tsatsaronis, and M. Moran, *Thermal Design and Optimization*, 1 edition. John Wiley & Sons, 1996.

[5] A. Abusoglu and M. Kanoglu, "Exergoeconomic analysis and optimization of combined heat and power production: A review," *Renew. Sustain. Energy Rev.*, vol. 13, no. 9, pp. 2295–2308, Dec. 2009.

[6] A. Valero, S. Usón, C. Torres, A. Valero, A. Agudelo, and J. Costa, "Thermoeconomic tools for the analysis of eco-industrial parks," *Energy*, vol. 62, pp. 62–72, 2013.

[7] A. Valero, F. Lerch, L. Serra, and J. Royo, "Structural theory and thermoeconomic diagnosis," *Energy Convers. Manag.*, vol. 43, no. 9–12, pp. 1519–1535, Jun. 2002.

[8] A. Modi, F. Bühler, J. G. Andreasen, and F. Haglind, "A review of solar energy based heat and power generation systems," *Renew. Sustain. Energy Rev.*, vol. 67, pp. 1047–1064, 2017.

[9] P. Palenzuela, D.-C. Alarcón-Padilla, and G. Zaragoza, "Large-scale solar desalination by combination with CSP: Techno-economic analysis of different options for the Mediterranean Sea and the Arabian Gulf," *Desalination*, vol. 366, pp. 130–138, 2015.

[10] B. Ortega-Delgado, L. García-Rodríguez, and D.-C. Alarcón-Padilla, "Thermoeconomic comparison of integrating seawater desalination processes in a concentrating solar power plant of 5 MWe," *Desalination*, vol. 392, pp. 102–117, 2016.

[11] R. Leiva-illanes, R. Escobar, J. M. Cardemil, and D. Alarcón-padilla, "Thermoeconomic assessment of a solar polygeneration plant for electricity, water, cooling and heating in high direct normal irradiation conditions," *Energy Convers. Manag.*, vol. 151, no. May, pp. 538–552, 2017.

[12] I. Sarbu and C. Sebarchievici, "General review of solar-powered closed sorption refrigeration systems," *Energy Convers. Manag.*, vol. 105, pp. 403–422, Nov. 2015.

[13] C. Torres, A. Valero, V. Rangel, and A. Zaleta, "On the cost formation process of the residues," *Energy*, vol. 33, no. 2, pp. 144–152, Feb. 2008.

[14] S. Usón, A. Valero, and A. Agudelo, "Thermoeconomics and Industrial Symbiosis. Effect of by-product integration in cost assessment," *Energy*, vol. 45, no. 1, pp. 43–51, 2012.

[15] C. Torres, A. Valero, L. Serra, and J. Royo, "Structural theory and thermoeconomic diagnosis," *Energy Convers. Manag.*, vol. 43, no. 9–12, pp. 1503–1518, Jun. 2002.

[16] A. M. Blanco-Marigorta, M. Victoria Sanchez-Henríquez, and J. A. Peña-Quintana, "Exergetic comparison of two different cooling technologies for the power cycle of a thermal power plant," *Energy*, vol. 36, no. 4, pp. 1966–1972, Apr. 2011.

[17] NREL, "System Advisor Model (SAM) Case Study: Andasol-1," pp. 1–10, 2013.

[18] G. Zak, A. Mitsos, and D. Hardt, "Master Thesis. Thermal Desalination : Structural Optimization and Integration in Clean Power and Water," Massachusetts Institute of Technology, 2012.

[19] K. Herold, R. Radermacher, and S. Klein, *Absorption Chillers and Heat Pumps*, 1st editio. CRC Press; 1 edition (January 18, 1996), 1996.

[20] R. A. Escobar, C. Cortés, A. Pino, E. B. Pereira, F. R. Martins, and J. M. Cardemil, "Solar energy resource assessment in Chile: Satellite estimation and ground station measurements," *Renew. Energy*, vol. 71, pp. 324–332, Nov. 2014.

[21] SimTech GmbH, *IPSEpro Process Simulation Environment*, Rev 5.0. SimTech Simulation Technology, 2011.

[22] C. Torres and A. Valero, "ExIO, Thermoeconomic analysis of thermal systems.," *CIRCE, Universidad de Zaragoza*, 2012. .

Nomenclature

A: solar field aperture area
BS: backup system
C : exergy cost
$\boldsymbol{C}_P$: exergy cost of the product
$\boldsymbol{C}_P^e$: exergy cost of product due to irreversibilities of the components
$\boldsymbol{C}_P^r$: exergy cost of product due to the residues allocation
c : unit exergy cost
$\boldsymbol{c}_e$: unit exergy cost of the external resources
$\boldsymbol{c}_R$: unit exergy cost of the residues
COP: coefficient of performance
CSP: concentrated solar power
CST: cold storage tank
E : exergy flow
ECT: exergy cost theory
FWP: feed water preheater
F: fuel
$\boldsymbol{F}_e$: vector of external resources
$\langle \boldsymbol{FP} \rangle$ matrix composed of distribution coefficients
G: generator
HP: high pressure
HST: hot storage tank
I: irreversibility
$\boldsymbol{K}_D$: diagonal matrix of unit exergy consumptions
k : unit exergy consumptions
LP: low pressure
MED: multi-effect distillation
P: product
PH: process heat plant
Poly 1: Polygeneration 1
REF: Refrigeration plant
SF: solar field
TES: thermal energy storage
$\boldsymbol{U}_D$: identity matrix
V_D : dissipative system components
y : distribution coefficients

Greek symbols

ψ : exergy efficiency
β_{ir} : residue cost distribution ratio

Design of a Calorimetric Facility to Asses Volumetric Receivers Employing a 42 kW High Flux Solar Simulator

Salvador Luque, José González-Aguilar and Manuel Romero

IMDEA Energy Institute, Avda. Ramón de la Sagra 3, 28935 Móstoles, Spain

Abstract

This paper presents the design of a new calorimetric facility for the experimental aerothermal assessment of volumetric receivers. The facility employs a 42 kW_e high flux solar simulator composed of 7 Xenon-arc lamps associated to as many ellipsoidal reflectors. An incident concentrated radiative power in excess of 14 kW_{th} is achieved at its focal point, with peak fluxes in excess of 3600 suns. A radiation homogenizer of square cross section is utilized upstream of the working section to uniformly heat the receiver aperture. Measured irradiance levels are discussed, and it is shown that the flow field non-dimensional governing parameters are highly representative of on-sun experiments at larger scales. The facility allows for the acquisition of comprehensive measurements to validate the design point operation of volumetric solar receivers, including absorber wall temperatures, air inlet and outlet temperatures, pressure drop, incident heat flux and thermal efficiency.

Keywords: Experimental Techniques, Performance Testing, Forced Convection, Thermal Radiation, Central Receiver Systems, Concentrating Solar Energy

1. Introduction

Solar receivers absorb incident concentrated sunlight and convert it to thermal energy at the temperature required by the downstream conversion process: mechanical, thermal, or chemical (Becker and Vant-Hull, 1991). To make them feasible for large-scale industrial deployment, it is expected that working fluid temperatures at receiver exit in excess of 720 ºC, thermal conversion efficiencies over 90%, minimum service life of 10,000 cycles, and overall costs below 150 USD per kilowatt of thermal power delivered ought to be achieved (Mehos et al, 2016). Operating temperatures play a conflicting role because receiver thermal losses typically become significant at the very high levels that are required for efficient downstream conversion processes.

Four heat transfer fluids have been researched in the development of solar power plants with central receiver systems: water (or steam, either saturated or subcritical), molten salts, sodium and air (Romero et al., 2002). The use of air has advantages in terms of abundance, availability, low environmental impact, and the ability to achieve very high temperatures without thermal degradation. In this context, volumetric receivers constitute a good alternative due to their functionality and geometric configuration. They operate as radiative-convective heat exchangers, generally at irradiance levels which can be approximately five times higher than those of tubular receivers (Romero et al., 2016). The goal is to achieve the so-called volumetric effect: a situation where the hottest part of the receiver is located deep inside its structure so that thermal emission losses from its outer surfaces (particularly the front face) are minimized (Boehmer et al., 1991).

Volumetric receivers are made of generally porous structures that enable concentrated sunlight to be absorbed and conducted within their solid volume, from where it is gradually transferred by forced convection to a heat transfer fluid that flows within (Ávila-Marín, 2011; Ho, 2017). Current design trends towards higher thermal efficiencies have led to the use of complex intricate geometries to maximize temperatures deep inside the structure and thus minimize frontal thermal emissions (Gómez-García et al., 2016). High (or selective) solar absorptance, high internal convective heat transfer, high (or directional) thermal conductivity, low radiative and convective thermal losses, mechanical durability at severe operating conditions, and, where possible,

doi:10.18086/swc.2017.04.10 Available at http://proceedings.ises.org

inexpensiveness of manufacturing, operation and maintenance are all desired features for volumetric receivers.

There exists, to the authors' knowledge, scarce experimental evidence of solar receivers achieving a significant volumetric effect, the exception being a double-layer selective receiver composed of an external silica square-channel monolithic honeycomb (transparent in the solar spectrum and absorbent in the infrared band) and an internal layer of solar absorbent silicon carbide particles (Menigault et al., 1991). It is thus possible that selective reflectance and absorptance technologies (Kribus et al., 2014) or pressurized systems (Pozivil et al., 2015) are thus required.

This paper describes the design of a new calorimetric facility for the measurement of steady-state thermal conversion efficiency in volumetric receivers. The facility and its associated techniques are expected to serve as an experimental platform for the evaluation and validation of such radiative-convective heat exchangers in highly operation-representative conditions. Absorber samples up to a maximum aperture area of 300 cm^2 can be tested in it, at an incident power of 14 kW_{th}, typical air mass flow rates of 10 g/s, and maximum air outlet temperatures of approximately 1200 ºC. The facility allows for fully-integrated evaluations of performance and thermal conversion efficiency in solar receivers. Measurements acquired in it can thus be placed at technology readiness levels of 5 to 6 (technology validated and demonstrated in relevant environment).

2. The 42 kW High Flux Solar Simulator

High-flux solar simulators allow for the possibility of conducting high temperature solar thermal and thermochemical research under controlled, stable and adjustable laboratory conditions. The solar simulator employed in this study consists of 7 Xenon arc lamps, arranged in a compact hexagonal layout (Li et al., 2014). Cathodes and anodes are mounted on electrode rods, and contained within quartz glass bulbs. Each lamp is connected to a 6 kW electrical power supply and associated to an ellipsoidal reflector that also acts as a radiation concentrator. Reflectors are made from polished aluminum in order to have a very high reflectivity surface, in turn protected by a transparent polymeric coating. The ellipsoids have semi-major and semi-minor axes of 1374 mm and 569 mm, respectively, and their truncation diameter is 750 mm. The working section aperture plane is situated at a distance of 2314 mm from the reflector. The focal length is 2500 mm. The solar simulator has been illustrated in Fig. 1. Axisymmetric radiation flux profiles are achieved with this configuration, with peak flux in excess of 3600 kW/m^2 and a total incident power of approximately 14 kW_{th} at the working section aperture.

Fig. 1: Left, frontal photograph of the high flux solar simulator. Right, attenuated photograph of the Xenon lamps in operation

High flux solar simulators have the advantages of stable and adjustable radiation intensity and heat flux. They have been employed in research on high-temperature solar thermal applications, including solar thermo-chemistry, in the temperature range between 250 and 2250 ºC. Artificial radiation sources with spectral distributions that are close to that of actual sunlight are typically employed, such as metal halide lamps (Codd et al., 2010) and Xenon arc lamps (Petrasch et al., 2007; Krueger et al., 2011; Li et al., 2015). They are commonly employed in conjunction with ellipsoidal reflectors that concentrate radiation onto their secondary focal plane. Light sources and reflector surfaces are the main factors affecting the optical performance of high-flux solar simulators. The electric arc size has a notable influence on the optical performance of solar simulators. Smaller arcs allow for reflectors that are more effective at redirecting radiation toward the target focus. For this reason, Xenon arc lamps are typically preferred in the design and development of high-flux solar simulators.

3. Experimental Facility

A schematic diagram of experimental facility is given in Fig. 2. The facility is composed of the following elements: a fluid inlet module which also acts as a radiation homogenizer, a working section which houses the heavily thermally insulated receiver, an air-water heat exchanger to lower the air temperature to 50 °C, a thermal mass flow meter, a secondary air inlet for volumetric flow control, an air filter, and a high mass flow rate high pressure blower (operated by means of a frequency converter) that supplies the necessary pressure difference to circulate air through the system. Orifice plates of various sizes are employed to adjust the volumetric flow rate through the absorber between 5 and 20 g/s. They are installed in both primary and secondary air flow inlets in order to allow for adjustable pressure drops in both channels, which operate hydrodynamically in parallel. The facility is modular in design to allow for a rapid interchangeability of the test components, instrumentation, and experimental configurations.

The nominal operating mass flow rate through the absorber is 10 g/s, which leads to an average flow velocity in its flow channels of 2.8 m/s. The resultant Reynolds number is approximately 80, well inside de laminar flow regime. The pressure loss is thus, to first order, directly proportional to the mean flow velocity (and thus mass flow rates) in each flow channel. As non-uniform heating of volumetric absorbers can cause a reduction in their thermal conversion efficiency due to the dependence of air properties on temperature (which causes the air stream to flow preferentially through colder channels, where viscosity is lower), a radiation homogenizer is used to generate a uniform incident radiative heat flux on the absorber aperture. A 10 kW nominal shell-and-tube heat exchanger, operating in a counter-flow configuration, is utilized to lower the air temperatures from 1227 °C (achieved at the receiver outlet) to and 50 °C (suitable for operation of the downstream blower).

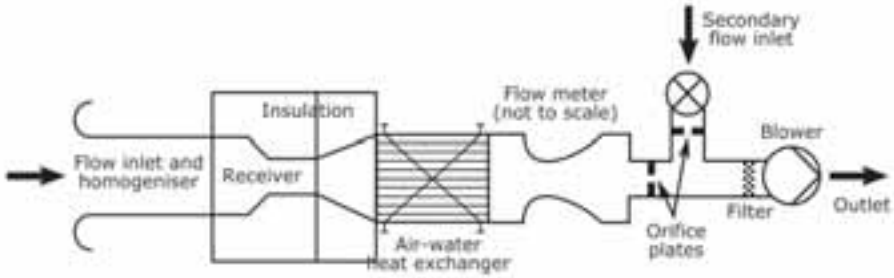

Fig. 2: Schematic diagram of the calorimetric experimental facility, with its main constitutive blocks labelled

Fig. 3: Left, frontal photograph of the absorber aperture plane (square lateral size is 125 mm). Right, three-dimensional view of the complete receiver, composed of the absorber plus a cup-shaped air collecting manifold

Two photographs of the baseline volumetric absorber experimentally characterized in this work are given in Fig. 3. It consists of a square-cell monolithic honeycomb module, manufactured from siliconized silicon carbide by Saint-Gobain High Performance Refractories[1], coupled to a cup that ducts the heated air towards the back of the facility. There are various experimental and numerical studies already conducted on this absorber (Téllez, 2003; Palero et al., 2008; Fend et al., 2013; Cagnoli et al., 2017), which therefore constitutes an adequate platform for the operational validation of new experimental facilities. The absorber has a 125 mm × 125 mm aperture and a

[1] Saint-Gobain IndustrieKeramik Rodental GmbH, Postfach 1144 D-96466 Rodental, Germany.

62.5 mm length. Absorber walls are 0.8 mm thick (nominal) and each flow channel is approximately 1.84 mm × 1.84 mm wide. The cross-sectional porosity of the absorber is thus 48.6%. Figure 4 illustrates the absorber assembly within the working section of the calorimetric facility. Sealing O-rings are distributed throughout the facility to prevent air leaks between the absorber aperture plane and the mass flow meter (such leaks would introduce unacceptably high uncertainties in the calculation of the absorber thermal conversion efficiency). During installation, the working section is placed on a highly accurate computer-controlled positioning table that moves along three axes. Careful alignment of the absorber aperture with the optical axis of the high flux solar simulator is achieved by employing a high precision cross level laser pointer. The inlet of the radiation homogenizer is situated exactly at focal point of the high flux solar simulator.

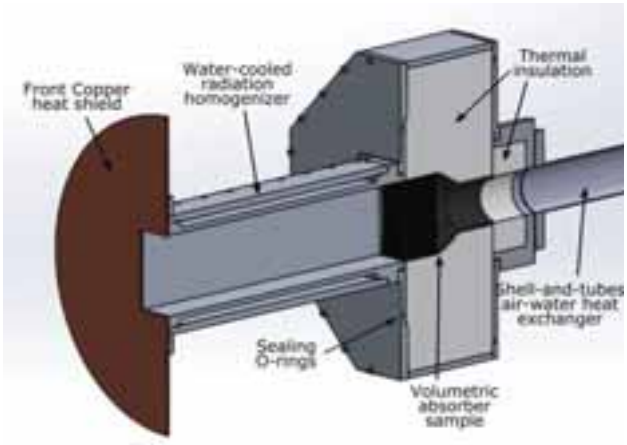

Fig. 4: CAD schematic diagram of the working section of the new experimental facility, with its main constitutive blocks labelled

4. Operating Conditions

A list of the operating conditions that can be achieved in the experimental facility is presented in Tab. 1, where comparisons to other experimental datasets at both smaller and larger scales are also given. Reynolds numbers have been calculated at the absorber aperture plane. Nusselt numbers and convective heat transfer coefficients have been obtained from correlations for thermal entry length solutions of the energy equation for internal laminar flows in square channels (Kays and Crawford, 2004). Averages have been taken along channel lengths.

Tab. 1: Typical operating conditions in the new experimental facility (at a scale of 42 kW_e) and comparison to values in the SolAir 200 on-sun experiments, from Téllez (2003), and to values achieved at a scale of 7 kW_e in a smaller solar simulator also at the Institute IMDEA Energy, reproduced from Luque et al. (2017)

Variable, units	7 kW_e scale	42 kW_e scale	SolAir 200
Absorber aperture, cm^2	4.5 – 9	156.3	2579
Total incident radiative power, kW	0.4 – 0.8	6.72	389
Maximum average radiation flux density, kW/m^2	1016	397.9	640
Mass flow rate, g/s	0.5 – 5	5 – 20	345
Mass flow rate per unit aperture area, $kg/(s\ m^2)$	1.3 – 2.1	0.7 – 2.6	~1.3
Maximum radiation per unit mass flow rate, kJ/kg	2500	1344	1128
Reynolds number (at inlet conditions)	50 – 250	62 – 248	~124
Average Nusselt number	3.0 – 3.24	3.02 – 3.15	~3.1
Average Biot number	0.52 – 2.92	0.57 – 2.27	~2.3
Technology readiness level (EU definition)	3 – 4	5 – 6	7 – 8

As shown in Tab. 1, the facility has been designed such that on-sun representative values of incident power per unit mass flow rate, Reynolds, Nusselt and Biot numbers can be achieved. Operating conditions that are highly representative of central receiver systems in actual solar towers are thus reproduced, whilst maintaining the advantages of operational flexibility and inexpensiveness of maintenance. The last row on the table shows technology readiness levels for the three experimental scales, based on the scale defined by the European Commission. The new experimental facility places itself between a smaller scale test bed for the aerothermal assessment of volumetric receivers already developed at the Institute IMDEA Energy (Luque et al., 2017), and actual on-sun central receiver experiments. It is thus expected that the flexibility and cost-effectiveness of the technique will allow for the validation of novel solar absorbers that show promise at the smaller scale, and prior to conducting on-sun tests, in order to de-risk the latter, typically resource-intensive, experimental campaign.

5. Instrumentation and Data Acquisition

The facility employs a dedicated instrumentation system based on an 8-slot National Instruments[1] CompactRIO platform. A total of 32 K-type thermocouples with 1 mm diameter Inconel sheaths have been placed throughout the facility, including measurement points on the radiation homogenizer walls and cooling water channels, on the intake module, on the absorber walls inner and outer walls, and in the exhaust module. Arrays of thermocouples were also placed at various position on the thermal insulating material in order to aid the calculation of heat conduction losses in it. The pressure drop across the absorber channels is measured by calibrated differential pressure transducers, and a thermal mass flow meter provides reliable mass measurement for the air flow.

Two radiation-shielded suction pyrometers are employed to accurately measure air inlet and outlet temperatures, immediately upstream and downstream of the absorber aperture and outlet planes, respectively. Their use is justified by the environment in which they operate and the fact that these measurements are key to the calculation of absorber thermal efficiency. Large amounts of radiation could affect unshielded thermocouples at those measurement planes: the radiation homogenizer outlet plane, where radiation from the high flux solar simulator is redirected and collimated, and the absorber exit plane, which is affected by intense thermal emissions from the hot inner walls of the facility.

A supervisory control and data acquisition system has been developed in National Instruments' LabVIEW for operation, hardware monitoring and data-logging in the experimental facility. Its main control window is shown in Fig. 5. It is divided in three main parts: on the left hand side, the user is presented with all control, monitoring and adjustment options for the 7 lamps of the high flux solar simulator. All information related to the facility instrumentation is displayed on the top right of the screen. Finally, the right lower part contains all options for the control and automated motion of the high precision three-axis positioning table. Safety operation interlocks have been included in the program to prevent hardware damage through user error.

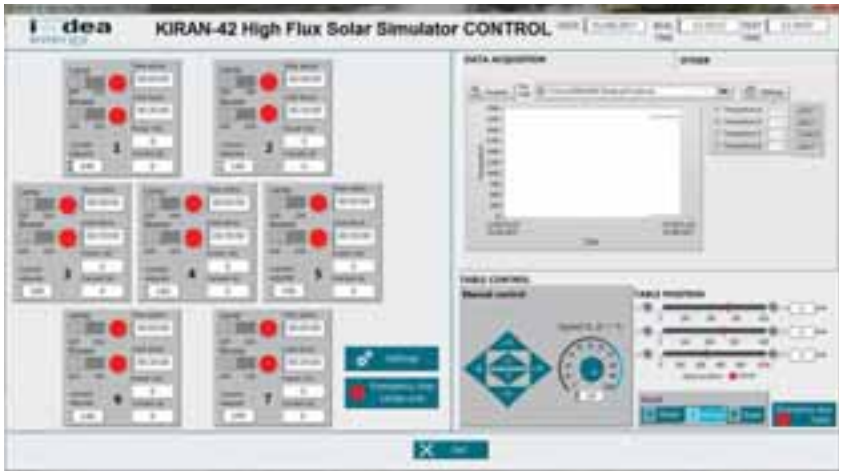

Fig. 5: Captured screen of the supervisory control and data acquisition (SCADA) software

[1] National Instruments Corporation, 11500 N Mopac Expy, Austin, Texas 78759, USA.

6. Radiation Conditioning on Absorber Aperture

Non-uniform heating of volumetric absorbers can cause a reduction in their thermal conversion efficiency (Pitz-Paal et al. 1997). The dependence of air properties on temperature causes the air stream to flow preferentially through colder channels, where viscosity is lower. Hotter flow channels then remain relatively uncooled, and the temperature imbalance can lead to a runaway effect that originates flow instabilities and hot spots on the absorber aperture. Orifice plates can be used to balance the flow by creating additional pressure loss in colder flow channels. When designing an experimental facility, a well-conditioned set-up requires the use of radiation homogenizers to produce a uniform incident heat flux on the absorber aperture.

Numerical ray-tracing simulations were then conducted during the design of the radiation homogenizer with the objective of maximizing the uniformity of the radiation profile at its outlet plane. The 7-lamp high flux solar simulator and the homogenizer were modelled in Tracepro[1]. The homogenizer was assumed to be a square cross-sectioned tube with a length of 500 mm and height and width both equal to 125 mm in this analysis. The mirrors were defined as perfect reflectors as the main goal was to assess the uniformity of radiation profiles rather than obtain actual values. In the ray-tracing simulation 100,000 rays per lamp were calculated, assumed to be emitted by a surface source located at the first focal point of each ellipsoidal reflector. The homogenizer inlet plane is situated exactly at the second focal point of the ellipsoidal reflectors.

Figure 6 shows the irradiance distribution on the outlet plane of the homogenizer, normalized with respect to the peak flux. The graph on the left hand side have been smoothed and averaged in groups of 8×8 pixels. The graphs in the middle show normalized heat flux profiles in the horizontal and vertical directions. On the right hand side the simulated rays are displayed in the setup. The analysis was conducted for all seven lamps both individually and in conjunction, but only selected results are shown for brevity. The simulations showed that moving the homogenizer closer to the ellipsoidal reflectors (i.e., ahead of the solar simulator focal point) results in a slightly smoother profile in horizontal direction, but a lower radiation level in the vertical direction. Moving the homogenizer away from the reflectors leads to an inverse horizontal profile, i.e., one where regions of maximum heat flux are found near the corners rather than in the center.

Single lamp analyses showed small areas in the center of the homogenizer outlet plane where irradiance was relatively lower than in their surroundings. This can be explained by the existence of a hole in the center of each the ellipsoidal reflector through which the lamp bulb electrical connections pass through. Simulations showed that these troughs could be reduced by moving the homogenizer away from the solar simulator focal point, but this led, again, to inverse radiation profiles. On the basis of this study, the final decision was to operate the radiation homogenizer with its inlet plane located exactly on the solar simulator focal plane. Numerical results showed that this configuration provided the best balance between homogeneity of the heat flux profiles and overall incident power on the absorber aperture.

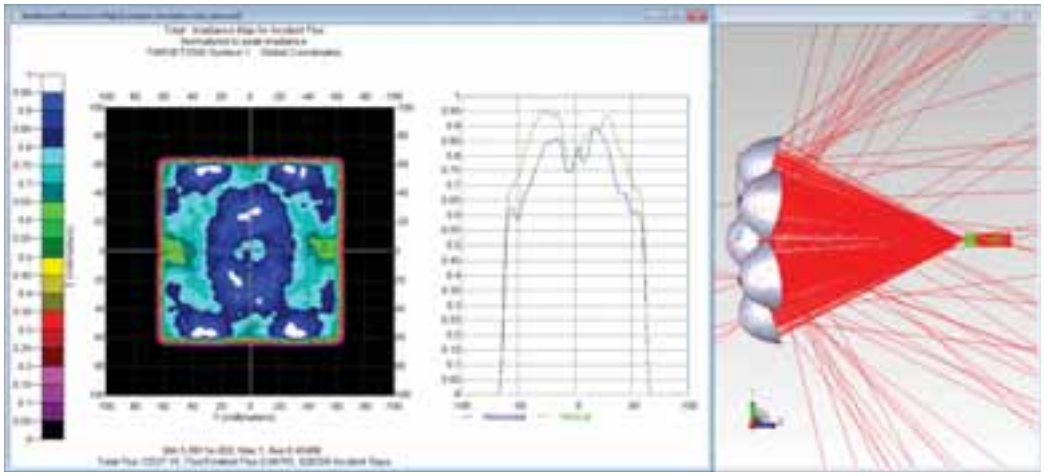

Fig. 6: Left, normalized heat flux map at the homogenizer outlet plane, for all seven lamps of the solar simulator. Center, normalized radiation profiles along the horizontal and vertical directions. Right, image of the simulated rays.

[1] Lambda Research Corporation, 25 Porter Road, Littleton, MA 01460, USA.

7. Incident Radiation Flux Distribution

The radiative flux density distribution at the outlet plane of the radiation homogenizer was acquired by direct measurements conducted with a Gardon radiometer (Gardon, 1953). The gauge traverses the measurement plane by means of an automated motion control mechanism that allows for high-spatial measurement resolution. At the homogenizer inlet plane, on the contrary, heat flux measurements were acquired by employing a water-cooled Lambertian target, in a procedure which was described in detail by Li et al. (2014). Radiation intensity on the Lambertian target was recorded by employing a high resolution CCD camera, which was calibrated against the Gardon radiometer.

Irradiance maps at the inlet and outlet of the radiation homogenizer are shown in Fig. 7. The white line in the right hand side figure indicates the actual size and relative location of the volumetric absorber aperture plane. It can be observed that the highly non-uniform and approximately Lorentzian radiation profile produced by the high-flux solar simulator is transformed to a square and relatively flat profile at the homogenizer outlet. The uniformity of the irradiance map at the homogenizer outlet was characterized by an average of 397.9 kW/m^2 and a standard deviation of 136.4 kW/m^2, both measured over a surface area of 125 mm × 125 mm (equal to the absorber aperture). The peak flux is 607.6 kW/m^2. Integration leads to an overall incident radiative power on the homogenizer outlet of 6.72 kW_{th}. This plane is approximately 2 mm upstream of the absorber aperture, so uniform heating of its front face is considered to be achieved.

There are, nonetheless, slight discrepancies with respect to results from the numerical ray-tracing simulations, especially noticeable in the region of high heat flux near the geometric center of the homogenizer outlet and the radiation trough that is found in the upper region of the channel (Fig. 7, right). This is attributed to two main effects: first, having a less reflective homogenizer than simulated, which leads to a lower level of homogenization of the outlet heat flux, and, second, to slight misalignments in the solar simulator with respect to the perfectly aligned numerically simulated configuration. Measurements showed that the points of maximum heat flux of all seven lamps where contained within a circular area of 18 mm diameter, whereas the simulation assumed perfect concentric alignment.

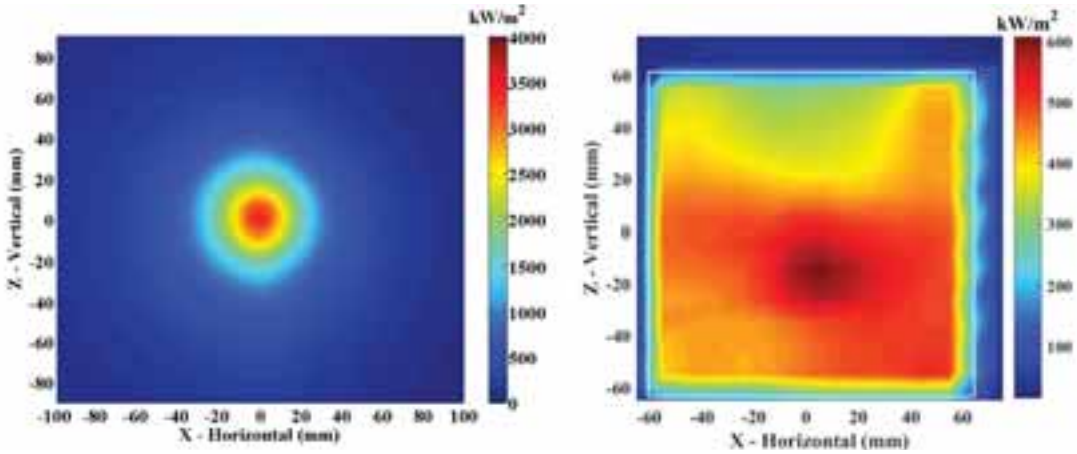

Fig. 7: Left, measurements of irradiance at the homogenizer inlet plane, reproduced from Li et al. (2014). Right, measurements of irradiance at the homogenizer outlet plane, conducted by traversing a Gardon radiometer

Laterally averaged irradiance distributions at the homogenizer inlet and outlet planes are shown in Fig. 8. Two curves are shown in the figure, one for Z-averaged data (in which averages have been taken along the vertical direction), and one for X-averaged data (in which averages have been taken along the horizontal direction). The edges of the absorber aperture are located at -62.5 mm and 62.5 mm. It can be observed that the X-averaged data shows the region of high heat flux that is close to the center of the absorber aperture, as well as the trough on the upper part. Z-averaged measurements presented in Fig. 8 also show a somewhat higher irradiance towards the right hand side of the absorber aperture.

In assessing whether or not the heat flux distribution on the absorber aperture can lead to the unstable operation of volumetric receivers, the receiver thermal conductivity was also shown to be an important factor to consider by Becker et al. (2006). In a theoretical and numerical study, it was demonstrated that sufficiently conductive

volumetric receivers could altogether avoid flow instabilities by allowing for an enhanced redistribution of heat within the absorber solid volume. As a result, the temperature difference between hot and cold flow channels is not sufficient for instabilities to occur. Considering that the volumetric absorber to be tested is made out of highly conductive siliconized silicon carbide, the heat flux profile at the homogenizer outlet was thus considered sufficient for the stable operation of the experimental facility in this initial aerothermal characterization test campaign.

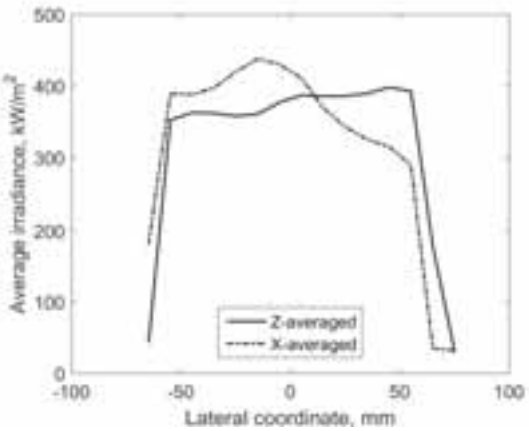

Fig. 8: Laterally averaged irradiance distributions at the radiation homogenizer outlet plane

8. Conclusions

A new calorimetric facility has been designed to investigate volumetric absorbers by employing a seven-lamp 42 kW high flux solar simulator, and is described in this paper. A modular design has been sought to allow for the quick interchangeability of components and experimental configurations. Incident radiation levels and internal flow field variables have been shown to be highly representative of central receiver systems in actual solar towers. Together with its associated techniques, the facility allows for fully integrated assessments of absorber radiative-to-convective heat conversion efficiencies, whilst maintaining the advantages of operational flexibility and inexpensiveness of maintenance.

It is envisaged that the facility will be used in investigations of novel volumetric absorbers that include gradual variations of convective heat transfer coefficients (implemented, for instance, by variable porosity configurations), gradual variations of thermal conductivity through the sample, or selective absorptance and reflectance profiles. Transient measurements are possible too. The technique is expected to allow for a more rapid experimental validation of such innovative concepts than has previously been possible. Experimental data will also be used for the validation of both high-fidelity numerical simulations and simplified analytical models of air solar receivers in high-irradiance high-temperature operation. Besides, the new facility can also serve as a platform for the validation of other type of central receiver systems for concentrated solar power applications, (for instance directly or indirectly heated tube and particle receivers) with minimal changes to the experimental apparatus.

9. Acknowledgements

Research leading to these results has received funding from the regional government of Comunidad de Madrid through project ALCCONES (S2013/MAE-2985), and from the European Union FP7 Programme through grant agreements 609837 and REA 291803 (Marie Curie Actions). Lena Bühre is thanked for substantial contributions relating to the radiation homogenizer numerical ray-tracing simulations. All are gratefully acknowledged.

10. References

Ávila-Marín, A.L., 2011. Volumetric receivers in solar thermal power plants with central receiver system technology: a review. Solar Energy 85(5), 891-910.

Becker, M., Vant-Hull, L., 1991. Thermal Receivers, in: Solar power plants. Berlin Heidelberg: Springer, pp. 163–198.

Becker, M., Fend, T., Hoffschmidt, B., Pitz-Paal, R., Reutter, O., Stamatov, V., Steven, M., Trimis, D., 2006. Theoretical and numerical investigation of flow stability in porous materials applied as volumetric solar receivers. Solar energy 80(10), 1241-1248.

Boehmer, M., Becker, M., and Sánchez, M., 1991. Development of volumetric air receivers, in: Proceedings of the Biennial Congress of ISES, Pergamon Press, Denver, Colorado, USA, pp. 2123-2128.

Cagnoli, M., Savoldi, L., Zanino, R., Zaversky, F., 2017. Coupled optical and CFD parametric analysis of an open volumetric air receiver of honeycomb type for central tower CSP plants. Solar Energy 155, 523-536.

Codd, D. S., Carlson, A., Rees, J., Slocum, A. H., 2010. A low cost high flux solar simulator. Solar Energy 84(12), 2202-2212.

Fend, T., Schwarzbözl, P., Smirnova, O., Schöllgen, D., Jakob, C., 2013. Numerical investigation of flow and heat transfer in a volumetric solar receiver. Renewable energy 60, 655-661.

Gardon R., 1953. An instrument for the direct measurement of intense thermal radiation. Rev. Sci. Instrum. 24(5), 366-370.

Gómez-García, F., González-Aguilar, J., Olalde, G., Romero, M., 2016. Thermal and hydrodynamic behavior of ceramic volumetric absorbers for central receiver solar power plants: A review. Renewable Sustainable Energy Rev. 57, 648-658.

Ho, C.K., 2017. Advances in central receivers for concentrating solar applications. Solar Energy 152, 38-56.

Kays W, Crawford M, Weigand B., 2004. Convective heat and mass transfer, fourth ed. McGraw-Hill Higher Education, New York, NY, USA.

Kribus, A., Gray, Y., Grijnevich, M., Mittelman, G., Mey-Cloutier, S., Caliot, C., 2014. The promise and challenge of solar volumetric absorbers. Solar Energy 110, 463-481.

Krueger, K. R., Davidson, J. H., Lipinski, W., 2011. Design of a new 45 kWe high-flux solar simulator for high-temperature solar thermal and thermochemical research. J. Solar Energy Eng. 133(1), 011013.

Li, J., González-Aguilar, J., Pérez-Rábago, C., Zeaiter, H., Romero, M., 2014. Optical analysis of a hexagonal 42 kW_e high-flux solar simulator. Energy Procedia 57, 590-596.

Li, J., González-Aguilar, J., Romero, M., 2015. Line-concentrating flux analysis of 42 kW_e high-flux solar simulator. Energy Procedia 69, 132-137.

Luque, S., Bai, F., González-Aguilar, J., Wang, Z., Romero, M., 2017. A parametric experimental study of aerothermal performance and efficiency in monolithic volumetric absorbers, in: AIP Conference Proceedings, 1850, 030034.

Luque. S., Santiago, S., Gómez-García, F., Romero, M., González-Aguilar, J., 2017. A new calorimetric facility to investigate radiative-convective heat exchangers for concentrated solar power applications. Int. J. Energy Res. X, 1-11.

Mehos, M., Turchi, C., Jorgenson, J., Denholm, P., Ho, C., Armijo, K., 2016. On the path to Sunshot: advancing concentrating solar power technology, performance, and dispatchability. Tech. Rep. NREL/TP-5500-65688, National Renewable Energy Laboratory, Golden, Colorado, USA.

Menigault, T., Flamant, G., Rivoire, B., 1991. Advanced high-temperature two-slab selective volumetric receiver. Solar energy materials 24(1-4), 192-203.

Palero, S., Romero, M., Castillo, J.L., 2008. Comparison of experimental and numerical air temperature distributions behind a cylindrical volumetric solar absorber module. J. Solar Energy Eng. 130(1), 011011.

Petrasch, J., Coray, P., Meier, A., Brack, M., Häberling, P., Wuillemin, D., Steinfeld, A., 2007. A novel 50 kW 11,000 suns high-flux solar simulator based on an array of Xenon arc lamps. J. Solar Energy Eng. 129(4) 405-411.

Pitz-Paal. R., Hoffschmidt, B., Boehmer, M., Becker, M., 1997. Experimental and numerical evaluation of the performance and flow stability of different types of open volumetric absorbers under non-homogeneous irradiation. Solar Energy 60, 135-150.

Pozivil, P., Ettlin, N., Stucker, F., Steinfeld, A., 2015. Modular design and experimental testing of a 50 kWth pressurized-air solar receiver for gas turbines. J. Solar Energy Eng. 137(3), 1-7.

Romero, M., Buck R., Pacheco, J.E., 2002. An update on solar central receiver systems, projects, and technologies. J. Solar Energy Eng. 124(2), 98-108.

Romero, M., González-Aguilar, J., Zarza, E., 2016. Concentrating solar thermal power, in: Goswami, D.Y., Kreith, F. (Eds.), Energy efficiency and renewable energy handbook, second ed. CRC Press, Boca Raton, Florida, USA, pp. 1237-1345.

Téllez, F.M., 2003. Thermal performance evaluation of the 200 kW_{th} "SolAir" volumetric solar receiver. Tech. Rep. 1024, CIEMAT (Centro de Investigaciones Energéticas, Medioambientales y Tecnológicas), Almería, Spain.

To beam or not to beam down

Sarah A. Miller[1]

[1] CSIRO Energy, Newcastle (Australia)

Abstract

Concentrating solar thermal (CST) technologies can be employed for high-temperature applications such as electricity generation, industrial process heat and solar thermochemistry. There has been on-going interest in tower reflectors or beam-down systems without any commercial systems in operation yet. This paper reviews the geometry of beam-down central receiver tower systems along with the resultant receiver flux distributions to develop an understanding of the opportunities for beam-down systems. It includes a qualitative analysis in terms of the field, tower, secondary reflector and receiver, as well other CST beam-down systems.

Although beam-down systems will have a lower optical efficiency than an equivalent tower system, there is also a trade-off between either power or energy collection and concentration, although there are design options to improve these. The application of beam-down systems may be suited to applications, such as solar thermochemistry, where the cost of the additional plant is warranted by the value of the products.

Keywords: Concentrating, solar, thermal, CST, beam-down tower, secondary, reflector, CPC, flux, power

1. Introduction

Concentrating solar thermal (CST) technologies can be employed for electricity generation, industrial process heat and solar thermochemistry (Blanco and Miller, 2016) and the choice of technology depends on a range of details required to meet the end-use specifications or overall cost envelope. One critical detail is the temperature requirements of the end-use, and point focus technologies provide the higher concentration ratios required for high-temperatures. While one limitation of dish CST technologies is the mass of the receiver in the focal point, the optical efficiency is better than central receiver systems. However central receiver tower systems are being increasing deployed for electricity generation because they are often more cost effective than other CST technologies.

While secondary reflectors can be employed in close proximity to linear receivers to improve the capture of reflected rays, they can also be used to achieve further concentration in point receivers, such as in a solar furnace, but with an overall loss in optical efficiency. There is growing interest in beam-down central receiver systems, where the rays reflected onto a tower mounted secondary reflector are further reflected down to the ground.

The beam-down concept is attributed to Rabl (1976) who proposed a tower reflector as an alternative to the tower boiler concept for a central receiver solar thermal electric conversion plant. He expected this could be accomplished without excessive optical losses and his preliminary estimates appeared favourable. He recommend that a detailed systems analysis be performed comparing the tower reflector with the power tower.

In 1991, Vant-Hull considered the beam-down concept as based on a Cassegrain reflector system. While he felt there may be obvious benefits in simplifying the tower and saving on pumping power and piping, there were also penalties and difficulties. The obvious loss of added reflection is that of the primary heliostat reflector, ~5%, although at higher flux densities on the secondary reflectors, this might more likely be 10%. If this 10% optical energy loss represents thermal energy absorbed by the secondary reflector, active cooling might be required to dissipate this heat. Vant-Hull assumed the secondary reflector area must be smaller than the primary reflector area, except “where cost is secondary to performance”, as for a solar furnace.

Vant-Hull (1991) considered 3 secondary reflectors shapes based on geometrical optics, finding:

- An elliptical (concave) reflector would need to be placed beyond the focal point of the heliostats, requiring a taller tower to reflect a more diffuse cone of rays (image) created by a longer optical path without any advantage
- A hyperboloidal (convex) reflector would need to be placed before of the focal point of the heliostats, requiring a shorter tower. The smaller the secondary reflector, the larger the reflected secondary sunshape image and lower the concentration. A further concentrator could be placed at the receiver, adding to the cost

doi:10.18086/swc.2017.04.11 Available at http://proceedings.ises.org

- A flat reflector would need to be placed anywhere up to the focal point of the heliostats, so long as the total optical path length does not change. The flat reflector system would have small, 5-10%, reflection losses but require a moderately large mirror.

In reference to beam-down system, he stated that "Although often recommended, when subjected to a comprehensive design and costing analysis, all such concepts have failed to date".

In 2000, Segal and Epstein considered both concave (ellipsoidal) and convex (hyperboloidal) tower reflectors for electricity generation system. They identified that elliptical reflectors require both higher tower, perhaps twice as high, and also a larger secondary reflector and directed their attention to hyperboloidal reflectors. In 2011, Segal stated that appropriately placed hyperboloidal and ellipsoidal tower reflectors can provide comparable results, although the hyperboloidal surface is definitely more effective. Although a "quadratic surface mirror always magnifies the sun image" and they highlight the importance of its linear magnification, it is noted that the flux density and concentration decrease as the beam area increases by the square of the linear magnification.

There has been on-going interest in beam-down systems for both electricity generation and solar thermochemistry. The purpose of this paper is to review work since 2000 with a view to understanding the opportunities for beam-down systems. This paper will focus on simple ray geometry of beam-down systems as well as receiver flux distributions that affect the resultant black-body temperature limit.

2. Simple ray geometry

In CST technologies, determination of receiver flux distributions requires ray-tracing involving the position of the sun and the properties of any reflectors, including consideration of the conical magnification of the sun upon reflection and the imperfections of the reflector structure and tracking. An example of the initial system design using simple ray geometry is shown in Figure 1 for a hyperboloidal secondary reflector. This geometry considers the rays from the edges and centre of the heliostat that is furthest from the tower (R_{max}). The heliostat is flat, although a curved heliostat can also be considered. The sun position and annual DNI intensity for Alice Springs, Australia, shown in Figure 2 highlights the range of zenith and azimuth angles that need to be considered in the design of CST systems.

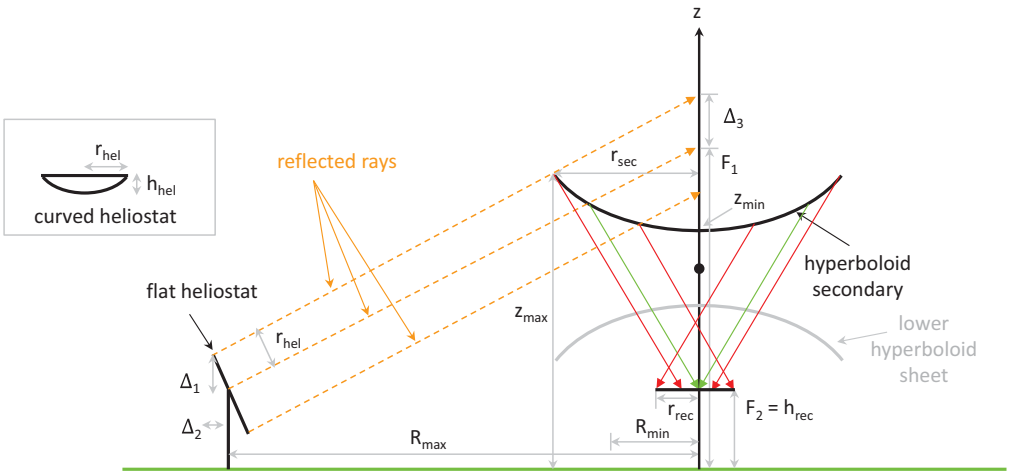

Fig 1: Geometry of beam-down tower system with hyperboloidal secondary reflector

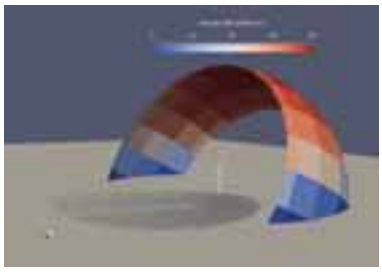

Fig. 2: Sun position diagram for Alice Springs, Australia (Potter et al., 2017)

The effect of eccentricity on the hyperbola size and shape is shown in Figure 3 for an upper focal height (F_1) of 75m for a heliostat radius of (a) 5m and (b) 1m, both at R_{max} = 150m. The vertex of the hyperbola changes with eccentricity but not heliostat radius. The radius of the hyperbola increases with increasing eccentricity and increasing heliostat radius. The linear magnification of the rays with the smaller heliostat will be less since the outer edge of the hyperbola is slightly closer to both the heliostat and the receiver.

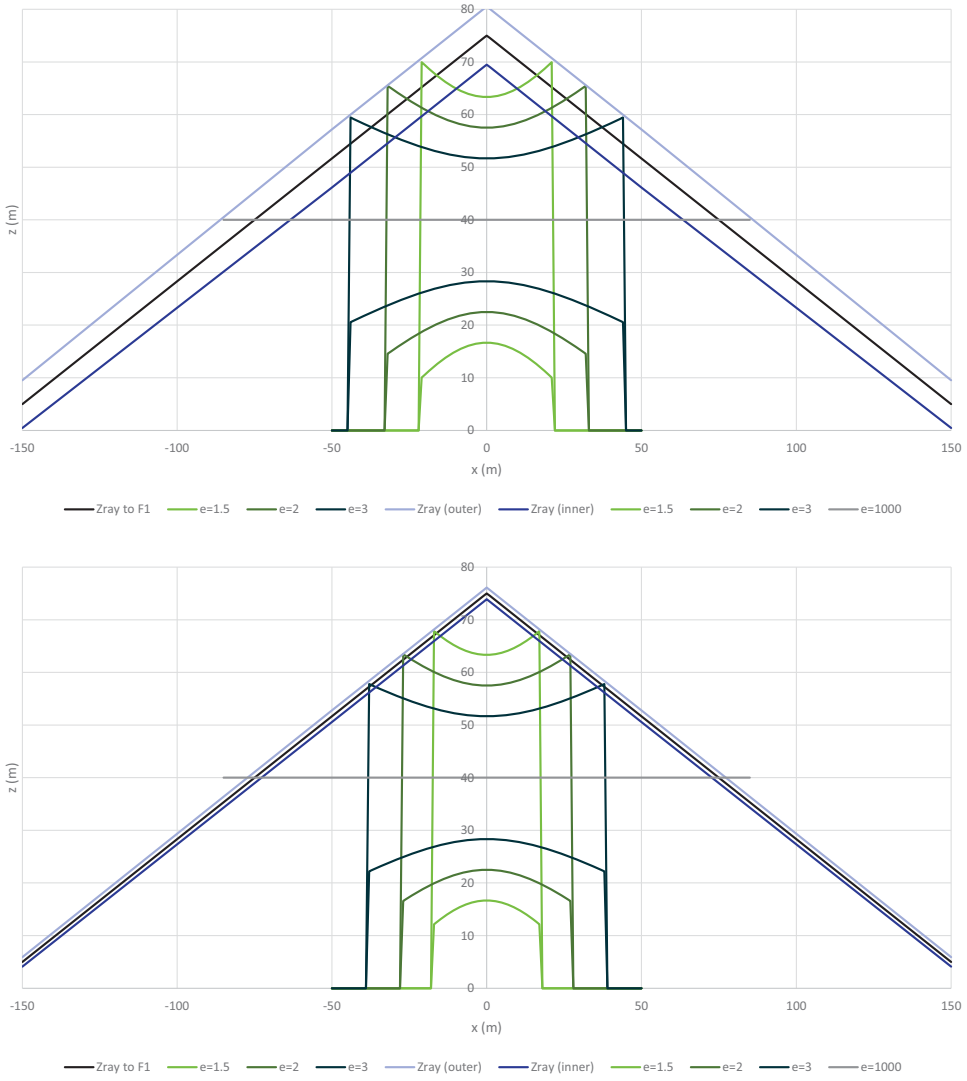

Fig. 3: Effect of eccentricity on hyperbola size and shape for heliostats of (top) 5m and (bottom) 1m (F1=75m, Rmax=150m)

3. Receiver flux distribution

In 2012, Vant-Hull stated there are 3 basic configurations for central tower concentrating solar power (CSP) systems defined essentially by the receiver; these being an external cylinder receiver, with a cavity receiver as principal alternative, and a beam-down concept as the third alternative. In 2014, he stated that "However there are substantial disadvantages which make the beam-down concept impractical except in a few very special situations", without clearly articulating the special situations. The tabulated results for a Gemasolar type system show the beam-down system has a receiver power of 124 MW_t, which is 91% of the original 137 MW_t. More dramatically, the concentration of the beam-down system without a compound parabolic concentrator (CPC) on the receiver is only 28. Adding a CPC gives a concentration of 390, which is still much lower than the original 736. The concentration of the beam-down system can be further increased by reducing the rim angle, which reduces the field size but the power is also significantly reduced. The effect of decreasing the field radius on decreasing the receiver incident power whilst increasing the concentration, and black-body temperature are shown in Figure 4.

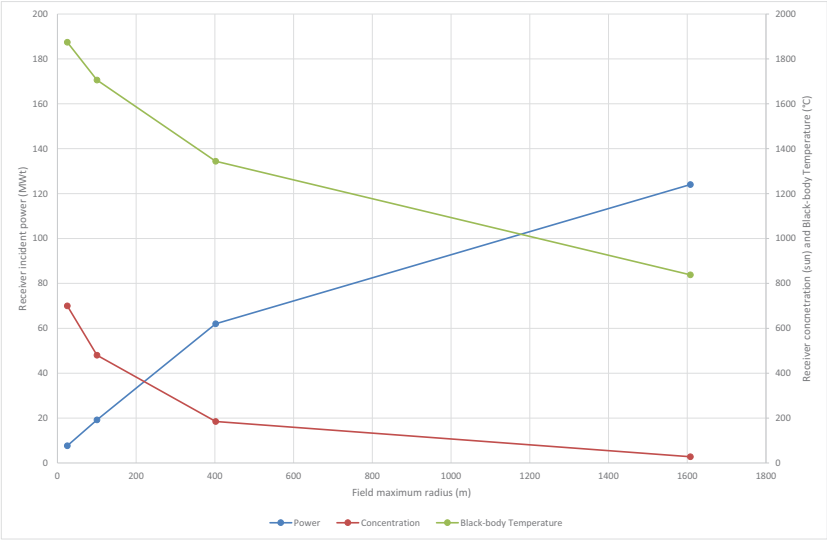

Fig. 4: Effect of field maximum radius on receiver incident power, concentration and black-body temperature (data from Vant Hull, 2014)

Circa 2000, the Weizmann Institute (Israel) built a 700kW experimental system with a secondary hyperboloidal reflector of 75m² and claims to use a CPC, with a magnification of 25, to attain average concentration of ~4000. Segal and Epstein (2003) published a concept for a 50MW ground reformer, involving an asymmetric surround field, hyperboloidal secondary reflector and a packed array of CPCs. The geometric concentration ratio of CPC aperture to heliostat mirror area is 12909. The pattern of rays arriving at the CPC aperture shows a high power density (25 MW or 3400 kW/m²) at the central CPC and low density (~4.8 MW or 653 kW/m²) in each of the outer 6 CPCs (see Figure 5).

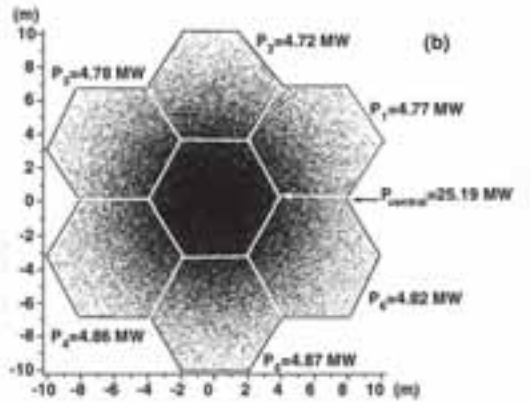

Fig. 5: Pattern of rays arriving at the CPC aperture for a 50MW ground reformer (Segal and Epstein, 2003)

Blackmon (2008) reports some details about a 10MW$_t$ "High Concentration Solar Central Receiver Demonstration Plant" for Zaafarana (Egypt) based on ideas from the Weizmann Institute. The system involves a tower-mounted reflector and CPC on the ground passing to volumetric air receivers, with quartz windows, coupled to a Brayton turbine system. This type of volumetric receiver is capable of operation at high concentrations of 2,000 to 10,000 suns. They determined that smaller heliostats were needed and selected 9.2 m² to achieve the required high concentrations at the receiver. Appendix C (Blackmon 2008) has the power from the solar field as 12.1 MW having 10.0 MW at the secondary reflector and 9.6 MW at the collector (presumably the CPC inlet). The equivalent concentration is 58.7 kW/m² at the secondary reflector and 1,013 kW/m² at the collector. Appendix E (Blackmon 2008) reported flux density at the aperture of the real CPC of 54 kW/m² (0.054 MW$_t$/m²), ranging from peak of 95 to edge of 30 kW/m². Blackmon designed and patented a number of features including the tripod-tower, the secondary reflector frame with heat recovery.

Circa 2007, Masdar Institute built 100 kW pilot plant based on a design from the Tokyo Institute of Technology (Hasuike et al., 2009). The total heliostat field aperture is 280.7 m², using small flat heliostats of 8.5 m² each, a hyperboloidal tower reflector composed of 45 flat mirrors mounted on a 19m tower. The original receiver was a

4.88mx4.88m (16'x16') near-lambertian ceramic tiled surface located 2.3m above ground to allow performance measurement (Mokhtar et al., 2014).

Mokhtar et al. (2014) report experimental analysis of the original Masdar system. They measure the optical performance in terms of flux, then compute the optical efficiency as well as both the receiver intercept factor (spillage) and thermal efficiency based on a model to determine optimum receiver aperture for a desired temperature. For a large receiver aperture of 1.71m (9.186m²), the peak optical efficiency appears ~48%, with the daily average over ~10 hours of sunshine given as 37%. The daily average mean flux density was given as 9.422 kW/m², corresponding to power of 86.55 kW, presumably at 300°C.

For a small receiver aperture of 1.06m (3.53m²), the peak optical efficiency appears circa 42%, with the daily average given as 32%. The daily average mean flux density was given as 20.9 kW/m², corresponding to power of 73.77 kW, presumably at 600°C. The higher temperature, at 2.2 times the concentration, results in a 15% loss of power.

Moktar (2011) calculated both the flux density and accumulative power with radius at the receiver plane. The peak flux density was 110 kW/m², decreasing to about 50 kW/m² at a radius ~0.75 m and decreasing to about 20 kW/m² at a radius ~1 m (Figure 6). The accumulative power is 80 kW at 0.75m and 105 kW at 1 m, reaching 130 kW at 3 m (Figure 7). However the large the receiver aperture, the greater the heat loss, so the useful radius is likely to be 1 m.

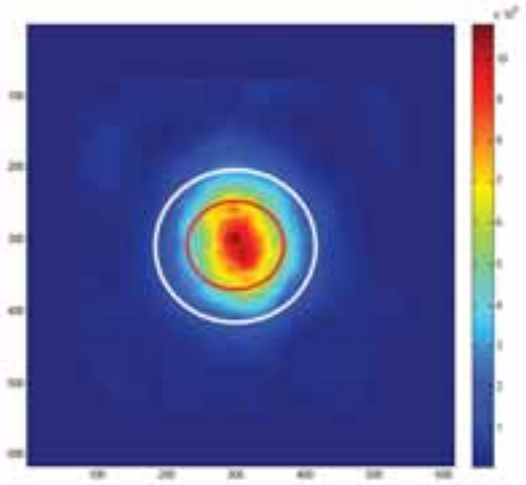

Fig. 6: Typical flux distribution [W/m²] at the receiver plane [distance in cm] (Moktar, 2011)

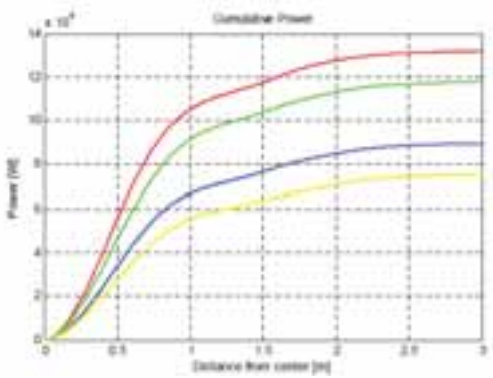

Fig. 7: Accumulative power [W] with radius at receiver plane at different times of the day (Moktar, 2011)

Grange at al. (2015) simulated the system giving an efficiency, from 77 % to 22 % depending on the solar zenith angle, appearing to be circa 68% at 40°. The simulated concentration was stated as ~150 suns at zenith angles of <40°. To improve the concentration, both a CPC and a cone were considered as a third-stage non-imaging concentrator. The power at the inlet to this final optical element was 143.2 kW at midday and 104.1 kW at 10am, being 71 and 52 kW/m² respectively. The 0.385 m² CPC led to a power loss of 5.2% at midday and 6.4% at 10am, but increased the concentration to 353 kW/m² and 253 kW/m² respectively. The 0.636 m² cone led to a power loss of 4.5% at midday and 5.5% at 10am, but increased the concentration to 215 kW/m² and 155 kW/m² respectively. Thus the CPC gave higher concentration, but also increased the power loss.

In 2012 Magaldi built a 100 kW thermal experimental system at Buccino (SA), Italy. CSP Today (2014) described the system concept being multiple 500 kWe modules. A photograph shows a hyperboloid type secondary reflector, being a 4-sided inverter pyramid on 4-legged tower system, with the receiver being directly underneath. The heliostats appear flat, but there are no optical details.

In 2016 Magaldi started operating a 2MW thermal system at S. Filippo Del Mela (ME), Italy. This is designed to produce 20.5 tons of steam daily, using 786 heliostats on a site of 2.25 hectares. The website says each module can store 8.2 MWh of thermal energy. Several modules can be combines to produce superheated steam at circa 500°. It indicates the 270 ton sand receiver-fluidised bed operates at 550-650°C.

Each module has 390 heliostats of 7m² each, or 2,730 m² (on a site of 12,000 m²), giving a thermal input of 1.05 MW, which equates to 0.384 kW_t/m^2.

Circa 2012, the University of Miyazaki (Japan) built a 100 kW experimental system (Kodama et al., 2014). The system has an elliptical secondary reflector, 4.6m diameter, mounted on a 16m tower. The heliostat field is a half circle around the tower. Each of the 88 heliostats units consists of 10 small mirrors with 50 cm diameters, giving a total area of mirrors is 176 m². The sunlight being beamed-up to the elliptical secondary reflector pass through the first focal point at 14 m height and returns to a second focal point plane 10 m above ground level (Figure 8).

Kodama et al. (2014) report using 78 of 88 heliostats, DNI was about 0.9 kW/m², 113 kW_t solar power was concentrated within an area of 1.3m × 1.3m at the second focal spot, being ~59 kW/m². Of this, 70 kW_t was concentrated within area of 0.6m × 0.6m, or 194 kW/m² (Figure 9). However, laboratory results suggest that a flux >1000 kW/m² is required to get 1400°C. Thus a CPC was proposed with a 0.75m inlet and 0.44m outlet, length of 1.525m, to achieve this. Kodama et al. (2016) reported testing this system on a fluidised bed of sand that had been pre-heated to 600°C. They achieved central bed temperatures of 1100°C, albeit with a non-uniform flux distribution (Figure 10a). They subsequently proposed that canting the CPC by an angle of 6-12 ° will provide a more even flux distribution (Figure 10b) and, with smaller particles, higher temperatures can be achieved.

Fig. 8: University of Miyazaki (Japan) tower with elliptical secondary reflector (Kodama et al., 2014)

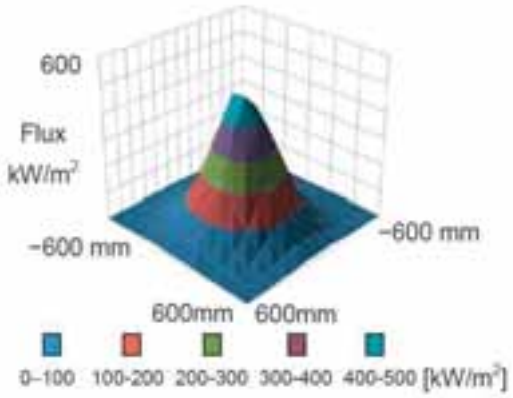

Fig. 9: Flux density from elliptical secondary reflector at CPC inlet (Kodama et al., 2014)

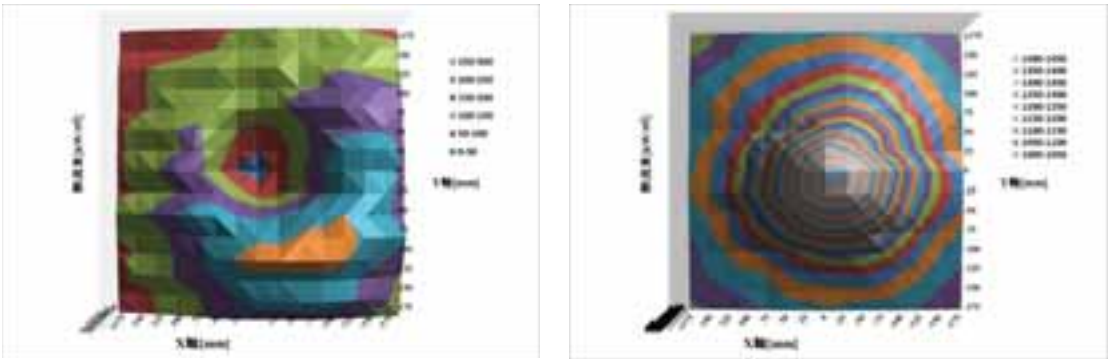

Fig. 10: Flux density 25 cm below CPC outlet (a) uncanted (b) canted (Kodama et al., 2016)

In 2013, Seigel and Ermanoski proposed a thermochemical water splitting system using a flat secondary reflector. This system places the particle-based receiver-reactor close to the flat secondary reflector to minimise image magnification and not need a terminal (CPC) concentrator for high concentration. In considering a 3MW thermal system capable of temperatures of 1500°C, they propose that the annual average collection efficiency can be 43% or more. They note the secondary reflector design will need to consider non-uniform incident flux of 20-140 kW/m². They emphasise the need for accurate, and possibly individually focused mirrors, choosing small heliostats of 1m².

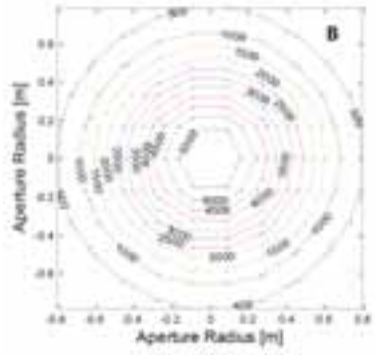

Fig. 11: Flux density from flat secondary reflector at receiver reactor inlet (Seigel and Ermanoski, 2013)

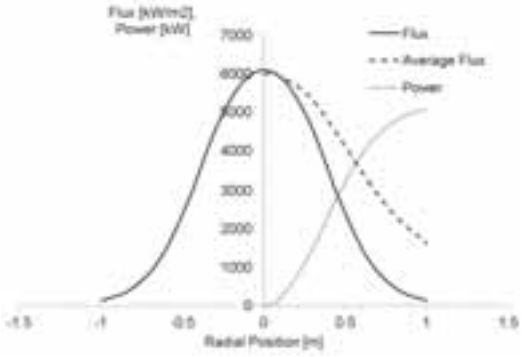

Fig. 12: Flux density, average flux and power with receiver reactor radius (Seigel and Ermanoski, 2013)

Hoffman (2011) also considered a flat secondary reflector and concave converging heliostats for a 1 MW, 1000 suns concentration, showing 2 MW and 4,000 suns concentration is achievable. He considers performance details for 4 days of the year, being solstice and equinox. The peak power output ranges from 1-2 MW, with peak concentrations of 2,000-4,000 and peak optical efficiencies of 39-50%.

In 2012, Leonardi undertook a detailed analysis of a beam-down central receiver system. The system has a symmetrical surround field, flat heliostats of either 5m or 1m radius, hyperboloidal secondary reflectors with eccentricities 1.5, 2.0 or 3.0 as well as considerations of a CPC. Ray-tracing to examine the sunshape at the upper and lower focus, she considers a conic bundle of perfectly rays reflected from the heliostat centre to the aim point (F_1). At low eccentricity, the sunshape is most spherical and the magnification is largest, resulting in the lowest concentration. At high eccentricity, as the secondary reflector becomes more flat, the sunshape is more elliptical and the magnification is unity, resulting in little concentration. Leonardi (2012) found that simplifying the optical analysis to only one conic bundle per heliostat results can lead to drastic approximations; with errors up to 35%.

Leonardi (2016) compares the use of flat and concave heliostat in beam-down systems, considering the secondary reflectors as hyperbolas with significant concavity (eccentricity, e=3), or flat (e=∞). The system has a symmetrical surround field with heliostats of 5m radius. The design point is solar noon at equinox, but also considers the annual efficiency. She finds that concave heliostats are beneficial, even when a hyperbola of small eccentricity (e=3) is considered. Concave heliostats provide a higher concentration, ~ 10 times, over a smaller receiver area, offering the possibility of avoiding a CPC. She deems that it may not be practical to have each heliostat with its own concavity in large solar fields (Figure 13).

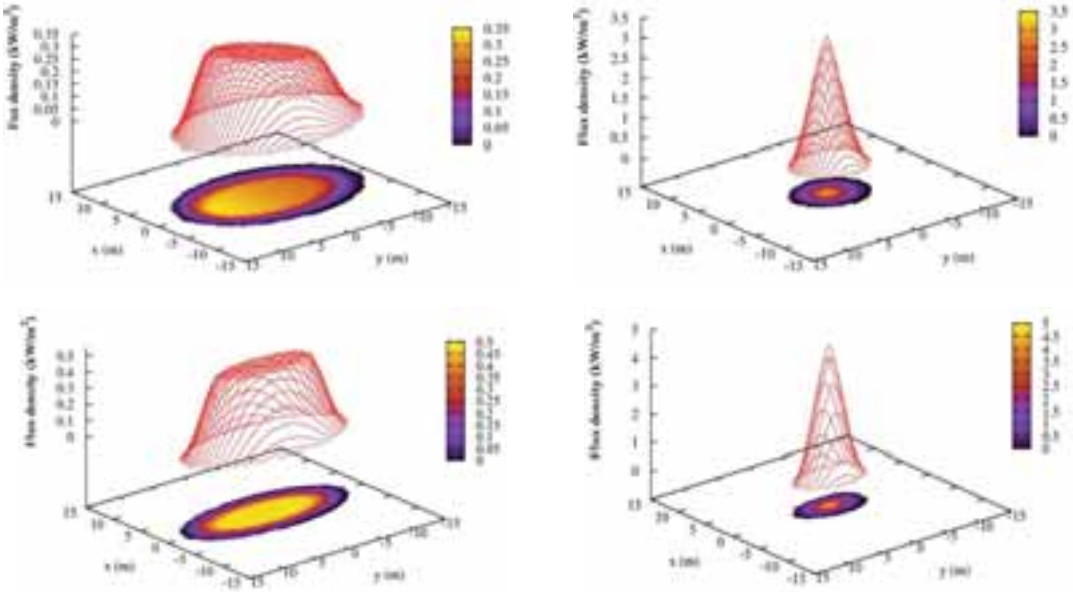

Fig. 13: Receiver flux density for (a) Flat heliostat, hyperbola eccentricity = 3 (b) Concave heliostat, hyperbola eccentricity = 3 (c) Flat heliostat, hyperbola eccentricity = ∞ (b) Concave heliostat, hyperbola eccentricity = ∞ (Leonardi, 2016)

A convex or hyperboloidal secondary receiver provides a higher annual energy collection than a flat secondary, particularly at low receiver radius (Figure 14). The relationship between concentration, black-body temperature and annual energy collection is shown in Figure 15. In this system, at the low receiver radius and high concentration, the field efficiency based on annual energy is 66.37 % in the case of concave heliostats and only 19.30 % in the case of flat heliostats. The field efficiency at the design point is 80.1 % for concave heliostats and 15.8 % for flat heliostats.

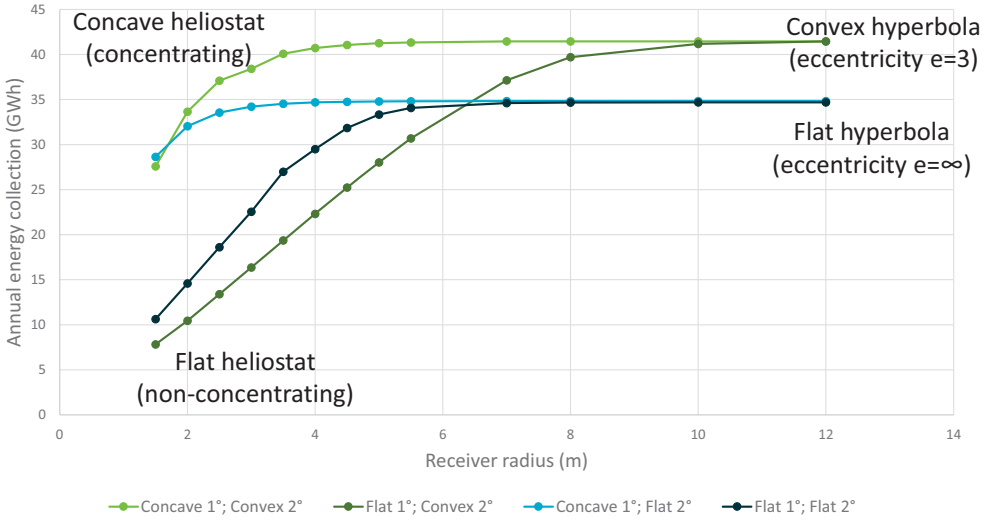

Fig. 14: Effect of receiver radius on annual energy collection (data from Leonardi, 2016)

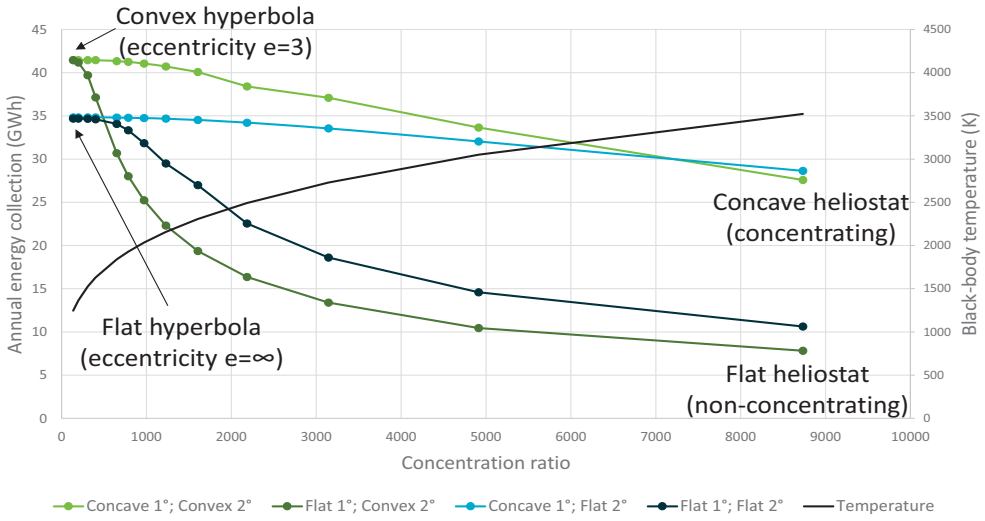

Fig. 15: Relationship between concentration, black-body temperature and annual energy collection (data from Leonardi, 2016)

4. Discussion

CST systems are often simple in concept and complex in detail, with subsystems that integrate to optimise power, energy, concentration and ultimately cost. CST beam-down systems have the added complexity of a secondary reflector. This paper has focused on central receiver tower systems and the following analysis considers the field, tower, secondary reflector and receiver, as well other CST beam-down systems.

Field

The literature reviewed in this paper suggests heliostat size plays an important role the design of CST beam-down systems with small heliostats giving less beam magnification. Reducing the size of the heliostats implies increasing the number of individually controllable heliostats in a heliostat field. While the number of heliostats may be

decreased by having different sized heliostats in the field, it is noted the greatest linear magnification occurs from the most distant heliostats.

The style or concavity of heliostats has been explicitly considered by Leonardi (2016). Concave heliostats provide a higher concentration over a smaller receiver area, offering the possibility of avoiding a CPC. She deems that it may not be practical to have each heliostat with its own concavity in large solar fields. . While increasing the number and concavity of heliostats increases the total cost, this may be offset by a system cost benefit.

Heliostat pedestal height has not been considered in this paper but it is noted that it is normally the minimum height to match the heliostat size. It is further noted that the heliostat height might need to be considered in terms of the height of the receiver.

The size of the heliostat field is normally dictated by the power sizing of the system. Where an application involves heating particles to heat a heat transfer fluid, it is possible to design multi-tower systems where a number of small fields are closely packed. This packing may be to (1) keep the size of each system small, (2) have the heat transfer fluid from each system accumulate to produce a large system and/or (3) have heat from one system pass to one or more systems to increase the temperature of the system.

In addition to the outer size of the heliostat field, a zone around the tower will be void of heliostats. While this zone will house the receiver, it may also need to house ancillary equipment such as pumps, heat exchangers and turbine, although these may also be sited underground.

The literature reviewed in this paper considers a range of heliostat field styles, being asymmetric surround, symmetric surround or polar wedge. While asymmetric surround fields are common for large solar thermal electricity plants, it is likely this will remain the case for large single-tower beam-down systems, while the other options remain under consideration for small multi-tower systems.

Tower

The tower height relative to the outer size of the heliostat field gives a rim angle, with a small rim angle having a relatively tall tower to field radius. This may also be considered in terms of the optical *f*-Number, which is the focal length divided by twice the field radius. Thus decreasing the field radius, whist keeping then focal length constant, decreases the rim angle and increases the *f*-Number. As shown by Vant Hull (2014, decreasing the field radius decreases the receiver incident power whilst increasing the concentration (Figure 4).

This paper has not considered the tower design options but notes that the tower may need to be a significant structure to support the secondary reflector to prevent imparting wind loads onto the mirror, thereby increasing aberration errors. Consideration should also be given to preventing soiling of the secondary mirrors as well as potentially needing to capture and/or dissipate heat to cool the secondary reflector.

Tower Reflector

The literature reviewed in this paper covers hyperboloidal, flat and ellipsoidal secondary reflectors. It is most common for researchers to consider the hyperbola. Leonardi (2012) compared different eccentricities and found that at low eccentricity, the sunshape is most spherical and the magnification is largest, resulting in the lowest concentration. At high eccentricity, as the secondary reflector becomes more flat, the sunshape is more elliptical and the magnification is unity, resulting in little concentration. In 2016 she found a convex or hyperboloidal secondary reflector provides higher annual energy collection than a flat secondary, particularly at low receiver radius.

Thus Leonardi and Vant Hull are both clear that there is a trade-off between either power or energy collection and concentration.

Seigel and Ermanoski (2013) considered flat secondary but located the receiver close “up the tower” close to the secondary. While this avoids losses due to magnification, it negates some of the common drivers for beam-don to have the receiver close to the ground. In this case the receiver aperture is the entrance to a reactor and having a CST particle reactor facing upwards has some advantages over a particle reactor facing downwards.

Kodama et al (2014) considered an elliptical secondary reflector but did not achieve the desired flux density. They added a CPC to increase the concentration by ~4-5 and then found they needed to cant the CPC 6-12° to provide more uniform flux distribution. Since they are using a semi-circular field, further consideration is required to determine whether canting the secondary reflector, more concentrating heliostats or a surround field provide alternative solutions.

Receiver

In this paper, the receiver is taken to be the focal or aperture plane. It is noted that CPCs are often considered as part of the receiver to increase the concentration. CPC may also provide a means of minimizing heat losses from the receiver by shielding the cavity from aperture wind and/or reducing convection currents.

It is noted that Leonardi (2012) proposes that concave heliostats offer the possibility of avoiding a CPC. Seigel and Ermanoski (2013) propose to locate the receiver close "up the tower" close to the secondary to avoid needing a CPC. The height of the receiver is an important consideration to avoid introducing additional shading of the solar field.

Other CST beam-down systems

Although this paper focuses on central receiver tower beam-down systems, the general concepts can also be applied to

- linear Fresnel systems, where a longitudinal receiver might be fixed and located near the ground
- parabolic trough systems, where longitudinal receiver might be integrated into or onto a torque bar at the vertex
- parabolic dish systems, where a cavity receiver might be integrated into or onto the structure at the vertex

A brochure in 2009 describes the CNRS solar furnace in Ordellio, France. This furnace has a more horizontal beam-redirection and is intended for research purposes. The heliostat field reflective area is given as 2136 m², with the elliptical secondary reflector area as 1830 m² and the receiver area as 0.29 m². This equates to a heliostat-to-secondary geometric concentration ratio of 1.17 and heliostat-to-receiver geometric concentration ratio of 7321. The thermal output is stated as 600 kW, equating to an average flux of 2026 kW/m². This flux equates to a black-body radiation temperature of 3371 K. Assuming a peak insolation of 1 kW/m², the thermal output relative to the heliostat area is 28.1%.

The peak and annual optical efficiency of a "conventional" CST collectors in large solar thermal electricity plants are

- parabolic dish: peak 94%, annual 87%
- central receiver tower: peak 63%, annual 51%
- parabolic trough: peak 72%, annual 59%
- linear Fresnel: peak 64%, annual 41%.

It is noted that the most significant proportion of the cost for large solar thermal electricity plants is for the CST collectors (Fernandez-García et al., 2016). The beam-down system increases this cost by adding the secondary reflector whilst reducing the overall optical efficiency. The beam-down system also either (1) reduces power and concentration or (2) requires more complex concentrating heliostats and/or more complex receiver by including a CPC. Thus the potential applications for beam-down systems must be able to tolerate thermal energy costs that are higher than equivalent large solar thermal electricity plants. These applications are likely to include solar thermochemistry where the additional cost is warranted by the value of the products.

5. Conclusion

Although beam-down systems will have a lower optical efficiency than an equivalent tower system, there is also a trade-off between either power or energy collection and concentration. The power or energy collection and concentration can be improved by using small, individually controlled heliostats, and keeping the rim angle and heliostat field outer radius small, with options of asymmetric surround, symmetric surround or polar wedge fields being options for small multi-tower systems. Convex or hyperboloidal secondary reflectors provides higher annual energy collection than a flat secondary, particularly at a low receiver radius. CPCs are often considered as part of the receiver to increase the concentration.

The beam down concept may be applied to CST systems other than central receiver tower systems. . The application of beam-down systems may be suited to applications, such as solar thermochemistry, where the cost of the additional plant is warranted by the value of the products.

6. References

Blackmon, J.B. (2008) "Tri-Lateral Noor al Salaam High Concentration Solar Central Receiver Program" report of

DOE Grant Number DE-FC36-02GO12030

Blanco, M.J. and Miller, S.A. (2016) "Introduction to concentrating solar thermal (CST) technologies" in Blanco, M. and L.R. Santigosa (eds.) Advances in Concentrating Solar Thermal Research and Technology. Woodhead Publishing, 2016. ISBN: 978-0-08-100516-3

CNRS (2009) "High Temperature Solar Energy" brochure from https://history.gtri.gatech.edu/history/files/media/other-publications/High_Temp_Solar_Energy_Pamphlet.pdf (downloaded on 29-Sep-2017)

CSP Today (2011) "Italian project shows strong potential for sand-based CSP" Posted on Apr 11, 2014" http://beta.csptoday.com/technology/italian-project-shows-strong-potential-sand-based-csp (accessed 16-Jun-2014)

Fernandez-García, A., Sutter, F., L. Martínez-Arcos, L., Valenzuela, L., and Sansom, C. (2016) "Advanced mirror concepts for concentrating solar thermal systems" in Blanco, M. and L.R. Santigosa (eds.) Advances in Concentrating Solar Thermal Research and Technology. Woodhead Publishing, 2016. ISBN: 978-0-08-100516-3

Grange, B., Kumar, V., Gil, A., Armstrong, P.R., Codd, D.S., Slocum, A. and Calvet, N. (2015) "Preliminary Optical, Thermal and Structural Design of a 100 kWth CSPonD Beam-down On-sun Demonstration Plant" Energy Procedia, 75, pp.2163-2168

Hasuike, H., Yuasa, M., Wada, H., Ezawa, K., Oku, K., Kawaguchi, T., Mori, N., Hamakawa, W., Kaneko, H. and Tamaura, Y. (2009) "Demonstration of Tokyo Tech Beam-Down Solar Concentration Power System in 100 kW Pilot Plant" In Proceedings of 15th International Symposium on Concentrated Solar Power and Chemical Energy Technologies, Berlin, Germany

Hoffmann, R.J. (2011) "Modeling of a novel solar down beam test facility utilizing Newtonian optics" UNLV Theses, Dissertations

Kodama, T., Gokon, N., Matsubara, K., Yoshida, K., Koikari, S., Nagase, Y., & Nakamura, K. (2014). "Flux measurement of a new beam-down solar concentrating system in Miyazaki for demonstration of thermochemical water splitting reactors" Energy Procedia, 49, 1990-1998

Leonardi, E. (2012) "Detailed analysis of the solar power collected in a beam-down central receiver system" Solar Energy, 86(2), 734-745.

Leonardi, E. (2016) "On the Use of Concave Heliostats in a Beam-Down Central Receiver System" International Journal of Energy Science, 6(1), 21-35

Magaldi (2016) "CSP – Concentrating Solar Power, STEM® - Solar Thermo-Electric Magaldi" http://www.magaldi.com/en/products-solutions/csp-concentrating-solar-power (accessed 13-Sep-2017)

Mokhtar, M. (2011) "The Beam-Down Solar Thermal Concentrator: Experimental Characterization and Modeling" Master of Science thesis, Masdar Institute of Science and Technology

Mokhtar, M., Meyers, S.A., Armstrong, P.R. and Chiesa, M. (2014) "Performance of a 100 kWth concentrated solar beam-down optical experiment" Journal of Solar Energy Engineering, 136(4), p.041007

Potter, D., Kim, J-S., Khassapov, A., Pascual, R., Hetherton, L. and Zhang, Z. (2017) "Heliosim: An integrated model for the optimisation and simulation of central receiver CSP facilities" SolarPACES, Santiago, Chile, 27-Sep-2017

Rabl A. (1976) "Tower reflector for solar power plant" Solar Energy 18(3), 269-271

Segal, A. (2011) "Optimization of heliostat field layout for the beam down optics" Report SFERA, WP.13, Task 2, July 2011 (last revision 30 July 2011)

Segal, A.; Epstein, M. (2000) "The optics of the solar tower reflector" Solar Energy 69, 229-241

Segal, A.; Epstein, M. (2003) "Solar ground reformer" Solar Energy 75 (2003) 479–490

Siegel, N. P., & Ermanoski, I. (2013) "A beam-down central receiver for solar thermochemical hydrogen production" In Proc. Solar. 2013. https://www.osti.gov/scitech/servlets/purl/1115952 (accessed 30-Mar-2017)

Vant-Hull, L.L. (1991) "Concentrator optics" In: Winter, C.-J., Sizmann, R.L., Vant-Hull, L.L. (Eds.), Solar Thermal Power Plants. Springer Verlag.

Vant-Hull, L.L. (2012) "Central tower concentrating solar power (CSP) systems" In: Concentrating solar power

technology: principles, developments and applications, Woodhead Publishing, Cambridge, UK.

Vant-Hull, L.L. (2014) “Issues with beam-down concepts” Energy Procedia 49, 257 – 264

7. Nomenclature

Symbol	Description	Units, range and sign convention
F_1	Upper focal height	m
F_2	Lower focal height	m
h_{hel}	Heliostat depth/height	m
h_{rec}	Receiver height	m
r_{hel}	Heliostat radius	m
R_{min}	Inner heliostat field void radius	m
R_{min}	Outer heliostat field limit radius	m
r_{sec}	Secondary reflector radius	m
r_{sec}	Receiver radius	m
z_{min}	Secondary reflector minimum height	m
z_{min}	Secondary reflector maximum height	m
Δ_1	Canted heliostat effective height	m
Δ_2	Canted heliostat effective width	m
Δ_3	Focal height of top of furthest heliostat	m

Experimental validation of a novel light-splitting technique for retrofitting CSP plants by hybridizing with CPV

Matthew Orosz[1], John Dale[1], and Todd Otanicar[1]
The University of Tulsa, Tulsa (USA)

Abstract

Photovoltaic (PV) solar power generation is expanding rapidly relative to Concentrating Solar Power (CSP) due to a faster decline in solar PV panel costs after manufacturing commenced in east Asia in the 1990s. One remaining advantage of CSP is thermal energy storage (TES) which allows for smoothing output and timed dispatch of power at utility scales, whereas PV power, which currently has lower investment and levelized costs, is dependent on battery storage that has not yet matured at a large scale. There are potential advantages in hybridizing the two technologies if the low investment cost and higher areal basis yield of PV can be combined with CSP's robust and scalable storage. Under the Advanced Research Projects Agency-Energy (ARPA-E) FOCUS program, our team developed a novel approach to achieve CSP-PV hybridization through an add-on package that can retrofit existing parabolic trough collector (PTC) plants with secondary spectrum-splitting optics and a concentrating PV (CPV) receiver. The dichroic filter transmits UV and IR solar irradiance to the standard evacuated tube heat collection element (HCE) while wavelengths that are optimally utilized by PV are reflected down to an actively cooled flow through CPV receiver. The fraction of solar energy remaining available for storage can be tuned between 20-100% through configuration of the extension and optical properties of the filter. An experimental section of a standard RP3 mirror parabolic trough and HCE outfitted with the upgrade demonstrates the proof-of-concept for the approach and validates key technical and economic performance targets. The results of these experiments are relevant to operators of CSP plants as a means of enhancing output and return on investment.

Keywords: Solar, CSP, PV, Thermal, Storage, Hybrid, Retrofit, Parabolic Trough, Dichroic filter, CPV

1. Introduction

Solar thermal, also known as concentrating solar power (CSP), and solar photovoltaic (PV) generation are competing approaches to viably and economically supply utility scale energy converted from sunlight. In the past decade market forces, technology and volume manufacturing in east Asia have resulted in PV power surpassing CSP in installed capacity and bankability, with PV projects competing for power purchase agreements (PPAs) at prices competitive with traditional sources (Bleich & Guimaraes, 2016). As penetration of grid-scale solar generation has increased since the 1980s, the phasing of daytime supply against 24-hour demand has led to an increased awareness of the value of energy storage in promoting and maintaining grid stability (Castillo & Gayme, 2014). CSP historically has been coupled with an economical grid-scale storage solution by capturing solar energy as heat, pre-conversion to electricity, in thermal energy storage (TES) typically using molten

doi:10.18086/swc.2017.04.12 Available at http://proceedings.ises.org

salts and other phase change materials (PCMs). Photovoltaics directly convert sunlight to electricity and therefore require batteries for energy storage. Due to nascence of technology for grid-scale battery deployment both the absolute and relative capacity of battery storage to solar generation lags for PV in comparison with CSP (Orosz, 2015). Whereas PV and CSP generation are technologically disparate conversion methods, there is a means of fusing the technologies to pair the advantages of PV's low investment costs with CSP's mature and scaleable thermal batteries. This paper describes an approach for separating the solar spectrum via the addition of an optical filter to the standard parabolic trough collector (PTC) CSP architecture and equipping the PTC with a secondary, linear, actively-cooled concentrating photovoltaic (CPV) receiver.

2. Spectrum Splitting Secondary Optics

Under the Advanced Research Projects Agency-Energy (ARPA-E) FOCUS program, several concepts for spectrum-splitting hybrid solar thermal and photovoltaic power are under investigation with the rationale of coupling with TES to promote grid stability. The conversion of photons into electricity is only marginally wavelength dependent for CSP technology; to a first order approximation the spectral response of optical and thermal elements in solar thermal conversion is flat. Approximately 70% of a photon's energy can be expected to be concentrated and captured as heat and from there conversion to electricity by endoreversible thermodynamic means is typically around 30% for a 390ºC steam Rankine cycle, for a combined efficiency of around 22% for a well matched solar field and power block (Lovegrove & Stein, 2012). Photovoltaics conversely have a distinctive spectral response due to the bandgap of the semi-conductor junction: longer wavelength photons below the bandgap energy (E_g) threshold fail to promote an electron into the conduction band, while high energy photons excite electrons into overshooting and relaxing back towards the band gap. Over 70% of the solar spectrum in a single junction PV cell is lost in heating up the device, however the quantum efficiency of conversion at the band gap approaches 90% and falls off from there towards higher wavelengths (Green, 1982). This suggests a simple logical framework for comparison of PV and CSP efficiency on the basis of spectral determinants: for any wavelength a photon would be optimally directed to PV where the quantum efficiency of the PV cell exceeds a baseline of 22%, and elsewhere directed to CSP. Calculating this in turn specifies the band edges for a dichroic filter interposed in the flux line of a PTC with transmission and reflection bands capable of splitting sunlight and directing photons of differing energies to their respective optimal targets. Following this procedure we specify a spectral response for an optical coating on borosilicate glass facets for reflecting (mainly visible and near IR) light downwards to a CPV receiver using single junction c-Si cells (E_g of 1.1 eV). The as-built performance of the filter at normal incidence is shown in Figure 1.

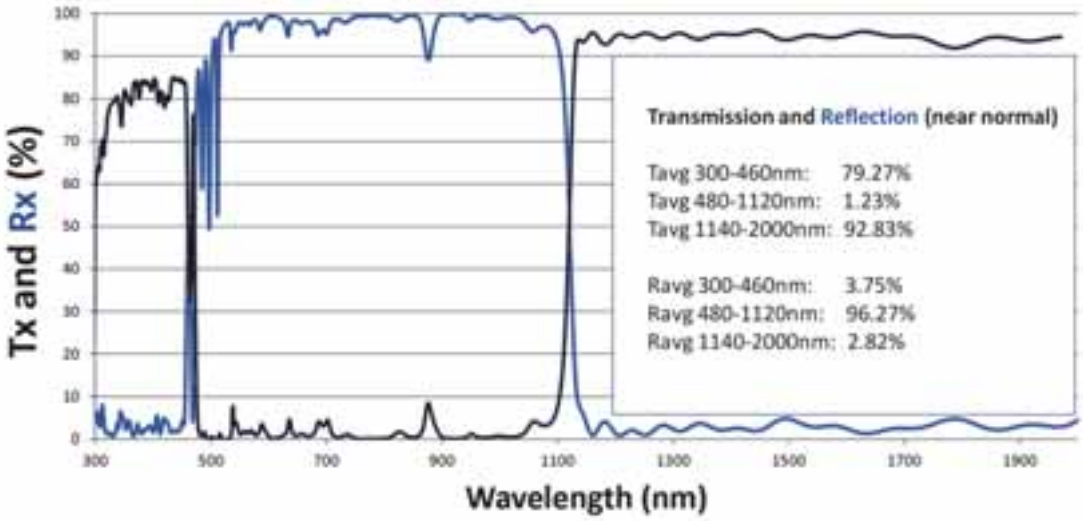

Figure 1. Spectral response of a dichroic filter for separating light into bands optimized for PV (blue) and CSP (black) receivers

It should be noted that efficiency is not necessarily the only determinant of the filter design. The selection of the band edges for reflection to the CPV receiver is subject to tuning as part of an optimization strategy considering component and system level efficiency and economic impacts - which may be site specific relating to the Rankine power cycle specifications and the physical properties of any connected thermal energy storage (TES) system. The retrofit can be flexibly adapted, by means of the dichroic filter spectral response and physical placement, to redirect design specific amounts and wavelengths of the solar spectrum within wide ranges.

3. CSP-CPV Retrofit Prototype

3.1. Design approach and component performance validation

To evaluate the potential for solar thermal and photovoltaic hybridization ("Retrosol") our team modelled and considered both ground-up designs and approaches that add filter and CPV components to an existing CSP platform (Matthew Orosz, Zweibaum, Lance, Ruiz, & Morad, 2016). The latter strategy has the economic advantage of requiring minimal investment since the primary optical and thermal infrastructure is already present, and the deployment of specialized concentrating PV panels is minor in extent relative to the solar field aperture due to the 50-100 concentration factor. Techno-economic dynamic modelling of a retrofit to a case study CSP plant in Bythe, CA indicates a potential increase in power output of 30% (O'Hern, et. al., 2017). To validate the concept and the previously developed performance models we designed a prototype for on-sun testing consisting of a standard inner set of RP3 mirrors (featured in many parabolic trough plant designs) focusing on a standard 70mm evacuated heat collection element (HCE) at a characteristic focal length of 1.7m – essentially a copy of the typical parabolic trough collector (PTC). The main components and design features are illustrated in Figure 2.

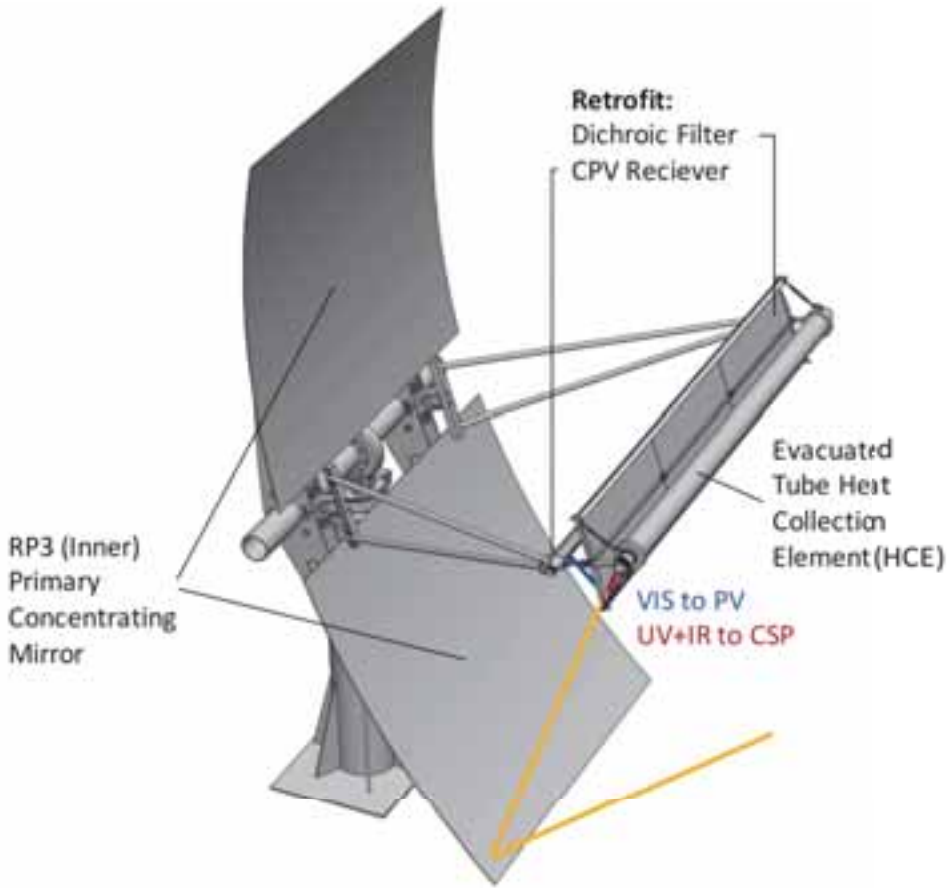

Figure 2. Prototype hybrid CSP-CPV collector using standard PTC architecture and adding dichroic filter and PV receiver as a bolt-on retrofit.

The rationale behind the design of the prototype for Retrosol is to combine the ability to experiment and collect research data with a platform that is reasonably similar to the operational Parabolic Trough Collector (PTC) power plants that would be candidates to retrofit with CPV. While PTCs are linear concentrators, there are some losses associated with walk off at the edge of the collectors that are insignificant at the length scales of 100m or longer assemblies common in CSP plants. For a single set of RP3 inner mirrors, this effect is significant and we therefore mount the PTC on an Azimuth-Zenith two-axis tracking platform such that the aperture is always normal to the sun. The use of RP3 mirrors as a primary reflector is consistent with the standard practice in PTC plants and the prototype features inner RP3 segments, a typical Schott-like Heat Collection Element (HCE), and a torque tube and arm design which is a combination of support structure that is in use in commercial plants (alongside space frame support structures). Whereas the typical PTC plant uses both inner and outer mirror segments and a single axis tracking layout, in order to operate at a reasonable scale for experimentation the prototype features only inner mirrors and uses a dual axis slewing drive for Azimuth-Zenith tracking to avoid dealing with walk-off effects on a small aperture of ~5m^2. This approach enables the project to achieve its R&D goals while demonstrating the appearance and geometry familiar to the CSP industry which can be leveraged during technology-to-market outreach. Conceptual design of the prototype following these principles has resulted in detailed part and assembly design and fabrication with installation at the North Campus facility of the University of

Tulsa, Oklahoma, USA.

Testing is achieved through I-V measurement of CPV receiver output and heat gain the HCE is measured as mass flow times heat capacity and temperature difference across the focal line.

3.2 Wind Load Analysis

In order to take appropriate steps towards a prototype design that would be compliant with relevant standards regarding safety and wind loading the team developed specifications using IEC 62817: Design Qualifications for Solar Trackers as a reference (IEC 2014). These included that the prototype structure should survive a 40 m/s (90 mph) wind and be operable in a 10m/s (22mph) wind. For this purpose a deflection of 1mm and 5mm are applied for operable and survival respectively. Wind loading is estimated using CFD flow simulation and deformation of the structure under the calculated static load is performed using finite element analysis.

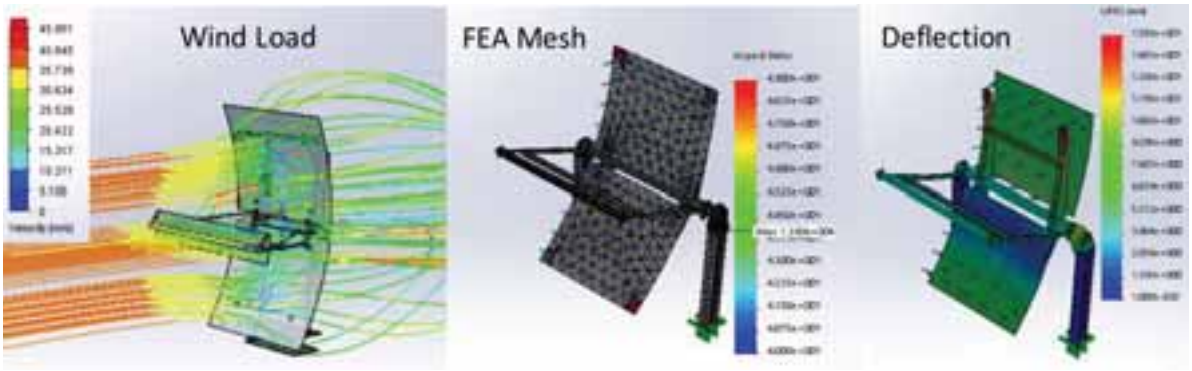

Figure 3 Design structural integrity and compliance with IEC 62817 uses simulated wind loading and finite element modeling

These analyses were used to investigate different mounting configurations and evaluate various design configurations for the mounting of the CPV receiver and dichroic filter. As a result of this process several changes were made to improve structural support of the receivers while also enabling them to be readily serviced and replaced in the field (an important consideration for operation and maintenance). This was a challenge due to the fact that there is a tradeoff between adding structure and shading the primary, and the fact that while the CPV receiver is intermediate between the torque tube and the HCE, a support that extends up from the torque tube supporting both CPV and HCE should be able to function while either one is removed. The updated configuration for mounting the CPV receiver meeting these requirements is shown below.

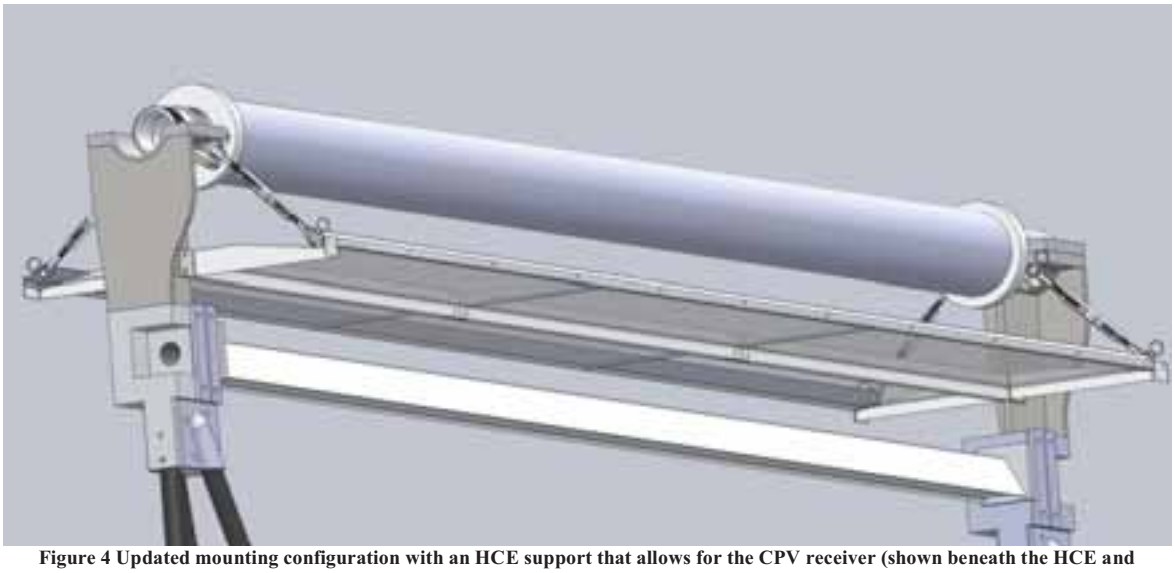

Figure 4 Updated mounting configuration with an HCE support that allows for the CPV receiver (shown beneath the HCE and dichroic secondary) to be removed for servicing from the side

3.3 CPV Receiver design

SunPower Maxeon back contact cells are deployed in the Retrosol CPV receiver as a low cost option that avoids the shading losses from dense front contacts (needed to convey increased current at concentration) of specialized concentrator cells. The solid copper substrate is suitable for managing the current generated at concentration. Because current increases nearly linearly with concentration and SunPower panels are nominally fused at 15A, the ~5A I_{mp} Maxeon cell nominally remains within its specifications if operated up to 10 suns and possibly can be operated at even higher concentration when e.g. the 125mm semi-square cell is sliced into 1/6th sections (Nesterenkov et. al., 2016).

The Retrosol prototype under development uses a 50mm width CPV receiver but to facilitate testing in parallel with construction, a version using the form factor of a Cogenra Solar T14 concentrator receiver was manufactured using 64 SunPower 1/6th form factor cells in series with customized interconnects made of bus wire and encapsulated using liquid silicones (Figure 5).

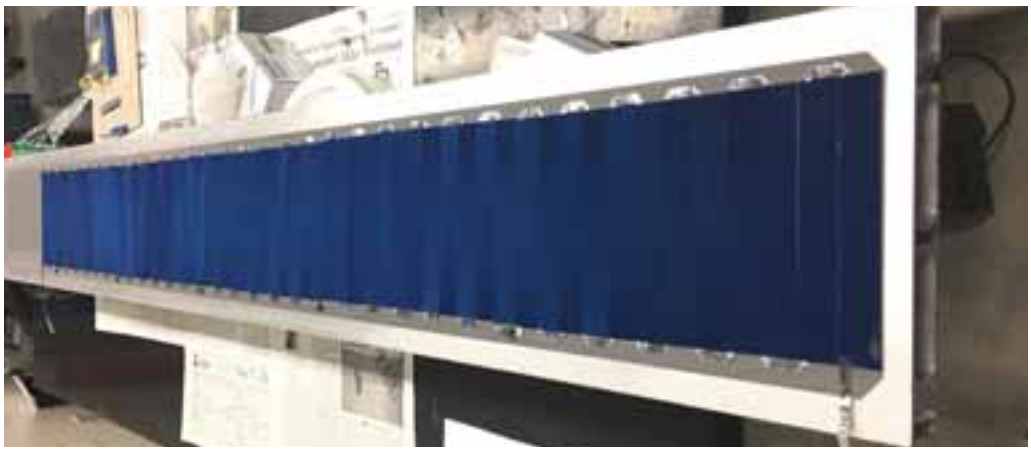

Figure 5. T14-type CPV receiver fabricated at TU using 1/6th SPWR Maxeon cells in series

Vopen (V)	39.59		Area:	0.17	m^2
Ishort (A)	0.985		Irradiance:	1031	W/m^2
Vmaxp (V)	31.41		Efficiency:	15.98%	

Imaxp (A)	0.891
Pmax (W)	28.01

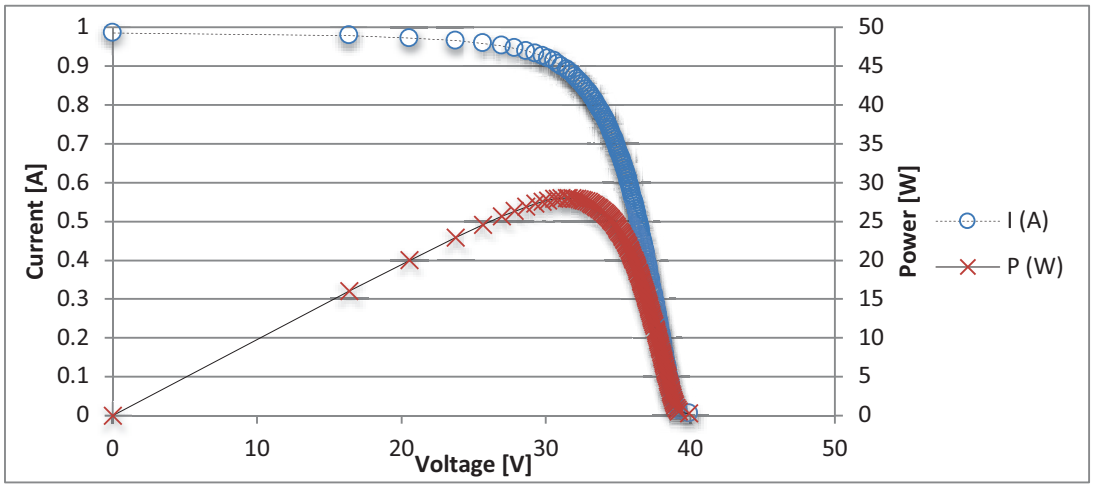

Figure 6. 64 cell SPWR Receiver benchmarked at 1-sun and ambient temperature (electrical data in table above)

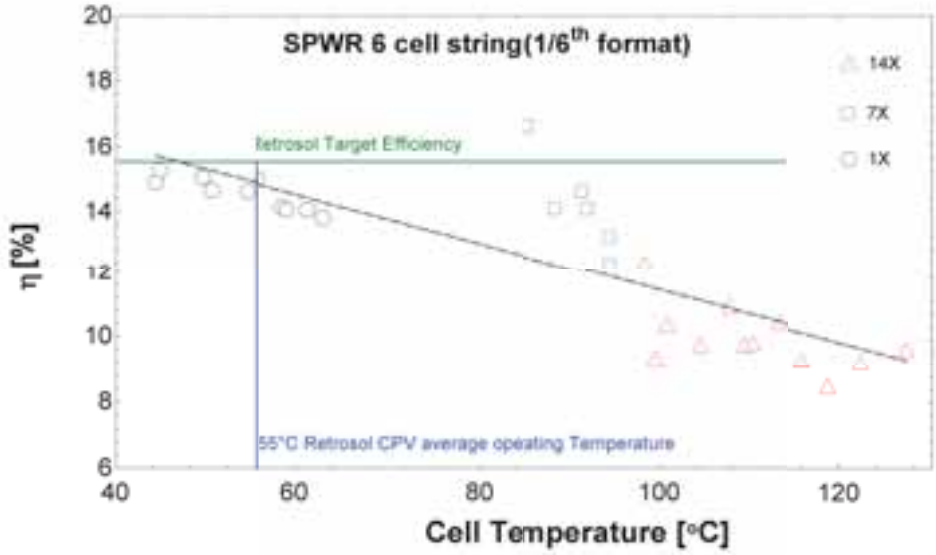

Figure 7. Test data for a 6-cell SPWR CPV Reciever at 1, 7 and 14X and a range of temperatures

Test sections of the SunPower T14 type CPV receiver were tested at 1, 7 and 14X (Figure 7) in a T14 concentrator (Morad, 2014), and the data indicates that concentration (at least up to 14X) is not significantly impairing receiver performance whereas temperature plays a driving role in CPV receiver efficiency. Further testing is underway but extrapolation of this dataset indicates that operational efficiencies at an average receiver temperature of 55°C will be approximately 95% of the targeted 15.8% efficiency.

3.4 Retrofit mounting considerations

The prototype provides an example of a design that uses a torque tube as the foundation for the attachment of mounting struts for the HCE. Torque tubes are a common design feature in parabolic trough collectors, beginning with the LS-2 design used at SEGS I-VII in California as well as troughs designed by Sener (Extrasol and Valle plants in Spain, Genesis in the US) and ENEA. Similar to these collectors, the prototype mounts the primary mirror

on cantilevered arms. The prototype is compatible with torque tube designs with the only modification being the U-bolt clamp to accommodate variation in torque tube diameters, which are generally standard pipe cross sections so only a few variants would be needed. Alternative designs in the market would require more modification to the attachment format. These include Flabeg's torque box design (Andasol plants in Spain and Kuraymat in Egypt) and Acciona (Nevada Solar One) and Abengoa (Solana, Mojave in the US) space frame mirror support structures. For these formats the prototype mounting structure would require additional modification to adjust the mode and orientation of the fixture to the frame elements, as well as variation in the length of the support. These aspects are considered to be relatively straightforward mechanical engineering challenges that could be addressed quickly with access (via partnership) to the relevant structural design drawings and documentation.

4. Prototype Evaluation

Figure 8 Prototype hybrid CSP-CPV system in on sun operation

Initial on-sun testing of the Retrosol prototype (Figure 8) has been dedicated to experiments that have benchmarked the durability of the ~65W 0.5m length CPV receiver section installed (no degradation of maximum power point output after daily use at operating temperatures) under conditions of 45x concentrated sunlight (reflected in the 500-1000nm band) and evaluating various power evacuation techniques. The remaining (~23%) of concentrated sunlight not utilized by the CPV receiver passes through the dichroic filter and is absorbed by the HCE. Because radiative and convective heat losses to the ambient are a function of operating

temperature (averaging around 300°C in the collector field) , the diversion of a significant portion of the solar spectrum to the CPV receiver results in a corresponding reduction in the efficiency of the HCE due to constant losses and less heat gain per unit length under lower incident irradiance (Figure 9). The dichroic filter effectively increases thermal losses by up to 30% at operating temperatures, however, this thermal efficiency penalty is compensated by the increased in-band quantum efficiency of the CPV receiver.

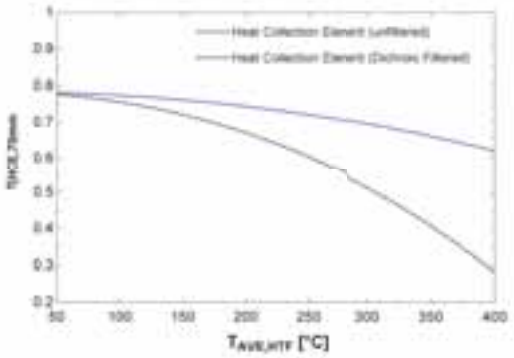

Figure 9 HCE performance pre (solid blue line) and post (dashed black line) retrofit

5. Summary and future work

This work describes technical aspects of an approach for modifying CSP power plants using linear PTC solar fields with the addition of hybrid CPV receivers for increased power output using spectrum-splitting secondary optics. A practical motivation for this exists as evidenced by the example of a CSP plant (SEGS II) which was decommissioned and redeveloped with PV. Retrofitting the existing solar field with a CPV receiver represents an alternative means to achieve PV conversion and increased capacity. The output improvement compared to investment requirement possible with this retrofit is comparatively advantageous as described in (O'Hern et al., 2017) and the validation of the performance simulation is carried out by component and system level validations, including those described in this work: spectral selectivity of the dichroic filter secondary optic and the CPV receiver efficiency at various concentrations and temperatures. The remaining components (standard HCE and CSP primary optics) are modelled using validated and well understood energy balance models based on (Forristall, 2003).

Future work includes translating the learnings from the proof of concept prototype to a full scale pilot on a collector assembly at an operating parabolic trough plant in partnership with a CSP operator to demonstrate the feasibility and benefits of retrofitting PTC plants with CPV receivers.

6. Acknowledgments

The information, data, or work presented herein was funded in part by the Advanced Research Projects Agency-Energy (ARPA-E), U.S. Department of Energy, under Award Number DE-AR0000729

7. References

Bleich, K., & Guimaraes, R. D. (2016). Renewable Infrastructure Investment Handbook: A Guide for Institutional Investors. *World Economic Forum*, *40117*(December).

Castillo, A., & Gayme, D. F. (2014). Grid-scale energy storage applications in renewable energy integration: A survey. *Energy Conversion and Management*, *87*, 885–894. https://doi.org/10.1016/j.enconman.2014.07.063

Commission, I. E. (2014). IEC 62817: Photovoltaic systems - Design qualification of solar trackers. International Electrotechnical Commission Sign in | Create account.

Forristall, R. (2003). *Heat Transfer Analysis and Modeling of a Parabolic Trough Solar Receiver Implemented in Engineering Equation Solver*. *Contract*. Golden, CO. Retrieved from http://www.mendeley.com/research/heat-transfer-analysis-modeling-parabolic-trough-solar-receiver-implemented-engineering-equation-solver-7/

Green, M. A. (1982). *Solar cells: operating principles, technology, and system applications* (Print.). Englewood Cliffs, NJ: Prentice-Hall, Inc.

Lovegrove, K., & Stein, W. (2012). *Concentrating solar power technology - Principle, developments and application*. *Woodhead Publishing Series in Energy: Number 21*. Woodhead Publishing.

Morad, R. (2014). *Solar Cogeneration of Electricity and Hot Water at DoD Installations ESTCP Project EW-201248 Final Report*. Mountain View.

Nesterenkov, A., Nesterenkov, P., & Nesterenkova, L. (2016). Fundamentals of designing hybrid concentrator solar systems. *AIP Conference Proceedings*, *1766*. https://doi.org/10.1063/1.4962073

O'Hern, H., Otanicar, T., & Orosz, M. (2017). Performance and economic optimization of hybrid solar thermal and photovoltaic power plants with dynamic simulation. In *30th International Conference on Efficiency, Cost, Optimisation, Simulation and Environmental Impact of Energy Systems*. San Diego.

Orosz, M. (2015). Photovoltaics and concentrating solar power : why hybridization makes sense. *SPIE Newsroom*, 1–4. https://doi.org/10.1117/2.1201508.006018

Orosz, M., Zweibaum, N., Lance, T., Ruiz, M., & Morad, R. (2016). Spectrum-splitting hybrid CSP-CPV solar energy system with standalone and parabolic trough plant retrofit applications. *AIP Conference Proceedings*, *1734*(June). https://doi.org/10.1063/1.4949170

Molten Carbonates Electrolyzer Model for Hydrogen Production Coupled to Medium/Low Temperature Solar Power Plant

Miguel A. Reyes-Belmonte[1], Alfonso Delgado[2], Elena Díaz[1], José González-Aguilar[1] and Manuel Romero[1]

[1] IMDEA Energy Institute, Móstoles (Spain)

[2] Universidad Autónoma de Madrid, Madrid (Spain)

Abstract

In this work, mathematical model of molten carbonates electrolyzer (MCEC) has been developed for its integration into concentrating solar power (CSP) plant. MCEC modeling has been based on electrochemical and thermodynamics approach using experimental information from a testing device. Despite the high temperature requirements for MCEC operation (above 500 ºC), heat generation during the electrolysis process reduces the requirement of external heat addition. Energy optimization approach using ASPEN HYSYS pointed out that MCEC stable operation could be achieved for a wide temperature range of the feeding steam by using smart heat recovery diagram. Temperature conditions that are covering from exothermal to thermoneutral working conditions have been explored depending on the input thermal and electrical requirements. MCEC model described in this work has been encoded into TRNSYS platform for transient performance evaluation. Optimal integration scheme of MCEC coupled to linear-Fresnel solar plant has been proposed and sized for the hydrogen production of a refueling station.

Keywords: High Temperature Electrolysis, Molten Carbonates, CSP Modeling, Hydrogen Production

1. Introduction

Concentrating Solar Power (CSP) consists in producing electricity through thermo-mechanical transformation by heating a working fluid using concentrating solar technologies (parabolic through, solar tower, parabolic dish or linear Fresnel (Lovegrove and Stein, 2012)). Later this fluid is expanded inside the turbine of a power cycle converting the thermal energy into mechanical power and electricity by its self-mounted generator. CSP deployment has been growing over the last few years as it is seen as one of the most promising energy options for the upcoming years. This is mainly due to its high flexibility on energy dispatch thanks to use of thermal energy storage (TES).

Apart from the wide variety of TES systems mainly focused on short- medium term thermal storage, an alternative way is considered based on production of energy carriers like hydrogen. In this case, hydrogen can be used either for compressed storage, transportation, electricity production using a fuel cell (Carrette et al., 2001), engine powering (Dimitriou and Tsujimura, 2017) or as a valuable product for chemical and oil companies. Despite the high interest and number of applications for hydrogen, its production is still considered a costly and high greenhouse gas emission process since most of hydrogen is still produced from fossil fuel sources. However, for becoming a true zero-emission energy carrier, hydrogen should be produced from renewable energy sources such as wind, solar energy (Sanz-Bermejo et al., 2014b) or biomass (Dincer and Acar, 2015). Several technologies can be used for hydrogen production from renewable energy sources such as biomass gasification, solar-driven direct water splitting, solar-driven high-temperature thermochemical water splitting, bio-derived liquids reforming or water electrolysis using renewable electricity (Ibrahim Dincer, 2012). Water electrolysis is based on water splitting into its components (hydrogen and oxygen) inside an electrochemical device (electrolyzer) by applying an electrical current. Low temperature water electrolysis is a mature technology and hydrogen plants based on alkaline or proton exchange membrane (PEM) electrolyzers are very common. Nevertheless, power consumption is relatively high (Zeng and Zhang, 2009). Therefore high temperature steam electrolysis is being developed as an alternative because it shows a decrease on the electrical power requirements in spite of an increase of thermal energy demands as steam temperature increases (Laurencin and Mougin, 2015). This is explained from kinetics point of view, since higher temperature is promoting electrode activity while reducing cell overvoltage what is translated into lower energy losses and

doi:10.18086/swc.2017.04.13 Available at http://proceedings.ises.org

more efficient process (Schiller et al., 2009). Two main electrolyzer technologies can be distinguished for high temperature electrolysis; these are Solid Oxide Electrolytic Cell (SOEC) and Molten Carbonates Electrolytic Cell (MCEC). These devices operate at temperatures above 500 ºC at higher power density than conventional low temperature electrolyzers. These characteristics allow more compact components and less number of units. SOEC and MCEC can work either as electrolyzer or as fuel cells improving grid stabilization in a near and likely future with high penetration of renewable energy sources.

In this work, an electrochemical and thermodynamic model for molten carbonates electrolyzer (MCEC) has been developed and validated with experiments from small lab demo prototype (Frangini et al., 2014). Due to the small size prototype, scaling-up design has been proposed and applied for larger power plants corresponding to commercial application of 400 kg/day for hydrogen production. This scenario corresponds to hydrogen requirements for municipality refueling station (Sanz-Bermejo et al., 2014a). Proposed model has been used to investigate the effect of working operative conditions (current density, steam temperature, conversion ratio…) on MCEC performance. Trends and limits found from that analysis will help choosing best operative conditions. Later, proposed model has been encoded as a TRNSYS component (Trnsys, 2007) for the dynamic analysis. Integration scheme for MCEC coupling to the solar plant has been proposed and energy recovery network optimized for system efficiency maximizing. Finally, solar plant requirements have been discussed for linear Fresnel coupling assessment.

2. Molten carbonates electrolyzer (MCEC) description

One of the main differences between SOEC electrolyzers and MCEC is the requirements of the second one on CO_2 feeding together with water steam. Water and carbon dioxide molecules decompose into H_2 and carbonate ion (CO^{3-}) at electrolyzer cathode. Simultaneously CO_3^{2-} diffusion occurs through the alkaline electrolyte made of lithium, sodium and potassium towards the anode resulting into CO_2 and O_2 (Hu et al., 2014). Chemical reactions occurring inside the MCEC are summarized in Table 1.

Table 1 MCEC involved reactions

Cathode	$H_2O + CO_2 + 2e^- \leftrightarrow H_2 + CO_3^{2-}$
Anode	$CO_3^{2-} \leftrightarrow CO_2 + ½\ O_2 + 2e^-$
Full conversion	$H_2O + O_2 \leftrightarrow H_2 + CO_2 + ½\ O_2$
ΔH_r (298 K)	285,8 kJ/mol

Nickel-based alloy with chromium and aluminum rate between 2-10 % is employed for the cathode due to its sintering resistance and mechanical properties (Bodén, 2007). The anode is made of NiO with lithium and MgO intercalated (Antolini, 2011; Hu et al., 2014) in order to avoid short-circuits into the cathode. Ceramic matrix made of $LiAlO_2$ (Hu et al., 2014) separates the cathode from the anode and supports the electrolyte LiNaK, which is a ternary eutectic mixture of molten carbonates Li_2CO_3-Na_2CO_3-K_2CO_3 (Frangini et al., 2014; Hu et al., 2014).

MCE concept is quite flexible and apart from H_2 and O_2 production as it is discussed in this work, it could operate for oxy-fuel combustion processes or methanation as it can be observed from Figure 1.

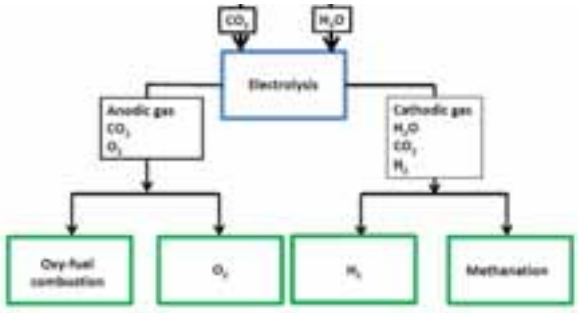

Figure 1 Applications of MCEC electrolyzer

2.1 Experimental device

Small lab-scale MCE was designed, developed and tested by ENEA (Frangini et al., 2014). This electrolyzer was made of a gold electrode with surface area of 0.2 cm^2 and a standard oxygen electrode of gold immersed in molten electrolyte and hold by alumina tube with a small hole at the bottom part. CO_2 and O_2 mixture in a relation of 2:1 with gold sheet of 1cm^2 surface was employed as counter-electrode. A mixture composed of alkaline molten carbonates Li_2CO_3-Na_2CO_3-K_2CO_3 with 43.5-31.5-25.0% molar ratio was used. This mixture has its melting point at 397 ºC. Several steady-state galvanostatic and cyclic voltammetric tests were performed for a temperature range between 500 ºC and 600 ºC as it can be seen on Figure 2. Experiments were performed by introducing different gas compositions of dry CO_2 and wet mixture in a 50:50 composition (p_{CO2}=0.5 atm; p_{H2O} =0.5 atm) at 120 ºC with a flow rate of 60 mL/min (Frangini et al., 2014).

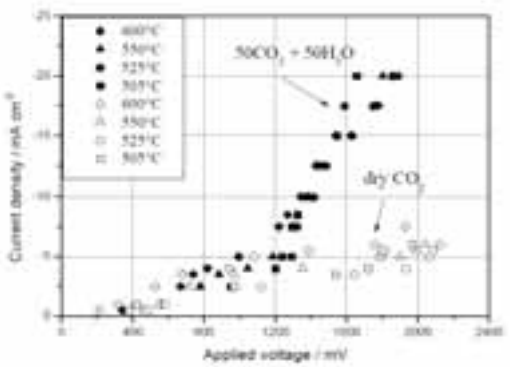

Figure 2 Applied voltage dependency according to experimental results at different temperatures (Frangini et al., 2014)

3. Mathematical model

MCE model was based on the electrochemical equations shown below.

3.1 Potential calculation: Nerst, reversible and thermoneutral

Reversible potential exchanged in a cell (eq. 1) depends on Gibbs free energy that changes with cell temperature *T* according to (eq. 2) (Brouwer et al., 2006; Petipas et al., 2013)

$$E_{REV} = \frac{\Delta_r G_T^0}{2 \cdot F} \quad \text{(eq. 1)}$$

Where *F* is the Faraday's constant equal to 96485.33 C mol^{-1}.

$$\Delta_r G_T^0 = 244800 - 49.18 \cdot T - 2.72 \cdot 10^{-3} \cdot T^2 \quad \text{(eq. 2)}$$

Nernst potential (eq. 3) depends on gases partial pressure in cathode and anode, according to electrolyzer operating pressure and spices composition (Brouwer et al., 2006).

$$E_N = E_{REV} + \frac{R \cdot T}{2 \cdot F} ln \left[\frac{p_{H_2,cat} \cdot p_{O_2,an}^{1/2} \cdot p_{CO_2,an}}{p_{H_2O,cat} \cdot p_{CO_2,cat}} \right] \quad \text{(eq. 3)}$$

Thermoneutral potential can be derived from (eq. 4)

$$E_{TN} = \frac{\Delta_r H_T}{2 \cdot F} \quad \text{(eq. 4)}$$

Where $\Delta_r H_T$ is the reaction enthalpy (eq. 5) given by (Petipas et al., 2013).

$$\Delta_r H_T = 238200 + 13.12 \cdot T - 3.53 \cdot 10^{-3} \cdot T^2 \quad \text{(eq. 5)}$$

3.2 Mass balance

Streams flow and composition can be determined using the following mass balance equations (eq. 6-10). On the first hand, hydrogen molar flow can be estimated according to Faraday's electrolysis law (eq. 6) (Petipas et al.,

2013).

$$n_{H2} = \frac{j \cdot S}{2 \cdot F} \quad \text{(eq. 6)}$$

Hydrogen production is proportional to current density j (A/cm^2) and electrodes active surface S (cm^2). Once hydrogen molar production has been determined, composition of involved species in the cathode can be determined by taking the standard conversion steam rate of the cell (x_{H2O}). Molar flow for cell feeding (n_{H2O}) can be calculated from (eq. 7).

$$n_{H_2O,cat} = \frac{n_{H_2}}{x_{H_2O}} \quad \text{(eq. 7)}$$

Considering that cell feeding is equimolar (0.5 H_2O + 0.5 CO_2) (eq. 8) can be derived (Frangini et al., 2014).

$$n_{CO_2,cat} = n_{H_2O,cat} \quad \text{(eq. 8)}$$

In a similar way, mass balance applied to electrolyzer anode results into (eq. 9) and (eq. 10).

$$n_{O2,an} = n_{H2} \cdot 0.5 \quad \text{(eq. 9)}$$

$$n_{CO2,an} = n_{H2} \quad \text{(eq. 10)}$$

3.3 Overpotential calculation

Electrolyzer working potential (E) can be determined as the sum of all system irreversibilities (eq. 11) (Brouwer et al., 2006) and includes ohmic losses (E_{ohm}), activation overpotential (η) and Nernst potential (E_N).

$$E = E_N + E_{ohm} + \eta(j) \quad \text{(eq. 11)}$$

Ohmic losses can be determined from Ohm law while the overpotential (η) is determined from Butler-Volmer expression (eq. 12) (Brouwer et al., 2006).

$$\eta = \frac{R \cdot T}{2 \cdot \alpha_A \cdot F} \cdot \sinh^{-1} \cdot \left(\frac{j}{2 \cdot j_{0,an} \cdot S} \right) + \frac{R \cdot T}{2 \cdot \alpha_C \cdot F} \cdot \sinh^{-1} \cdot \left(\frac{j}{2 \cdot j_{0,cat} \cdot S} \right) \quad \text{(eq. 12)}$$

Where j is the exchanged current (A/cm^2), α_c, α_A are transfer coefficients for cathode and anode while $j_{0,an}$ and $j_{0,cat}$ are the exchange currents of anode and cathode respectively. Due to the complexity on parameters fitting from Butler-Volmer equation and its later model programming (Sanz-Bermejo et al., 2015) simplified (eq. 13) has been proposed (Ulleberg, 2003) instead of (eq. 11).

$$E = E_{REV} + r \cdot j + s \cdot \log_{10}(t \cdot j + 1) \quad \text{(eq. 13)}$$

Where r, s and t parameters are referring to the ohmic resistance (r) and electrolyzer overpotential (s, t) that are depending on temperature.

3.4 Applied power

Electrical applied power (P) can be determined multiplying cell voltage (E), current density (j), surface (S) and the number of cells (N).

$$P = j \cdot N \cdot E \cdot S \quad \text{(eq. 14)}$$

3.5 Cell geometry

Cell dimensioning was addressed according to the following equations and considering that cells were arranged in a stack (Petipas et al., 2013; Yu et al., 2007). Unit volume depends on cell length (l), cell thickness (e_{cell}), endplate thickness (e_{plate}) and the number of cells (N) (eq. 15).

$$V = l^2 \cdot (N \cdot e_{cell} + 2 \cdot e_{plate}) \quad \text{(eq. 15)}$$

Number of stacks (eq. 16) are depending on unit volume and length.

$$N_{stack} \approx \left(\frac{\sqrt[3]{V}}{l} \right) \quad \text{(eq. 16)}$$

Number of cells per stack ($N_{cell/stack}$) can be calculated dividing the number of cells (N_{cell}) and stacks (N_{stack}). From abovementioned parameters, unit surface (S_{unit}) can be determined from (eq. 17).

$$S_{unit} = 4 \cdot \left(N_{stack} \right)^{1/2} \cdot l \cdot \left(N_{cell/stack} \cdot e_{cell} + 2 \cdot e_{endplate} \right) + 2 \cdot N_{stack} \cdot l^2 \quad \text{(eq. 17)}$$

3.6 Energy balance

Energy balance for the electrolyzer can be expressed according to (eq. 18).

$$K_s \cdot \frac{dT}{dt} = E \cdot j \cdot S \cdot (1 - \eta) - \frac{(T - 25)}{R} - n_{H_2O} \cdot c_{p\,H_2O} (T - T_{IN}) - n_{CO_2} \cdot c_{p_{CO_2}} (T - T_{IN}) \quad \text{(eq. 18)}$$

Left-hand side of the equation accounts for the temperature variation of the electrolyte whose thermal capacity was already characterized (An et al., 2016). On the right-hand side of the expression, the first term represents the gained thermal energy while the other terms are representing the energy losses. T is referring to the cell temperature while T_{IN} corresponds to the feeding temperature. Cell efficiency is determined as the ratio between thermoneutral potential (E_{TN}) and total potential (E).

3.7 Iterative solving method

MCE electrolyzer model has been derived from standard electrochemical and thermodynamics equations that are solved following the flow diagram presented on Figure 3. Design input parameters such as cell current density and steam conversion are needed for electrolyzer modeling, these parameters can be estimated from lessons learnt during experimental testing device (Frangini et al., 2014). Steam flowrate required for the electrolysis process was determined accordingly to the chosen conversion and desired hydrogen production. Main design criteria for MCE was based on hydrogen production rates for its later application, while from modeling results the number of cells, stack geometry, electricity consumption, production rates (CO_2, H_2, steam), cell temperature and the thermal energy released will be determined by solving material and energy balance equations (Petipas et al., 2013; Ulleberg, 2003).

3.8 Model fitting

Proposed model for MCEC has been calibrated using experimental data shown in Figure 2 what resulted into a series of fitting parameters for *r, s* and *t* (eq. 13). Family of coefficients was obtained due to temperature dependence of *r* and *t.* This allowed temperature-based equations definition shown in Table 2.

Table 2 Fitting coefficients proposal

Parameter	Value
r (Ω cm^2)	$-7.58 \cdot 10^{-5} \cdot T + 8.19 \cdot 10^{-2}$
s (V)	$2{,}18 \cdot 10^{-2}$
t (cm^2/mA)	$-5.69 \cdot 10^{-8} \cdot T + 6.62 \cdot 10^{-5} \cdot T - 1.91 \cdot 10^{-2}$

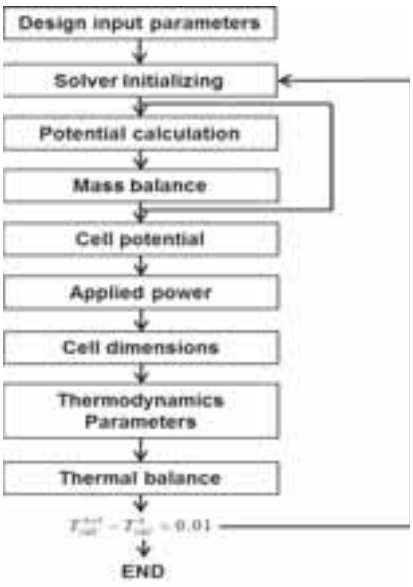

Figure 3 Solving diagram for MCEC characterization

4. Sensitivity analysis

MCEC performance has been explored using the model described above. Effects of conversion ratio, current density and feeding temperature on cell temperature and electrical power have been investigated by means of the sensitivity analysis shown on Figure 4. Data were obtained for 400 kg/day production of H_2 by fixing feeding temperature at 100 ºC (when not modified) and 60% conversion (when not modified).

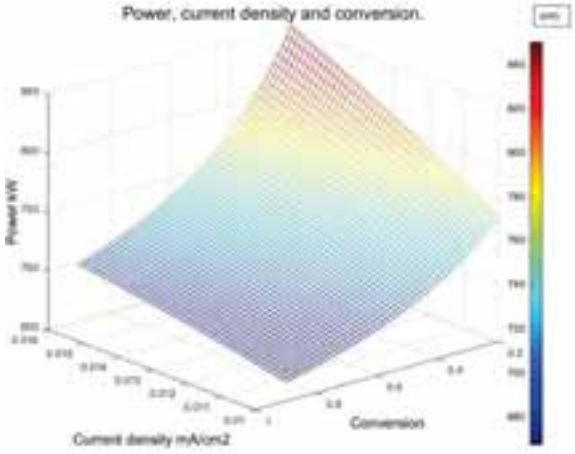

a. Given feeding temperature (100 ºC)

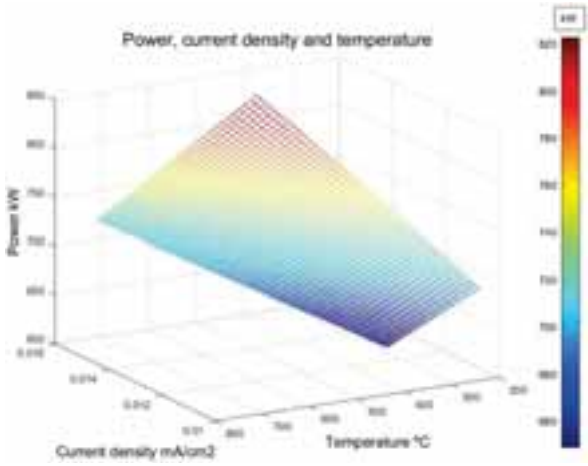

b. Given conversion rate (60%)

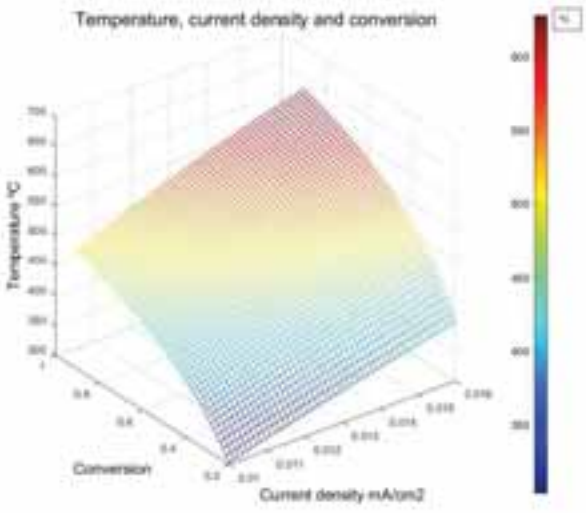

c. Given feeding temperature (100 ºC)

Figure 4 Working conditions effect on MCEC performance. Power consumption (top). Cell temperature (bottom)

As it can be observed from Figure 4-a, higher conversion rates and lower energy density currents would be desired in order to reduce electrical power consumption of the electrolyzer. Those conditions correspond to intermediate cell temperature range (400 ºC – 500 ºC) as it can be observed from Figure 4-c. This figure also gives an idea about the working range for the electrolyzer, since lowest cell temperature is limited to 400 ºC to avoid molten carbonates electrolyte freezing. Figure 4-b shows the effect of MCE feeding temperature (steam and CO_2) into electrical power consumption for a given conversion rate. As it can be observed, the lower is the feeding temperature of streams, the higher is the electrical power consumption for the electrolysis process. In other words, higher thermal input energy will be compensated with lower electrical power consumption of the electrolyzer which is the design target. Optimum working conditions for the electrolyzer should meet low density currents, with high conversion rates and high feeding temperatures.

5. Plant integration

As it was observed on Figure 4-b, high temperatures of the feeding streams to the electrolyzer are desired due to the lower electrical power consumption. In addition, MCE can operate under exothermal conditions which are increasing the temperature of the electrolyte cell. Thermal energy generated during the exothermal process can be mostly recovered using a heat exchangers network; the objective of this regeneration process is two-fold. On the one hand, it would increase the temperature of feeding streams (steam and CO_2) what will reduce electric power consumption of the MCEC. On the other hand, hot streams out of the electrolyzer will be cooled-down what is required for H_2 and O_2 separation processes whether using amines process or membranes.

Figure 5 shows the energy recovery network proposed for MCEC operation, this network was optimized using pinch-point methodology (Das, 2005) on ASPEN Energy Analyzer (AspenTech, 2017). This optimization was based on energy recovery maximizing from hot products streams (electrolyzer output) for input streams preheating (steam and CO_2) by using network of heat exchangers named as E-101, E-103, E-104, E-105 and E-106. Water from the network will be pumped into the system and firstly preheated by low temperature products stream at heat exchanger E-101. Later, water stream will be heated-up using external heat addition at E-102 in case of the electrolyzer operation cannot cover the thermal demand. This thermal power could be provided by external process heat as for example from concentrating solar power (CSP) plant. After external heat addition, heat exchanger network will be used for reaching the operation temperature of the electrolyzer. As it can be observed, membranes separation process (M-101 and M-102) has been proposed for CO_2 separation from products streams (H_2 + CO_2 for stream marked as 7 and O_2 + CO_2 for output stream 8). Separated CO_2 is recirculated back for electrolyzer feeding mixed with pumped water. Demister (component V-101) is considered for downstream cathode line for water droplets separation in those cases where the electrolyzer is operating with a conversion ratio lower than 100%. Condensed water is pumped back and mixed with feeding water stream. As

it can be observed, cathode stream (7) is cooled down while preheating feeding water through heat exchanger E-101; this will favor water droplets separation while reducing external heat addition on heat exchanger E-102. Furthermore, suitable temperature for membranes separation process M-101 will be expected after E-101 cooling down. Additional heat exchanger E-107 has been included as a heat sink for cooling down anode stream (8) to ensure low temperature for CO_2 separation on membrane M-102.

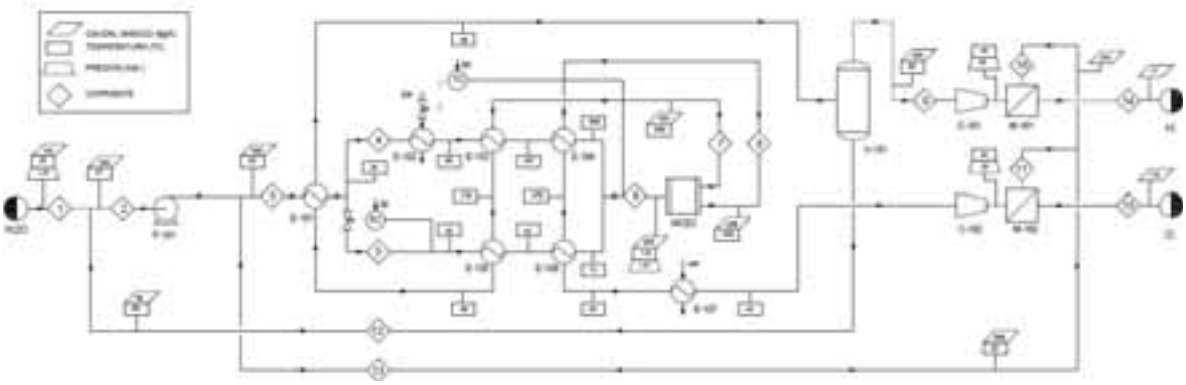

Figure 5 Energy recovery network of the MCEC

As it has can be observed on the diagram from Figure 5, feeding water stream mixed with CO_2 was separated into two streams (4 and 5) for optimizing preheating process what will reduce the external heat addition and optimizing heat exchangers network design. Mass flow splitting factor was optimized according to ASPEN HYSYS Energy Analyzer tool resulting into a ratio of 60% through the branch 4 and 40% trough branch 5 which optimized the annual cost of the system. Later, both streams were mixed again for electrolyzer feeding (branch 6). Electrolyzer feeding using separated branches was considered as well, but this option was discarded due to less efficient energy utilization resource according to pinch-point analysis.

6. TRNSYS integrated model

MCEC model described above has been programmed as a TRNSYS component (own created Type203) which will allow for performance evaluation under transient conditions and its coupling to a solar power plant. Mixer component numbered as Type210 was also developed to precisely account for energy balance when mixing streams with different fluids and with temperature dependent specific heat capacities.

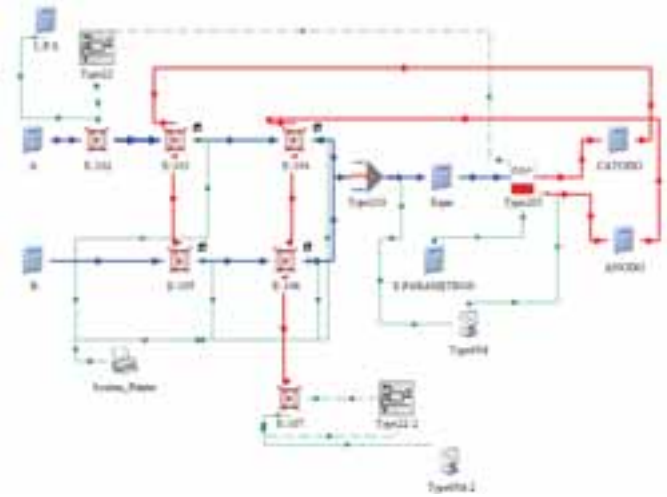

Figure 6 TRNSYS layout for MCEC developed model and auxiliaries

TRNSYS integrated model allowed to investigate the dynamic effect of warming-up the electrolyzer or its response to fluctuating temperature of feeding streams as it can be observed from Figure 7. Warming-up scenario is described on Figure 7-a, in this case the electrolyzer is fed at 1 bar and 100 ºC while molten

carbonates electrolyte are kept at initial temperature of 400 ºC (below that temperature will froze). As it can be observed, cell temperature will increase due to the exothermal electrolysis process till converging to 539 ºC cell temperature. Electrical power reduction as cell temperature is increasing is observed based on kinetics improvement and reversible potential reduction (Mazloomi et al., 2012). Figure 7-b shows electrolyzer time response against a change on feeding temperature according to sinusoidal temperature oscillation. As it can be seen, amplitude signal of 50 ºC on the feeding stream was dumped to less than 10 ºC for the electrolyte due to its thermal capacity. Similar effect on the time delay of temperature signal for the electrolyzer cell was found when varying the feeding temperature.

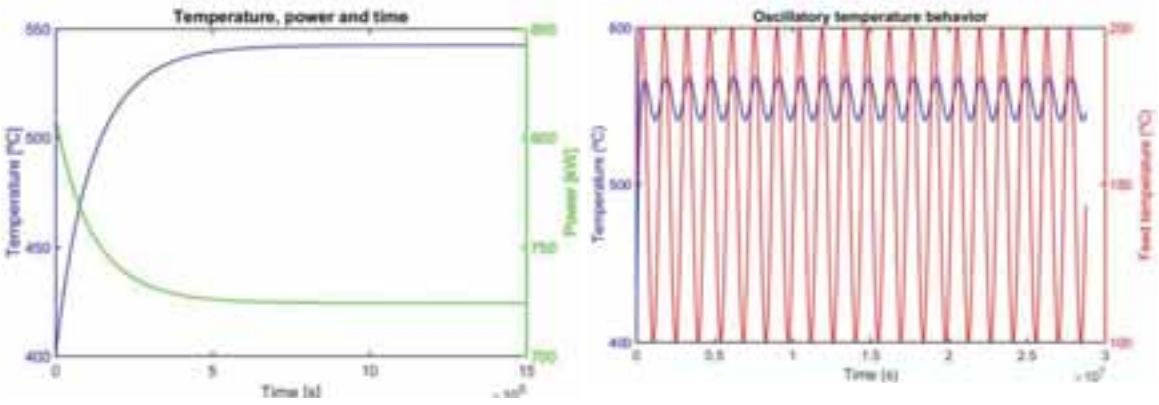

Figure 7 Time response of MCEC model programmed into TRNSYS. Electrolyzer warming-up (a). Fluctuating response (b)

7. Modelling results

Modelling results for commercial application using MCEC concept studied in this paper are presented on Table 3. Two different cases have been modelled, one corresponding to exothermal MCEC behavior with low feeding temperature and another one for thermoneutral working conditions. Working conditions for the exothermal case were taken from lessons learnt from experimental test data (Frangini et al., 2014), considering conversion ratio of 60% for current density of 0.014 A/cm^2 and low feeding temperature. Thermoneutral working conditions were determined from (eq. 4) considering cell temperature of 550 ºC. As it can be seen, the exothermal working mode consumes higher electrical power for the electrolysis process than thermoneutral mode (23% more). However, external thermal power requirements are one fourth of the thermoneutral needs at a lower temperature (40 kW at 110 ºC instead of 160 kW at 550 ºC from thermoneutral mode).

Table 3 Modelling results for commercial application

		Units	Exothermal	Thermoneutral
Assumptions	H_2 production	kg/day	400	400
	Current density	A/cm^2	0.014	0.0073
	Conversion rate	%	60	60
	Feeding temperature	ºC	110	550
Model calculation	Cell temperature	ºC	539	550
	Feeding steam	kg/h	248.2	248.2
	Feeding CO_2	kg/h	606.4	606.4
	Applied voltage	V	1.62	1.34
	Number of cells	-	319000	616000
	Electric power consumed	kW	726	593
	Required external thermal power	kW	40	160

According to results shown on Table 3, exothermal mode is suitable for low temperature applications since small amounts of thermal heat at low temperature are enough for hydrogen production using molten carbonates electrolyzer. For example, it could be coupled to low temperature CSP applications such as linear Fresnel collector according to diagram shown on Figure 8. In that case, dedicated linear Fresnel CSP plant is considered for external heat generation required for increasing temperature of feeding streams to the electrolyzer (heat exchanger named E-102 on Figure 5).

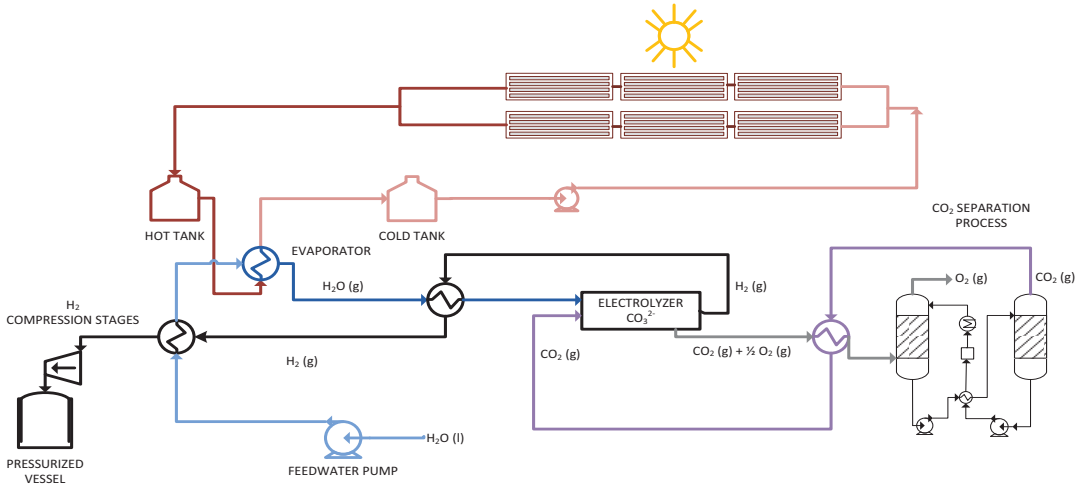

Figure 8 MCEC coupling to dedicated linear Fresnel CSP plant

8. Conclusions

In this paper it has been analyzed the application of molten carbonates electrolyzer cell (MCEC) for hydrogen production. Mathematical model has been developed based on electrochemical and thermodynamics equations and encoded as TRNSYS component for dynamic performance evaluation. MCEC model was completed considering experimental data from lab-scale demonstrator which also contributed to determine model assumptions (conversion ratio and operative cell temperatures). Sensitivity analysis performed on MCEC model demonstrated that operative conditions corresponding to high conversion ratios and low density currents were preferred due to the lower electricity requirements for the electrolysis process. However those conditions were leading to low cell temperatures what could damage the electrolyzer by freezing the electrolyte. It was also found that smart energy recovery network was required for input streams pre-heating for reducing external thermal power requirements, and in this case, splitting the mass flow into two streams (60% and 40%) will be beneficial according to pinch-point methodology. Dynamic response of TRNSYS model simulation showed how the electrolyzer was able to dump temperature fluctuations of the input streams while shifting its response due to molten carbonates thermal inertia.

9. Acknowledgments

The research leading to these results has received funding from EU FP7/2013-2017 under grant agreement n 609837 (FP7 IRP STAGE-STE). The authors would like to thank “Comunidad de Madrid” for its support to the ALCCONES project (S2013/MAE-2985) through the Program of R&D activities between research groups in Technologies 2103, co-financed by structural funds.

10. References

An, X., Cheng, J., Zhang, P., Tang, Z., Wang, J., 2016. Determination and evaluation of the thermophysical properties of an alkali carbonate eutectic molten salt. Faraday Discuss. 190, 327–338. doi:10.1039/C5FD00236B

Antolini, E., 2011. The stability of molten carbonate fuel cell electrodes: A review of recent improvements. Applied Energy 88, 4274–4293. doi:10.1016/j.apenergy.2011.07.009

AspenTech, 2017. Aspen HYSYS v8.8 [WWW Document]. AspenTech: Optimizing Process Manufacturing. URL http://www.aspentech.com/products/aspen-hysys/ (accessed 3.23.17).

Bodén, A., 2007. The anode and the electrolyte in the MCFC. KTH Chemical Science and Engineering.

Brouwer, J., Jabbari, F., Leal, E.M., Orr, T., 2006. Analysis of a molten carbonate fuel cell: Numerical modeling and experimental validation. Journal of Power Sources 158, 213–224. doi:10.1016/j.jpowsour.2005.07.093

Carrette, L., Friedrich, K.A., Stimming, U., 2001. Fuel Cells - Fundamentals and Applications, Fuel Cells. WILEY‐VCH Verlag GmbH. doi:10.1002/1615-6854(200105)1

Das, S.K., 2005. Process heat transfer. Alpha Science International, Harrow.

Dimitriou, P., Tsujimura, T., 2017. A review of hydrogen as a compression ignition engine fuel. International Journal of Hydrogen Energy 42, 24470–24486. doi:10.1016/j.ijhydene.2017.07.232

Dincer, I., Acar, C., 2015. Review and evaluation of hydrogen production methods for better sustainability. International Journal of Hydrogen Energy 40, 11094–11111. doi:10.1016/j.ijhydene.2014.12.035

Frangini, S., Felici, C., Tarquini, P., 2014. A Novel Process for Solar Hydrogen Production Based on Water Electrolysis in Alkali Molten Carbonates. ECS Transactions 61, 13–25. doi:10.1017/CBO9781107415324.004

Hu, L., Rexed, I., Lindbergh, G., Lagergren, C., 2014. Electrochemical performance of reversible molten carbonate fuel cells. International Journal of Hydrogen Energy 39, 12323–12329. doi:10.1016/j.ijhydene.2014.02.144

Ibrahim Dincer, 2012. Green methods for hydrogen production. International Journal of Hydrogen Energy 37, 1954–1971. doi:10.1016/j.ijhydene.2011.03.173

Laurencin, J., Mougin, J., 2015. High-Temperature Steam Electrolysis, in: Hydrogen Production. Wiley-VCH Verlag GmbH & Co. KGaA, Weinheim, Germany, pp. 191–272. doi:10.1002/9783527676507.ch6

Lovegrove, K., Stein, W., 2012. Concentrating solar power technology : principles, developments and applications. Woodhead Publishing.

Mazloomi, K., Sulaiman, N.B., Moayedi, H., 2012. Electrical Efficiency of Electrolytic Hydrogen Production. Int. J. Electrochem. Sci 7, 3314–3326.

Petipas, F., Brisse, A., Bouallou, C., 2013. Model-based behaviour of a high temperature electrolyser system operated at various loads. Journal of Power Sources 239, 584–595. doi:10.1016/j.jpowsour.2013.03.027

Sanz-Bermejo, J., Gallardo-Natividad, V., González-Aguilar, J., Romero, M., 2014a. Coupling of a Solid-Oxide cell unit and a linear Fresnel reflector field for grid management. Energy Procedia 57, 706–715. doi:10.1016/j.egypro.2014.10.226

Sanz-Bermejo, J., Muñoz-Antón, J., Gonzalez-Aguilar, J., Romero, M., 2015. Part load operation of a solid oxide electrolysis system for integration with renewable energy sources. International Journal of Hydrogen Energy 40, 8291–8303. doi:10.1016/j.ijhydene.2015.04.059

Sanz-Bermejo, J., Muñoz-Antón, J., Gonzalez-Aguilar, J., Romero, M., 2014b. Optimal integration of a solid-oxide electrolyser cell into a direct steam generation solar tower plant for zero-emission hydrogen production. Applied Energy 131, 238–247. doi:10.1016/j.apenergy.2014.06.028

Schiller, G., Ansar, A., Lang, M., Patz, O., 2009. High temperature water electrolysis using metal supported solid oxide electrolyser cells (SOEC). Journal of Applied Electrochemistry 39, 293–301. doi:10.1007/s10800-008-9672-6

Trnsys, 2007. TRNSYS 16: Volume 8 Programmer's Guide, in: Solar Energy Laboratory Univ. of Wisconsin-Madison (Ed.), TRNSYS 16 a TRaNsient SYstem Simulation Program.

Ulleberg, Ø., 2003. Modeling of advanced alkaline electrolyzers: A system simulation approach. International Journal of Hydrogen Energy 28, 21–33. doi:10.1016/S0360-3199(02)00033-2

Yu, L.J., Ren, G.P., Jiang, X.M., Yuan, J.Q., Cao, G.Y., 2007. Experiment and numerical simulation on the performance of a kw-scale molten carbonate fuel cell stack. Brazilian Journal of Chemical Engineering 24, 523–533. doi:10.1590/S0104-66322007000400006

Zeng, K., Zhang, D., 2009. Recent progress in alkaline water electrolysis for hydrogen production and applications. Progress in Energy and Combustion Science 36, 307–326. doi:10.1016/j.pecs.2009.11.002

Detrimental Effects of Dust Deposition in Pores of an Open Volumetric Air Receiver

Gurveer Singh[1] and Laltu Chandra[1#]

[1]Indian Institute of Technology Jodhpur, Jodhpur (India)

[#] corresponding author: chandra@iitj.ac.in

Abstract

Recently the novel concept of solar convective furnace based on open volumetric air receiver is proposed and evaluated for metals processing. The use of open volumetric air receiver is motivated by the need of hot air at about 750 K. It is well-accepted that the dust deposition will be a major challenge for implementation of open volumetric air receiver in the arid deserts, worldwide. In this paper, some of its detrimental consequences pertaining to flow instability and absorber temperature are presented. A pressure-drop correlation for straight pore based absorber is developed for analyzing the flow instability. A two-dimensional validated approach is adopted for analyzing the receiver overheating as a result of dust deposition forming a so-called insulation-type layer on the inner surface of absorber pore. The findings show stable flow regime with a uniform thickness of the deposited dust layer (100 μm & 200 μm) on the inner surface of a pore. The thickness of dust layer is more detrimental in view of substantial rise of absorber temperature and thus, the sustainability of the open volumetric air receiver needs to be addressed. The presented details are both encouraging and alarming, addressing some of the gaps and outlining the need of an in-situ cleaning approach for operating such a system in the arid deserts of India and worldwide.

Keywords:open volumetric air receiver, solar convective furnace, dust deposition, heat flux distribution

1 Introduction

Rajasthan and Gujarat in India are prosperous in terms of direct normal irradiance. This can be converted to heat or power using the concentrated solar thermal technologies. As an application, the concept of solar convective furnace system is being developed at IIT Jodhpur (Patidar et al., 2015). A three-dimensional view of this furnace for heat treatment of aluminum is shown in Fig. 1a. Here, the obtained hot air from an open volumetric receiver is introduced limiting the required temperature to 750 K for annealing of aluminium. The open volumetric air receiver based central receiver systems fulfill the same and even beyond 750 K (Romero et al., 2002). The desired volumetric heating effect may be manifested by applying a uniform heat flux throughout the absorber length. In such a case, the absorber temperature at the inlet will be lower than that of the outlet. Achieving such an ideal operating condition on the field condition is not possible. This is referred to non-volumetric heating and is a manifestation of heat flux non-uniformity along the axial and radial direction. For evaluating an open volumetric air receiver, which is open to atmosphere, the solar air tower simulator facility is installed at IIT Jodhpur as depicted in Fig. 1b. The porous absorbers of this receiver are exposed to concentrated solar irradiance with simultaneous cooling basing on the forced convection of air. The installed foot-piece, anchor-plate and nozzle ensure thermal uniformity of hot air at its outlet. The designed receiver aims to provide (a) a uniform outlet air temperature, (b) a stable flow condition and (c) the long-term operation in dusty environment. An open volumetric air receiver comprising of circular straight pore based cylindrical absorber is developed to fulfill these requirements, as far as possible, and is discussed subsequently. A review and challenges in achieving the volumetric effect in such a receiver is presented in e.g. (Gomez-Garcia et al.,2016; Capuano et al., 2015).

Even with volumetric or more so with a non-volumetric heating the desired stable flow limits the targeted high air temperature in an open volumetric air receiver (Kribus et al., 1996; Pitz-paal et al., 1997). The combined effect of high temperature and its non-uniformity leads to flow instability beyond a critical heat

doi:10.18086/swc.2017.04.14 Available at http://proceedings.ises.org

flux level. This is associated with the thermo-physical properties of air and in particular, the offered flow resistance at a high temperature. The concentrated solar irradiance on the open volumetric air receiver aperture is known to be quasi-Gaussian and thus centrally located absorbers are more prone to such an unwanted situation (Becker et al., 2006; Roldán et al., 2014). One way of mitigating the same is the use of an absorber with high thermal conductivity to reduce thermal gradient and the resulting change in fluid properties. Another challenge pertaining to its operation in the arid desert region is the deposition of dust having a low thermal conductivity of about 1-2 W/mK in absorber pores. This is likely to limit its installation in such areas of high potential, worldwide, and in particular the Thar-desert of India and the great desert of Middle-East. The deposition mechanism and a dust removal process were analyzed by Singh et al., (2016). The possible consequences of dust deposition are (a) the flow instability even at a low heat flux concentration, (b) the local or wide-area hot spot and (c) an eventual failure of open volumetric air receiver. Considering these aspects (a) the effect of uniform and non-uniform heat flux distribution on an absorber pore and (b) the detrimental consequences of the dust deposition in an absorber pore are discussed in this paper.

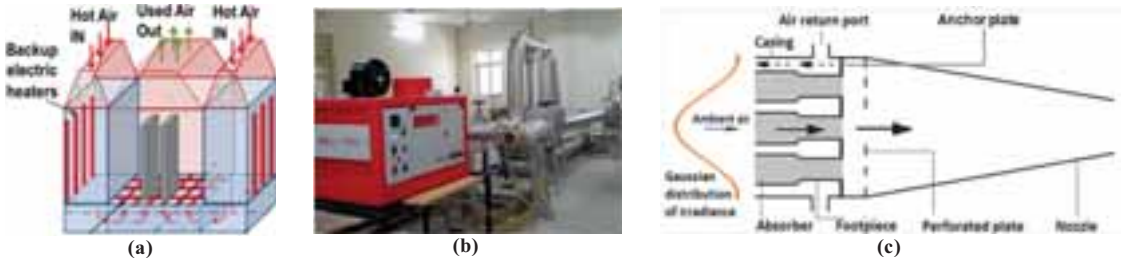

(a) (b) (c)

Fig. 1: (a) Schematic of solar convective furnace,(b) Solar air tower simulator facility at IIT Jodhpur, (c) Schematic of an open volumetric air receiver

2 Modeling and simulation

In this section the derived new pressure-drop coefficient based correlation is presented. Subsequently, the validated two-dimensional computational approach is used to address the above-mentioned objectives.

2.1 Pressure-drop Correlation

The porous absorbers in an open volumetric air receiver are made of metals, alloys and ceramics that are of foam or straight pore –type (Avila-Marin, 2011). The straight two-dimensional pore based absorbers offers a lower pressure-drop in comparison to that of a three-dimensional structures, which can be easily inferred in comparison to the Ergun equation. Thus, the straight pore based receiver is attractive for pressure-drop and are also less prone to the dust accumulation. There are a number of correlations to predict the pressure-drop (Δp) across the foam-type absorbers, which may not be applicable for the straight pore based absorber (Edouard et al.,2008). Therefore, several experiments and detailed analysis are performed to deduce a realistic correlation for Δp across the designed circular straight pore based open volumetric air receiver (Sharma et al., 2015a, 2015b). The employed cylindrical absorber and the receiver assembly are shown in Fig. 2b and 2c. The schematic of experimental setup for measuring the pressure-drop across an isolated absorber is shown in Fig. 2a. This consists of a blower, two connecting pipes each of length ~0.83 m, an absorber of length (L) ~0.0254 m, pore hydraulic diameter (d_p) ~0.002 m and porosity (ε) ~52%, a differential pressure transducer (Dwyer 475 mark III with an accuracy of about ±1.5%, a rotameter and a hot-wire anemometer (Fisher scientific make with an accuracy of about ±1%). The detailed analysis is presented in Singh et al. (2018). The authors' have also reported three dimensional numerical analyses with absorbers having porosities of 42, 52 and 62%. The obtained correlation based on these investigations is as follows:

$$\left.\begin{aligned} \Delta p &= k_p \times \frac{\rho_f \mathrm{v}_p^2}{2} \\ k_p &\approx 179.25 Re_p^{-0.588} \end{aligned}\right\} \qquad \text{(eq. 1)}$$

where,k_p is the pressure drop coefficient, ρ_f is the density of air, Re_p is the Reynolds number based on the hydraulic diameter (d_p) of circular straight pore and v_p is the average speed of air inside an absorber pore. The derived correlation is expressed in terms of Re_p, which includes fluid properties. It is well known that $\left(\Delta p/\rho_f v^2\right) \propto f\left(Re_p\right)$ for an incompressible fluid flow in a smooth straight pore (Fox et al., 2011). This can be also be inferred from the fact that a blower of large capacity is required to achieve a high mass flow rate through a given porous geometry. Thus, with the increasing velocity/mass flow rate of air or the corresponding Reynolds number the pressure-drop increases. This is also evident from eq. (1) in which including the proportionality constant k_p (a function of Reynolds number) the pressure drop scale with $v^{1.412}$.

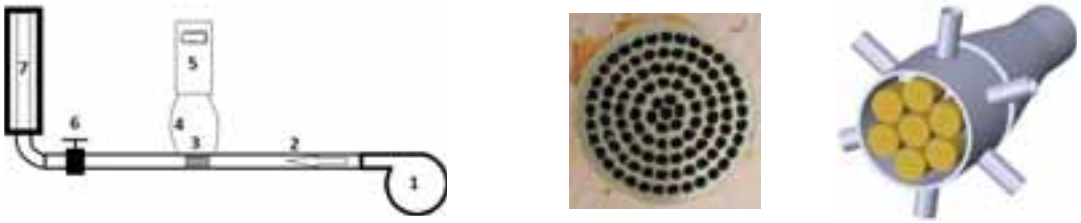

(a) (b) (c)

Fig. 2: (a) Schematic of experimental setup showing 1:blower, 2:pipe, 3:absorber, 4-5:differential pressure transducer with probes, 6:valve, 7:rotameter; (b) a circular straight pore based cylindrical absorber; (c) the receiver assembly.

2.2 Two-dimensional analysis: clean and partially blocked pore

The deposition of dust will enhance the thermal resistance in an absorber pore and as a consequence the temperature difference between solid and air will be higher than that of a clean pore. The thermal resistance between solid and air for a clean and partially blocked pore can be easily estimated as follows:

$$\left.\begin{aligned} R_{th\_cl} &= \frac{1}{h_{cl} A_{ps\_cl}} \\ R_{th\_bl} &= \frac{1}{h_{bl} A_{ps\_bl}} + \frac{\ln\left(d_{cl}/d_{bl}\right)}{2\pi k_d L} \end{aligned}\right\} \qquad \text{(eq. 2)}$$

where, R_{th} is the thermal resistance in the pore, h is the convective heat transfer coefficient in the pore, A_{ps} is the wetted surface area of the pore, d is the hydraulic diameter of the pore, subscripts cl and bl stands for clean and blocked pores, L is the length of the circular straight pore and k_d is the thermal conductivity of dust. In eq. (2) the offered conductive resistance by the absorber solid material is ignored basing on its high thermal conductivity (~ 100 W/mK) in comparison to that of dust (~ 1-2 W/mK). The porosity (ε) of absorber in terms of dust layer thickness can be obtained as

$$\varepsilon = \frac{A_c \times n_c + A_b \times n_b}{A_{cs}}, \text{where } A_c = \frac{\pi d_p^2}{4} \text{ and } A_b = \frac{\pi (d_p - 2t)^2}{4} \qquad \text{(eq. 3)}$$

where, A_c is the cross section area of a clean pore, A_b is the flow cross section area of a partially blocked pore, t is the thickness of dust layer, n_b is the number of partially blocked pores, n_c is the number of clean pores and A_{cs} is the cross section area of absorber. Therefore, if dust deposits then the porosity of absorber will be lower than that of a clean pore. This will offer higher resistance to flow and heat transfer for a given mass flow rate. For a simple analysis the uniform layer of deposited dust along the pore length is assumed. Because of the identical geometry only one pore will suffice to estimate its effect on the heat transfer. This is manifested as the rise of mean temperature difference between absorber material and air with thickness of dust layer as summarized in Table 1. The digits are rounded off to the first decimal point. In these calculations an average convective heat transfer coefficient is used, which ideally should vary along the length. Thus, the numbers are only representative in nature. The Table 1 confirms that the mean temperature difference between absorber solid and air will increase with the dust layer thickness as a result of the enhanced conductive resistance and decrease with

Re_p as a consequence heat transfer coefficient for a given thickness of dust layer. Thus the need for a more detailed analysis is realized. As the next step, a two-dimensional analysis, based on axisymmetry is performed with Ansys-Fluent.

Tab. 1: Mean temperature difference between solid and fluid in a partially blocked pore with a uniform dust layer thickness

Re_p	Dust layer thickness (Porosity in %)		
	100 µm (42%)	200 µm (33%)	300 µm (25%)
100	103.5 K	104.7 K	106.3 K
200	92.8 K	94.8 K	97.2 K
300	84.7 K	87.1 K	89.8 K

Assuming that all the pores are identical and are exposed to the same condition suffices modeling a single pore. The modeled single pore geometry comprises a fluid (air) domain with temperature dependent properties and a solid (brass) domain with constant thermo-physical properties for a clean pore. For a partially blocked pore the dust layer is introduced as a solid domain with thermo-physical properties of sand. This is sandwiched between the absorber and fluid domain (see Fig. 3a). Thus the dust-air and dust-solid interface is suitably modeled with consistent thermal boundary condition. The deposition of dust, in an ideal case, will be uniform along the length, however, in reality, a non-uniform profile is expected. To simulate these different scenarios, uniform dust layer (UDL) and non-uniform dust layer (NDL) distributions are assumed (Fig. 3a). Moreover, both the ideal volumetric and real non-uniform heating effects are modeled with uniform and non-uniform heat flux distribution on the circumference of pore. The solved continuity, momentum and energy equations are given in eq.(4) and the numerical setup is summarized in Table 2. This describes the adopted numerical scheme and the convergence criteria.

Fluid (air)

$$\nabla \cdot \vec{\mathrm{V}} = 0$$

$$(\vec{\mathrm{V}} \cdot \nabla)\,\vec{\mathrm{V}} = -\frac{\nabla p}{\rho_f} + \nu_f\,\nabla^2\,\vec{\mathrm{V}}$$

$$\left(\nabla \cdot \rho_f\,\vec{\mathrm{V}}\mathrm{H}_f\right) = \nabla \cdot \left(\frac{k_f}{c_{pf}}\nabla H_f\right)$$

Solid (absorber material/dust)

$$\nabla \cdot (k_s \nabla T) = 0$$

(eq. 4)

Tab.2: Numerical setup for two dimensional analysis

Mesh-type	**Mesh-size (in mm)**	**Numerical Scheme**	**Convergence**
Structured	0.015 mm -0.05 mm	First-order Upwind with SIMPLE algorithm	10^{-6}

The schematic in Fig. 3c and depicts (a) volumetric heating effect with a uniform heat flux and (b) non-volumetric heating effect or a field condition with a non-uniform heat flux distributions along the axial direction, ignoring the radial variation with a single pore. The latter is adopted from Roldán et al.(2014) as eq. (5) and is implemented as a user-defined function.

$$I(z) = I_0 e^{-\xi z} \text{ with } \xi_{3d} = \frac{3(1-\varepsilon)}{d_p} \qquad \text{(eq. 5)}$$

where, $I(z)$ is the heat flux at a given axial position along the flow direction, I_0 is the irradiance at the front face, ε is the porosity of an absorber, ξ_{3d} is the extinction coefficient (Wang et al, 2013; Wu et al, 2011). Also, the

radiation based heat loss from the front surface of absorber is introduced as a boundary condition using a user defined function. Different cases are analyzed with a dust layer thickness up to 200 µm depicting one to four successive layers of deposition (see Yadav et al., 2014). Each absorber pore is subject to the same Δp inferring the applied same suction by a blower. This assumes that a common blower for suction through a receiver comprise of several porous absorbers. The same is depicted with a schematic of a clean and a partly blocked pore in Fig. 3b. In the two-dimensional simulation, a total pressure of 15.8 Pa corresponding to $\dot{q}/\dot{m}_a$~200 kJ/kg for a power ($\dot{q}$) of 1.03 W is employed as the inlet boundary condition. Zero gage pressure is applied at the outlet. Thus the flow inside a clean and a partially blocked pore is driven by the same pressure-drop as in a real absorber. The resulting Re_p is about 175, 70 and 19 for the clean and partially blocked pores with uniform dust layer thickness of 100 µm (ε ~ 42%) and 200 µm (ε ~ 33%), respectively. The lower value of Re_p is a manifestation of the offered higher resistance to the flow by the blocked pore in comparison to the considered clean pore. Thus, the flow and thermal development length (~0.05 Re_p with Pr ~ 1) will be shorter in the partially blocked pore as compared to its clean counterpart. In realistic conditions, the dust deposition is generally non-uniform. To estimate the effect of such a distribution, the simulations with non-uniform dust layers are also performed. Here, the dust layer thickness is maximum (100 µm or 200 µm) at the inlet and reduces to zero at the outlet as shown in Fig. 3a.The generated coarse and fine meshes in a dust deposited pore are shown in Fig. 3e. The finest mesh having a resolution of 0.05 mm is preferred for further analysis based on a grid independence test.

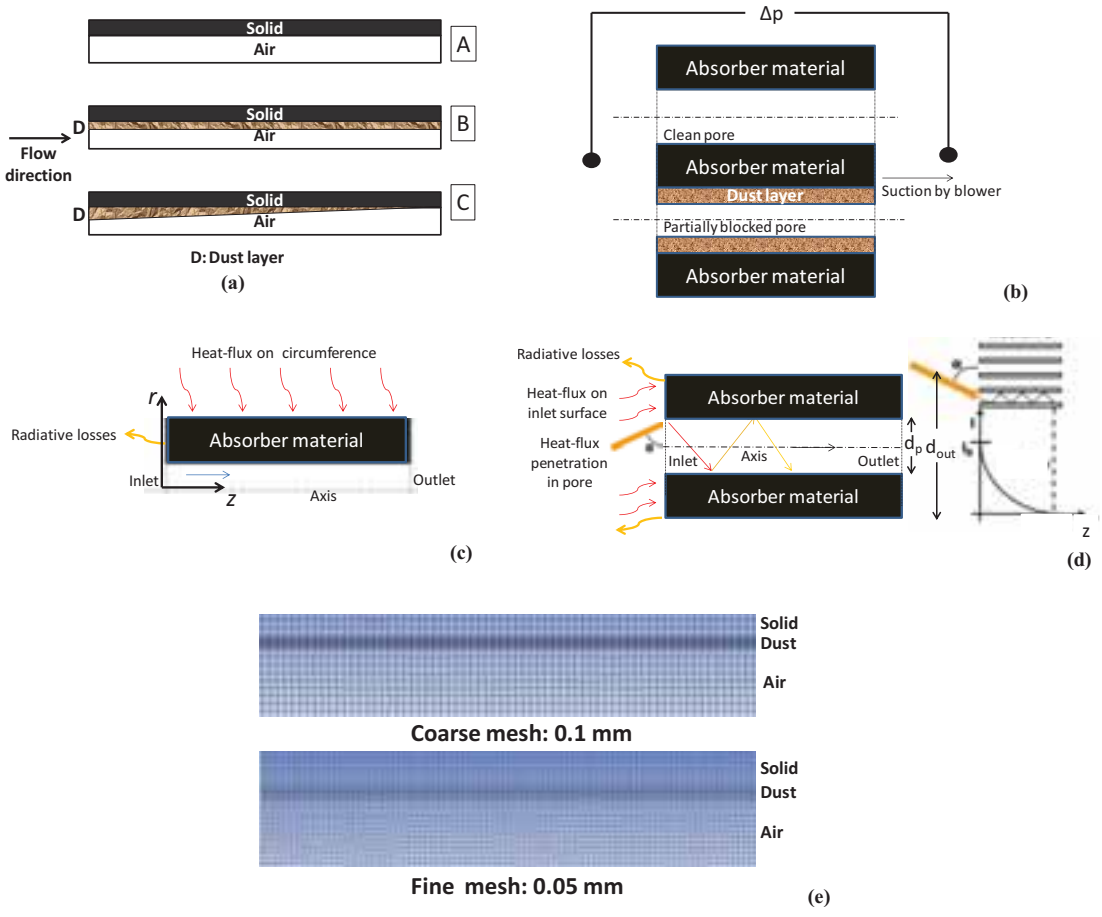

Fig. 3: (a) Geometries of A- clean pore, B.-pore with uniform dust layer (UDL), C- pore with non-uniform dust layer; (b) A schematic showing the same pressure drop across all absorber pores due to suction (c) Uniform distribution of heat flux on an absorber pore and (d) Non-uniform heat flux distribution on an absorber pore; (e) The generated meshes

3 Results and discussion

3.1. Two-dimensional analysis:validation and flow-instability with dust deposition

The employed axisymmetric numerical model is validated with the measured values of air temperature at the absorber outlet (T_{out}) with uniform or volumetric-type heating in laboratory bySharma et al., (2015a, 2015b). The comparative assessment in Fig. 4a shows a variation of less than 5% between the measured and computed values confirming the acceptability and quality of the performed analysis. The pressure-drop correlation as in eq. (1) is derived using experiments/computations under ambient condition and its applicability with heat input remains a question. To answer the same, simulations are performed using the validated numerical setup with uniform heat flux boundary conditions and Re_p < 300. A comparison between the computed and correlation based Δp is shown in Fig. 4b. This depicts that (a) the Δp increases with decreasing T_{out} that corresponds to a high mass flow rate of air or Re_p, (b) the derived correlation compares within 10-25% with the performed simulations for a T_{out} up to 900 K. One of the reasons for this error is the measurement uncertainty of about 2 Pa. This is substantial at a low mass flow rate and thus, differences are observed between experiment and computed values. Furthermore, the measured values will be affected by the curved streamlines at the inlet and outlet. Also, a comparison between the installed- rotameter and hot-wire anemometer based $\dot{m}_a$ values showed an uncertainty of about *5%*. These are some of the possible encountered errors. Also it is noted that a 5% of uncertainty in $\dot{m}_a$ corresponds to 10% uncertainty in pressure drop. Thus, the realistic pressure-drop correlation with its known limitations is used for flow stability analysis.

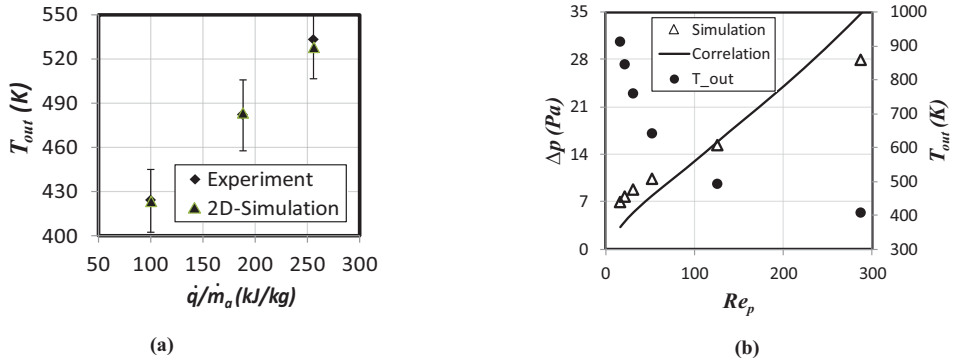

Fig 4: Comparison between (a) computed and measured air temperature at the absorber outlet and (b) computed and correlation (eq. (1)) based pressure-drop with different heat flux condition

For flow stability analysis the well-known quadratic pressure across the absorber is deduced by adopting the approach from Becker et al. (2006) and is presented in eq. (6). The detailed derivation of this expression considering a clean circular straight pore and the underlying assumption are reported in Singh and Chandra (2018). The instability is envisaged by the oscillatory nature of the difference between quadratic pressure-drop at a critical heat flux level. The investigation of the obtained expression clearly show that the non-existence of the same. The effect of dust deposition may be implicitly evaluated by updating the porosity of a partially blocked pore in eqn. (6) at the steady state.

$$\Delta p^2 = p_{inlet}^2 - p_{outlet}^2 = B'.\left(\frac{q_s''/\varepsilon\, T_{out} - \Sigma\beta\sigma T_{out}^5}{(T_{out} - T_0)}\right)^{1.412} \quad \text{where B}'=\left(\frac{179.25R\mu_0^{0.588}}{c_{pf}^{1.412}d_p^{0.588}T_0^{0.412}}\right) \qquad \text{(eq. 6)}$$

A variation of the derived expression for Δp^2 as in eq. (6) with respect to T_{out} and $\dot{m}_a$ is shown in Fig. 5. This illustrates that the pressure-drop decreases with mass flow rate of air or the corresponding Reynolds number for a circular straight pore. As a result, the outlet air temperature increases for the considered temperature dependent thermo-physical properties of air. Unfortunately, the analysis is not performed for the large scale receiver as the absorber design needs to be optimized. The work on the same is in progress. It is also inferred that for a given T_{out} the Δp^2 increases with the dust layer thickness or the decreasing effective absorber porosity

at a given mass flow rate of air. This is indicated by a dotted arrow. It must be emphasized that the estimated value of Δp^2 with eq. (6) compares well with that of the numerically analyzed values. This serves as an alternative validation of the derived expression. The difference between analytically and numerically obtained values of Δp^2 decreases with the mass flow rate of air, which is also inferred with the increasing values T_{out}. This is desirable in view of analyzing the flow instability. Higher values of Δp will lead to an elevated parasitic loss and the reduction in an overall efficiency, which is defined by Boddupalli et al. (2017). Thus, one of the consequences of dust deposition is the reduction of open volumetric air receiver performance or efficiency. Interestingly, with the uniform layer of dust deposition and the manifested volumetric heating effect no signature of flow instability is found, which is encouraging for implementing such a receiver design in desert regions and is a step towards optimization. The effect of non-uniform- dust deposition and heat flux distribution on the same will be investigated at a later date.

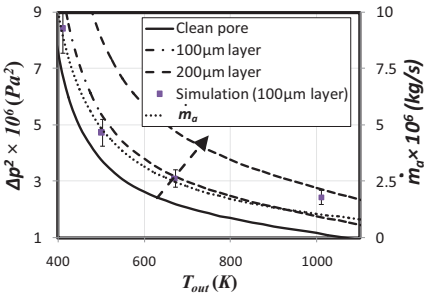

Fig. 5: Computed and eqn. (2) analyzed Δp^2 with clean and partly blocked pores.

3.2. Effect of dust deposition and heat flux distribution: air and absorber temperature

The simulations are performed with the clean and partly blocked absorberpores with an imposed fixed pressure drop across the absorber inlet and outlet (see Fig. 3b). This will allow one-to-one comparison between a clean and a partially blocked pore that are operating under an identical suction. The axial temperature variation of fluid and absorber material is shown in Fig. 6 for the cases with uniform and non-uniform heat flux distributions.

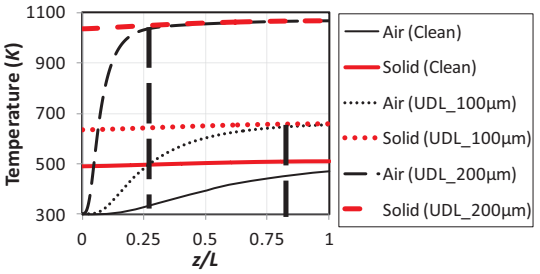

(a) Uniform heat flux(uniform dust layer, UDL)

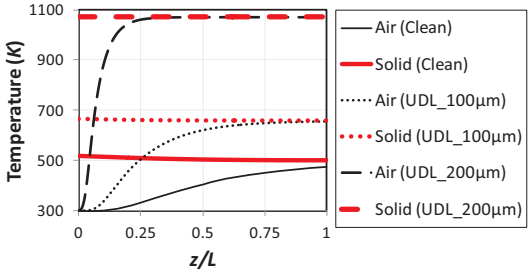

(b) Non-uniform heat flux(uniform dust layer, UDL)

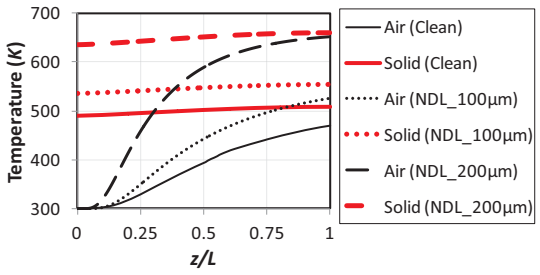

(c) Uniform heat flux (non-uniform dust layer, NDL)

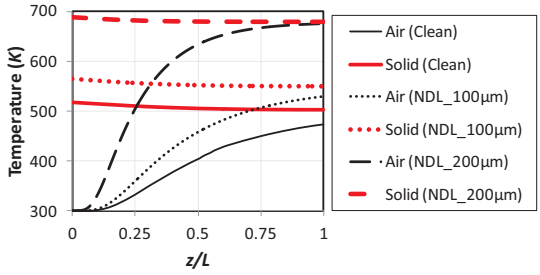

(d) Non-uniform heat flux (non-uniform dust layer, NDL)

Fig. 6: Axial temperature profile of fluid and solid with uniform and non-uniform dust layer thickness along the absorber pore

With the numerically imposed uniform heat flux along the pore length the desired volumetric heating effect is observed. This is inferred with an increasing solid temperature from the absorber inlet to outlet. Whereas with the employed non-uniform heat flux distribution along the pore length as in eq. (5) the highest absorber temperature is obtained at the inlet. This confirms the non-volumetric heating effect. The partially blocked pore shows a substantial increment in temperature with the applied pressure-drop attributed to the reduced mass flow rate. The temperatures of solid and air increase with the thickness of dust layer as expected. For the uniform dust layer a temperature rise of about 150 K and 580 K is found, which correspond to the thickness of 100 µm and 200 µm, respectively. For the non-uniform thickness of dust layer a temperature rise of about 40 K and 150 K is found, which correspond to 100 µm and 200 µm at the inlet, respectively. This is attributed to the decreasing mass flow rate of air in blocked pore for the applied pressure-drop and is substantiated by a shorter thermal development length (~ 0.05 Re_pPr) in blocked pore compare to its clean counterpart as depicted by the dotted vertical lines in Fig. 6a. Thus, it is concluded that the dust deposition is detrimental to long-term sustainable operation and also increases parasitic losses. Moreover, high surface temperature will lead to an elevated radiation based heat loss, which adds up to the losses. In essence, both the efficiency and durability of an open volumetric air receiver will be a concern in arid deserts.

Fig. 7: Temperature contours for a clean pore and for a partially blocked with uniform dust layer (UDL) thickness of 100 µm and the applied uniform heat flux along the pore length

The numerically analyzed solid and fluid temperature contours for a clean and a partially pore is shown in Fig. 7. The scale is preserved for a better visual comparison. As observed, the contours depict parabolic distribution of fluid temperature and its value increases with the axial position. As explained in Fig. 6a, it is clear that the fluid attains the solid temperature closer to the inlet for the blocked pore case in comparison to that of the clean pore. Thus, it may be inferred that the absorber solid will be exposed to a high temperature over a wider length with the blocked pore in comparison to the clean pore under a given operating condition. Thus, the need of in-situ cleaning is a must for mitigating the failure of such a system in arid deserts.

4 Conclusions

This paper aims at demonstrating the detrimental effect of dust deposition in an absorber pore of an open volumetric air receiver. A validated two-dimensional numerical approach is adopted for this purpose. The analyses reveal the following:

a. The uniform dust deposition may not encourage flow instability in the considered absorber. This is encouraging and allows expecting a stable operation of such a receiver in desert regions.

b. The dust deposition will increase parasitic and radiation based losses that are detrimental to overall efficiency of such a receiver. These can be easily inferred from the reduced pore diameter based Reynolds number and the computed higher temperature with a partially blocked pore in comparison to a clean pore.

c. The dust deposition will lead to an elevated temperature and thus the flow resistance. This will limit the operation of such a receiver in desert regions and confirms the need of an in-situ cleaning device.

5 Acknowledgements

The authors are thankful to Ministry of New and Renewable Energy (MNRE), Ministry of Human Resource Development (MHRD) and Indian Institute of Technology, Jodhpur (IITJ) for the provided financial and infrastructural support.

6. Nomenclature

c_{pf}	Specific heat at constant pressure for air (J/kgK)	Re_p	Reynolds number in an absorber pore
d_p	Hydraulic diameter of the pore (m)	T	Temperature (K)
H_f	Total enthalpy (J)	T_0	Temperature of air at the inlet of an absorber (K)
I	Heat flux along the z-direction (W/m^2)	T_{out}	Temperature of air at the outlet of an absorber (K)
I_0	Heat flux on the inlet surface of absorber (W/m^2)	$\vec{V}$	Velocity of fluid (m/s)
k_p	Pressure-drop coefficient (-)	v_P	Average speed in an absorber pore (m/s)
k_f	Thermal conductivity of fluid (W/mK)	ε	Porosity of absorber
L	Length of absorber (m)	ξ	Extinction coefficient (m^{-1})
$\dot{m}_a$	Mass flow rate of air (kg/s)	ρ_f	Density of air (kg/m^3)
p	Static pressure (Pa)	μ_0	Dynamic viscosity of air at inlet of absorber (kg/ms)
$\dot{q}$	Power on aperture (W)	Σ	Emissivity of brass
q''_S	Concentrated solar irradiance on the receiver aperture (W/m^2)	σ	Stephan-Boltzmann constant (W/m^{2}K^4)
R	Gas constant of air (J/kgK)		

7. References

Avila-Marin, A.L., 2011. Volumetric receivers in solar thermal power plants with central receiver system technology: a review. Solar energy 85(5), 891-910.

Becker, M., Fend, T., Hoffschmidt, B., Pitz-Paal, R., Reutter, O., Stamatov, V., Steven, M., Trimis, D., 2006. Theoretical and numerical investigation of flow stability in porous materials applied as volumetric solar receivers. Solar energy 80(10), 1241-1248.

Boddupalli, N., Singh, G., Chandra, L., Bandyopadhyay, B., 2017. Dealing with dust-Some challenges and solutions for enabling solar energy in desert regions, Solar Energy 150, 166-176.

Capuano, R., Fend, T., Hoffschmidt, B., Pitz-Paal, R., 2015. Innovative volumetric solar receiver micro-design based on numerical predictions. In ASME 2015 International Mechanical Engineering Congress and Exposition (Vol. 8, pp. 13-19).American Society of Mechanical Engineers.

Edouard, D., Lacroix, M., Huu, C.P., Luck, F., 2008. Pressure drop modeling on solid foam: State-of-the art correlation. Chemical Engineering Journal 144(2), 299-311.

Fox, R., McDonald, A., Pritchard, P., 2011. Fluid Mechanics. 8thed. New York: Wiley.

Gomez-Garcia, F., González-Aguilar, J., Olalde, G., Romero, M., 2016. Thermal and hydrodynamic behavior of ceramic volumetric absorbers for central receiver solar power plants: A review. Renewable and Sustainable Energy Reviews 57, 648-658.

Kribus, A., Ries, H., Spirkl, W., 1996. Inherent limitations of volumetric solar receivers.Journal of solar energy engineering 118(3), 151-155.

Patidar, D., Tiwari, S., Sharma, P., Pardeshi, R., Chandra, L., Shekhar, R., 2015.Solar Convective Furnace for Metals Processing. JOM 67(11), 2696-2704.

Pitz-Paal, R., Hoffschmidt, B., Böhmer, M., Becker, M., 1997.Experimental and numerical evaluation of the performance and flow stability of different types of open volumetric absorbers under non-homogeneous irradiation. Solar Energy 60(3), 135-150.

Roldán, M.I., Smirnova, O., Fend, T., Casas, J.L. Zarza, E., 2014. Thermal analysis and design of a volumetric solar absorber depending on the porosity. Renewable Energy 62, 116-128.

Romero, M., Buck, R., Pacheco, J.E., 2002.An update on solar central receiver systems, projects, and technologies.Journal of solar energy engineering 124(2), 98-108.

Sharma, P., Sarma, R., Chandra, L., Shekhar, R., Ghoshdastidar, P.S., 2015a. Solar tower based aluminum heat treatment system: Part I. Design and evaluation of an open volumetric air receiver. Solar Energy 111, 135-150.

Sharma, P., Sarma, R., Chandra, L., Shekhar, R., Ghoshdastidar, P.S., 2015b. On the design and evaluation of open volumetric air receiver for process heat applications. Solar Energy 121, 41-55.

Singh, G., Dhurwe, P., Kumar, R., Kumar L., Vaghela, N., Chandra, L., 2018. A step towards realizing open volumetric air receiver based systems in desert regions, Springer Proceedings in Energy, ICAER 2017 (to appear).

Singh, G., Chandra, L., 2018. On the flow stability in a circular cylinder based open volumetric air receiver for solar convective furnace. Energy Procedia, In: HEREM 2018 (To appear)

Singh, G., Saini, D., Chandra, L., 2016. On the evaluation of a cyclone separator for cleaning of open volumetric air receiver, Applied Thermal Engineering 97, 48-58.

Wang, F., Shuai, Y., Tan, H., Yu, C., 2013. Thermal performance analysis of porous media receiver with concentrated solar irradiation, Int. J. Heat and Mass Transfer 62, 247-254.

Wu, Z., Caliot, C., Flamant, G., Wang, Z., 2011.Coupled radiation and flow modeling in ceramic foam volumetric solar air receivers, Solar Energy 85(9), 2374-2385.

Yadav, N.K., Pala, D., Chandra, L., 2014. On the understanding and analyses of dust deposition on heliostat, Energy Procedia 57, 3004-3013.

Concentrating solar collectors integrated with low CO_2 emissions ultra supercritical power plants

Vittorio Tola, Mario Petrollese, Mario Cascetta and Daniele Cocco

University of Cagliari, Department of Mechanical, Chemical and Material Engineering, Cagliari (Italy)

Abstract

This paper focuses on the evaluation of the potential benefits arising from the integration of concentrating solar systems with coal-based Ultra Supercritical (USC) power plants with post-Combustion CO_2 Capture (PCC). In this study, the USC-PCC plant was integrated with a concentrating solar field with or without a thermal energy storage section. Different collector technologies (parabolic trough and linear Fresnel) and heat transfer fluids (direct steam generation and molten salts) were analyzed and compared. The performance of both solar field and power plant were evaluated by means of specifically developed models, by using data sets of a typical meteorological year for two sites in Italy and Morocco. A preliminary cost analysis was finally carried out.

Keywords: CSP plant, USC, CO_2 capture, parabolic trough, Linear Fresnel

1. Introduction

Worldwide, the Concentrating Solar Power (CSP) plants installed capacity is around 5000 MW, generated using parabolic troughs (83 %), solar towers (13 %), linear Fresnel reflectors (3.4 %) and single dish engines (0.02 %) [1]. Moreover, it is rapidly increasing with about 4000 MW of additional capacity under construction or development. [2]. Nowadays, different technologies and configurations are available for solar field (parabolic trough, linear Fresnel, solar tower and solar dish systems), power block (steam Rankine and ORC, Stirling engines, combined cycles, etc.), heat transfer fluid (thermal oil, molten salts, steam, etc.) and thermal energy storage (TES) systems (active, passive, two-tank, thermocline, etc.) [3,4]. Currently, parabolic trough collectors (PTC) are the most commercially proven technology for the solar field. Linear Fresnel collectors (LFC) are a viable alternative, despite a lower optical efficiency but requiring less land availability and capital costs [5,6]. Thermal oil is usually used as heat transfer fluid (HTF), but the maximum allowable temperature for these fluids is limited to about 400°C. For this reason, one of the main R&D activities in this field aims to overcome this limit by replacing it with Molten Salts (MS) or by using Direct Steam Generation (DSG) solar plants [7,8].

One of the most interesting options is represented by the integration of the solar field with a conventional power plant fed by fossil fuels through hybrid CSP plants [9]. A solar hybrid plant can utilize the existing infrastructure of a conventional power plant, thereby, reducing the investment cost and, consequently, the costs of electricity production. In addition, solar contribution in fossil plants allows to reduce fuel consumption and therefore CO_2 emissions [10]. Hybrid CSP plants can be found in North Africa and Middle East countries, where solar system have been integrated with combined cycles [11,12]. Moreover, with the aim to reduce CO_2 emissions, conventional power plants should require their integration with Carbon Capture and Storage (CCS) systems. In particular, coal-based steam plants require Post-Combustion CO_2 Capture (PCC) processes based on chemical absorption, especially with amine-based solvents, leading to a remarkable net efficiency penalty [13], in the order of 10-11 percentage points for the usual target of most CCS projects (90% CO_2 removal) [14,15]. Since low and medium temperature thermal energy can easily be produced by solar radiation, in recent years, several interesting options for integrating solar energy and CCS technologies have been studied aiming to mitigate the energy penalty generated by the large heat consumption required for solvent regeneration [16]. In particular, two main approaches are proposed: the first is the production of low-pressure steam for the solvent regeneration process (at about 130-140 °C). The advantage of using this approach is that, for a given fossil fuel input, steam production from solar energy reduces the extraction from the low-pressure (LP) turbine increasing its power output. The second

doi:10.18086/swc.2017.04.15 Available at http://proceedings.ises.org

approach is the production of high or intermediate pressure steam for the high-pressure (HP) and intermediate-pressure (IP) turbines. In this case, for a given fossil fuel input, steam production from solar energy raises the mass flow of the steam turbines and therefore increases the overall power output. Obviously, from a thermodynamic point of view, the latter is undoubtedly the preferred approach [17,18], although the best option also depends on climatic conditions and solar collector technology. The integration of solar systems both based on parabolic trough collectors and linear Fresnel collectors with PCC has been studied [18–20], demonstrating that solar integration improves the economic feasibility of CCS, especially for decreasing collector costs and increasing CO_2 emission prices [21,22].

In this framework, the present study evaluates the performance improvements of an Ultra Super Critical (USC) steam power plant with PCC integrated with concentrating solar collectors. USC systems represent the state of the art in the field of coal fired power plants, with conversion efficiencies above 45-46%, more than 5 percentage points greater than those of conventional steam power plants [23]. Firstly, the USC-PCC plant was integrated with a solar field based on LFC or PTC with DSG, without considering a thermal energy storage. Subsequently, the results were compared with those of an USC-PCC plant integrated with PTC using Molten Salts (PTC-MS) as HTF and a two-tank direct TES. The comparative analysis aims to evaluate the increase in USC-PCC energy production and global efficiency due to the solar energy contribution by considering two different locations: Sardinia (Italy) and Morocco. Finally, a preliminary cost analysis was also included, evaluating the levelized cost of energy (LCOE).

2. Configuration and performance of the solar field

As mentioned, a solar field based on parabolic trough (PTC) or linear Fresnel collectors (LFC) is considered in this paper. For both options, PTC and LFC collector line includes several modules connected in series and the different lines of linear collectors are connected in parallel to achieve the required thermal power output. Two different solutions based on direct steam generation or molten salts are compared. Table 1 reports the main geometrical and performance parameters assumed in this study [24].

Table 1 - Main characteristics of solar collectors.

	LFC (DSG)	PTC (DSG)	PTC (MS)
Module length/ width	44.8/16.56 m	100/5 m	100/5 m
Focal length F	7.4 m	1.8 m	1.8 m
Module collecting area A_C	513.6 m^2	470.3 m^2	470.3 m^2
Modules per line	16	8	8
Reference optical efficiency	0.665	0.745	0.745
Cleanliness efficiency	0.98	0.98	0.98
Inlet/outlet steam conditions (p=80bar)	175°C/500°C	175°C/500°C	175°C/500°C
Receiver thermal losses	$0.056\Delta T+2.13E\text{-}4\Delta T^2$ (EVA) $0.013\Delta T+6.251E\text{-}10\Delta T^4$ (SH)	$0.056\Delta T+2.13\ E\text{-}4\Delta T^2$ (EVA) $0.013\Delta T+6.251E\text{-}10\Delta T^4$ (SH)	Forristall model [25]

The performance of PTC and LFC are evaluated on a yearly basis and compared by means of a specifically developed simulation model starting from hourly data of Direct Normal Irradiation (DNI), solar position, air temperature and wind speed. Firstly, the actual thermal power incident into the receiver $\dot{Q}_{INC}$ is calculated according to the following equation:

$$\dot{Q}_{INC} = DNI \cdot A_C \cdot \eta_{OPT,R} \cdot IAM \cdot \eta_{END} \cdot \eta_{SHD} \cdot \eta_{CLN} \quad \text{(eq. 1)}$$

where $\eta_{OPT,R}$ is the reference optical efficiency, IAM the Incidence Angle Modifier, η_{END} the end-loss optical efficiency, η_{SHD} the shadow efficiency and η_{CLN} the surface cleanliness efficiency. Figure 1 shows the two IAM components in function of the longitudinal and transversal components θ_L and θ_T of the solar incidence angle θ. End loss optical efficiency is evaluated in function of collector length, focal height and longitudinal component θ_L. Shadow efficiency is considered only for the PTC cases and is evaluated in function of the distance between module rows and collector width.

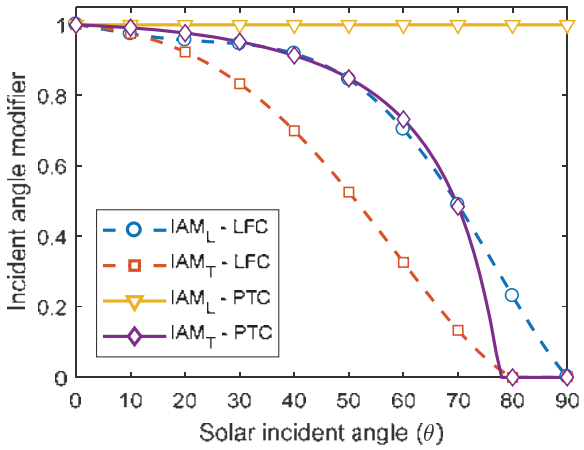

Figure 1 - Longitudinal and transversal IAM components

The thermal power $\dot{Q}_{SF}$ actually transferred to the HTF is calculated by applying the receiver energy balance:

$$m_R \frac{\partial h}{\partial t} + \dot{Q}_{REC,L} - \dot{Q}_{INC} = -\dot{Q}_{SF} = \dot{m}_{HTF}(h_{IN} - h_{OUT}) \quad \text{(eq. 2)}$$

Where the first term considers the thermal capacity of the HTF inside the tube and $\dot{Q}_{REC,L}$ represents the receiver thermal losses evaluated according to the specific correlations reported in Table 1 (ΔT is the temperature difference between the HTF temperature and the ambient temperature). A more detailed description of the simulation model can be found in [26]. Finally, a solar field control is introduced and the mass flow rate $\dot{m}_{HTF}$ is adjusted to meet the design point value of the loop outlet enthalpy. The latter is set to produce steam at 500 °C and 80 bar. For the DSG case, the overall steam production directly feeds the USC plant and the rated steam mass flow rate and the solar field aperture area are determined by setting a desired solar field power output under nominal conditions.

In case of molten salts as HTF, a direct two-tank TES system is considered: one tank stores the hot fluid while the other holds the exhausted cold fluid. The TES system is modelled by considering the mass and energy balance of each tank, as reported in the following equations:

$$\frac{\partial m_{TES}}{\partial t} = \dot{m}_{HTF,IN} - \dot{m}_{HTF,OUT} \quad \text{(eq. 3)}$$

$$m_{TES} \frac{\partial h_{TES}}{\partial t} = \dot{m}_{HTF,IN} h_{HTF,IN} - \dot{m}_{HTF,OUT} h_{TES} - \dot{Q}_{TES,L} \quad \text{(eq. 4)}$$

where m_{TES} is the HTF mass stored in the tank, $\dot{m}_{HTF,IN}$ and $\dot{m}_{HTF,OUT}$ are the inlet and outlet mass flow rate respectively, h_{TES} is the average HTF enthalpy inside the tank, $h_{HTF,IN}$ is the inlet HTF enthalpy and $\dot{Q}_{TES,L}$ are the TES thermal losses due to a not perfect insulation of the tanks. The HTF stored in the hot tank is then used to produce steam in a heat exchanger, simulated by considering a constant pinch point temperature difference (set to 10°C) and by applying a steady-state energy balance:

$$\dot{m}_{HTF}(h_{HTF,IN} - h_{HTF,OUT}) = \dot{m}_S(h_{S,OUT} - h_{S,IN}) \quad \text{(eq. 5)}$$

Where $\dot{m}_S$ is the steam mass flow rate, $h_{S,OUT}$ and $h_{S,IN}$ are the outlet and inlet steam enthalpy respectively. Therefore, thanks to the introduction of a TES system, the PTC-MS configuration slightly differs from the DSG case, as the steam mass flow rate produced is constant and does not depends on the solar energy availability. The thermal storage capacity (C_{TES}) is here expressed in terms of equivalent full-load hour of TES, which indicates the number of hours that the thermal storage section can supply energy to the heat exchanger to produce steam at nominal conditions. Moreover, in order to better exploit the TES storage an increase of solar field aperture area respect to the rated one is often recommended. Solar multiple (SM) is therefore used to represent the actual solar field thermal power as a multiple of the solar field reference thermal power. It is worth noting that the solar

multiple in case of DSG is always equal to one in this study. Two locations characterized by different DNI availability are considered in order to compare the energy performance and the cost-effectiveness of the solar field in different weather conditions. In particular, a site with a high DNI availability (Ouarzazate, Morocco, 2444 kWh/m²y) and one with a lower DNI (Cagliari, Sardinia, Italy, 1720 kWh/m²y) are evaluated. The data set for a typical meteorological year was obtained from the Meteonorm software, including DNI, solar azimuth and elevation, air temperature, relative humidity and wind velocity. Table 2 reports the main meteorological data of the chosen sites and the corresponding design conditions assumed for the solar field.

Table 2 - Meteorological data for the sites of Italy and Morocco and solar field design assumptions.

		Italy	Morocco
Available DNI	kWh/m^{2}y	1720	2444
Average ambient temperature	°C	17.2	18.8
Average wind velocity	m/s	3.96	3.80
Design DNI	W/m^2	800	900
Design elevation/azimuth angles	°	74.2/0.0	82.5/0.0
Design ambient temperature	°C	22.5	30.0

For both sites, Table 3 reports the main performance of a single line in terms of reference thermal power output and reference efficiency, as well as annual thermal energy production and average efficiency (the ratio of annual thermal energy production and annual available DNI), considering both LFC and PTC with DSG and PTC-MS. A decrease of about 9 percentage points in the reference efficiency and 17 percentage points in the average efficiency is observed in the LFC case compared to PTC with DSG. This is mainly due to the lower reference optical efficiency of the linear Fresnel collectors together with the effect of the transversal IAM, which is not present in the parabolic trough collectors. A reduction of about 3 percentage points in the reference efficiency is also detected by using PTC with molten salts instead of DSG, due to the higher HTF average temperature inside the receiver tube and the consequent increase of the receiver thermal losses. A more important decrease is observed in the annual performance due to both the higher receiver thermal losses and the higher thermal inertia of the molten salts. A reduction of 2-3 percentage points from Italy to Morocco cases is finally observed, because of different weather conditions and solar elevation. This difference rises up to 9 percentage points in the PTC-MS case. In fact, this case is characterized by a higher thermal inertia of the molten salts involving in the solar field due to the presence of a TES section. Consequently, a great increase of the energy spent to warm the molten salts in the first morning up to the nominal conditions occurs.

Table 3 - Performance of a single LFC and PTC line.

		LFC		PTC		PTC-MS	
		Ita	Mor	Ita	Mor	Ita	Mor
Collecting area	m^2	8217.6	8217.6	3762.4	3762.4	3762.4	3762.4
Reference thermal power	MW	4.030	4.720	2.118	2.469	2.020	2.370
Reference efficiency	%	61.30	63.82	70.36	72.92	67.11	70.00
Solar energy availability	GWh/y	14.12	20.08	6.47	9.19	6.47	9.19
Thermal energy production	GWh/y	5.85	8.91	3.77	5.66	2.53	4.43
Average efficiency	%	41.43	44.37	58.3	61.55	39.1	48.2

3. Configuration and performance of the USC plant with PCC

USC power plants are characterized by very hard operating conditions, reaching maximum steam pressures higher than 30 MPa and maximum steam temperatures up to 600-620 °C [27]. In recent years, several R&D studies focused on a further increase of the steam pressure and temperature with the aim of reaching overall plant efficiency as high as 50% [28]. The achievement of higher temperatures and pressures is closely related to the use of suitable advanced materials to withstand the harshest operating conditions [29,30]. A medium size plant (in the order of 450-500 MW_e) has been considered for this study. This size is lower than typical modern USC plant, but better matches with the integration with the solar field. The reference plant configuration is based on a superheated and double reheat steam cycle with ten regenerative steam extractions and four steam turbines: a very high-pressure turbine (VHPT), a high-pressure turbine (HPT), an intermediate pressure turbine (IPT) and a low-pressure turbine (LPT). Figure 2 shows a simplified scheme of the USC power plant.

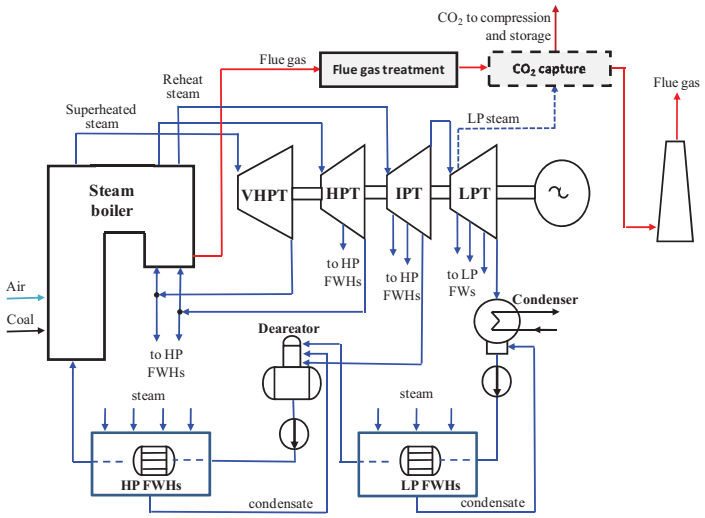

Figure 2 - Simplified scheme of the USC plant.

Performance of the plant have been assessed referring to a commercial coal, characterized by a carbon fraction slightly higher than 0.65 and a lower heating value of 25.03 MJ/kg. A coal power input of 1.0 GW was imposed. The plant is equipped with both a conventional flue gas cleanup (FGC) section (including a selective catalytic reduction denitrification system, baghouse filters and a low temperature flue gas desulphurization system) and a low temperature CO_2 removal section, based on a post-combustion chemical absorption process with amine-based solvents (MEA 30%wt), including an absorption and a regeneration column. To match CO_2 transport and storage requirements, the CO_2 removal section is also integrated with a conditioning and compression section to provide a high pressure (11 MPa) and high purity (99.7% by volume) CO_2 flow.

As in modern USC units, a maximum pressure of 33.5 MPa has been assumed, leading to a superheated (SH) steam pressure at the VHPT inlet of about 30 MPa. A minimum pressure of 4.2 kPa has also been assumed at the condenser. Superheated and reheat (RH) steam temperatures of 600 and 620 °C have been assumed, respectively. High temperature of the steam extraction allows to reduce to -1.5 °C the minimum temperature difference inside the high-pressure feedwater heat exchangers, whereas such a difference increases up to 1.5 °C inside the low-pressure feedwater heat exchangers. A deaerator pressure of 0.8 MPa has been assumed. Table 4 reportes the main characteristics of the plant and Table 5 summarizes its overall performance. The very high pressure of the first steam extraction (slightly lower than 15 MPa) allows to increase water temperature upstream of the economizer above 335 °C. The reference USC plant (without CCS) attains a net power output of about 465 MW with a corresponding net efficiency of 46.64%. The integration with the CO_2 removal section largely reduces the USC performance, mainly due to the large steam extraction (at about 4 bar) for solvent regeneration and to the power required by the CO_2 compression process.

Table 4 - Main characteristics of the USC plant.

Coal chemical power input	MW	1000
SH/RH1/RH2 steam temperatures	°C	600/620/620
SH/RH1/RH2 steam pressures	MPa	30.0/13.5/5.4
Cycle maximum pressure (boiler feedwater pump)	MPa	33.5
Cycle minimum pressure (condenser)	kPa	4.2
Deaerator pressure	MPa	0.8
BOP loss as steam turbine power fraction		0.02
High/low pressure heat exchangers minimum ΔT	°C	-1.5/1.5
MEA mass fraction	%	30
CO_2/MEA molar ratio		0.28
Reboiler specific thermal energy	MJ/kg_{CO2}	3.72

Table 5 - Overall performance of the USC plant.

		NO-CCS	CCS
Coal chemical power input	MW	1000	1000
- Steam turbines	MW	516.4	439.7
- Pumps	MW	16.1	16.1
Steam cycle output	MW	500.0	423.6
- Aux. absorptions and mechanical losses	MW	19.4	16.1
- Generator losses	MW	5.2	4.4
Gross power output	MW	475.4	403.1
- FGC section absorptions	MW	9.0	9.0
- CO_2 capture and compression	MPa	-	32.4
Net power output		466.4	361.7
Net efficiency		46.64	36.17
Plant availability	h/year	8760	8760
Energy production	GWh/year	4085.6	3168.5
CO_2 emissions	Mt/year	3.00	0.300
CO_2 specific emissions	g/kWh	734.3	94.7

In particular, a CO_2 removal efficiency of 90% requires about 320 MW_t, halving the LPT mass flow and reducing the USC power output by about 70 MW. This remarkable penalty combined with the power requirements of the CO_2 capture and compression section causes a noteworthy power output reduction of about 105 MW. Overall, the introduction of the PCC process reduces the energy production by about 25% and the USC efficiency by about 10.5 percentage points (from 46.6% to 36.2%). Obviously, the CO_2 specific emissions greatly benefit from the introduction of the CO_2 capture and compression section (decreasing from about 735 to about 95 g/kWh).

4. Performance of the integrated CSP-USC-PCC plant

To mitigate the energy penalty generated by the large heat consumption required for solvent regeneration, the USC-PCC plant has been integrated with concentrating solar collectors in a CSP-USC-PCC plant. The hybridization occurs through the production of intermediate pressure steam (80 bar and 500°C). The water is extracted downstream of the feedwater pump, it is pre-heated, vaporized and superheated in the solar field and then reintroduced downstream of the high-pressure turbine before entering in the second reheater. In particular, when solar energy is available, the IP steam produced by the solar field increases the mass flow rate of both IP and LP steam turbines allowing a greater power production but leading also to an off-design operation mode of the USC plant with a corresponding efficiency penalty. Moreover, the steam production from solar field causes both an increase of the LP turbine outlet pressure and a rise in the condenser thermal load, therefore, leading to a higher cooling water requirement or higher cooling water outlet temperature. Figure 3(a) shows the pressure and the condenser mass flow rate (the latter in percentage with respect to design conditions) in function of the ratio between solar field power output ($\dot{Q}_{SF}$) and fuel power input ($\dot{Q}_{USC}$). The condenser mass flow greatly increases with solar contribution and, therefore, in order to avoid an excessive increase in the condenser thermal load, a maximum value of the power ratio equal to 0.2 was considered in this study. The increase in steam pressure and mass flow leads to corresponding changes in the turbine power output owing to the sliding pressure operating mode of the steam turbine. Obviously, the USC-PCC-CSP net power output increases with the solar contribution and annual average performance of the power plant are greatly influenced by annual DNI availability. However, the USC power plant operates without solar energy integration for a large share of the annual operating hours, as concentrating solar collectors require a minimum available DNI (100-150 W/m^2). Moreover, during most of the solar field operating hours, the DNI is below its design value. Therefore, in the case of direct steam generation, the USC plant operates at reference conditions when no solar production occurs, while it operates in off-design conditions with the introduction of IP steam from solar field, with a corresponding cycle efficiency penalization. On the other hand, the use of molten salts as heat transfer fluid allows the introduction of a thermal storage at relative low costs. In this case, the steam production from the solar field is constant along the day with an important increase of the operating hours at on-design conditions.

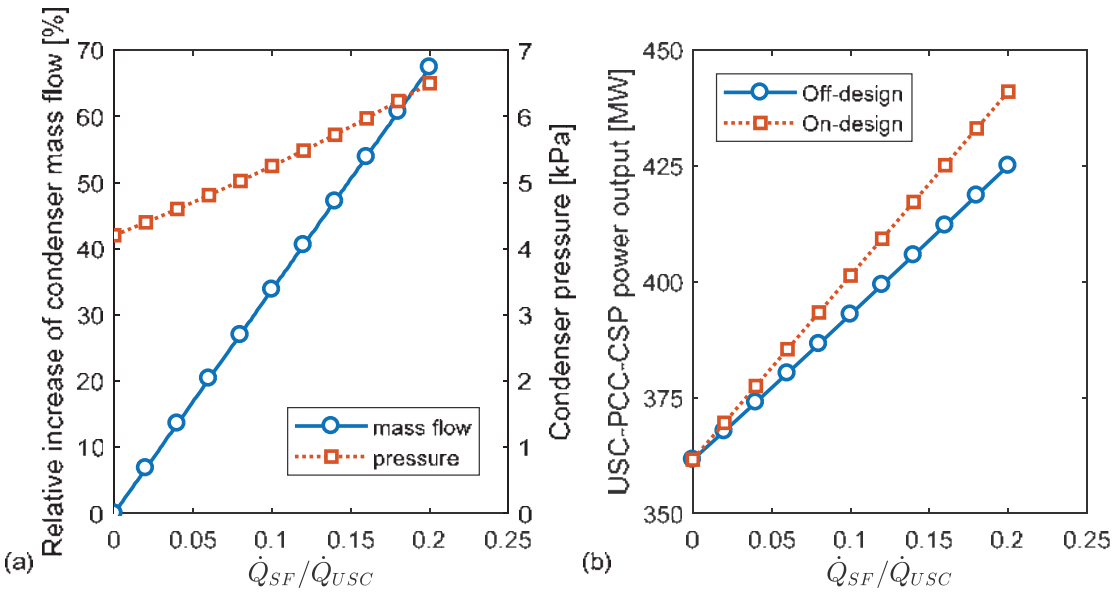

Figure 3 – (a) Relative increase of the condenser mass flow, condenser pressure and (b) power output of the USC-CCS-CSP plan as a function of the ratio between solar field power output and fuel power input.

The advantages in terms of efficiency and, thus, of net power output by working at on-design conditions instead of off-design is shown in Figure 3(b) as a function of the ratio between solar field power output and fuel power input. Figure 4(a) shows the annual performance of the system in terms of USC net energy production as a function of the ratio between the solar field power output and fuel power input in case of direct steam generation or molten salts as HTF (storage capacity equal to 4 hours and solar multiple equal to 1). The USC net energy production linearly increases with the solar contribution for all cases, and, as expected, the highest values are reached by adopting parabolic trough collectors. By referring to the Morocco case, an increase of 0.715 GWh in annual USC energy production for an increase of 1 MW of solar field reference thermal power is detected for PTC with DSG, 0.840 GWh/MW_{CSP} for the PTC-MS case and 0.590 GWh/MW_{CSP} for LFC solar field. Similar trends are observed by referring to the Italian site, although the lower DNI availability results in a lower solar contribution of 0.550 GWh/MW_{CSP}, 0.545 GWh/MW_{CSP} and 0.450 GWh/MW_{CSP} for the PTC-DSG, PTC-MS and LFC configurations, respectively. It is worth noting that for a given value of solar contribution, the overall collecting area increases by using LFCs instead of PTCs and by considering an Italian location instead of a Moroccan one.

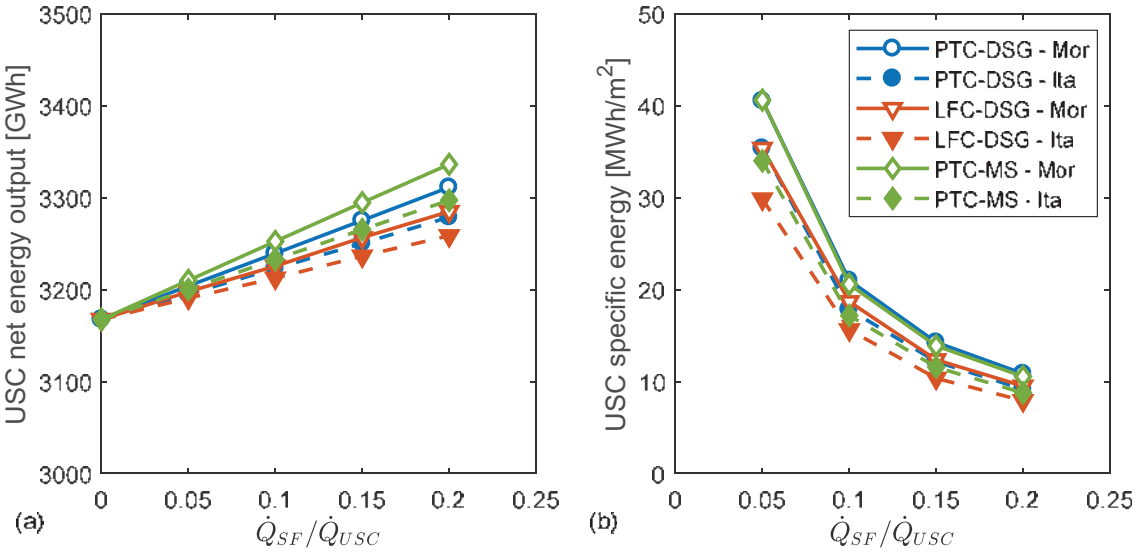

Figure 4 – (a) Annual USC-PCC-CSP energy production and (b) specific energy production as a function of the ratio between solar field power output and fuel power input.

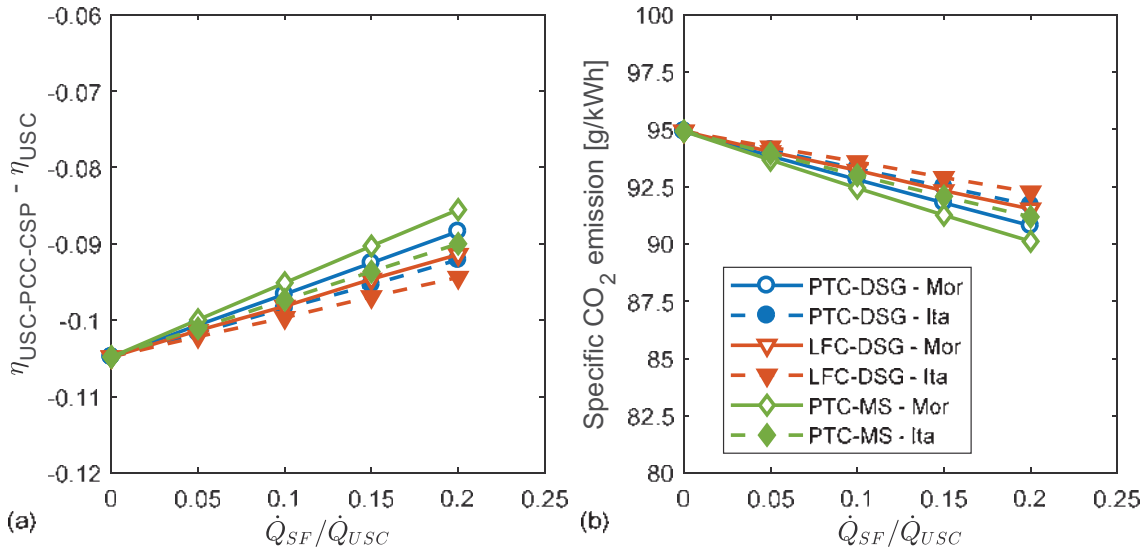

Figure 5 – (a) USC efficiency decrement and (b) specific CO_2 emissions as a function of the ratio between solar field power output and fuel power input.

For instance, for a solar contribution equal to 0.2, the overall collecting areas are about 304750 m^2 (81 loops) and 357430 m^2 (95 loops) for PTC in Morocco and Italy respectively, while the LFC solar field is characterized by a collecting area of 345140 m^2 (43 loops) in Morocco and 410880 m^2 (50 loops) in Italy. For this reason, Figure 4(b) depicts the specific annual energy production in terms of energy produced per unit area of solar field. The figure shows a marginal difference between the use of DSG and molten salts by referring to the Moroccan case. In fact, although as reported in Table 3 the average efficiency of the solar field using molten salts was lower than the use of PTC-DSG, they are substantially balanced by the higher USC efficiency resulting from the constant steam mass flow rate production of the solar field. On the other hand, the drop in solar field performance detected for the Italian case by using molten salts as HTF is predominant and the use of the PTC-DSG achieves the highest specific energy production. The main benefits arising from a solar integration are shown in Figure 5:

- the efficiency penalty due to the CO_2 removal section are partially balanced by the steam generation from the solar field (Figure 5(a));
- a further reduction of the specific CO_2 emissions is achieved thanks to the increase of annual energy production due to solar field without any further production of carbon dioxide (Figure 5(b)).

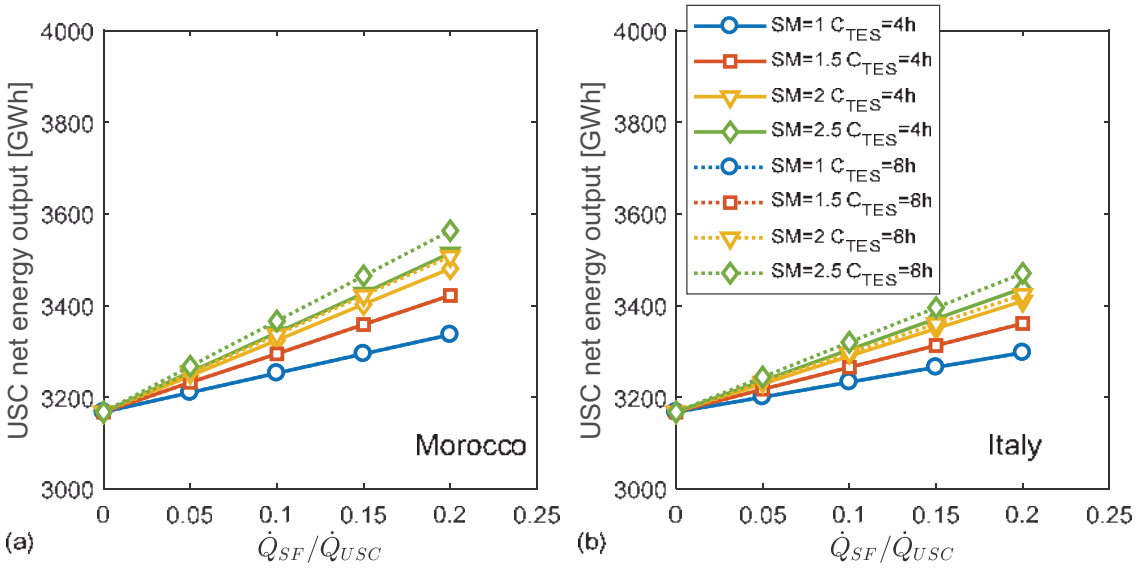

Figure 6 - Annual USC-PCC-CSP energy production as a function of the ratio between solar field power output and fuel power input for the Molten Salts case.

Both these performance indexes follow a linear increment with the increase in the solar field power output.
As mentioned, one of the advantages of introducing a TES system is the possibility to time shift the production of the solar field. In other words, with a TES system it is possible to increase the time of steam feeding to the USC by keeping a constant mass flow rate. As mentioned, other two important design parameters for the molten salts case are the storage capacity and the solar multiple. Figure 6 shows the annual energy production of the USC plant as a function of the solar contribution for different combinations of solar multiple and TES capacity. For solar multiples lower than 2, a TES capacity higher than 4 full-load hours do not introduced any benefits in terms of rising in energy production, independently form the plant location. On the other hand, with the rise in the solar multiple value, a higher storage capacity is required to store the surplus of energy produced by the solar field, especially during summer days. In particular, the increase of the TES capacity from 4 to 8 hours in Morocco results in an increase of about 15% of the annual steam production.

5. Preliminary economic analysis

A preliminary economic analysis was carried out to compare the energy production cost of the reference USC plant (with and without PCC) and the solar assisted configurations. In fact, the increment in the energy production with the solar integration also results in a rise of capital and operating costs. The economic analysis is based on the determination of the levelized cost of electricity (LCOE) for the various configurations considered. The LCOE was calculated by means of the following equation:

$$\mathrm{LCOE} = \frac{\mathrm{TCI_{USC}} + \mathrm{TCI_{PCC}} + \mathrm{TCI_{CSP}} + \sum_{n=1}^{N}\left(\mathrm{C_F} + \mathrm{C_{O\&M,USC}} + \mathrm{C_{O\&M,CSP}}\right)(1+\mathrm{i})^{-n}}{\sum_{n=1}^{N}\mathrm{E_E}(1+\mathrm{i})^{-n}} \qquad \text{(eq. 6)}$$

Where $\mathrm{TCI_{USC}}$, $\mathrm{TCI_{PCC}}$ and $\mathrm{TCI_{CSP}}$ are the total capital cost investment of the USC plant, PCC system and the CSP section (including solar field costs and, if present, TES costs) respectively, $\mathrm{C_F}$ is the annual cost of the fuel, $\mathrm{C_{O\&M,USC}}$ and $\mathrm{C_{O\&M,CSP}}$ are the operating and maintenance costs for the USC-PCC plant and solar section, $\mathrm{E_E}$ is the annual energy production, i is the annual interest rate and N is the expected operating lifetime.

Table 6 - Cost assumptions of the USC-PCC plant, solar field and TES section.

USC specific capital investment	1300 €/kW	Solar field specific cost	100-300 €/m^2
PCC specific capital investment	1170 €/kW	Piping specific cost	30 €/m^2
O&M cost of USC (% of TCI)	3%	Land cost	10 €/m^2
O&M cost of PCC (% of TCI)	2.5%	TES specific cost (only MS case)	625 €/m^3
Coal price	75 €/t	Molten salts cost	0.93 €/kg
Engineering cost (% of direct cost)	20%	O&M cost of solar section (% of TCI)	1.5%
Contingency cost (% of direct cost)	2%	Annual interest rate	7%
Insurance annual cost (% of TCI)	1%	Operating lifetime	20

Table 6 reports the main cost assumptions. In particular, the assumption of specific costs for the USC-PCC plant are taken according to [15], and for the CSP plant according to [31]. The solar field specific cost is not constant but ranges in the interval 100-300 €/m^2. In fact, the present economic analysis aims to evaluate the minimum capital cost of the solar field that allows to produce electricity at a lower LCOE than the reference USC-PCC plant. For a solar integration of 20% (that is the ratio between solar field power output and fuel power input equal to 0.2), Figure 7(a) shows the LCOE for the six different cases analyzed as a function of the solar field specific cost, as well as the LCOE obtained without considering any solar integration. Obviously, a linear increase of the LCOE is observed with the increase of the solar field specific costs. The LFC case always attains higher values of LCOE than PTC and a decrease of the solar field cost of about 60 €/m^2 should occurs to becomes competitive with PTC solar fields. The LCOE with solar integration in the Italian case always exceeds the LCOE of the USC-PCC plant even for the lowest solar field specific costs. On the other hand, the solar integration becomes cost effective for a solar field cost lower than 180 €/m^2 for the PTC-DSG case. The use of molten salts and the introduction of a TES section, despite the enhancement in annual energy production, increase the capital and operating costs and result less profitable than the direct steam generation.

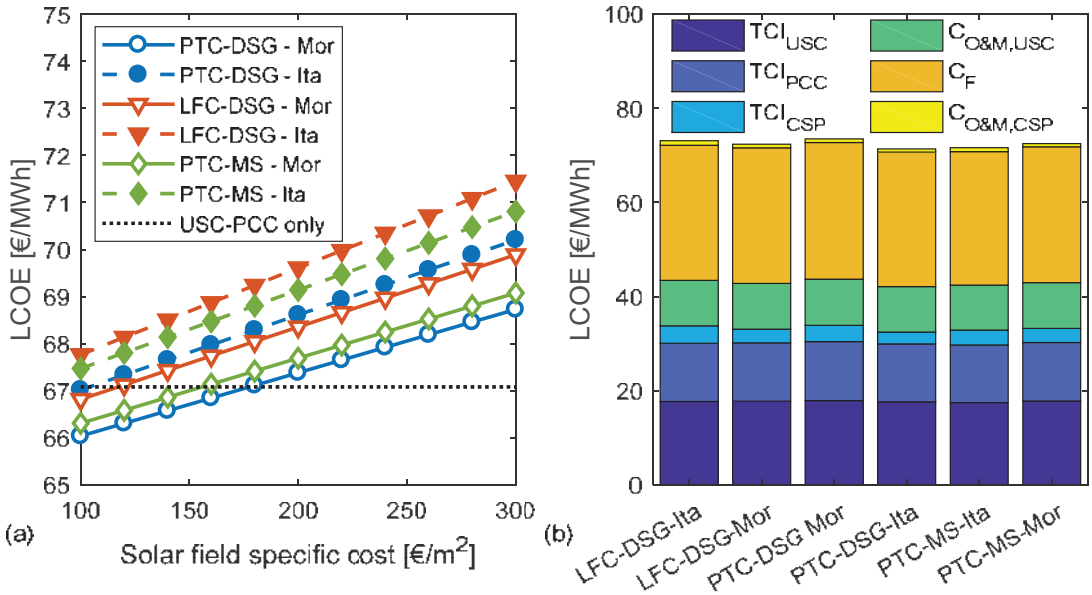

Figure 7 – (a) Levelized cost of electricity as function of the solar field specific cost and (b) influence of capital and operating costs on the determination of the LCOE.

It is worth noting that the influence of the solar field costs on the overall plant costs is marginal. As shown in Figure 7(b), by assuming a solar field specific cost of 200 €/m^2, the capital cost for solar integration contributes for about 5% of the overall LCOE while O&M costs of the solar section are lower than 1%. Finally, Figure 8 shows the levelized cost of energy in case of molten salts as HTF and different values of solar multiple and TES capacity. The figure demonstrates the not profitability to increase the storage capacity beyond 8 hours independently from the location, as the excess energy that cannot be stored due to the complete charge of the TES section is minimal (only for few summer days in case of C_{TES}=4h). Consequently, the rise in capital costs due to higher storage and HTF costs is not properly balanced by the increase in the energy production. On the other hand, an increment of the solar multiple to 1.5 could be a cost-effective solution if the solar field specific cost drops to 160 €/m^2 in the Morocco case. In this case, the benefits arising from a higher energy production becomes preponderant compared to the corresponding increment of the solar field capital costs.

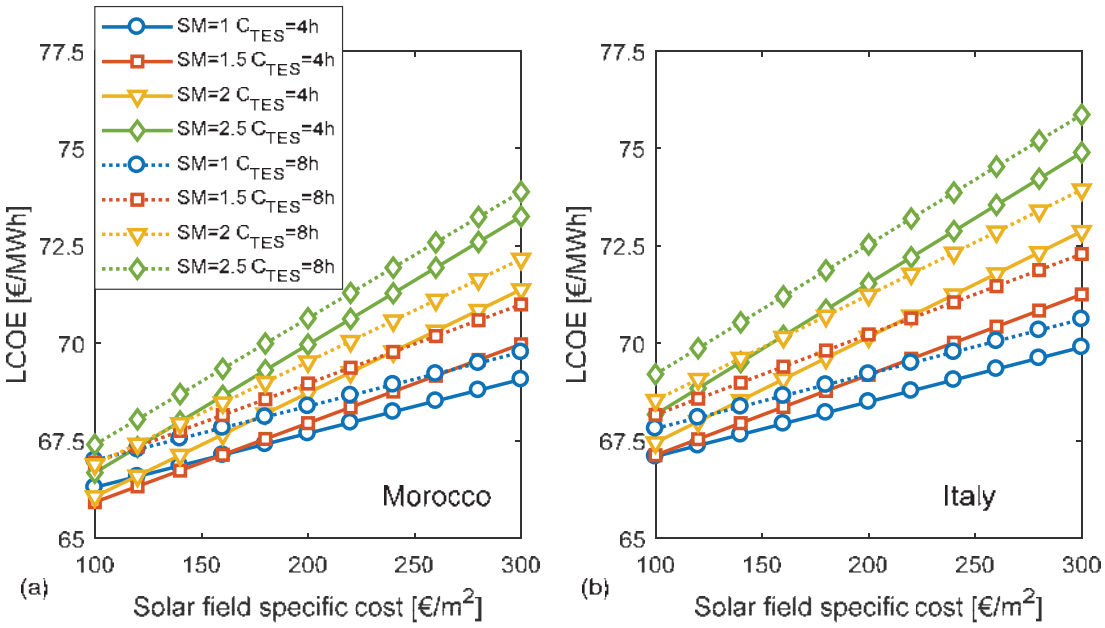

Figure 8 – Levelized cost of energy as function of solar field specific cost using molten salts in case of (a) Moroccan site and (b) Italian site.

6. Conclusions

The paper investigated the benefits arising from the integration of low CO_2 emission steam power plants with concentrating solar systems. Different solar field configurations were studied, varying both collector technology (parabolic trough or linear Fresnel) and heat transfer fluid (direct steam generation or molten salt with thermal energy storage). The achieved results proved that the energy produced by the solar field reduces the efficiency penalty due to CO_2 capture and compression system from about 10.5 percentage point (reference case without solar integration) to a maximum of about 8.5% (ratio between solar energy and fuel chemical energy equal to 0.2). As expected, better performance are achieved in Morocco in comparison to Italian site. The preliminary economic analysis demonstrated as, in Morocco, the solar integration in a USC-PCC plant becomes cost effective for a solar field costs lower than 180 €/m^2 for PTC-DSG case. A reduction of about 60 €/m^2 in solar field cost should occurs for LFC to becomes competitive with PTC solar fields. The use of Molten salts as HTF and the introduction of a TES section enhance the annual energy production but increase the capital and operating costs, resulting less profitable than the direct steam generation.

7. References

[1] Institute for Advanced Sustainability Studies (IASS). IASS Fact Sheet 2/2016 Concentrated Solar Power. 2016.

[2] Mehos M, Turchi C, Vidal J, Wagner M, Ma Z, Ho C, et al. Concentrating solar power: Gen3 demonstration roadmap 2017:1–140.

[3] Siva Reddy V, Kaushik SC, Ranjan KR, Tyagi SK. State-of-the-art of solar thermal power plants - A review. Renew Sustain Energy Rev 2013;27:258–73. doi:10.1016/j.rser.2013.06.037.

[4] Pelay U, Luo L, Fan Y, Stitou D, Rood M. Thermal energy storage systems for concentrated solar power plants. Renew Sustain Energy Rev 2017;79:82–100. doi:10.1016/j.rser.2017.03.139.

[5] Rovira A, Barbero R, Montes MJ, Abbas R, Varela F. Analysis and comparison of Integrated Solar Combined Cycles using parabolic troughs and linear Fresnel reflectors as concentrating systems. Appl Energy 2016;162:990–1000. doi:10.1016/j.apenergy.2015.11.001.

[6] Moghimi MA, Craig KJ, Meyer JP. Simulation-based optimisation of a linear Fresnel collector mirror field and receiver for optical, thermal and economic performance. Sol Energy 2017;153:655–78. doi:10.1016/j.solener.2017.06.001.

[7] Feldhoff JF, Schmitz K, Eck M, Schnatbaum-Laumann L, Laing D, Ortiz-Vives F, et al. Comparative system analysis of direct steam generation and synthetic oil parabolic trough power plants with integrated thermal storage. Sol Energy 2012;86:520–30. doi:10.1016/j.solener.2011.10.026.

[8] Schneider G, Maier H, Stenglein M, Schicktanz P, Stepper R, Schlipf D. Direct Molten Salt Linear Receiver CSP-concepts with MS-TES Compared with Direct Steam Generation Linear Receiver CSP-concepts with Solid Bed TES. Energy Procedia 2015;69:1412–20. doi:10.1016/j.egypro.2015.03.124.

[9] Behar O, Kellaf A, Mohamedi K, Belhamel M. Instantaneous performance of the first integrated solar combined cycle system in Algeria. Energy Procedia 2011;6:185–93. doi:10.1016/j.egypro.2011.05.022.

[10] Pramanik S, Ravikrishna R V. A review of concentrated solar power hybrid technologies. Appl Therm Eng 2017;127:602–37. doi:10.1016/j.applthermaleng.2017.08.038.

[11] Montes MJ, Rovira A, Muñoz M, Martínez-Val JM. Performance analysis of an Integrated Solar Combined Cycle using Direct Steam Generation in parabolic trough collectors. Appl Energy 2011;88:3228–38. doi:10.1016/j.apenergy.2011.03.038.

[12] Nezammahalleh H, Farhadi F, Tanhaemami M. Conceptual design and techno-economic assessment of integrated solar combined cycle system with DSG technology. Sol Energy 2010;84:1696–705. doi:10.1016/j.solener.2010.05.007.

[13] Lim Y, Kim J, Jung J, Lee CS, Han C. Modeling and Simulation of CO2 Capture Process for Coal-based Power Plant Using Amine Solvent in South Korea. Energy Procedia 2013;37:1855–62. doi:10.1016/j.egypro.2013.06.065.

[14] Goto K, Yogo K, Higashii T. A review of efficiency penalty in a coal-fired power plant with post-combustion CO2 capture. Appl Energy 2013;111:710–20. doi:10.1016/j.apenergy.2013.05.020.

[15] Tola V, Pettinau A. Power generation plants with carbon capture and storage: A techno-economic comparison between coal combustion and gasification technologies. Appl Energy 2014;113:1461–74. doi:10.1016/j.apenergy.2013.09.007.

[16] Zhao R, Deng S, Zhao L, Liu Y, Tan Y. Energy-saving pathway exploration of CCS integrated with solar energy: Literature research and comparative analysis. Energy Convers Manag 2015;102:66–80. doi:10.1016/j.enconman.2015.01.018.

[17] Jamel MS, Abd Rahman A, Shamsuddin AH. Advances in the integration of solar thermal energy with conventional and non-conventional power plants. Renew Sustain Energy Rev 2013;20:71–81.

doi:10.1016/j.rser.2012.10.027.
[18] Cau G, Cocco D, Tola V. Performance assessment of USC power plants integrated with CCS and concentrating solar collectors. Energy Convers Manag 2014;88. doi:10.1016/j.enconman.2014.09.040.
[19] Wang F, Zhao J, Li H, Deng S, Yan J. Preliminary experimental study of post-combustion carbon capture integrated with solar thermal collectors. Appl Energy 2017;185:1471–80. doi:10.1016/j.apenergy.2016.02.040.
[20] Cau G, Cocco D, Tola V. Chapter 84 Solar-Assisted Ultra-supercritical Steam Power Plants with Carbon Capture and Storage. Renew. Energy Serv. Mank. Vol II, vol. II, 2016, p. 933–47. doi:10.1007/978-3-319-18215-5.
[21] Zhao Y, Hong H, Zhang X, Jin H. Integrating mid-temperature solar heat and post-combustion CO2-capture in a coal-fired power plant. Sol Energy 2012;86:3196–204. doi:10.1016/j.solener.2012.08.002.
[22] Qadir A, Mokhtar M, Khalilpour R, Milani D, Vassallo A, Chiesa M, et al. Potential for solar-assisted post-combustion carbon capture in Australia. Appl Energy 2013;111:175–85. doi:10.1016/j.apenergy.2013.04.079.
[23] Yang Y, Wang L, Dong C, Xu G, Morosuk T, Tsatsaronis G. Comprehensive exergy-based evaluation and parametric study of a coal-fired ultra-supercritical power plant. Appl Energy 2013;112:1087–99. doi:10.1016/j.apenergy.2012.12.063.
[24] Morin G, Dersch J, Platzer W, Eck M, Häberle A. Comparison of Linear Fresnel and Parabolic Trough Collector power plants. Sol Energy 2012;86:1–12. doi:10.1016/j.solener.2011.06.020.
[25] Forristall R. Heat Transfer Analysis and Modeling of a Parabolic Trough Solar Receiver Implemented in Engineering Equation Solver 2003.
[26] Cau G, Cocco D. Comparison of medium-size concentrating solar power plants based on parabolic trough and linear Fresnel collectors. Energy Procedia 2014;45:101–10. doi:10.1016/j.egypro.2014.01.012.
[27] Bugge J, Kjær S, Blum R. High-efficiency coal-fired power plants development and perspectives. Energy 2006;31:1437–45. doi:10.1016/j.energy.2005.05.025.
[28] P. S. Weitzel, Tanzosh JM, Boring B, Okita N, Takahashi T, Ishikawa N. Advanced Ultra-Supercritical Power Plant (700 to 760C) Design for Indian Coal. J Chem Inf Model 2013;53:1689–99. doi:10.1017/CBO9781107415324.004.
[29] Natesan K, Park JH. Fireside and steamside corrosion of alloys for USC plants. Int J Hydrogen Energy 2007;32:3689–97. doi:10.1016/j.ijhydene.2006.08.038.
[30] Noguchi Y, Okada H, Semba H, Yoshizawa M. Isothermal, thermo-mechanical and bithermal fatigue life of Ni base alloy HR6W for piping in 700??C USC power plants. Procedia Eng 2011;10:1127–32. doi:10.1016/j.proeng.2011.04.186.
[31] Cocco D, Serra F. Performance comparison of two-tank direct and thermocline thermal energy storage systems for 1 MWe class concentrating solar power plants. Energy 2015;81:526–36. doi:10.1016/j.energy.2014.12.067.

Daylighting

Calculation of energy performance indices of daylight linked control systems by monitored data

Marco Beccali[1], Marina Bonomolo[1], Valerio Lo Brano[1] and Gaetano Zizzo[1]
[1]Università degli Studi di Palermo, Dipartimento Energia, Ingegneria dell'Informazione e Modelli Matematici, Palermo (Italy)

Abstract

The actual performances of Building Automation systems are often lower than the ideal ones. In order to investigate the actual performance of a Building Automation system for lighting control, a large stock of collected data, including indoor illuminance and absorbed electric power, have been presented and analysed in this paper. The measures have been taken during one year, in a laboratory located at the University of Palermo, where different lighting control systems, produced by two different manufacture companies, have been installed. As demonstrated in literature, many factors affecting energy savings' evaluation in lighting control systems are the position and the typology of the sensors and their configuration. Furthermore, using the collected data, a set of indices has been calculated. It is able to test the performance of the systems in terms of energy efficiency and fulfilment of visual comfort tasks, according to different natural light availability, lighting system configurations and time scenarios. Finally, the performances of the two above lighting control systems have been compared.

Keywords: Daylight control system, Building automation system, lighting, indices, daylight.

1. Introduction

The benefits of Building Automation and Control (BAC) systems are well-known and, for this reason, their application in both residential and commercial buildings and become very common. In several studies, potential energy savings due to BAC systems have been assessed (Ferrari and Beccali, 2017) and calculated by conventional methods sometimes suggested by technical standards, or by using simulation software. Parise and Martirano (Parise and Martirano, 2009) proposed a methodology to calculate energy consumption for lighting systems and the impact of the BAC systems promoting a comprehensive eco-design. In particular, the method mentioned above allows to satisfy in selected subareas lighting and energy performances and to provide design elements with a basic efficient control system suitable for a manual or automatic regulation. Asif ul Haq et al. (2014, a) developed a new method that is easy to apply but comprehensive at the same time and gives a good indication as to the potential of energy saving from daylight utilization. They gave a detailed description for applying it based on a simulated test project as an example. The same authors (Asif ul Haq et al., 2014, b) investigated the various control system types, the development of their associated technologies, the savings obtained from their application and the factors affecting their performance. They also presented a complete literature review, which demonstrated that lighting control systems can ensure important energy savings and reduction in electricity costs. Other researchers are beginning to study

doi:10.18086/swc.2017.05.01 Available at http://proceedings.ises.org

also the problem of an accurate and reliable calculation of these figures. Bellia et al. (2015) investigated the factors that influence the performance of Daylight-linked controls (DLCs) and did a review of the several aspects that must be considered during the design, installation, configuration and operating steps. P. Valíček, et al. (2015) explained the complexity in setting the system due to the usual different position of the task surface and the sensor commanding the system' operation. Chen et al. (2016) carried out a cost-benefit evaluation method for building intelligent systems underlining that the problems, like sensor faults and control strategy flaws, may result in low performance and that high energy consumptions and maintenance costs are needed as well. Doulas et al. (2014) presented a decision-making method capable of estimating the best position of a photosensor on the ceiling and its proper field of view (FOV) based on multiple criteria analysis, using three criteria:

- the correlation of the lighting levels between the working plane and the ceiling;
- the corresponding energy savings and the lighting adequacy (defined as the percentage of occupied time with total illuminance exceeding design illuminance)
- the influence of the control algorithm.

Their work is based on a high number of simulations with variable FOV and position of photosensors, performed to clarify the calculation procedure of the proposed methodology and on the measurement taken from a prototype photosensor with variable FOV through the use of a telescopic cylinder.

In general, since there are no standard rules among manufacturers of BAC systems, a trial-and-error method is often used by the contractors to obtain reliable dimming response. Moreover, commercial BACs, installed in residential or small offices to manage several functions of home services, often include functions of lighting control, acting as DLCSs. Their hardware and software configurations, as well as inaccurate commissioning, could not always allow reaching the desired tasks correctly; therefore, the systems could not work as expected. This lack of metric tools and methods, mainly regarding the assessment of the actual performances of such DLCs, is the object of the present research which presents an application and an extension of an original method carried out by the authors and presented by Bonomolo et al. (2017).

2. Objectives

The method is based on the calculation of a set of indices and has been developed for the assessment of the energy performance of DLC systems, starting from monitored data and aiming to consider both the influence of systems characteristics and the daylight availability in the room. In particular, the index named Over illuminance Avoidance Ratio (OAR) takes into account the excess of light that could be caused by the position of the detector. On the contrary, the index named Under illuminance Avoidance Ratio (UAR) takes into account the defect of light. The Artificial Lighting Demand (ALD) index is defined to evaluate the rate of lack of natural lighting and, therefore, the rate of required artificial lighting to achieve appropriate illuminance values on the working plan. Finally, the Energy Ratio of Illuminance (ERI) index, being the ratio of the electrical consumption for lighting and the ALD as mentioned above, is used to assess how close the performance

of the real DLC system is to the one of an ideal system.

In this paper, the application of the above-described method is presented using a broader set of data, collected during about a one-year-long period and relative to two DLC systems. The original contributions of the present work are: to further validate the method with reliable experimental data, to use the here described indices to make functional and energy performance comparisons between alternative DLCs that could be utilised in the same room even if these have been tested in different time.

3. Lighting system and daylight control systems

The measurement campaign has been carried out at the Solarlab laboratory (Figure 1), located at the third floor of the building hosting the DEIM (Department of Energy, Engineering of the information and Mathematical Models) of the University of Palermo (Italy) and described in detail in a previous work presented by Beccali et al. (2015). The laboratory has been equipped by a measurement instrumentation set. For measuring the indoor illuminance six indoor probes Delta Ohm HD 2021T (measuring range 0.02-20 klx) have been utilized. Two of them have been placed on two different points of the ceiling, two on opposite walls and, finally, two at the height of 0,80 m or 0,6. Furthermore, in order to measure apparent, active and reactive power, current and voltage a SIEMENS SENTRON Power Monitoring Device PAC3200 (Siemens, 2009) has been used. Data have been collected through the platform LabVIEW System Design.

Fig. 1: Some pictures of the laboratory, of the sensors used to measure indoor illuminance and the section with their location.

In order to test the DLC systems, four suspended luminaires equipped with LED (each one with a power of 54 W) have been installed. They are characterized by a power supply unit with DALI interface and are equipped with micro-lens optics in a polycarbonate cover. The nominal luminous is 3600 lm, and the initial LED luminaire efficacy is 92 lm/W. Also, four mono optic LED luminaires have been installed, with an initial luminous flux of 700 lm and with an efficacy of 50 lm/W. Both types of luminaires have a colour temperature of 3000 K and a colour rendering index ≥80. The lighting power density is 1.86 W/m^2 for the whole area and 2.9 W/m^2 for the zone considered in this work (where the three dimmable suspended luminaires are installed). Two different daylight linked control systems, produced by two manufacturers have been tested. The first one ("System A"), has been installed, in a first period, on the ceiling at about 1.60 m away from the window, close to one of the two photosensors Delta Ohm installed on the ceiling utilised for the measurements. This latter is characterized by an angle view of 180° longitudinally and 360° horizontally and, as in most lighting control systems, its positioning was not

optimized with a precise method but was installed simply following the manufacturer's suggestions. It is designed for being easily usable by anyone, also by not skilled personnel; indeed, its interface is very user-friendly. It was composed by a closed loop photosensor, a scenario programmer, a touch dimmer, three manual actuators and four basic controls (current switches). The second system ("System B") is equipped with a look-out open loop photosensor. It has been installed on the ceiling, following the installation handbook guidelines. This photosensor has been linked to a DALI electronic control ballast which send the signal to the luminaires. Figure 2 shows the pictures of the two photosensors.

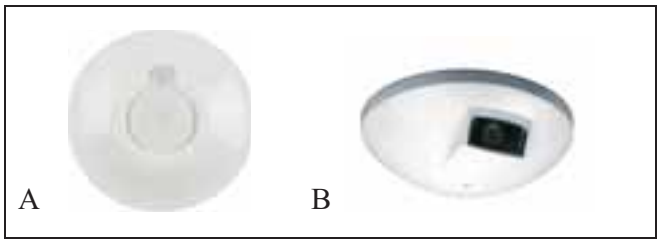

Fig. 2: Pictures of the closed loop sensor (A) and the open loop sensor (B).

In the first case, a target illuminance value can be set on the software menu after a "rapid" calibration of the photosensor, which is made with a remote-control device. After the measurement of the desired lighting level on the task area with a lux meter, the device sends a "calibration" command to the photosensor. This procedure has been made once with only artificial light and once with only daylight (without direct solar irradiance). It was the only option allowed by the software and naturally led to an approximate calibration of the system. Generally, it can be observed that with only artificial light or with diffuse daylight, a particular correlation between illuminance measured on the ceiling and on the work-plane is reliable only in case of low daylight levels (Bonomolo et al., 2017). The calibration of the second system has been shorter and more straightforward. It is based on the "memorizing" of "twilight points" (dimming the lamps to have task illuminance in the absence of daylight) and "daytime points" (dimming the lamps to have task illuminance in the presence of daylight). An accurate performance assessment of lighting and energy figures of a DLC system can be fulfilled by handling separate sets of natural and artificial illuminance data which together are present in the target area. This problem is easily solved in case of use of simulation software, which can separately calculate both the series. When data come from a real monitored space, a photosensor is no longer able to split the two contributions to the total illuminance. Moreover, provided that only an "ideal" system is able to ensure a constant illuminance setpoint over time, the actual contribution of artificial light becomes variable over the time. In assessing the artificial lighting contribution, it is possible to assume that the luminous flux is proportional to the power absorbed by the lighting system. The amount of artificial light has been calculated by applying a W/lx factor derived from measures made during the night-time. Natural lighting contribution has been estimated as the difference between the measured total illuminance and the calculated artificial illuminance.

4. Scenarios and configurations

During the measurement campaign, an office end-use has been tested. According to these case, as already said, several scheduled occupancy times, task level on the work-plane,

configurations and setup have been checked for each system. For the first part of the study, the installed luminaires have been controlled by the system A. In the last part, the System B has been tested. The electricity consumption has been calculated for two different control strategies: dimming and on-off. For the first case, consumption has been estimated merely using the measured power. In the second case, the energy consumption has been calculated assuming that the luminaires turn on when the illuminance value, due to the daylight contribution, is lower than the set-point value. Therefore, it has been taken into account the same time when the luminaires were turned on during the dimming case, but considering the absorbed power always at 100%. All the illuminance values have been calculated using the average of the measures taken by two pairs of photosensors (two in the ceiling and two on the work-plane). They have been placed in the task area where a good uniformity is observed. In total, 47 scenarios have been considered: 26 "office" scenarios with the system A and 21 with the system B. The illuminance target value has been set to around 500 lx on the work-plane at the height of 0.85 m.

5. The performance indices

The set of indices that are utilized to analyse and compare the DLC systems has been previously presented and commented in detail in another work (Bonomolo et al., 2017). Here, a brief description of them is provided. The first index is the Artificial Light Demand (ALD) (Eq. (1)) which is defined as the sum, during the operation time, of the differences between the illuminance target value on task area (E_{set}) and illuminance due to available natural light (E_{nat}), when this one is lower than the setpoint itself, times the hours:

$$ALD = \Sigma_{operation\ time} (E_{set} - E_{nat}) \times \Delta t \qquad \text{if} \quad E_{nat} < E_{set} \qquad \text{(eq. 1)}$$

This definition ensures that ALD changes according to the sky conditions for a given setpoint and a given period (for instance a day). Figure 3 shows this concept for two different days.

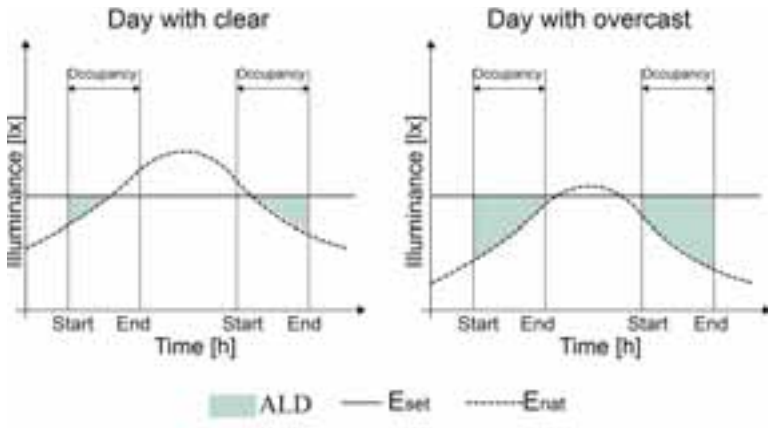

Fig. 3. Graphic scheme of ALD for two different days.

A normalization of energy consumption concerning the actual artificial light demand (ALD) is useful in comparing a DLCs operation with different hardware-software configurations (e.g. photosensors position) and calibration (Doulos et al., 2017). Moreover, it would be possible to make a comparison between different lighting systems. They would consume different amounts of energy according to their lighting efficiency and ability to

control the illuminance on the task area over time also according to the measured ALD. In this way, the second adopted index is the Energy Ratio of Illuminance (ERI) (Eq. (2)) as the ratio between the electricity consumption (ELEC measured in Wh) and ALD (lx·h) as follows:

$$ERI = \frac{ELEC}{ALD} \quad \left[\frac{Wh}{lx \cdot h}\right] \qquad \text{(eq. 2)}$$

If we look at an ideal system, the consumption due to lamps operation will be strictly proportional to the ALD by a factor k (Wh/lx·h) that can be intended to be a characteristic of the observed system and also a target value for the ERI of a real system. Indeed, in a real system, measured consumption could result in higher (or lower) than k·ALD and ERI will have a different result from k. In the tested systems the k value is 0.246 Wh/lx·h.
Anyway, it must be noted that when a system is not able to fulfil over the operation time the minimum E_{set} value (under-illuminated space), its electricity consumption is not related to the expected operating conditions and its low value is not reached thanks to its energy efficiency. At the same time, it is necessary to consider energy waste due to the quantity of "excess" of illuminance, which is highlighted by higher ERI values.
Two more indices can also account for values and times when the system provides an "excess" or a "deficiency" of illuminance for a given target value of illuminance on the task plane.

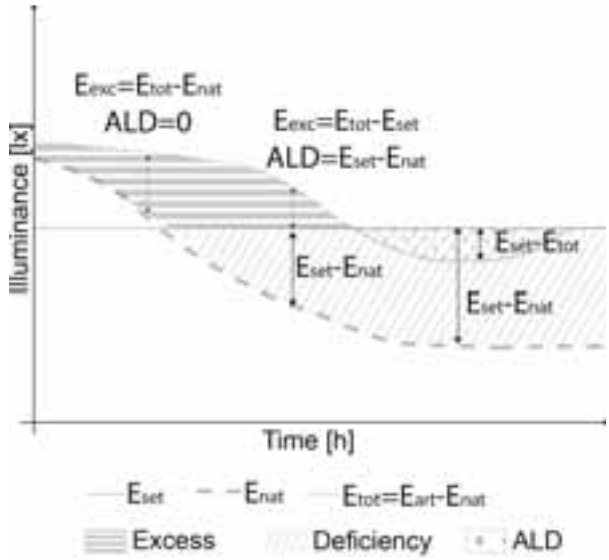

Fig. 4: Graphic scheme of the excess or the deficiency of illuminance compared to the illuminance target value on work-plane.

The index named OAR (Over illuminance Avoidance Ratio) is defined as the ratio, evaluated for an observed time period, between the minimum requirement of artificial light (ALD) and the sum of it plus the artificial light eventually provided in excess (E_{exc}).

$$OAR = \frac{ALD}{\sum_{t\,operation} E_{excess} \cdot \Delta t + ALD} = \frac{ALD}{\sum_{t\,operation} (E_{tot} - E_{nat})^{*} \cdot \Delta t} \qquad *\,\text{only if}\,(E_{tot} > E_{set}) \qquad \text{(eq. 3)}$$

where E_{tot} is the total illuminance due to the contributions of natural and artificial light.

Therefore, for a settled ALD, the higher the over-lighting (low values of OAR), the lower the capability of the system to fulfil the maintenance of the illuminance target value on

task area and thus the higher the related energy consumption.

If we want to account the "deficiency" of light, a UAR (Under-illuminance Avoidance Ratio) (Eq. (4)) index can be calculated. It can be defined as follows:

$$UAR = 1 - \frac{\sum_{t\ operation} (E_{set} - E_{tot}) \cdot \Delta t}{ALD} \qquad \text{(eq. 4)}$$

So, when a system does not cause much "under-lighting", E_{tot} is most of the time close to E_{set} and UAR will be close to 1. At the same time the closer E_{tot} to E_{nat} (when $E_{nat} < E_{set}$), the closer UAR to 0 which indicates the system has provided an insufficient contribution of artificial light..

As a result of previous considerations, to give a complete response to the performance of an observed system during the monitoring exercise, ERI, UAR and OAR indices must be considered together.–The scheme in Figure 5 shows how several combinations of the indices values can be interpreted as a system diagnosis checklist.

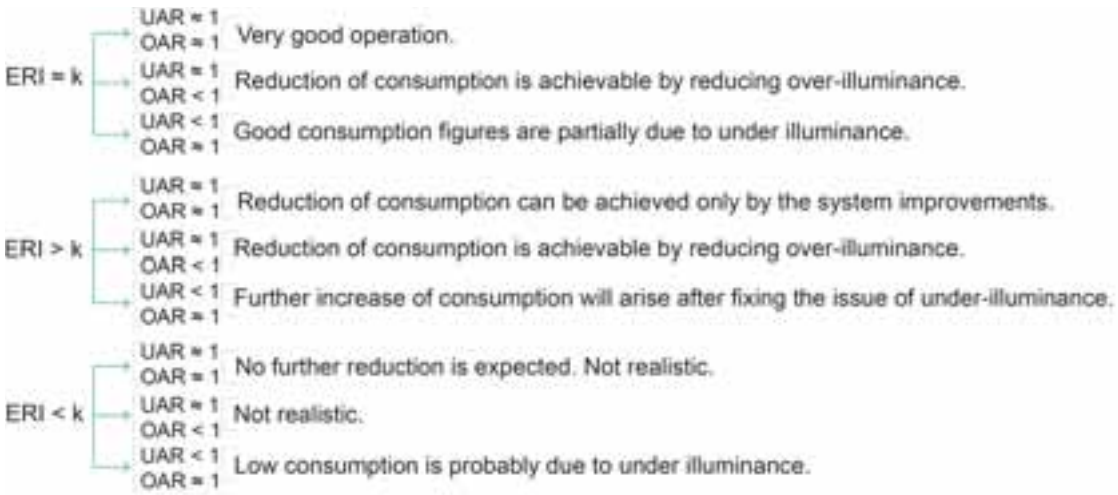

Fig. 5: Possible combinations of ERI, UAR, OAR and their meaning (Bonomolo et al. 2017).

For example, a system operating with an ERI close to the k value could have further improvement in its performance by avoiding a period of over illuminance (if the OAR resulted < 1). On the other side, if the measured UAR was <1 there is some "false" expectation of energy saving due to the occurrence of some under illuminance period.

6. Result and discussion/Data analysis

Two monitoring campaigns have been conducted from April 2016 to December 2016 and from May 2017 to July 2017. All the collected data have been analysed and the above indices have been calculated to test the actual performance of the systems for the different set-up, configurations and scenarios. In Table 1 some results of this calculation have been reported. It must be clarified that ALD values characterize the days when the systems worked. It ranges according to the season, the hours of the occupancy schedules and of the daily time. The scenarios reported in Table 1 are characterized by ALD values that range between 315 lx·h and 1797, for the System A, and from 322 and 1613 lx h, for the System B.

Tab. 1: Results for selected tested scenarios with dimming and on-off control.

System	Schedules	Date	ALD [luxh]	Dimmer control				On-off control			
				OAR	UAR	ELEC [Wh]	ERI [Wh/lxh]	OAR	UAR	ELEC [Wh]	ERI [Wh/lxh]
System A	09:00-13:00 14:00-18:00	04/10/2016	874	0.36	0.97	653.7	0.75	0.02	1.00	961.3	1.11
	09:00-13:00 14:00-18:00	05/10/2016	704	0.19	1.00	875.5	1.24	0.01	1.00	996.3	1.42
	09:00-13:00 14:00-18:00	06/10/2016	1221	0.52	0.97	622.8	0.51	0.03	1.00	824.0	0.68
	11:00-15:00 16:00-20:00	10/10/2016	1394	0.47	0.93	729.8	0.52	0.03	1.00	874.3	0.63
	8:00-12:00 13:00-17:00	12/10/2016	315	0.18	0.01	743.1	2.36	0.02	1.00	996.3	0.67
	8:00-12:00 13:00-17:00	13/10/2016	449	0.16	0.97	715.3	1.59	0.01	1.00	996.3	2.22
	10:30-14:30 15:30-19:30	17/10/2016	322	0.22	1.00	428.5	1.33	0.01	1.00	764.5	2.38
	07:00-11:00 12:00-16:00	18/10/2016	180	0.17	1.00	351.1	1.95	0.01	1.00	529.2	2.94
	07:30-11:30 12:30-16:30	20/10/2016	766	0.29	0.96	679.5	0.89	0.02	1.00	996.3	1.30
	07:00-11:00 12:00-16:00	21/10/2016	1114	0.61	0.82	460.1	0.41	0.03	1.00	779.3	0.70
	10:00-14:00 15:00-19:00	25/10/2016	919	0.66	0.93	425.3	0.46	0.03	1.00	745.7	0.81
	09:00-13:00 14:00-18:00	26/10/2016	561	0.36	0.96	460.2	0.82	0.01	1.00	807.7	1.44
	8:00-12:00 13:00-17:00	27/10/2016	458	0.38	0.91	300.7	0.66	0.02	1.00	457.5	1.00
	07:00-11:00 12:00-16:00	31/10/2016	553	0.59	0.84	317.4	0.57	0.02	1.00	710.1	1.28
	07:00-11:00 12:00-16:00	02/11/2016	973	0.74	0.79	373.5	0.38	0.02	1.00	633.4	0.66
	8:00-12:00 13:00-17:00	05/06/2017	469	0.62	0.97	195.60	0.42	0.21	1.00	792.7	1.10
	10:30-14:30 15:30-19:30	07/06/2017	1468	0.90	0.76	304.08	0.21	0.48	0.85	677.0	0.46
System B	07:00-11:00 12:00-16:00	06/06/2017	852	0.77	0.95	309.20	0.34	0.33	0.96	612.6	0.72
	07:30-11:30 12:30-16:30	08/06/2017	929	0.92	0.30	76.15	0.08	0.79	0.23	115.5	0.12
	07:00-11:00 12:00-16:00	09/06/2017	703	0.99	0.23	115.33	0.05	0.77	0.18	87.4	0.12
	07:00-11:00 12:00-16:00	10/06/2017	493	1.00	0.20	72.54	0.07	0.60	0.28	116.4	0.24
	10:00-14:00 15:00-19:00	11/06/2017	1431	0.71	0.61	317.53	0.22	0.58	0.73	457.3	0.28
	09:00-13:00 14:00-18:00	15/07/2017	457	0.71	0.58	187.70	0.41	0.51	0.53	320.5	0.44
	07:00-11:00 12:00-16:00	13/06/2017	1072	0.80	0.57	208.77	0.19	0.61	0.56	300.0	0.28
	8:00-12:00 13:00-17:00	06/07/2017	444	0.55	1.00	246.07	0.55	0.26	1.00	792.7	1.00
	8:00-12:00 13:00-17:00	12/07/2017	387	0.78	0.46	150.85	0.39	0.51	0.47	792.7	0.53
	09:00-13:00 14:00-18:00	13/07/2017	576	0.66	0.58	227.06	0.39	0.55	0.54	338.2	0.39
	07:00-11:00 12:00-16:00	17/07/2017	438	0.47	0.48	140.39	1.42	0.11	0.86	850.5	1.94
	09:00-13:00 14:00-18:00	18/07/2017	323	0.52	0.88	214.96	0.67	0.26	0.77	320.5	0.99
	09:00-13:00 14:00-18:00	21/07/2017	645	0.70	0.57	233.43	0.36	0.16	0.96	947.7	1.47

Starting to compare how the two systems worked, it can be noted that in some cases, they ran in a different way during scenarios with ALD very similar. For instance, there are for the scenarios with ALD of about 322 lx·h. The first one is related to the system A and presented an OAR of 0.22 and a UAR of 1. In the second one, for the system B, the calculated value of OAR was 0.52, and the one of UAR was 0.88. Similarly, for scenarios

with ALD of about 703 lx·h an OAR of 0.19 and a UAR of 1 have been calculated for the System A while for the system B the associated value of OAR was 0.99 an of UAR was 0.23. The graphs in Figure 6 show the relation between OAR and ALD indices for the two systems operated by the two control strategies. In general, high values of OAR corresponded to high values of ALD. It means that the systems worked better when there was low a contribution of daylight. So, in general, the higher the ALD, the lower the possibility of having over-lighting problems. The same is for the ON-OFF control case.

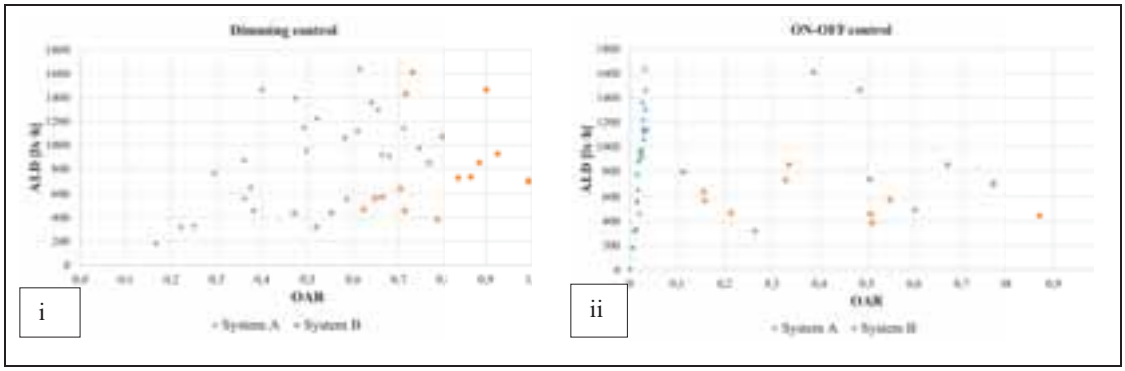

Fig. 6: Relationship between A.L.D and OAR indeces calculated in dimming and ON/OFF control for the two systems.

Generally, in dimming operation, system A had OAR lower than System B. For both systems a specific linear correlation with ALD can be observed. In ON-OFF operation (Figure 6ii) System A had a maximum of OAR equal to 0.07 (very poor result), while figures of System B are generally better, even if not well correlated with ALD. Also, observing figure 7i and 7ii, it can be noted that the higher ERI, the lower OAR values. It means that the system wastes energy over-lighting the room. On the other hand, small ERI values are coupled to low values of UAR (Figures 7iii and 7iv), because such energy "saving" is affected by an excessive under-lighting. The reason why correlations OAR vs ERI and UAR vs ERI are not very robust lays on the fact that the system can perform in under and over-lighting in the same day of operation. It can be noted that the System A in ON-OFF case did not have problems of under-lighting (Figure 7iv), but it had severe problems of over-lighting (Figure 7ii). As already noted looking at the calculated values, the System B had higher performances than the System A. Comparing the two control strategies, it can be observed that both systems had higher performances with dimmer control. Anyway, the gap between the performances of the two control strategies is more significant for System A. Indeed, the cloud of points calculated for the System B with dimmer control shifted slightly to higher values of OAR (Figure 7i). In the case of ON-OFF control, it is much more evident (Figure 7ii). The OAR values are very low for the System A (the highest value is 0.07). On the contrary, in the case of System B they are higher reaching value of 0.87), while, UAR are almost every time equal to1. In such a view it is useful to observe the ratio OAR/UAR vs ERI graphs. The higher the ratio, the higher is the influence of the under-lighting during the system operation. All the considerations related to the best performance of System B and the dimming control for both the systems are also confirmed in graph 7iii and 7iv. Also, the predominant behaviour of System A to provide exceeds of lighting (OAR/UAR very low) is confirmed.

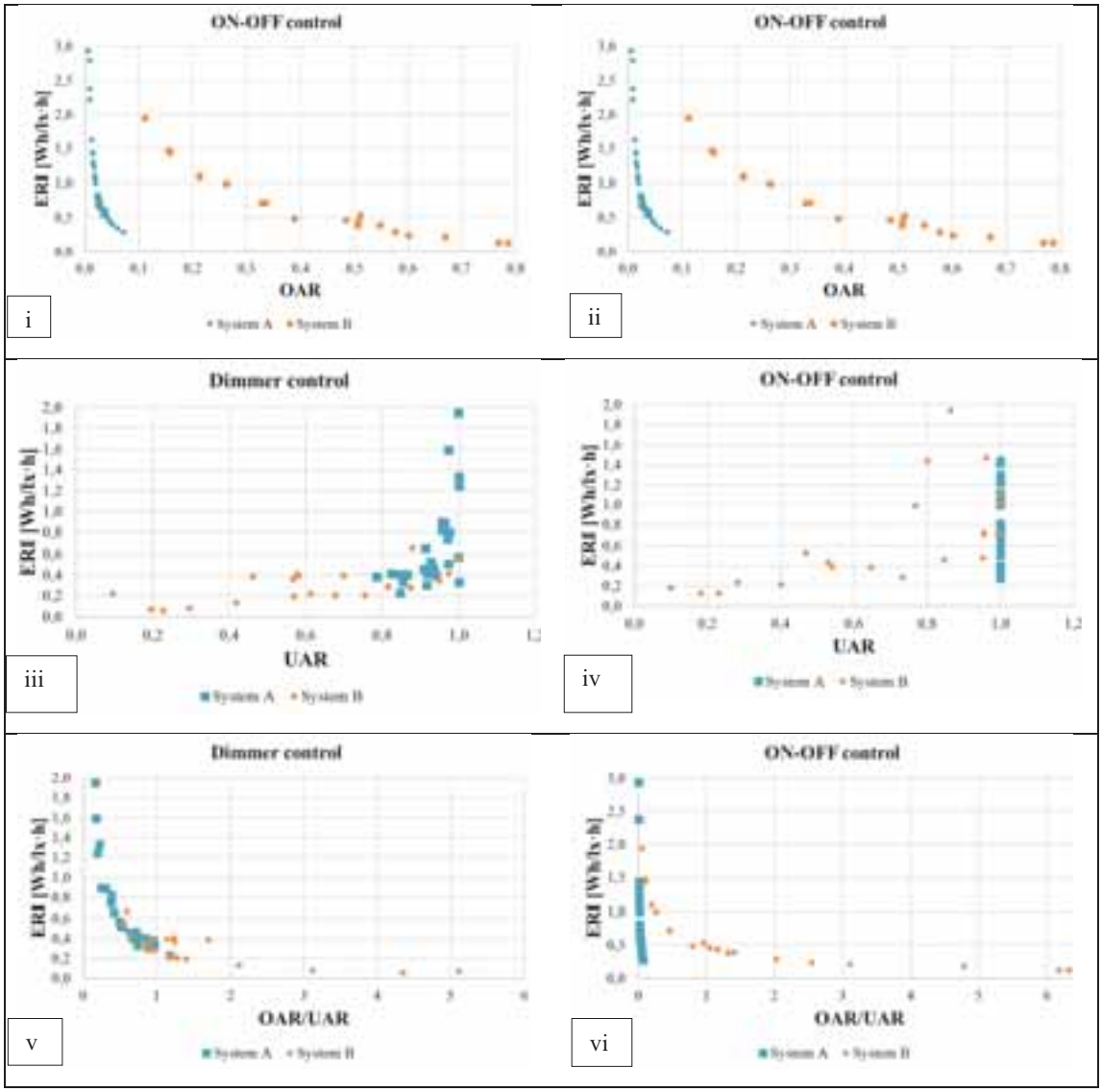

Fig. 7. Relation between ERI index and OAR index calculated in dimming control and ON/OFF control for the two systems.

The correlation between electricity consumption and ALD values (Figure 8) is helpful for analysing the ALD influence on the system performance. The ideal consumption has been calculated proportionally to the ALD. For this reason, the correlation is linear. On the contrary, looking at the actual consumption lines (both of System A and B), the correlation is not precisely linear as it is in the case of an ideal system (see the "ideal consumption" plot). It is because, as already said and observed, the control system did not work as expected and, some cases of incorrect operation associated to low values of UAR and the OAR have been found so, the consumption swung from the ideal figure. The more the points are closer to the ideal consumption line, the more a real generic system worked good. Moreover, the actual consumption regression lines shift from the ideal one by constant values because of the power absorbed by the control systems (around 18.3 W for the System A and about 10 W for the System B).

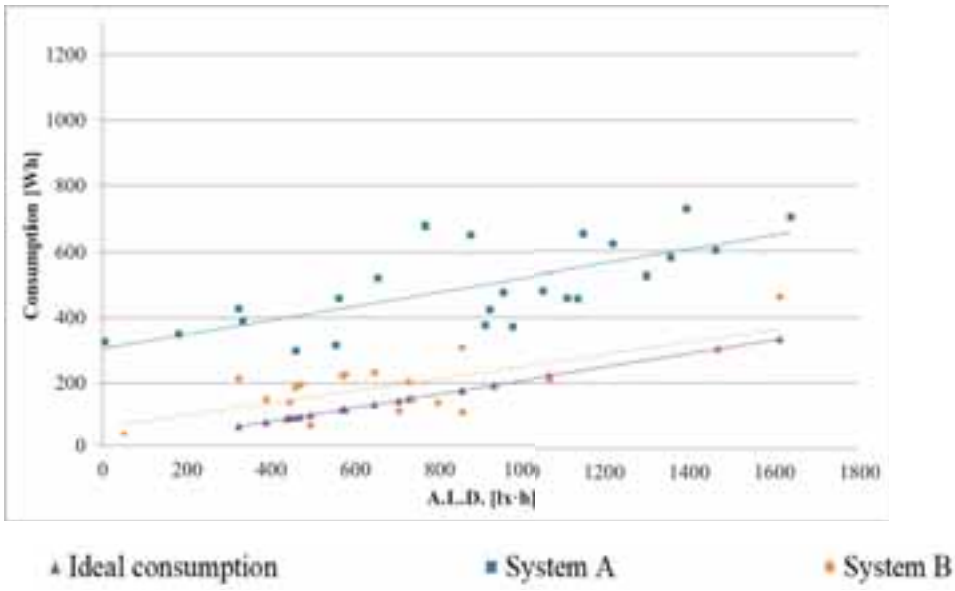

Fig. 8. Relationships between ALD index and the electricity consumption (systems A and B) and the ones for an ideal system..

7. Conclusions

This paper presents an experimental test of a new method developed by authors to evaluate the actual performance of two DLCs, based on the calculation of a set of indices. The index ERI has been used to account for the specific consumption *k* concerning the artificial light demand (ALD). Generally, it depends on the efficiency of the lamps, on the features of luminaries, electric systems and control systems. The indices OAR and UAR have been used to account their ability to maintain the target illuminance on the task area. The two systems have been tested under different operating conditions and control strategies (dimming and ON-OFF). In general, the closer the ERI index to the *k* factor the more the observed system works appropriately with very high values of UAR and OAR. The values of the indices have been calculated in different scenarios characterized by variable daylight availability and compared to have a picture of how each system performed. Furthermore, relationships between the indices have been carried out and analysed for large sets of data. In general, it has been proven the ability of the indices to highlight and analyse situations where consumptions far from the ideal ones are measured. For instance, it was possible to have evidence that a low specific consumption can be due to the inability of the system to fulfil the minimum target illuminance even though occasionally operated in over-lighting. Likewise, it can be noticed that the highest ERI values correspond to the lowest OAR values that means system is performing in over-lighting conditions. On the other hand, low ERI values are also coupled to very variable values of UAR. For this reason, it is useful to observe it as a function of OAR/UAR ratio. Accordingly, the higher the ratio, the more prevalent the under-lighting condition. In almost all the observed conditions System A performed worse than System B with a persistent behaviour characterized by frequent and relevant over-lighting. For both the systems the relationship between ALD and electricity consumption was only barely proportional. It was because the control system did not always work as expected in ideal cases (with UAR and OAR both equal to 1). Nevertheless, also through this approach, it has been possible to confirm the higher

efficiency of System B. Therefore, it can be affirmed that such method can be utilised to assess the system's performance on different days and, consequently, with different daylight conditions as well as different systems operating in similar daylight conditions. Further work will deal with the test of other commercial systems aiming also at a comparison of their performances in different seasons.

8. References

Bellia, L., Fragliasso, F., Pedace, A., Lighting Control Systems: Factors Affecting Energy Savings' Evaluation, Energy Procedia 78, 2645-2650, 2015

Beccali, M., Bonomolo, M., Galatioto, A., Ippolito, M. G., Zizzo, G., A laboratory setup for the evaluation of the effects of BACS and TBM systems on lighting, Renewable Energy Research and Applications, International Conference IEEE, 1388-1393, 2015

Bonomolo, M., Beccali, M., Brano, V. L., Zizzo, G., A set of indices to assess the real performance of daylight-linked control system. Energy and Buildings 149, 235-245, 2015

Chen, Z., Wang, F., Feng, Q., Cost-benefit evaluation for building intelligent systems with special consideration on intangible benefits and energy consumption. Energy and Buildings 128, 484-490, 2016

Doulos, L. T., Tsangrassoulis, A., Kontaxis, P. A., Kontadakis, A., Topalis, F. V., Harvesting daylight with LED or T5 fluorescent lamps? The role of dimming. Energy and Buildings, 140, 336-347, 2017

Doulos, L., Tsangrassoulis, A., Topalis, F. V., Multi-criteria decision analysis to select the optimum position and proper field of view of a photosensor, Energy Conversion and Management 86, 1069-1077, 2014

Ferrari, S., Beccali, M., Energy-environmental and cost assessment of a set of strategies for retrofitting a public building toward nearly zero-energy building target, Sustainable Cities and Society 32, 226-234, 2017

Parise, G., Martirano, L., Impact of building automation, controls and building management on energy performance of lighting systems. Industrial & Commercial Power Systems Technical Conference-Conference Record 2009 IEEE, 1-5, 2009

Siemens, SENTRON PAC Power Monitoring Devices, www.siemens.com/powermanagementsystem, 2009

a) ul Haq, M. A., Hassan, M. Y., Abdullah, H., Rahman, H. A., Abdullah, M. P., Hussin, F., Said, D. M., A review on lighting control technologies in commercial buildings, their performance and affecting factors, Renewable and Sustainable Energy Reviews 33, 268-279, 2014

b) ul Haq, M. A., Hassan, M. Y., Abdullah, H., Rahman, H. A., Abdullah, M. P., Hussin, F., A method for evaluating energy saving potential in lighting from daylight utilization, Power and Energy (PECon), 2014 IEEE International Conference (177-181), 2014

Valíček, P., Novák, T., Vaňuš, J., Sokanský, K., Martinek, R., Measurement of illuminance of interior lighting system automatically dimmed to the constant level depending on daylight, Environment and Electrical Engineering (EEEIC), IEEE 16th International Conference, 1-5, 2016

Studying the Impact of Colored Glazing Systems on Visual and Non-visual Performances in a Daylit Office

Xiaodong Chen[1], Xin Zhang[1], Jiangtao Du[2]

[1]School of Architecture, Tsinghua University, Beijing (China)

[2]School of Built Environment, Liverpool John Moores University, Liverpool (UK), j.du@ljmu.ac.uk

Abstract

This article presents a full-scale survey of the impact of colored/neutral glazing systems on occupants' visual and non-visual functions, as well as working performance in a daylit office in Beijing, China. Five glazing systems were investigated during a heating season from 17 November 2016 to 11 January 2017. Lighting measurements and subjective assessments were conducted to study the relationship between lighting conditions, glazing types, and visual and non-visual performances. Several key findings were achieved as follows: 1) According to visual performances, the blue glazing could be the best solution while the bronze glazing tends to be less acceptable; both grey and green glazing systems did not show significant differences from the clear glazing. 2) No clear divergences of non-visual performances can be found between various colored/neutral glazing systems. 3) The circadian light (CL) has an obvious link to occupants' non-visual performances. 4) Participants' working performance in a short-term GONOGO test will become worse when the blue glazing system is applied.

Keywords: Colored glazing; Visual and non-visual performances; Daylit office; Heating season; Beijing

1. Introduction

Daylighting has been recognized as a critical environmental factor in office buildings, due to its significant effects on workers' performances such as productivity, psychological and physiological aspects (Veitch et al., 2004; Aries et al., 2015). Studies of daylight's impact on occupants have recently become a focus in offices. Using a survey of ten office buildings in the Netherlands, Aries et al. (2010) found that workers' visual comfort and well-being can be substantially linked to configurations and installations of the external window, which can determine indoor daylighting conditions and view. Borisuit et al. (2014) pointed out that office occupants prefer to work with the occurrence of daylighting in terms of visual and non-visual functions. Another office survey in both winter and summer periods enhanced the importance of daylight availability and its positive influences on productivity, mood and sleep quality (Figueiro & Rea, 2016). As highlighted in a new report (Ticleanu & Littlefair, 2017) and a short commentary (Figueiro, 2013), nevertheless, more proofs would still be required to justify how daylight regulates sleep and mood, especially in the working spaces.

Due to the application of coated/tinted glass, currently, colored glazing systems can be broadly found in modern office buildings across the world (SLL, 2014; BSI, 2011). The primary function of these glazing systems is to adjust the external solar gains, and therefore help bring in a proper level of indoor thermal/visual comfort. In the meantime, the effect of those coated/tinted glazing systems on visual and color perception has been noticed (Bulow-Hube, 1995). A pilot study using scale models indicated that the neutral coated glazing with a high visual transmittance can receive more acceptances (Dubois et al., 2007). On the other hand, the colored coated glazing products in the current market can possibly distort the color appearances of daylight in modern buildings (Matusiak et al, 2012). Based on scale models and subjective assessments, a study showed that there is a preference for daylight filtered through colored window glazing and that the glazing color type may have a significant effect on arousal level of office workers (Arsenault et al., 2012). This study (Arsenault et al., 2012) also revealed that the bronze glazing receives more preferences than the blue and clear glazing. In the area of artificial lighting design, the light color temperature in working places does affect occupants' performance (Bellia et al., 2015). An interesting finding has been produced through a human experiment (Sahin & Figueiro, 2013): the narrow long-wavelength / red light (2568K) can obviously increase alertness and working performance during the daytime. However, few studies have been completed so far to fully explain how the broad-wavelength daylight combined with colored glazing works on human's psychological and biological functions.

Therefore, it is still necessary to carry on more investigations on the relationship between glazing types,

doi:10.18086/swc.2017.05.02 Available at http://proceedings.ises.org

daylighting and human performance in office buildings. Based on daylighting measurements and subjective assessment, this article presents a study in a full-scale office room with various glazing systems in Beijing, China. The aim is to investigate how the colored/neutral glazing affects the human visual comfort, non-visual functions including mood, alertness, well-being and relaxation and working performance.

2. Methods and materials

2.1. Office room, study design, and participants

During a heating season from 17 November 2016 to 11 January 2017, this study was conducted in an office room at the School of Architecture of Tsinghua University in Beijing (Lat: 39.9042° N, Long: 116.4074° E) in China (Figure 1). With a dimension of 6.2×3.2×3.8m, the office room has one side window facing south, and four sitting positions including A1 & A2 (working places for participants), B (for the person who did measurements and controlled the experiment) and T (for GONOGO test (section 2.4)). The reflectances of the room surface are 0.3 (floor), 0.88 (wall) and 0.88 (ceiling).

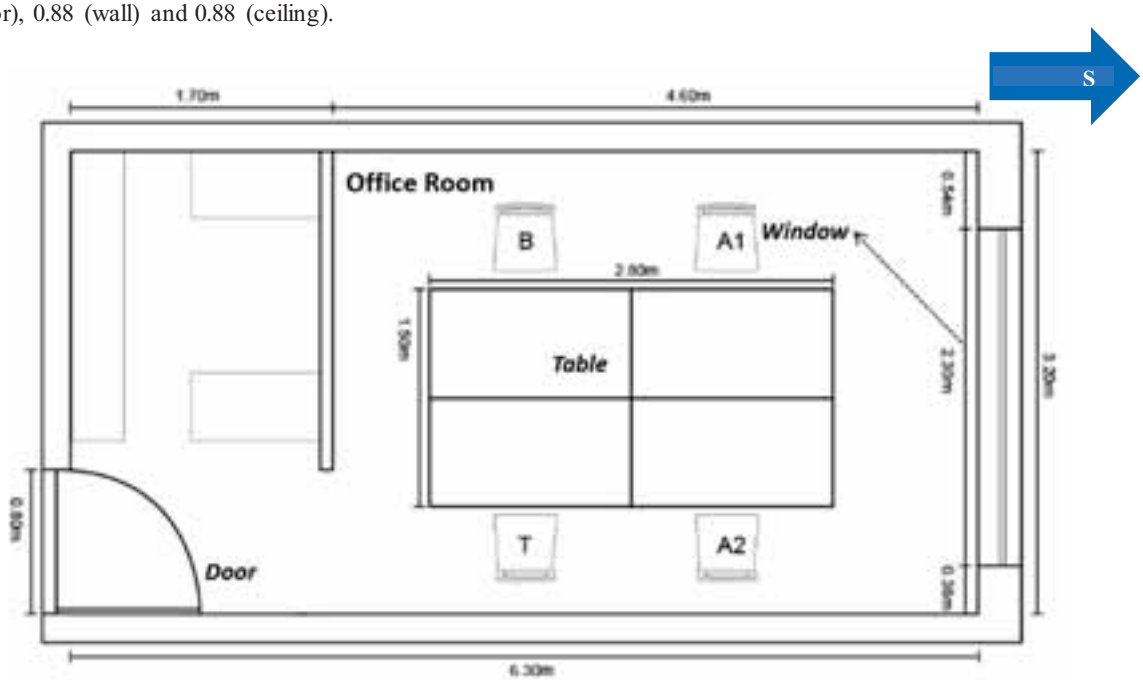

Fig. 1: Plan, dimensions, and sitting positions of the office room studied

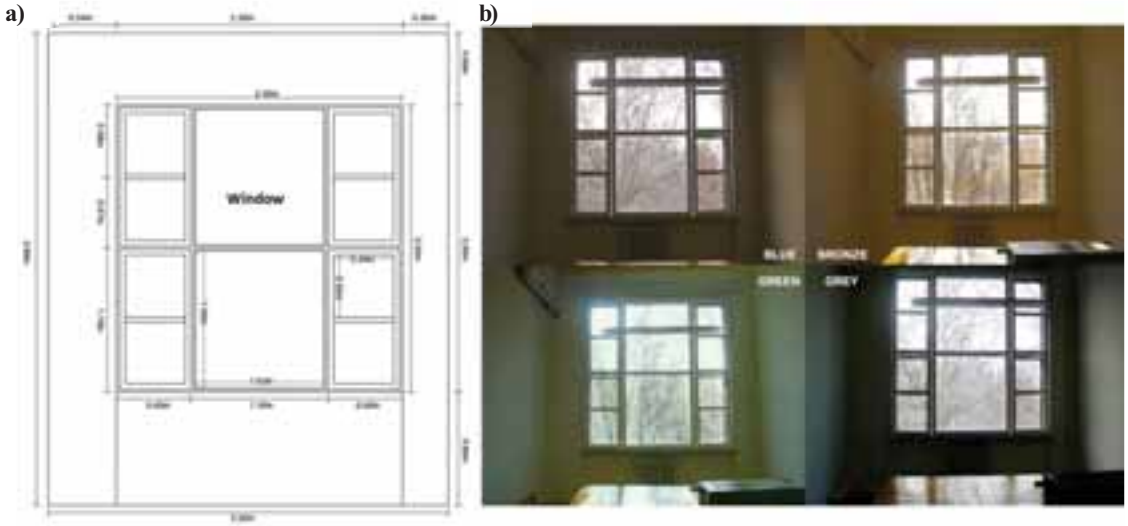

Fig. 2: Window configurations and dimensions (a); interior views of four glazing systems (blue, bronze, green and grey) (b).

Configures and dimensions of the side window can be found in Figure 2 (a). It has a dimension of 2.3×2.3m and a two-layer structure. The external layer is composed of single clear glazing and dividers, while the internal layer

adopts a removable structure with easily installed/dismantled glazing and dividers. Five types of glazing were studied including clear, blue, bronze, green and grey. They are typical products that can be found in current Chinese window market and have been widely used in modern non-domestic buildings. Except for the clear glazing, Figure 2 (b) displays pictures of the interior appearances with four glazing systems in the room. The transition spectrum of all glazing systems can be found in Figure 3. Then, overall visible transmittance (VT) values of them are 0.91 (clear), 0.55 (blue), 0.37 (bronze), 0.68 (green) and 0.22 (grey).

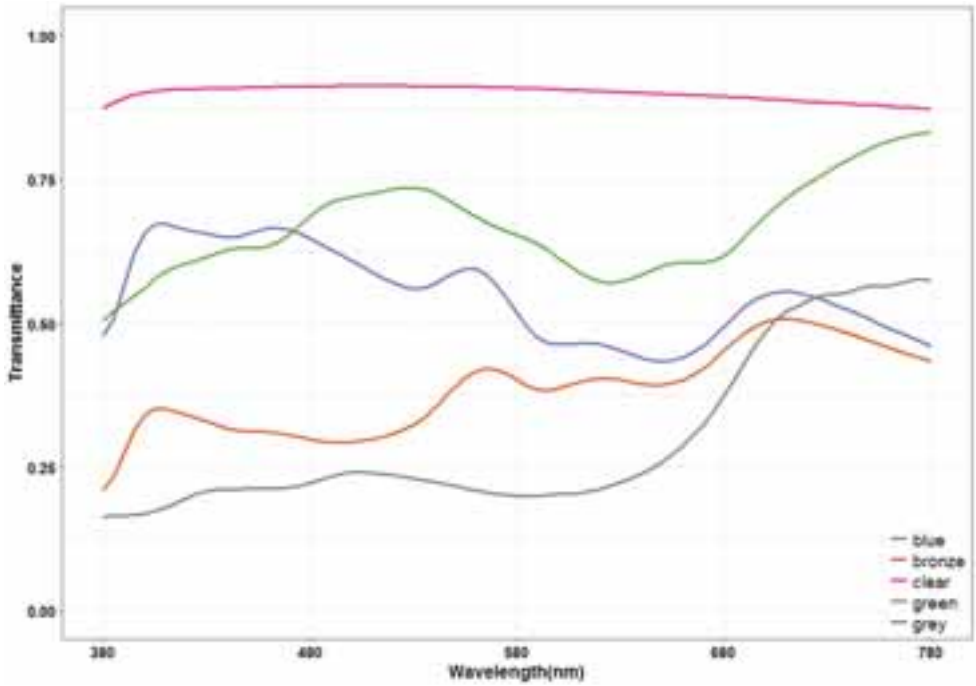

Fig. 3: Transmission spectrum of window glazing systems used in the office

A total of 17 participants were recruited from current students at Tsinghua University, with a mean age of 22.68 (±1.80) years. No participants should have medical and psychiatric diseases and sleep disorders. Each participant attended a five-day experiment, while only one type of glazing has been tested for each day. All participants were required to attend the experiment during a normal working time (8:30 – 16:00). The daily experiment was divided into two time-slots: 08:30-11:30 and 13:00-16:00, with a 1.5 hours lunch break in between. In order to control prior light exposure, each participant was asked to start his/her sleep earlier than 23:00 at the night before the testing day. During the experiment, the participants were just allowed to carry out regular office work in the office room, such as reading, writing, typing, etc. No food and drinks with caffeine or similar content can be taken on the testing day.

2.2. Light measurements and calculations

The experiment has been implemented under only daylighting conditions. No artificial lighting can be used in the experiment, even if the daylighting level was insufficient to meet the lighting standard at the working plane. The lighting condition was measured by a portable Illuminance Color Spectral meter (SPIC-200), in terms of three types of data: illuminance (lux), spectral distribution and correlated color temperature (CCT, K). The measured positions were the table and the vertical plane near the participant's eyes. Each meter reading was recorded every 10 minutes. Based on the collected light spectral distributions, Circadian Light (CL) and Circadian Stimulus (CS) were calculated according to a reference (Rea and Figueiro, 2016). The two values can be adopted as indicators of the nocturnal melatonin suppression due to the spectral response of the human circadian system. In addition, the indoor temperature and humidity were measured as a reference of thermal conditions.

2.3. Visual and non-visual assessment

Two VAS (visual analogue scale (Monk, 1989)) questionnaires were adopted to assess the visual and non-visual performances of participants. A paper-based VAS was used as a measuring tool for each question (scale range: 0-100mm).

The visual assessment questionnaire is composed of six questions: Q1, Lighting is comfortable? (0mm, extremely uncomfortable; 100mm, extremely comfortable); Q2, Room is bright? (0mm, very bright; 100mm, OK); Q3, Room is dark? (0mm, very dark; 100mm, OK); Q4, Glare? (0mm, intolerable; 100mm, no); Q5, Light color is comfortable? (0mm, extremely uncomfortable; 100mm, extremely comfortable); Q6, Color appearance is proper?

(0mm, absolutely not; 100mm, perfect). Four questions were given in the questionnaire for assessing non-visual performances as follows: Q1, Alertness (0mm, extremely sleepy; 100mm, extremely alert); Q2, Mood (0mm, very bad; 100mm, very good); Q3, Physical well-being (0mm, very uncomfortable; 100mm, very comfortable); Q4, Relaxation (0mm, very tense; 100mm, very relaxed). Each participant was asked to complete the two questionnaires every 45 minutes. Thus, a total of 16 questionnaires would be collected from each participant in each testing day. The feedbacks were statistically analyzed using IBM_SPSS(v23).

2.4. Working performance test

Participants' working performances in this experiment were tested using a computer GONOGO tool. This tool was produced by the authors according to fundamental GONOGO theories (Kreutzer et al., 2011). A GONOGO test is generally used to measure a participant's capacity for sustained attention and response control (Kreutzer et al., 2011).

In this study, the GONOGO test totally followed the method used in a human performance experiment (Sahin et al., 2014). Based on participants' responses via a computer mouse, this test lasted around 10 minutes. In each test, a smiling or frowning face was presented on a black background every 2-10 seconds. Participants were instructed to do the following actions: clicking the mouse when smiling face appears; stopping to respond when the frowning face occurred. The occurrence of smiling face will be around 70% of test time while only 30% of the time will be given to the frowning face. Once the participant clicks on the mouse, the face will disappear and the time from the face 'appear' to 'disappear' will be recorded. If the participant's response time is longer than 1 second, the face will vanish and therefore a 'miss' was recorded. In addition, a 'false alarm' will be recorded if the participant clicked the mouse before the face appears. In this study, each participant attended a GONOGO test every 90 minutes.

As mentioned in the experiment (Sahin et al., 2014), four GONOGO scores were adopted to measure the working performance: overall accuracy, mean response time, mean response time of the best 10% of response times, mean response time of the worst 10% of response times. A new value named as Tput was adopted in order to statistically analyze the collected data (Sahin et al., 2014), and it can be calculated through the algorithm: 100 × (# of valid responses) / (# of total responses) / median of the response times. A valid response used in the calculation did not include 'miss' and 'false alarm of an incorrect face shape'. Therefore, three Tput values can be achieved such as for a total test (Tput), the best 10% of response times (bTput) and the worst 10% of response times (wTput).

3. Results and discussions

This section includes results and discussions from lighting measurements, subjective assessments of visual and non-visual performances, as well as working performances using GONOGO in the office with various glazing systems.

3.1. Daylighting and color conditions

Figure 4 displays mean values of vertical illuminance and CCT near participants' eyes in terms of varying times and glazing types. Most of the time the grey and green glazing systems have higher illuminance levels than other types. The mean values of illuminance are 1454.3lux (±237.0) and 1407.7lux (±189.2) for grey and green glazing respectively. On the other hand, the lowest illuminance levels can be found with the blue and bronze glazing as follows: 701.1lux (±101.6) and 620.2lux (±86.3). The daylighting performance of clear glazing is in between (1025lux (±190.57)). It can be clearly noticed that a higher visual transmittance of glazing does not necessarily bring in a higher indoor illuminance. Certainly, external sky conditions are more critical. From around 10:00 to 15:00 all the glazing systems see a vertical illuminance above 500lux, whilst a higher illuminance (>1000lux) can be only found in a time slot of 12:00 -- 14:00. In the late afternoon (15:00—16:00) all the glazing types give rise to a lower illuminance level (<500lux). In general two peaks of illuminance variation occur at 10:45 and 13:45 for most of the glazing systems.

As for the mean values of CCT of light near participants' eyes, no big differences can be found in the daily testing time from 9:15 to 16:00. The blue glazing has the highest mean CCT of 5395.1K (±36.0), which could result in a relatively cold/blue lighting atmosphere. It is normal that the lowest mean CCT of 3986.2K (±54.8) occurs with the application of bronze glazing. This value will not be considered as 'warm', but 'neutral' or 'white'. However, the use of green, grey and clear glazing systems can lead to mean CCT values between 4000K and 5000K. A light color in this range tends to be called as 'cold white'. Interestingly the green and grey glazing systems achieve a similar CCT value: 4792K (±30.4) for green glazing; 4724.5K (±53.0) for grey glazing. The clear glazing,

nevertheless, has a slightly lower mean CCT of 4443.9K (±27.2). Accordingly, the three glazing systems might produce a similar light atmosphere in this office room during the testing time.

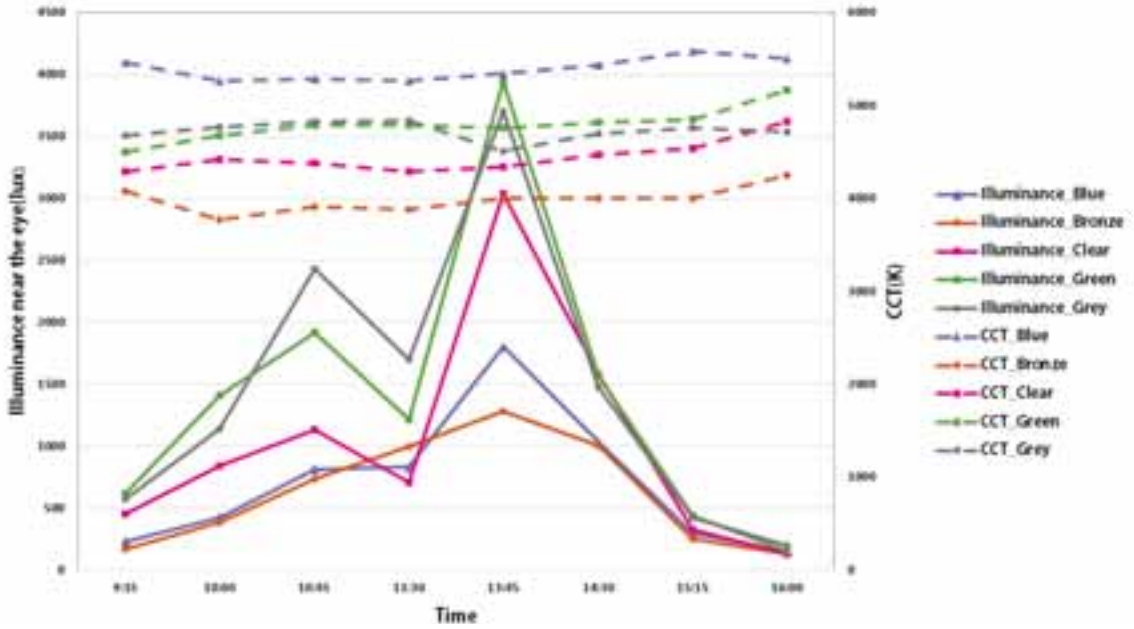

Fig. 4: Mean values of vertical illuminance and CCT (measured near the eyes of participants)

3.2. Visual performance

A 'five glazing types × eight times' repeated measures of variance (ANOVA) was performed using the feedback from the visual performance questionnaire including six questions (see section 2.3). A Post Hoc method (Least Significant Difference (LSD)) was used to further compare the main effects and interactions. The planned comparisons were performed to investigate whether the visual performances of five glazing types were significantly different from each other. All statistical analyses were completed using IBM SPSS (v23.0). The significance can be achieved based on $p < 0.05$.

Figure 5 & 6 display the impact of glazing type and times on the six questions of visual performance (ANOVA). For the visual performance, the assessment of seventeen subjects reveals a significant impact of glazing types on Q2 (Brightness) [$F(4, 678) = 4.468$, $p = 0.001$], Q3 (Darkness) [$F(4, 678) = 9.793$, $p < 0.001$], Q4 (Glare) [$F(4, 678) = 3.196$, $p = 0.013$], Q6 (Color appearance) [$F(4, 678) = 3.035$, $p = 0.017$]. The visual comfort (Q1) and color comfort (Q5) have no clear relationship with the glazing type ($p > 0.05$). Similarly, the time takes clear effects on the visual performances of Q2 (Brightness) [$F(7, 678) = 11.371$, $p < 0.001$], Q3 (Darkness) [$F(7, 678) = 9.465$, $p < 0.001$], and Q4 (Glare) [$F(7, 678) = 12.470$, $p < 0.001$]. No significant influence of time can be found for the Q1, Q5 and Q6 ($p > 0.05$). In addition, no significant interaction effects between glazing type and time were proved according to the feedback of six visual performance questions.

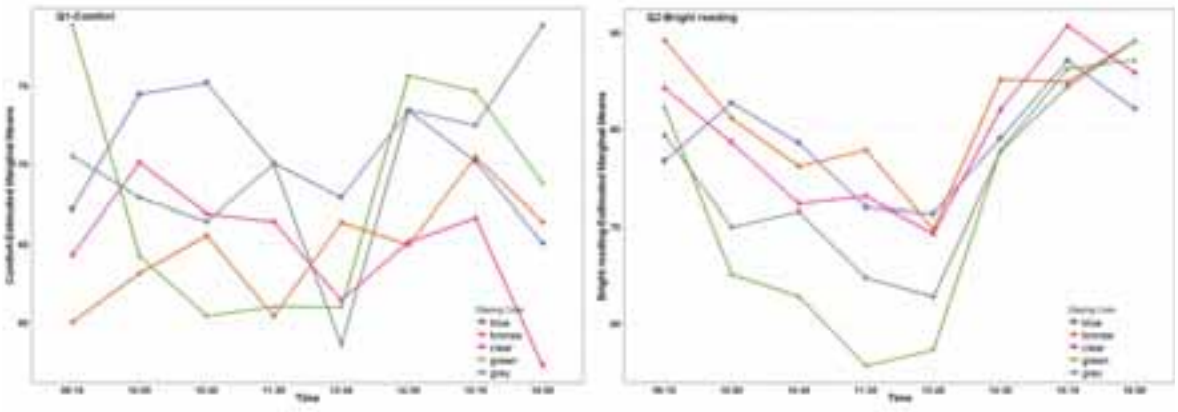

Fig. 5: Subjective assessments of visual performance (Q1--2): the impact of glazing types and time

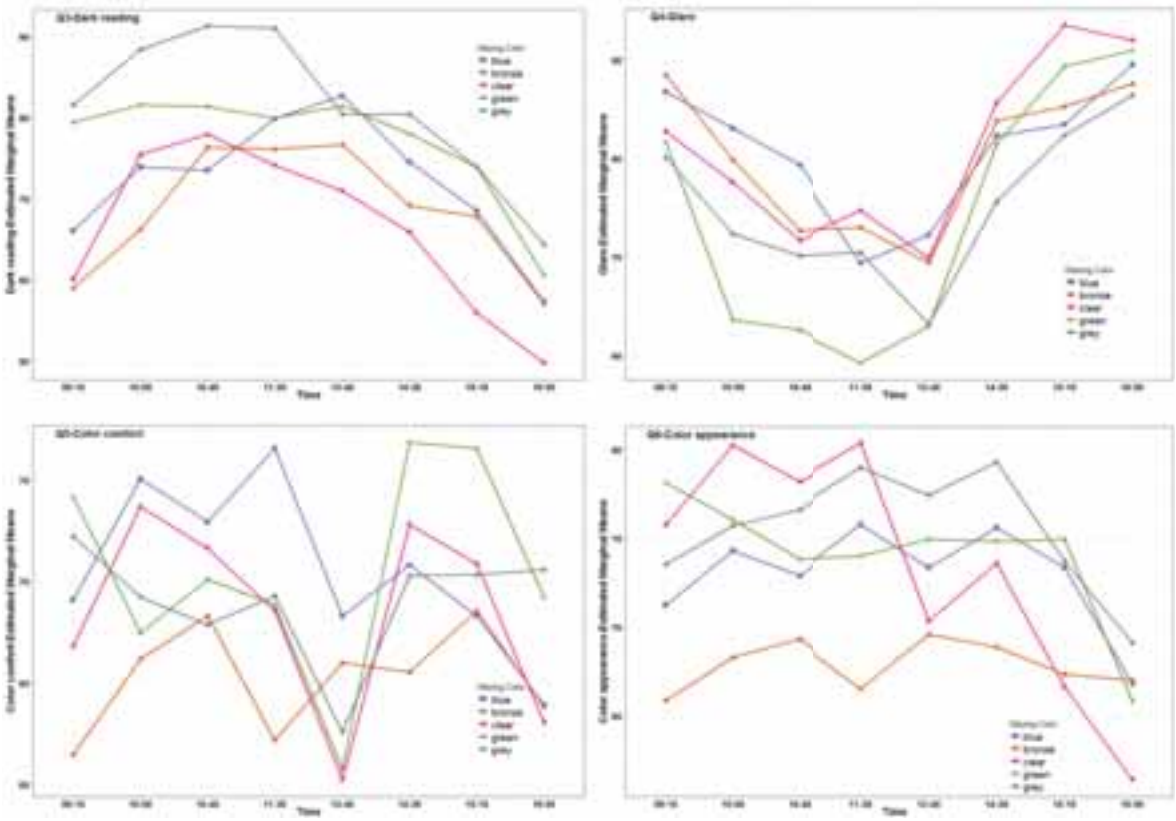

Fig. 6: Subjective assessments of visual performance (Q3--6): the impact of glazing types and time

Table 1 gives the multiple comparisons of visual performances between various glazing types (Post Hoc, LSD). Only the results with a significant difference have been presented ($p < 0.05$). For Q1 (comfort), the score of blue glazing is higher than both bronze and clear glazing ($p < 0.05$), whilst the score of bronze glazing is significantly lower than the grey glazing ($p < 0.05$). Even though the illuminance levels of blue and bronze glazing are similar, participants feel more comfortable with the occurrence of blue glazing. When compared with the clear type, the blue glazing can still receive a higher acceptance rate. The first feedback of comfort would support that participants in this office were more sensitive to the glazing's color than its visual transmittance and illuminance level. The questions Q2-4 focuses on the visual comfort and their feedback shows a similar statistical result. Compared with the green and grey glazing, generally, the blue, bronze and clear glazing would bring in a relatively darker lighting space and the lower risk to get glare problems in this office ($p < 0.05$). Taking Q2 (brightness) as an example, scores of blue, bronze and clear glazing are significantly higher than those of green and grey glazing. Interestingly, the clear glazing tends to deliver a darker lighting condition than the blue glazing ($p = 0.034$), although the former receives 40% higher illuminances than the latter. For the Q5 (color comfort), the only significant difference can be found between the blue, bronze and green glazing. Both blue and green glazing will give the participants a more comfortable color environment than the bronze type ($p = 0.026$ or 0.04). However, no clear differences of color comfort were achieved between the clear glazing and others ($p > 0.05$). On the contrary, the color appearance (Q6) shows an obvious difference between the bronze glazing and the blue, clear, green, grey glazing systems. The participants would agree that the bronze glazing can have a higher possibility to distort a normal color appearance even compared with the green glazing.

As regards Figure 5, 6 and Table 1, main effects of the time between various glazing systems also have some clear differences. It can be revealed that participants feel less comfortable (Q1) when the time is at 13:45 than 14:30 ($p = 0.023$) and 15:15 ($p = 0.013$). Also, participants would feel brighter when it is approaching the time 12:00, and therefore complaining of glare will start to increase at the same time. Also, the same feedback occurs for the color comfort (Q5): participants would feel less comfortable about the light color at 13:45 than other times, such as 10:00 ($p = 0.37$), 10:45 ($p = 0.42$), 14:30 ($p = 0.18$), 15:15 ($p = 0.15$). These findings indicated that under a higher illuminance level participants' comfort may not be linked with glazing color.

Tab. 1: Post-Hoc LSD: multiple comparisons of visual performances between glazing types (Sig. $p < 0.05$)

Dependent Variable	(I) Glazing type	(J) Glazing type	Mean Difference (I-J)	Std. Error	Significance
Q1-comfort	blue	bronze	6.00	2.603	.022
	blue	clear	5.88	2.603	.024
	bronze	grey	-5.13	2.599	.049
Q2-brightness	blue	green	6.77	2.638	.011
	bronze	green	9.88	2.634	.000
	bronze	grey	6.71	2.634	.011
	clear	green	7.74	2.634	.003
Q3-darkness	blue	clear	5.96	2.804	.034
	blue	grey	-9.23	2.804	.001
	bronze	green	-8.49	2.799	.003
	bronze	grey	-12.90	2.799	.000
	clear	green	-10.79	2.799	.000
	clear	grey	-15.19	2.799	.000
Q4-glare	blue	green	6.61	2.649	.013
	blue	grey	5.53	2.649	.037
	bronze	green	6.01	2.644	.023
	clear	green	6.98	2.644	.009
	clear	grey	5.90	2.644	.026
Q5-color comfort	blue	bronze	5.72	2.563	.026
	bronze	green	-5.26	2.558	.040
Q6-color appearance	blue	bronze	5.32	2.368	.025
	bronze	clear	-5.46	2.364	.021
	bronze	green	-6.21	2.364	.009
	bronze	grey	-7.68	2.364	.001

For the visual assessment, the application of blue glazing can generally benefit the occupants' performance and comfort, even compared with the normal glazing, i.e. clear product. In the contrast, the bronze glazing would receive the lowest acceptance rate when evaluating the visual performance. Other glazing types have no clear differences including green, grey and clear glazing. A higher illuminance level after 12:00 might increase occupants' discomfort.

3.3. Non-visual performance

Similarly, an analysis of the subjective feedback under 'five glazing types × eight times' were performed using ANOVA and LSD for the non-visual performance assessment including four questions (Q1-4). In addition, a correlation analysis (Pearson) was implemented between the circadian light and stimulus (Rea and Figueiro, 2016), and the four aspects of non-visual function. The significance can be achieved based on $p < 0.05$.

Figure 7 gives the subjective assessments of non-visual performance (Q1--4): the impact of glazing types and time. Different from the visual assessment discussed above, the ANOVA analyses exposed that there are no significant main effects of glazing type or time on the Q1 (alertness), Q2 (mood), Q3 (physical-wellbeing), and Q4 (relaxation). Also, it has not been found a clear interaction effect between glazing type and time exists. In Table 2, the LSD analyses show some differences of non-visual performance between various glazing systems. For the Q3 (physical well-being), scores of blue glazing are significantly higher than the clear one ($p = 0.035$). The blue glazing could make participants feel more comfortable than the clear type. Compared with the grey glazing, the clear glazing scores higher for the Q4 (relaxation) ($p = 0.046$). It could be reasonable that a relatively lower illuminance brought by the clear glazing would make occupants feel more relaxed. Based on both Figure 7 and Table 2, furthermore, it can be found that the alertness (Q1) can achieve a higher level at the time 11:30 than the

times 09:15 ($p = 0.030$), 13:45 ($p = 0.14$), 14:30 ($p = 0.005$) and 16:00 ($p = 0.003$). This indicates participants tend to be alerted with the time approaching the noon. At the time 13:45, a lower physical wellbeing (Q3) occurs compared with the time 15:15 ($p = 0.014$). This could be explained by one fact that these Chinese students would feel sleepy and tired at around 13:45 (a routine nap time for university students in China). The assessment of visual performances also shows a similar result as this finding.

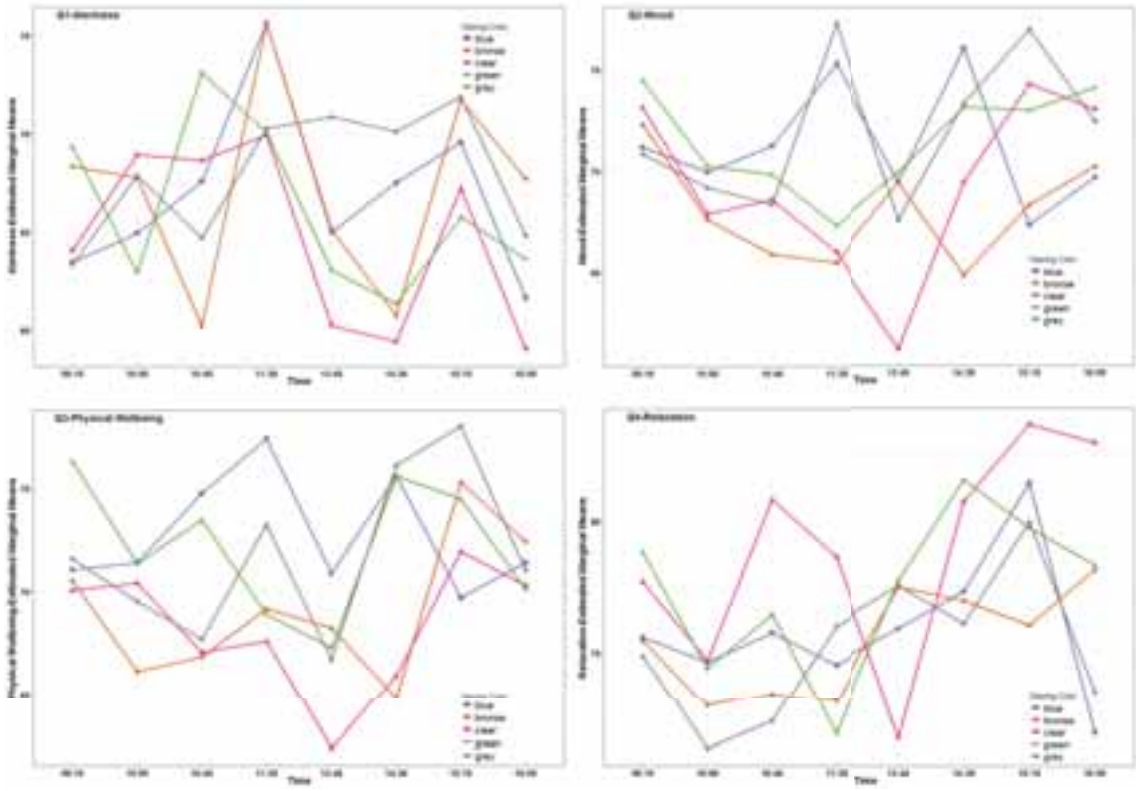

Fig. 7: Subjective assessments of non-visual performance (Q1--4): the impact of glazing types and time

Tab. 2: Post-Hoc LSD: multiple comparisons of non-visual performances between glazing types (Sig. $p < 0.05$)

Dependent Variable	(I) Glazing type	(J) Glazing type	Mean Difference (I-J)	Std. Error	Significance
Q3-physical wellbeing	blue	clear	4.48	2.114	.035
Q4-relaxation	clear	grey	3.68	1.843	.046

Tab. 3: Correlations between daylighting conditions and non-visual performances (Pearson Correlation)

		Alertness	Mood	Physical well-being	Relaxation
Circadian light (CL)	Correlation coefficient	-.041	-.136**	-.153**	-.147**
	Sig. (2-tailed)	.292	.000	.000	.000
	N	679	679	679	679
Circadian stimulus (CS)	Correlation coefficient	.002	.003	.013	-.066
	Sig. (2-tailed)	.962	.942	.739	.085
	N	679	679	679	679

Table 3 presents a correlation analysis (Pearson) between circadian light and stimulus (CL & CS) and non-visual

performances including four aspects. A clear link can be found between the circadian light, and mood (Q2, correlation coefficient = -0.136, $p < 0.001$), physical well-being (Q3, correlation coefficient = -0.153, $p < 0.001$) and relaxation (Q4, correlation coefficient = -0.147 $p = 0.001$). A higher level of circadian light may indicate a lower score of the three aspects. However, the circadian stimulus does not show any significant relevance to the three non-visual factors above ($p > 0.05$). In addition, the circadian light and stimulus have no clear relationship with the participants' alertness ($p > 0.05$). These analyses supported one fact that the Circadian Light should be used as an indicator of the non-visual effect of light instead of illuminance and CCT (Rea and Figueiro, 2016).

3.4. Working performances

An analysis of 'five glazing types × four times' ANOVA and LSD was performed for the GONOGO results (Figure 8 & Table 4). It has been found in Figure 8: there are significant main effects of glazing types on the 'mean response time' [$F(4, 339) = 2.246$, $p = 0.064$] and the 'Tput' [$F(4, 339) = 3.142$, $p = 0.015$]; however, no clear impacts from the glazing types can be found for the 'b-Tput', 'w-Tput', 'accuracy', 'average of best 10% response time', and 'average of worst 10% response time'. In addition, the main effect of time and the interaction effect between glazing types and time are not significant according to the working performance. The significance can be achieved based on $p < 0.05$.

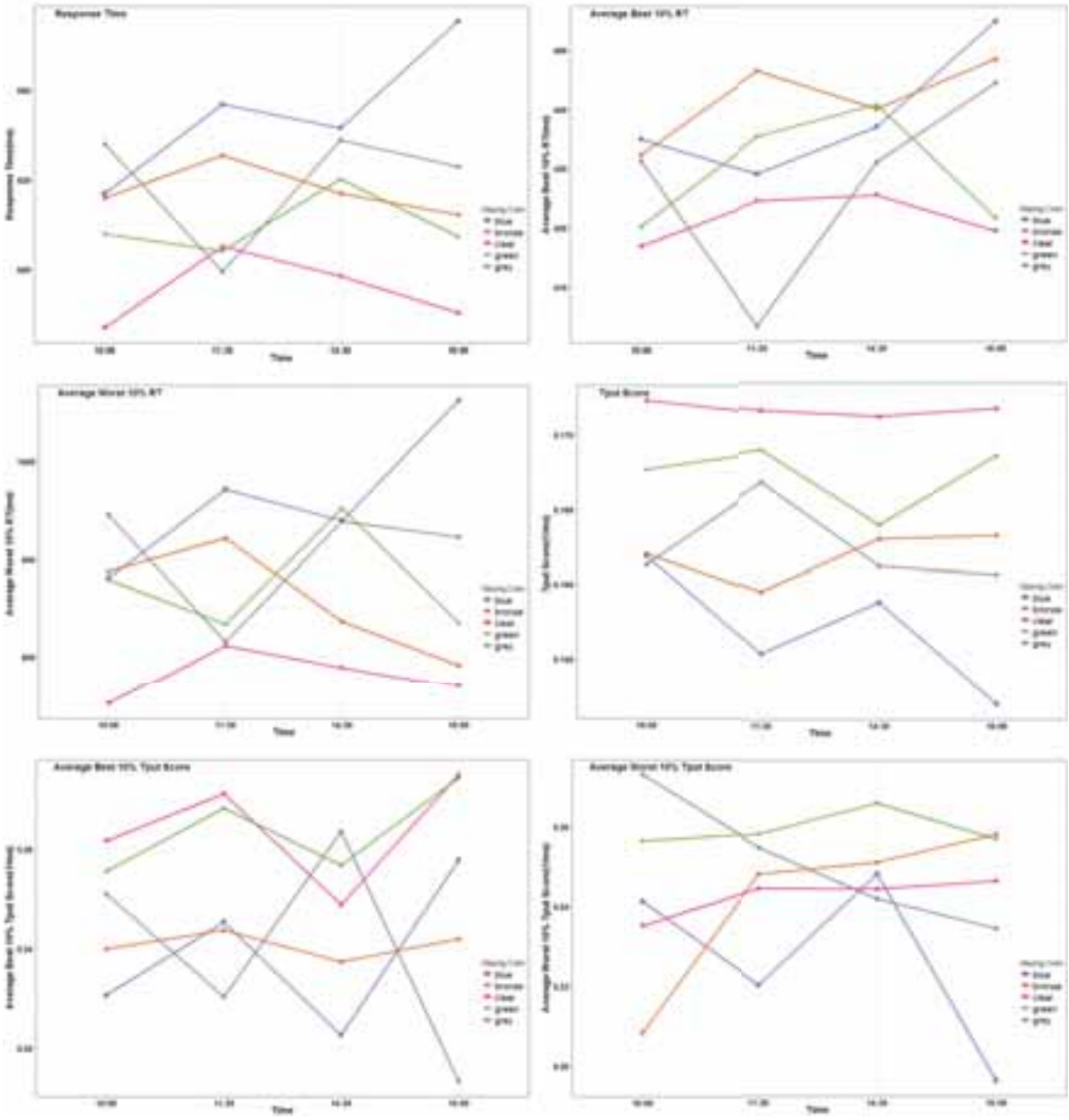

Fig. 8: Subjective assessments of GONOGO working performance: the impact of glazing types and time

Tab. 4: Post-Hoc LSD: multiple comparisons of working performances between glazing types (Sig. p<0.05)

Dependent Variable	(I) Glazing type	(J) Glazing type	Mean Difference (I-J)	Std. Error	Significance
accuracy	blue	clear	-.018846	.0093160	.044
	bronze	clear	-.020273	.0093160	.030
	clear	grey	.018703	.0093160	.046
mean response time	blue	clear	50.007639	17.2499604	.004
average 10% best response time	bronze	clear	20.289869	9.1630131	.028
average 10% worst response time	blue	clear	92.094608	36.0994601	.011
Tput	blue	clear	-.014707	.0044735	.001
	blue	green	-.010298	.0044735	.022
	bronze	clear	-.009767	.0044735	.030
	clear	grey	.009216	.0044735	.040
w-Tput	blue	green	-.032999	.0135124	.015

As shown in Table 4, the performance differences with various glazing systems are given (only results with a significance < 0.05 are available). The accuracy of clear glazing is higher than blue glazing ($p = 0.044$), bronze glazing ($p = 0.030$), and grey glazing ($p = 0.046$). Compared with clear glazing, blue glazing has less mean response time ($p = 0.04$) and average 10% worst response time ($p = 0.011$). These indicate that the blue glazing helps participants deliver a quicker response, but a lower working accuracy. The clear glazing nevertheless gives rise to an opposite result. Compared to clear glazing, bronze glazing can help to reduce average 10% best response time. However, no clear difference of mean response time can be found in the two glazing systems. As for the Tput, the clear glazing shows significantly higher scores than blue glazing ($p = 0.001$), bronze glazing ($p = 0.030$), and grey glazing ($p = 0.040$); the blue glazing performances worse than the green type. For the green and clear glazing, it is still unclear of which one performs better in terms of Tput. Since a higher Tput value is associated with a better working performance, the application of clear glazing seems to improve the working performance.

4. Conclusions

A full-scale survey in an office room was given in this article, focusing on the impact of five various glazing systems on occupants' visual, non-visual and working performances across a winter period only under the daylighting condition. The key findings can be drawn from results and discussions above:

1) For the visual assessments, the blue glazing could achieve higher performances according to visual/color comfort, glare, and color appearance; while the bronze glazing has been recognized as the least acceptable choice. The grey and green glazing did not show a significant difference from the clear glazing.

2) Generally, the five glazing systems have no big differences in terms of alertness, mood, and relaxation in the office. However, the blue glazing seems to bring in more positive effects than the clear glazing according to the performance of physical well-being.

3) This experiment has found some aspects of non-visual performances of occupants have a significant link to the circadian light (Rea and Figueiro, 2016).

4) The clear glazing could be considered as the best choice according to the working performance in this office. Even though the blue glazing would improve occupants' visual performance, its effect on the working performance should be paid attention to.

5) It could be exposed that with the occurrence of daylighting the non-visual measurements are very hard to achieve; a non-linear statistical model would be required. Except for GONOGO, more practical methods to test the human working performance (e.g. reaction time task) could be considered.

6) Under daylighting conditions, human performances (visual and non-visual aspects) relating to the light color

could be very difficult to clarify, especially when considering the fact that the color preference is linked to the cultural and ethnic backgrounds.

5. Acknowledgement

This project was supported by grant from the National Natural Science Foundation of China No. 51778322.

References

Arsenault, H., Hébert, Marc., Bubois, M-C. 2012. Effects of glazing colour type on perception of daylight quality, arousal, and switch-on patterns of electric light in office rooms. Building and Environment. 56, 223-231.

Aries, M. B. C., Veitch, J. A and Newsham, G. R, 2010. Windows, view, and office characteristics predict physical and psychological discomfort. Environmental Psychology. 30, 533-41.

Aries, M.B.C., Aarts, M.P.J, van Hoof, J., 2015. Daylight and health: A review of the evidence and consequences for the built environment. Lighting Research & Technology. 47, 6-27.

Bellia, L., Pedace, A., Fragliasso, F. 2017. Indoor lighting quality: Effects of different wall colours. Lighting Research & Technology. 39(3), 283-340.

Borisuit, A., Linhart, F., Scartezzini, J-L., Munch, M., 2014. Effects of realistic office daylighting and electric lighting conditions on visual comfort, alterness and mood. Lighting Research & Technology. 0, 1-18.

BSI, 2011. BS/EN 410:2011: Glass in building —Determination of luminous and solar characteristics of glazing.

Bulow-Hube, H. 1995. Subjective reactions to daylight in rooms: effect of using low-emittance coatings on windows. Lighting Res. Technol, 2: 37–44.

Bubois, M-C., Cantin, F., Johnsen, K. 2007. The effect of coated glazing on visual perception: a pilot study using scale models. Lighting Research & Technology. 39(3), 283-340.

Figueiro, M. G., Rea, M. S. 2016. Office lighting and personal light exposures in two seasons: Impact on sleep and mood. Lighting Research & Technology, 48(3), 352-364.

Figueiro, M. G. 2013. Opinion: Why field measurements of circadian light exposure are important. Lighting Res. Technol, 45, pp. 6.

Kreutzer, J. S., DeLuca, J., Caplan, B. 2011. Encyclopedia of Clinical Neuropsychology. Publisher: Springer-Verlag New York.

Matusiak, B., Anter, K.F., and Angelo, K. 2012. Color shifts behind modern glazing. Research report, Department of Architectural Design, Form and Colour Studies, NTNU, Norway.

Monk, T.H. 1989. A visual analogue scale technique to measure global vigor and affect. Psychiatry Research, 27, 89–99.

Rea, M. S and Figueiro, M. G. 2016. Light as a circadian stimulus for architectural lighting. Lighting Research and Technology.0, 1–14.

Sahin, L. & Figueiro, M.G. 2013. Alerting effects of short-wavelength (blue) and long-wavelength (red) lights in the afternoon. Physiological Behaviour, 116-117, 1-7.

Sahin, L., Wood, B. M., Plitnick, B., Figueiro, M. G. 2014. Daytime light exposure: Effects on biomarkers, measures of alertness, and performance. Behavioral Brain Research, 274, 176–185.

Ticleanu, C. 2017. Report describing initial literature review on circadian lighting. CIBSE report. www.cibse.org/knowledge/knowledge-items/detail?id=a0q0O00000CF7o9QAD. (last access: 10/09/2017).

Veitch, J. A., Charles, K. E., Newsham, G.R. 2004. Workstation design for the open-plan office. Institute for Research in Construction, National Research Council of Canada. www.nrc-cnrc.gc.ca/ctu-sc/ctu_sc_n61 (last access: 10/09/2017)

Study on the Effect of the Layout of Daytime Activity Space on the Annual Vertical Daylight Exposure on the Eye in Elderly Facilities

Bo Tang[1], Xin Zhang[2]

[1] School of Architecture, Tsinghua University, Beijing (China)

[2] School of Architecture, Tsinghua University, Beijing (China)

Abstract

Lighting has been identified as a significant environmental attribute responsible for promoting physical and mental health of the elderly. However, present guide and standard focuses mostly on horizontal illumination requirements for specific tasks, but less on vertical lighting. This study attempts to evaluate lighting quality of the daytime activity space in Beijing's elderly facilities from the configuration of vertical daylighting on the eye by DAYSIM simulation based on dynamic climate, and to analyze the influence of position orientation on vertical daylight exposure on the eye so as to explore the possibility and design technology to optimize the non-visual based lighting quality.

Keywords: daylight; vertical daylight exposure; activity space; elderly facilities;

1. Introduction

With the discovery of ipRGCs (intrinsically photosensitive retinal ganglion cells, a type of neuron in the retina of the mammalian eye) (Berson, Dunn et al., 2002), the effect of light on human physiological and psychological health has become research hotpot in the lighting field. Light causes circadian, hormonal and other behavioral responses, from shifting sleep timing, jet-lag and melatonin suppression to pupil constriction, light adaptation and physiological activation (Price and Peirson, 2014), and then influences alertness, tension and sleep quality (Münch, Kobialka et al., 2006).

Lighting has been identified as a significant environmental attribute responsible for promoting physical and mental health of the elderly (Shikder, Mourshed et al., 2012).With the growth of age, the elderly suffer from evident overall optical changes that can cause one or more visual diseases and result in reduced visual performance (Weale, 1992). Besides, with the discovery of non-visual biological effects, light can help the elderly defeat depression, circadian sleep-wake disorder and behavioral disturbances among elderly (Sloane, Figueiro et al., 2008). Therefore, specialized lighting for the elderly was urgently considered to satisfy their physical needs and to enhance their psychophysical health and well-being (Shikder, Mourshed et al., 2012).

With non-visual biological effects, researches on elderly's lighting for physiological and psychological health (alertness, mood, performance and sleep quality) is taken more seriously. Several studies were made and the effects of light on alertness and mood has been found that the high-light regime always results in better alertness and mood than control group (Boyce, Beckstead et al., 1997). Meanwhile it was investigated that lighting during daytime hours can influence the sleep quality during the night (Riemersma-van der Lek, Swaab et al., 2008). A significant positive correlation between vertical illuminance at the eye level and sleep quality was shown (Aries, 2005). Many studies, besides mentioned above, indicate that lighting levels of at least 1000 lux on the eye are needed for biological stimulation (van Bommel, 2006). Besides, the influences of CCT (Correlated Color Temperature) of light on mental performances was also aimed that the blue-enriched white light experimented within an office has improved the subjective measure of alertness, mood, performance and other indicators of wellbeing (Viola, James et al., 2008). The efficiency of good natural light in the architectural context has also been investigated in several studies (Beauchemin and Hays, 1996).

It has been evident that non-visual biological effect of light is not directly governed by the illuminance on the

doi:10.18086/swc.2017.05.03 Available at http://proceedings.ises.org

working plane, but by light entering the eye (van Bommel, 2006), namely vertical light exposure at the eye level, which means that both vertical illuminance at the eye level and its time should be counted. The light entering the eye causes non-visual biological effect and provides the time information (the moment when the light exposure exists and its lasting time) at the same time (Bierman, Klein et al., 2005), which will influence the former. However, levels of illumination for various tasks and spaces are widely discussed in guides and specific values are suggested in lux (CIEUK, 1997, Light, 2002), while detailed recommendations for vertical illumination and vertical light exposure at the eye level are lacking in most guides (Shikder, Mourshed et al., 2012).

Therefore, in this study it was suggested that investigation into the effect of vertical light exposure at the eye level on the elderly's physiological and psychological health should be carried out on the base of acknowledgement of the difference of vertical daylight condition in elderly facilities, and then help optimize the non-visual based lighting quality.

Since China entered an aging society in 1999, aging trend has been presented the characteristics of the huge elderly population, fast speed of growth and the increasing proportion of the oldest old. People over the age of 60 account for 16.15% of the country's population of 1.37 billion in 2015, up from 10.3% in 2000, and will be 33.6% in 2050, according to the National Bureau of Statistics of China (2016). The ageing population has already been recognized as one of the greatest challenges of the 21st century for housing on both side of quantity and quality. A number of new elderly facilities for not only housing and health care but also social care services need to be built and the quality of those existing need to be updated to accommodate the increased service levels the ageing population will require.

As one of the biggest cities in China, Beijing has many typical conditions and was selected as the location of the model in this study. Daytime activity space was taken due to its various vertical daylight conditions. Therefore, this study attempts to evaluate lighting quality of the daytime activity space in Beijing's elderly facilities from the configuration of vertical daylighting on the eye and the illuminance on the working plane (UDI) by DAYSIM simulation (Reinhart, 2011) based on dynamic climate, and to analyze the influence of position orientation on vertical daylight exposure on the eye so as to explore the possibility and design technology to optimize the non-visual based lighting quality. It must be illustrate that as a simulation the spectrum of light could not be considered, and in the simulation the element of time has been simplified.

2. Methodology

2.1 Building model and simulation

The building model was a unit of the activity room in the elderly facilities located in the urban area of Beijing (39.80 N/ 116.47 W), where there were no obstructions all around. According to the survey of the content and characteristics of the elders' activity in elderly facilities in Beijing, the model was built on the widely used standard column grid of 8.4m×8.4m, with the floor height of 3.6m (Fig. 1). The basic unit was formed as Fig. 1 shows, with the available space of 16m×16m×2.8m excluding the space occupied by beam, column and other facilities. According to the survey, the unit consisted of two rooms separated by a hallway. Considering the elders' requirement of daylight, the depth of the south room (8m) was larger than the north (6m), between which was a 2m-wide hallway to ensure that two wheelchairs could pass through meantime. And French window was used for more daylight.

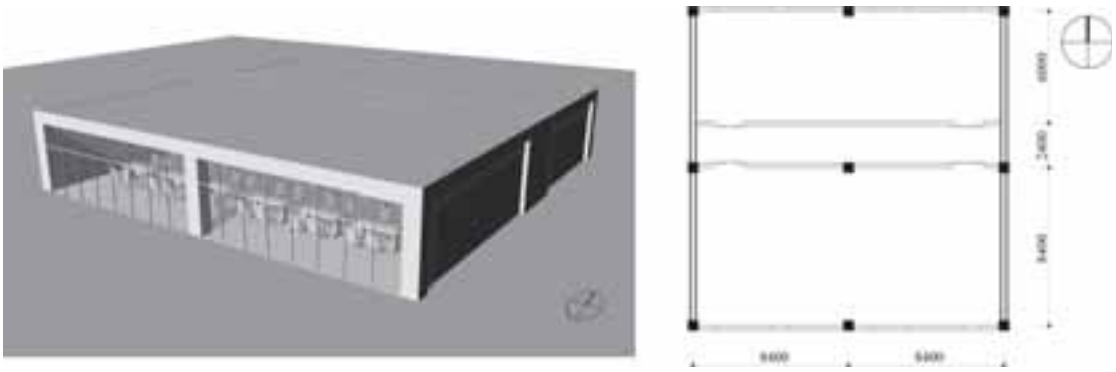

Fig. 1 perspective view and plan of the model

In the unit there were 3 typical furniture layout representing 3 common daytime activities in the elderly facilities (Tab. 1). The reflectances of the room surface are in Tab. 2.

Tab. 1 the three typical furniture layout

Type	1. Reading Room or Public Living Room	2. Classroom	3. Dining Room or Chess and Card Room
Plan	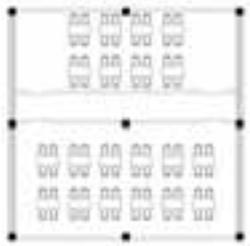	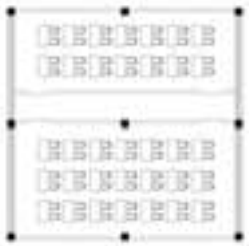	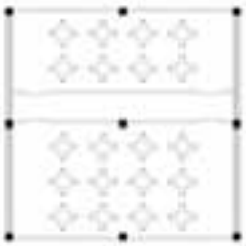
Activity samples			

Tab. 2 Parameters for simulation

Room orientation	South	North
Moulded dimension (Wide/Depth/Height)	16m/8m/2.8m	16m/6m/2.8m
Site description	Beijing_CHN(39.80 N/ 116.47 W)	
Hourly occupancy schedule	8:00-18:00 per day	
Obstructions	None	None
Mutual occlusion of the elderly	None	None
the Eye height of the elderly	1.15m	1.15m
the Height of work plane for UDI	0.8m	0.8m
Material reflectance		
Interior white wall	0.5	0.5
Furniture (wood)	0.3	0.3
Ceiling	0.7	0.7
Floor	0.2	0.2
Ground	0.2	0.2
Material Visual Transmittance		
Glazing DoublePane LowE Argon	0.65	0.65
Parameters of simulation precision		

ambient bounces	5	5
ambient divisions	1000	1000
ambient accuracy	0.1	0.1
direct sampling	0.2	0.2
direct relays	2	2

2.2 Daylight simulation

The relative daylight metrics were obtained by annual dynamic daylighting simulation software DAYSIM based on dynamic climate, with three typical furniture layout and simulation period of 8:00-18:00, according to the survey of elderly facilities. Two daylight metrics were used: the annual vertical daylight exposure on the eye (simplified as H_v in this paper) and Useful daylight illuminance (UDI).

In this study, the vertical daylight exposure on the eye instead of vertical illuminance on the space's surface of the elderly facilities was selected to reflect the distribution of vertical lighting. This is because the latter of the seats in space changes between different moments, which cannot be used as an evaluation standard, while the former is more objective (it considered the effect of time although it supposes that person always sit here). And it was suggested that higher vertical daylight exposure on the eye is recommended under consideration of UDI

Considering the complexity of vertical daylight situation which changes by time, situation, and orientation, only the positions of the elderly's eyes when they sat in the seat instead of the whole room were considered in this paper. And it was supposed that the elderly would sit on the same seat and look at the front during the whole daytime activity in a year, so that the vertical daylight exposure the elderly received could be represented by vertical daylight metrics of the positions of the elderly's eyes when they sat on the seat.

There's some point must be illustrate that the position of the elderly, namely the seats and tables' usage periods in different position, is far more complex than supposed, which are related to the seasons, weather, the horizontal illumination, layout of activities, etc, and there will significantly influence vertical daylight exposure on the eye. Therefore, the annual daylight exposure can proximately reflect this phenomenon but not totally.

Useful daylight illuminance (UDI) was invoked to be comparatively analyzed with the annual vertical daylight exposure on the eye. UDI evaluates luminous environment with the effective horizontal illumination (from 100 lux to 2000 lux) in work plane, which is irrelevant to the face orientation. Therefore, the simulation of the study, which presents health concept, was treated as an addition to UDI to some extent.

In order to get H_v, a series of vertical working planes including the seats' position were chosen as calculation plane, on which the points of 1.15m above the floor (the eye position of a sitting elderly) were finally considered. As for UDI, the calculation position in the model was at a horizontal working plane height of 0.8m above the floor. A calculation grid with 1600 points was evenly distributed across the plane. Other detailed parameters for the simulation were shown in Tab. 2.

2.3 Data analysis

Data analysis paid attention to the effect of position, orientation on H_v, the difference between H_v and UDI, and the difference between the glass hallway and opaque hallway. Besides, the material of walls, which are the solid wall (opaque, and reflectance is 0.5) and the glass wall (visual transmittance is 0.65), on both sides of the hallway was also compared to find how much it would influence the daylight environment.

Statistical analyses were performed using SPSS version 23.0 for Windows (IBM SPSS Inc., Chicago, IL). A two-sided p value<0.05 was considered significant. One-Way ANOVA (one-way analysis of variance, a technique that can be used to compare means of two or more samples) (Howell, 2002) was adopted to determine whether H_v of different groups (columns or rows) have a significant difference. When comparing H_v with UDI, as for the seats at one table, visual task happened mainly on the tabletop, so the average UDI of tabletop was calculated to approximately reflect the level of visual task lighting of the seats at the table. In order to compare easily, the average H_v of the seats at one table was also calculated similarly.

In order to analysis conveniently, each table and seat in the 3 type of plans was numbered as Tab.3 showed.

Tab. 3 numbers of tables/seats

Type	Plan	Table numbers	Seat numbers
1	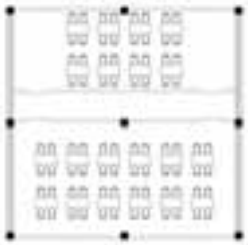	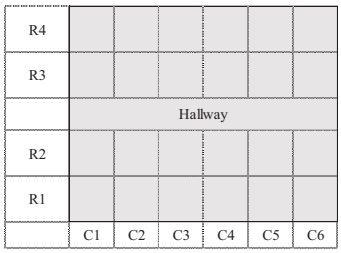	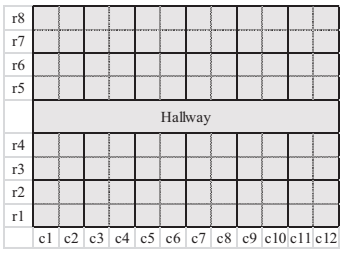
2	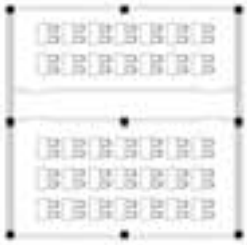	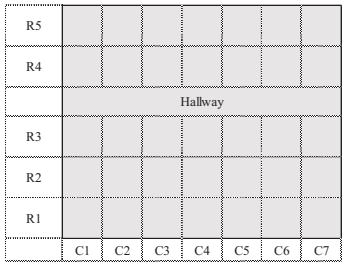	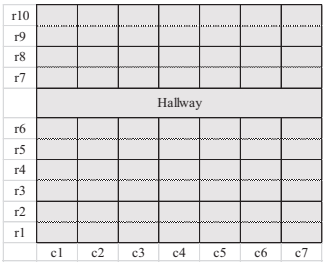
3		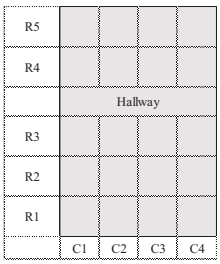	None

3. Results

3.1 Position and orientation

In this part, it was found that position orientation has a significant influence on annual vertical daylight exposure on the eye (H_v). For analyzing, position and orientation were discussed separately. Position was divided into the differences of the same row, the same column and whether in south or north, while orientation paid attention to whether facing or back to windows. And it is similar between the two different material of hallway, so in this part only the opaque hallway was discussed while the difference between the two hallway was shown in part 3.3.

According to H_v in all 3 types (Fig. 2.1 to 2.3), generally type-1 has the best evaluation (with MN of 4.2×10^6 lux·h) while type-2 has the worst (with Mean, simplified as MN, of 3.4×10^6 lux·h). And the distribution of H_v among the seats in type-2 is most uniform (with Standard Deviation, simplified as SD, of 2.5×10^6 lux·h) while the type-3 varies most (with SD of 4.4×10^6 lux·h).

Meanwhile, it was found that orientation of the room makes obvious effect on H_v. Generally the H_v of the seats in south room is higher than that in north room (with the MN of 5.5×10^6 lux·h in south vs 3.0×10^6 lux·h in north in type-1, 4.1×10^6 lux·h vs 2.4×10^6 lux·h in type-2, and 5.2×10^6 lux·h vs 2.4×10^6 lux·h in type-3), and varies more (with the SD of 5.8×10^6 lux·h in south vs 2.6×10^6 lux·h in north in type-1, 3.0×10^6 lux·h vs 9.8×10^5 lux·h in type-2, and 5.2×10^6 lux·h vs 1.9×10^6 lux·h in type-3).

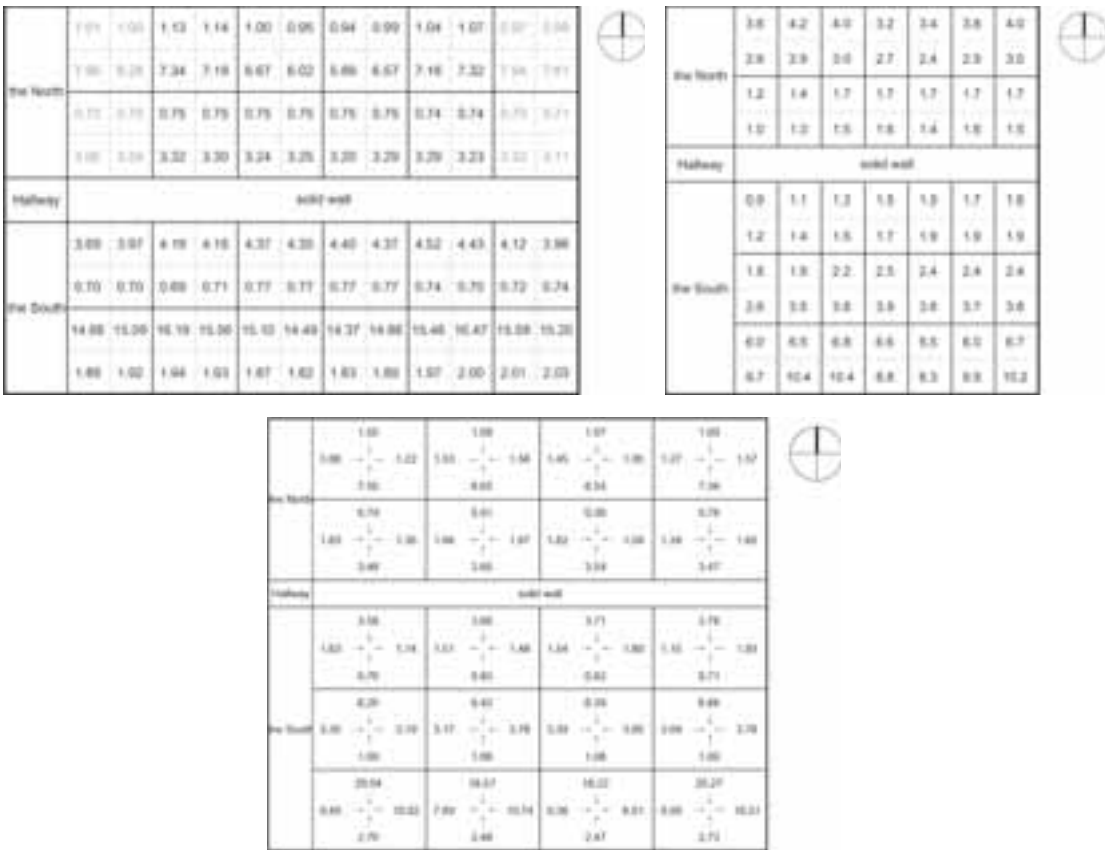

Fig. 2.1 to 2.3 the annual vertical daylight exposure on the eye (H_v, 10^6 lux • h) of each seat with solid walls on the side of the hallway, layout type-1 to type -3

Besides, there is a big difference among the seats in the same column. From the result of One-way ANOVA (Tab. 4), it was shown that there is a significant difference of H_v among the column (F_7=2265.063, $p<0.05$ in type-1, F_9=312.153, $p<0.05$ in type-2, and F_4=571.305, $p<0.05$ in type-3). Among the seats of the same orientation in one column, H_v decreased with the raise of the distance to windows (Fig. 3.1 to 3.4).

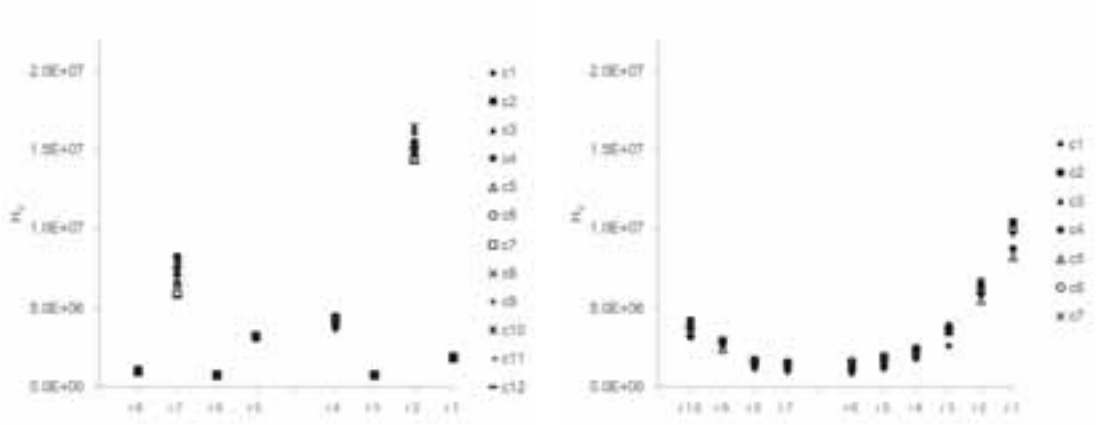

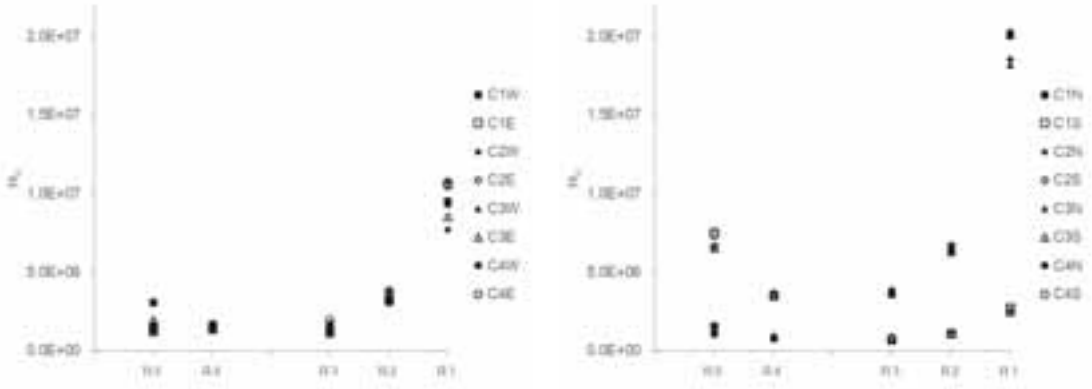

Fig. 3.1 to 3.4: the annual vertical daylight exposure on the eye of each seat (H_v, lux • h), layout type-1 to type -3

Note: 3.1 for type-1, 3.2 for type-2, and H_v in type-3 was divided into 2 parts: 3.3 includes seats westwards and eastwards, and 3.4 includes the north and south.

However, the H_v of the seats in the same row is similar according to One-way ANOVA result in Tab. 5 (F_{11}=0.007, p>0.05 in type-1, F_6=0.068, p>0.05 in type-2, and F_3=0.006, p>0.05 in type-3). In type-2, H_v among the seats in the row near the window varies more than those away from the window, and the conclusion is tenable in type-1 and type-3 when considering seat orientation (facing or back to windows). That is to say, within the 3 type plan, positions perpendicular to windows have more effect on H_v than positions parallel to windows.

Tab. 4 one-way ANOVA results (between columns)

		Sum of Squares	df	Mean Square	F	Sig.
Type-1	Between Groups	2053885838252480.000	7	293412262607497.000	2265.063	.000
	Within Groups	11399366119749.400	88	129538251360.789		
	Total	2065285204372230.000	95			
Type-2	Between Groups	449089154852403.000	9	49898794983600.300	312.153	.000
	Within Groups	9591226811834.930	60	159853780197.249		
	Total	458680381664238.000	69			
Type-3	Between Groups	197368045712237.000	4	49342011428059.300	571.305	.000
	Within Groups	1295508725153.260	15	86367248343.551		
	Total	198663554437390.000	19			

Notes: df: degree of freedom; F: F-test; Sig.: Statistical significance

Tab. 5 One-way ANOVA Results (between rows)

		Sum of Squares	df	Mean Square	F	Sig.
Type-1	Between Groups	2005104461408.360	11	182282223764.397	.007	1.000
	Within Groups	2063280099910820.000	84	24562858332271.700		
	Total	2065285204372230.000	95			
Type-2	Between Groups	2950000602991.090	6	491666767165.181	.068	.999
	Within Groups	455730392694777.000	63	7233815757059.960		
	Total	458680393297769.000	69			
Type-3	Between Groups	226823208655.060	3	75607736218.353	.006	.999
	Within Groups	198436731228735.000	16	12402295701796.000		
	Total	198663554437390.000	19			

Considering orientation of seats, there is a significant difference in type-1 and type-3 (type-2 has only one orientation). In type-1 (Fig. 3.1) between the two orientation——facing (r8, r6, r3 and r1) or back to windows (r7,

r5, r4 and r2), H_v of the former seats is obviously larger than the latter in general, with a difference of 6.4×10^6 lux·h on average (7.5×10^6 lux·h vs 1.1×10^6 lux·h). As for the seats at the same table, H_v between facing and back to windows differs by 6.1×10^6 lux·h (r7 vs r8), 2.5×10^6 lux·h (r5 vs r6), 3.5×10^6 lux·h (r4 vs r3), and 1.3×10^7 lux·h (r2 vs r1), among which it showed that the difference between facing and back to windows enlarges with the distance to windows. Besides, the difference between the two orientations in south room is larger than that in south.

In type-3 (Fig. 3.3 and 3.4) among the 3 orientation——facing (R1N, R2N, R3N, R4S and R5S), side-facing (towards west or east) or back to windows (R1S, R2S, R3S, R4N and R5N), generally H_v of the seat facing windows (8.0×10^6 lux·h) is the highest compared with side-facing (3.5×10^6 lux·h) and back to windows (1.3×10^6 lux·h). Meanwhile, within the seats side-facing windows, there is no significant difference between towards west or east generally (differs by 2.5×10^5 lux·h, about 7.5%). Similar with type-1, in type-3 the difference between the different orientations increased with the distance to window, and the difference between the three orientations in south room is larger than that in south (R1 in type-3 is the largest of SD 6.0×10^6 lux·h).

From the discussion it could be said that as for the elderly at the same table, the one facing windows has the highest H_v, and the one back to windows has the lowest, and that generally H_v of the elderly in south room is higher than the one in north. Thus, the elderly sitting in the seats close to and facing windows in south room (r2 in type-1, r1 in type-2 and R1 in type-3) can receive the most daylight, while the elderly in the seats away from and back to windows (r3 and r6 in type-1, r6 and r7 in type-2, and R3 and R4 in type-1) have the least daylight. Meanwhile, sitting at the same table, the elderly near windows have more individual differences than those away from windows.

3.2 Health evaluation by the annual vertical daylight exposure on the eye (H_v) vs Visual task lighting evaluation by UDI

Based on the comparison, Health evaluation (H_v) differs significantly from Visual task lighting evaluation (UDI). According to UDI in all 3 types (Fig. 4.1 to 4.3), generally type-1 has the best evaluation (with MN of 82.17%) while type-3 has the worst (with MN of 79.01%), which is a little different from H_v (type-2 is the worst). And the distribution of daylight among the seats in type-1 is most uniform (with SD of 9.18%) while the type-3 varies most (with SD of 17.15%), which is in common with H_v.

Meanwhile, according to UDI in all 3 types the north room is better than the south both in general evaluation (with MN of 87.04% in north vs 77.30% in south in type-1, 89.90% vs 75.51% in type-2, and 88.40% vs 72.75% in type-3) and uniformity (with SD of 4.01% vs 10.26% in type-1, 1.78% vs 15.18% in type-2, and 3.33% vs 19.62% in type-3). However, according to H_v the north has advantages in uniformity but disadvantages in general evaluation compared with the south (mentioned in Part 3.1).

the North	81.67	81.50	86.13	86.75	82.25	81.83
	90.17	90.88	91.00	91.00	91.00	90.33
Hallway	solid wall					
the South	88.11	88.58	87.42	87.50	87.67	85.78
	69.00	66.13	66.75	67.13	66.00	67.50

the North	4.53	4.20	3.66	3.60	4.15	4.38
	1.93	2.03	2.00	2.00	2.00	1.96
Hallway	solid wall					
the South	2.27	2.44	2.56	2.58	2.60	2.39
	8.40	8.91	8.32	8.24	8.97	8.71

the North	88.00	87.00	88.13	91.75	89.25	87.38	88.00
	90.50	91.50	91.75	91.50	91.75	91.50	90.63
Hallway	solid wall						
the South	85.83	87.67	88.67	88.50	88.17	87.83	85.17
	86.88	86.00	84.50	84.13	84.00	85.13	84.13
	55.50	53.33	53.33	57.00	54.50	52.50	53.00

the North	3.12	3.56	3.50	2.98	2.91	3.33	3.48
	1.07	1.36	1.57	1.64	1.54	1.61	1.61
Hallway	solid wall						
the South	1.02	1.20	1.42	1.59	1.70	1.78	1.73
	2.20	2.71	2.99	3.21	2.98	3.07	3.02
	7.84	8.43	8.58	7.71	6.89	7.93	8.48

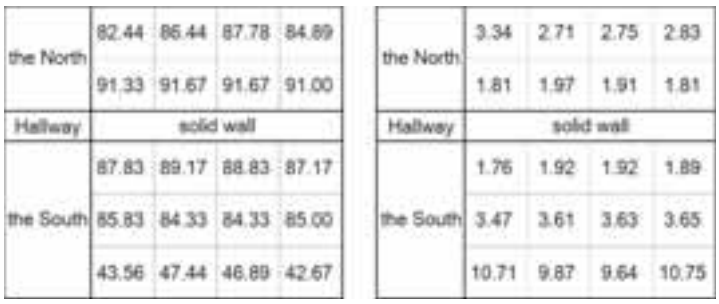

Fig. 4.1 to 4.3 Results of UDI (on left, %) and H_v (on right, 10^6 lux • h), Layout Type-1 to Type -3

Note: UDI refers to the average UDI on each desktop; and H_v is the average of the 4 seats at the table.

Besides, UDI showed that the tables near windows are more disadvantageous than others (with an average lack of 13.90% in type-1, 16.80% in type-2, and 22.88% in type-3), and those close to windows in the south-facing room (R1 in all 3 types) are the worst (with the MN of 67.08% in type-1, 54.17% in type-2, and 45.14% in type-3). On the contrary, as a result of H_v the seats close to window are more favorable than others, especially in the south-facing room (mentioned in Part 3.1). Moreover, even at the same table the elderly have a significant difference between each other because of the orientation of seats (mentioned in Part 3.1), which is not expressed by UDI, while discomfort and unwanted excessive levels of daylight such as glare is not considered in H_v.

3.3 Material of walls on both sides of the hallway

In general, solid walls on both sides of the hallway help increase the annual vertical daylight exposure (H_v), compared with glass walls. In type-1 and type-2, solid walls improve H_v on both sides of general level (by 5.8×10^4 lux·h in type-1 and 1.4×10^5 lux·h in type-2) and uniformity, while in type-3 the result is on the contrary (decrease 3.5×10^4 lux·h in type-3) (Tab. 6). Meanwhile, in the north room of type-1 and type-2 the improvement of using solid walls is better that in south (8.5×10^4 lux·h vs 4.1×10^4 lux·h in type-1 and 2.0×10^5 lux·h vs 9.4×10^4 lux·h in type-2). And in the north room of type-3 using solid walls decreases H_v, while in the south it increased. Besides, in general when using solid walls instead of glass walls, there is no significant difference between facing and back to windows but on the contrary a difference between near and away from windows (1.4×10^4 lux·h vs 1.0×10^5 lux·h in type-1, 1.0×10^5 lux·h vs 2.0×10^5 lux·h in type-2 and -1.4×10^5 lux·h vs 1.8×10^4 lux·h in type-3).

Tab. 6 descriptive statistics of H_v with the solid wall and the glass wall (10^6 lux·h), layout type-1 to type-3

			Solid wall	Glass wall	Difference				Solid wall	Glass wall	Difference
Type-1	MN	Whole	4.28	4.23	0.05	Type-2	MN	Whole	3.42	3.29	0.13
		North	3.04	2.96	0.08			North	2.38	2.18	0.20
		South	5.53	5.49	0.04			South	4.12	4.02	0.10
		Face	7.46	7.40	0.06			Face	/	/	/
		Back	1.10	1.05	0.05			Back	/	/	/
		Side-facing	/	/	/			Side-facing	3.42	3.29	0.13
	SD	Whole	4.65	4.66	-0.01		SD	Whole	2.53	2.59	-0.06
		North	2.57	2.61	-0.04			North	0.96	0.98	-0.02
		South	5.78	5.76	0.02			South	2.98	3.03	-0.05
		Face	4.75	4.76	-0.01			Face	/	/	/
		Back	0.49	0.55	-0.06			Back	/	/	/
		Side-facing	/	/				Side-facing	2.53	2.59	-0.06

			Solid wall	Glass wall	Difference

Type-3	MN	Whole	4.10	4.13	-0.03
		North	2.39	2.53	-0.14
		South	5.24	5.20	0.04
		Face	8.00	7.89	0.11
		Back	1.30	1.18	0.12
		Side-facing	3.55	3.73	-0.18
	SD	Whole	4.41	4.38	0.03
		North	1.93	1.90	0.03
		South	5.16	5.17	0.01
		Face	5.83	5.86	0.03
		Back	0.68	0.77	0.09
		Side-facing	3.13	3.06	0.07

Note: 'Whole' =all the seats in the type; 'North' and 'South' = the room orientations; the others= the seat orientations.

MN refers to Mean, and SD refers to Standard Deviation.

By comparison of H_v of each row in details, using solid walls instead of glass walls mainly changed seats in r6 (1.9×10^5 lux·h) and r8 (-3.5×10^4 lux·h) in type-1, seats side-facing windows in R4 in type-3 (1.3×10^6 lux·h), and seats back to windows in R3 in type-3 (1.7×10^5 lux·h). And remarkably the difference between type-3 and other types is caused by the large decreasing H_v of the seats side-facing windows in R4 (by 1.3×10^6 lux·h).

Therefore, in order to improve the daylighting quality of the elder away from windows especially in north-facing room, the solid walls on both sides of the hallway are recommended.

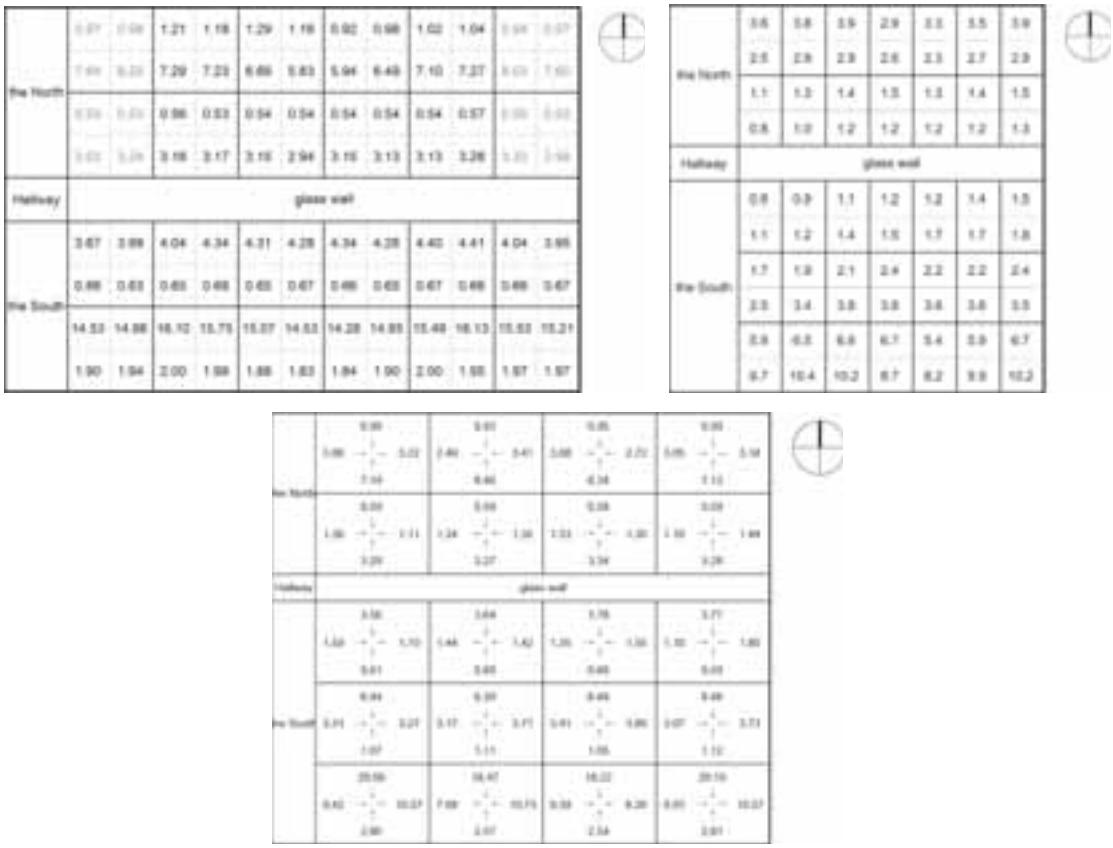

Fig. 5.1 to 5.3 the annual vertical daylight exposure on the eye (H_v, 10^6 lux • h) of each seat with glass walls on the side of the hallway, Layout Type-1 to Type-3

4. Conclusion

According to the discussion above, the main conclusions showed as follows:

- Position orientation has a significant influence on annual vertical daylight exposure on the eye (H_v);
- Health evaluation by the annual vertical daylight exposure on the eye (H_v) differs significantly from Visual task lighting evaluation by UDI, and both have shortage and need to be considered together;
- Compared with glass walls, solid walls on both sides of the hallway help improve the annual vertical daylight exposure (H_v) on both side of general level and uniformity.

All above can be applied to improve the daylight conditions for the elderly during activities. On one side, the layout of daytime activity space can be designed or redesigned to optimize the daylight quality based on non-visual effects. For example, a suitable room orientation and furniture layout of the space can be chosen according to the requirement of the activity. On the other side, the regulation of the elderly's activities can be optimized to realize the needs of the elderly and to avoid disadvantages.

Limitations and future work: in this paper, the regulation of the elderly's activities is simplified as a point, while actually it is more appropriate to describe it as a line. In other words, the movement of the elderly from one seat to another and from one room to another should be recorded so that the difference between different elderly will be more comparable. Some work has been made in this paper that if one always sit in the seat with the most/least vertical illuminance per hour, finally he will receive the H_v of 3.6×10^4 lux·h /2.0×10^3 lux·h in one day (for example in Sep. 23rd) and 1.8×10^7 lux·h /5.3×10^5 lux·h in a year (for example in type-1), which can somewhat reflect the influence of position on vertical daylight exposure on the eye in another view. With the real occupancy schedule of one's activities as well as his position record, specialized plan for improving his condition of vertical daylight exposure on the eye will be drawn up and the result of the improvement will be more efficient.

5. Acknowledgements

This study was supported by the Natural Science Foundation of China (Grant No. 51778322) and Tsinghua University (School of Architecture) -CIFI Joint Research Center for Sustainable Residential Developments, as well as Zhangyou Geracomium, Chaoyang District, Beijing.

6. References

Aries M. 2005. Human lighting demands:healthy lighting in an office environment. Technische Universiteit Eindhoven.

Beauchemin KM, Hays P. 1996. Sunny hospital rooms expedite recovery from severe and refractory depressions. Journal of Affective Disorders 40:49.

Berson DM, Dunn FA, Takao M. 2002. Phototransduction by Retinal Ganglion Cells That Set the Circadian Clock. Science 295:1070-1073.

Bierman A, Klein TR, Rea MS. 2005. The Daysimeter: a device for measuring optical radiation as a stimulus for the human circadian system. Measurement Science & Technology 16:2292-2299.

Boyce PR, Beckstead JW, Eklund NH, Strobel RW, Rea MS. 1997. Lighting the graveyard shift: The influence of a daylight-simulating skylight on the task performance and mood of night-shift workerst. Lighting Research & Technology 8:105-134.

CIEUK. 1997. TRE 123/1997 Low vision: lighting needs for the partially sighted.

Howell, D. C. 2002. "Statistical Methods for Psychology." Journal of the Royal Statistical Society 43(43): 324–325.

Illuminating Engineering Society of North America. 1998. Recommended Practice: Lighting and the Visual Environment for Senior Living. New York: Illuminating Engineering Society of North America.

Light TCCT. 2002. Light and lighting - Lighting of work places - Part 1 : Indoor work.

Münch M, Kobialka S, Steiner R, Oelhafen P, Wirzjustice A, Cajochen C. 2006. Wavelength-dependent effects

of evening light exposure on sleep architecture and sleep EEG power density in men. American Journal of Physiology 290:1421-1428.

National Bureau of Statistics of China. 2016. China Statistical Yearbook-2016. China Statistics Press.

Price LLA, Peirson SN. 2014. The first international workshop on circadian and neurophysiological photoreception, 2013: A physicist's perspective on the construction of standard units. Light & Engineering 22:24-27.

Reinhart, C. F. 2011. Simulation-based Daylight Performance Predictions. Building performance simulation for design and operation. E. M. Hensen and Roberto Lamberts.

Riemersma-van der Lek RF, Swaab DF, Twisk J, Hol EM, Hoogendijk WJ, Van Someren EJ. 2008. Effect of bright light and melatonin on cognitive and noncognitive function in elderly residents of group care facilities: a randomized controlled trial. Jama 299:2642-2655.

Shikder S, Mourshed M, Price A. 2012. Therapeutic lighting design for the elderly: a review. Perspectives in Public Health 132:282-291.

Sloane PD, Figueiro M, Cohen L. 2008. Light as Therapy for Sleep Disorders and Depression in OlderAdults. Clin Geriatr 16:25-31.

van Bommel WJ. 2006. Non-visual biological effect of lighting and the practical meaning for lighting for work. Applied Ergonomics 37:461.

Viola AU, James LM, Schlangen LJ, Dijk DJ. 2008. Blue-enriched white light in the workplace improves self-reported alertness, performance and sleep quality. Scandinavian Journal of Work Environment & Health 34:297-306.

Weale RA. 1992. The senescence of human vision: Oxford University Press.

The Daylight Performance of an Integrated Skylight and Shading Dome for the Tropics

Sopa Visitsak[1], Liliana O. Beltran[2] and Nattaree Sridaranon[1]

[1] Department of Building Innovation, Faculty of Architecture, Kasetsart University, Bangkok (Thailand)

[2] Department of Architecture, College of Architecture, Texas A&M University, College Station (USA)

Abstract

This paper evaluates the daylighting performance of an integrated skylight and shading dome with natural ventilation (SDV) for residential buildings in the tropics using the RADIANCE lighting simulation program and the Energy Plus Weather (EPW) file for Bangkok, Thailand. Indoor illuminance levels at work plane height of a simulation model with the SDV was compared to that of from similar physical scale model located in natural environment. A typical unit base case model (1.35 m x 1.35 m x 2.80 m) with a circular translucent opening (60% transmittance, r = 0.175 m) was developed to relate with sizing of available conventional roofing materials and typical residence room's height. Daylighting performance of the base case based on Daylight Autonomy (DA 300 lux) was compared to the original SDV and the modified SDVs, which the skylight plate replaced with different translucent materials (40%, 50%, and 60% transmittance). The results show that the modified SDVs' DA are all above 50%. Four typical units of the modified SVD (60% transmittance) were developed to represent an application and compare to a conventional translucent sheet in an extended residence area. The results confirm that the modified SDV has better daylighting quality than the translucent sheet which has similar opening area and light transmittance value (60%). With proper design and material selection, the modified SDV (60% transmittance) could significantly reduce direct sunlight, which is the cause of glare and heat problems for buildings in tropical climates.

Keywords: Daylight simulation, Radiance, Building innovation, Green technology, Sustainable architecture

1. Introduction

In Thailand, most indoor spaces in low rise buildings (e.g. single house, row house, townhouse, etc.) have low daylight levels. Using electric lighting is costly and not a sustainable solution. Conventional translucent sheets have been widely used but it is difficult to control the quality of daylight and always be a cause of significance problems such as heat, glare, and ultra violet, which may be harmful to eyes, artworks, and furniture. Although many products were developed for the use of natural light such as typical transparent and translucent roof sheets with optional of external or internal shading devices. There are limitations of thermal resistance and quality of daylight. Advanced materials and advanced technology devices such as glass reinforced polyester, insulated glass, double panes, low-e coating, laminated glass with a polymer dispersed liquid crystal (PDLC), hyperboloid skylights, dome skylights, tubular daylighting devices, with and without sun tracker and reflective materials have been developed to improve the daylighting performance and thermal insulation. However, the cost of those materials and products are expensive and may not be cost effective.

Fig. 1: An integrated skylight and shading dome with natural ventilation (SDV)

doi:10.18086/swc.2017.05.04 Available at http://proceedings.ises.org

We are proposing an integrated skylight and shading dome with natural ventilation (SDV) (Fig.1), which was developed from the previous one (without natural ventilation system) (Visitsak et al., 2014) as a sustainable solution that could reduce significantly problems of heat, glare, and ultra violet. The opening and the shading form were developed to responds to sunpath (Stein and Reynolds, 2000) for Bangkok, Thailand (latitude 13.76° N, longitude 100.52° E) in order to protect direct light (100%) throughout the year. The design also allows building occupants to perceive external view through the opening and be connected with the environment.

The objective of this paper is to evaluate the daylighting performance of the SDVs (original and modified) and typical translucent skylight using the RADIANCE lighting simulation program (Ward, 1996), which was found to be the most generally useful software package for architectural lighting simulation program (Reinhart and Fitz, 2006) as well as a highly optimized daylighting and energy modeling plug-in, DIVA-for-Rhino (v.4).

2. Methodology

The SDV consists of two main parts: 1) a circular metal skylight plate (r = 0.175 m, area = 0.096 m^2,) on a metal tube (height = 0.185m) with an opening area to allow only indirect sunlight and the opaque area to obstruct direct sunlight and 2) a transparent acrylic dome (88% transmittance), which the shading area for protecting direct sunlight is silver painted. The reflectance values of ceiling, walls, and floor are 70%, 70% and 20%, respectively. The process of conducting and comparing daylight performance of the original and modified SDVs and typical translucent skylight using simulation and Bangkok weather comprised 3 steps:

2.1. Calibration of simulation model (original SDV)

A physical scale model with the original skylight and shading dome (SDV) installed on the roof (Fig.2) was prepared and tested outdoor in Ayuthaya, Thailand (latitude 14.37° N, longitude 100.59° E). The model dimensions were 1.00 m wide x 1.00 m long x 2.30 m high. Indoor illuminance at work plane (0.80 m) on March 6th at noon, when the outdoor illuminance was similar to that of from Bangkok weather data (EPW), was used to calibrate with the results of simulation model using Bangkok weather data from Energy Plus Weather file (DOE, 2017).

(a) (b) (c)

Fig. 2: Simulation model of the skylight and shading dome (SDV): (a) Plan (b) Section and (c) Perspective

2.2. Daylighting performance: One unit (base case, original SDV, and modified SDVs)

A typical unit base case model with dimensions 1.35 m wide x 1.35 m long x 2.80 m high and a circular opening equivalent to the SDV's circular skylight plate (r = 0.175 m, area = 0.096 m^2) was developed to relate with sizing of available typical roofing materials and typical residence room's height. The daylighting performance at work plane (0.76 m) based on daylight autonomy (300 lux) during the occupied hours (8:00 a.m.-6:00 p.m.) throughout the year (Reinhart et al., 2006) of the base case with a circular translucent opening (60% transmittance) (Fig.3a) was compared to that of from the original SDV and modified SDVs, which the skylight plate (opaque part) was replaced with an alternative translucent material with different transmittance (40%, 50%, and 60%) (Fig.3b).

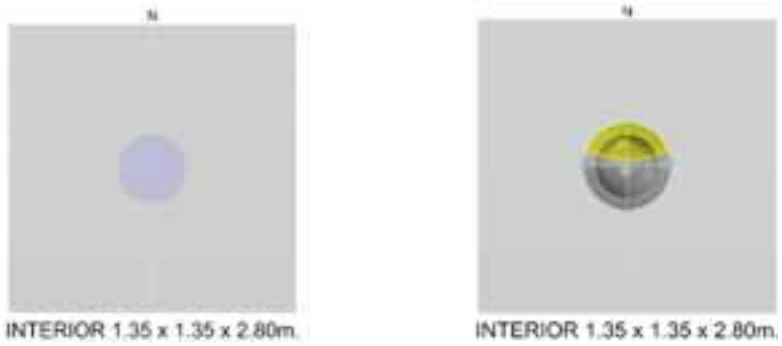

(a) (b)

Fig. 3: Simulation model: One unit (a) Base case (Circular translucent material, τ = 60%) (b) Original SDV & Modified SDVs (τ = 40%, 50%, and 60%)

2.3. Daylighting performance: Four units (translucent sheet vs. modified SDVs)

Four typical units with dimensions 2.70 m wide x 2.70 m long x 2.80 m high represent an application of a conventional translucent sheet (opening area = 0.38 m^2, 60% transmittance) in an extended residence area with typical cement roof sheets. The daylighting performance at work plane (0.76 m) of the translucent sheet installed on the roof (Fig.4a) based on Daylight Autonomy (DA300 lux), which represents percentage of annual daytime hours during the occupied hours (8:00 a.m.-6:00 p.m.) that a given point in the area is above 300 lux, was simulated and compared with the results from four modified SDVs (Fig.4b) with 40%, 50%, and 60% transmittance, which have equal opening area and placed 1.35m apart from each other, installed on roof.

The best modified SDV option (60% transmittance) from the previous step was used to simulate and compare daylighting performance results to the translucent sheet. The daylighting performance results include mean indoor illuminance on the summer solstices (Jun 21st at noon) when the external daylight is critical and mean Useful Daylight Illuminance that indicates percentage of occupied hours per year when daylight illuminance falls within a range from 300-3000 lux (UDI 300-3000 lux) (Nabil and Mardaljevic, 2005; 2006), as well as the daylighting metrics in LEED v4, which are Spatial Daylight Autonomy (sDA300/50%) (IESNA, 2012) that indicate percentage of the area that meets or exceeds 300 lux at least 50% of the occupied hours per year, and Annual Sun Exposer (ASE1000/250) (IESNA, 2012) that identified potential of discomfort and should be no more than 10% of the area exposed to direct sunlight more than 1000 lux for 250 hours per year.

In addition, simulation glare images for sitting eye level from the corner of the room for the translucent sheet and the best modified SDV (60% transmittance) as well as glare indices results of Daylight Glare Probability Index (DGP) (Wienold and Christoffersen, 2006), Daylight Glare Index (DGI) (Hopkinson, 1972), Unified Glare Index (UGR) (CIE, 1992), Visual Comfort Probability Index (VCP) (IESNA, 1993) and CGI/CIE Glare Index (Einhorn, 1969) on the four representative dates (Mar 21st, Jun 21st, Sep 21st, and Dec 21st) at noon were also simulated and compared.

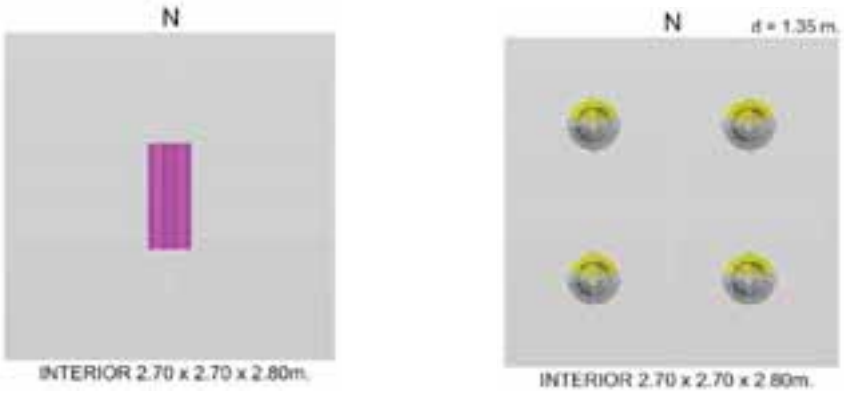

(a) (b)

Fig. 4: Simulation model: Four units (a) Translucent sheet (τ = 40%), (b) Modified SDVs (τ = 40%, 50%, and 60%)

3. Data analysis and results

3.1. Calibration of simulation model (original SDV) results

The indoor illuminance at work plane (0.80 m) of the physical scale model with the original skylight and shading dome (SDV) installed on the roof, which was located in Ayutthaya, (March 6, at noon) was used to calibrate with the results of simulation model using Bangkok weather file (March 6, at noon). Table 1 shows that the average indoor illuminance (125 lux) from simulation model, when the outdoor illuminance from Bangkok weather file (93,400 lux) is similar to the outdoor illuminance from field measurement (93,800 lux), corresponds to the indoor illuminance (129 lux) measured from the physical scale model. The results confirm that the simulation model is compatible with the physical scale model and could be used to modify and simulate daylighting performance of various conditions in the next step.

Tab. 1: Comparison of indoor and outdoor illuminance from simulations and field measurements (Mar 6, at noon)

Run	Simulation (BKK epw)		Measurement	
	Indoor Illuminance (lux)	Outdoor Illuminance (lux)	Indoor Illuminance (lux)	Outdoor Illuminance (lux)
1	126	93400	129	93800
2	128			
3	128			
4	122			
5	122			

3.2. Daylighting performance results: One unit (base case, original SDV & modified SDVs)

The simulation results of one unit (1.35 m wide x 1.35 m long x 2.80 m high) in Figs. 5 & 6 show Daylight Autonomy (300 lux) during the occupied hours (8:00 a.m.-6:00 p.m.) of the base case model with a circular translucent material (60% transmittance), the original SDV, and the modified SDVs, which the skylight plate (opaque part) was replaced with translucent material with different transmittance (40%, 50%, and 60%). As expected, the percentage of DA (300 lux) increases with the transmittance value. The percentages of DA (300 lux) of the original SDV and the modified SDVs (40%, 50% and 60% transmittance) are 0%, 2.44%, 6.72%, and 16.76%, respectively. Although they are all lower than that of the base case (60.4%), an alternative translucent material with different transmittance (40%, 50% and 60%) is effective and increases the percentage of Daylight Autonomy.

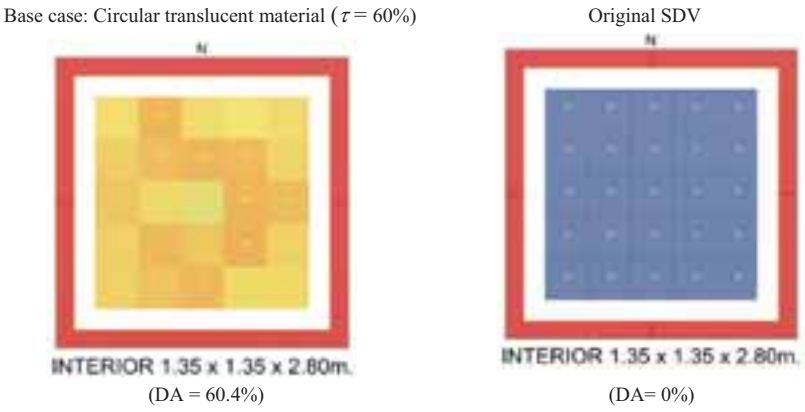

Fig. 5: Percentage of DA (300 lux) of one unit: Base case (Circular translucent material, τ= 60%) and Original SDV

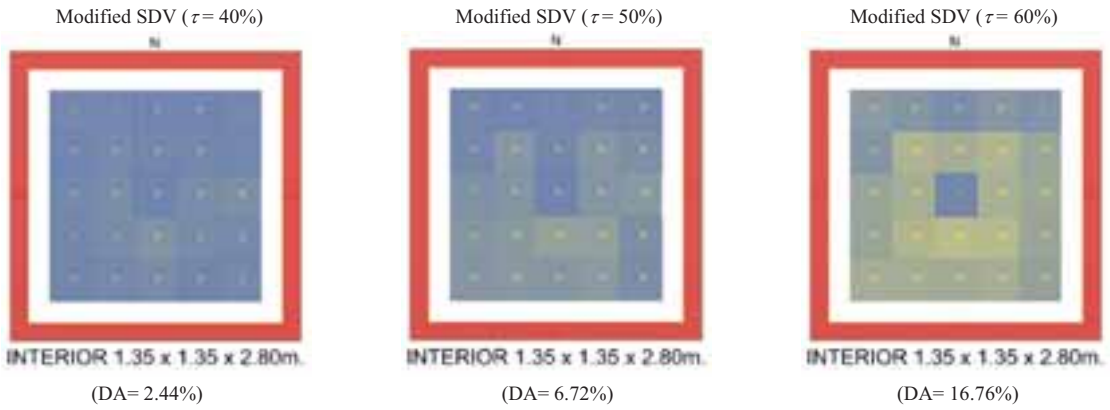

Fig. 6: Percentage of DA (300 lux) of one unit: Modified SDVs (τ= 40%, 50%, and 60%)

3.3. Daylighting performance results: Four units (translucent sheet vs. modified SDVs)

- *Daylight Autonomy (300 lux) results:*

In Fig.7, the results show that the percentages of Daylight Autonomy (300 lux) during the occupied hours (8:00 a.m.-6:00 p.m.) corresponds to the DA (300 lux) results in Figs. 5 & 6, which increase with the transmittance value. In addition they also increase with larger space for all cases. The percentages of DA (300 lux) of four units of the conventional translucent sheet (60% transmittance) and the modified SDVs (40%, 50% and 60% transmittance) increase to 86.57%, 52.64%, 66.3%, and 73.57%, respectively. Although the modified SDVs (40%, 50%, and 60% transmittance) have percentage of DA (300 lux) lower than that of the translucent sheet (60% transmittance), they are all above 50% DA (300 lux).

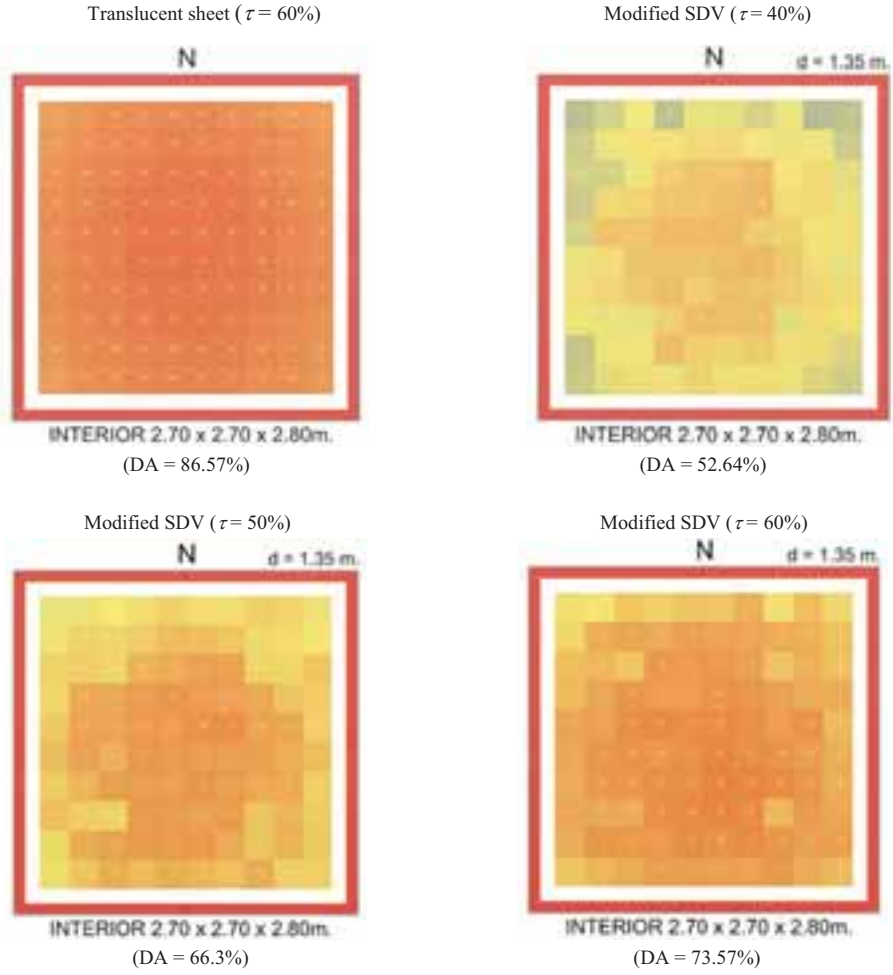

Fig. 7: Percentages of DA (300 lux) of four unit: Translucent sheet (τ= 60%) vs. Modified SDVs (τ= 40%, 50%, and 60%)

- *Mean illuminance results:*

Fig. 8 shows the results of mean illuminance on the June 21st (at noon) of the translucent sheet and the modified SDV with similar transmittance value (60%). Mean illuminance on the June 21st (at noon) of the translucent sheet is 1551 lux with illuminance level ranging between 1074-2148 lux for 98% of the area, which is much higher than the standard indoor illuminance requirements and that of the modified SDV with 60% transmittance. The mean illuminance of the modified SDV (60% transmittance) is 831 lux with illuminance level ranging between 537-1074 lux for 97% of the area. The results implies that the modified SDVs in larger space could provide sufficient daylighting and reduce incoming solar radiation significantly.

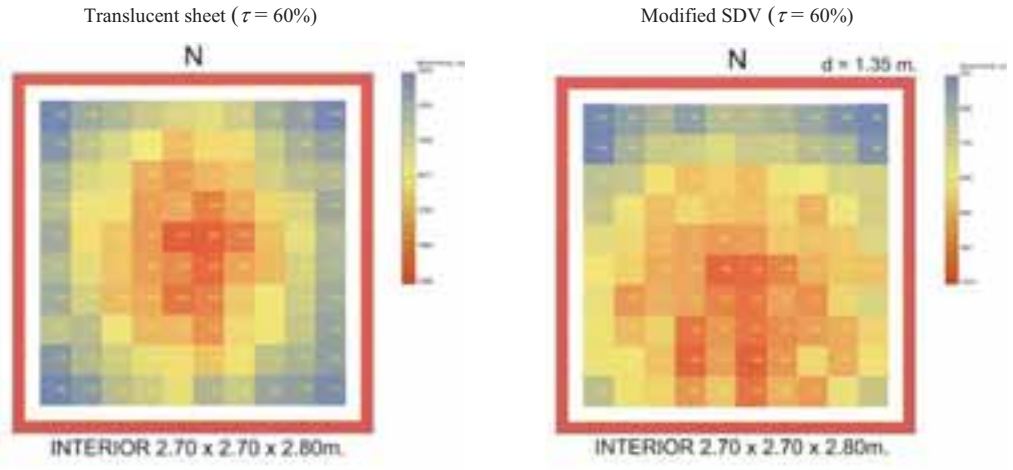

Fig. 8: Mean Illuminance of four units, Jun 21st at noon: Translucent sheet (τ= 60%) vs. Modified SDV (τ= 60%)

- *Mean Useful Daylight Illuminance (UDI 300-3000 lux) results:*

Simulation results in Fig.9 indicate percentages of occupied hours per year when daylight illuminance falls within a range from 300-3000 lux (UDI 300-3000 lux). For the translucent sheet (60% transmittance), there are 77% to 93% of the occupied hours per year that the partial areas have illuminance in the range from 300-3000 lux and the mean UDI (300-3000 lux) equals to 86.46%. The UDI (300-3000 lux) of the modified SDV (60% transmittance) vary from 50% to 85% and mean UDI (300-3000 lux) is 73.99%. UDI (300-3000 lux) of both cases are higher in the middle of the areas and spread out to lower value in the perimeters and in the corners of the areas.

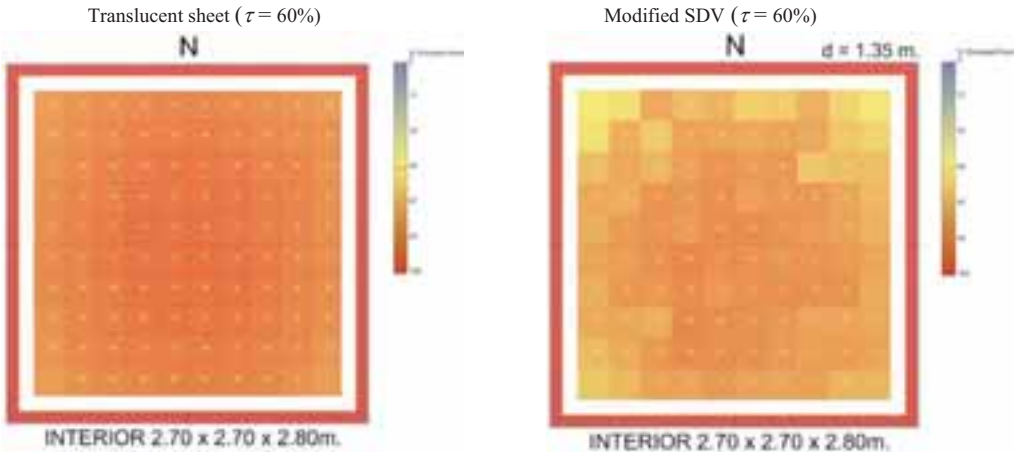

Fig. 9: Mean Useful Daylight Illuminance (UDI 300-3000 lux) of four units: Translucent sheet (τ= 60%) vs. Modified SDV (τ= 60%)

- *Spatial Daylight Autonomy (sDA300/50%) and ASE (1000/250) results :*

In Fig.10, the simulation results show that 100% the translucent sheet (60% transmittance) room area and 98% of the modified SDV (60% transmittance) room area have a *Spatial Daylight Autonomy* at 300 lux value for more than 50% of the occupied hours. For both cases, none of the areas are exposed to direct sunlight more than 1000 lux for 250 hours per year, which qualify for 3 LEED points in LEED v4.

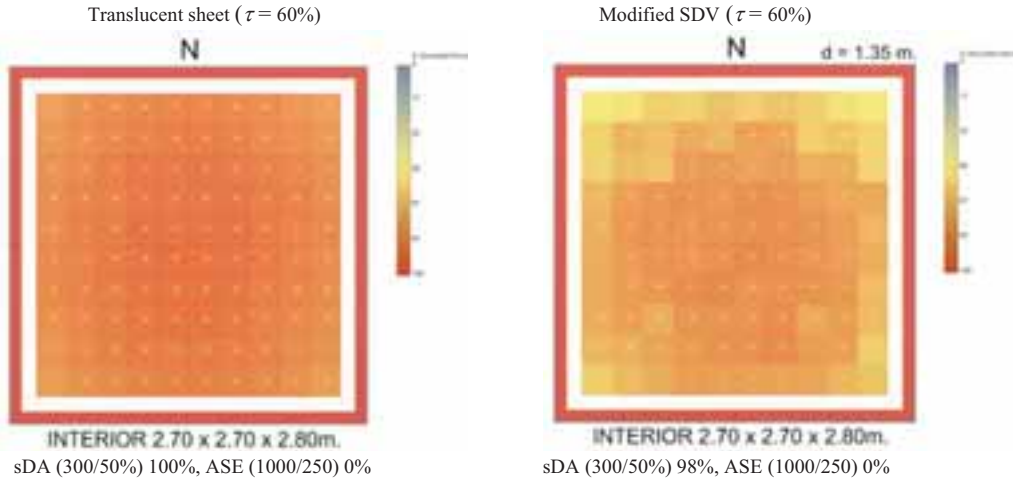

Fig. 10: Spatial Daylight (sDA 300/50%): Translucent sheet and Modified SDV (τ= 60%)

- *Glare Evaluations (DGP, DGI, UGR, VCP, CGI)*

In (Figs.11-12), the simulation glare images and glare indices *(DGP, DGI, UGR, VCP, CGI)* for sitting eye level from the corner of the room on Mar 21 st st, Jun 21 st st, Sep 21 st st, and Dec 21st (at noon) are presented. Green, Yellow, Orange, and Red colors that correspond to glare value ranges represent the levels of glare, which are imperceptible, perceptible, disturbing, and intolerable, respectively.

The results show that the glare value ranges of Daylight Glare Probability Index (DGP) and Daylight Glare Index (DGI) on all selected dates for the conventional translucent sheet (60% transmittance) and the modified SDV (60% transmittance) are imperceptible glare. Base case has higher DGP glare values and lower DGI glare values than the modified SDV, except on Dec 21st.

The results are different for Unified Glare Index (UGR), Visual Comfort Probability Index (VCP) and CGI/CIE Glare Index, which in general the modified SDV has better glare values than the translucent sheet (60% transmittance) for all selected dates. It implies that the modified SDV (60% transmittance) has less glare problems than the base case, especially on Dec 21st when the sun ray is lower. For base case, the results show significant problem of intolerable glare on Mar 21st , Jun 21st , and Sep 21st as well as disturbing glare on Dec 21st for the Visual Comfort Probability Index (VCP).

4. Conclusion

Daylighting performance of an integrated skylight and shading dome with natural ventilation (SDV) for the tropics and alternative materials were investigated using the RADIANCE lighting simulation program and the weather file (EPW) for Bangkok, Thailand. The daylighting simulation results show that, with proper design and material selections, the daylighting performance of the modified SDVs with part of the skylight plate replaced with an alternative translucent materials (40%, 50%, and 60% transmittance) are above 50% daylight autonomy (300 lux). The modified SVD with 60% transmittance provides appropriate indoor illuminance with mean UDI 73.99% of occupied hours in the range of 300-3000 lux as well as 98% of the area have a *Spatial Daylight Autonomy* at 300 lux value for more than 50% of the occupied hours without any of the areas are exposed to direct sunlight more than 1000 lux for 250 hours per year, which qualify for 3 LEED points. The modified SVD (60% transmittance) has better daylighting quality than a conventional translucent skylight with similar opening area and light transmittance value (60%). In addition, the modified SDVs could reduce glare problems and incoming solar radiation that exceeds indoor illuminance requirements, which is the cause of heat problem for buildings in tropical climates.

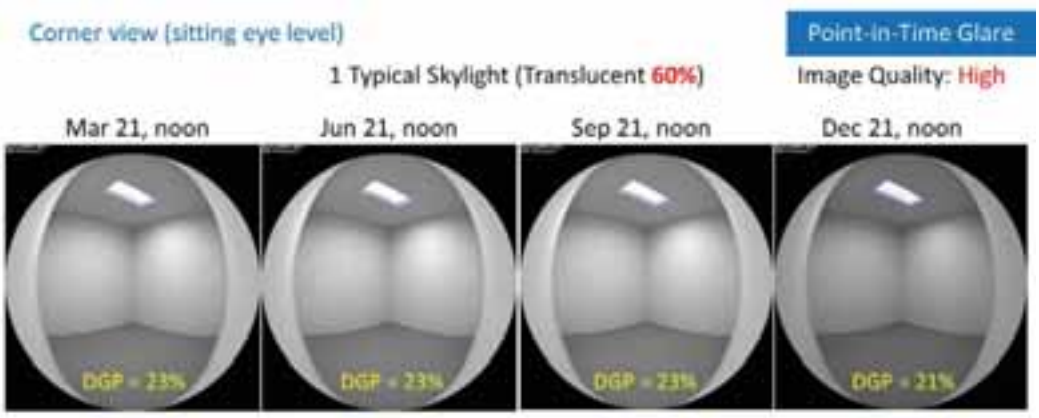

	DGP (Daylight glare probability)	DGI (Daylight Glare index)	UGR (Unified Glare Index)	VCP (Visual Comfort Probability)	CGI (CIE Glare Index)
Mar 21, noon	0.231562	13.956071	20.586311	35.631779	23.651011
Jun 21, noon	0.233975	14.053003	20.709019	34.567097	23.850048
Sep 21, noon	0.232480	14.007485	20.659151	35.103310	23.746941
Dec 21, noon	0.214668	13.039995	19.381838	45.800575	21.872459

Fig. 11: Glare evaluations: Translucent sheet (τ= 60%)

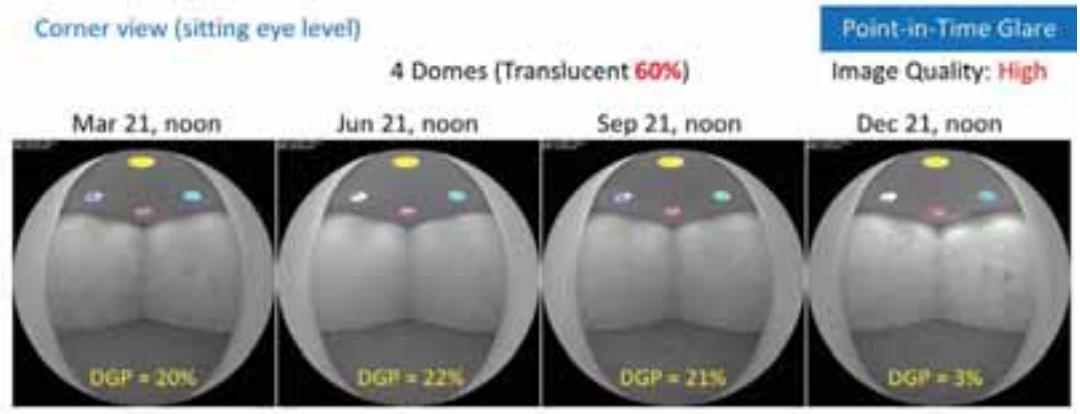

	DGP (Daylight glare probability)	DGI (Daylight Glare index)	UGR (Unified Glare Index)	VCP (Visual Comfort Probability)	CGI (CIE Glare Index)
Mar 21, noon	0.203701	15.725554	19.436243	55.547352	21.052660
Jun 21, noon	0.221535	17.005383	20.922939	42.045521	23.336435
Sep 21, noon	0.205238	15.808572	19.542120	54.609406	21.214691
Dec 21, noon	0.031514	10.794039	12.561081	89.084564	13.864660

Fig. 12: Glare evaluations: Modified SDV (τ= 60%)

5. Acknowledgement

This research was supported by Department of Architecture, College of Architecture, Texas A&M University, Building Innovation Department, Faculty of Architecture, and Graduate School at Kasetsart University, Thailand Research Fund and Thailand-United States Educational Foundation (TUSEF/Fulbright Thailand).

6. References

CIE, 1992. Discomfort Glare in the Interior Lighting, Technical Committee TC-3.13, Division 4, Interior Environment and Lighting Design. International Commission on Illumination.

Einhorn, H. D., 1969. A new method for the assessment of discomfort glare, Lighting Research and Technology 1 (4) 235–247.

IESNA,1993. IESNA Lighting Handbook, 8th edition. Illuminating Engineering Society of North America, New York, NY, USA.

IESNA, 2012. IES LM-83-12. Approved Method: IES Spatial Daylight Autonomy (sDA) and Annual Sunlight Exposure (ASE). Illuminating Engineering Society of North America, New York, NY, USA.

Hopkinson, R. G., 1972. "Glare from daylighting in buildings", Applied Ergonomics 4.

Nabil, A. and Mardaljevic, J., 2005. Useful daylight illuminance: A new paradigm for assessing daylight in buildings, Lighting Research and Technology, 37(1), pp. 41-59.

Nabil, A. and Mardaljevic, J., 2006. Useful daylight illuminances: A replacement for daylight factors, Energy and Buildings, 38(7), pp.905-913.

Reinhart, C. F. and Andersen, M., 2006. Development and validation of a radiance model for a translucent panel. J. Energy and Building. 38 (7), 890-904.

Reinhart, C. F. and Fitz, A., 2006. Finding from a survey on the current use of daylight simulations in building design. Journal of Energy and Building. 38 (7), 824-835.

Reinhart, C. F., Mardaljevic, J., & Rogers, Z., 2006. Dynamic Daylight Performance Metrics for Sustainable Building Design. Leukos, 3(1), 7-31.

Stein, B. and Reynolds, J.S., 2000. Mechanical and Electrical Equipment for Buildings, ninth ed. John Wiley & Sons, Inc., New York.

U.S. Department of Energy, 2017. EnergyPlus Version 8.8.0 Documentation, Auxiliary Programs, from https://energyplus.net/sites/all/modules/custom/nrel_custom/pdfs/pdfs_v8.8.0/AuxiliaryPrograms.pdf, retrieved on October 2, 2017.

Visitsak, S., Sridaranon, N., and Khedari, J., 2014. An Optimum Skylight and Shading Device Set. Proceedings of the International Conference, Grand Renewable Energy 2014 (GRE), Tokyo, August.

Ward. G., 1996. Radiance. Berkeley: Lawrence Berkeley National Laboratory.

Wienold J. and Christoffersen J., 2006. Evaluation methods and development of a new glare prediction model for daylight environments with the use of CCD cameras, Energy and Buildings 38: 743-757.

District Heating

Validation of a District Heating System Model and Simulation-Based Investigation of Bidirectional Heat Transport by Decentralized Solar Thermal Plants

Daniel Beckenbauer[1,2], Mathias Ehrenwirth[1,2], Michael Klärner[1], Wilfried Zörner[1] and Vicky Cheng[2]

[1] Institute of new Energy Systems, University of Applied Sciences Ingolstadt (Germany)

[2] Munich School of Engineering, Technical University of Munich (Germany)

Abstract

This work discusses a MATLAB/Simulink-based modelling approach for the simulation of bidirectional flow in district heating systems with decentralized solar thermal plants. Based on the results of a monitoring campaign of an operational district heating network with decentralized solar thermal plants, a simulation model of the system is validated. Modified components for pipes, thermal storages and network junctions are derived from the CARNOT toolbox and additionally validated by laboratory tests. These components are used to enhance the model for the simulation of a reversed flow in the district heating pipes. Based on this modification, a study is conducted to examine the performance of a return-supply feed-in compared to a return-return feed-in for different dimensions of solar thermal plants in the network. The comparison shows that for small plant sizes and low solar fractions, a pure return-return feed-in can be suitable, whereas for higher solar fractions, a return-supply feed-in increases the solar yield of the decentralized plants.

Keywords: district heating, modelling, bidirectional flow, decentralized solar thermal plants

1. Introduction

The integration of solar heat into district heating systems is a promising approach for the reduction of carbon dioxide emissions from domestic hot water and space heat consumption in urban areas. While large contiguous collector arrays are a cost effective way of supplying newly built areas and large ambitious renovation projects with solar heat, existing buildings and district heating networks in densely built-up quarters require adapted solutions to deal with the limited space. The decentralized integration of solar collectors and diurnal heat storages is one possible answer to this challenge. However, as this approach transforms the connected buildings from pure consumers to prosumers, a detailed planning of the design and operation of multiple plants interacting in one energy supply system is required. The simulation-based optimization of the hydraulic layout, the dimensioning and the control strategy is an essential step towards the realization of such projects.

Four major hydraulic schemes can be identified for the decentralized integration of solar heat. These are return-return (RR), supply-return (SR), supply-supply (SS) and return-supply (RS) feed-in (Schäfer et al. 2014). While the first three concepts do not lead to a change in the flow direction of the water circulating in the district heating pipes, the RS feed-in causes a reversed flow in the branches where decentralized heat generators are in operation. This operation mode is shown in Fig. 1, where the upper scheme represents the flow distribution when the central heating plant is the sole heat supply. The bottom scheme shows the same system while a decentralised heat generator is additionally active, which allows partly supplying other consumers in the system with the necessary nominal flow rate. While this feed-in strategy is very attractive due to the parallel operation of decentralised heat generators on the same supply and return temperature level as the central heating plant, it is on the other side more complex in terms of hydraulic layout and system operation. In some existing systems, additional solar pipes are used in parallel to the district heating supply and return pipe, allowing additional hydraulic design parameters (so called 2+1 or 2+2-systems). Examples can be seen in Mies and Rehrmann (2007) or Paulus and Papillon (2014). However, this leads to additional costs. Furthermore, for most existing district heating systems, it may be difficult to add another pipe in the ground. As this paper aims at renovation projects, this approach is not further discussed and the connection of the solar thermal plants to the existing district heating pipes is the focus of the work.

doi:10.18086/swc.2017.06.01 Available at http://proceedings.ises.org

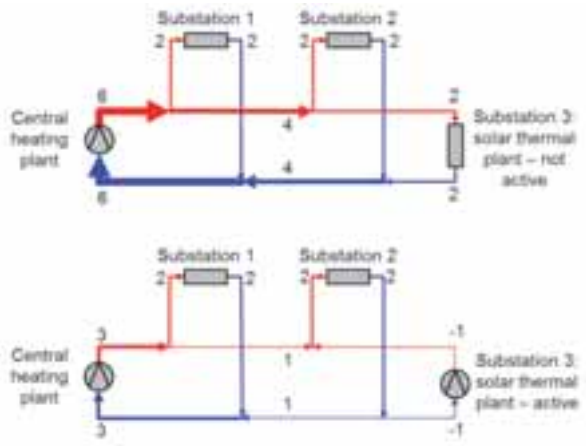

Fig. 1: Change in flow conditions during activation of a decentralized RS feed-in. Top scheme: solely supplied by central heating plant; bottom scheme: additional decentralized feed-in by solar thermal plant (numbers show nominal flow rates)

The CARNOT-toolbox in MATLAB/Simulink provides a block library with all necessary components to model heating systems – including district heating – for the conceptual design of these systems (Hafner et al. 1999). Due to the unidirectional information flow between Simulink blocks, it is, nevertheless, not straightforward to model the reversed flow in pipe connections between components like boilers, storages and heat exchangers. A modification and extension of the available CARNOT library is, therefore, necessary to enable the design of a district heating system with decentralized solar thermal plants utilizing an RS feed-in. One approach of such a modification is presented in this paper, validated by measurements and tested in a district heating network model.

2. Description of the existing district heating network

The basis of the system simulation is the metrological investigation of an existing, operational district heating network in Ingolstadt, Germany, which is shown in Fig. 2. The network was built in the 1970´s and was equipped with four decentralized solar thermal plants in 2016. It was decided to use single-cover flat-plate collectors in this case, to keep the investment costs on a low level. The standard CARNOT toolbox was used for designing this renovation project and all plants were equipped with comprehensive metrological equipment to measure the temperatures and volume flows in the systems as well as the heat flows in each branch continuously. While three plants have the same collector area of 71 m² and orientation, the hydraulic integration concepts differ. The similar sizing allows a comparison of the different utilization concepts:

- One solar thermal plant was installed on the roof of the main building (Hindenburg 57 – HB57), where the central heating plant is located. As the building has 85 residential units and, therefore, a high domestic hot water consumption, there is no need to feed in heat from the solar thermal plant into the network. Due to the high ratio of heat consumption to collector area and the resulting low operation temperatures, the plant can achieve a high annual yield of 42.5 MWh at the average local climate.
- Another system (Hindenburg 36 – HB36) is designed for pure feed-in and is very simple regarding the hydraulic layout and the control strategy. In addition, it has only small space requirements in the building, as it does not require a thermal storage, making it easy to integrate into the existing quarters. The feed-in strategy is a pure RR feed-in. The plant is directly connected via a plate heat exchanger to the main return pipe of the network passing by the building. Measurements show an average annual yield of 16.9 MWh at the current operation parameters of the network.
- Finally, there are two systems for a combined use, meaning that in a first step the solar heat is consumed directly in the building for domestic hot water preheating. Only if there is excess heat and the storage temperature reaches a certain level, the feed-in to the return of the network is activated. The plants achieve an annual yield of 26.6 MWh for the south oriented roof (Schubert 21 – SB21) and 31.8 MWh for the west oriented roof (Schubert 12 – SB12), where 21 m² vacuum tube collectors are additionally in operation. These collectors were already installed and integrated to the new plant. Local solar fractions for domestic hot water of the two plants are 73 % and 49 % respectively. During summer, this fraction increases up to monthly values of 140 %. The installed excess heat feed-in reliably transfers the heat into the district heating return.

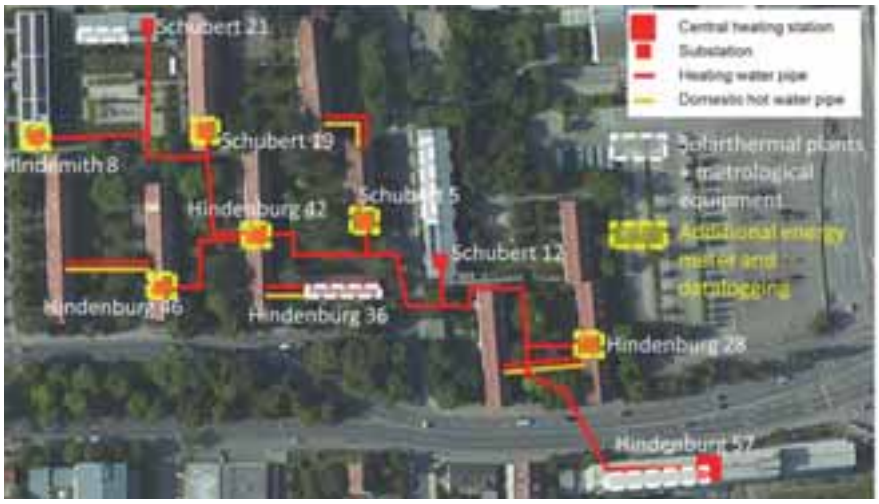

Fig. 2: Scheme of the existing district heating network with decentralized solar thermal plants

3. Description of the simulation model

Fig. 3 shows the layout of the complete district heating network model. The single components used in this model are introduced in the following section.

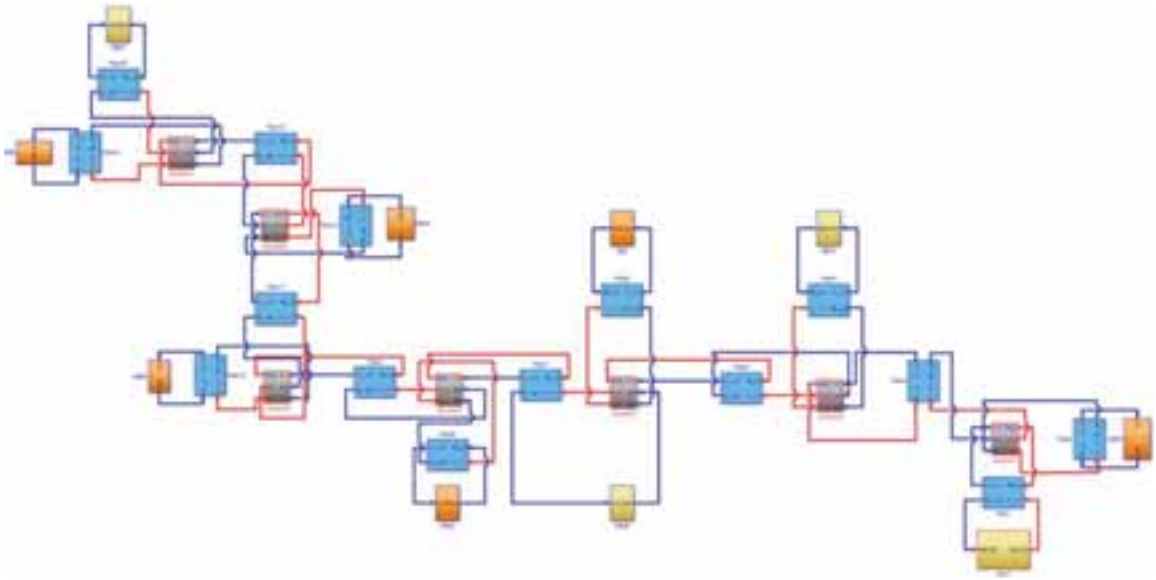

Fig. 3: Depiction of the district heating network simulation model with consumers (orange), producers/prosumers (yellow), pipes (blue) and network junctions (grey)

3.1 Pipe model

For the simulation of a district heating network with decentralized feed-in, four properties of the pipe model are particularly of interest:

- Calculation of the heat losses
- Calculation of the stored energy due to the thermal capacity of pipe and fluid
- Calculation of the time delays of the fluid flow in the network
- Ability to simulate a reversed flow in the pipe

To cope with these demands, a new setup of pipe model was developed based on Simulink. As the buildings and other system components are modelled in CARNOT, the thermo-hydraulic vector (THV) was the basis for the new calculation procedure. Besides the temperature and the mass flow, the THV contains several data, which are not relevant to the energy balance of the district heating network and can be simplified without losing accuracy in

this application. As the fluid is always pure water and pressure loss calculations are only of interest for the detailed system design but not for the conceptual layout and control strategy, only the temperature and the mass flow were selected and structured in a 2-component vector for all calculations in the network. To realize the reversed flow in Simulink, the pipe model consists of a *Supply*- and a *Return*-pipe, merged in one block. Fig. 4 shows the structure of this block. It is connected via the *Supply_in*, *Supply_out*, *Return_in* and *Return_out* ports to the superior model. Depending on the sign of the mass flow (positive = heat generation, negative = heat consumption), the *Switch* blocks conduct the information from the *Supply_in* port to the *Supply* pipe and the *Supply_out* port for standard operation. During a decentralized feed-in, the *Return* pipe is connected to the *Supply_in* and *Supply_out* ports to establish the reversed flow. The *Memory* blocks are used to break algebraic loops by adding a one integration step time delay. As the time step is always below 10 s (approximately 3 s in average), this does not lead to a significant error in the simulation.

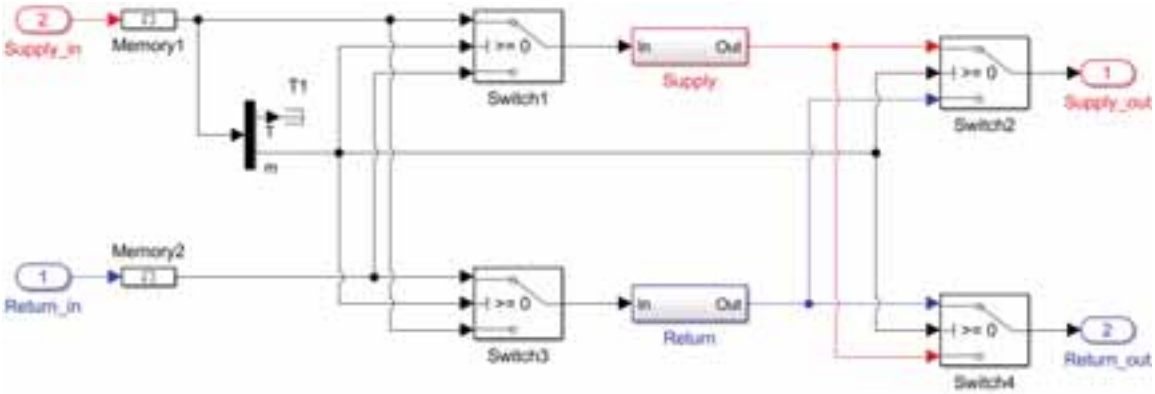

Fig. 4: Pipe block with *Supply* and *Return* pipe and *Switches* for change of the flow direction

Inside the *Supply* and *Return* blocks, several calculations are performed to emulate the pipe behavior (Fig. 5). The *Delay* sub-model takes the current mass flow of the fluid in the pipe, calculates the fluid velocity and, based on the pipe length, the transport delay from the inlet to the outlet. The temperature information at the inlet is then kept for the calculated delay duration until the fluid is conducted to the *Q_loss* and the *E_pipe* block. These blocks represent the energy balance at the pipe (losses through insulation, stored internal energy due to fluid, pipe wall and insulation capacity). Integrating the sum of these two terms after multiplication with the total pipe capacity leads to the time-dependent outlet temperature. The same calculation is performed in the *Return* pipe of the block.

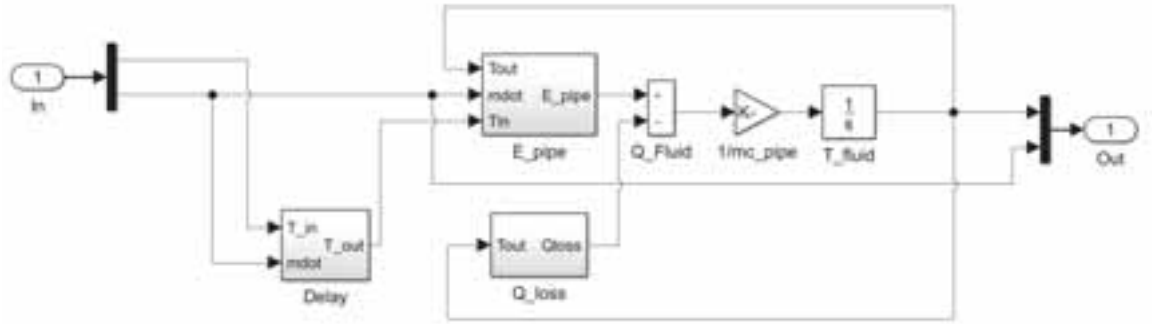

Fig. 5: Layout of a single pipe component with time delay, energy loss, energy balance of inlet and outlet and thermal node of the pipe

Some simplifications are introduced in this pipe model. Firstly, the heat capacity of the water is assumed to be constant at 4,188 J/(kgK). This is justified as the maximum deviation of the real value within the temperature range between 0 °C and 100 °C is less than 0.5 %. Secondly, the temperature of the pipe wall is assumed to be the same as the fluid temperature, which is acceptable if the thermal resistance of the pipe insulation is much higher than the thermal resistance of the pipe wall and the convective heat transfer between fluid and pipe wall. For thermal conductivities of the insulation material around 0.04 W/(mK) and thicknesses in the range of the pipe diameter, this assumption is sufficient. For the calculation of the insulation capacity, an average insulation temperature has to be defined. This results from the fact that when assuming a linear temperature gradient along

the insulation thickness, more than half of the insulation material mass is closer to ambient than to fluid temperature due to the increasing lateral surface at larger distances from the pipe wall. For a pipe with an insulation thickness equal to the inner diameter, this results in a weighted temperature of 37 % of the inner temperature compared to ambient, meaning that e.g. at 80 °C fluid and 20 °C ambient temperature, the average insulation temperature is only at 42 °C. To cope with this fact, 37 % of the total capacity of the insulation are added to the fluid capacity and set to fluid temperature whereas the other 63 % are neglected. Fig. 6 illustrates this correlation.

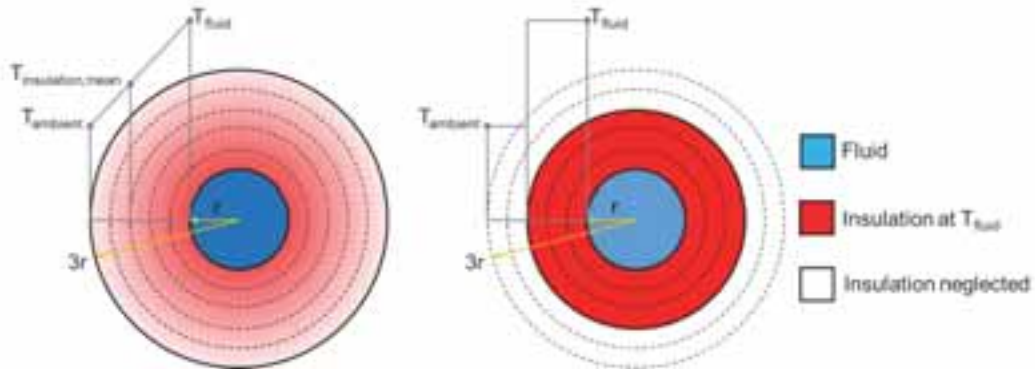

Fig. 6: Real (left) and discretized (right) temperature distribution across the pipe cross-section with equal stored energy

As the thermal conductivity of insulation materials can be highly dependent on the temperature, a temperature-conductivity function is introduced using a set of temperature-conductivity pairs and a linear interpolation between the known values. Equation 1 gives the heat loss of the pipe:

$$loss = \frac{2 \cdot \pi \cdot l}{ln\left(\frac{D+\frac{2 \cdot P_i}{100}}{D}\right)} \quad \text{(eq. 1)}$$

The thermal capacity of the fluid, the pipe wall and the insulation can be calculated by:

$$mc_f = l \cdot \frac{D}{2} \cdot \pi \cdot \rho_f \cdot c_f \quad \text{(eq. 2)}$$

$$mc_w = l \cdot D \cdot \pi \cdot t_w \cdot \rho_w \cdot c_w \quad \text{(eq. 3)}$$

$$mc_i = l \cdot \left[(0.5 \cdot D + \frac{D \cdot P_i}{100})^2 - (0.5 \cdot D)^2\right] \cdot \pi \cdot \rho_i \cdot c_i \quad \text{(eq. 4)}$$

The delay time of the fluid particle and temperature information between inlet and outlet of the pipe is given by:

$$delay = \frac{l}{\frac{\dot{m}}{\left(\frac{D}{2}\right)^2 \cdot \pi \cdot \rho_f}} \quad \text{(eq. 5)}$$

The change of the internal energy of the fluid in the pipe is:

$$\dot{E}_{fluid} = (T_{in} - T_{out}) \cdot c_w \cdot \dot{m} \quad \text{(eq. 6)}$$

With the change in internal energy and the loss, the new outlet temperature of the pipe can be calculated by:

$$T_{fluid} = \int \frac{1}{mc_{fluid} + mc_{wall} + 0.37 \cdot mc_{insulation}} \cdot (\dot{E}_{fluid} - \dot{Q}_{loss}) \delta t \quad \text{(eq. 7)}$$

With:

$\dot{m}$	*mass flow in the pipe*	*kg/s*
$mc_{w,\,f,\,i}$	*mass times thermal capacity of the pipe wall, fluid or insulation*	*J/K*
l	*length of the pipe*	*m*
D	*inner diameter of the pipe*	*m*
t_w	*wall thickness of the pipe*	*m*
P_i	*relative insulation thickness based on pipe diameter*	*m*
$\rho_{w,\,f,\,i}$	*density of the pipe wall material, fluid or insulation*	*kg/m³*
$c_{w,\,f,\,i}$	*specific thermal capacity of the pipe wall material, fluid or insulation*	*J/(kgK)*

Another simplification is to define the pipe as a one-node capacity along the pipe length. This results in the fact that a temperature gradient along the pipe length cannot be simulated in detail. In addition, the heating and cooling process of the pipe wall and insulation are neglected, as the temperature of these parts is assumed to be immediately at fluid temperature.

3.2 Network junctions

A dedicated *Junction* component is used for the pipe couplings of the network. As at every point in the network, there is a supply and a return temperature, this component has an "upper" and a "lower" node, representing these temperatures. The upper temperature is calculated as the mass-flow-weighted mean value of all incoming supply flows, whereas the lower temperature represents the mass-flow-weighted mean value of all incoming return flows. The decision of whether an incoming flow is directed to the upper or lower node depends on the sign of the mass flow. Similar to the pipe supply and return component, this is performed by *Switch* blocks in the *Junction*. As on the network level, the mass flows are calculated in a bottom-up approach from the single buildings back to the flow at the central heating station, the flow in branch one, connected to the junction is the sum of branch two and branch three. Fig. 7 shows the junction sub-model.

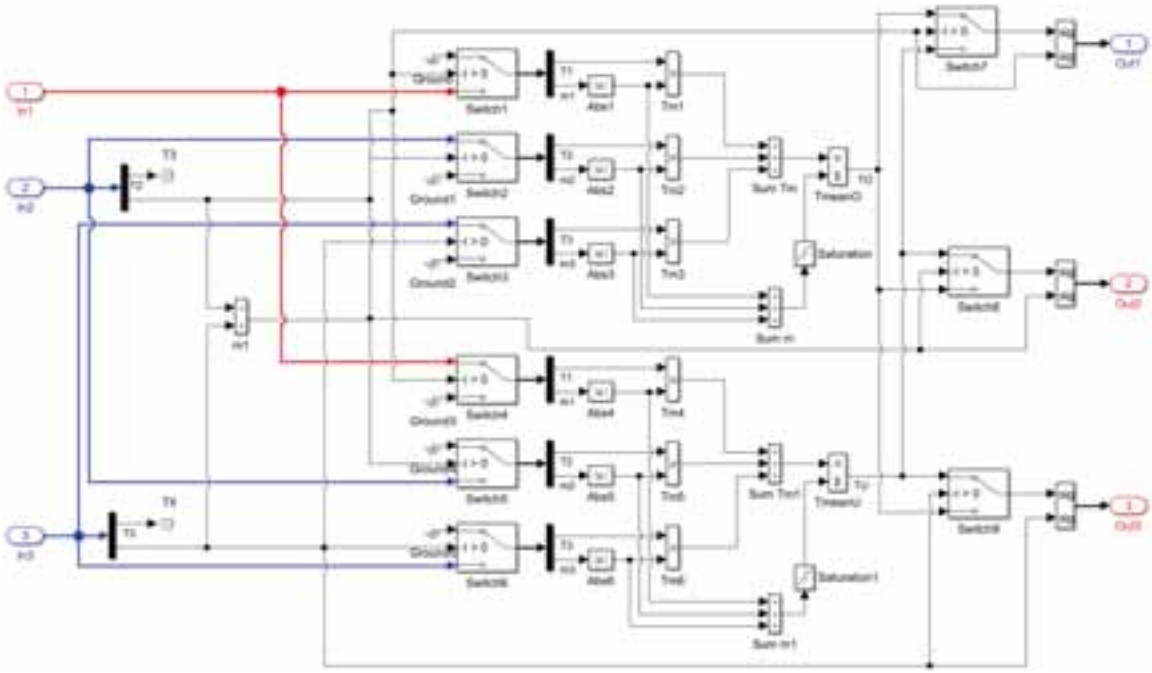

Fig. 7: Sub-model of a network junction

3.3 Substations

The connection of the modified network model to the CARNOT-based building models is realized by a hydraulic compensator that is based on the CARNOT storage model. Fig. 8 shows the sub-model with the relevant connections for space heating, domestic hot water storage, solar thermal plant and the bidirectional connection to the district heating network. Inside this block, the same *Switch*-based decision is performed like described for the pipe and the junction components, if there is currently a consumption from or a feed into the network. By selecting the storage connection heights either to a flow from top to bottom or vice-versa, the bidirectional flow is implemented.

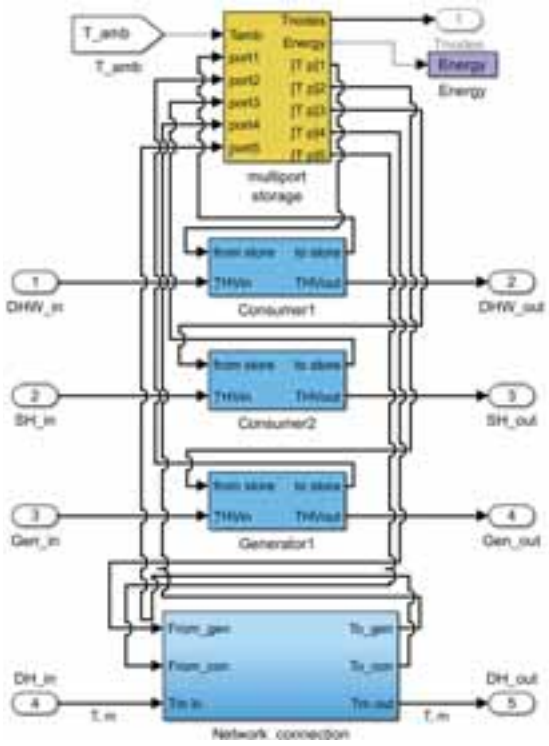

Fig. 8: Substation between modified district heating network model and CARNOT-based building model

4. Validation of the model

4.1 Description of the laboratory test

While the network junctions and the connections between district heating network and buildings can be solved by a purely logical approach, the pipe model includes physical properties, which need to be examined in detail. Due to the choice of a one-node model for the pipe, the question arises of how the pipe performs under a sudden temperature change e.g. caused by a reversion of the flow direction. To answer this question, a laboratory test was set up to validate the pipe model. The layout of the test rig is shown in Fig. 9. Main component of this test was a 2.12 m long copper pipe with an inner diameter of 20 mm and a wall thickness of 1 mm. The pipe was equipped with five thermocouples along the length and insulated with a 19 mm EPDM foam insulation. The parameters of the components are listed in Tab. 1. A computer-controlled thermostat maintained a constant inlet temperature at the pipe. A pump and a motor valve were used to set the volume flow in the circuit. To get an immediate temperature load on the pipe, the heated water was conducted through a bypass tube in the first step (green arrow), while cold water was flowing through the pipe (blue arrow). After starting the data logging, valve 2 and valve 1 were closed while valve 3 was opened and the 3-way-valve 4 set to connect the inlet with the pipe sample and to start the temperature load (red arrow). The temperatures of the inlet and outlet sensors as well as the five temperatures along the pipe and the ambient temperature were logged in a one-second interval. In addition, the volume flow was monitored with a magnetic flow meter (MID).

Tab. 1: Parameters of the laboratory test for validating the pipe model

Length of pipe in mm	2,120
Inner diameter of pipe in mm	20
Wall thickness of pipe in mm	1
Thickness of insulation in mm	19
Thermal conductivity of insulation in W/(mK)	0.04
Temperature sensor inlet / outlet	PT100 4-wire 1/10 DIN
Pipe temperature sensors	Thermocouple type T

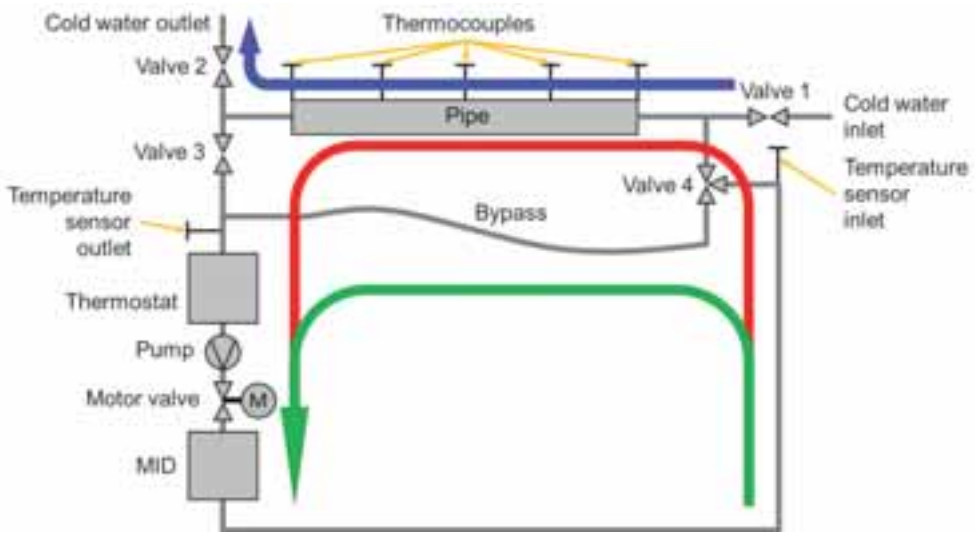

Fig. 9: Layout of the test rig for validating the pipe model

Several measurements were conducted to validate the model at different conditions. The conditions of the presented tests are listed in Tab. 2. In the test *Step Response*, the step response of the pipe was tested at a volume flow of 150 l/h and a sudden inlet temperature change from 22 °C to 47 °C. In the test *Heat Loss*, the pipe was heated up to 70 °C and then the volume flow set to zero to observe the cooling behavior.

Tab. 2: Conditions of the laboratory test for validating the pipe model

Test name	Initial temperature in °C	Inlet temperature in °C	Volume flow in l/h
Step Response	22	47	150
Heat Loss	71	-	0

4.2 Validation of the pipe model

The most interesting results of the first test are the time delay of the temperature change along the pipe length and the shape of the temperature curve after the heating process starts. Fig. 10 shows the comparison of the temperature sensors of the measurement compared with the outlet temperature of the simulation model for the scenario of a sudden inlet temperature increase from 22 to 47 °C. “Tin_measured” describes the measured temperature step at the inlet. “Tout_measured” is the measured value of the temperature at the outlet of the pipe. For the CARNOT pipe, two models were simulated. The first one has only one node (Tout_CARNOT_1). This leads to an instant but slow temperature increase at the outlet. The second model with 100 nodes (Tout_CARNOT_100) describes the time delay very well but shows a too steep temperature increase, when the hot fluid reaches the outlet-node. No node number could be found, where the time delay and the slope of the curve fitted the measured data. For the newly set up model, two variants were simulated, where the first one (Tout_w_I) includes the fractional capacity of the insulation and the second one (Tout_wo_I) only includes the fluid and pipe wall capacity. Due to the fast heating process, the model without insulation capacity fits the measured curve better than the other one. But still, the pipe including the insulation capacity is very close to the measured value and has a more realistic behavior than the CARNOT pipe model in this comparison. The fractional capacity of the insulation was also added to the capacity of the pipe wall in the CARNOT models for better comparison.

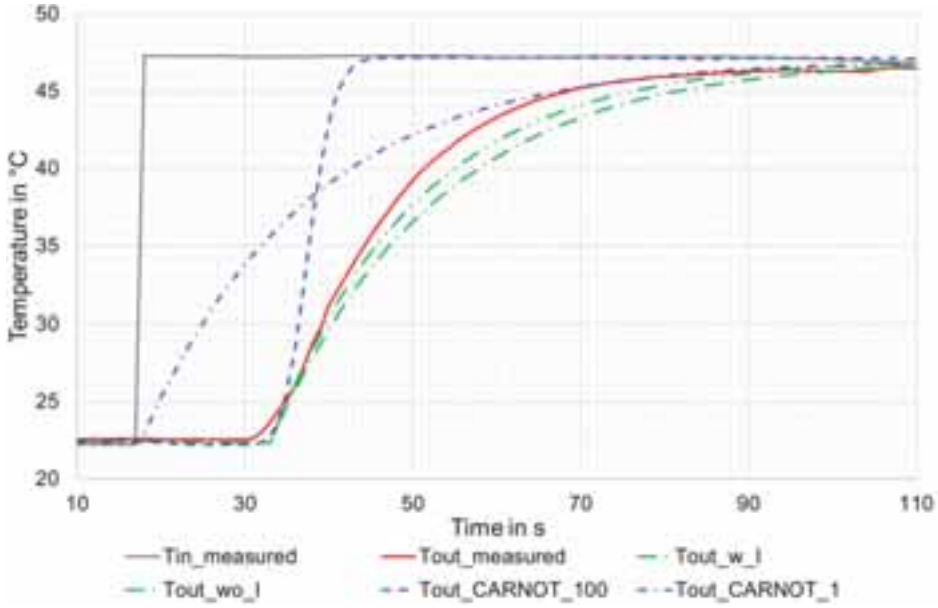

Fig. 10: Temperature curves over time for the step response from 22 to 47 °C

Another important information when discussing the control strategy of the district heating network is the stored energy in the pipes. Fig. 11 shows this energy for the measured pipe, the CARNOT pipe (1 node and 100 nodes) and the new model with insulation capacity. As expected from the faster temperature increase at the outlet, the CARNOT pipe model stores less energy than the measured pipe. The new model calculates slightly higher energies within the period of observation due to the overestimated contribution of the insulation but differs by only 6.3 % in this case.

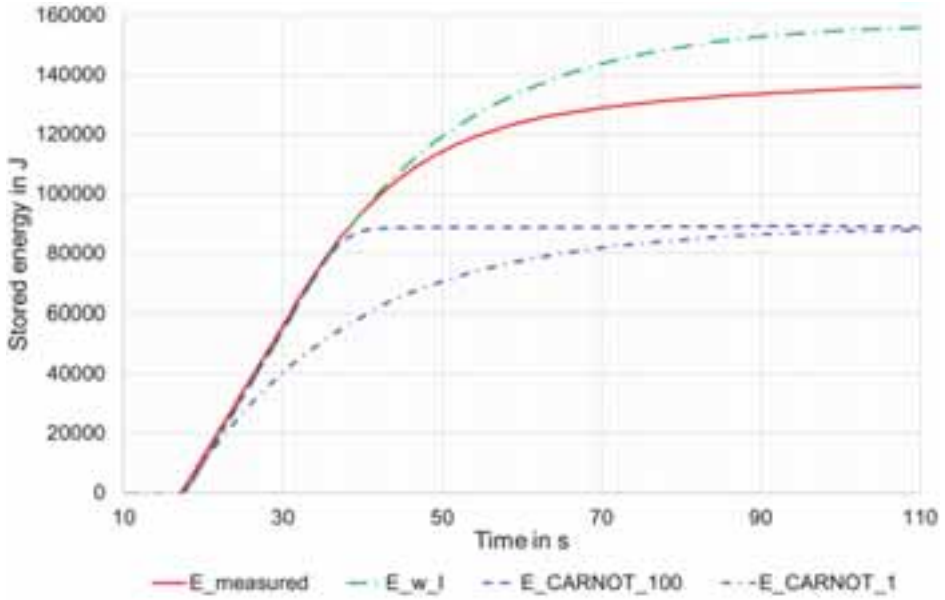

Fig. 11: Stored energy over time for the step response from 22 to 47 °C

The third important point is the calculation of the heat losses in the district heating network. The pipe in the laboratory test was heated up to a constant temperature of 71 °C and then cooled down by the losses through the insulation for approximately 50 minutes. As convection losses in the fluid at the ends of the pipe cannot be completely excluded, only the temperature sensor in the center of the pipe is evaluated. It could be seen that both models are within acceptable tolerance and the temperature loss is 0.8 % too low and 1.7 % too high for the new model and the CARNOT model respectively.

4.3 Validation of the system model

The validation of the complete network model is presented by two exemplary weeks (week 16 and week 20) in 2017. These two weeks represent both, higher and lower ambient temperatures as well as high and average irradiation in the collector plane (Tab. 3). This ensures that sufficient accuracy of the models is achieved under different conditions. The individual components, the overall system and the real control devices were validated in the model. The same collectors and solar stations are installed in all buildings. A distinction is only made in the length of the collector array piping, the array connection and the orientation of the collectors. In addition, the downstream components, e.g. buffer storage, and the connections to the existing local heating or hot water system in the basements are of different designs.

Tab. 3: Average ambient temperature and irradiation on the collector plane for two weeks in 2017

Week	Average ambient temperature in °C	Irradiation on collector plane in kWh/m²
16	4.6	23.9
20	16.1	46.1

In order to be able to make a reliable statement about all different concepts of solar thermal systems, the three different types of installations "local hot water use", "network supply" and "combined solution" are presented using the buildings HB57, HB36 and SB21. Of particular importance are the deviations of solar yields between measurement and simulation over a week, which are defined as follows:

$$Deviation\ in\ \% = \frac{E_{solar,simulated} - E_{solar,measured}}{E_{solar,measured}} \quad \text{(eq. 8)}$$

The measured network temperatures, cold water temperatures and domestic hot water consumption as well as the irradiation in the collector plane and the ambient temperature were set as boundary conditions for the simulations. Tab. 4 shows the results of the metrological investigation and the simulation. It can be seen that the deviations are below 4 % for all considered configurations. Therefore, it can be stated that the accuracy of the model is sufficient for further simulation studies and optimization of the existing network.

Tab. 4: Measured and simulated solar yields for the three plant concepts

	Measurement in kWh	Simulation in kWh	Deviation in %
Solar yield week 16 HB36	253	251	-0.8
Solar yield week 20 HB36	1,033	1,041	0.8
Solar yield week 16 HB57	671	693	3.3
Solar yield week 20 HB57	1,492	1,499	0.5
Solar yield week 16 SB21	386	381	-1.3
Solar yield week 20 SB21	591	611	3.4

5. Simulation study on decentralized feed-in

As the goal of this work is to define a Simulink-based model for the investigation of RS feed-in concepts, a simulation-based comparison based on the operational network is discussed. While in this network, only a RR feed-in could be implemented and the collector area is limited, the simulation model allows additional investigations of the influence of a RS feed-in and larger solar thermal plants. The following designs are compared based on a one-year simulation of the complete network:

- Type 1: Model of the real network and RR feed-in based on CARNOT toolbox
- Type 2: Model of the real network and RR feed-in based on new components
- Type 3: Model of the real network and RS feed-in based on new components
- Type 4: Model with optimized network operation and RR feed-in based on new components
- Type 5: Model with optimized network operation and RS feed-in based on new components
- Type 6: Model with larger collector arrays, optimized network operation and RR feed-in based on new components

- Type 7: Model with larger collector arrays, optimized network operation and RS feed-in based on new components

Type 1 represents the existing, operational network, using only CARNOT components. The operation strategy and the solar thermal plants are designed like in reality. Type 2 is the same but using the modified components for the network. Type 3 is based on type 2 but includes the change from a RR feed-in to a RS feed-in for the plants with combined utilization, while the pure feed-in plant (HB36) keeps the RR concept. Nevertheless, the network operation and plant dimensions are still the same. In type 4, the operation of the district heating system is improved in a way that reduced flow rates are set at the substations to keep the return temperature at an average value of 60 °C during the year, while using a 5 K lower supply temperature during summer. In the existing network, this is not yet implemented but would be possible. Type 4 uses the same RR strategy like type 1 and type 2 but includes a lower feed-in temperature threshold to adapt to the lowered return temperature. Type 5 is again the same as type 4 but with RS feed-in from type 3. Types 6 and 7 contain larger collector arrays as compared to types 4 and 5. The flat-plate-collector areas on the buildings HB57 and SB21 are tripled, as this would still be a feasible design in the existing network. Due to limited roof space, HB36 is kept at 71 m². SB12 has a large available roof area. For these types, the removal of the vacuum tube collectors and a flat plate collector area of 142 m² on the east and 142 m² on the west roof is discussed. This results in a total collector area of the network of 781 m² compared to 305 m² for the other types.

For the simulation study, average climate data for Ingolstadt were used. The thermal loads in the district heating network were derived from measurements of the load profile at the substations in combination with yearly energy consumption data. For the space heat demand, simulations of the buildings were included in the CARNOT model. Tab. 5 shows the solar yields for the plants of all types and their contribution to the heat production of the complete network.

Tab. 5: Annual solar yields and solar fraction of decentralized plants of the simulated system types

Type	Annual solar yield HB57 in MWh	Annual solar yield HB36 in MWh	Annual solar yield SB12 in MWh	Annual solar yield SB21 in MWh	Fossil heat production in MWh	Solar fraction in %
1	42.5	16.9	31.8	26.6	4,289	2.67
2	42.5	16.6	31.1	25.9	4,299	2.63
3	42.5	16.6	31.6	26.2	4,294	2.65
4	42.5	21.2	31.6	26.4	4,261	2.78
5	42.5	21.2	32.4	27.8	4,254	2.83
6	81.2	19.1	57.8	60.1	4,189	4.95
7	79.9	18.8	62.4	70.2	4,165	5.26

Several conclusions can be drawn from the simulation results. Firstly, due to the modified pipe components and resulting variations in the temperatures of the network, there is a difference of the solar yield between the pure CARNOT model and the modified model of 1.6 %. This is considered as acceptable within the scope of this work. Secondly, a RS feed-in has no benefit over the less complex RR feed-in in case of small solar fractions. For the existing network, it increases the solar fraction from 2.63 % to 2.65 %, which cannot compensate for the higher investment costs. The same applies for the existing network with reduced supply temperatures and optimized flow rates. For larger plants, the benefit increases. Type 7 produces 231.3 MWh of solar heat compared to type 6 with 218.2 MWh, meaning an increase of 6.3 %. Thirdly, it can be seen that the pure feed-in concept in HB36 produces less solar heat, when larger plants are connected via RS instead of RR feed-in. This is due to the reduced volume flow passing by the building, when the decentralized plant in SB21 is in operation and supplies the north-west part of the district. Therefore, a combination of the different feed-in concepts is to be avoided. Fourthly, the optimized system operation slightly increases the yield of the plants with partial feed-in but distinctly increases the yield of the pure feed-in plant, which only depends on the return temperature of the network.

6. Conclusions and outlook

For the simulation of district heating networks with decentralized solar thermal plants, a new MATLAB/Simulink-based model was set up. While for the solar thermal plants and the buildings, the standard CARNOT library was used, the network pipes, junctions and substations were modified to allow reversed flow in the network, as is necessary for the simulation of RS feed-in. The pipe model was validated in a laboratory test and shows satisfying performance, which is, in terms of the dynamic behavior of the pipe, closer to reality than the CARNOT pipe. Solar thermal plant models with different hydraulic concepts where validated based on a real district heating network in Germany and also show adequate accuracy. Based on the validated plant and pipe models, a simulation-based comparison was done, showing the difference between RR and RS feed-in for different plant sizes and network operation modes. It can be seen that small plants work well with RR feed-in, which is a simple and reliable configuration for the retrofit of a district. If higher solar fractions are desired, it is beneficial to use RS feed-in to increase the plant performance. Based on the introduced model, further simulation studies will be done to derive recommendations for decentralized solar thermal plants in different districts and to show the possible improvement in performance by an intelligent control strategy for the interaction of the plants.

7. References

Hafner, B. et al., 1999. Carnot Blockset Version 1.0 - Conventional and renewable energy systems optimization blockset - User's guide. Solar-Institut Jülich, Fachhochschule Aachen.

Mies, M., Rehrmann, U., 2007. Abschlussbericht für das Projekt Cohnsches Viertel Hennigsdorf.

Paulus, C., Papillon, P., 2014. Substations for decentralized solar district heating: design, performance and energy cost. Energy Procedia 48, 1076 - 1085.

Schäfer, K. et al., 2014. Dezentrale Einspeisung von Solarthermie in Wärmenetze - technische Analyse von realisieren Anlagen. 24. Symposium Thermische Solarenergie, Kloster Banz, Bad Staffelstein, 7th - 9th May 2014.

FLEXYNETS – A new district heating network concept for higher renewable and waste heat share

Ilyes Ben Hassine, Xavier Jobard[1], Linn Laurberg Jensen [2]

[1] University of Applied Sciences Stuttgart (Germany)

[2] PlanEnergi, Aarhus (Denmark)

Abstract

The FLEXYNETS project on low-exergy district heating and cooling systems has been started in summer 2015 in the framework of the European H2020 program. The project aims to develop a new generation of intelligent district heating and cooling networks that reduce energy transportation losses by working at temperature levels lower than 40 °C. Reversible heat pumps and chillers are used at laboratory scale to exchange heat with the DHC network on the demand side. In this way, the same network can provide contemporary heating and cooling. FLEXYNETS solutions integrates effectively multiple generation sources (including high- and low-temperature solar thermal, biomass, cogeneration and waste heat) where they are available along the DHC network. Two network types are considered in simulation: the classic supply-return type and the single-pipe system. This paper describes possible operation strategies and some control aspects related to the second network type.

Keywords: district heating/cooling, low temperature, low exergy, solar thermal feed-in, waste heat

1. Introduction

Traditional District Heating and Cooling (DHC) networks distribute energy from a centralized generation plant to a number of remote customers. As such, actual DHC systems suffer from significant heat losses, highly unexplored integration potential of different available energy sources into the same DHC network and high installation costs. Lowering the network temperature and including multiple distributed sources could reduce these issues. However, a distributed energy generation approach would also introduce issues for heat marketability and management. Hence, a true change of paradigm is needed to move from the "monopolistic" structure (for generation, distribution and trading) implemented in today's DHC networks, to a structure where multiple actors can play the role of energy providers and where even the final consumers can economically profit from their waste heat rejected to the network.

Centralized/High-level control solutions integrating multiple energy generation sources and sinks within a DH network are today under evaluation in a number of research and demonstration projects (ehub 2016, EnEff:Stadt 2016). However further innovations as the use of very low temperatures within the network loop, exploitation of pipelines storage capacity and bi-directional communication among multiple energy sources and sinks require further research at simulation level.

FLEXYNETS aims to develop a new generation of district heating and cooling networks, which will combine (i) multiple energy sources at different temperature levels, (ii) systems capable of using that heat efficiently (such as Organic Rankine Cycle (ORC) based polygenerative systems, absorption cooling systems) (iii) a low-temperature (<40°C) DH, and (iv) devices able to exploit such low temperature energy in residential buildings, like reversible heat pumps (see fig.1).

doi:10.18086/swc.2017.06.02 Available at http://proceedings.ises.org

Fig. 1 The FLEXYNETS concept with several prosumers connected to the main loop

Depending on the substation needs, heat is supplied to or removed from the network

The Flexynets concepts considers the low temperature network as infrastructure for storage and heat exchange between geographically dispersed (renewable) prosumers with different sizes. The decentralization of heat and cooling sources as well as the linking of several small networks to independent large systems are topics of high interest. While supplying energy to consumer substations is common in today´s systems, the reverse flow from prosumers into the network remains one of the challenging tasks.

In this paper we briefly go through state-of-the-art concepts for feed-in substations. We comment some weaknesses related to the return-supply feed-in strategy. The Assumption is that in order to facilitate the energy exchange within the system and to increase the share of renewable and waste heat sources, one needs to adapt/optimize the network side. Targets of the adaptation should be high distribution efficiency, high effectiveness of feed-in, less auxiliary energy for better primary energy factors.

In this context we propose the FLEXYNETS concept as an option for new 'liberalized' DHC networks where prosumers can easily feed (excess-) heat and enhance the primary energy balance of the whole system. The discussion of the results at the end of the paper is related to district heating and will be extended to cooling networks in the future.

2. Heat feed-in into DH systems

The substation

In accordance to SDH (2012) 0 "distributed" or "decentralized" means that the feed-in plant is not closely located to another major heat generator like a biomass or fossil fuel fired plant. These substations generally make use of the network fluid content instead of providing own storage capacities. Their size is mostly small with regard to the whole district heat demand. Among the feed-in principles described in 0 (2012) and Bucar et al. (2005), two concepts have been realized in the past twenty years: the return-return (RR) and the return-supply (RS) concept as shown in fig. 2.

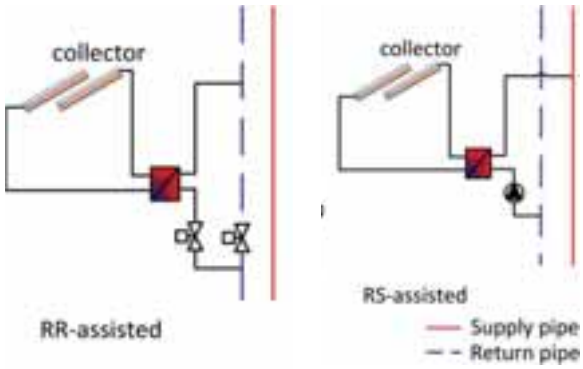

Fig. 2 The most common feed-in layouts

The solar collectors shown in fig. 2 are generally representative for every decentral heat source (waste heat incinerator, heat recovery etc.). The feed-in principles remain the same. In the RS case, the return temperature of the network remains low which is more advantageous/efficient for operating central CHP units. Among the nine European plants assessed in Schlegel (2014), seven are of RS type. In Hamburg Berne (Germany) a combined feed-in substation has been realized (Großmann, 2015) to work in winter and summer mode. In addition to the shortcomings of the RS concept that were discussed in Schlegel (2014), we want to highlight another aspect related to the control.

Due to the dynamic behavior of the network (consumers´ regulating valves, variable speed pumps), the control of RS substation becomes challenging. The pressure difference in two pipe networks changes by more than 30% within short fractions of time. The feed-in substation itself adds through head rise new dynamics to the whole system. The difficulty of regulating the flow under a fluctuating 'resistance' is demonstrated in fig. 3 (Gunnar 2014). The measurements show how the flow changes from no flow to maximum flow in the range of few percent of the pump speed.

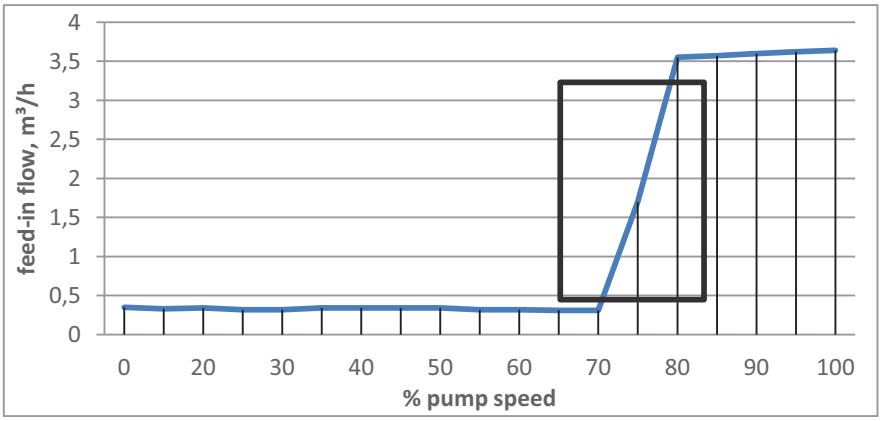

Fig. 3 Example of feed-in flow dependency on pump speed from a Swedish network

The problem is more relevant for small feed-in substations because they are generally equipped with (relatively) small feed-in pumps that are not able to cope with the network dynamics, at least not as able as high pressure/high flow pump stations which are common for large supply units. In substations without storages, supply interruptions due to too low or too high temperatures are common (Gunnar (2014), Eicker et al (2012)). Bucar (2005) reported about longer feed-in outages in Austrian networks due to too high pressure differences in the network.

This –among other reasons- may explain the decline of the reported solar gains in small size installations which is plotted in fig. 4.

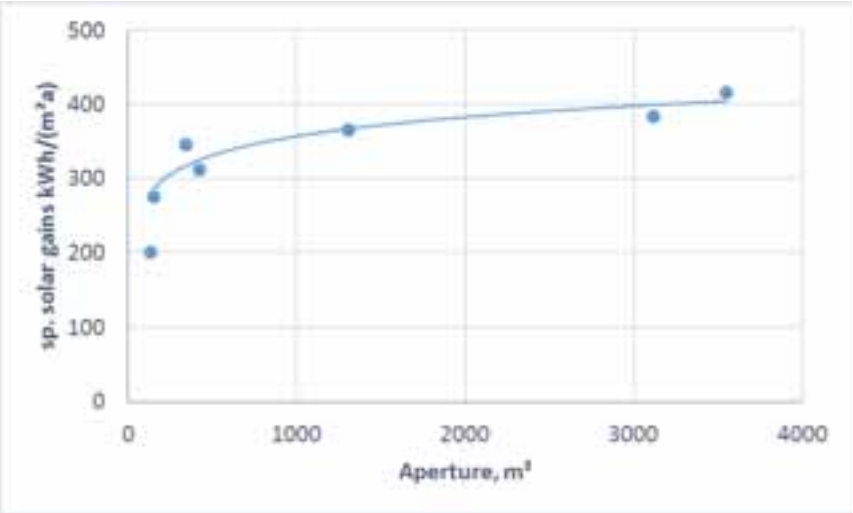

Fig. 4 Specific solar gains of seven European installations from Schlegel (2014)

The network

In conventional 2-pipe networks, the pump illustrated in fig. 2 needs to overcome the pressure difference between return and supply lines. This makes the feed pump power and rate depend on two factors: the governing network head and the substation location. Fig. 5 shows how much power is needed to supply approx. 200 kW of heat into a 6.3 km long DH network under different governing pressure differences. Fig 6 presents the pressure difference in a 13.5 km long network in the south of Germany. Halmdienst et al (2014) expect that substations which are closer to the main supplier need more power to provide the same heat amount to the network than those outside. However, we recognized in recent investigations within the FLEXYNETS project that the dimensions of the existing pipes as well as the flow direction (opposite or inline with main flow) are affecting.

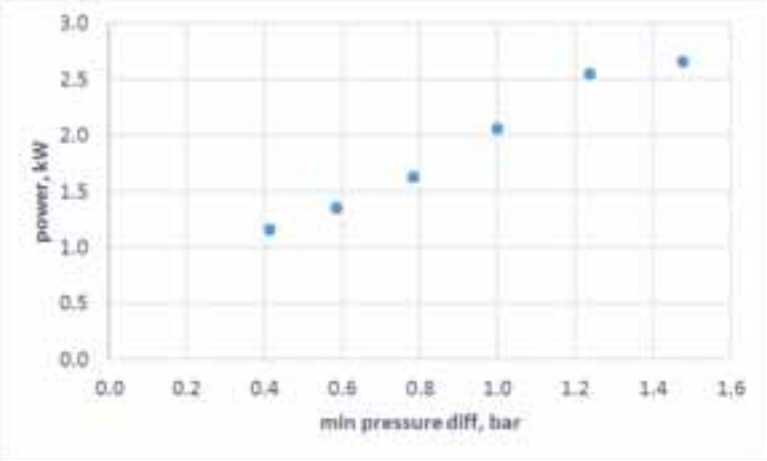

Fig. 5 Power requirements as function of lowest pressure difference

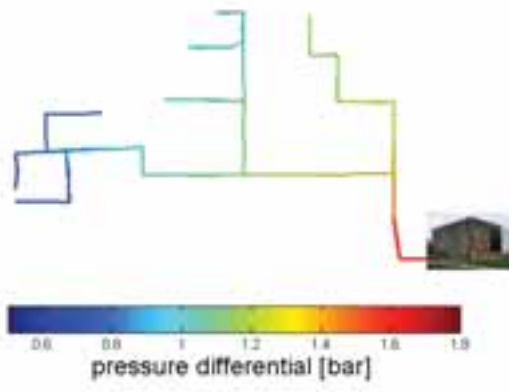

Fig. 6 Pressure profile in a tree-type network

3. The case study

With regard to the difficulties encountered in regulating feed-in substations, the following question arises: can the network be adapted/designed to facilitate (excess-) heat supply from decentralized prosumers with limited capacities? Keeping the auxiliary energy consumption low while assuring stability of supply is of course of high interest.

In the context of the FLEXYNETS project, two new network topologies were proposed as alternative to an existing 2-pipe system in the city of Aarhus in Denmark. The network contains -as part of the city DH system- more than 500 consumer substations and was aggregated to 23 nodes for the current study. The systems are simulated afterwards in TRNSYS and compared using some performance indicators.

The system aggregation

The map of the Aarhus south west area is shown in the left hand side of fig. 7. In order to aggregate the demands to 23 nodes, an affiliation function in the software program Termis is used. Termis is a hydraulic modeling tool that simulates the behavior of flow directions, pressure, and thermal conditions in a DH or Cooling network. The network from the geographic information system (GIS) tool and the demand points from the Heat Atlas is loaded in Termis as shape files. To affiliate the demand, the nodes are placed on different locations in the network chosen strategically for the affiliation of demand to be dependent on typology type. The nodes are placed manually by the best individual ability and evaluation in each case. The purpose of this process is to estimate the sum of the capacity of the collected demands in each of the chosen nodes for further analysis in TRNSYS.

In this way, the demands from the reference towns can be used in the analysis. The demands from Heat Atlas is an expression of actual demands for each building from these reference towns, in this case Aarhus. The Heat Atlas is developed by Aalborg University. It is designed to explore the possibility of development and application of a detailed mapping of the buildings' heating needs in Denmark. The Heat Atlas is developed for use in GIS software with the purpose to extract building data from the Building and Housing Register (BBR) and a number of heat consumption specifications that are developed by the Danish Building Research Institute (SBi). The Heat Atlas includes data such as construction year, building area and heat demand for each building.

The Danish reference towns are divided in areas according to the FLEXYNETS typologies, as seen in the figure. A GIS software is used as tool to establish the town or city boundary and the boundaries for the different typologies. For this purpose, municipality planning and the Heat Atlas is used. In Denmark, the data from the Heat Atlas, local planning and municipality planning is available for all towns and cities. Each reference town is divided into the different typologies based on the specific use category in the municipality planning.

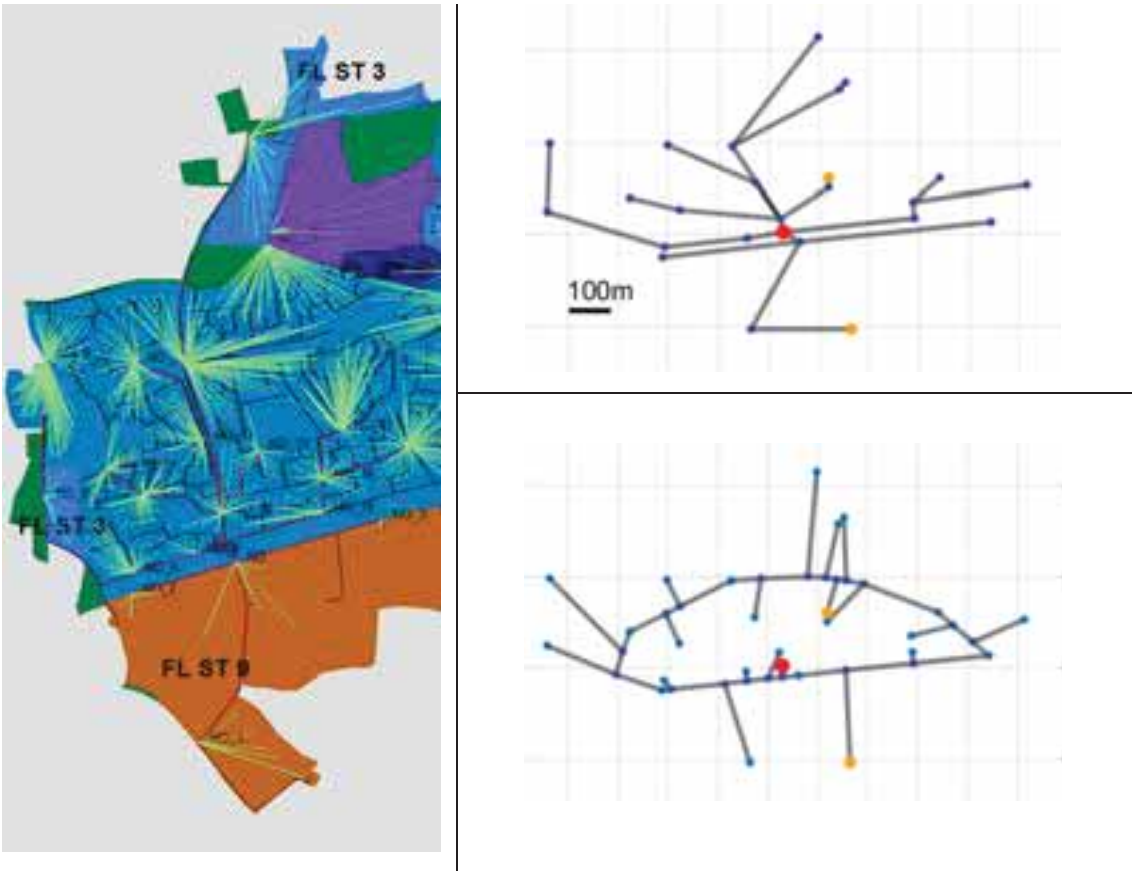

Fig. 7 Map of Aarhus SW (left), tree-type and loop-type network (right)

The network types

Additionally to the tree-type network of the south west of Aarhus (fig. 7), two additional models have been designed out of the loop-type system presented in the same figure. As can be seen in fig 8, the first model incorporates two loops (each for low and higher temperature) that are connected through a stratified storage tank. The system is called low-pressure type due to the low head difference between supply and return line. Storage inlets and outlets generally cause minor head losses in the range of <10 mbar. Feed-in substations inject hot water into the supply loop. In case of low demand, the injected heat can be stored in the central tank. The energy balance of the whole system is performed in the storage level, where heat can be removed or added via heat exchangers.

The operation of the feed-in pump is favorized by the fact, that other consumer substations circulate water in the same direction of flow. However, in real installations two aspects should be taken into account: a) the formation of small loops between two neighboring substations (one consumer and one producer) which may result in too low supply temperatures. b) the overflow of the feed-in pump due to high pressure rise in the consumer substations.

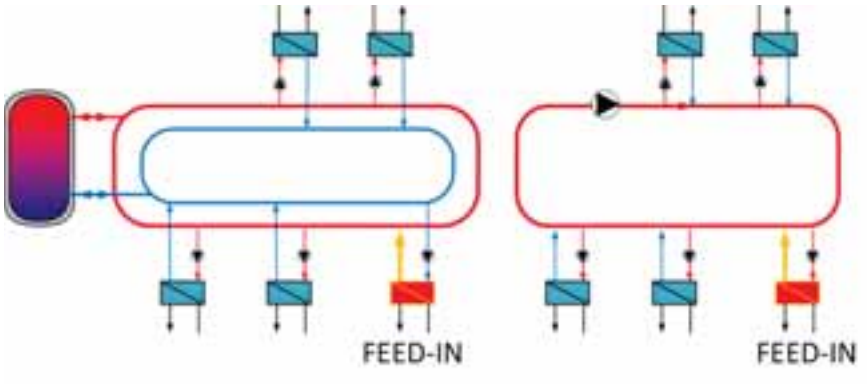

Fig. 8 Simple layouts of the loop-type networks

The second loop-type network contains a single circuit for both removal and feed of heat. At least one substation is needed to balance the network. The main loop pump recirculates water at high flow rates to e.g. compensate for the water cooling after each substation (in case of heat consumers). The feed-in concept is similar to the RR layout of fig. 2 where a part of the circulating volume is heated up and reinjected in the loop. Large differences between the inlet temperatures of the different substations are expected. If the consumers are equipped with heat pumps, their coefficients of performance (COP) will vary. The pump power requirements of the individual substations are assumed to be very low: the major head losses are due to the heat exchanger and service pipe friction.

General design and operational aspects

The modification from a conventional 2-pipe network to the proposed systems has some advantages for the operation of feed-in substations. Not only the power consumption of the decentral pump decreases, but also the flow control is expected to be more stable. This can be deduced from the open-loop behavior of the system. In fig. 9 the heat demand of the considered network is varied from full to partial by keeping both main and feed-in pumps at constant speed. If only 1/3 of the consumers are supplied, the decentral feed-in flow drops by 24% in the tree network compared to 11% in the low-pressure one. The same tendency is seen in the case of small variations. The single loop system exhibits the most robust behavior towards these variations. The substations are almost ‘decoupled’ from each other.

Fig. 9 Feed flow variation depending on demand decline

We also calculated the power needed to feed 32kW of heat into the three network types at different nodes. Head losses associated with mountings like heat meters and gate valves or pipe connections are not considered in this paper. The power requirements in the 2-pipe network are higher by a factor of five to ten than in the other two loop-based systems (see fig. 10). Also in the 2-pipe case, no clear dependency between the pumping power and the distance to the main supply node can be recognized. The power requirements logically depend on the distance to the consumers to be served, which can be variable depending on the current flow/demand situation. In the loop-based systems, the power consumption depends on the distance to the main loop. In other words, pipe friction in the service pipes presents the major head loss independent on the flow situation.

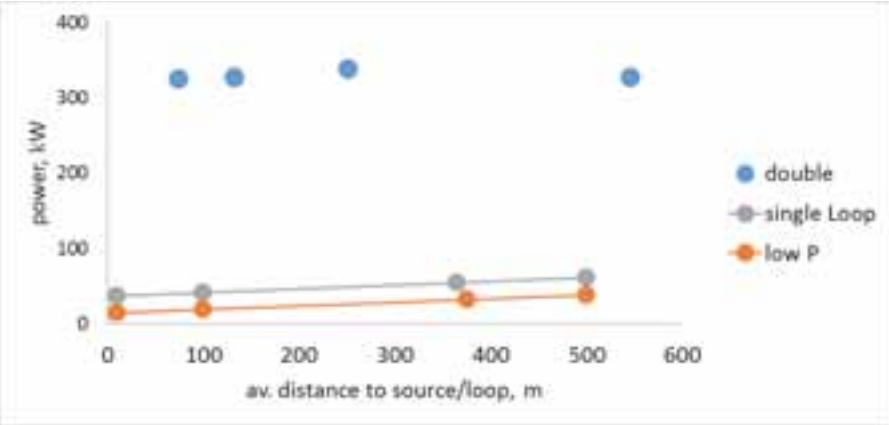

Fig. 10 Power requirements of feed-in pump at different nodes

The fluctuating (wavy) temperature profile in the case of single loop system made the control of the substations unstable. The heat pump model used was valid for a certain temperature range on the evaporator side. Many heat pumps would not be able to run adequately in case of too low temperatures. The study was therefore limited to the 2-pipe and low-pressure systems. The pipes were designed to a maximum velocity of 0.65m/s. The following table summarizes the obtained network sizes:

Table 1 Network dimensions

	2-pipe system	**Low-pressure system**
Length of pipes, m	6365.5	7313.5
Av. size of pipes	DN 150	DN 200
Total volume, m³	129.7	289.8

4. The simulation results

The system setup

The systems simulated in TRNSYS are the district heating networks of fig. 7. They distribute heat at low temperature (in a range between 20 °C and 30 °C) to decentralized heat pumps, which have to fulfil the heat demand of the buildings in the given area. The yearly heat demand is approximately 20.7 GWh with a peak load of approximately 6.0 MW. The network manager NM of the considered system is responsible for balancing the energy flows and owns the central supply station of the district heating grid that consists of a 2.2 MW gas-fired reciprocating engine that produces combined heat and power (CHP) and a 2.3 MW auxiliary gas boiler (GB) assumed here to have a constant efficiency of 80%. The NM is placed at the red dot of fig. 7. A 330 m³ central storage tank is used to buffer the heat supply by the CHP unit- Figure 11 shows the layout of the central heat supply station. In the low-pressure case, the central storage CS is directly connected to the network without any pump. The flow direction on the network side can be from top to bottom or reversed depending on the amount of feed-in. The CHP unit covers the base load whereas the gas boiler GB is operated during peak phases.

Two decentral substations supply heat to the network, that is gained out of two solar collector fields of different sizes (200 and 2000m² aperture). The solar pump is run in high flow mode (30l/hm²) and the feed-in temperature is regulated to 5K above the network temperature. The corresponding integration nodes are colored in orange in fig. 7.

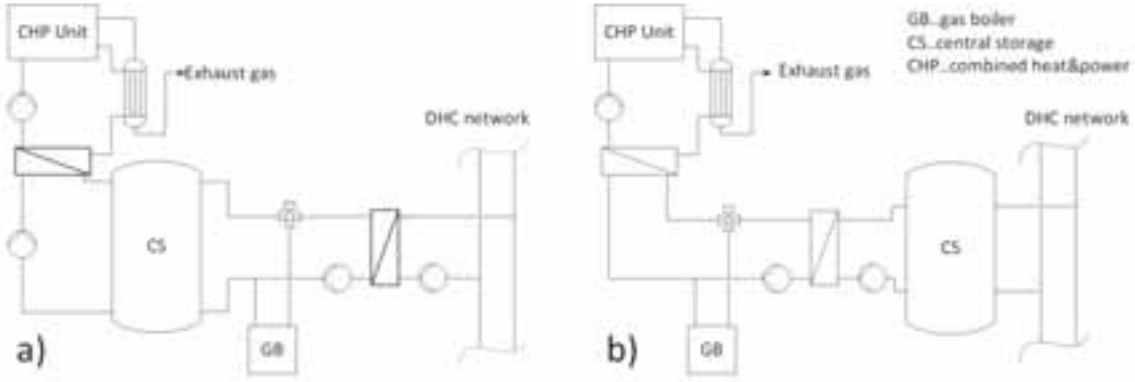

Fig. 11 Layout of main heat supply station in a) 2-pipe and b) low-pressure system

The water-to-water heat pumps use R407c as refrigerant and provide water to the buildings at 55-65°C. The performance of the heat pumps is affected by the temperature of the water supplied by the DH network. A higher network temperature increases the COP of the heat pumps, which turns into a lower power consumption of the compressors for a given heat demand of the buildings. As long as the power consumption is reduced, a higher amount of heat is extracted from the DH network.

Results

The two systems composed of the network, the main supply station, the consumer heat pumps and the solar feed-in substations were simulated over one year with a time step of 15 minutes. Due to the fact that the time constant of the hydraulic system is much lower than the simulation time step, continuous control of the feed-in pumps would be time intensive. We decided to run the pumps with an offset value that allow them to overcome the pressure difference at any time. The simulation study lead to the results of table 2.

The network pipe losses of the low-pressure system were higher than those obtained in the 2-pipe one. This can be explained by the larger size of pipes used as indicated in table 1. The main loop pipe with DN300 causes the major part of the losses. The average network temperature is slightly lower, which is reflected in the average COP of the heat pumps. The CHP unit produces more electric energy and enhances the primary energy balance of the system (lower PER). The solar gains of both small (200 m²) and large (2000m²) collector fields are comparable in the low pressure network. In the pressurized case, the larger installation feeds less heat than the smaller one. Further investigations are needed to find out if the feed-in flow is at nominal level in the 2000 m² installation.

Table 2 Simulation result summary

	2-pipe system	**Low-pressure system**
Users´ end energy, GWh	20.77	20.77
Net delivered energy, GWh	16.52	16.33
CHP thermal energy, GWh	13.74	13.42
CHP electric yield, GWh	13.48	13.22
Network heat losses, MWh	17.02	458.8
Average COP	4.88	4.67
Solar irrad., kWh/m²	1204	1204
Solar gains small, kWh/m²	446.16	462.56
Solar gains large, kWh/m²	427.61	460.28
Network pump consumption, MWh_{el}	71.98	24.45
Feed-in pump consumption, kWh_{el}	2519.8	288.1
Primary energy factor PER	0.638	0.648

When coming to the electric pump consumption, the low-pressure system is more advantageous and requires around one third of the energy needed in the other case. At feed-in substation level, the power requirements are much lower ($1/9^{th}$) which confirms the results presented in fig. 10. Here we need to repeat that only the heat exchanger and the pipe friction are considered to calculate the pressure drop. In reality, other substation mountings and pipe connection will lead to higher electric consumption.

5. Conclusion and outlook

The paper focuses on feed-in substations as measure to enhance the share of renewable and waste heat in DH networks. The weaknesses related to the flow stability in conventional 2-pipe systems are shortly discussed. In the context of the FLEXYNETS project, two alternative (loop type) topologies were suggested out of which the low-pressure one was considered in simulation.

The simulation results of the low-pressure system show some advantages related to the pump power demand. Considering the open loop response, the low-pressure system is expected to operate with higher stability and to reach higher feed-in rates over the whole year. This can be assessed by testing the dynamic flow behavior under real conditions and with discrete controllers. The Energy Exchange lab established by the project partner EURAC in Italy will allow to perform this kind of investigations. The lab recreates on a small scale the various stages involved during the operation of district heating and cooling systems, from heat generation and distribution to consumption by end customers. This enables it to investigate the best network management solutions as well as the supply of heat from several sources. The flexible lab infrastructure allows various configurations as well as hardware and control software to be tested.

Higher heat losses were calculated in the low-pressure system and were explained by the larger pipe size. It is planned to redesign the main loop taking the head losses (and not the flow velocity) into account and to check if the system can be optimized in both investment and operational costs.

6. References

SDH, 2012. Solar district heating guidelines, collection of fact sheets, WP3-D3.1 & D3.2, IEE

Bucar G. Gerhard Bucar; Karin Schweyer; Christian Fink; Richard Riva; Michael Neuhäuser, 2005: Dezentrale erneuerbare Energie für bestehende Fernwärmenetze. Berichte aus Energie- und Umweltforschung. Grazer Energieagentur

Frank Schlegel, 2014. Technisch-ökonomische Analyse und Bewertung von Anlagen zur dezentralen Einspeisung von Solarwärme in Fernwärmenetze. Masterarbeit am Institut für Energiewirtschaft und rationelle Energieanwendung, Stuttgart

Bastian Großmann, 2015. Erneuerbare Energien für das Wärmenetz: Projekte zur Einspeisung von dezentraler Energie. HanseWerk Natur GmbH

Gunnar Lennermo, 2014. Decentralised heat supply in District Heating Systems. DHC conference 2014, Stockholm

Ursula Eicker, Dirk Pietruschka, Ilyes Ben Hassine, Ruben Pesch, 2015. Simulationsbasierte Optimierung energieeffizienter Wärmenetze mit Umsetzung in EnEff:Stadt Ludwigsburg. Abschlußbericht

Christian Halmdienst, Klaus Lichtenegger, Daniel Reiterer, David Wöss, 2014. Bidirektionale Einbindung von Gebäuden mit Wärmeerzeugern in Wärmenetze Ergebnisbericht. AEE Arbeitsgemeinschaft Erneuerbare Energie NÖ-Wien

This project has received funding from the European Union's Horizon 2020 research and innovation programme under grant agreement No. 649820.

Solar district heating in Europe: supplying renewable zero-emission heat

Magdalena Berberich, Dirk Mangold

Solites, Steinbeis Research Institute for Solar and Sustainable Thermal Energy Systems, Stuttgart (Germany)

Abstract

District heating is one major approach to increase the overall energy efficiency in urban areas and an important platform to increase the share of renewable energies in the heat supply. Solar thermal energy is emission-free, available everywhere and offers stable operating costs for decades. Together, they can play an important role in the energy transition of the heating sector in Europe and beyond.

The integration of solar thermal systems into district heating offers different technical solutions, whereof some are applied since decades, some others, like decentral direct feed-in, are in evaluation. Generally, solar thermal systems are sensitive to the levels of the supply and return temperature and the detailed system integration, here especially regarding the hydraulics and the control strategy.

In the case that the solar thermal system is applied to combined heat and power productions, the overall system can be designed to the best economics if the electricity market, the dynamics in the heat consumption and the solar thermal production etc. are considered. The integration of a large heat storage volume might be helpful to separate production and supply powers and therefore can lead to a system with lowest heat cost, although the investment cost can be quite high. At least such complex systems ask for dynamic system simulation during the design phase to ensure best economics and to enable a risk analysis for varying prerequisites.

Keywords: Solar district heating, large-scale solar thermal system, smart cities

1. Introduction

Solar district heating (SDH) plants are a large-scale solar thermal technology supplying renewable, zero-emission heat from large collector fields via district heating networks to residential and industrial areas. Combined with large seasonal heat storages, the solar thermal plant can contribute to more than 50 % of the yearly heat demand even in high latitudes. The main market for SDH consists of plants with a solar fraction of up to 20 % of the yearly heat demand, including the application of a short-term heat storage or even without any heat storage.

New solar district heating projects show an interesting variety of technical concepts and operator models. This underlines also the high potential of district heating and cooling with renewable energy sources as flexible technical and organizational solution for the energy transition at local level.

2. Basic systems for solar thermal integration

A solar thermal plant can be connected to the district heating system by means of central feed-in or decentralized as shown in Figure 1. Central feed-in means the solar heat is integrated in the main heating central where the heat storage is located. The schematic in Figure 1 shows a seasonal heat storage; it depends on the size of the collector area and the performance of the additional heat productions in relation to the fluctuating heat demand if a smaller short-term heat storage can be sufficient or even neglected.

In the case of decentral feed-in of solar thermal heat, the solar collectors are placed at suitable locations and are connected directly to the district heating circuit. In several large solar thermal plants in Sweden, Austria and in a few first plants in Germany, a decentral feed-in of solar heat into district heating systems has been realized.

doi:10.18086/swc.2017.06.03 Available at http://proceedings.ises.org

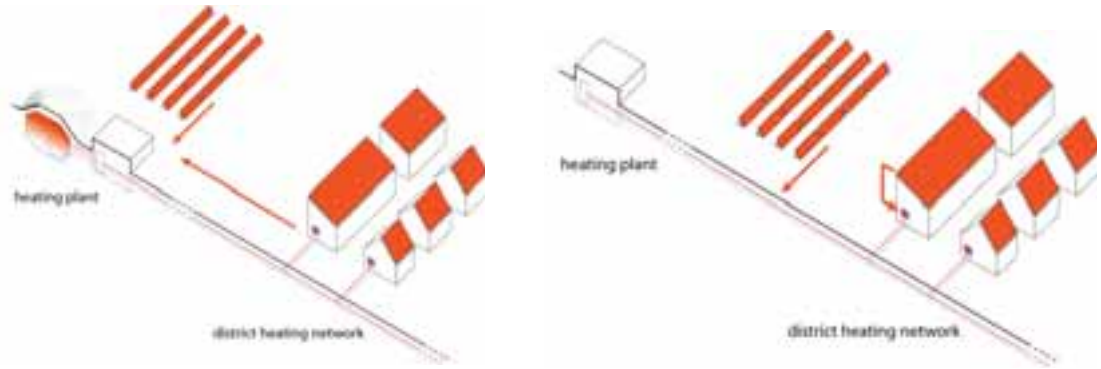

Figure 1: Schematic of central (left) and decentral (right) feed-in of solar thermal heat

For both, central and decentral feed-in of solar thermal heat in a district heating net, the solar thermal plant can be operated to produce the supply temperature or to preheat the fluid in the return flow. Figure 2 shows a basic schematic of a solar thermal plant for district heating. Usually it is applied for a solar thermal integration in the central heating plant. The broken grey line shows the system boundary for the solar system. To separate the solar circuit and the net circuit hydraulically a heat exchanger is applied. Often a heat storage is integrated into the system to store the heat from the solar collectors before it is transported to the additional heater and then delivered with the supply temperature to the district heating net.

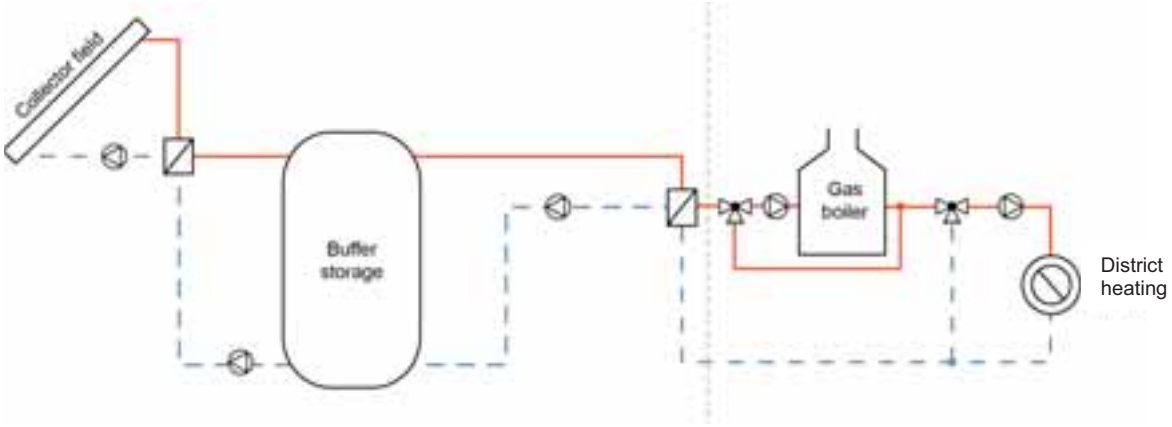

Figure 2: Schematic of a solar thermal plant for solar district heating

In case of delivering the supply temperature for the district heating net, the solar collectors only can produce heat if the solar irradiation is high enough.

In the case of preheating the return flow, the solar collectors heat up the return flow with a predefined temperature difference. For supplying the heat to the district heating net the fluid is heated up to the supply temperature by an additional heater (e.g. a gas boiler as shown in Figure 2). The variation of the solar irradiation can be balanced by a volume-flow control of the pumps in the solar circuit to keep the temperature of the preheated flow from the collector field to the buffer storage within the predesigned range.

The sizing of the buffer storage depends on several parameters like the intended solar fraction, the operation characteristics of the collector field and the dynamics of the heat demand in the district heating net and in the unload circuit of the buffer storage etc. The larger the intended solar fraction and the higher the complexity of the hydraulic system concept are, the more a dynamic simulation of the overall system is recommended.

3. Solar collector area

Within the last 30 years the technology for realizing large collector areas was developed, first by pilot plants that were supported by R+D funding. Within the last 10 years the technology is on its way to a state-of-the-art heating technology for utilities, energy companies, cooperatives etc. The developments differed due to different boundary conditions in different European countries. All developments comprise specialized collectors for district heating application. They cover up to about 12 m² of collector area per collector. Their internal hydraulic scheme is optimized to facilitate the realization of long collector rows by a simple connection of the collectors and to run these rows with low flow. This saves installation costs as well as electricity consumption of the solar circuit pumps. The following figures show different mounting systems of solar collector areas for district heating systems:

1. Ground mounted (Figures 3 and 4)
2. Roof integrated (Figure 5)
3. On roof (Figure 6)

Figure 3: Vacuum tube collectors in Büsingen, Germany

Figure 4: High-temperature flat plate collectors in Dronninglund, Denmark

Figure 5: Roof integrated solar thermal collectors on "solar@home"-building in Crailsheim, Germany

Figure 6: Solar collectors elevated on flat roof in Neckarsulm, Germany

Without regarding the cost for the ground, to mount the collectors on simple subconstructions directly on the ground offers the possibility to achieve the lowest cost for the realization of a solar collector area. The availability of ground is restricted especially in urban areas. Thus it might be also applicable to integrate the collectors in a roof. Figure 5 shows a so called "solar roof" that was realized within an energetic retrofitting of an old army building. The "solar roof" replaces the roof tiles and integrates roof windows, drip moulding, snow guard etc. Another possibility is to mount a collector field on a flat roof as shown in Figure 6. In this case, to achieve low cost for the subconstruction can be a challenge due to the statical requirements to carry especially the wind loads.

The market offers two main constructions of collectors, flat plate collectors and vacuum tube collectors (see Figure

3 and Figure 4). The specific products of the collector producing companies vary in performance and construction. To find the best suitable collector for a specific project it is recommended to invite offers from the solar companies and to decide according to the specific heat price. The solar heat price is calculated from the overall costs of the solar thermal plant in relation to the usable solar heat. To compare different offers, this usable solar heat should be calculated for all offers with the same simulation program, using the characteristic figures for every offered collector type according to test certificates like “Solar Keymark”, that is valid all over Europe (ESTIF, 2017).

4. System design

For a favorable performance of the solar thermal system, the overall system design is important. First of all the location of the solar thermal plant decides about the amount of solar irradiation that the collectors receive. The solar thermal plant is able to heat its inlet temperature only if the irradiation is high enough for that. The following Figure 7 shows the differences between the global irradiation of two cities in Germany over ten years, whereas Würzburg is a location with very good solar irradiation conditions and Hamburg is a location with quite low solar irradiation. The solar irradiation in the years 2007 to 2016 fluctuates with +4 to -6 % of the average in the ten years for Würzburg (broken line). For Hamburg, the variation comprises the range of +7 to -5 % of the average level. There is a significant difference in the global solar irradiation of the two locations, which is very variable over the ten years.

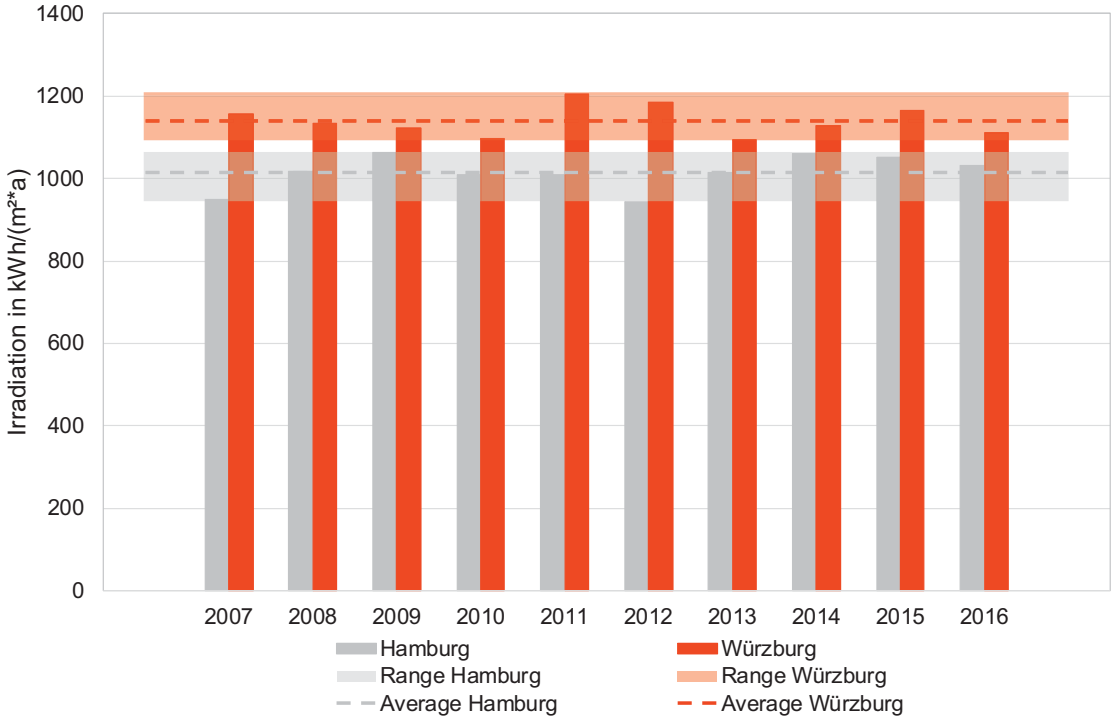

Figure 7: Yearly global solar irradiation in the years 2007 to 2016 for Würzburg and Hamburg (Deutscher Wetterdienst, 2017) on horizontal plane

Therefore, it is recommended to dimension a solar thermal plant using climate data of the location of the plant over a longer period, e.g. 10 years. By varying the solar irradiation in a sensitivity analysis within a system simulation program, its effect on the energy gain of the solar system can be analysed and valuated. If necessary, the solar thermal plant can be dimensioned with a safety factor to reach the needed solar heat gain even in years with poor irradiation.

In addition to that, the solar heat gain depends on the operation temperatures. The higher the average operation temperature of the collectors is, the lower the efficiency of the collectors gets because of higher heat losses of every collector. Therefore, the return temperature to the collector field and the needed supply temperature, which shall be produced by the collectors, are decisive for the achievable solar energy gain.

This correlation is shown in Figure 8 for high-temperature flat plate and vacuum tube collectors in the German market. The sample collector is a high-temperature flat plate collector with average specific values. The results are calculated with average climate data over 10 years (Meteotest, 2017) of the German city Frankfurt. The average net temperatures in the diagram are the yearly average for the arithmetic value of the supply and return temperatures of the regarded collector in every hour of the year.

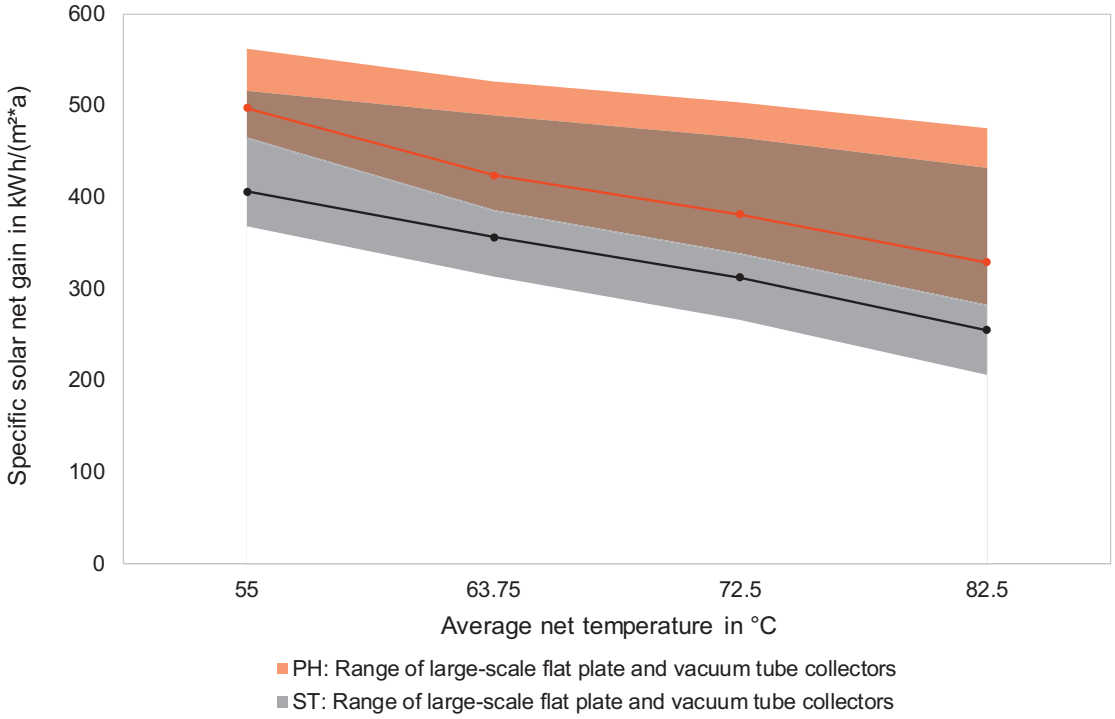

Figure 8: Usable solar heat of large-scale collectors in the German market with two different control strategies for the delivered temperature of the solar thermal plant: ST = heating up to the supply temperature, PH = preheating. The lines represent a sample collector (m²: brutto collector area)

In the preheating mode (PH, Figure 8), the solar thermal plant delivers heat at a lower temperature level than the supply temperature of the district heating net. Therefore, the solar thermal plant can produce heat even if the solar irradiation is low. The solar heat production in this mode mainly depends on the return temperature of the district heating net that should be heated by the solar thermal plant. This is visible by the strong reduction of the solar heat gain between the cases with 55 °C and 63.75 °C average temperature. The return temperature increases between these two cases from 40 to 50 °C in a yearly average.

A first idea of the performance of one single collector gives the Solar Keymark certificate (ESTIF, 2017). Each collector is tested and certified under standardized conditions with a constant average temperature in the collector. Neither the influence of the system integration nor the realistic supply and return temperatures are considered in the tests. In the certificate the performance indicators and yearly heat productions are declared for the climate data of four different locations in Europe.

As mentioned above, the solar irradiation influences the solar heat production of the collector field to a strong extend. This is shown in Figure 9 for the sample collector and with the application of the formerly mentioned climate data from Würzburg and Hamburg (see Figure 7).

The calculations of the solar heat production, whose results are shown in Figure 9, are based on a solar thermal system with a decentral feed-in and without a heat storage. This system is operated to deliver always the supply temperature of the district heating net. The average net temperature is 63.75 °C, in summer the supply temperature amounts to 75 °C and the return temperature to 55 °C. The results show the direct dependency of the solar heat gain on the solar irradiation and the strong variation from the average in single years. The variation around the 10-years-average lies in a range of +10 to -15 % for Würzburg and +20 to -14 % for Hamburg.

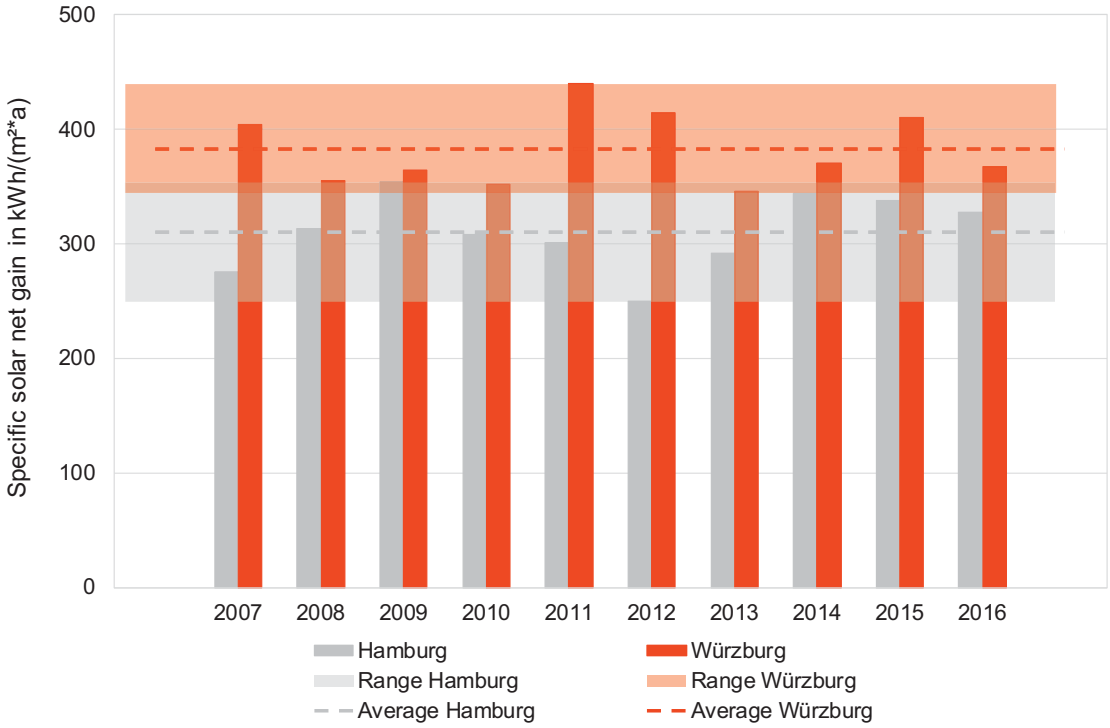

Figure 9: Calculated specific solar heat gain per m² brutto collector area of a sample collector with climatic data for the years 2007 to 2016 for the cities of Würzburg and Hamburg. The solar thermal plant is operated to always reach the supply temperature in a district heating network with 63.75 °C average temperature.

Such variations in the solar heat gain need to be considered when dimensioning a solar thermal plant. That is why the careful calculation of the solar heat gain with all available data and, in addition, based on realistic assumptions is essential for the feasibility of solar district heating systems. Compared to conventional heat producers, dynamic system behavior and the variations of the solar irradiation, the mass flow and the temperatures of the district heating net need to be considered in detail.

If a solar thermal plant is dimensioned to deliver the entire heat demand of the district heating net during the summer time, in most cases a short-term heat storage is necessary to store the heat from day to night and for the case of some cloudy days. In Europe the heat demand during summer usually is defined by tap water heating and the heat demand of industrial processes. The solar fraction of these solar thermal systems depends on the seasonal distribution of the yearly heat demand and is usually between 10 to 15 %. The higher the solar fraction, the more solar heat needs to be stored, not only for some days but for weeks. In case of high solar fractions of solar heat in the region of more than 40 % of the yearly heat demand, a seasonal heat storage is necessary, because the heat from summer has to be used in winter. Due to the longer storage time of the solar heat, the heat losses increase and the specific net solar heat gain of the collectors decreases. Figure 10 gives an example for the interrelations of the main parameters for such systems.

Therefore, it is assumed that the collector field comprises high temperature flat plate collectors of the sample type (see Figure 8), located in the city of Frankfurt in Germany. The collector field feeds in decentrally into a district heating net with a supply temperature of 78 °C in a yearly average and a yearly heat demand of 4 GWh/a. To increase the solar fraction of the yearly heat demand of the district heating net (see red line in Figure 10), the collector area has to be increased (see x-axis in Figure 10). The higher the solar fraction gets, the larger the heat storage volume has to be. The dashed grey line shows the specific storage volume in m³ water, related to the brutto collector area, that is necessary to reach the intended solar fraction. By mathematical variation, the specific storage volume was fitted to the respective collector area in a way that the storage volume is used completely and stagnation in the collector field is just avoided. For a solar collector area of 10,000 m² a solar fraction of 70 % of the yearly heat demand of the district heating net can be reached with a specific storage volume of 2.3 m³/(m² brutto collector area). In Figure 10, this specific storage volume is set to 100 % (see y-axis). The black broken

line in Figure 10 gives the specific solar net gain of the entire solar thermal system (see Figure 2). The solar net gain is the usable solar thermal energy that is fed into the district heating net. Heat losses by the storage etc. are subtracted already. The maximum value of 313 kWh/(m² a), equals 100 %, is quite low and caused by the overall system layout that asks for a feed-in of the solar net heat gain always on the supply temperature of the district heating net of 78 °C in a yearly average. This specific solar net heat gain declines with rising solar fraction due to rising heat losses of the necessary storage and rising average operation temperatures in the collector field.

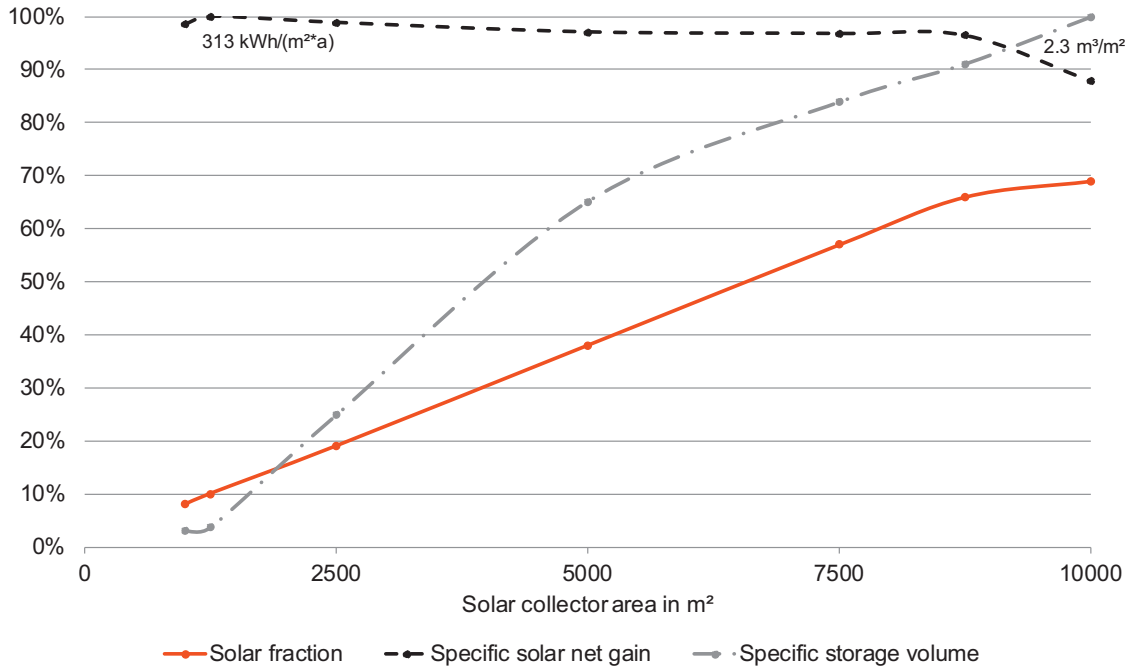

Figure 10: Correlation of solar collector area, specific heat storage volume, solar fraction of the yearly heat demand and solar heat gain for a solar thermal plant that feed in decentrally in a district heating net and always delivers the supply temperature of 78 °C in a yearly average (sample collector and weather data of the German city Frankfurt (see Figure 8))

For a real plant, possible next steps in the overall system design would be to change the system integration of the solar thermal system to a preheating mode (see Figure 8) or to integrate a heat pump into the solar system to unload the heat storage to lower temperatures. Both possibilities allow to reduce the operation temperatures of the solar collector field to reach higher specific solar net gains per year.

The results in the diagrams of chapter 4 are calculated with the Excel-calculation program SCFW ("ScenoCalc Fernwärme", in German: "ScenoCalc for solar district heating systems") which is free of charge and can be used for first assessments of SDH systems (Solites, 2017).

5. Market development in Europe

The first solar thermal plants that delivered heat to district heating nets were realized in Europe in the beginning 1980s driven by national research and demonstration programs as a reaction on the worldwide oil crises in the 1970s. Since then, the technical developments in different fields like the technologies for solar thermal collectors that are specialized for their application to district heating, the system integration of a solar collector field into district heating, the available heat stores, the possible operation modes of the solar thermal system etc. were immense. First large pilot plants were built in Sweden and Denmark, followed by a continuous development in Germany and other European countries like Austria etc.

In the last years, Denmark showed an impressive success story regarding solar district heating driven by national laws that increase the price for fossil gas if it is used only for heating. Since 2010 a capacity of more than 500 MW_{th} of solar thermal collectors has been newly installed. These solar thermal plants are connected to the heating central of a district heating net according or similar to the schematic system in Figure 2. The largest plant in operation

has a total collector area of 15 hectares and a thermal capacity of 100 MW_{th}. In other European countries, the market conditions of the heating and cooling sectors significantly differ from the particular situation in Denmark. But also in Germany, Austria and in other countries with starting markets large scale solar thermal plants become an economically competitive heat generation option for district heating. Figure 11 gives an overview of the market status of solar district heating in Europe.

Fig 11: Solar district heating market status in Europe (May 2016) (red dot: solar thermal system for district heating, blue dot: solar thermal system for district cooling, number: amount of solar thermal systems in respective European country) (Solites, 2016)

At the end of 2015, 252 plants with more than 350 kW_{th} nominal power were in operation in Europe. The total installed capacity amounts to 750 MW_{th}. Moreover, an increasing number of countries are following this trend and new markets have started to develop, for example in Italy, France and even in South Korea.

New solar district heating projects show an interesting variety of technical concepts and operator models: So called 'energy villages' are a solution for rural areas, where whole villages switch from individual, often oil-based heating systems to district heating systems for larger parts of the village. Local biomass plants combined with a solar thermal system are seen as one of the applicable renewable heat sources for such systems and operators are often cooperatives, municipalities themselves or their utilities. Solar district heating is, however, also an advantageous solution for new built or retrofit districts in innovative urban development projects. In several large solar thermal plants in Sweden and Austria a decentral feed-in of solar heat into the district heating has been realized. A decentral feed-in is in particular interesting for larger city district heating systems, where sufficiently large roof or infrastructure areas are available along the district heating lines.

The energy transition with its growing part of renewable power supply in the electricity nets in some European countries leads to an additional market push for solar thermal systems in district heating nets. More and more fossil-driven CHP-plants (CHP: combined heat and power) reach a shut down during the summer months due to uneconomic operation conditions that are caused by high amounts of renewable power in the electricity grids. The missing heat can be replaced by renewable solar thermal energy.

Economical competitiveness and heat generation costs between 30 and 50 Euro/MWh are reached whenever the solar thermal plants are sufficiently large (> 1 MW_{th}), the overall concept is kept simple (e.g. ground-mounted collector fields, see Figures 3 and 4) and the district heating system is operated at suitable temperatures (< 100 °C). In addition subsidies for the introduction of renewable energy sources into district heating are available in many

European countries. The low share of operation costs leads to a long term stability and calculability of heat generation costs for the whole operation period of typically 25 years.

6. The European SDHp2m project

SDHp2m stands for “Solar District Heating and actions from Policy to Market”. The project addresses market uptake challenges for a wider use of district heating and cooling systems (DHC) with high shares of renewable energy sources (RES). The action specifically focuses on the use of large-scale solar thermal plants combined with other RES in DHC systems (Solites, 2016).

The key approach of the project is to develop, improve and implement advanced policies and support measures for SDH in nine participating EU regions. In three focus regions Thuringia (DE), Styria (AT) and Rhône-Alpes (FR) the regulating regional authorities are participating as project partners to ensure a strong implementation capacity within the project. In six follower regions from BG, DE, IT, PL, SE the regulating authorities are integrated through letters of commitment. The project activities aim at a direct mobilization of investments in SDH and hence in a significant market rollout.

In each region, a stakeholder advisory group has been created, gathering market and policy actors to identify the actions that have to be taken to enable a market roll-out of SDH. A detailed action plan has been set up that the regional teams are implementing. The planning of activities by local actors at a regional level ensures the development and implementation of ideas adapted to the local framework. On the other hand, thanks to the international level of the project, know-how and experience from frontrunner regions are available and partners can exchange ideas and methods on how to tackle their challenges. Several factsheets are under development regarding the policy, financing and market development actions in each region.

Addressed market uptake challenges are: Improved RES DHC policy, business models and better access to plant financing, sustained public acceptance and bridging the gap between policy and market through market support and capacity building. Denmark and Sweden reach already today a high share of RES in DHC and are used as a role model for this project.

Some European countries supplement the market development for SDH by national market development projects. As an example, the German Federal Ministry for Economic Affairs and Energy started the project “Solnet 4.0”. Within this project, eight suppliers of solar thermal plants for district heating works together with SDH specialists, the German district heating industry federation AGFW e.V. and media suppliers to increase and strengthen the growing development of the German SDH market.

7. Perspectives

The technologies for large collector fields that can be integrated into district heating systems in Europe are already offered by at minimum eight companies. Further technical developments are necessary to further adopt the solar thermal technologies to district heating for centralized and decentralized feed-in. One of the main focuses of research lies in the system integration of large collector fields into complex district heating networks with several heating centrals, several combined heat and power plants etc. The energy transition leads to fundamental changes in the district heating technologies with good opportunities to integrate solar thermal as a heating technology into these systems. The technical questions how this integration should be realized are not yet answered. Within first pilot plants this new, broad field of research and development is investigated like in the new project “renewable district heating 2020 – the multifunctional district heating network as a heat hub” in the city of Hennigsdorf in Germany. The utilities of Hennigsdorf are going to raise the amount of renewable energies up to 100 % for their district heating net of about 50 km length that delivers about 120 GWh/a heat on a temperature level of up to 105 °C supply temperature. Therefore the utilities cooperate with technical consultancies and Solites as scientific experts to develop the technical-economical optimum for the overall district heating system and its operation strategy.

Safeguarding the SDH market development to a stable and durable market still is a comprehensive task that asks for huge efforts within the coming years - with Denmark as the only worldwide exception. These efforts mainly comprises non-technical developments. Some first European countries show that if the political will to further develop the SDH market is expressed clearly and in addition finds its way into market incentive programs and

long term stable market conditions, the district heating companies increasingly welcome solar thermal plants as a sustainable, future-proof heating technology and start their own way into a solar future. The possible variants are extensive: from a first small solar thermal plant to the 100 % renewable solution for whole (smart) cities.

8. References

Deutscher Wetterdienst, 07.09.2017, ftp://ftp-cdc.dwd.de/pub/CDC/observations_germany/

ESTIF – European Solar Thermal Industry Federation, 15.09.2017, http://www.estif.org/solarkeymarknew/index.php

Meteotest, Meteonorm: Einstrahlungsdaten für jeden Ort des Planeten, 22.08.2017, http://meteonorm.com/de/

Solites, 07.04.2016, Solar District Heating - The SDH projects website. http://solar-district-heating.eu/Home.aspx

Solites, 29.09.2017, ScenoCalc Fernwärme – Ertragsvorhersagetool für Solarthermie-Anlagen in Wärmenetzen, https://www.scfw.de/

The SDHp2m project has received funding from the European Union's Horizon 2020 research and innovation programme under grant agreement No 691624

The projects "Solnet 4.0" and "renewable district heating 2020 – the multifunctional district heating network as a heat hub" has received funding from the German Ministry for Economic Affairs and Energy on the basis of a decision by the German Bundestag

The sole responsibility for the content of this publication lies with the authors. It does not necessarily reflect the opinion of the funding organizations. Neither the funding organizations nor the authors are responsible for any use that may be made of the information contained therein.

Central versus Semi-decentralized Solar District Heating for Low Heat Demand Density Housing Developments in Germany

Isabelle Best, Janybek Orozaliev and Klaus Vajen

University of Kassel, Solar and Systems Engineering, Kassel, Germany

Abstract

District heating risks to lose competitiveness the lower the linear heat density of a district is. The distribution network needs to be highly efficient in order to ensure economic feasibility. The heat distribution temperatures are crucial to keep distribution heat losses as low as possible. For a new housing area in Germany consisting mainly of single family houses, solar district heating concepts at two different supply temperature levels of 70°C supply and 40°C supply are examined in terms of economic and efficiency aspects. Depending on the required temperature level of the heat supply concept the component's design differs. A system with 70°C supply temperature is based on a central heat supply with a heat pump and ground-mounted solar collectors, whereas the system with 40°C supply temperature is a semi-decentralized concept with central heat pump for space heating and decentralized solar thermal systems and electric back-up heaters for domestic hot water preparation.

Keywords: solar district heating, low heat demand density, ultra-low-temperature district heating

Abbreviations

BTES	Borehole Thermal Energy Storage
DH	District Heating
DHW	Domestic Hot Water
GSHP	Ground Source Heat Pump
HP	Heat Pump
PTES	Pit Thermal Energy Storage
SH	Space Heating
TTES	Tank Thermal Energy Storage
B / W	Brine /Water

1 Introduction

Future smart thermal energy systems are based on a combination of renewable technologies using wind, geothermal, and solar thermal power along with residual resources to meet the heat demand (Lund et al., 2014). District heating infrastructures and large thermal storages play an important role in future energy systems as demonstrated by various projects in Denmark in recent years (SDH solar district heating, 2017). The heat supply system should distribute heat with low heat losses. However, district heating risks to lose competitiveness the lower the linear heat demand density of a district is. The planned new housing area "Zum Feldlager" (Kassel, Germany) comprises of 131 buildings on a land area of 115,000 m². The housing area will consist mainly of single family houses, resulting in a low building density with a plot ratio of 0.25 according to (Persson and Werner; Persson and Werner, 2011). It represents a heat demand sparse area with a very low linear heat demand density of around $580\ \mathrm{kWh/(m_{trench} \cdot yr.)}$. In this case the distribution network needs to be highly efficient in order to ensure economic feasibility. The heat distribution temperatures are crucial to keep distribution heat losses as low as possible. Likewise, the heat supply system should include renewable energies, as much as possible.

Therefore, two solar district heating concepts for the new housing area "Zum Feldlager" at different supply temperature levels are examined in terms of economic and efficiency aspects in this study. In Denmark, the implementation of solar heat is characterized by large central ground-mounted solar thermal collector fields connected to thermal networks and seasonal storages. The opposite case occurs in Germany. A broad implementation of ground-mounted large-scale solar thermal collector fields in district heating systems is limited because of high land prices. Individual solar thermal systems are currently dominating the German market. Key issue is, under which boundary conditions a central solar district heating system is more beneficial than a semi-decentralized district heating system for very low linear heat density areas in Germany, like the housing development "Zum Feldlager". Accordingly, the heat generation costs have been calculated considering components' investment, system operating costs as well as maintenance and service costs for two exemplary heat supply systems.

doi:10.18086/swc.2017.06.04 Available at http://proceedings.ises.org

2 Boundary Conditions

2.1 Description of the New Housing Development

The planned new housing development "Zum Feldlager" (Kassel, Germany) comprises of 131 buildings on a land area of 115,000 m². The housing development will consist mainly of single family houses, resulting in a low building density with a plot ratio of 0.25 according to (Persson and Werner, 2011). The buildings were calculated to meet the requirements of the German KfW-70 low-energy building standard according to the Energy Saving Ordinance 2016 (Gesellschaft für Rationelle Energieverwendung e. V., 2016). This means that the buildings were designed to have a specific heating demand below $50\ \mathrm{kWh/(m^2 \cdot yr)}$. The space heating demand of each building was calculated according to the German standard DIN V 4108-6 (Deutsches Institut für Normung e. V., 2003). Additionally, the peak heating load for every building was computed according to DIN EN 12831 (Deutsches Institut für Normung e. V., 2012). Regarding the domestic hot water demand, demand profiles were generated by using a stochastic modelling tool developed by Jordan et al. for IEA SHC-Task 26, which takes into consideration the Gaussian-Distribution and different time scales to generate various load profiles (Jordan and Vajen, 2001). The total heat demand was calculated to amount $\approx 1{,}656\ \mathrm{MWh}/yr$, that comprises of one quarter DHW ($\approx 380\ \mathrm{MWh/yr}$) and of three quarter for space heating (SH) ($\approx 1{,}285\ \mathrm{MWh/yr}$). It represents a heat demand sparse area with a low linear heat demand density of around $580\ \mathrm{kWh/(m_{trench} \cdot yr)}$ assuming a total district heating (DH) pipe length of 2.89 km.

2.2 Generation of Heat Load Profile

Within the framework of the joint research project "Geosolare Nahwärmeversorgung für die Siedlung Zum Feldlager" the new building development and the corresponding semi-decentralized solar DH system was modelled with the software TRNSYS. Dynamic simulations were conducted in cooperation with the Fraunhofer Institute of Building Physics from Kassel. The model consists of all heat supply units, a simplified distribution infrastructure, and clustered consumers. The distribution infrastructure was simplified calculating the average pipe diameter of the district heating network branches and the corresponding pipe length. The characteristics of standard plastic jacket compound pipes with standard insulation were assumed. The 131 buildings were clustered in 22 building typologies and then displayed as single thermal zone models. According to design characteristics of each building type, there were various possibilities for the number of consumers of domestic hot water. These possibilities were sub-grouped into three main cases: typical single family houses, double single family houses and multi-family houses. All other possibilities were realized by taking into account multiplication factors for each case. Precise and realistic domestic hot water systems consisting of all system engineering components were designed in accordance to VDI 6002 (Verein Deutscher Ingenieure e. V., 2014) and VDI 2067 Blatt 12 (Verein Deutscher Ingenieure e. V., 2000). The resulting annual heat load profile is shown in Fig. 1. The space heating (SH) demand is depicted in blue, while the domestic hot water (DHW) demand is displayed in red. The heat load profile is taken as a base for system design and calculation of the central solar DH system (see section 2.3).

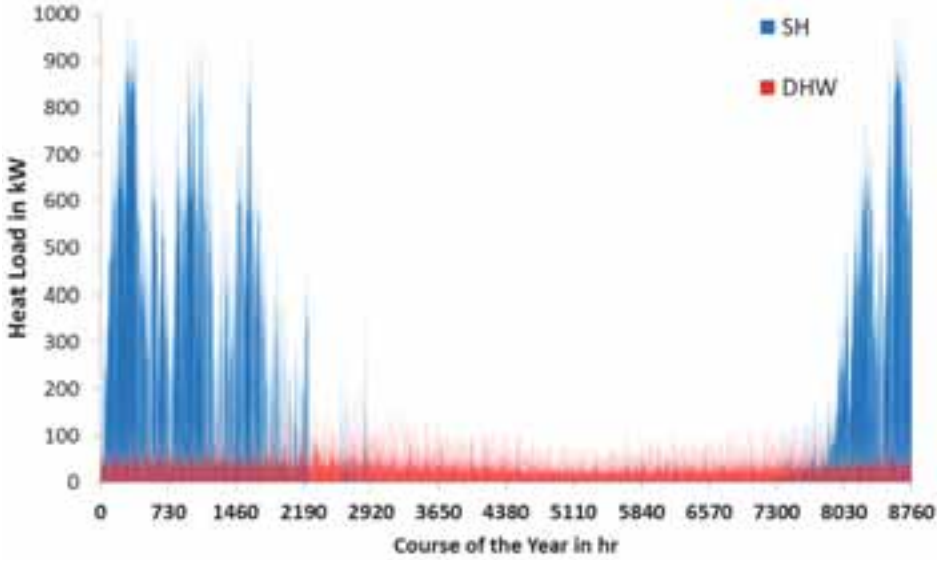

Fig. 1: Calculated hourly heat load profile of the housing development "Zum Feldlager", in blue the space heating demand, in red the domestic hot water demand

2.3 Design Requirements and Basis of Comparison

Both solar DH systems presented were designed to achieve a renewable heat supply of ≈ 80 % of the total heat demand of the new building development. Considering that the renewable energy already covered roughly 29% of gross electricity generation (total volume of electricity generated in Germany) in 2016, the electricity consumption of each solar DH system had to be below 427 MWh/yr. The number of buildings and inhabitants, as well as the DH geometry and pipe length were kept constant. Depending on the required temperature level of the heat supply concept the components´ design differs. Also, the heat distribution network design (pipe diameters, pumps) was adapted according to the distribution temperatures. The central solar DH system is compared to the semi-decentralized DH system for low heat density housing developments in Germany taking following criteria into account:

- Investment for heat supply components
  (decentralized versus central solar thermal system, heat pump, electric peak load heater,
  borehole thermal energy storage, pit thermal energy storage, tank thermal energy storage)
- Investment for the distribution infrastructure (material and burring costs for pipes)
- Prices for land area
- Maintenance and service costs
- Operating costs.

The discounted present value of capital costs, service and maintenance costs, and operating costs was calculated on a base period of 30 years including proportional reinvestments after 15 operating years (central heat pump, decentralized hot water storages, electric back-up heater, components of the uncovered collector field) with an interest rate of 5.6 %. All heat supply components, the DH infrastructure, pumps, the energy centre (centre building with utilities), site development costs, connection, and commissioning costs were considered. Furthermore, the characteristic operating costs were computed at the base of the results from dynamic simulations and static calculations. The maintenance and service costs were evaluated according to VDI 2067 Blatt 1, which recommends fixed rates of investment to calculate the maintenance and service costs depending on the technology used (Verein Deutscher Ingenieure e. V., 2012).

3 System Design

3.1 Central Solar District Heating System

The first concept introduced in this paper is similar to Danish systems like the DH system in Braedstrup and the German DH system in Crailsheim (Nußbicker-Lux, 2010; SDH solar district heating, 2017). The supply temperature of 70°C ensures DHW preparation and SH supply via a low-temperature district heating network. The heat supply system consists of (see Fig. 2):

- A central large-scale, ground-mounted collector field,
- A central heat pump supplemented by an electric peak load heater,
- A Pit Thermal Energy Storage (PTES),
- And a low-temperature district heating network of 70 °C supply and 40 °C return temperature.

The shown functional diagram of the heat supply concept shows only the main components and does not include heat exchangers, pumps, valves etc. for reason of simplicity (see Fig. 2). The district heating network is simplified and represented by a supply line and a return line. The DH network is operated throughout the year with a fixed supply temperature. A linear heat demand density of $576\ \mathrm{kWh/(m_{trench} \cdot yr)}$ was determined.

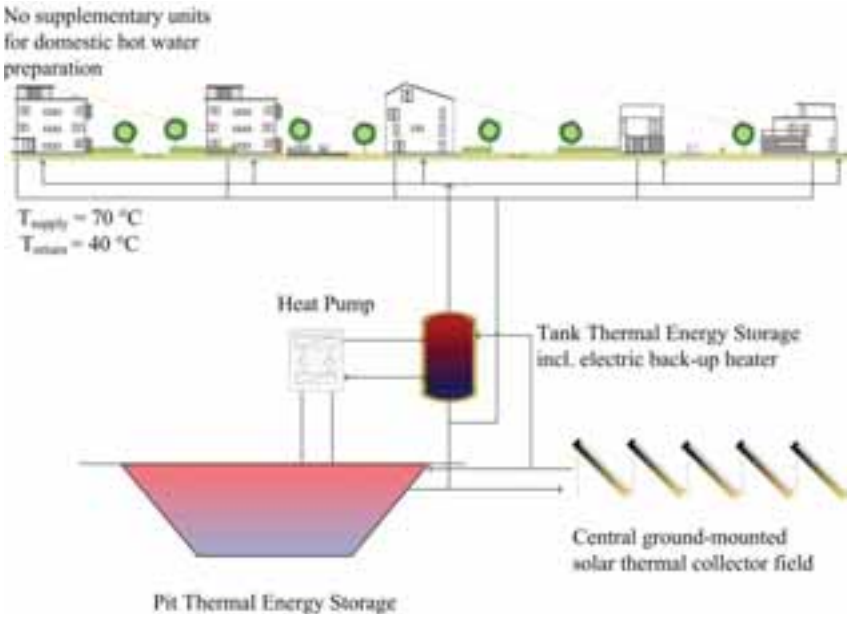

Fig. 2: Central solar district heating based on low-temperature district heating network

The solar thermal system was designed with the free software ScenoCalc Fernwärme 2.0 (Solites, 2017). The heat demand profile shown above served as a basis for the system design. The seasonal PTES is dimensioned in order to achieve a high solar fraction and at the same time low solar heat surplus. A specific storage volume of 3.3 m³/ m² collector area was found to be reasonable (via parameter variations) resulting in the lowest solar heat surplus. The collector field is connected through a heat exchanger to the PTES (heat exchanger temperature difference 5 K). An additional heat exchanger is assumed between the PTES and the DH network (heat exchanger temperature difference 5 K). In order to meet the requirements of renewable heat share of 80 %, the system was designed as follows:

Tab. 1: System design of the central solar district heating system

Component	Size
Flat plate collectors (ground mounted)	2,400 m²
PTES	8,000 m³
Heat Pump	593 kW_{th} (at W0/W35) / SPF 3.8
Tank Thermal Energy Storage (TTES)	100 m³
Electric peak load heater	740 kW nominal power
DH operating Temperatures	Summer: 70 °C / 40 °C Winter: 70 °C / 30 °C
Software for design and calculation	TRNSYS and ScenoCalc Fernwärme 2.0

3.2 Semi-decentralized solar district heating system

The second concept is a semi-decentralized concept based on an ultra-low-temperature district heating network. The supply temperature of 40°C ensures space heating. However, supplementary components for Domestic Hot Water (DHW) preparation are needed. A linear heat demand density of $432\ \mathrm{kWh/(m_{trench} \cdot yr)}$ has been determined, as only space heating is provided by the district heating.

The heat supply consists of (see Fig. 3):

- Distributed solar thermal systems (mounted on the building roofs) for DHW preparation,
- Uncovered solar thermal collector fields for thermal ground regeneration,
- A central Ground Source Heat Pump (GSHP) supplemented by an electric peak load heater,
- A Borehole Thermal Energy Storage (BTES),
- And an ultra-low-temperature district heating network with 40 °C supply and 25 °C return temperature.

Furthermore, a seasonal operating strategy is applied in order to keep distribution losses low. The heat network is operated during the space heating period from October to April only and distributed solar thermal systems on the building roofs combined with electrical back-up heaters ensure DHW preparation throughout the year. The GSHP and the DH is offline in the period of May to September. Only the thermal ground generation is operated through one DH branch. The uncovered solar collector field supplies the BTES with low temperature heat. Thus, the ground temperature is kept constant over the calculated 30 operating years. Also here, the shown functional

diagram of the heat supply concept shows only the main components and does not include heat exchangers, pumps, valves etc. for reason of simplicity (see Fig. 3). The district heating network is simplified and represented by a supply line and a return line.

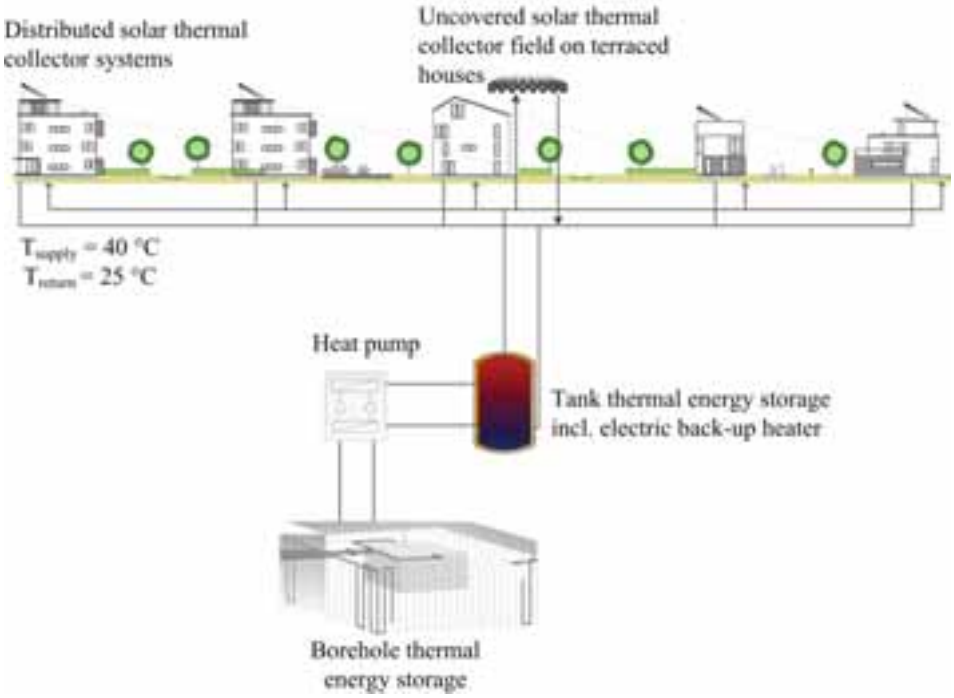

Fig. 3: Semi-decentralized solar district heating based on an ultra-low-temperature district heating network

The semi-decentralized solar DH system was modeled with the software TRNSYS (see section 2.2). The GSHP was designed to meet 60 % of the maximum heat load. The distributed solar collector systems are determined to ensure a solar fraction $f_{sol\ in}$ of ≈ 70 % (average solar fraction of the energy input into the hot water storage).

Tab. 2: System design of the semi-decentralized solar district heating system

Component	Size
Distributed solar DHW systems	820 m² (on the buildings roofs)
Distributed hot water storage tanks in buildings with electrical back-up heaters	300 l (for single family houses) to 1,700 l (for large multifamily houses)
BTES	92 boreholes, 120 m depth
Heat pump	593 kW_{th} (at W0/W35) / SPF 4.6
Tank Thermal Energy Storage (TTES)	20 m³
Electrical peak load heater	740 kW nominal power
Uncovered solar collectors for thermal ground regeneration	1,800 m² on several large building roofs
DH operating temperatures	Summer: - C / - °C Winter: 40° C / 25 °C
Software for design and calculation	TRNSYS

3.3 Network Design

The housing development has been sub-divided in three parts that are supplied by three DH branches. The DH network geometry was kept constant. For each building a connection capacity was determined. The piping network was designed for the maximum heat load. Depending on the heat supply system, it has been differentiated between two design temperature levels: for 70 °C supply and 40 °C return (temperature difference ΔT = 30 K) as well as for 40 °C supply and 25 °C return (ΔT = 15 K). Additionally, the piping manufacturer's recommendation (ISOPLUS) for maximum flow velocities were applied (Nussbaumer and Thalmann; Nussbaumer and Thalmann, 2014). According to the connected capacity a volume flow and the corresponding pipe diameter were computed for each branch. The resulting pipes sums up to 2.89 km pipe length. The connecting pipes were defined to have 1.71 km, while the transportation pipes were calculated to have 1.18 km. The following bar chart depicts the sum of supply and return pipe length (including the connecting pipes) broke down into nominal pipe diameter (see Fig. 4).

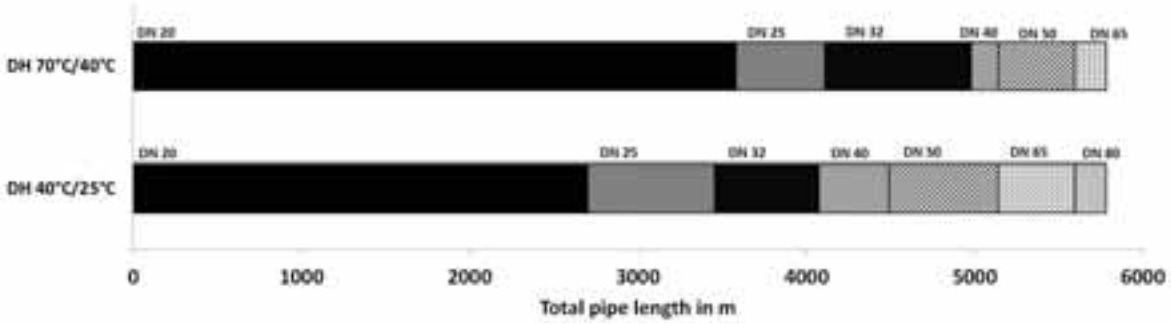

Fig. 4: Nominal pipe diameter distribution showing the sum of supply and return pipes

Based on the nominal pipe diameter (DN) distribution, the network costs were determined with a medium cost approach for new building developments for unmade terrain and rigid pipes after (Nast et al., 2009) (see Fig. 5, red dashed line). The medium cost approach was also approved by (Klöpsch et al., 2009) and can still be considered valid in 2017. Nevertheless, there is an optimization potential according to Manderfeld, who showed that specifically in rural areas the specific network construction costs can be reduced using for example flexible pipes (see grey dashed line) (Manderfeld et al., 2008). This data applies only for Germany, they may differ in other countries.

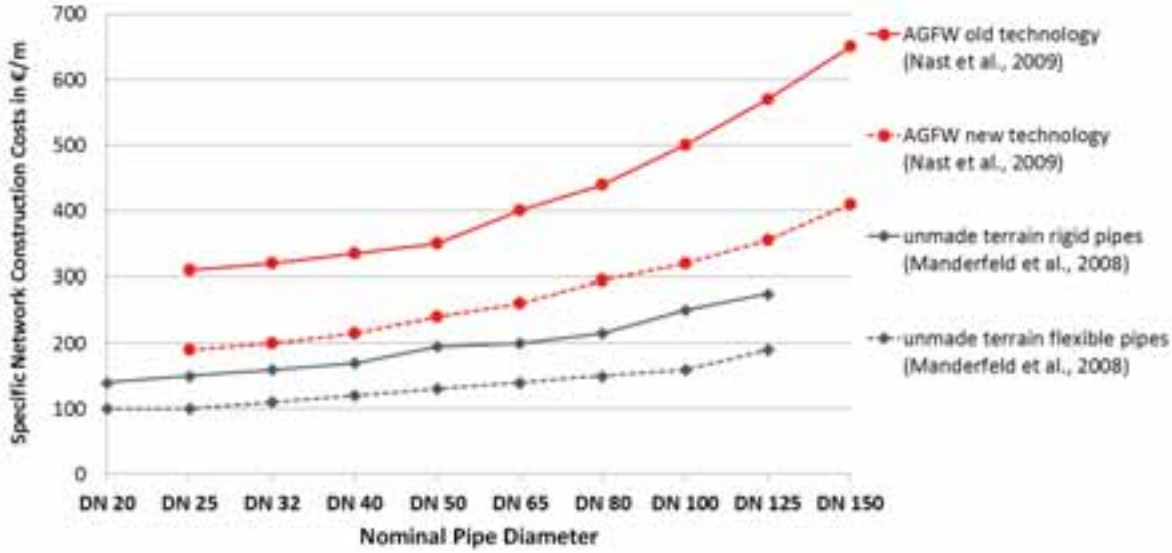

Fig. 5: Specific network construction costs including construction costs and pipe material costs

In operation a DH network shows a characteristic heat loss rate that depends mainly on the pipe type, pipe diameter, insulation, and the temperature gradient between the pipe and the surrounding ground. The relative heat distribution losses increase, the lower the linear heat demand density is. Consequently, the operating costs are affected. For this reason, the heat losses have been calculated and modeled for the two different heat supply systems taking single rigid pipes as a basis (Arbeitsgemeinschaft QM Fernwärme: Nussbaumer, Thomas et al., 2017).

4 System Efficiency

The central solar DH network was designed to meet the requirement of ≈ 80 % renewable heat supply of the total heat demand of the new building development. Thus the electricity consumption has to be below 427 MWh/yr. On the basis of the designed DH network ≈ 18 % distribution heat losses occur within one operating year (see section 3.3). The HP was assumed discharging the PTES from 40°C to 10°C, which results in a seasonal performance factor *SPF* of 3.8. The corresponding maximum electricity consumption of the HP was calculated to be ≈ 310 MWh/yr. taking distribution heat losses and auxiliary energy demand of the system into account. According to these assumptions, the solar collector field needs to ensure ≈ 40 % solar fraction of the total heat demand (fraction of solar energy that meets the heat demand including distribution heat losses). Thus, a large collector field of 2,400 m² of flat plat collector gross area was determined. This corresponds to a solar heat supply of ≈ 800 MWh/yr. to the DH network. The remaining ≈ 60 % of the heat demand are met by the HP. The seasonal storage,

which consists of 8,000 m³, causes ≈ 14 % heat losses, which are already subtracted from the yearly solar heat supply. The electrical peak load heater was assumed to supply only 4 % of the heat demand which shall be covered by the HP.

In contrast to the central DH system, the distributed solar collector systems were designed only for the DHW preparation. They were calculated to meet fully the DHW demand during the non-SH period, which allows keeping the DH network and the HP offline during this period. The simulation's results demonstrated a solar fraction of DHW demand $f_{sol\ out}$ of ≈ 58 % (average solar fraction of the DHW net energy). Besides this, the DHW is preheated via DH network during space heating period up to ≈ 29 % (fraction of the DHW net energy). The remaining ≈ 13 % are covered by electrical back-up heaters. Regarding the HP design, the approach was to keep supply temperatures of the DH network as low as possible in order to achieve a high seasonal performance of the HP and at the same time to avoid heat losses through the network. The calculations showed that a *SPF* of 4.6 (without peak load heater) is achieved following this approach (supply 40 °C return 25 °C). Add to this, only 5.5 % heat distribution losses occur through the DH network, due to the low operating temperatures and the seasonal operating strategy. The uncovered solar collectors (roof top installation) fully ensure thermal regeneration of the BTES during the non SH period. This means, the BTES is charged or rather regenerated with the amount of energy which was subtracted during space heating period. The total electricity consumption amounts to 413 MWh/yr., thus it meets the requirement of 80 % renewable heat supply. The resulting total electricity consumption of the different solar DH system is listed in the following table:

Tab. 3: Comparison of Electricity Consumption

Component	Central Solar DH system Electricity Consumption in MWh/yr.	Semi-decentralized Solar DH system Electricity Consumption in MWh/yr.
Heat Pump, DH heat losses	55	16
Heat Pump operating	251	294
DHW electrical back-up heaters	-	50
Central electrical peak load heater	47	16
Sum without auxiliary energy demand	***353***	***376***
Auxiliary Energy demand (pumps)	54	37
Total Sum	**407**	**413**

5 Economic Evaluation

Hereafter, the results of the economic evaluation are presented. This section examines the net annual costs without and with subsidies of the two different solar DH systems. Thereby, specific costs of the components are discussed. Also, the maintenance and service costs as well as the operating costs are considered. Additionally, the impact of land area prices and the type of seasonal storage are highlighted.

5.1 Net Annual Costs of the Central Solar DH System

The specific investment for each component was evaluated. First, the DH network costs for transportation pipes were calculated on the basis of the computed DN distribution of the network. The network was characterized by a majority of small diameters of DN 20 and DN 32. This results in an average 226 €/m pipe length (Nast et al., 2009) (see section 3.3) Together with costs for substations, house-lead-in costs, and network pumps, they build total investment for the central distribution infrastructure. Secondly, the central flat plate collector field was calculated based on a gross collector area of 2,400 m². Taking the economy of scale into account, specific collector costs of 380 €/m² were assumed. Furthermore, the pit storage (PTES) was examined. It was designed according to the Danish principle. The Danish pit storages are typically without surface sealing and only covered by insulation material and a canvas cover. Thus, costs of only 45 €/m³ water equivalent incur. However, as a result the seasonal storage cover is not usable as leisure space for example. Consequently, costs for land area use for the PTES installation and the collector field incurred (blue parts in the pie chart, see Fig. 6). Land area prices for green areas and for solar system installations were assumed according to standards in Kassel. The specific investment for each component is listed in the following table:

Tab. 4: Specific investment of the central solar DH system's components

Network construction costs	226 €/m_{tr}	(Nast et al., 2009)
Costs for substations	4,000 €/unit	(Stuible et al., 2016)
House-lead-in costs	3,600 €/unit	(Stuible et al., 2016)
Network Pumps	3,350 €/unit	(wilo, 2017)
Solar System Collector Costs	380 €/m²	(Verein Deutscher Ingenieure e. V., 2017)
PTES	45 €/m³ water equivalent	(Solites, 2016; Freistaat Thüringen Ministerium für Umwelt, Energie und Naturschutz, 2016)
Land area	8 €/m² for green areas, 15 €/m² for land areas for solar system installations	(BORIS Hessen, 2016)
HP	195 €/kW_{th}	(Lambauer et al., 2008; Wolf et al., 2014)
Peak load heater	100 €/kW	Assumption, expert knowledge

According to the specific investment the total annual investment was determined based on the system components design. The following figure shows the results of the detailed economic evaluation of the central solar DH system (see Fig. 6). The net annual heat costs comprise of operating costs, maintenance and service costs, as well as the investment. The bar chart shows the net annual costs without taken subsidies into account. In absolute values the total annual system costs are ≈ 415 k€/yr. Thereof 61 % are investment (252 k€/yr.), 22 % result from maintenance and service and only 18 % are caused by system operating. Thus, the fixed cost rate is 83 %.

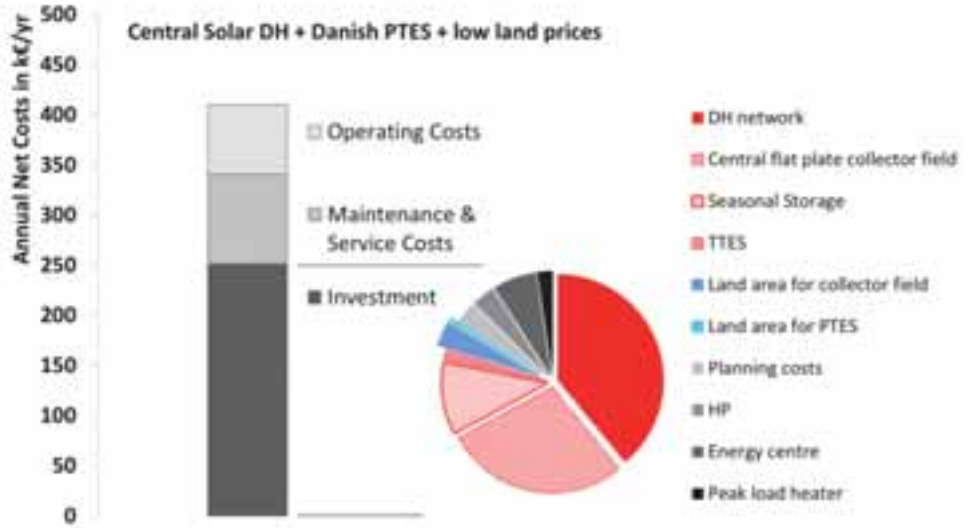

Fig. 6: Net annual costs for a central solar district heating system (left) and the breakdown of the investment (right) at a base period of 30 years

The break-down of investment demonstrates the three most cost-intensive system components: the DH network (39 %), the central collector field (28 %), and the pit storage PTES (11 %). The pie chart shows also several other points of expenses marked in grey. They are considered to be nearly constant through the different heat supply systems. They comprise of planning costs, the heat pump, the peak load heater, and the energy centre. Together they amount to 16 % of the investment. The land area costs represent an ideal situation and can be seen as a low cost approach. Nevertheless, they amount to 4 % of the total investment (marked in blue).

On top of the investment, maintenance & service costs and operating costs are added. The maintenance and service costs were evaluated according to fixed rates recommended by VDI 2067, whereas the operating costs represent the system operating characteristic. Here, the operating costs result only from the yearly electricity consumption, which mainly reflects the HP performance and secondly the auxiliary energy demand of pumps (see section 4). The HP achieves a SPF of 3.8 and supplies 60 % of the total heat demand. To sum up, the net annual costs amount to 415 k€/yr. This results in specific net heat generation costs of 249 €/MWh for a total heat demand of 1,665 MWh/yr. without subsidies.

5.2 Net Annual Costs of the Semi-decentralized Solar DH system

Similar to the economic evaluation of the central solar DH system, the calculations were conducted for the semi-decentralized solar DH. First the specific costs for system components were investigated. The DH network costs resulted to be almost the same as the costs of the central solar DH network, despite the lower temperature level and the smaller temperature difference of 15 K between supply and return. The DH network transportation pipes amount of average 233 €/m_{tr} (Nast et al., 2009), which is an increase of 3 % compared to the central solar DH system. The costs for substations as well as house-lead-in costs were assumed to be the same as previously shown. In contrast to the central solar DH system, distributed flat plate collector systems were planned of 820 m² in order to supply the DHW demand during non-space heating period. Thus, higher specific solar thermal system costs incur of 742 €/m² (Stuible et al., 2016). The BTES was designed in cooperation with the Institute of Geotechnics of the University Kassel, which computed the BTES to have 92 boreholes of 120 m depth. Specific costs of 63 €/m borehole depth were determined. The land area above the BTES was assumed to be still usable as green space, because the boreholes are installed 1 m under the surface. Consequently, no additional costs for land area occur.
The specific investment for each component is listed in the following table:

Tab. 5: Specific investment of the semi-decentralized solar DH system's components

Network construction costs	233 €/m_{tr}	(Nast et al., 2009)
Costs for substations	4,000 €/unit	(Stuible et al., 2016)
House-lead-in costs	3,600 €/unit	(Stuible et al., 2016)
Network Pumps	3,490 €/unit	(wilo, 2017)
Solar System Collector Costs	742 €/m²	(Stuible et al., 2016)
BTES	63 €/m borehole depth	(Institute of Geotechnics of the University Kassel)
Land area	-	
HP	195 €/kW_{th}	(Lambauer et al., 2008; Wolf et al., 2014, & requests for proposals of manufacturers)
Peak load heater	100 €/kW	assumption

The central solar DH system shall be compared with a semi-decentralized solar DH system, which was designed especially for the new building development "Zum Feldlager". Therefore, the net annual costs were examined similarly to the central solar DH system. The results are shown in the following diagram. Fig. 7 displays the net annual costs of the semi-decentralized solar DH system. The net annual costs consist of 64 % investment (284 k€/yr.). Furthermore, maintenance and service costs amount to 22 % of the total heat generation costs, which can be summed up to a fixed cost rate of 86 %. The investment is dominated also by three main system components: the DH network (37 %), followed by the BTES (31 %), and the distributed solar collector systems (17 %). In case of the semi-decentralized solar DH system the operating costs were determined via dynamic simulations (see section 2.2). Similar to the central solar DH system analyses, the specific electricity costs were assumed to be 0.17 €/kWh, which applies to large consumers. Regarding DHW preparation, the electricity consumption of the electrical back-up heaters was rated with 0.21 €/kWh, which applies to small consumers in Germany. The HP performance, thus the *SPF* has the largest impact on the operating costs. The electricity consumption of the HP is 310 MWh/yr. (*SPF* = 4.6) that generates costs of 68 % of total operating costs. This implies the distribution heat losses through the network already. To sum up, the net annual costs amount to 443 k€/yr.. This results in specific net heat generation costs of 266 €/MWh for a total heat demand of 1,665 MWh/yr. without subsidies.
In conclusion the semi-decentralized DH system shows 7 % higher net heat generation costs than the central solar DH system. However, this applies only for the given boundary conditions. Specifically, this applies for sites with very low land area costs and for the assumed seasonal storage type. In order to investigate the impact of these parameters on the total net heat generation costs, a sensitivity analysis was conducted.

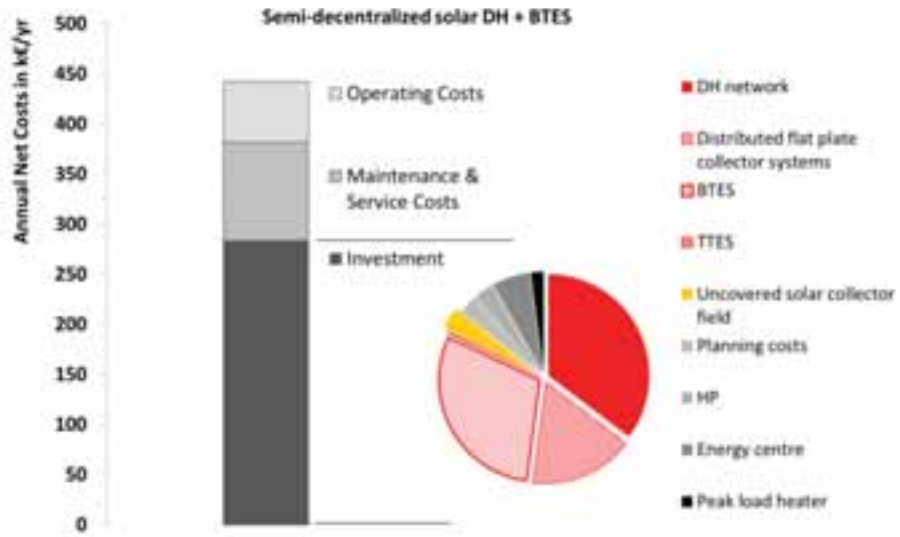

Fig. 7: Net annual costs of the semi-decentralized solar DH system for the new housing development „Zum Feldlager“ at a base period of 30 years

5.3 Sensitivity analysis of land area prices and PTES type

In Germany the availability of open space is restricted, which results in high land prices. In order to demonstrate the upper limit of heat generation costs, the land use for solar system installations (3.5 times the collector area) was calculated with land prices of 175 €/m² land area. This represents the land value of the district, where the new housing development “Zum Fedlager” will be build. Additionally, seasonal storages with surface sealing were realized in Germany in the recent years in order to be able to still use the area as leisure space. In case of PTES with a surface sealing, the specific costs increase significantly as demonstrated from various German projects (Solites, 2016). The specific costs can increase up to 200 €/m³ water equivalent (Freistaat Thüringen Ministerium für Umwelt, Energie und Naturschutz, 2016). For sensitivity evaluation reasons, the central solar DH system was calculated with a PTES with surface sealing applying 142 €/m³ water equivalent, which represents the average of several projects realized in Germany. The results of the sensitivity analysis are presented in the following bar chart (see Fig. 8). The light grey bars show the total net annual costs without subsidies (left axis) and the net heat generation costs (right axis). Besides this, the net heat generation costs considering subsidies are displayed by the striped bars. Compared to the initial event of the central solar DH (bar pair on the left side) the net heat generation costs increase about 38 % in case of high land area prices (second bar pair from the left). The semi-decentralized solar DH system was optimised to use as little land as possible. The distributed solar collector systems as well as the uncovered solar collector field for ground regeneration were planned as roof installations. No supplementary land is needed, which makes this heat supply concept competitive. In case of PTES with surface sealing, land costs are saved, because it is assumed that the storage cover can be used as leisure space (third bar pair). Despite this, the net heat generation costs do not increase significantly (5 % increase) compared to the second version of the central solar DH due to the high investment of the PTES with surface sealing. Considering subsidies, a new funding program (Wärmenetze 4.0, in English district heating 4.0) aiming at the implementation of sustainable and renewable DH systems entered into force end of September 2017. On this basis, subsidies of 30 % - 40% of the total investment can be received. This leads to the lowest specific heat generation costs of 198 €/MWh in case of the initial central solar DH system, and 207 €/MWh in case of the semi-decentralized solar DH system. Compared to the previous funding programme for renewable energies in Germany (KfW, 2016), this means a cost reduction of 10 % in case of the central solar DH system and 19 % in case of the semi-decentralized solar DH system.

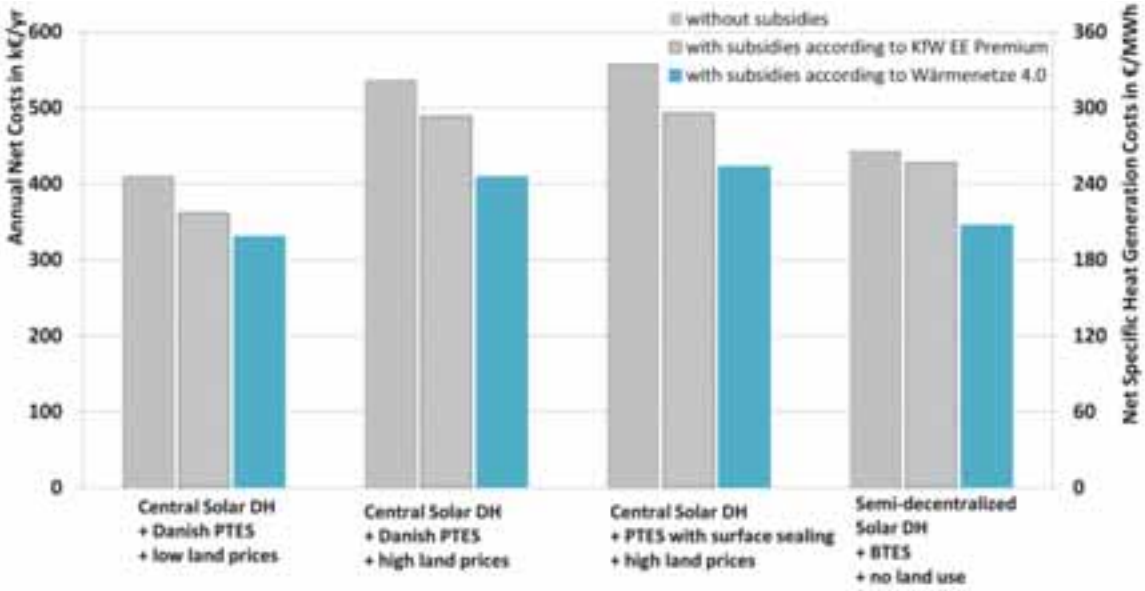

Fig. 8: Net annual costs and net heat generation costs of the central solar DH system under different PTES types and land prices compared to the semi-decentralized solar DH system with and without subsidies

In conclusion, in case of low land prices and a cost-efficient PTES without surface sealing a central solar DH system is 4 % less expensive than the semi-decentralized solar DH system taking subsidies according Wärmenetze 4.0 into consideration. Thus, the semi-decentralized is an economically competitive heat supply system under the given boundary conditions and assumptions. Without subsidies the central solar DH system is 6 % less expensive than the semi-decentralized solar DH system. Thus, in case of low land prices below 15 €/m², a central solar DH following the Danish example is slightly more beneficial than the semi-decentralized solar DH system from an economic point of view. In case of high land prices the heat generation costs of the central solar DH system increase about 30 % without subsidies and 24 % with the subsidies of the funding programme Wärmenetze 4.0. Thus, land prices have a high impact on the system feasibility and have to be considered within economic analyses.

6 Discussion

Two different solar district systems have been designed for the new building development “Zum Feldlager”, which represents a low heat density area. Both developed heat supply systems were designed under the precondition to achieve a renewable heat supply of ≈ 80 %. Key issue was to identify the preferable system from the economic point of view. Detailed economic analyses were conducted in order to determine the net heat generation costs of each system comprising of investment, maintenance and service as well as operating costs. At this point, it has to be said, that a medium cost approach was chosen. The specific costs for solar thermal collectors were considered conservatively. The maintenance costs are determined applying fixed percentages of investment according the German VDI 2067, which might be overestimating the costs in case of large systems. In conclusion, the economic analyses showed that the central solar district heating system is only favorable under specific boundary conditions: low land prices and low costs for the seasonal pit thermal energy storage. If the land prices are greater than 15 €/m², the semi-decentralized solar district heating system is to be preferred. In conclusion the semi-decentralized DH system shows 6 % higher net heat generation costs than the initial central solar DH system at low land prices (without subsidies). However, this applies only for the given boundary conditions. Specifically, this applies for sites with very low land prices and for the assumed specific solar thermal system costs. Due to the fact, that the central solar collector field makes 28 % of the investment of the central solar DH system (based on a PTES following the Danish examples), the specific solar thermal system costs represent a sensitive parameter. Furthermore, both heat supply systems were designed to achieve 80 % renewable heat supply. If this is not the requirement, the solar fraction can be reduced by lowering the collector area and likewise increasing the HP operating hours. This would lead to lower net heat generation costs. On the other hand, in case of lack of open space, the semi-decentralized solar DH system represents an energy efficient, sustainable and economic alternative to the central solar DH system.

Acknowledgment

The project partners greatly acknowledge the financial support of the project by the German Federal Ministry of Economic Affairs and Energy. (FKZ: 03ET1336C)

7 References

Arbeitsgemeinschaft QM Fernwärme: Nussbaumer, Thomas, Thalmann, S., Jenni, A., Ködel, J., 2017. Planungshandbuch Fernwärme ISBN 3-90870505-30-4. www.verenum.ch/Dokumente/PLH-FW_V1.0.pdf. Accessed 26 June 2017.

BORIS Hessen, 2016. Hessische Verwaltung für Bodenmanagement und Geoinformation. https://hvbg.hessen.de/immobilienwerte/boris-hessen. Accessed 9 October 2017.

Deutsches Institut für Normung e. V., 2003. Thermal protection and energy economy in buildings Part 6: Calculation of annual heat and annual energy use. https://www.beuth.de/de/vornorm/din-v-4108-6/63939447. Accessed 18 December 2017.

Deutsches Institut für Normung e. V., 2012. Heatings system in buildings - Method for calculation of the design heat load - Supplement 2: Simplified method for calculation of the design heat load and the heat generator capacity. https://www.beuth.de/de/norm/din-en-12831-beiblatt-2/150360566. Accessed 18 December 2017.

Freistaat Thüringen Ministerium für Umwelt, Energie und Naturschutz, 2016. Zukunft Sonne! Solarthermie und Fernwärme: Ein WEgweiser für die Praxis. Solites - Steinbeis Forschungsinstitut für solare und zukünftige thermische Energiesysteme, Stuttgart.

Gesellschaft für Rationelle Energieverwendung e. V., 2016. Energieeinsparverordnung EnEV 2016, Kassel.

Jordan, U., Vajen, K., 2001. Realistic Domestic Hot Water Profiles in Different Time Scales. Universität Marburg.

KfW, 2016. Merkblatt Erneuerbare Energien. KfW-Programm Erneuerbare Energien "Premium", Frankfurt.

Klöpsch, M., Besier, R., Wagner, A., 2009. Reicht für Kunststoffmantelrohre die Standarddämmung? Wirtschaftliche Dämmung von KMR. Euro Heat & Power (12), 46–54.

Lambauer, J., Fahl, U., Ohl, M., Blesl, M., Voß, A., 2008. Industrielle Großwärmepumpen - Potenziale, Hemmnisse und Best-Practice Beispiele. Institut für Energiewirtschaft und Rationelle Energieanwendung (IER).

Lund, H., Werner, S., Wiltshire, R., Svendsen, S., Thorsen, J.E., Hvelplund, F., Mathiesen, B.V., 2014. 4th Generation District Heating (4GDH). Integrating smart thermal grids into future sustainable energy systems. Energy 68, 1–11.

Manderfeld, M., Jentsch, A., Pohlig, A., Dötsch, C., Richter, S., Bohn, K., 2008. Abschlussbericht Forschungsvorhaben Fernwärme in der Fläche RDH (Rural District Heating) . Ermittlung des Fernwärmepotentials unter Berücksichtigung der neuester Verlegeverfahren und unterschiedlicher Energiedargebote in der Fläche der Bundesrepublik Deutschland.

Nast, M., Ragwitz, M., Schulz, W., Bürger, V., Leprich, U., Klinski, S., 2009. Ergänzende Untersuchungen und vertiefende Analysen zu möglichen Ausgestaltungsvarianten eines Wärmegesetzes. Ausarbeitung im Auftrag des Bundesministeriums für Umwelt, Naturschutz und Reaktorsicherheit. DLR, Fachhochschule für Wirtschaft Berlin (FHW), Öko-Institut, IZES, ISI, BEI. www.dlr.de/tt/Portaldata/41/Resources/dokumente/institut/system/publications/Endbericht_Waermegesetz-11.pdf. Accessed 18 December 2017.

Nussbaumer, T., Thalmann, S. Influence of system design on heat distribution costs in district heating. http://www.sciencedirect.com/science/article/pii/S036054421630113X?via%3Dihub. Accessed 18 December 2017.

Nussbaumer, T., Thalmann, S., 2014. Sensitivity of System Design on Heat Distribution Cost in District Heating. ISBN 3-908705-27-4. verenum and Swiss Federal Office of Energy, Zürich. www.ieabcc.nl/publications/IEA_Task32_DHS_Cost_Analysis.pdf. Accessed 18.12.17.

Nußbicker-Lux, J., 2010. Simulation und Dimensionierung solar unterstützter Nahwärmesysteme mit Erdsonden-Wärmespeicher. Dissertation.

Persson, U., Werner, S., 2011. Heat distribution and the future competitiveness of district heating. Applied Energy 88 (3), 568–576.

SDH solar district heating, 2017. Ranking List of European Large Scale Solar Heating Plants. http://solar-district-heating.eu. Accessed March 2017.

Solites, 2016. saisonalspeicher.de. Das Wissensportal für die saisonale Wärmespeicherung. Solites Steinbeis Forschungsinstitut für solare und zukunftsfähige thermische Energiesysteme. http://www.saisonalspeicher.de/. Accessed 9 October 2017.

Solites, 2017. ScenoCalc Fernwärme 2.0. SDH tools. Solites - Steinbeis Forschungsinstitut für solare und zukünftige thermische Energiesysteme. http://solar-district-heating.eu/ServicesTools/SDHcalculationtools.aspx. Accessed 9 October 2017.

Stuible, A., Zech, D., Wülbeck, H.-F., Sperber, E., Nast, M., Hartmann, H., Reisinger, K., Budig, C., Orozaliev, J., Pag, F., Vajen, K., Erler, R., Janczik, S., Kaltschmitt, M., Niederberger, M., 2016. Evaluierung von Einzelmaßnahmen zur Nutzung erneuerbarer Energien im Wärmemarkt (Marktanreizprogramm) für den Zeitraum 2012 bis 2014. Evaluierung des Förderjahres 2014.

Verein Deutscher Ingenieure e. V., 2000. Economic efficiency of building installations - Effective energy requirements for heating service water Blatt 12. https://www.beuth.de/de/technische-regel/vdi-2067-blatt-12/32138558. Accessed 19 December 2017.

Verein Deutscher Ingenieure e. V., 2012. Economic Efficiency of building - Fundamentals and economic calculation VDI 2067 Blatt 1. https://www.beuth.de/de/technische-regel/vdi-2067-blatt-1/151420393. Accessed 19 December 2017.

Verein Deutscher Ingenieure e. V., 2014. Solar heating for potable water - Basic principles - System technology and application in residential buildings Part 1/2.

Verein Deutscher Ingenieure e. V., 2017. Gründruck VDI 3988 Solarthermische Prozesswärme.

wilo, 2017. wilo-select. wilo-select.com. Accessed 2017.

Wolf, S., Fahl, U., Blesl, M., Voß, A., Jakobs, R., 2014. Analyse des Potenzials von Industriewärmepumpen in Deutschland. Institut für Energiewirtschaft und Rationelle Energieanwendung (IER).

Thermal Performance Analysis of a Solar Heating Plant

Jianhua Fan[1], Junpeng Huang[1], Ola Lie Andersen[1], Simon Furbo[1]

[1] Department of Civil Engineering, Technical University of Denmark, Kgs. Lyngby, Denmark

Abstract

Detailed measurements were carried out on a large scale solar heating plant located in southern Denmark in order to evaluate thermal performances of the plant. Based on the measurements, energy flows of the plant were evaluated. A modified Trnsys model of the Marstal solar heating plant was developed to calculate thermal performances of the plant. In the Trnsys model, three solar collector fields with a total solar collector area of 33,300 m^2, a seasonal water pit heat storage of 75,000 m^3, a simplified CO_2 HP, a simplified ORC unit and a simplified wood chip boiler were included. The energy consumption of the district heating net was modeled by volume flow rate and given forward and return temperatures of the district heating net. Weather data from a climate station on the site of the plant were used in the calculations. The Trnsys calculated yearly thermal performance of the solar heating plant was compared to the measurement result. Validity of the Trnsys model was analyzed. Recommendations are given with an aim to develop a Trnsys model that can be used to optimize design of a solar heating plant under different scenarios.

Keywords: Solar heating plant, Thermal performance, Monitoring, Trnsys simulations, Design optimization

1. Introduction

Modern district energy systems provide heating and cooling services using technologies and approaches such as combined heating and power (CHP), thermal storage, large scale heat pumps and solar heating. District energy creates synergies between supply and demand of process heating and cooling, space heating, cooling, domestic hot water and electricity. Tackling the energy transition of district heating to a sustainable future will require the intelligent use of synergies, flexibility, and short and long term energy storage solutions (Lund etc. 2014).

Denmark is one of the leading countries in district heating. Around 60% of Danish buildings are connected to district heating and district heating covers more than 50% of the total heating demand of Denmark (Nussbaumer & Thalmann 2014). The development of Danish district heating targets the transition from current 3rd generation district heating to the future 4th generation low temperature district heating with a large share of renewable energies. In 2009, a total 54,500 m^2 solar collectors were installed in Denmark, of which 35,000 m^2, i.e. 64%, were used in large solar district heating systems. In 2015, the solar collector areas installed in solar district heating plants reached 241,000 m^2, increased by 342% in six years. Supplemented by cogeneration technologies for biomass and large scale heat pumps fueled by electricity from wind power, it is possible to achieve a district heating and cooling system with 100% renewable energy. In these large scale solar heating plants, seasonal water pit thermal energy storages (PTES) are implemented. PTES is a viable solution of thermal energy storage both economically and environmentally since it is simple in construction and relatively cheap. Larger storage volumes lead to increased efficiency in practice, since the heat losses do not increase with the volume proportionally. With a large water pit heat storage, solar fraction of a district heating system could be significantly increased to for example 50% of the heat demand. Examples of large scale solar heating plants are the Marstal plant (33,300 m^2 solar collectors and 75,000 m^3 PTES), the Dronninglund plant (37,573 m^2 solar collectors and 60,000 m^3 PTES), the Vojens plant (70,000 m^2 solar collectors and 200,000 m^3 PTES) and the Gram plant (44,801 m^2 solar collector and 120,000 m^3 PTES) (PlanEnergi 2016).

Thermal behaviors of water pits have been investigated both experimentally and theoretically. Kielsgaard Hansen et al. (1983) investigated for the first time a small 500 m^3 pilot water pit heat storage at the campus of the Technical University of Denmark. Later, Kübler etc. (1997) presented investigations on a pilot heat storage of about 600 m^3 volume built in Rottweil. The pilot heat storage was applied as short term storage in connection with a combined heat and power (CHP) plant. The storage container was made of concrete with a stainless steel liner and mineral wool as insulation. The aim of the paper was to demonstrate the feasibility of the technology and to gain practical experience for the construction of larger stores. A gravel /water storage pit was built in Steinfurt, Germany (Pfeil M.

doi:10.18086/swc.2017.06.05 Available at http://proceedings.ises.org

2000). The ecological compatibility of the used materials in the storage was proved. Another focus of the paper was analysis of the cost-reduction potential of the PTES (Pfeil M. 2000). Thermal behavior of a model PTES was experimentally investigated in a test rig and numerically investigated by means of CFD simulations (Chang and Wu, 2017). The investigated PTES was a scaled down model that facilitates measurements on a test rig. However experimental investigations on thermal behaviors of large solar district heating plants in real operation were not found.

Theoretical investigations were carried out to gain knowledge and to optimize thermal performances of solar heating plants. Trnsys (Trnsys 2016) is used to calculate performance of a combined solar thermal and ground source heat pump (HP) system and to investigate different operation strategies of the system (Li H., 2018). Tian et al. investigated thermal performance of a solar heating plant with combined parabolic trough collectors and flat plate solar collectors. The focus of the investigation was on thermos-economic analysis of the plants with different types of collectors connected in series (Tian Z., et al. 2018). Cioccolanti et al. investigated performance of a solar trigeneration system for residential applications by means of a modelling study. The potential of a small scale concentrated solar Organic Rankine Cycle (ORC) plant coupled with an absorber was investigated using a Trnsys simulation analysis of a small scale 50 m^2 CPC solar field, a 3.5 kWe ORC and a 17.6 kWc absorption chiller to satisfy respectively heating, electricity and cooling needs of a residential user (Cioccolanti L., et al. 2018). However there is a lack of theoretical investigations on large scale solar heating systems with PTES.

The aim of the paper is to investigate thermal behaviors of the Marstal solar heating plant. The operation of the solar heating plant was monitored in detail in the period 2014-2016. Temperatures and fluid volume flow rates of the solar collector fields, the PTES storage, the heat pump and the district network were measured constantly. Energy flows in the plant were analyzed. A Trnsys (Trnsys 2016) simulation model of the solar heating plant is developed to investigate thermal performances of the plant. The calculated energy flows will be compared to the monitored energy flows with an aim to validate the simulation model. The Trnsys model could be used to optimize design of a solar heating plant under different scenarios in terms of levelized cost of heat (LCOH).

2. Monitoring of the plant operation

As shown in Table 1, the Marstal solar heating plant (Fig. 1) has been under continuous developments throughout the years. During the Sunstore 1 project in 1996, a 9045 m^2 solar collector field was installed with 12.53 m^2 large flat plate solar collectors produced by ARCON A/S. Additionally a 2100 m^3 accumulation tank was built as short term storage. Due to an increase of consumers of the solar heating plant, the Sunstore 2 project was introduced in 2001-2004 in which flat plate solar collectors of 8019 m^2were added in the plant. Heat produced by the collectors installed in Sunstore 1 and 2 is fed in the 2100 m^3 accumulation tank.

In 2012 the SUNSTORE 4 project was built. 15,064 m^2 solar collectors were installed and a 75,000 m^3 PTES was constructed, see Fig. 1. The aim of the Sunstore 4 project was to increase the solar fraction of the plant up to 55% of the thermal energy production, focusing on sustainability, increased efficiency and low costs. Marstal's 75,000 m^3 PTES was commissioned in 2012 and it has a capacity of 6.96 GWh according to PlanEnrgi (Jensen 2014). Heat produced by the collectors installed in the Sunstore 4 is fed in the 75,000 m^3 PTES. The operating temperatures vary depending on the season and the depth of the water layer, however the pond is designed to operate in a range of 10-90 °C. An electricity generator based on ORC and a CO_2 heat pump were added in the plant. The Organic Rankine Cycle (ORC) uses heat at around 300ºC produced by a wood chip boiler to generate electricity. The CO_2 heat pump utilizes heat from the water pit heat store as heat source to provide heating for the district heating network.

Detailed measurements were carried out in the period 2014-2016 to evaluate thermal performances of the plant. Temperatures and fluid volume flow rates of the solar collector fields, the PTES storage, the heat pump and the district network were measured constantly. The sensors in the inlet/outlet pipes of the PTES are located at the end of the transmission pipes 300 m away from the pit storage. Thirty-three temperature sensors were installed in the middle of the water pit storage to measure water temperatures at different levels. The volume flow rate is measured with flow meters in m^3/h with an accuracy of 2% (Schmidt 2013). The temperature sensors are PT resistance thermometers with an accuracy of +/- 0.1 K (Schmidt 2013).

Fig. 1: Bird view of the Marstal Solar heating plant

Tab. 1: Components of the Marstal solar heating plant

Sunstore 1	- 9,045 m^2 field consisting of arrays of 12.53 m^2 Arcon HT collectors (Collector field 1)
Sunstore 2	- 8,019 m^2 field consisting of arrays of 12.53 m^2 Arcon HT collectors (Collector field 2) -
Sunstore 4	- 15,064 m^2 field consisting of arrays of 13.88 m^2 Sunmark solar collectors (Collector field 3)
Other utilities	- 2,100 m^3 accumulation tank (Sunstore 1 & 2) - 75,000 m^3 water pit thermal storage (Sunstore 4) - 1,500 kW (produced heat) CO_2 heat pump - 4.15 MW wood chip boiler that runs a electricity producing Organic Rankine Cycle with a power of 750 kW

3. Dynamic simulations of plant thermal performances

A Trnsys model of the Marstal solar heating plant was developed in the Sunstore 4 project (Kate 2013). The Trysns model was modified in this paper to accommodate changes in the system, see Fig.2. The Trnsys model includes three solar collector fields with a total solar collector area of 32,138 m^2, an accumulation tank of 2100 m^3, a seasonal water pit heat storage of 75,000 m^3, a simplified CO_2 HP, a simplified ORC unit and a wood chip boiler. The energy consumption of the district heating net was modeled by volume flow rates and given forward & return temperatures of the district heating net. Forward temperatures of the district heating net are 72-74ºC in summer and 75-77ºC in winter. Temperatures of the fluid back to the plant vary in the range 33-41ºC from summer to winter. Weather data including total solar irradiance, diffuse solar irradiance and ambient air temperature from a climate station on the site of the plant were used in the calculations. In order to eliminate influence of initial conditions of the water pit heat storage, calculations were repeated for 2 years with a time step of 1 hour. Result from the 2nd year was used in the analysis.

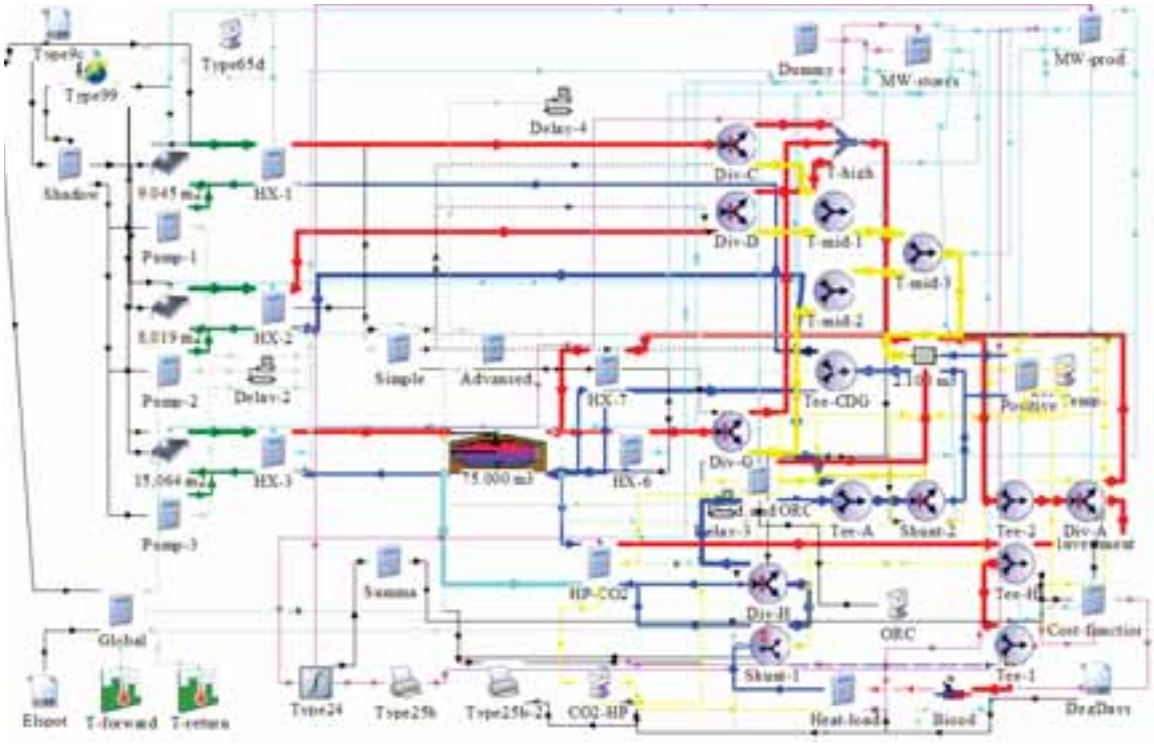

Fig. 2: The Trnsys model of the Marstal Solar heating plant

In the solar collector field model developed in Trnsys, parameters such as coefficients of the collector efficiency expressions, collector area, collector orientation, collector inclination and number of collectors per row are used as inputs. The following collector efficiency expression is used in the model.

$$\eta = \eta_0 K_\theta - \frac{a_1(T_m - T_a)}{G} - \frac{a_2(T_m - T_a)^2}{G} \qquad \text{(eq. 1)}$$

η_0: the start or the maximum efficiency, [-].
a_1: the first order heat loss coefficient, [W/(m^{2}K)].
a_2: the second order heat loss coefficient, [W/(m^{2}K^2)].
K_θ: incidence angle modifier, [-].
G: the total solar radiation, [W/m^2]
T_m: the mean temperature of the solar collector [ºC]
T_a: the ambient air temperature [ºC]

Table 2 show the coefficients of efficiency expressions for the collectors used in the solar collector fields. Collector efficiency for the collector field 1 is taken from a test report issued in 1991 (Fan etc., 2009). Collector efficiency expression of the collectors in the collector field 2 was reported by Vejen (2004). In the collector field 3, 13.88 m^2 flat plate solar collectors produced by Sunmark were installed. Efficiency of the collector was tested by SP Technical Research Institute of Sweden (2010).

Tab. 2: Collector efficiency expressions used in the Trnsys simulations

Collector field no.	Area, m2	η_0, -	a_1, W/(m^{2}K	a_2, W/(m^{2}K^2)
1	9045	0.76	3.5	0.002
2	8019	0.82	2.44	0.005
3	15064	0.80	3.43	0.015

The water pit thermal storage was modeled in Trnsys with a 2D multi-node storage model that includes both the water volumes at different layers and the ground soil around the storage. The Trnsys calculations starts with an uniform temperature of 35ºC for the store as the initial condition. Initial temperature of the ground was 8ºC.

Yearly thermal performances of the solar heating plant calculated by the Trnsys model were compared to the measurement results. Preliminary results calculated by the Trnsys model were analyzed.

4. Thermal performances of the solar collector fields

4.1 Analysis of the collector fields by the input/output method

Thermal performance of the solar collector fields were calculated by the Trnsys model with a time step of 1 hour. Fig. 3 shows the collector energy output of the solar collector field 1 in kWh/m^2/day as a function of the total solar radiation in kWh/m^2/day. It can be seen in Fig. 3 that there is a 2nd order polynomial function between the modeled collector field output and the total solar radiation on the collector panels. This is in good agreement with the collector efficiency expressions used in the calculations. The modeled outputs are however a bit scattered, which means that for the same total solar radiation on the collector panel the collector energy outputs are different. A possible explanation could be the varying collector fluid temperatures during operation. Even though there is the same total solar radiation on the panel the collector fluid temperature might vary depending on temperatures of the storage. A higher temperature of the storage means a higher temperature at the inlet of the collector field and thus a lower energy output of the field, vice versa. The measured collector outputs have a much larger deviations, most likely due to differences in collector operating temperatures and/or failures in operations of the systems. For instances there were some days with a daily total solar radiation in the range 3.5-5.5 kWh/m^2/day, however the collector outputs of the field were almost zero, indicating there was a failure or interruption in the collector field operation. There are also points with a significantly lower collector energy output than the modeled values, which could be caused by differences in collector inlet temperatures, uneven flow distribution among collector rows or malfunction of the controller etc. For the days when the collector field was in a good operation condition, the collector energy output follows nicely the trend with the simulations.

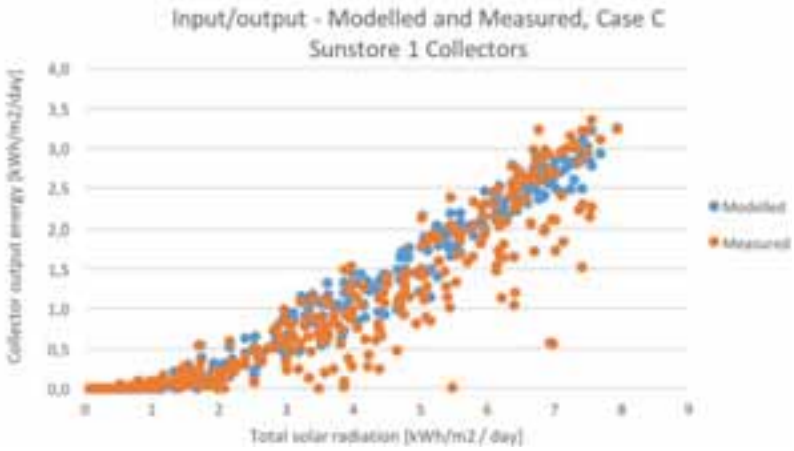

Fig. 3: Input/output diagram for the Sunstore 1 collector field with collector output [kWh/m^2/day] in 2015 as a function of total solar radiation [kWh/m^2/day]

The modeled and the measured collector energy output for the collector field 2 are shown in Fig. 4. There is a similar trend between the modeled collector energy output and the total solar radiation on the collector surface as it is for the collector field 1. With a change of the total solar radiation, the measured collector field output follows nicely a similar trend line as the modeled output does. The measured output has deviations of similar magnitude as the calculations. It is indicated that the solar collector field 2 has a much steadier operation than the solar collector field 1. It is shown that the solar collector model used in Trnsys is able to predict thermal performances of the solar collector fields with an acceptable accuracy.

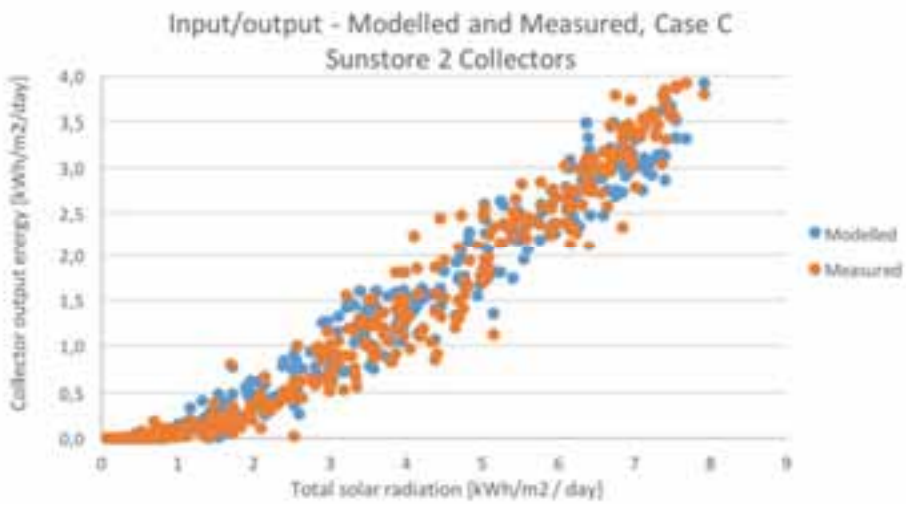

Fig. 4: Input/output diagram for the Sunstore 2 collector field with collector output [kWh/m^2/day] in 2015 as a function of Total solar radiation [kWh/m^2/day]

Fig. 5 shows the modeled and the measured collector energy output for the collector field 3 installed in the Sunstore 4 project. There is a similar trend between the modeled collector energy output and the total solar radiation on the collector surface as for the collector field 1 and 2, but the deviations of the data points are much larger. That indicates larger variations of collector field output for the same total solar radiation, which could be caused by large temperature variations at the bottom of the water pit thermal storage. Since the collector field 4 is connected to the water pit thermal storage, water is taken from the bottom of the water pit and is circulated through the solar collector field 4. Water temperature at the bottom of the water pit has a larger variation throughout the year. In summer or autumn when the water pit is almost fully charged, there is a higher temperature at the bottom of the water pit, for instance, 40-50ºC, while in spring or winter when the water pit thermal storage has been discharged, there is a lower temperature at the bottom of the water pit, for instance, 20-30ºC. A temperature difference of 20 K or more will result in different collector energy outputs even though the total solar radiation on the collector panels is the same. Deviations of similar magnitudes are also seen in the measured collector output that proves conclusion of the simulations. A detailed investigation on individual days is therefore necessary in the future in order to understand thermal behaviors of the solar collector field.

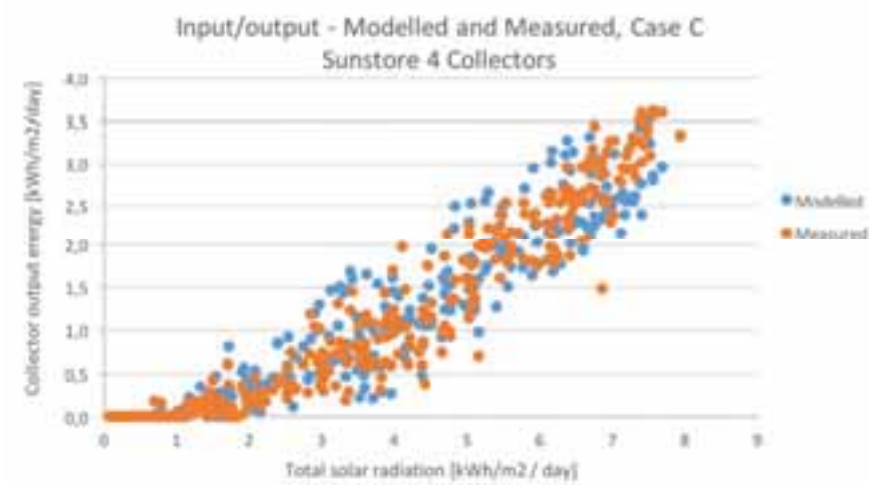

Fig. 5: Input/output diagram for the Sunstore 4 collector field with collector output [kWh/m^2/day] in 2015 as a function of Total solar radiation [kWh/m^2/day]

4.2 Daily collector energy outputs throughout the yearly

It is important to examine thermal behaviors of the collector fields throughout the year. Fig. 6 shows the measured and the calculated collector outputs [kWh/m^2/day] throughout the year for the Sunstore 1 Collectors. Not surprisingly there is a large variation of collector energy output throughout the year. At the start of the year, there was almost no solar heat produced by the field. After the middle of March, a significant increase of collector output is seen due to increasing solar irradiance in late spring. Throughout the summer and even late autumn there are notably solar heat

gains. The daily energy output of the collectors lies in the range 0.5-3.0 kWh per m^2. The calculated energy output agrees quite well with the measured ones, except an overestimation of the model occasionally in the summer and in the autumn (October).

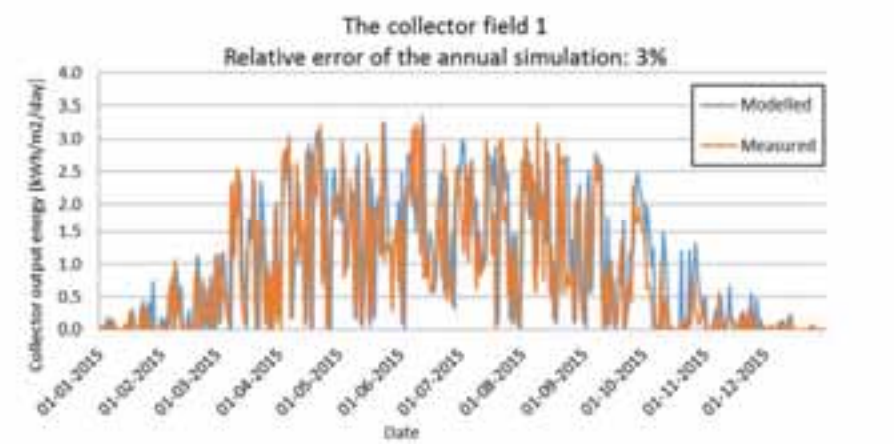

Fig. 6: The measured and the calculated collector outputs [kWh/m2/day] throughout the year 2015 for the Sunstore 1 Collectors

The measured and the calculated collector outputs for the collector field 2 and 3 are shown in Fig. 7 and 8 respectively. The Trnsys collector model predicts satisfactorily the energy outputs from the solar collector fields.

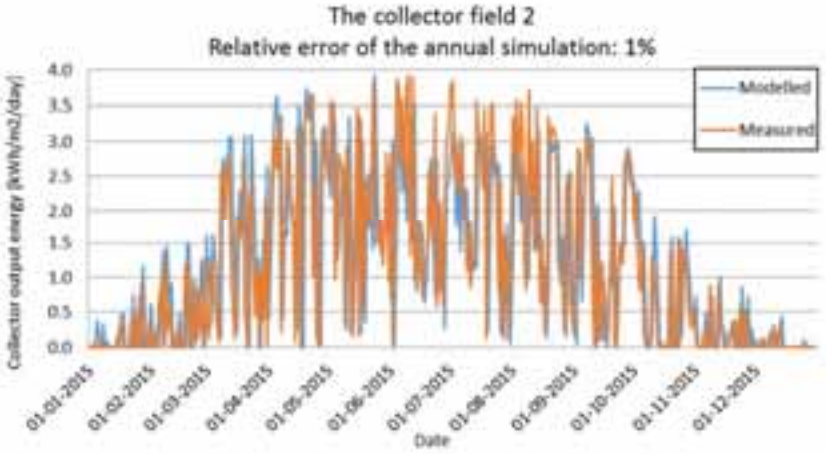

Fig. 7: The measured and the calculated collector outputs [kWh/m2/day] throughout the year 2015 for the collector field 2

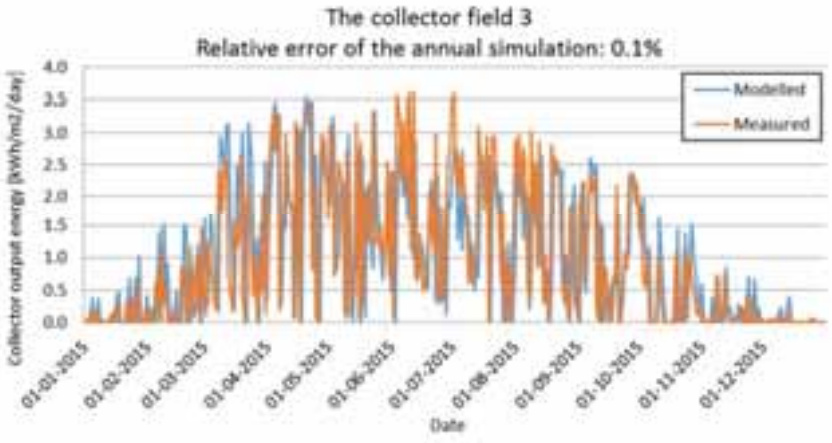

Fig. 8: The measured and the calculated collector outputs [kWh/m2/day] throughout the year 2015 for the collector field 3

4.3 Yearly collector energy outputs

The energy outputs of the collector fields are summarized and presented in Fig. 9. It is shown that the yearly energy outputs of the solar collector fields predicted by the Trnsys model agree well with the measured values. For the solar collector field 1, the Trnsys model predicts a yearly energy output of 3320 MWh in comparison to a measured value

of 3430 MWh. The deviation is 110 MWh, corresponding to a relative error of 3%. For the solar collector field 2, the accumulated energy output is measured to be 3617 MWh per year, while the Trnsys model calculates an energy output of 3600 MWh per year with a deviation of less than 1%. For the solar collector field in Sunstore 4, the measured and modeled energy outputs are respectively 5620 and 5624 MWh. Heat losses through the connection pipes account for 5-10% of the energy gain of the field and are therefore subtracted in the energy calculations. It can be concluded that the Trnsys model can predict satisfactorily the yearly energy outputs of the solar collector fields.

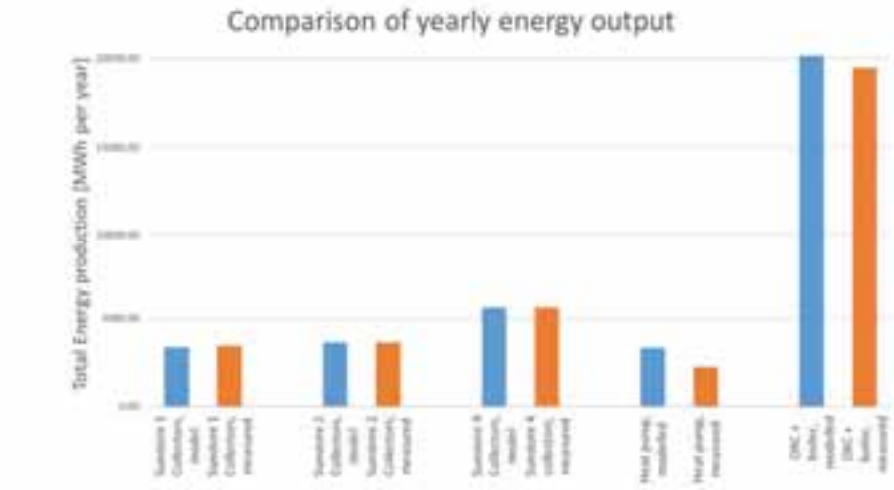

Fig. 9: The measured and the calculated yearly collector outputs in 2015 [kWh/m^2/day]

5. Thermal performances of the water pit thermal storage

Thermal behaviors of the water pit thermal storage were investigated experimentally by the monitored data and numerically by the Trnsys model. Fig. 10 shows a comparison of the measured and the calculated charge power of the PTES. A charge power of up to 55 MW was observed in the measurement in the middle of June because in June 2015 there was a lower consumption in the district heating net while on the other hand the solar irradiance was quite high. The Trnsys model underestimates the charge power of the PTES with a difference up to 12 MW. The significant error of the model is most likely caused by wrong prediction of water temperatures in the PTES, which could be a consequence of oversimplified models used in the calculations. Detailed investigation is therefore suggested for the future to identify the cause of errors. During the winter when there is a low solar irradiance, the model seems to overestimate the charge power.

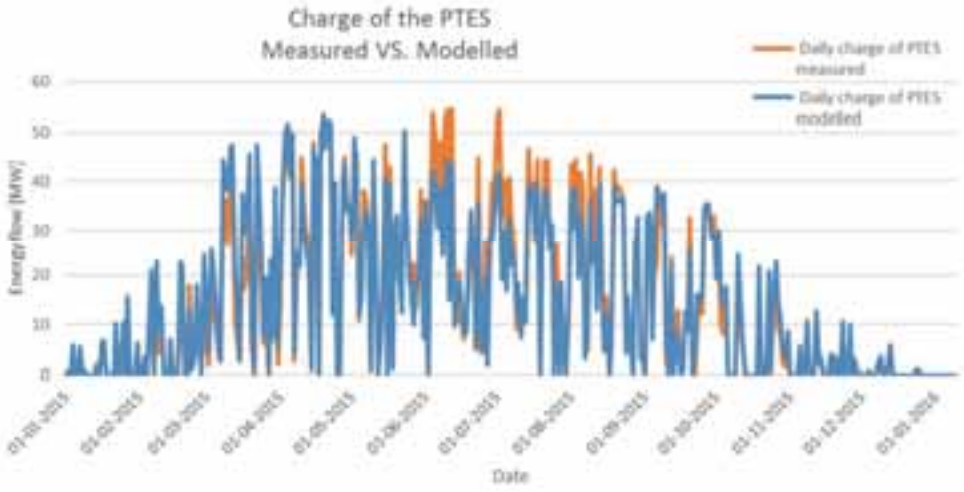

Fig. 10: The measured and the calculated charge power of the PTES in 2015

Fig. 11 show the measured and the modeled temperatures in the water pit thermal storage throughout the year. The measured temperature were shown as square or triangle dots. At the start of the year, there was a measured temperature of 62ºC at the top of the PTES, while the temperature was measured to be around 30ºC at the bottom of the PTES. Since there was a quite high temperature at the top of the PTES, heat was directly taken from the top of

the PTES and was mixed with hot water produced by the wood chip boiler or the backup oil burner so a mixed temperature of around 75-77ºC can be achieved for the district heating net. The direct discharge of the PTES continues except when temperatures at the top of the PTES drops below 50-55ºC or when price of electricity is sufficiently low. In that case, the heat pump will operate in order to utilize heat in the PTES with medium or low temperatures. The operation of the heat pump created a sudden decrease of temperatures at the bottom of the PTES. For instance, in the period from March 14 to March 21 there was a significant decrease of water temperatures at the bottom of the PTES. Due to discharge by heat pump, water temperatures at the top of the PTES was significantly decreased as well. In the middle of April the PTES reached a uniform temperature of 31-33ºC. After the middle of April thermal stratification was built up again by the use of heat pump since temperature of the water flowing from the heat pump back to PTES was much lower than 30ºC. The strategy for the discharge procedure was to extract heat from the PTES as much as possible. The benefit of the use of heat pump in April was not only a higher utilization ratio of the stored heat but also an empty PTES to store more solar heat for the coming summer. After the middle of May, temperatures in the store gradually increased. At the start of October, the PTES reaches the highest heat content. In the period October-December water temperatures in the store were kept quite constant.

The Trnsys modeled store temperatures were shown in curves in Fig. 11. It can be seen that the modeled temperatures follows the trend of developments as shown by the measurements. However there is quite a large difference between the modeled and the measured store temperatures, especially after the middle of April when heat pump cooled down the whole store to much lower temperatures. The likely cause of the difference could be oversimplification of the heat pump model or the control algorithm used in the Trnsys calculations. For an example, the operation of ORC unit has a significant influence on temperatures of the store since the ORC unit will be cooled by the store if there is not sufficient consumption of the district heating net. Whether the ORC unit will operate or not depends on an economical analysis of electricity generation by the manager of the plant. A detailed decision making algorithm for operation of ORC was difficult to obtain so the Trnsys model was not able to accurately determine the operation time of the ORC unit.

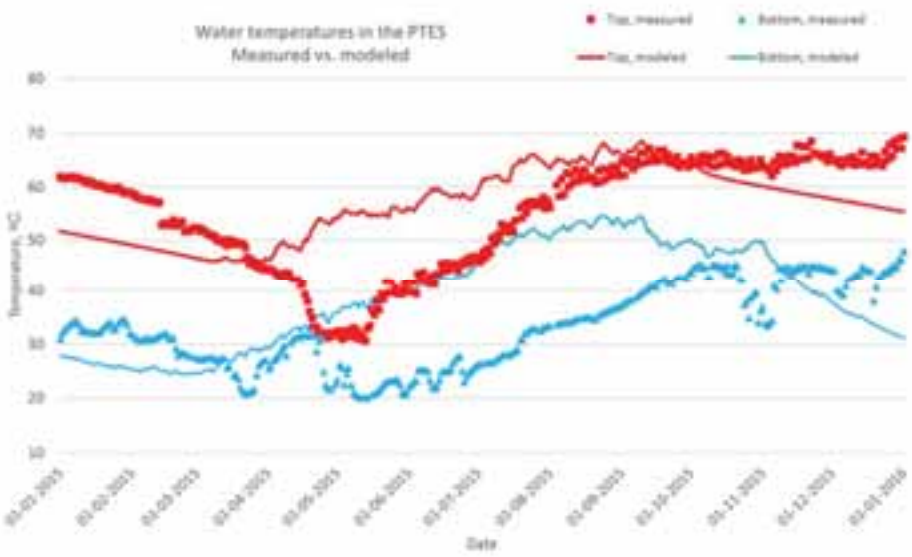

Fig. 11: The measured (orange) and the modeled (blue) temperatures through the top inlet/outlet on an hourly basis during year 2015

6. Conclusions

Detailed measurements were carried out on the Marstal solar heating plant. Based on the measurements, energy flows in the plant were calculated and thermal performance of the plant was analyzed. The monitored energy flows were compared to the energy flows calculated by a simplified Trnsys model of the plant. Preliminary results show that the Trnsys model predicts satisfactorily energy output of the solar collector fields. A max. deviation of 3% between the measured and the modeled energy output of the field was observed. A comparison between the measured and the modeled water temperatures in the PTES shows that the Trnsys model is able to predict the trend of temperature development in the store but fails to reproduce temperatures of the store especially in the period May-August. A likely cause of the error could be oversimplified heat pump model, inaccurate plant control algorithm etc. Detailed

investigation is therefore suggested for the future to improve the Trnsys model with focuses on the interaction between the heat pump, the ORC unit, the collector field and the store and on accurate inputs of boundary conditions of the model. The ultimate goal is to develop a Trnsys model that can be used to optimize design of a solar heating plant in terms of levelized cost of heat (LCOH).

7. References

Chang C., Wu Z., Navarro H., 2017, Comparative study of the transient natural convection in an underground water pit thermal storage, Applied Energy, 208, 1162-1173.

Cioccolanti L., Tascioni R., Bocci E., et al. 2018, Parametric analysis of a solar Organic Rankine Cycle trigeneration system for residential applications, Energy Conversion and Management, 163, 407-419.

Collector test report, 2010, SP Technical Research Institute of Sweden, SP 509301.

Fan J., Chen Z., Furbo S., Perers B., Karlsson B., 2009, Efficiency and lifetime of solar collectors for solar heating plants, ISES Solar World Congress 2009. Johannesburg, South Africa, p. 331-340

Jensen M.V., 2014. SUNSTORE ® 4 Design of the Water Storage The SUNSTORE Plant in Marstal. In Sunstore 4 Design of the Water Storage.

Kate D. Sunstore4. http://sunstore4.eu/, 2013. [Online; accessed 01-04-2017].

Kielsgaard Hansen, K., Nordgaard Hansen, P., Ussing, V., 1983. Seasonal heat storage in underground warm water stores. Report 134, Thermal Insulation Laboratory, Technical University of Denmark.

Kübler R., Fisch N., Hahne E., 1997, High temperature water pit storage projects for the seasonal storage of solar energy Journal, Solar Energy, 61, 97-105.

Li H., Xu W., Yu Z., et al. 2018, Discussion of a combined solar thermal and ground source heat pump system operation strategy for office heating, Energy and Buildings, 162, 42-53.

Lund, H., Werner S., Wiltshire R. etc. 2014, 4th Generation District Heating (4GDH) - Integrating smart thermal grids into future sustainable energy systems, Energy, 68, 1-11.

Nussbaumer T., Thalmann S., 2014, Status report on district heating systems in IEA concountries, Zurich, Switzerland, ISBN 3-908705-28-2.

Pfeil M., Koch H., 2000, High performance-low cost seasonal gravel/water storage pit, Solar Energy, 69, 461-467.

PlanEnergi, 2016, Long term storage and solar district heating, a presentation of the Danish pit and borehole thermal energy storages in Brædstrup, Marstal, Dronninglund and Gram, https://ens.dk/sites/.../sol_til_fjernvarme_brochure_endelig.pdf

Schmidt T., 2013. Sunstore 4 Technical Reports: Design of the measurement and evaluation program.

Tian Z., Perers B., Furbo S., et al., 2018, Thermo-economic optimization of a hybrid solar district heating plant with flat plate collectors and parabolic trough collectors in series, Energy Conversion and Management, 165, 92-101.

Trnsys, 2016. Trnsys Manual 17.0, LLC 22 North Carroll Street – suite 370 Madison, WI 53703 – U.S.A.

Vejen N.K., Furbo S., Shah L.J., 2004, Development of 12.5 m² Solar Collector Panel for Solar Heating Plants Solar, Energy Materials and Solar Cells, 84, 205-223.

Extension of Germany's Largest Solar District Heating System with Seasonal Thermal Energy Storage

Natalie Gohl, Dominik Bestenlehner and Harald Drück

Research and Testing Centre for Thermal Solar Systems (TZS)
Institute for Thermodynamics and Thermal Engineering (ITW)
University of Stuttgart, Stuttgart (Germany)

Abstract

This publication introduces several measures to extend and optimize Germany's largest solar district heating system with seasonal thermal energy storage, located in southern Germany in the city Crailsheim. The aim of the extension is to achieve a solar fraction above 50 % in order to reduce CO_2 emissions and to demonstrate the functional and economic attractiveness of solar district heating systems with seasonal thermal energy storage. The investigated measures comprise different concepts for the extension of the solar thermal collector area with high-efficiency flat-plate collectors and the extension of the borehole thermal energy store, which serves as seasonal thermal energy store in the system. As an alternative, the installation of an overground hot water thermal energy store is considered to increase the heat storage capacity. Other measures are the installation of a second heat pump as well as the reduction of the return flow temperature of the district heating grid. Further, combinations of the above mentioned measures are investigated. The effects of the specific measures are quantified by means of annual system simulations with the transient simulation software TRNSYS 17.

Keywords: solar district heating, seasonal thermal energy storage, high solar fractions, system simulation, TRNSYS

1. Introduction

The currently largest central solar district heating plant with seasonal thermal energy storage (CSHPSS) in Germany is located in Crailsheim, which is a small city with a population of about 33 000 in the south of Germany. The CSHPSS was built between 2004 and 2011 in two main construction phases. With an initially planned solar fraction of 50 %, the system is a flagship project for solar thermal district heating grids.

The CSHPSS in Crailsheim supplies heat to the district heating grid Hirtenwiesen II. Fig. 1 shows the development of the annual heat demand of the district heating grid as well as the solar fraction. Through the years, the heat demand of the district heating grid increased continually due to the construction and connection of new buildings. With over 7 000 MWh at the beginning of the year 2017, the heat demand is more than 1.7 times higher than the 4 100 MWh which were assumed in the original plans for the current stage of the heat generation system. The solar fraction reached a maximum of about 42 % in the year 2014, but due to the increasing heat demand, the solar fraction of the entire system is decreasing and was at a level of about 27.5 % in 2016. In order to enlarge the share of solar energy in the system, an extension and optimization of the solar district heating system is planned. Various measures to reach this aim were investigated with the help of transient system simulations, carried out with the simulation software TRNSYS 17. The aim of these measures is to achieve a solar fraction of more than 50 %. Finally, the most promising concept will be further investigated for implementation, considering ecological, technical, energetic as well as economical aspects. However, the focus of this publication lies only on the technical and energetic aspects.

More detailed descriptions of the CSHPSS in Crailsheim as well as the results of the system monitoring over the last years can be found in various publications, e.g. Bauer et al. (2009, 2013 and 2015), Bodmann et al. (2005) or Kurz and Schopf (2012).

doi:10.18086/swc.2017.06.06 Available at http://proceedings.ises.org

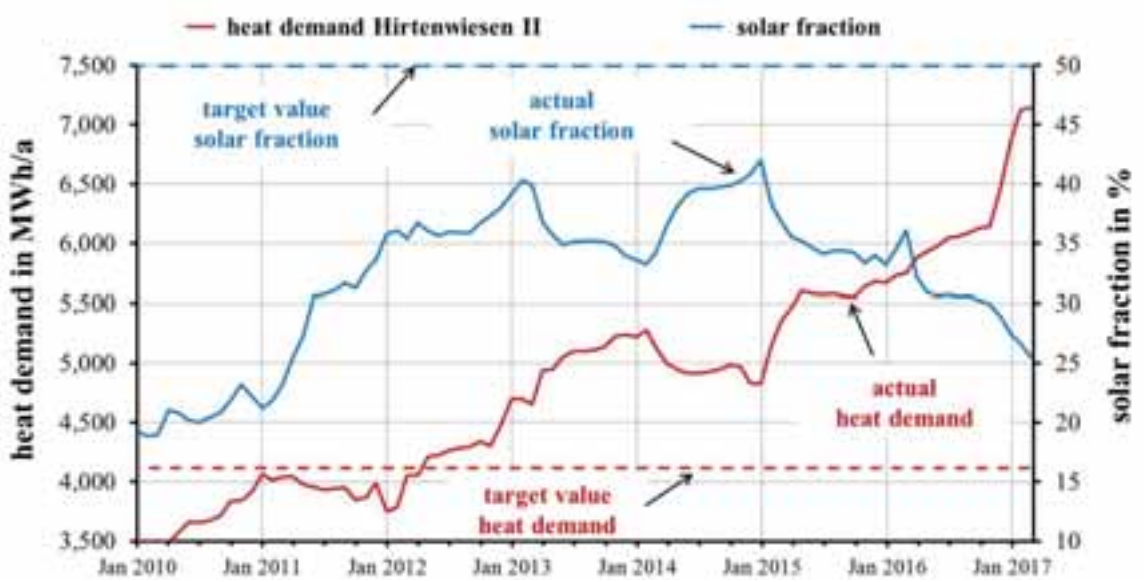

Fig. 1: Development of the heat demand and solar fraction of the district heating grid Hirtenwiesen II.

2. Reference system and methods

The simulation software TRNSYS 17 was used to develop and assess different measures and concepts for the extension and optimization of the CSHPSS in Crailsheim.

The performance of the existing system, see Fig. 2, which serves both as reference for the investigated concepts and as source of validation for the simulation model with monitoring data, is described in the sections 2.2 and 2.3. The definitions of the performance figures are defined in section 2.1. Finally, section 2.4 introduces the different investigated concepts.

2.1 Performance figures

Four performance figures are used in this publication in order to assess the performance of the system and specific components namely

- the solar fraction f_{sol},
- the efficiency of the borehole thermal energy store η_{BTES},
- the efficiency of the hot water thermal energy store η_{HWTES} and
- the seasonal performance factor of the heat pump SPF_{HP}.

The fraction of heat in the district heating grid Hirtenwiesen II covered with solar thermal energy is expressed using the solar fraction f_{sol}, which is defined as

$$f_{sol} = \frac{Q_{SHE} - Q_{HWI} - W_{HP,el}}{Q_{HWII}}, \qquad \text{(eq. 1)}$$

with

Q_{HWI} heat transferred to the district heating grid Hirtenwiesen I in order to prevent stagnation [MWh],

Q_{HWII} total annual heat consumption of the district heating grid Hirtenwiesen II [MWh],

Q_{SHE} solar heat transferred at the preheating solar heat exchanger [MWh] and

$W_{HP,el}$ electrical energy consumption of the heat pump [MWh].

The efficiency of the borehole thermal energy store η_{BTES} is described as

$$\eta_{BTES} = \frac{Q_{BTES,dischar}}{Q_{BTES,char}} \qquad \text{(eq. 2)}$$

with

$Q_{BTES,char}$ heat charged to the BTES over the period of one year [MWh] and

$Q_{BTES,dischar}$ heat discharged from the BTES over the period of one year [MWh].

The efficiency of the hot water thermal energy store η_{HWTES} is defined in an analogous manner.

In order to quantify the efficiency of the heat pump, the seasonal performance factor of the heat pump SPF_{HP} is used

$$SPF_{HP} = \frac{Q_{HP,cond}}{W_{HP,el}} \qquad \text{(eq. 3)}$$

with

$Q_{HP,cond}$ annual useful heat provided by the heat pump [MWh] and

$W_{HP,el}$ annual electrical energy consumption of the heat pump [MWh].

2.2 Description of the existing system

The CSHPSS in Crailsheim was built for the heat supply of a new part of the city erected on the area of a former military base. The current system setup is shown in a schematic design in Fig. 2 and is described in brief in the following.

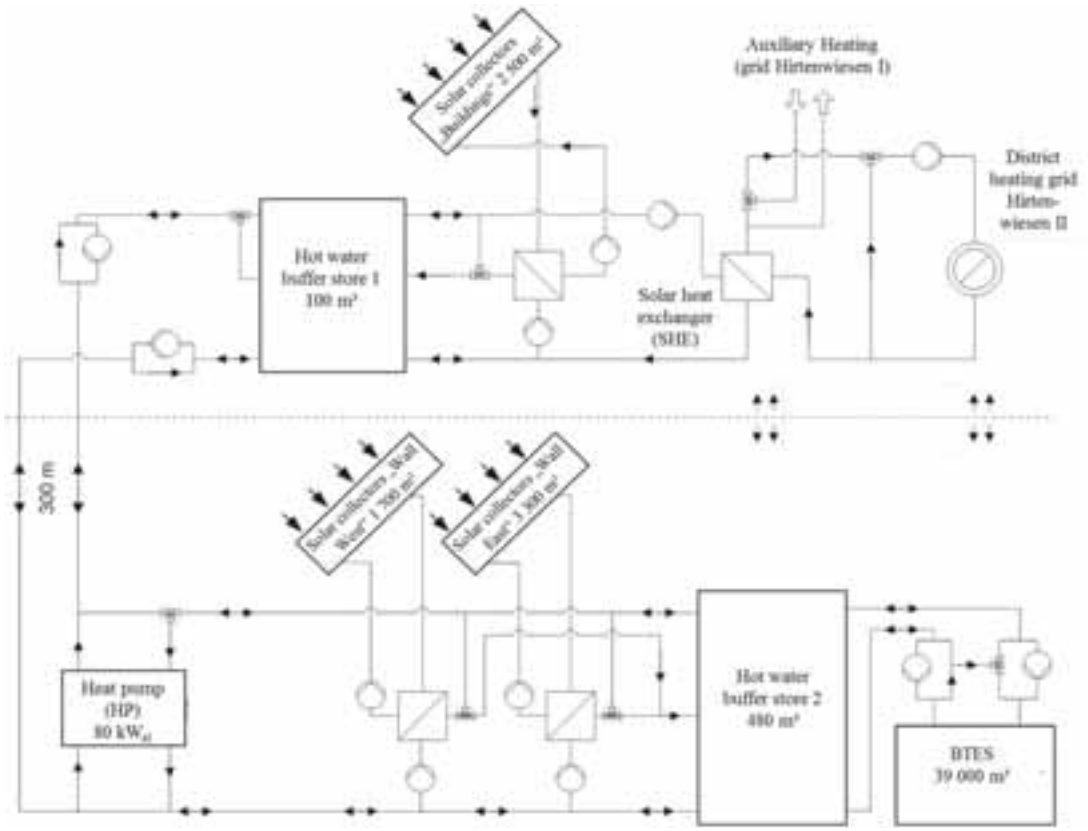

Fig. 2: Schematic design of the existing solar district heating system in Crailsheim.

The solar thermal system consists of three collector fields. Two collector fields are installed on noise barrier walls ("Wall West" and "Wall East") with a collector aperture area of 1 700 m² and 3 300 m², respectively. Additionally, there are flat-plate collectors mounted on the roofs of the former and retrofitted barracks buildings as well as on the local school building and gymnasium with a total collector aperture area of 2 500 m². The total thermal power output of the solar thermal systems is at present about 5.2 MW. A borehole thermal energy store with a volume of 39 000 m³ serves as seasonal thermal energy store. The BTES can be charged by the collector fields "Wall West" and "Wall East" via a hot water buffer store with a volume of 480 m³. In order to discharge the BTES to lower temperatures, a compression heat pump with an electrical power of 80 kW is installed. The second part of the system consists of a hot water buffer store with a volume of 100 m³, which is charged by the collector field installed on the buildings. If necessary, thermal energy can be transferred between the two buffer stores. The annual heat consumption of the solar district heating grid was 6 862 MWh in 2016.

2.3 Validation of the simulation model

Transient system simulations were carried out with the simulation software TRNSYS 17 based on a simulation model that was validated beforehand with extensive monitoring data from the years 2013 to 2016. Because the conditions in 2016 were nearest to the mean values of the considered years, the measured weather data of the year 2016 were used as input data for the simulation of the reference system. Tab. 1 shows the comparison between the measured and simulation data for the reference year 2016.

Tab. 1: Absolute and relative deviations between measurement and simulation data of the CSHPPS in the reference year 2016.

Quantity	Unit	Measurement	Simulation	Δx_{abs}	Δx_{rel} [%]
f_{sol}	[%]	27.5	28.3	- 0.8	- 2.9
η_{BTES}	[%]	57.3	63.6	- 6.3	- 11.0
SPF_{HP}	[-]	4.8	4.7	0.1	2.1
Q_{HWII}	[MWh]	6 862	6 861	1	0.0
Q_{SHE}	[MWh]	2 283	2 336	- 53	- 2.3
Q_{HWI}	[MWh]	175	158	17	9.7
$Q_{HP,cond}$	[MWh]	1 061	1 114	- 53	- 5.0
$W_{HP,el}$	[MWh]	221	235	- 14	- 6.3
$Q_{BTES,char}$	[MWh]	731	647	84	11.5
$Q_{BTES,dischar}$	[MWh]	419	411	7	1.7

Generally, there is a good consistence between measured and simulation data. The explanation for the relatively high deviations in the values concerning the BTES is the different conditions in the simulation and in reality. In the simulation, the time period is three years, where every year has the same boundary conditions. Only the third year of the simulation is used for the evaluation. Consequently, the final and initial temperature profiles of the BTES and the buffer stores at the beginning and the end of the year are exactly the same which is not the case in reality. The deviations in the heat transferred to the district heating grid Hirtenwiesen I can be explained by the fact, that the heat transfer is often controlled manually in reality, for example if the weather forecast predicts a hot and sunny day and the stores are already full. This behavior cannot be reproduced in the simulation.

2.4 Concepts for system extensions and optimization

Several single measures as well as their combinations were considered and assessed in order to increase the solar fraction of the CSHPSS in Crailsheim to a value above 50 %. Tab. 2 shows an overview of the single measures presented in this publication.

Tab. 2: Overview and description of possible measures for the extension and optimization of the solar district heating system.

Measure	Description
HFC	Installation of high-efficiency flat-plate collectors (HFC)
BTES	Enlarging of the borehole thermal energy store (BTES) from 80 to 160 borehole heat exchangers
HWTES	Integration of a seasonal hot water thermal energy store (HWTES) with a volume of 8 000 m³
HP	Installation of a second heat pump with a rated electrical power of 80 kW
RFT45	Reduction of the mean return flow temperature of the district heating grid from 48.1 °C to 45 °C
RFT40	Reduction of the mean return flow temperature of the district heating grid from 48.1 °C to 40 °C

One measure is the extension of the collector field energy output by the installation high-efficiency flat-plate collectors (HFC). Different collectors and combinations of collectors were simulated. Tab. 3 shows the resulting collector field power output of the four collector configurations HFC1 to HFC4.

Tab. 3: Total collector field power output[1] of the CSHPSS for the four different HFC configurations.

Collector configuration	Power output [MW]
HFC1	7.24
HFC2	7.17
HFC3	7.38
HFC4	7.34

As the solar gain is increased, the capacity of the seasonal thermal energy store should be increased as well. For that purpose two different measures were investigated: The first measure (BTES) extends the BTES by doubling the current number of borehole heat exchangers, the second measure integrates an overground seasonal hot water thermal energy store (HWTES) with a volume of 8 000 m³ into the system. In order to increase the thermal energy extracted from the BTES and therefore its efficiency, the integration of a second heat pump (HP) with the same rated electrical power of 80 kW as the existing heat pump was investigated.

The volume weighted mean return flow temperature of the solar district heating grid was 48.1 °C in the year 2016, according to monitoring data. A reduction of the mean return flow temperature would increase the efficiency of the collectors as well as reduce the heat losses of the grid and the thermal energy stores and therefore increase the solar fraction of the system. Simulations with mean return flow temperatures of 45 °C (RFT45) and 40 °C (RFT40) were carried out.

3. Simulation results

The actual configuration of the CSHPSS with the measured weather data of the year 2016 serves as the reference system for all simulations. Due to the assumption that more buildings will be connected to the district heating grid in the following years, an annual heat consumption of the district heating grid Hirtenwiesen II of 7 000 MWh is assumed for the simulations. Due to the slightly higher heat consumption, the solar fraction of the reference system is reduced to 27 %.

Fig. 3 shows the solar fraction, the seasonal performance factor of the heat pump as well as the efficiency of the BTES for simulations with all four HFC configurations and all of their possible combination with one additional measure. Generally, the differences between the HFC configurations are relatively small at about 2-3 %-points

[1] Basis: Solar Keymark certificates: Power output of the collector module at a temperature difference between collector and ambience of 50 K.

between the configurations HFC2, which shows the lowest solar fractions, and HFC3, which shows the highest solar fractions. Regarding the single measure HFC, the solar fraction can be increased by 11 %-points compared to the reference system to a total value of 38 %. The extension of the BTES has no positive influence on the solar fraction. The reason for this is that the energy output of the heat pump is not increased as well. Consequently, more heat is charged to the BTES, but the amount of heat that is discharged from the BTES does not increase in the same magnitude. This also leads to a decrease in the efficiency of the BTES but also to the best seasonal performance factor of the heat pump in both measures BTES and HWTES. The reason for the higher performance of the heat pump are the higher temperatures in the BTES and therefore a smaller temperature lift for the heat pump. The installation of a second heat pump has the opposite effect than the extension of the storage capacity. The seasonal performance factor decreases significantly due to lower BTES temperatures while the efficiency of the BTES increases significantly due to the higher heat pump power output.

The most promising measure in terms of increasing the solar fraction is the reduction of the mean return flow temperature of the district heating grid to a value of 40 °C. This leads to an increase of the solar fraction by at least 5 %-points compared to the measure HFC, depending on the collector configuration. However, none of the concepts shown in Fig. 3 turned out to be sufficient to obtain a solar fraction of 50 %. Accordingly, other concepts combining several measures have been investigated.

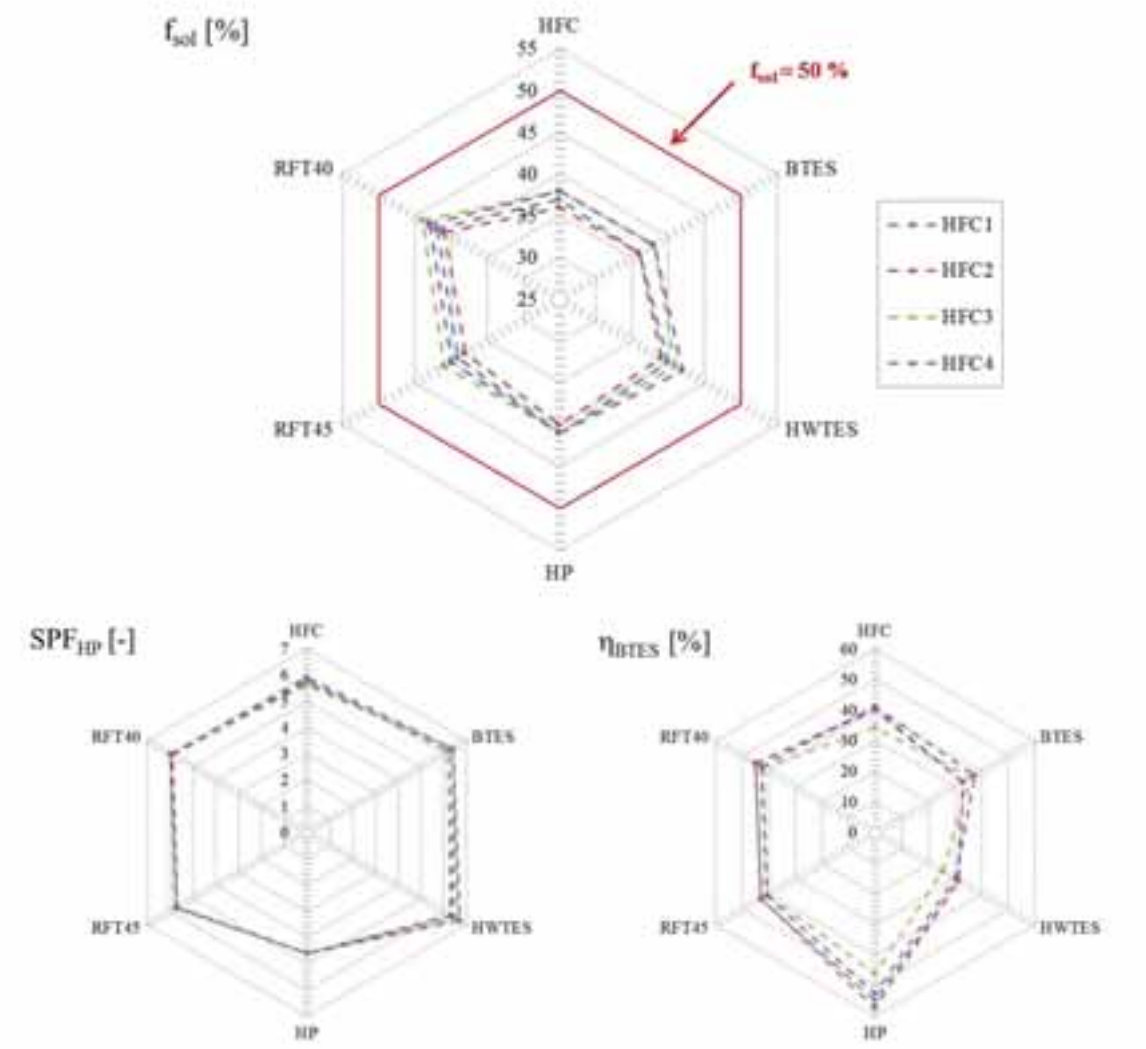

Fig. 3: Simulation results for selected investigated system concepts.

The installation of a HWTES was preferred compared to the extension of the BTES, consequently only concepts including a HWTES are shown in Fig. 4. Additional to the performance figures shown in the previous figure, the efficiency of the HWTES is presented in Fig. 4.

Like before, the concepts including a second heat pump have a positive effect on the efficiency of the BTES. Since the BTES and the HWTES are installed in parallel and the heat pump can discharge both, the efficiency of the HWTES is increased as well. The seasonal performance factor of the heat pump on the other hand is reduced due to lower temperatures in the stores.

With the concept using a HTES, a second heat pump as well as the reduction of the mean return flow temperature of the district heating grid to 45 °C a solar fraction of 50 % can only be reached using the collector configuration HFC3. A further reduction of the mean return flow temperature to 40 °C leads to a further increase of the solar fraction to or above 50 %, except for HFC2 with a solar fraction of 49 %. High solar fractions of almost 50 % can also be reached with the collector configurations HFC3 and HFC4 by a combination with the measure RFT40, without the installation of a second heat pump. However, the installation of a second heat pump is recommended because it leads to an extension of the effectively usable storage capacity of the CSHPSS.

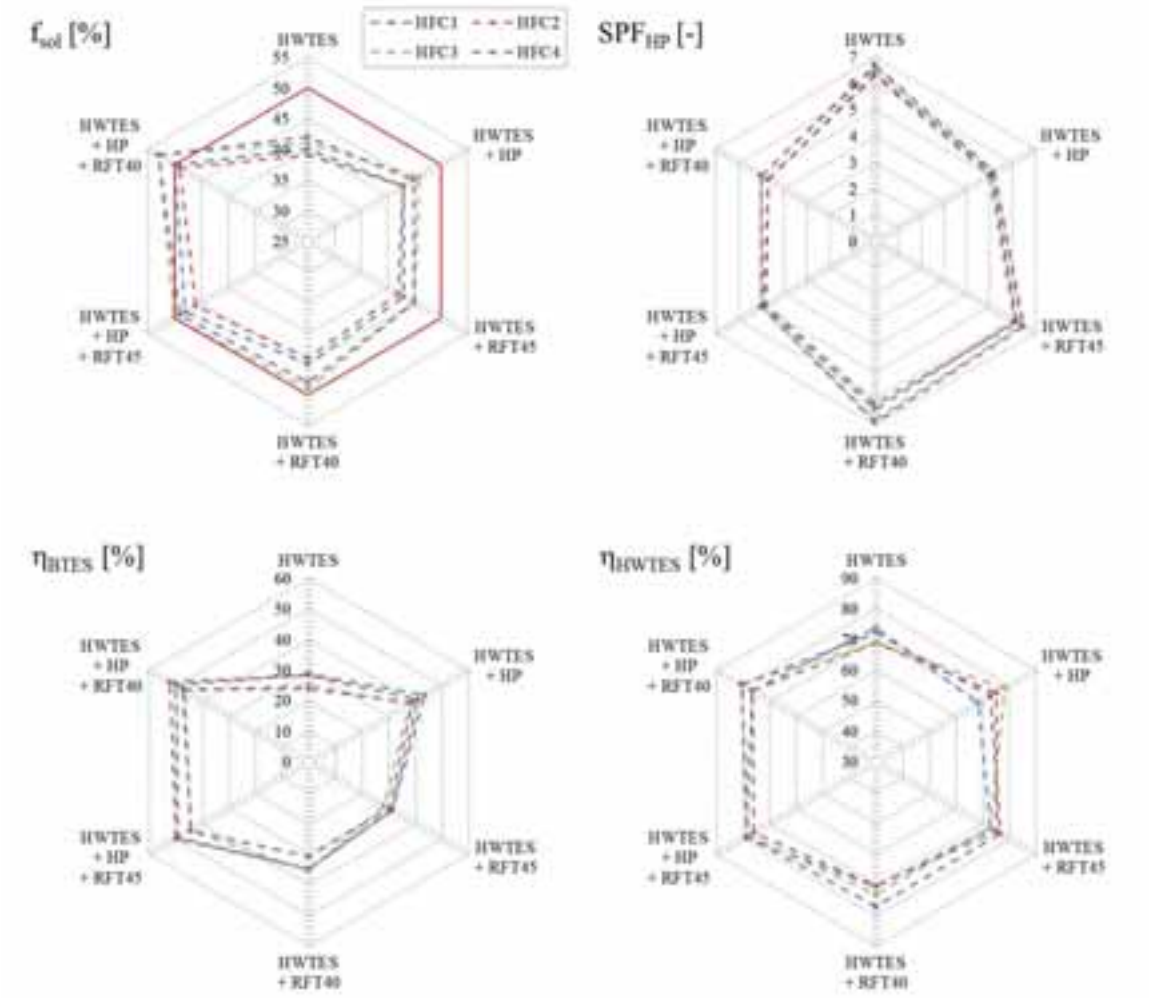

Fig. 4: Simulation results for selected investigated system concepts.

Conclusions

The concepts assessed regarding the extension and optimization of the solar district heating system in Crailsheim were presented and discussed in this publication. The concepts which lead to a solar fraction of around 50 % comprise the option of enlarging the solar thermal system with high efficient flat plate collectors (HFC) with a collector area of about 2 500 m² as well as the integration of a second heat pump (HP) with an electrical power of 80 kW and a hot water thermal energy store (HWTES) with a volume of 8 000 m³. A further increase of the solar fraction above 50 % can be achieved by the additional reduction of the return flow temperature of the district heating grid to 40 °C.

Considering the simulation results, the owner of the CSHPSS intends to extend the system with an enlargement of the collector area, a HWTES and a second heat pump. Additionally it is planned to introduce measures which offer the consumers incentives to reduce the return flow temperature of their heat transfer stations. The detailed planning of the enlargement of the CSHPSS is currently in progress, considering amongst other issues different locations and hydraulic integrations of the HWTES, as well as an adaption and optimization of the control strategy.

Acknowledgement

The activities described in this publication are being supported by the German Federal Ministry for Economic Affairs and Energy (BMWi) based on a decision of the German Bundestag by Projektrräger Jülich (PtJ) under the grand number 0325869B (research project CROW: Extension and Optimization of the solar district heating system Hirtenwiesen II in Crailsheim and accompanying research on solar district heating and seasonal thermal energy storage). The authors gratefully acknowledge this support and carry the full responsibility for the content of this publication.

References

Bauer, D. et al., 2009. Solar unterstützte Nahwärme und Langzeit-Wärmespeicher (Juni 2005 bis Juli 2008), Final research report of national project funded by the Federal Ministry for the Environment, Nature Conservation and Nuclear Safety under grant-no. 0329607J

Bauer, D. et al., 2013. Solarthermie2000plus: Wissenschaftlich-technische Begleitung des Förderprogramms Solarthermie2000plus zu solar unterstützter Nahwärme und Langzeit-Wärmespeicherung (August 2008 bis September 2012), Final research report of national project funded by the Federal Ministry for the Environment, Nature Conservation and Nuclear Safety under grant-no. 0329607P

Bauer, D. et al., 2015. Solarthermie2000plus: Wissenschaftlich-technische Begleitung des Förderprogramms Solarthermie2000plus zu solar unterstützter Nahwärme und Langzeit-Wärmespeicherung (Januar 2013 bis September 2015), Final research report of national project funded by the Federal Ministry for Economic Affairs and Energy under grant-no. 0325998A

Bodmann, M. et al., 2005. Solar unterstützte Nahwärme und Langzeit-Wärmespeicher (Juni 2005 bis Juli 2008), Final research report of national project funded by the Federal Ministry for the Environment, Nature Conservation and Nuclear Safety under grant-no. 0329607F

Kurz, S., Schopf, M., 2012. “Solar unterstützte Nahwärmeversorgung Crailsheim Hirtenwiesen II” Final research report of national project funded by the Federal Ministry for the Environment, Nature Conservation and Nuclear Safety under grant-no. 0329607H

Appendix: Units, Symbols and Abbreviations

Tab. 4: Symbols

Quantity	Symbol	Unit
Collector area	A	m^2
Solar fraction	f_{sol}	%
Heat charged to BTES	$Q_{BTES,char}$	MWh
Heat discharged from BTES	$Q_{BTES,dischar}$	MWh
Heat provided by the heat pump	$Q_{HP,cond}$	MWh
Heat to the district heating grid Hirtenwiesen I	Q_{HWI}	MWh
Heat consumption district heating grid Hirtenwiesen II	Q_{HWII}	MWh
Heat charged to HWTES	$Q_{HWTES,char}$	MWh
Heat discharged from HWTES	$Q_{HWTES,dischar}$	MWh
Heat transferred through solar heat exchanger	Q_{SHE}	MWh
Seasonal performance factor of the heat pump	SPF_{HP}	-
Electric energy consumption of the heat pump	$W_{HP,el}$	MWh
Absolute deviation	Δx_{abs}	MWh, %, -
Relative deviation	Δx_{rel}	%
Efficiency of the BTES	η_{BTES}	%
Efficiency of the HWTES	η_{HWTES}	%

Tab. 2: Abbreviations

Abbreviation	
BTES	Borehole thermal energy store
CSHPSS	Central solar heating plants with seasonal thermal energy storage
HFC	High-efficiency flat-plate collector
HP	Heat pump
HWTES	Hot water thermal energy store
RFT40	Mean return flow temperature 40 °C
RFT45	Mean return flow temperature 45 °C
TRNSYS	Transient systems simulation software

Potential Analysis On Solar District Heating in China

Junpeng Huang[1], Jianhua Fan[2] and Simon Furbo[2]

1 Department of Civil Engineering, Technical University of Denmark, Copenhagen (Denmark)

2 Department of Civil Engineering, Technical University of Denmark, Copenhagen (Denmark)

Abstract

Abstract: This paper analyzes the potential of solar district heating (SDH) in China from the perspective of incentive policy making, selection of technology solutions, regional adaptability and economic feasibility for clean heating. Based on the analyzation, this paper proposes a road map for the development of SDH, and predicts its market potential in China.

Key words: solar district heating, potential analysis, road map, 13th-Five-Year Plan

1. The urgency moving from coal to clean energy

China's urbanization rate is currently only 54.8%, leaving a huge potential for future growth. Over the past decade, increasing heating requirements have led to the fast deployment of district heating systems in big cities, as shown in Fig.1, the heating area increased from 2.5 billion m^2 to 6.7 billion m^2 in the past 10 years from 2005-2015. Meanwhile although rural population has been decreasing, rural energy demand most notably for heating has also been increasing steadily. This rise has been on par with economic development and improvements in lifestyle. District heating is therefore increasingly being deployed to meet heating loads in rural regions.

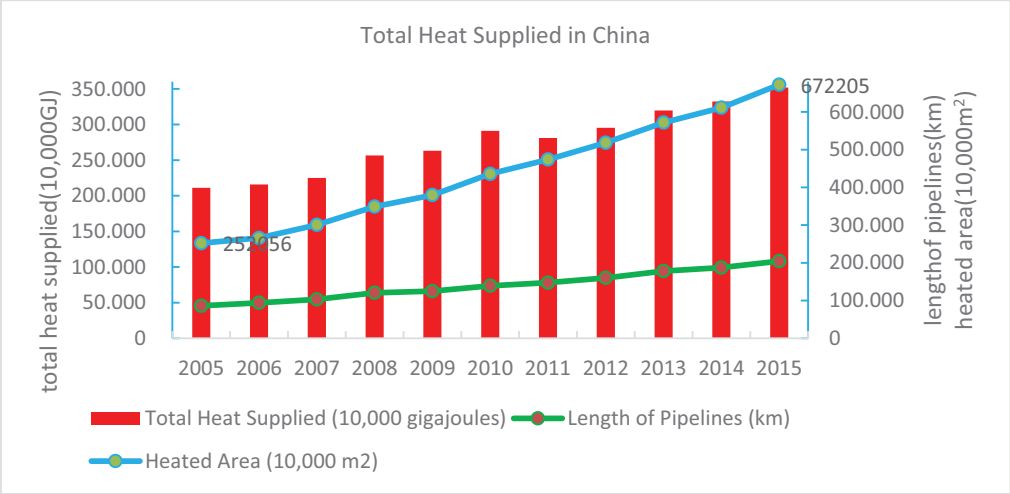

Fig. 1: Growth of the heating capacity in China[1]

To cope with the rapidly increasing demand for heating, authorities have deployed district heating systems throughout north of the country. However, as shown in Fig.2, district heating systems in China are coal intensive, accounting for 81%[2] of the total heating energy, which caused serious air pollution. It's reported that over 366,000 people died earlier from diseases in China in 2013 caused by air pollution due to burning of coal[3].

doi:10.18086/swc.2017.06.07 Available at http://proceedings.ises.org

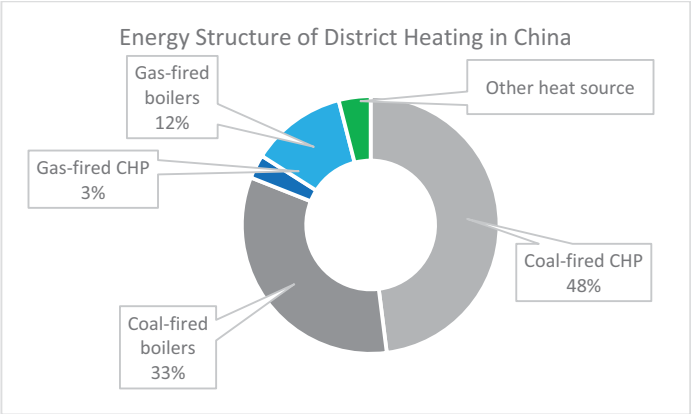

Fig. 2: Energy structure of district heating in China

According to the Sino-US Joint Statement on Climate Change[4], China will reach its CO_2 emission peak in 2030, and will increase the share of non-fossil energy to 15% by 2020, 20% by 2030. But there is a big gap from the objectives until now. Only taking Beijing as an example, by the end of 2015, the proportion of renewable energy in total heating energy consumption is only 0.8%. To increase the proportion of non-fossil fuels accounted for primary energy consumption, large-scale using solar heating is imperative.

2. Why solar district heating

50% of total air pollution source comes from coal consumption in China, especially in rural area, raw coal (~80% bituminous and ~20% anthracite) is often consumed in stoves with low efficiency. In 2013, Chinese government published Air Pollution Control Action Plan, which set a target for coal reduction, by 2017, consumption of coal will fall to below 65% in terms of total energy consumption. Beijing-Tianjin-Hebei Province, the Yangtze River Delta and the Pearl River Delta will try to achieve negative growth of total coal consumption.

To fulfill this target quickly and effectively, the government takes two main strategies which are called Coal to Gas and Coal to Electricity, with a subsidy policy on clean heating transformation. Now, these two strategies are widely used under the emission reduction pressure and being stimulated by subsidy policy. From the actual implementation effect of view, these two strategies may reduce the raw coal combustion temporarily, but there're still problems on the real effect of reducing air pollution and the sustainability of policy.

2.1. Coal to Gas is difficult to be applied widely

Coal to Gas in power plants was first implemented in Beijing and quickly adopted by other cities. However, currently most of them have suspended or canceled the initiative, mainly because natural gas is still scarce and costly in China.

High natural gas prices, increased burden of heating companies, it is difficult for long-term stable operation. In addition to the initial expenditure for transformation of equipment, the using cost is also great. The price of natural gas per kWh is about 3-5 times the price of coal with the same thermal value. Due to fuel costs rose sharply, and government subsidies declined year by year, many small heat companies which have completed the coal to gas transformation tend to change back to coal-fired boilers.

Evidence show that Coal to Gas also indirectly results in wind power curtailment and PV power curtailment. At present, the wind power and PV installed mainly concentrated in the "Three North" area (northeast, northwest, North China), accounting for 77% and 68% of the country with large-scale centralized development. During heating season due to the output power of CHP is determined by heat demand, which makes the CHP units less flexible, power supply surplus, which leads to huge wind and PV power

curtailment. According to "China Building Energy Annual Development Research Report 2017"[5], in "three North" area, the amount of abandoned wind power in 2015 was 9.48 TWh, 8.34 TWh and 16.55TWh, accounting for 99.9% of the total abandoned wind power. From the time distribution point of view, 67% of the country, more than 90% of the northeastern region, wind power curtailment occurred in the heating season.

In 2016, the natural gas gap between supply and demand reached 60 billion m^3 in China, and it's estimated that the gap will reach 130 billion m^3 by 2020, which means there would be not enough gas supply for a lot of households installed gas boilers when the heating demand reaches to peak. Natural gas is currently easy to be accessed in urban areas, but the infrastructure for gas supply in rural area is still under plan or under construction. Coupled with the difficulty of laying the gas pipe network, high costs, not sufficient gas production and other factors, the Coal to Gas strategy is difficult to be applied widely.

2.2. Coal to Electricity is difficult to be sustained

Coal to Electricity means replacing coal-fired boilers with low-temperature air-source and ground-source heat pumps, in some cities, including regenerative electric boilers, but direct heating types of electric heater are prohibited by this program. The government will provide about $3,600 subsidies per household for heating equipment, and additional 0.6 US cent per kWh electricity price subsidies in heating season, almost reducing 2/3 cost for using electric heating equipment.

But the Coal to Electricity is also in dispute on cleanness and the sustainability of subsidy policy.

Most of the electricity used in Beijing, Tianjin and Hebei comes from the off-peak electricity in Inner Mongolia, and the main source is coal. The implementation of Coal to Electricity is a method with rob Peter to pay Paul, and finally pollution will eventually be grafted to the western region.

Another disputation is the heavy financial burden. Taking Beijing as an example, it is expected that there will be 1.1 million households finishing the Coal to Electricity transformation at the end of 13th -5-Years Plan. If calculating in accordance with maximum subsidy of 10 thousand kWh per household, the government needs 334 million US dollars in the following years. In addition, to reduce the burden on the residents, the government must invest substantial money to improve thermal insulation performance for the residents' houses.

So, the Coal to Electricity is not a problem for cities with higher economic level, but it is unsustainable in economically backward areas. Therefore, coal reduction cannot engage in "one size fits all", and solar-aided energy systems that integrating multi-energy types and multi-heat sources, such as geothermal energy, biological energy and other clean energy should also be valued to replace the scattered coal combustion.

2.3. Advantages of solar district heating

Compared with Coal to Gas and Coal to Electricity technologies and policies, SDH is the only strategy to substitute fossil energy completely, which will also improve energy security by reducing energy imports, especially natural gas importation for China.

The most advantage of SDH for end users is the great operating cost savings. In a combination system of solar and gas boiler, solar will contribute 66.6% energy cost savings by saving gas consumption[22] in Hebei area, for a solar combined with air-source heat pump heating system, solar will contribute 45.6% energy cost savings in Xi'an City[23].

SDH can also create local jobs related to the manufacturing, commercialization, installation and maintenance of solar thermal systems.

3. Feasibility of SDH in China

3.1. Stringent environmental protection pressure national wide

To deal with the serious air pollution problem, the Chinese government has made systematic favorable

policies for clean energy space heating.

Fig. 3: Favorable policy structure for clean heating in China[6]

The detailed indexes and targets which address clean heating issued by different government departments:

Table.1 Regulations and Plans on Clean Heating and Renewable Development in China

Regulations and Plans	Indexes and Targets
Solar Energy Development 13th-5-Years Plan	In 2020 and 2030, non-fossil energy accounted for 15% and 20% of the primary energy consumption. In 2020, the number of large SDH stations in suitable areas reached more than 200, the total area of collector is more than 4 million square meters. Combined with the construction of New Countryside, more than 3 million demonstration projects of solar hot water and solar heating in rural areas will be promoted nationwide.
Renewable Energy Development13th-5-Years Plan	In 2020 and 2030, the proportion of non-fossil energy in primary energy consumption reached 15% and 20% respectively. In 2020, all types of renewable energy substitute about 1.5 tce in heating and civilian fuels, in which, solar thermal utilization (heating and hot water) reached 800 million square meters, equivalent to 96 million tce.
Energy Development 13th-5-Years Plan	In 2020, the supply capacity of non-fossil energy reached 750 million tce, the proportion of non-fossil energy consumption increased to more than 15%.
Building Energy Efficiency and Green Building Development 13th-5-Years Plan	In 2020, renewable energy substitutes conventional energy consumption accounted for more than 6% in civil buildings. The new solar thermal application area will reach to more than 2 billion square meters in buildings.
Suggestions on Promoting Renewable Energy Heating	In 2020, renewable energy heating area reached 3.5 billion square meters, Beijing, Tianjin and surrounding areas up to 1 billion square meters, Solar heating reached 400 million square meters nationwide.
Air Pollution Prevention and Control Action Plan (2013-2017)	In 2017, the proportion of non-fossil energy consumption increased to 13%.

3.2. Choose suitable region

China has abundant solar resources, equivalent to 1.7 trillion tons of standard coal equivalent (tce) per year[7], but most Chinese cities are densely populated with high land price and limited places for installation of solar collectors. So, at the beginning phase for solar district heating(SDH) in China, the most suitable area for developing large-scale solar heating is the area with rich solar resources, longer heating period, many free lands available, and no power grids and gas pipe network coverage, such as Tibet, Gansu, Tsinghai provinces.

In the outskirts of the central city, as well as rural areas without municipal heating infrastructure, it is also appropriate to develop small SDH pants to reduce the use of coal, while creating the conditions for using of rural biomass and municipal solid waste incineration.

3.2.1 North urban area

Heating in urban areas of northern China is mostly district heating, including many city level heat supply network and community level heat supply network. According to the heat source and size, heating systems can be divided into cogeneration, regional coal fired boiler, gas boiler, residential area coal-fired boiler, gas boiler, heat pump residential district heating etc.; And household gas stove, household coal stove, air conditioning heating, direct electric heating etc.

The heating area of Chinese cities reached 12.6 billion m^2, and the energy consumption of heating in northern cities was 184 million tce, accounting for 21% of total building energy consumption in 2014. In 2001~2014, the heating area of northern urban buildings increased from 5 billion m^2 to 12.6 billion m^2, increased by 1.5 times, the total energy consumption increased less than 1 times, the total energy consumption growth was significantly lower than the growth of construction area. The heating energy consumption per square meter decreased from 22.8kg tce/m^2 in 2001 to 14.6kg/m^2 in 2014, and the energy consumption per square meter decreased by 34%[25-26].

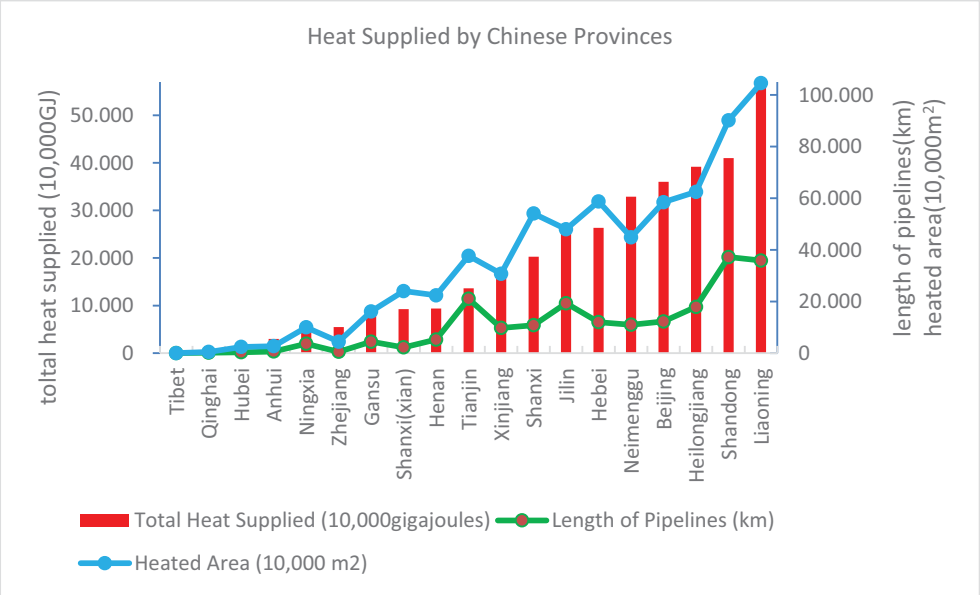

Fig. 4: Heat supplied by Chinese Provinces[1]

The vast existing heating area means great potential for clean heating transformation, and a good opportunity for solar heating, but there're great challenges from the economic point of view.

Affected by the welfare heating system under the planned economy, most residential heating systems are single pipe vertical series system, in which vertical imbalance is serious, uneven heat and cold between high

and low stories of buildings, difficult to achieve heat charging by metering. At the same time, heating equipment obsolete, poor reliability, lack of advanced heat metering means[12].

"Heat" as a commodity is not accepted by users and part of enterprise, it is difficult for users to change from the welfare heating system to buy heat, auxiliary heat metering equipment is expensive, the reform from the tandem network to metering per household is difficult.

The urban area has large population density, high land price, and limited installation space for solar collectors. In the short term, it is not the best choice for developing SDH. But the heating demand of urban area is large and the users are concentrated. The economic and environmental benefits from SDH are more significant, which will be the focus of future development.

3.2.2 North Rural areas

The northern rural heating mainly relies on heated brick bed, hot wall, household coal stove, gas stove, electric heating and solar assisted biomass boiler heating in some developed rural area around Beijing and Tianjin, some rural areas also develop small district heating systems.

Zhang Wei of Tianjin University summarizes the current heating technologies, heating fuel in north rural area, household evaluation of indoor thermal comfort, and the distribution of heating technologies based on a survey to rural residential buildings in the cold area between 2007 and 2010[27]. As shown in Fig.5, small coal fired boilers and heated brick beds are the main heating solution for rural area, accounting for 84% in total.

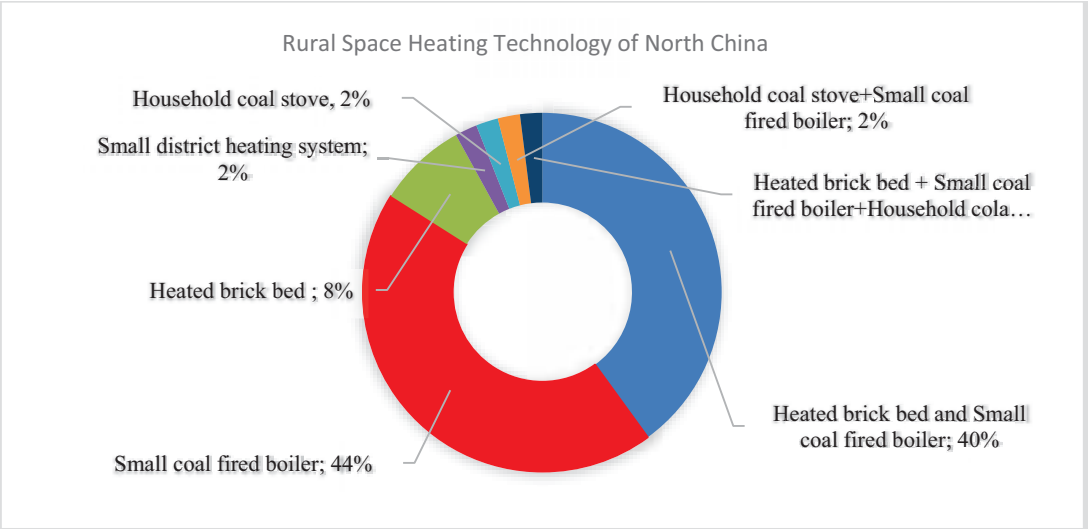

Fig. 5: Rural Space Heating Technologies in North China

There are many deficiencies for current heating solutions in rural heating in North China, such as low indoor temperature, large heating energy consumption, serious pollution and so on. Energy utilization rate of heated brick bed and hot wall is about 60%, stove is only 40%, while no insulation measures for heating pipes, the heat loss of pipelines is large. Heating safety is not guaranteed, the improper operation or design easily lead to gas leakage, and even explosion accident, stove heating easily leads to carbon monoxide poisoning[28].

In terms of district heating in rural area, Shandong province is far more developed than other provinces. Beijing, Shanxi, Liaoning, Heilongjiang and Hebei have developed rapidly.

Rural and small towns in northern China are good places for developing large-scale SDH projects due to cheap lands, backward heating pipe network infrastructures, serious air pollutions caused by raw coal burning, and the great pressure to improve quality of life.

3.2.3 South Area

Air conditioning is still the largest portion of household heating in South China, reaching 30%[1]. Due to the short heating time in South China, even if the heating effect is not good, many families still use air conditioning as the only heating source, to save a large amount of installation of other heating equipment. Household gas-fired boilers and electric floor heating accounted for 1% and 0.1% in southern households, respectively. The heat pump as a relatively new product, accounting for only 0.03%. With characteristics of energy saving and environmental protection, more suitable for the southern climate, heat pumps are currently the fastest growing household heating products in the South. Affected by the rainy, not enough sunshine time and other factors in the south, solar heating applications are relatively limited, accounting for only 0.005%.

Short heating time in southern China, usually about 1-3 months, household heating dominates, not conducive to develop SDH. In order to reduce operating costs, residential property management companies are also considering adding a solar collector field on the existing heating system.

3.3. Choose suitable technologies

Although China shares 71% of the total installation of solar collectors in the world, but no more than 0.3% of solar collectors have been used for solar heating[8], as shown in Fig.6, there're only 154,971m^2 solar collectors used for heating, accounting for 0.3% of the annual production in 2014 in China. Most of solar collectors were used in rural area as a home appliance, solar water heaters.

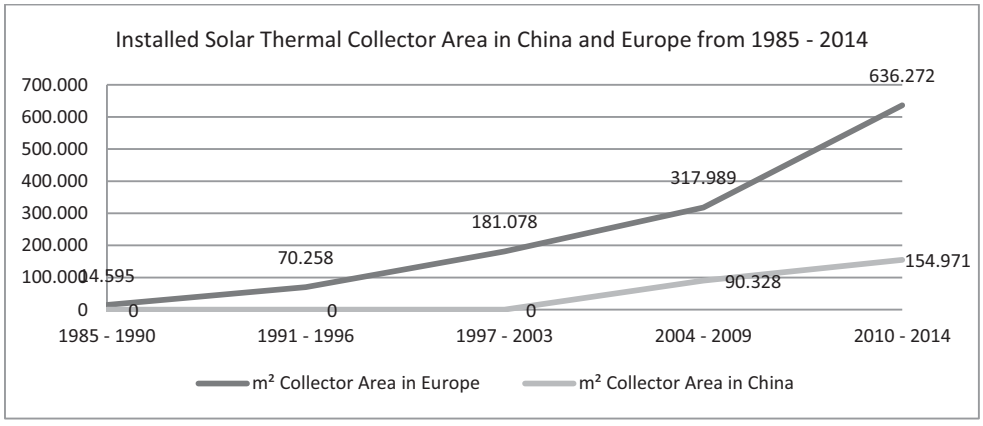

Fig. 6: China-EU collector installation area for solar heating[9]

3.3.1 Centralized solar heating system is better than household solar heating

Solar heating has been used for more than 10 years in China, and is widely used in rural areas as household heating in the early stage. In recent years, solar heating has gradually developed into schools, public buildings and residential communities etc. Without municipal heating.

Year 2016, we conducted a post-survey on some solar household heating projects in Beijing rural villages(Fig.7). The on-site survey reveals that solar heating system can save more than 50% of the coal burning annually, but it doesn't run steadily. Caused by the easily damaged all-glass vacuum tube solar collectors and bad installation, there're lots of deficiencies found after 2 years' installation, e.g. leaking in the pipelines and water tanks. The operation and maintenance of household heating system mainly conducted by the user personal, due to lack of professional knowledge, many users face the helplessness when the system fails. But it is easier to build a regional operation and maintenance service points in a centralized heating station than decentralized household heating.

A farmhouse heated by solar energy

A village with solar heating

Fig. 7: Typical household solar heating project in rural areas of Beijing

After more than 10 years of rural solar heating pilot and experience accumulation, from the economy, safety and operation and maintenance work convenience point of view, the author thinks that district heating with solar and biomass as the main heat source is more suitable than household heating in rural areas.

3.3.2 Flat plate solar collector is better than all-glass vacuum tube solar collector

The authors investigated many solar heating projects in northern China. All-glass vacuum tube solar collectors are mostly used in those household solar heating systems. Due to poor maintenance and improper operation, the real life span for all-glass vacuum tube solar collectors is only 2-3 years. Many all-glass vacuum tube solar collectors are broken for overheat or freezing in the first year since installation. The Investigation Report on Solar Heating Demonstration Projects in Mentougou of Beijing (ICA, 2010) gives the same suggestions, for solar heating projects, flat plate solar collector with simple structure, long service life and low maintenance rate should be preferentially selected.

3.3.3 Solar heating can prolong the life of existing ground source heat pump system

In the past more than 10 years, part of local Chinese government in cold northern area promoted ground source heat pump (GSHP) heating, only in Shenyang City, GSHP heating area reached 59.41 million square meters in 2012, accounting for nearly 1/3 of the city's total heating area. But now, there are many residential communities with GSHP heating system cannot get normal heating because of long term imbalance between heating and cooling.

Because heating load in winter is greater than cooling load in summer in cold areas, the heat extracted from the underground soil by GSHP systems is much greater than the heat injected to the soil, which makes the soil temperature decreasing yearly. The lower soil temperature will decrease the system's evaporation temperature in winter, reduce the heating capacity, and increase the energy consumption. According the Study on Heat Balance of Ground Source Heat Pump in Severe Cold Area[11], when soil temperature decreases by 1℃, the energy consumption of the GSHP will increase by 3-4%.

Solar collectors can be added to those dysfunctional GSHP systems to form a hybrid energy heating system. With proper control strategies, this hybrid energy system can achieve direct solar heating, direct heat pump heating, heat injection from solar collectors in summer and heat extraction by GSHP in winter, and prolong the life span of GSHP systems, at the same time improve the system energy efficiency.

3.4. Economic feasibility

There are mainly two district heating models in China – district boiler heating and district CHP heating, the fuel is coal or gas. This paper selects a Chinese standard building (heating index: 50W/m^2) in Xi'an as a sample, with 10^6 m^2 heating area, 50MW heating load. Suppose the efficiency of coal fired boiler is 0.68,

gas fired boiler is 0.9; pipe network transmission efficiency is 0.9. The heating mode is setting as single heat source, double pipe heating system. Based on a 25 years' payback time, we can calculate the heat price and analysis the economy for different district heating technologies[13].

Based on land cost, energy price, O&M cost etc. in China, we analyze the economy of SDH in China with successful models from Denmark. The annual global solar irradiance is 1247.4KWh/m^2.a in Xian, total district heating load is 144 GWh/a, heating time is 2900 hours, designed solar fraction is 20%, the price for different energy in Xi'an is shown in Table.2.

Table.2 Basic assumptions and price structure in Xi'an

Biomass	29.5$/MWh
Electricity	149.6$/MWh
Power grid price	225.0$/MWh
Bank loan interest rate	5%
Years of investment	25 Year

According to the above design parameters and prices of fuels, we analyzed the economy for four SDH systems in China by means of the SUNSTORE4-Feasibility-Evaluation-Tool[12]. And the heating prices is shown in Fig.8 based on 25 years' payback time. Solar collector area is 144,300 m^2 for all district heating systems, the volume of PTES is 288,600 m^3, BTES is 1,154,400 m^3, and TTES is 31,746 m^3.

Table.3 Four types of SDH technologies combination

Types	Technologies combination
SDH1	Solar + Biomass + HP + Pit Thermal Storage
SDH2	Solar + Biomass + Pit Thermal Storage
SDH3	Solar + Biomass + HP + Borehole Storage
SDH4	Solar + Biomass + Tank Thermal Storage

Coal is the mainly energy source in China, but the heating price of coal fired CHP is very high, so government allocates large amount of subsidy to coal fired CHP to maintain price competitive advantage. we calculate the heating price for traditional district heating technologies, heating price is very high, but the price of SDH systems are relatively low. SDH not only will save a lot of fossil fuels, but also reduce the heating price.

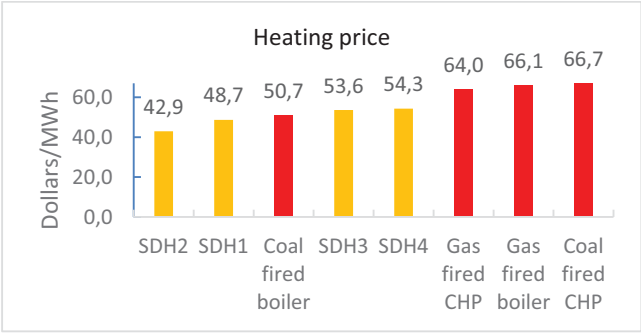

Fig. 8: Heating price of different district heating systems

From Fig.8, we can conclude that the heating prices of gas fired CHP, Gas fired boiler and coal fired CHP are very high; comparing heating price of the eight district heating systems, in the 50MW heating load condition, the heating price of SDH2 is the lowest, with a price 42.9$/MWh, then SDH1, with a price 48.7$/MWh; and the price of coal fired CHP is the highest, the heating price is 66.7$/MWh. Generally, the heating price of SDH systems is lower than traditional CHP and gas fired boiler district heating. So SDH has

price competitive advantage in China.

4. Major barriers

Although SDH has many benefits, it is still very difficult to implement this environmentally friendly clean heating technology in China. The major barriers include no demo project, and lack of mature supply chain support such as design, construction and operation of SDH plants. Besides the above-mentioned barriers, there're two facts for development of SDH in China.

4.1. Backward idea

When promoting SDH, the most common voice is that "land price is high" in China, this centralized solar heat station needs to take up a lot of land, completely inconsistent with China's national conditions. The reality is that, from an economic point of view, compared with conventional agriculture, the economic benefits of solar heat stations are much higher than those of agriculture, and due to the arrangement of collectors, a large interval distance is required, which makes the land can still develop livestock and facilities agriculture. In addition, in the sparsely populated, resource-poor Tibet, Gansu and other regions, as well as some areas with strict ecological protection requirements, SDH is the best choice.

4.2. Difficult to be connected into existing heating pipe networks

District heating technology in China is still the second generation, supply and return water temperature is higher in main pipe network, it's difficult for solar heating to be connected into existing heating pipe networks without a heat pump or reheat device[17~18]. In addition, space heating is mandatory in heating season as a livelihood project in China, but there's no heating demand in the rest of the year, which means a waste of solar energy in summer, or will increase the payback time of a SDH system. Therefore, to make full use of solar energy, improve annual solar fraction, building a seasonal heat storage facility is necessary[19~20].

5. Huge market potential

China's district heating capacity shows an increasing trend year by year, which is in line with the level of China's economic development, the demand for improving indoor thermal comfort in winter is becoming higher. Not only compulsory heating in North, the voice for heating in South in winter is also stronger in recent years. It can be predicted that district heating load will further increase in near future. Based on the analysis to the data of district heating capacity in recent ten years, we can get the annual growth rate of district heating capacity, about 9%, we can predict the district heating capacity development trend in future 5 years by this growth rate. By 2020, China's district heating capacity will reach 727,100 MW, an increase of 254,544 MW compared with 2015, see Figure 10.

Assuming the annual solar irradiance is 800 W/㎡, the efficiency of high performance flat plate heat collector is 0.6, transmission efficiency of pipe network is 0.9, the average daily sunshine hours was 7 h, the share of SDH used in clean energy heating is 5%, 10%, 15%, 20%, we can calculate the market potential and environmental benefit from the clean transformation of existing district heating network and newly installed district clean heating network.

By calculation shown in Table 4, when clean heating accounts for 5% of total district heating capacity and SDH accounts for 5% of clean heating, SDH installation capacity is 1,200 MW, and the maximum installation area of solar collector is 1.5 million m^2. When clean heating accounts for 20% of total district heating capacity and SDH accounts for 20% of clean heating, SDH installation capacity would reach to 19,000 MW, and the maximum installation area of solar collector would be 23.8 million m^2.

Table.4 Potential SDH capacity and solar collector area in the clean transformation of existing district heating system

SDH loads and Solar collector area in existing district heating system（10^3MW）				
	DH-5%	DH-10%	DH-15%	DH-20%
SDH-5%	1.20	2.35	3.55	4.75
SDH-10%	2.40	4.70	7.10	9.50
SDH-15%	3.60	7.05	10.65	14.25
SDH-20%	4.80	9.40	14.20	19.00
Solar collector area（10^6m^2）				
	DH-5%	DH-10%	DH-15%	DH-20%
SDH-5%	1.50	2.94	4.44	5.94
SDH-10%	3.00	5.88	8.88	11.88
SDH-15%	4.50	8.81	13.31	17.81
SDH-20%	6.00	11.75	17.75	23.75

Note: DH-5% represents clean heating account for 5% in clean heating transformation of existing district heating capacity, SDH-5% represents SDH account for 5% in clean heating capacity. The rest are similar.

6. Conclusions

By above technical and economic analysis, we can summarize a SDH development road map as shown in Table.5.

Table. 5 SDH Development Road Map in China

Steps	Pilot demonstration	Technology accumulation	Technology innovation
Years	2017-2020	2021-2025	2026-2030
Target market	Rural area, small villages, towns	Industrial parks, large residential communities	Small cities, integration with existing heating network
Technology application	Solar + GSHP, Solar + Tank Thermal Storage, high performance flat plate solar collector	Low temperature heating, remote monitoring, seasonal heat storage	System integration, large scale solar district heating

Northern China owns the basic conditions for the implementation of SDH with a developed district heating network. With the national energy saving renovation of existing buildings and clean energy transformation of existing district heating system, development of low temperature heating technology, and more stringent restrictions to coal-fired boilers, heating enterprises must actively look for clean energy alternative to fossil energy, and SDH will be the best choice. There are already some enterprises begin to build pilot and demonstration projects in Tibet, Beijing suburbs and other regions. It is expected there would be many SDH projects finished by the end of 2017.

Even though there are many challenges for SDH in China, we still believe that the implementation of SDH is an inevitable requirement for economic development and environmental protection. The next five years would be the best time to promote SDH with the mature technologies, favorable policies, and huge market potential.

7. References

1.http://data.stats.gov.cn/easyquery.htm?cn=C01&zb=A0B05&sj=2015
2.*Jiang Yi*. Study on China's Building Energy Conservation Strategy. "China Engineering Science", 2011, 13 (06): 30-38. "China Construction Annual Development Research 2015")
3.https://www.healtheffects.org/ （GBD MAPS Working Group. Burden of Disease Attributable to Coal-Burning and other Major Sources of Pollution in China. 2016. HEALTH EFFECTS INSTITUTE）

4.http://news.xinhuanet.com/world/2015-09/26/c_1116685873.htm
5.Tsinghua University Building Energy Conservation Research Center. 《China Building Energy Annual Development Research Report 2017》. China Construction Industry Press. Beijing (2017)
6.http://zfxxgk.nea.gov.cn (National Energy Administration of China)
7.《Assessment method for solar energy resources》QX/T89-2008
8.Werner Weiss, Monika Spork-Dur, Franz Mauthner. Solar Heat Worldwide 2017(Global Market Development and Trends in 2016 Detailed Market Figures 2015). IEA Solar Heating & Cooling Programme, (2017)
9.http://www.mohurd.gov.cn/xytj/ （Annual Report of Urban Construction of China(2013)）
10.http://sunstore4.eu/ (DESIGN OF THE OVERALL ENERGY SYSTEM OF THE DEMONSTRATION PLANT AT MARSTAL FJERNVARME)
11.Li Ying.Study on heat balance of ground source heat pump in Severe Cold Area[J]; Journal of Jilin Architectural and Civil Engineering Institute. (2012)
12.http://sunstore4.eu/use-results/sunstore4-tool/
13.*Tan Dalu, Zhao Shiqiang*.《GONGCHENGJINGJIXUE》. Wuhan University of Technology. 2012
14. *Huang Jianchun*. Economic Analysis on the status of urban central heating and research on heating system optimization and energy-saving measures. 《Chang'an University》, 2008
15. *Zhou Zhisheng*. Economic Analysis of Cogeneration Technology. 《Jilin University》, 2015
16. http://zfxxgk.nea.gov.cn (National Energy Administration of China)
17. *X Yang，H Li，S Svendsen*. Decentralized substations for low-temperature district heating with no Legionella risk, and low return temperatures. 《Energy》, 2016, 110:65-74
18. *Du Lijuan*. Research and application of low temperature heating technology. 《BEIJING UNIVERSITY OF CIVIL ENGINEERING AND ARCHITECTURE》, 2016
19. *C Flynn, S Kai*. Influence of location and design on the performance of a solar district heating system equipped with borehole seasonal storage. 《Renewable Energy》, 2015, 81:377-388
20. *B Sibbitt* et al. The Performance of a High Solar Fraction Seasonal Storage District Heating System – Five Years of Operation. 《Energy Procedia》, 2012, 30(1):856 - 865
22. Zhang Chen, Study On Combined Heating System Of Solar Energy And Gas Wall Hung Boilers In Baoding,2014, University Of Hebei

23. Shen Zhenyu, Xuan Yongmei, Energy Consumption Analysis Of Solar Air Source Heat Pump Heating And Hot Water System, School of environmental and chemical engineering, Xi'an Polytechnic University, 05 issue of 2016, Refrigeration & Air Conditioning,p544-548

24. Tang Jiayao, Heating System Reform And Regulatory Innovation, Urban Development Research, 2016, 23 (3): 43-48

25. Annual Report On the Annual Development Of Building Energy Conservation In China 2015, Building Energy Conservation Research Center Of Tsinghua University

26. Annual Report On the Annual Development Of Building Energy Conservation In China 2016, Building Energy Conservation Research Center Of Tsinghua University

27. Zhang Wei. Study on heating energy consumption of rural residence in cold area. Tianjin University, 2011

28. Li Yanjun. Study on heating mode of rural residence in Northwest China. Xi'an University Of Architecture And Technology, 2014

Implementation of large solar thermal system into district heating network in Chemnitz (Germany)

Nirendra Lal Shrestha[1], Thorsten Urbaneck[1], Thomas Oppelt[1], Bernd Platzer[1], Thomas Göschel[2], Ulf Uhlig[2] and Holger Frey[2]

[1] Chemnitz University of Technology, Department of Mechanical Engineering, Professorship Technical Thermodynamics, 09107 Chemnitz (Germany)

[2] inetz GmbH, Augustusburger Straße 1, 09111 Chemnitz (Germany)

Abstract

The interest on solar thermal systems in district heating networks has been growing all over the world for several years. The integration of solar heat into the district heating network along with the conventional combined heat and power plant requires special concepts. This contribution describes the recent implementation of a large-scale solar heating system into a low-temperature network in the city center of Chemnitz. The technical specification of different subsystems such as the solar collector fields, the two-zone thermal energy storage and the heat transfer substation for auxiliary heating is presented. Special features of this plant are e.g. the use of water in the complete system and the extraction of heat from the return line of the main district heating network. First monitoring results are presented for the period from May to September 2017. In general, the system works as expected and a solar fraction of 21 % could be reached in the observed period. A potential for optimization is identified e.g. related to the network return temperature.

Keywords: large-scale solar heating system, district heating, low-temperature, network, two-zone storage, heat transfer substation, auxiliary heating system

1. Introduction

In order to achieve the national and international energy and climate goals, the potential of solar energy should be exploited. A large-scale solar district heating is a sustainable and environmentally friendly solution for the supply of thermal energy in urban quarters. The AGFW, the German industry association for district heating and cooling, predicts that there will be an expansion of solar thermal systems with 800,000 m^2 of collector field area in the district heating systems until 2020 in Germany (IKZ, 2017). The integration of solar thermal energy in a district heating system along with the existing cogeneration plant enables many advantages such as the reduction of non-renewable primary energy consumptions, of the CO_2 emissions and of the operating costs of the system.

This paper is intended to describe the implemented solution in Chemnitz, Germany. Chemnitz is a typical East German industrial city with a large-scale district heating system. This hot water system was planned as a municipal heating system in 1928 and had grown steadily until 1990. The heat generation in this system is based on a very high share on combined heat and power (CHP), which is produced by large lignite blocks. For ecological and energy policy reasons, it is very important to find solutions for the cities which are currently supplied by such conventional district heating systems. A favorable situation was present in Chemnitz from 2009 to 2011. It was recognized that the Brühl quarter (part of the northern city centre of Chemnitz) had to be renovated completely including the infrastructure due to the condition of the buildings (Municipality of Chemnitz, 2017). A brief description of the urban design situation is available online (Staedtebaufoerderung, 2017). The main problem was the very high vacancy rate of residential and commercial units which exceeded 50 %. Hence, several major steps were taken to preserve the quarter and to fundamentally improve the social conditions. The authors (Urbaneck et al., 2015) got involved for a complete restructuring of the heat supply, in particular to increase the share of renewable energies. First, the building structure and the heat consumers

doi:10.18086/swc.2017.06.08 Available at http://proceedings.ises.org

as well as possible renewable energy sources were analyzed. A preliminary study (2011-2012) lead to the design of the heat supply concept with measures to increase energy efficiency and the use of solar thermal energy showing the best results (Urbaneck et al., 2015). The concept has been implemented as proposed except a few technical modification. In summer 2016, the plant was put into operation. The pilot plant consists of a heat transfer substation with two solar collector fields, a two-zone storage, a district heating connection as well as a low temperature network for the quarter with the house connection stations (Fig. 1). The monitoring and analysis are carried out as part of the project "Solar district heating for the Brühl district in Chemnitz – accompanying research (SolFW)" which is located in the 6th energy research program of the German federal government. Further objectives and tasks can be found online (Urbaneck, 2017).

Fig. 1: Scheme of the supply station at the Georgstrasse, Chemnitz, Source: inetz 2016.

2. Solar heating system concept

The quarter (Hertelt et al., 2012) covers an area of more than 10,000 m^2 and includes mainly apartment buildings with around 1300 residential units. About 25 % of the buildings are subjected to preservation order. A low-temperature network with a supply and return temperature of 70 and 40 °C, respectively (design-supply temperature of 70 °C at an ambient temperature above 0 °C, linear rise to 80 °C at -14 °C ambient temperature) was built. Moreover, heat exchangers (pre-heating and post-heating stage, Fig. 2) decouple the quarter hydraulically from the existing main district heating network. The temperature reduction in the network enables the efficient use of solar thermal energy. That means, a "low-temperature island" is created in the city and in the district heating area. Additionally, in order to achieve low return temperatures, special heat transfer stations for the apartment residential units were chosen which are based on a solution by Mahler (Mahler, 2004). The construction of a supply station (transfer station between the existing district heating system (primary line) and the low-temperature network) with relatively large collector fields and a relatively large storage brings several advantages in the present urban situation:

- using existing brownfield areas close to the quarter,
- effective realization of construction measures outside the residential area,
- the reduction of specific investment costs due to large units,
- a central operation and
- no problems related to buildings being subject of a preservation order.

The structure of the transfer station is shown in Fig. 2. The main components of this supply station are described in the following sections.

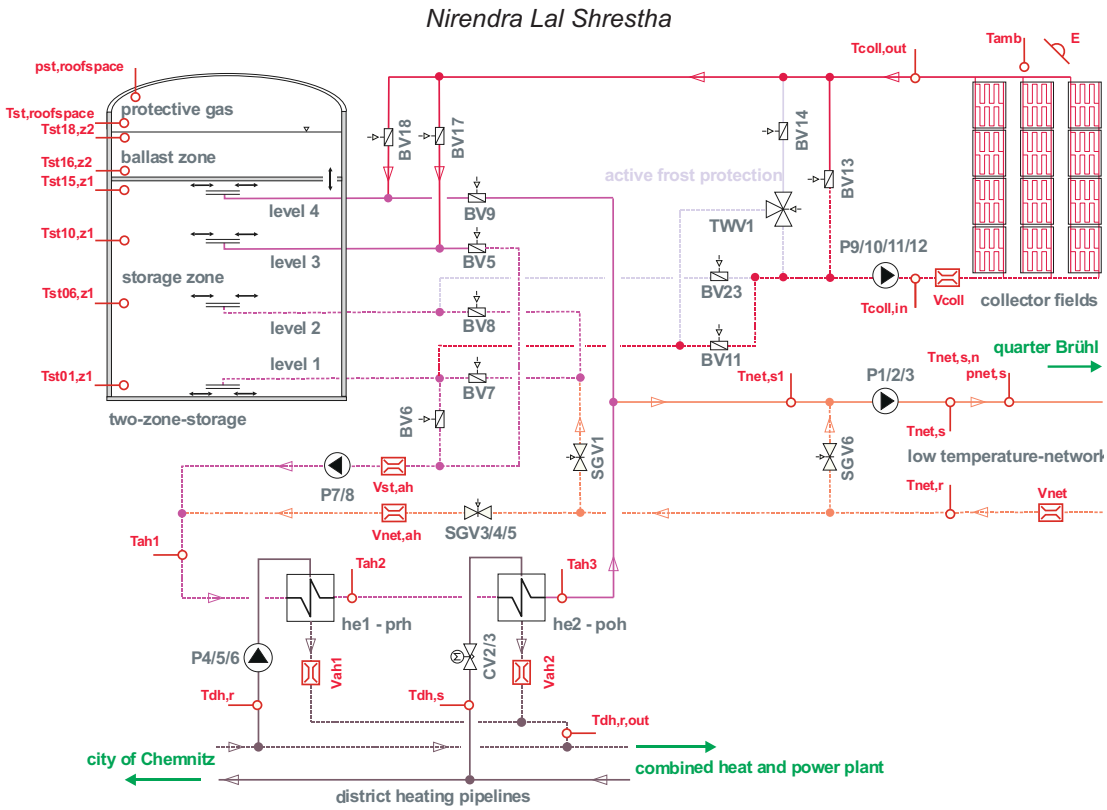

Fig. 2: Structure of the transfer station (supply center).

2.1 Solar thermal field

The large flat plate solar collectors were installed in two fields (north and south) based on the model of systems in Denmark (Holm, 2000) and cover a collector aperture area of 2093 m^2 (Fig. 3). The collectors were mounted on the ground with a tilt angle of 35° and field azimuths of 0° and -30° (south and north field, respectively). Two sizes of solar collectors provided by Wagner Solar GmbH, were installed for charging the storage and for supplying hot water directly to the network (Tab. 1).

Tab. 1: Parameters of the collector fields.

	Collector field south	Collector field north
Aperture area	1007 m^2	1086 m^2
Collector type	Wagner WGK133AR, Wagner WGK80AR	Wagner WGK133AR, Wagner WGK80AR
Number of rows	10	17
No. of WGK133AR	79	86
No. of WGK80AR	4	3

The special feature of the Chemnitz solar system is that water is used as heat transfer medium in the two solar fields. Additionally, there is no hydraulic separation between the solar fields, the storage and the customer's heating surface (e.g. radiator, floor heating). This reduces the heat and temperature losses along the supply path and increases the collector efficiency. Furthermore, a faster availability and the reduction of auxiliary energy requirements are achieved. In the collector, the heat transfer is improved due to the thermo-physical properties of water. From a practical point of view, deaeration is facilitated leading to simple and efficient operation. Cost reduction can be achieved by eliminating large heat exchangers, avoiding water-glycol mixtures, omission of pumps and valves on the secondary side, etc. However, in minus temperatures during winter the collectors must be heated with low heat amounts from the network in order to keep them frost-free. In the SolFW project, this active frost protection (Fig. 2) which was previously practiced only with compound parabolic concentrators (CPC) by Paradigma (Paradigma, 2016) is to be investigated in detail.

The solar fields are operated with matched flow. The specific volume flow rate is 15 l/(m^2·h) at maximum and controlled between 30 % and 100 %. The aim is for each string to reach the desired supply temperature of ca. 70 °C. This is performed by the setting of regulating valves being located at the outlet of each collector row. These valves are adjusted in such a way that the desired flow distribution is reached in nominal operating conditions. The control strategy (on the system side) ensures supply temperatures of 70 °C – 80 °C (possibly higher). In case of stagnation, the solar fields are separated from the system.

Fig. 3: South solar collector field and two-zone storage (left) and north collector field (right) in the Brühl system, Chemnitz.

2.2 Storage

For buffering short-term solar surpluses and as short-term storage for the CHP plants, a welded flat bottom tank was installed above the ground close to the south field (Fig. 3). It is constructed as two-zone storage according to a patent application by Thümmler (Thümmler, 2014) with a thermal useful volume of 1000 m^3 (storage zone) and a volume in the ballast zone of approx. 500 m^3. It is possible to store hot water with a charging temperature of up to 108 °C in the tank with stratification. The high temperature is possible due to the hydrostatic load of the upper zone (ballast zone) which increases the pressure in the lower storage zone and thus influences the boiling temperature of the water to be stored. The increased temperature leads to a higher storage capacity. The two zones (Fig. 2) are separated by a rigid and tightly sealed intermediate ceiling with insulation. For pressure balance, both zones are interlinked by a pipe system. Thus, the static pressure in the storage zone is always above the boiling pressure and evaporation or cavitation are prevented reliably. Additionally, this design helps in absorbing the volume difference due to expansion of water in the storage tank or the entire distribution system.

The total height of the storage is 20 m and the two zones are separated at the height of 13.4 m. The inner diameter of the storage is approx. 10 m. and it is insulated with mineral wool being 0.50 m thick. The outer surface of the insulation was covered by aluminum trapezoidal profiles. Furthermore, in order to charge and discharge the storage at different temperatures, four radial diffusors with diameters of 1.4 m are arranged in different levels.

This new construction of the storage is one of the first of its type being built in a solar district heating system. To avoid a contact of the water surface in the storage with air, nitrogen is injected in the roof space inside the tank.

2.3 Heat transfer substation

Since the solar energy yield can only cover the demand on favorable summer days, auxiliary heat for charging the storage and direct supply of the low-temperature network is provided by the existing district heating system. For this purpose, a two-stage system was installed in the heat transfer substation. The first group of heat exchangers (pre-heating stage, Tab. 2) contains two parallel plate heat exchangers for transferring heat from the main district heating return line. Depending on the return temperature from the low-temperature network or the storage (Tah1 in Fig. 3) and the current temperature of the main return line (Tdh,r), pre-heating can be conducted. Then the water with the temperature Tah2 flows to the post-heating stage where two parallel shell and tube heat exchangers supply heat from the main supply line in order to reach the desired supply temperature.

Tab. 2 Technical parameters of the heat transfer substation (Source: Requirements specification for Brühl district heating, AIC Ingenieurgesellschaft für Bauplanung Chemnitz GmbH, 2015).

plate heat exchangers (pre-heating)		**shell and tube heat exchangers (post-heating)**	
capacity	2.7 MW	capacity	3.3 MW
primary side:		*primary side:*	
allowable operating over pressure	25 bar	design pressure	25 bar
max. allowable operating temperature	140 °C	design temperature	160 °C
inlet- / outlet temperature	60/50 °C	inlet- / outlet temperature	120..130/63..65 °C
max. pressure loss	0.20 bar	max. pressure loss	0.25 bar
secondary side:		*secondary side:*	
allowable operating over pressure	16 bar	design pressure	16 bar
max. allowable operating temperature	140 °C	design temperature	160 °C
inlet- / outlet temperature	45/57 °C	inlet- / outlet temperature	60/80..108 °C
max. pressure loss	0.25 bar	max. pressure loss	0.25 bar

2.4 Network

A buried two-pipe network connects the buiding's heat transfer substations to the supply center and distributes heat with constant/annually varying supply temperature. Most of the pre-insulated pipes with sizes from DN25 to DN250 have been newly laid since 2014. So far, the owners of 198 out of 259 buildings (76 %) have taken up the connection offer by the utility inetz. The current load of the connected buildings amounts to 12.6 MW. This is about 200 % of the load expected for the first stage of network construction which was assumed for designing the solar plant (Urbaneck et al., 2015).

3. Monitoring results

Although the operation of the solar plant started from August 2016, the recording of all the required parameters has been only available since May 2017 onwards. Therefore, at first the thermal behavior of the system from May to September 2017 is shown and evaluated:

- The continuous supply of the low-temperature network is depicted in Fig. 4. The supply temperature is slightly above 70 °C, which is due to the safety reasons. The return temperature is in the range of 52…63 °C. Several factors are responsible of this higher return temperature, e.g. the supply being used only for domestic hot water systems during the summer period, maintaining the network temperature in the low-temperature circuit and fluctuations in the charging cycles of the transfer station.
- The daily sums for the output of collector field (sum of north and south field), auxiliary heating demand and demand of the low-temperature network are shown in Fig. 5. The solar thermal system has been designed for the first stage of network construction (Urbaneck et al., 2015). As the interest of building owners exceeded the expectations, the number of connections and thus the load values (Fig. 5) already correspond to the second stage of construction. Therefore, the output of the collector fields can be seen below the network demand. Even during summer, auxiliary heating is necessary. No off-peak periods (e.g. vacation) can be detected in the analyzed period. The base daily demand is 10…15 MWh/day.
- The relatively high return temperatures in the low-temperature network (Fig. 4) have an effect on the auxiliary heating system (Fig. 6). A fluctuating temperature profile can be seen (mainly because of the control behavior of the pre-heating stage). The increase of the temperature to the desired value is mainly performed in the post-heating stage because the return temperature of the low-temperature network is close to the temperature of the main return line being used as heat source in the pre-heating stage.
- The daily sums of thermal energy transferred by the auxiliary heating system (stages 1 and 2) are depicted in Fig. 7. The pre-heating stage covers ca. 15 % of the total auxiliary heat demand. It is expected that during the heating season from autumn to spring, the return temperature in the network

will be lower which leads to an increasing contribution of the pre-heating stage to the total auxiliary heat supply.

- The desired supply temperature is hold ready in the upper level of the storage zone (Fig. 8). However, fluctuations between 65 and 82 °C can be observed due to the operation of the collector fields and the auxiliary heating system.
- The high return temperature of the network has an effect on the operation of the collector fields. During the day, the outlet temperature of the solar collector in the south field is between 70 °C and 80 °C (Fig. 9) and sometimes it exceeds 80 °C for a few hours. The inlet temperature is in the range of 50…60 °C (Fig. 10). The design temperature difference between the inlet and outlet of the collector field with nominal operation is 30 K. However, the observed temperature differences are often lower (ca. 20 K, Fig. 11) due to high return temperatures in the network.
- Fig. 12 and Fig. 13 show a regular behavior with respect to the solar collector yield. There are a few outliers which indicate temporary malfunction. Generally, the fluctuation range is relatively narrow and confirms continuous operation of the solar plant.

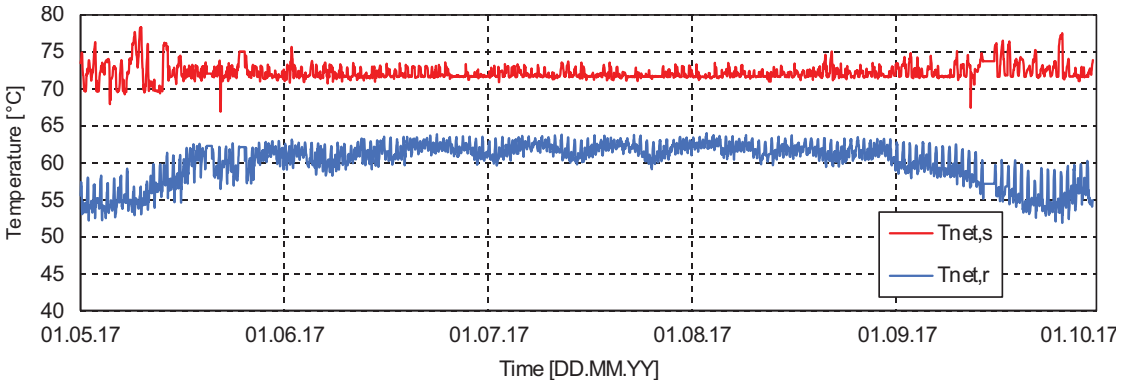

Fig. 4: Temperatures in the course of time, supply and return of low-temperature network (hourly mean values).

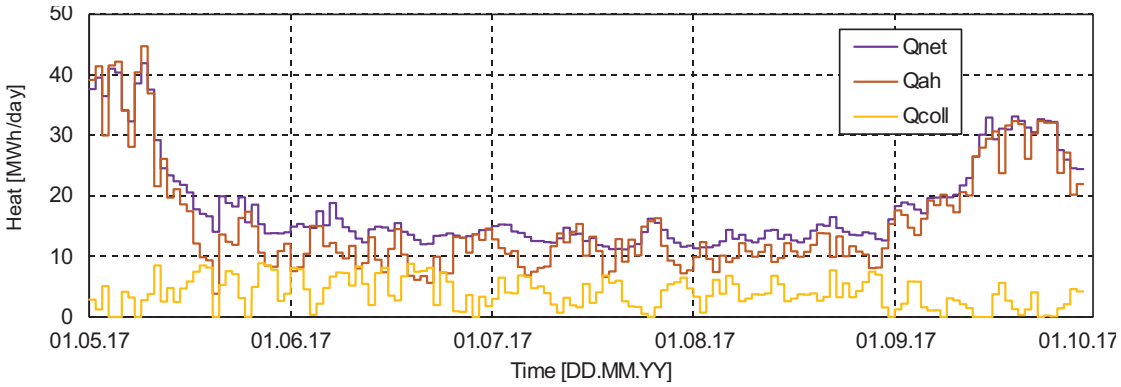

Fig. 5: Daily heat sum, output of collector field, auxiliary heating demand, demand of low-temperature network.

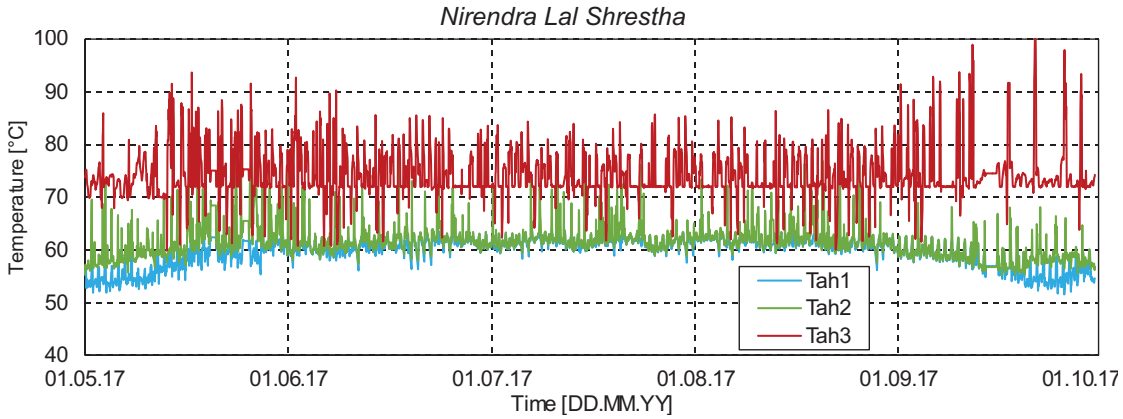

Fig. 6: Temperatures in the course of time, auxiliary heating circuit (hourly mean values).

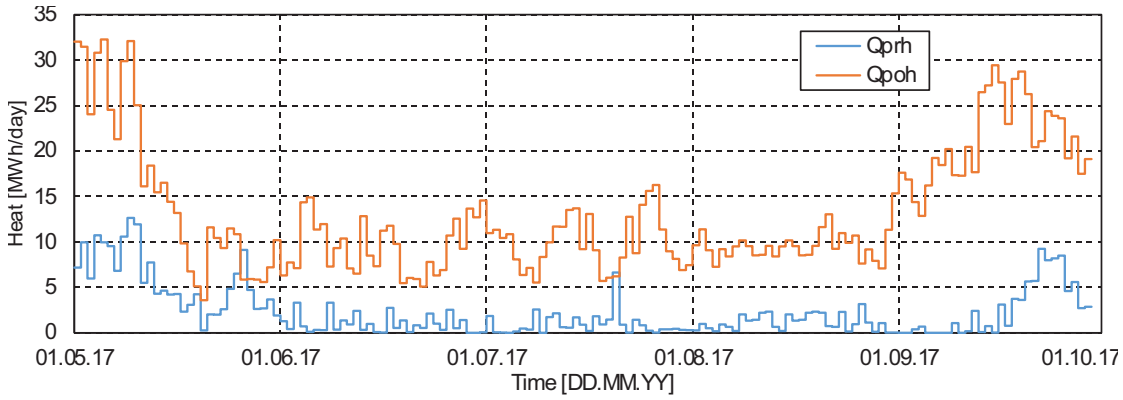

Fig. 7: Daily heat sum, auxiliary heating stages 1 and 2.

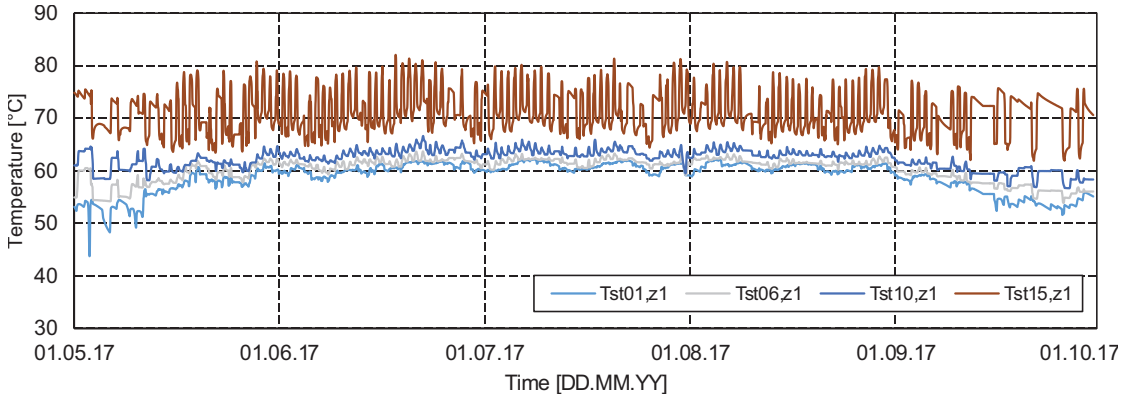

Fig. 8: Temperatures in the course of time, two-zone storage (hourly mean values).

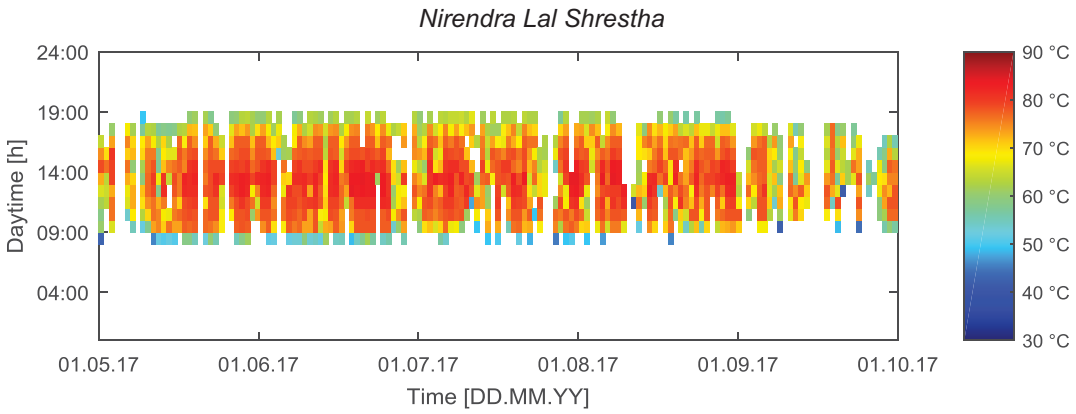

Fig. 9: Temperatures in the course of time, outlet temperature of the south collector field (hourly mean values during matched flow operation).

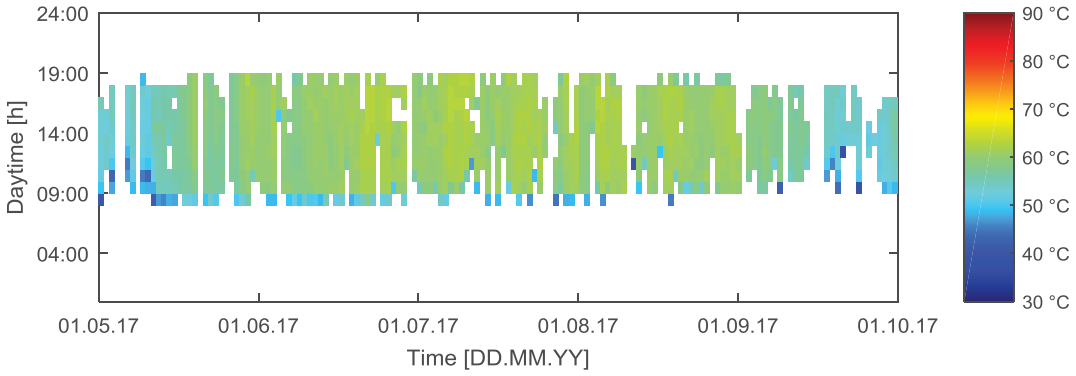

Fig. 10: Temperatures in the course of time, inlet temperature of the south collector field (hourly mean values during matched flow operation).

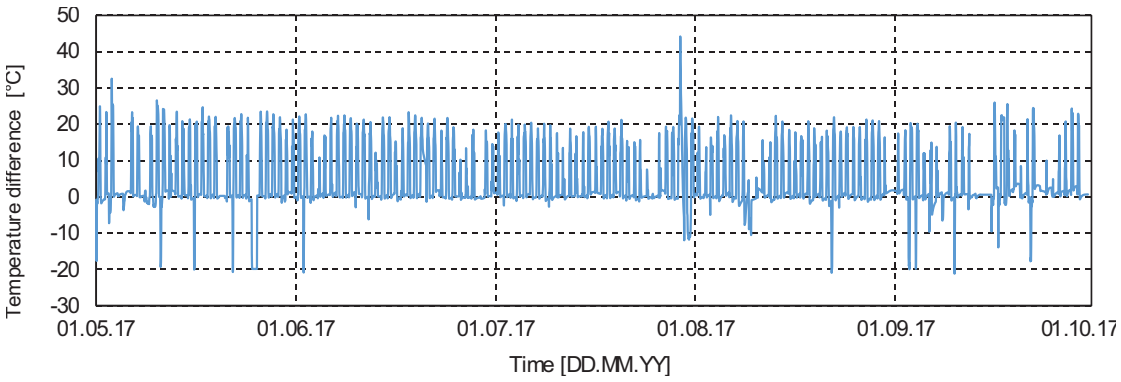

Fig. 11: Temperature differences of the south collector field in the course of time (hourly mean values).

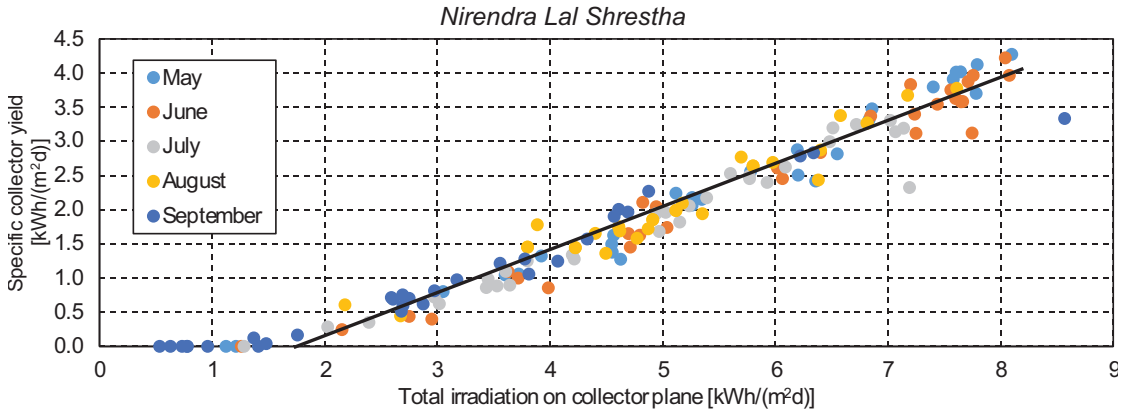

Fig. 12: Solar collector yield depending on the total irradiance on the collector surface in south field, 2017.

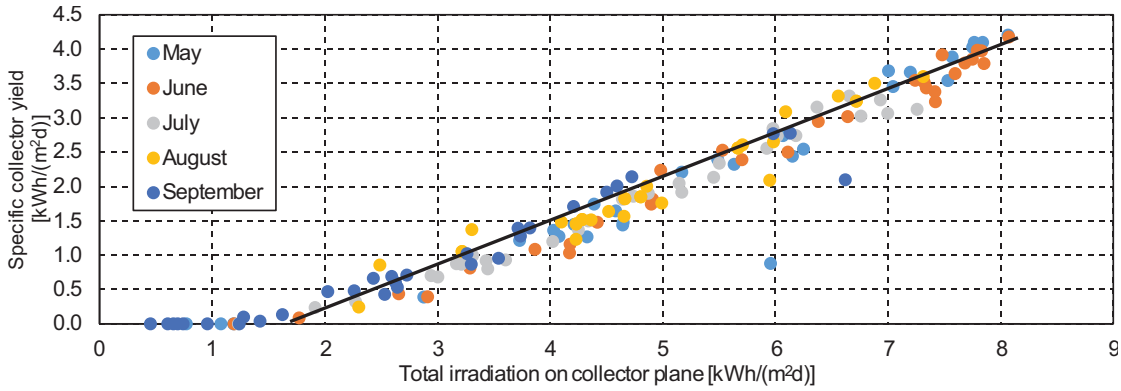

Fig. 13: Solar collector yield depending on the total irradiance on the collector surface in north field, 2017.

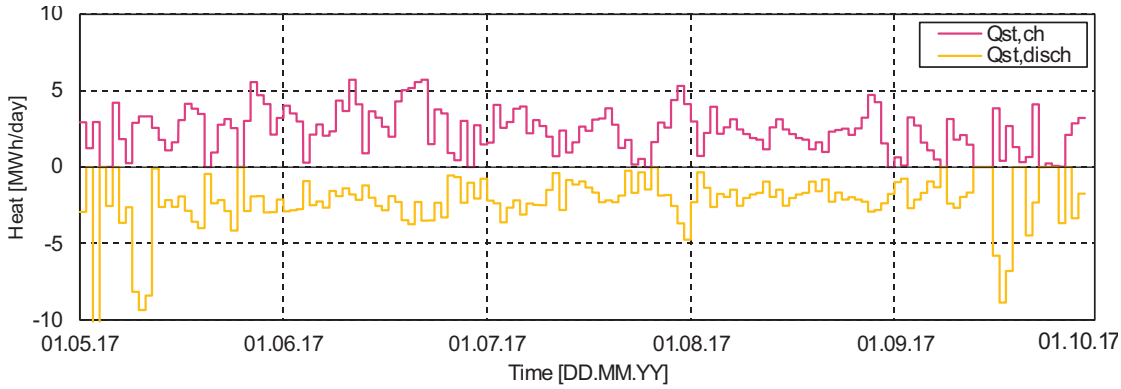

Fig. 14: Daily heat sum, charging and discharging of the storage.

On the basis of the monitoring data from May to September 2017, the heat quantities were calculated and are listed in Tab. 3. Furthermore, the key figures were listed which facilitate the evaluation:

- The summed yield of the solar collector fields is 599 MWh from May to September. In the design phase, a specific collector yield of about 402 kWh/(m²·a) was simulated for a net collector area of 1800 m² (Urbaneck et al., 2015). Thus, 71 % of the predicted yield was achieved so far. The solar fraction for the analyzed summer period amounts to 21 %, which is quite small because the solar collector field has been designed for the first stage of network construction. However, the second stage of construction has been reached faster than expected.

- The difference in yield between the south field with ideal south orientation and the north field with an azimuth of -30° (east) is quite small with about 4 %. The azimuth of -30° was chosen for avoiding shading by the main district heating pipes (Fig. 1).
- The high return temperature of the network during the analyzed period lead to a relatively low share of the pre-heating stage in the total auxiliary heat supply.

Tab. 3: Heat quantities and key figures.

Heat		**Key figures**	
Generation:		specific collector yield (north field) [kWh/m^2]	281
yield from collector field (north field) [MWh]	305	specific collector yield (south field) [kWh/m^2]	292
yield from collector field (south field) [MWh]	294	solar fraction [%]	21
auxiliary heating (stage 1) [MWh]	356	share of stage 1 in auxiliary heating [%]	15
auxiliary heating (stage 2) [MWh]	2037	share of stage 2 in auxiliary heating [%]	85
Consumption:		collector field efficiency (south) [%]	39.9
supply to low-temperature network [MWh]	2808	collector field efficiency (north) [%]	39.6
losses [MWh]	184		

4. Conclusions

In this paper, the implementation of large flat plate solar collectors into a low-temperature district heating network is presented. First monitoring results for the period from May to September 2017 show that the system in general operates as expected. The return temperature of the network has a very high influence which has been known since the 1990s. Optimization measures are planned here. Further work will be conducted for improving e.g. control of the auxiliary heating system. It is possible to transfer this concept to other urban quarters. Moreover, with the scale-up of collector area and storage capacity, higher solar fraction can be achieved. Therefore, this concept is one useful technical solution for large-scale heating systems.

5. Acknowledgements

The project underlying this report is funded by the German Federal Ministry for Economic Affairs and Energy under the code 0325871 following a decision by the German parliament. Special thanks also go to the Project Management Jülich for supporting the project. The sole responsibility for the report's contents lies with the authors.

6. References

Hertelt, J., Heller, M., Dilger, M., 2012. Städtebauliche Planungsstudie zur Entwicklung des Gebietes "Brühl-Boulevard" in Chemnitz [Urban design study for the development of the area "Brühl-Boulevard"in Chemnitz, in German]. Albert Speer & Partner GmbH, C&E Consulting and Engineering GmbH.

Holm, L., 2000. Experiences and results from Marstal district heating plant. In: Frankovic, B. (Editor): International Congress Energy and the Environment 2000 – 17th Scientific Conference on Energy and Environment. Opatija (Croatia), Proceedings, Vol. 1, p. 157-164. - ISBN 953-6866-00-6.

IKZ. http://www.ikz.de/detail/news/detail/vorhersagbarer-waermeertrag/, (accessed on 25.02.2017).

Mahler, B., 2004. Ganzheitliche Optimierung von solaren Nahwärmenetzen mit Langzeit-Wärmespeicher

[Holistic optimization of solar district heating networks with long-term heat storage, in German], PhD thesis. VDI-Verlag, Düsseldorf.

Municipality of Chemnitz. http://www.chemnitz.de/chemnitz/de/die-stadt-chemnitz/stadtentwicklung/entwicklung-bruehl/index.html., (accessed on 02.08.2017).

Paradigma. http://www.paradigma.de, (accessed on 15.05.2016).

Staedtebaufoerderung - Federal Institute for Research on Building, Urban Affairs and Spatial Development within the Federal Office for Building and Regional. http://www.staedtebaufoerderung.info/StBauF/DE/Programm/AktiveStadtUndOrtsteilzentren/Praxis/Massnahmen/Chemnitz/Chemnitz_node.html. Internet-Plattform zum Städtebauförderprogramm Aktive Stadt- und Ortsteilzentren (in German), (accessed on 25.08.2017).

Thümmler, E., 2014. DE102013111543 A1.

Urbaneck, T.; Oppelt, T.; Platzer, B.; Frey, H.; Uhlig, U.; Göschel, T.; Zimmermann, D.; Rabe, D., 2015. Solar District Heating in East Germany – Transformation in a Cogeneration Dominated City. Energy Procedia, Vol. 70, pp. 587–594. - doi: 10.1016/j.egypro.2015.02.090.

Urbaneck, T. www.solfw.de. Project website, (accessed on 27.07.2017).

7. Nomenclature

ah	auxiliary heating	P	pump
amb	ambient	poh	post-heating
BV	butterfly valve	prh	pre-heating
ch	charging	Q	heat
coll	collector(-field)	r	return
CV	control valve	s	supply
dh	district heating	SGV	sliding gate valve
disch	discharging	st	storage
E	solar radiation (measurement)	T	temperature (measurement)
he	heat exchanger	TWV	Three-way valve
net	network	V	volume flow rate (measurement)
p	pressure (measurement)	z	zone

Drake Landing Solar Community: 10 Years of Operation

Lucio Mesquita[1], Doug McClenahan[1], Jeff Thornton[2], Jarrett Carriere[3] and Bill Wong[3]

[1] CanmetENERGY/Natural Resources Canada, Ottawa (Canada)

[2] Thermal Energy System Specialists (TESS), Madison (USA)

[3] LEIDOS Canada, Ottawa (Canada)

Abstract

Drake Landing Solar Community is a Canadian solar district heating system with seasonal thermal storage. The demonstration project, designed to achieve over 90% solar fraction, was commissioned in the summer of 2007, reaching its 10th year of operation in 2017. The present work describes the system and its operation, presenting simulated and measured performance indicators for 10 years of operation, together with relevant operational data. Monitoring has proven the design simulations to be generally very accurate. During the last 5 years, the measured average solar fraction was 96%, including 100% achieved during the 2015-2016 heating season. The ability to easily access and view detailed system operating data combined with the ability to compare actual operation against predicted has proven to be extremely valuable for the successful commissioning and the efficient operation of energy systems at DLSC. Overall, the system has successfully demonstrated the reliable operation of a high solar fraction solar district heating system with seasonal thermal storage in a very cold climate. Although that Drake Landing system is too small to be economically competitive with the current very low price of natural gas in North America, subsequent feasibility studies show that larger systems of similar design can deliver solar energy at about half the cost compared to Drake Landing.

Keywords: Solar district heating, seasonal heat storage, borehole thermal energy storage, BTES, Drake Landing, high solar fraction, monitored performance.

1. Introduction

In Canada, space and domestic water heating account for more than 80% of greenhouse gas emissions in the residential sector. Despite that and the good levels of annual solar irradiation available in the most populated areas of the country, adoption of solar thermal technologies has been slow. This is partly due to the seasonal mismatch between the solar resource and the heating load, in particular for space heating applications. The Drake Landing Solar Community (DLSC) project was created to demonstrate the technical feasibility of achieving conventional fuel energy savings of more than 90% by using solar energy collected and stored during the summer to provide residential space heating during the following winter (seasonal storage). The system was commissioned in late June 2007, achieving 10 years of space heating operation during the 2016-2017 winter.

2. System Description

DLSC consists of 52 detached homes in Okotoks, Alberta (latitude 50.73N, longitude 113.95W). Each home has a detached garage behind the house, facing onto a lane (Figure 1). Each garage has been joined to the next garage by a roofed-in breezeway, creating 4 continuous roof structures, as seen on Figure 2. On those roof structures, 2293 m^2 (gross) of flat-plate solar collectors were installed.

The houses are located along two streets running east-west. Six different house models were available to buyers, with an average above-grade floor area of 145 m^2. The houses were built to meet Canada's R-2000 performance standard, with upgraded building envelopes, including higher insulation, low-e argon filled double panel windows and improved air tightness and construction details. The higher standard was estimated to reduce space heating load by 30% when compared to baseline houses at the time of construction. Space heating is supplied to the 52 houses through 4 parallel branches of a 2-pipe district heating system. An integrated air handler and heat recovery ventilator, incorporating fans with electronically commutated motors and a large water-to-air heat exchanger, supplies forced-

doi:10.18086/swc.2017.06.09 Available at http://proceedings.ises.org

air heating and fresh air. An independent, 2-collector, solar domestic hot water system, backed-up with a high-efficiency gas-fired water heater, supplies service hot water.

Fig. 1: View of houses with adjoined garages and houses street view

Fig. 2: Aerial view of Drake Landing Solar Community

A seasonal borehole thermal energy storage (BTES) field was installed under a corner of a neighborhood park and covered with a layer of insulation beneath the topsoil. The BTES is composed of 144 boreholes, each 35 m deep and radially plumbed in 24 parallel circuits, each with a string of 6 boreholes in series. Each series string is connected in such a way that the water flows from the centre to the outer edge of the BTES when storing heat, and from the edge towards the centre when recovering heat, so that the highest temperatures will always be at the centre. Figure 3 shows the borehole field under construction and currently, as a landscaped park.

Most of the solar district energy system mechanical equipment (pumps, controls, auxiliary gas boilers, etc.) is in a dedicated building (Energy Centre, at top right corner of Figure 2), which also houses two short-term thermal storage (STTS) tanks with a combined water volume of 240 m^3. The STTS acts as a buffer between the collector loop, the district loop, and the BTES field, accepting and dispensing thermal energy as required. A 22 kW photovoltaic array is installed on the roof of the energy centre (not visible in Figure 2, as the picture was taken before its installation)

The specially designed air-handlers and separate water heating systems allow the district system to operate at low temperatures, leading to increased effective storage capacity and higher collector performance. Typically, the supply temperature for the district heating system is below 40°C, and return below 30°C.

Fig. 3: Borehole field under construction and currently, as a landscaped park

A schematic diagram of the system is shown on Figure 4, and more details on its design and early results of operation can be found elsewhere: McClenahan et al. (2006), Wong et al. (2006) and Sibbitt et al. (2012, 2015).

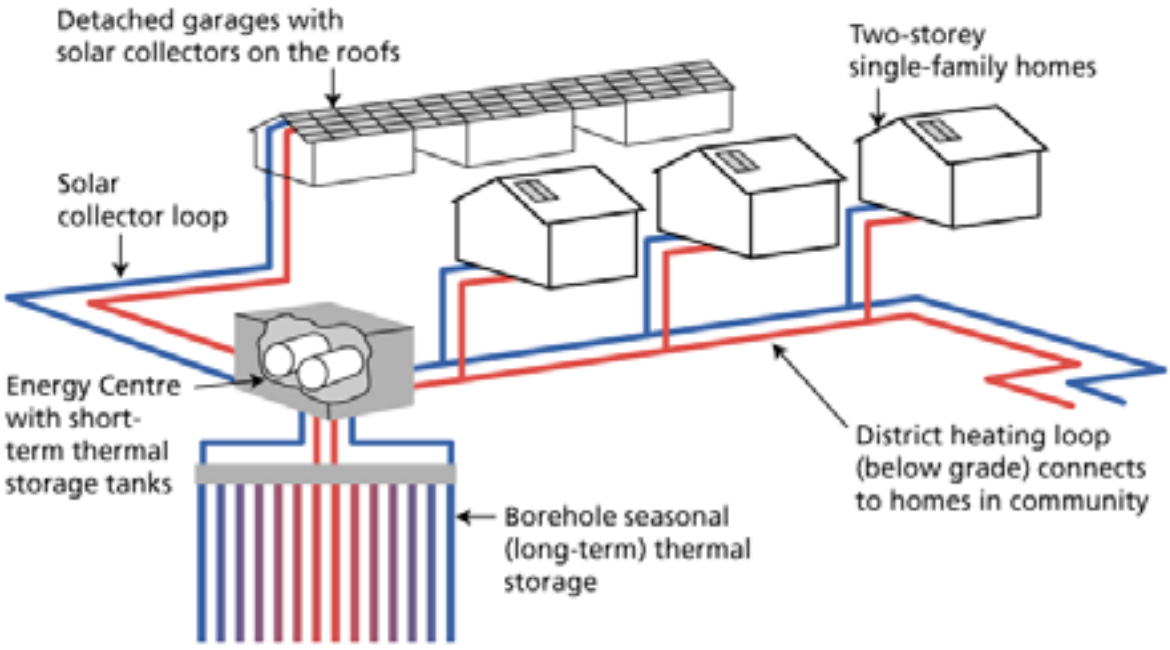

Fig. 4: Schematic diagram of the solar seasonal storage heating system at Drake Landing Solar Community

3. System Performance Results

3.1. Simulated system performance

During the design phase, a detailed TRNSYS model was developed to simulate the system operation. The model includes solar collectors, heat exchangers, short-term and bore-hole storage, piping, controls and district heating system. The house heating loads were calculated using ESP-r, and the results used as input into TRNSYS. Simulations were done both with 50 years of historical weather data and by repeating the typical meteorological year, CWEC – Canadian Weather for Energy Calculation, for the site. Both analysis predicted average solar fractions above 90% over 50 years of operation. The TRNSYS simulations were used to optimize some of the main design parameters, such as solar collector area, short-term storage size and number and depth of boreholes. Table 1 presents the results of the simulated 10 years of operation with repeated CWEC data.

The results of 50 years simulations using the same load and weather data show very little change beyond the 10th year of operation. Therefore one can see the results for the 10th year on Table 1 as the final steady state condition for the simulations. The system reaches a maximum solar fraction of 91%, with an all pumps electrical COP of 46. COP calculations are based on home heating load as a way to compare its values to distributed heat pump systems. Two different COPs are defined: COP_{ss}, based on the solar and storage pumps electricity consumption and the solar

contribution to the houses heat load, and COP_{ap}, based on all pumped electricity consumption and the houses heat load.

$$COP_{ss} = {(Q_h f)}/{E_{ss}} \quad \text{(eq. 1)}$$

$$COP_{ap} = {Q_h}/{E_{ap}} \quad \text{(eq. 2)}$$

Tab. 1: Summary of simulated system performance

Year of Operation (Jan-Dec)	1	2	3	4	5	6	7	8	9	10
Heating Degree-Days (18°C ref.)	5200	5200	5200	5200	5200	5200	5200	5200	5200	5200
Homes Heating Load (GJ)	2328	2328	2328	2328	2328	2328	2328	2328	2328	2328
Horizontal. Global Irradiation (GJm^{-2})	4.97	4.97	4.97	4.97	4.97	4.97	4.97	4.97	4.97	4.97
Incident Global Irradiation (GJm^{-2})	6.08	6.08	6.08	6.08	6.08	6.08	6.08	6.08	6.08	6.08
Collected Solar Energy (GJ)	4480	3830	3630	3550	3520	3510	3490	3490	3480	3470
Collector Efficiency[1]	0.32	0.27	0.26	0.25	0.25	0.25	0.25	0.25	0.25	0.25
Energy into BTES (GJ)	3030	2390	2200	2110	2080	2060	2050	2040	2030	2020
BTES Efficiency[2]	0.09	0.23	0.35	0.40	0.41	0.43	0.43	0.45	0.45	0.45
Solar Energy to District Loop (GJ)	1670	1930	2140	2230	2230	2270	2280	2300	2300	2300
Total Energy to District Loop (GJ)	2530	2530	2530	2530	2530	2530	2530	2530	2530	2530
Solar Fraction	0.66	0.76	0.85	0.88	0.88	0.90	0.90	0.91	0.91	0.91
Solar and Storage Pumps Electricity Consumption (GJ)	46	47	47	46	45	45	45	45	45	45
All Pumps Electricity Consumption (GJ)	53	54	53	52	52	52	51	51	51	51
COP_{ss}	33	37	43	45	45	46	47	47	47	47
COP_{ap}	44	43	44	45	45	45	45	45	45	46

Although the results on Table 1 were obtained with the TRNSYS model developed at the time of system design, many efforts have been made to improve and calibrate the model. McDowell and Thornton (2008) performed an initial model calibration during the first year of operation, and additional efforts are currently under way to review and calibrate the model by comparing the results between measured and modeled energy performance results using measured weather and load data as inputs to the model.

[1] Based on gross area
[2] Apparent efficiency; does not account for year-to-year change in stored energy

3.2. Measured system performance

DLSC operation has been closely monitored since its commissioning in 2007 and a summary of the performance measurements between July 1, 2007 and June 30, 2017 is presented on Table 2. The annual collector efficiency has remained relatively constant over the period at approximately 34%, based on the gross area of the collectors and the collected energy measured at the heat exchanger in the energy centre. In the first year of operation, most of the collected energy (2610 of 4470 GJ) was sent to the BTES. Although the BTES only returned 152 GJ (6%) of the input energy for heating later in the first year, 1520 GJ of solar energy was also supplied directly from the STTS. Together, 1670 GJ of solar energy, out of a total of 3040 GJ was delivered to the district loop, giving a solar fraction of 55%. In the next 3 years, the BTES returned a greater fraction of the heat supplied to it, reaching 54% in the fourth year, allowing the solar energy contribution to the load to increase to 60% in year two, 80% in year three and 86% in year four. In year 5, the solar fraction increased to 97%, but the heat returned from BTES dropped to 36% of the heat supplied to it. Such low BTES contribution happened again in 2015-2016, when the system reached 100% solar fraction and the house heating loads were the lowest for the 10 years of operation. During the last 5 years, the average solar fraction was 96%, including 100% achieved during the 2015-2016 heating season.

Tab. 2: Key measured performance indicators for the first 10 seasons of operation

Year of Operation (Jul-Jun)	**2007 2008**	**2008 2009**	**2009 2010**	**2010 2011**	**2011 2012**	**2012 2013**	**2013 2014**	**2014 2015**	**2015 2016**	**2016 2017**
Heating Degree-Days (18°C ref.)	5060	5230	4890	4910	5480	4580	5300	4860	4130	4760
Homes Heating Load (GJ)	2790	2470	2400	2700	2100	2380	2520	2160	1840	2340
Horizontal. Global Irradiation (GJm^{-2})	4.63	4.96	4.65	4.58	4.75	4.70	4.63	4.57	4.50	4.26
Incident Global Irradiation (GJm^{-2})	5.82	6.07	5.49	5.45	5.67	5.55	5.55	5.41	5.48	5.06
Collected Solar Energy (GJ)	4470	4390	4270	4060	4430	4330	4290	4340	4360	3920
Collector Efficiency[1]	0.34	0.32	0.34	0.33	0.34	0.34	0.34	0.35	0.35	0.34
Energy into BTES (GJ)	2610	2710	2500	2260	2520	2570	2460	2680	2670	2270
BTES Efficiency[2]	0.06	0.21	0.35	0.54	0.36	0.51	0.56	0.42	0.32	0.54
Solar Energy to District Loop (GJ)	1670	1790	2030	2460	2050	2430	2780	2390	2270	2550
Total Energy to District Loop (GJ)	3040	2960	2550	2860	2120	2490	3030	2500	2270	2750
Solar Fraction	0.55	0.60	0.80	0.86	0.97	0.98	0.92	0.96	1	0.93
Solar and Storage Pumps Electricity Consumption (GJ)	133	135	126	120	81	72	84	64	65	72
All Pumps Electricity Consumption (GJ)	153	156	145	138	93	83	97	74	79	78
COP_{ss}	12	11	15	19	25	32	28	33	28	31
COP_{ap}	18	16	17	20	23	29	26	29	23	30

[1] Based on gross area
[2] Apparent efficiency; does not account for year-to-year change in stored energy

Measured irradiation has been consistently lower than CWEC typical meteorological year numbers. Solar collectors have performed better than estimated through the simulations. Those discrepancies are currently under closer investigation. COP values have improved considerably since the beginning, mostly due to control strategies that reduced pump electricity consumption. Lower initial COP values were due to higher pump consumption and the fact that the BTES was being charged for the first time. The system has consistently produced COP results above 28. Moreover, the electricity consumption for pumps is almost entirely off-set by onsite PV generation. Unlike PV, however, the solar thermal system with seasonal storage delivers energy when it is mostly needed, without seasonal imbalances. Overall, the system has surpassed performance expectations and has operated with a high level of reliability.

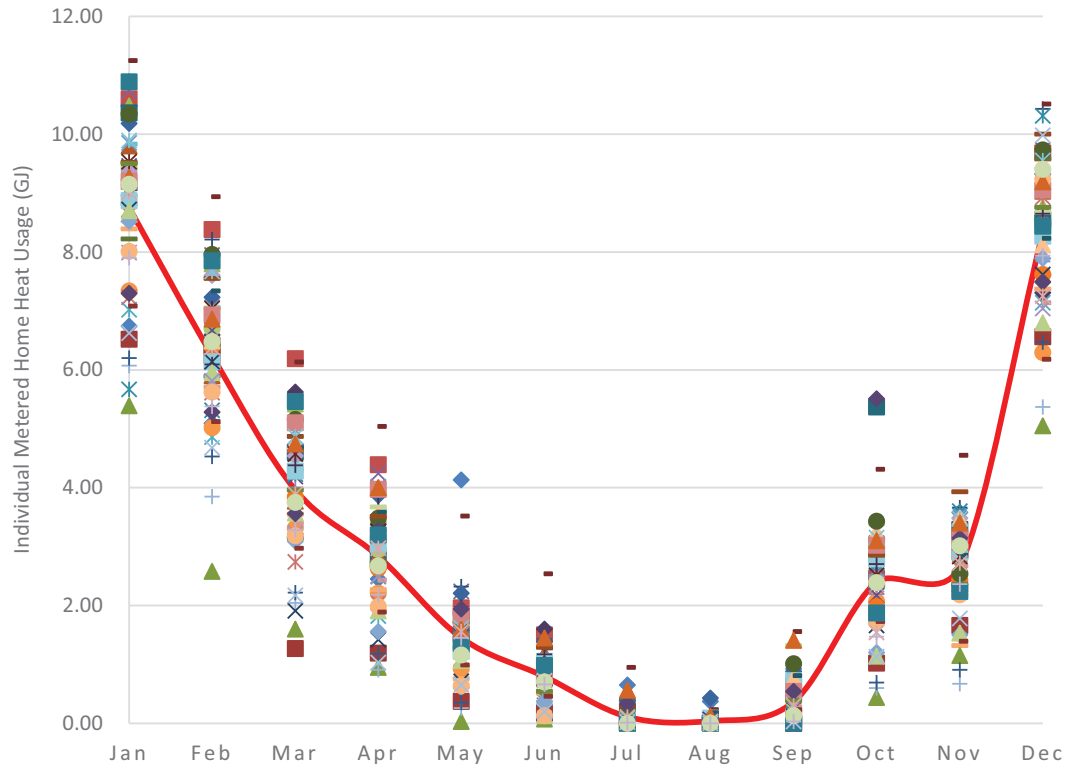

Fig. 5: Monthly metered heat usage for each one of the 52 houses for the calendar year of 2016

The individual heat metering results shown in Figure 5 show a large variation in heat usage among the 52 houses, even though there is not a significant difference in house sizes or construction. However, many other variables can lead to such variations, such as thermostat settings, and internal and solar passive heat gains. The original design heat load estimates showed that internal gain and passive solar represent about half of the contribution to the total heat load. It should be noted, however, that despite large individual variations, the average annual heat usage for the 52 houses is very close to the design value. For the initial 10 years, the average heating load for the 52 houses has been metered at 2370 GJ/year, compared to 2328 GJ/year simulated.

4. System Operation and Control

DLSC is controlled and monitored through METASYS, a building automation system (BAS) developed by Johnson Controls. Data is recorded every 10 min and the system operation is followed remotely by the project utility partner, ATCO and by researchers at CanmetENERGY Ottawa. There are no operators on site, and a number of alarms are set in the BAS, providing immediate awareness of operational issues. Figure 6 shows a functional diagram for DLSC with the system monitoring points.

The control system is designed to initiate and maintain collector loop operation whenever there is sufficient incident solar energy available. Initial operation each day warms up the collector loop, bypassing the glycol-water plate-frame

heat exchanger. When the collector loop fluid is hot enough, the flow is directed to the heat exchanger, transferring the heat to the water loop connected to the STTS. Thermal stratification is important in both the BTES and the STTS to allow the high temperature water to be available for space heating needs while supplying relatively low temperature glycol to the collectors. Both glycol and water collector loops utilize variable speed pumps. The control system was initially designed to vary the flow rate to achieve a 15°C temperature rise in the glycol loop and the water side pump would mimic the glycol side flow rate. This strategy enhances stratification in the STTS while reducing pump electricity consumption.

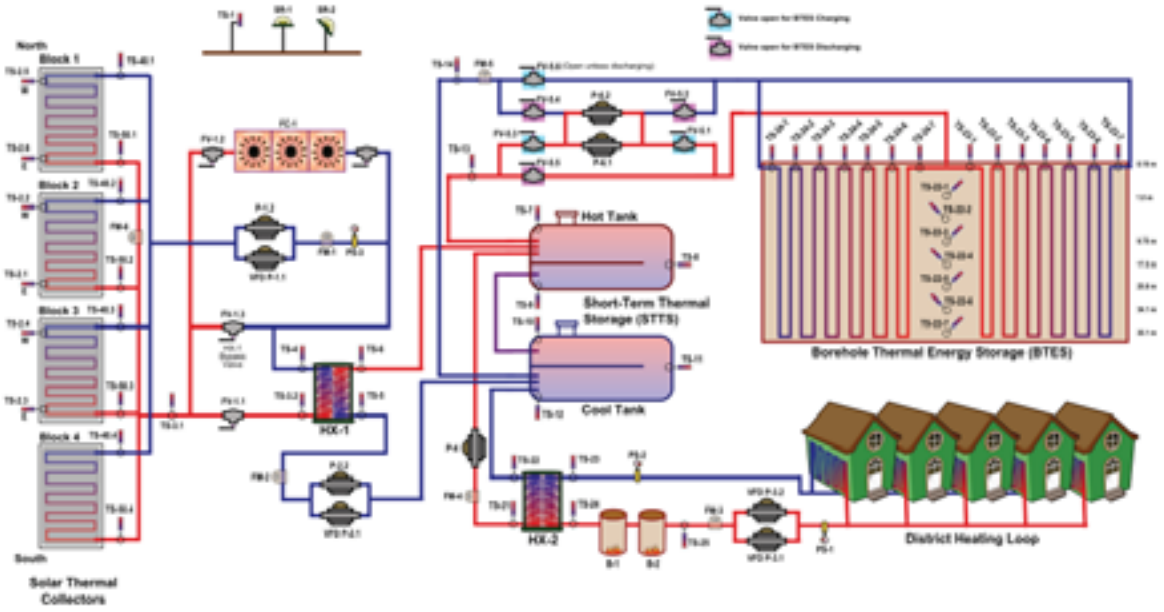

Fig. 6: Functional system schematic with monitoring points

One of the goals of the project is to evaluate control strategies that can optimize net energy production, maximizing the amount of collected energy and reducing power consumption for pumps. The solar collection pumps (primary glycol and primary water) account for more than 45% of all the electricity used for pumps (Table 3), despite the fact that the glycol loop was designed with a relatively low maximum flow rate of 25 l/hm^2. Therefore, during the years of system operation, a number of experiments were conducted to evaluate, through different control strategies, the impact of primary circuit flow reduction on electricity usage and thermal performance.

Tab. 3: Pump electricity consumption (GJ) for 2016-2017

Description	Pump					
	Primary Glycol	Primary Water	District Loop	STTS to HX	BTES	Total
Annual Consumption (GJ)	26.16	10.81	6.38	7.99	26.85	78.19
Percentage of Total	33.5%	13.8%	8.2%	10.2%	34.3%	-

Power consumption vs pump speed was measured for each one of the pumps equipped with variable frequency drives (VFD). Figure 7 shows, as expected, the marked increased in electrical power that follows an increase in pump speed.

The main strategy to reduce power consumption has been to increase the set temperature differential through the glycol loop, which leads to lower flow rates and pump speed. This effect can be observed on Figure 8. Compared to 2010-2011, both 2015-2016 and 2016-2017 show less hours of operation at high flow rates, which translates into a reduction of electricity usage. With negligible impact on collector annual efficiency, the electricity savings are calculate to be approximately 50% of the amount used with the original control strategy.

For the BTES pump the approach has been to use a predictive manual control, preventing energy from being moved from the STTS to the BTES if a cold front is forecasted, and only charging the BTES in the winter if the top temperature in the hot tank surpasses 60°C.

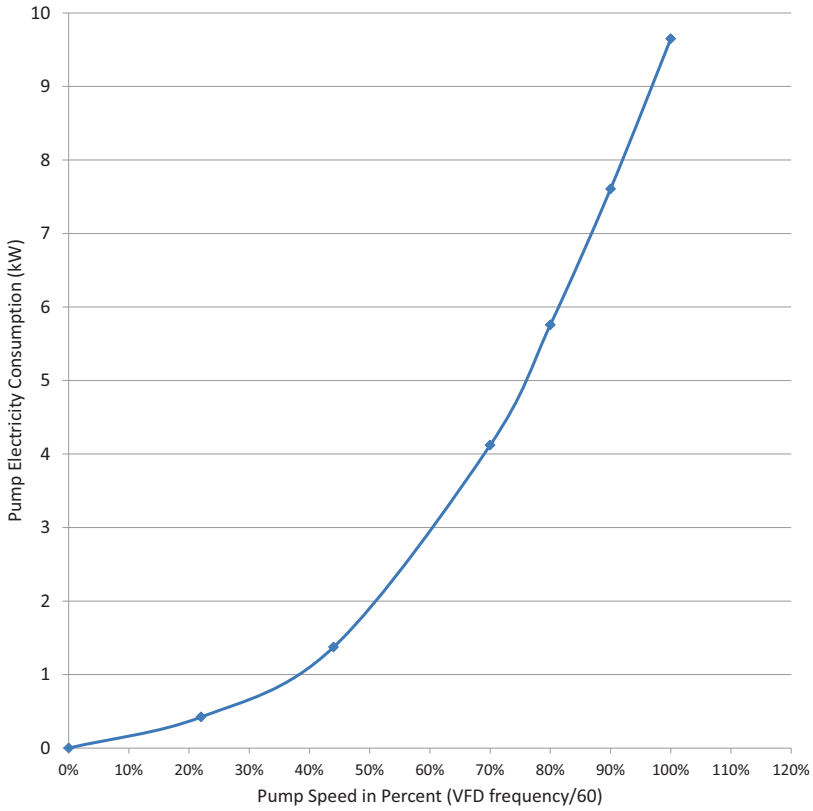

Fig. 7: Measured glycol pump (P1.1) electricity consumption as function of VFD setting

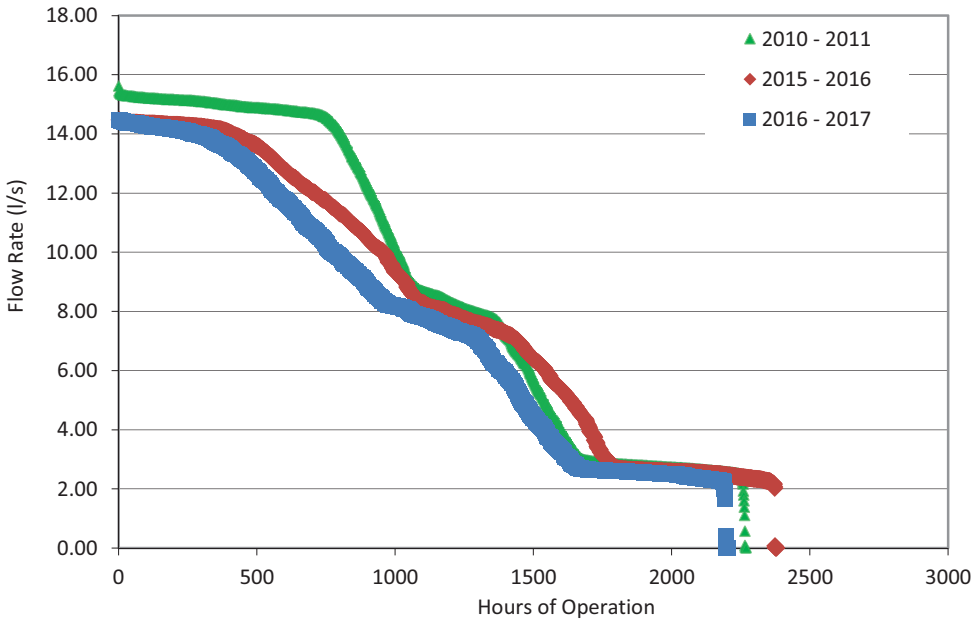

Fig. 8: Numbers of hours of operation at different flow rates for the glycol pump (P1.1) (selected years)

When space heating is required, energy from the STTS heats the district loop fluid through a second plate-frame heat exchanger. If there is insufficient energy in the STTS to meet the anticipated heating requirement, heat is transferred from the BTES into the STTS to meet the requirement. If the stored water temperature is insufficient to meet the current heating load, natural gas fired boilers raise the temperature of the district loop as required. When there is more heat in the STTS than is required for space heating in the short-term, water is circulated from the STTS through the BTES to store heat for later use. Figure 9 shows the heat supply to the system based on type of source for the

2016-2017 operational year. In this particular year, which was somewhat typical, direct solar was responsible for 48% of the energy supplied, while indirect solar, i.e., energy extracted from the BTES, accounted for 45% and the boilers for 7% of the supply.

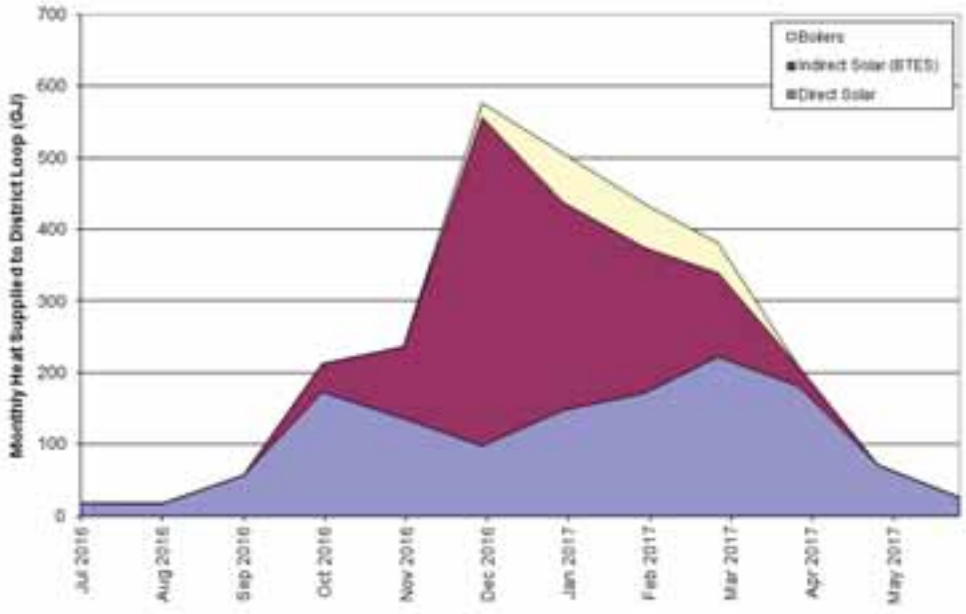

Fig. 9: Heat supply to the district loop in 2016-2017, according to the source

As mentioned previously, the home air handlers were designed to deliver the necessary amount of heat at a relatively low temperature. This, and the fact that the district heating system does not supply domestic hot water, allows the system to operate at low temperatures. The district loop supply water temperature is varied linearly from 37°C for ambient air temperatures of -2.5°C or above to 55°C for ambient air at -40°C. Variable water flow rates are also used in the district loop to allow a wide range of space heating loads to be met while facilitating efficient use of solar heat over a range of source and load temperatures, and limiting pump electricity consumption. Figure 10 shows the weekly average supply and return temperatures for 2016-2017. The slightly higher temperatures in the summer months are not indicative of operation set points. When the district loop is not operational in the summer, the surrounding air heats up the temperature sensors, which are located in the mechanical room close to the heat exchanger. Ambient temperatures in the mechanical room are usually close to 40°C in the summer.

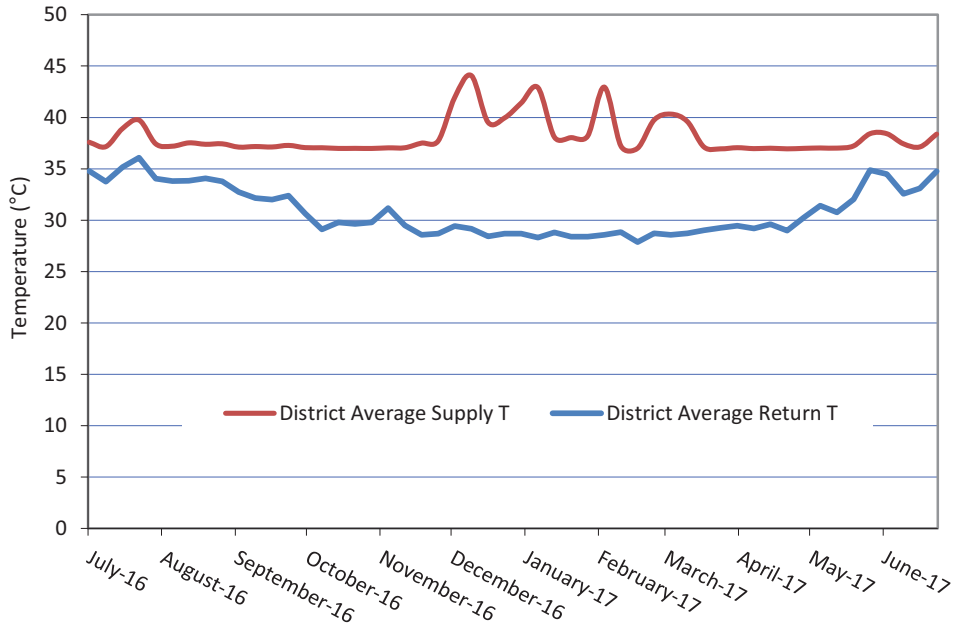

Fig. 10: Weekly average supply and return district loop temperatures for 2016-2017

Low supply and return district loop temperatures improve the effective thermal capacity of the BTES. In most cases, the BTES is able to meet the demand, with the exception of stretches of extreme cold days, which require higher supply temperature and thermal power. Figure 11 shows the maximum and minimum yearly temperatures for sensors located in the water piping at the top of the boreholes, with 24-1 and 23-1 being closest to the centre, and 24.7 and 23.7 being closest to the edge of the BTES (see Figure 6). Charging and discharging of the BTES is done in a way to promote thermal stratification within the BTES, with higher temperatures at the centre.

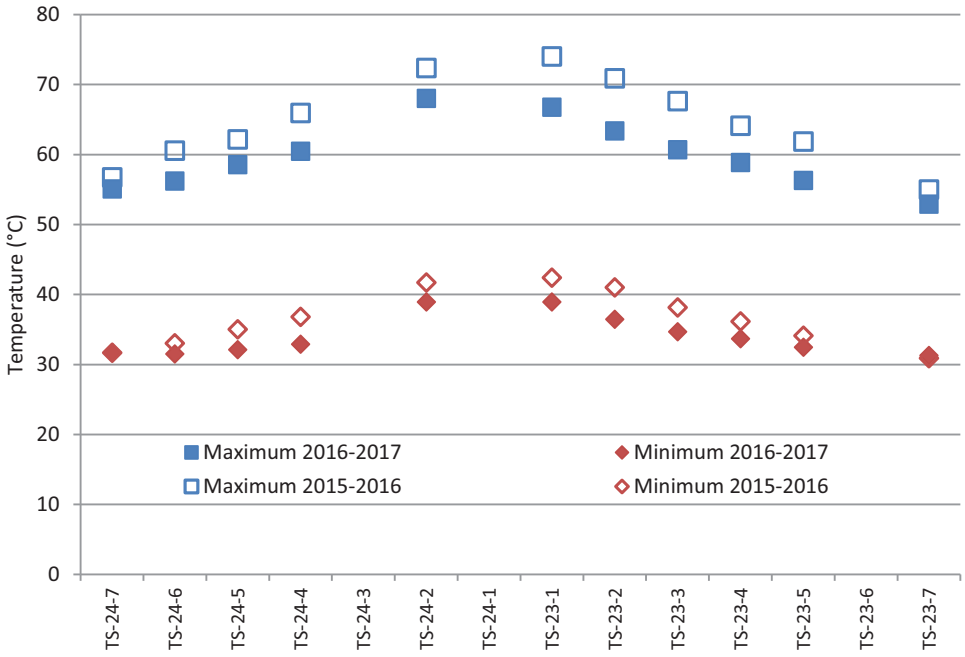

Fig. 11: Maximum and minimum yearly temperatures for sensors located at the top of the boreholes

During those 10 years of operation, DLSC has not experienced a stagnation episode in its glycol loop. This is mostly because there is enough capacity in the BTES to absorb all the energy produced. Nonetheless, the system is equipped with dry coolers that can reject enough heat to prevent the system from reaching a boiling state. The favourable conditions have resulted in longer glycol life and the fluid has not been replaced since the initial charge in 2007. Figure 12 shows the results of glycol pH and reserve alkalinity analysis throughout the last 10 years.

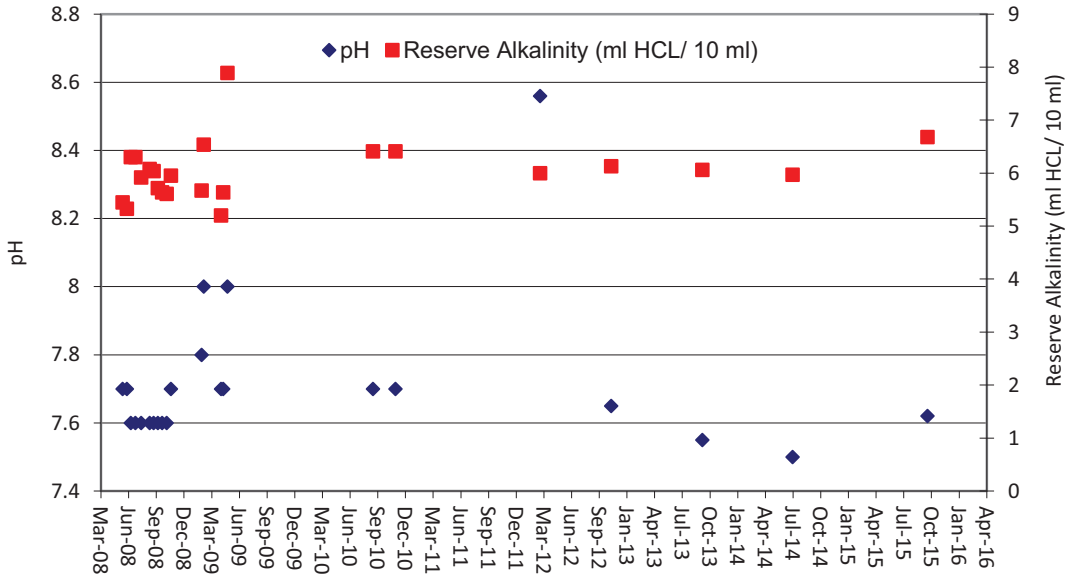

Fig. 12: Glycol pH and reserve alkalinity

5. Lessons Learned and Future Outlook

Overall, the system has successfully demonstrated the reliable operation of a high solar fraction solar district heating system with seasonal thermal storage in a very cold climate. In ten years of operation, only 2 of 798 solar collectors have been replaced and regular testing of the propylene glycol-water heat transfer fluid shows negligible deterioration, indicating many more years of service can be expected.

Adjustments and improvements have been implemented, such as better controls. Issues that could have led to significant performance and reliability problems were corrected early on. For example, a design oversight of the outlet ports in the upper half of one of the short term storage tanks led initially to lower thermal performance. It was promptly identified and corrected. This underlines the importance of technical and financial resources for monitoring and correction of eventual issues, common in pilot systems with this level of complexity. Careful design is seldom enough.

The DLSC builder, land developer and municipality were included in the project planning process from the beginning. This proved to be the right approach since their experience with and understanding of the home buyer's perspective had a significant positive influence on important design decisions throughout the process. It was also valuable in building confidence in the project regarding the market acceptance of the unfamiliar technologies being applied.

The homes were sold very quickly, with a long waiting list of potential buyers wanting to move into the community. People who live in the community are very pleased with it and they have adapted very well to the constant attention from outside, including opening their homes to people from over 20 countries around the world as far away as South Korea, China, and Chile. DLSC house values have increased in step with conventional homes in the area. The builder, the utility, the land developer and the municipality have all expressed interest in participating in the implementation of similar projects in the future.

As with the other utilities, district heating loop piping needs be installed before the houses are built. Shut-off valves in the utility easement near the street should be considered for subsequent projects to simplify the line installation and connection process for the builder.

It is essential to have committed partners. In significant projects, unexpected issues will almost certainly arise, however, with high levels of dedication and commitment, teams can identify acceptable paths forward which can be successfully executed. Some of the unexpected issues the DLSC team faced included severe construction site flooding, lower than expected reliability for some conventional equipment and some components that didn't actually perform to specification.

The ability to easily access and view detailed system operating data combined with the ability to compare actual operation against predicted is extremely valuable for the successful commissioning and the efficient operation of energy systems such as that used at DLSC. Going well beyond the obvious benefits of fine tuning control set points and identifying failed sensors and mechanical components, the availability of these data has identified inoperative control logic, inadvertent use of "temporary" set points, instances where plumbing modifications were warranted and opportunities to reduce electricity consumption with improved control logic. The performance and financial implications can be very significant if issues like these are not corrected.

Using the system data in conjunction with the TRNSYS design simulation has raised confidence in the ability to predict the energy performance of similar systems. Monitoring has proven the design simulations to be generally very accurate. Refined simulations have been subsequently used to perform feasibility studies for follow-on projects using similar designs. The simulation model has also been used to look for evidence of soil drying within the borehole field and conclude that no significant change has taken place in the bulk properties of the soil or in the performance of the seasonal storage.

Drake Landing system is too small to be economically competitive with the current very low price of natural gas in North America. However, subsequent feasibility studies show that larger systems of similar design can deliver solar energy at about half of the cost compared to Drake Landing, and additional work is underway to improve cost performance further. Current work includes model refining, O&M cost evaluation, and predictive control analysis and test implementation.

6. Nomenclature

Heat load (GJ)	Q
Coefficient of Performance	COP
Electricity consumption (GJ)	E
Solar Fraction	*f*
Subscripts	
Solar and Thermal Storage	ss
All Pumps	ap
Houses	h

7. Acknowledgements

The Government of Canada (CanmetENERGY, the Program of Energy Research and Development, the ecoENERGY Technology Initiative and the Energy Innovation Program) has provided funding for the construction, monitoring and technical support for DLSC. We also acknowledge the continuing effort of the operations and maintenance team including ATCO, Sterling Homes, the Town of Okotoks, J. E. Taylor Plumbing, Nu-Air, BCC HVAC Tech, Quigley Electric, and Johnson Controls. We would also like to acknowledge all of the organizations who made the design and construction of this project possible through their funding support, cash, in-kind contributions and dedicated efforts.

8. References

McClenahan, D., Gusdorf, J., Kokko, J., Thornton, J., Wong, B., 2006. Okotoks: Seasonal Storage of Solar Energy for Space Heat in a New Community. Proceedings of ACEEE 2006 Summer Study on Energy Efficiency in Buildings, Pacific Grove, CA USA.

McDowell, T.P. and Thornton, J.W., 2008. Simulation and Model Calibration of a Large-Scale Solar Seasonal Storage System. Proceedings of SimBuild 2008, Third National Conference of IBPSA-USA, Berkeley, CA USA.

Sibbit, B., McClenahan, D., Djebbar, R.,Thornton, J., Wong, B., Carriere, J., Kokko, J.,2012. The Performance of a High Solar Fraction Seasonal Storage District Heating System – Five Years of Operation, Energy Procedia, 30, 856-865.

Sibbit, B., McClenahan, D., Djebbar, R., Paget, K., 2015. Groundbreaking Solar: Drake Landing Solar Community, ASHRAE - High Performing Buildings, Summer 2015, 36-46.

Wong, W.P., McClung, J.L., Snijders, A.L., Kokko, J.P., McClenahan, D., Thornton, J., 2006. First Large- Scale Solar Seasonal Borehole Thermal Energy Storage in Canada, Proceedings of Ecostock Conference, Stockton, NJ USA.

IEA SHC Task 55: Towards the Integration of Large SHC Systems into DHC Networks

Anna Katharina Provasnek,[1] Sabine Putz[1]

[1] R&D Department/SOLID, Graz (Austria)

Abstract

Solar thermal large-scale installations provide less than 1% of heat for DHC networks globally. The interest into solar thermal energy installations increases, but still strong measures are necessary to promote the technology across countries and energy policy frameworks. So how can the share of solar thermal energy be increased in district heating and cooling networks globally? Today, technical, economic, and policy measures still restrict a profound market development and limit the integration of large scale solar systems into different types of energy networks despite the huge potential of the technology to provide heat based on renewable sources. The new IEA SHC Task 55 extends research towards district heating and cooling networks, main system components and hybrid technologies. Additionally, the Task provides a new platform for scientists and industry partners to share their knowledge and solve pressing technical, political, and economic questions.

Key-words: IEA SHC Task 55, solar thermal large-scale installations, solar thermal systems, solar energy, district heating, district cooling

1. Introduction

Renewable energies such as solar provide promising business opportunities for companies. Innovation efforts at the right spot and at the right time can boost business success. Even international stock indices are aware of the economic strength of energy company efforts towards sustainability-oriented measures (Provasnek et al. 2015). However, increasing project dimensions require increasing technical capabilities and business model reliability. The cost competitiveness of solar thermal heating and cooling technologies is defined by several factors. Among these are initial costs of the solar thermal system, proper maintenance, or prices of alternatives. Solar thermal large-scale installations suitable to be integrated into district heating networks face these challenges on a much larger scale than well-established residential solar thermal systems. For decades, countries such as Denmark or Austria have paved a way to upscale solar thermal systems up to GW sizes, with a number of implications due to system sizes.

Several technical design characteristics determine the specific energy output of solar thermal systems, such as collector field losses, low temperature operations, or low return temperatures into solar collectors critical to storage losses. One major specific problem of regions with strong seasons are system and operational losses during winter times. The integration of solar thermal large-scale applications into district heating networks is problematic: Solar radiation is low while temperatures of the district heating networks are high (90°C – 140°C flow temperature). Additionally, the performance of collectors and their performance in field constructions do not correspond to their designated lab test results. Storages, hybrid technologies (industrial waste heat, heat pumps, or storage types) and optimized system components have to be aligned with all-year system requirements of district heating and cooling networks to guarantee a high solar fraction.

The IEA SHC Task 55 is a follow up Task of the successfully terminated IEA SHC Task 45. The former task provided research results on technical-economic parameters of large scale solar thermal plants (TASK 45, 2014). The new task integrates past findings and extends research towards district heating and cooling networks, main system components and hybrid technologies. Additionally, the new Task provides a new platform for scientists and industry partners to share their knowledge and solve pressing technical, political, and economic problems. It aims to provide options on how to best integrate solar thermal large-scale installations in combination with hybrid technologies (such as seasonal heat storages or adsorption heat pumps) into district heating and cooling networks. It is central to focus on the integration of solar thermal systems into network technologies, and on challenges which limit current integration efforts.

doi:10.18086/swc.2017.06.10 Available at http://proceedings.ises.org

2. IEA SHC TASK 55: Structure and Strategy

The international cooperation on the integration of solar thermal large scale installations into district heating and cooling networks is structured into four subtasks, A, B, C, and D. Subtask A focuses on district heating network requirements and options to integrate solar thermal heating or cooling installations. Economic analyses, hybrid technology applications, or control strategy challenges are major points of research. Subtask B elaborates on the specific components of such systems, testing and monitoring projects as well as quality aspects of integrated components. Subtask C emphasize the design of solar thermal systems. Projects elaborate on simulation tools, collector designs or modular conception and construction measures. Finally, Subtask D promotes and disseminates project results and know-how on SDH/SDC systems including hybrid technologies. It contributes business models, market analyses and best practice examples. Experts on Task 55 key research areas exchange their main fields of expertise in half-year cycles between 2016 and 2020, and aim to stimulate the growth and realization of a strong SDH/SDC industry. Strategic steps to reach set objectives are high attendance rates at Task 55 Meetings, active dissemination on most well-known industry platforms, increasing numbers of experts involved into Task 55 project work activities and active participation in the International Energy Agency on local and international levels.

3. Network Analyses and Integration

The overall district heating or cooling network and integration aspects are central as soon as the solar share of a DHC system reaches a level where the operation of the network and the other supply units is influenced significantly.

Best practice examples and case studies of existing, newly integrated and planned SDH and SDC systems with large (>5%) solar fraction (typically of > 0,5MWth up to GWth), including characteristics such as typical network temperatures, summer/winter load ratio, pressure level, collector fields, seasonal storages, hybrid-technology implementation, hydraulics and control strategies are central to analyze the network and integration strategies. Case studies, including potentials and barriers for the integration of solar thermal systems can show possible transition strategies from no to 100% solar thermal supply. System challenges in the network especially affect the hydraulics and the interaction with other supply technologies.

Technical and operational parameters of district heating systems differ across countries. In China, typical water supply temperatures range from 115-130°C, whereas in Denmark 66-115°C apply. In Germany, temperatures range from 90-113°C. Water return temperatures range from 50-80°C in China, 38-67°C in Denmark, and 30-60°C in Germany. Chinese networks show losses of 20-50%, whereas Denmark has 19.8% and Germany on average 13%. The volumes of networks in China have doubled since 2000 with rapid expansions, in Denmark networks are at the age between 24-54 years, whereas in Germany, some networks are close to 100 years old (IRENA, 2017).

The inclusion of solar thermal devices into diverse, complex heat distribution systems is ambitious, but doable. Solar thermal installations are based on renewable heat with minimal environmental impact. Disadvantages of the technology are the irregularity of solar irradiation (on which the heat yield depends) and the typically negative correlation between solar heat supply and heat demand. These disadvantages can be met by the use of storage tanks. Furthermore, heat production can be supported by the use of heat pumps. Complex heat generation and distribution systems incorporate many types of heat sources. The control of both the solar thermal systems and the heat distribution network constitutes a major challenge. Standard strategies of independent linear controllers for individual subsystems are not appropriate for control of transient modes. By disregarding the couplings between the systems, changes in operating conditions in one system can lead to oscillations and suboptimal behavior in others, which again can have repercussions on the first system. Unpredictable behaviors when integrating solar thermal systems into DH networks can be met by subordinate model-predictive control approaches.

Simple linear controllers do not account for dead time (delay), which is unavoidably present in large thermal systems fed by renewable sources. By a model-based approach, dead time can be explicitly taken into account in control strategies. Since the velocity-dependent throughput time corresponds to the heating time in the collector, one has some level of control over the outlet temperature by properly adjusting the mass flow. Adding an electrically operated heat pump to the system allows to decouple (to some extent) outlet temperature and heat flux. With a model-based control approach it is thus possible to independently prescribe target values both for outlet temperature and heat flux (within technical and physical limits). By setting the target values for critical system quantities, a superordinate predictive control system can make best use of all components and avoid unwanted situations, such as loaded storage tanks at a time when considerable solar yields are possible (Lichtenegger, et al. 2015).

Necessary conditions to use these predictive control measures to integrate a solar thermal system into a district

heating network are (Lichtenegger, Unterberger, 2015):

- Sufficient knowledge of the system,
- Reliable forecasts for solar irradiation,
- Reliable forecasts for ambient temperature and heat demand,
- Significant device for heat storage,
- The system has non-trivial heat demand characteristics.

International research projects on elementary components of the integration of solar thermal systems are heat portfolio, BiNe2+, UrbanDHExtended, OptENgrid, or BIGSOLAR. A switch to renewable energy sources for district heating and cooling can help meet rising urban energy needs, improve efficiency, reduce emissions and provide cost-effective temperature control. Under calculated conditions, DHC offers a cost-effective and energy efficient option. There is significant potential to upgrade existing systems and create new networks using solar thermal large-scale systems (IRENA, 2017).

4. Components testing, system monitoring and quality assurance

Operational conditions of components in large solar thermal plants usually differ from conditions under which components were originally tested in laboratories. Based on findings of IEA SHC TASK 45 Subtask C - which focused on system configurations, system performance, tools and guidelines for operating strategies, and models for ESCo services – the parameter are scaled up to much bigger sizes (Putz, Provasnek, 2016). Plant-specific characteristics, such as the azimuth, inclination, hydraulic effects, differentiated flow rates of parallel collector arrays, or characteristics of the heat transfer media determine how solar thermal systems operate. To reduce the uncertainty on the performance of solar thermal systems and to increase the planning reliability of systems to be integrated into DHC networks, current test methods have to be scrutinized and the actual operating conditions have to be put into consideration.

One major research project named `MeQuSo´ provides Task 55 with data on In-situ tests of the power output of large collector arrays to assess the thermal performance of the deployed collectors under real operating conditions in the field. By monitoring the performance of different collector types, assessments on the quality of individual products and external influences in the field are possible. Existing measurement data of solar thermal plants are not sufficient to improve current collector test approaches, since the needed quantities might not be measured and the accuracy might not be adequate. This is certainly true for radiation, since precise measurement of radiation is not always mandatory for control systems of solar thermal plants. A solar thermal plant called `Fernheizwerk´ was equipped with high precision measurement equipment to meet the data quality requirements of the project MeQuSo. Test results show that the field performance of a number of collectors differ highly from tests performed in the laboratory. Findings provide more accurate efficiency values under real operating conditions in the field, a higher reliability of the expected solar yield, and will lead to performance improvements of future collectors, collector arrays, and components of the total solar thermal system (Doll, Ohnewein, et. al 2016).

5. Design of the Solar Thermal System and of integrated Hybrid Technologies

The design of solar thermal systems defines their architecture, modules, and interfaces. The data on the design have to focus on the demand of specified requirements. Ideally, theory on system design and product development merge and are transported to the market, leading to innovative large-scale solar installations suitable for SDH. Core steps include the analysis, architecture and engineering of solar thermal components. Hybrid technologies can help to shape the change into DHC solar thermal innovation. Elements from new solar thermal system designs can be combined with technologies of the status quo. Hence, two technologies are combined with one another.

New systems can be based on a first simulation of solar thermal systems and their components, such as storage, piping, and hybrid technologies such as heat pumps. The project at hand elaborates on characteristics of collector array units, large and seasonal storages, hydraulics, and heat pumps within system operations. Large scale collector fields are simulated and compared to related measurements in field tests. Optionally, the simulation tool can be corrected. Next, parameters of seasonal storages are calculated and guidelines for the design and construction of different storage types identified. Hydraulics within systems are sensitive to a variety of parameters. These parameters have to be optimized. Piping within large systems and options for a modular conception and construction

of very large systems have to be investigated. The subsequently developed modes provide new findings for performance surveillance, system design, and system control measures.

Steps to evaluate and optimize the design of solar thermal systems include:

- Investigation of measured long-term field performance in relation to standardized collector test information
- Development of tools/models for annual performance predictions at different operating conditions and field designs
- Solar radiation modelling
- Assessment of different collector types for large collector fields
- Investigation of system performance and control for a collector field with series connection of different collector types
- Investigations on influence of the design of the solar collector loop on the thermal performance of solar collector fields
- Analyzing pressure loss and flow distribution in collector components, collectors, and collector fields

Focusing on renewable energy sources, solar thermal energy can be generated by more than one renewable source at a time. Examples are sources of solar, biomass, or geothermal. The hybrid energy generation module of solar and geothermal or solar and waste heat hybrid module are attractive, as they are abundant in nature and from the industry, and are very much environmentally friendly (TASK 55, 2017).

A component critical to solar thermal large-scale systems and their hybrid systems are thermal storages for achieving high penetration levels. It increases the capacity factors or value of such energy systems and are therefore core to any system design (IRENA, 2017).

6. Dissemination of SDH/SDC and of Hybrid Technologies in New Markets

Business activities on solar thermal energy are increasingly important contributors to the energy economy. Current firms on the market are major sources of innovation, business development, and of new jobs. Securing financial success for newly designed large scale solar thermal installations is still a challenge, as they are built upon intellectual capital rather than on physical assets, which are still to be built. However, several companies are willing to `go boldly where no one has gone before´ with solar thermal energy installations. For these companies it is central to identify sources of financing and new business models.

One instrument to assist in the availability of financing are promotion activities for large SHC installations coupled with existing DHC networks. Additionally, including industrial waste heating (and cooling) sources with the other technologies of heat pumps, geothermal heat and thermal energy storages are attractive, innovative combinations. Exemplary business models for these solar thermal and hybrid technologies are to be elaborated, as well as best practice examples of already existing installations.

Besides, promising are also new industrial markets for solar heating and cooling systems, which need training material in order to diffuse the technologies. Most countries could scale up renewable energy substantially in district heating and cooling. In a few countries, such as Denmark and Switzerland, renewable energy already provides more than 40% of district heat supply. Renewable energy such as solar thermal energy and hybrid technologies could theoretically satisfy all DHC demand in 2030. However, a realistic potential for deployment differs from country to country. China could realize a 24% renewable share in district heat generation, split equally between geothermal, bioenergy and solar. In Denmark, the already high renewable share of 42% could reach 73%. The country is and will remain a global leader in large-scale solar energy, which can be expanded to meet 13% of total district heat demand by 2030, complemented by hybrid technologies of geothermal and bioenergy. In Germany, solar heat could reach a share of 6% in DH networks by 2030.

7. Summary and Outlook

IEA SHC TASK 55 focuses on very recent efforts of a number of stakeholders to increase the share of solar thermal large-scale installations in district heating and cooling systems. District heating systems spilt the local production of energy and its consequences (such as CO2 emissions) from its consumption. Despite already being considers as more environmentally friendly than conventional single energy systems, district heating systems can still increase their

environmental performance by integrating renewable sources. Optimizing system operation, achieving economies of scale, integrating large scale storage and holistic system designs are essential to accelerate the deployment of cost-effective solar thermal assisted DHC systems. As the systems of solar thermal and geothermal large scale improve and grow, DHC systems will also offer increasingly attractive synergies.

Mismatches between load patterns and the supply from solar radiation can already be balanced to a great extent with thermal storage facilities. Storages are expected to become integral, with DHC systems coming to play a pivotal role in enabling variable renewable sources. Solar thermal large-scale applications are only used in a few places today but have significant potential. Countries such as China become increasingly dependent on variable renewables due to pollution crises. Next steps have to promote demonstration projects for the new technologies. Due to the limited number of systems already in place (despite in Denmark), the availability and suitability of renewable resources for DHC is often unclear. For solar district cooling technologies, demonstration projects will have a significant positive effect on investors´ and customers´ trust into the technology.

As installations in Denmark have shown for decades, large scale solar thermal systems are a promising technology. However, several challenges are still to be met: Which approaches are most promising in integrating such systems, how should the DHC systems be designed, which components fit best into the system and which business models actually meet most stakeholders´ needs? Examples of already existing installations and elaborations on promising new markets and market developments are much needed fields of expertise. IEA SHC TASK 55 tackles these challenges and will provide answers to all questions by mid-2020.

8. References

Doll, W., Ohnewein, P., Krammer, S., Prem, G., Tschopp, D., Stelzer, R., 2016. PRECISE MEASUREMENT OF LARGE COLLECTOR ARRAYS FOR THE DEVELOPMENT OF IN-SITU TEST METHODS.

IEA SHC TASK 45, http://task45.iea-shc.org/, 09.10.2017.

IEA SHC TASK 55, http://task55.iea-shc.org/, 09.10.2017.

IRENA (2017), Renewable Energy in District Heating and Cooling: A Sector Roadmap for REmap, International Renewable Energy Agency, Abu Dhabi.

Lichtenegger, K., Unterberger, V., Gölles, M., Muschick, D., Höftberger, E., Gerardts, B., Krammer, S., Wöss, D., 2015. Inclusion of solar thermal devices in complex heat distribution systems – a look from the model-predictive control point of view.

Provasnek, A. K., Schmid, E., Geissler, B., & Steiner, G., 2016. Sustainable corporate entrepreneurship: Performance and Strategies toward Innovation. Business Strategy and the Environment. DOI: 10.1002/bse.1934

Putz, S., Provasnek, A.K., 2016. Results of IEA SHC Task 45 Subtask C “Systems - Configurations, Operating Strategies, Financing Issues“. Journal of Energy Procedia. DOI: 10.1016/j.egypro.2016.06.199

DH Networks - Concept, Construction and Measurement Results of a Decentralized Feed-In Substation

Toni Rosemann[1], Martin Heymann[1], Karin Rühling[1] and Bernd Hafner[2]

[1] Institute of Power Engineering, Professorship of Building Energy Systems and Heat Supply
Technische Universität Dresden, Dresden

[2] Viessmann Werke GmbH, Allendorf (Eder)

Abstract

The paper presents the concept and measurement results of a solar thermal pilot plant for decentralized feed-in to a 2nd generation district heating network. Ambitious conditions for both target temperature level and pressure difference are fulfilled with a return line to supply line feed-in (RL/SL) design. The use of water as solar liquid requires an active frost protection using return line district heating water. The stagnation state is investigated by the application of distributed temperature sensing (DTS). The measurement results include one frost protection and almost one feed-in season.

Keywords: solar thermal, decentralized feed-in, stagnation, frost protection, control concept, measurements

1. Introduction

Decentralized feed-in of solar thermal gains can contribute to the decarbonisation and flexibilisation of modern district heating networks (e.g. Heymann, et. al., 2017). The development of standards concerning network feed-in substations and their control concepts is the research goal of the ongoing research project "Kostenreduktionspotential beim Ausbau der Solarisierung von Fernwärmenetzen durch Standardisierung"[1]. These standards are derived from practical experiences of the planning, the commissioning and the operation of pilot plants – including the solar thermal system and the substation itself – as well as simulations studies.

In this paper the design and control concept of a pilot plant is presented which is in operation at the Centre for Energy Technology (CET) in Dresden since November 2016. The network feed-in substation is connected to a 2nd generation network (according to Annex X classification Rosa, et. al., 2014) and was developed in cooperation with the local network operator as part of a feasibility study for larger collector fields. The pilot plant is designed for the RL/SL feed-in into the district heating network - the most common and most flexible type of decentralized network integration.

This paper presents detailed measurement results and details of the control algorithms for the three main operation modes (hereafter referred to as states) of the network feed-in substation:

- *Feed-in* of solar energy,
- *Stagnation* and
- Active *Frost Protection* for the water-based solar circuit.

[1]Founded by Federal Ministry for Economic Affairs and Energy FKZ 0325553A.

doi:10.18086/swc.2017.06.11 Available at http://proceedings.ises.org

2. Concept of the District Heating Network Feed-in Substation

The pilot plant is connected to the primary district heating network of the city with a nominal pressure stage of PN25 and the nominal target feed-in temperature is 110 °C. Therefore solar vacuum tube collectors working according to the heat pipe principle are used in the collector field (CF). The collector field consisting of six subfields C1..C6 has a total gross area of 84 m² (total aperture area 48 m²) and an inclination of about 31° facing south. The design heat flow rate is 30 kW based on a total incline irradiance $G_{t,i}$= 1000 W m^{-2} and collector field temperatures of 115/70°C. The subfields C1..C6 are connected in series (see Fig. 1).

The circulation pump in the solar circuit Pu_{STS} is a speed-controlled pump group where only one pump is used in main operation at a time and where the other pump is hold as a spare component. The redundancy is important to guarantee the functionality of frost protection. The compressor-based pressure maintenance is connected to the system in the supply line of the collector field through stagnation cooler. This cooler is built as a finned tube radiator which limits the maximum steam spread in case of stagnation, reduces the design volume of the common additional auxiliary vessel and thereby the design volume of the pressure maintenance expansion vessel.

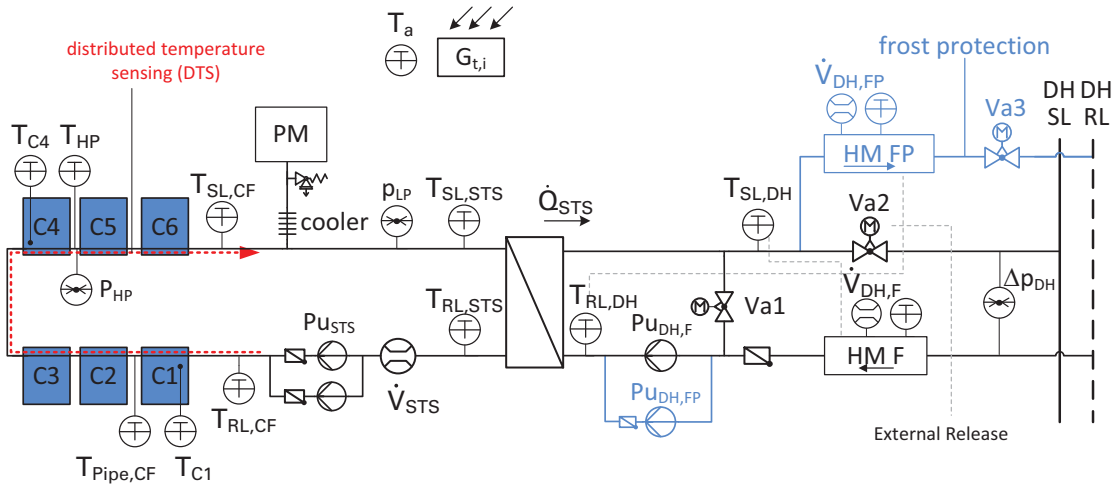

Fig. 1: Schematic of the feed-in substation (Ta – ambient temperature, C – collector, CF – collector field, DH – district heating, HM – heat meter, F – feed-in, FP – frost protection, HP – highest point, LP – lowest point, PM – pressure maintenance, Pu – pump, Va – valve, STS – solar thermal system)

The speed-controlled feed-in pump $Pu_{DH,F}$ is necessary to overcome the pressure difference Δp_{DH} in the DH network and generates the feed-in volume flow. The proper selection of this component is essential to assure the feed-in of the solar yields into the network. This is often complicated due to the lack of information about Δp_{DH}, $T_{SL,DH}$ and $T_{RL,DH}$ at the feed-in point for the course of the year and the future development of these values. Before feed-in the bypass valve Va1 will be opened to heat up the medium in the district heating side of the substation to prevent cold plugs in the network but will be closed during feed-in. It can also be opened during times of partial load/low irradiance to raise the RL temperature $T_{RL,DH}$ when the speed-controlled pumps reach their minimal flow rate. The valve Va2 is used to realize an external unblocking. If necessary the network operators can withdraw the release signal and prevent/stop the feed-in by closing the valve and shut of the pumps. The valves Va2 and Va3 are used to switch the flow direction between RL/SL in the state *Feed-in* (Va2 open, Va3 closed) and RL/RL for heating the STS in the state *Frost Protection* (Va2 closed, Va3 open). A separate frost protection pump $Pu_{DH,FP}$ is used because of different design parameter for the RL/RL frost protection heating (low discharge head) and due to redundancy.

A minimum sensor equipment is necessary for the plant operation. It consists of five temperature sensors ($T_{SL,CF}$ $T_{SL,STS}$ $T_{RL,CF}$ and $T_{SL,DH}$, T_a), the radiation sensor $G_{t,i}$ as well as two heat meters. The heat meter HM F measures the heat fed into the network. The volume flow signal $\dot{V}_{DH,F}$ of the feed-in heat meter is used for a control loop by an analogue module. There is a second heat meter HM FP, which measures the heat required for frost protection. These two separate heat meters are necessary as long as no bidirectional heat meter is available on the market that is certified for billing.

The monitoring package consists of additional temperature sensors, three pressure sensors (p_{HP}, p_{LP}, Δp_{DH}), a flow meter $\dot{V}_{STS}$, as well as a distributed temperature sensing system (DTS see Herwig, Rühling, 2014). The DTS uses an optical sensor cable, which is attached to the collector pipe of the system in order to measure the temperature distribution with a high spatial and time resolution. This is helpful for detailed analysis of the states *Frost Protection* and *Stagnation*.

3. State Feed-In

3.1 Controller

In order to operate the network feed-in substation in the *Feed-in* state a set of three controllers is used (see Tab. 1). The controller C1 is used for the matched-flow control of the collector field output temperature $T_{SL,CF}$ by adapting the pump speed of Pu_{STS}. This controller compensates changes mainly in the radiation $G_{t,i}$ and the return line temperature $T_{RL,STS}$. The objective is to keep the heat exchanger input temperature $T_{SL,STS}$ higher than the setpoint of the feed-in temperature $T_{SL,DH}$ – to guarantee heat transfer – and to keep the average temperature of the solar thermal system low to minimize losses.

Tab. 1: Closed-loop PI-controllers for state Feed-in

Name	Control variable	Setpoint	Output
C1	$T_{SL,CF}$	115..120°C	speed Pu_{STS}
C21	$T_{SL,DH}$	110°C	setpoint C22
C22	$\dot{V}_{DH,F}$	results from control signal of C21	speed $Pu_{DH,F}$

The two general main tasks of controlling the feed-in pump $Pu_{DH,F}$ are:

- to guarantee a stable volume flow $\dot{V}_{DH}$ despite the strongly changing pressure difference of the network Δp_{DH} but corresponding to the current solar yields and
- to operate with minimal power consumption.

A cascaded controller is used (see Fig. 2 left) to achieve both tasks. The temperature controller C21 finds a solution for the equation (eq. 1) by adjusting the volume flow setpoint $\dot{V}_{SP}$ of the controller C22 and thereby the volume flow $\dot{V}_{DH}$. The inner controller compensates any change of the pressure difference of the network $\Delta p_{DH.}$ This is energetic efficient, because the pump speed is changed to manipulate $\dot{V}_{DH}$ directly instead of using a throttling or bypass valve. The volume flow signal of the heat meter HM F can be used directly e.g. through an additional analogue module, depending on the kind of heat meter and the achievable update interval. The tested substation works well when controllers are updated every four seconds.

$$T_{SP} = T_{SL,DH} = \frac{\dot{V}_{SP} \cdot \varrho \cdot c_p}{\dot{Q}_{STS}} + T_{RL,DH} \quad \text{with } T_{SP} \text{..setpoint for } T_{SL,DH}, \dot{V}_{SP} \text{..setpoint for } \dot{V}_{DH} \qquad \text{(eq. 1)}$$

The compensation of the variable pressure difference Δp_{DH} by using the volume flow controller C22 (see Fig. 2 Right) is realized in three steps:

1. The setpoint volume flow is reached at the actual pressure difference $\Delta p_{DH,1}$ (steady state)
2. The volume flow $\dot{V}_{DH}$ differs from the setpoint as a result of the disturbing pressure difference $\Delta p_{DH,23}$. The feed-in temperature $T_{SL,DH}$ will differ from its setpoint as well. (instationary)
3. The controller C22 compensates the pressure difference variation and the feed-in temperature will not be affected. (stationary)

The volume flow signal $\dot{V}_{DH}$ of the HM F can also be used to find the right pump speed to overcome the pressure difference Δp_{DH} when the feed-in starts (Rosemann, et. al., 2017a). The integration of this signal into the plant control as described above is recommended because of the low additional costs for reading out this signal and the high advantages for solving the common technical pressure difference Δp_{DH} problems in district heating networks (Lennermo and Lauenburg, 2015).

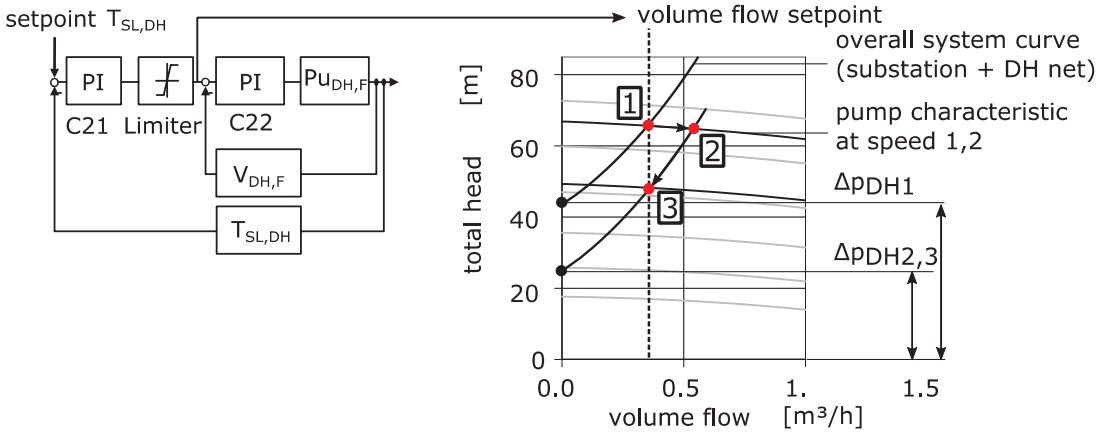

Fig. 2: Left: Cascade controller for the feed-in temperature TSL,DH
Right: Characteristic curves of the feed-in pump PuDH,F and the operation points 1..3
during the control action of C22 reacting on a step of ΔpDH
(1 – Starting point, 2 – after step of ΔpDH without reaction of C22, 3 – Final stage after correction of the pump speed)

3.2 State Machine

For the correct operation of a district heating network feed-in substation, the controller and actuators of the plant have to be de-/activated and set to corresponding values at the right moment. This task is solved with a state machine (see Fig. 3). A state is a set of actor and controller settings which structures the operation of the plant into sequential steps. The entry point of the state machine is "Start". There is always only one active state. The active state checks the criteria pointing to the connected states and starts a transition if the logical expression of all criteria is true. Global states are special states that always check their entry criteria because of their high priority, which is used e.g. for safety technology. States can consist of substates. This is used to cluster states to visualize their coherence (e.g. to heat up the solar thermal system is always a part of the feed-in).

A criterion is based on measurements of physical values and durations. A duration can be based on a physical criterion (additional time criterion, "How long is a physical condition met") or on the active time of a state (τ_{State}, "How long is a state active"). The parameters of the criteria depend on the concrete plant and its constraints.

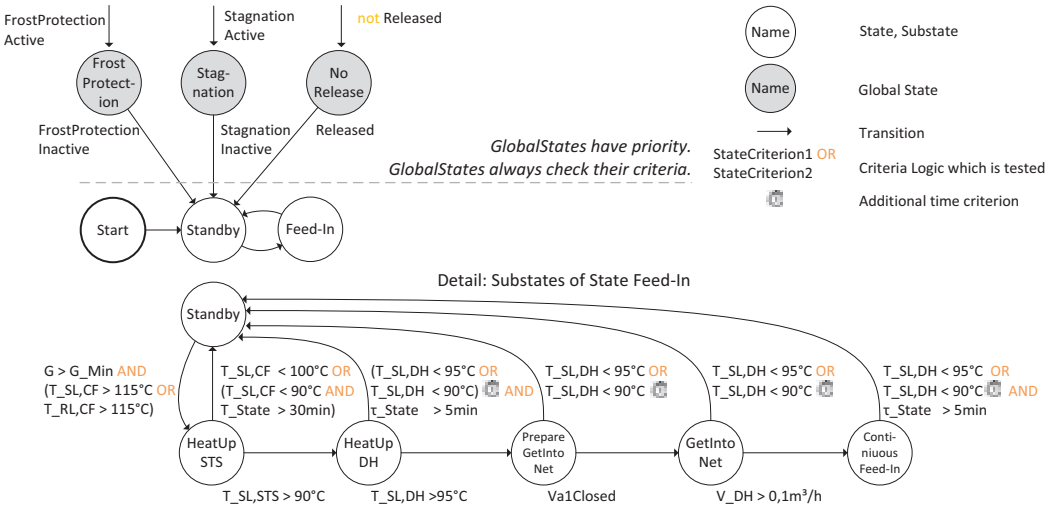

Fig. 3: State diagram of the net feed-in substation with detailed substates of the state Feed-in
Released – External release signal is true and feed-in allowed
G_Min – minimal radiation threshold calculated on basis of the collector curve
The criteria for Stagnation and Frost protection are discussed in the corresponding section.

Tab. 2: Description of the substates for the state Feed-in and controller activity (○ – inactive, ● - active)

State	Description	C1	C21	C22
Standby	Default State with no activity of the plant (night, cloudy day, winter day)	○	○	○
HeatUpSTS	When high temperatures are detected in the collector field, Pu_{STS} is activated and the hot fluid is moved into the network feed-in substation.	●	○	○
HeatUpDH	When the hot plug reaches the heat exchanger, the district heating side of the network feed-in substation is heated up by opening the bypass valve Va1 and starting the feed-in pump $Pu_{DH,F}$.	●	○	○
PrepareGetIntoNet	The bypass valve Va1 is closed.	●	○	○
GetIntoNet	The pump speed $Pu_{DH,F}$ rises until a volume flow $\dot{V}_{DH}$ is detected.	●	○	●
ContinuousFeed-In	Hot water heated by the collector field is fed into the district heating network	●	●	●

3.3 Measurement results

The exemplary measurement results of the state *Feed-in* (see Fig. 4) start at 8:00 of 22th of June and end at 18:00 with an average radiation of 530 W m^{-2} and an average ambient temperature of 31 °C.

The plant is operated according to the state machine described above with the substates from Tab. 2. In the morning, the system starts in *Standby* until $T_{CF,SL}$ or $T_{CF,RL}$ exceeds 115 °C. The collector field return line temperature $T_{RL,CF}$ is remarkable higher than the collector field supply line temperature mainly due to shading of C6. From 9:20 to 10:00 the active state falls back to *Standby*. The fallback is triggered by the low solar thermal supply line temperature $T_{SL,CF}$ < 90 °C criterion. This undesired behavior sometimes happens due to mentioned collector temperature variation during the heat up and is a specialty of the collector field design of the pilot plant. After reaching the state *HeatUpSTS* again the hot medium is transported to the heat exchanger and the district heating side gets heated up. During the *Continuous Feed-in* from 11:20 to 17:10 three different disturbances occur, which are well compensated. $T_{SL,DH}$ very accurately reaches its dynamic setpoint:

- 12:00, 15:50 – Peaks in the pressure difference Δp_{DH} are compensated by the pump speed adaption of the controller C22.
- 13:30 - The rising of the return line temperature $T_{RL,DH}$ by 10 K is compensated with a higher volume flow $\dot{V}_{DH}$ by the controller C21.
- 14:30 – The radiation starts to drop caused by clouds. The solar volume flow $\dot{V}_{STS}$ is reduced by the controller C1. The high thermal capacity of the collector and the medium as well reduces the sensitivity to radiation disturbances.

The continuous volatility of the district heating return line temperature $T_{RL,DH}$ is caused by the periodic opening and closing of the control valve of a district heating substation located in the long stub pipe to the district heating network.

In the evening the feed-in temperature $T_{SL,DH}$ falls below 95 °C and the feed-in is stopped by falling back to *Standby*. During the day 82 kWh solar thermal energy where fed into the district heating network mainly at the desired feed-in temperature of 110 °C. The current amount of heat fed into the network from January to September 2017 – without final optimization of the state machine and controller – is 8.556 kWh.

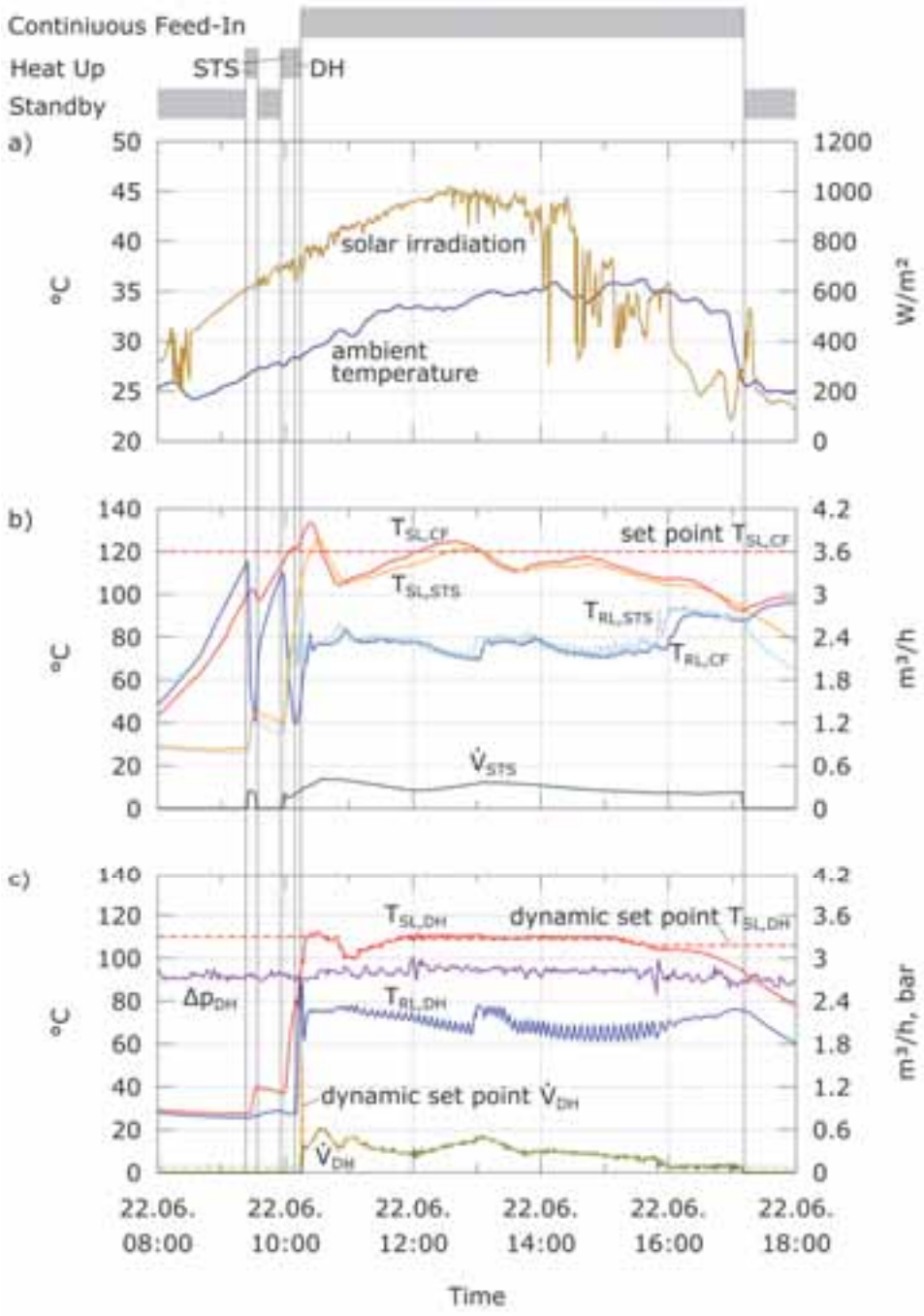

Fig. 4: Measurement data for state Feed-in,
a) ambient, b) solar system, c) district heating side

4. State Active Frost Protection

4.1 Controller and State Machine

The frost protection has to prevent all parts of the installation from cooling down to a temperature near the melting point of the solar liquid. To achieve this, a lower limit for the medium temperature in the solar system of 5 °C is defined. If any of the temperature criteria goes below this threshold, the state *Frost Protection* is activated. This state is defined as a global and is checked in every iteration.

If activated, heating water from the district heating return line flows through the district heating side of the station and back to the return line via the frost protection branch with the heat meter. The separate pump $Pu_{DH,FP}$ (see Fig. 1), which is installed in parallel to the feed-in pump $Pu_{DH,F}$, is used for this issue. The frost protection stops and returns to the *Standby* state, when all observed sensors exceed the upper threshold value of 10 °C and a minimum runtime is reached.

The tested variants concerning the details of the state *Frost Protection* made during the winter season 2016/2017 are shown in Tab. 3. First tests were done with the activation of the pumps when any of the collector field temperatures falls below the lower limit. These temperatures are reported by sensors installed in the piping of the supply and return line ($T_{SL,CF}$ $T_{RL,CF}$) and sensors in the connection pipes of the collector field (T_{HP}, $T_{Pipe,CF}$). The pumps are stopped if all measured temperatures go above the upper threshold. It has been shown, that a minimum runtime of 13 min is necessary to assure at least one turn of the fluid through the solar thermal system. Furthermore detailed evaluations using the DTS showed that under some conditions the collectors cool down faster than the piping of the collector field (see Rosemann, et. al., 2017b). Therefore two collector sensors CS (T_{C1}, T_{C4}) had been included in the scanning routine to detect low medium temperature within the collectors.

Tab. 3: Tested criteria for the de-/activation of the state Frost protection (○ – on, ● - off, | - "or", & - "and")

Name	Frost protection	Criteria	Pump activity	
			Pu_{STS}	$Pu_{DH,FP}$
5 °C	Enter	$(T_{SL,CF} \mid T_{RL,CF} \mid T_{Pipe,CF} \mid T_{HP}) < 5$ °C	●	●
	Exit	$(T_{SL,CF}$ & $T_{RL,CF}$ & $T_{Pipe,CF}$ & $T_{HP}) > 10$ °C	○	○
5 °C, 13min	Enter	$(T_{SL,CF} \mid T_{RL,CF} \mid T_{Pipe,CF} \mid T_{HP}) < 5$ °C	●	●
	Exit	$(T_{SL,CF}$ & $T_{RL,CF}$ & $T_{Pipe,CF}$ & $T_{HP}) > 10$ °C AND RUNTIME $Pu_{STS} > 13$ min	○	○
5 °C, 13min, CS	Enter	$(T_{SL,CF} \mid T_{RL,CF} \mid T_{Pipe,CF} \mid T_{HP} \mid T_{C1} \mid T_{C4}) < 5$ °C	●	●
	Exit	$(T_{SL,CF}$ & $T_{RL,CF}$ & $T_{Pipe,CF}$ & T_{HP} & T_{C1} & $T_{C4}) > 10$ °C AND RUNTIME $Pu_{STS} > 13$ min	○	○

4.2 Measurement results

In Fig. 5 the measurement data for the operation of the frost protection using the latest level of development are shown (5°C. 13min, CS). The measurement period starts at midday of the 8th of February and ends at midday the day after. The average ambient temperature was -2.7 °C, at minimum -4.7 °C and the sky was clouded. The upper chart illustrates temperature profiles gained from the sensors of the solar thermal system and the collector field. The lower chart contains the temperature values on the district heating side.

The temperatures in the collector field increase in the afternoon due to solar gains and are dropping constantly afterwards. The solar gains only effect the sensors located directly next to the collectors. The temperature in the 25 m long connection pipe between C1 and C2 $T_{Pipe,CF}$ is not raised. At 19:50 $T_{Pipe,CF}$ triggers the first frost protection period (#1). All other frost protection periods (#2 to #4) are triggered by the collector sensor T_{C4}.

The solar pump operates at its maximum speed ($\dot{V}_{STS}$) when the state *Frost Protection* is active. The volume flow on the district heating side $\dot{V}_{DH}$ is controlled in order to reach a supply line temperature of 20 °C in the

solar circuit. The temperatures on the district heating side $T_{RL,DH}$ and $T_{SL,DH}$ are very low, almost at room temperature.

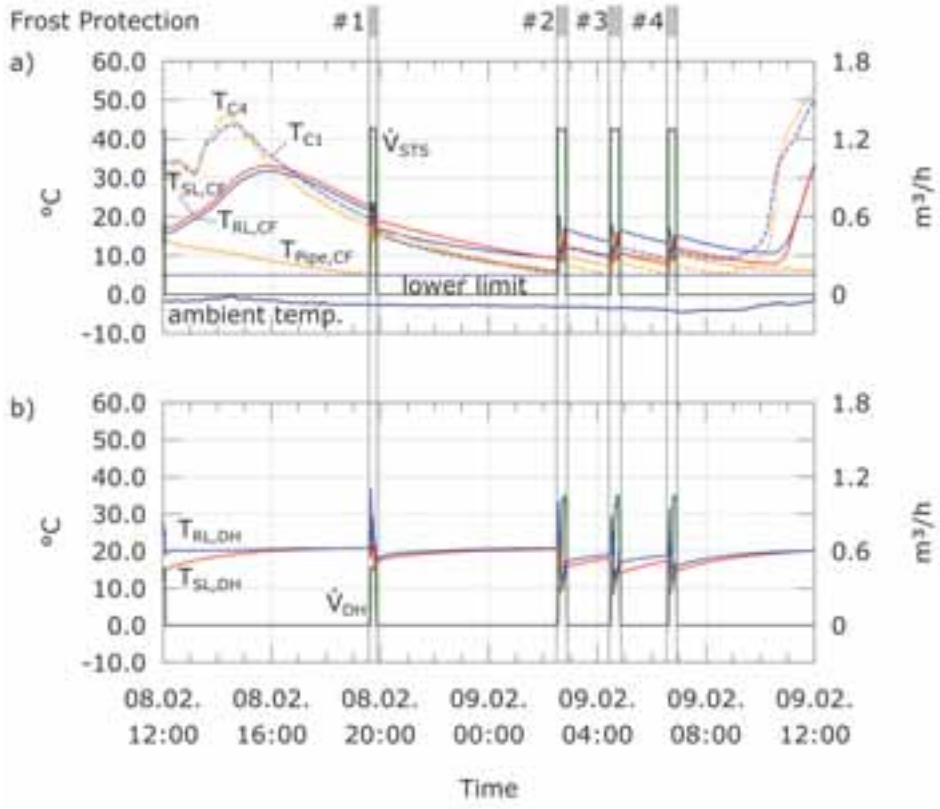

Fig. 5: Measurement data for state Frost Protection, a) solar system, b) district heating side

The solar thermal plant is connected to the district heating network via a long stub pipe. In the presented time period the connected consumers have no heat demand and the return line cools down. The frost protection can be guaranteed anyway, because it's little heat demand and the big transfer surface of the heat exchanger. Overall a heat demand for the frost protection of 4 kWh was measured at that day.

Fig. 6 shows the daily heat demand for the frost protection over the daily ambient temperature for the whole winter season. Days with a relatively high irradiation (> 1,2 kWh/m² in collector plane) are colored red, others blue. As expected the heat demand for frost protection increases with decreasing ambient temperatures. This demand is clearly reduced at days with high solar gains. The frost protection starts at daily average ambient temperatures of about 3 to 5 °C. The heat demand can go up to 14 kWh per day at very cold days with daily average ambient temperatures under -5 °C.

For the optimized and save variant of the state *Frost Protection* (✖ 5 °C, 13min, CS) only 9 days with a heat demand are available. The heat demand added up to 273 kWh for the whole winter season, which is about 2 – 3% of the annual heat output fed into the district heating system. This is in the range of known plants with active frost protection.

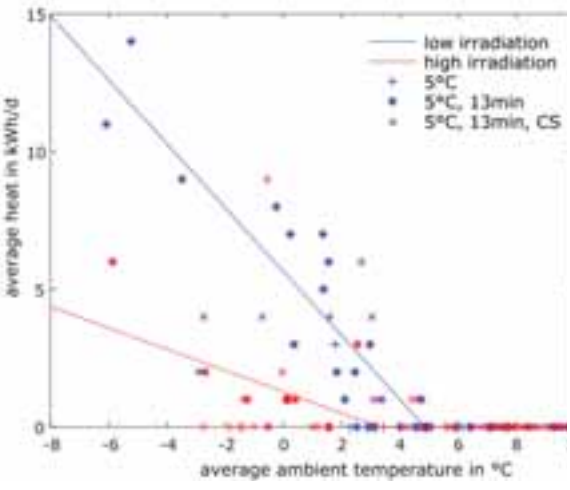

Fig. 6: Statistical evaluation of the frost protection season in winter 2016/17, daily average, low irradiation < 1,2 kWh/m² in collector plane per day ≤ high irradiation

5. State Stagnation

5.1 Controller and State Machine

The operation of a solar thermal system can stop during the day even though there is a solar irradiation. This can occur because of a case of damage, a plant maintenance or the operator of the district heating network withdraws the release signal. The stagnation concept has to ensure an intrinsic safety of the installation to handle this issue. Stagnation is detected by the state machine observing the collector field supply line temperature $T_{SL,CF}$. If it exceeds the limit of 138 °C for more than 5 min or if it exceeds 140 °C the state *Stagnation* is activated. This mainly stops the solar circulation pump. No other switching operation is necessary. The stagnation cooler should limit the produced steam volume and the compressor pressure maintenance should take this volume and keep the pressure in the tolerated range.

The state *Stagnation* is left when $T_{SL,CF}$ falls below 120 °C for more than 5 min or under 110 °C. The *Stagnation* state is implemented as global state.

5.2 Measurement results

Fig. 7 shows a test of the state *Stagnation* at the 5th of September 2017. It was a warm (up to 25 °C) and sunny day with some clouds during midday (maximum 1000W/m² in collector surface). Subfigure a) shows ambient conditions, Subfigure b) pressures at the lowest and highest point in the system (p_{LP}, p_{HP}) and the filling level of the expansion vessel (V_{PM}). Subfigure c) includes temperatures of the collector field (where T_{C6} is measured with the DTS), the calculated boiling temperature under the conditions at the highest point and the volume flow in the solar thermal system $\dot{V}_{STS}$. Subfigure d) is a carpet plot of the DTS with the time on the x-axis and the position in the collector field on the y-axis. The temperature is color coded (dark-blue means cold, light-blue means feed-in temperature, green means boiling temperature, red means superheated steam).

In the morning the system starts in *Standby* until one temperature of the collector field exceeds 115 °C. From 10:00 to 10:50 the solar and afterward the district heating side is heated up followed by the state *Feed-In*. At 12:00 the release signal is withdrawn manually and the system changes to *Standby*. At about 13:00 the state machine recognizes the state *Stagnation*. Using the DTS, which can measure the temperature not only at discrete locations, the boiling temperature is already reached at 12:30 in C5 and C6. The filling level sensor V_{PM} also recognizes a fast increase from 14 to 28% at this point in time, which means that first steam is produced here. Solar liquid displaced by the spreading steam bubble can only flow in the direction of the supply line into the pressure maintenance due to the plant configuration.

The equalizing of the pressure values at the highest p_{HP} and lowest point p_{LP} in the system between 12:30 and 13:00 is very interesting. This results from the falling water level when the steam fills the supply line and finally reaches the stagnation cooler at the lowest point. The pressure maintenance keeps the pressure level at the lowest point constant and thus increases the pressure at the top of the system p_{HP}. This behavior can reduce the dynamic of the beginning stagnation because the boiling temperature is slightly increased.

According to subfigure d) at about 13:00 the boiling point is reached in all collectors and all connection pipes between C2 and C6. When C1 is filled with steam a steam front fills about 8 m of the connection pipe between C1 and C2. The cool water in the connection pipe is pushed in C2 and C3 and temporary causes a condensation here. When the steady state is reached in C1 the steam front in the connection pipe condenses again and sucks in steam from C2 into the connection pipe. At first in C1 the steam is superheating, because here are the lowest dynamics. Shortly before 15:00 the superheating also occurs in C5 and C6 and at 16:00 in C4. In C2 and C3 there is boiling liquid for the whole measurement day.

At 16:30 the maximum filling level of the expansion vessel is reached with 65%. The stagnation cooler can safely limit the produced volume of steam. The solar irradiation is decreasing in the evening hours. Starting from 17:30 the steam front is declining, which makes the pressure at the highest point p_{HP} decrease again. At 18:15 subcooled liquid reaches the collector field and the steam condenses very fast and empties the expansion vessel. This causes a short and small underrun of the allowed pressure level p_{LP}. The state *Stagnation* is left.

The presented stagnation test (and several others) shows that the *Stagnation* state can be handled safely. Produced steam is condensed in the stagnation cooler. The compressor pressure maintenance can take all of the produced steam volume and can mostly keep the pressure in the desired range.

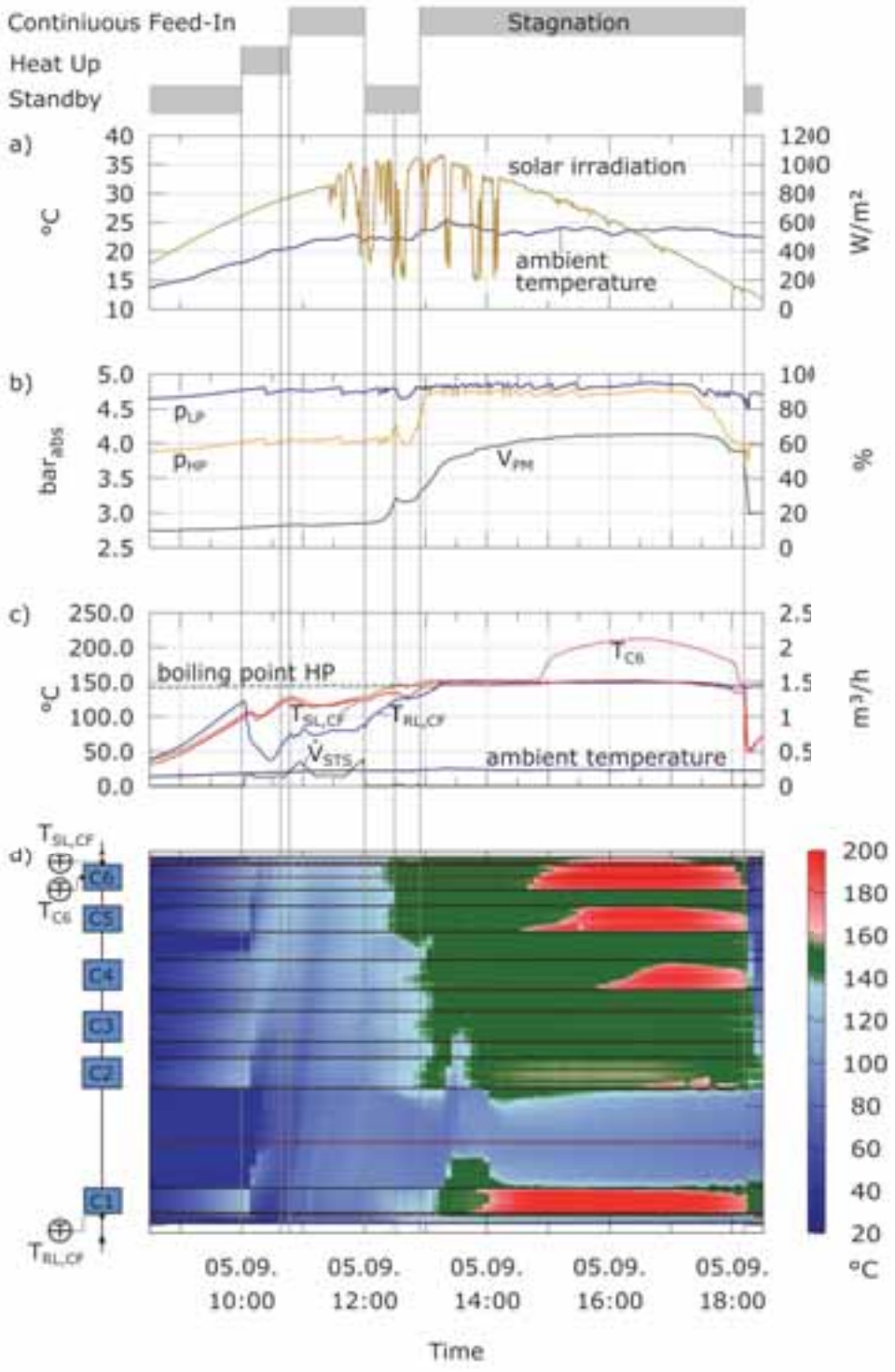

Fig. 7: Measurement data for stagnation, a) ambient, b) pressure maintenance, c) solar system, d) DTS of the collector field

6. Conclusions/Prospects

The planning of the pilot plant, the realization and the operating experience of almost one year have already provided valuable information which can be used for standardization of decentralized feed-in substations. There is a need for clarification with the district heating companies regarding the control accuracy of the feed-in temperatures. A high control accuracy of the feed-in temperature always is reached at the expense of a higher variation of the feed-in volume flow and vice versa. For solar thermal systems, a higher temperature tolerance especially in the morning during heat up or during phases of clouds would ease the general operation. Especially for district heating systems with a crucial solar fraction a high variation of the feed-in volume flow can cause hydraulic problems and interference.

The use of water as solar liquid is feasible with an active frost protection in the winter season. It is necessary to take the different cooling behavior of the collectors and the piping into consideration. A well designed separate stagnation cooler combined with a small additional auxiliary vessel can safely limit the steam spread and protect the membrane of the expansion vessel. This combination can reduce the design volume of the expansion vessel thus reduce investment costs.

Solar thermal gain prognoses will be possible after the validation of a simulation model for the decentralized solar thermal feed-in substations. It is intended to make simulations studies regarding the generalization of the current control concept (state machine) and a model predictive control concept. The commissioning of a combined supply and feed-in substation connected to a low temperature district heating network in Berlin Adlershof[1] is in progress. This will extent the monitoring portfolio of the research project.

7. References

Lennermo, G., Lauenburg, P., 2015. Variation in Differential Pressure at a District Heating Prosumer Substation, 3nd International Solar District Heating Conference, Toulouse

Herwig, A., Rühling, K., 2014. Fiber-Optic Distributed Temperature Sensing Of Large Hot Water Storage Tanks. 15th International Symposium on District Heating and Cooling, Stockholm

Heymann, M., Rühling, K., Felsmann, C., 2017. Integration of Solar Thermal Systems into District Heating – DH System Simulation, Energy Procedia, 116, Seoul doi:https://doi.org/10.1016/j.egypro.2017.05.086

Rosa, A. D., Li, H., Svendsen, S., Werner, S., Persson, U., Rühling, K., Felsmann, C., Crane, M., Burzynski, R. and Bevilacqua, C. 2014. Annex X Final Report: Toward 4th Generation District Heating, Tech. rep., IEA DHC|CHP

Rosemann, T., Löser, J., Rühling, K., 2017a. A New DH Control Algorithm for a Combined Supply and Feed-In Substation and Testing Through Hardware-In-The-Loop, Energy Procedia, 116, 416-425. doi:https://doi.org/10.1016/j.egypro.2017.05.089

Rosemann, T., Heymann, M., Rühling, K., Hafner, B., 2017b. Dezentrale Solarthermieeinspeisung in das Fernwärmeprimärnetz - Feldversuch in Dresden, Euroheat & Power, number 9, pages 24 - 27

[1] Founded by Federal Ministry for Economic Affairs and Energy FKZ 03ET1155B.

8. Appendix: Units and Symbols

Table 4: Symbols

Quantity	Symbol	Unit
Area	A	m^2
Global irradiance or solar flux density	G	$W\ m^{-2}$
System mass	m	kg
Mass flow rate	$\dot{m}$	$kg\ s^{-1}$
Pressure (absolute)	p	bar
Pressure difference	Δp	bar
Heat	Q	kWh
Heat flow rate	$\dot{Q}$	kW
Temperature	T	°C
Efficiency	η	
Time	τ	s

Table 5: Abbreviations and subscripts

Quantity	Symbol
Ambient	a
Collector	Col
Collector field	CF
Collector sensor	CS
District heating	DH
Feed-in	F
Frost protection	FP
Heat meter	HM
Highest point in system	HP
Lowest point in system	LP
Network feed-in Substation	NFS
Pressure maintenance	PM
Pump	Pu
Return line	RL
Valve	Va
Solar thermal system	STS
Supply line	SL

Barriers and opportunities to maximize the share of solar thermal energy in district heating networks – approaches within the IEA SHC Task 55, Subtask A and selected preliminary results

Ralf-Roman Schmidt[1], Markus Gölles[2], Anna Katharina Provasnek[3], Paolo Leoni[1], Sabine Putz[3]

[1] AIT Austrian Institute of Technology GmbH, Vienna (Austria)

[2] BIOENERGY 2020+ GmbH, Graz (Austria)

[3] S.O.L.I.D. Gesellschaft für Solarinstallation und Design mbH, Graz (Austria)

Abstract

The integration of large and very large solar thermal plants in district heating (DH) networks gained increasing attention in recent years. However, the integration poses some challenges, especially for large shares of solar heat. This contribution gives an overview of the approach chosen within Subtask A of the IEA SHC Task 55 for assessing the impact of high shares solar thermal energy on the overall district heating and cooling network and different integration aspects in order to maximize the share of solar thermal energy. This includes:

- Collection and analyses of case studies for assessing the technical requirements of large shares
- Economic analyses of overall DHC networks, their supply strategies, transition strategies, heat demand and energy price scenarios
- Analyses of DHC network hydraulics, evaluation of hybrid technologies and possible supply points for large solar thermal installations
- Overall DHC network control strategies and other measures for increasing solar thermal fractions

This contribution describes the used approach and selected preliminary results

Keywords: solar district heating; case studies; integration aspects; transition strategies; network performance; hydraulics; control strategies; return temperature reduction.

1. Introduction

In recent years, megawatt-scale solar thermal (ST) supply to district heating (DH) or district heating & cooling (DHC) systems have gained increasing attention. This alternative energy is available almost everywhere (unlike e.g. deep geothermal energy or industrial waste heat) and thus it can contribute to satisfy the increasing energy demands of districts and cities. Further on, the use of solar thermal supported DHC networks has benefits on an environmental (reduced emissions and air pollution) and systemic level (e.g. DHC infrastructure and local economy). It can make use of synergies in the urban context (suitable integration into urban environment) and can increase energy supply security (reduced fuel imports, diversification of the energy mix).

A breakdown of fuel use in DHC systems worldwide shows that 43.2% are fueled by natural gas, 43% are based on coal and its products, followed by oil (4.3%), biofuel and waste (6.5%), or nuclear energy (0.2%). Solar based energy supply accounts for far less than 0.01% globally. Still, the share of energy based on renewable sources has been growing (IRENA, 2017). The presence of solar thermal supported DHC networks is highly diverse across countries. E.g. Denmark is well known for its integration of large solar thermal plants into local DH networks. Other countries, such as Austria, are about to implement even bigger solar thermal district heating systems.

In a simulation study[1] for Austria, Denmark, Germany and Italy, a technical potential between 3% and 12% solar share in 2050 has been estimated (*solar share = heat supplied by solar thermal collectors / overall heat supply to*

[1] http://www.sunwindenergy.com/solar-thermal/solar-thermals-role-2050-energy-mix

doi:10.18086/swc.2017.06.12 Available at http://proceedings.ises.org

the end customers). However, the integration of large solar thermal systems into existing and new DH networks faces several challenges, especially the high network temperatures and the seasonal mismatch between supply and demand, e.g. (BDEW 2017). This is especially relevant as soon as the solar share reaches a level, where the operation of the network and the other supply units are influenced significantly.

The solar heating and cooling (SHC) technology cooperation programm (TCP) of the international energy agency (IEA) was established in 1977 to promote the use of all aspects of solar thermal energy by international collaborative effort of experts from various countries[1]. Its primary activity is to develop research projects (Tasks) to study various aspects of solar heating and cooling. Task 55 of the SHC TCP provides a platform for practitioners and scientists to elaborate the benefits and challenges of solar district heating (SDH) and solar district cooling (SDC) systems[2]. Hence, SHC Task 55 elaborates options and measures to realize sophisticated SDH and SDC plants.

2. Methodology

The activities in IEA SHC Task 55 are funded through a task-sharing approach, where each participant contributes resources in-kind (for example personnel or materials)[3]. The task-sharing approach allows to connect existing national and international projects via the international platform and thus benefit from international experience and exchange. More than 25 international experts share their expertise on SDH and SDC systems, requirements and integrational challenges, existing district energy systems face when integrating large amounts of solar thermal energies. Task 55 is separated into the following 4 Subtasks: **A**: Network Analyses and Integration, **B**: Components Testing, System Monitoring and Quality Assurance, **C**: Design of the Solar Thermal System and of Hybrid Components and **D**: Promotion and dissemination of SDH/SDC and hybrid technologies in new markets.

This contribution describes the approach and selected preliminary results within Subtask A. It focusses on the assessment of the impact of solar thermal technologies on the overall district heating and cooling network and integration aspects in order to analyze barriers and opportunities for maximizing the share of solar thermal energy.

Subtask A is separated as follows:

1. Assessment of technical requirements of existing and newly integrated large scale Solar DHC networks. Aim is to understand the boundary conditions and parameters (technical, economical etc.) enabling high shares of solar thermal supply to DHC networks.
2. Economic analyses of overall DHC networks, their supply strategies, transition strategies, heat demand and energy price scenarios. Aim is to understand possible pathways from zero (or very little) solar shares to high or very high shares (e.g. 20-70%). Here, especially economic parameters should be analyzed.
3. Analyses of DHC network hydraulics, evaluation of hybrid technologies and possible supply points for large solar thermal installations. This part focusses on technical aspects of the integration, building upon existing analyses and case studies on solar thermal integration measures.
4. Assessment of overall DHC network control strategies and other measures that can support the integration of solar thermal energy and thus increase the solar thermal share.

Due to its interdisciplinary scope, activities in Subtask A will be performed in collaboration with other SHC Tasks (e.g. Task 52 on "Solar Heat and Energy Economics in Urban Environments"[4]) and the IEA TCPs on District Heating and Cooling (DHC) and Combined Heat and Power (CHP)[5]. For the later, one main cooperation will be established to the new Annex TS2 on "Implementation of Low Temperature District Heating Systems"[6].

[1] https://www.iea-shc.org/
[2] http://task55.iea-shc.org/
[3] https://www.iea.org/media/impag/FAQs_new.pdf
[4] http://task52.iea-shc.org/
[5] http://www.iea-dhc.org
[6] http://www.iea-dhc.org/the-research/annexes/2017-2020-annex-ts2-draft.html

3. Selected preliminary results

The runtime of Task 55 is from September 2016 to End August 2020. During the first year, the work in Subtask A focuses mainly on the set-up of the overall structure including a detailed work plan as well as analyzing and consolidating the international activities and projects from the Task 55 participants. Within this contribution, some selected preliminary results can be presented.

3.1. Assessment of technical requirements of existing and newly integrated large scale SDH/SDC – collection and analyses of case studies

Initially, best practice examples and case studies of existing, newly integrated and planned SDH and SDC systems with large (>5%) solar fractions (typically of > 0,5MWth up to GWth) will be collected. The case studies are collected via supporting projects from the IEA SHC Task 55 partners as well as through a dedicated internet research. A template for the data collection was set up with focus on:

- temperature and pressure ranges of both networks and solar systems
- solar thermal share
- storage size
- efficiency of the solar systems
- economic parameters (which will be used in the section 3.2)
- demand structure and possible additional summer demand (e.g. from adsorption chillers) .

Analyzing and comparing the existing case studies, potentials, challenges and barriers for the integration of solar thermal systems will be analyzed. The following aspects should be handled:

- What overall supply mix is the most economic/ ecologic for covering the heat demand in a given network?
- How to transform the DH network towards a maximum share of ST (and other low carbon sources?)
- What is the impact of different boundary conditions (energy prices, demand development …)?
- Evaluation of the system`s performance (e.g. Primary energy consumption and Socio-economic benefits)

3.2 Economic analyses of overall DHC networks, their supply strategies, transition strategies, heat demand and energy price scenarios

Based on the results of 3.1 and other case studies, possible transition strategies supporting a maximum share of solar thermal supply will be derived.

One very prominent example is the transformation strategy developed for the city of Graz (Austria). Fig. 1, left illustrates that current energy generation for district heating (DH) in Graz, Austria, is primarily based on waste heat from fossil-fired combined heat and power (CHP) plants. Due to low prices on the European electricity market, the operation of the CHP plants became increasingly uneconomic. Hence, the operator of the main CHP plant in Graz recently announced its closure in 2020. As a result, almost 80% of the overall heat production in the Graz DH network has to be replaced by new energy sources.

For developing future supply options, the city of Graz initiated a wide stakeholder process (Götzhaber et al 2017). This process resulted in a bunch of measures including the project “BIG Solar Graz” which is supposed to have a share of about 20% on the overall DH supply in Graz – see Fig. 1 right.

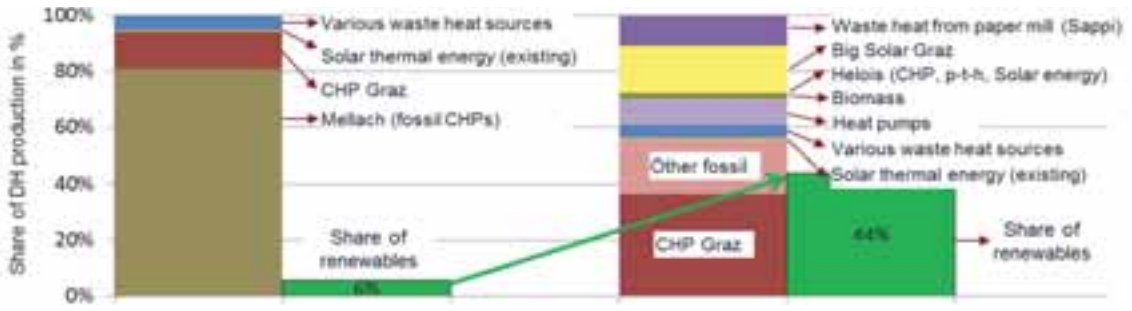

Fig. 1: Transformation strategies, example: Graz, left: current situation of the DH network in Graz, right: possible future supply mix (Prutsch 2017, translated, p-t-h = power-to-heat)

Current energy used for heating and domestic hot water in residential and service buildings in Graz is estimated at 2,400 gigawatt hours per year (GWh/a). In total, 1,100 GWh/a (2013) are provided by DH. While Graz receives 935 GWh per year, corresponding to 39% of the cities heat demand, the remaining 165 GWh/a are distributed beneath the southern communities around Graz, which are obtaining heat from DH mainly in winter. It is planned to further increase the share of DH up to 56% until 2030. Operating temperatures vary seasonally. The system is operated with flow temperatures up to 120°C in winter and up to 75°C in summer. The return flow temperature is on average 60°C. The DH network is operating all seasons throughout the year in Graz, whereas the southern communities are not supplied in summer.

The concept to integrate high solar thermal fractions into the DH network named "BIG Solar" aimed to investigate a maximum solar fraction applicable (e.g. (Poier 2017)). It is limited to the basic condition of having a competitive heat price compared to other sources of heat generation, such as from gas boilers for DH in Graz. Therefore, the size and capacities of key components, namely the collector field, the pit storage, and the absorption heat pumps (AHPs) were simulated in a certain range. Simulations aimed at identifying a system optimum for dimensioning each component and ultimately for the whole system.

First, for estimating the overall potential of the concept the heat load profile of DH in Graz was divided into two shares. A low temperature share for the basic heat load, provided either from solar and the storage directly and from the storage via the AHPs indirectly and a high temperature share, which is mainly for peak load especially in winter, provided by high temperature sources such as gas or biomass boilers. According to the calculation, the BIG solar share may be roughly at 55% of DH in Graz with current boundary conditions. Moreover, by taking into account that only one part of the energy is supplied by solar and the other part is supplied by the driving energy for the thermal AHPs from an auxiliary heating source, the pure solar output would be 33%. Therefore, detailed investigations of the concept were performed up to a solar fraction of 30%. TRNSYS, the transient system simulation software tool was applied to run multiple up to a maximum solar fraction of 30% in order to identify the technical and economic optimum. A series of simulations for collector field sizes between 20,000 m² up to 1 Million m², pit storage sizes between 100,000 m³ up to 2 Million m³ and 3 different sizes of AHPs (0, 50 and 100 MW heat output) were performed and evaluated. The multiple simulations with different parameter resulted in a techno-economic optimum of 450,000 m² collector field area, a seasonal heat storage capacity of 1,800,000 m³ and AHPs with a total heat capacity of 100 MW for the DH network of the city of Graz.

The use of AHPs is a key element in the system. On the one hand, AHPs are used to raise the temperature from the seasonal storage, when the storage is already partly emptied and temperature is lower than the minimum necessary 80 to 90°C for DH. On the other hand, AHPs accelerate the cooling down process of the seasonal pit storage, which means higher collector-efficiency at lower temperatures and therefore they lead to an essential yield improvement of the specific net solar heat production. The solar thermal concept also foresees an auxiliary heating component, which serves to power the generator of the AHPs and raises the temperature from the BIG Solar system up to the required 120°C for DH in winter.

Technical limitations such as the maximum capacity of the DH transport line, current heat and temperature loads, or future loads of waste heat from industries, were taken into account. Furthermore, a comprehensive cost evaluation was performed by using capital budgeting. The most important economic key performance indicators (KPIs) such as net present value (NPV), internal rate of return (IRR), discounted payback period (DPB) and levelized cost of energy (LCOE) were calculated and evaluated for different financing scenarios.

To sum up, simulations show that the BIG Solar concept is technically and economically feasible. The economic analysis shows that a heat price is comparable to other heating sources for DH in Graz. Although such a system has high upfront investment costs, the payback-time is moderate and economically reasonable, even in the light of neglected environmental benefits. Moreover, the project has flexible parameters. Given the boundary conditions in Graz such as land availability, the size of the solar thermal system can vary between 150,000 and 650,000 m² respecting the adaptation of sizes of the pit storage and the AHPs by feasible and economic sound price ranges (Reiter, Poier, et al. 2017).

The study on solar thermal large-scale installations integrated into the DH network of the city of Graz was one of the first analyses undertaken. Next to the study, a range of analyses named ´BSX-BigSolarX´ have been performed. Results indicated flexible parameters and techno-economically feasible collector field sizes similar to parameters identified in Graz. A number of study results will be available in upcoming Task 55 expert meetings.

3.3 Analyses of DHC network hydraulics, evaluation of hybrid technologies and possible supply points for large solar thermal installations

The technical integration options of the solar thermal energy will be evaluated from a hydraulic point of view. This is including the differentiation between central and decentral supply into existing networks as well as different local hydraulic connections and supply options. Also, the related challenges in the network performance will be evaluated considering the interaction with other supply technologies. Fig. 2 shows possible supply points for solar collectors in a DH network.

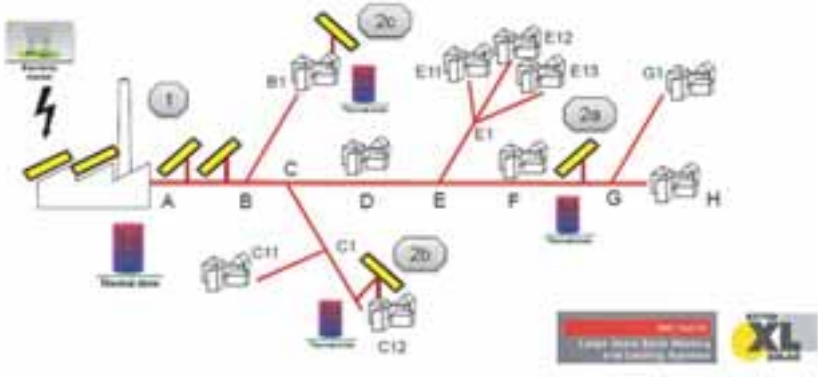

Fig. 2: Possible supply points for solar collectors in a DH network (from IEA SHC Task 45)

The *central* solar thermal systems are typically installed in combination with other heat-only or CHP plants and provided with a thermal storage unit, e.g. (SDH Guidelines 2012). As contribution to IEA SHC Task 55, the project partner PlanEnergi described the possible supply schemes of central solar systems; the most efficient solutions have to be identified in each case according to more parameters, among others:

- network supply and return temperature
- Solar system supply temperature
- Storage charge level and location of the possible storage charging/discharging points
- Boiler operational flexibility to return temperature fluctuations

The connection of *decentral* solar thermal systems is investigated in detail by (Schäfer et al. 2015), who analyzed the state of the art identifying 31 case studies in Austria, Denmark, Germany, and Sweden, and evaluated the potential and barriers for optimizing the integration. In the most cases (29), the connection is return-to-supply, in one case return-to-return, and in one case both options are possible. Contrarily to central collectors, the storage unit is not necessarily present in the decentral plants. Simulations allowed identifying the size of the existing users' connections as a possible hydraulic bottleneck limiting the solar share: in one case study, the solar collectors cannot entirely integrated into the network if the aperture exceeds 25% of the available roof area. Such issues can be faced adding new appropriate connections or/and storage units. As expected, the best solutions are highly case-sensitive.

However, while the network parameters considered in the existing studies are essentially the supply and return temperatures and the thermal load, a more complete investigation should take into account further aspects playing as well an important role in the integration of solar thermal systems. In particular, a solution-oriented approach to hydraulics cannot exclude the topology of the entire network and the (possible) supply points: the effects and the potential of the integration of decentral solar systems are in fact expected not to be the same in a linear, a ring, or a mash network, as well as they will vary according to the location of the supply point [Köfinger et al 2016]. For supply points outside the city center, hydraulic limitations might apply due to small pipe diameters in outskirt network branches. In some cases, the possibilities for bidirectional flows in line networks should be also investigated.

3.4 Overall DHC network control strategies and other measures for increasing solar thermal fractions

Another focus of Subtask A is on the assessment of measures for increasing the solar fraction. In doing so, the following measures should be considered:

Short term flexibility measures: In district heating networks, normally two distinct customer side heating load peaks occur at almost the same time of the day typically as morning and evening peaks (see Fig 3, right). This requires the intervention of additional peak boilers, usually operated with fossil fuels at high costs. Solar thermal energy has its supply peak usually directly in-between the morning and evening peak and therefore can only partly be used for covering the heating load, especially in summer times, when the solar thermal supply surpasses the heat demand. Short term flexibility measures for overcoming this mismatch include centralized and customer side storages, the utilization of the network as storage and customer side load shifting, with all measures mentioned being state-of-the art.

In (Schmidt and Basciotti 2014), those measures have been analysed and compered based on a literature review and network simulations of a typical rural heating network in Austria. The results can be summarized as follows:

- Centralized storage tanks are already used in many DH networks for various reasons (as back-up, for decoupling heat and electricity production in CHP and for peak load reductions) and represent a suitable measure for short term flexibility at a high economic viability.
- Smaller distributed storages at the customer side have a high storage capacity and the additional potential to reduce the pumping energy. However, they are very investment cost intensive and difficult to implement.
- The utilization of the network as storage is promising due to the very low investment costs and the resulting fast amortization, however, restrictions on the network side (i.e. the thermal expansion due to the additional temperature changes causes stress in the pipes and other system components) allow only limited number of temperature changes and lead to the risk of piping leakage respectively.
- Implementing load shifting for larger loads (e.g. hotels, swimming pools, shopping centre) is another conceivable measure resulting in a cost effective generation of short term flexibility. However, the practical implementation on a large scale needs further investigation.

In conclusion, for improving the supply of solar thermal energy in DH networks, the penetration of short-term flexibility measures and their cost-effectiveness need to be improved, including the development and integration of new technologies (e.g. storages, controls), services (including customer involvement) and business models. Also measures for forecasting the flexibility of the DH network need to be develop in order to be included in the overall system management.

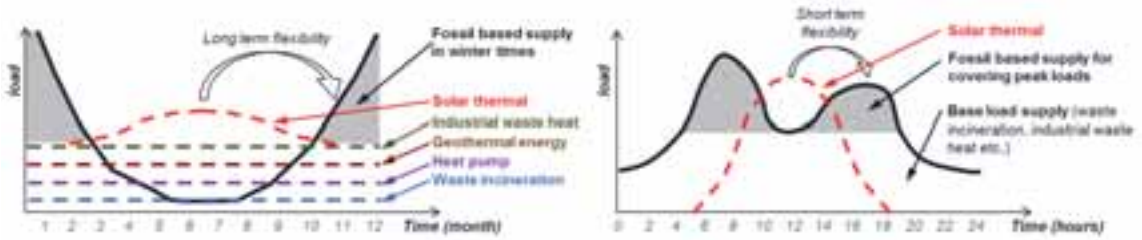

Fig. 3: Mismatch between the DH network demand and seasonal (left) and daily (right) behavior of different heat sources

Long term flexibility measures: Beside the short term mismatch, a major barrier for integrating solar energy and other renewable heat sources (such as geothermal energy and ambient heat) as well as waste heat in DH networks is their seasonal mismatch to the demand profiles (see Fig. 3, left). Here, two cases have to be differentiated: First, DH networks with very low operational costs in summer, i.e. the base load is covered by heat pumps, geothermal energy or industrial waste heat. For economic reasons, those sources should not be turned off or operated on part load for allowing solar energy to be integrated. As a consequence, every notable solar supply in summer times needs to be either cooled to the ambient or stored for transition times or winter. This applies also for a base load supply by waste incineration, having a “must-run” condition.

Second, DH networks where the base load is covered by supply units that consume fuels, e.g. fossil fired CHP plants or biomass plants. Here, the solar energy can actually safe operation costs and could be economically beneficial. However, subsidies and profits on the electricity markets from CHP plants might require those plants to run as well in summer times. Also very large shares of solar energy, i.e. exceeding 20% of the overall heat supplied to the network, need to be stored in a seasonal storage anyways, e.g. (Winterscheid et at 2017).

For this purpose, various seasonal storage systems are available nowadays, including aquifer, borehole, pit, tank storages, e.g. (SDH Guidelines 2012). However, these systems have up to now mainly been integrated in small/rural networks or building clusters in Germany, Denmark and Sweden. For increasing the long term storage capacity of larger, urban DH networks, the disadvantages of seasonal storages, especially the mismatch of the maximum storage temperature to the typical network temperature level, the high space requirements and the high investment costs need to be overcome.

One example for the integration of seasonal storages is the urban DH network Linz (Austria). Here, available industrial waste heat from a steel mill cannot be fed directly into the network during summer times since a waste incineration plant already covers the whole summer load and has a must-run condition (Pauli 2016). As a consequence, the integration of a seasonal storage was investigated for shifting the summer surplus waste heat into the transition time. Within a pre-study (Muser et al 2015) possible locations, geometries and costs of a seasonal storage for the Linz DH network have been analysed. Based on this study, two different operational scenarios for the integration of this seasonal storage have been analysed (Köfinger et al 2017): First, a "simple" operation strategy of the seasonal storage, where the storage is mainly charged in the summer and discharged in autumn/winter. Further on, a "strategic" operation strategy has been developed, allowing also short term charging/discharging and as a consequence also to enhance the operation of the existing CHP plants and reduce the use of the peak load boiler. Whereas the "simple" charging strategy the 1.8-fold storage capacity can be used, for the strategic charging strategy, this value goes up to 4.4 and therefore increases its economic feasibility. As a consequence, in a best case scenario a payback period of ~20 years could be achieved, although various uncertainties (especially electricity prices) apply. Together with high investment costs of about 100 mil. Euros, the investment risk for the storage is unacceptable high in the particular case. However, smaller DH networks with lower network temperatures and lower investment costs have already proven to be realizable.

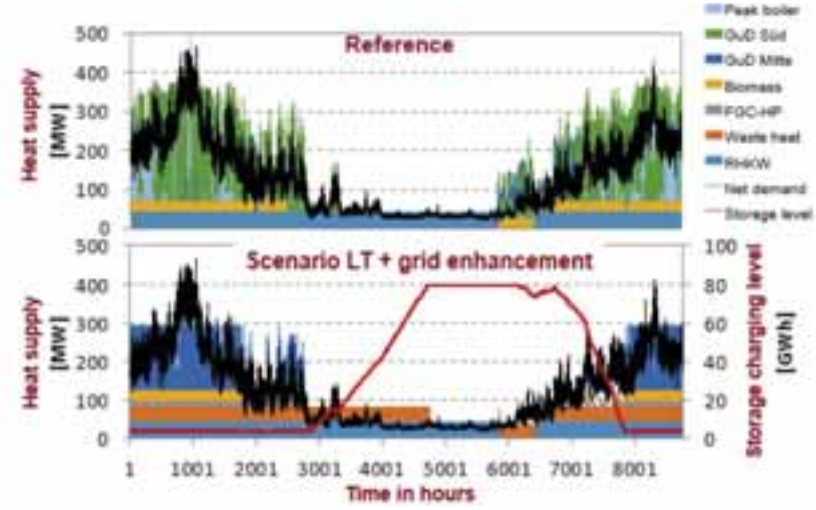

Fig. 4: Simulation based evaluation of the integration of a seasonal thermal storage in the DH network of Linz (Austria) for improved waste heat utilization, top: reference scenario without seasonal storage, bottom: integration of the seasonal storage in a low temperature scenario with enhancement of the network (Köfinger et al 2017)

Control strategies for an efficient integration of solar thermal plants into district heating networks: The operation of a district heating network incorporating different producers with at least one being a solar thermal plant and different consumers in any case goes along with several control problems to be considered.

At *first*, the scheduling (load respectively energy management) of the different producers and possibly also consumers has to be managed properly, i.e. a strategy which is able to plan ahead the use of the different components is necessary. This is especially important when slowly reacting and/or weather dependent heat

producers, such as solar thermal plants, or relevant energy storages, as it is the case in both the short and long term flexibility measures previously mentioned, have to be considered. Thus a high-level control has to decide the general mode of operation and adjust the reference values for different process variables, such as for example the required outlet temperature of the collector field. In most practical applications this high-level control is specifically adjusted to the particular heating network and bases on various standard controllers and additional expert rules. Within the last years it got increasingly popular to incorporate weather forecasts, however, with the control algorithms still basing on specific expert rules.

A very promising alternative approach is the application of a model predictive controller (MPC). MPC bases on mathematical models used to predict the future behaviour of the system for different courses of the manipulated variables. This allows to determine the optimal future course of the manipulated variables, thus in the specific case of a district heating network with different producers and consumers the optimal future operational strategy. This prediction is periodically repeated always using updated values for the state of the different components. The different approaches for MPCs for (bidirectional) heating networks mostly base on mixed-integer linear programs (MILP), since not only continuous states but also discrete states, e.g. for the activation and deactivation of specific producers, have to be considered, e.g. (Moser et al 2017). The resulting optimization problem of the MPC, formulated as mixed-integer linear program (MILP), has to be solved by appropriate MILP solvers. In order to provide the MPC with the future heat demand of the consumers or for example the future solar yield to be expected additional forecast methods have to be applied. Within the Task both control approaches, control strategies based on expert rules as and different MPC approaches, as well as forecast methods for the future heat demand or the solar yield to be expected are considered.

Second, it must be ensured that the heat produced by the different producers is properly fed into the district heating network and transported to the corresponding consumers. If there would be only one (central) heat producer in a network, this would be comparatively simple. In this case the pumps supplying the network would aim for setting the differential pressure in such a way that the supply is ensured even for the most distant consumer. However, in the general case, this is more complex, since it has to be ensured that the pumps of the individual producers do not work against each other. At first it has to be distinguished between producers which need to feed into the network immediately, since they cannot store the heat produced locally, and producers coupled with a buffer and consequently able to temporarily store the heat produced. One common approach is to use heat producers with buffer storages for maintaining the differential pressures, while the others regulate the mass flows of the feeds to ensure that their heat is properly transferred to the heating network. In detail, the finally applied approaches strongly depend on the actual heating network and there is also no systematic approach available in literature.

Third, the mode of operation of the collector field chosen by the high-level control (load respectively energy management) has to be realized by the respective low-level control at the solar collector site as efficiently as possible. Strictly speaking the outlet temperature of the collector field respectively the different sub-fields has to be controlled by adjusting the flow rate to the current radiation. This is in general done by varying the pump speed. Additionally, the individual fields are typically equipped with adjustable balancing valves in order to ensure an adequate flow distribution in the individual subfields. These valves can either be adjusted manually for nominal operation or be driven by a servomotor in order to achieve an adequate flow distribution for every operating condition and thus avoid exergy losses by mixing flows with different temperatures. The controllers applied typically are simple linear PID controllers, which in some are enhanced by a static feedforward control signal for the pump speed based on a static model for the heat output of a solar collector representing a static energy balance, where the parameters are determined in a standardized collector test (EN12975-2) and can be found in the datasheet. In research more advanced approaches can be found, e.g. (Camacho et al, 2007), but they have not reached a wide practical distribution up to now. A promising approach, also using mathematical models describing the collector field but explicitly aiming for practically manageable complexity, is presented in another article within this conference proceedings (Unterberger et al, 2017).

Measures for reducing the return temperatures: The potential for the utilization of solar thermal, but also other alternative heat sources such as industrial waste heat, geothermal energy and heat pumps, in DH networks is strongly correlated to the temperature level at which the networks are operated. Currently, many “traditional” existing DH networks are not designed for a significant share of solar thermal energy due to the relatively high network temperatures, often between 60°C (return) and 120°C (supply). Fig. 4 compares “traditional” high temperature DH networks with low temperature systems enabling higher shares of solar thermal energy.

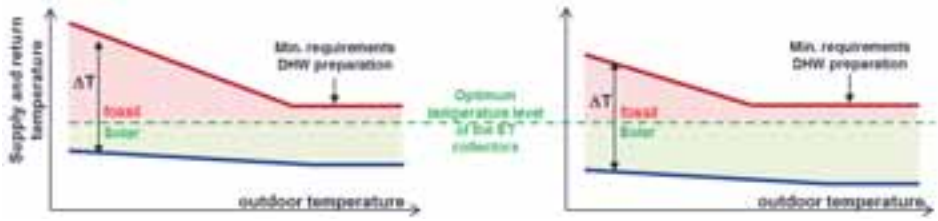

Fig. 5: Schematic description of the influence of the temperature level of the district heating network on the potential for the utilization of solar thermal energy (left: high supply and return temperatures in the DH network result in a limited potential of solar thermal energy, right: decreasing return and supply temperatures enable an increasing share of solar thermal energy)

Most of the technical measures for transforming traditional DH networks towards low temperature systems are well known, mature and in principle straightforward in their implementation. They can be distinguished in following areas:

- building side optimization such as hydraulic balancing and the correct use of thermostatic radiator valves
- Detecting and minimizing errors and faults in substations and domestic hot water preparation
- cascading (using the return flow of high temperature customers as a supply to low temperature customers)

Within Subtask A business models, existing strategies and the impact of different approaches from the participating parties as well as from literature should be analysed in detail within the Task. Here, a strong link to the currently starting IEA DHC Annex TS2 on low temperature district heating systems will be established.

4. Discussions

Based on the preliminary results, a literature review and stakeholder discussions, following analyses of the strengths, weaknesses, opportunities and threats (i.e. SWOT analyses) for the integration of solar energy into DH networks can be summarized:

Strengths: Besides being free of any emissions such as CO_2, NO_x or others (including noise), the main asset of solar thermal energy supply to DH networks is the good availability and the very low operation cost in combination with fuel independency and long term stability. Compared to other renewable sources, especially biomass, the required specific land use area is very low, e.g. (Poier 2017). The DH network temperatures in summer times are in general lower, supporting the efficiency of the collectors. Thermal driven adsorption chillers can increase the summer demand and thus absorb a possible surplus heat in summer times. The solar thermal components as well as different centralized and decentralized integration concepts are state-of-the-art and well proven in various DH networks already. Further on, producers of components for solar thermal collectors and system installers are often available regionally, resulting in high local added value.

Weaknesses: Additional to the high specific investment costs of solar thermal energy systems, the main disadvantage is the supply competition to other renewables (e.g. heat pumps, geothermal energy), waste heat (e.g. from industrial processes) and pants with must-run condition (e.g. waste incineration) in summer times. Seasonal storages for shifting the summer surplus heat to transition or winter time are available, but difficult to integrate in urban DH networks. Further on, higher network temperatures in winter times reduce the efficiency of the collectors. Also the integration of thermal driven adsorption chillers require higher network temperatures. For reaching significant solar shares, the systems require large areas that are limited and costly in an urban context. Larger and low-priced areas are likely to be far from the city center and thus additional investment costs for transport pipes and hydraulic limitations for supplying to outskirt network branches might apply.

Opportunities: For different reasons, many DH network operators are working continuously on the reduction of their network temperatures and this will increase the efficiency or solar thermal systems by trend. The utilization of large shares of other renewable or alternative heat sources (such as heat pumps, geothermal energy and waste heat) in DH networks supports the integration of seasonal storages. Finally, for accomplishing the COP21 targets, direct or indirect subsidies (e.g. CO2 taxes) for solar thermal energy are either already in place or are currently discussed in some countries.

Threats: One main threat are the long payback times of the systems, reducing the flexibility in the overall system. Further on, large and exposed collector areas might be damaged due to more frequent extreme weather events due

to the climate change, resulting in by trend lower heat energy supplied the network and higher maintenance cost. Finally, the price of the land for installing the collectors might increase, as soon as the land owner get aware of the aim of the intended land use and want to increase their own profit – especially if only limited areas are available.

5. Conclusion & outlook

Solar thermal energy is one of the few renewable heat sources, that is available almost everywhere and can bring multiple benefits to DH networks (on an environmental and systemic level) with very low operation costs and risks. However, the integration of large solar thermal systems into existing and new DH networks faces several challenges, especially the high specific investment costs, the mostly very high network temperatures and the seasonal mismatch between supply and demand.

Task 55 of the IEA Solar heating and cooling technology cooperation program provides a platform for practitioners and scientists to elaborate the benefits and challenges of solar district heating (SDH) and solar district cooling (SDC) systems. As part of Task 55, Subtask A focusses on the assessment of the impact of solar thermal technologies on the overall district heating and cooling network and integration aspects in order to analyze barriers and opportunities for maximizing the share of solar thermal energy.

During the first year, the work in Subtask A focuses mainly on the set-up of the overall structure including a detailed work plan as well as analyzing and consolidating the international activities and projects from the Task 55 participants. However, some preliminary results already show the strengths (especially small running costs), weaknesses (especially the high specific investment costs and a competition to renewable or must-run base load supply), opportunities (especially decreasing temperature levels and possible subsidies) and threats (especially long payback times) for a large scale integration of solar energy into existing and new DH networks. More results from Subtask A can be expected in the next years.

The international cooperation between IEA SHC Task 55, Subtask A and the IEA DHC TCP will lead to a more holistic understanding of integrated systems with a clear focus on achieving a high share of solar thermal supply in DH networks by following up on some best-practice examples from Denmark and the current discussions in Graz. Both TCPs show significant expertise, which in the past had mainly been focused on each system individually. In a future energy system, the different sectors have to be highly integrated to reflect developments not only in Task 55, but also in other IEA TCPs.

Finally, it should be mentioned, that the integration of solar thermal energy can trigger some significant synergies: most of the measures supporting the integration of solar thermal energy also support the integration of other renewable and alternative energy sources such as heat pumps, geothermal energy and industrial waste heat. Although being in competition to each other, especially seasonal storages are a key element for the other sources as well. Additionally, the integration of various heat sources and efficiency measures will require an overall management strategy, supporting also the integration of solar thermal energy.

6. References

Basciotti, D. and Schmidt, R.R.: “Peak reduction in district heating networks: A comparison study and practical considerations”, The 14th International Symposium on District Heating and Cooling, Stockholm, Sweden, September 7th to September 9th, 2014;

BDEW Bundesverband der Energie- und Wasserwirtschaft e.V.; Strategiepapier „Zukunft Wärmenetzsysteme", Berlin, 15. Juni 2017, https://www.bdew.de/internet.nsf/id/E8B05091DDD5F238C12581540039C159/$file/BDEW-Strategiepapier%20Zukunft%20W%C3%A4rmenetzsysteme.pdf

Camacho, E.F., Rubio, F.R., Berenguel, M., Valenzuela, L., 2007. A survey on control schemes for distributed solar collector fields. Part II: Advanced control approaches, Solar Energy, 81, 1252-1272

Götzhaber, E.; Meißner, E.; Moravi, G.; Prutsch, W.; Schlemmer, P.; Schmied, R.; Slivniker, B.; Zimmel, M.: Wärmeversorgung Graz 2020/2030, Wärmebereitstellung für die fernwärmeversorgten Objekte im Großraum Graz, Statusbericht 2017. https://www.grazer-ea.at/cms/upload/warmeversorgung2020.30/wrmeversorgung_graz_statusbericht_2017_compressed.pdf

IRENA (2017); Renewable Energy in District Heating and Cooling: A Sector Roadmap for REmap, International Renewable Energy Agency, Abu Dhabi. www.irena.org/remap .

Köfinger, Markus: "Simulation based evaluation of large scale waste heat utilization: Optimized integration and operation of a seasonal storage in the district heating network of Linz (Austria)", Smart Energy Systems and 4th Generation District Heating, 12-13. September 2017, Copenhagen; http://www.4dh.eu/images/1_20170913_Presentation_-_FDHS_Linz.pdf

Köfinger, Markus: „Rahmenbedingungen zur Integration dezentral anfallender (Ab-) Wärmequellen in Wärmenetze", final report Open Heat Grid, 2016

Moser A, Muschick D, Lichtenegger K, Gölles M, Hofer A. Model predictive control of a solar- and biomass-based district heating network. in Nachhaltige Gebäude. Band 12. Graz: Leykam. 2017. (Science. Research. Pannonia). (in German).

Muser, Christoph; Drucker, Petra; Samhaber, Wolfgang; Jung, Martin; Spendlingwimmer, Robert: Groß-Wärmespeichers für Linz; Abschlussbericht der Sondierung, 2015, Report from: Klima- und Energiefonds, Projektnummer: 843937,

Pauli, Hubert: Abwärmeintegration im Linzer Wärmesystem; 2. Praxis- und Wissensforum Fernwärme & Fernkälte, 15. November 2016, Vienna (Austria); https://www.ait.ac.at/fileadmin/mc/energy/downloads/News_and_Events/2016_11_15_2.Praxis_und_Wissensforum_FWK/B3_Pauli__Future_DH_System_AIT_15_Nov_16_Pauli_V3.pdf

Poier Hannes: BIG SOLAR GRAZ – Results of a techno-economic feasibility for solar district heating; 3rd international conference on Smart Energy Systems and 4th generation district heating, Copenhagen, 12–13 September 2017; http://www.4dh.eu/images/3._Hannes_Poier.pdf

Prutsch, W.; Götzhaber, W.; Papousek, B.; 2017; Fernwärme als Schlüssel zur Wärmewende oder Sackgasse?" - Der Zukunftsprozess Fernwärmeversorgung Graz 2020/2030; Fernwärmetage 2017; Velden, 16.3.2016 (in German).

Reiter, P.; Poier, H.; Holter, C; 2017; „IEA Heat Pump Conference 2017"; Stichting HPC 2017.

Schäfer, K.; Mangold, D; Pauschinger, T.: Dezentral. Dezentrale Einspeisung in Nah- und Fernwärmesysteme unter besonderer Berücksichtigung der Solarthermie. Report from: Deutsches Bundesministerium für Wirtshcaft und Energie, Forschungsvorhaben 03ET1039C, 2015.

Solar district heating guidelines. SDH Solar District Heating. August 2012, http://solar-district-heating.eu/

Unterberger, V., Muschick, D., Gölles, M., 2017. Model-based control strategies for an efficient integration of solar thermal plants into district heating grids. Proceedings Solar World Congress 2017, 29 October – 02 November 2017, Abu Dhabi, UAE, 2017.

Winterscheid, Carlo; Dalenbäck, Jan-Olof; Holler, Stefan: Integration of solar thermal systems in existing district heating systems, In Energy, 2017, ISSN 0360-5442, https://doi.org/10.1016/j.energy.2017.04.159

Simulations of a Solar-Assisted Block Heating System

Artem Sotnikov[1], Christian K. Nielsen[2], Chris Bales[3], Jan-Olof Dalenbäck[4], Martin Andersen[3] and Emmanouil Psimopoulos[3]

[1] Lucerne University of Applied Sciences and Arts, Horw (Switzerland)

[2] PlanEnergi, Copenhagen (Denmark)

[3] Högskolan Dalarna, Borlänge (Sweden)

[4] Chalmers University of Technology, Gothenburg (Sweden)

Abstract

Two types of simulation software TRNSYS and Polysun are studied to check their suitability for solar district heating system planning. A reference case, a part of the Vallda Heberg district heating system is modelled in both tools and results are compared with available measured data and with each other. Models are successfully calibrated. TRNSYS and Polysun models have deviations in main key figures compared to the reference case less than 2% and less than 8% respectively. A sensitivity analysis of key parameters shows that the two tools give similar results.

Keywords: solar thermal, district heat, dynamic simulation, TRNSYS, Polysun,

1. Introduction

Approximately 10% from EU heat market is covered by district heating (Dalenbäck, 2011), thus giving solar district heating a good potential to also be implemented in existing networks.

Furthermore, there are examples where the employment of solar thermal technology in combination with biomass combustion can supply 100% renewable district heating (Faninger, 2000). However, there are a number of obstacles for the wide spread implementation of solar district heating (SDH) systems, namely: high investment costs, technological difficulties and lack of engineering experience (Dalenbäck, 2011).

Considering complexity of the systems, usage of new technologies and the lack of engineering experience, computer modeling of the solar district heating systems is a key to successful system implementation. It is achieved through market available computer simulation software or self-developed tools. Several studies have been made employing such tools, of which the scope and purpose vary.

Considering the wide implementation of simulation software for the design and the optimization of solar district heating systems, it is important to investigate how applicable available tools are. In the present study two different tools are compared TRNSYS 17 (Klein, 2012), originally developed at SEL, and Polysun (Rezaei et al., 2009), developed by Vela Solaris. The base case for this investigation is a part of the solar-assisted block heating system for a new building area in Vallda Heberg, Sweden.

1.1. Aims

The main aim of the study is to determine how applicable Polysun and TRNSYS are for simulation of block heating solar systems, which include advanced controlling strategies and/or complex hydraulics. In order to do this, different aspects should be considered. Available component models should be detailed and robust enough to build such system in the given boundary conditions. It should be possible to calibrate the model with the real system. Changing of the boundary conditions and sensitivity analysis of different components should lead to well-explained changes in the system model performance.

1.2. Methodology

As a base case, sub-station 1 (SS1) of the Vallda Heberg district heating system was chosen. The models, in TRNSYS 17 and Polysun, were constructed based on drawings, known properties and operational strategies of

Selection and/or peer review under responsibility of Scientific Committee
doi:10.18086/swc.2017.06.13 Available at http://proceedings.ises.org

the sub-station. The whole study is performed taking into perspective the boundary conditions, assumptions and limitations of the available data and models.

The system has been monitored to evaluate and fault-find the system. Based on data of the monitoring system and weather data of the Swedish Metrological and Hydraulic Institute (SMHI) for the monitoring period, input files have been constructed for the models in order to calibrate them using the measured energy, flows and temperatures. For the calibrated models, sensitivity analyses for key parameters were performed using Meteonorm weather data. The process and results of calibration as well as the models` reactions in sensitivity analyses were used to determine applicability, usability and limitations of the tools for the given case.

2. Description of the system

The local district heating system comprises one central heating plant (HP) for which the details are listed below in table 1 (the left part). It features a 250 kW wood pellet boiler (and an oil boiler for back-up) and four substations (SS1-4) connected to the primary culvert (PC).

Buffer storage tanks are installed in the central heating plant and in each substation. There are 108 m^2 evacuated tube solar collectors (ETC) on the heating plant and 570 m^2 flat plate roof-integrated solar collectors (FPC) in connection to the substations. Solar heat is targeted to cover 40% of the end-use of space heating and domestic hot water.

The focus of this study is SS1 with secondary distribution culvert and connected houses, of which the details are shown below in table 1 (the middle part).

Tab. 1: Details of the central heating plant (HP) and of substation 1 (SS1) at Vallda Heberg, Sweden

Heating plant (HP)		**Substation 1 (SS1)**		**Load (SS1)**	
Key characteristics	**Values**	**Key characteristics**	**Values**	**Key characteristics**	**Values**
Installed storage volume	15 m^3	Installed storage volume	15 m^3	Single family houses	19
Installed collector area	108 m^2 (ETC)	Installed collector area	142 m^2 (FPC)	Heating area per house	140 m^2
Collector Slope (β)/Azimuth(α)	70°/30°	Collector Slope (β)/Azimuth(α)	27°/30°	Heating area total	2660 m^2
PC design operating temperatures (S/R)	75°C/50° C	Load capacity solar HEX	85 kW	Specific demand heat	59 kWh/(m^2·yr)
PC pipe diameter ØPC	100 mm	Load capacity auxiliary HEX	165 kW	Specific demand electricity	34 kWh/(m^2·yr)
Load capacity solar HEX	65 kW	PC connection pipe diameter ØCP	50 mm	SC length (total)	938 m
Load capacity biomass boiler	250 kW			SC target temperature	58°C
Load capacity oil boiler (backup)	500 kW			SC pipe diameter Øsc	63 mm
Load capacity PC HEX	1000 kW				

The secondary heat distribution system between the substation and the buildings is a so called GRUDIS 2-pipe system (Zinko 2004) where hot water is circulated in plastic (PEX) pipes, similar to a standard DHW circulation

system. The pipes are located in an insulating (styrofoam) box buried in the ground, with fig. 1 showing the distribution to the houses and the placement of the sub-station as well as heat meter points.

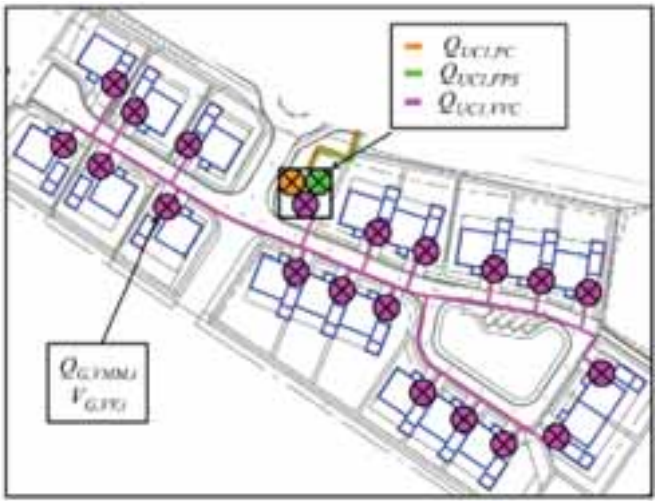

Fig. 1: Drawing of distribution network and houses connected to SS1 (Olsson and Rosander, 2014)

142 m^2 aperture area of flat plate collectors are connected to SS1. 38 m^2 on the roof of the substation, while the second field 104 m^2 located on multi-family buildings. The solar collectors deliver heat to the storage tanks via an external heat exchanger, as the collector loop fluid is a water-glycol mixture. One pump is controlled on each side of the heat exchanger by matched flow rate. The fixed solar collector flow rate is 0.38 l/min per m^2 aperture area. The pumps are controlled based on "sensors" in storage, collector outlet and heat exchanger outlet. To obtain stratification, two inlet heights to the storage are possible from the charging loop. Fig. 2 shows how the different loops are connected by heat exchangers.

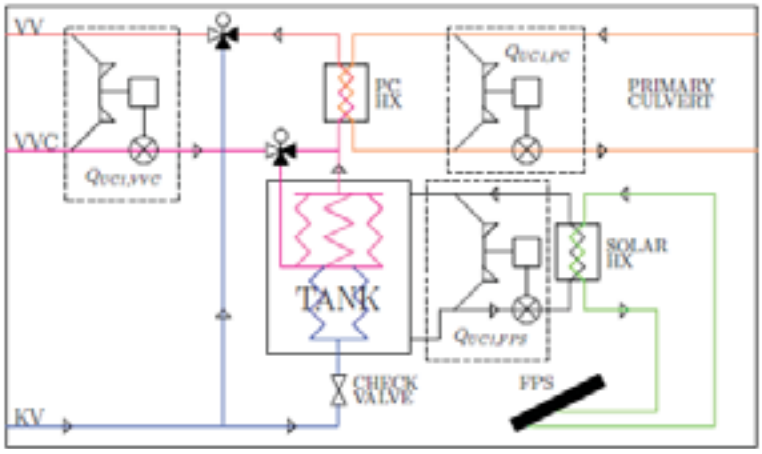

Fig. 2: Schematic drawing of SS1 with installed heat meters (Olsson and Rosander, 2014)

The circulation pump is running at constant flow. The cold water inlet of the loop is supplied through the storage to be pre-heated. If the storage temperature is high enough, the DHW circulation will pass through the storage as well. The primary culvert delivers heat to the secondary distribution loop via a heat exchanger when the solar heat of the sub-station is not sufficient to maintain 58°C outlet temperature. If the temperature after this heat exchanger is more than 60°C (due to high temperatures in the storage tank), cold water is mixed to lower the supply temperature.

The load is represented by a group of single-family houses and the DHW-circulation in the secondary culvert (SC). Details of the load are shown in table 1 (the right part).

All buildings are designed as passive houses according to the Swedish standards, i.e. well insulated buildings with air tight envelopes, and supply and exhaust ventilation with heat recovery is applied in all buildings (Jimmefors and Östberg, 2014). Roof overhang and balconies provide sun shading to reduce solar gains in the summer period.

Each house has two floors, and a total heated area of 140 m^2. The hot water circulation of the secondary culvert is connected to each individual building. The hot water is delivered directly for tapping and for heated appliances (e.g. washing machines). The circulating flow is passing through the floor heating loop in the bathroom and utility room without control (ie all year) as well as through a heat exchanger coupled via a thermostat controlled water-glycol loop that delivers heat to an air heating coil. Space heating is provided by the air heating coil to the supply air, which is pre-heated by the exhaust air using a rotating heat recovery unit.

2.1. Monitoring system

The monitoring system is logging every hour. Temperatures, flow rates and energy rates (and total quantities) are measured to evaluate the system performance of houses, distribution network and heating plant/substations. Incoming solar energy and auxiliary energy from heating central and hot water circulation losses are monitored at the substation, as shown in fig. 2. The DHW and space heating loads are measured in all houses. Temperature to and from houses are measured as well.

In 2014 the whole area of Vallda Heberg had a low heat demand, corresponding well to the design values. The measured yearly load of sub-station was 59 kWh/(m^2 living area) including circulation losses. Distribution losses are a large share of the yearly load (25 %), especially due to the low space heating demand of the buildings.

Solar fraction of SS1, SF (eq. 1), is calculated by the supplied solar (Qsolar) compared to load (Qload) as the relative saving of energy from the main heating plant:

$$SF = \frac{Q_{solar}}{Q_{load}} \qquad \text{(eq. 1)}$$

The actual solar utilization and solar fraction are larger than what is measured in the sub-station directly, due to the evacuated tubular collectors installed at the main heating plant. The specific collector performance of the flat plate collectors connected to SS1 was 297 kWh/(m^2·yr).

3. The models

The system models have been created based on known system properties and the available monitored data. Measured temperature levels and flow rates were used as a guideline when setting the controls of the model. Monitored data concerning energy consumption of the area has been used to calibrate the load parts of the model (space heating and distribution losses) and to create a load input file (domestic hot water). The monitored data for energy to the substation from heating plant and flat plate solar collectors are used to calibrate the supply parts of the models.

A hot water pattern input file has been constructed using DHWCalc (Jordan and Vajen, 2003) so that it matches the measured monthly demand data for all 19 houses of the network. The cold water inlet temperature variation during the year is based on information from the provider (8 to 16°C – January coldest) as this temperature is not measured.

Weather data of 2014 from SMHI has been collected on hourly basis as input file for the calibration process. This includes direct and global solar radiation data for horizontal surfaces for the area constructed by SMHI based on interpolation of values of other Swedish locations (SMHI, 2015).

The calibration itself has been based on monthly energy balances, due to the large uncertainties when combining short time interval interpolated weather data, limited measurement points and general assumptions.

3.1. TRNSYS and Polysun models

TRNSYS is a component based dynamic simulation tool, where the user combines component models and user defined equations and controls. The timestep used is 3 minutes. Integration and convergence tolerances are 0.001 relative.

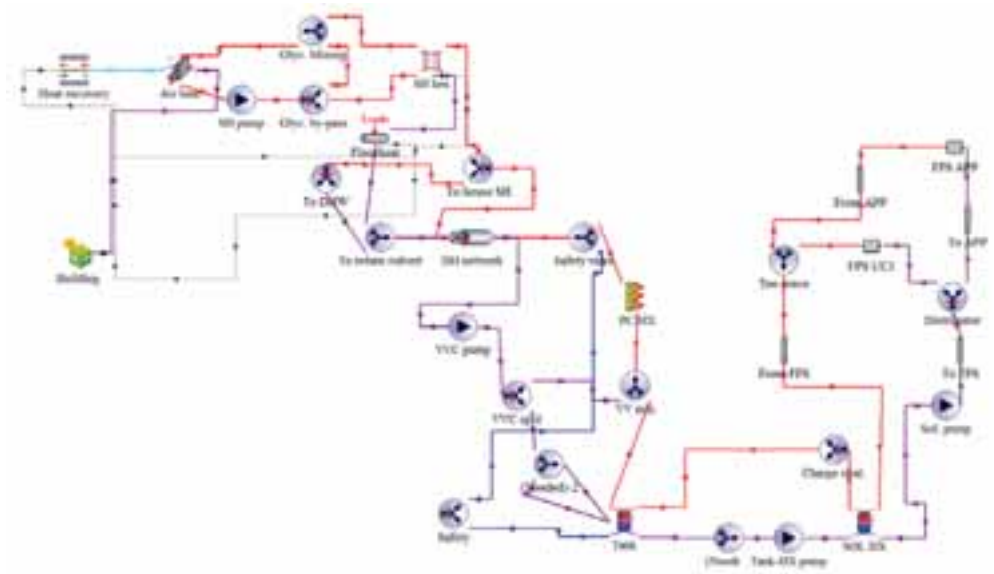

Fig. 3: System model in TRNSYS

Polysun is a dynamical simulation tool, which is used principally for design and planning of renewable energy systems. Polysun uses variable timestep. The largest timestep is chosen which satisfies convergence criteria, but not larger than 3 min and 12 min for day and night respectively.

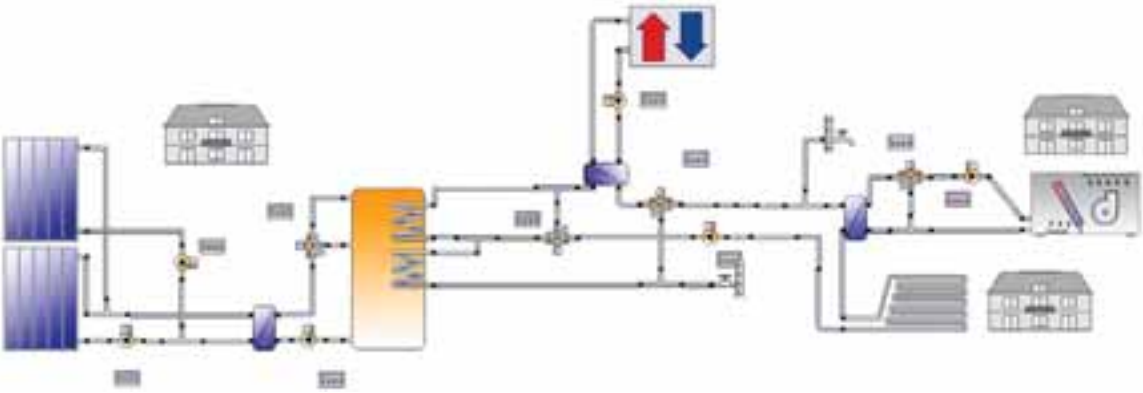

Fig. 4: System model in Polysun

The main components of SS1 are storage, heat exchangers and solar collectors. Other modelled components include pumps, valves and collector loop pipes.

The solar collectors are modelled as two flat plate collector components using the parameters for the installed collectors from Solar Keymark certificates. The pipe lengths to the two fields are included to simulate thermal capacity, time dependency and heat losses. The flow is distributed to the two fields dependent on collector area, so that the area specific flow rates are the same for both fields.

Even though the storage is cubic in reality, it is modelled as a vertical cylinder. Real inlet and outlet heights are used both for tank charge- and discharge.

In TRNSYS the distribution pipe is simulated using Type 951 buried twin pipe in the ground (Thornton 2012), comprising supply and return pipe inside one shell of insulation. In Polysun an existing pipe model was extended to simulate buried pipes. Each pipe has a separate shell. The models assume circular shape while the real twin pipe has rectangular insulation. The part of the flow which is due to DHW tapping is withdrawn from the flow at the end of the secondary culvert. The rest of the flow is for space heating with no flow bypassing the houses.

In TRNSYS one two-zone building is modelled to simulate an average of the 19 space heating loads of the 19 buildings. The flow rate to the building is thus one nineteenth of the total flow in the secondary culvert, after

DHW has been extracted. When the hot water returns to the network pipe the flow rate is multiplied by 19 again, while assuming that the return temperature is valid for the whole flow. In this way the space heating demand of the simulated building acts as average of all buildings in the network.

In TRNSYS inputs for outer area of walls in different directions and air volume of the two zones have been modelled based on drawings of the house. Windows and shading (provided by roof overhang and balcony) are accounted for. Internal gains are added to the main area (i.e. not bathroom) based on known electricity consumption (70 % is expected to be gained as heat) and the average number of inhabitants (4 seated at rest). The yearly measured average electricity consumption is 4700 kWh per house. One zone is bathroom including floor heating, and the other zone comprises all other indoor areas, which are heated by mechanical ventilation only. All of the hot water circulation initially passes through a glycol heat exchanger, then through the floor heating. The glycol loop heatsup the inlet air via a heat exchanger after it is pre-heated by ventilation heat recovery unit. There is a bypass valve in the glycol circuit that is controlled by a room thermostat, and thus varies the addition of heat to the inlet. The heat recovery efficiency is a function of the ambient air, and the unit is turned off at ambient temperatures above 16°C.

In Polysun the space heating load is modelled as two one-zone buildings. The first building model represents the living area with a fan-coil heating system. The second building model represents a bathroom and a floor heating system. There is no flow separation since the first building represents total load of living areas of all 19 buildings, the second building represents total load of bathrooms of all 19 buildings.

In Polysun the same boundary conditions for building as in TRNSYS are considered, but since one building represents 19 buildings it is scaled down. The actual size is chosen during model calibration. For the living room internal gains are increased. These gains represent gains from bathroom, since there is no connection between the living area and the bathroom in the model.

3.2. Assumptions / simplifications in the models

Pressure drops are generally neglected, as pressure is not the driving force of flows in the models. This causes issues when controlling valves, as the flows rates are controlled upstream. Thus hydronic diverting valves are controlled based on equations, which are working ideally. Pipes and valves without flow during normal operation have been neglected. The primary culvert heat exchanger is modelled to give constant outlet temperature (perfect flow control on primary side).

In TRNSYS external heat exchangers are modelled without thermal capacity and heat loss coefficients. Heat losses of the solar heat exchanger lumped together with the return pipe of the solar loop. The UA value is constant for the solar heat exchanger. Pipes in solar loop have constant loss coefficient.

In Polysun, the main simplification is the use of two one-zone building models instead of one two-zone building model. So heat gains from bathroom to living area are not modelled. Heat exchangers are modeled without thermal capacity. Two independent buried pipes are used to model secondary culvert, therefore pipe thermal interaction is not considered.

Only modelling one house and one distribution pipe is a big simplification, and it is only possible in this study because the dynamic effects of the space heating elements are not the focus of this study.

3.3. Calibration

A few unknown properties were found by parameter identification based on comparison with monthly heat balances.

For TRNSYS model room set-point temperature of air heating, maximum heat recovery efficiency (80 %) and maximum external shading share (80 %) were estimated in this way. External shading is activated when solar radiation on the wall surface is above 200 W/m^2 until it decreases to less than 120 W/m^2. Floor heating was simulated using an active floor layer. The parameters of the floor were calibrated to reach around 200 W all year from water circulation to bath zone. Heat loss coefficient of pipe in solar loop was calibrated to monthly values of solar gains.

For Polysun model sizes of buildings which represent living area and bathroom were defined by parametric identification. Set-point temperature of air heating was also estimated in this way. Thickness of insulation of buried pipe was defined based on losses in distribution system. Thickness of insulation of pipes in solar loop was

calibrated to monthly values of solar gains.

3.4. Simulated versus measured

Fig. 5 shows how the measured loads and solar gains of the block-heating system correspond to the simulated values on a monthly basis. Solar gains correspond very well, which is partly due to the calibration process. Considering loads, simulated values correspond well with measured values for simulations performed with TRNSYS. The simulated values obtained in simulations with Polysun show minor deviations due to the application of the one-zone model, as mentioned earlier.

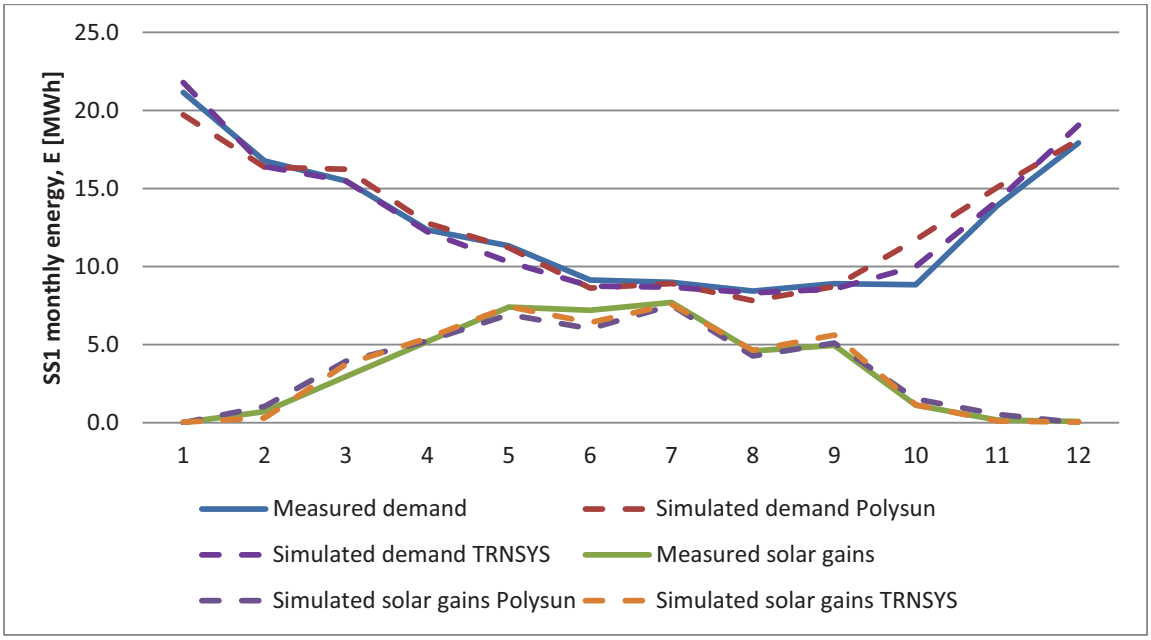

Fig. 5: Measured vs. simulated in TRNSYS and Polysun heat loads and solar heat to storage for SS1 in 2014

4. Model comparison

Table 2 and 3 below show comparison between measured and simulated values of key figures. The simulation results obtained with TRNSYS show very good agreement at production and load sides. Relative deviation on an annual basis for each key figure is lower than 1.5 %.

Polysun model has the highest deviation from measured value for space heating, which was partly compensated by calibrating distribution losses to achieve expected solar performance. Therefore, production side has very good agreement with measured data. Relative deviation on an annual basis is lower than 1.5 %.

Tab. 2: Monitored and simulated in TRNSYS yearly key figures, and the deviation between these values

Parameter	Monitored [MWh]	Simulated [MWh]	Deviation [MWh]	Deviation, %
Space Heating	71.9	72.6	0.7	1.0
DHW	45.2	44.7	-0.5	-1.2
Distribution losses	36.1	36.5	0.4	1.2
Solar to storage	42.1	42.5	0.4	0.8
Primary culvert heat	111.1	110.6	-0.5	-0.4

Tab. 3: Monitored and simulated in Polysun yearly key figures, and the deviation between these values

Parameter	Monitored [MWh]	Simulated [MWh]	Deviation [MWh]	Deviation, %
Space Heating	71.9	77.5	5.6	7.8
DHW	45.2	44.4	-0.8	-1.6
Distribution losses	36.1	33.5	-2.6	-7.3
Solar to storage	42.1	42.1	0	0
Primary culvert heat	111.1	113.1	2	1.2

5. Sensitivity analysis

For the sensitivity analysis weather data for a standard average year shall be used. For this purpose, Meteonorm data for this location is chosen. Therefore, the first study is sensitivity of the models to different weather data. Figure 6 and 7 show how simulated values for energy demand and solar gains vary according to the choice of weather data.

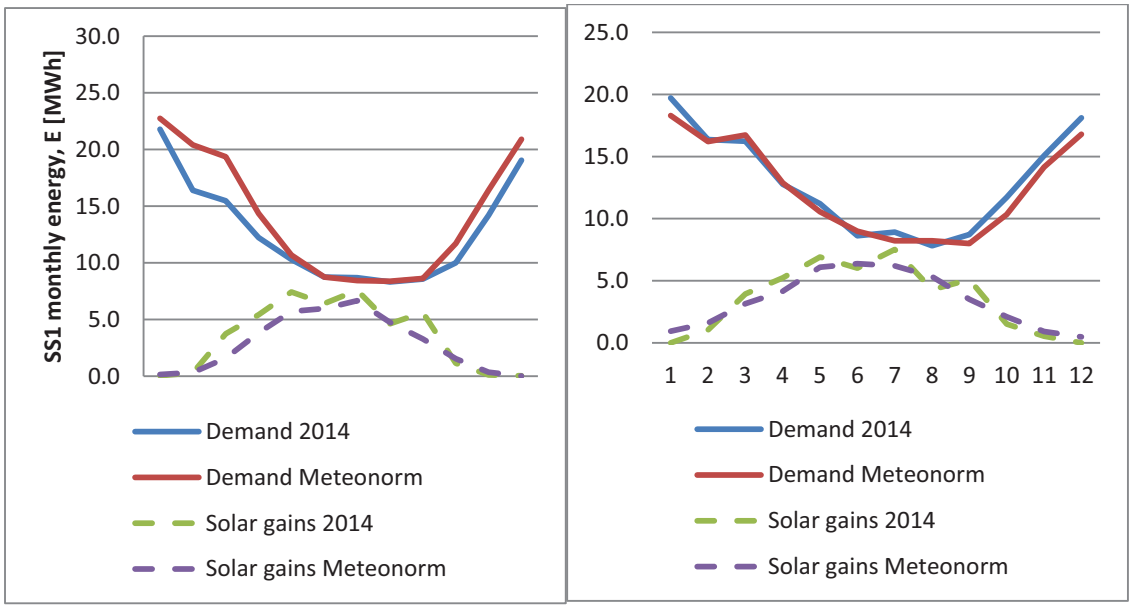

Fig. 6 and 7: Comparison of Polysun (left) and TRNSYS (right) simulated 2014 data with Meteonorm data: heat loads and solar heat to storage for SS1.

The Meteonorm average year is colder and has lower solar radiation level than 2014. It corresponds very well with TRNSYS results: annual total demand is higher and annual solar gains are lower with the weather data of the Meteonorm average year.

Polysun shows that even though shapes of the curves are similar to ones from TRNSYS, the absolute values do not reflect adequately the change of weather data. The main reason for it is an uncertainty in the building model, namely thermal performance of the one-zone model the size of which was calibrated according to thermal behavior of 19 multi-zone buildings.

Since the main focus of this study is to evaluate how Polysun can simulate the collector field and the substation as well distribution network and how close it can get to TRNSYS results, further sensitive analysis is done based on key figures normalized to the basic case simulated with the Meteonorm average year. In this way an influence of the uncertainty of the building model can be eliminated and other parts of the model can be studied.

Thus sensitivity analysis consists of two parts. The first part is a study of an influence of density of the heating network on the solar fraction of the sub-station and distribution losses in the system. The density of a distribution network is a relationship between the number of houses and the length of the distribution network. For the present

study the number of building is constant and equal to the actual number of buildings at the site. The length of the distribution network is varied from 0.5 to 2.5 times of the actual length. The study showed a good agreement between both tools, as shown in the fig. 8.

The second part of the sensitivity analysis is a study of the influence of different collector field sizes and storage tank sizes on performance of the system in terms of solar energy supplied to the system from the store. Collector field size is varied from 0.5 to 2 times of the basic case. A relative storage volume (storage volume / collector aperture area) is varied for each collector field size from 0.5 to 2 times of the basic case. In this way a matrix of 25 systems is built.

In the fig. 9 matrix results for solar energy supplied to the system from storage are shown. For all cases Polysun results are close to TRNSYS showing consistency between tools.

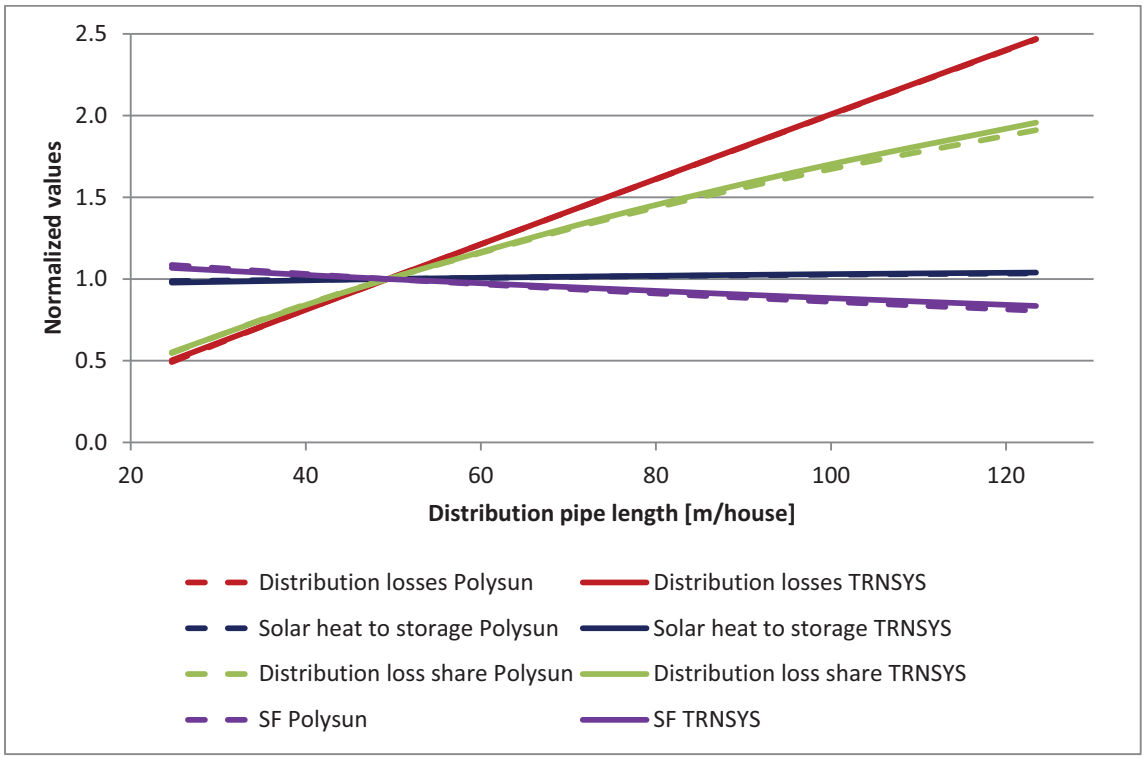

Fig. 8: Sensitivity analysis of influence of heating network density on district heating system performance (solar fraction, value of distribution losses, solar energy to the system and share of distribution losses in total demand) for TRNSYS and Polysun models

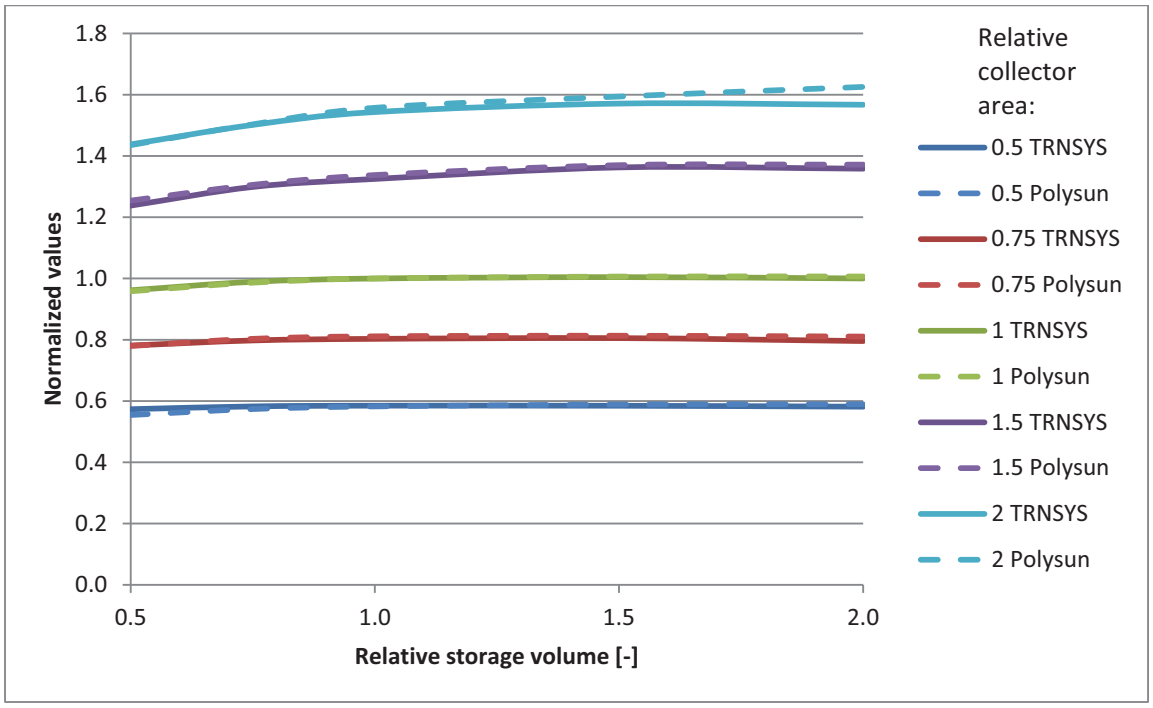

Fig. 9: Sensitivity analysis of influence of collector and storage sizes on system performance for Polysun and TRNSYS models.

6. Conclusion

Applicability of Polysun and TRNSYS for simulation of block heating solar systems was studied by comparison with measured data and performing a parametric study. As a reference case Vallda Heberg decentralized solar district heating system was chosen. It was proven that if enough measured data is available and controlling strategy as well as main system parameters are known it is possible to calibrate models in Polysun and TRNSYS with high degree of accuracy. Relative deviations of all annual key figures of both tools compare to the real case are low and monthly values are also in good agreement. Relative deviations of annual key figures for TRNSYS and Polysun are < 2% and < 8% respectively.

In order to compare model behaviors a sensitivity analysis was performed. First of all, instead of actual weather data Meteonorm average year data was used. With the new weather data TRNSYS showed expected performance. Since the year 2014 was rather warm, total demand for the average year is higher than for 2014. For the same changes in boundary conditions Polysun showed poor agreement – total demand for the average year approximately equals to the one in 2014 and is significantly higher than TRNSYS. It means that the building model in Polysun does not respond adequately to change in the weather data. The main reason is that the one-zone building model is not suitable to simulate such complex case (multi-zone building with complex interaction between zones).

Then two cases were studied; influence of a density of the heating network on a solar fraction of the sub-unit and distribution losses in the system; and influence of different collector field sizes and storage tank sizes on performance of the system in terms of solar energy supplied to the system and a solar fraction. In order to eliminate influence of the building model, key figures were normalized to the base case and plots were built based on these normalized values (fir. 8 and fig. 9). The plots show very good agreement between Polysun and TRNSYS. It means that Polysun simulates the changes in the same way as TRNSYS for collector and store sizes as well as pipe length/energy density of the network.

Acknowledgement

The study was supported by Seventh Framework Programme of the European Union, support for training and career development of researchers (Marie Curie), Solar Heat Integration Network (SHINE) project (Jordan, et al. 2014). The study was performed in scope of SHINE work package one (Bales, et al. 2014).

7. References

Bales, C., et al., 2014. Seven Phd Studies on Solar District Heat. EuroSun 2014. Aix-les-Bains, France.

Dalenbäck, J.-O., 2011. Large-scale solar heating - DH. European Solar Thermal Technology Panel. Munich, Germany.

Duffie, J. A., Beckman, W. A., 2006. Solar Engineering of Thermal Processes, third ed. John Wiley and Sons, New Jersey.

Faninger, G., 2000. Combined Solar-Biomass District Heating in Austria. Solar Energy 69, 425-435.

Jimmefors, H., Östberg, J., 2014. Energy Performance and Indoor Climate Investigations in the Passive House Residential Area Vallda Heberg. Master Thesis, Gothenburg, Sweden, Chalmers University of Technology.

Jordan, U., et al., 2014. SOLNET - Phd-Scholarships and Courses on Solar Heating. EuroSun 2014. Aix-les-Bains, France.

Jordan, U., Vajen, K., 2003. Manual. DHWcalc. Tool for the Generation of Domestic Hot Water (DHW) Profiles on a Statistical Basis. Version 1.10. Kassel, Germany, University of Kassel.

Klein, S. A., et al., 2012. TRNSYS Users Manual, Version 17. Madison, Wisconsin, University of Wisconsin Solar Energy Laboratory.

Olsson, H., Rosander, A., 2014. Evaluation of the Solar-Assisted Block Heating System in a Passive House Resindential Area. Master Thesis, Gothenburg, Sweden. Chalmers University of Technology.

Rezaei, S. H., Witzig A., Marti J., 2009. Design Methodology for Combined Solar and Geothermal Heating. ESTEC. Munich, Germany.

SMHI. 2015. http://strang.smhi.se/ (accès le 2015).

Thornton, J.W, et al., 2012. TESSLibs 17. GHP Library Mathematical Reference. Madison, Wisconsin, Thermal Energy System Specialists.

Zinko, H., 2004. Grudis-Tekniken för Värmegles Fjärrvärme. Stockholm, Sweden, Svensk Fjärrvärme AB.

Performance and Optimization of a Novel Combined Solar Heating Plant with Flat Plate Collectors and Parabolic Trough Collectors in Series for District Heating

Zhiyong Tian, Bengt Perers, Simon and Jianhua Fan

Department of Civil Engineering, Technical University of Denmark, Brovej Building 118, Lyngby, 2800, Denmark

Abstract

More than 1.3 million m^2 solar heating plants are in operation in Denmark by the end of 2016. Most existing collectors in the solar heating plant are flat plate collectors. To maximize the advantages of flat plate collectors and parabolic trough collectors in large solar heating plants for a district heating network, a novel combined solar collector field with 5960 m^2 flat plate collectors (FPC) and 4039 m^2 parabolic trough collectors (PTC) in series has been constructed in Taars, Denmark. The design domain variables of the combined solar heating plant require to be considered in the optimization routine to get the optimal performance of such plant. A validated TRNSYS-Genopt model was set up to optimize key design parameters and investigate the potential performance of the combined solar heating plant. It is found that the design concept of hybrid solar heating plants with flat plate collectors and parabolic trough collectors in series can be feasible in Denmark. The results of optimal design parameters could guide engineers and designers in the design, construction and control of large-scale combined solar heating plants.

Keywords: combined solar district heating plants, flat plate collectors, parabolic trough collectors, LCOH.

1. Introduction

Large scale solar district heating plants have gained great success in Europe, particularly in Denmark. Denmark is the frontrunner country in the large scale solar district heating plants. Most solar collectors in the existing solar heating plants in Denmark are ground mounted flat plate collectors. A hybrid solar heating plant with flat plate collectors and parabolic trough collectors was put into operation in August of 2015. The aim of this study is to optimize the hybrid solar heating plant based on the Levelised Cost Of Heat (LCOH).

2. Case study

The Taars solar heating plant was put into operation in August of 2015, consisting of a 5960 m^2 flat plate collector field and a 4039 m^2 parabolic trough collector field in series [1]. Figure 1 briefly illustrates the basic principle of the plant. The solar collector fluid of the parabolic trough collectors is water, while that of FPC is a 35% glycol/water mixture. The return water from the district heating network is heated up to 70°C by the heat exchanger connected to the flat plate collector field. Then the water from the flat plate collector field is heated to the required temperature by going through the parabolic trough collector field. The orientation of parabolic trough collector axes is 13.4° towards west from south. The parabolic trough collectors track the sun rays from east to west when the collectors work during the daytime. There are six rows of parabolic trough collectors and the row distance is 12.6 m. The length of each row is about 120 m. The parabolic trough collectors were delivered by Aalborg CSP A/S. The orientation of the flat plate collectors is south and the collector row distance between flat plate collectors is 5.67 m. The tilt of flat plate collectors is 50°. The flat plate collectors consist of two types of flat plate collectors, namely HTHEATboost 35/10 and HTHEATstore 35/10, delivered by Arcon-Sunmark A/S. Half of flat plate collectors are HTHEATboost 35/10, while the other half is HTHEATstore 35/10. The backup heat resource is two natural gas boilers. Two tanks with a total volume of 2430 m^3 are used as heat storage for several days in the summer. The lessons from the operation are that the parabolic trough collectors have to be defocused in several sunny days in summer because of limited heat storages and heat demand. A validated TRNSYS model was developed to optimize the hybrid solar heating plant to reach the minimum nLCOH [2]. The yearly DNI and global

doi:10.18086/swc.2017.06.14 Available at http://proceedings.ises.org

radiation in the Design Reference Year are 1150 and 1030 kWh/m^2 respectively. The typical heat demand is 20167 MWh per year.

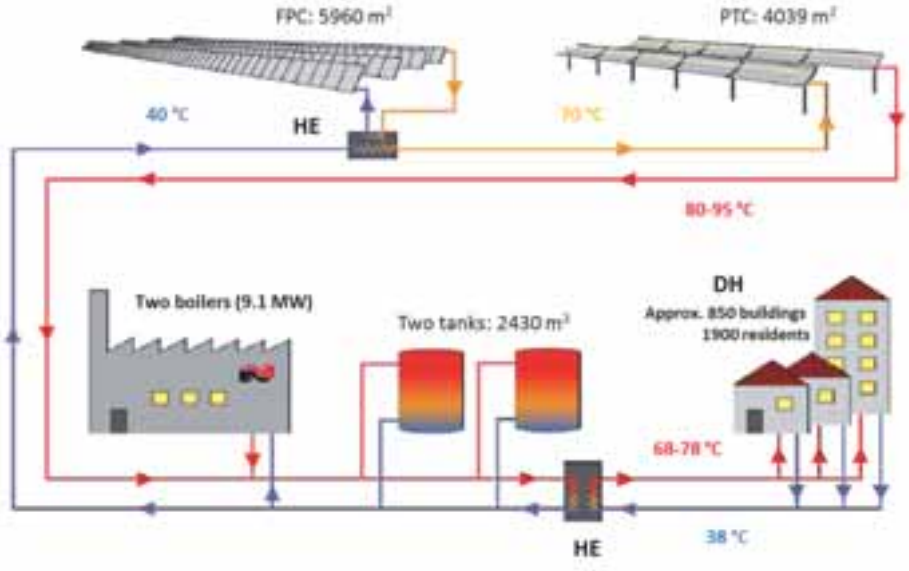

Fig.1.Illustration of the Taars solar heating plant [3].

3. Method

LCOH definition has two boundary conditions for the solar district heating network in this study. One boundary condition is elaborated only for the solar collector field and heat storage. Other boundary condition not only includes the solar collector field and heat storage, but also takes conventional heat supply into consideration. The former is called by net LCOH (nLCOH). nLCOH is used in this study and can be expressed as equation below: I_s is the initial cost, DKK; T is the lifetime, 30 years; r is the discount rate, 3%; P_s is the operation and maintenance cost, SE is the energy produced, kWh. The operation and maintenance cost of the flat plate collector field every year is assumed as follows: a) 2 DKK/MWh heat produced for maintenance fee; b) 1.5 kWh electricity/100kWh heat produced for operation (2.3 DKK/kWh electricity). The operation and maintenance cost of the parabolic trough collector field every year is assumed to be 0.8% of the initial cost. The initial cost of the flat plate collector field without foil was assumed as 2180-2400 DKK/m^2 (500-10000m^2). The cost of the flat plate collector field with foil was assumed as 7.6% higher than that of the flat plate collector field without foil. The cost of the parabolic trough collector field is 40-70% higher than that of the flat plate collector field. Detail information is shown in the reference [4].

$$nLCOH = \frac{I_s + \sum_{t=1}^{T} P_s \cdot (1+r)^{-t}}{\sum_{t=1}^{T} SE \cdot (1+r)^{-t}} \quad (1)$$

4. Results and conclusions

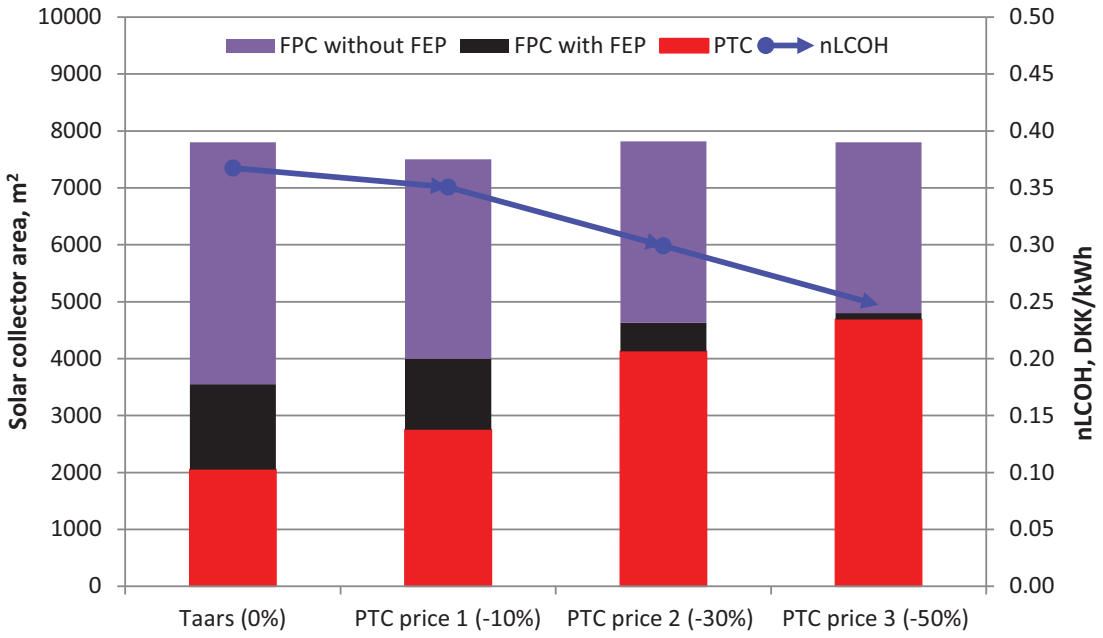

Fig.2. Minimum LCOH and optimal parameters based on different prices of the PTC [4].

Fig.2 shows the optimal solar collector area for different scenarios. The Taars bar shows optimal solar collector area for the reference case. Different scenarios for different parabolic trough collector price levels are also investigated, if the the price of the parabolic trough collector field decreases by 10%, 30% and 50% in the future. All the scenarios show that the design concept that the hybrid heating plant with flat plate collectors and parabolic trough collectors can be feasible in Denmark. Further information please find in the published papers.

5. Acknowledgements

The first author really appreciates the China Scholarship Council (No.201506120074) for the financial support for the PhD study at the Technical University of Denmark. Special thanks are expressed to Aalborg CSP A/S (Andreas Zourellis, Jan Holst Rothman, Steffen Rovsing Møller and Per Aasted) for the information provided. This work is a part of an EUDP project financed by the Danish Energy Agency and the IEA-SHC Task 55 "Towards the Integration of Large SHC Systems into DHC Networks".

6. References

[1] Aalborg CSP A/S, “Aalborg CSP,” *http://www.aalborgcsp.com/*, 2017. [Online]. Available: July.2017.

[2] Z. Tian, B. Perers, S. Furbo, and J. Fan, “Analysis and validation of a quasi-dynamic model for a solar collector field with flat plate collectors and parabolic trough collectors in series for district heating,” *Energy*, Sep. 2017.

[3] Z. Tian, B. Perers, S. Furbo, and J. Fan, “Annual measured and simulated thermal performance analysis of a hybrid solar district heating plant with flat plate collectors and parabolic trough collectors in series,” *Appl. Energy*, vol. 205, pp. 417–427, 2017.

[4] Z. Tian, B. Perers, S. Furbo, and J. Fan, “Thermo-economic optimization of a hybrid solar district heating plant with flat plate collectors and parabolic trough collectors in series,” *Manuscript*, 2017.

MODEL-BASED CONTROL STRATEGIES FOR AN EFFICIENT INTEGRATION OF SOLAR THERMAL PLANTS INTO DISTRICT HEATING GRIDS

Viktor Unterberger[1,2], Daniel Muschick[1] and Markus Gölles[1]

[1] BIOENERGY 2020+ GmbH, Graz (Austria)

[2] Institute for Automation and Control, Graz University of Technology, Graz (Austria)

Abstract

The integration of solar thermal plants into district heating grids requires advanced control strategies in order to utilize the full potential in terms of efficiency and least operating effort. State-of-the-art control strategies cannot completely fulfill this since they are not able to consider the physical characteristics of the different components, nor do they take information on future conditions and requirements into account properly. A promising attempt for improvement is the application of model-based control strategies together with practicable forecasting methods for both the solar yield as well as the heat demand. This contribution will present the results of several projects performed on the development of suitable mathematical models, forecasting methods and control strategies relevant for the integration of solar thermal plants into district heating grids.

Keywords: model-based control strategies, forecasting methods, solar thermal plants, district heating grids

1. Introduction

Modern large-scale solar thermal plants are increasingly used as heat sources for heating grids. In urban environments, they are also often set up with local buffer storages and the possibility to directly supply local consumers with heat. In this specific case an additional bi-directional transfer station can be used which allows the supply of the local consumers with heat from the grid in case there is too little solar energy available. The most beneficial operating strategy of such a configuration first of all depends on the point of view: For the operator of the solar thermal plant, who is responsible for the supply of the local consumers, maximizing the on-site consumption will be most beneficial, since the prizes for heat fed into and taken from the heating grid typically differ significantly. For the operator of the heating grid, generally a different operating strategy would be most beneficial, since all other components and parties have to be taken into account. This contribution will focus on control strategies for an efficient integration from the point of view of the solar thermal plant operator, but also parts relevant for the district heating grid operator will be outlined.

The most important part of the solar thermal plant is the collector field. In the most general case, this solar collector field consists of several subfields connected in parallel that can differ in size. These differences in size have their origin in the optimization of the collector area under the local constraints of the place of installation which are often encountered in urban areas. In order to ensure an adequate flow distribution in the individual subfields, and to avoid exergy losses by mixing flows with different temperatures, the individual fields are typically equipped with adjustable balancing valves. These valves can either be adjusted manually for nominal operation or be driven by a servomotor in order to achieve an adequate flow distribution for every operating condition.

There are two major challenges to be faced when controlling such plants. The first challenge is to use the generated heat in an economically optimal way. The price for selling heat to the grid is typically lower than the price for buying it back, so an effective buffer management strategy is necessary which ensures the heat supply to the consumers while maximizing profits. The decision whether the heat currently generated should be stored in the buffer storage or be fed into the district heating grid determines the required feed temperature. When feeding into the grid, a minimum feed-in temperature must be provided by the plant; when feeding the local consumers via the buffer storage, a lower feed temperature is normally sufficient and thus a higher efficiency in the collectors can be obtained, a point that needs to be considered in the buffer management strategy.

The second challenge is to keep the outlet temperature of the solar collector field within certain boundaries and

doi:10.18086/swc.2017.06.15 Available at http://proceedings.ises.org

adjust it quickly regarding the mode of operation (store the heat in the buffer storage vs. feeding it into the district heating grid) even for fast changing ambient conditions. This is difficult because of several factors: first, there are delays between the control actions and the resulting outlet temperature changes, and the actuators are usually slow. Second, the outlet temperature depends on the accumulated influence of the solar irradiation during the transition time of the water through the collectors, thus requiring control strategies incorporating some kind of memory to obtain a good outlet temperature control performance.

To deal with these challenges, state-of-the-art control systems of solar thermal plants are often hierarchically structured. On a high-level basis, typically a set of rules defines the general mode of operation (e.g. feeding the heat into a district heating grid vs. storing it in the local buffer storage). On the low-level basis, control tasks such as controlling mass flows and temperatures are mainly handled separately for each subfield using simple linear PID controllers, which in some cases are enhanced by additional expert rules and, for example in the case of controlling the solar collector output temperatures, by energy balance calculations. On both control levels typically neither the non-linear and coupled characteristics of the different components are considered, nor is information on future conditions and requirements taken into account. Thus the default strategies applied on both levels usually do not yet utilize the full potential of modern solar thermal plants, mainly resulting in efficiency losses, even unused solar energy and increased operating efforts due to the need of frequent re-parametrization by the operators.

For both control levels, the most promising alternative approach would be the development and application of appropriate model-based control strategies combined with a good forecast of the expected heat generated by the plant and the heat demand of the local consumers.

Model-based control strategies base on mathematical models describing the fundamental static or dynamic characteristics of the different components and systems and thus allow an explicit consideration of the physical characteristics of the different components. In the case of high-level control, the specific method of model predictive control can also take information on future conditions and requirements into account. The models for most of the components and systems of interest available prior to the beginning of the work underlying this contribution were either too complex (used for comprehensive simulation studies) or too simple (static mass and energy balances). For this reason, the development of mathematical models suitable to serve as a basis for model-based control strategies represents a necessary part of the overall control development.

Furthermore, the available forecasting methods for solar yield and heat demand were in most of the cases mathematically by far too complicated, tailored for a specific application and very often not adaptive. Thus, they cannot serve as a general basis for model-based control strategies, which is why the development of general, simple and adaptive forecasting methods for the solar yield as well as the heat demand is another prerequisite for the final application of model-based control strategies.

This contribution presents a summary of the results of several projects performed on the development and validation of mathematical models suitable for model-based control strategies (section 2), forecasting methods for both the load demand as well as the solar yield (section 3) and control strategies relevant for the integration of solar thermal plants into district heating grids from the point of view of the solar thermal plant operator (section 4). Finally, section 5 sums up the results and draws a short conclusion.

2. Mathematical modelling

The modelling for the low-level control focusses on the correlation of pressure differences and mass flows in hydraulic components as well as the heat transfer, i.e. the temperature levels especially at the outlet of the components or systems as functions of the inlet temperature, ambient conditions and mass flows. The modelling for the high-level control focusses on heat storage and heat loss and aims at mathematically more simple models usable in optimization problems such as those formulated in model predictive control. Appropriate models for all relevant components in a solar thermal plant (buffer storage, collector fields and all hydraulic components for the heat distribution such as piping, pumps and valves) respectively control levels were developed, of which the model of the buffer storage as well as the solar circuit and its components are described exemplarily in this section.

2.1 Buffer storage

Buffer storages are used in order to decouple the occurrence of heat production from heat consumption at least at a certain degree. The mathematical modelling of buffer storages is primarily important for the high-level controller in order to estimate the available heat in the buffer within the next hours.

The modelling of buffer storages can be conducted in different levels of detail. In literature, models ranging from three-dimensional partial differential equations used for computational fluid dynamic (CFD) simulations, to single ordinary first-order differential equations can be found. In the next section three model of different detail are described: a detailed model primarily useful for simulation purposes (PDE model); the simplest possible model that is usually used for high-level, optimization-based control purposes (single integrator model); and a new, purpose-built linear hybrid model that combines the advantages of both for more accurate prediction results (hybrid model).

PDE model

A reasonable compromise of complexity and accuracy when considering a typical cylindrical buffer storage is to neglect the radial temperature dependency and assume a constant temperature at a specific axial (vertical) position. This assumption is supported by the usual mechanical construction of inlets aiming at a good radial distribution of entering fluids and thus minimal axial mixing. This leads to a mathematical model of one partial differential equation with only one spatially dependent variable (typically the temperature), where all relevant mechanisms of heat transfer are considered, e.g. (Cruickshank, 2009; Hemmer, 2014; Zlabinger, 2017). In simulations, the differential equation should preferably be solved implicitly in order to increase numerical stability and reduce computational effort. Typically, all model parameters can be determined from geometrical data and data sheets, but if they are not available or if the geometries are exceedingly complicated, it could be easier to determine some model parameters experimentally. This typically also would lead to an improved reproduction of the energy losses to the environment.

Fig. 1 shows results of an exemplary experimental verification of the model described in (Hemmer, 2014) performed with a commercially available buffer storage with a capacity of 1500 l. In the beginning, the upper third of the boiler got heated up to 70°C while the two lower thirds remained at ambient temperature. In the next step the lower part got heated up via an internal heat exchanger. In order to evaluate the simulation results, 12 vertically distributed temperature sensors have been installed. Despite the challenging setup the model describes the measured behaviour sufficiently well.

A model like this can be used for simulation purposes and even in a predictive high-level control not based on linear optimization. However, such controllers typically are computationally expensive and cannot rely on standard solvers. A simpler prediction model for the future available heat is thus required.

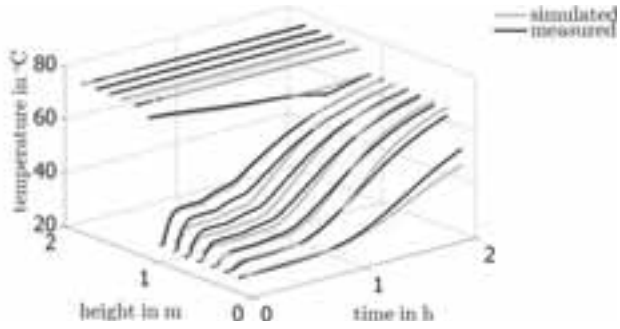

Fig. 1: Exemplary comparison of measured (black) and simulated (grey) vertical temperature distribution in a buffer storage while transferring heat via an internal heat exchanger in the lower third of the buffer.

Single integrator model

The single integrator model is the simplest approach for a linear model of a buffer storage and describes the dynamic behavior of the buffer storage on the basis of a simple energy balance

$$\frac{dE_{\mathrm{stor}}}{dt} = \sum \dot{E}_{\mathrm{in}} - \sum \dot{E}_{\mathrm{out}} \qquad \text{(eq. 1)}$$

with the stored energy as state variable E_{stor} and the in- $\dot{E}_{\mathrm{in}}$ and outgoing $\dot{E}_{\mathrm{out}}$ energy flows as inputs.

This model describes the energy content of typical cylindrical buffer storages sufficiently well to be used in model predictive control strategies with approximately constant inlet temperatures during the optimization horizon and comparatively quick charging and discharging cycles, where a detailed description of the losses is not crucial (Moser, 2017). But as soon as different, varying temperature levels or long-term operating cycles have to be taken into account, a more complex model has to be considered.

Hybrid model

In (Zlabinger, 2017) a more detailed but still linear approach is suggested, which is able to consider a finite number of different inlet temperatures and in- and outlets at different heights as well as all relevant mechanisms of heat transfer (convective heat input and output at predefined heights, axial heat conduction, environmental losses and natural convection). It is a hybrid, linear model that divides the buffer volume into different zones with constant mean temperatures and variable heights. The quantities of heat stored within these zones represent the continuous state variables of the system, and are described by simplified energy balances. The energy flows to the connected consumers and from the producers constitute the input variables. Depending on the heights of the zones in relation to the heights of the in- and outlets, different energy flows have to be considered. They are selected depending on additional discrete state variables that are used to distinguish between the different operating states. In the simplest form of the model, the consumers' return temperatures and the producers' feed temperatures are assumed to be constant, but through further case differentiation, varying inlet temperatures can be represented as well. Finally, the model can be described in the form of a mixed logical dynamic model (Bemporad and Morari, 1999), which is well-suited for the design of model predictive controllers for the high-level control as discussed in chapter 4.

2.2 Solar Circuit

The solar circuit in general consists of pipes, a pump, valves and several subfields, made up of multiple solar collectors, connected in parallel. It is connected to other hydraulic circuits via a heat exchanger. All these components have to be described through their thermal characteristics (heat transfer) as well as their hydraulic characteristics (correlation of pressure differences and mass flows) as described next.

Thermal characteristics

The thermal characteristics of pumps, valves and insulated pipes can be neglected for control purposes since no relevant heat transfer occurs. Only the thermal characteristics of the solar collector subfields are of major importance, for which several models of different levels of complexity already exist. On the one hand there exists a static model for the heat output of a solar collector based on a static energy balance, where the parameters are determined in a standardized collector test (EN12975) and can be found in the datasheet. This model is sometimes already used in today's control strategies in order to calculate a static feedforward control signal for the pump, and can be incorporated into solar yield forecasting methods (see section 3).

On the other hand there are more sophisticated dynamic models, such as models consisting of two coupled partial differential equations for the fluid and the absorber temperature of the collector, e.g. (Camacho et al., 2007a). Such more complicated models are often linearized in an operating point in order to obtain linear models. These linear models represent the dynamics of the outlet temperature of the collector field depending on the inlet temperature and the solar irradiation (Lemos et al., 2014) and can be used for model-based outlet temperature controllers. In several articles, the complicated models are used in combination with model-predictive controllers, e.g. (Camacho et al., 2007b; Lemos et al., 2014), but still more at an academic level or implemented in small-scale demo plants (Andrade et al., 2015).

Hydraulic characteristics

The hydraulic characteristics, namely the correlation of pressure differences and mass flows of the individual components in the solar circuit, play an important role for the low-level control. For pipes, valves and pumps simple models describing their static as well as their dynamic characteristics are summarized in (Unterberger et al., 2017). A turbulent flow regime can be assumed for all these components. When considering collector fields consisting of several large flat plate collectors this is different. The collector fields experience different flow regimes varying from laminar to turbulent as well as transition regimes between them. Thus, it is not sufficient to describe the correlation between pressure difference and mass flow through a purely quadratic equation. Another challenge in modelling the hydraulic characteristics of solar collector fields is the influence of the

temperature. Due to the significant rise in temperature of a fluid flowing through a collector, its viscosity and density are highly affected. This effect even increases further when an anti-freeze mixture is used. This results in varying hydraulic resistance values depending on the temperature levels and temperature increases.

These challenges can be dealt with by expressing the pressure difference over a subfield Δp_{subf} as a combination of the pressure difference in a laminar flow regime Δp_{lam} and the pressure difference in a turbulent flow regime Δp_{turb}:

$$\Delta p_{\mathrm{subf}} = \Delta p_{\mathrm{lam}} + \Delta p_{\mathrm{turb}} \qquad \text{(eq. 2)}$$

The pressure difference in the laminar regime Δp_{lam} is based on the friction along a straight pipe of constant cross section described by the Darcy-Weisbach equation (Rouse, 1946). This is a linear correlation between the pressure difference Δp and the mass flow $\dot{m}$ for a certain fluid temperature T. The correlation depends on the pipe parameters diameter and length and is proportional to the temperature dependent kinematic viscosity of the fluid $\nu(T)$. The constant parameters, diameter and length can be combined in a constant parameter $R_{0,\mathrm{lam}}$,which has to be determined experimentally for a specific temperature T_0:

$$p_{\mathrm{lam}} = \frac{\nu(T)}{\nu(T_0)} R_{0,\mathrm{lam}}\, \dot{m} \qquad \text{(eq. 3)}$$

The pressure difference in the turbulent regime Δp_{turb} is represented by an empirical formula usually used to describe the pressure drop due to an abrupt change in the pipe cross section as e.g. caused by a bezel. It is a correlation between the pressure difference and the square of the mass flow, with the constant parameter $R_{0,\mathrm{turb}}$, experimentally determined for a specific temperature T_0, and the density of the fluid ρ:

$$p_{\mathrm{turb}} = \frac{\rho(T_0)}{\rho(T)} R_{0,\mathrm{turb}}\, \dot{m}^2 \qquad \text{(eq. 4)}$$

In practical applications, using the mean temperature between inlet and outlet of a solar collector usually provides a sufficiently accurate approximation of the correlation.

If a balancing valve is installed at the entry of the collector subfield, it is useful to describe the hydraulic characteristics of the collector subfield together with the balancing valve. In this case, both the laminar as well as the turbulent temperature independent coefficients ($R_{0,\mathrm{lam}}, R_{0,\mathrm{turb}}$) are modelled as a function of the valve position. This in turn allows calculating the valve position necessary to obtain a desired mass flow through the subfield given a specific pressure difference provided by the pump, which is useful for feedforward control strategies.

A comparison of the model with measurement data for a single collector subfield with an overall size of 172 m² is shown in Fig. 2 for stepwise changes of the plug position of a balancing valve.

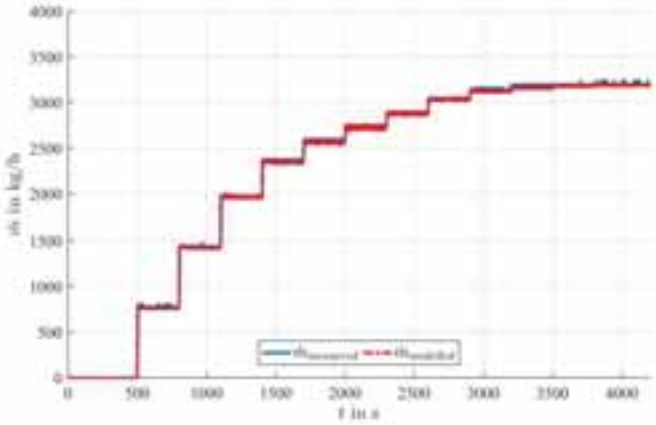

Fig. 2: Exemplary comparison of the measured (blue) and the modelled (red) mass flow through a solar collector field (172 m²) for stepwise changes of the plug position of a balancing valve at its inlet at a constant rotational speed of the pump.

3. Forecasts

The high-level controller, which is often called energy or load management system, of the solar thermal plant should incorporate forecasts for both the expectable solar yield and the expectable heat demand of the consumers in order to optimally plan generation, storage and consumption of heat.

Many different approaches for performing these forecasts can be found in literature, but almost all of them are highly academic and very complex. They are often tailor-made for specific configurations, require high computational effort and, due to their complexity, a comprehensive mathematical educational background of the implementing control engineers. Therefore, most of them are inappropriate to be widely used in practical implementations.

To be practical applicable, the forecasting methods first of all need to be general in order to cover a big variety of systems. Furthermore, the methods should be easy to implement and use little computational resources so that they can be integrated into the PLCs typically used for controlling solar thermal plants. Finally, the methods need to be able to adapt to varying conditions such as shading or changing consumer behavior. In this section, methods for predicting the future heat demand and the future solar yield are presented which fulfill these requirements and are thus usable in both solar thermal plants and district heating grids.

3.1 Forecasting method - heat demand

The method for forecasting heat demand presented in (Nigitz and Gölles, 2017) is based on the empirical analysis of the correlation between weather data and heat load data of several types of consumers. The analysis revealed that there exists an approximately linear correlation between load demand and ambient temperature and that there is a characteristic dependency of the heat load on the time of the day. Furthermore, it was also found that the individual days of the week do not have to be considered explicitly, but a distinction between working days and weekends/holidays turned out to be necessary.

The method predicts the heat demand of the consumers and corrects it by using the current prediction error as well as basic expert knowledge. The method itself is based on a linear regression model for each hour of the day describing the dependency of the heat demand on the ambient temperature. The parameters of the regression model are updated every hour taking into account the actual heat flow and the ambient temperature of the previous days, where only similar days are considered (work days or weekends/holidays). The only inputs necessary for the method are the measured heat flow supplied to the consumers and the predicted ambient temperature, provided e.g. from a weather service provider. This means that no parameterization is needed and no complex model of the connected buildings or the consumer behavior is necessary. Fig. 3 shows an exemplary forecast for the heat demand of a local consumer connected to the buffer storage of a thermal solar plant, compared to the actual load demand.

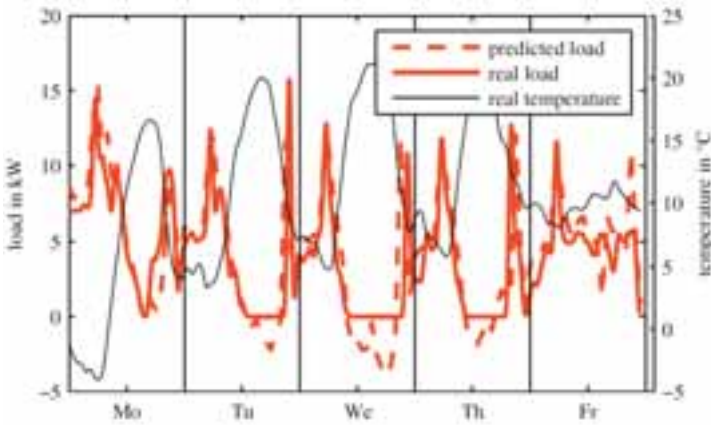

Fig. 3: Exemplary prediction of the load demand of an on-site consumer (connected load: 35 kW) compared to the actual (measured) load demand together with the (measured) ambient temperature for a representative work week.

3.2 Forecasting method - solar yield

The method developed to forecast the solar yield is based on an extensive analysis of weather data and measurement data from a large-scale solar thermal plant. The analysis showed that the static collector model

(see section 2.2) with the model parameters from the datasheet, determined according to European Standard EN12975, does not directly lead to satisfying results but represents a suitable basis to forecast the solar yield. This is because the model parameters are only valid for stationary conditions in the laboratory and not for the dynamic conditions occurring in the daily operation. Furthermore, these model parameters would have to change over time because of polluted collector surfaces decreasing the optical efficiency, or because of the decay of materials leading to higher convective heat losses of the collector.

For this reason the method developed is based on the static collector model, but continuously estimates the collector parameters based on previous data. Like the method for forecasting the future heat demand, the method to forecast the future solar yield is based on linear regression models for each five minutes of the day describing the dependency of the solar yield on the ambient temperature, the global solar irradiation and the absorber temperature.

The parameters of the static collector model are adapted every five minutes, taking into account the past values of the measured solar yield, the measured ambient temperature as well as the measured global solar irradiation. By doing so, the pollution of the collector fields, the decay of the materials as well as the influence of local shading is automatically considered. In addition, no manual parameterization efforts or complex dynamic models are necessary. The only inputs necessary for the method are the measured solar yield and both the predicted and measured values for ambient temperature as well as global solar irradiation.

Fig. 4 shows an exemplary forecast of the solar yield for a sunny summer day of a subfield with 172 m² built in 2009, compared to the expected solar yield calculated with the static collector model with the parameters taken from the datasheet of the manufacturer as well as the actual measured solar yield. For this verification, real weather forecast data from the company *meteoblue AG* (https://www.meteoblue.com) was used, which provides weather information world-wide. This method will be extended by a correction approach in order to react on prediction deviations, which is for example necessary in case of very cloudy days.

It can be seen that the static model with the parameters taken from the datasheet would indicate the solar yield before 8 am as soon as global solar irradiation is predicted, not considering the heating up phase of the collector subfield. Furthermore, most of the time the static model is overestimating the solar yield. Only in the afternoon the prediction of the static collector model seems accurate. In fact this has its origin in the course of the predicted global solar irradiation which in the afternoon is below the measured one compensating the general overestimation of the collector efficiency. In contrast, the predicted solar yield resulting from the developed forecasting method with the parameters based on previous measurement data describes the real generated solar yield of the subfield throughout the day very well.

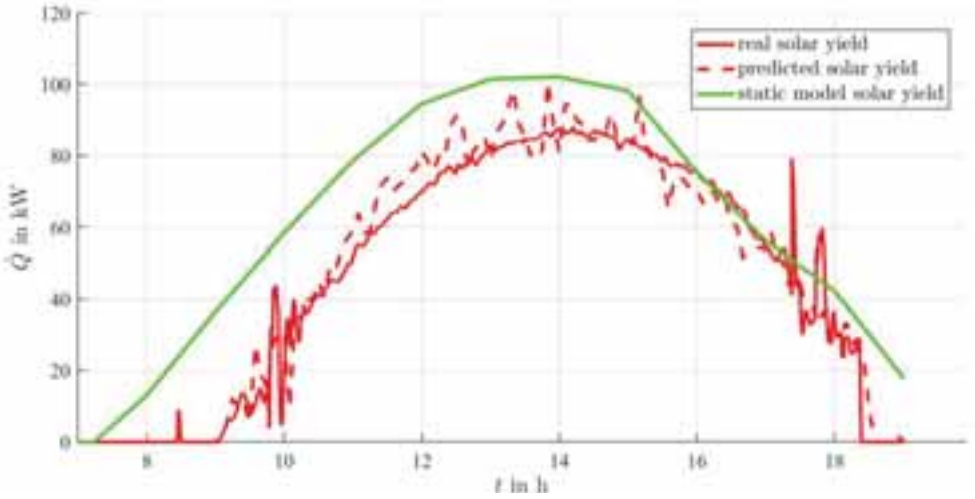

Fig. 4: Comparison between the measured solar yield, the predicted solar yield and the solar yield calculated with the static model and the parameters taken from the datasheet for a collector field of 172 m².

4. Control

The control of a solar thermal plant connected to a heating grid and local consumers must handle multiple aspects. Locally, a high-level controller must decide when to feed heat into the grid, when to store it locally and when to consume heat from the grid. A low-level controller must take care of temperature and mass flow control in the solar collectors, and of the heat distribution to and from the local buffer storage. At the heat transfer station, a grid controller must handle the feeding of heat into the grid or the transfer of heat from the grid to the local buffer storage. Such bidirectional heat transfer stations are still a matter of research, and often two transfer stations are operated in parallel, one for each task.

The different model-based controllers developed base on different methods from control theory. Fig. 5 shows the main idea of a model predictive controller used for the high-level control providing the reference values for all the underlying low-level controllers.

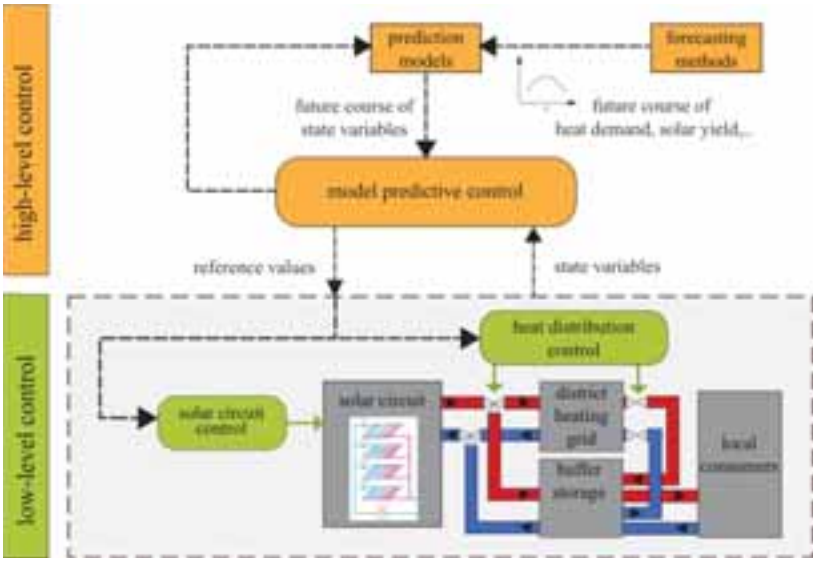

Fig. 5: Schematic overview of the interactions of the different control systems addressed

As an example for the different low-level controls to be considered, the control of the most important part, the solar circuit is discussed in more detail. The task of the low-level controller of the solar circuit is to realize the reference values given by the high-level control as efficiently as possible. In case of the solar collector circuit, this only influences the desired collector outlet temperature, which is different depending on the mode of operation of the plant - feeding the heat into the district heating grid requires a higher outlet temperature than storing it in the local buffer storage.

The desired outlet temperature of the solar circuit is realized by the model-based solar circuit control. It controls the pump in such a way that the mass flow necessary to achieve the desired outlet temperature is reached. In case there are motor-driven balancing valves installed in the subfields, these can be used to individually control the mass flows through the individual fields, and the controller has to adjust the valves appropriately. One possible control concept to accomplish this task will be described next, first for the case that controllable balancing valves exist in each collector subfield, then for the case where no motor-driven balancing valves exist.

In a first step, the mass flows through the N individual subfields ($\dot{m}_{1,\mathrm{des}}$ to $\dot{m}_{N,\mathrm{des}}$) necessary to achieve the desired outlet temperature $T_{\mathrm{out,des}}$ are calculated based on a thermal model of the solar collector field, e.g. the static collector model based on the energy balance mentioned in section 2. This requires the knowledge of (measured or predicted) influencing variables such as the global solar irradiation G, the ambient temperature T_{a} and the inlet temperature to the collector subfields T_{in}. The parameters of the thermal models for each subfield can be continuously estimated according to the forecasting method for the solar yield in order to consider shading, pollution of the collector surface or decay of materials.

In addition to this static calculation, the individual desired mass flows are continuously updated by a temperature controller. The temperature controller compares the current outlet temperatures of the individual subfields $T_{1,\mathrm{out}}$ to $T_{\mathrm{N,out}}$ with the desired outlet temperature $T_{\mathrm{out,des}}$. Based on this comparison, the desired mass

flows calculated in the first step are either in- or decreased. In the simplest case, the temperature controller consists of very slowly adjusting PI controllers, but also more sophisticated, model-based control techniques could be used.

In the second step, the sum of the desired mass flows, together with the nominal positions of the valve plugs φ^*_1 to φ^*_N are used to set the rotational speed of the pump n_P and, as a consequence, the differential pressure Δp_P. The nominal positions of the valve plugs are chosen between 80-100%, where 0% corresponds to a closed valve and 100% to an open valve. They should be chosen as high as possible in order to avoid unnecessarily increased pressure losses, but keeping in mind that controllability is reduced when the valve is opened too much because the valve will have less effect on the mass flow closer to the opened state.

The results of the two steps, the desired mass flows and the differential pressure of the pump, are used in a third step to determine the individual actual valve plug positions. In order to realize the adjusted desired mass flows, a feedforward controller for the valves is used. In this feedforward controller the valve positions φ_1 to φ_N necessary to accomplish the desired mass flows are determined based on the differential pressure provided by the pump and the hydraulic model of the solar collector subfield (see section 3). In the simplest case this feedforward control can be implemented neglecting the hydraulic couplings between the subfields, but even more extensive control techniques using graph-based algorithms, e.g. (Hassine and Eicker, 2014), could be used which take into account the hydraulic couplings by solving the equations simultaneously.

In case of larger model deviations, an additional slow controller could compare the actual valve positions (φ_1 to φ_N) with the nominal ones (φ^*_1 to φ^*_N) in order to adjust the rotational speed of the pump. Fig. 6 shows a schematic representation of the described strategy for the solar circuit control.

In case that there exist no motor-driven balancing valves in the solar circuit, the control strategy can be simplified to steps one (calculating the desired mass flows) and two (choosing the rotational speed of the pump), by adding a control loop comparing the overall outlet temperature of the solar circuit with the desired one, and adjusting the rotational speed of the pump accordingly.

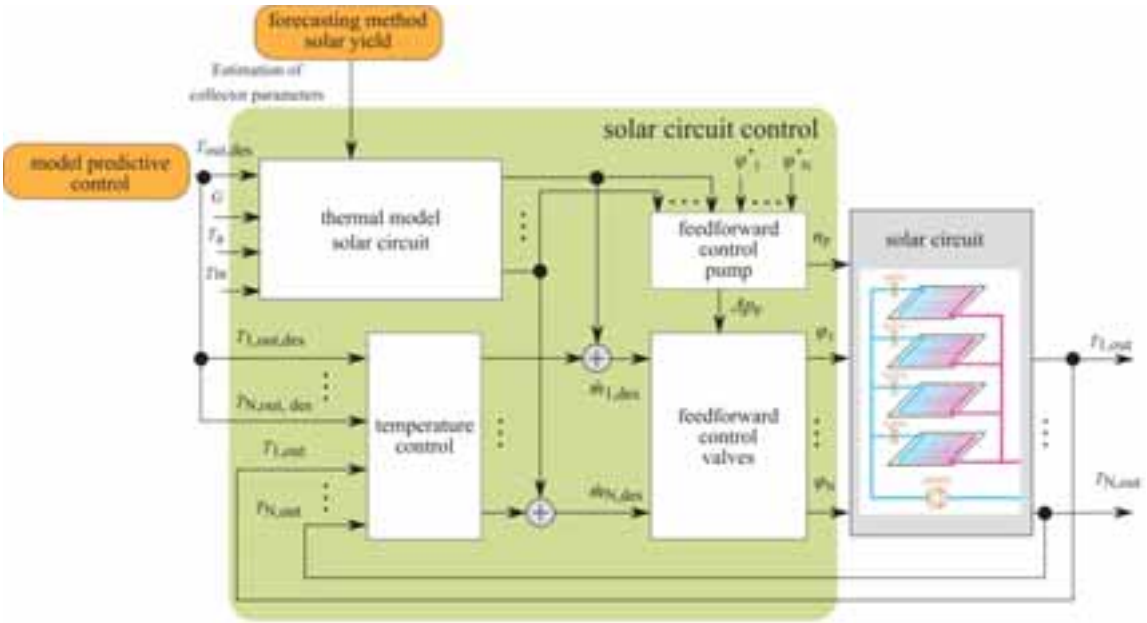

Fig. 6: Control approach for the low-level control of the solar circuit.

5. Conclusion and outlook

In order to efficiently integrate solar thermal plants into district heating grids challenges regarding the hydraulic control and the load management have to be dealt with. State-of-the-art control strategies cannot cope with these challenges in optimally since they are neither considering the non-linear and coupled characteristics occurring in such hydraulic systems, nor do they take into account future weather conditions and therefore cannot control the

systems in a predictive manner. Instead, they can only react when a control deviation has already occurred. A promising approach for improvement is the application of model-based control strategies together with practicable forecasting methods for both the solar yield as well as the heat demand.

In this contribution models, forecasting methods as well as control strategies for solar thermal plants were presented exemplarily and verified with either measurement or simulation data, already showing good results. Some of the presented approaches such as the forecasting methods can serve as a basis for developing similar methods for the heating grid as well. Future investigations have to address the cooperation of the solar thermal plant with the district heating grid: for example the interactions of the high-level controllers in charge of the respective load management. This issue is relevant for all kinds of consumers also acting as producers, and is still a topic of current research.

6. References

Andrade, G.A., Álvarez, J.D., Pagano, D.J., Berenguel, M., 2015. Nonlinear controllers for solar thermal plants: A comparative study. Control Engineering Practice, 43, 12 – 20.

Bemporad, A. and Morari, M., 1999. Control of systems integrating logic, dynamics, and constraints. Automatica, 35, 407–427.

Camacho, E.F., Rubio, F.R., Berenguel, M., Valenzuela, L., 2007a. A survey on control schemes for distributed solar collector fields. Part I: Modeling and basic control approaches. Solar Energy, 81, 1240-1251.

Camacho, E.F., Rubio, F.R., Berenguel, M., Valenzuela, L., 2007b. A survey on control schemes for distributed solar collector fields. Part II: Advanced control approaches. Solar Energy, 81, 1252-1272.

Cruickshank, A., 2009. Evaluation of a stratified multi-tank thermal storage for solar heating applications. Doctoral Thesis, Queen's University, Kingston, Canada.

Hassine, I. B. and Eicker, U., 2014. Control Aspects of Decentralized Solar Thermal Integration into District Heating Networks. Energy Procedia, 48, 1055 – 1064.

Hemmer, J., 2014. Modelling and control of buffer storages in biomass heating systems. Master's thesis, Graz University of Technology. (in German).

Lemos, J.M., Neves-Silva, R., Igreja, J.M., 2014. Adaptive Control of Solar Energy Collector Systems. Springer, International Publishing.

Moser, A., 2017. Model predictive control of a bidirectional, solar and biomass-based district heating grid. Master's thesis, Graz University of Technology. (in German).

Nigitz, T. and Gölles, M., 2017. A simple short-term forecasting method for small-scale heat producers. To be submitted to Journal of Applied Energy in December 2017.

Rouse, H., 1946. Elementary Mechanics of Fluids. John Wiley and Sons, New York.

Unterberger, V., Muschick, D., Loidl, A., Gölles, M., Horn, M., 2017. Modelling and flatness-based control of hydraulic heat distribution systems. Submitted to Journal of Control Engineering Practice in September 2017.

Zlabinger, S., 2017. Modelling of buffer storages as basis for the development of model-predictive control strategies in heating systems. Master's thesis, Graz University of Technology. (in German).

Domestic Solar Water Heating

Theoretical and experimental investigation of polymeric solar-thermal flat-plate collectors

Mathias Ehrenwirth[1,2], Daniel Beckenbauer[1,2], Michael Klaerner[1], Christoph Trinkl[1], Wilfried Zoerner[1] and Vicky Cheng[2]

[1] Institute of new Energy Systems (InES), University of Applied Sciences Ingolstadt (Germany)

[2] Munich School of Engineering (MSE), Technical University of Munich (Germany)

Abstract

In this paper, a novel approach for manufacturing cost effective polymeric solar-thermal collectors is described. The approach known as Twin-Sheet-Thermoforming (TST) is suitable for mass-production and enables a significant cost saving potential compared to conventional, metal-based collectors. Based on an absorber made of acrylonitrile butadiene styrene (ABS), a collector prototype was set-up and tested according to EN ISO 9806:2013. The results were compared to data available both from literature and market available polymeric collectors. The tested prototype shows a higher solar-thermal efficiency compared to market available polymeric collectors and a similar efficiency compared to laboratory prototypes recently described in literature. Against this background, the production and manufacturing costs of polymeric solar-thermal collectors become increasingly important, as these costs directly affect the Levelized Cost of Heat (LCOH) of a solar-thermal system equipped with such collectors.

Keywords: Solar-thermal flat-plate collector, Collector Efficiency, Polymeric Materials, Experiment

1. Introduction

Currently, solar-thermal systems are facing two challenges: On the one hand, the low commodity prices for oil and gas on the world market cause longer payback periods for solar-thermal systems. On the other hand, heating with other renewable energy sources (e.g. heat pumps in combination with photovoltaic systems) becomes economically more attractive. In order to remain competitive compared to other heat generation systems, prices for solar-thermal systems must be significantly decreased. According to Ivancic et al. (2014), current heat generation costs of solar-thermal systems have to be halved to become cost competitive with heat generated by fossil fuels (*fossil fuel parity*). To achieve this goal, different approaches are currently pursued, e.g. increasing the collector efficiency or decreasing the installation costs with so-called *plug-and-function* systems. Further cost reduction can be realized by utilizing cost-effective, polymeric materials on both collector and system level. In this study, the efficiency of a solar-thermal collector based on a polymeric absorber is investigated.

2. State of science and technology

2.1. Polymeric collectors described in scientific literature

The application of polymeric materials for solar-thermal collectors and systems has been subject of various scientific publications. Next to economic key figures like investment and operating costs, the thermal efficiency of polymeric collectors is of major importance for cost effective solar-thermal systems. However, the thermal efficiency of polymeric solar-thermal flat-plate collectors is limited by the physical properties of polymeric materials such as low temperature and pressure resistance.

Martinopoulos et al. (2010) determined the efficiency[1] of a polymeric collector (absorber area: 1.25 m^2) both experimentally and with a numerical flow simulation (CFD). A 10 mm thick honeycomb plate made of polycarbonate (PC) was the basis for the absorber. Two acrylic, rectangular, 8 mm wide pipes were used as header channels and connected with the absorber. The same 10 mm thick honeycomb PC plate was used for the backside insulation of the collector. To minimize the thermal losses to ambient, a special nanogel was used, enabling the overall heat transfer coefficient of the insulation to be lowered to 0.018 W $m^{-1}K^{-1}$. The authors used a 3 mm thick transparent PC plate as a front cover. A circumferential, 30 mm thick insulation made of extruded

[1] $\eta = \frac{\dot{Q}_{out}}{\dot{Q}_{in}} = \frac{\dot{m} \cdot c_p \cdot (T_{out} - T_{in})}{A \cdot I}$

doi:10.18086/swc.2017.07.01 Available at http://proceedings.ises.org

polyurethane (PUR) minimized the thermal losses towards ambient. Black colored water was used as the heat transfer fluid (HTF). The efficiency of this collector is shown in Fig. 4 **(**blue curve**)**. The authors point out the importance of a well-designed inlet of the absorber. In case of a poorly designed inlet, the HTF may not be equally distributed across the whole area of the absorber. As a result, the remaining air inside the collector will deteriorate the heat transfer from the absorber to the HTF, resulting in a decrease of the collector efficiency.

Based on the work of Martinopoulos et al. (2010), Missirlis et al. (2014) investigated different manifold configurations in order to determine the optimal position of both the in- and outlet. The highest efficiency could be obtained with a setup where both the in- and outlet pipe are aligned with the orientation of the honeycombed absorber sheet. The efficiency curve of this setup is shown in Fig. 4 (red curve).

Sandnes and Rekstad (2002) carried out experimental investigations on a combined photovoltaic and solar-thermal (PV/T) collector (absorber area = 0.48 m^2). The twin-wall shaped polymeric absorber made from polyphenylene ether (PPE) was filled with a ceramic granulate to increase the heat transfer between absorber and the HTF. A 4 mm thick sheet of glass was used ($\tau \approx 0.9$) as a front cover. The HTF was pumped to the upper manifold of the collector, from where it trickled down through the granulate-filled absorber due to the gravity. The efficiency curve of this collector is shown in Fig. 4 (grey curve).

Ariyawiriyanan et al. (2013) tested five different (unglazed) polymeric collectors to determine both the influence of the material and the aperture area on the thermal efficiency. Three absorbers had the same aperture area (1.30 m^2) but were made from different polymeric materials. The remaining two absorbers were made from polyvinyl chloride carbon black (PVC-CB) and had an aperture area of 1.8 and 2.0 m^2, respectively. According to the results from an outdoor-measurement, the authors suggest to choose an absorber material with a high thermal conductivity. In addition, a correlation between increasing aperture area and collector efficiency was found. The efficiency of the 2.0 m^2 absorber made from PVC-CB is shown in Fig. 4 (yellow curve).

Chen et al. (2015) also adopted the principle of extruded twin-wall sheets as the basis for a polymeric absorber. The absorber (aperture area: 1.16 m^2) consisted of an 8 mm thick twin-wall sheet. An additional 4 mm thick twin-wall sheet was used as a front cover, a 20 mm thick foam material was used as the backside insulation. Both the absorber and the glazing twin-wall sheet were made of transparent PC. In their study, the authors mention one general disadvantage of connecting extruded twin-wall sheets with header channels made from different materials: Due to different coefficients of thermal expansion, leakage may occur at higher operating temperatures. To absorb the incoming irradiation, a black coating was applied to the transparent absorber. The authors were able to demonstrate that the position of the coating (either top or bottom surface of the twin-wall plate) hardly affects the thermal efficiency. The efficiency of the absorber is shown in Fig. 4 (black curve).

2.2 Market available polymeric collectors

The approaches described above resulted in some market available polymeric solar-thermal flat-plate collectors. A honeycomb structure is used as an absorber (gross collector area: 0.95 m^2) in case of the *One Sun One World* solar collector. The structure is surrounded by a frame made from multiple polymeric parts which are welded together (Buchinger and Barek, 2015). In between the polymeric absorber and the transparent, polymeric glazing, a honeycomb matrix is inserted to mechanically support the glazing and to prevent large deflections of the glazing (e.g. in case of snow load). In addition to the support function of the matrix, the convective losses can be reduced by using such a honeycomb matrix (Hollands, 1965). An identical honeycomb matrix is used between the backside of the absorber and the backside cover of the collector. In this context, the encapsulated air inside the single cells of the honeycomb matrix acts like an insulator to minimize the backside losses to ambient. The efficiency curve of the *One Sun One World* collector was determined according to EN ISO 9806:2013 (One Sun One World GmbH, 2015) and is shown in Fig. 5 (blue curve).

The collector *Eco Flare 3M*, patented by the Israeli manufacturer *Magen Eco Energy*, is composed of a large number of individual plastic pipes (Sessler et al., 2011). The individual risers connect the two manifolds of rectangular cross-section. The efficiency curve of the collector (gross collector area: 2.25 m^2) was determined according to DIN EN 12975-2:2006 (Magen eco energy, 2011) and is shown in Fig. 5 (red curve).

The Norwegian company *Aventa AS* utilizes an extruded twin-wall plate of polyphenylene sulfide (PPS) as a basis for an polymeric absorber (Rekstad, 2012). A special feature of this collector (gross collector area:

2.65 m^2) is the arrangement of the two manifolds. Both of them are located below the absorber to ensure a proper self-draining when integrating the collector into a drain back system (DBS). The front-side glazing is made of a PC plate. The glazing, absorber and the backside insulation (mineral wool) are held together by a frame made of aluminum profiles. The efficiency curve of the collector was determined according to DIN EN 12975-2:2006 (Aventa AS, 2014) and is shown in Fig. 5 (grey curve).

In conclusion, the application of polymeric materials in solar-thermal collectors has been investigated in depth in scientific literature. Some of these concepts have been adopted by manufacturers of polymeric collectors and further developed. It is worth mentioning that all concepts presented in scientific literature as well as all market available polymeric collectors utilize pre-fabricated, semi-finished products (e.g. twin-wall-plates, pipes, etc.) as the basis for a polymeric absorber. The main advantages of this approach relates to the fact that these semi-finished products are widely used across several different industries (e.g. automotive or aerospace technology), yielding relatively low component costs. However, this approach also lead to some disadvantages. Firstly, the assembly of different parts yields higher production costs, either due to higher personnel or machine costs. Secondly, leakage problems may occur in case of insufficient sealing (e.g. welding) between the connection of single components or due to different coefficients of thermal expansion. Due to the lower raw material costs of polymeric materials compared to metals, the replacement of metallic materials (e.g. copper, aluminum, etc.) yields a cost saving potential. However, the manufacturing of polymeric absorbers and collectors should be linked with the materials applied to unleash the full potential of polymers. Some of the disadvantages described above can be compensated by utilizing a modern manufacturing technique for polymeric materials such as the Twin-Sheet-Thermoforming (TST) process. The manufacturing of a polymeric absorber based on this approach is described subsequently.

3. Setup of a polymeric absorber by means of the Twin-Sheet-Thermoforming manufacturing process

Deviating from common approaches described in scientific publications, a highly automated manufacturing process was chosen for mass production of polymeric absorbers. By comparing the respective advantages and disadvantages of several different polymeric manufacturing processes, the Twin-Sheet-Thermoforming (TST) manufacturing process was found to be the most suitable approach for manufacturing polymeric solar-thermal absorbers. The major advantages of the TST process compared to other processes such as injection molding, extrusion, blow molding or single-sheet-thermoforming are the low unit costs and the high reliability of the process (Ehrenwirth et al., 2016). The necessary process steps for manufacturing a polymeric absorber with the TST process are shown in Fig. 1. The major requirement for the TST is a molding tool that contains two halves. Starting from an initial position with both mold halves open (c.f. Fig. 1-a), two polymeric plates (e.g. made of PP, PC, etc.) are inserted and clamped by a mount (c.f. Fig. 1-b). In the next step, both the upper and lower plate are heated up by means of radiators (c.f. Fig. 1-c). The necessary temperature depends on the type of material used and the level of local deformation. Therefore, the temperature across the plate may vary. Prior to further processing, the radiators have to be removed out of the processing zone (c.f. Fig. 1-d). Subsequently, a vacuum is applied to both polymeric sheets (c.f. Fig. 1-e). The combination of the vacuum applied and the viscous material yields the plates to adopt the form of the mold halves (c.f. Fig. 1-f). Afterwards, the mold halves are closed, sealing together the upper and lower part of the absorber (c.f. Fig. 1-g). As soon as the final shape cooled down, the mold halves re-open (c.f. Fig. 1-h). Cutting away manufacturing remnants leads to the final polymeric absorber (c.f. Fig. 1-i). Applying both appropriate glazing to the front side and an insulation to the backside of the absorber finalizes the process (c.f. Fig. 1-j).

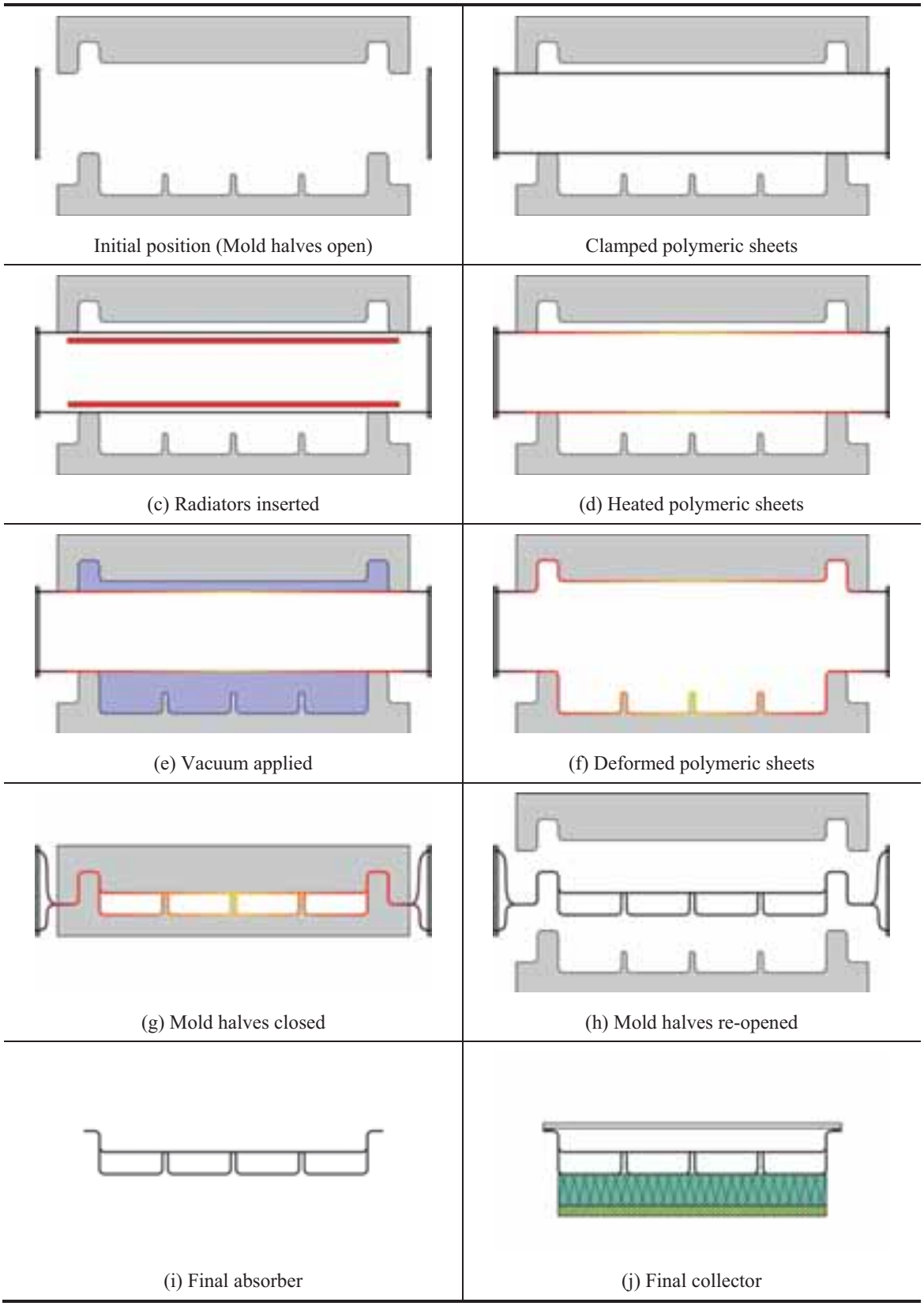

Fig. 1: Necessary process steps for manufacturing a polymeric absorber.

Based on the procedure described above, a prototype was set-up. A 4 mm thick front cover made of glass was glued onto the absorber (c.f. Fig. 2, grey part). A 30 mm thick insulation made from PUR minimizes the heat losses towards the backside (c.f. Fig. 2, crosshatched part). Special profiles made from aluminum were utilized to build a frame, encapsulating the glazing, absorber and the insulation (c.f. Fig. 2, dark blue parts). For both the back and side walls, 4 mm thick transparent walls made from poly(methyl methacrylate) (PMMA) were used. Temperature sensors were applied on the backside of the absorber ($T_{Absorber}$), the insulation ($T_{Insulation}$), the back wall ($T_{Backside}$), the outer side of the glazing ($T_{Glazing}$) as well as the side wall (T_{Side}) to monitor the temperature of these components during testing. Thermocouples (type T) were used, positioned in the center of each component and fixed with adhesive aluminum tape.

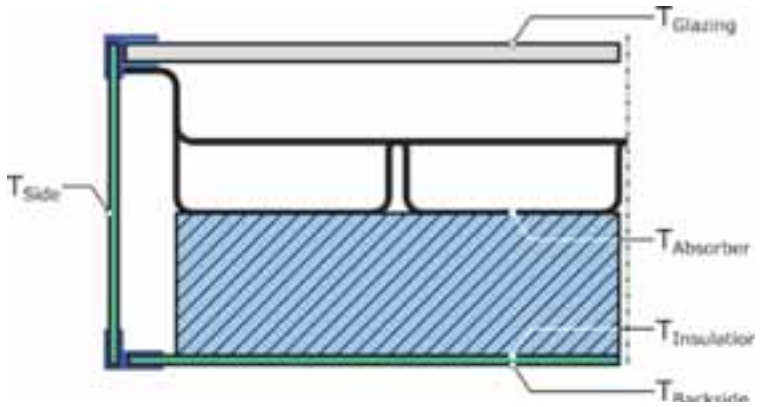

Fig. 2: Cross sectional view of the collector prototype.

The properties of this prototype are summarized in Tab. 1 (last column) and compared with information available from other studies. Comparing the different parts such as absorber, insulation and glazing reveals that the mounted prototype is similar to approaches described in recent studies.

Tab. 1: Properties of polymeric collectors described in previously cited studies vs. tested prototype (last column). Empty cells indicate that no information is available regarding the specific property. Crossed-out cells (—) indicate that the corresponding collector does not include the specific property.

		Martinopoulos et al. (2010), Missirlis et al. (2014)	Sandnes and Rekstad (2002)	Ariyawiriyanan et al. (2013)	Chen et al. (2015)	Tested prototype investigated in this study
Absorber	Area	1.30 m^2	1.30 - 2.00 m^2	0.50 m^2	1.20 m^2	1.32 m^2
	Thickness	10 mm			8 mm	8 mm
	Material	PC	PPO	PVC-B, PB, PP-R, PVC-CB	PC	ABS
	Type	Honeycomb	Twin-wall	Twin-wall	Twin-wall	Twin-Sheet-Thermoforming
Insulation	Thickness (back)	10 mm	50 mm		20 mm	30 mm
	Material (back)	PC + nanogel	Mineral wool		Polyfoam	PUR
	Thickness (side)	30 mm	—		—	—
	Material (side)	PUR	—		—	—
Glazing	Thickness	3 mm	4 mm	—	4 mm	4 mm
	Material	PC	Glass	—	PC	Glass
	Type	Plate	Plate	—	Twin-wall	Plate

The efficiency of the tested prototype was determined according to EN ISO 9806:201 using the university`s solar simulator. Fig. 3-a shows the setup of the test rig. The HTF is pumped through the tested prototype (2) by means of a pump (1). An array of special lamps (not shown in the sketch) provides an irradiation with a spectrum similar to the sunlight towards the collector. The energy absorbed by the collector is removed w of a heat exchanger (3) to provide constant inlet temperatures. The volume flow rate is monitored with a magnetic-inductive flow sensor (4). Deviating from EN ISO 9806:201, an additional reservoir (9) was included to the system. As this reservoir is open to the atmosphere, the operating pressure inside the system is a function of the difference in height between collector and reservoir (Pascal`s principle). This setup was chosen to prevent damages to the prototype in case of over-pressure. During the test, the inlet (5) and the outlet temperature (6) as well as the ambient temperature (7) were monitored with temperature sensors. Furthermore, the in-plane irradiation is recorded by means of a pyranometer (8). A photo of the prototype during testing can be seen in Figure 5-b.

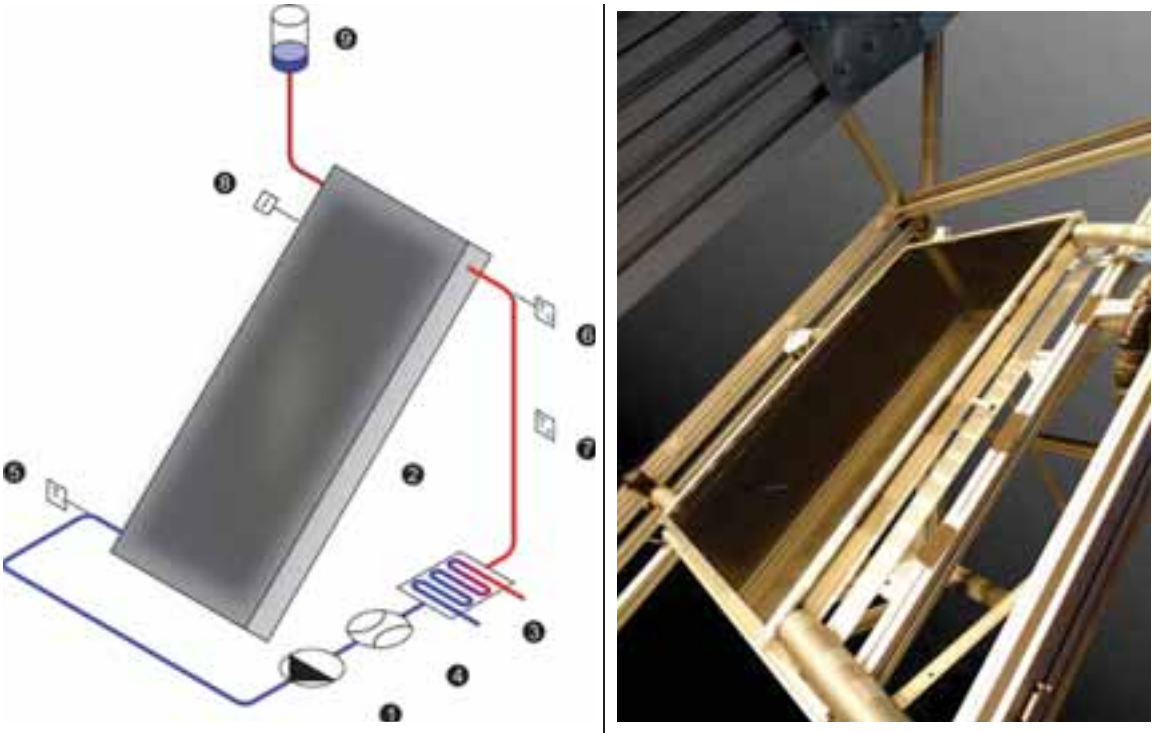

(a) Scheme of the collector test rig (b) Photo of the tested prototype

Fig. 3: Determination of the solar-thermal efficiency according to EN ISO 9806:2013.

4. Results and discussion

The efficiency curve of the tested prototype in relation to data available from literature is presented in Fig. 4 (green curve). The measured efficiency curve is well comparable with the results reported by Martinopoulos et al. (2010). Following the advices given by Missirlis et al. (2014), the efficiency of the prototypes could be improved by means of an arrangement of the in- and outlet pipe into and out of the manifolds. A comparison of the tested prototype with market available collectors reveals the highest solar-thermal efficiency of all polymeric collectors analyzed for temperatures $(T_{mean} - T_{amb}) / I < 0.07\ m^2KW^{-1}$ (c.f. Fig. 5). During measurement of the solar-thermal efficiency of the prototype, the temperatures of each component of the collector were recorded. Tab. 2 (first four rows) shows the steady-state temperatures for different inlet temperatures. Except for the lowest inlet temperature (24.2 °C), the absorber always reaches the highest temperature measured, followed by the glazing and the insulation. Between the insulation and the backside wall, only a small difference in temperature is observed (0.2 °C – 1.4 °C). The temperatures of the side walls are ranging at similar levels as the backside wall.

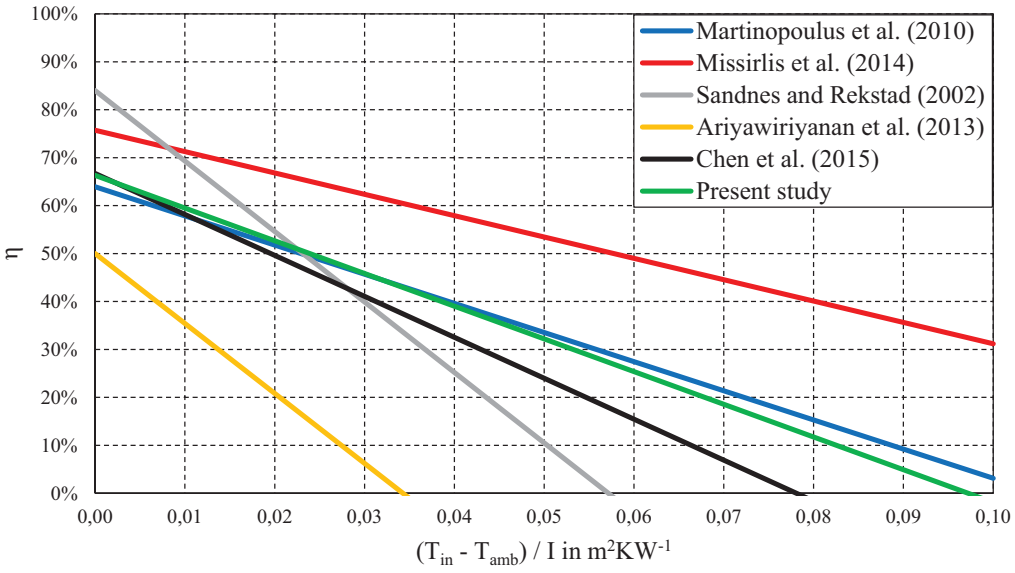

Fig. 4: Efficiency curve of the tested prototype (green curve) contrasted with data available from literature.

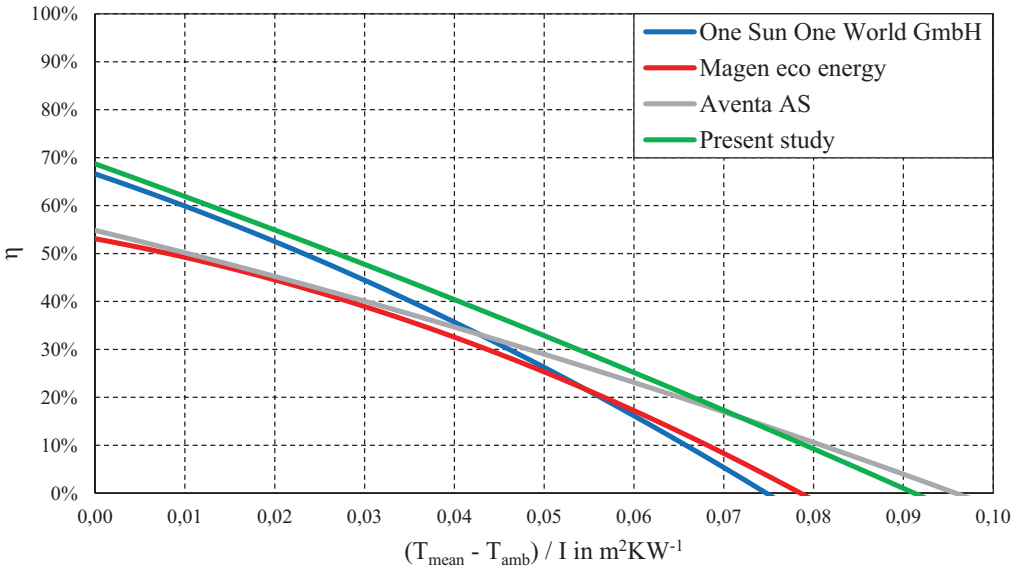

Fig. 5: Efficiency curve of the tested prototype (green curve) compared with market available polymeric collectors (data source: One Sun One World GmbH (2015), Magen eco energy (2011) and Aventa AS (2014)). The efficiency of *One Sun One World* solar collector was determined according to EN ISO 9806:2013, the efficiency of the collectors from *Magen Eco Energy* and *Aventa AS* according to DIN EN 12975-2:2006. For a comparability of the efficiency determined according to different standards, the ratios η_0, a_1 and a_2 were multiplied by the ratio of the aperture surface area to the gross collector area in the case of *Magen Eco Energy* and *Aventa AS*.

In addition to the case of HTF flowing through the absorber, the component temperatures were evaluated in case of dry stagnation for two different values of irradiation (c.f. Tab. 2, last two rows). Special attention is attributed to the maximum absorber temperature (93.6 °C), as this temperature is of crucial importance for the polymeric material used. In case of ABS, the maximum permissible temperature for permanent operation ranges between 95 °C and 105 °C (Bonten, 2014, p. 199).

Tab. 2: Measured component temperatures for different inlet temperatures in case of a filled absorber and for different values of irradiation in case of an empty absorber (dry stagnation).

T_{Inlet} in °C	T_{Outlet} in °C	$T_{Ambient}$ in °C	$T_{Glazing}$ in °C	$T_{Absorber}$ in °C	$T_{Insulation}$ in °C	$T_{Wall\ (back)}$ in °C	$T_{Wall\ (left)}$ in °C	$T_{Wall\ (right)}$ in °C	I in W/m²
24.2	30.7	26.5	35.5	30.1	28.5	28.1	29.6	27.5	852.5
35.9	41.5	26.4	38.3	40.4	28.9	28.1	29.9	28.0	853.4
50.5	55.1	27.1	43.2	53.7	31.5	30.3	31.6	29.8	852.1
65.1	68.4	26.6	47.3	67.3	32.2	30.8	32.0	29.9	851.9
Dry stagnation		26.6	64.3	93.6	33.7	31.9	32.9	31.3	879.3
Dry stagnation		27.5	54.7	88.7	33.5	31.6	31.6	29.9	635.0

5. Summary and Outlook

Within this paper, a polymeric solar-thermal absorber made of ABS was produced by means of the Twin-Sheet-Thermoforming manufacturing process. Based on a literature research, characteristic properties of both polymeric absorbers and other main components of polymeric solar-thermal collectors were identified and taken into account when setting up an appropriate prototype. The evaluation of the solar-thermal efficiency according to EN ISO 9806:2013 indicates competitive results compared to different concepts of polymeric collectors both described in scientific literature and market available collectors. Against this background, the production and manufacturing costs of polymeric solar-thermal collectors become increasingly important, as these costs directly affect the Levelized Cost of Heat (LCOH) of a solar-thermal system equipped with such collectors. As a technology capable of mass-production, the utilization of the highly automated TST for manufacturing polymeric solar-thermal collectors enables a significant cost-reduction. However, due to material limitations (such as low pressure and temperature resistance), polymeric solar-thermal collectors must always be considered as part of an entire solar-thermal system. Extending the application of polymeric materials to other parts of a solar-thermal system (e.g. pipes, heat storage, etc.) can therefore lead to further cost reductions. The determination of the LCOH of such a polymeric solar-thermal system is therefore subject of further research.

6. References

Ariyawiriyanan, W., Meekaew, T., Yamphang, M., Tuenpusa, P., Boonwan, J., Euaphantasate, N., Muangchareon, P., Chungpaibulpatana, S., 2013. Thermal Efficiency of Solar Collector Made from Thermoplastics. Energy Procedia 34, 500–505. 10.1016/j.egypro.2013.06.778.

Aventa AS, 2014. Summary of EN 12975 Test Results, annex to Solar Keymark Certificate: Licence Number: 011-7S2409F. Aventa AS.

Bonten, C., 2014. Kunststofftechnik: Einführung und Grundlagen, 1st ed. Carl Hanser Fachbuchverlag, s.l., 497 pp.

Buchinger, R., Barek, M., 2015. Thermischer Solarkollektor, 32 pp.

Chen, G., Doroshenko, A., Koltun, P., Shestopalov, K., 2015. Comparative field experimental investigations of different flat-plate solar collectors. Solar Energy 115, 577–588. 10.1016/j.solener.2015.03.021.

Deutsches Institut für Normung e.V., 2006. Thermal solar systems and components – Solar collectors – Part 2: Test methods; German version EN 12975-2:2006, 2006th ed., 135 pp.

Deutsches Institut für Normung e.V., 2013. Solar energy - Solar-thermal collectors - Test methods (ISO 9806:2013); German version EN ISO 9806:2013, 2013rd ed.

Ehrenwirth, M., Klärner, M., Reiter, C., Trinkl, C., Zörner, W., Hoellenriegel, W., 2016. Untersuchungen zur Fertigungstechnik und Kollektorkonstruktion für Vollkunststoff-Kollektoren: Abschlussbericht, 127 pp. https://www.tib.eu/de/suchen/id/TIBKAT%3A887789994/Untersuchungen-zur-Fertigungstechnik-und-Kollektorkonstruktion/?tx_tibsearch_search%5Bsearchspace%5D=tn.

Hollands, K., 1965. Honeycomb devices in flat-plate solar collectors. Solar Energy 9 (3), 159–164. 10.1016/0038-092X(65)90089-7.

Ivancic, A., Mugnier, D., Styri-Hipp, G., Weiss, W., 2014. Solar Heating and Cooling Technology Roadmap. Renewable Heating & Cooling. http://www.rhc-

platform.org/fileadmin/user_upload/Structure/Solar_Thermal/Download/Solar_Thermal_Roadmap.pdf.
Magen eco energy, 2011. Summary of EN 12975 Test Results, annex to Solar Keymark Certificate: Licence Number: 011-7S1599F. Magen eco energy.
Martinopoulos, G., Missirlis, D., Tsilingiridis, G., Yakinthos, K., Kyriakis, N., 2010. CFD modeling of a polymer solar collector. Renewable Energy 35 (7), 1499–1508. 10.1016/j.renene.2010.01.004.
Missirlis, D., Martinopoulos, G., Tsilingiridis, G., Yakinthos, K., Kyriakis, N., 2014. Investigation of the heat transfer behaviour of a polymer solar collector for different manifold configurations. Renewable Energy 68, 715–723. 10.1016/j.renene.2014.03.008.
One Sun One World GmbH, 2015. Summary of EN ISO 9806 Test Results, annex to Solar Keymark Certificate: Licence Number: 011-7S2586F. One Sun One World GmbH.
Rekstad, J., 2012. Arrangement for a solar collector plate, solar collector plate, solar collector module, and solar collector system.
Sandnes, B., Rekstad, J., 2002. A photovoltaic/thermal (PV/T) collector with a polymer absorber plate. Experimental study and analytical model. Solar Energy 72 (1), 63–73. 10.1016/S0038-092X(01)00091-3.
Sessler, M., Waisman, A., Plaschkes, M., 2011. Solar Collector, 28 pp.

Simulation Study on the Optimization of Solar Water Heating System in Passive Solar House - Case Study

Tao Li, Yanfeng Liu, Dengjia Wang, Yong Zhou, Juan Li

Xi'an University of Architecture and Technology, Xi'an (China)

Abstract

The design of the active solar heating system is different in the passive solar room due to its passive additional heat. The passive additional heat affected the active solar heating system thermal performance. So the optimization of the system is necessary. In this paper, a solar heating building with active and passive combination as the object of study. The TRNSYS simulation model of solar heating system was established. The accuracy of the simulation model was verified by field test of indoor thermal environment for three consecutive days in the heating season. Under the condition of typical meteorological data, the indoor thermal environment of the whole heating season was simulated and compared under four different conditions. The results show that when the active and passive solar heating technology coexists, the indoor air temperature has been significantly improved. The design of the active system does not take into account the influence of the passive solar room. The design parameters and operating parameters of the system were analyzed by simulation in this paper. The research can provide the basis for the optimization of the active solar heating system in the passive solar room, which is beneficial to the popularization and application of solar heating technology.

Keywords: Optimization research, SWHS, TRNSYS, Passive solar house

1. Introduction

Almost all of China's heating areas are solar energy resources rich areas, with solar heating conditions. Therefore, solar heating should be the village buildings heating and energy conservation priority development direction. Active solar hot water heating technology has been correspondingly mature, many areas have formed corresponding demonstration buildings (Wang et al., 2014; Yu et al., 2014; Zheng and Han, 2013). The corresponding technical specifications and evaluation criteria have been formed (GB 50495-2009; GB/T 50604-2010; Zheng et al., 2012), to provide the basis for engineering application and construction. In addition, many studies on solar hot water heating systems at domestic and abroad, mainly in the system components optimization, operation control analysis and system evaluation research (Shukla et al., 2013; Wang et al., 2015). The research on system component optimization mainly included thermal collectors, water tanks and heat exchangers.

Although these studies provide a reference for the design and application of solar hot water heating systems, these studies are less concerned with passive solar construction. Due to the larger additional heat of the passive solar room, the heating needs of the building had significant difference between the day and night, and the heat storage capacity of the active system had a great influence (Liu and Wang, 2016). At the beginning of the design, the calculation method of the average heat consumption was used to determine the design parameters of the active solar heating system (GB 50495-2009). It shows that active solar heating system design in the passive solar building is not reasonable.

In order to obtain optimization design parameters of active solar heating systems in the passive solar rooms. The TRNSYS system simulation model was established in this paper. The influence of the design parameters and operating parameters of the typical meteorological year on the solar energy assurance rate and indoor thermal environment of the whole heating season were compared and analyzed. For the passive solar rooms' active solar heating systems to provided the basis for optimization. It was conducive to the promotion and

doi:10.18086/swc.2017.07.02 Available at http://proceedings.ises.org

application of solar heating.

2. The demonstration project

2.1. The demonstration project of solar heating system with passive solar house

The study object consists of two types of passive solar rooms, included thermal storage walls and additional sun-space. The photo of the exterior feature of the demonstration project was shown in Fig. 1. The external envelope of the building is a brick wall with 240mm thick. A 50mm thick XPS thermal insulation layer on the South wall, and 80mm thick XPS thermal insulation layer on other walls. The roof consists of 160mm thick Reinforced concrete and a 100mm thick XPS thermal insulation layer. The ground consists of a 150 mm thick Reinforced concrete and a 60 mm thick XPS thermal insulation layer. All of the windows adopt plastic steel material Insulating glass, on both sides containing 16mm thick air layer and 4mm thick glass. Southward, Northward and other directions to the windows with the height of 1800mm, 1500mm and 900mm respectively. The building plane is shown in Fig. 2. The basic parameters of the passive solar house are shown in Table 1.

The active solar heating system is designed for heating the demonstration building. Included 7 flat plate heaters modules with a total area of 14 m^2, a storage tank of 200 L volume, a thermal collector circulating water pump, a heating circulating water pump, water segregator and collector, controller and floor heating end etc. Radiant floor heating using DN15 coil, spacing 300mm.

Fig. 1: Photo of the exterior feature of the demonstration project

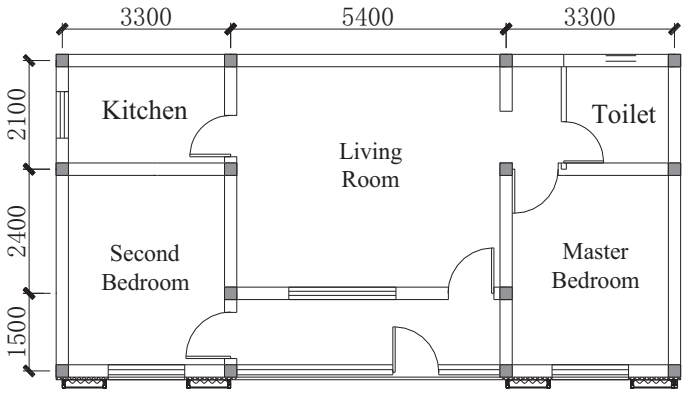

Fig. 2: Plane layout and size of the demonstration project (unit: mm)

Tab. 1: The components of the passive solar house

Types	Component	Descriptions
Trombe wall	Air vent	Size: 200mm×200mm, locate upper and lower three and two respectively
	Glazing	4mm thick simple glass
	Coating	10mm thick red corrugated sheet iron
	Air layers	100 mm thick

Attached sunspace	Sunspace	There are windows with a size of 1800mm×2100mm on the wall
	Glazing	The attached sun-space covered with 5mm wire glass

3. TRNSYS modeling and validation

3.1 Thermal performance simulation model

Used TRNSYS17.1 (TRNSYS 17.1) to build the simulation model of the combined active and passive solar heating system, as shown in Fig. 3. The building model in the system model was built in Google SketchUp according to Section 2.1.1. And imported it in the TRNBuild to set parameters, further as an external file for Type 56. There are two house connected forms in the actual building. The demonstration building has the same house type, so one house of the building was chosen to build model. Assume that the walls of the two rooms are adiabatic. Building adopted floor radiant heating. Living room, master bedroom and second bedroom belonged active heating room, other rooms were non-heating. The heating temperature of the heating room was set at 18 °C. The main TRNSYS components and parameters adopted were explained in Table 2.

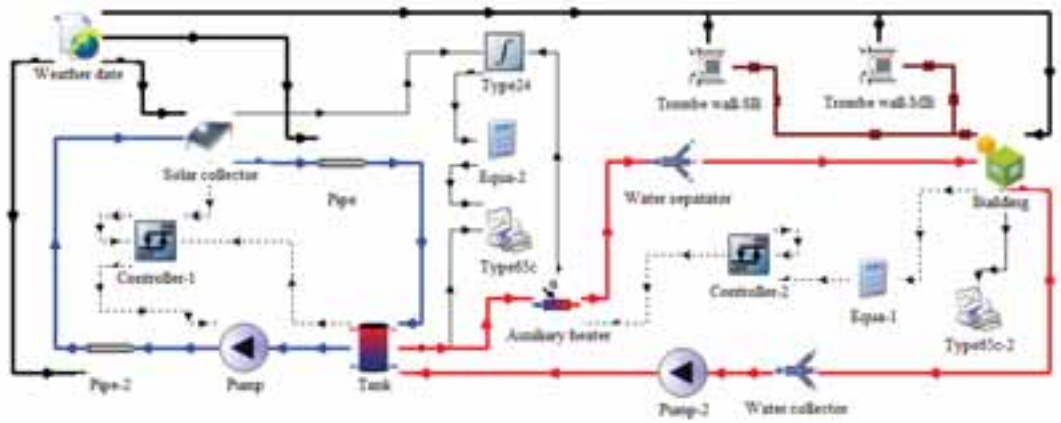

Fig. 3: TRNSYS modeling

Tab. 2: The main TRNSYS components and parameters

Name	Component	Main parameters	Descriptions
Weather date	Type 15-2	Number of surfaces: 2; slope of surface-1: 30°; slope of surface-2: 90°.	The external file contains the TMY-2 weather date of Gangcha. Used for the optimization analysis.
Weather date in test conditions	Type 99	The measured meteorological conditions during the test were inputted.	Used for the model validation.
Building	Type 56	The room air exchange rate: 0.5 h^{-1}; the active layer of 3 rooms were added.	The building model was built in Google Sketch Up, and imported to TRNBuild for setting the parameters. For the thermophysical properties please see Table 1.
Tank	Type534	Tank volume: 0.2m^3, tank height: 0.9m, number of tank nodes: 2, outer tube diameter: 0.025m, length of coiled tubes: 5.7m, HX cross sectional area: 0.45m^2, coil diameter: 0.3m.	There has a heat exchanger in the tank.
Controller	Type73	Collector area: 14m^2, collector slope: 30°.	The thermal performance parameters obtained from the manufacture.
Auxiliary heater	Type 6	Maximum heating rate: 10800 kJ h^{-1}, efficiency of auxiliary heater: 0.95.	Used for supplying the auxiliary heater

		Base case: set point outlet temperature: 40 °C.	
Trombe wall	Type 36b	Wall height: 2.9m, wall width: 1.5m, wall thickness: 0.33m, vent outlet area: 0.2m^2.	Used for calculating the energy of trombe wall flow to MB and SB.

3.2 Tests and model validation

A demonstration project of solar heating in Northwest China is taken as the research object. One dwelling with active and passive solar heating was test under the overall heating modes operating conditions. Conducted a three-day continuous test on April 25 - 27, 2016. Test contents had outdoor weather conditions, the indoor temperature of various function rooms of the two buildings and solar heating system operating parameters etc. The main parameters of the test included: the global solar irradiance on the inclined collector surface and the horizontal surface, ambient temperature, indoor temperature of various function rooms, the inlet and the outlet temperature of each device, flow rate of each system. Time interval of the data acquisition was 30 min. The measuring instruments and corresponding accuracies are listed in Table 3.

Tab. 3: Measuring instruments for the tests

Test instruments and type	Accuracy	Measurement parameter
Solar pyranometer (TBD-1) Recrding meter(QTS-4)	±8.789 W m^{-2} ——	Solar radiation intensity
Thermo recorder(TR-72ui)	±0.2 °C	Indoor and outdoor air temperature
Ultrasonic flowmeter(PH204)	±1.0% rdg	Flowrate of the pipes
Thermocouple thermometer(CENTER309)	±(1 °C+0.3% rdg)	Import and export temperature of main components

Meteorological conditions of weather data were tested as the input meteorological conditions for the model validation. According to the reference Denget al. (2016), the meteorological conditions were added to the input data in order to remove the initial thermal inertia of the building since the begins in the heating season in this area. Comparion of heating room master bedroom indoor air temperature test data and simulation data, as shown in Fig. 4. It can be seen that the overall correlation is good, although there is still a certain gap in temperature. It may be due to the following reasons: The opening and closing time of the ventilation holes of the heat storage wall was not set; residents and testers into and out of the room led to the actual increase in the amount of cold air penetration etc. During the test, the maximum relative error between the master bedroom test and the simulated temperature was 8.9% and the average of the relative error was 3.7%. Therefore, the simulation results show that the calculation error can be accepted, the simulated model can be trusted in the later analysis.

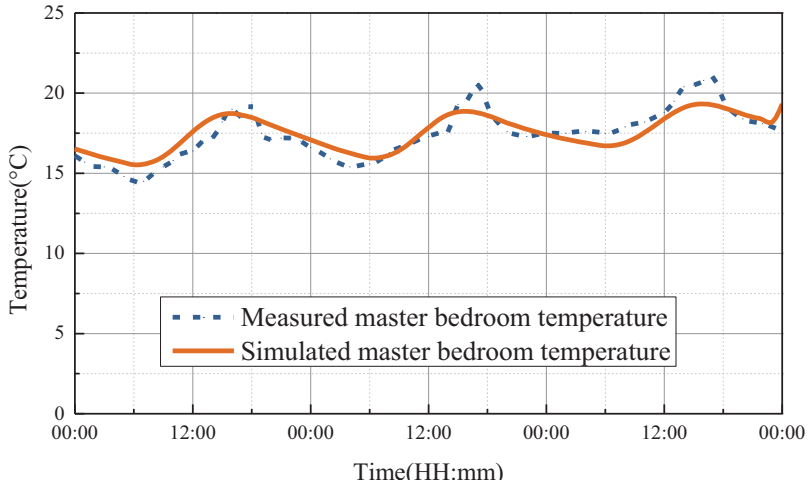

Fig. 4: Comparison of the simulated master temperature with the measured values during the test period

4. Optimizing the results and discussion

4.1. Comparison of indoor thermal environment during heating season

Simulated and compared the building with or without a passive solar room and active solar heating system, the master bedroom air temperature comparison shown in Fig. 5. It can be seen that the difference among the four types of indoor air temperature at the beginning and the end of the heating season was smaller. At the beginning and end of the heating season, the outdoor temperature was higher and the solar radiation intensity is larger, the heat load of the building was smaller, and the passive solar room had a higher additional heat. The passive additional heat can meet the heat required for the building basically. During the middle of the heating season, the indoor air temperature of the active system was significantly higher than that without the active system, the average temperature difference between the two is 14 °C or more. Because in the middle of the heating season, the outdoor temperature was lower, the building heat load was larger, the passive additional heat can not meet the heat supply of the building needs. The active solar heating system can provide a higher heat supply to meet the indoor temperature requirements. In addition, throughout the heating season, the active and passive combination of solar heating had the higher indoor temperature than other types, the average temperature can reach 19.8 °C. So the active and passive combination of solar heating technology is the most effective way to enhance the indoor thermal environment.

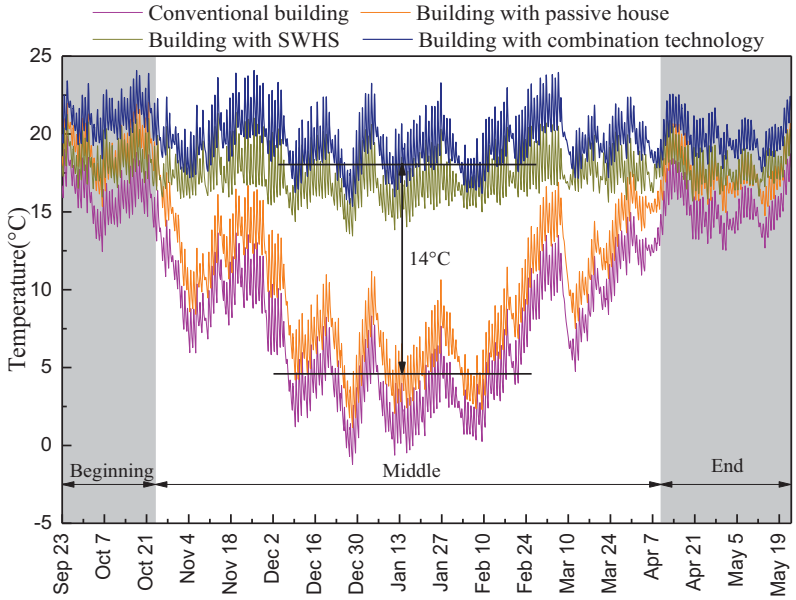

Fig. 5: Comparisonof air temperature in master bedroom

4.2. System design parameters optimization and comparison

(1) System capacity

In the building with or without passive components under different system capacity conditions (Solar collector area and storage tank volume). Compared the solar guarantee rate and indoor air temperature, as shown in Figure 6. It can be observed that the active and passive combination technoledge had more higher solar energy assurance rate and indoor temperature than the active solar heating significantly. Passive solar components for the building to provide a certain amount of heat, used to enhance the indoor temperature, and further reduced the amount of auxiliary heat, thereby enhancing the solar guarantee rate. In addition, in the active and passive combination heating technology, the solar energy guarantee rate increased with the system capacity increasing, the growth of initial stage was larger. When the system capacity reaches 49-700 (m^2-L), solar guarantee rate and master bedroom temperature increase gradually slow with the increasing in system capacity. At this point, the corresponding solar guarantee rate of 48.59%, master bedroom air average temperature of 20.16 °C. Therefore, a reasonable system capacity design is not only conducive to enhance the solar energy assurance rate and indoor thermal environment, but also to avoid blindly increase the system capacity and thus reduce the initial investment of system.

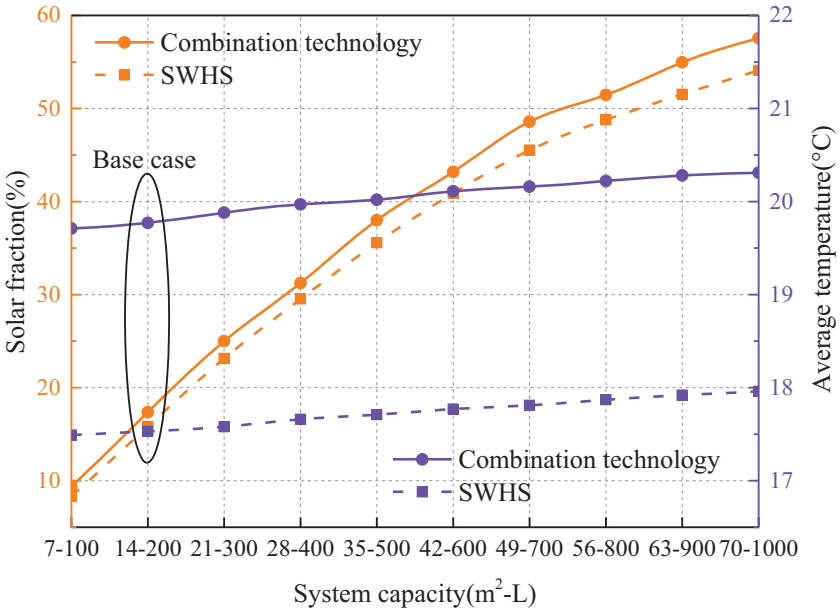

Fig. 6: Comparison of solar fraction and averagetemperature with the change of system capacity

(2) Tank volume

Under the condition of the building with or without passive components when the storage tanks had different storage capacities. The solar energy assurance rate and indoor air temperature had compared. Shown in Fig. 7. Similar to the system capacity change, the active and passive combination technolege can made higher solar energy assurance rate and indoor air temperature than only the active system. The average temperature of the indoor air increased slowly as the tank volume increaseing. The outlet temperature of the auxiliary heater was set to a constant value, affected the heating system inlet temperature directly, so the indoor air average temperature change was relatively small. The initial stage of changes of water tank volume , solar heating guarantee rate increased faster; with the further increased in the volume of the tank, solar heating guarantee rate growth rate gradually slow. It can be observed when the tank volume to a certain extent, although the storage capacity of the tank will become larger, but the system can gradually increase to the maximum heat storage capacity. Further increase the tank volume can not affect the stored heat amount of solar heating system. So the tank volume can be determined in a certain range. Do not have to increase the initial investment in the tank.

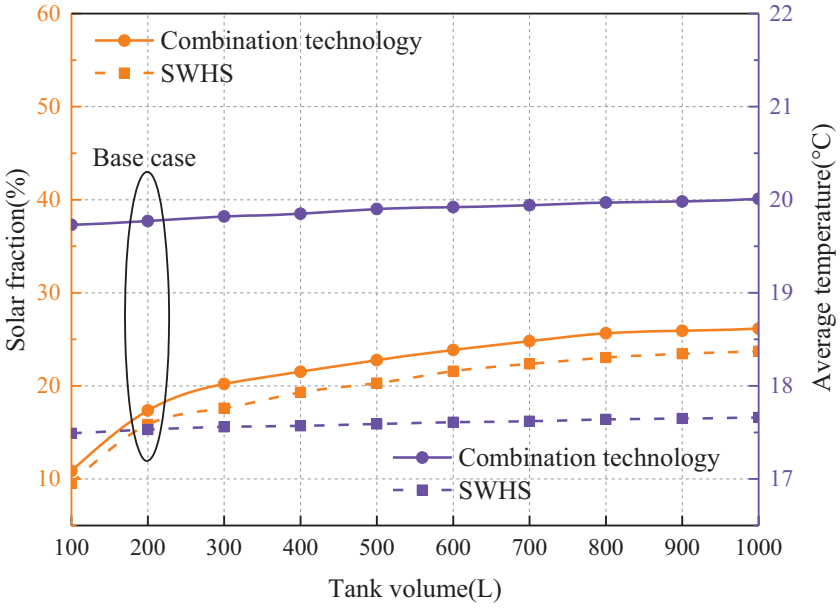

Fig. 7: Comparison of solar fraction and averagetemperature with the change of tank volume

(3) Solar collector area

Under the conditions of the building with or without passive components of different solar collector area. Comparison of the solar energy assurance rate and indoor air temperature shown in Fig. 8. When solar energy collector area changed, the average temperature of indoor air and solar heating guarantee rate changed similar to the changes of tank volume. With the increasing in solar collector area, the system heat collection increased. The heat of needed to store will increase gradually. But the tank capacity was limited, its thermal storage capacity was limited, and can not be stored excess heat of the system. Therefore, in order to meet the required heat supply in the night or rainy days of building. Need to increase the area of solar collectors also need increase the relative capacity of the system.

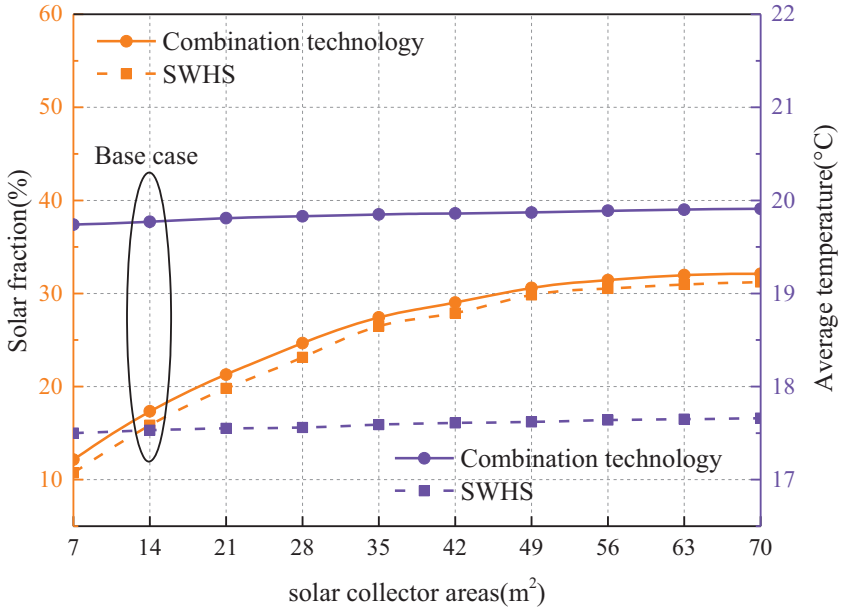

Fig. 8: Comparison of solar fraction and averagetemperature with the change of solar collector areas

Based on the comparative analysis of the above system design parameters. It can be observed that increasing the system's single component capacity can increase in the early play a certain effect. But blindly increased, will only increase the system investment costs, and not the relative gains. Should be combined with the system as a whole, while changing the design parameters of the system components to get more efficient solar heating system design. At the same time, should be combine with the system economic analysis in the follow-up study, and further evaluation of the system.

4.3. System operation parameter optimization and design

Under the conditions of the building with or without passive components of different auxiliary heaters set the outlet temperature conditions. Compared to the solar guarantee rate and the indoor air temperature, as shown in Fig. 9. The solar energy assurance rate decreased as the auxiliary heater sets the outlet temperature increasing, while the indoor average temperature increased as the auxiliary heater sets the outlet temperature increasing. When the tank outlet temperature can not reach the auxiliary heater set temperature, auxiliary heater operation will result in auxiliary heat increasing, resulting in reduce solar energy assurance rate. When the outlet temperature is set above 45 ° C, the indoor air temperature is almost unchanged. As the heating room has a set indoor temperature value, when the indoor temperature reaches the set value, the auxiliary heater to stop running. Auxiliary heat was no longer changed, solar guarantee rate remained stable.

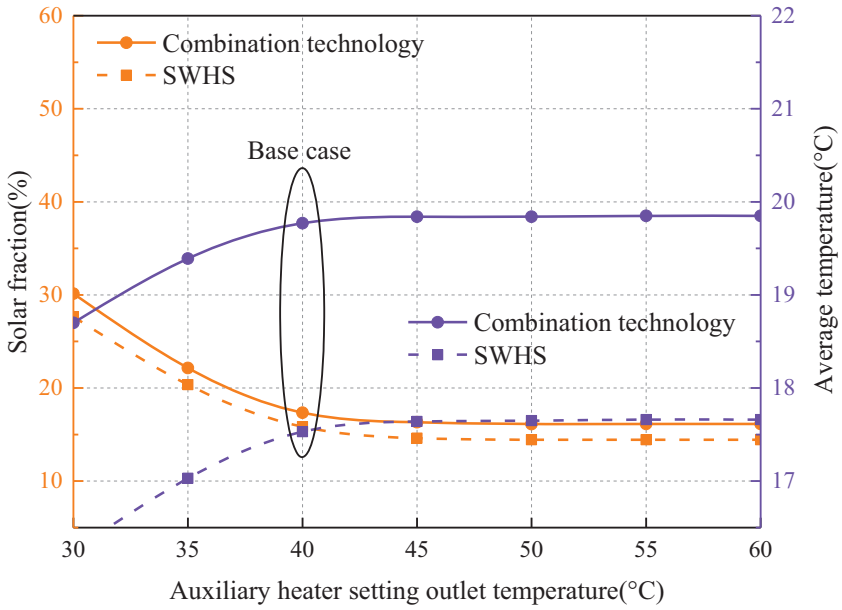

Fig. 9: Comparison of solar fraction and averagetemperature with the change of auxiliary heater setting outlet temperature

5. Conclusion

The indoor heating effects of SWHS in passive solar house were analysed, by means of dynamic simulation using TRNSYS software. The results have been well validated by comparison to the results of the demonstration short-term test in April 25-27. During the test, it was found that the maximum relative error of the master room test and simulated temperature was 8.9%, and the average relative error was 3.7%. Contrasted the four types of building indoor thermal environment, found that active solar heating technology had a significant role to enhance the indoor environment temperature.

Based on the simulation and optimization of the design parameters and operating parameters of the active SWHS in the passive solar building, it is found that: When the area of the solar collector and the size of the thermal storage tank are increasing in proportion, the growth rate of the indoor air temperature and the solar guarantee rate is gradually reduced. Only increased the capacity of the storage tank and solar collector area, can not enhanced the indoor thermal environment and increased the solar guarantee rate significantly. Reasonable outlet temperature settings of auxiliary heater had a greater impact on system performance. These findings can provide a basis for the application of active solar heating systems in passive solar rooms.

6. Acknowledgements

We wish to thank the national key research projects (No.2016YFC0700400) and the National Natural Science Foundation of China (Nos. 51378411, 51678468 and 51590911).

7. References

Deng, J., Tian, Z. Y., Fan, J. H., Yang, M., Furbo, S., Wang, Z. F., 2016. Simulation and optimization study on a solar space heating system combined with a low temperature ASHP for single family rural residential houses in Beijing. Energy Build. 126, 2-13.

GB 50495-2009, China National Standard, Technical code for solar heating system. China Architecture & Building Press, Beijing.

GB/T 50604-2010, China National Standard, Evaluation standard for solar water heating system of civil buildings. China Architecture & Building Press, Beijing.

Liu, Y.F., Wang, D.J., 2016. Design principle and technology of solar heating. China Architecture &

Building Press, Beijing, pp.103-113.

Shukla, C., Sumathy, K., Erickson, P., Gong, .J. W, 2013. Recent advances in the solar water heating systems: A review. Renew. Sustain. Energy Rev. 19, 173-190.

TRNSYS, A Transient Simulation Program, Version 17.1, University of Wisconsin Solar Energy Laboratory, Madison, WI, 2012.

Wang, D.J., Liu, Y.F., Wang, Y.Y., Liu, J.P., 2014. Numerical and experimental analysis of floor heat storage and release during an intermittent in-slab floor heating process. Appl. Therm. Eng.62, 398-406.

Wang, Z.Y., Yang, W.S., Qi, F., Zhang, X. M., Zhao, X. D., 2015. Solar water heating: From theory, application, marketing and research. Renew. Sustain. Energy Rev. 41, 68-84.

Yu, Z., Ji, J., Sun, W., Wang, W., Li, G. Q., Cai, J.Y., Chen, H.F, 2014. Experiment and prediction of hybrid solar air heating system applied on a solar demonstration building. Energy Build. 78, 59-65.

Zheng, R. C, Han, A. X, 2013. The present situation and development of solar energy heating technology in China. Construction Science and Technology, 1, 12-16.

Zheng, R. C., Lu, B., Li, Z., He, T., 2012. Technical handbook for solar heating. China Architecture & Building Press, Beijing, pp. 243-269.

Education and Workforce Development

Example of an innovative initiative for education in thermal energy storage: INPATH-TES project

Gabriel Zsembinszki and Luisa F. Cabeza

GREiA Research Group, INSPIRES Research Centre, University of Lleida, Pere de Cabrera s/n, 25001 Lleida (Spain)

Abstract

Following the EC SET-Plan Education and Training Roadmap, the goal of INPATH-TES is to create a network of academia, research institutes and small and medium-sized enterprises (SMEs) to implement a joint PhD programme on Thermal Energy Storage (TES) technologies. The project consortium consists of 22 partners from academia, industry and SMEs from 14 different countries. The final result of such a network is to educate professionals on these technologies for the European research and industry institutions. Some of the main challenges identified so far consist of the development of the programme, the implementation of the programme in each country/institution, and to ensure the continuity of the programme after EU funding ends.

Keywords: Thermal energy storage, PhD programme, e-learning

1. Introduction

According to the European Commission (EC) SET-Plan Education and Training (E&T) Roadmap (JRC Coordination, 2014), there is a need for more efficient education in the area of thermal energy storage (TES). To meet the needs and fill the gaps identified by the SET-Plan E&T Roadmap, the project "Innovative Pathway for PhD research in Thermal Energy Storage" (INPATH-TES), coordinated by the University of Lleida, Spain, was launched in May 2015 (www.inpathtes.eu). The project is funded within the framework of the research and innovation programme Horizon 2020 by the EC.

The goal of INPATH-TES is to create a network of academia, research institutes and small and medium-sized enterprises (SME) to cooperate in defining and implementing a joint PhD programme on TES technologies. The final result of such a network will be the qualification of professionals for European research and industry institutions interested in hiring personnel with expertise in TES technologies. The specific objectives and outcomes of INPATH-TES project are:

- to establish a unique PhD programme in the field of TES starting year 2017,
- to develop at least 20 ECTS equivalent common training modules,
- to develop four technology oriented PhD courses,
- to establish one annual joint workshop for PhD students,
- to aim at graduating 28 PhD students per year at year 2021, and
- to exchange at least 14 PhD students per year between industry and academia.

The INPATH-TES consortium consists of 22 partners from 14 European countries, and has the presence of 14 universities, 3 research institutes, 3 industries, and 2 SMEs. Currently, they are the core of a future larger network of excellent R&D institutions, and industries for co-funding and industrial placement, sharing infrastructure capacities, and enhancing mobility of students.

doi:10.18086/swc.2017.08.01 Available at http://proceedings.ises.org

2. Approach for the PhD programme in TES and main results

The INPATH-TES work plan is divided in six work packages, being either coordination or support activities. Main coordination activities contain the development, maintaining and updating of the PhD programme in TES and the implementation of the PhD programme. Main support activities are stakeholder involvement, expansion of partnerships, framework for monitoring and evaluation of INPATH-TES as well as intellectual property rights, and regulatory issues.

A total of curriculum 14 courses are currently being developed by the consortium that can be implemented from a global perspective in ECTS awarding institutions. The courses can be grouped as follows:

- Basic common PhD courses: Research and PhD, Introduction to thermal energy storage, Thermal energy storage materials, Testing and characterisation of thermal energy storage materials, and Heat and mass transfer and sizing of energy storage devices.
- Common technology specialisation courses: Thermal energy storage applications for buildings, Demand side management concepts and energy storage, Large scale and industrial energy storage, and Energy policy and market development.
- Research management, dissemination, and communication courses ("soft skills"): Intellectual property and patenting ideas, Idea to product development, Dissemination and communication of R+D+I, Funding of research and project management, and Management and entrepreneurship.

2.1. Description of the courses

2.1.1. Research and PhD

The main objective of this course is to introduce the students to the basic aspects related to the scientific method, and provides the students with the details on the concepts of research, development and innovation (R+D+I). Specifically, the course provides an introduction to the different research methods and exposes the differences between the definition of PhD and industrial PhD. Concepts such as Responsible Research and Innovation (RRI), management of the research data, and the Intellectual Property Rights (IPR) are also dealt with in detail. The students also have the opportunity to learn how to correctly write a CV (academic and industrial one) and supporting statements.

2.1.2. Introduction to TES

The course will introduce students to thermal energy storage (TES), from thermophysical properties of materials used in TES systems to their implementation into the energy system. Thus, it will introduce the energy system and policy drivers, describing the technologies that can be used for storing energy, and focusing on fundamentals of thermal energy storage, its technologies, and its role in the energy system, while providing details on thermodynamic properties of materials. The learning philosophy of this course is to provide students enough information in order, for them, to be able to analyse a problem related to thermal energy storage and have a first idea on how to solve it by TES.

2.1.3. Thermal Energy Storage Materials

The purpose of this course is to provide an overview of thermal energy storage materials and their properties. It will also introduce a selection methodology as a tool for selecting TES materials performing the best for a certain application. Numerical models will be introduced for design and calculation of composite structures including TES materials, in order to perform an optimal selection regarding energy efficiency. Numerical models at micro/nano-scale for TES materials can provide better understanding of the heat and mass transfer phenomena on small scales. This knowledge can be applied to the design of new energy storage materials. A continuous learning philosophy is adopted in this course, with emphasis on problem solving through application of thermal engineering fundamentals - energy balances and thermodynamics. This course will be linked to other courses such as building or industrial applications.

2.1.4. Testing and characterisation of Thermal Energy Storage Materials

The course focuses on the characterization of energy storage materials and on the methods that could be used for testing them. It will provide the theoretical background and standard of characterization, describing also the

instrumentation and the parameters that have to be measured. Thermal and structural characterization technologies have been subdivided in conventional and "in house". Such technologies are the objects of the lessons of the course with the aim to offer a complete overview on: Differential Scanning Calorimetry (DSC); Thermogravimetric Analysis (TGA); T-history methodology and stability analysis for heterogeneous materials; technologies for measuring morphological, structural and specific solid properties, thermal diffusivity, thermal conductivity, thermal expansion, rheological properties, volatility and vapour pressure. Lab scale, experimental and in-situ procedures for thermal response, compatibility, flammability and mechanical testing will be given also.

2.1.5. Heat and Mass Transfer and Sizing of Energy Storage Devices

This course provides the INPATH-TES students with basic and advanced knowledge in heat transfer. It addresses such topics as multi-dimensional heat transfer, mass transfer, heat transfer with phase change, thermal design and component modelling. It is envisioned that since the PhD programme allows enrolling students with very different background, their entrance level knowledge in heat transfer may significantly vary. For this reason, the learning material includes such very basic items as fundamental heat transfer modes, thermal properties of materials, and heat transfer enhancement. On the other hand, students with an appropriate background would proceed directly to the lessons on basic numerical methods for thermal problems, analysis and modelling of heat transfer with phase change, and study of specific effects related to heat transfer in phase-change materials. Mass transfer by diffusion and convection is included as the theoretical basis for thermochemical energy storage. An advanced student will also acquire broad knowledge and practical tools in principles of thermal design, modelling and optimization of heat transfer equipment in general and sensible, latent and thermochemical energy storage devices, in particular.

2.1.6. Intellectual Property and Patenting Ideas

The purpose of this course is to provide the students enrolled in the INPATH-TES PhD programme with all fundamental aspects of Intellectual Property (IP) in general, and of patents in particular. The first part of the course is designed to provide an overview of IP and the reasons why it is considered an important economic and cultural asset in today's life and economy. Another important subject of the first part of the course is devoted to the definition of the dissemination, exploitation and communication plan. The second part of the course focuses on some basics concepts regarding patents, such as the relevant parts of the patent system and how to make use of patent information to encourage innovation and economic growth, patent classification, and the main tools available for patent information search. Besides this, the course also explains the different ways to apply for a patent, and presents some relevant case studies for a better understanding of the theoretical information presented.

2.1.7. Idea to Product Development

The objective of the course is to provide the methodology required to develop a product starting from the preliminary idea. The structure of the course starts with an introduction (with the need for innovation), then it describes the idea generation, idea screening, idea development and testing, followed by the business analysis, finishing with the technical implementation of a new idea.

2.1.8. Dissemination and Communication of R+D+I

This course aims at providing the students sufficient skills and information needed to locate and successfully apply for suitable sources of research funding, and to introduce them to the basics of project management, dissemination, exploitation and communication. Specifically, the course presents the different types of funding available and where these sources of funding can be found, how networking can help in locating funding, how to prepare and write a proposal, and how proposals are evaluated. Furthermore, the course also presents the different stages of the lifecycle of a project and explains the main skills required in managing a project. Finally, the purpose and definition of the research dissemination, exploitation and communication plan are also provided.

2.1.9. Funding of Research and Project Management

This course aims at providing the students sufficient skills and information needed to locate and successfully apply for suitable sources of research funding, and to introduce them to the basics of project management,

dissemination, exploitation and communication. Specifically, the course presents the different types of funding available and where these sources of funding can be found, how networking can help in locating funding, how to prepare and write a proposal, and how proposals are evaluated. Furthermore, the course also presents the different stages of the lifecycle of a project and explains the main skills required in managing a project. Finally, the purpose and definition of the research dissemination, exploitation and communication plan are also provided.

2.1.10. Management and Entrepreneurship

This course provides an introduction to Management and Entrepreneurship for course participants with a technical background. The topics covered in this course are prototype to market roadmap (business ideas), business planning (innovation concept), entrepreneurship (start-up company), managing firms for growth, and building soft skills in management and entrepreneurship. By the end of this course, participants will be able to generate business ideas, assess opportunities, formulate business strategies, find their first customers, procure funding for start-ups and manage firms for growth. Soft skills such as teamwork, leadership and communication for management and entrepreneurship are covered as well.

2.1.11. Thermal Energy Storage Applications for Buildings

In this course, the main building integration strategies of TES systems as passive and active solution for energy saving and indoor thermal comfort conditions are introduced and discussed. The key evaluation methodologies, e.g. experimental assessment and modelling-simulation approach, are also presented and deeply analysed. Then, the most significant research contributions are described and the uttermost promising future trends are outlined. Finally, the student is driven to select the proper TES solution with varying the main constraint of several research problems and also the district scale application is discussed, in cooperation with other two courses of the same PhD programme (Course 12 and Course 13).

2.1.12. Demand Side Management Concepts and Energy Storage

Demand side management (DSM) is based on two essential features, namely energy efficiency and of increasing importance, the role of demand side response. Energy efficiency is essential if we are to deliver zero carbon and low energy solutions for society. Changes to human behaviour and control systems are increasingly proving to be critical if energy savings, as a result of technological development, can be maximised. Often technology improvements are let down by the human involvement and hence it is important that those involved with research into the development and implementation of technologies understand demand side management. Demand side response addresses variable electricity and heat load management, whether driven by variable renewable energy or batch/cyclic demand and supplies. The course will cover the subject at macro – city level, down to buildings. It will outline legislative and incentive programmes, discuss the financial aspects and conclude with case studies of DSM.

2.1.13 Large Scale and Industrial Energy Storage

This course aims at providing the students with information about the use of thermal energy storage technologies in large-scale and industrial applications. The course begins with an introductory overview of examples of the integration of thermal energy storage in production and energy facilities, specifically in energy-intensive industries, concentrating solar power, and district heating and cooling. The students will be introduced to recent research progress in terms of innovative materials, container designs and concepts for systems integration for large-scale TES. Specific demonstration and operational, real-world projects as well as collection and analysis of in-field performance data will be discussed in detail. Different numeric simulation exercises give an introduction to the computer aided TES design and integration using realistic scenarios. The course will delve into environmental and economic aspects of large-scale TES installations, specifically introducing the use of LCA, LCC and further analyses in these studies, and will close with several real-world examples of applications in large-scale thermal energy storage. Common issues with industrial installations will be presented, including the scalability of R&D results.

2.1.14 Energy Policy and Market Development

The energy policy and market development course takes a holistic approach in looking at how thermal energy storage can solve issues identified at EU policy level. It commences by providing insights into energy policy

with particular reference to renewable energy policies, and examines this further by considering "good" and "poor" policies. Then in a heuristic fashion, it looks at the theory and real-life examples of how market development tools can be used to identify and develop new opportunities for TES in the context of energy efficiency and renewable energy technology policies. The course also examines how best to inform policy through key skills such as networking, influencing and communication, and how this can be enabled by being close to the customer and aware of predicted future market developments.

Each of these courses is composed of various topics, and each topic is then composed of different lessons. The lessons can then be “tailor-packaged” to meet the needs of each of the PhD supervisors for their PhD candidates. The developed learning material is implemented in the constructive alignment perspective in the EIT (European Institute of Innovation and Technology)/KIC InnoEnergy pedagogical methodology of student-centred learning, aligned teaching, and active learning (Biggs and Tang, 2011).

2.2. Online learning platform

An e-learning repository platform has been commissioned to host all the learning materials that will be delivered in the PhD curricula. The pedagogical methodology in student centred learning consists of careful design by the teachers of the intended learning outcomes (ILOs) assessed with the achieved learning outcomes (ALOs) assessment questions (EIT handbook, 2016). The online learning platform self-learning section consists of recorded learning videos, recorded lectures, automatically corrected exercise, remote lab, filmed study visits and online literatures. Randomized automatically corrected calculation exercises are to be programmed so that students may test their skills and knowledge at their convenience.

Based on the specific content generation and delivery needs of the project, as well as the demands of the consortium’s partners, the following main functionalities have been delivered: set of tools for content creation and co-creation between partners; server for content storage and indexation; tools for application of the agreed pedagogical methodology; system for achieving the 3 stages material review (content, methodology, IT) process; front-end, autonomous, self-operating content delivery system which allows the student to follow the courses with no needed for the professor to intervene for ensuring the due learning process; tracking mechanism of student progress, including completion of exercises and results, plus generation of a report; generation of certificate after completion of each course’s lesson; complimentary online manual and instructional videos for solution understanding and operation.

2.3. Web-based platform

The internet has become a powerful tool for reaching a wide range of groups of people and websites provide the best way of transmitting information. The website has been developed by one of the INPATH-TES partners, TCD, and the domain of the website is www.inpathtes.eu (see Figure 1). The website is a web-based platform designed for external communication and dissemination. This includes a general description of the project along with a more detailed explanation of its specific objective, partners’ logos and links to their own websites, a list of project results such as scientific papers and newsletters published during the project life-time, information related to how to enrol on the PhD programme, a description of the training material that is being developed, information regarding past and future events, links to other relevant European projects and international platforms, and contact information.

Currently, only students belonging to the core members of the INPATH-TES project can register and take lessons from the online learning platform. However, external people from academia or companies may also take courses from the platform in the near future. Enrolments will be possible by filling up the form that will be made available on the project website, and after paying the corresponding fees.

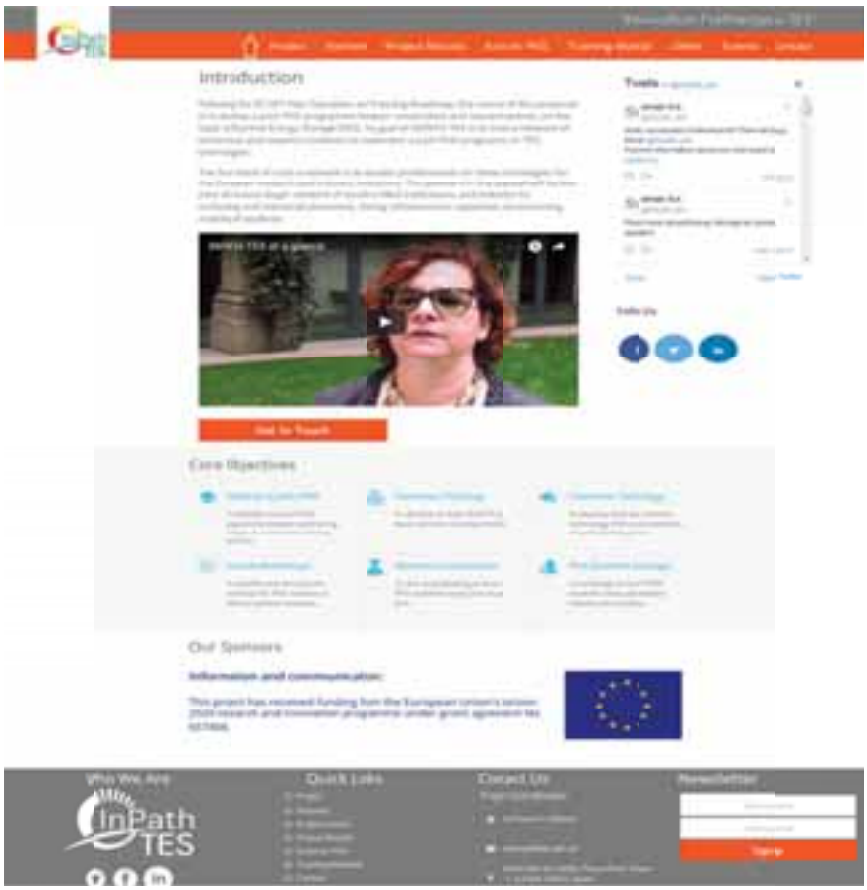

Fig. 1: Image of the website of the project

2.4. INPATH-TES label

The students willing to achieve the recognition of INPATH-TES label should contact two partner universities or institutions to join their own doctoral programme under joint PhD supervision, also called co-tutelle, and achieve the needed milestones. To be awarded the INPATH-TES label, the PhD candidate must fulfil the following requirements:

- To take at least 20 ECTS from lessons within the INPATH-TES programme.
- To perform at least 2 months of internship or secondment to a third partner from the INPATH-TES consortium for at least 2 months.
- To publish at least 1 scientific journal paper with co-authors from 3 institutions from INPATH-TES consortium.
- To have attended at least one annual INPATH-TES workshop/training school.

3. Main challenges

During the development of the project, some difficulties and challenges have been encountered, which can be summarized as follows:

- Development of the programme.
- The implementation of the programme in each country/institution.
- Two levels of work: PhD programme and Master of Science (MSc) programme.
- To ensure the continuity of the programme after EU funding ends.

The main difficulties regarding the development of the programme consisted in the fact that the contents of the proposed curriculum should respond to the needs and gaps identified by the SET-Plan, and at the same time they

must meet the needs of industry. On the other hand, the presence of many members who are not from academia required additional efforts to successfully adapt and implement the innovative EIT pedagogical methodology into the material developed. Last but not least, the development of a new e-learning platform for hosting the online learning material, and the need for 100% online assessment activities that does not require the presence of lectures, accounted for an additional degree of difficulty.

With regards to the implementation of the PhD programme, right from the beginning of the project the consortium collected the main information related to the PhD programme on the topic of the project in each of the academic institutions participating in the project, as well as others that are in close relationship with research centres also participating in the INPATH-TES project. After collecting all the information, the consortium reached to the conclusion that although there are some common items in all countries regulations, it is very difficult to define a unique implementation agreement for a joint PhD programme able to fit all requirements from each country. Consequently, the INPATH-TES consortium proposed to carry out doctoral theses in a co-tutelle regime as an alternative way to fulfil the main project objectives. A co-tutelle is an agreement on joint supervision at PhD level (also known as co-tutoring). Such agreements can be reached between the two cooperating universities, the PhD candidate, and the candidate's supervisors. The co-tutelle agreement regulates enrolment, supervision and the evaluation of the candidate's doctoral degree thesis. The PhD candidate must be enrolled in both universities, and must have at least one supervisor at each university. Furthermore, the PhD candidate must have a period of stay at both institutions. The thesis must have the logo of both institutions, and the cooperation agreement must be specified. Usually a single public presentation of the thesis is sufficient, which must comply with the rules that are in force at the institution where the presentation is to be given. The PhD candidate shall receive a diploma from each institution. This kind of PhD is well recognised in most of the partners' regulations. Therefore, at least 30 bilateral agreements are being negotiated between partner universities, and currently there are already a few students enrolled in co-tutelle PhDs.

Besides the development of a PhD programme, one of the aims of the project is to also implement a joint Master on TES. There is a big opportunity found in the fact that there is no other master on TES around the world, and that we have developed high quality material during the project. Unfortunately, today it is not possible to have an international joint Master programme outside the Erasmus Mundus programme, therefore the consortium decided to start by implementing a non-university Master programme, but apply in the near future for an Erasmus Mundus. Next step would be to apply for a university Master on TES by one of the universities members of the consortium. Here the biggest challenge would be to ensure its long term sustainability, but this is basically based on the number of students the Master would have each year, and the high specialization of the Master makes it difficult to convince the authorities of its sustainability. Therefore the first step would be to implement a non-university Master on TES at one of the consortium universities with the participation from the other consortium members as lecturers. We expect that after a short period of success of the Master will be the best way to go a step further to get a university master on TES or even a university joint Master on TES with participation of as many partners as possible in a joint-degree.

Finally, one of the main challenges of the project refers to the long-term sustainability of the project, once funding from the EU ends. INPATH-TES has the aim to continue as many years as International Network on TES with a joint-PhD programme and a joint-Master programme. Currently, the consortium is working on the development of a strategy to address this issue. The main problems to address consists in how to provide the funding necessary to meet the costs related to the e-learning platform and for maintaining, updating and reviewing the learning material, and also to establish an appropriate governance structure for the future network. The consortium is considering two possible options: continuing as network, based in one of the partners (now it is the University of Lleida), or creating a non-profit association. In any case, the membership is based on current partners that are the core of the future network of this project on the long-term. For the future sustainability of the project, there will be a membership fee applied to all members. However, the core members will avail a membership discount if they take responsibility of improving, maintaining and updating the learning material. New members are always welcome to join our network, under terms and conditions that will be agreed by the core members.

4. Conclusions

The INPATH-TES project was launched in May 2015 with the main goal to create a network of academia, research institutes and SMEs to implement a joint PhD programme on Thermal Energy Storage (TES) technologies. The proposed PhD curriculum aims to meet the needs and fill the gaps identified by the SET-Plan E&T Roadmap, through providing qualified professionals specialized in TES technologies for European research and industry institutions.

A curriculum consisting on 14 courses has been proposed, which are currently being developed by the consortium. Through active engagement with different stakeholder groups in the project, research and market oriented inputs to the PhD topics were set up in the training courses.

All the leaning material is being implemented in the "flipped classroom" perspective in the EIT/KIC InnoEnergy pedagogical methodology of student-centred learning, aligned teaching and active learning. An e-learning repository platform is being developed, which has the functionality of hosting recorded learning videos for efficient learning.

The main challenge that has been identified is the implementation of the joint PhD programme in each of the participating countries. Although all participating countries in INPATH-TES are within Europe, differences in the regulatory framework for establishment of PhD programme subsist. In order to overcome this problem, the consortium decided to define different bilateral agreements between partner universities for joint supervision of PhD students. Another important challenge of the project is how to ensure the continuity of the programme after EU funding ends. By creating further synergies between INPATH-TES and other global organisations and initiatives, extension of the partnership and exchange of students are foreseen.

5. Acknowledgements

The authors would like to thank the Catalan Government for the quality accreditation given to their research group (2014 SGR 123). GREA is certified agent TECNIO in the category of technology developers from the Government of Catalonia. This study has received funding from European Union's Horizon 2020 research and innovation programme under grant agreement Nº 657466 (INPATH-TES). The work is partially funded by the Spanish government ENE2015-64117-C5-1-R (MINECO/FEDER).

6. References

Biggs J., Tang C., 2011. Teaching for Quality Learning at University. 4th ed. Milton Keynes: Open University Press.

EIT handbook, 2016. 'Quality for learning' EIT Quality Assurance and Learning Enhancement Model: Handbook for planning, labelling and reviewing EIT-labelled masters and doctoral programmes. Revised ed. European Institute of Innovation and Technology (EIT) as a body of the European Union. Available at [2017-10-06]: https://eit.europa.eu/sites/default/files/eit_label_handbook.pdf.

JRC Coordination: Georgakaki A., von Estorff U., Peteves S.D., 2014. Strategic Energy Technology (SET) Plan Roadmap on Education and Training. Luxembourg: Publications Office of the European Union.

Solar photocatalytic treatment of rain: from laboratory scale to real sanitary use in elementary school into economic unfavorable urban areas from Mexico City

Fabiola Mendez-Arriaga[1,2] and Rafael Almanza[2]

[1] Centro de Ciencias Aplicadas y Desarrollo Tecnológico (CCADET), UNAM, Mexico City, (Mexico).

[2] Engineering Institute, UNAM, Mexico City (Mexico)

Abstract

Important number of elementary schools in Mexico have not basic sanitary infrastructure: drinking water supply, sewer system or electricity service are not full available for the scholar community. On the other hand, hydric stress is remarkably worry in urban dense poor areas, as the case of the Iztapalapa municipality in Mexico City. In this condition, the development of sustainable technologies such the rainfall harvesting and solar photocatalytic treatment is a promising strategy against the water scarcity. This work shows the design, construction, installation and startup of a solar photocatalytic reactor as treatment of harvested rainfall for final use in an elementary school from an unfavorable economic urban area in Mexico City.

Keywords: Heterogeneous Solar Photocatalysis, TiO_2, rainfall, urban areas.

1. Introduction

The Mexico City metropolitan sector is one of the largest urban agglomerations in the world. With more than 21.2 million metropolitan population (18% of country's inhabitants), Mexico City has an unpredictable model of generation, carrying, supply and availability of basic public services such as drinking water, gas, transportation, food, hospitals, electricity, etc. In this big city, the social disparities and economic inequalities are strong remarkable among their residents. One of the most critical and detrimental situation is observed in the infrastructures of basic services in elementary schools predominantly into unfavorable economic areas. The most recent national census reflects 207,682 elementary schools attending more than 25 million of students among primary and secondary school age children (ages 2 to 15) (INEGI, 2014). Almost 50% of the elementary schools in México do not have drainage networks, 31% show deficiencies in drinking water accessibility, 11.2% express nonexistence of electricity facilities and 12.8% display entire absence of toilets.

Specifically in Mexico City there are 8,141 elementary schools attending around 13,151,297 students. More than a half of those schools (51.8%) belong to the public administration and 3.5% do not have drinking water facilities. Several students are used to return at home during the 30 minutes break between lessons in order to use the own toilets and lavatories if available in their houses. The inexistence of drinking water networks as well as the remarkable hydric stress are part of the sanitary problem for a large number of scholars and teachers. Figure 1 shows the availability´s coverage of basic facilities in elementary schools in Mexico City (INEGI, 2014)

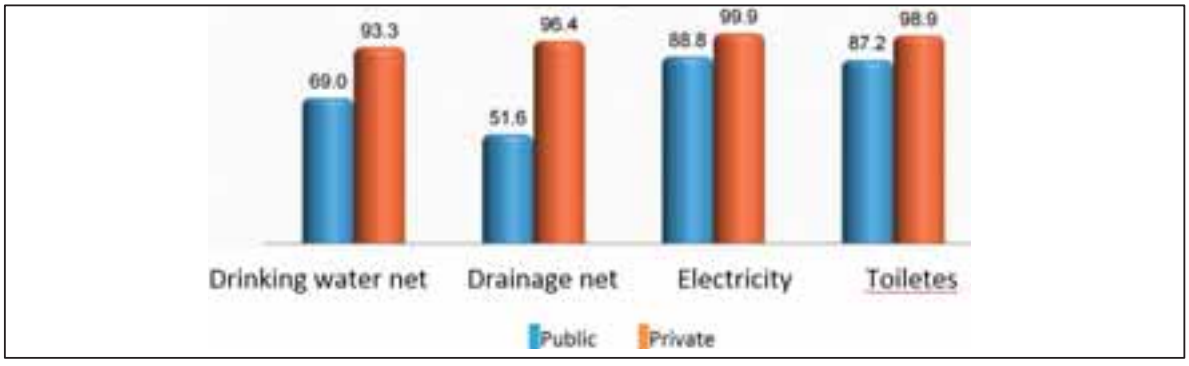

Fig. 1: Availability´s coverage of basic services in elementary schools in Mexico City (INEGI, 2014).

A rainfall-harvesting project is not under consideration as part of the public water supply in any governmental plan. Mexico City wastes approximately 1,000 million of m^3 of rainwater per year. In contrast, the Mexico city´s principal drinking water source, the Cutzamala system, has around 728 million of m^3 of capacity (SACM, 2017). Some estimations show that only 10% of the harvested rainfall is available and used within the same period of collection.

doi:10.18086/swc.2017.08.02 Available at http://proceedings.ises.org

On the other hand, the solar photocatalytic process has shown effective results as water treatment for effluents containing a huge variety of recalcitrant contaminants. Recent papers shows the increasing interest on this field applying the solar technologies to heat up, purify or pasteurize harvest rainwater at laboratory scale (Saran, 2018; Reyneke, 2017). Some of the most interesting goals for the scientific, engineering and academic community are to increase the efficiency of the harvest systems as well as to reduce the cost of the water treatment by means of sustainable solar technologies. This study shows the application of the well-known and mature solar photocatalytic process TiO_2 based at large scale in a real case of study inside of an elementary school placed into a high hydric stress zone in Mexico City.

2. Real case study: "Luis Braille" primary School

This school is located in Iztapalapa district, one of the most densely populated regions in the northeast of Mexico City as showed in Figure 2. This school belongs to the public administration. Twenty-six teachers attend around 550 students per each two timetables (morning, 8:00–13:00 and evening, 13:00- 18:00). The school has 4 bathrooms, 1 computer zone, 21 classrooms, 1 gymnasium or sport area, 1 parking among others facilities, etc. The Figure 2 shows the school localization and its physical boundaries.

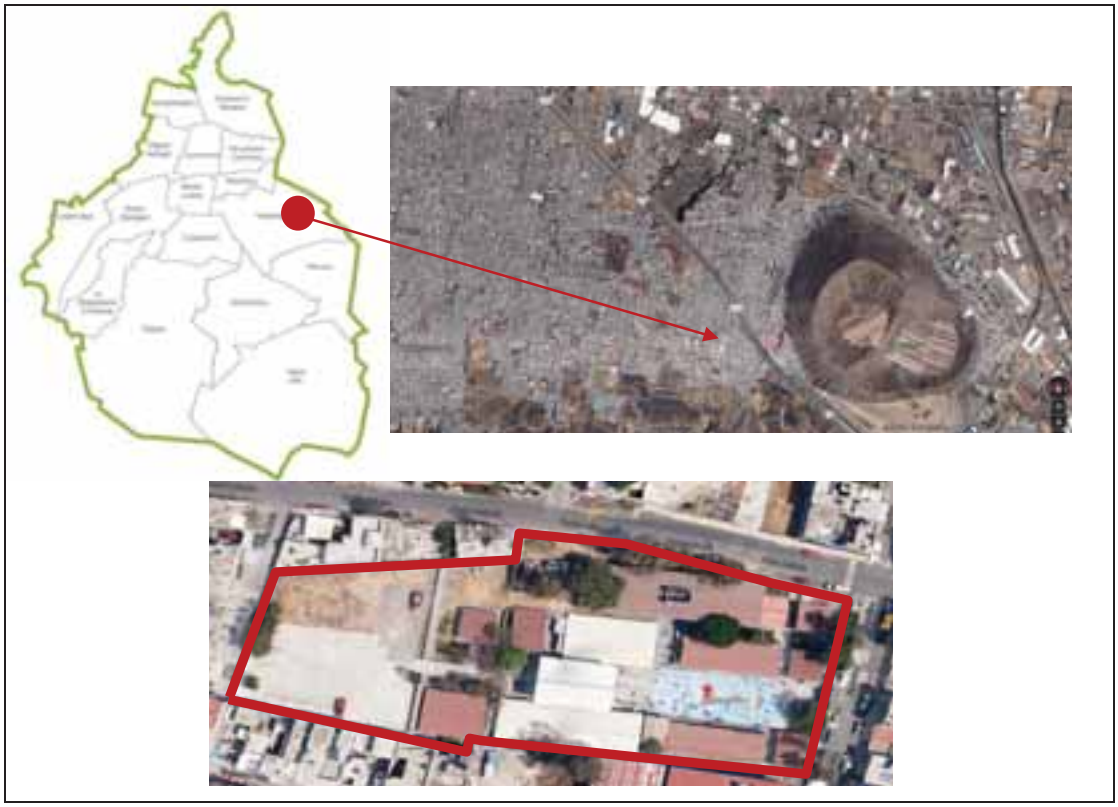

Fig. 2: Luis Braille elementary school in Iztapalapa district.

Municipal drinking water network is not available in this school. Acquisition of 10,000 liters of tap water shipped by a container truck or "pipa" is reach with around 50 dollars per week.

The water container truck does not offer any chemical/biochemical safe certificate of quality. The school has a cistern with capacity of 30,000 L as shown in Figure 3 (central photography). However, the maintenance of this reservoir is scarce and very often it remains empty or dirty.

Fig. 3: Sport area (left), cistern (center) and toilet building (right).

3. Design and on-field analysis

Initial step was the visual field inspection of the installations inside the school in order to evaluate the technical feasibility. Figure 4 shows the observations carried out in the parking area by technicians and researchers involucrate in this project. Noteworthy requirements taken into account during the on-field assessment were: a) accessibility of a south oriented large area; b) availability of solar free irradiated space without or as minimum as possible shades; and c) suitability of a large rainwater caption surface. Authorities, teachers and members of the Parents Association, whom showed deep involvement and interest amongst the research project, were also present during the field inspection.

Fig. 4: Parking area (left) and visual-technical inspection (right).

A crucial element of the school founded during the on-field analysis was a free large border wall (20 m length) south oriented in perfect conditions as supporter of the photoreactor. Figure 5 (left) shows this wall. The volcanic stones observed in the image were a “natural” stop limit to the occupation and self-construction progress of the neighborhoods (called in Mexico as “paracaidistas”) long time ago. Nearby this wall, there are no pedestrian cross or student presence due to the eventual occurrence of reptiles or arachnids adapted to the large accumulation of foliage. Thus, this isolated area was an excellent option for the operation of the photoreactor saved of damage for the football balls or other normal items used inside the school. On the other hand, the top roof cover of the playground was also a very important facility observed. Figure 5 (right) shows the roof cover of the playground. The long surface exposed for caption of rainwater allows harvest water previous filtration of dust and small particles following the photochemical treatment.

Fig. 5: Enclosing wall south oriented inside the school (left) and rainfall roof caption surface (right).

4. Rainfall treatment by solar heterogeneous photocatalysis

Advanced oxidation processes are based on the presence and reactivity of the hydroxyl radical (•OH) generated at

standard ambient temperature and pressure (25°C and 1 atm) with or without catalyst and/or presence of chemically reactive energy (Méndez-Arriaga, 2009). Among the AOP's, the heterogeneous photocatalysis with TiO_2, have shown highlighted efficiencies on removal of a wide type of persistent, recalcitrant, and emergent contaminants. Oxidation of organic compounds by means of TiO_2 is achieved by hydroxyl radical generation through the e^-/h^+ pair generated when the semiconductor is exposed to UV radiation.

On the other hand, contaminants present in rain are strong different in composition and content between annual season, stages or places. In an urban environment, most of the pollutant substances presents in rainfall are in relationship to the previous immediate quality of the air due to the "washing" effect during precipitation. In general, the direct employment of harvested rainfall is not preferable without previous physical and/or chemical treatment. Dissolved particulate substances and microorganism coming from the atmosphere are hazardous health compounds. In this project, an additional consecutive physicochemical conventional process (activated carbon and UV irradiation) follows the photochemical treatment train in order to guarantee the drinkable quality of the final effluent. Figure 6 depicts the full treatment train for both usages washbasin and drinking water.

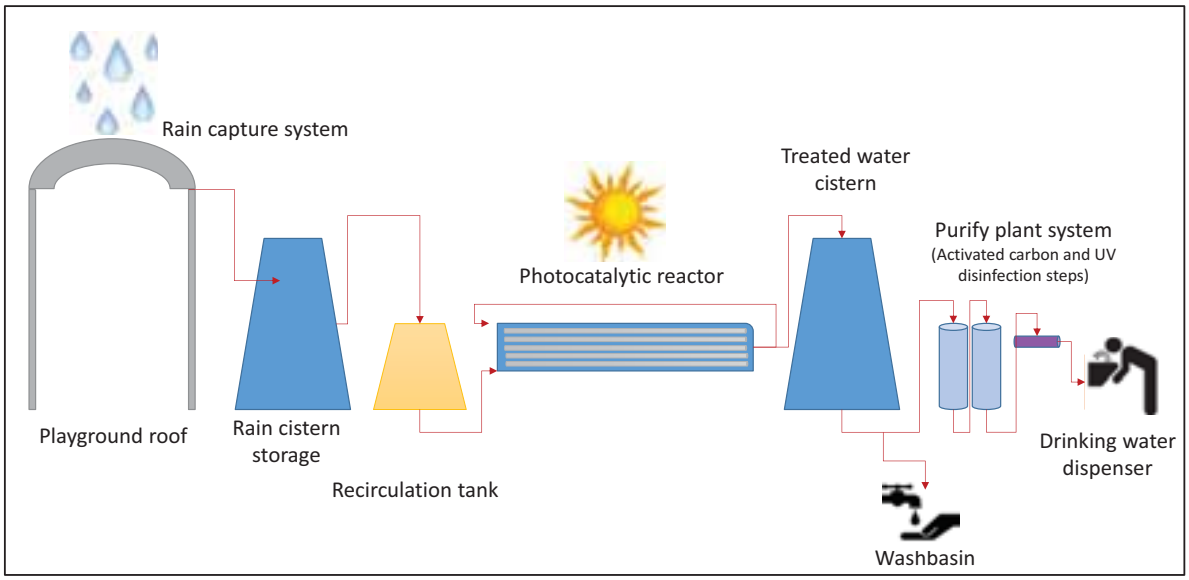

Fig. 6: Full treatment train (solar photocatalytic reactor and conventional physicochemical filters) for harvested rainwater

5. Solar photocatalytic reactor design

The solar photocatalytic reactor was designed with 10 compound parabolic collectors (CPC´s) disposed in parallel configuration. The basic components of the photoreactor are:

i) centrifugal pump (½ HP),

ii) storage cistern of harvested rainfall of 10,000 L of capacity (243 cm length, 238 cm extern diameter, 8.2 mm thick),

iii) sixty Duran glass pipes (5.08 cm inner diameter and 150 cm length) with TiO_2 (Degussa P25) thermally attached

iv) storage cistern of treated water of 10,000 L of capacity(243 cm length, 238 cm extern diameter, 8.2 mm thick).

Grupo Iddea Co. designed the layout of photoreactor and the virtual sketch (Figure 7a and 7b respectively), developed the hydraulic and electric systems and installed the full prototype.

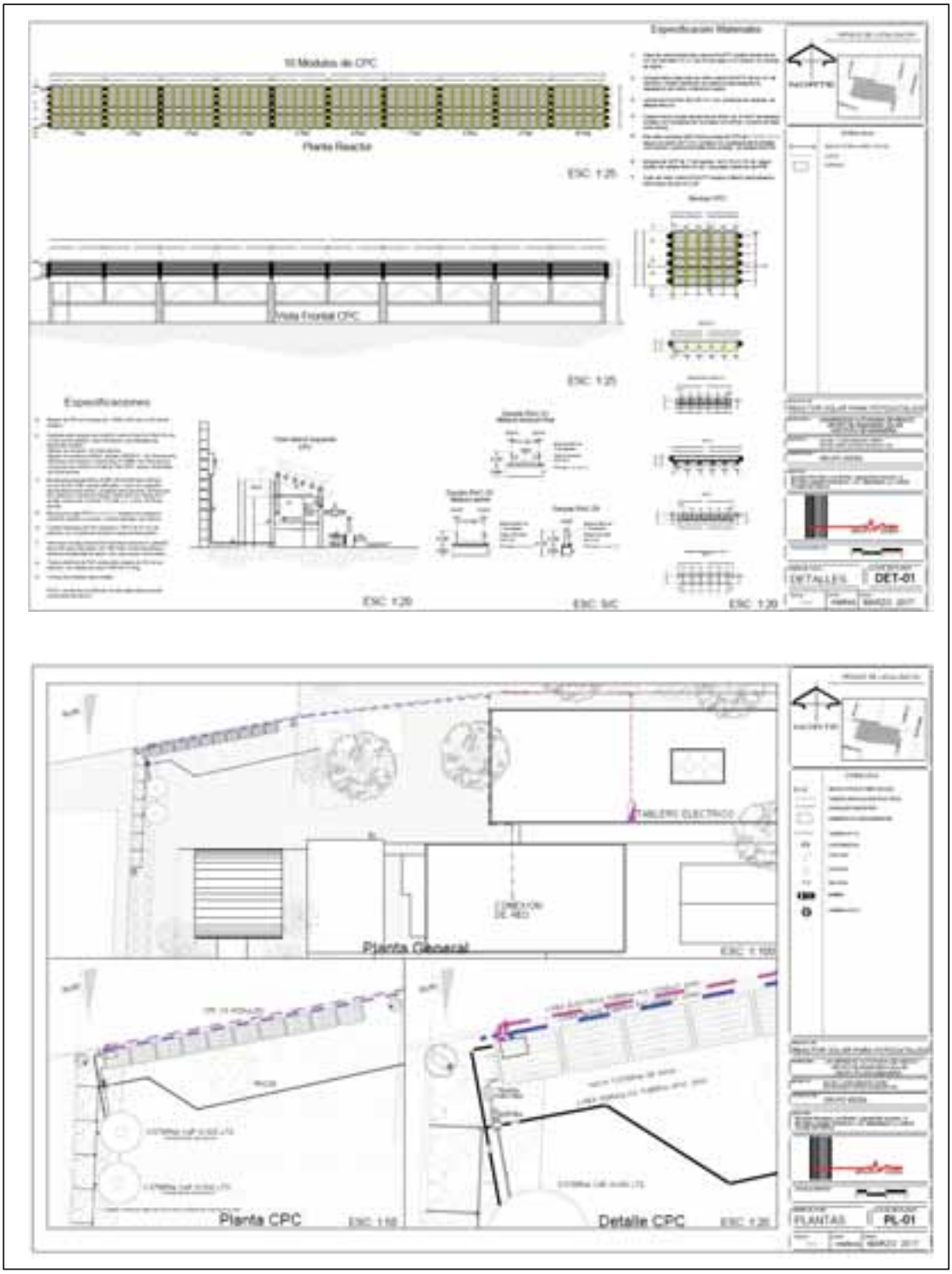

Fig. 7a: Layout and compound parabolic collector details

Fig. 7b: Digital sketch of the photocatalytic treatment system

6. Reactor construction, installation and startup

The photochemical reactor was constructed and installed in several stages per separated sections of the overall system following specific aims:

a) Fabrication of metallic structures for support and base of photo-reactors (see Figure 8);

b) Design of Compound Parabolic Collector and profile manufacture in fiber board outdoor material by jet stream water cutting system (see Figure 9 left and center);

c) Conformation of the high reflective mirror geometry through 99.5% aluminum film (see Figure 9, on the right);

d) Titanium dioxide (Degussa P25) thermal impregnation (150ºC, 4 h) on the internal pipe glass wall (5.08 cm ID Schott Duran glass);

e) Assembly of metallic structures and reflective aluminum mirror (see Figure 11);

f) Installation of hydraulic and pump system comprising the potable treatment system and final use (facet/dispenser) devices (see Figure 12);

g) Design of rain capture system on the roof of the outdoor play area (see Figure 13, left and center);

h) Installation of on-line measurement instruments (pH, OD, conductivity, salinity, temperature, total solids suspended, etc) and computational acquisition system (see Figure 13, right).

Figure 8 shows the manufacturing process for the construction of the metallic base of photoreactors including a finish detail of praimer and paint covering in order to avoid the outdoor damage.

Fig. 8: Metallic structures constructing.

Figure 9 depicts the one sun concentration geometry of the composed parabolic collector (CPC) of the photoreactor as well as the water jet cutting for construction of ribs to support the aluminum film along linear focus of the CPC.

Fig. 9: 1 sun CPC geometry (left), jet stream water cutting system (center), aluminum film adjust (right).

Figure 10 shows the shipping stage of all the premanufactured and separated pieces and devices from the laboratory at Engineering Institute in Coyoacan district until the elementary school in Iztapalapa municipality for the installation of the prototype. The Figure 10 also depicts the enthusiasm and collaboration of the students and academic community, which was interested to learn on the photochemical concepts and operation of the prototype.

Fig. 10: Transport of prefabricated pieces and helpfulness involvement of enthusiastic student in the school

Figure 11 illustrates the integration of one module consisted on the metallic base, aluminum reflectors and Duran glass pipes with catalytic activity. Ten modules with 6 glass pipes were hang on the wall south oriented making sure horizontal level and 19° inclination in each module.

Fig. 11: Parts joint and aliening-fastening on the wall

Figure 12 depicts a section of the hydraulic system including the harvest rain container, the closed recirculation tank and the treated water cistern together with the centrifugal pump and PVC pipelines to the photoreactor.

Fig. 12: Hydraulic system and pump test.

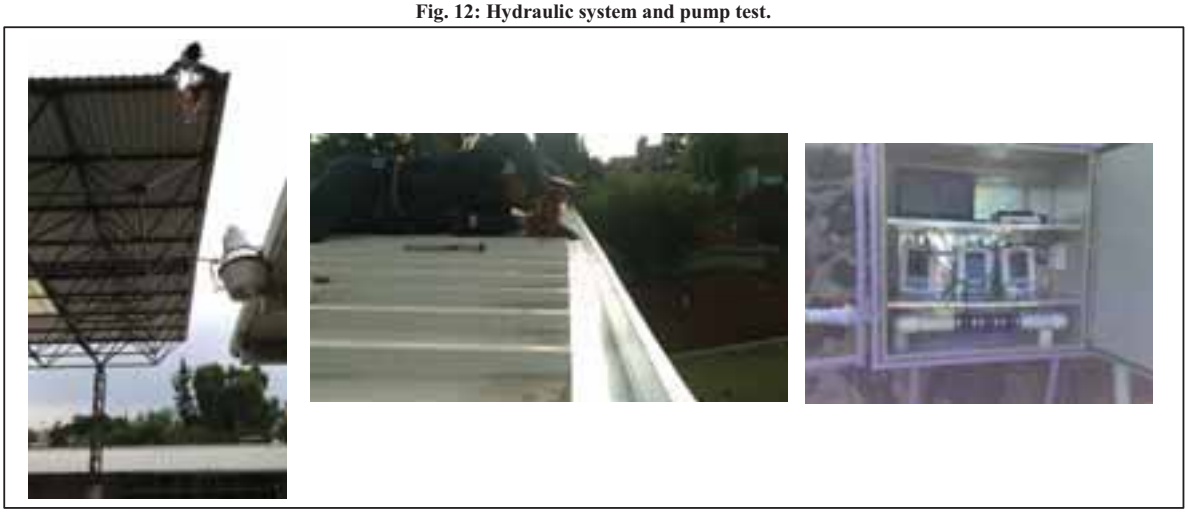

Fig. 13: Rainwater collection system (left and center) and on-line chemical measure instruments (right).

The harvest rain system was built with a semi-squared laminate canalization (20 m length) welding on the metallic top structure of the roof to 10 m altitude as depicted in Figure 13 (left and center). After that, the PVC pipeline reached connection to the storage tank with 45° inclination and previously crossing three cellulose glass paper filters consecutively attached.

The harvest rainwater flowed through the system till the pH, dissolved oxygen and conductivity sensors placed on the left side of the photoreactor. The measures during the photocatalytic treatment were recorded on line as well as the data of the UV-radiometer simultaneously acquired. Figure 13 (right) shows the chemical parameters measure system.

Fig. 14: Photochemical treatment system coupled to potable water train system and drinking water dispensers

Figure 14 shows the complete photocatalytic prototype including the conventional purification water system and the drinking water dispenser. The design, construction and startup of the prototype lasted 6 months. Following steps into the project consist on the assessment of the initial chemical quality of the harvest rainwater including the evaluation of inorganic ions (phosphorus, sulfates and nitrates among others), metals and organic compounds as well as the characterization of microorganism eventually presents. Effect of the photocatalitic treatment and optimization of residence solar irradiated time is also part of the goals during next rainy season during May, June, July and August 2018. Part II of this paper covers such results into the forthcoming ISES congress.

7. Conclusion

The solar photocatalytic science is a mature high efficient demonstrable knowledge applied for environmental remediation yet able to reach industrial scales and commercial proposes. However still there is a lack of examples with studies in real contexts to assess the potential scopes of this technology as the solar thermal and photovoltaic technologies did many years before. The solar photocatalytic research opens the opportunity to contribute against the water contamination and scarcity in unfavorable and marginal urban sectors.

8. Acknowledgement

Authors acknowledge the support of the Consejo Nacional de Ciencia y Tecnología, CONACyT for the postdoctoral fellow to F.M-A as well as the financial support to the Secretaria de Ciencia, Tecnología e Innovación de la Ciudad de México under projects SECITI/048/2016 and CM-SECITI/109/2017. Finally, authors thank the economic support of UNAM with the project PAPIIT 6106.

9. References

INEGI, 2014. Censo de Escuelas, Maestros y Alumnos de Educación Básica r Especial (CEMABE) Resultados definitivos. https://www.uv.mx/personal/kvalencia/files/2013/09/INEGI-2014-Censo-Escolar.pdf (October 20, 2017).

SACM, 2017. Sistema de Aguas de la Ciudad de México (SACM)

http://www.sacmex.cdmx.gob.mx/storage/app/media/index/LeySustentabilidad.pdf (October 20, 2017).

Méndez-Arriaga, F., 2009. Advanced oxidation processes, (photocatalysis, photo-fenton and sonolysis) for removal of pharmaceutical pollutants in water. Doctoral Thesis. Universitat de Barcelona.

Reyneke, B., 2017. Application of solar pasteurization for the treatment of harvested rainwater. Master of Science Thesis. Stellenbosch University. South Africa.

Saran, S., Arunkumar, P., Devipriya, P., 2018. Disinfection of roof harvested rainwater for potable purpose using pilot-scale solar photocatalytic fixed bed tubular reactor. Water Science and Technology. DOI 102166/ws.2017.097

Clustering methodology for defining a short test sequence for whole system testing of solar and heat pump systems

Diego Menegon[1], Anton Soppelsa[1] and Roberto Fedrizzi[1]

[1] Eurac Researc, Bolzano (Italy)

Abstract

Dynamic whole system testing methods are currently applied to evaluate the performance of heating and cooling system. One major obstacle to the implementation of such dynamic test methods is the cost connected to the experimental phase. To define a short test sequence, an original implementation of "k-medoid" clustering has been implemented. The paper investigates on the length of the sequence and how the days should be described to achieve effective results. A family of solar assisted heat pump systems has been generated by varying the collector field area and storage tank volume and studied via numerical simulations.

The results show that the days can be described as a function of average temperature and global horizontal irradiation. The simulation of different sequence lengths shows that a six-day sequence can be used to test the system with a possible deviation of results lower than 8% if compared to the annual simulation. The deviation is reducing with a higher number of clusters.

Keywords: Clustering; short test sequence, solar and heat pump system.

1. Introduction

In the contest of reducing the heating and cooling consumption, the system efficiency plays an important role. In a complex system composed by different energy sources and variable distribution, often driven by renewable energy, the performance of the entire system does not correspond to the "sum" of the single components performance, as the way the components interact among themselves has itself an impact on the performance and needs to be correctly considered. For this motivation, dynamic methods capable of assessing entire systems are used to characterize the system performance by different research institutes (Haller et al. 2013). The main advantage of this method is that the entire system is installed in the test chanber and realistic working conditions are used to study its performance. In this way, it is possible to perform a reliable evaluation of the system performance as-a-whole.

To reduce the cost of experimental phase, short test sequences (between 6 to 12 days) are defined to represent the seasonal boundary conditions. To arrange such short sequence, the literature presents different methodologies:

- Iterative definition of the sequence with the aim of attaining proportionality to the annual performance.
- Selection of days with temperature and radiation profiles corresponding to the monthly average conditions.
- Selection of days using some sort of weather data classification.

In the first approach, an optimization program reduces the deviation between the test bench data and the annual simulation of a system model. In addition to the fact that the method relies directly on a model of the system, it requires to perform a different optimization for every weather condition required to reproduce the weather pattern at the given location (unless the test it is referred to only one condition). The second approach is more easy to be implemented but in some cases it could not be able to perform a direct evaluation of performance, see for example (Haberl et al., 2009). For the last approach, different methodologies can be identified, i.e. classification into bins or classification with clustering. For example, the clustering has been adopted also for the definition of short sequence for the simulation of combined heat and power systems (Domínguez-Muñoz et al. 2011) and for heat pump systems (Huchtemann et al. 2016).

doi:10.18086/swc.2017.08.03 Available at http://proceedings.ises.org

In the development of the PLPE procedure (Menegon et al. 2017), we have investigated different methodologies. The first option was to create classes in according to the procedure developed for the test of components (Menegon et al. 2014). The method organizes the boundary conditions into multidimensional classes and a proportional part of the so-obtained distribution is selected. The good results obtained for the component test were not replicable when applied to the entire systems. Therefore, we decided to explore other techniques. Clustering, among the options we have considered, has the advantage that the weather conditions are classified without performing model simulations. In addition, the sequence corresponding to a certain climate can be easily be calculated. This study employs extensively numerical simulation of entire systems to verify the validity of the selections performed with clustering.

In particular, section 2 presents the clustering methodology while its application to the definition of test sequences of different duration is presented in the section 3. Different sequences are defined for the climate of Bolzano and Zurich. The section 4 presents the SAHP system to which the clustering procedure has been applied. The results and concluding remarks are finally given in section 5.

2. Method

The purpose of clustering is to group a set of objects in such a way the objects in the same group (called cluster) are closer, or more similar, to each other more than to those in other groups. In other words intra-cluster similarity is higher than inter-cluster similarity. In the case of this application, the objects to be classified are the days of a given weather file (long one year). The literature presents different algorithms and the authors have applied the Partitioning Around Medoids (PAM also called k-medoids) algorithm et al. 2007).

The user selects a number of clusters “N” and the algorithm classifies the objects into the “N” clusters. To apply the algorithm, the objects need to be described by a number of numerical variables, which are used to map every objects into a point in an M-dimensional coordinate space. Sometimes, the geometrical representation can be used to graphically represent the objects in the clusters.

The algorithm starts by defining randomly “N” initial medoids and the initial clusters are computed assigning every point in the cloud to one of these clusters. The clusters boundaries are then modified following an iterative process that tries all the possible combinations of point and cluster. The final clusters outline is obtained minimizing the total Euclidean distance between the cluster points and the medoid of the cluster they belong to. As the unit of measure used to characterize the objects along the dimension are different, data is usually moved (removing the mean) and scaled (by the reciprocal of the standard deviation) to avoid unit of measure bias. In this way, the object could be described by variables of different normalized physical quantities.

At the end of the iterative process, the “N” clusters are produced and the representative objects should be selected. Both the centroid and the medoid could represent the cluster: the centroid is the geometric center while the medoid is the nearest object to the centroid. For a discrete dataset, the centroid could not be part of the dataset. As in our case the points represent day of the years, the sequence is created selecting the medoids.

To understand better the application of the method, an example of classification of events with the clustering is given in Table 1: 15 objects, representing day of the year described by their mean temperature and irradiation, were randomly generated. Willing to select 3 representative days out from these 15, the method divides the objects into 3 clusters and then we select as representatives the clusters medoids.

Tab. 1: Example of clustering. 15 objects with their characteristics and cluster identity.

Day	Temperature [°C]	Irradiation [Wh/m^2]	Cluster
1	1.91	2376.85	0
2	9.90	2694.12	1
3	5.98	751.26	1
4	8.86	5.65	1
5	0.14	1048.74	0

6	2.57	1929.99	0
7	4.30	210.95	0
8	0.45	161.38	0
9	8.64	1454.36	1
10	0.58	5923.16	2
11	0.69	4057.67	2
12	3.77	6457.90	2
13	3.72	2715.89	0
14	6.00	4473.34	2
15	0.95	4764.96	2

Figure 1 shows the graphical representation of clusters indicating with different colors the different clusters. The centroids are indicated with a yellow point and the medoids are encircled. The centroids can be quite far or very close to a member of the dataset but usually they do not belong to the dataset. In this example, the sequence would be created with the temperature and irradiance profiles of objects 6, 9 and 15.

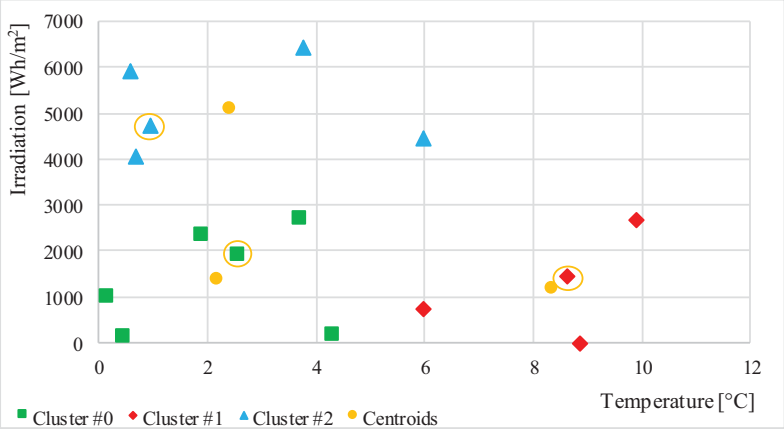

Fig. 1: Six-day and ten-day sequence defined with clustering of the climate of Bolzano.

In our procedure, the annual performance is directly extrapolated from the sequence performance, that is the performance of the tested system under the boundary conditions assembled from the short sequence. As the number of objects per cluster is usually not the same, the extrapolation of seasonal performance is done weighing the energy performance on the specific day by the size of the clusters it belongs to:

$$Q_{seas} = \sum_{i=1}^{n_{cluster}} n_{el,cluster,i} \cdot Q_i \qquad \text{(eq. 1)}$$

Where Qi is the energy measured during the event corresponding to the i-th Medoid and $n_{el,cluster,i}$ is the size of the i-th cluster, i.e. the number of objects it contains. The equation is valid for the thermal energies (SH, SC, DHW, collector and so on) and for the electric consumptions.

The medoid load is not equal to the cluster average load. In this way, the eq.1 does not give exactly the cluster load energy. In the PLPE method, the load is fixed and therefore we can apply a scaling factor to the medoid load. This factor (one value for each cluster) compensates for the deviation between the medoid energy and the cluster average energy.

$$L_{sc(i)} = \frac{E_{Simulations.Day(i)}}{E_{Simulations.Cluster(i)}} \cdot N_{Days.In.Cluster(i)} \qquad \text{(eq. 2)}$$

The scaling factor (Lsc) scales the space heating space cooling loads. The scaling factor is lower when a 3D or 4D coordinates are used then a 2D coordinate system.

The sequence defined with clustering would be closed to a correct representation of the whole year performances when the performances are linearly dependent from the boundary conditions. This because the days are selected considering the nearest object of geometric center of each cluster and the consumptions and loads are built through discrete integration.

As example, considering one-dimensional case where the consumption (W) is linearly dependent from the temperature, the consumption can be described as:

$$W = \alpha \cdot \mathrm{T} + \beta \qquad \text{(eq. 3)}$$

Where the parameters α and β are the coefficients of the linear dependence.

The total consumption is a sum of the "i-th" consumptions, and each "i-th" consumptions could be described as a function of the "i-th" temperatures with the equation:

$$W_{tot} = \sum_{i=1}^{N} W_i = \sum_{i=1}^{N} (\alpha \cdot T_i + \beta) = \alpha \cdot \sum_{i=1}^{N} (T_i) + \beta \cdot N \qquad \text{(eq. 4)}$$

In this case, the geometric center corresponds to the average temperature and the last summation could be substituted with the average temperature multiplied by the number of objects:

$$W_{tot} = \sum_{i=1}^{N} W_i = (\alpha \cdot \bar{T} + \beta) \cdot N \qquad \text{(eq. 5)}$$

The total consumption could be calculated directly from the geometric center of the boundary condition (in this case one temperature). The same demonstration could be performed with a multi-dimension problem when the consumptions are linearly dependent from more boundary conditions.

3. Short Sequence

As we have seen in the methodology section, the days have to be compared in terms of some characteristics that became the coordinates for the method. Days can be characterized by profiles of temperature, irradiance (with its different components), relative humidity, wind speed and so on. Not all these variables have the same influence on an heating and cooling system performance. For example, in a SAHP system the temperature and the irradiance profile have a higher effect than the wind speed. To reduce the number of variables that identify an object, the average ambient temperature and total irradiation on the horizontal surface are considered, describing a 2D coordinates. This classification is the simplest possible. Other solutions are given by adding the space load to the classification. Other options could be using 3D and 4D clustering where the 3D clustering considers the temperature, irradiance and heating and cooling load (in one vector using the sign to discriminate between heating and cooling), while the 4D considers the temperature, the irradiance and the heat and cooling loads separately.

In addition, the sequence length should be determined. The results presented in the literature show that longer sequences are more representative of the whole season. However, it is important to remark that the sequence length is a trade-off between accuracy and cost. To verify the influence of the sequence length in our application, we defined sequences of 6, 8, 10, 12 and 24 days.

In this study, we present the results for the climates of Bolzano and Zurich. The sequences are used as boundary condition of a family of reference numerical models of a solar assisted heat pump system (SAHP). The reference models were generated by varying, the collector area and the tank storage volume.

Fig. 1 shows the effect of changing the number of clusters: six clusters (green triangular points) and ten clusters (red diamonds points). With a different number of cluster, the shapes of the clusters changes and therefore different days are selected. It is possible that one specific day is selected by both classifications, although this is not generally the case (in the figure, one triangle - with coordinates 22°C, 7322 Wh/m^2 - is hidden by one diamond). With a larger number of clusters, a wider range of temperature and irradiation are covered. This happens because the dataset is relatively uniform and therefore medoids are quite uniformly distributed which means that increasing their number will cover better points at the boundary of the dataset. The other way round, with only few cluster the extreme conditions could not be reached.

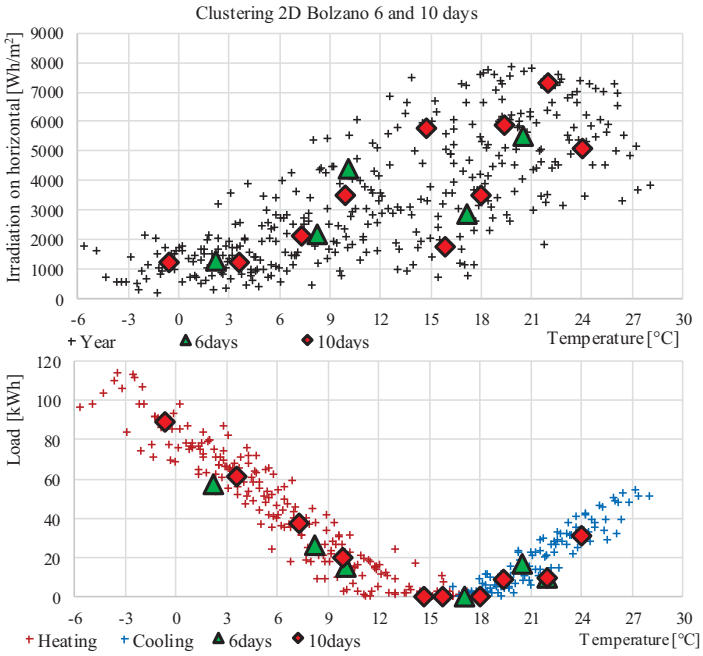

Fig. 2: Six-day and ten-day sequence defined with 2D clustering of the climate of Bolzano.

Fig. 2 shows the identification of the sequence for Zurich. The green triangular points identify the selection with 2D coordinates (T and GHI), the red diamonds points identify the selection with 3D coordinates (T, GHI and Load) and the blue circle points identify the selection with 4D coordinates (T, GHI, Heating and cooling load). The figure in the left shows the days of the year as function of the average temperature and global horizontal irradiation while the right figure shows the days as a function of the average temperature and the space load distinguished into cooling (blue points) and heating (red points).

The different coordinates of the days (2D, 3D, 4D) modify the geometry of the problem and therefore the selections are different.

In the climate of Zurich, the 2D clustering does not considers days with space cooling load. The 3D clustering selects only one day with very low load (1.6 kWh) while the 4D clustering selects two days with cooling load (one with 1.6 kWh and the other one with 25.5 kWh). The reason for this fact is that only few events require cooling. Using the 2D clustering, the load is more influenced by the temperature and irradiation while the 3D clustering gives more importance to the load. The 4D clustering gives equal importance to the cooling and heating load since the coordinates are normalized. This means that in a climate like Zurich where the heating load is about 30 time the cooling load, this selection would give the same number of days to the heating and to the cooling season, resulting in an unbalanced selection.

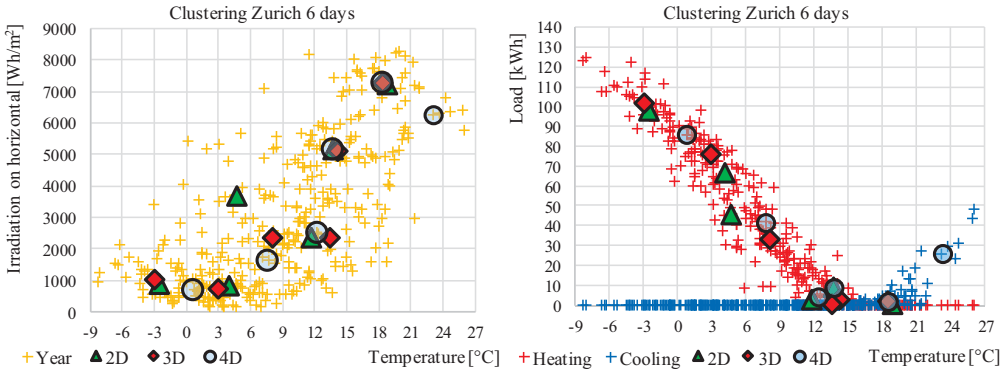

Fig. 3: Identification of six-day sequences defined with different coordinates. Zurich climate.

In addition to the information given with previous figures, Fig. 4 shows how the 2D and 3D coordinate systems affect the boundary conditions profiles. The figure present the two six-day sequence defined in the climate of

Bolzano. The 2D clustering presents the temperature profile higher than the 3D clustering and as consequence the heating load is lower and the cooling load is higher. The temperature profiles are smoothed between two days.

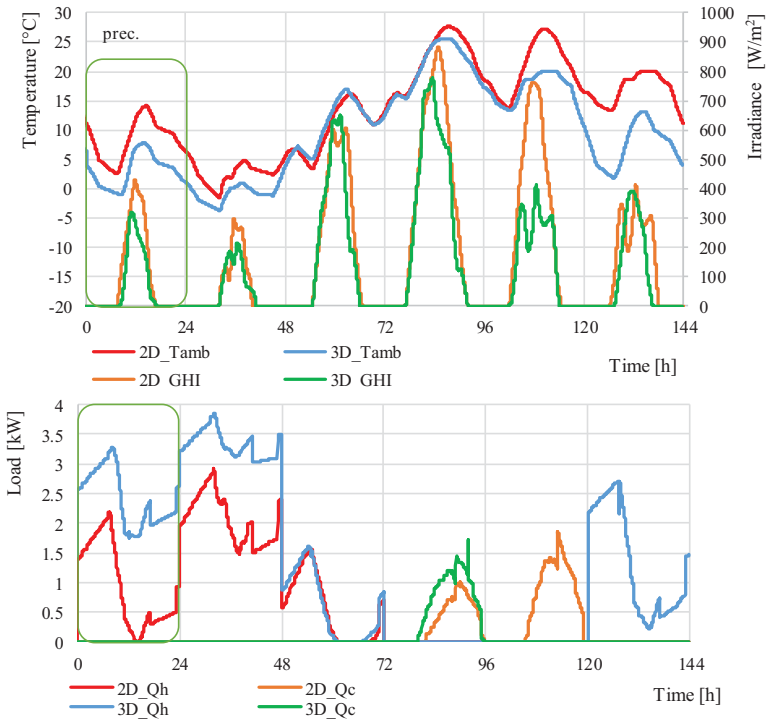

Fig. 4: Comparison of six-day sequences profiles defined with different 2D and 3D coordinates. Bolzano climate.

4. Simulation

The clustering was tested simulating a family of SAHP systems (see figure 5). The study considers different configurations of collector area (8 m^2 or 16 m^2) and storages volume (700 l or 1500 l). The volume of 700 l is obtained connecting in series a 500 l and a 200 l storages while the 1500 l volume is obtained with the combination of a 1000 l and 500 l storages.

The system was modelled with Trnsys (Klein and et al. 2012) and the components were validated with laboratory tests or with monitoring data (Bettoni 2013). The figure presents the layout and the models of the system:

- The heat pump model (type 847) is based on a performance map (as a function of inlet temperatures and flows).
- The collector model (type 1) considers the collectors' parameters calculated in the certification test of one commercial collector. The type 1 is coupled to a moving average to introduce inertia effects.
- The Storages model (type 340) is a commercial type (Drück and Pauschinger 2006).
- The building model is type 56.
- The weather file is read with the type 109 for the simulation of the whole year. The sequence' weather data is read with type 9.
- The dry-cooler model (type 880) was developed by (Besana 2009; Bettoni 2013).
- Other traditional models are the pipes (type 31), circulation pump (type 110), mixing and tempering valves (type 11) and heat exchanger (type 5b).

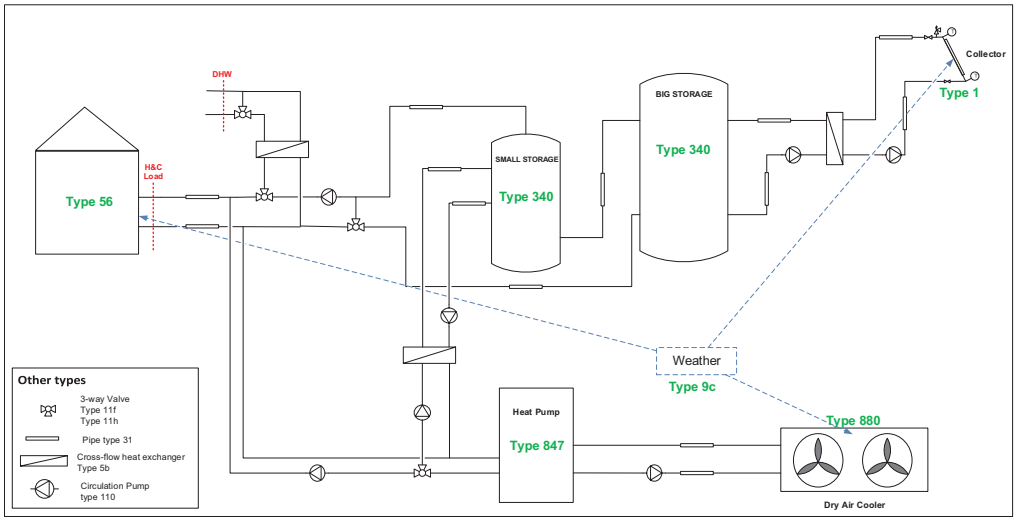

Fig. 5: System layout and component models.

The sequences are the boundary condition for the simulation of this system. The selection with the clustering method does not give any advice on the order of the sequence. The days are ordered in the same order as they occur in the year starting from the winter and ending the sequence with the autumn conditions. The last day of the sequence is used to precondition the whole sequence.

The simulation set-up considers the combination of:

- Climates of Bolzano and Zurich.
- 6, 8, 10, 12 and 24 day.
- 2D, 3D and 4D coordinates.
- System configurations (collector area and storage volume).

In parallel to the sequence simulation, also the whole year was simulated. The values extrapolated from the short sequence are compared with those calculated from annual simulation. The deviation between the values extrapolated from the short sequence and the annual simulation with:

$$\delta X = \frac{X_{short\ sequence} - X_{annual\ simulation}}{X_{annual\ simulation}} \qquad \text{(eq. 6)}$$

Where X represents one of the selected performance figures among thermal energy (load or source), electrical consumption, seasonal performance factor and solar fraction.

Six-day sequence are defined also for Rome and Gdansk.

5. Results

Figure 6 and Figure 7 show the SPF deviation (eq.6) as a function of the number of clusters for the climate of Bolzano and Zurich for the different plant configurations. The figures show the total SPF value calculated with the annual simulation. In general, the deviation of SPF decreases as the number of clusters increase. Table 2 and Table 3 report the SFP deviation RMSD and span (the difference between the maximum and minimum value). These values help to understand how much the trend could variate by selecting a different number of clusters. The cells of the two tables are colored in order to highlight in green the smallest values (best case) and in red the highest values (worst case).

The first outcome, is that the 4D clustering presents the highest deviation. As it was noticed before discussing the points in figure 3 (section 3), the 4D coordinate system gives an unbalanced selection (the days with heating load have the same weight as the days with cooling load also if the two loads are different). The 2D clustering represents better the selection in the climate of Zurich while the 3D represents better the selection in the climate of Bolzano.

The second outcome is that the configuration with the 700 l storage has a lower deviation than that with the 1500 l storage while the configuration with 8 m^2 of collector has a lower variation than the case with 16 m^2. In general,

we expect the sequence to be less accurate in case of high collector area. In the short sequence, more consecutive days with high irradiation could not be present while it occurs during the summer season. In this case, the stagnation could be neglected by the short sequence because the storage does not have enough energy to stagnate. Besides the effect of collector area, also the effect of the storage volume has to be considered. If we examine the extreme case of high collector area and very low storage volume, the system would use the solar energy by the end of the day when it has been produced since the solar energy cannot be stored. Therefore, a short sequence could be representative since no stagnation occurs due to consequent days with high irradiation. Increasing the volume, this effect starts to be noticeable. In fact, all the sequences simulated for the case of system with 700 l are more accurate than those with 1500 l.

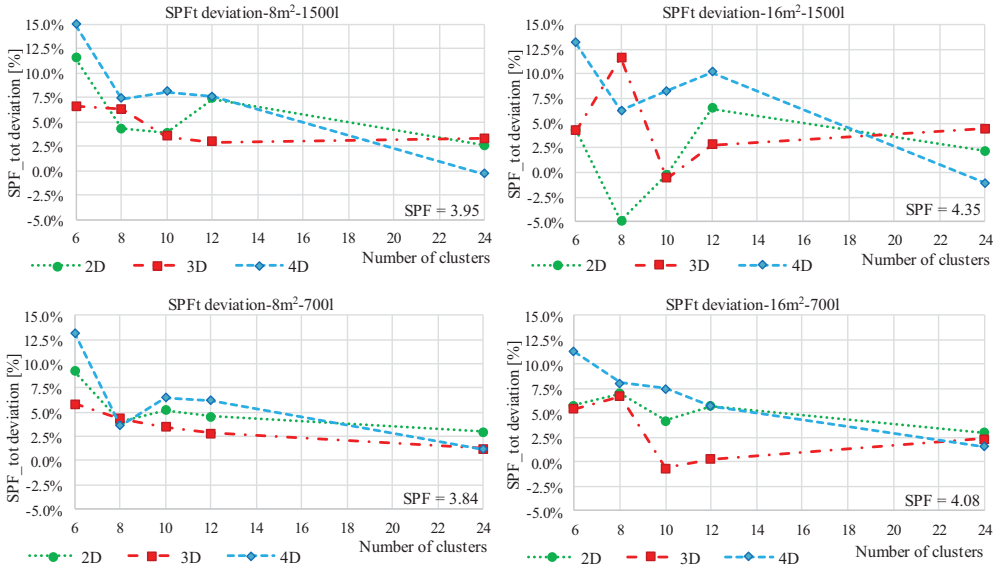

Fig. 6: Total seasonal performance factor as a function of the number of cluster and M-dimensional coordinates. Simulation of a SAHP system with different collector field and storage volume. Bolzano Climate.

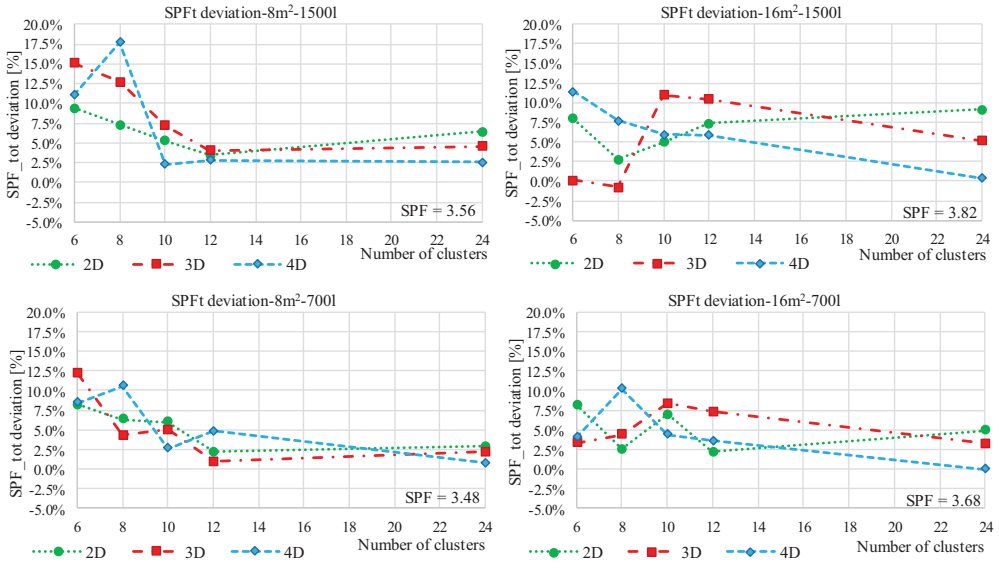

Fig. 7: Total seasonal performance factor as a function of the number of cluster and M-dimensional coordinates. Simulation of a SAHP system with different collector field and storage volume. Zurich Climate.

Tab. 2: RMSD in the different coordinate systems.

		2D	3D	4D		2D	3D	4D
Climate	**Stor.\Size**	**8m²**	**8m²**	**8m²**		**16m²**	**16m²**	**16m²**
BZ	**1500**	6.7%	4.8%	9.0%		4.2%	6.0%	8.8%
ZU	**1500**	6.7%	9.8%	9.6%		6.9%	7.2%	7.2%
BZ	**700**	5.2%	3.9%	7.3%		5.4%	4.1%	7.6%
ZU	**700**	5.6%	6.3%	6.5%		5.5%	5.7%	5.5%

Tab. 3: RMSD in the different coordinate systems.

		2D	3D	4D		2D	3D	4D
Climate	**Stor.\Size**	**8m²**	**8m²**	**8m²**		**16m²**	**16m²**	**16m²**
BZ	**1500**	0.35	0.14	0.6		0.5	0.53	0.62
ZU	**1500**	0.21	0.39	0.55		0.24	0.45	0.42
BZ	**700**	0.24	0.16	0.46		0.16	0.3	0.4
ZU	**700**	0.21	0.39	0.34		0.22	0.19	0.38

The system considered in this study presents the possibility to satisfy the space heating and domestic hot water loads with the solar energy or the heat pump, while the space cooling is satisfied only with the heat pump. The cooling SPF does not depends from the collector area and the storage volume and in the climate of Bolzano is quantified in 4.22. The figure 8 presents the trend of the deviation of the cooling SPF. This figure presents the same scale of the ordinate axis of figure 6 to show that the variation of cooling SPF is much lower than the total SPF and the deviation could be considered not dependent from the number of clusters. The reason is that the performance of the heat pump is close to be an affine dependence of the air temperature. We have shown with eq.3 to eq.5 that the clustering is nearly optimal in such a case.

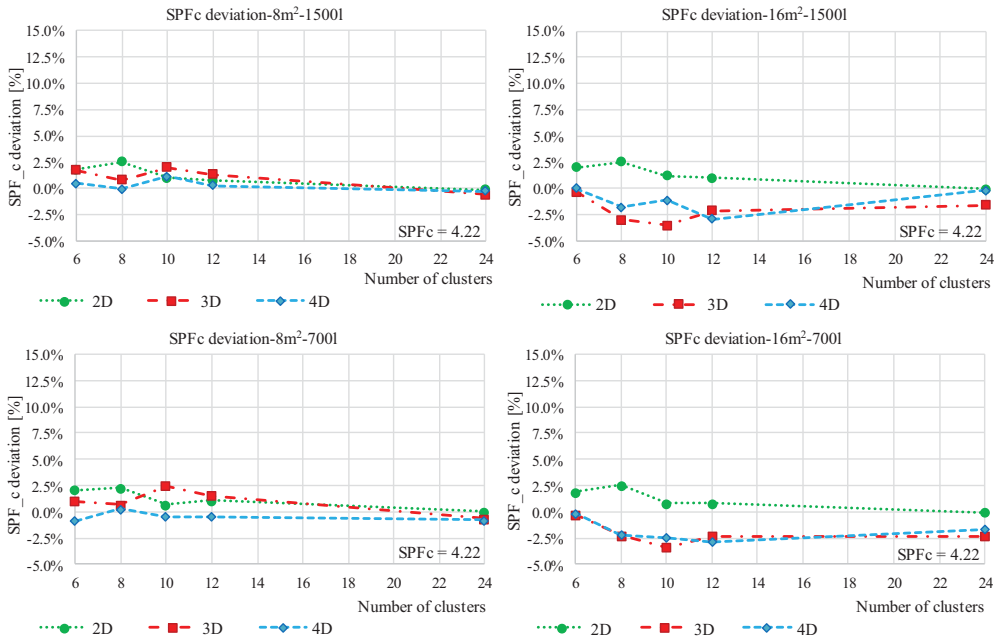

Fig. 8: Total seasonal performance factor as a function of the number of cluster and M-dimensional coordinates. Simulation of a SAHP system with different collector field and storage volume. Bolzano Climate.

Regarding the solar fraction, figure 9 presents the result of Zurich. The solar fraction is well reproduced for lower storage volume or collector area. The clustering with a 2D selection represents better the solar fraction with the only exception of Zurich with 16 m^2 and 1500 l (the sequence deviates from the annual simulation about 10 %). The cooling solar fraction is 0 since the plant uses only a compression chiller and not thermally driven chillers.

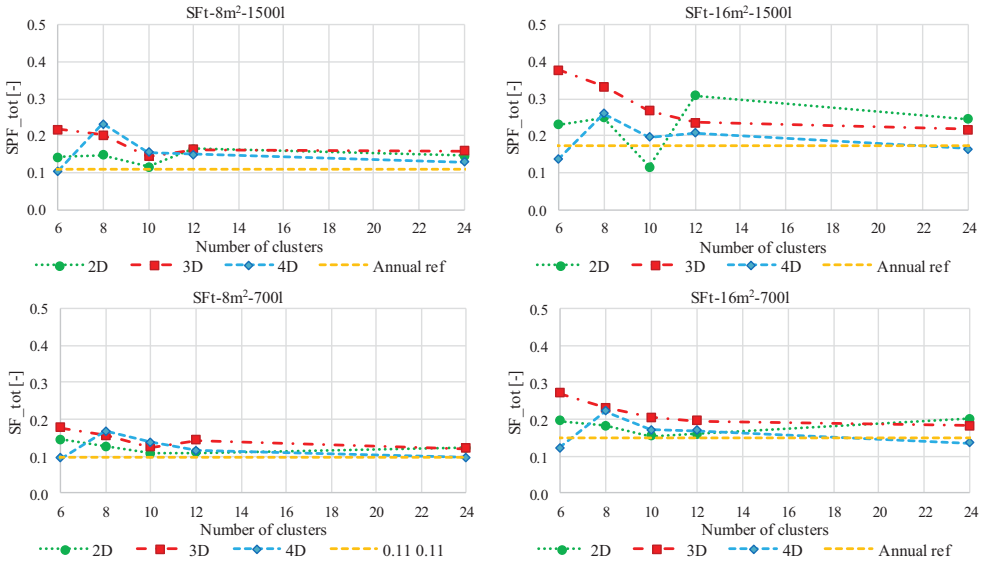

Fig. 9: Total solar factor as a function of the number of cluster and M-dimensional coordinates. Simulation of a SAHP system with different collector field and storage volume. Zurich Climate.

A shorter sequence is more attractive in terms of the cost connected to the testing phase but presents the highest uncertainty. In any case, the results presented previously showed that 2D or 3D coordinate system have a deviation lower than 10% with respect to the annual simulation. The 2D clustering was used to define a six-day sequence for other climates. Table 2 presents the total seasonal performance factor calculated with six-day sequence and with the annual simulation. The climates considered are Bolzano, Zurich, Gdansk and Rome. The highest deviation is 7.85% obtained for the climate of Zurich while the lowest deviation was obtained for the Roman case. This lower deviation could be also explained by the smaller collector area (16m^2 were not considered in this case since it would have not represented a good system design).

Tab. 4: Deviation of total SPF of six-day sequences defined with 2D clustering.

	Bolzano 16m²-1500l	**Zurich 16m²-1500l**	**Gdansk 16m²-1500l**	**Rome 8m²-1500l**
Six day	4.43	4.12	3.85	4.79
Annual	4.21	3.82	3.62	4.82
Deviation [%]	5.22%	7.85%	6.35%	0.62%

6. Conclusion

The purpose of this paper is to clarify the methodology used in the PLPE procedure to define a short test sequence starting from the annual weather data. The PLPE procedure is a method to perform dynamic test of entire heating and cooling systems in an objective way which is easily applicable to different climates and that allows a direct extrapolation of the seasonal results from the short test.

The underlying tool at the heart of the procedure is clustering. The days are grouped into clusters wherein each object is more similar to each other than to those in other clusters. To build the sequence, for each cluster, the

medoid, i.e. the closest object to the geometric centre, is selected. The days can be described with different quantities and the optimal solution is to consider the daily average temperature and the daily irradiation on horizontal surface. In the sequence, the days are ordered with the same order they occur in the year starting from the winter days and concluding with the summer days.

The sequence defined with clustering represents correctly the seasonal performances when those are linearly dependent to the boundary conditions; this could be a good approximation of heat pump system while for solar system the performances are not linearly dependent from boundary conditions.

Different system configurations have been simulated with sequences of different sizes. The deviation of the seasonal performance figures calculated with the short sequence and compared with the ones calculated with an annual simulation decreases as the number of clusters is increased. To that, we have noticed an influence on the accuracy given by the collector area and the storage volume. The deviation between the short sequence performance and the annual performance increases with increasing the collector area and the volume of storage.

A six-day sequence defined with 2D clustering has been defined for the climates of Bolzano, Zurich, Gdansk and Rome and the expected deviation is lower than 8%.

The main advantage of adopting the clustering is that the simple application of the methodology does not require any iterative simulation and therefore a test sequence can be defined for each climatic condition where the test would be performed.

The clustering could be used also for reducing the computational time for large parametric simulations. In that case the user can chose the proper number of clusters.

References

Besana, Francesco. 2009. “Heat Rejection Problematic in Solar Combi+ System.” PhD Thesis, Bergamo: Universitá degli studi di Bergamo.

Bettoni, Davide. 2013. “Design and Assessment of Optimised Control Strategies for Solar Heating and Cooling Systems.” PhD Thesis, Bergamo: Universitá degli studi di Bergamo.

Domínguez-Muñoz, Fernando, José M. Cejudo-López, Antonio Carrillo-Andrés, and Manuel Gallardo-Salazar. 2011. “Selection of Typical Demand Days for CHP Optimization.” *Energy and Buildings* 43 (11): 3036–43. doi:10.1016/j.enbuild.2011.07.024.

Drück, Harald, and T. Pauschinger. 2006. *MULTIPORT Store-Model*. Type. http://www.trnsys.de/download/en/ts_type_340_en.pdf.

Gan, Guojung, Chaoqun Ma, and Jianhong Wu. 2007. *Data Clustering: Theory, Algorithms, and Applications*. 10th ed. ASA-SIAM Series on Statistics and Applied Probability. Philadelphia: SIAM.

Haberl, R., E. Frank, and P. Vogelsanger. 2009. “Holistic System Testing-10 Years of Concise Cycle Testing.” In *ISES 2009*, 351–360. http://www.solarenergy.ch/fileadmin/daten/publ/202_Haberl_Frank_Holistic_System_Testing_FullPaper.pdf.

Haller, M.Y., R. Haberl, T. Persson, C. Bales, P. Kovacs, D. Chèze, and P. Papillon. 2013. “Dynamic Whole System Testing of Combined Renewable Heating Systems – The Current State of the Art.” *Energy and Buildings* 66 (November): 667–77. doi:10.1016/j.enbuild.2013.07.052.

Huchtemann, K., H. Engel, P. Mehrfeld, M. Nürenberg, and D. Müller. 2016. “Testing Method for Evaluation of a Realistic Seasonal Performance of Heat Pump Heating Systems: Determination of Typical Days.” In *CLIMA 2016*. Aalborg, Denmark.

Kaufman, Leonard, and Peter J. Rousseeuw. 2005. *Finding Groups in Data: An Introduction to Cluster Analysis*. Hoboken, NJ: John Wiley & Sons.

Klein, S. A., and et al. 2012. *TRNSYS 17 Volume 4 Mathematical Reference*. SEL (Solar Energy Laboratory, Univ. of Wisconsin-Madison), TRANSSOLAR(TRANSSOLAR Energietechnik GmbH), CSTB (Centre Scientifique et Techniquedu Bâtiment), TESS (Thermal Energy Systems Specialists).

Menegon, Diego, Anton Soppelsa, and Roberto Fedrizzi. 2017. “Development of a New Dynamic Test Procedure for the Laboratory Characterization of a Whole Heating and Cooling System.” *Applied Energy* 205 (November): 976–90. doi:10.1016/j.apenergy.2017.08.120.

Menegon, Diego, Alice Vittoriosi, and Roberto Fedrizzi. 2014. “A New Test Procedure for the Dynamic Laboratory Characterization of Thermal Systems and Their Components.” *Energy and Buildings* 84 (December): 182–92. doi:10.1016/j.enbuild.2014.07.085.

Solar Energy Education and Skill Development for Enhancing Quality of Life in Developing Countries

Namrata Sengar[1], Christopher Sansom[2], Douglas Halliday[3] and Deepak Gadhia[4]

[1] University of Kota, Kota (India)

[2] Cranfield Universiy, Cranfield (UK)

[3] Durham University, Durham (UK)

[4] MSA Renewtech, Vadodara (India)

Abstract

Worldwide, around more than one billion people are without access to electricity and around three billion people use solid biomass for cooking, water heating and heating their homes. Majority of the developing countries of the world receive more than 5 kWh/m^2 of global solar irradiation per day, which can be utilized for a variety of applications such as providing electricity, cooking, drying, water heating, space heating etc. Use of solar energy can provide pathways for social and economic development of communities without triggering climate change but it requires consistent growth and efforts in providing solar energy education and skill development. The paper discusses the inclusion of solar energy education at school level and in higher education, the solar awareness programs and establishing a skilled chain for installation, repair and maintenance of solar systems at regional/community level. It also discusses some of the initiatives being taken in India.

Keywords: Solar education, solar awareness, skill development, socio-economic development, employment.

1. Introduction

Energy is linked to almost every aspect of life in one form or another. According to the report of World Energy Council worldwide more than one billion people are without access to electricity (WEC 2016). Around 3 billion people use solid biomass for cooking, water heating and heating their homes and over 4 million people die prematurely from illness attributable to the household air pollution from cooking with solid fuels as per World Health Organization (WHO 2016). For sustainable development of communities in developing countries it is essential that clean, safe and affordable energy is made available. In order to provide clean lighting source and clean fuel for cooking to billions of people in this world, apart from technical and financial support, awareness and knowledge dissemination is important. The implementation of policies and schemes can only be successful if people are willing to accept the technology. Majority of the developing countries of the world receive more than 5 kWh/m^2 of global solar irradiation per day, which can be utilized for a variety of applications such as providing electricity, cooking, drying, water heating, space heating etc. Use of solar energy can provide pathways for social and economic development of communities without triggering climate change but it requires consistent growth and efforts in providing solar energy education and skill development. Solar energy education at school levels can help in enhancing the awareness and increasing the acceptability of solar systems into the society for various applications. Inclusion of solar energy education in technical courses in higher education may provide the deeper understanding of solar technologies, enhance the research and development and produce innovations for use of solar energy to solve local problems. Further, there is need for awareness programs for communities and development of chain of local persons who can install, repair and maintain solar systems. These measures may help to a large extent in improving the quality of life of many communities through solar lighting, solar cookers, dryers, distillation stills etc. and at the same time provide employment opportunities to many. According to a study by Karakul (2016) during last two-three decades there has been rise in unemployment as the links between education system and economic system has been loosened. The links between education system and economic system may be strengthened by educating according to the needs of the economy. Though solar and wind energy accounted for only 4% of power generation in 2014, but it is estimated by

doi:10.18086/swc.2017.08.04 Available at http://proceedings.ises.org

2060 it will account for 20% to 39% of power generation as per World Energy Council (2016). According to Ciriminna et. al. (2016) with the prospective rise of solar economy it becomes important to think on solar energy education. They have discussed about a multi-disciplinary graduate course on solar energy.

With the above aspects in mind, the present paper discusses the course structures for inclusion at school level and in higher education, the solar awareness programs and establishing a skilled chain for installation, repair and maintenance of solar systems at regional/community level. The basis has been taken as the educational system in India, it may be replicated in other developing countries as well.

2. Solar energy for improving lives

Worldwide many communities are still struggling for basic facilities from which clean and affordable energy supply is one. According to World Bank (2015), more than one billion people are living without electricity and another one billion face the problem of unreliable and inadequate supply of electricity. Mainly kerosene lamps are used for lighting lamps which provides dim light and is polluting. Around three billion people use polluting fuels like wood, charcoal, coal, dung and kerosene for cooking and heating applications. It is estimated that around four million deaths take place each year due to indoor and outdoor air pollution caused by use of polluting fuels. Most of this population lives in rural areas of developing countries of sub-Saharan Africa, Pacific region, south and east Asia and are poor. Energy availability is closely linked with social and economic development. Absence or inadequate availability of clean energy affects health care, availability of clean water, education, information, communications, environment, agricultural or industrial growth and productivity. Most of the time of women and children is spent is picking wood and carrying water. It deprives them of quality time for studying, recreation, leisure and following creative interests. It hinders their productivity and economic growth also. Access to affordable, clean and adequate energy is essential to reduce poverty, promote welfare and meet the goals of climate change mitigation.

Here solar energy can play an important role as solar energy can directly or indirectly meet most of the energy needs for electric power, heating, cooling, cooking, drying, desalination, transportation etc. Further, it is interesting to observe that most of the developing countries facing the problem of energy access lie in high solar radiation receiving areas of the world. According to Renewables global status report (2016) many countries have started programs for installing off grid and on grid solar PV home lighting systems. Countries such as Kenya, Uganda and Tanzania in Africa; China, India, Bangladesh and Nepal in Asia; Brazil and Guyana in Latin America are seeing rapid expansion of small-scale renewable systems. Solar PV systems with battery storage or grid integration can provide clean and reliable supply of electric power to most of the countries. Further, solar thermal applications can be used for cooking, drying, heating, water treatment, distillation etc. Major global energy use for heat is fossil fuel-based, so solar energy has a huge potential to be used for providing heat. With deployment of solar technologies deep to the rural communities in developing countries, the pace of socio-economic growth can be increased.

3. Solar education

Among many challenges in penetration of solar technologies is reluctance and hesitation of the people. This requires more involvement of people at local level in designing, installation, operation and maintenance of the solar systems. Involving local communities will result in better support, developing region based solutions and sustainability of the projects. Here role of solar education becomes very important. The penetration of solar systems will be smooth and very fast if the new generation as student gains knowledge about the principle, working and maintenance of the systems. Solar education in itself involves application of various scientific and technological principles which will make studies more practical and interesting.

3.1 School level

At school level some theory and experiments on solar energy may be included in the science/physics laboratory, after the student has learnt basics of heat transfer and electricity. The instruments and equipment to be used in the experiments need not be expensive and of very high accuracy. These should be meant to provide students with the fundamental knowledge and inculcate an interest in use of solar energy. The theory and experiments may include

- Observing photovoltaic effect through small solar panel
- Types of solar cells
- Study of I-V characteristics of solar panel
- Estimation of maximum power point and fill factor
- Charging of battery by solar panel
- Effect of shading on power of PV panel
- Effect of tilt on power of PV panel
- Study of PV power during different times of a day
- Differentiating between flat plate and concentrating solar collectors
- Study of box type solar cooker
- Study of parabolic solar cooker
- Study of solar distillation still
- Study of solar dryer,
- Study of Fresnel lens, etc.

The solar PV based experiments involve basic principles of electricity and the learning outcome will be greater understanding of these principles. These experiments mainly require a small size solar panel, a multimeter or voltmeter and ammeter, a resistance box and connecting wires. The students will learn the use of voltmeter and ammeter, understand about dc electricity provided by solar panel, plot I-V characteristics, concepts of short circuit current and open circuit voltage, maximum power point and fill factor. Study of variations of PV power with shading, tilt and time of day will help the students understand the effect of varying solar radiation on the panel.

Fig. 1: A simple experiment to study characteristics of solar cell

The solar thermal experiments give insight to the students about green house effect of glass, transmission, reflectance and absorbance of different materials. The students can learn about beam, diffuse and global solar radiation, optical and thermal properties of materials in a simple manner through solar collectors. A simple hot box solar cooker involves explanation of optical property and heat trap property of glass, black absorber coating on a good thermal conducting material and reduction of heat losses through thermal insulating material. Like this, numerous experiments can be designed according to age group of the students for explaining them various principles. The experiments are generally very simple and safe, and cost of the experiments mainly lies between $20-70. Teachers and students may be motivated to design the systems and study them. Most of the systems may be made from inexpensive materials. Some of the entrepreneurs may

also come up with suitable low cost experimental kits for the schools so that the students learn the fundamentals of science in a more effective way through experiments on solar systems.

Fig.2: Fresnel lens experimental set up

Fig. 3: Solar lantern with solar panel

Fig.4: Demonstration of cooking through parabolic solar cooker to village school students

Fig. 5: Demonstration of solar hot box cooker in village school

3.2 Higher Education

Inclusion of solar energy education in scientific/technical courses in higher education may provide the deeper understanding of solar technologies, enhance the research and development and produce innovations for use of solar energy to solve local/regional problems.

At the level of higher education many institutes in India offer B.Tech. and M. Tech. courses in renewable energy and recently some have started courses with specialization in solar energy. As solar energy is an extensive field covering materials, power generation, thermal applications, building design, modeling, simulation etc. it is required that a full- fledged master's course specialized in solar energy is run. In India M.Tech. is a two years course of four semesters, which includes a research project of around six months to twelve months. The course on solar energy consists of theory, experiments, seminars and project work mainly on

- Solar radiation –Physics of the Sun, solar constant, spectral distribution and variation of extraterrestrial radiation, air mass, beam, diffuse and global solar radiation, irradiance, solar insolation. Solar radiation on the earth surface - spectral energy distribution of solar radiation. Depletion of solar radiation - Absorption, scattering, atmospheric attenuation. Measurement through pyranometer, pyrheliometer, albedometer. Solar radiation geometry - Earth-Sun angles – Solar angles. Sunrise, sunset, solar day length, tilt factors, solar radiation on horizontal and tilted surfaces. Angles for tracking surfaces. Average and clear sky radiation, beam and diffuse components of hourly, daily and monthly radiation, radiation on sloped surfaces- isotropic and anisotropic sky, radiation augmentation, beam radiation on moving surfaces, effects of receiving surface orientation, utilizability.
- Fundamentals of materials- Electronic and atomic structures, atomic bonding in solids, structure of metals and ceramics, density computations, polycrystalline and amorphous materials. Polymeric structures, thermosetting and thermoplastic polymers, copolymers, polymer crystallinity, semiconductors, imperfections in solids. Diffusion mechanisms, factors affecting diffusion, diffusion in ionic and polymeric materials, phase diagrams, solubility limit, phase, microstructure, phase equilibria. Mechanical properties, concepts of stress and strain, Hooke's law, tension, compression and shear. Stress-strain diagram and thermal stresses, elasticity, effect of temperature, fracture and failure. Electrical, optical, thermal and magnetic properties of materials.
- Fundamentals of power generation- Power scenario-world and India, thermodynamic cycles, their importance and use, Carnot, Rankine cycle, modified Rankine cycle, Brayton cycle, Stirling cycle , Binary cycles, Combined cycles, reheat, regeneration and supercritical. Load duration curves, location of power plants, types of power plants- Steam, hydroelectric, diesel, gas, nuclear, biomass, solar and wind, relative advantages and disadvantages of different modes of power production, energy conversion and losses, power plant economics.
- Heat and mass transfer- One dimensional energy equations and boundary conditions – Three dimensional conduction equations - Extended surfaces – Critical thickness of insulations – Overall heat transfer coefficient. Convection-Momentum and energy equations, turbulent boundary layer heat transfer –Mixing length concepts, turbulent model – K - ε model. Analogy between heat and momentum transfer – Reynolds, Colburn and Von Karman. High speed flows. Radiation - Gases and vapour. Solar radiation – Sky radiations, solar radiation through fenestrations – Estimations. Phase change heat transfer, heat exchanger. Finite difference formulation of steady and transient conduction problems. Application of heat transfer in solar thermal system and its components.
- Energy audit and management- Role of energy conservation and energy efficiency. Energy Conservation Act- 2001, Electricity Act, Bureau of Energy Efficiency, energy and exergy analysis. Energy management and audit-need, objectives, types, methodology and phases, instruments used and report preparation. Material and energy balance, energy action planning, financial management, project management. Electrical system- losses, demand side management, factors affecting energy efficiency and minimizing losses in compressed air system, motors, fans and blowers, pumps and pumping systems, lighting system. Fuels and combustion, efficient utilization and energy saving opportunities. Thermal systems, cogeneration, heat exchangers, waste heat recovery, energy performance assessment of buildings and commercial establishments, financial analysis.
- Solar collectors- Radiation transmission through glazing, optical properties of cover systems, transmittance transmittance-absorptance product and its angular dependence, spectral dependence of transmittance. Flat Plate Collectors- components, basic energy balance equations, temperature distribution, collector overall heat loss coefficient, collector efficiency factor, collector heat removal factor, flow factor, critical radiation level, collector tilt and orientation, mean fluid and plate temperatures, effective transmittance- absorptance product, effect of dust and shading, heat capacity effects, liquid heaters, air heaters, measurements of collector performance, collector characterization and tests, practical considerations. Concentrating collector configurations, concentration ratio, thermal and optical performance of concentrating collectors, cylindrical absorber arrays, optical characteristics of non-imaging collectors, orientation, absorbed energy and performance of CPC collectors, linear imaging concentrators, ray trace method, incidence angle modifier, energy balance, paraboloidal concentrators, central receiver collectors, practical considerations.

- Solar photovoltaics- Semiconductors, charge carriers, carrier concentration, drift, diffusion, light absorption, recombination of carriers, solar cell design for high fill factor, properties of efficient solar cells, lifetime and surface recombination effects, efficiency and band gap, spectral response, parasitic resistance effects, temperature effects, efficiency limits for photovoltaic conversion. Crystalline silicon solar cell- manufacturing process, multicrystalline solar cells, photovoltaic modules, thin film silicon solar cells, high efficiency III-IV multijunction solar cells, amorphous silicon, Cu(InGa)Se_2 solar cells, Cadium Telluride solar cells and modules. Dye-sensitized solar cells, introduction, fabrication, new developments, approach to commercialization. measurement and characterization of solar cells and modules, rating PV performance.
- Solar thermal applications- Active and passive systems, auxiliary energy, natural and forced circulation systems, integral collector storage systems, testing and rating of water heaters, solar cookers-types, design components, factors affecting performance, Indian and international testing procedures. Solar process loads, energy storage, sensible, latent and chemical energy storage systems, solar dryers- types, direct gain, indirect gain, design components, application areas, solar distillation- design fundamentals, efficiency and practical considerations. Solar cooling: Fundamentals of refrigeration and air conditioning, solar absorption cooling, combined solar heating and cooling, solar industrial process heat. Solar thermal power plants: low, medium and high temperature power generation systems, thermal conversion systems, solar chimney power plant, central receiver power plant.
- Energy efficient buildings- Thermal comfort, factors affecting thermal comfort, comfort parameters, Climatic conditions, climate zones, heat flow calculations in buildings. Building heating and cooling- active methods, solar heating systems- liquid and air systems. solar energy- heat pump systems, phase change and seasonal storage systems, solar and off-peak storage systems, solar air-conditioning. Passive and hybrid methods for heating and cooling, insulation, shading, sunspace, storage walls and roofs, ventilation, evaporative and nocturnal cooling, earth–air tunnel, solar chimney, active collection-passive storage hybrid systems, heat distribution in passive buildings, Energy conservation building code. Building integrated photovoltaic systems.
- Solar power generation- Photovoltaic systems: Configuration and applications, grid –independent for small devices, PV systems for remote consumers of medium and large size, decentralized grid-connected PV systems, central grid connected PV systems. Components of PV systems-battery storage, charge controller and inverters. Design methodology for SPV system, system sizing. Installation, troubleshooting and safety, Economic analysis.
- Modeling and simulation- system, experiment, model, simulation - definition, importance, application areas, advantages, disadvantages and difficulties, types of models. Steps of modeling process-problem analysis, model formulation, model abstraction, defining variables, solving, execution, verifying, analysis of results. Verification and validation, Solar energy modeling techniques-, Brief introduction to the software used for simulation in solar energy field, comparative review of software for solar photovoltaics, solar thermal systems and buildings. Use of software such as TRNSYS, PVSYST, PVSOL, SAM, SOLTRACE, HOMER, Meteonorm etc.

The seminars focus on advancements in solar technologies, research and development, policy changes and their impact on industry and society. During project work student has to opt for a problem related to research depending on technical, industrial or society requirement.

At master's level students need to learn the principles and technologies with more depth and accuracy. More practical trainings, hands-on workshops and industrial collaborations improve the quality of the course and learning by the students. In order to improve the engineering education Royal Academy of Engineering,UK and FICCI, India have started Higher Education Partnership Project. This scheme involves partnership between Indian and UK universities and industry. In this scheme University of Kota has been awarded a project entitled "Enhancing teaching and research and development in Solar Energy Materials and Technologies through Capacity Building and Collaborative Research Projects" for its M.Tech. (Solar Energy) course. During this project instead of taking one major research problem, it was decided to carry out several minor research projects with involvement of students. This helped the students in gaining the skills. Solar based systems have been designed and developed through use of mainly locally available materials. The systems have been tested on-field for their performance and their economic analysis has been done. The

systems have been developed after analysing the requirement of the lower and middle income households and cottage industries of developing countries like India, which face the problem of availability of fuel in adequate amount and pollution due to solid fuel use. The system designed and tested are- solar cookers, solar distillation stills, solar dryer, solar PV cooler, solar PV induction cooker and solar water heater. The research projects aim at providing a solution to some regional/community level problem through use of solar energy. This promotes innovation, entrepreneurship and spin-out companies.

Fig. 6: Developed small size solar water heater for cottage textile industry of Kota

Fig.7: Solar dryer developed by students

Fig. 8: Design development and study of solar distillation stills with different absorber coatings

Fig. 9 Developed large size solar cooker/solar hot case

Fig. 10: Design, development and study of solar PV air cooler

Fig. 11: Developed solar PV induction cooker

4. Solar awareness and skill development

The Government of India has set a target of renewable energy capacity of 175 GW by 2022. 100 GW of this

is planned through solar energy, 60 GW through wind energy, 10 GW through small hydro power, and 5 GW through biomass-based power projects. Out of the 100 GW target for solar, 40 GW is expected to be achieved through decentralized rooftop projects, 40 GW through utility-scale solar plants and 20 GW through ultra-mega solar parks. For achieving this target it is necessary to address the availability of skilled manpower and capacity building.

In 2015Government of India announced the National Policy for Skill Development and Entrepreneurship. It envisages a major role of private sector as shared responsibility for skill development in the country. The Ministry of Skill Development and Entrepreneurship has been creating Skill Councils in various domains. The initial funding for the Sector Skill Council is by the government through National Skill Development Corporation (NSDC) with 10% contribution from the industry. It becomes a self-sustainable body over a period of 3-5 years. Skill Council for Green Jobs (SCGJ) has been created in 2015, promoted by the Ministry of New and Renewable Energy (MNRE) and Confederation of Indian Industry (CII). In a report by SCGJ the skill gap is assessed as around 0.4 million for solar engineering, procurement and construction, 0.2 million for solar operation and maintenance, 36 thousand for solar off-grid and 16 thousand for solar thermal applications. SCGJ is offering various courses related to solar PV installations such as solar PV installer (Suryamitra), solar PV installer (Electrical), solar PV installer (Civil), solar PV rooftop entrepreneur, solar proposal evaluation specialist and rooftop solar grid engineer etc. for reducing the skill gap (SCGJ reports, 2016)

Apart from government initiatives, many not for profit organizations are also working for solar awareness and skill development such as Barefoot College. Barefoot college is exemplary as it involves women from rural areas, train them in solar technologies and empower them. They have trained more than 750 engineers in more than 1300 villages worldwide and have provided light 0.5 million people with light. Some companies are using their corporate social responsibility fund to disseminate solar systems which is also promoting solar awareness. Academic institutions and departments of science and technology hold workshops, exhibitions and competitions for spreading the knowledge.

5. Challenges and suggestions

Solar education and skill development are important for sustaining the deployment of solar systems deep into the regions waiting for access to clean energy. The various schemes and projects die out if proper measures are not taken. It is important the training should focus on both the technical aspects as well as engaging community, explaining and managing finances, knowledge of policies and project implementation. There can be several challenges in the way of solar education and skill development, overcoming those require following steps

- Understanding local needs
- Engaging communities and women
- Maintenance of quality of training programs
- Development of specialized solar courses
- Research and development as per local problems
- Involving industries as partner with academic institutions to enhance skills
- More hands-on training
- Monitoring and assessing the skills
- Support for entrepreneurship
- Reducing bureaucracy and corruption in implementation of skill development schemes
- Motivating rural communities to be self-reliant
- Sustained effort by government, academic institutes, industries and society.

Terrapon-Pfaff (2014), Dóci (2015) and Bossink (2017) have stressed on continuous evaluation and learning to develop sustainable prototypes as per need and engagement of the community and following chain of up

scaling and making it commercial with industry. So, solar education and skill development will be a continuous process involving evaluation and improvements.

6. Conclusions

Solar energy holds the potential to improve the quality of life of people in developing countries. Solar energy education and skill development are important for promoting the solar energy technologies to the communities without access to clean energy in developing countries. Solar energy education can easily form a part of school curriculum with simple theory explaining scientific principles involved and simple low cost experiments for practical understanding. In higher education, advanced and in-depth study of solar energy will help students get equipped with designing, improving and innovating new solar systems as per the need of local communities. Skill development initiatives can form a part of government's action plan, and industries and academic institutes can play a significant role in it. With these measures, it will be important to monitor, evaluate and assess the quality and need of programs. Further, involvement of local communities is essential for sustainability of the projects.

Acknowledgement

Authors gratefully acknowledge the support of Royal Academy of Engineering, UK and FICCI, India.

7. References

WEC 2016 https://www.worldenergy.org/wp-content/uploads/2016/10/World-Energy-Scenarios-2016_Full-Report.pdf accessed on 12/10/2017.

WHO 2016 http://www.who.int/mediacentre/factsheets/fs292/en/ accessed on 12/10/2017.

Ciriminna, R., et.al. 2016. Rethinking solar energy education on the dawn of the solar economy. Renew. Sust. Energy Rev. 63, 13-18.

Karakul, A.K., 2016. Educating labour force for a green economy and renewable energy jobs in Turkey: A quantitive approach. Renew. Sust. Energy Rev. 63, 568-578.

World Bank Support to Electricity Access FY 2000-2014: An independent evaluation, http://www.worldbank.org accessed on 13/10/2017.

Banerjee S.G. 2015. Power for all: Electricity access challenge in India, World Bank, http://dx.doi.org/10.1596/978-1-4648-0341-3.

Renewables 2016 global status report: REN21Renewable Energy policy network for the 21st centuary, http://www.ren21.net/wp-content/uploads/2016/05/GSR_2016_Full_Report_lowres.pdf accessed on 13/10/2017

http://niti.gov.in/writereaddata/files/writereaddata/files/document_publication/report-175-GW-RE.pdf accessed on 14/10/2017

http://sscgj.in/ accessed on 14/10/2017

http://sscgj.in/wp-content/uploads/2016/06/renewable-energy-solar-skill-gap.pdf, accessed on 14/10/2017

http://sscgj.in/wp-content/uploads/2016/06/SCGJ-skill-gap-report.pdf accessed on 14/10/2017

https://www.barefootcollege.org/solution/solar/ accessed on 14/10/2017

Bossink B.A.G., 2017. Demonstrating sustainable energy: A review based model of sustainable energy demonstration projects, Renew. Sust. Energy Rev. 77, 1349-1362. doi:10.1016/j.rser.2017.02.002

Dóci, G., Vasileiadou, E., 2015. Let's do it ourselves- Individual motivations for investing in renewables at community level, Renew. Sust. Energy Rev., 49, (2015) 41-50. doi:10.1016/j.rser.2015.04.051

Terrapon-Pfaff, J. et. al., 2014. A cross-sectional review_Impacts and sustainability of small-scale renewable energy projects in developing countries, Renewable and Sustainable Energy Reviews, 40, 1-10. doi:10.1016/j.rser.2014.07.161

Digital Media to contribute to the development and dissemination of renewable energy systems

Alex Zahnd[1,2], Christoph Pimmer[1], and Urs Groebhiel[1]

[1] University of Applied Sciences and Arts Northwestern Switzerland (Switzerland)

[2] RIDS-Nepal/Switzerland, (Nepal/Switzerland)

Abstract

Awareness raising and education regarding the use and application of renewable energy systems is a key issue in many development projects. The goal of this practice-based research was to explore the potentialities of locally developed instructional videos on tablet PCs to create awareness about renewable energy systems and to train mostly illiterate communities in extremely secluded areas to operate and maintain these systems. To do so, a case study was carried out in the Nepalese Himalayan Mountains. The observational mixed-method evaluation indicates (a) that, upon initial instruction, local people were able to handle videos on tablets PCs well. In addition, (b) after studying the tablet-based videos, small groups of workers were able to carry out concrete manual and analytical tasks regarding the development and operation of renewable energy systems; the findings also suggest that villagers' understanding of more complex tasks was enhanced significantly by showing videos a second time; and (c), the facilitated screening of instructional videos with a battery-charged handheld projector in public areas allowed the whole community to participate, watch, and engage in awareness raising and learning processes.

The pilot study supports the tentative conclusion that videos, which are produced locally and shared via mobile technologies, can serve as viable means in raising awareness and creating learning opportunities regarding the use of sustainable energy systems in extremely remote communities with a predominantly illiterate population. Further research is needed to corroborate the findings of this exploratory and small-scale pilot study.

Keywords: digital media, instructional video, awareness raising, education, skill training, tutoring, low literacy, renewable energy systems, mobile learning

doi:10.18086/swc.2017.08.05 Available at http://proceedings.ises.org

1. Introduction and background

1.1 Challenges in the introduction and maintenance of renewable energy systems

The importance of implementing, operating and maintaining renewable energy systems is widely recognised. It is, perhaps most prominently, reflected in the sustainable development goals: Goal 7 highlights the access to affordable, reliable, sustainable and modern energy for all (SDG Goals, n.d.). The health-related, economic, educational and social benefits of sustainable and renewable energy systems are particularly important in low-income contexts. For instance, solar-based lighting would provide extra time for families to generate income and would allow children to do homework in the evening, let alone the health and ecological benefits of banning lighting sources such as open fire or kerosene lamps (The World Bank, 2016). However, the reality is still bleak for 20% of the global population who lack access to modern electricity and the 3 billion people who rely on wood, coal, charcoal or animal waste for cooking and heating (SDG Goals, n.d.).

The implementation of renewable energy systems in low resource contexts and elsewhere goes far beyond the introduction of new technologies. A change affects the overall system and often results in a novel configuration of actors, organization and practices which is in many cases, not a straightforward but a lengthy and dynamic developmental process (Negro et al., 2012). Accordingly, it is key to not only work together with local communities, but also to make them fully understand and drive these changes (Reid et al., 2009, Jerneck and Olsson, 2013). To do so, local people need to acquire the technical knowledge of building and maintaining renewable and sustainable systems. In addition, they also need to understand the underlying ecological, health-related and economical motives for this transformation.

A change in beliefs and practices requires systematic awareness raising, exposure and education. The organisation and realisation of these measures in the settings under investigation, i.e., the remote, underdeveloped and high-altitude villages in the North-West Nepalese Himalayan Mountain districts of Humla and Jumla, is a complex and challenging endeavour for a number of reasons. Yet the logistics of organising training events in the scattered villages are problematic, as it takes days of walking to reach these villages. This condition is further aggravated by the fact that many of the local people have very limited or no literacy or numeracy skills, which inhibits the value of written instructions and operation manuals. To address these contextual constraints, extended time and effort is needed, which, as past projects have shown, often exceeded budgets and time frames of smaller initiatives. Conventional training can be also problematic because it can reinforce existing power imbalances. Tensions can be created for example by community leaders who prioritise friends and relatives in the recruitment process (i.e., groups who are often more interested in receiving the per diem than in the training content) at the expense of the actual target group, as prior research has shown (Zossou et al., 2009).

1.2 Producing local videos to share local knowledge in community development context

One way in which awareness raising and training activities can be supported are videos. Video is seen as a powerful tool in development work, because it can attract people's attention, addresses barriers of illiteracy and it is reflective of the narrative culture and the oral traditions which are conspicuous characteristics in many rural contexts (Lie and Mandler, 2009). In addition, it can reach many people at the same time (Zossou et al., 2009). Although video has been applied in development cooperation for more than 30 years, recent developments, such as decreased costs and improved usability, have resulted in an increase in the use of this technology (Lie and Mandler, 2009). Advances in mobile and portable technologies have also widened dissemination and screening opportunities, for example by using handheld, battery-powered projectors (Cai et al., 2013, Kumar et al., 2015), or by directly distributing videos on users' personal mobile devices (Vashistha et al., 2016).

In development and low-resource settings, videos are being used for manifold purposes including capacity building and awareness raising (Lie and Mandler, 2009) across a wide range of disciplines, such as agriculture (Gandhi et al., 2007), health (Kumar et al., 2015) and climate change (Plush, 2013). In context of the present research, both training and awareness raising were of relevance. The idea was to use short videos to support the technical training regarding the implementation, operation and maintenance of a community-owned village drinking water system. Other videos were aimed at educating and raising the awareness of local communities regarding the underlying causes and benefits of this transformation.

However, despite the identified opportunities and potentialities, there is still relatively little systematic research on the use of videos in very marginalised and remote settings. Yet, there are a number of good-practice principles that

can guide and inform practitioners in the development and deployment of persuasive, educational and awareness raising videos.

In the video production process, it is recommended to follow the principles of participatory design, which requires the close involvement of the target group from the very beginning (Kumar et al., 2015). Local participation is important because it ensures the appropriateness of the verbal and visual language and it enhances the persuasiveness of the video (Lie and Mandler, 2009). For example, in an Indian agricultural extension service context, videos which featured farmers who spoke the same dialect and accent and who had similar levels of education as the target group were much more trusted by the audience than the ones which involved educated and outside experts. In the same vein, farmers were more convinced to adopt a new agricultural technique if they realised that peers to whom they could relate had already endorsed and implemented this practice (Gandhi et al., 2007). Another influencing factor was the type of content. It was witnessed that videos which featured engaging forms of content such as concrete demonstrations, testimonials and entertainment were clearly preferred over videos in classroom-style lectures (Gandhi et al., 2007).

In the training itself, it is important not to conceive videos as self-explanatory and standalone tools. Instead, it has been suggested to combine them with hands-on practical tasks and printed materials to help increase the understanding of the video content (Lie and Mandler, 2009). For example, a quasi-experimental study found that although both video training and traditional lecture-based demonstration increased agricultural knowledge of men and women, only the combination of these two methods decreased the pre-existing gender knowledge gap (Cai et al., 2013). In addition, the screening of videos should be facilitated, for example in the form of moderated group training sessions at the community level. Facilitators should seek to trigger reflection and enhance learning by highlighting the main points, moderating the discussions, raising questions and collecting feedback (Lie and Mandler, 2009). The value of facilitation is confirmed in the empirical literature: Whereas the screening of videos alone was received poorly and resulted even in people leaving the events, yet minimal facilitation positively impacted their interest (Gandhi et al., 2007). If need be, the facilitator can also screen the whole video or specific sequences a second time (Lie and Mandler, 2009), which is relevant because it was found that the audience frequently required a second viewing to better grasp the contents (Gandhi et al., 2007).

An emerging body of studies has confirmed the instructional value of videos, and especially of participatory videos, in sensitizing and educating local communities. For example, the facilitated screening of participatory videos in an agricultural extension project in rural India increased the adoption of certain agricultural practices by a factor seven while being 10 times more cost-effective in comparison to common training and visit-based extension services (Gandhi et al., 2007). The authors emphasised that it was not the technology but the people and social dynamics which ultimately triggered the change (Gandhi et al., 2007). Positive effects were also achieved through the facilitated screening of farmer-to-farmer videos of a rice parboiling process to communities in Benin. The video caused 95% of the audience to improve their practices compared to about 50% who received the conventional training (as a 2-day community workshop). No differences were found between people who only watched the video and people from a third cohort who watched the video and attended the training. This underscored the value of video as the most effective instructional means.

Open video screening is also considered a more democratic form of education compared to closed training sessions. Research from Benin has shown that neither ethnic group, age, number of dependents in the household, education level, perceived importance of and motivation for the topic, experience, religion and membership in a farmer organization influenced the participation in the viewing practices (Zossou et al., 2009). However, not all studies confirmed the superiority of facilitated video screening over traditional training methods (Cai et al., 2015, Cai et al., 2013). Although a participatory video on nutrition, which was shown to smallholder farmers in Malawi, increased the participants' knowledge as much as the control group with the conventional demonstration, it was less effective in changing the farmers' nutrition practices in the short term. Reasons were seen in the video cohorts' inability to taste and smell the food (Cai et al., 2015).

2. Approach and evaluation methods

2.1 Research question

The research questions were centred on the feasibility of using locally produced, participatory videos in very remote areas of the Nepalese Himalaya region. Concretely, they were formulated as:

(1) Whether, and if so how, can poorly literate and illiterate people in extremely secluded areas access and handle videos on tablet PCs?

(2) Whether, and if so how, can poorly literate and illiterate people in extremely secluded areas use participatory videos on tablet PCs to learn and perform concrete manual and analytical tasks regarding the installation, operation and maintenance of renewable energy systems?

(3) Whether, and if so how, can the screening of videos with battery powered handheld projectors during community meetings engage and raise the awareness of poorly literate and illiterate people in extremely secluded areas?

2.2 The setting: an extremely remote and poor Nepalese mountainous area

The practice-based research was carried out in the remote Nepalese mountain village of Syada (210 families and at 2'750 meters above sea level). It can be reached either by an 8-10 day trek from the nearest road or by a one-hour airplane flight to Simikot from Nepalgunj in the South and an additional one-day trek. The research site is in the district of Humla, which ranks among the country's three least developed districts regarding poverty, gender inequality and deprivation (CBS and ICIMOD/MENRIS, 2003). The Swiss-Nepalese NGO RIDS-Nepal/Switzerland has been working and partnering with the Syada village community since 2003 in small scale community development projects. The request of the village community to build a village drinking water system in 2015 in partnership with RIDS-Nepal formed the jumping-off point for this practice-based research project.

Fig. 1: Syada Village's (yellow pin) geographical location, in the northern part of Humla district, ©2017 Google Earth / 2017 CNES / Airbus Image Landsat / Copernicus Image © 2017 Digital Globe.

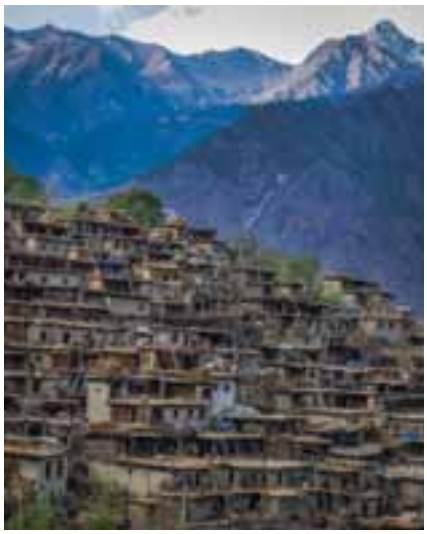

Fig. 2: Syada Village in northern Humla with 210 farmer families 2750 meters above sea level.

2.3 The production and use of the videos

The design and use of the videos was informed by the findings of the literature described in the previous sections. The videos were filmed and cut by RIDS-Nepal/Switzerland, a Swiss-Nepalese NGO. The local cameraman and video editor, who was from one of these remote villages, was trained and supervised by the NGO. The training and production took place in the form of face-to-face working phases, e-mail communication and Skype calls from the RIDS-Nepal head quarter in the Jumla district, when Internet was available. A number of 23 videos was produced (RIDS-Nepal/Switzerland 2017). The videos featured local actors directly from the communities who explained the rationale for and benefits of implementing renewable energy systems in story-like narratives and demonstrated specific tasks. The task-oriented videos adhered to the following design principles: providing a brief verbal overview of the process; an itemization of the required resources; step by-step instructions in which the local actors

demonstrated how a task was carried out (Gandhi et al., 2007). The use the videos was combined either with practical instructions and follow-up hands-on tasks, or in the community setting in which it was actively facilitated by a member of RIDS-Nepal/Switzerland, as specified in the following.

2.4 Task 1: Accessing and handling of videos on tablet PCs

First, local people were instructed regarding how to handle and use the tablet PCs. The RIDS-Nepal/Switzerland staff invited small groups of 4-6 people to participate in this learning event. Each group was informed about the activity. Then the staff member demonstrated the handling of the tablet to the group, which included the following steps: (1) switch on the tablet and log in; (2) navigate to the video folder; (3) select the correct video; (4) adjust volume (5) start playing the video (see Task 2). Then the tablet was switched off and handed over to the group with the task to repeat this step-by-step process. Each of the steps was evaluated on a scale from one to five. One signified that the step was not accomplished and great difficulties were experienced. Five meant that the step was very well accomplished. This procedure was carried out two times, i.e. with two groups in each of the four villages involved.

Fig. 3: Task 1: people handling the tablet PC

2.5 Task 2: Videos to learn and perform manual and analytical tasks

The second task consisted of the evaluation of the extent to which the groups were able to perform concrete manual and analytical tasks after watching short, tablet PC-based instructional videos. The first video (Task 2a) explained the evaluation of the suitability of a village owned water source. The goal was to learn how to determine systematically whether or not a spring provides sufficient water throughout the year so that it can be used as the village's central water source for their village drinking water system. This process involved several steps ranging from organizing and collecting the necessary items (two different sized buckets and a stopwatch) to measure the water source and calculating the water flow per minute.

Fig. 4: Task 2a: Village-owned water source measurement

The second video (Task 2b) required a group of female and male participants from the respective villages to moderate a process to identify suitable positions for tap stands in their village. First, a video was shown to the groups regarding how to organize and moderate this procedure. Water tap stand identification is a complex process, which requires the consideration of several infrastructural, social and cultural aspects. The final decision needs to be taken and supported by all community members. For example, a certain distance to houses and fields needs to be maintained to ensure that excess water would not flow into the people's premises. Upon viewing the video, the group moderated this process. Together with the community they developed a social map of the village on a rooftop of one of the houses (Figure 5). They used diverse items (e.g., stones, wooden sticks, charcoal, and leaves) to map the major infrastructure such as houses, walking paths, temples, fields and forest in and nearby the village as accurately as possible. On this basis, the community discussed locations for each of the water tap stands. The selection of the location of each tap stand was organized in the form of a democratic decision-making process.

Fig. 5: Task 2b: Social Mapping - Village water tap stand identification led by one of the participants

In each of the tasks, the video was shown to a group of about 4-6 people. This was followed by a question-and-answer session moderated by a facilitator from RIDS-Nepal/Switzerland. Then the participants performed the task. The task water measurement was more complex and thus the participants watched the video and carried out the associated hands-on water source measuring tasks two times (evaluated as a first and second trial). The accomplishment of steps and other criteria, for example the involvement of a sufficient number of female participants in the tap stand identification process, was evaluated according to a predetermined schedule on a scale of 1-5.

2.6 Task 3: Videos publically screened through a handheld, battery powered projector to raise awareness and educate communities

Also Task 3 was managed by an NGO staff who organised a community meeting. The video featured messages on the importance of a holistic community development (HCD) approach, the "Family of 4", which included the four basic and most often identified needs of the local village communities to be addressed as part of a long-term village development process. The four pillars of the "Family of 4" HCD are: (1) a toilet for each family; (2) a smokeless metal stove in each household; (3) basic indoor lighting powered by tapping into one of the locally available renewable energy resources and transformed through a contextualised renewable energy technology (such as solar PV, wind turbine or small hydro power plant; (4) clean and sufficient drinking water from the village-based water tap stands. After watching the video, facilitator asked the community the following questions: (1) name the four different "Family of 4" programs; (2) list the sequence of implementation, (3) explain the rationale behind the sequence, and (4 a to d) explain how the short- and long-term impact on families and community differ if 4, 3, 2 or only 1 of the "Family of 4" programs would be implemented. The video screening took place (see Figure 6) in the evening, using a tablet PC, a battery-powered handheld projector and an improvised screen (a white cotton sheet). After screening the video, the NGO staff asked up to 6 people (each 3 women and men respectively) the predefined questions. Apart from the answers elicited from the persons who were explicitly addressed, further discussions were stimulated and a number of additional people shared their opinion or experience. In this sense, the level of knowledge was evaluated as a collaborative product of the community.

Fig. 6: Task 3: Public video screening, awareness raising and educating the whole village community

The evaluation of all of the three tasks was carried out according to a predetermined assessment protocol. The participants' responses and actions were evaluated based on a set of previously developed criteria. For example, the step "collecting items" in the task water measurement was evaluated according to the following scheme: 5 points if all 4 items were collected, 4 points if 3 items were collected etc. The evaluator also took field notes, which were collected and analyzed in addition to the quantitative data.

3. Results

3.1. Task 1: Accessing and handling of videos on tablet PCs

The evaluation regarding the handling of the tablet was carried out in four villages with two pilot groups each. The results indicate that, in total, the small groups managed to handle the tablets well, with an average (mean) of 3.9 out of 5 points (Table 1). The more difficult tasks appeared to be the navigation to the video folder and the adjustment of the volume. It was also observed that women had more difficulties in using tablet PCs and they needed more support and repeated instructions. However, the most remarkable differences were found between villages and not between tasks. One village (4) scored particularly low. This might be explained by the fact that this village had an especially high number of poorly literate and illiterate people. According to RIDS-Nepal/Switzerland's evaluation, Village 4 could be also qualified as the least developed village from the cohort involved.

Tab. 1: Task 1 Accessing and handling of videos on tablet PCs

	Group 1				**Group 2**				
Steps / Villages	**Village 1**	**Village 2**	**Village 3**	**Village 4**	**Village 1**	**Village 2**	**Village 3**	**Village 4**	**Means**
Switch on tablet	5	5	5	2	5	4	4	3	**4.1**
Login	5	3	5	2	5	3	5	4	**4.0**
Navigate to video folder	4	4	5	1	4	4	4	3	**3.6**
Select correct video	5	5	4	2	5	5	4	4	**4.3**
Adjust volume	4	3	3	1	5	4	4	3	**3.4**
Play video	4	4	4	2	5	4	4	3	**3.8**
Means	**4.5**	**4**	**4.3**	**1.7**	**4.8**	**4**	**4.2**	**3.3**	

3.2 Task 2: Videos to learn and perform manual and analytical tasks

The video instructions on tablet PCs were regarded highly by the involved participants and, with a few exceptions, the tasks were carried out well (Table 2). It was observed that the group which found the videos particularly useful was illiterate women. This could be explained by the fact that their illiteracy and social position excluded them otherwise from similar participatory learning and community events.

Table 2 shows the participants' performance regarding the individual steps of the task water source measurement. As indicated, this task was more complex and the participants thus watched the video and carried out the associated tasks two times (labelled here as trial 2). In comparison with the first trial (Mdn = 3), showing the video a second time significantly enhanced the performance of the participants (Mdn = 5), as determined through a Wilcoxon signed ranks test ($Z=-3.704$ $p<.000$).

Tab. 2: Task 2a Water Measurement

	Trial 1				**Trial 2**				
Steps / Villages	**Village 1**	**Village 2**	**Village 3**	**Village 4**	**Village 1**	**Village 2**	**Village 3**	**Village 4**	**Means**
Organize equipment	4	4	4	4	5	5	5	5	**4.5**
Measure time	4	3	3	1	5	5	5	3	**3.6**
Measure water flow	4	4	3	2	5	5	4	3	**3.8**
Calculate water flow	3	3	3	2	4	4	5	3	**3.4**
Means	**3.8**	**3.5**	**3.3**	**2.3**	**4.8**	**4.8**	**4.8**	**3.5**	

The most difficult step was the calculation of the water flow (in litres per second), as it involved the solving of an arithmetic problem. This required the facilitator to demonstrate the task in addition to viewing the video at the measuring site in the second trial. However, after this demonstration, participants were able to calculate this measure rather easily, as some of them had a mobile phone with a calculator. In general, it was observed that younger men who had mobile phones and were familiar with the calculator app understood the calculation task better than elder people and women.

In the task water tap stand identification (Task 2b), the participants organised a group of villagers to develop a map of the village and to discuss and agree on the distribution of the water tap stands. In this task (like in the task water measurement), differences appeared to be more pronounced between groups (villages) than between steps, as can be seen in table 3. In particular in Village 1 and Village 2, the people and spokespersons were more actively engaged than in Village 3, which resulted in better results (Table 3).

Tab. 3: Task 2b Water tap stand identification through social mapping as a whole community

Steps / Villages	Village 1	Village 2	Village 3	Village 4	Means
Organise people & materials	5	4	4	4	**4.3**
Correct mapping	4	4	2	4	**3.5**
Identification of tap stand locations	5	5	2	4	**4.0**
Justification of tap stand locations	4	3	1	3	**2.8**
Means	**4.5**	**4.0**	**2.3**	**3.8**	

3.3 Task 3: Videos on handheld projectors to sensitize and educate communities

The public screening of the videos in each of the four communities raised considerable interest and the events were very well visited - with a total of approximately 380 participants (about 140 in Village 1, 120 in Village 2, 60 in Village 3 and 60 in Village 4). The video was received very well and participants requested to watch it at least two times. Again, illiterate women in particular provided positive feedback. They indicated that the spoken and visualised instructions helped them understand the rationale behind and the benefits of the "Family of 4 " HCD project concept, thus overcoming their illiteracy constraints and being active members of the village's awareness and knowledge building processes. As can be seen in Table 4, the quality of the responses from the community participants was found to be satisfactory. The importance and prioritisation of each of the "Family of 4" HCD programs was explained well. However, the participants had more difficulties in explaining the relation of the individual programs, and even more so, the possible synergistic benefits of the "Family of 4" programs (Questions 4a to c). The observations also point to helpfulness and persuasiveness of additional testimonies provided by some people who described their personal experience and especially the benefits that they experienced with the "Family of 4" programs.

Tab. 4: Task 3: "Family of 4" Holistic Community Development Concept Video

Questions / Village	Village 1	Village 2	Village 3	Village 4	Means
Q1: Name all four "Family of 4" programs	3.5	2.7	3.0	2.0	**2.8**
Q2: Describe implementation prioritization	3.5	2.7	3.0	2.0	**2.8**
Q3: Describe importance of each measure	4.0	3.3	3.3	3.0	**3.4**
Q4a: Describe benefits 4 measures	3.5	2.0	2.0	2.5	**2.5**
Q4b: Describe benefits 3 measures	3.0	2.0	2.0	2.0	**2.3**
Q4c: Describe benefits 2 measures	3.5	2.7	2.7	2.5	**2.8**
Q4d: Describe benefits 1 measures	3.5	3.7	3.3	3.5	**3.5**
Means	**3.5**	**2.7**	**2.8**	**2.5**	

4. Discussion and conclusion

The findings of this practice-based study point to the feasibility and value of using locally produced awareness raising and educational videos for poorly literate and illiterate people in very isolated and secluded mountainous areas in the design, implementation and use of sustainable renewable energy systems. The videos were received very well by the individual study participants and the community as a whole. The public screening produced considerable effects in terms of interest, and increased awareness and collectively building up new knowledge. It was observed that the people in the community frequently wanted to view the video more than one time (as in the study of Gandhi et al., 2007), which, as the findings of the present study indicate, enhanced their understanding of the content significantly.

The findings also suggest that, upon initial instruction, local people were able to handle videos on the tablet PCs well. In addition, the tablet-based videos enabled small groups of workers to carry out concrete manual and analytical tasks regarding important community development measures for their village. The increased levels of knowledge and practical skills resonate with results from prior studies (Cai et al., 2015).

Perhaps the most genuine value offered by the videos was to allow groups of people, especially females and older people, with otherwise severely constrained educational and participatory opportunities, to acquire knowledge and to engage in central social processes in the community. This confirms previous research, for example from Benin, which revealed the democratising potentialities of public video screening, especially in comparison to closed training sessions (Zossou et al., 2009).

The qualitative observations indicate that one key to success was the incorporation of story-like elements (Lie and Mandler, 2009), which was regarded highly by the viewers. It was also observed that the testimonies and the local "good practice" examples demonstrated in the videos, such as a clean and hygienic kitchen, had a persuasive impact on the participants who appeared to transform their practices as could be often seen in the follow-up visits. However, this aspect was not measured systematically. Another practice-based observation was that, in the cultural context under investigation, the use of songs in the videos allowed the creators to highlight delicate and critical issues in the respective communities, such as the importance of gender equality, e.g. with regard to firewood collection, and the damaging exposure of women to indoor air pollution. Drawing on this insight, the project team has decided to film and incorporate songs about individual developmental measures in the production of future videos.

Although this study points to the feasibility and potential of using videos in highly secluded areas, the validity of the findings is constrained by a number of limitations which were mostly tied to the particularities of working in an extremely remote area. Firstly, only the immediate reception and knowledge output was measured and no longer-term transformation or knowledge effects were considered in the research design (for practical and logistical reasons). This is a constraint because prior research has shown that increased knowledge does not automatically amount to changes in local practices (Cai et al., 2015). In addition, the measurement was carried out on a group level, which causes bias with regard to the performance of individual members and needs to be viewed critically in terms of reliability. Moreover, although a detailed evaluation framework was developed a priori, the measurement was constrained in that only one observer, though experienced in the local culture and language, evaluated the tasks and no interrater-agreement could be taken into account. These constraints mean that the findings can only be considered preliminary in nature and further and more robust research is warranted. Finally, any generalization has to be treated with caution, given the socio-cultural particularities of these communities. Yet, we believe that future research can draw on these insights and this work can provide a jumping-off point for future investigations.

5. References

Cai, T., Abbott, E. & Bwambale, N. The ability of video training to reduce agricultural knowledge gaps between men and women in rural Uganda. Proceedings of the Sixth International Conference on Information and Communications Technologies and Development: Notes-Volume 2, 2013. ACM, 13-16.

Cai, T., Chiwasa, H., Steinfield, C. & Wyche, S. Participatory video for nutrition training for farmers in Malawi: an analysis of knowledge gain and adoption. Proceedings of the Seventh International Conference on Information and Communication Technologies and Development, 2015. ACM, 29.

CBS and ICIMOD/MENRIS 2003. Districts of Nepal. Indicators of Development. Update 2003. . Central Bureau of Statistics (CBS), Nepal and International Centre for Integrated Mountain Development (ICIMOD/MENRIS).

Gandhi, R., Veeraraghavan, R., Toyama, K. & Ramprasad, V. Digital green: Participatory video for agricultural extension. Information and Communication Technologies and Development, 2007. ICTD 2007. International Conference on, 2007. IEEE, 1-10.

Jerneck, A. & Olsson, L. 2013. A smoke-free kitchen: initiating community based co-production for cleaner cooking and cuts in carbon emissions. *Journal of cleaner production,* 60**,** 208-215.

Kumar, N., Perrier, T., Desmond, M., Israel-Ballard, K., Kumar, V., Mahapatra, S., Mishra, A., Agarwal, S., Gandhi, R. & Lal, P. Projecting health: Community-led video education for maternal health. Proceedings of the Seventh International Conference on Information and Communication Technologies and Development, 2015. ACM, 17.

Lie, R. & Mandler, A. 2009. *Video in development. Filming for rural change. CTA and FAO 2009.* [Online]. Available: https://cgspace.cgiar.org/bitstream/handle/10568/63643/Video_in_Development.pdf?sequence=1&isAllowed=y

Negro, S. O., Alkemade, F. & Hekkert, M. P. 2012. Why does renewable energy diffuse so slowly? A review of innovation system problems. *Renewable and Sustainable Energy Reviews,* 16**,** 3836-3846.

Plush, T. 2013. Fostering social change through participatory video: A conceptual framework. *Development Bulletin (Canberra),* 75**,** 55-58.

Reid, H., Alam, M., Berger, R., Cannon, T., Huq, S. & Milligan, A. 2009. Community-based adaptation to climate change: an overview. *Participatory learning and action,* 60**,** 11-33.

SDG Goals. n.d. *Goal 7: Ensure access to affordable, reliable, sustainable and modern energy for all* [Online]. Available: http://www.un.org/sustainabledevelopment/energy/.

The World Bank. 2016. *Sustainable Development Goal on Energy (SDG7) and the World Bank Group* [Online]. Available: http://www.worldbank.org/en/topic/energy/brief/sustainable-development-goal-on-energy-sdg7-and-the-world-bank-group.

Vashistha, A., Kumar, N., Mishra, A. & Anderson, R. Mobile Video Dissemination for Community Health. Proceedings of the Eighth International Conference on Information and Communication Technologies and Development, 2016. ACM, 20.

Zossou, E., Van Mele, P., Vodouhe, S. D. & Wanvoeke, J. 2009. Comparing farmer-to-farmer video with workshops to train rural women in improved rice parboiling in central Benin. *Journal of agricultural education and extension,* 15**,** 329-339.

Energy Storage in Buildings

Comprehensive analysis of thermal utilization of solar wall system

Qintai Jiao[1] ,Kun Qin[1] ,Wenjing Qiao[2] ,Shuhuai Wang[3] ,Daojing Xu[1]

[1] Jiangsu sunrain solar energy Co.,Ltd.,Lianyugang(China)

[2] Xi`an Technological university,Xi`an(China)

[3] Beijing micoe solar energy technology Co.,Ltd.,Lianyugang(China)

Abstract

This paper introduces a energy saving solar wall ventilation heating system.We measure the temperature of each part of the system and analyze the performance of the system.Results indicate that,Under the same conditions, the solar wall system has a high efficiency in the high volume of air delivery, while in the case of low air supply, the heating efficiency is lower;The air volume of the system is inversely proportional to the temperature rise.;The solar wall system has good energy saving effect and good economic benefit.

Keywords：Solar wall system，Energy conservation，Economy

1.Introduction

With the rapid development of the economy ,the energy and environmental pressure which people are facing is increasing.Solar energy as an ideal renewable energy is applied in the construction field.Solar wall system is effective integration of solar air heating technology and building integration,which provides an ecnonmic and applicable solution for heating and ventilation,and is with such prominent advantages as low cost,low energy consumption,low maintenance cost and high air quality.The paper investigate the thermal performance in actual building,application results and benefit analysis by experimental research and theoretical analysis.

2.Overview of solar wall research system

2.1. System introduction

The solar wall ventilation heating system studied in this paper is located in lianyungang, jiangsu province(Fig.1), which is the office of sunrain solar energy Co.,Ltd.The office heating area is 97.5m^2, office wall toward the south, with 25m^2 to install solar wall system, metope is exposed.

Fig.1 solar wall testing system

Fig.2 90°irradiation

Fig.3 wind speed and ambient temperature

doi:10.18086/swc.2017.09.01 Available at http://proceedings.ises.org

2.2. Principle of system operation

The system adopts the automatic control mode, when the cavity temperature reaches the set temperature , then the fan is started, and the air supply air temperature is set at 20℃

2.3. Data collection and testing methods

2.3.1. Measurement of irradiation strength

TBQ - 2 to measure Solar radiation(Fig.2).

2.3.2. Measurement of wind speed and ambient temperature

EC-1A to measure wind speed and pt100 to ambient temperature(Fig.3).

2.3.3. Solar wall system temperature measurement

The internal wall temperature and indoor temperature were tested respectively(Fig.4).

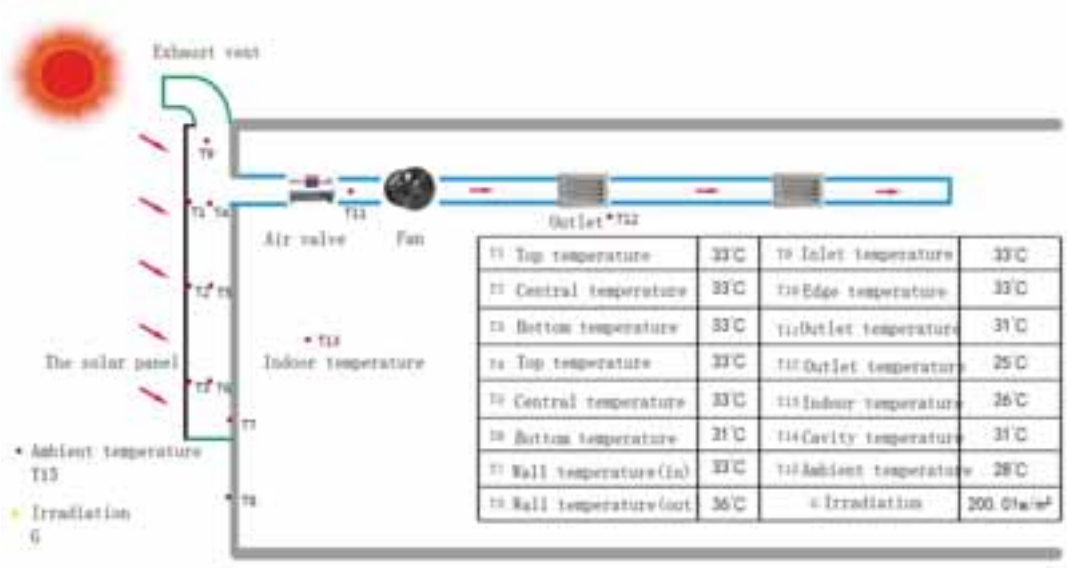

Fig.4 Temperature distribution of solar wall test system

3.Thermal performance of solar wall test system

3.1. Solar panel and cavity temperature

Figure 5 shows the change of cavity temperature and the surface temperature of solar wall panel during the solar wall system operation.From the diagram, the temperature of the solar panel and the temperature of the cavity are consistent with the variation of solar radiation.When the solar radiation intensity is greatest at noon, the temperature of the solar wall panel and the cavity temperature reach the maximum.In the morning and evening, the temperature of the cavity is low due to the small amount of solar radiation.During the operation of the system, the temperature of the cavity is up to 40℃, which is 30℃ higher than the outdoor environment, and the effect of temperature rise is obvious.

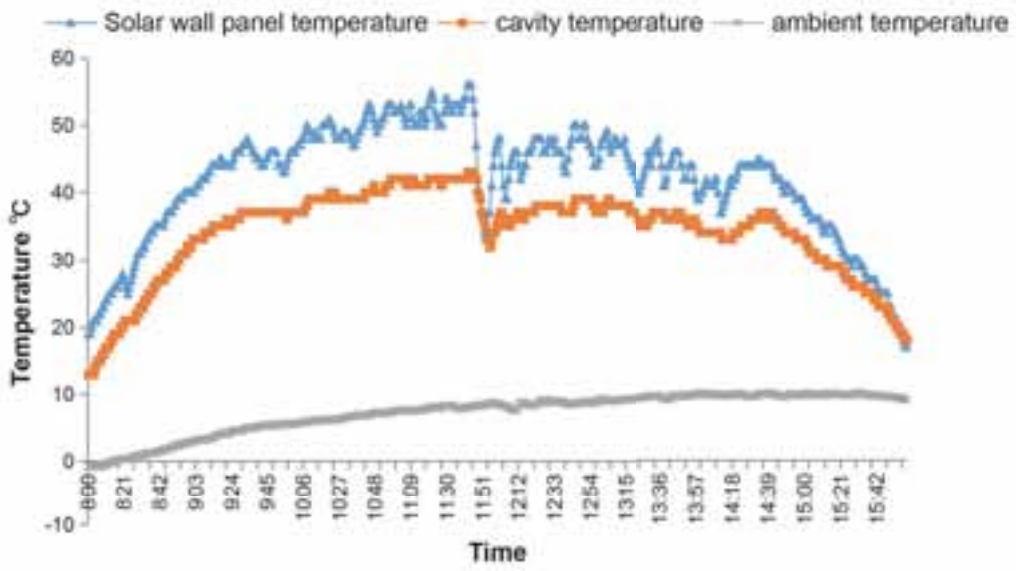

Fig.5 cavity temperature and the surface temperature of solar wall

3.2. Deliver temperature

Figure 6 shows the change of deliver temperature during the operation of the solar wall system in local heating period(Nov 14, 2016 ~Mar 27, 2017, total 134 days [1]).Figure illustrates the deliver temperature up to 48℃ during work, and the average working time from 8:30 ~ 16:00, with an average of seven hours.The results show that the solar wall heating system is stable and reliable in the better working conditions.

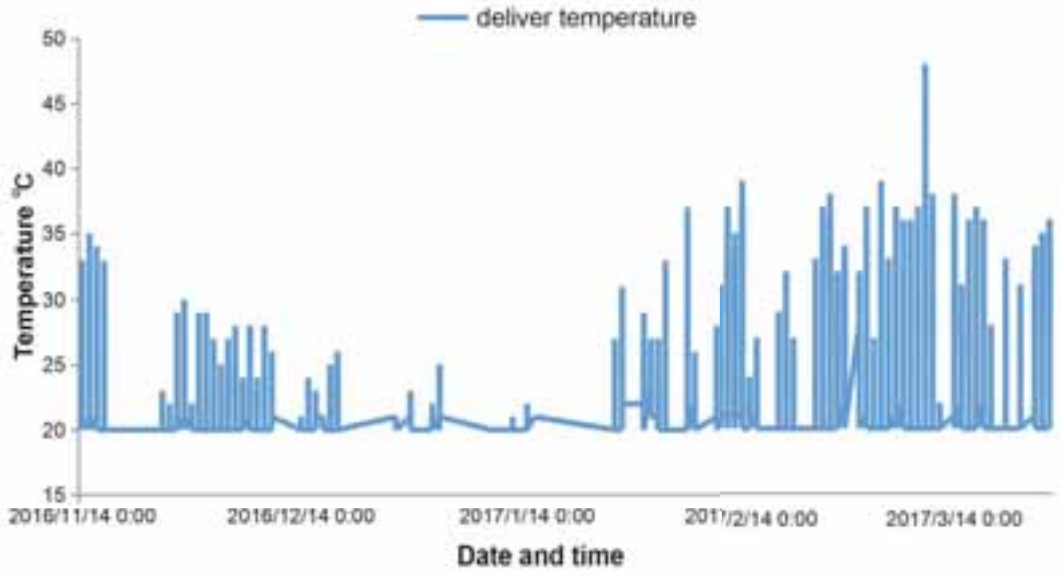

Fig.6 deliver temperature during heating period

3.3. Performance analysis

The save energy Q refers to the heat provided by the solar wall during a heating period

The heat provided by solar wall system in unit time：

$$Q = c * \rho * mv * \Delta T \text{ (eq. 1)}$$

The heating efficiency of solar wall heating system in unit time is calculated by

$$\eta = \frac{Q}{A * H} \text{ (eq. 2)}$$

As shown in figure 7, when the radiation is high, the instantaneous heat efficiency of the system decreases, and when the radiation intensity decreases, the instantaneous heat efficiency of the system is increased.Because the heat efficiency is proportional to the temperature rise and inversely proportional to the radiation intensity,When the magnitude of the decrease of radiation is greater than that of temperature rise, the efficiency will be increased. While when the amplitude of radiation rise is greater than that of temperature rise, the efficiency will decrease.

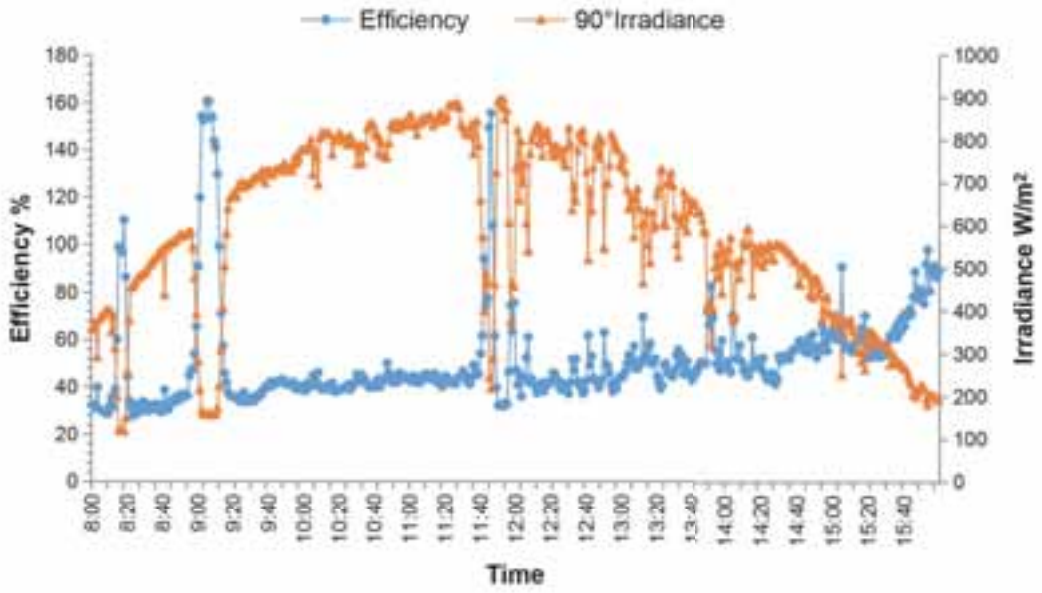

Fig.7 Efficiency and Irradiance

3.4. The effect of air flow on the system

It can be seen from figure 8 that under certain conditions, the heat efficiency is high in high air flow and low heat efficiency in low air flow.This result is consistent with figure 9.In this way, we can use the efficiency curve to calculate the energy of the section through irradiation

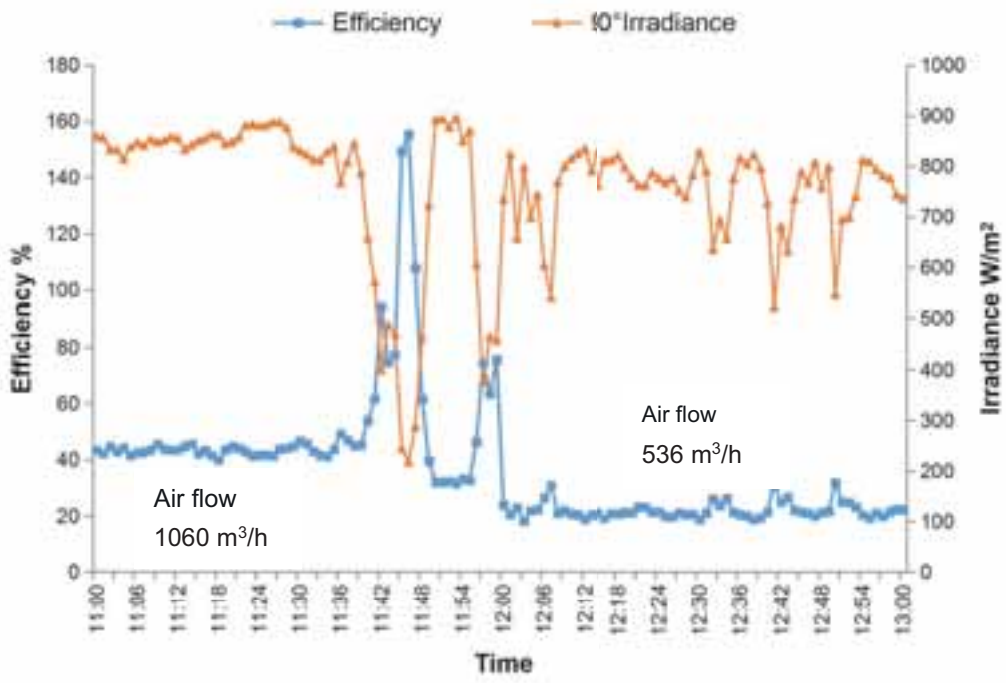

Fig.8 Efficiency for solarwall at various wind speeds

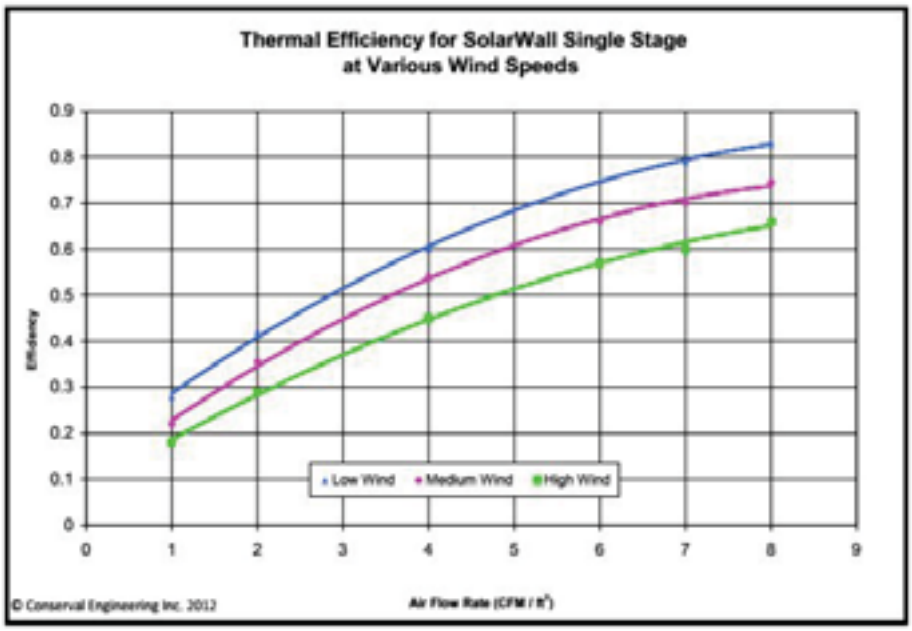

Fig.9 Efficiency for solarwall at various wind speeds[2]

According to the figure 10 analysis, under certain conditions, the solar wall system under the condition of high air flow, the deliver temperature rise is smaller, and under the condition of low air flow, the deliver temperature rise is larger. You can compare the temperature rise certification curve, as shown in figure 11.

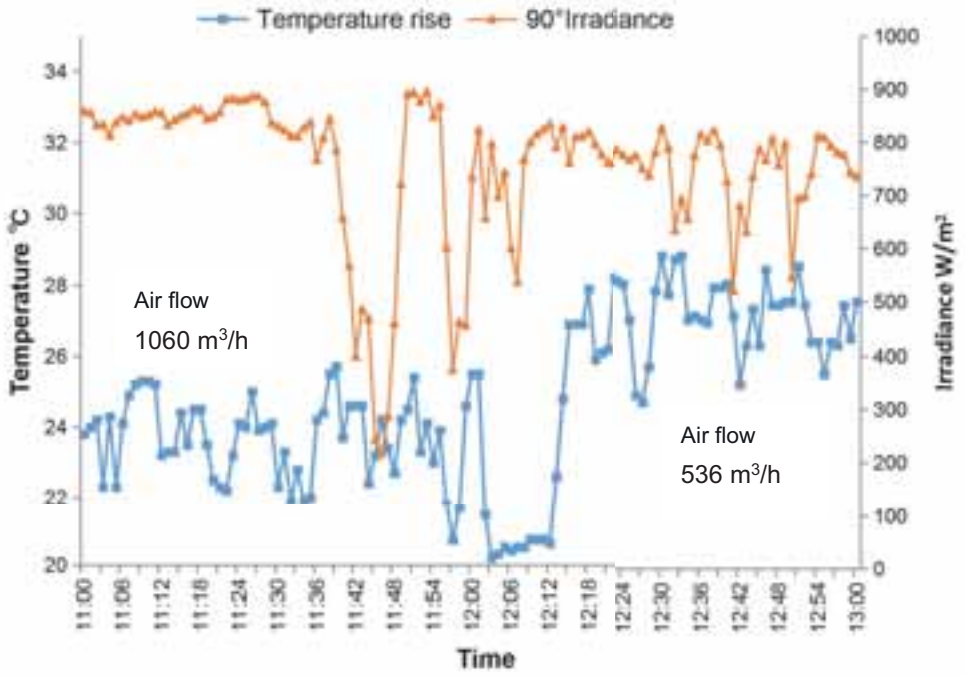

Fig.10 Temperature performance for solarwall wint wind variance

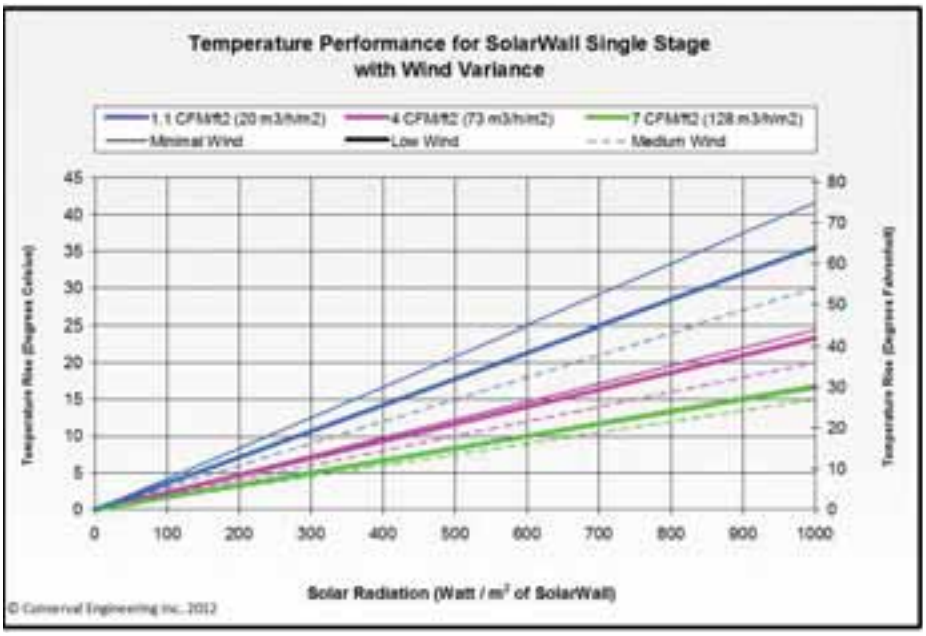

Fig.11 Temperature performance for solarwall wint wind variance[2]

Practical application can not blindly pursue high efficiency and increase the air volume, it will lead to the deliver temperature is low, thereby reducing the body's comfort, so in the later application according to different types of engineering deal with the relationship between air flow and temperature rise, maximize the benefits.

4.economy evaluation

The economic evaluation index of solar wall system includes the fund saving in life span and the payback time N[3].The two methods are calculated as follows：

$$SAV = PI * (\Delta Q_{SAV} * C_C - A * DJ) - A \quad \text{(eq. 3)}$$

$$PI = \frac{1}{d-e}\left[1-(\frac{1+e}{1+\mathrm{d}})^n\right] \quad \text{(eq. 4)}$$

payback time N，That is, when the formula SAV is equal to zero, the value of N,the calculation formula is as follows:

$$N = \frac{\ln\left[1-\frac{A(\mathrm{d}-e)}{\Delta Qsav - A \bullet DJ}\right]}{\ln\left(\frac{1+\mathrm{e}}{1+\mathrm{d}}\right)} \quad \text{(eq. 5)}$$

The above formula can be used to calculate the payback time N=2.3 years.

5.Conclusion

This paper studies the solar wall system in lianyungang,the following conclusions can be obtained by statistical analysis of the application of solar wall system

1.The solar wall system has good thermal performance, and system efficiency is inversely proportional to irradiation;The air flow is proportional to the efficiency, inversely proportional to the temperature rise.

2.The solar wall heating system can provide 48℃ heating air in the heating season, with an average working time of 7 hours per day, and 13640MJ energy in the heating season.

3.This solar wall heating system has good economic benefits and the payback time is two to three years.

References

[1] GB 50736-2012,Civil building heating ventilation and air conditioning design specification[S].

[2] SAHWIA.SLOAR AIR COLLECTOR CERTIFICATE 1001[EB/OL].http://sahwia.org/solar-a-mark/view-certifications/,2012-07-31.

[3] Ruicheng.ZHENG.Technical manual for solar heating and heating engineering[M].china building industry press，2012：240-247.

Nomenclature

Quantity	Symbol	Unit
Specific heat	*c*	J kg^{-1} K^{-1}
Density	ρ	kg m^{-3}
Air flow	*mv*	m3/s
Temperature difference	*ΔT*	K^{-1}
Area	*A*	m^2
Heat	*Q*	J
Irradiance	*E, H*	W m^{-2}
Efficiency	η	
Total energy saving cost	SAV	yuan
discount factor	PI	
discount rate	d	
fuel cost escalation rate	e	
project life	n	
heating delived	∆ Qsav	J
Fuel cost	Cc	Yuan J^{-1}
Total initial costs	*Aa*	yuan
O&M expense ratio	DJ	

Experimental and numerical investigation of heat transfer inside an air cavity with a Phase Change Material side

Abdelouhab Labihi[1,4], Hassan Chehouani[1], Faiçal Aitlahbib[1], Brahim Benhamou[2,3], Andrei-Stelian Bejan[4], Cristiana-Verona Croitoru[4], Ilinca Nastase[4]

[1] LP2M2E Laboratory, Faculty of Sciences and Techniques, Cadi Ayyad University, Marrakech (Morocco)

[2] National Center of Studies and Research on Water & Energy (CNEREE), Cadi Ayyad University Marrakech (Morocco)

[3] Energy Process Research Group at LMFE, Faculty of Sciences Semlalia, Cadi Ayyad University, Marrakech (Morocco)

[4] Technical University of Civil Engineering Bucharest, CAMBI Research Center, Faculty of Engineering for Building Services, Bucharest (Romania)

Abstract

A numerical model was developed to study the coupling of heat transfer in the PCM and the air inside the enclosure. The solidification of the initially melted PCM induces a natural convection of air flow inside the cavity. We present in this work the heat transfer behavior between a chosen phase change material (PCM) incorporated in a thin right wall and a square enclosure filled with air whereas the left one is kept at ambient temperature. The solidification of the PCM generates a latent heat inducing a natural convection air flow inside the cavity and compensating the heat loss. The numerical analysis leaded to a Nusselt number correlations depending on constant Stefan number. Nusselt number is given as a function of a Rayleigh number and dimensionless temperature difference between hot and cold sides. These correlations have been established since there is a lake in the literature to evaluate the natural convection heat transfer coefficient between air and a PCM wall. The parametric domain covered the range of Rayleigh number between $3.4\ 10^5$ to $4.\ 10^7$ with Prandtl number Pr = 0.73 and Stefan number Ste=0.41.

Keywords: Energy Management; Phase Change Material; Natural Convection; Solidification Phase Front; Active Wall; Heat Storage.

NOMENCLATURE

A	Aspect ratio e/L	**Greek symbols**	
C	Specific heat of PCM	ε	Temperature jump
a	Thermal diffusivity		
C_{Pg}	Specific heat of air	ρ	Density
e	PCM thickness	ν	Cinematic viscosity
F	PCM fraction	λ	Thermal conductivity
Fo	Fourier number		
H	Latent heat	Δ	Step
g	Gravity	ψ	Stream function
Nu	Nusselt number	**Subscripts**	
PCM	Phase Change Material	C	Cold
t	Time	H	Hot
T	Temperature	g	Gas
U,V	Velocity components	l	Liquid
x,y	Cartesian coordinates	m	Melting
Ste	Stefan Number $Ste = \frac{C_{pcm}\ (T_m - T_C)}{H}$		

doi:10.18086/swc.2017.09.02 Available at http://proceedings.ises.org

1. Introduction

The adaptation of large-scale energy storage solutions are a prerequisite for the development of renewable energy. Thus, to achieve an efficient energy mix, it is necessary to manage the balance between production and demand to ensure optimal service. Except in very specific cases, it is difficult to store electricity directly. It must therefore be transformed into another form of energy more easily stored. One of those ways of storing thermal energy consists in using a phase change material (PCM). The energy is then stored in the form of latent heat through the melting of these materials and then released through the solidification process (Dinçer and Rosen 2002, Zalba et al. 2003). The Thermal Energy Storage (TES) method is commonly used to save energy and to improve the comfort level in buildings. This explains the growing interest of the scientific community to elucidate both numerically and experimentally the thermal performance of a PCM layer incorporated in a part of the building envelope.

The configuration of an enclosure with one side integrating a PCM layer has been rarely addressed despite its wide application such as in optimal utilization of energy (Tan et al. 2002, Ho et al. 2005) and thermal protection (Cao and Faghri 1990). The solidification of the PCM will provide a latent heat inducing a natural convection air flow inside the cavity. In this way, the study of the influence of the PCM wall on the coupled flow and heat transfer in the cavity provides both scientific and practical interests. An issue may arise in the study of this problem. Are the existing correlations applicable to describe the heat transfer between the PCM wall and air in the cavity?

Buoyancy-driven flow in a closed cavity without PCM wall has been studied widely because of the applications in nature and engineering. Many heat transfer correlations have been proposed for imposed temperature or boundary heat flux of the most common cases of rectangular, cylindrical or other regular geometries (Davis1983, Ostrach 1988, Shilei 2014, Gracia 2015). However, there are few studies regarding the solidification/melting effect of a PCM integrated in a boundary on the convective heat fluid inside the cavity. (Zhang and Bejan 1989) reported experimentally and analytically, the melting process of enclosed paraffin heated at a constant rate from the side with an air space 30 mm left at the top of the enclosure. They predicted overall Nusselt number relationship agrees reasonably well with the existing empirical correlation. (Wang et al. 1999) investigated experimentally the melting process of polyethylene glycol in a rectangular enclosure heated from vertical wall. An air gap of 12.7 mm was maintained between the assembled unit and all sides of the container. It was shown that the temporal Nusselt number variation distinguishes three different heat transfer regimes during the melting process. (De Gracia et al. 2013) have studied the convective heat transfer between an air flow and a phase change material plate. They found that the correlation used in the literature to determine the heat transfer coefficient in the case of the PCM is no longer valid. They introduced a correction coefficient in the correlation expression to account for the presence of the PCM.

(Lipnicki and Weigand 2012) studied experimentally and theoretically the natural convection and ice solidification in an annular enclosure. They found that the influence of the contact layer between the frozen layer and the cold surface is of significant importance for the solidification process. To predict the heat transfer coefficient, they used a conventional correlation given by (Vahl Davis and Thomas 1970). A previous work has been conducted to highlight the thermal performance of a Keeping Warm System (KWS) incorporating a PCM wall (Ait lahbib and Chehouani 2015). The studied configuration demonstrated the effect of the PCM discharge where the solidification plays a great role on the heat transfer in the KWS cavity.

As latent thermal energy storage represents smart efficient thermal energy storage, such technique can be used in many domestic and industrial sectors depending on PCM thermophysical properties such as latent heat, melting point and conductivity. During the development of useful applied PCMs, many different groups of phase change materials have been studied, including inorganic compounds (salt and salt hydrates), organic compounds such as paraffin's, fatty acids and even polymeric materials. In comparison to inorganic PCMs, organic substances could serve as important heat storage media because of their several advantages including their ability to melt congruently, their self nucleation and the fact they don't have a problem of separation on melting. A relevant aspect is the useful life of this category of PCM and the number of cycles they can withstand without any degrading of their properties. (Hadjieva et al. 1992) used three paraffin mixtures and confirmed that there was no effect of the cycles on the properties of paraffin. (Gibbs and Hsnain 1995) also

verified that neither the cycles nor contact with metals degrade the thermal behavior of paraffin thus they have excellent thermal stability.
The aim of this work is to propose useful heat transfer correlation in a widely used configuration of air cavity incorporating organic paraffin side. In this way both experimental and numerical studies have been carried out for the given configuration. The developed numerical model treats the coupling of the natural convection inside an air square enclosure with only conduction in the PCM side aiming to provide a comprehensive evaluation of the effectiveness of PCMs wall in industrial applications. Nusselt number was calculated as a function of the Rayleigh number, the temperature difference between both sides of the cavity in PCM during the solidification process.

2. Experimental setup and methodology

Experimental setup consists mainly of an enclosure cavity, electrical resistance, insulation material, PCM package, thermocouples and the data acquisition system (Figure 1).

In this study, the enclosure cavity has (10x10x10) cm^3 as geometric dimensions. It was differentially heated across two vertical walls; while the remaining side walls were thermally insulated. The hot wall was heated by an electrical resistance. The cold wall consists of an aluminum plate kept at the temperature T_C by controlled circulating water from a constant temperature bath. All the external surfaces of the test apparatus were insulated with polystyrene insulation material of 4 cm thickness to reduce heat losses from the sides to the surroundings. Four K-type thermocouples with accuracy of 0,2 °C were assembled in the hot and cold walls at various locations along the length, and two others were placed in the center of the gas cavity and the layer of PCM respectively. Temperature was constantly monitored for loading data every 5s via data acquisition system (Fig. 2 and 3).

Fig. 1: Experimental setup. 1) The enclosure cavity. 2) The cold wall. 3) Temperature regulator. 4) Data acquisition, 5) Heating system, 6) Computer.

Experiment have been undertaken to evaluate the numerical model validity. In our disposal, we selected the PCM60 provided by KAPLAN ENERGY-France which is a carboxylic acid that has the properties given in Table 1. We have no data on the thermal conductivity of the solid and liquid states. Their values are measured by the method of transient hot wire. This method is the best known and most widely used for measuring the thermal conductivity of fluid and solid medium because of its rapidity and ease of implementation. The principle of this technique is to heat by Joule effect a filiform element (probe) of very small radius immersed in the fluid to be characterized and measure the temperature rise in the vicinity of the probe versus time via a sensor associated therewith. Indeed, the transfer to the sample center is assumed to be unidirectional.

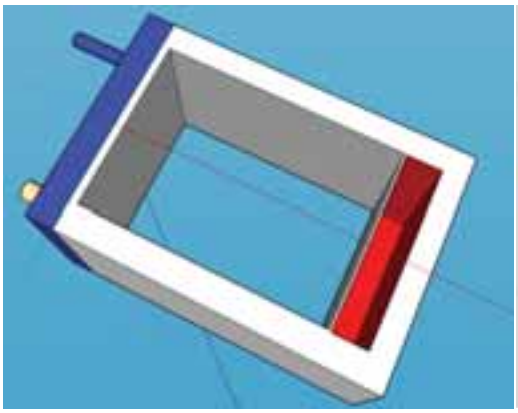

Fig. 2: Inside of the experimental square cavity.

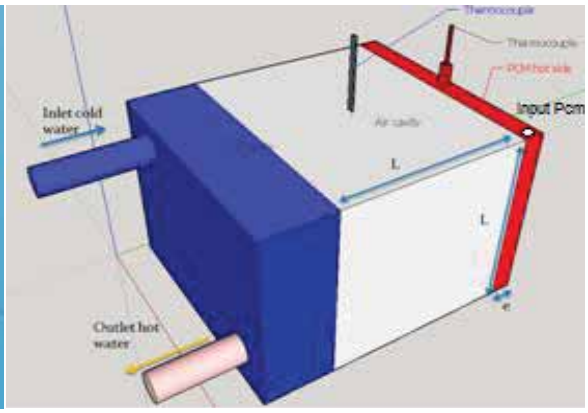

Fig. 3: Experimental square mode.

3. Model formulation and Numerical Solution

The 2D geometry used in the present study is shown in Figure 4. The thickness of PCM is equal to e and the cavity length is L. We define the aspect ratio parameter as A=e/L. The square enclosure is filled by air, cooled from the left side at T_C, insulated from the bottom and the top and heated from the right side by the PCM which is initially at T_H. The PCM is insulated from the top, bottom and right sides.

The following assumptions are made in the present study:

- The natural convection within the melt part of the PCM is negligible and can be ignored.
- All the thermophysical properties of the air are assumed constant except the density giving rise to the buoyancy forces (Boussinesq approximation). These thermophysical properties are taken at the reference temperature T_C.
- The thermo physical properties of the PCM are different for the solid and liquid phases and dependent on phase fraction.
- The PCM behaves ideally and is homogenous and isotropic.

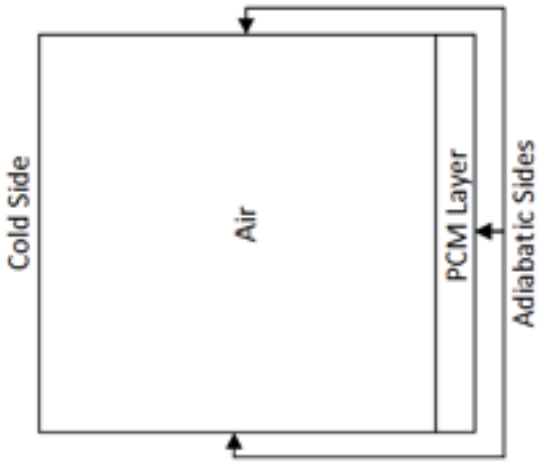

Fig. 4: Physical model

For the air inside the cavity, the equations describing the flow and heat transfer are written as follows:

- Continuity equation

$$\frac{\partial U}{\partial x} + \frac{\partial V}{\partial y} = 0 \quad Eq.1$$

- Momentum equations:

$$\frac{\partial \mathrm{U}}{\partial \mathrm{t}} + \mathrm{U}\frac{\partial \mathrm{U}}{\partial \mathrm{x}} + \mathrm{V}\frac{\partial \mathrm{U}}{\partial \mathrm{y}} = -\frac{1}{\rho_g}\frac{\partial \mathrm{P}}{\partial \mathrm{x}} + \nu_g\left(\frac{\partial^2 \mathrm{U}}{\partial \mathrm{x}^2} + \frac{\partial^2 \mathrm{U}}{\partial \mathrm{y}^2}\right) \quad \mathrm{Eq.2}$$

$$\frac{\partial V}{\partial t} + U\frac{\partial V}{\partial x} + V\frac{\partial V}{\partial y} = -\frac{1}{\rho_g}\frac{\partial P}{\partial y} + \nu_g\left(\frac{\partial^2 V}{\partial x^2} + \frac{\partial^2 V}{\partial y^2}\right) - \left[1 - \beta\left(T_g - T_C\right)\right]g \quad Eq.3$$

- Energy equation

$$\rho_g C_{pg}\frac{\partial T_g}{\partial t} + \rho_g C_{pg}\left(U\frac{\partial T_g}{\partial x} + V\frac{\partial T_g}{\partial y}\right) = \lambda_g\left(\frac{\partial^2 T_g}{\partial x^2} + \frac{\partial^2 T_g}{\partial y^2}\right) \quad Eq.4$$

Using an enthalpy-porosity method with the previous assumptions, the energy equation in the PCM wall reads as:

$$\rho_{pcm}\, C_{pcm}\,\frac{\partial T_{pcm}}{\partial t} = \lambda_{pcm}\left(\frac{\partial^2 T_{pcm}}{\partial x^2} + \frac{\partial^2 T_{pcm}}{\partial y^2}\right) - \rho_{pcm}\, H\frac{\partial f}{\partial t} \quad Eq.5$$

The properties of the PCM are updated following the values taken by the liquid fraction after each time step. Thus:

$$\rho_{pcm} = f\rho_l + (1-f)\rho_s \quad Eq.6$$

$$\lambda_{pcm} = f\lambda_l + (1-f)\lambda_s \quad Eq.7$$

For the density in the PCM layer was modeled by (Labihi et al. 2017). These authors proposed a new formula, ρ_{eff}, takes into account the PCM and the air layer resulting from volume contraction.

$$\rho_{eff} = \frac{\rho_{pcm}\, L^* + \rho_g \delta}{L} \quad Eq.8$$

where ρ_{pcm} is calculated using the Eq. 6

The governing equations are completed by the following initial and boundary conditions:

- $\mathrm{t} = 0$, all the intial values (U,V,T) in the gas are in steady state natural convection inside the closed cavity with differentially heated vertical walls. $\mathrm{T_{pcm}} = \mathrm{T_H}$ and $\mathrm{f} = 1$ (the PCM is liquid).
- $\mathrm{x} = 0, \mathrm{T_g} = \mathrm{T_C}, \mathrm{U} = \mathrm{V} = 0.$
- $\mathrm{x} = \mathrm{L} + \mathrm{e}, \frac{\partial \mathrm{T_{pcm}}}{\partial \mathrm{x}} = 0, \frac{\partial \mathrm{f}}{\partial \mathrm{x}} = 0, \mathrm{U} = \mathrm{V} = 0.$
- $\mathrm{y} = 0$ or $\mathrm{y} = \mathrm{L}, \frac{\partial \mathrm{T_g}}{\partial \mathrm{y}} = 0, \frac{\partial \mathrm{f}}{\partial \mathrm{y}} = 0, \mathrm{U} = \mathrm{V} = 0.$
- $\mathrm{x} = \mathrm{L}, \mathrm{T_g} = \mathrm{T_{pcm}}, \mathrm{U} = \mathrm{V} = 0, \lambda_g \frac{\partial \mathrm{T_g}}{\partial \mathrm{x}} = \lambda_{pcm} \frac{\partial \mathrm{T_{pcm}}}{\partial \mathrm{x}},$
- $\mathrm{f} = \frac{\mathrm{T}-\mathrm{T_s}}{\mathrm{T_l}-\mathrm{T_s}}$ with the correction f $\begin{cases} 0 \text{ if } \mathrm{f} < 0 \\ 1 \text{ if } \mathrm{f} > 1 \end{cases}$.

The time discretization is performed using the simple first-order Euler implicit scheme. The sets of algebraic equations resulting from the numerical scheme were solved iteratively using the Gauss-Seidel method.

- ***Mesh grid analyses***

In order to ensure grid independent solutions, a series of trial calculations were conducted for different grid distributions with an uniform mesh cells in both PCM and Air cavities.

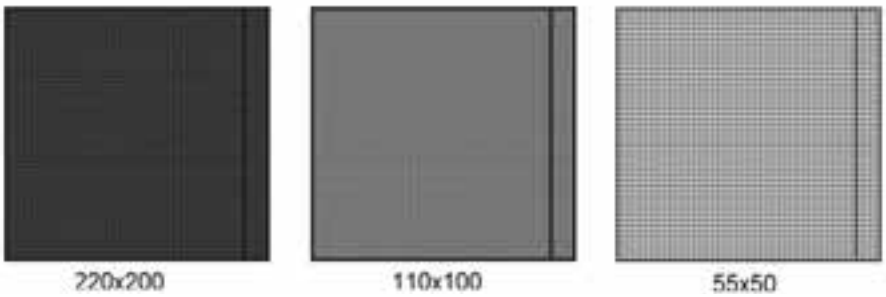

Fig. 5: Different Mesh grids sizes

To evaluate the grid size effect on numerical results, we conducted a series of trial calculations with 50X55, 100X110 and 200X220 nodes (Fig. 5) for a cavity with L=10cm and e=1cm. we calculated for each case the average Nusselt number at hot and cold side and the relative error issues between the different grid size chosen. Table 1 shows the thermophysical properties of RT55 product by RubiTherm used in this study.

Tab. 1 Thermo-physical propreites for RT55

T_m (K)	324.15 - 329.15
ρ_l ($kg\ m^{-3}$)	770
ρ_s ($kg\ m^{-3}$)	880
λ ($Wm^{-1}K^{-1}$)	0.2
H ($kJ\ kg^{-1}$)	170
C ($J\ kg^{-1}K^{-1}$)	2000

Table2 presents the different results founded of this comparison. We can note that the solution is very sensible when we use 50X55 mesh grids cells (up to 6%of difference) contrariwise, the obtained by 100X110 and 200X220 are practically the same.
The mesh 100X110 was adopted on the numerical computations in this study.

Tab. 2: Grid evaluation results

	$\overline{Nu}$ Hot Side	$\overline{Nu}$ Cold Side			Hot Side	Cold Side
55x50	13.15	13.135	Relative Error (%)	55x50 Vs 110x100	5.17	5.16
110x100	13.82	13.81		55x50 Vs 220x200	6.03	6.02
220x200	13.94	13.928		110x100 Vs 220x200	0.81	0.81

- ***Validation of the initial state***

In order to validate the initial flow and heat transfer in the cavity with PCM melted at constant T_H, we used two correlations for the average Nusselt number defined as:

$$\mathrm{Nu} = \frac{\mathrm{hL}}{\lambda_g} \quad \mathrm{Eq.9}$$

Where h is the average convective heat coefficient through the hot side of the cavity.

Table 3 compares the obtained Nusselt number with those calculated using the empirical correlations established respectively by (Eckert and Carlson 1962) and (Lankhorst 1991) for $\mathrm{Ra} = 5.32\ 10^6$. Since the relative error is less than 3%, our numerical model adopted in this study could be considered valid.

Tab. 3: Validation of the numerical model.

	$\overline{Nu}$	Relative error
This study	13.82	-
(Eckert and Carlson 1962)	14.139	2.3%
(Lankhorst 1991)	13.517	2.19%

4. Results and discussion

The experimental results were presented in our previous work (Labihi et al 2017). We found that the numerical simulation results match well with the experimental measurements. For that we conclude that the numerical model be considered valid along the process.

Due to the lack of empirical information about the heat transfer coefficients in the same studied configuration, authors used to use differentially heated wall cavity literatures correlation which is not representing the real physical processes of heat exchange between PCM and air cavity. In order to obtain correlations capable of characterizing the transient heat transfer process inside such cavity a simulation runs were carried out to obtain correlations of heat transfer rate via Nusselt number, with Rayleigh number Ra and the differnce dimensionless temperature between the hot and cold sides Θ.

In this study we define Ra number by the following formula $R_a = \frac{\rho g \beta L^3 (T_H - T_c)}{\alpha \mu}$ and $\Theta = \frac{T(t) - T_c}{T_H - T_c}$
Where $T(t)$ is the average temperature at hot side in each time.

In order to get a significatif range of Ra number we have chosen to vary L and not $(T_H - T_c)$ always keeps the same aspect ratio $A = \frac{e}{L} = 0.1$. Heat transfer at the hot interface between air and PCM is thoroughly inspected in the defined range $3.4\ 10^5 < Ra \leq 4.3.10^7$ with $Ste = 0.41$, $T_H = 50$ °C and $T_C = 20$ °C.

A simulation series was carried out with L=6, 10, 14 and 18cm. Figure 6 present the liquid fraction as a function of Θ for different Ra numbers. Despite the fact that we have the same formal report we can see that the solidification process (Θ from 0.6 to 0) is not the same when we change L. whereas the curves are very close to one another for Θ greater than 0.6. That can be explaining by the fact of volume contraction due to the difference between the density liquid/solid.

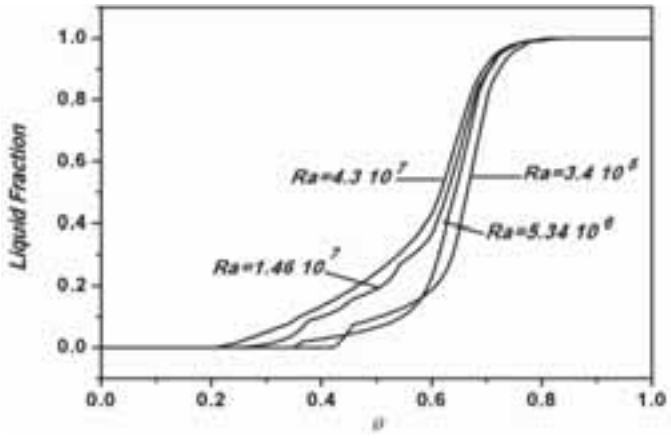

Fig. 6 Liquid fraction as function of Θ

The figure 7 shows the methodology that we use to find the correlations. to find an equation Nu as a function of Θ for different Ra number. We can see that the Nu number have a non-linear curve as function of Θ also we have some perturbation in the curves. The Nu perturbation becomes important when Ra increase.

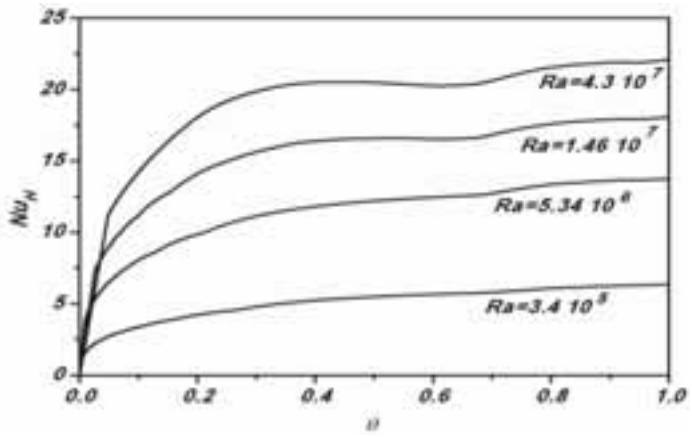

Fig. 7: Nusselt number evolution with dimensionless temperature for Ste=0.41

By using a non linear fitting for the curves issued in Figure 7.A new correlations between the dimensionless Nusselt number as a function of dimensionless Temperature Θ were made and presented in table 4.

Tab. 4: Nusselt number correlations at hot side as function of θ for different Rayleigh numbers

L (cm)	Ra	$\overline{Nu}$
6	$3.4\,10^5$	$6.7\,\theta^{0.3}$
10	$5.34\,10^6$	$14.88\,\theta^{0.283}$
14	$1.46\,10^7$	$19.67\,\theta^{0.254}$
18	$4.3\,10^7$	$23.50\,\theta^{0.213}$

5. Conclusion:

It is generally agreed that the intensive investigations undertaken in the last decades have given latent heat significant advantages especially organic PCM. We choose for this study a Rubitherm RT55 paraffin We conduct a numerical simulation where several assumptions had to be made in order to create a correlation model as close as possible to the realized experiment such as the invariability of PCM volume. Also knowledge of all the properties of the paraffin and the experimental validation would obviously provide more accurate results. Nevertheless, the coupling of convection of heat transfer in a cavity with solidifying PCM was successful and proposed correlation can be definitely used as a prediction in industrial or engineering fields. Hence, it can help for material selection step during design providing an economical advantage in saving time and money.

Based on the Numerical results and the correlated equations, the following conclusions could be drawn:

- The solidification process accurse early in time and tend to begin from the bottom to the top by following convection air loop.
- To have more Ra values we heed to vary L not the temperature difference between hot and cold side
- The contraction of volume in PCM layer affect the heat transfer processes from a Ra number to another despite the same aspect ratio in all cases.

For Ste=0.47 we see that we can write a new correlation for Nu number as function of Θ and Ra as the following formula:

$$Nu = aRa^n\theta^m$$

In future work we will exanimate a range of Ste values in order to write a general correlation of Nu number as a function of Ste, Ra andΘ.

5. Acknowledgement

This study is a part of the RafriBat project financially supported by the PARS grant from the Hassan II Academy of Sciences and Techniques, Morocco and

This work was supported by the grants of the Romanian National Authority for Scientific Research, CNCS – UEFISCDI, project number PN-III-P2-2.1-PED-2016-1154.

6. References:

A. Labihi, F. Aitlahbib, H. Chehouani, B. Benhamou, M. Ouikhalfan, C. Croitoru, I. Nastase, , 2017, Effect of phase change material wall on natural convection heat transfer inside an air filled enclosure, In Applied Thermal Engineering, Volume 126, Pages 305-314.

AM. Lankhorst, 1991, Laminar and turbulent natural convection in cavities: Numerical and experimental validation, PhD thesis University Delft.

Alvaro, G, Damien, D, Castell,A,and, Luisa F. C, 2013, transfer coefficient between an air flow and a phase change material Joseph Virgone, A correlation of the convective heat plate, J. Applied Thermal Engineering, Volume 51, Issues 1–2, Pages 1245-1254.

B.M. Gibbs, S.M. Hasnain, ,1995, DSC study of technical grade phase change heat storage materials for solar heating applications, Proceedings of the 1995 ASME/JSME/JSEJ International Solar Energy.

Cao,Y, and Faghri, A., 1990, Thermal protection from intense localized moving heat fluxes using phase-change material, Int. J. Heat Mass Transfer 33 .1271–1238.

Dinçer, I, Rosen M.A., 2002, Thermal Energy Storage, John Wiley & Sons, New York.

De. G,and Davis,V, 1983, Natural convection of air in a square cavity: a bench mark numerical solution, Int. J. Numer. Methods Fluids, 249-264.

E.R. Eckert, W.O. Carlson, 1961, Natural convection in a layer enclosed between two plates with different temperatures. Int. J. Heat Mass Transfer,106-120.

F. Aitlahbib, H. Chehouani, 2015, Numerical study of heat transfer inside a Keeping Warm System (KWS) incorporating phase change material. Appl Therm Eng; 75:73-85.

Gracia,A., Cèsar Fernández, Albert Castell, CarlesMateu, Luisa F. Cabeza, 2015, Control of a PCM ventilated facade using reinforcement learning techniques, Energy and Buildings, Volume 106, 1, 234-242.

Ho, C.J, Chiu, S.Y, and Lin J.F., 2005, Heat transfer characteristics of a rectangular natural circulation loop containing solid–liquid phase-change material suspensions, Int. J.Numer. Methods Heat Fluid Flow 15,441–461.

M. Hadjieva, S. Kanev, J. Argirov, 1992, Thermophysical properties of some paraffins applicable to thermal energy storage, Solar Energy Mater. Solar Cells 27, 181–187.

Ostrach,S., 1988, Natural convection in enclosure, J. Heat Transfer 110, 1175e1190.

R. W. Thomas, G. de Vahl Davis, 1970, Natural convection annular and rectangular cavities – a numerical study, in: Proc. 4th Int. Heat Transfer Conference, Paris 4, Paper N.C. 2.4.

Shilei, L,Shangbao, L, Jingyu, H, and Xiangfei, K,2014, Establishment and experimental verification of PCM room's TRNSYS heat transfer model based on latent heat utilization ratio,J. Energy and Buildings, Volume 84, Pages 287-298.

Tan, G.H, and Ho C.J, 2002, Experiments on thermal behaviors of a natural circulation loop with latent heat storage under cyclic pulsating heat load, Heat Mass Transfer 39,11–17.

Wang,Y., Amiri,A, and Vafai,K.,1999, An experimental investigation of the melting process in a rectangular enclosure,J. International Journal of Heat and Mass Transfer 42, 3659-3672.

Z. Lipnicki, B. Weigand, 2012, An experimental and theoretical study of solidification in a free-convection flow inside a vertical annular enclosure, Int. J. Heat Mass Transfer, 55, pp. 655–664.

Zhang, Z., and, Bejan A., 1989, Melting in an enclosure heated at constant rate, J.International of Heat and Mass Transfer 32, 1063e1076.

Zalba, B, Marin J.M. Cabeza L.F., Mehling H., 2003, Review on thermal energy storage with phase change: materials, heat transfer analysis and applications, J.Appl.Therm. Eng. 23,251–283.

Grid Integration of Variable Renewable Energy Systems

Reliability Analysis of Photovoltaic Systems with LEDs Integrated in Lighting Applications

Laurentiu Fara[1,2], Dan Craciunescu[1], Paul Sterian[1,2], Andreea Bobei[1] and Florin Dragan[1]

[1]Polytechnic University of Bucharest, Bucharest, Romania

[2]Academy of Romanian Scientists, Bucharest, Romania

Abstract

This paper is dedicated to the analysis of a PV system based on LEDs application from the point of view of its qualitative and quantitative reliability. This reliability study was conducted based on: 1) the RAMS (Reliability, Availability, Maintenance, and Safety) model applied to a PV system by using a simulation SYNTHESIS platform developed by ReliaSoft, and 2) the simulation of the LED lighting system using the SYNTHESIS platform and TM-21 Calculator software developed by ENERGY STAR. The purpose of the reliability analysis was to obtain a more stable and long-lasting operation of a PV system regarding reliability, maintainability, availability and degradation of the system.

Keywords: Reliability, Maintainability, Availability, Degradation, PV system, LEDs, simulation tools, RBD

1. Introduction

Due to various incentive programs and local market conditions in several European countries, as well as around the world, the PV systems represent a widespread solution for residential houses and other autonomous applications. This approach raises new and important issues related to the efficiency, reliability and safety of the PV systems, either autonomous or integrated in the electrical grid (Huffman and Antelme, 2011; DeGraaff et al., 2011).

In the case of grid-connected PV systems, the occurrence of system failures may affect the operation of other interconnected systems, that is why a thorough reliability analysis of such systems should be carried out (Kececioglu, 1991; IEC International Standard, 1995; Ishii et. al., 2011). The reliability analysis also makes it possible to establish an acceptable maintenance plan for both the user and the system as efficiently as possible (Crow, 2003, 2004). However, a reliability analysis is often missing from the feasibility study of photovoltaic systems or is treated superficially due to an incomplete methodological approach or lack of specific simulation tools (Herrmann et. al. 2010), (Hoffmann and Koehl. 2012). A PV system for LED lighting applications has been analysed (Popescu et al., 2009; Stanciu et al., 2015; Sterian, 2000, 2012), (Handbook, 2010). To overcome the reported inconveniences, it is envisaged the reliability analysis, using RAMS (Reliability, Availability, Maintainability, and Safety) statistical models through accelerated testing and application of stress levels (Nelson 1998; Kijima, 1989; Mettas, 2000; Holley et al., 1996). Starting from ground studies, the failures of PV systems have shown that manufacturers do not correctly perform reliability analysis of their PV modules' lifetime. For this reason, a small part of the PV modules fails before the lifetime specified by the manufacturer (Meydbray et. al., 2008). Reliability analysis applies to both PV systems, and simple systems, such as LED-based lighting lamps (Collins et al., 2009).

The authors proposed and carried out the reliability analysis of solar cells for specific meteorological conditions (Meydbray et al 2008; McMahon, 2004; Aoki et. al. 2010; Dhere et. al. 2010) To assess the reliability of the integrated PV system with LED lighting applications, its operating characteristics have been used for a time period (Wohlgemuth, 2011), and in the case of the simple LED lighting system there were used thermal characteristics of the studied LED lamp (Kim et al., 2006; Handbook, 2007) .

The most relevant analyzes proposed by the authors in this paper are based on Reliability Block Diagrams (RBDs) required for development of RAMS for studied PV systems. RBD diagrams have been developed for: 1)definition of PV systems, 2)description of interdependence between components, 3)identification of how they degrade / fail, and 4)appreciation of how the PV system reliability is influenced.

doi:10.18086/swc.2017.10.01 Available at http://proceedings.ises.org

2. Background, state of the art and simulation tools

2.1. Background

The reliability of a product can be defined as the probability of performing its tasks without incidents within a specified time, under previously established conditions. On this basis, the quality of a product is determined, the reliability concept being applied in almost all areas of engineering, in the preventive maintenance of systems and their components. It is envisaged the modeling of the product's lifetime, represented by the time it has worked successfully or its time until the moment of failure. For the purpose of accurately determining the lifetime, it has been proposed an accelerate product testing (qualitatively or quantitatively during its lifetime) (Wohlgemuth, 2003; Dhere, 2005).

Qualitative accelerated testing only provides information about system malfunctions or ways of failure. Qualitative tests do not quantify the system's life (or reliability) characteristics under normal conditions of utilization, but provide valuable information on the type and level of demands to use during a later quantitative test. In qualitative accelerated testing, the expected result consists in identifying deficiencies and ways of failure without predicting the life of the product under normal conditions of utilization (Crow 2008; DeGraaff, et. al. 2011; Copper, 2016).

Accelerated quantitative testing involves the estimation of product lifetime characteristics, obtained under normal conditions of utilization after an accelerated test. High Accelerated Life Test (HALT) provides various information about the product and its failure mechanisms. Accelerated quantitative testing consists of tests designed to quantify the life characteristics of a product, component or system under normal conditions of utilization, and to provide information on determining the reliability of the system (probability of system failure under various conditions, life expectancy, average lifetime). It can be used to carry out risk assessments or for comparison of different design methods (Hoffmann and Koehl, 2012).

Two acceleration methods were designed (Hoffmann and Koehl, 2012) for use of: 1) acceleration rate and 2) stress acceleration, in order to obtain time data on product failure at an accelerated rate. For products where use of acceleration rate is impractical, a second method can be applied, in which the normal stress level of a product is exceeded.

2.2. State of the art

The reliability of photovoltaic systems and their components/elements (solar cells, PV modules, electrical storage systems, inverters, regulators, etc.) are the key issues in manufacturing performance and financially competitive photovoltaic installations. For this purpose, a number of methods for testing and improving the reliability of PV products have been studied (Nelson, 1998; Mettas, 2000), such as: 1) the accelerated test method for solar cells (Desombre, 1980); 2) analysis of defect detection and degradation mechanisms detection for solar cells (Kijima, 1989), as well as PV systems and their components (Vazquez and Rey-Stolle, 2008); 3) energy production forecasting based on the rate of failure and degradation of PV systems and their applications (Holley et al., 1996).

In this paper the authors proposed in this paper to integrate some of these methods by using a specialized complex simulation platform, namely SYNTHESIS, which allows a physical and statistical approach for PV products; it is envisaged the development of a highly useful RAMS methodology, both in research and in the efficient design of PV systems and their applications (Wohlgemuth, 2003; Van Weeran, 2013; Granata et al., 2009).

2.3. Methodology

In order to perform a fairly accurate reliability analysis of the PV systems and their components, the authors of this paper have chosen to use the SYNTHESIS simulation platform developed by **ReliaSoft (**Synthesis Platform, 2017)**.** The simulation methodology is intended to explain how the simulation platform modules work. On this basis the obtained results regarding: 1) solar cell, 2) PV system, including its components, 3) LED lighting system and 4) integrated PV system can be understood. The following modules of the simulation platform were used in the analysis:

a) The **Weibull++ software tool** is the industry standard in life data analysis (Weibull analysis) for many companies around the world. This software performs life data analysis using multiple lifetime distributions with a clear and concise, reliability-oriented interface. The features of Weibull++ provide the most comprehensive set of tools available for life data reliability analysis. The software supports all types of data and all distributions commonly used throughout the product's lifetime.

b) The **ALTA software tool** provides an intuitive way of complex and powerful mathematical models for quantitative analysis of accelerated life tests. Accelerated lifetime testing techniques, combined with powerful data analysis methodologies, reduce testing time for the product, thus providing faster product launch times, lower product development costs, as well as lower warranty costs.

c) The **BlockSim software tool** provides a comprehensive platform for the reliability, availability, maintenance and related products analyzes. The software provides a graphical interface that allows modeling of both simple and complex systems and processes using reliability block diagrams (RBDs), failure tree analyzes (FTAs), or combinations of both approaches. Using accurate calculations and / or discrete events simulation, BlockSim facilitates a wide range of analyzes: 1) system reliability analysis, 2) identification of critical components (important for reliability), 3) optimal allocation of reliability, 4) system maintenance analysis (determining the optimal intervals for preventive maintenance); 5) analyzing the availability of the system (determining the operating time, availability / unavailability), 6) performing calculations for obstacle identification, production capacity estimation, etc.; 7) estimating the cost of the life cycle.

d) The **RENO software tool** is a platform that allows complex analyzes for any probabilistic or deterministic scenario. Chart models can be created for complex reliability analyzes, risk and safety analyzes, decision making, or maintenance planning. The Monte Carlo simulation methods offer a number of definitions and constructions that allow modeling of the examined situations. Simulation results can be applied to estimate/optimize risk analysis, complex modeling of reliability and maintenance planning.

e) The **RGA software tool** allows the application of reliability enhancement models for data analysis from both development tests and on-site repair systems. In the development phase, the software allows to quantify the increase in reliability achieved for each product prototype and also provides advanced design, planning, and reliability enhancement management methods. The software also offers opportunities for ground-based system analysis, including a test utility for system reliability.

For a deep understanding of LED PV applications, the authors used the TM-21 Calculator software developed by ENERGY STAR to study the reliability of LED systems. The main feature of this software is the application of temperature stress levels that allow the establishment of lumen maintenance degradation during the lifetime of these products.

3. Modeling and numerical simulation of PV system components using RAMS analysis. Discussion of the results

3.1. Basic concepts

The studied integrated PV system is defined as a PV application, which uses a consumer for LED lighting application (see Fig.1). The implementation of the RAMS analysis of the PV system was performed using the modeling and simulation SYNTHESIS platform for system reliability (Craciunescu et al., 2017). When it is analyzed the reliability of studied solar cells, the simulation module used in the SYNTHESIS platform was Weibull / ALTA. This module statistically addresses reliability issues through statistical repartitions and together with the ALTA module contributes to the accelerated life tests. For the analysis of the PV system / LED lighting application studied in the paper, the BlockSim simulation module was used within the same platform. The simulation of the PV systems is based on the RBD diagram, as well as on the component types and the way they are arranged in the system.

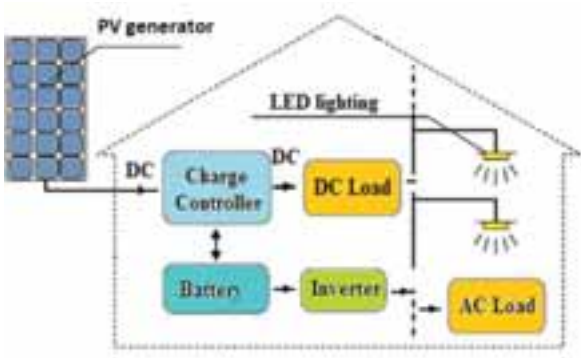

Fig. 1 PV integrated system concept

For a rigorous understanding of the RAMS analysis for the PV integrated system, it was analyzed the highlighting of solar cell degradation. By performing a statistical analysis based on the Weibull, Exponential and Normal repartitions, it was possible to estimate the most frequent events (characterized by main meteorological parameters: solar irradiance, temperature and humidity) that contribute to the most probable degradation of solar cells during their lifetime. The statistical approach was correlated with the accelerating lifetime method by stressing solar cells using different meteorological parameters (Fig. 2). The present study considered only the three meteorological parameters mentioned above, which have an essential role in cell degradation.

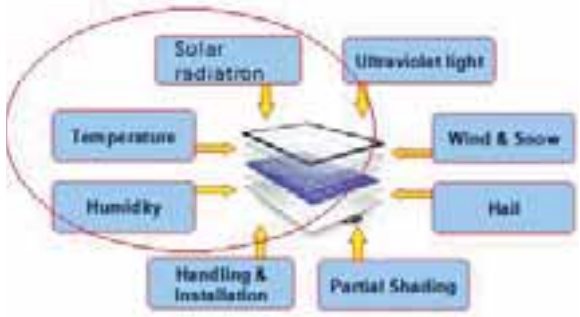

Fig 2. Accelerated stress test diagram

3.2. Reliability analysis of solar cells

Reliability analysis of solar cells has been developed based on the accelerated testing method, which has certain advantages: 1) avoiding testing in real and more severe conditions that can lead to cell degradation / failure, 2) determining the frequent reasons that determine cell failure. Highly Accelerated Stress Screening (HASS) aimed at identifying defects in as short time as possible compared to the standard method (based on cell monitoring and results analysis), which may take several months / years. Accelerated testing (HASS) can be performed with either a weather parameter (e.g. temperature / solar irradiance) or combined with few weather parameters (such as temperature, humidity and solar irradiance). Within this paper the HASS analysis was implemented in the version of the three key meteorological parameters.

The authors' study also looked at establishing the best statistical reparation used to make the most accurate predictions of the of solar cells life time. Three types of statistical repartitions, namely Weibull, Exponential and Normal, were evaluated using the SYNTHESIS software, and based on the correlation cause (determined by one of the three main meteorological parameters) - occurrence (characterized by the degradation degree of the solar cell) it was possible to obtain the probabilities for the three repartitions (the black curve defines the Weibull repartition, the green one defines the Normal repartition, and the purple one defines the Exponential repartition), using the HASS test. In Fig. 3a the curves of the mentioned statistical repartitions were obtained. It can be seen that Weibull repartition is the closest to the values of the three main meteorological parameters. The accelerated test has highlighted that the most influential meteorological parameter in solar cell degradation (characterized by most occurrences) is temperature, followed by humidity and further by

solar irradiance. Fig. 3b shows the temporal evolution (in hours) of the degradation level of solar cells for two operating modes: under stress conditions (purple continuous curve) and in standard conditions (blue continuous curve).

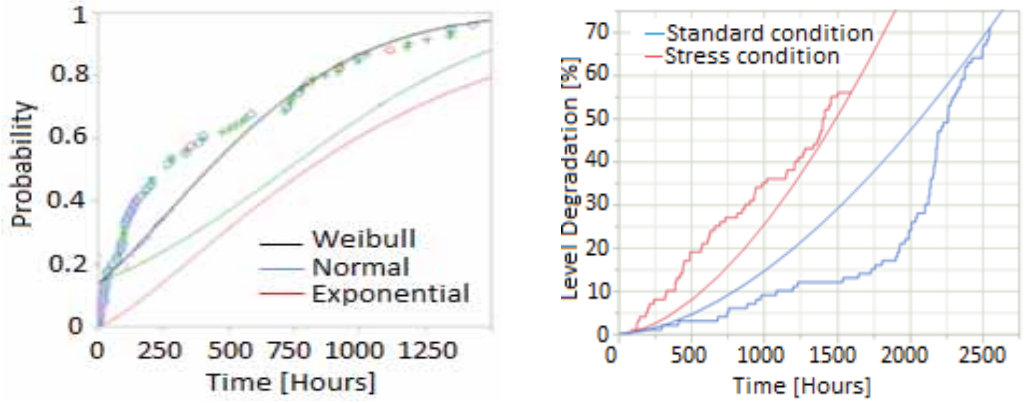

a) b)

Fig.3 a) The life distribution of solar cells for different distribution function b) Degradation level of solar cells simulation in different conditions (standard and stress)

Using the stress results of the HASS test (purple curve in Fig. 3b), it was possible to determine by numerical simulation in the SYNTHESIS platform, the limit value of the cell operating time in normal conditions, respectively 1600 hours, according to the curve in Fig. 4a. The accelerated test also enabled the probable number of solar cell failures (see Fig. 4b) within the range of 1000-2800 hours, with a higher concentration between 1500-2800 hours according to the results from Figure 4a; the linear dependence defines the expected failures curve based on Weibull repartition.

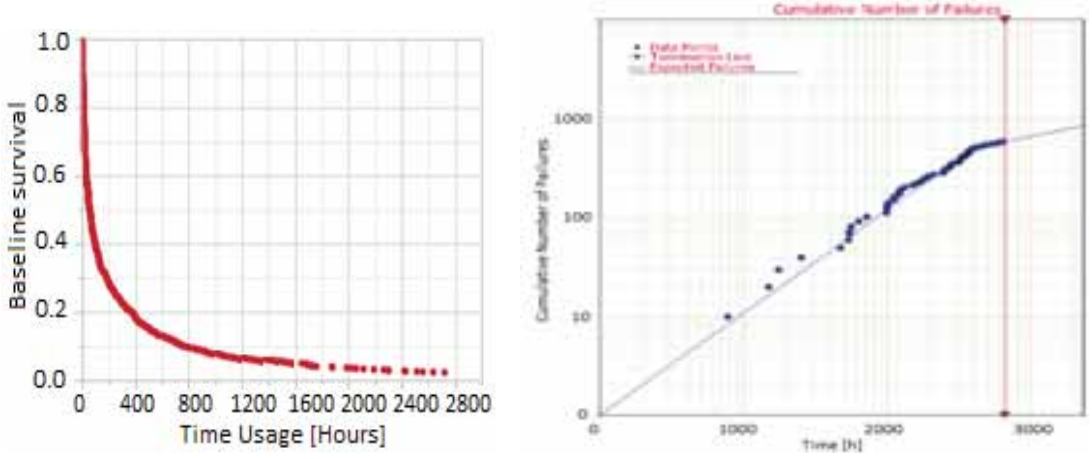

a) b)

Fig. 4 a) Baseline survival of solar cells module simulation in stress conditions b) Cumulative number of failures as function of time

3.3. RAMS analysis of the PV system

The analyzed PV system consists of a set of components, arranged to achieve the established performance and to provide acceptable reliability. The reliability characteristics of the PV system and its components can be presented in RBD-type diagrams illustrating their possible failures. These failures are due to a facile analysis of the failures risk.

The RAMS analysis for the photovoltaic system aimed to determine how the system and its components worked over a 5000-hour period (about 5 months). For this purpose, it was analyzed the time evolution of the PV generator efficiency, as well as of the PV system's battery efficiency. There were noted high fluctuations for the efficiency of PV generator, slower fluctuations in battery efficiency based on Fuzzy Logic Controller (FLC) and Maximum Power Point Tracking (MPPT) methods (see Fig. 5). The LED lighting system (electric consumer) will be discussed further in section 3.5.

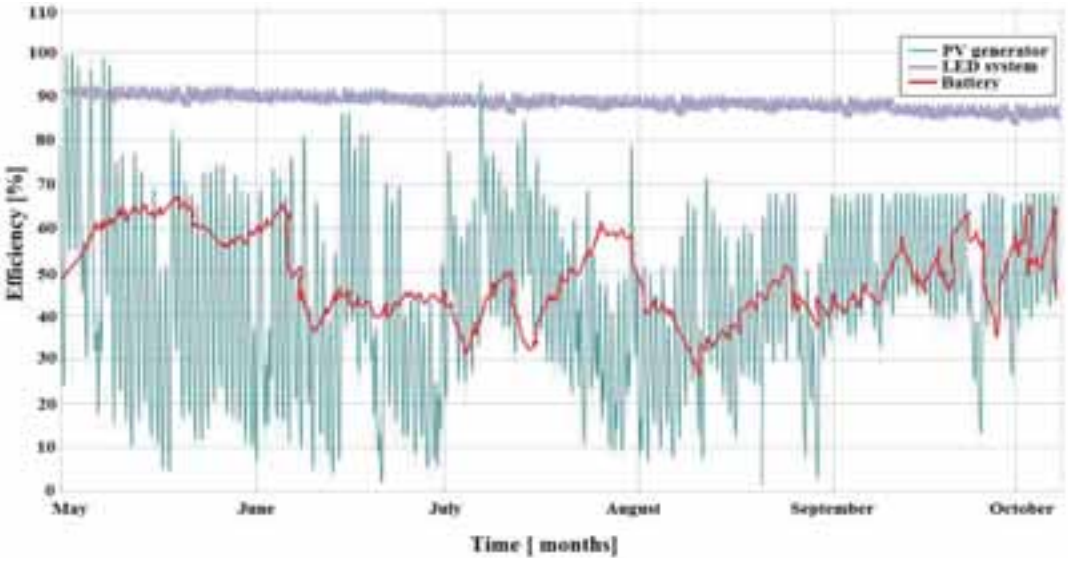

Fig. 5 Efficiency and functionality of a PV system for its main three components: 1) PV generator 2) battery and 3) electrical load

Using the results obtained in Fig. 6a we could establish the availability diagram of the PV system giving the operation time and unavailability periods (when the PV system is not working). The unavailability periods are usually small; after 3000 hours of operation there is a 500-hour period when the PV system has to be repaired due to different failures. In Fig. 6a there are also analyzed the main components of the PV system (PV modules, battery and load) to be maintained. The complex analysis of defect risks and preventive planned maintenance of the components aims at avoiding spontaneous malfunctions and premature degradation of the PV system.

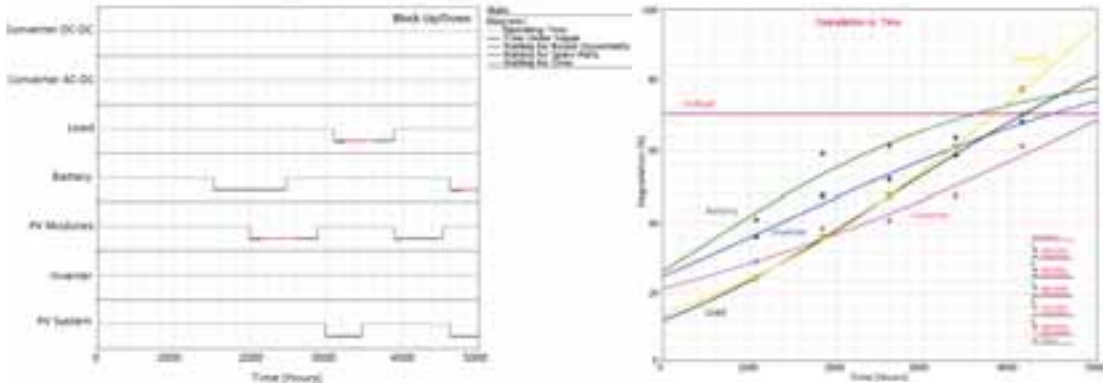

a) **b)**

Fig. 6 a) PV system availability / unavailability diagram b) Degradation of system components based on availability / unavailability diagram

In Fig. 6b the level of degradation for each component of the PV system is presented. Although, excepting the inverter, all other components exceed the critical threshold to the end of the test (3500-4500 hours); however, two components, respectively the PV modules and the storage system, are the most vulnerable to failure (exceeding the critical level much earlier). The simulation tools allowed to obtain the efficiency degradation analysis of the PV system (see Fig. 7a). A good PV system is characterized by small fluctuations of the time evolution of efficiency, determining a usual degradation based on normal operation requirements for the analyzed simulation period (5000 hours).

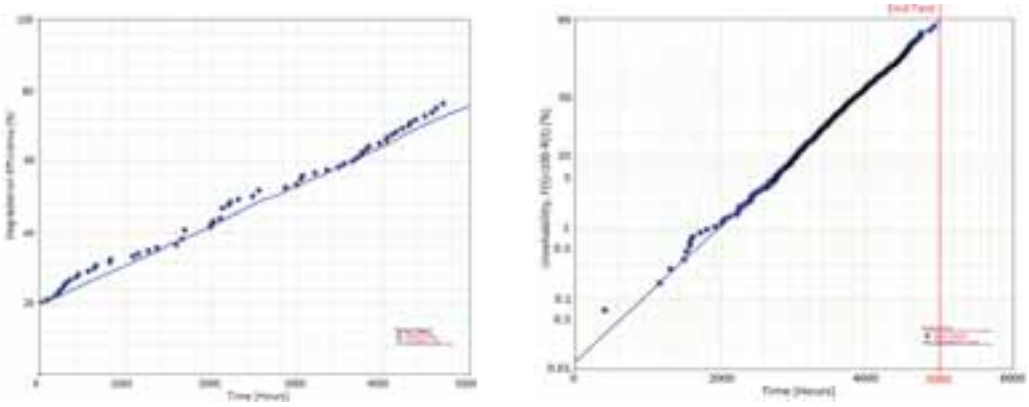

a) b)

Fig. 7. a) Time degradation of PV system efficiency b) Statistical unreliability of the PV system in time

The probability of non-functioning of the PV system over time is sensitive after 2000 hours of the product use (see Fig. 7b). It is noted the role played by this diagram in RAMS analysis; when the components of the PV system start to degrade, the number of failures increases, that leads to the need for more frequent interventions (repairs) on the PV system.

The RAMS approach, based on the SYNTHESIS simulation platform, was able to obtain preliminary information on the time behavior of the PV system and its components (from the point of view of its reliability and maintenance) which could be very useful for its proper design.

3.4. Failure analyses for the LED lighting system

The operation of LEDs is strongly influenced by the thermal conditions that can cause LED degradation. The evaluation of LED degradation is performed by the lumen degradation method, in which higher internal temperatures are produced without heat sink. The RAMS analysis of typical LED lamps, as the one in Fig. 8, is possible with the help of two software environments, namely: 1) TM-21 Calculator developed by ENERGY STAR - to determine LED lamp degradation, and 2) SYNTHESIS simulation platform - to assess the failure of each component of the LED lamp (TM-21 Calculator, 2017; Synthesis Platform, 2017).

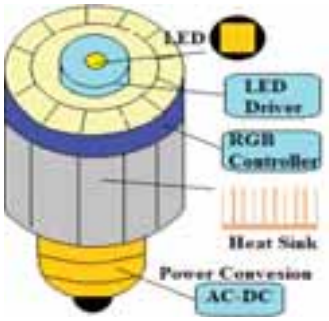

Fig 8. Concept of a typical LED lamp

According to Fig. 9a, at a test temperature of 140 ^{o}C, the lumen flux reaches 60% of its total value; it corresponds to a 2200 hours operation (based on a 5000-hour range for which the simulation was performed). It is remarked that the life duration of the LED lamp was reduced by roughly 1500 hours in the temperature range of 80-140 $^{\circ}$C.

The SYNTHESIS platform, in particular the BlockSim software tool, was used to obtain the degradation diagram of the LED lamp, as shown in Fig. 9b, useful in testing of several efficient cooling systems, which can help to increase the reliability of the LED system. It is noticed that, under standard operating conditions, the LED lamps are getting closer to the critical degradation limit, while using the Heat Sink the LED lamp component functioning is removed from the critical area.

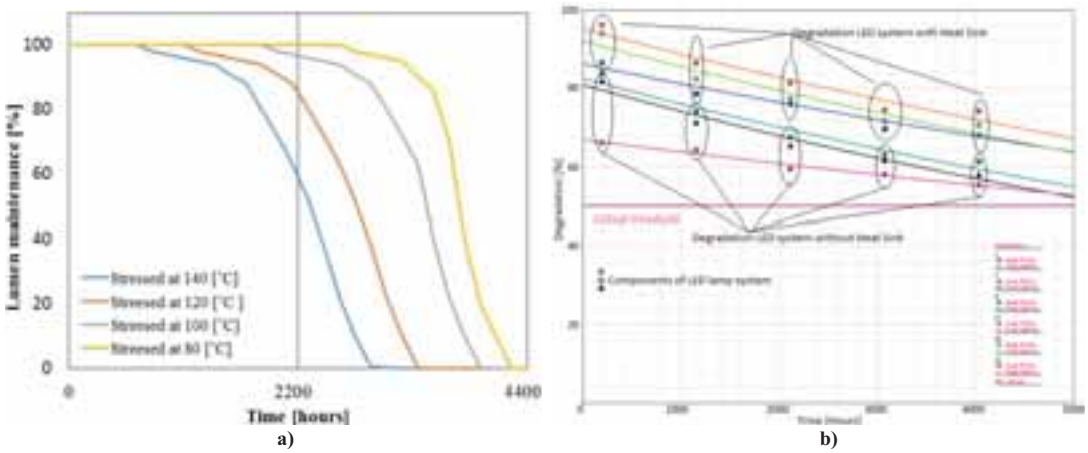

Fig. 9: a) The degradation curve of lumen maintenance [%] for the whole LED lamp, represented by life duration (hours) depending on four values of test temperature (stress). b) Degradation diagram of the LED lamp components

3.5. RAMS analysis specific to a PV system

A PV system based on LED lighting application has been studied. Analysis of the PV integrated system was possible using the availability / unavailability diagram of its components (Fig. 10). This diagram describes the interdependence between the components and defines how the system works. An important parameter of the availability / unavailability diagram is the power load LED system that is influenced by the operating mode (using either serial, parallel or mixed type configurations). Each component of the PV system is characterized by a repairable block, parameterized in the BlockSim simulation module.

A feature of the Up / Down diagram is the planning of the PV system maintenance; thus, as a result of prompt interventions in order to repair its components, spontaneous or irreversible failures are eliminated, the system thus becoming functional over the entire lifetime.

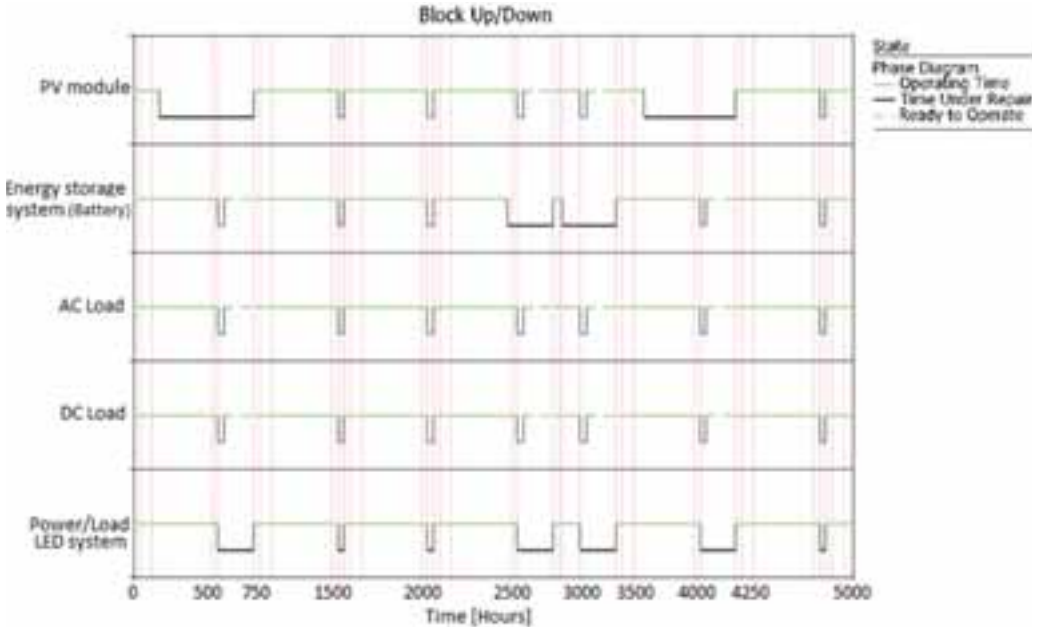

Fig. 10: Diagram of the availability / unavailability (Up / Down) of the PV integrated system

The failure rate for each component of the PV system was also being studied. The highest failure rate is presented, by the PV modules, respectively LED systems, according to the results in Fig. 11. This is due to

the specific configurations for these components (series, parallel or mixed) that increase their failure rate compared with other components (battery, inverter, regulator, etc.).

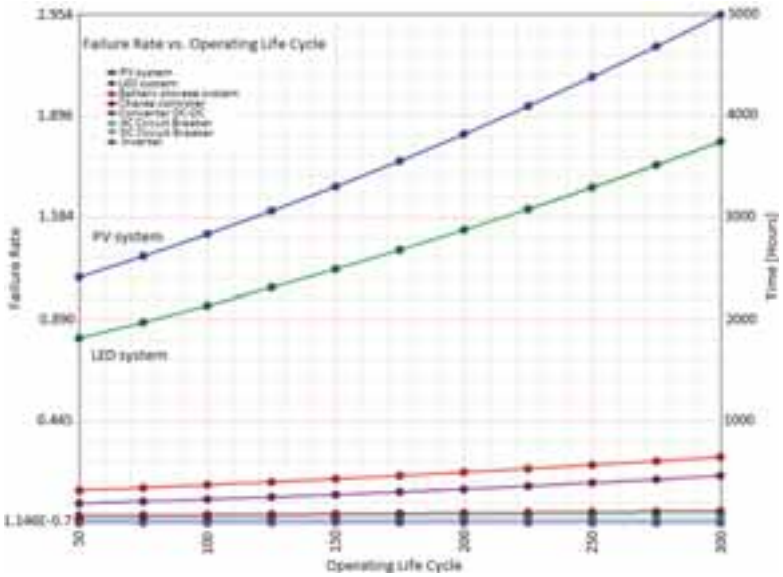

Fig. 11: Time evolution (in hours) of components failure rate of the PV system depending on operating life cycle

4. Concluding remarks

The authors have proposed the reliability analysis of a PV system for a LED lighting application using a performance SYNTHESIS simulation platform, which allowed the system to function more accurately by identifying probable defects in certain components of the system.

This contribution is based on an original approach of RAMS reliability analysis. It was considered the adaptation of Up / Down reliability block diagrams (RBD) from *the reliability theory and applications* for a photovoltaic system in order to determine its functionality and availability and to establish its duration of non-functionality (required to implement the PV system maintenance). The obtained results of this study are in good agreement with the reliability published studies from the point of view of the methods used (Huffman et al., 2009; DeGraaff et al., 2011; Crow 2004; Crow 2003; Collins et al., 2009; Copper et al., 2016; Vazquez et al., 2008).

The main results obtained by the authors in this article could be synthesized as follows:

- the simulation of the solar cells operation on an accelerated test basis (under the influence of three essential meteorological parameters: solar irradiance, temperature and humidity) allowed to put in evidence the normal operating time under normal / stress conditions, defining the initial degradation time of stressed solar cell (determined by a possible degradation of the cell's I-V characteristics). The Weibull most probable statistical repartition has also been identified using a proper solar cells testing; on this basis, the operating duration in which a significant concentration of defects is achieved, was determined.

- the simulation of the PV system operation allowed to obtain information on the availability / unavailability of the system, based on a RBD diagram. Using this diagram, PV components that may exhibit a higher rate of degradation (PV modules, electrical battery) during operation are identified. Also, useful information on degradation of the PV system was obtained (based on the efficiency degradation curve and the non-functional curve).

- the simulation of the LED lamp allowed to study the temperature influence on the lifetime and the degradation of the lamp components.

- the simulation of PV system operation for the LED lighting application allowed also to use the Up/Down diagram as maintenance schedule for elimination of spontaneous or irreversible failures,

The results obtained by the authors were partially validated by other authors research studies, regarding the availability and degradation of analyzed systems (Mahdi et al., 2017; Lavrova et al., 2015).

In order to increase the reliability of the PV system and its components, it is necessary to develop an elaborated failure management strategy that involves knowing the initial level of reliability and developing efficient solutions for planning and assessing the probable risks of failure. The essential directions for such a strategy could be as follows:

- experimental accelerated testing of the PV system under the influence of possible degradation factors;

- identifying the cause of failure in experimental conditions, that is intended to isolate possible failures occurring in the PV system;

- implementing effective corrective actions to significantly reduce the failures of the PV system.

Acknowledgment

The authors are grateful for the financial support of Ministry of Research and Innovation, Romanian Executive Agency for Higher Education, Research, Development and Innovation Funding (UEFISCDI), no. 34/2016 contract, SOLHET project “High-performance tandem hetero-junction solar cells for specific applications”.

5. References

Huffman D.L., Antelme F., 2009. Availability analysis of a solar power system with graceful degradation. Proc. of the Reliability and Maintainability Symposium, Fort Worth, TX.

DeGraaff D., Lacerda R.,. Campeau Z, 2011. Degradation Mechanisms in Si Module Technologies Observed in the Field; Their Analysis and Statistics. Presentation at PV Module Reliability Workshop, NREL, Denver, Golden, USA.

Kececioglu, D.B., 1991. Reliability Growth, Reliability Engineering Handbook. fourth ed, Vol. 2, Prentice-Hall, Englewood Cliffs, New Jersey, pp. 415-418.

IEC International Standard, Reliability Growth- Statistical test and estimation methods, IEC 1164 International Electrotechnical Commission, 1995

Ishii, T., Takashima, T., Otani, K., 2011. Long-term performance degradation of various kinds of photovoltaic modules under moderate climatic conditions. Prog. Photovolt: Res. Appl., 19, 170.

Crow, L.H., 2004. Evaluating the Reliability of Repairable Systems. IEEE Proc. Annual Reliability and Maintainability Symposium, 73-80.

Crow, L.H., 2003. Methods for Reducing the Cost to Maintain a Fleet of Repairable Systems. IEEE Proc. Annual Reliability and Maintainability Symposium, pp. 392-399.

Herrmann, W., Bogdanski, N., Reil, F., Kohl, M., Weiss, K., Assmus, M., Heck, M., 2010. PV module degradation caused by thermo-mechanical stress: Real impacts of outdoor weathering versus accelerated testing in the laboratory. Proc. Vol. 7773, Reliability of Photovoltaic Cells, Modules, Components, and Systems III; 777301

Hoffmann, S., Koehl, M., 2012. Effect of humidity and temperature on the potential-induced degradation. Prog. Photovolt: Res. Appl., 22, 173–179

Popescu A., Miclos S., Savastru D., et al. 2009. J. Optoelectron. Adv. M. 11(11), 1874

Stanciu A. E., Cotoros D. L., Cristea L., Baritz M., 2015 J. Optoelectron. Adv. M. 17(7-8), 1146.

Sterian PE., 2000 Fotonica. Printech;

Sterian A. and Sterian P, 2012 "Mathematical Models of Dissipative Systems in Quantum Engineering", Mathematical Problems in Engineering, vol. 2012, Article ID 347674, 12 pages, doi:10.1155/2012/347674

Power Semiconductor Reliability Handbook, 2010, Alpha and Omega Semiconductor.

Holley, W., Agro, S. Galica, J., Yorgensen, R. 1996. UV stability and module testing of non-browning experimental PV encapsulant. IEEE Photovoltaic Specialists Conference

Nelson, W., 1998. An Application of Graphical Analysis of Repair Data. Qual. Reliab. Eng. Int., 14, 49-52.

Kijima, M., 1989. Some results for repairable systems with general repair. J. Appl. Probab., 20, 851—859.

Mettas, A., 2000. Reliability Allocation and Optimization for Complex Systems. Proc. of the Annual Reliability & Maintainability Symposium.

Meydbray, Y., Wilson, K., Brambila, E., Terao, A., Daroczi, S., 2008. Solder joint degradation in high efficiency all back contact solar cells. IEEE Photovoltaic Specialists Conference.

Collins, E., Miller, S., Mundt, M., Stein, J., Sorensen, R., Granata, J., Quintana, M. 2009. A reliability and availability sensitivity study of a large photovoltaic system. IEEE Photovoltaic Specialists Conference.

Meydbray, Y., Wilson, K., Brambila, E., Terao, A., Daroczi, S., 2008. Solder joint degradation in high efficiency all back contact solar cells. IEEE Photovoltaic Specialists Conference.

McMahon, T., 2004. Accelerated testing and failure of thin-film PV modules. Prog. Photovolt: Res. Appl, 12, 235-248.

Wohlgemuth, J., 2011. Tutorial/short course on reliability: PV cells, modules, and systems. IEEE Photovoltaic Specialists Conference. Seattle, WA.

Aoki, Y., Okamoto, M., Masuda, A., Doi, T., 2010. Module performance degradation with rapid thermal-cycling. Proc. of Renewable Energy.

Dhere, N., Pethe, S., Kaul, A., 2010. Photovoltaic module reliability studies at the Florida Solar Energy Center. IEEE International Reliability Physics Symposium.

Kim S. K., Kim S. Y., Choi Y. D., 2006 Proceedings of 10th Intersociety Conference on Thermal and Thermomechanical Phenomena in Electronic Systems, pp. 377-379,.

Handbook, 2007, Lumileds, understanding power led lifetime analysis. Technical report, Philips Lumileds Lighting Company.

Crow, L.H., 2008. A Methodology for Managing Reliability Growth During Operational Mission Profile Testing. IEEE Proc. Annual Reliability and Maintainability Symposium, 48-53.

Dhere, N., 2005. Reliability of PV modules and balance-of-system components. IEEE Photovoltaic Specialists Conference.

Copper, J. K., Bruce, A., 2016. Calculation of PV System Degradation Rates in a Hot Dry Climate. Asia Pacific Solar Research Conference, Canberra, Australia.

Desombre, A., 1980. Methodology for a reliability study on photovoltaic modules. Proc. of the third European Commission, PV Solar Energy Conference. Cannes, France. 741-745.

Vazquez, M. Rey-Stolle, I., 2008. Photovoltaic module reliability model based on field degradation studies. Prog. Photovolt., 16, 419.

Wohlgemuth, J., 2003. Long-term photovoltaic module reliability. NCPV and Solar Program Review Meeting, NREL/CD-520-33586, 179-183

Van Weeran, N., 2013. Degradation of photovoltaic modules in Alice Springs, Australia. Undergraduate Thesis, School of Photovoltaics and Renewable Energy Engineering, The University of New South Wales.

Granata, J., Boyson, W., Kratochvil, J., Quintana, M., 2009. Long-term performance and reliability assessment of 8 PV arrays. IEEE Photovoltaic Specialists Conference.

Craciunescu D., Fara L., Sterian P., Bobei A. Dragan F., 2017 Optimized Management for Photovoltaic Applications Based on LEDs by Fuzzy Logic Control and Maximum Power Point Tracking, Nearly Zero Energy Communities, Springer Proceedings in Energy, DOI 10.1007/978-3-319-63215-5_23

TM-21 Calculator platform. https://www.energystar.gov/sites/default/files/ENERGY%20STAR%20TM21%20Calculator%20rev%2002-08-2016%20clean_0.xlsx. Accessed October 2017.

Synthesis Platform. http://www.reliasoft.com/synthesis/downloads.htm. Accessed October 2017.

Mahdi I., Chalah S. Nadji B., 2017, Reliability study of a system dedicated to renewable energies by using stochastic petri nets: application to photovoltaic (PV) system, 4th International Conference on Energy and Environment Research, ICEER 2017, 17-20 July 2017, Porto, Portugal, Energy Procedia 136, 513–520.

Lavrova O., Flicker J., Johnson J., Armijo K., Gonzalez S., Schindelholtz E., Sorensen R., Yang B., 2015 PV Systems Reliability: Final Technical Report, Sandia Report-SAND2015-376607.

A multi-criteria analysis of bidirectional solar district heating substation architecture

Nicolas Lamaison[1, 2], Roland Bavière[1, 2], David Chèze[1, 2], Cédric Paulus[1, 2]

[1] CEA LITEN - 17 Rue des Martyrs, 38054 Grenoble (France)

[2] INES - 50 Avenue du Lac Léman, 73375 Le Bourget du Lac (France)

Abstract

Decentralized surplus feed-in of solar heat into a District Heating Network (DHN) is here addressed. The heat collected from solar panels located on rooftops of DHN connected buildings may either be used locally for domestic hot water and space heating or fed into the heating network. Two-way substations able to transfer heat from and into the network seem then to be required utilities of future DHN. In that context, two equally important questions were identified: i) what should be the specifications and architecture of such solar fed bidirectional substations? and ii) what is the impact of decentralized reinjection on the network operation? The former is addressed in the present paper while the latter is an ongoing study not presented here. In the present work, first a discussion on the specifications and architecture of such bidirectional substations led to the conclusion that architectures for which the solar heat is entirely reinjected into the DHN without local consumption seem more feasible. Second, a Modelica-based modeling framework of the bidirectional substation is presented and preliminary results highlight the potential of reinjection on the DHN. The results presented here are part of the first year work in the frame of the European project 'THERMOSS'.

Keywords: Solar Feed-In, Decentralized, Substation, District Heating, Dynamic Modeling, Modelica, Prosumers

1. Introduction

In the "2way District Heating" course of action from the 4GDH concept (Lund et al., 2014), decentralized feed-in of solar heat from prosumers, i.e. customers reinjecting heat into a district heating network (DHN), seems to be a promising solution to increase the share of renewable energy of DHNs. The latter is especially true in dense urban areas with limited ground surface. Reinjection of solar heat will maximize the use of well-exposed customers' rooftops while minimizing the cost by mutualizing the equipment via the DHN.

However, when scattered heat reinjections occur in a DHN, new problematics arise. Among the most decisive ones, prosumers must decide whether it is interesting to consume or feed-in the collected solar energy, they must control their reinjection temperature in a context of variable differential pressure and the DHN operating company must deal with distributed reinjection points.

Among the various reinjection principles (see Fig. 1), the Return to Supply line (R/S) variant highlighted in Fig. 1a, seems to be the best option since it leads to the lowest temperature in the solar panels without modifying the network return temperature (Lennermo and Lauenburg, 2016; Schäfer et al., 2014). However, R/S feed-in implies to overcome the local differential pressure between the return and supply lines, which usually exhibits significant variations due to rapid load fluctuations. Moreover, the feed-in temperature must be superior or equal to the local network supply line value. The latter constraints on the local differential pressure and the local supply temperature involve at the bidirectional substation level the use of at least a variable speed pump and a finely tuned control strategy.

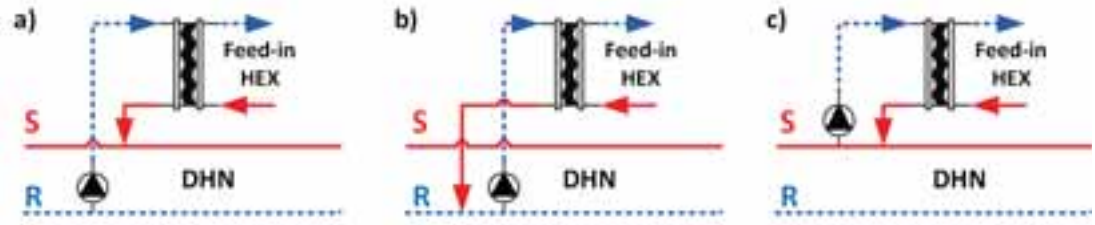

Fig. 1: Schematic of two-way substation feed-in strategies into a DHN – a) Return/Supply (R/S), b) Return/Return (R/R) and c) Supply/Supply (S/S)

doi:10.18086/swc.2017.10.02 Available at http://proceedings.ises.org

More than only considering decentralized reinjection like in Brange et al. (2016) or Heymann et al. (2017), it is of great importance to consider both the local consumption and reinjection of the excess heat as in Paulus and Papillon (2014) and Pietra et al. (2015). The local consumption possibility together with the local differential pressure and supply temperature constraints presented previously lead to the requirement of innovative control algorithm at the substation level (Rosemann et al., 2017). At the network level, the operation with multiple prosumers also becomes more challenging with the creation of new pressure cones for example (Brand et al., 2014) that may lead to flow stagnation in some parts of the network and even possible flow reversal at the main generator (Heymann et al., 2017). Additionally, the traditional critical differential pressure driven operation becomes more difficult to implement (Hassine and Eicker, 2014).

In this context, it seems necessary to address the question of bidirectional substation at both the substation and network levels. Thus, on the one hand, the present study addresses the specifications, architectures, and modeling of a two-way substation for a multi-family building including the possibility of local consumption. On the other hand, work on the influence of decentralized reinjection on the network's performance is ongoing but not presented here. These two studies are meant to be connected in future work by implementing the model developed in the first task into the network of the second task.

The present paper thus addresses the problem at the substation level. It firstly deals with the specifications and architectures of bidirectional substations. Features such as the location of the hydraulic separation between the network and the building, local consumption of the heat or total feed-in and control strategies are combined to build an exhaustive list of possible configurations. Secondly, a promising setup is chosen from that table based on a multi-criteria analysis. Finally, a modeling framework for the simulation of bidirectional substations is presented with preliminary results. Contrarily to most publications on this topic in the open literature, Modelica programming language is here used rather than TRNSYS (Paulus and Papillon, 2014), NetSim (Brand et al., 2014) or in-house tools (Pietra et al., 2015) since it has native multi-physical modeling capabilities (i.e. thermo-hydraulic) and allows for implementing new components. Both the details of the two-way substation and the impact of these prosumers on the network are thus studied using the Modelica "Standard" Library, together with the "Buildings" (Wetter et al., 2014) and the "DistrictHeating" (Giraud et al., 2015) libraries.

2. Bidirectional Substation Specifications

2.1. Initial Considerations

As previously discussed, the problem here addressed is the decentralized reinjection of solar heat on a DHN using R/S feed-in (see Fig. 1). The solar collectors are assumed to be on the rooftop of a multi-family building, equipped with a unique bidirectional substation (see Fig. 2). Variants relying on individual bidirectional stations at the apartment level have been discarded from this study due to prohibitive cost and increased complexity. Indeed, solar bidirectional substations seem more appropriate for multi-family buildings rather than for individual apartments (Rosemann et al., 2017) since it simplifies the hydraulic connections at the building level while reducing the costs. It also reduces the number of reinjection points in the DHN, aggregate heat inputs and thus simplifies the operation of the network.

Fig. 2 Two-way substation in multi-family building prosumers

The multi-family building considered in the present study consists in 3 floors with 2 apartments of 3 people per floor. Each apartment has a height, width and length of respectively 2.5m x 10m x 7m leading to an overall footprint of the building of 7.5m x 10m x 14m. A preliminary calculation leads to an overall space heating (SH) nominal power of about 42kW based on a consumption of 100W/m² (poorly insulated buildings built in the 80's in western European climate) and an overall domestic hot water (DHW) nominal power of 60kW. The latter is obtained using the daily draw-offs from COSTIC (2016), i.e. about 150 liters for an apartment of 3 people, and the "DHWcalc" calculator (Jordan and Vajen, 2005) to obtain distributed daily or yearly profiles. The maximum 10 minutes average from this profile is 16kW/apartment leading to the 60kW for the entire building when accounting for a simultaneity coefficient of 0.62. The solar collector field has an area of 80m², which covers one side of the rooftop with a 30° of inclination angle. The building solar production would reach 56kW with an assumption of 700W/m² of production based on IEA SHC recommendations (IEA SHC, 2004).

The rest of the present section is dedicated to the question of the architecture of such two-way substation. Fig. 3 summarizes schematically the challenge posed here with the bidirectional substation connected to the DHN, to the SH and the DHW loops, and to the solar collector field. The question to address in the following parts is how to do so.

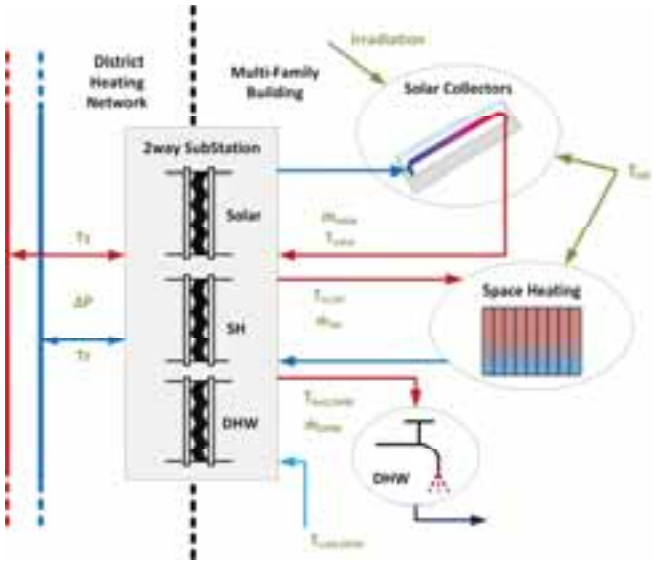

Fig. 3: Overview of the boundary conditions to account for in the design of the two-way substation

2.2. Selection of Features

In the present section, an exhaustive list of possibilities regarding the architecture of the substation will be established through the combinations of three features. Then, the purpose will be to select the most promising ones based on various criteria. The three selected features to characterize the bidirectional substations are the following:

- Feature 1: Type of connection to the DHN, i.e. location of the hydraulic separations for SH and DHW
- Feature 2: Possibility or not to reuse the heat locally, i.e. connection with the solar field
- Feature 3: Control strategy associated to the reinjection of heat.

Tab. 1 presents the three possibilities listed for Feature 1 'Network Connection', Feature 2 'Local Usage' and Feature 3 'Control Strategy'. In this Table, the substation is represented by a grey rectangle. More specifically, the section of the substation dedicated to SH and DHW production is highlighted by a 'SH/DHW' tag while the section dedicated to the solar heat is referred by a 'Solar' tag. The different features will be combined in the next section.

Feature '1', referred as C for Connection, deals with the location of the hydraulic separation between the DHN and the consumer (SH and DHW). Here is the list of possibilities for Feature '1':

- C0: There is no hydraulic separation between the DHN and the consumer inside the bidirectional substation;
- C1: A single heat exchanger in the bidirectional substation performs the hydraulic separation between the DHN on one side and the DHW and SH loops of the consumer on the other side. C1' indicates that

DHW production is then collective for the entire building while C1'' indicates that DHW production is decentralized at the apartment level;

- C2: Two heat exchangers in the bidirectional substation perform the hydraulic separation respectively between the DHN and the DHW loop and between the DHN and the SH loop of the consumer.

Feature '2', referred as U for Usage, deals with the local consumption of the produced heat, i.e. the connection between the consumer and the solar field. It is worth mentioning here that the hydraulic separation between the solar field and the DHN will always be performed with a heat exchanger in the two-way substation:

- U0: The produced heat is entirely reinjected into the DHN;
- U1: The produced heat is partly used locally for DHW preparation and partly reinjected in the DHN;
- U2: The produced heat is partly used locally for DHW preparation and SH and partly reinjected in the DHN.

Feature '3', referred as S for Strategy, deals with the strategy/control associated to the reinjection (feed-in), i.e. the link between the substation and the DHN. The following possibilities are further detailed later:

- S0: A pump and a 2-way valve in series;
- S1: A pump and a 2-way valve as bypass;
- S2: Two pumps and a hydraulic separator.

Tab. 1: Possibilities for Features 1, 2 and 3 - The gray rectangle represents the bidirectional substation perimeter, the 'SH/DHW' tag represents the substation part dedicated to SH and DHW while the 'Solar' tag represents the substation part dedicated to the solar heat

FEATURE 1: HYDRAULIC SEPARATION between DHN and SH+DHW (Network Connection)		
C0	**C1**	**C2**
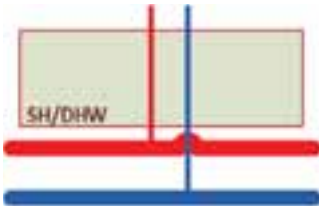	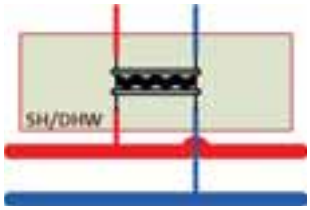	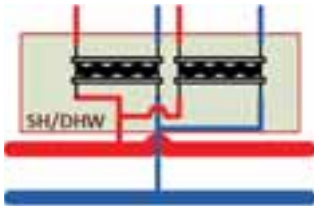
FEATURE 2: SOLAR FIELD CONNECTION (Local Consumption)		
U0	**U1**	**U2**
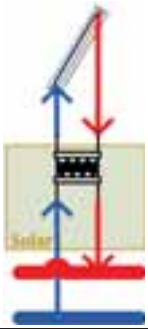	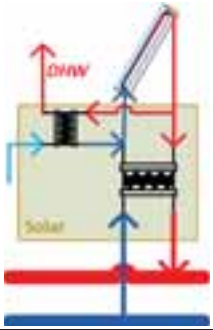	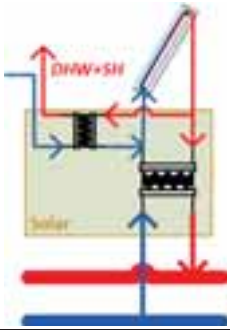
FEATURE 3: FEED-IN ARCHITECTURE (Control Strategy)		
S0	**S1**	**S2**
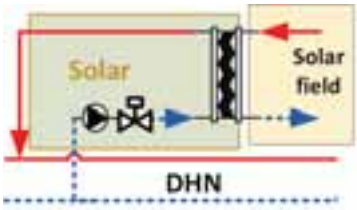	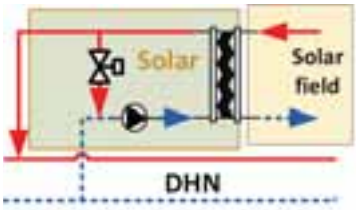	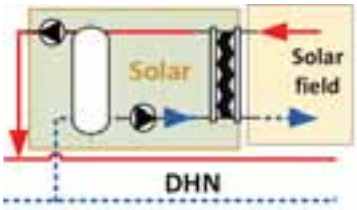

2.3. Features Combinations

As a first step, the two Features ('C' and 'U') are combined resulting in the configuration table Tab. 2. Fig. 4 Fig. 5 show examples of such combined configurations with the two parts 'SH/DHW' and 'Solar' inside the bidirectional substation. Additionally, here are the considerations to account for when combining these first two features:

- If there is no hydraulic separation between the DHN and the building in the bidirectional substation (C0), then each apartment is equipped with an individual small scale one-way substation with a DHW heat exchanger and a SH heat exchanger in parallel, as highlighted in configuration C0U0 of Fig. 4
- If there is no hydraulic separation between the DHW and SH loops in the bidirectional substation but they are themselves separated from the DHN (C1), then if the DHW production is individual, each apartment is equipped with an individual small scale one-way substation with only a DHW heat exchanger (C1''), as highlighted in configuration C1''U0 of Fig. 5

Tab. 2: Possible configurations for solar source bidirectional substation based on Features 1 and 2

DHN Connection	Local usage		
	U0	U1	U2
C0	V	X	X
C1'	V	V	V
C1''	V	X	V
C2	V	V	V

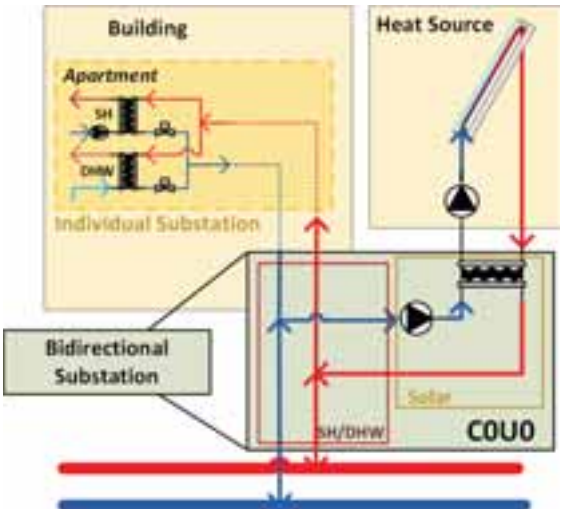

Fig. 4: C0U0 configuration with individual SH/DHW substation in each apartment

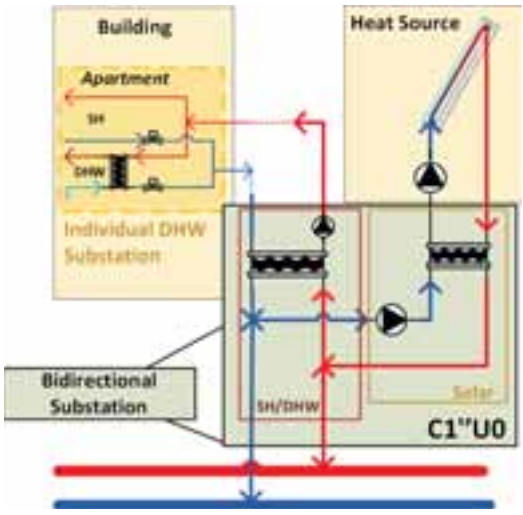

Fig. 5: C1''U0 configuration with individual DHW substation in each apartment

It is observed in Tab. 2 that three configurations, namely C0U1, C0U2 and C1''U1 are unrealistic. Indeed, for the first two, since in configuration C0 the bidirectional substation has no heat exchanger separating the network from the building, individual one-way substations (from network to consumer) are needed in each apartment. Thus, if local usage is implemented, it means that each individual substation needs to handle the solar heat produced. The latter seems inappropriate as explained in Section 2.1 (cost and complexity issues). Similarly in configuration C1''U1, since DHW is not separated from SH at the substation level and is produced individually in each apartment, it means that in order to be able to reuse the solar heat for DHW preheating, an extra heat exchanger is needed in each apartment, which is again rather costly.

For all the other feasible combinations, various criteria listed below have been considered and Tab. 3 summarizes the performance of each of these configurations for these criteria:

- Cost: Related to i) the pressure and temperature levels in the building (lower if hydraulic separation present in the substation), ii) the necessary equipment in the two-way substation (amount of pumps, valves, heat exchangers), and ii) the necessary equipment in the building (extra individual substation for DHW production or indirect space heating)

- Operation: Related to the operation of the solar field with respect to the DHN and the consumers. Simpler if the solar production is decoupled from the consumer part (U0 solutions)
- Ownership: Related to who owns what in the overall system, i.e. is the barrier between the DHN operating company and the consumer clear? In the case of local consumption (U1 and U2), it is clear if the solar field belongs to the consumer but not clear if it belongs to the DHN company.
- Extra DHW production in the apartments: Related to the requirement of an extra hydraulic separation between SH or DHN water and DHW water outside of the two-way substation. This is linked to the location of the hydraulic separation.
- Sanitary loop Requirement: Related to the requirement of a sanitary loop for DHW production. If individual DHW substations are used, sanitary loop is not needed.

Tab. 3: Performance criteria for the selection of the most promising architecture

	C0U0	C1'U0	C1''U0	C2U0	C1'U1	C2U1	C1'U2	C1''U2	C2U2
Cost	+/-	+/-	-	+	+/-	+	+/-	--	+
Ownership	+	+	+	+	+/-	+/-	+/-	+/-	+/-
Operation	+	+	+	+	+/-	+/-	+/-	+/-	-
Extra DHW production needed	Yes	Yes	Yes	No	Yes	Yes	Yes	Yes	No
Sanitary loop required	No	Yes	No	Yes	Yes	Yes	Yes	No	Yes

In general, operation and ownership are easier if there is no local usage of the produced solar heat (U0 solutions) since the DHN could then own the decentralized solar fields and operate them at wish, as common generators (but of small size). Solutions involving additional individual substations (C0 and C1'') are more costly but do not require sanitary loops and allow for individual metering. C2U1 also seems interesting since it does not increase drastically the number of components while allowing self-consumption of the locally generated heat. However, that configuration is more complex to operate.

2.4. Selected Architecture

For the continuation of the present study, configuration C2U0, i.e. with the hydraulic separation for both the space heating and the DHW performed in the bidirectional substation and with no local consumption, has been selected for the following reasons:

- In this configuration, the DHN operator could rent the building's rooftop to install the collector field and would then operate it at wish to suit the entire DHN operation;
- In this configuration, the operation of the consumer part of the substation remains as usual;
- It is cost efficient since the hydraulic separation is performed at the building scale and thus individual one-way substations are not necessary. Additionally, since the hydraulic separation is performed at the building scale, the building's piping would run at lower pressure and temperature;
- It presents the simplest operational scheme / control strategy.

The selected configuration C2U0 is shown on Fig. 6. On this Figure, control strategy S0 (see Tab. 1) of the last feature, i.e. Feature '3', has been superimposed to the C2U0 configuration. In general, the main objective of the control strategy is to obtain a feed-in temperature level above the local supply temperature in the DHN, while fulfilling the following constraints:

- Obtain the lowest temperature in the solar field to reach high efficiencies;
- Overcome the strongly varying local flow resistance, i.e. differential pressure drop;
- Well adjust the feed-in flow rate so that the feed-in rate matches the strongly varying heat rate produced by the solar field.

As highlighted in Schäfer et al. (2014), the challenge here lies in the combination of two parameters with strong and fast variations, i.e. the solar heat production and the local differential pressure drop. In general, if a speed controlled pump alone is used to maintain the targeted temperature, too many startup/shutdown cycles are noticed when the differential pressure exhibits strong variations.

In control strategy S0 (see Tab. 1), the pump is responsible for the pressure differential while the valve is applied to regulate the flow in order to meet the targeted temperature. This method exhibits good performance but the control valve results in higher electricity demand for the pump. In control strategy S1 (see Tab. 1), the pump is responsible for the pressure differential and the 2way valve used as shunt is responsible for the feed-in flow and temperature. The feed-in pump, shall only have enough pressure head to exceed the differential pressure. The cold temperature on the hot side of the heat exchanger is higher than it needs to be resulting in lower solar field efficiency. Finally, in control strategy S2 (see Tab. 1), the hydraulic separator divides the system into two hydraulic loops. The pump located after the extraction is used for temperature control while the other one targets a pressure differential set point. The solution turns out to be a good approach for solving the problems. However, the cost is high as the use of additional components (extra pump and hydraulic separator).

A 3-way valve solution is also possible but was not selected here because of the fast-varying differential pressure, impossible to handle using a 3-way valve (Lennermo et al. (2014).

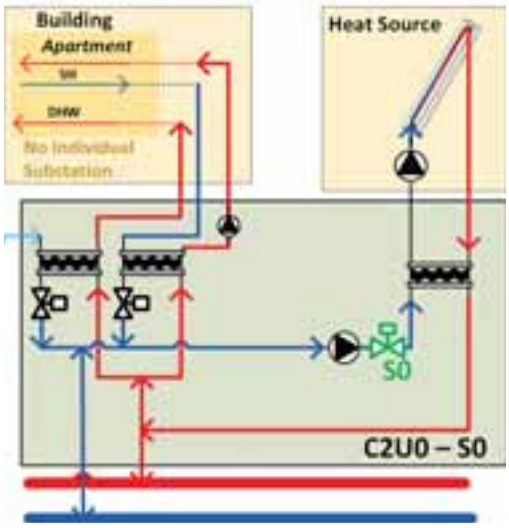

Fig. 6: Bidirectional Substation configuration C2U0 with control strategy S0

As a conclusion of the present section, the performed assessment led to the selection of configuration C2U0 as promising architecture for a bidirectional substation. In this configuration, the hydraulic separation between both the building SH and SHW loops and the DHN is performed in the substation and the solar heat is entirely reinjected in the DHN. Three control strategies have been identified and will be compared in future work. The next section presents the modeling framework developed and the associated preliminary results obtained.

3. Modelling Framework

3.1. Modelling

This section aims at presenting the framework developed for the comparison of the bidirectional substation architectures and control strategies in the frame of the 'THERMOSS' project. It is based on the open source modelling language Modelica used in the commercial simulation environment Dymola. Modelica is an acausal (equation-base) and object-oriented programming language with a large and fast-growing community both for industrial and academic applications (Schweiger et al., 2017). Modelica has native multi-physical modelling capabilities (thermo-hydraulic), is structured in libraries enabling exchange of methods in the scientific community and allows for implementing new components. Moreover, the Annex 60 project from the IEA (Wetter, et al., 2015) promotes the development of computational tools for building and community energy systems based on Modelica and FMI standards, motivating the choice of this modelling framework. As mentioned in the introduction, the Modelica "Standard" Library for its common connectors and fluid ports, the "Buildings" library

(Wetter et al., 2014) for its general building and solar panels models and the "DistrictHeating" library (Giraud et al., 2015) for its heat exchanger and piping models will be used.

As highlighted previously in Fig. 3, the bidirectional substation is surrounded by four boundary conditions blocks, namely the space heating needs, the domestic hot water draw-offs, the solar gains and the network operating conditions. Thus, the present section begins with the core model of the bidirectional substation and then continues with the description of these four boundary conditions blocks.

Bidirectional substation

It is composed of three heat exchangers and associated valves, two pumps (for SH circulation and for the reinjection) and connection piping as shown in Fig. 6. The heat exchangers are discretized in nz elements and the heat exchange in each element 'i' is calculated as $\dot{Q}_i = (UA/nz).\Delta T$ with a constant overall heat transfer capacitance UA and the local temperature difference ΔT between the hot and cold streams. The overall heat transfer capacitance for each heat exchanger is obtained based on nominal operating conditions (see Tab.4). It is worth mentioning that the network side is the hot side for both the DHW and the SH heat exchangers while it is the cold side for the Solar heat exchanger The heat exchangers are modeled with no flow resistance, the pressure drop being entirely considered in the associated valves model. For the latter, a quadratic model is assumed. Finally, regarding the pumps, they are both considered to run at constant speed with the flow rate modulation being performed by the feed-in valve (see S0 in Fig. 6) in the case of the feed-in pump and a thermostatic valve for the SH, as explained in the next paragraph.

Tab. 4: Nominal operating conditions for the Heat Exchangers of the bidirectional substation

Heat Exchanger	$T_{hot,in}$ [°C]	$T_{hot,out}$ [°C]	$T_{cold,in}$ [°C]	$T_{cold,out}$ [°C]	DTLM [°C]	Power [kW]	UA [kW/K]
Solar	90	60	50	85	7.2	56	7.8
DHW	80	50	10	55	31.9	60	1.9
SH	80	50	45	70	7.2	42	5.8

SH needs

The boundary condition dealing with the space heating demand is modeled with i) a heating system and ii) a mono-zone building. For the former, it is connected to the SH pump and is composed of a thermostatic valve and a radiator modelled using the "RadiatorEN442_2" model from the library "Buildings" (Wetter et al., 2014). In this model, the transferred heat is computed using a discretization along the water flow path, and heat is exchanged between each compartment and a uniform room air and radiation temperature. The mono-zone building is modeled using the "mixed air" model (Wetter et al., 2011) from the library "Buildings" (Wetter et al., 2014). The latter considers a perfectly mixed air in the room and takes into account heat exchange through convection, conduction, infrared radiation and solar radiation. Internal heat gains due to occupation (latent heat), lighting (radiation) and home appliances (convection) are included in the model. Constant single-flow ventilation is considered with a flow-rate of about 0.4 room volume per hour. For the present study, the dimension of the building considered were listed in Section 2.1. The total glazed area for the building represents 1/6 of the building living area, shared as follows, 50% on the South wall, 15% on the West wall and 35% on the East wall. The envelope of the building (layers composition and infiltration) can be set to follow various French thermal regulations (RT2000, RT2005, RT2012).

DHW draw offs

For now, the water draw-off system is considered without sanitary loop. As explained initially, the daily or annual (depending on the simulation) profile of draw-offs are obtained from the software DHW calc (Jordan and Vajen, 2005) from Task 26 of IEA which distributes DHW draw-offs throughout the year or the day with statistical means, according to a probability function. The mean daily DHW consumption was obtained from a report of COSTIC (2016) based on the type of apartment and the number of people living in it. Additionally, a correction of the cold water temperature is also included in the simulations using the model of Burch and Christensen (2007).

Network

The network side inputs are the local differential pressure and supply temperature. It was explained beforehand that these two variables are decisive regarding the control scheme of the two-way substation. In the present model, these two variables can either be set to constants to study specific operational conditions or set to follow real DHN variations. For the latter, data were collected in the frame of the THERMOSS project at the DHN of San Sebastian, Spain. Fig. 7 below presents these data for three days with a time step of 15 minutes.

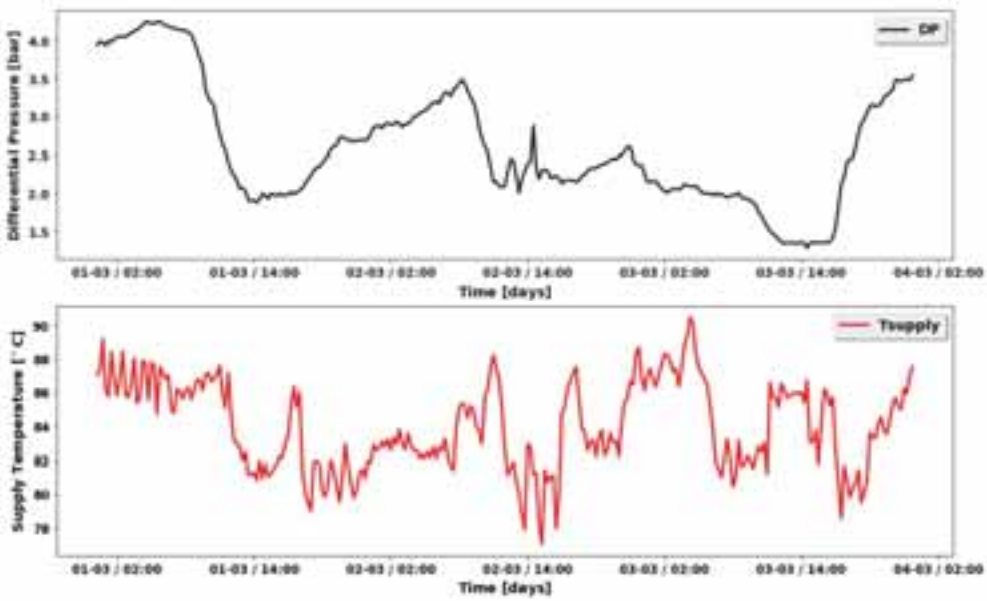

Fig. 7: Differential pressure and Supply Temperature variations in the DHN of Giroa-Veolia in San Sebastian

Solar field

The solar field on the rooftop is modeled using the 'SolarCollectors' package from the Buildings library which models a solar thermal collector according to the ASHRAE93 test standard (ASHRAE93, 2010). The package proposes different pre-defined solar panels set of characteristics. The flat plate panel Guandong Fivestar Solar Energy Co, FS-PTY95-2.0 (area of 2m²) is thus used together with Glycol47 as working fluid. The collector area is discretized and considered to be 80m² for a tilt of 30° as explained in Section 2.1. A solar pump with variable speed is considered. That pump is set to start above a given level of solar irradiance (100W/m²) and is controlled so that the outlet temperature from the solar field remains around 85°C.

Overall model

Fig. 8 presents the final Modelica-based framework built for the bidirectional substation simulations. The core block, i.e. the bidirectional substation, is surrounded by the four boundary conditions blocks described previously, i.e. the network inlets, SH needs, DHW draw-offs and solar gains.

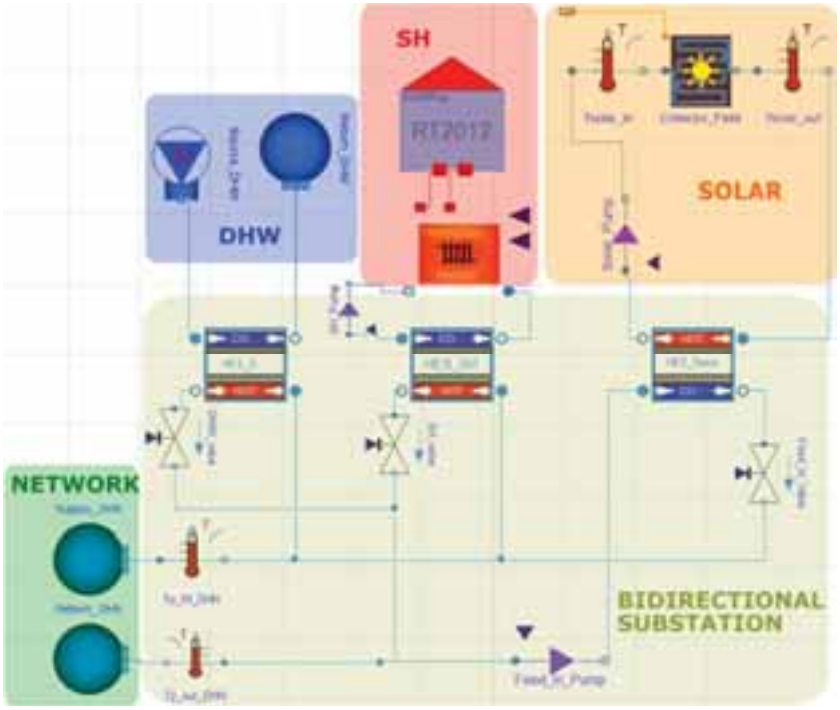

Fig. 8: Overall Modelica-based framework developed

3.2. Preliminary results

In the present study, the modeling framework discussed in the previous section is used to highlight the potential of solar heat reinjection from the multi-family building described in section 2.1. For that preliminary results, only the SH, DHW and Solar boundary conditions blocks were simulated. The location selected for the simulation is San Sebastian, Spain. Monthly energy gains/consumptions results are shown in Fig. 9. From this Figure, it can be calculated that if a configuration allowing for local consumption (U1 or U2) is chosen, up to 19.7MWh/yr could be consumed locally by the building while up to 41.2MWh/yr could be reinjected in the DHN. If a configuration with no local consumption is chosen as C2U0 for example, up to 60.9MWh/yr could be reinjected in the DHN. Future detailed simulations including the bidirectional substation together with the different control strategies discussed in section 2.4 will allow calculating which part of these potential amounts can effectively be used locally and reinjected into the DHN.

At this point, it is worth mentioning that at the level of the DHN, the usage of bidirectional substation is rational energetically speaking in two different situations. The first one is in the case that an inter-seasonal storage is installed on the DHN so that the decentralized contributions from excess heat of different prosumers are collected during summer (see Fig. 9) and reinjected in the DHN during winter. The second one is in the case where the reinjection from few prosumers allow reducing the centralized heat production for the DHW of all the consumers of the DHN, even during summer.

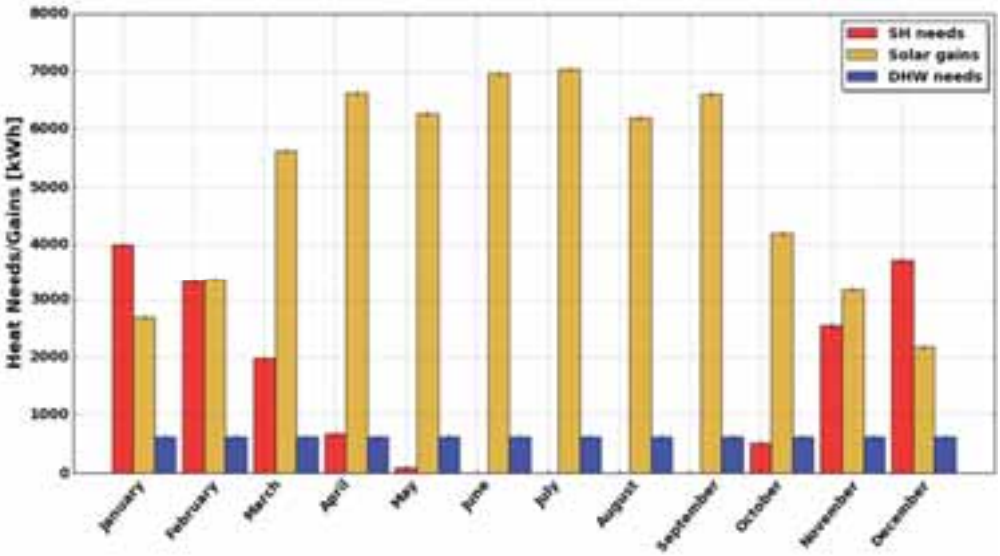

Fig. 9: Simulated solar production and SH and DHW needs for a multi-family building of 6 apartments and a flat plate solar collector area of 80m² located in San Sebastian

4. Conclusion

The present paper has set the basis towards the development of a solar bidirectional substation able to reinject/consume heat on/from a district heating network. Firstly, the main specifications of this bidirectional substation were established, i.e. Return to Supply decentralized feed-in, multi-family building scale, both able to consume and reinject heat. Secondly, features such as the type of connection to the network and the type of local consumption were combined to build an exhaustive list of potential architectures, and the most promising one was selected from a multi-criteria analysis. For this architecture, the hydraulic separation between both the building SH and SHW loops and the DHN is performed in the substation and the solar heat is entirely reinjected in the DHN. Finally, a modeling framework built to study and compare different architectures and control strategies was presented together with preliminary results highlighting the reinjection potential from multi-family building equipped with solar bidirectional substation.

In the frame of the European project 'THERMOSS', variants of the selected architecture with the various control strategies discussed will be compared using the presented modeling framework. Additionally, the impact of multiple reinjection points on the DHN operation will be studied at the network scale in order to have a complete picture of the development of bidirectional substations.

5. Acknowledgements

This project has received funding from the European Union's Horizon 2020 research and innovation program under grant agreement No 723562. The authors also wish to thank Bosch Thermotechnik GmbH and Giroa-Veolia for their valuable inputs.

6. References

ASHRAE93, 2010. ASHRAE 93-2010 -- Methods of Testing to Determine the Thermal Performance of Solar Collectors (ANSI approved).

Brand, L., Calvén, A., Englund, J., Landersjö, H., Lauenburg, P., 2014. Smart district heating networks – A simulation study of prosumers' impact on technical parameters in distribution networks. Appl. Energy 129, 39–48. doi:10.1016/j.apenergy.2014.04.079

Brange, L., Englund, J., Lauenburg, P., 2016. Prosumers in district heating networks – A Swedish case study. Appl. Energy 164, 492–500. doi:10.1016/j.apenergy.2015.12.020

Burch, J., Christensen, C., 2007. Towards development of an algorithm for mains water temperature, in: PROCEEDINGS OF THE SOLAR CONFERENCE. AMERICAN SOLAR ENERGY SOCIETY; AMERICAN INSTITUTE OF ARCHITECTS, p. 173.

COSTIC, 2016. besoin-eau-chaude-sanitaire-habitat-individuel-et-collectif.pdf (Guide Technique : Les besoins d'eau chaude sanitaire en habitat individuel et collectif).

Giraud, L., Baviere, R., Vallée, M., Paulus, C., 2015. Presentation, Validation and Application of the DistrictHeating Modelica Library. pp. 79–88. doi:10.3384/ecp1511879

Hassine, I.B., Eicker, U., 2014. Control Aspects of Decentralized Solar Thermal Integration into District Heating Networks. Energy Procedia, Proceedings of the 2nd International Conference on Solar Heating and Cooling for Buildings and Industry (SHC 2013) 48, 1055–1064. doi:10.1016/j.egypro.2014.02.120

Heymann, M., Rühling, K., Felsmann, C., 2017. Integration of Solar Thermal Systems into District Heating – DH System Simulation. Energy Procedia, 15th International Symposium on District Heating and Cooling, DHC15-2016, 4-7 September 2016, Seoul, South Korea 116, 394–402. doi:10.1016/j.egypro.2017.05.086

Jordan, U., Vajen, K., 2005. DHWcalc: Program to generate domestic hot water profiles with statistical means for user defined conditions, in: ISES Solar World Congress. pp. 1–6.

Lennermo, G., Lauenburg, P., 2016. Distributed heat generation in a district heating system. Presented at the International Conference on Solar-Heating and Cooling, Gleisdorf, Austria.

Lennermo, G., Lauenburg, P., Brand, L., 2014. Decentralised heat supply in district heating systems : Implications of varying differential pressure. Presented at the The 14th International Symposium on DH and Cooling, September 7th to September 9th, 2014, Stockholm, Sweden.

Lund, H., Werner, S., Wiltshire, R., Svendsen, S., Thorsen, J.E., Hvelplund, F., Mathiesen, B.V., 2014. 4th Generation District Heating (4GDH). Energy 68, 1–11. doi:10.1016/j.energy.2014.02.089

Paulus, C., Papillon, P., 2014. Substations for Decentralized Solar District Heating: Design, Performance and Energy Cost. Energy Procedia 48, 1076–1085. doi:10.1016/j.egypro.2014.02.122

Pietra, B.D., Zanghirella, F., Puglisi, G., 2015. An Evaluation of Distributed Solar Thermal "Net Metering" in Small-scale District Heating Systems. Energy Procedia, 6th International Building Physics Conference, IBPC 2015 78, 1859–1864. doi:10.1016/j.egypro.2015.11.335

Rosemann, T., Löser, J., Rühling, K., 2017. A New DH Control Algorithm for a Combined Supply and Feed-In Substation and Testing Through Hardware-In-The-Loop. Energy Procedia, 15th International Symposium on District Heating and Cooling, DHC15-2016, 4-7 September 2016, Seoul, South Korea 116, 416–425. doi:10.1016/j.egypro.2017.05.089

Schäfer, K., Schlegel, F., Pauschinger, T., 2014. Decentralized feed-in of solar heat into district heating networks - a technical analysis. Presented at the 2nd SDH-Conference, Hamburg, Germany.

Schweiger, G., Larsson, P.-O., Magnusson, F., Lauenburg, P., Velut, S., 2017. District heating and cooling systems – Framework for Modelica-based simulation and dynamic optimization. Energy. doi:10.1016/j.energy.2017.05.115

Wetter, M., Fuchs, M., Grozman, P., Helsen, L., Jorissen, F., Lauster, M., Dirk, M., Nytsch-geusen, C., Picard, D., Sahlin, P., Thorade, M., 2015. IEA EBC Annex 60 Modelica library an international collaboration to develop a free open-source model library for buildings and community energy systems. Presented at the BS2015, pp. 395–402.

Wetter, M., Zuo, W., Nouidui, T.S., Pang, X., 2014. Modelica Buildings Library. J. Build. Perform. Simul. 7, 253–270.

A Multicriteria Approach for the Integration of Renewable Energy Technologies and Thermal Energy Storage to Support Building Trigeneration Systems

Eduardo A. Pina, Miguel A. Lozano, Luis M. Serra

GITSE-I3A, Department of Mechanical Engineering, University of Zaragoza, Zaragoza (Spain)

Abstract

Trigeneration systems benefit from process integration to achieve primary energy savings, reduction of pollutant emissions, and reduction of unit costs relative to conventional separate production. Achieving such benefits requires an appropriate design procedure. The issue is that finding the best configuration that minimizes total annual cost is not enough anymore, as the environmental concern has become an ever-present theme in the design and synthesis of energy systems. The minimization of costs is often contradictory to the minimization of environmental impact. Multiobjective optimization tackles the issue of conflicting objectives by providing a set of trade-off solutions, or Pareto solutions, that can be examined by the decision maker, so that the best configuration can be selected for a given scenario. This paper proposes a mixed integer linear programming model (MILP) to determine the optimal configuration and hourly operation of trigeneration systems considering the effects of thermal energy storage (TES) and hourly variations of solar radiation, energy supply prices, energy demands, and CO_2 emissions. The objective functions to be minimized are the total annual costs and the total annual CO_2 emissions. Initially, the objective functions were evaluated separately. Then, the Pareto curve was obtained for the minimization of total annual cost subject to CO_2 emissions restrictions. The trade-off solutions were analyzed and the preferred solutions were selected, achieving results close to the optimal solutions with reasonable sacrifices for both objectives.

Keywords: buildings, multicriteria, photovoltaics, solar thermal energy, thermal energy storage, trigeneration.

1. Introduction

Environmental awareness, depletion of fossil fuels resources, and economic aspects are some of the factors that motivate the development of alternative energy systems. Process energy integration is regarded as an effective way to achieve primary energy savings and reduction of pollutant emissions relative to conventional separate production (Mancarella, 2014; Serra et al., 2009). Trigeneration systems benefit from process integration, producing electricity (and/or mechanical energy), heating, and cooling from a common resource. There is a large potential for the incorporation of trigeneration systems in the residential-commercial sector (Liu et al., 2014; Rong and Su, 2017).

In the design of trigeneration plants, two fundamental issues must be addressed (Lozano et al., 2009; Wakui et al., 2016): the synthesis of the plant configuration (installed technologies and capacities, etc.) and the operational planning (strategy concerning the operational state of the equipment, energy flow rates, purchase/selling of electricity, etc.). Finding the optimal configuration of trigeneration systems in building applications is a complex task, given the wide variety of technology options available and great diurnal and annual fluctuations in energy demands and energy prices. Other factors that further increase complexity are: (i) the incorporation of renewable energy technologies, such as photovoltaic panels and solar thermal collectors, which are characterized by intermittent behavior and non-simultaneity between production and consumption; (ii) the incorporation of TES units, which allow to decouple production from consumption; and (iii) conflicting objectives, as the minimization of environmental burdens is often contradictory to the minimization of costs.

Nowadays, sustainability-related issues are ever-present themes in the design of energy systems. Therefore, a purely economic analysis is not sufficient anymore. Multiobjective optimization tackles the issue of conflicting objectives by providing a set of non-dominated solutions (Pareto Frontier), which provides flexibility and allows the decision maker's judgement into the optimization problem (Andiappan, 2017).

doi:10.18086/swc.2017.10.03 Available at http://proceedings.ises.org

One of the most important steps in the optimization problem is data collection, since the quality of the data given as input to the model will directly affect the results obtained. In this regard, it is essential to maintain the same level of detail for all aspects of the model; however, this information is not always easily obtained or identified. In the case of hourly optimization problems, Pina et al. (2017) argued the difficulty of finding hourly CO_2 emissions data associated with the electricity available in the Spanish electric grid, as opposed to the well-established hourly electricity prices. Because the authors could not find appropriate CO_2 emissions data on an hourly basis, a constant annual average was considered; as a result, it was necessary to consider a constant electricity price as well, as it is not consistent to evaluate electricity prices on an hourly basis and electricity CO_2 emissions on a constant annual value.

This work improves the optimization model proposed by Pina et al. (2017) to include hourly electricity prices and the corresponding hourly CO_2 emissions, instead of constant annual values. The MILP model determines the optimal configuration and optimal operation of trigeneration systems, considering the effects of thermal energy storage and hourly variations of solar radiation, energy supply prices, energy demands, and CO_2 emissions associated with the electricity from the electric grid. A multiobjective optimization procedure is presented, taking into consideration the minimization of the total annual cost and total annual CO_2 emissions. The MILP model provides a Pareto frontier, a set of solutions representing the optimal trade-offs between the economic and environmental objectives, in which there can be no increase in one objective without a decrease in the value of the other. The solutions along the Pareto curve were analyzed and the preferred trade-off solutions were selected.

2. Solar assisted trigeneration system

The synthesis of trigeneration systems begins with the definition of a superstructure (Iyer and Grossmann, 1998; Lozano et al., 2010; Yokoyama et al., 2015). The first step in defining the superstructure is to identify design targets, that is, the types and quantities of resources available (e.g. fuels, electricity from the electric grid) and desired products (energy demands of the consumer center that the system must attend), as well as possible restrictions (e.g. permission or not to sell electricity to the grid). Then, the superstructure can be established, considering potential technologies and the feasible connections between them, based on appropriate process integration. Once the superstructure is defined, additional and more specific data are incorporated; this step plays an essential role, since the quality of the data collected will directly affect the results of the optimization model. After the optimization procedure, the superstructure will be reduced to its optimal configuration. These three steps are presented in the following subsections.

2.1. Energy demands

The consumer center considered in this study is a multifamily building located in Zaragoza, Spain. The complex is composed of 100 dwellings, each one with 100 m² surface area. The energy demands of the consumer center are assumed to be known beforehand: the annual electricity, heating, and cooling demands are 254,963 kWh, 573,503 kWh, and 113,989 kWh, respectively. The electricity demand is required all year round. The heating demand is composed of domestic hot water, required all through the year, and space heating, required from November to April. The cooling demand is only required in the summer months (from June to September).

The study covers the period of one year. It was considered that the energy demands and the operation of the system are described by 12 representative days d (NRD = 12) each one composed of 24 consecutive periods h (NP = 24) of 1-hour duration ($NHP(h)$ = 1). Each representative day d is attributed to a month of the year, so the number of representative days d per year is equal to the number of days in the corresponding month ($NRY(1, 2, 3, ..., 12)$ = 31, 28, 31, …, 31). Two additional representative days were included to account for extreme demand situations, as described in Pina et al. (2017); what these extreme representative days do is increase the technologies' installed capacity for safety power margin, with impact on the annual fixed cost, but not on the annual operation cost.

2.2. Superstructure

The superstructure of the trigeneration system considered in this study is depicted in Fig. 1. Natural gas F_p, electricity purchased from the grid E_p, and solar radiation F_{pv} and F_{st} are the resources that can be used by the system to attend the electricity E_d, heating Q_d, and cooling R_d demands of the consumer center. Heat can be

produced at two temperature levels: low-temperature heat is only used to cover the heating demand, while high-temperature heat can also be used for cooling production. The cogeneration module GE (natural gas reciprocating engine coupled to a heat recovery system) consumes natural gas F_c and produces electricity W_c, low-temperature heat Q_{cc}, and high-temperature heat Q_{cr}; also, a portion of the total heat produced can be dissipated to the environment Q_{cl}. The gas boiler GB consumes natural gas F_a and produces low-temperature heat Q_{ac} and high-temperature heat Q_{ar}. The photovoltaic panels PV produce electricity W_{pv} from the incident solar radiation F_{pv}. The single-effect absorption chiller ABS uses high-temperature heat Q_{abs} to produce cooling R_{abs}; this technology also consumes a small quantity of electricity W_{abs}. The reversible heat pump HP and the solar thermal collectors ST are assumed to operate in two operation modes according to the month of the year:

- From January to May and from October to December: The HP operates in heating mode (HPQ), consuming electricity W_{hp} to produce low-temperature heat Q_{hp}. The ST produces low-temperature heat Q_{stc} from the incident solar radiation F_{st};
- From June to September: The HP operates in cooling mode (HPR), consuming electricity W_{hp} to produce cooling R_{hp}. The ST can produce low and/or high-temperature heat Q_{stc} and Q_{str}, respectively.

Both operation modes consider the possibility of dissipating heat from the ST Q_{stl}. Finally, two thermal energy storage tanks are considered, one for low-temperature heat (TSQ) and another for cooling (TSR). Energy can be charged to/discharged from the TSQ Q_{in}/Q_{out} and TSR R_{in}/R_{out}. Energy losses Q_s and R_s are proportional to the stored energy S_q and S_r, respectively, and to an hourly energy loss factor.

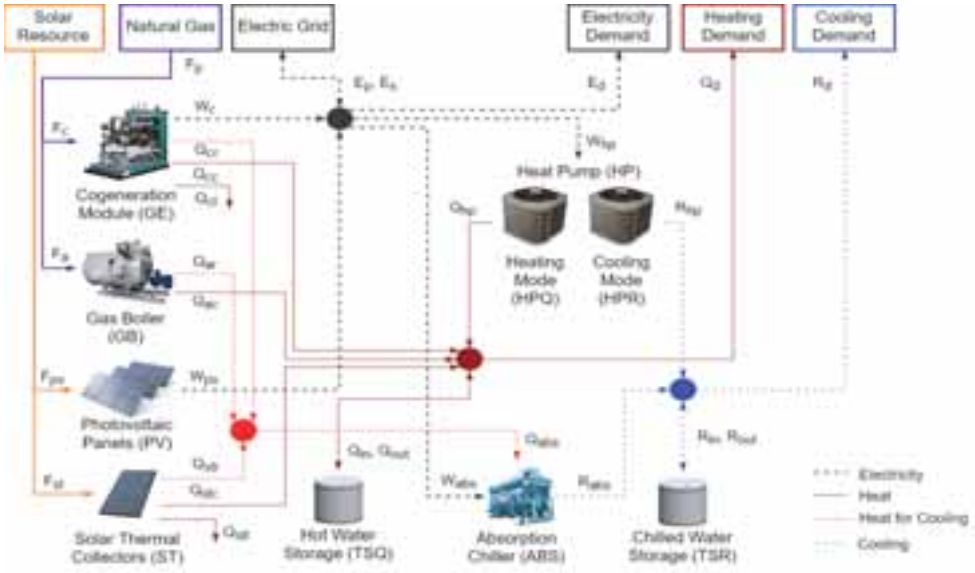

Fig. 1: Superstructure of the trigeneration system

2.3. Data collection and elaboration

Once the superstructure is established, it is necessary to provide more specific information about the system in line with the objective of the analysis. In this regard, in order to contemplate the technical, economic, and environmental aspects of the incorporation of potentially installable technologies, including renewable energy technologies and thermal energy storage units, in the building trigeneration system analyzed herein, the following information is required:

(i) Technical data

All technologies included in the superstructure are commercially available. The equipment can modulate up to nominal load, except for the non-manageable ones (PV and ST). Performance variations with ambient and operation conditions are taken into consideration. Table 1 presents the technologies' main technical parameters obtained from the manufacturers' catalogs. The PV has a maximum power of 0.260 kW, module efficiency of 15.51%, and total surface area of 1.60 m². The ST presents thermal performances of k_0 = 0.789, k_1 = 3.834 W/(m²·K), and k_2 = 0.011 W/(m²·K²), and total surface area of 5.04 m². The hourly unit productions per square

meter of the PV panels and ST collectors were evaluated as explained in Pina et al. (2017).

Table 1: Technologies' technical parameters

Parameter	Value	Parameter	Value
GE Electric power efficiency, α_w	0.26	HP Cooling/heating capacity ratio, *RCAPrq*	0.90
GE Thermal efficiency, α_q	0.61	ABS COP, *COPabs*	0.69
GB Thermal efficiency, η_q	0.95	ABS unit electricity consumption, *kwabs*	0.03
HP COP in heating mode, *COPhpq*	3.24	TSQ hourly energy loss factor, *fpacuQ*	0.01
HP COP in cooling mode, *COPhpr*	3.19	TSR hourly energy loss factor, *fpacuR*	0.01

Based on the geometry of the buildings, a total roof top area of 2000 m² is available for the installation of PV panels and ST collectors. PV and ST are installed with a tilt of 35º and 30º, respectively. Considering their surface areas and tilt, it was possible to determine the roof top area occupied by each square meter of PV and ST: the PV unit surface area usage is equal to 3.1250 m² roof/m² PV and the ST unit surface area usage is equal to 2.2676 m² roof/m² ST.

(ii) Economic data

Table 2 presents the unit investment cost *CI* of each technology *i* included in the superstructure. These values were obtained from manufacturers' catalogs (including taxes) and multiplied by a simple module factor that took into account transportation, installation, connection costs, etc. An operational lifetime *nyr* of 20 years was considered for all equipment. An amortization and maintenance factor *fam* of 0.15 yr^{-1} and an indirect costs factor *fic* of 0.20 were considered (Ramos, 2012).

Table 2: Technologies' economic and environmental data

Technology *i*	Unit Investment cost *CI*	Unit CO_2 emissions *CO2U*	Technology *i*	Unit Investment cost *CI*	Unit CO_2 emissions *CO2U*
GE	2700 €/kW_{el}	65 kg CO_2/kW_{el}	PV	264 €/m²	285 kg CO_2/m²
GB	77 €/kW_{th}	10 kg CO_2/kW_{th}	ST	578 €/m²	95 kg CO_2/m²
HP	481 €/kW_{th}	160 kg CO_2/kW_{th}	STQ	150 €/kWh	150 kg CO_2/kWh
ABS	518 €/kW_{th}	165 kg CO_2/kW_{th}	STR	300 €/kWh	300 kg CO_2/kWh

Gas and electricity rates were taken from a real Spanish distributor (EDP, 2017). The gas price is constant all through the year c_g = 0.057 €/kWh LHV (with taxes). In the case of the electricity purchase price c_{ep}, a time-of-use tariff is applied with three time periods, namely on-peak, mid-peak, and off-peak, whose rates are given in Table 3. The selling price of electricity c_{es} was assumed to be the same as the purchase price c_{ep}.

Table 3: Electricity prices in €/kWh, with taxes (EDP, 2017)

Annual period	On-peak		Mid-peak		Off-peak	
	Hours	c_{ep}	Hours	c_{ep}	Hours	c_{ep}
Winter (Jan-Mar, Nov-Dec)	19-22	0.183	9-18, 23-24	0.156	1-8	0.122
Summer (Apr-Oct)	12-15	0.183	9-11, 16-24	0.156	1-8	0.122

(iii) Environmental data

Table 2 presents the unit CO_2 emissions *CO2U* of each technology *i* of the superstructure. The *CO2U* values were obtained from the literature (Carvalho, 2011; Guadalfajara, 2016; Ito et al., 2009; Ralui et al., 2014).

In terms of CO_2 emissions, the environmental cost associated with the consumption of natural gas is constant throughout the year *kgCO2g* = 0.252 kg CO_2/kWh; this is a Spanish national value obtained from IDAE (2014). *Red Eléctrica de España* (REE, 2017) provides data on the national electric demand, generation, and associated emissions on a 10-minute basis. We have processed this information to obtain the hourly CO_2 emissions associated with the electricity available in the grid for each representative day, as shown in Fig. 2.

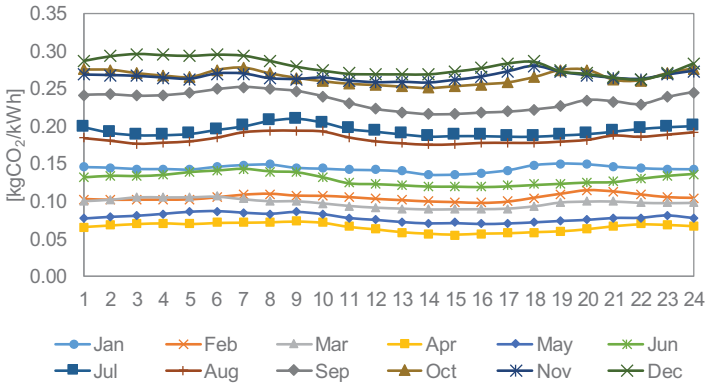

Fig. 2: Hourly CO_2 emissions of the electricity in Spain for each representative day, in kg CO_2/kWh (REE, 2017)

3. Mathematical model

Having defined the superstructure of the trigeneration system, it is necessary to develop a mathematical model, representing the behavior and performances of all elements in the superstructure, to determine the optimal configuration and optimal operation modes of the system. A MILP model was developed using the software LINGO (Schrage, 1999). Two objective functions are included: the first considers the economic aspects of the trigeneration system through the total annual cost, while the second considers the environmental impact in terms of the total annual CO_2 emissions.

The economic objective is to minimize the total annual cost C_{tot}, which consists of the annual fixed cost C_{fix} and the annual operation cost C_{ope}.

$$Min\ C_{tot} = C_{fix} + C_{ope} \tag{1}$$

The annual fixed cost is expressed by Eq. (2)

$$C_{fix} = fam \cdot (1 + fic) \cdot \sum_i CI(i) \cdot CAP(i) \tag{2}$$

in which the *fam*, *fic*, and *CI* were given in Section 2 (*CI* values are given in Table 2).

As explained earlier, it was considered that the year was divided into *NRD* representative days *d*, each one composed of *NP* consecutive hourly periods *h* of *NHP(h)* duration. Throughout the year there are *NRY(d)* days for each representative day type *d*. The annual operation cost includes fuel costs and the purchase/sale of electricity, as expresses Eq. (3):

$$C_{ope} = \sum_{d=1}^{NRD} \sum_{h=1}^{NP} NRY(d) \cdot NHP(h) \cdot \left(F_p(d,h) \cdot c_g + E_p(d,h) \cdot c_{ep}(d,h) - E_s(d,h) \cdot c_{es}(d,h)\right) \tag{3}$$

Regarding the environmental objective, the goal is to minimize the total annual CO_2 emissions $CO2_{tot}$, which is composed of the annual fixed emissions $CO2_{fix}$ and the annual operation emissions $CO2_{ope}$.

$$Min\ CO2_{tot} = CO2_{fix} + CO2_{ope} \tag{4}$$

The annual fixed emissions, annualized for the equipment's operational lifetime *nyr* is expressed by Eq. (5)

$$CO2_{fix} = \sum_i CO2U(i) \cdot CAP(i)/nyr \tag{5}$$

in which the *CO2U* values of each technology *i* are given in Table 2.

The annual CO_2 emissions associated with the operation of the system is expressed by Eq. (6). The first and second terms within the parenthesis correspond to the emissions associated with the purchase of natural gas and electricity, respectively, while the last term corresponds to the avoided emissions due to the selling of electricity.

$$CO2_{ope} = \sum_{d=1}^{NRD}\sum_{h=1}^{NP} NRY(d)\cdot NHP(h) \cdot \left(F_p(d,h)\cdot kgCO2_g + E_p(d,h)\cdot kgCO2_e(d,h) - E_s(d,h)\cdot kgCO2_e(d,h)\right) \quad (6)$$

The objective functions are subject to equipment constraints (capacity limits and production restrictions), balance equations, and electric grid constraints (permission to purchase/sell electricity). The reader is referred to Pina et al. (2017) for a detailed explanation of the restrictions.

4. Single-objective optimization

The two objective functions were initially evaluated separately. Table 4 gathers the main results obtained for the minimization of total annual costs and total annual CO_2 emissions.

For the optimal annual cost solution, all candidate technologies were included except for the PV and ST; further, the TSQ installed capacity is so small (0.4 kWh) that it could be dropped out. Regarding the annual investment cost, 47% is due to the installation of HP, followed by the ABS with 29%, and the GB with 10%. Taking into account the annual CO_2 emissions relative to the manufacturing of each device, the HP also accounts for the highest share, 46%, followed by the ABS with 28%, and the TSR with 21%. This configuration heavily relies on natural gas (363,285 kWh/yr) and electricity from the electric grid (355,040 kWh/yr). Further, all electricity produced by the GE is consumed, so that there is no selling.

Table 4: Main results of the single-objective solutions

Technology	Optimal annual cost (B)			Optimal annual CO_2 emissions (A)		
	Installed capacity	**Investment cost [€/yr]**	**CO_2 emissions [kgCO_2/yr]**	**Installed capacity**	**Investment cost [€/yr]**	**CO_2 emissions [kgCO_2/yr]**
GE	4.2 kW_{el}	2050.8	13.7	0.0 kW_{el}	-	-
GB	204.8 kW_{th}	2838.1	102.4	49.3 kW_{th}	683.1	24.6
HP	162.1 kW_{th}	14,031.7	1296.5	269.6 kW_{th}	23,343.1	2156.9
ABS	94.0 kW_{th}	8761.6	775.2	48.8 kW_{th}	4554.4	403.0
PV	0.0 m²	-	-	461.2 m²	21,873.1	6571.6
ST	0.0 m²	-	-	246.5 m²	25,618.8	1170.7
TSQ	0.4 kWh	10.8	3.0	314.0 kWh	8449.1	2354.8
TSR	39.9 kWh	2148.9	598.9	0.0 kWh	-	-
Annual fixed	C_{fix} / $CO2_{fix}$	29,841.9	2789.8		84,521.6	12,681.6
Energy service	**Consumption [kWh/yr]**	**Energy cost [€/yr]**	**CO_2 emissions [kgCO_2/yr]**	**Consumption [kWh/yr]**	**Energy cost [€/yr]**	**CO_2 emissions [kgCO_2/yr]**
Natural gas	363,285.1	20,557.7	91,547.8	124.2	7.0	31.3
Purchased electricity	355,040.0	54,667.3	60,728.1	355,919.7	54,606.8	63,048.5
Sold electricity	-	-	-	9348.0	1505.1	1521.3
Annual operation C_{ope} / $CO2_{ope}$		75,225.0	152,275.9		53,108.7	61,558.5
Total annual C_{tot} / $CO2_{tot}$		**105,066.9 €/yr**	155,065.7 kgCO_2/yr		137,630.2 €/yr	**74,240.1 kgCO_2/yr**

In the case of the optimal annual CO_2 emissions solution, all technologies were included except for the GE and TSR. Compared with the optimal annual cost configuration, the installed capacity of the HP has increased, while the capacities of GB and ABS have decreased. This configuration heavily relies on electricity from the electric grid (355,920 kWh/yr), while there is virtually no consumption of natural gas (124 kWh/yr); also, a part of the electricity produced (9348 kWh/yr) is sold to the grid. It is interesting to note that all roof top area is used for the installation of PV and ST, which suggests that it could be interesting to increase its availability. Moreover, compared with the optimal annual cost solution, there was a significant shift in the use of thermal energy storage, from 39.9 kWh of TSR to 314.0 kWh/yr of TSQ. Looking at the annual investment cost, 30% is due to

the installation of ST, followed by the HP with 28%, and the PV with 26%. In the case of the annual CO_2 emissions relative to the manufacturing of each device, the three highest contributions are 52% PV, 18% TSQ, and 17% HP.

The optimal CO_2 emissions configuration presents a total annual cost 31% higher than the optimal annual cost solution, while CO_2 emissions are 52% lower. The shift towards a more environmentally sound configuration incurs an increase of 183% in the annual fixed cost and 354% in the annual CO_2 emissions relative to the manufacturing of the equipment. These are offset by a better energy usage during the operation of the system, translated into a decrease of 29% in the annual operation costs and 59% in annual CO_2 emissions relative to the operation of the system.

Analyzing the annual operation of the optimal annual cost solution, the GE, GB, HP, and TSQ operate all year round, the TSR operates all summer, and the ABS operates from July to September. Of the total electricity consumed, 8.4% is produced by the GE and the rest is purchased from the electric grid. Regarding the heat production, the HP and the GB are the major producers, with 48.4% and 38.6%, respectively. The produced cooling comes almost entirely from the HP (91.7%), being the ABS responsible for supplying peak demands in July and August. Considering the total cooling produced by the system, 4.5% is stored.

Focusing on the optimal CO_2 emissions solution, the HP operates all year except for May, the ABS operates all summer except for September, and the TSQ is used all year round. The GB operates marginally in June to attend heat peak demands. It is worth mentioning that there is dissipation of heat from the ST Q_{stl} in May (4977 kWh/yr). The PV panels account for 23.6% of the electricity consumed, while the rest is purchased from the grid. Of the total electricity produced by the PV, 8.7% is sold to the grid, generating economic benefits. The HP is responsible for 76.2% of the heat produced by the system, followed by the ST with 23.8%; the GB has a negligible share. Of the total heat produced, 26.7% is stored in the TSQ. Cooling is produced mostly in the HP (87.9%) and the rest is covered by the ABS with solar heat from the ST.

The optimization model also determines the hourly operation of the system for each representative day. As an example, Fig. 3 presents, for the optimal annual cost solution, the hourly productions of (a) electricity, in the month of January, (b) heating, in the month of January, and (c) cooling, in the month of July.

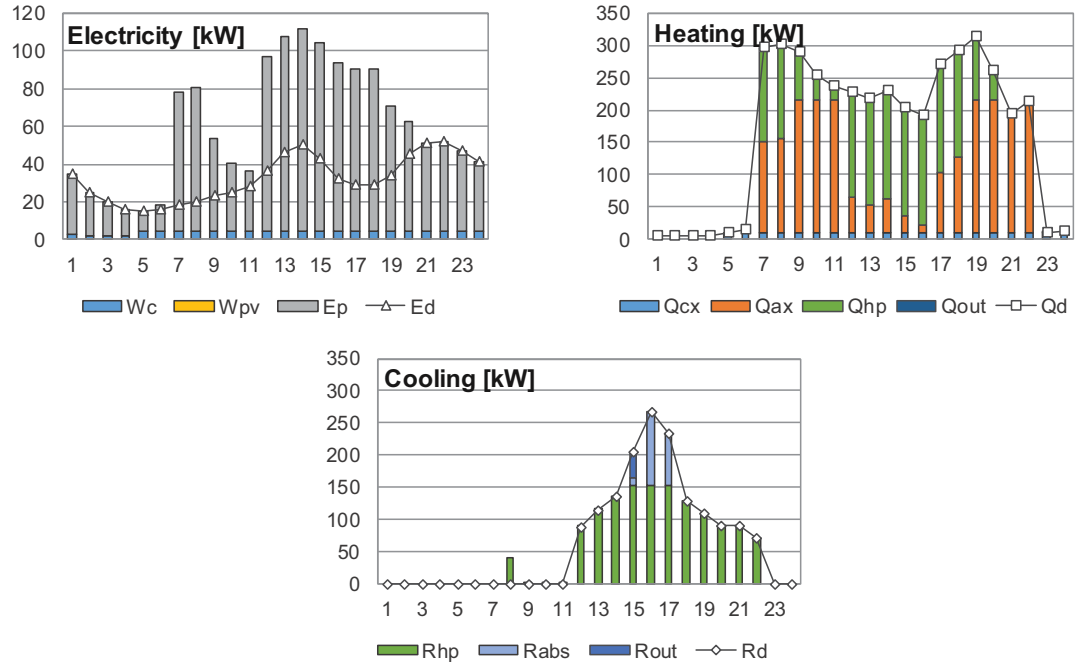

Fig. 3: Hourly production for a representative day of (a) electricity in January, (b) heating in January and (c) cooling in July. Optimal annual cost configuration

In January, only electricity E_d and heating Q_d are required by the consumer center. As can be seen from Fig. 3, the GE operates all through the day producing electricity W_c and heat Q_{cx}; particularly, between hours 6 and 24,

it operates at full load. Also, electricity is purchased from the grid E_p throughout the day. It is interesting to note the increase in the purchase of electricity at hours 7 and 8, which are the last two hours of off-peak rate. Apart from the electricity demand E_d, electricity is consumed by the HP from hour 6 to 20 for heat production Q_{hp}. The HP's load increases in the afternoon, after hour 11; it also complements heat production when the GB is at full load, e.g. hours 9 to 11 and 19 to 20. As already mentioned, the TSQ is used but with negligible shares.

In the month of July, cooling is required from hour 12 to 22. However, as presents Fig. 3, cooling production begins earlier in the day (e.g. hour 8), being stored in the TSR for later use. The ABS operates marginally with heat from the GB at hours 12 and 13, and more significantly from hour 15 to 17, when the HP is at full load. The TSR has one significant charge at hour 8 and one significant discharge at hour 15.

5. Multiobjective optimization

The issue is that economic costs and environmental concern are generally conflicting objectives, which means that the optimal solution for one is not the best for the other, as was demonstrated in Section 4. Multiobjective optimization is used to optimize a problem with two or more conflicting objectives, identifying trade-off solutions among them. These trade-off solutions, also known as non-dominated solutions, constitute the Pareto set, in which no improvement in one objective can be achieved without sacrificing the other (Andiappan, 2017).

Pareto optimization has been extensively applied in the literature concerned with multicriteria problems and many methods are available for solving multiobjective optimization problems. Some methods involve converting the multiobjective problem into a series of single optimization problems. An important question is the role of the decision maker in the procedure. In this regard, *a posteriori* methods for generating Pareto-optimal solutions are preferred. Among them, the ε-constraint has been applied by various authors to the optimization of energy supply systems (Buoro et al., 2013; Carvalho et al., 2012; Fazlollahy et al., 2012; Gebreslassie et al., 2012). In this approach, the problem is optimized with respect to one of the objective functions, while upper/lower bounds are set for the rest of the objective functions. The problem is repeatedly solved for different ε values, obtaining the different trade-off solutions that compose the Pareto set. Based on the Pareto curve obtained, the decision maker has more flexibility to judge the different trade-off solutions and make a more informed decision.

In this paper, the optimization model was solved for the total annual cost objective, subject to CO_2 emissions constraints. The Pareto set obtained is limited by Lim_{sup} = 155,066 ton CO_2/yr (optimal annual cost solution) and Lim_{inf} = 74,240 ton CO_2/yr (optimal annual CO_2 emissions solution). The interval between superior and inferior limits have been subdivided and the model was repeatedly solved. Table 5 presents the ε values considered in the analysis, starting from the optimal annual cost solution (point B), towards the optimal annual CO_2 emissions solution (point A). Along the Pareto curve, different solutions are obtained with different configurations and installed capacities. Fig. 4 shows the Pareto curve obtained, in which equal symbols represent the same configuration (with different installed capacities). As can be seen from Table 5, a total of 33 ε values were evaluated, obtaining 9 different configurations.

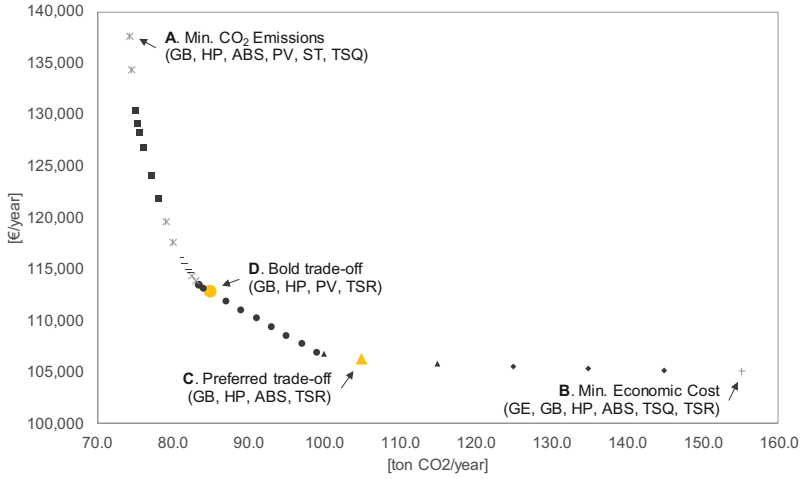

Fig. 4: Pareto curve – Annual economic cost vs. annual CO_2 emissions

Table 5: Trade-off solutions obtained with the ε-constraint method considering economic cost and CO_2 emissions

	ε-CO_2 emissions [tonCO_2/yr]	Economic cost [€/yr]	Installed capacities								Marginal cost [€/tonCO_2]	Average cost [€/tonCO_2]
			GE	GB	HP	ABS	PV	ST	TSQ	TSR		
(**B**)	155.1	105,067	4.2	204.8	162.1	94.0	-	-	0.4	39.9	-	-
	145.0	105,126	3.5	193.5	176.8	83.8	-	-	-	40.0	5.9	5.9
	135.0	105,254	3.1	171.6	201.9	66.3	-	-	-	40.2	12.8	9.3
	125.0	105,453	1.1	169.0	209.8	60.9	-	-	-	40.2	19.9	12.8
	115.0	105,771	-	163.6	218.7	54.7	-	-	-	40.3	31.9	17.6
(**C**)	105.0	106,266	-	140.0	244.6	36.7	-	-	-	40.4	49.5	24.0
	100.0	106,690	-	113.6	273.6	16.6	-	-	-	40.6	84.7	29.5
	99.0	106,916	-	91.8	297.6	-	1.5	-	-	40.7	226.6	33.0
	97.0	107,745	-	91.8	297.6	-	88.1	-	-	40.7	414.4	46.1
	95.0	108,574	-	91.8	297.6	-	174.7	-	-	40.7	414.4	58.4
	93.0	109,403	-	91.8	297.6	-	261.3	-	-	40.7	414.4	69.9
	91.0	110,232	-	91.8	297.6	-	347.9	-	-	40.7	414.4	80.6
	89.0	111,060	-	91.8	297.6	-	434.4	-	-	40.7	414.4	90.7
	87.0	111,889	-	91.8	297.6	-	521.0	-	-	40.7	414.4	100.2
(**D**)	85.0	112,718	-	91.8	297.6	-	607.6	-	-	40.7	414.4	109.2
	84.0	113,170	-	86.6	303.3	-	640.0	-	-	35.3	452.0	114.0
	83.5	113,472	-	75.3	315.6	-	640.0	-	-	23.6	604.3	117.4
	83.0	113,932	-	74.5	316.6	-	634.9	7.1	-	22.7	919.2	123.0
	82.5	114,392	-	74.5	316.6	-	629.4	14.6	-	22.7	920.5	128.5
	82.3	114,631	-	72.6	316.6	-	626.8	18.2	1.9	22.7	953.8	131.3
	82.0	114,884	-	69.7	317.3	-	624.5	21.4	4.8	22.0	1012.7	134.4
	81.5	115,424	-	63.2	320.9	-	620.3	27.1	11.4	18.6	1080.2	140.8
	81.0	116,005	-	59.8	320.8	0.4	615.0	34.5	18.5	18.1	1163.3	147.7
	80.0	117,605	-	56.1	312.6	19.2	603.9	49.7	43.1	-	1599.3	167.0
	79.0	119,643	-	55.8	296.4	30.4	589.2	70.0	89.4	-	2038.6	191.6
	78.0	121,862	-	55.6	285.2	37.4	570.5	95.8	121.1	0.9	2218.4	217.9
	77.0	124,221	-	54.7	267.8	39.3	552.9	120.0	172.6	14.8	2359.3	245.4
	76.0	126,850	-	52.9	260.4	41.4	530.4	151.1	201.1	19.0	2629.2	275.5
	75.5	128,282	-	52.8	253.2	42.7	520.2	165.1	228.8	24.0	2863.0	291.8
	75.3	129,301	-	62.7	265.0	47.8	519.3	166.3	231.0	5.8	4076.3	303.6
	75.0	130,498	-	63.0	269.6	48.8	513.4	174.5	247.2	-	4789.6	317.6
	74.5	134,365	-	54.3	269.6	48.8	480.2	220.2	267.0	-	7734.3	363.7
(**A**)	74.2	137,630	-	49.3	269.6	48.8	461.2	246.5	314.0	-	12,562.0	402.9

The graphs in Fig. 5 show the installed capacities of each technology along the Pareto curve, from the optimal annual cost to the optimal annual CO_2 emissions solution. The analysis of the trade-off solutions that constitute the Pareto curve obtained shows that each technology was included in at least one configuration; on the other hand, no configuration included all eight technologies simultaneously. The GB and the HP were included in all solutions obtained and the TSR was included in most solutions. From the optimal annual cost configuration (B), as CO_2 emissions are forced down towards the environmental optimal (A), there is a shift in the installed capacities of GB and HP: the former decreases, while the latter generally increases. GE is only included at CO_2 levels higher than 125 ton CO_2/yr, and even so with relatively small installed capacities. For total annual emissions below 99 ton CO_2/yr, PV panels begin to be incorporated. ST collectors are included at even lower overall emissions levels, 83 ton CO_2/yr, closely followed by the TSQ at 82.25 ton CO_2/yr. There are two different ranges in which the ABS is included: for CO_2 levels higher than 100 ton CO_2/yr and lower than 91 ton CO_2/yr. It is interesting to look into the role the ABS plays in each scenario: at the higher CO_2 emissions range, the ABS is driven with heat produced with natural gas (Q_{cr} and mostly Q_{ar}); on the other hand, at the lower range, the ABS is driven exclusively with heat from the ST (Q_{str}). It is worth noting that GE was not included in any solution simultaneously with PV and/or ST.

From the analysis of the trade-off solutions obtained, point C in Fig. 4 and Table 5 was selected as preferred intermediate solution because of its good trade-off between both criteria: it achieves a 32.3% reduction in CO_2 emissions with an increase of only 1.1% in costs relative to the optimal cost configuration (B). Moreover, solution C includes only GB, HP, ABS, and TSR. Compared with the optimal annual cost solution (A), there is a

reduction in the installed capacities of GB and ABS and an increase in the installed capacity of HP. As a result, the system consumes 75.7% less natural gas and purchases 31.4% more electricity from the electric grid. By supporting a higher sacrifice for the economic objective, point D in Fig. 4 and Table 5 can also be identified as an interesting trade-off solution: it achieves a 45.2% decrease in CO_2 emissions with an increase of 7.3% in costs relative to the optimal cost configuration (B). The configuration includes GB, HP, PV, and TSR.

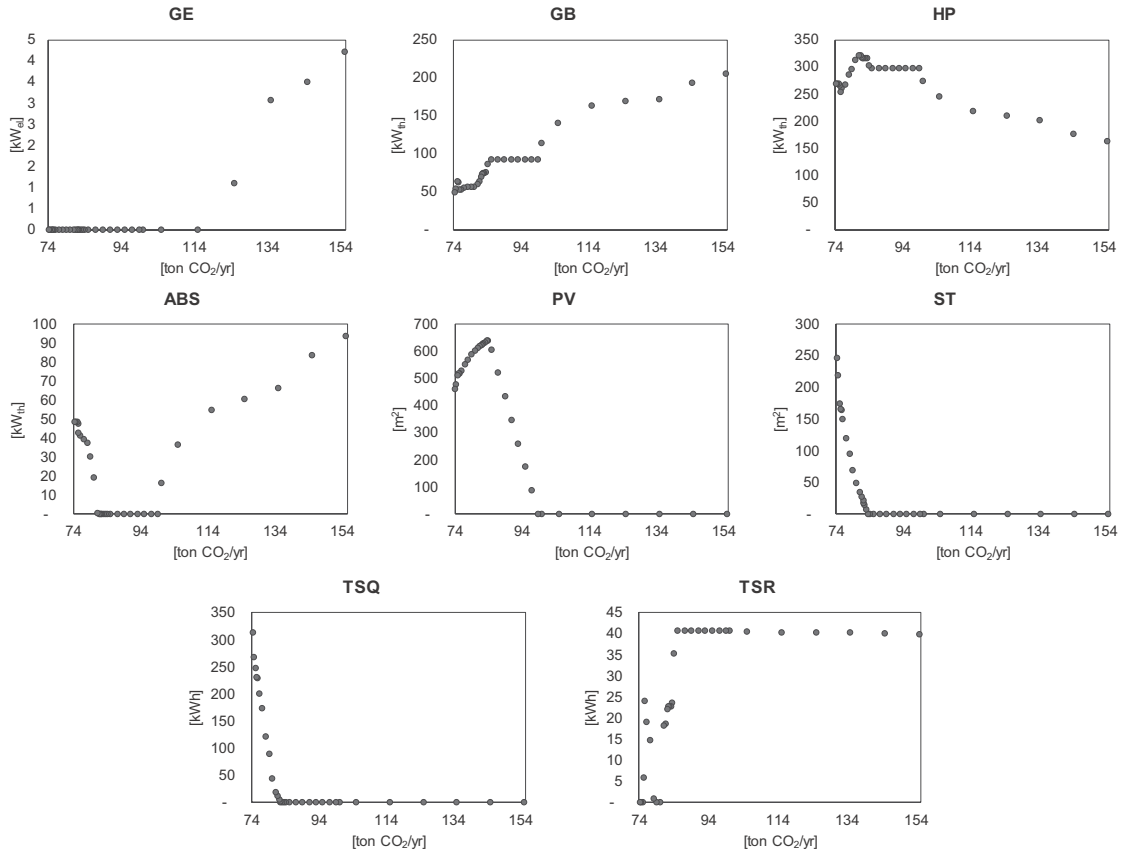

Fig. 5: Installed capacities along the Pareto curve

Table 5 also presents the marginal and average costs of each solution, in €/ton CO_2. The marginal cost represents the cost of moving from one solution to the next in the Pareto curve, while the average cost represents the cost of moving from the optimal annual cost solution (B) to any other. These could be interesting indices to measure the effort the decision maker is willing to make in order to move towards a more environmentally sound configuration. As can be seen from Table 5, it is no surprise that both the marginal and the average costs increase as the system shifts towards more environmentally sound configurations. Moving from one optimum to the other (B → A) involves an average cost of 402.9 €/ton CO_2. However, taking the trade-off solution C into account, the average cost of moving from B to C is only 24.0 €/ton CO_2.

Based on the different circumstances under which the system operates, for instance local subsidies for CO_2 emissions savings and/or stock market prices of CO_2 emissions, the marginal cost could be used to select among the various trade-off solutions obtained. Solution C presents a marginal cost of 49.5 €/ton CO_2. Ensuring a higher economic compensation for CO_2 emissions savings would enable other solutions to be chosen, such as solution D with 414.4 €/ton CO_2.

6. Conclusions

This paper tackled the issue of conflicting objectives in the synthesis of trigeneration systems including renewable energy technologies and thermal energy storage. A MILP model was developed using the optimization software LINGO including two objective functions: minimize the total annual cost and minimize the total annual CO_2 emissions. Both objectives take into account a fixed term, relative to the manufacturing and

installation of the equipment, and a variable term, relative to the hourly operation of the system. The model was applied to a multifamily building located in Zaragoza, Spain.

At first, the objective functions were minimized separately, obtaining the optimal annual cost solution and the optimal annual CO_2 emissions solution. The optimal solutions presented fundamentally different configurations: the optimal cost configuration included cogeneration, whereas the optimal CO_2 emissions configuration included renewable energy technologies. Then, the ε-constraint approach was employed to identify the intermediate trade-off solutions that compose the Pareto curve. As a result, it was possible to identify trade-off solutions that were close to the single-objective solutions with reasonable sacrifices for both objectives; for example, the preferred trade-off solution selected in this study achieved a 46.2% reduction in total annual CO_2 emissions with only an 8% increase in total annual cost relative to the optimal annual cost configuration. This procedure demonstrated the importance of the decision maker in evaluating the trade-off solutions in search for the configuration that best suits the objectives of the analysis.

In the synthesis of energy systems, the quality of the data used plays a central role because it directly affects the results of the optimization model. However, in multiobjective optimization problems, it is essential to maintain all objective functions at the same level of detail. This issue was highlighted in a previous paper by Pina et al. (2017), in which the price of the electricity from the grid and the associated CO_2 emissions were considered constant throughout the year. The present paper improved the optimization model proposed in that work by incorporating hourly electricity prices and CO_2 emissions per kWh, for each representative day. As a result, it was shown that the system takes advantage of the different electricity prices and emissions at different hourly periods to achieve more interesting results in accordance with the objective function.

It is also important to maintain the closest level of detail as possible with regard to the elaboration of the optimization model. For example, it is known that the electricity tariff is generally composed of a power term and an energy term; however, what would be the appropriate counterpart to the power term for CO_2 emissions? Due to the lack of an appropriate value, the authors opted to consider only the energy term in the calculations. Nevertheless, we do recognize having applied an amortization and maintenance factor over the operational lifetime of the system with no equivalent in the CO_2 emissions objective function. These issues should be explored in further studies.

Further work could explore the interconnection with the electric grid, considering local policies on the permission to sell/inject electricity to the grid and its effects on the optimal configuration and operation of the system. Moreover, more technologies could be included in the superstructure, namely prime movers (e.g. microturbines, fuel cell), RES (e.g. wind power, biomass), and energy storage units (e.g. electrical batteries).

7. Acknowledgements

This work was developed in the frame of the research project ENE2014-57262-R, partially funded by the Spanish Government (Energy Program), the Government of Aragon (Spain) and the EU Social Fund (FEDER Program). Eduardo Pina acknowledges financial support from the Brazilian Federal Government and CNPq Science Without Borders Program.

8. References

Andiappan V. State-Of-The-Art Review of Mathematical Optimisation Approaches for Synthesis of Energy Systems. Process Integration Optimization Sustainability. Published Online 13 August 2017. (doi:10.1007/s41660-017-0013-2).

Buoro D, Casisi M, De Nardi A, Pinamonti P, Reini M. Multicriteria optimization of a distributed energy supply system for an industrial area. Energy 2013; 58:128–137.

Carvalho M. Thermoeconomic and environmental analyses for the synthesis of polygeneration systems in the residential-commercial sector. PhD Thesis, University of Zaragoza, 2011.

Carvalho M, Lozano MA, Serra LM. Multicriteria synthesis of trigeneration systems considering economic and environmental aspects. Appl. Energy 2012; 91:245–254.

EDP, 2017. Gas and Electricity Prices - Liberalized Market [WWW Document]. Gas Electr. Prices - Lib. Mark. URL http://www.edpenergia.es/es/hogares/gas-y-electricidad/precios/mercado-libre/ (accessed 8.31.17).

Fazlollahi S, Mandel P, Becker G, Maréchal F. Methods for multi-objective investment and operating optimization of complex energy systems. Energy 2012; 45:12-22.

Gebreslassie BH, Guillén-Gosálbez G, Jiménez L, Boer D. Solar assisted absorption cooling cycles for reduction of global warming: A multi-objective optimization approach. Sol. Energy 2012; 86:2083–2094.

Guadalfajara M. Economic and environmental analysis of central solar heating plants with seasonal storage for the residential sector. PhD Thesis, University of Zaragoza, 2016.

IDAE, 2014. Factores de emisión de CO_2 y coeficientes de paso a energía primaria de diferentes fuentes de energía final consumidas en el sector de edificios en España.

Ito M, Komoto K, Kurokawa K. A comparative LCA study on potential of very-large scale PV systems in Gobi desert. Conf. Rec. IEEE Photovolt. Spec. Conf. 000729–000732, 2009.

Iyer RR, Grossmann IE. Synthesis and operational planning of utility systems for multiperiod operation. Computers and Chemical Engineering 1998; 22:979–93.

Liu M, Shi Y, Fang F. Combined cooling, heating and power systems: A survey. Renew. Sustain. Energy Rev. 2014; 35:1–22.

Lozano MA, Ramos JC, Carvalho M, Serra LM. Structure optimization of energy supply systems in tertiary sector buildings. Energy and Buildings 2009; 41:1063-1075.

Lozano MA, Ramos JC, Serra LM. Cost optimization of the design of CHCP systems under legal constraints. Energy 2010, 35:794- 805.

Mancarella P. MES (multi-energy systems): An overview of concepts and evaluation models. Energy 2014; 65: 1–17.

Pina EA, Lozano MA, Serra LM. Multicriteria synthesis of trigeneration systems assisted with renewable energy sources and thermal energy storage. ASME Paper POWER-ICOPE2017-3103, 10 pages, 2017. (doi:10.1115/POWER-ICOPE2017-3103).

Raluy RG, Serra LM, Guadalfajara M, Lozano MA. Life cycle assessment of central solar heating plants with seasonal storage. Energy Procedia 2014; 48:966-976.

Ramos JC. Optimización del diseño y operación de sistemas de cogeneración para el sector residencial comercial. PhD Thesis, University of Zaragoza, 2012.

REE, 2017. Demanda y producción en tiempo real [WWW Document]. Demanda y Prod. URL http://www.ree.es/es/actividades/demanda-y-produccion-en-tiempo-real (accessed 8.31.17).

Rong A, Su Y. Polygeneration systems in buildings: A survey on optimization approaches. Energy and Buildings 2017; 151:439–454.

Schrage L. Optimization modeling with LINGO. Lindo Systems, 1999.

Serra LM, Lozano MA, Ramos J, Ensinas AV, Nebra SA. Polygeneration and efficient use of natural resources. Energy 2009; 34:575–586.

Wakui T, Kawayoshi H, Yokoyama R. Optimal structural design of residential power and heat supply devices in consideration of operational and capital recovery constraints. Appl. Energy 2016; 163:118–133.

Yokoyama R, Shinano Y, Taniguchi S, Ohkura M, Wakui T. Optimization of energy supply systems by MILP branch and bound method in consideration of hierarchical relationship between design and operation. Energy Conversion and Management 2015; 92:92–104.

Operational Analysis of a 34 kWp Grid-connected PV System Considering Local Weather Measurements in Central Brazil

Sergio P. Pimentel[1], Enes G. Marra[1], Wallisson C. Nogueira[1], Marcelo N. Bousquet[2], Augusto P. Neto[3] and Antonio J. M. de Rezende[4]

[1] Federal University of Goias, Goiania (Brazil)

[2] Transenergia Sao Paulo, Itatiba (Brazil)

[3] JMalucelli Energia, Curitiba (Brazil)

[4] Espora Energetica S/A, Apore (Brazil)

Abstract

More and more distributed generations systems have been connected to the power system in Brazil, especially PV systems in the range between a few units (residential) to hundreds (power plants) of kW. On that context, this work is related to operational analysis of a new 34 kWp grid-connected PV system based on local weather conditions measured in the city of Goiania, located in Central Brazil. The PV system had been installed by a research and development project approved by ANEEL (Brazilian Electrical Energy Agency) and it was the first rooftop solar plant installed at UFG (Federal University of Goias) and also among other public universities from Central Brazil. After some basics operational tests, that 34 kWp grid-connected PV system started to work continuously on January 2017 after being registered and authorized by local grid utility. Since then an amount of 4.4 MWh has been generated and fed into the power distribution line up to middle of October 2017. Results registered during February 2017 from an existing and active PV plant were chosen to present a possible operational analysis. At the end, the energy and power performance profiles from grid-connected PV system are discussed in terms of weather measurements and conditions. As a fully one operational year from 34 kWp grid-connected PV system has not been concluded yet, authors still working on its performance analysis.

Keywords: PV systems, Weather measurements, Distributed generation, Grid-connected PV system, Renewable energy, Solar inverter.

1. Introduction

Grid-connected photovoltaic (PV) systems have been regulated in Brazil since 2012 (main document had been reviewed in 2015) by the net metering mechanism related to Distribution Generation (DG) systems (Aneel, 2015). After that almost 25 MWp of new grid-connected PV systems have been installed (Aneel, 2017a).

Although there is a clear growing up of installed PV systems, such amount of power does not represent a huge contribution from solar resources considering the fully power generation capacity in Brazil nowadays. According to Tab. 1, renewables resources represent 78.5% of Brazilian power generation capacity up to now (October 2017). This is already known around the world and that is why Brazil has been always cited in renewable global reports or outlooks.

Tab. 1: Official Brazilian power generation capacity up to October 2017 (Aneel, 2017a).

Energy resource	Solar	Nuclear	Foreign	Wind	Biomass	Oil & Fossils	Hydro	Total
Installed power capacity (GW)	0.31 (0.2%)	1.99 (1.2%)	8.17 (5.0%)	11.50 (7.1%)	14.24 (8.8%)	26.89 (16.5%)	99.40 (61.2%)	162.47 (100%)

doi:10.18086/swc.2017.10.04 Available at http://proceedings.ises.org

However, solar energy (exclusively from PV power plants) represents the lowest contribution (approx. 0.312 GW) of total power capacity in Brazil. It is even lower than the 8.17 GW imported (and paid for) from neighbor countries (Paraguay, Argentina, Uruguay and Venezuela, in descending order). That is obviously an encouraging reason for increasing solar power plants in Brazil over the next years. Considering its geographical localization on Earth, its annual weather conditions and size of its territorial area, Brazil could produce even much more electrical energy from solar resources for sure. Fig. 1 presents an overview of five geopolitical regions of Brazil edited from original file published by (Macedo, 2007) and also its annual global horizontal solar radiation per day estimated by (NREL, 2005). Actually those conclusions are not so new anymore since academics, professionals, foreign and local companies, public agencies, grid utilities and politicians recognize that Brazil still has an unexplored potential for power generation from solar and wind resources.

Fig. 1: Brazilian geopolitical regions (left) and its estimated global horizontal solar radiation (right) (Macedo, 2007; NREL, 2005).

Even under an unofficial (but real) political and economic crisis registered during last years that affects new regulations and investments, step by step solar and wind resources have been more and more explored in Brazil. For example, a new record of power generated by wind plants installed in the Northeast of Brazil was stablished during the beginning of September 2017 (approx. 6.8 GW) but it will not last very long since new wind plants are expected to be added to the Brazilian power grid until 2020 (ONS, 2017). In addition, Brazilian agency ANEEL (National Agency of Electrical Energy) officially predicts that new solar (residential and commercial) power plants will also provide plus 3.2 GW to Brazilian power grid among the 2017-2024 years (Aneel, 2017b).

Under that context, this work is related to operational analysis of a new 34 kWp grid-connected PV system based on local weather conditions measured in the city of Goiania, located in Central Brazil. Central Brazil corresponds to entire Central-West and a part of North geopolitical regions presented in Fig. 1. Also from Fig. 1 it can be concluded that city of Goiania has an estimated annual global horizontal solar radiation around 5.0-6.0 kWh/m2 per day. These estimated values suggest a considerable potential for exploring the annual available solar energy source in terms of electrical energy production.

Some results from that 34 kWp grid-connected PV system operation are presented and discussed in terms to propose a possible operational analysis related to such DG systems. Energy and power performance profiles are also discussed in terms of weather measurements and conditions. At the end, some conclusions are presented.

2. Grid-connected PV system description

Fig. 2 shows the basic topology of the DG system covered by this work. It is based on a 34 kWp grid-connected PV system and composed by 145 PV panels (235 W, 60 cells, poly c-Si) connected (in series and parallel associations) with 8 single-phase power inverters. The PV panels and power inverters have been manufactured by SUN EARTH (model TPB 156×156-60-P) and ELTEK (models Theia 2.9 HE-t and 4.4 HE-t), respectively.

That new 34 kWp grid-connected PV system corresponds to a rooftop structure and its installation was provided by a research and development (R&D) project executed by UFG (Federal University of Goias). The R&D project was financially supported by four local power companies: Espora Energetica; Transenergia Sao Paulo;

Transenergia Renovavel; and Caldas Novas Transmissao (Pimentel, 2017). This R&D project was approved by ANEEL and it proudly became the first rooftop solar grid-connected power plant installed at UFG and also among other public universities from Central Brazil.

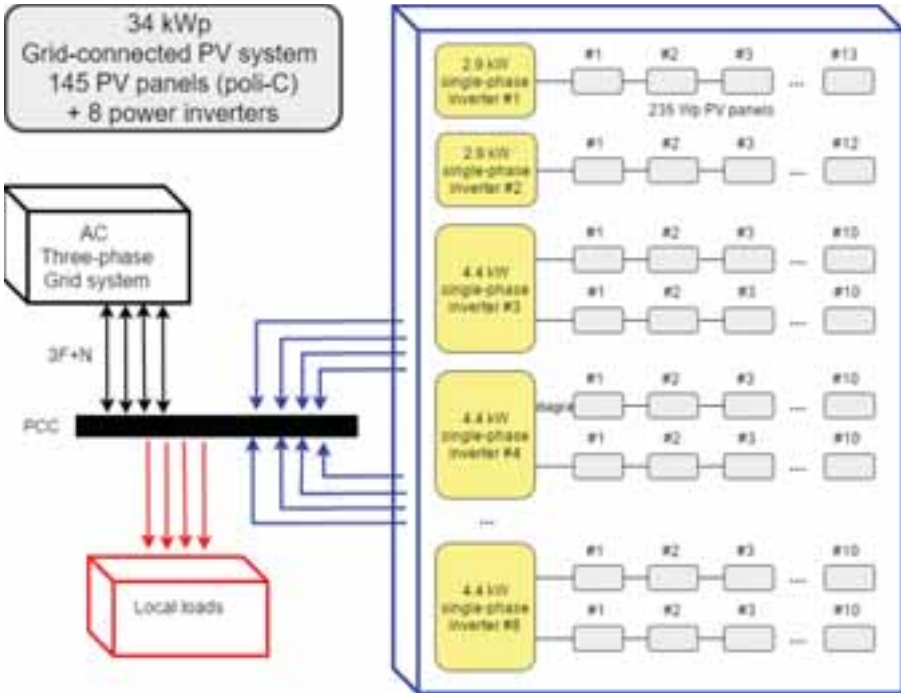

Fig. 2: Basic topology of the 34 kWp PV grid-connected system installed at Goiania (Brazil).

After some basics operational tests during the end of 2016, the 34 kWp grid-connected PV system started to work continuously on January 2017 after being registered and authorized by local grid utility. All the power inverters are connected to the PCC (Point of Common Coupling) which is also connected to the AC three-phase power line based on four wires (more typical situation) and with nominal parameters 220/380 V and 60 Hz. The shunt connection of local loads corresponds to all electrical circuits that feed a three-floor building construction from Electrical, Computer and Mechanical Engineering School (EMC) at UFG.

Fig. 3: A 180° panoramic view from the 34 kWp rooftop PV grid-connected system on April 2017 (autumn).

In addition, Fig. 3 presents a 180° panoramic view from the PV panels related to the 34 kWp rooftop PV grid-connected system during afternoon on April 2017 (autumn). It can be noticed that PV panels had been installed with different orientation and inclination angles. A part of them are faced to North direction (with +15° deviation) with a 10° of inclination (following rooftop's inclination). Others PV panels are faced to South direction with the same deviation and inclination angles. The reason of such different installation procedures is related to R&D objectives and it justifies why nominal power 34 kWp would be never reached all over the year.

3. Power and energy measured performance

It is known that some aspects related to energy production and its performance can be monitored and saved for future numerical analysis. Otherwise other aspects related to local weather conditions can be also involved by that PV system analysis as they could limit overall system performance (Raj, 2016).

This paper discusses the influence of local weather conditions on the operational analysis of an existing 34 kWp PV grid-connected system (presented in Figs. 2 and 3). Its daily operation can be freely accessed by Internet connection through the address (http://200.137.220.91/index.htm) after typing the code 'visitante' into both user name and password fields (from login screen). The web interface (created by power inverters' manufacture)

could be describe as a supervisory system and it provides the amount of power and energy produced by power plant or by each of power inverters during a period of time. Fig. 4 presents a print screen from such supervisory system as it appears on October 15th, 2017. It can be noticed the shapes from total PV power output over the last seven days and also a summary of energy and power over the last twelve months.

Fig. 4: A screen from supervisory system related to 34 kWp grid-connected PV system as it appears on October 15th, 2017.

An amount of registered data from local weather conditions and PV power performance during February 2017 was considered to support the analysis presented in this work. Then Fig. 5 presents the daily electrical energy provided by the 34 kWp PV system to the PCC (as shown in Fig. 2) during February 2017. The biggest and lowest registered values of energy occurred in days 15 (176.3 kWh) and 16 (71.3 kWh), respectively. However, the AC output peak power from a 34 kW (nominal) PV system had a different behavior with lower variations all over the days. Even so, the biggest output peak power value occurred in day 12 (32,7 kWp) and in the same day with a 'poor' energy production (75,4 kWh).

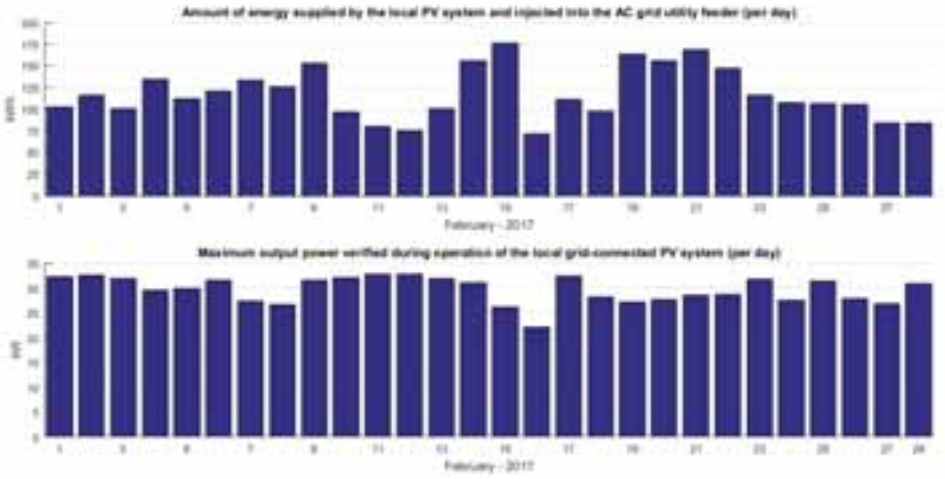

Fig. 5: Daily energy production and output power peak from a 34 kWp PV grid-connected system on February 2017.

Those conclusions suggest that both energy production and maximum power may be used to describe some PV system performance. However, they are not directly dependent just because they are determined by different local weather variables and/or power inverter capability. These issues are described during the next section.

4. Influence of registered local weather conditions

It is well known the direct relationship between power or energy performance from any PV system and the available weather conditions during a period of time. As this particular 34 kWp grid-connected PV system was related to a R&D project, an autonomous local weather station had been also purchased and installed alongside with its PV panels. Fig. 6 presents a general view from local weather station installed closed to the PV panels.

Fig. 6: Local weather station installed alongside the 34 kWp grid-connected PV system at UFG (Goiania, Brazil).

The weather station showed in Fig. 6 automatically collects values from seven different weather sensors during an interval of 10 seconds and registers an average of those captured values over one minute. Each average value from all seven weather variable is then added to a table that could be accessed by user through a serial or IP port. Besides time, the weather measured variables are: wind speed; wind direction; air temperature; relative humidity; precipitation; global solar horizontal irradiance; and atmospheric pressure.

All variable values registered by local weather station since July 2015 are available to visualization (and for free downloading) from an Internet portal through the address: https://sites.google.com/site/sfvemcufg/weather-station. Updates involving data registered by local weather station and its sharing are weekly made by authors of this work. Some of these data had been considered by authors to analyze the operation points from the 34 kWp grid-connected PV system power plant and are presented below.

Fig. 7 presents the horizontal global solar irradiance and air temperature exactly at the 34 kWp grid-connected PV system power plant during February 2017. It can be noticed that from February 12th to February 17th, both local weather variables have distinct behaviors than other days. For that reason, this period of six consecutive days from entire month had been chosen for a more detailed analysis.

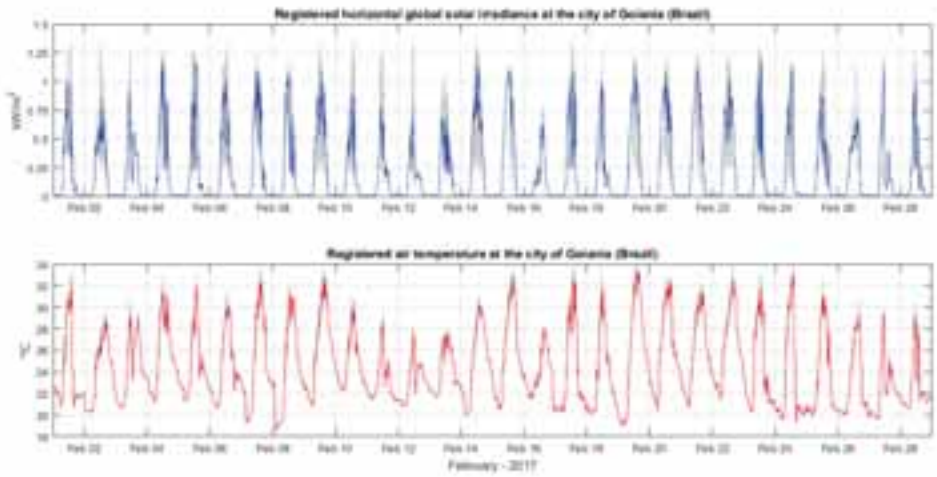

Fig. 7: Local horizontal global solar irradiance (top) and air temperature (bottom) at Goiania (Brazil) during February 2017.

Fig. 8: Amount of local precipitation per minute (blue) and accumulated (red) at Goiania (Brazil) during February 2017.

During the entire month of February 2017, a cyclic oscillation had been verified on air temperature in Fig. 7 (bottom). It suggests that power inverters operation probably had been not limited by temperature. Those peaks verified on horizontal global solar irradiance (not the average blue curve) could explain a possible power saturation on power inverters. It can be noticed that highest values verified in Fig. 5 (bottom) occurred on the same days which global solar horizontal irradiance reached 1.1 kW/m2 (or higher) in Fig. 7 (top).

As February corresponds to a summer season in the city of Goiania and it means a lot of raining days (at least on that of Earth), the oscillations on energy production verified in Fig. 5 (top) can be compared with the local precipitation presented in Fig. 8. And it can be also noticed that significate rains were scattered along the month and have not influenced those energy production oscillations. Even for that period from Feb-12 to Feb-17 that reflects a distinct behavior from the rest of the month, the accumulated precipitation had just a slightly transition over the days 12 and 13.

However, Fig. 8 shows only the precipitation measurements over the month and not how many cloudy were those days (or that distinct period). Fig. 9 exhibits the correspondent part of Fig. 7 related to period from Feb-12 to Feb-17 and Tab. 2 describes this period in terms of energy and weather conditions.

It can be concluded from Fig. 9 that ‘low’ solar irradiance and ‘low’ air temperatures were verified on days 12, 13 and 16. Then, they were probably cloudy days and affected the energy production presented in Fig. 5 (top). In addition, the constant behavior of output power in Fig. 5 (bottom) could be determined by the MPPT capability from power inverters (Hosseini, 2016; Killinger, 2016).

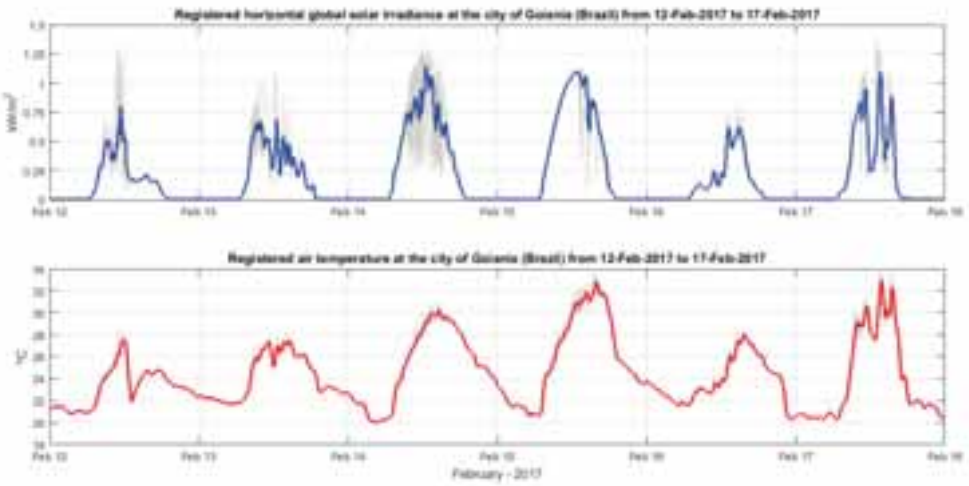

Fig. 9: Particular distinct behaviors verified on local horizontal global solar irradiance (top) and air temperature (bottom) during a period of six consecutive days of February 2017 at the city of Goiania (Brazil).

Tab. 2: Power performance and weather conditions measurements registered during operation of the 34 kWp PV grid-connected system from 12-Feb-2017 to 17-Feb-2017.

Day	Energy from PV system	Output power from PV plant	Daily air temp. range	Effective rain duration	Solar irrad. (average peak)
12-Feb-2017	075.4 kWh	32.7 kW	~ 21-28 ºC	~ 1 h (at 1 pm)	~ 0.8 kW/m²
13-Feb-2017	100.6 kWh	31.8 kW	~ 22-27 ºC	< 1 h (at 7 pm)	~ 0.7 kW/m²
14-Feb-2017	155.9 kWh	31.1 kW	~ 20-30 ºC	~ 1 h (at 3 am)	~ 1.2 kW/m²
15-Feb-2017	176.3 kWh	26.2 kW	~ 21-34 ºC	-	~ 1.1 kW/m²
16-Feb-2017	071.3 kWh	22.1 kW	~ 22-28 ºC	< 1 h (at 10 pm)	~ 0.6 kW/m²
17-Feb-2017	111.6 kWh	32.4 kW	~ 20-34 ºC	~ 1 h (at 6 pm)	~ 1.1 kW/m²

In addition, Tab. 3 presents some values obtained by performance parameters related to PV systems during February 2017. The daily (and monthly) amounts of energy produced by PV power plant, its capacity factor (CF) and the verified performance ratio (or productivity) are presented.

Tab. 3: Daily (specific) and monthly performance parameters registered by 34 kWp grid-connected PV system on February 2017.

Period of time	AC electrical energy produced (kWh)	PV power plant capacity factor (CF)	PV plant performance ratio (kWh/kWp or h)
Feb 12th	75.40	9.24%	2.22
Feb 13th	100.60	12.33%	2.96
Feb 14th	155.90	19.11%	4.59
Feb 15th	176.30	21.61%	5.19
Feb 16th	71.30	8.74%	2.10
Feb 17th	111.60	13.68%	3.28
All month	3302.60	14.45%	97.14

Considering the selected distinct period of six days from Feb-12 to Feb-17, the effects of daily variations on weather conditions can be cleared verified. A capacity factor of 15.0% (average) and a performance ratio around

5 h (average) have been obtained. Such values are typical on good PV systems and they were expected since PV panels and power inverters have been recently manufactured. Among specific days presented in Tab. 3, Feb-15 can be selected as most representative day from a PV system in the city of Goiania during a summer. High solar irradiance and clear sky (no clouds) over a long period of time have been observed during that day. The amounts of CF and performance ratio achieved on Feb-15 are also in accordance with the expected values from Fig. 1 (right) considering the localization of 34 kWp grid-connected PV system.

Considering a higher period of time, Fig. 10 presents some daily CF values observed from April 2017 to October 2017 on the same 34 kWp grid-connected PV system. As it was previously concluded, an average CF value around 15.0% still being observed on 34 kWp grid-connected PV system. Even so, some low FC values have been also noticed from May to August, a period of year related to dry season (no raining) in the city of Goiania. Such reduction can be explained by two typical weather conditions related to that dry season: higher amount of accumulated impurities on the PV panels; and lower solar irradiance over the days (winter). Future measurements from FC values may present the expected efficiency degradation from PV panels over the years.

Fig. 10: Curve of daily capacity factor values observed on 34 kWp grid-connected PV system from April to October 2017.

5. Conclusions

Some operational results from a 34 kWp grid-connected PV system installed in the city of Goiania (Central Brazil) have been presented and discussed.

As the number of installed grid-connected PV systems in Brazil has been increasing over that last five years, this paper described a new 34 kWp grid-connected PV system installed in the city of Goiania (Central Brazil).

After some basics operational tests, that 34 kWp grid-connected PV system started to work continuously on January 2017 after being registered and authorized by local grid utility. Since then an amount of 4.4 MWh has been generated and fed into the power distribution line up to middle of October 2017.

Some operational results observed on this solar power plant during February 2017 have been presented and discussed. For the same 34 kWp grid-connected PV system, a method for validating operational results from PV systems based on weather measurements has been also proposed and discussed.

From presented results, it can be concluded that days with low solar irradiance and low air temperatures cannot be related to raining days only. Some cloudy days may have same aspects and they can also affect seriously the power production from PV panels. Over the next months, the authors concluded that the clearness factor verified during daylight actually has more impact on the efficiency of PV panels than the presence of raining. This conclusion is valid in the city of Goiania since its average temperature does not significantly varies over a year.

Besides, the constant behavior of output power from 34 kWp grid-connected PV system over an intermittent solar month as observed during February 2017 can validate the MPPT capability from power inverters and its efficiency considering the accomplish of DC input voltage range specified by manufacturer.

Some performance parameters related to PV systems have been also calculated. A capacity factor of 15.0% (average) and a performance ratio around 5 h (average) have been obtained. Such values are typical on good PV systems and they were expected since PV panels and power inverters have been recently manufactured.

As a fully one operational year from 34 kWp grid-connected PV system has not been concluded yet, authors still working on its power inverters and weather conditions monitoring, on energy performance parameters analysis and on reliability of solar power plants.

6. Acknowledgments

This work had been developed within the context of all activities related to a R&D project registered with Brazilian agency ANEEL (National Electrical Energy Agency) by code PD-3033-002/2014 and sponsored by the local companies: Espora Energetica S/A; Transenergia Sao Paulo S/A (TSP); Transenergia Renovavel S/A (TER) and Caldas Novas Transmissao (CNT).

7. References

Aneel, 2015. Resolucao normativa nº 687 (in Portuguese). URL (last time accessed on April 03rd, 2017): www2.aneel.gov.br/cedoc/ren2015687.pdf

Aneel, 2017a. BIG - Banco de informacoes de geracao (in Portuguese). URL (last time accessed on October 13th, 2017): http://www2.aneel.gov.br/aplicacoes/capacidadebrasil/capacidadebrasil.cfm

Aneel, 2017b. Nota Tecnica n° 0056/2017-SRD/ANEEL (in Portuguese). URL (last time accessed on September 19th, 2017): www2.aneel.gov.br/cedoc/ren2015687.pdf

Hosseini, S., Taheri, S., Farzaneh, M., Taheri, H., 2016. An approach to precise modeling of photovoltaic modules under changing environmental conditions. 2016 IEEE Electrical Power and Energy Conference (EPEC), Ottawa, pp. 1-6. DOI: 10.1109/EPEC.2016.7771772

Killinger, S., Müller, B., Saint-Drenan, Y. M., McKenna, R., 2016. Towards an improved now casting method by evaluating power profiles of PV systems to detect apparently atypical behavior. 2016 IEEE 43rd Photovoltaic Specialists Conference (PVSC), Portland, pp. 0980-0985. DOI: 10.1109/PVSC.2016.7749757

Macedo, F., 2007. Brazil Labelled Map. URL (last time accessed on October 02nd, 2017): https://commons.wikimedia.org/wiki/File:Brazil_State_Map.svg

NREL, 2005. Brazil – Annual Global Horizontal Solar Radiation. URL (last time accessed on October 02nd, 2017): https://openei.org/wiki/File:NREL-brazil-glo.pdf

Pimentel, S. P., 2017. Sistema Fotovoltaico – EMC/UFG (in Portuguese). URL (last time accessed on October 02nd, 2017): https://sites.google.com/site/sfvemcufg/home

ONS, 2017. Geracao eolica bate recorde no nordeste nos primeiros dias de setembro (in Portuguese). Published by Brazilian agency ONS (National Power Energy Operator). URL (last time accessed on October 13th, 2017): http://ons.org.br/Paginas/Noticias/20170905-recordegeracaoeolica.aspx

Raj, A., Gupta, M., Panda, S., 2016. Design simulation and performance assessment of yield and loss forecasting for 100 kWp grid connected solar PV system. 2nd International Conference on Next Generation Computing Technologies (NGCT), Dehradun, India, 2016, pp. 528-533. DOI: 10.1109/NGCT.2016.7877472

Inverter testing and evaluation according to the Brazilian standards; experiences gained in the first two years of operation of the first Brazilian laboratory equipped for this purpose

José C. de S. Almeida Neto[1], André R. Mocelin[1], Roberto Zilles[1], João T. Pinho[2]

[1] Instituto de Energia e Ambiente / Universidade de São Paulo, São Paulo (Brazil)

[2] Grupo de Desenvolvimento de Alternativas Energéticas / Universidade Federal do Pará. Belém (Brazil)

Abstract

This work presents the experience gained with the testing of photovoltaic grid-tie inverters to evaluate their compliance with the Brazilian standards. The experience was obtained during the first two years at the Laboratory of Photovoltaic Systems of the Institute of Energy and Environment of the University of São Paulo - LSF/IEE/USP, the first laboratory in Brazil equipped to perform these tests.

Since the LSF is the first laboratory to apply the Brazilian standards procedures, there is still uncertainty if the inverters available international market are able to comply with all the aspects of the standards.

The approach focus on the experiences with inverters that did not comply with the Brazilian standards concerning one or more of its aspects, the difficulties encountered during the tests, and the firmware implementation needed to solve inverter nonconformity with the standards.

By reviewing the data obtained, this work aims to evaluate if the criteria required by the Brazilian standards is obtainable by the inverters that already exist in the market. In case there are non-conformities, the interaction with the inverters technical team will show what are the most critical aspects of the standards, and if they can be implemented in the existing inverters.

To back up the analysis, the laboratory infrastructure is briefly described, mostly to establish the power range and main characteristics of the inverters that can be tested using the LSF infrastructure.

Keywords: Grid tied inverter, equipment evaluation, Brazilian standard.

1. Introduction

Distributed power generation is becoming usual in Brazilian distribution grids, and thus grid-connected systems need compliance with the Brazilian standards, regarding the connection interface and energy quality. The inverters in a photovoltaic system are mainly responsible for establishing the connection and delivering the generated power to the grid. In order to evaluate the string inverters sold in the Brazilian market, the Instituto Nacional de Metrologia, Qualidade e Tecnologia – INMETRO (National Institute of Metrology, Quality and Technology), established a labeling program for inverter evaluation according to the standards NBR 16149, 16150, NBR IEC 62116 of the Associação Brasileira de Normas Técnicas – ABNT (Brazilian Association of Technical Standards) and the INMETRO Normative Regulation Number 357.

To support the inverter labeling program the Laboratory of Photovoltaic Systems of the Institute of Energy and Environment of the University of São Paulo was accredited by INMETRO to test grid-tie inverters and guarantee their compliance to the standards.

This scenario presents a specific challenge for inverters already available in the international market, mostly because for these products to enter the Brazilian market they would need to comply with a new standard specific for that country, where there was still no data available for the inverter performance under the Brazilian criteria.

During the first two years, different inverter brands and models were tested at the laboratory, and although most models showed compliance to the standards, a few cases showed non-compliance with one or more aspects of the standards.

This work presents the data obtained during inverter testing. The main attempt is to inform international inverter manufacturers about the aspects of the Brazilian standards and which aspects will require hardware and software reengineering in order for the inverter to be commercialized in the Brazilian market.

doi:10.18086/swc.2017.10.05 Available at http://proceedings.ises.org

2. Brazilian standards

The Brazilian standards NBR 16149 and NBR 16150 dictate most of the features of photovoltaic systems´ connection to the power grid, except for the anti-islanding aspect, which is fully described in the NBR IEC 62116, and DC polarity inversion and photovoltaic overload, which are described in the INMETRO Normative Regulation Number 357. All the tests for the conformity criteria are listed in Tab. 1, and are briefly described in the following items.

Tab. 1: Inverter tests according to Brazilian regulation.

Number	Test	Reference standard
1	Flicker	ABNT NBR 16149 and 16150
2	DC-Component injection	
3	Harmonics and wave distortion	
4	Power factor	
5	Reactive power injection/demand	
6	Over/undervoltage	
7	Over/underfrequency	
8	Power control under overfrequency conditions	
9	Reconnection	
10	Automatic out-of-phase reconnection	
11	Active power modulation	
12	Reactive power modulation	
13	Photovoltaic system grid disconnection	
14	Fault ride-through – FRT	
15	Polarity inversion protection	INMETRO nº 357 normative
16	PV overload	
17	Anti-islanding	ABNT NBR IEC 62116

2.1. Test 1: Flicker

The flickering caused to the electric system by the inverter is evaluated during the tests. For the criteria used and test procedures the Brazilian standards make reference to the international standards IEC 61000-3-3, IEC 61000-3-11 and IEC 61000-3-5. This is the only test with direct reference to international standards and all inverters tested in the laboratory complied with this aspect.

2.2. Tests 2, 3, and 4: DC-Component injection, harmonics and wave distortion, power factor

Tests 2, 3, and 4 are grouped together because of the similarity in their procedures. These three tests require de measurement of DC component, harmonics, and power factor of the current injected to the grid for different inverter loading conditions. Tab. 2 presents the conformity criteria for the three tests. It is important to mention that the DC component and harmonics are calculated using the inverter current fundamental component.

Tab. 2: Criteria for tests 2, 3 and 4 for inverter evaluation in Brazil.

Test	Criteria	Limit
2	DC component	< 0.5 %
3	Total harmonic distortion	< 5.0 %
	Odd harmonics – 3^{rd} to 9^{th}	< 4.0 %
	Odd harmonics – 11^{th} to 15^{th}	< 2.0 %
	Odd harmonics – 17^{th} to 21^{st}	< 1.5 %
	Odd harmonics – 23^{rd} to 33^{rd}	< 0.6 %
	Even harmonics – 2^{nd} to 8^{th}	< 1.0 %
	Even harmonics – 10^{th} to 32^{nd}	< 0.8 %
4	Power factor	0.98 lead ~ 0.98 lag

2.3. Test 5: Reactive power injection/demand

The fifth test requires the inverter to operate controlling the reactive power flowing between the inverter and the grid. This control is done regarding the actual active power injected into the grid. The Brazilian standards describe two types of reactive power control. The first type of control is referenced as a power factor curve, and in this mode the inverter is required to change its power factor according to a ramp function related to the active power delivered to the grid. The inverter installer should be able to configure the ramp function in the inverter, with the default values for the test as shown in Fig. 1. The second type of control consists of maintaining a fixed proportion between the reactive power flowing and the active power injected into the grid. This is the same as maintaining a fixed power factor during inverter operation, but the standard requires the installer to input a percentage value for the reactive/active power relation and not a fixed power factor value. Fig. 2 shows the expected operation for the inverter in the second type of control.

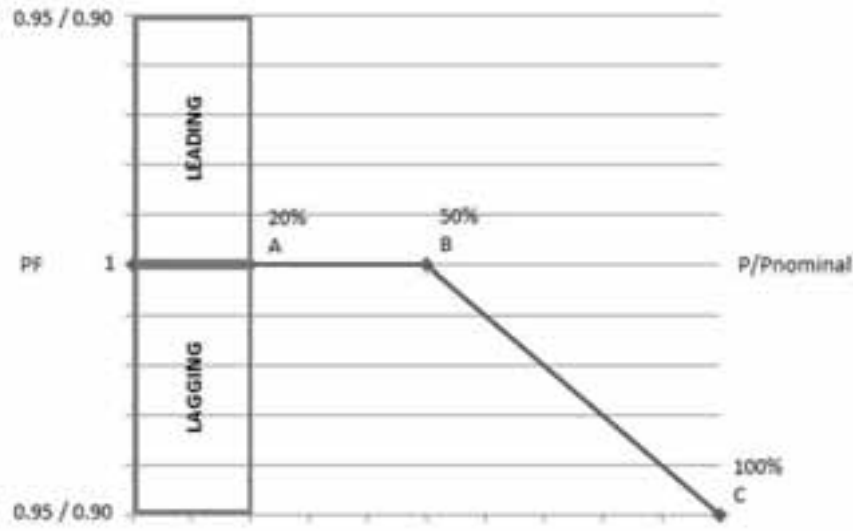

Fig. 1: Reactive power control as a power factor ramp.

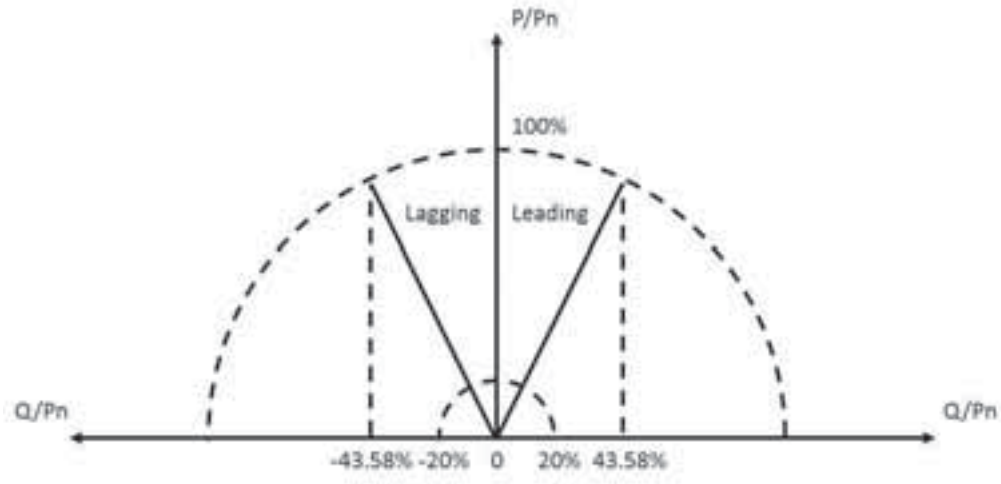

Fig. 2: Reactive power control as a fixed proportion of the active power injected to the grid.

The first type of control is mandatory for inverters with rated power above 3 kW and less or equal to 6 kW; for inverters with rated power equal or above 6 kW, the manufacturer may choose between the two types of control to be implemented in the equipment. Inverters with rated power under 3 kW are not required to have a reactive power control routine.

For the conformity criteria in the first control type, the inverter should be able to attain the power factor values within a ± 0.025 tolerance of the expected values for the injected power above 20 % of the inverter rated power. The second type of control has the same directive but with ± 2.5 % tolerance regarding the expected reactive power.

2.4. Tests 6 and 7: Over/undervoltage, over/underfrequency

The 6º and 7º tests evaluate the inverter regarding the interruption of power injection during abnormal grid conditions. In these tests, the inverter should detect the voltage and frequency values outside the normal operation range and cease to inject power into the grid within the respected time limits. Tab. 3 summarizes the criteria for these tests.

Tab. 3: Grid operation values and power injection interruption time limits for tests 6 and 7.

Voltage range (% V_{rated})	Power injection interruption time limit
$V_{grid} < 80$ %	0.4 s
80 % ≤ V_{grid} ≤ 110 %	Normal operation
110 % < V_{grid}	0.2 s
Frequency range	Power injection interruption time limit
$f_{grid} < 57.5$ Hz	0.2 s
57.5 Hz ≤ V_{grid} ≤ 62.0 Hz	Normal operation
62.0 Hz < V_{grid}	0.2 s

2.5. Test 8: Power control under overfrequency conditions

Test eight requires the inverter to control the active power injected into the grid according to the grid frequency. For frequency values between 60.0 Hz and 60.5 Hz the inverter is required to maintain the power injection unaltered, but for frequency values between 60.5 Hz and 62.0 Hz the inverter must reduce the power injected to the grid according to Eq. 1.

$$\Delta P = [F_{grid} - (F_{rated} + 0.5)] * R \qquad \text{(eq. 1)}$$

where:

ΔP is the active power variation, expressed in percentage, based on the active power injected at the moment the frequency exceeds 60.5 Hz (P_M);

F_{grid} is the actual grid frequency;

F_{rated} is the rated grid frequency;

R is the active power reduction factor, expressed in percentage by Hz, adjusted on - 40 %/Hz.

Also, once an overfrequency event is detected and the injected power is reduced, the inverter is required to reestablish the normal power injection only when the grid frequency returns to a value between 60.0 and 60.1 and maintains this value for at least 5 minutes. When the frequency stabilizes, the inverter is allowed to increase the power injection at a maximum rate of 20 % P_M/minute.

The Brazilian standards divide this test procedure in two parts. The first part corresponds to seven frequency points that evaluate the inverter response to overfrequency events. The second part corresponds to the eighth point that evaluates the power injection gradient. Fig. 3 shows the frequency points and the expected injected power; the power injection gradient is evaluated during the transition between points 8 and 1.

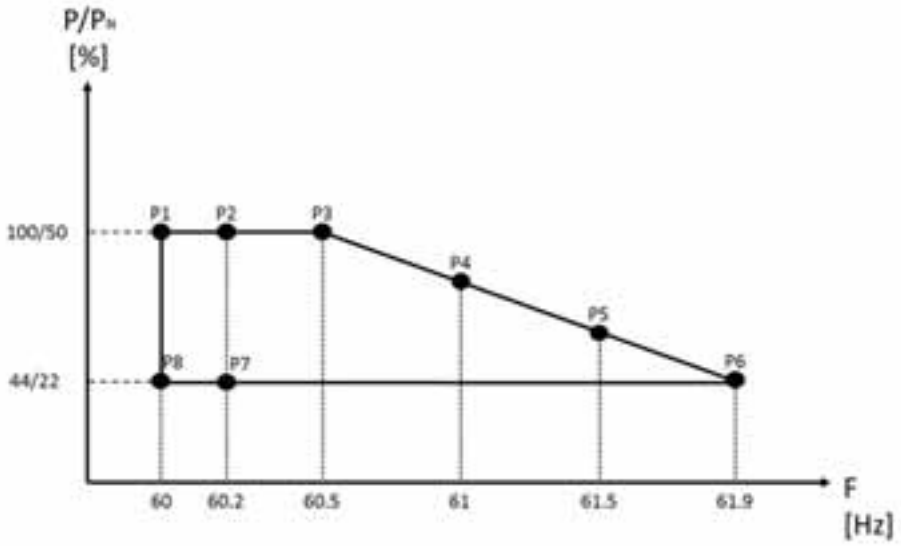

Fig. 3: Frequency points and inverter response for test 8.

The inverter presents conformity with the test requirements if the values measured are as expected in Fig. 3 with a ± 2.5 % tolerance.

2.6. Test 9: Reconnection

This test requires the inverter to reconnect to the grid once the normal operation conditions are detected. The inverter is required to reconnect within 20 to 300 s after the grid returns to normal. After the over and undervoltage tests the reconnection time is measured to verify this test criteria.

2.7. Test 10: Automatic out-of-phase reconnection

This test requires the inverter to withstand two pulses of out-of-phase grid voltage. In the first pulse, the grid voltage waveform skips 90º and, in the second pulse, the waveform skips 180º. The inverter is considered in conformity with this requirement if after each of these events it still injects power into the grid normally.

2.8. Tests 11, 12, and 13: Active power modulation, reactive power modulation, photovoltaic system grid disconnection

Tests 11, 12, and 13 are grouped together because their procedures make use of telecommunication protocols to send commands to the inverter. By using external commands test 11 evaluates if the inverter is capable of limiting the power injected into the grid according to the operator necessity. Test 12 makes use of external commands to evaluate if the inverter is able to operate with reactive power control as described in Fig. 2. These two tests are only required for inverters with rated power above 6 kW. Test 13 is required for all inverters and consists of sending commands for the inverter to start and stop the power injection into the grid.

The Brazilian standards do not establish a communication protocol and require the inverter manufacturer to provide the inverter with a protocol of his choice and all the equipment needed for testing.

2.9. Test 14: Fault ride-through – FRT

Test 14 requires that inverters with rated power equal or over 6 kW withstand voltage sags without disconnecting from the grid. Fig. 4 shows the criteria for the sags duration and inverter expected response regarding the sag event duration.

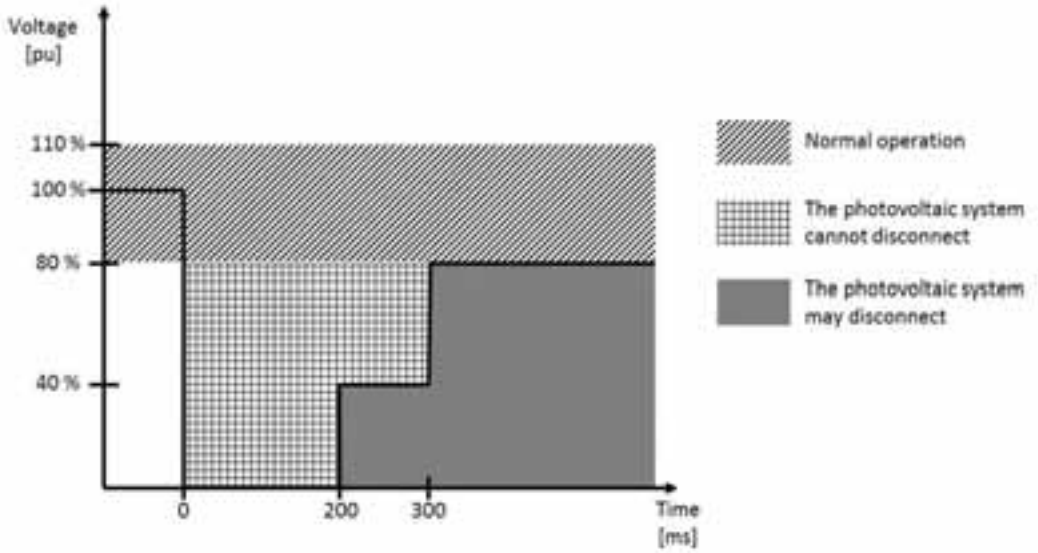

Fig. 4: Inverter response regarding voltage sag duration.

2.10. Tests 15 and 16: Polarity inversion protection, PV overload

Test 15 and 16 are grouped together because their test proceedings are similar and they are both discussed in the INMETRO Normative nº 375. These tests consist of operating the inverter for a period with the DC input polarity inverted, or with an overall DC input capacity 20 % above the inverter rated active power, for each test respectively. After the abnormal operation period, the inverter is operated in normal conditions. The inverter is considered in conformity if after the abnormal conditions it is able to inject power into the grid normally and there is no visible damage to it.

2.11. Test 17: Anti-islanding

The ABNT NBR/IEC 62116, which is a translation of the IEC 62116 standard, describes the anti-islanding test characteristics and procedures. For this test, the inverter is required to detect the absence of grid voltage and stop to provide power to the local load. The procedure takes several test conditions, which vary in power injected by the inverter and the percentage consumed by the local RLC load, but once the grid voltage disconnection occurs the inverter needs to stop the power injection in at least 2 seconds.

3. Laboratory infrastructure

In order to test grid-tie inverters the Laboratory of Photovoltaic Systems of the Institute of Energy and Environment of the University of São Paulo developed a test bench that is composed mainly of: a Solar Array Simulator (SAS) DC power supply, a grid simulator AC power source, a RLC load bank, and a power analyzer. The equipment used in the laboratory and the connection diagram are shown in Fig. 5 and Fig. 6, respectively.

Fig. 5: LSF String Inverter test equipment. From left to right: S.A.S DC power source, grid simulator AC power source, and RLC load bank.

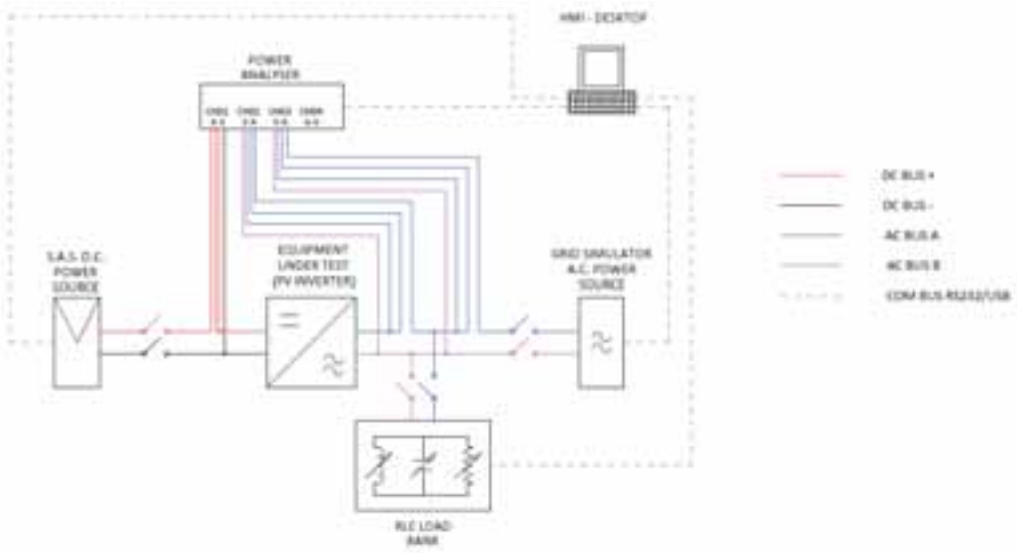

Fig. 6: Laboratory inverter test setup connection diagram.

The test bench equipment allows for testing single-phase inverters with maximum rated power up to 10 kW, as the current INMETRO normative only applies to inverters with rated power equal to or below 10 kW.

4. Inverter test experiences

During the first two years, the laboratory tested 15 inverters with rated power between 250 W and 5,000 W. Among the inverters tested, nine showed conformity with all the tests required by the labeling program, and the others showed nonconformity in one or more tests. Tab. 4 summarizes the inverters tested in the order they were tested, and the conformity criteria.

Tab. 4 shows that the inverters presented nonconformity in tests 2, 3, 4, 5, 6, 7, 8, 13 and 17. Inverters numbers 4, 6, 7 and 8 did not have further development on their firmware, but the manufacturers from inverters 9 and 10 requested to use the laboratory infrastructure to collect data and improve their firmware.

It is important to notice that inverter number 4 is a micro-inverter, designed for use connected directly to a photovoltaic module. This equipment did not have a communication port or telecommunication system that an operator could use to configure its operation or send any type of commands; so it immediately showed nonconformity with test 13.

Tab. 4: Inverters tested and their conformity with the standards.

Inverter	Rated Power (W)	Conformity with the standards?	Nonconformity for tests
1	1,500	Yes	--------
2	3,000	Yes	--------
3	4,600	Yes	--------
4	250	No	6; 7; 13
5	2,000	Yes	--------
6	700	No	3; 4; 8
7	1,500	No	2; 3; 4; 8
8	2,000	No	3; 4; 8
9	4,600	No	3; 5; 8; 17
10	5,000	No	5; 8
11	4,600	Yes	--------
12	1,000	Yes	--------
13	1,500	Yes	--------
14	3,000	Yes	--------
15	5,000	Yes	--------

4.1. Inverter nº 9

Inverter number nine had its firmware updated for harmonic distortion compliance with the Brazilian standards. Fig. 7 shows the results for the 4 evaluations of the harmonic distortion firmware update. The inverter technical team made each update based on the previous results. For the first three evaluations, the inverter presented one or more current harmonics over the limits established by the ABNT NBR 16149. At the fourth evaluation the firmware update lead to an inverter operation in conformity with the Brazilian standard.

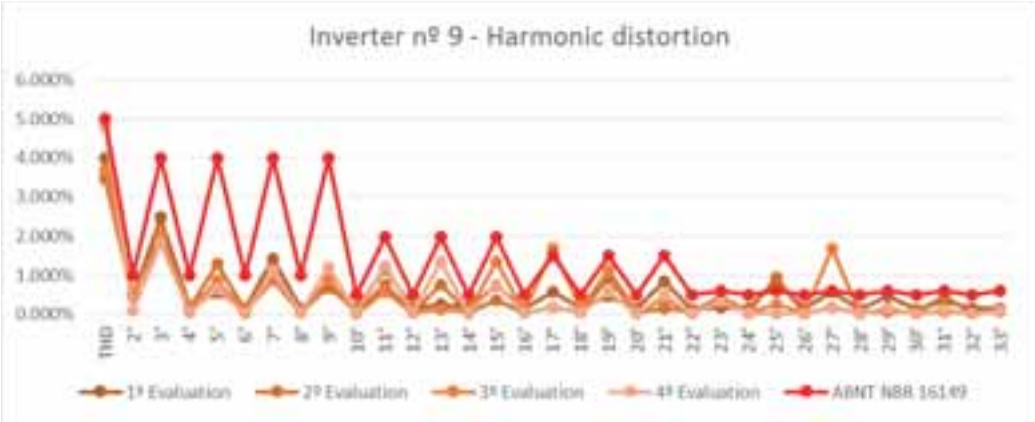

Fig. 7: Harmonic distortion evaluation results for firmware update on inverter nº 9.

After confirming the compliance with the requirements of test 3, the inverter technical team requested to evaluate the power control on overfrequency. At first, the inverter firmware did not present such control. The fourth firmware update implemented the power control required by test 8. One trouble found in this implementation was the misinterpretation of the power injection gradient. During the second evaluation, it was discovered that the value used for the power injection gradient was the inverter rated power and not the P_M value specified by the standard. With this result, the technical team developed a fifth firmware update, which presented conformity for test 8. Fig. 8 and Fig. 9 show the gradient test results for the three evaluations of inverter number nine.

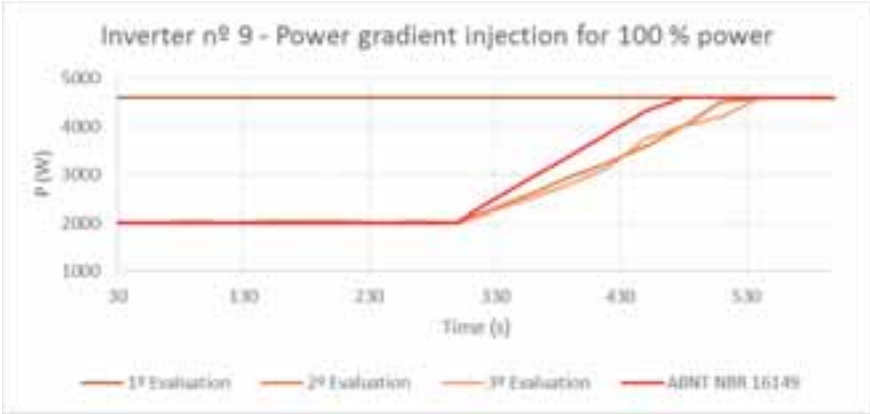

Fig. 8: Power injection gradient evaluation results for inverter nº 9 with 100 % rated power.

Fig. 9: Power injection gradient evaluation results for inverter nº 9 with 50 % rated power.

With inverter nº 9 in conformity with the requirements of tests 3 and 8, the technical team requested the evaluation for the power factor curve. Fig. 10 shows the results for the first and second evaluations of the power curve. At the first evaluation the inverter presented power factor values very close to the standard upper limit, so the technical team implemented a sixth firmware update to bring the values closer to the standard.

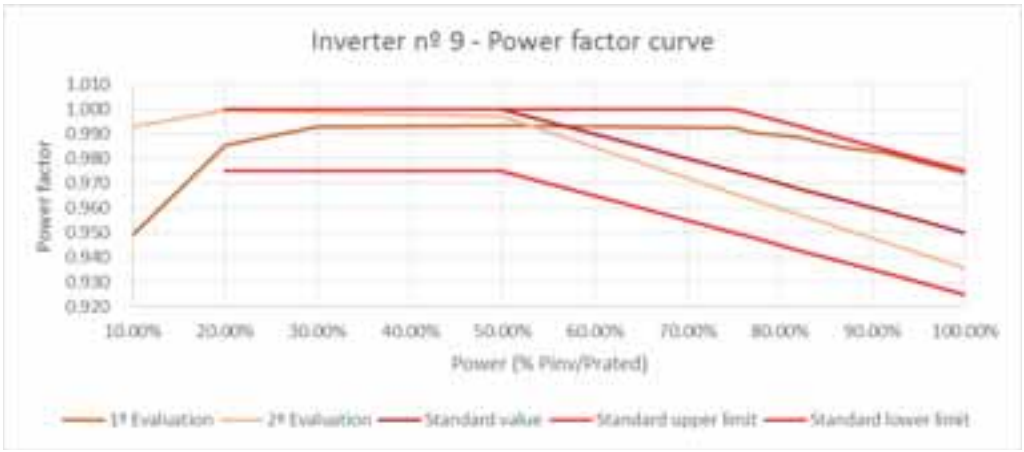

Fig. 10: Power curve evaluation results for inverter nº 9.

Although the inverter did not show conformity with the requirements of test 17, once the inverter showed conformity with tests 3, 5, and 8, the manufacturer did not request additional evaluations and firmware updates.

4.2. Inverter nº 10

Similar to inverter number nine, the inverter number ten also went through firmware updates in order to comply with aspects of the Brazilian standards. The first update was regarding the requirements of test 8. Likewise the values presented by inverter nº 9, inverter nº 10 also used the rated power instead of the P_M value in order to apply the power injection gradient. The inverter technical team then implemented a firmware update in order to comply with test 8. After the first update, the inverter showed compliance with the test requirements but started to present instability problems such as random disconnections from the grid. To correct this problem, the technical team developed a second firmware update to eliminate the inverter operation instability and add the power factor curve operation.

Fig. 13 shows that the firmware update implemented the power factor curve successfully; also, the update solved the disconnection problems. Yet, Fig. 11 shows the power injection gradient did not attain the inverter rated power during the 3rd evaluation, and the equipment was considered in nonconformity with the requirements of test 8. After this firmware implementation, the inverter manufacturer did not request further evaluations for this equipment.

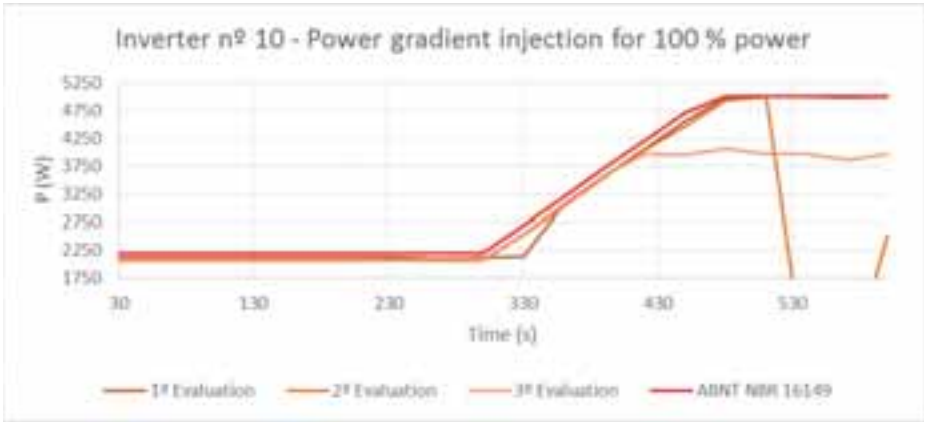

Fig. 11: Power injection gradient evaluation results for inverter nº 10 with 100 % rated power.

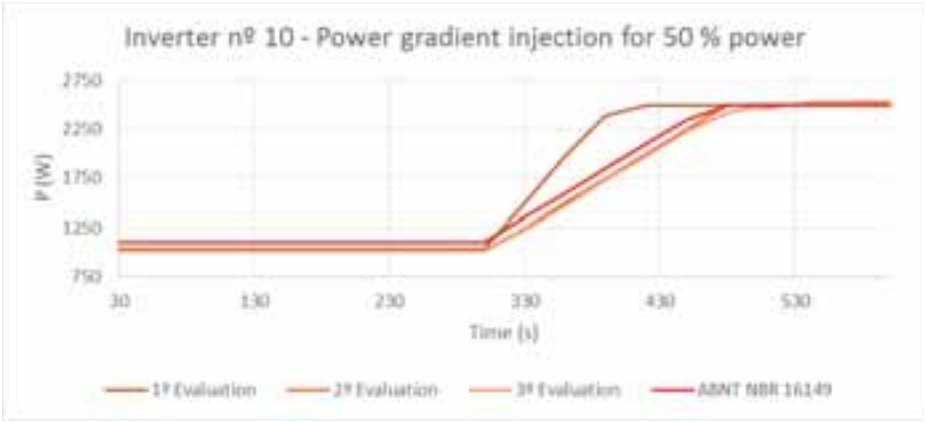

Fig. 12: Power injection gradient evaluation results for inverter nº 10 with 50 % rated power.

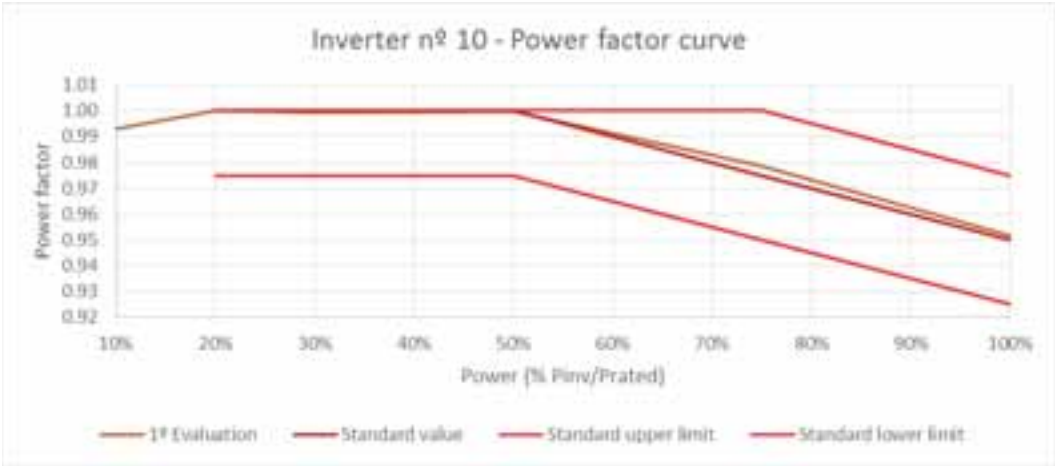

Fig. 13: Power curve evaluation results for inverter nº 10

5. Conclusion

The Brazilian standards evaluate inverters in different aspects: power quality, grid interaction, and safety. Most of the inverters tested in the laboratory were able to present conformity with all the standards requirements. Some of the inverters tested showed nonconformity with different aspects of the standards, but the experience with the manufactures´ technical teams showed that it is possible for equipment already available in the market to attain conformity with the Brazilian standards by firmware update.

The results showed in section 4 back the conclusion where it is possible for equipment already available in the market to receive firmware development in order to comply with the Brazilian criteria. The results also inform manufacturers which aspects should be included in the inverter firmware and how the equipment should perform

under test conditions.

It is important to mention that micro-inverters usually do not have a communication port or telecommunication system able to send commands to change the inverter operation, which leads to a nonconformity with the requirements of test 13 and make firmware update unavailable.

As for the most critical aspects of the Brazilian standards, the power control in overfrequency, the power factor curve, and the harmonic distortion requirements showed to be more difficult to attain for the inverters that did not comply with the aspects of the standards.

The Brazilian standards have a rigorous criteria, some types of inverters, like micro-inverters, won't be able to comply with the all the aspects without hardware and software implementations, this could impact in the equipment cost and performance. So for future challenges there is the question that all types of inverters should comply with one general standard or there should be a specify criteria for each type of inverter. Also there is the question about the limit levels of the standards and the discussion of which ones should be revised, for example, inverter n° 9 at the first firmware implementation showed a power factor curve within the limits required by the standard, but the second implementation showed an improvement on the inverter power curve, so a more restrict limit level could help inverter manufacturers to provide equipment with better performance to the market.

6. References

Agência Nacional de Energia Elétrica, ANEEL, 2012. Resolução normativa nº 482 de 17 de Abril de 2012.

Agência Nacional de Energia Elétrica, ANEEL, 2015. Resolução normativa nº 687. 24 de Novembro de 2015.

Almeida Neto, J. C. S., 2017. Avaliação de conformidade de inversores para micro e mini geração fotovoltaica: a implantação da NBR 16150 e NBR IEC 62116. Dissertação (Mestrado em Ciências) – Programa de Pós-Graduação em Energia da Universidade de São Paulo, São Paulo.

Associação Brasileira de Normas Técnicas, ABNT, 2012. ABNT NBR IEC 62116 - Procedimento de ensaio de anti-ilhamento para inversores de sistemas fotovoltaicos conectados à rede elétrica.

Associação Brasileira de Normas Técnicas, ABNT, 2013. ABNT NBR 16149 - Sistemas fotovoltaicos (FV) - Características da interface de conexão com a rede elétrica de distribuição. 2013.

Associação Brasileira de Normas Técnicas, ABNT, 2013. ABNT NBR 16150 - Sistemas fotovoltaicos (FV) - Características da interface de conexão com a rede elétrica de distribuição - Procedimento de ensiao de conformidade.

Instituto Nacional de Metrologia, Normalização e Qualidade Industrial, INMETRO, 2011. Portaria nº 004 de 04 de Janeiro de 2011.

Instituto Nacional de Metrologia, Normalização e Qualidade Industrial, INMETRO, 2014. Portaria nº 357 de 01 de Agosto de 2014.

International Electrotechnical Commission, IEC, 2008. IEC 62116, Utility-interconnected photovoltaic inverters - Test procedure of islanding prevention measures

International Electrotechnical Commission, IEC, 2013. IEC 61000-3-11, Electromagnetic compatibility (EMC) - Part 3-11: Limits - Limitation of voltage changes, voltage fluctuations and flicker in public low-voltage supply systems - Equipment with rated current ≤ 75 A and subject to conditional connection.

International Electrotechnical Commission, IEC, 2013. IEC 61000-3-3, Electromagnetic compatibility (EMC) - Part 3-3: Limits - Limitation of voltage changes, voltage fluctuations and flicker in public low-voltage supply systems, for equipment with rated current ≤16 A per phase and not subject to condition.

International Electrotechnical Commission, IEC, 2013. IEC 61000-3-5, Electromagnetic compatibility (EMC) - Part 3-5: Limits - Limitation of voltage fluctuations and flicker in low-voltage power supply systems for equipment with rated current greater than 75 A.

Integrating Desalination with Thermal and Electrical Systems

Dynamic Numerical Simulation of a Mechanical Vapour Compression (MVC) Desalination System That Use Renewable Source Energy

Sergio Morales-Ruiz[1], Joaquim Rigola[1], Jesús Castro[1], Carles Oliet[1] and Assensi Oliva[1]

[1] Heat and Mass Transfer Technological Center (CTTC) - Universitat Politècnica de Catalunya
Terrassa - Barcelona (Spain)

Abstract

This paper presents a numerical model to analyse the thermal and fluid dynamic behaviour of a mechanical vapour compression MVC desalination system, which uses renewable energy to supply the electricity required by the whole system. The reason to use renewable energy is that the MVC desalination system has been though to work in remote places, where an electric grid is not available. The transient and steady-state of the desalination system are evaluated taking into account the variability of the renewable energy sources (solar energy). A scalability study has been carried out to find the relation between the variability of the renewable energy sources and the capacity of the desalination system (distilled water production). Different components which making up the desalination system are considered in the numerical simulation, all of them are solved in a coupled way by mean of an object-oriented tool called NEST. The influence of the feed seawater conditions is also analysed on the system performance.

Key-words: MVC desalination unit; Numerical modelling; Dynamic performance; Renewable source energy.

1. Introduction

The MVC desalination method is an evaporation and condensation process that occurs at low pressure, which requires a compression work to increase the saturation temperature of the vapour. The trend is to use low evaporation temperatures (between 50 to 70^{o}C) to reduce the risk of corrosion and scale deposition (El-Khatib 2004). The compressed vapour is condensed and its latent heat is transferred to the feed seawater. The applicability of MVC desalination systems in remote places where there is not possible a connection to an electric grid depend on the use of renewable energy sources. However, the renewable energy means variability in the power given. This variability should be well defined to avoid damage and establish secure partial working operation of the desalination system. The MVC desalination is used at low and medium scale in comparison with other techniques such as: multistage flash desalination (MSF) or reverse osmosis (RO) (Ettouney, 2006).

The numerical modelling presented in this paper is applied to analyse the thermal and fluid dynamic behaviour of a MVC desalination system, which uses renewable energy source (solar energy) to supply the electric requirements of the system. The electrical energy is used to feed the mechanical compressor, a heater, a group of pumps and the control panel of the system. The well-known variability of renewable sources of energy is considered in the performance system study. Also, the influence of the boundary conditions on the execution of the unit along the time is analysed.

2. Dynamic modelling

The desalination system has been divided in four different subsystems, following the strategy proposed by Bodalal (2010) and Mazini (2014). The first subsystem is the evaporator and condenser, in which the evaporation and distillation processes are performed. The second is the vacuum and deareation subsystem, where the low pressure is achieved and non-condensed gas (Oxygen) is stripped. The third subsystem is the mechanical compressor, which is modelled to know its energetic requirement in function of the desalination performance and the climatic conditions. The last subsystem is the heat exchangers, which preconditioning the feed seawater flow temperature, taking advantage of the heat contained in the distilled water and brine flows at the outlet of the evaporator/condenser.

The evaporator and condenser subsystem is modelled describing it as a brine block, vapour space block, and a tube bundle. A schematic representation of these blocks is depicted in Figure 1, together with the others

doi:10.18086/swc.2017.11.01 Available at http://proceedings.ises.org

subsystems. The vacuum and deareation subsystem is modelled assuming that there are a liquid block, a vapour space block and a package zone, which are depicted in Figure 2. The compressor has been modelled following the mechanical model of a rotatory lobe compressor (blower), which uses the geometric configuration and the relation between velocity (rpm) and the displacement by revolution (cfr) of the compressor.

3. Mathematical formulation

The mathematical formulation of the evaporator/condenser subsystem is based on mass, and energy balance conservation equations.

$$\frac{dm_V}{dt} + \frac{dm_B}{dt} + \dot{m}_B + \dot{m}_{Do} - \dot{m}_{Fi} = 0 \qquad \text{(eq. 1)}$$

$$\frac{dm_V h_v}{dt} + \frac{dm_B h_B}{dt} + \frac{dm_{VT} h_T}{dt} + \dot{m}_B h_B + \dot{m}_{Do} h_{Do} - \dot{m}_{Fi} h_{Fi} = 0 \qquad \text{(eq. 2)}$$

Mass and energy conservation equations of vapour space

$$\frac{dm_V}{dt} + \dot{m}_D + \dot{m}_{v2} + \dot{m}_{nc} - \dot{m}_V - \dot{m}_{nc} = 0 \qquad \text{(eq. 3)}$$

$$\frac{dm_v h_V}{dt} + \dot{m}_D h_V + \dot{m}_{v2} h_V + \dot{m}_{nc} h_V - \dot{m}_V h_V - \dot{m}_{nc} h_V = 0 \qquad \text{(eq. 4)}$$

Mass, energy and salt conservation equation of the brine lump

$$\frac{dm_B}{dt} + \dot{m}_B + \dot{m}_{Fr} - \dot{m}_{Fo} - \dot{m}_C = 0 \qquad \text{(eq. 5)}$$

$$\frac{dm_B h_B}{dt} + \dot{m}_B h_B + \dot{m}_{Fr} h_B - \dot{m} h_{Fo} - \dot{m}_C h_B = 0 \qquad \text{(eq. 6)}$$

$$\frac{dm_B X_B}{dt} + \dot{m}_B X_B + \dot{m}_{Fr} X_B - \dot{m}_{Fo} X_{Fo} - \dot{m}_C X_C = 0 \qquad \text{(eq. 7)}$$

Mass of the bundle tubes and energy conservation equation of the vapour condensed inside tubes, assuming that there is not heat accumulation in solid walls.

$$\frac{dm_T}{dt} = 0 \qquad \text{(eq. 8)}$$

$$\frac{dm_{VT} h_T}{dt} + \dot{m}_{Do} h_{Di} - \dot{m}_{Do} h_{Do} = -\dot{Q}_e \text{ evaluating } \dot{Q}_e = U_T A_T (T_D - T_B) \qquad \text{(eq. 9)}$$

The heat transferred between the vapour condensed inside of the bundle tubes and the fluid outside of tubes is defined in function of the global heat transfer coefficient, transfer area and the difference temperatures. Assuming that the tubes cannot accumulate salt on the external surface, then

$$\dot{m}_C X_C - \dot{m}_{Fr} X_B = 0 \qquad \text{(eq. 10)}$$

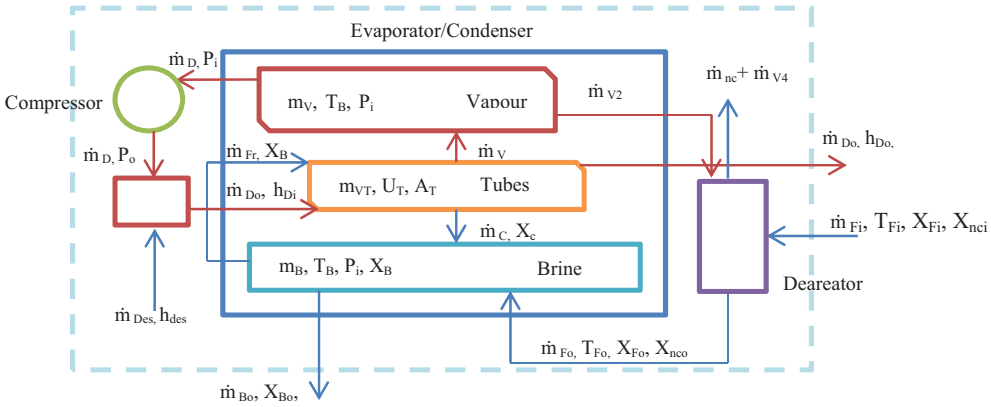

Fig. 1: Schematic representation of the MVC desalination system and evaporator/condenser subsystems

The mathematical formulation of the vacuum and deareation subsystem is based on the same mass, energy and salt balance conservation equations applied on the vapour, liquid and packed zone. The conservation equations are applied on the package zone assuming that there is not accumulation of mass, energy or salt on it. Some extra relations are used to define the value of the non-condensable gas stripped, the flash evaporation, the mass flow condensed into the package and the mass flow at the outlet of the deareator (Suryanarayana, 2011).

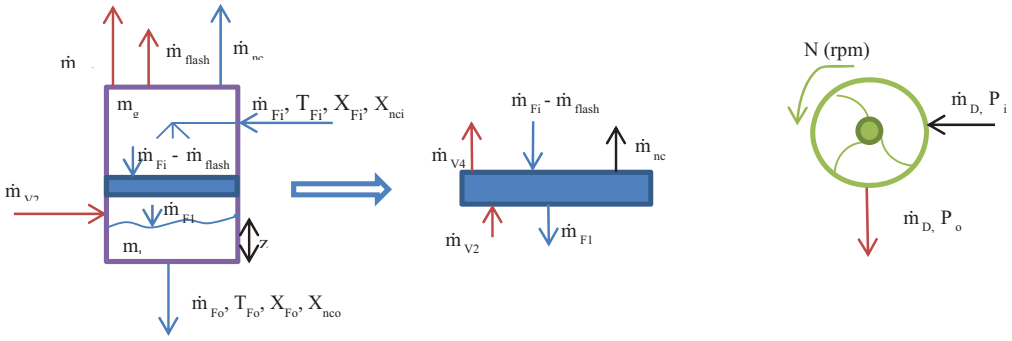

Fig. 2: Schematic representation of the deareator subsystem (including a detail of the package zone) and the compressor

$$\frac{\partial m_g}{\partial t} + \dot{m}_{v4} + \dot{m}_{v3} - \dot{m}_{flash} - \dot{m}_{v2} = 0 \quad \text{(eq. 11)}$$

$$\frac{\partial m_l}{\partial t} + \dot{m}_{Fo} - \dot{m}_{F1} = 0 \quad \text{(eq. 12)}$$

$$X_{nco}\frac{\partial m_l}{\partial t} + m_l\frac{\partial X_{nco}}{\partial t} + \dot{m}_{Fo}X_{nco} - \dot{m}_{F1}X_{nc1} = 0 \quad \text{(eq. 13)}$$

$$\frac{\partial m_g h_g}{\partial t} + \dot{m}_{v4}h_g + \dot{m}_{v3}h_f - \dot{m}_{flash}h_g - \dot{m}_{v2}h_g = 0 \quad \text{(eq. 14)}$$

$$\frac{\partial m_l h_{fo}}{\partial t} + \dot{m}_{Fo}h_{fo} - (\dot{m}_{Fi} - \dot{m}_{flash})h_{fi} - \dot{m}_{v3}h_f = 0 \quad \text{(eq. 15)}$$

Assuming that there is not accumulation on package zone:

$$\dot{m}_{F1} - (\dot{m}_{Fi} - \dot{m}_{flash}) - \dot{m}_{v3} = 0 \quad \text{(eq. 16)}$$
$$\dot{m}_{v4} + \dot{m}_{v3} - \dot{m}_{v2} = 0 \quad \text{(eq. 17)}$$
$$\dot{m}_{F1}X_{nc1} + \dot{m}_{nc} - (\dot{m}_{Fi} - \dot{m}_{flash})X_{nci} = 0 \quad \text{(eq. 18)}$$
$$\dot{m}_{F1}h_{f1} - \dot{m}_{v3}h_f - (\dot{m}_{Fi} - \dot{m}_{flash})h_{fi} = 0 \quad \text{(eq. 19)}$$
$$\dot{m}_{v4}h_g + \dot{m}_{v3}h_f - \dot{m}_{v2}h_g = 0 \quad \text{(eq. 20)}$$

Where:

$$\dot{m}_{v3}h_{fg} = \dot{Q}_{cond} = \alpha_i A_i (T_{sat} - T_{fi}) \quad \text{(eq. 21)}$$

$$\dot{m}_{flash} = \frac{C_p\,(T_{sat} - T_{fi})}{h_{fg}}\,\dot{m}_{Fi} \quad \text{(eq. 22)}$$

$$\dot{m}_{nc} = K_l A_c \Delta X_{Ln} \quad \text{(eq. 23)}$$

Evaluating: $\Delta X_{Ln} = \frac{[(X_{nci} - X^*_{nci}) - (X_{nco} - X^*_{nco})]}{ln[(X_{nci} - X^*_{nci})/(X_{nco} - X^*_{nco})]}$

$$\dot{m}_{Fo} = f(valve) = \sqrt{2gz}\,A_{valv}\,\rho \quad \text{(eq. 24)}$$

The compressor (blower) model is based on the root blower laws, in which the volumetric flow, velocity, power and the displacement by revolution values are related:

$$\dot{V} = cfr * (rpm - Slip_{corrected}) \quad \text{(eq. 25)}$$
$$Power = [0.00436 * cfr * rpm * (P_o - P_i)] + Friccional\ loss \quad \text{(eq. 26)}$$

The ideal gas law is used to evaluate the inlet pressure at the compressor as function of the vapour mass contained into the evaporator, the temperature of the vapour and the volume occupied.

$$P_i = \frac{1}{V_v}\frac{m_v}{M}RT \quad \text{(eq. 27)}$$

The heat exchangers are evaluated in function of heat flux transferred between flows (distilled water, brine and feed seawater) to obtain the temperatures of each one, using the overall heat transfer coefficient (U), the logarithm mean temperature difference (LMTD) and the transfer area (A_{Hex}). Assuming the hypothesis that there is not heat losses in the heat exchangers, the heat transferred should be equal to the heat flux obtained or delivered for the flow.

$$Q_{exchanged} = U\, A_{HEX}\, LMTD = \dot{m}\, C_p(T_{in} - T_{out}) \qquad \text{(eq. 28)}$$

4. Numerical resolution

The group of equations is solved by means of the in-house object-oriented tool called NEST, which is capable to link and solve different elements that making up a system (Damle, et. al., 2011; Farnós, et. al., 2014). The MVC desalination system that is presented in this paper has different components: an evaporator/condenser, a compressor, a deareator, two heat exchangers and a group of pumps. Although in this numerical platform each component is an object, the whole system resolution is carried out iteratively by solving all its components and transferring the appropriated information between them (see Figure 3).

A dynamic model based on mass, energy and salt balances and applied to internal components of the MVC desalination system has been implemented to analyse the transient behaviour of the MVC desalination system, which uses renewable source energy.

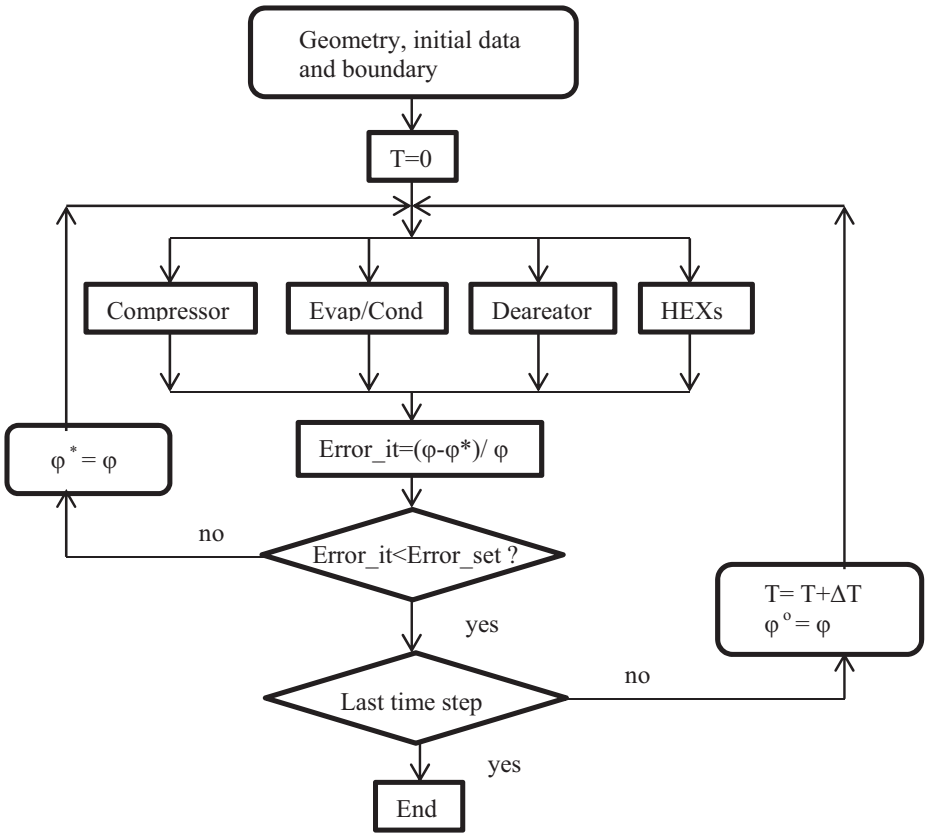

Fig. 3: Global algorithm to solve the MVC desalination unit

5. Results

A numerical analysis has been carried out to define the specific average consumption of the MVC desalination systems analysed. A value of 15.08 kW/m^3 has been defined including the power required by the compressor, pumps and heater of the whole system. A scalability study using three different units, each one with a production capacity of 100, 200 and 400 m^3/day of distilled water, has given 14.98, 15.07 and 15.19 kW/m^3,

respectively. All these values are in agreement with technical literature data (Plantikow, 1999). The numerical results expressed in a percentage relation between the energy used and the distilled water production is depicted in Figure 4. This graphic shows the capacity of supplying distilled water in function of the energy source variability; as an example a reduction of 70% in the energy source represents a decreasing of 58% in the production capacity of distilled water. This value is in agreement with data proposed by Plantikow (1999) for a specific case in which evaporation occurs at 60°C.

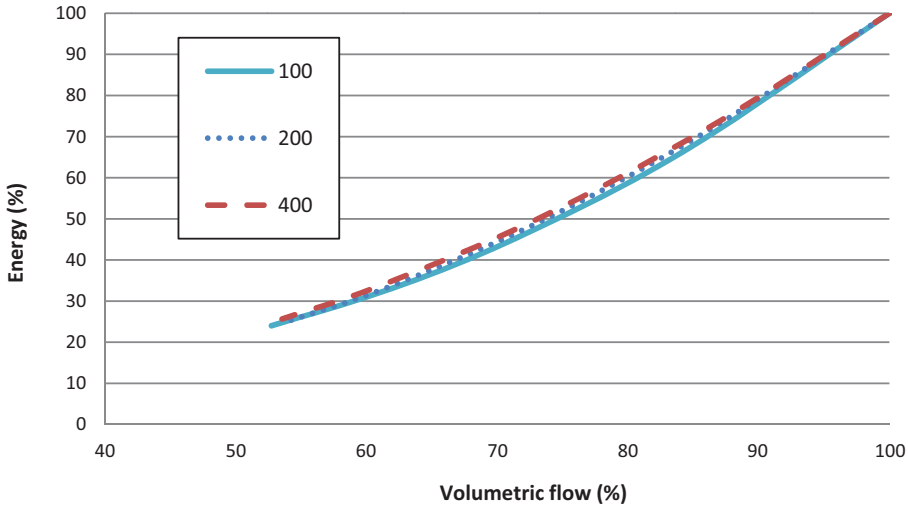

Fig. 4: Percentage relation between energy requirement and volumetric flow demand of the MVC desalination system

A virtual prototype desalination unit capable to produce 1m^3/day of distilled water has been used to evaluate the preliminary results under dynamic conditions. Three different cases have been used to evaluate the thermal behaviour of the MVC desalination unit, in which an evaporation temperature about 60°C has been used.

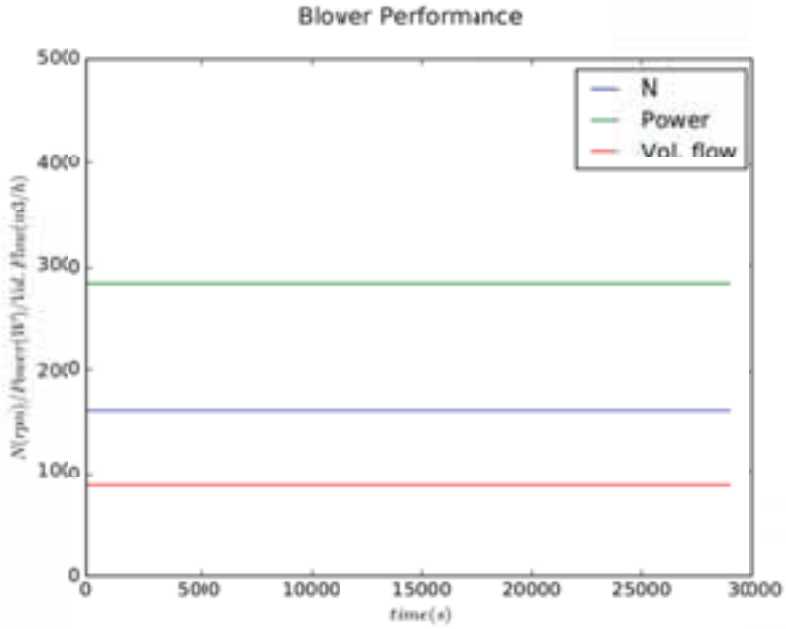

Fig. 5: Compressor (blower) performance: Velocity (N), Power availability (Power) and Volumetric Flow (Vol. Flow)

The first case consist of evaluating the energy required to produce 1m^3/day of distilled water, assuming a complete availability of the energy and constant power (a hypothetical condition: how if the unit will be connected with an electrical grid). The power, the velocity and the volumetric flow of the compressor are shown in Figure 5. A constant power produces not variations in the velocity and the volumetric flow, which produce

that the MVC desalination unit works in stable conditions using a constant mass flow of feed seawater during the working time. The total mass of the seawater required to produce 1m^3 of distilled water is depicted in Figure 6, together with the mass of brine and distilled water produced in the process.

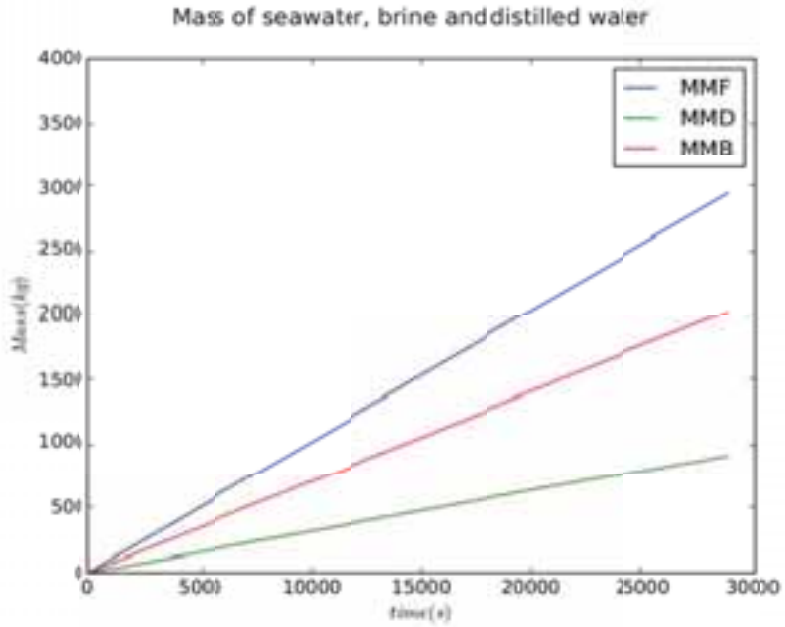

Fig. 6: Masses used by the MVC desalination unit along 8 hours: distilled water (MMD), brine (MMB) and seawater (MMF)

The pressures and the temperatures in the evaporator and condenser of the MVC desalination unit keep their values along the process, achieving a steady state conditions until produce the quantity of distilled product defined. In this case a power of 2850W is required to produce around 1m^3 of distilled water in 8 working hours.

The second case consists of analysing the influence of the energy availability and variability on the compressor performance and their effect on the thermal behaviour of the MVC desalination system. The solar energy is used as source energy of the MVC desalination system in which the energy availability is obtained from meteorological data, assuming that the desalination plant works in Barcelona-Spain (See Table 1).

Tab. 1: Meteorological data for Barcelona on June

Hour	Radiation (W/m^2)	Ambient Temperature (^{o}C)
9:00	515	17.2
10:00	684	18.1
11:00	771	19.8
12:00	860	20.6
13:00	811	21.1
14:00	801	21.9
15:00	734	22.0
16:00	722	20.9

A group of photovoltaic devices should be used to transform the solar radiation in electrical energy, which will be used to feed the compressor and pumps. The radiation data is a parameter needed to evaluate the energy

source, together with the photovoltaic panel efficiency and the effective area used. The electric power evaluated is used to calculate the compressor velocity and the volumetric flow displaced. A sunny day of June has been chosen to evaluate the energy availability and variability along the day. Eight hours have been simulated with the aim of obtaining 1.0m^3/day of distilled product.

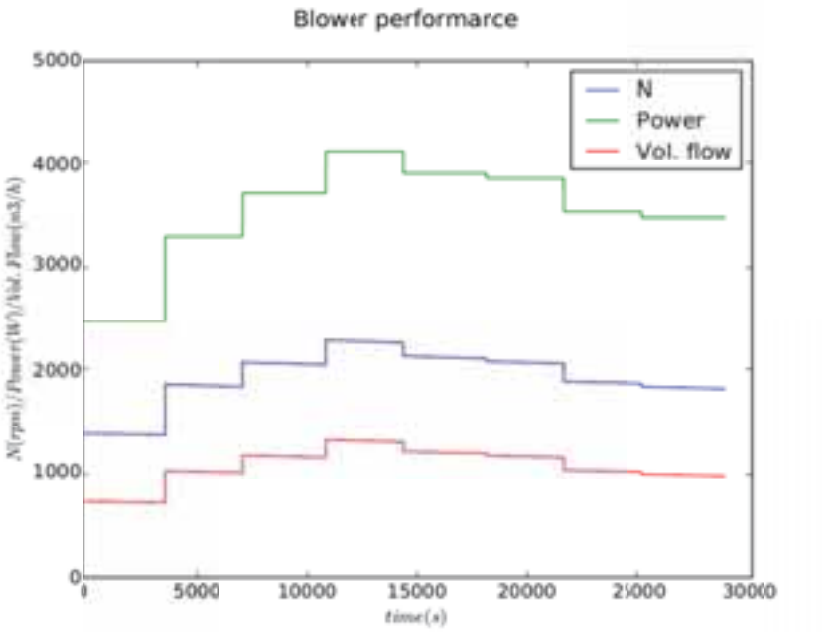

Fig. 7: Compressor (blower) performance: Velocity (N), Power availability (Power) and Volumetric Flow (Vol. Flow)

The compressor performance and the thermal behaviours of the MVC desalination unit are described in next figures. The velocity of the compressor and the volumetric flow are function of the solar energy available, which is defined by a power profile that manages the compressor performance along the 8 working hours.

The volumetric flow moved from the compressor to the evaporator/condenser defines the thermal behaviour of the MVC desalination unit, which requires a specific quantity of the seawater to feed the unit and to produce the distilled water. The mass flows used by the MVC desalination unit are depicted in Figure 8.

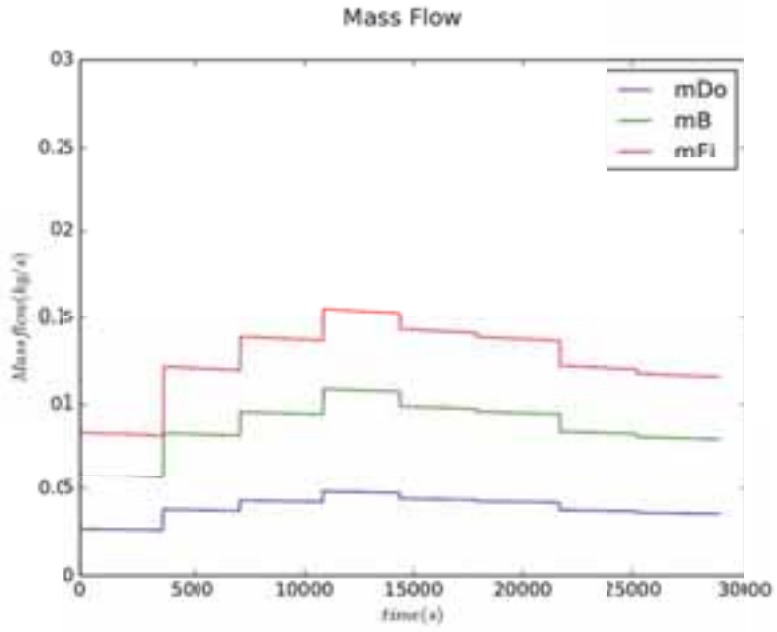

Fig. 8: Mass flows used by the MVC desalination unit: distilled water (mDo), brine (mB) and feed seawater (mFi)

The total mass of seawater needed to produce 1.0 m3 of distilled water (final product) together with the quantity of brine produced in the desalination process can be obtained after integrating the mass flows along the time. The masses of seawater, brine and distilled water are shown in Figure 9, a slight change can be observed if the results are compared with the results of the case with constant power (see Figure 6).

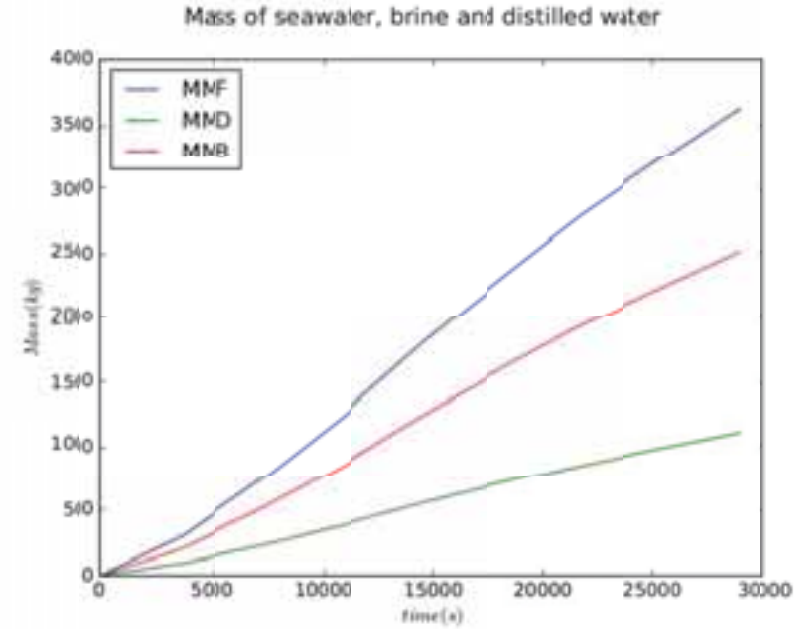

Fig. 9: Masses used by the MVC desalination unit along 8 hours: distilled water (MMD), brine (MMB) and seawater (MMF)

The salt concentration of the recirculation, brine and feed seawater flows are shown in Figure 10. A constant salt concentration value of the feed seawater at the inlet is used, whilst the salt concentration values of recirculation and brine flows present a slight decrease following the same tendency of the pressure in the evaporator.

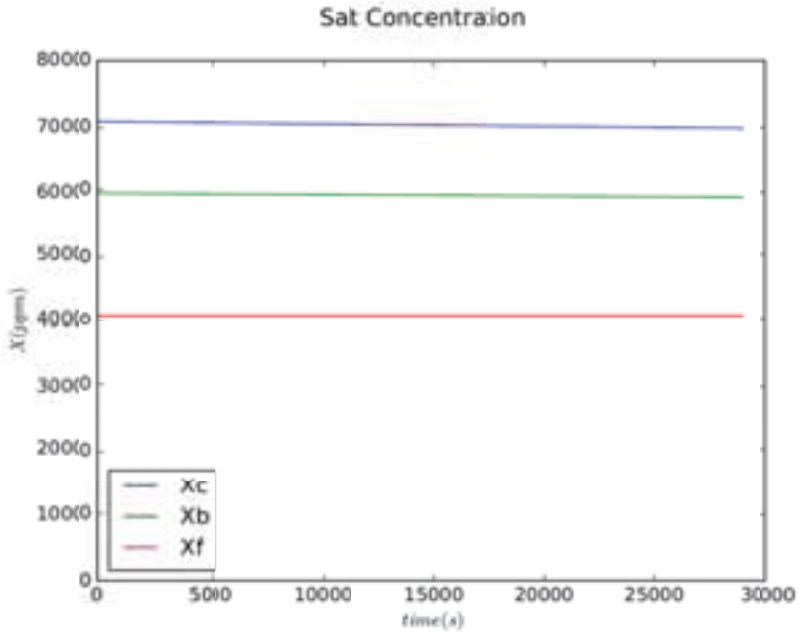

Fig. 10: Salt concentration in the evaporator/condenser: recirculation flow (Xc), brine flow at the outlet (Xb) and feed seawater flow at the inlet (Xb)

The temperatures and pressures into the evaporator/condenser are shown in Figure 11. The vapour, brine and feed seawater temperatures present a stable behaviour as consequence of the evaporation pressure (Pinlet) and condensation pressure (Poutlet) used in the process. A small decrease in the evaporation pressure and temperature are detected, which produces that the differential pressure increase its value, reducing the volumetric flow in the compressor and the mass flows in the MVC desalination unit (see Figures 7 and 8).

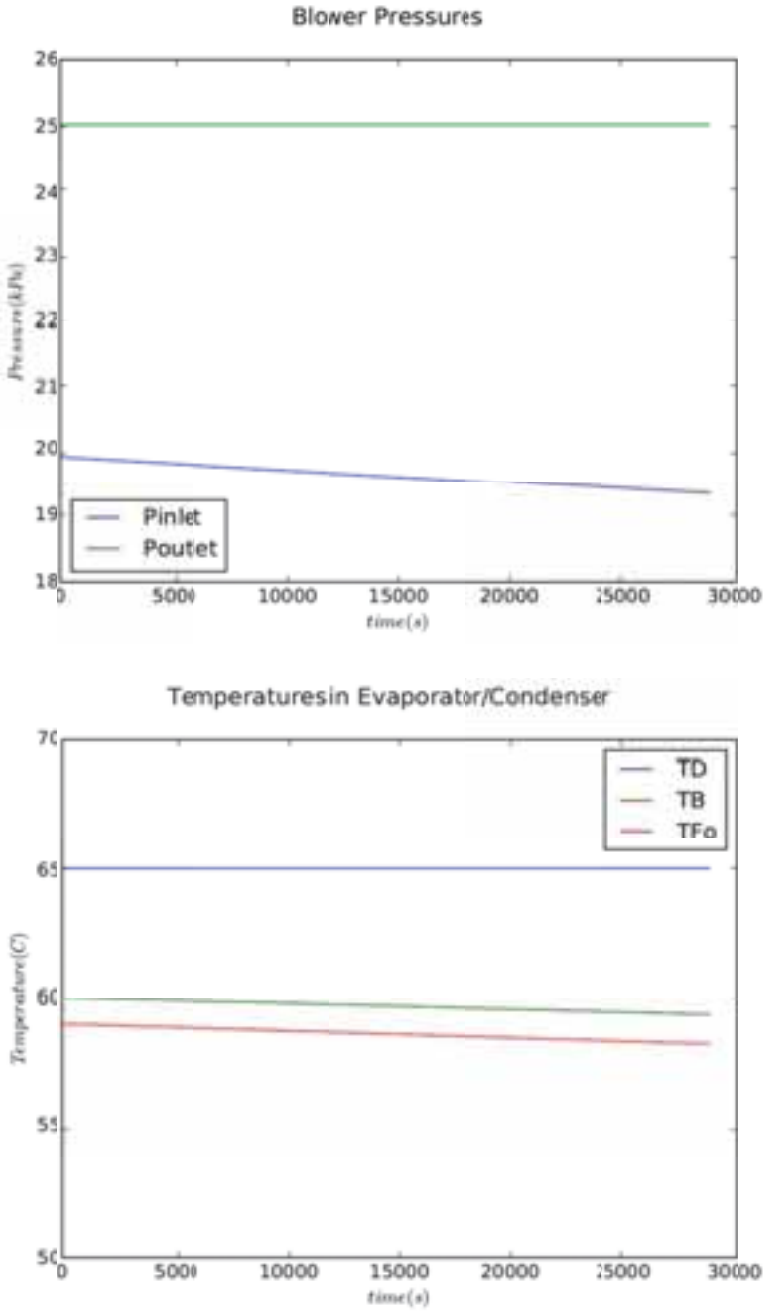

Fig. 11: Temperatures in the evaporator/condenser: vapour (TD), brine (TB) and feed seawater (TFo) and pressures in the blower

The energy transferred between the feed seawater, the distilled water and brine flows in the heat exchangers produce that the seawater increases its temperature from T_{CW} to T_{FI}, whilst the distilled water and brine flows decrease their temperatures from T_D and T_B to T_{DO} and T_{BO}, respectively. The temperature profiles are function of the different mass flows used by the MVC desalination unit, as consequence of the power variability along the working time. These temperatures are shown in Figure 12.

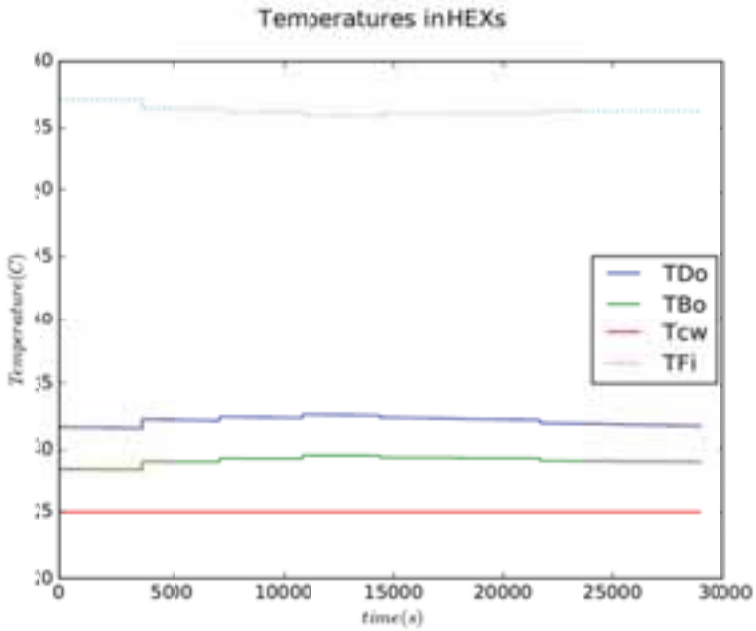

Fig. 12: Temperatures in the heat exchangers of the flows along 8 hours: distilled water at the outlet (TDo), brine at the outlet (TBo), preheating seawater at the outlet (TFi) and feed seawater at the inlet (Tcw)

The third case consists of analysing the influence of the boundary conditions, the feed seawater temperature (T_{CW}) and its salt concentration (X_f) at the inlet of the system, on the distilled water and brine flows at the outlet of the system. Regularly a change in the boundary conditions is applied, details in Table 2.

Tab. 2: Boundary conditions applied in function of time

Hour	Seawater Temperature T_{cw} (^oC)	Salt Concentration X_f (ppm)
1	25.0	41000
2	25.5	42000
3	26.0	42500
4	27.0	43000
5	27.0	43000
6	26.5	42500
7	26.0	42000
8	25.0	41500

The numerical results of the third case are depicted in Figures 13 and 14. The salt concentration of the brine flow (Xb) at the outlet of the unit and the salt concentration of the recirculation flow (Xc) are shown. The salt concentration values tend look for a new steady-state condition along the time, keeping the difference regarding to the salt concentration of the feed seawater at the inlet.

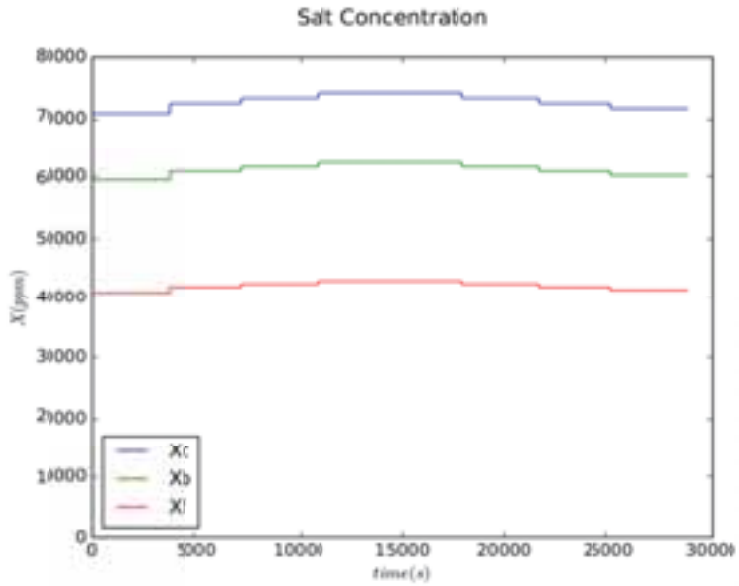

Fig. 13: Dynamic behaviour of the salt concentration in the MVC desalination system

The temperatures of the distilled water, brine and feed seawater flows after pass through the preconditioning heat exchangers are shown in Figure 14. The temperature profiles of the flows depend on the feed seawater conditions (T_{CW}) at the inlet of the MVC desalination unit.

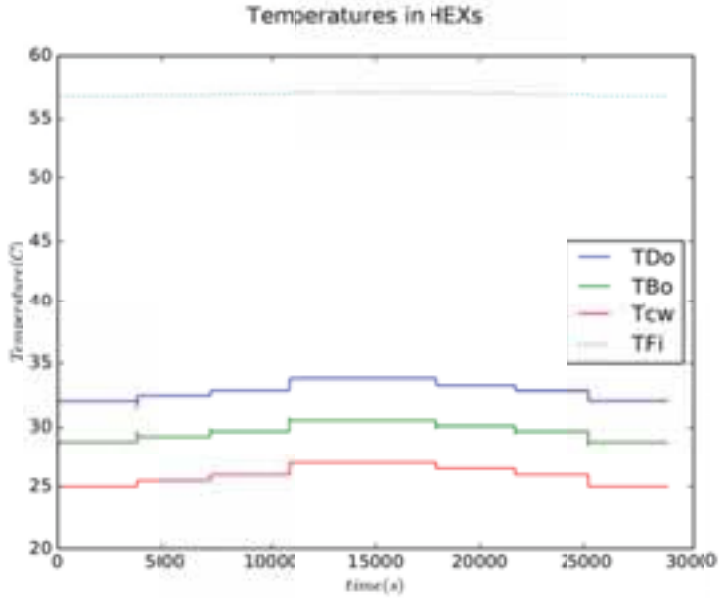

Fig. 14: Dynamic behaviour of the temperatures in the heat exchangers of the MVC desalination system

6. Conclusions

A model to simulate the dynamical behaviour of a MVC desalination unit has been implemented and the numerical results have been presented in this paper. The numerical model proposed is a powerful tool to evaluate the thermal and dynamical performance of the MVC desalination unit working under variable conditions. Three different cases have been simulated with the aim of describing the compressor and MVC desalination unit performance under different conditions of power or boundary conditions.

The mass flows used by the MVC desalination unit depend on the energy used by the compressor during the working period, whilst the temperatures, pressure and salt concentrations into the evaporator/condenser are independent of this value.

The salt concentrations of the flows into the evaporator/condenser depend on the boundary conditions applied at the inlet of the MVC desalination system. The third case shows the variation of the salt concentration of the brine in function of the salt concentration of the feed seawater (X_f).

The temperatures of the distilled water and brine flows at the outlet of the system and the preheated seawater temperature at the inlet of the evaporator/condenser are function of the mass flows used by the MVC desalination unit and depend on the feed seawater temperature (T_{CW}) at the inlet of the precondition heat exchangers.

Acknowledgement

The authors gratefully acknowledge the financial support provided by the Spanish Government “Ministerio de Economía y Competitividad, Secretaria de Estado de Investigación, Desarrollo e Innovación”, Research project F-00394; Ref RTC-2014-2056-5.

7. References

Bodalal, A., Abdul_Mounem, S.A., Salama, H.S., 2010, Dynamic modeling and simulation of MSF desalination plants, Jordan Journal of Mechanical and Industrial Engineering, Vol. 4, Number 3, 394-403.

Damle, R., Rigola, J., Pérez-Segarra, C.D., Castro, J., Oliva, A., 2011, Object oriented simulation of reciprocating compressors: Numerical verification and experimental comparison. International Journal of Refrigeration, 34, 1989-1998.

El-Khatib, K.M., Abd El-Hamid, A.S., Eissa, A.H., Khedr, M.A., 2004, Transient model, simulation and control of a single –effect mechanical vapour compression (SEMVC) desalination system, Desalination, 166, 157-165.

Ettouney, H., 2006. Design of single-effect mechanical vapor compression. Desalination. 190, 1-15.

Farnós, J., Castro, J., Morales, S., Garcia-Rivera, E., Oliva, A., Kizildag, D., 2014, Preliminary results of a 7kW single-effect small capacity pre-industrial LiBr-H2O air-cooled absorption machine, Conference Proceedings EuroSun 2014, Aix-les-Bains (France).

Mazini, M.T., Yazdizadeh, A., Ramezani, M.H., 2014, Dynamic modeling of multi-effect desalination with thermal vapor compressor plant, Desalination, 353, 98-108.

Plantikow, U., 1999, Wind-powered MVC seawater desalination – operational results, Desalination, 122, 291-299.

Suryanarayana, K.V., Sharma, K.V., Sarma, P.K., Dharma, V., Reddy, D.M., 2011, Experimental analysis of heat and mass transfer in a two stage jet cum packed bed deareator, Int. Journal of Material Research, Electronics and Electrical Systems, Vol. 4, Number 1-2, 91-106

Integrating Renewable Technologies into Buildings

Architectural Morphology and potential use of renewable energy at urban and building scale

Raul F Ajmat[1-2], Victoria Longhini[1-2], Santiago Lombana[1], Matías Kauffman[3], Jose Sandoval[1-4]

[1] Institute of Lighting, Environment and Vision, San Miguel de Tucuman (Argentina)

[2] Faculty of Architecture and Urban Planning, University of Tucuman, S.M. de Tucuman (Argentina)

[3] BECA Group, Auckland, (New Zealand)

[4]Department of Lighting, Light and Vision, Faculty of Engineering and Technology, University of Tucuman, San Miguel de Tucuman (Argentina)

Abstract

The environmental impact generated by the residential sector on energy consumption is estimated at approximately 40%. Architecture and urban planning practice is on the front line directly applying best-case evidence-based solutions to make the most of conserving and generating energy. The excessive and inevitable growth of cities derived in both high and low rise building in most of urban central areas to accomplish social and regular housing demands. Simultaneously, a sustained development of clean energy production technologies and computer simulation allows for an increasingly more accurate prediction of the potential that the architectural morphology possesses on the production of clean energies. High rise buildings bring together: possibilities of high density housing, daylighting access limitations in low floor apartments and issues related with the exploitation of solar irradiation for renewable energy purposes.

Today's powerful building simulation tools can be leveraged for energy modeling during early design phases and even to shape the morphology of tomorrow's cities. For further reductions in building energy consumption, energy simulations done during conceptual design have potential to impact long term energy use both in architecture and urban planning. This paper reviews early conceptual designs of buildings and their interaction with the immediate built environment looking at the consequences in terms of daylight availability and the potential of irradiation use for clean energy generation.

Keywords: Architectural morphology, Residential housing, Simulation, Daylighting, Renewable energy.

1. Introduction

Planning and Building Codes play a decisive role in regulating the development of urban environments. The regulations of urban planning and environmental management of urban land and other rights should guarantee citizens the right to natural light, as a basic human right. (Bautista, G., 2012).

Building simulation is a powerful tool which can be used at all steps of architectural design complementing and fostering innovations in the field of geometry (Gillchcrist, R., 2010) (Mascaró, J.J.; 2010).

Its predictive capabilities have been reflected in many areas of architectural design and energy assessment of buildings and urban environments. (Ajmat, R. 2008).

This paper seeks to explore the potential energy savings and energy production due to solar radiation under different proposed scenarios: buildings as isolated units and buildings within the urban environment.

That is why, knowing how and to what extent buildings' density of the city affects or diminishes the chances of capturing solar radiation, will allow better planning and generate new appropriate policies for better land use.

doi:10.18086/swc.2017.12.01 Available at http://proceedings.ises.org

2. Methodology

Two study cases of the city of San Miguel de Tucuman, in Northwest Argentina are presented. Particular attention is paid to its central area which does not escape the global trend of massive densification often to the detriment of its environmental quality.

For this study both the global environment and the local level of San Miguel de Tucuman were analyzed in the first stage from the legal and morphological point of view.

The starting point of this methodology is the generation of geometries using appropriate software (Autocad and SktechUp) optimized to work modeling morphological and volumetric scenarios; then processing the incidence of radiation on the surfaces (Ecotect or Revit) and finally the post-processing of results with the aid of spreadsheets and graphic interface (Excel) for the presentation of data.

As mentioned previously two different approaches were taken into consideration:

Case A: Building as a unit complying with social housing requirements

Case B: Buildings as part of the urban grid complying with a particular Code of Urban planning

2.1 Case A:

Building as a unit complying with social housing requirements:

The analysis of case A was based in social housing of two different locations. One located in Tucuman (NW Argentina) -Figure1-the other in Berlin (Germany) -Figure 2-:

Case Study A1.: Tucumán (Argentina)

Figure 1 Left: aerial view of the neighborhood- Right: Picture of one block

The case study selected is the COPIAAT II a neighborhood in the south of the city of San Miguel de Tucumán, Argentina, which was built in 1996 by the Provincial Institute of Housing and Urban Development.

It has 14 blocks of 9 flats each. Each block has 3 levels (lower plan plus 2 storeys) with 3 flats per level.

The average energy demand (ED) for each of the blocks was calculated based on the consumption of each appliance with its approximate power (W) and hours of use (h) per day. The annual ED of each flat is 2991.7 kWh / yr. It is observed that the highest energy consumption corresponds to the air conditioning equipment with a demand of 600 kWh/yr. This implies 49,85 kWh/m2 per year of energy consumption. This is a consideration of a mean value for the same type of units; however, it depends on the level of exposure of its surfaces to the environment and to the different U-values one can consider (or a mean U-value). Notwithstanding, the aim of this study is focused in generating a methodology that cooperates in the first stages of architectural design in the analysis of the link between morphology and clean energy generation potential

Values of annual ED:

Energy demand per flat 2991.7 kWh/yr.

Energy demand in communal spaces 522 kWh/yr

Total energy demand per block 27447 kWh/yr

Case Study A.2: Housing Block Altoner Strasse 4-14 - Berlin, Germany

Architect: Oscar Niemeyer

Location: Hansa Viertel, Berlin, Germany

Figure 2 Left: aerial view of the neighborhood- Right: Picture of the block

"In response to Stalin Allee, a street-neighborhood built in East Berlin with a strong ideological load, Hansa Viertel, a neighborhood designed through an international competition, emerged in West Berlin. It is proposed first of all to give an answer to the question of homelessness in Berlin. The answer must be in the area of housing design, but also in the area of construction and use of new materials.

The organization of the competition invites many German and foreign architects to carry out the projects, with the aim of making an international exhibition of architecture, in the style of the Weissenhof. With this approach and the specific problem of housing, Hansa Viertel is a laboratory in which the proposals experience all types: towers, blocks and detached houses with and without patio. The general arrangement is characterized by the rigid orientation of the buildings, both North-South and East-West, in order to obtain good lighting in all rooms. The proposals of linear blocks are of great interest, highlighting the projects of Frizt Jaenecke and Sten Samuelson, Oscar Niemeyer, Egon Eiermann, Pierre Vago and Walter Gropius. (Moya Gonzalez et al, 2015)

For this case, the energy demand was taken from the one stipulated by the Ministry of Environment of Germany

Values of annual ED: (For social housing dwellings considering water heating with electricity)

Flats for 2 inhabitants with heating 2800 kWh / yr per flat. That means 46,66 kWh/m2 and per year

Flats for 3 inhabitants with heating 3900 kWh / yr per flat. That means 43,33 kWh/m2 and per year

Flats for 4 inhabitants with heating 4400 kWh / yr per flat. That means 40,00 kWh/m2 and per year

Energy Estimations

Flats Type B (2) x 12 = 12 flats x 2800 kWh / yr = 33600 kWh / yr

Flats Type C (3) x 54 = 54 flats x 3900 kWh / yr = 210600 kWh / yr

Flats Type D (4) x 12 = 12 flats x 4400 kWh / yr = 52800 kWh / yr

Total energy demand = 297000 kWh / yr

Methodology for Case A

The study of morphological alternatives linked to energy possibilities is the basis for an environmentally responsible and energy efficient architecture. The shape of a building should not be indifferent to the potential for energy production from renewable sources. Recent computer tools allow new ways of conceiving a building from a morphological perspective. In this study the first step consisted in a geometric analysis in order to build the base case geometry in a friendly interface which can interact with different software (Sketch up). Later the Rhinoceros 3D Software together with the Grasshopper Plug-In make it possible to import the building model and work its morphology parametrically, that is to say, using generative algorithms. The main interface for algorithm design in Grasshopper is the node-based editor. The information goes from component to component by means of cables that connect outputs with inputs.

Starting from the traditional block studied, formal alternatives are proposed, maintaining the number of units and surfaces of each one. A systematization of the simulation process has been studied in order to automate the modeling and the process to obtain output data. This methodology can be applied to various case studies of any city. Once representative geometries of each scenario are generated, the potential of solar radiation on top of the roof of buildings is determined using a graph computer model that works on the basis of hourly weather data. The plug-in Insight was used in this case. This methodology allows us to try different geometries for the block during the very first steps of design, analyzing the potential of solar radiation and, consequently, the potential for the production of clean energy. The whole process is described in Figure 3

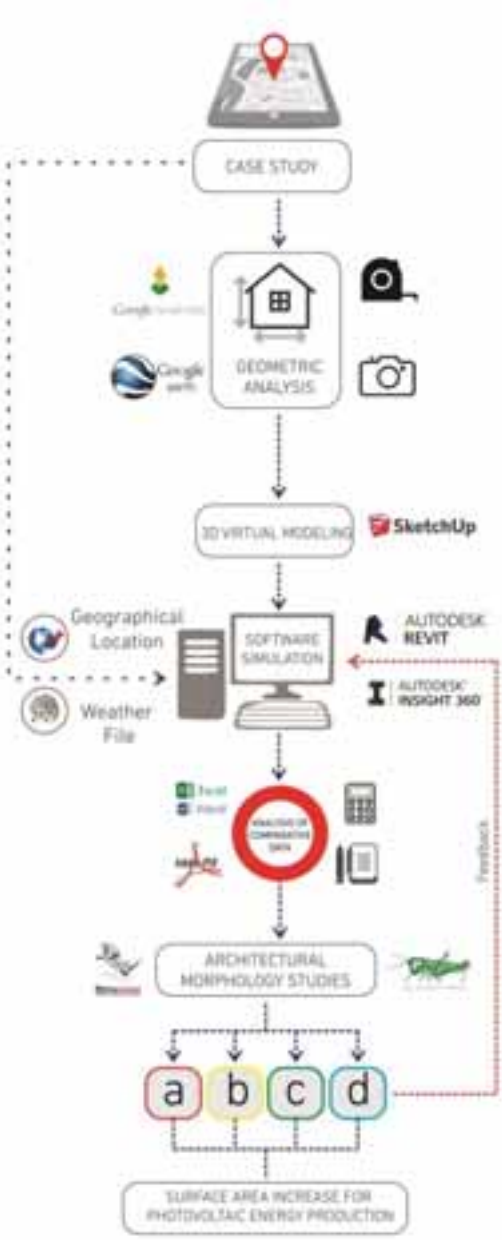

Figure 3 Scheme of the simulation process for case A

Results for Case A

The results of the simulations show the incidence of radiation in different surfaces Figures 4 and 5. However, since the horizontal surfaces are most suitable for the placement of photovoltaic panels, they have been taken as reference in order to make a comparison of the solar-based energy production potential. The alternatives analyzed show the increase of production surfaces that could be obtained from different morphological operations. In that sense, it has been taken as an indicator of the percentage of coverage of the energy demand of the housing complexes under study. Comparatively it can be observed that in the case of Berlin can go over 300% which makes it possible to cover energy demand reaching almost 100%. In the case of Tucumán with smaller scale housing blocks carrying out the same morphological operations only increase up to 65% of the surface. However, due to the potential of irradiation of the climate of Tucumán the possibilities of coverage of the demand are significantly greater reaching 150% coverage of it. In fact the base case has the possibility to cover the excess demand.

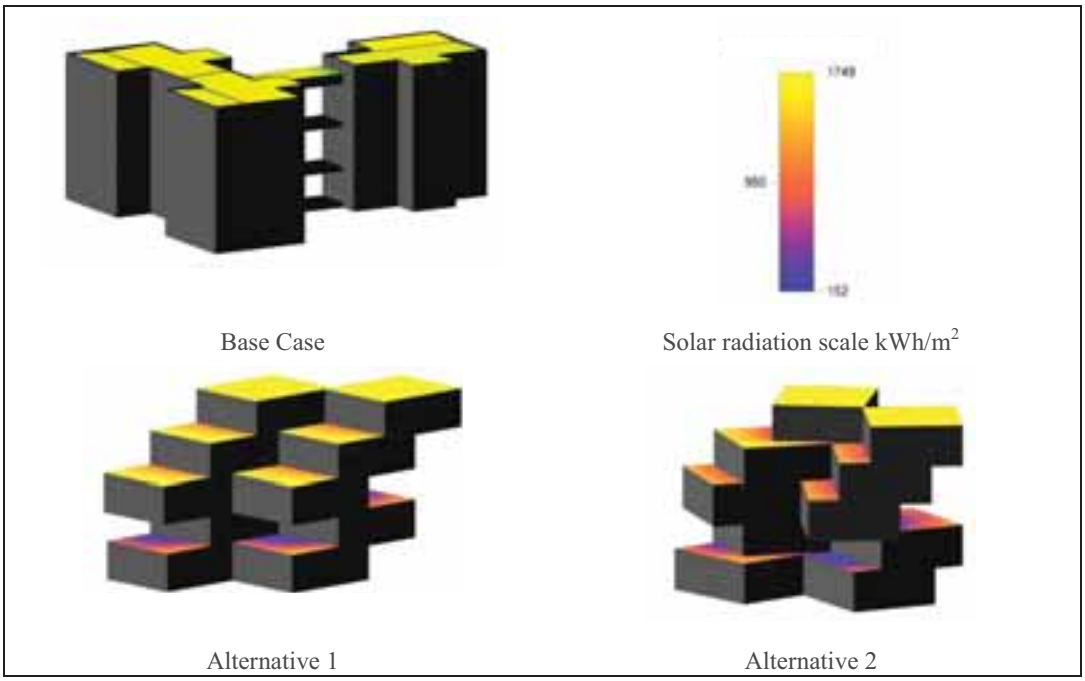

Figure 4: Results of radiation due to morphology exercises for Tucuman-Argentina

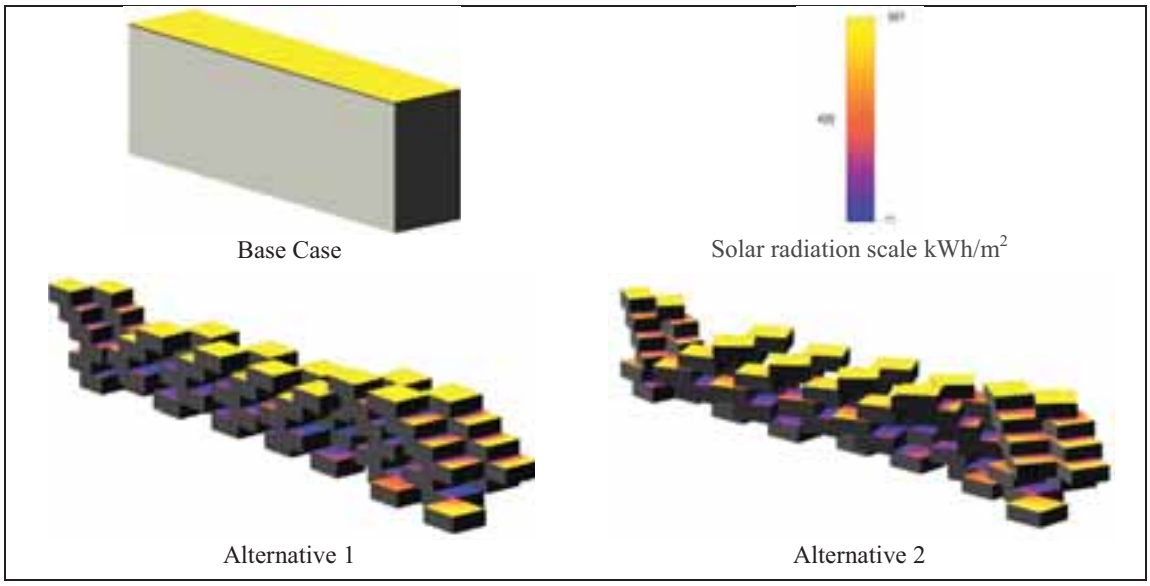

Figure 5: Results of radiation due to morphology exercises for Berlin-Germany

	CASE	SURFACE	CUMULATIVE RADIATION	ENERGY DEMAND	ENERGY PRODUCTION	PERCENTAGE OF ENERGY DEMAND FULFILLED
BERLIN		1080 M2	1.066.432 Kwh	295.900 Kwh	149.234 Kwh	50,50%
		3542.7 M2	1.902.773 Kwh	295.900 Kwh	266.362 Kwh	90,16%
		3782.3 M2	2.084.340 Kwh	295.900 Kwh	291.666 Kwh	98,64%
TUCUMAN		179.4 M2	310.309 Kwh	27.447 Kwh	43.328 Kwh	158%
		295.9 M2	353.764 Kwh	27.447 Kwh	49.520 Kwh	181%
		240.5 M2	288.544 Kwh	27.447 Kwh	40.488 Kwh	148%

Figure 6: Summary of annualized radiation due to morphology exercises for both locations.

2.2 Case B:

Buildings as part of the urban grid complying with a particular Code of Urban planning

This exercise aims to explore the potential of energy savings and the production of energy from solar radiation with the application of the current Code of Urban Planning of Tucumán under different scenarios proposed. Solar energy plays an important role in replacing fossil fuels to generate electricity without emitting pollutants and without the need for fuel. (Li, 2014).

For this study the current environmental legislation was analyzed in the first stage in order to know how and to what extent the density of construction of the city affects or diminishes the possibilities of capturing the solar radiation, as well as the generation of new appropriate policies for a better use of the land. For example, we consider the morphology of a solar facade as a building component that is feasible to generate energy and allows the entry of daylight into the interior spaces, a key aspect of the design of such facades is the determination of total energy benefits. (Li & Lam, 2008).

This work has a previous data base generated and processed to be able to obtain the different scenarios proposed (Ajmat et al, 2011). The sector to work is selected, the morphological proposals are generated and the simulation of surface radiation is carried out. The starting point of this methodology is the generation of appropriate software geometries; then processing the incidence of radiation on surfaces and finally post-processing the results with the help of spreadsheets and graphical interface for data presentation. (Hui,2001) (Mesa et al,2010)

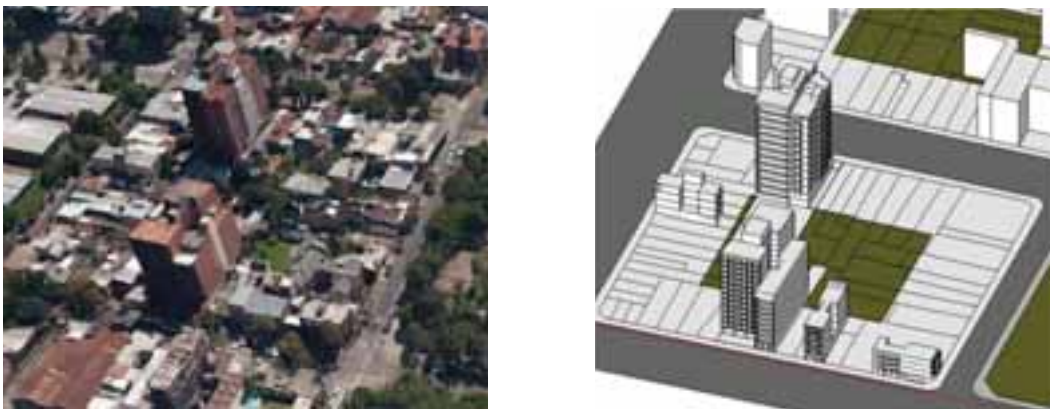

Figure 7: Left: Aerial view of urban sector for simulations - Right: Sketch up model to be exported for calculations.

Methodology for Case B

The proposed Simulation Process (Figure 7) is based on a sequence of data that can be modified at different points, leading to the obtention of data from different scenarios or typologies simultaneously. It analyzes in a first step the basic information of the grid of the city, this information is checked against what the Urban Planning Code proposes for each sector of the city and through a processing of it with different software. It can provide a number of scenarios necessary to carry out studies of the morphology of the city or a selected city sector. Once the necessary information is obtained for each scenario, it is modeled in both 2D and 3D (at this point there is a Loop regarding modifications that can be made on the information data base of the model that result in automatic changes on the 3D morphology of it). Finally the analysis with the calculation of solar radiation and shadows of the 3D model is performed using the appropriate climate file and its geographic location. Once the results are obtained we can review the initial model and make modifications to obtain different morphological alternatives for the same scenario and thus compare different performances.

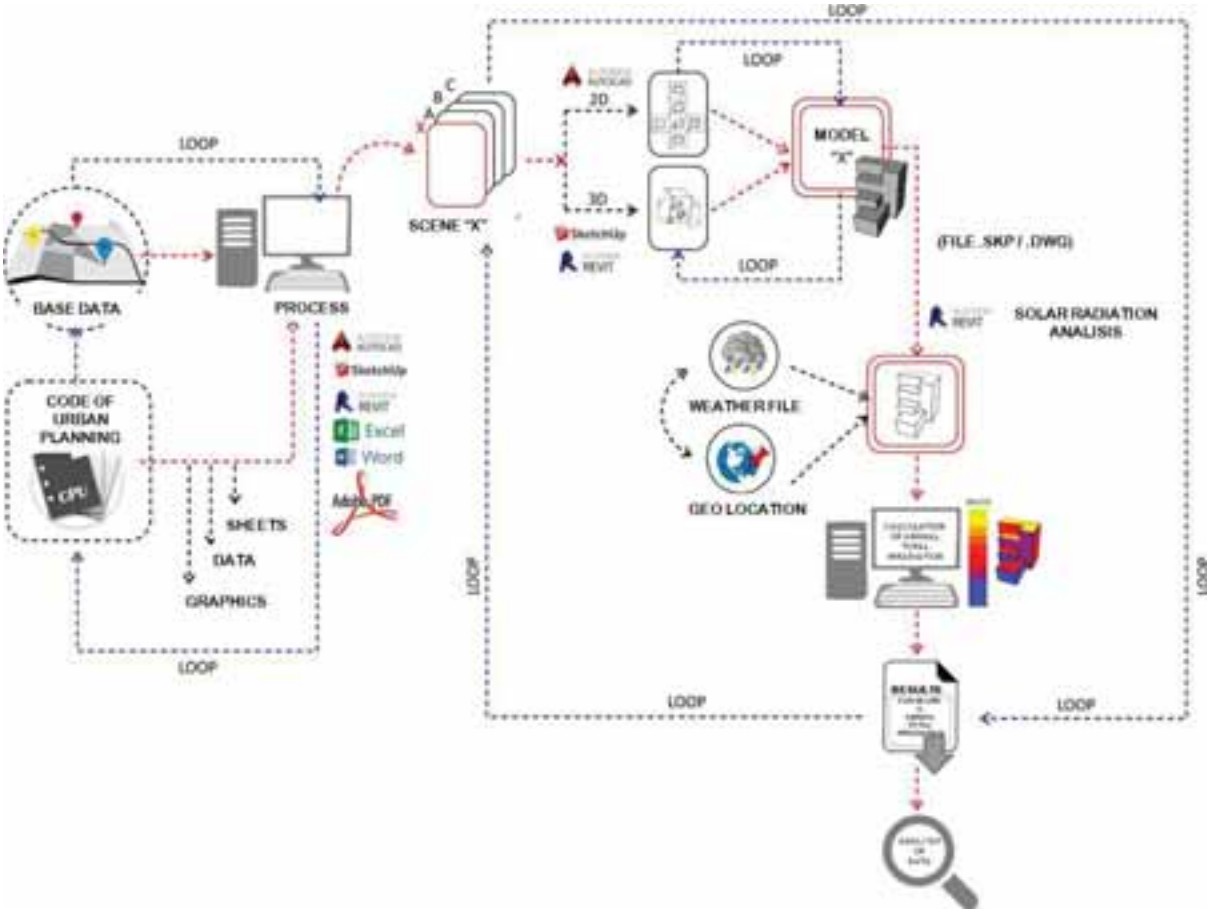

Figure 8 Scheme of the simulation process for case B

Two scenarios were simulated in order to analyze the potential and limitations of the urban densification process: Maximum built surface until the lateral limits and therefore a certain height can be reached. This was identified as: Scene 1. Minimum built surface with maximum height. This was identified as: Scene 2.

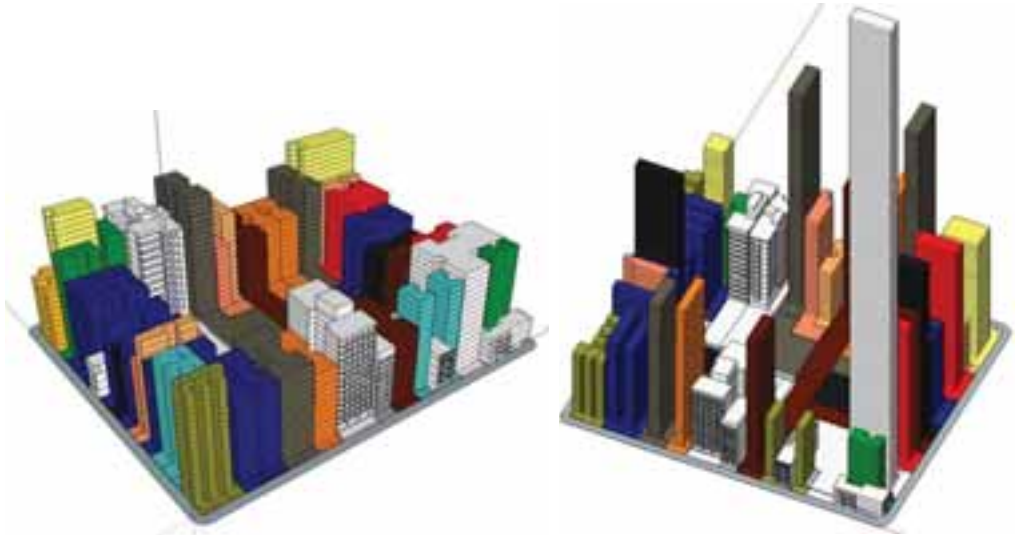

Figure 8 Left: Scene 1 Maximum area constructed minimum height-Right: Minimum area constructed maximum height

Results for Case B

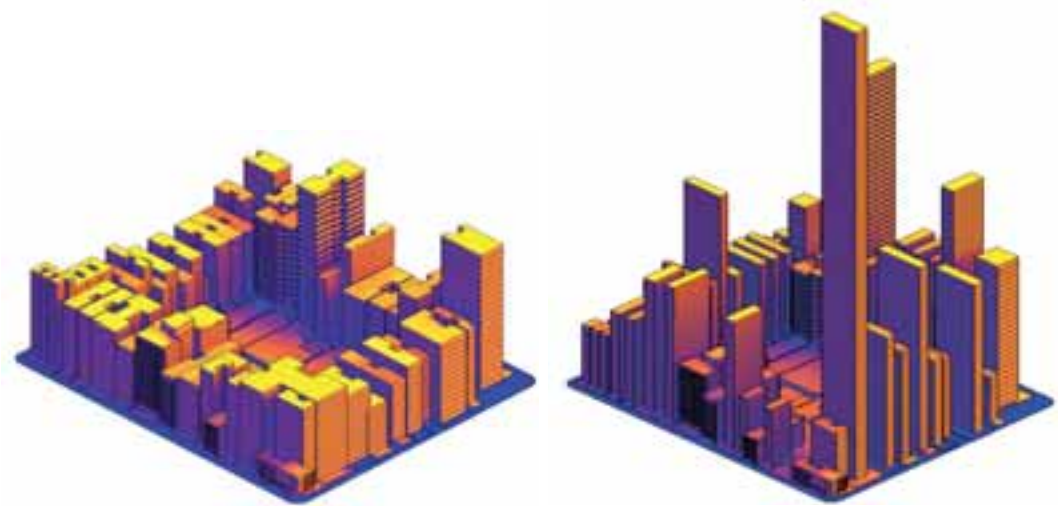

Figure 9 Left: Results of Solar Radiation for Scene 1 Right: Results of Solar Radiation for Scene 2

Based on this modeling, geographic and climate data are loaded. Then it proceed to the calculation of irradiation. As for the area in square meters considered for both cases we observe that Scene 2 is a 14% greater in surface than Scene1. This consideration is made since a greater surface can accumulate a higher radiation amount, however the obstructions due to the morphology of the buildings must be considered too. When analyzing the results Scene 2 exceeds Scene 1 by 6%with respect to amount of accumulated solar radiation per square meters. We can say from these comparisons that for the cases studied Scene 2 exceeds Scene 1 by 19% with respect to its total annual irradiation capacity from the point of view of morphology (Table 1).

Table1: Results comparison between scenarios

	Scene 1: Minimum Height	**Scene 2: Maximum Height**	**Differences %**
Total study surface area [m^2]	506116.57	587776.40	13.89
Study average insolation value [kWh/ m^2]	224.34	238.53	5.95
Total study insolation value [kWh/yr]	113541961.94	140201310.76	19.02

3. Discussion

Case A

The influence of the morphological dispositions can be observed in the first place in the possibilities of extension of the surfaces exposed to the radiation. It is also observed that the type of morphological arrangement, even if it enlarges the surface, can generate shadows thrown between parts of the same building when moving from a compact to a more disaggregated shape. In any case there are direct consequences on the potential of solar energy exploitation. Terrestrial coordinates and the local climate characteristics also influence the availability of the solar resource. It is for this reason that the role of the designer of architectural form must be appropriately combined with local site and local climate considerations. Since we have limited ourselves here to the analysis of the horizontal surface, the behavior of the other surfaces of the architectural form are still to be experimented in order to develop the shape of future buildings..

Case B

It is evident that both the shape and height of each building and the ordering between plots influence the capacity of a city to make the most of solar energy. Urban building codes fulfill a very specific role; the future possiblities of production of clean energy will comply with it and consequently the reduction of carbon dioxide emissions (De Schiller, 2002). In Case B two extreme scenarios of application of the building code of San Miguel de Tucumán were studied. The study of the minimum height scenario is perhaps the most feasible due to the technological possibilities, since the case of maximum height does not seem to be possible execution in all the plots. However, using the minimum and maximum values allowed by the Urban Planning Code of San Miguel de Tucumán, make it possible to question this code, since when generating the scenarios, the morphology of the resulting set of buildings does not seem to come from a basis of criteria, norms and guidelines to be taken into account to improve habitability and solar conditions, but, to restrict densification, raising the problem of land use from the real estate point of view. Thus, the possibilities offered by the technology and the characteristics of the ground where these buildings are located, and not the regulations provided by codes and ordinances, which actually limit urban growth, which give rise to the urban morphology resulting from the city. But the methodology which has been produced would allow simulating an unlimited number of combinations and probabilities with a costless time investment. This would allow us to experiment with new regulations within the code or to test the possibilities of collecting solar energy from a new building to be built in a given context.

4. Conclusions

A methodology of evaluation of the architectural and urban morphology in relation to the potential use of renewable energy has been presented. It is valuable at the scale of building and city in order to assess the influence that the form has on the availability of surface for the capture of solar energy. In both cases - building and city - morphological operations allow designers to increase the possibility of a greater and better use of solar energy whether this is by surface increase or by the study of the shadows that buildings throw each other (Kamal & Smiriti, 2014). From the results obtained we can verify the importance of urban morphology and therefore the influence of city planning codes in terms of the availability of natural light and the potential use of irradiation for energy generation.

This approach arises from the search for strategic solutions, given the need to create conditions of habitability in areas of high density population as well as in the interior and exterior of buildings; which today seems to lack effective solutions. Therefore, a simplified process that facilitates consideration of the morphology and size of future constructions is a valuable goal sought by designers. The possibilities offered by simulation as a prediction tool are significant; energy simulations carried out during the initial stages of design have the potential to impact on long-term energy consumption. On the other hand, we are challenged as architects of the cities of the coming century challenging formal innovation and creativity in relation to the interaction between buildings.

A systematic simulation process to analyze the consequences of densification, an output of the current building trends, applying a methodology to investigate the real effects of the implementation of the urban planning codes enable.

- The analysis of the production potential of clean energy.

- Pre visualization and study of the habitability of particular situations (courtyards within high-rise buildings).

- To propose new legislation that addresses problems of habitability and sustainability.

-To challenge the established morphological paradigms of low and high rise buildings.

5. References

Ajmat, R; 2008 “Precision daylight and thermal modeling of shading devices” PhD Thesis. Institute of Energy and Sustainable Development, De Montfort University, United Kingdom.

Ajmat, R. et al; 2011. “El Edificio en Altura: su acondicionamiento ambiental”, Facultad de Arquitectura y Urbanismo de la Universidad Nacional de Tucumán, Cátedra de Acondicionamiento Ambiental II. Tucumán, Argentina.

Bautista, G 2012 Los derechos ciudadanos, Editorial El Ateneo, Buenos Aires, Argentina

De Schiller, S.; 2002. "Transformación urbana y sustentabilidad"; publicación Revista Urbana; 2002.

Gillchcrist, R. 2010 Sustainable Strategies for High rise Buildings , Skidmore, Owings & Merril , Worls Conference Sustainable Cities in the vertical age, India, 2010

Hui, S.;2001. Hui, Sam CM.Renewable Energy 24. “Low energy building design in high density urban cities”.Department of Architecture, The University of Hong Kong, Pokfulam Road, Hong Kong, China.

Kamal, M.; Smiriti, S 2014 Emerging trends in tall buildings design. Environmental Sustainability through Renewable Energies Technology; Civil Engineering & Architecture Vol 2, N°3, pg 116-120.

Li, D; Chong, B.; Chan, W.;Lam, J. 2014 “An analysis of potential applications of wide-scale solar energy in Hong Kong” General Research Fund from the Grant Council of the Hong Kong Special Administrative Region, China.

Li, D; Lam, J. 2008 “An analysis of building energy performances and benefits using solar façades” Building Energy Research Group, Department of Building and Construction, City University of Hong Kong, Hong Kong SAR, People’s Republic of China

Mascaró, J.J.; 2010. Mascaró, J.J.; Pelisser N.; Vieira M. “El diseño de la ciudad y la iluminación natural”. Jornadas Argentinas de Iluminación Luz.

Mesa, N.; 2010.Mesa, Néstor A.; Arboit, Mariela; Herrera, Ma. Marta; De Rosa, Carlos.“La eficiencia energética de la alta densidad edilicia en ciudades de trama ortogonal”–IV Conferencia Latinoamericana de Energía Solar, Cusco, Perú.

Moya González, L y otros (2015) “La Vivienda Social en Europa, Alemania, Francia y Países Bajos desde 1945” Escuela Técnica Superior de Arquitectura, Avenida Juan de Herrera, 4. 28040 Madrid, Ed Mairea Libros, ISBN 10: 978-84-936485-3-4

6. Acknowledgements

The authors would like to thank: the National Agency for the promotion of science and technology, the National Research Council and the University of Tucuman, Argentina for their continuous encouragement and financial support given for this research work.

Mobile HIL Test Bench for Low Cost Radiative Heating and Cooling Collectors

Irina Mitina, Reiner Braun[1], Antoine Dalibard, Tobias Erhart, Ilyes Ben-Hassine and Ursula Eicker
Centre for Sustainable Energy Technology Research,
University of Applied Sciences Stuttgart – HFT Stuttgart,
Schellingstr.24, 70174 Stuttgart, Germany, reiner.braun@hft-stuttgart.de

Abstract

This paper presents a mobile hardware-in-the-loop (HIL) test bench that has been developed to simulate a solar assisted cooling and heating system for residential buildings in hot climates. The main component of the system is a low cost uncovered solar collector that is used for the production of night radiative cooling or daytime heating energy (hardware component). The collector was designed for low cost housing projects in Egypt, whose cooling and heating demand was modeled using the program TRNSYS (software component). The design and construction of a mobile HIL test bench is presented together with some performance results from the HIL-tests in cooling mode.

Keywords: HIL test bench, space heating and cooling, solar absorber, radiative cooling

1. Introduction

Low cost renewable heating and cooling systems are of prime importance for developing nations with high population densities and limited financial resources. As an example, Egypt is one of the fastest growing countries worldwide, the population increased from 21 million in 1950 to 98 million in 2017 and is currently ranked on place 14 by total population size worldwide. For the year 2050 a total population for Egypt of 153 million it is expected (UN, 2017). Due to this fast population increase, the state of Egypt is facing many social and economic problems. Providing decent and affordable housing for the lower and middle class and the adaptation of the energy system will be two of these challenges for the future.

During the past few years, Egypt has been suffering from recurrent electricity cut-offs, mainly in summer because of the large cooling demand (Elharidy et al., 2013). The national demand has been exceeding the available produced power from generation plants since 2011.

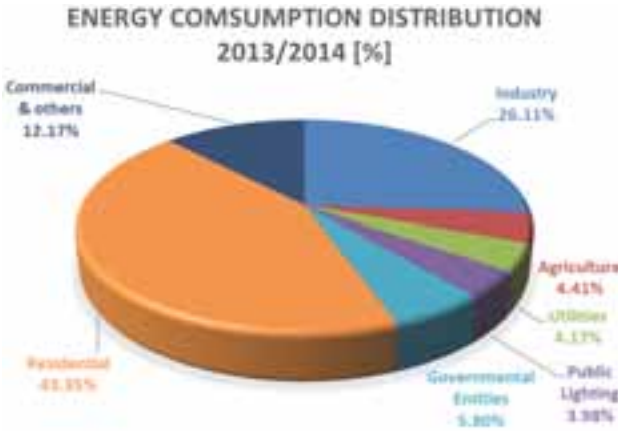

Fig. 1: Electricity-shares sold in Egypt (on all voltage levels) according to the purpose of usage 2013/2014 (Egyptian Electricity Holding, 2014)

Fig. 1 shows the electrical energy consumption distribution among the different sectors in Egypt. The greatest share of the total nationally generated electricity is consumed in residential buildings (43.4%). When considering only the medium and low voltage levels, the residential consumption reaches 51.3% of the total energy sold from the national electricity distribution companies (Egyptian Electricity Holding, 2014).

[1] Corresponding author

doi:10.18086/swc.2017.12.02 Available at http://proceedings.ises.org

Urbanized dense cities lead to higher local ambient temperatures. As a result of this, the use of air-conditioning (AC) units for cooling has immensely increased in Egypt. Conventional AC units represent the major energy consumption of the residential energy demand (Xing Lu et al., 2016, Attia et al., 2012). On the other hand, in winter electric water heating accounts for large shares of electricity demand, even in warm-climate countries. Nowadays, cooling in residential buildings in Egypt is provided by not very efficient split units, which number grows very rapidly (Attia et al. 2012). This leads to frequent electricity cut-offs in summer (Elharidy et al., 2013). Integration of renewable energies to the space cooling and heating in residential buildings could be an environment-friendly and sustainable solution.

Within the research project NightCool, funded by the German Federal Ministry of Education and Research (BMBF), a concept for a low-cost system for heating and cooling applications was developed and simulated in detail.

The developed system consists of uncovered solar collectors for the energy production and an activated ceiling for the energy distribution. Fig. 2 shows the principles of the energy supply system for direct cooling (left) and direct heating (right). The space cooling is achieved at night by circulating the heat transfer fluid in the collectors (radiative cooling) while the space heating is provided during the day by converting the solar energy into useful heat. Since these collectors are not expensive, such a heating and cooling system results to be low-cost. The advantages of such a simple system lie in simple installation and low energy costs (Eicker and Dalibard, 2011), which is very important for solar thermal systems in order to achieve a higher market penetration (IEA SHC Task 54).

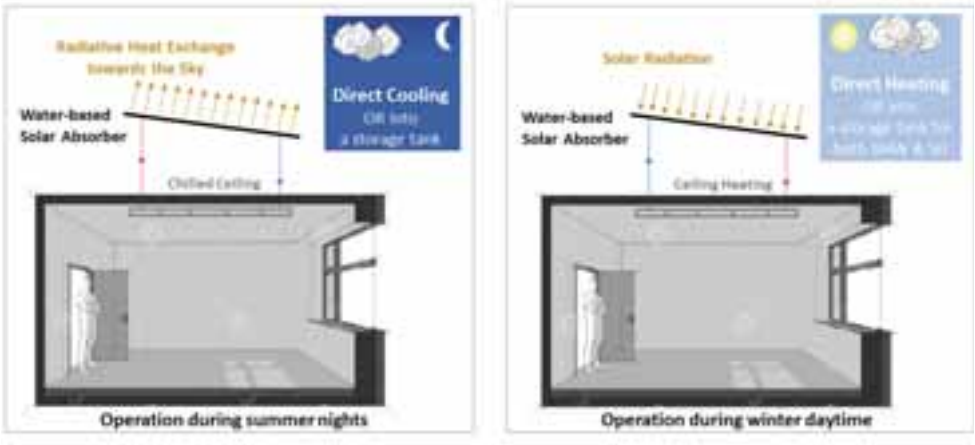

Fig. 2: Energy supply system that provides space cooling in summer (left) and space heating in winter (right)

In order to investigate the potential and limits of such a system, a mobile HIL test bench has been designed and constructed. The present paper aims to show the advantages of using such a HIL environment show its limitations and give some insights for further improvements.

2. Motivation to build a mobile HIL test bench

2.1. Motivation to build a mobile HIL test bench

As before mentioned, the project NightCool aimed to develop a low-cost system for heating and cooling applications for Egyptian climate conditions. The estimation of the achievable return temperatures as well as the cooling power by using solar collectors for radiative cooling applications needs adequate physical collector models.

ISO 9806:2017 specifies test methods for the thermal performance characterization of fluid heating collectors for steady-state and quasi-dynamic conditions (ISO 9806, 2017). Based on this test method parameters for the parameterization of collector models within the simulation environment TRNSYS such as Type 203 (PVT collectors) (Bertram et al., 2011) or Type 1289 (flat plat collectors) can be determined. The deviation between measured collector power output on a test stand and simulated power can vary between night and daytime (Cremers et al., 2015). Especially for night time radiative cooling, the collector parameters determined according to ISO 9806:2017 are not sufficient enough to develop control strategies only by using a simulation model.

The motivation to build the HIL test bench in the NightCool project can be summarized as follows:

- The thermal performance of solar collector at night cannot be modelled accurately with existing available models so that their performance needs to be measured and not simulated.
- Test new market available solar thermal collectors (which thermal performance is not specified by the producer)
- Test the integration of such collector into different systems and for different buildings construction (light or heavy) and achieve a realistic estimation of the dynamics of the system, scalable and adaptable to different kind of loads etc.
- Dimension the system components and optimize the control before it can be installed on a bigger scale

Following table summarizes the main functionalities of the mobile HIL test bench and the benefit by setting up a small scale test environment.

Tab. 1: Main functionalities of the mobile HIL test bench and the need and benefit

Functionality	Need and benefit
Conduct collector performance tests under real conditions and conduct tests of solar collectors at night time	Various solar collectors of different constructions from different producers (basically swimming pool absorbers are recommended) can be tested and a collector with a highest thermal potential and best integration suitability (easily connected hydraulic connections, appropriate mechanical properties, etc.) can be defined For the cooling application, it is essential to know also the cooling potential of different solar collectors. This information is missing in technical data sheets, it can be obtained experimentally.
Analysis of the dynamic behaviour of system components	It is important to understand the behaviour of the solar collector and the building to define optimal control algorithms.
Development and test of control algorithms for heating and cooling systems depending on the defined system	The control algorithm of a system can be easily implemented in a simulation environment such as TRNSYS either for cooling or heating application. An optimal set of parameters such as the set point temperatures to turn on or of the system.
Optimize building construction elements so that they are appropriate for the suggested cooling/heating system	By changing building parameters in the building model on the simulation environment an optimal distribution system can be defined (activated heating and cooling ceiling, floor heating or others)
Estimation of achievable thermal comfort e.g. temperature and relative humidity and analysis of the activation capability of building mass to act as energy storage through different distribution systems e.g. activated ceilings	Direct feedback from the simulation model helps analyse comfort parameters and gives insight into the architectural concept of active and passive measures (active and passive building design).

3. Mobile HiL test bench

3.1. Working principle and construction

The mobile HIL test bench has been designed and constructed within a research project aiming to develop a low-cost space heating and cooling system for Egyptian climate conditions. The working principle of the HIL test bench (Figure 3) is based on hardware-in-the-loop (HIL) simulation, a technique that is used in the development and test of real-time embedded systems. The mobile HIL-Box consists of an uncovered solar collector (hardware component) and a building simulation model (software component). It enables to conduct real-time measurements and simulations to calculate at each time step the dynamic change of the system parameters such as room temperature and ceiling temperature, as well as the cooling or heating power. The solar collector is replaceable, so that different solar collectors can be tested. The building and the distribution system are defined in the simulation environment TRNSYS (www.trnsys.com). Thus, an optimal solar system combination, solar collector (collector-type, -size, etc.) and

building properties (construction, size, materials, etc.) can be chosen. In other words, the HIL test bench enables to optimize the building and the system at the early planning stage.

The main weather data (ambient temperature T_a, relative humidity RH, horizontal global irradiance G_{hor}, net long-wave radiation G_L and wind velocity w) and system parameters (inlet and outlet temperature T_{in} and T_{out}, flow rate $\dot{m}$) are measured and acquired by several ethernet input modules connected with the software LabVIEW. The measured data are given as inputs to the TRNSYS building model which calculates the building behavior and the system response, such as room temperature T_{room} and the outlet temperature of the cooling ceiling T_{cc}. In the hydraulic system the simulated T_{cc} is the same as the inlet collector temperature T_{in}. It is read in LabVIEW and transmitted as set-point temperature via an analog output module to the temperature control unit (TCU). The TCU regulates then the fluid inlet temperature of the solar collector, i.e it sets the inlet temperature equal to the T_{cc} Based on the temperature difference ($T_{in} - T_{out}$) and the fluid flow rate the cooling or heating power of the solar collector can be calculated.

$$Q = \dot{m} c_p (T_{out} - T_{in}) \qquad \text{(eq. 1)}$$

where c_p is the fluid heat capacity.

In the next step, the collector response and the weather data are measured and the procedure is repeated (see Figure 3).

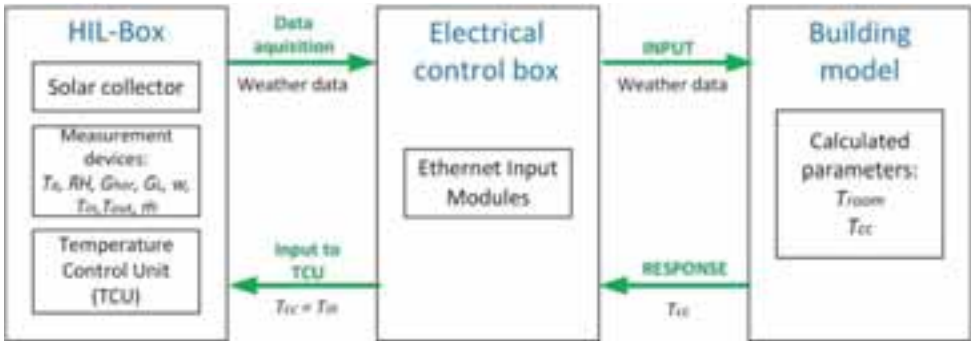

Fig. 3: Working principle of the HIL test bench

The measuring box is shown in Figure 4 and its main components are listed in Table 2.

Tab. 2: List of the main components of the HIL test bench

Number	Component	Manufacturer
1	Solar collector, length 1,8 m	AQSOL
2	Temperature control unit Variocool VC 2000	Lauda
3	Pyrgeometer LP PIRG 01	Delta Ohm
4	Pyranometer LP PYRA 02	Delta Ohm
5	Anemometer "Windgeber – compact" 4.3519.00.161	Thies Clima
6	Temperature and relative humidity sensor HD9008TRR	Delta Ohm
7	Air vent valve	Solar
8	Temperature sensor	Omega
9	Ball valve	-
10	Valve Motor	Oventrop
11	3-way diverter valve Tri-M TR	Oventrop
12	Magnetic inductive flow sensor induQ	SIKA
13	Flexible pipes	-
14	Copper tubes	-
15	Roller Shutter	Turtle24
16	Electric control box	Consists of many components

Fig. 4: HIL test bench: a) general view closed, b) general view open, c) and d) weather station, e) hydraulic system, f) electric control box

The simplified hydraulic scheme of the HIL test bench is shown in Figure 5. The solar absorber is connected to the temperature control unit Lauda and the thermal fluid, forced by the pump, circulates through the absorber. The flow rate is regulated by a valve with motor. The valve can be partly closed to reduce the flow rate. When the valve is closed completely, there is no flow through the absorber.

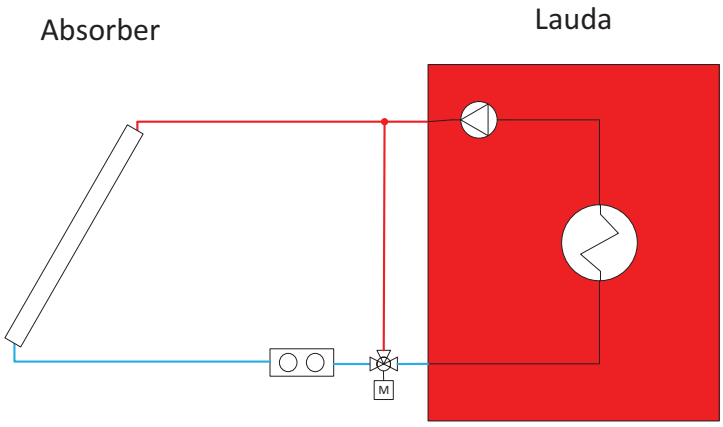

Fig. 5: Simplified hydraulic scheme of the HIL test bench (Lauda is the temperature control unit)

3.2. Data communication

The coupling between LabVIEW and TRNSYS requires a data communication between two softwares, which is achieved by the means of ASCII files (text files read and written by both programmes). The different steps of this communication has been programmed in LabVIEW and are shown in Figure 6.

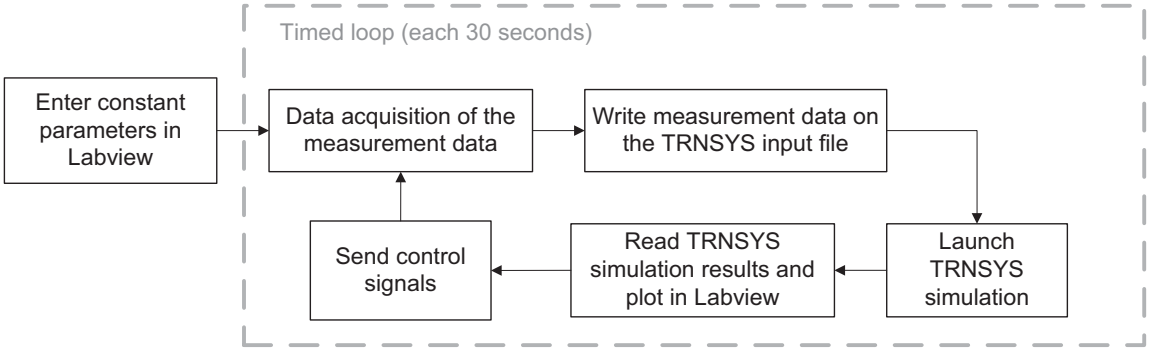

Fig. 6: Data communication steps between Labview and TRNSYS for the HiL configuration

In the first step, the parameters which remain constant during the whole HIL test have to be entered by the user in the LabVIEW graphical interface in order to define the system size as well as the main control parameters. In addition the path locations of the necessary different files have to be defined.

In the second step, the measurement data are acquired in LabVIEW via the I/O modules and written in a ASCII file to be read in TRNSYS. The data required by TRNSYS are listed in Table 3.

Tab. 3: Data transferred from LabVIEW to TRNSYS

Variable	Name	Unit
Ambient air temperature	Tamb	°C
Ambient air relative humidity	RH	%
Horizontal solar irradiance	Gh	W/m²
Effective sky temperature	Tsky	°C
Collector outlet fluid temperature	TcolOut	°C
Collector mass flow rate	mdotCol	kg/h
Collector aperture area	Acol	m²
Specific heat of the collector fluid	cp	kJ/kgK
Density of the collector fluid	rho	kg/m³
Pipe diameter	dpipe	m
Pipe length	Lpipe	m
Building orientation	TURN	°

Then the TRNSYS program is run and the LabVIEW program stops until the simulation is finished. At the end of the simulation, the main results are written by TRNSYS in a text file, read by LabVIEW and shown for visualization (see Figure 7).

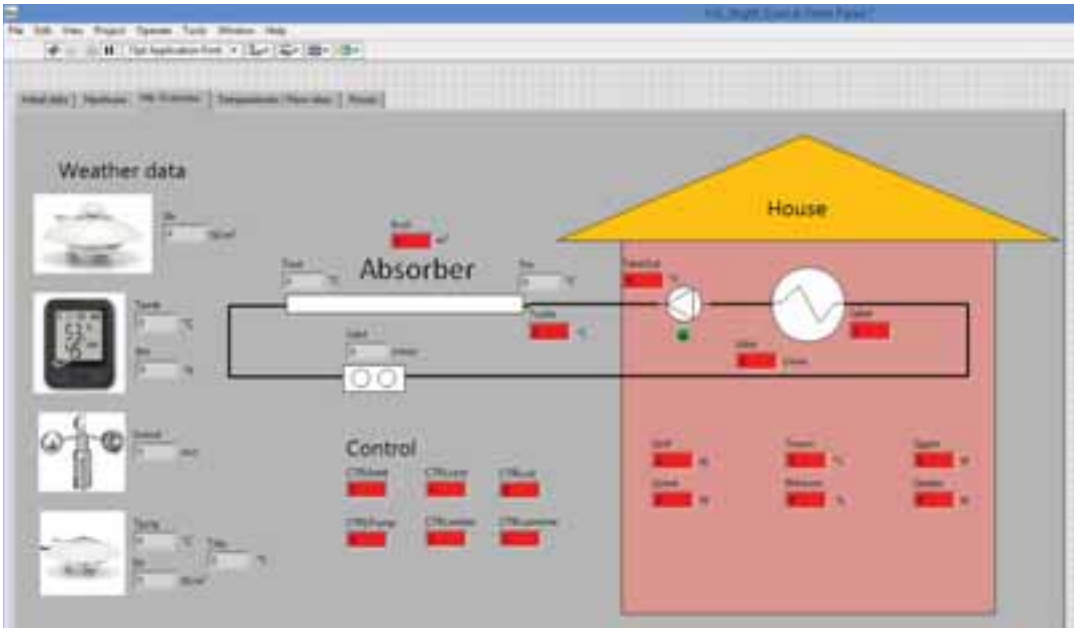

Fig. 7: Screenshot of the HiL visualization in Labview (grey: measurement data, red: simulated data)

The data that are passed from TRNSYS to LabVIEW are listed in Table 4.

Tab. 4: Data communicated from TRNSYS to LabVIEW

Variable	Name	Unit
Outlet fluid temperature of the building heating/cooling distribution system	TdistOut	°C
Collector inlet temperature (after pipe)	TcolIn	°C
Building room temperature	Troom	°C
Control signal of the pump	CTRLpump	[0/1]
Heating/cooling power transferred to the building (+/-)	Qdist	W
Relative humidity of room air	RHroom	%
Infiltration gains	Qinf	W
Ventilation gains	Qvent	W
Radiative internal gains	QgainRad	W
Convective internal gains	QgainConv	W
Total solar radiation absorbed at all inside surfaces of zone	Qtsabs	W
Control signal heating	CTRLheat	[0/1]
Control signal cooling	CTRLcool	[0/1]
Control signal collector	CTRLcol	[0/1]
Control signal season	CTRLseason	[0/1]
Control signal winter	CTRLwinter	[0/1]
Control signal summer	CTRLsummer	[0/1]

Depending on the simulation results, the appropriate control signals of the inlet temperature to the solar collector and the flow rates are sent via the I/O modules.

4. Example of measurement results

In this section, some results obtained in cooling mode with the developed HIL test bench are shown exemplarily. The test bench has been operated for commissioning tests during one week between the 12th and the 19th of June 2017 for a typical Egyptian building and under the climate conditions of Stuttgart.

4.1. Constant parameters

The main constant parameters assumed for the test of the measurement box are summarized in Table 5.

Tab. 5: Main constant parameters

Parameters	Value	Unit
Collector area	70	m²
Fluid density	1043	kg/m³
Fluid specific heat	3.675	kJ/kgK
Cooling set point	22	°C
Activated ceiling area	114	m²
Initial building temperature	23.5	°C

4.2. Weather data

Figure 8 shows the main measured weather data during the considered period: the ambient temperature T_{amb}, the sky temperature T_{sky} which is calculated with the help of the downward longwave radiation measured with the pyrgeometer and the global irradiance on the horizontal plane G_h.

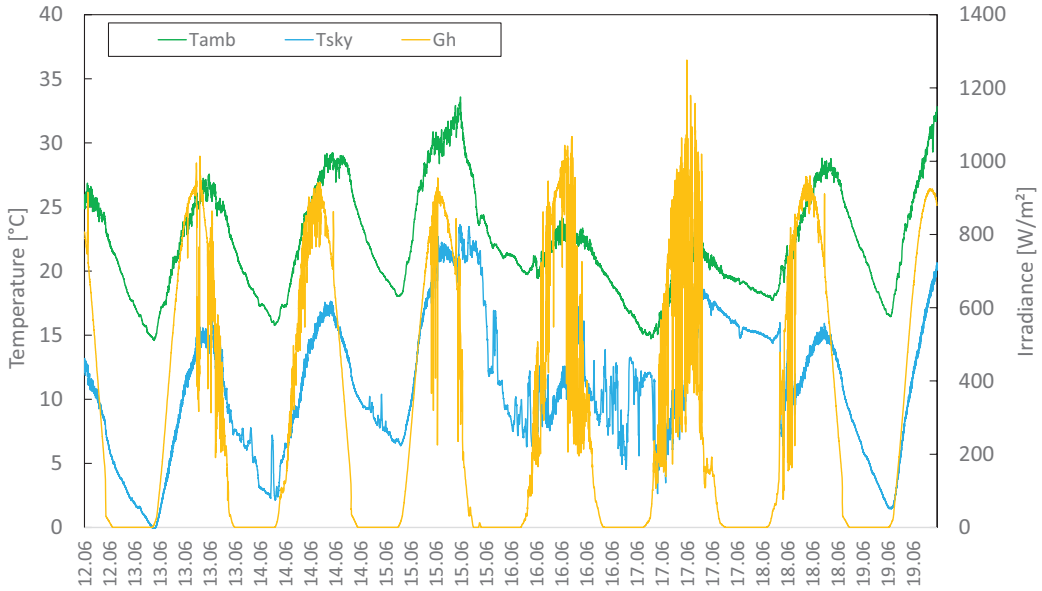

Fig. 8: Main weather data during the measurement period

4.3. Collector operation

Figure 9 shows, in addition to the ambient and sky temperatures, the main collector measured values: the inlet and outlet temperatures T_{in} and T_{out} as well as the volumetric flow rate V_{dot}. The collector is operated in cooling mode, i.e. at night according to a defined control strategy.

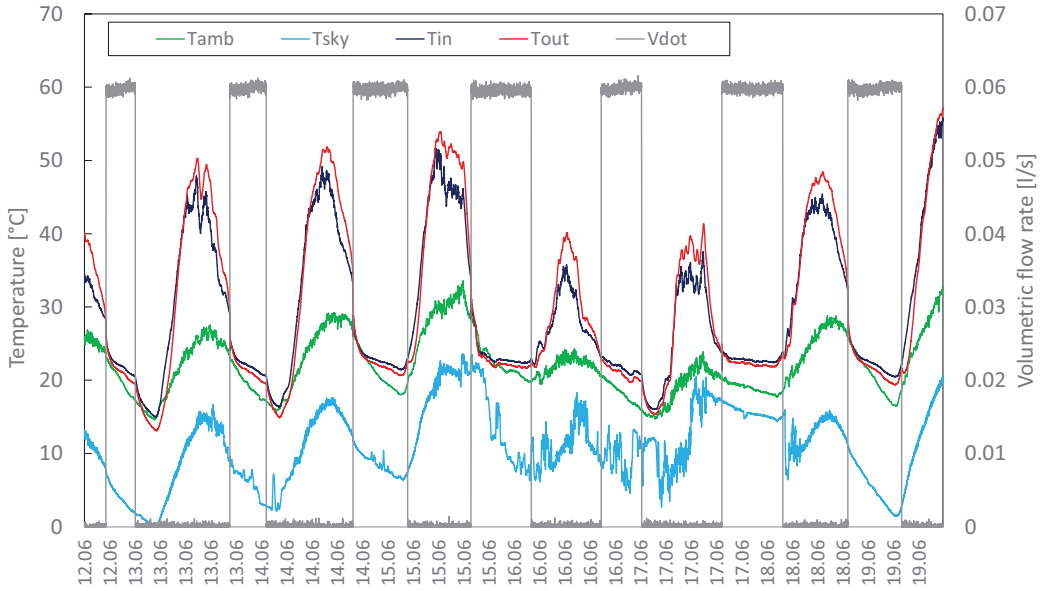

Fig. 9: Collector operation during the measurement period

4.4. Building behavior

Figure 10 shows the simulated building temperature T_{room}, the collector specific power $Q_{dotColSp}$ transferred to the building, as well as the total building specific gains $Q_{dotGains}$. The collector specific power is based on the collector area (70 m²) whereas the building specific gains are based on the apartment floor area (115 m²). $Q_{dotColSp}$ is defined positive when cooling is provided to the building. $Q_{dotGains}$ includes the internal gains, the solar gains, as well as the ventilation and infiltration gains.

It can be seen that the building temperature T_{room} increases suddenly when the collector pump is switched ON at the beginning of the night. This is due to the still hot fluid which is in the pipes and the collector and is pumped to the building causing a temperature increase in the room. This can be easily solved by appropriate changes on the control parameters.

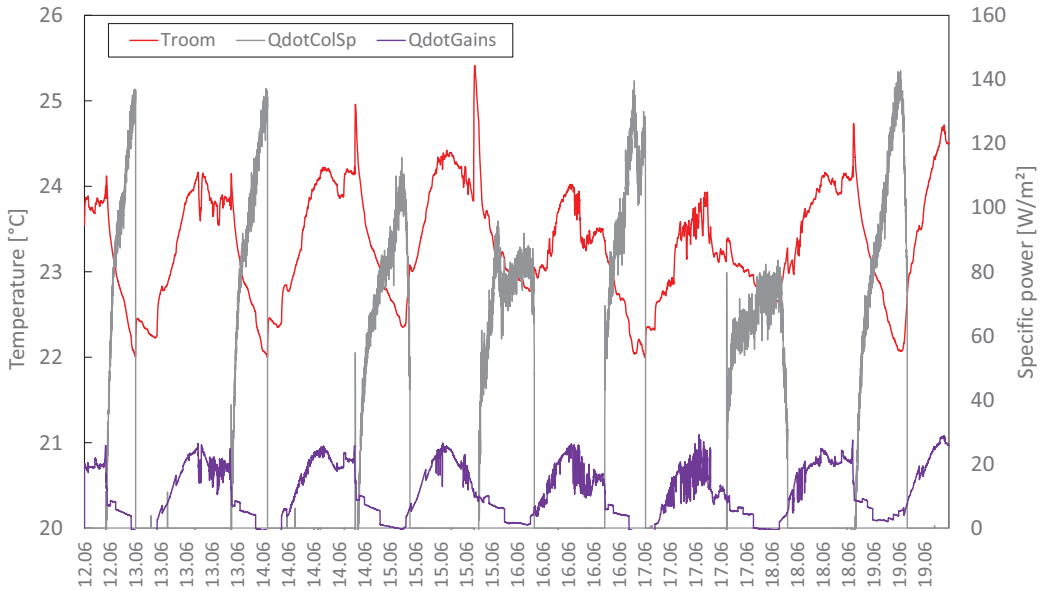

Fig. 10: Main building results during the measurement period

In order to see the influence of the investigated system on the building temperature, a reference system (i.e. without collectors) has been simulated. Figure 11 shows the room temperatures of the reference system and the night cooling system for the three first nights of the considered measurement period. Due to the control problem mentioned earlier,

the room temperature of the radiative cooling system is higher at the beginning of the night (i.e. the building is actually heated up) than the reference system. When the cooling power of the collector is positive (i.e. the building is cooled down), the room temperature is lower than the reference system. The pump is stopped when this temperature reaches 22°C.

Due to the chosen distribution system (thermally activated ceiling), both temperatures merge together as soon as the collectors are not operated. Indeed, the activated ceiling of the TRNSYS building model assumes a unique thermal coupling to the building air node. Therefore, the cooling provided by the collectors cannot be transferred to the building thermal mass, causing a quick drop in the room temperature which has no effect on the room temperature during day time. A better option would be in this case to connect the collector loop to an activated concrete core so that the building thermal mass can be cooled down during the night and therefore providing additional thermal comfort during the day.

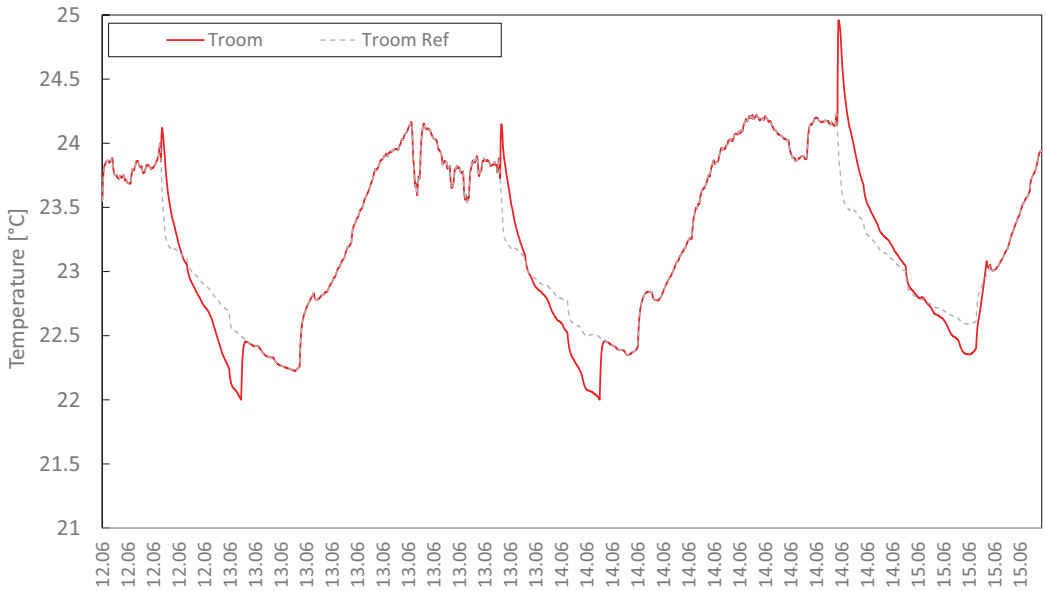

Fig. 11: Comparison of the room temperatures with the night cooling system (red line) and without (grey dashed-line)

4.5. Summarized results

Table 6 shows the main summarized measurement results over the considered measurement period. These values have been averaged or integrated only during the collector operation, i.e. when the collector pump was running (see Figure 9).

Table 6: Summarized main measurement results over the considered period

Parameter	Value	Unit
Collector mean specific cooling power	75.9	W/m²
Mean sky temperature	9.3	°C
Mean ambient temperature	20.3	°C
Mean wind velocity	0.3	m/s
Mean downward longwave radiation	363.2	W/m²
Total cooling energy (one collector)	8,9	kWh

5. Conclusions and outlook

The present paper presents a mobile Hardware in the Loop test bench that allows to test solar assisted heating and cooling systems based on low cost uncovered solar collector for the Egyptian climate. This test bench can be used for collector testing and for system testing in a hardware in the loop configuration. The measurement results show that a 70 m² collector could provide an average of 76 W cooling power per square meter and would be suitable for the cooling of a 120 m² apartment. With the developed test bench, many kind of collector integrations can be tested for different building constructions and system definitions. Also the control algorithm of the system can be tested and optimized before the implementation in real systems.

The developed test bench will be transported to Egypt and further used for both collector and system testing at the German University of Cairo (GUC). In particular the following improvements will be done by modifying the systems in the TRNSYS model:

- Activate the building thermal mass (Type 56) by changing from chilled ceiling to activated ceiling
- Integrate a water store in the system for domestic hot water preparation
- Add a water storage to store the cold at night and use it during the day
- Modify the control so that the collector energy yield is increased

6. Acknowledgements

The project NightCool was supported by the German Federal Ministry of Education and Research (BMBF). Support code: 01DH14021.

7. References

Attia, S., Evrard, A. Gratia, E., 2012. Development of benchmark models for the Egyptian residential buildings sector. In: Applied Energy 94, pp. 270–284.

Bertram E., Kirchner M., Rockendorf G.. “Solare Gebäudewärmeversorgung mit unverglasten photovoltaisch-thermischen Kollektoren, Erdsonden und Wärmepumpen für 100% Deckungsanteil, Kurzbezeichnung: BiSolar-WP, Hameln/Emmerthal, (2011) Final Report.

Cremers J., Eicker U., Palla N., Jobard X., Klotz F., and Mitina I.. PVT Integral – Research Project. Multivalente PV sowie thermische Kollektoren zur Kälte-, Wärme- und Stromerzeugung und Szenarien für die Gebäudeintegration. Project duration 2012 – 2015. (2015) Final Report.

Egyptian Electricity Holding Company. Annual Report 2013/2014. English. Ministry of Electricity and Renewable Energy - Arab Republic of Egypt.

Eicker Ursula and Dalibard Antoine. Photovoltaic–thermal collectors for night radiative cooling of buildings. In: Solar Energy Volume 85, Issue 7, July 2011, pp. 1322-1335.

Elharidy et al. Facing the Growing Problem of the Electric Power Consumption in Egyptian Residential Building Using Building Performance Simulation Program. In: Building Simulation - Towards Sustainable & Green Built Environment. Egyptian Group for Energy in Buildings and Environmental Design Research. Cairo, June 2013.

IEA SHC Task 54. Price Reduction of Solar Thermal Systems. Project duration October 2015-October 2018. Solar Heating & Cooling Programme International Energy Agency.

ISO 9806:2017, 2017. Solar energy -- Solar thermal collectors -- Test methods. International Organization for Standardization (ISO).

United Nations, Department of Economic and Social Affairs, Population Division (2017). World Population Prospects: The 2017 Revision, Key Findings and Advance Tables. Working Paper No. ESA/P/WP/248.

Xing Lu et al. Cooling potential and applications prospects of passive radiative cooling in buildings: The current state-of-the-art. In: Renewable and Sustainable Energy Reviews 65 (2016), pp. 1079–1097.

Active Solar Chimney (ASC) - Numerical and experimental study of energy storage and evaporative cooling

José Carlos Frutos Dordelly[1], Mike Coillot[1], Mohamed El Mankibi[1], Ricardo Enriquez Miranda[2], Maria José Jimenez[2], Jesus Arce Landa[3]

[1] ENTPE – Université de Lyon, Vaulx-en-Velin (France)

[2] CIEMAT, Almeria (Spain)

[3] CENIDET – Cuernavaca (Mexico)

Abstract

Research in the domain of renewable energies has been showing increasing consideration of energetic sustainability due to the escalation of global environmental concern. This paper focuses on implementing an energy storage solution in a hybrid ventilation system. Solar Chimneys constitute an effective technology used in green building architecture that capitalizes on solar energy to provide thermal comfort and air quality. The study centers on the effects of the organic paraffinic Phase Changing Material (PCM) RT-44 panel upon the thermal performance of a laboratory prototype and a stand-alone solar chimney. Furthermore, a numerical model has been established, which solves the thermal exchange of a PCM integrated multi-layered wall. The mass balance of the aerodynamic model of the chimney channel is calculated and input into a coupled model.

Keywords: energy storage, green energy, green house emission, PCM, solar chimney

1. Introduction

For the past years, natural ventilation has increasingly taken into consideration new energy-efficient strategies for thermal comfort as well as air quality improvement. One of the main objectives of the COP21 – Sustainable Innovation Forum meetings (information available at: http://www.cop21paris.org/) has been to decrease energetic consumption and to implement of green energies in order to reduce greenhouse gas emissions.

1.1 Overview

In its simplest design, a Solar Chimney is a channel used to evacuate hot air from a building via a closed conduct at a higher elevation. By means of the greenhouse effect, temperature rises across the canal and induces a thermal updraft. Most recent designs, as the one proposed by Arce, Jiménez, *et al.*, 2009, have made modifications to add elements such as a glazing or an opposite collector wall, both of which maximize the incoming solar energy and improve the chimney's performance. The use of solar chimneys is only profitable during the day, when solar energy heats the chimney and the air within it. Thus far, the induced airflow created in the chimney has been used for ventilation almost exclusively in hot countries.

The chimney acts like a heat engine converting heat generated by a collector into kinetic flow. The main task of the collector is to absorb solar energy for heating air and release it as solar radiation decreases. The initial driver of a solar chimney is the temperature difference between the inside of the building and the inside of the conduit, which causes a density variation. Several previous studies (Bansal, Mathur and Bhandari, 1993; Mathur *et al.*, 2006; Jianliu and Weihua, 2013; Naraghi and Blanchard, 2015) have proven that mass flow rate is directly related to solar radiation. Other investigations focused on the effect of solar radiation intensifiers on the performance of solar chimneys (Shahreza and Imani, 2015), however few have investigated the possibility of after-sundown utilization or the possibility of implementing this ventilation system in cold climate environments.

1.2 Active Solar Chimney

The objective of the study is to analyze the effectiveness of energy storage devices, in particular organic phase changing materials (PCMs), on solar chimneys for after-sundown utilization. The activation (transition from passive to PCM enhanced ventilation) of this technology is achieved through the implementation of these PCM panels.

The interest of phase changing materials lies in their superior energy storage capacity per unit of volume in

doi:10.18086/swc.2017.12.03 Available at http://proceedings.ises.org

comparison to conventional building materials. This type of material stores energy in its latent form. A rise in temperature up to the range of 40 – 44 °C will induce a change of state of the material from solid to liquid. The melting phase is an endothermic process, where heat is absorbed for the phase changing. Furthermore, the stored energy is released during the solidification process once temperature drops. The selected RT44 PCM panel has a heat storage capacity of 250 kJ/kg (or 70 Wh/kg) for a combination of latent and sensible heat in a temperature range of 35°C to 50°C.

Overall, paraffinic phase change materials for implementation in solar chimneys could be an economically viable option for hybrid design solutions to create a healthy indoor environment within residential buildings through renewable solar energy. The aim if this analysis is to evaluate the thermal performance of PCMs for residential purposes particularly after sundown.

Fig.1a represents a simple solar chimney as developed by Arce *et al.*, 2015, which is the basis of our model that integrates the PCM panels as shown in Fig.1b. This study will focus on the macro encapsulated organic PCM panels (bottom) filled with RT44 (top) shown in Fig.1c.

(a) (b) (c)

Figure 1: (a) Solar chimney built by Arce et al. (b) PCM panel integrated solar chimney. (c) Top - Organic paraffinic PCM in solid state. Bottom - macroencapsulated panel.

2. Numerical approach

The system is modeled by a heat transfer model and a pressure code. The first model integrates a multi-layered wall containing PCM and the second by analyzes the air temperature, speed and pressure distribution.

2.1 PCM integrated multi-layered wall

The model was developed using a finite-difference Crank-Nicholson implicit method, which follows a central difference scheme at time $t_{n+1/2}$ and a second order central difference for the space derivative at position x_i by setting the new variable $\bar{T}$:

$$\bar{T}_i = \frac{T_i^{t+\Delta t} + T_i^t}{2} \qquad (eq.1)$$

This method was chosen over other finite-differences approaches due to its faster convergence and its superior stability properties, especially at higher time steps (Δt) however, at the expense of a higher computational cost. Since we test our system over a large time interval, stability must be assured. Unstable approaches are not well suited due to these large time steps. The following expressions allows us to define a mathematical resolution that considers four different types of nodes: nodes in contact with the exterior environment, nodes in contact

with the internal channel, nodes within a solid material and the nodes in the interfaces between materials. The system is defined as follows:

$$\begin{cases} T_1^t = \left(1 + \frac{\lambda_1\gamma_1\Delta t_1}{\Delta x_1^2} + \frac{h_{ext}\gamma_1\Delta t_1}{\Delta x_1}\right)\bar{T}_1 + \frac{\lambda_1\gamma_1\Delta t_1}{\Delta x_1^2}\bar{T}_2 - \frac{h_{ext}\gamma_1\Delta t_1}{\Delta x_1}T_{ext} - \frac{\gamma_1\Delta t_1}{\Delta x_1}\left(\alpha_{clo}\varphi_{clo} + \alpha_{glo}\varphi_{glo}\right) & (eq.2) \\ T_i^t = -\frac{\lambda_i\gamma_i\Delta t_i}{2\Delta x_i^2}\bar{T}_{i-1} + \left(1 + \frac{\lambda_i\gamma_i\Delta t_i}{\Delta x_i^2}\right)\bar{T}_i - \frac{\lambda_i\gamma_i\Delta t_i}{2\Delta x_i^2}\bar{T}_{i+1} & (eq.3) \\ T_j^t = -\frac{\lambda_{j-1}\Delta t_{j-1}}{\vartheta\Delta x_{j-1}^2}\bar{T}_{j-1} + \left(1 + \frac{\lambda_{j-1}\Delta t_{j-1}}{\vartheta\Delta x_{j-1}^2} + \frac{\lambda_{j+1}\Delta t_{j+1}}{\vartheta\Delta x_{j+1}^2}\right)\bar{T}_j - \frac{\lambda_{j+1}\Delta t_{j+1}}{\vartheta\Delta x_{j+1}^2}\bar{T}_{j+1} & (eq.4) \\ T_n^t = -\frac{\lambda_n\gamma_n\Delta t_n}{\Delta x_n^2}\bar{T}_{n-1} + \left(1 + \frac{\lambda_n\gamma_n\Delta t_n}{\Delta x_n^2} + \frac{h_{int}\gamma_n\Delta t_n}{\Delta x_n}\right)\bar{T}_n - \frac{h_{int}\gamma_n\Delta t_n}{\Delta x_n}T_{int} - \frac{\gamma_n\Delta t_n}{\Delta x_n}\left(\alpha_{clo}\varphi_{clo} + \alpha_{glo}\varphi_{glo}\right) & (eq.5) \end{cases}$$

Eqs. 2-5 are solved by the following matricial equation and solving for $T_i^{t+\Delta t}$ in the previous eq.1:

$$T_i^t = A\bar{T} + Bu \qquad (eq.6)$$

2.2 Modelling of PCM Non-linearity in a multi-layered wall

In order to account for the non-linear behavior of phase changing materials, several options were considered. Some studies have explained the behavior of phase changing materials by setting three different working phases: solid, liquid and transitory state (Li and Liu, 2014). Studies such as the one carried out by Mirzaei and Haghighat, 2012 have modelled the behavior in similar ways and adding a discretization along the PCM layer to simulate the progressive phase change of the material. Other articles have opted to work on different approaches such as DTA (Differential thermal analysis) (Zhou, Zhao and Tian, 2012) and DSC (Differential scanning calorimetry) tests (Kheradmand *et al.*, 2016), both techniques in which the difference in the amount of heat required to increase the temperature of a sample and reference is measured as a function of temperature. This last technique was chosen over other options since the data from the test can be simply input into the code instead of calculated at each time interval; thus reducing the calculation time of the numerical model.

(a) **(b)** **(c)**

Figure 2: (a) Preparation of solid state RT44 material. (b) Sample setup for DSC analysis. (c) DSC test machine

The results of the DSC test for the Rubitherm RT44 phase changing material are shown in Fig.3. This test was carried out at a cooling/heating speed of 0.05°C/min, according to the expected charge/discharge speed of the panels in the chimney. The specific heat of the RT44 material is input to each node of the discretization as a function of temperature $C_p(T)$, allowing a more specific evolution along the PCM layer. Specific heat is calculated using the following expression:

$$C_p(T) = \frac{DSC(T)_s}{\varphi} \qquad (eq.7)$$

2.3 Pressure code – Airflow calculation model

The aerodynamic behavior and the heat exchange of the fluid within the conduct are influenced by the boundary wall temperature. This model employs a pressure code for the calculation of airflows throughout the

conduct and is based on the following simplifications:

- Airflow through the channel has been assumed one-dimensional. Only the vertical component parallel to the height of the chimney are considered.
- No losses are considered throughout the air channel. The mass conservation equations only take into account the exchanges between adjacent volumes and boundaries.
- Density is not constant and behaves according to the Boussinesq approximation as a function of temperature to account for the buoyancy driven flow.

The pressure code follows an iterative resolution based on the Newton-Raphson method. The mass balance $\dot{m}$ of a cell i connected to cells j of a domain is expressed by the following equation:

$$\sum_{k=1}^{j} \dot{m}_{ik} = 0 \qquad (eq.8)$$

The mass flow rate depends on the pressures of the neighboring cells. The mass exchange between common interfaces will serve to calculate the new pressure distribution through several iterations until convergence is reached. Density fluctuates due to temperature differences between adjacent zones, which leads to buoyancy driven flow. This phenomenon causes light hot air to rise and flow out while cooler air flows in. The system is solved by using Bernoulli's principle; taking the reference pressure on the lower boundary of the cell P_0 and according to the hydrostatic gradient, the pressure due to stack effect P_i only at height z is:

$$P_i = P_{o,i} - \rho_i g z \qquad (eq.9)$$

$$\rho_i = \rho_0 \frac{T_0}{T_0 + T_i} \qquad (eq.10)$$

where T_0 corresponds to a reference temperature and T_i the air temperature of the cell. Boundaries between volumes are written in terms of ΔP to account for the interaction between adjacent volumes. This substitution is then input into the mass conservation equation in order to satisfy the expression in equation 7 and rewritten in terms of Bernoulli:

$$\sum_{k=1}^{j} \dot{m}_{ik} = \sum_{k=1}^{j} \rho_{ik} \left[C_d W \sqrt{\frac{2\Delta P_i}{\rho_{mean}}} \right] \qquad (eq.11)$$

where C_d is a discharge coefficient inherent to the system and W the perpendicular surface to the flow. Calculation of unknown pressures is derived by application of mass balance equations in each node. The solution of the system, as stated before, is based on a Newton-Raphson iterative method. Each cell pressure is adjusted to satisfy mass balance. The new cell pressures are computed from the previous estimated pressures and a correction vector P_{corr} as follows:

$$P_{iter+1} = P_{iter} - P_{corr} \qquad (eq.12)$$

P_{corr} is calculated using:

$$P_{corr} = J^{-1}\, x\, Mb \qquad (eq.13)$$

where Mb is a mass balance vector when considering no source terms, computed by the following expression:

$$Mb_j = \sum_{k=1}^{j} Q_{ik} \rho_{ik} \qquad (eq.14)$$

and J is the Jacobian matrix calculated by:

$$J_{ij} = \frac{\partial Mb_j}{\partial P_j} \qquad (eq.15)$$

The convergence of the aerodynamic model is given by a convergence factor, which is defined by a correction vector in order to end iterations. This correction factor was set to $\varepsilon = 0.001$.

2.4 Model coupling

The data obtained in the previous sections and equation systems share information through a Matlab Simulink interface called HYBCELL (El Mankibi *et al.*, 2006, 2015) which displays the temperature evolution, pressure distribution and air flow across the chimney.

From an initial temperature distribution, aerodynamic model computes pressures and flow distributions. These results will allow new temperature calculations by changing convective heat fluxes. The model was developed to run with meteorological data from Lyon.

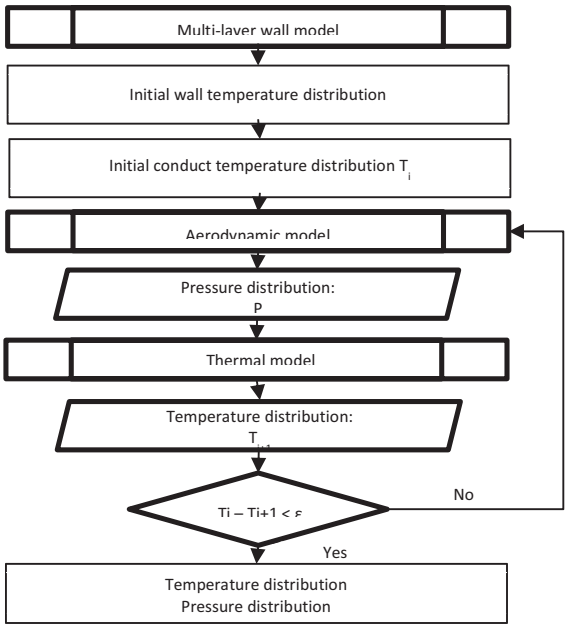

Figure 3: Flowchart of the coupled model.

3. Experimental procedure

3.1 Laboratory set-up

In order to analyze and validate the numerical models, a laboratory prototype was developed. The prototype is based on the chimney built by Acre et al. (Arce, Jiménez, *et al.*, 2009; Arce, Xaman, *et al.*, 2009) at the Almeria Solar Platform (PSA). The laboratory prototype is made from 5cm-wide polystyrene plates, supported by an aluminum beam structure (3cm cross section). The prototype is connected to one of the sections of the Guarded Hot Box (shown in Fig.3) in order to simulate the temperature in a controlled volume.

(a)

(b)

Figure 4: Laboratory prototype showing (a) the prototype and the both sides of the Hot Guarded Box and (b) ongoing experiment with PCM panels.

3.1.1 Experimental protocol

Fig. 5 below shows the protocol used for the experimentation. The experimental protocol is composed of seven consecutive phases of 6 hours each (0.25 days), completing a full cycle in roughly 1.75 days. Phases depend on the state of the opening (open/closed) for natural ventilation, and heating provided by the halogen lamps, which simulate solar radiation. The lamps are evenly distributed over the 3m glass face of the chimney and provide a net heat flux of 700 W/m².

Phase 1 corresponds to the initialization of the system. In this stage, the outlet is closed and there is no present heat source. Phase 2 was designed to charge the panels in order to ensure the melting process of PCMs. Phase 3 allows air circulation by opening the outlet and maintaining the heat source. Phase 4 removes the heat source while allowing air circulation. Phase 5 reinitializes the system. Phases 6 and 7 work in the same way as phases 2 and 4.

Phase 1 : Initialization

Phase 2 : Heating Only

Phase 3 : Chimney Activation

Phase 4 : Ventilation only

Phase 5 : Initialization

Phase 6 : Heating only

Phase 7 : Ventilation only

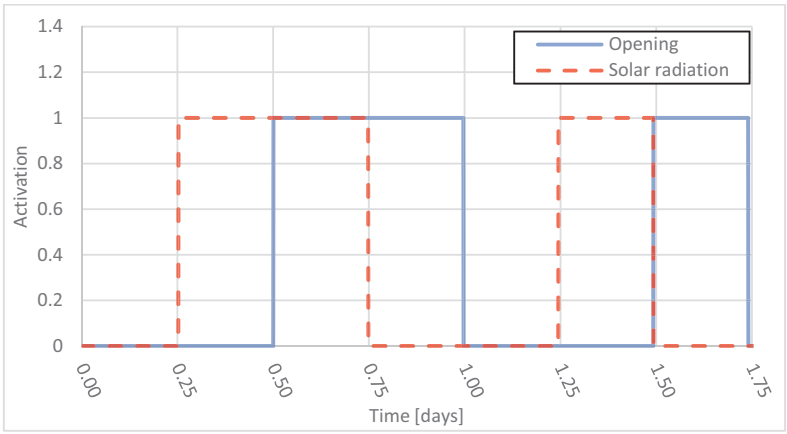

Figure 5: Experimental protocol showing the Boolean behavior between the outlet (open/closed) and the solar gain (on/off)

3.1.2 Laboratory test results

Outlet mass flow rate, air gap temperature and temperature difference between inlet and outlet, are some of the most important quantities for the design of a solar chimney. Outlet airflow for no PCM and PCM integrated solar chimney (ASC) are shown in Fig. 6-8. The results represent two continuous cycles from the experimental protocol. The results shown below were carried out under two different conditions: input temperature set by the Hot Guarded Box and no input temperature, thus following the exterior temperature.

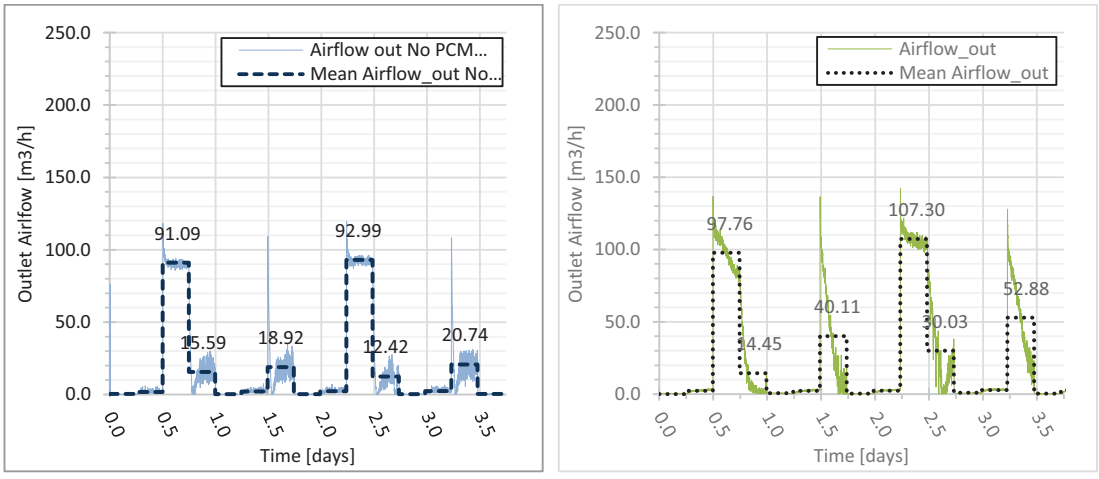

(a) **(b)**

Figure 6: Outlet airflow results for (a) 09/05/2017 No PCM Solar chimney for a set temperature of 17°C (Cycle 5 No MCP) and (b) 16/08/2017 RT44 PCM integrated Solar Chimney for a set temperature of 17°C (Cycle 4 MCP)

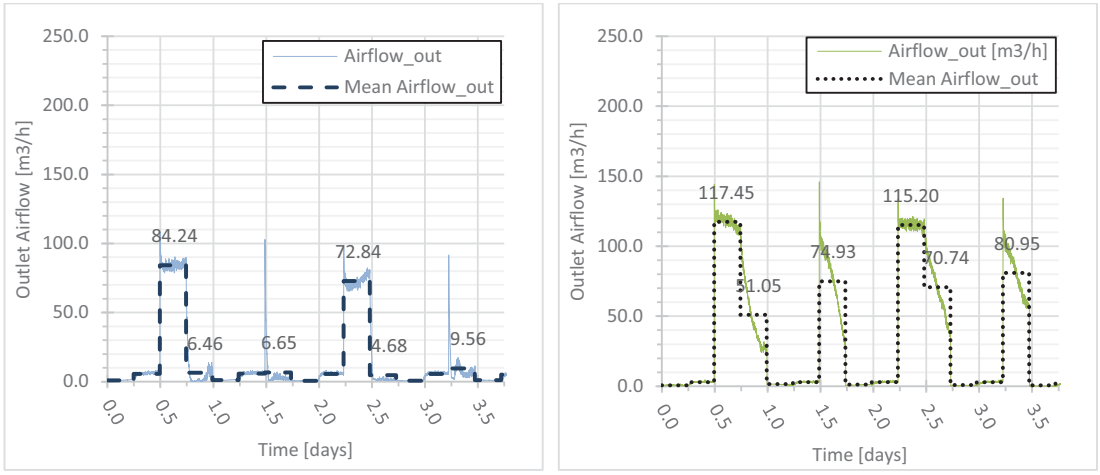

Figure 7: Outlet airflow results for (a) 25/07/2017 No PCM Solar chimney following exterior temperature (Cycle 7 No MCP) and (b) 23/08/2017 RT44 PCM integrated Solar Chimney following exterior temperature (Cycle 5 MCP) – Max outside temperature of 42°C

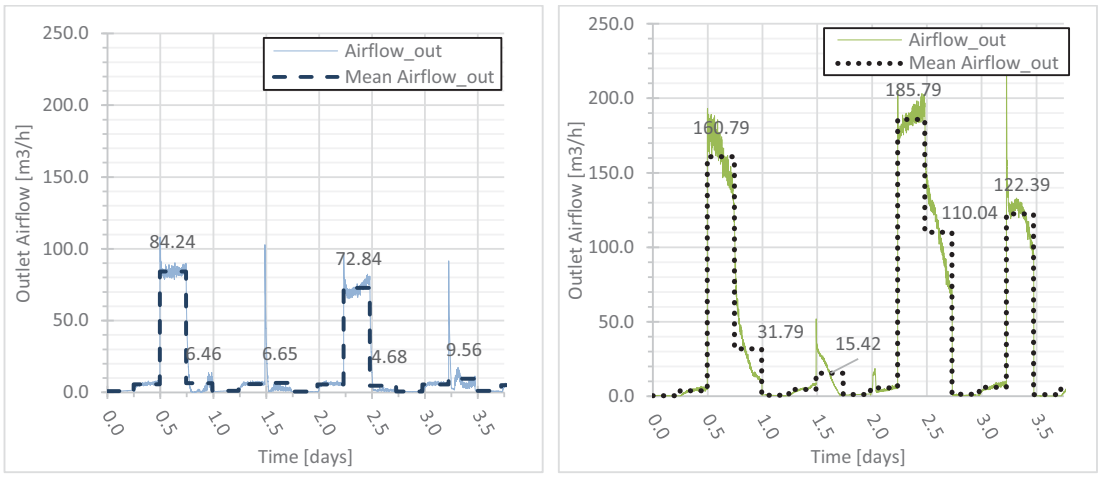

Figure 8: Outlet airflow results for (a) 25/07/2017 No PCM Solar chimney following exterior temperature (Cycle 7 No MCP) and (b) 15/06/2017 RT44 PCM integrated Solar Chimney following exterior temperature (Cycle 3 MCP) – Max outside temperature of 45°C

The results demonstrate the influence of the different stages of the experimental protocol on the outlet mass flow rate. The impact of the PCMs is particularly noticeable during ventilation only phases (4 and 7). Solar chimney mass flow rate values drop dramatically during the aforementioned phases, as shown in Fig. 6a – 8a. The polystyrene structure provides no thermal inertia to the system, which causes a drop in outlet mass flow rate as soon as there is no longer a heat source. In turn, ASC results (as shown in Fig. 6b – 8b) display a slow decrease of mass flow rates between phases. The PCM panels work as expected, absorbing available energy during each charging phase and releasing once the source is withdrawn.

Additionally, ASC results display as well, an overall higher mean mass flow rate across all phases of the experiment. In some cases, up to a twofold increase of mass flow rate can be noted for the active solar chimney.

3.2 In-situ experimentation

The stand-alone chimney was developed in Almeria in 2009. The latest iteration of the system is 5.60 m tall, 1.20 m width and 0.52 m deep. The chimney is composed of a 0.15m thick concrete absorbing plate, thermal insulation behind the concrete plate, a 5mm thick glass cover to reduce convective and radiative losses to the environment, a wood casing, and a driving air protection; which generates a fall of pressure near the exit and,

at the same time aids the extraction of air. The prototype is shown in Fig 9. (Arce *et al.*, 2015).

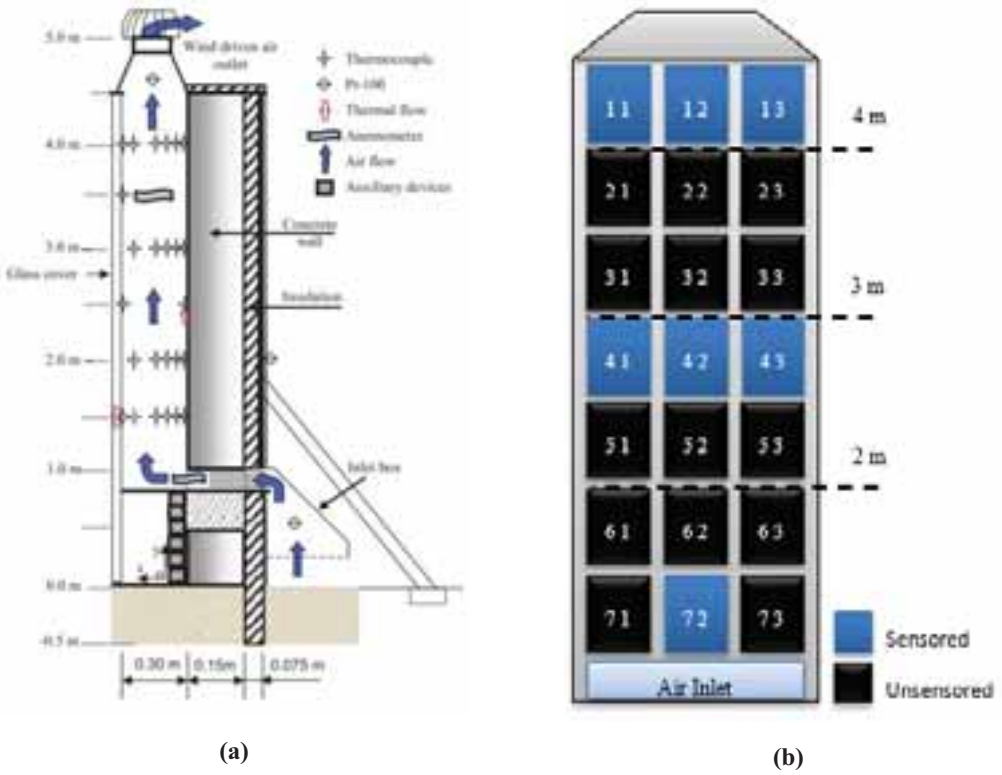

Figure 9: (a) Lateral view of the PSA solar chimney and the instrumentation set up by Arce et al. and (b) Panel distribution on the PSA solar chimney

3.2.1 PCM implementation

The dimensions of the Almeria solar chimney, as well as the cable distribution do not allow the placement of PCM panels on the perpendicular sides to the glazing. The panels are distributed over the concrete collector wall as shown in Fig. 4b in a matrix manner. The sensors are placed in the center of the panel, over and behind at three different levels: inlet panel (72) at 1,25m, center of the solar chimney (41, 42 and 43) at 2,75m and the outlet panels (11, 12 and 13) at 4,25m. The panels' southern surfaces were painted matte black in order to maximize the absorption of solar radiation and to ensure the phase change.

3.2.2 Instrumentation

The experimental instrumentation used for the different measurements of the solar chimney is detailed in the technical note published by Arce et al. (Arce, Jiménez, *et al.*, 2009). Platinum thermoresistance (PT100, 1/10 DIN) sensors are used to record surface temperature of the panels via a four-wire connection. These sensors consist of a very small sensing element embedded in a slim rubber substrate. The sensors were glued to the center of the panels as marked in Fig.9b and painted black matte to integrate them as much as possible with the corresponding surface.

A data acquisition system with the following characteristics is being used: 16-bit A/D resolution, range of measurements fitting sensor output, modules distributed to minimize wiring, based in Compact Field Point modules manufactured by NATIONAL INSTRUMENTS.

The Solar Platform of Almeria counts with its own meteorological station, which measures data ever second. Data is averaged and recorded every minute. Further details concerning the meteorological station can be found in the aforementioned article.

3.2.3 Mass flow rate

The results presented below show the exterior temperature and wind speed for the period from October 6 to

October 9 in 2016 and 2017 respectively.

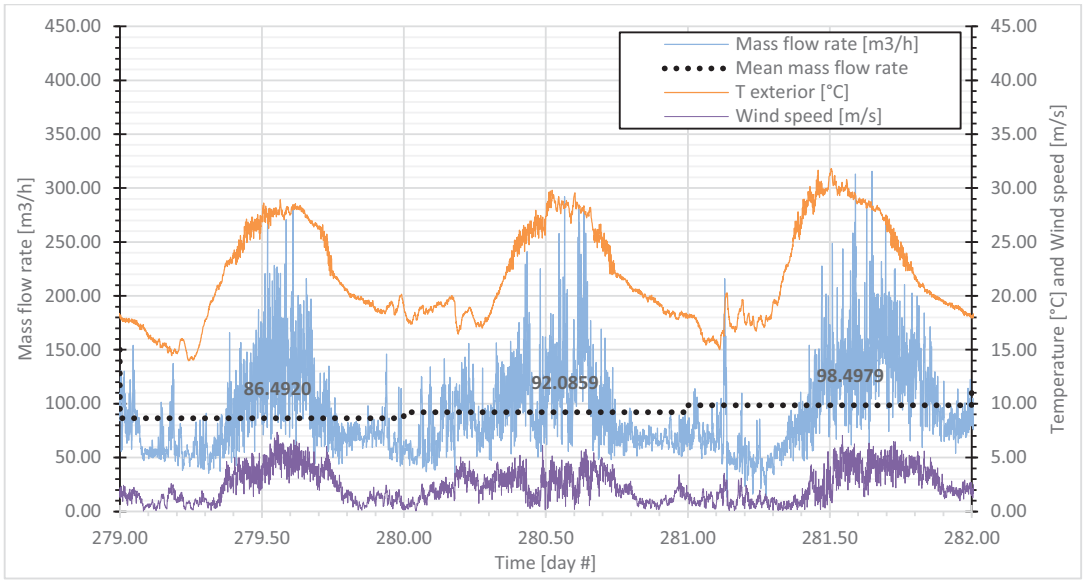

(a)

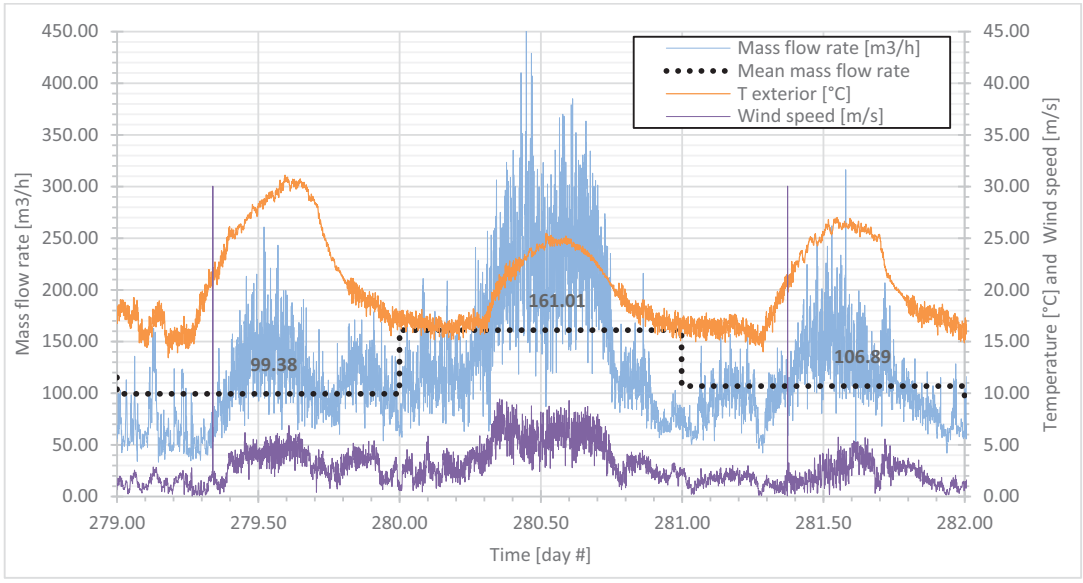

(b)

Figure 10: Influence of exterior temperature and wind speed on the mass flow rate for (a) Arce et al. solar chimney and (b) PCM integrated solar chimney

Fig. 10 (a) and (b) show an increase in mass flow rate for the PCM integrated solar chimney for the same period between both year samples. For this specific period, the overall mass flow rate is higher across the three days. The maximum and minimum differences are 62.98 m^3/h and 8.39 m^3/h respectively. The maximum temperature from the three days in 2016 is approximately 30°C, thus there is a +5°C difference in relation to the results of 2017. The highest mass flow rate values for the PCM integrated solar chimney are obtained at 25°C where wind speed has a mean wind speed of 6.5 m/s.

3.2.4 Panel surface temperature distributions

Fig. 11 (a) – (c) show the panels' surface temperature evolution for the period from October 6 to October 9 2017. In Fig. 11 (a) and (b) the phase change can be appreciated through temperature evolution of curves 12, 42 and 72 back. This phenomenon starts as soon as the temperature approaches 40°C. Once the material is fully melted temperature continues to rise until it reaches the maximum level. When solar radiation decreases

and outside temperature starts to drop, the surface temperature of the panel falls as well until it drops to 44°C. At this point, the stored energy is being released from the PCM and thus, the temperature decrease occurs at a slower rate. Moreover, Fig. 11 (c) represents the temperature evolution of the outlet level of the solar chimney. At this level, surface temperatures do not reach the phase change range. This is explained by the lack of direct sunlight due to the shadow of the top level of the solar chimney.

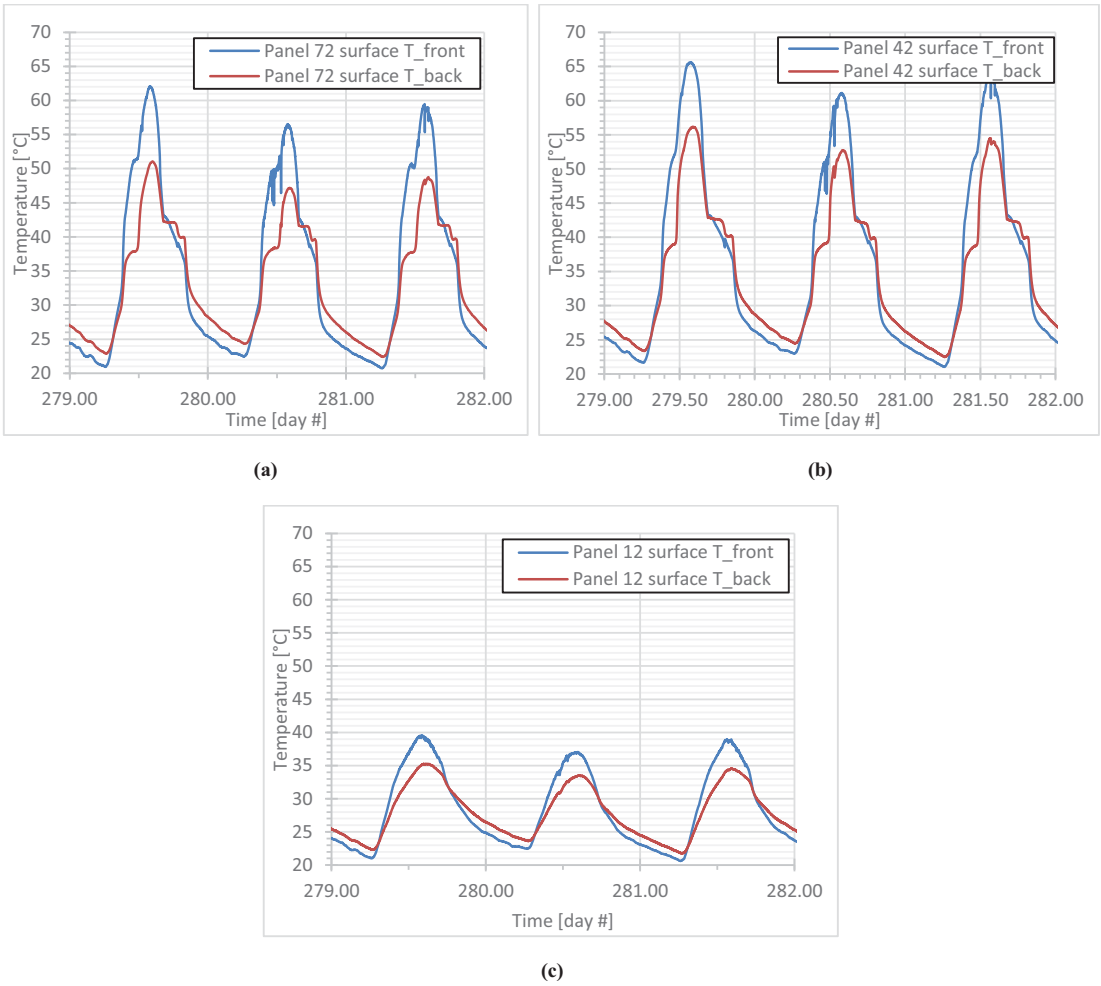

Figure 11: Frontal and back surface temperatures of the PCM panel integrated in the solar chimney at three different levels (a) inlet, (b) mid-level and (c) outlet.

4. Conclusions

An experimental study of the implementation of RT44 phase changing material panels was carried out for a solar chimney prototype under laboratory and in situ conditions. Laboratory results show a clear influence of solar radiation on the outlet mass flow rate when integrating PCMs to the solar chimney. Moreover, the interest of phase changing materials can be appreciated in these results since the mass flow rate slowly decreases once there is no longer a heat source. Outlet mass flow rate shows a steady reduction rather than the abrupt drop observed without PCM. Although the decrease is cut by the duration of each stage of the experimental protocol, its effect on mass flow rate is noteworthy. After the PCM has completed the melting process and the heat source is taken away, surface temperatures and air temperatures follow as well a slow discharge.

The increase in mass flow rate is proportional to the energy stored by the PCMs. Lower mean mass flow rates are the result of unattained melting temperatures at one or several levels of the active solar chimney. Further studies will act on the optimization of the laboratory parameters such as the heat source and the time lapses.

In situ results are yet inconclusive and require additional tests in order to validate the wind speed and melting assumptions made in order to explain the differences between the results obtained by Arce et al. and the Active

Solar Chimney. Results, even though promising, are yet to be optimized to obtain a better performance. Thus far, it can be concluded that the undercharge of the system can have an impact on the performance of the chimney. The chimney is oriented to the south; this will be particularly impactful during winter when the chimney receives an almost absolute impact of the sun. A better exposure to the sun and lower ambient temperatures will show the performance of the active solar chimneys under disadvantageous conditions.

Finally, the numerical analysis aims to describe the behavior of the phase changing materials through the combination a multi-layered wall. Further studies will emphasize in the validation of the numerical model via the experimental data obtained by both experimental procedures.

5. References

Arce, J., Xaman, J. P., *et al.* (2009) 'A parametric study of conjugate heat transfer of solar chimney', *Proceedings of the ASME 3rd International Conference on Energy Sustainability 2009, ES2009*, 1, pp. 605–612. doi: 10.1115/ES2009-90387.

Arce, J., Jiménez, M. J., *et al.* (2009) 'Experimental study for natural ventilation on a solar chimney', *Renewable Energy*, 34(12), pp. 2928–2934. doi: 10.1016/j.renene.2009.04.026.

Arce, J. *et al.* (2015) 'Thermal performance analysis of a solar chimney , based on the experimental study of the main driving variables in a physical prototype', *Paper conference*, (October), pp. 385–395.

Bansal, N. K., Mathur, R. and Bhandari, M. S. (1993) 'Solar chimney for enhanced stack ventilation', *Building and Environment*, 28(3), pp. 373–377. doi: 10.1016/0360-1323(93)90042-2.

Jianliu, X. and Weihua, L. (2013) 'Study on solar chimney used for room natural ventilation in Nanjing', *Energy and Buildings*. Elsevier B.V., 66, pp. 467–469. doi: 10.1016/j.enbuild.2013.07.036.

Kheradmand, M. *et al.* (2016) 'Experimental and numerical studies of hybrid PCM embedded in plastering mortar for enhanced thermal behaviour of buildings', *Energy*, 94, pp. 250–261. doi: 10.1016/j.energy.2015.10.131.

Li, Y. and Liu, S. (2014) 'Numerical study on thermal behaviors of a solar chimney incorporated with PCM', *Energy and Buildings*. Elsevier B.V., 80, pp. 406–414. doi: 10.1016/j.enbuild.2014.05.043.

El Mankibi, M. *et al.* (2006) 'Prediction of hybrid ventilation performance using two simulation tools', *Solar Energy*, 80(8), pp. 908–926. doi: 10.1016/j.solener.2005.08.003.

El Mankibi, M. *et al.* (2015) 'Numerical modeling of thermal behaviors of active multi-layer living wall', *Energy and Buildings*. Elsevier B.V., 106, pp. 96–110. doi: 10.1016/j.enbuild.2015.06.084.

Mathur, J. *et al.* (2006) 'Experimental investigations on solar chimney for room ventilation', *Solar Energy*, 80(8), pp. 927–935. doi: 10.1016/j.solener.2005.08.008.

Mirzaei, P. A. and Haghighat, F. (2012) 'Modeling of phase change materials for applications in whole building simulation', *Renewable and Sustainable Energy Reviews*. Elsevier, 16(7), pp. 5355–5362. doi: 10.1016/j.rser.2012.04.053.

Naraghi, M. H. and Blanchard, S. (2015) 'Twenty-four hour simulation of solar chimneys', *Energy and Buildings*. Elsevier B.V., 94, pp. 219–226. doi: 10.1016/j.enbuild.2015.03.001.

Shahreza, A. R. and Imani, H. (2015) 'Experimental and numerical investigation on an innovative solar chimney', *Energy Conversion and Management*. Elsevier Ltd, 95, pp. 446–452. doi: 10.1016/j.enconman.2014.10.051.

Zhou, D., Zhao, C. Y. and Tian, Y. (2012) 'Review on thermal energy storage with phase change materials (PCMs) in building applications', *Applied Energy*. Elsevier Ltd, 92, pp. 593–605. doi: 10.1016/j.apenergy.2011.08.025.

Experimental Comparison on the Energy Performance of Semi-Transparent PV Facades Under Continental Climate

Zissis Ioannidis[1], Konstantinos Kapsis[1], Annamaria Buonomano, Andreas Athienitis[1,] Eftsratios Dimitrios Rounis[1] and Ted Stathopoulos[1]

[1] Dept. of Building, Civil and Environmental Engineering, Concordia University, Montreal (Canada)

[2] *Department of Industrial Engineering, University of Naples Federico II, Naples, (Italy)*

Abstract

Semi-Transparent Photovoltaic panels (STPV) have become an important element in the building integration of photovoltaic panels (BIPV). STPV panels can be integrated on double skin facades (DSF) and insulating glazing units (IGU) acting as their exterior layer, generating electricity, controlling the solar heat gains and utilizing daylight. In addition, a mechanically ventilated DSF integrating STPV panels (DSF-PV), can cool down the PV panels, increase their efficiency but also use the preheated air to enhance the thermal efficiency of the mechanical system connected to the DSF-PV. Two virtually identical STPV are integrated on a DSF-PV and a IGU-PV respectively and their electrical performance is evaluated experimentally. Under the same exterior and interior conditions, it is found that the DSF-PV has a 3% greater electrical performance than the IGU-PV and if the cavity of the DSF-PV is selectively ventilated, the DSF-PV can generate more than 9% of electric power than the IGU-PV.

Keywords: Double Skin Façade, IGU, STPV, BIPV, BIPV/T, Semi-Transparent, PV

1. Introduction

It is very common for both commercial and residential modern buildings to use curtain wall systems as part of their envelope design. A well-designed curtain wall system is able to seal the building, protect it from weather phenomena and provide to the building the modern architectural aesthetics. The large transparent facades are preferred due to the reduced cost and the great appreciation of daylighting, as the sun light can penetrate deeper into the building. This architectural tendency is likely to remain, due to the low cost of the curtainwall application and the fact that more studies link daylight and view to the outdoors with increased worker productivity, well-being (Veitch and Galasiu 2011) and reduced lighting loads (Tzempelikos and Athienitis 2007). Highly glazed facades may maximize the daylight potentials of the building but they may require an oversized mechanical system, as excessive solar gains may lead to increased cooling loads during the day and low insulation may lead to increased heating loads during the night, adding to the thermal and visual discomfort of the occupants.

The disadvantages of highly glazed facades may be minimized or overcome by either integrating photovoltaics (PV) on windows or by adding an additional exterior layer forming in this way a double skin façade (Miyazaki, Akisawa, and Kashiwagi 2005). Solar cells may be used instead of reflective coating or ceramic frits to reduce the solar gains, forming in this way semi-transparent photovoltaics (STPV) that could be integrated on parts of the façade of the building (James, Jentsch, and Bahaj 2009; Qiu et al. 2009). As a result, solar heat gains may be reduced, maintaining at the same time adequate levels of daylight, provide view to the outdoors (Vartiainen 2001) and generate electricity.

When PV cell overheating is of concern, instead of a window with a sealed cavity (IGU), a ventilated one can be utilized, turning the façade into a Double Skin Façade integrating photovoltaics (DSF-PV). The possibility of recovering the heat from within the DSF-PV, along with the electricity generation and the daylight transmission, gives the opportunity to the creation of an active façade (Gaillard, Giroux-Julien, et al. 2014). As the air circulates behind the PV cells, it cools down the cells through convection, reducing the temperature of the cells and increasing their

doi:10.18086/swc.2017.12.04 Available at http://proceedings.ises.org

electrical efficiency.

STPV façades could have a substantial effect on the daylighting/lighting performance as well as energy and peak power demand reduction on highly-glazed office buildings. The objective of this study is to experimentally investigate the energy performance of two prevailing STPV façade configurations: i) curtain wall systems incorporating STPV insulated glazing units (IGU-PV), ii) Double Skin Façade incorporating STPV technologies on the outer skin (DSF-PV). The study focuses on offices in a continental climate region (Northeastern United States and Southeastern Canada) and it is part of a bigger effort to provide input to the design guidelines for the utilization of advance fenestration technologies that will help to achieve net-zero energy building performance targets and beyond, through energy conservation and renewable energy generation.

2. Literature review on experimental investigation

A series of experiments have been held to characterize the performance of windows and double skin facades integrating photovoltaic panels. Single, double and ventilated windows have been investigated, while the majority of the studies used amorphous silicon (a-Si) photovoltaic panels. The experiments were mainly focused on the electrical performance of the integrated photovoltaics, but many studies focus as well on the thermal and daylight performance of such systems.

2.1 Windows integrating Photovoltaic

To assess the electrical performance of amorphous silicon STPV modules, the Sandia model was first validated experimentally by Peng et al, with indoors and outdoors experiments (Peng et al. 2015b). It is reported that Sandia model is able to predict the electrical output of the STPV modules on a sunny day but in order to predict the electricity production on an overcast day a spectral correction should be applied to correctly simulate the performance of the STPV windows. It is reported that a comprehensive spectral correction function is needed to be developed in the future.

An experiment was set-up by Robinson and Athienitis (2009), integrating STPV on a double glazing window in Montreal (Robinson and Athienitis 2009) focusing on its electrical and daylight performance. A design methodology for optimizing the electricity generation and the daylight utilization was validated showing the potentials of south facing STPV facades.

In addition to the electrical performance, the thermal performance of a double glazing STPV module was studied under standard test conditions and outdoor conditions (Park et al. 2010). For an increase of 1ºC of the PV module, it is observed that the temperature coefficient (β) is 4.8% and 5.2% under STC and outdoor conditions respectively (irradiance of 500W/m^2). It is also reported that the type of glass used at the STPV window does not affect the electrical performance of the module but affects the thermal performance of the system.

A comparison is held between an a-Si STPV double glazing unit and common single and double glazing units in terms of their electrical and thermal performance (Liao and Xu 2015). Liao and Xu focused mainly on the room and façade dimensions to develop a model and later validate it with field experiments in order to simulate it with the use of Energy Plus. Amorphous silicon STPV windows are found to be better suited for small rooms with high WWR or tall rooms. It is also found that they perform better than single and double-glazing units, mainly because they reduce the cooling loads of the interior zone.

The SHGC of STPV modules and STPV windows was measured using a calorimetric box in a solar simulator (Chen et al. 2012). Three laminated and two double glazing units with amorphous and micromorph are tested in the Solar Simulator and it is reported that it is sensitive to the spectrum of the solar simulator and the reflection properties of the absorber plate. It is also reported that the SHGC reduces significantly for incident angles greater than 45º.

In addition, a hot-box is used by He et al. (He et al. 2011) to compare an amorphous single-glazing PV window to a ventilated double-glazing PV window. With an electrical efficiency of less than 5% and with a packing factor of 0.8 the SHGC of the IGU integrating STPV is 46.5% in comparison to the single glazing STPV. A CFD analysis is held using ANSYS FLUENT and RNG k-epsilon turbulence model. The difference between the experiments and the model created, for the total heat gains, is 11.7% and 2.7% for the ventilated double-glazing PV window and the single-glazing respectively and the estimated temperature difference is less than a degree C for both cases.

A ventilated thin-film PV window is experimentally assessed and verified using a developed ESP-r simulation model that is then used to compare the STPV window with a simple absorptive glazing (Chow, Qiu, and Li 2009). For an electrical efficiency of less than 5%, the STPV window is compared to an a-Si STPV product available in the market and an to absorptive glazing. It is shown that the see-through PV installation can reduce the consumption of the HVAC by 28%.

An exterior experimental facility was set up by Olivieri et al (2013), to assess the electrical, thermal and daylighting and behavior of an STPV window (Olivieri et al. 2014). It is reported that the transparency of the PV window is not the most important factor concerning the electrical performance. Four a-Si STPV modules with visible transmittances between 0.1 and 0.4 have been experimentally compared to a reference glass. All four modules present higher SHGC, approximately 40% larger heat losses and the U-values are almost double in comparison to the reference glass.

The optimal packing factor of STPV windows for office buildings in central China was investigated, for different room lengths, WWRs and orientations (Xu et al. 2014), analyzing its electrical, thermal and daylighting performance. A parametric analysis is performed, using Energy Plus, to identify the impact of different cell coverages into the energy consumption of the zone, stating that the selection of the optimal configuration can reduce the energy consumption up to 13% in comparison to the least favorable configuration.

2.2 Double Skin Facades integrating Photovoltaic

The integration of PV on DSF is an idea that has recently received the attention of the academic community. The majority of the research is focused on naturally ventilated DSF integrating STPV made out of amorphous silicon.

Peng et al, set-up an experimental facility in Hong Kong, consisting of a DSF integrating see-through a-Si PV (Peng et al. 2015a; Peng, Lu, and Yang 2013). The DSF has a cavity width of 400mm that is created between a double glazed see-through PV and the interior window and inlets at the top and the bottom, both at the exterior side. Four different operation modes of the dampers and the interior window were experimentally investigated showing that the temperature of the air at the outlet can be more than 2ºC higher than the one at the inlet. It is also reported that the SHGC for the different operation modes are between 0.1 and 0.13.

The same experimental facility was later used to validate a developed simulation model, based Energy Plus (Peng et al. 2016). For a cool-summer Mediterranean climate zone, a thickness between 0.4m and 0.6m could be recommended as the optimal cavity width while the DSF-PV, used 50% less net-electricity than other glazing systems. In addition, it is highlighted that the future of the DSF-PV is promising because of the decrease of the prices and the increase of the efficiencies of the PVs.

Three prototype DSFs integrating semi-transparent photovoltaics are tested and a comparison between the thermal response of the semi-transparent photovoltaics and the air inside the cavity is presented (Gaillard, Ménézo, et al. 2014). The two-storey West North-West DSF of the building is designed to increase the electrical performance of the semi-transparent photovoltaics installed by utilizing the stack effect (Gaillard, Giroux-Julien, et al. 2014). As reported by the experimental data collected under real conditions, in a span of a year, the behavior of the system can be predicted by using simple relationships.

An experimental facility was built in Hong Kong to compare the energy performance of a Double Skin Façade (DSF) and an insulation glass unit (IGU) integrating semi-transparent photovoltaics (Wang et al. 2017). The thermal

performance of the IGU integrating STPV was found to be better by 2% than the naturally ventilated DSF integrating photovoltaics (DSF-PV), although the authors mentioned that an appropriate ventilating mode for the DSF-PV would potentially result into better thermal performance.

In Table 1, the available state of the art is shown, presenting the experimental research performed on windows and double skin facades integrating semi-transparent photovoltaics. The available literature is also analysed presenting the different type of PV utilized, the types of windows used and whether the DSF is mechanically or naturally ventilated. In addition, the focus of the study is presented along with whether any simulation models are used. The last row states the location of the experimental facility, if it is an exterior one, or if the experiments are performed on a solar simulator.

Table 1 Available literature on experimental research perfromed on windows and DSF integrating PVs

Study	PV				Window				DSF		Focus			Simulation				Location
	a-Si	Mono-Crystaline	Poly-Crystalline	Micromorph	Single	Double	Triple	Ventilated	Mechanically ventilated	Naturally Ventilated	Electrical	Thermal	Daylighting	Numerical model	Energy Plus	ESP-r	CFD	
J. Peng et al (2015)	✓										✓							Solar Simulator
L.Robinson and A.Athienitis (2009)			✓			✓					✓		✓	✓				Montreal
K. E. Park et al (2010)			✓			✓					✓	✓						Solar Simulator
W. Liao and S. Xu (2015)	✓					✓					✓	✓		✓	✓			
F. Chen et al. (2012)	✓			✓	✓	✓					✓	✓						Solar Simulator
W. He et al (2011)	✓				✓	✓		✓			✓	✓					✓	Hefei
T. T. Chow et al (2009)	✓							✓			✓	✓				✓		Hong Kong
Olivieri et al (2014)	✓				✓						✓	✓	✓					Madrid
S. Xu et al (2014)					✓						✓	✓	✓		✓			Wuhan
J. Peng et al (2013)	✓									✓		✓						Hong Kong
L. Gaillard et al (2014)			✓							✓		✓		✓				Toulouse
J. Peng et al (2015)	✓									✓	✓	✓						Hong Kong
M. Wang et al (2017)	✓					✓				✓	✓	✓	✓		✓			Hong Kong

Based on the Mataro Library in Barcelona, Mei et al, developed a dynamic thermal model on TRNSYS for a DSF integrating STPV (Mei et al. 2003). For a 15% transparency and an assumed as constant transmittance-absorptance of 0.8 STPV panel a thermal model was developed. It is reported that the air at the outlet of the DSF-STPV can reach

50°C in summer and 40°C in winter and this preheated air can be introduced into the HVAC system to reduce the heating load by 12%. Based on the same building the potential to use a desiccant cooling machine in combination with the DSF-PV is investigated (Mei et al. 2006). The 70°C heated air within the DSF can be fed into the desiccant cooling machine and regenerate the sorption wheel, resulting into an average COP of 0.518 during the summer season. The approach of four different terms describing the ventilation gains, the transmission losses and the temperature components are used in a steady state analysis to simulate the Mataro Library DSF-PV (Infield, Mei, and Eicker 2004) (Infield et al. 2006). In this way, monthly U and g values have been derived and the energy thermal gains have been calculated.

An integral (electrical, thermal and daylight) simulation model is used to carry out an annual performance study for an architype office building located at Toronto, Canada (Kapsis and Athienitis 2015). The model is experimentally-verified. The analysis demonstrates that the use of STPV façades have the ability to generate enough electricity to cover the annual electricity demand of the building on electric lighting and plug loads. In case of STPV/T or double skin façade, a significant amount of heat (in the form of preheated outdoor air) could be also generated. The heated air could be used to a solar assisted air-source heat pump that could be used to partially cover the heating and cooling demands of the building. Moreover, the use of STPV/T or double skin façade reduces the heat losses through the building skin during the heating season.

3. Experimental set-up

Two virtually identical semi-transparent photovoltaics (STPV) are used for this experimental set-up, located in Montreal, Canada (45° 30' N / 73° 35' W). The first STPV is used as the exterior layer of a DSF forming in this way a DSF-PV and the second one is used as the exterior layer of an Insulating Glazing Unit (IGU-PV). For each STPV, 48 cells of 17.80% nominal efficiency are used and are distributed in 8 rows with 6 cells in each row. In Figure 1, the experimental test cell is presented, showing the IGU-PV on the left side and the DSF-PV on the right. An automated damper with a Belimo actuator (0-5V) is integrated underneath the DSF-PV and is controlled to ventilate the DSF-PV. The test cell faces towards the south, while the south view of the façade is shown on the panoramic picture of Figure 1. It can be seen that most of the days of the year, the sky-scraper at the east, south-east shades the test cell, in the early morning and for a couple hours after the solar noon the test cell is shaded by the building that is located at the south, south-west.

The characteristics of the STPV modules are presented in Table 2 and the layers of the first and the second STPV are show in Figure 2. Both the STPV have the same layers: glass, Ethylene-vinyl Acetate (EVA), PV cells, EVA and glass. The dimensions of both the STPV panels is 1.968m by 0.992m and the PV cells used are square and have sides of 15.6cm, while the seven transparent strips have a width of approximately 10.3cm. In this way, 63.4% of the area is covered by the cells and the remaining 36.6% is transparent. The insulating glazing unit is assembled with a hard low emissivity coating at the back of the STPV. The space between the STPV and the double glazing is vacuum and 13mm wide.

The cavity of the DSF-PV is 17cm wide and the back layer of the DSF-PV extends from the bottom of the test-cell to a height of 1.90m. The top of the DSF-PV is sealed and a plenum is used to collect the air and drive it through a manifold (Figure 3). A rectangle FLST 25.4cm by 25.4cm (10in by 10in) flow meter by Dwyer is flashed at the middle of this manifold and its location is selected to be at distance from previous and later elbows that could affect the flow.

Both the systems are integrated on the test-cell using mullions and pressure plates that are mainly used in curtainwall applications. On the interior side of the DSF-PV, the double glazing that is used as the interior layer of the DSF-PV, is mounted following the same principal. In this way, the mullion in its width acts as the spacer between the internal and external layer of the DSF-PV and makes it easy for the integration on buildings.

Thermocouples (T-type) are place on the interior side of the STPV and on both sides of the clear IGU of the DSF-PV. In addition, thermocouples are placed in the middle of the cavity, approximately 8.75cm from each side and in the vertical direction. The thermocouples are placed at the same heights in all layers and are evenly distributed along the

height of the DSF-PV (Figure 3). Because the dampers are located underneath the exterior layer of the DSF-PV, the thermocouples on the DSF-PV start at the second height level. Similarly, because of the manifold, the thermocouples on the interior layer stop before the last height level. In Figure 3, all sixteen of the height levels of the thermocouples are shown with each color indicating a different layer.

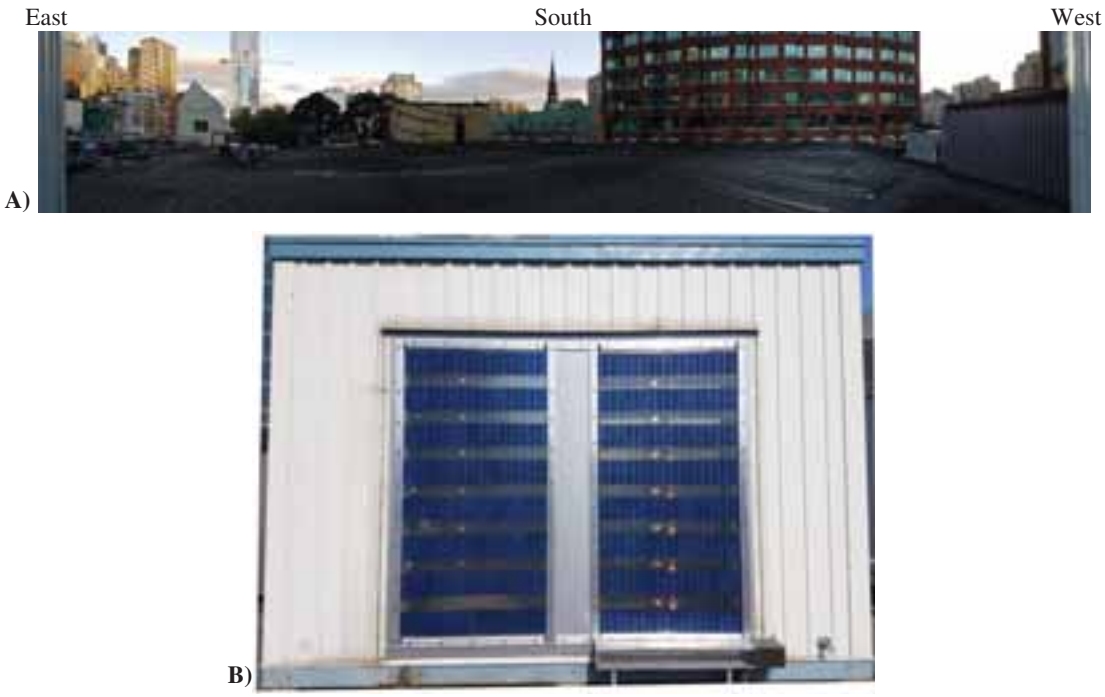

Figure 1 A) View from the south façade of the test-cell, where the STPV are integrated. B) The IGU-PV is installed on the left and the DSF-PV is on the right. The mechanical dampers are shown under the DSF-PV installation.

Table 2 Electrical data of the STPV integrated on the DSF-PV and the IGU-PV

	STPV #1 (DSF-PV)	STPV #2 (IGU-PV)
I_{sc}	8.55 A	8.57 A
V_{oc}	29.90 V	29.98 V
P_{max}	186.39 W	187.95 W
eff	10.6 %	10.7 %
		*under Standard Test Conditions

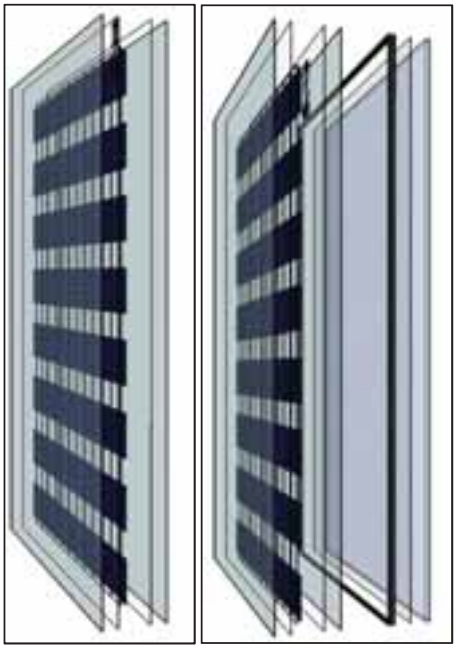

Figure 3 Layers of the STPV used at the DSF-PV (Left) and of the IGU-PV (Right).

Figure 3 Thermocouples are placed on four layers on the DSF-PV (Left) and on the IGU-PV (Right).

For the IGU-PV, thermocouples were installed on the side of the IGU that faces the room, distributed in the same way as they are on the DSF-PV. The data acquisition system used is the LabView using national instruments (NI). For the thermocouples the NI 9213 module is used (National-Instruments 2016). For the accurate measurement of the power output of the DSF-PV and the IGU-PV, an identical electric assembly was set up for each PV module. This assembly consist of a charge controller with maximum power point tracker (MPPT) a battery of 12 V and 110 Ah and a dump load (TE Connectivity 2005). The multi-stage MPPT solar charge controllers used are the Solar Boost SB3024i (Blue Sky Energy Inc. 2009) and the battery is the 8A31DT AGM sealed (MK Battery 2015). The voltage of each PV module is measured with a NI 9223 module (National Instruments 2016) and a shunt resistor (Riedon Inc. 2018) is used to measure the current flowing from the PV. The electrical configuration and connections are shown in Figure 4. The selection of shut resistor was based on the range and precision of the voltmeter. In our case a NI 9213 was used to measure the voltage difference (range of $\pm$78 mV) and using a safety factor of two (2) over the short circuit current from the PV (~16 A), the value of the shunt resistor was calculated to be 5 mΩ. For the selection of the battery, an empirical rule was used to calculate the battery capacity (Ah), which is equal to the watt peak of the STPV multiplied by the daily solar exposure and the days of battery autonomy of the system, divided by the battery loss factor, the depth of discharge and the battery voltage. In order the MPPT to supply the battery with the maximum current possible, the battery should not be full and this is why a single day of battery autonomy was preferred. Assuming that the PV average daily solar exposure is three hours, the battery loss is 0.85 and the depth of discharge is 0.5 the battery capacity is calculated to be approximately 110 Ah. A resistor is used as dump load to release, in the form of heat, the total electricity generated by the STPV and stored at the battery, during the night, when the heating loads from the resistors will not interact with the STPV experiments. For a 1 Ω resistor and a 12 V battery supply, a 144 W resistor should be used, instead a 300 W resistor was selected to avoid the overheating of the resistor.

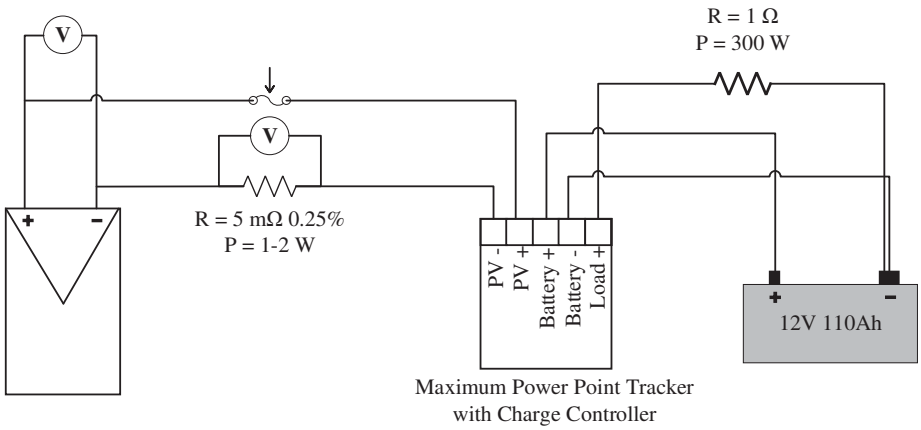

Figure 4 Schematic showing the electrical connection between the STPV, the MPPT and the batteries. The location of the shunt resistors used for the current measurement and the resistors used as a dump load is shown.

4. Experiments and result discussion

The test-cell and the experimental set-up described earlier, is used to characterize the electrical performance of the DSF-PV and the IGU-PV. In addition, a comparison is held between their performance under the same exterior and interior condition.

Experiments that are presented in this paper are for a series of eight (8) consecutive days, under different weather conditions and under different ventilation strategies for the cavity of the DSF-PV. The average velocity within the cavity and the incident solar radiation for these days are presented in Table 3. From Table 3, it can be extracted that for all the monitored days, the DSF-PV out-performs the IGU-PV by a 3% to 10% difference, depending on the strategy selected for the ventilation of the cavity of the DSF-PV.

From the same table, it can be seen that clear sky days are Day 1,4,6,7 and 8 and the overcast days are Day 2, 3, 5. If the cavity is ventilated, the electricity production of the STPV integrated on the DSF is greater than this of the IGU-PV by 7.27% to 9.20%. The days that the cavity is ventilated but the sky is overcast (Day 2 and 3), the electrical performance of the DSF-PV is approximately 4.5% greater than the IGU-PV. Lastly, when the cavity is closed, the difference between the electricity generated by both the STPV, is the smallest encountered but is still between 3.6% and 4.1%. On the last column of Table 3, the percentage of the time that the power of the DSF-PV is greater than the Power of the IGU-PV is presented showing that more than 87% of the time, the DSF-PV performs better than IGU-PV

In Figure 5, a comparison of the power produced and the current generated by the DSF-PV and the IGU-PV is depicted for Day 1 between 7:00 AM and 2:40 PM. The shaded with different colors zones, represent time-periods where different average velocities within the cavity were measured, due to different fan operation.
As it can be seen, the power generation between 7:30AM and 8:00AM drops and this is because of the shading that is provided to the test-cell by the sky-scraper presented in Figure 1. For the same reason, the power drops after 2:15PM, where the building located at the south-west shades the test-cell. The power of the IGU-PV drops first, as it is located on the west side of the test-cell.
When the cavity of the DSF-PV starts to be ventilated, the power generated by the DSF-PV starts to be greater that this of the IGU-PV. The current generated by both the STPVs is almost identical, and this is because the STPV are similar and under the same incident solar radiation. On the other hand, the difference of the power generated by the integrated STPVs should be correlated to the voltage difference created by each system and thus the temperature their cells, as the operating voltage of the STPV panels is dependent on the temperature of the cells.

For the same day (Day 1), the power generated by the DSF-PV and IGU-PV and the voltage at which this power is generated is shown in Figure 6. It can be seen that the DSF-PV operated at a higher voltage of about 2 V than the

IGU-PV. Consequently, the power generated by the DSF-PV is approximately 10 W higher than this of the IGU-PV, for the majority of the time, resulting in the average 9.20% difference presented in Table 3.

Table 3 Experimental data for eight (8) consecutive days in Montreal.

	Average Velocity within the Cavity	Average Incident Solar Radiation (W/m^2/day)	Average diffuse Solar Radiation (W/m^2/day)	Electricity generated by the DSF-PV (Wh/day)	Electricity generated by the IGU-PV (Wh/day)	Daily Difference	Percentage of time $P_{DSF}>P_{IGU}$
Day 1	1.25 m/s	194	44	704.01	644.67	9.20%	96.49
Day 2	0.65 m/s	156	70	561.06	537.31	4.42%	93.81
Day 3	1.10 m/s	156	77	462.91	442.40	4.64%	89.27
Day 4	closed	201	46	637.04	611.58	4.16%	91.24
Day 5	1.20 m/s	170	61	637.62	594.39	7.27%	95.72
Day 6	closed	203	29	754.09	725.23	3.98%	89.85
Day 7	closed	201	25	768.62	741.85	3.61%	87.58
Day 8	1.20 m/s	192	31	742.65	683.23	8.70%	97.72

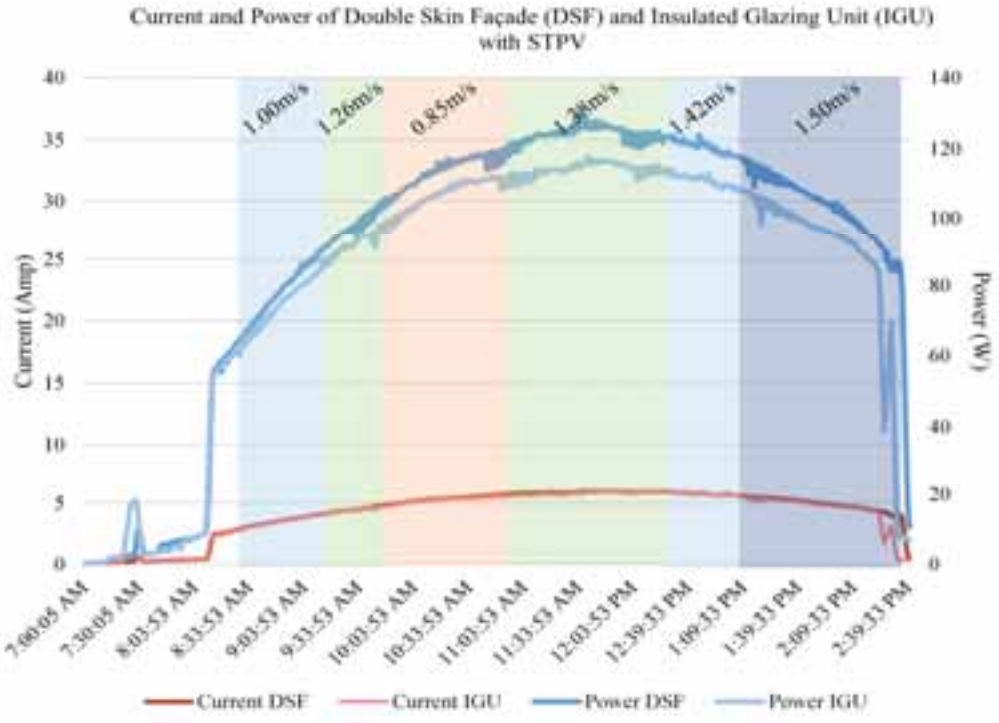

Figure 5 Power production and current of the STPV panels integrated on the DSF and the IGU on Day 1, with an average velocity within the cavity of approximately 1.25m/s.

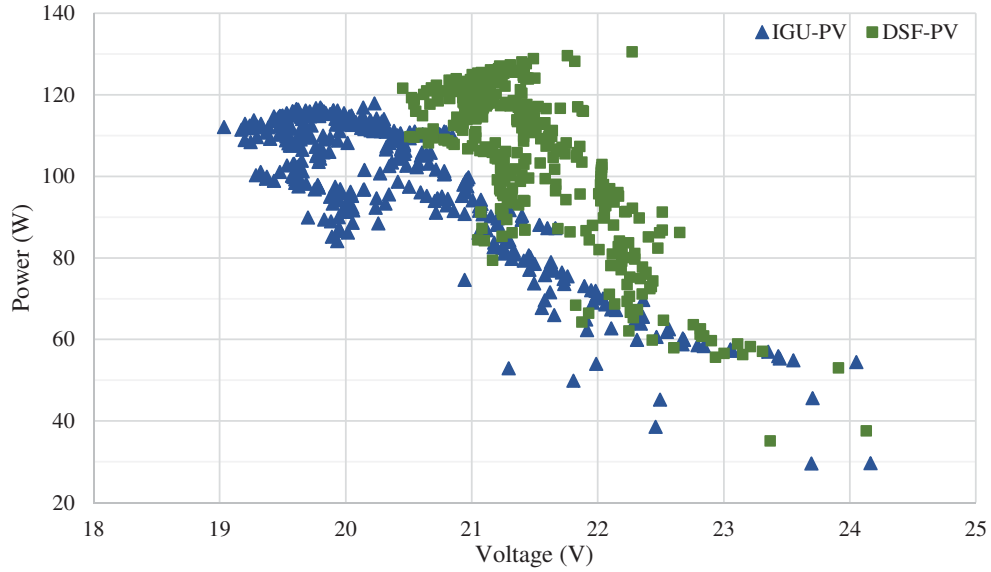

Figure 6 Power production of the STPV panels integrated on the DSF and the IGU in comparison to their voltage output on Day1, with an average velocity within the cavity of approximately 1.25m/s.

5. Conclusions

This study is focused on assessing the electrical performance of two similar STPV panels under the same exterior and interior conditions, integrated on different systems. An exterior experimental facility is set up to monitor the electrical performance of the STPV panel integrated on the exterior layer of a DSF and on an IGU, forming in this way a DSF-PV and an IGU-PV.

It should be noted, that the study presents some limitations. One of these is the short duration of the experiment. In the contrary, these days are around the September equinox and thus makes it easier for the results to be used for future studies and simulations. Also, the eight (8) monitored days that are presented in this manuscript are part of a longer experiment that is set-up to run for a whole year, in Montreal (Canada). Annual results can be later used, with more confidence to simulate IGU-PV and DSF-PV under different climatic conditions.

During the monitored days, the STPV integrated on the DSF out-performs the one integrated on the IGU. For all the eight (8) monitored days that the experiment lasted, the electrical performance of the DSF-PV presented increased values between 3% and 9% depending on the ventilation strategy of the cavity of the DSF-PV and the incident solar radiation. Even when the DSF-PV is not ventilated and acts as a buffer zone, the electrical performance of the STPV panels is 3% to 4.5% greater than this of the IGU-PV.

6. Acknowledgments

The authors would like to acknowledge the support of Unicel Architectural, Canadian Solar and the Hydro Quebec Industrial Chair.

7. References

Blue Sky Energy Inc. 2009. “SB3024i Datasheet.” Retrieved April 30, 2018 (http://www.blueskyenergyinc.com/uploads/pdf/SB3024(D)iL_Datasheet_(2017)_1.pdf).

Chen, Fangzhi, Stephen K. Wittkopf, Poh Khai Ng, and Hui Du. 2012. “Solar Heat Gain Coefficient Measurement

of Semi-Transparent Photovoltaic Modules with Indoor Calorimetric Hot Box and Solar Simulator." *Energy and Buildings* 53:74–84.

Chow, Tin Tai, Zhongzhu Qiu, and Chunying Li. 2009. "Potential Application Of 'see-Through' solar Cells in Ventilated Glazing in Hong Kong." *Solar Energy Materials and Solar Cells* 93:230–38.

TE Connectivity. 2005. "HSC100 METAL HOUSED POWER RESISTOR." Retrieved April 30, 2018 (http://www.te.com/commerce/DocumentDelivery/DDEController?Action=srchrtrv&DocNm=1625999&DocType=Customer+Drawing&DocLang=English).

Gaillard, Leon, Stéphanie Giroux-Julien, Christophe Ménézo, and Hervé Pabiou. 2014. "Experimental Evaluation of a Naturally Ventilated PV Double-Skin Building Envelope in Real Operating Conditions." *Solar Energy* 103:223–41.

Gaillard, Leon, Christophe Ménézo, Stéphanie Giroux, Hervé Pabiou, and Rémi Le-Berre. 2014. "Experimental Study of Thermal Response of PV Modules Integrated into Naturally-Ventilated Double Skin Facades." *Energy Procedia* 48:1254–61.

He, Wei et al. 2011. "Experimental and Numerical Investigation on the Performance of Amorphous Silicon Photovoltaics Window in East China." *Building and Environment* 46(2):363–69. Retrieved (http://dx.doi.org/10.1016/j.buildenv.2010.07.030).

Infield, David, Ursula Eicker, Volker Fux, Li Mei, and Jürgen Schumacher. 2006. "A Simplified Approach to Thermal Performance Calculation for Building Integrated Mechanically Ventilated PV Facades." *Building and Environment* 41(7):893–901.

Infield, David, Li Mei, and Ursula Eicker. 2004. "Thermal Performance Estimation for Ventilated PV Facades." *Solar Energy* 76(1–3):93–98.

James, P. A. B., M. F. Jentsch, and A. S. Bahaj. 2009. "Quantifying the Added Value of BiPV as a Shading Solution in Atria." *Solar Energy* 83(2):220–31.

Kapsis, Konstantinos and Andreas K. Athienitis. 2015. "A Study of the Potential Benefits of Semi-Transparent Photovoltaics in Commercial Buildings." *Solar Energy* 115:120–32. Retrieved (http://dx.doi.org/10.1016/j.solener.2015.02.016).

Liao, Wei and Shen Xu. 2015. "Energy Performance Comparison among See-through Amorphous- Silicon PV (Photovoltaic) Glazings and Traditional Glazings under Different Architectural Conditions in China." *Energy* 83:267–75. Retrieved (http://dx.doi.org/10.1016/j.energy.2015.02.023).

Mei, Li, David Infield, Ursula Eicker, and Volker Fux. 2003. "Thermal Modelling of a Building with an Integrated Ventilated PV Facade." *Energy and Buildings* 35(6):605–17.

Mei, Li, David Infield, Ursula Eicker, and Dennis Loveday. 2006. "Cooling Potential of Ventilated PV Facade and Solar Air Heaters Combined with a Desiccant Cooling Machine." 31:1265–78.

Miyazaki, T., a. Akisawa, and T. Kashiwagi. 2005. "Energy Savings of Office Buildings by the Use of Semi-Transparent Solar Cells for Windows." *Renewable Energy* 30:281–304.

MK Battery. 2015. "8A31DT AGM Battery." Retrieved April 30, 2018 (http://www.mkbattery.com/images/8A31DT.pdf).

National-Instruments. 2016. "NI 9213 Datasheet." Retrieved April 29, 2018 (http://www.ni.com/pdf/manuals/374916a_02.pdf).

National Instruments. 2016. "NI 9223 Datasheet." 1–12. Retrieved April 30, 2018 (http://www.ni.com/pdf/manuals/374223a_02.pdf).

Olivieri, L., E. Caamaño-Martin, F. Olivieri, and J. Neila. 2014. "Integral Energy Performance Characterization of Semi-Transparent Photovoltaic Elements for Building Integration under Real Operation Conditions." *Energy and Buildings* 68:280–91.

Park, K. E., G. H. Kang, H. I. Kim, G. J. Yu, and J. T. Kim. 2010. "Analysis of Thermal and Electrical Performance of Semi-Transparent Photovoltaic (PV) Module." *Energy* 35(6):2681–87.

Peng, Jinqing et al. 2016. “Numerical Investigation of the Energy Saving Potential of a Semi-Transparent Photovoltaic Double-Skin Facade in a Cool-Summer Mediterranean Climate.” *Applied Energy* 165:345–56.

Peng, Jinqing, Lin Lu, and Hongxing Yang. 2013. “An Experimental Study of the Thermal Performance of a Novel Photovoltaic Double-Skin Facade in Hong Kong.” *Solar Energy* 97:293–304.

Peng, Jinqing, Lin Lu, Hongxing Yang, and Tao Ma. 2015a. “Comparative Study of the Thermal and Power Performances of a Semi-Transparent Photovoltaic Façade under Different Ventilation Modes.” *Applied Energy* 138:572–83.

Peng, Jinqing, Lin Lu, Hongxing Yang, and Tao Ma. 2015b. “Validation of the Sandia Model with Indoor and Outdoor Measurements for Semi-Transparent Amorphous Silicon PV Modules.” *Renewable Energy* 80.

Qiu, Z. et al. 2009. “Performance Evaluation of the Photovoltaic Double Skin Facade.” *11th International IBPSA* 2251–57.

Riedon Inc. 2018. “Precision Current Resistor / DC Current Shunts.” Retrieved April 30, 2018 (https://riedon.com/media/pdf/RS.pdf).

Robinson, Leanne and Andreas Athienitis. 2009. “Design Methodology For Optimization Of Electricity Generation And Daylight Utilization For Façade With Semi-Transparent Photovoltaics.” *11th International IBPSA Conference, Building Simulation 2009* 811–18.

Tzempelikos, Athanassios and Andreas K. Athienitis. 2007. “The Impact of Shading Design and Control on Building Cooling and Lighting Demand.” *Solar Energy* 81(3):369–82.

Vartiainen, Eero. 2001. “Electricity Benefits of Daylighting and Photovoltaics for Various Solar Facade Layouts in Office Buildings.” *Energy and Buildings* 33:113–20.

Veitch, Jennifer A. and A. D. Galasiu. 2011. “The Physiological and Psychological Effects of Windows, Daylight and View at Home.” *National Research Council of Canada* 60.

Wang, Meng et al. 2017. “Comparison of Energy Performance between PV Double Skin Facades and PV Insulating Glass Units.” *Applied Energy* 194:148–60. Retrieved (http://dx.doi.org/10.1016/j.apenergy.2017.03.019).

Xu, Shen, Wei Liao, Jing Huang, and Jian Kang. 2014. “Optimal PV Cell Coverage Ratio for Semi-Transparent Photovoltaics on Office Building Façades in Central China.” *Energy and Buildings* 77:130–38.

Influence of Solar Radiation on Classroom Environment in High Latitude and Rich Solar-Resource Areas

Jing Jiang[1], Dengjia Wang[1], Yanfeng Liu[1], Yaowen Chen[1] and Jiaping Liu[2]

[1] School of Environmental and Municipal Engineering, Xi'an University of Architecture and Technology, Xi'an (China)

[2] School of Architecture, Xi'an University of Architecture and Technology, Xi'an (China)

Abstract

Understanding of the knowledge of classroom temperature distribution is critical to design of solar system terminal. The temperature non-uniformity caused by solar radiation is not negligible, especially in high-latitude and strong radiation areas. This paper presents a detailed and comprehensive experiment in a primary and secondary school in northwestern China that was used to determine the thermal distribution and validate a simulation model. The temperature variations in both the vertical and horizontal directions were analyzed in detail. The indoor air temperature distribution was investigated with a systematic simulation of different conditions, including five solar radiation intensity levels, four southern external walls thicknesses and five window-to-wall area ratios. The results showed that the average air temperature difference in the vertical direction was nearly 3.0°C, whereas it was approximately 1.0°C in the horizontal direction. The optimal results of the non-uniform temperature distribution can provide the basis for determining the parameters of thermal design and heating system settings in primary and secondary school classrooms.

Keywords: Temperature distribution, simulation, classroom, non-uniform, in-situ measurement,

1. Introduction

Healthy and comfortable microclimate conditions are essential in any type of environment, but schools in particular are buildings, in which a high level of environmental quality can considerably improve attention, concentration, learning, listening and performance (Corgnati et al. 2007; Corrado and Astolfi, 2002).The need to provide good environments in commercial and educational buildings relies on the fact that people spend more than 90% of their time indoors. Students spend approximately 30% of their life in schools (Valeria et al. 2012), so researching the thermal environment in schools is essential. Existing research on indoor thermal environments has primarily focused on thermal comfort in the whole environment; information on indoor temperature distribution is limited, as current studies on indoor temperature distribution have concentrated on urban office and residential buildings (Srebric et al. 2008; Catalina et al. 2009). However, primary and secondary schools are different because students have a higher metabolic rate, classrooms have a higher density of personnel, and classroom time is relatively fixed. Thus, current distribution laws may not apply to primary and secondary school classrooms in northwestern China due to the unique indoor thermal environment requirements for students; it is essential that it need to study these temperature distributions.

Indoor temperature distribution is not only affected by interior personnel and equipment but also by factors such as wall thickness, materials and window-to-wall ratios etc. The latter factor is significantly influenced by solar radiation and other outdoor parameters. Because of economic underdevelopment, improving the indoor thermal environment of primary and secondary schools has primarily relied on renewable solar energy resources. This provides the basis and foundation for the study of classroom temperature distribution under different conditions for the construction of solar buildings.

Computational fluid dynamics (CFD) is a proven and effective simulation tool for predicting and analyzing buildings with reliable results. Building temperature and other parameters are strongly affected by the outdoor environment and the building envelope properties, which can be simulated and predicted using CFD (Desta and Janssens, 2004). Currently, CFD consistently provides a convenient method for indoor thermal environment evaluation and design for offices (Stamou and Katsiris, 2006), lecture halls(Cheng et al. 2003), and industrial

doi:10.18086/swc.2017.12.05 Available at http://proceedings.ises.org

premises (Rohdin and Moshfegh, 2007). Catalina (Catalina et al. 2009) showed test results for wall surface temperatures to be consistent with thermal boundary conditions. Rundle (Rundle et al. 2011) simulated indoor air temperature distribution given the temperature boundary condition of the outside wall surface and the heat flux boundary condition of the indoor heat source. In addition, because of the complex nature of windows, research has rarely considered the natural convection and radiation coupling of windows and the indoors. Behnia (Behnia et al. 1990) considered the effect of solar radiation and change of temperature inside the glass when modeling windows. Ismail (Ismail and Henriquez, 2003) simulated a corridor with a window inside of an air flow and temperature distribution and then analyzed the building energy consumption and use of solar energy. CFD is essential when studying the heat transfer properties of glass and room air flow and temperature effects.

A comprehensive test was conducted to determine the temperature distribution features of primary and secondary school classrooms with enriched solar energy resources in an actual passive solar classroom. On the basis of the actual test, temperature distribution is simulated through Fluent. There was a high degree of concurrence between the measured and the simulated results. The indoor air temperature distribution was investigated with a systematic simulation of different conditions, including different solar radiation intensity levels, southern external walls thicknesses levels and five window-to-wall area ratios. Therefore, the non-uniform characteristics of temperature change provided the foundation for the construction designs of solar buildings and system heating settings.

2. Methods

2.1. Experimental classroom

The experimental classroom was located in Huangzhong County (latitude:36°34′N, longitude:101°49′E, altitude: 2645m), Qinghai, China, where the average annual air temperature and precipitation were 5.1°C and 509.8mm, respectively, as provided by a meteorological station.

The experimental classroom is shown in Fig. 1. The east, west and north walls were constructed of 20 mm of plaster, 300 mm of aerated bricks, 20mm of polystyrene board and 20 mm of plaster. The roof and ground structures were constructed with 200 mm of steel-reinforced concrete and 50 mm of aerated concrete and 100 mm of poured concrete and 80mm of polystyrene board, respectively. The heat transfer coefficient of the windows was 1.1 (W m-2 K-1). The size of the south window was 2.3m×1.8m×2; the north window was 1.8m×0.9m×1.The north door was 2.1m high×0.9m wide in the front and back of the classroom.

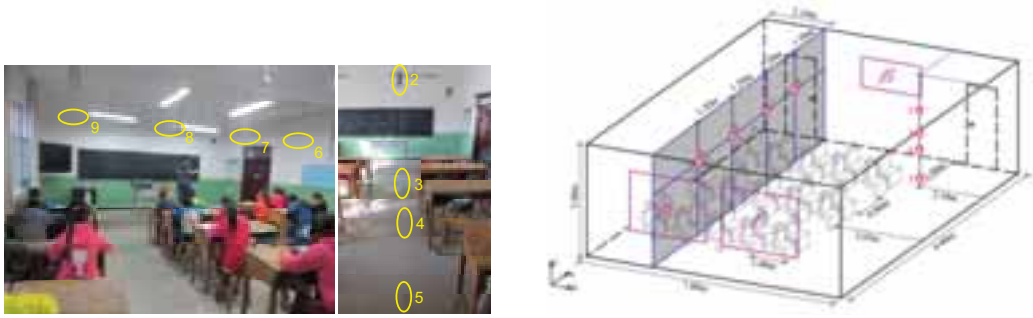

(a) Layout of experimental classroom (b) A real-scale 3-D model of the experimental classroom

Fig. 1: Measurement locations and dimensions of the experimental classroom

2.2. Measuring parameters, instruments and experimental procedure

The outdoor temperature and relative humidity were simultaneously measured according to the indoor classroom measurements by means of a portable automatic meteorological station located on the roof of the school building. The indoor environment measurements were automatically recorded every 10 minutes over 24h every day for a total of seven days (from 5 to 11 December 2015). Tab. 1 summarizes the characteristics of the equipment. The measurement equipment was fitted to the classroom to collect indoor environmental variables, such as air temperature, relative humidity, air velocity. The equipment was placed at eight locations inside the classroom and at one outdoor location without disturbing class activities and far from any heat sources, such as projectors or computers. The detailed measurement points are shown in Tab. 2 and correspond to Fig. 1.

Tab. 1: Measuring equipment specifications

Parameters	Instrument	Model	Accuracy	Operating method
Solar radiation intensity	Solar pyranometer	TBD-1	±8.789 W m^{-2}	Automatic recording every 10 min
Outdoor air temperature and relative humidity	Portable automatic meteorological station	Vantage Pro2	±0.5°C/±5%	
Indoor air temperature and relative humidity	Recording thermometer	TR-72U	±0.2°C/±5%	
Wall surface temperature	Thermocouple thermometer	CENTER309	±(0.3%rdg)+1°C	

Tab. 2: Measurement details of monitored positions at the cross-section shown in Fig. 1

Monitored position(P)	Measured items	Notes
1(Not shown)	Outdoor air temperature, Wind velocity, Solar radiation, etc.	Portable automatic meteorological station placed on roof (open space)
2	Indoor air temperature	Height:2.30m
3		Height:1.60m
4		Height:1.10m
5		Height:0.25m
6/7/8/9	Indoor air temperature	Height:2.30m

2.3. Computer simulation

Physical model. A real-scale 3-D model (shown in Fig. 1) of the experimental classroom was created with two modules: for fluid computational domains such as inside and outside air, and solid computational domains such as walls, roof and floor. Energy and Standard *k*-*ε* Turbulence Models were selected.

Model simplifications. 1) Humidity was not taken into consideration; 2) Air exchange between the inside and outside of the classroom was neglected because natural ventilation was negligible for the closed experimental classroom; and 3) The heat processes of the east wall, west wall and roof were considered to be adiabatic.

Governing equations. CFD is a numerical methodology that solves the governing equations of fluid flow by using a finite volume method to convert partial differential equations into a set of algebraic equations (Molina-Aiz et al. 2010; Zhang et al. 2016). It is based on the resolution of the governing equations of three conservation laws that include mass, energy, and momentum transport equations as follows (Versteeg and Malalasekera, 1995):

$$\frac{\partial(\rho\delta)}{\partial t} + div(\rho\mu\delta) = div(\Gamma_\delta \cdot grad\delta) + S_\delta \qquad \text{(eq. 1)}$$

where δ is the universal variable; ρ, μ, Γ_δ and S_δ are the density (kg m^{-1}), velocity vector (m s^{-1}), generalized diffusion coefficient (m^2 s^{-1}), and source term (W m^{-1}), respectively. This presents as a continuity equation when δ is 1, an energy equation when δ is T and a momentum equation when δ is u, v, w (m s^{-1}) with velocities in the directions of x, y, and z, respectively.

Initial and boundary conditions. Five types of boundary conditions were defined: the outside air temperature (T_{out}), the air temperature of the north corridor (T_c), the radiant sky temperature (T_{sky}), the surface convective heat transfer coefficient (h_o) and the soil surface temperature (T_f). The initial temperature of the inside air was set as an average value at 8:00 during the experimental period.

The air temperature (including T_{out} , T_c)changed over time; the conduction equation was solved inside the walls and can be fitted based on the experimental data during the entire day as follows:

$$T_{out} = 268.7 - 6.9 \times \cos(0.000073\tau + 5.2) \qquad R^2 = 0.9173 \qquad \text{(eq. 2)}$$

from 8:00(t=0 s $\tau = t + 3600 \times 8$) to 18:00(t=36000s)

$$T_c = 276.8 - 0.5 \times \cos\left(0.000073\tau - 26.3\right) \qquad R^2 = 0.7222 \qquad \text{(eq. 3)}$$

where τ is the time(s) and $28800 \le \tau \le 36000$; R^2 is the degree of fitting.

The heat transfer of the exterior wall can be determined by the convective heat transfer coefficient that can be calculated by eq. (4).

$$K_0 = \frac{1}{\frac{1}{h_i} + \sum \frac{d}{\lambda} + \frac{1}{h_o}} \qquad \text{(eq. 4)}$$

where K_0 is the heat transfer coefficient, W m^{-2} K^{-1}; h_i and h_o are the heat transfer coefficients of the inner and outer wall surfaces, respectively, W m^{-2} K^{-1}; d is the thickness of the wall, m; and λ is the thermal conductivity coefficient, W m^{-1} K^{-1}.

The thermal radiant exchange with the sky influences the heat balances of the exterior wall. It is therefore necessary to determine the radiant sky temperature T_{sky} (Tang et al. 2003). The following proposed empirical formula (Berdahl and Fromberg, 1982) was used:

$$T_{sky} = \varepsilon_{sky}^{0.25}\left(T_a + 273\right) \qquad \text{(eq. 5)}$$

$$\varepsilon_{sky} = 0.74 + 0.006T_{dp} \qquad \text{(eq. 6)}$$

where T_a is ambient air temperature, K.

The dew point temperature T_{dp} has the following empirical correction expressed in degrees Celsius(Cook,1985):

$$T_{dp} = 26.14 + 16.99C + 1.8893C^2 \qquad \text{(eq. 7)}$$

$$C = \ln\left(Rh \cdot Pa\right) = \ln\left(Rh\right) - 8.0929 + 0.97608\left(T_a + 42.607\right)^{0.5} \qquad \text{(eq. 8)}$$

where Rh is the relative humidity, %; and Pa is the saturation vapor pressure of the air at any air temperature.

The final fitting equation of T_{sky} is below:

$$T_{sky} = 276.8 - 6.8 \times \cos\left(0.000073\tau + 5.2\right) \qquad R^2 = 0.8498 \qquad \text{(eq. 9)}$$

To conveniently validate and utilize the established simulation model, the floor was regarded as playing a constant wall temperature role.

The evaluation of the metabolic rate in the school building was obtained from Havenith (Havenith, 2007), who studied the metabolic rate and clothing insulation of children and adolescents. The metabolic rate was set at 52 W m^{-2} in accordance with a simple writing task or sedentary activity. The total heat release of a human body was set at 76 W per person (Srebric et al. 2008). The temperature around the body was simulated by a given body surface heat flux.

2.4. Model applications

Once the computer simulation was validated, it was used to predict the thermal environment with different conditions in terms of varying solar radiation intensities, south external wall thicknesses and window-to-wall area ratios, as listed in Tab. 3. The same model parameters, initial and boundary conditions and solving methodology were used in all models.

Tab. 3: Different cases of different conditions for simulation

(a) Five cases of solar radiation intensity for simulation

Case	Solar radiation intensity level(W m^{-2})
1	800
2	600(Case validation)
3	400
4	200

5	100

(b) Four cases of thickness of the south wall for simulation

Case	Thickness of the south wall(mm)
1	240+20
2	370+20(Case validation)
3	520+20
4	630+20

(c) Four cases of window-to-wall area ratio for simulation

Case	Area ratio of window to wall	Length(m) × Width(m) × Number
1	0.3(Case validation)	2.3×1.8×2
2	0.4	2.4×2.4×2
5	0.5	2.8×2.5×2
3	0.6	3.0×2.8×2
4	0.7	3.2×3.2×2

3. Results and discussion

3.1. Measuring results and analysis

Ambient air conditions. Fig. 2 shows the indoor and outdoor air temperatures along with the solar radiation intensity for one measured day. During the day, the maximum global and direct radiation levels were 557 W m^{-2} and 470 W m^{-2}, respectively. The mean outdoor air temperature and relative humidity were -1.3°C and 54.6%, respectively. The air temperature ranged between 6.1°C and 13.4°C, with an average of 8.7°C during the day. The relative humidity ranged between 16% and 74% and the air velocity ranged from 0 to 0.49 m s^{-1}. However, the variations in global solar radiation, outdoor air temperature and indoor air temperature ranged from 0 to 557 W m^{-2}, from -6.2°C to 8.1°C, and from 6.1°C to 13.4°C, respectively, with averages of 284 W m^{-2}, 1.8°C and 10.8°C during the school day.

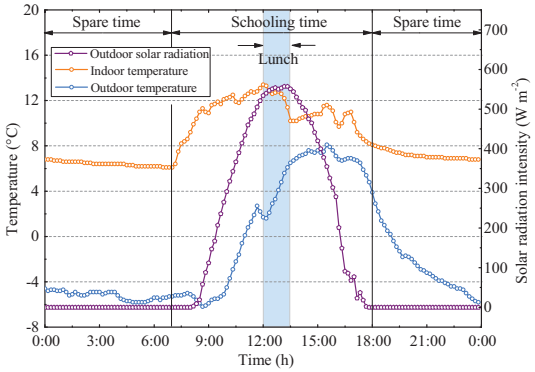

Fig. 2: Indoor and outdoor air temperatures and solar radiation intensity

Vertical temperature distribution. There are considerable differences in ambient building temperatures that also influence the distribution of temperature fields inside buildings. According to the measured temperature data, there was significant non-uniformity in the temperature field distribution inside the measured building. The uneven distribution of the temperature field was analyzed in the vertical and horizontal directions.

The temperature variation in the vertical direction is shown in Fig. 3(a). The building temperature field, as

observed in the temperature distribution, shows significant non-uniformity in the vertical direction. The measured temperature at 2.3 m was consistently higher than the other locations. The temperature at 1.6m was slightly higher than at 1.1m but substantially less than at 2.3 m. Obviously, the temperature is the lowest at ground level. It can be seen from the diagram that the change tendency of the four lines is roughly the same. The temperature decline was primarily due to students leaving the room for recess, lunch and nap. Heated air moves upward in the classroom, the heat loss of human body at 1.1~1.6m makes the temperature higher than at ground level (0.25m).

To facilitate analysis, the measured temperature data at representative timings (8:00, 10:30, 12:00, 12:30, 14:30, and 16:10) were selected for assessing non-uniformity. The temperature values at different points are shown in Fig. 3(b). It can be seen that the tendency of the temperature distribution was generally similar. The mean temperature during the school day (from 7:00 to 18:00) was calculated. In the range of 0.25 to 1.1m, the rate of temperature increase was greater due to the heat dissipation from the human bodies to the indoor environment at 2.0 °C m^{-1}. Because of the lower personnel density, the rate of temperature increase reached 0.8 °C m^{-1} at 1.1 to 1.6m.

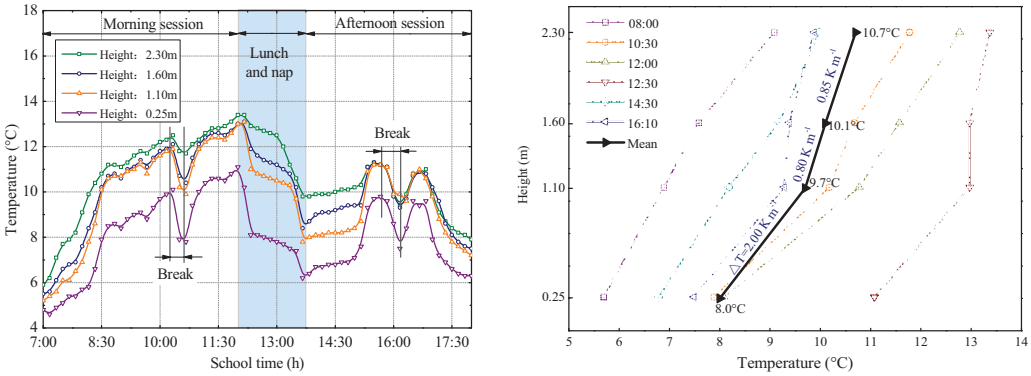

(a) Temperature variation (b) Temperature distribution at different times

Fig. 3: Temperature distribution in vertical direction

Horizontal temperature distribution. The temperature at the south measuring point was generally higher than the north. The average value was 11.4°C, 10.9°C, 10.8°C and 10.7°C from south to north in turns. It can be seen from Fig.4 (a). that the tendency of the temperature distribution was generally similar except for the curve at P9. Because the P9 point was located in the south, the influence of solar radiation was the strongest. From 16:00 to 17:00, the temperature at P9 rose sharply.

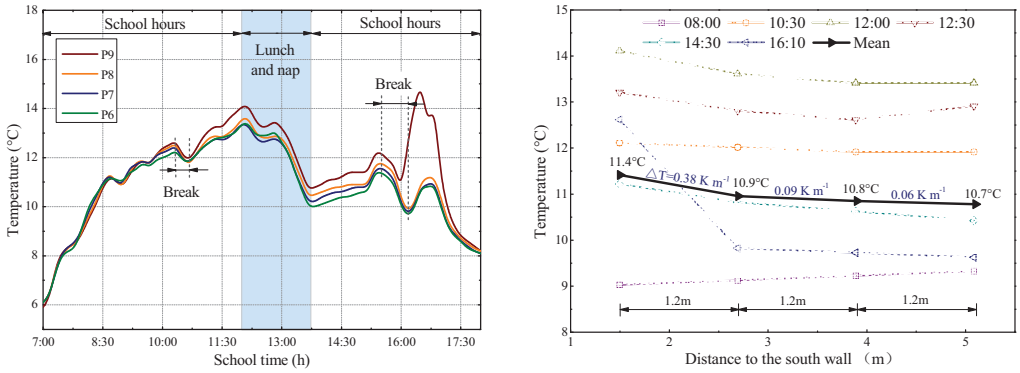

(a) Temperature variation (b) Temperature distribution at different times

Fig. 4: Temperature distribution in horizontal direction

The temperature values at different points are shown in Fig. 4(b). It can be seen that the tendency of the temperature distribution was generally similar except at 8:00 and 16:10. At 8:00, the temperature elevated from south to north due to less solar radiation. With the increase of solar radiation, the temperature increased rapidly at the south end of the room. At 16:10, the temperature at south rises sharply. The differences between the northern and southern temperatures are caused by the increased heat loss on the north side due to differences on both sides of the outdoor environment temperature in the winter and the increased solar radiation heat gain in

the south. Based on the above, solar radiation intensity plays a decisive role in the south - north temperature distribution differences.

3.2. Model validation

To verify the differences between the measured and simulated results and verify the reliability of the simulation and the measurements, a comparative analysis of the measured and simulated temperature values between 1.1 m and 1.6 m are shown in Fig. 5. It can be seen that the simulated temperatures at each measurement position concurred with the experimental temperatures, with the same trend over the measurement period. For example, the temperature tendencies of the measurement and the simulation at P3 in the morning and at P4 in the afternoon are shown in Fig. 5(a) and Fig. 5(b), respectively. It can be seen that the mean simulated results were higher than the measured results by 0.3°C to 0.4°C; the mean simulated and measured temperatures at P3 in the morning were 11.7°C and 11.3°C, and the mean simulated and measured temperatures at P4 in the afternoon were 9.9°C and 9.6°C, respectively. This small difference was caused by objective factors. Although the simulation closely adheres to the actual situation, there are certain simplifications that cannot be fully considered such as various indoor objects and accidental disturbances. In addition, the specific locations of the actual measuring points are not precisely the same as the simulation locations.

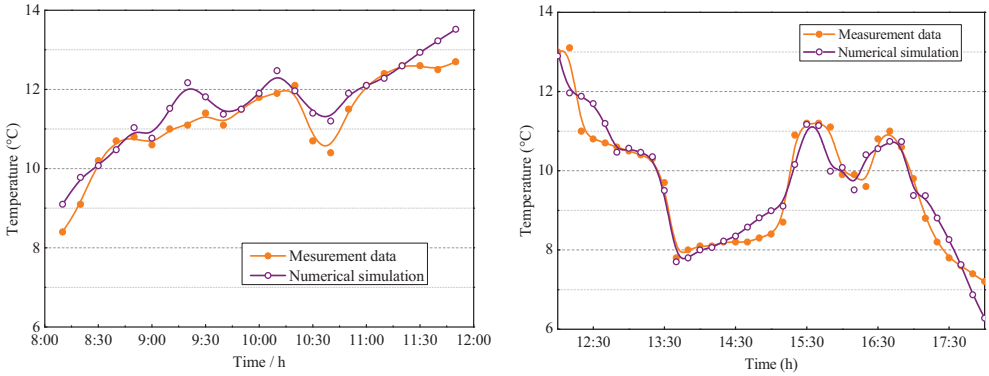

(a) Verification of P3 at 1.6m in the morning (b) Verification of P4 at 1.1m in the afternoon

Fig. 5: Comparison of the temperature distribution obtained by simulation and in-situ measurements

3.3. Simulated temperature distribution

Different solar radiation intensity levels. Fig. 6(a) shows the temperature changes of different positions at a height of 1.1m. The temperature at the same location essentially shows a linearly increasing trend with increasing solar radiation intensity. The temperature amplification differs with the increase of solar radiation at different locations from the south wall; the closer to the south wall, the greater the slope of increased temperature. The temperature increased by 2.3°C, 2.1°C and 1.9°C from distances of 0.8m, 3.3m and 5.8m to the south wall, respectively, when the solar radiation increased in100 W m^{-2} increments. At 3.3 m from the south wall, the temperature increased by 14.7°C when the solar radiation increased from 100 W m^{-2} to 800 W m^{-2}. The temperature increased by 0.7°C and 1.0°C at different locations from distances of 0.8m to 3.3m and from distances of 3.3m to 5.8m at a solar radiation of 600 W m^{-2}. The temperature gradient is lower when closer to the south wall and greater when further away.

Different thicknesses of south external wall. The simulation was carried out under the following conditions: a solar radiation of 600 W m^{-2}, a window-to-wall area ratio of 0.3, and a time of 12 noon. Fig. 6(b) shows the temperature changes of different positions at height of 1.1m.The temperature at the same location shows a trend of initial decrease and subsequent increase with the increase of south wall thickness. When the wall thickness is increased from 260mm to 390mm, the temperature significantly decreases by 5°C at 3.3 m distance to the south wall. When the wall thickness is increased from 390mm to 540mm, temperature slightly decreases by less by 1°C. When it increased from 540mm to 650mm, the temperature only decreases by 0.2°C. In short, the impact on indoor temperature is significant with increasing south wall thickness, but the indoor temperature will eventually rise when the wall thickness increases to a certain extent.

Different window-to-wall area ratios. The simulation was carried out under the following conditions: a solar radiation of 600 W m^{-2}, a 540-mm south wall thickness, and a time of and 12 noon. Fig. 6(c) shows the temperature changes of different positions at height of 1.1m. The temperature at the same location essentially

showed an increasing trend with the increased window-to-wall area ratios. The temperature growth trends differed with the increase of the window-to-wall area ratio at different positions to the south wall. At 0.8m from the south wall, the temperature increase was greater with an area ratio of 0.3 to 0.4 and more gradual with an area ratio of 0.4 to 0.7; the further from the south wall, the more gradual the temperature variation. This may be due to an increase in the area of the window. The window increases the quantity of heat but simultaneously contributes to heat loss because it is poorly constructed for heat gain and loss reduction.

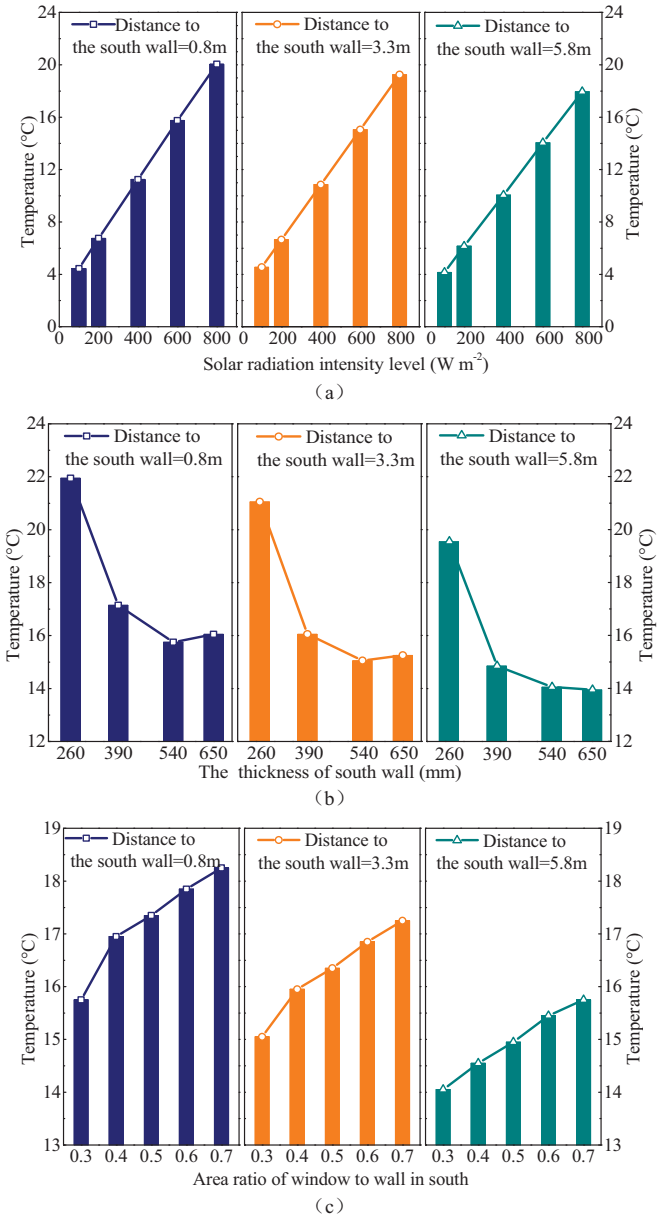

Fig. 6: The evolution of temperature distribution under different simulation cases

4. Conclusions

A computer simulation model using the finite-volume-based commercial software Fluent was used to evaluate classroom temperature distributions. Experiments were conducted in an experimental primary school classroom in northwestern China to validate the simulation model. The simulated results concurred with the measured temperatures. The validated computer simulation model was applied to predict classroom temperature distributions with various conditions. The following conclusions were obtained:

(1) Based on the measured temperature data, there is significant non-uniformity in the temperature field

distribution inside the measured building. The vertical direction of the average air temperature in the classroom was nearly 3.0°C; the horizontal direction of the average temperature was approximately 1.0°C.

(2) Within the range of 0.25m to 1.10m in vertical direction, the temperature gradient was approximately 2.0 °C m^{-1}, whereas the temperature gradient was reduced to 0.8 °C m^{-1} at 1.10 to 2.30m. The closer to the south wall, the more obvious the temperature difference in horizontal direction. From 1.5m to 2.7m, 2.7m to 3.9m, and 3.9m to 5.1m, the temperature gradients were 0.38, 0.09 and 0.06 °C m^{-1}, respectively.

(3)The simulated results showed that the indoor temperature changed when the solar radiation intensity was varied; the temperature trends were linear. The temperature gradient is lower when closer to the south wall and greater when further away.

(4)The indoor temperature changed when the thickness of the south wall was varied and the temperature trends were non-linear. The temperature at the same location shows a trend of initial decrease and subsequent increase with the increase of south wall thickness. So a thinner south wall was preferable.

(5)The indoor temperature changed when the window-to-wall area ratio was varied, and the temperature at the same location essentially showed an increasing trend. At different positions, however, the temperature growth trends differed with an increase of window-to-wall area ratio; the further the distance from the south wall, the more gently the temperature varied.

Acknowledgements

The research was supported by the National Key Research Project (Project No. 2016YFC0700400), and the National Natural Science Foundation of China (Project Nos. 51678468 and 51590911).

References

Behnia, M., Reizes, J.A., Davis, G., 1990. Combined radiation and natural convection in a cavity with a transparent wall and containing a non-participant fluid. Int J Numer Meth Fl. 10, 3205-3225.

Berdahl, P., Fromberg, R.,1982. The thermal radiance of clear skies. Sol Energy. 29, 299-314.

Catalina, T., Virgone, J., Kuznik, F., 2009. Evaluation of thermal comfort using combined CFD and experimentation study in a test room equipped with a cooling ceiling. Build Environ. 44, 1740-1750.

Cheng, K.W.D., Djunaedy, E., Chua, Y.I., Tham, K.W., Sekhar, S.C., Wong, N.H., Ullan, M.B., 2003. Thermal comfort study of an air-conditioned lecture theatre in the tropics. Build Environ. 38, 63-73.

Cook, J., 1985. Passive Cooling. MIT Press, Cambridge.

Corgnati, S.P., Filippi, M., Viazzo, S., 2007. Perception of the thermal environment in high school and university classrooms: Subjective preferences and thermal comfort. Build Environ. 42, 951-959.

Corrado, V., Astolfi, A.,2002. Environmental quality assessment of classrooms. In: Proceedings of EPIC 2002 AIVC international conference, Lyon, 251-256.

Desta, T.Z., Janssens, K.,2004. CFD for model-based controller development. Build Environ. 39, 621-633.

Havenith, G.,2007. Metabolic rate and clothing insulation data of children and adolescents during various school activities. Ergonomics. 50, 1689-1701.

Ismail, K.A.R., Henriquez, J.R.,2003. Modeling and simulation of a simple glass window. Sol Energ Mat Sol C. 80, 355-374.

Molina-Aiz, F.D., Ftnassi, H., Boulard, T., Roy, J.C., Valera, D.L.,2010. Comparison of finite element and finite volume methods for simulation of natural ventilation in greenhouses. Comput Electron Agr. 72, 69-86.

Rohdin, P., Moshfegh, B., 2007. Numerical predictions of indoor climate in large industrial premises a comparison between different κ-ε models supported by field measurements. Build Environ. 42, 3872-3882.

Rundle, C., Lightstone, M., Osthuizen, P., 2011. Validation of computational fluid dynamics simulations for atria geometries. Build Environ. 46, 1343-1353.

Srebric, J., Vukovic, V., He, G., Yang, X.,2008. CFD boundary conditions for contaminant dispersion, heat transfer and airflow simulations around human occupants in indoor environments. Build Environ. 43, 294-303.

Stamou, A., Katsiris, I., 2006. Verification of a CFD model for indoor airflow and heat transfer. Build Environ. 41, 1171-1181.

Tang, R.S., Meir, I.A., Etzion, Y.,2003. Thermal behavior of buildings with curved roofs as compared with flat roofs. Sol Energy. 74, 273-286.

Valeria, D.G., Osvaldo, D.P., Michele, D.C., 2012. Indoor environmental quality and pupil perception in Italian primary schools. Build Environ. 56, 335-345.

Versteeg, H.K., Malalasekera, W., 1995. An introduction to computational fluid dynamics. Longman Group Ltd, London.

Zhang, X., Wang, H.L., Zou, Z.R., Wang, S.J., 2016. CFD and weighted entropy based simulation and optimisation of Chinese Solar Greenhouse temperature distribution. Biosyst Eng. 142, 12-26.

Development of Automation Models for the Intelligent Use of PV Energy and Energy Storage in Regarding to Air Quality and Comfort in Buildings

Alexander-Nicolai Köhler[1], Markus Fischer[1], Andreas Böttcher[1] and Bolli Björnsson[1]

[1] University of Applied Sciences Fulda, Fulda (Germany)

Abstract

The so-called "Plus-Energy-House" can make an important contribution to the future through a more efficient use of energy. In cooperation with numerous partners from the industry as well as the Fulda University of Applied Sciences (Fulda UAS), a multifunctional school building which meets the requirements of a Plus-Energy-House was built. Intelligent energy management achieves a high level of self-consumption and an energy excess. This paper explains the energy concept of the building, which consists of numerous components. These include for example, prediction algorithms for generating as well as using PV energy and a computer vision (CV) system, which integrates the human as a thermo-technical component in the energy concept of the building.

Keywords: Plus Energy House, Control, Prediction Algorithm

1. Introduction

The recent years have shown that the current method of energy production and energy consumption is not sustainable. As a result, energy transition in the Federal Republic of Germany is currently a very relevant issue of today's world. Energy transition defines the transition from unsustainable fossil fuels and nuclear energy to a sustainable and environmental friendly energy supply through renewable energies (Verbruggen, 2014). An important goal is to reduce the social, health and ecological problems caused by the conventional energy industry. A decarburization of the energy industry plays a significant role in stopping global warming. (Lüdeke-Freund, 2014) (Poizot and Dolhem, 2011) (Armaroli and Balzani, 2007) Therefore, a basic change in thinking of energy production and the use of energy has to follow in the future. (Mertens, 2011) The construction and housing sector provides a great energy saving potential. Currently, about 40 percent of the total primary energy consumption is spent on it (Ministry of Environment, Energy and Climate Protection, 2013). As shown by Köhler, Fischer and Lambeck (2014) the technology of the so-called "Plus-Energy-House" can make a major contribution to that. A plus energy house produces more energy than it needs for heating and the entire household electricity by using modern energy technologies in conjunction with energy storage (Lüdeke-Freud and Opel, 2014). Combining the technology of plus energy houses with additional energy optimization systems, further improvements are possible regarding energy consumption.

2. Application

A new multifunctional school building (see Figure 1) was built on the campus of the Johannes-Keppler-School in Neuhof (Germany) in cooperation with the manufacturer "Bien Zenker" as well as numerous other partners from industry and the handicrafts (Figure 1). It is in conformity with the requirements of a plus-energy-house. Fulda UAS is using the building for research purposes.

doi:10.18086/swc.2017.12.06 Available at http://proceedings.ises.org

Fig. 1: Front view of the school building

The modern, energy-saving and efficient house contains numerous systems that produce, store and distribute the required energy for the operation of the building in an intelligent way. For example, there is a photovoltaic system on the roof of the building. The generated energy can be used for operation, stored in a battery or fed into the grid. To ensure the lowest possible energy consumption, only highly efficient and energy-saving systems are used inside the building. A ventilation system with heat recovery ensures ideal air quality. An infrared heating system is used to heat the building. The control of actuators such as lighting, blinds as well as some sensors e.g. temperature, CO2, brightness or presence is done by a radio bus system.

The use of special prediction algorithms enables the prediction of energy generation and energy consumption in the building and helps to optimize the energy usage. In addition, the use of special camera systems to predict the CO2 concentration and room temperature help to improve the energy balance. The camera system makes it possible to determine the number of persons in the building. With the help of a Computer Vision (CV) system (see 4.1) the influence of the room temperature and the CO2 concentration can be calculated by the persons inside the building and their change can be predicted.

3. Efficient energy management

3.1. Three pillars concept

The energy of the building is used sensibly. As a result, only a little energy is taken from the public grid and the own consumption is increased. To achieve this, the energy concept is based on *three* fundamental pillars.

First, efforts are necessary to save as much energy as possible. The built-in highly efficient technologies contribute significantly to energy saving. It is important to reduce the energy consumption of the building as much as possible. Energy should only be used when necessary. For example, make contacts and presence detectors are installed inside the building, which allow some consumers to be switched off if there is no one inside.

Secondly, the storing of the energy has to be made possible. The photovoltaic system generates energy only during the day. As there is no solar energy available at night, it must be saved during the day time. This increases the self-consumption of the generated energy and thus has a decisive influence on the autonomy of the building. A battery system can be used for this purpose. In addition, the building has a special cement flooring, which has a high heat capacity.

The *third* priority is the preventive use of excessive energy. The excessive energy is used where it is required in the near future, e.g. for heating or ventilating the building. The battery has only a limited capacity. In spring, summer and autumn the capacity is enough to supply the building at night without any power from the grid. In the winter, the infrared heating requires a lot of energy that the battery cannot cover. That is when the usage - optimization is put to use. There is a sufficient number of sunny days in the winter time, when the photovoltaic

system produces enough energy. On these days surplus energy which is normally fed into the grid, is to be effectively used in the building in order to prevent energy consumption at a later time.

3.2. Use of prediction algorithms

Renewable energy has many advantages like low environmental impact and endless resources. However, there are also some disadvantages. For example, the energies are highly weather-bound and therefore not always available. This makes it necessary to store and use such time-dependent energy. It would be ideal to adjust the power consumption to the power generation. Thus, the produced energy could be consumed concurrently, peak loads would be reduced and stored energy would be available longer. To realize this, it is advantageous to forecast the produced energy by suitable methods to plan their use in advance. Thus, the energy consumption of the produced energy can be tracked by PV forecasts and suitable activation of electric loads. On the one hand this prevents unwanted load peaks and on the other hand economic losses of the system. The basis for a forecast-based operating method are suitable methods to predict the PV production in order to plan the usage of the generated energy better.

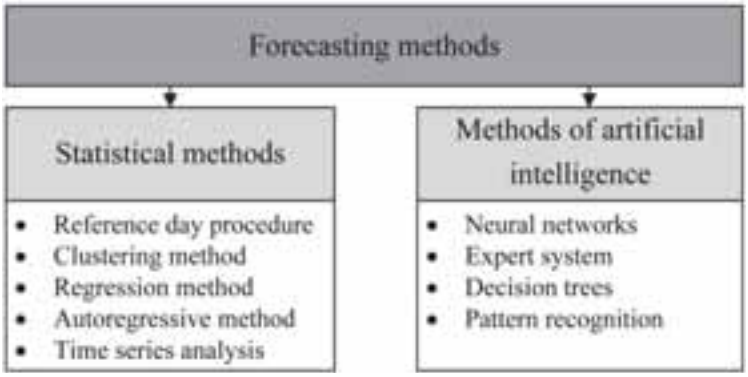

Fig. 2: Overview of typical forecasting methods (Köhler, Fischer and Lambeck, 2014)

There are two typical types of forecasting methods, as Figure 2 shows. Statistical methods use mathematical combinations of historical data combined with information on the influencing variables to predict the future behavior of consumers. However, if no expedient prediction can be made because of unavailable influence factors, it could be helpful to use methods of artificial intelligence. Methods of artificial intelligence learn patterns of behavior with the help of historical data and project these as a function of the expected operating conditions into the future. To select the optimal forecasting method for a particular application, it is also important determine the required time horizon of the forecast. Short-term forecasts (forecast horizon for one day) can be created on the basis of measurements and current data. In contrast to long-term forecasts (forecast horizon for several months) where mostly methods of artificial intelligence are used. These learn the different patterns of behavior based on historical data and project them into the future. Sometime various forecasting methods can work differently for certain sectors of the influencing factors. Because of this, combined or cascaded models are increasingly used. These include a number of methods. Each of them operates only for certain input variables and complement each other. A combination of different methods for a forecast can improve the forecasting accuracy. (Prokhorova and Heimel, 2013) (Theil, 1966) (Schlittgen, 2001)

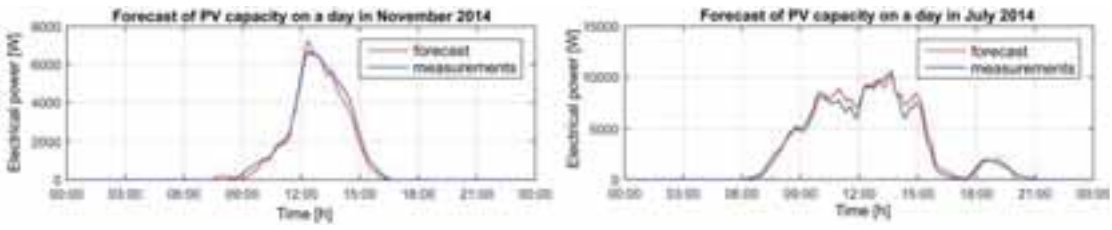

Fig. 3: Comparison between simulation and measurements on two days (Köhler, Fischer and Lambeck, 2016)

4. Comfort and air quality for people

A major problem in well-insulated buildings is the air quality. The high insulation makes the air exchange with the environment more difficult. This has advantages and disadvantages. One advantage is that the energy, like heat from humans, remains inside the room. A disadvantage is that old depleted air remains inside the building. For these reasons, various systems have been integrated into the building, which also significantly increase the energy efficiency.

4.1. Use of prediction algorithms

Figure 4 shows that an average person with a light activity produces a heat current of 120 W. This results in a daily heat output of about 2.9 kWh per day 8 (24 hours). This factor is multiplied many times due to the many students inside the public building. Accordingly, this would be a heat flux of 3000 W at an average of 25 students. (Specht, 2005) Thus, the human is a part of heating system which is an important factor in the control of heating and ventilation.

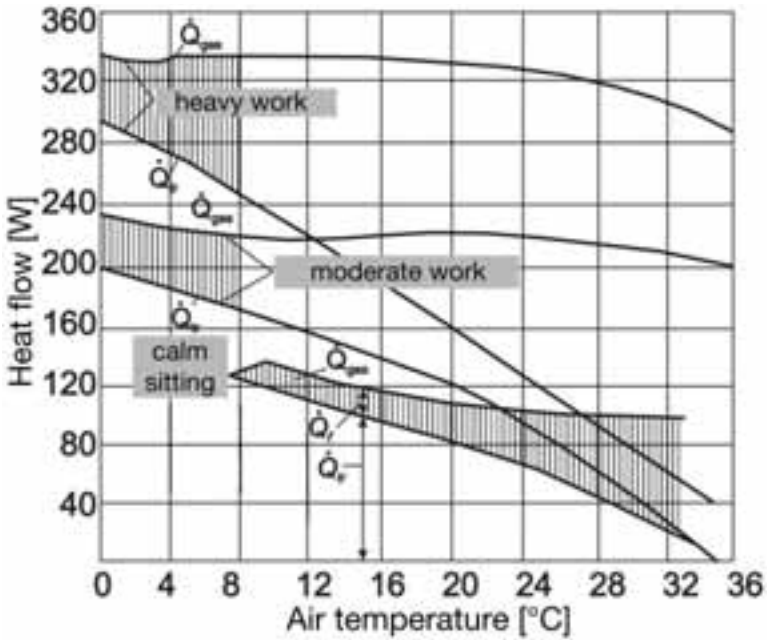

Fig. 4: Heat emission of humans (Specht, 2005)

A Computer Vision (CV) system (ADBF-Vision) was developed to recognize the number of people in the room. Depending on the number of detected persons in the room, the heating is throttled and unnecessary energy is saved. The Viola-Jones algorithm, which was originally presented in 2001 by Paul Viola and Michael Jones as a possible solution for the problem of facial recognition, is used to realize the recognition of persons. (Behera and Mohapatra, 2015) information on this development, refer to (Böttcher and Köhler, 2017). This can also be applied to detect other objects.

The algorithm gains high acceptance because of the comparatively high computational efficiency that allows real-time image processing. In one iteration, a migrating window moves over the input image pixel by pixel. After completion of a run, the image can be scaled into a smaller format or the mask can be enlarged. The image area inside the movable window is analysed step by step. The Haar wavelets developed by Alfred Haar are processed (see figure 5). These are folding masks. The black and white areas represent the sign for the summation of the brightness values of the covered pixels.

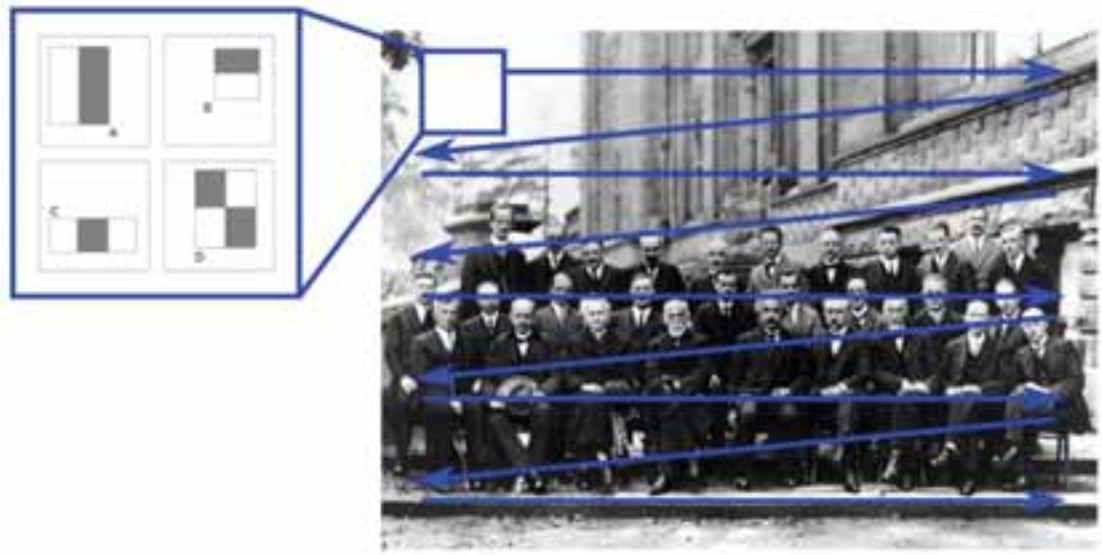

Fig. 5: Bewegliches Fenster und Haar Kaskadenmuster (Zhenyu, 2012)

The object detection is based on the cascade filter. Within a position of the moving window, different Haar-cascade elements are applied according to the state of the filter on this area. The individual results of the masks are summed. If a specific threshold is exceeded, the area is passed on to the following level. If the threshold for matching with the masks falls to a certain level, the content of the window is not checked anymore for correspondence and the window moves. If the content of the windows can exceed the required threshold in all levels of the filter, it is included in the result set of the detected objects. Therefore, it is possible for the algorithm to search for possible facial shapes inside the movable window (figure 6). For further information on this development, please refer to (Böttcher and Köhler, 2017).

Fig. 6: Person detection inside the classroom

4.2. Carbon dioxide (CO2) and temperature

Various studies have shown that the air quality in classrooms is poor and that CO2 concentration is too high, especially during the winter months. This can lead to tiredness or lack of concentration for teachers and pupils. The amount of CO2 depends on the activity of the people inside the room. Breathing air contains about 4 percent by volume CO2. This corresponds to 18 to 20 l/h CO2 per person (Benedix, 2006). In contrast to water vapor, the exhaled CO2 is not absorbed by surfaces. It accumulates completely in the air. During a lesson, it leads to an increase of the CO2 concentration from 400 ppm up to 2000-2500 ppm. The maximum permitted

CO2 limit in public areas is 1500 ppm according to DIN 1946-2. The CO2 and temperature sensors as well as the computer vision (CV) system allow a predictive control of the ventilation. Thus, it is possible to maintain the air quality inside the room under efficient conditions.

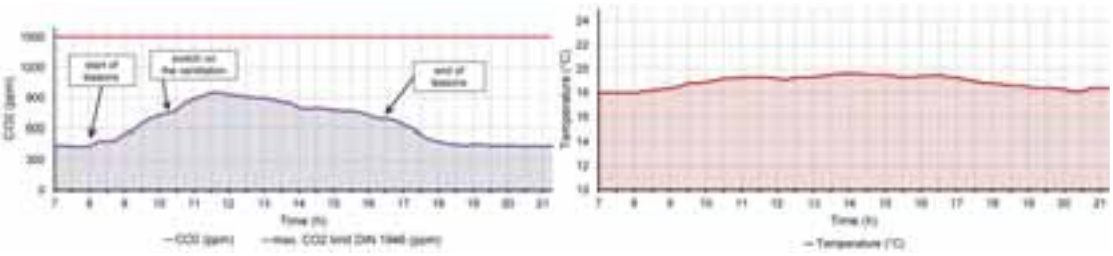

Fig. 7: measurements of carbon dioxide (CO2) and temperature for one day in school

5. Conclusion and prospects

The energy management of the multifunctional school building has already proved over the past few years that intelligent, predictive control strategies allow an environmental friendly operation of the building and an efficient use of renewable energies. In particular, the low energy consumption of the building as well as a high part of renewable energy in the total energy consumption should be highlighted. The strategies used to regulate temperature and CO2 concentration leads to an ideal air quality and comfort.

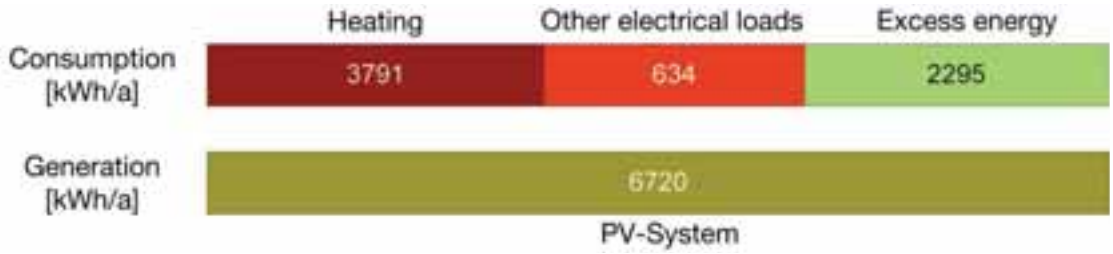

Fig. 6: energy balance

Through integrating the Computer Vision system into the existing automation unit, further energy saving potentials will be realized in the near future. A statement about the level of energy saving or an improvement in air quality can only be made when the system is operating in the building over a longer period of time. In the future, it is also important to coordinate the integrated systems and optimize their functions in order to increase the efficiency of the building.

6. References

Armaroli, N., Balzani, V., 2007. The Future of Energy Supply: Challenges and Opportunities. Printed in: Angewandte Chemie International Edition 46.

Behera, H., Mohapatra, D., 2015. Computational Intelligence in Data Mining - Volume 1. Springer-Verlag. Berlin – Heidelberg.

Benedix, R., 2006. Bauchmie – Einführung in die Chemie für Bauingenieure. B.G. Teubner Verlag. Wiesbaden. 2006.

Böttcher, A., Köhler, A.-N., 2017. Konzeption und Realisierung eines Bildverarbeitungssystems zur Personenerkennung. University Fulda.

Köhler A.-N., Fischer M., Lambeck S., 2014. Einsatz innovativer Bussysteme für ein intelligentes Energiemanagement in Plus-Energie-Häusern. SPS IPC Drives. Nuremberg.

Köhler A.-N., Fischer M., Lambeck S., 2016. Forecasting models for an intelligent use of renewable energy based on the prediction of PV energy. EuroSun 2016. Palma.

Lüdeke-Freund, F., Opel, O., 2014. Energie – Nachhaltigkeitswissenschaften. Springer-Verlag. Berlin – Heidelberg.

Mertens, K., 2011. Photovoltaik – Lehrbuch zu Grundlagen, Technologie und Praxis. Carl Hanser Verlag. Munich.

Ministry of Environment, Energy and Climate Protection, 2013. Bauen und wohnen. Article of 25.09.2013.

Poizot, P., Dolhem, F., 2011. Clean energy new deal for a sustainable world: from non-CO2 generating energy sources to greener electrochemical storage devices. Printed in: Energy and Environmental Science 4.

Prokhorova, A., Heimel, S., 2013. Prognoseverfahren für die Energiewirtschaft: Klassifizierung und Anwendungsbereiche verschiedener Modelle. Zeitschrift für Energiewirtschaft Recht Technik und Umwelt. Edition ½.

Schlittgen, R., 2001. Zeitreihenanalyse. 9th Edition. Oldenbourg Verlag. Munich.

Specht, E., 2005. Der Mensch als wärmetechnisches System. Otto-von-Guericke-Universität. Magdeburg.

Theil, H., 1966. Applied Economic Forecasting. 2nd Edition. Amsterdam.

Verbruggen, A., 2014. Could it be that Stock-Stake Holders Rule Transition Arenas? Im Hürdenlauf zur Energiewende. Springer-Verlag. Berlin – Heidelberg.

Zhenyu Y.: Viola-Jones Face Detection. https://sites.google.com/site/5kk73gpu2012/assignment/viola-jones-face-detection. Version: 2012.

PVT-GSHP Hybrid Tri-Generation System for Net Zero Energy Buildings

E. J. LEE[1,2*†], E. C. KANG[1], K.S. LEE2, M. Ghorab[3], L. YANG[3], E. ENTCHEV[3]

[1] Korea Institute of Energy Research, Daejeon(Republic of Korea)

[2] University of Science and technology, Daejeon(Republic of Korea)

[3] Natural Resources Canada, CanmetENERGY, Ottawa(Canada)

Abstract

One way to improve the efficiency of renewable energy system is by integrating two or more devices or so called the hybrid system. In this study, the change of the Ground Source Heat Pump (GSHP) seasonal performance factor will be observed when it is integrated with Photovoltaic-Thermal (PVT) to meet the multiple loads of house and office. Basically, the strategy to get this efficiency improvement is by combining the water outlet of GSHP which firstly heated by desuperheater and the output of PVT in one (preheat) tank. In the solar preheat tank, the heat from PVT will be added through heat exchanger as the supplementary to the hot water which is previously from city water passing desuperheater of GSHP. The final output of GSHP with the heat addition from PVT and the efficiency of stand-alone GSHP will be compared. GSHP-PVT hybrid system has the lowest energy consumption followed by GSHP stand-alone and reference case (simple sum of house and office) with 31.8 kWh/m^2-yr, 78.7 kWh/m^2-yr and 107 kWh/m^2-yr

Keywords: *Ground Source Heat Pump (GSHP), Photovoltaic-Themal (PVT), Multi-Load, Energy, Net Zero Energy Building(nZEB)*

1. INTRODUCTION

The requirement for alternative low-cost and efficient energy sources has triggered people to the development of Ground Source Heat Pump (GSHP) system for residential and commercial heating and cooling applications. Earth temperature always stable throughout the year and this is also the reason why GSHP is very attractive. The heat pump on GSHP system operates using the same cycle as a vapor compression refrigeration cycle. Both systems absorb heat at a low temperature level and reject it to a higher temperature level. The difference between these two systems is that a refrigeration application is only concerned with the lower temperature effect produced at the evaporator, while a heat pump may be concerned with both cooling effect produced at the evaporator as well as the heating effect produced at the condenser in GSHP system. A reversing valve system is used to switch between heating and cooling modes by changing the refrigerant flow direction. GSHP system can be seen in Fig.1

A photovoltaic-thermal or PVT module is a combination of photovoltaic cells with a solar thermal collector, forming one device that converts solar radiation into electricity and heat simultaneously. The excess heat that is generated in the PV cells is removed and converted into useful thermal energy. The PVT system can produced efficiency up to 75% as the efficiency of PVT increases and the cell temperature is decreased. PVT can be distinguished into two types based on the manufacturing process: PVT collectors and PVT panels. PVT collectors are very similar in appearance to a regular solar thermal collector, consisting of a PV-covered absorber in an insulated collector box with a glass cover. PVT panes on the other hands are similar in appearance to regular PV panels. Due to lack of extra insulation and a glass cover, PVT panes have a lower thermal efficiency but higher electrical yield. Fig.2 shows the PVT panels. In this study, two cases will be compared which are GSHP system and GSHP coupled by PVT system in order to perform the annual performance analysis.

doi:10.18086/swc.2017.12.07 Available at http://proceedings.ises.org

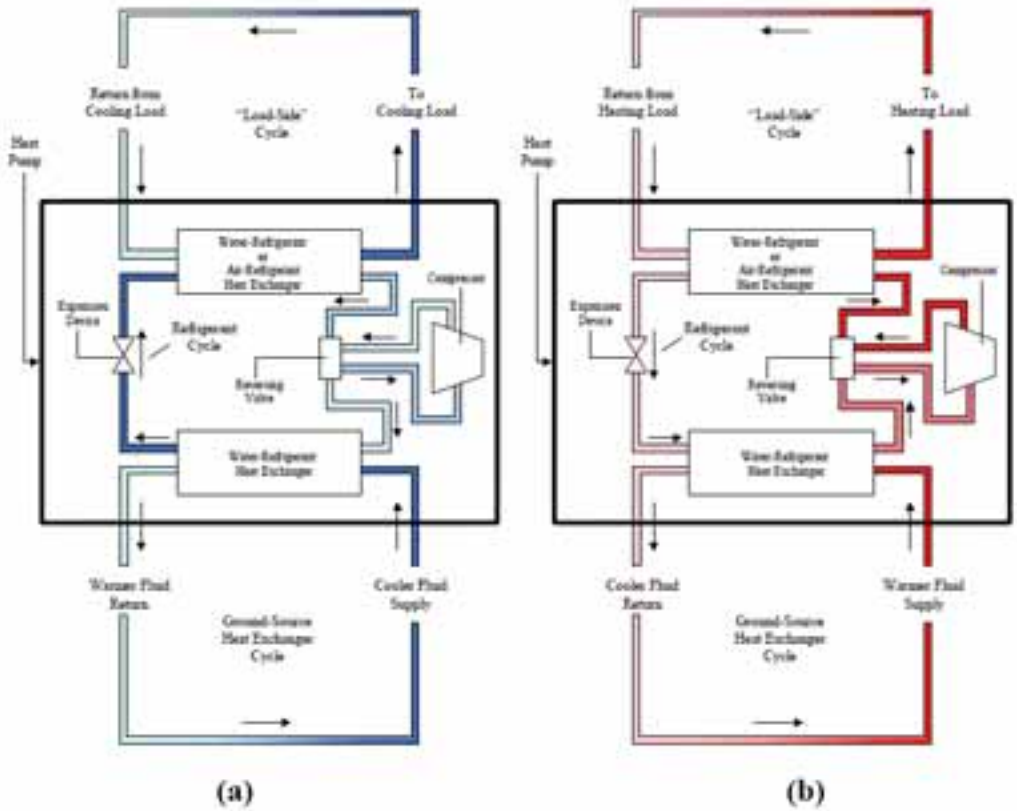

Fig.1. Ground Source Heat Pump (GSHP) Cycle in (a) Cooling mode and (b) Heating Mode

Fig.2. PVT Module

2. MICRO-GENERATION SYSTEM MODELING FOR EACH CASE STUDIES

In this study, three systems will be introduced for applications in residential and commercial buildings. Case one is simple sum of residential and commercial buildings (house and office) heating/cooling demand. Both thermal loads of residential and commercial buildings are provided by boiler and chiller system also fan coil unit as presented in Fig.3. The fan coil unit is located inside the building and a duct system is used to distribute the cooling/heating air inside the building. Domestic hot water (DHW) tank in installed inside the house and connected with the boiler via pipelines. This case will be the reference case for this simulation study.

Case two is a load sharing system with Ground Source Heat Pump (GSHP) to meet the combined load of houses and offices. Case two is load sharing hybrid system of GSHP integrated with PVT module. Load sharing in this case means houses and offices will use one system to provide heating and cooling demand instead of using separate system for each house and office. In case one, as presented in Fig.4, uses GSHP system to provide the heating/cooling demand instead of boiler/chiller system (conventional system). The desuperheater of GSHP is used to preheat the city water for DHW usage. A hot water storage tank is equipped to provide space heating and DHW heating. A gas burner is located at the bottom of the tank to provide supplementary heat in cases where GSHP alone cannot provide sufficient heat in very cold days or to heat the DHW water in summer. Water from the hot water tank is supplied to the two buildings through pipelines for DHW demand loads. In this case, the city water has enough pressure to flow the water in the system without using a pump. A cold water storage tank is used in the cooling season to provide chilled water for the cooling coils. Three way valves are used to switch between GSHP heating and cooling loops in winter and summer cooling seasons.

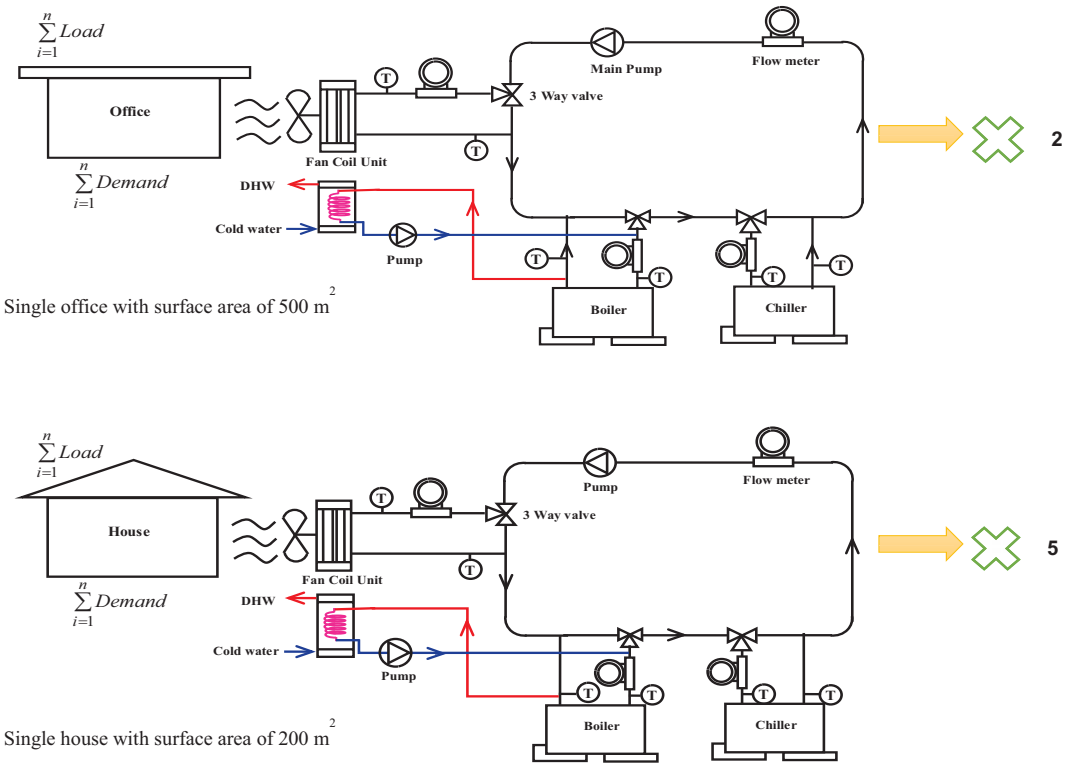

Fig.3. Simple Sum of Residential and Commercial Buildings System

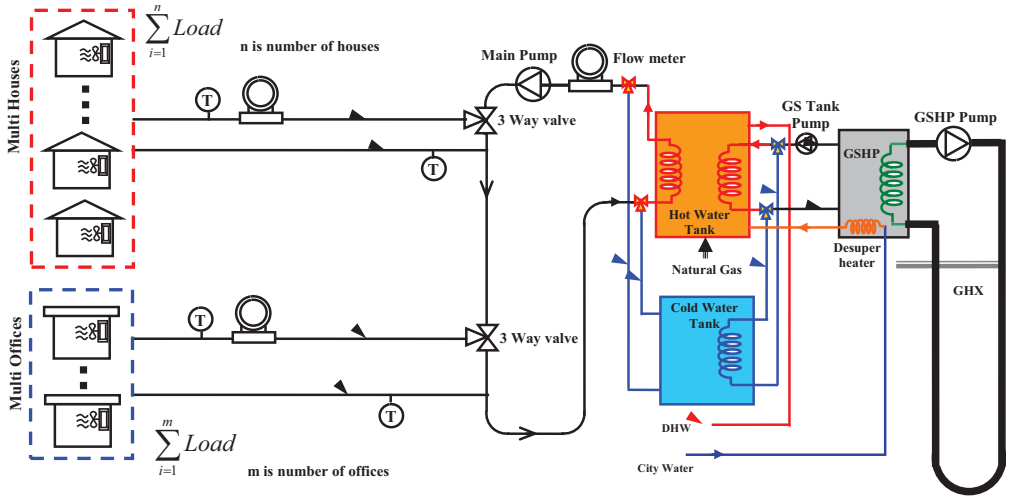

Fig.4. Load Sharing (Houses & Offices) Using GSHP System

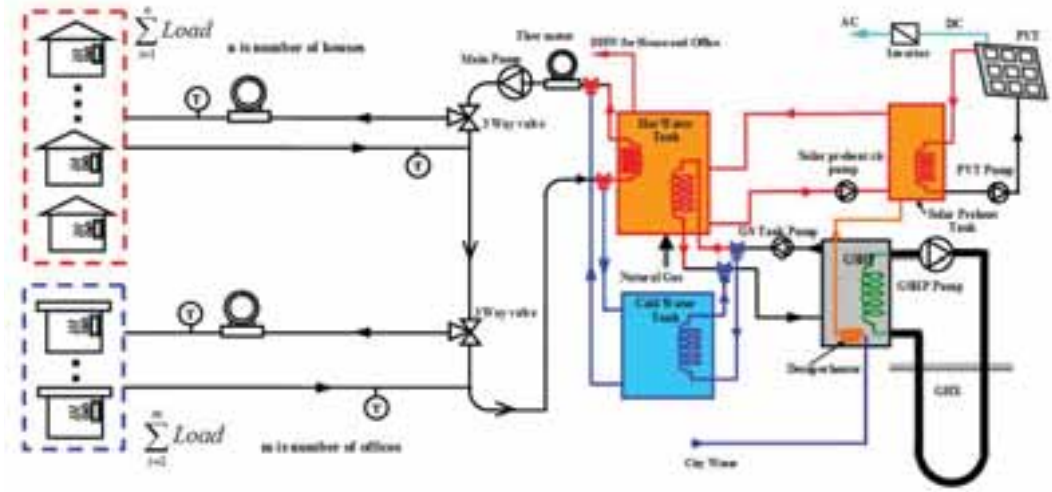

Fig.5. Load Sharing (Houses & Offices) Using Hybrid Micro-Generation System (GSHP-PV/T)

Tab. 1. Summary of Modelling Cases

Cases	Heating/Cooling Systems			Remarks
	Cooling	Heating	DHW	
Case 1	Chiller + Fan-Coil	Boiler + Fan-Coil	Boiler + DHW Storage Tanks	Simple Sum Loads (House + Office)
Case 2	GSHP - Fan-Coil	GSHP - Fan-Coil	GSHP (DSH) + Storage Tanks	Load Sharing
Case 3	GSHP - Fan-Coil	PV/T- GSHP- Fan-Coil	PV/T-GSHP (DSH) + Storage Tanks	Load Sharing

Case three is a hybrid micro-generation system integrating a photovoltaic thermal system to a GSHP system. PVT panels can generate both electric and thermal energy. The generated energy can be used to reduce the electrical power import from the grid to houses and offices and also used for space and water heating. There are many possible ways to integrate the PVT's thermal system to the GSHP system. In this study, system configuration with solar preheat-tank as shown in Fig.5 was chosen for the present study. The collected solar thermal energy is stored in a preheat-tank for two purposes: preheat the DHW and transfer the heat to the hot water storage tank in condition where the preheat-tank bottom temperature is few degree Celsius higher than the top of hot water storage tank. The remaining part of the system is same as that in case one.

Tab. 1 presents a summary of different modeling case studies and the corresponding technologies used for space heating, space cooling and DHW heating

3. SIMULATION AND ANALYSIS METHODOLOGIES

In the present study, all hybrid system models analysis from previous chapter are done by TRaNsient SYStems (TRNSYS-17) which is a popular software platform for advanced dynamic building energy simulation. TRNSYS library includes a large database of component models related to buildings, thermal and electrical energy system, input and output data management and other dependent functions. All components models in this study were selected from TRNSYS libraries and enhanced with latest manufactures' system performance data. Additional models were developed for some components that are not present in the TRNSYS libraries such as PV module, GSHP desuperheater and etc. A PVT module has 2.56m2 dimension, 295W electrical output and 1535W thermal output.

Based on that approach, detailed simulation models were developed and applied for all three cases. In order to evaluate the load sharing system performance, multi-building block consists of five identical houses (with floor area 200m^2 each) and two identical houses (with floor area of 500m^2 each) were introduced. The building specifications meet the building envelope requirements for climate zone 4 recommended by ASHRAE Standard 90.1-2007.

For systems serving multiple buildings, it will typically have a lower thermal peak than the sum of thermal peaks of each homogeneous house and office. This is mainly due to the fact that individual buildings reach their respective thermal peaks at different times during the day. A load diversification factor is commonly used to take this phenomenon into consideration in load estimation and equipment sizing for systems that serve a number of mixed buildings. This factor is commonly in the range of 0.90 and tends to be lower when the central system serves a mix of office and residential buildings with peak demand occurring at different times.

The simulation models were run with Incheon, South Korea weather data over a year to simulate and analyze the energy systems' performance. The energy consumption results from the TRNSYS simulations were then used for energy and cost analyses to evaluate and compare the performance of various systems (cases)

4. ENERGY ANALYSIS RESULTS AND DISCUSSION

In this section, simulation results of the case one, case two and case three systems that serving multiple buildings (five houses and two offices) will be presented and discussed. While the houses are identical to the house studied in the previous section with a floor area of 200 m2 per house, the office is enlarged and each has a floor area of 500m2. The total combined floor area with five houses and two offices is 2000 m2.

Both thermal and non-HVAC electric loads of the simulated houses and offices were analysed through appropriate time series methodology prior to the system simulation models development. The houses and offices were assumed to be separated from each other with no thermal interaction between them. Both type of buildings are square shaped and are assumed with a single interior zone in the simulations. The domestic hot water volume assumption was according to ASHRAE-124 recommendations for residential and small office buildings. Following "Office of Energy Efficiency Statistics and Analysis", NRCan, Non-HVAC electric loads

were developed based on "average" consumption of a detached house and a small office in Canada which is 43.9 kWh/m^2-yr. Those are presented in Tab. 2:

Tab. 2. Annual Thermal Load and Non-Electric Load Intensities

Load Intensity (kWh/m^2-yr)	Building Blocks Five Houses + Two Offices(5x200 m^2 + 2x500 m^2=2000 m^2)	
Weather data	Incheon, South Korea (TMY2 weather data)	
DHW	8.6	6.6%
Space Heating	47.2	36.1%
Space Cooling	31.2	23.8%
Non-HVAC Electricity	43.9	33.5%
Total	*130.9*	*100%*

Initial simulation study found out that if a GSHP system integrates with PVT panels only, the PVTs thermal and electrical energy generations are restricted by the volume and temperature of the solar pre-heat tank directly and building thermal demand indirectly. Therefore, it may be more efficient to design a GSHP-PV/T system with combination of both PVT and PV panels rather than installing PVTs only. In this way, the electricity generation will not be restricted or reduced by the thermal demand compare to systems with all PVT panels. In addition, it is anticipated that the initial capital cost could be reduced as PV panels are usually cost less than PVTs. For this reason, 5 GSHP-PVT systems (Case 3) with various combinations of PVT and PV panels were simulated, as shown in Tab. 3:

Tab. 1. GSHP-PVT Systems for Simulation Study

Number of PV Panels	Number of PVT panels	
	0	60
0	GSHP	GSHP-PVT60-PV0
120	GSHP-PVT0-PV120	GSHP-PVT60-PV120
240	GSHP-PVT0-PV240	GSHP-PVT60-PV240

Tab. 2. Energy Analysis of Multiple-Building for Each Case Study

Incheon (Multiple Buildings)		Five Houses + Two Offices (5x200 m^2 + 2x500 m^2 = 2000 m^2)						
Energy Intensity (kWh/m^2-yr)		Case 1	Case 2	Case 3				
		SIMPLE SUM (REFERENCE)	GSHP	PVT=60 PV=0	PVT=0 PV=120	PVT=60 PV=120	PVT=0 PV=240	PVT=60 PV=240
Space + DHW Heating	N. Gas	55.9	3.6	0.7	3.6	0.7	3.6	0.7
	Electricity	-	13.5	11.8	13.5	11.8	13.5	11.8
Space cooling	Electricity	16.2	8.6	7.9	8.6	7.9	8.6	7.9
Fans		4.2	5.3	6.0	5.3	6.0	5.3	6.0
Pumps		0.8	3.8	3.1	3.8	3.1	3.8	3.1
Non HVAC (lighting, equip.)		43.9	43.9	43.9	43.9	43.9	43.9	43.9
Electricity Production		0	0.0	-3.8	-19.0	-22.8	-38.0	-41.8
Total (Net) Energy Use		*107.6*	*78.7*	*69.8*	*59.7*	*50.8*	*40.7*	*31.8*
Energy Savings		-	*28.9*	*37.8*	*47.9*	*56.8*	*66.9*	*75.8*

Energy Savings (%)	-	*26.9%*	*35.1%*	*44.5%*	*52.8%*	*62.1%*	*70.4%*

The result shows that the reference case (Case 1) has the highest total energy consumption at 107.6 kWh/m2-yr followed by GSHP system at 78.7 kWh/m2-yr and GSHP-PVT systems are showing better energy consumption compared to others ranged from 31.8 kWh/m2-yr until 69.8 kWh/m2-yr. The main reason why GSHP-PVT has better energy consumption is because this system only use small amount of natural gas for auxiliary burner inside the hot water burner and also GSHP-PVT system produced electricity so that reduced the net amount of energy consumption. Those results are shown in Tab. 4 and Fig. 6

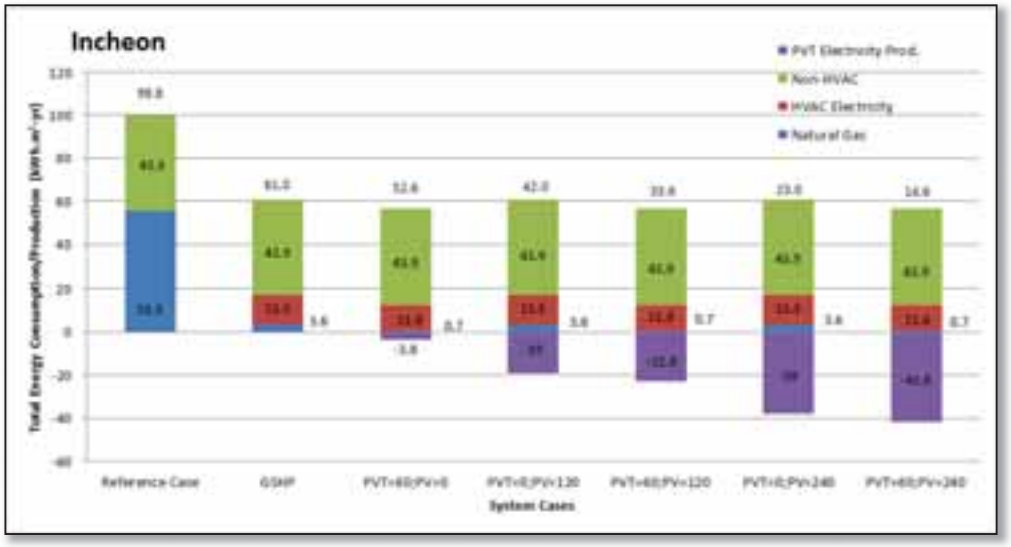

Fig. 6. Energy Analysis Results for Each Study Case

Based on those Tab. and graph, the system performance is evaluated and presented in COP values for the three studied cases. The COP is the ratio of the total energy delivered to the buildings (which includes space heating, space cooling, and DHW energy as well as electricity production if any) to the total consumed energy (natural gas and electricity) in the respective period as shown in Tab. 6

Tab. 3. System Performance (COP) For Multi-Building Cases In Incheon

Incheon	COP		
	Heating Period	Cooling Period	Overall/Annual
Reference System	0.92	1.47	1.08
GSHP	2.87	2.09	2.50
GSHP-PVT60-PV0	3.09	2.56	2.85
GSHP-PVT0-PV120	3.42	2.64	3.05
GSHP-PVT60-PV120	3.70	3.24	3.49
GSHP-PVT0-PV240	3.97	3.19	3.59
GSHP-PVT60-PV240	4.30	3.92	4.13

The result in Tab. 5 shows that Case 3 which is GSHP-PVT system has the highest COP ranged from 2.56 to 4.30 followed by GSHP system (Case 2) and simple sum of residential and commercial buildings (case 1). This result indicates that hybrid system has a better performance compared to conventional system and GSHP-PVT is the best combination. One of the reasons is the additional contribution from solar energy to produce electricity so that electricity that consumed from the grid can be reduced as shown in Tab. 6

Tab. 4 Annual Electricity Generation and Supply of Various GSHP-PVT system

Incheon	PV/T Electricity Generation		System Electricity Supply	
	Used by System	Exported to Grid	Supplied by PV/T	Supplied by Grid
Reference System	-	-	-	100%
GSHP	-	-	-	100%
GSHP-PVT60-PV0	100.0%	0.0%	5.2%	94.8%
GSHP-PVT0-PV120	83.4%	16.6%	21.1%	78.9%
GSHP-PVT60-PV120	80.5%	19.5%	25.2%	74.8%
GSHP-PVT0-PV240	62.3%	37.7%	31.5%	68.5%
GSHP-PVT60-PV240	60.0%	40.0%	34.4%	65.6%

The results in Tab. 6 indicate that the PV/T panels, depending on its capacity, meets 5.2% to 34.4% of the total electrical loads in Incheon. The remaining 65.6% to 94.8% required electricity is imported from the grid. Increase of the PV/T capacity certainly reduces the hybrid MG system's dependency on the electric grid, on the other hand this will result high initial capital costs

5. CONCLUSION AND FURTHER WORK

In this study, three different renewable and hybrid micro-generation cases were analyzed for application in combination of residential and commercial buildings. Five houses and Two Offices were selected in this study to perform the annual energy performance for each technology. Based on the result in previous chapter, we can conclude that:

• The total energy consumption of all the studied GSHP-PV/T systems (Case 3) is lower than that of the GSHP system (Case 2), and also the reference case (case 1) due to the use of geothermal and solar renewable energies. The overall system performance (COP) increases with the increase of the PV/T panels.

•The simulation results show that it is more efficient to design a GSHP-PVT system with combination of both PVT and PV panels. The PVT panels (operated with thermal-load control strategy) are primary used for covering part of the building heating loads and the PV panels (operated when there is solar radiation available) are mainly used for generating electricity for building usage. In this way, the electricity generation will not be restricted or reduced by the thermal demand compared to systems with all PVT panels. Any excessive electricity could be sold to the grid for additional income or stored in batteries for later use.

• Due to the PV/T electricity production is intermittent and not synchronized with the building demand, the GSHP-PV/T systems not only require electricity from the grid, but also have excessive electricity to be exported to the grid. The amount of electricity imported and exported to the grid is dependent on the number of the PV/T panels integrated to the systems.

• The GSHP-PV/T systems are able to meet 5.2%-34.4% of the building total electric load in Incheon. The remaining electric load is met by the grid. Increase the number of PV/T panels certainly reduces the system dependency on the electric grid.

• For the simulated GSHP-PV/T systems, between 60% and 100% of the PV/T generated electricity is used by the buildings themselves and the remaining 0% to 40% excessive electricity is exported to the grid. The

percentage of exported electricity increases with the increase of the PV/T panel numbers.

For Further work, an artificial intelligence (AI) control strategy to be embedded in a gateway wireless platform for optimal control of the hybrid system will be developed to further apply the new concept of energy cloud. The strategy will be simulated and investigated for variety of system sizes and applications. The hybrid systems will be optimized and the optimal component and system configurations will be simulated and assessed for maximum utilization. Variety of simulations will be conducted using system integration optimization technique to approach real life situations where a group of multi-type buildings will be served by the hybrid energy system in load sharing applications. Further, and more in depth, economic analyses will be performed to investigate the viability of the hybrid energy systems in selected scenarios and their impact on the overall installation and operation costs.

6. ACKNOWLEDGEMENT

This research was supported by a grant(code# 17CTAP-C096424-03) from Technology Advancement Research Program (TARP) funded by Ministry of Land, Infrastructure and Transport of Korean government & This work was supported by Korea Energy Agency(KEA) grant funded by the Ministry of Trade, Industry & Energy, Republic of Korea in 2015 (No. 201605010001)

7. REFERENCES

E. Saloux, A. Teyssedou, M. Sorin 2013. “Analysis of photovoltaic (PV) and photovoltaic/thermal (PV/T) systems using the exergy method” Energy and Buildings Journal, Vol.67, pp.276

Entchev, E. Yang, L. Ghorab, M. 2013. “Photovoltaic Thermal-Ground Source Heat Pump Simulation Study, Second year report”. CanmetERNERGY-Ottawa, Natural Resources Canada.

Lee, E.J. Kang, E.C. Cho, S.Y. Entchev, E. Yang, L. Ghorab, M. Performance Assessment and Integral Effect Test of Fuel Cell – Ground Source Heat Pump and Photovoltaic Thermal – Ground Source Heat Pump. Annex54-KIER- subtask B report. Available from: http://www.annex-54.sharepoint-live.de

Lee, E.J. Kang, E.C. Cho, S.Y. Entchev, E. Yang, L. Ghorab, M. Performance Assessment and Integral Effect Test of Fuel Cell – Ground Source Heat Pump and Photovoltaic Thermal – Ground Source Heat Pump. Annex54-KIER- subtask C report. Available from: http://www.annex-54.sharepoint-live.de

Dott, R., M. Haller, H, J. Ruschenburg, F. Ochs and J. Bony, 2012, IEA-SHC Task 44 Subtask C technical report: The Reference Framework for System Simulation of IEA SHC task 44 / HPP Annex 38: Part B: Buildings and Space Heat Load, IEA-SHC, Paris, www.iea.org/task44

Stegman M., Bertram E., Rockendorf G. & Janben S., 2011. Model of an Unglazed photovoltaic thermal collector – based on standard test procedures. Proc. Of ISES Solar World Congress 2011, Solar Heating and Cooling, International Solar Energy Society (ISES), p.252-260, Kassel, Germany

Clean Energy Project Analysis: RETScreen Engineering & Cases Textbook Ground-Source Heat Pump Project Analysis Chapter, Minister of Natural Resources Canada

Switchable Windows - Spectral Transmission and Switching Times

Philippe Lemarchand[1], Eoin McLean[1] and Brian Norton[1]

[1] Dublin Institute of Technology, Dublin (Ireland)

Abstract

The switching time and spectral transmission in fully clear and fully opaque states of polymer dispersed liquid crystals (PDLC), suspended particle device (SPD) and electrochromic (EC) switchable windows were evaluated to assess their suitability to control solar heat transmission though glazed façade and comfort to building occupants. The transmission measurement on a SPD film showed a very effective absorption modulation in the visible range but fast decrease in the near infrared region. The switching speed was demonstrated to be related strongly to wavelengths. A SPD film with a larger absorption and faster switching speed in the infrared region was shown to be preferable to control solar heat transfer through glazings and thermal comfort. The PDLC window did not modulate transmission but rather modulated scattering. In the opaque state, the PDLC window was highly scattering resulting in spectral transmission varying at short distances from the window while being constant in the far field. The switching speed measurement demonstrated that liquid-based switchable windows can respond as fast as the eye to have the potential to control spontaneous glare. The EC window demonstrated a lower absorbance efficiency than the SPD in the visible range but appeared to have a much higher efficiency in the infrared region measured. EC windows are characterized by their slow switching speed when compared to SPD and PDLC. This makes them unsuitable for spontaneous glare control and are more suited to predictive solar heat gain control over a defined time horizon. With the increasing integration of adaptive technologies into building facades and to predict the energetical and ambient performance of such buildings and the impact on the occupants' comfort, this paper emphasises on the importance to provide spectral performance information of switchable windows.

Keywords: switchable window, spectral transmission, switching speed, adaptive façade, solar control.

1. Introduction

Switchable windows switch between a clear and an opaque transparent state by controlling light absorption, reflection and/or scattering. EC, liquid crystal (LC) based and electrophoretic or SPD technologies are the most promising for manufacturing large area electrically activated switchable windows for control of solar energy through building and vehicle glazings.

The coefficient of solar energy transmittance (g-value) or solar heat gain coefficient (SHGC) and shading coefficient are determined knowing the incident solar insolation and the spectral transmittance of glazing over the entire solar spectrum (Geymard, 2007; Gueymard and duPont, 2009; Waide and Norton, 2003). These coefficients vary significantly with the incident solar insolation. With adaptive windows dynamically adapting their optical transmission these coefficients will vary furthermore. As visible light transmission and scattering is modulated, indoor lighting conditions vary with illuminance, colour rendering index and daylight glare probability (Wienold, 2010) the affected quantities. It is therefore important to disaggregate the impact of the visible component of the spectrum affecting indoor lighting and glare, and the infrared component of the spectrum contributing to the indoor thermal performance via solar gain and the greenhouse effect further affecting the cooling and heating loads of the building and occupants' comfort.

Switchable windows do not prescribe requirements on switching times. For building application, the short time change of glare (visible wavelength) and solar heat (infrared wavelengths) incident on a surface typically vary with the passage of watery clouds. Considering an instant change of the solar irradiance by the passing of a cloud, the required switching time for switchable windows would correspond to the human response to light. Presumably, switchable windows would need to switch as fast as the eye response, i.e. 13ms to 80ms (Lewis, 2014), to have a spontaneous control of the glare.

The human sensation of heat given by the heat index varies by 8°C when moving from shade to sunlight (NWSWFO,

doi:10.18086/swc.2017.12.08 Available at http://proceedings.ises.org

2004). Moreover, the human skin response time to cold is 0.1°C/s (Jones, 2009) and discomfort is perceived with only 1°C difference to body temperature which is felt in the order of 10 seconds (Kenny, 1998). Consequently, the 8°C difference felt from shadow to sunlight brings a sensation of discomfort in the order of 1.25 seconds which would then be the desired response time to solar heat transfer (infrared wavelength) through the switchable glazing.

Knowing the spectral transmission and switching time performances of switchable windows as further studied below can potentially enable to appropriately and more accurately control such adaptive technologies with the desired building energy performance and occupant comfort.

2. Methodology: sample characteristics and optical setups

2.1. Sample characteristics

The EC EControl™, SPD SmartGlass™, PDLC SmartGlass™ glazings as well as SPD and PDLC films (without glass panes) presented in Tab. 1 and Fig. 1 were characterized. The EC glazing was electrically switched by its controller applying between -1Vdc and +2Vdc measured at the window's electrodes. The window transmissions provided by the manufacturer are measured according to DIN EN 410 within the 380-780nm region. The EC window were specified to be 50% and 10% in the transparent and opaque state respectively with a tolerance of +/-2%. Both the SPD and PDLC films and glazing were electrically switched between 0Vac and 110Vac. Consequently, the EC and SPD films worked either in a transparent mode when turned ON or into an opaque mode when turned OFF, the window appearing tinted with a dark blue colour. The LC films were in their transparent state when turned ON, and exhibited a milky-white tint when turned ON and were consequently in their opaque mode. A Lambda900 spectrophotometer was used to measure the full and scattered transmission through the SPD and PDLC films, the glazings and each individual component forming the SPD and PDLC glazings. Due to the size of the EC glazing that could not fit in the Lambda900, a second dedicated optical setup was used. This setup was used to measure the optical transmission of the EC glazings and the switching time of the SPD, PDLC and EC glazings.

Tab. 1: SPD, PDLC and EC tested samples.

Sample name	Shape	Size	Thickness Configuration
SPD glazing	Flat	L=28cm, H=18cm	4mm glass/~1mm space/4mm glass
PDLC glazing	Flat	L=28cm, H=18cm	4mm glass/~2mm space/4mm glass+silver coating
EC glazing	Flat	L=32cm, H=32cm	4mm glass/~1mm space/4mm glass/cavity/4mm low-E coated glass
SPD film	Flat	L=5cm, H=5cm	ITO/SPD film/ITO
PDLC film	Flat	L=5cm, H=5cm	ITO/PDLC film/ITO

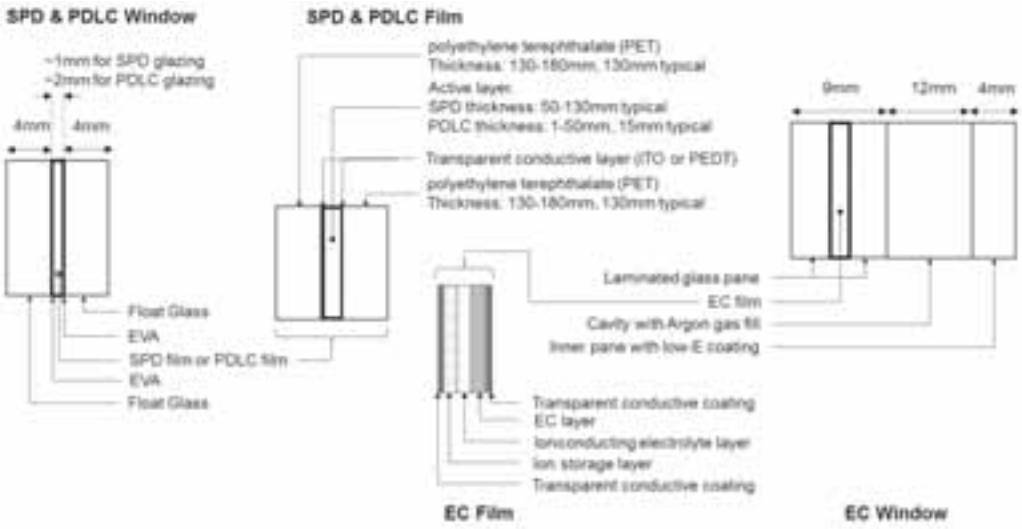

Fig. 1: Schematic of the tested SPD and PDLC films and SPD, PDLC and EC windows

2.2. Lambda900 spectrophotometer for film transmission analysis

Fig. 2 and Fig. 3 represent the reference beam (1) and the sample beam (2) within the Lambda900, with same optical path length (D≈36cm) from their respective cuvette holder to the integrating sphere (IS) aperture of diameter Φ=5mm. Wavelengths from 250nm to 2500nm were scanned in 1nm steps to look at the film ultraviolet (UV), visible (VIS), near-infrared (NIR) and short-wave infrared (SW-IR) transmission and compare them with the optical bench

setup results. Absorbance calibration was done in air. For measurement of all transmitted light, a maximum of scattered light was collected for the switchable film (SPD or LC film with ITO layers on both sides and no glass) located flat at the integrating sphere aperture entrance. All forward scattered light sketched in Fig. 4 was collected by the integrating sphere. Transmission in the far-field (~36cm from the IS) was achieved by setting the film flat at the cuvette or further named "sample port" (SP). The cone angle θt of collected transmission is reduced to θt ≈0.15º as illustrated in Fig. 5. The cone angle in that configuration being close to 0º, transmission measurements are considered to correspond to the specular and direct (0º) transmissions.

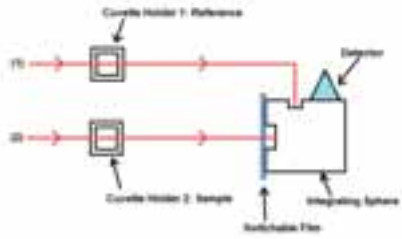

Fig. 2: Film scattered transmission measurement at the Lambda900 integrating sphere.

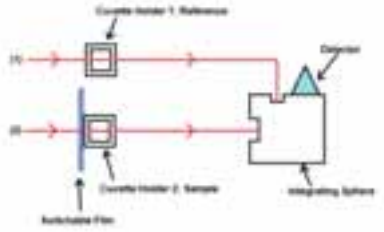

Fig. 3: Far field film transmission at the cuvette in Lambda900.

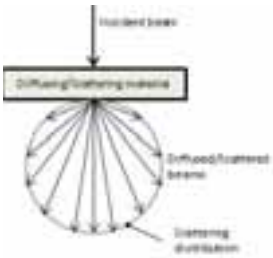

Fig. 4: Scattered transmission sketch. The doted circle represents the irradiance distribution of the scattered light.

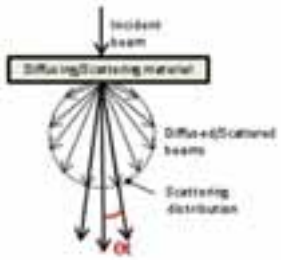

Fig. 5: Far field transmission sketch.

$$\eta_{abs} = \frac{T_{clear} - T_{opaque}}{T_{clear}} = 1 - \frac{T_{opaque}}{T_{clear}} \quad \text{(eq. 1)}$$

$$T_{scatt}(\%) = T_{IS}(\%) - T_{SP}(\%) \quad \text{(eq. 2)}$$

$$\alpha = \frac{\pi * D_p}{\lambda} \quad \text{(eq. 3)}$$

The dynamic light attenuation when switching ON and OFF the samples could be obtained from the transmission curves. The relative attenuation of the signal can be seen as the relative absorption efficiency η_{abs} of the film expressed by (eq. 1. As calculated by (eq. 2, the difference between transmission measurements at the IS port (T_{IS}) and sample port (T_{SP}) provided information on the percentage transmission affected by scattering. (eq. 3 describes the scattering dimension less parameter α with D_p the diameter of a spherical particle and λ the wavelength. The parameter α enables to distinguish three types of scattering: 1) Rayleigh scattering for $\alpha << 1$; 2) Mie scattering for $\alpha \approx 1$ and 3) geometric scattering for $\alpha >> 1$. With the incident light wavelength of the same order as the particles' sizes. The condition where α≈ Mie scattering (α≈1) enables to have a view of the particles size distribution across the studied film. Once the switchable film is in position, transmission measurements in clear and opaque states are separated by several minutes (~5minutes) to ensure the films in their opaque state reach their thermodynamic equilibrium and are optically stable.

2.3 Optical bench setup and its validation with float glass and EVA transmission

A solar simulator and integrating sphere fibre connected to a handheld spectrometer was used to i) determine the absorption contribution of glass and EVA layers in the final glazing, ii) to ensure the optical bench setup results coincide with the Lambda900 spectrophotometer and iii) to measure the switching time of the EC, SPD and PDLC glazing. A first sample, named 'FGEVAFG' hereafter, comprised of an ethylene-vinyl acetate (EVA) layered in between two float glass (FG) panes 6mm thick was measured in transmission using both setups. The absorption measurement of a single 6mm FG pane further enabled the determination of the transmission of the EVA layer only.

Both transmission measurements at the IS and SP of the Lambda900 were perfectly matching between 250nm and 2500nm, demonstrating no scattering occurred. Transmission measurements compared using the optical bench setup validated the setup results between 385nm and 1020nm (see Fig. 6).

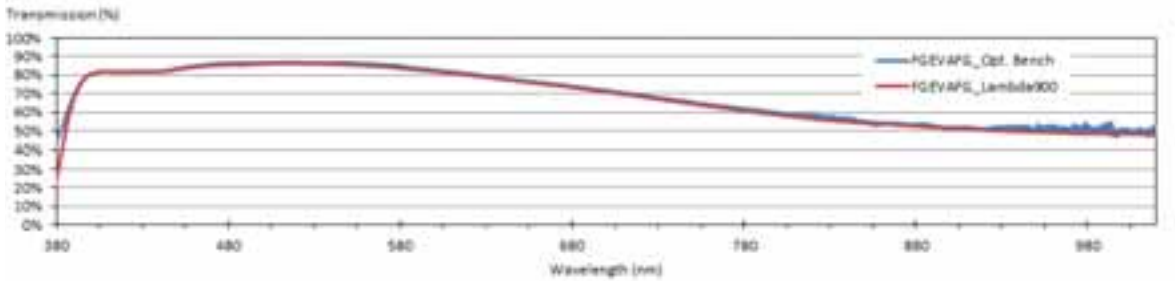

Fig. 6: FG-EVA-FG transmission and optical bench setup validation.

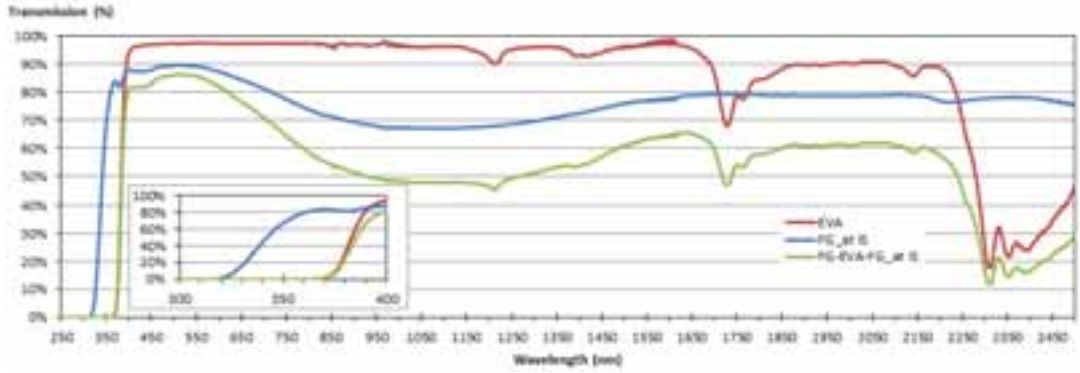

Fig. 7: Transmission of 4mm float glass (FG), FG-EVA-FG sample and EVA layer.

The absorbance (Ab) of the float glass and the FGEVAFG sample measured, the transmission of the EVA layer was calculated using (eq. 4.

$Ab_{FGEVAFG} \approx A_{FGEVAFG} + R_{FG} \approx R_{FG} + A_{EVA} + 2 * A_{FG}$ discarding multiple internal reflections $Ab_{FG} = A_{FG} + R_{FG}$ and $Ab_{FGEVAFG} - 2 * Ab_{FG} \approx A_{EVA} - R_{FG}$ leading to:

$$T_{EVA}(\%) = \frac{100}{10^{Ab_{FGEVAFG} - 2*Ab_{FG}}} * 10^{-R_{FG}} \qquad \text{(eq. 4)}$$

(eq. 4 requires the spectral reflection at the air-FG interface R_{FG} approximated using the Fresnel reflection in (eq. 5 for unpolarized light (Albregtsen, 2008) and considering the known refractive index of BK7 available between 300nm and 2500nm (Polyanskiy, 2016).

$$R_s = \left|\frac{n_1 * \cos\theta_i - n_2 * \cos\theta_t}{n_1 * \cos\theta_i + n_2 * \cos\theta_t}\right|^2 = \left|\frac{n_1 * \cos\theta_i - n_2 * \sqrt{1 - \left(\frac{n_1}{n_2} * \sin\theta_i\right)^2}}{n_1 * \cos\theta_i + n_2 * \sqrt{1 - \left(\frac{n_1}{n_2} * \sin\theta_i\right)^2}}\right|^2$$

$$R_p = \left|\frac{n_1 * \cos\theta_t - n_2 * \cos\theta_i}{n_1 * \cos\theta_t + n_2 * \cos\theta_i}\right|^2 = \left|\frac{n_1 * \sqrt{1 - \left(\frac{n_1}{n_2} * \sin\theta_i\right)^2} - n_2 * \cos\theta_i}{n_1 * \sqrt{1 - \left(\frac{n_1}{n_2} * \sin\theta_i\right)^2} + n_2 * \cos\theta_i}\right|^2$$

$$R = \frac{R_s + R_p}{2} \qquad \text{(eq. 5)}$$

In the equations above, the subscripts 's' and 'p' respectively denote the perpendicular and parallel electric field direction of the light electromagnetic wave. The subscripts 'i' and 't' refer to the incident and transmitted angles θ at the air-FG interface of respective refractive index n_1 and n_2.

The resulting EVA transmission curve in Fig. 7 showed relatively flat transmissions of above 95% from 430nm to 1650nm and ≈ 90% from 1850-2200nm. Strong absorption bands occurred in the 1655-1750nm and 2325-2400nm ranges. The glazing thickness is mostly comprised of glass. The FGEVAFG sample transmission showed that the

choice of glass highly affects the overall glazing performance– most importantly the NIR, SW-IR ranges and the consequent solar transmission. The UV cut-off wavelengths of float glass and EVA were respectively noted around 320nm and 370nm. The EVA, absorbing UV, acts as a protective filter for particles embedded into switchable windows but UV sensitive particles would still deteriorate under long-term UV exposure (Czanderna, 1996).

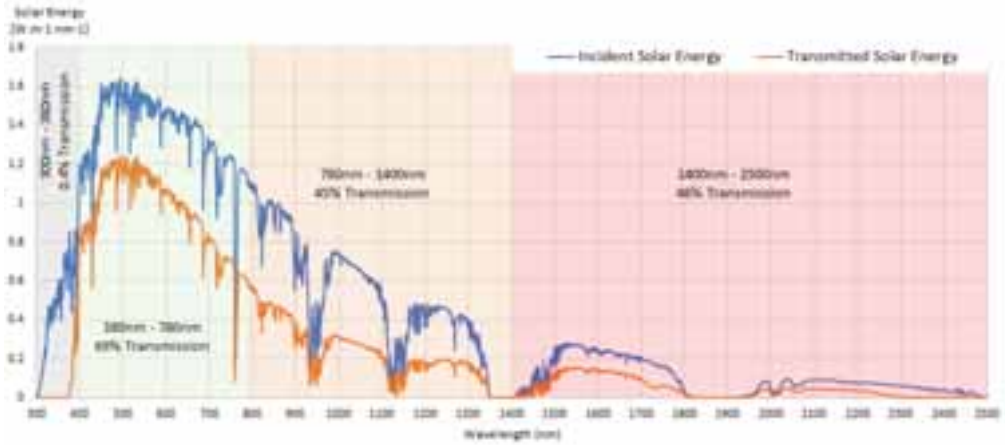

Fig. 8: Solar energy spectrum incident and transmitted through 12mm of the measured clear float glass and 0.4mm EVA layer.

Knowing the absorbance of the float glass and the EVA layers enabled the calculation of the Napieran attenuation coefficient of the materials and simulation of the transmission through three glass panes 4mm thick and two EVA layers 0.2mm thick (see Fig. 8). This configuration, similar to the EC window without the active EC film and the low-E coating, enabled an understanding of the amount of solar energy available for transmission modulation by a switchable film. The measured clear float glass showed ~69% transmission in the visible and strong absorption in the NIR and SW-IR regions with transmission to ~45% and ~46% respectively. The transmitted solar energy was about 371W.m^{-2}, 145W.m^{-2}and 47W.m^{-2} in the respective wavelength ranges. The EVA layer absorbing UV, ~0.4% transmission is calculated between 300nm and 380nm, representing ~120mW.m^{-2}. Simulation on clearer glass such as the Planiclear^{TM} from Saint-Gobain demonstrated transmission of about 1.2%, 83%, 63% and 63% in the UV, VIS, NIR and SW-IR respectively and therefore enabling a larger fraction of the solar energy to be modulated by an active film integrated between the two EVA layers.

3. Spectral transmission analysis

3.1. SPD and PDLC films

The SPD film tested, about 0.35mm thick, is mainly made of a polymer (most likely PMMA) for which absorption bands occurred around 1657nm, 2143nm and 2328-2450nm in Fig. 9 and again for the PDLC film in Fig. 10. The transmission curves at both the IS and SP positions for the ON state were matching, meaning reflections from all internal interfaces and absorption are the only occurring phenomena. In the OFF state, particles in random orientations strongly absorb light in the visible and NIR range. The transmission curves at the IS and SP showed differences in the transmitted blue and NIR wavelength ranges. Plotting the scattered transmission (difference between the two curves), a Poisson distribution was obtained between 760nm and 2250nm with a maximum of the particles having a size about 1µm corresponding to the particles length (Saxe et al. 2003) and confirming this difference is attributable to a Mie scattering process ($\alpha \approx 1$ in eq. 2).

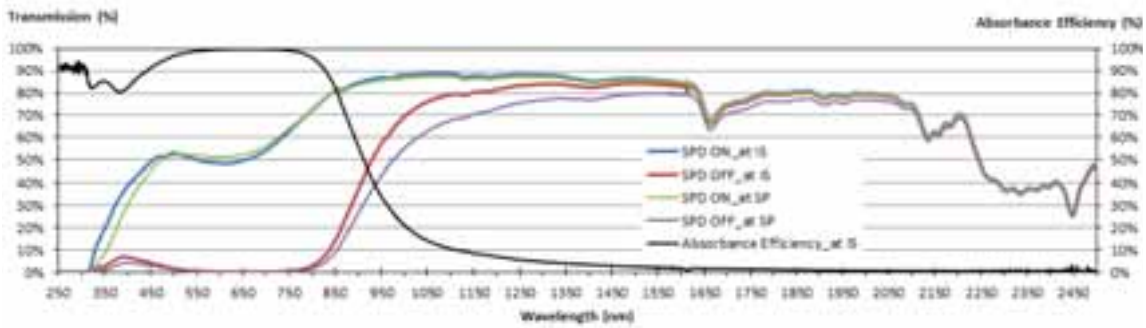

Fig. 9: SPD film transmission and absorbance efficiency

Multiplying the transmission curve by the global solar irradiance at an air-mass of 1.5 (ASTM, 2012), the spectral solar irradiance and solar energy transmitted through the SPD film (i.e. without glazing and interfacing EVA) in the transparent and opaque states was obtained and summarised in Tab. 2.

Tab. 2: Global solar energy modulated by the SPD film.

		Transmitted solar energy (W/m^2)			
Spectral range (nm)	Global solar energy (W/m^2)	Transparent	Opaque	Solar energy modulated (W/m^2)	Fraction of solar energy modulated (%)
280 - 379.5	32.1	6.5	1.1	5.4	16.9%
380 - 780	535.5	274.0	8.4	256.6	49.6%
781 - 1400	323.8	272.8	166.7	106.1	32.8%
1401 - 2500	101.9	76.0	74.9	1.2	1.1%
280 - 2500	993.3	629.4	251.1	378.3	38.1%

Fig. 9 shows the SPD window highly modulated transmission in the wavelength range from 390nm to 820nm with transmission varying from 50% to 70% above 450nm and averaging at 51.2% transmission over the visible range (380nm-780nm). The SPD showed a strong absorption from 1000nm to 2100nm with a modulation efficiency continuously decreasing below 30% from above 1000nm and below 10% above 1350nm. In Tab. 2, the SPD film appeared to modulate 16.9% of the UV light (280nm-380nm) with $6.5W.m^{-2}$ of solar UV transmitted in the transparent state. Considering the ~$120mW.m^{-2}$ transmitted through the simulated glazing, between $4mW.m^{-2}$ and $24mW.m^{-2}$ is transmitted in the opaque and transparent modes. To mitigate degradation of the SPD film, exposed to ~$850mW.m^{-2}$ after 4mm glass and 0.2mm EVA layer, or other materials within the occupant environment, UV protection is initially achieved with float glass and EVA layers forming the window and would benefit from the potential addition of a UV filter. In the transparent state, about half of the solar energy in the visible range is absorbed which significantly limits the fraction of natural light entering the occupant environment on cloudy days. With 49.6% of visible solar energy controllable, this is the spectral band most effectively controlled by the SPD film. In the near-infrared (781-1400nm) the SPD still modulated 32.8% of the input solar energy but a high $166.7W.m^{-2}$ solar energy was transmitted in the opaque state and represented more than 51.4% of the solar energy in that range. This implies that there is significant infra-red solar heat transfer in the switched-mode that is ostensibly intended to reduce solar gain. SPD materials with an absorption efficiency in the NIR similar to current performances within the visible range could lead to an additional 16.8% to the current modulation capability. The latter represents an additional 51.2% of energy modulable through a glazing integrated the active film. For the simulated glazing with 12mm glass thickness and 0.4mm EVA layer, it represents an additional 4.3% solar (280-2500nm) energy modulation compared to 4.9% for a clearer glass such as the Planiclear^{TM}. Considering the film thickness and the low dynamic absorption of SPD material above 1400nm, only 1.1% of the solar energy in the short-wave infrared (1400-2500nm) could be modulated with more than 73% of the solar energy transmitted through the SPD independently of the SPD optical state. The 780nm-2500nm solar range containing 42.6% of the $1kW.m^{-2}$ global solar energy and ~34% of the solar energy transmitted through the simulated window, innovative SPD materials with an efficient dynamic control of the infrared range would significantly contribute to the infrared solar heat transfer modulation offered by switchable windows. Overall, in the 280-2500nm range, the SPD film could modulate 38.1% of the solar energy passing through a glazing

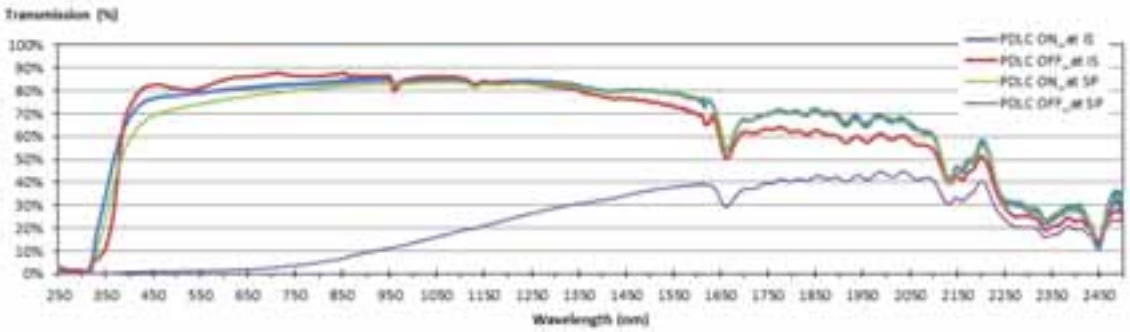

Fig. 10: PDLC film transmission.

Transmission results on the PDLC film shown in Fig. 10 demonstrated very similar transmission in the clear and opaque state over the entire scanned range when measured at the integrating sphere. This result led to conclude that light passing through the film is not further absorbed nor significantly more reflected when switching ON or OFF the film. However, when setting the film at the sample port, transmission is highly reduced in the OFF state meaning

that 1) almost all visible light passing through the film in the OFF state is scattered (giving the milky-white appearance) and 2) that the transmission loss mechanism in the OFF state is uniquely related to the distance between the detector and the film until the cone angle becomes small enough (close to 0 radian) that the transmission will not change anymore.

3.2. EC window transmission

The EC window transmission curves for both the opaque and transparent states are shown in Fig. 11 together with the absorbance efficiency. In the transparent state, the EC window tested, demonstrated transmission in the visible (380-780nm), near-infrared (780-1020nm) and solar (380-1020nm) ranges of 50.1%, 50.8% and 29.2% respectively. In the opaque state, the EC window transmission went down to 15.3%, 14.9% and 0.8% at the respective range. The transmission tolerance in those ranges were ±1.0%, ±1.1% and ±4.9% due to the intensity of the source, the fluctuation of the lamp, the sensitivity of the spectrometer and the signal noise in the various wavelength ranges. While the 50.1% visible transmission in the transparent state of the window was matching the manufacturer information, the 15.3±1.0% transmission in the opaque state was not matching the 10±2% transmission. A possible cause of this, suggested by the manufacturer, was the lack of sunlight exposure of the glazing and switching in the time leading up to the test. The EC glazing requires UV sunlight exposure to allow it to fully darken. This encourages further understanding of the influence of outdoor solar conditions and temperature on the glazing transmission and switching speed capabilities. In the visible range the window has an absorbance efficiency varying from about 70% at 380nm down to 50% at 480nm before rising to nearly 95% at 780nm. The signal noise in the opaque mode did not allow a clear transmission measurement above 880nm but it appeared the window absorbance efficiency tends to 100% up to 1020nm likely due to the low-E reflective coating in the fifth glass surface of the window. A measurement of the EC film only using the Lambda900 is desirable to have a higher accuracy of results over the entire solar range.

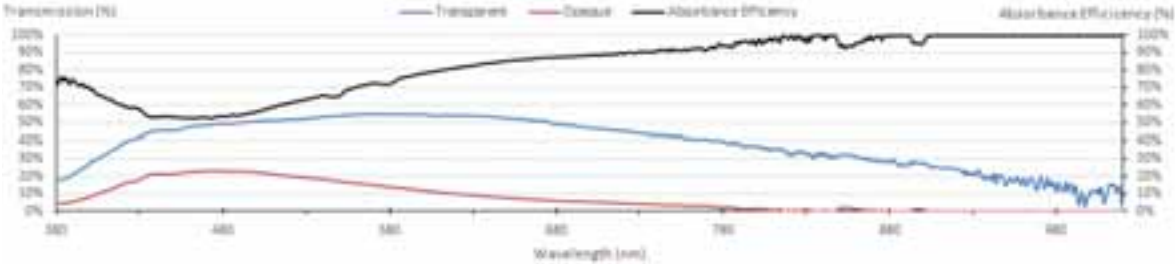

Fig. 11 EControl EC Window – Transmission in the transparent and opaque states and absorbance efficiency

Similar to the SPD film, the global solar irradiance transmitted through the EC window in the transparent and opaque states was obtained in Fig. 12 and the solar energy summarised in Tab. 3.

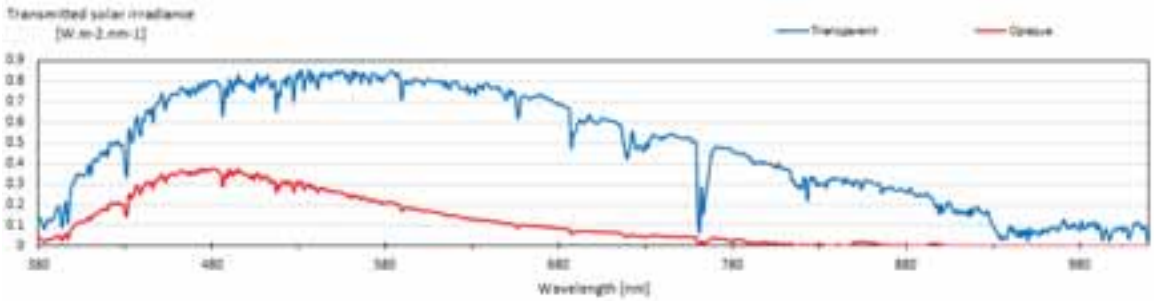

Fig. 12: Calculated solar irradiance transmitted through the EC window in the transparent and opaque states

Tab. 3: Global solar energy modulated by the EC window.

		Transmitted solar energy (W/m^2)			
Spectral range (nm)	Global solar energy (W/m^2)	Transparent	Opaque	Solar energy modulated (W/m^2)	Fraction of solar energy modulated (%)
380-780	535	258±6	70±6	188	35.1%
780-1020	188	50±9	1±9	49	26.1%
380-1020	723	308±8	71±8	237	32.8%

Similar to the SPD film in the transparent state, Tab. 3 shows that the EC window transmission in the visible range

significantly limits the fraction of natural light entering the occupant environment on cloudy days. With 35.1% of visible solar energy controllable, this is the spectral band most effectively controlled. In the near-infrared (780-1020nm) the fraction of solar energy modulated goes down to 26.1% with about 50W.m^{-2} solar energy transmitted in the transparent state and 0-10 W.m^{-2} in the opaque state. Such low transmission in the infrared in both states is the result of the film light absorption and the light reflection from the low-E coating on the fifth glass surface. Such configuration would allow the window to significantly reject infra-red solar heat transfer but still be able to modulate a small portion of the solar energy in that region. Thus, it is convenient for climates with a high solar irradiance. In low to moderate solar irradiance conditions, the window would benefit from modulating a larger fraction of the solar range as more visible light and infrared solar heat passing through the window might be required. Overall, the EC window could control 32.8% of the solar energy contained within the 380nm-1020nm range.

4. Switching time of SPD, PDLC and EC windows

In principle, the complete switching time between fully clear to fully opaque is identical at all wavelengths due to the time it takes for the SPD particles and LC molecules to rotate or the ions to be fully absorbed by the EC layer according to the voltage applied. However, the relative spectral switching time further on called "switching time" varies according to the intensity of the source and the spectral transmission in the transparent and opaque states at the wavelength considered. Using the optical bench setup, the switching time of the SPD, PDLC and EC windows could be measured. When switching the windows, the light transmission change with time, was observed rising and decreasing similar to the charging and discharging curves of an electronic Resistor-Capacitor (RC) circuit. As illustrated in Fig. 13, the time τ was defined as the time required for the window to reach 63% of its final state (transparent or opaque). The defined switching time 3τ is the time required to reach 95% of the transition and 5τ for 99% of the transition.

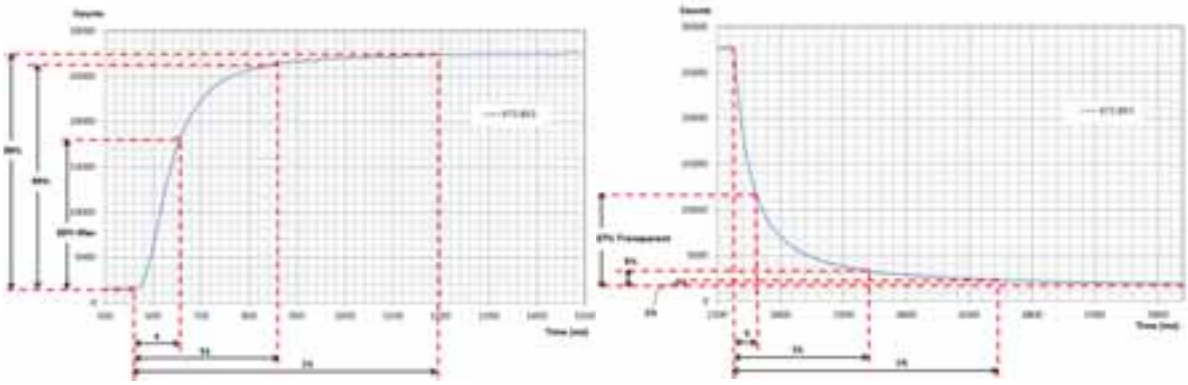

Fig. 13: (left) Switching ON time (τ_{up}) and (right) switching OFF time (τ_{down}) definition. Examples with the SPD glazing at 473nm.

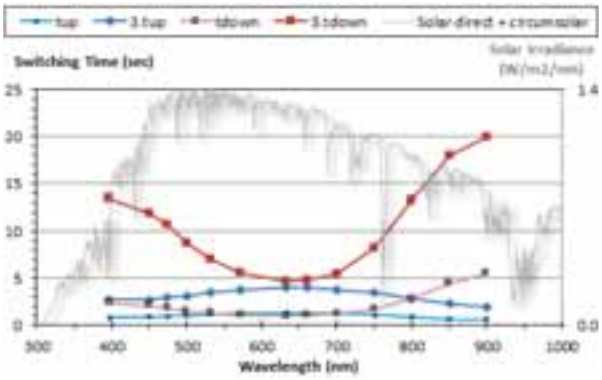

Fig. 14: SPD window switching ON and OFF times.

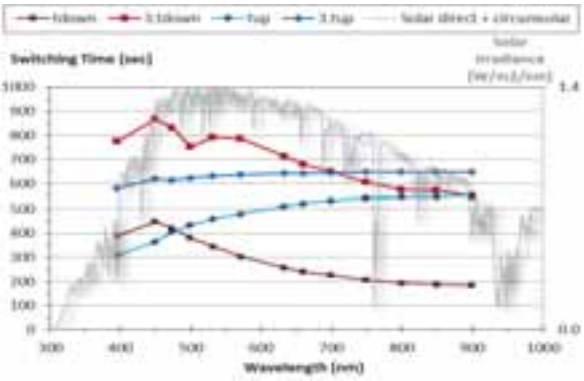

Fig. 15: EC window switching ON and OFF times.

$$f = \frac{3\tau_{down}}{3\tau_{up}} \qquad \text{(eq. 6)}$$

Fig. 14 compares the up (to transparent state) and down (to opaque state) switching times of the SPD glazing with the solar spectrum. The curves show opposite behaviours affected by a factor f defined in (eq. 6). In the 400-700nm region the transmission switches from 48.54% to 1.27% (Lemarchand, 2014). Simultaneously the "f" factor

decreased from x4.9 at 400nm to a minimum x1.17 at 633nm, before it started strongly picking up in the infrared region. At 900nm, the switching "down" time was x10.7 longer than the switching "up" time. Particles are forced to align with the electrical fields between the conductive layers when the window is switched ON. Reversely, when turned OFF, the voltage across the SPD film drops to 0Vac, the electrical field disappears and the particles are free to naturally disperse in random orientations within the Brownian fluid forming the SPD film. It was then expected, as the experiment confirmed, that the switching ON time would be much shorter than the switching OFF time. The switching ON time could not be calculated theoretically due to a lack of information on the particle composition but this one was expected to be in the hundreds of milliseconds – this was also confirmed by the results obtained in Fig. 14. Using Hsu et al. (2005) equations, the theoretical switching OFF time was calculated to be about 1100ms or 2000ms respectively for ethanol and propanol as the organic fluid considered. In the OFF state the window appeared with a dark blue tint as a direct consequence of the particle rotating and reaching a chaotic order. The time it took for the particles to rotate could then be best visualised in transmission when looking at the blue wavelengths, meaning at wavelengths the particles are efficiently absorptive but with the least absorption. The τ_{down} time measured at 450nm and 473nm were 2100ms and 1800ms respectively and match with the particle rotation time order of magnitude expected. Strongly absorbed wavelengths have their transmitted intensities reach a minimum even before the particles finish their rotation, consequently reducing the switching OFF time. This appeared in Fig. 14 from 572nm to 700nm with a factor below x1.5. The particles being increasingly transparent as the incident infrared wavelength is increased, the intensity variation tends to zero and the switching OFF time tends to infinite.

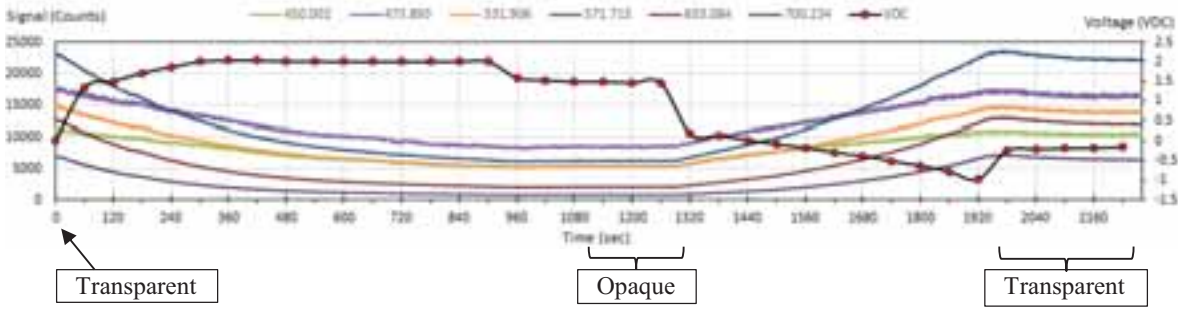

Fig. 16: EC window voltage and transmission variation in time at selected wavelengths.

Fig. 16 illustrates the intensity variation of the transmitted light at specific wavelengths when switched from transparent to opaque and from opaque to transparent. The voltage measured at the window electrodes is plotted on the secondary axis. In the initial transparent state the window was not operated for 7 days prior the experiment and voltage was 0Vdc. When switching off the window, the voltages rises up to +2Vdc after ~ 5 minutes and remained constant until the windows reached its opaque state with the voltage reduced down to +1.5Vdc. At this stage, it is believed the window acting as a capacitor was fully "charged" and retained the +1.5Vdc. Small crystallite systems such as those used in EC windows have been shown to behave more like capacitor than faradaic systems and this may offer an explanation for this apparent discharging behaviour (Ho et al. 1997). A plot of charge versus applied voltage could aid in better understanding this behaviour. Switching the window to the transparent state reduced the voltage to just above +0Vdc. The voltage continued decreasing to -1Vdc when the window reached a maximum transmission. Once the transparent state was reached, the voltage flattened just below 0Vdc. The final transmission state was slightly lower than the initial state but it is believed that, should the transmission and voltage measurements be monitored over a longer period, the transmission would have equalised and the voltage reached 0Vdc.

Fig. 15 shows a $3\tau_{down}$ switching times of the EC window from transparent to opaque varying from 867 seconds at 450nm down to 549 seconds at 900nm. Switching from opaque to transparent resulted in curves in the opposite trend. The τ_{up} increased from 308 seconds at 400nm to 552 seconds at 900nm. The $3\tau_{up}$ switching time to the transparent state varied from 582 seconds to 648 seconds at the respective wavelength. The $3\tau_{up}$ values appeared relatively constant across the visible range. A switching speed of this order makes EC windows unsuitable for instantaneous glare control and reactive rule based control (RBC). The ambient temperature at the time of testing was 21°C and EC switching time is known to decrease with an increase in temperature (LBNL, 2006) such as in the warm condition of sunny climates. Whilst this slow switching speed may be seen as a disadvantage, it is worth noting that this slow switching speed would be imperceptible to building occupants. The rapid switching of SPD and PDLC would however be noticeable and may have an impact on occupant comfort as they experience rapid changes of their environment. To mitigate such issues, controllers can adjust the switching speed to control the desired indoor lighting condition. A slow switching EC window, if properly controlled offers the possibility to modulate visible light and

heat transmittance without any obvious change in the window appearance. A model predictive control (MPC) strategy, with an appropriate time horizon, could offer the possibility of using the slow response time of the EC window combined with expected building conditions over the prediction time horizon to maintain a comfortable occupant environment, primarily by reducing heat gain in the IR range. This type of system is likely to perform better in cooling dominated climates where a constant glare reduction is required rather than a strategic glare control.

Switchable windows need to switch in the visible range as fast as the eye response, i.e. 13ms to 80ms, for the user to have spontaneous control of the glare. Measurements on the SPD glazing showed that 95% of the full transmission change occurred with switching times of ~0.5s and ~1 second when respectively switching ON and OFF the window. These switching times were consequently 6 to 77 times too long to instantly control glare to the eyes visible response. Moreover, considering a perception of discomfort can be perceived in the order of 1.25 seconds, it would be preferred to have a similar response time in the infrared to instantaneously control solar heat transfer through the switchable glazing. A faster switching speed, achievable with increased absorption from the particles, would then be preferable for wavelengths above 800nm.

Tab. 4: PDLC switching time.

Wavelength (nm)	378	396	473	532	572	633	660	850	900
Average Switching OFF time (ms)	25	25	30	35	50	45	55	40	45
Average Switching ON time (ms)	15	15	15	15	15	15	15	15	15

As shown in Tab. 4, the switching time for PDLC under applied voltage was as low as 15ms but is likely to be even faster and wavelength dependent as the recorded values were limited by the spectrometer integration time. For the same window size the SPD required 300-400ms which was at least 20 to 25 times longer. The relaxation time of the LC molecules was at least 2-3 times longer than the switching ON time. Due to their light scattering properties, PDLC windows are primarily applied as indoor privacy walls. The control of glare and thermal response from outdoor conditions is not relevant in that particular case but LC based windows with an embedded dye absorbing the desired wavelength range such as the Licrivision^{TM} product from Merck (2017) enable control of glare, solar heat transfer and the desired window colour. The fast switching speed of the PDLC windows is noted to be as fast as the human eye response (13ms to 80ms) and LC based technologies are consequently ideal for glare control.

5. Conclusion

The SPD window highly modulated the transmission from 390nm to 820nm with 51.2% transmission over the visible range in the transparent state. It also showed a strong absorption and low modulation efficiency in the infrared range reaching below 30% efficiency from above 1000nm and below 10% above 1350nm. These results led to 49.6%, 32.8% and only 1.1% of the solar power dynamically controllable respectively in the visible, near-infrared and the short-wave infrared wavelength range. Using the simulation results of a glazing formed of three 4mm thick glass panes and two EVA layers 0.2mm thick, improving on the SPD film dynamic absorption efficiency by 16.8% within the near-infrared range could lead to additional modulation of up to 51.2% of the transmitted solar energy within the 780nm-1400nm range. This is equivalent to an additional modulation of the solar energy transmitted from 4% to >5% according to the clearness of the glass used. The switching time was shown to be strongly dependent on the wavelength. Switching to the transparent state, the 3τ switching time varies from 200ms to 400ms but, most importantly varies from 450ms to 2000ms when switching the window to the opaque state. The measured 1800ms switching time to the opaque state at 473nm is in concordance with the theory. In the visible range, the 3τ switching time of the SPD window is in average 4 to 66 times slower than the human eye response. Increasing the switching speed in the visible range would further help instantaneous glare control. To match the estimated 1.25 seconds required for a human to feel some discomfort from instantaneous solar heat transfer variation due to the passing of clouds, engineering windows with a faster and stronger modulation over a wider wavelength range starting at 800nm is preferable. Scattering effects were low for SPD windows but were the major physical effect of PDLC windows and indicated the need to specify the distance between the detector and the window when referencing optical transmission. The switching time to the transparent state of the PDLC was below 15ms but also varies from 25ms to 55ms according to the wavelength when turning back the window to its opaque mode. In both case this switching time is sufficiently fast to control glare but, due to its milky-white appearance, is most appropriate for privacy rather than façade glazings. However, a UV filter with a wavelength cut-off at 380nm would provide additional protection where both EVA and PMMA are highly transparent and consequently extend the service lifetime of building integrated switchable windows and protect from the degradation (colour fading) of indoor materials. The switching

time of the EC window appeared particularly dependant to the wavelength when switching the window to the opaque state while it appeared relatively uniform when switching to the transparent state. It should be noted that these times may be expected to decrease with an increase in temperatures above the 21ºC measured during testing and with an increased exposure to sunlight. These switching times are slow compared to SPD and PDLC windows and for this reason they should not be subject to the same control methodologies. Switching times of this order make them unsuitable for instantaneous glare control and better suited to predictive control where heating/cooling or lighting demand can be predicted in advance of the required switching operation. The EC window was able to modulate only 32.8% of the solar energy within the 380nm-1020nm range making it more suited to climates with high solar irradiance. An increase in the transmission levels, particularly in the infra-red range, would make it more suitable in climates that may require greater levels of visible light and solar heat gain.

6. References

Albregtsen, F. (2008). *Reflection, refraction, diffraction, and scattering*. [online] Available from https://www.uio.no/studier/emner/matnat/ifi/INF-GEO4310/h09/undervisningsmateriale/imaging-kap2.pdf [Accessed June 2016].

ASTM - American Society for Testing and Materials (2012). *Reference Solar Spectral Irradiance: Air Mass 1.5*. [online] Available from http://rredc.nrel.gov/solar/spectra/am1.5/ [Accessed June 2016].

Czanderna, A. W. & Pern, F. J. (1996). Encapsulation of PV Modules Using Ethylene Vinyl Acetate Copolymer as a Pottant: A Critical Review. *Solar Energy Materials and Solar Cells,* 43**,** pp. 101-181.

Jones, L. (2009). "Thermal touch." Scholarpedia 4(5): 7955.

Kenny, L. W. (1998). Part VI - General Hazards, Chapter 42 - Heat and Cold: Physiological responses to the thermal environment, Encyclopedia of Occupational Health and Safety 4th Edition.

Gueymard, C. A. (2007). Advanced Solar Irradiance Model and Procedure for Spectral Solar Heat Gain Calculation. ASHRAE Transactions, 113 (1), pp. 149-164.

Gueymard, C. A. & duPont, W. C. (2009). Spectral effects on the transmittance, solar heat gain, and performance rating of glazing systems. Solar Energy, 83, pp. 940–953.

Ho, K. et al., 2006. Proceedings of the Third Symposium on Electrochromic Materials, Electrochemical Society.

Hsu, H.-Y., Sharma, N., Ruoff, R. S. & Patankar, N. A. (2005). Electro-orientation in particle light valves. *Nanotechnology* 16 (2)**,** pp. 7.

LBNL (Lawrence Berkeley National Laboratory), 2006. PIER Final Project Report: A Design Guide for Early-Market Electrochromic Windows. PIER Final Project Report, (May), pp.1–58. Available at: www.energy.ca.gov [Accessed October 15, 2017]

Lemarchand, P, Norton, B & Doran, J. (2014, Nov 27). 'Smart Switchable Technologies for Glazing and Photovoltaic Applications', Energy Procedia, Volume 57, Pages 1878-1887.

Lewis, T. (2014). New Record for Human Brain: Fastest Time to See an Image. Live Science.

Merck (2017). Liquid Crystal Window Technology. [online] Available from https://www.licrivision.com/en/LCW_solar_control_glazing.html [Accessed Oct. 2017].

NWSWFO (National Weather Service Weather Forecast Office). (2004). "Heat Index." from http://www.nws.noaa.gov/os/heat/heat_index.shtml [Accessed Oct. 2017]

Polyanskiy, M. (2016). Refractive index database. [online] Available from http://refractiveindex.info/ [Accessed June 2016].

Waide, P. A. & Norton, B. (2003). Variation of Insolation Transmission With Glazing Plane Position and Sky Conditions. ASME Journal of Solar Energy Engineering, 125 (2), pp. 182-189.

Wienold, J. (2010). Daylight Glare in Offices. Fraunhofer-Verlag.

PERFORMANCE ASSESSMENT OF A SOLAR-ASSISTED, GROUND-COUPLED ABSORTION HEAT PUMP UNDER DIFFERENT SCENARIOS IN SUMMER AND WINTER OPERATION

Andrés Macía[1], Luis A. Bujedo[1], Teresa Magraner[2], César Chamorro[3]

[1] CARTIF Technology Centre, Parque Tecn. de Boecillo, 205, 47151, Boecillo, Valladolid (Spain)

[2] Energesis Center, Poligono Industrial San José de Valderas, 28918, Leganés, Madrid (Spain)

[3] Valladolid University, Paseo del Cauce, 59, 47011, Valladolid (Spain)

Abstract

This work describes a novel HVAC system consisting in a solar-assisted ground-coupled absorption heat pump. The aim of this work is to analyze, using a TRNSYS simulation program, the influence of different design parameters, such as the area of the solar collectors; the building occupancy and the using schedule, as well as an assessment of the influence of the weather conditions in the energy performance of the installation during winter and summer season. Finally, an annual analysis of the energy transferred by the main elements of the installation (solar collectors, boiler, geothermal heat exchange, generator, condenser, evaporator, radiant floor) under the actual operating conditions was carried out.

Keywords: Solar energy, solar cooling, sustainable HVAC, geothermal heat exchange, absorption heat pump, radiant floor, TRNSYS

1. Introduction

The building sector consumes almost 120 EJ per year worldwide, representing 30% of total final energy consumption in all sectors of the economy and half of the world's electricity demand. Despite the great efforts of politicians to improve the energy efficiency of buildings, energy use in this sector has increased by almost 20% since 2000. Fossil fuels (coal, oil and natural gas) used directly inside buildings and in the generation of electricity represent a significant part of the energy used. The building sector represent almost 30% of global CO_2 emissions and 36% of the final energy consumed in buildings is used for heating (IEA 2015).

The European Union has identified the building sector as a key sector to achieve the 20/20/20 objective (Reduce greenhouse gas emissions by 20%, achieve that renewable energies cover 20% of final energy consumption and achieve 20% savings in energy demand by 2020), as well as to achieve a reduction of greenhouse gas emissions from 80% to 95% by 2050. To achieve these goals, heating and cooling technologies that use renewable energy as an energy source will play a vital role within a sustainable energy system. This has been identified by the European Commission as a "no-return" point in its energy roadmap towards 2050, as it can provide a "local production" of energy. Renewable energies, in addition to being a decentralized system and a highly available energy sources, has also a significant economic impact: about half of the investment will go to the bottom of the value chain, job creation and economic growth at the local level (Ivanic et al. 2014).

As explained above, there is an interest in integrating different renewable technologies to cover the heating and cooling needs in the building sector, and thus help to reduce the demand of fossil source in this sector. Thus, this work is focused on the energy assessment of an installation, which integrates solar energy and geothermal energy with an absorption heat pump, as a way to cover the heating and cooling demand in an office building. In this paper has done several simulation and the idea is to identify the influences of different parameters such as area solar collector, occupancy of the building and weather conditions (different localization) in the performance of the installation.

2. Installation description

doi:10.18086/swc.2017.12.09 Available at http://proceedings.ises.org

The facility under study is located in one of the buildings of the CARTIF technology center in Boecillo Technology Park, Valladolid (41º north latitude and 720 m altitude), Spain. It is a building of tertiary use with an approximate area of 1200 m^2.

The main elements of the experimental installation are: The single-effect, lithium bromide - water (BrLi / H_20) absorption heat pump, THERMAX LT 1; a solar field composed by 42 vacuum tube solar collectors, Vitosol 300; a geothermal energy exchanger consisting in 12 vertical boreholes; and an energy storage system based on water tanks. The system was described in detail by (Macia et al. 2013). The characteristics of the main elements of the system are listed in Table 1.

Tab. 1: Main characteristics of experimental installation

Element	Characteristics
Absorption chiller (Thermax LT1)	35 kW
COP nominal	0.7
Vacuum tube solar collectors (Vitosol 300)	84 m^2
Borehole heat exchanger	12 boreholes
Depth of borehole	100 m
Energy storage system (water)	8 m^3
Radiant floor	1200 m^2

The main novelty of the installation is that the absorption heat pump is connected simultaneously to a geothermal field and to a solar collector field, which allows its use throughout the year with two modes of operation (summer and winter):

Summer: The heat pump condenses with the geothermal exchange; evaporator is connected to the cooling radiant floor system that is distributed throughout the building and the generator is connected to both the solar storage tanks and the gas boiler.

Winter: The evaporator of heat pump is connected to the geothermal exchange, condenser is connected to heating radiant floor which supports the conventional systems installed in the building and the generator is connected to the solar tanks or to the boiler, when there is not enough temperature in the tanks. Figure 1 shows the scheme of the installation.

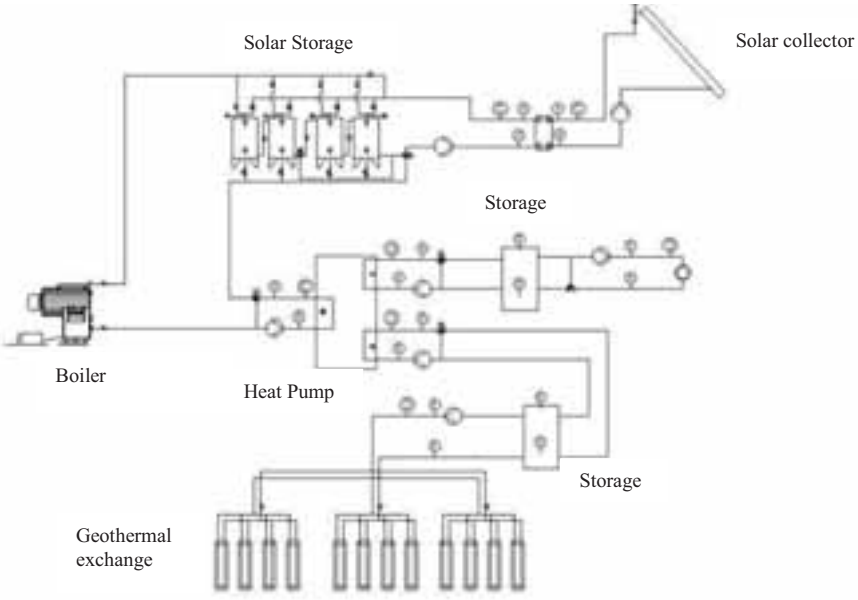

Fig. 1: Schema of experimental installation

3. Simulation approach

In this paper an analysis of the operation of the installation is done under different scenarios, both in summer and winter season. The scenarios that will be analyzed are: influence of solar collector's area; building occupancy, schedule and influence of the weather conditions in the performance of the installation. Finally, an annual analysis of the energy transferred by the main elements of the installation under the actual operating conditions is carried out.

In Figure 2 is possible to observe a schematic of the model developed in TRNSYS for the simulation of the installation, and how the components of the installation are interrelated, from the weather conditions to the building. The simulation model was validated with experimental data collected in actual working conditions of the experimental installation in summer and winter operation modes.

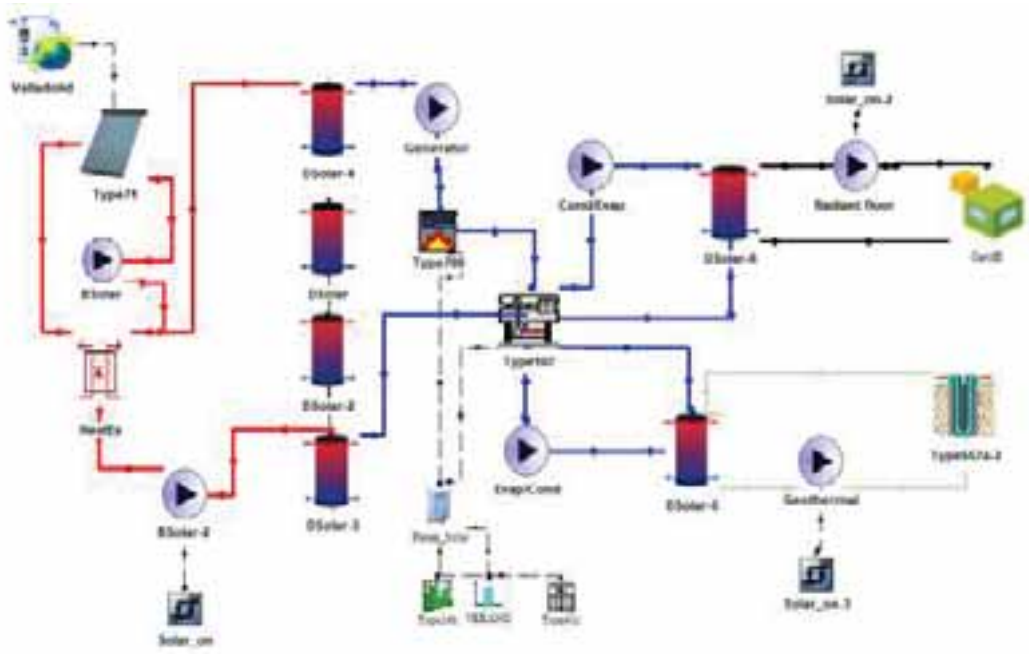

Fig. 2: Diagram of TRNSYS model of experimental installation

The TRNSYS Model is a transient system simulation program with a modular structure that was designed to solve complex energy systems problems by breaking the problem down into a series of smaller components known as Types (Klein 2004). Figure 2 depicts the TRNSYS model scheme developed to simulate the experimental plant. The main modules are described below.

To simulate the performance of the Thermax LT1 absorption chiller, type 107 was used. Since this type uses a catalogue data look up approach to predict the output of the absorption chillers, and the default data file of the type differs from real operation of the installation, several data files of absorption chillers were created, according to the manufacturer technical data.

Type 71 was used to simulate the solar collectors of the solar field. Since standard efficiency curves are calculated for a single solar collector in clear days, at normal sun incidence and nominal flow rate of the water, a few correction factors are introduced in the model, in order to account for series connection, clouds, etc.; details regarding the correction algorithms are given in the TRNSYS documentation. In addition, since evacuated-tube collectors are optically asymmetric, the model takes into account some biaxial Incidence Angle Modifiers (IAM) coefficients for both beam and diffuse radiation. These adjusting parameters are available for any collector tested (ASHRAE 2003) or European Standards (EN12975 – 2:2006)

The natural gas fired boiler used as auxiliary heater is represented by Type 700 in TRNSYS library. The boiler is activated only when its upstream water temperature is lower than a fixed set-point. A vertical ground heat exchanger model must analyze the thermal interaction between the duct system and the ground, including the

local thermal process around a pipe and the global thermal process through the storage and the surrounding ground. Ground heat exchanger has been modeled using the known as 'duct ground heat storage model' (Claesson et al. 1981). This model assumes that the boreholes are placed uniformly within a cylindrical storage volume of ground. There is convective heat transfer within the pipes, and conductive heat transfer to the storage volume. Also U-tube pipe parameters correspond to the properties of polyethylene pipes DN 32 mm PE100.

Type 4 is used to simulate the thermal energy storage water tanks. Simulation is based on the assumption that the tanks can be divided into N fully-mixed equal sub-volumes. The storage tanks are also equipped with a pressure relief valve, in order to account for boiling effects. The model takes into account the energy released by the fluid flowing through the valve, whereas the corresponding loss of mass is neglected. The temperatures of the N nodes are calculated on the basis of unsteady energy and mass balances. For the radiant floor system in the building, TRNSYS type 56 component was used. Building was simulated using TRNBUILD taking into account internal gains by occupancy, working schedule and the radiant floor was simulated as active slab. Weather conditions are represented by the Typical Meteorological Year (TMY) for Valladolid (Spain). Temperatures, wind speeds and solar radiations at regular time intervals are read by a data processor to generate direct and diffuse radiation outputs for a number of surfaces with arbitrary orientation and inclination.

The control strategy that has been developed for the summer and winter operation simulation may be separated in four principal components, each one with its own conditions.

The solar field consists of several elements: solar collectors, primary pump, secondary pump, heat exchanger and storage tanks. The primary pump switches on between 9:00 and 20:00 h every day. The secondary pump has two conditions that it has to carry out before switch on: the first condition is that primary pump is switched on, and the second condition is that the outlet temperature of the solar collectors is higher than the solar storage tanks temperature.

The control for the switch on of the absorption heat pump has to achieve three simultaneous conditions: *Schedule*: The building is occupied between Monday and Friday from 7:00 to 15:00, so the heat pump only operates on these days. *Solar conditions*: In this simulation the installation only operates with solar energy, without the boiler back up. The solar condition is that temperature of storage tank is above the set point generator temperature. *Demand condition*: Summer, heat pump is only in operation when evaporator storage tank temperature is between 8ºC and 15◦C. Winter, heat pump is switch on when condenser storage tank is between 28º and 30ºC.

The control for the switch on of the pump of the geothermal heat exchanger has to fulfill two conditions: that absorption heat pump is in operation and that the temperature of the condenser storage tank is above the condenser set point temperature (summer season) or the temperature of evaporator storage tank is under evaporator set point temperature (winter season).

The control for the switch on of the pump of the radiant floor circuit has to fulfill two conditions: the building occupancy schedule, and the temperature of the evaporator storage tank being between10ºC and 15ºC in summer or condenser storage tank being between 28ºC and 30ºC.

4. Results

On this section, the assessment of three scenarios during winter and summer are analyzed, solar collector area, building occupancy and weather conditions. For the simulation, the summer season is from 1st June to 30th September, and winter season is from 1st October to 31th of May.

Performance of the installation will be evaluated in terms of some indicators described by (Macia, 2016) such us solar fraction defined by equation 1, solar efficiency defined by equation 2, and COP of the heat pump, defined by Equation. (3).

$$Solar\ fraction = \frac{Q_{solaruseful}}{Q_{gen}} \quad \text{(eq. 1)}$$

$$Solar\ efficieny = \frac{Q_{solaruseful}}{Q_{solaresource}} \quad \text{(eq. 2)}$$

$$COP_{summer} = \frac{Q_{evap}}{Q_{gen}}, COP_{winter} = \frac{Q_{cond}}{Q_{gen}} \quad \text{(eq. 3)}$$

Where Q_{evap}, Q_{gen} and Q_{con} are the energy transferred to the evaporator, generator and condenser of the heat pump, calculated by integrating numerically the respective heat flows. $Q_{solaresource}$ is the total amount of solar energy captured by the solar field during the considered period of time. $Q_{solaruseful}$ is the useful energy used for the installation. Qevap evaluated through equation (4).

$$Qevap = \sum \dot{m}_p \, C_p \left(T_{eva,i} - T_{eva,o}\right) \Delta t \quad \text{(eq. 4)}$$

Where $\dot{m}_p$ is the flow through the evaporator. C_p is the fluid specific heat capacity. $T_{eva,i}$ is the inlet temperature to evaporator. $T_{eva,o}$ is the outlet temperature to evaporator and Δt is the time interval.

4.1 Performance of the installation for different solar collector area

One of the difficulties when designing these types of installations is to know the best relation between the area of solar collectors and the power of the heat pump. For this reason, it has been decided to make seasonal simulations (summer and winter) of the installation for several areas of solar collector. Figure 3 shows the relation between the solar fraction (%), solar efficiency and solar collector area for summer (a) and winter (b).

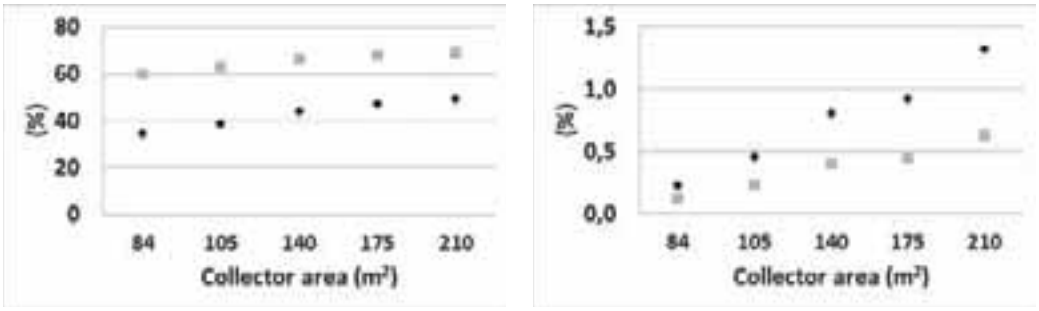

a. Summer, solar fraction (●) solar efficiency (■) b. Winter, solar fraction (●) solar efficiency (■)

Fig. 3: Relation between solar fraction and solar collector area for summer and winter

In summer, when the solar collector area increases from 84 m^2 to 210 m^2, the solar fraction increases from 34% to 50%, which means that 50% of the energy demand of the heat pump is covered by solar energy. In figure 3a, it can be seen, that by increasing the area from 175 m^2 to 210 m^2, the solar fraction does not change, and it is in accordance with (Eicker et al. 2014), who say that the solar fraction increases until achieve the saturation. This demonstrates that in order to avoid overcosts in this kind of installations, the design must be done with caution, and always trying to undersize in order to achieve higher hours of operation with a lower investment. In figure 3b is clear that, although the solar collector area increase from 84 m^2 to 210 m^2, the solar fraction just rises from 0.2% to 1.4% and with solar efficiency less than 1%.

These results show that it is possible to use this installation in both summer and winter seasons. The using of absorption heat pump in winter with other auxiliary energy source is feasible, because it will have higher performance than using the energy of the boiler in a direct way for the heating of the building by the radiant floor. In addition, the primary energy consumption is reduced when it is compared to conventional installations.

4.2 Performance of the installation as function of building occupancy

A simulation has been carried out to know if there is any influence of the building occupation schedule on the solar efficiency and solar fraction of the installation. . The schedules were chosen to cover the most common work schedules in Spain, which according to (Nogareda et al. 2014) are: morning and afternoon 40.2%, morning 28.7%, 24 hours 7.2% , morning or afternoon 14.5%, just nights 1.7%, just afternoon 4.6% and 3.1%

corresponding to other work schedules. The five schedules of occupation defined for the simulations are listed in table 2.

Tab. 2: Schedule of building occupancy, absorption heat pump and radiant/cooling floor whole year

Schedule	Days of working	Schedule of building	Schedule of heat pump	Schedule of radiant/cooling floor
1	Monday to Friday	07:00 – 15:00	07:00 – 15:00	09:00 – 15:00
2	Monday to Friday	07:00 – 15:00	04:30 – 11:30	04:30 – 12:00
3	Monday to Friday	07:00 – 15:00	20:00 – 6:00	20:00 – 06:00
4	Monday to Friday	06:00 – 20:00	06:00 – 20:00	06:00 – 20:00
5	Monday to Friday	24 hours	24 hours	24 hours

The figure 4 shows the result of the simulation for both season summer and winter. The assessment was done with two indicators: solar fraction, solar efficiency.

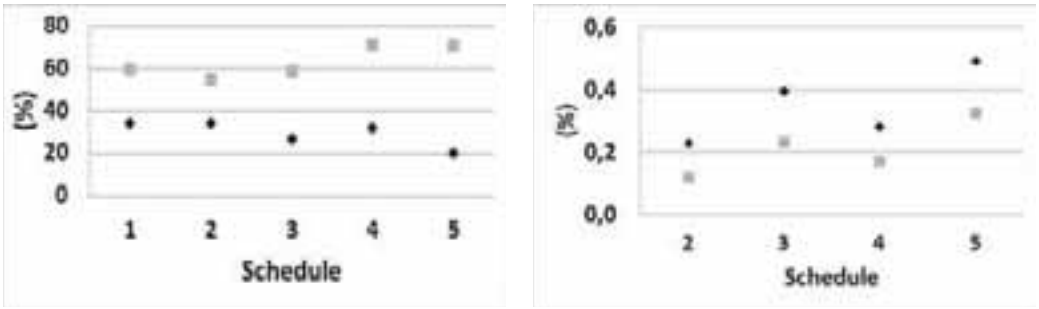

a. Summer simulation **b. Winter simulation**

Fig. 4: Solar fraction (●) and solar efficiency (■) of installation as function of schedules.

In summer, when comparing the 24 hour operating hours (schedule 5) and the CARTIF schedule (schedule 1), the efficiency of the installation is higher in the 24 hour schedule with 70% compared to CARTIF with 60%. This result shows that is better from the solar energy use point of view keep the building open 24 hours. On the other hand, the solar fraction changes from 35% in the CARTIF schedule to only 20% solar fraction in the 24 hour schedule. This decrease in the solar fraction is due to the increase in the energy demand of the generator to cover the 24 hours of operation, causing that the solar installation does not have the sufficient capacity and it is necessary a greater support of the auxiliary energy, CARTIF schedule to 24 hours schedule the generator demand increases 2.6 times.

In winter, with 84 m^2 of solar installation, the solar fraction for any of the simulated schedules is less than 0.5%, demonstrating the need for an auxiliary energy source to cover demand.

4.3 Performance under different weather conditions.

To make an analysis of the influence of climatic conditions on the performance of the installation, simulations for different weather conditions were carried out. For the selection of cities to be simulated, the climatic severity index has been taken into account, according to the Technical Building Code (CTE, 2006) the climatic severity of a locality is the quotient between the energy demand of any building in that locality and the energy demand of same building in a reference locality. The advantage of making the geographic classification based on the index of climatic severity, (Rodríguez, 2015) is that in contrast to the degrees day total year; this index takes into account other variables as the radiation.

According to (Rodríguez, 2015) with the use of the climatic severity index it is possible to discriminate between cold areas of Europe with high solar radiation in winter and other areas with low solar radiation in summer, that having classification by degrees days would not be possible differentiate.

According to the classification explained before, it has been decided to do the simulation for six different cities, each one belonging to a different zone. They are: Valladolid, Seville, Stuttgart, London and Oslo and Medellin.

For the simulations in different climatic conditions, the same characteristics of the heat pump, the building and the same characteristics of the soil have been considered for all the locations. Only the slop of the solar field has been modified according to the latitude of each of the cities. The analysis only has been focused on the influence of both solar radiation and climatic conditions, on the performance of the installation and the heat pump, as well as the solar fraction. The results of simulations are depicted in figure 5.

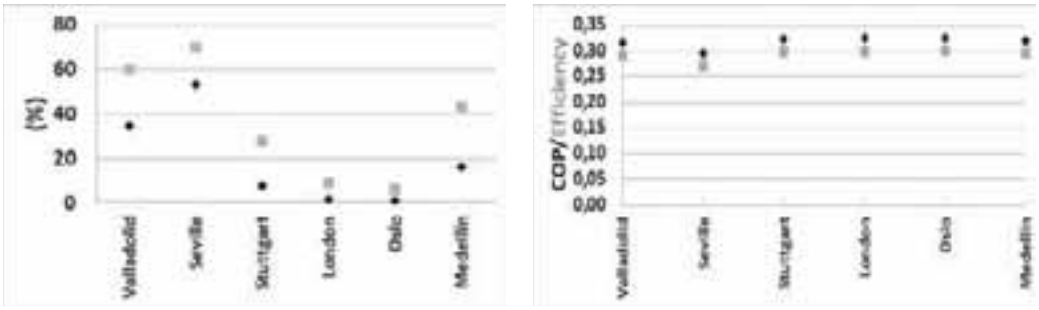

a. Solar fraction (■) solar efficiency(■)

b. COP(■), installation efficiency (■)

Fig. 5: Solar fraction, solar efficiency, COP of installation as function of weather conditions

Solar efficiency in Valladolid and Seville is greater than 60%, which means that more than 60% of the energy of solar field becomes useful energy for the installation. In Oslo and London the efficiency is less than 9% showing that useful solar energy is negligible and it would be necessary to increase the collector area to increase the solar fraction. The results of simulation during winter season for the main elements of installation are presented in table 3.

Tab. 3: Energy of main elements of installation during winter season

City	Q_{boiler} (kWh)	$Q_{solaresource}$ (kWh)	Q_{useful} (kWh)	Q_{gen} (kWh)	Q_{con} (kWh)	Q_{eva} (kWh)	Q_{floor} (kWh)	Q_{geo} (kWh)
Valladolid	8666	16974	20	8686	11486	1800	10425	1968
Seville	6701	21751	372,9	7122	9389	1509	6673	1203
Stuttgart	9545	11047	0	9768	12965	2010	9456	2463
London	9217	9545	0	9278	12270	1913	9456	2184
Oslo	11196	8198	0	11118	14808	2272	11892	3197

The amount of solar energy used by the heat pump during winter (solar useful energy) for three cities Stuttgart, London and Oslo is zero and all energy demand must be covered by the boiler. On the other hand, for Valladolid the contribution did not reach even 1% of total energy demand. A greater contribution was achieved in Seville, with 5% of the total demand of the generator. These results indicated that for the demand conditions of the heat pump with 84 m^2 of solar collector, the solar fraction is zero or very low.

When comparing the solar energy (Qsolar) in Table 3 among the different cities, it is seen that in Seville is where there is a greater uptake with 21750 kWh, but of this energy the contribution to the installation is only 372 kWh, which represents a total of 21378 kWh of solar energy were not used. Oslo on the other hand, it was the city with a lower solar energy with 8198 kWh, this is due to the few hours of solar radiation in winter. This result suggests that in winter the solar energy should be given another use, such as the preheating of the supply water to the boiler.

In table 3, it can also be seen that the demand for radiant floor is higher in Oslo (11892 kWh) being almost double the demand of Seville (6673 kWh), it is expected since the weather conditions in Oslo are more severe than in Seville. The coefficient of operation of the heat pump (COP) in all cities was 1.32 and there is no influence of external conditions on the performance of the pump, one of the reasons is that its three exchanges (generator, condenser and evaporator) are not affected by the external conditions, since the conditions of the

ground, the conditions of the radiant floor and the conditions of the boiler have been considered equal in all the locations.

4.4 Annual energy balance

Finally, after all the simulations carried out in previous section such as: the influence of the building's schedule, the area of solar collector and the study of the influence of the weather conditions on the performance of the installation. On this section, an analysis of the energy flows by each one of main element of the installation during one year of operation under CARTIF conditions (schedule, location) was done.

Figure 6 display the energies exchanged in each one of the main elements of the installation both in summer and winter season.

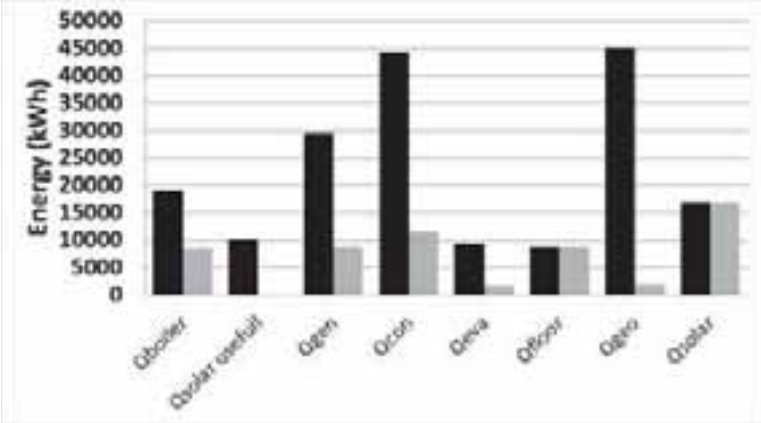

Figure 6. Energy season by each element of installation, summer (■) winter (■)

A holistic analysis of Figure 6 shows that there is a greater exploitation of the facility in summer than in winter, since the energies transferred in all elements are greater in summer. The solar useful energy during the winter is almost null even though the solar energy (Qsolar) is even greater than the energy transferred by the boiler, this result suggests to search another use to the solar energy captured, although it is not possible to use it directly in the installation for the temperature conditions necessary for its use, if it is possible to use all "free" energy as preheater of the supply water entering the boiler or for the floor heating in a direct way.

Another result of Figure 6 that should be paid attention, is the energy exchanged with the geothermal field (Qgeo). In the summer, the facility exchange 23 times more energy to the terrain than it absorbs in winter (45008 kWh versus 1968 kWh). This result suggests a more detailed analysis of the geothermal field and its performance over the years in order to avoid saturation of the soil, due to the decoupling between the energy transferred in summer and winter, coefficient of heat transfer is reduced.

5. Conclusions.

In winter, increasing the solar collecting area in Valladolid does not have a significant effect on the solar fraction, the energy captured goes from 17 MWh to 18 MWh, which can be an energy to be used for preheating the supply water to the boiler or to domestic hot water (DHW) of the building. On the contrary, in summer, if the solar collector area increases from 84m^2 to 210 m^2, the solar fraction increases from 34% to 50%, but above 175 m^2 the solar fraction is practically constant. This demonstrates that to avoid over costs of this type of installations, the design must be done with great care and always trying to undersize to achieve higher hours of operation with a lower investment.

The simulations allow concluding that the occupation schedule of the building has an influence on the solar fraction and yield, showing that with more hours of occupation, a higher efficiency is obtained, but the solar fraction decreases.

The analysis of the weather conditions shows that the use of solar energy in winter for this type of facilities,

with demand of high temperatures is negligible in all simulated cities, this result suggest that in winter it should be look for other uses for the solar energy in order to increase the useful energy during this season. In summer, on the other hand, in cities such as Seville, solar fractions are achieved in excess of 50% and solar efficiency in excess of 60%. In northern cities, both summer and winter, solar yields remain low; giving to think that perhaps this type of facilities have a better exploitation in countries of the Mediterranean.

96% of the total annual energy transferred to the geothermal field corresponds to its operation during the summer, when the heat pump capacitor exchanges with it. This result suggests a more detailed analysis of the geothermal field and its performance over the years to avoid a saturation of the terrain, generating a degradation of the terrain due to the lag between summer and winter

6. Acknowledgements

This work has been done thanks to support of two institutions CARTIF Foundation and Iberoamerican Sciences and Technology Program for the Development (CYTED).

7. References

Claesson, J. Hellstrom, G. 1981. Model Studies of Duct Storage Systems,

CTE 2006. Spanish building code. (available at https://www.codigotecnico.org/)

Eicker, U., Pietruschka, D., Haag, M., Schmitt, A., 2014. Energy and Economic performance of solar cooling systems worldwide. Energy procedia 57, 2581-2589.

IEA (International Energy Agency) 2015. Building Energy Performance Metrics. OECD/IEA, Paris. Available at: https://www.iea.org/publications/freepublications/publication/building-energy-performance-metrics.html (Last accessed: April 2017)

Ivanic A., Mugnier D., Weiss W. 2014. Solar heating and technology roadmap-European Technology platform on renewable heating and cooling .RHC.

Klein, S.A. TRNSYS 16, 2004. A Transient System Simulation Program, Solar Energy Laboratory, University of Wisconsin, Madison, USA

Macía A., Bujedo L.A., Magraner T., Chamorro C. 2013. Influence parameters on the performance of an experimental solar-assisted ground-coupled absorption heat pump in cooling operation. Energy and Buildings, 66, 282-288.

Macia, A. 2016. Análisis y caracterización de una instalación de calefacción y refrigeración solar usando una bomba de calor de absorción LiBr/H_2O condensada/evaporada mediante un intercambiador geotérmico cerrado. PhD thesis, Valladolid University. Spain

Methods of Testing to Determine the Thermal Performance of Solar Collectors,ASHRAE Standard, no. 93-2003 (2003) 2–42.

Nogareda, C., Nogareda, S., Solorzano, M.2014. Jornadas y horarios de trabajo. Madrid. Instituto Nacional de Seguridad e Higiene en el Trabajo. España

Rodriguez, J.. “Economical and primary energy optimization of solar thermally driven heat pump systems along Europe”. Tesis doctoral, Universidad de Valladolid, 2015. España.

Standard Reference: EN 12975-2:2006, Thermal Solar Systems and Compo-nents – Solar Collectors – Part 2: Test Methods. 2006. Directive: 89/106/EEC, EuropeanCommittee for Standardization, Brussels, Belgium,.

Experimental Investigation of Thermal Enhancements for a Building Integrated Photovoltaic/Thermal Curtain Wall

Eftsratios Dimitrios Rounis, Zisis Ioannidis, Olesia Kruglov, Andreas Athienitis and Konstantinos Kapsis

Dept. of Building, Civil and Environmental Engineering, Concordia University, Montreal (Canada)

Abstract

Building integrated Photovoltaic/Thermal (BIPV/T) systems provide a cost-effective way of incorporating solar technologies on buildings for the generation of electricity and useful heat, by replacing common building materials. Air-based systems are generally better suited for large façade or roof installations, they are however, less efficient in extracting heat from the PV due to the thermo-physical properties of air and therefore need enhancements for their thermal performance. This study investigates ways of enhancing air-based Building Integrated Photovoltaic/Thermal (BIPV/T) systems, focusing on the use of multiple-inlets and presents the development and initial testing of a BIPV/T curtain wall prototype. The testing of the prototype showed superior performance for the double-inlet versus the single-inlet configuration, thermally (up to 18% higher thermal output), lower peak PV temperatures (reduced by up to 3.6ºC) and a marginal increase in electrical output due to enhanced cooling.

Keywords: Building Integrated PV/Thermal, thermal enhancements, experimental performance

1. Introduction

The building sector is responsible for approximately 40% of the global energy consumption (Agathokleous & Kalogirou, 2016). Incorporation of solar technologies for electricity and useful heat production on buildings is essential for the design of net-zero energy buildings and for reducing the energy footprint of retrofits.

Photovoltac/Thermal (PV/T) hybrid systems combine the generation of electricity and useful heat. The photovoltaic layer of such a system also acts as the absorber and a circulating fluid removes part of the excess heat from it, which may be then utilized by various means, depending on the fluid's outlet temperature and delivery rate. PV/T systems have been found more efficient than independent PV or thermal collectors covering the same surface area (Kumar & Rosen, 2011a).

Building-Integrated Photovoltaic/Thermal systems come from the integration of PV/T with the building envelope. This integration may have several advantages over using PV/T systems as stand-alone (Yang & Athienitis, 2016). Apart from the architectural integration and the superior aesthetic result, the PV panels replace the outer shell materials (roof shingles, siding, concrete or masonry panels for façade etc.), increasing the cost effectiveness of the installation and the whole system functions as a building envelope element. A BIPV/T system must fulfill the requirements of the building envelope in terms of heat, air, water and moisture control (Jelle & Breivik, 2012). Integration with the façade or the roof may offer a larger installation area, which would otherwise not be available for use, although BIPV/T systems cannot be optimally oriented and tilted as opposed to stand-alone PV/T systems.

Ventilation and cooling of building integrated PV is essential since they do not have the same wind-driven cooling potential as racked PV (Bloem, 2008; Fossa et al, 2008). An air channel formed between the PV layer and the rest of the wall section for the ventilation of the system may serve two purposes: the cooling of the PV to prevent a decrease in electrical efficiency, and the collection of the preheated air for various purposes. Fan-assisted convection has been found to be more efficient in cooling the PV and extracting heat, in comparison to natural convection, especially in larger systems (Kaiser et al, 2014).

Depending on the coolant, BIPV/T systems are divided into water and air-based systems. Water based systems have greater heat exchange effectiveness. They require special casing and piping and are generally limited to smaller scale roof applications to avoid leakage and freezing issues within the wall section. Air-based systems on the other hand are easier to install and maintain, they do not pose leakage or freezing issues and can be adapted to different kinds

doi:10.18086/swc.2017.12.10 Available at http://proceedings.ises.org

of facades and roofs. However, due to the thermo-physical properties of air they are less efficient in the extraction of excess heat from the PV. There have been several studies on ways to enhance the thermal performance of PV/T and BIPV/T systems, which are discussed in the next section.

BIPV/T systems currently hold a small share of the PV installations. Usually, a harmonic architectural integration with an existing façade or roof is enough to characterise the system as integrated. However, there are few examples of systems that entirely replace the typical wall or roof structure of a building (Athienitis et al, 2011; Chen et al, 2010). The lack of more examples like those is mainly due to the fact that there is no current BIPV/T standard related to its integrated performance and function as a building envelope element.

This study presents the development and initial testing of a BIPV/T prototype, which was designed based on existing curtain wall practices and intended for full building integration. The main purpose was to be able to test and compare different thermal enhancements on the same experimental prototype, and provide design insight on fully integrated air-based BIPV/T systems. The initial experimental test set-up focuses on the effect of different PV module transparencies, the introduction of an additional air intake and the use of a flow director on the electrical and thermal performance of the prototype. The use of fins and varying channel depth will also be incorporated and studied in the future.

2. BIPV/T Thermal Enhancements

2.1 Air based systems thermal enhancements

Air-based systems are generally more suitable for envelope integration and large-scale applications, but less efficient in heat extraction than water-based systems. Several researchers have looked into ways of enhancing the thermal performance of air-based systems. These enhancements may only involve geometric and/or flow optimization, or the addition of material elements such as double glazing, fins or other porous media. Most of the proposed enhancements were applied to a reference PV/T system (Fig.1), while others refer to specific prototypes.

Fig. 1: Typical PV/T configuration

The criteria for enhancement vary among studies. For naturally ventilated systems with no heat collection the goal is to enhance the electrical output and PV durability by reducing the PV temperatures. This is generally achieved by optimizing the collector's aspect ratio (length over depth) for which the velocity of the buoyancy driven flow is maximized, but it may also involve the optimum tilt angle (Brinkworth, 2000; Brinkworth et al, 2000; Brinkworth & Sandberg, 2006; Brinkworth, 2006; Gan, 2009). In general, studies on naturally ventilated systems agree on a 10-15 cm optimum channel gap and a 45^{o}-55^{o} tilt angle.

The enhancement of mechanically ventilated systems varies considerably, depending on whether the priority is given to either the electrical output, or the thermal output, or a balance between the two and whether the consumption of the cooling system is also considered. Several researchers have investigated the optimal aspect ratio of the collector length to the collector depth and the optimal flow for air-based PV/T systems (Kaiser et al, 2014; Bambrook & Sproul, 2012; Zogou & Stapountzis, 2011). In addition, some studies include the effect of pressure drop within the collector (Bambrook & Sproul, 2012) and within the ducting that connects the PV/T to the HVAC system (Farshchimonfared et al, 2015). The suggested optimal flows vary between 0.026-0.050 kg/m2s, and the optimal channel depth between 0.025-0.090 m.

The practice of adding one or more glazing layers over the PV layer has been studied as a means to increase the thermal output of the system by reducing the wind induced heat losses (Hegazy, 2000; Tiwari et al, 2006; Sopian et al, 2000). The boosted thermal performance comes at the cost of the electrical, due to the higher PV temperature and the reduced solar radiation transmitted through the extra glazing (occasionally due to the formation of condensation on the outer glazing). The PV temperatures can be decreased with a double-pass configuration, by placing the PV

layer between two air channels, independent or connected. Tripanagnostopoulos (2007) suggested that, unless the system is optimized for thermal output, glazed PV/T systems are not recommended, due to PV overheating and poor electrical performance.

Heat extraction from the PV layer can be further enhanced with the use of material elements inside the air channel. These elements could either be fins in contact with the absorber that act as heat sinks (Othman et al, 2007), or fins set on the back surface which induce turbulence and boost the convective heat transfer (Kumar & Rosen, 2011b; Tonui & Tripanagnostopoulos, 2006). Other elements can be porous media, such as a metallic mesh (Pantic et al, 2010; Yang & Athienitis, 2014), honeycomb heat exchanger (Hussain et al, 2015), and suspended thin metal sheet [24] which further increase the radiative and convective area. These techniques have been proven very effective in removing heat from the PV, as opposed to the reference design (Fig. 1). However, a major limitation is that they cannot be used for systems with long channels due to the added flow resistance in the air channel and consequent increase of fan consumption.

Most of the aforementioned studies has been based on small scale experimental models (collector length generally 1-1.5 m), the behaviour of which could be different in larger scale applications. This is primarily due to the formation of a thermal boundary layer and a consequent temperature rise of the PV layer along the collector, leading to non-uniform PV temperature distribution and lower performance of the collector.

One major issue that is raised is the lack of common criteria for the enhancement and optimization of the systems. Usually the enhancement refers to the PV/T system without considering the integration with the mechanical system (heat pump, direct heat supply, heat exchanger, desiccant cooling etc.) and the corresponding requirements in terms of flow and fluid temperature, along with limitations for allowed PV temperatures. Furthermore, it is difficult to have a clear comparison between the various proposed systems due to the difference in dimensions and testing conditions, while the proposed numerical models are usually case specific and the convective correlations are not generally applicable.

2.2 Multiple-inlet BIPV/T

A more recent method of thermal enhancement is the introduction of more than one air intakes along the collector's channel. This technique is based upon the breaking of the thermal boundary layer and taking advantage of the introduced entrance effects. The convective heat exchange from the PV layer to the air stream is enhanced and more uniform PV temperatures can be achieved by regulation of the inlet flow distribution. The concept of a multiple-inlet BIPV/T evolved from the hybrid unglazed transpired collector (UTC) - PV/T system introduced by Athienitis et al (2011), which is installed at the mechanical penthouse of the John Molson School of Business (JMSB) building of Concordia University in Montreal. This system consists of custom PV modules attached onto a layer of UTC.

A double-inlet system was numerically investigated by Yang & Athienitis (2014). Convective heat transfer correlations were developed based on the testing of an experimental single-inlet prototype in an indoors solar simulator facility, which were used for the simulations of the performance of a two-inlet system. The addition of a second inlet increased the thermal efficiency of the system by 5%, reduced the maximum PV temperatures and marginally increased the electrical efficiency. Rounis et al (2016) proposed a method of modelling multiple-inlet BIPV/T systems and simulated the performance of a single and a multiple-inlet BIPV/T system for a large-scale office building application. Results showed that the multiple-inlet system had the lowest and most uniform PV temperatures, as well as higher electrical and thermal efficiency. Mirzaei et al. (2014) investigated experimentally the role of cavity flow on the performance of naturally ventilated BIPVs placed on inclined roofs. The experimental configurations included a flat and a stepped arrangement, which was essentially a multiple-inlet formation. It was found that the PV temperatures were significantly lower for the stepped configuration (multiple-inlet) cases, as opposed to the flat roof.

3. BIPV/T Prototype Development

A BIPV/T prototype was designed at Concordia University and developed in collaboration with Unicel Architectural and Canadian Solar, based on the curtain wall façade system. The prototype (Fig. 2) represents part of a full BIPV/T curtain wall façade. The purpose of the prototype was to address issues of architectural and structural integration, but also to investigate and compare experimentally different configurations and performance enhancement methods. The objective of this effort would be to provide insight on the development of a BIPV/T design and performance standard.

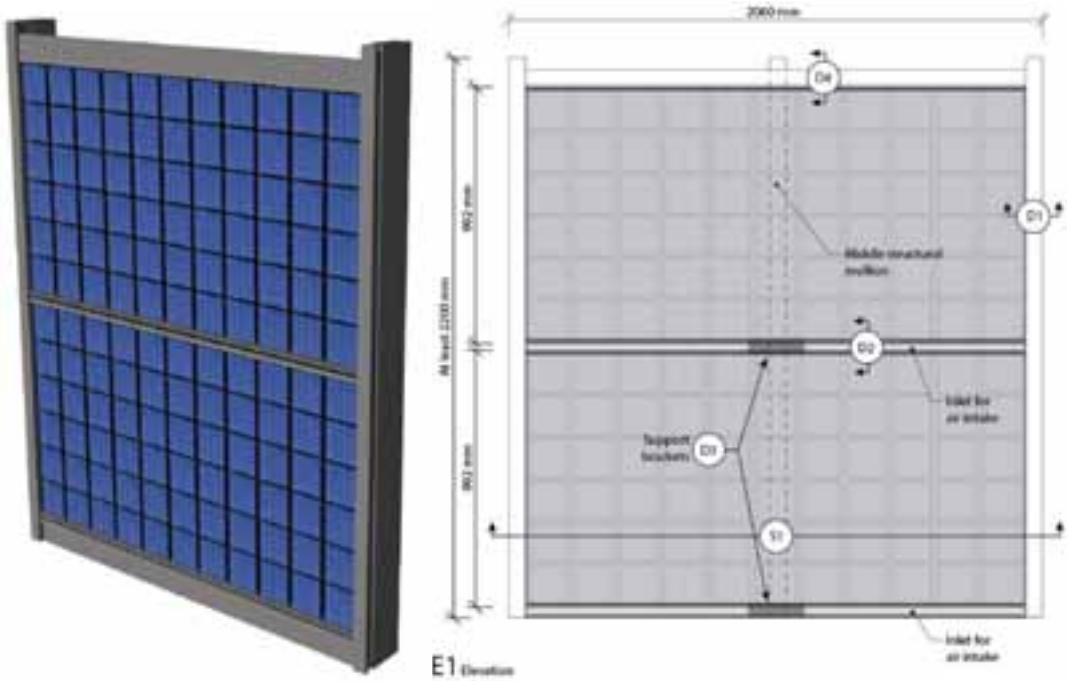

Fig. 2: BIPV/T curtain wall concept

The BIPV/T curtain wall prototype consists of a metal frame, two frameless PV modules and a 2-inch rigid insulation sandwiched between aluminum sheets. The metal frame was fabricated by Unicel Architectural using commercial mullion extrusions. The frameless, semi-transparent PV modules were provided by Canadian Solar. Two sets of semi-transparent PV modules were used, one with 66 cells and one with 72 cells, in order to investigate the effect of different transparencies on the prototype's performance.

A second inlet was introduced between the two PV modules, while the PV panels were placed horizontally to take advantage of the entrance effects of the second inlet flow. The panels were fixed with pressure plates at the side and top mullions and a shorter middle mullion was used to reduce counter deflection and provide extra support for the dead load of the panels.

Figure 3 demonstrates the cross side section of the prototype and the building envelope functions of its layers.

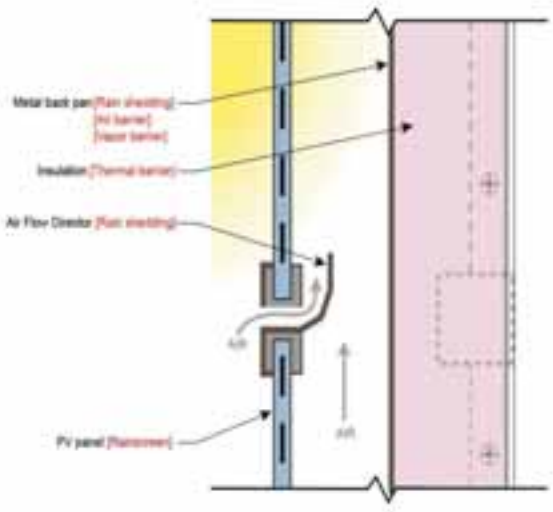

Fig. 3: BIPV/T curtain wall cross section

The prototype was designed with a reduced height to fit the test platform, but is considered as part of a story-high, or taller, system. Regarding the flow of the air channel, several aspects were considered. The primary factor that dictated the overall flow design was the introduction of a second inlet between the PV panels. The opening of the inlet was roughly estimated by previous analysis (Rounis et al, 2016) to approximately provide one third of the total

flow when fully open. Furthermore, air flow directors were used (Fig. 3) to direct the air stream of the second inlet closer to the surface of the top PV module. This also acted as a measure against rain penetration. Finally, a custom manifold was built and connected to holes opened on the top mullion, at the top side of the collector. This consisted of four take-offs from the collector connected to the main duct of the air collection unit. The number of take-offs was a compromise between flow uniformity and reduction of the structural integrity of the top mullion.

4. Experimental Process and Preliminary Results

The experimental prototype was tested in the Concordia University indoor Solar Simulator (Fig. 4). The Solar Simulator consists of a lamp field which emulates the sun light and a test bench upon which the test specimens are placed. The 8 metal halide lamps that comprise the lamp field can be moved individually in the horizontal and vertical axis and can produce irradiance intensities from 500 to 1200 W/m2 with a uniformity of up to 97% (Kapsis et al, 2016). The spectral quality of the lamps fulfills the specifications of ISO 9806. Both the lamp field and the test platform can rotate between a horizontal and vertical orientation to accommodate testing cases varying between flat roofs, tilted roofs and vertical facades. The experiments carried out for the experimental process presented here was in the vertical position, corresponding to a façade integrated BIPV/T.

This paper includes the results from testing conditions similar to the Nominal Operating Cell Temperature (NOCT) conditions, namely:

- Average solar radiation, G=842 W/m2
- External wind velocity, Vwind=1 m/s
- Ambient temperature, Tamb=20ºC

Two sets of PV modules were used (66 and 72 cell) and for each set, three configurations were tested: single inlet (with the middle inlet covered), double-inlet without the flow director and double inlet with the flow director installed. For each configuration, three total mass flow rates were investigated, namely, 400 kg/hr, 500 kg/hr and 600 kg/hr, with corresponding average channel velocities of 0.5 m/s, 0.62 m/s and 0.74 m/s. The most important results from this first set of experiments are presented in the following sections.

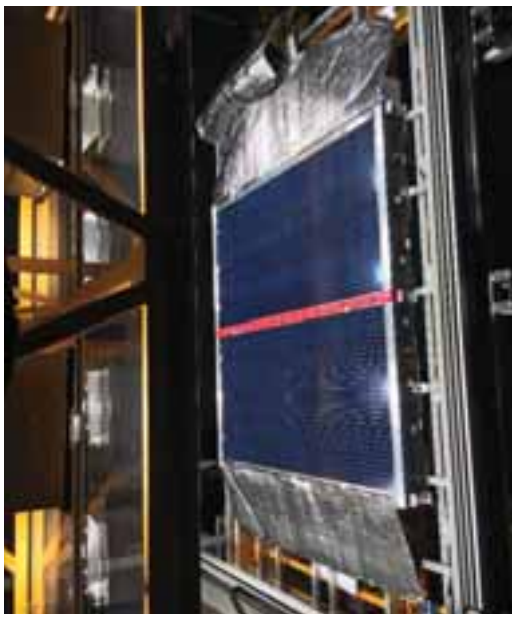

Figure 4: The BIPV/T prototype during testing in a vertical position at the Concordia University Solar Simulator

4.1 Effect of transparency

As expected the set of more transparent modules (66-cell) had lower electrical output of about 10-11% versus the 72-cell set, but the higher amount of radiation transmitted to the back absorber resulted in a 5-10% higher thermal output and slightly higher outlet temperature (up to 0.7ºC). The peak PV temperatures for the 72-cell set were higher

by 0.6°C - 3.6°C, due to the higher radiation absorbed by a larger PV cell area. These results agree with previous investigations (Bloem, 2008; Vats et al, 2012). The choice of packing factor in a real application would depend on the desired electrical and thermal output.

4.2 Effect of second inlet and flow director

The introduction of the second inlet may increase the thermal output by up to 18% and the outlet temperature by 1°C (for a collector of 2 m height). The system's performance was further enhanced with use of a flow director, which directed the flow entering from the second inlet closer to the surface of the upper PV module, extracting more heat and further reducing its temperature. The electrical efficiency was marginally increased and the peak PV temperatures are lower by up to 1.6°C, depending on the flow rate. These results are in accordance with the experimental work of Yang & Athienitis (2014)

Figure 5 presents the electrical and thermal efficiencies and the peak PV temperatures for the three configurations at the 600 kg/hr flow air collection rate. The results were similar for the other flow rates tested, as well as for the 66-cell set.

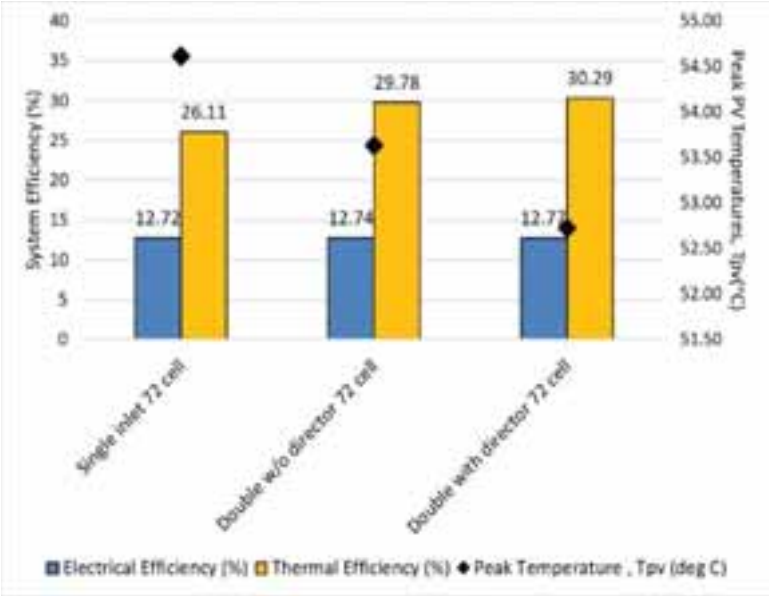

Figure 5: Electrical efficiency, thermal efficiency and peak PV temperature for the three configurations of the 72-cell set, at 600 kg/hr total mass flow rate (0.75 m/s average channel velocity)

5. Conclusion

This study focused on thermal enhancement techniques for air-based BIPV/T systems and presented the initial testing of a BIPV/T curtain wall prototype, with semi-transparent PV and multiple-inlets. The prototype has been developed to both provide design guidelines for fully integrated façade and roof BIPV/T systems and investigate the performance and applicability of various thermal enhancement techniques.

The initial testing of the prototype has shown that the introduction of a second inlet may increase the thermal output by up to 18%, decrease the peak PV temperatures by up to 3°C and marginally increase the electrical output, as opposed to the case of a reference single-inlet system. The double-inlet system's performance was further boosted by an air flow director element, which directed the flow closer to the surface of the second PV module. The use of higher transparency PV modules increased the thermal output, by 5-10% and the outlet air temperature but the electrical output was decreased by 10-11%. The differences in performance for the single and double-inlet systems are expected to be more prominent in larger scale applications.

This is part of a larger study involving the comparison of different enhancement techniques for air-based systems as well as the development of design guidelines for BIPV/T that may lead to a BIPV/T performance standard. Future work includes the investigation of more thermal enhancement techniques applied to the prototype, such as the use of fins and varying channel depth. A collective comparison of the tested methods will be carried at the end of the experimental procedure. Furthermore, models will be developed and validated according to the experimental results

for the simulation of full scale systems and the suitability of already developed convective coefficient relations will be evaluated.

6. Acknowledgements

The authors would like to acknowledge the support of Unicel Architectural, Canadian Solar and the Hydro Quebec Industrial Chair.

7. References

Agathokleous, R. A., & Kalogirou, S. A. (2016). Double skin facades (DSF) and building integrated photovoltaics (BIPV): A review of configurations and heat transfer characteristics. *Renewable Energy*, *89*, 743–756.

Athienitis, A. K., Bambara, J., Neill, B., & Faille, J. (2011). Design and performance of a photovoltaic/thermal system integrated with transpired collector. *ASHRAE Transactions*, *117*(PART 2), 403–410.

Bambrook, S. M., & Sproul, A. B. (2012). Maximizing the energy output of a PVT air system. *Solar Energy*, *86*(6), 1857–1871.

Bloem, J. J. (2008). Evaluation of a PV-integrated building application in a well-controlled outdoor test environment. Gan, 2009)*Building and Environment*, *43*(2), 205–216.

Brinkworth, B. (2000). Estimation of flow and heat transfer for the design of PV cooling ducts. *Solar Energy*, *69*(5), 413–420.

Brinkworth, B. J., Marshall, R. H., & Ibarahim, Z. (2000). A validated model of naturally ventilated PV cladding. *Solar Energy*, *69*(1), 67–81.

Brinkworth, B. J., & Sandberg, M. (2006). Design procedure for cooling ducts to minimize efficiency loss due to temperature rise in PV arrays. *Solar Energy*, *80*(1), 89–103.

Brinkworth, B. J. (2006). Optimum depth for PV cooling ducts. *Solar Energy*, *80*(9), 1131–1134.

Chen, Y., Athienitis, A. K., & Galal, K. (2010). Modeling, design and thermal performance of a BIPV/T system thermally coupled with a ventilated concrete slab in a low energy solar house: Part 1, BIPV/T system and house energy concept. *Solar Energy*, *84*(11), 1892–1907.

Fossa, M., Menezo, C., & Leonardi, E. (2008). Experimental natural convection on vertical surfaces for building integrated photovoltaic (BIPV) applications. *Experimental Thermal and Fluid Science*, *32*(4), 980–990.

Farshchimonfared, M., Bilbao, J. I., & Sproul, A. B. (2015). Channel depth, air mass flow rate and air distribution duct diameter optimization of photovoltaic thermal (PV/T) air collectors linked to residential buildings. *Renewable Energy*, *76*, 27–35.

Gan, G. (2009). Effect of air gap on the performance of building-integrated photovoltaics. *Energy*, *34*(7), 913–921.

Hegazy, A. A. (2000). Comparative study of the performances of four photovoltaic / thermal solar air collectors. *Energy Conversion and Management*, *41*.

Hussain, F., Othman, M. Y. H., Yatim, B., Ruslan, H., Sopian, K., Anuar, Z., & Khairuddin, S. (2015). An improved design of photovoltaic/thermal solar collector. *Solar Energy*, *122*, 885–891.

Ioannidis, Z., Buonomano, A., Athienitis, A. K., & Stathopoulos, T. (2017). Double Skin Façades Integrating Photovoltaic Panels: A Comparative Analysis of the Thermal and Electrical Performance. *Energy & Buildings*. http://doi.org/10.1016/j.enbuild.2017.08.046

Jelle, B. P., & Breivik, C. (2012). State-of-the-art building integrated photovoltaics. *Energy Procedia*, *20*(1876), 68–77

Kaiser, A. S., Zamora, B., Mazon, R., Garcia, J. R., & Vera, F. (2014). Experimental study of cooling BIPV modules by forced convection in the air channel. *Applied Energy*, *135*, 88–97.

Kapsis, K., Athienitis, A. K., & Harrison, S. J. (2016). Determination of solar heat gain coefficient for semi-transparent photovoltaic windows: an experimental study. *ASHRAE Transactions*, *125*.

Kumar, R., & Rosen, M. A. (2011a). A critical review of photovoltaic-thermal solar collectors for air heating. *Applied*

Energy, *88*(11), 3603–3614.

Kumar, R., & Rosen, M. A. (2011b). Performance evaluation of a double pass PV/T solar air heater with and without fins. *Applied Thermal Engineering*, *31*(8-9), 1402–1410.

Mirzaei, P. A., Paterna, E., & Carmeliet, J. (2014). Investigation of the role of cavity airflow on the performance of building-integrated photovoltaic panels. *Solar Energy*, *107*, 510–522.

Othman, M. Y., Yatim, B., Sopian, K., & Abu Bakar, M. N. (2007). Performance studies on a finned double-pass photovoltaic-thermal (PV/T) solar collector. *Desalination*, *209*(1-3 SPEC. ISS.), 43–49.

Pantic, S., Candanedo, L., & Athienitis, A. K. (2010). Modeling of energy performance of a house with three configurations of building-integrated photovoltaic/thermal systems. *Energy and Buildings*, *42*(10), 1779–1789.

Rounis, E. D., Athienitis, A. K., & Stathopoulos, T. (2016). Multiple-inlet Building Integrated Photovoltaic/Thermal system modelling under varying wind and temperature conditions. *Solar Energy*, *139*, 157–170.

Sopian, K., Liu, H. T., Kakac, S., & Veziroglu, T. N. (2000). Performance of a double pass photovoltaic thermal solar collector suitable for solar drying systems. *Energy Conversion and Management*, *41*(4), 353–365.

Tiwari, A., Sodha, M. S., Chandra, A., & Joshi, J. C. (2006). Performance evaluation of photovoltaic thermal solar air collector for composite climate of India. *Solar Energy Materials and Solar Cells*, *90*(2), 175–189.

Tonui, J. K., & Tripanagnostopoulos, Y. (2006). Improved PV/T solar collectors with heat extraction by forced or natural air circulation. *International Journal of Hydrogen Energy*, *31*(15), 2137–2146.

Tripanagnostopoulos, Y. (2007). Aspects and improvements of hybrid photovoltaic/thermal solar energy systems. *Solar Energy*, *81*(9), 1117–1131.

Vats, K., Tomar, V., & Tiwari, G. N. (2012). Effect of packing factor on the performance of a building integrated semitransparent photovoltaic thermal (BISPVT) system with air duct. *Energy and Buildings*, *53*, 159–165.

Yang, T., & Athienitis, A. K. (2016). A review of research and developments of building-integrated photovoltaic/thermal (BIPV/T) systems. *Renewable and Sustainable Energy Reviews*, *66*, 886–912.

Yang, T., & Athienitis, A. K. (2014). A study of design options for a building integrated photovoltaic/thermal (BIPV/T) system with glazed air collector and multiple inlets. *Solar Energy*, *104*, 82–92.

Zogou, O., & Stapountzis, H. (2011). Experimental validation of an improved concept of building integrated photovoltaic panels. *Renewable Energy*, *36*(12), 3488–3498.

Assessment of Solar and Farming Systems Integration into Tropical Building Facades

Abel Tablada[1], Ian Chaplin[1], Huang Huajing[1], Vesna Kosoric[2,3], Siu-Kit Lau[1], Yuan Chao[1], and Stephen Siu-Yu Lau[1]

[1] Department of Architecture, National University of Singapore, (Singapore)

[2] BauLab GmbH, (Switzerland)

[3] Daniel Hammer Architekt FH AG, (Switzerland)

Abstract

Singapore has committed to reducing greenhouse gases emissions as a part of the Paris Agreement. Increasing energy and food self-sufficiency through integration of solar and vertical farming systems into buildings' envelope could play a significant role in achieving Singapore's targeted reductions. This paper focuses on the design optimization of the façade systems that are to be installed at the Tropical Technologies Laboratory at the National University of Singapore. In particular, the paper presents the results related to five performance indicators which include solar energy and farming potential as well as the impact of the façade design on the indoor daylight conditions, shading and thermal performance. The multi-criteria decision analysis (MCDA) method VIKOR was adopted in the evaluation of the created design alternatives. The results from the computational simulations on radiation, daylight, and thermal conditions were used as inputs. Final optimal façade design is selected for four types of facades according to BIPV and farming systems arrangements for north and south orientations.

Keywords: BIPV, vertical farming, façade systems, solar architecture, tropical architecture

1. Introduction

Singapore has a high dependency on energy and food imports in order to cope with the growing domestic demand. Despite the currently favourable political and market conditions in the region, there are arguments, mainly for security reasons, for a gradual increase of locally produced food and energy in the future. Given the high population and urban density of the city-state, a limited land area available for conventional agriculture, as well as a lack of mineral resources, Singapore is seeking both the alternative solutions to reduce the dependency on imports and the means by which to meet the commitments of the United Nations Framework Convention on Climate Change Paris Agreement (United Nations, 2015) in combating the intensity of greenhouse gas (GHG) emissions and preventing them from peaking by 2030. Therefore, the contribution of the urban environment in increasing Singapore's self-sufficiency through the application of Building Integrated Agriculture (BIA) and Building Integrated Photovoltaic (BIPV) systems could play a crucial role in achieving those goals.

More than 90% of power production in Singapore is generated from fossil fuels. As for renewable energy sources, the rooftop integration of PV panels is very limited and does little to increase the share of renewable energy. Façade integration is therefore necessary to achieve a significant increase of solar energy production. Land in Singapore is scarce and expensive and although solar irradiation is much lower on vertical surfaces than on horizontal surfaces (at cca. -48.5% (for east) up to -64.3% (south)) (Khoo et al., 2014) façade integrations may justifiably present a sustainable solution. The design of façade integrations is a complex task requiring careful consideration and good optimization of various parameters such as: the tilt, shading effects, position, visibility from the inside and the outside of the building, accessibility, function, and overall aesthetics. Another factor to consider is that façade integration often relies on custom-made PV panels, hence, the attending costs, although exhibiting a gradual downward trend, still pose an important challenge in the design of façade integrations. Façade surfaces are visually more dominant than the rooftops of high-rise buildings and offer a

doi:10.18086/swc.2017.12.11 Available at http://proceedings.ises.org

wider range of aesthetically pleasing, high-quality solutions that can in turn serve as a positive influence on the behavior of the people and provide motivation for furthering similar projects.

Urban farming has recently come into attention since it represents a significant step towards reconnecting food producers and consumers. By shortening the food mile, urban farming saves time, reduces costs as well as GHG emission related to food transportation. At the same time, urban farming provides city residents with fresh ingredients, enabling a healthier life style and creating a more pleasant living environment. Urban farming also creates educational and interacting opportunities for city dwellers. Additionally, farming in the city may contribute to rainwater storage thus alleviating urban storm water flooding and run-off.

Several studies have been conducted on the integration of PV panels into building facades in Singapore (Luther and Reindl, 2014; Saber et al., 2014). The application of farming systems on building facades from the construction point of view was reported by Suparwoko and Taufani (2017) but there are no other references on the façade arrangement and the potential yield. The integration of both solar and farming systems on building facades was investigated by Tablada & Chao (2016) and Tablada et al. (2017) at the urban and façade scales respectively.

This paper therefore focuses on the design optimization of the productive solar façade (PSF) systems to be installed at the Tropical Technologies Laboratory (T2 Lab) located at the university campus. The research is based on the hypothesis that the performance of building facades should exceed the traditional functions of indoor–outdoor boundary and climatic regulation by also providing a portion of the energy and food that residential buildings demand. BIPV and vertical farming systems provide dual benefits: on one hand, they help produce electricity and food, and on the other, act as a passive device for solar gains reduction and the improvement of both visual and thermal comfort indoors.

The development of a PSF prototype involving both BIPV and BIA systems should employ a holistic iterative process that includes conflicting quantitative and qualitative parameters. The aim of the said process is to arrive at an optimal solution – a solution that meets and balances specific architectural and techno-economic requirements but also allows for different constraints that elements such as safety, accessibility and others may additionally impose. For the purposes of this study, the VIKOR method is employed (Opricović and Tzeng, 2004; Opricović and Tzeng, 2007). It is a multi-criteria compromise method that enables comparisons and assessment of otherwise incommensurable or conflicting criteria while offering relatively easy modelling and flexibility according to the preferences of the decision-maker (Kosorić et al., 2011; Krstić at al., 2012), especially if the decision maker has a complex structure and/or insufficiently clear preference in the optimisation process. MCDA VIKOR method used in this paper will therefore help provide a comprehensive evaluation and selection of the optimal design alternatives. Grasshopper parametric simulation tool (McNeel, 2010) is used together with necessary plug-ins to calculate several environmental performance criteria for the analysed cases on north and south façade orientations.

2. Method

2.1. Optimization method framework

Figure 1 presents the overall MCDA framework followed in this study. The first step is to define the potential façade components for the BIPV, vertical farming and the fenestration or voids. A series of preliminary simulations and technology selection is carried out for each system based on the available reference literature and discussions with local experts for both BIPV and BIA. Thereafter, the design strategy and decision goals are identified considering the potential PSF installation in residential buildings.

Quantitative and qualitative assessment criteria are also defined as well as the weights for each criterion. The impact of the façade design on sunlight availability for the BIPV and farming systems, as well as on indoor daylight conditions, shading and thermal performance are also taken into account by conducting computational simulations using Grasshopper's plug-ins.

While always accounting for the coherence with the overall building logic, mainly geometrical, functional and aesthetical characteristics of residential buildings, the design alternatives are then generated for two types of facades: (1) facade wall and (2) facade with balcony. Both façade systems are analyzed separately for four orientations: north, south, east and west. This paper presents the results for north and south oriented façade

walls. The façade design alternatives were developed according to the T2 Lab dimensions and layout. As shown in figure 2, eight test bed cells are located inside a 60 m2 building and are also used for other investigations of tropical technologies.

Optimal design alternatives are selected by means of the VIKOR (MCDA) method i.e the method was used to evaluate the PV integration design variants, rank determined alternatives, and then select a compromise solution Q from a set of m alternatives: A1, A2... Am, while those alternatives were evaluated on the basis of a set of n criteria functions. The alternative with the lowest Q value represents the compromise solution. This means that the said solution achieves a compromise between 2 decision making strategies: maximum group benefit defined by the value Sj (a better alternative is considered good according to the majority of criteria), and minimum of maximum deviation of ideal values defined by the value Rj (a better alternative must not be very bad according to any criteria). Vikor method also verifies "acceptable advantage" and "acceptable stability" of variant 'optimality' (Opricović and Tzeng, 2004). The details of the VIKOR method applied in this study can be found in Tablada et al. (2017).

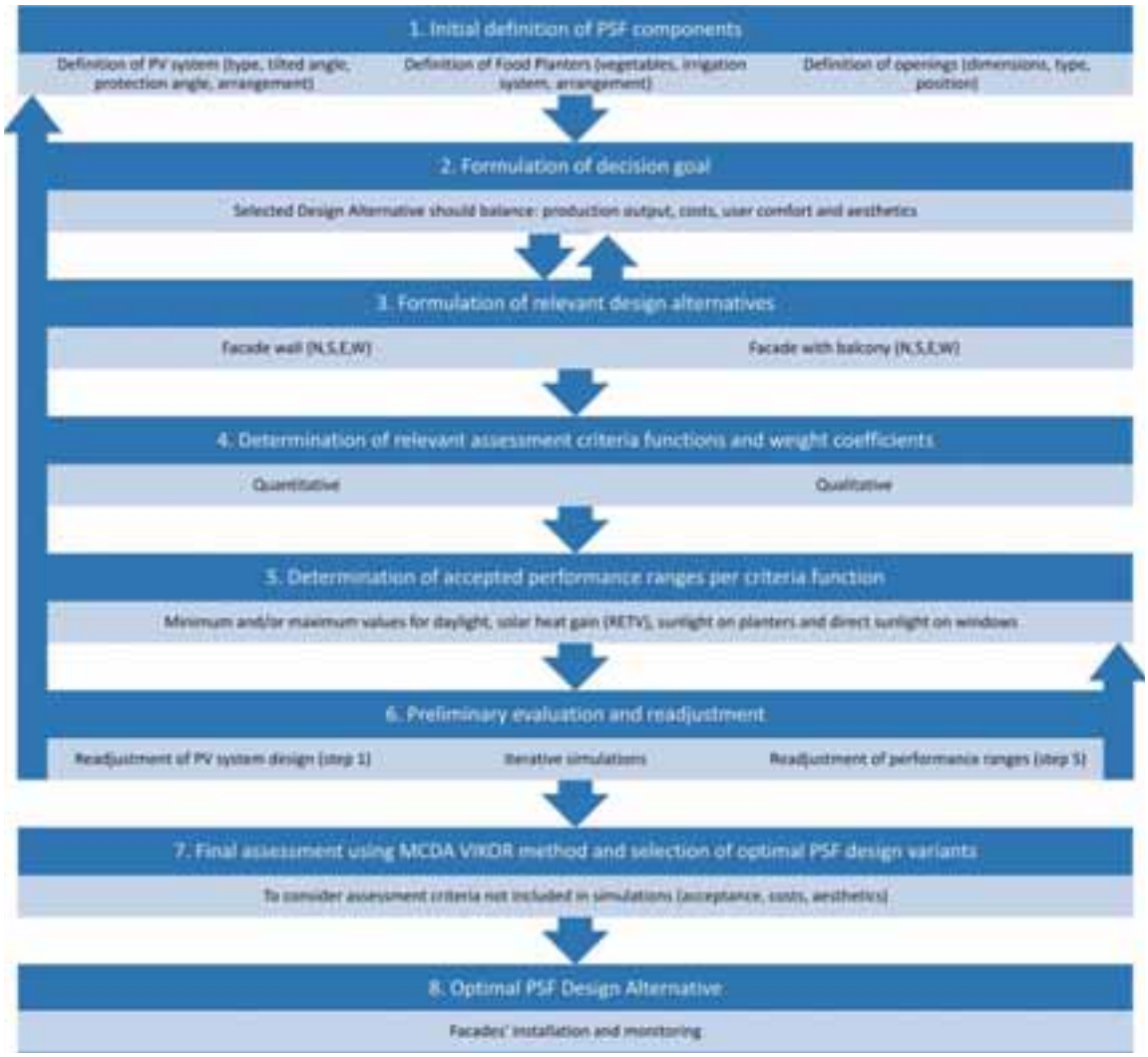

Fig. 1: Overall methodology for the development and optimization of the Productive Solar Façade (PSF) systems.

2.2. Model and simulation setup

Figure 3 presents four façade arrangements for façade wall and façade with balcony types. The façade arrangements are the following: façade with a single PV panels attached on top of the façade (I-F), façade with two PV panels attached to the top of the façade (II-F), façade with a single PV panel attached to the planter of the level above (I-P) and façade with two PV panels attached to the planter of the level above.

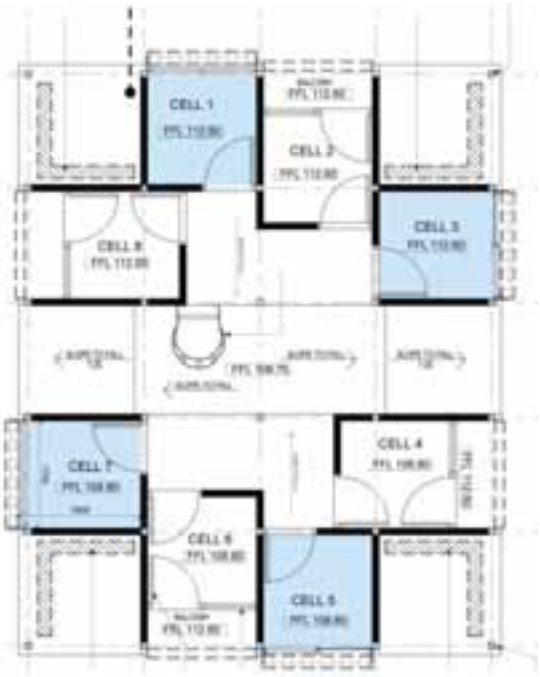

Fig. 2: Floor plan of the Tropical Technologies Laboratory (T2 Lab). Highlighted the cells analysed in this study. Adapted from: AWP Architects based on author's preliminary design.

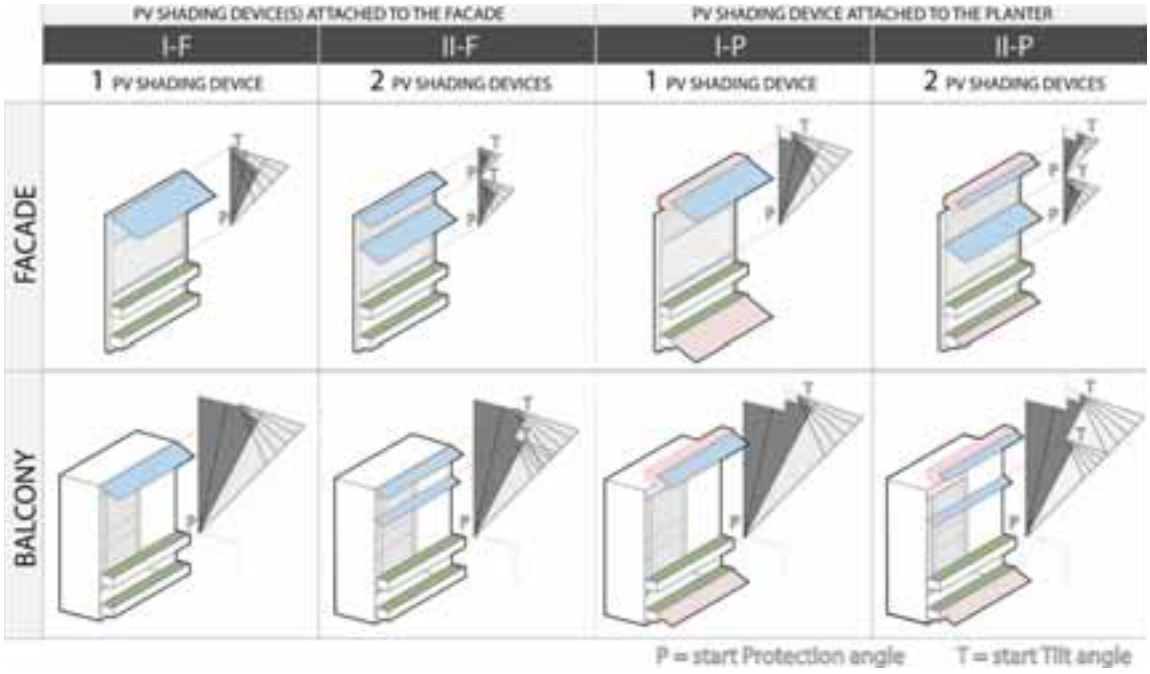

Fig. 3: Types of PV configurations and corresponding start of the protection and tilt angle.

A modular façade is used in order to obtain a high-quality sustainable solution: a cost-effective, time-efficient, and flexible multifunctional façade. Considering the restrictions of the building site - the typical floor to floor height of a Housing Development Board (HDB) flat of 2.8m, the module will be 2.8 m in height (2.6 m ceiling height) and 1.8 m in width. According to the Approve Document by the Building and Construction Authority (BCA) (BCA, 2017), the height of a barrier should not be less than 1.0m in order to protect people from falling from height. However, in order to have more design alternatives (e.g., to provide more space for planters installed at the lower part of the module), a window sill height of 1.1m is considered in this study which will

allow accommodating planters at the height of 100mm, 300mm, 500mm, 700mm and 900mm, in two or three rows, with a minimum height difference of 400mm between planters. A trapezoid cross-sectional planter will be used in the case of multiple-row planters, making it possible to provide more sunlight for lower level plants, while allowing more growing space for plants below. The size of the planter is set to be 190mm high and 150mm wide.

Optimizing the design of BIPV as shading devices on different façade orientations requires a careful definition of the objectives of the façade elements. The shading BIPV elements should be able to maximise the electricity generation and solar irradiance protection while allowing required illuminance levels in the interior, view towards the exterior and a minimum required amount of sunlight on the planters and BIPV on the same and lower stories respectively. The most influential geometrical parameter in achieving an optimal design alternative is the protection angle which together with the tilt angle defines the width of the BIPV shading element. The protection angle is defined as the angle between the vertical plane of the façade and the outside end of the BIPV shading element. The angle is taken from the bottom of the window for single shading and also on top of the lower shading for the cases with double BIPV shading as shown in figure 3. The protection angle should be understood as a response to the incidence angle; the angle of the sun to a specific target at a moment in time.

This study takes into account the minimum protection angle required by the Building Code Authorities of Singapore (BCA, 2008), through the Residential Envelope Transmittance Value (RETV) calculations. Additionally, for extreme incidence hours a minimum threshold of direct sunlight hours was set to before 8:30 and after 16:30. Lastly the minimum for the range of the protection angles was set so that no substantial impact on the operative temperature would be gained above a temperature of 28°C. Through this optimization the ideal intersection of protection and tilt angle of the shading device was arrived at. For the north and south orientation, protection angles from 28° to 37° met the specified requirements. For south the specific angle of 28° is only sufficient to comply with RETV requirements in combination with a tilt angle of 50°.

2.3. Farming considerations

A selection of leafy vegetables and herbs was deemed suitable for cultivation on building façades since the whole final produce is edible and usually shallow-rooted which makes it space-efficient. Additionally, leafy vegetables and herbs are less prone and less vulnerable to the attack of pests than fruited vegetables.

There are several factors affecting the growth of vegetables, including light, temperature, water and cultural practices. Among them, light is the key factor as it drives photosynthesis and affects plant development, morphology and yield (Inada and Yabumoto, 1989). With regards to the building façade farming, the demand for light is the most crucial factor to be considered due to the inconsistent light condition of building façades. Among the most common locally grown leafy vegetables, shade-tolerant crops with a lower daylight demand like Leaf Lettuce (Lacttuca Sativa) and Kangkong (Ipomea Aquatica), should ideally be grown on building facades. Also, most species of herbs like sage and basil are also quite suitable for the building façade cultivation.

Daily light integral (DLI), expressed in mol/m²· day, is defined as the total number of photo-synthetically active photons that plants receive in 1 sqm of growing space in one day. DLI reflects the combined result of the light intensity and duration of the photoperiod. Compared to other measuring methods, DLI is more accurate in determining the exact lighting condition for plants and is therefore commonly used in the agricultural industry. Commercial farms aim to keep minimum DLI of 10-12 mol/m²· day for optimum growth of plant (Morgan, 2016). A DLI of 12-13 mol/m²· day or higher is generally required for lettuce production (Dorais, 2003). The optimal DLI for production of sweet basil is about 28.8 mol/m²· day (Beaman, Gladon, & Schrader, 2009). Although leaf lettuce normally needs 12-13 mol/m²· day or more to achieve maximum production, it can still be grown with as little as 4-10 DLI. However, its quality is usually low below 8 mol/m²· day (Schiller, 2017)(Glenn, Cardran, & Thompson, 1984). Hence, 8 mol/m²· day is set as the minimum DLI requirement for lettuce growth. Converting the DLI to illuminance levels, this is equivalent to 10 000 lux.

2.4. Simulation settings

Combining the 3d-modeling software Rhinoceros with the programming software Grasshopper supports the parametric design generation. Utilizing these combined instruments the results of over 1.000 plausible cases can be approximated precisely, without requiring intermittent manual interference. The plug-ins Ladybug and Honeybee (Roudsari & Pak, 2013; Grasshopper3d.com, 2017) utilize the flexibility of Grasshopper to read local

weather data, add detailed design information and run these through validated software such as Daysim (Reinhart and Walkenhorst, 2001) (Lagios et al., 2010), Radiance (Ward and Shakespeare, 1998) and Energyplus (Crawley et al., 2011) (Jakubiec & Reinhart, 2011), In return these results can be read, disseminated, organized and visualized by Ladybug and Honeybee in Grasshopper.

Since PSF has multiple quantifiable performance indicators, a multi-objective optimization process was chosen supported by VIKOR. This method chooses the optimal result by balancing 5 conflicting performance indicators: daylight autonomy (DA), energy flow, electricity potential of the PV shading device(s), farming potential and view angle. A fitness value indicating the performance of each case on each indicator is established by comparing their results with the highest (100%) and lowest value (0%) returned by all cases. Strict requirements were predefined for each performance indicator according to literature and local regulations. This ensured overall quality of all cases within the VIKOR optimization process and reduced the total amount of cases by around 90%.

DA is defined as the percentage of time during the year in which a certain pre-defined illuminance value (200 lux) is achieved from 8 AM till 5 PM. Since the size of the testbed cell is reduced in comparison to actual room dimensions in residential buildings, an equivalent DA was used instead of the actual values obtained in the simulations. The energy flow is defined as the interior net heat gain (heat gain minus heat loss, kWh). Electricity potential is defined as the potential electricity generation from the PV panel taking the lowest incident radiation on the PV multiplied with the total area of the shading device, as the PV cells are connected in series. At this stage no definition was made regarding the type of PV and also other performance coefficients affecting electricity generation were not considered. Farming potential is defined as the percentage of days per year where planter area receives DLI > 8 mol/m²· day. View angle is defined as the average view angle from two points inside the testbed cells towards the exterior. The two points are located at 1.5m from the façade at 1.17m and 1.56m height from the floor, which correspond to sitting and standing viewing height for an overall height of 1.68m. The obstruction effect from the planters and the PV panels are taken into account. A minimum of 20° was set as required for all cases.

3. Results

This section summarises the results obtained for the north and south oriented Façade Wall. Figure 4 presents the preliminary design of the optimal cases for four types of façade arrangements: I-P, I-F, II-P and II-F (see figure 3 for nomenclature). For the 4 façade types the optimal position of the planters is at 100mm and 700mm from the floor level. This assure the best sunlight access to both planters disregarding the dimensions and positions of the PV panels. The optimal position of the planters for the 4 façade types stands at 100mm and 700mm from the floor level respectively. This ensures the best access of sunlight to both planters disregarding the PV panel dimensions and position. The optimal solution for north and south orientation is the same - a single PV attached to the planter above with a protection angle of 28° and a tilt angle of 50°. Higher position of the PV panel with respect to the upper window allows higher value of Daylight Autonomy (DA), however, in order to achieve the required solar protection according to the RETV, the tilt angle should be larger than the recommended 30° from the horizontal position (Luther and Reindl, 2014) (Saber et al., 2014) for Singapore facades. The second and third best cases for south and north oriented façades respectively are those with a single PV attached to the top of the façade. Double PV configurations are not favourable for any of the two façade orientations, especially for the north façade. The small dimension of the upper PV panel results of in the need to avoid overshadowing on the panel underneath. However, such small dimension may not be feasible and cost-effective.

Figure 5 presents the results of five performance indicators for each optimal case of the four façade arrangement types. The left-side axis displays actual values of each performance indicator while the right-side axis presents fitness values relative to the best and worst cases per façade type. The fitness value (Fv) is defined as:

$$Fv = (PI - Min) * (100 / (Max - Min) \quad \text{(eq. 1)}$$

Where PI is the obtained value per performance indicator, Min and Max are the minimum (worst) and maximum (best) values on the list of cases per façade arrangement type.

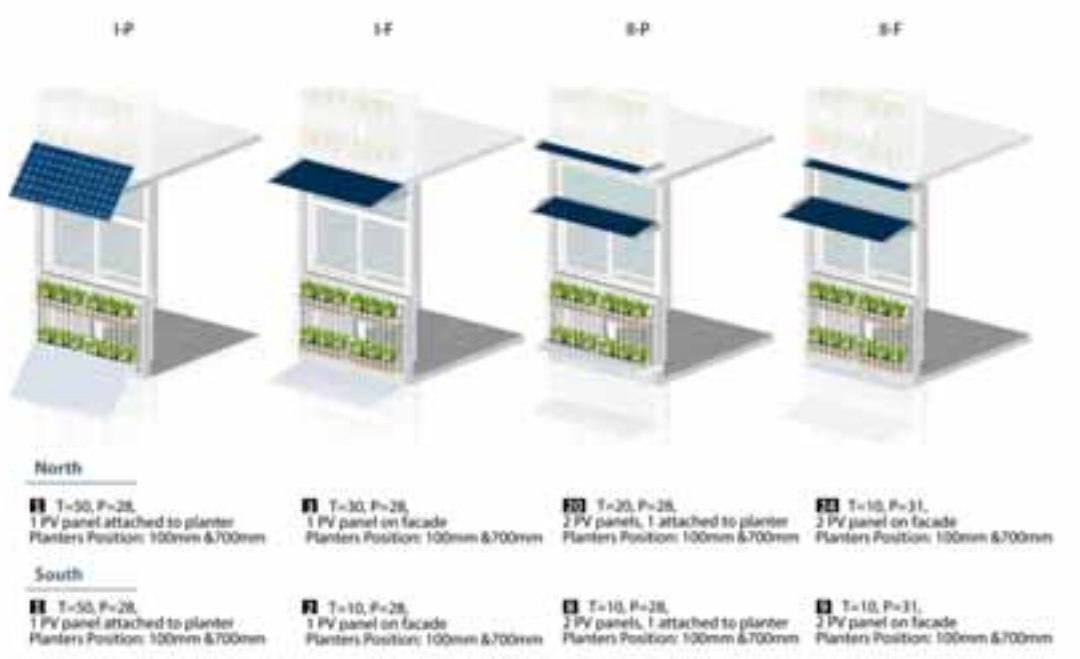

Fig. 4: Best cases per type, with overall rank and specifications for north and south orientations.

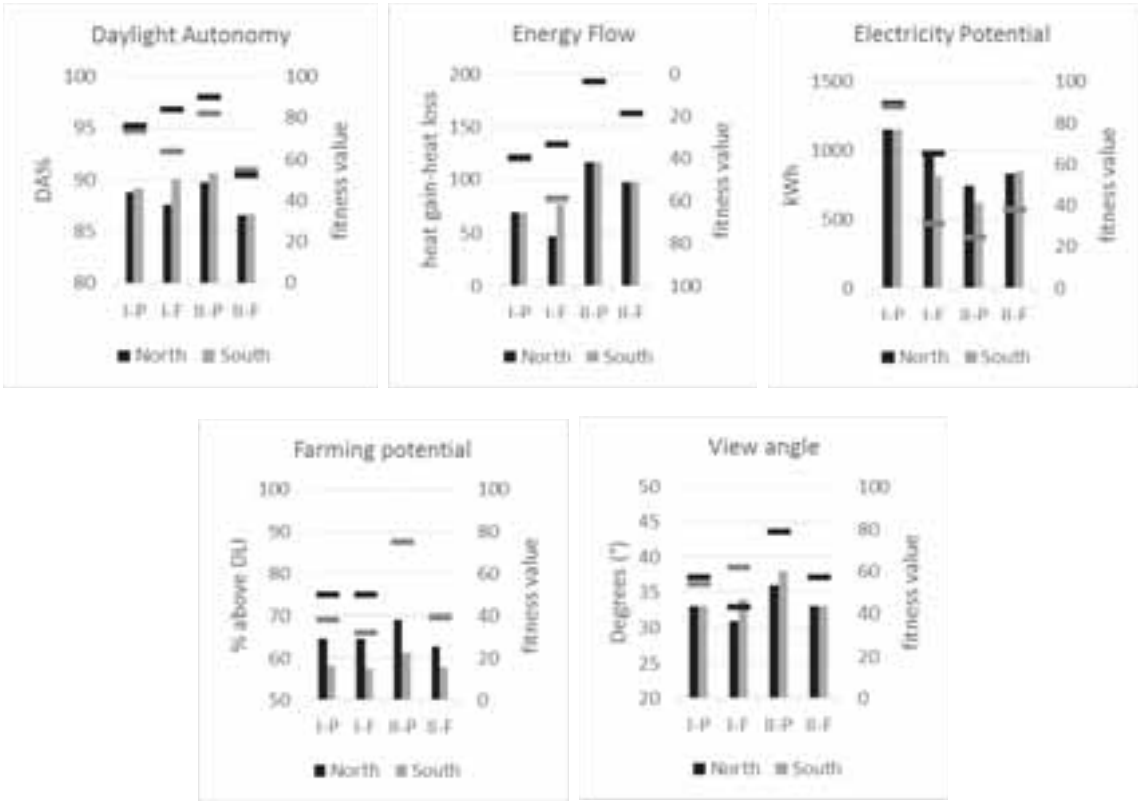

Fig. 5: Performance indicators for four façade types on north and south orientations. Bars correspond to left-axis values and lines represent fitness value.

Regarding DA, all cases achieve values above 85% representing the time period in a year with the average illuminance levels above the threshold of 200 lux. The performance in two cases when PVs are attached to planters above (I-P and II-P) is better (fitness value > 75%) than in the two cases where PVs are attached to the

highest point of the façade. Larger separation of PVs from the upper window allows higher penetration of diffuse daylight. South façade arrangements receive higher illuminance levels than north façade arrangements.

With regards to the energy flow indicator, the lower the value of the net heat gain from the exterior, the better its performance and fitness value. Also, in terms of this indicator, the number of PV panels has a higher impact than their position on the façade. A single panel will provide better protection from solar radiation than two panels. Sunlight inter-reflection between the two panels and the reflection of the lower panel towards the interior may be the reason for the higher heat gain. Only in cases when a single PV is attached to the façade, substantial differences on energy flow exist in relation to the facade orientation.

As for electricity potential, once again, a single PV panel will perform better than two panels. If two PV panels are utilized, then the top device, although small, shades the bottom one during the hours in which the incidence angle is smaller than the protection angle. Since PV cells are connected in series, the shaded cell will define the overall electricity production by lowering it. The differences are more evident between the cases I-P and II-P with fitness values around 90% and 25% respectively. The electricity potential on the north façade is overall higher, most likely due to frequently clear skies from March to September equinoxes. If we consider a conventional 13% efficiency Si-monocrystalline PV module the estimate of electricity generation of the optimal cases of north I-P, I-F, II-P and II-P are 150 kWh, 130 kWh, 97 kWh and 108 kWh respectively which represent 48%, 48%, 33% and 34% of the same PV module type and area located on a rooftop without obstruction.

The four façade types exhibit smaller differences regarding the farming potential. In all cases the percentage above the required DLI is not higher than 70%. However, DLI values are substantially higher for the north than the south façade orientation. For the latter, the fitness values are around 40% or below except in the II-P case. The last performance indicator considered at this stage of the study is the view angle from the interior. Facades with PV panels attached on the planters above provide higher view angles, which is well within expectations considering the higher position of the panels with respect to the upper window.

Figures 6 presents fitness value for all façade types facing north and south respectively. The average fitness value of the optimal case I-P is 62.0% and 59.1% for north and south orientations respectively. The average fitness values for the second best façade type are 56.0% and 48.5% for north and south orientation respectively. Figure 7 presents the fitness values of the two best and worst cases for north façade orientation.

At this stage, the strategy to determine the best among facade types presupposes that all criteria used are of equal importance. Consequently, since the selection of the optimal solution strongly depends on the criteria weight coefficients, all five criteria used were allocated the same weight of 0.2. However, different weights may be applied for east and west façade orientations given the larger exposure of glass windows to direct solar radiation. For these orientations, the weight of criteria functions with larger value variation –for example, those related to the energy flow- will be proportionally higher than the weights of criteria functions with smaller variation.

4. Conclusions

This paper describes the design optimization of SPF facades with the integration of PV and farming systems and analyses the performance of four façade types for north and south orientations. The facades systems are to be installed at the Tropical Technologies Laboratory at the National University of Singapore. The impact of the façade design on five performance indicators - daylight autonomy, energy flow, PV electricity potential, farming potential and view angle - are obtained from computational simulations and subsequently used as inputs in the MCDA method VIKOR.

The above results reflect the values relative to facade types deemed to be the best, and are not representative of all instances. However, a comparison with the fitness values of other cases of the same type has served as a confirmation of trends. With these practical considerations in mind, the following conclusions can be made:

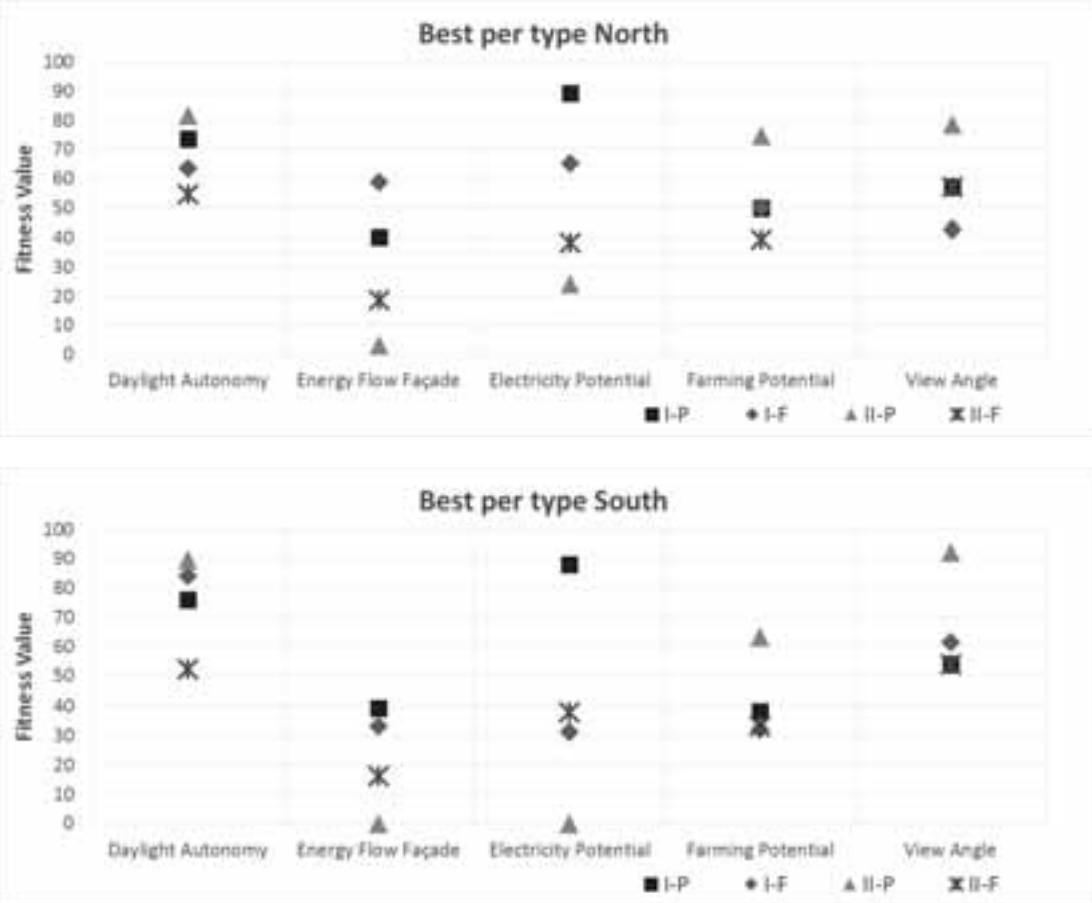

Fig. 6: Performance indicators of the optimal facade designs for north (top) and south (bottom) orientations

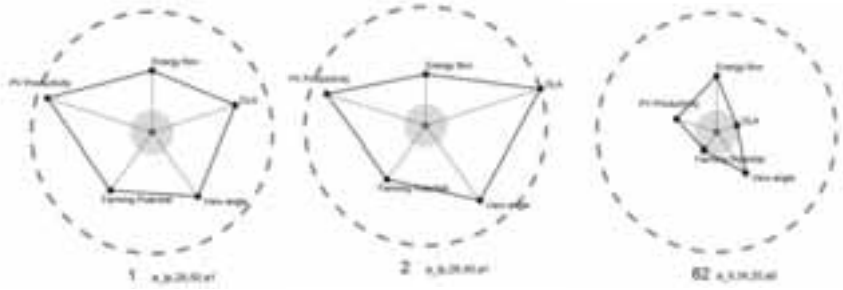

Fig. 7: The two best and worst cases for north, small (0%) to large (100%) circle represents fitness value.

- The optimal position for BIPV shading device is next to the planters at the above level. This position maximizes solar energy yield while also achieving a high fitness value for other four performance indicators related to food production and indoor visual and thermal conditions. The result indicates that even with no farming system installed, the best compromise between solar energy yield and indoor conditions is achieved by using the lower portion of the façade of the level above for the installation of larger sun-exposed PV panels.
- For north and south façade orientation, systems with two rows of PV panels will produce less electricity than the system with one row of PV panels. With two PV shading devices, the topmost device shades the bottom one during the hours in which the incidence angle from the vertical plane is smaller than the protection angle. It should be noted this occurs around midday when the incident solar radiation is at its highest.

- Overall, north facades achieve slightly higher fitness value than south facades. Farming potential on north facades is higher than on south facades as the planter area receives the required Daily Light Integral for longer periods of time during the year. Similar trend is observed for the electricity yield potential although not for all cases.

The results of the study prove the importance of using a holistic approach and a multiple objectives criteria analysis in the design of such complex façade systems, especially for BIPV and BIA systems which compete for receiving the maximum sunlight. The VIKOR optimization method helped obtain a solution according to a tight set of requirements. It also created a framework that enabled iterative strategic learning based on reciprocity and the understanding of project strengths and weaknesses. The impact of the façade systems on indoor visual and thermal conditions in residential buildings are also crucial and are not to be ignored or underestimated. Otherwise, the benefits of the electricity and vegetable production are minimised or reversed.

The study will continue with further analysis aimed at finding the optimal façade design alternatives for east and west orientation. In addition, the same optimisation process will be applied for the façades with balcony that already have solar protection to a certain degree. Different BIPV configurations and dimension are expected for those façade types and orientations. In this first part, the design process of SPF was focused and based mainly on quantitative parameters, resulting in optimal solutions with balanced technical performance. The subsequent steps will include costs and qualitative criteria, which will ensure sophisticated sustainable high-quality solution in terms of both techno-economic performance and architectural value.

5. Acknowledgements

This research is funded by City Developments Limited (CDL), Singapore. The authors would like to acknowledge the collaboration of Thomas Reindl and Veronika Shabunko from Solar Energy Research Institute of Singapore (SERIS) and Hugh Tan from Department of Biological Sciences, NUS.

6. References

Beaman, A. R., Gladon, R. J., & Schrader, J. a., 2009. Sweet Basil Requires an Irradiance of Biomass Production. HortScience, 44(1), 64–67.

Building and Construction Authority, 2008. Code on envelope thermal performance for buildings. Version 3Rb Jan 2008.

Building and Construction Authority, 2017. Approved Document: Acceptable Solution - Issued by Commissioner of Building Control under Regulation 27 of the Building Control Regulations. Version 6.3 April 2017.

Crawley, D.B., Lawrie, L.K., Winkelmann, F.C., Buhl, W.F., Huang, Y.J., Pedersen, C.O., Strand, R.K., Liesen, R.J., Fisher, D.E., Witte, M.J., Glazer, J.. 2001. EnergyPlus: creating a new-generation building energy simulation program. Energy and Buildings 33: 319-331. doi:10.1016/S0378-7788(00)00114-6

Dorais, M., 2003. The use of supplemental lighting for vegetable crop production: Light intensity, crop response, nutrition, crop management, cultural practices. Canadian Greenhouse Conference, 1–8.

Glenn, E. P., Cardran, P., & Thompson, T. L., 1984. Seasonal effects of shading on growth of greenhouse lettuce and spinach. Scientia Horticulturae, 24(3–4), 231–239.

Grasshopper3d.com, 2017. Ladybug + Honeybee. [online] Available at: http://www.grasshopper3d.com/group/ladybug

Inada, K., & Yasumoto, Y., 1989. Effects of light quality, daylength and periodic temperature variation on the growth of lettuce and radish plants. Japanese Journal of Crop Science, 58(4), 689–694.

Jakubiec, A., & Reinhart, C. F., 2011. DIVA 2.0: Integrating daylight and thermal simulations using Rhinoceros 3D, DAYSIM and EnergyPlus. In Proceedings of BS2011 (pp. 2202–2209). Sydney, Australia: IBPSA.

Khoo, YS., Nobre, A., Malhotra, R., Yang, D., Rüther, R., Reindl, T., Aberle, AG., 2014. Optimal orientation

and tilt angle for maximizing in-plane solar irradiation for PV applications in Singapore. IEEE Journal of photovoltaics 4 (2), 647-65.

Kosorić, V., Wittkopf, S. and Huang, Y., 2011. Testing a design methodology for building integration of photovoltaics (PV) using a PV demonstration site in Singapore. Architectural Science Review, 54 (3), 192-205.

Krstić, A., Kosorić, V. and Golić, K., 2012. Potential for reduction of CO2 emissions by integration of solar water heating systems on student dormitories through building refurbishment. Elsevier-Sustainable cities and society, 2, 50-62.

Lagios, K., Niemasz, J., and Reinhart, C.F., 2010. Animated Building Performance Simulation (ABPS), Linking Rhinoceros/Grasshopper with Radiance/DAYSIM. Proceedings of SimBuild 2010, New York City.

Luther, J., Reindl, T., 2014. Solar Photovoltaic (PV) Roadmap for Singapore (A Summary), Solar Energy Research Institute of Singapore, Singapore.

McNeel, R. (2010). Grasshopper - Generative Modeling with Rhino. McNeel North America, Seattle, USA.: http://www.grasshopper3d.com/

Opricović, S. and Tzeng, G. H., 2004. The compromise solution using MCDM methods: a comparative analysis of VIKOR and TOPSIS. European Journal of Operational Research, 156 (2), 445-55.

Opricović, S. and Tzeng, G. H., 2007. Extended VIKOR method compared to outranking methods. European Journal of Operational Research, 178 (2), 514-29.

Reinhart, C.F., and Walkenhorst, O., 2001. Validation of Dynamic RADIANCE-based Daylight Simulations for a Test Office with External Blinds. Energy and Buildings 33 (7): 683-97.

Roudsari, M. S., & Pak, M., 2013. Ladybug: a parametric environmental plugin for grasshopper to help designers create an environmentally-conscious design. In Proceedings of the 13th International IBPSA Conference. Retrieved from http://www.ibpsa.org/proceedings/BS2013/p_2499.pdf

Saber E. M., Lee, S. E., Manthapuri, S., Wang Y., Deb, C., 2014. PV (photovoltaics) performance evaluation and simulation-based energy yield prediction for tropical buildings. Energy 71, 588-595.

Schiller, L., 2017. Is my plant getting enough light? Retrieved September 7, 2017, from http://www.ceresgs.com/is-my-plant-getting-enough-light/

Suparwoko & Taufani, B., 2017. Urban Farming Construction Model on the Vertical Building Envelope to Support the Green Buildings Development in Sleman, Indonesia. Procedia Engineering. 171, 258-264.

Tablada, A., Kosoric, V., Lau KS, Lau S., Yuan S., 2017. Productive facade systems for energy and food harvesting: prototype optimisation framework. 33rd Passive Low Energy Architecture Conference (PLEA), Edinburgh.

Tablada, A., Zhao X., 2016. Sunlight Availability and Potential Food and Energy Self-sufficiency in Tropical Generic Residential Districts. Solar Energy 139, 757–769.

United Nations / Framework Convention on Climate Change, 2015. Adoption of the Paris Agreement, 21st Conference of the Parties, Paris: United Nations.

Ward, G., and Shakespeare, R., 1998. Rendering with radiance. The Art and Science of Lighting Visualization. Morgan Kaufmann Publishers, Ann Arbor.

Bricker project: Power, Heating and Cooling for Public Non-Residential Buildings Feeding with RES

Fredy Vélez[1], Javier Antolín[1] and Juan Ramón de las Cuevas[2]

[1] CARTIF Technological Center, Valladolid (Spain)

[2] ACCIONA Construction S.A., Seville (Spain)

Abstract

Existing non-residential buildings represent a valuable asset in Europe. These buildings account for 25% of the total building stock in Europe and comprise a more complex and heterogeneous sector compared to the residential one. The public non-residential building stock represents an average 31% of the total non-residential sector in Europe. Understanding the energy use and CO_2 emissions in the non-residential sector is complex as end-uses such as lighting, ventilation, heating, cooling, refrigeration, IT equipment and appliances vary greatly from one building category to another within this sector. The average specific energy consumption in the non-residential EU27 sector is 280kWh/m^2 (covering all end-uses). A retrofitting solution package for existing public-owned non-residential buildings is needed in order to achieve a drastic reduction of the energy consumption (beyond 50%) and GHG emissions in this sector. This retrofitting package is based on; Envelope retrofitting solutions for demand reduction through made-to-measure façades, innovative insulation materials and high performance windows and zero emissions energy production technologies based on a cogeneration system fed with locally available and clean renewable sources. The retrofitting solution package is implemented in three real demonstration multi-buildings complexes, located in different climate conditions in three different European Countries and with different end-uses: Sanitary, Educational and Administrative.

Keywords: Energy efficiency, Renewable energies, Tri-generation, Zero energy buildings

1. Introduction

Existing non-residential buildings represent a valuable asset in Europe. These buildings account for 25% of the total building stock in Europe and comprise a more complex and heterogeneous sector compared to the residential one. The retail and wholesale buildings comprise the largest portion of the non-residential stock, while office buildings are the second biggest category with a floor space corresponding to one quarter of the total floor space. Understanding the energy use and CO2 emissions in the non-residential sector is complex as end-uses such as lighting, ventilation, heating, cooling, refrigeration, IT equipment and appliances vary greatly from one building category to another within this sector. The average specific energy consumption in the non-residential EU27 sector is 280kWh/m^2 (covering all end-uses).

Over the last 20 years in Europe, electricity consumption in European non-residential buildings has increased by a remarkable 74%. This is compatible with technological advances over the decades where an increasing penetration of IT equipment, air conditioning systems etc. means that electricity demands within this sector is on a continuously increasing trajectory. Buildings vary remarkably in terms of size where large variations are expected in the non-residential categories.

The ownership profile in the non-residential sector is heterogeneous. Private ownership can span from as low as 20% to 90% from country to country and also from one building type to another. The public non-residential building stock represents an average 31% of the total non-residential sector in Europe (Based on the survey "Europe´s buildings under the microscope" by BPIE in 2011.).

On the other hand, the heating and cooling of buildings take a large share in the energy consumption. The average energy consumption in the non-residential sector, such as public and industrial buildings, is estimated to be at least 40% greater than in the residential sector in Europe. Some reasons for this general increase are for example an increase in comfort habits, currently still low energy costs, architectural trends (glazed areas in

doi:10.18086/swc.2017.12.12 Available at http://proceedings.ises.org

buildings) and slowly changing in climate conditions. This rising demand for cooling and air-conditioning in buildings involves unfavourable fossil fuel consumptions as well as upcoming stability problems in the electricity supply in Mediterranean countries, which in turn demands for costly upgrading of the grids to handle electricity peak power demand situations.

Therefore, integrating technologies to make existing buildings more energy efficient is the challenge that the EU-funded BRICKER research project is addressing. The project consists of retrofitting showcase public buildings in Spain, Turkey and Belgium to achieve at least 50% reduction in energy consumptions compared to the values before renovation.

2. Demonstration buildings

The demonstration buildings are in use and the goal is to demonstrate the performance of the technologies and systems developed within the project. BRICKER combines various active and passive technologies to achieve energy efficiency in innovative ways. (In this case a tri-generation system capable of providing power, heating and cooling simultaneously). The system's activation heat will be produced using parabolic solar collectors working on a high temperature and biomass boilers adapted to the specificities of each demo site and its surroundings.

The demonstration buildings of this project BRICKER are 3, and are located in the geographical areas trying to cover the diversity of Europe. These buildings can be seen in Fig. 1 and are concretely located in Caceres (Spain), Liege (Belgium) and Aydin (Turkey). The idea behind the project is to demonstrate the operation of the technologies and systems developed and to achieve energy savings of more than 50% compared to the initial values prior to renewal. The investment costs associated are expected to be at most 20% of the total costs of a building compared to those due to a new one located on the same site, and return of investment around 7 years. All this can be seen reflected for each concrete case of each demonstration building below.

Fig. 1: Location of demonstration buildings in the BRICKER project

2.1. Demonstration building in Caceres:

- Building: Administrative offices of the Government of Extremadura.
- Renovation: 1 administrative building of a set of 7 buildings.
- Useful area: 8,480 m^2.
- Occupation: 300 workers.
- Electrical savings: 60%.
- Return of investment: 7 years.
- Associated investment cost: 13.4%.

Fig. 2: Administrative offices in Caceres

2.2. Demonstration building in Liege:

- Building: School of Engineering of the University of Liege.
- Renovation: 2 blocks of an academic complex formed by 7 buildings.
- Useful area: 23,000 m^2.
- Occupation: 1,200 students.
- Electrical savings: 86%.
- Gas savings: 75%.
- Return of investment: 7.2 years.
- Associated investment cost: 9%.

Fig. 3: School of Engineering in Liege

2.3. Demonstration building in Aydin:

- Building: AHU Hospital; Adnan Menderes University.
- Renovation: 1 building of the university hospital complex composed by 4 blocks.
- Useful area: 19,467 m^2.
- Occupation: 600 patients y 450 workers.
- Energy savings: 51%.
- Return of investment: 7 years.
- Associated investment cost: 10%.

Fig. 4: AHU Hospital in Aydin

3. Core of BRICKER project

Tri-generation concept or CCHP (Combined Cooling, Heating and Power) is the simultaneous production of mechanical power, heating and/or cooling from one primary fuel by coupling with thermally activated cooling technologies that take the waste heat from CHP for producing cooling.

Thermally activated cooling utilized for CCHP systems primarily refers to sorption refrigeration; it employs waste heat produced in the process of power generation as the driving force to power a sorption refrigeration device. Some energy demand for refrigeration is thus shifted from electrical to thermal energy, and primary energy consumption is also reduced. Another difference between sorption systems and conventional vapour compression systems is the working fluid used. Most vapour compression systems commonly use chlorofluorocarbon refrigerants (CFCs), because of their thermo-physical properties. It is through the restricted use of CFCs, due to depletion of the ozone layer that will make sorption systems more prominent. However, although sorption systems seem to provide many advantages, vapour compression systems still dominate all market sectors. In order to promote the use of sorption systems, further development is required to improve their performance and reduce cost.

Power generation system is an Organic Rankine Cycle (ORC) whose operation principle is the same as the conventional Rankine cycle, but in this case, the working fluid is an organic compound of low boiling point instead of water, thus decreasing the temperature needed for evaporation. A pump pressurizes the liquid fluid, which is injected into an evaporator (heat source) to produce a vapour that is expanded in a turbine connected to a generator. Finally, the output vapour is condensed and sucked up by the pump to start the new cycle. ORC heat source could come from renewable sources (solar, biomass, geothermal…), the ORC unit is able to produce electricity (DC) for self-consumption or for the grid, and another heat source at lower temperature (from the condensation side) than can be used for heating. If the heat source from the condensation is also used for cooling (using a sorption machine), we have a tri-generation system.

Most of the commercial installations of concentrating solar collectors are for large scale solar power generation in steam turbines. Large collectors and systems with high operating temperatures are targeted for optimal steam cycle efficiency. However, Parabolic Trough Collectors (PTCs) are also suitable for the medium temperature and medium size applications and for industrial process heat, desalination, solar air conditioning and distributed power generation with Cogeneration turbines or internal combustion engines. For state of the art, we refer to small (roof mountable) parabolic trough collectors commercially available today, because the larger parabolic trough can simply not be used on rooftops. These small parabolic troughs are optimized for the temperature range 100-200°C. This temperature range has a very large potential for industrial process heat and solar cooling. For small power plants where ORC and solar are combined, the temperature range should be increased up to the temperature range 250 to 300°C, i.e. at least 50°C above the current optimization range. Therefore, in the framework of the BRICKER project, the development, testing and integration of a parabolic through collector and whole solar fields to feed the cogeneration unit that works with a heat source of 250 +/- 30ºC, is also developed.

Several factors such as the heat sources available, the existing conventional systems and the new energy systems to be installed in the buildings within this project, the economic restrictions and the cooling and heating needs among others has been studied and has allowed to identify which of the solutions/configurations fitted better within the BRICKER concept. As has been mentioned before the main objective of BRICKER is the installation of a tri-generation system to provide energy in an optimal way to the building, so for that and following the original concept of a tri-generation system, the unique option is limited to use the residual energies coming from the BRICKER energy system to produce in this case cooling, and in this particular case has been concluded that the only option available is the utilization of the residual heat coming from the ORC in form of water condensation to feed the chiller unit as primary heat source. This limitation together with the need to produce chilled water at certain range of temperatures to feed the terminal units already installed has reduced the possibilities to only two, which are the installation of an adsorption chiller unit (Fig. 5) or on the other hand the installation of a single effect absorption chiller unit (Fig. 6). These two possibilities can be seen in the pictures below.

Fig. 5: Integration of an adsorption chiller

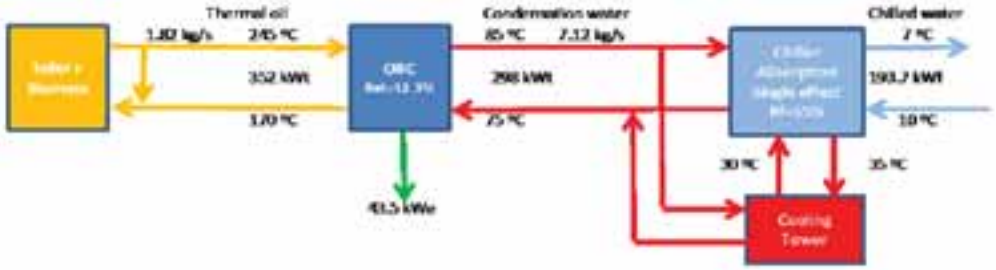

Fig. 6: Integration of an absorption chiller

The difference between them is mainly the activation requirements but also the working principle as one is using a liquid as sorption material and the other is using a solid.

Demo cases analyzed are two public buildings located in Spain (Caceres) and Turkey (Aydin). The first one is an administrative building of around 8,150 m^2 while the second one is a big hospital with a surface of more than 50,000 m^2. Due to their similar weather conditions (both located in the south of Europe) with hot summer periods, but also in the case of the hospital due to their specific conditions with cooling needs during the whole year, it is assumed the necessity of systems which provide the buildings with cooling capacity. In both cases original cooling systems are based on conventional heat pump systems which consume high amounts of electricity. So the idea is with the implementation of thermally activated cooling technologies within the BRICKER system to cover cooling needs of the buildings with the corresponding reduction of electricity consumption due to the less use of the conventional systems.

Many options are available and have been studied in terms of thermally activated cooling technologies, each of them with their own characteristics and limitations. After analyzing the different options and taking into account the boundary conditions imposed by each demo case has been concluded that the most suitable option is to install an adsorption chiller unit for both buildings. This selection has been due to the necessity to meet the original concept of tri-generation, in which is needed to make use of the residual energies coming in this specific project from the ORC water condensation at low temperature (70 ºC in cogeneration mode) as primary heat source. This limitation of temperature together with the possibility to get higher electrical performances in the ORC in comparison with the other thermally activated technologies (lower temperatures in the condensation side, makes the ORC to work with higher electrical performances), makes this selection as the most suitable. Other options such as the open cycle systems have been discarded due to the necessity to feed the terminal units at a given temperature (10 - 15 ºC). In the same way, the absorption units have been discarded due the operating limitations to work below 80 ºC in which the ORC develops their full potential in cogeneration mode. In addition, these machines have lower performances at working temperatures in the range between 80 - 90 ºC.

Although the selected technology has been the same for both demo cases (an adsorption chiller unit), it could be noticed that each has their own peculiarities. In the case of the Spanish demo case, the chiller unit has been dimensioned with the idea to cover all the cooling needs of the building, accomplishing the project economical restriction (only requiring additional support during occasional peak loads through a conventional heat pump system). In the Turkish demo case, due to their higher demand in terms of cooling, the idea is to cover only a little portion of it, so the selection is only based on the restrictions coming from the ORC (thermal energy limitations) and the economical ones.

4. Conclusions

Finally, two main conclusions can be drawn:

1. Energy use in public non-residential buildings represents a high proportion of the EU energy consumption and CO_2 emissions for the non-residential sector. In particular, hospitals, offices and educational buildings represent the highest levels of energy intensities of public-owned buildings.

2. Concerning the energy retrofitting solutions to be proposed for this target group, aiming at achieving nearly zero energy buildings, the scope must be related to systemic and integrated approaches involving:

a. Energy demand reduction by envelope optimization techniques (to decrease electrical and gas dependence).

b. Development and integration of Combined heat and Power (renewable based) solutions to produce both distributed heat and electricity at building and district level, according to the locally available resources.

c. Integration and optimization of the systems and its operation in cost effective way for the life cycle.

To sum up, the heart of this project is the development of innovative Combined Heating, Cooling and Power (CHCP) systems tailored to the specific needs of each demo building combining and adapting in the best way different subsystems (ORC units, parabolic through collectors, biomass boilers, sorption units) and locally available renewable sources (solar and/or biomass) as an example of high efficiency and renewable energy alternative, suitable for those buildings and districts with relevant electricity, heating and/or cooling needs.

5. References

Deng, J., Wang, R.Z., Han, G.Y., 2010. A review of thermally activated cooling technologies for combined cooling, heating and power systems.

Buildings Performance Institute Europe (BPIE), 2011. Europe´s buildings under the microscope.

Pongsid Srikhirin, Satha Aphornratana, Supachart Chungpaibulpatana, 2001. A review of absorption refrigeration technologies.

Studies on Optimal Application of Building-Integrated Photovoltaic/Thermal Facade for Commercial Buildings in Australia

Siliang Yang[1], Francesco Fiorito[2], Alistair Sproul[3] and Deo Prasad[4]

[1] Faculty of the Built Environment, UNSW, Sydney NSW 2052, Australia

[2] Department of Civil, Environmental, Land, Building Engineering and Chemistry, Polytechnic University of Bari, 70125 Bari, Italy

[3] School of Photovoltaic & Renewable Energy Engineering, UNSW, Sydney NSW 2052, Australia

[4] Cooperative Research Centre for Low Carbon Living (CRC-LCL), Sydney NSW 2052, Australia

Abstract

Both electrical power and useful thermal energy can be obtained from building-integrated photovoltaic/thermal systems (BIPV/T) which have the potential to reduce the energy consumption of buildings. Double-skin façades (DSF) have been implemented for enhancing energy efficiency as well as improving indoor thermal comfort. This paper explored the performance of a combination of BIPV/T and DSF, which included the thermal performance of this novel building envelope as well as the indoor comfort performance through a simulation analysis for a test building in Sydney, Australia. To date, the work has focused on two operation modes of the BIPV/T-DSF system comprising fan-driven ventilation mode in summer time and non-ventilation mode in winter. A comparative simulation analysis of the two operation modes and the building without adopting the BIPV/T-DSF system was presented in terms of the thermal response of the indoor space.

Keywords: Building-integrated Photovoltaic/Thermal System, Double-skin Façade, Commercial Building, Energy Efficiency, Indoor Thermal Comfort

1. Introduction

The world is in the process of rapid development, with increasing heavy industrial production as well as increasing building construction, all of which is contributing to the rapid increase of energy consumption. Energy demand from the building sector accounts for 40% of energy consumption globally and consequently emits approximately 1/3 of the greenhouse gas emissions (United Nations Environment Programme, 2016). The total energy consumption of commercial buildings in Australia was 3.5% of the national gross energy consumption in 2009 and this proportion is expected to rise by 24% over the period 2009 to 2020 (Council of Australian Governments, 2012). Building façades are a key component linking buildings and the outdoor environment, which significantly affects air-conditioning energy use for heating and cooling (Peng, Lu, Yang, Song, & Ma, 2015). High heating and cooling energy consumption is due to the poor thermal insulation properties of building façade (Papaefthimiou, Syrrakou, & Yianoulis, 2006). Thus, exploring high performance building façades is important to improve energy efficiency of commercial buildings.

The utilization of renewable energy technologies in buildings is an effective solution to combat the increase in energy consumption (Chwieduk, 2017). Solar energy is one of the most widely applied renewable energy approaches for increasing energy sustainability in the building industry (Mekhilef, Saidur, & Safari, 2011). Solar photovoltaic/thermal (PV/T) systems, integrated into building façade, can form a cohesive design, construction and energy solution for buildings (M. D. Bazilian, Leenders, Ree, & Prasad, 2001). Both electrical power and useful thermal energy can be obtained from the PV/T system hence contributing to the reduction of

[1] Corresponding author. Tel.: +61 (02) 9385 6372; Mob.: +61 (0) 415 680 589.
E-mail address: siliang.yang@unsw.edu.au

doi:10.18086/swc.2017.12.13 Available at http://proceedings.ises.org

the energy consumption of a building (Yang & Athienitis, 2012). Double skin façades, have been effective for enhancing energy efficiency as well as improving the indoor thermal comfort (Marques da Silva, Gomes, & Rodrigues, 2015). This type of façade solution has become a globally widespread option for implementing sustainable energy and an architecturally attractive option for the building envelope (Ghaffarianhoseini et al., 2016). Quite a few researchers have generally reported the factors of that affecting the power efficiency of the BIPV system (e.g. typology of the materials, PV module temperature, and packing factor of PV module) (M. Bazilian, Kamalanathan, & Prasad, 2002; Oliver & Jackson, 2000; Vats, Tomar, & Tiwari, 2012). A few studies have reported both the thermal and electrical efficiency of the BIPV/T system but, the outcomes in cold climates have predominated and only a small number investigated a range of climatic conditions (Athienitis, Bambara, O'Neill, & Faille, 2011; Chen, Athienitis, & Galal, 2010; Chow, Hand, & Strachan, 2003; Pantic, Candanedo, & Athienitis, 2010; Yang & Athienitis, 2015). Further a few studies lately reported the performance of PV efficiency of a BIPV/T-DSF envelope, but little research has been done on understanding of indoor thermal comfort and energy performance of the building adopting BIPV/T-DSF system (Charron & Athienitis, 2006; Peng, Lu, & Yang, 2013; Saadon, Gaillard, Giroux-Julien, & Ménézo, 2016). Most of field studies were conducted under the indoor test conditions, which were not absolutely reliable (Fossa, Ménézo, & Leonardi, 2008; Yang & Athienitis, 2015).

Neither building-integrated photovoltaic/thermal (BIPV/T) nor double-skin façade (DSF) is novel. However, little research or real application of the hybrid mechanism of BIPV/T and DSF has been conducted in both academic and industrial settings (Peng, Lu, Yang, & Han, 2013). Therefore, this research project aims to investigate the overall performance of a BIPV/T system integrated with a DSF. In particular the electrical and thermal performance of this novel building envelope as well as the impact of this envelope solution on indoor thermal comfort performance of the commercial buildings is investigated.

2. Methodology

This paper examined both experimental field measurements and computational simulation for building-integrated photovoltaic/thermal double-skin façade (BIPV/T-DSF). The computational model was validated against experimental results reported in the literature. This model was then used to simulate a commercial building in Australia. The system parameters were adjusted to optimize the performance of the BIPV/T-DSF and the indoor thermal condition of the building. A long-term system performance and indoor thermal comfort then can be predicted confidently by using the validated computational model.

The building with BIPV/T-DSF system was modelled in TRNSYS (thermal modelling software). TRNSYS is widely used visual based software for transient simulations of solar thermal energy systems and any dynamic simulation including buildings (Kamel & Fung, 2014).

A model of the BIPV/T-DSF was developed in TRNSYS and validated by using experimental results taken from the existing published studies by Peng et al. (Peng et al., 2016; Peng, Lu, & Yang, 2013; Peng, Lu, Yang, & Ma, 2015). They have conducted the series field studies of a test bed with a ventilated BIPV/T-DSF under different ventilation modes in Hong Kong. This BIPV/T-DSF system uses a double-glazed semi-transparent a-Si PV module (Peng, Lu, & Yang, 2013). The diagram of the BIPV/T-DSF is shown in Fig. 1. As can be seen, the DSF consisted of two cavities which were separated by a vertical insulation board; at this point, the two air cavities were used for the comparative analysis for different modes of ventilation without affecting one another. Two ventilation modes used for model simulation and model validation, are shown in Tab. 1.

Tab. 1: Specifications of the selected ventilation modes for model validation (Peng, Lu, & Yang, 2013).

Ventilation Modes	Specifications
Non-ventilated mode (mode 1)	All inlet and outlet louvers were closed and the internal windows were opened, air-conditioner was turned off.
Buoyancy-driven ventilation mode (mode 2)	The inlet and outlet louvers on left hand side (cavity 1) were closed, while the inlet and outlet louvers on right hand side (cavity 2) were opened; all internal windows were closed; indoor air temperature was maintained at 22°C by use of the air-conditioner.

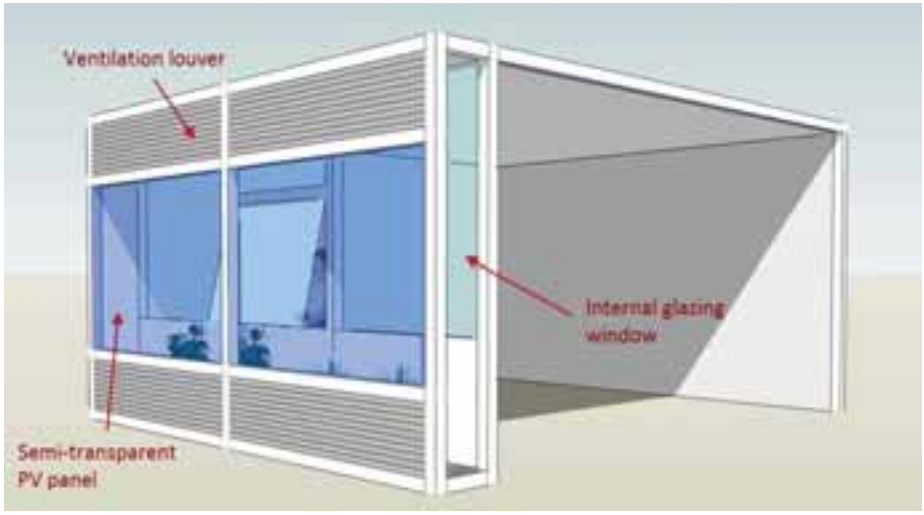

Fig. 1: Schematic diagram of the BIPV/T-DSF system for the test bed (Peng et al., 2016).

3. Modelling and Model Validation

The key dimensions of the BIPV/T-DSF system and the physical characteristics of the PV panel (semi-transparent) used are given in Tab. 2 and Tab. 3 respectively.

Tab. 2: Key dimensions of the BIPV/T-DSF system (Peng et al., 2016).

Parameters	Values
Width of PV panel	1.1 m
Height of PV panel	1.3 m
Thickness of PV module	0.006 m
Width of louver	1.1 m
Height of louver	0.5 m
Depth of air flow duct (air cavity)	0.4 m
Dimension of the test bed (W x L xD)	2.4 x 2.5 x 2.3 m
Orientation	Due south

Tab. 3: Physical characteristics of the semi-transparent a-Si PV panel (Peng et al., 2016).

Parameters	Values
Maximum power under STC (W_p)	85
Open circuit voltage, V_{oc} (V)	134.4
Short circuit current, I_{sc} (A)	1.05
Voltage at the maximum power point, V_{mp} (V)	100
Current at the maximum power point, I_{mp} (A)	0.85
Efficiency, η (%)	6.2
Power temperature coefficient, T_k (%/K)	-0.21
Dimensions (L x W x D), (mm)	1300 x 1100 x 6
Transmittance in visible lighting range (%)	7
Thermal conductivity, ($Wm^{-1}K^{-1}$)	0.486
Infrared emittance	0.85

The test model was established in TRNSYS based on the experimental parameters provided in Tab. 2 and Tab. 3. Real-time meteorological data (on-site historical weather data for Hong Kong) of the site during the experiment was provided by the authors (Peng et al.), which was used for the TRNSYS simulation. Fig. 2 shows the model of the BIPV/T-DSF in the TRNSYS Simulation Studio (the user interface to create the simulation model).

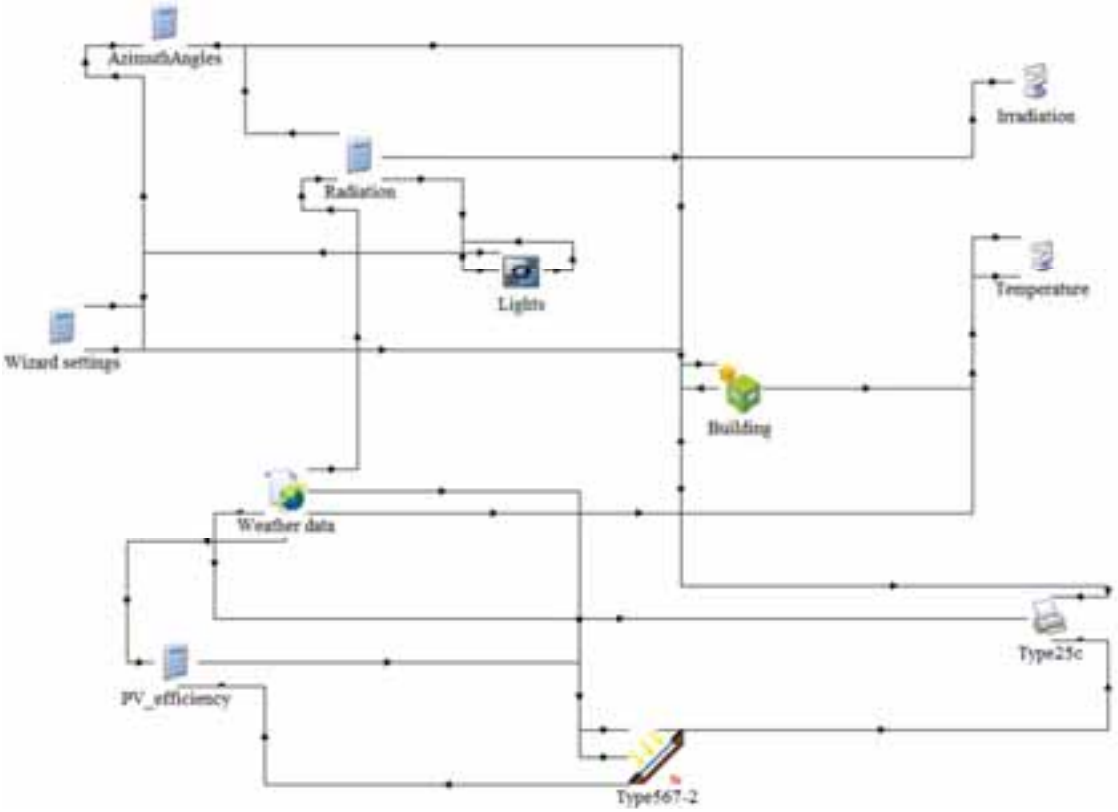

Fig. 2: Schematic of the testing building model integrated with the BIPV/T-DSF system in TRNSYS.

Type 56 (the "building" icon in Fig. 2) included the details of the building model such as building geometry, type of construction, and optical data of the window glazing. The glazed semi-transparent PV panel used in the test bed was symbolized by Type 567-2 (the corresponding PV module in TRNSYS) which was connected to the test bed (Type 56) in the TRNSYS model. Because the semi-transparent PV panel model is not available in TRNSYS, a glazing model with the exact identical thermal and optical properties of the semi-transparent a-Si PV panel was created and replaced the outer window on the DSF. As such, the electricity production of the PV was calculated separately.

3.1. Validation of the Model in Non-Ventilated Mode

The PV module (back-surface) temperature is a major feature that is closely related to the output power of the PV panel, which is mainly affected by the ambient conditions, primarily the solar radiation as well as the ambient temperature (Chikate & Sadawarte, 2015). Therefore, the PV module temperature of the BIPV/T-DSF system from the simulation was compared with the experimental result (Peng, Lu, & Yang, 2013). In addition, the indoor air temperature is a crucial indicator for indoor thermal comfort which was also compared accordingly. The available experimental results of the non-ventilated mode (mode 1) were from Jan 5 to Jan 7, 2013. The simulation in the TRNSYS model was in accordance with the same time period and the comparative results are shown in Fig. 3 and Fig. 4 accordingly.

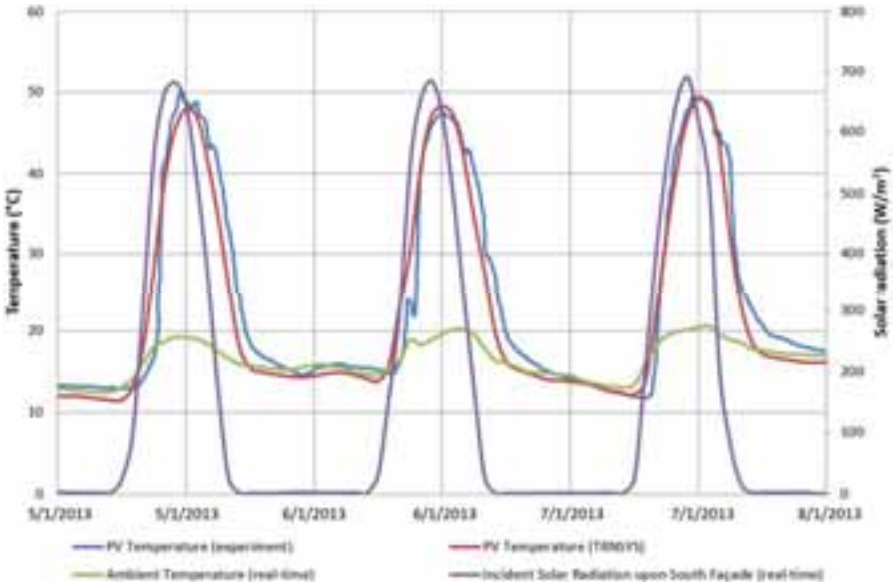

Fig. 3: PV module temperature comparison in Mode 1 (non-ventilated).

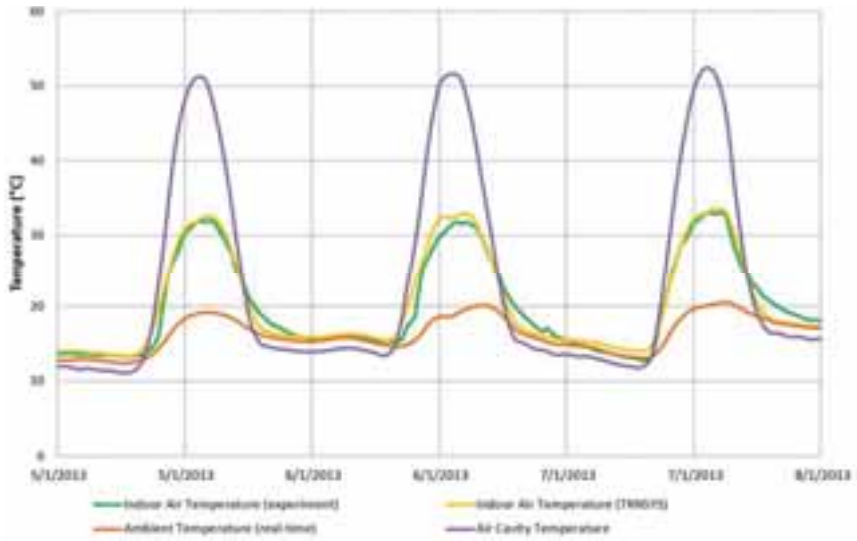

Fig. 4: Indoor air temperature comparison in Mode 1 (non-ventilated).

As can be observed in Fig. 3, the simulated PV module temperature and the measured PV module temperature (72 hours' results) show good agreement although a certain extent of discrepancy exists. The hourly Mean Bias Error (MBE) and Cumulative Variation of Root Mean Squared Error (CVRMSE) (ASHRAE, 2002) were used as the criteria for assessing the acceptability of the agreement between simulated and measured data. The MBE and CVRMSE are calculated as:

$$\boldsymbol{MBE} = \frac{\sum_{i=1}^{Np}(\boldsymbol{M_i}-\boldsymbol{S_i})}{\sum_{i=1}^{N_P}\boldsymbol{M_i}} \qquad \text{(eq. 1)}$$

$$\overline{\boldsymbol{M_P}} = \frac{\sum_{i=1}^{N_P}\boldsymbol{M_i}}{\boldsymbol{N_P}} \qquad \text{(eq. 2)}$$

$$\boldsymbol{CVRMSE_{(P)}} = \frac{\sqrt{\sum_{i=1}^{N_P}((\boldsymbol{M_i}-\boldsymbol{S_i})^2/\boldsymbol{N_P})}}{\overline{\boldsymbol{M_P}}} \qquad \text{(eq. 3)}$$

Where M_i and S_i are measured and simulated data at instance "i" respectively; p is the interval (e.g. monthly, weekly, daily and hourly); N_p is the number of values at interval p (e.g. $N_{month} = 12$, $N_{day} = 365$, $N_{hour} = 8760$) and $\overline{M_p}$ is the average of the measured data (Raftery, Keane, & Costa, 2011). The both hourly acceptance

thresholds of MBE and CVRMSE are ±10% and ≤30% respectively. For the PV module temperature, the MBE and CVRMSE were 4.55% and 14.48% respectively, so the simulated results of PV module temperature were acceptable. Similarly, as shown in Fig. 4, the hourly values of indoor air temperature also show good agreement with the experimental results and the corresponding hourly MBE and CVRMSE were -1.02% and 5.5% respectively. Thus, the TRNSYS model for mode 1 was deemed validated.

3.2. Validation of the Model in Buoyancy-Driven Ventilation Mode

The available experimental results for the buoyancy-driven ventilation mode were from Jan 28 to Jan 31, 2013. The right-hand side cavity (cavity 2) was selected. As the indoor condition was constantly maintained at 22°C through air-conditioning, the indoor air temperature in this operation mode was not be analyzed. The PV module back surface temperature on this cavity (PV module 2) and internal surface temperature of the corresponding internal window (window 2) were selected and simulated in the TRNSYS model through the same time period of the experiment and the comparative results are shown in Fig. 5 and Fig. 6 accordingly.

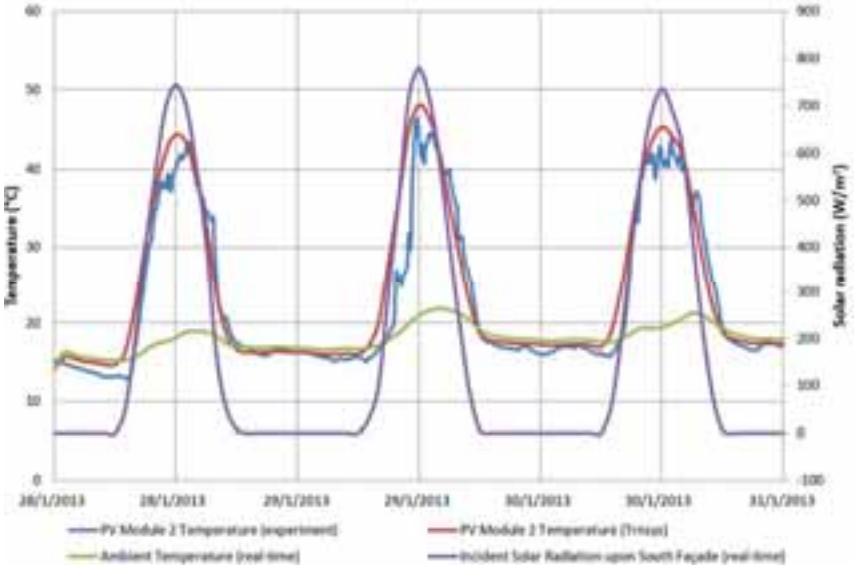

Fig. 5: PV module temperature comparison in Mode 2 (buoyancy ventilation).

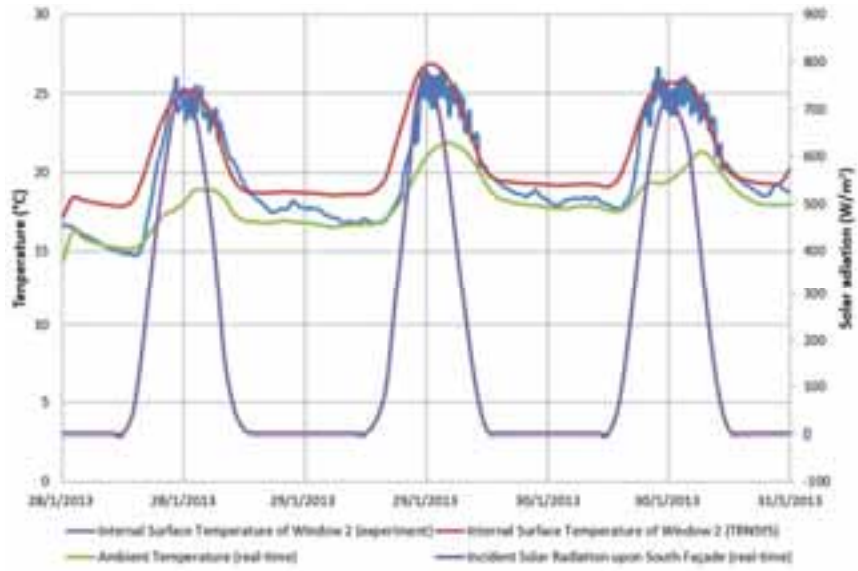

Fig. 6: Comparisons for internal surface temperature of Window 2 in Mode 2 (buoyancy ventilation).

As shown in Fig. 5, the hourly values of PV module temperature show acceptable agreement with the

experimental results and the corresponding hourly MBE and CVRMSE were -4.85% and 11.6% respectively. Comparison of the simulated and measured hourly internal surface temperature of window 2 shows obvious differences during the troughs, in which the simulated values are consistently exceeding the measured values and the biggest difference reached about 3°C in Fig. 6. A likely explanation is the different thermal behaviors between the used window glazing in TRNSYS and the experiment as the experimental information of the window was not available (Peng, Lu, & Yang, 2013), a float glass was assigned to window 2 in the TRNSYS model. In addition, it is difficult to model natural ventilation directly in TRNSYS. This could be done by coupling with the external plug-in such as TRNFlow and CONTAM, but it is outside the scope of this stage of study. As an alternative, the buoyancy-driven ventilation in the cavity was modelled in terms of the constant mass flow rate as the window speeds during the 72 hours were basically floating at 2m/s according to the real-time weather data, so the simulated curve (internal surface temperature of window 2) was much steadier than the curve of measured values. Moreover, the related MBE and CVRMSE were -5.51% and 7.28% respectively, which were acceptable and hence the TRNSYS model for mode 2 was deemed validated.

4. Preliminary Numerical Simulation Model for the BIPV/T-DSF in Australia

In terms of the validated TRNSYS model, a preliminary numerical simulation model has been developed for investigating the thermal performance of the novel BIPV/T-DSF system and its impact on indoor thermal comfort of a commercial building in Sydney, Australia. A building model was built in TRNSYS which was based on the experimental test bed but facing due north in Sydney. The building fabric, except for the PV glazing of the simulation model was modified in the generic design for a better evaluation of the indoor thermal response by use of the BIPV/T-DSF. In order to understand the performance of the BIPV/T-DSF system, the indoor air temperature under the typical days in summer and winter were analyzed accordingly.

4.1. Fan-Driven Ventilated Operation in Summer

A fan-driven ventilating operation for the model building in Sydney was modelled in TRNSYS using a constant mass flow rate (1.35 kg/hour from the validated model in section 3.2) for a steady state of analysis for 72 hours' simulation. In this operation mode, there was no air-conditioning in the building model, the inlet and outlet louvers on the both cavities were opened to allow buoyancy ventilation, which was then compared to the building model operated without the BIPV/T-DSF system. In order to eliminate other uncertainties which might interfere the simulation results, the internal gains from people, equipment and lightings were not included in the models.

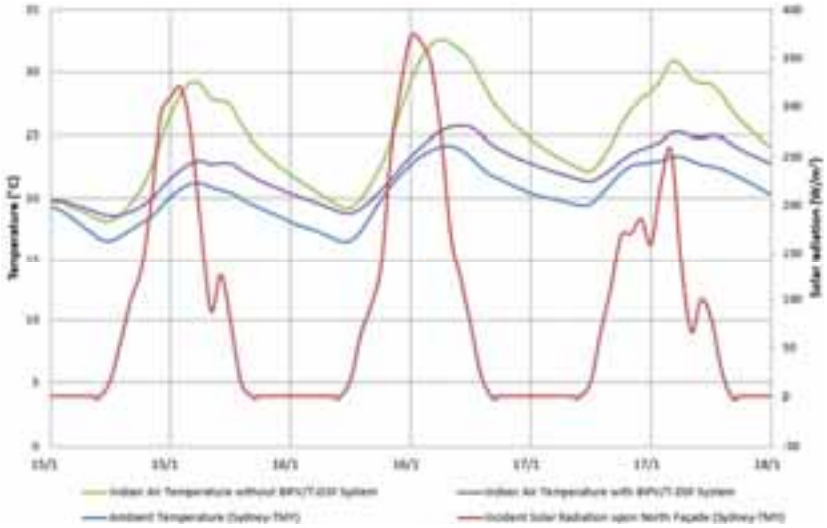

Fig. 7: Comparisons for indoor air temperature with/without BIPV/T-DSF system in summer.

Fig. 7 presents the indoor air temperatures with/without the application of BIPV/T-DSF system for the building model from Jan 15 to Jan 18 in the typical summer days in Sydney. It was found that the indoor air temperature of the building either with or without the BIPV/T-DSF system was always higher than the ambient temperature

throughout the day. The main reason is that the accumulations of solar heat gain led to a higher indoor air temperature than ambient temperature. However, the building model that utilized the BIPV/T-DSF system has significantly lower indoor air temperature than the building model without a BIPV/T-DSF and reached a maximum temperature of 6°C lower during the daytime. This indicated the BIPV/T-DSF system can reduce the indoor air temperature and assist in reduce the thermal load on the mechanical cooling system.

4.2. Non-Ventilated Operation in Winter

Based on the results in section 4.1, all the louvers and windows of the BIPV/T-DSF system were closed for winter to avoid the heat loss through the ventilation. The comparisons between the building adopting and not adopting the non-ventilated BIPV/T-DSF system were compared from Aug 15 to Aug 18 for typical winter days in Fig. 8. It can be seen that the indoor air temperature of the building model either with or without BIPV/T-DSF system was always higher than the ambient temperature, and the indoor air temperature can be maintained at a comfort level during the daytime. Clearly, the temperature drops at night time due to the heat loss through the building fabric, while the BIPV/T-DSF system brought the thermal buffer benefit that played a passive heating role in winter, but the ventilated operation of the cavity can be used for the higher solar radiation days (i.e. Aug 15 and Aug 17) to maintain a lower and comfort indoor air temperature. The non-BIPV/T-DSF case has an overheating issue during the peak daytime and the highest indoor temperature reached about 42°C on Aug 15.

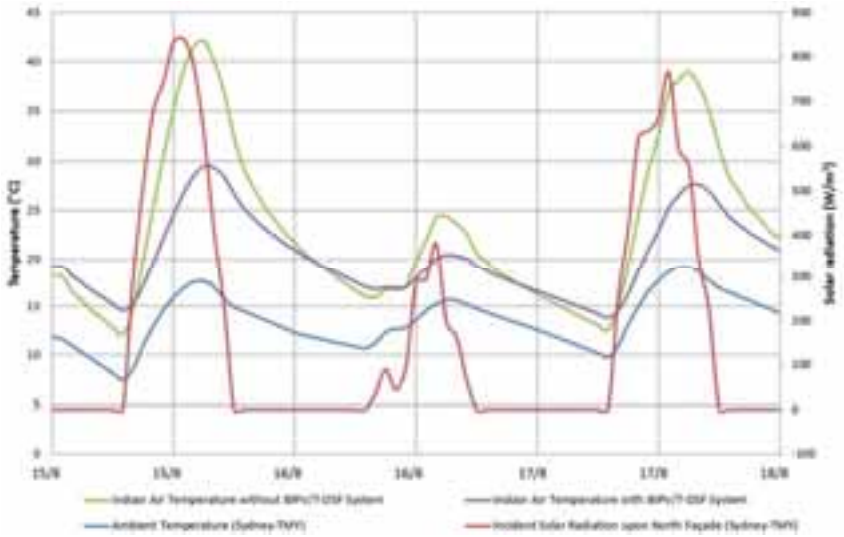

Fig. 8: Comparisons for indoor air temperature with/without BIPV/T-DSF system in winter.

5. Conclusions

The simulation results show that BIPV/T-DSF system gives not only good thermal performance in terms of buffering the building from summer heat gains, but reduces heat loss as well as overheat of building during winter time in the subtropical climate areas in southern hemisphere like Sydney. These are preliminary studies of the novel building façade technology that remains provisional since they are parts of the ongoing research. Further studies will concentrate on developing the specific strategies for maximizing its thermal and electrical performance, and optimizing the long term indoor thermal comfort using the strategies.

Acknowledgements

The authors would like to acknowledge the financial support provided by the Faculty of Built Environment, University of New South Wales (Australia) and the Cooperative Research Centre for Low Carbon Living (CRC-LCL). The authors also would like to express the deepest gratitude to Dr. Jinqing Peng for providing the indispensable input data of the test bed.

References

ASHRAE. (2002). Guideline 14-2002 *Measurement of Energy and Demand Savings*. Atlanta, Georgia: American Society of Heating, Ventilating, and Air Conditioning Engineers.

Athienitis, A. K., Bambara, J., O'Neill, B., & Faille, J. (2011). A prototype photovoltaic/thermal system integrated with transpired collector. *Solar Energy, 85*(1), 139-153. doi:10.1016/j.solener.2010.10.008

Bazilian, M., Kamalanathan, H., & Prasad, D. (2002). Thermographic analysis of a building integrated photovoltaic system. *Renewable Energy, 26*(3), 449-461.

Bazilian, M. D., Leenders, F., Ree, B. G. C. V. d., & Prasad, D. (2001). Photovoltaic cogeneration in the built environment. *Solar Energy, 71*(1), 57-69.

Charron, R., & Athienitis, A. K. (2006). Optimization of the performance of double-façades with integrated photovoltaic panels and motorized blinds. *Solar Energy, 80*(5), 482-491. doi:10.1016/j.solener.2005.05.004

Chen, Y., Athienitis, A. K., & Galal, K. (2010). Modeling, design and thermal performance of a BIPV/T system thermally coupled with a ventilated concrete slab in a low energy solar house: Part 1, BIPV/T system and house energy concept. *Solar Energy, 84*(11), 1892-1907. doi:10.1016/j.solener.2010.06.013

Chikate, B. V., & Sadawarte, Y. A. (2015). *The Factors Affecting the Performance of Solar Cell*. Paper presented at the International Journal of Computer Applications (0975-8887), Maharashtra, India.

Chow, T. T., Hand, J. W., & Strachan, P. A. (2003). Building-integrated photovoltaic and thermal applications in a subtropical hotel building. *Applied Thermal Engineering, 23*(16), 2035-2049. doi:10.1016/s1359-4311(03)00183-2

Chwieduk, D. A. (2017). Towards modern options of energy conservation in buildings. *Renewable Energy, 101*, 1194-1202. doi:10.1016/j.renene.2016.09.061

Council of Australian Governments. (2012). *Baseline Energy Consumption and Greenhouse Gas Emissions in Commercial Buildings in Australia (Part 1)*. Canberra: Department of Climate Change and Energy Efficiency.

Fossa, M., Ménézo, C., & Leonardi, E. (2008). Experimental natural convection on vertical surfaces for building integrated photovoltaic (BIPV) applications. *Experimental Thermal and Fluid Science, 32*(4), 980-990. doi:10.1016/j.expthermflusci.2007.11.004

Ghaffarianhoseini, A., Ghaffarianhoseini, A., Berardi, U., Tookey, J., Li, D. H. W., & Kariminia, S. (2016). Exploring the advantages and challenges of double-skin façades (DSFs). *Renewable and Sustainable Energy Reviews, 60*, 1052-1065. doi:10.1016/j.rser.2016.01.130

Kamel, R. S., & Fung, A. S. (2014). Modeling, simulation and feasibility analysis of residential BIPV/T+ASHP system in cold climate—Canada. *Energy and Buildings, 82*, 758-770. doi:10.1016/j.enbuild.2014.07.081

Marques da Silva, F., Gomes, M. G., & Rodrigues, A. M. (2015). Measuring and estimating airflow in naturally ventilated double skin facades. *Building and Environment, 87*, 292-301. doi:10.1016/j.buildenv.2015.02.005

Mekhilef, S., Saidur, R., & Safari, A. (2011). A review on solar energy use in industries. *Renewable and Sustainable Energy Reviews, 15*(4), 1777-1790. doi:10.1016/j.rser.2010.12.018

Oliver, M., & Jackson, T. (2000). The evolution of economic and environmental cost for crystalline silicon photovoltaics. *Energy Policy, 28*(14), 1011-1021.

Pantic, S., Candanedo, L., & Athienitis, A. K. (2010). Modeling of energy performance of a house with three configurations of building-integrated photovoltaic/thermal systems. *Energy and Buildings, 42*(10), 1779-1789. doi:10.1016/j.enbuild.2010.05.014

Papaefthimiou, S., Syrrakou, E., & Yianoulis, P. (2006). Energy performance assessment of an electrochromic window. *Thin Solid Films, 502*(1-2), 257-264. doi:10.1016/j.tsf.2005.07.294

Peng, J., Curcija, D. C., Lu, L., Selkowitz, S. E., Yang, H., & Zhang, W. (2016). Numerical investigation of the energy saving potential of a semi-transparent photovoltaic double-skin facade in a cool-summer Mediterranean climate. *Applied Energy, 165*, 345-356. doi:10.1016/j.apenergy.2015.12.074

Peng, J., Lu, L., & Yang, H. (2013). An experimental study of the thermal performance of a novel photovoltaic double-skin facade in Hong Kong. *Solar Energy, 97*, 293-304. doi:10.1016/j.solener.2013.08.031

Peng, J., Lu, L., Yang, H., & Han, J. (2013). Investigation on the annual thermal performance of a photovoltaic wall mounted on a multi-layer façade. *Applied Energy, 112*, 646-656. doi:10.1016/j.apenergy.2012.12.026

Peng, J., Lu, L., Yang, H., & Ma, T. (2015). Comparative study of the thermal and power performances of a semi-transparent photovoltaic façade under different ventilation modes. *Applied Energy, 138*, 572-583. doi:10.1016/j.apenergy.2014.10.003

Peng, J., Lu, L., Yang, H., Song, A., & Ma, T. (2015, 25 to 27 August). *182: Investigation on the overall energy performance of an a-si based photovoltaic double-skin facade in Hong Kong.* Paper presented at the Proceedings of the 14th International Conference on Sustainable Energy Technologies, Nottingham, UK.

Raftery, P., Keane, M., & Costa, A. (2011). Calibrating whole building energy models: Detailed case study using hourly measured data. *Energy and Buildings, 43*(12), 3666-3679. doi:10.1016/j.enbuild.2011.09.039

Saadon, S., Gaillard, L., Giroux-Julien, S., & Ménézo, C. (2016). Simulation study of a naturally-ventilated building integrated photovoltaic/thermal (BIPV/T) envelope. *Renewable Energy, 87*, 517-531. doi:10.1016/j.renene.2015.10.016

United Nations Environment Programme. (2016). Sustainable Buildings and Climate Initiative: Promoting Policies and Practies for Sustainability. Retrieved from http://www.unep.org/sbci/AboutSBCI/Background.asp

Vats, K., Tomar, V., & Tiwari, G. N. (2012). Effect of packing factor on the performance of a building integrated semitransparent photovoltaic thermal (BISPVT) system with air duct. *Energy and Buildings, 53*, 159-165. doi:10.1016/j.enbuild.2012.07.004

Yang, T., & Athienitis, A. K. (2012). *Investigation of performance enhancement of a building integrated photovoltaic thermal system.* Paper presented at the Proceedings of the Canadian Conference on Building Simulation, Halifax, Canada.

Yang, T., & Athienitis, A. K. (2015). Experimental investigation of a two-inlet air-based building integrated photovoltaic/thermal (BIPV/T) system. *Applied Energy, 159*, 70-79. doi:10.1016/j.apenergy.2015.08.048

Whole System Design of an Energy Efficient Residential Pool System

Jianzhou Zhao[1], Jose I. Bilbao[1], Edward D. Spooner[2] and Alistair B. Sproul[1]

[1] School of Photovoltaic and Renewable Energy Engineering, UNSW, Sydney (Australia)

[2] School of Electrical Engineering and Telecommunications, UNSW, Sydney (Australia)

Abstract

The impact of low-speed filtration on the performance of salt water chlorinators, pool cleaners, and the pool water quality, based on experimental and modelled data, is investigated. Results show that a typical salt water chlorinator and pressure pool cleaner do not work well for flow rates of less than 1 litre s^{-1} and 1.3 litre s^{-1} respectively. With the implementation of a robotic pool cleaner, energy savings of more than 70% can be obtained by operating the filtration system at around 1 litre s^{-1} with a correctly adjusted chlorinator setting. This does not compromise the system performance and achieves a largely improved water quality. Furthermore, it is shown that a small photovoltaic system can provide nearly all the energy required by such energy efficient pool system. This PV powered pool filtration system achieves a discounted payback period (DPP) of 5.4 years in comparison to the grid supplied pool filtration system (the Business as Usual (BAU) scenario).

Keywords: low-speed pumping; pool chlorinator; pool cleaner; high-efficiency pool filtration.

1. Introduction

With the rapid growth of residential energy consumption and peak electricity demand, it is important to investigate the energy saving potential in households and so achieve higher energy efficiency. Studies have shown that households with a swimming pool have higher energy demand than households with no pools (Elnakat et al., 2015; Fan et al., 2015). The savings in pump energy used for solar pool heating was previously investigated by the authors and the results showed that operating the system at a lower flow rate reduced the pumping energy by 60%, without materially affecting the pool thermal performance (Zhao et al., 2018). This paper will investigate how to improve the energy efficiency of the pool filtration system by evaluating the performance of the whole system. Such system could achieve significant savings in energy and cost, which therefore enables its energy load to be supplied by a typical photovoltaic system.

2. Background

Presently, there are approximately 1.1 million residential pools in Australia (DEE, 2016) and the total annual electricity demand is estimated be 2100 GWh per year (EES, 2008). This corresponds to approximately 2 million tonnes of carbon emissions per year (DEE, 2017). Operating the pool filtration system under low flow conditions have been recognized as an energy efficiency retrofit by the industry and many swimming pool have adopted this measure (DOE, 2018). Further, numerous studies have investigated the operation of pool filtration under low pump speed (Springer and Rohe, 1996; Sproul, 2005; Cunio and Sproul, 2008; Hameiri et al., 2009) with reported savings of as much as 80%. In addition, the use of a small photovoltaic system to power the low-energy pumping system was examined by Sproul (2005) and the system achieved a 14 year payback period.

Although it is clear that significant amounts of energy could be saved by operating the pool filtration system under low flow conditions, the impacts on other system components such as the salt water chlorinators and the pool cleaners have not been widely reported. In addition to this, the associated effects on pool water quality yet have not been quantitatively examined. According to a recent report prepared for the Department of the Environment and Energy (DEE) of the Commonwealth of Australia, the most common type of Australian pool is a salt water pool (60%) which relies on a chlorinator for sanitation (Woolcott Research and Engagement, 2016). The electrolysis process in the salt water chlorinator has been studied by Khouzam

doi:10.18086/swc.2017.12.14 Available at http://proceedings.ises.org

(2008); this process produces two gases, hydrogen gas and chlorine gas. The hydrogen gas is not soluble in water and therefore gets carried out of the chlorinator by the water flow, into the pool, and eventually into the environment. On the other hand, the chlorine gas, which is highly soluble in water, reacts with water to produce the hypochlorous acid (HOCl). The hypochlorous acid is known as free chlorine, which is an effective disinfectant in the pool. As in most cases, the same pump is used to both filter and chlorinate the water. One possible problem of operating the standard salt water chlorinators at low flow rate is that as the water flow reduces, the hydrogen gas produced accumulates in the chlorinator instead of being flushed out into the pool. Typically, chlorinators are designed to detect this dangerous situation and will switch off the chlorinator and the pump. Hence under these conditions, the pool sanitation deteriorates.

Additionally, a pressure pool cleaner powered by the filtration pump is also susceptible to low water flow operation, as the flow through the cleaners is shared with the pool skimmers or returns. Thus, to fulfill the cleaning task, the pump needs to run at a high speed for a certain period of time, which limits the extent to which the pool filtration can be completed at low flow rate using high-efficiency pumps.

Thus, it is the aim of this study to estimate the energy savings of the pool filtration system by taking the whole system into consideration. In particular, the low flow operation of the salt water chlorinator and the pressure pool cleaner are investigated to examine potential efficiency gains. To the authors' knowledge, there is no information available regarding the minimum operating flow rate of the chlorinator as well as its energy usage. Furthermore, energy efficient operating scenarios are proposed and the feasibility of utilising a PV system is analyzed.

3. Experimental system

Experiments were carried out on an existing domestic pool filtration system in Sydney Australia (Figure 1). The system has an eight-star variable speed water pump (Viron eVo P280), a controller, a salt water chlorinator (Hurlcon VX11T), an oversized cartridge filter (Viron CL400), and a pressure pool cleaner (Polaris 360) operated by the filtration pump. During the experiment key system parameters were monitored, which included the electrical power of the pump and chlorinator; water flow rates through the pump and the pressure pool cleaner; the pressure drop across the pump and the filter. A manually adjustable 3-way valve is located at the discharge of the chlorinator, which can change the proportion of water flow into the cleaner.

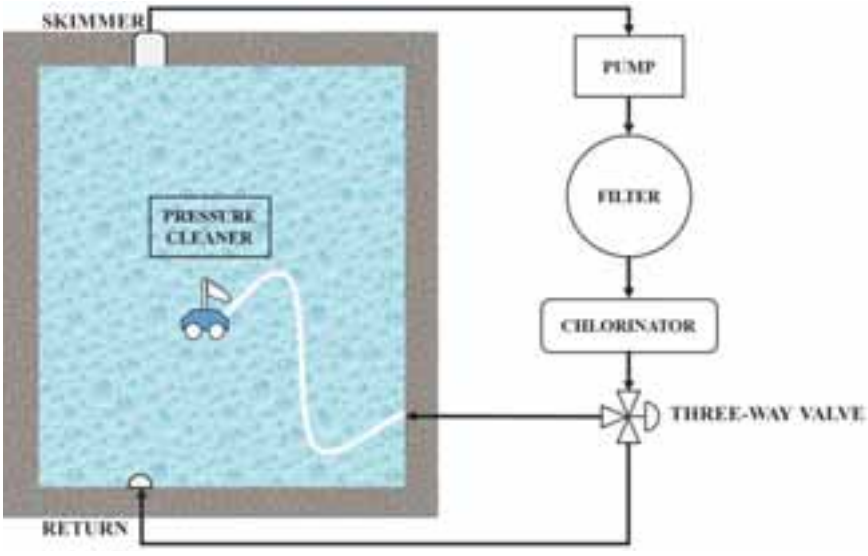

Figure 1: Pool filtration system layout.

The controller coupled to the pump was used to set the operating schedule as well as the pump speed so that the system performance could be investigated under multiple operating scenarios, with different pump speeds

and running times. The details of the operating scenarios are presented in Table 2. A robotic cleaner (Zodiac, 2017) was also retrofitted to replace the existing pressure cleaner in order to evaluate further energy saving opportunities.

Under each operating scenario, the water quality and cleaning effectiveness were examined qualitatively and quantitatively according to the requirements as per the Australian Standard AS3633 (1989) and NSW Government (2013) (Table 1). Based on the measured water quality, the chlorinator setting was adjusted manually using the controller until an acceptable water condition was obtained. Notice that as the pool water quality is affected by pool chemical levels as well as ambient factors including solar irradiance, the location of the pool, and its surroundings (Khouzam, 2008), the scenarios were varied out during the summer period to minimize variations due to the ambient weather conditions. Specifically, each scenario was carried out for 5 consecutive days with similar weather conditions (sunny and warm) and the daily water quality check was performed at 9 am.

Table 1: Recommended pool water chemical concentrations (Standards Australia, 1989; NSW Government, 2013).

Parameters	Recommended range	
Free chlorine (ppm[1])	Pool temperature < 26°C	> 2
	Pool temperature ≥ 26°C	> 3
pH	7 – 7.8 (Optimum: 7.2 – 7.6)	
Total alkalinity (ppm)	60 – 200	
Isocyanuric acid (ppm)	30 – 50	
Calcium hardness (ppm)	0 – 500	
Total dissolved solids (ppm)	1000 – 2000	
Turbidity	0.5 (NTU[2])	

4. Operating the whole pool filtration system at low flow

In order to assess the energy savings of running the variable speed pump at low speed, the comparison was made to the standard single speed pump investigated by Cunio and Sproul (2008). The Hurlcon 1500 W single speed pump was assumed to operate the same pool filtration system. The system operating point was obtained by overlaying the pump working curve with the measured system curve of the existing filtration system. The operating point was approximately 4.3 litre s^{-1} at a head of 18.5 m. For such a single speed pump to fully turnover the pool once every day as required by the Australian Standard AS3633 (1989), the daily pump energy is 3.6 kWh/day. This is comparable to the data reported by DEE (2016), which stated that "*Australian households with a pool use on average 1352 kWh per year (3.7 kWh/day) powering pool pumps used for filtration.*".

Figure 2 shows the daily required pump running time calculated based on one pool turnover and the measured pump efficiency (pump efficiency was calculated as the ratio of measured hydraulic and electrical power). Also shown is the daily pump energy savings in comparison to the single speed filtration by operating the variable speed pump over its flow rate range. Note that the daily energy consumption of the variable speed filtration was calculated based on the measured power usage and the required running time at each flow rate. As can be seen, lowering the flow rate leads to a significant increase in the daily running time while the pump efficiency decreases drastically. However, even at the minimum flow rate, one pool turnover can still be accomplished within 24 hours.

[1] Parts per million. One ppm is equivalent to 1 milligram of something per litre of water (mg/l).
[2] Nephelometric Turbidity Units.

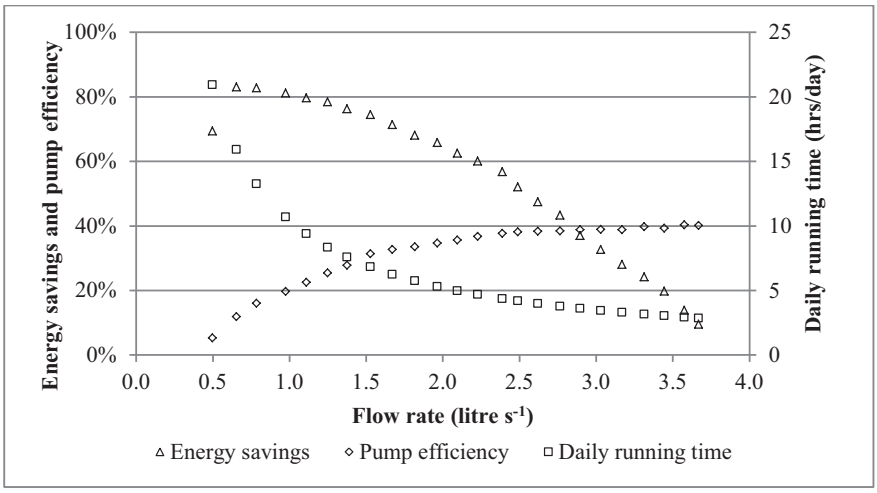

Figure 2: Pump energy savings in comparison to the BAU case, daily running time and measured pump efficiency.

Notice that even if the pump efficiency reduces by half, by operating the variable speed pump at a flow rate between 0.7 litre s^{-1} to 1 litre s^{-1}, pump energy savings of over 80% can still be obtained. This amount of pump energy savings matches the finding reported by Sproul (2005) and Cunio and Sproul (2008). However, the 80% energy savings were only contributed by the pool filtration pump, it is essential to adopt the whole system approach by taking other main system components into consideration, e.g. the pool chlorinator and the cleaner as shown in Figure 1.

Figure 3 shows the pressure drop across various system components. It can be seen that more than half of the total system pressure drop is due to the pipe and fittings. These include components that cause large pressure drop like the pool "eyeballs" (water inlet fittings), bends and tee pieces, and the three-way valve. It is also interesting to see that for flow rates below 1.7 litre s^{-1} (pump speed of less than or equal to the default low speed), the pressure drop across the oversized cartridge filter is very small and therefore can be neglected. This confirms that oversizing the pool filter could reduce the overall pressure loss and achieve a better energy efficiency (NRDC, 2013). In addition, the existing pressure pool cleaner accounts for noticeable pressure loss, which is about one-third of the total system pressure. In comparison to the filtration system without the pressure pool cleaner, this reduces the flow rate under a specific pump speed and leads to a longer daily filtration period to change over the same amount of water. Though the pump uses lower power, the daily energy is more.

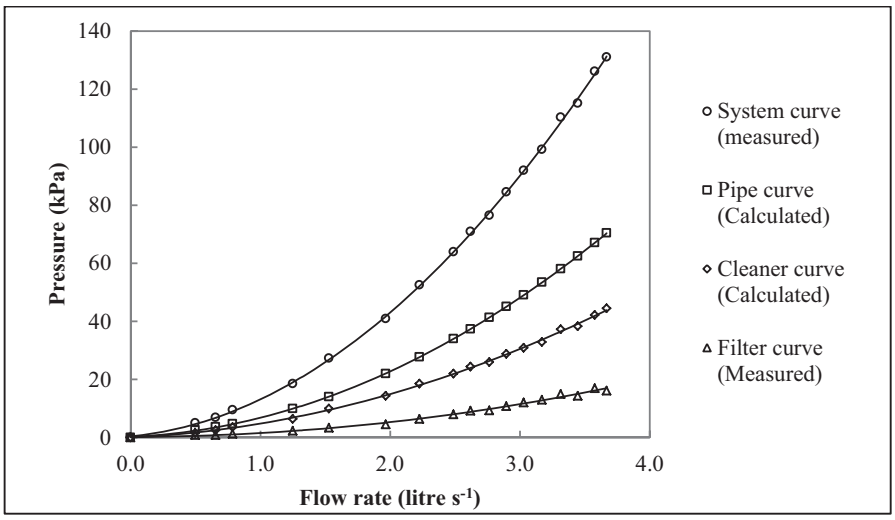

Figure 3: Pressure drop across the pool filtration system components.

By operating the pool filtration system under various scenarios, the energy savings achieved at low flow conditions can be examined along with the associated effects on key system components. Table 2 shows the experimental results obtained by operating the whole pool filtration system under 7 scenarios. Also shown is the chlorinator setting for maintaining an acceptable pool water quality as per the Australian Standard AS3633 (1989) for all scenarios. The Business as Usual (BAU) scenario is also presented, in which the variable speed pump was running at the highest speed and the chlorinator was at the highest setting. Notice that for scenario G, the pressure pool cleaner was disconnected and a robotic pool cleaner was used. Under this scenario, all flow was diverted through the pool returns by adjusting the three-way valve.

Table 2: Experimental results of the whole pool filtration system operating under different scenarios.

Scenarios	A	B	C	D	E	F (BAU)	G
Pump speed (RPM)	900	950	1150	1450	2075	2850	750
Cleaner type	Pressure cleaner						Robotic cleaner
Filtration time (hrs/day)	14 (11 for one turnover)	10	8	6	4	4 (2.8 for one turnover)	10
Schedule	5am – 7pm	7am – 5pm	8am – 4pm	9am – 3pm	10am – 2pm	10am – 2pm	7am – 5pm Robotic cleaner (11 am – 12 pm)
Flow rate (litre s^{-1})	0.97	1.03	1.30	1.73	2.58	3.67	1.07
Chlorinator working?	N	Y					
Chlorinator setting (out of 8)	N/A	3	4	5	8	8	3
Proportion of flow through pool returns	0%	0%	0%	24%	50%	65%	100%
Water chemistry	Poor	Good					
Water turbidity	3.2	0.82	0.45	0.41	0.43	0.4	0.24
Skimmer effectiveness and water clarity	Poor			Ok for small and lightly polluted pools.	Good		Perfect
Manual clean?	Y						N
Pool filtration system load (pump + chlorinator) (kW)				0.29	0.62	1.36	0.12 (before 11 am and after 13 pm) 0.19 (11 am to 13 pm)
Daily energy usage (kWh/day)				1.8	2.6	5.5	1.5

The pool chlorinator stopped working when the flow rate dropped below 1 litre s^{-1} due to insufficient flow and hydrogen accumulation. Hence under scenario A (flow rate of 0.97 litre s^{-1}), the pool water condition was heavily compromised – an unbalanced water chemical level and a turbidity of 3.2 NTU that was more than 6 times the recommended value of 0.5 shown in Table 1. This implies that 80% of savings of pump energy is actually not practical at a flow rate between 0.7 litre s^{-1} to 1 litre s^{-1}. This is due to the hydrogen accumulation in the salt water chlorinator, which is shut down under such circumstances.

In terms of the pressure pool cleaner, the operating flow rate for achieving the proper wheel rotations (28 – 32 RPM) was approximately 1.3 litre s^{-1} (Polaris, 2017). As seen from Table 2, under scenario A and B (flow rates of less than 1.3 litre s^{-1}), even if all flow was diverted into the pressure cleaner, its motion was still constricted and debris accumulated in the pool. By contrast, with proper adjustments of the existing three-way valve to meet the recommended flow range of the pressure cleaner, it was feasible to operate the pressure cleaner under scenario C to F. However for scenario C, the skimmer effects were heavily compromised since all flow was passed through the pressure cleaner. As a result, debris accumulated on the pool surface and this affected the pool clarity. The situation may get worse for heavily polluted areas.

From the whole of system performance perspective, it is more acceptable to operate the pool under scenario D (pump speed of 1450 RPM), where the three-way valve was adjusted to divert most of the flow (76%) through the pressure cleaner while still allowing some (24%) to allow the normal pool returns ("eyeballs"). This enabled the skimmer box and the pressure cleaner to be effective while running at the same time, therefore obtaining an appropriate pool condition. Notice that under scenario D, occasional manual cleaning was still needed to pick up the debris on the pool surface, especially during windy days.

After the robotic pool cleaner was retrofitted to replace the existing pressure cleaner, a significant improvement of pool cleanliness was observed (Figure 4). With the 4WD system, the robotic cleaner was able to climb on the pool steps and walls easily and perform cleaning without losing traction. In addition, since the water flow through the main pump was no longer needed to supply the pressure cleaner, all water flow was diverted via the normal pool returns and this allowed the skimmer box to operate more effectively. As a result, no manual work was required under this scenario to catch debris on pool surface nor to sweep the steps.

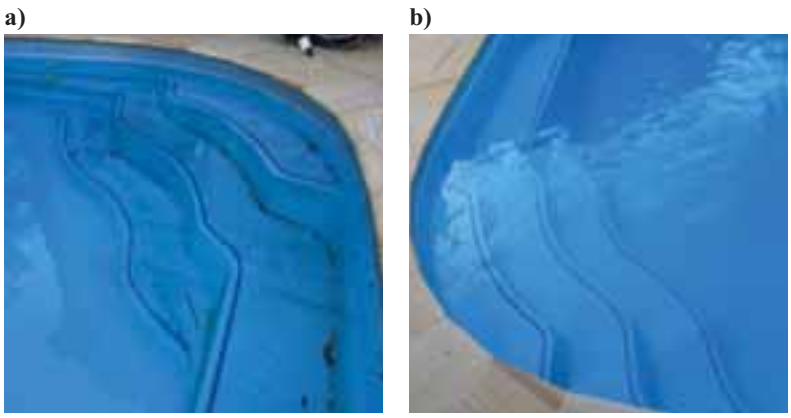

Figure 4: Conditions of pool steps when the filtration system was operating under a) BAU scenario with a pressure cleaner, b) scenario G with a robotic cleaner (both with no manual cleaning) after a 24-hour period.

Apart from the improved water clarity, it was also encouraging to see that the robotic cleaner was highly energy efficient and additional energy savings were obtained. Figure 5 shows the measured daily energy usage of the whole system operating under different scenarios. Notice that under these scenarios, all the system components were experimentally examined to work appropriately and the water quality was checked as acceptable.

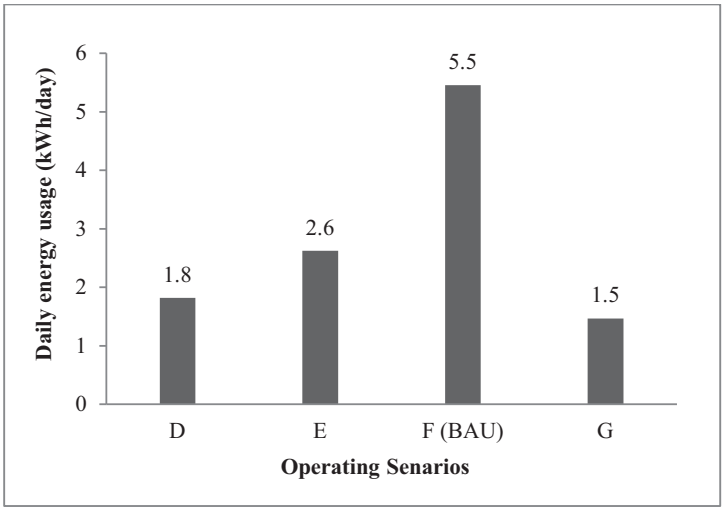

Figure 5: Measured daily energy usage of the whole pool filtration system operating under various scenarios.

For all scenarios with the pressure pool cleaner in use, the whole filtration system operating under scenario D consumed the least daily energy of 1.8 kWh/day. With a robotic cleaner in use (scenario G), the daily energy usage of the whole system was reduced to around 1.5 kWh/day. This is less than 30% of the BAU scenario (energy use of 5.5 kWh/day).

Assuming the pool filtration system is running year-round to maintain the pool conditions, the simple payback period of the whole system under the proposed energy efficient scenarios was calculated. Considering a variable speed pump (AU$1,500 including installation) as a retrofit option to the existing pool filtration system, operating the whole system at the minimum flow as required by the pressure cleaner (scenario D) has a simple payback period of approximately 3.4 years based on the electricity price of 0.323 AU$/kWh (Energy Australia, 2017). This is less than the average pool pump lifetime of approximately 7 years (DEE, 2016), making it an ideal energy saving option for pool owners. For the energy efficient scenario G where a robotic cleaner is retrofitted, it takes around 6.5 years to pay back the total capital cost of the variable speed pump and the robotic pool cleaner. This is nearly double the payback of scenario D since the robotic pool cleaner costs about the same as the variable speed pump (AU$1,550). If low-cost robotic pool cleaners were developed, operating a variable speed pump at the lowest flow that suits the chlorinator (scenario G) would obtain a lower payback and therefore become a better solution considering its superior cleaning quality as demonstrated above.

5. PV operated swimming pool filtration system

Previous results showed that operating the pool filtration system under energy efficient scenarios (D & G) achieves significant energy savings and acceptable paybacks in comparison to the BAU scenario. It is also interesting to investigate the feasibility of running the whole system from a PV array. The simulation was carried out using NREL's System Advisor Model (SAM) (NREL, 2017a) and the PV system was sized based on the BAU high-speed operation of the pool filtration system (scenario F in Table 2) in Sydney. The filtration system was assumed to operate year-round and the PV array was assumed to be connected to the grid. The key assumptions and parameters are shown in Table 3.

Table 3: Assumptions and parameters of the PV system sized based on the BAU scenario (F).

Nameplate capacity	2 kW
Array orientation	North
Array tilt	34°
PV module	Suntech Power STP250-20/Wd
Number of PV modules	8
Modules per string	8
Strings in parallel	1
Inverter	Solar Power: YS-2000TL 277V
Shading loss	0%
Soiling loss	5%
DC power loss	3%
AC loss	1%
Total module area	13 m^2

Figure 6 shows the power generated by the PV system at three different dates near to the: a) Spring (Autumn) Equinox, b) Summer Solstice, and c) Winter Solstice. Notice that two days around each date are presented to demonstrate the system performance under i) cloudy and ii) clear weather conditions. Also shown is the pool filtration system loads under BAU scenario, scenario D, and scenario G. The associated daily operating schedules and the energy loads are presented in Table 2.

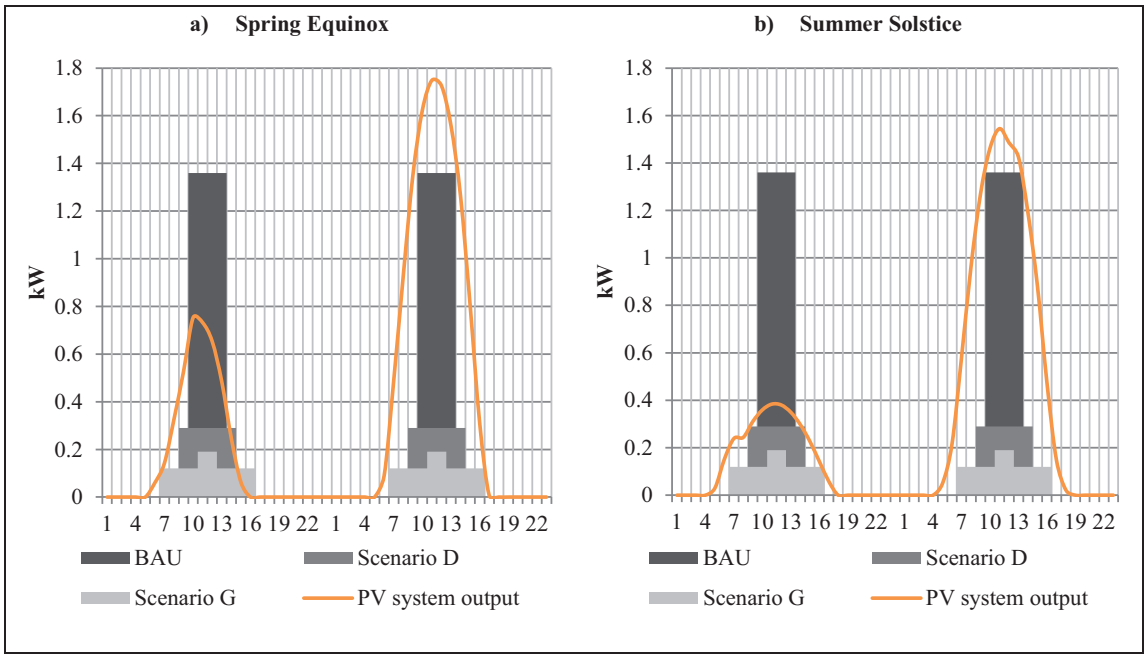

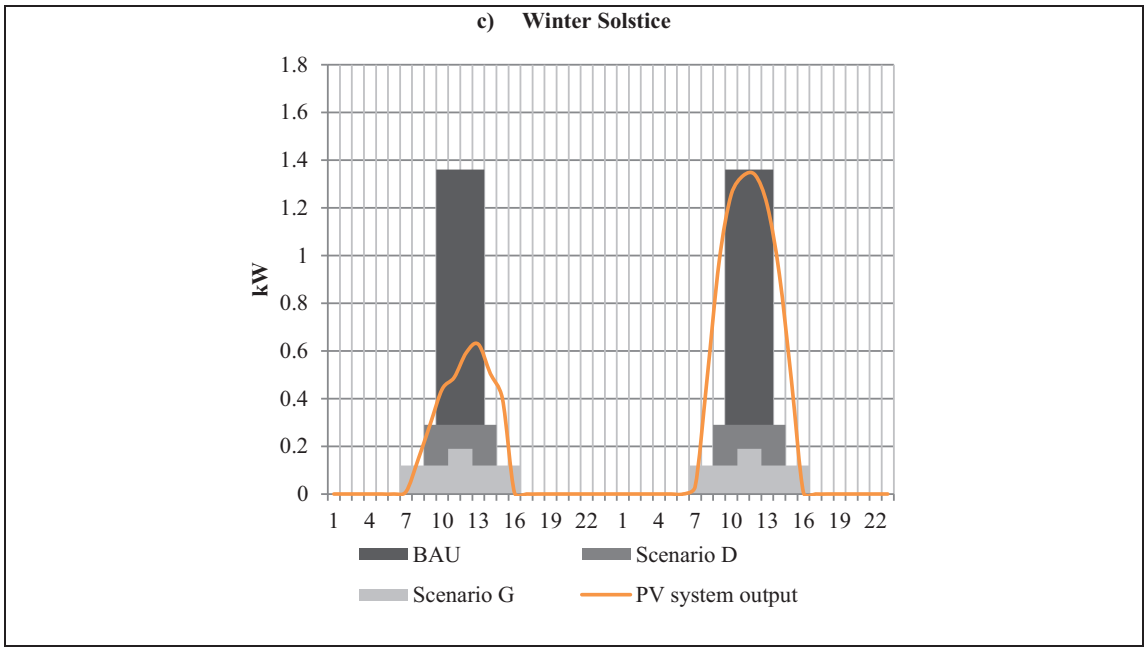

Figure 6: PV system output and pool load under scenario D, G, and BAU for different sun positions in the southern hemisphere (left: cloudy day; right: clear day).

It is clear from Figure 6 that on cloudy days, a majority of the pool load under the BAU scenario cannot be met by the PV system due to the significant decrease in the power generated. As seen from the SAM simulation results shown in Table 4, 423 kWh of electricity must be supplied annually by the grid under the BAU scenario and this leads to a PV fraction of only 45% (proportion of period where the pool filtration system load is completely covered by the PV system). By contrast, the same PV system is more likely to power the pool filtration system operating under energy efficient scenarios (D & G) even with bad weather. In both of these cases, only a small amount of electricity is sourced from the grid while the pool load can be fully supplied by the PV system for more than 90% of the total operating period (Table 4).

Table 4: SAM simulation results of the pool filtration system operating under BAU scenario (both grid and PV powered), scenario D, and scenario G.

	BAU+Grid	BAU+PV	Scenario D (PV+Variable speed pump+Pressure cleaner)	Scenario G (PV+Variable speed pump+Robotic cleaner)
PV system output (kWh/yr)	0	3017		
Excess PV output (kWh/yr)	0	1,454	2,391	2,547
Electricity from grid (kWh/yr)	1,986	423	9	19
Period with full load covered by PV (hrs/yr)	0	651	2,083	3,399
PV fraction	0	45%	95%	93%

Based on the results shown in Table 4, the net present values (NPV) and the discounted payback periods for the PV powered pool filtration systems were calculated relative to the BAU case: single speed pump, pressure cleaner, and grid-supplied system (BAU+Grid). The following parameters and assumptions were made for the calculations:

- Cost of system components:
  - Single speed pump: AU$ 775 (DEE, 2016).
  - Pressure pool cleaner: AU$ 720 (supplier).
  - Variable speed pump: AU$ 1,500 (supplier).
  - Robotic pool cleaner: AU$ 1,550 (supplier).
  - PV system: AU$ 5,868 (NREL, 2017a).
- The lifetime of both pool cleaners are assumed the same as that of a typical pool pump, therefore all need to be replaced every 7 years (DEE, 2016).
- All the PV electricity generated is assumed to be self-consumed by the household.
- The discount rate is 5% (Drury et al., 2011).
- The grid electricity price is 0.323 AU$/kWh (including GST) (Energy Australia, 2017)
- The grid electricity price is assumed to increase by 3% each year (Kai, 2017).
- The typical PV lifetime is 25 years (NREL, 2017b).

Table 5: Capital costs, net present values (NPV), and discounted payback periods (DPP) for PV powered pool filtration systems compared to BAU grid supplied system.

	BAU+Grid (Grid+Single speed pump+Pressure cleaner)	**BAU+PV** (PV+Single speed pump+Pressure cleaner)	**Scenario D** (PV+Variable speed pump+Pressure cleaner)	**Scenario G** (PV+Variable speed pump+Robotic cleaner)
Capital costs	AU$ 1,495	AU$ 7,363	AU$ 8,088	AU$ 8,918
NPV (relative to BAU+Grid)	AU$ 0	AU$ 13,288	AU$ 19,465	AU$ 17,649
DPP (years)		6.5	5.0	5.4

From Table 5, it can be seen that although the more efficient options have high upfront costs, the discounted payback periods for the two PV powered energy efficient systems (scenario D & G) are very attractive. In terms of scenario D, it has the highest NPV difference relative to the BAU grid supplied system and thus it is the most cost-effective solution. The whole system cost can be paid back in just 5 years, which is the shortest amongst three PV powered system considered. As for scenario G, due to the additional costs of the robotic pool cleaner and more electricity is purchased from the grid (Table 4), it needs around 5 months more for the whole system to pay back in comparison to scenario D. Nevertheless, it starts generating profits 1 year earlier than the BAU PV powered system (BAU+PV) and the discounted payback period is less than a quarter of the standard lifetime of a PV system. Considering that better pool quality and simpler pool maintenance can be achieved under scenario G, it is also an appropriate energy efficiency design of a residential pool filtration system.

6. Conclusion

The study presents for the first time the results of a typical residential pool filtration system operating under various scenarios. The water flow rate was varied under different scenarios and the pool chlorinator was adjusted accordingly to deliver different chlorine production rates. For lower flow rates and longer running times, the rate of chorine production was reduced in comparison to the high flow rate operation. The pool water was also tested to ensure that the key water chemistry such as free chlorine and pH levels met the Australian Standard AS3633 (1989) for all flow rates considered in this paper.

Experimental results revealed that over 80% of the pump energy could be saved by operating a variable

speed pump at flow rates of less than 1 litre s^{-1}. However, at such flow rates, the salt water chlorinator and the pressure pool cleaner were identified not working properly and this led to unsatisfactory pool water conditions. For the pool filtration system considered in this study (with the pressure pool cleaner in use), it is more appropriate and energy efficient to operate the whole system at a flow rate of 1.7 litre s^{-1} with a properly adjusted chlorinator setting (scenario D). The associated energy use is 1.8 kWh/day, which is approximately 33% of the energy use of the BAU scenario. In addition, the energy use reduces to 1.5 kWh/day with a robotic cleaner and the pool cleanliness is also substantially improved. For these energy efficient pool filtration systems, its load can be supplied by a small PV system. With no export of the PV electricity, it takes around 5 years and 5.4 years respectively for scenario D (pressure pool cleaner in use) and scenario G (robotic cleaner in use) to payback the initial investment (both refer to the discounted payback period with the replacement of pool system components taken into consideration). These discounted payback periods are less than 25% of the PV system lifetime.

Approximately 70% of the swimming pools in Australia are operated by single speed pumps (DEE, 2016). If all of these pools were retrofitted to the energy efficient scenarios considered in this study, total energy savings of more than 1000 GWh and carbon reductions of nearly 1 million tonnes could be obtained annually (DEE, 2017). Further, if all the low energy pool filtration systems were powered by PV systems where possible, total peak demand reductions of approximately 1 GW could be realized in Australia.

Except during periods of experimentation, the pool under study was operated under low flow conditions for approximately two swimming seasons. During this time water quality tests were undertaken, and readings were always in the acceptable range to maintain healthy swimming conditions as per the Australian Standard AS3633 (1989). In all circumstances, the filtration flow rates and pump run times were set so that the full volume of pool water was filtered once per day, as required by the Australian Standard AS3633 (1989). We would propose that provided this methodology was adhered to and that pool chemistry levels were maintained, the findings of this study should be generally applicable to different pool sizes, climates, and pool usage. However further studies of different pools would be useful to further verify the approach used in this paper.

7. Acknowledgements

This research is funded by the CRC for Low Carbon Living Ltd supported by the Cooperative Research Centre program, an Australian Government initiative. One of the authors (JZ) acknowledges scholarship funding provided by the Cooperative Research Centre for Low Carbon Living Ltd, as well as a scholarship from the Research Training Program of the Australian Government.

8. References

Cunio, L. N., Sproul, A. B., 2008. Optimising energy use in a domestic pool system. 3rd International Solar Energy Society Conference 2008 (ISES 2008), 46th Australian New Zealand Solar Energy Society Conference, 2008.

DEE, 2016. Consultation Regulation Impact Statement - Swimming Pool Pumps. Proposed Energy Labelling and Minimum Energy Performance Standards. Department of the Environment and Energy, Commonwealth of Australia.

DEE, 2017. National Greenhouse Accounts Factors. Department of the Environment and Energy, Commonwealth of Australia.

DOE, 2018. Installing and Operating an Efficient Swimming Pool Pump. Energy Saver, Office of Energy Efficiency & Renewable Energy, An office of U.S. Department of Energy. Available: https://www.energy.gov/energysaver/installing-and-operating-efficient-swimming-pool-pump, [Accessed April 29th 2018].

Drury, E., Denholm, P., Margolis, R., 2011. Impact of Different Economic Performance Metrics on the Perceived Value of Solar Photovoltaics. National Renewable Energy Laboratory (NREL), Golden, CO.

EES, 2008. Energy use in the Australian residential sector 1986-2020. Energy Efficient Strategies Pty Ltd (EES). Department of the Environment, Water, Heritage and the Arts, Commonwealth of Australia.

Elnakat, A., Gomez, J. D., Roberts, J., Wright, M., 2015. Big data analysis of swimming pools' impact on household electric intensity in San Antonio, Texas. International Journal of Big Data Intelligence, 2, 250-261.

Energy Australia, 2017. Energy Price Fact Sheet NSW Residential (Electricity). Available: https://secure.energyaustralia.com.au/EnergyPriceFactSheets/Docs/EPFS/PriceFactSheet_ENE390949SR.pdf, [Accessed July 10th 2017].

Fan, H., MacGill, I. F., Sproul, A. B., 2015. Statistical analysis of driving factors of residential energy demand in the greater Sydney region, Australia. Energy and Buildings, 105, 9-25.

Hameiri, Z., Spooner, E. D., Sproul, A. B., 2009. High efficiency pool filtering systems utilising variable frequency drives. Renewable Energy, 34, 450-455.

Kai, S., 2017. Energy prices—the story behind rising costs. Parliament of Australia. Available: http://www.aph.gov.au/About_Parliament/Parliamentary_Departments/Parliamentary_Library/pubs/BriefingBook44p/EnergyPrices, [Accessed September 28th 2017].

Khouzam, K. Y., Electrolysis of salt water for chlorine production by photovoltaic power. Power and Energy Society General Meeting-Conversion and Delivery of Electrical Energy in the 21st Century, 2008 IEEE, 2008. IEEE, 1-8.

NRDC, 2013. Appliance Efficiency Pre-Rulemaking on Appliance Efficiency Regulations: Docket Number 12‐AAER‐2F ‐ Residential Pool Pumps and Motors. NRDC's Response to CEC's Invitation to Participate in the Development of Appliance Energy Efficiency Measures. Natural Resources Defense Council.

NREL, 2017a. System Advisor Model, National Renewable Energy Laboratory, U.S. Department of Energy.

NREL, 2017b. Useful Life, Energy Technology Cost and Performance Data for Distributed Generation. National Renewable Energy Laboratory, U.S. Department of Energy. Available: http://www.nrel.gov/analysis/tech_footprint.html, [Accessed June 22nd 2017].

NSW Government, 2013. Swimming Pool Chemistry Testing Frequency. Environmental Health, New South Wales Government. Available: http://www.health.nsw.gov.au/environment/factsheets/Pages/swimming-pool-chemistry.aspx, [Accessed September 8th 2017].

Polaris, 2017. Polaris 360 Owner's Manual. Available: http://www.polarispool.com.au/pressure/polaris-360, [Accessed May 22nd 2017].

Springer, D., Rohe, F., 1996. Field Studies of Two-Speed and PV-Powered Pumps and Advanced Controls for Swimming Pools. ACEEE Summer Study on Energy Efficiency in Buildings "Profiting from Energy Efficiency".

Sproul, A. B., Design of PV powered, high efficiency pool pump systems. ANZSES solar energy conference, 2005.

Standards Australia, 1989. AS 3633-1989 - Private Swimming Pools - Water Quality. SAI Global.

Woolcott Research and Engagement, 2016. Pool Pumps: An Investigation of Swimming Pool Pumps in Australian and New Zealand, A research report prepared for the Department of the Environment and Energy. Commonwealth of Australia.

Zhao, J., Bilbao, J. I., Spooner, E. D., Sproul, A. B., 2018. Experimental study of a solar pool heating system under lower flow and low pump speed conditions. Renewable Energy, 119, 320-335.

Zodiac, 2017. Zodiac VX50 4WD Robotic Pool Cleaner. Available: https://www.zodiac.com.au/vx50-4wd, [Accessed March 3rd 2017].

Low to Medium Temperature Thermal Storage

Development and Testing of a Thermo-chemical Energy Store - Results of a Five year Research Project -

Sebastian Bonk, Henner Kerskes, Harald Drück
Institute of Thermodynamics and Thermal Engineering (ITW)
Research and Testing Centre for Thermal Solar Systems (TZS)
University of Stuttgart, Stuttgart (Germany)

Abstract

During the five-year research project EnErChem, a new solar heating system has been developed, aiming to supply the demand for space heating of energy efficient buildings completely based on solar thermal energy. Within the research project engineers and material scientists from universities and industry cooperated interdisciplinary. The aim was the further development of a concept of efficient long term heat storage based on improved storage materials. Composite storage materials based on the combination of hygroscopic salts and zeolite granulates have been developed. To fully use the properties of the developed storage materials a robust reactor design has been developed. Based on this design a prototype store has been built and experimentally investigated in a "hardware in the loop" (HIL) test environment. The developed design of the thermal energy store and the experimental results of the thermal energy store operation are presented in this paper.

Keywords: thermo-chemical heat storage, thermal energy store, adsorption, solar heating, high solar fraction, testing, hardware in the loop

1. Introduction

Solar assisted space heating systems are already well established on the market. These systems are usually able to cover between 30 % and 50 % of the building's total heat demand using solar radiation. To increase the solar fraction of space heating systems towards covering the complete heat demand using solar radiation as the only energy source, efficient heat storage is a crucial aspect. The main part of already well established systems is a sensible heat store based on hot water. Due to continuous heat losses during the storage period high efficient long term heat storage based on sensible heat is not possible.

For the purpose of highly effective long-term heat storage the technology of thermo-chemical heat storage has the advantage of high energy storage densities and minimal heat losses during energy storage over long time periods. Hence, adsorption heat storage, a sub category of thermo-chemical heat storage, has been under intensive research in recent years (Engel et al. 2017, Mette et al. 2014a, Kerskes et al. 2012, Cuypers et al. 2012, Zondag et al. 2012, Jähnig et al. 2006). Within the research project EnErChem, funded by the German Federal Ministry for Economic Affairs and Energy (BMWi), the development of this technology was conducted. In this project material scientists from ITC (Institute of Chemical Technology, University of Leipzig) partners from industry (Vaillant GmbH, Chemiewerk Bad Köstritz) and process engineers from TZS/ITW (Research and Testing Centre for Thermal Solar Systems, Institute of Thermodynamics and Thermal Engineering, University of Stuttgart) were working collaboratively on the development of enhanced sorption storage materials and on the development of the thermo-chemical heat store itself. Both scientific fields are crucial for the implementation of a thermo-chemical heat store with a high energy density.

Previous work on development of thermo-chemical heat stores stated the need for improvement regarding the robustness and efficiency of the charging and discharging process. Additionally enhanced sorption storage materials show a significant change of their thermal characteristics, influencing the charging and discharging process of the thermo-chemical heat store. This paper shows the improvement of the charge and discharge operation of the developed thermo-chemical heat store due to the newly developed reactor design and discusses the impact of the changed thermal characteristics of the storage material on the thermo-chemical heat store operation.

doi:10.18086/swc.2017.13.01 Available at http://proceedings.ises.org

2. Enhanced sorption storage materials

With a commercial zeolite material as a basis, the sorption properties have been improved systematically by ion exchange and the impregnation with salts (Nonnen et. al. 2016). Figure 1 shows the energy storage density related to the material volume of the commercially available zeolite 13X (Na-X, KÖSTROLITH 13XBFK, Chemiewerk Bad Köstritz), the corresponding Ca^{2+}-ion-exchanged zeolite Ca-X, as well as the salt-impregnated zeolite composite 15 $CaCl_2$/Ca-X on the basis of the ion-exchanged zeolite Ca-X.

Due to the ion-exchange, the storage density Q_V of the zeolite can be increased by approximately 15 % to about 145-180 kWh m^{-3} (desorption at temperature of T = 110 °C and partial pressure of water vapor of $p_{w:}$ <0.2 mbar; adsorption at T = 30 °C/p_w: 5-25 mbar). Furthermore a profound understanding on the interaction between zeolite and salt could be obtained from investigations on the composite material (Nonnen 2016). Experiments at partial pressure of water vapor below the deliquescence of $CaCl_2$ show, that adsorption centers of the zeolite were covered by salt. Consequently, the storage density is decreased compared to the pure zeolite material. For water vapor pressures exceeding the deliquescence humidity of $CaCl_2$, the storage density of the composite material increases. Due to the formation of a salt solution, the energy storage takes place by simultaneous water adsorption by the zeolite and water absorption by the salt solution.

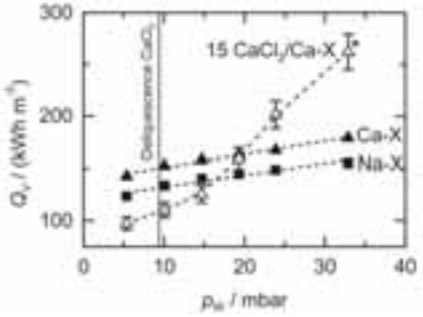

Fig. 1: Energy storage density Q_v of selected storage materials as a function of water vapor pressure p_w. Experimental conditions: desorption at 110 °C, < 0.2 mbar water vapor pressure, adsorption at 30 °C, 5-35 mbar water vapor pressure (Nonnen et al. 2016)

While the adsorption kinetic remained unchanged after the ion-exchange in the zeolite, the salt-impregnated zeolite changed its adsorption kinetic vastly. Figure 2 demonstrates this change, showing the results of an adsorption experiment in a packed bed reactor at a water vapor partial pressure of 24 mbar, an air mass flow rate of 0.3 kg h^{-1} resulting in a mass flow rate per cross section area storage material of 330 kg m^{-2} h^{-1}.

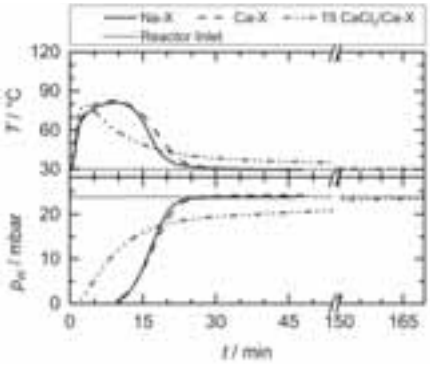

Fig.2: Comparison of a temperature T and water vapor pressure p_w at the outlet of a fixed bed reactor during adsorption for the storage materials Na-X, Ca-X and 15 $CaCl_2$/Ca-X (Nonnen et. al. 2016)

All three materials are showing a maximum temperature lift of about 50 K. While the water vapor breakthrough for the Na-X and Ca-X zeolites is begins after 9 min, it starts already after 2 min for the composite 15 CaCl2/Ca-X and extends over a time period more than 5 times as long as for the salt free zeolites. This characteristic is a challenge for the application of the material in a thermo-chemical heat store.

In addition to the steps of material development and laboratory characterization, the process for large-scale manufacturing of the composite has been developed by the industrial partner Chemiewerk Bad Köstritz. Material batches of 150 liters up to 200 liters have been produced. The produced material was inserted in the newly developed store and experimentally investigated in a “hardware in the loop“ (HIL) test facility under representative operation conditions described in section 5.

3. Development of improved storage design

The implementation of continuous charging and discharging process of the thermo-chemical energy store has been realized as an open adsorption process with material transport. The thermo-chemical energy store consists of three main parts: The storage vessel, a material conveyor system and an external reactor unit (cf. Figure 3). Charged and discharged material is stored separately in a thermally uninsulated, water vapor proof vessel. For charging and discharging the material is transported via the material conveyor system (e.g. vacuum exhauster transport system) to the external reactor unit. In the reactor unit the storage material flows gravity driven through the reactor and leaves the reactor unit at the bottom where it is collected and transported back to the appropriate part of the storage vessel.

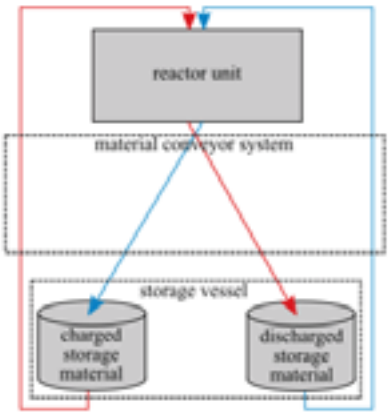

Fig. 3: Schematic view of the thermo-chemical store components

This concept has been applied by Kerskes et al. (2012) and Mette et al. (2014a). It shows a great potential for the realization of a high thermal performance thermo-chemical heat storage. The earlier work also addresses challenges regarding the robust operation and efficiency during charging and discharging of the storage material in the external reactor. A semi batch operation mode has been suggested by Kerskes et al. (2012) to implement an interruption-free operation. The experimental work on the semi batch operation has been limited to operation modes with a constant storage material mass flow rate. An introduction of a process controlled storage material mass flow rate based on the temperature measured in the reactor has been identified as the most promising improvement for a stable reactor operation. The implications resulting from a temperature based storage material mass flow control in a single stage reactor as used in previous work and further challenges regarding the efficiency of the charging and discharging process led to the development of an improved reactor design based on a two stage reactor.

Improvement of the reaction behaviour through reactor splitting

During charging and discharging the reactor is operated in a semi batch operation mode (see figure 3 left). Small portions of storage material are extracted discontinuously at the bottom of the reactor. Fresh storage material falls from a buffer vessel at the top of the reactor into the reactor bed. The air streams through the reactor bed in cross flow.

To ensure that the storage material always leaves the reactor completely charged/discharged it has to stay in the reactor bed until the adsorption process is completed everywhere in the material batch. In practice this state is hardly achievable. Due to grain size deviations, zones with unevenly distributed air flow are present. The increased friction between the storage material and the reactor walls creates zones with lower material flow. These influences lead to different timings of water vapor breakthrough in different parts of the reactor. Therefore a buffer zone at the bottom of the reactor is necessary where the charging/discharging of all parts of the material is completed. Furthermore the buffer zone provides the possibility to transfer the sensible heat of the storage material to the air stream during discharging.

The impact of introducing a buffer zone in a single stage reactor shall be explained with an adsorption example. The example sequence is based on a dynamic simulation of the adsorption process. The used storage material is the zeolite Na-X. The storage material enters the reactor with a temperature $T_{s\text{-}in}$ = 20 °C and a water loading of X_s = 84 g/kg. The reactor is crossed with a humid air stream with a mass flow rate of $\dot{m}_f$ = 300 kg/h. The humid air enters the reactor with a temperature of $T_{f\text{-}in}$ = 30 °C and the specific humidity of $x_{f\text{-}in}$ = 6 g/kg corresponding to water vapor pressure of approximately 9.4 mbar. At the beginning of the adsorption sequence the reactor is completely filled with fresh storage material. The reactor control initiates an exchange of one storage material portion (1.0 liter) if the trigger

temperature T_{ME} is lower than $T_{f\text{-}in}$ + 1.8 K. Figure 3 shows a scheme of the single stage reactor as well as the time series for specific humidity, temperatures and the binary signal for storage material exchange (ME) in the reactor.

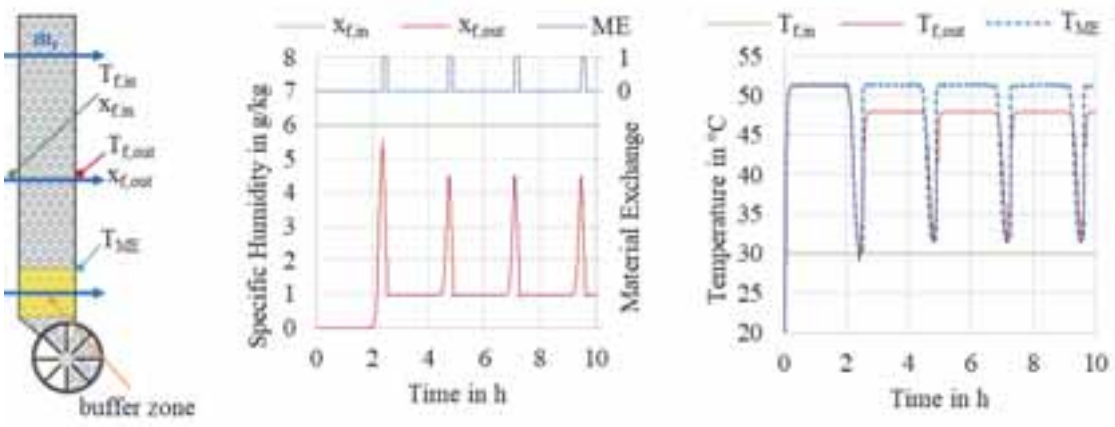

Fig. 3: Simulation results of an adsorption sequence in a single stage reactor

The process illustrated in figure 3 shows that in a single stage reactor the introduced buffer zone has multiple disadvantages. Since the reactor depletes as a whole, all storage material portions above the buffer zone are exchanged after each other. This leads to a short drop of the outlet temperature $T_{f,out}$. Since the buffer zone is not filled with fresh material the specific humidity of the air stream is not adsorbed in the buffer zone. Therefore after the initial period the specific humidity in the mixed air stream behind the reactor has a value of at least 1.0 g/kg. Since there is no temperature lift in the buffer zone the temperature in the mixed air stream behind the reactor ($T_{f,out} \approx 48$ °C) is also lower compared to the temperature during the initial period of 51 °C.

To overcome the disadvantages of the single stage reactor the reactor has been split up into two stages: a main reactor and a pre-reactor (see figure 4 left). In this two stage reactor the air first flows through the pre-reactor, is redirected at the outlet of the pre-reactor and then enters the main reactor. The storage material enters the main reactor first and is moved to the pre-reactor after leaving the main reactor. The introduced buffer zone is now placed in the bottom part of the pre-reactor. Analog to the single stage reactor the storage material portions will be exchanged based on the trigger temperature at the top of the buffer zone.

For the comparison of the single stage reactor with the double stage reactor the same adsorption sequence has been applied. The sum of the reactor bed thickness of the double stage reactor equals the reactor bed thickness of the single stage reactor. The cross area of each, the main reactor and pre-reactor is equal to the cross area of the single stage reactor. Therefore the pressure drop over the whole reactor remains similar. Figure 4 shows the calculation results. In the double stage reactor the specific humidity and the temperature at the outlet of the pre-reactor are specified in addition to the quantities at the inlet and outlet of the whole reactor.

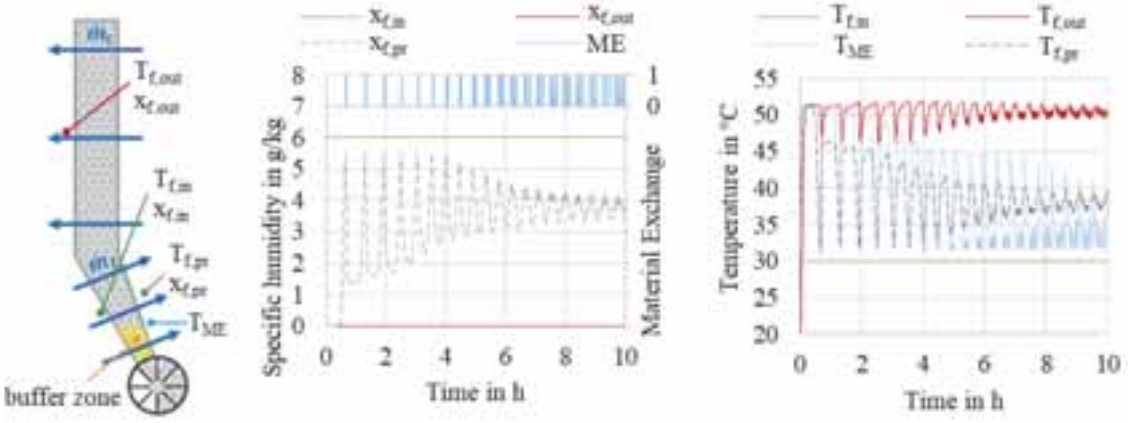

Fig. 4: Simulation results of an adsorption sequence in a double stage reactor

Due to the lower reactor bed thickness of the pre-reactor the specific humidity at the outlet of the pre-reactor rises and the temperature falls already after a period of about 0.5 h. The adsorption in the pre-reactor is completed and the first storage material portion is exchanged. Since the main reactor is still filled with fresh material this has no impact

on the specific humidity at the outlet of the reactor. The exchange of the storage material portion causes a short reduction of the outlet temperature. The entering storage material in the upper part of the reactor has a temperature of 20 °C and has to be heated up to the process temperature. During the whole sequence the water vapor is completely adsorbed in the two stage reactor and the mixed air stream temperature at the reactor outlet remains nearly at the maximum of 51 °C. In this way the introduced buffer zone does not have a negative impact on the reactor performance.

4. Experimental investigation of the improved storage design

For demonstration and performance testing of thermo-chemical energy storage device with the newly developed reactor unit with a two stage reactor, a “hardware-in-the-loop” (HIL) test facility has been built. The HIL test facility consists of an air loop, a heat load emulation loop and an electrical power source. With the air loop a humid air stream with a defined specific humidity in the range from 3 to 16 g/kg, a temperature in the range of 15 to 30 °C and a mass flow rate up to 200 kg/h can be provided to the reactor of thermo-chemical energy store. In the heat load emulation loop thermal oil is circulated with a mass flow rate between 100 and 250 kg/h. For tempering of the oil an electrically heated thermostat is used for heating with a power up to 4 kW and for cooling with a power up to 2.5 kW in a temperature range from 20 to 200 °C.

In the HIL test facility the thermo-chemical storage has been operated under real application conditions. Adsorption and desorption experiments have been carried out in application scale. All ingoing and outgoing energy fluxes were measured based on the measurement of temperatures, mass flow rates and humidities, which allowed an energetic balancing under dynamic operating conditions.

Developed reactor unit with a two stage reactor

The newly developed reactor unit consists of four key components: the two stage reactor (consisting of main and pre reactor), air heat exchanger, charge heat exchanger (or electrical heating rod) and discharge heat exchanger. All key components are placed in a common thermal insulation (cf. Figure 5). During operation ambient air enters the reactor unit through the air heat exchanger and is preheated by the exiting air stream. Thus the air heat exchanger decouples the reactor operation temperature level from the ambient temperature. Afterwards the air flows through the charge heat exchanger, which is only active during charging, and enters the reactor through the pre-reactor. The air steam is deflected in a duct behind the pre-reactor and led through the main reactor. Finally it flows through the discharge heat exchanger, only active during the discharge operation, which is placed directly after the main reactor.

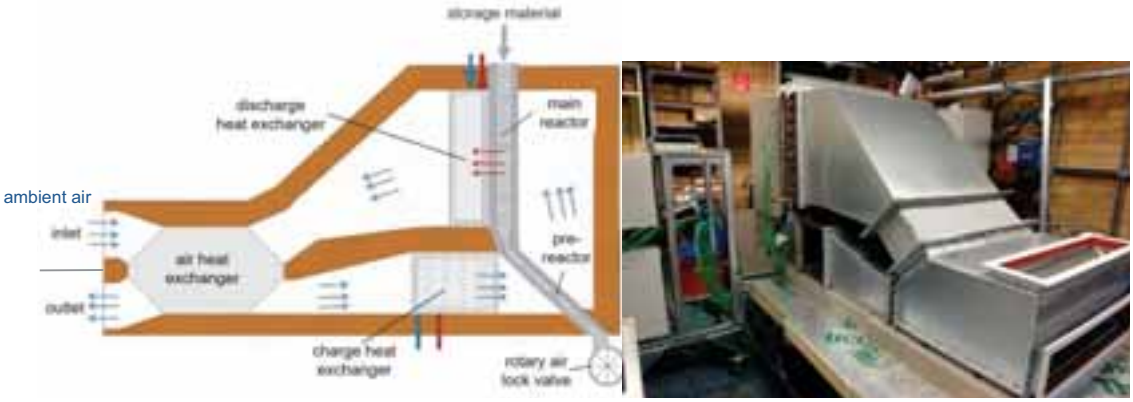

Fig. 5: Sketch of the reactor unit with a two stage reactor (left) and the reactor unit during construction integrated in the “hard ware in the loop” (HIL) test environment (right)

The reactor accommodates approximately 24 liters of storage material. The pre-reactor has a cross area of 0.245 m^2 and a bed depth of 0.02 m. The main reactor has a cross area of 0.49 m^2 and a bed depth of 0.05 m. A buffer vessel at the top of the reactor unit contains additionally 90 liters of storage material. The storage material enters the reactor unit from the buffer vessel and is conveyed through the reactor driven by gravity. The dosing of the storage material is handled by a customized rotary air lock valve. The rotary air lock valve is operated discontinuously triggered depending on the temperature behind the pre-reactor. The volume of each rotary air lock valve chamber is 0.7 liters, which corresponds to the storage material portions which are extracted at once.

In the experimental setup a vacuum exhaust transport system has been added at the outlet of the rotary air lock valve.

This system transports the charged/discharged storage material into a storage vessel, where it is stored water vapor tight until the next test sequence. As storage vessels for the charged and discharged storage material two metal bins have been used. The transport from the storage vessel to the buffer vessel is done manually before the beginning of a test sequence.

The newly developed reactor unit has been operated in a fully automated mode under realistic conditions in approximately 50 adsorption and desorption experiments, each with a duration between 4 and 20 hours. During discharging the set value for the reactor unit is the flow temperature of the heat load emulation loop. The reactor control adapts the air mass flow rate through the reactor to match the reactor adsorption output to the heat demand of the discharge heat exchanger. The mass flow rate and the return temperature of the heat load emulation loop were applied as boundary conditions. During charging the temperature at the inlet of the pre-reactor is the set value. To attain the required pre-reactor inlet temperature in this operation mode the air mass flow rate is adapted to the available charging power and the outlet temperature of the main reactor.

5. Results of HIL experiments

The following questions have been experimentally investigated in the HIL test facility:

- Is the reactor unit able to provide the expected thermal power?
- Is the reactor unit operating robust when dynamic heating demand is applied during discharging?
- Can the theoretically available energy storage density of the storage material be fully used in the reactor unit?
- Is efficient operation with the commercially available Na-X zeolite and the newly developed composite material 15$CaCl_2$/Ca-X in the reactor unit possible?

Reactor unit operation with different storage materials

A series of adsorption and desorption experiments have been successfully conducted with the commercially available zeolite Na-X and with the newly developed composite material 15 CaCl2/Ca-X.

In the results of the desorption experiments shown in figure 6 the storage material is desorbed at a temperature of 180 °C. The air mass flow rate through the reactor unit is controlled to provide a defined fluid temperature measured at the reactor inlet of $T_{f\text{-}in}$ = 192 °C. A portion of the storage material is released, when the fluid temperature measured at the outlet of the pre-reactor bed $T_{f\text{-}pr}$ reaches 180 °C. Figure 6 shows the temperatures and the specific humidity during desorption of the zeolite Na-X and during desorption of the composite material 15 $CaCl_2$/Ca-X.

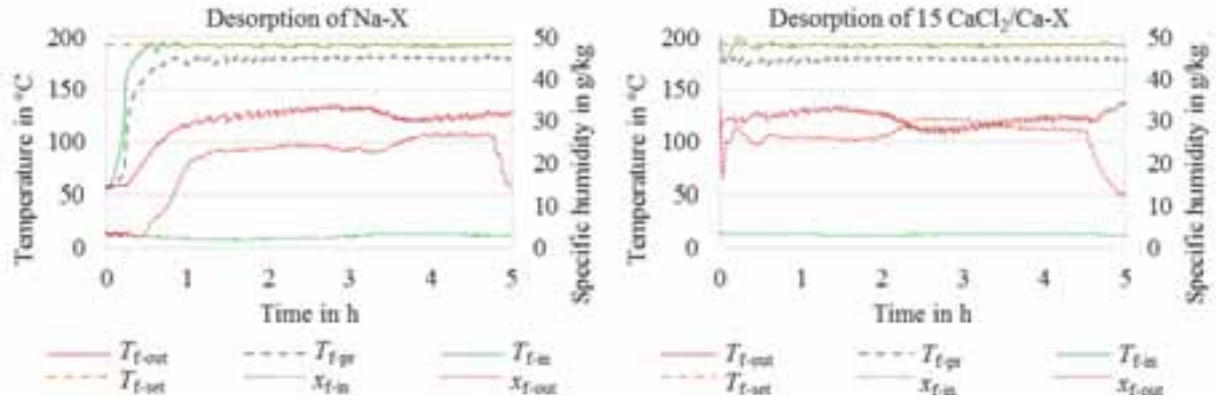

Fig. 6: Mean temperatures in the reactor unit as well as specific humidity and temperatures at the inlet and outlet of the reactor unit during a stationary desorption of Na-X zeolite (left) and the composite 15CaCl2/Ca-X (right)

As shown in figure 6 a stable desorption process continues over a period of about 5 hours for both storage materials. In both sequences similar fluid output conditions are reached over the major part of the shown period. The fluid temperatures at the reactor outlet ($T_{f\text{-}out}$) are in both cases in the range from 110 °C to 140 °C. The reactor outlet specific humidity is in both experiments in a similar range from 22 g/kg to 30 g/kg. After a starting period of approximately 1 hour (not included in the shown desorption of 15 $CaCl_2$/Ca-X) a stationary operation of the reactor is reached and continues until the buffer vessel at the top of the reactor runs out of storage material.

In the adsorption experiments shown in figure 7 the storage material has been discharged during an adsorption process with an air mass flow rate through the reactor unit of approximately 110 kg/h. The mean thermal output

power of the reactor unit during the adsorption process was 680 W. Due to control errors the specific humidity deviates slightly in the two shown experiments resulting.

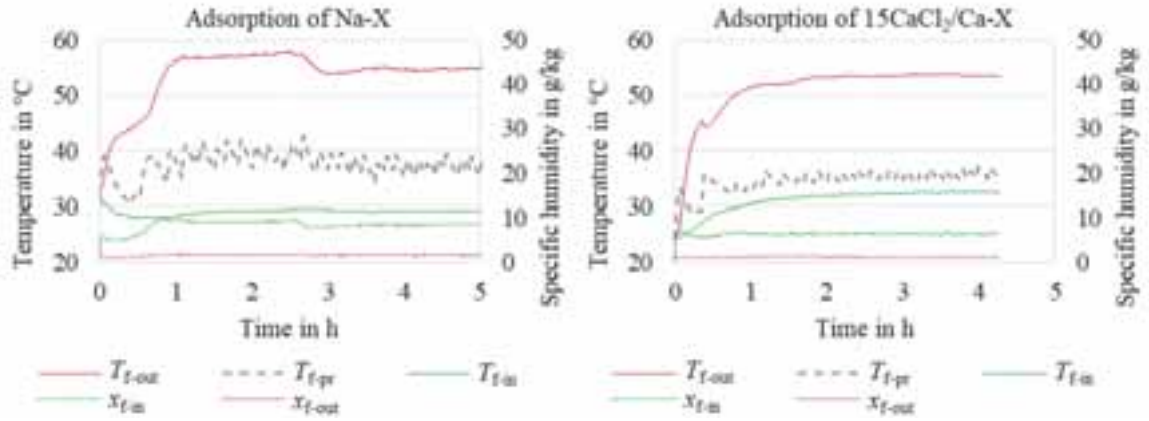

Fig. 7: Mean temperatures in the reactor unit as well as specific humidity and temperatures at the inlet and outlet of the reactor unit during a stationary adsorption of Na-X zeolite (left) and the composite 15CaCl2/Ca-X (right)

As shown in figure 7 in both experiments a stationary outlet temperature of approximately 54 °C has been reached after 3 hours of operation. After a period of approximately 20 to 30 minutes the material exchange starts in both cases. The process is stationary after approximately 1 hour. The temperature $T_{f\text{-}pr}$ at the outlet of the pre-reactor is slightly lower during the adsorption of the 15 $CaCl_2$/Ca-X compared to the adsorption of Na-X. This behavior is consistent with the results measured in a fixed bed reactor, which have been shown in figure 2. Although the zeolite-salt composite 15 CaCl2/Ca-X has a slower reaction kinetic, the double stage reactor design compensates this limitation and allows a stationary charging and discharging process.

Measured reactor unit output power

To determine if the reactor unit is able to provide the expected heat flow rate, multiple adsorption experiments have been conducted. In this series of experiments the specific humidity has been varied in the range from 5.5 g/kg to 13.5 g/kg. The heat load demand has been varied in the range from 500 W to 1800 W. As reference the theoretical heat flow rate is used which is calculated based on the measured water uptake from the air stream and the standard adsorption enthalpy of the Na-X zeolite of h_{ads} = 3456 kJ/kg determined by Mette et al. (2014b). The reactor unit output power is determined based on measured inlet and outlet temperatures and mass flow rate of the heat load emulation loop. Figure 8 shows the comparison between the theoretical heat flow rate and the measured reactor unit output power.

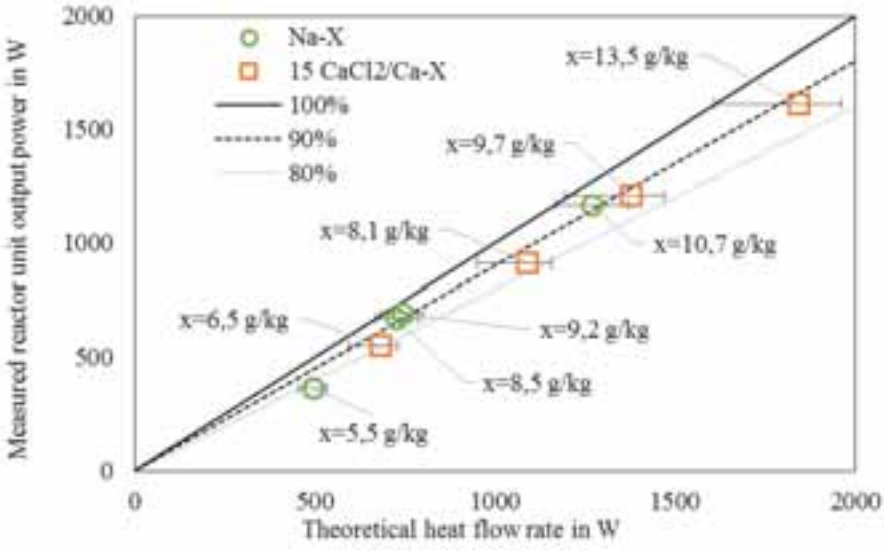

Fig. 8: Comparison of the measured reactor unit output power to the theoretical heat flow rate or power respectively obtainable for Na-X zeolite and the composite 15CaCl2/Ca-X at given boundary conditions

As shown in figure 8 in the most experiments the measured reactor unit output for the zeolite Na-X has reached

approximately 90 % of the theoretical heat flow rate. Operation conditions with lower humidity and operation with the zeolite salt composite 15 $CaCl_2$/Ca-X leads to a slight degradation of the efficiency. In this cases the measured reactor unit output is about 80 % of the theoretical heat flow rate.

Robustness of reactor unit operation

To ensure a robust operation of the reactor unit adsorption experiments with varying heat demand have been conducted. The heat demand variation has been applied through variation of the mass flow rate in the heat load emulation loop. Small deviations of the specific humidity in the air stream entering the reactor constitute an additional disturbance representing a dynamic environment. Figure 9 shows the results of an adsorption experiment.

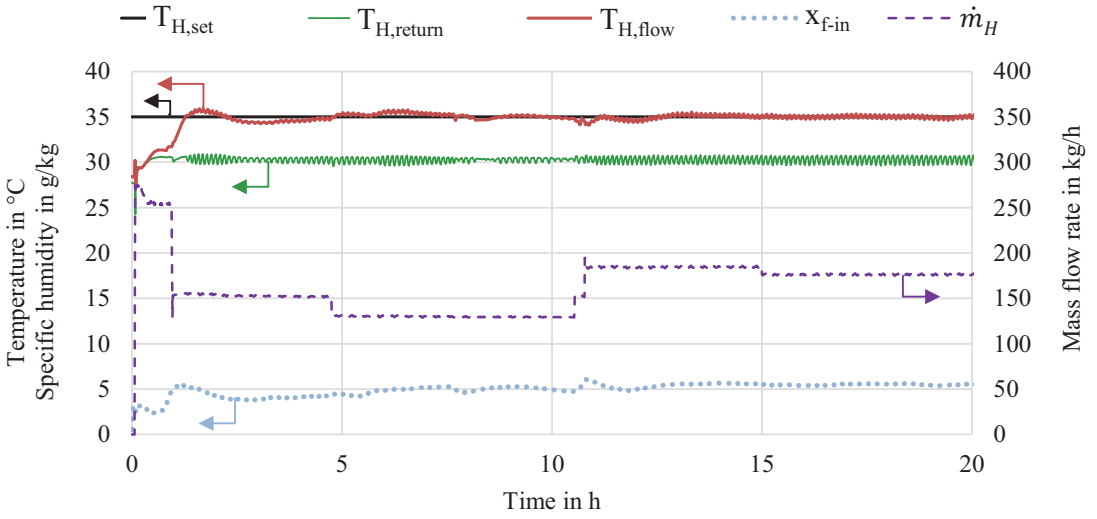

Fig. 9: Temperatures and the mass flow rate in the heating loop of the reactor unit and specific humidity at the inlet of the reactor unit during adsorption of Na-X zeolite with variations of the heat demand

The results show that the reactor unit managed to provide the required flow temperature of $T_{H\text{-}set}$ = 35 °C with only small deviations. The reactor unit control adapted the mass flow rate of the air through the reactor adequately and with it the required thermal power of the reactor. Thus both deviations due to the variation of the humidity and the variation of the heat demand were compensated.

Degree of storage material capacity utilization

The introduction of a pre-reactor with a buffer zone at the bottom theoretically allows to utilize the full storage material capacity. Therefore experiments have been conducted to investigate the degree of storage capacity utilization.

During adsorption and desorption operation of the reactor unit in the HIL test facility material samples of approximately 10 g have been extracted for analyses from the storage vessel. The samples have been taken from the storage vessel after finishing the experiment from volume portions of 10 l each. The water loading of the samples has been determined using a halogen moisture analyzer from the manufacturer Mettler Toledo. All samples were desorbed in the moisture analyzer to reference conditions (T_{ref} = 180 °C, $x_{f\text{-}ref}$ = 7.2 g/kg), where the change of the water loading between the state after the experiment and the reference conditions has been measured. From the change in the water loading the water loading at the end of the experiment has been calculated.

The theoretical storage capacity of the storage material is being utilized when the material reaches the equilibrium water loading at the given conditions. The equilibrium water loading has been calculated from the isotherms (Mette et al. 2014b) of the zeolite Na-X for each sample. The equilibrium was calculated according to the conditions ($T_{f\text{-}pr}$, $x_{f\text{-}in}$) in the lower part of the pre-reactor during the residence time of the material sample in the pre reactor. Figure 8 shows the results of the comparison of water loading X_s measured in samples and the calculated equilibrium water loading during an exemplary adsorption and desorption sequence. The samples are displayed over the normalized volume fraction. The normalized volume fraction is the total storage material volume used in the sequence divided by the reactor volume.

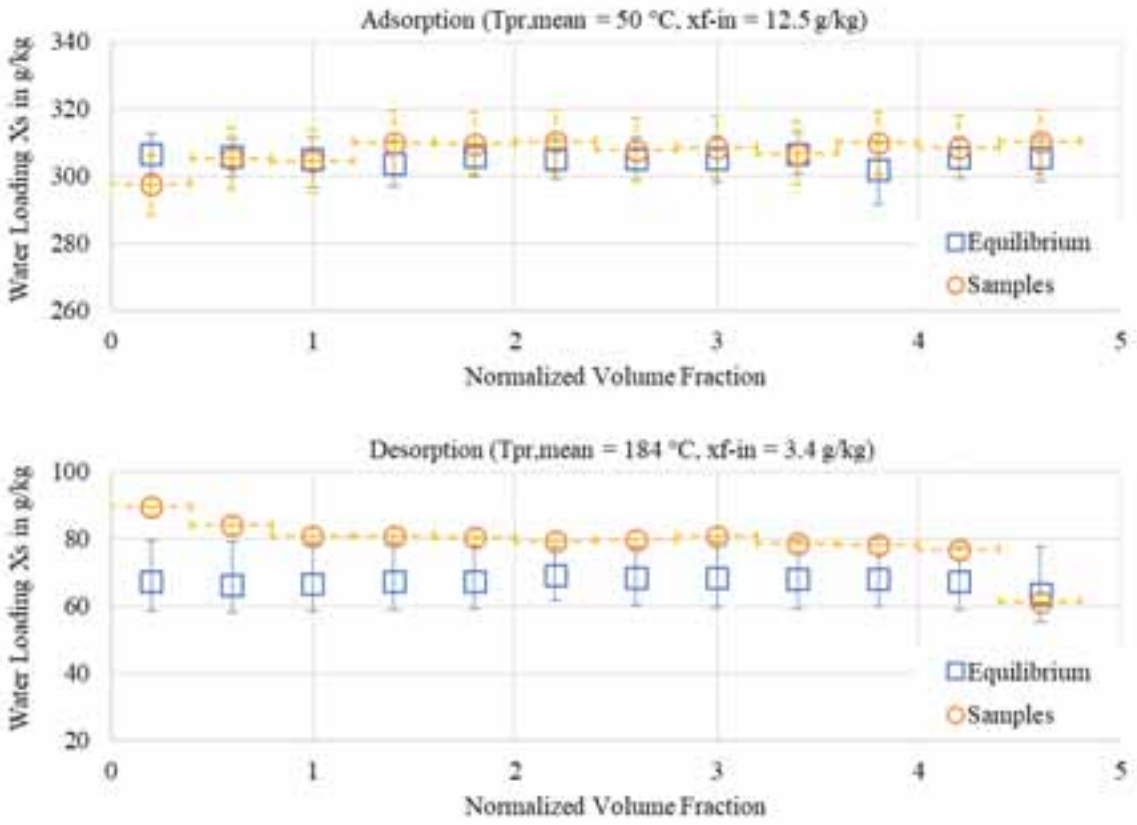

Fig. 1: Measured water loading of Na-X after an adsorption and desorption sequence in the reactor unit compared with the water loading of Na-X reached in equilibrium

The results for the adsorption experiment show that the measured and calculated equilibrium water loading matches well within the error margin of the experiment. In the shown desorption sequence the measured water loading is approximately 10 g/kg higher than the calculated equilibrium water loading. The measured water loading lift between the shown desorption and adsorption is 228 g/kg. Compared to the maximum water loading lift of 238 g/kg this shows a 96 % degree of storage capacity utilization. This experiment shows further that the charging and discharging of the storage material is robust over multiple filling volumes of the reactor. Only the first probe shows lowered water loading compared to the average values.

The shown experiment has been conducted for a combination of more than 10 adsorption and desorption sequences. The degree of storage capacity utilization in all experiments is in the range from 92 to 98 %.

6. Conclusions

Zeolites and zeolite salt composites are promising energy storage materials applicable for seasonal heat storage. Both storage materials have a high energy storage density but show different characteristics regarding the adsorption kinetic. Therefore a new reactor unit design has been developed. In this design the reactor is split into two stages: the main reactor and the pre-reactor. This two stage reactor allows an efficient and robust charging and discharging of the storage material under dynamic operation conditions.

For experimental investigation of the newly developed reactor unit a HIL test facility has been built up. The experiments carried out in the HIL test facility are an important step from laboratory to demonstration scale. The developed thermo-chemical store has been operated in the HIL test facility in a fully automated mode under realistic conditions. In stationary adsorption and desorption experiments using the pure zeolite Na-X and the zeolite salt composite 15 $CaCl_2$/Ca-X the expected operation behavior of the reactor unit has been confirmed. During discharging the rector unit shows an efficient operation: More than 80 % of the theoretical rector unit output power has been obtained for all investigated settings of humidity. Furthermore it has been shown, that approximately 95 % of the theoretical value of energy storage density provided by the storage material could be utilized with the newly developed two stage reactor design.

7. References

Cuypers R. MERITS: More Effective use of Renewables Including compact seasonal Thermal energy Storage. In: Innostock, editor. Proceedings of Innostock 2012, 12th International Conference on Energy Storage; 2012.

Engel, G.; Asenbeck, S.; Köll, R.; Kerskes, H.; Wagner W.; van Helden, W.: Simulation of a seasonal, solar-driven sorption storage heating system. Journal of Energy Storage Volume 13, October 2017, Pages 40-47, https://doi.org/10.1016/j.est.2017.06.001, 2017.

Jähnig D, Wagner W, Isaksson C. Thermo-chemical storage for solar space heating in a single-family house. In: EcoStock, International Conference on Thermal Energy Storage, editors. 10th International Conference on Thermal Energy Storage, EcoStock 2006. [Pomona, NJ]; 2006.

Nonnen, T.; Beckert, S.; Gleichmann, K.; Brandt, A.; Unger, B.; Kerskes, H.; Mette, B.; Bonk, S.; Badenhop, T. Salg, F., Glaeser, R. (2016): A Thermochemical Long-Term Heat Storage System Based on a Salt/Zeolite Composite. In: Chem. Eng. Technol. 39 (12), S. 2427–2434. DOI: 10.1002/ceat.201600301.

Nonnen, T.: Salz/Zeolith-Komposite für die Sorptionswärmespeicherung (engl.: Salt/Zeolite Composites for Sorption Heat Storage). Dissertation, Leipzig, 2016

Mette, B.; Kerskes, H.; Drück, H.: Experimental and Numerical Investigations of Different Reactor Concepts for Thermochemical Energy Storage. Energy Procedia, Volume 57 (2014), Pages 2380–2389, 2014

Mette, B.; Kerskes, H.; Drück, H.: Müller-Steinhagen, H.: Experimental and numerical investigations on the water vapor adsorption isotherms and kinetics of binderless zeolite 13X, International Journal of Heat and Mass Transfer, Volume 71, April 2014, Pages 555–561, ISSN 0017-9310, http://dx.doi.org/10.1016, 2014

Kerskes, H.; Mette, B.; Bertsch, F.; Asenbeck, S.; Drück, H.: Chemical energy storage using reversible solid/gas-reactions (CWS) – results of the research project, Energy Procedia, Volume 30, 2012, Pages 294–304, ISSN 1876-6102, http://dx.doi.org/10.1016/j.egypro.2012.11.035, 2012

Zondag H, Kikkert B, Smeding S, Boer R de, Bakker M. Prototype thermochemical heat storage with open reactor system. In: Innostock, editor. Proceedings of Innostock 2012, 12th International Conference on Energy Storage; 2012.

Acknowledgment

The activities described in this paper were supported by the German Federal Ministry for Economic Affairs and Energy (BMWi) based on a decision of the German Bundestag by Projektträger Jülich (PtJ) under grant numbers 03ESP402A (research project „EnErChem“: Development and testing of a long term sorption heat store for domestic heating). The authors gratefully acknowledge this support and carry the full responsibility for the content of this paper.

Performance Evaluation of a Demonstration System with PCM for Seasonal Heat Storage: Charge with Evacuated Tubular Collectors

Gerald Englmair[1], Simon Furbo[1], Weiqiang Kong[1], Mark Dannemand[1], Jianhua Fan[1] and Zhifeng Wang[2]

[1]Department of Civil Engineering, Technical University of Denmark
[2]Institute of Electrical Engineering, Chinese Academy of Sciences

Abstract

A seasonal heat storage with phase change material (PCM) for a solar space heating and domestic hot water combisystem was tested in automated operation during charge with solar collectors. A water tank was operating as buffer heat storage. Based on measurements during a representative day with sunshine, the storage system performance was evaluated regarding charge with solar heat. It shows the system behavior during typical operation resulting from the control strategy. Heat transfer rates from the solar collector array (22.4 m^2 aperture area) to the heat stores reached a peak of 19 kW, when PCM was melted. 30 kWh of heat was transferred to the 750 l water volume as it heated up. Afterwards 46 kWh of heat was transferred to the segmented PCM storage. In total 56 % of the total irradiation on the tilted collector plane was utilized to heat the storage units. During PCM charge heat transfer fluid temperatures were increasing with the state of charge. This is in contrast to maximization of solar yield. However, the energy conversion efficiency (65 %) of the collector array was satisfying. By considering pump electricity consumption, an overall performance ratio of 30.8 was obtained.

Keywords: Solar combisystem; Seasonal heat storage; Demonstrator; Performance evaluation; Measurement.

1. Introduction

Sodium acetate trihydrate (SAT) can be utilized for heat storage in a solar combisystem for space heating and domestic hot water supply. It can be melted in sunny periods with solar heat, the PCM can cool down to the ambient temperature without solidifying and remain stable in supercooled state. The solidification can be initiated and the heat of fusion released later when heat is in demand. This concept was successfully applied to flat prototype heat storage units (Dannemand et al., 2016). SAT has a melting point of 58°C and a latent heat of fusion of 264 kJ/kg (Meisingset & Grønvold, 1984). The heat content of SAT composites was experimentally investigated by Kong et al. (2016).

A seasonal PCM heat storage demonstration system (Fig. 1) was designed based on calculations with a TRNSYS model (Dannemand et al., 2015). Four 150 l heat storage units have been assembled to a latent heat storage stack. They were tested for their ability to supercool in a stable way after being charged with a fluctuating heat source (Englmair et al., 2016). The system was built at the solar heating test facility of the Technical University of Denmark. Heat from a solar collector array, 7 panels of evacuated tubular collectors with an aperture area of 22.4 m^2, was used to charge a 750 l water tank (buffer storage). The excess yield of the collector array was utilized to heat up the latent heat storage. This additional storage volume aims to preserve heat for periods with shortage of solar energy supply.

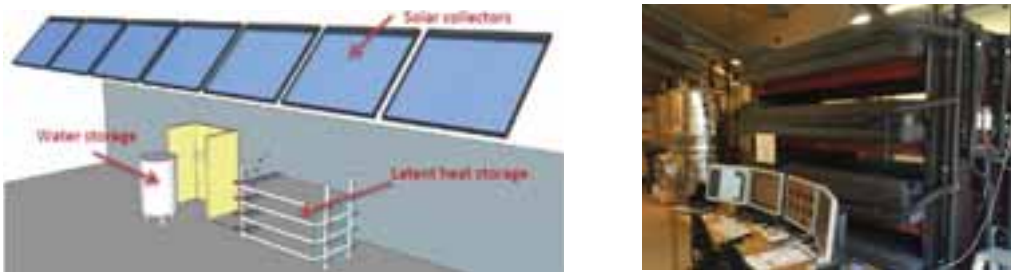

Fig. 1: Overall system design: Schematic drawing (left); Photography of water tank and PCM heat storage (right).

doi:10.18086/swc.2017.13.02 Available at http://proceedings.ises.org

Using evacuated tubular collectors as a heat source for seasonal PCM heat storage is a novel approach. The heat transfer to the buffer storage and the PCM units are of special interest, since the solar source is fluctuating and therefore an optimized control strategy has to be found. Therefore data from a sunny day (9th of September 2015) where the system was operating with the designed control strategy was analyzed. The performance evaluation was based on measured heat transfer rates and monitoring of pump electricity consumption.

Nomenclature:

Symbol	**Quantity**	**Unit**
G	global irradiance	[W/m^2]
H	global irradiation	[Wh/m^2]
P	electrical power	[W]
PR	performance ratio (daily)	[-]
$\dot{Q}$	heat transfer rate	[W]
Q	heat	[Wh]
T	temperature	[°C]
W	electrical work	[Wh]
η	efficiency	[-]

Subscript	**Quantity**
aperture	aperture area (collector field)
charge	buffer charge and PCM charge loops
charge buffer	buffer charge loop
charge PCM	PCM charge loop
coll	solar collector
coll loop	solar collector loop
P	pump
total	tilted surface (collector field)

2. Method

2.1 Hydraulic configuration

The solar collector array was formed with 7 panels of Thermomax HP 450 (heat pipe evacuated tubular solar collectors) from Kingspan Renewables. Each panel consisted of 30 tubes. The 7 panels were connected in 2 parallel circuits. One circuit with 4 panels in series and one with 3 panels in series as illustrated in Fig 2. Equal fluid flow rate in each collector panel was realized by means of regulation valves. A CM3 pyranometer from Klipp & Zonen was used for G_{total} measurements in between the two parallel collector circuits (location marked with the green star). A copper-constantan thermocouple (TT-type) was used for measurement of the collector outlet temperature (location marked with the red star). Because of its location in Denmark (latitude: 55.89), an inclination angle of 45° was chosen. The azimuth angle of the collector array was 12° towards east.

Fig. 2: Collector setup (schematic drawing).

Inside the building heat was transferred from the collector loop via a plate heat exchanger, operated in counter flow. At the secondary side, 2-way control valves were set in order to realize either buffer storage or

PCM charge. TYFOCOR LS (propylene-glycol and water mixture) was used as solar collector fluid and water was filled in the secondary side. In Fig. 3 operation schemes for the operation modes are drawn. Active pumps and open valves are marked in green; inactive pumps and closed valves in red.

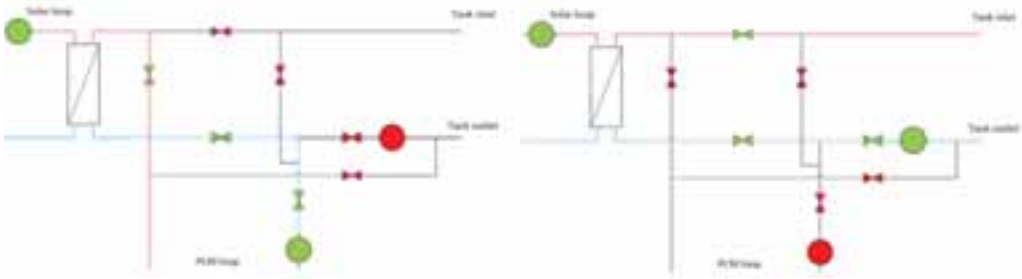

Fig. 3: Operation scheme with marked active components: PCM charge (left); buffer storage charge (right).

The forward pipe from the heat exchanger to the collector array was 21.5 m, the return pipe was 14 m. 8 meters of the forward and of the return pipe was inside of the building of the demonstration system and the rest was outside the building. Forward and return pipe in between the heat exchanger and the water tank were both 4.5 m long. From the heat exchanger to the PCM heat storage units the forward pipe reached 7-9 m and the return pipe reached 10-12 m, depending on the number of PCM units in charge. 20 mm (outer diameter) copper pipes in the collector loop and ¾" carbon steel pipes in the secondary loops were installed. Pipework, valves and the heat exchanger were insulated with 19 mm of elastomeric foam.

All hydraulic loops were equipped with magnetic induction flow meters (class 2) in the return flow, copper-constantan thermocouples (TT-type) for temperature measurements, thermopiles (TT-type) for temperature difference measurements and motor valves. Regarding to the norm (EN 1434), the maximum measurement error of class 2 flow sensors was 2.5 % in the operation range. This accuracy was proved by tests for all flow meters installed. Electricity consumption was detected by an installed wattmeter for each pump.

2.2 Operation sequence

The collector loop pump was activated when the temperature difference between the collector outlet temperature and the temperature at the bottom of the water storage exceeded 10 K (lower threshold value). The water tank was charged until a temperature of 55°C was reached in the middle of the water tank. This value was chosen as the upper threshold value for the control. Buffer storage charge stopped 5 minutes after either the lower or upper threshold value was met.

When the upper threshold for the buffer storage was met, collector loop circulation stopped until a collector outlet temperature of 70°C was measured. Then the PCM charge mode was activated. Melting of SAT composites required higher temperature, therefore previous buffer storage charge was beneficial. In order to achieve the full melting of the PCM, which is required for stable supercooling, inlet temperatures to the PCM units of up to 93 °C and high water flow rates were applied.

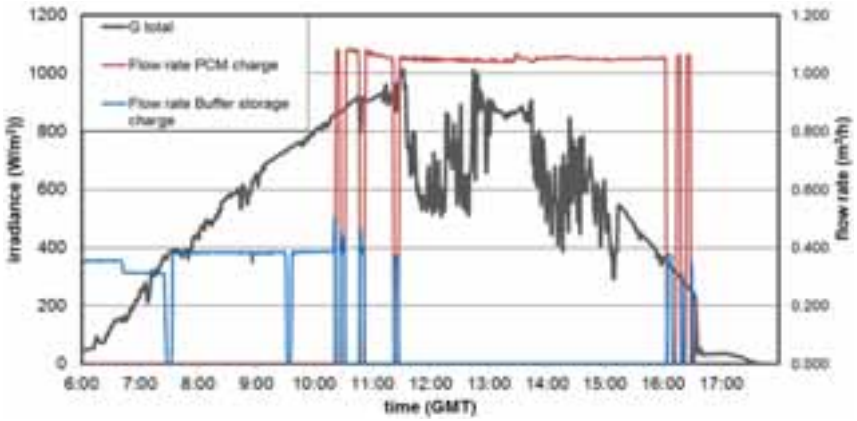

Fig. 4: Development of irradiance on the collector array and water flow rates applied.

Fig. 4 shows the flow rates applied on the secondary side of the plate heat exchanger. At 7:30 h the operation mode was switched from manual to automated control. The buffer storage was charged with a flow rate of 6.3 l/min (blue curve). Although at 10:15 h the buffer storage was already heated up, some periods of additional demand around noon and in the evening were detected by the control system. The collector array was shaded from 16:20 h on. As a consequence, the operation stopped with a short delay. A water flow rate of about 16.5 l/min (red curve) was applied when the PCM storage was charged. Due to the limited heat exchange capacity rates of a single PCM unit (Englmair et al., 2016) the units were charged in parallel.

2.3 Performance evaluation

The evaluation was based on heat transfer rates in the charging loops. In Fig. 5 the thermopiles (TP) mark the location where the heat transfer rates were evaluated. Also inlet-and outlet temperature measurements were located there. Beside temperature difference, measured flow rates, temperature dependent densities and specific heat capacities (resulting from temperature measurements) of the heat transfer fluids (solar collector fluid and water) were used for calculation.

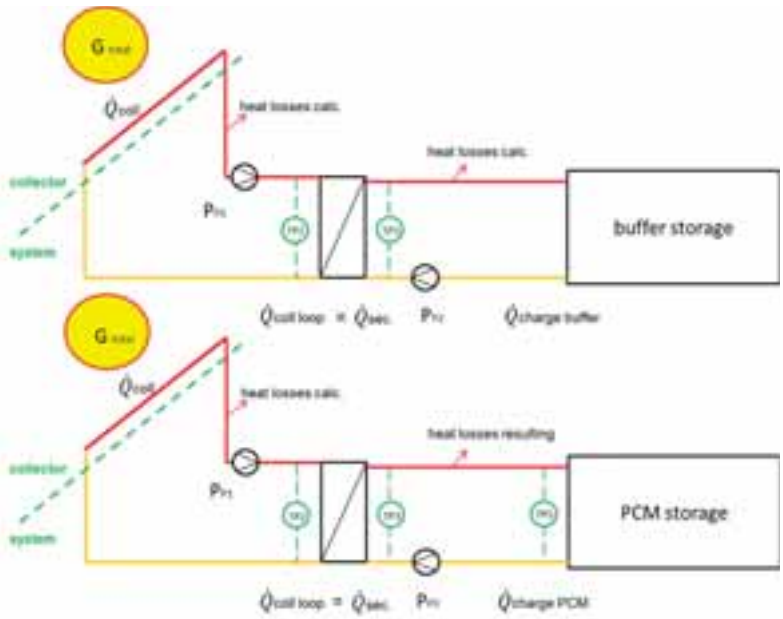

Fig. 5: Schematic evaluation model.

Pipe heat losses between the solar collector and the heat exchanger and between the heat exchanger and the buffer storage are included in the analyses. The heat loss in the solar collector loop was determined by calculations based on length, diameter and insulation thickness for the pipes and on measured temperatures. The heat loss in the PCM charge loop was resulting from the difference of heat transfer rates between TP3 and TP5. Thermal collector power was resulting from adding pipe heat losses to the calculated heat transfer rates at the plate heat exchanger.

Transferred heat was resulting from integration of heat transfer rates over time, considering the duration of each charging period.

As reference for evaluation, the solar potential was defined by the daily solar irradiation ($H_{aperture\ total}$) on the aperture area of the tilted collector surface. The course of the solar irradiance (G_{total}) is drawn in Fig. 4 (grey curve). The overall energy conversion efficiency was defined by the ratio of heat transferred to the sink (Q_{charge}) and the solar potential (formula no. 3).

$$\eta_{collector} = \frac{Q_{coll}}{H_{aperture\ total}} \quad (1)$$

$$\eta_{system} = \frac{Q_{charge}}{Q_{coll}} \quad (2)$$

$$\eta_{overall} = \frac{Q_{charge}}{H_{aperture\ total}} \quad (3)$$

Energy conversion efficiency at the collector (formula no. 1) and heat transfer efficiency in the system (formula no. 2) were based on the system border to the collector array, defined in Fig. 5. This approach enabled a closer look on the dependency of heat losses to the water temperatures during the two charging modes.

In terms of electrical power, control plays a minor role in solar heating systems. Therefore the consumption of pumps (marked in Fig. 5) was evaluated with the following performance ratios:

$$PR_{charge\ buffer} = \frac{Q_{charge\ buffer}}{W_{P1\ charge\ buffer} + W_{P2}} \quad (4)$$

$$PR_{charge\ PCM} = \frac{Q_{charge\ PCM}}{W_{P1\ charge\ PCM} + W_{P3}} \quad (5)$$

$$PR_{charge\ overall} = \frac{Q_{charge\ buffer} + Q_{charge\ PCM}}{W_{P1} + W_{P2} + W_{P3}} \quad (6)$$

As reference, their electrical work was logged during charging periods (indicated by the flow rates in Fig. 4). The collector loop pump (P1) was in operation during all periods, while P2 operated during buffer storage charge and P3 during PCM storage charge.

3. Results and discussion

On the selected day, the system was only in charging operation. Heat transfer rates, the daily energy balance as well as efficiency values were evaluated.

3.1 Heat transfer rates

In Fig. 6 the development of heat transfer rates of the collector loop (black marks), of the buffer storage charge loop (blue marks) as well as of the PCM charge loop (red marks) are drawn over time. The collector loop power followed G_{total} (grey curve in Fig. 4). During PCM charge peak values of up to 19 kW were reached when the mode has been activated (10:15 h), as well as during cascading of the number of PCM units (13:30 h – 14:00 h) in the charging loop.

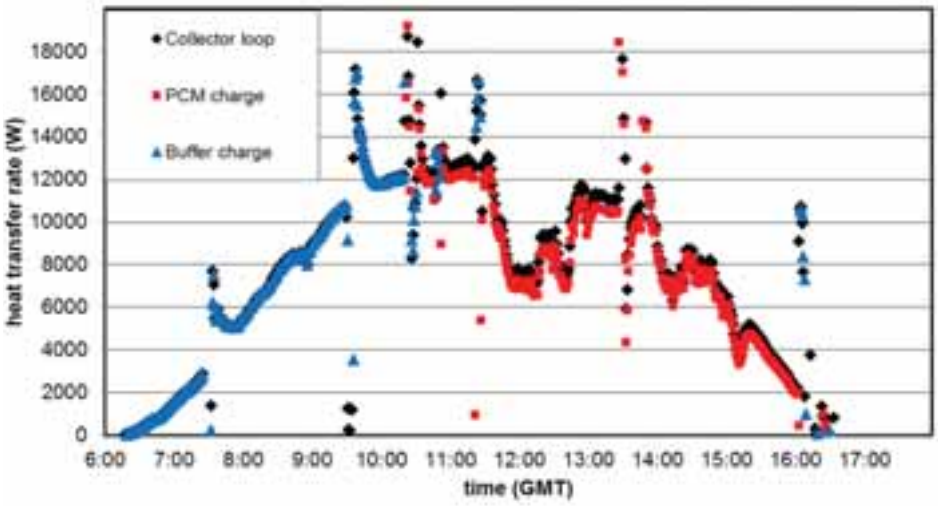

Fig. 6: Heat transfer rates during the course of the day.

Because the buffer storage is situated close to the plate heat exchanger, the collector loop power almost equaled to the heat transferred to the water tank. Buffer storage charge was interrupted two times before noon. Significant heat losses occurred in the PCM charge loop. The total duration of heat transfer was 10 hours.

The data were noisy through to the setting of the control system. Cascading of PCM units during PCM storage charge is necessary to match the fluctuating collector power with the limited heat transfer capacity of

PCM units. In contrast, intermediate buffer storage charge during periods of PCM storage charge only happened due to small internal temperature changes in the water tank. This cooled down the collector array and system components (collector loop, plate heat exchanger, pipework). Therefore a temperature hysteresis for full buffer charge (end criterion: 60°C, start criterion: 50°C) was implemented in the control after the present initial tests.

3.2 Daily energy balance

The energy balance was analyzed by integration of the heat transfer rates over time. Fig. 7 shows the solar potential (black curve) compared to the transferred heat during the course of the day. The difference between the collector loop energy (red curve) and the calculated collector output (red dotted curve) was a result of the pipe heat losses in the collector loop. During the total period of operation, the solar potential was 135 kWh. From this potential 79 kWh of energy was supplied by the collector loop to the heat storage system. 76 kWh (53 % of the solar potential) of heat was stored. Most heat was transferred to the PCM modules (46 kWh) in the period from 10:30 h to 16:00 h. This means an average net heat transfer rate of 9 kW. To the buffer tank (green curve) the highest share of energy (25 kWh) was transferred until 10:00 h, while the rest was transferred later, in four short periods.

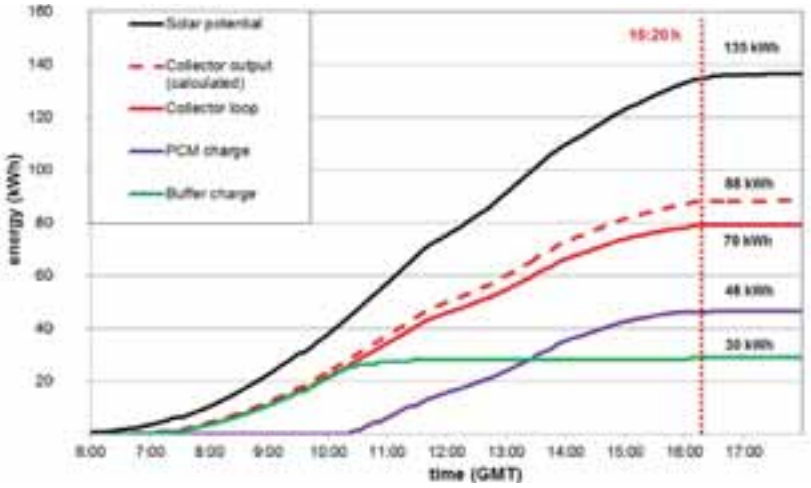

Fig. 7: Development of heat transfer during the course of the day.

During buffer storage charge only minor heat losses occurred in the system (collector loop and charging loop), while significant heat losses (8 kWh) occurred during the charge of the PCM units with high solar collector fluid and water temperatures.

The buffer storage charge means an average temperature increase of 35K in the water tank (750 l), which was considered to be sufficiently high to cover the heat demand of an energy efficient single family house throughout the following day. Full charge of a single PCM unit (from solid state at ambient temperature) required 27.4 kWh (Englmair et al., 2016). However, since up to 3 PCM units were charged in parallel, 2 consecutive sunny days are assumed to be necessary to ensure full PCM unit heat up to a uniform temperature of 80°C. Only in this way the supercooling ability of charged PCM units can be enabled.

3.3 Energy efficiency

Based on the daily energy balance, average energy efficiency factors are obtained:

$$\eta_{collector} = 0.65; \qquad \eta_{system} = 0.86; \qquad \eta_{overall} = 0.56$$

As a result of energy conversion of the collector, 65 % of the solar potential was transferred in form of heat to the system. The system efficiency was 86 % on the reference day. 10 % of heat in the collector loop and 4 % of heat in the secondary loop were dissipated via heat losses to the ambience. So, in total 56 % of the solar potential was transferred to the heat sink.

Further information can be seen from the course of energy efficiencies in context to the collector outlet temperature in Fig. 8. The energy conversion efficiency at the collector (grey scattered curve) was low until

9:00 h. During this period and all components of the collector loop as well as the heat transfer fluids were heating up. Peak values occurred due to changes of operation modes. After 9:00 h $\eta_{collector}$ reached a level of above 65 %. Because of rising heat transfer fluid temperatures (indicated by the collector outlet temperature – red curve) $\eta_{collector}$ fell throughout the day. Shifts between buffer and PCM charge modes (Fig. 4) caused collector outlet temperature jumps. During PCM charge the heat transfer fluid temperatures were coupled to the state of PCM unit charge.

After 15:00 G_{total} and the efficiency values fell down dramatically and the heat transfer fluid temperatures remained high. When the operation stopped, heat remained in the hot heat transfer loops and in the solar collector.

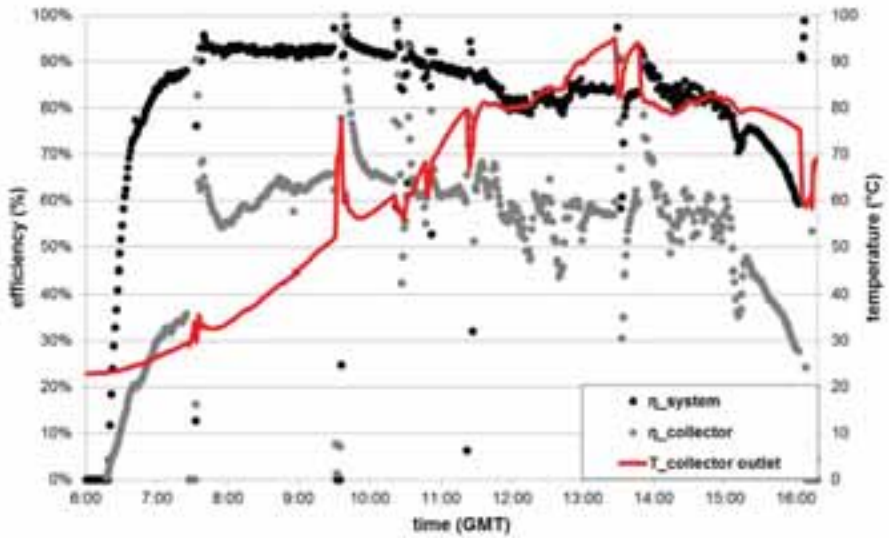

Fig. 8: Development of system efficiency, energy conversion efficiency at the collector and collector outlet temperature during the course of the day.

The system efficiency (black scattered curve) showed similar behavior. After the pipework was heated up (until 7:30 h), η_{system} remained above 90 % during buffer storage charge. During PCM charge, when heat transfer fluid temperatures raised and a longer pipework was used, η_{system} was in the range of 80-90 % for long time. Lower values were observed around noon, when G_{total} was fluctuating at lower level than before noon. Decreasing system efficiency after 15:00 h was a result of lower heat transfer rates at high fluid temperatures. This means that during that period a high share of heat was dissipated to the ambience.

Longer periods of buffer storage charge (lower heat transfer fluid temperatures) at the end of the day (when G_{total} is decreasing) would maximize the daily energy yield. Increased η_{system} and $\eta_{collector}$ values would be resulting. However, PCM unit charge is beneficial after the buffer heat storage is sufficiently heated for domestic heating applications.

3.4 Pump efficiency

The secondary loop pump (P2) was powered with 8 W to achieve the set water flow rate during buffer charge. To match the heat transfer capacity rate of the solar collector fluid at the heat exchanger to the water, a collector loop pump power of 70 W was required. During PCM charge the pumps were set at 90% of their maximum operation speed to enable high fluid flow rates. The collector loop pump power reached 390 W and the secondary loop pump (P3) was operating at 120 W. The resulting electricity consumptions are given in Tab. 1:

	W_{P1} (Wh)	W_{P2} (Wh)	W_{P3} (Wh)
Buffer charge	167	22	none
PCM charge	1716	none	548
Overall charge	1883	22	548

Tab. 1: Pump electricity consumption during charging periods.

The electrical power consumption of pumps during PCM charge (about 5 hours of operation) was 2.5 kWh, while for buffer storage charge only 0.2 kWh were consumed. Based on the previous definitions, the following performance ratios were resulting:

$PR_{charge\ buffer}$ = 154; $PR_{charge\ PCM}$ = 19.1; $PR_{charge\ overall}$ = 30.8

The highest performance ratio was occurring during buffer storage charge (154), while the performance ratio during PCM module charge was about 8 times lower. The overall charge performance ratio was 30.8. It was found that the electricity consumption for PCM charge can be lowered by application of different pump types. Also, a reduction of flow rates during PCM charge could lower the electricity consumption. However, this would lower the heat transfer in the PCM units.

4. Conclusions

A demonstration system on seasonal heat storage, utilizing the principle of stable supercooling of SAT, was tested for its functionality during charge on a representative sunny day. System control enabled interplay between solar collectors, buffer heat storage and PCM heat storage:

- The applied collector array enabled sufficiently high heat transfer for both, buffer storage and PCM charge. The heat transfer reached peak values of more then 12 kW in both operation modes. When modes were changed or interrupted, heat transfer rates of up to 19 kW occurred.
- During PCM charge the HTF temperatures were increasing with the state of PCM charge. This is in contrast to maximisation of solar yield. Since the number of PCM units in operation was variable, no restrictions for heat transfer from the collector array were observed.
- Regarding to the required high collector outlet temperatures (up to 95°C) during PCM charge, the energy conversion efficiency of the collector array was satisfying. 65 % of the solar potential was converted into heat and transferred to the system.
- 76 kWh (86 %) of available heat was stored. During buffer storage charge only minor pipe heat losses occurred. 46 kWh of heat were charged to the PCM storage when 8 kWh (10% of available heat) were dissipated via hydraulic components to the ambience.
- The PCM charge performance ratio (19.1) and therefore also the overall performance ratio (30.8) were quite low, although standby consumptions of pumps and of the control system were not considered in their calculation.

The resulting operation sequence proved functional system behavior. Significant heat losses due to a long pipework, frequent mode-switches and rather high pump electricity consumption during PCM charge were identified as areas for potential improvements.

5. Acknowledgements

This research was funded by the European Commission (Grant Agreement N_295568) as part of the Seventh Framework Programme through the former COMTES project. The work was also supported by the PhD program of the Sino Danish Center for Education and Research (SDC). We thank our partners from Nilan A/S and the Graz University of Technology for sharing knowledge and discussions as well as the research technicians Troels V. Kristensen and Claus Aagaard for their practical support.

6. References

Dannemand, M., Dragsted, J., Fan, J., Johansen, J. B., Kong, W., & Furbo, S., 2016. Experimental investigations on prototype heat storage units utilizing stable supercooling of sodium acetate trihydrate mixtures. Applied Energy, 169, 72–80.

Dannemand, M., Schultz, J. M., Johansen, J. B., & Furbo, S., 2015. Long term thermal energy storage with stable supercooled sodium acetate trihydrate. Applied Thermal Engineering, 91, 671–678.

Englmair, G., Dannemand, M., Johansen, J. B., Kong, W., Dragsted, J., Furbo, S., & Fan, J., 2016. Testing of PCM Heat Storage Modules with Solar Collectors as Heat Source. Energy Procedia, 91, 138–144.

Kong, W., Dannemand, M., Johansen, J. B., Fan, J., Dragsted, J., Englmair, G., & Furbo, S., 2016. Experimental investigations on heat content of supercooled sodium acetate trihydrate by a simple heat loss method. Solar Energy, 139, 249–257.

Meisingset, K. K., & Grønvold, F., 1984. Thermodynamic properties and phase transitions of salt hydrates between 270 and 400 K III. CH3CO2Na·3H2O, CH3CO2Li·2H2O, and (CH3CO2)2Mg·4H2O. The Journal of Chemical Thermodynamics, 16(6), 523–536.

EXPERIMENTAL AND THEORETIC INVESTIGATIONS OF THERMAL BEHAVIOR OF A SEASONAL WATER PIT HEAT STORAGE

Jianhua Fan[1], Junpeng Huang[1], Angelos Chatzidiakos[1], Simon Furbo[1]

[1] Department of Civil Engineering, Technical University of Denmark, Kgs. Lyngby, Denmark

Abstract

Seasonal heat storages are considered essential for district heating systems because they offer flexibility for the system to integrate different fluctuating renewable energy sources. Water pit thermal storages (PTES) have been successfully implemented in solar district heating plants in Denmark. Thermal behavior of a 75,000 m^3 water pit heat storage in Marstal solar heating plant was investigated experimentally and numerically. Temperatures at different levels of the water pit storage and temperatures at different depths of the ground around the storage were monitored and analyzed. A simulation model of the water pit storage is built to investigate development of temperatures in and around the storage. The calculated temperatures are compared to the monitored temperatures with an aim to validate the simulation model. Thermal stratification in the water pit heat storage and its interaction with the ground are elucidated by calculations using the validated CFD model.

Keywords: Solar heating plants, Seasonal water pit thermal storages (PTES), Experimental investigations, Computational fluid dynamics (CFD), Thermal stratification

1. Introduction

Heat storages are considered essential for a district heating system with a large share of renewable energies due to the flexibility they offer to accommodate the fluctuating nature of the renewable energy sources such as wind and solar energy. The most promising heat storage solutions are tank storage systems, water pit thermal storage (PTES), aquifer thermal energy storage (ATES), borehole storage (BTES) and water-gravel pit storage (Pavlov and Olesen 2012, Heller 2000). Moreover, cases of latent heat storage using phase change materials are also investigated but there are still some barriers to overcome before applying them to large scale (Sharma etc 2009). Large scale water pit thermal energy storages are viable solutions both economically and environmentally since these stores are simple in construction and relatively cheap. Larger storage volumes lead to increased efficiency in practice, since the heat losses do not increase with the volume proportionally. With a large water pit heat storage, solar fraction of a district heating system could be significantly increased to for example 50% of the heat demand of the district heating network. PTES have been successfully used in district heating plants in Denmark, for example, in Marstal (75,000 m^3), Dronningland (60,000 m^3), Vojens (200,000 m^3) and Gram (120,000 m^3).

Thermal behaviors of water pits as seasonal heat storages have been investigated both experimentally and theoretically. Kielsgaard Hansen et al. (1983) investigated first a small 500 m^3 pilot water pit heat storage at the campus of the Technical University of Denmark. Later, Kübler et al. (1997) presented investigations on a pilot heat storage with about 600 m^3 volume built in Rottweil. The pilot heat storage was applied as short term storage in connection with a combined heat and power (CHP) plant. The storage container was made of concrete with a stainless steel liner and mineral wool as insulation. The aim of the paper was to demonstrate the feasibility of the technology and to gain practical experience for the construction of larger stores. A gravel /water storage pit was built in Steinfurt, Germany (Pfeil M. 2000). The ecological compatibility of the used materials in the storage was proved. Another focus of the paper was analysis of the cost-reduction potential of the PTES (Pfeil M. 2000). Thermal behavior of a model PTES was experimentally investigated in a test rig and numerically investigated by means of CFD simulations (Change and Wu, 2017). The investigated PTES was a scaled down model that facilitates measurements in a test rig. Thermal behaviors of PTES in real operation with a volume as large as 70,000 m^3 was not found.

Marstal's PTES was developed, based on the experience from the small demonstration water pits, and funded under the SUNSTORE 4 project, as part of the "EU flag projects" (Kate 2013). Its aim is to increase the solar fraction of the plant up to 55% of the thermal energy production, focusing on sustainability, increased efficiency and low costs.

doi:10.18086/swc.2017.13.03 Available at http://proceedings.ises.org

Marstal's 75,000 m^3 PTES was commissioned in 2012 and it has a capacity of 6.96 GWh according to PlanEnrgi (Jensen 2014). The operating temperatures vary depending on the season and the depth of the water layer, however the pond is designed to operate in a range of 10-90 °C.

The aim of the paper is to investigate thermal behavior of the large water pit heat storage in Marstal solar heating plant. Temperatures at different levels of the water pit storage and temperatures at different depths of the ground around of the storage were monitored and analyzed. A simulation model of the water pit storage is built to investigate development of temperatures in and around the storage. The calculated temperatures are compared to the monitored temperatures with an aim to validate the simulation model. Thermal behavior of the water pit heat storage and its interaction with the ground are elucidated.

2. Measurements of the PTES in Marstal

Located in a small island Ærø in the southern part of Denmark, the 75,000 m^3 water pit heat storage has an outer dimension of 98 m × 98 m excluding the dam around the storage, see Fig. 1. The depth of water in the storage is 16 m. An illustration of the design of the water pit thermal energy storage is given in Fig. 2. After commissioning of the PTES in 2012, detailed measurement have been carried out in in the period 2014-2016 to evaluate thermal performances of the storage. The following monitoring equipment is installed on the water pit heat storage:

‹ Temperature and volume flow sensors in inlet/outlet pipes
‹ Temperature sensors inside the water storage at different levels
‹ Temperature sensors in the ground at different depths
‹ A heat flux sensor in the floating top cover

Fig. 1: Bird view of the water pit heat storage in Marstal Solar heating plant

The sensors in the inlet/outlet pipes are located at the end of the transmission pipes 300 m away from the pit storage. The volume flow rate is measured with flow meters in m^3/h with an accuracy of 2% (Schmidt 2013). The temperature sensors are PT resistance thermometers with an accuracy of +/- 0.1 K (Schmidt 2013).

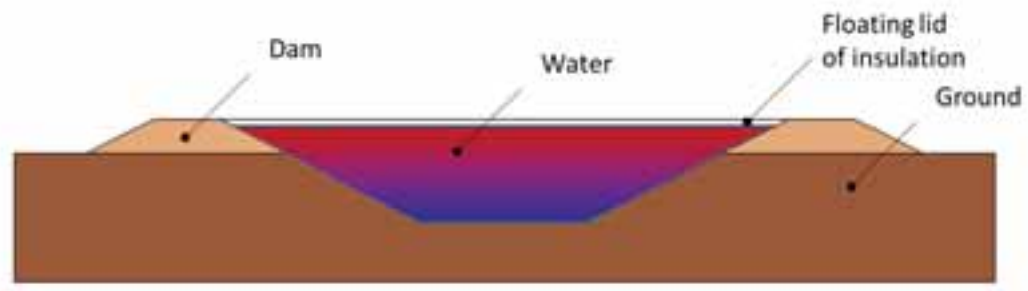

Fig. 2: Illustration of the design of a water pit thermal energy storage

The placement of the sensors in the water pit heat storage are indicated as circles in Fig. 3, where sensors A1 and A2

measure water temperatures of the store at different depths, while the sensors B, C and G measure temperatures of the ground at different levels. Moreover, at A1 a heat flux sensor is installed in the lid including one temperature sensor on the top and one temperature sensor on the bottom surface of the insulation layer.

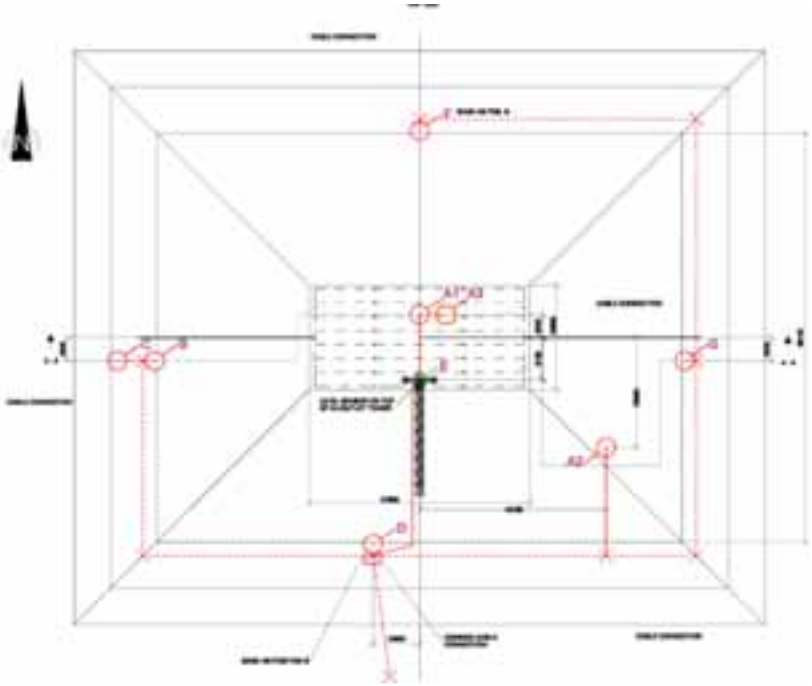

(A)

Fig. 3: Schematic illustration of the measurement sensors

3. Numeric method

A simplified CFD model of the water pit heat storage in Marstal is built using a commercial CFD software Ansys Fluent (Ansys 2016). The model includes the water volume in the store and the inlet/outlet openings. An inlet/outlet pipe with three inlet/outlet openings is placed in the middle of the PTES. Fig. 4 shows mesh of the simplified CFD model of the PTES. Grid lines on the side and the bottom surfaces of the PTES and grid lines on two vertical cut planes across the middle of the inlet/outlet pipe are presented. In the area around the inlet/outlet pipe, a denser mesh is assigned in order to better resolve fluid flow and heat transfer caused by inlet and outlet flows. In total 1.6 million hexahedron elements were used to mesh the model.

Fig. 4: Mesh of the simplified CFD model of the PTES in Marstal

Heat loss coefficients for the top cover is determined based on given design of the floating lid and on measurements by a heat flux sensor at A1 while heat loss coefficients and boundary conditions for the side and the bottom surfaces of the store are evaluated by transient simulations using a simplified 2D CFD model of the ground around the store. Fig. 5 shows the 2D model of the water pond and the ground around the pond. It is assumed that the pond is symmetrical therefore only half of the water pond is modelled. The whole model has a dimension 74 m * 41 m with an aim to minimize the thermal influence of the pond on the bottom and the side boundary surfaces. Since temperature at the bottom and the side boundary surface of the 2D model is not influenced by the pond during the investigated 4 months period, these boundary surfaces are defined as adiabatic walls.

The 2D model calculates the heat transfer between the water pond surface and the ground around the store, which is used to determine heat loss coefficients of the bottom and the side surface of the PTES. The obtained heat loss coefficients are used as input in calculations using the 3D CFD model of the PTES.

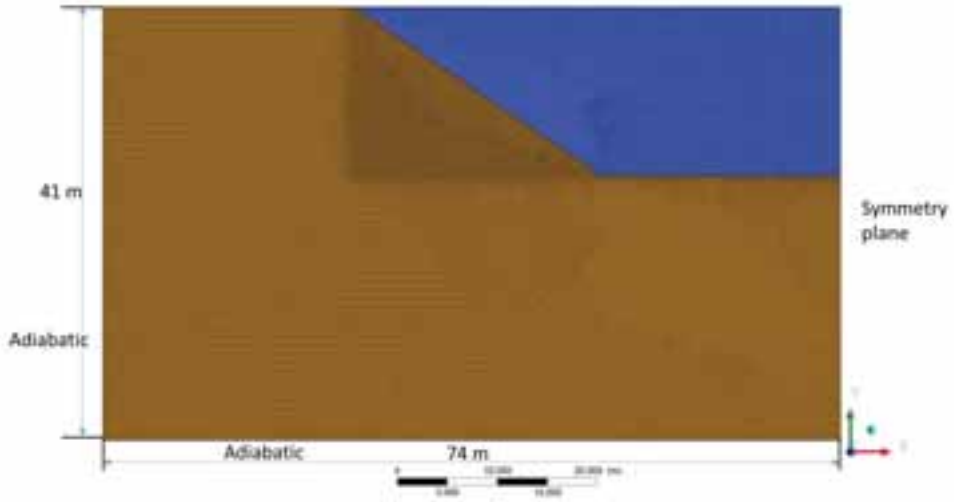

Fig. 5: A 2D ground model including the water pond and the ground around the pond

Water is used as the heat storage media. Properties of water and their dependences on temperature are shown as follows:

Density, [kg/m^3] $$\rho = 863 + 1.21 * \mathrm{T} - 0.00257 * \mathrm{T}^2 \quad (1)$$

Dynamic viscosity, [kg/(ms)] $$\mu = 0.0007 * (\frac{T}{315})^{-5.5} \quad (2)$$

Thermal conductivity, [W/(mK)] $$\lambda = 0.375 + 8.84 \times 10^{-4} * T \quad (3)$$

Specific heat, [J/(kgK)] $$Cp = 4432.6 - 1.819 * \mathrm{T} + 0.0033 * T^2 \quad (4)$$

where T is fluid temperature, [K].

Calculation of Rayleigh number shows that the flow in the PTES is laminar in most parts of the store, therefore the laminar model is used in the calculation. Transient CFD calculations are performed with Boussinesq approximation. The PRESTO and second order upwind method are used for the discretization of the pressure and the momentum/energy equations respectively. The SIMPLE algorithm is used to treat the pressure-velocity coupling. The transient simulations start with a temperature distribution in the PTES determined by measurements. A zero velocity field is assumed at the start of all simulations. The calculation is considered convergent if the scaled residual for the continuity equation, the momentum equations and the energy equation are less than 10^{-3}, 10^{-3} and 10^{-6} respectively. The simulation runs with a time step of 5 s and a duration of 7-10 h.

4. Heat losses from the store

One important boundary of the model is thermal losses of the store which consists of two heat losses: losses from the top floating cover to the ambient air and losses from water in the pond to the ground. Heat loss from the top cover of the store is determined based on measurement by a heat flux sensor placed on the cover and properties of the

insulation material, see location A1 in Fig. 3. Since it is only a single point measurement at a fixed location, precise measurement of heat losses for the whole cover is difficult. For instance, the measurement is not able to measure extra heat losses caused by periodic ventilation of the top cover, thermal bridges through the manhole, joints and extra heat losses caused by decreased insulation property of deformed insulation material observed in some places of the cover. The measured heat loss from the cover is therefore modified with an aim to achieve an energy balance of the water pond in a measurement period of one year. The heat fluxes of the floating cover used in the paper are in the range of 22-34 W/m^2.

Tab. 1: Heat fluxes from the top floating cover

Days calculated by the 3D CFD model	Heat flux from the top cover [W/m^2]
October 07	34
August 03	24.2
February 18	22
April 22	24.2

From Table 1, it can be seen that among the four days investigated, the heat flux is the largest on October 07 and the smallest on February 18. It can be explained by the temperature difference between the water at the top layer of the pond and the ambient air. On October 07, the water pond had a relatively higher temperature due to charging during the summer while the ambient air temperature is around 10-20ºC. In February 18, the ambient air temperature is much lower and the temperature at the top layer of the pond was significantly decreased due to discharge of the PTES throughout the winter.

Heat losses from the PTES to the ground are more difficult to measure since it is influenced not only by yearly fluctuation of the ambient air temperature, but also by heat transfer in the soil. In order to locate a ground boundary of the water pond that is not influenced by temperatures of the water pond, a large amount of soil volume has to be included in the CFD model. As a result, the CFD model might be extremely large, making it too time consuming to carry out CFD simulations. In this paper, heat transfer between the water pond and the ground is calculated in a separate 2D model, see Fig. 5. In the 2D model, measured temperatures at different layers of the water pond were used as initial conditions of the store. Fig. 6 shows temperature distribution in a vertical cut plane of the ground around the PTES. View of the whole water pond is shown in the figure to the left while a magnified view of the upper corner of the PTES is shown to the right.

The 2D ground model calculates the heat transfer between the water pond surfaces and the ground around the store, which is used to determine heat loss coefficients of the water pond surfaces. The heat loss coefficients are used as input in the 3D CFD model of the PTES.

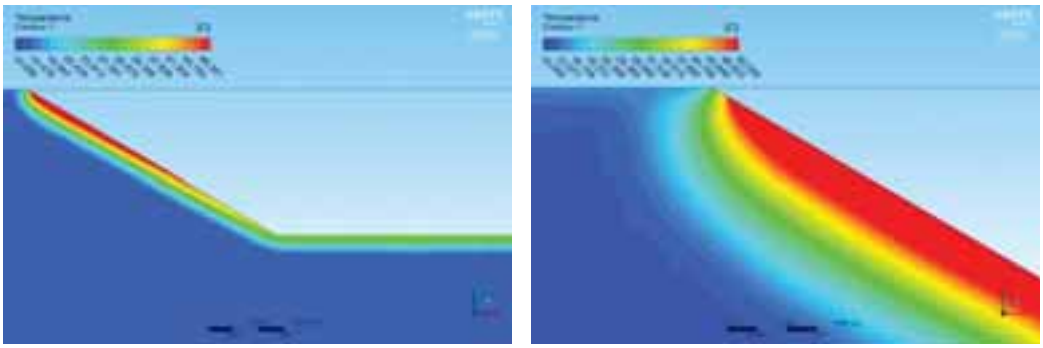

Fig. 6: Temperature distribution in a vertical cut plane of the ground around the PTES (left: side and bottom surface, right: a magnified view of the upper corner of the PTES)

Fig. 7 shows the calculated heat transfer coefficients between the sides of the water pond and the ground soil. The blue curve and the orange curve show respectively the heat transfer coefficients obtained by the simplified 2D model and the coefficients used in the 3D CFD model by means of a user defined function. As shown in Fig. 7, the heat loss coefficient of the sides of the PTES is around 0.15 W/m^2/K at a depth of 16 meters. The heat loss coefficient increases slightly with a decrease of the depth. At a depth of 2 meters, the heat loss coefficient is around 0.2 W/m^2/K. For surface area within 2 meters deep, the heat loss coefficient increases significantly due to the influence of ambient

conditions. At the bottom surface of the PTES, the heat loss coefficient is found to be 0.1 W/m^2/K.

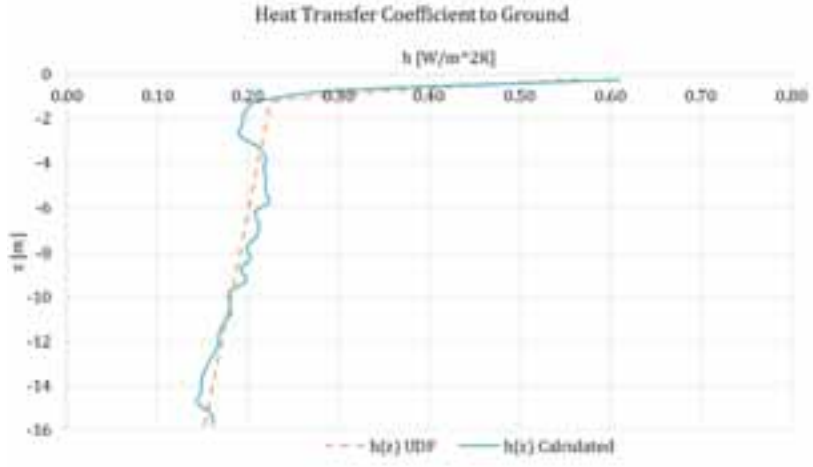

Fig. 7: Heat transfer coefficients between the sides of the water pond and the ground soil.

The 2D ground model was also used to determine soil temperature around the water pond. Since temperature of the ground around the store depends on both the depth of the soil and the time of the year, the distribution pattern of the temperatures was determined by calculation using the 2D ground model, while the absolute level of the temperature was determined by measurements at the location B.

Fig. 8 shows ground temperatures on the side of the water pond in different times of the year. Among the investigated four periods, the ground soil temperature is the highest in October and the lowest in February, which indicates a strong influenced by the temperatures of the pond and the ambient air. A clear pattern can be seen from the curves: relatively lower temperature at both the top and the bottom of the pond and higher temperature around 6 m below the ground surface. A lower temperature at the bottom of the pond could be explained by strong thermal stratification in the pond. Due to thermal stratification, temperature of water layer at the bottom of the pond is relatively lower, therefore a lower temperature is observed at 16 m below the ground surface. While a lower temperature close to the ground surface could be explained by cooling of soil by the ambient air with a lower temperature.

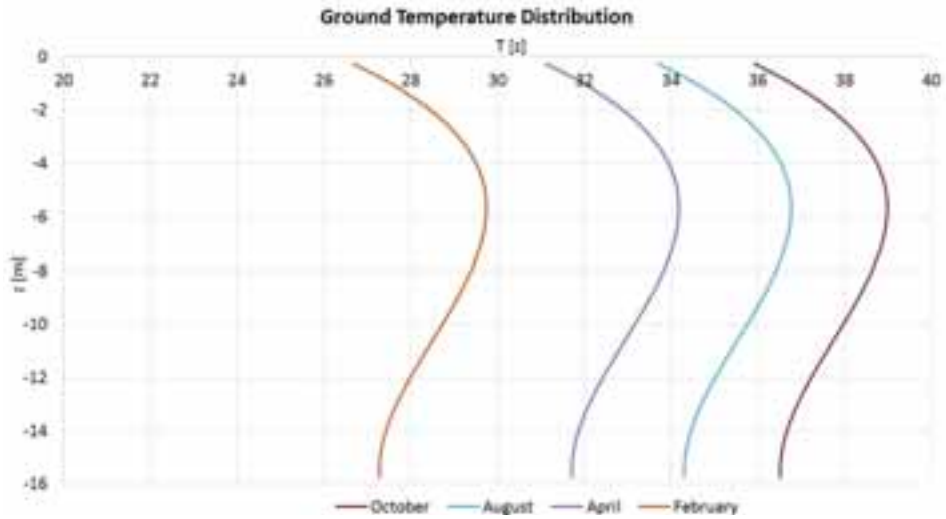

Fig. 8: Ground temperature on the side of the water pond

5. Thermal stratification in PTES

Validity of the CFD model is investigated by comparing the CFD calculated thermal behaviors of the PTES with the measurements. The investigation was carried out for 4 scenarios including two discharges and two charges of the PTES, see Table 2. In the CFD simulations measured temperatures of the water pond and the ground were used as initial conditions of the PTES. The transient flow rate and temperature of the inlet flow to the PTES were measured

and used as boundary conditions for the inlets by means of user defined functions. During charge of the PTES, the average temperatures of the inlet flow are 83.3ºC and 77.3ºC on August 03 and April 22 respectively. The average discharge temperature are 44.4ºC and 36.5ºC respectively on October 07 and February 18. The CFD calculated temperatures at the outlet and at different levels of the pond were compared to the measured ones.

The CFD model is able to calculate heat transfer and the convective, buoyance driven flow in the PTES. The development of water temperature is elucidated by means of the transient CFD simulations. Thermal stratification in the store during charge and discharge of the store is evaluated.

Tab. 2: Heat fluxes from the top floating cover

Days calculated by the 3D CFD model	Initial pond T at the bottom, ºC	Initial pond T at the top, ºC	Average ground T 2.5 m from pond surface, ºC	Average inlet T, ºC	Measured energy, MWh
October 07	44	82	37.8	Discharge, 44.0	24.2
August 03	52	79	35.6	Charge, 83.3	68.9
February 18	30	51	33.0	Discharge, 36.5	14.6
April 22	33	71	28.5	Charge, 77.3	95.3

5.1. Charge of the PTES

Fig. 9 shows the measured and the CFD predicted charge power of the PTES for the charge case on August 3. There is a satisfactory agreement between the CFD model and the measurements. The difference between the measured energy flow and the calculated energy flow is within 10%.

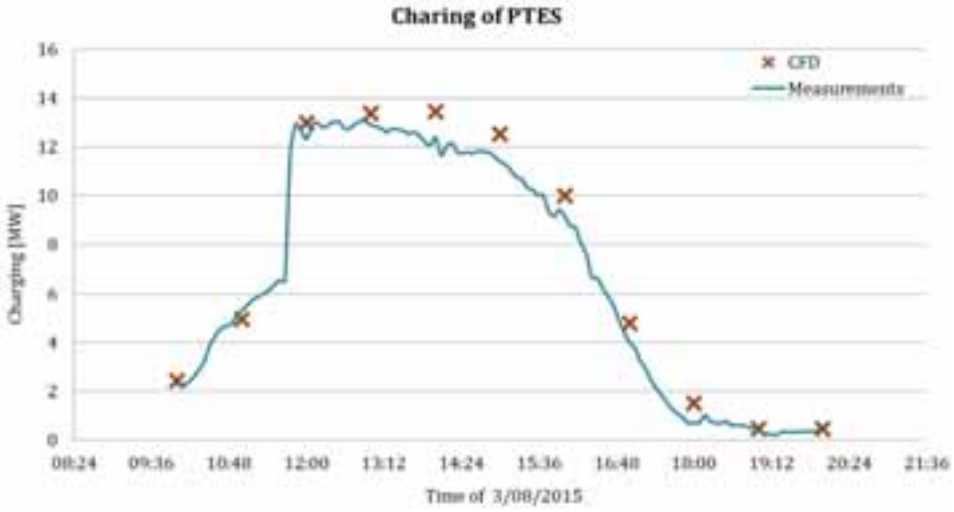

Fig. 9: Measured and CFD predicted charge power of the PTES for the case on August 3

Fig. 10 shows the measured and the CFD predicted temperature distributions in the PTES for the case on August 3. Both the initial temperatures and the temperature distribution of the pond at the end of the calculation are presented. The measured temperatures are shown as scatted dots while the CFD calculated temperatures are shown as curves. A comparison between the measured and the CFD calculated temperatures is shown for the location A1 and A2 respectively in the figure to the left and the figure to the right. Since the depths of the water are 16 meter at the location A1 and 8 meters at the location A2, the scales of the two figures are different. It is shown that water at the same level of the pond has almost identical temperatures. Based on the measured initial temperatures at different levels of the water pond in the start of the charge period, a regression is made to find a function between the water temperature and levels of the pond. The function is used as initial conditions in the CFD model by means of user defined functions.

There is generally a good agreement between the measured and the CFD calculated temperatures at the end of the charge period (20:00) at different locations of the pond. An exception is found at the level of 4 m below the ground surface on the location A2 where the water temperature was measured to be approx. 85ºC in comparison to a CFD calculated temperature of around 75ºC. A likely cause of the big difference could be false measurement of the sensor.

As water temperatures at the top of the pond are approx. 80ºC, it is very unlikely that temperature of the water 4 meter below the surface has a temperature higher than temperature of the water on the top of the pond. Therefore measurement data of the false sensor was not included in the investigations.

In the right figure of Fig. 10, it is shown that measured temperature of water at the top surface of the pond has a lower temperature than water 1-4 meter below the water surface, indicating a higher heat loss from the top cover at the location A2 than the average heat loss used in the CFD model.

It should be noted that temperature of the water pond increases slightly during charging in the investigated period. Such a change of temperature during charge in one day is too small to fully validate the CFD model. CFD calculation of charging in more than one day would better elucidate validity of the CFD model but the corresponding simulation time would increase significantly, therefore was not applicable for the present study. However such long term calculations are recommended for the future by means of parallel computing on super computers.

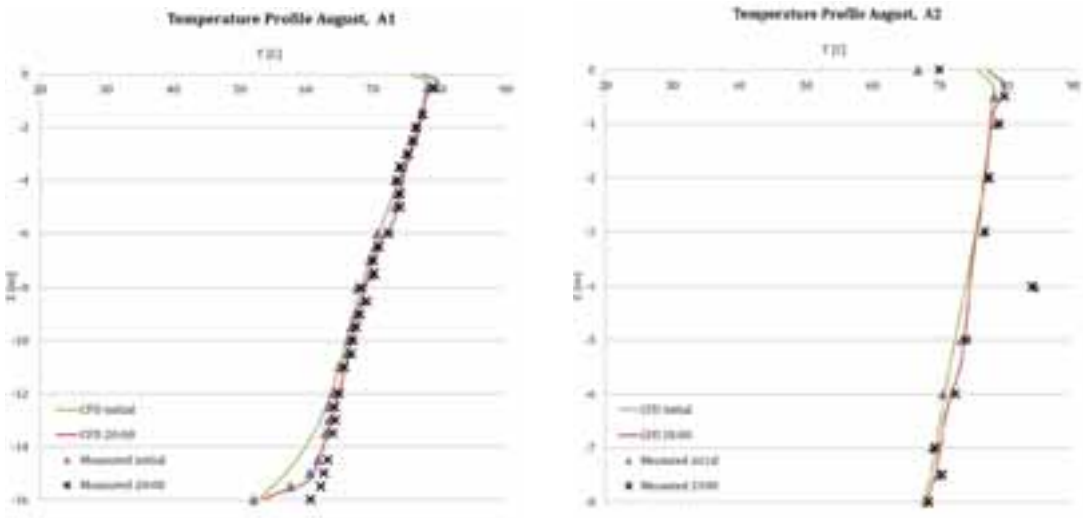

Fig. 10: Measured and CFD predicted temperature distribution in the PTES for the charge case on August 3

Fig. 11 shows temperature plots in the water pond at different times of the day. Temperature distributions at the start of the charge period (10:00) and in the middle of the day (14:00) are shown respectively in Fig. 11A and 11B. As shown in Fig. 11B, there are inlet flows with a temperature of 85ºC in the top inlet and in the middle inlet. After entering the top inlet opening, the hot fluid rises up and tends to flow along the top surface of the pond. Around the middle inlet opening, the inlet hot fluid mixes with relatively colder water in the PTES, resulting in a mixing region above the inlet opening. The mixing region is limited to a small area around the inlet disc indicating a good conservation of thermal stratification in the pond.

Fig. 12 shows regions in the pond where there is a larger fluid movement. Not surprisingly, larger fluid movement is observed in the three regions: around the top inlet opening, the middle inlet opening and the exit. The fluid velocity close to the inlets are in the range of 4-8 cm/s, which are considered to be higher enough to destroy thermal stratification. Since the region with a disturbing fluid velocity is rather limited, thermal stratification in the pond is kept during charge of the pond. It is interesting to note that around the top inlet opening the region with a higher fluid movement looks like a disc, indicating spreading of the hot fluid along the top surface of the PTES. That fluid pattern means well function of the inlet opening since the hot fluid has a higher temperature than the water temperature at the top of the pond and therefore should be directed by the inlet to the very top of the pond.

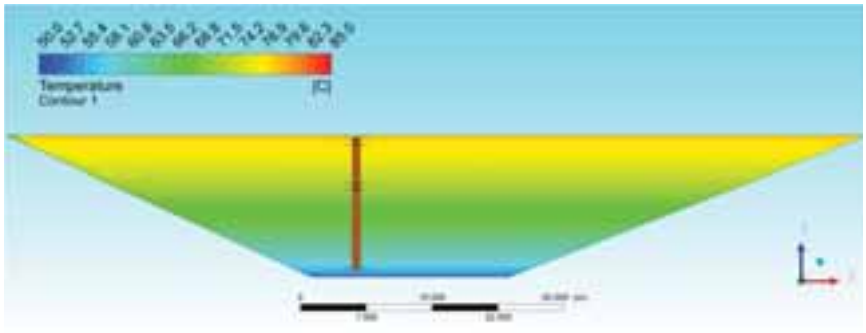

(A) Thermal stratification at 10:00

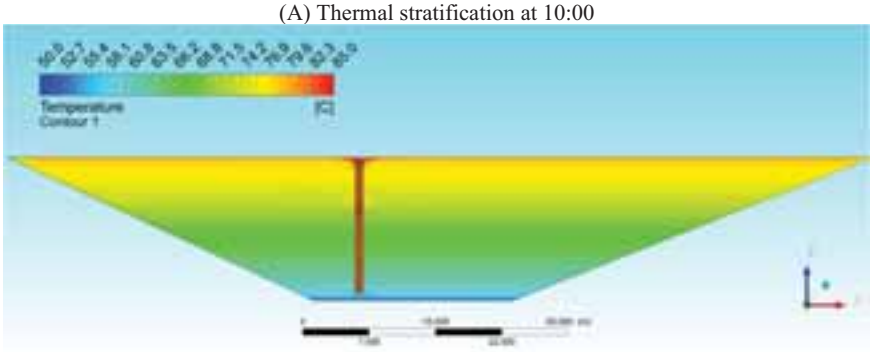

(B) Thermal stratification at 14:00

Fig. 11: Temperature plots of the water pond during charge on August 3

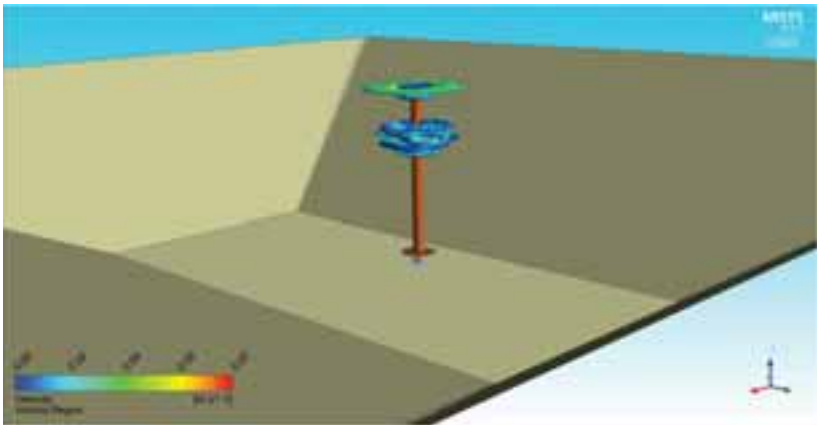

Fig. 12: Illustration of regions with a larger fluid movement for the charge case on August 3

5.2. Discharge of the PTES

Fig. 13 shows the measured and the CFD predicted discharge power of the PTES for the discharge case on October 7. There is a satisfactory agreement between the CFD model and the measurements. The difference between the measured energy flow and the calculated energy flow is within 5% except at the very start of the simulation. There is a large difference of approx. 0.4 MW between the measured and the calculated discharge power. A large deviation at the start of the simulation could be due to over simplified initial conditions of the PTES in the CFD model.

Fig. 13: Measured and CFD predicted discharge power of the PTES for the discharge case on October 7

Fig. 14 shows temperature distribution in the water pond at 21: 00 October 7. A clear thermal stratification in the pond can be observed. At the start of the October the pond was already quite fully charged. Water temperatures are 80-87ºC in the top of the pond, 70-76ºC in the middle and 40-45ºC at the bottom of the pond. During discharge, hot water is taken from the top of the pond, cooled down by the district heating network and returns through the bottom inlet of the pond. Since the inlet water is around 44ºC, close to the water temperature at the bottom of the pond, there is almost no mixing induced by the inlet flow. It is also confirmed by Fig. 15 where regions with a fluid velocity larger than 3 cm/s can be seen. Around the inlet opening at the bottom, the mixing region is very much limited. It can concluded that the current inlet/outlet design is able to minimize mixing during discharge from the top and the bottom openings when the PTES is fully charged.

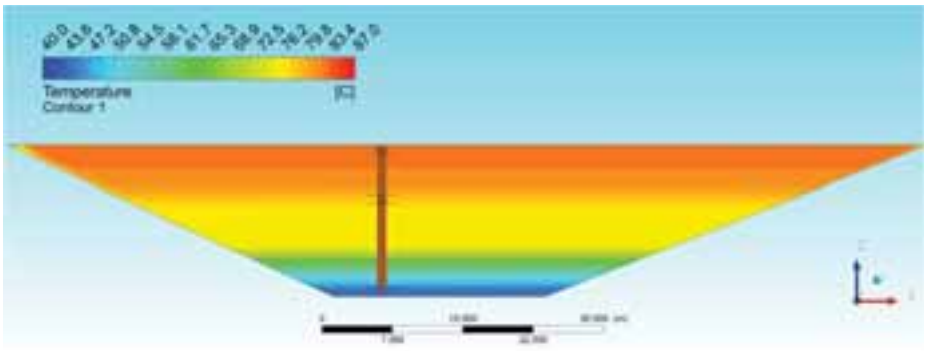

Fig. 14: Temperature plot of the water pond at 21:00 for the discharge case on October 7

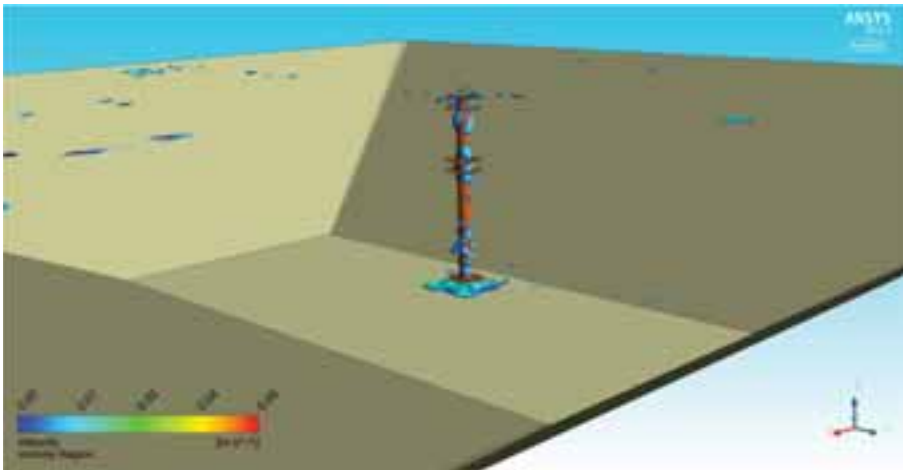

Fig. 15: Illustration of regions with a larger fluid movement for the discharge case on October 7

Fig. 16 shows temperature distribution in the water pond at 6:00 February 18 during discharge. After discharge throughout the winter, temperature of the pond was significantly decreased. Water temperature at the top of the pond was decreased to 48-53ºC while the water temperature was in the range 28-32ºC below the middle opening. During

the discharge, heat is taken from the top of the pond as for instance heat source of a heat pump. On the hot side of the heat pump, the district heat water is heated from 40ºC to 80-85ºC. On the cold side the heat pump, water is cooled down from 48-53ºC to around 40ºC before flowing back to the pond through the bottom inlet opening. Since the inlet water temperature is higher than the water temperature at the bottom of the pond, a significant mixing at the lower part of the pond is observed, see Fig. 17. Due to buoyancy forces, the incoming water with a higher temperature rises along the inlet/outlet pipe while water on the edge of the pond with a relatively lower temperature flows down to the bottom of the pond, creating a big circulation and a quite uniform temperature at the lower part of the pond. The circulation is shown by the stream lines in Fig. 18.

Velocity vectors in the water pond during discharge on February 18 are shown in Fig. 18. A clear uprising flow is seen along the inlet/outlet opening. After reaching the middle opening where there is a water layer with higher temperature, the flow turns to flow horizontally.

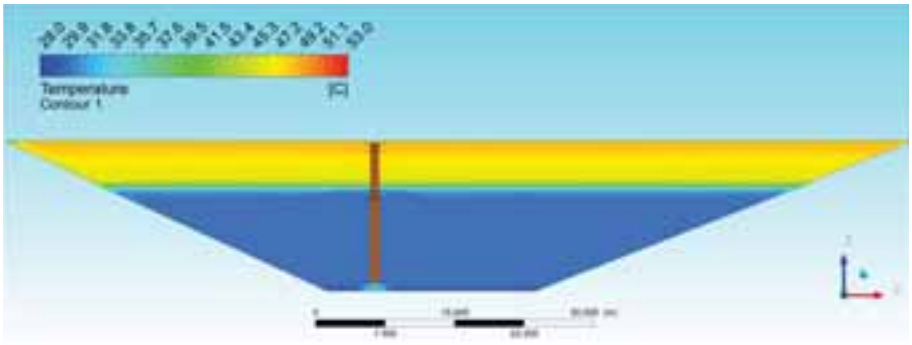

Fig. 16: Temperature plot in the water pond at 6:00 for the discharge case on February 18

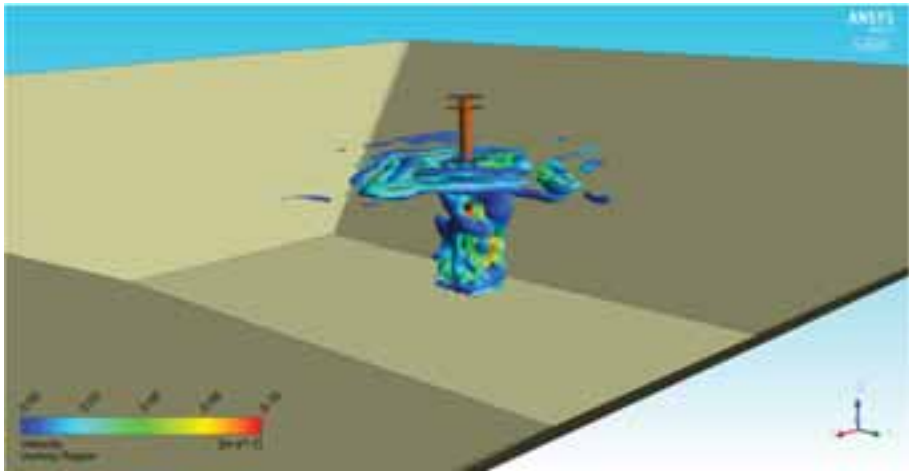

Fig. 17: Illustration of regions with a larger fluid movement for the discharge case on February 18

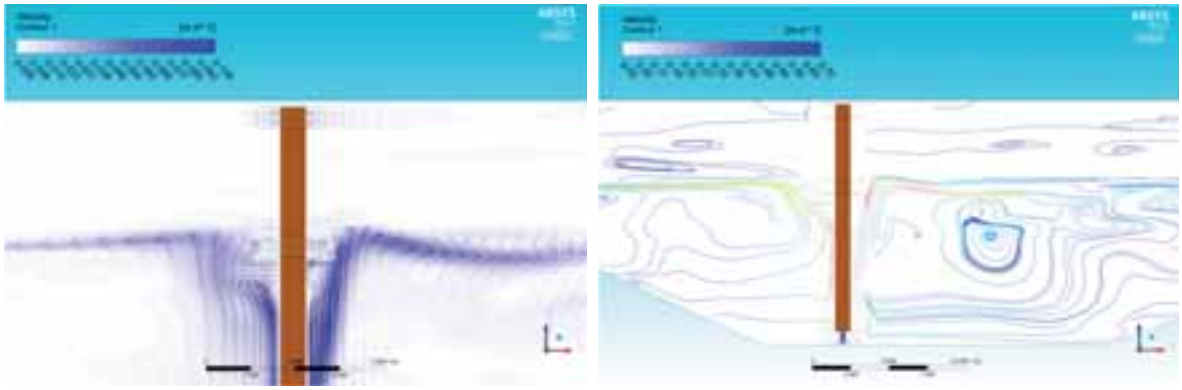

(A) Velocity vectors showing the uprising flow (B) Stream lines shown a big circulation

Fig. 18: Velocity vectors and stream lines in the water pond during discharge on February 18

For the investigated scenario, the inlet temperature is much higher than the temperature at the bottom of the pond,

thus creating strong mixing and destroying stratification at the lower part of the pond. If the middle inlet opening was used as inlet, a better thermal stratification in the pond could be achieved. However it should be mentioned that temperature of water from the heat pump varies depending on operation conditions of the heat pump. The return temperature could be much lower under some conditions, for instance a return temperature from the heat pump in the range of 15-25ºC is likely to happen. Consequently it will be advantageous to have the inlet at the bottom inlet opening. It is therefore interesting to investigate these scenarios in detail in the future.

6. Conclusions

Thermal behaviors of the 75,000 m^3 water pit heat storage in Marstal solar heating plant were investigated experimentally and numerically. Temperatures at different levels of the water pit storage and temperatures at different depths of the ground around the storage were monitored and analyzed. A simulation model of the water pit storage is built to investigate development of temperature in and around the storage. The calculated temperatures are compared to the monitored temperatures with an aim to validate the simulation model. The results show that the CFD models predict satisfactorily temperatures in the PTES for both charge and discharge operations. However it is recommended for the future to carry out a long term simulation in order to achieve a more detail validation of the CFD models.

Calculations of fluid flow and heat transfer in the PTES by the CFD model show that the inlet/outlet openings work properly during charge with minimal mixing region created in the PTES around the inlet/outlet openings. While for discharge of PTES, the ability of the inlet/outlet arrangement to keep thermal stratification strongly depends on temperature of water returned to the PTES. If temperature of the flow back to the PTES is much higher than the temperature at the bottom of the pond, strong mixing will be created, thus destroying stratification at the lower part of the pond. If the return temperature is lower than temperature at the bottom part of the PTES, it will be advantageous to have the inlet at the bottom inlet opening. It is therefore recommended to investigate these scenarios in future studies.

7. References

Ansys Inc., 2016. Ansys Fluent release 17.0, Southpointe, 2600, Ansys Drive, Canonsburg, PA 15317, USA.

Heller A., 2000. 15 Years of R&D in central solar heating in Denmark. Solar energy, 69, 437-447.

Chang C., Wu Z., Navarro H., 2017, Comparative study of the transient natural convection in an underground water pit thermal storage, Applied Energy, in press.

Jensen M.V., 2014. SUNSTORE ® 4 Design of the Water Storage The SUNSTORE Plant in Marstal. In Sunstore 4 Design of the Water Storage.

Kate D. Sunstore4. http://sunstore4.eu/, 2013. [Online; accessed 01-04-2017].

Kielsgaard Hansen, K., Nordgaard Hansen, P., Ussing, V., 1983. Seasonal heat storage in underground warm water stores. Report 134, Thermal Insulation Laboratory, Technical University of Denmark.

Kübler R., Fisch N., Hahne E., 1997, High temperature water pit storage projects for the seasonal storage of solar energy Journal, Solar Energy, 61, 97-105.

Pavlov, G.K., Olesen, B.W., 2012. Thermal energy storage -A review of concepts and systems for heating and cooling applications in buildings: Part 1-Seasonal storage in the ground. HVAC&R Research, 18, 515-538.

Pfeil M., Koch H., 2000, High performance-low cost seasonal gravel/water storage pit, Solar Energy, 69, 461-467.

Schmidt T., 2013. Sunstore 4 Technical Reports: Design of the measurement and evaluation program.Sharma A., Tyagi V. V., Chen C. R., Buddhi D., 2009. Review on thermal energy storage with phase change materials and applications. Renewable and Sustainable Energy Reviews, 13, 318–345.

RADIAL DIFFUSERS IN STRATIFIED HOT WATER STORES: GEOMETRY OPTIMIZATION WITH CFD

Fabian Findeisen[1*], Thorsten Urbaneck[1], Bernd Platzer[1]

[1] Chemnitz University of Technology, Department of Mechanical Engineering, Institute of Mechanics and Thermodynamics, Professorship Technical Thermodynamics, 09107 Chemnitz, Germany

Abstract

This abstract deals with thermal energy stores for solar and district heat supply systems and presents numerical results for the performance of radial diffusers in a new type of overground storage tank which has a floating ceiling. The influence of the position of the radial diffuser in the thermal store was investigated revealing significant potentials regarding thermal stratification and storage efficiency. The optimization of the diffuser geometry led to a new free-form radial diffuser, which allows charging temperatures up to 98 °C. A Large Eddy Simulation (LES) illustrated the development of the stratification.

Keywords: CFD, district heating, floating ceiling, geometry optimization, heat supply, hot water, LES; charging device, radial diffuser, solar heating, thermal energy storage, thermal stratification

1. Introduction

Sensible thermal energy stores can make heat surpluses available to the consumer if necessary. A thermal stratification inside the storage tank is achieved by separating water with different temperatures through buoyancy. In a store operating according to the displacement principle, a water exchange takes place by direct charging and discharging. Radial diffusers can serve as charging devices. They consist of radial plates guiding the flow through a narrow gap horizontally into the cylindrical storage tank. For use in solar thermal systems an operation via matched flow is recommended to realize constant loading temperatures.

Numerical results will be presented for a new storage design proposed by Urbaneck et al. (2016) offering numerous benefits compared to other storage types. Here especially the effect on the temperature distribution inside this storage tank will be discussed using Computational Fluid Dynamics (CFD). The main novelty of the construction is an indoor protected floating ceiling, with the upper charging device directly attached to it. A flexible connection allows the free movement of the floating ceiling between a top and bottom dead center. During charging of the tank a gravity current occurs directly at the ceiling, which is an essential prerequisite for a good thermal stratification as will be shown later in this paper. The design is illustrated in fig. 1c. In comparison, fig 1a and 1b show examples of conventional storage types where the radial diffuser is mounted in a fixed position resp. floating (e.g. Hedbäck, 1993).

A demonstrator of the new storage design was already built in cooperation with industrial partners. By now, experiments are in progress to prove the high stratification quality and the very low heat losses. The investigations are part of the OBSERW project (Urbaneck et al., 2017).

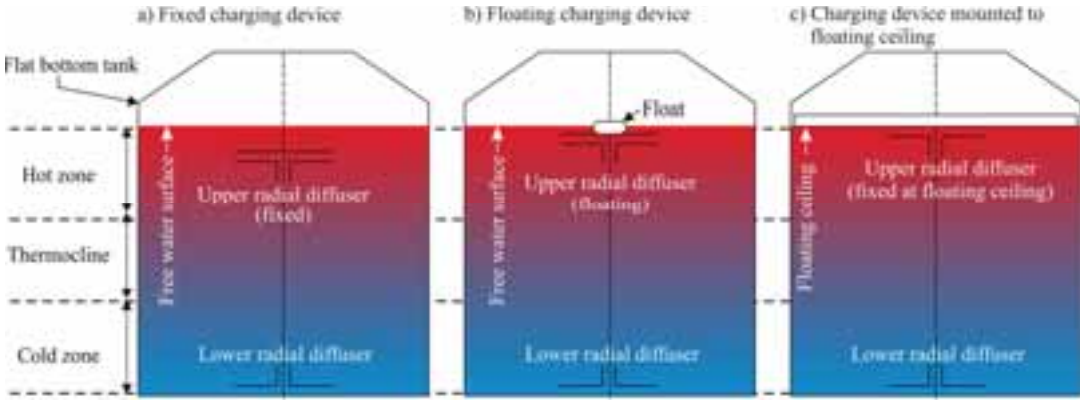

Fig. 1: Thermal energy storage with different possibilities of mounting the charging device in the store

doi:10.18086/swc.2017.13.04 Available at http://proceedings.ises.org

2. CFD model and boundary conditions

A two-dimensional axisymmetric model was used to perform the simulations with Ansys CFX. The CFD model takes buoyancy into account. The k-ω-SST model serves as a turbulence model. Additional production and dissipation terms capture the effects of density gradients on the turbulent flow. Fig. 2 presents the simulation model. Findeisen et al. (2016) describes the modeling in detail. The boundary conditions at the inlet as well as the initial condition in the tank are determined by the operating conditions in tab. 1 (assumption: constant volume flow and constant charging temperature).

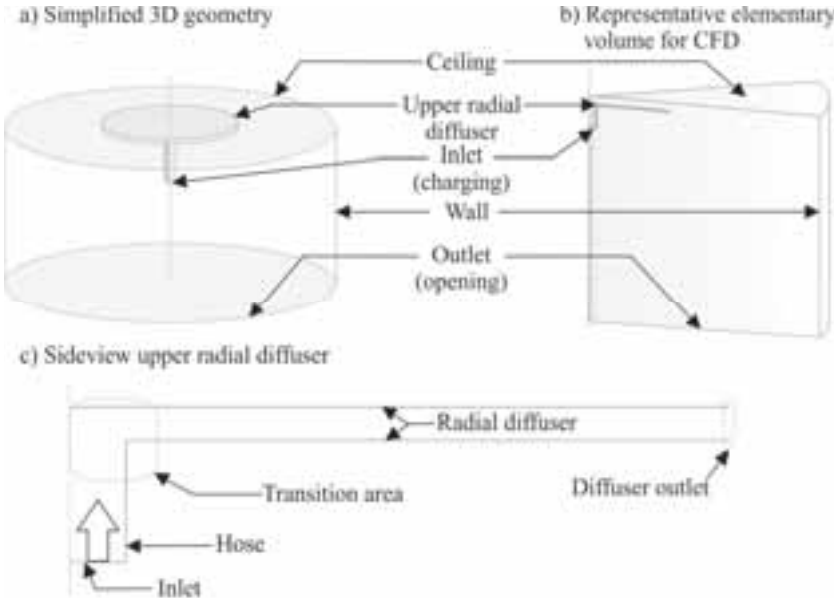

Fig. 2: Schematic view of the simulation model

Tab. 1: Operation conditions and geometrical parameters of the demonstrator

$\dot{V}_{in}$ [m³/h]	19.44	T_{in} [°C]	70	$h_{diffuser}$ [mm]	40	d_{store} [m]	5.12
V_{store} [m³]	116.76	T_{store} [°C]	40	d_{hose} [mm]	68.8	$d_{diffuser}$ [m]	0.96

3. Influence of the position of the charging device

Radial diffusers in flat bottom tanks are usually floating or mounted fix in the store without any moving parts (fig. 1a, b). Thus, the diffusor is located below the water surface, resp. the storage ceiling. To investigate the influence of reducing this distance, especially by mounting the charging device directly to the ceiling, a simplified simulation model was used, which does not consider a free water surface. It assumes a constant velocity profile at the entry of the tank (corresponds to the outlet of the charging device). Hence, the radial diffuser is not yet simulated.

Fig. 3 illustrates the calculated temperature fields for three different cases. As the distance towards the ceiling increases, the thermocline grows and the average temperature in the hot zone decreases while an unfavorable non-isothermal free stream due to convection develops. This free stream causes strong mixing of hot charging fluid and cooler storage fluid significantly reducing the layering quality.

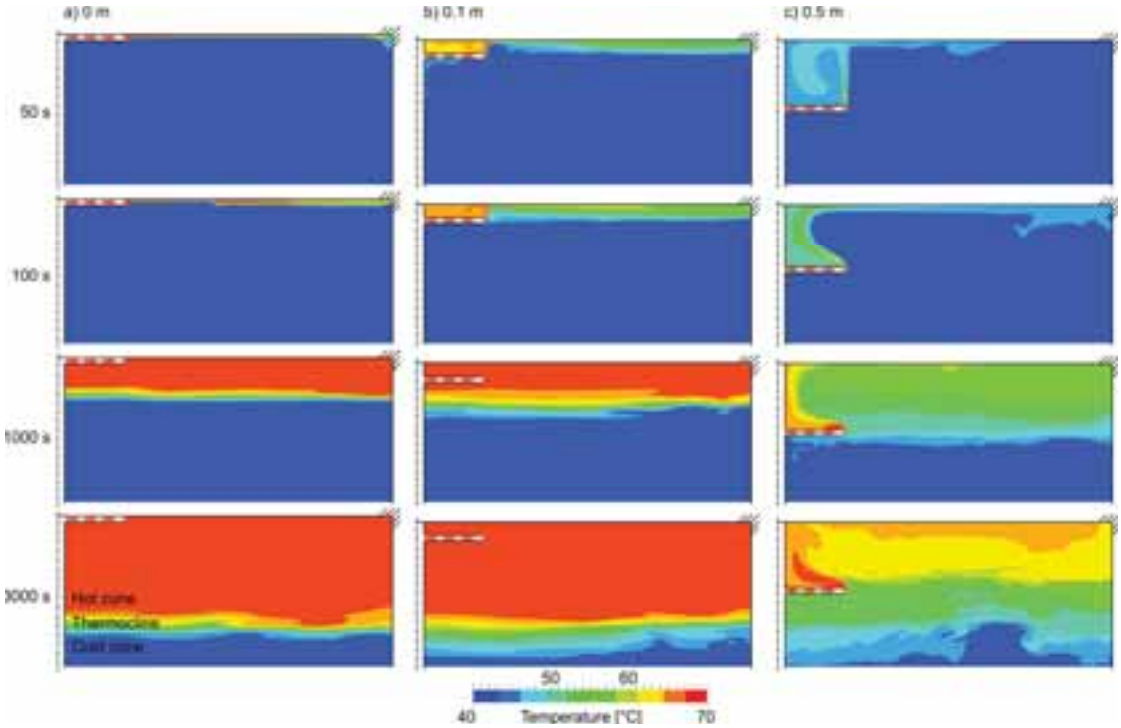

Fig. 3: Evolution of the calculated temperature field inside the storage tank for different distances between the charging device and the ceiling

To determine the quality of the stratification the volume averaged temperature in the hot zone as well as the average height of the thermocline are used for evaluation. The height corresponds to a volume averaged height over the entire radius of the simulation model according to the 90/10%-principle (Findeisen et al., 2016). Tab. 2 compares the results obtained. The thermocline doubles its height if the distance between diffuser and ceiling increases to 10 cm and is more than tenfold its height if the distance is 50 cm. At the same time the average temperature in the hot zone drops to 69.64 °C, resp. 67.42 °C. Thus, the stratification quality strongly depends on the position of the charging device.

Tab. 2: Results for different distances between the radial diffuser and the ceiling after 3000 s of charging

Distance between radial diffuser and storage ceiling [m]	0.0	0.1	0.5
Average thermocline height (90/10%-Method) [m]	0.09	0.18	0.99
Average temperature in the hot zone [°C]	69.99	69.64	67.42

Furthermore, since the hot fluid cannot be removed from above the charging device, the corresponding storage volume as well as the heat stored there is unusable. In addition, as soon as the hot fluid cools down, thermal inversion can permanently destroy the stratification in the tank. Charging directly along the storage ceiling completely eliminates these drawbacks and therefore promises substantial improvements, also because the floating ceiling is well insulated.

4. Investigation of the discharging- and charging behaviour

With a minimal distance between the charging device and the floating ceiling, hot water is sucked in directly along the ceiling in case of discharging, which allows the full use of the hot zone. But mounting the charging device to the ceiling goes along with an elimination of a hydrostatic pressure relief above the charging device. Since the store operates with a maximum temperature up to 98 °C this means that there is a risk of falling below the steam pressure limit. The pump is in feed mode, the charging device sucks in and thus discharges the storage tank. Hereby, the flow can be disrupted by local steam formations (e.g. cavitation) or other transient effects, which can lead to operational failures or even a breakdown of the entire discharging system. In order

to ensure operational safety during discharging, it is therefore necessary to optimize the diffuser geometry in order to minimize the local pressure drop. There is usually no risk for the charging behavior. Instead, for this operational case the influence of different diffuser geometries on the quality of the thermal stratification will be investigated.

The various geometries of charging and discharging systems (CDS) are shown in fig. 4. Starting from a reference case with a sharp edge from the connection hose to the diffuser and straight diffuser walls (CDS_0) the transition area between the hose and the radial diffuser will be modified. Hence, CDS_1 has a round transition with a constant radius and CDS_2 to CDS_4 have a free from transition area. Furthermore, different diffuser styles (CDS_2a/b) as well as build-in parts (CDS_5) and guiding plates at the outlet are part of the study. Besides of the demonstrator (tab. 1) the investigation also considers three representative storage sizes (tab. 3).

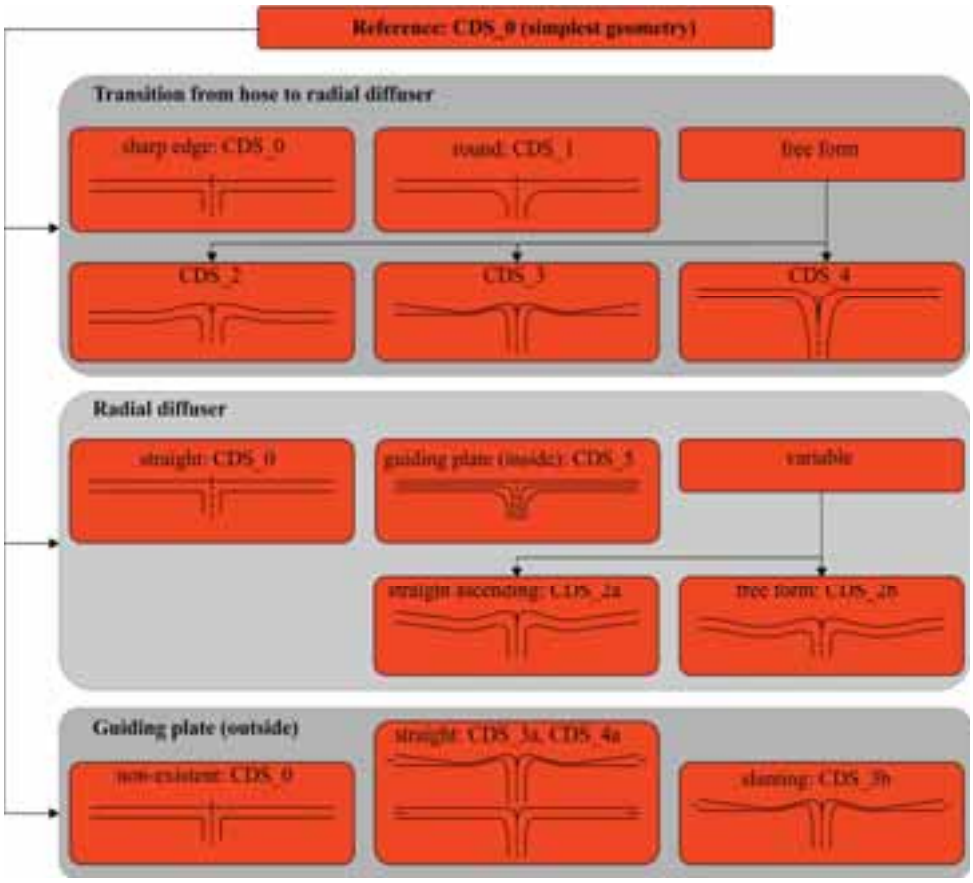

Fig. 4: Investigated diffuser shapes

Tab. 3: Overview of simulated storage sizes

Name	V_{store} [m³]	d_{store} [m]	$d_{diffuser}$ [m]	$h_{diffuser}$ [mm]	d_{hose} [mm]	$\dot{V}_{in}$ [m³/h]	*Fr* [-]	*Re* [-]
demon-strator	116	5.12	0.96	40	68.8	20	0.57	4209
store 1	1000	10.84	2.00	80	200.0	167	0.86	17658
store 2	3500	16.46	3.60	120	371.0	583	0.91	34334
store 3	6000	19,69	5,00	120	486,0	1000	1,12	42378

4.1 Discharging behaviour

Aim of the study is to improve the flow inside the charging device since the pressure in the radial diffuser must not fall below the steam pressure limit. Thus, it is important to minimize the local pressure drop. Besides of different storage sizes the investigation also takes into account different atmospheric pressure levels.

The minimum absolute pressure inside the charging device for three different atmospheric pressure levels and the steam pressure limit for 95 °C, resp. 98 °C is illustrated in fig. 5 for selected geometries. Whether the pressure falls below the steam pressure of 98 °C strongly depends on the atmospheric pressure. Whereas for 0 m above sea level (a.s.l.) there is only a risk for the reference diffusor with a sharp edge (CDS_0), in case of 500 m a.s.l. nearly every simulated geometry case, except of the optimized free form CDS_4, falls below the limit. For an atmospheric pressure level according to 1000 m a.s.l. the pressure in CDS_1, resp. CDS_4 is above the steam pressure only if the liquid temperature is reduced to 95 °C.

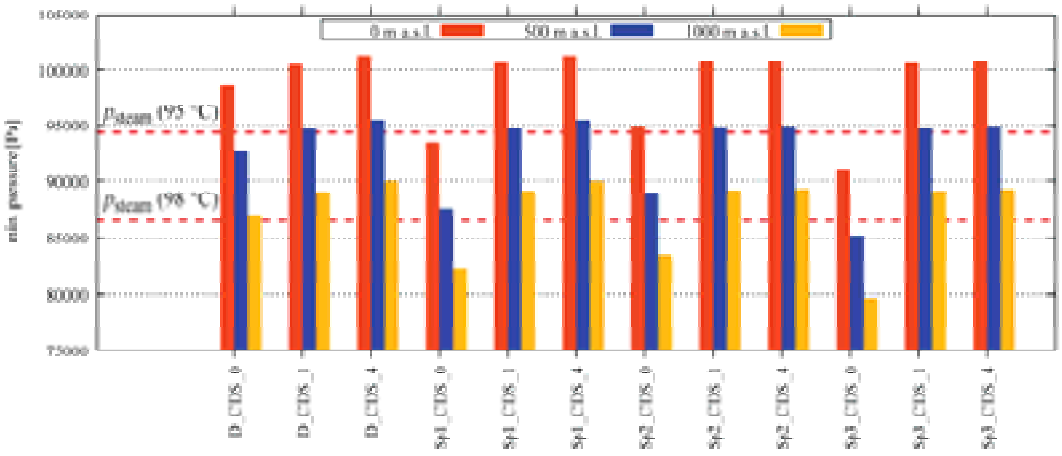

Fig. 5: Minimum static pressure inside the radial diffuser for different atmospheric pressure levels

Fig. 6a shows the pressure field for the reference radial diffuser CDS_0 with a sharp edge between the connection of the hose and the radial diffuser, where the pressure drops locally for about 10 kPa. As a result of the geometry optimization, the free form diffuser CDS_4 (fig. 6b) reduces the local pressure drop to 1.2 kPa. This value corresponds exclusively to the dynamical pressure conversion due to the acceleration of the fluid. Thus, by using a free form diffuser the local pressure drop inside the charging device can be minimized.

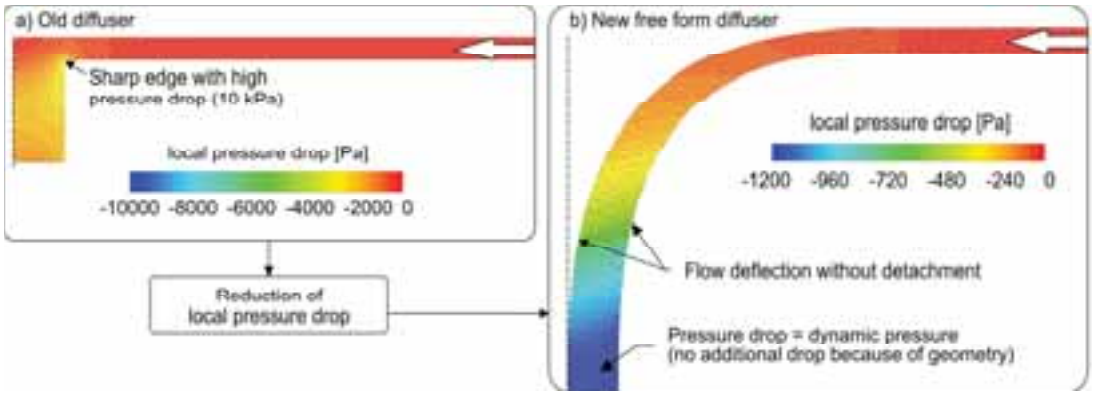

Fig. 6: Local pressure drop in a radial diffuser during discharging with 98 °C hot water; CDS_0 (a) and CDS_4 (b)

4.2 Charging behaviour and development of the thermal stratification

The diffuser shapes were also investigated regarding their performance during charging of the tank. Fig. 7 displays the temporal evolution of the averaged height of the thermal stratification using the example of the demonstrator. It is important to notice, that the criteria is not valid until the thermal stratification is fully developed. This is the case during the first 500 s. In the further development no significant differences can be observed between the investigated diffuser shapes. The same yields for the other simulated stores (fig. 8). There is no remarkable difference between the geometries. Since the stratification quality is already very high

due to the direct mounting of the diffuser at the ceiling no further improvements can be observed. Thus, a very high stratification quality is possible and independent of the diffuser geometry. But, as test simulations with different diffuser heights suggests, this counts only as long as there are no negative velocities at the diffuser outlet because of suction effects. The dimensioning of the radial diffuser is therefore still important.

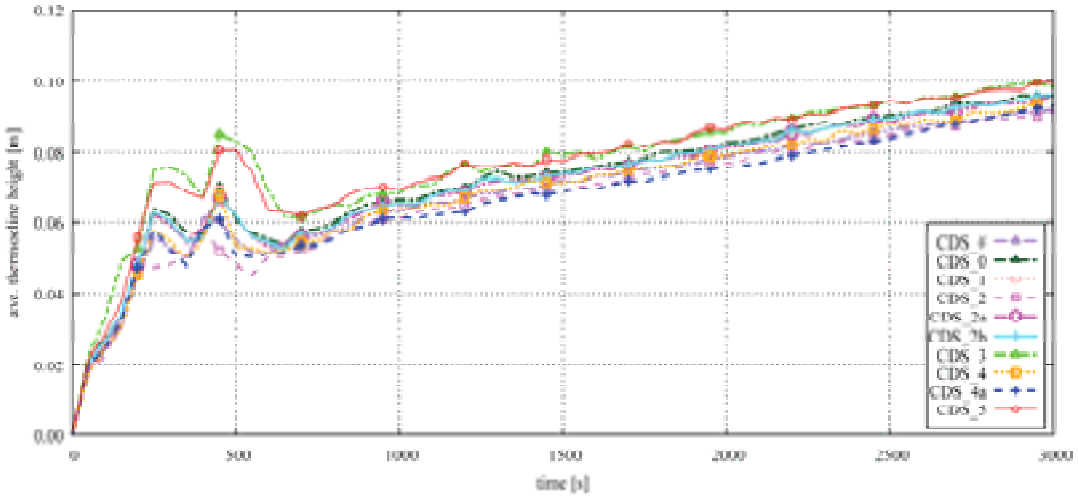

Fig. 7: Temporal evolution of the average height of the thermocline for different diffuser geometries in the demonstrator

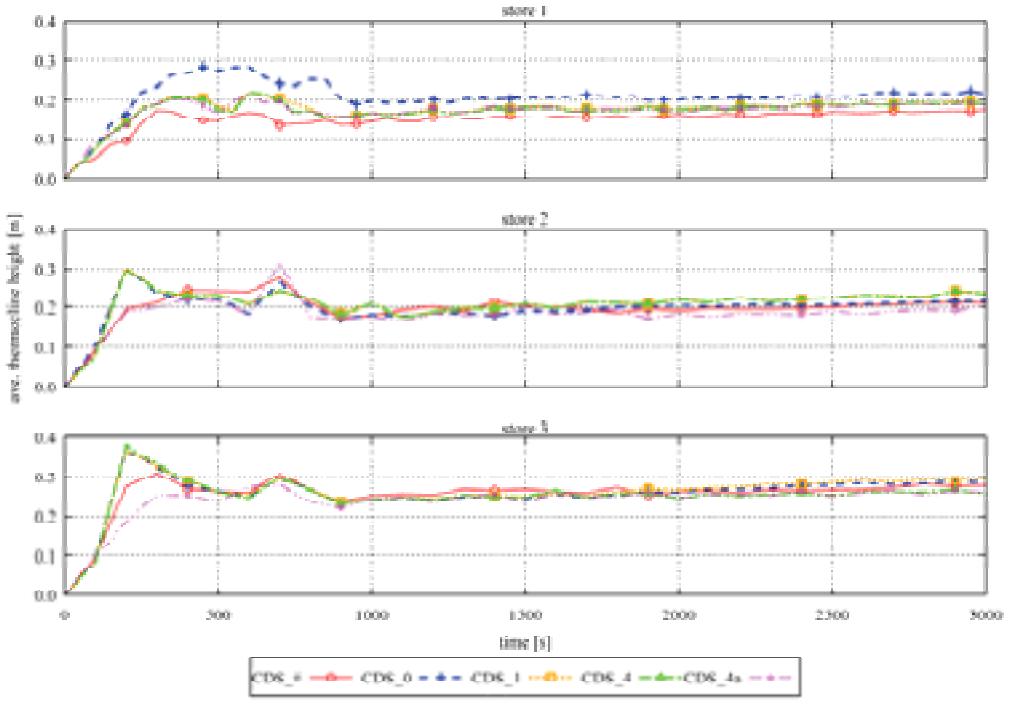

Fig.8: Temporal evolution of the average height of the thermocline for selected diffuser geometries in stores with a volume of 1000, 3500 and 6000 m³

To understand the underlying mechanisms and to illustrate and clarify effects that determine the resulting thermocline height a Large Eddy Simulation (LES) was performed. Fig. 9a shows the density current with its characteristic properties. The result pointed out, that there are mainly two mixing areas. The first one is situated along the height of the radial diffuser (fig. 9c) and the second one is located below the radial diffuser (fig. 9d). Interesting is, that, at least in flat bottom tanks with relatively high diameters, the collision of the density current against the side wall did not significantly influence mixing.

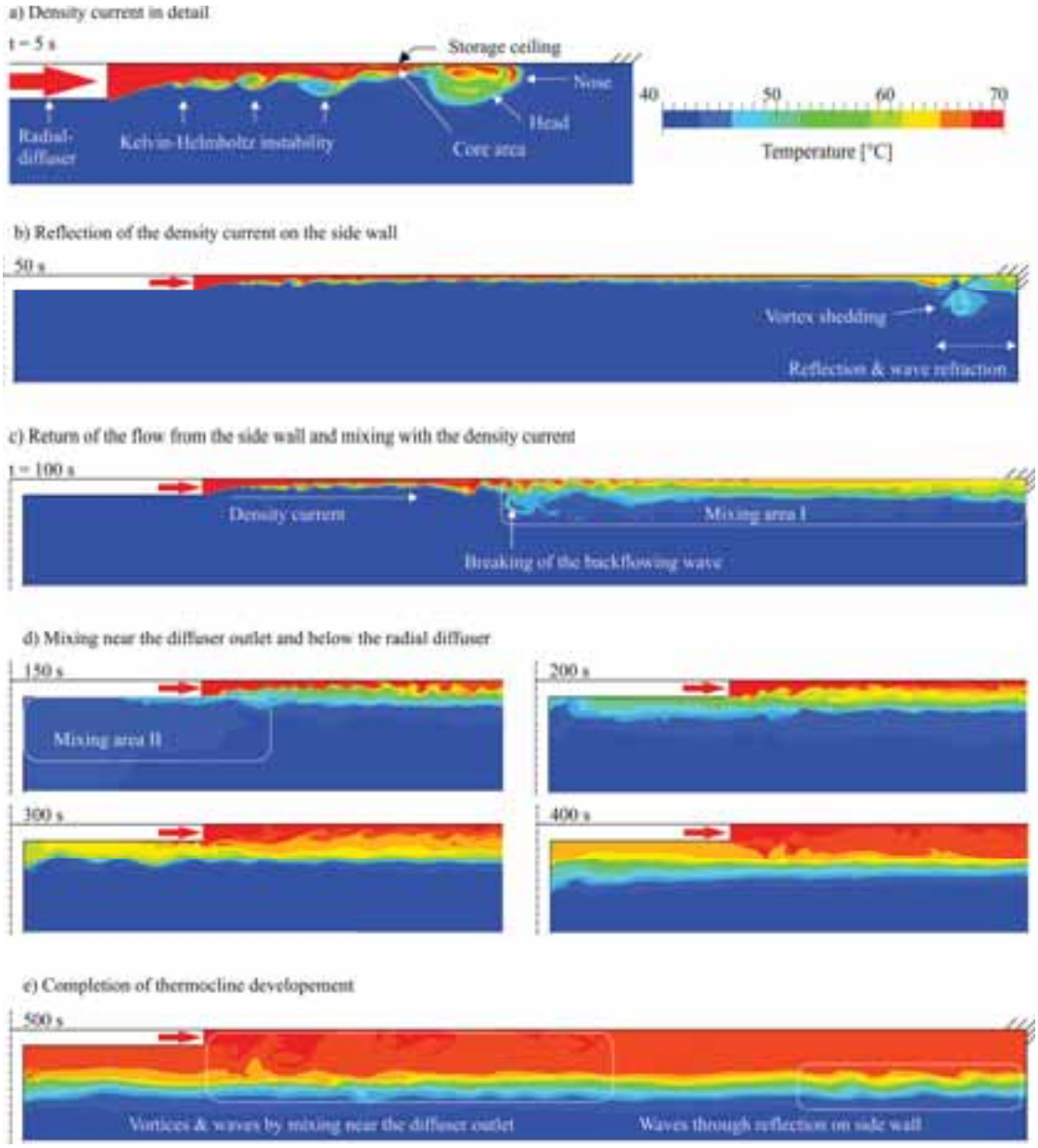

Fig. 9: Temperature field in the cross section area of the cylindrical storage during the development of the thermal stratification

To summarize the results regarding the charging behaviour fig. 7 illustrates the correlation between stratification quality and the Froude number *Fr* used for the radial diffuser design (Findeisen et al., 2017), resp. the storage volume and the height of the diffuser. Due to the high density difference and the moderate loading volume flow a rather conservative design with $Fr = 0.57$ is present in the demonstrator. In store 3, the Froude number is significantly higher at 1.06, but still within the framework of the usual recommendation of $Fr \approx 1$ (Urbaneck, 2012). It can be seen, that the height of the thermocline increases by a factor of about three with a double Froude number. Since in the examples shown the same difference in density exists, here, the height of the thermocline mainly depends on the impulse of the flow.

The diffuser height has a similar tendency to the Froude number on the stratification quality. This correlation is obvious. As previously stated, for the same density differences the impulse of the volume flow rate is decisive and the diffuser height now determines the flow impulse as the outflow velocities are quiet similiar. The LES simulation illustrated this correlation qualitatively (fig. 9): The mixing area I is approximately as high as the gap at the diffuser outlet and the final thermocline has approximately twice the height. The additional mixing occurs in the mixing area II. The differences between the different diffuser variants of store

1 and 2 as well as between the variants of store 3 are also determined by mixing area II (because of vertical speed differences in the near field; see Findeisen et al., 2017).

The compact storage tanks considered in this study have a height to diameter ratio of about one. In larger storage tanks likely more mixing takes place due to the increasing mixing surface on the underside of the jet. On the other hand, in stores with a significantly smaller diameter compared to their height other effects dominate (Lohse, 2012).

The results show for a specific operating point that the stratification quality depends on the store diameter, the Froude number and the diffuser height, which is already contained in the Froude number. In addition to the diffuser height, the Froude number also considers the operating parameters. It is therefore well suited for the dimensioning of radial diffusers. In general, buoyancy forces should outweigh inertia forces and therefore smaller Froude numbers should be preferred. In the present case a more conservative interpretation is recommended as the very low thermocline height of the demonstrator proves.

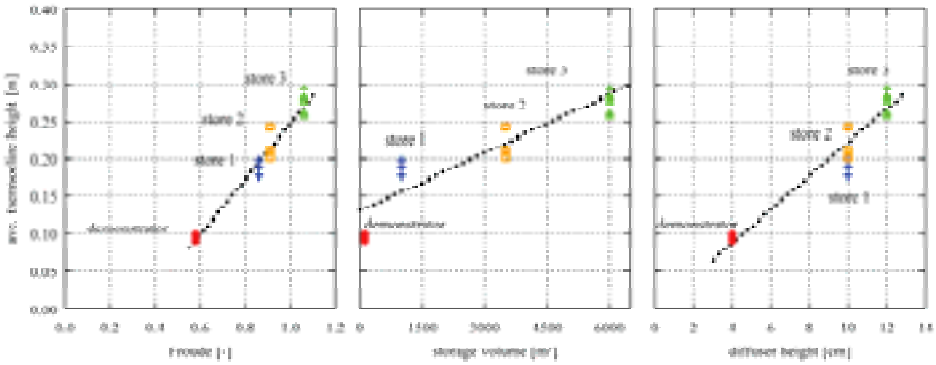

Fig. 9: Results of the average height of the thermocline from all simulated diffuser geometries after 3000 s for different Froude numbers, storage volumes and diffuser heights

5. Conclusion and Outlook

The performance of radial diffusers with different shapes was investigated for a single design point in different hot water storage sizes using CFD. Due to an optimized position of the diffuser in the tank the thermal stratification could be significantly improved. This offers various other advantages and underlines the benefits of a new storage type with a floating ceiling. A new free-form radial diffuser with a flow optimized shape was presented, which enables charging and discharging with temperatures up to 98 °C by reducing the risk of falling below the steam pressure limit. Furthermore, the application of LES identified mixing areas during the beginning of the loading process determining the resulting stratification quality.

6. Acknowledgement

The realization of the project and the scientific work is supported by the German Federal Ministry for Economic Affairs and Energy (BMWi) on the basis of a decision by the German Bundestag (FKZ: 03ET1230B). The authors gratefully acknowledge this support and carry the full responsibility for the content of this paper.

7. References

Findeisen, F., Urbaneck, T., Platzer, B., 2016. Radiale Diffusoren in Warmwasserspeichern – Funktionale Optimierung mittels CFD, Teil 1: Grundlagen und Modellierung. HLH, 10, 20-28. ISSN 1436-5103.

Findeisen, F., Urbaneck, T., Platzer, B., 2017. Radiale Diffusoren in Warmwasserspeichern – Funktionale Optimierung mittels CFD, Teil 2: Optimierung des Be- und Entladeverhaltens. HLH, 2, 25-33. ISSN 1436-5103.

Hedbäck T., Hedbäck, A., 1993. DE 43005 867.

Lohse, R., Urbaneck, T., Brämer, C., Platzer, B., 2012. Effecks During Loading of Hot Water Storages with a High Asped Ratio. Euro Heat & Power, English Edition. 3, 42–47. – ISSN 1613–0200.

Urbaneck, T., Platzer, B., Findeisen, F., 2016. Warmwasserspeicher – Stand der Technik und Entwicklungen. HLH, 07-08, 16-21. ISSN 1436-5103.

Urbaneck, T. et al., 2017. www.obserw.de [Accessed 3 Oct. 2017].

Urbaneck, T., 2012. Kältespeicher: Grundlagen, Technik, Anwendung. Oldenbourg Verlag. ISBN 3486719882.

Cycling test of liquid sorption thermal energy storage using sodium hydroxide

Benjamin Fumey[1], Robert Weber[1] and Luca Baldini[1]

[1] Empa, Dübendorf (Switzerland)

Abstract

In this paper results of an absorption heat storage cycling test are presented. The specific application is long term heat storage, the test setup is based on a spiral finned tube heat and mass exchanger constructed of stainless steel type 1.4571 and the absorbent working pair is sodium hydroxide and water. A total of 7 cycles are performed at approximately 13.5 hours of absorption and 17 hours of desorption time per cycle. Average concentration of sodium hydroxide in the solution is 48 wt% after desorption and 27 wt% after absorption. Comparison of thermal performance among different cycles is made. No clear tendency of cycling improvement or degradation is found.

Keywords: Absorption heat storage, Long term thermal energy storage, Sodium hydroxide / Water, Cycling test, Spiral finned tube heat and mass exchanger

1. Introduction

Heat storage based on sorption process has the prospective for compact thermal storage without suffering loss during storage time. Much research has been done towards this goal, accompanied by several IEA Technology Collaboration Programs [van Helden et al. 2015]. Sorption heat storage operates as a chemically driven heat pump, storing not heat, but the potential to regain heat at elevated temperatures. Applied sorption materials are generally categorized into adsorbents referring to solid sorbents and absorbents referring to liquid sorbents. Categorization is made from an application perspective whereby the sorbate, frequently taken to be water, adheres to the surface of solids and diffuses into liquids. Theoretical work on absorption materials shows promising potential for heat storage application [Hui, et al. 2011], and is seen to have good potential for building integrated heat storage [N'Tsoukpoe, et al. 2009, Tatsidjodoung, et al. 2013, Zhang, et al. 2014]. Common absorbents considered are the aqueous salts lithium bromide (LiBr) [N'Tsoukpoe et al. 2013, Mortazavi et al. 2015], lithium chloride (LiCl) [Bales et al. 2008], calcium chloride ($CaCl_2$) [Quinnell, et al. 2011, Le Pierrès, et al. 2011] and sodium hydroxide (NaOH) [Weber and Dorer, 2008]. First heat storage prototypes for solar heating have been built based on the conventional falling film tube bundle heat and mass exchanger (HMX) [N'Tsoukpoe et al. 2013, Fumey et al. 2015a]. Nevertheless, various issues related to the required large concentration difference in a single cycle process have led to poor operation results. Challenges include regrouping of droplets due to high viscosity of the absorbent working pair as well as high surface tension and high contact angle. Thus, system performance has generally been unsatisfactory, and it is recognized that new HMX concepts are required [N'Tsoukpoe et al. 2013, Daguenet-Frick, et al. 2017]. In contrast to solar sorption chilling machines [Ibarra-Bahena and Rosenberg, 2014] not cold, but heat is sought and not a full cycle but a time interrupted process is at hand. Absorption heat storage performance is measured in respect to energy density and temperature lift [Fumey et al. 2015b]. Energy density is dependent on the degree of absorbate difference between charged and discharged absorbent working fluid and temperature lift is dependent on the concentration of absorbent in the working fluid. High concentration leads to increased temperature lift. A HMX for absorption heat storage must reach maximum absorbate uptake in a single pass process in order to prevent temperature drop due to concentration reduction through mixing of charged absorbent solution with semi discharged solution. Experiments have shown that substantially more exposure time of absorbent solution to absorbate is required then commonly possible in absorption chiller type HMXs [Fumey et al, 2017]. Alternative HMX designs are suggested by [Michel et al. 2017] and [Fumey et al, 2017].

doi:10.18086/swc.2017.13.05 Available at http://proceedings.ises.org

In this paper the cycling test results of a spiral finned tube HMX design as described in [Fumey et al., 2017] made of stainless steel type 1.4571 and operated with aqueous NaOH are presented and compared in respect to important performance parameters with focus on possible degradation.

2. Setup description

In this absorption process, HMX operation is under exclusion of non-condensing gasses. Fig. 1b shows the finned tube heat exchanger used both as absorber and desorber (A/D) as well as evaporator and condenser (E/C). Dual function is possible due to the time separated processes of evaporation and absorption and the process of desorption and condensation. Both, in absorption and desorption operation, aqueous NaOH is introduced to the top of the A/D spiral fin and flows down, channeled along the fin as illustrated in Fig. 1a. In absorption mode, water follows the same principle on the E/C unit whereby it is evaporated by means of low temperature heat source and in turn absorbed on the aqueous NaOH. The heat of vapor condensation as well as to a smaller part the heat of dilution is released at concentration dependent elevated temperature to the heat transfer fluid (HTF). In desorption mode the revers process is followed; heat from the HTF is released to the absorbent, whereby water is evaporated from the aqueous NaOH solution. The water vapor is in turn condensed on the E/C unit and the heat released to the respective HTF. Depending on the NaOH concentration and the temperature difference between A/D and E/C unit absorption or desorption takes place.

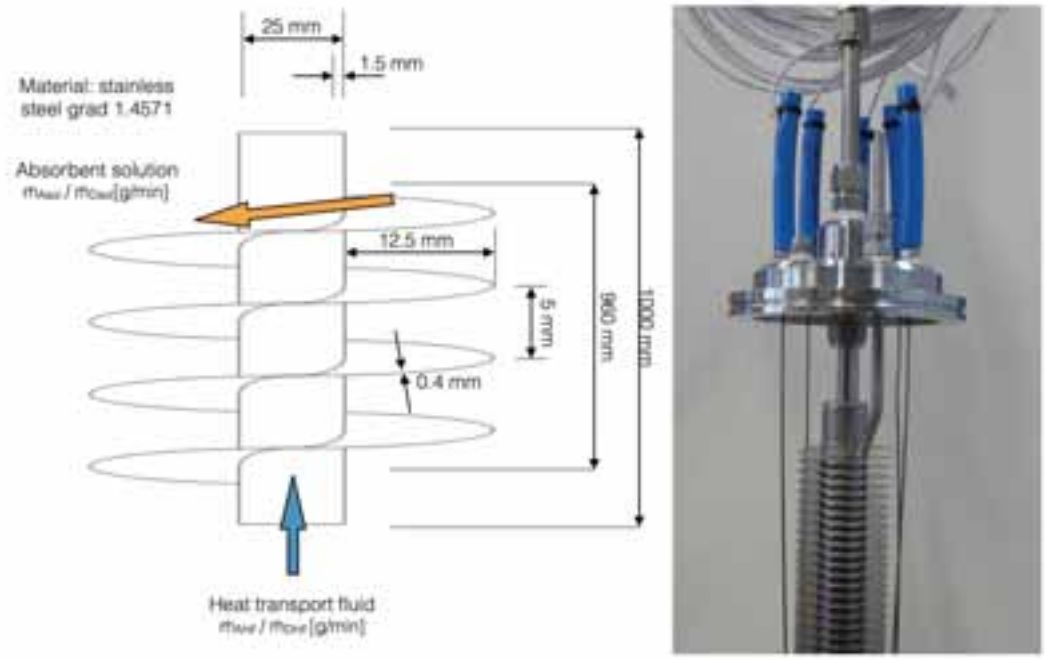

Fig. 1: a) Illustration of the finned tube heat exchanger with absorbent solution flow indicated by the orange arrow and HTF by the blue arrow (left). b) Finned tube heat exchanger showing the sorbent supply tube on the top most fin as well as installed temperature sensors. The HTF flows through the center tube (right).

The benefits of the spiral finned tube heat exchanger are, the long exposure time, large surface area, slow flow of the absorbent and resulting thin film, adjustability of exposure time, film thickness control by absorbent flow regulation, and continuous process both in absorption as well as desorption.

In the lab scale HMX test facility, two spiral finned tubes as A/D and E/C units are installed in two separate chambers respectively as shown in Fig. 2. The two chambers are interconnected in order to enable water vapour exchange and the HMXs are supplied with heat and cold from two thermostat/cryostat baths. These operate as solar heat source and ambient heat sink in desorption also referred to as charging mode as well as low temperature heat source and building heat demand in absorption or discharging mode. Gear pumps circulate the heat transfer fluids, supplied to the bottom of the HMX, in counter flow to the absorbent and absorbate and flow is regulated with buoyancy flow regulators. Both absorbent and absorbate are sourced from plastic canisters at atmospheric pressure. The containers are seen in Fig. 2 at the bottom center. The blue canister holds the absorbent (aqueous NaOH) and the white canister holds the absorbate (water). This is strongly in contrast to the

conventional approach in closed sorption systems where both sorbent and sorbate are stored under low pressure conditions with removal of all non-condensing gasses. Absorbent is dosed to the absorber by a tubing pump seen above the blue canister. Mass flow is monitored by electronic scale placed underneath the absorbent canister. Absorbate is supplied to the E/C chamber from the respective canister by pressure difference between the ambient to the low pressure in the chamber and re-circulated on the HMX using a gear pump. Both absorbent and absorbate are removed from the low pressure HMX chambers by vacuum lock. These consist of a container each connected to the respective chamber via ball valve. The absorber / desorber vacuum lock is indicted in Fig. 2 bottom left. Absorbent and absorbate flows from the HMX into the vacuum lock by gravitational force. Periodically, the interconnecting valves are closed, the lock aired and the working fluids released to plastic container. Prior to opening the valve again, the lock is evacuated. This setup enables periodic sampling without interrupting the continuous operation. Detailed results of initial operation tests are presented in [Fumey et al. 2017].

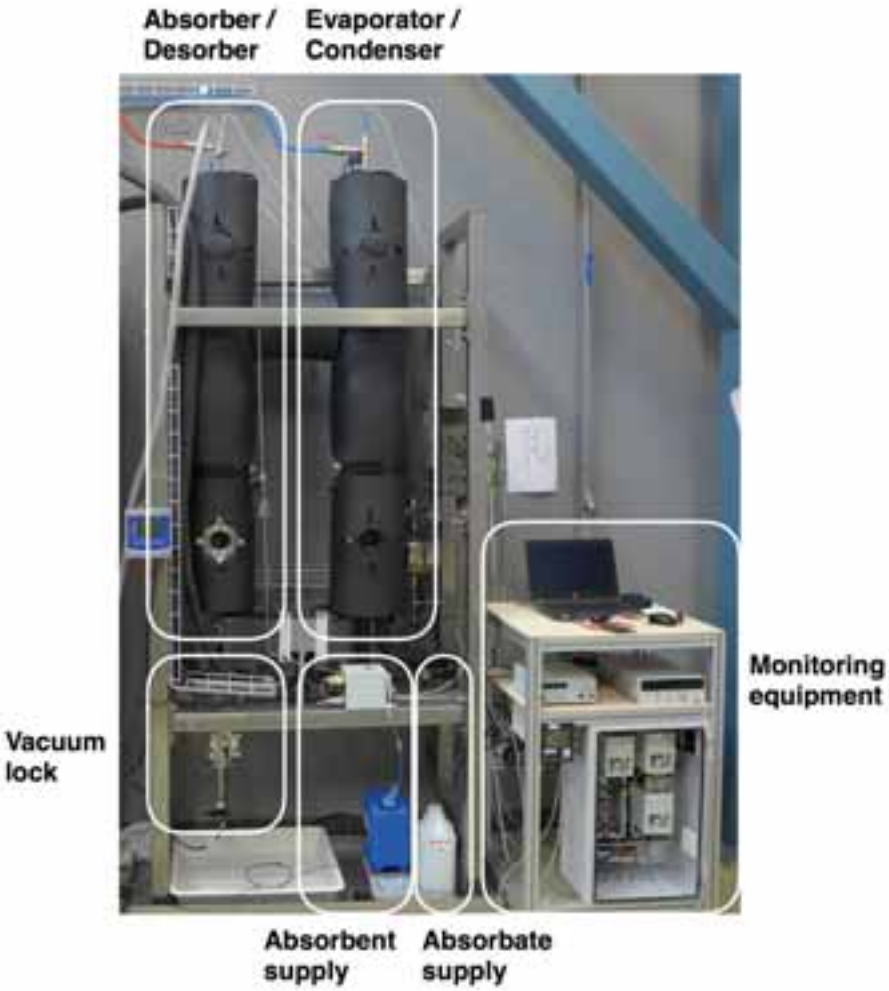

Fig. 2: Test setup including the absorber / desorber composition on the left top, the evaporator / condenser unit on the right top, the absorbent vacuum lock on the left bottom, the absorbent and absorbate supply on the bottom center and the monitoring equipment to the bottom right.

3. Testing procedure

Seven absorption and desorption cycles are undertaken in the described setup and performance is compared in terms of deviation of effective temperature difference from the theoretical temperature difference for a given absorbent concentration. Theoretical values are represented by the equilibrium curve (see Fig. 3-6). This test distinguishes itself from the former tests reported in that both absorbent solution and absorbate are continuously reused. This approach leads to a dependence of absorption performance on the preceding desorption process and

may lead to an accumulation of possible performance depredators. In absorption, the absorbent flow is 6 g/min, the A/D HTF supply temperature is 28 °C at a flow of 200 g/min and the E/C supply temperature is 25°C at a flow of 800 g/min. In desorption the absorbent flow is 8 g/min, the A/D HTF supply temperature is 65 °C at a flow of 800 g/min and the E/C supply temperature is 10 °C at a flow of 1200 g/min. The test duration for a single cycle in absorption is approximately 13.5 hours and the desorption duration is 17 hours due to the greater mass of diluted aqueous NaOH to be transported. One complete absorption and desorption cycle is tested per week resulting in a total test duration of 7 weeks. No absorbent or absorbate is added or removed from the solution during the test series. Both absorbent and absorbate are stored under atmospheric pressure and exposed to air.

4. Results and discussion

Fig. 3 shows the process performance with reference to the ideal equilibrium state of the cycling test with temperature difference between the A/D and E/C unit on the x-axis and the absorbent concentration on the y-axis. Average values of the cycles are shown. The dashed line shows the theoretical equilibrium between the temperature difference and the concentration. In Fig. 3 the red x values show the maximum temperature difference between the absorbent and evaporation temperature during absorption in dependence of the concentration. Due to the varying concentration in the cycling tests, the maximum absorption temperature varies. Performance is measured in dependence of horizontal distance from the equilibrium line. The red + values show the final resulting concentration in the absorption process plotted against the minimum temperature difference between A/D and E/C HMX. As with the x values, performance is measured in dependence of horizontal distance to the equilibrium. Closer fit to the equilibrium line shows good performance in terms of effective mass transfer. The blue o values show the resulting concentration of the desorption cycles. As with the absorption results, close fit to the equilibrium line is desired.

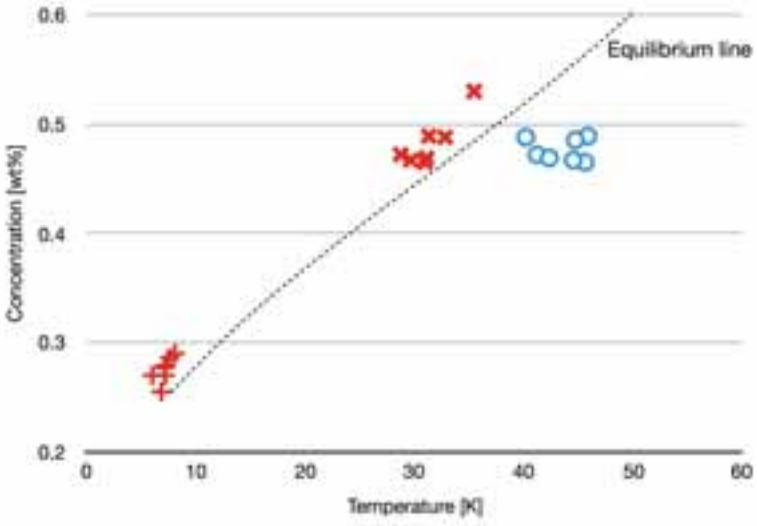

Fig. 3: Overview of resulting concentration/temperature difference pairs recorded during cycle testing in absorption and desorption mode. Red x representing beginning of absorption, red + end of absorption and blue o end of desorption (beginning of desorption is omitted as initial absorbent concentration do not correspond to charging temperatures).

Fig. 4 to 6 show details of the results presented in Fig. 3 for the different operation regimes, beginning and end of absorption as well as end of desorption process, with indication of cycle number for analysis of cycling performance and standard deviation. Fig. 4 shows the maximum temperature increase in respect to concentration in absorption. As expected the temperatures are lower than the equilibrium. Part of this temperature drop is due to water vapor mass diffusion resistance in evaporation, as well as vapor transport from A/D unit to E/C unit and diffusion into the absorbent. It is yet unclear what portion of the total temperature drop is due to this effect.

Test A1 shows a substantially higher temperature gain due to the starting concentration of 53 wt%, temperature increase is directly dependent on absorbent concentration. Nevertheless, it also shoes a large temperature deviation from equilibrium. Interesting is to note that the first 3 cycles have a stronger temperature deviation than the following 4 cycles. Nevertheless, there is no clear tendency observed, highlighting a potential effect of cycling. The least temperature difference is seen at test A5, with tests A6 and A7 showing again an increase. The dashed line is parallel to the equilibrium line with a temperature offset of 4 K representing an average temperature deviation from equilibrium through the set of cycles.

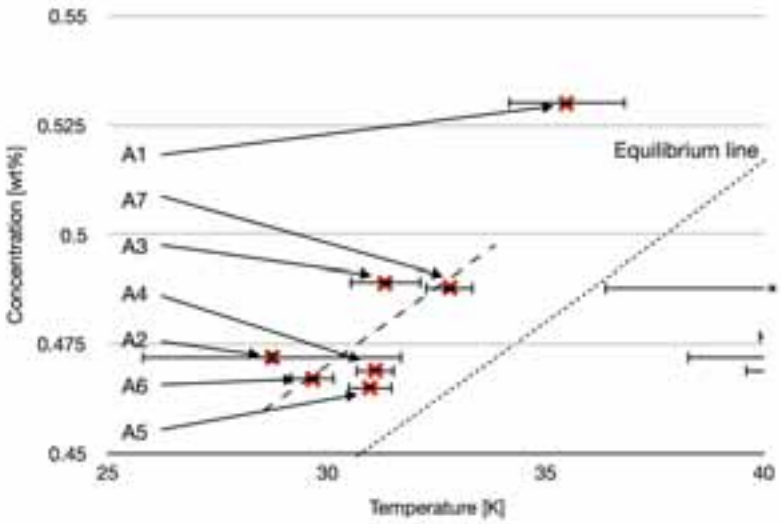

Fig. 4: Focus of Fig. 3 on the maximum temperature increase in respect to the concentration in the absorption process. All values are numbered according to their cycle. The dashed line shows a 4 K offset to the equilibrium line.

Fig. 5 shows the resulting concentration in respect to the minimum temperature difference between the absorber and the evaporator. This is approximately 7 K. As in Fig. 4 there is no trend of degradation or improvement visible across the cycles. Apart from cycle A1 and A6, all results show approximately the same offset to the equilibrium line of approximately 3 K as indicated by the dashed line parallel to the equilibrium line. The concentration difference results from the slightly varying temperature difference between the cycles.

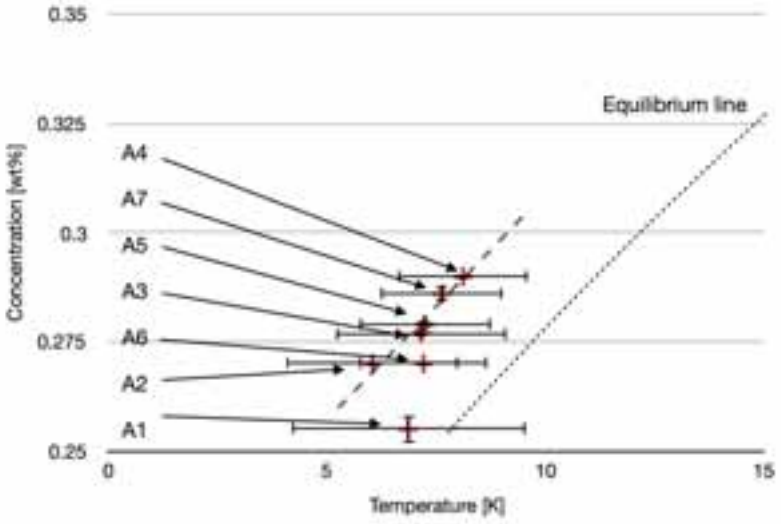

Fig. 5: Focus of Fig. 3 on the minimum concentration reached in absorption modus. All values are numbered according to their cycle. The dashed line shows a 3 K offset to the equilibrium line.

Fig. 6 shows a close up of the resulting concentration in respect to the temperature difference in the desorption process. Compared to the absorption results in figures 4 and 5 there is a greater average deviation from the equilibrium line in the desorption process. It appears that more time is required in order to reach a closer fit to

the equilibrium line. As in absorption, mass transport resistance is three fold; desorption, vapor transport and condensation. Assuming that vapor transport resistance and water phase change on the E/C unit is equal in the absorption as well as the desorption process, it may be concluded that there is a greater mass transport resistance in desorption than in absorption. The dashed line shows an offset of 9 K. As for absorption, there is no clear degradation trend to be recognized in desorption.

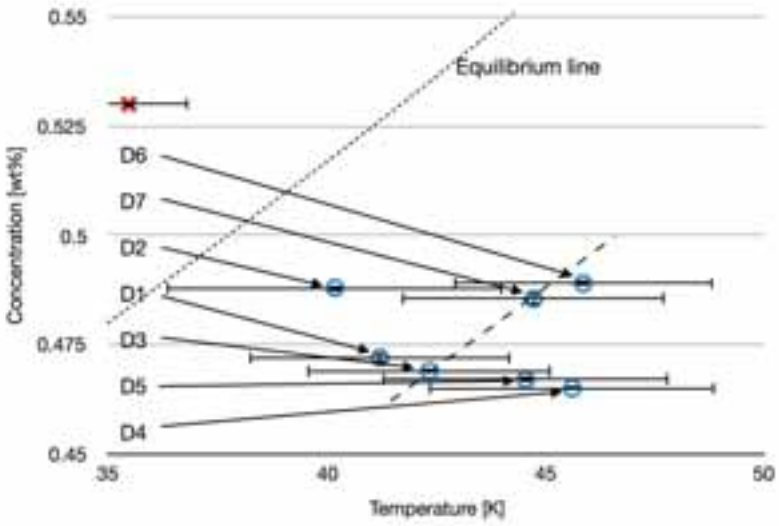

Fig. 6: Focus of Fig. 3 on the maximum concentration reached in desorption modus. All values are numbered according to their cycle. The dashed line shows the 9 K offset to the equilibrium line.

From the illustrated results it is shown that in respect to performance there is no clear trend of degradation or improvement.

It can be seen that even though both absorbent and absorbate are exposed to air in storage, no performance loss is encountered. On a system level this is a very important result, due to the large potential of system simplification and reduction of component costs.

5. Conclusion and outlook

In this paper a cycling test of 7 cycles is presented based on a spiral finned tube heat and mass exchanger for absorption heat storage. Results show good cycling stability without any clear degradation of the process. Storage of both absorbent and absorbate at ambient pressure is seen to be a promising approach for substantial reduction of system complexity and cost. Further work will include measurement over increased number of cycles with chemical analysis of absorbent in between the cycles.

6. Acknowledgements

We gratefully acknowledge financial support by the Swiss Comission for Technology and Innovation (CTI) through the Swiss Competence Center for Energy Research Heat and Electricity Storage.

7. References

B. Fumey, R. Weber, L. Baldini, 2017, Liquid sorption heat storage – A proof of concept based on lab measurements with a novel spiral fined heat and mass exchanger design, In Applied Energy, Volume 200, Pages 215-225,

Bales C., 2008, Final report of subtask B chemical and sorption storage the over- view, Available from: http://archive.iea-shc.org/publications/ downloads/task32-b7.pdf

Benjamin Fumey, Robert Weber, Paul Gantenbein, Xavier Daguenet-Frick, Ian Hughes, Viktor Dorer, 2015b, Limitations Imposed on Energy Density of Sorption Materials in Seasonal Thermal Storage Systems, In Energy Procedia, Volume 70, Pages 203-208,

Benoit Michel, Nolwenn Le Pierrès, Benoit Stutz, 2017, Performances of grooved plates falling film absorber, In Energy, Volume 138, 2017, Pages 103-117,

Fumey B., Weber R., Gantenbein P., Daguenet-Frick X., Stoller S., Fricker R., Dorer V., 2015a, Operation Results of a Closed Sorption Heat Storage Prototype, Energy Procedia, Volume 73, 324-330

Jonathan Ibarra-Bahena and Rosenberg J. Romero, 2014, Performance of Different Experimental Absorber Designs in Absorption Heat Pump Cycle Technologies: A Review, Energies, 7, 751-766

K. Edem N'Tsoukpoe, Hui Liu, Nolwenn Le Pierrès, Lingai Luo, 2009, A review on long-term sorption solar energy storage, In Renewable and Sustainable Energy Reviews, Volume 13, Issue 9, Pages 2385-2396

K.E. N'Tsoukpoe, N. Le Pierrès, L. Luo, 2013, Experimentation of a LiBr–H2O absorption process for long-term solar thermal storage: Prototype design and first results, In Energy, Volume 53, Pages 179-198,

Le Pierrès N., Liu H., Luo L., 2011, CaCl2/H2O absorption seasonal storage of solar heat, Proceedings of the international conference for sustainable energy storage, Belfast, Ulster, Feb 21-25.

Liu Hui, N'Tsoukpoe K. Edem, Le Pierres Nolwenn, Luo Lingai, 2011, Evaluation of a seasonal storage system of solar energy for house heating using different absorption couples, In Energy Conversion and Management, Volume 52, Issue 6, 2011, Pages 2427-2436,

Mehdi Mortazavi, Rasool Nasr Isfahani, Sajjad Bigham, Saeed Moghaddam, 2015, Absorption characteristics of falling film LiBr (lithium bromide) solution over a finned structure, In Energy, Volume 87, Pages 270-278

Parfait Tatsidjodoung, Nolwenn Le Pierrès, Lingai Luo, 2013, A review of potential materials for thermal energy storage in building applications, In Renewable and Sustainable Energy Reviews, Volume 18, Pages 327-349

Quinnell J.A., Davidson J.H., Burch J. 2011, Liquid calcium chloride solar storage: concept and analysis, Journal of Solar Energy Engineering.

R. Weber, V. Dorer, 2008, Long-term heat storage with NaOH, In Vacuum, Volume 82, Issue 7, Pages 708-716

Wim van Helden, Motoi Yamaha, Christoph Rathgeber, Andreas Hauer, Fredy Huaylla, Nolwenn Le Pierrès, Benoit Stutz, Barbara Mette, Pablo Dolado, Ana Lazaro, Javier Mazo, Mark Dannemand, Simon Furbo, Alvaro Campos-Celador, Gonzalo Diarce, Ruud Cuypers, Andreas König-Haagen, Stephan Höhlein, Dieter Brüggemann, Benjamin Fumey, Robert Weber, Rebekka Köll, Waldemar Wagner, Xavier Daguenet-Frick, Paul Gantenbein, Frédéric Kuznik, 2016, IEA SHC Task 42 / ECES Annex 29 – Working Group B: Applications of Compact Thermal Energy Storage, In Energy Procedia, Volume 91, Pages 231-245,

Xavier Daguenet-Frick, Paul Gantenbein, Jonas Müller, Benjamin Fumey, Robert Weber, 2017, Seasonal thermochemical energy storage: Comparison of the experimental results with the modelling of the falling film tube bundle heat and mass exchanger unit, In Renewable Energy, Volume 110, Pages 162-173,

Xiaoling Zhang, Minzhi Li, Wenxing Shi, Baolong Wang, Xianting Li, 2014, Experimental investigation on charging and discharging performance of absorption thermal energy storage system, In Energy Conversion and Management, Volume 85, Pages 425-434

Thermal Performance Testing of Outdoor Hot Water Stores for Long-term Thermal Energy Storage

Markus Gerschitzka[1], Dominik Schmidt, Dominik Bestenlehner[1], Roman Marx and Harald Drück[1]

[1] University of Stuttgart, Institute of Thermodynamics and Thermal Engineering (ITW)
Research and Testing Centre for Thermal Solar Systems (TZS)
Pfaffenwaldring 6, 70550 Stuttgart, Germany

Abstract

This contribution describes a model-based thermal performance test method for outdoor hot water stores for long-term thermal energy storage. For this purpose an existing TRNSYS model for indoor hot water stores is modified. In particular, local variations of the ambient temperature and the influence of solar irradiation are taken into account. A parameter identification process is proposed, which makes it possible to determine the parameters of the model required for the characterization of the thermal performance of an outdoor installed hot water store. The test method has been developed for an outdoor installed hot water store with a volume of 12 m^3, a vacuum thermal insulation and a transparent thermal insulation as well as for an outdoor installed 100 m^3 hot water store with a conventional thermal insulation. The functionality of the test method is confirmed by measured data, plausibility checks of the model parameters and a comparison to theoretical values determined based on material properties. Furthermore, the influences of the minimization algorithm on the results of the parameter identification process are investigated.

Keywords: Hot water store for outdoor installation, thermal performance test method, parameter identification

1. Introduction

Overground hot water stores with volumes in the range of 10 m^3 to 500 m^3 are an attractive technology for efficient and long-term thermal energy storage due to their relatively low surface to volume ratio compared to stores with smaller volumes. Applications of such stores range from SolarActiveHouses (Gerschitzka et al., 2016) to buffer stores in solar district heating systems (Bauer el al., 2010). In the last decade, several demonstration projects with stores in a volume range of 10 m^3 to 500 m^3 were planned, built and monitored within national and international research projects (Bauer et al., 2010, 2016). These stores are often placed overground and outside due to their large size. The resulting dynamic changes in the ambient conditions and novel effects on the heat losses, such as wind and irradiation, compared to a common indoor installation, require a modification and extension of already existing methods for the performance testing of hot water stores. Hence, in this contribution a model-based thermal performance test method for outdoor hot water stores is developed and validated. An existing TRNSYS model for indoor installed hot water stores (Drück, 2006) is modified. In particular, local variations of the ambient temperature and the influence of solar irradiation are taken into account. A parameter identification process is proposed, which makes it possible to determine the parameters of the model required for the characterization of the thermal performance of an outdoor hot water store for long-term thermal energy storage. The new test method was applied to a 12 m^3 hot water store with a vacuum thermal insulation combined with a transparent thermal insulation (TTI) as well as to a 100 m^3 hot water store with a conventional thermal insulation, see figure 1. Both stores were built for demonstration purposes in the context of two German research projects. The stores are equipped with measuring sensors for the determination of the ambient conditions and the store's thermal behaviour. Especially the temperatures inside the storage medium, outside the stores and on the outer surface of the thermal insulations are measured. Furthermore, the wind speed and the solar irradiation are recorded.

doi:10.18086/swc.2017.13.06 Available at http://proceedings.ises.org

Fig. 1: Outdoor installed thermal energy stores with a water volume of 12 m³ (left) and 100 m³ (right)

The store with a volume of 12 m³ was developed as part of the German national research project „StoEx“ (Development of a large-volume, low-cost hot water store with high-efficient thermal insulation for outdoor installation; PTJ grant number: 0325992B). The aim of this project was the development of an advanced hot water store for outdoor installation. A significantly reduced heat loss rate compared to conventionally insulated thermal energy stores was achieved by the use of the high-efficient thermal insulation techniques vacuum thermal insulation and transparent thermal insulation (Gerschitzka et al., 2015a). The store was tested at a novel outdoor test facility especially designed for thermal performance testing of large-scale outdoor installed thermal energy stores (Gerschitzka et al., 2016). The project was carried out by the Research and Testing Centre for Thermal Solar Systems (TZS) of the Institute of Thermodynamics and Thermal Engineering (ITW) of the University of Stuttgart and the company Sirch Tankbau-Tankservice-Speicherbau GmbH from Germany.

The 100 m³ store was developed as part of the German national research project “OBSERW” (Overground stores in segmental construction for district heating systems; grant number: 03ET1230C). The partners of the project are the Professorship of Technical Thermodynamics of the Faculty of Mechanical Engineering of the Chemnitz University of Technology (TUC/TT), the Research and Testing Centre for Thermal Solar Systems (TZS) of the Institute of Thermodynamics and Thermal Engineering (ITW) of the University of Stuttgart and the company farmatic Anlagenbau GmbH from Germany. Within the project a so-called flat bottom hot water store using a thermal insulation based on polyurethane recycling material is developed (Urbaneck and Platzer, 2015). Regarding the store construction, a novel floating ceiling combined with a CFD-optimized charging device is investigated (Findeisen et al., 2016, 2017). Further topics of the research project OBSERW are the laboratory and application scale tests of the sealing material required for the segmental construction (Gerschitzka et al., 2015b).

2. Test method for outdoor hot water stores

The application of well-known test methods for indoor installed hot water stores to outdoor installed stores, e. g. of the test methods according to EN 12977-3 (2012) and EN 12977-4 (2012) is not appropriate since these methods are designed for smaller store volumes up to 5 m³ and for quasi steady state ambient indoor conditions. Additionally, no effects on the heat losses due to the outdoor specific installation are considered such as the decreased heat losses by solar gains. Furthermore, the charging and discharging capacity required to perform the test sequences of these methods is usually not available on-site. Therefore, a modified calculation procedure is developed regarding the determination of heat losses of outdoor installed hot water stores. For this calculation a model based on an extension of the proven TRNSYS Multiport Store-Model by Drück (2006) is used. A novel calculation of the outer surface temperature of the store is considered.

The Multiport Store-Model uses a one dimensional finite difference method to calculate the temperature of the storage medium. The storage medium is discretized along the store height in volume segments characterized by a node representing the temperature of these segments. The temperature of each node is determined by solving the energy balance for all nodes of the store's volume. This is a common approach to model the thermal behaviour of such stores for system simulation studies. A more detailed description of the Multiport Store-Model is given in (Drück, 2006, 2007). The original Multiport Store-Model considers the heat losses of the store medium for each volume segment by a linear approach between the heat flux of the heat losses and the temperature difference between the ambience and the store medium, according to eq. 1. The parameter (UA) represents the heat loss rate. Usually the inner surface temperature of an indoor installed hot water store is assumed to be the storage medium temperature.

$$\dot{Q}_{\mathrm{hl}} = (UA) \cdot (\vartheta_{\mathrm{sto}} - \vartheta_{\mathrm{amb}}) \qquad \text{(eq. 1)}$$

An outdoor installation of a hot water store requires a more detailed approach for the calculation of the heat losses. This is caused by the fact, that the heat flux of the solar irradiation, the convective heat transfer by wind and the heat capacity of the thermal insulation influence the outer surface temperature of the store. Hence, an extension of the Multiport Store-Model is necessary. This extension is done by an afterwards explained novel calculation method using a more detailed calculation of the store's outer surface temperature.

2.1. Calculation of the outer surface temperature

The thermal behaviour of a store's outer surface can be characterized by a multi-node calculation. Each node represents the temperature of a certain area of the outer surface of the store. Eight separate surface temperatures of the store's lateral area in circumferential direction are considered. A vertical temperature distribution within the considered specific surface area is neglected. The outer surface temperatures can be calculated by determining the heat transfer between the outer store surface and the ambience as well as the thermal capacities. The considered heat transport phenomena are the heat transfer by solar and thermal irradiation, a temperature and wind speed dependent convective heat transfer and an internal heat transfer inside the material of the outer surfaces in the circumferential direction.

The model parameters of the surface temperature calculation are the effective heat capacity C_{eff} of the store's thermal insulation, the transmittance-absorptance-product $(\tau_{\mathrm{g}}^{*}\alpha_{\mathrm{a}}^{*})$ and the heat transfer coefficient from the store surface to the ambience h_{ext1} respectively the coefficient of the temperature dependence of heat transfer coefficient h_{ext2}. Furthermore, a wind speed and irradiation dependency of the surface temperature can be included by the parameters h_{w1} and h_{w2}. Concerning the calculation of the incidence angle, depended on solar irradiation, the reflectance of the ambience ρ_{amb}^{*} and the incidence angle modifier K_{b} are of importance. A heat transfer by thermal irradiation between the store's surface and the ambience respectively the sky can be considered by the parameter ϵ^{*}. If there is a transparent thermal insulation on the outer store surface, a heat transfer between different surfaces in circumferential direction can occur. This heat transfer can be considered by the parameter $h_{\mathrm{int,i\rightarrow j}}$ between two neighboring segments.

Assuming only a small change of inner energy compared to the incoming solar irradiation and heat losses of the outer store surface, the energy balance of one surface segment can be approximated according to eq. 3. The subscription is exemplary for a north orientated surface segment. The aim of eq. 3 is to calculate the surface temperature ϑ_{sur} of one segment based on the knowledge of the input values and the temperature of the surface $\vartheta_{\mathrm{sur,old}}$ from the time step before. Considering all individual segment equations, an equation system occurs.

$$\begin{aligned}
\vartheta_{\mathrm{sur,N}} = {} & \vartheta_{\mathrm{sur,old,N}} \\
& + \{\left(\tau_{\mathrm{g}}^{*}\alpha_{\mathrm{a}}^{*}\right)_{\mathrm{N}} \cdot A \cdot (K_{\mathrm{b,N}} \cdot G_{\mathrm{hem,dir,N}} + G_{\mathrm{hem,diff,N}} + 0.5 \cdot \rho_{\mathrm{amb}}^{*} \cdot G_{\mathrm{glob}}) \\
& - A' \cdot h_{\mathrm{ext1,N}} \cdot (\vartheta_{\mathrm{sur,old,N}} - \vartheta_{\mathrm{amb}}) - A' \cdot h_{\mathrm{ext2,N}} \cdot (\vartheta_{\mathrm{sur,old,N}} - \vartheta_{\mathrm{amb}})^{2} \\
& + A'' \cdot h_{\mathrm{int,N\rightarrow NO}} \cdot \left(\vartheta_{\mathrm{sur,old,NO}} - \vartheta_{\mathrm{sur,old,N}}\right) \\
& + A'' \cdot h_{\mathrm{int,N\rightarrow NW}} \cdot (\vartheta_{\mathrm{sur,old,NW}} - \vartheta_{\mathrm{sur,old,N}}) \\
& - A' \cdot h_{\mathrm{w1,N}} \cdot w \cdot G_{\mathrm{hem,N}} - h_{\mathrm{w2,N}} \cdot A' \cdot w \cdot (\vartheta_{\mathrm{sur,old,N}} - \vartheta_{\mathrm{amb}}) \\
& - 0.5 \cdot \epsilon^{*}{}_{\mathrm{N}} \cdot \sigma \cdot A' \cdot [\left({T_{\mathrm{sur,old,N}}}^{4} - {T_{\mathrm{amb}}}^{4}\right) + ({T_{\mathrm{sur,old,N}}}^{4} - {T_{\mathrm{sky}}}^{4})]\} \cdot \Delta t \; / \; C_{\mathrm{eff,N}}
\end{aligned} \qquad \text{(eq. 3)}$$

The incidence angle modifier K_b of the direct irradiation is defined by eq. 4 (Fischer, 2011; Bosanac, 1992). The incident angle Θ between the sun and the normal of the TWD area of each segment is calculated in TRNSYS. The coefficient r_0 is used for the fitting of the incident angle modifier.

$$K_b = 1 - [\tan(\Theta/2)]^{1/r_0} \quad \text{(eq. 4)}$$

The areas A, A' and A'' are multiplied with the corresponding heat transfer coefficients. The sky temperature T_{sky} is calculated according to Swinbank (Fischer, 2006) for the assumption of clear sky. To get a workable number of model coefficients, only the heat transfer coefficient $h_{int,i\rightarrow j}$ is individually determined for all segments. The remaining parameters are equal for all segments. The input values of the surface temperature calculation are the ambient temperature, the global solar irradiation, the diffuse solar irradiation in the horizontal and the wind speed.

In the novel and extended Multiport Store-Model, the calculated local mean surface temperatures are used for the calculation of the heat losses instead of the ambient temperature, according to eq. 5. The mean surface temperature $\bar{\vartheta}_{suf}$ is calculated by the average of all eight individual segment temperatures.

$$\dot{Q}_{hl} = (UA) \cdot (\vartheta_{sto} - \bar{\vartheta}_{suf}) \quad \text{(eq. 5)}$$

In addition to the integration of the surface temperature's calculation into the original Multiport Store-Model (Drück, 2006), two further changes are introduced. On the one hand, the original store model is modified in such a way, that an ambient temperature of the bottom and an ambient temperature of the top can be set as input value. On the other hand, a non-homogeneous temperature distribution in the storage medium is introduced at the initial time step. The possibility of starting the calculation with an inhomogeneous temperature distribution is particularly useful for parameter identification on the basis of in-situ measuring data.

The parameters of the store model, relevant for the thermal behaviour of a long-term thermal energy storage, remain the heat loss rate of the store mantle $(UA)_{man}$, the heat loss rate of the store bottom $(UA)_{bot}$, the heat loss rate of the store top $(UA)_{top}$ and the effective thermal conductivity of the storage medium in a vertical direction k_{eff}. The store model input values are the store's surface temperatures, determined by the novel surface temperature model, and the ambient temperature for the mantle, the bottom and top of the store. It is assumed, that the heat losses of the store don't influence the temperature of the transparent thermal insulation respectively the outer surface temperature of the store.

2.2. Process of parameter identification

The procedure of determining the model parameters of both models, the store and surface temperature model, regarding the thermal behaviour of a long-term thermal energy storage is separated into two individual parameter identification processes. Figure 2 shows the basic approach of such a parameter identification process for a dynamic model (Fischer, 2011). The output values of the model calculation and of the measurement are compared using a target value. Afterwards, an optimization algorithm searches for a minimum of the target value by varying the model parameters.

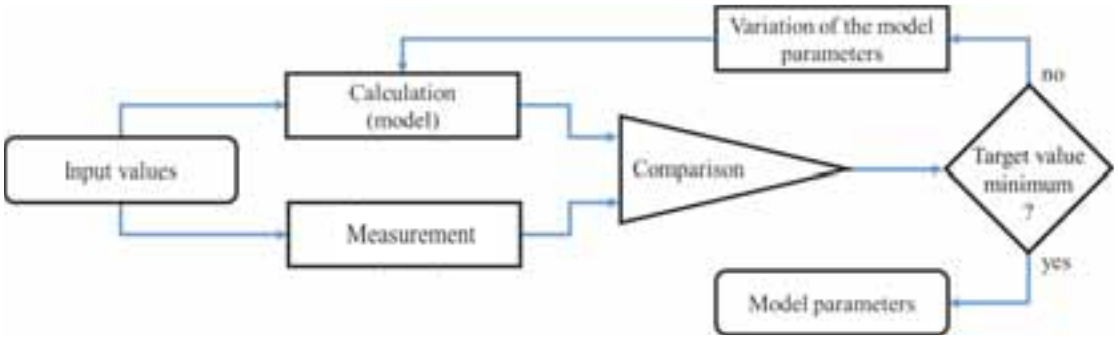

Fig. 2: Schematic process of a parameter identification

In this investigation, several Matlab integrated optimization algorithms are tested. Especially for the dynamic parameter identification of solar collector models in TRNSYS several well working optimization algorithms are known (Bales, 2002; Fischer; 2011, Bosanac, 1992). Because of the similarity to a solar collector, the transparent thermal insulation is also calculated in a time-dependent, dynamic way.

The parameter identification process of the surface temperature model uses the mean quadratic deviation of measured ($\vartheta_{m,j,i}$) and calculated ($\vartheta_{c,j,i}$) surface temperatures as target value. The parameter identification process of the store model uses the mean quadratic deviation of measured ($\vartheta_{m,j,i}$) and calculated ($\vartheta_{c,j,i}$) store medium temperatures as target value. Equation 6 defines the target value with a constant reference temperature ϑ_{ref} of 10 °C. The reference temperature is used to obtain a dimensionless target value. The value N_{MS} is the amount of considered sensors and the value N_{TS} is the amount of measuring time steps during the considered stand-by test.

$$f' = \sqrt{\sum_{i=1}^{N_{TS}} \left(\frac{\sum_{j=1}^{N_{MS}} \left(\vartheta_{m,j,i} - \vartheta_{c,j,i}\right)^2}{N_{MS} \cdot N_{TS} \cdot {\vartheta_{ref}}^2} \right)} \qquad \text{(eq. 6)}$$

This approach for the calculation of the target value is similar to the calculation method in (John, 2002), in which the heat loss rates of a store with a volume of 85 m³ is successfully identified by parameter identification with the Multiport Store-Model.

The charging and discharging characteristics of the Multiport Store-Model with volumes between 5 m³ and 100 m³ are assumed to be equal to stores with volumes lower than 5 m³. This is indicated in (John, 2002), due to a validation of the Multiport Store-Model for a store with a volume of approximately 85 m³. Hence, no modifications in the Multiport Store Model regarding the charging and discharging characteristics are necessary. Model parameters for the charging and discharging characteristics are for example the height of the input and output flow ports, the number of nodes in the store volume and a local turbulent thermal conductivity (Drück, 2007). However, the currently known test methods according to EN 12977-3 (2012) and EN 12977-4 (2012) for the identification of the charging and discharging parameters are again not applicable to stores with volumes greater than 5 m³ for the previously mentioned reasons. The following investigations only consider the thermal behaviour of a long-term thermal energy store respectively a stand-by heat loss test of a store, so these charging and discharging model parameters don't have to be identified.

With the above-described procedure for determining the model parameters three stand-by tests of the store with a volume of 12 m³ and with a vacuum and transparent thermal insulation are exemplary analyzed. These tests include a stand-by test with an inhomogeneous starting temperature distribution in the vertical direction (test 1), a stand-by test with a homogeneous starting temperature distribution (test 2) and a stand-by test with a homogeneous starting temperature distribution and an additional thermal insulation of the bottom of the store (test 3). The mean daily irradiation sum in the horizontal is 5.59 kWh m^{-2} d^{-1} for the duration of 26 days of test 1, 4.54 kWh m^{-2} d^{-1} for the duration of 18 days of test 2 and 2.72 kWh m^{-2} d^{-1} for the duration of 16 days of test 3. The maximum uncertainty of the eleven Pt100 temperature sensors, used for measuring the vertical temperatures in the store, and the eight Pt100 temperature sensors, used for measuring the horizontal surface temperatures of the TTI, is ± 0.35 K. The maximum uncertainty for the pyranometer is ± 1.5 % of the measured value and 0.2 m s^{-1} for the windspeed sensor. A digital data acquisition system measures the measuring values with a time step of 60 s.

3. Results

The following chapter describes a model sensitivity analysis of the surface temperature model and the results of the parameter identification process for measuring data of the three stand-by tests of the thermal energy store with a volume of 12 m³ and with transparent and vacuum thermal insulation.

3.1. Analysis of the model sensitivity

Due to the dynamic parameter identification of the surface temperature model, typical sensitivity analysis methods for the parameters of the model equation cannot be applied. Therefore, an alternative sensitivity analysis method, called morris method (Morris, 1991), is used to identify the main parameters of the models. A

further explanation of the morris method and its extension can be found in (Campolongo et al., 2005; Cropp and Braddock, 2002; Saltelli et al., 2004). The method was successfully implemented in Matlab and tested by means of several test functions compared to literature results. The results of the morris method for the surface temperature model parameter identification show, that the main parameters are $(\tau_g^* \alpha_a^*)$, C_{eff}, h_{ext1}, h_{ext2}, ϵ^*, ρ_{amb}^* and r_0. The parameters h_{w1}, h_{w2} and all individual $h_{\text{int,i}\rightarrow\text{j}}$ seem to be of small importance. This is indicated in figure 3 (left) by a high value of μ'. A high value of σ' indicates a strong dependency on other parameters or a nonlinear model equation. The range in which the parameters are investigated in the morris method is equal to the range of the parameter identification process.

Further investigations also show, that all eight individual $h_{\text{int,i}\rightarrow\text{j}}$ cannot not be neglected completely, but can be assumed to be equal for all segments. This finding was confirmed by means of several individual parameter identification processes with a stepwise decrease of the amount of fitting parameters. Exemplary results of the morris method for a decreased amount of parameters are shown in figure 3 on the right side. Only the parameters $(\tau_g^* \alpha_a^*)$, C_{eff}, h_{ext1} and $h_{\text{int,i}\rightarrow\text{j}}$ are considered. It can be concluded, that due to the parameter reduction the heat losses are characterized completely by h_{ext1}, which is now the most relevant parameter.

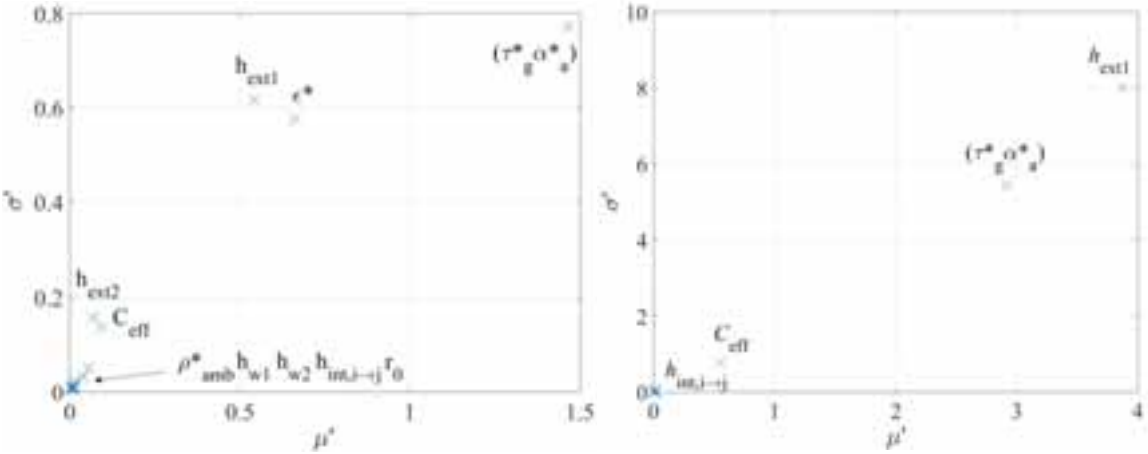

Fig. 3: Results of the morris method ($p' = 50$, $r' = 2000$, stand-by test 1) for the surface model with all (left) and a reduced amount (right) of parameters

Further investigations concerning the parameter identification process of the surface model show, that there is an influence of the solution algorithm on the target value. A comparison of several Matlab integrated minimization algorithms implemented in the parameter identification process was done. Generic algorithms, especially the particle swarm algorithm, and direct search and simulated annealing methods were investigated. However, these algorithms and methods show no or only slight advantages concerning the target value and the simulation time, compared to the standard interior-point algorithm for the parameter identification of the surface model. Hence, the interior-point algorithm was used for all following parameter identifications.

A second sensitivity analysis, based on the fit results of the parameter identification process for each month of one year of measuring data, is determined. Table 1 summarizes the mean parameter values for all fits for one year and the corresponding standard deviations. The parameter $\bar{h}_{\text{int,i}\rightarrow\text{j}}$ represents the average of all individual parameters $h_{\text{int,i}\rightarrow\text{j}}$.

Tab. 1: Selected deviations derived from the cross correlation matrix and mean parameter values of the store model for a monthly parameter identification of one year

	$(\tau^*{}_g \alpha^*{}_a)$ in [-]	C_{eff} in kJ K^{-1}	h_{ext1} in W m^{-2} K^{-1}	h_{ext2} in W m^{-2} K^{-2}	$\bar{h}_{\text{int,i}\rightarrow\text{j}}$ in W m^{-2} K^{-1}	ϵ^* in [-]	ρ_{amb}^* in [-]	r_0 in [-]
mean value	0.60	119.44	3.51	$2.1 \cdot 10^{-2}$	183.37	$4.70 \cdot 10^{-3}$	$2.4 \cdot 10^{-1}$	$3.4 \cdot 10^{-2}$
standard deviation	0.14	25.47	0.54	$1.2 \cdot 10^{-4}$	45.15	$7.79 \cdot 10^{-5}$	$2.4 \cdot 10^{-2}$	$3.0 \cdot 10^{-2}$

It can be concluded, that the standard deviation of most of the parameters is in an acceptable range for the interpretation of the results, expect the parameter r_0. The results of parameter r_0 indicate, that the modelling of the incidence angle modifier strongly depends on the season of the year.

3.2. Results of the parameter identification process

Table 2, table 3 and table 4 show a summary of the parameters determined for the surface temperature model and the store model for all stand-by tests mentioned above by means of parameter identification. The determined overall heat loss rate $(UA)_{\mathrm{ov}}$, which is summed up by $(UA)_{\mathrm{man}}$, $(UA)_{\mathrm{top}}$ and $(UA)_{\mathrm{bot}}$, is 6.410 W K^{-1} for the stand-by test 1, 6.618 W K^{-1} for the stand-by test 2 and 5.038 W K^{-1} for the stand-by test 3. The lower overall heat loss rate of the stand-by test 3 results from the additional thermal insulation at the bottom of the store. The higher value of the effective thermal conductivity k_{eff} compared to the material value of water can be explained due to several stratification devices integrated in the store and the store's lateral walls made of steel, which increase the thermal conductivity in the vertical direction. The quite similar results of the overall heat loss rate and of the store's effective thermal conductivity for all three experiments indicate, that the procedure for modeling dynamic ambient conditions respectively for identifying the model parameters provides reasonable and reproducible results.

Tab. 2: Summary of store model parameters and target values

Test	$(UA)_{\mathrm{man}}$ in W K^{-1}	$(UA)_{\mathrm{top}}$ in W K^{-1}	$(UA)_{\mathrm{bot}}$ in W K^{-1}	$(UA)_{\mathrm{ov}}$ in W K^{-1}	k_{eff} in W m^{-1} K^{-1}	f in [-]
1	2.412	0.122	3.874	6.410	1.553	0.087
2	1.876	0.142	4.599	6.618	1.595	0.009
3	2.404	0.053	2.582	5.038	1.611	0.022

Tab. 3: Summary of surface model parameters and target values (part 1)

Test	$(\tau^*{}_{\mathrm{g}}\alpha^*{}_{\mathrm{a}})$ in [-]	C_{eff} in kJ K^{-1}	h_{ext1} in W m^{-2} K^{-1}	h_{ext2} in W m^{-2} K^{-2}	$\bar{h}_{\mathrm{int,i\rightarrow j}}$ in W m^{-2} K^{-1}
1	0.670	136.093	3,928	0.011	199.488
2	0.695	135.876	4.657	0.010	171.235
3	0.574	110.780	3.561	0.026	164.316

Tab. 4: Summary of surface model parameters and target values (part 2)

Test	ϵ^* in [-]	ρ^*_{amb} in [-]	h_{w1} in s m^{-1}	h_{w2} in J m^{-3} K^{-1}	r_0 in [-]	f in [-]
1	0.010	0.231	0.019	1.172	0.028	0.427
2	0.006	0.239	0.018	0.939	0.016	0.369
3	0.004	0.230	0.005	0.492	0.023	0.312

If the averaged sum of the heat loss rate of the mantle and the top for all three experiments is converted to an effective thermal conductivity with the assumption of an one-dimensional heat transfer, a calculated effective thermal conductivity for the vacuum thermal insulation of $13.3 \cdot 10^{-3}$ W m^{-1} K^{-1} is obtained. This value is 11 % higher than the value expected from laboratory measurements of $12.0 \cdot 10^{-3}$ W m^{-1} K^{-1} (Gerschitzka et al., 2016).

The value of the effective heat capacity used in the surface temperature model exceeds the theoretically expected value of a cylindrical metal sheet with same dimension as the store's outer surface steel sheet by 10 %. This indicates, that a part of the pourable filling material of the vacuum thermal insulation also acts as a thermal capacity.

The values of the heat transfer coefficient from the surface to the ambience are within the expected range of free convection at a vertical cylinder. The transmittance-absorptance-product for all stand-by tests falls below the theoretical value of an incidence angle of 90° by 18 %. This can be explained due to the simplified calculation of the incidence angle modifier by only one parameter for all segments. The remaining coefficients of the surface model are within the expected range.

The target value according to eq. 6 multiplied by ϑ_{ref} can be interpreted as mean deviation between the calculated and the measured temperatures of the store and surface temperature model. According to this interpretation, the mean deviation of 0.39 K from the calculated and measured temperatures of the store parameter identification shows very good results and the mean deviation of 3.70 K from the calculated and measured temperatures of the surface parameter identification shows acceptable results.

For an exemplary presentation figure 4 shows the measured and calculated temperatures of the south-orientated surface of the transparent thermal insulation and the hemispherical respectively diffuse solar irradiation for the first three days of the stand-by test 1. Despite some deviation during the time of maximum temperatures, the results of the calculation of the southward-orientated surface temperature fit quite well. It has to be considered, that only the hemispherical und diffuse solar irradiation, the wind speed and the ambient temperature are available as input values. Furthermore, the surface temperature model does not take shadings into account. These occur in the morning and evening of the considered days and are caused by the horizon and neighboring buildings.

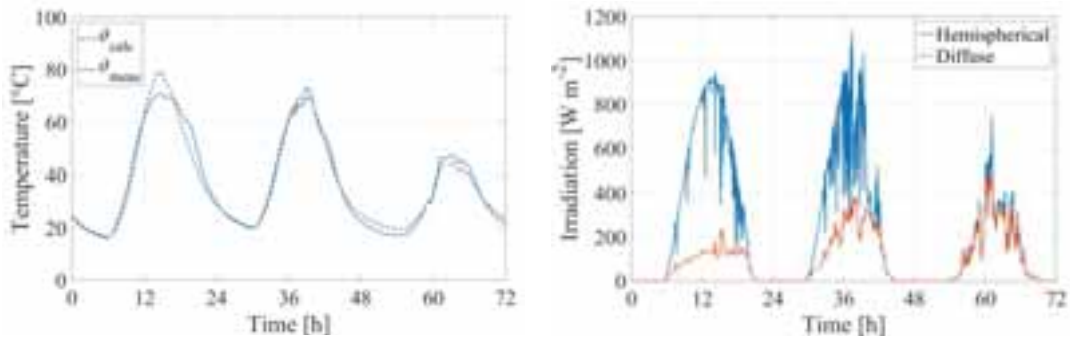

Fig. 4: Measured and calculated temperature of the south orientated surface of the transparent thermal insulation (left) and the south orientated hemispherical respectively diffuse solar irradiation (right)

If the previous calculation method for the heat losses of the store according to equation 1 is used, the determined heat loss rate of the store mantel $(UA)_{\mathrm{man}}$ is on average 30 % lower than the heat loss rate of the store mantle for all three stand-by tests calculated according to equation 5. The reduction of $(UA)_{\mathrm{man}}$ is 38 % for the stand-by test 1, 33 % for the stand-by test 2 and 19 % for the stand-by test 3. These results correspond with the mean daily radiation sum for the three stand-by tests. The heat loss rate decreases, because the positive effect of a lower temperature difference over the vacuum thermal insulation is taken into account for the parameter identification of the heat loss rate. Derived from these results, the importance of the consideration of the surface temperature calculation for the heat loss rate determination can be seen.

4. Conclusions

It can be summarized, that additional effects for the characterization of the heat losses of an outdoor installed hot water store have to be taken into account compared to an indoor installed one. These effects can be described by means of the developed combination of the surface temperature model and the store model. The novel calculation of the outer store surface temperature is applied to separate surface segments of the store's lateral area in circumferential direction. These surface temperatures are used for the calculation of the heat losses of the modified store model derived from the well-known Multiport-Store Model from TRNSYS. An evaluation of both model parameter identification processes using three stand-by tests show reasonable and reproducible results, compared to theoretical, material based values. Based on the identified model parameters of both models, the detailed characterization of the heat losses of outdoor installed hot water stores for long-term

thermal energy storage is possible. A comparison of the identified model parameters using the previous and the novel surface temperature calculation method shows, that the dynamic ambient conditions can have a significant influence on the heat loss rate of a hot water store. A mean change of the mantel heat loss rate of 30 % in the parameter identification process due to the surface temperature calculation cannot be neglected.

Future work will deal with the development of a more detailed node model for the surface temperature calculation, especially to account for a vertical temperature gradient. It is also planned to optimize the surface temperature model for thermal energy stores in outdoor installation with no transparent thermal insulation, especially for the 100 m^3 store of the project OBSERW. For stores of this kind, the influence of the wind speed could be more relevant for the surface temperature calculation than for stores with transparent thermal insulation.

References

Bauer, D., Marx, R., Nußbicker-Lux, J., Ochs, F., Heidemann, W., Müller-Steinhagen, H., 2010. German central solar heating plants with seasonal heat storage. Solar Energy 84 (2010) 612-623.

Bales C., 2001. Parameter identification manual for trnsys models at SERC. Technical report. Högskolana Dalarna, ISSN 1650-1497, EKOS Publication, 2001:3 Internskrift.

Bauer, D., Marx, R., Drück, H., 2016. Solar district heating systems for small districts with medium scale seasonal thermal energy stores. Energy Procedia 91 (2016) 537-545.

Bosanac, M., Brunotte, A., Sprikl, W., Sizmann, R., 1992. The use of parameter identification for flat-plate collector testing under non-stationary conditions. Renewable Energy, Vol. 4, No. 2, pp, 217-222, 1994.

Campolongo, F., Cariboni, J., Saltelli, A., Schoutens, W., 2005: Enhancing the morris method. In: Proceedings of the 4th International Conference on Sensitivity Analysis of Model Output (SAMO 2004), Santa Fe, New Mexico.

Cropp, R., Braddock, R., 2002: The new morris method: an efficient second-order screening method. Reliability Engineering & System Safety, Volume 78, Issue 1, October 2002, Pages 77-83.

Drück, H., 2006. Multiport Store-Model for TRNSYS – Stratified fluid storage tank with four internal heat exchangers, ten connections for direct charge and discharge and an internal electrical heater. TRNSYS Description Type 340, V.1.99F, [Online: http://www.trnsys.de/download/de/ts_type_340_de.pdf, 08.03.2017].

Drück, H., 2007. Mathematical modelling and experimental testing of hot water stores for thermal solar systems. Dissertation. University of Stuttgart, Shaker Verlag, ISBN 978-3-8322-6215-0, ISSN 0945-0726.

EN 12977-3, 2012. Thermal solar systems and components – Custom built systems – Part 3: Performance test methods for solar water heater stores.

EN 12977-4, 2012. Thermal solar systems and components – Custom built systems – Part 4: Performance test methods for solar combistores.

Findeisen, F., Urbaneck, T., Platzer, B., 2016. Radiale Diffusoren in Warmwasserspeichern – Funktionale Optimierung mittels CFD; Teil 1 Grundlagen und Modellierung. HLH Lüftung/Klima Heizung/Sanitär Gebäudetechnik Springer 67. Jg. (2016) Heft 10 S. 20-28. – ISSN 1436-5103.

Findeisen, F., Urbaneck, T., Platzer, B., 2017. Radiale Diffusoren in Warmwasserspeichern – Funktionale Optimierung mittels CFD; Teil 2 Optimierung des Be- und Entladeverhaltens. HLH Lüftung/Klima Heizung/Sanitär Gebäudetechnik Springer 68. Jg. (2017) Heft 2 S. 25-33. – ISSN 1436-5103.

Fischer, S., 2011. Dynamic testing of solar collectors with special attention to the incidence angle modifier and reduction of testing time. Dissertation. University of Stuttgart, Shaker Verlag, ISBN 978-3-8440-0601-0, ISSN 0945-0726.

Gerschitzka, M., Lang, S., Bauer, D., Drück, H., 2015. Development of a high-efficient long-term thermal energy store for outdoor installation. In Proceedings: 9th International Renewable Energy Storage Conference, IRES 2015, Düsseldorf (Germany).

Gerschitzka, M., Marx, R., Lang, S., Bauer, D., Drück, H., 2015. New developments related to thermal insulation materials and installation techniques for over ground seasonal thermal energy stores. In Proceedings: 13th International Conference on Thermal Energy Storage, Greenstock 2015, Peking (China).

Gerschitzka, M., Lang, S., Rieder, M., Sirch, M., Marx, R., Bauer, D., Drück, H., 2016. Development of a large-volume, low-cost hot water store with high-efficient thermal insulation for outdoor installation. Final report. Institute of Thermodynamics and Thermal Engineering, University of Stuttgart, [Online: http:// www.itw.uni-stuttgart.de/forschung/veroeffentlichungen/10rnsys10ogy_publikationen/index.html, 08.03.2017].

John, R., 2002. Validierung eines Rechenmodells für Großspeicher zur Auslegung solarer Heizsysteme. Dissertation. Fachbereich Physik, Phillips-Univerität Marburg.

Morris, M., 1991: Factorial sampling plans for preliminary computational experiments. Technometrics, Vol. 33, No. 2, (May, 1991), pp. 161-174.

Saltelli, A., Tarantola, S., Campolonga, F., Ratto, M., 2004: Sensitivity analysis in practice – A guide to assessing scientific models. Book. John Wiley & Sons Ltd, ISBN 0-470-87093-1.

Urbaneck, T., Platzer, B., 2015. Overground storages in segmental construction for district heating systems (OBSERW) – Project overview. In Proceedings: 13th International Conference on Thermal Energy Storage, Greenstock 2015, Peking (China).

Nomenclature

A	Projected area of the TTI [m^2]	A'	Area of the TTI [m^2]
A''	Cross section area of the TTI [m^2]	C_{eff}	Effective thermal capacity of one TTI segment [kJ K^{-1}]
f'	Target value [-]	$G_{\mathrm{hem,dir}}$	Direct hemispherical solar irradiance [W m^{-2}]
$G_{\mathrm{hem,diff}}$	Diffuse hemispherical solar irradiance [W m^{-2}]	G_{glob}	Global solar irradiance [W m^{-2}]
h_{ext1}	Heat transfer coefficient from store to the ambience [W m^{-2} K^{-1}]	h_{ext2}	Temperature dependent heat transfer coefficient from store to ambience [W m^{-2} K^{-2}]
$h_{\mathrm{int,i\rightarrow j}}$	Heat transfer coefficient within the TTI [W m^{-2} K^{-1}]	$\bar{h}_{\mathrm{int,i\rightarrow j}}$	Mean heat transfer coefficient within the TTI [W m^{-2} K^{-1}]
h_{w1}	Parameter of the wind speed dependency of the TTI heat losses [s m^{-1}]	h_{w2}	Parameter for the wind speed and irradiation dependency of the TTI heat losses [J m^{-3} K^{-1}]
K_{b}	Incidence angle modifier [-]	k_{eff}	Effective thermal conductivity of the storage medium water [W m^{-1} K^{-1}]
p'	Discretization parameter of the morris method [-]	N_{TS}, N_{MS}	Number of time steps, number of measuring sensors [-]
$\dot{Q}_{\mathrm{hl}}$	Heat flux caused by the heat losses of the store [W]	r'	Number of runs of the morris method [-]
r_0	Fitting parameter for the incidence angle modifier [-]	T_{amb}	Ambient temperature [K]

T_{sky}	Sky temperature [K]	$T_{\mathrm{suf,old}}$	Surface temperature of the TTI at the previous time step [K]
(UA)	Heat loss rate [W K^{-1}]	$(UA)_{\mathrm{bot}}$	Heat loss rate of the bottom of the store [W K^{-1}]
$(UA)_{\mathrm{man}}$	Heat loss rate of the mantle of the store [W K^{-1}]	$(UA)_{\mathrm{top}}$	Heat loss rate of the top of the store [W K^{-1}]
$(UA)_{\mathrm{ov}}$	Overall heat loss rate of the store [W K^{-1}]	w	Wind speed [m s^{-1}]
ϑ_{amb}	Ambient temperature [°C]	$\vartheta_{\mathrm{calc}}$	Calculated temperature [°C]
$\vartheta_{\mathrm{c,j,i}}$	Calculated temperature of the sensor j at the time step i [°C]	$\vartheta_{\mathrm{m,j,i}}$	Measured temperature of the sensor j at the time step i [°C]
ϑ_{ref}	Reference temperature for the target value calculation [°C]	ϑ_{sto}	Store temperature of the storage medium water [°C]
ϑ_{suf}	Surface temperature of the TTI [°C]	$\bar{\vartheta}_{\mathrm{suf}}$	Mean surface temperature of the TTI [°C]
$\vartheta_{\mathrm{suf,old}}$	Surface temperature of the TTI at the previous time step [°C]	$\vartheta_{\mathrm{meas}}$	Measured temperature [°C]
ϵ^*	Parameter of the emittance of the TTI [-]	${\rho^*}_{\mathrm{amb}}$	Ground reflectance of the ambience [-]
$({\tau^*}_{\mathrm{g}}{\alpha^*}_{\mathrm{a}})$	Transmittance-absorptance-product of the TTI [-]	μ'	Evaluation parameter of the parameter relevance [-]
σ'	Evaluation parameter of the parameter correlation to other parameters [-]	σ	Stefan-Boltzmann constant [W m^{-2} K^{-4})]
Δt	Time step [h]	Θ	Incidence angle [°]

Acknowledgment

The activities described in this paper were supported by the German Federal Ministry for Economic Affairs and Energy (BMWi) based on a decision of the German Bundestag by Projektträger Jülich (PtJ) under grant numbers 0325992B (research project „StoEx“: Development of a large-volume, low-cost hot water store with high-efficient thermal insulation for outdoor installation) and 03ET1230C (research project “OBSERW”: Overground storages in segmental construction for district heating systems). The authors gratefully acknowledge this support and carry the full responsibility for the content of this paper.

Aging and Lifetime Assessment of Polyethylene Liners for Heat Storages – Effect of Liner Thickness

Michael K. Grabmann[1], Gernot M. Wallner[1], Wolfgang Buchberger[3], David Nitsche[2]

[1] Institute of Polymeric Materials and Testing, University of Linz, Linz (Austria)

[2] Institute of Analytical Chemistry, University of Linz, Linz (Austria)

[3] AGRU Kunststofftechnik GmbH, Bad Hall (Austria)

Abstract

This paper deals with the global aging behavior and lifetime assessment of polyethylene liner materials for seasonal heat storages. Hot water aging experiments at elevated temperatures of 95, 105 and 115°C were carried out using specimens with various thicknesses of 100, 500 and 2000 µm. The aging indicator strain-at-break was monitored for up to 1500 days. The experimental hot water data were fitted by potential and Arrhenius equations referring to thickness and temperature dependency. By merging both equations a semi-empirical model was established and used for lifetime estimation of polyethylene liner materials. The low divergence of the lifetime values between experimental and calculated failure data indicates the high accuracy of the thickness/temperature-model. A lifetime value of 18 years was derived for 3 mm thick polyethylene based liner materials for solar district heating systems.

Keywords: Polyethylene liner material, Seasonal heat storage, Thickness/temperature depending model, Lifetime.

1. Introduction

The share of polymeric materials for hot water seasonal heat storages increased steadily due to lower material costs and installation costs compared to stainless steel (Köhl et al., 2012). A better competitiveness especially for big storage volumes greater than 20.000 m³ is given by replacing steel with polymeric liner materials (Heller, 2000). Regarding the material grades, the most common polymeric liner materials are based on special polyethylene grades (PE-RT) or polypropylene random copolymers (PP-R) (Grabmayer, 2014). Improved long-term stability against thermo-oxidation given by stabilization packages is essential to ensure functionality and durability at service temperatures of up to 95°C for more than 20 years (Schramm and Jeruzal, 2006; Paranovska and Pedersen, 2016). While polypropylene materials exhibit a more critical degradation behavior in hot air environment than in hot water, interestingly a reverse phenomenon was reported for polyethylene liner grades (Grabmayer, 2014).

Oven aging tests at elevated temperatures are commonly performed to evaluate the long-term thermo-oxidation behavior of polymeric materials (Gijsman, 1994; Kahlen et al., 2010a; Olivares et al., 2010; Celina, 2013). Enhanced temperatures result in accelerated aging processes with reduced experimental time (Kahlen et al., 2010c, 2010d; Olivares et al., 2010) (Kahlen et al., 2010a; Olivares et al., 2010). Polymer aging is strongly influenced by diffusion limited oxidation (Audouin et al., 1994). Hence, a reduction of the specimen thickness leads to accelerated aging processes (Gugumus, 1996; Grabmayer et al., 2015).

So far, no comprehensive studies on temperature and thickness depending global aging behavior of polyethylene liner materials were published. Hence, it is the main objective of this paper to establish a thickness/temperature model using ultimate failure data. Lifetime assessment under service-relevant loading conditions should be executed for typical liner thicknesses of 2 and 3 mm. This is of utmost importance to clarify the durability of polymeric liner materials and to compare polyolefin liner materials for large solar-thermal district heating systems with seasonal heat storages.

doi:10.18086/swc.2017.13.07 Available at http://proceedings.ises.org

2. Methodological approach

2.1 Materials, aging conditions and characterization methods

A commercial polyethylene high density grade was used. Details as to the molecular structure, morphology and the stabilizers are given in Grabmayer (2014) and Beißmann et al. (2013). The PE grade was extruded to a 2 mm thick sheet by AGRU Kunststofftechnik GmbH. Specimen with various thicknesses of 100 and 500 µm and a length of at least 150 mm were manufactured by using an automated planning technique (Grabmayer et al., 2015). Additionally, ISO 5A specimens with a thickness of 2000 µm were prepared by die-punching.

Due to the more critical aging behavior in water than in air, primarily hot water exposure was performed. The specimens were aged in closed stainless steel vessels with integrated specimen holder at temperatures of 95, 105 and 115°C using a Binder FED53 (Tuttlingen, Germany) heating chamber with forced circulation. Whenever specimens were removed from the vessels, the deionized water was changed. Four specimens were examined per aging interval.

To assess the aging behavior, tensile tests were carried out at ambient conditions using a screw-driven universal testing machine at a deformation rate of 50 mm/min. For various polymeric materials used in solar energy engineering the ultimate mechanical properties strain-at-break or tensile strength are highly sensitive indicators to monitor both, physical and chemical aging phenomena (Wallner et al., 2004; Povacz et al., 2014; Povacz et al., 2016). As aging indicator, strain-at-break was evaluated over the aging period. Ultimate failure was defined when strain-at-break values dropped below the strain-at-yield value ($\varepsilon_b < \varepsilon_y$). The limit value for ε_y was 20% for all investigated specimen thicknesses.

2.2 Modelling the thickness/temperature dependency

A semi-empirical model describing the effect of specimen thickness and exposure temperature on global aging behavior was evolved. Therefore, experimental failure data for specimens of various thicknesses (100, 500 and 2000 µm) at aging temperatures of 95, 105 and 115°C were applied. The thickness and temperature dependency was considered separately and merged. Hülsmann and Wallner (2017) used a similar approach to describe the temperature and thickness dependent water vapor permeation in photovoltaic encapsulation materials.

By using a potential function (eq. 1) the thickness dependency of the failure data was fitted. The effect of temperature on global aging behavior was considered by the well-established Arrhenius model (eq. 2). Both equations give the endurance time ($t_{endurance}$) as a function of thickness (d) or temperature (T) considering material specific constants (A, B, C), the activation energy (E_A) ant the gas constant (R).

$$t_{endurance} = B * d^C \qquad \text{(eq. 1)}$$

$$\ln t_{endurance} = \ln A + \frac{1}{T} * \frac{E_A}{R} \qquad \text{(eq. 2)}$$

The thickness and temperature dependent endurance time is calculated by a two dimensional model (eq. 3). Here, variables with index "0" are experimental values whereby C and E_A are calculated material specific constants from eq. 1 and 2.

$$t_{endurance} = \frac{t_0}{d_0^C} * e^{\frac{E_A}{R}*\left(\frac{1}{T}-\frac{1}{T_0}\right)} * d^C \qquad \text{(eq. 3)}$$

2.3 Lifetime assessment

For lifetime estimation a cumulative damage approach was used, established by Wallner et al. (2016) for black-pigmented PP solar absorber materials. The lifetime assessment approach is based on the simulation of temperature loading profiles for liner materials, the extrapolation of experimental aging data from elevated temperatures to service relevant temperatures and the accumulation of damages at different temperature levels. Temperature loading profiles for seasonal heat storages are dependent on the plant type. As minimum temperature level 50°C was considered for the storage temperature in winter months. Temperature of the storage system increases during warm-weather months and reaches maximum temperature level of 85°C in summer (see Fig. 1). Comparable loading profiles were assumed by Ochs (2008) and deduced for seasonal pit storages in Denmark (Paranovska and Pedersen, 2016).

Experimental aging data obtained at 115, 105 and 95°C were extrapolated to service relevant temperatures (50

to 85°C) using the linear Arrhenius fit approach. Various aging processes and temperature degradation mechanisms as described by Gugumus (1999), Celina et al. (2005), Hoàng and Lowe (2008) and Kahlen et al. (2010c, 2010d) were neglected. According to ISO 13760 a cumulative damage model was used to calculate lifetime values. The theoretical temperature loading profile was transformed to frequency distributions. The lifetime was derived by weighting the frequency distributions with extrapolated endurance times.

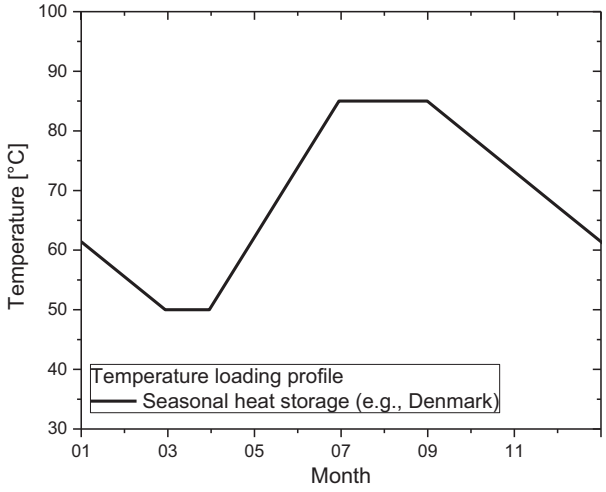

Fig. 1: Assumed temperature loading profile for a seasonal heat storage in Northern hemisphere.

3. Results and discussion

3.1. Hot water aging behavior of the PE liner material

Aging data for up to 900 days in hot air and hot water for micro- and macro-sized specimens are based on previous investigations of Grabmayer et al. (2014). The main result of this study was that the investigated polyethylene liner material revealed a more critical aging behavior in hot water than hot air. Based on these results it was decided to focus on hot water aging. While all specimens were embrittled at 115°C within up to 443 days, no failure for 2000 µm specimens at 95°C were obtained within 1500 days of exposure. These aging experiments are still ongoing.

Figure 2 depicts strain-at-break values of the investigated 100 and 500 µm thick PE liner grade as a function of aging time in hot water at elevated temperatures. Ultimate failure with strain-at-break values below yield point (20%) is indicated with open symbols in the chart. The unaged 100 and 500 µm specimens revealed high ductility with strain-at-break values up to 1400%. Due to different specimen thickness, the unaged 500 µm specimens exhibited slightly lower strain-at-break values. A significant drop in strain-at-break values appeared after initial aging within the first few days. This drop was more pronounced for the 100 µm specimens at all investigated exposure temperatures. This reduction in ultimate strain is presumably related to crystallization effects and higher intersperulitic, internal stresses. In course of aging, strain-at-break values leveled off at about 750 and 1250% for 100 and 500 µm thick specimens, respectively. These plateaus are more pronounced for thicker specimens and lower exposure temperatures. Subsequently, a drop of strain-at-break values was observed resulting in ultimate failure for 115 and 105°C exposure. Interestingly, for 95°C aging experiments a second plateau with strain-at-break values of 25 to 150% was obtained before embrittlement occurred. Ultimate failure first appeared at 115°C after 91 days for 100 µm specimens. Increasing specimen thickness resulted in longer aging times up to 278 and 443 days for 500 and 2000 µm specimens, respectively. Hence, diffusion limited oxidation processes as postulated by Audouin et al. (1994) or Celina (2013) were also ascertained for the investigated PE grade. An less pronounced effect of specimen thickness on endurance times was also described by Grabmayer et al. (2015) for different polypropylene grades. The experimental failure times of the investigated PE liner material of different thicknesses are summarized in Table 1. Up to 1500 days no embrittlement occurred at an exposure temperature of 95°C for 2000 µm specimens. In 115°C hot water a reduction of thickness from 2000 to 100 µm (factor 20) and 500 to 100 µm (factor 5) resulted in a 4.9 and 3.1

times accelerated aging, respectively. Acceleration factors of 5.5 and 2.7 were deduced by exposing to hot water at 105°C. For aging in 95°C hot water an acceleration factor of 3.1 was derived for a thickness reduction from 500 to 100 µm. Compared to data provided by Grabmayer et al. (2015) or Povacz (2014) for polypropylene, for the investigated PE liner material a more pronounced specimen thickness dependency on global aging behavior for similar thickness reduction and exposure temperature was obtained. The acceleraton factors are below 2 for PP specimen with comparable thickness. Based on these results, it was unambiguously confirmed that localized aging effects play a significant role in polyethylene oxidation as pointed out by Audouin et al. (1994) or Celina (2013).

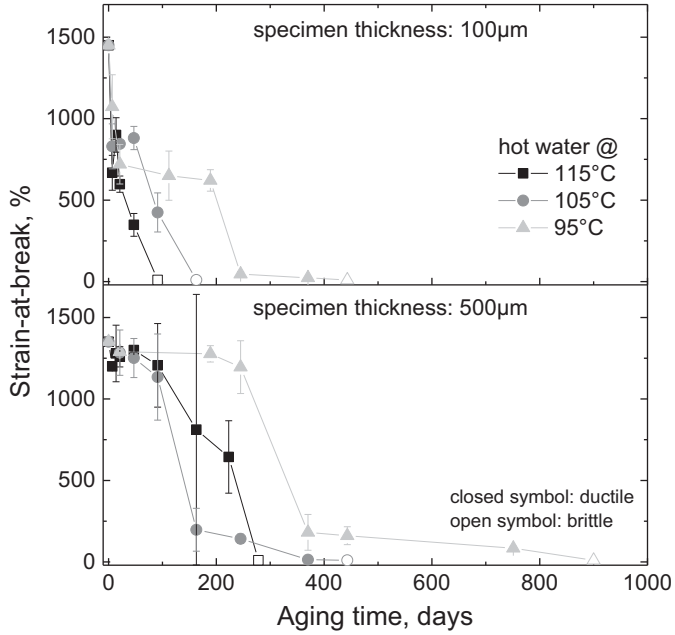

Fig. 2: Strain-at-break of micro-sized PE specimens with a thickness of 100 and 500 µm as a function of aging time exposed in hot water at 115, 105 and 95°C.

Tab. 1: Embrittlement times of PE liner specimens with varying thickness in hot water at 115, 105 and 95°C.

Specimen thickness, µm	Failure time in days in hot water at		
	115°C	105°C	95°C
100	91	163	245
500	278	443	751
2000	443	900	> 1500

3.2. Theoretical model for thickness and temperature dependency

The experimental aging data in hot water at different temperatures and for various PE specimen thicknesses were used to evolve a semi-empirical model. Therefore, the factors specimen thickness and exposure temperature were considered separately and finally merged to a two-dimensional model. Figure 3 depicts the dependency of failure time as a function of specimen thickness in hot water at 115, 105 and 95°C. The fits of the experimental data with potential functions resulted in high coefficients of determination. No embrittlement was observed for 2000 µm specimens in 95°C hot water within 1500 days, so fit parameters gathered from 115 and 105°C aging data were used to implement the model. A significant temperature dependent difference was deduced for the fit parameter B. The material specific constant C was calculated and determined with 0.5522 for the semi-empirical model. For C a temperature induced deviation of <5% was ascertained. Hence, an arithmetic value was deduced and used for the two-dimensional model. The validity and reliability of this parameter will be further improved by continuation of the aging experiments at 95°C.

Experimental aging data and related Arrhenius fittings as a function of temperature are plotted in Fig. 4. Slightly thickness dependent E_A/R-ratios ranging from 7.1 to 10.4 x10^3 K were derived. The E_A/R-ratios were lower for the thinner specimen, which already failed at all investigated temperautres. Due to non-failure of 2000 µm thick

specimens at 95°C within 1500 days, extrapolation was done by only two aging data points resulting in a higher E_A/R value. By using Arrhenius fit parameters gathered from 100 and 500 µm thick specimens an average value of 7.1 x10³ K was used for the two-dimensional model. A specimen thickness dependent E_A/R-ratio can be implemented in the semi-empirical model finishing aging experiments at 95°C. The obtained activation energies are in the range from 59 to 86 kJ/mol. These values are comparable to data given for polyolefins (Kahlen et al., 2010b), but slightly lower than data for specific polyethylene grades (Anderson and Freeman, 1961; Peterson et al., 2001; Gao et al., 2003; Mueller and Jakob, 2003).

As zero or reference values the endurance time at a thickness of 500 µm and a temperature of 105°C were selected. These reference values resulted in best reproduction of experimental values and lowest deviations between theoretical and experimental endurance times. The comparison of the experimental and theoretical values of thick specimens at low temperatures (2000 µm at 105°C and 500 µm at 95°C) revealed a deviation of about 10%, reflecting the uncertainty of the model. Improved accuracy will be achieved by continuation of the experiments at 95°C until ultimate failure of 2000 µm specimens. Figure 5 depicts the calculated endurance times depending on various specimen thicknesses and a wide range of hot water temperature based on equation 3. It can be clearly seen for the plotted range, that the specimen thickness has also a significant impact on the failure times. At 95°C the expected endurance time is compared to 100 µm specimens a factor of 5 and 7 higher for 2 and 3 mm liners, respectively.

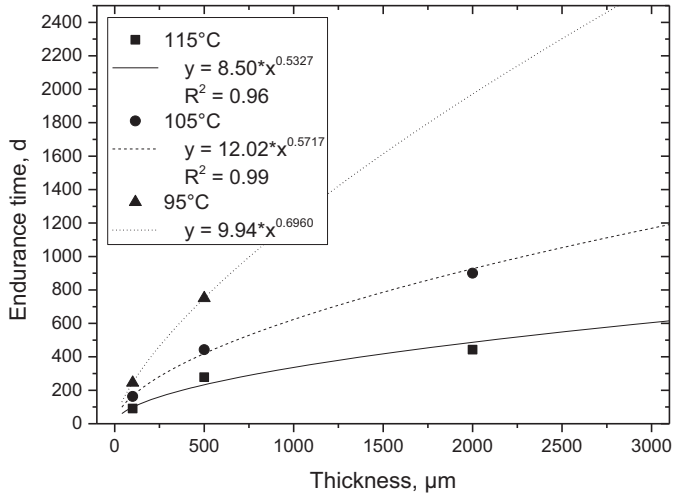

Fig. 3: Experimental endurance time dots and potential fit for aging of PE specimens with varying thickness in hot water at 115, 105 and 95°C.

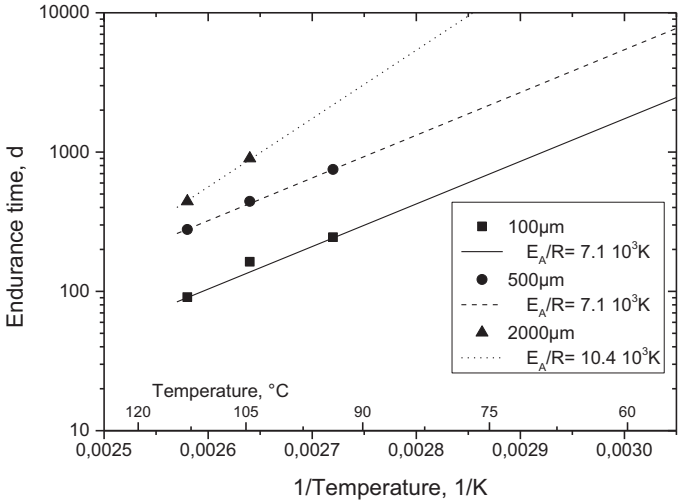

Fig. 4: Experimental endurance time dots and Arrhenius fit for 100, 500 and 2000 µm thick specimens at different temperatures.

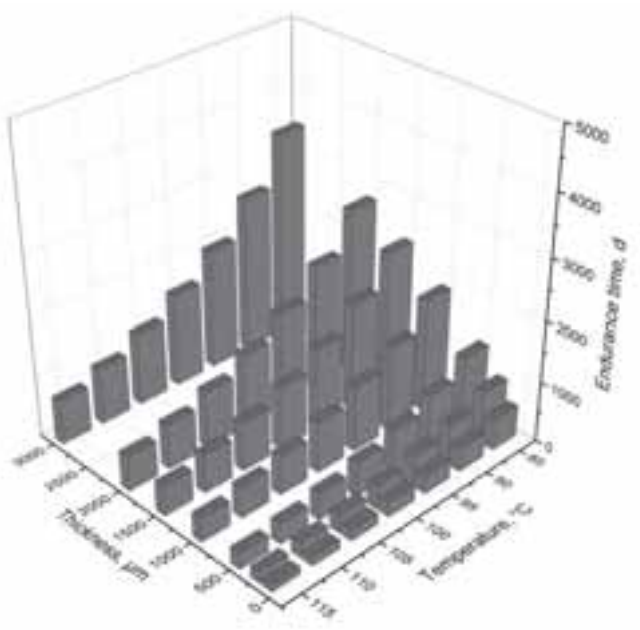

Fig. 5: Calculated endurance times of the investigated polyethylene liner material depending on specimen thickness (100 to 3000 µm) and hot water temperature (85 to 115°C).

3.3 Estimated lifetimes for PE liners

To deduce the lifetime of polyethylene liner materials experimental and theoretical, temperature dependent endurance times were considered. In Fig. 6 the experimental (filled symbols) and theoretical (open symbols) endurance times are displayed for a commercially relevant liner thickness of 2 mm and the reference thickness 500 µm. Additionally, theoretical embrittlement times for a 3 mm thick PE liner are plotted. The closed grey symbol indicates the current maximum exposure time of the non-failed 2000 µm specimens in hot water at 95°C. A good agreement of experimental and theoretical endurance times was obtained with slightly (~10%) overestimated theoretical embrittlement times for the 2 mm thick specimen. By weighting the temperature dependent endurance times with the frequency distribution of the seasonal heat storage lifetime values of 7, 15 and 18 years were obtained for liner thickness of 500, 2000 and 3000 µm. The lifetime values of this study are slightly lower than lifetime estimates published by Paranovska and Pedersen (2016) for polyethylene liners in seasonal storages of Danish solar district heating systems. The deviation of <20% is attributable to different aging and evaluation procedures and other polyethylene material formulations. However, the results of our and the Danish study are in a comparable lifetime range.

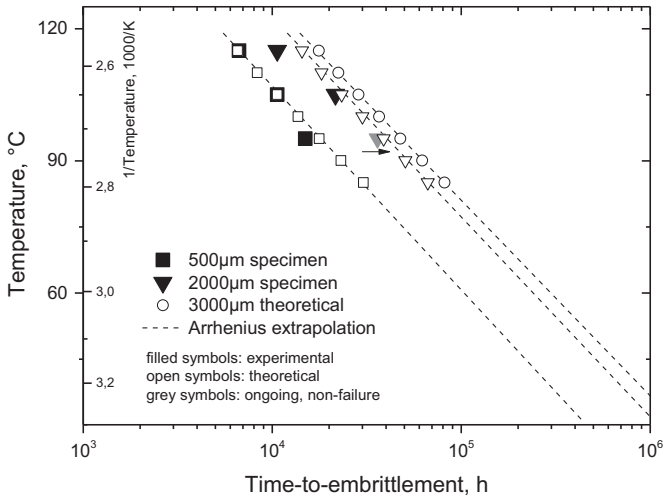

Fig. 6: Experimental and calculated failure times for 500 and 2000 µm thick PE liners.

4. Summary and conclusion

To assess the lifetime of a polyethylene liner material grade, experimental failure data of 100, 500 and 2000 µm thick specimens were gathered at elevated temperatures in hot water. The experimental aging data were used to implement a semi-empirical thickness/temperature-model using a potential and an Arrhenius fit. As a result endurance times for polyethylene liner specimens in a wide range of thickness and temperature (100 to 3000 µm, 85 to 115°C) were derived. Lifetime values were deduced by weighting the endurance times with a temperature loading profile of seasonal heat storages in Danish solar district heating systems.

The polyethylene specimens were exposed to the more critical environment hot water at 95, 105 and 115°C. The strain-at-break values dropped within the first aging interval which was mainly attributed to physical recrystallization mechanisms. After the initial drop a plateau was obtained which was more pronounced at lower exposure temperatures and for thicker specimens. Ultimate failure characterized by full embrittlement was significantly thickness and temperature dependent. A factor of 5 and 3 shorter embrittlement times were discerned by reducing specimen thickness by a factor of 20 and 5 (2000 to 100 µm, 500 to 100 µm), respectively. Similar acceleration factors were obtained for the exposure temperatures of 95 and 105°C. This thickness dependency was fitted with potential functions with a slightly temperature dependent exponent. The effect of temperature was described by an Arrhenius fit. Minor differences in activation energy for hot water exposure at 115 and 105°C were calculated. The implemented two-dimensional model for thickness and temperature dependency was corroborated.

Lifetime values of 15 and 18 years were deduced for PE liners with a thickness of 2 and 3 mm, respectively. Compared to published values for currently used polyethylene liner materials a slightly lower performance was obtained for the investigated polyethylene grade mainly related to differences of the material grade, aging conditions and the failure criterion. Hence, it is concluded that current PE grades reveal sufficient performance for pit storages. However, for insulted tank storages with higher operating temperatures a new class of polymeric liner materials has to be developed. As described in an associated study (Grabmann et al., 2017) polypropylene copolymers are a potential alternative.

5. Acknowledgment

This research work was performed in the cooperative research project SolPol-4/5 entitled “Solar-thermal systems based on polymeric materials” (www.solpol.at). The project is funded by the Austrian Climate and Energy Fund (KLI:EN) within the program "Neue Energien 2020" and administrated by the Austrian Research Promotion Agency (FFG).

6. References

Anderson, D.A., Freeman, E.S., 1961. The kinetics of the thermal degradation of polystyrene and polyethylene. J. Polym. Sci. 54 (159), 253–260.

Audouin, L., Langlois, V., Verdu, J., 1994. Role of oxygen diffusion in polymer ageing: kinetic and mechanical aspects. Journal of Material Science 29, 569–583.

Beißmann, S., Stiftinger, M., Grabmayer, K., Wallner, G., Nitsche, D., Buchberger, W., 2013. Monitoring the degradation of stabilization systems in polypropylene during accelerated aging tests by liquid chromatography combined with atmospheric pressure chemical ionization mass spectrometry. Polymer Degradation and Stability 98 (9), 1655–1661.

Celina, M., Gillen, K.T., Assink, R.A., 2005. Accelerated aging and lifetime prediction. Review of non-Arrhenius behaviour due to two competing processes. Polymer Degradation and Stability 90 (3), 395–404.

Celina, M.C., 2013. Review of polymer oxidation and its relationship with materials performance and lifetime prediction. Polymer Degradation and Stability 98 (12), 2419–2429.

Gao, Z., Amasaki, I., Kaneko, T., Nakada, M., 2003. Calculation of activation energy from fraction of bonds broken for thermal degradation of polyethylene. Polymer Degradation and Stability 81 (1), 125–130.

Gijsman, P., 1994. The long-term stability of polyolefins. Dissertation.

Grabmann, M.K., Wallner, G.M., Grabmayer, K., Buchberger, W., Nitsche, D., 2017. Effect of thickness and temperature on the global aging behavior of polypropylene random copolymers for seasonal heat storages. submitted to Solar Energy.

Grabmayer, K., 2014. Polyolefin-based Lining Materials for Hot Water Heat Storages. Dissertation.

Grabmayer, K., Beißmann, S., Wallner, G.M., Nitsche, D., Schnetzinger, K., Buchberger, W., Schobermayr, H., Lang, R.W., 2015. Characterization of the influence of specimen thickness on the aging behavior of a polypropylene based model compound. Polymer Degradation and Stability 111, 185–193.

Grabmayer, K., Wallner, G.M., Beißmann, S., Braun, U., Steffen, R., Nitsche, D., Röder, B., Buchberger, W., Lang, R.W., 2014. Accelerated aging of polyethylene materials at high oxygen pressure characterized by photoluminescence spectroscopy and established aging characterization methods. Polymer Degradation and Stability 109, 40–49.

Gugumus, F., 1996. Thermooxidative degradation of polyolefins in the solid state. Part 2: Homogeneous and heterogeneous aspects of thermal oxidation. Polymer Degradation and Stability. Polymer Degradation and Stability 52 (2), 145–157.

Gugumus, F., 1999. Effect of temperature on the lifetime of stabilized and unstabilized PP films. Polymer Degradation and Stability 63 (1), 41–52.

Heller, A., 2000. 15 Years of R&D in central solar heating in Denmark. Solar Energy 69 (6), 437–447.

Hoàng, E.M., Lowe, D., 2008. Lifetime prediction of a blue PE100 water pipe. Polymer Degradation and Stability 93 (8), 1496–1503.

Hülsmann, P., Wallner, G.M., 2017. Permeation of water vapour through polyethylene terephthalate (PET) films for back-sheets of photovoltaic modules. Polymer Testing 58, 153–158.

Kahlen, S., Jerabek, M., Wallner, G.M., Lang, R.W., 2010a. Characterization of physical and chemical aging of polymeric solar materials by mechanical testing. Polymer Testing 29 (1), 72–81.

Kahlen, S., Wallner, G.M., Lang, R.W., 2010b. Aging behavior and lifetime modeling for polycarbonate. Solar Energy 84 (5), 755–762.

Kahlen, S., Wallner, G.M., Lang, R.W., 2010c. Aging behavior of polymeric solar absorber materials – Part 1. Engineering plastics. Solar Energy 84 (9), 1567–1576.

Kahlen, S., Wallner, G.M., Lang, R.W., 2010d. Aging behavior of polymeric solar absorber materials – Part 2. Commodity plastics. Solar Energy 84 (9), 1577–1586.

Köhl, M., Meir, M., Papillon, P., Wallner, G.M., Saile, S. (Eds.), 2012. Polymeric Materials for Solar Thermal Applications. Wiley-VCH, Weinheim.

Mueller, W., Jakob, I., 2003. Oxidative resistance of high-density polyethylene geomembranes. Polymer Degradation and Stability 79 (1), 161–172.

Ochs, F., 2008. Abschlussbericht zum Vorhaben „Weiterentwicklung der Erdbecken-Wärmespeichertechnologie“. FKZ 0329607 E. BMU, Germany.

Olivares, A., Rekstad, J., Meir, M., Kahlen, S., Wallner, G.M., 2010. Degradation model for an extruded polymeric solar thermal absorber. Solar Energy Materials and Solar Cells 94 (6), 1031–1037.

Paranovska, I., Pedersen, S., 2016. Lifetime Determination for Polymer Liners for Seasonal Thermal Storage. https://universe.ida.dk/meetupfiles/download/?meetupNumber=310923&filename=Lifetime%20Determination%20of%20Polymer%20Liners%20for%20seasonal%20Thermal%20Storage.pdf. Accessed 08.2017.

Peterson, J.D., Vyazovkin, S., Wight, C.A., 2001. Kinetics of the Thermal and Thermo-Oxidative Degradation of Polystyrene, Polyethylene and Poly(propylene). Macromol. Chem. Phys. 202 (6), 775–784.

Povacz, M., 2014. Black-pigmented polypropylene absorber materials - Aging behavior and lifetime modelling. Dissertation.

Povacz, M., Wallner, G.M., Grabmann, M.K., Beißmann, S., Grabmayer, K., Buchberger, W., Lang, R.W., 2016. Novel Solar Thermal Collector Systems in Polymer Design – Part 3. Aging Behavior of PP Absorber Materials. Energy Procedia 91, 392–402.

Povacz, M., Wallner, G.M., Lang, R.W., 2014. Black-pigmented polypropylene materials for solar thermal absorbers – Effect of carbon black concentration on morphology and performance properties. Solar Energy 110, 420–426.

Schramm, D., Jeruzal, M., 2006. PE-RT, a new class of polyethylene for industrial pipes. Plastic Pipes Conference Association, Proceedings Plastics Pipes XIII 2006.

Wallner, G.M., Povacz, M., Hausner, R., Lang, R.W., 2016. Lifetime modeling of polypropylene absorber materials for overheating protected hot water collectors. Solar Energy 125, 324–331.

Wallner, G.M., Weigl, C., Leitgeb, R., Lang, R.W., 2004. Polymer films for solar energy applications—thermoanalytical and mechanical characterisation of ageing behaviour. Polymer Degradation and Stability 85 (3), 1065–1070.

Increasing the Photovoltaic Self-Consumption by Integration of an Ice Storage into a Mono-Split-Air Conditioning Unit

Carsten Heinrich[1], Myrea Richter[1], Felix Stelzer[2] and Mathias Safarik[1]

[1] Institute of Air Handling and Refrigeration (ILK Dresden), Dresden (Germany)

[2] Technische Hochschule Nürnberg Georg Simon Ohm, Nuremberg (Germany)

Abstract

Photovoltaic-driven air conditioning systems offer a lot of advantages over solar-thermal driven cooling systems. An open issue is the missing linkage between PV and AC system regarding the different temporal peaks of electricity generation and cooling demand. The paper presents investigation results of an ice storage coupled with a mono-split air-conditioning unit. Resulting average energy efficiency ratios of charging process are between 2.8 and 3.4. Maximum ice fraction was limited due to evaporator – storage geometry to 55 %. Between an ice fraction of 55 down to 5 % a cooling rate of 2 kW was achieved for discharge process.

Keywords: PV-cooling, ice storage

1. Introduction

The number of installed air-conditioning (AC) systems is rapidly increasing worldwide. About 130 million units a year are sold (Holley, 2014). The majority (about 120 million) are lower capacity units. A number of unfavorable effects are associated with the desired gain in comfort: (1) increasing electricity demand and thereby an increasing emission on greenhouse gases (indirect emissions), (2) direct greenhouse gas emissions due to usage of refrigerants with high global warming potential (GWP), (3) distinct peak loads in the grid.

To reduce the impact of solar-driven cooling technologies have been developed and applied in the last ten to fifteen years. In the past the focus was set to solar-thermal systems, due to the use of natural refrigerants (mainly water/lithium bromide) and the cost benefits of thermal collectors. The number of solar-thermal driven cooling systems increased but on low level. Only about 1000 systems are installed worldwide (Mugnier, 2015). A higher dissemination is impeded by high investment costs and complexity of those systems.

On the opposite distinct cost reductions have been achieved in the photovoltaic (PV) sector. Present electricity generation costs of PV-systems turn PV-driven cooling systems into an economic scenario. Investigations within the EvaSolK project revealed lower carbon dioxide abatement costs for PV-driven compression refrigeration systems compared to solar-thermal driven single stage refrigeration systems (Wiemken et al., 2012).

An issue of the majority of existing PV-driven cooling systems is the missing linkage of PV and AC system. Generally the PV-system is operated grid-connected, feeding in electricity during the period of high solar radiation around midday. In residential area AC-systems start operation in the late afternoon when people come home (see Figure 1, left figure). Hence, in countries with a high dissemination of rooftop PV-systems (e.g. Australia (Council, 2016)) the demand peak of AC systems is not noticeable reduced, but during midday an oversupply of electricity is fed in into the grid.

To balance the temporal divergence between electricity generation and cooling demand an integrated energy storage is required. Thermal cold storages offer a number of advantages compared to batteries: Materials are inexpensive and free of risk to the environment. Thermal losses can be regarded as far less relevant if storage is located in the air conditioned room. Using ice storages the required volume can be decreased to suitable sizes. Depending on the concept, maximum cooling capacity provided to the room can be significantly increased in case of parallel operation of storage discharge and outdoor unit.

doi:10.18086/swc.2017.13.08 Available at http://proceedings.ises.org

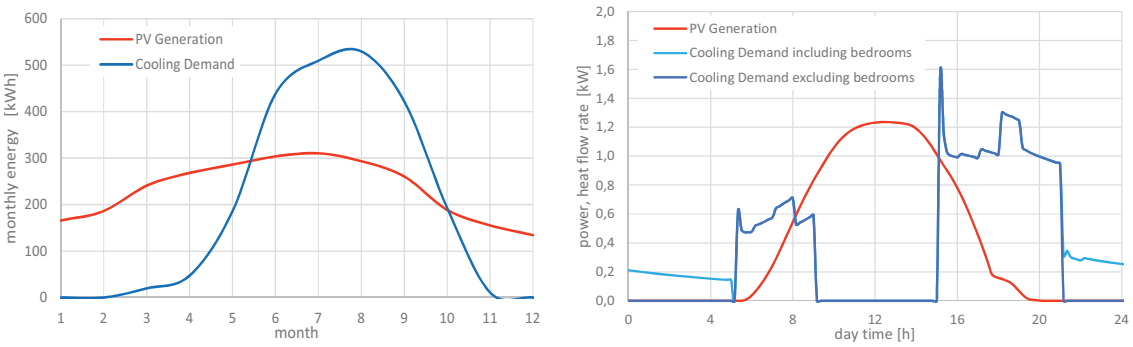

Figure 1: Seasonal (left figure) and daily (right figure) PV electricity generation and cooling demand in a residental building. source: ILK Simulation results for a residential building in Lisbon / Portugal using Modelica - BuildingsLibrary

2. System Concepts and Storage Dimensioning

System Concepts

A standard mono-split AC system consists respectively of an outdoor and an indoor installed unit, linked by a low pressure liquid and low pressure suction gas tube. From refrigeration side the outdoor unit contains compressor, condenser and electric expansion valve and the indoor unit the air-cooling evaporator.

Integration options of an ice storage into mono-split-AC-system can be characterized by

- storage position (outdoor, indoor or inside indoor unit)
- charging by direct evaporation process or via secondary cycle (brine, refrigerant)
- discharging using direct air contact (integration into indoor unit), external melting process (water cycle using the water of the ice storage) or an integrated heat exchanger (using the refrigeration or brine cycle)
- realization of direct cooling mode by usage or by bypassing the storage

Varying the mentioned characteristics lead to a number of cycle options which even increases if valves, bypasses or pumps are taken into account to achieve a more flexible operation.

A number of boundary conditions resulting from market situation and trends, legal regulations and technical standards influences the selection process. Some main aspects are discussed below:

- Required technical solutions are not yet available on the market or in a reasonable cost ranges: Discharge process using the ice storage water by external melting process can be combined with standard air cooler units. But using water in the air cooler is not common in Mono-Split systems so far. Discharge process using the refrigeration cycle requires very low capacity refrigerant pumps with a high pressure rating. There are no standard refrigeration products including such pumps on the market. Pumps from other applications have to be adapted.
- Efficiency requirements arising from legislation and quality labels: The European product regulation requires seasonal cooling efficiency ratios (SEER) calculated according to DIN EN 14825 of > 7 and > 8.5 from 01.01.2019 for air conditioning units with a cooling capacity of less than 12 kW. The German quality label *Blauer Engel* requires an EER Cooling > 4.6. The direct cooling operation will be the minor operation mode of a mono-split-unit with integrated ice storage. Avoiding barriers in the product marketing requires an appropriate cycle design to fulfill these criteria.
- Requirements to refrigerant usage: European F-Gas Regulation requires the usage of refrigerants with a global warming potential < 750 from 01.01.2025 in small scale air-conditioning units. *Blauer Engel* requires the usage of non-halogen refrigerants. Within a progressive intensification of regulations the usage of natural refrigerants gain in importance. Almost all refrigerant with a GWP < 750 that can be applied in split systems are flammable. Therefore the refrigerant charge needs to be limited.

Based on an assessment matrix using the upper characteristics further theoretical and experimental analysis were

focused on a small number of preferred options. Table 1 contains three promising options, including their advantages and drawbacks.

Table 1: Preferred integration options - system description and remarks

system description	remarks
option 1: 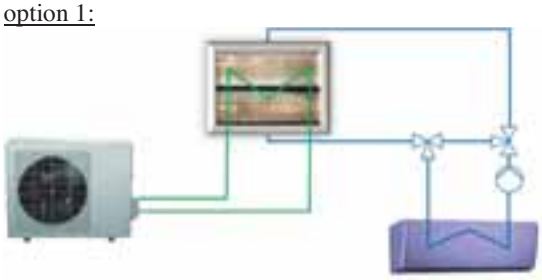 - direct charging using an evaporator in the ice storage - discharge using the water of the storage in an hydraulic cycle, indoor unit is replaced to a water based air cooler unit	advantages: - standard products can be applied, no refrigerant pumps required, no development of a specific indoor unit is required - cost efficient solution - simple control - ice melting direction inverse to freezing direction - air cooler surface temperature can be controlled by return flow addition in the water cycle for controlled dehumidification drawbacks: - poor cooling efficiency in direct cooling mode - thermally inertial system, especially not recommendable for heating mode
option 2: 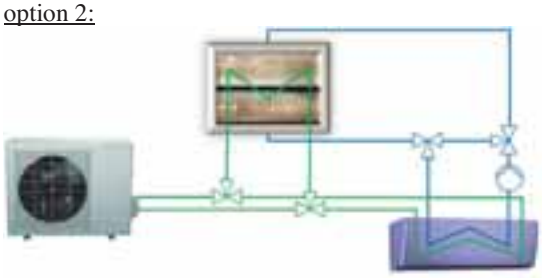 - option 1 is extended by an parallel refrigerant cycle to the indoor unit.	advantages: - direct cooling and heating mode as efficient as in common mono-split systems - extended operation flexibility (e.g. parallel operation of direct cooling and storage discharge is possible) drawbacks: - non-standard indoor unit required - more complex control algorithms required
option 3: 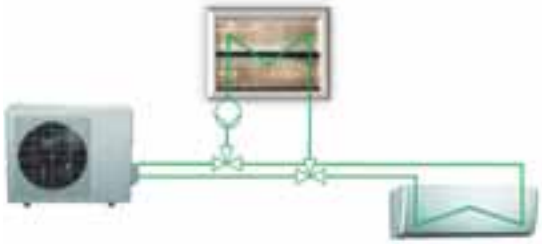 - option 2 is extended by an additional refrigerant pump for discharge process, indoor unit is changed to standard split indoor unit, water cycle is removed	advantages: - standard indoor unit - no water cycle - direct cooling and heating mode as efficient as in common mono-split systems drawbacks: - refrigerant pump availability - discharge process probably less efficient - difficult dehumidification control

Storage Dimensioning

The mono-split unit including an ice storage is connected to a photovoltaic system as well as to the grid, increasing photovoltaic self-consumption and decreasing grid peak loads. The storage should allow equalizing the daily shift between solar irradiation and cooling demand.

A simple algorithm can be applied for storage size estimation

- creation of a building model and definition of surface area and orientation for photovoltaic installation
- definition of a lower radiation limit $E_{PVSurf,low}$, which will account for any cooling generation using electricity from the grid
- daily integration of cooling demand for the condition $E_{PVSurf} < E_{PVSurf,low}$

$$Q_{CD,grid,day,i} = \int_0^{24\text{h}} \dot{Q}_{CD} \quad \text{if } E_{PVSurf} < E_{PVSurf,low} \qquad \text{(eq. 1)}$$

- analysis of the class frequency distribution of $Q_{CD,grid,day,i}$ and selection of a proper storage size

For theoretical investigations a typical single family house according to the German building standard EnEV2016 was selected and modelled (Richter, 2016). The low radiation limit on the southern roof surface area was defined by $E_{PVSurf,low} = 200\ \mathrm{W/m^2}$. Simulation was done for the German site Mannheim.

In different scenarios building heat capacity was used as thermal storage. In case of sufficient solar radiation the building was cooled during absence of inhabitants to 20.0, 22.5 and 25.0 °C, respectively. Figure 2 represent the distribution of daily integrated cooling demand requiring energy from the grid for different scenarios: (1) building is only cooled in case of cooling demand (people are at home), (2 – 4) building is cooled to 25, 22.5 or 20 °C during the day in case of sufficient photovoltaic electricity generation.

Results from Figure 2 are: Cooling demand with electricity consumption from the grid occurs for 131 days a year (case 1). If building is used as thermal storage the number of days is reduced to 126, 125 and 114 (case 2 – 4). Considering only larger cooling demands the number of days decreases. Counting only days with cooling demands $Q_{CD,grid,day} > 5$ kWh (all days below vertical blue lines), the number is reduced to 38, 24, 12 and 3 (case 1 – 4). That means integrating an ice storage with a thermal capacity of 5 kWh in case 1, the number of days with electricity consumption from the grid for cooling generation can be reduced from 131 to 38 days. For the remaining 38 days the cooling demand with electricity consumption from the grid is largely reduced. Using the building as additional thermal storage, the consumption from the grid or the cold storage capacity can be reduced further. But using the building envelope as thermal storage correlates with an increasing total cooling demand, due to additional thermal losses to ambience.

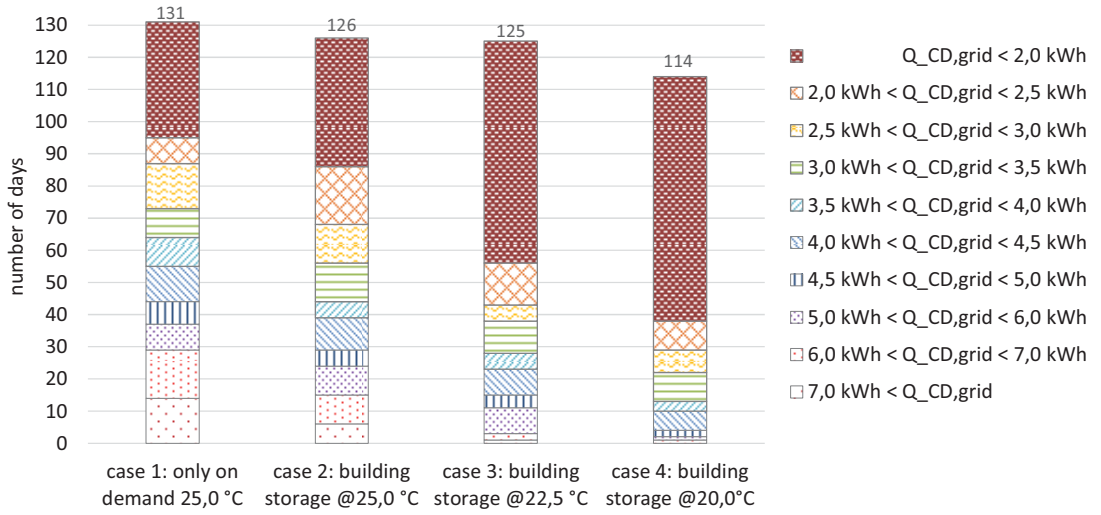

Figure 2: Distribution of daily cooling demand with energy demand from grid

3. Experimental Investigations – Integration Option 1

Motivation and experimental set up

Characteristic data for mono-split-AC-units are limited to air conditioning conditions and are only available as function of room and ambient conditions. Ice growth on evaporator during charging mode and melting during discharging mode represent non-uniform, three dimensional and dynamic processes. Furthermore, mono-split-AC-units include a number of implemented operation and safety algorithms, designed for building cooling (and heating) and dehumidification only. Hence, an evaluation of the operation of a mono-split-AC-unit with integrated ice storage requires experimental analysis.

Experimental investigations focused on

- evaluation of operation control and safety algorithm issues connected with the operation with distinctly lower evaporation pressure and non-corresponding response signals from indoor unit
- operational limits of the outdoor unit in case of distinctly lower evaporation pressures
- cooling capacity and cooling efficiency during charging process for different evaporators, different part

load factors and an increasing state of charge

- evaluation of operation in direct cooling mode (building cooling without changing the ice content within the storage)
- evaluation of influence on cooling characteristics and operational stability in case of partly charge and discharge storage cycles

For the experimental investigations, a test rig was built. The design includes options for extension to investigate a number of further integration options. A simplified piping and installation scheme to investigate option 1 is shown in Figure 3. It includes the outdoor unit (1), ice storage vessel (2), ice storage evaporator (3), hydraulic cycle for discharge mode (4), electrical water heater simulating cooling demand (5), additional manually and electronically controlled expansions valves (6) and an additional unit to directly control the compressor speed in the outdoor unit.

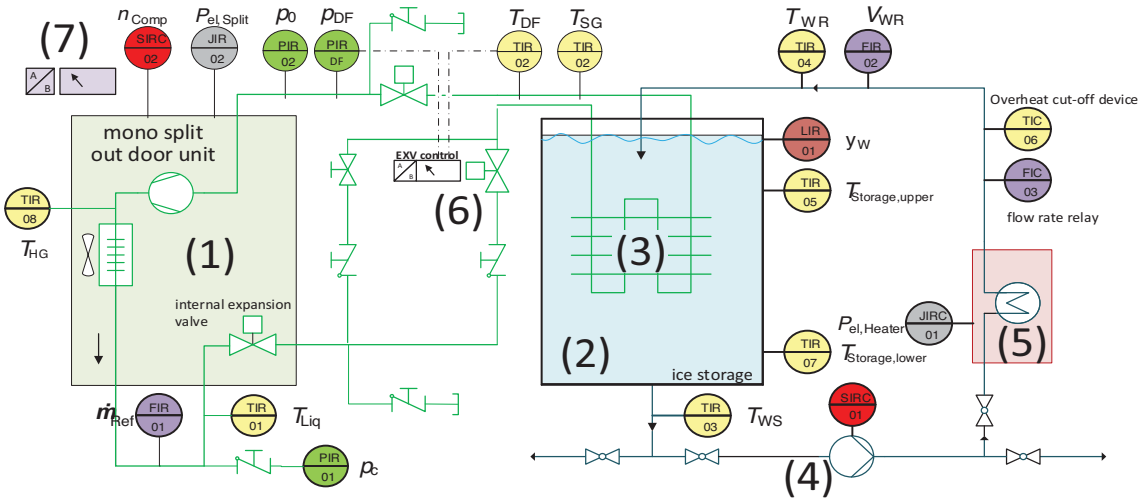

Figure 3: Piping and installation scheme of test rig to investigate the integration option 1 - direct charge process and discharge process applying external melting

Component dimensioning was carried out according to the results of a residential building simulation. A maximum cooling capacity of 2.5 kW is required. An oversized mono-split-outdoor-unit with a rated cooling capacity of 4.0 kW (Fujitsu AOYG 14LMCA) was selected to compensate the required lower evaporation temperature. The installed test rig is shown in Figure 4. Two different evaporator types have been investigated. The selection criteria focused on market availability and price. Table 2 gives relevant geometry parameters..

Table 2: Relevant geometry parameters of evaporators investigated

	tube and fin	finned tube
tube length	2 x 6.2 m, in series	4 x 4.95 m, in parallel
tube outside surface	0.39 m²	0.51 m²
fin water side area	2.32 m²	0.91 m²
total water side area	2.71 m²	1.42 m²
mean fin length	9.8 mm	11.1 mm
refrigerant volume	5.8 l	5.0 l

Refrigerant cycle operation is measured by high pressure liquid medium temperature in front of expansion valve inlet T_{Liq}, suction gas temperature at evaporator outlet T_{SG}, hot gas temperature as tube surface temperature at compressor outlet T_{HG}, condensing pressure p_C in front of expansion valve inlet, evaporation pressure p_0 between evaporator outlet and compressor inlet and refrigerant mass flow rate $\dot{m}_{Ref}$ in front of expansion valve inlet. Furthermore, split-unit power input $P_{el,split}$, which includes power demand for compressor / inverter, electronic

control unit and fan. Compressor speed n_{Comp} and expansion valve opening is taken from split unit service tool, connected to electronic control unit.

Storage and water cycle is measured by upper and lower storage water temperature $T_{Storage,up}$ and $T_{Storage,low}$, return water temperature in front of storage inlet T_{WR}, supply water temperature behind storage outlet T_{WS} , water volume flow rate $\dot{V}_{WR}$ in front of storage inlet and storage liquid level height by an optical system y_W. Additional the power input of electrical heater $P_{el,heater}$ is measured.

If not mentioned differently, all temperatures are measured using PT100 sensor types, directly in the fluid.

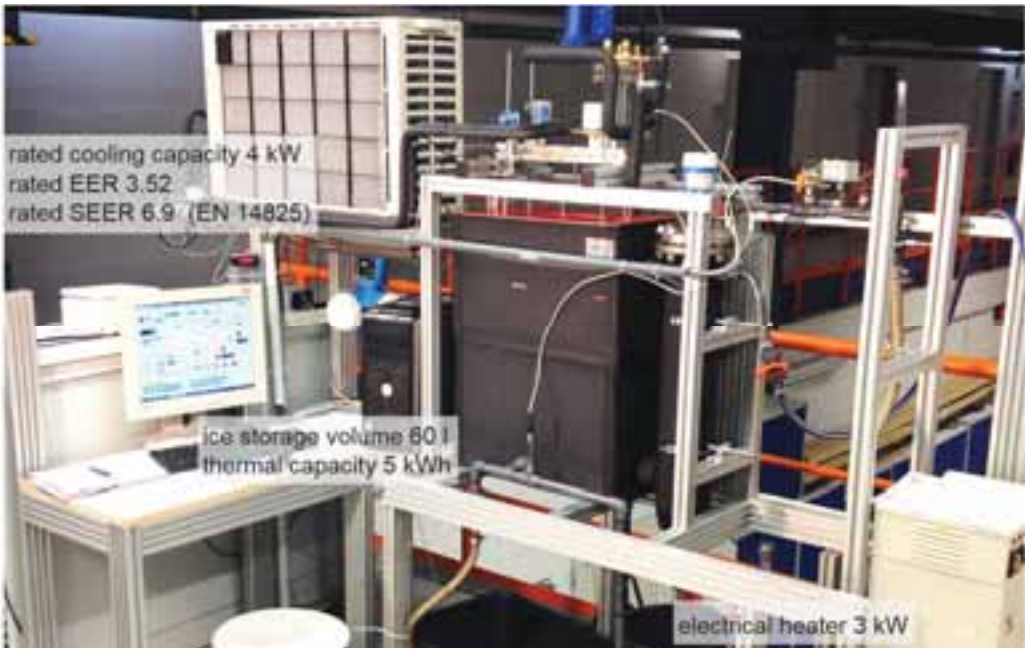

Figure 4: Photo of the test rig

Data post processing

Cooling capacity $\dot{Q}_{\mathrm{Ref,charge}}$ during charging process is calculated under the consumption of subcooled condenser outlet and superheated evaporator refrigerant state. These conditions have been proved for the whole measurement period, except a not fully liquid refrigerant state at condenser outlet for a short period after compressor start:

$$\dot{Q}_{\mathrm{Ref,charge}} = \dot{m}_{\mathrm{Ref}} \cdot \left(h_{\mathrm{gas}}(p_0,\ T_{\mathrm{SG}}) - \ h_{liq}\left(p_{\mathrm{C}}, T_{\mathrm{Liq}}\right)\right) \qquad \text{(eq. 2)}$$

Energy efficiency ratio of charging process EER_{charge} is calculated using cooling capacity and total power consumption of split unit. If convective heat transfer is enforced by pumping the water in the cycle during the sensible cooling phase, the electrical power demand of the pump has to be included.

$$EER_{\mathrm{charge}} = \dot{Q}_{\mathrm{Ref,charge}} \,/\, \left(P_{\mathrm{el,split}} + P_{\mathrm{el,pump}}\right) \qquad \text{(eq. 3)}$$

Ice fraction x_{Ice} of the storage is calculated based on the density difference between liquid and solid phase of water. A reference temperature T_{R} is defined for reference conditions of storage level height $y_{\mathrm{liq,TR}}$ and liquid water density $\varrho_{\mathrm{W,TR}}$.

$$x_{Ice} = \ \left(y/y_{\mathrm{liq,TR}} - 1\right)/\left(1 - \varrho_{\mathrm{W,TR}}/\varrho_{\mathrm{Ice}}\right) \qquad \text{(eq. 4)}$$

Discharge capacity $\dot{Q}_{\mathrm{discharge}}$ is calculated by the enthalpy difference resulting from the temperature difference between storage inlet and outlet. Required mass flow rate is calculated based on the measured volume flow rate in front of the storage inlet $\dot{V}_{WR}$ and the corresponding temperature T_{WR}.

$$\dot{Q}_{\mathrm{discharge}} = \mathrm{V}_{\mathrm{WR}} \cdot \varrho_{\mathrm{W}}(T_{WR}) \cdot \left(h_{\mathrm{W}}(T_{\mathrm{WR}}) - \ h_W(T_{\mathrm{WS}})\right) \qquad \text{(eq. 5)}$$

Overall discharge heat transfer value $G_{\mathrm{discharge}}$ is calculated under the consumption of an ice surface temperature T_{IceSurf} of 0 °C.

$$G_{\mathrm{discharge}} = \dot{Q}_{\mathrm{discharge}} \cdot \ln((T_{\mathrm{WR}} - T_{\mathrm{IceSurf}})/(T_{\mathrm{WS}} - T_{\mathrm{IceSurf}})) \,/(T_{\mathrm{WR}} - T_{\mathrm{WS}}) \qquad \text{(eq. 6)}$$

All media properties for water and the refrigerant R410A are calculated using *CoolProp* (Bell et al., 2014).

Results – Charging Process

The charging process is investigated for both evaporator types varying the outdoor unit part load factor. Initial storage temperature is kept constant at 18 °C. Test rig is located in the main test hall of the institute. Ambient temperature depend on test hall temperature and varied in the measuring period between 20 and 25 °C. The charging process is terminated in case of ice fraction of 80 % or in case a further ice growth could lead to storage damages.

Figure 5 shows the cooling capacity versus ice fraction for both evaporator types and for varying outdoor unit part load factor (plf). Maximum achieved ice fractions are 75 % for the finned tube evaporator and 55 % for the tube and fin evaporator. The cooling capacity decreases with increasing ice fraction and with decreasing outdoor unit part load factor. The decreasing cooling capacity as function of ice fraction is more distinct for the tube and fin evaporator. The cooling capacity decreases from 0 to 50 % ice fraction to about 60 to 65 %. For the finned tube evaporator the cooling capacity decrease for the same ice fraction range to about 80 to 85 %.

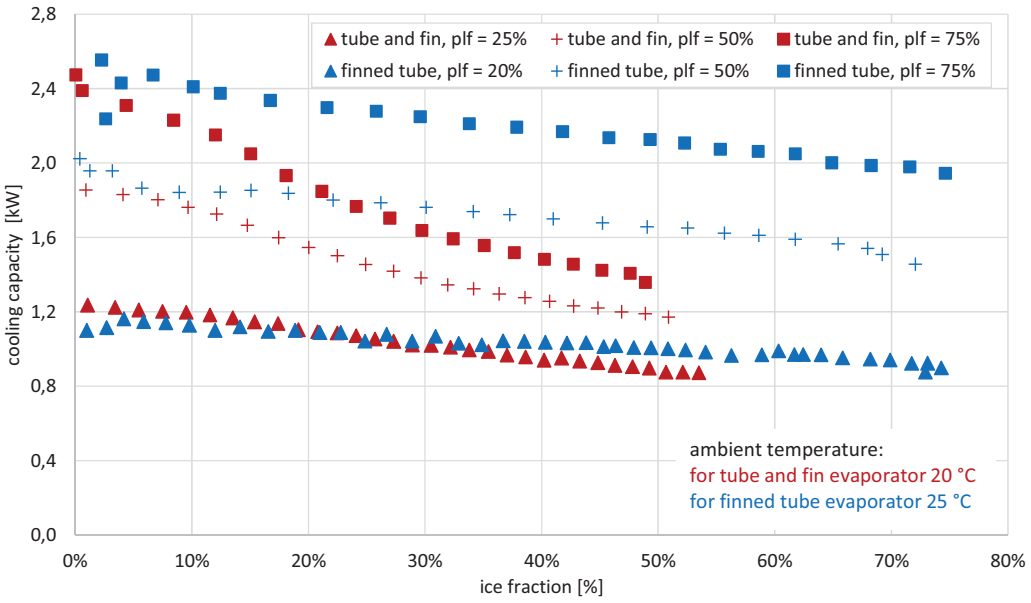

Figure 5: Ice storage charging process - cooling capacity versus ice fraction with variation of outdoor unit part load factor

Figure 6 shows the energy efficiency ratio (EER) of the charging process versus ice fraction for both evaporator types and for varying outdoor unit part load factor. The EER varies between 2 and 4.4. It decreases with increasing part load factor and increasing ice fraction. The EER for the split-unit at a part load factor of 75 %, an ambient temperature of 25 °C and an indoor temperature 25 °C can be estimated using the catalog data (Swegon, 2016) and the info sheet for SEER calculation according to eco design regulation (Fujitsu, 2015) to 6.0.

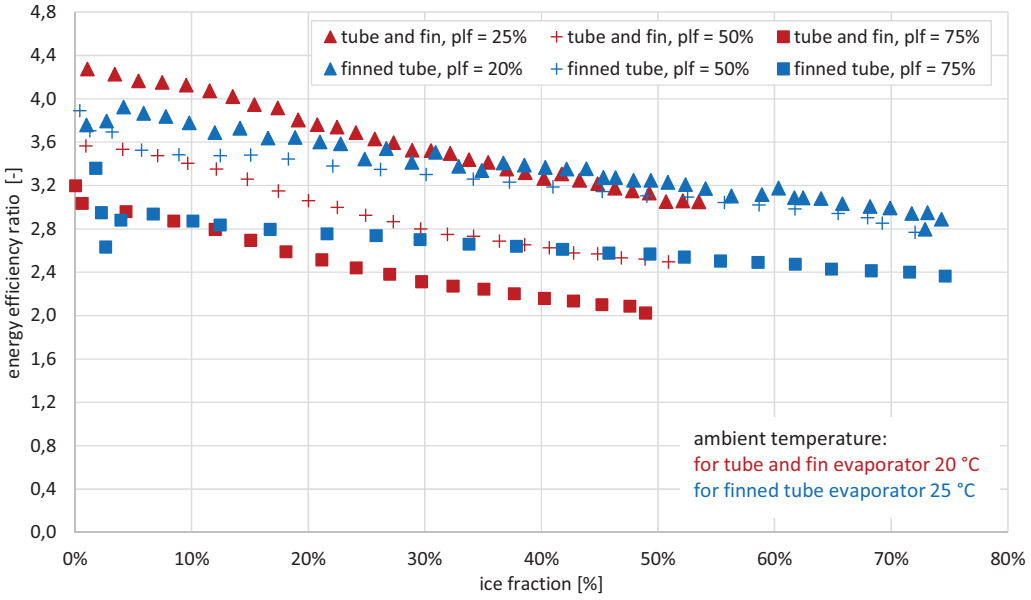

Figure 6: Ice storage charging process - energy efficiency ratio versus ice fraction with variation of outdoor unit part load factor

In Figure 7 charging time and average energy efficiency ratio between a storage temperature of 15 °C and an ice fraction of 50 % are shown as function of outdoor unit part load factor. Charging times for the finned tube evaporator are 40 to 45 minutes lower compared to the fin and tube evaporator for the same part load factors. For part load factors lower than 60 % a strong dependency between charging time and part load factor can be observed. A further increase of the part load factor result in only minor reductions of the charging time.

Average energy efficiency ratios for the defined charging range and ambient temperature of 20 and 25 °C vary between 2.4 and 3.9. Outdoor unit part load factor and average energy efficiency ratio show approximately a linear dependency.

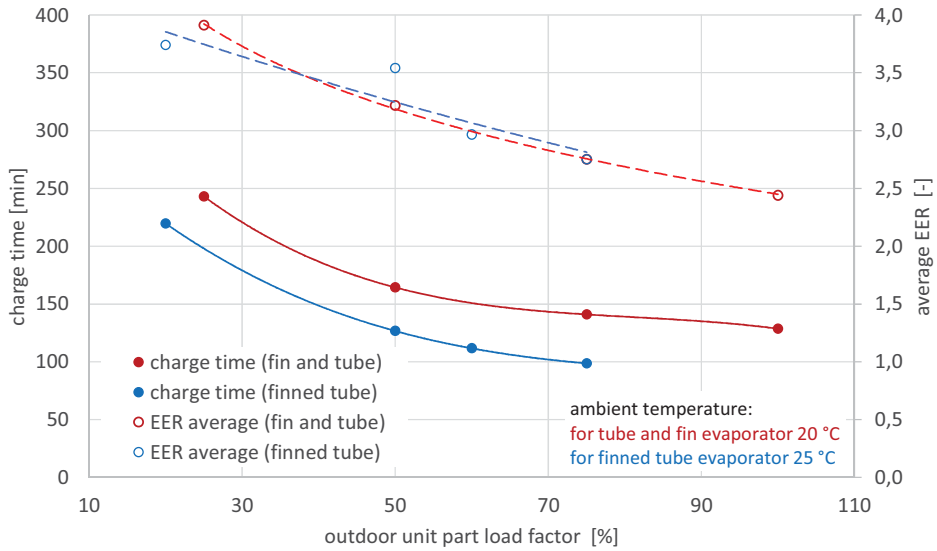

Figure 7: Charge time from 15 °C to 50 % ice fraction and average energy efficiency ratio versus outdoor unit part load factor

Results – Direct Cooling Mode

In direct cooling mode the cooling capacity supplied by the outdoor-unit is directly transferred to the water cycle. Ideally no change of storage state of charge occurs. Cooling capacity is limited by the heat transfer conditions in the storage. Heat transfer is characterized by forced convection due to the storage water flow rate. Evaporation temperature has to be limited to avoid ice growth on the surface. In this case the cooling capacity supplied by the outdoor-unit exceeds the cooling capacity transferred to the water cycle.

Figure 8 shows the maximum cooling capacity and the corresponding energy efficiency ratio depending on the storage volume flow rate for the finned tube evaporator. Maximum cooling capacity increases with increasing water flow rate, due to the improving heat transfer conditions. Energy efficiency ratio decreases with increasing cooling capacity due to the higher part load factor in the outdoor unit.

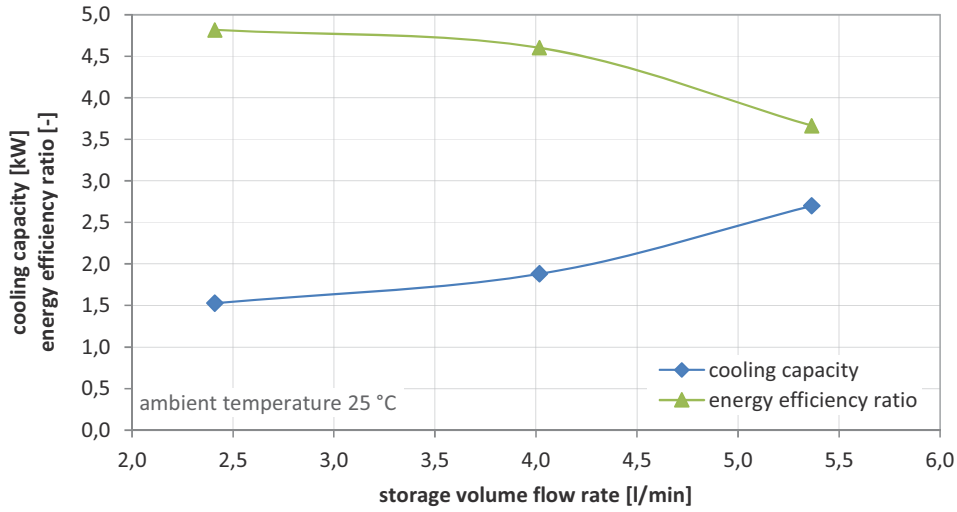

Figure 8: Maximum cooling capacity and energy efficiency ratio versus water volume flow rate for finned tube evaporator

4. Summary and Discussion

Based on daily characteristic of cooling demand and photovoltaic electricity generation in residential buildings the integration of a cold storage into the AC-system can significantly increase photovoltaic self-consumption. Integrating the ice storage into a mono-split-AC-system is a potential option. The system benefits from the high energy efficiency and low investment cost of mono-split-systems. Using an assessment matrix approach the large number of conceivable integration options is reduced to a few technically promising and economically feasible options. Three basic options were presented and discussed. Option 1, charging the storage with an evaporator, discharging the storage with a water cycle using external melting process, was experimentally investigated.

No additional modifications of the outdoor-unit were required. Only a mass flow sensor was implemented between condenser and expansion valve. A successful interaction, an efficient and stable operation of the outdoor unit with the connected storage was achieved after installation of additional refrigeration and electronic components. The required refrigerant charge had increased by about 100 g of R410A. As mono-split-units are designed to operate at evaporation temperatures above 0 °C, some protection functions had to be outwitted.

Charging process at part load factors between 20 and 75 %, ambient temperatures between 20 and 25 °C result in energy efficiency ratios between 2.0 and 4.4. In direct cooling mode in case of maximum achievable cooling capacity at given water flow rate and an ambient temperature of 25 °C energy efficiency ratios between 3.5 and 4.8 were achieved.

The efficiency during charging process is acceptable as in many cases there are not a lot of other applications for self-consumption during the day. For direct cooling mode the required efficiency ratio of 4.6 according to the German quality label *Blauer Engel* (EER = 4.6 at 27 °C room temperature and 35 °C ambient temperature) will be achieved only in low part load ranges.

Based on the obtained results, integration option 1 is a convenient integration option if cooling by storage discharge mode is the predominant operation. If direct cooling becomes more important, integration option 2 becomes more relevant.

5. Outlook

The test rig has been extended to experimentally investigate integration option 2 and 3. Other evaporation types will be included in the investigation. For an economic operation a suitable controller is required including forecast

algorithms taking building behavior, weather and photovoltaic electricity generation into account.

For controller design and optimization a simulation model library have been developed in Modelica. Based on Modelica BuildingSystems models (Nytsch-Geusen et al., 2017) for buildings, weather, radiation processing and photovoltaic generators were created. Based on ThermoFluidILK and using results from experimental investigations a wide range of pure split-unit and split-units with integrated ice storages model have been implemented.

6. Acknowledgment

The investigations were carried out in the SolarSplit project (funding code 0325900A). It is managed by the project management organization Jülich (PTJ) and financially supported by German Federal Minister of Economics and Technology (BMWI) within the 6th Energy Research Program of the German Federal Government.

7. References

Bell, I.H., Wronski, J., Quoilin, S., Lemort, V., 2014. Pure and Pseudo-pure Fluid Thermophysical Property Evaluation and the Open-Source Thermophysical Property Library CoolProp. Industrial & Engineering Chemistry Research 53, 2498–2508.

Fujitsu, 2015. Information Sheet (Lot. 10) - ASYG14LMCA / AOYG14LMCA. Swegon - Fujitsu.

Holley, A.M., 2014. Global Trends in Air Conditioning. Chillventa.

Mugnier, D., 2015. Worldwide overview on Solar cooling and SHC tasks 48, 53, in: Chinese Solar Cooling Conference.

Nytsch-Geusen, C., Inderfurth, A., Moeckel, J., Mucha, K., Tugores, C.R., Raedler, J., Thorade, M., 2017. Modelica BuildingSystems Library (Version 2.0.0-beta).

Richter, M., 2016. SolarSplit: Gebäudeenergiebedarf und Rückschlüsse auf notwenige Speichergrößen (No. ILK-B-5-16-0369). ILK Dresden.

Swegon, 2016. Montage- und Betriebsanleitung Wärmetauschersteuerung INV-DX Fujitsu Single-Split.

Wiemken, E., Safarik, M., Zachmeier, P., Schweigler, C., Nienborg, B., Elias, A.R.P., 2012. Evaluierung der Chancen und Grenzen von solarer Kühlung im Vergleich zu Referenztechnologien, in: EuroSun 2012, ISES-Europe Solar Conference. Rijeka, Croatia.

STUDY ON SEASONAL AND SHORT-TERM THERMAL ENERGY STORAGE USING A PHASE CHANGE MATERIAL EMULSION FOR DISTRICT HEATING APPLICATIONS

G. Rinaldi[1], A. Lazaro[2], M. Delgado[2], J.M. Marin[2], C. Peñalosa[2], M. A. Lozano[2], L. M. Serra[2], V. Verda[1]

1. Department of Energy, Politecnico di Torino, Torino (Italy)

2. GITSE-I3A, Department of Mechanical Engineering, University of Zaragoza, Zaragoza (Spain)

Abstract

Thermal energy storage systems are necessary to increase the flexibility and the share of renewable energy sources in district heating systems. The use of latent heat storage materials (PCM) can reduce the volume of the storage and at the same time the storage temperature needed for a given heat storage. This work studies since a technical viewpoint the potential application of Thermal Energy Storage using "low cost" emulsion of latent heat storage material in district heating for: central heat storage in Solar District Heating systems (seasonal) and de-centralized heat storage (short-term). Results obtained for the seasonal application showed slight improvement achieved by the latent heat storage system using the selected "low-cost" PCM emulsion. On the other hand, the de-centralized TES unit using the PCM emulsions integrated into the DH grid increased the thermal performance and allowed the connection of additional buildings in a saturated grid.

Keywords: District Heating, thermal energy storage, latent heat, phase change materials emulsion, solar thermal.

1. Introduction

In the European Union (EU), buildings account for 40% of the total energy consumption (European Union, 2010), which suggests a great potential for energy savings. In this regard, the EU Directive on energy efficiency (European Union, 2012) recognizes district heating and cooling networks, as key elements for improving the energy efficiency. Thus, the 4th generation of district heating (DH) systems, i.e. low temperature district heating (LTDH), is being developed in order to accomplish the European goals as well as the target of fossil fuel free by 2050 established by some countries, e.g. Denmark. Lower distribution temperatures and more flexible elements of the network provide heat to low-energy buildings and allow the integration of low-temperature heat sources (Fevrier et al., 2012), as it is the case of solar thermal energy. In northern and central European countries, e.g. Denmark, Germany or Austria, new installations also supply heat for the space heating needs. The approach of central solar heating plants with seasonal storage (CSHPSS) is the storage of solar thermal energy from the period of higher offer (summer) to be consumed in the periods of higher demand (winter). These installations are integrated into district heating systems that supply heat for a large number of dwellings and reach a solar fraction about 50% or higher (Nielsen, 2014).

Thermal energy storage systems (TES) cover a central role in this scenario, increasing the efficiency of the energy systems in which they are integrated and the potential utilization of new renewable energies (RES). Although TES themselves do not save final energy, they are able to "move" heat and cold in space and time, correcting the mismatch between supply and demand allowing: a) energy conservation by exploiting new RES; b) peak shavings both in electric grids and DH grids; c) power conservation by reducing the required power of energy conversion machines; d) reduced GHG emissions (IEA, 2014)

The study of thermal energy storage systems (TES) has been a very intensive branch of research in the last decades. Even though the most commonly used method remains based on sensible heat, the latent heat storages, based on the employment of phase change materials (PCM), are an attractive solution, because they provide higher storage density and smaller temperature difference between the absorbed and the released heat than sensible heat storage. Recently, a new class of latent heat fluids, phase change slurries (PCMs), have been analyzed because of their promising role. The main advantage of PCMs is their applicability either as thermal storage medium and/or heat transfer fluid (HTF). They can be continually pumped in charging/discharging cycle, without the necessity of an additional fluid, reducing the losses and increasing the heat transfer thanks to

doi:10.18086/swc.2017.13.09 Available at http://proceedings.ises.org

the high ratio surface/volume. These slurries are two-phase fluids composed by a PCM dispersed phase in a carrier fluid, usually water. Based on the nature of the dispersed phase, among the PCMs are mentioned the PCM emulsion, ice slurries, microencapsulated PCM slurries (mPCM), clathrate slurries and shape-stabilized PCM slurries (Delgado et al., 2012).

This work studies the potential application of Thermal Energy Storage (TES) using a low-cost emulsion of latent heat storage material (PCM emulsion) in central solar heating plants with seasonal storage (CSHPSS). Furthermore the main outcomes of a second analysis on the application of PCM emulsions into short term de-centralized TES into low temperature district heating (LHTD) networks are presented. The study is made from a technical feasibility viewpoint, analysing the physical advantages and constraints. No economic feasibility analysis is presented due to the lack of appropriate economic information.

2. Thermal energy storage materials: PCM emulsions

The PCM emulsions are mixture of two immiscible fluids whose one forms the continuous phase in which the other part is dispersed in small droplets. They are dispersions with particle size distribution between 1-1000 nm thermodynamically unstable. Usually for energy applications the oil-in-water type, more precisely the paraffin-in-water, is selected because of its suitability given by lower viscosities and higher conductivities than the water-in-oil combination (Edelen, 2012). The properties of a paraffin emulsion depend on many factors like the preparation method, which influences the particle size distribution of the paraffin, and on the surfactants used. The emulsifiers are indispensable components of a PCM emulsion since they provide the kinetical and thermo-mechanical stability between the two phases. The addition of these organic molecules lowers the interfacial tension between the oil and the water and, consequently, lowers the energy required to manufacture the emulsion. Furthermore, the surfactants form a protective layer around the oil droplets preventing coalescence, particles breaking and other instability phenomena like creaming, flocculation and sedimentation. (Shao et al., 2015).

In the current study, two “low cost” paraffinic emulsions were considered. Emulsion 1 is a paraffinic emulsion produced by an oil company, as by-product of the petrochemical industry that has been chosen as test material. This PCM slurry is an anionic emulsion of paraffin with an oleic consistence, with a solid content of about 60% of paraffin, and white color. The thermophysical properties of the selected paraffinic emulsions have been experimentally characterized (Figs. 1-3) applying the methods shown in Table 1, available in the Thermophysical Properties Characterization Lab at the GITSE-I3A facilities in the University of Zaragoza. From the study with the DSC (heating process) and with the T-History (cooling process), the whole phase transition behavior of the Emulsion 1 has been characterized. The phase change occurs in the temperature range of 30 – 50 ºC. Such a wide melting range is due to its by-product nature which enables the cost reduction of the material. However, thermal and rheological properties are not optimal. The enthalpy-temperature curve has been determined (Fig. 1), obtaining a phase change enthalpy value of $h_{sl} \cong 140\ \mathrm{kJ/kg}$. Some hysteresis between the melting and solidification curves was observed, as well as a slight but not significant subcooling. The specific heat curve of the Emulsion 1 as a function of the temperature was also obtained as shown in Fig. 3. Its value outside the change of phase is about 3.2 kJ/(kg K), which is rather poor and lower than the water specific heat. The measured density range of the Emulsion 1 was 0.9372 kg/m^3 at 20 $^{\circ}$C - 0.8704 kg/m^3 at 60 $^{\circ}$C.

Table 1: Properties and equipment used for the characterization of the considered PCM emulsion (Delgado et al., 2015)

Property	Method	Accuracy	Sample size	Equipment
Enthalpy	T-history/DSC	< 10%	≈ 10 g	T-history / DSC 200F3 Maia (Netzsch)
Phase change ΔT	T-history	0.2 K	≈ 10 g	T-history
Specific heat	DSC/T-history	< 1%	≈ 20 mg – 10 g	DSC 200F3 Maia (Netzsch)
Viscosity	Reometer	0.1 nN·m	0.5 cm^3 – 30 cm^3	Reometer AR-G2 TA
Density	Densimeter	< 1%	> 1 cm3	Densimeter DM-40 (Mettler-Toledo)

Subsecuently, a second PCM emulsion, called Emulsion 2, has also been considered in this study for analyzing the applicability of PCM emulsions in Central Solar Heating Plants with Seasonal Storage (CSHPSS. Indeed the advantages obtained with the employment of a PCM usually derive from its utilization as close as possible to the phase transition. For this reason, the study of a second emulsion with a more convenient temperature range of

the phase change has been evaluated to explore the potential utilization of PCM emulsions in this application.

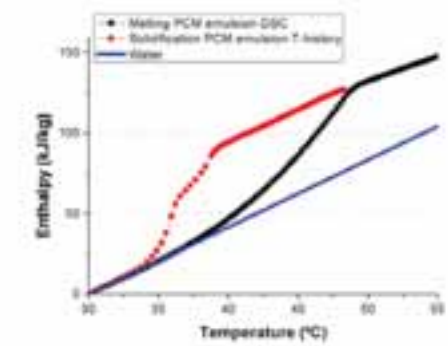

Fig. 1: Enthalpy vs temperature (Emulsion 1)

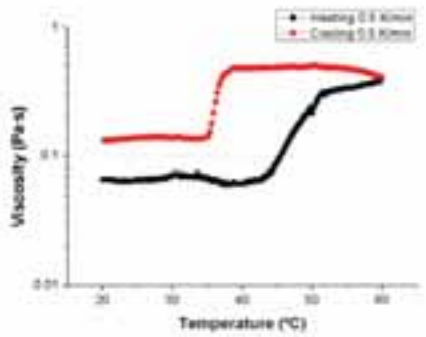

Fig. 2: Viscosity vs. temperature (Emulsion 1)

This Emulsion 2 is a hypothetical material with the same density, thermal conductivity and viscosity values than those experimentally measured for Emulsion 1, but with the curves c_p-T and h-T moved 10 ºC in order to get the phase change in the temperature range of 40 ºC to 60 ºC, as shown in Fig. 3.

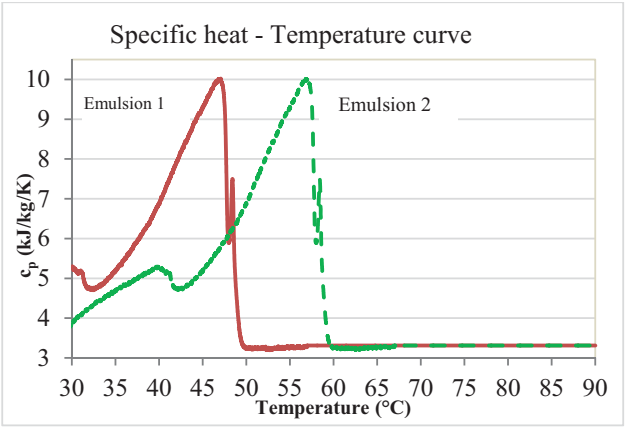

Fig. 3: Specific heat vs temperature curves for the emulsions considered (Emulsion 1 and Emulsion 2).

3. Mathematical model for the evaluation of Central Solar Heating Plants with Seasonal Storage using PCM emulsion as thermal energy storage

The model developed to evaluate the performance of Central Solar Heating Plants with Seasonal Storage (CSHPSS) using PCM emulsion as Thermal Energy Storage (TES) material in the seasonal storage is based on the *simple model* for the predesign of CSHPSS, built on the Engineering Equation Solver (EES, 2016) and developed by Guadalfajara et al. (2015). This model is based on an approximate calculation of the solar collector field production and of the capacity of the seasonal thermal energy storage on a monthly basis and using water as TES working fluid, to match production and demand, as well as to perform easily parametric analysis for the evaluation of CSHPSS. Fig. 4 shows the system scheme and identifies the main energy flows that appear in the system model.

The radiation received, Q_r, over the solar collector is harvested and the production of the solar field, Q_c, is calculated simulating its hourly operation during a representative day of the month. It is considered a complete mixture in the thermal energy storage, i.e. without stratification; so that it keeps uniform the seasonal storage (accumulator) temperature, T_{acu}, along the calculation period, which is a month in the proposed method. With this approach the considered temperature in the tank is lower than the top temperature and higher than the bottom temperature. This approach slightly underestimates the performance of the system, because the estimated temperature of the inlet water of the solar collector is higher than the real value, provoking a reduction of the solar collector efficiency. Nevertheless, the study developed by Braun et al. (1981) revealed that stratification effects have a negligible effect on the performance of CSHPSS. The solar collector performance and the heat losses, Q_l, of the seasonal storage are calculated considering the tank temperature at the beginning of the month.

In a seasonal storage tank, the premise of considering constant the water tank temperature along the month is reasonable due to its high thermal inertia (high volume). A monthly energy balance is used to calculate the temperature in the thermal energy storage at the end of the month. This temperature, water tank temperature at the end of the month, is used to calculate the solar collector performance in the next month.

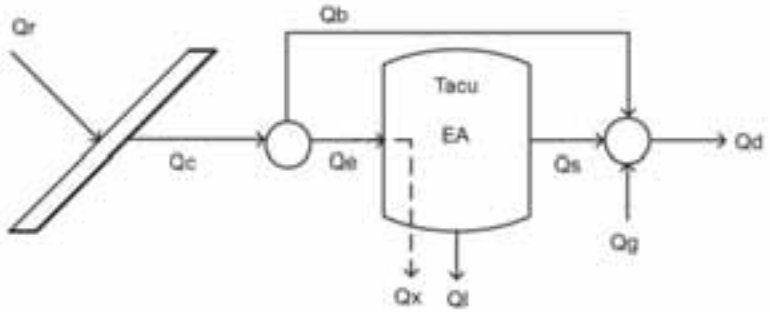

Fig. 4: Energy flow chart of the *simple model* of central solar heating plants with seasonal storage (Guadalfajara et al., 2015)

The monthly operation of the seasonal storage tank has two different operation modes during the year: i) charge and ii) discharge. The charge mode occurs when the production of the solar field, Q_c, is higher than the heat demand, Q_d. Consequently, part of the collected heat is used to attend the immediate demand, Q_b, and the surplus of the collected heat is sent to the seasonal storage for its later consumption, Q_e. In the discharge mode, the heat demand, Q_d, is higher than the production of the solar collector field, Q_c, and the seasonal storage tank is first discharged, Q_s. If it is not sufficient, the auxiliary system, Q_g, provides the required heat to cover the demand. The thermal energy storage operation is constrained by two temperature limits, T_{min} and T_{max}. When the limit of the minimum temperature is reached, the thermal energy storage cannot be discharged anymore and the auxiliary system provides the required heat, Q_g, to fulfill the demand. The thermal energy storage cannot be either charged over the maximum temperature. When it achieves this maximum temperature limit, part of the heat production is rejected, Q_x, to avoid overheating and equipment damage. As the thermal energy storage is warm, the heat losses to the environment, Q_l, are also calculated. The thermal energy accumulated in the storage tank is denoted by the variable EA, and its maximum value EA_{max} depends on the temperature limits. A complete description of this model as well as its validation can be found in Guadalfajara et al. (2015) and Guadalfajara (2016). Note, that this model is suitable for studying the employment of water as storage medium. Although the overall framework of the model has been maintained, several modifications have been required for testing the performance of a different material and especially when considering a PCM emulsion (Rinaldi, 2016).

Thus, replacing the current storage material (water) with the investigated PCM emulsions requires using their properties, obtained from the thermo-physical characterization of the PCM emulsions (Delgado et al., 2015), in the equations related to the storage and to the secondary circuit. While the density of the emulsions, $\rho_{em}(30°C)$ = 921.5 kg/m^3, and their conductivity, λ_{em} = 0.4 W/m/K, were assumed constant in all the analyzed cases, the viscosity depends on the shear stress. However, to minimize the pressure losses, the working fluid conditions have been created in order to attain the lowest viscosities of the curve (~0.05 Pa·s; see Fig. 2). Moreover, when a PCM emulsion is used as storage material, the latent heat of the phase transition is exploited for storing or discharging thermal energy, and it has been necessary to consider the enthalpy-temperature curves measured with the DSC and T-History (Fig. 1).

Additionally, a second modification was implemented. In the model developed by Guadalfajara et al. (2015) it was considered that the fluid circulating through the solar collector transfers the collected heat to the water of the seasonal storage through a heat exchanger with effectiveness, E_{ff} = 0.9. This value is used to calculate the heat exchanger inlet and outlet temperatures. Substituting the heat storage medium with a PCM emulsion, a heat transfer study was required due to the significant different properties of the secondary fluid affecting the efficiency of the process. Consequently, a specific flat-plate heat exchanger was modeled. For a detailed explanation see Rinaldi (2016).

3.1. Base case

The considered base case taken as a reference for the analysis presented in this paper is a CSHPSS, in which a water tank is a seasonal thermal energy storage system (sensible heat), located in Zaragoza, Spain (latitude 41.6º North) supplying heat for space heating and domestic hot water to a community of 1000 dwellings of 100 m^2 each. The input data required few public available data (Guadalfajara et al., 2015): annual demand of domestic hot water, Q_{DHW}, and space heating, Q_{SH}; latitude of the location of the plant; monthly average of daily global radiation on a horizontal surface, H (monthly data); monthly average of daily medium, minimum and maximum ambient temperatures, Ta_{ave}, Ta_{min} and Ta_{max} (monthly data); cold water temperature from the net, T_{net} (monthly data); ground temperature, T_{ter}; and ground reflectance, ρ_g.

The design data for the base case, which were selected based on manufacturers' catalogues, existing plants and bibliographic information, are presented in Table 2.

Table 2: Design parameters for the base case with water as storage material (Guadalfajara et al., 2015; Rinaldi, 2016).

	Parameter	Value		Parameter	Value
Solar Collector Field	RAD: ratio collector area / demand	0.6 m^2/(MWh/yr)	Seasonal Storage	RVA: ratio volume / area	6 m^3/m^2
	A: area of solar collectors	3210 m^2		V: volume of seasonal storage	19,260 m^3
	η_0: optical efficiency	0.816		T_{min}: minimum storage temperature	30ºC
	k_1: 1st order heat loss coefficient	2.235 W/(m^2·K)		T_{max}: maximum storage temperature	90ºC
	k_2: 2nd order heat loss coefficient	0.0135 W/(m^2·K^2)		RHD: ratio height / diameter	0.6 m/m
	β: tilt	45º		U_{acu}: heat transfer coefficient	0.12 W/(m^2·K)
	γ: orientation	0º		A_{acu}: heat transfer area	4101 m^2
	m_s: solar field flow rate	20 kg/(h·m^2)		$\rho \cdot c_p$: heat capacity	4.18 MJ/(m^3·K)
				EA_{max}: storage capacity	1342 MWh
Flat Plate Heat Exchanger	E_{ff}: heat exchanger effectiveness	0.90		Φ: corrugation factor	1.22
	A_{ht}: total heat exchange area	73.78 m^2		N_{pl}: number of plates	42
Annual Heating Demand	Q_{SH}: annual space heating demand	4060 MWh/year	District Heating	T_{sup}: supply temperature	50ºC
	Q_{DHW}: annual DHW demand	1290 MWh/year		T_{ret}: return temperature	30ºC
	Q_d: annual demand	5350 MWh/year		T_{DHW}: DHW temperature	50ºC

Primary design variables considered in the model are: solar collector's area, A (or RAD, which is the ratio of the area of the solar field, m^2, divided by the annual demand in MWh/year), and the volume of the seasonal storage tank, V (or RVA, which is the ratio of the volume of the seasonal storage tank, m^3, divided by the area of the solar field in m^2). The RAD and RVA values for the base case were selected to obtain a significant solar fraction, higher than 50%, avoiding stagnation and heat rejection during the summer period.

Secondary design variables are: the efficiency curve parameters (η_0, k_1, k_2) taken from a manufacturer's catalog (Arcon, 2013) of large solar collectors employed in CSHPSS; tilt, β, and orientation, γ, of the solar collectors, which values were defined considering the geographical coordinates of the plant location; the specific mass flow rate of the working fluid circulating through the solar collectors, m_s, based on the low-flow model (Peuser at al., 2010), characterized by a nominal flow rate of 12-20 l/(h·m^2), and suitable for larger solar thermal installations, since it favors a higher temperature spread between outlet and inlet in the solar collector and pumping savings in the solar field; the temperature of the water supplied to the district heating network, T_{sup} and the temperature of the water returning from the district heating network, T_{ret}, which values were selected considering a high efficiency district heating network (Nielsen, 2014); the minimum and maximum temperatures allowed in the storage tank, T_{min} and T_{max}, and its global heat transfer coefficient for the calculation of the heat losses, U_{acu}. The seasonal storage has been modeled considering a global heat transfer coefficient value of 0.12 W/(m^2·K), in agreement with the specialized literature (Raab et al., 2003; Raab et al. 2005). The seasonal storage is assumed as an underground cylindrical tank with a shape ratio RHD = 0.6 (height divided by diameter). Once the volume is known, the other dimensions can be calculated. The flat plate heat exchanger, consisting of N_{pl} = 42 thin corrugated plates, was modeled following technical specification of manufacturers (ALFA LAVAL, 2015; SWEP, 2015) and recommendations of specialized bibliography (Marin and Guillen, 2013). It has been sized considering the maximum energy flow which has to be handled (in the considered base case location the maximum solar heat production occurred in July 1st at 13 hours), the corresponding inlet and outlet temperatures, the same water mass flow rate in both sides, an effectiveness E_{ff} = 0.90, and a corrugation factor Φ with a typical value of Φ = 1.22.

(i) Comparison of CSHPSS base case behavior: water vs. PCM emulsions

Once the model of the flat plate heat exchanger was implemented in the *simple model*, it was possible to analyze the heat transfer phenomenon when operating with PCM emulsions. Table 3 shows the comparison of the plate heat exchanger working with water in both sides (water-water) or with the investigated PCM emulsions in the secondary side (water-emulsion)

Table 3. Heat transfer study results and comparison of plate heat exchanger performance: water-water vs. water-emulsions.

$\dot{m}_{sto}$= 20.5 kg/s	Water	Emulsion 1	Emulsion 2
v_{sto} (m/s)	0.5362	0.5793	0.5793
Re_{sto}	2633	42.01	42.01
Pr_{sto}	5.53	551.6	551.6
α_{sto} (W/(m^{2}K))	14047	2890	2939
U (W/(m²K))	6346	2313	2344
E_{ff}	0.9067	0.7382	0.7505
Δp_{distr} (Pa)	131317	403012	403012

The results indicate a relevant decrement in the heat exchanger effectiveness when working with the PCM emulsions, caused by the drop of the Reynolds number and, consequently, of the global heat transfer coefficient.

This phenomenon is due to the high viscosity (0.05 Pa·s) of the investigated material compared to the water. The significant rise of the Prandtl number highlights that the momentum diffusivity dominates the heat transfer in the PCM emulsions, while the pure conduction diffusivity in the fluid is low. Choi et al. (1994) reported that the local convective heat transfer coefficient varies slightly in forced convection heat transfer with phase-change-material slurries. However, the lack of experimental study and literature about test of PCM emulsions in plate heat exchangers does not permit to consider this factor. Consequently, the heat convective coefficient of the emulsion and the overall heat transfer performance of the plate heat exchanger experience a significant reduction. This phenomenon affects the operation of the global CSHPSS plant since the solar collected heat is not well discharged and utilized. Another important aspect, related to the utilization of the PCM emulsion in the secondary circuit, is the pressure losses. Just analyzing the distributed pressure drop (Δp_{distr}) that occurs in the heat exchanger, they result almost four times higher than those generated by the water circulation in the same circumstances. The high viscosity of the studied PCM emulsion arises to be one of the critical factors on which it is necessary to work for achieving a satisfactory behavior.

Table 4. TES comparison: water vs. PCM emulsions (Annual results. Base case, T_{max}= 90°C, V= 19260 m^3, A= 3210 m^2).

	Water	Emulsion 1	Emulsion 2	*Annual energy flows*	Water	Emulsion 1	Emulsion 2
PHE E_{ff}	0.9067	0.7504	0.7641	Q_x (MWh/y)	0	0	0
$EA_{max,calc}$ (MWh)	1153	1167	1180	Q_l (MWh/y)	148.8	140.2	138.5
Solar fration and efficiencies				Q_{aux} (MWh/y)	2359	2368	2342
SF	0.5591	0.5574	0.5622	Q_c (MWh/y)	3140	3122	3146
η_{coll}	0.5706	0.5673	0.5717	Q_e (MWh/y)	1244	1252	1263
η_{sto}	0.8803	0.8880	0.8904	Q_s (MWh/y)	1095	1111	1125
η_{sys}	0.5435	0.5419	0.5466	Q_b (MWh/y)	1896	1870	1883

Table 4 illustrates the results obtained from the annual calculation of the CSHPSS. As can be observed, in these circumstances the substitution of the water with the PCM slurry in the storage does not represent any significant benefit. The storage temperature along the year with both water and emulsion does not reach the maximum fixed constrain (T_{max}= 90°C) and it remains below 82°C in all the cases, for water and for both PCM emulsions. In terms of solar fraction, SF, and global efficiencies, Emulsion 2 presents a slightly improved performance while Emulsion 1 is even slightly worse than water. Even though the solar heat transferred to the secondary circuit Q_c diminishes in the case of Emulsion 1 compared to the case of water-water, surprisingly the calculated energy accumulated in the storage ($EA_{max,calc}$) is higher. This was mainly due to two factors: the decrease of the heat losses in the storage (Q_l), due to the lower temperatures in the seasonal storage tank when using PCM

emulsions as TES, and the change in the collector efficiency curve along the year (Rinaldi, 2016). Although the yearly solar collector field efficiency (η_{coll}) is reduced and, consequently, the yearly solar heat collected (Q_c), the solar field presents a greater performance in the summer months, when a significant share of energy is stored, due to the lower temperature in the seasonal storage when operating with PCM emulsions. The critical feature that was recognized in the utilization of the PCM emulsion in this particular case is the large operating temperature range. Indeed, the advantages obtained with the employment of a PCM usually derive from the utilization of the material always close to the phase transition. The chart of the cp_{em} of the PCM emulsions as the function of temperature (Fig. 3) shows that the cp_{em} outside the change of phase is about 3.2 kJ/(kg K), which is a rather poor value and lower than the water specific heat. Accordingly, the benefits linked to handling PCM materials are limited by the running conditions of this application since it has to operate mostly out of the melting-solidification stages.

(ii) Sensitivity analysis of CSHPSS operation with PCM emulsions

From the first two steps of the calculation procedure, the results highlight that two are the main obstacles which make difficult the exploitation of the real PCM emulsion as seasonal storage material: a) the high viscosity and b) the incompatibility between the phase change temperature and the operating conditions of the storage. Thus, a sensitive analysis was performed based on the base case design, decreasing only the seasonal storage upper limit (T_{max}) and varying this parameter from T_{max}= 80°C until the minimum allowed temperature, T_{max}= 60°C, for discharging heat to the DH grid.

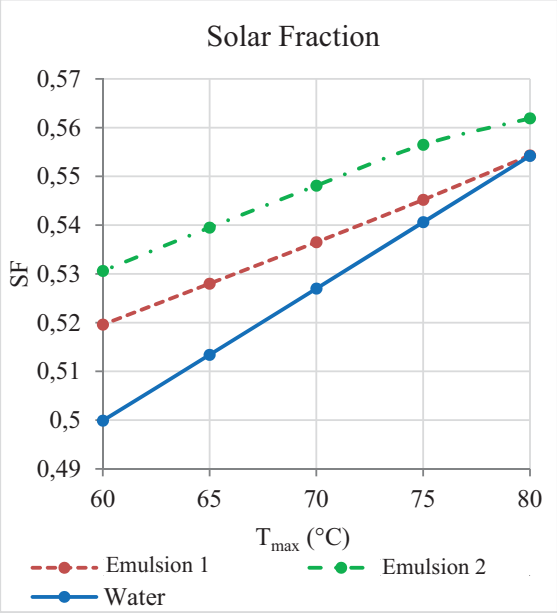

Fig. 5. Base case: Solar fraction (SF) versus T_{max} of TES.

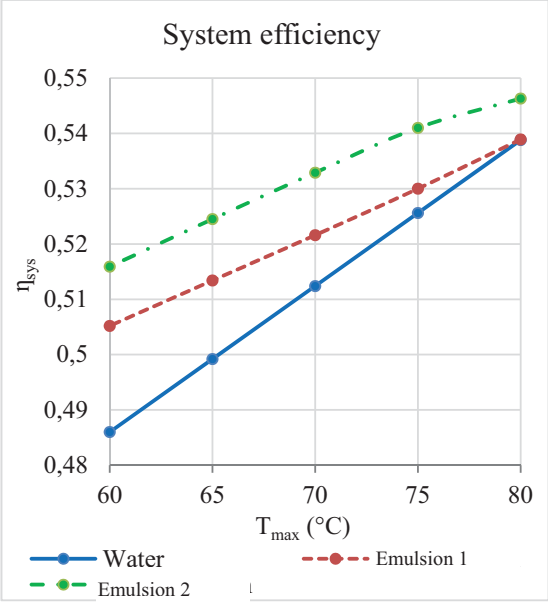

Fig. 6. Base case: System efficiency, η_{sys}, versus T_{max} of TES.

As shown in Figs. 5 and 6, the benefit coupled with the replacement of water with the studied emulsions grows moving T_{max} towards values closer to the phase transition. This benefit is particularly interesting in the case of Emulsion 2, in which enables to achieve a 6% higher of solar fraction with respect to the water as TES material thanks to the increased efficiency of the system. The growing heat capacity of the PCM emulsions working closer to the phase transition permits to accumulate more thermal energy in the same volume (see Table 5). Nevertheless, from results shown in Table 5 it is possible to note that when the maximum allowed temperature in the seasonal storage is T_{max}= 60°C, some solar heat is rejected. However, this phenomenon is significantly lower when PCM emulsions are employed and particularly operating with Emulsion 2, generates a reduction of about 40% in heat rejection compared with the water case. In order to avoid heat rejection when working with the Emulsion 2 and T_{max}= 60°C, the volume of the seasonal storage tank should be increased about 8540 m^3, requiring a seasonal storage tank of 27,800 m^3 (Rinaldi, 2016). However, in this later case 305 MWh/y would be still rejected if the seasonal storage tank were operating with water. An additional volume of about 8740 m^3, reaching a tank volume larger than 36,500 m^3, would be required in order to avoid heat rejection when water is used as storage medium and T_{max}= 60°C. In these conditions, the volume of the seasonal storage with Emulsion

2 would be about 25% smaller than when operating with water. Additionally, note in Table 5 that the heat transfer in the flat plate heat exchanger operating with PCM emulsions, being worse than operating with water (Table 3), increases due to the higher specific heat values, since the operation temperature range is more favorable and closer to the phase change.

Table 5. TES comparison: water vs. PCM emulsions when T_{max}= 60°C (Annual results, Zaragoza, V= 19260 m^3, A= 3210 m^2).

	Water	Emulsion 1	Emulsion 2	*Annual energy flows*	Water	Emulsion 1	Emulsion 2
PHE Eff	0.9067	0.7907	0.8073	Q_x (MWh/y)	567.9	421.5	343.2
$EA_{max,calc}$ (MWh)	668	815.4	884	Q_l (MWh/y)	120	118	121.4
Solar fration and efficiencies				Q_{aux} (MWh/y)	2676	2570	2511
SF	0.4999	0.5196	0.5306	Q_c (MWh/y)	3362	3319	3303
η_{coll}	0.6110	0.6032	0.6003	Q_e (MWh/y)	1318	1315	1307
η_{sto}	0.9089	0.9103	0.9071	Q_s (MWh/y)	629.9	776	842.3
η_{sys}	0.4860	0.5052	0.5159	Q_b (MWh/y)	2044	2004	1996

3.2. Geographic analysis of CSHPSS operation with PCM emulsions

Since the CSHPSS performance is strongly related to the climate conditions as well as to the heat demand characteristics, the assessment of a plant situated in a different European climatic zone, as it is the case of Oslo (Norway), was also analyzed. The location of the CSHPSS highly influences the design process and parameters of the whole system. Considering a colder area than the south of Europe, the heat demand rises because of the higher space heating requirements, caused by the more severe winters, as well as its distribution (SH demand) along the year. Moreover, the solar radiation decreases and consequently, the solar energy production per area of solar collector falls down making necessary the installation of a larger solar field surface per MWh of heat demanded (i.e. increase of RAD). Furthermore, the lower average environmental temperature along the year reduces the collector efficiency because of the higher heat losses with the surroundings. In regard to the seasonal storage, colder climates need relative smaller storage per unit area of solar collector (i.e. smaller RVA ratio). Warmer locations, present higher accumulation requirements per area of solar collector because of the shorter heating period and of the larger solar energy yielded in summer (Guadalfajara, 2016). Thus, the CSHPSS placed in Oslo (latitude 59.93º North), sized according to the criteria previously adopted for the plant in Zaragoza (1000 dwellings of 100 m^2 each, T_{max}= 90°C, SF~0.5, no heat rejection), owns the specific design parameters listed in Table 6. The rest of the parameters are the same shown in Table 2.

Table 6: Design parameters for the CSHPSS in Oslo with water as seasonal TES material (1000 dwellings of 100 m^2 each, T_{max}= 90°C, SF~0.5, no heat rejection) (Rinaldi, 2016).

CSHPSS Oslo **(latitude 59.93º North)**							
Solar collector field		*Seasonal storage*		*Flat plate heat exchanger*		*Annual heating demand*	
RAD	1.39 m^2/MWh	RVA	1.75 m^3/m^2	E_{ff}	0.9	Q_{SH}	6427 MWh/y
A	11,383 m^2	V	19,920 m^3	A_{ht}	342.47 m^2	Q_{DHW}	1769 MWh/y
β	60°	A_{acu}	4196 m^2	N_{pl}	116	Q_d	8197 MWh/y
γ	0°	Ea_{max}	1389 MWh				

The heat transfer problems occurring when operating with PCM emulsion in the seasonal TES already explained in subsection 3.1 were also observed in this case. Indeed, the change of the equipment dimensions does not vary the worsening heat transfer performance utilizing the PCM emulsions instead of water. As already noticed, the heat exchanger effectiveness working with the Emulsion 2 appears improved respect to the Emulsion 1 because of its higher average specific heat in the working temperature range (Rinaldi, 2016). A comparison of the behavior of the CSHPSS located in Oslo operating with different seasonal storage materials (water and PCM emulsions) are shown in Table 7. As occurred in the base case analysis, the Emulsion 1 does not provide any enhancement of the overall system efficiencies. Additionally, the seasonal storage with this PCM emulsion as storage material has a lower heat storage capacity than with water. Consequently, the main benefit linked to the employment of a PCM is lost as well as the possibility of the application of this solution in the studied conditions (large temperature range). In contrast, interesting outcomes have arisen from the CSHPSS calculations using the Emulsion 2. From a first look to Table 7, there is a slight increase of the overall plant performance as well as of the component performances coupled with the higher maximum storage capacity of

the seasonal TES (EA_{max}). Thus, it is observed an appreciable rise of the solar production Q_c (+74 MWh/y) and the decrease of the tank losses Q_l (-6.4 MWh), obtaining as a consequence some heat rejection (Q_x= 28.2 MWh).

Table 7. TES comparison: water vs. PCM emulsions (Annual results. Oslo, T_{max}= 90°C, V= 19,920 m^3, A= 11,383 m^2).

	Water	Emulsion 1	Emulsion 2	*Annual energy flows*	Water	Emulsion 1	Emulsion 2
PHE E_{ff}	0.8951	0.7525	0.7600	Q_x (MWh/y)	0	0	28.2
$EA_{max,calc}$ (MWh)	1372	1350	1419	Q_l (MWh/y)	194.1	187.8	187.7
Solar fration and efficiencies				Q_{aux} (MWh/y)	4129	4148	4077
SF	0.4958	0.4935	0.5021	Q_c (MWh/y)	4254	4282	4328
η_{coll}	0.3755	0.3780	0.3820	Q_e (MWh/y)	1468	1495	1538
η_{sto}	0.8678	0.8744	0.8779	Q_s (MWh/y)	1274	1255	1322
η_{sys}	0.3584	0.3567	0.3630	Q_b (MWh/y)	2786	2787	2790

The explanation to these effects can be found evaluating the seasonal storage temperature (T_{acu}) along the year (Fig. 7). Indeed, the higher specific heat of the PCM emulsion during the phase change generates lower storage temperatures. This fact reduces the heat losses of the tank, which are larger in a cold climate. Furthermore, since the storage temperature affects the solar field efficiency, its decrement leads to higher collector performances despite the worse solar heat transfer through the PHE, thanks to the lower temperature of the working fluid when the PCM emulsion is used. The most profitable solution in order to avoid the heat rejection is the reduction of the solar field area. Since the collector production is more effective, a smaller surface area of solar collectors can be installed for generating the same amount of solar heat avoiding heat rejection. The value obtained was 11,040 m^2, which is 335 m^2 smaller than the required for satisfying the heat demand employing water in the Seasonal TES. Despite the smaller solar field, the whole plant operation with the Emulsion 2 is even slightly more efficient than operating with water, reaching very similar values to those shown in Table 7.

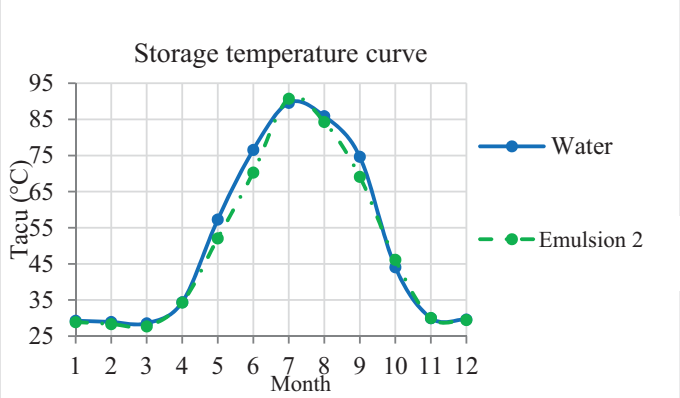

Fig. 7. Monthly temperatures of the water and Emulsion 2 in the seasonal TES

From the conclusions achieved studying the base case, working with temperatures closer to the phase transition of the emulsion would allow to accomplish more relevant advantages. Consequently, a sensitivity analysis lowering T_{max} of the Oslo seasonal TES has been carried out in order to create a more favorable state for the PCM emulsion operation.

As shown in Figs. 8 and 9, and similarly to the base case, the performance of the yearly plant operation continually gets worse with the decrease of the seasonal TES maximum temperature, T_{max}. Indeed, the volume of the seasonal TES is kept unchanged (V= 19,920 m^3). It has been sized to be appropriate for reaching T_{max} = 90 ºC. Thus, when limiting T_{max} to a lower value, the seasonal TES is not able of storing all the collected solar energy and there is heat rejection, reducing the solar fraction and the system efficiency. However, Figs. 8 and 9 show that this decay is smaller for the PCM emulsions, particularly for the Emulsion 2. Note that the lower is T_{max}, the better is the paraffinic emulsions performance and, consequently, the lower is the reduction of SF and η_{sys} compared to the water case. Further, note that the whole SF and η_{sys} variations along the sensitivity study are less significant in the Oslo case in comparison with the sensitivity analysis of the base case (Figs. 5 and 6). These observations show that in cold climate the variation of T_{max} has a less important impact on the overall

efficiencies, due to the improvement of the solar collector efficiency when lowering the seasonal TES temperature, which provokes an increased solar production. The reduction of the storage temperature can be performed substituting the water with the PCM emulsion or by lowering $T_{max.}$

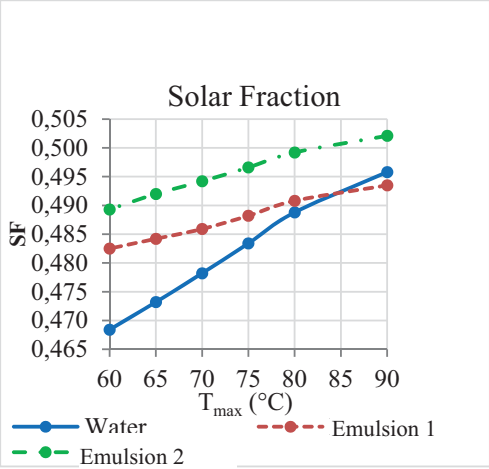

Fig. 8. Oslo case: Solar fraction (SF) versus Tmax of TES.

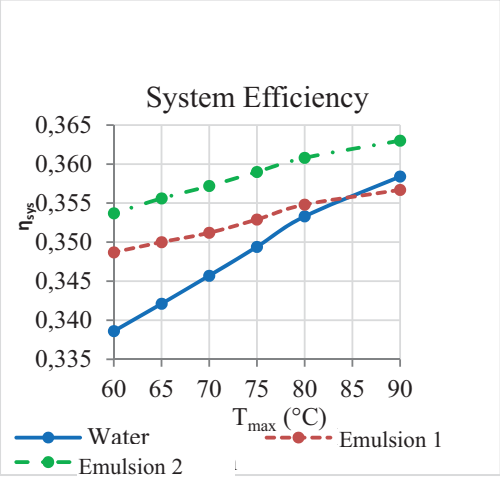

Fig. 9. Oslo case: System efficiency, Πsys, versus Tmax of TES.

In the Oslo case, the required collectors surface area, for a seasonal TES using Emulsion 2 as storage material with T_{max}= 60°C, avoiding heat rejection (Q_x= 0 MWh/y), and maintaining unchanged the volume of the seasonal TES (V = 19,920 m^3), is A = 7270 m^2. This represents a reduction of the solar collector area of about 36%, in comparison with the design value at T_{max} = 90°C (Table 6). As a consequence, the obtained solar fraction is obviously lower, SF = 0.4192, when T_{max}= 60°C. If the storage material employed in these operating conditions and with these last design values were water instead of Emulsion 2, there would be a significant heat rejection (Q_x = 192.8 MWh/y) requiring a seasonal TES 28% larger, i.e. with a volume of 25,450 m^3. These results show that significant reductions in seasonal TES volume could be achieved when using PCM emulsions with appropriate properties. The narrower is the temperature range of the seasonal TES the better is the behavior of the PCM emulsion thanks to the longer period working at the phase transition.

4. Integration of de-centralized TES with PCM emulsion into LTDH

This section presents the results of a research carried out on the improvement that a utility of Low Temperature District Heating (LTDH) can undergo when a tank of thermal energy storage is integrated into its network. The performance of two different cases, with water and with a PCM emulsion, have been analyzed and compared within a set of 40 residential buildings consisting of twenty-five apartments each, i.e. 500 dwellings, located in Zaragoza (Spain). A detailed heat transfer model of the storage tank was established to determine the actual behavior of a system TES-DH in de-centralized storage application. The chosen configuration is a typical cylindrical tank with internal coils through which the DH water flows to carry out the charge and discharge processes. The outcomes show the benefit of the operation with either water or PCM emulsion as storage materials, with a noticeable advantage for the PCM emulsion. See Rinaldi (2016) for further details of the model and the analysis.

The results obtained show that a de-centralized TES unit integrated into the DH grid is able to curtail the peak demand and, consequently, to reduce the mass flow that the network has to handle. This solution allows the connection of additional buildings in a saturated grid.

Concerning the additional new area that could be connected to the district heating (DH) network thanks to the de-centralized TES unit, it has been possible to maintain a regular nominal power supplied by the DH without raising the production during the peak hours. Furthermore, this solution permits to move the heat production to the night where the electricity costs and requirements are lower. Additionally to the potential economic benefits, the installation of de-centralized storages allows to the power unit to operate more regularly and provide the peak energy that otherwise should be supplied by auxiliary units (e.g. boilers).

In respect to the PCM emulsions as storage medium, it has been shown that their use provides remarkable

benefits in relation to the conventional use of water. These positive effects are due to the favorable working conditions due to the phase change of the PCM. According to the priority of the system design and to the main objective pursued, the particular advantages are: 1) Accumulation of a greater amount of thermal energy than water in the same configuration of the system, generating a smoother operation with less abrupt changes in the mass flow circulating in different hours. Thus, higher TES temperature during the discharge hours guarantees an easier control of mass flows variation. Additionally, the flat-plate heat exchanger in the customers substation works better thanks to the greater temperature at the heat exchanger inlet, $T_{HE,in,}$ also when part of the heat is delivered by the TES. 2) Reduction of the storage volume and, consequently, of the investment costs in order to achieve the same system operation than that attained using water. 3) Reduction of the nominal monthly DH power and, therefore, the additional mass flow rate that the existing DH pipes have to handle with the connection of the new area. Fig. 10 shows an example of the results obtained (Rinaldi, 2016).

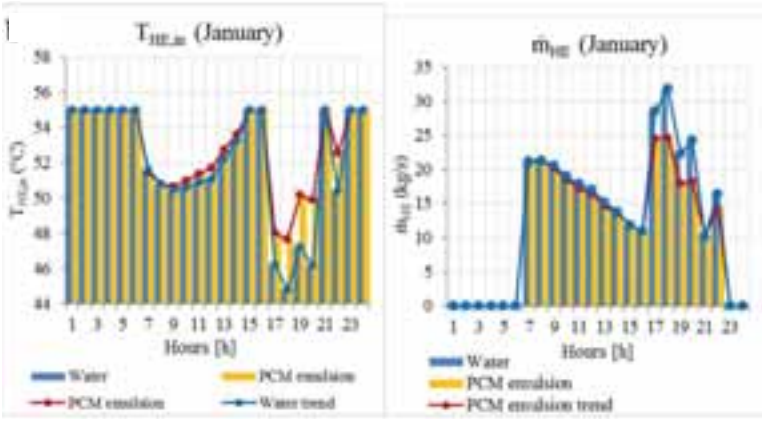

Fig. 10 Example of the results obtained in the case of Vsto,eff=180 m^3 in Zaragoza (Spain)

5. Conclusions

The potential application of Thermal Energy Storage using a low-cost emulsion of latent heat storage material (PCM emulsion) in two different District Heating applications has been studied from a technical viewpoint. It has not been presented an economic analysis due to the lack of appropriate economic information.

The analysis of the behavior of CSHPSS operating with two different PCM emulsions has been performed for several scenarios in different climates (Zaragoza, Spain and Oslo, Norway). The study revealed that the wide temperature working range of this application makes non-optimal the operation with the analyzed PCM emulsions, particularly with Emulsion 1. The operation of the CSHPSS operating with the improved Emulsion 2 has shown some advantages. The temperature stabilization produced by the phase change, especially along the charging process, improved the solar field production and, consequently, the overall system performance and the solar fraction, as well as the storage efficiency. Thus, the material properties enhancements that are necessary to seek for the application of PCM emulsions in CSHPSS are: i) higher density; ii) lower viscosity; and iii) more suitable h-T and c_p-T curves: all the phase transition temperature range has to be included in the working interval of the STES, higher c_p values outside solidification-melting window, higher c_p peak, reduced phase transition range for a more relevant temperature stabilization.

The connection of de-centralized TES units has demonstrated to be a valuable solution for the peak shaving of the thermal demand and for the decrement in the DH mass flow permitting additional connections. The usage of the analysed PCM emulsion improved the overall system operation thanks to the temperature stabilization generated by the change of phase, and to the greater thermal storage capacity of the TES. The hydraulic transients resulted less abrupt and the mass flow changes smoother. This suggested an easier regulation of the DH-TES connection and more regular working conditions, allowing higher efficiencies of the components.

Acknowledgements

This work was developed in the frame of the research project ENE2014-57262-R, partially funded by the Spanish Government (Energy Program), the Government of Aragon (Spain) and the EU Social Fund (FEDER Program) and the use of Servicio General de Apoyo a la Investigación-SAI, Universidad de Zaragoza.

References

ALFA LAVAL, 2015. Gasketed plate-and-frame heat exchangers [WWW Document]. URL http://www.alfalaval.com (accessed: December 2015).

ARCON, 2013. Arcon HT-SA 28/10. [WWW Document]. URL http://www.arcon.dk (accessed: February 2013)

Braun J.E., Klein S.A., Mitchell J.W., 1981. Seasonal storage of energy in solar heating. Solar Energy 26, 403–411.

Choi E., Cho Y., Lorsch H.G., 1994. Forced convection heat transfer with phase-change-material slurries: turbulent flow in a circular tube. International Journal of Heat and Mass Transfer. 37, 207-215.

Delgado M., Lazaro A., Mazo J., Zalba B., 2012. Review on phase change material emulsions and microencapsulated phase change material slurries: Materials, heat transfer studies and applications. Renewable and Sustainable Energy Reviews 16, 253-273.

Delgado M., Lazaro A., Mazo J., Penalosa C., Dolado P., Zalba B., 2015. Experimental analysis of a low cost phase change material emulsion for its use as thermal storage system. Energy Conversion and Management. 106, 201–212.

Edelen A.N., 2012. Characterization of Stable Paraffin Emulsions for Use as Phase Change Slurry in Cool Thermal Energy Storage. Research report. Ritsumeikan Asia Pacific University.

EES, 2016. Engineering Equation Solver. F-Chart Software. [WWW Document]. URL http://www. fchart.com/ (accessed: February 2016).

European Union, 2010. Directive 2010/31/EU of the European Parliament and of the Council of 19 May 2010 on the energy performance of buildings (recast). Off. J. Eur. Union, pp. 13-35.

European Union, 2012. Directive 2012/27/EU of the European Parliament and of the Council of 25 October 2012 on energy efficiency. Off. J. Eur. Union, pp. 1-56.

Fevrier N., Froning S., Landolina S., Trigg L., Werner S., 2012. Strategic Research Priorities for Cross-cutting Technology. Section 2: “District Heating and Cooling”. European Technology Platform on Renewable Heating and Cooling, Brussels.

Frederiksen S., Werner S., 2013. District Heating and Cooling. Studentlitteratur AB.

Guadalfajara M., Lozano M.A., Serra L.M., 2015. Simple calculation tool for central solar heating plants with seasonal storage. Solar Energy 120, 72–86.

Guadalfajara M., 2016. Economic and environmental analysis of central solar heating plants with seasonal storage for the residential sector. PhD Thesis, Universidad de Zaragoza, Spain.

IEA, 2014. Energy Storage Technology Roadmap. Technology Annex. [WWW Document]. URL http://www.iea.org (accessed: November 2015).

Marin J.M., Guillen S., 2013. Diseño y cálculo de intercambiadores de calor Monofásicos. Paraninfo Ediciones, Spain (in Spanish).

Nielsen J.E., 2014. A booming market for solar district heating. In: SHC 2014, International conference on Solar Heating and Cooling for Buildings and Industry, Beijing, China.

Peuser F.A., Remmers K.H., Schnauss M., 2010. Solar Thermal Systems. Successful Planning and Construction. Earthscan.

Raab S., Mangold D., Heidemann W., Müller-Steinhagen H., 2003. Simulation study on solar assisted district heating systems with solar fractions of 35%. In: ISES Solar World Congress 2003, Göteborg, Sweden.

Raab, S., Mangold, D., Müller-Steinhagen, H., 2005. Validation of a computer model for solar assisted district heating systems with seasonal hot water heat store. Solar Energy 79, 531–543.

Rinaldi G., 2016. Study on “low-cost” PCM emulsion as Thermal Energy Storage material for District Heating applications. MSc Thesis, Politecnico di Torino, Italy.

Shao J., Darkwa J., Kokogiannakis G., 2015. Review of phase change emulsions (PCMEs) and their applications in HVAC systems. Energy and Building 94, 200-217.

SWEP, 2015. Products [WWW Document]. URL http://www.swep.net (accessed: December 2015).

Performance of a domestic oil storage tank during charging and discharging cycles

Ashmore Mawire[1], Adedamola B. Shobo[2]

[1] North-West University (Mafikeng Campus), Private Bag X2046, Mmabatho 2745, South Africa

[2] Department of Mathematics, Science and Sports Education, University of Namibia, Ongwediva, Private Bag 5507, Oshakati, Namibia

Abstract

The overall experimental thermal performance for complete charging and discharging cycles of a 40 L Sunflower Oil storage tank is presented. Results of two complete charging and discharging cycles are presented. The oil is heated electrically using a copper spiral coil in thermal contact with electrical heaters. A spiral copper coil immersed in a water bath discharges the stored thermal energy. The first complete cycle charges at a low flow-rate of 0.6 L/min and discharges at a high flow-rate of 1.7 L/min. The second cycle charges at a high flow-rate of 1.8 L/min and discharges at a high flow-rate of 1.7 L/min. The charging energy and exergy rates for the first cycle are higher than that of the second cycle, however, the discharging energy and exergy rates are higher for the second cycle. Total stored energy and exergy values for the charging period are higher for the first cycle as compared to the second cycle. The stored energy and exergy are discharged more efficiently in the second cycle. The overall energetic and exergetic efficiencies of the second cycle are higher than those of the first cycle suggesting that a high charging and discharging flow-rate is essential to increase the overall efficiency of the system.

Keywords:Charging; Discharging; Energy; Exergy; Oil Storage Tank

1. Introduction

Two widely adopted thermal energy storage (TES) systems for domestic applications are sensible heat TES (SHTES) and latent heat TES (LHTES) (Dincer and Rosen, 2002). These systems are essential to cater for the mismatch between energy supply and demand especially when intermittent energy resources like solar energy are involved. LHTES has advantages of a high energy storage density and controlled charging and discharging temperatures but it suffers from some disadvantages such as high cost, low thermal conductivity and supercooling in some phase change materials (PCMs), only to mention a few. When issues of cost outweigh the issues of energy storage density and temperature controlled applications, SHTES seems to be the most viable option. Water is the mostly used SHTES for low temperature applications, however, its use is limited to applications below its boiling point so it cannot be used for medium to high temperature applications without pressuring the storage vessel. Thermal oils have been used in recent years for domestic and industrial applications (Mussard and Nydal, 2013; Mussard et al., 2013; Mawire et al. 2009, Bruch et al., 2014; Bruch et al., 2017) . The advantages of these oils are that they can be used for higher temperatures and they exhibit better thermal stratification as compared to water.

Previous studies (Mawire et al., 2014; Mawire, 2016) have focused on the use of Sunflower Oil as a TES medium since it is cheap, it is readily available locally in most countries in the world, it is food grade and environmentally friendly and it has comparable characteristics to commercially available thermal oils. In previous studies smaller storage tanks were used to characterize the performance of Sunflower Oil using separate charging, discharging and heat retention cycles. Energy, exergy and thermal stratification related quantities were evaluated in these separate cycles and the overall thermal performance for a complete charging and discharging cycle was not evaluated which is necessary for a complete understanding of the end user application. Besides this, the previously reported storage tanks were smaller for any real sustainable practical purpose and some initial storage charging conditions were not similar within experimental error limits.

In a bid to understand the overall thermal performance of a domestic oil storage tank during complete charging and discharging cycles, an experimental setup is presented in this paper under two cases and different TES

doi:10.18086/swc.2017.13.10 Available at http://proceedings.ises.org

parameters are evaluated. The aim is to evaluate the energetic and exergetic performance of the TES system for the two complete charging and discharging cycles. The first complete cycle charges the storage tank at a low flow-rate of 0.6 L/min and discharges it at a high flow-rate of 1.7 L/min. In the second complete cycle, the storage tank charges at a high flow-rate of 1.8 L/min and discharges it at a high flow-rate of 1.7 L/min.

2. Experimental setup and procedure

The experimental setup and procedure for the charging and discharging experiments is shown in Fig. 1 and the main components of the experimental setup are shown in the photograph of Fig. 2. The insulated storage tank (i) is 40 litres and it contains Sunflower Oil. During charging with the electric heater in thermal contact with an oil circulating copper coil, valves (1) and (2) are opened while valves (3), (4), (5), (6) are closed. During discharging, valves (4), and (5) are opened while valves (1), (2), (3) and (6) are closed. The HTF flow rate is controlled by adjusting the frequency of the circulating pump (c) via the VLT microdrive (b). The maximum temperature of the electric heating unit (d) is adjusted by the temperature controller module (e). The flow of the HTF is from the top of the tank to the bottom during both charging and discharging cycles and this is measured with a positive displacement flow meter (f). 5 radial K thermocouples measure the temperature distribution at five different axial positions. Thermocouples T11-T15 measure the temperatures at the top of the storage tank such that an average temperature at the top of the storage is determined. Other average temperatures for levels 2-5 are determined in a similar manner.

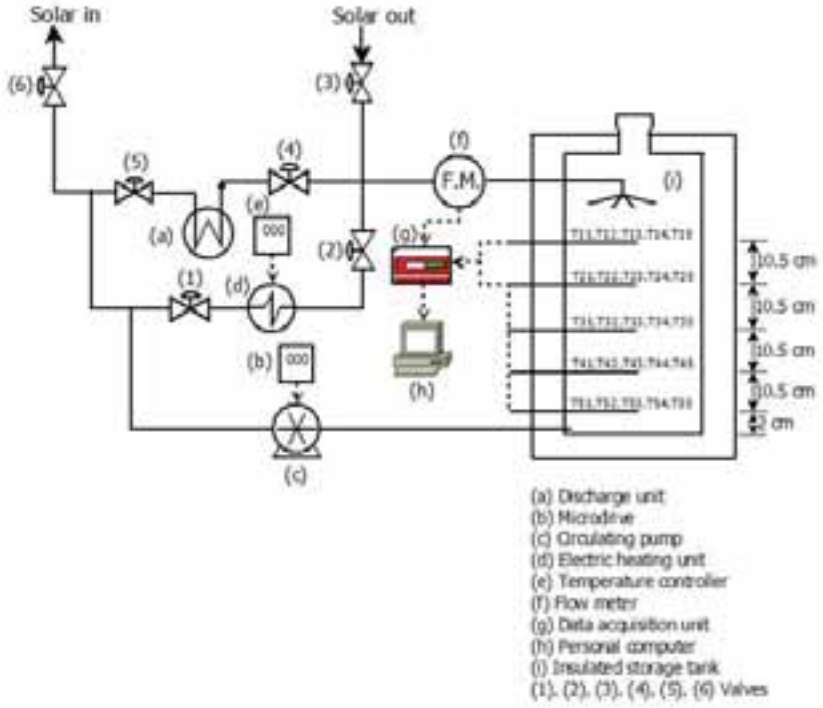

Figure 1: Experimental setup

Firstly it was ensured that the average temperature of the storage tank was around 40 ^{o}C by slightly charging it if it was below this temperature, or discharging it if it was above this temperature. Charging was performed by opening valves (1) and (2) in Fig. 1, while the other valves were left closed. For discharging, valves (5) and (4) were opened while the other valves were closed. During each charging cycle, the temperature controller for the electrical heater was set to 250 ^{o}C and the flow-rate was set to a desired value by adjusting the frequency of the microdrive. Charging was continued until the top of the storage tank attained an average temperature of just above 190 ^{o}C. After this, discharging was immediately done by opening valves (5) and (4) and the discharging cycle was stopped when the temperature of the water bath (which contained 3 liters of waters) fell to just below 100 ^{o}C.

Figure 2: Photograph of experimental setup showing the main components. (1) Insulated storage tank (2) Electrical heater with copper spiral coil (3) Control valves (4) PID temperature controller (5) Discharging coil (6) Datalogger

3. Thermal performance parameters

The charging energy rate depends on the inlet and outlet charging temperatures of the storage tank and is expressed as

$$\dot{E}_{ch} = \rho_{av} c_{av} \dot{v}_{ch} (T_{chin} - T_{chout}) \quad (1)$$

where ρ_{av} is the temperature dependent average density of the oil at the start and end of charging, c_{av} is the temperature dependent average density of the oil at the start and end of charging, $\dot{v}_{ch}$ is the volumetric charging flow-rate, T_{chin} is the inlet charging temperature at the top of the storage tank and T_{chout} is the outlet charging temperature at the bottom of the storage tank. The total energy stored in stored tank can be estimated by integrating Eq. (1) from the start of charging to the end of charging for each small temperature measurement interval and this can be expressed as (Alam; 2015; Jegadheeswaran et al., 2010)

$$E_{ST} = \int_{t_{ini}}^{t_f} \rho_{av} c_{av} \dot{v}_{ch} (T_{chin} - T_{chout}) dt \quad (2)$$

and the charging exergy rate is given as (Jegadheeswaran et al., 2010)

$$\dot{E}_{xch} = \rho_{av} c_{av} \dot{v}_{ch} \left[(T_{chin} - T_{chout}) - \left(T_{amb} \ln \frac{T_{chin}}{T_{chout}} \right) \right] \quad (3)$$

where T_{amb} is the ambient temperature. The total charging exergy is also evaluated by integrating Eq. (3) and it is expressed as

$$E_{XCHT} = \int_{t_{ini}}^{t_f} \rho_{av} c_{av} \dot{v}_{ch} \left[(T_{chin} - T_{chout}) - \left(T_{amb} \ln \frac{T_{chin}}{T_{chout}} \right) \right] dt. \quad (4)$$

The discharging energy rate can be expressed as

$$\dot{E}_{dis} = \rho_{av} c_{av} \dot{v}_{dis} (T_{disin} - T_{disout}) \quad (5)$$

where $\dot{v}_{dis}$ is the discharging volumetric flow-rate, T_{disin} is the discharging inlet temperature from the storage tank to the discharging coil and T_{disout} is the discharging outlet temperature from the discharging coil to the storage tank. The total energy discharged from the stored tank can be estimated by integrating Eq. (5) from the start of discharging to the end of discharging for each small temperature measurement interval and this can be expressed as (Alam, 2015, Jegadheeswaran et al., 2010)

$$E_{DIST} = \int_{t_{ini}}^{t_f} \rho_{av} c_{av} \dot{v}_{dis} (T_{disin} - T_{disout}) dt. \quad (6)$$

The discharging exergy rate is expressed as (Alam; 2015; Jegadheeswaran et al., 2010)

$$\dot{E}_{xdis} = \rho_{av} c_{av} \dot{v}_{dis} \left[(T_{disin} - T_{disout}) - \left(T_{amb} \ln \frac{T_{disin}}{T_{disout}} \right) \right]. \quad (7)$$

The total exergy discharged is obtained by integrating Eq. (7) and this is expressed as

$$E_{XDIST} = \int_{t_{ini}}^{t_f} \rho_{av} c_{av} \dot{v}_{dis} \left[(T_{disin} - T_{disout}) - \left(T_{amb} \ln \frac{T_{disin}}{T_{disout}} \right) \right] dt \quad . \tag{8}$$

The overall energy efficiency can be expressed by the ratio of the total energy discharged to the total energy stored and this is expressed as (Alam, 2015; Jegadheeswaran et al., 2010)

$$\eta_e = \frac{E_{DIST}}{E_{ST}}. \tag{9}$$

The overall exergy efficiency can also be expressed as the ratio of the total exergy discharged to the total charging exergy and this is given as

$$\eta_{ex} = \frac{E_{XDIST}}{E_{XCHT}}. \tag{10}$$

The exergy factor (Mawire and Taole, 2014) can be expressed as the ratio of the exergy charging/discharging rate to the ratio of the energy charging/discharging rate and it is given as

$$E_{XF} = \frac{\dot{E}_{xch}}{\dot{E}_{ch}} \quad \text{or} \quad E_{XF} = \frac{\dot{E}_{xdis}}{\dot{E}_{dis}}. \tag{11}$$

The variation of the density and the specific heat capacity with temperature is given as (Mawire, 2016; Mawire et al., 2014)

$$\rho_s = 930.62 - 0.65T \tag{12}$$

and

$$c_s = 2115.0 + 3.13T. \tag{13}$$

4. Results and discussion

Fig. 3 shows two experimental charging plots using the same flow-rate of 0.6 L/min with almost the same initial conditions to test the repeatability of the experimental results. The plots for the two tests are almost identical for the charging temperatures at the top and the bottom of the tank (T_{chin} and T_{chout}), for the top level of the storage tank (T_1) and for the middle of the storage tank (T_3). Small deviations between the two tests are due slightly different initial conditions and the measurement errors due to the accuracies of the thermocouples used in the measurements. It can thus be concluded that the experimental results are reproducible and reliable within the experimental error limits.

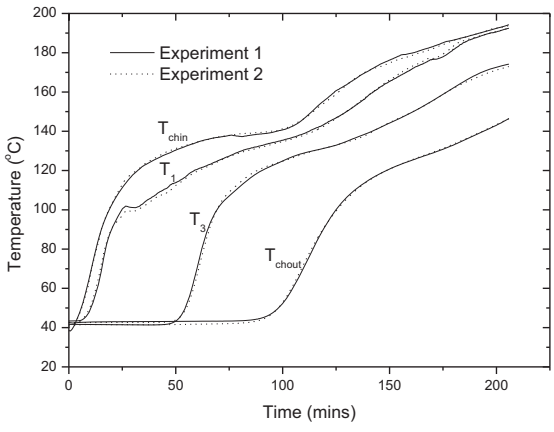

Figure 3: Repeatability charging experiments with a flow-rate of 0.6 L/min.

Fig. 4 shows the temperature profiles along the height of the storage tank for the two complete charging and discharging cycles. For case 1, the temperature profiles show evident layering of the storage tank levels due to the lower charging flow-rate which promotes a larger degree of thermal stratification. The higher flow-rate shows lower temperature differences between adjacent levels due to the larger flow-rate which promotes a higher degree of heat transfer during charging and thus a loss of thermal stratification. Case 2 is charged for a

longer period because of the higher flow-rate that causes the upper limit charging temperature of about 190 °C at the top of the storage to be achieved later. The temperature variations for case 1 during charging show a characteristic flattening of the profiles particularly at the top possibly due to heat losses and radial thermal conductivity, thus slowing down the rate of axial heat transfer. Discharging temperature profiles are almost identical for both cases although case 1 has a more thermally stratified distribution at the onset of discharging. Slightly higher TES temperatures are obtained at the end of discharging for case 1 as compared case 2 possibly due to the more thermally stratified distribution

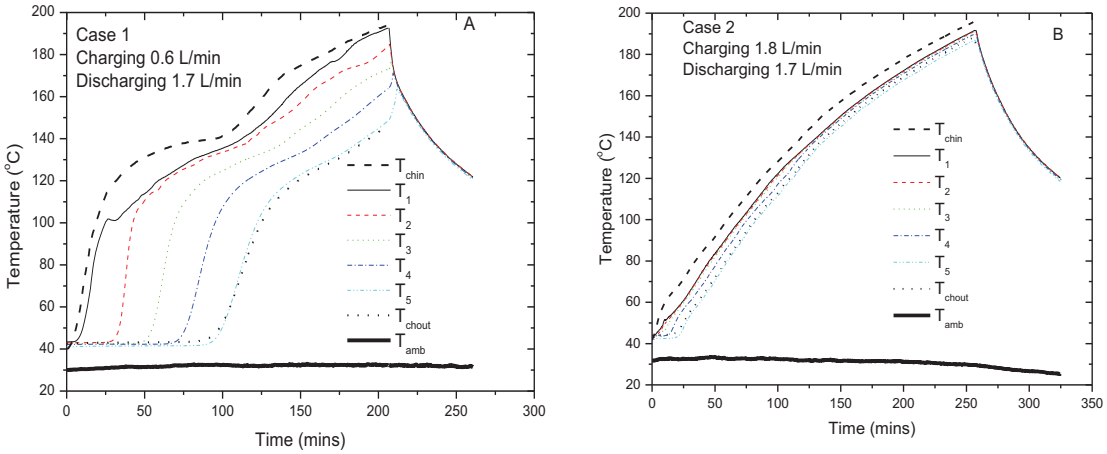

Figure 4: Temperature profiles along the height of the storage tank for experimental charging and discharging cycles case 1 (A) and case 2(B).

Table 1: Thermal performance parameters for the two cases

Parameter	**Case 1**	**Case 2**
Charging flow-rate (L/min)	0.6	1.8
Initial average storage temperature, T_{iniav} (°C)	42.4	43.1
T_{1av} at the end of charging (°C)	193.0	191.5
Average charging ambient temperature, $T_{ambchav}$	31.9	31.8
Average discharging ambient temperature, $T_{ambdisav}$	32.0	27.2
Charging time (mins)	206	258
Discharging time (mins)	54	60
Total energy stored, E_{ST} (MJ)	17.28	12.69
Total exergy stored, E_{CHXT} (MJ)	3.41	2.67
Discharging flow-rate(L/min)	1.7	1.7
Maximum charging energy rate (W)	2920	560
Maximum charging exergy rate (W)	490	180
Maximum charging exergy factor (-)	0.31	0.35
Maximum discharging energy rate (W)	3000	3800
Maximum discharging exergy rate (W)	550	950
Maximum discharging exergy factor (-)	0.18	0.25
Total energy discharged , E_{DIST}(MJ)	3.70	4.69
Total exergy discharged, E_{XDIST} (MJ)	0.88	1.25
Overall energy efficiency, η_e(-)	0.21	0.37
Overall exergy efficiency, η_{ex}(-)	0.26	0.47

Table 1 shows the thermal performance parameters for the two cases The total energy and exergy values stored during the charging period for case 1 are higher as compared to case 2 due to the larger degree of thermal stratification in case 1. It is clear that the higher charging flow-rate results in low values of the total energy and exergy stored due to a loss in thermal stratification. Due to a smaller temperature difference between the top and the bottom of the storage tank for the higher charging flow-rate, the maximum charging energy and exergy rates for case 2 are lower as compared to case 1. Even though, the energy and exergy rates for case 1 are

higher than that of case 2, the maximum exergy factor for case 2 is larger than that of case 1 due the higher average thermal energy storage temperatures for case 2. This suggests that more quality energy stored is at a higher flow-rate due the increase in the heat transfer rate. For the discharging period, case 2 with the higher temperatures induced by the higher charging flow-rate shows higher values of the total discharged energy and exergy. The overall energy and exergy efficiencies for case 2 are higher as compared to case 1, suggesting that the storage tank should be charged with a high flow-rate which increases the rate of heat transfer thus enabling high TES temperatures to be obtained. These higher temperatures ensure that the energy and exergy is discharged more efficiently with a high discharging flow-rate. Charging with a high flow-rate, however, comes at an expense of increasing the charging time with the currently imposed charging conditions. The overall energy efficiencies increase from 0.21 to 0.37 for case 1 to case 2 and the corresponding exergy efficiencies increase from 0.26 and 0.47 respectively. The exergy efficiencies are seen to be higher than the energy efficiencies which also agrees with previous simulated studies (Mawire et al., 2010) done on an oil/packed bed TES system. Although thermal stratification is important in storing maximum energy and exergy, it seems to be outweighed by the maximum temperature (due to high rate of heat transfer) that can be achieved which improves the overall storage efficiency.

5. Conclusion

An experimental study on the overall experimental thermal performance for two complete charging and discharging cycles of a 40 L Sunflower Oil storage tank has been presented. The oil was heated electrically using a copper spiral coil in thermal contact with electrical heaters. A spiral copper coil immersed in a water bath discharged the stored thermal energy. The first complete cycle charged at a low flow-rate of 0.6 L/min and discharged at a high flow-rate of 1.7 L/min. The second cycle charged at a high flow-rate of 1.8 L/min and discharged at a high flow-rate of 1.7 L/min. The charging energy and exergy rates for the first cycle were higher than that of the second cycle due to the larger degree of thermal stratification induced by the lower flow-rate. The discharging energy and exergy rates were higher for the second cycle due to the higher heat transfer rates which resulted in higher storage tank temperatures. Total stored energy and exergy values for the charging period were higher for the first cycle as compared to the second cycle due to the higher degree of thermal stratification in the first cycle. The stored energy and exergy was discharged more efficiently in the second cycle. The overall energetic and exergetic efficiencies of the second cycle were higher than those of the first cycle suggesting that a high charging and discharging flow-rate is essential to increase the overall efficiency of the system. Although thermal stratification was important in storing maximum energy and exergy, it seemed to be outweighed by the maximum temperature (due to high rate of heat transfer) that could be achieved which improved the overall storage efficiency..

Acknowledgements

The authors would like to acknowledge the National Research Foundation (NRF) of South Africa for funding to carry out this research under the Incentive Funding for Rated (IFRR, Grant No: 90638) researchers scheme.

References

Alam TE. Experimental investigation of encapsulated phase change materials for thermal energy storage. PhD Thesis 2015, University of South Florida, USA.

Bruch A, Fournigue JF, Couturier R. Experimental and numerical investigation of a pilot-scale thermal oil packed bed thermal storage system for CSP power plant. Solar Energy 2014;105:116–25.

Bruch A, Molina S, Esence T, Fourmigue JF, Couturier R. Experimental investigation of cycling behaviour of pilot-scale thermal oil packed-bed thermal storage system. Renewable Energy 2017;103:277–85.

Dincer I, Rosen, MA. Thermal energy storage: systems and applications. first ed. 2002, Wiley, UK.

Jegadheeswaran S, Pohekar SD, Kousksou T, Exergy based performance evaluation of latent heat thermal storage system: a review, Renewable and Sustainable Energy Reviews 2010;14: 2580–95.

Mawire A, McPherson M, Van den Heetkamp RRJ. Thermal performance of a small oil-in-glass tube thermal energy storage system during charging. Energy 2009;34:838–49.

Mawire A, McPherson M, Van den Heetkamp RRJ. Discharging simulations of a thermal energy storage (TES) system for an indirect solar cooker. Solar Energy Materials and Solar Cells 2010;94:1100–106.

Mawire A, Taole S, Phori A. Performance comparison of thermal energy storage oils for solar cookers during charging. Applied Thermal Engineering 2014;73:1321–29.

Mawire A, Taole S, Phori A. Performance comparison of thermal energy storage oils for solar cookers during charging. Applied Thermal Engineering 2014;73:1321–29.

Mawire A, Performance of Sunflower Oil as a sensible heat storage medium for domestic applications. Journal of Energy Storage 2016;5:1–9.

Mussard M, Nydal O. Comparison of oil and aluminum-based heat storage charged with a small-scale solar parabolic trough. Applied Thermal Engineering 2013;58:146–54.

Mussard M, Gueno A, Nydal O. Experimental study of solar cooking using heat storage in comparison with direct heating. Solar Energy 2013;98:375–83

Development of Overground Hot Water Stores in Segmental Construction for Solar and District Heating Systems within the Project OBSERW

Thorsten Urbaneck[1*], Fabian Findeisen[1], Jan Markus Mücke[1], Bernd Platzer[1], Markus Gerschitzka[2], Stephan Lang[2], Dominik Bestenlehner[2], Harald Drück[2], Timo Herrmann[3], Robert Beyer[3]

[1] Chemnitz University of Technology, Department of Mechanical Engineering, Institute of Mechanics and Thermodynamics, Professorship Technical Thermodynamics, 09107 Chemnitz, Germany

[2] University of Stuttgart, Institute of Thermodynamics and Thermal Engineering, Research and Testing Centre for Thermal Solar Systems, 70550 Stuttgart, Germany

[3] Farmatic Tank Systems, Kolberger Str. 13, 24589 Nortorf, Germany

Abstract

Thermal energy stores can significantly improve the efficiency and environment-friendliness of the heat supply. Therefore, a high demand for cost-effective storage systems with low energy losses exists. This contribution deals with thermal energy stores for heat supply systems and presents a new aboveground store in segmental construction that allows temperatures up to 98 °C. The construction of a demonstrator is part of the OBSERW project, where researchers show the advantages of this technology, particularly regarding thermal insulation and storage efficiency.

Keywords: district heating, floating ceiling, heat supply, hot water, segmental construction, solar heating, thermal energy storage, thermal stratification

1. Introduction

Thermal energy stores can make heat surpluses available to the consumer if necessary. A thermal stratification inside the storage tank is achieved by separating water with different temperatures through buoyancy. In a storage tank operating according to the displacement principle, a water exchange takes place by direct charging and discharging.

Significant potential for optimization can be identified by comparing currently available storage technologies, in particular pressure vessels and flat-bottom tanks as illustrated in fig. 1 and 2. Pressure vessels (b) allow higher storage densities as well as higher temperature differences but often have low storage volumes, higher heat losses and higher investment costs. However, flat-bottom tanks (a) combine large volumes with relatively low costs. A drawback is that a second zone, respectively a higher fill level is required to apply a hydrostatic load. Furthermore, for safe operation low-pressure steam or an inert gas in the attic is mandatory. This leads to higher heat losses, unfavorable thermal stratification and operation conditions plus unused storage volume. A new storage tank design eliminates these disadvantages and offers numerous benefits. A demonstrator was already built in cooperation with industrial partners as part of the OBSERW project (see also Urbaneck et al., 2017), which will be presented here.

doi:10.18086/swc.2017.13.11 Available at http://proceedings.ises.org

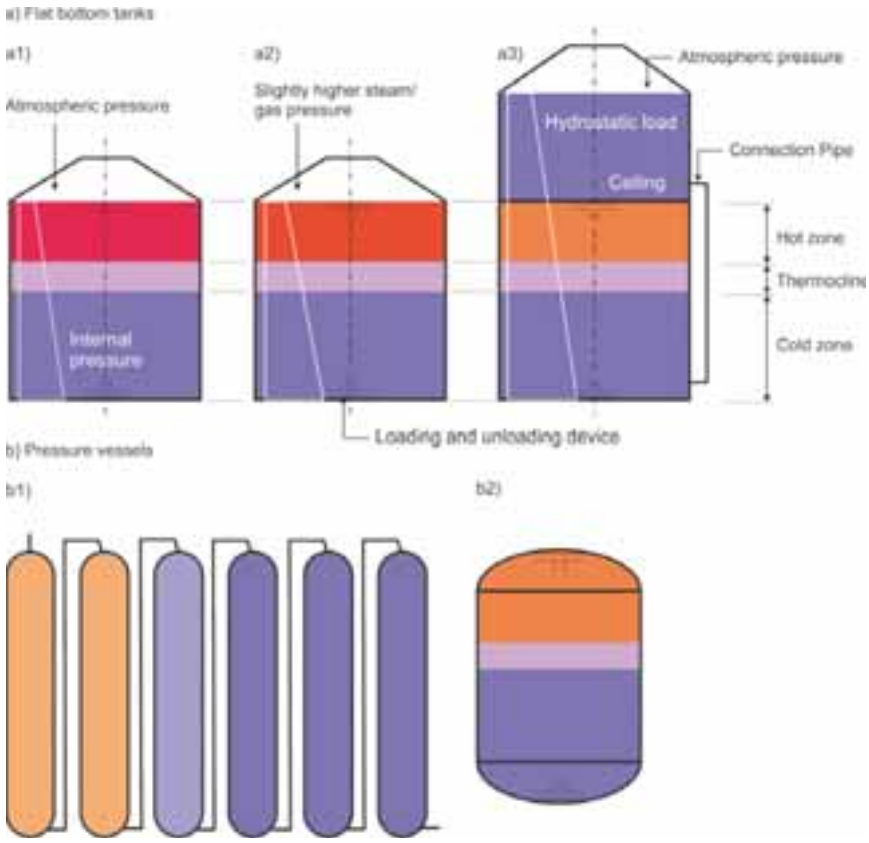

Fig. 1: Overview of storage tank constructions, Urbaneck et al. (2016b)

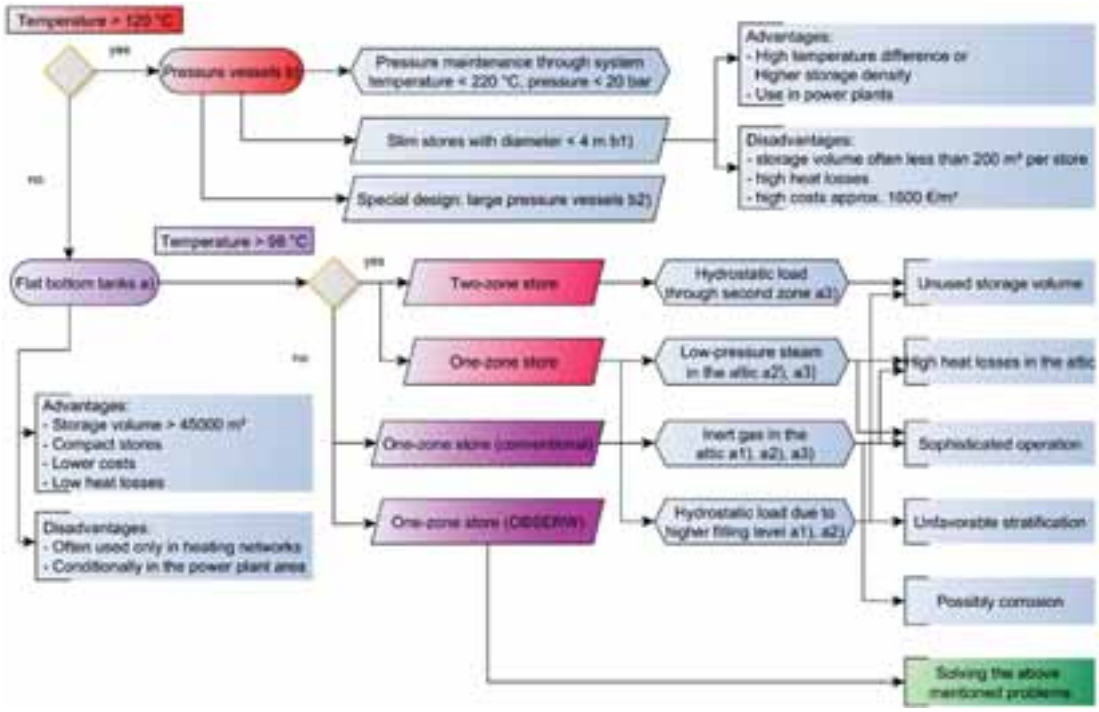

Fig. 2: Systematization and characterization of large hot water storage tanks, Urbaneck et al. (2016b)

2. New Storage Tank Design with a Floating Ceiling

In contrast to welded flat-bottom tanks, respectively pressure vessels a storage tank design with bolted and sealed segments has already proven to be advantageous for large cold water storages (Urbaneck, 2012) for the following reasons:

- use of storage tanks at ambient pressure for cost reasons compared to pressure vessels (use of thin-walled metal sheets, minimization of material),
- thereby avoiding classification in pressure vessels (avoidance of cyclical checks, etc.), storage tanks are considered as a building with simple permission,
- elimination of excavation in comparison to underground reservoirs (strong cost reduction),
- significant reduction of problems with regard to the accumulation of moisture in the thermal insulation (reduction of the thermal resistance of the thermal insulation, impairment of the long-term durability),
- easy geometric design with sufficient storage tank height (essential prerequisite for operation with thermal stratification),
- more efficient construction technology and logistics and therefore faster production,
- unproblematic use in many places (e.g. no geological requirements).

In principle, this storage tank design is also of interest for hot water storage tanks. However, this technology cannot be transferred to high operating temperatures (up to 98 °C) or use in local and district heating systems without further research and development work. Thus, several adaptions of the design are necessary.

The main novelty of the new construction is an indoor protected floating ceiling with the upper loading device (e. g. a radial diffuser) attached directly to it, as shown in fig. 3. A flexible connection allows the free movement of the floating ceiling between a top and bottom dead center. During charging of the tank a gravity current occurs directly at the ceiling, which is an essential prerequisite for a good thermal stratification (Findeisen et al., 2017a). When discharging, hot water is sucked straight along the ceiling, which allows the full use of the warm zone. The aim is to operate the storage tank with a maximum temperature of 98 °C. The elimination of a hydrostatic pressure relief means that there is a risk of falling below the steam pressure limit. This has to be avoided, as it could lead to cavitation or other transient effects during discharging. A free-form radial diffuser lowers the local pressure drop due to its flow-optimized shape and thus improves operation safety as recently shown by Findeisen et al. (2017b, c). A flexible sealing and the pressure compensation pipe ensure volume and pressure compensation in both storage tank and attic. This allows the storage in combination with a pressure-increase or pressure-reduction installation, to provide functions such as pressure maintenance as integration into heat supply networks (Urbaneck and Platzer, 2015). The pressure compensation pipe is also used for independent ventilation (e.g. during commissioning) and secures the storage tank against overpressure and underpressure. This may also occur, e.g., when the appliance is not in use and the water level falls while the floating ceiling rests on the support (bottom dead center). The floating ceiling and the flexible sealing avoid a gas input into the storage water and thus help to avoid corrosion in the system. Furthermore, flexible sealing lips are located at the edge of the ceiling to suppress free convection between the ceiling and the storage tank wall. As a result, heat losses are reduced and the flexible sealing is less thermally stressed. For the construction of the ceiling, bolted and sealed segments are provided which can be easily filled with a blow-in thermal insulation material. The use of plates is also conceivable. Compared to other constructions, the thermal insulation is located directly on the hot zone, which is topologically the best solution. The storage roof protects the thermal insulation from weather influences. Since the attic can be equipped with ventilation, drying is possible if humidification occurs (e.g. temperature falls below dew point in winter).

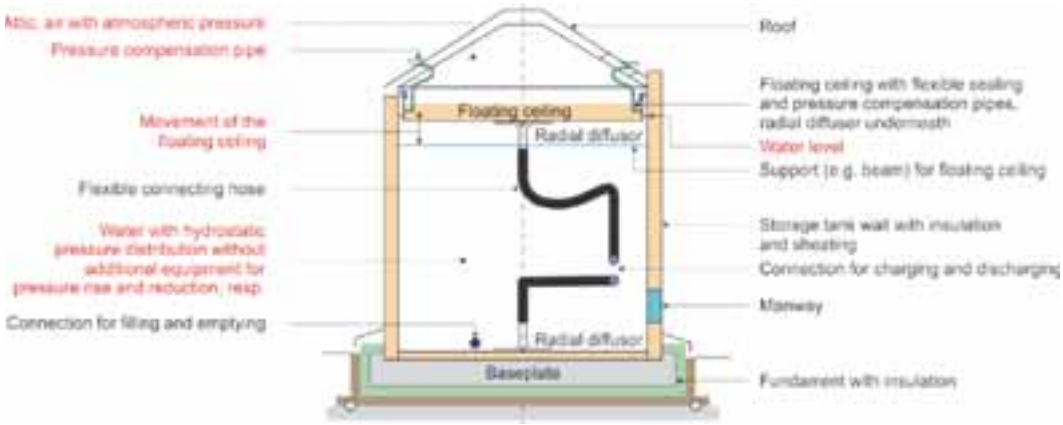

Fig. 3: Aboveground thermal energy store with floating ceiling and directly mounted radial diffuser, Urbaneck et al. (2016a)

3. Concept and Project Organization

The aim of the project is the development of a storage tank in segmental construction as proposed in fig. 3 with a volume from 500 to 8000 m³ that should be suitable for the following applications:

- district heating networks with central heating power plants and combined heat and power generation, used in the grid area (typically for short-term storage),
- local heating networks with decentralized combined heat and power plants (typically for short-term storage),
- large solar heating systems (short- and longterm storage),
- systems with industrial waste heat.

For a tank design which meets these goals several sub-problems must be solved. First, temperature- and water vapour diffusion-resistant roof and wall structures must be designed, with a special focus on the seal between the floating ceiling and the tank wall. In addition, improvements to the thermal insulation design must be undertaken, including the use of innovative substances and the elimination of thermal bridges. Advances in charging and discharging design are required. Finally, methods for better integration into existing networks, and reduced cost, on-site manufacturing procedures should be developed.

The consortium carrying out this project consists of the following partners:

- Chemnitz University of Technology, Professorship Technical Thermodynamics (TUC/TT): accompanying research and coordination of the collaborative project;
- University of Stuttgart, Institute of Thermodynamics and Thermal Engineering, Research and Testing Centre for Thermal Solar Systems (ITW/TZS): accompanying research;
- Farmatic Tank Systems (FTS), Nortorf (Germany): practical oriented development and demonstration.

Fig. 4 shows the procedure to solve the named subproblems. After defining requirements and three typical storage tank sizes, in a first stage fundamental investigations of the materials were carried out by Lang et al. (2016) and Gerschitzka et al. (2016). Furthermore, Urbaneck et al. (2016b) and Findeisen et al. (2017) verified the benefits regarding storage tank design and loading behavior. In a second and ongoing stage, practical tests on a special test rig in the laboratory (fig. 5) help to understand the characteristics of multilayered wall structures in detail. In the third stage, theoretical and practical results are transferred to the demonstrator. Here, many different tests are in progress to secure the technical feasibility and to prove the substantial benefits compared to other storage tank technologies. For this purpose, accompanying measures are provided.

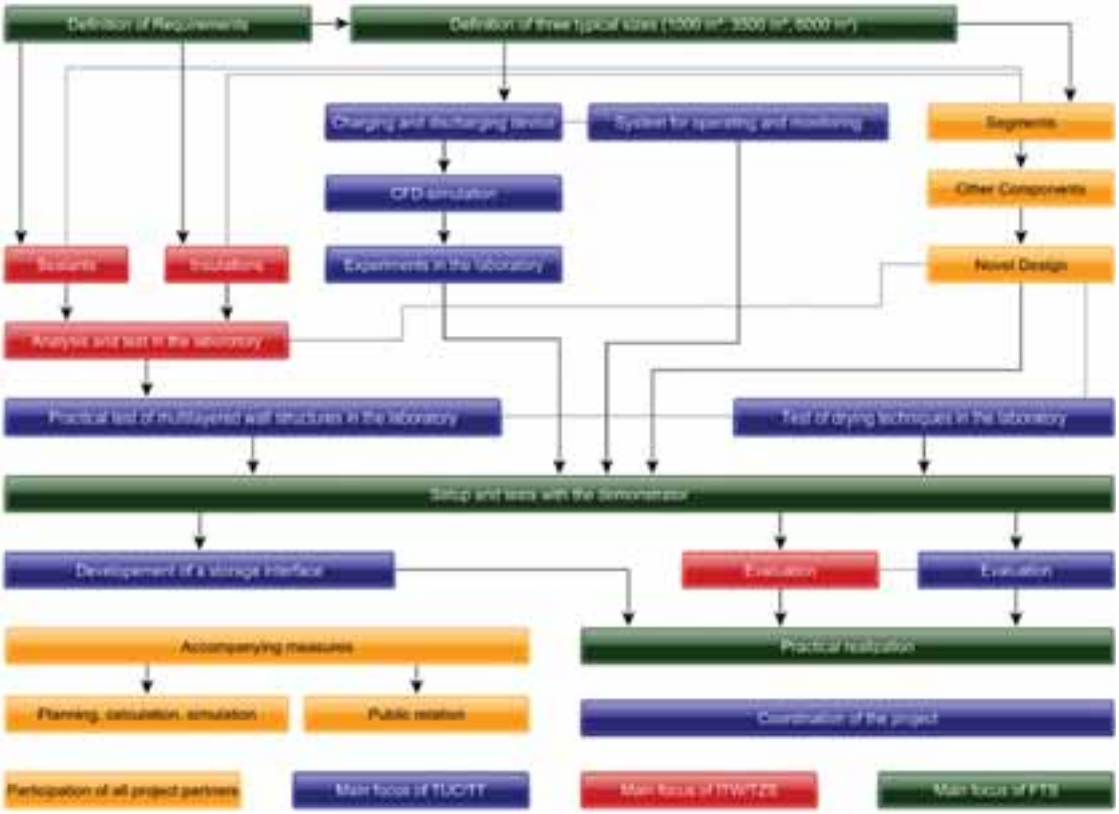

Fig. 4: Overview of the division of work and the procedure in the project, Urbaneck et al. 2016b

Figure 5: Test rig for practical testing of multi-layered wall structures in Chemnitz, enamelled and sealed wall segment (left), pivoting wall cut-out with thermal insulation and cladding panel in the vertical position during the test (right)

Fig. 6 to 8 shows the segmental wall construction, the thermal insulation of the floating device as well as the charging devices in an early state of construction. Fig. 9 presents the final construction of the demonstrator.

After filling the tank and performing first charging tests with hot water, it appears that

- the sealed wall construction is watertight (leakage tests successful),
- the floating ceiling and the flexible sealing work as expected and
- a high stratification quality can be achieved (hot water tests successful).

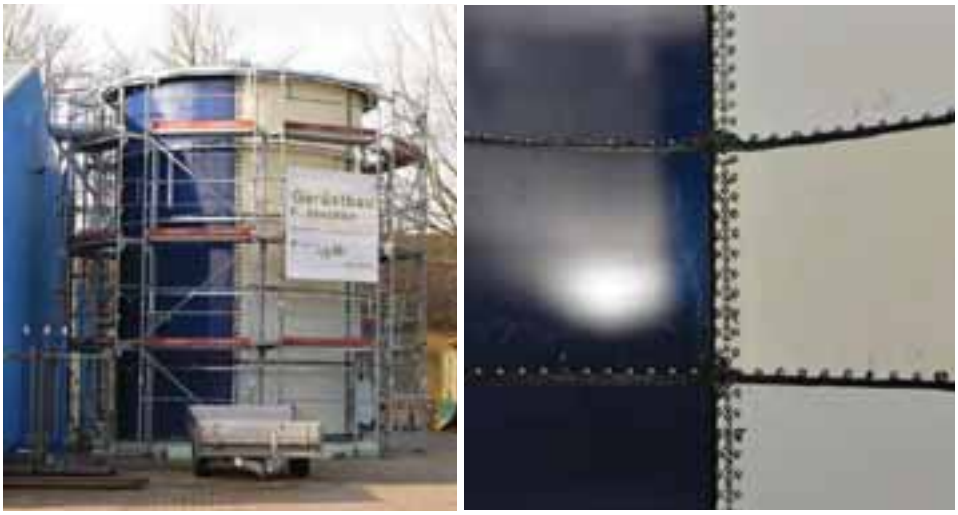

Figure 6: Demonstrator in Nortorf, Germany (left), approx. 100 m³, single-zone storage tank, test of different coatings, interior view (right), April 2016

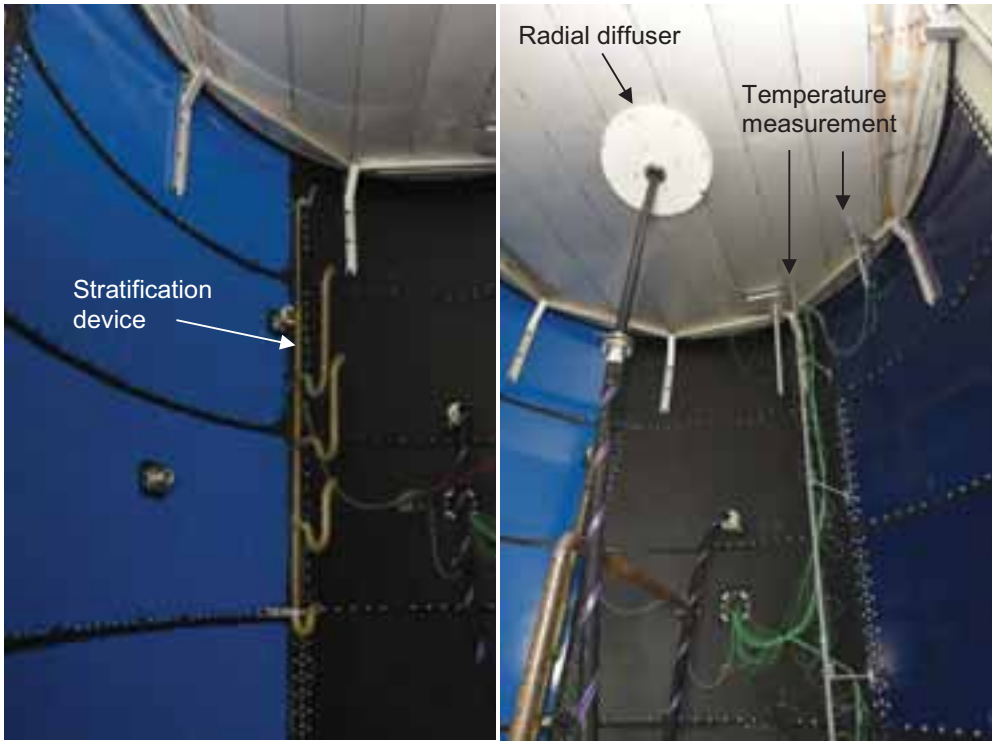

Figure 7: Stratification device (left), radial diffuser with flexible EPDM-hose and temperature measurement probes (right), February 2017

Figure 8: Laying of XPS panels on the PUR foam of the floating ceiling in the attic during the construction, July 2017

Figure 9: CAD-Visualization (left), panelling with trapezoidal sheet metal (right), July 2017

4. Conclusion and Outlook

A project for the development of a novel thermal energy storage tank type with a floating ceiling was presented. The design has multiple advantages. Besides a very efficient thermal insulation at the top of the tank it ensures protection of the thermal insulation by avoiding practical problems like moisture penetration. The simple design provides significant benefits compared to other storage types. However, because of the thin-walled construction and the project objectives, the wall structure as well as installations and peripherals need further research and development. The direct integration of solar thermal systems is intended. By now, the construction process is finished. First tests showed, that the design is suitable to operate as an aboveground hot water store in segmental construction for solar and district heating systems. Ongoing work is focused on tests regarding stratification quality and external heat losses.

5. Acknowledgement

The realization of the project and the scientific work is supported by the German Federal Ministry for Economic Affairs and Energy (BMWi) on the basis of a decision by the German Bundestag (FKZ: 03ET1230B). The authors gratefully acknowledge this support and carry the full responsibility for the content of this paper.

6. References

Findeisen, F., Urbaneck, T., Platzer, B., 2017a. Radial diffusers in stratified hot water stores: Geometry optimization with CFD. In Proceedings: International Conference on Solar Heating and Cooling for Buildings and Industry, SHC 2017, Abu Dhabi (VAE).

Findeisen, F., Urbaneck, T., Platzer, B., 2017b. Radiale Diffusoren in Warmwasserspeichern – Funktionale Optimierung mittels CFD, Teil 2: Optimierung des Be- und Entladeverhaltens. HLH, 2, 25-33. ISSN 1436-5103.

Findeisen, F., Urbaneck, T., Platzer, B., 2017c. Radiale Diffusoren in Warmwasserspeichern – Funktionale Optimierung mittels CFD, Teil 3: Detaillierte Untersuchung des Beladeverhaltens. HLH, 6, 19-27. ISSN 1436-5103.

Gerschitzka, M., Marx, R., Lang, S., Bauer, D., Drück, H., 2015. New developments related to thermal insulation materials and installation techniques for over ground seasonal thermal energy stores. In Proceedings: 13th International Conference on Thermal Energy Storage, Greenstock 2015, Peking (China).

Lang, S., Bauer, D., Drück. H., 2016. Neue Untersuchungen zu Wärmedämmstoffen für thermische Energiespeicher. 5. Fachforum Thermische Energiespeicher, Ostbayerisches Technologie Transfer Institut e.V. (OTTI), Regensburg (Hrsg.), 53-55.

Urbaneck, T., Uhlig, U., Göschel, T., 2012. Kraft-Wärme-Kälte-Kopplung mit großen Kaltwasserspeichern. 1. VDI-Fachkonferenz - Thermische Energiespeicher in der Energieversorgung (CD), Düsseldorf: VDI Wissensforum GmbH, 2012. ISBN 978-3-942980-93-7

Urbaneck, T., Platzer, B., 2015. Overground storages in segmental construction for district heating systems (OBSERW) - Project overview. In Proceedings: 13th International Conference on Thermal Energy Storage, Greenstock 2015, Peking (China).

Urbaneck, T.; Findeisen, F.; Mücke, J.; Marx, R.; Lang, S.; Bauer, D.; Rohde, T.; Hoffmann, F.; Gebhardt, S.; Fischer, M.; Beyer, R., 2016a. Oberirdische Tankspeicher in Segmentbauweise (OBSERW) – Vorstellung des Projektes. 5. Fachforum Thermische Energiespeicher, Ostbayerisches Technologie Transfer Institut e.V. (OTTI), Regensburg (Hrsg.), 93-100.

Urbaneck, T., Platzer, B., Findeisen, F., 2016b. Warmwasserspeicher – Stand der Technik und Entwicklungen. HLH, 07-08, 16-21. ISSN 1436-5103.

Urbaneck, T. et al., 2017. www.obserw.de [Accessed 3 Oct. 2017].

Medium/High Temperature Thermal Storage for Electricity Production with CSP Systems

Moisture-triggered ambient-temperature carbonatization of main group II metal oxides under elevated CO_2 pressure

Georg Gravogl[1,2], Christian Knoll,[2,3] Werner Artner,[4] Elisabeth Eitenberger,[5] Gernot Friedbacher,[5] Andreas Werner,[6] Michael Harasek,[3] Peter Weinberger,[2] Danny Müller,[2]* Ronald Miletich[1]

[1] Institut für Mineralogie und Kristallographie, University of Vienna, Althanstraße 14, 1090 Vienna, Austria

[2] Institute of Applied Synthetic Chemistry, TU Wien, Getreidemarkt 9/163-AC, 1060 Vienna, Austria

[3] Institute of Chemical, Environmental & Biological Engineering, TU Wien, Getreidemarkt 9, 1060 Vienna, Austria

[4] X-Ray Center, TU Wien, Getreidemarkt 9, 1060 Vienna, Austria

[5] Institute of Chemical Technologies and Analytics, TU Wien, Getreidemarkt 9/164, 1060 Vienna, Austria

[6] Institute for Energy Systems and Thermodynamics, TU Wien, Getreidemarkt 9/302, 1060 Vienna, Austria

danny.mueller@tuwien.ac.at

Abstract

The reversible reaction of metal oxides with CO_2 forming metal carbonates with concomitant release of energy is considered as a promising concept for thermochemical energy storage. One major advantage of thermochemical energy storage materials is the possibility of a lossless mid-term and long-term storage of waste heat. Metal carbonates provide high-energy densities and were so far investigated for their application in high-temperature processes. Inspired by the carbonatization of (main group II) metal oxides in nature during mineralization and CO_2 fixation in the presence of moisture under elevated pressures, the Me (II) oxides (Me = Mg, Ca, Sr, Ba) were investigated with respect to their reactivities with CO_2 at pressures up to 55 bar and ambient temperature. Whereas for MgO none of the applied conditions yielded any formation of a carbonate phase, the other oxides revealed appropriate reactivities by forming corresponding carbonates under considerably mild reaction conditions.

Keywords: main group II oxides, main group II carbonates, low-temperature carbonatization, in-situ powder X-Ray diffraction, thermochemical energy storage

1. Introduction

Reliable energy supply has become a fundamental in today's society. Although notable efforts were made within the last decade to decrease the ecological footprint of the global energy supply by supporting sustainable energy sources, fossil raw materials are still the fundamental resource for energy production. (Shine, 2005) Aiming for an increased awareness of sustainable energy management the International Energy Agency (IEA) reported in 2011, that the global energy loss in form of waste heat during electricity generation accounts for approximately 66 %. (IEA, 2011) This stimulated equally politics and science to focus on a reduction and recycling of waste heat to contribute to a more efficient energy management. (IEA, 2014; Arce et al., 2011)

A major challenge for waste heat management is the temporal mismatch between heat production and consumption. (Solé et al., 2012) Therefore, a feasible approach towards a more efficient energy balance could be the storage of so far unused waste heat, allowing for a decoupling of production and consumption in space and

doi:10.18086/swc.2017.14.01 Available at http://proceedings.ises.org

time. (Zhang et al., 2016) The concept of thermal energy storage enables the transfer of excess energy to a suitable storage medium, thus preserving the stored energy for the case of a sudden demand. (Bauer et al., 2012; Abedin, 2011) Several methods categorized according to the used storage medium, are known for this purpose. Whereas sensible (Dinker et al., 2015) and latent heat storage (Zalba et al., 2003) transferring the heat to a liquid or solid storage medium, respectively to a phase-change material are mainly suitable for low- to medium-temperature storage, thermochemical energy storage (TCES) offers a much larger temperature compatibility, being tunable by the applied storage reaction. (Abedin, 2011; Cot-Gores et al., 2012) By charging the storage material (*A*, Eq.1) with the waste heat its dissociation is forced, liberating a reactive gas (*B*, Eq.1) as H_2O, CO_2, O_2, NH_3, … Once the formed decomposition product (*C*, Eq. 1) is contacted with the reactive gas under suitable reaction conditions, the back-reaction takes place, discharging the stored energy. A general equation for a thermochemical energy storage reaction is given in Eq.1.

$$A + \Delta H \leftrightharpoons B + C \tag{1}$$

Compared to sensible and latent heat storage, thermochemical storage offers - besides the broad applicable temperature range (between room-temperature and 1200 °C in *e.g.* concentrating solar power plants (Prieto et al., 2016)) - notably higher energy densities, decreasing amounts of necessary material. Moreover, it avoids insulation of the material once charged, as until contacted with the reactant no discharging will occur. The possibility of lossless storage lends TCES-materials for mid-term to long-term storage applications, (Xu, 2014) where *e.g.* waste heat is continuously stored but liberated periodically to fit heat-demands going beyond the daily process routine. For such applications a storage at preferably room-temperature would be desirable, followed by a discharging of the material at low-temperatures avoiding a preheating of the material.

A class of TCES-materials featuring relatively high energy contents are metal carbonates, (Kyaw et al., 1996; Yamauchi et al., 2007) commonly investigated for application at elevated temperatures in combination with *e.g.* concentrating solar power plants. (Reich, 2014; Rhodes et al., 2015) Recently we could demonstrate, that various metal oxides (obtained from decomposition of the corresponding carbonates) undergo carbonatization already at moderate temperatures in the presence of moisture and by increasing the partial pressure of CO_2 to 55 bar. (Müller et al., 2017a)

Main-group II metal oxides were so far mainly known as TCES-materials with respect of being considered for hydrate reactions. In order to broaden the scope of applicability, the process of CO_2 sequestration in rock mineralization (Fagerlund et al., 2012; Sissmann et al., 2014; Yamauchi et al., 2007; Morales-Flórez et al., 2015) inspired this endeavour reported here. Carbonatization reactivity at low-temperatures and elevated CO_2 pressures were studied aiming for novel low-temperature carbonate TCES-materials for mid- and long-term storage.

2. Results and Discussion

2.1 Carbonatization of MgO

Among the different main-group II metal oxides in particular MgO appears to be perfectly suitable for an application in thermochemical energy storage due to its availability as industrial raw material. It is known from earlier studies on the hydration behavior of MgO, which also have been aiming for a TCES-process, that the calcination conditions determine the reactivity of the material. Previous work on $Mg(OH)_2$-calcination resulted in calcination conditions providing a notably reactive material (Müller et al., 2017b), which was also used in the current low-temperature carbonatization study.

Successful carbonatization of MgO was already reported for reactions at temperatures around 575 °C (Fagerlund et al., 2012). Nevertheless, at ambient temperatures under the applied conditions varying from 8 bar wet CO_2 in the *in-situ* P-XRD setup (see experimental) to 55 bar wet CO_2 in the autoclave, in none of the experiments terminated after 2 h any detectable trace of $MgCO_3$ has been found. The same negative result accounts for experiments at temperatures up to 60 °C in the autoclave. The most likely explanation for the absence of any reactivity is the relatively high energetic barrier of the CO_2-absorption, which cannot be overcome by simply

increasing the CO_2-pressure. In order to investigate even higher CO_2-pressures under supercritical conditions, MgO was exposed to H_2O and kept for 4 h in a supercritical CO_2-reactor at 150 °C, 150 bar. In this case a complete conversion to $Mg(OH)_2$ can be observed, but still no reaction with CO_2 and hence no carbonate formation occurs.

A notable kinetic hindrance was already reported in literature (Hu et al., 2011) not only for the CO_2-absorption on the MgO surface, but also for the H_2O dissociation on a MgO surface forming $Mg(OH)_2$. To exclude, that the carbonatization of MgO is hampered by a required intermediate formation of $Mg(OH)_2$, all experiments were repeated using $Mg(OH)_2$ as a precursor material. Nevertheless, even the choice of reactant material reveals to be not critical for the observed absence of any significant carbonatization.

Most recently it was shown, that the energetic barrier of the H_2O-dissociation on the MgO surface could be notably decreased by the dotation of the MgO lattice with a degree of dotation by up to 10 % of Ca^{2+}-ions (Müller et al., 2017c). In order to derive, whether a similar effect could also be observed in the case of the carbonatization, samples of $Mg_{1-x}Ca_xO$ with Ca-contents x = 0-1 were moistened and kept for 2 h at 55 bar in the autoclave. The phase composition of the different samples after 2 h reaction time is shown in Figure 1.

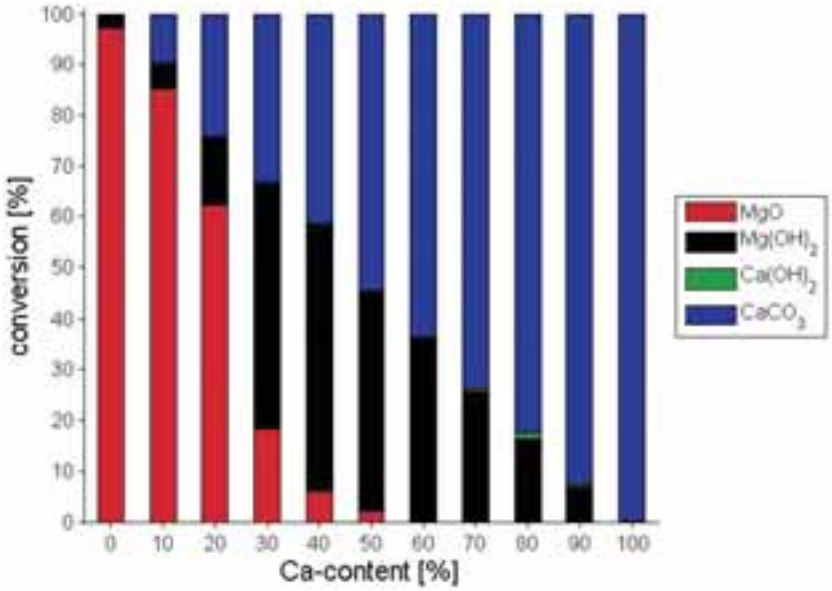

Fig. 1: Phase composition after 2 h reaction time of the $Mg_{1-x}Ca_xO$ samples in the presence of moisture at 55 bar CO_2

Phase analyses as carried out by means of X-ray powder diffraction gave evidence for significant conversion to carbonate for the Ca^{2+}-doped MgO materials, with a selective carbonate formation on the Ca^{2+}-components. Starting from the sample with 10 % Ca^{2+}-dotation, the complete amount of Ca^{2+}-dopant was carbonated, whereas the MgO component remained unchanged, or was partially hydrated forming $Mg(OH)_2$. The same result was obtained, when the mixed hydroxides $Mg_{1-x}Ca_x(OH)_2$ were used as starting material for carbonatization (see figure 2).*

* The phase composition of a comparable experiment regarding the reactivity of both the mixed oxides $Mg_{1-x}Ca_xO$ and hydroxides $Mg_{1-x}Ca_x(OH)_2$ in the absence of moisture are shown in Figure S1 and S2.

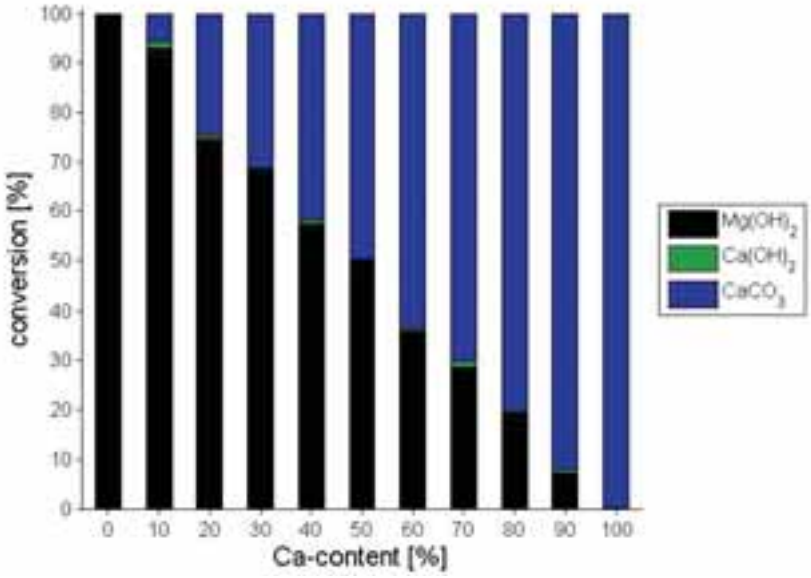

Fig. 2: Phase composition after 2 h reaction time of the $Mg_{1-x}Ca_x(OH)_2$ samples in the presence of moisture at 55 bar CO_2

This allows for the conclusion, that although a Ca^{2+}-dotation can effectively promote the H_2O dissociation, no similar catalytic effect is found in the case of the CO_2-absorption.

2.2 Carbonatization of CaO

Based on the promising carbonatization results of the Ca^{2+}-doped MgO samples, and demonstrating the favorable transformation of the CaO components to the corresponding carbonate within 2 h at 55 bar and room-temperature, as a result both the time dependency of the reaction and the influence of the moisture concentration has been investigated.†

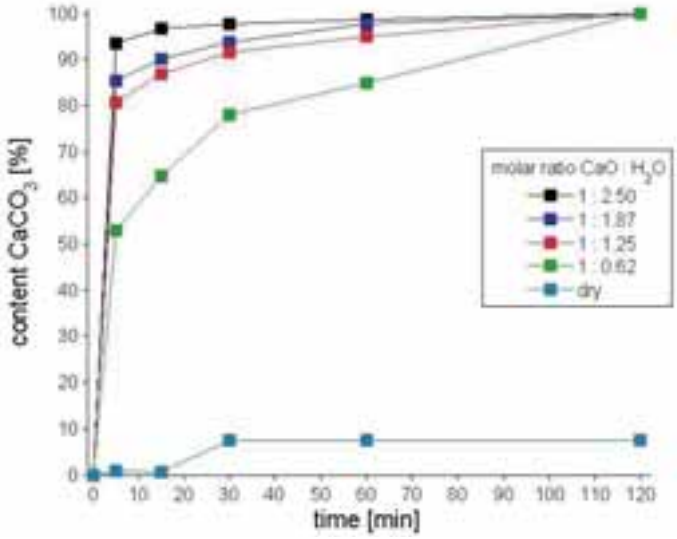

Fig. 3: Time- and moisture dependent carbonatization of CaO at 55 bar CO_2

Figure 3 shows the time dependent increase of the $CaCO_3$-concetration for 5 different moisture concentrations, ranging between 0 and 2.5 molar equivalents of H_2O per equivalent CaO. Without additional moisture, the initial

† Prior experiments on CaO-carbonatization in the P-XRD at 8 bar of wet CO_2 resulted only incomplete conversion to 34 % $CaCO_3$ after 120 minutes. (Müller et al., 2017a)

CaO is converted to 9 % into $CaCO_3$, keeping this phase composition constant over the observed time. Already after 5 minutes, more than 50 % of CaO are carbonated for the various amounts of added H_2O. In the case of 2.5 equivalents of H_2O even 94 % $CaCO_3$ had formed. The CaO phase was completely carbonated after 120 minutes for all investigated variations of H_2O contents. As even in the case of molar deficits of H_2O the complete carbonatization of CaO to $CaCO_3$ takes place, it indicates that H_2O appears to have only a catalytic role in the process, otherwise no quantitative $CaCO_3$ formation would have been possible. According to the SEM-images shown in figure S3 an increasing amount of H_2O present during the carbonatization promotes the observable fragmentation of the particles, facilitating easier access of reactive gas CO_2 to the remaining CaO.

Once a fully reversible reaction, which is potentially suitable for a TCES-process, has been identified another intriguing aspect is the cycle stability of the process. To assess the reproducibility of the quantitative CaO-carbonatization, the same sample of $CaCO_3$ was calcined at 900 °C for 1 h and re-carbonated in the autoclave at 55 bar in the presence of 0.62 equivalents H_2O for 120 minutes in 7 subsequent cycles. The phase composition of a representative sample after each cycle is shown in Figure 4.

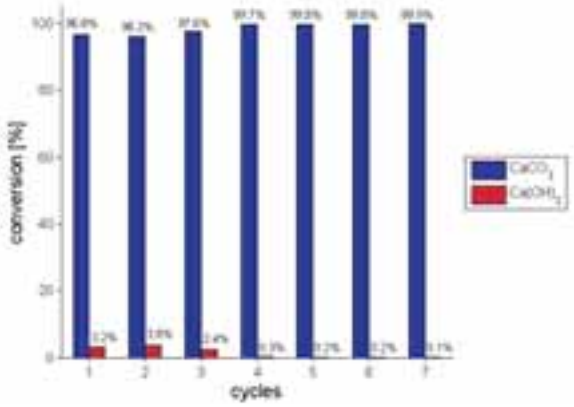

Fig. 4: Phase composition during cycle-stability test of $CaCO_3$ / CaO

For all 7 cycles after 120 minutes the carbonatization was found nearly quantitative, only in the first 3 cycles a small residue of <4 % $Ca(OH)_2$ could be observed. The reduction of the residual CaO is attributed to an increasing degree of particle fragmentation with the number of cycles, which in turn decreases the diffusion pathways for any volatile component. In the SEM-images in Figure 5, a fragmentation of the particles on repeated carbonatization / calcination process could be observed. In Figure 5a – showing CaO after the first calcination – a rather uniform particle size distribution is found. With increasing number of cycles also a fraction of smaller particles is observed, which results from the mechanical stress originating from the volume work accompanying the transformation from CaO to $CaCO_3$.

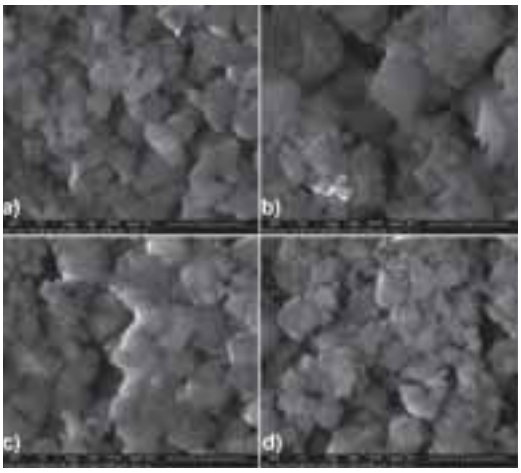

Fig. 5: SEM images of various stages of the cycle stability test a) CaO after first decomposition of $CaCO_3$ b) $CaCO_3$ after 1 cycle c) $CaCO_3$ after 4 cycles d) $CaCO_3$ after 7 cycles. Image size 9 x 9 µm

As the reaction $CaCO_3 \leftrightarrow CaO + CO_2$ revealed an attractive reactivity and cycle stability, subsequent investigations will focus on determination of the thermochemical parameters and energy density under the applied low-temperature carbonatization conditions.

2.3 Carbonatization of SrO

A direct comparison of the carbonatization behavior of MgO and CaO suggests an increased CO_2-affinity moving towards the heavier alkaline earth cations, correlating with the increased ionic radii. Attempted carbonation of SrO in the absence of H_2O failed both under 8 bar and 55 bar of CO_2, which could be anticipated based on the prior experience. In contrast, P-XRD patterns of the sample in the presence of moisture under 8 bar CO_2 reveal an interesting behavior as shown in Figure 6.

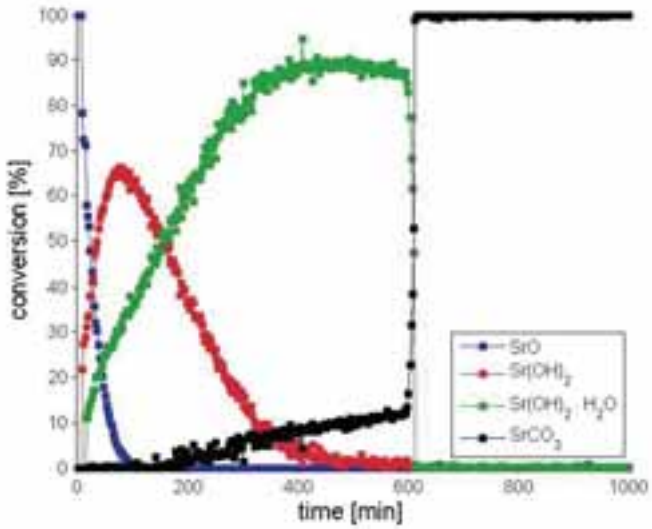

Fig. 6: Time-dependent phase composition of SrO during carbonatization in the presence of moisture at 8 bar CO_2

SrO is very hygroscopic, transforming immediately in the presence of H_2O to crystalline $Sr(OH)_2$ (red symbols). It directly hydrates yielding the monohydrate phase $Sr(OH)_2 \cdot H_2O$ (green symbols). This hydration process occurs simultaneously, and after 500 minutes the intermediate $Sr(OH)_2$ completely converted to $Sr(OH)_2 \cdot H_2O$. In parallel to this process after approximately 180 minutes the carbonatization starts at a nearly exact 1:1 ratio of $Sr(OH)_2$ to $Sr(OH)_2 \cdot H_2O$. The XRD pattern provides evidence for the formation of $SrCO_3$ as new phase (black symbols). Within the next 400 minutes the $SrCO_3$ phase augments slightly up to about 12 %, when suddenly the carbonatization gets significantly accelerated and the conversion is completed within a short time interval (*i.e.* 15 minutes). This spontaneous acceleration of the carbonatization rate was found to be reproducible on repeated experiments.

Apart of this unexpected carbonatization behavior, SrO behaves also different with respect to the role of H_2O in the process. Whereas in the case of CaO H_2O seems to have only a catalytic impact – under-stoichiometric H_2O amounts still allow for quantitative carbonatization of CaO, – in the case of SrO the intermediate $Sr(OH)_2 \cdot H_2O$ is the apparently critical reactive species. Once enough $Sr(OH)_2 \cdot H_2O$ had formed, the carbonatization starts from the surface of the particles, most likely forming a thin layer of $SrCO_3$ on the particle surface. As this $SrCO_3$ layer is denser than the original hydroxide phase, it acts as a barrier for diffusion of water and CO_2 into the inner bulk of the particles. A likely explanation for the observed sudden acceleration of the carbonatization rate is the formation of micro-cracks, mechanical changes including fragmentation of the particles as caused by the volume work and strain occurring at the interface between the hydrous phase and the carbonate.‡ Table S1 provides the corresponding crystallographic cell-parameters for SrO, $Sr(OH)_2$, $Sr(OH)_2 \cdot H_2O$ and $SrCO_3$. This interpretation is supported by SEM-images of SrO material before and after carbonatization (figure 7), as the images reveal a

‡ The carbonation of $Sr(OH)_2 \cdot H_2O$ to $SrCO_3$ goes along with an expansion of the cell about 68 %.

notable particle fragmentation during the carbonatization process.

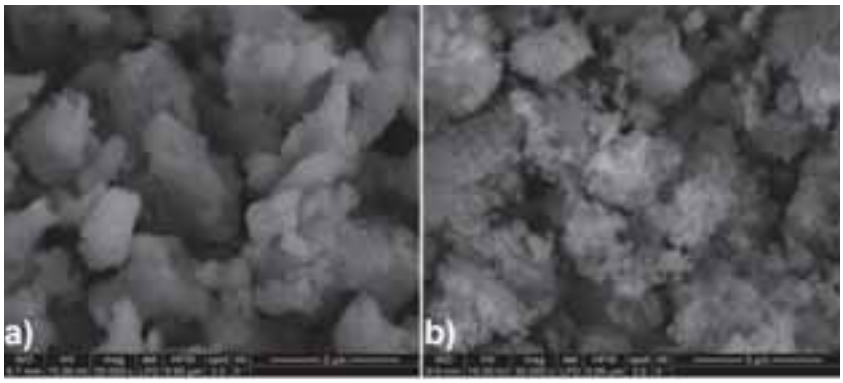

Fig. 7: SEM-images of a) SrO before carbonatization and b) $SrCO_3$ after carbonatization. Image size 9 x 9 µm

The same carbonatization experiment was repeated under 8 bar of wet CO_2, using a mixture of $Sr(OH)_2 \cdot 8H_2O$ (50 %) and $Sr(OH)_2 \cdot H_2O$ (50 %) as starting material in order to derive, whether a higher hydrate coordination around the Sr^{2+}-cation would significantly enhance the progress of the carbonatization process.

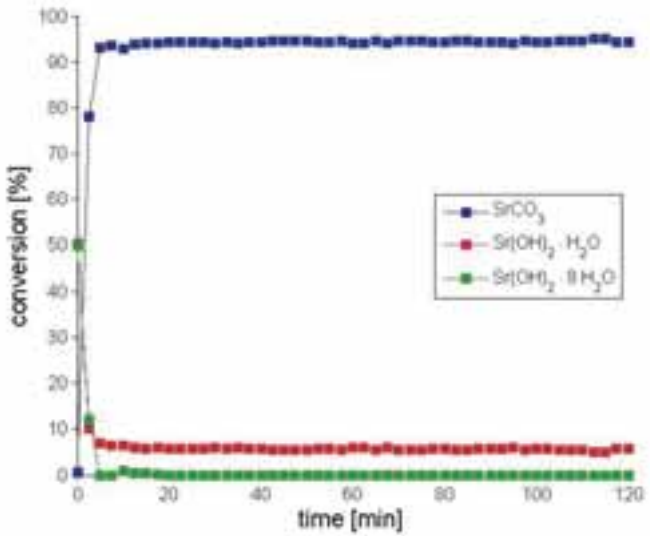

Fig. 8: Time-dependent phase composition of a mixture of $Sr(OH)_2 \cdot 8H_2O$ (50 %) and $Sr(OH)_2 \cdot H_2O$ (50 %) during carbonatization in the presence of moisture at 8 bar CO_2

Figure 8 reveals, that within 6 minutes the complete amount of $Sr(OH)_2 \cdot 8H_2O$ and 82 % of the $Sr(OH)_2 \cdot H_2O$ phase were converted into $SrCO_3$. The residual $Sr(OH)_2 \cdot H_2O$ was found inert towards further carbonatization within the next 120 minutes. This different carbonatization behavior allows for the conclusion, that carbonatization is favored by the higher hydrate coordination of Sr^{2+}.

2.4 Carbonatization of BaO

Based on the chemical similarity between Sr^{2+} and Ba^{2+} and the fact, that both form hydrated hydroxides, the behavior of BaO reacting with wet CO_2 was expected to be similar to that observed for SrO.

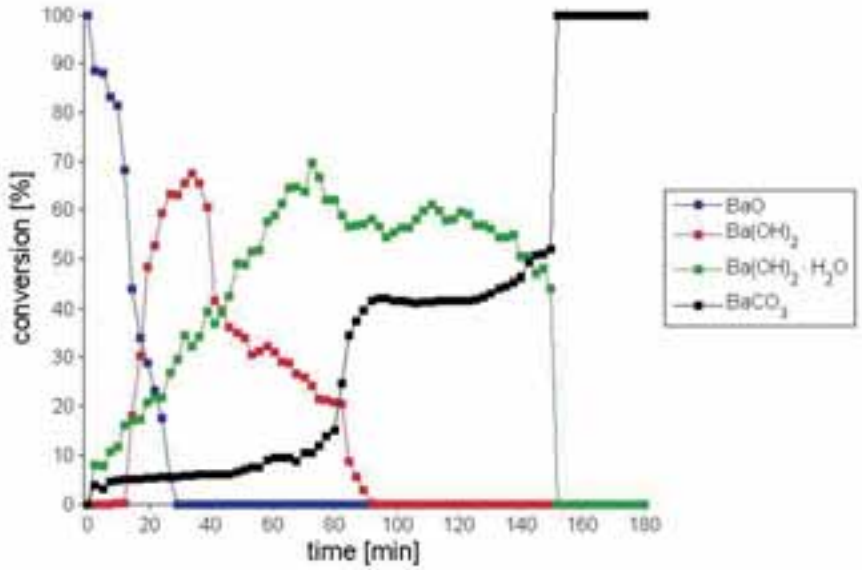

Fig. 9: Time-dependent phase composition of BaO during carbonatization in the presence of moisture under CO_2 atmosphere

Whereas in the case of SrO the carbonate formation initiated after formation of a 1:1 mixture between hydroxide and hydroxide monohydrate, in the case of BaO already after 2 minutes a small amount of the $BaCO_3$-phase is found. This may be attributed to a higher CO_2-affinity of Ba^{2+}, but also to the much faster conversion of BaO into the hydroxide and hydroxide monohydrate. In fact, the conversion of $Ba(OH)_2$ to $Ba(OH)_2{\cdot}H_2O$ is under the applied conditions so fast, that for the first 15 minutes only the $Ba(OH)_2{\cdot}H_2O$ – originating from the immediate hydration of the former $Ba(OH)_2$ – is observed. After that time also the $Ba(OH)_2$ phase increases, converting to the $Ba(OH)_2{\cdot}H_2O$ within 90 minutes. The carbonatization seems in the case of Ba^{2+} not as strictly related to the hydroxide monohydrate as in the case of Sr^{2+}. In fact, after the initial formation of around 5 % $BaCO_3$, the carbonate formation occurs via a two-step process with an intermediate plateau-phase: After 75 minutes the carbonatization rate increases, decelerating again once 42 % of $BaCO_3$ were formed. After 50 minutes of a nearly constant $BaCO_3$ content, only slightly increasing towards the end to 52 % $BaCO_3$, within 2 minutes a spontaneous completion yielding 100 % of $BaCO_3$ occurs. Based on the present data no final explanation of this in the series so far unique carbonatization process is possible.[§]

Also for Ba^{2+} a mixed sample of $Ba(OH)_2{\cdot}8H_2O$ (50 %) and $Ba(OH)_2{\cdot}H_2O$ (50 %) was compared regarding their carbonatization behavior (Figure 10).

[§] Table S2 provides the corresponding crystallographic cell-parameters for BaO, $Ba(OH)_2$, $Ba(OH)_2{\cdot}H_2O$ and $BaCO_3$.

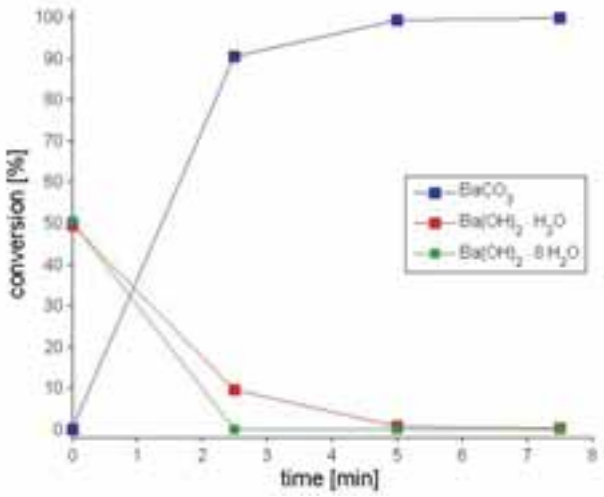

Fig.10: Time-dependent phase composition of a mixture of $Ba(OH)_2 \cdot 8H_2O$ (50 %) and $Ba(OH)_2 \cdot H_2O$ (50 %) during carbonatization in the presence of moisture at 8 bar CO_2

In the case of Ba^{2+} the carbonatization of both hydroxides is completed already within 5 minutes. Nevertheless, also in this case a slightly higher reactivity for the $Ba(OH)_2 \cdot 8H_2O$ is found, as after 2.5 minutes the complete octahydrate phase was carbonated, whereas still 12 % of $Ba(OH)_2 \cdot H_2O$ were present.

3. Conclusion

In the present study main group II oxides were investigated for their reactivity towards CO_2 in the presence of moisture at ambient temperature and elevated pressures up to 55 bar of CO_2. The aim of this approach was the investigation of a carbonatization process for main group II oxides regarding their application as long-term thermochemical storage materials with discharging of the stored energy near to ambient temperature.

From the investigated series of MgO, CaO, SrO and BaO, all oxides apart from MgO were found to carbonate under the applied conditions at the given time scales. The best performance was observed for CaO, transforming quantitatively to the corresponding carbonate in the presence of moisture at 55 bar CO_2 within 120 minutes. Repeated calcination / carbonatization of the material under the same conditions revealed a very appealing cycle stability of the process, although a concomitant particle fragmentation was observed, which can be attributed to the volume work involved into the reaction. In case of SrO the hydrate coordination sphere around the Sr^{2+} seems to have a notable impact on the calcination behavior. Treated with 8 bar wet CO_2, SrO was hydrated immediately to $Sr(OH)_2$ in a first step and consequently to $Sr(OH)_2 \cdot H_2O$, which was then the active phase reacting with CO_2 to form $SrCO_3$. An initial slow conversion rate observed for the carbonatization was suddenly accelerated and is assigned to particle changes, most likely due to the formation of micro-cracks and fragmentation. Additional experiments using $Sr(OH)_2 \cdot H_2O$ and $Sr(OH)_2 \cdot 8H_2O$ in carbonatization further supported the postulated importance of the hydrate coordination sphere around the cation, as in contrast to the monohydrate the octahydrate was quantitatively carbonated within 6 minutes. In the case of BaO a much higher carbonatization reactivity than for SrO, reaching complete conversion after 150 minutes, was found. Although, the reaction involves the intermediate formation of $Ba(OH)_2$ and $Ba(OH)_2 \cdot H_2O$, the carbonatization mechanism seems different, as a two-step carbonatization with an intermediate plateau was observed. Also in the case of Ba^{2+} the hydrate coordination sphere around the cation promotes the carbonatization.

Based on the present work regarding a general feasibility of an ambient-temperature carbonatization for main group II oxides, within a next step the thermochemical data and energy densities for the materials under the selected process parameters will be established. A further in-depth investigation of the impact of H_2O on a molecular level during the carbonatization process, as well as on the detailed carbonatization mechanisms for SrO and BaO is currently ongoing.

4. Experimental

4.1 Material

MgO (calcined from $Mg(OH)_2$,), CaO (calcined from commercially available $Ca(OH)_2$) and the mixed $Mg_{1-x}Ca_xO$ were prepared by thermal decomposition of the commercially available (or in the case of $Mg_{1-x}Ca_x(OH)_2$ freshly precipitated) hydroxides. All other materials were commercially obtained and used as supplied.

4.2 X-Ray Powder Diffraction

The powder X-ray diffraction measurements were carried out on a PANalytical X'Pert Pro diffractometer in Bragg-Brentano geometry using Cu $K_{\alpha1,2}$ radiation and an X'Celerator linear detector with a Ni-filter. For *in-situ* monitoring of experiments an Anton Paar XRK 900 reaction chamber was used. The sample was mounted on a hollow ceramic powder sample holder, allowing for complete perfusion of the sample with the reactive gas. The sample temperature is controlled directly via a NiCr-NiAl thermocouple and direct environmental heating. The diffractograms were evaluated using the PANalytical program suite HighScorePlus v4.6a. (Degen et al., 2014) A background correction and a $K_{\alpha2}$ strip were performed. Phase assignment is based on the ICDD-PDF4+ database ((http://www.icdd.com), the exact phase composition, shown in the conversion plots, was obtained via Rietveld-refinement incorporated in the program suite HighScorePlus v4.6a. (Degen et al., 2014) All phase quantifications based on P-XRD are accurate within ±5 %. For the carbonization experiments the pressure in the sample chamber was adjusted to 8 bar, maintaining a constant flow through the chamber of 0.4 L CO_2 min^{-1}. To investigate the carbonation in the presence of moisture, the CO_2 was passed through an external moisturiser. The CO_2 was bubbled through a 20 cm high water tank followed by a droplet-separator before contacting the sample in the reaction chamber. At the entrance of the reaction chamber the gas had a dew-point temperature of 23.2 °C with a constant sample temperature of 25 °C.

4.3 Carbonation in the reactor

For the carbonation of the metal oxides at higher CO_2 pressure a stainless-steel autoclave with a volume of 0.19 L was used. A small amount of the metal oxides (around 250 mg) was placed in a glass-vial with perforated cap to avoid cross-contamination during pressure release and moistened with 200 µL H_2O. The reactor was pressurized with CO_2 at 55 bar unless otherwise stated, controlling the internal pressure with the integrated manometer of the reactor. The carbonation process was stopped after the specified reaction time by releasing the CO_2.

4.4 Scanning Electron Microscopy

SEM images were recorded on gold coated samples with a Quanta 200 SEM instrument from FEI under low-vacuum at a water vapor pressure of 80 Pa to prevent electrostatic charging.

5. References

1. Keith Shine, J.F., Kinfe Hailemariam, Nicola Stuber, 2005. Alternatives to the Global Warming Potential for Comparing Climate Impacts of Emissions of Greenhouse Gases. climatic change 3, 281-302.
2. IEA, 2011. Co-generation and Renewables. Solutions for a low-carbon energy future. https://www.iea.org/publications/freepublications/publication/co-generation-and-renewables-solutions-for-a-low-carbon-energy-future.html
3. IEA, 2014. Heating without global warming: Market developments and policy considerations for renewable heat.
4. Arce, P., et al., 2011. Overview of thermal energy storage (TES) potential energy savings and climate change mitigation in Spain and Europe. Applied Energy 8, 2764-2774.
5. Solé, A., et al., 2012. Parameters to take into account when developing a new thermochemical energy storage system. Energy Procedia 380-387.
6. Zhang, H., et al., 2016. Thermal energy storage: Recent developments and practical aspects. Progress in Energy and Combustion Science 1-40.

7. Bauer, T., et al., 2012. Thermal Energy Storage Materials and Systems. Annual Review of Heat Transfer 15, 131-177.
8. Ali H. Abedin, M.A.R., 2011. A Critical Review of Thermochemical Energy Storage Systems. The Open Renewable Energy Journal 42-46.
9. Dinker, A., M. Agarwal, and G.D. Agarwal, 2015. Heat storage materials, geometry and applications: A review. Journal of the Energy Institute
10. Zalba, B., et al., 2003. Review on thermal energy storage with phase change: materials, heat transfer analysis and applications. Applied Thermal Engineering 3, 251-283.
11. Cot-Gores, J., A. Castell, and L.F. Cabeza, 2012. Thermochemical energy storage and conversion: A-state-of-the-art review of the experimental research under practical conditions. Renewable and Sustainable Energy Reviews 7, 5207-5224.
12. Prieto, C., et al., 2016. Review of technology: Thermochemical energy storage for concentrated solar power plants. Renewable and Sustainable Energy Reviews 909-929.
13. J. Xu, R.Z.W., Y. Li, 2014. A review of available technologies for seasonal thermal energy storage. Solar Energy 610-638.
14. Kyaw, K., H. Matsuda, and M. Hasatani, 1996. Applicability of Carbonation/Decarbonation Reactions to High-Tempereture Thermal Energy Storage and Temperature Upgrading. Journal of Chemical Engineering of Japan 1, 119-125.
15. Yamauchi, K., N. Murayama, and J. Shibata, 2007. Absorption and Release of Carbon Dioxide with Various Metal Oxides and Hydroxides. Materials Transactions 10, 2739-2742.
16. Reich, L., 2014. Towards Solar Thermochemical Carbon Dioxide Capture via Calcium Oxide Looping: A Review. Aerosol and Air Quality Research
17. Rhodes, N.R., et al., 2015. Solar Thermochemical Energy Storage Through Carbonation Cycles of $SrCO_3$/SrO Supported on $SrZrO_3$. ChemSusChem 22, 3793-3798.
18. Müller, D., et al., 2017a. Low-temperature carbonation of metal oxides. Journal of Materials Science, submitted.
19. Fagerlund, J., J. Highfield, and R. Zevenhoven, 2012. Kinetics studies on wet and dry gas–solid carbonation of MgO and $Mg(OH)_2$ for CO_2 sequestration. RSC Advances 27, 10380.
20. Sissmann, O., et al., 2014. Enhanced Olivine Carbonation within a Basalt as Compared to Single-Phase Experiments: Reevaluating the Potential of CO_2-Mineral Sequestration. Environmental science & technology 10, 5512-5519.
21. Morales-Flórez, V., et al., 2015. Hydration and carbonation reactions of calcium oxide by weathering: Kinetics and changes in the nanostructure. Chemical Engineering Journal 194-200.
22. Müller, D., et al., 2017b. An in-situ powder X-Ray diffraction study on the rehydration-reactivity of low temperature calcined $Mg(OH)_2$. Applied Energy, submitted.
23. Hu, X.L., et al., 2011. Trends in water monomer adsorption and dissociation on flat insulating surfaces. Physical Chemistry Chemical Physics 27, 12447.
24. Müller, D., et al., 2017c. Calcium Dotation Facilitates Water Dissociation in Magnesium Oxide. Advanced sustainable materials, submitted.
25. Degen, T., et al., 2014. The HighScore suite. Powder Diffraction S2, S13-S18.
26. http://www.icdd.com,

6. Appendix

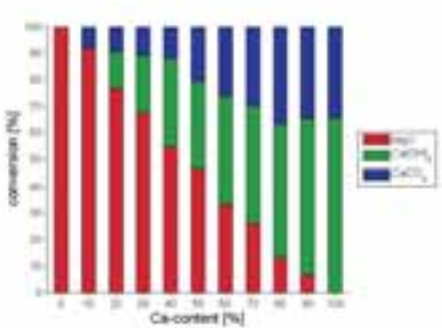

Fig. S1: Phase composition after reaction time of 2h of the $Mg_{1-x}Ca_xO$ samples in the absence of moisture at 55 bar CO_2

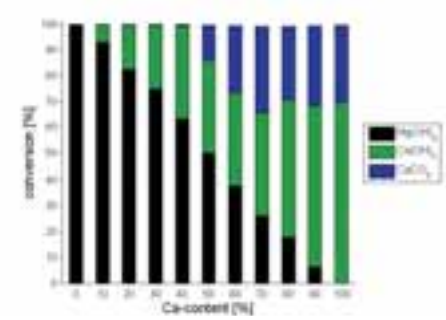

Fig. S2: Phase composition after reaction time of 2h of the $Mg_{1-x}Ca_x(OH)_2$ samples in the absence of moisture at 55 bar CO_2

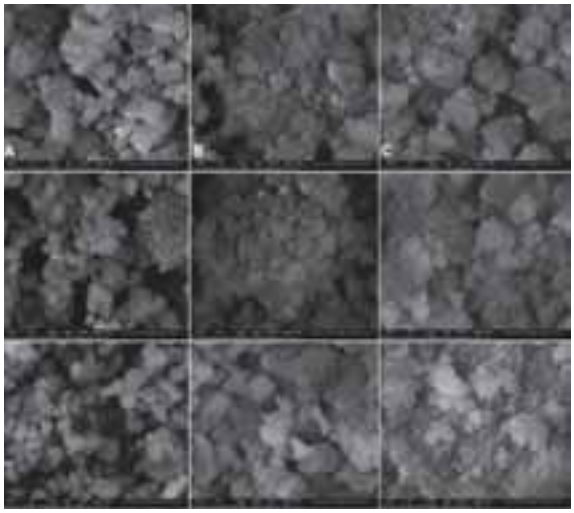

Fig. S3: SEM images of the moisture-dependent CaO carbonatization. In column A the carbonatization in the absence of H_2O, in column B in the presence of 1.25 equivalents and in column C in the presence of 2.5 equivalents is shown. Images are compared for the starting materials (first row), after 30 minutes (second row) and after 120 minutes (third row). Image size 9 x 9 µm

Tab. 1: Cell-parameters of $Sr(OH)_2$, $Sr(OH)_2 \cdot H_2O$ and $SrCO_3$

	SrO	$Sr(OH)_2$	$Sr(OH)_2$ H_2O	$SrCO_3$
	cubic	ortho-rhombic	ortho-rhombic	ortho-rhombic
Space group	$F\,m\,\bar{3}\,m$	P n a m	P 2_1 a m	P m c n
Nr°	225	62	26	62
a [A]	5.1615(3)	9.8889(5)	6.7131(7)	5.090(2)
b [A]	5.1615(3)	6.1202(6)	6.1981(6)	8.358(2)
c [A]	5.1615(3)	3.9184(4)	3.6478(4)	5.997(4)
α [°]	90	90	90	90
β [°]	90	90	90	90
γ [°]	90	90	90	90
V[A^3]	137.51	237.15	151.78	255.13

Tab. 2: Cell-parameters of BaO, $Ba(OH)_2$, $Ba(OH)_2 \cdot H_2O$ and $BaCO_3$

	BaO	$Ba(OH)_2$	$Ba(OH)_2$ H_2O	$BaCO_3$
	cubic	mono-clinic	ortho-rhombic	ortho-rhombic
Space group	$F\,m\,\bar{3}\,m$	$P\,1\,2_1/n\,1$	$P\,m\,c\,2_1$	$P\,m\,c\,n$
Nr°	225	14	26	62
a [A]	5.5391	9.3396(2)	3.8947(4)	5.319(9)
b [A]	5.5391	7.8550(2)	6.3657(6)	8.905(8)
c [A]	5.5391	6.7267(2)	6.9523(7)	6.435(9)
α [°]	90	90	90	90
β [°]	90	95.607(2)	90	90
γ [°]	90	90	90	90
V[A^3]	169.95	491.13	172.36	304.85

Metal oxides for thermochemical energy storage – From gas-triggered isothermal cycling to low-temperature applications with increased O_2 pressure

Christian Knoll,[1,2] Georg Gravogl[1,3], Werner Artner,[4] Elisabeth Eitenberger,[5] Gernot Friedbacher,[5] Andreas Werner,[6] Ronald Miletich,[3] Peter Weinberger,[1] Danny Müller,[1]* Michael Harasek[2]

[1] Institute of Applied Synthetic Chemistry, TU Wien, Getreidemarkt 9/163-AC, 1060 Vienna, Austria

[2] Institute of Chemical, Environmental & Biological Engineering, TU Wien, Getreidemarkt 9, 1060 Vienna, Austria

[3] Institut für Mineralogie und Kristallographie, University of Vienna, Althanstraße 14, (UZA 2), 1090 Vienna, Austria

[4] X-Ray Center, TU Wien, Getreidemarkt 9, 1060 Vienna, Austria

[5] Institute of Chemical Technologies and Analytics, TU Wien, Getreidemarkt 9/164, 1060 Vienna, Austria

[6] Institute for Energy Systems and Thermodynamics, TU Wien, Getreidemarkt 9/302, 1060 Vienna, Austria

danny.mueller@tuwien.ac.at

Abstract

Metal oxides providing various, reversibly accessible oxidation states are in the focus as auspicious materials for high-temperature thermochemical energy storage (TCES) materials. Among all principally suitable metal oxides due to equilibrium temperature and, in particular, reaction rate and reversibility, only the couple Co_3O_4 / CoO and to a smaller extend Mn_2O_3 / Mn_3O_4 are considered as suitable candidates. Based on recent studies on isothermal TCES-cycles, the impact of temperature and increased O_2-pressure on the reaction rate was investigated by varying the O_2-partial pressure in the low-temperature oxidation of the reduced oxide. Whereas Mn_3O_4 was found to react too slow for a process at lower temperatures, CoO was found suitable. For an increase of the O_2 pressure to 6 bar between 500 – 550 °C an attractive oxidation behavior was observed. At 900 °C Co_3O_4 / CoO could be cycled within 4.5 minutes between both oxidation states by changing the atmosphere from N_2 to O_2 and vice versa.

Keywords: cobalt oxide, manganese oxide, non-ambient pressure, in-situ powder X-Ray diffraction, thermochemical energy storage

1. Introduction

The different technologies suitable for thermal energy storage are defined according to the storage process as sensible (Dinker et al., 2015), latent (Zalba et al., 2003) and thermochemical heat storage (Abedin, 2011; Cot-Gores et al., 2012). The latter provides the highest storage densities and has the potential for loss-less storage, once the material was charged. The necessary smaller amounts of material – related to the higher storage densities compared to other techniques, – as well as the enormous applicational flexibility due to the large temperature range being tolerated, are additional advantages of this technique. (Yan, 2015)

The loss-less storage ability of thermochemical energy storage materials (TCES-materials) is an intrinsic feature, as no discharging of the storage occurs in the absence of the reactive gas. The broad operational temperature

doi:10.18086/swc.2017.14.02 Available at http://proceedings.ises.org

profile of TCES-materials is given by the equilibrium temperatures of the applied substance classes. By ranking the materials following to the involved reactive gases such as H_2O, NH_3, H_2, CO_2 or O_2, the field of application for TCES-materials ranges from low-temperature storage with temperatures below 100 °C (van Essen et al., 2009; Knoll et al., 2017) (mostly hydrated salts for *e.g.* civil engineering applications as in an energy self-sufficient building) to medium-temperature storage using ammoniates or hydrides and to temperatures between 800-1200 °C (T. Yan, 2015), using carbonates or oxides in combination with *e.g.* concentrating solar power plants. (Pardo et al., 2014)

Oxides suitable for TCES require several stable oxidation states of the metal, reversibly accessible via redox-reactions. During the charging of the storage material the metal is reduced, while discharging in the presence of O_2 leads to a restorage of the (initial) higher oxidation state (see equation 1).

$$M_xO_{y+n} + \Delta H \leftrightarrow M_xO_y + \frac{n}{2} O_2 \quad (1)$$

Although, metal oxides are investigated with respect to their thermochemical properties since the 80's, only a few suitable oxides are known due to the necessary reversibility of the redox-process. Candidate materials promising for application are the couple Co_3O_4 / CoO, as well as Mn_2O_3 / Mn_3O_4 considering reversibility, toxicity issues, temperature range and reaction time. A variety of studies was reported in particular for the cobalt system, covering cycle stability tests (Agrafiotis et al., 2014), composite materials, (Agrafiotis et al., 2016a), (Agrafiotis et al., 2015a; 2015b; Karagiannakis et al., 2016) materials optimization via spinel-phases (Babiniec et al., 2015; Block et al., 2014; LiuPrewitt, 1990), mechanical stress (Karagiannakis et al., 2016), etc. Although, Mn_2O_3 is also widely known for TCES purposes, (Carrillo, A. J. et al., 2014) due to the slower reaction kinetics, (Alonso et al., 2013; Chen et al., 2013) as well as the minor performance compared to the cobalt-system. Most efforts focussed on the dotation of Mn_2O_3 with iron (Carrillo, A. J. et al., 2015;Wokon et al., 2017), forming perovskites, or the combination with Co_3O_4 for a combined system. (Agrafiotis et al., 2016b)

Theoretically suitable metal oxides such as ZnO, (Palumbo, 2001) Fe_2O_3 or V_2O_5 feature equilibrium temperatures well above 1500 °C (Pardo et al., 2014), hampering both their routine investigation for storage processes, and their combination with conventional concentrating solar power plants. In order to expand the portfolio of redox-TCES materials, experimental approaches combining TCES with syngas production (Muthusamy et al., 2014), or the application of peroxide / oxide reactions (Carrillo, A. J. et al., 2016) were reported for energy storage in literature.

Apart from their potential of bridging non-operational times in concentrating power plants, the interest in oxidic TCES-materials relates mainly to their high storage density. Recently we could demonstrate (Müller et al., 2017), that between 830 - 930 °C a regime of coexistence between CoO and Co_3O_4, depending on the O_2-concentration, allows for isothermal TCES-cycles. Moreover, both CoO and Mn_3O_4 start oxidation under O_2-atmosphere already below 500 °C. Materials of high storage densities would be highly appreciated for applications around these temperatures. To enhance the reaction rate and obtain a material, which would combine fast reaction rates with high energy densities and a broad perspective of applicability, in the present study the impact of temperature on the isothermal redox-cycle, and the effect of an increased oxygen partial pressure on the oxidation rate was investigated by an *in-situ* powder diffraction (P-XRD) study.

2. Experimental

2.1 Material

Cobalt(II,III) oxide (99.995%), cobalt(II) oxide (99.99%), manganese(IV) oxide (99.99%) and manganese(II, III) oxide (97%) were obtained from Sigma-Aldrich and used as supplied.

2.2 X-Ray Powder Diffraction

The powder X-ray diffraction measurements were carried out on a PANalytical X'Pert Pro diffractometer in Bragg-Brentano geometry using Cu $K_{\alpha1,2}$ radiation and an X'Celerator linear detector with a Ni-filter. For *in-situ*

experiments at elevated pressures an Anton Paar XRK 900 reaction chamber, operable between ambient pressure and 12 bar was used. The sample was mounted on a hollow ceramic powder sample holder, allowing for complete perfusion of the sample with the reactive gas. The sample temperature is controlled directly via a NiCr-NiAl thermocouple and direct environmental heating. For the *in-situ* experiments at ambient pressure an Anton Paar HTK 1200N sample chamber was used. The sample temperature is controlled via a Pt 10 % RhPt thermocouple and direct environmental heating. The diffractograms were evaluated using the PANalytical program suite HighScorePlus v4.6a. (Degen et al., 2014) A background correction and a $K_{\alpha 2}$ strip were performed. Phase assignment is based on the ICDD-PDF4+ database ((http://www.icdd.com), the exact phase composition, shown in the conversion plots, was obtained via Rietveld-refinement incorporated in the program suite HighScorePlus v4.6a. (Degen et al., 2014) All quantifications based on P-XRD are accurate within of ±5 %.

2.3 Thermal Analysis

For thermal analysis of the redox-reactions a Netzsch TGA/DSC 449 C Jupiter ® equipped with a water vapour furnace including an air-cooled double jacket was used. The oven operates between 25 °C and 1250 °C, regulated by an S-type thermocouple. Oxygen and nitrogen gases were 99.999 % and obtained from Messer. For all measurements under air a mixture of 21 % O_2 and 79 % N_2 was applied. The gas flow was set to 25 ml min^{-1}, controlled and mixed with Vögtlin Instruments "red-y" mass flow controllers. A sample mass of 20 mg in an open Al_2O_3 crucible was used for all experiments with heating and cooling rates of 10 °C min^{-1}. The DSC was calibrated according to the procedure suggested by Netzsch, using the In, Sn, Bi, Zn, Al and Ag standards provided by the manufacturer.

2.4 Scanning Electron Microscopy

SEM images were recorded on gold coated samples with a Quanta 200 SEM instrument from FEI under low-vacuum at a water vapor pressure of 80 Pa to prevent electrostatic charging.

3. Results and Discussion

3.1 Isothermal oxidation of CoO triggered by variation of the reactive gas

Based on the previously identified window of coexistence between CoO and Co_3O_4, selected temperatures between 880 °C and 920 °C were chosen to determine the reaction rate by isothermal thermogravimetry / differential scanning calorimetry (TG / DSC). The isothermal reduction of Co_3O_4 under N_2 with subsequent oxidation by changing the atmosphere to O_2[*] was investigated at five temperature levels for each two cycles (figure 1).

[*] The redox-reaction of Co_3O_4 under gas-change conditions was confirmed to be highly comparable for 20 consecutive cycles (figure S1).

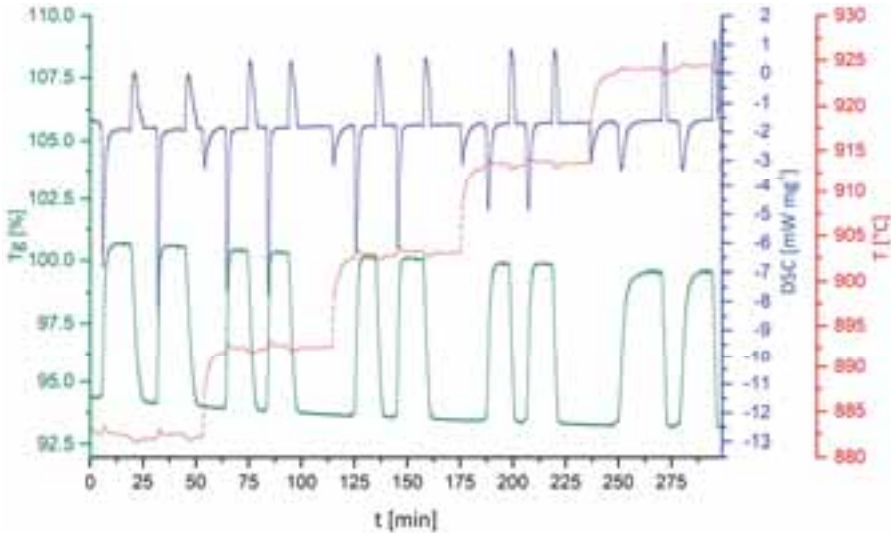

Fig. 1: TG / DSC of isothermal redox-cycles of Co_3O_4, triggered by variation of the atmosphere at 880, 890, 900, 910 and 920 °C. Reduction occurs under N_2-atmosphere, oxidation under O_2-atmosphere.

The averaged reaction times for reduction and oxidation, obtained from figure 1, are given in table 1.

Tab. 1: Average reaction times for isothermal reduction of Co_3O_4 (under N_2) and oxidation of CoO (under O_2), calculated from the differential scanning calorimetry data

	880 °C	**890 °C**	**900 °C**	**910 °C**	**920 °C**
Oxidation [min]	3.92 ± 0.40	3.35 ± 0.03	4.54 ± 0.11	4.95 ± 0.03	6.91 ± 0.28
Reduction [min]	7.07 ± 0.15	5.58 ± 0.05	4.62 ± 0.08	3.96 ± 0.08	3.41 ± 0.19

Except the spike for the oxidation time at 890 °C, an apparent linear correlation between reaction time and temperature is obtained. The oxidation time doubles with increased isothermal temperature almost nearly over the whole investigated temperature range, whereas the reduction time is exactly halved. Based on the herein obtained results the most suitable temperature for such an isothermal TCES-process is identified with 900 °C, where oxidation and reduction of the material are taking equal times.

The presented isothermal redox-cycling between 880 - 920 °C with the optimum at 900 °C represents a notable improvement regarding the earlier investigations, where oxidation was accomplished within 10.4 minutes at 848 °C and the complete reduction accounted for 23 minutes. (Müller et al., 2017)

3.2 Isothermal oxidation of CoO

The second objective of the current study on isothermal redox-reactions for thermochemical energy storage was the combination of low-temperature oxidation of CoO at around 500 °C under increased O_2-pressure. The isothermal oxidation under varied oxygen contents at ambient pressure was selected as a starting point. In order to compare the reactivity towards O_2 in the desired temperature regime, samples of CoO were oxidized at 500, 520 and 550 °C using an atmosphere with 21 % O_2 (synthetic air) and 100 % O_2.

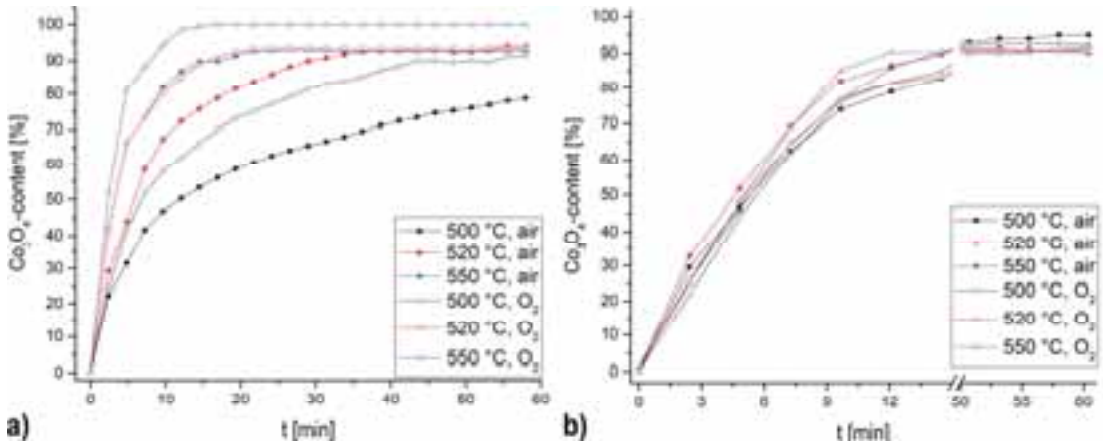

Fig. 2: Oxidation rate of CoO at several temperatures and O_2-concentrations for a) a CoO-sample obtained from thermal decomposition of Co_3O_4 under N_2 b) a commercial CoO sample

A concentrating plot of the different oxidation rates for CoO – obtained from Co_3O_4 by thermal reduction of the material under N_2 at 890 °C for 5 minutes – is shown in figure 2a. Especially for the series at 500 °C a notable difference in oxidation rate between the measurement under air and O_2 is found. The impact of the O_2 concentration with increasing temperature is superimposed by the thermal contribution, leading to a nearly identical oxidation rate observed in the experiments at 520 °C under O_2 and 550 °C under air.

In principle both a Co_3O_4 initially reduced to CoO and a CoO prepared on an industrial scale should be feasible for a Co-based TCES process. For comparison, the same series of oxidation experiments was repeated using a commercial sample of CoO (figure 2b). Interestingly, a completely different picture is observed in this case. The chemically identical sample provides much faster oxidation rates with conversions above 80 % under all applied conditions within the first 15 minutes. The reason for this behavior was found in the SEM-images of both precursors, showing for the Co_3O_4 (figure 3a) large sintered agglomerates, whereas the CoO (figure 3b) consisted of small, isolated particles. The different O_2-concentrations, as well as the various temperatures, have no impact on the initial particle morphology (see figure S2).

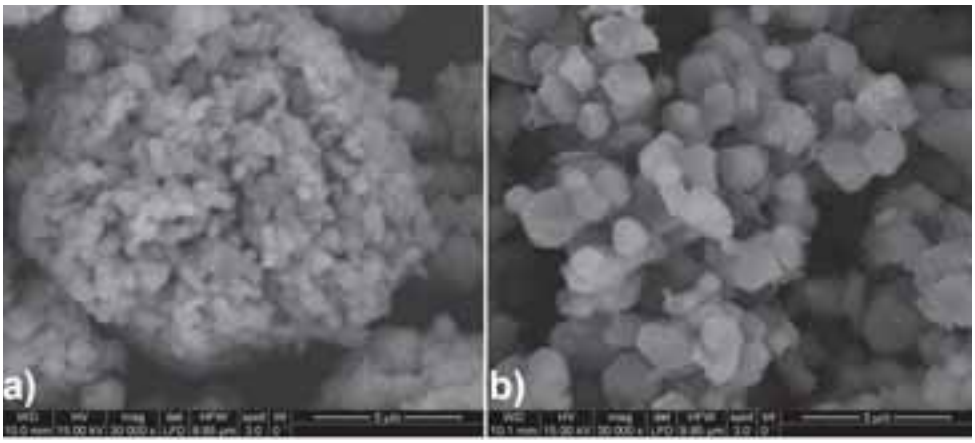

Fig. 3: SEM-images of a) commercial Co_3O_4 b) commercial CoO. Image size 9 x 9 µm

3.3 Isothermal oxidation of CoO under elevated O_2 pressure

In order to facilitate investigations on the impact of an increased oxygen pressure, which is higher than the atmospheric one, Co_3O_4 that has been *in-situ* reduced under N_2 was used for the experimental approach. Although, the commercial CoO sample would provide faster reaction rates, no reliable results would have been obtained even with a high-end laboratory P-XRD setup.†

The oxidation rates for the experiments under ambient pressure, 3 bar and 6 bar O_2‡ are shown in figure 4, which reveals a rate-enhancing effect of the increased O_2 pressure for all three temperature levels. Obviously, the largest influence on the oxidation is observed for 500 °C (figure 4a). By applying 3 bar O_2 the conversion within the first 15 minutes is enhanced about 20 %. 6 bar O_2 result in a quantitative Co_3O_4 formation after 30 minutes, the reaction rate being only slightly faster than for 3 bar.

In case of the series at 520 °C, O_2 oxidation under ambient pressure and 3 bar O_2 reveal only slight differences in the reaction rate. At 6 bar O_2 an increased oxidation within the first 6 minutes leads to quantitative Co_3O_4 formation after 15 minutes. Finally, at 550 °C the temperature increase predominates over the increased pressure, as both 3 bar and 6 bar O_2 yield a complete oxidation - 3 bar after 12 minutes, 6 bar after 8 minutes.

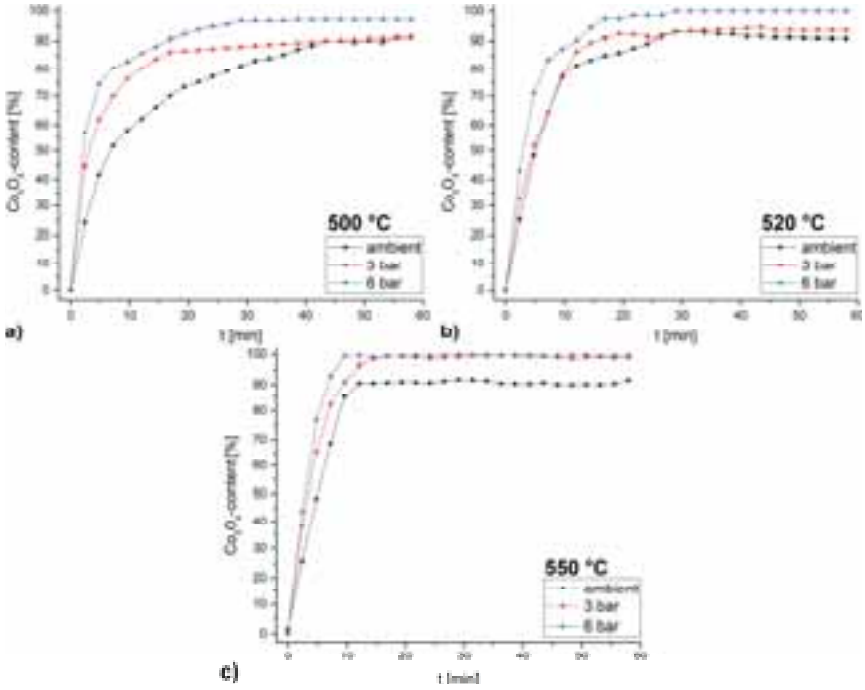

Fig. 4: Oxidation rate of CoO at different pressures and temperatures at a) 500 °C b) 520 °C c) 550 °C

Based on these results a lower oxidation temperature for CoO in a TCES-process seems feasible, increasing the reaction rate by moderately enhanced pressure. For technological processes elevated pressure is always correlated with much higher expenditures regarding the process design. Using only 6 bar O_2 – for all three temperatures yielding a notable enhancement of the conversion rate – may be still worth the efforts aiming for an oxide-based

† This limitation – also slightly affecting the accuracy of the phase-determination for the high Co_3O_4-contents – is attributed to the overlap of significant peaks in the diffractograms of the two Co-phases, as well as the high fluorescence of the Co-containing samples in combination with the available Cu K_α-radiation (see figure S3). To ensure the data quality, a minimum measurement time of 2 minutes per diffractogram was necessary.

‡ Although, the used Anton Paar XRK 900 would tolerate pressures up to 12 bar, applying a higher pressure than 6 bar O_2 extends due to radiation absorption and the fluorescence background the measurement time notably, so within one diffractogram the transformation from CoO to Co_3O_4 is completed. For similar measurements under higher pressures a different X-Ray source or a synchrotron would be needed.

medium-temperature TCES-process.

The only drawback of the increased pressure is the promoted sintering of the material, which is already evidenced in the SEM-images of the Co_3O_4 samples, oxidized at 550 °C and various pressures (see figure 5). Nevertheless, this changed particle morphology so far was not found to decrease the reactivity of the material on repeated cycling.

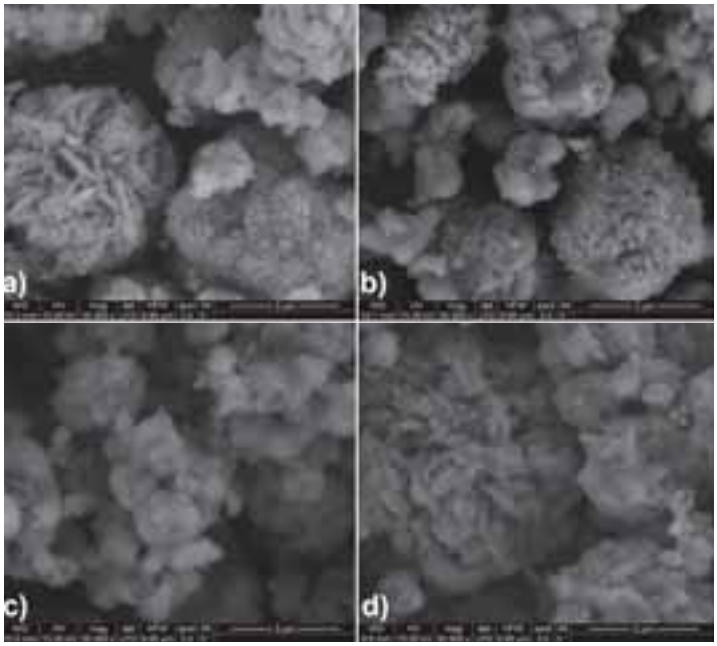

Fig. 5: Particle morphology of Co_3O_4 after oxidation at 550 °C and varied O_2 pressures a) Co_3O_4 starting material b) ambient pressure c) 3 bar O_2 d) 6 bar O_2. Image size 9 x 9 µm

3.4 Isothermal oxidation of Mn_3O_4

Similar to the study on the isothermal oxidation of CoO, a series was carried out also on Mn_3O_4 which was oxidized at different temperatures (470 °C, 500 °C, 520 °C, 550 °C) and ambient pressure under synthetic air and pure oxygen (figure 6).

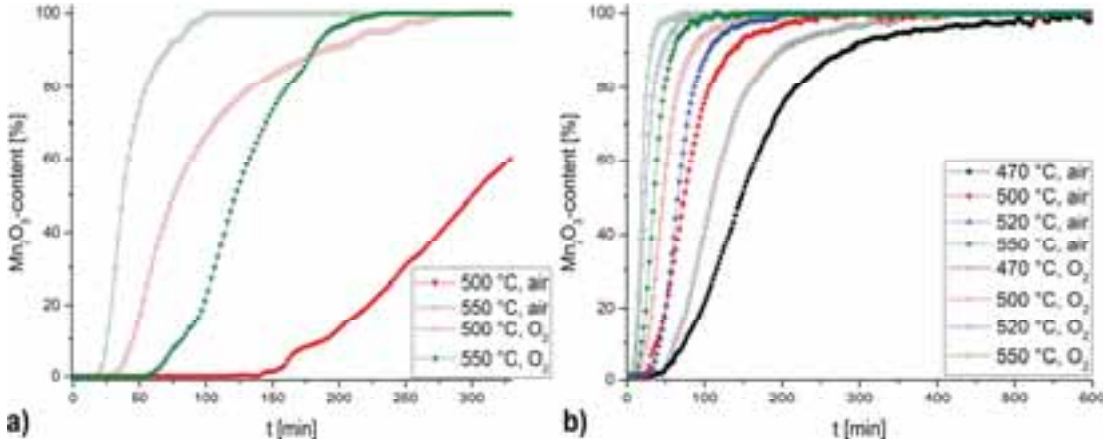

Fig. 6: Oxidation rate of Mn_3O_4 at various temperatures and O_2-concentrations for a) a Mn_3O_4-sample obtained from thermal decomposition of MnO_2 under N_2 b) a commercial Mn_3O_4 sample

Similar to the Co-system also for Mn_3O_4 a notable difference between the *in-situ* reduced sample under N_2 (figure 6a) and the commercially obtained Mn_3O_4 (figure 6b) was found. For the freshly reduced Mn_3O_4 at 500 °C under

air within 330 minutes only 62 % of Mn_2O_3 are formed, whereas O_2 enables complete conversion to Mn_2O_3. Still a notable difference is observed at 550 °C, where both air and O_2 result in complete re-oxidation.

In the case of the commercial Mn_3O_4 a clear trend towards faster oxidation rates, both with increased temperature and O_2-content is found. Similar to CoO also for Mn_3O_4 temperature increases the oxidation rate more efficiently than a higher O_2 concentration. Comparable oxidation rates in this case are found at 550 °C under air and 520 °C under O_2.

4. Conclusion

In the present study the redox-couple Co_3O_4 / CoO was investigated with respect to an isothermal redox-cycle, triggered by changing the atmosphere from N_2 to O_2 between 880 – 920 °C. A reasonably linear correlation was found between the reduction / oxidation times and the applied temperature. Within the investigated temperature range the best conditions for an isothermal redox-cycle were found at 900 °C, as both reduction and oxidation take place quantitatively within 4.5 minutes. This represents an improvement of the so far reported results on isothermal cycling.

Based on former results an isothermal low-temperature oxidation of CoO between 500-550 °C under increased O_2-pressure was attempted, allowing for the application (only discharging) of a TCES-material featuring a high energy density at medium-temperatures. Increasing the O_2-pressure during oxidation from ambient conditions to 6 bar resulted in an attractive increase of reaction rate, discharging the CoO (oxidation to Co_3O_4) quantitatively at 500 °C within 24 minutes, at 550 °C within 8 minutes.

Elevated pressures during the oxidation process allow for a shift of the discharging reaction towards lower temperatures. This enables the application of the *per se* attractive high energy density of metal-oxide redox-reactions at temperatures, where they so far could not be operated, as the oxidation (discharging) required higher temperatures. This could be attractive for complementing an existing process with thermochemical energy storage, when pressurized air / oxygen is already available, or when a storage material with high energy density and a fast reaction rate is required at lower temperatures.

Mn_3O_4 was found to be too slow in its oxidation under all investigated conditions to be competitive in comparison to CoO.

5. References

1. Dinker, A., M. Agarwal, and G.D. Agarwal, 2015. Heat storage materials, geometry and applications: A review. Journal of the Energy Institute
2. Zalba, B., et al., 2003. Review on thermal energy storage with phase change: materials, heat transfer analysis and applications. Applied Thermal Engineering 3, 251-283.
3. Ali H. Abedin, M.A.R., 2011. A Critical Review of Thermochemical Energy Storage Systems. The Open Renewable Energy Journal 42-46.
4. Cot-Gores, J., A. Castell, and L.F. Cabeza, 2012. Thermochemical energy storage and conversion: A-state-of-the-art review of the experimental research under practical conditions. Renewable and Sustainable Energy Reviews 7, 5207-5224.
5. T. Yan, R.Z.W., T. X. Li, L.W.Wang, Ishugah T. Fred, 2015. A review of promising candidate reactions for chemical heat storage. Renewable and Sustainable Energy Reviews 13-31.
6. van Essen, V.M., et al., 2009. Characterization of Salt Hydrates for Compact Seasonal Thermochemical Storage. 825-830.
7. Knoll, C., et al., 2017. Probing cycle stability and reversibility in thermochemical energy storage – $CaC_2O_4 \cdot H_2O$ as perfect match? Applied Energy 1-9.
8. Pardo, P., et al., 2014. A review on high temperature thermochemical heat energy storage. Renewable and Sustainable Energy Reviews 591-610.
9. Agrafiotis, C., et al., 2014. Exploitation of thermochemical cycles based on solid oxide redox systems for thermochemical storage of solar heat. Part 1: Testing of cobalt oxide-based powders. Solar Energy 189-211.
10. Agrafiotis, C., et al., 2016a. Exploitation of thermochemical cycles based on solid oxide redox systems for thermochemical storage of solar heat. Part 5: Testing of porous ceramic honeycomb and foam

cascades based on cobalt and manganese oxides for hybrid sensible/thermochemical heat storage. Solar Energy 676-694.
11. Agrafiotis, C., et al., 2015a. Exploitation of thermochemical cycles based on solid oxide redox systems for thermochemical storage of solar heat. Part 2: Redox oxide-coated porous ceramic structures as integrated thermochemical reactors/heat exchangers. Solar Energy 440-458.
12. Agrafiotis, C., et al., 2015b. Exploitation of thermochemical cycles based on solid oxide redox systems for thermochemical storage of solar heat. Part 3: Cobalt oxide monolithic porous structures as integrated thermochemical reactors/heat exchangers. Solar Energy 459-475.
13. Karagiannakis, G., et al., 2016. Cobalt/cobaltous oxide based honeycombs for thermochemical heat storage in future concentrated solar power installations: Multi-cyclic assessment and semi-quantitative heat effects estimations. Solar Energy 394-407.
14. Babiniec, S.M., et al., 2015. Investigation of LaxSr1−xCoyM1−yO3−δ (M=Mn, Fe) perovskite materials as thermochemical energy storage media. Solar Energy 451-459.
15. Block, T., N. Knoblauch, and M. Schmücker, 2014. The cobalt-oxide/iron-oxide binary system for use as high temperature thermochemical energy storage material. Thermochimica Acta 25-32.
16. Liu, X. and C. Prewitt, 1990. High-temperature X-ray diffraction study of Co_3O_4: Transition from normal to disordered spinel. Physics and Chemistry of Minerals 2,
17. Carrillo, A.J., et al., 2014. Thermochemical heat storage based on the Mn_2O_3/Mn_3O_4 redox couple: influence of the initial particle size on the morphological evolution and cyclability. J. Mater. Chem. A 45, 19435-19443.
18. Alonso, E., et al., 2013. Kinetics of Mn_2O_3–$Mn_3O_4$and Mn_3O_4–MnO Redox Reactions Performed under Concentrated Thermal Radiative Flux. Energy & Fuels 8, 4884-4890.
19. Chen, S., et al., 2013. Synthesis of Mn_2O_3 microstructures and their energy storage ability studies. Electrochimica Acta 360-371.
20. Carrillo, A.J., et al., 2015. Improving the Thermochemical Energy Storage Performance of the Mn_2O_3/Mn_3O_4 Redox Couple by the Incorporation of Iron. ChemSusChem 11, 1947-1954.
21. Wokon, M., A. Kohzer, and M. Linder, 2017. Investigations on thermochemical energy storage based on technical grade manganese-iron oxide in a lab-scale packed bed reactor. Solar Energy 200-214.
22. Agrafiotis, C., M. Roeb, and C. Sattler, 2016b. Exploitation of thermochemical cycles based on solid oxide redox systems for thermochemical storage of solar heat. Part 4: Screening of oxides for use in cascaded thermochemical storage concepts. Solar Energy 695-710.
23. Möller, S. and R. Palumbo, 2001. The Development of a Solar Chemical Reactor for the Direct Thermal Dissociation of Zinc Oxide. Journal of Solar Energy Engineering 2, 83.
24. Muthusamy, J.P., N. Calvet, and T. Shamim, 2014. Numerical Investigation of a Metal-oxide Reduction Reactor for Thermochemical Energy Storage and Solar Fuel Production. Energy Procedia 2054-2057.
25. Carrillo, A.J., et al., 2016. Revisiting the BaO_2/BaO redox cycle for solar thermochemical energy storage. Phys. Chem. Chem. Phys. 11, 8039-8048.
26. Müller, D., et al., 2017. Combining in-situ X-ray diffraction with thermogravimetry and differential scanning calorimetry – An investigation of Co_3O_4, MnO_2 and PbO_2 for thermochemical energy storage. Solar Energy 11-24.
27. Degen, T., et al., 2014. The HighScore suite. Powder Diffraction S2, S13-S18.
28. http://www.icdd.com,

6. Appendix

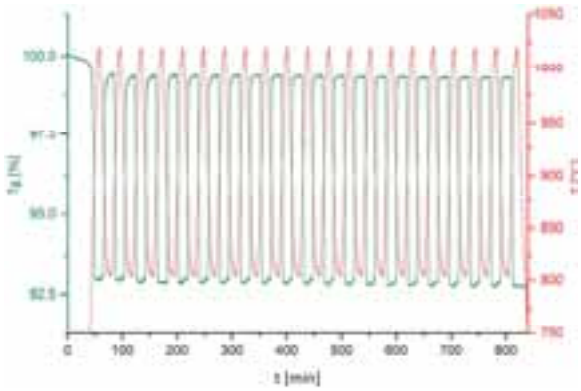

Fig. S1: 20 consecutive redox-cycles of Co_3O_4 under alternating atmosphere (N_2 vs. O_2)

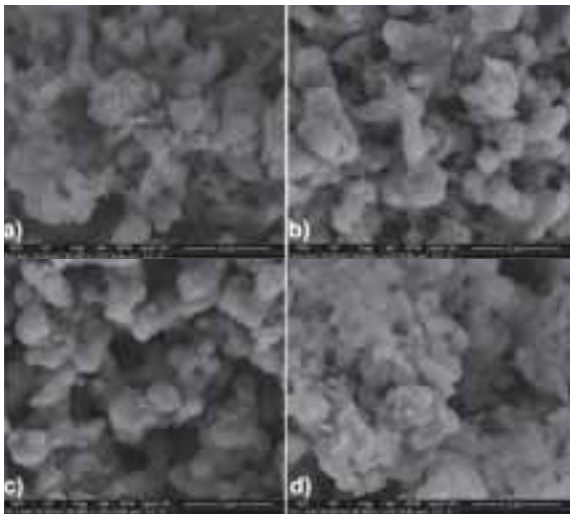

Fig. S2: SEM images of different Co_3O_4 samples after the oxidation in the P-XRD a) CoO after oxidation under air at 500 °C b) CoO after oxidation under air at 550 °C c) CoO after oxidation under O_2 at 500 °C d) CoO after oxidation under O_2 at 550 °C. Image size 9 x 9 µm

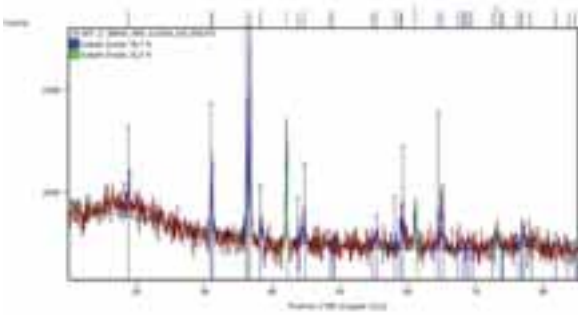

Fig. S3: P-XRD of a mixed CoO / Co_3O_4 sample, showing the moderate signal-to-noise ratio for the weaker peaks due to the X-Ray fluorescence of Co

Thermo-physical properties of NaCl – Na_2CO_3 – NaOH as a high-temperature sensible heat storage medium

Gowtham Mohan, Mahesh Venkataraman and Joe Coventry

Research school of engineering, Australian National University, Canberra (Australia)

Abstract

A novel ternary salt mixture composed of sodium chloride, sodium carbonate and sodium hydroxide (Na-Cl-CO_3-OH) was developed for high-temperature sensible thermal energy storage (HTSTES) application. The melting point and the heat capacity of the Na-Cl-CO_3-OH mixture was measured using a differential scanning calorimeter. The final melting temperature of the blend was estimated as 347.3°C. The average heat capacity of the blend was calculated as 1.50 J g^{-1} K^{-1} by following the ASTM standard E1269. The mass loss of the molten salt mixture was studied up to 1000°C using a thermogravimetric analyser in three different atmospheres, and the salt was found to be stable over 700°C. In terms of cost, Na-Cl-CO_3-OH mixture costs approximately 4.5 USD/kWh, around 60% less than the commercial "solar salt" nitrate salt mixture.

Keywords: Molten salt, sensible energy storage, thermophysical properties, mixed-anion.

1. Introduction

Thermal energy storage (TES) plays a vital role in the effective and efficient use of concentrated solar power (CSP) to provide steady output and meet intermittent electricity demands. The storage media is the most important component in any thermal energy storage (TES) system (Kuravi et al., 2013). Molten salts are extensively used thermal storage media and heat transfer fluid (HTF) in CSP plants due to their favourable thermo-physical properties. Current state-of-the-art CSP plants utilise "solar salt" (60 wt. % $NaNO_3$ – 40 wt. % KNO_3) and HITEC salt (53 wt. % KNO_3 – 40 wt. % $NaNO_2$ – 7 wt. % $NaNO_3$) for TES due to their acceptably low melting point and reasonable heat capacity (Ushak et al., 2015). Several recent CSP research programs have focused on developing high-temperature, and high-efficiency CSP plants incorporating advanced power cycles such as the supercritical Rankine, supercritical CO_2, and air-Brayton cycles. Selection of the HTF and TES media plays a crucial role in developing a modern CSP plant. The current generation molten salts (solar salt and HITEC) decompose around 600°C, which is insufficient for high-temperature power cycles (Gil et al., 2010; Kenisarin, 2010; Medrano et al., 2010), although a slight extension in the operating temperature is possible with meticulous atmospheric control (Olivares, 2012). Thus, development of new high-temperature molten salts with high thermal stability, specific heat capacity, reasonable melting point, and low cost is vital to support advanced power cycles. For the operating temperature range between 500°C and 700°C, mixtures of carbonates, chlorides, fluorides and hydroxides can potentially be exploited for high temperature sensible thermal energy storage (HTSTES). Several researchers attempted to develop HTSTES molten salt mixtures with carbonates (Olivares et al., 2012; Wu et al., 2011), chlorides (Wei et al., 2015), fluorides (Forsberg et al., 2007), and also mixed anions (Wang et al., 2015). Most of these mixtures had one or all of the following issues: (i) high melting point, (ii) low heat capacities, and (iii) an expensive salt component.

In this research work, a ternary salt mixture with a mixed anion configuration, and sodium (Na) cation (NaCl – Na_2CO_3 – NaOH), was developed based on the FactSage prediction reported by Gomez (Gomez, 2011) for latent heat storage. To the best of the authors' knowledge, this mixture has not been investigated as a sensible heat storage media. In this research work, we assume the thermal storage system is in the 'two-tank' configuration, as shown schematically in Figure 1. Note, Figure 1 includes a heat exchanger between the storage tank and the receiver, which allows for a separate heat transfer fluid (HTF) in the receiver (such as sodium). This particular mixture is interesting for HTSTES because of three important factors: firstly, low predicted melting point with inexpensive materials; secondly, the use of sodium (Na^+) as the cation for all three salts, which allows compatibility with an elemental sodium HTF for direct-contact heat exchange (Venkataraman, 2017); and finally, presence of large proportion of NaOH augments the specific heat capacity of the molten salt mixture. The key thermo-physical properties, such as, melting point, heat capacity, and thermal stability of this

doi:10.18086/swc.2017.14.03 Available at http://proceedings.ises.org

ternary mixture were experimentally determined, and its commercial suitability for HTSTES application has been assessed.

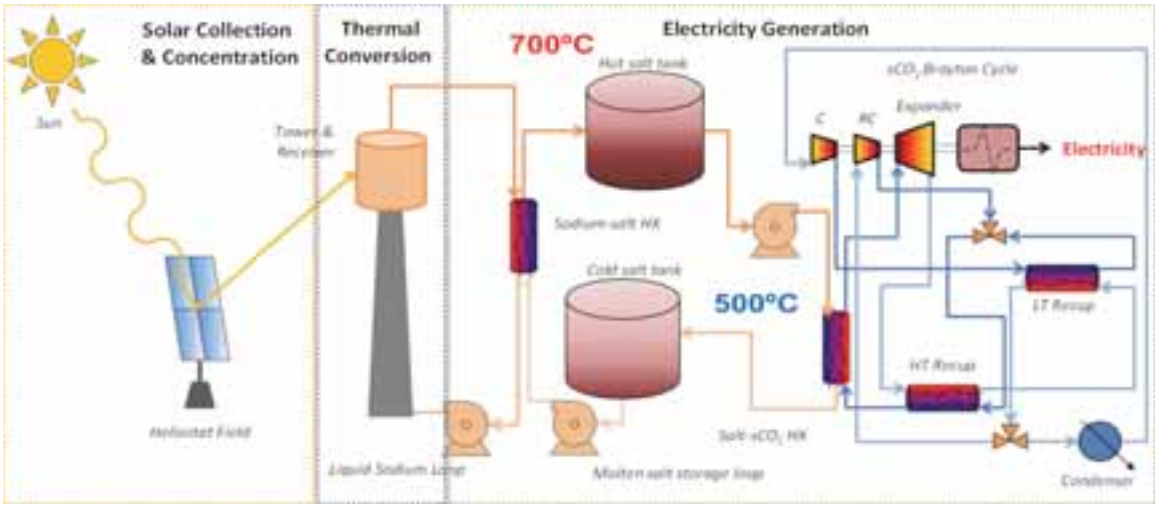

Fig. 1: Schematic diagram of proposed next-gen two-tank CSP power plant

2. Experimental procedure

A ternary mixture of NaCl – Na_2CO_3 – NaOH (Na-Cl-CO_3-OH) (mass ratio- 24.68:15.67:59.65) was synthesised. The three salts — NaCl (>99% purity, ACS grade), Na_2CO_3 (>99.5% purity, ACS grade), and NaOH (>98% purity) — were procured from Alfa Aesar and stored under nitrogen flow to avoid moisture absorption. The salt components were weighed in proportion to the FactSage prediction, then blended by hand-grinding inside a glove box using a mortar and pestle for 30 min.

The ground mixture was used directly in a Netzsch Pegasus DSC 404 to determine the melting point and heat capacity. Graphite crucibles with lids were utilised for the DSC experiments to attain faster heat transfer into the salt mixtures. The melting point and heat capacity measurements were conducted using SiC and Pt-Rd furnaces respectively at a heating/cooling rate of 10 °C/min and 20 °C/min respectively with 50 ml/min of nitrogen purge. The heat capacity of the sample was determined by following ASTM standard E1269 with a sapphire disk as the reference.

The mass loss of the salt mixture was tested using a Q600 SDT TG/DSC (TA instruments). Experiments were conducted from room temperature to 1000°C at a heating rate of 10°C/min in three different atmospheres (nitrogen, argon and air), at a flow rate of 50 mL/min. Each sample of about 5-10 mg was placed into an 85 μL alumina crucible and covered with a perforated lid.

3. Results and discussions

3.1. Determination of melting point

The melting point of the Na-Cl-CO_3-OH mixture was predicted as 320°C by FactSage. Fig. 1(a) shows the DSC curve with onset and peak melting temperatures, and multiple endothermic peaks suggesting that the mixture is off-eutectic. It is evident from Fig. 2 that complete melting of the ternary mixture takes place around 347.3°C. The freezing of the salt mixture begins at 325°C, and this difference between the melting and freezing temperatures is due to sub cooling. Four continuous heating and cooling cycles were run for each sample. The fusion between the salts in the mixture was achieved during the first heating cycle, and the melting point determined from the three subsequent cycles.

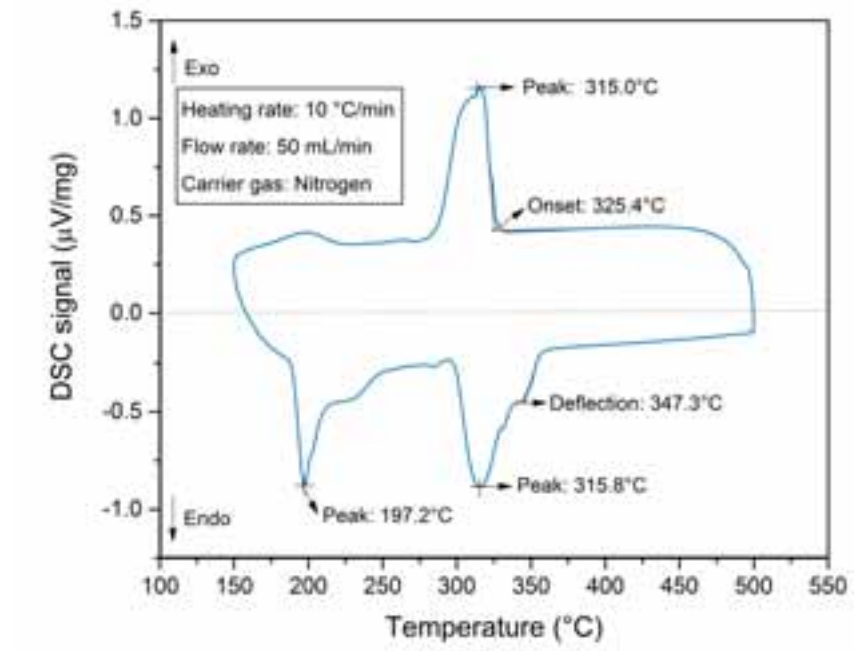

Fig. 2: Melting point analysis of Na-Cl-CO_3-OH mixture in a nitrogen atmosphere

3.2. Heat capacity measurement

The experimental measurement of specific heat capacity, c_p in the DSC followed the ASTM E1269 standard with a sapphire disk as the reference. The specific heat capacity measurement method was validated by correlating the heat capacity values obtained for a unary salt (NaCl) with the theoretical values (Chase-Jr, 1998) in the temperature range 400 – 600°C. The maximum variation between the experimental and theoretical values was less than ±2%, as presented in Fig. 3. The heat capacity of the mixed anion ternary was measured above the liquidus temperature between 450 and 600°C as shown in Fig. 4. The experiments were conducted in a nitrogen atmosphere at 50 mL/min, and measured over 10 heating-cooling cycles. The average heat capacity of the mixture is 1.508±0.005 J g^{-1} K^{-1}, which is similar to the commercial 'solar salt' mixture. Values for average specific heat capacity is first averaged across all 10 cycles, and then averaged across the measurement temperature range. The error value (±0.005) is the standard deviation from the mean of the temperature averaged values across the 10 heat capacity measurements. The liquid heat capacity values (J g^{-1} K^{-1}) of Na-Cl-CO_3-OH are fitted into a polynomial function for convenience of use. Polynomial regression is used to fit curves to the c_p data with good agreement, and therefore, within the nominated temperature ranges, specific heat capacity can be taken as follows:

$$c_p = aT^3 + bT^2 + cT + d \quad (1)$$

where temperature T is the salt temperature in °C and the coefficients are given in Table 1. The R^2 value from the regression analysis is also given.

Tab. 1: Polynomial coefficients for the heat capacity

Mixture	Validity	a	b	c	d	R^2
NaCl – Na_2CO_3 – NaOH	455 – 600	$-3E^{-7}$	0.000516	0.281139	52.45630	0.972

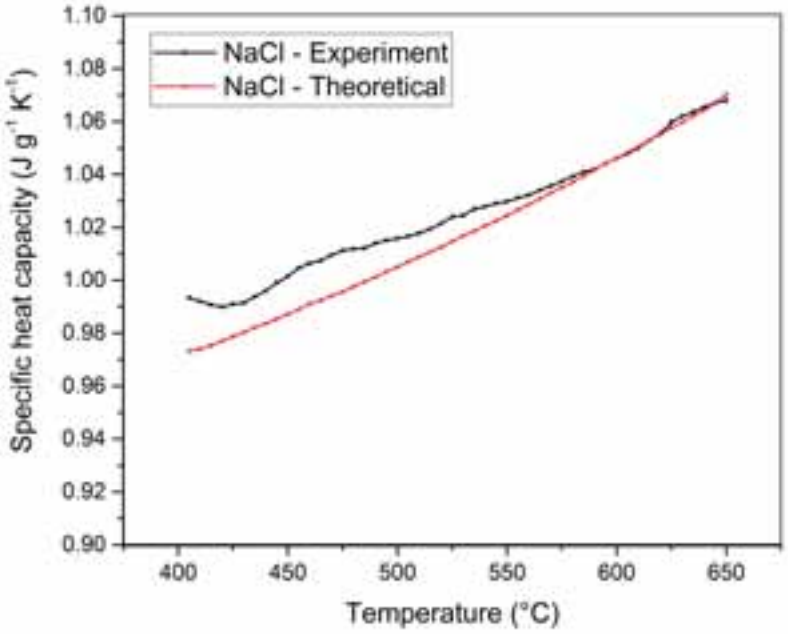

Fig. 3: Validation of heat capacity measurement with NaCl

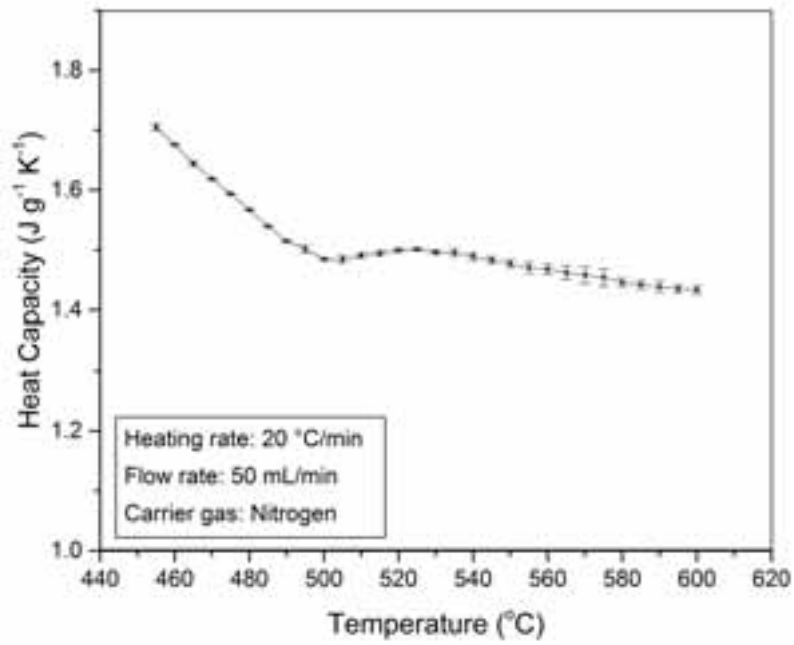

Fig. 4: Heat capacity measurement of Na-Cl-CO_3-OH mixture in a nitrogen atmosphere

3.3. Mass loss testing of the ternary mixture

Both thermal stability and mass loss due to vaporisation of the molten salt are important considerations for solar thermal application. Here we distinguish between the physical decomposition of the salt (thermal stability) and mass loss due to vaporisation caused by high vapour pressure. The mass loss of the salt mixture was measured in three different atmospheres with a flow rate of 50 mL/min using the DSC-TGA equipment. The experiments were conducted up to 1000°C from room temperature as shown in Fig. 3. An initial mass loss is observed due to evaporation of absorbed moisture during sample loading process. The tested salt mixture showed excellent stability over 700°C in inert atmospheres. In the presence of air, the ternary mixture reacts and increases in mass as shown in Fig. 5. This may be due to the interaction between NaOH and CO_2, leading to the formation of Na_2CO_3 (Zeman, 2007). Fig. 6 shows that pure liquid NaOH reacts with air at higher temperatures, causing a

change in mass, which reaffirms the previous statement. It is evident from the tests, that the Na-Cl-CO_3-OH mixture shows promising thermal stability as a HTSTES media for modern high-temperature CSP plants.

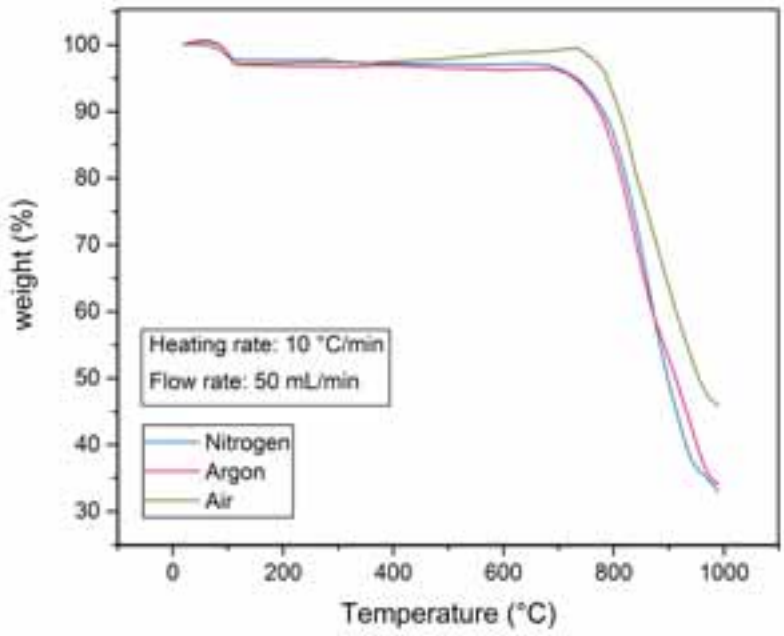

Fig. 5: Thermal stability of ternary mixture in three atmospheres

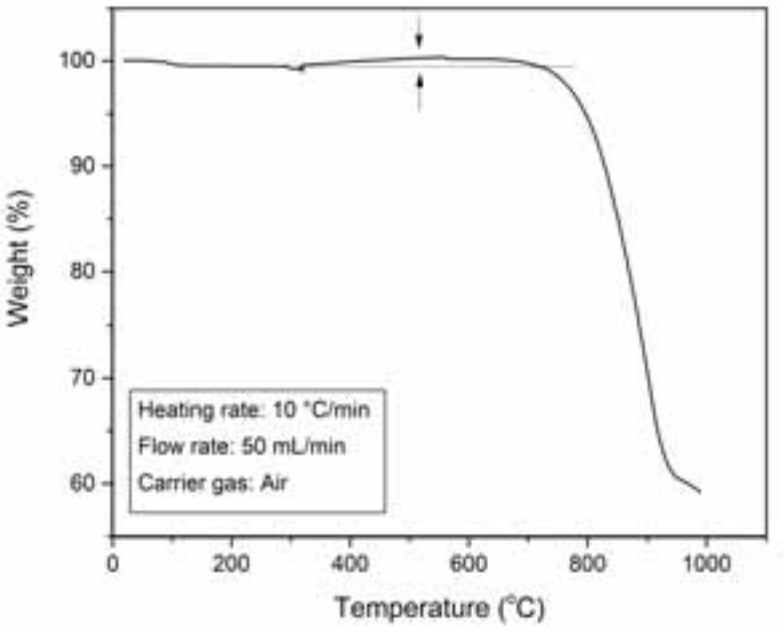

Fig. 6: Thermal stability of NaOH in air

3.3. Economic analysis

The cost of the storage media is one of the important parameter in the selection process. The costs of individual salt components considered in the study, as well as the reference case 'solar salt', are shown in Table 2. All the values shown in the table are adjusted to December 2016 currency using the PPI (producer price index) commodity data for industrial chemicals provided by Bureau of Labor Statistics (BLS) (BLS, 2016). The cost of each salt mixtures was calculated in terms of USD/tonne and USD/kWh, assuming operating temperature range between 500°C and 700°C. Prices were obtained from industrial suppliers. The total cost of the salt mixture was 390 USD/tonne and 4.5 USD/kWh, which is approximately 60% cheaper than the 'solar salt'.

Tab. 2: Cost of individual salts, as in Dec 2016. PPI: average Purchaser Price Index provided by (BLS, 2016)

Material	Cost (USD/tonne)	Source
NaCl	49	52 USD/tonne in Mar'16 (Industrial minerals, 2016). PPI = -6%
Na_2CO_3	324	320 USD/tonne in Sep'15 (Industrial minerals, 2016). PPI = 1%
NaOH	550	550 USD/tonne in Dec'16 (Alibaba, 2016)
Solar Salt	950	950 USD/tonne in Dec'16 (SQM, 2016)

4. Conclusion

The current state-of-the-art storage media decomposes around 600°C, and there is therefore a need for new storage media with thermal stability over 700°C to support modern high-efficiency CSP plants. In this research work, a new ternary mixture was developed and its thermo-physical properties evaluated for HTSTES applications. The molten salt mixture displayed acceptable melting point (<350°C), good heat capacity (1.50 $J\ g^{-1}\ K^{-1}$) and excellent thermal stability (>700°C). Most importantly, the ternary mixture was more economical (4.5 USD/kWh) that the nitrate 'solar salt' blend used in many current CSP plants. The experimental results indicate that Na-Cl-CO_3-OH mixture is a promising candidate for future HTSTES applications. The corrosion behaviour of containment materials and interacting surfaces is an important issue which needs to be addressed, before this mixed anion salt mixture can be recommended for use in high-temperature CSP systems.

5. References

Alibaba, December 2016 (www.alibaba.com).
Industrial Minerals, March 2016 (www.indimin.com).
Personal communication from SQM Europe M.V, December 2016.
PPI Commodidy Data for industrial chemicals, Bureau of Labor Statistics (URL: www.data.bls.gov).
Chase-Jr, M.W., 1998. NIST-JANAF Thermochemical Tables. Journal of Physical and Chemical Reference Data Fourth Edition(Monograph 9), 1-1951.
Forsberg, C.W., Peterson, P.F., Zhao, H., 2007. High-Temperature Liquid-Fluoride-Salt Closed-Brayton-Cycle Solar Power Towers. Journal of Solar Energy Engineering 129(2), 141.
Gil, A., Medrano, M., Martorell, I., Lázaro, A., Dolado, P., Zalba, B., Cabeza, L.F., 2010. State of the art on high temperature thermal energy storage for power generation. Part 1—Concepts, materials and modellization. Renewable and Sustainable Energy Reviews 14(1), 31-55.
Gomez, J.C., 2011. High-Temperature Phase Changer Materials (PCM) Candidates for Thermal Energy Storage (TES) Applications. National Renewable Energy Laboratory NREL/TP-5500-51446.
Kenisarin, M.M., 2010. High-temperature phase change materials for thermal energy storage. Renewable and Sustainable Energy Reviews 14(3), 955-970.
Kuravi, S., Trahan, J., Goswami, D.Y., Rahman, M.M., Stefanakos, E.K., 2013. Thermal energy storage technologies and systems for concentrating solar power plants. Progress in Energy and Combustion Science 39(4), 285-319.
Medrano, M., Gil, A., Martorell, I., Potau, X., Cabeza, L.F., 2010. State of the art on high-temperature thermal energy storage for power generation. Part 2—Case studies. Renewable and Sustainable Energy Reviews 14(1), 56-72.
Olivares, R.I., 2012. The thermal stability of molten nitrite/nitrates salt for solar thermal energy storage in different atmospheres. Solar Energy 86(9), 2576-2583.
Olivares, R.I., Chen, C., Wright, S., 2012. The Thermal Stability of Molten Lithium–Sodium–Potassium Carbonate and the Influence of Additives on the Melting Point. Journal of Solar Energy Engineering 134(4), 041002-041002.
Ushak, S., Fernández, A.G., Grageda, M., 2015. Using molten salts and other liquid sensible storage media in thermal energy storage (TES) systems. 49-63.
Venkataraman, M., Mohan, G., Coventry, J., Buoyancy-driven direct contact heat exchange between a sodium HTF and a molten salt storage media for solar thermal application, SolarPACES 2017, Santiago, Chile.
Wang, T., Mantha, D., Reddy, R.G., 2015. Novel high thermal stability LiF–Na2CO3–K2CO3 eutectic ternary system for thermal energy storage applications. Solar Energy Materials and Solar Cells 140, 366-375.

Wei, X., Song, M., Wang, W., Ding, J., Yang, J., 2015. Design and thermal properties of a novel ternary chloride eutectics for high-temperature solar energy storage. Applied Energy 156, 306-310.
Wu, Y.-t., Ren, N., Wang, T., Ma, C.-f., 2011. Experimental study on optimized composition of mixed carbonate salt for sensible heat storage in solar thermal power plant. Solar Energy 85(9), 1957-1966.
Zeman, F., 2007. Energy and material balance of CO_2 capture from ambient air, Environmental Science and Technology, 41, 7558-7563.

Lab-scale demonstration of thermochemical energy storage with NH_3 and impregnated-loaded zeolites

Danny Müller,[1*] Christian Knoll,[1,2] Georg Gravogl,[1,3] Andreas Werner,[4] Michael Harasek,[2] Ronald Miletich,[3] Peter Weinberger[1]

[1] Institute of Applied Synthetic Chemistry, TU Wien, Getreidemarkt 9/163-AC, 1060 Vienna, Austria

[2] Institute of Chemical, Environmental & Biological Engineering, TU Wien, Getreidemarkt 9, 1060 Vienna, Austria

[3] Institut für Mineralogie und Kristallographie, University of Vienna, Althanstraße 14, 1090 Vienna, Austria

[4] Institute for Energy Systems and Thermodynamics, TU Wien, Getreidemarkt 9/302, 1060 Vienna, Austria

danny.mueller@tuwien.ac.at

Abstract

High energy densities are one key-feature of thermochemical energy storage materials. Among the substance classes featuring the highest energy densities are oxides and carbonates, having both operational temperature profiles between 800 °C - 1200 °C. Comparable high energy contents are provided by the reaction between ammonia and (transition) metal salts, operable in a medium-temperature range between 150 °C - 450 °C. Due to the toxicity of ammonia a closed cycle preventing the release of ammonia to the surrounding environment would be necessary.

Herein, $CuSO_4$ and $CuCl_2$ are investigated in a laboratory scale reactor for their application in thermochemical energy storage with ammonia as reactive gas. In the current setup after 80 seconds peak temperatures of 312 °C and 238 °C respectively were measured. To circumvent the notable volume expansion during the reaction with ammonia, both copper salts were loaded on zeolite 13X, yielding matrix-supported composite materials. Operation of those materials in the laboratory scale reactor under ammonia revealed, that the rapid temperature increase and the high peak temperatures could be retained, simultaneously simplifying the handling of the materials.

Keywords: copper salts, copper ammoniates, laboratory scale reactor, thermochemical energy storage

1. Introduction

Increased awareness of a necessary reduction of greenhouse gasses in relation to energy production stimulated an ongoing reorientation of the energy market. (IEA, 2014, Paris agreement, 2015) Environmentally benign energy production with increasing percentages of renewable energy, a sustainable energy management and a responsible use of the produced energy led to a multiplicity of innovative approaches, complying the climate targets. (Keith Shine, 2005) Related to this development are also the increase of energy efficiency, especially in context of electricity production, as according to the IEA about 2/3 of the therefore used energy are lost in form of waste heat. (IEA, 2011)

Optimizing the waste heat management encouraged research to develop recycling methods for so far lost waste heat. (Bauer et al., 2012; Hasnain, 1998) One auspicious approach due to its broad application profile is the thermal storage of waste heat by sensible, (Zhang et al., 2016) latent (Zalba et al., 2003) or thermochemical energy storage materials. (Abedin; A.H. 2011; Cot-Gores et al.; 2012, T. Yan, 2015) Thermochemical energy storage (TCES) takes a very prominent position amongst these approaches, as highest storage densities, loss-less storage, a broad

doi:10.18086/swc.2017.14.04 Available at http://proceedings.ises.org

operational temperature profile and fast reaction times allow for a flexible application in domestic and industrial environments, compatible with waste heat temperatures between 30 °C and above 1200 °C.(T. Yan, 2015)

Depending on the available waste heat source, the suitable materials may be selected from an ample catalogue of principally suitable reactions, ranked according to their storage density and application temperature.(Deutsch et al., 2016) On the lower end of the temperature spectrum are located salt hydrates for *e.g.* application in energy efficient housing projects,(van Essen et al., 2009) whereas the high temperature end around 800 °C - 1200 °C is covered by carbonates and oxides, complementing *e.g.* concentrating solar power plants (CSP) during non-operational times. (Pardo et al., 2014) For the medium temperature region between 150 °C - 450 °C so far mainly hydroxide / oxide reactions (Criado et al., 2014) or metal hydrides were considered. (T. Yan, 2015)

A so far widely neglected class of TCES-materials operating in this temperature range are (transition) metal salt ammoniates, featuring notably high storage densities, comparable to redox-active metal oxides. Although, first reports on reactions of NH_3 with salts for energy storage purposes date back to the 80's, (Dunlap, 1982) until today only a handful of publications dealing with the reaction between $CoCl_2$, (AidounTernan, 2001; Trudel et al., 1999) $MnCl_2$ (Jiang et al., 2016) or $ZnCl_2$ and NH_3 (Dunlap, 1982) is known. Concepts for NH_3 in energy storage technology relate mainly on the NH_3 formation / splitting in combination with solar power. (Dunn et al., 2012; Lavine et al., 2016; Lepinasse-Spinner, 1994; Lovegrove et al., 1999; 2004)

One major obstacle of NH_3 is its inherent toxicity. Therefore, to enable thermochemical energy storage based on NH_3-metal salt reactions, a closed reactor design, avoiding any release of NH_3, would be necessary. For this purpose, in the present work a feasibility study of a NH_3-based storage reaction, using $CuSO_4$ / $CuCl_2$ loaded on zeolite 13X in a hermetically closed laboratory scale reactor, is presented.

2. Experimental

2.1 Material

$CuSO_4$ was obtained by drying $CuSO_4 \cdot 5H_2O$ for 3 h at 400 °C in an electric furnace. All other materials were commercially obtained and used as supplied.

The copper-loaded zeolites **13X-SO_4** and **13X-Cl** were prepared by soaking zeolite 13X for 30 minutes in a saturated solution of $CuSO_4 \cdot 5H_2O$ or $CuCl_2 \cdot 2H_2O$. The zeolite was rinsed with water and dried for 2 h at 150 °C under vacuum, before the soaking procedure was repeated. After rinsing with water, the loaded zeolite was dried for 2 h at 400 °C and stored after cooling in a desiccator. The Cu-loading was determined gravimetrically and by X-Ray fluorescence spectroscopy with 0.16 g $CuSO_4$, and 0.09 g $CuCl_2$ per gram of zeolite.

For preparation of the partially reduced copper-loaded zeolites, dried samples of **13X-SO_4** and **13X-Cl** were soaked for 15 minutes in a 10 % aqueous solution of $N_2H_4 \cdot H_2O$. Due to the exothermic reaction no additional heating was necessary to keep the reaction constantly at 65 °C.

2.2 Thermal Analysis

For thermal analysis a Netzsch TGA/DSC 449 C Jupiter ® equipped with a water vapour furnace including an air-cooled double jacket was used. The oven operates between 25 °C and 1250 °C, regulated by an S-type thermocouple. NH_3 gas was 99.98 % and obtained from Messer. The gas flow was set to 100 ml min^{-1}, controlled and mixed with Vögtlin Instruments "red-y" mass flow controllers. A sample mass of 10 mg in an open aluminum crucible was used for all experiments with heating and cooling rates of 10 °C min^{-1}. The DSC was calibrated according to the procedure suggested by Netzsch, using the In, Sn, Bi, Zn, Al and Ag standards provided by the manufacturer.

2.3 Reactor-setup

For the experiments in a closed system a reactor consisting of two separated chambers connected via a tap was used. Both chambers had an inner diameter of 40 mm and a length of 200 mm. The reaction chamber was fitted with a manometer to monitor the internal pressure, as well with two K-type thermocouples positioned in the middle of the chamber (T1 and T2) and a further K-type thermocouple on the outside (T3). The reaction chamber

was loaded with the dried copper salt / copper-loaded zeolite and the whole system was evacuated for 10 minutes. The tap between reaction chamber and NH_3-chamber was closed, and NH_3 liquified in the NH_3-chamber being cooled down to – 50 °C. After 10 minutes the tap to the NH_3 cylinder was closed and the NH_3-chamber warmed to room-temperature. Once the reactor had established a thermal equilibrium with the surrounding, the tap between NH_3-chamber and reaction chamber was opened to start the reaction (discharging of the storage material). Due to the excess of NH_3 during all experiments a pressure of 6 bar was obtained in the system.

For all experiments 250 ml of material were charged to the reactor.

2.4 Scanning Electron Microscopy

SEM images were recorded on gold coated samples with a Quanta 200 SEM instrument from FEI under low-vacuum at a water vapor pressure of 80 Pa to prevent electrostatic charging.

3. Results and Discussion

3.1 Reaction between NH_3 and $CuSO_4$ / $CuCl_2$

The reaction between NH_3 and $CuSO_4$ / $CuCl_2$ – although, mainly in aqueous solutions – is a well-known, colorful reaction for demonstration of simple coordination chemistry in undergraduate-laboratories. Even in the case of mixing the aqueous solutions of NH_3 and $CuSO_4$ an increase of the reaction temperature is observed.

For the gas-solid reaction between NH_3 and $CuSO_4$ / $CuCl_2$ energy-densities of 1.77 MJ kg^{-1} and 2.20 MJ kg^{-1} were obtained by differential scanning calorimetry. These values are highly comparable to the benchmark of metal-oxide redox-reactions, featuring the highest energy densities among the various TCES-materials. Even more important for a potential TCES-material, thermogravimetry evidenced a full reversibility of the NH_3- coordination, thus by heating the formed ammine-complexes to 350 °C the initial copper salts are restored (see figure S1). Based on the decomposition of the copper-ammine complexes their composition was determined as $[Cu(NH_3)_4]SO_4$ and $[Cu(NH_3)_6]Cl_2$, thus $CuSO_4$ reacting with 4 equivalents of NH_3, $CuCl_2$ with 6.

The experimental setup selected for the gas-solid reaction between NH_3 and the anhydrous copper salts on a laboratory scale is shown in figure 1.

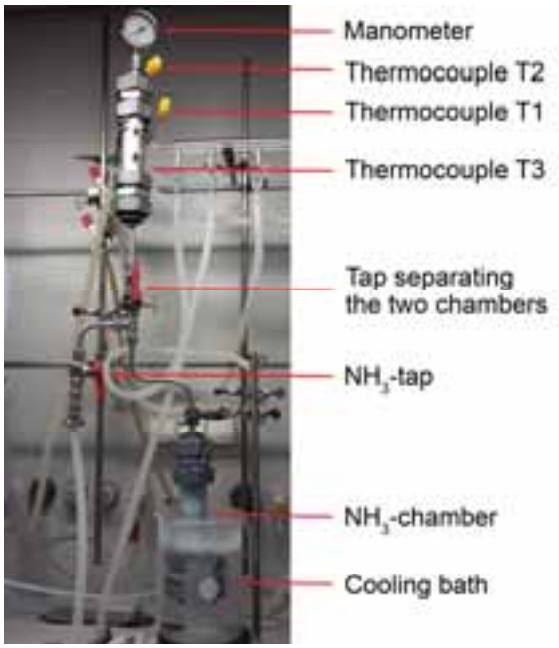

Fig. 1: Laboratory scale reactor for the gas-solid reaction between NH_3 and copper salts in a closed system

Based on the necessity of a closed system preventing the release of NH_3, a reactor with two chambers, separated

by a tap, was selected. The copper salt is situated in the reaction chamber (upper part). After evacuation of the complete system the tap between the two chambers is closed and NH_3 is condensed into the precooled NH_3-chamber. Once the NH_3-tap is closed, the NH_3-chamber is warmed to room-temperature and the reaction is started by opening the tap between the two chambers. The temperature gradient during the reaction was monitored by the 3 thermocouples T1-T3, T1 and T2 placed inside, in the middle of the reactor, T3 on the outside to follow the heat conductance. Due to the NH_3-excess used, through all experiments a constant pressure around 6 bar was obtained.

In figure 2 the temperature plots for the formation of $[Cu(NH_3)_4]SO_4$ (figure 2a) and $[Cu(NH_3)_6]Cl_2$ (figure 2b) are given.

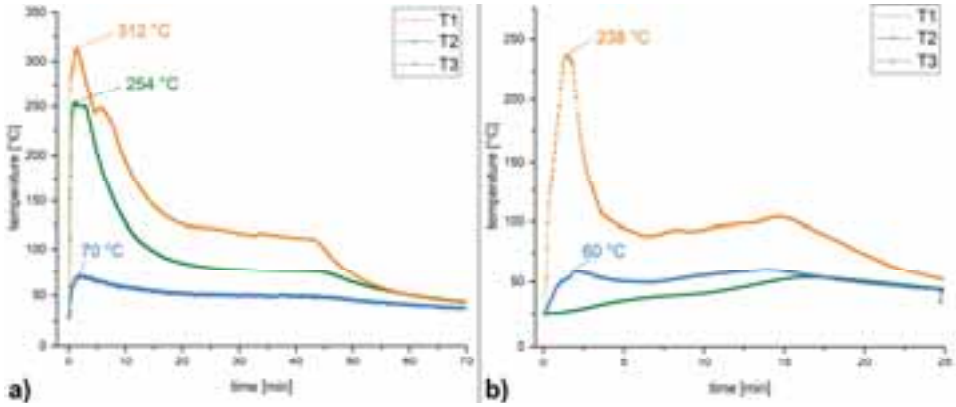

Fig. 2: Temperature plots for the formation of a) $[Cu(NH_3)_4]SO_4$ and b) $[Cu(NH_3)_6]Cl_2$ in the reactor

For both experiments starting with the opening of the tap between the two chambers an extremely fast increase of the internal temperature is observed. For $CuSO_4$ the peak temperature of 312 °C* is reached after 80 seconds, after 10 seconds T1 exceeds already 160 °C. In the case of $CuCl_2$ a peak temperature of 238 °C was reached after 90 seconds.

Both experiments are highly encouraging, as such extremely fast reactions with concomitant high temperature differences are notably rare for thermochemical energy storage materials. Nevertheless, the packed bed using the pure metal salts in the reaction chamber cannot be considered ideal, as due to the extreme volume work during the reaction a compacting / sintering process of the material occurs, deteriorating permeability of the packed bed and thus hampering the completeness of the reaction. In the case of $CuSO_4$ after the reaction the former loose powder had turned into a solid brick, which had to be removed mechanically from the reaction chamber. Additionally, from the bottom to the top of the packed bed the completeness of reaction was notably affected: Whereas, in the bottom the dark blue $[Cu(NH_3)_4]SO_4$ was formed, on the top only a slight blue color of the former white material was observed. The kinks and sudden increases in the temperature profile are attributed to the volume work of the material, varying permeability of the continuously expanding packed bed.

In the case of $CuCl_2$, although with the observed peak temperature of 238 °C the melting point of $[Cu(NH_3)_6]Cl_2$ was not exceeded, due to partial overheating near to the bottom of the reaction chamber a dark black-bluish molten residue in the reactor was formed immediately. As the thermocouple T1 was above this molten mass, the observed peak temperature was lower than in the case of $CuSO_4$ (see figure S2). Additional, nearly 2/3 of the reactors' content did not react, as the NH_3 could not pass the molten salt / ammoniate mass. Therefore, also thermocouple T2 featured only very low temperatures and the temperature in the reactor had dropped within 25 minutes significantly.

The slow decrease of the temperature profile, retaining for some extended period temperatures above 100 °C, followed by a sudden decrease of the temperature is caused by the stepwise reaction of the copper salts with NH_3. As seen from the thermogravimetric decomposition in figure S1, for the consecutive addition or removal of each of the NH_3-ligands different equilibrium / decomposition temperatures are found. Therefore, with the initial temperature rise the reaction temperature is too high to allow for complete reaction. Coming to lower

* The difference between T1 and T2 is attributed to the linear progression of the reaction zone and sintering of the material, notably affecting permeability of the packed bed.

temperatures, the further coordination of NH_3 is enabled, still releasing notable heat and thus keeping the temperature almost constant unless the reactant is consumed.

In figure 3 a time-dependent series of infrared-images, visualizing the temperature increase and slow decrease during the reaction of NH_3 with $CuSO_4$ at the outside of the reactor is shown.

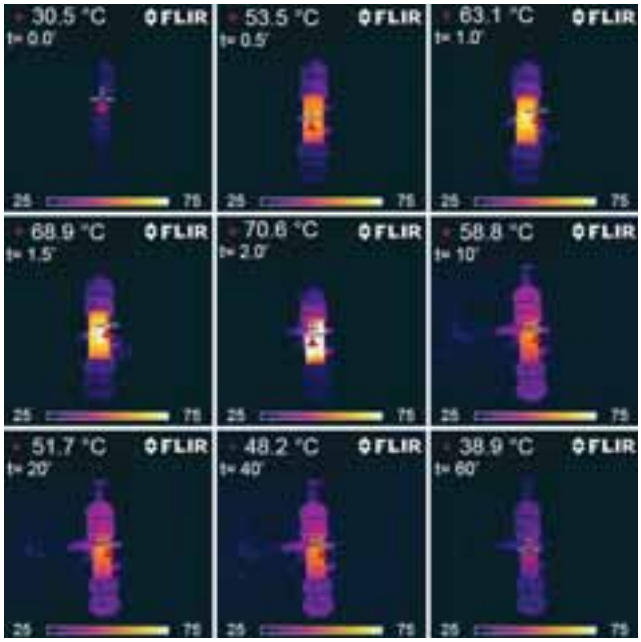

Fig. 3: Infrared-images of the reactor during the reaction of NH_3 with $CuSO_4$ at different time steps as indicated

Already after 30 seconds the temperature of the reactor walls had increased about 23 °C, reaching its maximum of 70.6 °C after 120 seconds. For the next 50 minutes a nearly constant temperature of 50 °C was observed. The temperature distribution in the IR-image after 40 minutes clearly shows, that the reaction was still ongoing.

The extreme volume work occurring on coordination of NH_3 to both copper salts becomes evident comparing the crystallographic parameters for the four different materials in table 1 (although, for $[Cu(NH_3)_4]SO_4$ only the monohydrate is found in the ICSD-database).

Tab. 1: Crystallographic parameters for $CuSO_4$, $CuCl_2$ and the corresponding NH_3-complexes

	$CuSO_4$	**$CuCl_2$**	**$[Cu(NH_3)_4]SO_4 \cdot H_2O$**	**$[Cu(NH_3)_6]Cl_2$**
	orthorhombic	monoclinic	orthorhombic	tetragonal
Space group	*P* n m a	*C* 1 2/m 1	*P* b n m	*F* 4/m m m
Nr°	62	12	62	139
Z	4	2	4	4
a [Å]	8.3976(1)	6.9038(9)	12.12	10.375(7)
b [Å]	6.70382(9)	3.2995(4)	10.66	10.375(7)
c [Å]	4.82443(8)	6.824(1)	7.07	9.481(11)
α [°]	90	90	90	90
β [°]	90	122.197(8)	90	90
γ [°]	90	90	90	90

V [Å^3]	271.6	131.54	913.44	1020.54

Based on the unit-cell volumes given in table 1, for $CuSO_4$ a 3.4-fold, for $CuCl_2$ a 3.9-fold volume expansion during the reaction with NH_3 is obtained.

To circumvent, or at least decrease the expansion of the material, causing considerable issues on larger (or applicational) scale, allow for a better permeability of the packed bed and control the temperature release during the reaction, the impregnation of zeolite 13X with $CuSO_4$ and $CuCl_2$ was chosen.

3.2 Reaction between NH_3 and matrix-supported $CuSO_4$ / $CuCl_2$

The $CuSO_4$ / $CuCl_2$ loaded zeolite samples (**13X-SO_4** and **13X-Cl**) were obtained as described in the experimental section, having a greenish-brown color after drying in the furnace (see figure S3). The copper-loading was determined gravimetrically and by X-Ray fluorescence spectroscopy with 0.16 g $CuSO_4$, and 0.09 g $CuCl_2$ per gram of zeolite.

Of course, the better handling and limited volume expansion goes to the expense of a much lower copper content compared to the pure salts, relating to a lower energy content and thus decreased reaction temperature. Due to the matrix-support also the heat transfer is affected. Therefore, externally copper-coated samples were prepared by reducing the external layer of copper-salts on the zeolite by hydrazine hydrate (see experimental), which should improve the thermal conductivity of the material.

To compare the performance of the various matrix-supported copper salts in the reactor, the same approach as described for the pure copper salts was chosen. In figure 3 the temperature plots of the experiments using **13X-SO_4** (figure 4a) and **13X-Cl** (figure 4b), and their partially reduced equivalents **13X-SO_4_Cu** (figure 4c) and **13X-Cl_Cu** (figure 4d) are shown.

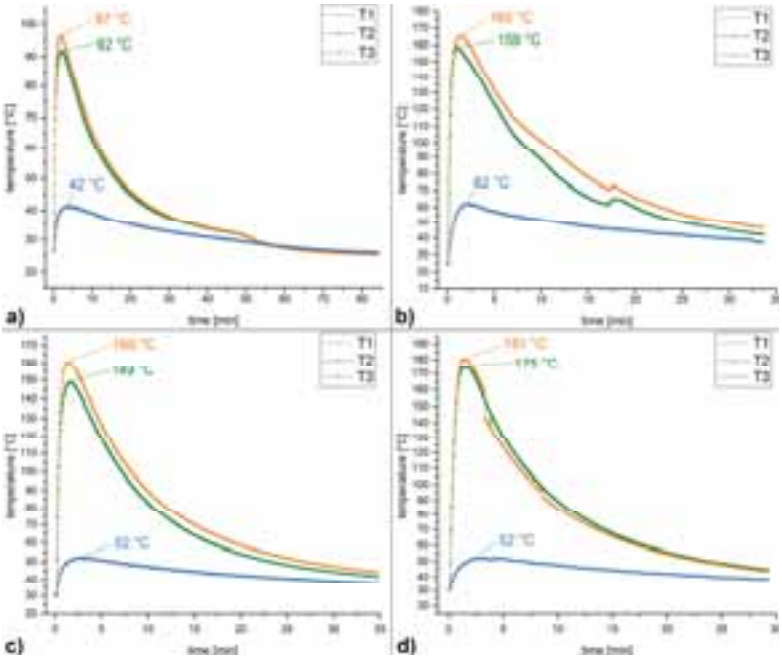

Fig. 4: Temperature plots for the reaction of NH_3 with a) 13X-SO_4 b) 13X-Cl c) 13X-SO_4_Cu d) 13X-Cl_Cu in the reactor

The prior observed temperature rise after opening the tap between the two chambers was also found in the present experiments, in all cases reaching the maximal temperature within 90 seconds. This finding is very promising, stating, that although the copper salts was heavily ‘diluted’ by loading on the matrix, its performance is still outstanding for a TCES-material. In these experiments also the temperature difference between T1 and T2 was reduced, as a notably better permeability of the packed bed was achieved. It should be emphasized, that due to the

particle shape of the zeolite the contact between thermocouple and material was less efficient as in the previous experiments. In this respect, the partial reduction of the copper salts on the zeolite matrix, yielding a better thermal conductivity was found quite efficient, as in the experiments with **13X-SO_4_Cu** (figure 4c) and **13X-Cl_Cu** (figure 4d) notably higher peak temperatures were observed. Especially, in the case of **13X-SO_4_Cu** (figure 4c) the impact of the external Cu-coating increased the measured temperature about 60 °C. The discontinuities in the temperature plots of **13X-Cl** and **13X-Cl_Cu** are attributed to slight movements of the packed bed, affecting the contact between thermocouple and zeolite particles.

A control experiment with a mixed packed bed loading of **13X-Cl** and 10 % copper turnings (figure S4) showed a decreased temperature output (figure S5) even compared to the experiment using unmodified **13X-Cl**. It seems, that in the case of the matrix-loaded copper salts even a further 10 % dilution has a negative impact on the highest achievable reaction temperature.

The use of matrix-supported copper salts in the reactor experiments turned out to be quite promising, as still the fast temperature increase and notably high peak temperature was retained, at the same time avoiding the volume expansion of the material during the reaction.

4. Conclusion

The reaction between NH_3 and $CuSO_4$ / $CuCl_2$ was investigated for their feasibility as thermochemical energy storage process. Initial requirement was the operation in a closed system to prevent release of NH_3 to the surrounding environment due to its toxicity. For this purpose, a two-chamber reactor setup with the reaction chamber and the NH_3-chamber – loaded by condensation of NH_3 at -50 °C – was chosen.

For the pure copper salts 80 seconds after beginning of the reaction the peak temperatures of 312 °C ($CuSO_4$) and 238 °C ($CuCl_2$) were obtained. Such an abrupt and remarkable temperature increase is quite outstanding and very promising for a high-end technological applicability of thermochemical storage materials. The reaction temperature is kept for about 40 minutes around 100 °C, as the stepwise coordination of NH_3-ligands to the copper salts continuously releases heat until the reaction is complete. The only and major drawback of such an operation is the extreme volume work during the reaction accounting up to a 3.9-fold volume expansion in the case of $CuCl_2$. This causes a sintering and condensing of the packed bed, affecting completeness of the reaction due to very limited permeability of the bed and complicates the handling, as the reacted material needs mechanical force to be removed from the reactor. In the case of $CuCl_2$ due to initial high reaction temperatures, exceeding locally the melting point of the $[Cu(NH_3)_6]Cl_2$ the reaction product is obtained as massive solid.

To allow for a better handling, but retain the promising reactivity, both $CuSO_4$ and $CuCl_2$ were loaded on zeolite 13X, resulting in matrix-supported copper salts. In this case the volume expansion during the reaction is nearly eliminated, concomitantly retaining high initial peak temperatures and fast energy release on reaction with NH_3. To ensure a better heat conductivity, partial reduction of the copper on the outside of the zeolite particles was accomplished by treatment of the composite materials with hydrazine hydrate. The thereby obtained externally copper coated, copper salt loaded materials revealed a much better thermal conductivity, leading to the observation of higher peak temperatures.

As the main objective of the present work was a feasibility study on the reaction of NH_3 with copper salts, respectively matrix-supported copper salts, the main subject of continuative studies will be the optimization of the heat output / heat transfer. Design and operation of the reactor / process will need some improvement to efficiently use and transfer the released heat.

5. References

1. IEA, 2014. Heating without global warming: Market developments and policy considerations for renewable heat.
2. Treatie, U.N., 2015. Paris agreement, No. 54113,
3. Keith Shine, J.F., Kinfe Hailemariam, Nicola Stuber, 2005. Alternatives to the Global Warming Potential for Comparing Climate Impacts of Emissions of Greenhouse Gases. climatic change 3, 281-302.
4. IEA, 2011. Co-generation and Renewables. Solutions for a low-carbon energy future. https://www.iea.org/publications/freepublications/publication/co-generation-and-renewables-solutions-for-a-low-carbon-energy-future.html
5. Bauer, T., et al., 2012. Thermal Energy Storage Materials and Systems. Annual Review of Heat Transfer 15, 131-177.
6. Hasnain, S.M., 1998. Review on sustainable thermal energy storage technologies, Part I: heat storage materials and techniques. Energy Conversion and Management 11, 1127-1138.
7. Zhang, H., et al., 2016. Thermal energy storage: Recent developments and practical aspects. Progress in Energy and Combustion Science 1-40.
8. Zalba, B., et al., 2003. Review on thermal energy storage with phase change: materials, heat transfer analysis and applications. Applied Thermal Engineering 3, 251-283.
9. Ali H. Abedin, M.A.R., 2011. A Critical Review of Thermochemical Energy Storage Systems. The Open Renewable Energy Journal 42-46.
10. Cot-Gores, J., A. Castell, and L.F. Cabeza, 2012. Thermochemical energy storage and conversion: A-state-of-the-art review of the experimental research under practical conditions. Renewable and Sustainable Energy Reviews 7, 5207-5224.
11. T. Yan, R.Z.W., T. X. Li, L.W.Wang, Ishugah T. Fred, 2015. A review of promising candidate reactions for chemical heat storage. Renewable and Sustainable Energy Reviews 13-31.
12. Deutsch, M., et al., 2016. Systematic search algorithm for potential thermochemical energy storage systems. Applied Energy 113-120.
13. van Essen, V.M., et al., 2009. Characterization of Salt Hydrates for Compact Seasonal Thermochemical Storage. 825-830.
14. Pardo, P., et al., 2014. A review on high temperature thermochemical heat energy storage. Renewable and Sustainable Energy Reviews 591-610.
15. Criado, Y.A., M. Alonso, and J.C. Abanades, 2014. Kinetics of the CaO/Ca(OH)2Hydration/Dehydration Reaction for Thermochemical Energy Storage Applications. Industrial & Engineering Chemistry Research 32, 12594-12601.
16. Dunlap, R.M., *Thermochemical energy storage and mechanical energy converter system*. 1982, Google Patents.
17. Aidoun, Z. and M. Ternan, 2001. Pseudo-stable transitions and instability in chemical heat pumps: the NH3–CoCl2 system. Applied Thermal Engineering 10, 1019-1034.
18. Trudel, J., S. Hosatte, and M. Ternan, 1999. Solid–gas equilibrium in chemical heat pumps: the NH_3–$CoCl_2$ system. Applied Thermal Engineering 5, 495-511.
19. Jiang, L., et al., 2016. Experimental investigation on a $MnCl_2$ –$CaCl_2$ –NH_3 thermal energy storage system. Renewable Energy 130-136.
20. Dunn, R., K. Lovegrove, and G. Burgess, 2012. A Review of Ammonia-Based Thermochemical Energy Storage for Concentrating Solar Power. Proceedings of the IEEE 2, 391-400.
21. Lavine, A.S., et al., 2016. Thermochemical energy storage with ammonia: Aiming for the sunshot cost target. 050028.
22. Lepinasse, E. and B. Spinner, 1994. Production de froid par couplage de réacteurs solide-gaz I: Analyse des performances de tels systèmes. International Journal of Refrigeration 5, 309-322.
23. Lovegrove, K., H. Kreetz, and A. Luzzi, 1999. The first ammonia based solar thermochemical energy storage demonstration. Le Journal de Physique IV PR3, Pr3-581-Pr3-586.
24. Lovegrove, K., et al., 2004. Developing ammonia based thermochemical energy storage for dish power plants. Solar Energy 1-3, 331-337.

6. Appendix

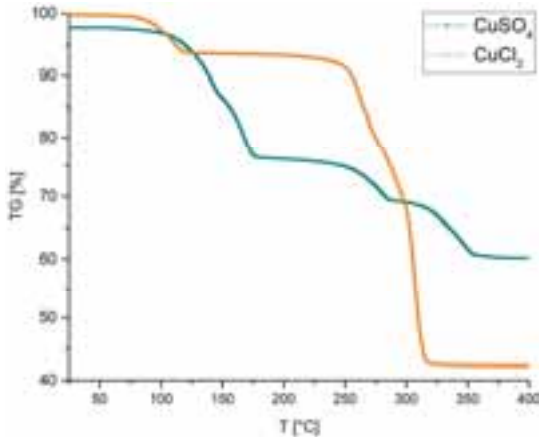

Fig. S1: Thermogravimetric decomposition of $[Cu(NH_3)_4]SO_4$ and $[Cu(NH_3)_5]Cl_2$

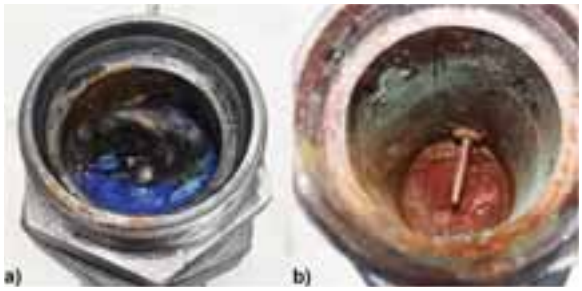

Fig. S2: Molten residue of $[Cu(NH_3)_6]Cl_2$ after the reaction a) molten residue on the bottom b) unreacted $CuCl_2$ on the top with thermocouple T2

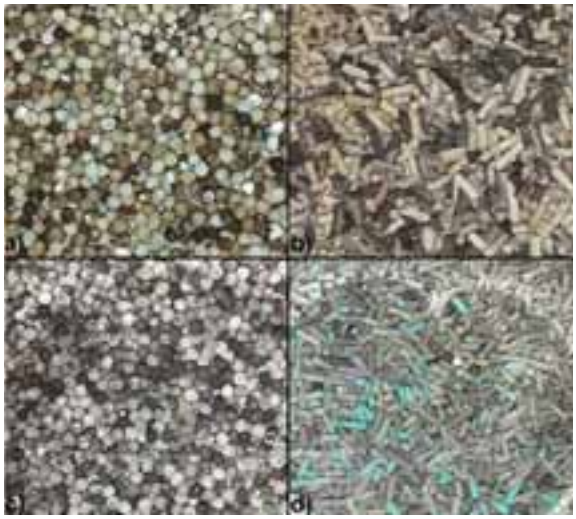

Fig. S3: Images of copper-impregnated zeolite 13X a) 13X-SO_4 b) 13X-Cl, c) 13-X-SO_4 after reaction with NH_3, c) 13-X-Cl_2 after reaction with NH_3

Fig. S4: A mixed packed bed loading of 13X-Cl and Cu-turnings

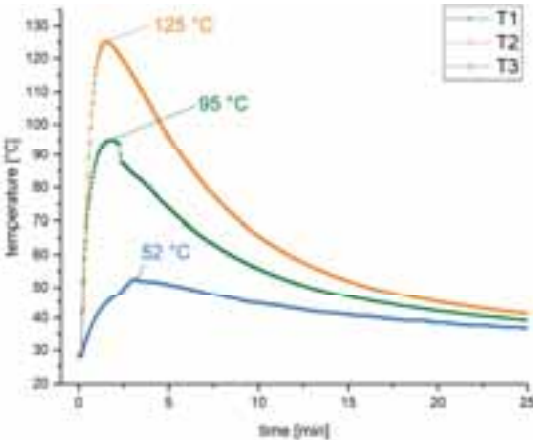

Fig. S5: Temperature plot for the reaction of NH_3 with a mixed packed bed loading of 13X-Cl and Cu-turnings

Experimental Investigation of Thermal Perfomance for Selected Oils for Solar Thermal Energy Storage and Rural Cooking Application

Karidewa Nyeinga[1], Denis Okello[1], Tabu Bernard[1,2], Ole Jorgen Nydal[3]

[1]Department of Physics, Makerere University, Uganda
[2]Department of Physics, Gulu University, Uganda
[3]Department of Energy & Process Engineering, Norwegian University of Science & Technology (NTNU), Norway.

Abstract

The thermal performance of locally available oils in Uganda have been experimentally investigated to determine their suitability for heat transfer and solar thermal energy storage. Sunflower oil and palm oil, both local vegetable vegetable oils and Shell thermia B, commonly used in the local industries as a heat transfer fluid were used in the study. The oils were heated in an insulated tank until temperatures close to their smoke points were attained and then heating was stopped; the tank temperature was recorded for 24 hours during the cooling. The second experiement involved charging the oil in a self-circulating system without the aid of a pump. It was observed that the vegetable oils gained heat faster than thermia B. Sunflower oil retained heat for a longer period compared to palm oil and thermia B. The total amount energy stored by sunflower was equally higher than palm oil while thermia B had the least energy stored. The results show that sunflower oil is the most suitable oil for solar thermal storage and heat transfer.

Key words: vegetable oil, sunflower, palm oil, thermia B, solar energy storage, cooking.

1. Introduction

Solar thermal storage systems for rural cooking applications require suitable heat transfer fluids capable of transferring heat to the storage during charging and to the cooker during discharging (Lovseth 1997; Heetkamp 2002). The choice of fluid for heat transfer depends on the storage medium and the choice for heat extraction. There are industrial fluids available for heat transfer in large scale solar thermal plants. However, such fluids are expensive for rural applications and therefore will increase the cost of the system. Air and water have been used as heat transfer media with rock bed storage systems as reported by (Okello et al. 2016; Nyeinga, et al. 2016). However, air has low heat capacity and water may pause high risks since it vaporizes at high temperatures and therefore not suitable for rural cooking application.

Vegetable oils can be used as both heat transfer fluid and heat storage medium for solar cooking applications. The advantage with vegetable oils is that they are not risky even if there are leakages in the system. Mawire et al. (2014) explored the use of sunflower as heat transfer medium; they studied the charging of the oil using high and low flow rates. For cooking applications, the interest is in oils which are capable of attaining temperatures of about $200^{o}C$. In this paper, thermal properties of selected oils were investigated

2. The Experimental set-up and procedure

2.1. Oil samples

Local vegetable oils namely refined sunflower oil and refined palm oil were used in this study in addition to thermial B, a mineral oil but readily available in the country. Table 1 shows the thermo-physical properties of the selected oils. It can be observed that the vegetable oils have high densities and specific heat capacities compared to thermia B.

doi:10.18086/swc.2017.14.05 Available at http://proceedings.ises.org

Tab. 1: Thermo physical properties of the selected oils adapted from Mawire et al. (2014)

	Density $\left(kgm^{-3}\right)$	**Specific heat capacity** $\left(Jkg^{-1}K^{-1}\right)$	**Thermal conductivity** $\left(Wm^{-1}K^{-1}\right)$
Refined sunflower oil	$930.62-0.65T$	$2115.00+3.13T$	$0.061+0.018e\left(-T/26.142\right)$
Refined palm oil	$925.00-0.66T$	1861	0.1721
Thermia B	$870.00-0.65T$	$1798.00+3.58T$	$0.118+0.018e\left(-T/168.660\right)$

3.2. Determination of heat retention capacity

A cylindrical tank of about 4.5L fitted with a 1.5kVA electrical heater was used to heat 4L of the selected oil samples in turn. Three K-type thermocouples fitted in the tank at a distance of 5cm apart were used to measure the temperature along the tank. The thermocouples were connected to a TC-08 data logger interfaced with computer as shown in figure 1. The heater was connected to a 240V a.c main and the oil in the tank was heated to a temperature close to its smoke point and the heater switched off. The temperature of in the tank was recorded for about 25 hours.

Fig. 1: Showing the experimental setup. The oil is heated in an insulated tank and thermocouples connected to a data logger and a computer were used to monitor and record the temperature during heating and cooling.

The quantity of heat energy, Q stored in oil at any time is expressed as:

$$Q=\rho vc\left(T-T_o\right) \qquad \text{(eq. 1)}$$

where ρ, c, v are average density of the oil, average specific heat capacity of the oil and volume respectively. T is the average temperature at time, t and T_o is the initial temperature. The average temperature of the oil in the storage tank was considered in the computation of the energy content of the tank since the storage tank was short.

3.3. Self circulating charging unit

Figure 2 shows a storage tank of internal diameter 18cm and height 40cm made of steel and a boiler of internal diameter 18cm and height 20cm made of mild steel oriented at 60^o to the horizontal. The storage tank was charged based on self-circulating system. The main advantage with a self-circulating system is that you avoid the

use of pumps. A continuous copper pipe of internal diameter 0.9cm and total length measuring 150cm was inserted from the top of the storage tank to the bottom through the boiler.

Fig. 2: A self circulating system consisting of a storage tank and a boiler. Sunflower oil was used in the boiler and the three types of oil where put in the storage tank one after the other. The storage was filled with each type of oil and this got heated in the boiler and thereby charging the storage.

Seven k-type thermocouples each at an interval of 5cm were placed at the central axis of the storage tank. The storage tank was filled with 10 litres of sunflower oil followed by palm oil and finally thermia B as a heat storage fluid respectively. The boiler was filled with 4 litres of refined sunflower oil. An electrical heater of 1.5 kVA was used for heating the oil in the boiler. The temperature of the boiler was maintained in the range of $230^{o}C - 240^{o}C$ (just below the smoke point of sunflower oil) manually, by switching the electrical heater on and off. The storage tank was charged for 6 hours.

The total energy, *E* stored in a tank of, *n* segments during the charging process is given by

$$E = \rho c \sum_{i=1}^{n} v_i \Delta T_i \qquad \text{(eq. 2)}$$

where ρ, c are the density of the oil and the specific heat capacity of the oil respectively; v_i is the volume of oil in the i^{th} segment and T_i is temperature difference between two adjacent nodes of the i^{th} segment of a stratified tank.

3. Results and discussions

4.1 Heat retention

Refined sunflower oil and palm oil were both heated to a maximum temperature of about $236^{o}C$; these temperatures are slightly below their smoke points. Thermia B was heated to a maximum temperature of $220^{o}C$. After heating the oils to their maximum temperatures, the heater was switched off and the tank allowed to cool. Figure 4 shows the temperature profiles during heating and cooling. Refined sunflower oil and refined palm oil showed a rapid increase in temperature during the heating while thermia B gained heat slowly.

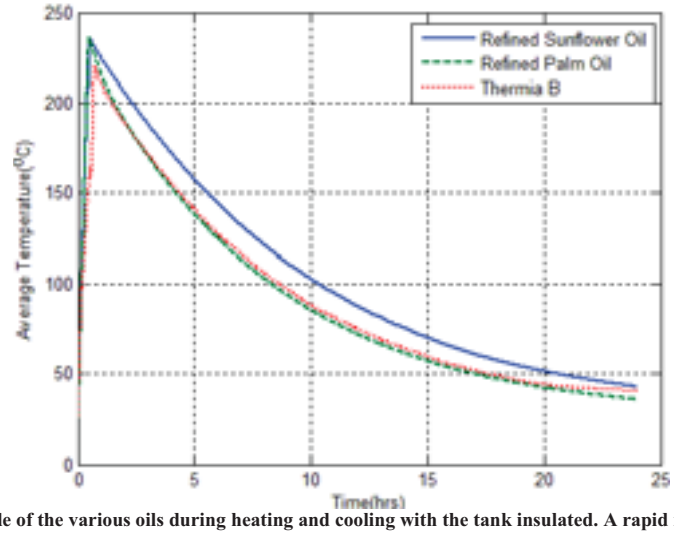

Fig. 4: Temperature profile of the various oils during heating and cooling with the tank insulated. A rapid increase in temperature of sunflower oil and palm oil are observed during heating. After 24hours, the temperature of sunflower oil can be seen to be higher than for palm oil and thermia B.

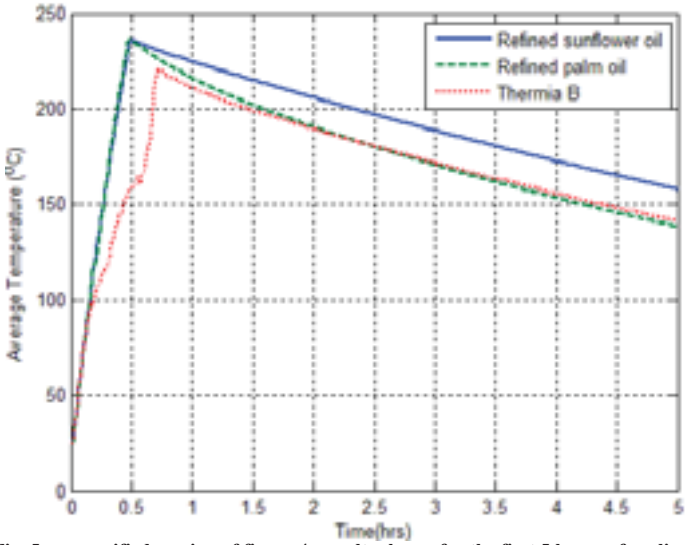

Fig. 5: a magnified version of figure 4; results shown for the first 5 hours of cooling.

Both refined sunflower oil and refined palm oil reached a maximum temperature of about $236^{o}C$ in 30 minutes. This high increase in temperature is attributed to fact that both refined sunflower oil and refined palm oil have high densities and specific heat capacities. However, thermia B took longer to attain its average maximum temperature of $220^{o}C$ in about 45 minutes because it has low density and specific heat capacity and this can be clearly seen in figure 5 which is an amplified version of in figure 4.

For solar thermal storage systems with cooking applications, we are interested in charging the storage in the shortest possible time since the solar radiation keeps varying with time. Fluids which can retain the heat for a longer period are to be preferred since this allows cooking to be done even after sunset. Both refined sunflower oil and refined palm oil absorbed heat faster than thermia B; but refined refined sunflower retains heat better than palm oil.

4.2 Energy distribution

Figure 6 shows the energy distribution during heating and retention computed using equation 1. The maximum energy attained by refined sunflower was 1.6MJ in 30 minutes, while for refined palm oil was 1.4MJ in 30 minutes, and thermia B attained the maximum energy of 1.2MJ in 45 minutes.

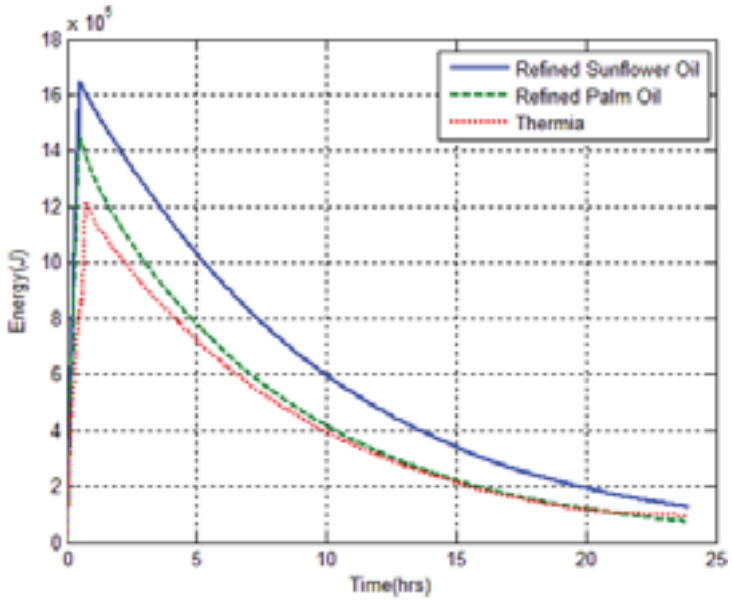

Fig. 6: energy distribution over time for oils heated for 30-45 minutes and thereafter the heater was switched off and allowed to cool for about 24 hours in an insulated tank.

From figure 6, it can be observed that at the end of the 24 hours, sunflower oil had much more energy than both palm oil and thermia B. This furthers shows that sunflower oil is more suitable for solar thermal energy applications.

4.3. Temperature profiles during charging

Figures 7 shows the temperature profiles in the storage tank based on the self-circulating charging system for 6 hours.

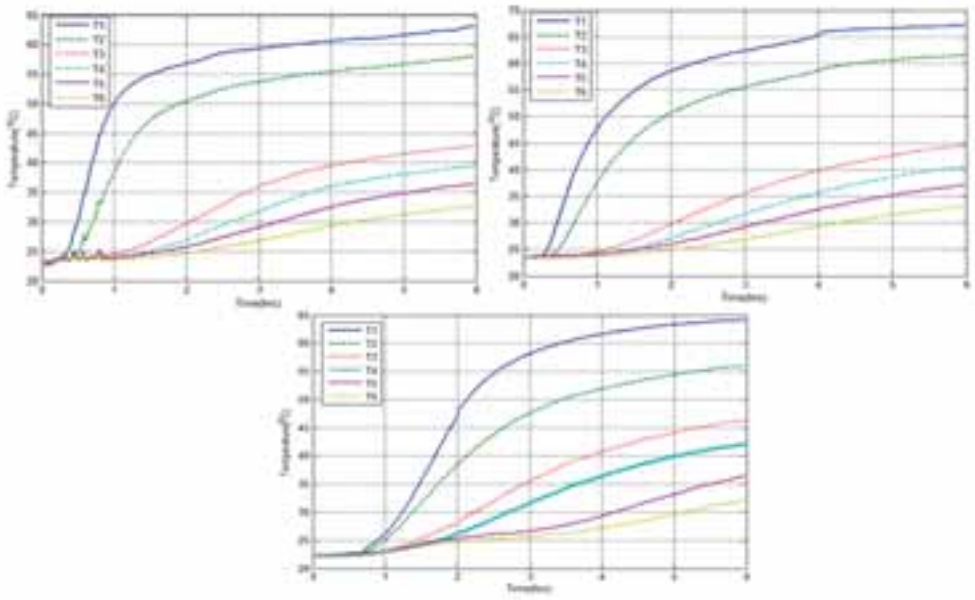

Fig. 7: Temperature profiles during charging of the storage tank using a self-circulating system for 6 hours using a self-circulating system. T_1 is temperature at the top of the storage while T_6 is at the bottom. The storage tank was not insulated since the aim was to compare the temperatures during charging of the three different oils under the same conditions.

In the first one hour, sunflower oil and palm charged very fast and attained temperatures of about $50^{o}C$ at the top of the tank; however, in the same period thermia B had a temperature below $30^{o}C$ at the top. The observed high rate of charging attained by sunflower oil and palm oil is attributed to their high densities and specific heat capacities which agrees with similar findings by Mawire et al. (2014).

4.4. Thermal energy profiles during charging

Figure 8 shows the energy distribution in the storage tank for the three different oils during charging by a self-circulating system. The energy profiles for both refined sunflower oil and refined palm oil increased rapidly in the first one hour until their peak values were attained.The maximum energy for refined sunflower oil was $0.13MJ$ attained in about 1.5 hours while for refined palm oil was $0.12MJ$ attained in about 2 hours. The energy profile for thermia B increased gradually until it attained a peak value of $0.10MJ$ in about 3 hours. The high energy gained in sunflower in a short time is again associated to its high density and specific heat capacity.

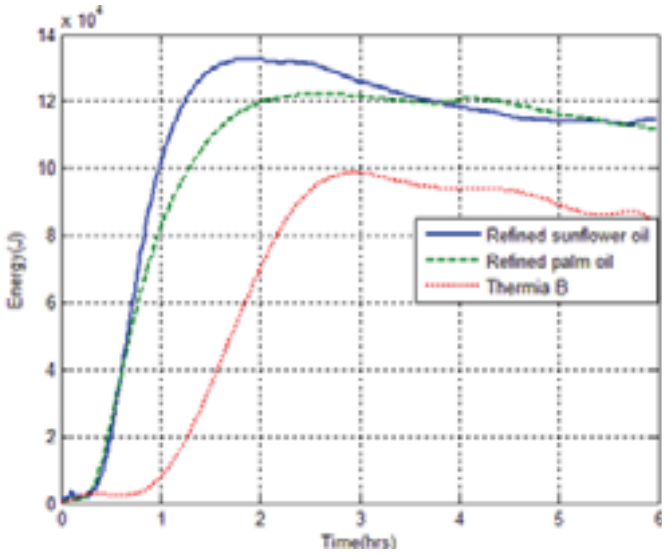

Fig.8: thermal energy stored in the tank by refined sunflower, refined palm oil and thermia B during charging for 6 hours using a self-circulating system. Sunflower oil the highest energy and thermia B had the least energy.

The drop in energy after 2.5 hours can be attributed to the fact that the density and specific heat capacity for oil decreases and increases respectively with increasing temperature; but the decrease in density overrides the increase in specific heat capacity as cited by Esteban et al. (2012).

5. Conclusion

The thermal performance of refined sunflower oil, refined palm oil, and thermia B was experimentally studied. The results show refined sunflower oil and palm oil gained heat faster than thermia B. However, refined sunflower oil retained more heat than palm oil. For solar energy applications, the solar radiation may be available over a period of time and therefore sunflower oil would be more suitable since it can absorb the heat faster and retain it longer. Further studies should be carried out on a hybrid storage system consisting of rock pebbles and sunflower oil. This will cut down the cost of the storage since rock pebbles are readily available and cheap. We also recommend further work on the number of cycles the sunflower oil can be heated and cooled without any major changes in its properties.

6. Acknowledgement

The authors would like to thank NORAD and the Energy & Petroleum (EnPe) Project-Norway, for the financial support received to carry out this research. Further thanks to all project partners for their contribution in this research.

7. References

Ashmore Mawire, Abigail Phori, Simeon Taole, 2014. Performance comparison of thermal energy storage oils for solar cookers during charging. Applied Thermal Engineering, Vol. 73, pp. 1323-1331.

Denis Okello, Ole J. Nydal, Karidewa Nyeinga and Eldad J. K. Banda, 2016. Experimental investigation on heat extraction from a rock bed heat storage system for cooking applications. Journal of Energy in Southern Africa; Vol.27, No.2, pp.30-37

Esteban B, Riba JR, Baquero G, Rius A and Puig R, 2012. Temperature dependence of density and viscosity of vegetables oils. *Biomass and bioenergy*. 42:164-171.

Heetkamp van den R.R.J. 2002. The development of small solar concentrating systems with heat storage for rural food preparation. Physica Scripta T97, pages 99-106.

Karidewa Nyeinga, Ole J. Nydal, Denis Okello, and Eldad J. K.B. Banda, 2016. Dynamic model of a small scale concentrating solar cooker with rock bed heat storage. Journal of Energy in Southern Africa; Vol.27, No.1, pp.20-27.

Lovseth J. Small, multi-purpose concentrating solar energy systems for villages, 1997. Proceedings ISES 1997 Solar World Congress, 7:108-177.

Test campaign and performance evaluation of a spiral latent storage module with Hitec® as PCM

M.M. Rodriguez-Garcia[1], E. Rojas[2] and R. Bayón[2]

[1] Ciemat - Plataforma Solar de Almería, Almería (Spain)

[2] Ciemat - Plataforma Solar de Almería, Madrid (Spain)

Abstract

A modified spiral plate heat exchanger for its use as thermal energy storage (TES) has been selected using Hitec® salt as storage medium within the activities of the REELCOOP project (7th Framework program of the European Union Ref N. 608466, www.reelcoop.com). After its installation at one of the storage test facility at PSA (Plataforma Solar of Almería) and its commissioning, the test campaign has been performed. The testing procedures and the results evaluation are presented in this paper. For a better understanding of the phase change process, thermal analyses of the commercial Hitec® salt have been carried out.

Keywords: Latent storage, spiral heat exchanger, Hitec® as phase change material.

1. Introduction

A modified design based on a spiral plate heat exchanger used as latent thermal energy storage module was proposed in the Prototype #3 of the REELCOOP project. In this project an organic ranking cycle (ORC) using parabolic trough solar collectors is to be driven with direct steam generation combined with a biogas boiler. In order to keep producing power in the necessary transient time to change from solar field to biomass boiler a latent storage module was included as part of this plant. The reliable phase change material (PCM) used to meet the temperature range needed for both ORC and solar field is the Hitec® salt.

Previous results regarding the phase change material selection were presented by Rodriguez-Garcia et al., 2016a, where several candidates PCMs in the range of 130 ºC to 170 ºC were studied. The commercial Hitec® salt was selected because it was the only one that showed chemical stability under cycling and despite its relatively low phase change enthalpy.

In the EuroSun congress (Rodriguez-Garcia and Rojas, 2016b) the settlement of the problems addressed during the commissioning was presented: mainly the filling of the spiral thermal energy storage module and the presence of water remaining from a previous mandatory pressure test.

In this paper the test campaign of the spiral storage module with Hitec® salt as PCM and a preliminary evaluation of the results are presented. Moreover, further thermal analyses of Hitec® like differential scanning calorimetry (DSC) measurements, melting/freezing cycles in the oven under air down to 40 ºC together with the analysis of salt composition after the cycles are presented as well.

2. Facility description

Patented by Rivas et al. (2011), the module tested in the REELCOOP project is an adaptation of a commercial spiral plate heat exchanger, due to limitations in budget and project time frame. With 825 mm external diameter and 1000 mm height, the spiral heat exchanger used as TES module has volume at the water/steam channel of 205 liters, and 230 liters at the molten salt channel. For more information see Rodriguez-Garcia and Rojas, 2016b.

The testing facility was designed to operate in both charging (see Fig. 1(a)) and discharging modes (see Fig. 1(b)) with water as heat transfer fluid (HTF). In nominal conditions, for the charging (discharging) mode a steam generator (water heater) provides saturated steam (warm water) to the storage module where energy is transferred to (from) the PCM. The storage module provides a mixture of steam and liquid water in an undetermined ratio or steam quality. This water-steam flow is later mixed with liquid water at known temperature and flow. The resulted

doi:10.18086/swc.2017.14.06 Available at http://proceedings.ises.org

water-liquid flow and its temperature are measured and the thermal cycle is closed.

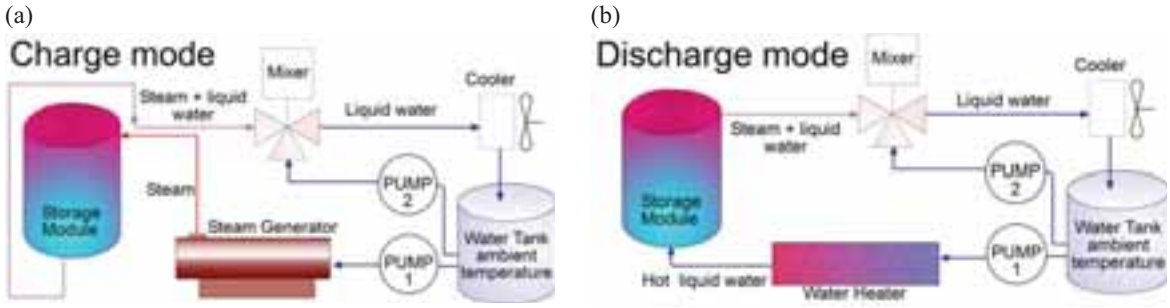

Fig. 1 Charge (a) and discharge (b) operation mode schemas of the test facility at Plataforma Solar de Almería. The facility is composed by: a water tank; a steam generator that provides saturated steam; an electric water heater; two pumps; a mixer; and a water cooler.

The pressure in the whole loop is given by the steam generator in charge or by the boiler in discharge and controlled by a pressure regulating valve situated at the mixed inlet. A 0.5 MPa pressure drop was calculated.

Theoretically, during the charge operation saturated steam at 150 °C enters the storage module prototype (TES) through the A2 conduction (see Fig. 2) and, once the heat is transferred to the PCM, saturated water at 140 °C exits the TES module through the A1 pipeline. During the discharge, the operation takes place in the contrary flow direction: saturated water at 130 °C enters the TES through the A1 conduction and, after evaporating in the TES, saturated steam at 130 °C leaves the module through A2. Tab. 1 shows a summary of the nominal operation conditions for both charge and discharge modes.

Tab. 1: Nominal operation conditions for the charge and discharge modes at TES module.

Charge mode				
	Temperature [°C]	Pressure [MPa]	Flow [kg/s]	Water phase
Inlet (A2)	150	0.47	0.04	Saturated steam
Outlet (A1)	140	0.36	0.04	Saturated water
Discharge mode				
	Temperature [°C]	Pressure [MPa]	Flow [kg/s]	Water phase
Inlet (A1)	130	0.27	0.05	Saturated water
Outlet (A2)	130	0.26	0.05	Saturated steam

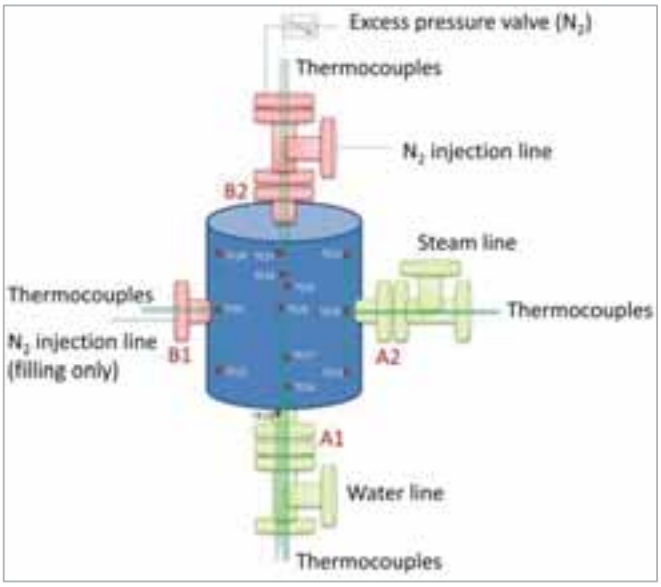

Fig. 2: TES module temperature sensors.

While water flow is measured with vortex flowmeters, steam flow is measured with a Coriolis-type flowmeter. The storage module tested here did not allow including temperature gauges at different radial positions, but at the center and outer radius of the equipment. The final distribution is shown in Fig. 2.

3. Storage module test campaign

After commissioning, test campaign took place from 23/11/2016 to 15/01/2017. The most remarkable aspects of the preoperational tests and the TES module filling with the selected PCM where presented in Rodriguez-Garcia and Rojas, 2016b. In this section, the thermal performance tests are presented, comparing the results with that theoretically expected. While January, 9th has been taken as reference day, the most important results are also observed in the rest of the days. A further work will present the details of repeatability and quality of the whole test campaign.

3.1. Charge mode

In this operation mode water should go into the storage module as saturated steam through the lateral upper entrance (A2 in Fig. 2) and flow through the spiral channel from the largest diameter to the smallest one. Along its way, water is expected to loss energy by melting the solid PCM, placed in the alternate spiral channel, and to condensate. The saturated water should be drained by gravity to the bottom.

During the commissioning testing days, some experience had to be acquired to control pressure and temperature inside the TES module. PCM temperature gauges showed the PCM did not melt when operating at nominal conditions, and hence, a change in the operation strategy had to be adopted by having 170 °C set point for the steam generator and adjusting the circuit pressure to the corresponding saturated steam pressure (0.89 MPa). Nominal mass flow was not achieved due to limitations in the steam generator.

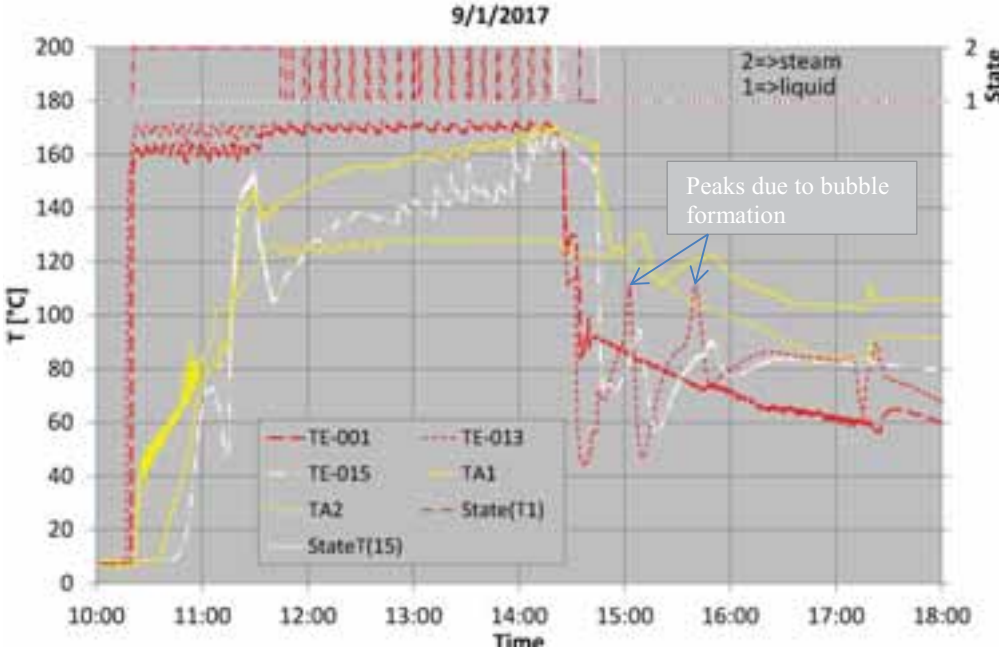

Fig. 3: Charging and discharging operation

In charging processes the steam generator continuously provides steam at 170 ºC and at a much lower pressure than 0.8 MPa, which is the saturation pressure at that temperature. Therefore, the mean HTF temperature within the module at its entrance increases with time as expected (TA1 and TA2 in Fig. 3). When the loop pressure was adjusted to get up to 0.8 MPa, the system reacts by changing the temperature at the outlet pipe of the module (TE-015) with a sudden drop down. Temperatures close to the outlet but within the module (TA1 and TA2) show a certain decrease, but not so important. When the gauge pressure becomes 0.4 MPa, the initial 0.025 kg/s steam decreases to 0.01 kg/s, which is in the range of the minimum steam mass flow the flowmeter can detect. 'State(T1)' variable shows if the water at the temperature (TE-001) prior to enter the storage module is steam (associated to value 2) or liquid (associated to a value 1). Working at pressures so close to saturation ones, implies that it may happen, as shown in Fig. 3, that steam is easily condensed prior to be supplied to the storage module.

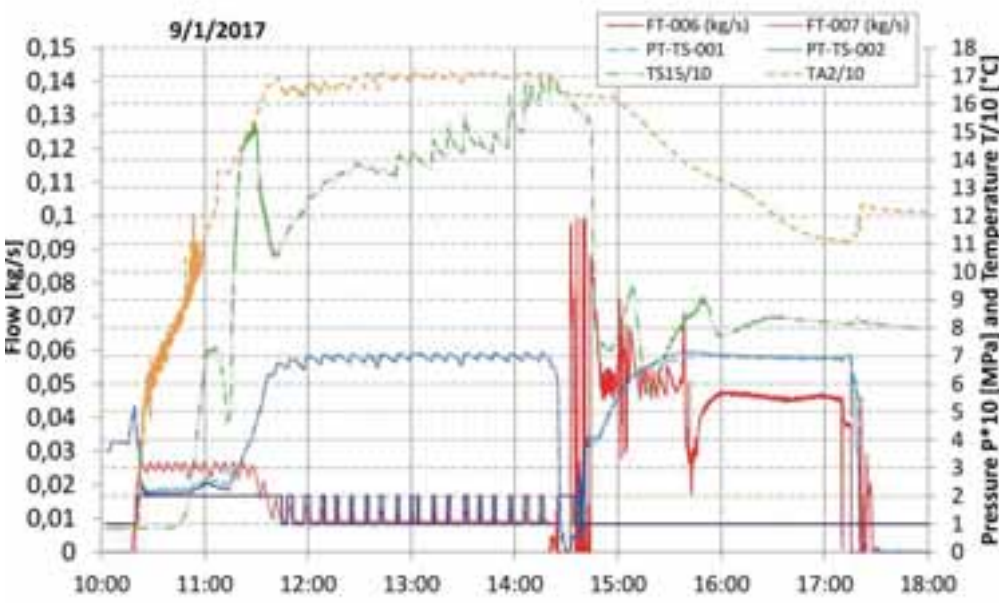

Fig. 4: Charging and discharging operation (flow, pressure and temperature/10)

3.2. Discharge mode

During the discharge, the operation takes place in the contrary flow direction: according to specifications saturated water at 130 °C enters the TES through the A1 conduction; being constant the power provided to the TES and producing, after evaporating in the TES, saturated steam at 130 °C. In this last case particular problems were found due to the electrical water heater used to preheat the water up to 130 °C, and finally, its set-point temperature had to be reduced to 85 °C in order to avoid an undesirable bubbles formation around the electrical resistance in the water heater. Temperature in the storage module was 160 °C, with a corresponding saturation pressure of 0.61 MPa, which is 0.2 MPa lower than the pressure in the circuit. Due to the imposed pressure loop, the water exiting the TES during the discharge is in liquid phase, even after exchanging enough energy with the PCM to be evaporated. Therefore, the foreseen methodology of testing and evaluation for discharging could not be applied.

3.3. Temperatures in the PCM

In the PCM channel of the storage module there are 6 thermocouples installed (see Fig.2): three in the central PCM channel (purple lines in Fig. 5) and another three close to the outer module surface at the opposite side at the horizontal entrance/exit of the HTF to the module (yellow lines in Fig. 5). These temperatures should reflect the fact that the PCM changes phase at a certain point.

According to the HITEC® study reported at 4.2 below, during charging (melting process) two phase transitions should be observed in the PCM: one at 90 ºC –which may correspond to a solid to solid transition- and another one at 140 ºC –corresponding to solid to liquid phase change-. The transition at around 90 ºC is observed in all these 6 thermocouples by a change in their profile slope. The 140 ºC transition is clearly observed only in TE-024. TE-027 may show a short of changing slope at that temperature but due to the fluctuations in the data it cannot be assured with certainty. TE-022 shows a transition but at around 130 ºC and TE-023, TE-025 and TE-026 seem to have no more transition but the one at 90 ºC.

During discharging (freezing the PCM) the above mentioned study supports to have two transitions: one at 140 ºC (liquid to solid) and another one at 60 ºC (corresponding to solid to solid phase change). The difference in the temperature at which the solid to solid transition takes placed is due to the supercooling effect. In discharging is the solid to liquid transition the one that is clearly identified in all the thermocouples that achieved 140 ºC. TE-024, TE-025 and TE-026 in the 9/1/2017 test, which is being used as example, do not reach but 160 ºC when the recording of experimental data stopped.

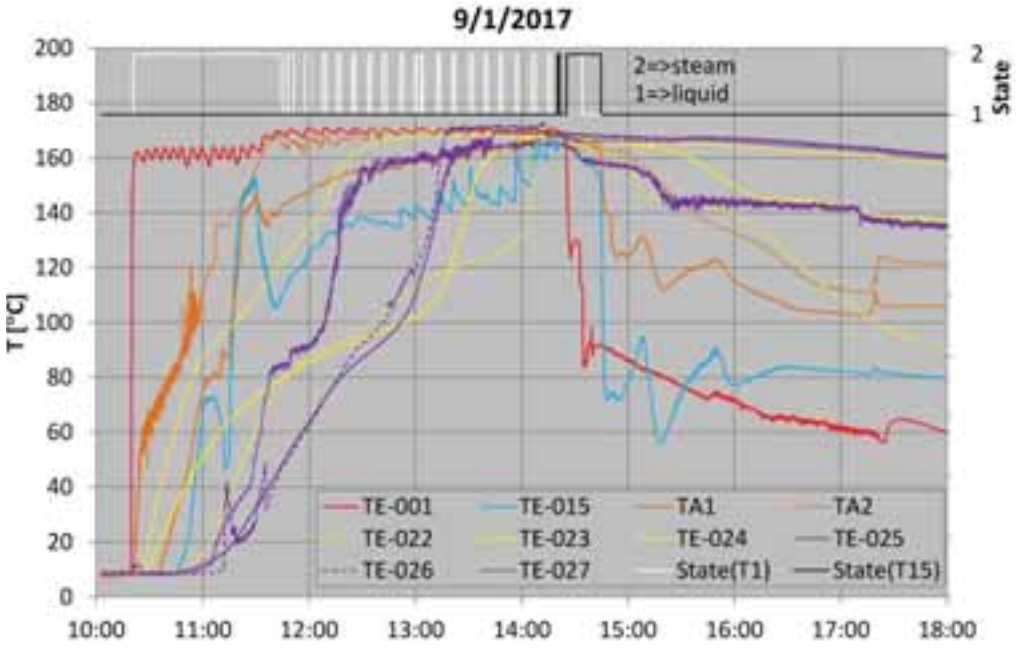

Fig. 5: PCM temperatures for charging and discharging on 9/1/2017.

During **charging**, temperature at the bottom (TE-022) and the top (TE-024) show the same profiles up to around 90 ºC, from which the steam boiler starts providing non-continuous steam at low mass flow and the value of the temperature gauges at the top began to increase more slowly than the bottom ones, reaching the solid to liquid transition temperature –around 140 ºC- 36 minutes later. This delay can be explained by considering that the steam supplied to the module stagnates at the upper part and, since steam has a poor heat transfer coefficient without changing phase, the PCM at this upper part requires more time to reach the same temperature level than at the bottom part when it condensate.

This inhomogeneous melting of the PCM within the storage module imposes a problem when determining the end of charging process. Depending on the period of time considered for charging, one of the following situations can occur at that point: part of the PCM at the top is still solid; part of the PCM at the bottom is superheated; or part of the PCM at the top is still solid and part at the bottom is superheated.

Looking at the temperatures or the state of the HTF at the exit of the storage module during charging (TE-016), this question is not clarified either. The end of charging may be assumed when steam is detected at the exit of the storage module; in this case the PCM gauges show a superheating behavior coming close and to around 170 ºC.

Discharging is assumed to start after a transition time, in which valves are closed/open to change to discharging HTF loop. In the case of the tests performed on 9/1/2017, at 15:37 pressure at the loop reaches 0.7 MPa but the cold mass water flow does not stabilized till 15:58 (see Fig. 4), thus discharging is assumed to start at that time. As mentioned in 3.1, due to the affordable loop pressure the water during discharge cannot be converted to steam, therefore the state of the corresponding HTF at the storage module exit does not give any clue on the end of discharging process.

Looking at PCM average temperatures, we can see that the three average profiles decrease their values with a different velocity as it happens during charging. While the PCM at the bottom of the storage module achieved the solidification temperature, 140 ºC, the PCM at the top of the module did not achieve such temperature when we stopped recording experimental data.

3.3. Thermal losses analysis

Idle thermal losses were expected to be calculated by the difference in discharged energy from a fully to a partially charged TES module situation, coming the partially charged situation from leaving the TES module for a certain time without any manipulation. As already mentioned, stablishing the end -and thus the associated energy- in a discharge process is not reliable due to the inhomogeneous behavior of the PCM. Thus, another procedure has to be applied.

One method for calculating idle thermal losses is to turn off all heating sources and track the rate of temperature

decay in average along certain time. By knowing the mass and enthalpy of storage media in the vessel, an estimation of the heat losses can be made by calculating the enthalpy variation in water and PCM from the starting time to the final time.

In Fig. 6 experimental results of the evolution of temperature during one week is shown. In those testing days some adjustments to the data acquisition system were performed so data is not continuously recorded along the whole day. These experimental data (- markers) is linked between them by an interpolation line. In this Figure, several "plateaus" at different temperatures can be observed for both water and PCM. It has been assumed that these plateaus are the result of a phase change occurring in the influence volume of the corresponding thermocouple. When the thermocouple is inserted in the PCM, the plateaus do not correspond necessary to its expected solid to liquid (around 140 °C) nor to its solid to solid (around 60 ºC) transitions, but keeps its temperature constant because some PCM around changes phases in spite that the PCM directly in contact does not. This assumption is a certainty with the thermocouples placed in water: no phase change takes place in the water at certain time period, but a plateau can be observed due to the phase change occurring in the adjacent PCM.

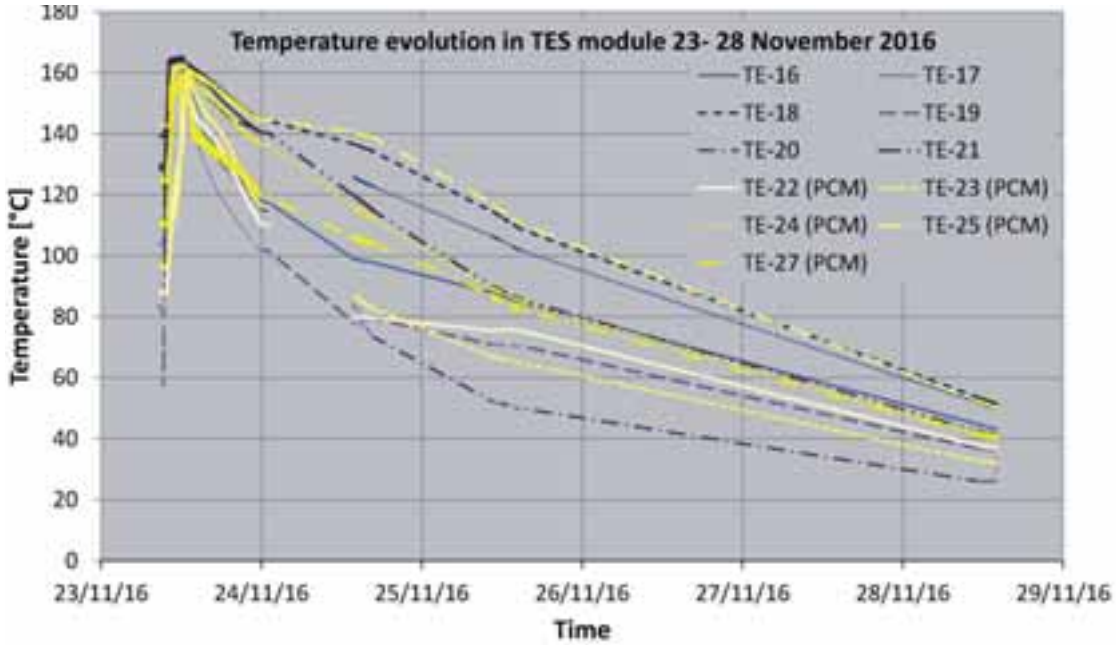

Fig. 6: Temperature evolution of water and PCM during the thermal losses test.

From these data, an estimation of 1.45 kW power thermal losses mean value has been found. This value is calculated by adding the thermal losses associated to the stainless steel conforming the TES module (25.6 kWh), the thermal losses of the PCM (23 kWh), those of the water (127.871.05 KWh) and knowing that these thermal losses have occurred along 121.78 hours. For sake of simplicity, ambient temperature has been considered the mean ambient temperature during the experiment (20 °C).

According to the authors, this method of calculating idle thermal losses by adding the idle thermal losses of the different components of the tank along a long period of time is the only possible way of calculating thermal losses of the while system, since it is not possible to define a representative temperature nor of the prototype nor of its surface in contact with ambient. This fact implies that it is not possible calculating a heat lost coefficient for a given TES module temperature (or time step) but just a mean value along a long period of time.

3.4. Charging and discharging power and stored energy

As already mentioned there is not a clear definition of the points at which charging and discharging processes end, since the storage module does not behave as a whole.

In Figure 7 the charging power for 9/1/2017 is shown. It is calculated by the mass flow measurement and the enthalpy change given by the HTF outlet conditions and HTF inlet conditions. Keeping in mind that the steam boiler provides steam at pulses, the obtained shawtooth profile is expected. The very low values from 11:25 onwards are due to the already mentioned decrease in steam mass flow production due to pressure loop and the limitations of the steam boiler. If there were not these disadvantages, a constant charging power would be expected.

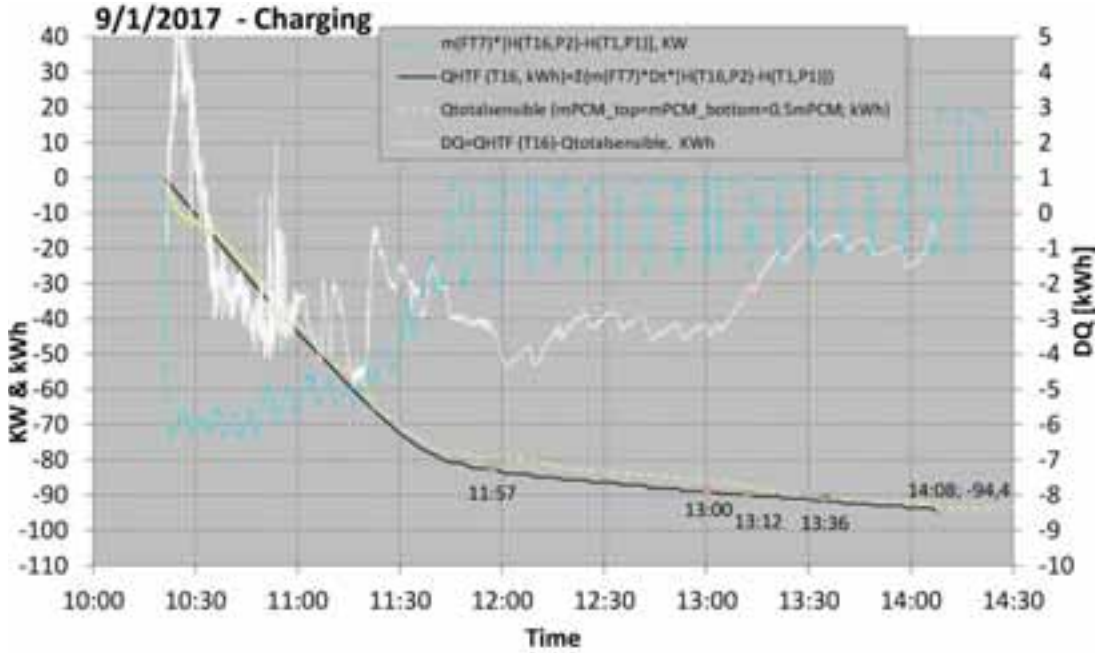

Fig. 7: HTF charging power, energy supplied by the HTF and estimated energy used for sensible heat.

In order to calculate the energy supplied by the HTF to the storage module, the above mentioned curve has been integrated in time (Q_{HTF}(T16), [kWh]). At the end of charging process, the HTF has supplied around 94.4 kWh to the whole system. Part of this energy has been used for increasing the temperature of the storage module ($Q_{sensible}$), [kWh], part for dealing with thermal losses (Q_{lost}),[kWh], and part has been stored in form of latent heat, by changing the phase of the PCM from solid to liquid (Q_{latent}), [kWh], i.e.,

$$Q_{HTF} = Q_{sensible} + Q_{lost} + Q_{latent} \qquad \text{(eq. 1)}$$

The sensible energy required to increase the temperature, $Q_{sensible}$, takes into account that the storage module is made of 1410 kg stainless steel (c_p=500 kJ/kgK) and 410 kg of HITEC (c_p=1560 kJ/kgK), which means that steel mass is more than 3 times PCM mass, while its heat capacity is around three times lower, giving similar thermal losses for both materials.

Considering that, as mentioned above, that mean heat loss power is 1.45 kW, the resulting energy for the latent heat is 1 kWh, which implies 9 kJ/kg specific latent heat of the PCM, which is much lower than the one expected up to now. This result makes Hitec salt not the most appropriate candidate for its use as PCM.

The main conclusion obtained is that with a module of this type it is necessary to know with certain accuracy a thermal map of the PCM. The storage module tested here did not allow including temperature gauges at different radial positions, but at the center and outer radius of the equipment. This would allow a better definition of the phase change moment for the different parts of the TES module, since one of the main conclusions of this work is the difficulty in defining ends of charging and discharging processes when inhomogeneous phase change processes take place.

4. Performance studies of Hitec® salt

As stated in a previous work (Rodríguez-García and Rojas, 2016), the selected PCM implemented in the spiral storage module was the commercial eutectic salt mixture Hitec® ($NaNO_3$-KNO_3-$NaNO_2$; 7/53/40 % w) (http://www.coastalchem.com/). This salt mixture has the melting point at 142 °C with a reported enthalpy of fusion of about 83 kJ/kg and is expected to be thermally stable up to 535 °C (http://stoppingclimatechange.com). Despite its relatively low phase change enthalpy, this salt was finally selected because its melting temperature fits the operating temperature range of the storage module but also because it has proven to be chemically stable upon daily melting/freezing cycles under inert atmosphere (Rodríguez-García and Rojas, 2016).

4.1. DSC measurements

For a preliminary stability study a Hitec® sample previously dried at 120 ºC for 48 hours was subsequently cycled between 130 ºC and 150 ºC at 2 ºC/min except for the first heating that was performed at 10 ºC/min. The resulting

curves are plotted in Fig.8 and the temperatures and enthalpies calculated for each cycle are recorded in Tab. 2.

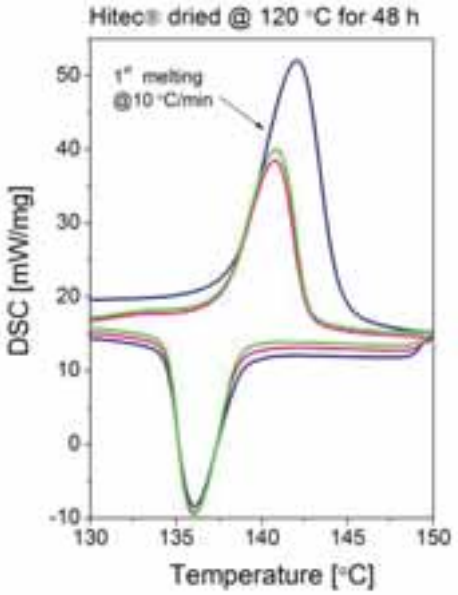

Fig. 8: Three DSC melting/freezing cycles performed from 130 ºC to 150 ºC for Hitec® commercial mixture dried at 120 ºC for 48 h.

Tab. 2: Results of DSC measurements displayed in Fig. 8

Cycle	$T_{melt-peak}$	ΔH_{melt}	$T_{freez-peak}$	ΔH_{feez}
1st	142 ºC*	56 kJ/kg*	136 ºC	51 kJ/kg
2nd	141 ºC	57 kJ/kg	136 ºC	49 kJ/kg
3rd	141 ºC	60 kJ/kg	136 ºC	47 kJ/kg
(*) Performed at 10 ºC/min				

As we can see thermal behavior is maintained during cycling and not only in terms of temperatures but also in terms of enthalpies. In this way, the mean melting temperature obtained is about 142 ºC while the freezing temperature is 136 ºC. This small difference between melting and freezing is usually observed in DSC measurements and does not correspond to any supercooling phenomenon. As for the enthalpy values they remain constant for all cycles being the values slightly higher for melting (57 kJ/kg) than for freezing (49 kJ/kg). It is important to remark that the melting enthalpy obtained experimentally is no higher than 60 kJ/kg and hence rather lower than the expected theoretical value of 80 kJ/kg. On the other hand the peak of the first heating cycle is much larger than the other peaks because this run was performed at 10 ºC/min and the others at 2 ºC/min. However the thermal result of this run is similar to the results of the other ones.

DSC measurements were also performed for Hitec® salt previously dried at 120 ºC for 48 hours in the temperature interval 50 ºC-160 ºC at 10 ºC/min rate. The curves obtained for the first heating and the second heating /cooling runs are displayed in Fig. 9. During the first heating run, we observe a sharp peak at around 131 °C that could correspond to adsorbed water evolution together with a broad peak corresponding to the melting of the bulk salt powder. During the first DSC run not much information about sample thermal properties can be obtained since the main goal is to make it homogeneous. During the second heating/cooling runs, if temperature is decreased down to 50 ºC, in addition to the melting/freezing process at ~140 ºC other transition is observed at 93 ºC upon heating and at 119 ºC upon cooling. It is interesting to note that the additional transition observed in the heating run (at 93 ºC) has an enthalpy almost in the range of the melting process. This would explain the plateau displayed by some of the thermocouples recording temperatures inside the REELCOOP P#3 storage prototype at a temperature lower than the melting one.

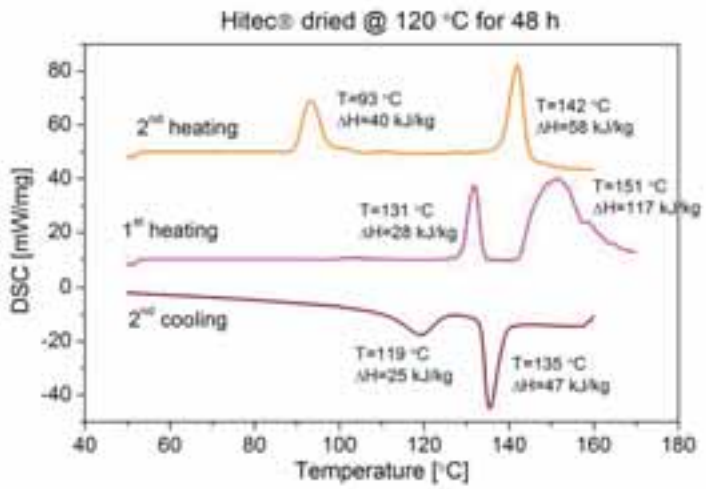

Fig. 9: DSC curves for 1st heating and 2nd heating/cooling runs for HITEC® mixture previously dried @ 120 ºC for 48 h.

4.2. Thermal cycles under air

In order to confirm that Hitec® has a transition that takes place at a temperature lower than the melting one, various daily heating/cooling cycles between 40 ºC and 170 ºC were performed under air in an oven with forced ventilation and hence with strict temperature control. Fig. 10 displays one of these cycles where it can be seen not only a shoulder at around 140 ºC that corresponds to the eutectic phase change but also other shoulder at lower temperature with apparently similar size. The shoulder associated to the melting/freezing transition appears at the same temperature during both heating and cooling processes, which confirms that Hitec® does not present supercooling. For the shoulder at lower temperature we can see that it appears at 90 ºC during the heating and at 60 ºC during the cooling. This is in agreement not only with the plateaus observed at around 90 ºC in the temperature curves recorded during the charging of REELCOOP P#3 storage prototype (Fig. 1.b) but also the DSC heating scan of Fig. 9. The fact that this transition appears at a lower temperature (60 ºC) during the cooling can be due to a supercooling phenomenon. This can be the reason why it was not observed in DSC scans since they were only performed down to 50 ºC and usually supercooling effect is larger in this kind of measurements due to the small amount of sample they use. On the other hand, since the oven has forced ventilation and Hitec® remained melted at 170 ºC for about 10 h and hence enough time and temperature to evolve any adsorbed water, this low temperature shoulder can be more likely associated to a solid to solid transition than to water exchange.

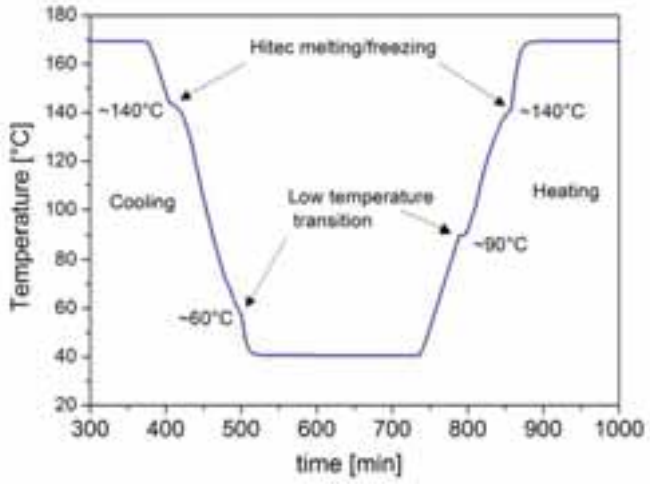

Fig. 10: Close view of a temperature-time curve for a daily heating/cooling cycle of a Hitec® sample between 40 ºC and 170 ºC.

4.3. Studies of thermal degradation

Hitec® salt is not a medium chemically stable since its components can react between them or with their environment (atmosphere or metallic walls) through processes strongly temperature dependent. One of the widest studies of Hitec® thermal degradation was published by Roche in 1980. This author observed that the main indicator of Hitec® degradation is the decrease of nitrite ions which leads to an increase of melting temperature in the salt mixture. Actually if all nitrites were converted in nitrates the final salt composition would be the eutectic mixture $NaNO_3$-KNO_3 47/53 %-w whose melting point is 220 ºC.

According to Roche 1980, the main degradation reactions of Hitec® mixture are the following:

$$(Na,K)NO_2 + \frac{1}{2}O_2 \leftrightarrow (Na,K)NO_3 \qquad \text{(eq. 2)}$$

$$5(Na,K)NO_2 \leftrightarrow 3(Na,K)NO_3 + (Na,K)_2O + N_2 \qquad \text{(eq. 3)}$$

The first one (eq. 2) is the oxidation of nitrite to nitrate by the oxygen, which is expected to take place in open systems exposed to air, whereas the second one (eq. 3) is the so called nitrite *thermolysis* in which nitrate, oxide and nitrogen are produced. In this case the presence of oxygen is not required and hence this reaction can take place in closed systems.

Assuming that only these two reactions are involved in Hitec® degradation, Roche (1980) obtained the thermodynamic equations governing the equilibrium and with them he calculate the mole percentage of all species involved in the equilibrium (nitrites, nitrates and oxides) as function of temperature for different environments. In this way, when molten Hitec® is kept under air at temperatures below 500 ºC, the predominant species are the nitrates and hence the risk of nitrite oxidation is very high. However, at temperatures above 500 ºC, nitrites become more stable and reaction (2) can even be reversed with the corresponding evolution of oxygen. For the case of oxides they start only appearing above 850 ºC. In contrast, if molten Hitec® is kept under N_2 with a very little amount of oxygen (0.001 atm) the amount of nitrites at 500 ºC increases dramatically (from 2.6 % in air to 27.3 % in N_2), which are good news, whereas oxides can appear already at 600 ºC increasing the corrosion risk and the possibility of other degradation reactions (Roche, 1980). It must be taken into account that these results correspond to the equilibrium composition of the molten Hitec but thermodynamic equations do not give any information about how long it takes until such equilibrium state is reached. For that information the kinetics of these degradation reactions must be studied.

In this way Olivares (2012) performed kinetic studies of Hitec® thermal degradation under different gas atmospheres by means of thermogravimetric analysis. In general it can be said that Hitec® seems to be stable under any gas atmosphere for temperatures lower than 370 ºC and this stability range is extended to about 470 ºC if it is kept under inert atmosphere (Ar or N_2). Under either O_2 or air atmospheres nitrites undergo slow oxidation at 370 ºC-390 ºC through eq. 2 but this process is not observed when inert gases are used. However, for all atmospheres once 450-500 ºC is reached, gas emission is produced although the strong weigh loss begins at about 610 ºC. The gases evolved during weight loss are NO, NO_2, O_2,, N_2, which are the expected products of both nitrate and nitrite thermal degradation. Roche 1980 also performed various test for determining Hitec® degradation rate under different atmospheres by monitoring the variation of NO^{2-} molar percentage versus the number of days it had been kept at a certain temperature. Again they obtained that degradation of Hitec® starts to be important at temperatures above 300 ºC not only under N_2 but also under air atmosphere. However, due to the operating conditions of the storage module of REELCOOP P#3 prototype, the highest working temperature of molten Hitec® is not expected to exceed 180 ºC. Therefore kinetic results of Olivares 2012 and Roche 1980 are not valid in our case. Moreover, the degradation experiments performed by both authors were not correlated to any kinetic equation and hence their extrapolation to low temperature region cannot be done directly.

Fortunately, it has been found in the literature that Freeman described the degradation kinetics of both $NaNO_2$/$NaNO_3$ (Freeman 1956) and KNO_2/KNO_3 systems (Freeman 1957) with similar equations. Therefore we can assume that the same expressions could be used for describing the thermal degradation of Hitec® mixture. By combining the experimental results of Roche (1980) and the kinetic equations of Freeman (1956 and 1957) for nitrites degradation, it was possible to obtain the dependence of the kinetic constant with temperature and hence estimate the degradation of Hitec® under air at temperatures close to the melting point. As displayed Fig. 11.a, in the time scale of a year, Hitec® mixture undergoes strong degradation under air when kept at temperatures higher than 400 ºC whereas for operation temperatures of 300 ºC, nitrite mole fraction remains at its initial value (0.49). When degradation curves of Hitec® are calculated for lower temperatures (see Fig. 11.b), degradation time scale has to be increased to several years. In this case we can see that for temperatures below 200 ºC, Hitec® shows no

decrease in nitrite content and hence no significant degradation should be expected for at least 10 years of operation in that temperature range.

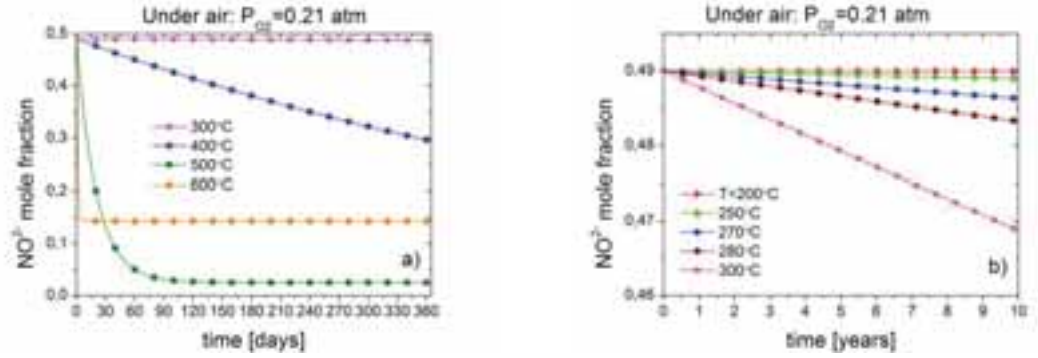

Fig. 11: Expected Hitec® degradation under air in the temperature range: 600 ºC-300 ºC (a) and in the range: 300 ºC-200 ºC (b).

From these calculations we can conclude that Hitec® mixture can be kept under ambient air without any risk of degradation due to nitrite oxidation when used as PCM for latent storage in the range of its melting temperature. However, although salt degradation is not expected in the presence or air, the metallic container might not behave in the same way and hence undergo corrosion due to the presence of air or to the molten salt itself. This could change the behavior of Hitec® salt and promote its degradation. This was one of the reasons why REELCOOP P#3 prototype inner cavity was kept under N_2 in order to avoid any atmosphere undesirable degradation process either in the salt or in the material container. The other reason was preventing moisture to be in contact with Hitec® mixture since we observed that it is quite hygroscopic in solid state.

In order to confirm that no degradation happened in Hitec® salt upon short-term cycling, we analyzed the composition of some samples by ionic chromatography before and after either consecutive or daily cycles performed under air or inert atmosphere (N_2 or Ar). The results in terms of ionic weight percentage are recorded in Tab. 3. The analysis of ionic composition of Hitec® showed a slight decrease of nitrite concentration after 50-60 daily melting/freezing cycles. However, the increase in nitrate composition is not so clear especially if we take into account that cation percentages do not remain constant. Hence, since the values are close to the theoretical ones, these variations could be within the limits of the experimental error specially if we take into account that the results for the cycles under air are the same as the results for the cycles under inert atmosphere.

Tab. 3: Results of Hitec® analysis by means of ionic chromatography.

	Na^+[w-%]	K^+[w-%]	NO_3^-[w-%]	NO_2^-[w-%]
Theoretical composition	15.2	20.4	37.6	26.7
As received Hitec® salt	17	18	33	31.7
After 5 consecutive cycles in air	16	20	36.5	28.7
After 25 consecutive cycles in air	16	19	35.8	28
After 60 daily cycles in air	17	20	37.4	26.7
After 50 daily cycles in N_2	17	20	37.5	25.8
After 53 daily cycles in Ar	17	20	37.3	26

5. Conclusions

In this article the experimental results of the REELCOOP project have been evaluated. In this project a PCM thermal energy storage with a spiral geometry is used. In terms of the behaviour of the storage prototype, it can be said that inhomogeneous melting/solidification processes of the PCM takes place due to the stagnation of steam in the upper part of the module. This inhomogeneous melting/solidification processes implies that the charging and discharging processes are difficult to be defined and limited in time, which results in not very accurate charge and discharge power and thermal losses calculations.

The obtained values for power and stored energy are much lower than the expected ones: 50 kWth as the lowest expected power against the 13 kWth as the largest experimentally calculated; 6 kWh expected thermal capacity against 1 kWh experimentally observed. This mismatch may be due to a lower specific latent heat of the PCM (9 kJ/kg) than the expected from DSC measurements (around 50 kJ/kg).

In spite of a well-designed insulation not only around the prototype but also by reducing thermal bridges by having two well-isolated storage module supports, thermal losses are 1.44 kW. Thermal losses related to the steel (tank and channeling) are of the same order as the ones of the PCM.

Considering the above, we have to conclude that neither the module design nor the PCM are appropriate options for storing latent energy.

The performance studies carried out Hitec® have shown that this salt does not display supercooling while its corresponding melting enthalpy is much lower than the reported value (55 kJ/kg vs. 80 kJ/kg). Hitec also displays an additional transition at a temperature lower than the melting temperature which is most probably associated to a solid-solid and not to water evolution. Kinetic calculations and salt analysis after short-term cycling have demonstrated that Hitec® was not expected to degrade due to nitrite to nitrate conversion during the prototype testing period.

The mismatch between the results obtained of the PCM at laboratory level -with small amounts of PCM and well controlled ambient conditions- and those obtained in a medium size storage module shows the importance of manufacturing prototypes and avoid claiming feasibility of materials for storing energy just by laboratory results.

6. Acknowledgements

The authors would like to acknowledge the E. U. through the 7th Framework Program for the financial support of this work under the REELCOOP (Renewable Electricity cooperation) project with contract number: 608466, the DETECSOL project (Ref. ENE2014-56079-R) with ERDF funds, and the operation, instrumentation and maintenance departments at the PSA for their collaboration during the development of this work

7. References

Freeman E. S., 1956. The kinetics of the thermal decomposition of sodium nitrate and of the reaction between sodium nitrite and oxygen, Journal of Physical Chemistry 60 (11), 1487-1493.

Freeman E. S., 1957. The kinetics of the thermal decomposition of potassium nitrate and of the reaction between potassium nitrite and oxygen, Journal of the American Chemical Society 79 (4), 838-842.

Olivares R., 2012. The thermal stability of molten nitrate/nitrite salt for solar thermal energy storage in different atmospheres. Solar Energy 86, 2576-2583.

Rivas E., Rojas E., Bayón R., inventor, Ciemat, assignee. 2011 Aug. 11. Módulo de almacenamiento térmico basado en calor latente con altas tasas de transferencia de calor. Spanish patent P201131378.

Roche M., 1980. L'utilisation d'un mélange de sels fondus pour le stockage de chaleur, Revue Phys. Appl. 15, 895-902.

Rodríguez-García M.M., Bayón R., Rojas E., 2016a. Stability of D-mannitol upon melting/freezing cycles under controlled inert atmosphere. Energy Procedia 91, 218-225.03

Rodríguez-García M.M., Rojas, E. 2016b. Testing a new design of latent storage. 11th ISES EuroSun 2016, International Conference on Solar Energy for Buildings and Industry. Palma de Mallorca, Spain. 11-14 October 2016.

Rojas et al., 2011, Definition of standardised procedures for testing thermal storage prototypes for concentrating solar thermal plants. SFERA project. Available at http://sfera.sollab.eu/downloads/JRA/WP15/Deliverable15.2_StandardisedTestingProcedures.pdf

http://stoppingclimatechange.com/MSR%20-%20HITEC%20Heat%20Transfer%20Salt.pdf

Net Zero Energy Buildings

Renovation of Swedish single-family houses from the 1960s and 1970s to net-zero energy buildings – Case study

Tomas Ekström[1,2], Ricardo Bernardo[1], Henrik Davidsson[1] and Åke Blomsterberg[1]

[1] Department of Architecture and the Built Environment, Division of Energy and Building Design, Lund University, Lund 221 00, Sweden

[2] NCC AB, Malmö 205 47, Sweden

Abstract

This paper evaluates whether a net-zero energy building (NZEB) can be attained by implementing on-site renewable electricity production when renovating to Passive House level. The assessment is based on the Swedish single-family housing stock constructed between 1961 and 1980, using two case study houses and three locations. Specific conditions of the houses, such as the type of heat generation and available roof area for installation of a photovoltaic system, determine whether a NZEB renovation is possible. Overall, the assessment showed that it is not cost-effective to aim for NZEB when implementing a PV system, based on the alternatives in this study.

Keywords: energy renovation, NZEB, single-family houses, renewable energy

1. Introduction

Single-family houses (SFHs) constructed between 1961 and 1980 account for approximately one-third of the total energy use, 31 TWh, for space heating and domestic hot water (DHW) in Swedish SFHs. These houses account for about 40 percent of the total energy use in buildings (Swedish Energy Agency, 2015b). There are roughly 715,000 houses from this period (Statistics Sweden, 2015) and they are largely homogeneous in technical terms, with low levels of thermal insulation, and ventilation with heat recovery is rare (Boverket, 2010a). The average energy use for houses from this period is about 40 percent higher than SFHs constructed between 2011 and 2013 (Swedish Energy Agency, 2015a). Many of these houses need to be renovated (Boverket, 2010b), providing an excellent opportunity to incorporate energy efficiency measures, to reduce both operational cost and greenhouse gas emissions related to energy use. A continuation of this is to also implement local renewable energy production to further reduce energy use.

National and international goals for a sustainable future are part of the overall objective to reduce greenhouse gas emissions and mitigate global warming and climate change (European Commission, 2011, SOU, 2016). The Swedish Government has set a target of a 50 percent reduction in total energy use per heated floor area by 2050, compared to the level in the reference year 1995 (Sahlin, 2006). Because of limitations in existing buildings, such as limited space, economic considerations, or preserving cultural heritage values, a 50 percent reduction of energy use is not possible in all buildings. To compensate for this, energy use must be reduced by more than 50 percent in some buildings to achieve an average of 50 percent energy use reduction. One way to achieve this is to renovate existing buildings to net-zero energy buildings (NZEB) whenever possible.

The purpose of this study was to determine whether a net-zero energy building (NZEB) could be attained for SFHs from 1960s and 1970s by implementing on-site renewable electricity production when implementing an extensive renovation package to Passive House level, based on the Swedish Passive House standard, FEBY 12 (Erlandsson et al., 2012).

doi:10.18086/swc.2017.15.01 Available at http://proceedings.ises.org

2. Method

A photovoltaics (PV) system for local renewable electricity production was installed on two reference houses to ascertain the viability of a NZEB renovation. The assessment involved comparing the electricity production from the PV system to the energy demand of the buildings after implementing extensive renovation packages to Passive House level. The reference houses were evaluated in three different locations in Sweden – from Malmö in the south (55.52 N, 13.37 E) to Kiruna in the north (67.82 N, 20.33 E).

When the Passive House standard is applied, thermal transmission and ventilation losses are reduced by about 70 percent (Ekström and Blomsterberg, 2016). The renovation measures used to achieve the Passive House level renovation are presented in Table 1. Based on the type of heat generation commonly used in Swedish SFHs from this period, the reference houses were evaluated with two alternatives: electric heating and a ground source heat pump. Non-electric heating such as pellets and district heating were excluded because of their reliance on other energy sources. Three locations were chosen to determine whether the difference in solar radiation and ambient conditions, such as temperature, impacted the possibility of achieving NZEB. These locations were Malmö in the south, Östersund located in central Sweden, and Kiruna in the north.

Table 1. Description of the Passive House renovation level with renovation measures and the required performance level.

	Renovation level	Passive House
Building envelope	Facades	New
	External walls	0.10 ±0.02 W/(m²·K)
	Roof	0.10 ±0.02 W/(m²·K)
	Foundation	Improved, see Table 3
	Cellar walls	+200 mm thermal insulation
	Windows	0.80 W/(m²·K)
	Doors	0.80 W/(m²·K)
	Thermal bridges	Calculated
	Airtightness, at ± 50 Pa	0.3 l/(s·m²)
	Drainage	New
Installations	Ventilation system	Balanced, with heat recovery
	Ducts	New air ducts
	Heating system	New, depends on heat generation used
	Heat generation	New, depends on evaluated heat generation
DHW	Heater	New
	Pipes	New
	Fixtures	New
	Household purpose electricity	Not included, new energy efficient appliances and lighting assumed

Two case study buildings represented the SFH building stock from the period (Table 2). These houses were used in earlier studies of energy savings potential (Ekström and Blomsterberg, 2016) and cost-effectiveness (Ekström et al., 2017) of renovations aimed at reaching Passive House level. More detailed information about the renovation measures can be found in those papers. The impact of renovation measures on the building envelope of the reference houses is shown in Table 3.

Table 2. Description and visualization for the two case study buildings before renovation.

Reference house 1		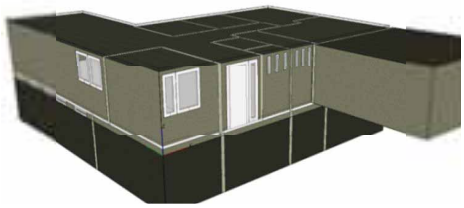
Year built:	1965	
Roof area:	169 m², inclination < 5 °	
A_{temp}:	230 m^2	
Ventilation:	Passive stack ventilation	
Description: One-storey house with a cellar and a pent roof, lightweight concrete walls and a concrete slab foundation.		
Reference house 2		
Year built:	1977	
Roof area:	80 m² + 80 m², inclination 45 °	
A_{temp}:	142 m^2	
Ventilation:	Balanced ventilation, with heat recovery	
Description: One-and-a-half storey house with a ridged roof, 45°, wood frame structure walls insulated with mineral wool and a concrete slab foundation.		

Table 3. Section drawings of the reference houses before and after implementing the passive house renovation packages.

Reference house 1		Reference house 2	
Before renovation	**After renovation**	**Before renovation**	**After renovation**
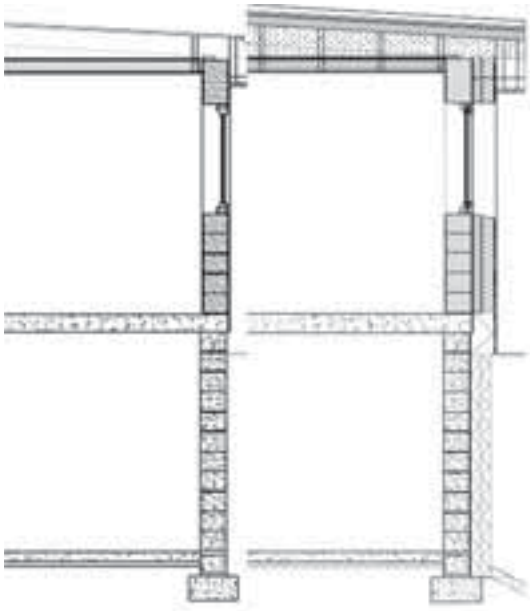		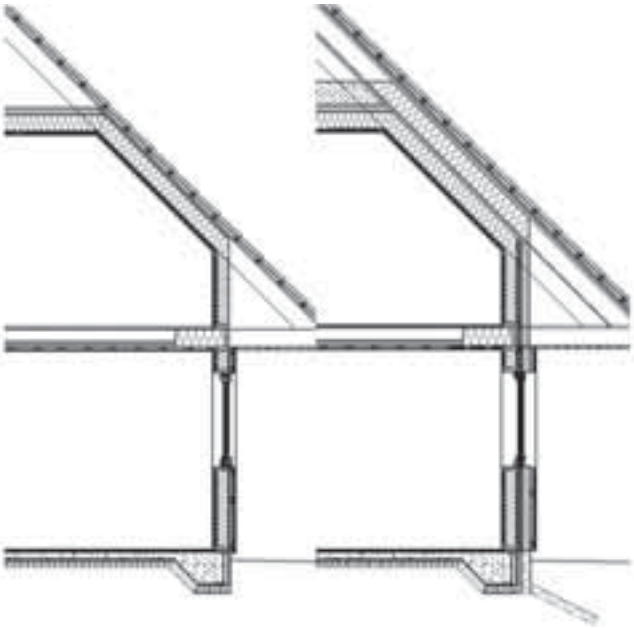	

The building simulations include detailed models of the reference houses, with zones for each room. A specific building model was used for each alternative in the assessment. The input data regarding structures, thermal transmittance, airtightness, inhabitants, internal heat gains and shading was gathered from and prioritised as follows: 1) specific data for reference house; 2) Passive House requirements (Erlandsson et al., 2012); and 3) Sveby (Levin, 2012) was used for normalised user-related input data. The reference houses were assumed to be inhabited by two adults and two children. Weather data files included in the building energy simulation program (*IDA ICE 4.7*) from *SMHI (Swedish Meteorological and Hydrological Institute)*, with long-term measurements of climate and weather, were used for each location in the simulations. In Swedish conditions cooling is not commonly used in residential buildings, so is excluded from the analysis.

On-site production of renewable energy was evaluated by simulating the performance of the PV system, to ascertain whether it could cover the annual energy demand of the houses. A validated dynamic building energy simulation tool, *IDA ICE 4.7* (EQUA, 2016) was used to simulate energy demand, and the simulation program *SAM 2017.1.17* (NREL, 2017) was used to simulate the production from the PV system. The nominal efficiency of the PV panels was assumed to be 20.6 percent and an expected service life of 25 years (Lindahl, 2014), with a temperature coefficient of -0.3 percent per degree increase and an inverter with a maximum conversion efficiency of 96 percent. The PV panels were placed with the same tilt as the existing roof. The simulations used hourly values to compare self-consumption of the electricity from the PV system. The definition and equation for calculating the self-consumption, or solar fraction, used in this study is presented in equation (1):

$$\text{Solar fraction (\%)} = \frac{\text{energy from PV to load}}{\text{energy load}} \quad (1)$$

The total energy demand that production from the PV system needs to cover is the demand for household electricity, space heating, domestic hot water and facility electricity. The demand for household electricity is based on the annual average use in Swedish SFHs, 5900 kWh, and the domestic hot water demand is based on the normalised annual use in Swedish SFHs of 20 kWh per heated floor area, Sveby (Levin, 2012). The energy demand for space heating and facility electricity was simulated in *IDA ICE 4.7* for the specific case study buildings at the different locations and with the different types of heat generation. The assumed variation in the domestic hot water demand for the evaluation is presented in Figure 1 and Figure 2. Variation in household electricity demand was assumed as shown in Figure 3 and Figure 4.

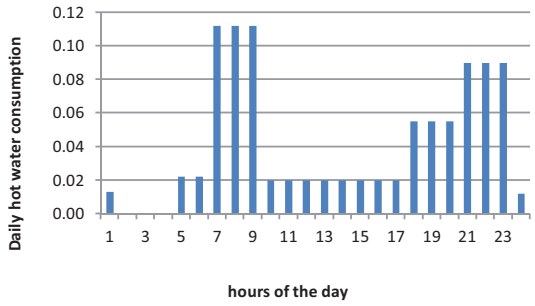

Figure 1. Daily variation of DHW consumption based on a simplification (Bernardo et al., 2012).

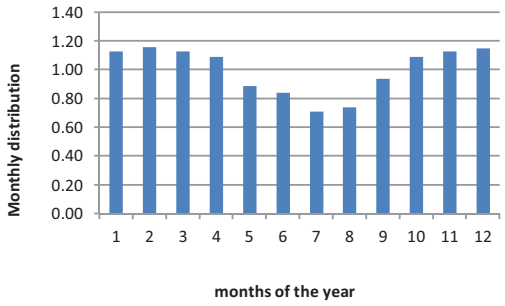

Figure 2. Annual variation of DHW consumption based on FEBY12 (Erlandsson et al., 2012).

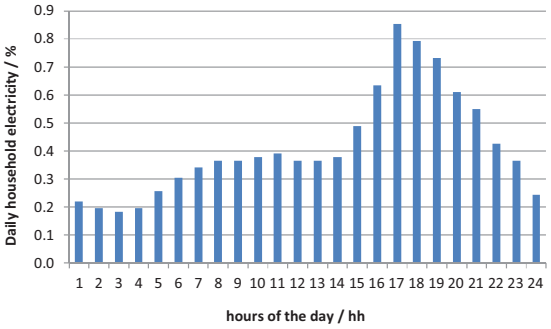

Figure 3. Assumed daily profile for household electricity use based on measurements of Swedish passive houses. This is not included in specific energy use (Nilsson and Westberg, 2012).

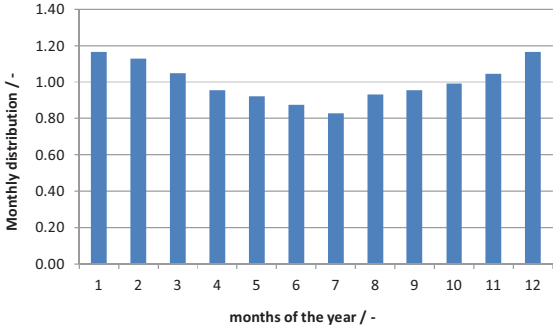

Figure 4. Assumed yearly distribution of household electricity use based on measurements of Swedish passive houses (Nilsson and Westberg, 2012).

The economic analysis, using the software *"Investment calculation for photovoltaics"* (Stridh, 2016), calculated the life cycle cost as net present value and internal rate of return. The investment cost of the system is based on the average prices, €1850 per installed kWp including VAT, presented in the software. A Government grant is available for installation of a PV system on a SFH, covering 20 percent of the investment costs (Svensk författningssamling 2016:900, 2009), which was included in the economic calculation. It was assumed that a loan was taken to cover the investment cost. The interest rate of the loan was assumed to be two percent higher than inflation, so the real interest rate used in the calculations of net present value was two percent.

The total price per kWh for bought electricity in Sweden is based on several parameters. In addition to the electricity price, there is also the grid service price, electricity certificate (Swedish Energy Agency, 2016), electricity tax (Swedish Tax Agency, 2017) plus VAT. The fixed fees were not included since they do not change with the energy demand, so they are not impacted by the reduced energy use from the renovation measures.

To determine the electricity price, information was gathered regarding average annual grid service price per kWh and monthly electricity prices per kWh for the variable price rate for SFHs (Statistics Sweden, 2017). The average electricity price depends on the electricity demand of the house – if the heat generation is based on electricity, electricity demand is higher and price per kWh lower, and if non-electric heat generation is used, electricity demand is lower and price per kWh higher. Only houses using electric heating were included in this study, so only electricity prices for such houses were included. Average electricity prices are about €0.13 per bought kWh for houses using electric heating (Figure 5). The price increase above inflation was assumed to zero.

The selling price for electricity sold to the grid, presented in Figure 6, was estimated based on the average price of €0.05 per kWh in *"Investment calculation for photovoltaics"*. Also included is the electricity certificate of €0.013, compensation for the grid owner of €0.005, certificate of origin of €0.0005, and a tax subsidy of €0.06 available for the first 15 years of production. All costs were estimated in Swedish Crowns (SEK) and converted to Euro (€) with a conversion rate of SEK 10 for €1.

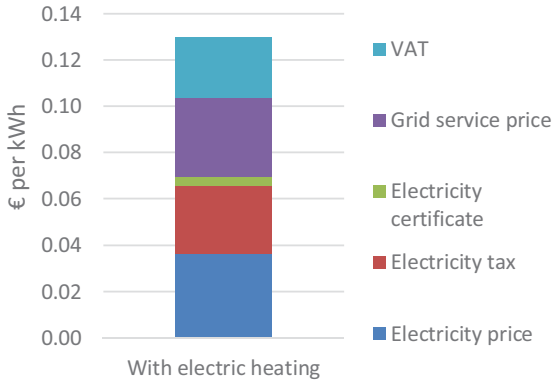

Figure 5. Average annual price for electricity bought from the grid for houses using electricity for heat generation.

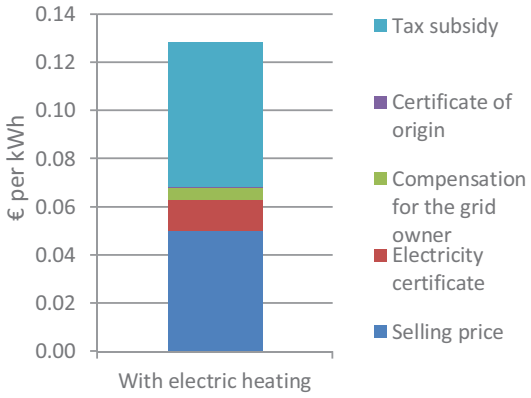

Figure 6. Average annual price for electricity sold to the grid for houses using electricity for heat generation.

3. Results and discussion

Results are presented, in Table 4 for Reference house 1 and in Table 5 for Reference house 2, as annual electricity demand (including space heating, domestic hot water, facility electricity and household electricity), annual electricity production from the PV system and self-consumption, based on the hourly demand and production. The aim was for the annual electricity production to equal that of the energy demand, to attain the NZEB level. The results are shown per location and type of heat generation. Also presented are the system size and the peak power of the evaluated systems. Alternatives presented in red do not attain the NZEB level.

Table 4. Results from simulation of the PV system production for Reference house 1 with roof tilt of < 5 degrees. Alternatives presented in red do not attain the NZEB level.

Heat generation	Location	PV system size m²	Peak power kWp	Annual demand kWh	Annual production kWh	Self-consumption %
Electric heating	Malmö	114*	23.5	18 400	19 000	31.1
	Östersund	114*	23.5	25 400	16 900	25.0
	Kiruna	114*	23.5	30 600	14 200	21.3
Ground source heat pump	Malmö	65	13.4	10 200	10 900	34.6
	Östersund	90	18.4	12 600	13 200	30.1
	Kiruna	114*	23.5	14 900	14 200	25.4

*Maximum available roof area.

Table 5. Results from simulation of the PV system production for Reference house 2 with roof tilt of 45 degrees and east-west orientation. Alternatives presented in red do not attain the NZEB level.

Heat generation	Location	PV system size m²	Peak power kWp	Annual demand kWh	Annual production kWh	Self-consumption %
Electric heating	Malmö	90	18.4	12 800	13 200	33.1
	Östersund	131	26.8	16 100	17 000	29.0
	Kiruna	163*	33.5	18 700	18 000	26.3
Ground source heat pump	Malmö	57	11.7	8 600	8 700	35.9
	Östersund	82	16.8	9 800	10 700	32.8
	Kiruna	98	20.1	10 800	10 800	29.6

*Maximum available roof area.

The results show that fulfilling the aim of a NZEB building depends both on location and type of heat generation. In the case of Reference house 1, the PV system was limited by the size of the roof in three cases: for electric heating in Östersund and Kiruna, and for the ground source heat pump in Kiruna. For Reference house 2, this was only the case for electric heating in Kiruna. The results reflect both the increased demand for space heating in the colder climate and the reduced production from the PV system in the northern parts of Sweden.

The results from the life cycle cost calculations are presented, in Table 6 for Reference house 1 and in Table 7 for Reference house 2, with the investment cost for each system and as net present value and internal rate of return. The results are shown per type of heat generation and location. Alternatives presented in red are not profitable.

Table 6. Profitability calculations for the implementation of PV systems on Reference house 1, presented with investment costs, net present value and internal rate of return. Alternatives presented in red are not profitable.

Heat generation	Location	Investment cost (€)	Net present value (€)	Internal rate of return (%)
Electric heating	Malmö	35 250	680	2.2
	Östersund	35 250	- 4 300	0.7
	Kiruna	35 250	- 10 200	- 2.4
Ground source heat pump	Malmö	20 100	710	2.4
	Östersund	27 600	- 3 100	0.8
	Kiruna	35 250	- 9 900	- 1.2

Table 7. Profitability calculations for the implementation of PV systems on Reference house 2, east-west orientation, presented with investment costs, net present value and internal rate of return. Alternatives presented in red are not profitable.

Heat generation	Location	Investment cost (€)	Net present value (€)	Internal rate of return (%)
Electric heating	Malmö	27 600	- 2 900	0.9
	Östersund	40 200	- 9 300	- 0.5
	Kiruna	50 300	- 17 200	- 1.9
Ground source heat pump	Malmö	17 600	- 1 100	1.4
	Östersund	25 200	- 5 500	- 0.4
	Kiruna	23 000	- 11 000	- 2.2

The cost-effectiveness is also shown to be dependent on both the location and type of heat generation. It is only cost-effective to install a PV system with a size to attain NZEB for Reference house 1 in Malmö in the south of Sweden. This is the case with both types of heat generation, although the investment cost for the electric heated house is higher.

4. Conclusion

Overall, the assessment showed that it is not cost-effective to aim for NZEB when implementing a PV system, based on the alternatives in this study, assuming a lifetime of 25 years and no electricity price increase above inflation. In many cases, the NZEB level could be attained with the roofs available, but this depended on the location and type of heat generation of the houses.

In this study, the aim was to maximise annual PV production, therefore the PV panels were installed flat on the roof for Reference house 1. The tilt of the PV system could be optimized to increase production per panel and cost-effectiveness. However, by doing this, the total annual PV production is reduced because of the limited space, so the NZEB level would not be attained.

5. References

BERNARDO, R., DAVIDSSON, H. & KARLSSON, B. 2012. Retrofitting Domestic Hot Water Heaters for Solar Water Heating Systems in Single-Family Houses in a Cold Climate: A Theoretical Analysis. *Energies* 5(10), 2012**,** 4110-4131.

BOVERKET 2010a. Energi i bebyggelsen - tekniska egenskaper och beräkningar - resultat från projektet BETSI (Energy in the existing building stock - technical properties and calculations - results from the BETSI project). www.boverket.se: Boverket.

BOVERKET 2010b. Teknisk status i den svenska bebyggelsen – resultat från projektet BETSI (The technical status of the existing building stock - results from the BETSI project). www.boverket.se.

EKSTRÖM, T., BERNARDO, R. & BLOMSTERBERG, Å. 2017. Cost-effective passive house renovation packages for Swedish single-family houses from the 1960s and 1970s. *Submitted to Energy and Buildings, 2017-08-02*.

EKSTRÖM, T. & BLOMSTERBERG, Å. 2016. Renovation of Swedish Single-family Houses to Passive House Standard – Analyses of Energy Savings Potential. *Energy Procedia,* 96**,** 134-145.

ERLANDSSON, M., RUUD, S., SANDBERG, E., BLOMSTERBERG, Å., EEK, H. & INGULF, O. 2012. Kravspecifikation FEBY12 - Bostäder (Requirement specification FEBY12 - Residential buildings). Sveriges Centrum för Nollenergihus.

EUROPEAN COMMISSION 2011. Energy Roadmap 2050.

LEVIN, P. 2012. Sveby - Branschstandard för energi i byggnader (Sveby - trade standard for energy in buildings).

LINDAHL, J. 2014. National Survey report of PV Power Applications in Sweden 2014. Swedish Energy Agency.

NILSSON, F. & WESTBERG, F. 2012. *Energianvändning i lågenergihus - Analys av mätningar från 97 lägenheter med passivhusteknik.* Master of science, Lunds universitet.

SAHLIN, M. 2006. Nationellt program för energieffektivisering och energismart byggande [National Programme for Energy Efficiency and Energy-Smart Construction, in Swedish]. *In:* GOVERMENT (ed.).

SOU 2016. Initiativet Fossilfritt Sverige [Fossil free Sweden initiative, in Swedish] - Dir. 2016:66.

STATISTICS SWEDEN. 2015. *Number of dwellings by type of building 1990-2013* [Online]. http://www.scb.se/: Statistics Sweden. Available: http://www.scb.se/en_/Finding-statistics/Statistics-by-subject-area/Housing-construction-and-building/Housing-construction-and-conversion/Dwelling-stock/Aktuell-Pong/87476/374826/ [Accessed 2016-04-22 2016].

STATISTICS SWEDEN. 2017. *Prices on electricity and transmission of electricity (network tariffs)* [Online]. Available: http://www.scb.se/en/finding-statistics/statistics-by-subject-area/energy/price-trends-in-the-energy-sector/prices-on-electricity-and-transmission-of-electricity-network-tariffs/ [Accessed 2017-05-19 2017].

STRIDH, B. 2016. *Investeringskalkyl för solceller (Investment calculation for photovoltaics)* [Online]. Mälardalens högskola. Available: http://www.mdh.se/forskning/inriktningar/framtidens-energi/investeringskalkyl-for-solceller-1.88119 [Accessed 2017-06-07 2017].

SWEDISH ENERGY AGENCY 2015a. Energy statistics for one- and two-dwelling buildings in 2014 ES 2015:06. www.energimyndigheten.se.

SWEDISH ENERGY AGENCY 2015b. Summary of energy statistics for dwellings and non-residential premises for 2014. www.energimyndigheten.se.

SWEDISH ENERGY AGENCY. 2016. *Elkundens bidrag till förnybar elproduktion (Elcertifikat) (Electricity customers contribution to renewable electric production)* [Online]. www.energimyndigheten.se. Available: http://www.energimyndigheten.se/fornybart/elcertifikatsystemet/om-elcertifikatsystemet/elkundens-bidrag-till-fornybar-elproduktion/ [Accessed 2017-05-19 2017].

SWEDISH TAX AGENCY. 2017. *Skattesatser på bränslen och el under 2017 (Tax rates on fuel and electricity during 2017)* [Online]. https://skatteverket.se. Available: https://www.skatteverket.se/foretagochorganisationer/skatter/punktskatter/energiskatter/skattesatserochvaxelkurser.4.77dbcb041438070e0395e96.html [Accessed 2017-05-19 2017].

SVENSK FÖRFATTNINGSSAMLING 2016:900 2009. Förordning (2009:689) om statligt stöd till solceller. *In:* MILJÖ- OCH ENERGIDEPARTEMENTET (ed.).

Modeling, Construction and Monitoring of a Plus-Energy Building in Dubai

Giuseppe Franchini, Giovanni Brumana, Antonio Perdichizzi

Department of Engineering and Applied Sciences, University of Bergamo, Dalmine (Italy)

Ali Shaheen, Mohammed Bin Neshooq, Shaikhah Alfalasi

Mohammed Bin Rashid Space Centre, Dubai (UAE)

Abstract

This work presents the performance analysis of the very first Energy+ building in Dubai certified by the German Passive House Institute. The analysis is presented as comparison between numerical predictions and the first available monitored data. Trnsys is the software used to create the energy model, including both thermal envelope and HVAC system. The use of highly insulating materials, together with a design aimed to reduce the solar heat gains, allows for minimizing cooling loads. A 40 kW PV field, coupled to a 25 kWh battery storage and to a high-efficiency air-cooled electric chiller, fulfills the electric and cooling demand, making the building energy-autonomous. The study demonstrates the high accuracy of the energy model, able to predict precisely the building cooling loads, the energy production and the cooling system performance. The Energy+ building, inaugurated in November 2016, is a pioneering pilot-project and it represents an advance in the field of sustainable construction for all Arabic area.

Keywords: energy+ building, solar cooling, PV, monitoring system, dynamic simulation.

1. Introduction

In many developed countries, buildings and their use are responsible for approximately one-third of the total primary energy consumption and carbon emissions. Governments and scientific communities are aiming for new paradigms for energy-efficient buildings: the goal is to reduce the environmental impact of the construction sector (Nejat et al., 2015). Many authors investigated the design principles for high-efficient buildings in cold climates (Thalfeldt et al., 2013; Justo Alonso et al., 2015). More recently, the interest in the development of passive buildings has grown also for hot regions (Fokaides et al., 2016; Schnieders et al., 2015).

The development of sustainable solutions goes through the construction of more and more efficient buildings. At this regard, new concepts have gained wide international attention, such as Passive Houses, Nearly Zero Energy Buildings, Net Zero Energy Buildings and Energy+ Buildings (Marszal et al., 2011). The first step in order to comply with all high-efficiency standards is to reduce the energy consumption in buildings. Passive design strategies contribute to improve the interior comfort conditions, reducing the requirement of energy supply from active systems (Rodriguez-Ubinas et al., 2014).

Besides the development of well-insulated thermal envelopes, an improvement of the building sustainability can be achieved by using high-efficiency cooling technologies coupled with renewable energy sources. Several types of solar cooling systems have been investigated in the open literature (Nanda and Panigrahi, 2016; Ghaith and Abusitta, 2014). Among the available technologies, the option based on compression chiller driven by a PV field assisted by a battery pack is highlighted. A remarkable comparison between this solution and thermal solar cooling systems was done by Lazzarin (2014). The results show that the performance is today comparable but the PV has a greater adaptability. Recently, huge investments in the electric storage technology have led to the spread of batteries for building applications and to the development of off-the-grid or stand-alone houses (Okoye and Solyalı, 2017; Fara and Craciunescu, 2017).

doi:10.18086/swc.2017.15.02 Available at http://proceedings.ises.org

In the Gulf area, the United Arab Emirates is one of the most active countries in the promotion of actions aiming to ensure a sustainable development while preserving the environment. The UAE Vision 2021 National Agenda focuses on improving the quality of air, preserving water resources, increasing the contribution of clean energy and implementing green growth plans. The UAE Energy Plan 2050 is an ambitious strategic plan aiming to cut carbon dioxide emissions by 70 per cent, to increase clean energy use by 50 per cent and to improve energy efficiency by 40 per cent by the middle of the century. Within this framework, the Government of Dubai is implementing policies and strategies in order to promote the energy efficiency and the use of renewable energy resources (Al-Amir and Abu-Hijleh, 2013). Recently, in the construction sector the Mohammed Bin Rashid Space Centre (MBRSC), a Dubai government R&D organization working in various fields of the scientific research including aerospace projects, started a Sustainable Energy Program. The goal was to build an autonomous house representing a model for the real-estate sector in the region. This project is the result of the collaboration of different players: the team of MBRSC engineers and scientists, University of Bergamo (modeling, simulations and scientific supervision), Casetta & Partners (executive design) and Wolf System (builder company). The present paper reports the modeling and simulation activities carried out to dictate the design choices for the building construction. All technologies used in this house are presented and the preliminary results of the monitoring data are shown. The building construction was completed in a record time of less than 100 days and was inaugurated in November 2016 by H.H. Sheikh Mohammed bin Rashid Al Maktoum, Vice President and Prime Minister of the United Arab Emirates, and ruler of the Emirate of Dubai.

2. Building description

The building is a two-floor office structure, with geometry and orientation aiming to reduce as much as possible the primary energy consumption. To do that, the surface to volume ratio is minimized. The solar irradiation on the walls during the day and across the seasons is accurately evaluated. A small patio shrinks the radiation on the glazed elements and keeps shaded the office areas. This solution allows for avoiding window shields even in daylight hours. The diffuse light naturally illuminates the 550 m^2 floor surface and – at the same time – the solar gains are minimized. A timber trimmed structure is designed to support a photovoltaic field (see Fig, 1), to promote the ventilation on PV modules and to shade the flat roof. The outline elements of the windows are protruding to limit direct radiation.

Fig. 1: The Energy+ Building unveiled in November 2016.

A lightweight load bearing structure made by wood supports timber walls and roof. The walls are designed to reduce as much as possible the building cooling load. The balance between mass and insulation improves the energy performance: the insulation thickness is designed to minimize thermal transmittance and the phase shift is controlled by adding mass layers. Walls are painted with a special reflective paint to curtail the absorption of solar radiation on the outer layer. Similarly, the roof is treated with a reflective film and infrared reflector films are inserted inside the walls. Windows are specific for warm climates with very low U and G values to limit the solar gains (see Table 1).

The prefab European timber platform frame technology made possible to realize the building in less than 100 days. The building envelope has been designed according to the Passive House standard and the energy systems have been selected to reach the level of Energy+ Building. Power supply is ensured by the rooftop PV field. A battery pack is available to store electricity during light hours and to supply electricity after sunset. The building is virtually off-grid (power import is possible for emergency) and the electric overproduction is delivered to the grid.

Table 1. Envelope thermal properties.

	unit	value
U_{wall}	W/(m^2 K)	0.063
Wall thickness	m	0.603
Wall solar absorptance	%/100	0.3
U_{roof}	W/(m^2 K)	0.061
Roof thickness	m	0.566
Roof solar absorptance	%/100	0.2
$U_{-value,w}$	W/(m^2 K)	0.7
$G_{-value,w}$	%/100	0.294

A high-efficient air-water reversible heat pump - specifically designed for hot-humid climates - meets the cooling and dehumidification demand, and the production of domestic hot water. The cooling system is based on a combination of three different technologies: floor cooling, mechanical ventilation and fan-coils. The radiant floor cooling maintains a high level of comfort, the air handling unit with high-efficient heat recovery controls temperature and humidity of the inlet air, and the fan-coils fulfill the cooling peak loads. The integration of high-efficient technologies both in the thermal envelope and energy systems is the key of the project performance.

3. Building model

The design of high-efficiency buildings in hot climates requires the accurate prediction of the cooling demand and of the energy plant performance. Fundamental is the development of simulation tools for assessing the building energy performance (Harish et al., 2016; Mihai et al. 2017). In a well-insulated building, the internal loads play a crucial role. The prediction of the energy consumption due to the electrical equipment is very important, as documented by Widen (2014). Moreover, Hoxha and Jusselme (2017) showed the relevance of using efficient lights and appliances adapted to new high-efficiency buildings. Furthermore, the analysis of occupancy reveals its relevant impact on the energy performance (Blight and Coley, 2013).

In the energy-efficient buildings a primary interest is the comfort perception: predictive techniques for quantifying and qualifying the indoor comfort are included in several building models (Wang et al., 2017; Satake et al., 2016). Frequently the goal of a high level of comfort perception is achieved through radiant floor cooling systems (Zhao et al., 2016).

The models developed for the simulation of building envelop and solar cooling system performance are based on Trnsys v.17. Weather data with hourly resolution have been provided by the Mohammed Bin Rashid Space Center.

3.1 Envelope model

The detailed architectural building model is based on Trnsys Multizone Building Type and developed by the 3D cad software Google Sketch Up®, with the plug-in Trnsys3D for geometry and shading. The building model includes 10 homogeneous thermal zones and all main comfort parameters are listed in Table 2.

Table 2. Comfort settings and internal gains.

	unit	value
Set point temperature	°C	24
Set point RH	%	50
Mean ventilation ratio	Vol/hr	0.60
HX efficiency	%	80
Infiltration	Vol/hr	0.06
Lighting (peak)	W/m^2	5
Internal gains (peak)	kW	6
Occupancy	Nr.	20

In the computer model the technical data of all the construction materials have been included, thus allowing a realistic prediction of the building envelope behavior. Internal loads due to lights and appliances have been carefully evaluated. The occupancy is considered as an average attendance including random occurrence of overload events.

The Trnsys model allowed to predict the cooling demand all over the year. This is crucial for a correct sizing of the energy plants. The simulation results show the strong impact of latent loads due to high relative humidity levels. The dehumidification demand influences both the peak load and the annual demand respectively by 60% and 30% (Table 3). The total cooling load and the latent load are shown in Fig 2: the peak cooling demand is about 27 kW. The short load duration curve (limited to 4000 hours per year) testifies the high performance of the building envelope.

Table 3. Building cooling loads.

Peak Load		
	unit	value
Air Load - sensible	kW	6.83
Air Load - latent	kW	20.49
Floor Load	kW	8.42
Total Load	kW	27.03

Annual Load		
	unit	value
Air Load - sensible	kWh	7954.6
Air Load - latent	kWh	11920.7
Floor Load	kWh	13844.5
Total Load	kWh	33719.9

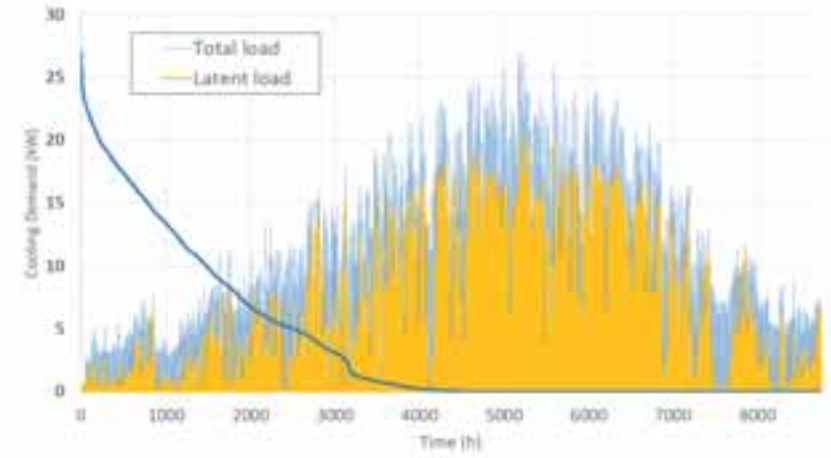

Fig. 2: Cooling load and duration curve.

In addition to the calculation of the global building performance, the Trnsys model permits to carry out detailed analysis of the thermal behavior of each single wall. For instance, Figure 3 reports for two consecutive summer days the temperature trends of a portion of flat roof not shaded by PV modules. It can be noted that, in spite of a strong temperature variation in the external side (with peak higher than 42°C), the temperature level on the internal side is predicted to be stable at 25°C.

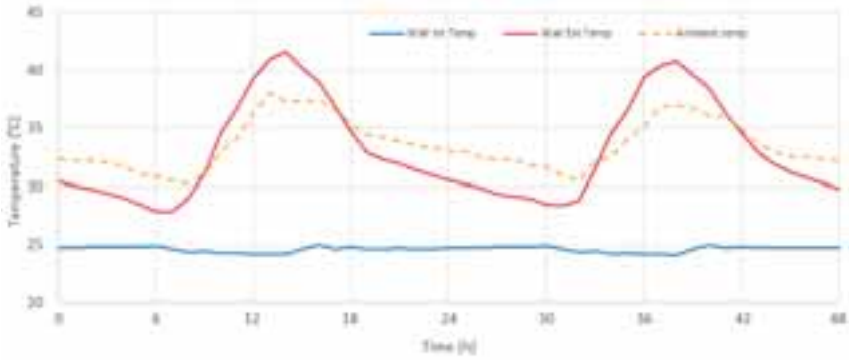

Fig. 3: Roof temperature.

Fanger's comfort parameters were also considered to improve the design quality. Table 4 shows the calculated comfort indexes: the excellent level is achieved thanks to the integration of different air conditioning systems. The predicted mean vote is very near to the ideal value (0) and the maximum deviation (0.27) is very small compared to the comfort region (-0.5 to 0.5) range. Furthermore, the value of the percentage of person dissatisfied is close to the minimum value.

Table 4. Building comfort parameters.

	Unit	Max	Min	Average
Mean Radiant Temperature	°C	24.23	22.34	23.66
Operative Temperature	°C	24.11	22.25	23.75
Predicted Mean Vote	[-3 ; 3]	0.26	-0.27	0.16
Percentage of Person Dissatisfied	% [5 ; 100]	6.51	5.00	5.69

3.2 Energy system model

The energy system is based on multi-crystalline PV panels coupled to a battery pack. Power PV-generated drives an air-cooled reversible heat pump and all technical devices. An electric energy storage (battery pack) has been designed to ensure the autonomous operation, assuring 24/7 power supply to A/C system, lighting and appliances. The electricity overproduction is exported into the grid when batteries are at full capacity. An additional small thermal energy storage (1 m^3 cold tank) compensates for cooling load fluctuations. The specifications of the PV system are reported in Table 5.

Table 5. PV field and battery specifications.

	unit	value
Area	m^2	268
Nominal efficiency	-	14.9%
Efficiency modif. temp.	1/°C	-0.0041
Voltage at P_{max}	V	30.5
Open circuit voltage	V	37.6
Battery capacity	kWh	25

The cooling plant model includes the heat pump performance map provided by the manufacturer. The chiller is designed to operate with an outdoor temperature up to 50 deg. C and the cooling capacity was selected to fulfill the peak demand of the building. The chiller specifications are reported in Table 5.

Table 6. Chiller specifications.

	unit	value
Chiller capacity*	kW	27.51
COP*	-	2.38
Power input*	kW	11.55
Cold tank volume	m^3	1
Tank insulation (EPS)	m	0.2

* Ambient temperature 30 deg. C; chilled water 7-12 deg. C.

The results of the transient simulation carried out for a one-year period are shown in Table 7. It can be seen that power consumption for air conditioning is about half of the total electricity consumption. The electricity production to meet the off-the-grid requirement results to be more than twice the Net-Zero Energy standard (export = import over one-year period). This has a heavy impact on the design of the photovoltaic field. Because the energy import must be zero at any time, PV system must be large enough to ensure the energy autonomy of the building.

Table 7. Electric production and consumption.

	unit	value
Chiller consumption	kWh	11400.3
Light and appliances	kWh	11914.7
Total electric load	kWh	23315.0

	unit	value
PV production	kWh	56460.2
Grid import	kWh	0.0
Grid export	kWh	33123.7

The simulation results document that the battery charge level (see Fig. 4) is always above 60% of the full capacity (25 kWh), even in the peak periods. The power demand exhibits a daily peak of about 3 kW in the winter months, whilst the annual peak taking place in August (when the cooling demand is maximum) is 10 kW. The daily curves of power production and consumption are shown in Figure 5. The energy demand is met according to the following priority order: by PV (when available and sufficient), by batteries and, in the last case, by import from the grid (emergency only). Power consumption for appliances and lighting depends on the occupancy and the activities in the thermal zones. The PV field drives the heat pump as priority and the surplus recharges the battery pack. The electricity overproduction, when the battery level is full, is delivered to the grid according to a net-metering scheme. Figure 6 shows the annual energy fluxes: PV production, total power consumption (heat pump, lighting and appliances) and the export to the network on a monthly basis. In winter months, when the cooling request is low and the heat pump efficiency is high thanks to the low ambient temperature, the electric energy delivered to the grid is around 70% of the global PV production. During the warm season this ratio decreases to 50%.

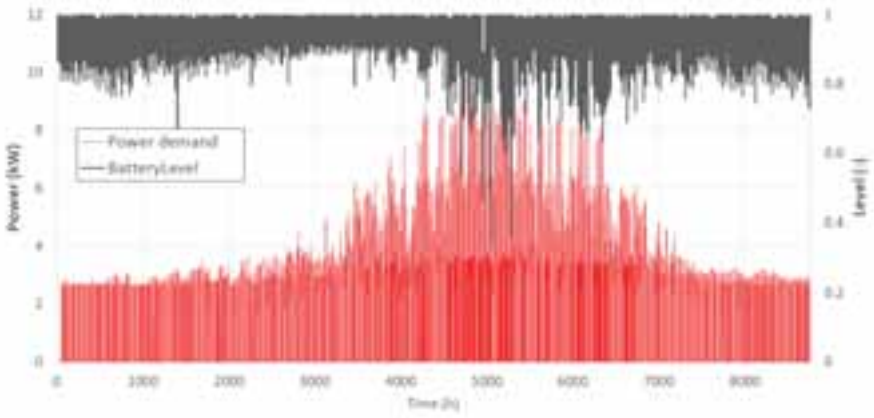

Fig. 4: Power demand and battery level.

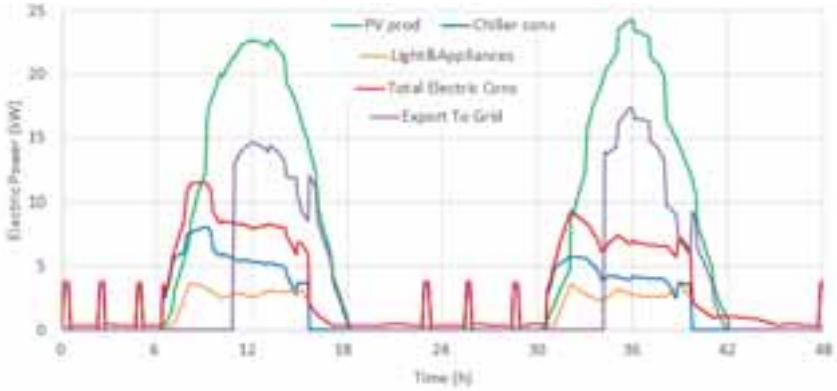

Fig. 5: Power demand and production.

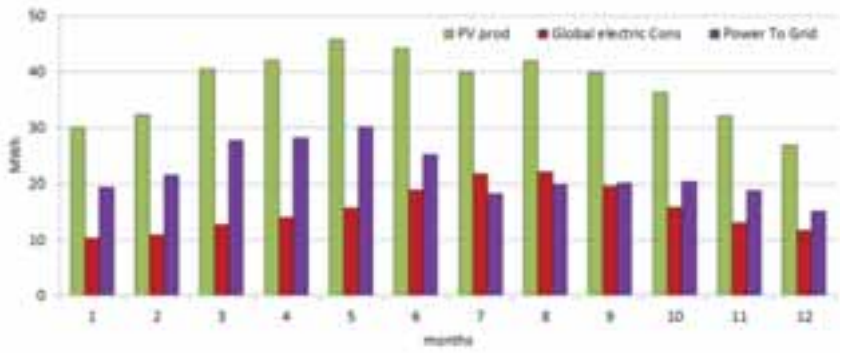

Fig. 6: Monthly energy production, consumption and export.

4. Comparison model prediction vs. monitoring data

The Plus-Energy building has been fully instrumented. A monitoring system has been installed for a remote real time access to all collected data (with a frequency of 1 sample per second). This equipment makes possible to monitor with high level of detail the building energy performance under real operating conditions. The monitoring system includes thermocouples in the wall layers, thermo-hygrometers in the rooms, power meters on the PV field, the battery package and all electric boards, temperature and flow rate sensors in all circuits of the HVAC system. Table 8 summarizes the main monitoring data.

Tab. 8: Monitoring System Equipment

Weather	Ambient temperature, Ambient humidity, Global solar radiation
Building Envelope	Room temperatures, Humidity, CO_2, External/Internal side Walls/Roof temperature
PV Field & Grid	PV production, Grid Import/Export, Appliances and auxiliary consumption
Cooling Plant	Cooling production, Chiller electric consumption, AHU in/out temperatures, Floor cooling in/out temperatures

It has to be reminded that this building is a pioneering pilot-project. The goal is to prove that new sustainable construction standards are possible in the UAE and that this is a viable solution to reduce the carbon footprint in the region. The monitoring activity is fundamental to demonstrate that the predicted performance is confirmed under real operating conditions. Moreover, the measurement campaign is important also for the model validation. Currently, the monitoring activity is going on and some weeks of collected data are available for analysis. This paper reports the comparison between the model predictions and the first available data.

Figures 7-10 show the simulation results and the experimental data for two consecutive days in September. Figure 7 refers to the cooling demand. The curves related to the model prediction (dashed line) and the measurements (solid line) exhibit a very good superposition: the model appears able to estimate the peak values, the hourly trend and the daily integral value. As mentioned before, in addition to the overall thermal loads the Trnsys model can predict the trend of detailed parameters, like wall and roof temperatures. Figure 8 shows the trend of internal and external temperatures for the well-insulated roof. The daily pattern for the outer side temperature (influenced by the incident solar radiation and the ambient temperature) is well predicted, in spite of a small time shift. The inner side temperature is perfectly estimated.

Moving to the energy systems, Figure 9 reports the 48-hour trend of the PV production and the power consumption due to light and appliances and for the chiller operation. The chart shows a small underestimation of the PV power output (-9.5% as integral value), whilst the power consumption for lighting and electrical equipment is very well predicted. A far as the chiller consumption is concerned, the monitored data show slightly different patterns during the day and higher peak levels. The hourly variation of the power input is related to the trend of the real cooling demand documented in Fig. 7, while the higher peak levels and the higher daily integral values indicate a lower-than-expected chiller efficiency (-12.8%).

As mentioned in the previous paragraphs, when the batteries are full charged the electricity surplus is supplied to the grid. Figure 10 shows the power export compared to the PV production. The model exhibits a good capability to predict the amount of electricity delivered to the grid and the time interval of the power exchange. When the battery package is full (at 11.30 a.m.) the model predicts an instantaneous shift to the exportation mode, whilst monitoring data show a soft ramp starting 2 hours before achieving the full capacity condition: this is due to the control system of the electric storage that is not implemented in the model. Nevertheless, the integral value of the exported electricity is well predicted: the error model vs. monitoring is only 2.0%.

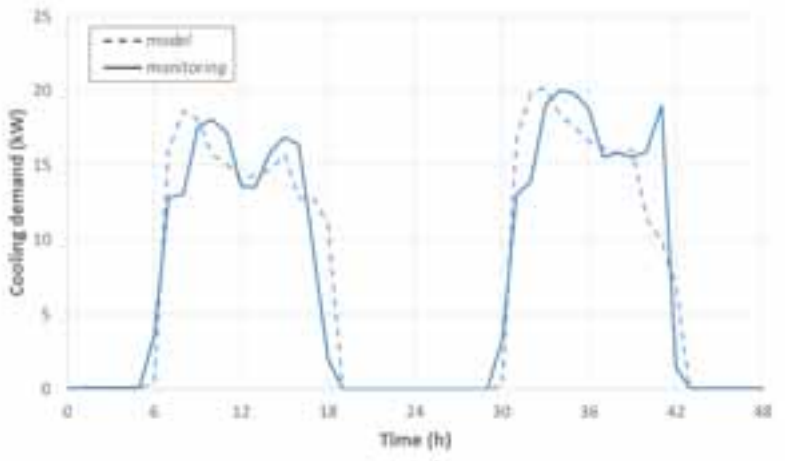

Fig. 7: Cooling demand (model vs. monitoring).

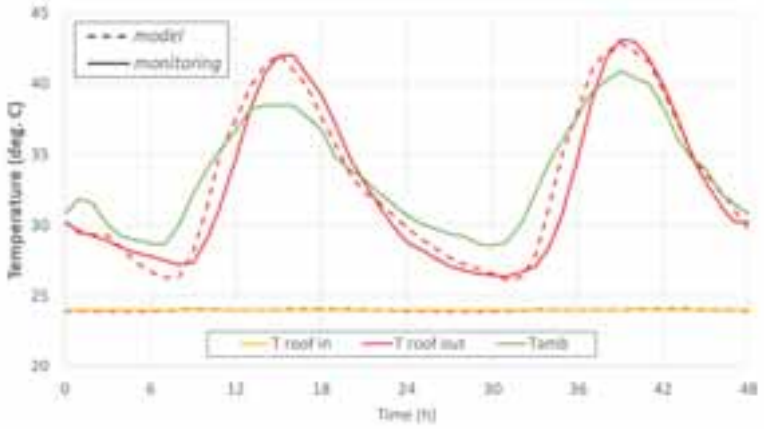

Fig. 8: Roof temperature (model vs. monitoring).

.

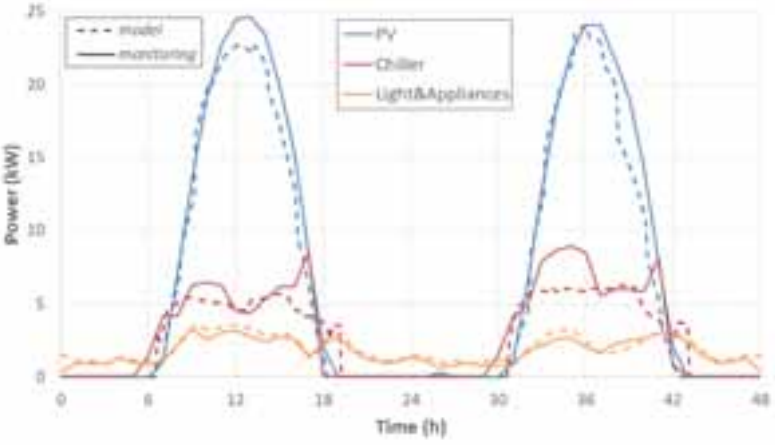

Fig. 9: Power production and consumption (model vs. monitoring).

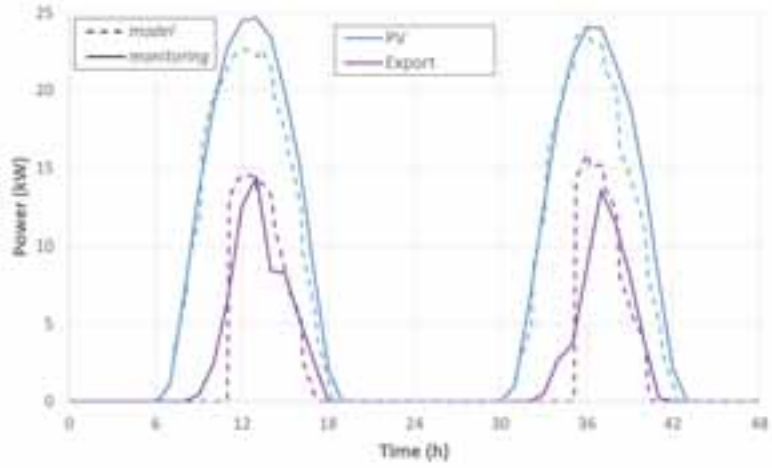

Fig. 10: PV production and electricity export (model vs. monitoring).

5. Conclusions

This work presents the very first Energy+ building certified by the Passive House Institute in the Dubai area. The building is a pioneering pilot-project aiming to prove that high comfort levels can be achieved by using solar energy as unique energy source. A 40 kW PV field, coupled to a 25 kWh battery storage and to a high-efficiency air-cooled electric chiller, fulfills the electric and cooling demand, making the building energy-autonomous. A preliminary activity of modeling and simulation dictated the design of the building envelope and of the energy systems. Trnsys is the software used to create the energy model and to predict the building performance. Starting from its inauguration, the building has been monitored to measure the actual performance under real operating conditions. The first available measurements confirm that the model predictions are very accurate and very close to the monitoring data. Therefore, it can be concluded that the expected targets in terms of energy savings and carbon footprint reduction have been successfully achieved.

6. References

Nejat P., Jomehzadeh F., Mahdi Taheri M., Gohari M., Majid M.Z.A., 2015. A global review of energy consumption, CO2 emissions and policy in the residential sector (with an overview of the top ten CO2 emitting countries). Renewable and Sustainable Energy Reviews 43, 843-862.

Thalfeldt M., Pikas E., Kurnitski J., Voll H., 2013. Façade design principles for nearly zero energy buildings in a cold climate. Energy and Buildings 67, 309-321.

Justo Alonso M., Liu P., Mathisen H. M., Ge G., Simonson C., 2015. Review of heat/energy recovery exchangers for use in ZEBs in cold climate countries. Building and Environment 84, 228-237.

Fokaides P. A., Christoforou E., Ilic M., Papadopoulos A., 2016. Performance of a Passive House under subtropical climatic conditions. Energy and Buildings 133, 14-31.

Schnieders J., Feist W., Rongen L, 2015. Passive Houses for different climate zones. Energy and Buildings 105, 71-87.

Marszal A.J., Heiselberg P., Bourelle J.S., Musall E., Voss K., Sartori I., Napolitano A., 2011. Zero Energy Building – A review of definitions and calculation methodologies. Energy and Buildings 43, 971-979.

Rodriguez-Ubinas E., Montero C., Porteros M., Vega S., Navarro I., Castillo-Cagigal M., Matallanas E., Gutiérrez A., 2014. Passive design strategies and performance of Net Energy Plus Houses. Energy and Buildings 83, 10-22.

Nanda A. K., Panigrahi C. K., 2016. A state-of-the-art review of solar passive building system for heating or cooling purpose. Frontiers in Energy 10(3), 347-354.

Ghaith F. A., Abusitta R., 2014. Energy analyses of an integrated solar powered heating and cooling systems in UAE. Energy and Buildings 79, 117-126.

Lazzarin R. M., 2014. Solar cooling: PV or thermal? A thermodynamic and economical analysis. International Journal of Refrigeration 39, 38-47.

Okoye C. O., Solyalı O., 2017. Optimal sizing of stand-alone photovoltaic systems in residential buildings. Energy 126, 573-584.

Fara L., Craciunescu D., 2017. Output Analysis of Stand-alone PV Systems: Modeling, Simulation and Control. Energy Procedia 112, 595-605.

Al-Amir J., Abu-Hijleh B., 2013. Strategies and policies from promoting the use of renewable energy resource in the UAE. Renewable and Sustainable Energy Reviews 26, 660-667.

Harish V. S. K. V., Kumar A., 2016. A review on modeling and simulation of building energy systems. Renewable and Sustainable Energy Reviews 56, 1272-1292.

Mihai M., Tanasiev V., Dinca C., Badea A., Vidu R., 2017. Passive house analysis in terms of energy performance. Energy and Buildings 144, 74-86.

Widén J., 2014. Improved photovoltaic self-consumption with appliance scheduling in 200 single-family buildings. Applied Energy 126, 199-212.

Hoxha E., Jusselme T., 2017. On the necessity of improving the environmental impacts of furniture and appliances in net-zero energy buildings. Science of The Total Environment 596, 405-416.

Blight T. S., Coley D. A., 2013. Sensitivity analysis of the effect of occupant behaviour on the energy consumption of passive house dwellings. Energy and Buildings 66, 183-192.

Wang Y., Kuckelkorn J., Zhao F. Y., Spliethoff H., Lang W., 2017. A state of art of review on interactions between energy performance and indoor environment quality in Passive House buildings. Renewable and Sustainable Energy Reviews 72, 1303-1319.

Satake A., Ikegami H., Mitani, Y., 2016. Energy-saving Operation and Optimization of Thermal Comfort in Thermal Radiative Cooling/Heating System. Energy Procedia 100, 452-458.

Zhao K., Liu X. H., Jiang Y., 2016. Application of radiant floor cooling in large space buildings–A review. Renewable and Sustainable Energy Reviews 55, 1083-1096.

Non-stationary thermal performance evaluation of external façade walls under central European summer conditions

Mitja Košir[1], Luka Pajek[1], Blaž Hudobivnik[2], Mateja Dovjak[1], Nataša Iglič[1], David Božiček[1], and Roman Kunič[1]

[1] University of Ljubljana, Faculty of Civil and Geodetic Engineering, Ljubljana (Slovenia)

[2] Leibniz Universität Hannover, Institute for Continuum Mechanics, Hannover (Germany)

Abstract

Thermal response of building envelope exerts a substantial influence on the formation of overall indoor comfort conditions as well as on the energy performance of buildings. For the majority of Central and Northern European countries it can be said that legislators as well as designers focus primarily on the optimization of building performance in heating season. Nevertheless, predictions for the future show the potential for large increase in cooling demand due to overheating of buildings. In this context, the focus of the presented work was to evaluate the non-stationary performance of different façade walls (lightweight and heavyweight construction systems) during typical Central European summer conditions. In addition to the influence of wall composition, the impact of orientation and high intensity passive cooling on thermal response was also investigated. The results showed differences in the summer time performance of lightweight and heavyweight envelopes, whereas lightweight façade walls had worse summer time thermal response. Furthermore, substantial differences in thermal behaviour of east, south and west faced walls were identified, with wall orientation having greater effect in the cases of walls with higher thermal transmittance and when constant ventilation regimes were used. However, among all the analysed parameters, high intensity passive cooling was identified to have the greatest influence on the summer time thermal behaviour of façade walls.

Keywords: external façade walls, transient thermal performance, night-time ventilation, thermal mass, FEM thermal analysis, Central European climate

1. Introduction

Indoor thermal environment in buildings during cooling season is becoming an ever more increasing concern in EU due to projected increase in the application of active cooling in the decades to come (STRATEGO, 2015). Current statistical data for EU (RESCUE, 2014) show that active cooling systems are installed in 7% of the total floor area in case of residential buildings, while the share for the tertiary sector is 40%. In the light of increasing influence of climate change and ever-higher demands for indoor occupant comfort, the growth in space cooling applications and their potential influence on energy consumption could be substantial. As an alternative, less energy demanding solutions for providing adequate indoor thermal conditions during summer time should be investigated in order to evaluate their overall efficiency. Best results can be attained by passive solutions on the level of building envelope, such as high thermal mass, and on the level of building functioning, for example night-time ventilation (Santamouris et al., 2010). Both approaches have a large potential in reduction of overheating occurrence, especially in temperate (i.e. Central Europe) and cold (i.e. Northern Europe) parts of Europe. In order to evaluate the potential influence of such passive solutions during free-run conditions (i.e. building is not mechanically cooled), a non-stationary analysis must be used due to the dynamic nature of the thermo-physical problem.

Several studies have investigated summer time thermal response of different construction types, with most of them studying lightweight constructions (i.e. constructions that lack or have low thermal mass). The overheating of buildings during cooling season most likely occurs in timber buildings (Adekunle and Nikolopoulou, 2016), in buildings located in highly urbanized environments (due to the occurrence of heat islands) (Paolini et al.,

doi:10.18086/swc.2017.15.03 Available at http://proceedings.ises.org

2016), in hot climates (Stazi et al., 2017) or in the case of a combination of all the stated. Pekdogan and Basaran (2017) investigated thermal performance of external walls during winter and summer. They emphasized that heat loss and gain values were significantly reduced with thicker insulation and that different thermal insulation positions (external, internal, sandwich) and wall orientations influenced the heat flow through the wall. Similar study was also conducted by Tzoulis and Kontoleon (2017), which highlighted that varying wall orientation has lower effect on the value of decrement factor compared to the time lag. Therefore, the composition and orientation of building's external wall are extremely important in the context of overheating prevention.

The objective of the analysis presented in this paper was to evaluate the thermal response of selected typical external façade walls under Central European (i.e. Ljubljana, Slovenia) summer time climatic conditions. The importance of thermal insulation position and wall composition, especially the presence or absence of thermal mass, was already emphasized by Al-Sanea and Zedan (2011). In this context, the executed study focused on the investigation of the influence of multi-layer wall composition on its non-stationary thermal response and consequential indoor conditions. Special focus was on the performance of walls with low U values (U = 0.20 $Wm^{-2}K^{-1}$), which are becoming a standard in Central Europe for the newly constructed as well renovated buildings. Simultaneously, the effect of high intensity passive cooling (i.e. night-time ventilation) and façade orientation was included in the analysis and their effect on thermal response of walls was evaluated. Calculations were conducted by an in-house developed finite element method.

2. Methodology

2.1. Selection of wall construction systems

The selected heavyweight (HWC) and lightweight (LWC) external wall construction types were analysed. As a representative construction of typical LWC envelope systems, a wall used in timber-framed buildings was selected. Such wall construction consists of an external thermal insulation and additional thermal insulation between elements of the wood load-bearing construction. Both the internal and external surfaces are finished with a construction board (e.g. OSB board). For a HWC, multiple materials, such as brick, reinforced concrete (RC), stone and hollow brick as a load bearing construction layer were investigated (Hudobivnik et al., 2016). Nonetheless, for the purpose of the presented analysis only the HWC with RC load bearing construction will be presented. In the case of RC, HWC thermal insulation is placed on external (RC_E) or internal surface (RC_I) of the load bearing construction. Because all the analysed façade walls and results of their thermal performance simulation have to be directly comparable, each construction system was, unless otherwise specified, insulated with appropriate thermal insulation thickness in order to have identical overall thermal transmittance of 0.20 $Wm^{-2}K^{-1}$.

2.2. Climate data and time interval of analysis

Calculations were made using climate data for the city of Ljubljana (46°03'N, 14°30'E), Slovenia. Necessary weather parameters (i.e. hourly air temperatures and solar radiation data) were obtained from EnergyPlus weather files (EnergyPlus, 2016) and were directly transferred into the numerical model. Ljubljana has a typical Central European climate with slight influence of northern Mediterranean due to the relative proximity of the Adriatic Sea. According to Köppen-Geiger climatic classification, it is classified as Cfb and can be described as a fully humid, warm temperate climate with cold winters and warm summers. According to ASHRAE Standards 90.1 and 90.2 (ASHRAE Standards 90.1-2004, 2004; ASHRAE Standards 90.2-2004, 2004) the climate of Ljubljana may be designated as type 5A. The average monthly air temperature (T_{avg}) varies between 20.4°C in July and – 1.2°C in January, while the average monthly maximum air temperatures ($T_{max,avg}$) reach up to 26.4°C, and minimum monthly average air temperatures ($T_{min,avg}$) reach down to – 4.9°C. The average daily global horizontal solar irradiation (G_{sol}) varies between the maximum values of 359 Whm^{-2} (July) and 73 Whm^{-2} (December). The climatological averages of Ljubljana for the period between 2005 and 2014 are presented in Figure 1. If the historical overview of trends in the average yearly values of T_{avg}, $T_{max,avg}$ and $T_{min,avg}$ are observed for the last 54 years (Fig. 2), it becomes evident that ambient air temperatures are on the rise. In regards to the observed trend it can be concluded that for the location of Ljubljana the importance of overheating protection is on the rise, while the duration of heating period is being reduced (Pajek and Košir, 2017). The stated underlines the importance of the proposed study.

The executed analysis was conducted for the summer period between the 21st of June and 11th of August with a

model's 10 days warm up period. In order to clearly present the calculated results, only a short period between the 2nd and 10th of August will be presented. During this time the external air temperatures were extremely high with daily maximums reaching above 30°C, while the last three days mark the beginning of a cooler period.

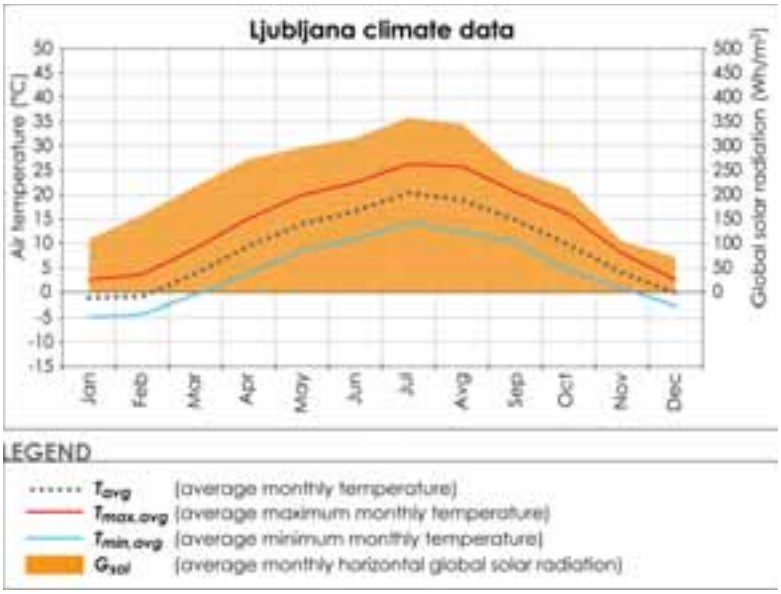

Fig. 1: Climate characteristics of Ljubljana (2005-2014 period).

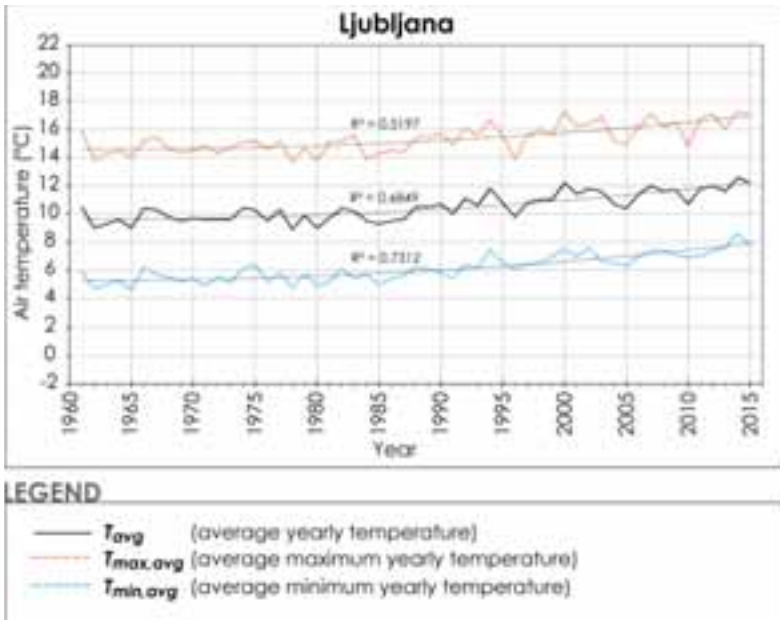

Fig. 2: Historical (1961-2015) overview of increase in average temperatures in Ljubljana.

2.3. Model and boundary conditions

The numerical model used to study the non-stationary response of the selected wall constructions was modelled in computer algebra system Mathematica (Wolfram Research, Inc., 2013) with finite element code derived using AceGen (Korelc, 2011) and finite model solved by AceFEM (Korelc, 2011). The model represents a 1 m^2 (i.e. 1 m by 1 m) of the external wall with an associated building interior of 2 m^3 and a 3.6 mm thick air boundary layer. The mass of internal partitions and furnishing as well as all internal heat gains were appropriately scaled in order to represent a typical residential house. The numerical model characteristics are presented in Figure 3 and in more depth also in a paper by Hudobivnik et al. (2016).

Additional model boundary conditions were defined in order to accurately study the non-stationary thermal behaviour of selected wall types. Solar radiation heat gains on wall's external surface were calculated, and the

constant solar absorptivity of the exterior surface was set as $\alpha = 0.40$ (solar reflectance $\rho = 0.60$), as suggested by Al-Sanea and Zedan (2011) for light-coloured surfaces (e.g. beige, cream, sand, etc.), commonly used in External Thermal Insulation Composite System (ETICS) façade renderings. In addition, the radiation losses to the environment were considered. Heat gains from occupants and appliances (including their intensity and timetable of occurrence) in internal space were defined in accordance with the values stated for residential buildings (living rooms and kitchens) in EN ISO 13790, Annex G (EN ISO 13790:2008, 2008, p. 137). Natural ventilation (0.7 ACH) as well as high intensity passive cooling (0.7/7.0 ACH) were taken into account, because ventilation regime has a significant impact on internal thermal conditions, consequently affecting heat flow through wall construction. When high intensity passive cooling is used, it is presumed that, during periods when external air temperatures are higher than internal, lower values of ventilation rates are applied (i.e. 0.7 ACH). The value of minimal ventilation rate in the simulations was defined in accordance to EN 15251 (EN 15251:2010, 2010) standard recommendation for residential buildings. In addition to the above, the orientation of façade walls was modified as well in order to evaluate the influence of received solar radiation on the thermal response of analysed walls. Orientations from east-northeast (azimuth 75°) through south (azimuth 180°) to west-northwest (azimuth 285°) were calculated in 15° steps (Fig. 3).

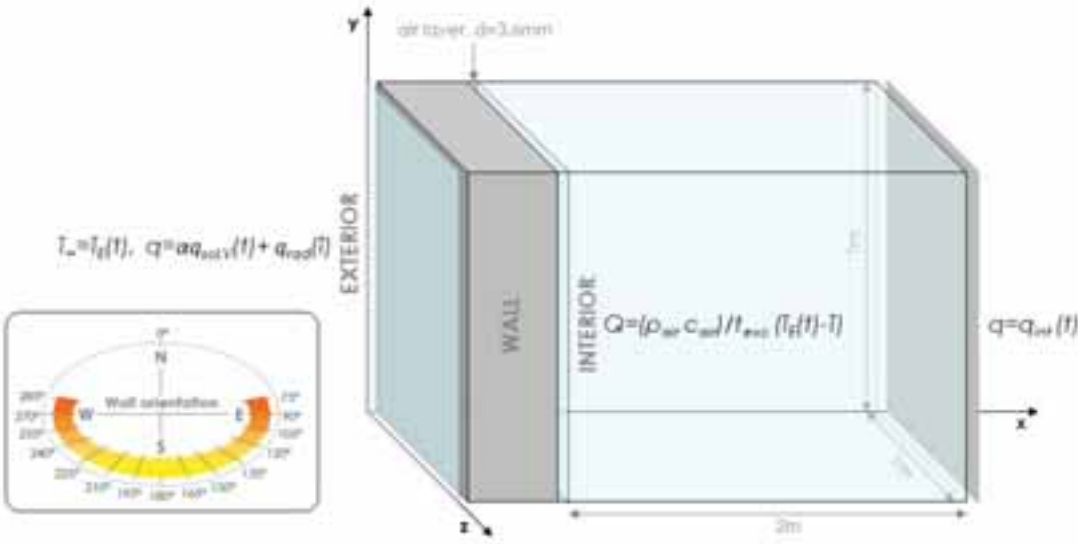

Fig. 3: Numerical model and boundary conditions with representation of analysed wall orientations.

3. Results and discussion of non-stationary analysis

The objective of the executed study was to evaluate the thermal performance of three different external façade walls (i.e. LWC, RC_E and RC_I) in relation to their loadbearing construction system type and thermal insulation position as well as wall orientation and the influence of ventilation regime (i.e. constant or high intensity passive cooling natural ventilation). The numerical model used to simulate the thermal response of the analysed external walls was run under summer climatic conditions in Central Europe (Ljubljana, Slovenia) with presumption that the building is not actively cooled and is therefore in a free-run mode. The latter enabled a study on the influence of the analysed passive strategies (i.e. wall composition, orientation and ventilation mode) on the internal temperatures. Specifically, the internal wall surface temperature was monitored (T_{surf}).

3.1. Influence of high intensity passive cooling on the internal temperatures

The results (Fig. 4) showed that indoor air change intensity has a significant impact on heat flow through external multi-layer building envelopes and the corresponding internal surface temperatures. Therefore, the effect of (natural) ventilation should not be neglected in the evaluation of the thermal response of building envelopes, especially when high intensity night ventilation is used as a passive cooling strategy (i.e. buildings in a free-run mode). When using constant ventilation rates (i.e. 0.7 ACH) for the south faced wall (i.e. azimuth 180°), the highest average T_{surf}, during the analysed period of 28.9°C was reached equivalently in the case of LWC and RC_I (Fig. 4). In the case of RC_E the average T_{surf} is 1.8 K lower (i.e. 27.1°C). In the case of externally insulated wall RC_E the average daily surface temperature fluctuations are the lowest ($\Delta T_{surf\_mean,RCE,0.7ACH} = 0.82$

K), which is the consequence of high thermal mass positioned on the internal side of the building envelope. In the other two cases, where thermal mass is positioned on the external side (RC_I) or there is overall lack of thermal mass (LWC), the average daily surface temperature fluctuations are higher and are $\Delta T_{surf\_mean,LWC,0.7ACH}$ = 1.58 K and $\Delta T_{surf\_mean,RCI,0.7ACH}$ = 1.68 K for LWC and RC_I, respectively.

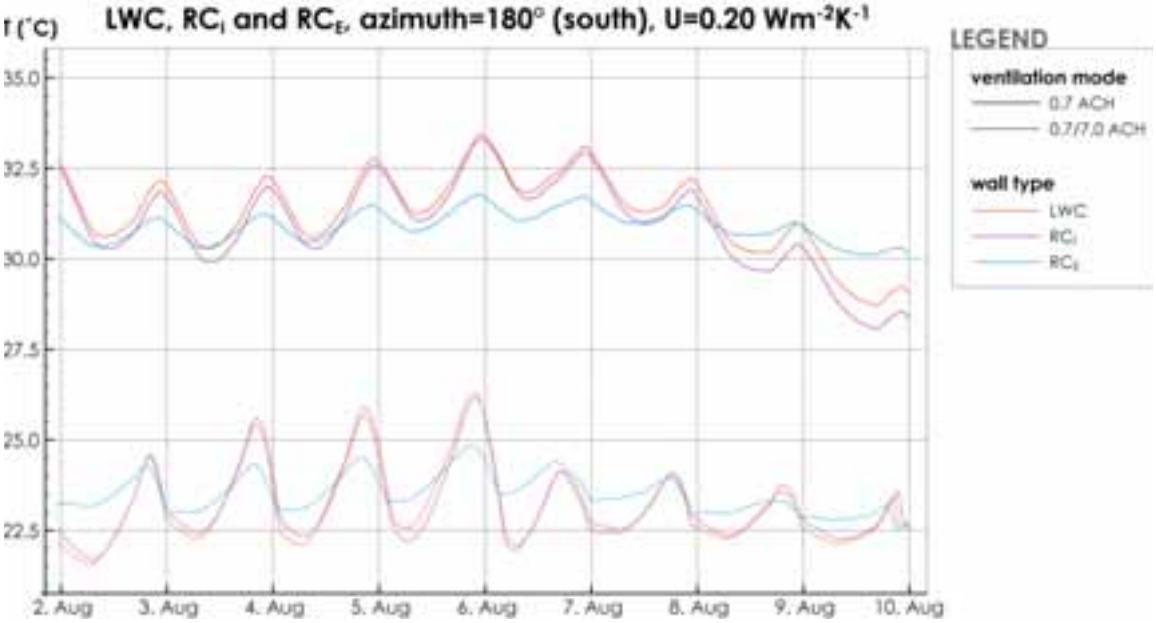

Fig. 4: Impact of high intensity passive cooling (0.7/7.0 ACH) in comparison to constant ventilation (0.7 ACH) on the internal surface temperatures for RC_E, RC_I and LWC at U = 0.2 $Wm^{-2}K^{-1}$ and azimuth 180° (south).

Observing the thermal response of the same three constructions under high intensity ventilation regime (i.e. 0.7/7.0 ACH) in Fig. 4, it can be noticed that the maximum T_{surf} in each case drops by approximately 7 K, compared to the case with constant ventilation. Nonetheless, all three constructions exhibit higher average fluctuations of surface temperature under high intensity ventilation regime, which amount to $\Delta T_{surf\_mean,RCE,0.7/7ACH}$ = 0.96 K, $\Delta T_{surf\_mean,LWC,\ 0.7/7\ ACH}$ = 2.23 K and $\Delta T_{surf\_mean,RCI,\ 0.7/7\ ACH}$ = 2.39 K. However, the mentioned increase in ΔT_{surf_mean} is most pronounced in the cases of LWC and RC_I constructions, which lack thermal mass on the internal side. The comparison between LWC (i.e. timber framed wall), RC_E and RC_I façade envelopes with and without the application of high intensity passive cooling demonstrated that, although passive cooling is beneficial in all cases, its absolute effectiveness on the indoor thermal conditions is, however, primarily still dependent on the selection of building envelope type. For example, observing Fig. 4 it can be seen that RC_E exhibits lower surface temperature fluctuations in both cases, whereas the maximum T_{surf} is always reached in the case of LWC, which is 33.3°C and 26.2°C without and with high intensity ventilation, respectively. This means that passive cooling was far more efficient in the case of RC_E than it was with LWC as well as RC_I façade walls, as a result of internally positioned thermal storage capacity in case of RC_E.

3.2. Influence of wall orientation on the internal temperatures

In the next stage of the analysis the influence of wall orientation was investigated for each of the three wall compositions using constant and high intensity ventilation mode. The main point of interest was to study how the combination of external temperatures and received solar radiation influences the internal surface temperatures with respect to the ventilation mode. Wall orientation as a variable was altered from east-northeast (i.e. azimuth = 75°) and west-northwest (i.e. azimuth = 285°) in steps of 15°. The results for each of the constructions are presented in Figs. 5–7.

The results in Fig. 5 represent variations of T_{surf} for RC_E wall construction as a function of orientation and ventilation regime. During the entire analysed period, the maximum T_{surf} in the case of RC_E with constant ventilation (i.e. 0.7 ACH) was reached at azimuth 255° and amounted to 33.5°C, while the minimum T_{surf} of 29.1°C was achieved at azimuth 75°. The mentioned orientations define the upper and lower boundary of a family of curves defining the extent of T_{surf} for all analysed orientations. The average difference between the upper and lower boundary of the defined envelope is 1.7 K. Moreover, several orientations presented in Fig. 5

give similar results. For instance, such orientations are western azimuths between 240° and 270° and east-southeast to south azimuths between 105° and 180°. In the case of RC_E with high intensity ventilation (0.7/7.0 ACH), the overall maximum and minimum T_{surf} of 25.3°C and 22.4°C are reached at different orientations of 240° and at azimuths between 90° and 150°, respectively. The average difference between the upper and the bottom line of a family of curves during the entire analysed period is 0.2 K. From the results presented in Fig. 5 it becomes evident that in the case of high intensity ventilation the impact of wall orientation is no longer significant.

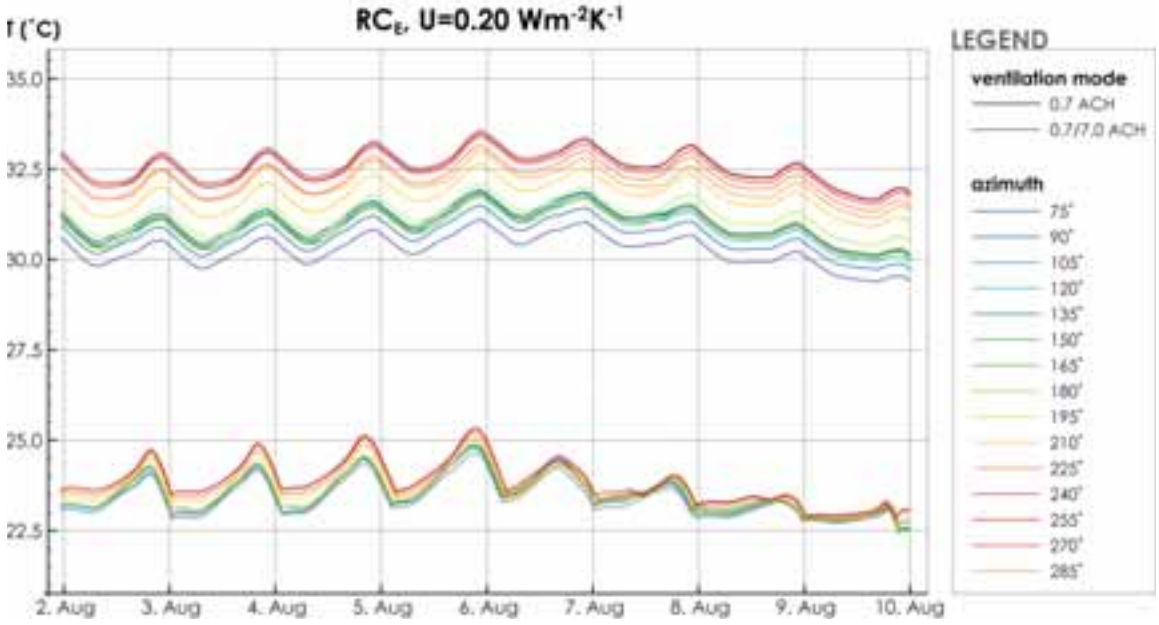

Fig. 5: Impact of wall orientation and ventilation mode (0.7 or 0.7/7.0 ACH) on the internal surface temperatures of RC_E with U value of 0.2 $Wm^{-2}K^{-1}$.

Fig. 6 shows the results for the RC_I construction, where variations of T_{surf} as a function of wall orientation and ventilation regime can be examined. During the entire analysed period, the maximum and minimum reached temperatures for RC_I in the case of constant ventilation (0.7 ACH) and at different orientations are 35.0°C (at azimuth 240°) and 27.1°C (at azimuth 75°), respectively. The average difference between the upper and the bottom line of a family of curves for RC_I during the entire analysed period is 2.0 K. In the same manner as it was observed in the case of RC_E, several orientations for RC_I construction presented in Fig. 6 give similar results. These orientations are again western azimuths between 240°and 270° (maximum T_{surf}) and eastern-southern azimuths between 105°and 180° (minimum T_{surf}). In the case of high intensity ventilation (0.7/7.0 ACH), the maximum and minimum reached temperatures at different orientations for RC_I are 26.6°C (at azimuths 240° and 270°) and 21.4°C (at azimuth 90°), respectively. The average difference between the upper and the bottom line of a family of curves is 0.4 K, effectively making orientation irrelevant when high intensity ventilation is used.

Finally, the results for the LWC wall construction are presented in Fig. 7, where variations of T_{surf} as a function of wall orientation and ventilation regime can be observed. During the entire analysed period, the maximum and minimum reached T_{surf} for LWC in the case of constant, 0.7 ACH ventilation and at different orientations are 35.1°C (at azimuth 255°) and 27.7°C (at azimuth 75°), respectively, while the average difference between the upper and the bottom line of a family of curves for LWC during the entire analysed period is 1.9 K. The same as in the cases of RC_E and RC_I, several orientations for LWC construction presented in Fig. 7 give similar results. These orientations are western azimuths between 240° and 255° and eastern-southeastern azimuths between 105° and 180°. In the case of high intensity ventilation (0.7/7.0 ACH), the maximum (i.e. 26.5°C) and minimum (i.e. 21.4°C) T_{surf} are reached at azimuths between 240° and 255° and at azimuth 105°, respectively, while the average difference between the upper and the bottom line of a family of curves is 0.3 K. Altogether, the results for LWC and RC_I are almost identical.

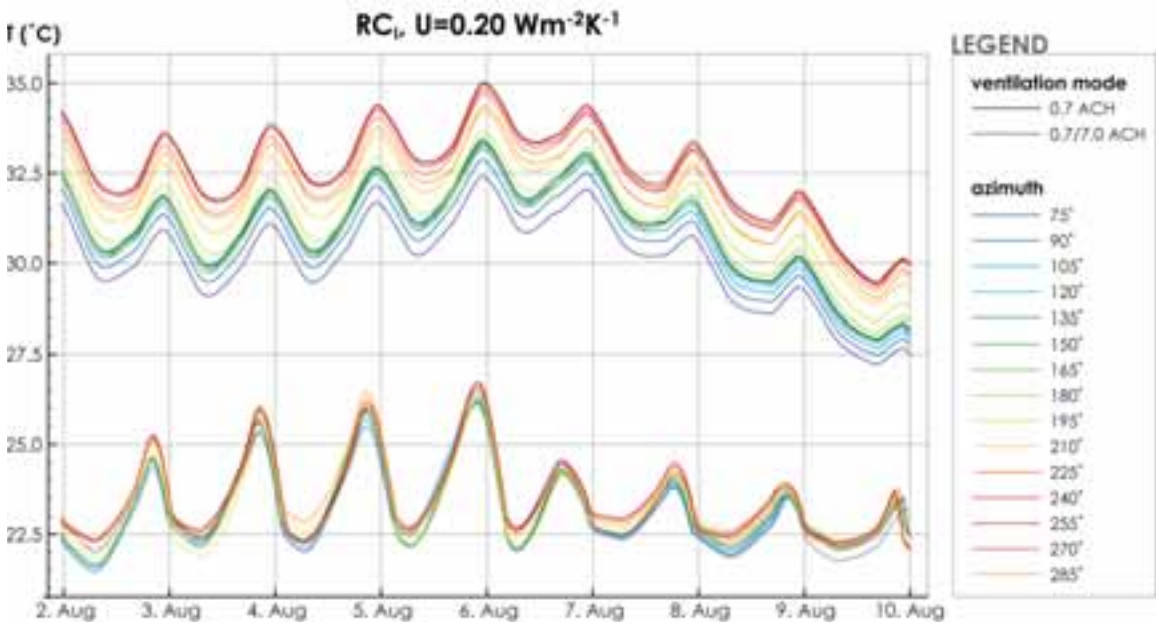

Fig. 6: Impact of wall orientation and ventilation mode (0.7 or 0.7/7.0 ACH) on the internal surface temperatures of RC_I with *U* value of 0.2 $Wm^{-2}K^{-1}$.

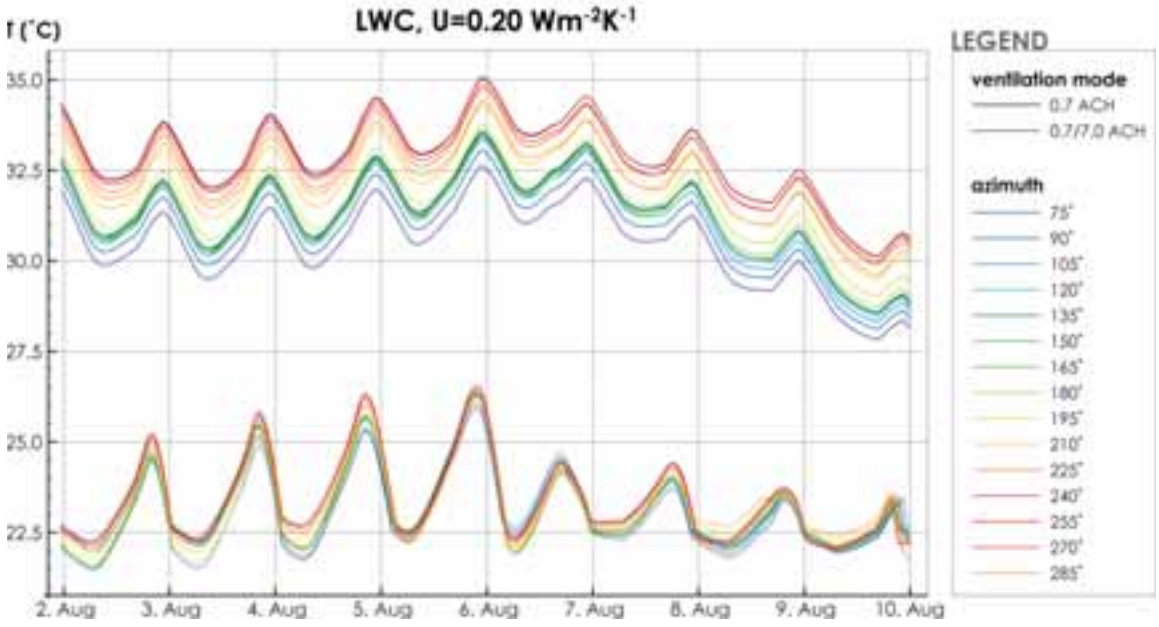

Fig. 7: Impact of wall orientation and ventilation mode (0.7 or 0.7/7.0 ACH) on the internal surface temperatures of LWC with *U* value of 0.2 $Wm^{-2}K^{-1}$.

The influence of wall orientation plays a role in performance of the analysed constructions as clear differences in internal surface temperatures can be identified at different orientations (Figs. 5–7). In general, for cases with constant natural ventilation (0.7 ACH), eastern orientations (i.e. azimuths 75–90°) exhibited up to 3 K lower T_{surf} in comparison to western oriented walls (i.e. azimuths 240–270°), while southern orientations fall between the two extremes. The orientation plays an insignificant role when high intensity passive cooling is used (Figs. 5–7) as average differences between minimum and maximum T_{surf} for all three analysed cases do not exceed 0.3 K, which is a tenfold reduction in comparison to constant ventilation mode. In general, the externally insulated wall with internally positioned thermal mass (i.e. RC_E) outperforms both lightweight (i.e. LWC) as well as internally insulated (i.e. RC_I) wall constructions in regards to their thermal response. Despite this fact, it should be stressed that constructions with higher thermal mass on the internal side cool down much slower when constant ventilation is applied. This effect can be observed if the results for RC_E and RC_I (or LWC) are

compared (Figs. 4–7) for the days from 8th till 10th of August. Such thermal behaviour is in this case unfavourable. However, if high intensity ventilation is used, the RC_E wall construction outperforms LWC and RCI even in this respect.

In the case of well insulated envelopes, solar gains through façade walls generally have moderate impact on the overall thermal performance. The results presented above were made for constructions with thermal transmittance of 0.2 $Wm^{-2}K^{-1}$. However, thermal response would be different if higher thermal transmittance of the wall was used, as was demonstrated by a study conducted by Corrado and Paduos (2016). Therefore, section 3.3 discusses this issue on the example of RC_E.

3.3. Discussion

Because the analyses presented in previous chapters were made with a fixed U value of 0.2 $Wm^{-2}K^{-1}$, it was of further interest to investigate how higher U value would influence the thermal response of the wall construction in regards to its orientation and ventilation mode. Therefore, an additional study was made with the RC_E wall construction, where its U value was set to 0.6 $Wm^{-2}K^{-1}$. The results presented in Fig. 8 are plotted as an envelope of a family of curves made for the wall orientations with azimuths between 75° and 285° for U values of 0.2 and 0.6 $Wm^{-2}K^{-1}$. The results in Fig. 8 show that wall orientation plays much greater role, when thermal transmittance of the construction is higher and even more so, if constant ventilation regime (i.e. 0.7 ACH) is used. In particular, the average difference between the upper and the bottom line of a family of curves for constant ventilation and U = 0.6 $Wm^{-2}K^{-1}$ is 3.3 K, while for U = 0.2 $Wm^{-2}K^{-1}$ this value is equal to 1.7 K. In the case of high intensity ventilation (i.e. 0.7/7.0 ACH) the average difference between the upper and the bottom line of a family of curves for U = 0.6 $Wm^{-2}K^{-1}$ is 0.8 K, while for U = 0.2 $Wm^{-2}K^{-1}$ this value is equal to 0.2 K. Comparing RC_E constructions in Fig. 8 at azimuth 180° (i.e. south) it can be said that in the case of constant ventilation higher U values of walls can results in lower T_{surf} and faster thermal response (e.g. the T_{surf} is reduced faster during the cooling down period from 8th to 10th of August). However, the situation is reversed when high intensity ventilation is used.

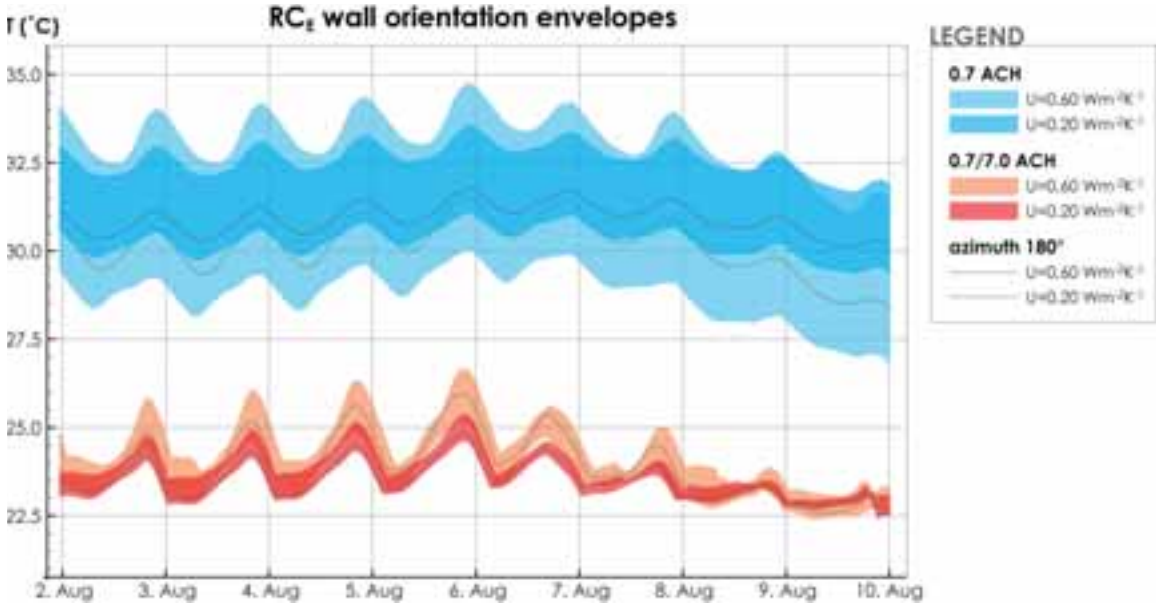

Fig. 8: Comparison of wall orientation envelopes of internal surface temperatures for RC_E at different ventilation modes (0.7 and 0.7/7.0 ACH) and different U values (0.60 and 0.20 $Wm^{-2}K^{-1}$).

Observing Fig. 8 it can be concluded that in temperate climate it would be better to use higher thermal transmittance of walls in order to better control indoor wall surface temperatures during summer. Conversely, buildings in such climate zones are mostly optimized for the winter conditions, thus having low or extremely low U values. The latter is also prescribed by the legislation. Therefore, high intensity cooling can play a vital role in enhancing the summer time thermal performance od wall constructions with low U values, as using it results in a better performing construction (i.e. lower T_{surf}) (Fig. 8). This specifically applies to all the considered orientations under the presumption that high intensity ventilation (passive cooling) is used.

The results of the conducted study showed that even in cases with low *U* values of the walls, orientation of the façade has an impact on the thermal response of non-transparent building envelope elements. In particular, substantial differences between east, south and west orientations were identified. Especially the south-west orientation of the façade was shown as extremely unfavourable in the case of LWC and RC_I. Although wall composition (especially thermal mass) and orientation play a role in the thermal response of the analysed façade walls, high intensity passive cooling proved as the most decisive factor, whereas the potential of diurnal temperature fluctuations is used to passively cool down buildings. Nevertheless, even here the effectiveness is linked to the configuration and type of the façade wall.

4. Conclusions

The trend of using lightweight building envelope components, especially in residential buildings, will probably continue during the forthcoming years (Kitek Kuzman et al., 2013). The biggest growth is expected in the market of timber framed and cross-laminated construction systems. Consequentially, the importance of assuring satisfactory thermal response of such envelope systems during summer conditions will become crucial. The latter is highlighted through the presented study as LWC external façade wall systems have been shown to exhibit inferior thermal performance in comparison to externally insulated heavy weight envelopes (HWCs). In the light of EU policies for the reduction of building stock's influence on the energy consumption and the decrease of environmental impact, it is crucial to develop and implement passive solutions for the reduction of cooling loads. Results of the conducted analysis show that lack of thermal mass in lightweight construction systems should be addressed. In addition, it was shown that, although both wall composition and orientation influence the thermal response of the façade envelope, the greatest effect can be achieved by using appropriate passive cooling ventilation technique. After all, prospective solutions can be found in applications of materials with high thermal storage potential and relatively small thickness in the form of interior cladding (Jeanjean et al., 2013). However, in this context the appropriate use of PCMs (Kheradmand et al., 2016) and/or other efficient enhancements of thermal performance of lightweight constructions (Pajek et al., 2017) can be a viable alternative as well. The findings of the conducted study can represent guidelines for design decisions when the objective is to design better performing buildings. Although each building is unique, set in its individual environmental context, the general performance principle of selected wall constructions remains the same.

References

Adekunle, T.O., Nikolopoulou, M., 2016. Thermal comfort, summertime temperatures and overheating in prefabricated timber housing. Build. Environ. 103, 21–35. doi:10.1016/j.buildenv.2016.04.001

Al-Sanea, S.A., Zedan, M.F., 2011. Improving thermal performance of building walls by optimizing insulation layer distribution and thickness for same thermal mass. Appl. Energy 88, 3113–3124. doi:10.1016/j.apenergy.2011.02.036

ASHRAE Standards 90.1-2004, 2004. Energy Standard for Buildings Except Low-Rise Residential Buildings.

ASHRAE Standards 90.2-2004, 2004. Energy-Efficient Design of Low-Rise Residential Buildings.

Corrado, V., Paduos, S., 2016. New equivalent parameters for thermal characterization of opaque building envelope components under dynamic conditions. Appl. Energy 163, 313–322. doi:10.1016/j.apenergy.2015.10.123

EN 15251:2010, 2010. Indoor environmental input parameters for design and assessment of energy performance of buildings addressing indoor air quality, thermal environment, lighting and acoustics.

EN ISO 13790:2008, 2008. Energy performance of buildings Calculation of energy use for space heating and cooling.

EnergyPlus, 2016. Weather Data [WWW Document]. URL energyplus.net/weather (accessed 8.2.16).

Hudobivnik, B., Pajek, L., Kunič, R., Košir, M., 2016. FEM thermal performance analysis of multi-layer external walls during typical summer conditions considering high intensity passive cooling. Appl. Energy 178, 363–375. doi:10.1016/j.apenergy.2016.06.036

Jeanjean, A., Olives, R., Py, X., 2013. Selection criteria of thermal mass materials for low-energy building construction applied to conventional and alternative materials. Energy Build. 63, 36–48. doi:10.1016/j.enbuild.2013.03.047

Kheradmand, M., Azenha, M., de Aguiar, J.L.B., Castro-Gomes, J., 2016. Experimental and numerical studies of hybrid PCM embedded in plastering mortar for enhanced thermal behaviour of buildings. Energy 94, 250–261. doi:10.1016/j.energy.2015.10.131

Kitek Kuzman, M., Grošelj, P., Ayrilmis, N., Zbašnik-Senegačnik, M., 2013. Comparison of passive house construction types using analytic hierarchy process. Energy Build. 64, 258–263. doi:10.1016/j.enbuild.2013.05.020

Korelc, J., 2011. AceGen and AceFEM user manual, University of Ljubljana, 809 2011. [WWW Document]. URL http://symech.fgg.uni-lj.si/ (accessed 6.30.16).

Pajek, L., Hudobivnik, B., Kunič, R., Košir, M., 2017. Improving thermal response of lightweight timber building envelopes during cooling season in three European locations. J. Clean. Prod. 156, 939–952. doi:10.1016/j.jclepro.2017.04.098

Pajek, L., Košir, M., 2017. Can building energy performance be predicted by a bioclimatic potential analysis? Case study of the Alpine-Adriatic region. Energy Build. 139, 160–173. doi:10.1016/j.enbuild.2017.01.035

Paolini, R., Zani, A., MeshkinKiya, M., Castaldo, V.L., Pisello, A.L., Antretter, F., Poli, T., Cotana, F., 2016. The hygrothermal performance of residential buildings at urban and rural sites: Sensible and latent energy loads and indoor environmental conditions. Energy Build. In Press, Corrected Proof. doi:10.1016/j.enbuild.2016.11.018

Pekdogan, T., Basaran, T., 2017. Thermal performance of different exterior wall structures based on wall orientation. Appl. Therm. Eng. 112, 15–24. doi:10.1016/j.applthermaleng.2016.10.068

RESCUE, 2014. EU District cooling market and trends. Capital Cooling under the framework of the RESCUE project co-funded by the IEE programme of the EU. [WWW Document]. URL www.rescue-project.eu/fileadmin/user_files/WP2_Reports/RESCUE_WP_2.3_EU_COOLING_MARKET.pdf (accessed 4.6.17).

Santamouris, M., Sfakianaki, A., Pavlou, K., 2010. On the efficiency of night ventilation techniques applied to residential buildings. Energy Build. 42, 1309–1313. doi:10.1016/j.enbuild.2010.02.024

Stazi, F., Tomassoni, E., Di Perna, C., 2017. Super-insulated wooden envelopes in Mediterranean climate: summer overheating, thermal comfort optimization, environmental impact on an Italian case study. Energy Build. 138, 716–732. doi:10.1016/j.enbuild.2016.12.042

STRATEGO, 2015. Enhanced heating and cooling plans for 2010 and 2050 (cofounded by Intelligent Europe Programme, Project number IEE/13/650) [WWW Document]. URL www.heatroadmap.eu/resources/STRATEGO/STRATEGO%20WP2%20-%20Executive%20Summary%20%26%20Main%20Report.pdf

Tzoulis, T., Kontoleon, K.J., 2017. Thermal Behaviour of Concrete Walls Around all Cardinal Orientations and Optimal Thickness of Insulation from an Economic Point of View. Procedia Environ. Sci., Sustainable synergies from Buildings to the Urban Scale 38, 381–388. doi:10.1016/j.proenv.2017.03.119

Wolfram Research, Inc., 2013. Mathematica version 9 [WWW Document]. URL http://www.wolfram.com/mathematica/ (accessed 6.30.16).

Design, Development and Thermal Performance Analysis of Ultra-Low Heat Loss Triple Vacuum Glazing

Saim Memon[1], Philip C. Eames[2]

[1] London South Bank University, London (UK)

[2] Loughborough University, Loughborough (UK)

Abstract

Heat loss through windows of buildings is one of the significant causes of high-energy consumption that require intervention to advance their thermal performance in a move towards net-zero energy buildings. High-performance triple vacuum glazing features ultra-low heat loss that maintains the transparency, regardless of tiny pillar spots, and slimness due to its narrow evacuated cavities. This study reports the design and development of high-vacuum system with the modified vacuum cup which provides an effective pump-out hole sealing and has an achievable vacuum pressure of $4.02 \cdot 10^{-5}$ Pa. A new dual-edge seal (low temperature melt 186˚C) consists of Cerasolzer CS186 alloy as a main and J-B Weld epoxy steel adhesive as a support seal is developed and the triple vacuum glazing (area of 300·300mm) samples are fabricated, in which the vacuum pressure of 4.8×10^{-2} Pa is achieved. A 3D FEM of the fabricated triple vacuum glazed is developed and the centre-of-pane and overall U-value of 0.33$Wm^{-2}K^{-1}$ and 1.05 $Wm^{-2}K^{-1}$, respectively, are predicted.

Keywords: Smart Window, Vacuum Glazing, High-Vacuum System, Finite Element Modelling, Sustainable Building, Solar Energy, Energy Efficiency.

1. Introduction

An increase of global annual average surface temperature to 0.99˚C in 2016 (Lee et al, 2017) is due to the CO_2 level that reached 400 ppm, breaking the 1950's level threshold of 300 ppm (Andric et al, 2017). More than 30 % of the total global final energy consumption is in the building sector (Piccolo and Simone, 2015). Advanced insulation technologies and retrofitting measures have already minimized the building energy consumption but yet require more energy-efficient technologies that bring the building sector towards zero-carbon sustainable buildings (Memon and Eames, 2017). To achieve this, glazed windows are of particular interest in this paper specifically in cold arid climate. It's one thing a need of high visual light transmittance, above 70%, and reasonable solar heat gain coefficient, G-Value, range from 0.4 to 0.7 through glazed windows and another thing a significant heat loss through glazed windows. The heat loss through glazed windows is the result of the heat transfer by conduction, convection and radiation and is determined by the thermal transmittance value (U-value). Smart glazing technologies such as thermotropic glazing or double air-filled glazing have identical U-values of 2.7 $Wm^{-2}K^{-1}$ (Allen et al, 2017). A smart double glazing with low-e glass and a photochromic coated glass achieved a G-value of 0.26 and U-value of 1.58 $Wm^{-2}K^{-1}$ (Wu et al, 2017). Glazed windows with cavities filled with heavy gases (Argon, Krypton or Xenon) improves thermal performance from 3.5 to 1.4 $Wm^{-2}K^{-1}$, depends on the cavity thickness, e.g. the best predicted U-value of the Xenon-gas filled double glazing at the cavity width of 20mm was reported to be 1.4 $Wm^{-2}K^{-1}$ (Manz, 2008). Aerogel-gas filled double glazing made of granular aerogel sandwiched in a 16mm wide polymethyl methacrylate (PMMA) double skin-sheet and two 12mm layers of krypton gas between two glass sheets (total cavity thickness of 38 mm) achieved the best possible U-value of 0.5 $Wm^{-2}K^{-1}$ (Baetens et al, 2011). Due to its semi transparency, greater thickness than conventional glazing and high cost of aerogel materials, they were not deployed in the UK.

doi:10.18086/swc.2017.15.04 Available at http://proceedings.ises.org

Vacuum glazing has the potential to provide a clear transparent view except for tiny dots due to support pillars, narrow width of about 8.3 mm and the space between the two glass sheets is evacuated to a pressure of less than 0.1 Pa rather than including any medium or material (Memon, 2014). With vacuum glazing, the centre-of-pane U-value can be reduced down to 0.8 $Wm^{-2}K^{-1}$ (Eames, 2008) when evacuating the space between two low-e coated glass panes, e.g. tin-oxide coating emissivity of 0.15. A pressure of less than 0.1 Pa reduces gaseous conductive and convective heat transfer to a negligible level (except heat conduction through support pillars and edges) and radiative heat transfer can be reduced using soft low-e coatings, e.g. silver coating emissivity of 0.02. To reduce the U-value below 0.5 $Wm^{-2}K^{-1}$, a concept of triple vacuum glazing was reported by Wuethrich (2005). In this paper, the design, development, fabrication methods and U-value predictions of a new dual-edge sealed triple vacuum glazing are reported. A dual-edge seal is hermetic and it consists of Cerasolzer alloy CS186 as a main seal and J-B weld epoxy steel resin as a support seal (Memon et al, 2015). A triple vacuum glazing consists of three SnO_2 coated k-glass sheets, air-tight sealed around the edges, with evacuated two narrow (0.15mm high) cavities having a pressure of 0.01 Pa. A regular square array of stainless steel support pillars, typically 0.15mm high and 0.3mm diameter spaced at 24mm, maintains the separation of three glass sheets under the effects of atmospheric and vacuum pressure.

2. High-Vacuum System Design and Development

A high-vacuum system was designed for the fabrication of ultra-low heat loss triple vacuum glazing as shown in Fig. 1. A dry type turbo-molecular with backing pump with an achievable pressure of $5 \cdot 10^{-6}$Pa was chosen. This is because the vacuum pump should be of an oil free/dry type as the contamination in the oil type with oil molecules could occur on the surfaces of tubes, valves, hose and/or vacuum cup preventing an effective vacuum level from being achieved. A turbo-molecular vacuum pump has a pumping speed of 200-300litre/min. The ATV (Atmosphere to Vacuum) transducer type 979, connected to the PDR 900 digital pressure measurement readout, is used in the present study for the measurement of vacuum pressure in the designed vacuum system. This pressure gauge is located at the closest possible location to the vacuum cup to measure the approximate pressure in the cavity/cavities of the triple vacuum glazing as illustrated in Fig. 2. The ATV transducer enables measurement of a wide pressure range from ultrahigh vacuum ($1.33 \cdot 10^{-8}$ Pa) to atmospheric pressure ($101.33 \cdot 10^{3}$Pa). In order to regulate or isolate the gas load either from the vacuum pump or Nitrogen gas cylinder, a Swagelok adapter is assembled; angle valves were located at the two positions of U joint as shown in Fig. 1.

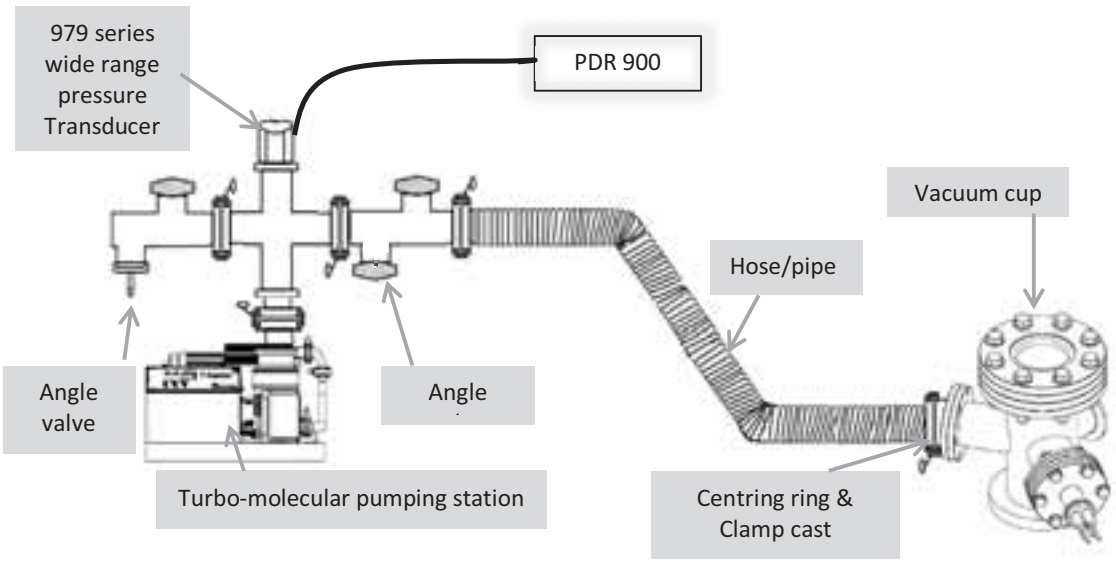

Fig. 1: A schematic diagram of the vacuum system showing the turbo-molecular pump connected via hose to the vacuum cup.

The laboratory vacuum glazing fabrication system developed as shown in Fig. 2. This is based on the design presented in Fig. 1. The vacuum system was experimentally tested and the minimum achievable vacuum pressure was recorded to be $4.35 \cdot 10^{-5}$ Pa. This deviates by 7.7% with the ultimate vacuum pressure of the turbo molecular pump due to the internal space conductance.

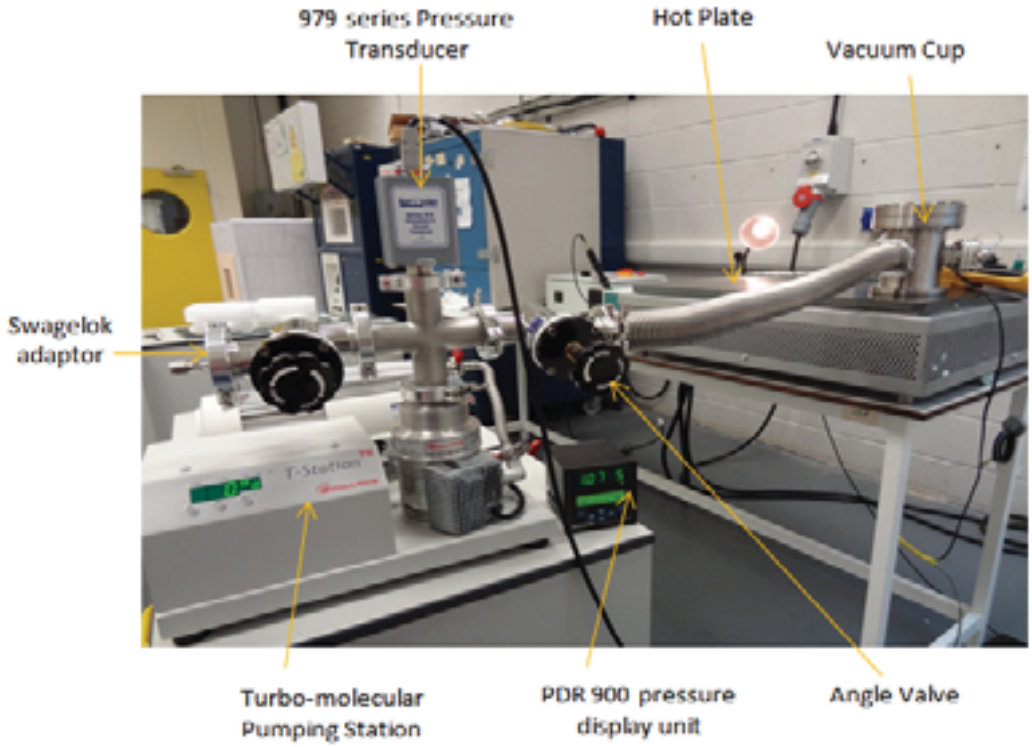

Fig. 2: A photograph of the vacuum system developed based on the design presented in Fig.1.

The vacuum cup was designed and constructed with dimensions of 100 mm diameter and 150 mm height for evacuation and pump-out hole sealing of the triple vacuum glazing as shown in Fig. 3. CF (conflat) metal seal flanges were used to provide an ultra-high vacuum (more than $1 \cdot 10^{-7}$Pa) seal between the two components. Only two CF flanges were used on the vacuum cup with an O ring seal on other joints. The modified pump-out mechanism, as illustrated in Fig. 3, requires a square cover slip (around 10·10mm) pre-soldered with Cerasolzer alloy (CS186) to be placed over the pump-out hole. Heating block, cartridge heater and thermocouple mounted on a metallic rod controlled through a supporting Y shaped block provides up and down motion of up to 10mm. A K type thermocouple fixed to the heating block measures the approximate glass disc/square temperature. Heat transfer at high vacuum occurs through both radiation and conduction due to the contact of the heating block over the glass disc. The required temperature should be approximately 40˚C more than the melting temperature of the pump-out sealing material to seal the pump-out hole. In this modified design, the risk of dislocation of the heating block and the degradation of O rings due to continuous heating in the vacuum cup was reduced. Different types of materials such as silicone, Buna-N, Teflon or Viton are available, among which the Viton type is capable of sustaining temperatures up to 250˚C. The Viton O ring decomposes at temperature above 250°C causing ingress of gas molecules from the atmosphere, to reduce this the O ring was selected to be around 100mm in diameter, placing the O ring sufficiently away from the heating element to avoid degradation.

Fig. 3: Photographs of the vacuum cup system for the evacuation and sealing of the pump-out hole of a triple vacuum glazing.

3. Fabrication Method

A multiple stage fabrication method was developed, in which a number of samples were fabricated by using a newly developed dual-edge (low melt-temperature i.e. 186˚C) seal. It consists of 10mm wide Cerasolzer CS186 as a main hermetic seal and a 4mm wide J-B Weld epoxy steel resin as a support seal. This is because, under temperature gradients and high internal compressive and external tensile stresses, such support seal provides mechanical strength to the main seal. The fabrication method developed is as follows: (a) the glass sheets and glass-square cover slip for pump-out hole sealing were prepared by drilling a pump-out hole on the upper glass sheet, cleaning all three glass sheets with water, isopropanol and acetone and shaping the glass-square cover slip (Zhao et al, 2007); (b) the main seal around the periphery of bottom and middle glass sheet and on the glass-square (18mmx18mm) was uniformly soldered; (c) the support pillars (0.15mm in height and 0.3mm in diameter) in the square array spaced at 24mm on the middle and lower glass sheets were placed (d) the three glass sheets were joined together by heating at 186˚C for up to 2 hours in the oven (e) the assembly was allowed to cool down to ambient temperature of around 21˚C followed by the use of epoxy J-B Weld to form the support seal (f) Two cavities between three hermetically sealed glass sheets were evacuated, using the high vacuum pump-out system, shown in Fig. 1; and (g) after the evacuation of ~ 6 hours at 50˚C the pump-out hole was sealed by heating the glass square using the cartridge heater located inside the vacuum cup pump-out assembly. The hot plate was used to maintain the narrow temperature gradients on the glass surfaces to avoid glass facture.

4. Experimental Results

A fabricated sample of size 300 mm·300 mm, shown in Fig. 2a, is a result after four repeated trials and the sealing characteristics were found similar where the stress patterns, due to internal compressive and external tensile stresses, across the support pillars were observed indicated a vacuum-tight seal. The evacuated pressure achieved was $4.8 \cdot 10^{-2}$ Pa when subjected to the hot-plate temperatures set to 50˚C as it improved the out-gassing and avoided any damage to the glass sheets due to temperature gradients. However, temperature control has significance as when it increases above 50˚C a high level of internal compressive stresses and external tensile stresses were observed that may cause a glass fracture. The evacuation pressure and hot plate temperature readings were recorded with respect to time at which the diaphragm and turbo-molecular pump achieves its ultimate pumping speed of up to 61 litres/sec as illustrated in Fig. 2b.

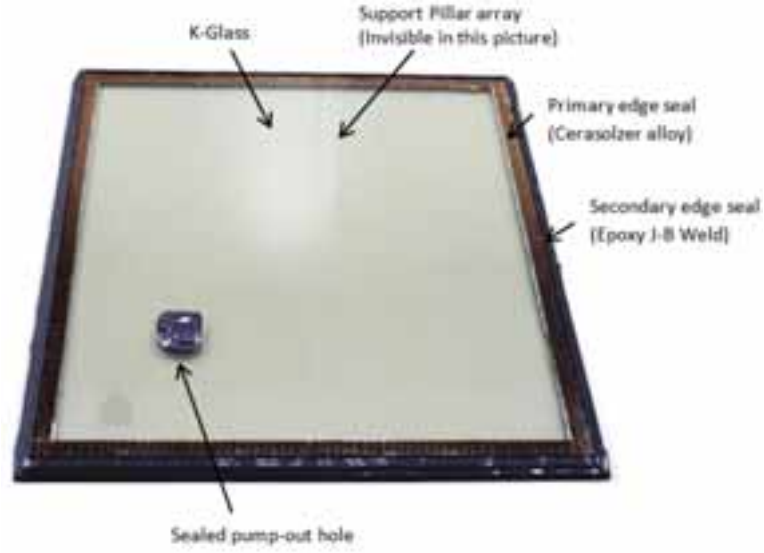

(a)

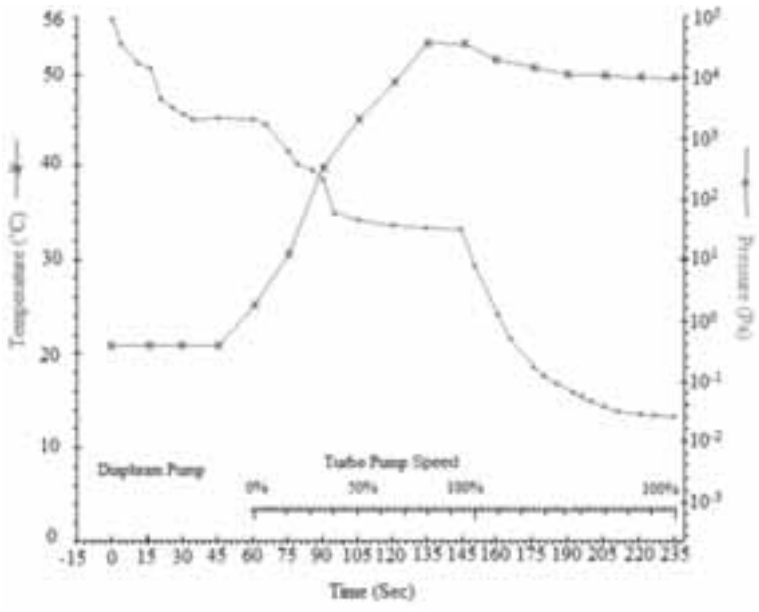

(b)

Fig. 2: (a) Fabricated dual-edge sealed triple vacuum glazing (300mm˙300mm) and (b) the evacuation pressure and hot plate temperature readings with respect to the increment of pumping speed with diaphragm to the full-load pumping speed with turbo-molecular pump.

5. Thermal Performance Predictions

A 3D finite-element model was developed, initially reported in Memon et al (2015), to predict the thermal performance based on the achievable vacuum pressure of $4.8 \cdot 10^{-2}$ Pa of the fabricated sample of size 300 mm·300mm. In order to reduce the computational time, only one quarter (150 mm·150 mm) of the triple vacuum glazing sample was modelled and simulated. The ASTM weather indoor and outdoor boundary conditions were employed in which the indoor and outdoor surface air temperatures were set to be at 21.1˚C and -17.8˚C respectively in winter conditions. The internal and external surface heat transfer coefficients were set to 8.3 $Wm^{-2}K^{-1}$ and 30 $Wm^{-2}K^{-1}$ respectively. The total U value and centre-of-pane U value equations employed are expressed in eq. 1 and eq. 2.

$$U_{centre} = \frac{1}{Rsi_{centre} + \frac{A_{centre}(Ti_{centre} + To_{centre})}{Q_{centre}} + Rso_{centre}} \quad (eq.1)$$

$$U_{total} = \frac{1}{Rsi_{total} + \frac{A_{total}(Ti_{total} + To_{total})}{Q_{total}} + Rso_{total}} \quad (eq.2)$$

Where, Rsi and Rso are the indoor and outdoor glazing surface thermal resistances, in m^2KW^{-1}. A_{centre} (m^2) is the total glazing area minus the edge of glass areas (Fang *et al*, 2007). The thermal conductivity of Cerasolzer CS-186(Primary seal) and J-B Weld (secondary support seal) employed in the 3D finite element model are 46.49 $Wm^{-2}K^{-1}$ and 7.47 $Wm^{-2}K^{-1}$, respectively. The details of the experimental measurements of thermal conductivities of the edge sealing materials are reported elsewhere (Memon, 2017).

The centre-of-pane and overall U-value of 0.33 $Wm^{-2}K^{-1}$ and 1.05 $Wm^{-2}K^{-1}$ for the fabricated triple vacuum glazing sample were predicted at the evacuated pressure of $4.8 \cdot 10^{-2}$ Pa having three k glass sheets (thermal conductivity of each 4mm thick glass 1 $Wm^{-1}K^{-1}$) coated with SnO_2 layer on the inner glass surfaces (emissivity of 0.15). The G value was predicted to be 0.71. It was predicted in (Manz et al, 2006 and Fang et al, 2010) and demonstrated here that the glazing size, due to edge effects, influences the total U-value. A typical cold side isotherm of the model is shown in Fig 3a and the temperature distribution across support pillars is shown in Fig. 3b.

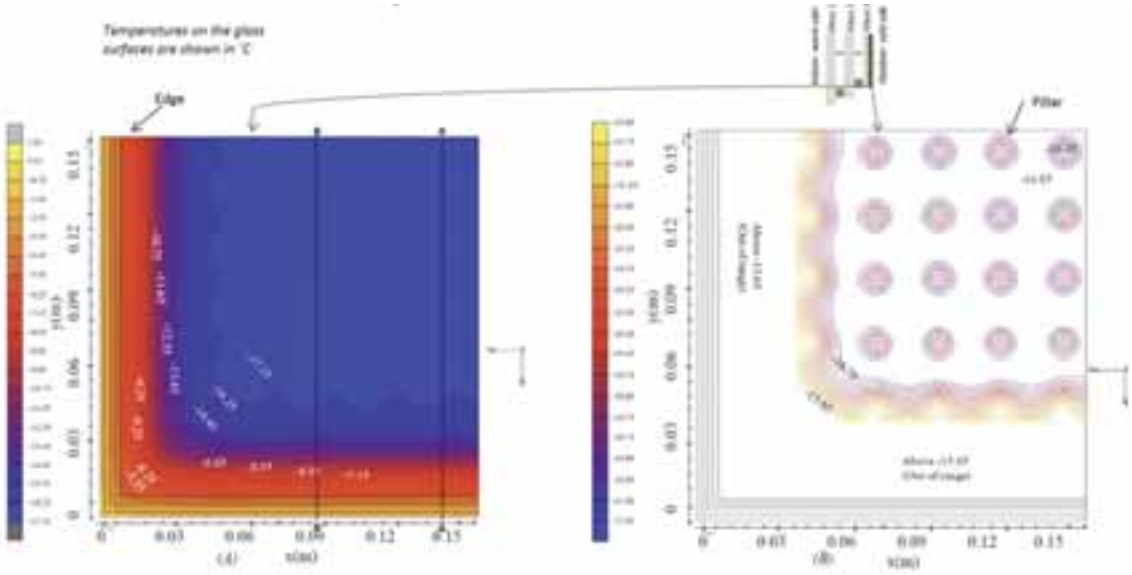

(a) (b)

Fig. 3: The isotherms on the cold glass surface illustrates (a) the temperature changes from the edge sightline towards the centre of glass and (b) the temperature changes around support pillars on the centre of glass area of the triple vacuum glazing.

6. Conclusions

The experimental testing results have shown the achievable vacuum pressure in the vacuum system to be $4.35 \cdot 10^{-5}$ Pa. This deviates by 7.7% with the ultimate vacuum pressure of the turbo molecular pump due to the molecular air flow conductances through the vacuum system. A vacuum cup designed to reduce the risk of dislocation of the heating block and the degradation of O rings due to continuous heating with the pump-out hole evacuation. The outcome of the design and development of high-vacuum system was the successful fabrication of ultra-low heat loss triple vacuum glazing with a pump-out hole sealing material using Cerasolzer CS-186. A new method of fabricating triple vacuum glazing based on a low melt temperature (186ºC) dual-edge seal was designed and experimentally validated, consisting of Cerasolzer CS186 alloy as a main seal and J-B Weld epoxy steel resin as a support seal. A vacuum pressure of $4.8 \cdot 10^{-2}$Pa was achieved. A 3D FEM of the fabricated design of triple vacuum glazing was developed in which the centre-of-pane and overall U-values of a triple vacuum glazing (300mm·300mm) were predicted to be 0.33$Wm^{-2}K^{-1}$ and 1.05 $Wm^{-2}K^{-1}$, respectively, based on three SnO_2 coated K-glass sheets, these results are in agreement with the preceding reported results. Triple vacuum glazing has the potential in future, if manufactured at the mass production level, because of its slimness (12.6 mm) compared to the conventional glazings and due to its lowest achievable thermal transmittance value.

7. References

Allen, K., Connelly, K., Rutherford, P. and Wu, Y., 2017. Smart windows—Dynamic control of building energy performance. Energy and Buildings, 139, pp.535-546.

Andric, I., Pina, A., Ferrão, P., Fournier, J., Lacarrière, B. and Le Corre, O., 2017. The impact of climate change on building heat demand in different climate types. Energy and Buildings, 149, pp 225-234.

Baetens, R., Jelle, P. Gustavsen, A. 2011. Aerogel insulation for building applications: A state of the art review. Energy and Buildings, 43, pp 761-769.

Eames, P. C. 2008. Vacuum glazing: Current performance and future prospects. Vacuum, 82 pp 717-722.

Fang, Y., Hyde, T. J., Hewitt, N., 2010. Predicted thermal performance of triple vacuum glazing. Solar Energy, 84, pp 2132-2139.

Fang, F., Eames, P. C., Norton, B., Hyde, T. J., 2006. Experimental validation of a numerical model for heat transfer in vacuum glazing. Solar Energy, 80, pp 564-577.

Lee, J.R., Raymond, B., Bracegirdle, T.J., Chadès, I., Fuller, R.A., Shaw, J.D. and Terauds, A., 2017. Climate change drives expansion of Antarctic ice-free habitat. Nature, 547(7661), pp.49-54.

Memon S. 2014. Analysing the potential of retrofitting ultra-low heat loss triple vacuum glazed windows to an existing UK solid wall dwelling. Int. Journal of Renewable Energy Development, 3(3), pp 161-174.

Manz, H. 2008.On minimizing heat transport in architectural glazing. Journal of Renewable Energy, 33, pp 119-128.

Memon, S., Farukh, F., Eames, P. C., Silberschmidt, V. V. 2015. A new low-temperature hermetic composite edge seal for the fabrication of triple vacuum glazing. Vacuum, 120, pp 73-82.

Memon, S. 2017. Experimental measurement of hermetic edge seal's thermal conductivity for the thermal transmittance prediction of triple vacuum glazing, Case Studies in Thermal Engineering, 10, pp 169-178.

Manz, H., Brunner, S., Wullschleger, L., 2006. Triple vacuum glazing: Heat transfer and basic mechanical design constraints, Solar Energy. 80, 1632-1642.

Memon, S and Eames, P.C. 2017. Solar Energy Gain and Space-Heating Energy Supply Analyses for Solid-Wall Dwelling Retrofitted with the Experimentally Achievable U-value of Novel Triple Vacuum Glazing. Journal of Daylighting, 4 (1), pp 15-25.

Piccolo, A. and Simone, F., 2015. Performance requirements for electrochromic smart window. Journal of Building Engineering, 3, pp.94-103.

Wu, L.Y., Zhao, Q., Huang, H. and Lim, R.J., 2017. Sol-gel based photochromic coating for solar responsive smart window. Surface and Coatings Technology, 320, pp.601-607.

Zhao, J. F., Eames, P. C., Hyde, T. J., Fang, Y., Wang, J. 2007. A modified pump-out technique used for fabrication of low temperature metal sealed vacuum glazing. Solar Energy 81, pp 1072-1077.

Study of Photovoltaics and Solar Thermal for Nearly Zero Energy Mediterranean Villas

Andreu Moià-Pol[1], Víctor Martínez-Moll[1] ,Vincent Canals[1],Rashid Nazmitdinov[2,1], Artem Morzhukhin[3]

[1]University of Balearic Islands, Physics department, P. Mallorca (Spain)

[2] BLTP, Joint Institute for Nuclear Research, 141980 Dubna, (Russian Federation)

[3] Dubna University, Dubna, Moscow Region (Russian Federation)

Abstract

The development of modern nearly zero-energy buildings (NZEB) has become possible due to the combination of high quality architecture design and the addition of renewable energies (especially solar thermal and photovoltaic). The Renewable energies can cover all the energy consumption of the year. Solar thermal with Heat Pump and photovoltaic (PV) systems for buildings have been designed to achieve different values of the fraction of primary energy saving. The Flat Plate Collectors (FPC) for Solar Thermal (ST) and Solar Photovoltaic (PV) have to be used in order the system to have higher efficiency with zero energy consumption. 13 different combinations have been studied in order to obtain higher savings with minimum investment.

Keywords: Zero Energy Buildings, Solar Thermal, Photovoltaic, heat pump, combisystems,

1. Introduction

The Article 9 of the European Union Directive 2010/3 which was incorporated in Spanish legislation requires that by the 31st December 2020, all new constructions must be nearly zero-energy buildings. This requires a new concept and a big effort to be made by the construction sector, mainly engineers and architects.

Recently, increasing efficiency of the heat pumps for Heating, Cooling and Domestic Hot Water with decrease in electric PV costs have provided a new model: solar-electric heat pumps. The ST energy has lost installed power during the last few years against other technologies, like PV. The development of modern net zero-energy buildings (NZEB) has become possible not only through the progress made in new renewable energies and construction technologies and techniques, but as well it has also been significantly improved by the combination of heat pump and solar systems (Moià-Pol et alt 2012). There are some simulation programs that can be useful to simulate different combinations of technologies and make it easy to choose the best in each case in order to archive the highest efficiency and renewable energy usage. (fraction). Counting that a modern compression machine with an evaporator up to 7ºC (usually at Mediterranean weather), has a 3-5 Coefficient of Performance (COP), with a Seasonal Coefficient of Performance over 5, and according to the Directive 2010/31/EU it's considered to be similar to another kind of Renewable energy. The actual cost of thermal production with Heat Pump is similar to the Solar Thermal, depending on the working temperatures, refrigerant and quality of the machine (ASHRAE). In Mediterranean areas almost all the villa houses have a swimming pool, Heating Ventilation and Air Conditioning system for a higher comfort. Some of these houses need to warm the outdoor pool in order to extend the swimming period in autumn and spring months, which is translated into a higher energetic demand. This kind of houses according to the Spanish law (CTE) have to use waste energy or renewable energies for the heating system of Domestic Hot Water (DHW) and the pool. For this it´s necessary a bigger installed surface of solar collectors which will allow to take profit of the solar collectors all the year, with a low overheating. However, in order to avoid a big energy consumption, it´s necessary to insulate and cover the pool, and not use it during the coldest Mediterranean months (December, January and February), when the average temperature is lower than 10ºC. The energy of the solar collectors can be used to help the heating system.

doi:10.18086/swc.2017.15.05 Available at http://proceedings.ises.org

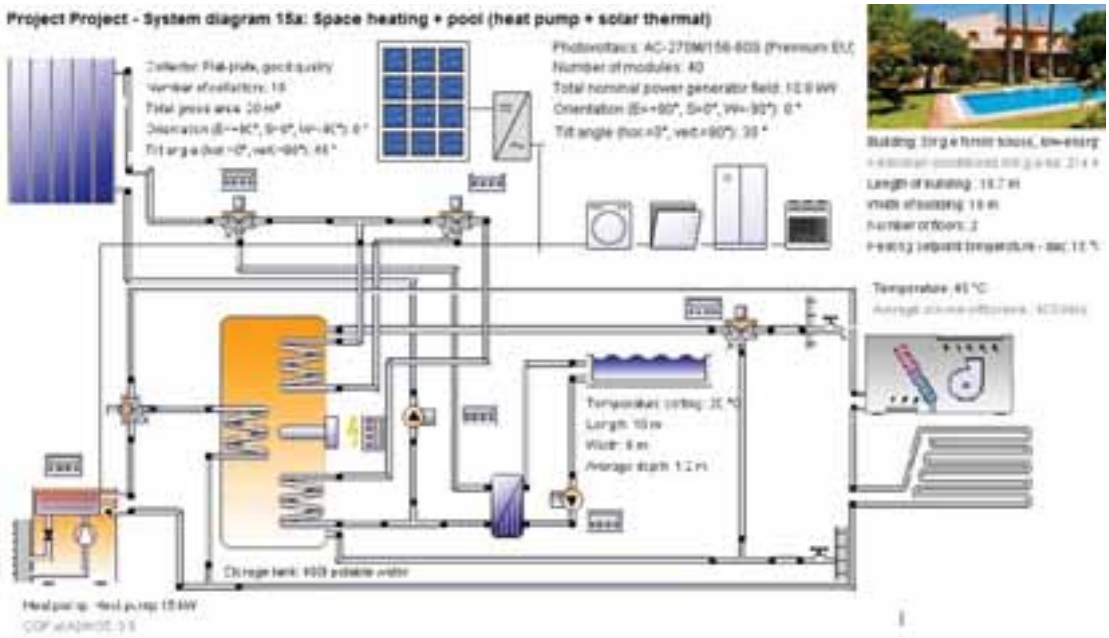

Fig. 1: Thermal system with Polysun

Tab. 1: Annual average temperatures, global horizontal irradiation and Heat Pump C.O.P.for Mallorca

	Jan.	**Feb.**	**March**	**April**	**May**	**June**	**July**	**August**	**Sept.**	**Oct.**	**Nov.**	**Dec.**	***Year***
H kWh/m²	65	79	126	159	196	208	214	188	140	106	66	57	**1604**
Temp.°C	9.4	10	11.1	12.8	16.7	20.6	23.9	24.4	21.7	17.8	13.3	10.6	**16.1**
C.O.P.	3.22	3.26	3.33	3.42	3.54	3.53	3.41	3.39	3.50	3.55	3.44	3.30	**3.41**

2. Simulation and Results

The study case house has a built surface of 400 m^2, of which only 300 m^2 require heating and cooling: the simulation has been made supposing a need for simultaneous heating for 150 m^2 with Fan coils and Radiant system. The pool has a surface of 80m^2 with a volume of 120 m^3. There is a limitation of useful surface for the installation of Solar Collectors -only one roof of 160 m^2 is available. However we have to take into account shadows and the distance between the Solar Collectors which leave us with a useful surface of nearly 80 m^2. This limitation has been taken into account in all the scenarios. The PV system has been designed with monocrystalline panels equivalent to an efficiency of 166 W/m^2 (η =16,60 %) and the solar thermal with good Flat Plate Collectors (A_0 = 0,807, A_1= 3,075, A_2= 0,022) .

The FPC sends the excess of energy to the pool, increasing the set point temperature, and consequently extending the swimming season. In the investment cost there have only been considered the solar collectors, structure, pipes and cables, without storage tank, heat pump and batteries, in order to be able to compare without auxiliary systems or other necessary elements for the basic system. However, PVT system wasn't analyzed due to limited roof surface; the results showed that it was better to use PV and ST systems with higher efficiency. The cost of the PV in Spain for medium systems (5- 20 kWp) is about 1500 €/kWp (including installation work, cable, structure and inverter without storage), similar to other EU countries, like Germany and Italy (source EIA and REN21, 2016), with efficient solar panel (15 to 20%) the price in square meter will be near 300 €/m^2.

Solar Thermal cost varies greatly according to the installation peculiarities (distances, roof,..) and other factors (labor, components,..) . In Spain a pumped system of FPC can cost from 300 to 600 €/m^2 (including pipes, pump and control system). Apart from that we have to add the storage. For Spain a storage system between 50-180 L/m^2 is recommended. Pumped systems until 6 m^2 are very expensive with the thermosiphon being cheaper. For larger systems the bigger the surface the cheaper are the prices per square meter.

The best scenario is a combination between Solar Thermal and Photovoltaic: in our case between 12-16 m^2 of FPC will provide the 16% of all the thermal energy, with almost 100% of the DHW and 31% of the pool and heating system. The PV will provide a 70% of the electricity for the heat pump. PV system has a peak power near 9-11 kWp in order to provide the electricity for the HVAC and use the excess for the rest of the

consumption. The FPC has a surface of 16 m^2 and the PV of 58 m^2, almost four times bigger.

The designers are working in two scenarios: the first one connected to the grid with batteries and the other a grid system without batteries in order to have the maximum energy production and less CO_2 emissions. The batteries increase a 33% the cost of the PV system (Gallo et al. 2014). Solar thermal technology has to be designed with storage and the advantage in Spain is that PV doesn't need storage, the excess can go to the grid free or with a low charge. For this reason the storage is a better option which offers higher savings.

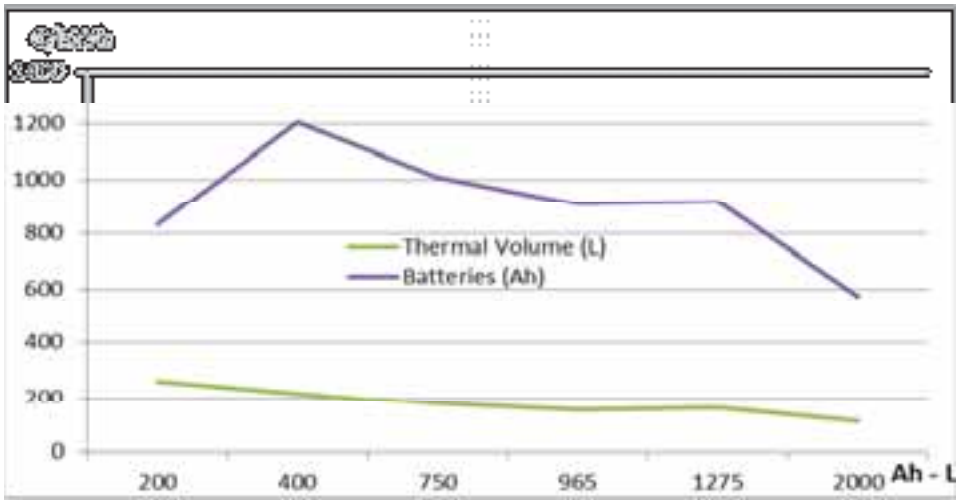

Fig. 2: Cost of Energy Storage Batteries vs. Thermal Storage water (Spanish prices from local suppliers)

In our case, it´s better to increase the storage with thermal energy (water tanks and pool) and install a few batteries in order to increase the self-consumption: the installation cost is 5 times cheaper. Grid parity has been achieved in Spain and the integration of PV systems in nearly ZEB is feasible today (Gallo et alt 2014). The system doesn´t overheat or waste electricity if we provide a good control system. The available roof limits the solar fraction so for higher solar fraction we need a bigger surface or most efficient heat pumps, for instance shallow geothermal or other combinations could be 100% with renewable energies. The PV has a better perspective, for two reasons: the simplicity of systems and the possibility to share the punctual excess (some days or months) to the grid with the net metering policies. Figure 3 has the results of 13 combinations and two different qualities of FPC and PV, Invest (high quality-first brand) and Invest 2 (lower quality-second brand). The Invest and savings are higher when we use the best quality brands. The efficiency of the solar system is the main difference, the initial investment has an average of 18% of difference and the savings are nearly a 47%.

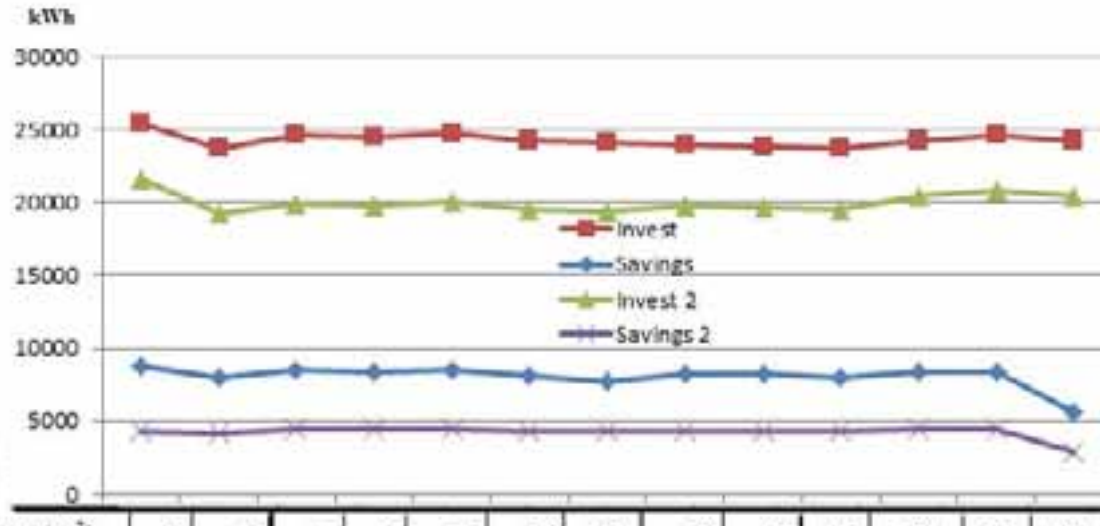

ST (m^2)	0	8	12	14	16	18	20	22	24	26	30	36	64
PV(kWp)	14	10.8	10.5	10	9.72	9	8.5	8	7.5	7	6.82	5.9	0

Fig. 3: Energy invest of the solar system (without components) with savings for 13 scenarios and 2 prices

Table. 2: Different studied scenarios with ST ,PV, investment, savings and solar fraction for ST and PV for a Villa in Mallorca

ST(m^2)	**0**	**8**	**12**	**14**	**16**	**18**	**20**	**22**	**24**	**26**	**30**	**36**	**64**
PV(m^2)	**84**	**65**	**63**	**60**	**59**	**54**	**51**	**48**	**45**	**42**	**41**	**35**	**0**
Invest	25410	23668	24672	24539	24805	24273	24140	24006	23873	23740	24236	24654	24200
Savings	8471	7749	8176	8143	8209	7897	7470	7995	7946	7667	8094	8110	5418
Invest 2	21600	19200	19950	19800	19980	19500	19350	19800	19650	19500	20430	20775	20400
Savings 2	4370	4182	4491	4510	4422	4362	4370	4375	4373	4373	4466	4477	2904
ST (Fraction)	0%	8%	12%	14%	16%	17%	19%	23%	26%	25%	29%	34%	66%
PV(Fraction)	86%	72%	73%	71%	70%	66%	60%	62%	59%	57%	58%	54%	0%

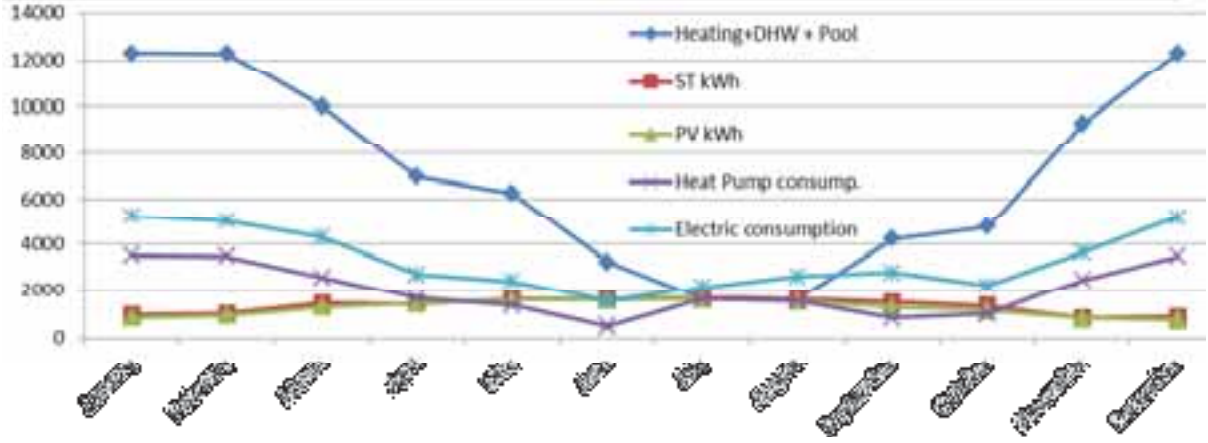

Fig.4: Annual energy simulated results in Final energy [kWh]

The total investment is less than a 5% of the total cost of the villa, which is technically and economically feasible so as to arrive to almost zero energy buildings.

3. Conclusions

The two solar technologies, Photovoltaic and Solar Thermal, are necessary for NZEB from a technical and an economic point of view. The investment cost and savings are better according to the monthly demand. In these cases the best scenario is 14 m^2 of Solar Thermal and 9 kWp of Photovoltaic. Limited space for solar systems make it necessary to use more efficient systems, however with a good control strategy, batteries and overheating systems are not necessary.

4. References

Recast, E. P. B. D. (2010). Directive 2010/31. EU of the European Parliament and of the Council of, 19.

Andreu Moià Pol, Víctor Martínez Moll, Miquel Alomar Barceló, Ramon Pujol Nadal. Solar and heat pump systems. An analysis of several combinations in Mediterranean areas. Proceedings of the Eurosun 2012, Rijeka, Croatia.

1999 ASHRAE Handbook. HVAC Application. Chapter 31. Energy Resources, American Society of Heating, Refrigeration, and Air-Conditioning Engineers, Inc.

CTE http://www.codigotecnico.org/ Spanish Technical Building Code and http://www.idae.es

Polysun. http://velasolaris.com

Gallo, A.; Téllez, M.B.; Prodanovic, M.; González-Aguilar, J.; Romero, M. "Analysis of net zero-energy building in Spain". Integration of PV, solar domestic hot water and air-conditioning systems". Energy Procedia, 2014, 48, 828-836 Proceedings of SHC 2013.

REN21 Renewable Energy Policy Network for the 21st Century. Advancing the global Renewable Energy Transition.

Simulation and Monitoring Results of two MFHs in PH Standard with Heat Pump, Solar Thermal and PV

Fabian Ochs[1], Georgios Dermentzis[1], Alexandra Ksiezyk[1]

[1] University of Innsbruck, Unit Energy Efficient Buildings, Innsbruck

Abstract

In the city of Innsbruck, the project Vögelebichl of the social housing company Neue Heimat Tirol (NHT), consists of two multi-family houses (MFH) in Passive House (PH) Standard and aims at operation with minimum CO_2 emissions for heating and domestic hot water (DHW) preparation. Net zero energy building (NZEB) was the goal of NHT for this project. The heat emission system, a floor heating with very low flow temperature, together with very well insulated heat distribution network allows a high performance of the ground water sourced heat pump (HP). The separate DHW distribution with flat-wise fresh water preparation is also designed for minimum possible flow temperature. DHW preparation is covered by solar thermal (ST) to a large extend. The electricity demand of the HP should be covered as much as possible by on-site PV. The optimum configuration of ST and PV with respect to energetic and economic performance was determined by means of simulation in a previous study Ochs et al. 2014. This paper presents the technical details of the two MFHs, the hydraulic concept and monitoring results after the first two years of operation, and a monthly primary energy evaluation.

Keywords: nearly zero energy building, Passive House, Multi-Family House, Heat Pump Solar Thermal, PV

1. Introduction

1.1 EPBD - Heat pump and PV for nZEBs

The recast of the European building directive (EPBD Recast, 2010) defined the path to nearly zero energy buildings (nZEB). Three aspects are addressed:

- New buildings will have a very high energy performance.
- The remaining very low energy demand will be provided to a very significant share by renewable energies and
- Cost-optimal levels for minimum energy performance are requested.

Hence, the aim of the EPBD recast is the minimization of the residual energy demand and achieving maximum reduction of CO_2-emissions considering economics. Hence, future buildings should have a very high-energy performance, such as Passive Houses and should be operated with a heat pump together with significant amount of energy from cost-effective renewable energy sources (PV and/or solar thermal).

However, the implementation of the EPBD in the member countries is far less ambitious (see BPIE 2016). The more important is it to demonstrate best practice examples and highlight non-renewable primary energy and CO_2-savings.

A dominating concept to reach the zero energy balance over an annual period for a nearly Zero Energy Building (nZEB) is the combination of solar PV systems and heat pumps. In the IEA HPT Annex 49, a follow-up of the Annex 40 heat pump integration options for nZEBs are investigated as well as the design and control for heat pumps in nZEB and the integration into energy systems. Solar thermal can be relevant as it is technically and economically less challenging to store heat compared to storage of electricity. Storage is relevant in order to reduce the remaining electricity usage in winter, which has generally a higher fossil (and/or nuclear) share. Hence, nZEBs should be evaluated considering the time of electricity usage from the grid.

doi:10.18086/swc.2017.15.06 Available at http://proceedings.ises.org

1.2 nZEB vs. NZEB

The goal of both, nZEBs and NZEBs are comparable in the sense that CO_2-emissions and non-RE primary energy use shall be minimized, nevertheless, the definitions differ quite much in detail and the performance might be quite different eventually.

nZEB: nearly zero Energy Building according to EPBD, 2010, see above. Each member state has a national definition, with significant differences with respect to the energy use considered (heating, cooling, DHW, auxiliary, appliances), the maximum limits, the conversion factors etc. (see BPIE, 2016).

NZEB: Net Zero Energy Building, generally a NZEB is a "grid-connected building which produces the same amount of energy on-site by renewable energy sources as it consumes on annual basis." (IEA SHC Task 40, IEA HPT Annex 40). There is a fuzziness in this definition regarding the interpretation of the system boundary, the energy flows, the weighting/conversion factors etc.

Usually, Net Zero includes

- Heating (and cooling)
- DHW
- aux. energies (MVHR, pumps, control, etc.)

but excludes appliances. Even though appliances, have a large contribution to the overall electricity consumption (1500 kWh/a to 4500 kWh/a depending on the number of persons per household for a typical central European household, Statistik Austria 2016, BEDW 2013).

According to this definition, a NZEB can consume relative high amount of (electric) energy in winter, when correspondingly a large PV area produces this amount as excess electricity in summer. This means, that according to the NZEB concept, the electric grid is considered as a loss free seasonal storage, which is obviously not the case. In order to account for this weakness in this concept, additional performance indicators such as the load match factor or fraction of PV own consumption are suggested.

Remark: „net-zero“ as a goal can be a misleading concept, anyway as optimization for net-zero may lead to one storey buildings, because reaching the net zero balance is more difficult compared to a multi-storey building (with smaller roof and façade area related to treated area). However, MFHs, which are more compact, are favorable from the overall energetic and macro-economic point of view, compare also Feist et al. 2014.

1.3 Monthly primary energy values

A possible approach of balancing primary energy demand and CO_2 emissions of a building with renewable energy generation is shown schematically in Fig. 1.Solar thermal (ST) energy is used to reduce the energy demand (heating, DHW + storage and distribution losses) that has to be covered by e.g. a heat pump (HP). Onsite PV can be used directly for appliances and auxiliary energies or to drive the HP, for higher own consumption a battery storage is required, which is subject to losses.

For the electricity mix, the share of renewables within the time frame of consideration (e.g. 20 years) should be included and not as usually done the current or past status. A significantly increased share of renewable electricity can be expected in the near future in particular in summer (PV), while in winter only a moderate increase is likely (further extension of wind power) unless seasonal storage capacities are strongly build up.

If a large number of buildings use heat pumps (and ST) for space heating and DHW preparation and produce electricity (with PV), both, the purchased electric energy and the share of renewables in the electricity mix and thus the CO_2 conversion factor of the electricity are dependent. Electricity that is used on site is not available in the grid and an increased share of fossil fuels in the energy mix have to be considered. PV electricity sold to the grid will replace fossil fuels more likely in winter, spring and autumn than in summer.

Heating and DHW preparation do not yet contribute significantly to the electric grid load in central European countries such as Germany and Austria (electric heating and heat pumps have a share in the range of 5 %, BEDW 2013, Statistik Austria, 2016)

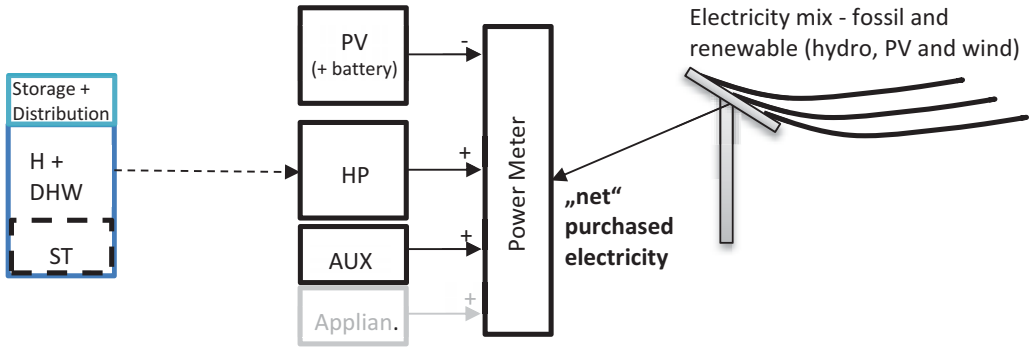

Fig. 1. One of different possible approaches for the energy balance for the calculation of the net energy balance with Heating (H) and domestic hot water (DHW) demand covered partly by ST; the remaining demand is covered by a heat pump (HP), which is partly powered by onsite PV, the remaining electricity demand for the HP auxiliary energies (and appliances) is covered by the grid with volatile shares of renewable electricity

Due to the volatile share of renewable energy in the grid (see e.g. the energy balance for Germany in 2015 (e.g. data from ENTSO-E), a net energy balance to evaluate different efficiency and energy concepts can be misleading.

National conversion factors for PE/CO_2 are not purely based on facts, but are partly politically motivated. They differ significantly between the EU member states and are subject to change, e.g. Germany (ENeV) 1.8 since 2016 (2.4 before), Austria 1.91 since 2015, 2.62 before (OIB-6, 2015, (OIB-6, 2011). Seasonal variations are not considered at all. Instead, a monthly evaluation based on monthly primary energy factors is proposed, which can be used to calculate a more representative environmental impact. The specific primary energy e_{PE} is

$$e_{PE} = f_{PE} \cdot w_{el} \qquad \text{(eq. 1)}$$

With different shares of hydro, wind, PV and fossil energy the primary energy conversion factor can be calculated on monthly basis.

$$f_{PE} = f_{PE,hyd.} \cdot \frac{w_{el,hyd.}}{w_{el}} + f_{PE,wind} \cdot \frac{w_{el,wind}}{w_{el}} + f_{PE,PV} \cdot \frac{w_{el,PV}}{w_{el}} + f_{PE,fos.} \cdot \frac{w_{el,fos.}}{w_{el}} \qquad \text{(eq. 2)}$$

Tab. 1: Monthly primary energy factors calculated exemplarily for two cases, A: a share of 10 % hydro, 10 % wind and 10 % PV, and the load of a PH with a HP for heating and DHW preparation as shown in Fig. 2 and B a share of 10 % hydro, 10 % wind and 10 % PV; $f_{PEhyd.}$ = 0.01 kWh_{PE}/kWh_{el}; f_{PEwind} = 0.05 kWh_{PE}/kWh_{el}; f_{PEPV}= 0.1 kWh_{PE}/kWh_{el}; $f_{PEfos.}$ = 2.4 kWh_{PE}/kWh_{el}

	Jan	Feb	Mar	Apr	May	Jun	Jul	Aug	Sep	Oct	Nov	Dec	av.
A: 10-10-10	2.01	1.96	1.89	1.60	1.33	1.20	1.18	1.28	1.53	1.78	1.92	2.01	**0.8**
B: 10-30-30	1.53	1.42	1.23	0.50	0.08	0.08	0.08	0.08	0.33	0.98	1.33	1.54	**1.6**

Remark: A more detailed paper showing in detail the approach and the method of the PE-model and discussing the assumptions and implications is under preparation. The method can be applied to CO_2-emissions in the same way.

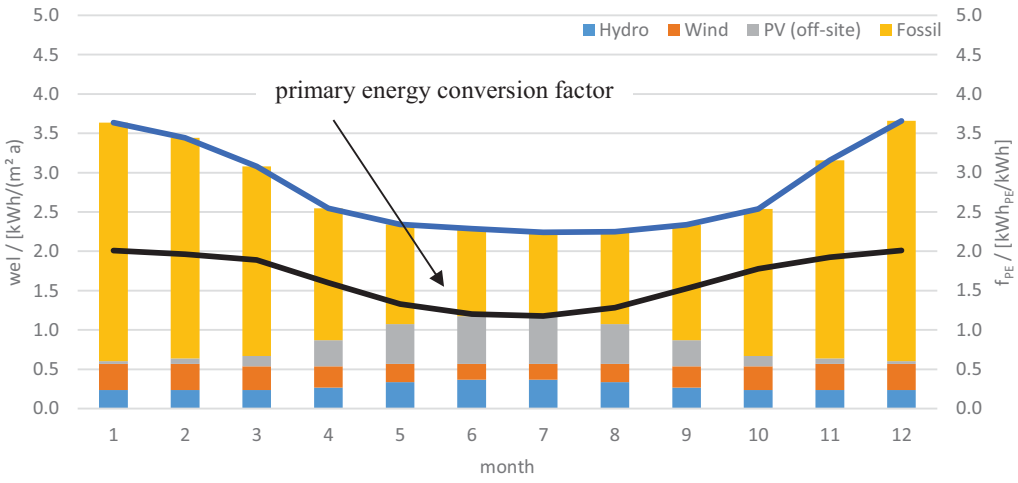

Fig. 2. Monthly share of renewables (hydro, wind, PV, fossil) and corresponding primary energy conversion factor, example of a PH with a HP for heating and DHW preparation with a share of 10 % hydro, 10 % wind and 10 % PV in the electricity mix

2. NZEB Project NHT Vögelebichl in Innsbruck

For the Passive House project Vögelebichl in Innsbruck (two multi-family houses with together 26 flats of the social housing company NHT see Fig. 3 and Fig. 4) the optimum share of PV and Solar Thermal (ST) was determined for the given boundary conditions. One roof of the multi-family houses is covered by PV (16 KWp) only. The other roof space was partly used for PV and partly for solar thermal (ST). The primary energy demand was determined for different shares of solar thermal collectors with regard to the maximum available unshaded roof space. For the optimal performance of the ground water heat pump a low temperature distribution system (floor heating) and separate DHW loop with decentral heat exchanger was proposed. Compared to the 2-pipe system, the 4-pipe system allows better performance of the HP and offers the possibility for some cooling in summer. Instead of the initially proposed 4 pipe system a 3 pipe system with common return pipe of the DHW and the heating loop was installed.

By means of a simulation study the share of PV (max 19 KWp) and solar thermal collectors (ST) was varied in order to determine the maximum possible energy yield considering PV and ST system efficiencies including heat pump performance and distribution losses. The optimal design (from energetic point of view) was found to be 74 m² ST and correspondingly 53 m² PV on the north roof, see Ochs et al. 2014.

Tab. 2: Characteristic data of the two buildings NHT Vögelebichl (as planed)

	North	South
No. of Flats	16	10
Treated area	1269.8 m²	818.8 m²
Heating Demand (PHPP)	13.5 kWh/(m² a)	17.0 kWh/(m² a)
Heating Load (PHPP)	12.0 W/m²	13.9 W/m²
PV size	8.5 kWp	16 kWp
ST area	50 m² (ca. 35 % of roof area)	-

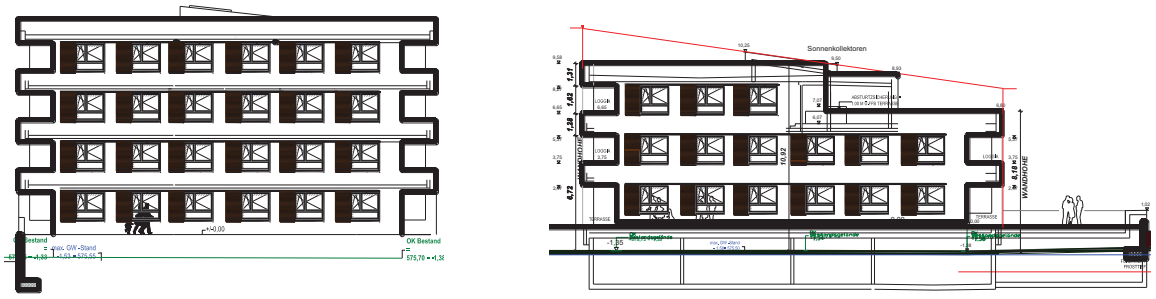

Fig. 3. West view of the two multi-family houses in Innsbruck Vögelebichl, NHT Tirol; two multi-Family PHs with ground water heat pump and PV (and opt. ST for DHW) with 4 pipe distribution system, low temperature system and fresh water modules in each flat

Fig. 4: Photos of the two MFHs in PH Standard (source: NHT)

During the final design process and the construction of the two buildings, some parameters changed with respect to the original planning. The treated area is 1295.6 m² (North) + 853.2 m² (South). The ST area is 73.6 m² (North) and the PV area is 52.5 m² (North) + 99.8 m² (South). The floor heating flow temperature is 30 °C (30/26 °C instead of 28/24 °C) and DHW flow temperature is 55 °C. A 3-pipe system (common return flow of floor heating and DHW) was realized (instead of the proposed 4-pipe system).

Fig. 5 shows a simplified hydraulic scheme including the GW heat pump (two stage), solar thermal collector field (SC) as well as the low temperature heat distribution and the separate decentral fresh water preparation (DHW plate HX). The double stage heat pump is equipped with a hydraulic circuit enabling hot gas (HG) de-superheating. Depending on the operation mode (heating or DHW preparation), the flow of the heat pump enters the buffer store (BS) at the top or at 1/3 of the height from the top. The combined return of the heating and DHW loop enters the large 6 m³ buffer store depending on the temperature level either at the bottom or at about 1/3 of the height of the store in order to enhance stratification. The electric backup heater (BH) is currently not used.

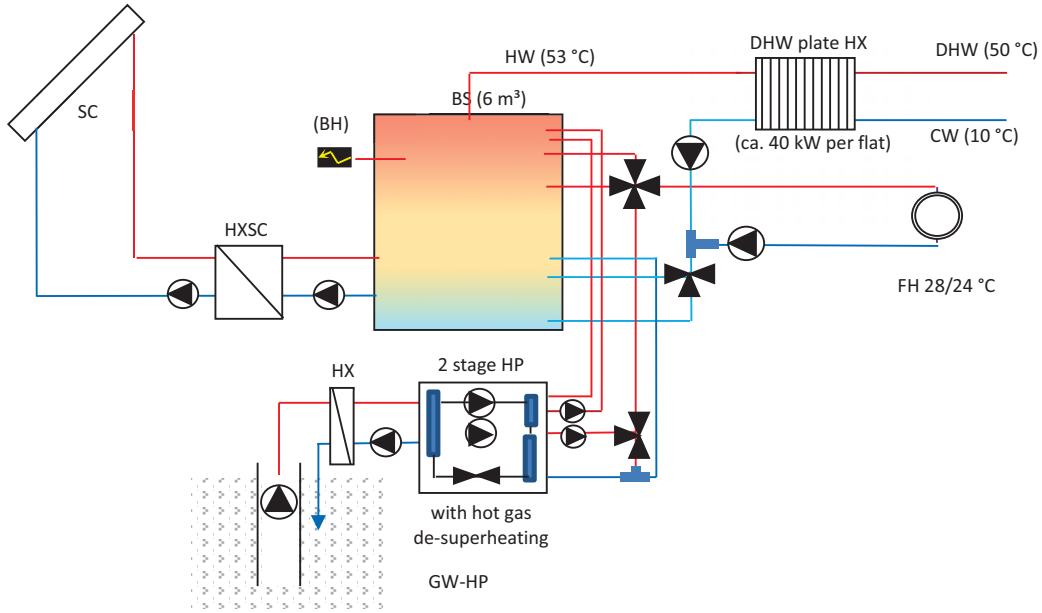

Fig. 5: Simplified Hydraulic Scheme with Solar Collectors (SC), Buffer Store (BS), 2-stage ground water heat pump (HP) with hot gas HG) de-superheating in heating mode with floor heating (FH) and decentral heat exchanger (HX) for domestic hot water (DHW) preparation

3. Monitoring Results

3.1 Climate

The climate during the monitoring period was rather typical. However, there was a relative cold January in 2017. The other months were in the range of average years. During the heating period in average the measured ambient temperature was 2.6 K higher than the design climate used in PHPP. The measured global horizontal solar radiation was with 1192 kWh/(m² a) very close to the design values.

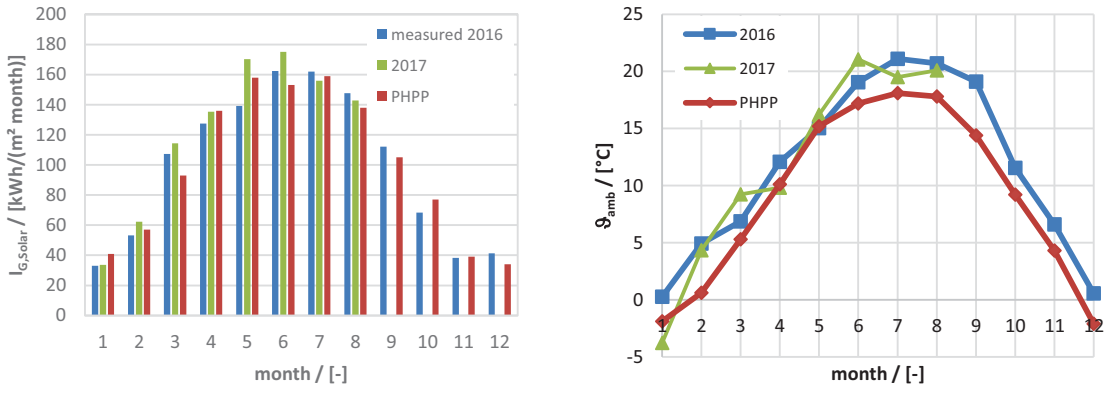

Fig. 6: Measured and design (PHPP) global horizontal solar radiation (left) and ambient temperatures (right)

3.2 Indoor Temperatures

The monitoring system is connected to the building management system (BMS), data of every relevant flow and return temperature, mass flow and energy flow is stored every 15 min. In addition, the temperature is recorded in each flat of the south building. The average temperature of the north building can be estimated by comparing the

measured extract air temperature of the south and the north building. The monthly temperatures are reported in the following figure:

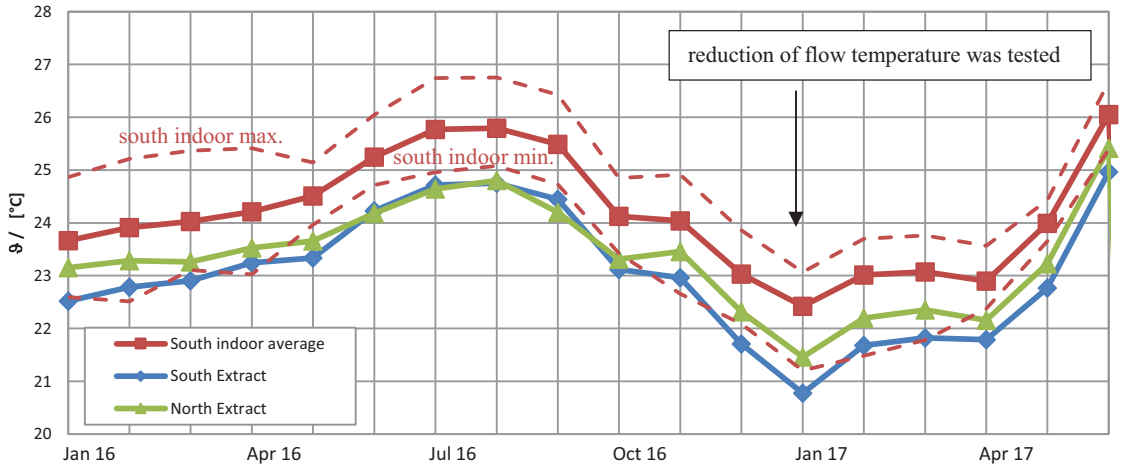

Fig. 7: Measured average, max. and min. indoor temperatures of 9 (of 10) flats of the south building and the corresponding extract air temperature as well as the extract air temperature of the north building

By comparing the average south building temperature and the extract air temperature of the south building and seeing that the extract air temperature of the north building is in winter about 0.5 K higher than the extract air of the south building, it can be expected that the average indoor temperatures were also slightly higher in the north building. In winter 2017, the average indoor temperature of the south building was in the range of 23 °C, while it can be expected that the temperature of the north building was in the range of 23.5 °C, which is 3.5 K higher than the design value. The difference between maximum and minimum indoor temperature of the flats of the south building was reduced significantly in the second winter (with 1.1 K compared to 2.4 in the first months).

In early winter 2017 (month 13 in Fig.7) the flow temperature of the floor heating system was reduced in order to reduce distribution losses. However, at least this sudden change in the indoor temperature together with the fact that January 2017 was a very cold month (average temperature -3.8 °C) was not accepted by most of the tenants and as consequence the flow temperature had to be increased again. It remains an open question, whether a smoother change of the temperature would have been recognized or not.

3.3 Energy Balance

The thermal energy balance for both buildings is shown in Fig. 8 for 2016. The HD for both buildings is with 31.1 kWh/(m² a) higher than design value of 12.2 kWh/(m² a) acc. to PHPP calculations (14 kWh/(m² a) for the south (853.2 m²) and 11 kWh/(m² a) for the north (1295.6 m²) building).

The main reason for an increased heating demand in the first year of operation is usually the construction moisture. Hence, it can be expected that the average annual heating demand decreases with respect to the first year of operation and will settle within the second year. In addition, the influence of the actual climate (compared to the reference climate) and the elevated indoor temperatures have to be considered. Furthermore, deviations from design values might be caused by the user (window ventilation, shading, occupation, equipment). Finally, the actual construction could differ from the design in terms of air-tightness, thermal bridges etc., but this can be practically excluded as the principles of Passive House design were followed and quality control such as blower door tests was conducted.

It is obvious that during the first winter of operation of such a building, there are effects that should be considered with care and general conclusions should be avoided. A HD closer to the design value can be expected for the next winter season, which is already indicated by the significantly lower HD in winter 16/17 than winter 15/16.

The domestic hot water demand (DHW) was with 24.7 kWh/(m² a) slightly higher than the design value, distribution losses are included and cannot be quantified by the available measurement equipment. Storage losses can be determined by energy balancing of measured heat flows from HP, ST, DHW and heating, and were relatively high: 1030 kWh/month in average throughout the measurement period, which is about a factor of three higher than expected even when a storage with relative poor insulation is assumed.

ST covers summer load including losses, so there is (theoretically) no need for HP operation in summer and PV electricity production can only be used for auxiliary energies and appliances (theoretically).

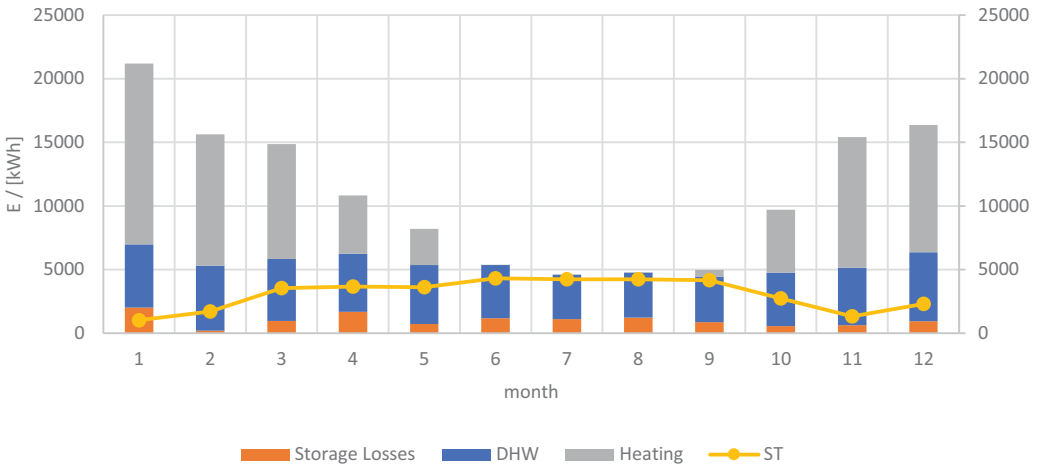

Fig. 8: Thermal energy balance (year 2016), DHW and heating is measured at storage outlet and this includes distribution losses

3.4 Heat Pump Performances

The performance of the ground water heat pump was with an SCOP of 2.9 poorer than expected. HP operation was not optimal for several reasons: heating and DHW flow/return temperatures were higher than planned. The two-stage compressor HP with de-superheating was operated mainly in DHW mode in the first winter. De-superheating contributed with 17 % to the total energy delivered by the HP. Storage stratification was poor in some operation modes and storage (and pipe) losses were too high. The ground water pump (well) was slightly over-dimensioned. Thermal losses of the HP were 16 % in winter and the HP was operated in summer without significant contribution (because of high contribution of ST, see above). The control of the HP and the system was optimized during summer 2016 and in winter 2016/2017 the COP could be increased to 3.4. Further system optimization is possible and an improved sCOP can be expected for 2017.

The average monthly temperature deceases from spring/autumn towards winter because of the higher share of operation in heating mode with flow temperatures of about 35 °C compared to the higher temperatures in DHW mode, see Tab. 3. The calculated monthly average COPs follow the trend of the measured COPs (based on values of 2017) but there is an offset of about 0.7 in average. This remaining difference between the calculation and the measurement can be explained by thermal losses and by the auxiliary electricity demand of the circulation pumps and the well pump and the temperature drop in the heat exchanger. An average COP of 3.6 to 3.7 can be expected based on the calculated values, while from the measurements an average COP of not more than 3.3 to 3.4 can be expected.

Tab. 3: Measured monthly COP in the heating season vs. calculated with Carnot performance factor of 0.5 acc. to data sheet; DHW mode in Mar. and Oct. with 60 °C, 50 % heating and 50 % DHW mode in Jan. and Dec.

	Jan	Feb	Mar	…	Oct	Nov	Dec
Meas. 2016	2.8	2.7	2.9		3.1	3.4	3.4
Meas. 2017	3.7	3.1	2.6				
Calc.	3.9	3.5	3.1		3.5	3.7	4.0
ϑ_{cold}	9	8	7		12	11	10
ϑ_{hot}	50	55	60		60	55	50

3.5 Performance of ST and PV

The performance of both, ST and of PV was relatively good. For a fair comparison, PV electricity has to be converted to thermal energy by means of running the heat pump with PV electricity and charging the storage. So

$$q_{PV} = sCOP \cdot w_{el,PV} \qquad \text{(eq. 3)}$$

Peak power limits and storage losses have to be accounted for. Furthermore, ST delivers temperatures up to 95 °C while with a heat pump the maximum temperature is below 60 °C. The power of the heat pump is limited (here 40 kW_{th}, correspondingly ca. 12 kW_{el}), i.e. for higher power (peak power of PV is ca. 23 kW_{peak}) either direct electric heating rods (with COP = 1) or batteries (with storage losses) have to be used.

A thermal energy storage is required for domestic hot water preparation, but for heating the HP could work directly on the floor heating system (ST contribution to heating is anyway very limited as can be seen in Fig. 8). Assuming 250 l per household, the 26 flats with a simultaneity factor of 0.2 and 50 % distribution losses, a storage volume of about 2 m³ would be sufficient. Hence, the additional volume of 4 m³ can be accounted to the solar thermal system. However, if the electricity generated by the PV area should also be used for DHW preparation (and heating) also in this case thermal energy storage would be required.

In this case, where ST is used for DHW preparation in summer, the monthly COPs of the heat pump should not be taken for further comparisons as the performance of the heat pump in summer was poor because of the very high contribution of ST and correspondingly low contribution of the HP. Therefore, the delivered energy is calculated with the average COP, which is with 2.9 rather low for a ground water heat pump. In this comparison, storage losses are disregarded and then the performance of both ST and PV (+ HP) is in the same order of magnitude as shown in Fig. 9. The specific yield of solar thermal without loses is q_{ST} = 500.8 kWh/(m^2_{ST} a) and reduces to $q_{ST\text{-}loss}$ = 336.5 kWh/(m^2_{ST} a) if all storage losses are accounted to the ST. The specific yield of PV is $q_{PV(COPav)}$ = 484.5 kWh/(m^2_{ST} a) based on the average COP of 2.9 and is $q_{PV(COPM)}$ = 428.5 kWh/(m^2_{ST} a) based on the monthly measured COPs (from 2016). With improved system design and control, a COP of the GW_HP of at least 3.2 should be possible (see section above) which would give PV a slight advantage over ST on annual basis, but ST would still perform slightly better in winter.

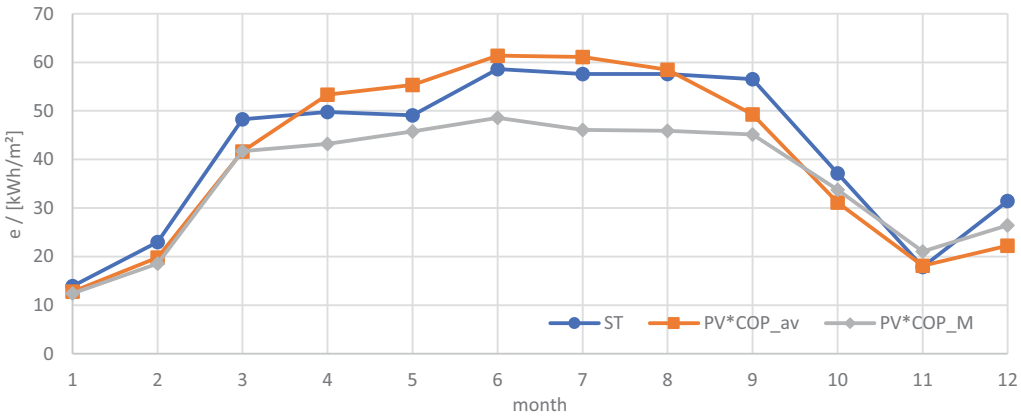

Fig. 9: Specific thermal energy (related to 1 sqm. of ST or PV, respectively) delivered by ST and by PV (with HP, with average and monthly COP of 2.9) (year 2016), storage losses are excluded

3.6 Electricity Consumption and Auxiliary Energies

The electricity consumed by the HP for heating and DHW is shown in Fig. 10. Aux. energies (pumps, MVHR, control, monitoring, etc.) are relative high. Electricity consumption is 15.3 kWh/(m² a) or 33 MWh w\o aux. and 22.9 kWh/(m²) or 49 MWh w\ aux. energy.

It can be seen in Fig. 10 that the first optimization measures proposed after the first winter already led to significantly reduced energy demand for heating and DHW and also to reduced auxiliary energy demand (5.6 MWh in December compared to 9.7 MWh in January, but still further optimization is required. The ambient temperature (and thus the heating degree days) and the global solar radiation were comparable in January 2016 and December 2016, see section 3.1, above.

PV yield is 167.6 kWh/(m^2_{PV} a) or 27 MWh or 12.6 kWh/(m^2_{AT} a) and is not even sufficient to cover the electricity for the heat pump. For heat pump and the auxiliary energies almost double the PV field size would be required. In December (where the el. consumption could already be significantly reduced with respect to January), on monthly basis, PV can cover 30 % of the electricity consumed by the heat pump and only 22 % if aux. energies are included. The remaining electricity has to be purchased from the grid.

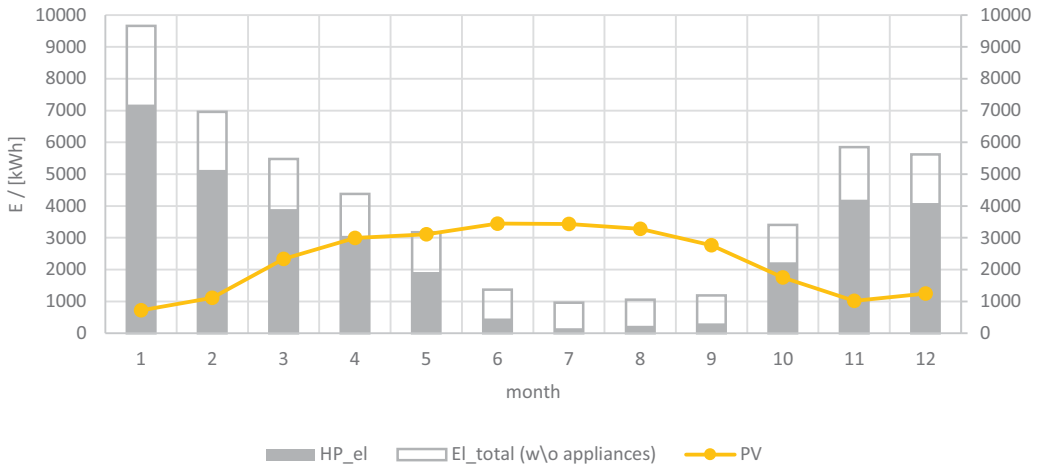

Fig. 10: Electric energy consumed by HP (grey bars), with auxiliary energies (white bars, appliances not included), and monthly electric energy produced by PV, monitoring results from 2016

4. Discussion

4.1 NZEB for heating, DHW (without appliances)

The goal of achieving a net zero energy balance (NZEB) for heating and DHW was not reached in the first monitoring period (2016) for several reasons: The higher HD in the first year (mainly because of construction moisture) and the relative high thermal losses of the storage led to a higher load. Furthermore, control settings were not optimal (e.g. not enabling good stratification) resulting in rel. poor performance of the heat pump. During the first year of monitoring some improvements were implemented and an increased performance of the HP can be expected. By avoiding thermal bridges of pipes and valves and convection (by heat traps) and by reducing storage set pint temperature, storage losses can be reduced.

If the heating demand can be reduced to PH-level (i.e. 15 kWh/(m² a)) and if further storage losses can be limited, higher solar fraction can be expected and the load for the heat pump can be reduced. If moreover, because of reduced set points and improved stratification, better performance of the HP can be achieved and finally aux. energies can be reduced, the electricity consumption could be reduced from ca. 22.8 kWh/(m² a) to the design level of ca. 11.8 kWh/(m² a). With all these possible improvements and optimization measures, the goal of NZEB could be achieved, as is shown in the prediction in Fig. 11. The annual yield of PV (167.6 kWh/(m^2_{PV} a) or 12.6 kWh/(m^2_{AT} a)) is enough to cover the consumed electricity on annual basis. However, the remaining purchased electricity in December would still be 3.1 MWh or 71 % (compared to 4.4 MWh or 78 % from the measurements).

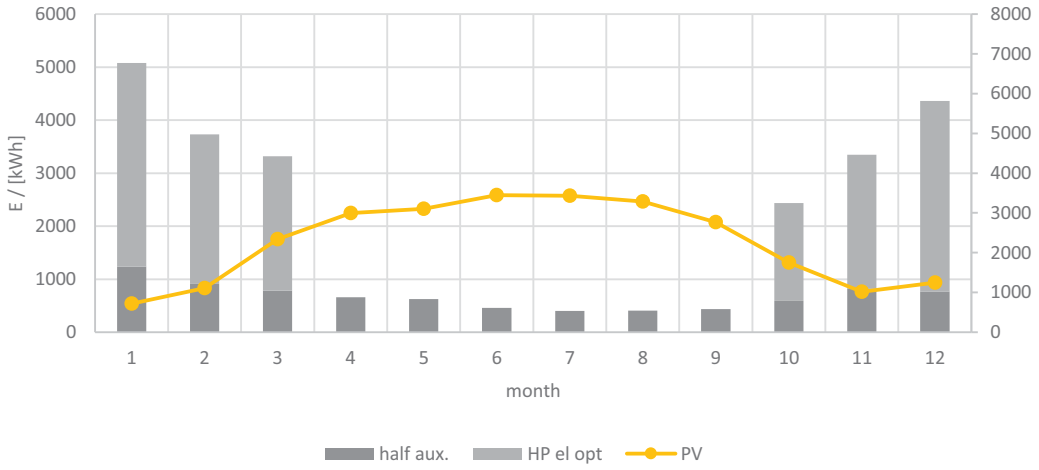

Fig. 11: Net-zero energy balance; prediction after optimization (50 % of auxiliary energies with respect to measurements, HD acc. to PH standard and improved HP performance (sCOP = 3.7)) Load is 25.2 MWh or 11.8 kWh/(m² a); PV yield is 167.6 kWh/(m^2_{PV} a) or 12.7 kWh/(m^2_{AT} a), respectively

4.2 NZEB for heating, DHW and appliances

Annual PV yield is not enough to cover appliances, even if only 1500 kWh/a are assumed per household (appliances are not measured, but European average is about 1500 kWh/person/year, see above in section 1.2). The monthly balance after optimization (prediction) but including appliances is shown in Fig. 12. If appliances are included, the net balance cannot be fulfilled. It is obvious, that in the winter months there is no PV electricity left for HP and auxiliary energies. Instead, 100 % has to be purchased from the grid. Only in summer, there is slight PV excess electricity which can be used to cover auxiliary energies and a small amount of PV has to be sold to the grid (again on basis of monthly balance). If higher consumption of appliances are assumed (e.g. 2500 kWh), on monthly basis, there would be no excess PV at all.

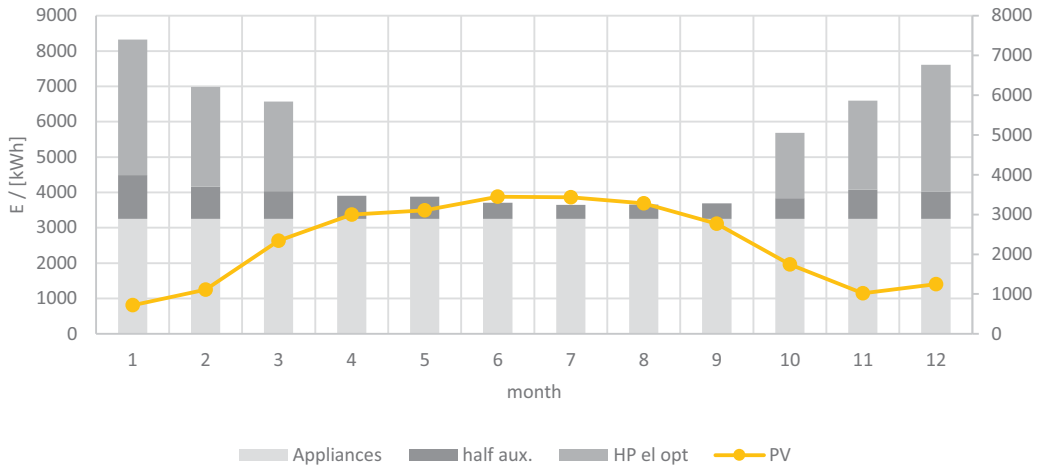

Fig. 12: Prediction of electric energy balance after optimization (as in Fig. 11 but with appliances; 1500 kWh/household; remark: electricity consumption for appliances is not measured (contract between electricity provider and the tenants); 64.3 MWh or 29.9 kWh/(m^2_{AT} a), respectively

For a NZEB with appliances, PV must be used in addition in the façades. An additional theoretical area of 300 m² (ca. 45 kW_{peak}) would be required in the south facades.

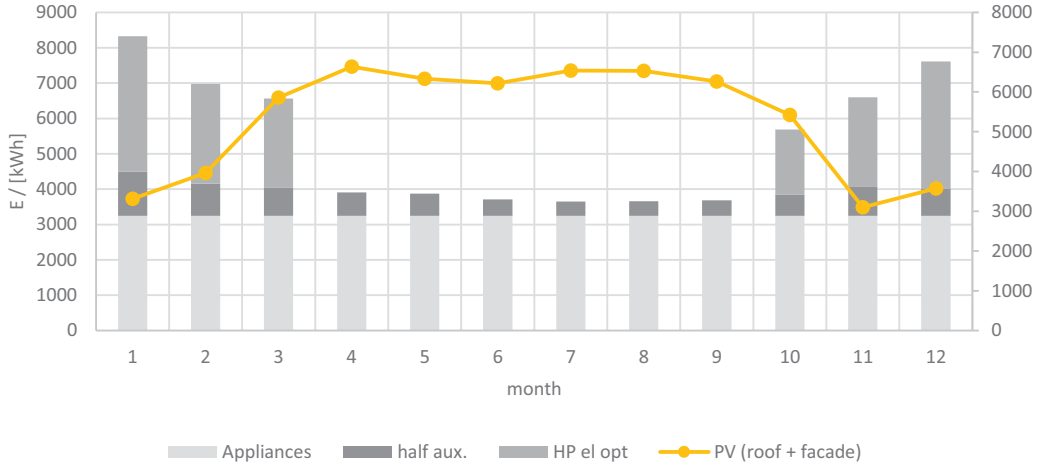

Fig. 13: Prediction of electric energy balance after optimization with appliances (as in Fig. 12) but with additional theoretical 300 m² PV on south facades (ca. 45 kW_{peak})

4.3 PE balance

The specific primary energy (e_{PE}) for heating and DHW production with the HP, for the case with the improved system, with appliances without and with 300 m³ of PV in south facades is calculated assuming two scenarios, see section 1.3:

- case A with 10 % hydro, 10 % wind and 10 % PV and
- case B with 10 % hydro, 30 % wind and 30 % PV.

It can be seen in Fig. 14 that in scenario B with higher share of renewables in the grid(all together 70 %), the additional PV in the façade yields less primary energy savings then in the case A with all together 30 % of renewables. In scenario A the additional PV in the façade reduces the annual specific PE demand from 32.7 $kWh_{PE}/(m^2\ a)$ to 15.2 $kWh_{PE}/(m^2\ a)$, or by 53.5 % while in scenario B, it reduces from 21.9 $kWh_{PE}/(m^2\ a)$ to 11.2 $kWh_{PE}/(m^2\ a)$ or by 49.2 %. As discussed in section 1.3, the state of the art is using a constant primary energy conversion factor, e.g. 1.91 as in At (OIB). PE savings with a constant PE conversion factor are 58 % (13.8 $kWh_{PE}/(m^2\ a)$ with compared to 32.9 $kWh_{PE}/(m^2\ a)$ without PV in the facade). With constant primary energy conversion factor, savings are accounted for with the same weighting independent of the season. Therefore, savings in summer are overrated.

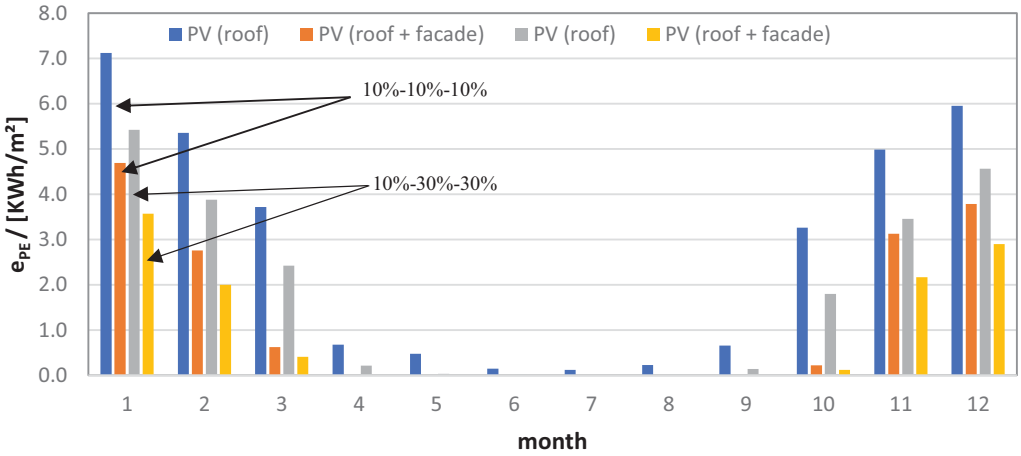

Fig. 14: Specific primary energy (e_{PE}) for heating and DHW production with the HP, improved system, with appliances without and with 300 m³ of PV in south facades for case A with 10 % hydro, 10 % wind and 10 % PV and case B with 10 % hydro, 30 % wind and 30 % PV.

5. Conclusions and Outlook

Two MFHs in PH Standard were implemented with solar thermal and heat pump system and PV to achieve maximum primary energy savings. Thus, the project can represent a best practice example for future nZEBs. PH standard is key for achieving real nZEB/NZEB level. ST has energetic benefits over PV in case of relatively small systems (i.e. $f_{sol}(DHW) < 40$ %). However, system complexity increases and a well-tuned control strategy is of major importance. Stratification of the buffer storage is crucial for optimal performance of the solar thermal plant and the heat pump. Obviously, storage size (i.e. volume) and connections must be carefully designed in order to avoid excessive storage losses. The reduction of the flow and return temperatures and the minimization of the distribution losses is also very relevant. Finally, also auxiliary energies have to be kept to minimum level.

In the paper monitoring results of the buildings (heating and DHW demand) and of the system (distribution losses, performance factors, solar thermal and PV yield) are reported and improvements after the first year of operation were discussed and design recommendations based on monitoring data and simulation results were given.

Net zero energy balance (for heating and DHW and auxiliary energies) could not be achieved during the first year of monitoring (2016), but predictions based on results after some improvements show that with it could be achieved. However, it is also highlighted in the paper, that electricity of appliances cannot be excluded from the energy balance and that NZEB do not significantly reduce winter grid load.

The mismatch between (electricity) demand and PV yield has to be considered, e.g. by means of different electricity prices for purchase and sell or by seasonal/monthly primary energy conversion factors. A method is discussed allowing to compare different nZEB/NZEB concepts considering the time (season) of the electricity purchase from the grid in order to be able to optimize concepts towards reduced non-renewable primary energy demand or CO_2 emissions in winter when renewable electricity is rare. In this sense, also concept of net zero energy buildings (NZEB, e.g. IEA SHC Task 40) can be critically discussed.

There is a need to develop design guidelines for HP design, HP and system control. Performance monitoring for fault detection and system optimization is strongly recommended.

6. Acknowledgements

This project is financially supported by Neue Heimat Tirol (NHT), Innsbruck, Austria. Building design optimization, PHPP calculations and PH certification was done by PHI Innsbruck.

The financial supports from the Austrian Ministry for Transport, Innovation and Technology and the Austrian Research Promotion Agency (FFG) through the IEA Research Cooperation to this work are gratefully acknowledged.

7. References

BPIE, NEARLY ZERO ENERGY BUILDINGS DEFINITIONS ACROSS EUROPE, EPISCOPE project (IEE/12/695/SI2.644739), 2016 (http://bpie.eu/uploads/lib/document/attachment/128/BPIE_factsheet_nZEB_definitions_across_Europe.pdf)

BEDW, Wie heizt Deutschland, BEDW-Studie zum Heizungsmarkt, Juli, 2016.

BEDW, Energie-Info, Stromverbrauch im Haushalt, Berlin, 2013.

Directive 2010/31/EC (EPBD), of European Parliament and of the Council of 19 May 2010 on the energy performance of buildings (recast).

IEA HPT Annex 40 Heat Pump Concepts for Nearly Zero Energy Buildings, https://www.annex40.net/, 2017

IEA SHC Task 40 / IEA EBC Annex 52: IEA EBC-SHC joint project 'Towards Net Zero Energy Solar Buildings, 2015

IEA HPT Annex 49 http://heatpumpingtechnologies.org/annex49/, 2017

Feist, Wolfgang, Passivhaus – das nächste Jahrzehnt. In: Tagungsband zur 18. Internationalen Passivhaustagung, Aachen, April 2014.

OIB-6 Richtlinie 6, Energieeinsparung und Wärmeschutz, Österreichisches Institut für Bautechnik, 2011

OIB-6 Richtlinie 6, Energieeinsparung und Wärmeschutz, Österreichisches Institut für Bautechnik, 2015

Ochs Fabian, Dermentzis Georgios, Feist Wolfgang, Minimization of the Residual Energy Demand of Multi-storey Passive Houses – Energetic and Economic Analysis of Solar Thermal and PV in Combination with a Heat Pump, Energy Procedia Volume 48, 2014, Pages 1124-1133

Statistik Austria, Bundesanstalt Statistik Österreich, 2016

https://www.statistik.at/web_de/statistiken/energie_umwelt_innovation_mobilitaet/energie_und_umwelt/energie/energieeinsatz_der_haushalte/index.html, 2017

On Behavioral Action Hierarchy for Understanding Occupants' Attitudes Driving Indoor Thermal Comfort in Office Buildings

Jessica Romanelli[1] and Anna Laura Pisello[1,2]

[1] CIRIAF – Interuniversity Research Center, University of Perugia, Perugia (Italy)

[2] Department of Engineering, University of Perugia, Perugia (Italy)

Abstract

Occupant behavior is one of the major factors influencing building energy consumption and contributing to uncertainty in building energy use prediction and simulation. Currently, the understanding of occupant behavior is insufficient in building design, operation, and retrofit, leading to incorrect simplifications in modeling and analysis. Recently, the need to integrate social science aspects into energy research has brought more awareness about the role of occupants in buildings and how their actions may be driven. Within this study, we identify a sort of behavioral actions' temporal sequence in a form of timing priority action logic to represent progressive occupants' decisions. This work will contribute to the scientific investigation about the impact of occupants' behavior in building energy assessments by determining a novel behavioral action hierarchy, useful for future advanced algorithm development in dynamic thermal-energy building simulation.

Keywords: Occupants' Behavior, Hierarchy Actions, Buildings' energetic behavior, Continuous monitoring

1. Research Background

The energy-efficiency analysis of buildings today takes into account building energy behavior underestimating the human factor. One of the main objectives of the research is therefore to analyze the behavior of occupants (in terms of their energy need) to understand how this affects the overall energy performance and how much it affects the difference between the expected energy consumption and the actual energy consumption.

Occupational Behavior, for example in offices, include a number of actions that can significantly affect energy consumption, such as adjusting thermostat settings, opening / closing windows, opening / closing curtains or shutters, switching on / off heating / cooling systems and finally moving from one room to another. In addition, behavioral habits, such as changes in clothing, drink consumption and different metabolism, directly affect the individual comfort that influences energy consumption.

The behavior of occupants in buildings is a multidisciplinary research topic that covers social and behavioral sciences, building physics, detection and control technologies, computational science and statistics. One of the greatest difficulties in collecting information is the lack of standardized data as well as privacy issues.

In order to overcome the uncertainty of occupant behavior, (O'Brien and Gunay, 2015) have proposed a design method for modeling actions to make people better adaptive to natural light and shading of a construction of a simulation of energy performance in a building. (Fabi, 2012), on the other hand, investigate the collection of numerous data obtained from experimental campaigns aimed at verifying the predictive precision of the various existing window-opening models in buildings.

Considering also the behavior of occupants on the manual adjustment system according to the presence of shadows, (Yao et al., 2015) have developed a stochastic model for integration with EnergyPlus (dynamic design software). Their results have shown that frequent and inappropriate use of open-cast walls in buildings has resulted in a decrease in internal thermal comfort.

Because of the uncertainty of occupant behavior, the results of dynamic-thermal-energy simulation often greatly vary from the actual energy consumption of the building. (Eguaras-Martínez,et al., 2014) indeed suggested that inclusion or exclusion of occupant behavior in simulations can result in differences up to 30%.

doi:10.18086/swc.2017.15.07 Available at http://proceedings.ises.org

A comparison between the energy consumption simulated at the design stage and the energy measured for the LEED certification (Leadership in Energy and Environmental Design), shows a significant error (mean square error of 18%) in a group of 62 buildings. The forecast error is even greater for low-energy buildings using passive systems, such as natural ventilation; in this case, the behavior of occupants could compromise the final energy consumption. Therefore, the behavior of occupants is one of the main sources of uncertainty in predicting the use of energy.

(Motuziene and Vilutiene, 2013) used four different employment profiles of housing in Lithuania, to show that the heating strategies can lead to savings of up to 31%. In addition, high efficiency can be achieved by optimizing energy consumption during vacation periods. For example, South Korean dorms use up to 31.5% less energy when they are not unoccupied. (Webber et al., 2001) observed, in offices in Washington DC and San Francisco, only 44% of the computers, 32% of monitors and 25% of the printers were turned off at night.

The quantification of energy saving imputable to occupant behavior remains a primary challenge. It was estimated that savings could be made between 10% and 20% for home and between 5% and 30% for commercial buildings (ie private offices) by acting on occupant behavior.

Previous Scientific Research has shown that the role of Occupant Behavior has a major influence on the energy performance of the building. In this work, an office building has been monitored for more than one year in terms of indoor-outdoor microclimate and energy needs. More in details, several rooms were monitored with similar characteristics in terms of their intended use, dimensional characteristics, exposure, constructive features, and presenting devices. By analyzing several key boundary conditions, occupants can be considered as peers (equal) by being related to formation, age, habits and customs and carrying out similar activities.

2. Research Scope

Compared to the state of the art, this study attempts to analyze and identify a sort of timing priority sequence in occupant behavior triggering after perceiving a potential discomfort situation.

Determining the sequence of actions that include subjectivity is complex, especially in the analysis of the progressive feeling-to-decision-to-action of occupants. Therefore, this work will contribute to the scientific research envisaged in the Annex 66 program, which aims to identify the state of the art in terms of Occupational Behavior modelling in buildings energy prediction.

The goal is therefore to determine a temporal hierarchy of behavioral actions that is also valid for a predictive and reliable energy evaluation, since the typical reactions may be energy-needy and their time prediction influences building final energy use.

3. Methodology

The methodology implemented in this paper consists of the following main steps:

- *Definition of the research statement,*
- *Selection of the case study,*
- *Continuous experimental monitoring of the main parameters of the internal microclimate and occupancy within each office during a year from April 2016 to March 2017,*
- *Statistical analysis of data and comparison of results.*

The following sections describe the above-mentioned work phases.

3.1. Field Monitoring

In order to study and analyze the different behavior of "peers" and the hierarchy of actions that are carried out within the building, they were considered a group of peers working in some office buildings that houses the University Research Center "CIRIAF" (Perugia, Italy). In particular, five office environments characterized by the same orientation, same architectural layout, size, construction technology, and HVAC system were selected. Consequently, the behaviors of the occupants were continuously monitored by means of special sensors installed in the various offices

selected as a case study.

More in detail, the experimental monitoring system was installed in September 2015 and consists of internal microclimate sensors capable of collecting data such as indoor air temperature, workplace illumination, electrical consumption, door / window opening. Therefore, data on the behavior and daily habits of occupants were collected and analyzed in terms of the use of electricity, lights on / off, opening / closing of doors / windows. In particular, the aforementioned monitoring system consists of a set of Wireless Network Sensors (WSNs), consisting of five indoor microclimate monitoring stations, each equipped with several sensors and a collector node (Fig. 1) connected to the cable sensors. The monitoring stations are located each within the five offices. Nodes communicate the data collected via radio to a collection gateway and then they are real-time available within the office web portal managed by the authors.

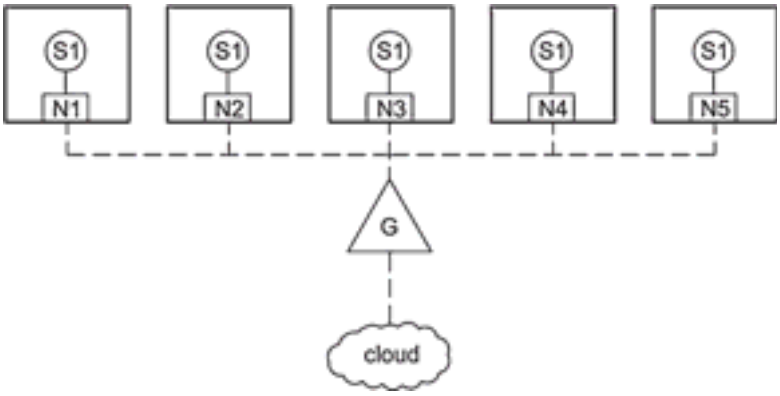

Fig. 1. Functional Diagram of the Wireless Monitoring System (n = nodes, S = sensors, G = Gateway, 1-5 = Monitored Offices (Pisello et al., 2016)

For the purpose of this research work, four types of sensors have been used in order to analyze the following internal parameters (Fig. 2):

- O*pening / closing of doors and windows (magnetic sensors),*
- I*lluminance level above the desk (luxmeter),*
- *Indoor air temperature (air temperature probe),*
- *Use of electricity (amperometer).*

Each sensor can record data every five minutes by sending the signal it to its node and finally to the gateway.

Fig. 2. Sensors installed in each office: (a) opening and closing windows, (b) luxmeter, (c) air temperature probe, (d) ammeter (Pisello et al., 2016).

4. Case Study

The building selected as a case study is represented by a building hosting the Research Center of the Department of Engineering of the University of Perugia, Italy (Latitude: 43 °'0'0'0 " N; Longitude: 12 ° 21'03 ' 'E) (Fig. 3). It has a two-story rectangular plan, which houses ground floor laboratories, while all the offices of researchers and professors are located at the first floor. The five monitored offices are all located on the first floor and are oriented to the South-West; they have rectangular plan and have the same dimensions (about 4 × 4 × 2.9-h m). Each office has two windows-doors on the South-West façade facing a terrace connecting all the rooms at the same floor. Lighting system is characterized by 4 ceiling lamps manageable from the entrance of each office as 2 groups of 2 lamps. The HVAC system is a centralized heating-cooling air system for the whole building. Each office is provided with a thermostat able to regulate both temperature (+/- 3°C compared to the setpoint centralized temperature) and air volumes (in a graduate scale of 3 steps).

The heating season is officially operating from 10-15 to 04-15, while summer cooling operates from 06-15 to 09-30 by law. Then, every office occupants may regulate their ambient thermostat according to personal needs and occupational perceptions of occupants.

In each office there are two or three computers and two or three people. (Fig. 3-4)

Fig. 3. Planimetry of Monitoring Offices (Pisello et al., 2016).

Fig. 4. Typical Offices (Pisello et al., 2016).

4.1 Data analysis scheme in the building

This analysis, which considers peers as occupants having similar characteristics (in terms of age, occupation, activity, and timetable) under the same environmental conditions, highlights how the attitudes and personal habits of different occupants differently affect the overall building behavior given their intrinsic variability. The table below describes (Tab. 1) the main features of each monitored office.

Tab. 1. Main features for each monitored Office.

Room	People in the office (n°)	Doors/Windows	PCs
1	3	1 D, 1 W	3 pc
2	2	1 D, 1 W	2 pc
3	2	1 D, 1 W	2 pc
4	3	1 D, 1 W	3 pc

Considering all the possible actions that can be taken, such as resulting in energy consumption or a different behavior of the building, the analysis was carried out by identifying macro categories and focusing on the opening and closing of the door and the window. The aim was to identify, where possible, a temporal correlation between the thermal discomfort and the occupation action.

First, the processing of collected data was carried out with reference to the continuously monitored weather data provided by the weather station positioned on the roof of the building that houses the offices.

Specifically, the correlation level analysis between the monitored internal parameters and the external microclimate was performed considering the outside air temperature, the total solar radiation on horizontal plane, the maximum internal temperature and the opening / closing of the doors / windows. The analysis of how internal parameters are influenced by external environmental conditions shows that there is always a time shift between the maximum incident solar radiation and the maximum internal temperature, as expected. From the monitored data analysis, the maximum incident solar radiation occurs between 11:00 am and 1:00 pm on average, while the maximum internal temperature is recorded between 3:00 pm and 6:00 pm. Of course, there are exceptional cases due to the use of technological installations and / or the change of external atmospheric conditions to vary this trend. additionally, the analysis of collected data has been made by considering the behavior of occupants in order to assess how personal attitudes and specific peer peaks can affect internal environmental parameters equal conditions.

In this regard, 12-month monitoring data, specifically from April 2016 to March 2017, were analyzed and the Global Maximum Incident Solar Radiation and the External Temperature were identified as the two key variables for each day. At the same time, the maximum internal temperature and external temperature and global radiation were selected as indoor feedback every day. For each day, based on these data, the opening of the door and the window timing was assessed and correlated to radiation and temperature profiles and peaks, by also investigating the time span of the action and the possible consequential relation.

5. Results and Discussion

5.1. Analysis of occupants' behavior

As mentioned, the present study aims to demonstrate that peers, i.e. persons of the same age, origin, activity and working hours, have different behavior from the thermo-energy point of view despite their theoretical similarities and the common work environment and how they react to environmental stimuli by implementing a temporal series of actions.

Room 1 and Room 3 office occupants often use window and door opening to adjust the temperature (openings normally coincide with indoor maximum indoor temperatures). Room 2 Office users do not use the window opening (there is only one opening in June at the peak of the measured temperature, about 30 ° C, and during September), but they act on the door opening to respond to the condition of overheating discomfort and adjust the internal temperature.

In "Room 4" office, the sensor data show that except for a few times, the window remained open throughout the day, even at night. In this case, the measurement was considered as not significant as this result may be due to a malfunction of the sensor or, if not, the action of opening the window is not a result of temperature variation.

However, occupants of the "Room 4" office used door opening as a solution to counteract environmental discomfort caused by rising temperature in the room. The Room 5 office is a synthesis of the previous ones; the opening of the window is recorded for long periods (especially during Spring and Summer), while the door opening does not always happen at the temperature peaks.

Another highlighted information to note is the behavior of the occupants of the office "Room 3", which, between May and June, with a temperature around 25°C, have constantly used the opening of the window while always closing the door. However, the internal temperature was on average around 25°C. It is likely that the opening of the window was not due to the air conditioning of the room, but to the need for occupants to breathe fresh outside air due to the pleasant temperature. As said many times, despite the fact that the "occupants" are potentially "peers", it emerges that the action is subjective or linked to its momentary and personal perception, privacy, etc. The following charts show the results of how each office occupants (Room1-2-3-4-5) react to the conditions just described.

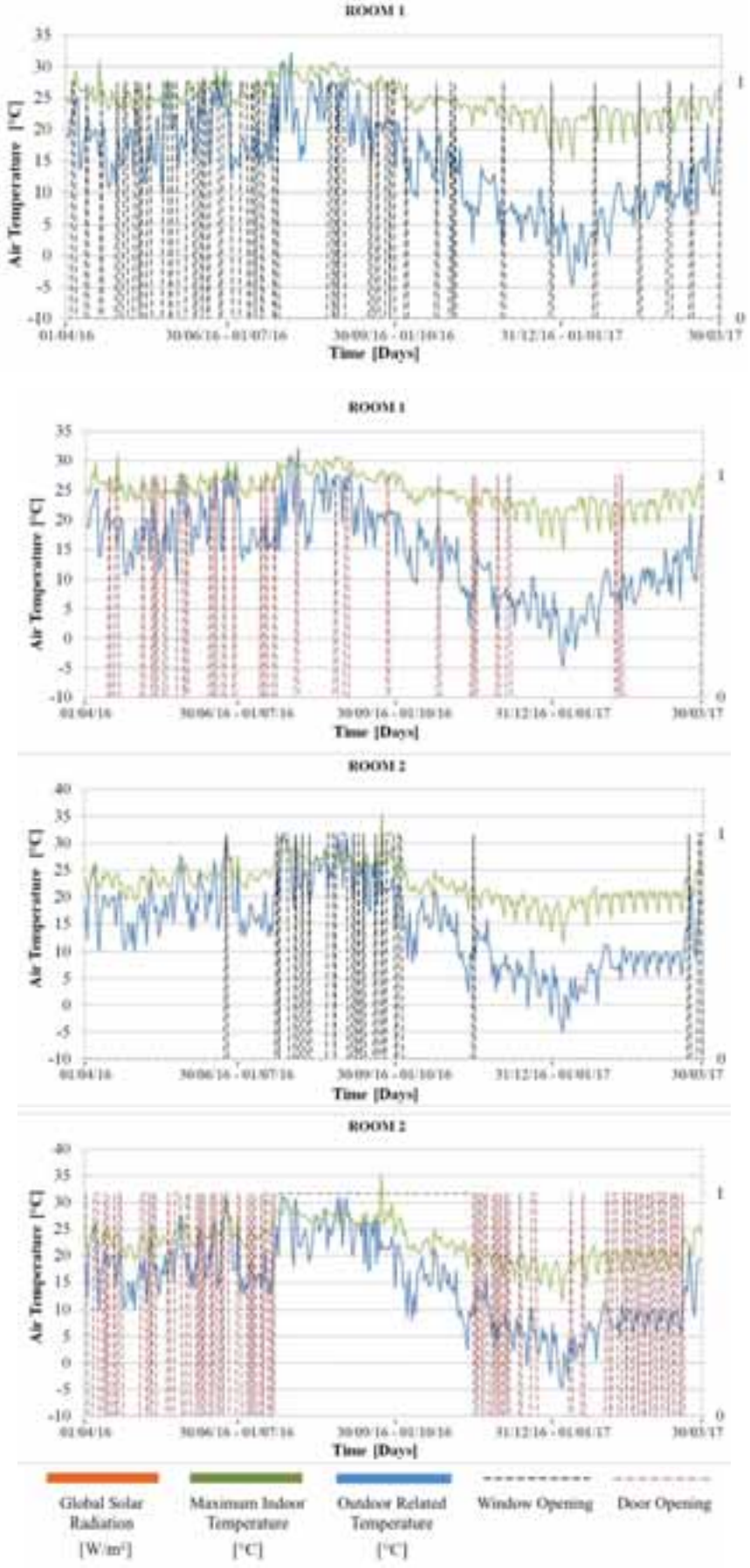
ROOM 1
Air Temperature [°C]
Time [Days]
ROOM 1
Air Temperature [°C]
Time [Days]
ROOM 2
Air Temperature [°C]
Time [Days]
ROOM 2
Air Temperature [°C]
Time [Days]
Global Solar Radiation [W/m²]
Maximum Indoor Temperature [°C]
Outdoor Related Temperature [°C]
Window Opening
Door Opening

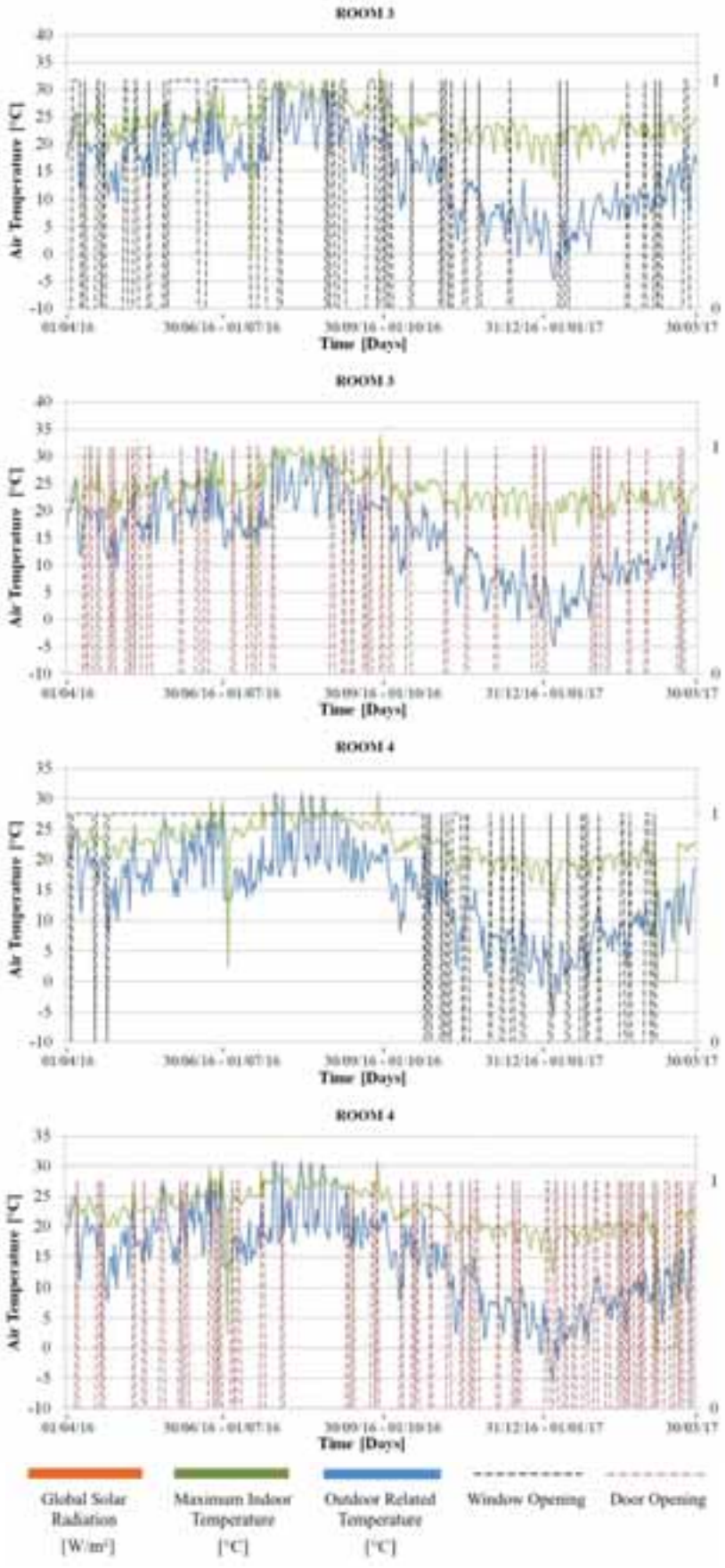
ROOM 3
Air Temperature [°C]
Time [Days]
ROOM 3
Air Temperature [°C]
Time [Days]
ROOM 4
Air Temperature [°C]
Time [Days]
ROOM 4
Air Temperature [°C]
Time [Days]
Global Solar Radiation [W/m²]
Maximum Indoor Temperature [°C]
Outdoor Related Temperature [°C]
Window Opening
Door Opening

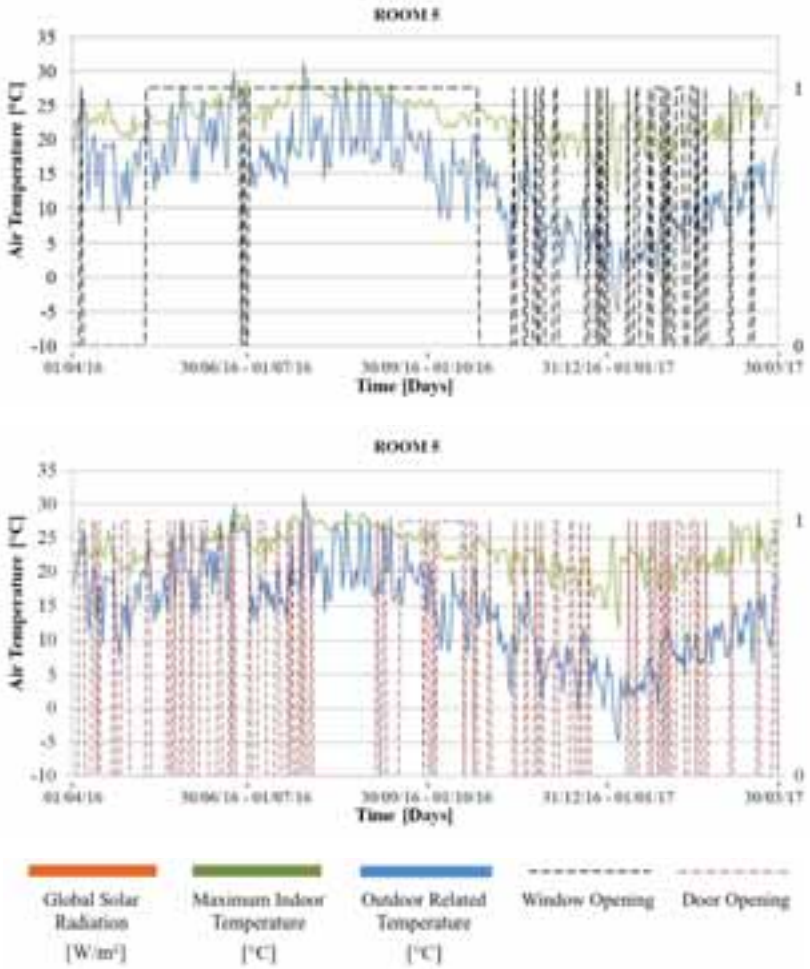

A further point to note is that the analysis of the opening of doors and windows at the maximum internal temperature is not significant during the winter season where the maximum indoor temperatures are consistently higher than the external ones and the user's action is not directly proportional to the discomfort.

The occupants are also able to use the thermostat (user autonomy ± 3 ° C) to raise the temperature during working hours as a measure of the minimum internal temperature. However, a sensor has not been installed yet, that monitors user action on the thermostat itself.

Analyzing the results, there is a clear difference in actions at the Maximum Solar Radiation (W / m²) that normally does not correspond to a condition of internal discomfort and therefore a noticeable non-action (Fig. 5). The Maximum Solar Radiation is recorded around 12:00pm-1:00pm daily, the time when the indoor temperature is normally lower. The Maximum Indoor Temperature, however, occurs almost always in the afternoon. This constancy is justified by the specific orientation of the offices being analyzed and the internal gains progressively heating the room.

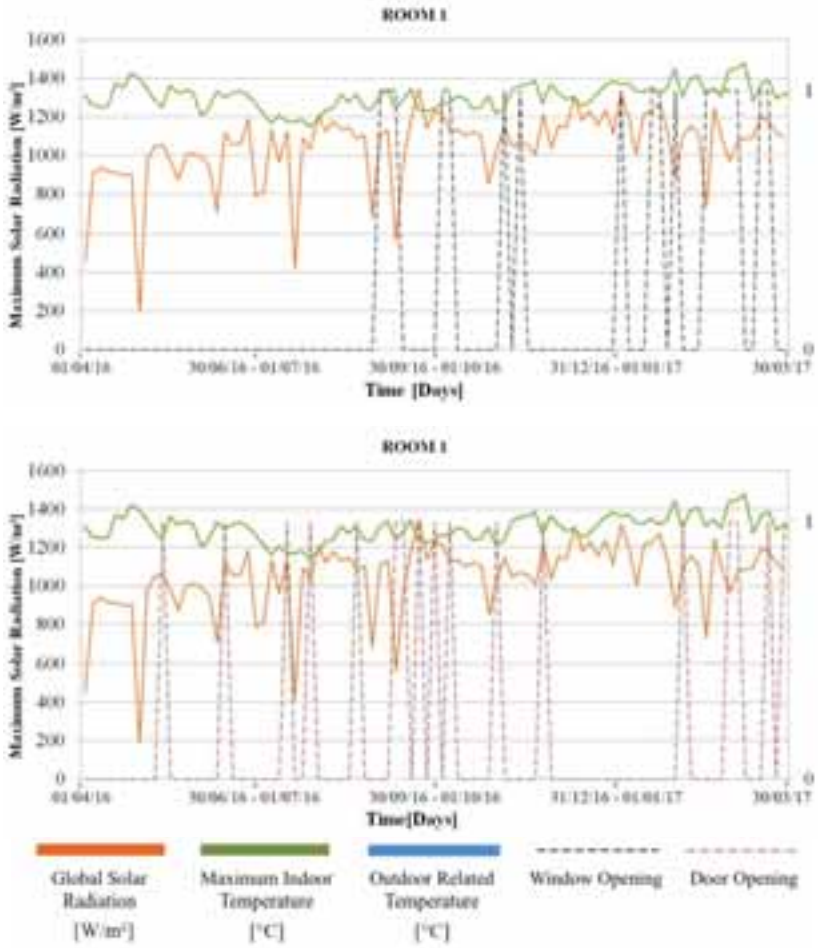

Fig. 5. Door and Window's Opening related to the Maximum Solar Radiation and Indoor Temperature.

In the following table, a synthesis of one year actions collected data for each office is described (Tab. 2).

Tab. 2. Results for each office of the analysis considering 365 days including 16 holidays.

Rooms	External Global Solar Radiation (W/m²)			Maximum Interior Temperature (°C)		
	Door	**Window**	**Door + Window**	**Door**	**Window**	**Door + Window**
1	37	52	12	32	74	21
2	148	28	28	137	34	34
3	47	99	15	48	94	17
4	74	237	42	69	233	32
5	103	188	94	106	203	89

5.2. Temporal Hierarchy Actions

Analyzing the results of occupancy actions, attention was focused on registered actions and time correspondence with recorded discomfort.

Starting from the specific action, it was analyzed whether the specific action occurred at the maximum internal temperature or if there was a time shift when the action was coming.

Results in Figs. 6-7 show how, starting from a situation of discomfort, subjective actions of the occupants are implemented. The subjectivity consists of the type of action, e.g. the fact that some occupants facing high internal temperature were opening the door while others, for privacy reasons, only managed the window. A further result is represented by the fact that not all the occupants reacted at the same moment of maximum internal temperature, but that

within a given temporal order (5-10-15 minutes) the action was usually widely implemented. However, the goal is to extend the time interval, up to about 2h, in order to understand and identify a possible recurring attitudes in the actions. The work in progress consists of the elaboration of an algorithm to quickly locate this correlation.

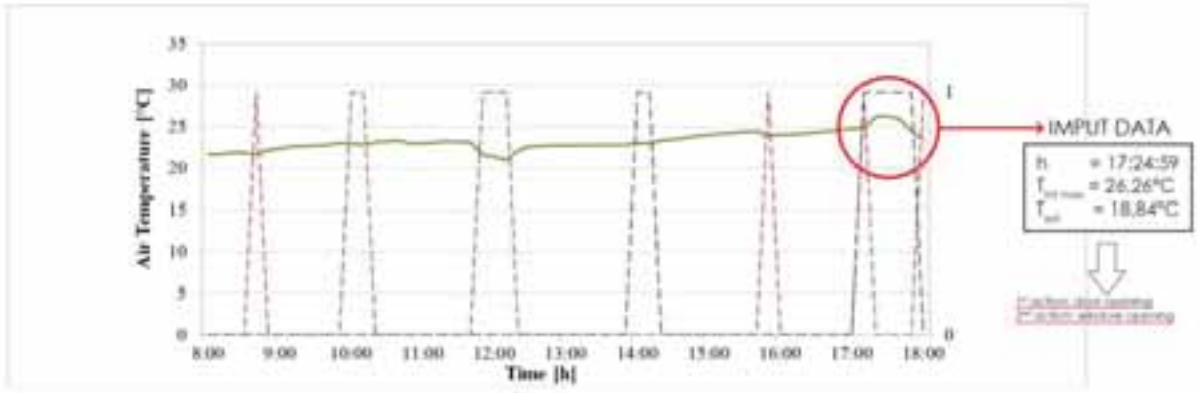

Fig.6: Daily Hourly table where are indicated Occupants' actions when the indoor temperature is maximum.

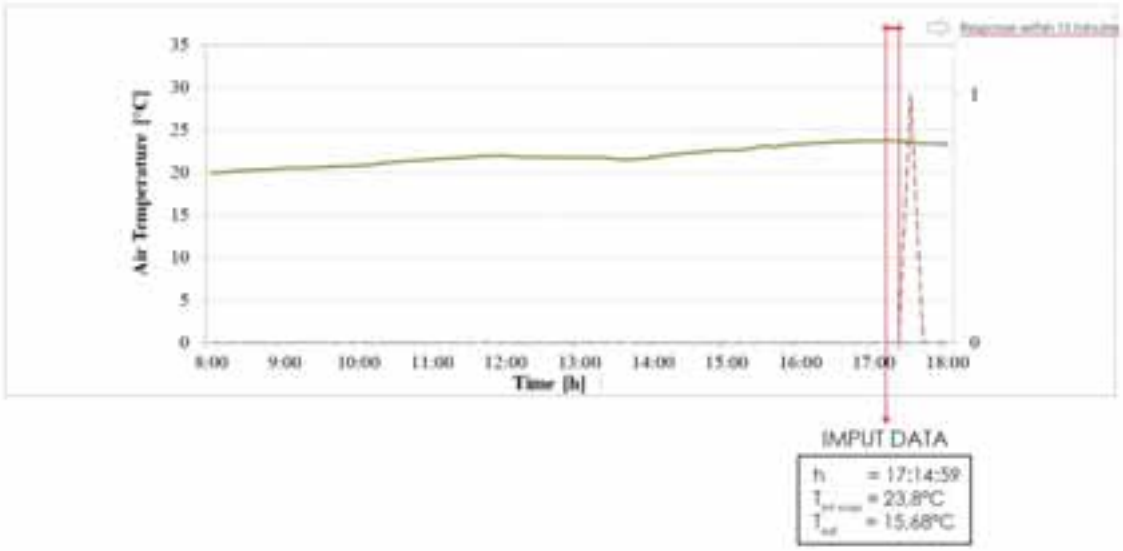

Fig. 7: Daily Hourly table where are indicated Occupants' actions with 15 minutes' time reaction range after the maximum indoor temperature.

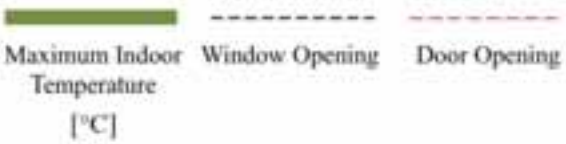

6. Conclusion and Future Development

The present study analyzed the possibility of establishing a sequence in the actions of occupants of an office building in order to assess the impact of subjectivity and time-hierarchy of user actions responsible for the variability of indoor air temperature in close proximity to each working station.

The results show how, in discomfortable situations, the subjective actions of the occupants find a common matrix of doing a subjective action. Subjectivity was found in the type of action, i.e. in the fact that for example some occupants reacted to high internal temperature with opening the door, while others, for privacy, the window.

Another result is that not all occupants reacted at the same time, but within a given time order (5-10 to 15 minutes) the action was completed. It is also important to note the difference in the actions at the maximum solar radiation (W/m²) that normally does not match an internal discomfort and therefore a noticeable non-action.

Being the subject of deep interest and study, the understanding of occupant behavior represents a new opportunity to shape the future evolution of building energy prediction models and technology, to improve the energy efficiency and comfort of occupants of buildings,.

7. Acknowledgements

This work was supported by the CIRIAF Interuniversity Research Center of the University of Perugia, Department of Engineering, on the PhD. The authors would like to thank Luigi Metelli S.p.A for supporting their research entitled COOL CRETE. This work has been carried out also within the framework of IEA-EBC Annex 66 “Definition and Simulation of Occupant Behavior in Buildings”.

8. References

Eguaras-Martínez, M., Vidaurre-Arbizu, M., Martín-Gómez, C., 2014. Simulation and evaluation of building information modeling in a real pilot site. Appl Energy, 114,475–484.

Fabi, V., Andersen, R.V., Corgnati, S., Olesen, B.W., 2012. Occupants’ window opening behavior: a literature review of factors influencing occupant behavior and models. Build. Environ. 58, 188–198.

Heck, S., Tai, H., 2014, Sizing the Potential of Behavioral Energy-Efficiency Initiative in the US Residential Market Report, McKinsey Company.

Hong, T. Lin, H.W., 2013. Occupant Behavior: Impact on Energy Use of Private Offices. Ernest Orlando Lawrence Berkeley National Laboratory ReportLBNL-6128E.

Hong, T., Sarah, C., Lange, T., D’Oca, S., Yan, D., Corgnati, S.P., 2015. Advances in research and applications of energy-related occupant behavior in buildings. Energy Build, 116, 694-702.

Martinaitis, V., Zavadskas, E.K., Motuzien˙e, V., Vilutien˙e, T., 2015. Importance of occupancy information when simulating energy demand of energy efficient house: a case study. Energy Build. 101, 64–75.

Motuziene, V.,Vilutiene, T., 2013. Modelling the effect of the domestic occupancyprofiles on predicted energy demand of the energy efficient house.Procedia Eng, 57:798–807.

O’Brien, W., Gunay, H.B., 2015. Mitigating office performance uncertainty of occupant use of window blinds and lighting using robust design. Build. Simul, 8-6, 621–636.

Pisello, A.L., Castaldo, V.L., Piselli, C., Fabiani, C., Cotana, F., 2016. How peers’ personal attitudes affect indoor microclimate and energy need in an institutional building: Results from a continuous monitoring campaign in summer and winter conditions, Energy Build., 126, 485-497.

Pothitou, M., Kolios, A.J., Varga, L., Gu, S., 2014. A framework for targeting house hold energy savings through habitual behavioral change, Int. J. Sustainable Energy, 686-700, h HYPERLINK "http://dx.doi.org/10.1080/14786451.2014.936867" HYPERLINK "http://dx.doi.org/10.1080/14786451.2014.936867"ttp://dx.doi.org/10.1080/14786451.2014.936867.

Schakib-Ekbatan, K., Fatma Zehra, C., Schweiker, M., Wagner A., 2015. Does the occupant behavior match the energy concept of the building? Analysis of a German naturally ventilated office building. Build Environ, 84:142–150.

Turner, C., Frankel, M., U.G.B Council 2008, Energy Performance of LEED for New Construction Buildings, New Buildings Institute, Vancouver, WA.

Webber, C.A., Roberson, J.A., Brown, R.E., Payne, C.T., Nordman, B., Koomey, J.G., 2001. Field surveys of office equipment operating patterns, in: Lawrence Berkeley National Laboratory Report, LBNL-46930.

Yan, D., O’Brien, W., Hong, T., Feng, X., Burak Gunay, H., Tahmasebi, F., Mahdavi, A., 2015. Occupant behavior modeling for building performance simulation: current state and future challenges, Energy Build. 107, 264–278, http://dx.doi.org/10.1016/j.enbuild.2015.08.032.

Yao, D.H.C. Chow, R.Y. Zheng, C.W. Yan, Occupants impact on indoor thermal comfort: a co-simulation study on stochastic control of solar shades, J. Build. Perform. Simul. 2015

Off-Grid Energy Supply

Solar Energy Development and Implementation in Nigeria: Drivers and Barriers

D Abdullahi[1], S Suresh[2], S Renukappa[3], and D Oloke[4]

School of Architecture and Built Environment, Faculty of Science and Engineering, University of Wolverhampton, WV1 1LY

Abstract

The over dependency on fossil fuel in Nigeria could be one big reason for the total failure of the power sector. The country's economic development which depends on productivity output is in peril due to the imminent energy crisis from gas shortage, vandalism, diminishing fossil fuel reserve and energy insecurity. Therefore, a strategic initiative to diversify the power sector into the energy mix to withstand the socioeconomic development has not indicated a positive progress. The insufficient electricity generation at the highest point was only in capacity put at 5000 MW in April 2015 to support a teeming population of about 184 million people. Nigeria is endowed with plentiful natural resources in which solar energy received more attention due to its potential, especially the rural communities. It is estimated that the solar potential deposit raises to 4,849, 782 kWh/m^2 days for the entire country of around 923,768 km2 areas. The theoretical framework is based on critical literature reviews being part of a PhD research. The research discusses the motivational drivers to the solar energy development and the barriers hindering the implementation. The key drivers were climate change, energy demand, power sector reform Act, energy security, supply versus demand conflicts, job opportunities, technology growth and market potentials. On the other hand, the key barriers are technical, social, economical, institutional and political. Recommendations of measures to surmount the barriers to facilitate implementation are also proffered.

Keywords: Solar energy, energy access, solar barriers, solar drivers, implementation

1. Introduction

There is little or no doubt that access to electricity is crucial to people, not only in the urban developed cities, but also to the development of rural areas. Even though, Nigeria is the biggest producer of Oil and Gas in Africa, 65% of its population lives in rural areas as peasant farmers without access to electricity (Duke, et al. 2016). Surprisingly, the total installed solar power in Germany is seven times more than the highest peak ever generated electricity from all sources in Nigeria, being 5000 MW in April 2015 (Edkins, et al. 2014). Nigeria located on the equator is within a high sunshine belt where solar radiation is potentially well distributed, especially over the Northern part of the country (Okoye and Taylan, 2017). Even though, the solar radiation distribution varies from 3.5kWh/m2/day within the coastal area and 7.0 kWh/m2/day in the northern part of the country (Ohunakin, et al., 2014). This result to earn the country a total solar radiation of 4,849, 782 kWh/m2 day covering the area of 923, 768 Km2of landmark (Akinyele, et al. 2007). Despite the potential solar radiation in the country, the technology is yet to find a sustainable strategy to be harnessed and put into the energy mix to solve the alarming energy crisis especially the electricity.

2. Status of Solar Energy in Nigeria

The whole of the continent is blessed with a great sunshine radiation, excluding the large areas of tropical rainforests (the Guinean Forests of West Africa and much of the Congo Basin), since desert and savannah regions of Africa stand up as the Earth's largest cloud-free area. The eastern Sahara/northeastern Africa is particularly noted for its world sunshine records: the area experiences not only the greatest mean annual duration of bright sunshine approximately as much as 4,300 hours, which is equal to 97% of the possible total but also the highest mean annual values of solar radiation (the maximum recorded was over 220 kcal/cm²) (Edkins, et al. 2014).

The distribution of solar resources across Africa is uniform, with more than 85% of the continent's landscape receiving a global solar horizontal irradiation at or over 2,000 kWh/ (m² year). Also, the theoretical reserves of Africa's solar energy are estimated at 60,000,000 TWh/year, which accounts for almost 40% of the global total, thus definitely making Africa the most sun-rich continent in the world (Nevin, 2016). Declining solar equipment

doi:10.18086/swc.2017.16.01 Available at http://proceedings.ises.org

costs are expected to significantly increase solar installations in Africa with an industry projection forecasting that the continent's annual PV market will expand to 2.2 GW by 2018 (Obeng, 2015).

Furthermore, harvesting solar energy in Africa tend not to be found within the equatorial and subequatorial climate zones, that are located in the western part of Central Africa usually near the equator, but that extends as far north and south as the 8th or 9th parallel in both hemispheres, since they are systematically linked with almost permanent cloud cover and only intermittent bright sunshine (Sharife, 2014). Therefore, African countries that entirely lie in this wet-humid zone, such as the Republic of the Congo, Equatorial Guinea, Gabon, Liberia and Sierra Leone are by far the least favoured in solar power of the entire continent. In contrast, many perpetually sunny African nations like Egypt, Libya, Niger and Namibia could rely on developing their tremendous solar resources on a large scale and at reduced prices (Sharife, 2014).

Tab.1: Maximum/minimum yearly global solar radiation in Nigeria (kWh/m2/day)

Stations	Location Longitude	Location Latitude	Altitude M	Maximum A	Minimum B	Monthly Average
Abeokuta	7.25	3.42	150	4.819	3.474	4.258
Abuja	9.27	7.03	305	5.899	4.359	5.337
Akure	7.25	5.08	295	5.172	3.811	4.485
Azare	11.8	10.3	380	6.028	5.022	5.757
Bauchi	10.37	9.8	666.5	6.134	4.886	5.714
Benin city	6.32	5.677.52	77.52	4.615	3.616	4.202
Calabar	4.97	8.35	6.314	4.545	3.324	3.925
Enugu	6.47	7.55	141.5	5.085	3.974	4.539
Ibadan	7.43	3.9	227.23	5.185	3.622	4.616
Ilorin	4.48	4.58	307.3	5.544	4.096	4.979
Jos	9.87	4.97	1285.58	6.536	4.539	5.653
Kaduna	10.6	7.45	645.38	6.107	4.446	5.672
Kano	12.05	8.53	472.14	6.391	5.563	6.003
Katsina	13.02	7.68	517.2	5.855	3.656	4.766
Lagos	6.58	3.33	39.35	5.013	3.771	4.256
Lokoja	7.78	6.74	151.4	5.639	4.68	5.035
Maiduguri	11.85	13.08	383.8	6.754	5.426	6.176
Makurdi	7.73	8.53	112.85	5.656	4.41	5.077
Minna	9.62	6.53	258.64	5.897	4.41	5.427
New Bussa	9.7	4.48	152	5.533	4.15	4.952
Nguru	12.9	10.47	342	8.004	6.326	6.66
Ubudu	6.63	9.08	305	5.151	3.375	4.224
Oweri	5.48	7.03	120	4.649	3.684	4.146
Port Harcourt	4.85	7.02	19.55	4.576	3.543	4.023
Serti	7.5	11.3	610	4.727	3.972	4.488
Sokoto	13.02	5.25	350.75	6.29	5.221	5.92
Wari	5.52	5.73	6.1	4.237	3.261	3.748
Yola	9.23	12.47	186.05	6.371	4.974	5.774

Source: Emodi and Boo, 2015

Table 1 above, is a view of Nigerian maximum and minimum sun radiation in various zones with highest radiation in the North-East Zone Nguru, Maiduguri, Kano and Azare in Bauchi state. However, other cities also possess high sun radiation making it equally potential for solar energy resources. Even the leas radiation

cities such as Warri and Calabar, the solar energy can potentially be harnessed by many users for household and small and medium businesses.

Figure 1 bellow shows the solar radiation distribution across Nigeria, where each zone is labelled to ascertain solar radiation contribution if the technology is harnessed. The three-different solar zone can be defined viz: Zone I, II and III where each zone having a diverse level of radiation that can be articulated for a specific project selection across the 36 states of the federation. It is evident that Zone I which comprises the states in the northeast zone have the highest solar radiation occurrence with excellent solar PV potential. Equally, zone II, which consist of the North-central and North-West have viable solar radiation while zone III has low solar radiation potential for big solar project selection in the country.

Figure 1: Solar Irradiation levels in Nigeria

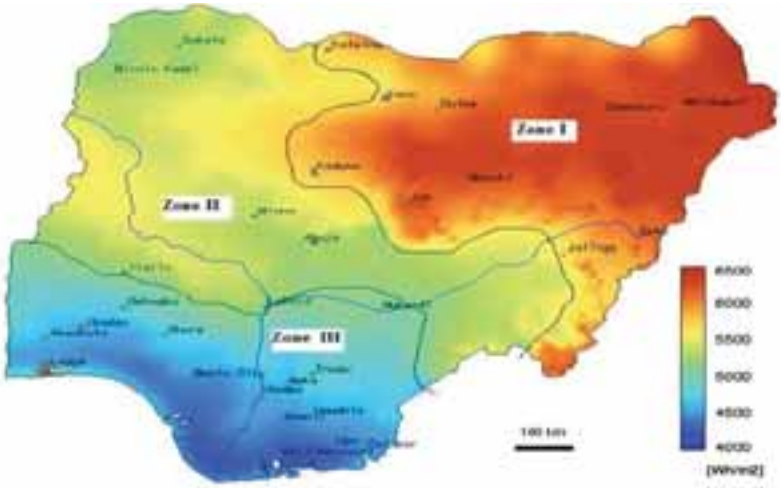

Source: NESP, 2015

It is evident that the northern part of Nigeria can generate substantial solar energy as seen in table1; with annual radiation rising up to 6.966 maximum in Nguru Yobe state in the North- East and 3.78 minimum in the Wari Delta state, South- South of Nigeria. The next table will show the major solar projects both public and private with license to generate, operate and commercialise solar energy in Nigeria.

3. Solar Energy Projects in Nigeria

There are more than 58 energy mix projects going on in Nigeria, of which 35 are Solar-based from licensed solar energy promoters, including rural electrification projects, with a total capacity of 115 MW of Photovoltaic combining mini-grids and stand-alone installed (ECN, 2014). The Solar-based projects are installed for residential and commercial purpose respectively. Even though, the Ministry of Power launch a project in 2014, known as ‘‘Operation Light Up Rural Nigeria’’ most of the Solar projects is targeted for rural communities which are estimated only 10% of the population have access to electricity. Other off-grid projects include the 37 Federal Universities and University teaching hospital projects are underway to complement the electricity supply. Four of the Universities and a teaching hospital has already signed the Engineering, Procurement and Construction (EPC) agreement to develop mini-grid solution to power facilities of up to 9.3MW of solar PV and 5,760 battery cells will be deployed for the projects. Other projects are monitored by the federal ministry of power and the rural electrification agency, energy commission and the regulator (NERC) accordingly (ECN, 2018).

Tab 2; Major Solar projects in Nigeria

S/N	Name of Solar projects	Capacity (MW)	Type	Location	Proponent
1	Anjeed Kafanchan Solar Ltd	50	Solar	Kaduna	Anjeed Innoval Ltd
2	PV Grid – tied generator system	50	Solar	Osun	Book Solar Investment
3	Ever Power Solar power plant	50	Solar	Kaduna	Quaint Global Energy
4	Solar Farm Projects	200	Solar	Borno	Borno State Govt.
5	Solar Farm at Kado	59	Solar	Kaduna	Synergent powershire
6	Solar Indep. Power Project	100	Solar	Bauchi	Nigerian Solar Capital
7	Solar PV Power Projects	50	Solar	Sokoto	Geo Envi. services
8	Solar Farm Projects	30	Solar	Katsina	Katsina State Govt.
9	Japanese Grand Solar Power	0.9	Solar	FCT	Fed.Min. of Power
10	On-Grid Solar Power	200	Solar	FCT	99 Effect Energy Ltd
11	PV-Solar Farm Kankia	20	Solar	Katsina	Katsina State Govt.
12	Solar Project Danmarke	75	Solar	Zamfara	SPGS Power Ltd
13	Solar Power Plant Panyam	50	Solar	Plateau	CT Cosmos Ltd
14	Solar Farm Riko, Jibiya	10	Solar	Katsina	Sinosum Investment
15	Solar Gen. Plant Damaturu	1000	Solar	Yobe	GOPA Int.Energy Cslt
16	PV Power Plant FCT Area	100	Solar	FCT	LR-Aaron Power Ltd
17	Shiroro Solar Power Projects	300	Solar	Niger	N/South Power Co.Ltd
18	Solar Power Plant Irewole	50	Solar	Osun	Remix Energy Ltd
19	Solar Power Plant, Bakura	150	Solar	Zamfara	PV Bakura
20	Solar Power Plan Owo	25	Solar	Ondo	Secusafe Limited
21	Solar Farm Gusau	50	Solar	Zamfara	Sinosun Investment
22	Solar Farm Kiru	40	Solar	Kano	Bravos Energy Res.
23	Solar Project Kankia	125	Solar	Katsina	Nova Solar 5 Farms
24	Solar Energy Projects Udi	1200	Solar	Enugu	Motir Seapire Energy
25	Solar Power Plant, Ilorin South	150	Solar	Kwara	Oroceram Limited
26	Solar Power Plant, Paiko LGA	150	Solar	Niger	Oroceram Limited
27	Solar Power Plant, Dutse	75	Solar	Jigawa	PAS Dutse Ltd
38	Solar Power Plant Hadejia	75	Solar	Jigawa	PAS Dutse Ltd
39	Solar Power Projects Gwa AC	100	Solar	FCT	Enerlog Limited
30	Solar Projects, Yabo	100	Solar	Sokoto	KVK Power
31	Solar Power Plant, Kankia	80	Solar	Katsina	Pan African Solar Ltd
32	Solar Power Plant, Bakura	300	Solar	Zamfara	Bakura Energy Ltd
33	Solar Plant Kokona	50	Solar	Nasarawa	Afringia Power Ltd
34	Solar Power Plant, Numan	35	Solar	Adamawa	Hill Crest Env. Mgt Ltd
35	Renewable Energy Owo	10	Solar	Ondo	Gottpower Limited

Source: ECN, 2016; FME, 2016, NERC, 2016

The table above shows some solar energy promoters, they have applied, met the requirement stipulated by the Federal Ministry of Power, Nigerian Electricity Regulatory Commission and other Ministries, Departments and Agencies responsible for initiation of solar energy initiatives in Nigeria. The approval and issuance of licenses to solar energy companies is an indicator of the government and it agencies commitment to achieving a sustainable energy mix. The next paragraph will discuss factors that drives the solar energy implementation in Nigeria.

4. Drivers for solar energy initiatives in Nigeria

Beside the location of Nigeria on a belt where solar radiation is high, there are other factors which help in driving the opportunity for the deployment of solar energy initiative in the country.

Tab 3: key drivers for solar energy in Nigeria.

Drivers	Drivers Remarks
Sustainability demands (CO_2 footprint and Climate change)	Climate change is the main driver for solar energy and other renewable and the main trigger for the called for the Millenium Development Goals (MDGs) and Sustainable Development Goals (SDGs) over the Years (Uken, 2013). Nigeria is lying on the coastline of about 800 km, with sea level raised to 0.2 m and approximately 3400km sq. several kilometres of land have been found to lose annually (Ohunakin, et al. 2014). The raising of the sea level and the desertification is resulting from the burning issues of the rapid greenhouse emission caused by the other unsustainable means of electricity. The application and development of solar PV, could reduce the impact to a minimal level while tapping the free and clean energy and making our environment friendly, more sustainable and green (Darmani, et al. 2014).
Increased energy demand	Growth is expected to reach 270 million by 2030 at an average annual rate growth of 4.0% between 2000 and 2030. Population growth, therefore, is the main driver vis – a - vis the energy demand and the socioeconomic activities measured by the GDP (Oseni, 2012). Therefore, the rapidly growing demand for energy will create more opportunities for solar PV development in Nigeria, since the conventional source will be inadequate to feed the high demand of the energy in the country. Solar energy deployment is also a very big opportunity for the rural area socioeconomic activities, because most the rural communities are neither connected nor faced with an epileptic supply of electricity (Sambo and Bala, 2012).
Power Sector Reforms Laws	The Electric Power Sector Reform Act (EPSRA) 2005, made provisions of law, to allow private individuals to construct, operate, own and generate electricity not exceeding 1000 kW at a site without a license (Amankwah, 2015). The order for the exception is meant to ease the process protocol and delays in acquiring licenses and to empower young entrepreneurs to invest in the standalone power generation. The facility is also part of the electricity expansion of a national grid, facilitation of off-grid power system, generates renewable energy and coordinates other energy mix (Ohunakin, et al. 2014). The abundance of solar radiation makes solar potentially the most important source driven by the high demand of population in the country (Okoye and Taylan, 2017).
Energy Security and access	Nigeria is estimated to have 80% demand/supply gap in electricity, and it is also, estimated that only 10% of the rural communities have access to the electricity from the national grid (Aliyu, et al. 2015). Most public and private businesses are run by self-generated electricity using gasoline and diesel generators which emit high unhealthy greenhouse gases to the environment and unbearable noise to the society. Electricity energy is lost via a transmission through distribution to the end users (Emodi, 2015). Frequent, high voltage cable vandalism, cable theft, illegal connections, and inadequate maintenance of the power sector facilities and lack of trained human capacity development (Ohunakin, et al. 2014). Therefore, solar PV and solar thermal constitute safe, enabling, reliable and affordable alternative energy widely used.
To Neutralise the energy conflict	The Nigerian power sector plant is crippled with the inconsistence in the supply and demand of gas to power plant's equipment. The common cause is associated with sabotage and destruction by the militants around the oil and gas producing area; Niger Delta (Sambo and Bala, 2012. The solar energy source is free from sunlight, and requires no transport as it is produced near where it is consumed (Aliyu, et al. 2015). Therefore, the ability to generate, transmit and develop the solar energy free of conflict zone can be a pushing factor for solar and other renewable energy technology deployment and implementation in Nigeria.
Job Creation and Opportunities	The promotion of solar energy in Nigeria will contribute enormously to poverty reduction by engaging young people in local communities to participate and benefit from the opportunity in skills development, technology transfer and investment opportunities (Darman, et al. 2014). Many alternative energy pilot projects in developing countries give positive evidence of impact on socioeconomic development, especially the rural communities in Nigeria with abundant, natural resources Ohunakin, et al. 2014). The increase in the investment in the solar battery manufacturing, installations, maintenance and repair skills, and the manufacture of various solar devices leads to the creation of massive job opportunities.

Source: Alam, et al. 2010; Darmani, et al. 2014; Ohunakin, et al. 2014; Uken, 2013 and Zahedi, 2011; Akinyele, et al. 2017; Okoye and Taylan, 2017.

Tab. 4: Other drivers for solar energy in Nigeria

Drivers	Drivers Remarks
Local value-added potential	Developing countries like Nigeria will yield local added value for solar energy penetration, considering that less than 40% of the population are connected to the national grid. Most of the population is in the rural area where fuel wood is the main source of energy (Emodi and Boo, 2015). There is a potential for the solar applications technology to be developed locally by the rural dwellers to support an energy mix in various forms such as cooking, water pumping and other agricultural activities (Dittmar, 2008). Solar energy is also potential for promoting socioeconomic stability, skill acquisition and job creation.
Growth in Education and Technology	Growth in technology and widespread of technical knowledge of solar technology could be a reason driving the initiative in Nigeria (Amankwah, Amoah, 2015). Besides, energy research centres in Nsuka, Sokoto, Lagos, Ilorin, Bauchi and Port Harcourt are the roots to awareness and skills development for solar and other renewable energies in Nigeria (Oseni, 2012). The growth in technical knowhow about the technology locally, is a pulling actor potentially responsible for continued interest in solar energy.
Stakeholders Involvement	Solar and other renewable energy projects cannot succeed without the intervention of local stakeholders. When local entrepreneurs, explicitly integrates their investment towards solar energy technology, the success of the technology is achievable (Zahedi, 2011; Marques and Fuinhas, 2011. Therefore, local investors, entrepreneurs and end users are encouraged to fully participate in the promotion, generation, production and implementation of solar energy in Nigeria to help mitigate the appalling electricity shortage in the country (Ohunakin, et al. 2014).
Financing opportunities and Market potential	One of the barriers to solar and renewable implementation in developing countries are the inability to penetrate a market because the technology is yet to be known and accepted in many countries including Nigeria (Rettere and Kelley, 2010). However, incentive mechanism such as subsidies towards the initial financial cost of solar could play a vital role in promoting the technology. In Nigeria, solar projects are funded by World Bank Projects, Central Bank of Nigeria (CBN), USAID, and many other international development funding institutions to support the promotion and development of solar energy (Ohunakin, et al. 2014). These projects drive interest from young entrepreneurs and investors to diversify into the energy mix to support the mitigation of power outage in the country.

Source: Darmani, et al. 2014; Dittmar, 2008; Marques and Fuinhas, 2011; Ohunakin, et al. 2014; Uken, 2013; Akinyele, et al. 2017; Okoye and Taylan, 2017.

The table above discussed the driving forces for solar energy implementation in Nigeria. Each country's location might have potential factors that drive the implementation of the solar energy initiative. For developing countries solar energy can bring major benefits for socio-economic development, especially in the rural communities where access to electricity has become the biggest challenge. A switch from other oil and gas energy sources can reduce the over dependency on oil and gas supply with issues of insecurities and vandalisation. In the south and other developed countries gain the advantages to driving the renewable energy from international climate change agreements like the Kyoto Protocol, SDGs and from socioeconomic interest. In other words, fast economic growth countries like China, India, and Brazil are mandated to meet their energy demand while the poorer nations must meet the international poverty reduction goals which implies the reduction of energy poverty especially in the rural areas in Africa particularly Nigeria. These forces include the declining cost of RET capital cost, integration of private public partnership in the energy industry, growth in population and the increase in demand for energy, needs for the mitigation of climate change and the achievement of the SDGs targets, energy security, job creation and financing opportunities for RET projects by international organisations.

5. Key Barriers to Solar Initiatives in Nigeria

Despite the many benefits that can be accrued from the use of solar energy potential and uses, is still very low. The major impediments to the solar energy initiative's adoption are series of barriers identified through critical review of literature which makes it difficult to implement.

Table 4; Barriers to Solar energy implementation in Nigeria

Barriers category	Barriers	Remarks	Sources
Technical Barriers	Lack of skilled personnel, lack of code of standard, lack of maintenance and operation, lack of training facilities and entrepreneur's development mechanism, lack of reliable framework for sustainability.	The barriers lead to poor plans, poor standard, and constraints of the competitive market, inadequate knowledge to know-how for the technology and risk of acceptance resulting in technology locked -up.	Sambo & Bala, 2012; Painly, 2001; Luthra, et al. 2015. Ozoegwu, 2017
Social; Cultural Behaviour	Lack of consumer awareness about the product, lack of understanding of benefit of solar PV and public resistance to chance for new technology.	The barrier, affect the market projection negatively, cultural and religious faith controversies towards economic development and sustainability.	Pasqualetti, 2011; Pollmann, et al. 2014; Akinwale, et al. 2014. Akinyele et al. 2017
Economic/ Financial Barriers	Lack of access to capital, credit to consumers and financial instrument. Lack of support to R & D, high interest rate, import duties subsidies to support local manufacturing.	At the early stage, solar projects need incentives to encourage entrepreneurs. The barriers make it difficult to adopt and sustain due to financial constraints.	Shaaban & Petinrin, 2014; Emodi &Boo, 2015; Kar & Sharma, 2015.
Institutional / Legal barriers	Institutional barriers, legal framework, regulatory issues, non-integration of energy mix, non-participation of private sector, poor R & D culture and stakeholder's non-interference.	High risk of uncertainty for solar support, lobbies against RET, a poor mechanism to reach the institutional policy makers for improvement and negative perception about the technology.	Aliyu, et al. 2015; Charles, 2014.
Political/ Policies Issues	Lack of long term policies, lack of political will to diversify into clean energy, constantly changing of government and re-shuffling of institutions.	These barriers serve as a deterrent to future planning for solar and other renewable energy adoption and sustainability. There is the fear of uncertainty in government.	Sambo & Bala, 2012; Ohunakin, et al. 2014; Painuly, 2001.
Market Distortions Issues	Trade barrier for new product, energy sector controlled, lack of access to diversified technology, lack of facilities and backup technology, non-market oriented research for solar energy technology and application.	The barriers cause hindrance to market penetration and hence new technology failed at some point.	Ohunakin, et al. 2014; Fagbenle, et al. 2011. Ikejemba and Schuur, 2016

Even though, Nigeria possesses potential driving factors for solar energy players to promote the initiatives throughout the country, the deployment and implementation of the initiatives still faces major obstacles making the implementation very challenging. It is hoped that the private sector participation will help the government to come out with an achievable solar energy roadmap. The next section will discuss the method by which this research was carried out

6. Methodology

The method adopted for this inquiry was based on desk study, otherwise recognised as literature-based from peered-reviews. Rather, many of secondary based were searched from published resources 2003 through 2017, with key articles obtained from PsyCho Info, ERIC, ProQuest, Science Direct, SocSci Search, EBSCO and COPAC, which are systematically narrowed to a search of any information related to the driving factors responsible for solar energy initiatives and the barriers which served as an obstacle for the implementation. Relevant literature was themed for critical analysis in order to produce a research outcome. The outcome from the critical literature review is analysed and discussed in the next paragraph.

7. Findings

From the literature, it is evident that Nigeria has huge potentials for solar energy almost throughout the year especially the North-East zone of the country. In accordance with literature findings, the factors driving the solar energy technology include a demand for a sustainable environment to achieve the SDGs, increase in energy demand due to increase in population, Power sector reforms Act, which suggested energy mix, challenges of energy security and access, job creation, financing and market potential, the establishment of energy research centers and stakeholders in the public private partnership deals. Even though, the drivers failed the potential for solar energy initiatives in Nigeria, the industry is encircled by barriers which makes the implementation difficult and almost impossible. Lack of skill personnel, consumer awareness about the product, lack of access to financing, lack of institutional framework, lack of long term policies for sustainable energy and trade barriers are hindering the deployment of solar energy initiatives in Nigeria. The Nigerian socio-economic activities cannot achieve its maximum potential unless the electricity challenges are adequately address by harnessing the available solar energy potential.

8. Conclusion and Recommendation

In conclusion, Nigeria, being a country within the belt of high solar radiation, a huge potential for solar energy could be grabbed to help support the epileptic conventional electricity in the country. The country possessed enormous solar energy drivers, making it a big opportunity to harness the potential solar energy to integrate into other renewable available in the country. In spite of the driving forces for the solar radiation in the country, the implementation process is constricted with many barriers, making it implementation chances very narrow. Even though, the power sector reform saw a progress for diversifying strategy to help bailout the power sector, to the energy mix, the progress indicator traced little or no significant to nearly achieving its objectives.

The Nigerian government together with integration of public private partnership (PPP) need to aggressively pursue measures to mitigate the barriers for sustainable solar energy initiatives in the country by supporting local solar panels and batteries manufacturers and distributors. The abundant solar energy in Nigeria need to be harnessed effectively and integrated with other renewable energy such as wind, biomass and mini-grid to help solve the electricity challenges tumbling the economic development of the country.

9. References

"Data on Renewable Energy Discussed by Researchers at University of Nigeria (The status of solar energy integration and policy in Nigeria)", 2017, Energy Weekly News, pp. 301.

Abam, F.I., Nwankwojike, B.N., Ohunakin, O.S. & Ojomu, S.A. 2014, "Energy resource structure and on-going sustainable development policy in Nigeria: a review", International Journal of Energy and Environmental Engineering, vol. 5, no. 2, pp. 1-16.

Akinwale, Y.O., Ogundari, I.O., Ilevbare, O.E. and Adepoju, A.O., 2014. A Descriptive Analysis of Public Understanding and Attitudes of Renewable Energy Resources towards Energy Access and Development in Nigeria. International Journal of Energy Economics and Policy, 4 (4), pp. 636-646.

Akinyele, D.O., Rayudu, R.K. & Nair, N.K.C. 2015, "Development of photovoltaic power plant for remote residential applications: The socio-technical and economic perspectives", Applied Energy, vol. 155, pp. 131-149.

Akinyele, D.O., Rayudu, R.K. & Nair, N.K.C. 2017, "Life cycle impact assessment of photovoltaic power generation from crystalline silicon-based solar modules in Nigeria", *Renewable Energy,* vol. 101, pp. 537-549.

Alam Hossain Mondal, M., Kamp, L.M. & Pachova, N.I. 2010, "Drivers, barriers, and strategies for implementation of renewable energy technologies in rural areas in Bangladesh—An innovation system

analysis", Energy Policy, vol. 38, no. 8, pp. 4626-4634.
Aliyu, A.S., Dada, J.O. & Adam, I.K. 2015, "Current status and future prospects of renewable energy in Nigeria", Renewable and Sustainable Energy Reviews, vol. 48, pp. 336-346.
Amankwah, Amoah, J., 2015. Solar Energy in Sub- Saharan Africa: The Challenges and Opportunities of Technological Leapfrogging. Thunderbird International Business Review, 57 (1), pp. 15-31
Charles, A., 2014. How is 100% renewable energy possible in Nigeria? Global Energy Network Institute (GENI), 1 (619), pp. 595-0139.
Emodi, N.V. and Boo, K.J., 2015. Sustainable energy development in Nigeria: Current status and policy options. Renewable and Sustainable Energy Reviews, 51, pp. 356-381.
Energy Commission of Nigeria (2016) Stakeholders [Online]. [Accessed 12 February 2017]. Available at: http://www.energy.gov.ng/.
Fagbenle, R.O., Katende, J., Ajayi, O.O. & Okeniyi, J.O. 2011, "Assessment of wind energy potential of two sites in North-East, Nigeria", Renewable Energy, 36 (4) pp. 1277-1283.
Kar, S.K. & Sharma, A. 2015, "Wind power developments in India", Renewable and Sustainable Energy Reviews, 48 pp. 264-275.
Luthra, S., Kumar, S., Garg, D. & Haleem, A. 2015, "Barriers to renewable/sustainable energy technologies adoption: Indian perspective", *Renewable and Sustainable Energy Reviews,* vol. 41, pp. 762-776.
Nasirov, S., Silva, C. & Agostini, C. 2015, "Investors' Perspectives on Barriers to the Deployment of Renewable Energy Sources in Chile", Energies, vol. 8, no. 5, pp. 3794-3814.
Nigeria: NERC condemns absence of renewable energy policy in NIGERIA 2014, , Athena Information Solutions Pvt. Ltd.
Obeng, G. Y. (2015). Solar photovoltaic rural electrification: Assessing energy poverty and impacts on quality of life in Ghana. Unpublished doctoral thesis, KNUST, Kumasi, Ghana.
Ohunakin, O.S., Adaramola, M.S., Oyewola, O.M. & Fagbenle, R.O. 2014, "Solar energy applications and development in Nigeria: Drivers and barriers", Renewable and Sustainable Energy Reviews, vol. 32, pp. 294-301.
Okoye, C.O. & Taylan, O. 2017, "Performance analysis of a solar chimney power plant for rural areas in Nigeria", *Renewable Energy,* vol. 104, pp. 96-108.
Osinowo, A.A., Okogbue, E.C., Ogungbenro, S.B. & Fashanu, O. 2015, "Analysis of Global Solar Irradiance over Climatic Zones in Nigeria for Solar Energy Applications", Journal of Solar Energy, 2015, pp. 1-9.
Oyedepo, S.O. 2012, "On energy for sustainable development in Nigeria", Renewable and Sustainable Energy Reviews, vol. 16, no. 5, pp. 2583.
Ozoegwu, C.G., Mgbemene, C.A. & Ozor, P.A. 2017, "The status of solar energy integration and policy in Nigeria", Renewable and Sustainable Energy Reviews, vol. 70, pp. 457-471.
Painuly, J.P. 2001, "Barriers to renewable energy penetration; a framework for analysis",*Renewable Energy,* vol. 24, no. 1, pp. 73-89.
Pasqualetti, M.J. 2011, "Social Barriers to Renewable Energy Landscapes", Geographical Review, vol. 101, no. 2, pp. 201-223.
Pollmann, O., Podruzsik, S. and Fehér, O., 2014. Social acceptance of renewable energy: Some examples from Europe and Developing Africa. Society and Economy, 36 (2), pp. 217-231.
Sambo, A.S. and Bala, E.J., 2012. Penetration of Solar Photovoltaic into Nigeria's Energy Supply Mix. In World Renewable Energy Forum (WREF).
Shaaban M, Petinrin, J. O. 2014. Renewable energy potentials in Nigeria: Meeting rural energy needs. Renewable and Sustainable Energy Reviews, 29:72-84.
Udoakah N. Y. -O. 2014. Sustainable meeting the energy needs of Nigeria: The renewable options. IEEE International Conference, IEEE, pp. 326-332.

Direct Drive Photovoltaic Milk Chilling: Two Years of Field Experience in Kenya

Robert Foster[1], Brian Jensen[2], Abdul Faraj[3], Johnson Kyalo Mwove[3], Brian Dugdill[1], Bruce Knight[1b], Wendy Hadley[1],

[1] Winrock International, Arlington, Viriginia (USA)

[1b] Winrock International, Naivasha (Kenya)

[2] SunDanzer, Inc., Tucson, Arizona (USA)

[3] Egerton University, Department of Dairy and Food Sciences, Njoro (Kenya)

Abstract

Direct drive solar milk chillers have been successfully developed and demonstrated with two and a half years field of operational experience in the Nakuru milk shed of Kenya. These innovative solar farm milk chillers (FMCs) are the first such units ever to be deployed and have been successfully operating with no issues or failures. The FMCs enable dairy farmers to boost incomes by selling chilled evening milk which would otherwise not be sold to dairy processors the next morning due to overnight spoilage. Milk is a highly nutritious, but perishable food, the storage quality of which cannot be improved once it has left the farm; thus, it is imperative to chill milk to below 10°C within 4 hours after milking at the point-of-production (on the farm) to protect quality. The solar FMC technology as been used to chill from about 25 to 40 liters of milk overnight to about 4°C. No overnight solar chilled milk was rejected by milk buyers in the 2-year study (traders and dairy cooperatives) and farmer incomes were significantly increased by over 30 percent.

Keywords: photovoltaics, direct drive solar refrigeration, milk chilling, Kenya

1. Introduction

SunDanzer Refrigeration, Inc. (SDZR) and Winrock International (WI) have partnered to develop and deploy the world's first solar farm milk chillers (FMCs) to help East African dairy farmers sell their evening milk to dairy processors that otherwise would spoil or forced consumed. The ***Photovoltaics for Sustainable Milk for Africa through Refrigeration Technology (PV-SMART)*** project aims to tackle off-grid milk cooling under the United States Agency for International Development (USAID) Powering Agriculture Energy Grand Challenge Program (PAEGC). PV-SMART began in 2013 to develop the world's first on-farm solar milk chiller. The SDZR/WI team is working in collaboration withthe County Governments of Baringo, the Department of Dairy and Food Science and Technology at Egerton University, and with dairy cooperatives and LLCs in Mogotio and Ngorika, and with the Happy Cow dairy processor in Nakuru. Chloride-Exide is the local firm representing SDZR and installing the FMCs.

Direct drive PV refrigerators were developed nearly 20 years ago and are commonly used for vaccine refrigerators for remote clinics (Foster, 2001). This project has scaled up this concept to develop an affordable direct drive with thermal ice storage capable of chilling up to about 40 liters of evening milk. The project has piloted 80 of these innovative milk chillers in Kenya and two units in Rwanda with UNIDO, allowing farmers to sell between 5 to 40 extra liters per day of higher quality evening milk. This results in additional farmer income, ranging from US$60 to US$500 extra incomes per month, depending on the number of cows per farm. Solar equipment investment payback averages about 6 to 12 months for these smallholder farmers based on increased evening milk sales.

There are over 850,000 smallholder dairy farmers in Kenya, about 85 percent of who do not have access to the national electric power grid. Diesel fuel is expensive and logistics difficult to deliver to small rural dairy farmers and uneconomical to use for small scale refrigeration. Thus, there has not been an economical method available for on-farm milk chilling for the vast majority smallholder dairy farmers in Kenya and other less developed regions globally. The typical Kenyan dairy farmer has about 3 to 5 cows, producing an average of about 8 liters per day of milk per cow (typically ~60% as morning milk and ~40% as evening milk). Dairy cooperatives have an

doi:10.18086/swc.2017.16.02 Available at http://proceedings.ises.org

organized morning milk collection system, but normally do not accept evening milk since by morning due to high bacteriological counts growing overnight. Due to the lack of on-farm refrigeration, evening milk is either forced consumed, sold cheaply to nearby neighbors or hawkers, or spoils. Only about 40% of milk produced nationally is processed in Kenya.

Fig.1: Dairy farmer training for solar farm milk chillers (FMCs) in Ngorika, Kenya.

This failing in upstream milk production causes milk spoilage and lost farm earnings. It also causes poor quality milk and further losses in earnings along the downstream dairy value chain. Of the milk that does arrive, much of it still has a high bacterial count due to lack of refrigeration, resulting in poor quality dairy products. Farmers could receive a premium price for better quality, refrigerated milk; dairy processors could charge a premium for better quality products if milk can be kept cool all the way from cow to consumer; especially during the all-important first four hours after milking that determine quality.

In order to enhance the value of milk from remote producers, *PV-SMART* has developed an affordable solar powered farm milk chiller (FMC) so these producers can deliver cool milk rather than warm to the central collection stations. The farmers also use FMCs on the farm to preserve other produce such as eggs, meat, fruits and vegetables. Besides demonstrating the technology proof of concept, *PV-SMART* is also working with stakeholders like Kenyan SACCOs (Savings and Credit Cooperative Associations) to provide financing for solar technologies like FMCs that can increase on-farm productivity and incomes. Farmers often need access to technology and credit on reasonable terms to finance the initial purchase of solar power systems, which have higher capital costs but lower operating costs when compared to traditional remote generation energy technologies like diesel gen-sets.

PV-SMART has a four-phase implementation strategy for developing, disseminating, and financing FMCs in Kenya:

- Year 1—Technology Development: Designed and tested prototype solar farm milk chiller (FMC) by scaling up an off-the shelf photovoltaic refrigerator (PVR) model. Surveys were conducted of smallholder dairy farmer's needs, and besides milk chilling, a wire basket was added for perishable household food items, as well as two 5V USB ports for daytime cell phone, radio, and LED lantern charging.

- Year 2—Pilot Phase 1: Piloted the world's first solar FMCs to 39 smallholder dairy farms in Baringo and Nyandarua Counties of Kenya. A baseline control unit was also installed at the Egerton University (EU) Department of Dairy and Food Science for more in-depth testing and milk quality evaluations. Field evaluations and farmer surveys were conducted by EU.

- Year 3— Field Testing Pilot Phase 2: Based on Phase 1 field experience, design and testing of a next generation prototype was developed with 40 units deployed to Kenya and 2 in Rwanda with UNIDO: (i) design adaptations notably moving from a ground to roof mounted PV system; (ii) established a local dealer network with Chloride-Exide; and (iii) begin financing units to farmer with Kenyan Savings and Credit Cooperative Associations (SACCOs), starting with Skyline SACCO in Mogotio. Demonstrations are also expanding to new regions with Mercy Corps and GiZ, including for camel milk chilling.

- Year 4— Commercial Rollout Phase 3: Planning is underway to expand the solar FMC technology commercially in Kenya with Chloride-Exide. Encourage more SACCOS to finance FMCs to more dairy farmers throughout Kenya. Expand FMCs to Rwanda and Tanzania.

2. Direct Drive Photovoltaic Refrigeration

The SunDanzer solar FMC is a direct drive refrigeration unit with no batteries that uses thermal phase change material (ice) energy storage. The technology was originally developed in support of NASA's future planetary mission's refrigeration requirements 20 years ago (Ewert, 2002), and later commercialized for vaccine battery free refrigeration. This is accomplished by integrating water as a phase-change material into a well-insulated refrigerator cabinet and by developing a microprocessor-based control system that allows direct connection of a PV panel to a fixed or variable speed dc compressor. By storing ice in the walls of the refrigerator, it eliminates the needs for electro-chemical energy storage. The solar refrigerator uses a vapor compression cooling cycle with an integral thermal storage liner, PV modules, and a controller. The Kenyan solar FMC employs a fixed speed dc compressor. By storing ice in the walls of the refrigerator, it eliminates the needs of battery storage; ice never wears out and provides sufficient energy storage to cool 40L of milk overnight.

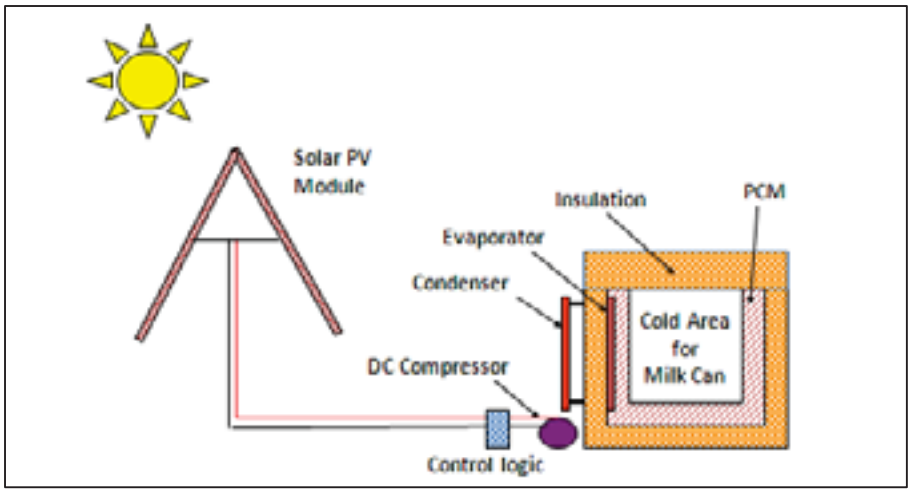

Fig. 2: Solar direct drive refrigerator with DC compressor and E-W "fixed tracking" array (Foster, 2015).

In addition to increasing the quality of product for farmers, the solar FMC has two 5 V USB plug ports capable of charging cell phones, radios, and solar lanterns which farmers use for themselves or rent out. Likewise, there are dietary and health benefits for farmer families to store vegetables, fruits, meat, etc. in the solar FMCs, which also reduces the frequency of trips to town to purchase fresh produce.

Fig. 2: PV Powered Chiller Using Thermal Ice Storage and Brine Bags to Chill Evening Milk

Figure 1. Rooftop PV Installation for Mogotio Dairy Farmer FMC

2.1. "Fixed Tracking" Array

The solar FMC system also uses an innovative East-West "fixed tracking" array to maximize compressor run time and not daily energy production. Conventional tracking increases both capital and operating costs due to additional hardware and maintenance requirements for moving parts. While a conventional equatorial facing PV array power output is well over the required power requirements for the FMC at solar noon; the East-West array's output wattage supplies the required compressor power for a longer period. Thus, increasing compressor run time providing longer operating hours for farmers to chill more milk. While this approach does not maximize energy usage, it does maximize ice production over the course of the day. PV prices have come down sufficiently that fixed tracking is a viable economic option over tracking without the future maintenance concerns. This type of approach works especially well in equatorial latitudes like Kenya. This simple approach provides reliable performance [4].

Fig. 5. FMC PV array (510 Wp) with unique East-West fixed tracking array under test at Egerton University Dairy Science Unit.

With the compressor running most of the daylight hours due to the E-W "fixed tracking" array (the array is not actually moving like a conventional tracker, but is fixed with half the array facing East and the other half facing West to maximize daily compressor run time). Ice is formed and stored into the walls of the PVR. Thus, there is no need for expensive battery storage and replacements. Ice does not wear out. Testing at New Mexico State University for NASA and SDZR on an early prototype PVR with ice storage was successful [2] and led to the development of direct drive vaccine PVRs using ice storage. The proven PVR technology was then increased in size for larger scale milk chilling.

In order to maximize heat transfer, the solar FMC incorporates brine bags, which do not freeze at 0°C, that are placed around the milk cans to increase heat transfer and cool milk quickly. Milk naturally contains antibacterial agents to protect the suckling young from potential infectious diseases; these antibacterial agents also slow bacteriological growth – the cause of milk souring. This effective natural protection is called the lactoperoxidase system, and has both bacteriostatic and bactericidal effects against some milk spoilage microflora for about the first four hours after milking. Bacteriological growth is further retarded when milk temperatures fall below 10°C and is essentially halted at 4°C. The FMC chills 25 liters of milk down to 10°C in a couple of hours, and the milk temperature by morning is about 4°C [4].

Since dairy farmers typically milk cows twice a day, once in the morning (~60%) and again in the evening (~40%), evening milk must be consumed or sold to neighbors or hawkers at a cut price. Even so, much of the evening milk spoils overnight. About 60% of milk in Kenya is not processed mostly due to the lack of on-farm chilling options. Solar FMCs increase farmer incomes from selling milk that would otherwise spoil, and some innovative dairy processors making cheese and yoghurt who need better quality product offer a Quality Milk Payment system incentive to dairy farmers. Solar chilling provides farmers the means to improve their milk quality and overall sales.

Fig. 6: Kenyan dairy farmer with her solar farm milk chiller (FMC), which has become a prized possession in her home.

3. Operational Findings

WI in collaboration with Egerton University Dairy and Food Sciences Department has been monitoring and evaluating (M&E) the performance and benefits of the Solar FMCs installed on the Mogotio and Ngorika Cooperative dairy farms. *PV-SMART* team is also monitoring solar irradiance at Ngorika and Egerton University sites. A few selected milk cans have a Hobo data logger installed on them to monitor milk can temperature data. The temperature probe is installed on the can with foam over it so that it measures true milk can temperature only.

The findings are based on milk can temperature data collected, co-op milk sales, surveys with the end-users, milk can temperature data, and field observations by the WI and Egerton University team. All of the original 40 piloted solar FMCs have functioned for 2.5 years with no failures, and no failures in the next 40 Phase 2 units as well. There was one Phase 1 unit which had a refrigerant leak upon delivery due to springing a refrigerant leak over some extremely rough roads traversed for delivery; this was easily repaired by a local refrigeration technician from Chloride-Exide for US$40 and the unit has functioned with no issues ever since. The solar FMC technology couples mature PV technology with mature vapor-compression technology and is very reliable.

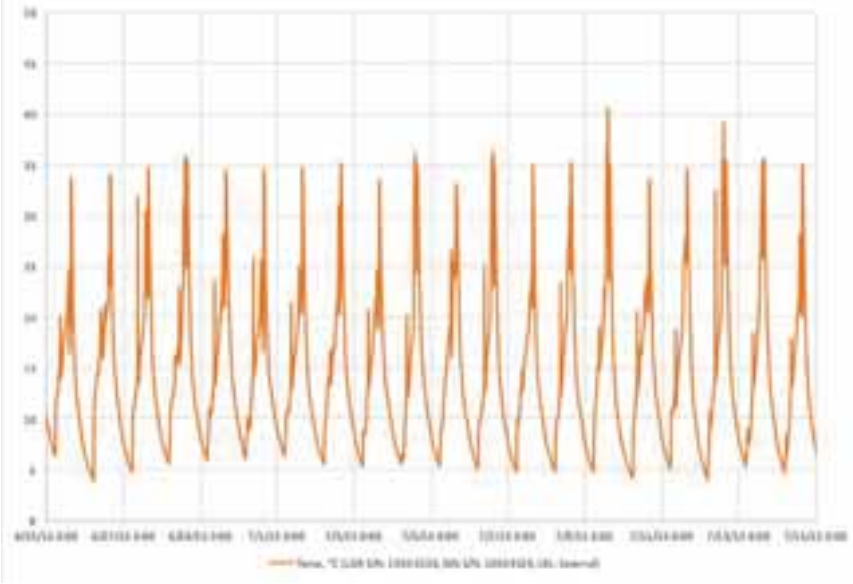

Fig. 7: Example Daily Milk Can Temperature Cycles (daytime high when can is drying in the sun and nightimg low with milk).

Milk temperature: The FMCs work well to chill 25 liters of evening milk to 4^{O}C and lower. If some milk is not removed the next morning and left throughout the day, small quantities of milk can freeze, indicating the prototype FMC may have 'spare' cooling capacity for Kenya. The figure below shows daily milk cooling cycle for one of the farmers, milk temperature is repeatedly cooled to about 5°C. Note that the farmer puts the milk can outside in the direct sunlight for drying after cleaning so the can heats up to above ambient peak temperatures during the daytime.

4. Impacts and Results

PV-SMART is piloting 80 solar FMCs in Baringo, Kisumu, Nakuru, Nyandarua, and Wajir counties, as well as one control unit at Egerton University. The first 40 Phase 1 Pilot solar FMCs have operated flawlessly in the Nakuru milkshed of Kenya with no equipment failures in the first 2.5 years. The second Phase Unit are being installed from August – November, 2017.

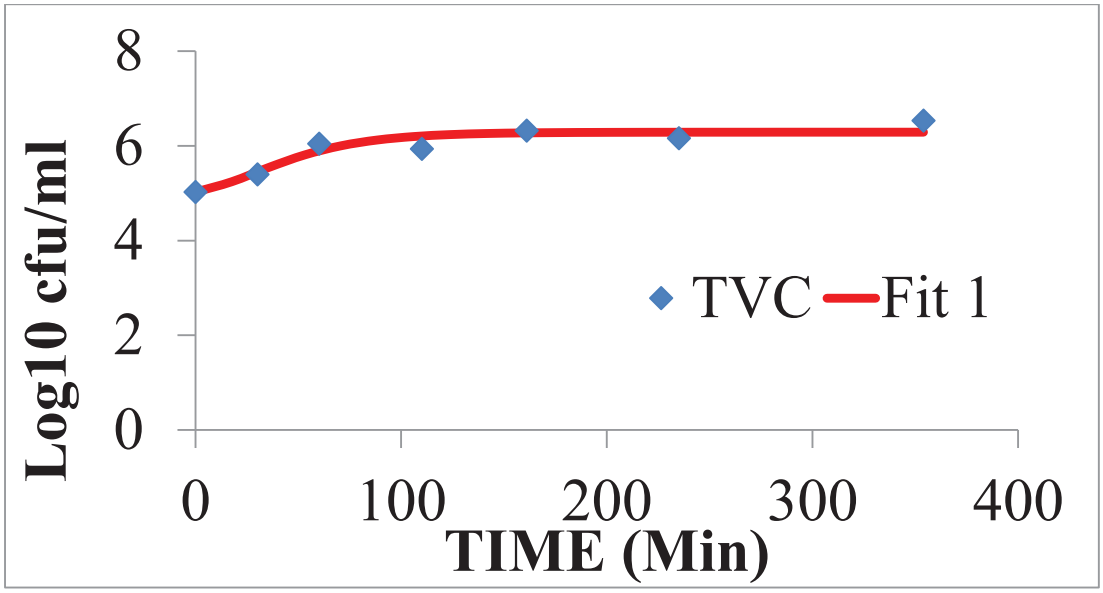

Fig. 8: Total Viable Count (TVD) of Bacteria shows that once the milk is introduced to the solar milk chiller, bacteria growth is halted.

The average dairy farmer chilled about 25 L of evening milk to 4°C; a few farmers chill as much as 40 L every night. Milk quality is maintained after milking and there have been zero rejections of solar chilled milk for any of the participating dairy farmers using solar FMCs, unlike from before. An informal farmer-to-farmer milk supply network was also organically created by solar FMC owners with excess capacity provided to their neighbors through FMC sharing (rent, barter, or purchase).

Over 92 percent of Mogotio farmers (lower elevation and hotter climate) and 67 percent of Ngorika farmers (higher elevation and cooler climate) reported increased milk sales directly attributable to chilling evening milk using solar FMCs. Other on-farm production factors include a severe drought in 2017 reducing forage and milk production for some farmers.

FMC field evaluations were conducted by WI in collaboration with the Department of Dairy and Food Science and Technology at Egerton University for units installed at the Mogotio Farmers' Cooperative Society Ltd. and New Ngorika Milk Producers Ltd. The farmer companies collect, bulk and deliver milk to two processors in Nakuru: Happy Cow Ltd and New Kenya Cooperative Creameries Ltd. Both are piloting quality-based milk quality payment (QBMP) schemes to incentivize farmers to improve milk quality. Based on solar FMC experience to date the key findings are below and summarized in Tables 1, 2, and 3.

- All 40 Phase 1 FMCs performed well and according to design, i.e. chilled 25 kg of warm evening milk to <10^{O}C within two hours, and to <4^{O}C by next morning collection.

- Some farmers were chilling up to 40 kg milk in plastic barrels to <10^{O}C prior by next morning collection – indicating potential to chill more than the designed 25 kg milk (ambient conditions vary).
- Some milk collector-transporter-farmers use the FMC to aggregate and chill up to 40 kg evening milk from 3 to 5 nearby farmers, charging additional KES 2 (~2 US cents) per kg.
- After homestead use of evening milk (for home and calves), the Phase 1 users are selling between 2 and 45 kg 'extra' milk daily – indicating gross incremental income gains ranging from KES 1,800 to 40,500 (US$18 to 400) per month based on an average farmgate milk price of KES 30/kg. Cows produce milk in the evening regardless of whether there is a market or not.
- Two head of household ladies earn 'extra' income from FMCs charging neighbour's cellphones - ~KES10 per charge x 10 = KES100 (US$1) per day.
- The FMC kept milk fresh until morning with zero rejections reported in two years.

Table 1: Evening Milk Sales Increased Dramatically to Dairy Processors

Location	Did Milk Sales increase?	Evening Milk Usage and Sales			
		Before FMC Installation		AfterFMC Installation	
		Home Consumption	Local sales	Home consumption /local sales	Sales to Dairy Processors
Mogotio n=19	No (7.7%	69%	31%	8%	92%
	Yes (92.3%)				
Ngorika n=20	No (16.7%)	27%	73%		100%
	Yes (66.7%				

Table 2: Comparison of milk stored in the Solar FMC

Parameter	Farm 1		Farm 2		Bench Sample	
	Evening	Morning	Evening	Morning	Evening	Morning
Room Temperature °C	19.0	17.4	20.6	19.1	19.1	18.1
Milk Temperature °C	29.6	3.5	28.4	0.2	29.5	17.2
Acidity (% Lactic acid)	0.162	0.174	0.155	0.164	0.161	0.195
pH	6.64	6.59	6.59	6.57	6.64	6.24

Table3: Milk quality change during overnight storage from Egerton University Dairy Lab

Parameter	Farm 1	Farm 2	Bench Sample
Time in storage (Hours)	14.946 ± 0.168a	15.361 ± 0.298a	14.946 ± 0.168a
Titratable acidity (%LA)	0.012 ± 0.012b	0.009 ± 0.006b	0.033 ± 0.022a
pH	-0.042 ± 0.170a	-0.021 ± 0.018a	-0.239 ± 0.167b
Log 10 CC	0.808 ± 1.273b	0.914 ± 0.865b	3.373 ± 1.403a
Log 10 TVC	1.023 ± 0.997b	0.950 ± 0.587b	3.946 ± 1.015a
Red figures indicate did not meet KEBS norms.			

The key takeaway is that the solar FMC works and improves on-farm milk quality at point-of-production on the farm potentially enabling more quality milk to enter the dairy supply chain. The returns from investing in solar FMCs appear are under a year, even for smallholder dairy farmers. WI is working with the Skyline SACCO and other partners to finance solar FMCs in 2017 as there is a good business case with relatively low repayment default risk facilitated by the well embedded existing milk 'check-off' repayment system.

Thus, milk quantity and potential incremental gross earnings gain at current milk prices is excellent for these pilot units, with simple payback ranging anywhere from six months to one year depending on user milk production. From the initial surveys users sell between 5 and 45 liters of extra evening milk each day, indicating gross incremental income gains ranging from US$50 to $650 per month. Kenyan small scale financial credit institutions (SACCOs) have begun financing PVRs during Phase 2 of PV-SMART at an initial selling price of about US$1,850 per installed unit if roof mounted (pole mounting is more). The final commercial price may vary. Field surveys found that 83 percent of the Phase 1 pilot FMC farmers felt the solar FMC technology was worth the initial cost and is a worthwhile investment. Financing is key as over 70 percent of small holder farmers prefer a short-term (1 year) loan mechanism to purchase solar FMCs.

5. Conclusions

PV direct drive solar milk chillers (FMCs) have been successfully introduced and used in Kenya with zero failures in the first 2.5 years of operation. There is a significant increase in amount of milk sold and the farmer income accruing from the extra liters of milk sold. Smallholder dairy farmers have sold between 5 and 40 extra liters of evening milk each day, depending on their dairy herd size. The FMC kept milk fresh until morning with zero rejections reported from the milk collection center. Resulting farmer income gains ranged from US$60 to $500 per month, with expected FMC payback typically in less than a year. This type of solar milk chilling uses no batteries and has no regular maintenance requirements. There are over 5 million smallholder dairy farmers in East Africa who can benefit from this technology, not to mention the millions more of other off-grid smallholder dairy farmers in the rest of Africa, Asia, and Latin America that can also benefit from solar FMCs to improve livelihoods and delivered milk quality.

6. References

Foster, R., Ghassemi M., Cota A., 2009. Solar Energy, Renewable Energy and the Environment Series, Volume 2, Taylor and Francis Publishing, CRC Press, ISBN: 13:9781420075663, Boca Raton, Florida, August, 2009.

Foster, R., Estrada L., Bergeron D., 2001. “Photovoltaic Direct Drive Refrigerator with Ice Storage: Preliminary Monitoring Results,” ISES Solar World Congress, Adelaide, Australia.

Ewert, M., Bergeron D., Foster R., Estrada L., LaFleur O., 2002. "Photovoltaic Direct-Drive Battery-Free Refrigerator Field Test Results," SOLAR 2002, ASES, ASME, NPSC, Reno, Nevada.

Foster, R., Jensen B., Dugdill B., Knight B., Faraj A., Mwove J., and Hadley, 2015. “Solar Milk Cooling: Smallholder Dairy Farmer Experience in Kenya,” ISES Solar World Congress, Daegu, South Korea.

Integration and management of solar energy for electric vehicle charging station

Asif Khan[1], Saim Memon[1], Tariq Sattar[1]

[1] London South Bank University, London (United Kingdom)

Abstract

A rise of electric vehicles and consequent increase of charging stations in the UK has widely been acknowledged due to its negligible carbon emissions leading to the transformation of low-carbon economy. A dynamic increase in the wind and solar power systems installation and grid-integration to the charging stations of electric vehicles has led uncertainty issues in the power distribution grid e.g voltage fluctuations, transients/harmonics. This paper addresses the uncertainty scenario aiming to contribute and propose a potential model focusing on the design of the route in which solar electric power is delivered to the electric vehicle charging station. A specialised system containing an electrical control system is proposed using MATLAB and SIMULINK. A system was designed for improving the interaction among electric-vehicle charging points and battery storage system in which electrical control system assists in developing the correct duty cycle in order to stabilise and regulate the voltage at the DC/DC power conversion station. The proposed system is very effective and significant contribution in understanding and reducing the load on the converter untimely enabling reduction of charging time for electric vehicles. The implemented electrical control system manages the electric power on the grid such as during the peak times it draws power from the batteries and then charges up the batteries in the off-peak times. A constant voltage is achieved on the micro grid irrespective of fluctuations in solar energy generation and in the load.

Keywords: Solar system, Power conversion, Electric vehicles, storage system, charging station

1. Introduction

Around 550000 hybrid electric vehicles are reported to be registered in 2015 by the centre of solar energy and hydrogen research (Shaaban et al, 2015). The storage energy based electric-vehicles are classified into plug-in hybrid electric vehicles (Han et al, 2017).The main factor in the revolution of electric-vehicles is due to the improvement in power electronics components, better performance of electric machines and the storage system (Shen et al, 2014). The power electronics components such as switches, converters and drives increase the performance of power conversion. Beside this, development of software for hybrid electric vehicles is a silent revolution. The hybrid electric vehicles combine the motor of propulsion and ICE (Guan and Chen, 2017). An increase of plug-in electric vehicles are due to the several reasons such as it generates no carbon emissions due to the usage of no fossil fuels and long-term sustainable mission of transforming cities towards 100% renewable and make cities better economically (Yu, 2017 and Zhang, 2016) because the carbon dioxide emissions was 407.70 ppm in May 2016 and is continuously increasing (Cheng et al, 2015). Currently, the state of art uses to charge up the batteries in the hybrid electric vehicles are fuel cells, regenerative breaking system, and the vehicles charging station. These vehicle charging stations are connected to the National transmission energy network (Dubarry et al, 2017). Charging up the electric vehicles from the distribution network is not suitable as it increases the electrical demand on the network and creates power flow issues on the distribution network such as transients, harmonics and voltage reductions (Sheng et al, 2017). The power supply to the electric-vehicles can be AC or DC type. AC type power flow is not suitable for the electric-vehicle (EV) charging station as it increases charging time. The DC type power flow reduces the charging time and increases the performance of the electric-vehicles (Tan, 2016) and (Yong, 2015). DC power flow system also reduces the power losses due to shorter in length for the EV charging station. The purpose of designing such system is to reduce the power flow issues such as voltage fluctuations and transients/harmonics and issues at the existing transmission system. The DC grid is fed from the solar energy where power generation is always fluctuating, therefore, a control system required that transmits the signal at a very faster rate (Liu and Sun, 2014).

doi:10.18086/swc.2017.16.03 Available at http://proceedings.ises.org

This paper presents the Simulink model for the solar storage system that transmits high DC voltage to the charging station. This is due to the unpredictable power generation from the solar system, it is a challenge to supply the constant required voltage to the electric vehicle. Beside this, quality ratings and stability are the main factors to charge up the large numbers of electric vehicle instantly. Due to these issues imbalances occur and harmonics and voltage sags arise. The research investigates the voltage efficiency and power flow management of solar energy transmission to the electric-vehicle charging station. This system has the ability to manage the power flow between generation and the loads. Under normal conditions, it is connected to the solar energy system and the storage battery bank and can be linked with fuel generator if required.

2. Methodology

A PV solar system of nominal energy geneation capacity 200 kWh is simulated on MATLAB/SIMULINK in which the 200 kWh storage system is added to balance the energy demands during the higher temperatures and low irradiance.This storage system is charged up from the solar system and the fuel generator. The fuel generator has the energy generation capacity 200 kWh that charging up the storage system after the energy falls to 60%. The storage system supplies power to the electric-vehicle charging station during the disturbances. The electric-vehicle charging station has maximum power consumption capacity of 103.50 kWh consisted of four charging points. DC/DC power conversion is carried out by using insulated gate bipolar transistors (IGBT) where MATLAB function coding environment is used to control the frequency of the IGBT and to stabalize the voltage from the solar system. By using low pass filter, spikes and transients are mitigated to achieve power quality. It is investigated how the temperature, irradiance, and over loading affects the power regulation on the system. Specifically, voltage instability and the transients are investigated. Programmable protection circuit breakers are placed to protect the charging terminal. Controlled power conversion system and analytical techniques are implemented to control the power flow in the system.

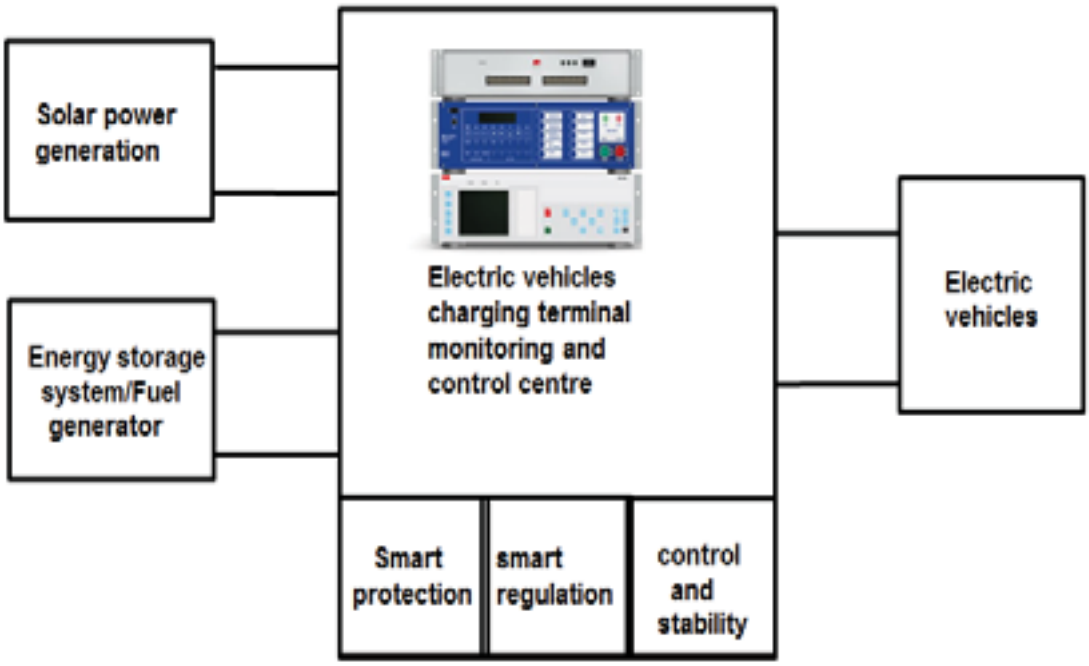

Fig. 1: illustrates the schematic model of the proposed system in which solar energy/storage system are maintaining the energy demands at the electric-vehicle charging station, smart monitoring and control system are used to convert and regulate the power flow from the storage and the solar system consisting of controlled DC/DC converter that is connected with the energy resources and the electric-vehicle loads

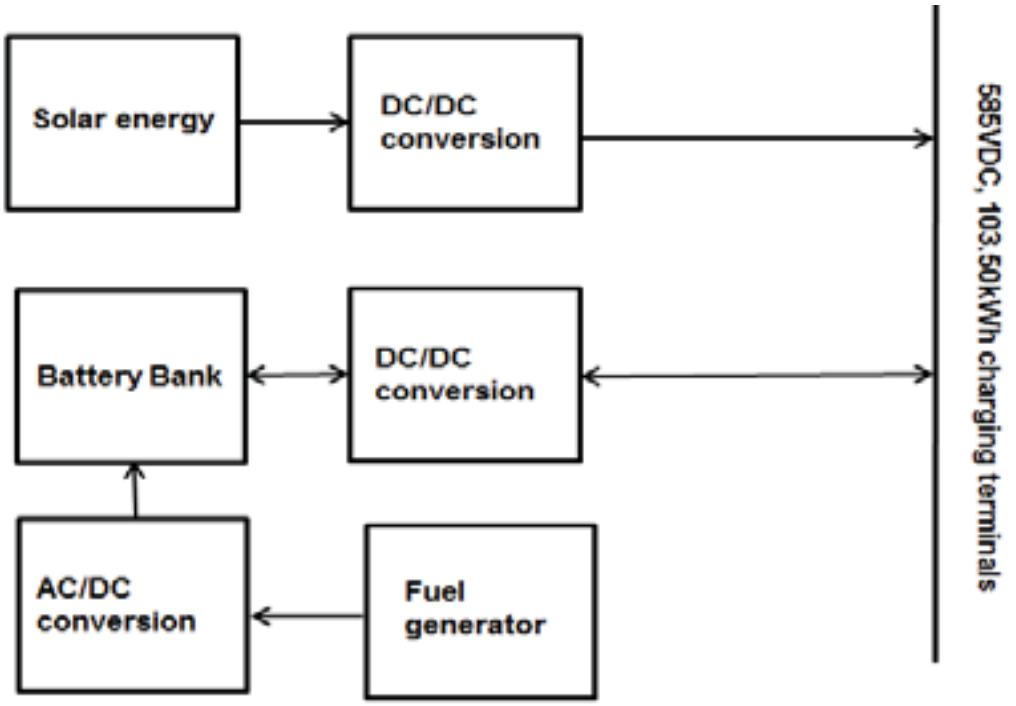

Fig. 2: is the block diagram of the power conversion for the solar system, fuel generator and the storage system in which the power flow between the storage system and the charging station is considered to be dual flow, meaning storage system can supply and receive energy from the charging station.

3. Discussion

The proposed structure consists of solar energy system, monitoring and control structure, measurements units, energy storage system, fuel based electric power generation system and power conversion system. The EV charging terminal consists of programmable protection system and a voltage regulator that assists to supply the quality power. The electric-vehicle charging station is receiving the electric power from the solar and storage system. The nominal power generated by the solar system is 200 kWh. The voltage from the solar system is converted to 585VDC that reduces the charging time for the electric vehicles. Irradiance and temperature block is used to provide sun power to the panels. Input from the irradiance is varying. Voltage source converters are used to convert the power from the solar farm. Then this power was added to the DC/DC converter station where a buck-boost converter is placed to balance the voltage. Low pass filter is applied to remove the transients and harmonics. It also supports to control the current and maintain the DC voltage level. A bi-directional converter is placed between the DC microgrid and the battery bank that charges up and discharges the batteries from the microgrid and it monitors the power flow at the grid and battery bank. During the peak time, battery storage system is dependent on the solar power generation unit, the fuel generator takeover to meet the energy demand. This topology is considered to improve the power flow on the transmission network due to the reduction in harmonics and voltage fluctuations. Transients and spikes arise in the system are also due to the installations of super capacitors at the electric-vehicles storage system. This reduces the efficiency of the power flow on the system because inductively behaves superlative at lower frequencies and capacitance load show good performance at higher frequencies. Due to DC power system, there is no phase shift between current and voltage but the voltage stability needs attention which can be maintained by supplying the correct pulses to the power converter switches.

List of energy converters connected to the electric-vehicle terminal.

- DC/DC energy conversion system for the solar energy system.
- AC/DC energy conversion system from the fuel generator.
- DC/DC power conversion system for the storage system.
- Monitoring and control centre energy measurement and regulation system

The DC/DC buck converters are used to transmit the regulated voltage to the electric-vehicles. To create the mathematical formulation constant voltage and constant power is assumed to be flowing out from the energy converter terminals. The constant voltage is achieved by applying the 50 kHz frequencies at the converter switches. The resistance of the tranmsitted conductor is considered constant. The capacitance and inductance are neglected due to DC type power flow system.

The power flow into the terminals is splitted into three subsets $\{V, R, P\}$ and the constant controlled voltage is received from the solar system/storage system. Branches of the terminal for voltage source converters are represented by $V = N \times N$ included the constant resistance of the conductor. The electric vehicle charging terminal converts the 585VDC into the voltage required to charge the electric-vehicle batteries and the supercapacitors. The terminal voltage and current admittance matrix on the system $G \in R^{N \times N}$ is expressed as follows,

$$\begin{bmatrix} I_V \\ I_R \\ I_P \end{bmatrix} = \begin{bmatrix} G_{VV} & G_{VR} & G_{VP} \\ G_{RV} & G_{RR} & G_{RP} \\ G_{PV} & G_{PR} & G_{PP} \end{bmatrix} . \begin{bmatrix} V_V \\ V_P \\ V_R \end{bmatrix} \quad \text{(eq. 1)}$$

Where $\mathbf{I_R} = -\mathbf{D_{RR}}.\mathbf{V_R}$ (eq. 2)

For the electric-vehicle charging terminal singular matrix can be written as shown in equation 3. Where B is the susceptance and D_{RR} is a diagonal matrix is for admittance.

$$V_R = -(D_{RR} + G_{RR})^{-1}(G_{RV} .\ V_V + G_{RP} . V_P) \quad \text{(eq. 3)}$$

$$I_P = J_P + B_{PP}. V_P \quad \text{(eq. 4)}$$

The voltage received from the storage/solar system is 585VDC. Power links are evaluated by the following equations where I_P is the current level and V_P is the voltage flow on the system.

$$P_P = \text{diag}(V_P) . I_P \quad \text{(eq. 5)}$$

The storage system is balancing the power flow on the system during the peak times and reduction in power generation from the designed solar system. The electric-vehicle charging terminal detects the power deficiency and switches ON the storage system. P_P is evaluated to

$$\mathbf{P_P} = \mathbf{diag}(\mathbf{V_P}) . (\mathbf{J_P} + \mathbf{B_{PP}}. \mathbf{V_P}) \quad \text{(eq. 6)}$$

With $\mathbf{J_p} = \mathbf{G_{PV}} - \mathbf{G_{PR}}. (\mathbf{D_{RR}} + \mathbf{G_{RR}})^{-1}. \mathbf{G_{RV}}) . \mathbf{V_V}$ (eq. 7)

$$B_{PP} = G_{PP} - G_{PR}. (D_{RR} + G_{RR})^{-1}. G_{RP} \quad \text{(eq. 8)}$$

The voltage in the terminals can be set by the solving the equation 9.

$$\mathbf{V_P} = \mathbf{B_{PP}^{-1}}. \left(\mathbf{diag}\left(\mathbf{V_P^{-1}}\right) . \mathbf{P_P} - \mathbf{J_P}\right) \quad \text{(eq. 9)}$$

To investigate the V_P, let consider $T \rightarrow R_P$

$$TV_P = B_{PP}^{-1}. (\text{diag}(V_P^{-1}) . P_P - J_P) \quad \text{(eq. 10)}$$

The voltage is stabilised at the monitoring and control centre in order to maintain the energy flow for the electric-vehicles at the station. The reduction in voltage is maintained by correcting the applied frequency to the converter switches. Fuel generator is connected with the battery to maintain the power storage on the storage system during the energy shortages.

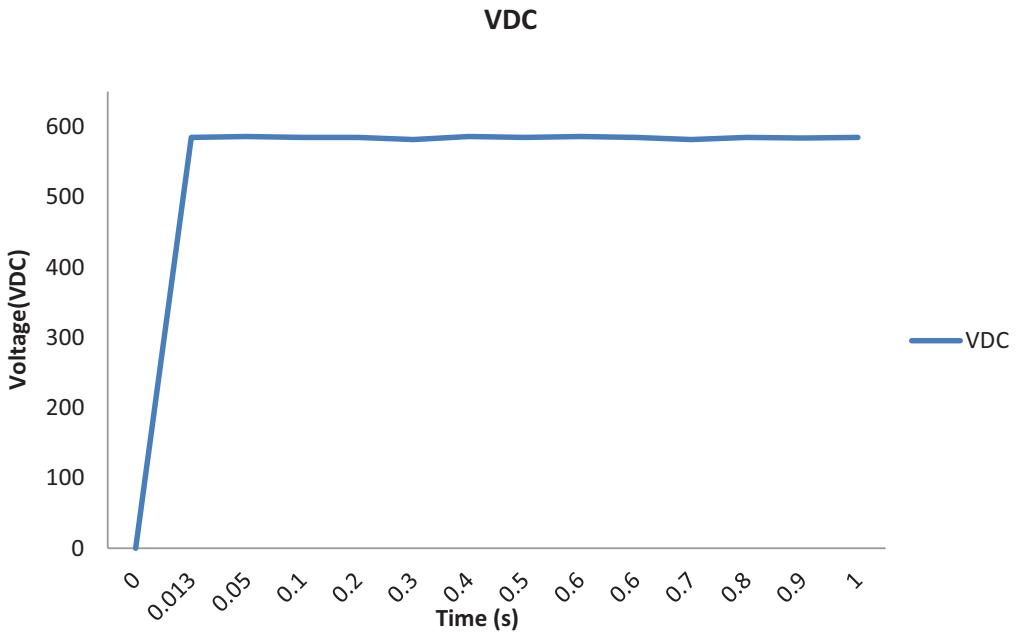

Fig. 3: The voltage output from the DC/DC converter of solar energy system

Tab. 1: The energy generation and storage capacity.

Energy resources	Capacity
Solar system	200kWh
Storage system	200kWh
Fuel Generator	200kVA

3.1 System performance

With the rapid increase in power consumption at the EV charging terminal, following are the three issues linked with the storage/solar system.

- Quick energy supply from the storage system into the EV charging terminal
- Quick energy injection from the solar system to the charging station.
- Dynamic behaviour instead of long term serving capacity of the storage system.

There are four EV charging points taken for this system. These charging points are associated with the faster charging because of connection with the higher DC voltage of 585 VDC. The charging point consumes 50 kWh, 43 kWh, 7 kWh, 3.5 kWh. The proportion is selected based on the charging points being installed several places in the UK such as 2×50 kWh and 1×43 kWh in Toddington Dunstable at M1 motorway and similar are installed at the china town at London, charter street at Leicester and many other places in the UK. The batteries in the electric vehicles support to run the machines, but the batteries take longer to charge up. During the running period engine are used to charge up the batteries in the electric vehicles. To solve the faster charging for the EV batteries a new system is investigated. Higher voltage DC power supply is found more appropriate to solve this issue. The investigated system has the features to supply the energy during peak/off-peak times at the EV charging station by means of solar and storage system.

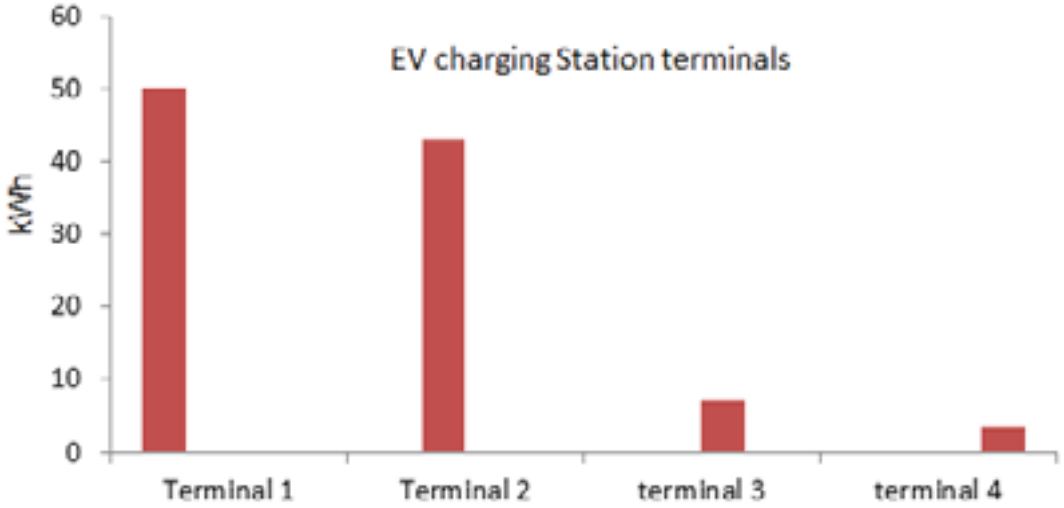

Fig. 4: Illustrates the Electric vehicles charging points at the EV station.

There are four scenarios considered to examine and analyse the energy system performance.

- When the solar system is independently supplying power to the EV charging terminal. In this case, the storage system is in off-mode. This is the best feature as energy demand is completely achieved by the renewable energy/solar system. This system also improves the environment by minimising the carbon emissions generated from the fuel generator. The energy losses are very small due to the shorter length of the electric power transmitted conductor. This scenario has the capacity to meet the energy demands at the EV station during the Peak and off-peak times.

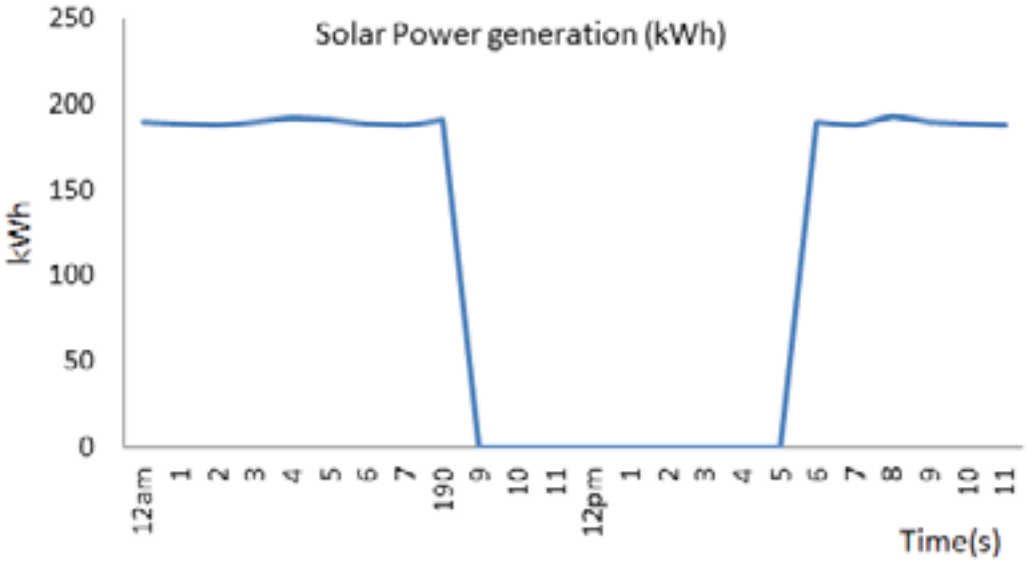

Fig. 5: The power generation by the solar system between 9pm and 5am no power is generated by the solar system. In this case the storage system and fuel generator will meet the energy demands at that time.

- The generated energy from the solar system is charging up the solar system in peak times. In this case, the EV charging terminal is consuming the energy at full capacity.

- When the storage system and fuel generator are meeting the energy demands at the EV charging station. At this point, the solar system is in off-mode and not generating any power. Fuel generator

charges up the storages when energy level falls below 60%. Storage system degradation is normally measured by three main features, such as the depth of discharge, temperature, and the conditions of charge. These three factors affect the performance of batteries used in the storage system.

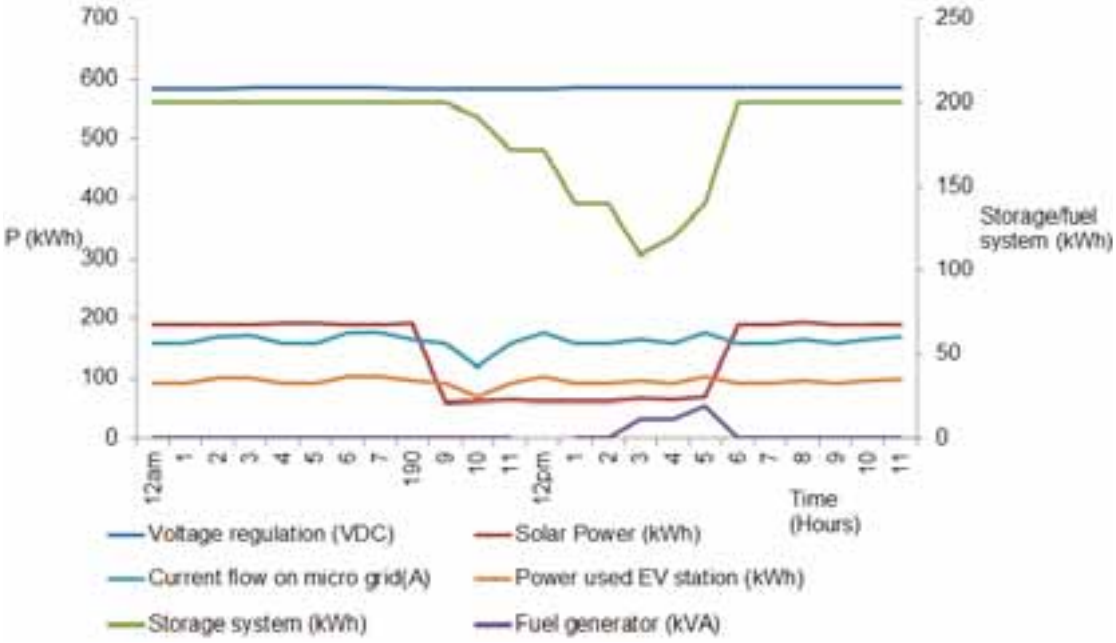

Fig. 6: The energy management at the EV charging station. In this case, the nominal power from the solar system is mitigated from 9pm to 5am where storage system is independently meeting the energy demands at the EV station. Fuel generator switched ON to charge up the storage system as the energy level falls below 60%.

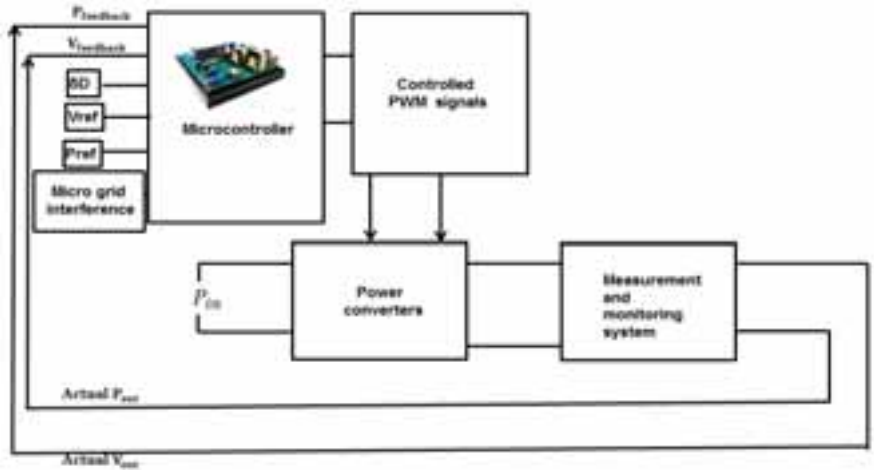

Fig. 7: The implemented control system to apply the correct duty cycle for regulating the voltage.

4. Simulation Results

The spikes and oscillations are detected in the voltage due to the usage of inductance and capacitance in the DC/DC power conversion and on the load side. The lower switching frequency created the higher ripples in the power supply because of the DC/DC buck converter and control system implementation in the electric vehicle charging terminal is featuring to supply the converted and regulated voltage to the electric vehicles. It is noticed that the higher inductance values reduing the losses and created lower ripples currents and to removes the transients low pass filter are used that are improving the sum of power flow relates to the numbers of vehicles being charged up at the electric-vehicles charging station. The losses in the entire

system are very lower due to the shorter length of the transmitted conductor. At the start of the simulation, a transient in the voltage is noticed due to charging up of inductance, the capacitance in the converters and in the line. Power availability is maintained constantly at the electric-vehicle charging station irrespective of changes in temperature/irradiance at the solar charging station. The controllable bidirectional converter is maintaining the power on the EV charging terminal and charges up the storage system. To measure the power flow, measurements components are used at several points of the system. The circuit breaker is used to protect the system from the faults and short circuit current. The system is enabling the electric-vehicles to be charged up all the time from the terminal.

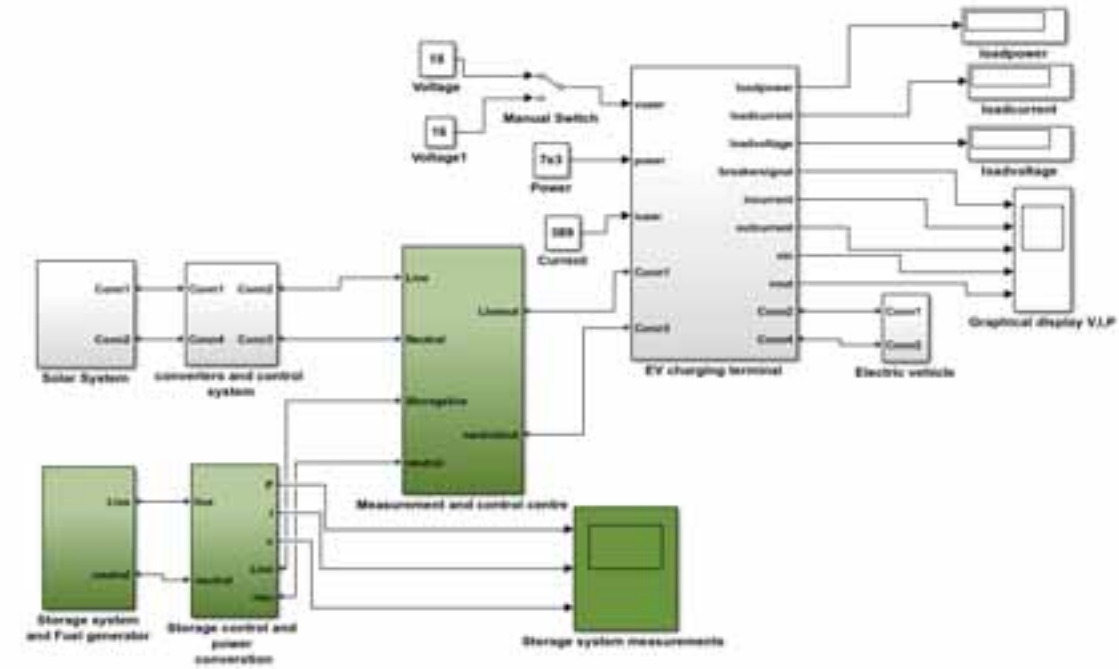

Fig. 8: The simulation model of the complete system.

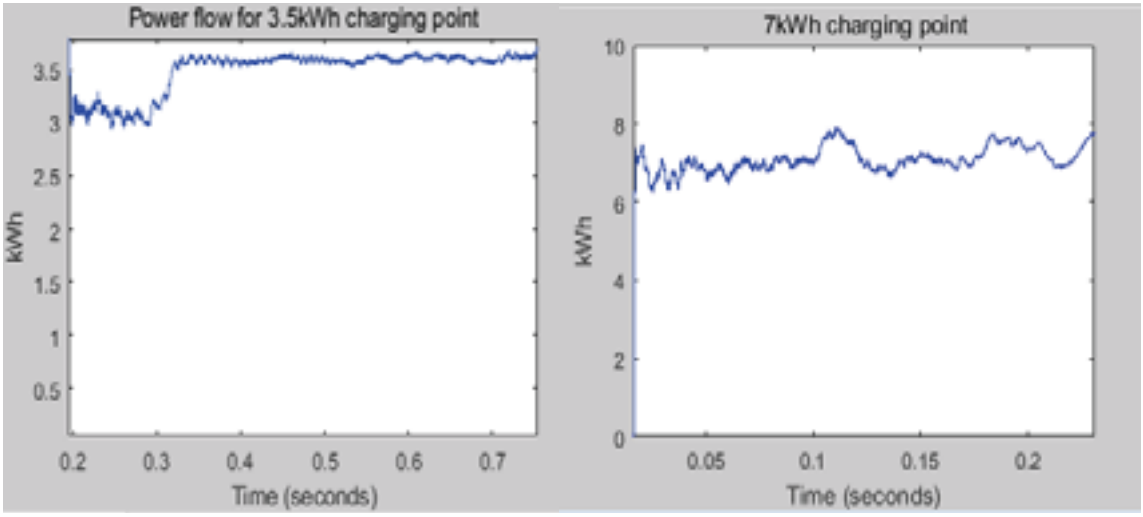

(a) **(b)**

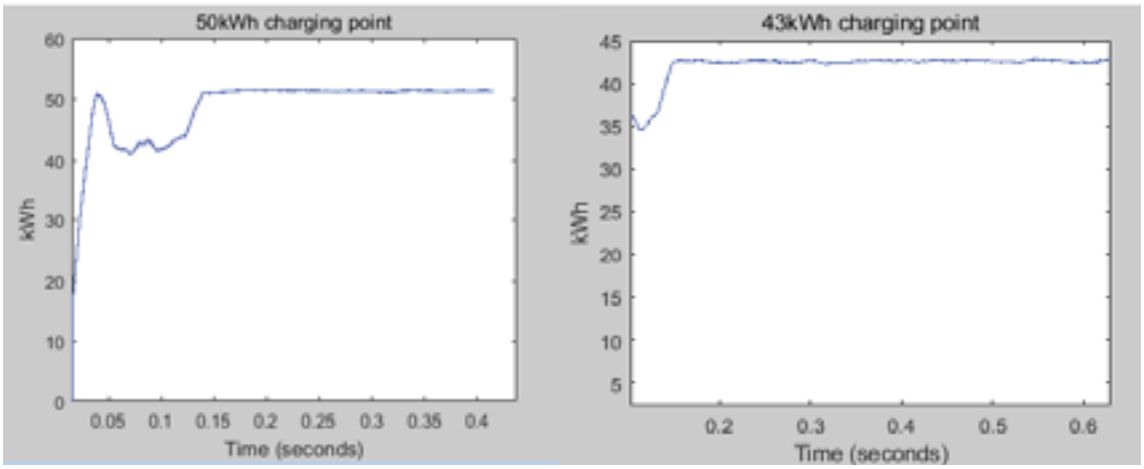

(c) (d)

Fig. 9: Illustrates the power consumption at the electric-vehicle charging station during the fully operational mode. (a) Power utilised by 3kWh charging point from the solar power system. (b) shows the 7kWh charging point power consumption. (c) Energy consumption by 50 kWh charging point. (d) Energy used by 43kWh charging point.

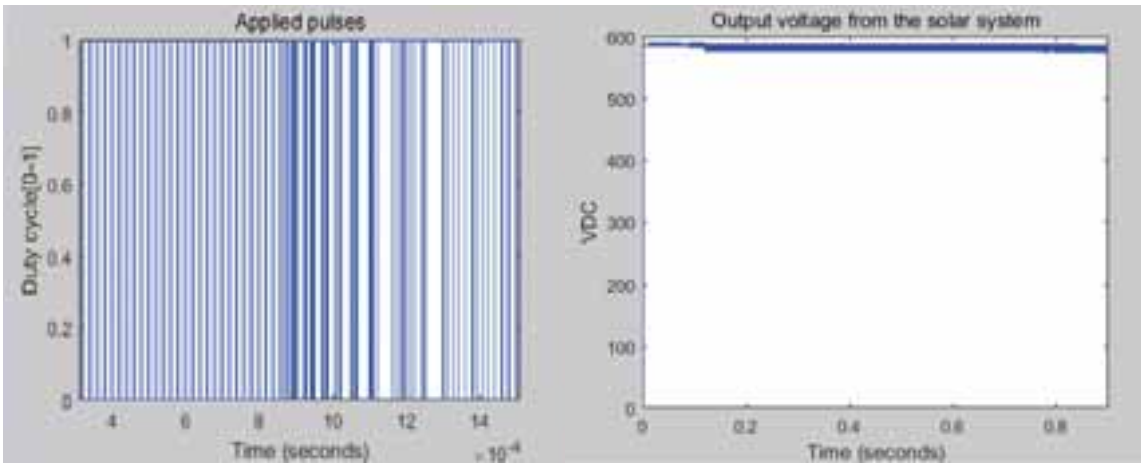

(a) (b)

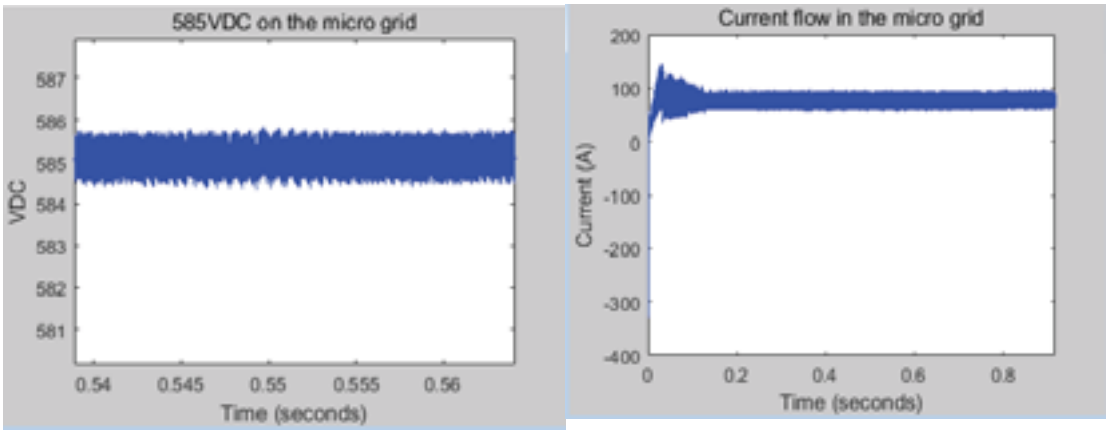

(c) (d)

Fig. 10: The voltage regulation achieved at the charging terminal from solar system/storage system. (a) Duty cycle applied to stabilise the fluctuated voltage from the solar system (b) 585VDC on the microgrid. This is controlled voltage from the solar system (c) The oscillations in the voltage level. (d) Current flow analysis on the simulated system.

5. Conclusion

A solar energy based electric-vehicle charging station is proposed in this paper. The proposed system is capable of managing the regulated voltage to supply the required energy during the peak/off-peak times. The applied electrical control techniques improve the voltage performance irrespective of the intermittent solar energy due to the changes in irradiation/temperature. The applied electrical control system is the advancement of maximum power point tracking algorithm based incremental conductance. The advancement is the addition interference between the solar, storage and fuel based energy generation system with the micro grid control centre and the application of higher frequency to achieve the quality results. The regulation in voltage is achieved by applying the correct duty cycle to the DC/DC power converter switches where the spike/oscillations and transients are minimised by using the low pass filters. It is found that losses in the system are reduced to 1% due to shorter transmission conductor length and lesser implementation of power converters After examining the simulation results, it is concluded that DC high voltage based electric-vehicle charging station reduces the charging time for the batteries of the electric vehicle. The simulation results are validated by the mathematical modelling and theoretical analysis. During the normal environmental conditions, the solar system has generated the electrical energy at full capacity that is considered to be sufficient for the EV charging station. The direction of future work is to incorporate the communication system at the electric-vehicle charging station to examine the energy flow from the solar/storage system. This communication should be linked with the smart sensors that are implemented at several points such as DC/DC solar converter, DC/DC storage converters and at the grid. This will improve the protection for the EV charging terminal during the disturbances from solar/storage or at the converters.

6. References

Cheng, L., Chang, Y. and Huang, R., 2015. Mitigating voltage problem in distribution system with distributed solar generation using electric vehicles. IEEE Transactions on Sustainable Energy, 6(4), pp.1475-1484.

Dubarry, M., Devie, A. and McKenzie, K., 2017. Durability and reliability of electric vehicle batteries under electric utility grid operations: Bidirectional charging impact analysis. Journal of Power Sources, 358, pp.39-49.

Guan, J.C. and Chen, B.C., 2017. Adaptive Power Management Strategy for a Four-Mode Hybrid Electric Vehicle. Energy Procedia, 105, pp.2403-2408.

Han, J., Kum, D. and Park, Y., 2017. Synthesis of predictive equivalent consumption minimization strategy for hybrid electric vehicles based on closed-form solution of optimal equivalence factor. IEEE Transactions on Vehicular Technology.

Liu, H. and Sun, J., 2014. Voltage stability and control of offshore wind farms with AC collection and HVDC transmission. IEEE Journal of Emerging and selected topics in Power Electronics, 2(4), pp.1181-1189.

Shaaban, M.F., Eajal, A.A. and El-Saadany, E.F., 2015. Coordinated charging of plug-in hybrid electric vehicles in smart hybrid AC/DC distribution systems. Renewable Energy, 82, pp.92-99.

Shen, J., Dusmez, S. and Khaligh, A., 2014. Optimization of sizing and battery cycle life in battery/ultracapacitor hybrid energy storage systems for electric vehicle applications. IEEE Transactions on industrial informatics, 10(4), pp.2112-2121.

Sheng, M., Zhai, D., Wang, X., Li, Y., Shi, Y. and Li, J., 2017. Intelligent Energy and Traffic Coordination for Green Cellular Networks With Hybrid Energy Supply. IEEE Transactions on Vehicular Technology, 66(2), pp.1631-1646.

Tan, L., Wu, B., Rivera, S. and Yaramasu, V., 2016. Comprehensive dc power balance management in high-power three-level dc–dc converter for electric vehicle fast charging. IEEE Transactions on Power Electronics, 31(1), pp.89-100.

Yu, H. and Stuart, A.L., 2017. Impacts of compact growth and electric vehicles on future air quality and urban exposures may be mixed. Science of The Total Environment, 576, pp.148-158.

Yong, J.Y., Ramachandaramurthy, V.K., Tan, K.M. and Mithulananthan, N., 2015. Bi-directional electric vehicle fast charging station with novel reactive power compensation for voltage regulation. International Journal of Electrical Power & Energy Systems, 64, pp.300-310.

Zhang, N., Hu, Z., Dai, D., Dang, S., Yao, M. and Zhou, Y., 2016. Unit commitment model in smart grid environment considering carbon emissions trading. IEEE Transactions on Smart Grid, 7(1), pp.420-427.

IMPROVING THE UTILIZATION FACTOR OF ISLANDED RENEWABLE ENERGY SYSTEMS

Mark A. Stambaugh[1], Alex Zahnd[2], Rick Sturdivant[3], and James Yeh[3]

[1] RIDS-USA, Post Falls, ID, USA

[2] RIDS-Nepal, RIDS-Switzerland, Nepal/Switzerland

[3] Dept. of Eng. and Computer Science, Azusa Pacific University, Azusa, CA, USA

Abstract

Although all energy produced by grid-tied renewable energy systems can be delivered to the grid for consumption by a wide user base, energy delivered by an islanded renewable energy system is limited by the time varying consumption of those served. A set of metrics is proposed to better evaluate this impact on the economic value of the system. This impact can be very significant in developing countries.

Smart systems can reduce energy consumption during periods of high demand through load shedding, but this technology is expensive and unproven in the context of a developing country. Smart systems typically do not add loads during periods of low demand, partly due to the incremental cost of electrical energy from non-renewables. A prioritized dump load control scheme is proposed that strategically diverts excess energy in a 100% renewable energy system to a set of loads useful to the community, first to satisfy the needs of the most valuable use, then to the next most valuable use, etc. A low cost architecture including hardware and software is introduced as a means to implement this scheme, appropriate in the context of developing communities so their economies can more rapidly evolve.

Keywords: 100% Renewables; Hybrid renewable energy system; Islanding; Pico-Hydro; Prioritized Dump Load; Holistic Community Development

1. Metrics Used to Evaluate Performance of Islanded Renewable Energy Systems

Renewable energy systems powered by 100% renewable resources do not run continuously at full capacity due to maintenance, variable weather conditions such as wind and solar irradiance, and variable availability of water to run hydro turbines. Utilization factor k_u is defined (Sivanagaraju and Sreenivasan, 2010) as the energy generated divided by the plant capacity (nameplate kW power rating) integrated over a period of time. It is used to evaluate the design and operational performance of an energy system, to derate its benefits, and to determine its unit cost through an economic life cycle cost analysis over the power plant's lifetime. According to Bhattacharyya (2013) the utilization factor of micro/mini hydro systems in India can be low due to the unavailability of sufficient water during the dry season versus what is available during the monsoons.

Renewable energy producers can usually deliver all their available power if connected to a large scale utility grid. Conversely, renewable energy producers in an islanded system can deliver no more than what can be consumed at that time, assuming we consider energy storage as a load while being charged. Either energy production must be reduced in times of low consumption, or excess energy must be dissipated in dump loads. Solar energy production is reduced by letting the operating voltage rise from its maximum power point toward V_{OC}. Wind and hydro energy production is typically reduced through braking, regulating the supply of water, or by diverting excess energy to dump resistors heating air or turbine exhaust water, with no use to the users. The latter, shown in Figure 1, is very common in Nepal for micro and pico-hydro systems.

doi:10.18086/swc.2017.16.04 Available at http://proceedings.ises.org

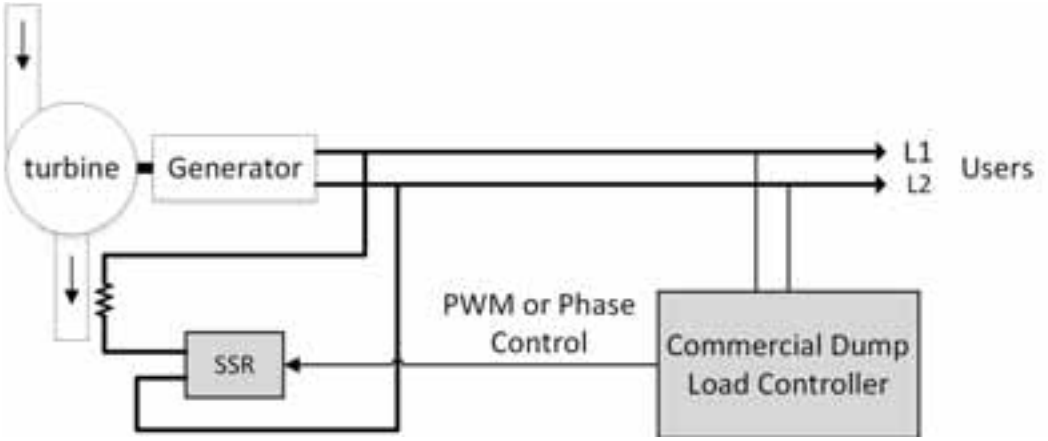

Fig. 1: Traditional Diversion in Pico or Micro Hydro Facilities in Developing Countries

Fig. 2: Traditional water heater "dumb" dump load in MHP (micro-hydro-power) plant in Nepal

Fig. 3: Resistive water heater elements are used to dissipate energy into the turbine's exhaust water.

The value of an islanded renewable energy system must be derated by any diversion or reduction in production required during times of low demand. Although this could be lumped into the utilization factor k_u, that would hide the impact of limited demand. Therefore, two new measures are introduced, the 'production factor' k_p, and the 'consumption factor' k_c.

The production factor k_p is defined as

$$k_p = \frac{E_p}{P_{capacity} * T} \qquad \text{(eq. 1)}$$

Where E_p is the islanded system's energy (MJ) that could have been produced at the pertaining meteorological and environmental conditions if consumption was unconstrained. $P_{capacity}$ is the nameplate power rating of the system. T is the time k_p is evaluated over.

The consumption factor k_c is defined as

$$k_c = \frac{E_d}{E_p} \qquad \text{(eq. 2)}$$

Where E_d is the energy actually delivered to useful loads.

$$E_d = P_{capacity} * T * k_u \quad \text{for grid-tied systems} \quad \text{(eq. 3)}$$

$$E_d = P_{capacity} * T * k_p * k_c \quad \text{for islanded systems} \quad \text{(eq. 4)}$$

k_p is the derating factor due to limits on power generation due primarily to variable and less than optimum weather and water supply, while k_c is the derating factor due to variable consumption in an islanded renewable energy system.

Sivanagaraju and Sreenivasan (2010) also define the load factor as the ratio of average demand to the maximum demand. Although somewhat related to consumption factor k_c, its denominator is the maximum energy demand, not the demand that could have been supported by the system under the environmental conditions over the evaluation period. Consumption factor k_c is a more appropriate metric to understand the impact of limited consumption.

RIDS-Nepal has been working in the Jumla district in Northwest Nepal since 1996, and has observed that during the day most people are working in the fields, so the value of k_c is so low during these periods that production is not warranted. Indeed, many of the hydroelectric systems in this region are shut down during the day to reduce wear and resulting repair and maintenance costs. Furthermore, RIDS-Nepal has observed that the turbine capacity of many of these systems is considerably more than the peak demand of the village it serves, so they are purposely run with constricted water flow to reduce maintenance and the amount of excess energy dumped into the river as heat. RIDS-Nepal has observed that in some cases the turbines are run at approximately 50% of their capacity while still satisfying the peak load. Furthermore, the village consumption varies over the 16 hours the system operates (4pm – 8am), from near its peak (~45% of capacity) consumption for ~4 hours around dinner (5pm - 9pm), to only ~10% of peak to provide minimal lighting throughout the rest of the day (4pm – 5pm) and night (9pm – 8am).

$$k_c \cong \frac{(0.45*4)+(0.045*12)}{24} \quad \text{(eq. 5)}$$

$$k_c \cong 0.10 \quad \text{(eq. 6)}$$

This surprisingly low consumption factor k_c significantly impacts the sustainability of these systems in several ways. First, the funding of operations and maintenance expenses are more difficult to justify due to the reduced benefits delivered by the system. Second, the reduced utilization during the day, and the resulting shutdown of the system during that period, stymies the economic development needed to ease the burden of the needed tariffs. Indeed, RIDS-Nepal has observed that many of the pico- and micro-hydro systems in this area are in service for only a few months to as much as 2 years maximum until significant maintenance expenses arise, at which time the system becomes inoperable or its performance significantly degrades.

The effect of consumption factor k_c is not limited to hydro and wind renewable energy systems. Once a solar system's batteries are fully charged, any excess production must be curtailed or dumped, reducing k_c. Although not as drastic as the example of hydro systems in the Jumla district described above, it can still be significant.

2. Improving the Consumption Factor in Developing Countries

The developed world is just now addressing the consumption factor k_c through smart metering which can shed optional loads or shift demand to times of low consumption. Although not directly increasing the consumption factor, load shedding allows a higher base load than normally could be supported without brownout, which does directly increase the consumption factor k_c. Unfortunately not all loads are considered to be optional by the consumers, so the impact of load shedding is limited.

Adding demand where there otherwise was little, which we'll call "Load Adding" as opposed to "Load Shedding", is not normally used, partly due to the incremental cost of electricity with non-renewable energy sources.

Many micro-grids in the developing world are powered by 100% renewables since hydrocarbon-based fuels are so expensive, especially considering transportation costs. 100% renewable energy sources have an exceedingly low incremental cost of electricity delivered, assuming system capacity isn't exceeded. Incremental energy

utilization is also very valuable in developing nations, for example to help solve basic needs such as:

- Powering pumps to supply clean water or irrigation
- Heating water for hygiene and cooking
- Maintaining the temperature of the slurry in a high-altitude biogas digester to the needed mesophilic (~25°C - ~40°C) or even thermophilic conditions (~40°C - ~60°C) for optimum performance
- Refrigerating fruit for long term storage
- Heating air and powering grow lights in greenhouses to provide year-long nutrition.

This list is not exhaustive, and each village will have to determine the most valuable uses of this excess energy based on their particular needs. Due to low incremental cost and the high value of energy utilization, load adding not only can, but should, be used in islanded pic/micro-grids in developing countries.

3. Prioritized Useful Dump Load Control

Given the number of potential uses for inexpensive, excess energy in the developing world, some mechanism is needed to ensure that the energy is routed to the most valuable load. Due to the dynamic nature of the consumer load profile, the mechanism has to be automatic, with no required decision making by distributed customers to turn useful loads on and off. Because production and consumption are already being balanced in many islanded systems, usually by heating water in dump loads useless to the users, the prioritization of a set of useful dump loads is pursued in this paper.

3.1 Simple Useful Dump Load Control

Figure 4 shows the schematic of a low cost and context-appropriate scheme using ubiquitous water heater thermostats to route excess power to the highest priority useful load needing power as determined by the temperature setting of the thermostat mounted to the water bath associated with that load. For example, thermostat TH1, solid state relay SSR1, and water heater element WHE1 are the components needed to support the highest priority useful dump load. For example, WHE1 and TH1 might be mounted to a hot water tank in a community bathing facility. Similarly TH2, SSR2, and WHE2 are needed to support the next highest priority useful dump load, and SSR3 and WHE3 would be needed to support the lowest priority load which must be able to absorb all available power.

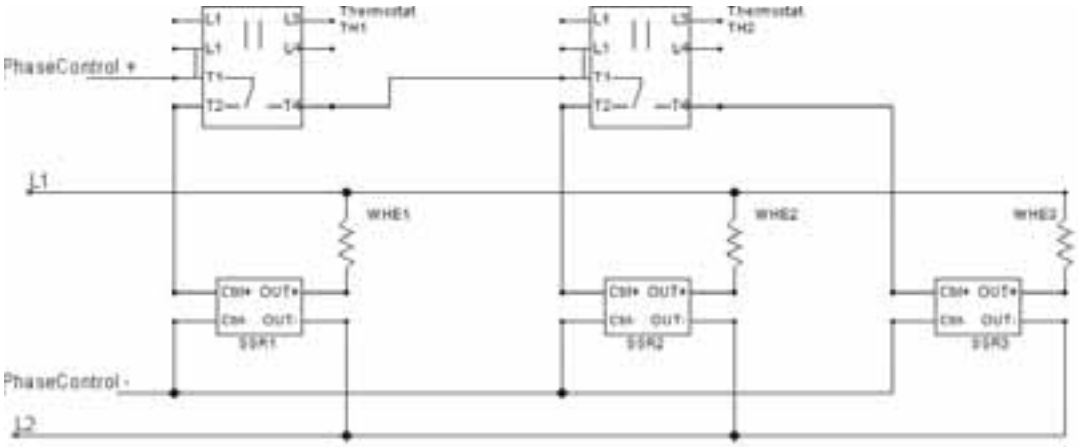

Fig. 4: Example Hardware Architecture of Simple Dump Load Control

This scheme can utilize a high percentage of all the available power generated by a 100% renewable energy system during periods of low consumption in the village served. This helps justify operation of the system 24 hours a day, increases the value of the facility, provides consistent energy to drive economic development, and helps the local population justify the funds needed to maintain the system. This scheme routes excess energy to

a set of useful dump loads, starting with the highest defined priority load needing power, and shifting power to the next highest priority load once the first useful dump load is met, e.g. the water is hot enough, etc. Conceptually there is no limit to the number of useful dump loads that can be included to obtain values of k_c approaching unity, a 10x improvement over the k_c seen by RIDS-Nepal in Northwestern Nepal.

This scheme's primary advantage is its simplicity and use of ubiquitously available hardware. However, water heater thermostats are not particularly accurate, have significant fixed hysteresis, and have limited range making them inappropriate for regulating the temperature in some applications, e.g. the lower limit of most hot water thermostats is too high for heating a greenhouse. Furthermore, the priority and temperature thresholds cannot practically be adjusted throughout the day and seasons. All these disadvantages can be addressed with a programmable dump load controller.

3.2 Programmable Useful Dump Load Control

The temperature accuracy, hysteresis, and range issues can be addressed by using electronic temperature sensors on the water bath associated with each useful dump load. Temperature sensors utilizing a DS18B20 integrated circuit are inexpensive, ubiquitous, reliable, and accurate. They are easily connected to a wide range of microcontrollers using the 1-wire serial interface standard. Figure 5 shows a hardware architecture implementing such a system.

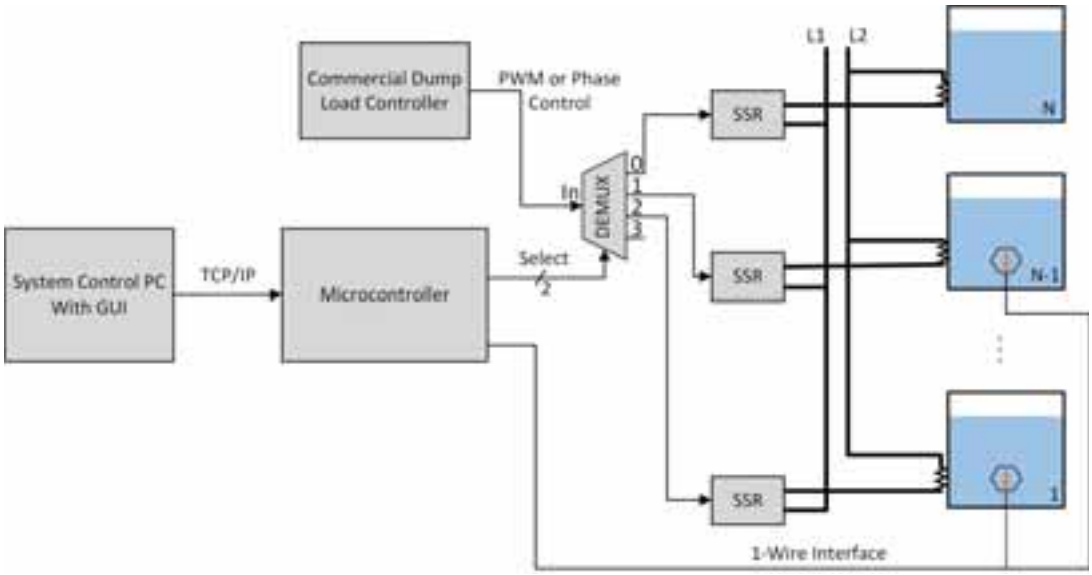

Fig. 5: Example Hardware Architecture of Programmable Dump Load Control

Figure 6 shows an example of the software architecture in the programmable controller. Grey objects are included to show how the firmware entities map to hardware.

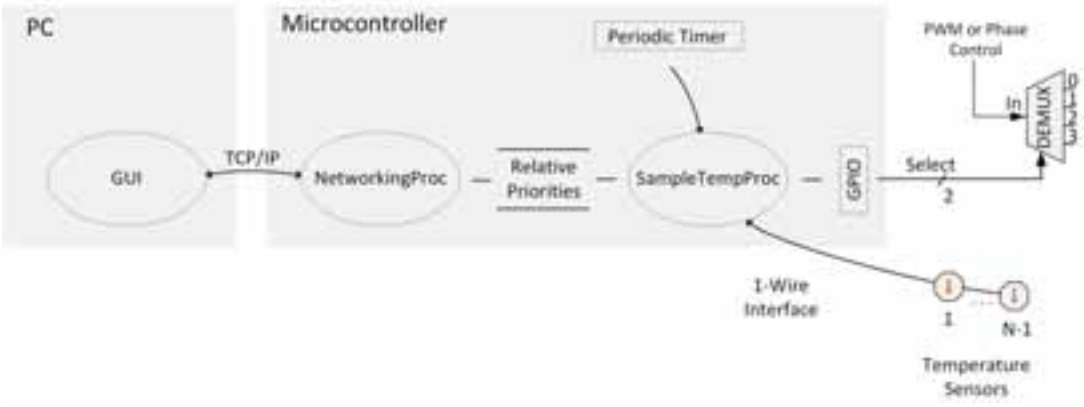

Fig. 6: Microcontroller Firmware Architecture

The PWM or phase control signal from the commercial dump load controller is used to modulate the amount of power consumed by the useful dump loads. Useful dump loads on either DC or AC lines can be supported with the selection and configuration of the appropriate commercial dump load controller and SSRs.

A System Control PC, located at a convenient place in the village such as the pay-as-you-go vending office, provides a GUI used to specify the relative priority and temperature thresholds of the various useful dump loads using a time, date, and/or season schedule. This schedule can be easily modified by local operators based on village requirements. The current prioritization and threshold information is communicated over a TCP/IP communication channel to the NetworkingProc process on the microcontroller. The use of TCP/IP allows this microcontroller to reside close to the useful dump loads, while the PC and GUI can be at a location more convenient to the villagers.

All useful dump loads incorporate a temperature sensor except the lowest priority one which must be able to continuously absorb all potential excess power. For example resistive elements could be included in greenhouses to heat the air or soil by several degrees. There are a large number of rugged, waterproof, and low cost temperature sensors available utilizing the DS18B20 temperature sensor IC. Their accuracy is typically 0.5 to 1 °C which should be quite acceptable and much more accurate than thermostats used in hot water heaters. Although the 1-wire serial interface is slow, the temperature of the water bath or air associated with each load changes slowly, so the sensors can be sampled at a relatively slow periodic rate by the SampleTempProc process. This process determines the highest priority dump load needing additional power, and updates a set of GPIO pins to drive the 'Select' value to the demultiplexer (DEMUX) as shown in figure 5. The demultiplexer routes the PWM or phase control signal to the appropriate SSR.

1-wire interface drivers are available for many microcontrollers. Hysteresis can be controlled programmatically based on village input via the GUI.

Figure 5 only shows dump loads utilizing tanks of water and water heater resistors, suitable for a wide range of useful loads including hot water for bathing and cooking, and to stabilize a biogas digester at its optimum temperature. However, other loads can also be used since the DS18B20 thermometers are accurate over a wide range and can measure other substances including soil or air. For example, a solid state refrigeration unit could be used to maintain the temperatures of apples in cold storage.

Fig. 7: Warm/hot water as "useful" dump load for improved personal hygiene, very welcomed in cold areas.

Fig. 8: Heating water for increased anaerobic process in the production of biogas and heating a high-altitude greenhouse.

4. Summary

The current utilization factor for many pico and micro hydro systems in Northwest Nepal is a surprisingly low value of around 10% based on observations by an NGO working in the area, RIDS-Nepal. This low utilization significantly impacts the benefits of the systems making it difficult for the villagers served to grow economically and to maintain and operate them.

Two different 'smart' dump load control schemes are described that can utilize the energy that would otherwise be wasted. One scheme using hot water heater thermostats is extremely simple, inexpensive, and context-appropriate. However, it hard-wires a fixed prioritization among the loads and suffers from fixed hysteresis and relatively poor temperature accuracy. The other scheme uses a small microcontroller, DS18B20 based temperature sensors, a PC-based GUI, and SSRs. It removes the limitations of the water heater thermostat implementation. Although more complex than the simple scheme, it is still context-appropriate.

RIDS-Nepal is planning to implement the microcontroller-based solution in a pico-hydro facility in the village of Moharigaun in the Jumla district of Nepal. Useful dump loads will be used:

- To heat bathing water for showers and personal hygiene to eradicate the most common skin sicknesses
- To maintain the temperature of a high-altitude biogas digester for an increased anaerobic process under mesophilic (~25°C - ~40°C) or even thermophilic conditions (~40°C - ~60°C)
- To heat water to reduce the amount of wood needed to cook rice and tea
- To heat and power grow lights in a greenhouse to improve year-round nutrition.

Extensive monitoring will be employed to quantitatively measure the impact of the prioritized dump load control scheme.

Fig. 9: The village of Moharigaun in the remote North-East of the Jumla district of Nepal will use a variety of useful dump loads

5. References

Bhattacharyya, Subhes, 2013, Rural Electrification Through Decentralised Off-grid Systems in Developing Countries. Springer, London.

Sivanagaraju, S., Sreenivasan, G., 2010. Power System Operation and Control. Dorling Kindersley, Noida, India.

REVIEW OF SOLAR ENERGY INCLUSION IN AFRICA: CASE STUDY OF NIGERIA

[1#]Ukoba, Kingsley; [1]Eloka-Eboka, A.C and [1]Inambao, F.L

[1]University of Kwazulu-Natal, Durban, (South Africa)

[1#]ukobaking@yahoo.com

Abstract

This work reviews solar energy inclusion in Africa using Nigeria as a case study. It reviewed studies made on viability, challenges and solutions associated with making solar energy a viable energy option in Nigeria. The study highlighted data on current industry capacity of solar energy, installed PV capacity, and solar energy application distribution. It sheds light on solar energy initiatives and projects in Nigeria and solar energy capacity development in Nigeria. Success stories of solar energy and solar cell fabrication in Nigeria are presented. Existing government policies and legislation are discussed. The authors consider the challenges faced and the current and future prospects of solar power in Nigeria, and make recommendations regarding the speedy and seamless inclusion of solar energy in Nigeria and Africa as a whole.

Keywords: solar, domestication, Nigeria, energy, Africa

1. Introduction

Sub-Sahara Africa is home to about 85 % of the 1.3 billion people in developing countries without access to electricity [1], with an estimated electrification rate of 64 % in urban and 13 % in rural areas [2]. Sub-Sahara Africa has many of the world's least electrified nations [3, 4]. A total of 70 % of such those without access to electricity reside in countries like Nigeria where the rural populace is mostly affected [5]. Nigeria is ranked seventh in world population and cannot provide electricity access to her populace both in the urban and rural areas [6, 7]. Nigeria's rural population is estimated to be about 42 % of the total population [8]. Over 60 % of the Nigerian population does not have power supply, with 40 % not on the nation's grid [9, 10]. The Nigerian grid supply of electricity is on average six hours per day rationed among inhabitants of the cities [11]. Almost all rural dwellers in Nigeria have little or no access to electricity. The majority of the electricity supply in Nigeria is generated by Kainji dam which produces about 3.2×10^8 W and 9.6×10^8 W at its peak [12, 13]. This is due to underperforming hydro dams in the country. Another factor is the high cost of distribution across the country which covers an area of 924 000 km^2 [14]. There is no uniformity in distribution of grid connection and electricity in Nigeria. About 61.2 % of households in Lagos in South-West are without access to electricity. The figure is different in Taraba in North-East where 81.3 % lack access to electricity [15]. Similarly, South-South have 61.2 % and South-East has 60 %. About 38.1 % of the rural population, 12.1% of the rural poor and 29.8% of the urban poor in Nigeria have access to electricity [16].

Erratic power supply has caused many of the inhabitants and companies in Nigeria to generate their own power. Nigeria has about 32 outages in a month with over 35 hours' outage of electricity supply [17]. Figure 1 shows the electrical outages per month and average duration in Africa [18]. Erratic supply is due to high energy losses caused by physical deterioration of the facilities for transmission and distribution, and theft of power equipment. Other causes are vandalism, the high cost of electricity production, insufficient metering system and ease of by-passing of the metering system by the consumers, poor billing system and low available capacity (only 40 % of the installed capacity of 6 000 MW) [19].

Individuals have resorted to using generators powered by petroleum fuel or diesel. This accounts for the increase in the price of petroleum products price by 70 % in 2012 [20]. The cost of generators has risen on a regular basis from 5.8 % in 2007 to 7.6 % in 2009 [21]. Generators also increase environmental pollution [22]. Electricity access has direct links to clean drinking water, good health and agricultural activities for rural dwellers [23, 24]. The lack of electricity has created, and is still responsible for, high levels of underdevelopment and poverty in the rural areas [25, 26]. Several studies attest to the fact that stable and affordable electricity contributes to higher levels of economic development [27-33].

doi:10.18086/swc.2017.16.05 Available at http://proceedings.ises.org

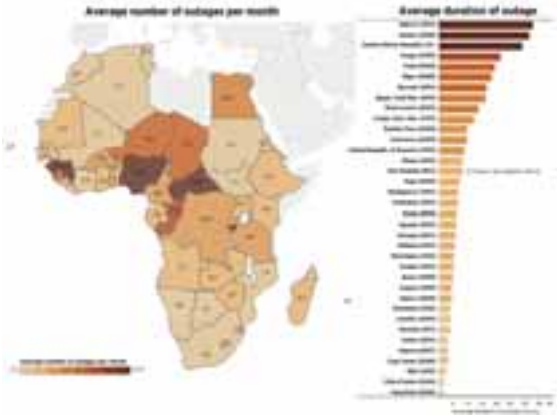

Fig. 1: Electrical outages per month and average duration in Africa [18]

Renewable energy is a tool that can end global electricity problems because supply exceeds world electricity demand [34]. It is an energy source that can be renewed indefinitely. Renewable energy sources include solar, ocean tides, geothermal, wind, hydro, and biomass [35-37]. They are used as electricity, thermal energy, fuels, mechanical force and hydrogen. These energy sources are obtained from non-fossil and non-nuclear sources [38]. They are sustainable and not harmful to the environment. Table 1 shows the vast potential of solar energy inclusion in Nigeria, shedding light on Nigeria's solar energy resources. From the data in Table 1 one can see that Nigeria only needs 0.1 % of the total solar radiation converted at 1 % efficiency to be able to meet her energy demand [39]. On average, Nigeria gets solar radiation of 20 MJ/m^2/day with minimal variation all year.

Tab. 1: Nigeria's solar energy resources [39]

Resource type	Reserves		Production	Domestic utilization
Natural units	Energy units	Energy units (BTOE)		
Solar Radiation	3.5 KWh/m^2/day to 7.0 KWh/m^2/day (4.2 million MWh/day using 0.1% Nigeria land area)	5.2 (40 years and 0.1% Nigeria land area)	Approximately 6 MWh/day solar Photovoltaic	Approximately 6 MWh/day solar Photovoltaic

Power generation involves the conversion of energy from an available source (sun in this case) to electrical energy in a form that is suitable for distribution, consumption and storage [40]. Solar PV is capable of powering off-grid single homes, and mini-grids incorporating from several kW to many MW [18]. Power generation using solar energy can be done in two ways, namely, solar-thermal conversion [41] and solar electric (photovoltaic) conversion [42]. Solar energy is one of the renewable energy endowments of Nigeria [43]. It can be used for powering remote villages disconnected from the nation's grid and its power can also be fed into the national grid [44]. Solar energy is used in rural clinics, powering of schools, vaccine refrigeration, street lighting, traffic lights, kiosks, among others. Solar technology is gradually being implemented in Nigeria. It is already implemented for solar crop drying, solar incubators, solar chick brooding, solar evaporative cooling and so on.

Renewable energy is capable of solving Nigeria's energy challenges [45, 46]. Several studies have looked at the viability and challenges of implementing solar energy in Nigeria. Chilakpu [47] examined renewable energy sources benefits, potentials and challenges in Nigeria. The study stated that renewable energy improves the security of a country, and reduces greenhouse gases. The study aligned with Körbitz [48] in stating that renewable energy reduces greenhouse gases by at least 3.2 kg carbon dioxide equivalents per one kilogram of biodiesel. The study observed that the challenges working against the full-scale implementation of solar energy in Nigeria include available technology, the political climate, and the weather conditions of the country. Körbitz study dwells

most on hydropower and fails to shed light on other renewable energy sources, especially solar energy. Olaoye et al. [49] studied the energy crisis in Nigeria and suggested a renewable energy mix as a solution. Attention was given to the installed capacity and licensing of on-grid power generation companies. The study provided two tables which summarized the renewable energy potential of Nigeria. The data provided is limited to the capacity of solar PV panels in Nigeria. Ajayi and Ajanaku [50] examined the energy challenge and power development in Nigeria and proposed a way forward. The study suggested that 80 % of hydropower in the country is untapped, and 5.5 KW-hr/m^2/day of solar radiation is not being utilized as well as unexploited wind energy resources and the gases being flared. The study believes that utilizing these resources will put an end to the energy challenge of Nigeria. Akinboro et al. [51] studied solar energy installations in Nigeria in terms of their prospects, problems and solutions. The study set out to study the use of solar energy as an alternative energy source in Nigeria. Emphasis was on stand-alone and hybrid installations and the problems encountered during domestic and industrial solar installation. In the end, the study was only able to enumerate the challenges confronting the implementation of solar energy, its prospects and possible solutions. However, the study shed light on waste generated from gas turbines, diesel plants, solar plants, biogas plants, nuclear and small hydropower plants. There was no mention of solar installations as stated in the beginning of the study. Ezugwu [52] discussed renewable energy in Nigeria with a focus on their sources, problems and prospects. The study was able to theoretically discuss the key renewable energy sources but lacked relevant data regarding Nigeria. Emodi and Yusuf [53] discussed the need for standardization of renewable energy technologies in Nigeria. They opined that renewable energy technologies are imported into Nigeria and there are no existing local standards. The study recommended standardization as a solution to check the influx of renewable energy technologies into Nigeria. Ikem et al. [54] studied integration of renewable energy sources into the Nigerian national grid as being a way out of the power crisis. It suggested a way forward for Nigeria's government to improve the current power supply of the country by investing in renewable energy. The study encouraged the government to review the power sector. Ozoegwu et al. [43] studied the status of solar energy integration and policy in Nigeria. It did a good job in reviewing the past, the current and future status of solar integration in Nigeria. It was able to combine several data related to solar energy in Nigeria. This provided a firm basis for the case of giving solar energy a high priority in mitigating the energy problem of Nigeria. Table 2 grouped the different categories of solar PV applications under different headings.

Tab. 2: Categories of Solar PV applications (adapted from [18])

Item	**Stand-alone**			**Grids**		
	DC		**AC**	**AC/DC**		**AC**
System	Solar lighting Solar kits or system lanterns	DC	AC solar system: single-facility AC systems	Nano-grid grid Pico-grid	Micro-Mini-	National/regional grid
Application	**Off-grid**			**Off-grid or on-grid**		**On-grid**
	Lighting	Lighting and appliances	Lighting and appliances	Lighting and appliances, emergency power	All uses (including industrial)	All uses (including industrial)
Key component	Generation, storage, lighting, phone charger	Generation, storage, DC special appliances	Generation, storage, lighting, AC appliances, building wiring	Generation plus single phase distribution	Generation plus three phase distribution	Generation plus three-phase distribution plus transmission

Typical size	0.10 W	11 W to 5 kW	100 W to < 5 kW	5 kW to 1 MW	Residential (100 W to < 5 kW) Mini grid (5 kW to < 1 MW) and Utility scale (> 1 MW)

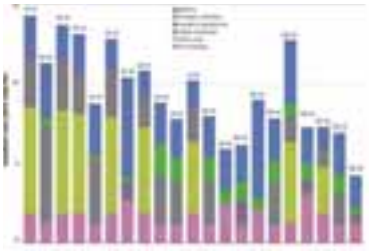

Fig. 2: Small solar system (<1 kW) cost breakdown by cost component, 2012-2015 [18]

Figure 2 presents the cost breakdown for sub-1 kW where the data are available. Battery costs account for the largest single share of these Small Household Solar Supply (SHS), with a simple average of 29 % of the total costs (USD 2.7 /W). The PV modules themselves, as well as the lighting fixtures and wiring, average around 20 % (USD 2.2 /W) of the total installed costs together, soft costs 22% (USD 2/W), other hardware 21% (USD 2 /W) and the charge controller 7% (USD 0.7/W).

Several researchers have proposed various ways in which the technology of solar can be used in Nigeria. This includes but is not limited to the following: Cota et al. [55] proposed the use of solar energy for street lighting and water pumping in the rural community of Igbelaba and Jigawa state. Kumar et al. [56] presented suggestion for replacing the usage of fossil fuel energy with solar energy for street lighting of Fugar city in Edo state of Nigeria. Ike Chinelo et al. [57] suggested the use of solar to power security lights in school hostels in Nigeria.

1.1 Data on solar energy capacity in Nigeria

The industry capacity of solar energy was a total of 33 active companies by 1999. There are no vendors or contractors for the supply and installation of solar equipment. Nigeria cannot boast of a company that manufactures the major components of solar systems, not even the basic solar cells [58]. However, NASENI assembles PV panels in Karachi, close to Abuja. Nevertheless, the country can boast about 200 installed solar PV installations with a capacity of about 3.5 kW to 7.2 kW [59]. This is insignificant when compared with the population of Nigeria and installed capacity in other Africa countries like South Africa. Figure 3 provides a vivid picture of installed solar PV capacity in watts per capita in Africa in 2015.

A survey was conducted in the northern part of Nigeria to show the application distribution [58]. It shows that domestic water pumping accounts for 57%, domestic lighting and rural for 8%, experimental room air conditioning for 1%, rural clinic refrigeration of clinic items like vaccines and lighting of the clinic and surrounding for 24%, and communications (TV and radio) for 10% (see Table 3).

In terms of installed PV in regions of Nigeria, Lagos has the highest with 23.6% closely followed by Yobe state with 16.3%. Kano and Akwa Ibom have 8.6%. The funding of such installations is principally by the federal government, state, local government, and international donors like the European union, Mobil and in some states like Lagos by private individuals. There are about one or two PV installations working or moribund in the 26 states out of the 36 states in Nigeria including the capital Abuja [59].

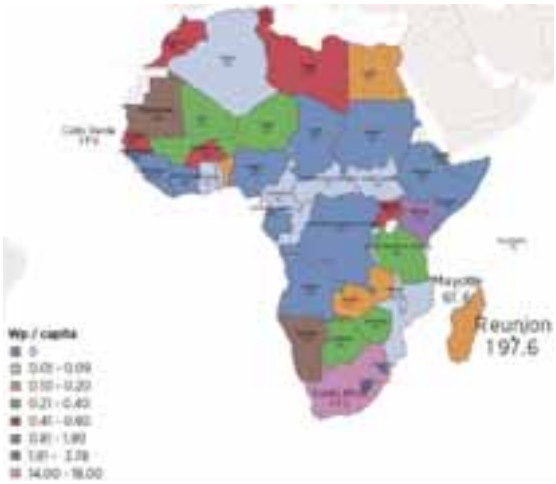

Fig. 3: Map of installed solar PV capacity in watts per capita, 2015

Tab. 3: Installed capacity of PV technology in Nigeria [59]

S/N	APPLICATIONS	PV CAPACITY (%)
1.	Residential (mostly lighting)	6.9
2.	Rural electrification and Television	3.9
3.	Commercial lighting and equipment	3.1
4.	Street, Billboard and other lighting	1.2
5.	**All lighting**	15.1
6.	Industrial	0.4
7.	Health center/clinic	8.7
8.	Telecom and radio	23.6
9.	Water pumping	52.2
	Total	**100**

2. Solar Project initiative in Nigeria

Some striking projects on solar energy have been executed in Nigeria. The Jigawa state government embarked on a project of rural electrification of the state [60]. This was funded 60 % by the United States government through USAID and department of Energy (DOE) and 40 % by the Jigawa state government. This project demonstrated inclusive solar usage for electricity generation in rural communities. The project targeted water supply, education, health, agriculture, security, opportunities for trade and commerce [61]. Several PV water pumping, electrification, and solar thermal installations have been executed by Sokoto Energy Research Center (SERC) and the National Center for Energy Research and Development (NCERD) under the supervision of the Energy Commission of Nigeria (ECN) [62]. A breakdown of the pilot projects by ECN include the 7.2 kWp solar-PV village electrification in Kwalkwalawa in Sokoto state, 1.87 kWp village electrification and TV viewing centre in Iheakpu, 1.5 kWp water pumping scheme in Nangere, Sokoto state. Solar dryer projects in Nigeria include: 2-tonnes solar rice dryer in Adani, Enugu state and 1.5 tonnes solar forage dryer in Yauri, Kebbi state.

The World Solar Programme designed for promotion of solar energy penetration worldwide has also provided about five high priority projects in Nigeria. They are; (i) the solar village; (ii) the upgrading of facilities and personnel of renewable energy R & D establishments, and development of renewable energy curricula; (iii) training workshops and colleges in renewable energy technologies (solar-PV and solar-thermal); (iv) Rural health

delivery and potable water supply using solar-PV; and (v) International Solar Energy Institute. The projects are threatened by inadequate funding. As a result, only projects (i) and (iv) have made significant progress.

2.1 Solar energy capacity development in Nigeria

The federal government of Nigeria has mandated the ECN with the responsibility to carry out research and development of the nation's energy needs. ECN has two centers dedicated to renewable energy spread evenly in the north and south of the country, namely, the National Centre for Energy Research and Development (NCERD) at Nsukka, in the south of Nigeria, and the Sokoto Energy Research centre (SERC) in Sokoto state, in the north of Nigeria. Apart from the research and development mandate of the centres, they are also responsible for personnel development, dissemination and promotion of renewable and alternative energy technologies. The other government agencies that have renewable energy components in their mandates are: Federal Department of Meteorological Services (FDMS), Power Holding Corporation of Nigeria (PHCN). Others are Project Development Institute (PRODA) Enugu, Nigerian Building and Road Research Institute (NBRRI), Federal and state owned Universities and Polytechnics, and the Federal Institute of Industrial Research, Oshodi (FIIRO), National Centre for Energy Research and Development (NCERD), Nsukka, Centre for Energy Research and Training (CERT), located in Ahmadu Bello University, Zaria, Centre for Energy Research and Development (CERD), located in Obafemi Awolowo University, Ile-Ife.

Some successes have been achieved in solar energy technology development in the country. These include, but are not limited to, solar crop dryers of various capacities. Worthy of note is the 2-tonne capacity rice dryer developed at the NCERD and a 2-tonne capacity forage dryer constructed by the SERC. Also, a solar manure dryer for poultry waste developed by NCERD, Nsukka. The dryer was able to reduce moisture content of manure from 71 % to 35 % in 22 hours of peak solar intensity of 600 W/m^2. Flat and concentrated solar cookers have been constructed and tested at NCERD and SERC. The flat plate cooker attained a record cooking time of 4.5 minutes at solar intensities of 850 W/m^2. Solar water heaters comprising horizontal and vertical tanks with natural circulation have also been constructed and are available at Usman Danfodiyo University, Sokoto, and solar chick brooders at NCERD, Nsukka.

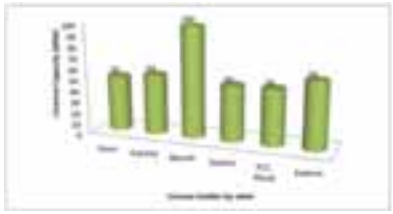

Fig. 4: Nigerian Electricity Regulatory Commission licensed solar power projects in Nigeria

Licenses for solar energy projects in the country have been awarded by the Nigerian Electricity Regulatory Commission as shown in Figure 4. As at 2014, seven companies have been awarded licenses in different states of Nigeria. Bauchi has the highest capacity with 100 MW awarded to Nigeria Solar Capital Partners. Kaduna have two licenses awarded to Quaint Global Nigeria Ltd and Anjeed Kafanchan Solar Ltd with a capacity of 50 MW and 10 MW respectively. Others are Lloyd and Baxter LP in Abuja, KVK Power Pyt Limited in Sokoto state, Pan African Solar in Katsina and Rock Solar Investment Company in Osun state. Due to fluctuation in generation capacity caused by water shortages in the dry season, Shiroro Hydroelectric Power Station in Niger State of Nigeria plans to construct a 300 MW PV solar power plant.

Some memorandums of understanding have been signed for solar projects in Nigeria. New Horizon Energy Resources proposed the building of a 100 MW solar plant in Nasarawa. Delta state government signed an MoU with Yutal Li Ltd for a 100 MW solar power plant in 2016 in addition to a 300 MW power plant signed for in 2014 with SkyPower FAS Energy. The federal government of Nigeria also signed a 300 MW solar power with Super Solar.

2.1.1 Solar cell fabrication and research in Nigeria

Limited work has been done on materials for solar cell fabrication and thin film growth in Nigeria at Obafemi Awolowo University (OAU, Ile Ife) and NCERD, Nsukka respectively and in some laboratories in the country.

Soboyejo and Kana have led some research studies at Africa University of Science and Technology (AUST, Abuja) and Sheda Science and Technology Complex (SHESTCO, Sheda), on organic solar cell materials fabrication. Fabian Ezema has worked extensively on Chemical Bath Deposition (CBD) for solar cell deposition at the University of Nigeria, Nsukka. The National Agency for Science and Engineering Infrastructure (NASENI) is also worthy of mention in terms of solar cells research and development and solar panels. NASENI, in Nigeria is leading the effort to make solar panels available at a reduced cost. It has a dedicated solar panel assembly plant in Karachi, Nigeria. Most of the solar PV studies conducted in Nigeria are on solar PV components and system testing, pilot plants and other application projects. The KwalkwalaWa 7.2 kW village electrification in Sokoto state is the largest single pilot plant established by the Energy Commission. It is used for pumping water, powering health centres and rural lighting and entertainment. Other developments include solar air heaters, solar stills for water purification, solar absorption and absorption refrigerators.

2.1.2 Solar data collection in Nigeria

Efforts are being intensified in solar energy data collection in Nigeria. Data such as solar radiation intensities (such as global, direct and diffuse), relative humidity, precipitation and ambient temperatures have been collected for over 64 towns by the Meteorological Services Department. About 33 % of these stations have been in existence for over 50 years. About twelve research institutes and centres located in and outside universities in the country are also involved in solar data collection and analysis. The Energy Commission is currently developing an Energy Data Bank for renewable energy data.

3. Existing government policies and legislation

A National Energy Policy was developed in 2003 by the Nigerian government, primarily for efficient management of the country's energy resources. It focuses on conventional and renewable energy sources for sustainable development of the country with full private sector participation.

The policy is summarized as; extensive crude oil and natural gas exploration and development shall be pursued with the view to increasing their reserves base to the highest level possible. Lastly, the nation shall continue to engage extensively in the development of electric power with the view to making reliable electricity available to 75 % of the population by 2020; as well as to broaden the energy options for generating electricity.

The Nigerian Electricity Regulatory Commission and the Rural Electrification Agency were established in 2005 with in order to liberate the electricity sector. The Nigeria Renewable Energy Master Plan (REMP) is a policy aimed at making electricity more available through renewable energy. It envisions renewable energy providing a minimum of 10 % of total energy consumption in Nigeria by 2025 [63]. It was produced in 2006 with United Nations Development Programme support, and outlined the road map for more renewable energy usage in Nigeria's quest to meet her energy demands and improve grid reliability and security [64]. The policy hopes to meet this goal by providing an enabling platform for renewable energy, legal instruments, technical-know-how, manpower, infrastructure and the markets.

The objectives are; expanding access to energy services and raising the standard of living, especially in the rural areas; Stimulating economic growth, employment and empowerment; Increasing the scope and quality of rural services, including schools, health services, water supply, information, entertainment and stemming the migration to urban areas; Reducing environmental degradation and health risks, particularly to vulnerable groups such as women and children; Improving learning, capacity-building, research and development on various renewable energy technologies in the country; and Providing a road map for achieving a substantial share of the national energy supply mix through renewable energy.

4. Challenges

The high cost of implementation of renewable energy technologies, particularly solar, is the major impediment militating against their widespread use [65]. High cost is not unconnected to the fact that nearly all the parts are imported from overseas at a very high cost. Most of the personnel and technologies are sourced abroad [58]. The key challenges facing the successful deployment of solar energy technologies can be grouped into cost, policy,

technical, people and environment. Some of the key challenges of solar energy in Nigeria are discussed below. Firstly,cost plays a major role in the life of people and the success or failure of a technology. Nigeria is a developing country home to both rich and poor, living in rural and urban areas. Initial investment in the cost of solar energy infrastructure is one of those factors militating against penetration of solar energy in Nigeria. The lack of adequate funding for solar energy development poses a high risk to the success of solar energy in Nigeria. Also, the general absence of comprehensive national energy policy. Nigeria has never formulated a comprehensive energy policy; only sub-sectoral policies have been formulated. Since such a policy is pivotal to using energy efficiently and solar energy, the lack of such a policy has, to a large extent, contributed to the lack of attention to solar energy. Thirdly, lack of technological capability is an issue in penetration of solar energy in Nigeria. The bulk of the technologies for solar energy are imported thereby increasing the high investment cost of solar energy. Cultural and low level of public awareness is also another challenge. The cultural inclination in some parts of Nigeria coupled with public awareness of renewable energy sources and technologies in Nigeria and their benefits, both economically and environmentally, are generally low. Consequently, the public is not well-equipped to influence the government to begin to take more decisive initiatives in enhancing the development, application, dissemination and diffusion of renewable energy resources and technologies in the national energy market.

5. Prospects for solar energy in Nigeria

Geographically, Nigeria lies within a high sunshine belt on longitude 3º and 14º East of Greenwich and latitude 4º and 14° north of equator [66] and thus has enormous solar energy potential [67]. The country has an annual average daily solar radiation of about 5.535 KW/m^2 /day [68]. The minimum average is about 3.55 kW/m^2/day in Katsina in January. It is 3.4 kW/m^2/day for Calabar in August. And the maximum average is 8.0 kW/m^2/day for Nguru in May [69]. This puts the solar radiation figure at an average of 19.8 MJ/m^2/day and is fairly distributed.

The country's annual average daily sunshine is 6.25 hours per day, the coastal areas are 3.5 hours and 9.0 hours at the far northern boundary [70]. Nigeria receives about 4.851 x 10^{12} KWh of energy per day from the sun [71]. This is equivalent to about 1.082 million tons of oil equivalent (mtoe) per day, and is about 4 000 times the current daily crude oil reduction, and about 13 000 times that of natural gas daily production based on energy units. This huge energy resource from the sun is available for only about 26 % of the day. This data couple with the prevailing efficiencies of commercial solar-electric generators and if solar collectors or modules were used to cover 1% of Nigeria's land area of 923 773km^2, it is possible to generate 1.804 x 10^{15} kWh of solar electricity per year. This is over one hundred times the current grid electricity consumption level in the country [72]. The annual solar energy insolation is 27 times the nation total conventional energy resources in energy units. This is over 117 000 of the electric power generated in 1998 in Nigeria [40]. Only about 3.7 % of Nigeria's land area is required for solar energy to meet the electricity demand of the country.

5.1 Future prospects

Though the bulk of the prospects for solar energy in Nigeria are in the off-grid areas and rural electrification, some areas on the grid and in urban areas also hold some prospects. Areas that provide opportunities for application include, but are not limited to: power plants, non-thermal electricity generation, large scale and family scale cooking, heating, drying of farm produce, water purification, clean water provision for humans and animals, aerospace development of the country, provision of light arms and ammunition for the Nigeria Army especially as they combat Boko haram terrorism and militants in the Niger Delta of the country. The future prospects of solar PV are shown in Figures 5 and 6.

The major focus on renewable energy in Nigeria is on transportation and electricity generation. Electricity generation from renewable energy in Nigeria is estimated to be 9.74 % for 2015, 18 % for 2020 and 20 % for 2030. However, electricity generation using solar is projected to be 1.26 % for 2015, 6.92 % for 2020 and 15.27 % for 2030. The targets of renewable electricity from solar alone is projected to be 12.96 %, 38.43 % and 76.36 % for these years. This shows that solar progressively dominates in the long-term. Figure 6 shows the targets for solar PV application in Nigeria for year 2020 and 2030.

Figure 6 shows the targets for solar thermal energy application in Nigeria for year 2015, 2020 and 2030. This is too dismal to be commended even in the long-term.

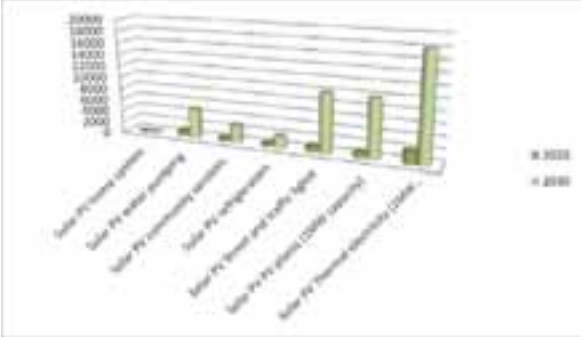

Fig. 5: Solar PV application in Nigeria for year 2020 and 2030

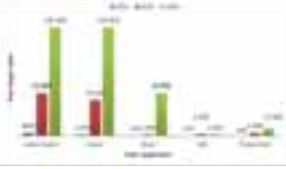

Fig. 6: Targets for solar thermal energy application in Nigeria for year 2015, 2020 and 2030

For example, consider the targets for solar cookers. Suppose each solar cooker is constructed to cook for five people as proposed by Saxena et al. [73]. With a population growth rate of 3.2 % per annum, the population in 2015, 2020 and 2030 population becomes 186 458 723, 218 263 539 and 299 073 660 respectively. The penetration level which represent the percentage of the population supplied with solar cooking energy becomes 0.0054 %, 0.1145 % and 0.2508 % respectively. Although this figure indicates a rising trend into the future, the penetration level is minor and does not reflect the energy crisis in Nigeria. This is because in 2014 about 80 % of the population were exposed to health issues. Many of these health issues arose from the heating and cooking used in the rural setting, using mainly biomass and waste resources. The maintenance-free and cheap nature of solar box cookers makes them well suited to developing countries.

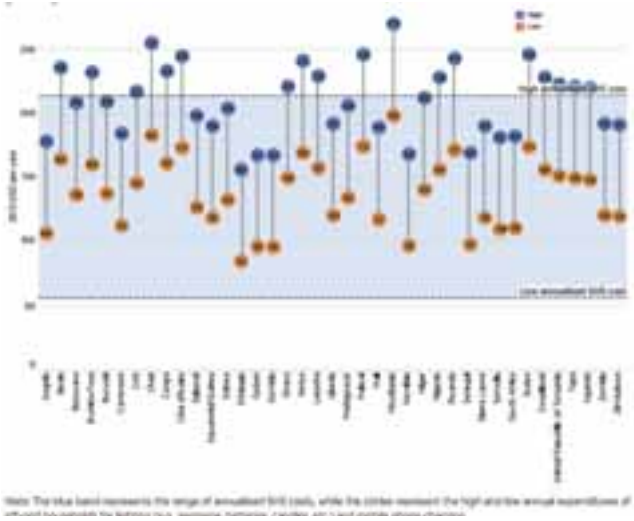

Fig. 2: Africa annual off-grid household expenditure on lighting and mobile phone charging compared to solar home system (< 1 kW) annualized costs, by country in 2015 [18]

Figure 8 gives the annual expenditure for off-grid lighting and mobile phone charging in Africa in 2015. The blue band represents the range of annualized solar system costs. Circles represent the high and low annual expenditures of off-grid households for lighting (e.g., kerosene, batteries, candles, etc.) and mobile phone charging. Expenditure in Nigeria is USD 140 per year. The lowest expenditure in Africa is in Ethiopia (USD 84) and the highest is

Mauritania (USD 270). Therefore, solar systems can be a very economical solution for powering homes in Africa

6. Conclusion

Nigeria has the capacity to use solar energy to end the problem of an erratic power supply facing her. This work has been able to shed light on solar energy domestication in Nigeria, reviewing work that has been done relating to solar energy in Nigeria, and the prospects and challenges of the technology. A lot of brilliant studies have been conducted. Well-articulated policies have been made and signed with memorandums of understanding on the part of the government but well monitored implementation seems to be an issue working against the full success story of solar energy utilization in Nigeria. Research into in-country fabrication of solar cells, thin films and solar panels is highly recommended for both public and private partnership in Nigeria. The windows of opportunities for solar energy inclusion in Nigeria are enormous. These are: solar power generation, increased internally generated revenue through manufacture of solar panels, capacity building in the field of solar energy technologies, supply of renewable energy equipment and accessories, and contracts in solar energy projects. The rest of Africa can benefit from the success story of Nigeria if well implemented.

7. Recommendation

More education should be conducted to sensitize the populace on the benefits of solar energy and the government should encourage more research on solar energy, especially the setting up of and/or funding of solar cells research centres.

Acknowledgements

The financial assistance of the National Research Foundation and The World Academy of Science (NRF-TWAS) of South Africa is acknowledged.

References

[1]Kaygusuz, K., 2012. Energy for sustainable development: A case of developing countries. Renew. Sustainable Energy Rev. 16(2),1116-1126.

[2]Scarlat, N., Motola, V., Dallemand, J. F., Monforti-Ferrario, F. and Linus Mofor, 2015. Evaluation of energy potential of municipal solid waste from African urban areas. Renew. Sustainable Energy Rev. 50, 1269-1286.

[3]Karekezi, S., 2002. Poverty and energy in Africa—a brief review. Energy Policy. 30(11-12), 915-919.

[4]Wolde-Rufael, Y., 2005. Energy demand and economic growth: the African experience. J. Policy Model. 27(8), 891-903.

[5]Bazilian, M., Nussbaumer, P., Rogner, H.H., Brew-Hammond, A., Foster, V., Pachauri, S., Williams, E., Howells, M., Niyongabo, P., Musaba, L. and Gallachóir, B.Ó., 2012. Energy access scenarios to 2030 for the power sector in sub-Saharan Africa. Utilities Policy, 20(1),1-16.

[6.]Bongaarts, J., 2009. Human population growth and the demographic transition. Philos. Trans. R. Soc. B. 364(1532), 2985-2990.

[7]Apulu, I., A. Latham, and R. Moreton, 2011. Factors affecting the effective utilisation and adoption of sophisticated ICT solutions: Case studies of SMEs in Lagos, Nigeria. J. Syst. Inf. Technol. 13(2), 125-143.

[8]Oseni, M.O., 2011. An analysis of the power sector performance in Nigeria. Renew. Sustainable Energy Rev. 15(9), 4765-4774.

[9]Obadote, D. Energy crisis in Nigeria: technical issues and solutions. In Power sector prayer conference. June 27-29, 2009.

[10]Aliyu, A.S., A.T. Ramli, and M.A. Saleh, 2013. Nigeria electricity crisis: Power generation capacity expansion and environmental ramifications. Energy. 61, 354-367.

[11]Oyedepo, S.O., 2012. On energy for sustainable development in Nigeria. Renew. Sustainable Energy Rev.16(5), 2583-2598.

[12]Ohunakin, O.S., 2010. Energy utilization and renewable energy sources in Nigeria. J. Eng. Appl. Sci. 5(2), 171-177.

[13]Mohammed, Y.S., Mustafa, M., Bashir, N. and Mokhtar, A.S., 2013. Renewable energy resources for distributed power generation in Nigeria: a review of the potential. Renew. Sustainable Energy Rev. 22, 257-268.

[14]Sambo, A.S., 2009. Strategic developments in renewable energy in Nigeria. International Association for Energy Economics, 16(3), 15-19.

[15]Ohiare, S., 2015. Expanding electricity access to all in Nigeria: a spatial planning and cost analysis. Energy Sustainability Soc. 5(1), 8.

[16]Usman, Z.G. and S. Abbasoglu, 2014. An overview of power sector laws, policies and reforms in Nigeria. Asian Trans Eng. 4(2), 6-12.

[17]Oseni, M.O., Power outages and the costs of unsupplied electricity: evidence from backup generation among firms in Africa. In Proceedings USAEE/IAEE Conference, Austin Texas. 2012.

[18]IRENA, Solar PV in Africa: Costs and Markets. 2016.

[19]Sambo, A., 2012. Nigeria's long term energy demand outlook to 2030. J. Energy.

[20]Onakoya, A.B., Onakoya, A.O., Jimi-Salami, O.A. and Odedairo, B.O., 2013. Energy consumption and Nigerian economic growth: An empirical analysis. Eur. Sci. J. 9(4).

[21]Ohiare, S., Financing rural energy projects in developing countries: a case study of Nigeria. PhD thesis, De Montfort University, Leicester, UK, 2014.

[22]Guttikunda, S.K. and R. Goel, 2013. Health impacts of particulate pollution in a megacity—Delhi, India. Environ. Dev. 6, 8-20.

[23]Zhang, J., Mauzerall, D.L., Zhu, T., Liang, S., Ezzati, M. and Remais, J.V., 2010. Environmental health in China: progress towards clean air and safe water. The Lancet, 375(9720), 1110-1119.

[24]Epstein, T.S. and D. Jezeph, 2001. Development—there is another way: a rural–urban partnership development paradigm. World Dev. 29(8), 1443-1454.

[25]Kanagawa, M. and T. Nakata, 2008. Assessment of access to electricity and the socio-economic impacts in rural areas of developing countries. Energy Policy. 36(6), 2016-2029.

[26]Kaygusuz, K., 2011. Energy services and energy poverty for sustainable rural development. Renew. Sustainable Energy Rev. 15(2), 936-947.

[27]Iyke, B.N., 2015. Electricity consumption and economic growth in Nigeria: A revisit of the energy-growth debate. Energy Econ. 51, 166-176.

[28]Jaunky, C.V., 2006. Income elasticities of electric power consumption: Evidence from African countries. Regional and Sectoral Econ. Stud. 7, 25-50.

[29]Akinlo, A.E., 2009. Electricity consumption and economic growth in Nigeria: evidence from cointegration and co-feature analysis. J. Policy Model. 31(5), 681-693.

[30]Ogundipe, A.A. and A. Apata, 2013. Electricity consumption and economic growth in Nigeria. J. Bus. Manage. Appl. Econ.11(4).

[31]Aliero, H.M., Ibrahim, S.S. and Shuaibu, M. 2013. An empirical investigation into the relationship between financial sector development and unemployment in Nigeria. Asian Econ. Financ. Rev. 3(10), 1361.

[32]Okoligwe, N. and Ihugba, O.A. 2014. Relationship between electricity consumption and economic growth: Evidence from Nigeria (1971-2012). Acad. J. Interdiscip. Stud. 3(5), 137.

[33]Dantama, Y.U., Abdullahi, Y.Z. and Inuwa, N. 2012. Energy consumption-economic growth nexus in Nigeria: an empirical assessment based on ARDL bound test approach. Eur. Sci. J. 8(12).

[34]Ellabban, O., Abu-Rub, H. and Blaabjerg, F. 2014. Renewable energy resources: Current status, future prospects and their enabling technology. Renew. Sustainable Energy Rev. 39, 748-764.

[35]Ibidapo-Obe, O., and Ajibola, 2011. Towards a renewable energy development for rural power sufficiency. In Proceeedings International Conference on Innovations in Engineering and Technology (IET 2011), August 8th – 10th, University of Lagos.

[36]Panwar, N., Kaushik, S. and Kothari, S. 2011. Role of renewable energy sources in environmental protection: a review. Renew. Sustainable Energy Rev. 15(3), 1513-1524.

[37]Johnstone, N., Haščič, I. and Popp, D. 2010. Renewable energy policies and technological innovation: evidence based on patent counts. Environ. Resour. Econ. 45(1), 133-155.

[38]Twidell, J. and Weir, T. Renewable energy resources. 2015: Routledge.

[39]Ojosu, J., 1990. The iso-radiation map for Nigeria. Solar Wind Technol. 7, 563-75.

[40]Emodi, N.V. and Boo, K.-J. 2015. Sustainable energy development in Nigeria: Overcoming energy poverty. Int. J. Energy Econ. Policy. 5(2).

[41]Reif, J.H. and Alhalabi, W. 2015. Solar-thermal powered desalination: Its significant challenges and potential. Renew. Sustainable Energy Rev. 48, 152-165.

[42]Archer, M.D. and Green, M.A. 2015. Clean electricity from photovoltaics. second ed. Imperial College Press, London.

[43]Ozoegwu, C., Mgbemene, C. and Ozor P., 2017. The status of solar energy integration and policy in Nigeria. Renew. Sustainable Energy Rev. 70, 457-471.

[44]Milosavljević, D.D., Pavlović, T.M. and Piršl, D.S. 2015. Performance analysis of A grid-connected solar PV plant in Niš, republic of Serbia. Renew. Sustainable Energy Rev. 44, 423-435.

[45]Nwofor, O. and Dike. V. 2016. Objective criteria ranking framework for renewable energy policy decisions in Nigeria. in IOP Conference

Series: Earth and Environmental Science. IOP Publishing.

[46]Sambo, A., 2016. Enhancing renewable energy access for sustainable socio-economic development in sub-Saharan Africa. J. Renew. Altern. Energy Technol. 1(1).

[47]Chilapku, K.O., 2015. Renewable energy sources: its benefits, potentials and challenges in Nigeria. J. Energy Technol. Policy. 5, 21-24.

[48]Körbitz, W., 1999. Biodiesel production in Europe and North America, an encouraging prospect. Renew. Energy. 16, 1078-1083.

[49]Olaoye, T., Ajilore, T., Akinluwade, K., Omole, F. and Adetunji, A., 2016. Energy crisis in Nigeria: Need for renewable energy mix. American J. Electrical Electron. Eng. 4(1), 1-8.

[50]Ajayi, O.O. and Ajanaku, K.O. 2009. Nigeria's energy challenge and power development: the way forward. Energy environ. 20(3), 411-413.

[51]Akinboro, F., Adejumobi, L. and Makinde, V. 2012. Solar energy installation in Nigeria: Observations, Prospect, problems, and solution. Trans. J. Sci. Technol. 2(4), 73-84.

[52]Ezugwu, C., 2015. Renewable energy resources in Nigeria: Sources, Problems and prospects. J. Clean Energy Technol. 3(1), 68-71.

[53]Dike, V.N., Opara-Nestor, C.A., Amaechi, J.N., Dike, D.O. and Chineke, T.C., 2017. Solar pv system utilization in Nigeria: Failures and possible solutions. Pac. J. Sci. Technol. 18(1), 51-61.

[54]Ikem, I.A., Ibeh, M.I., Nyong, O.E., Takim, S.A. and Osim-Asu, D., 2016. Integration of Renewable Energy Sources to the Nigerian National Grid-Way out of Power Crisis. Int. J. Eng. Res. 5(8), 694-700.

[55]Cota, O.D. and Kumar. N.M. 2015. Solar energy: a solution for street lighting and water pumping in rural areas of Nigeria. In Proceedings of International Conference on Modelling, Simulation and Control (ICMSC-2015).

[56]Kumar, N.M., Singh, A.K. and Reddy, K.V.K. 2016. Fossil fuel to solar power: A sustainable technical design for street lighting in Fugar City, Nigeria. Procedia Comput. Sci. 93, 956-966.

[57]Ike Chinelo, U., Okeke, C.C. and Okeke, S. 2013. Technical Report on The Design and Installation of a 1KVA Solar Energy Powered Security Light in The Dora Akunyili and Stella Okoli Female Hostels of Nnamdi Azikiwe University, Awka, Using Monocrystalline Panels. Int. Referred J. Eng. Sci. 2(8), 47-50.

[58]Bala, E., Ojosu, J. and Umar, I. 2000. Government policies and programmes on the development of solar-PV Sub-sector in Nigeria. Nigerian J. Renew. Energy. 8(1&2), 1-6.

[59]Iloeje, O. 2002. Renewable energy development in Nigeria: status & prospects. In Proceedings of a National workshop on energizing rural transformation in Nigeria: scaling up electricity access and renewable energy.

[60]Oparaku, O., 2002. Photovoltaic systems for distributed power supply in Nigeria. Renew. Energy. 25(1), 31-40.

[61]Nwofe, P., 2014. Utilization of solar and biomass energy-A panacea to energy sustainability in a developing economy. International J. Energy Environ. Res. 2(3), 10-19.

[62]Charles, A., 2014. How is 100% renewable energy possible for Nigeria. Global Energy Network Institute (GENI), California

[63]Scenario, N., East, M. and Cedex, P. 2015. World energy outlook 2014 factsheet. Paris: International Energy Agency.

[64]Akuru, U.B. and Okoro. O.I. 2010. Renewable energy investment in Nigeria: a review of the renewable energy master plan. In Energy Conference and Exhibition (EnergyCon), 2010 IEEE International.

[65]Bridgwater, A.V., 2003. Renewable fuels and chemicals by thermal processing of biomass. Chem. Eng. J. 91(2-3), 87-102.

[66]Simeon, P.O., Jijingi, H.E. and Ngabea, S.A. 2016. Conscientious management of soil humus and water: a major condition for purposeful mechanisation of field crop husbandry in tropical rain forest of Nigeria. Manage. Econ. Eng. Agric. Rural Dev. 16(4), 317-326.

[67]Adeyemo, S., 1997. Estimation of direct solar radiation intensities. Nigerian Soc. Eng. Tech. Trans. 32(1), 1-9.

[68]Fadare, D., 2009. Modelling of solar energy potential in Nigeria using an artificial neural network model. Appl. Energy. 86(9),1410-1422.

[69]Medugu D.W. and Yakubu, D. 2011. Estimation of mean monthly global solar radiation in Yola-Nigeria using angstrom model. Adv. in Appl. Sci. Res. 2(2), 414-421.

[70]Adaramola, M.S., 2012. Estimating global solar radiation using common meteorological data in Akure, Nigeria. Renew. Energy. 47, 38-44.

[71]Ani, V.A., 2013. Optimal sizing and application of renewable energy sources at GSM Base station site. Int. J. Renew. Energy Res. 3(3), 579-585.

[72]Ikuponisi, F.S. 2004. Status of renewable energy in Nigeria. In A background brief for an International Conference on Making Renewable Energy a Reality. 2004.

[73]Saxena, A., Pandey, S. and Srivastav, G. 2011. A thermodynamic review on solar box type cookers. Renew. Sustainable Energy Rev. 2011. 15(6), 3301-3318.

Other Innovative Components and Systems

Direct vaporization of an organic fluid in a parabolic trough solar collector

Simone Dugaria[1], Matteo Bortolato[1] and Davide Del Col[1]

[1] Department of Industrial Engineering (DII), University of Padova, Padova, Italy

Abstract

An innovative solar receiver for linear concentrating collectors is used for the direct vaporization of a low GWP halogenated fluid. Experiments have been conducted to determine the thermal performance of the collector during vaporization of an organic fluid that can be adopted for ORC cycle. The mass flow rate and the subcooling of the halogenated fluid entering the receiver have been varied, along with the outlet vapor quality and saturation pressure. The results of the experimental campaign reveal that the solar collector is able to vaporize this halogenated fluid at 85°C with 73% efficiency. A numerical model of the collector has been developed and validated against the experimental data. The estimated thermal performance of the collector is in good agreement with the experimental tests. The mean relative error in the prediction of the thermal efficiency of the collector results within 2%.

Key-words: HCFO-1233zd(E); solar direct vaporization; parabolic trough collector

Nomenclature

Symbols

A_a	Aperture area, m^2
c_{II}	Specific heat of the secondary fluid, J K^{-1} kg^{-1}
DNI	Direct Normal Irradiance, W m^{-2}
h	Specific enthalpy, J kg^{-1}
h_L	Specific enthalpy of the saturated liquid, J kg^{-1}
h_{LV}	Latent heat of vaporization, J kg^{-1}
$\dot{m}$	Mass flow rate, kg s^{-1}
p	Pressure, Pa
q	Heat flow rate, W
T	Temperature, °C
T_m^*	Reduced mean temperature, K m^2 W^{-1}
x	Vapor quality, -

Greek symbols

$\alpha_{r,coat}$	Absorbance of the coating layer, -
ρ_c	Reflectance of the collector's mirror, -
γ_r	Receiver intercept factor, -
η_{col}	Collector thermal efficiency, -

Subscripts

I	Primary fluid (HCFO-12333zd(E))
II	Secondary fluid (Cooling water)
HE	Heat Exchanger
in	Inlet
R	Receiver
out	Outlet

1. Introduction

Organic Rankine Cycle (ORC), unlike the traditional steam Rankine cycle, can work with low temperature heat sources, by using an organic fluid instead of water as working fluid (Peris et al., 2015). The selection of the organic working fluid (OWF) is a crucial choice in determining the performance and the cost of the system (Chen et al., 2010). For ORC systems coupled to low-grade heat sources, HFC-245fa has been considered by many authors the best choice (Cataldo et al., 2014, Quoilin et al., 2011). This is a common working fluid used in commercial ORCs generating mechanical power from low-temperature heat sources and for high-temperature heat pumps. Despite the excellent thermodynamic performance of HFC-245fa for the exploitation of low-grade heat source the growing sensitivity of the society on environmental issues will increasingly limit its use due to its high GWP (1030 according to Molés et al., 2015). Moles et al (2014) identified the halogenated fluid HCFO-1233zd(E) as valuable candidate for the future replacement of HFC-245fa in various applications. Despite the presence of the chlorine in its molecule, it presents an extremely small value (0.00034) of ODP (Patten and Wuebbles, 2010), due to its very short atmospheric lifetime. Its GWP value was recently reported to be lower than one (Myhre et al., 2014).

Besides the theoretical studies (Giuffrida, 2014, Heberle et al., 2016, Molés et al., 2014), very few experiments on the use of HCFO-1233zd(E) as HFC-245fa drop-in replacement for ORC have been presented in the literature. Eyerer et al. (2016) studied the applicability of HCFO-1233zd(E) as substitute for HFC-245fa in ORC system supplied by a heat source at 120 °C by comparing cycle efficiency and power output. The authors concluded that HCFO-1233zd(E) can be successfully used to replace HFC-245fa without major modifications in the system. It was found that the use of HCFO-1233zd(E) can lead to an increase of 6.92% in the thermal efficiency with

doi:10.18086/swc.2017.17.01 Available at http://proceedings.ises.org

constant condensation and evaporation temperatures and constant isoentropic expansion efficiency. However, the net electric power generated by the ORC was 12.17% lower due to the largest volumetric flow rates of the HCFO-1233zd(E) required for the use of the system designed for HFC-245fa. In the work of Molés et al. (2016), an experimental evaluation of the working fluid HCFO-1233zd(E) as HFC-245fa replacement in ORC systems for low-temperature heat sources at different operating conditions has been conducted. Thermal and electrical powers resulted lower for HCFO-1233zd(E) than those for HFC-245fa at the same volumetric flow rate, due to the fact that the different densities of the working fluids. However, the net electrical efficiency was similar for both working fluids, ranging from 5% to 10%.

The exploitation of solar radiation can significantly contribute to reduce the consumption of conventional (non-renewable) energy sources and relieving associated environmental problems. A solar thermal system can be combined with ORC system according to two configurations: coupling with direct vaporization of the OWF or by using an intermediate solar circuit to heat a heat transfer fluid and evaporate the OWF in a separate heat exchanger. In a solar powered ORC system with direct vaporization of the OWF, the solar receiver coincides with the evaporator. By adopting this configuration is possible to simplify the system layout as the intermediate loop for transferring the heat from the solar collector to the OWF is no longer needed. It is expected that the direct vaporization of the OWF in the solar receiver allows to convert the solar energy collected by the solar system into the thermal energy of the OWF with a higher efficiency. In fact, this process takes place without the irreversibility associated with the heat transfer occurring in the heat exchanger/evaporator of the indirect vaporization. This aspect is particularly important in ORC systems where the temperature differences between the heat source and environment are quite low (around 100 °C).

Although, the feasibility of conventional steam Rankine cycles with direct vaporization of water in parabolic trough collectors (PTCs) has been extensively demonstrated (Eck et al., 2003, 2007), it has not yet been proved with organic fluids. This paper presents the experimental and numerical results on the direct vaporization of the halogenated fluid HCFO-1233zd(E) in an innovative aluminum flat absorber for medium temperature linear concentrating solar collectors.

2. Experimental apparatus and campaign

The small parabolic trough concentrator considered in this work is asymmetrical since the reflective optics extends from the vertex line to the mirror rim (Figure 1). This concentrator has been installed at the Solar Energy Conversion Lab of the Industrial Engineering Department, University of Padova (45.416°N, 11.883°E). The present concentrator exhibits an aperture width of 2.9 m, a rim angle of 78°, a focal length of 1.81 m and a trough length of 2.4 m, resulting in an aperture area slightly lower than 7 m^2. The reflecting optical system is made up by four back silvered glass facets arranged in two rows, which have a nominal reflectance of 96%, as provided by the manufacturer. Due to the small dimensions of the prototype, it is equipped with a two-axes solar tracking system to have the beam radiation normal to the aperture area without any cosine loss. The motion is governed by a solar algorithm when approaching the sun and by a sun sensor to achieve the best alignment.

Figure 1. Asymmetrical parabolic trough linear solar concentrator installed in the Solar Energy Conversion Lab of the University of Padova.

Figure 2. Bar-and-plate flat receiver arranged on the support bar of the collector under concentrated solar radiation during a test run.

The particular geometry of the parabolic trough concentrator is suitable to be coupled with a receiver provided with a flat geometry absorber. The innovative receiver considered in this work has been manufactured with bar-and-plate technology and is provided with an internal offset strip turbulator (Bortolato et al., 2016). The combined use of a high thermal conductivity material and a passive heat transfer enhancement technique in the absorber is a promising solution for linear concentrating devices. In order to minimize the incidence angle of the concentrated beams on the flat receiver, the optimal concentration plane of this system is 45° tilted with respect to the plane containing the focal line and the normal to the aperture area. The receiver presents a length equal to 1.2 m, which corresponds to half of the total trough length, and a width of 70 mm, thus, the resulting geometrical concentration ratio of the concentrating collector is equal to 42 (Figure 2).

2.1 Test facility

The test facility has been designed in order to measure the thermal efficiency of the solar concentrating collector during the vaporization of the fluid. A primary loop, where the halogenated fluid flows, is arranged on board the concentrating collector (Figure 3). The heat provided by the concentrated solar irradiance is dissipated through a heat exchanger to a secondary loop with cooling water. Both the loops are thermally insulated to limit heat losses towards the surroundings. The laboratory is equipped with a measuring system of the solar irradiance including a first class pyrheliometer mounted on a high precision solar tracker that is used to measure the direct normal irradiance (DNI). An anemometer measures the wind speed on the horizontal plane and the ambient air temperature is gauged by a Pt100 resistance temperature detector (RTD).

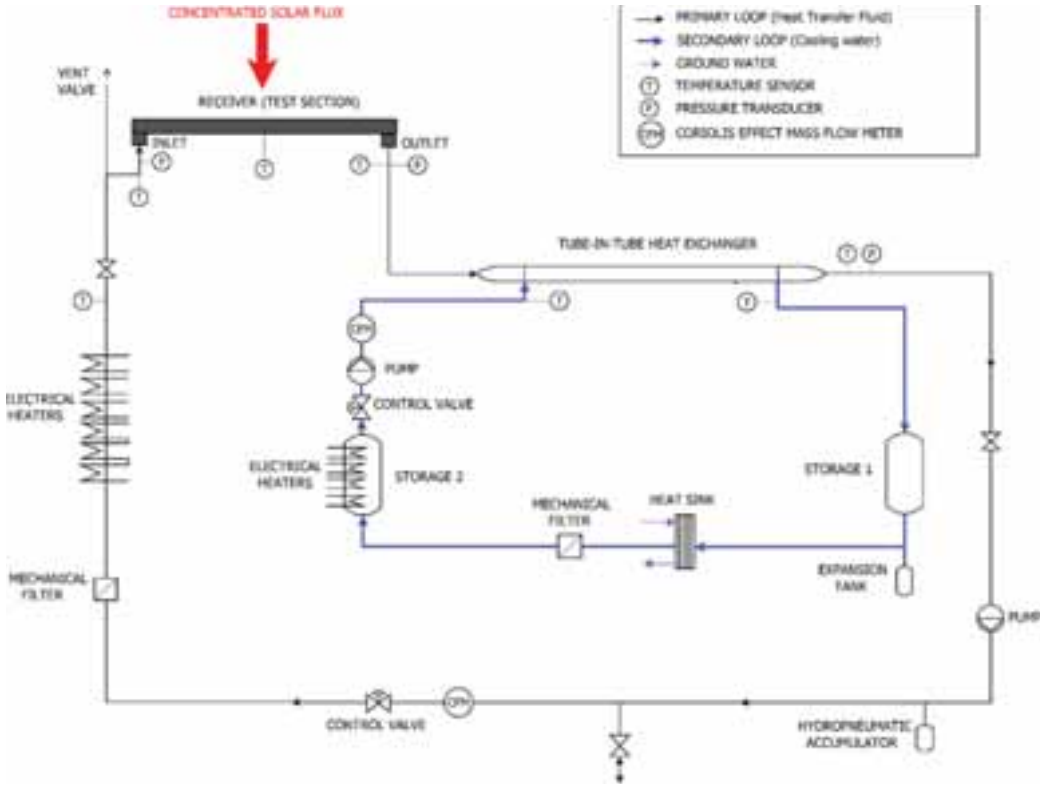

Figure 3. Sketch of the experimental test rig.

In the primary loop, after exiting the receiver, the heat transfer fluid (HCFO-1233zd(E)) enters a tube-in-tube heat exchanger, where the HCFO-1233zd(E) flows inside the inner tube, while the coolant (water) flows in the annulus. The pressure of the primary loop is regulated by a hydropneumatic accumulator with a fluoroelastomer diaphragm: this device plays an important role in direct vaporization tests as the working pressure determines the temperature of the generated vapor. Before entering the receiver, the halogenated fluid passes through a pre-heating section which consists of a electrical heater connected to a solid-state relay which is governed by a PID temperature controller. Temperatures and pressures of the organic fluid at inlet and outlet of the receiver and downstream of are measured by Pt100 RTDs and high precision absolute pressure transducers. Since the presence of a turbulator may penalize the hydraulic performance, accurate measurements of pressure drop have also to be carried out. In the

secondary loop, the controls on the cooling water mass flowrate and inlet temperature are useful to achieve constant conditions of the primary working fluid at the inlet of the receiver. The temperatures of the water at the inlet and at the outlet of the tube-in-tube heat exchanger are measured by Pt100 RTDs. All the measured quantities are recorded by a data logger with sampling rate of 3 s and the collected data are reduced in a MATLAB environment by calculating the fluid properties with NIST Refprop Version 9.0 (Lemmon et al., 2010).

2.2 Experimental technique and data reduction

The test methods to determine the thermal performance of solar concentrating collectors, namely the steady state method in the ASHRAE 93:2010 standard and the quasi dynamic method in EN ISO 8609:2013 standard, refer only to liquid or air heating devices. This means that the useful heat gained by the working fluid can be calculated considering its temperature increase inside the solar collector. There are no standard procedures to experimentally define the thermal efficiency of a solar concentrating collector performing direct steam generation, when a latent heat transfer is involved. The procedure proposed by Bortolato et al. (2016), has been adopted to evaluate the thermal performance of the concentrating solar collector during the vaporization of the halogenated fluid. During the test runs, the organic fluid enters the test section as subcooled liquid and its thermodynamic condition is completely determined by the temperature and pressure measurements at the inlet of the receiver. The fluid exits the receiver as saturated vapor and then it is condensed and subcooled in the tube-in-tube heat exchanger. The thermodynamic state of the halogenated fluid at the outlet of the receiver under saturated conditions can be experimentally defined by applying the energy balance to the heat exchanger, under the reasonable hypothesis of negligible heat losses towards the surroundings. The saturation temperature is assumed equal to the temperature measured at the outlet of the receiver because, during the two-phase test runs, the pressure drop across the receiver is very small.The specific enthalpy $h_{out,R,I}$ and of vapor quality $x_{out,R,I}$ of the saturated steam at the outlet of the receiver can be expressed as reported in the following expressions

$$h_{out,R,I} = h_{out,HE,I}\left(T_{out,HE,I}, p_{out,HE,I}\right) + \frac{\dot{m}_{II}\, c_{II}\left(T_{out,HE,II} - T_{in,HE,II}\right)}{\dot{m}_I} \qquad (2.1)$$

$$x_{out,R,I} = \frac{h_{out,R,I} - h_L\left(T_{out,R,I}\right)}{h_{LV}\left(T_{out,R,I}\right)} \qquad (2.2)$$

The experimental results are presented in a diagram plotting the experimental thermal efficiency η_{col}, as a function of the reduced mean temperature T_m^* along with the obtained efficiency curve of the collector.

$$\eta_{col} = \frac{q_I}{\mathrm{DNI}\, A_{ap}} = \frac{\dot{m}_I\left(h_{out\,R,I} - h_{in\,R,I}\right)}{\mathrm{DNI}\, A_{ap}} \qquad (2.3)$$

$$T_m^* = \frac{\frac{\left(T_{out\,R,I} + T_{in\,R,I}\right)}{2} - T_{amb}}{\mathrm{DNI}} = \frac{T_{m\,R,I} - T_{amb}}{\mathrm{DNI}} \qquad (2.4)$$

In order to express the reduced mean temperature under two-phase flow, it is required the introduction of the equivalent mean temperature of the fluid during direct vaporization of the fluid. Since the working fluid enters as subcooled liquid, both sensible and latent heat transfers occur inside the receiver of the solar concentrating collector. Hence, the equivalent mean temperature of the fluid shall be assumed as a weighted average temperature based on the enthalpy changes associated to the sensible and latent heat transfers (Equation 2.5).

$$T_{m\,eq,I} = \frac{\left(\frac{T_{out,R,I} + T_{in,R,I}}{2}\right)\left(h_L\left(T_{out,R,I}\right) - h_{in,R,I}\right) + T_{out,R,I}\left(h_{out,R,I} - h_L\left(T_{out,R,I}\right)\right)}{h_{out,R,I} - h_{in,R,I}} \qquad (2.5)$$

2.3 Experimental uncertainty analysis

Before the test campaign, the primary loop is evacuated and then filled with HCFO-1233zd(E). After a preconditioning period of 20 min, during each test sequence, that lasts for 3 hours minimum, the collected data are averaged every 10 min and the following criteria have been satisfied during tests:

- the inlet temperature of the subcooled liquid is kept stable within ±1 °C as compared to its mean value;
- the HCFO-1233zd(E) mass flow rate is kept stable within ±2% as compared to the mean value;
- the thermodynamic vapor quality at the outlet of the receiver must be higher than 0.1.

The uncertainty analysis has been performed in agreement with the guidelines provided by the “Guide to the

Expression of Uncertainty in Measurement" (International Organization for Standardization, 2008). Type B uncertainties of the measured parameters are reported in Table 1 with a level of confidence of 95%.

Table 1. Type B uncertainty of measured parameters during direct vaporization in bar-and-plate flat receiver under concentrated solar radiation.

Ambient air temperature	± 0.07°C
Fluid temperature in primary and secondary loops	± 0.035°C
Coriolis effect mass flow meters	± 0.3 kg h^{-1} (cooling water) ± 0.07 kg h^{-1} (HCFO-1233zd(E))
Pressure of the fluid in the primary loop	± 0.023 bar
Direct normal irradiance	± 3% of measured value
Wind speed	± (0.1 m/s + 1% of measured value)

With respect to the parameters which are not directly measured, their combined standard uncertainty can be calculated by applying the law of error propagation with level of confidence of 95%. Type A uncertainty is the standard deviation of the mean and, in the present tests, it comes out considering 200 readings collected over the averaging time period of 10 min.

2.4 Experimental results

The experimental tests have been carried out during the month of August 2016 at the average evaporation pressure of 7.5 bar corresponding to 85°C saturation temperature. During the tests, the ambient temperature was in the range 28 – 35°C and the values of the direct normal irradiance were between 700 W m^{-2} and 920 W m^{-2}. The mass flow rate of the halogenated fluid has been varied between 46 kg $h^{-1}$and 106 kg h^{-1}. The experimental results show that the collector thermal efficiency η_{col}, calculated according to Equation 2.3, was around 73%. Figure 4 reports the effects of the outlet vapor quality on the collector efficiency during the vaporization of the halogenated fluid Considering that the extended uncertainty of the collector efficiency is ±3%, it can be concluded that the outlet vapor quality has a negligible effect on the collector efficiency. This remarkable result suggest that it is possible to vaporize almost completely the halogenated fluid in the bar-and-plate receiver without any losses of efficiency. In Figure 5, where the thermal efficiency of the collector is plotted against the inlet subcooling, it can be noted that also the inlet subcooling did not significantly affect the efficiency of the solar collector.

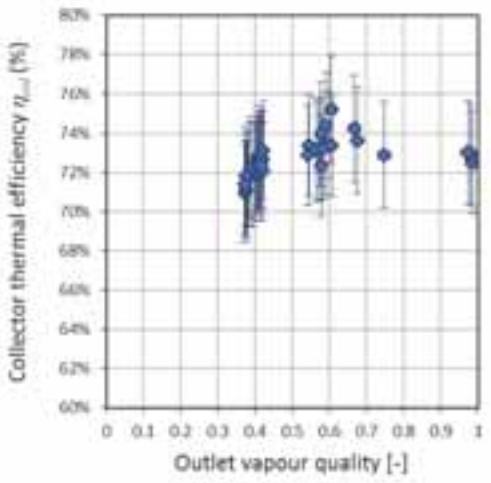

Figure 4. Experimental thermal efficiency of the solar collector as a function of the outlet vapor quality.

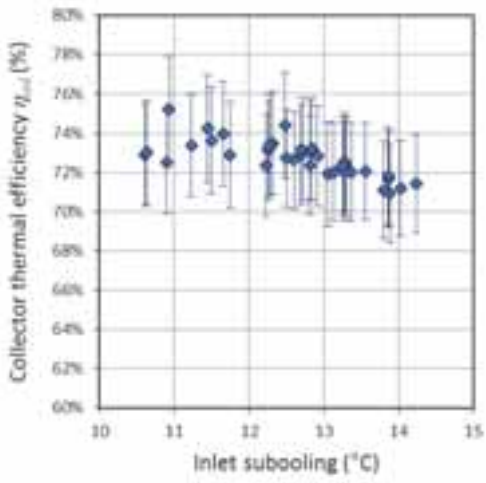

Figure 5. Experimental thermal efficiency of the solar collector as a function of the inlet subcooling.

Figure 6 reports the pressure drop through the bar-and-plate flat receiver as a function of the mass flow rate during the vaporization test runs of the halogenated fluid. This Figure provides only a general trend of the pressure drop, because the plotted values are lower than the experimental uncertainty of the pressure transducers. Anyway, the result shows that the designed absorber is capable of vaporize the fluid HCFO-1233zd(E) with a limited pressure drop, implying a low electrical consumption for the circulating pump.

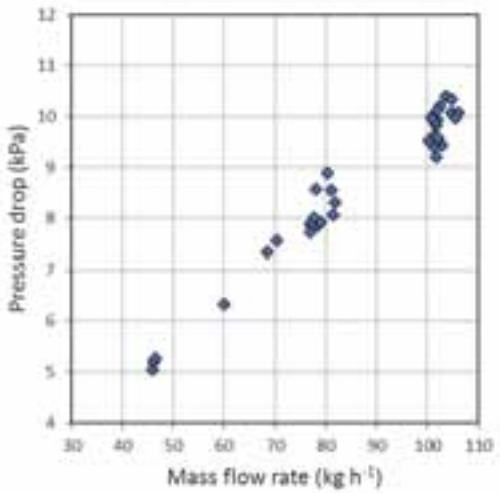

Figure 6. Pressure drop through the receiver as a function of the mass flow rate during vaporization.

3. Numerical model

A numerical model of the solar absorber system is developed in order to predict the performance of the receiver installed in a linear concentrating system. The receiver has been discretized along its length in several segments. Each segment constitutes a control volume where a zero-dimensional steady-state energy balance is applied. The zero-dimensional thermal resistance network is reported in Figure 7, where the external surfaces (front, back and lateral) of the absorber, the external surface of the insulation layer on the back of the receive, the internal surface of the absorber in contact with the fluid and the fluid itself constitute the thermal nodes of the model.

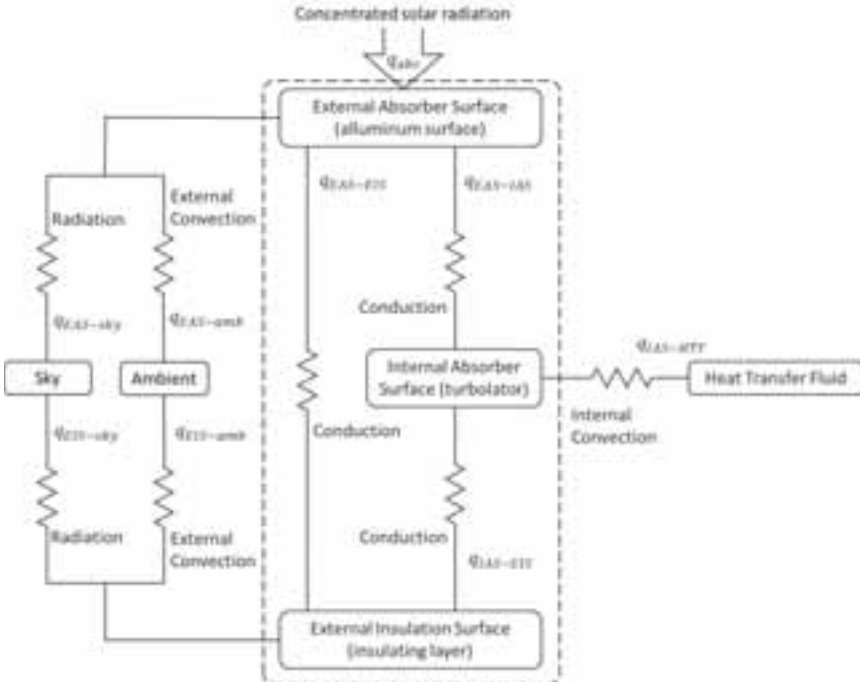

Figure 7. – Thermal resistance network representing the dimensionless model of the bar-and-plate flat receiver.

In the model, the effective incident concentrated solar radiation, net to the losses in the optical concentration, is mainly absorbed by the surface coating of the absorber and the absorbed heat flow rate q_{abs} has been considered as:

$$q_{abs} = DNI\ A_a \alpha_{r,coat} (\rho_c \gamma_r) \qquad (3.1)$$

Some energy absorbed into the coating is conducted through the absorber and transferred to the fluid $q_{EAS\text{-}HTF}$ by convection or by vaporization, while the rest is conducted through the insulating layer to the back surface $q_{EAS\text{-}EIS}$.

The remaining energy is lost directly to the environment by convection and radiation ($q_{EAS\text{-}amb}$, $q_{EIS\text{-}amb}$, $q_{EAS\text{-}sky}$, $q_{EIS\text{-}sky}$). The model assumes that all temperatures, heat flow rates and thermodynamic properties are uniform around the perimeter of the receiver. With reference to Figure 7, the energy balance equations are determined by conserving energy at each surface of the receiver cross-section:

$$q_{abs} = q_{EAS-amb} + q_{EAS-sky} + q_{EAS-IS} + q_{EAS-EBS} \quad (3.2)$$

$$q_{IAS-HTF} = q_{EAS-IS} - q_{IS-EIS} \quad (3.3)$$

$$q_{EAS-EIS} + q_{IAS-EIS} = q_{EBS-amb} + q_{EIS-sky} \quad (3.3)$$

Correlations for heat transfer in single- and two-phase flows are implemented in the energy balances depending on the flow conditions in each control volume. Convective losses from the outer surface of the absorber have been modelled considering a forced convection mechanism in which the wind speed plays the main role. Radiative heat losses to the environment depend on the difference between the temperature of the external surface of the receiver and the apparent temperature of the sky assumed 8 °C below the ambient air temperature (Forristall, 2003).

The heat transfer from the external to the internal (turbulator) surface of the absorber can be treated as heat conduction in a rectangular cross section hollow body with the inner and outer surfaces at constant temperatures. In the considered receiver, given the high conductivity of the aluminum, which the absorber is made, it is reasonable to assume that the internal surface temperature is fairly constant.

Finally, to calculate the heat flow rate gained by the heat transfer fluid in the absorber, two heat transfer mechanism have been considered. Convective liquid heating occurs when the fluid is subcooled or saturated liquid and the wall temperature of the inner surface is lower than the saturation temperature, while a two-phase heat transfer occurs when the temperature of the internal surface in contact with the fluid is above its saturation temperature. To calculate the convective heat transfer coefficient when the liquid is heated, the procedure proposed by Manglik and Bergles (1995) is adopted. In the two-phase heat transfer, vaporization of the fluid can occur already in the presence of undercooled liquid. The formulation proposed by Liu and Winterton (1991) at the average vapor quality between inlet and outlet conditions of the control volume is applied to calculate the heat transfer coefficient between the inner wall and the vaporizing fluid.

The numerical model is implemented in Matlab® in a block diagram Simulink® environment. The thermophysical properties of the fluids are calculated with NIST Refprop Version 9.0 (Lemmon et al., 2010). The model includes the parameters used to describe the concentrator's optical performance (i.e. the nominal reflectance of the mirrors, optical properties of the external surface of the receiver), the geometric properties of the receiver and of its internal turbulator. The inputs of the model are the direct normal irradiance, the temperature and the velocity (wind speed) of the ambient air, the inlet temperature and mass flow rate of the heat transfer fluid in the receiver, assuming that it is always in conditions of subcooled liquid and its saturation pressure. The model estimates the temperatures at each of the considered thermal nodes in each receiver's segment as long as the convergence criteria based on the local and global thermal balances are not satisfied. Once the convergence is reached, the model provides the useful heat flow rate gained by the fluid, the average fluid temperature, the outlet temperature and vapor quality for each segment of the receiver, and finally, the thermal efficiency of the solar thermal collector.

3.1 Model validation

The results of the numerical simulations are compared against experimental data to assess the accuracy of the model. The difference between the estimated value of the collector efficiency and the collect data are plotted as function of the mass flow rate of the halogenated fluid. Figure 8 shows that the estimated thermal performance of the collector is in good agreement with that determined through the experimental tests. The prediction of the thermal efficiency displays a prediction error within 2%.

The validated numeric model has been used to perform an estimation of thermal performance of the collector including vaporization of the halogenated fluid up to a saturation temperature of 120 °C. The result of these simulations is shown in Figure 13. For these simulations, the values of the mass flow rate are assumed according to the inlet subcooling, so that the outlet vapor quality resulted between 0.55 and 0.6. This is done to prevent the onset of dryout phenomenon and the use of the Liu and Winterton (1991) outside its validity range. The ambient temperature is considered equal to 30 °C. From the numerical predictions, it results that it is possible to vaporize

the halogenated fluid HCFO-1233zd(E) inside the modelled receiver at a saturation temperature of 130 °C with a thermal efficiency of solar collector higher than 65%. Even though, the experimental efficiency curve plotted in Figure 9 is extended from its original range of definition, it results in very good accordance with the simulated efficiency curve.

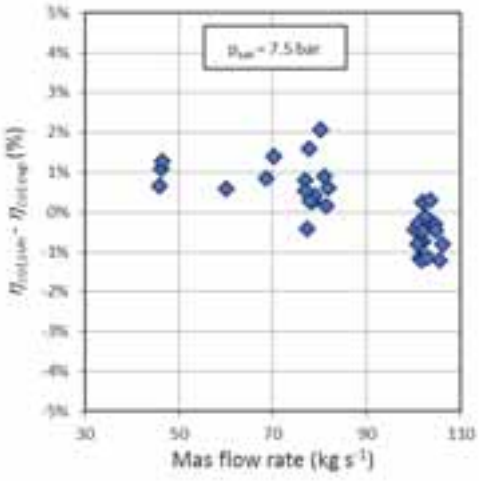

Figure 8 – Difference between simulated and measured values of the collector efficiency as a function mass flow rate.

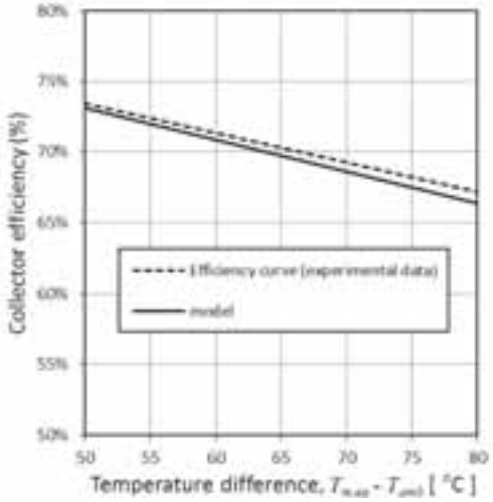

Figure 9. Simulated and experimental efficiency curves as a function of the temperature difference between the calculated mean condition of the fluid and the ambient.

4. Conclusions

An innovative solar receiver for linear concentrating collectors has been experimentally tested for the direct vaporization of a low-GWP halogenated fluid. The conducted experiments allow to determine the thermal performance of the collector composed by a parabolic trough concentrator and the flat solar receiver. During the tests the mass flow rate and the subcooling of the halogenated fluid entering the receiver have been varied to obtain different values of the outlet vapor quality.

The results of the experimental campaign reveal that the solar collector is able to vaporize the HCFO-1233zd(E) at 7.5 bar saturation and outlet vapor quality between 0.37 and 0.98 with a mean efficiency of 73%. In the present operating conditions, the mass flow rate and the subcooling of the halogenated fluid entering the receiver display a negligible influence on the performance of the collector.

A numerical model of the receiver has been developed in Matlab®. This model divides the receiver in several segments and is capable to estimate the temperatures at each thermal node in each receiver's segment providing the heat flow rate gained by the fluid, the average fluid temperature, the outlet temperature and vapor quality at each segment of the receiver, and finally, the thermal efficiency of the solar thermal collector. The results of the numerical simulations were compared against experimental data to validate the model. The estimated thermal performance of the collector is in good agreement with the experimental tests. The prediction of the thermal efficiency of the collector displays error within 2%. The model can be used to perform an estimation of thermal performance of the collector with vaporization of the halogenated fluid up to 120°C saturation temperature. It results that it is possible to vaporize the halogenated fluid HCFO-1233zd(E) at an outlet vapor quality between 0.55 and 0.6 with a thermal efficiency of the solar collector higher than 65%.

5. References

Bortolato, M., Dugaria, S., Del Col, D., 2016. Experimental study of a parabolic trough solar collector with flat bar-and-plate absorber during direct steam generation. Energy 116, Part 1, 1039-1050.

Cataldo, F., Mastrullo, R., Mauro, A.W., Vanoli, G.P., 2014. Fluid selection of Organic Rankine Cycle for low-temperature waste heat recovery based on thermal optimization. Energy 72, 159-167.

Chen, H., Goswami, D.Y., Stefanakos, E.K., 2010. A review of thermodynamic cycles and working fluids for the conversion of low-grade heat. Renewable and Sustainable Energy Reviews 14, 3059-3067.

Eck, M., Uhlig, R., Mertins, M., Häberle, A., Lerchenmüller, H., 2007. Thermal load of direct steam-generating absorber tubes with large diameter in horizontal linear fresnel collectors. Heat transfer engineering 28, 42-48.

Eck, M., Zarza, E., Eickhoff, M., Rheinländer, J., Valenzuela, L., 2003. Applied research concerning the direct steam generation in parabolic troughs. Solar Energy 74, 341-351.

Eyerer, S., Wieland, C., Vandersickel, A., Spliethoff, H., 2016. Experimental study of an ORC (Organic Rankine Cycle) and analysis of R1233zd-E as a drop-in replacement for R245fa for low temperature heat utilization. Energy 103, 660-671.

Forristall, R., 2003. Heat Transfer Analysis and Modeling of a Parabolic Trough Solar Receiver Implemented in Engineering Equation Solver.

Giuffrida, A., 2014. Modelling the performance of a scroll expander for small organic Rankine cycles when changing the working fluid. Applied Thermal Engineering 70, 1040.

Heberle, F., Schifflechner, C., Brüggemann, D., 2016. Life cycle assessment of Organic Rankine Cycles for geothermal power generation considering low-GWP working fluids. Geothermics 64, 392-400.

International Organization for Standardization, 2008. ISO/IEC Guide 98-3:2008; Uncertainty of Measurement -- Part 3: Guide to the Expression of Uncertainty in Measurement (GUM:1995), Geneve, Switzerland.

Lemmon, E.W., Huber, M.L., McLinden, M.O., 2010. NIST Standard ReferenceDatabase 23: Reference Fluid Thermodynamic and Transport Properties - REFPROP. 9.0.

Liu, Z., Winterton, R.H.S., 1991. A general correlation for saturated and subcooled flow boiling in tubes and annuli, based on a nucleate pool boiling equation. International Journal of Heat and Mass Transfer 34, 2759-2766.

Manglik, R.M., Bergles, A.E., 1995. Heat transfer and pressure drop correlations for the rectangular offset strip fin compact heat exchanger. Experimental Thermal and Fluid Science 10, 171-180.

Molés, F., Navarro-Esbrí, J., Peris, B., Mota-Babiloni, A., 2016. Experimental evaluation of HCFO-1233zd-E as HFC-245fa replacement in an Organic Rankine Cycle system for low temperature heat sources. Applied Thermal Engineering 98, 954-961.

Molés, F., Navarro-Esbrí, J., Peris, B., Mota-Babiloni, A., Barragán-Cervera, Á, Kontomaris, K., 2014. Low GWP alternatives to HFC-245fa in Organic Rankine Cycles for low temperature heat recovery: HCFO-1233zd-E and HFO-1336mzz-Z. Applied Thermal Engineering 71, 204-212.

Molés, F., Navarro-Esbrí, J., Peris, B., Mota-Babiloni, A., Kontomaris, K., 2015. Thermodynamic analysis of a combined organic Rankine cycle and vapor compression cycle system activated with low temperature heat sources using low GWP fluids. Applied Thermal Engineering 87, 444-453.

Myhre, G., Shindell, D., Bréon, F.M., Collins, W., Fuglestvedt, J., Huang, J., et al., 2014. Chapter 8: anthropogenic and natural radiative forcing, in Stocker, D., Qin, G.-., Plattner, M., Tignor, S.K., Allen, J.B., et al. (Eds.), Climate Change 2013: The Physical Science Basis : Working Group I Contribution to the Fifth Assessment Report of the Intergovernmental Panel on Climate Change. Cambridge University Press, New York.

Patten, K.O., Wuebbles, D.J., 2010. Atmospheric lifetimes and Ozone Depletion Potentials of trans-1-chloro-3,3,3-trifluoropropylene and trans-1,2-dichloroethylene in a three-dimensional model. Atmospheric Chemistry and Physics 10, 10867-10874.

Peris, B., Navarro-Esbri, J., Moles, F., Gonzalez, Mota-Babiloni, A., 2015. Experimental characterization of an ORC (organic Rankine cycle) for power and CHP (combined heat and power) applications from low grade heat sources. Energy 82, 269-276.

Quoilin, S., Orosz, M., Hemond, H., Lemort, V., 2011. Performance and design optimization of a low-cost solar organic Rankine cycle for remote power generation. Solar Energy 85, 955-966.

Water production from the atmosphere in arid climates using low grade solar heat

Vincenzo Gentile[1], Marco Simonetti[1], Pietro Finocchiaro[2], Gian Vincenzo Fracastoro[1]

[1] Politecnico di Torino, Turin (Italy)

[2] Solarinvent srl, Catania (Italy)

Abstract

Water scarcity is a severe problem that involves large areas of the World. The possibility to extract water from atmosphere is more and more investigated as a fascinating solution to face this problem in arid climates. A day-night thermodynamic cycle is here investigated to produce water from air using low temperature heat in an adsorption bed typically used for air dehumidification in DEC systems. The system can be easily integrated with a solar thermal collector and waste heat at 50-80 °C. The preliminary results of the experimental tests of a prototype that gives the possibility to simultaneously exchange heat and mass through the adsorbing mass are here presented.

Keywords: Atmospheric water harvesting, adsorption material, solar energy, water production,

1. The problem of access to water resources

Water scarcity is not a new problem, but the rise of the fresh water demand in the last years poses this issue as the critical challenge for the next 20 years. The OECD Environmental Outlook 2050 estimates that by 2050 water demand will increase by 55%, BRICS and developing countries plays a fundamental role in this scenario: respectively with an increase by 700% and 400%. Main actors of this increase are the domestic, manufacturing and power sector, driven by the increase of population, evaluated up to 33%, that will be concentrated in developing countries. (UNESCO, 2015). Cities are the areas in which the water challenge will most be played: in 2014 54% of the global population lived in cities and by 2050 it will be more than 65% (UNDESA, 2014). This water demand is mainly satisfied by the extraction from the available surface and groundwater source, that are yearly recharged by the hydrologic cycle. Figure 1 depicts the world condition in 2015 in terms of water withdrawal as a percentage of the renewable resources.

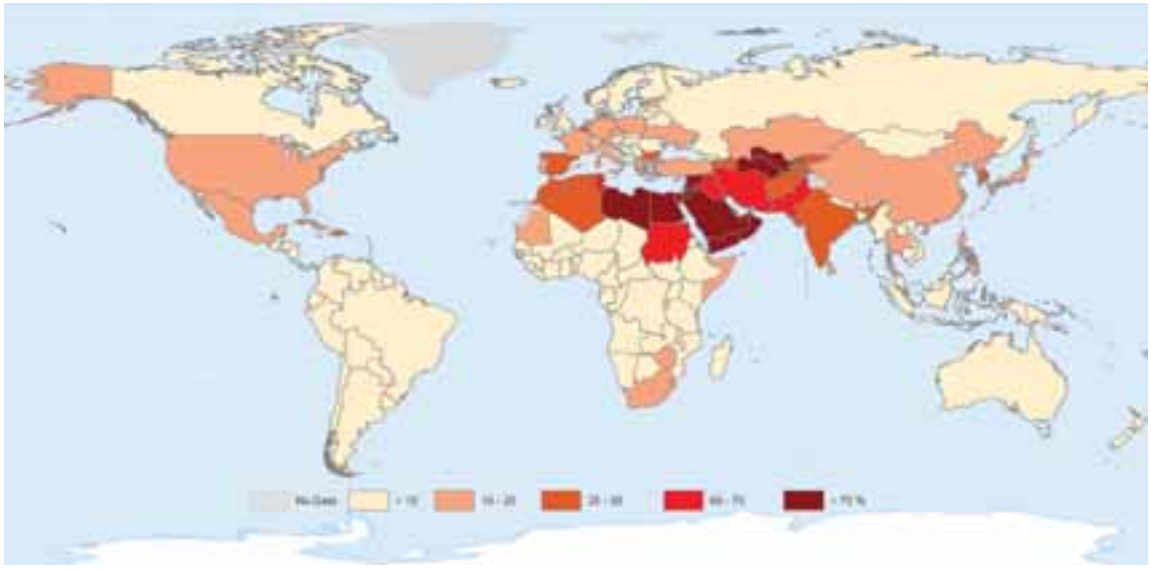

Figure 1. Percentage of withdrawal of renewable water resource in 2015

doi:10.18086/swc.2017.17.02 Available at http://proceedings.ises.org

The map shows clearly that the regions in which water issues presently are and will appear in the future more severe are North-Africa, Arabic peninsula, Middle East, and India in which there's a higher population density. In these regions water withdrawal overcomes 60% of the total renewable resource. Despite sub-Saharan region appears not involved in this issue, the uncontrolled rapid urbanization happened between 1990 and 2012 have reduced the percentage of population that have a direct access to piped water. In this case the problem of fresh water access is rather an infrastructure issue then a resource deficiency.

Up to now, the alternatives to satisfy the increase of water demand are to dig deeper to access available water resources or exploit other innovative solutions such as the use of reclaimed water or the reverse water osmosis process for sea-water desalination, that appears as the most promising solution for that problem (UNESCO, 2015). The use of technologies for wastewater treatment and water desalination are research object of many scientific research (Youssef et al., 2016; Siddiqui et al., 2016; Chiavazzo et al., 2017). The typical solutions become economically feasible for large plants only. Moreover, they are quite energy intensive, being based on the use of fossil fuels and, causing a large carbon footprint of the produced fresh water. Further on, it appears evident that persons that lack the access to water will also likely lack the access to electricity or other fuels to power decentralized solutions. There are a lot of countries nevertheless in which both the distance from brackish or polluted water resources is an obstacle for these alternatives, arid areas of inner region of North-Africa and the Arabic peninsula commonly face this problem. The atmosphere, containing 12,900 km^3 of fresh water in the form of water vapor, could be an alternative to this situation and should be considered as a valid renewable source of fresh water. Just for comparison, liquid fresh water at the earth surface is about 110,000 km^3 and superficial rivers, which represent the first source for human use, 2,107 km^3 (El-Ghonemy, 2012).

2. Water extraction from atmosphere

The possibility to use ambient air as water source has been already studied and tested in different research activities (El-Ghonemy, 2012). There are two main valid options:

- Use a refrigeration cycle based on vapor compression heat pumps or absorption chillers, to cool the air under dew point and condense the moisture (Margini et al., 2015)
- Use sorption materials to subtract the water vapor contained in the atmosphere. Afterwards the material is regenerated and the water is condensed at ambient temperature (William et al., 2015)

The system proposed in this paper is based on the second approach, a thermodynamic cycle is investigated as a feasible and practical solution driven by solar renewable energy, and experimental tests are carried out to investigate relative potentialities.

A fundamental role in this cycle is played by the heat provided at low temperature, 50-80°C, that can be easily and economically produced by low temperature solar technologies: flat-plate or evacuated tube solar collectors. This way of producing heat has high compatibility with such regions that are characterized by arid climate conditions, in which the problem of water scarcity is frequently coupled with a huge amount of solar radiation. Furthermore, the low level of temperature of the heat supply opens the access to a huge amount of *"alternative"* heat sources, such as waste heat or thermal cascade from other technological processes.

The cycle alternates two different successive phases as shown in Figure 2:

- *Adsorption*. Water vapor capture from the atmospheric air exploiting adsorption material such as silica gel, Zeolite, addicted clay, etc…
- *Desorption*. Very hot and humid air stream production by the regeneration of the adsorption material providing heat to the system.

The hot and humid flux is then condensed in a dry cooler at the outdoor ambient temperature. To have significant production of water during condensation it's necessary to produce an air stream reaching a sufficient level of temperature and humidity so that the environment might be accepted as an effective condenser. This consideration has to deal with the physics behind adsorption/desorption of water vapor in the material. Humid air when exposed to adsorption or desorption transformations moves along an isenthalpic line. This means that variation of air moisture content is always linked to a variation of air temperature: during adsorption, moisture content reduces and air temperature increases; conversely, during desorption moisture content increases and air temperature

reduces. For instance, if we want to have a condensing stream at the ambient temperature of 35°C, the saturation point corresponds to about 36.5 g kg^{-1} (point 3 in Figure 3). The only way to reach points on the saturation line above this reference point with an isenthalpic transformation is to have at the inlet of the desorption phase air at temperature around 50°C with the same moisture content (point 1). Anyhow, the moisture content at the saturation is very poor (point 2 iso-H) and just a reduced amount of water would be condensed (4-5 g/kg).

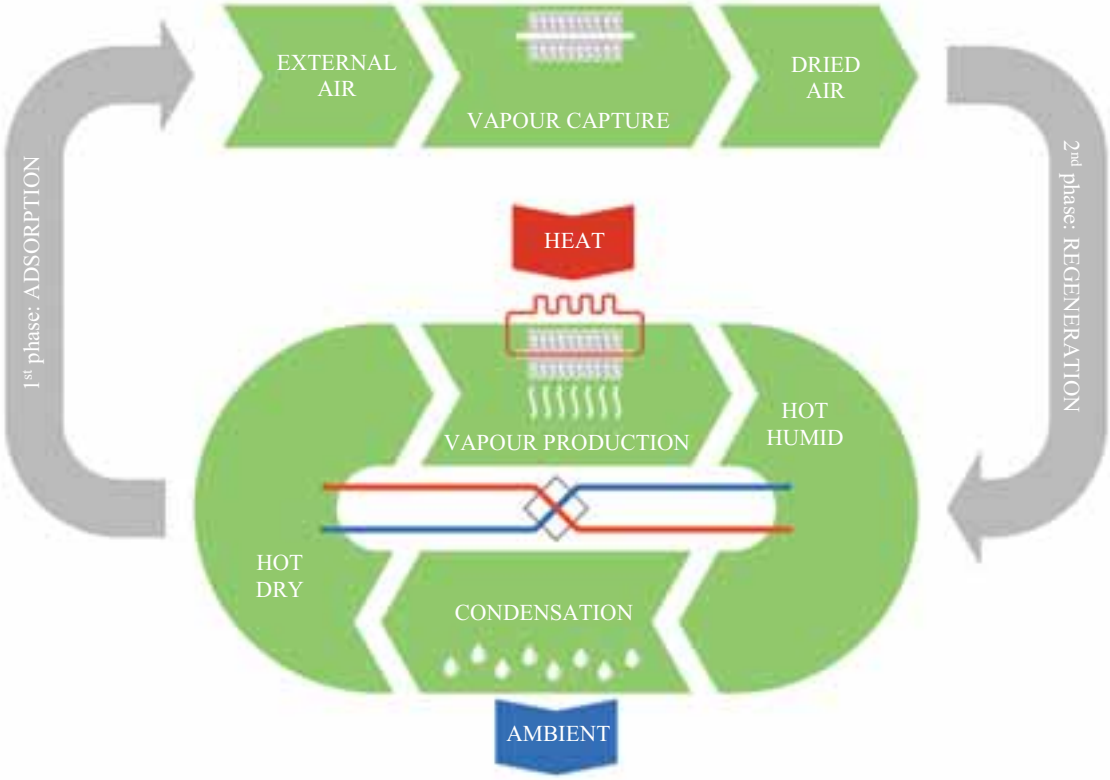

Figure 2. Conceptual scheme of the adsorption/desorption cycle

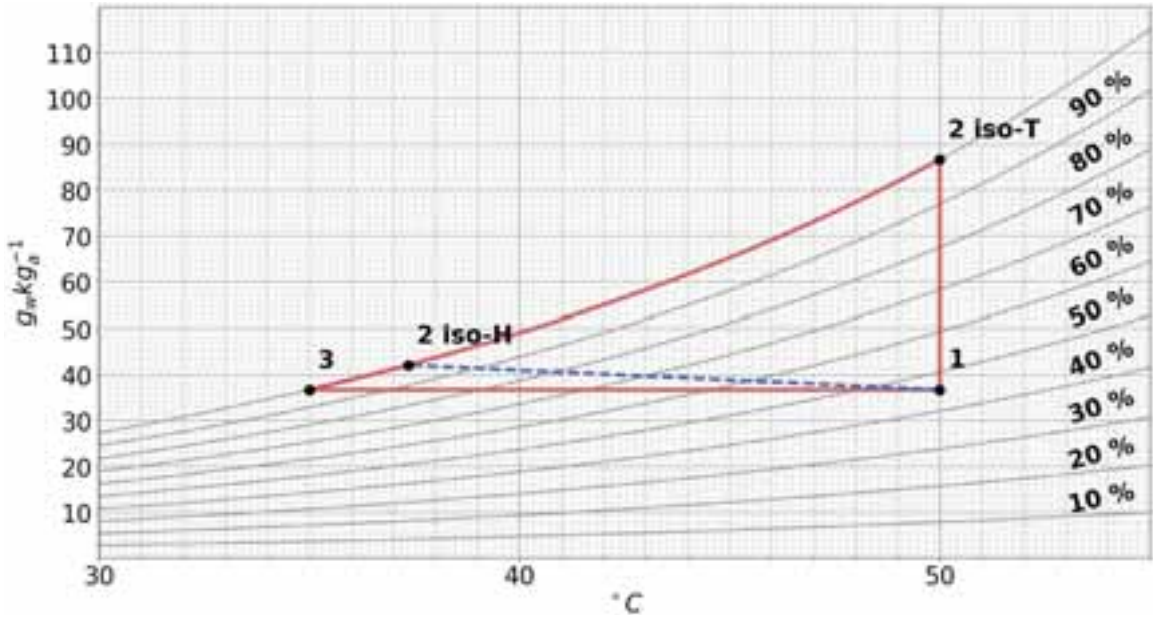

Figure 3. Comparison between a desorption with an isenthalpic (iso-H) or isothermal behavior (iso-T)

A different solution is when the sorption material follows a desorption transformation with an isothermal behavior

(2 iso-T). The specific humidity difference, starting from the same regeneration starting point (1), exceeds 40 g kg^{-1}, far more than the 5 g kg^{-1} given by the isenthalpic transformation. Obviously, this huge difference will require an equivalent amount of energy to allow the movement of water molecules from sorption material to the air. This amount of energy is slightly above the latent heat of water evaporation multiplied by moisture content difference. The point is that, to obtain the point 2 iso-T one has to supply an amount of heat equivalent to the latent heat, but always at the same temperature, 50°C. On the contrary, if point 2 iso-T had to be reached by an isenthalpic line the heat supply temperature would be above 70°C. This gives important advantages in terms of efficient utilization of solar thermal source at low temperature (flat plat or evacuated tubes), and limits the design problem only to the thermal requirement from the source.

To realize an isothermal transformation a system is required, that gives the possibility to exchange at the same time heat and mass. To do this, the sorption material such as Silica gel, Zeolite, etc. can be arranged in a finned heat exchanger (HX-ADS) (Finocchiaro et al., 2016; Simonetti et al., 2016). The heat to the adsorption heat exchanger is supplied by water circulation at 50-80°C, and a quasi-isothermal regeneration occurs. A fan circulates the air flow through the HX-ADS in a closed loop, thus permitting to continuously subtract water from the sorption material. The quasi-isothermal regeneration (line 1-2 iso T) is fundamental to obtain a hot and humid air stream from which water vapor can be easily condensed using ambient temperature in a dry cooler.

After this stage the air is cooled down by a double step thermal exchange: first by a heat recovery to reheat the regeneration stream and second by the condenser at the environment temperature. According to the thermodynamic cycle described in Figure 2 and Figure 3, around two liters of water can be collected from the treatment of an air volume of 100 m^3. In Table 1 different commercial solutions using vapor compression or absorption chillers are compared, in order to cool down the air to the dew point obtaining liquid water. Main differences of the proposed solution are the thermal supply at lower temperature, and lower specific consumption in terms of primary energy.

Table 1. Comparison of the proposed solution to existing commercial product and not.

	PROPOSED SOLUTION	AWA MODULE SEAS	WATER GEN	WATER FROM AIR	DESICCANT WHEEL	US 8584480
Technology	Adsorption material regeneration	Chiller (r134a)	Chiller (r134a)	Chiller (r134a)	Adsorption material regeneration	Absorption chiller (Li-Br)
Energy Supply	Heat	Electricity	Electricity	Electricity	Heat	Heat
Technology source	Solar thermal; waste heat; biomass	Fossil fuel; electricity power	Fossil fuel; electricity power	Fossil fuel; electricity power	thermal	Waste heat from diesel
Specific consumption	0,6 kWh_{th} lt^{-1}	0,6 kWh_{el} lt^{-1}	0,33 kWh_{el} lt^{-1}	0,33 kWh_{el} lt^{-1}	19 kWh_{th} lt^{-1}	-
Minimum supply temperature	55°C	-	-	-	80°C	100°C
Production in arid climate	+++	+	+	+	-	+
Use of renewables	+++	Indirect by RES	Indirect by RES	Indirect by RES	++	+
Use of waste heat	+++	None	None	None	++	++

3. Prototype

In the laboratory of the Energy Department (DENERG) of Politecnico di Torino a prototype has been assembled composed by and adsorption heat exchanger (Figure 4), and a condenser with a heat recovery system Figure 5. The adsorption system contains about 20.5 kg of silica gel grain with an average diameter of 3 mm. The heat is supplied to that system by a water circulation between 50-80 °C, produced by an electric resistance of 1.25 kW. The condenser is composed by an air to air heat recovery system and an air to water radiator which is used to condense the hot and humid stream, through cold water taken from water network, at around 20°C.

Integrated-Circuite temperature sensors LM35CAZ, with a precision of ± 0.2°C, monitor air and water temperature through the cycle. The RH sensor is a thermoset polymer capacitive type with on chip conditioning HIH4000-4 sensor monitors humidity at the inlet and outlet of the adsorption heat exchanger with

a precision of ± 3.5%. The air flow is driven by a centrifugal fan, at variable velocity with a maximum power consumption of 43 W, and an air flow rate range 0-100 $m^3 h^{-1}$. The two parts, adsorption/desorption packed bed and the condenser, are connected by a flexible duct: the outlet of the adsorption heat exchanger with condenser's inlet, and the condenser's outlet with the adsorption stage's inlet.

Figure 4. Adsorption heat exchanger

Figure 5. Condenser and heat recovery system

4. Experimental Tests

The testing procedure and preliminary results of the prototype operation are here presented.

Each test, as explained in the concept of the cycle, is composed by two successive phases. First the outdoor air circulates at the maximum flow in the adsorption bed, until equilibrium with adsorption material is reached with the air inlet condition, and the material can be considered as "quasi-saturated". Due to the prototype design this phase takes tens of hours, during which only the air at the inlet and outlet are monitored, in terms of temperature and humidity. After that, hot water starts to circulate through the coil of the adsorption heat exchanger and heats up the material. When the desired temperature is reached, flexible ducts are connected to the condenser and the fan is turned on. The regeneration starts, and humidity and temperature at each step of the cycle and the inlet/outlet water temperature are monitored. Finally, condensation starts, and water droplets are collected in a recipient, Figure 6. At the end of each test the water is discharged and the total amount is finally weighted with a high precision scale.

Figure 7 shows data monitored during the adsorption phase. This part of the test had a duration of more than 18 hours, with an average air inlet temperature of 22 °C and an average inlet air humidity of 8 g kg^{-1}. The outlet air from the adsorption bed reached a maximum temperature of 37.5 °C after around two hours from the start of the test, showing as the combination of a very high amount of sorption mass (20.5 kg) and a low air flow rate (100 $m^3 h^{-1}$) leads to a huge inertia of the system. In this phase outlet air moisture content drops down to 1 g kg^{-1} at the beginning of the test. The adsorption phase is stopped when outlet moisture content is around the inlet value. Figure 8 and Figure 9 shows data monitored during the desorption phase, that have a duration of about 6.5 hours. This phase has been divided in 5 successive intervals in which, between each other there isn't air flow but only hot water circulation. These intervals are visible in the graphs by the unshaded band, in this way at each interval the desorption starts at higher temperature. Condensation temperature is between 15 and 20°C depending on the

temperature of the water network. Air flow rate have changed from 50 to 100 $m^3\ h^{-1}$ during the desorption phase. The moisture content of the air had a big variation in each interval from 100 to 30 g kg^{-1}.

In Figure 10 to Figure 14 the cycle on the psychrometric chart is depicted for each interval of the desorption phase. It can be noticed that:

- Maximum moisture content at the outlet of the bed reduces progressively in each interval as consequence of the reduction of water contained in the adsorption material (red points)
- Air in the condenser always reaches the saturation condition, and all points fall on the 100% line of relative humidity (pale blue points)
- The temperature difference between the outlet of the bed and the outlet of the heat recovery system increases, following the increase of the sensible thermal exchange (red and yellow points)
- There's a big temperature difference between the inlet to the bed and the outlet of the heat recovery system caused by high thermal losses that occur in the path through the flexible duct that connect these two components. (blue points)

The total amount of water obtained from this test is equal to 2.318 kg. Starting from electrical power of the resistance (1.25 kW_{el}) and the total period of active desorption, 220 minutes, the thermal consumption is found to be 4.583 kWh_{th}. Then, the specific consumption results in 1.98 $kWh_{th}\ lt^{-1}$, that is 3.3 times the ideal value found through the thermodynamic analysis shown in Table 1. It has to be considered that numerous thermal losses occur in that system, the highest being in the duct between the condenser's outlet and the sorption bed's inlet, that can be estimated from the temperature difference between these two points, equal to 0,5 kWh lt^{-1}, or 25% of the total amount.

Another point is that the definition of the thermal specific consumption parameter in terms of total values, total thermal energy consumed and total water condensed, does not consider the transient behavior of the packed bed. In other terms, despite the thermal power provided to this system is always constant, the production of water decreases in time as the reduction of moisture content difference between inlet and outlet of the sorption bed. As a result of that, specific thermal consumption is not constant but an increasing function of the operating time. This behavior has been estimated in Figure 15, where positive difference of the air moisture content in the desorption phase is compared with a specific energy indicator, e_{th}, defined as follow:

$$e_{th} = \frac{P_{th}}{\dot{Q}_a * (X_{out} * \rho_{out} - X_{in} * \rho_{in})} = \left[\frac{Wh}{gr_{H_2O}}\right]$$

This function has two characteristic behaviors in time:

- *Continuous increase*. For each interval the increase is strictly correlated to the reduction of the outlet moisture content. This variation is very consistent such that at the end of each interval the final value is many times larger than the initial one.
- *Step behavior*. The reduction of internal moisture content of the sorption material amplifies the continuous increase between each interval. Instead the increase of the regeneration temperature between each interval shift down the initial value of the specific energy consumption. In this case the temperature and the duration of the hot water circulation period between each interval plays a fundamental role that is strictly related to the diffusive resistance of the water vapor in the micropore of the sorption material.

The correct management of heat in the regeneration phase has a large influence on the efficiency of the process, and thermal consumption can be reduced by an optimized control strategy.

Figure 6. Water droplets formation during condensation are collected in a basin.

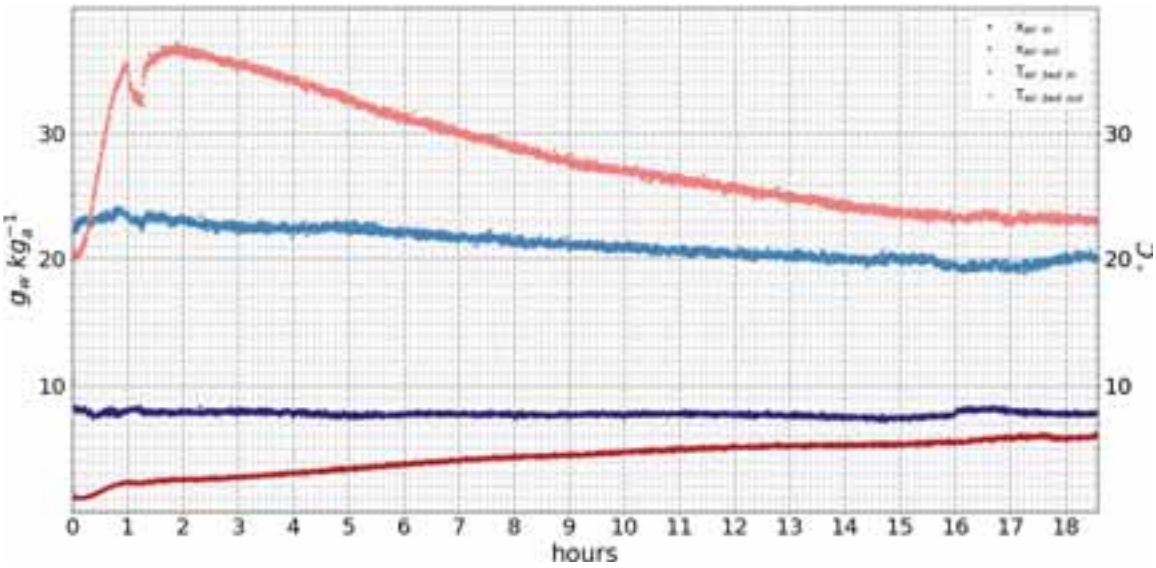

Figure 7. Air temperature and humidity profile during adsorption phase of the test

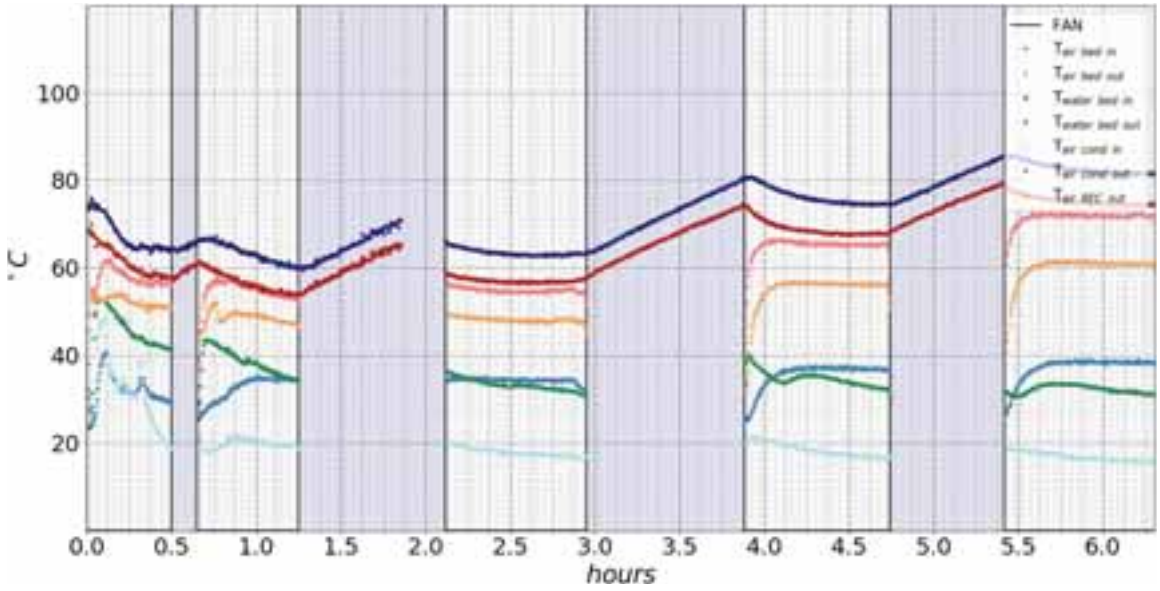

Figure 8. Air and water temperature profile during desorption phase of the test

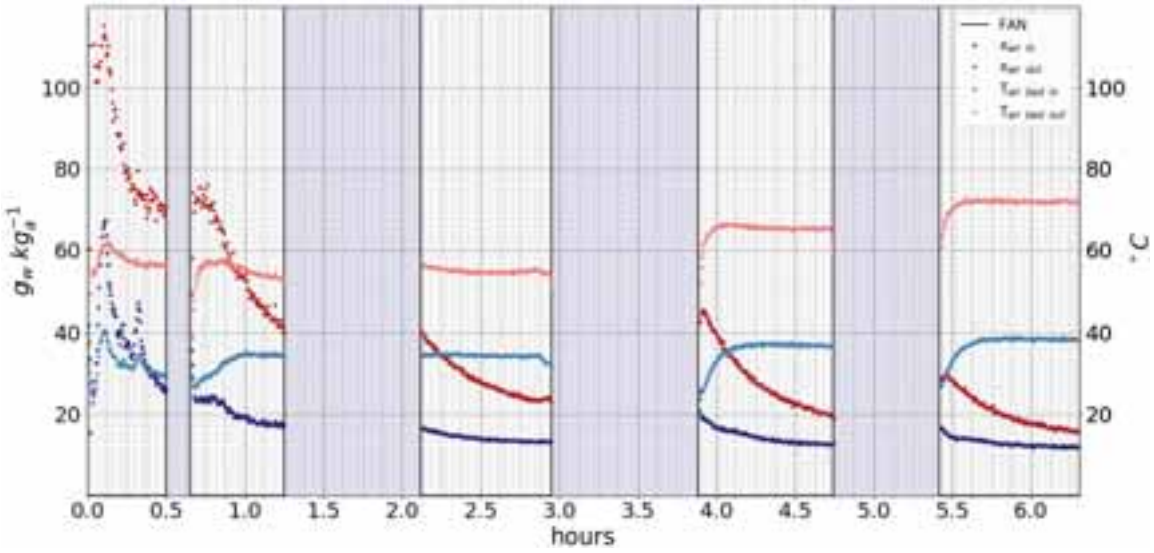

Figure 9. Air temperature and humidity profile during desorption phase of the test

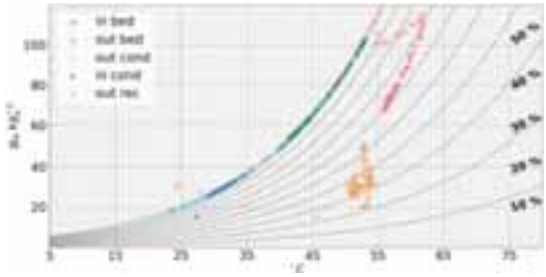

Figure 10. Cycle represented on psychrometric chart during the 1st part of the desorption

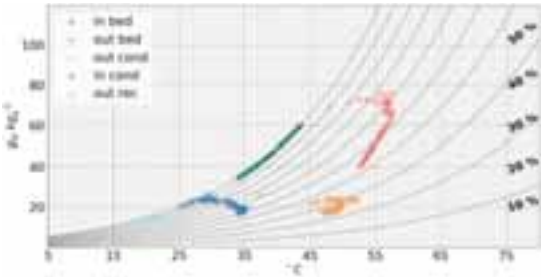

Figure 11. Cycle represented on psychrometric chart during the 2nd part of the desorption

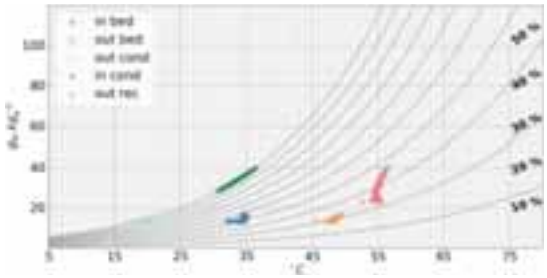

Figure 12. Cycle represented on psychrometric chart during the 3rd part of the desorption

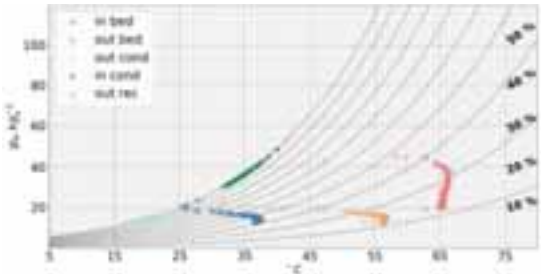

Figure 13. Cycle represented on psychrometric chart during the 4th part of the desorption

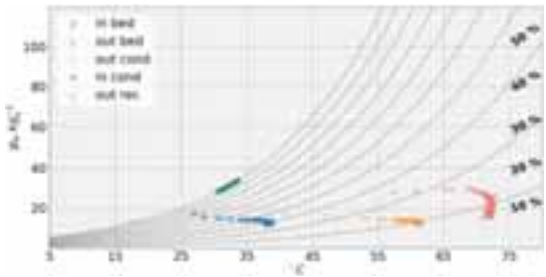

Figure 14. Cycle represented on psychrometric chart during the 4th part of the desorption

Table 2. Desorption interval

INTERVALS	Interval duration	Reg Temperature	Air Temperature
	min	°C	°C
1st	30	65	57
2nd	36	60	53
3nd	50	63	56
4th	49	74	65
5th	55	81	71

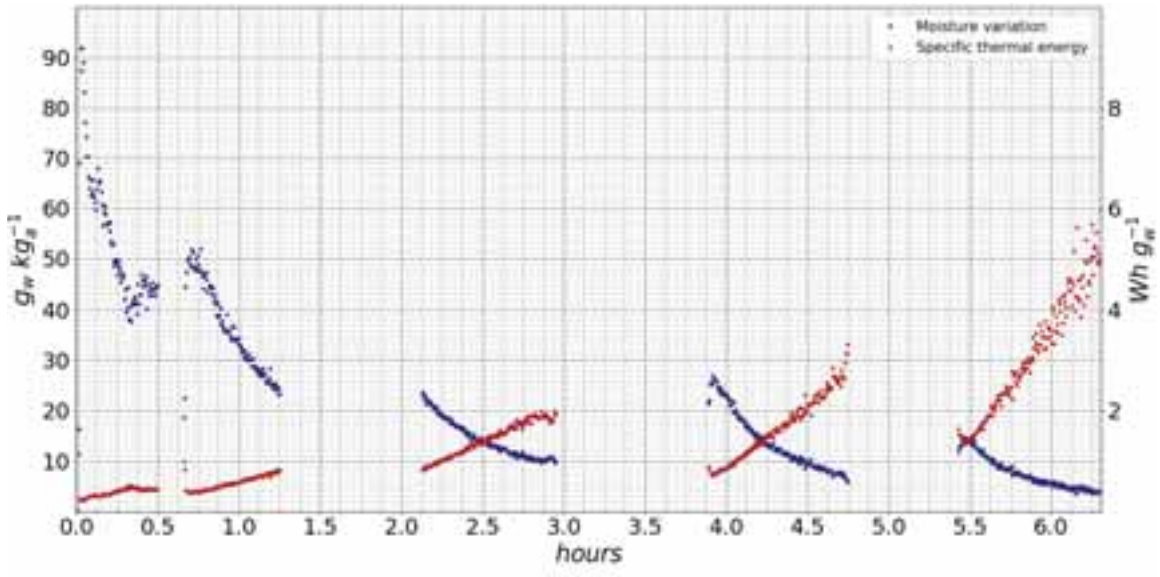

Figure 15. Evaluation of the specific thermal consumption of the desorption test (red), based on the variation of moisture content between inlet and outlet of the bed (blue).

5. Conclusion

The goal of this research is to demonstrate the feasibility of a system that catches the water vapor from air for many hours, such as a nocturnal period, and condenses this vapor using low temperature (50-80°C), solar heat. The prototype here presented has been tested in the laboratory of Energy Department (DENERG) of Politecnico di Torino. Preliminary results showed the capability to concentrate the water vapor contained in outdoor air for 18 of hours in the sorption material. Afterwards, with the use of heat under 80°C this vapor was released in about one fifth of the time to an air stream and condensed in order to obtain liquid water. A quantity of 2.318 lt of water has been obtained with an energy consumption of 4,625 kW_{th} of heat for an active period of operation around 3,7 hours.

Efficiency and performances of the process can be increased, and different strategies will be implemented to increase the efficiency of the system and reach values close to the theoretical value of 0,6 $kW_{th}\ lt^{-1}$, such as: the increase of ducts insulation; reduction of the length of air ducts; improvement of the regeneration strategy. New tests will be carried out with different outdoor temperatures and moisture contents, in order to simulate different climatic conditions such as in hot humid and arid countries. Also, the condensation temperature will be varied in a range of temperature between 15-35°C. Chemical test on water will be carried out in order to understand the best treatment needed to transform it in potable water.

Finally, we may say that the experiment has validated the concept on which this type of machine is based, and has shown an encouraging prospective.

6. References

E. Chiavazzo, M. Morciano, F. Viglino, M. Fasano, P. Asinari, Feb. 2017. Performance analysis of a water distiller. DENERG Politecnico di Torino.

A.M.K. El-Ghonemy, 2012. Fresh water production from/by atmospheric air for arid regions, using solar energy: Review. Renewable and Sustainable Energy Reviews 16, 6384-6422.

Finocchiaro P., Beccali M., Gentile V., 2016. Experimental results on adsorption beds for air dehumidification. International Journal of Refrigeration 63, 100-112.

A. Margini, L. Cattani, M. Cartesegna, L. Magnani, 2015. Production of water from the air: the environmental sustainability of air-conditioning systems through a more intelligent use of resources. The advantages of an integrated system. Energy Procedia 78, 1153-1158.

F. R. Siddiqui, N.A.S. Elminshawy, M.F. Addas, 2016. Design and performance improvement of a solar desalination system by using solar air heater; Experimental and theoretical approach. Desalination 399, 78-87.

Simonetti, M., Gentile V., Fracastoro, G.V., Freni, A., Calabrese, L., Chiesa G., 2016. Experimental testing of the buoyant functioning of a coil coated with SAPO34 zeolite, designed for solar DEC (Desiccant Evaporative Cooling) systems of buildings with natural ventilation. Applied Thermal Engineering 103, 781-789.

UNDESA (United Nations Department of Economic and Social Affairs), 2012. Back to our Common Future: Sustainable Development in the 21st Century (SD21) project.

UNESCO, 2015. The United Nations World Water Development Report 2015. WWAP(United Nations World Water assessment program.

G.E. William, M.H. Mohamed, M. Fatouh, 2015. Desiccant system for water production from humid air using solar energy. Energy 90, 1707-1720.

P.G. Youssef, S.M.Mahmoud, R.K. Dadah, 2016. Numerical simulation of combined adsorption desalination and cooling cycle with integrated evaporator/condenser. Desalination 392, 14-24.

Table 3. Symbols legend

Quantity	Symbol	Unit
Temperature	*T*	°C
Moisture content	*X*	$g_w\ kg_a^{-1}$ _
Relative humidity	*RH*	%
Enthalpy	*h*	$kJ\ kg^{-1}$
Volume	*V*	m^3, lt
Energy	*E*	kWh
Specific energy	*e*	$Wh\ g_w^{-1}$
Power	*P*	kW
Air flow rate	$\dot{Q}$	$m^3\ h^{-1}$
Density	ρ	$kg\ m^{-3}$
Time	*t*	h
Mass	*M*	kg

Table 4. Subscripts legend

Quantity	Symbol
Isoenthalpic	*iso-H*
Isotherm	*iso-T*
Water	*w*
Air	*a*
Thermal	*th*
Electrical	*el*
Inlet	*in*
Outlet	*out*
Condenser	*cond*
Heat recovery	*REC*
Adsorption packed bed	*bed*
Adsorption	*ADS*
Regeneration	*REG*

All-weather snow machine driven by solar energy

Michael Joemann[1], René Völkel[1], Clemens Pollerberg[1], Lorenzo Podesta[2] and Francesco Besana[2]

[1] Fraunhofer UMSICHT, Oberhausen (Germany)

[2] NeveXN s.r.l., Rovereto (Italy)

Abstract

Technical snowmaking is the only solution to run ski slopes at the beginning and at the end of the winter season if natural snow is missing. However, technical snowmaking has several shortcomings e. g. high water and power consumption. Furthermore, with current snowmaking technology, snow can only be produced below wet-bulb temperatures of approx. -2.5 °C for compressed air and water guns or below approx. -4 °C for fan guns. This paper presents the concept of a snow machine which can be driven by renewable energy sources, able to produce high quality snow at temperatures above 0 °C, in all-weather conditions, and even in high summer season. The proprietary technology is based on a steam jet ejector chiller (SJEC) and uses the triple point of water. The thermal energy for the ejector can be provided by solar collectors or by a biomass steam boiler. Water is the only working fluid in the entire refrigeration system, which guarantees an ecologically friendly concept for the snow supply. Within the paper, the first operational experiences of the prototype as well as performance figures are presented. Furthermore, a concept for the solar circuit of a solar-assisted snow machine is presented. Subsequently, the system design and system performance of a solar-assisted machine will be evaluated for different scenarios. The evaluation is based on simulation results gathered with a model based on mass and energy balances.

Keywords: Technical snowmaking; steam jet ejector chiller; solar-assisted; all-weather conditions

1. Introduction

At the beginning and at the end of the winter season, natural snow is often missing and ski slopes are closed. The missing snow delays the opening of ski resorts, and represents a serious threat for the multibillion-dollar ski tourism industry, resulting in great losses for the economy of the mountain regions. Technical snowmaking is the only solution to run the ski slopes, but it has several shortcomings e. g. high water and energy consumption. Energy is consumed mainly to generate compressed air and to pump water. Typically, 67 % of all energy consumed in a ski resort is used for snowmaking (Smith 2010). A study, which evaluated the energy consumption of ski resorts in Finland, indicates that the average electricity consumption for slope services including lift operation, lighting and snowmaking amounts to approximately 34.6 MWh/a per hectare of snowed slope. The share of snowmaking is high with an average energy consumption of approximately 24.1 MWh/a (Timonen and Ikkunassa Oy 2010). Beside ski resorts, another sector which is dependent on technical snowmaking is indoor ski domes. The specific energy demand for snow production and air cooling in indoor ski domes is even higher as they are operated all year round even at high ambient temperatures.

1.1. Technical snow generation – State of the art

There are several physical processes to produce technical snow. The available processes split into nozzle atomization of water, cooling technology or cryotechnology (Fuhrmann 1996). Snowmaking via nozzles is the most common way. Snowmaking systems via nozzles can be divided into following subspecies: compressed air and water guns (internal and external mixing guns), and fan guns. Compressed air and water guns can be mounted on the ground or on a tower. These systems require pressurized water and compressed air from an external source which is usually supplied by a central facility via a piping network. In contrast, fan guns use electric driven axial fans to propel the water droplets to a huge distance and only require a small amount of compressed air which is nowadays usually provided by an on-board air compressor. Fan guns typically have one or more rings of nozzles which inject water into the fan air stream. Some separate nozzles are fed with a compressed air and water mixture and provide the nucleation points for the snow crystals. For both systems the production of snow works by the atomization of water into myriad water particles (droplets). A water-compressed air mixture is ejected from a

doi:10.18086/swc.2017.17.03 Available at http://proceedings.ises.org

nozzle at a pressure of 5 to 10 bar. During the expansion of the water-compressed air mixture the temperature decreases and the water droplets freeze. Aside from the cooling effect by expansion, the water droplets are also chilled by convection and evaporative cooling. The ice nucleation occurs on impurities in the water droplets. The ratio of water and compressed air has a significant influence on the consistency of the snow. By regulating this ratio, either a dry and powdery snow, a wet and heavy snow, or an ice glaze can be obtained (Pierce, JR. 1954). While a relatively low ambient temperature favors the snowmaking process and decreases the necessary compressed air volume flow, a higher snowmaking temperature increases the need for compressed air. A calm wind is advantageous in order to enable a rapid removal of the crystallization heat. The two main factors, which have influence on the effectiveness of snow production are air temperature and humidity, both combined in the wet bulb temperature. Higher air humidity results in a longer cooling time of water droplets to reach the nucleation temperature. With nozzle based systems snow can only be produced with low wet-bulb temperatures. The borderline temperature where compressed air and water guns (snow lances) can start operation is approx. -2.5 °C and the borderline temperature of fan guns is approx. -4 °C (Fuhrmann 1996). These requirements impede the use of traditional technical snowmakers in many critical situations. According to a study from 2011 assessing the energy use of mobile snowmaking at Swedish ski resorts, the energy demand to produce 1 m^3 of snow is 0.58 – 0.72 kWh_{el} for snow lances and 0.97 – 1.94 kWh_{el} for fan guns. The snow production capacity varies for the tested lances between 13 and 22 m^3/h and for the fan guns between 15 and 34 m^3/h. Thus fan guns are more energy demanding but reach a higher snow production capacity (Rogstam and Dahlberg 2011).

1.2. All-weather snow machines

At wet bulb temperatures above approx. 0 °C some kind of active cooling process is required to produce snow, either refrigeration technology or cryotechnology. Cryotechnology uses a cryogenic medium (e.g. liquid nitrogen (LN) or liquid air) which is mixed in the snow cannon with compressed air and water. The cryogen is required to cool the water droplets for snow generation at ambient temperatures above 0 °C. Alternatively, a room can be chilled with cryogen. Then ordinary snow guns can be used to generate the snow in the chilled room. Cryotechnology is complex and expensive, thus this type of snow production is only used for very special purposes (e. g. snow production in summer as part of events) and thus not suitable for large scale snow production.

In the last decades temperature independent snow machines, also called »all-weather snow machines«, based on different cooling technologies and processes have been developed. Compared to traditional snowmaking technology via nozzles, snow production at temperatures above °C is energy demanding and the systems are technologically more complex. These are the main reasons why all-weather snow machines are currently not widespread. Most of the available all-weather snow machines are electrically driven and produce ice in different forms (e.g. blocks, ice cubes, flake ice, plate ice) which is crushed afterwards to small flakes. However, the snow quality is not comparable with natural snow or snow from nozzle systems, because just big chunks of ice are crushed. The snow is not as fine as natural snow and has sharp edges. In contrast, snow machines based on ice slurry generators produce snow by separating ice crystals from an ice slurry. The snow quality of these machines is much closer to natural snow. At present several types of ice slurry generators exist (cf. (Kauffeld et al. 2005)):

- Mechanical-scraper type with rotating knifes, scrape blades, rotating brushes or screws
- Vortex-flow type with oscillatory moving cooled wall method
- Direct-injection or direct heat exchange type
- Fluidized-bed ice generator
- Vacuum freezing method
- Super-cooling water method

The main functionality of the different principles is described in (Kauffeld et al. 2005). Up to date mechanical-scraper method and vacuum freezing method are used for snow generation. Tab. 1 shows a comparison of market available all-weather snow machines.

The snow quality of snow machines based on ice slurry generators differs, too. With the mechanical-scraper method, the slurry has a slush consistence (cf. (Mogilevsky 2013)). Snow generated with the vacuum freezing method is smoother than ice, which is scraped from a surface, as the ice is generated by formation of crystals in water at the triple point conditions. However, for both technologies, main challenges are the ice separation from the slurry and to produce dry and groomable snow.

Tab. 1: On the market available all-weather snow machines (Source of Data: (Eikevik 2017), (Dieseth 2016))

Company	SnowTek	TechnoAlpin / KTI	IDE	SnowMagic
Product name	SnowGen	SF220	VIM100	SnowMagic 100
Country of origin	Finland	Italy	Israel	USA
Principle	Ice Slurry (scraper type)	Flake ice	Ice Slurry (vacuum freezing)	Flake ice
Type	Mobile	Stationary	Mobile	Mobile
Capacity	220 m³/d (approx. 9.2 m³/h)	220 m³/d (approx. 9.2 m³/h)	200 m³/d (approx. 8.3 m³/h)	200 m³/d (approx. 8.3 m³/h)
Power consumption	280 kW	227 kW	250 kW	248 kW
Water consumption	1.4 l/s (approx. 5.0 m³/h)	1.5 l/s (approx. 5.4 m³/h)	1.3 l/s (approx. 4.7 m³/h)	1.6 l/s (approx. 5.8 m³/h)
Working fluid	Ammonia	Ammonia	Water	N/A
Size	1 x 40' container + snow separator	2 x 40' containers	1 x 40' and 1 x 20' containers + snow separator	N/A
Energy per m³	30.5 kWh/m³	24.8 kWh/m³	20.4 kWh/m³	29.8 kWh/m³
References	Winter Olympics in Sochi 2014	Winterberg (GER) Sjusjøen (NO)	-	Ski resorts in Japan and USA

Fig. 1 illustrates a process scheme of an all-weather snow machine based on an ice slurry generator with vacuum freezing method. Such a system consists of an evaporator where the ice slurry is generated, a snow separator, a compressor, and a condenser. In the evaporator, water is taken to the triple point condition namely the point that occurs at 0 °C and 6.1 mbar by reducing the evaporator pressure with a compressor. In these conditions, the liquid, ice and vapor phases of water coexist in a stable equilibrium. The compressor feeds the water vapor against a higher pressure into the condenser where it is liquefied again. Some of the water in the evaporator freezes forming a water and ice mixture called ice slurry. The ice slurry is fed to the snow separator, where water and ice crystals are separated.

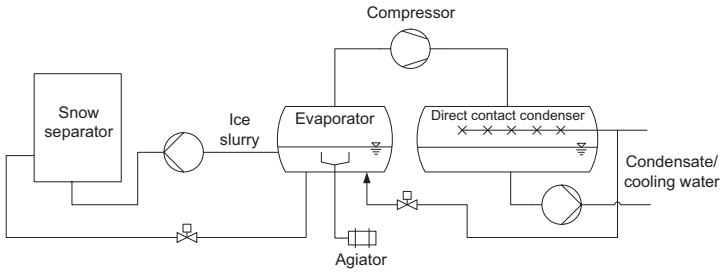

Fig. 1: Exemplary process scheme of an all-weather snow machine based on ice slurry generator with vacuum freezing method

Such a system has been realized by the company IDE Technologies Ltd. from Israel. The vacuum ice maker (VIM) of IDE uses an mechanical driven centrifugal compressor to create a vacuum in the evaporator where the ice slurry is generated. The suction vapor is fed to a direct contact condenser (mixing condenser). The direct contact condenser is cooled by a chilled water spray (coolant). The chilled water is produced by a conventional electric driven water chiller. A large surface area packing is installed in the condenser to increase the heat transfer between vapor and coolant. The liquid consisting of condensate and the sprayed coolant is fed via a coolant pump to the water chiller. The water vapor taken from the evaporator is replaced by chilled water. The ice slurry is pumped to the snow separator, where snow is separated from water. The water from the snow separator flows back to the evaporator. The IDE-system uses electricity as main driving energy to run the centrifugal compressor and the water chiller for condensation of the coolant. (IDE 2017), (Ophir et al. 2011)

1.3. All-weather snow machine based on steam jet ejector technology

An alternative concept for technical snow production based on an ice slurry generator with vacuum freezing method is presented in this paper. The system uses a thermally driven steam jet ejector to feed the water vapor from the evaporator to the condenser. The main components of an ejector are the motive nozzle, the mixing chamber and the diffuser. In the ejector an expansion of a motive steam takes place through a jet nozzle. Thereby the expansion of the motive steam is accompanied by a large increase in velocity up to Mach numbers of 3 to 4. The motive steam entrains the water vapor from the evaporator through momentum exchange. In a following diffuser, the kinetic energy of the mixed vapor streams consisting of motive steam and water vapor from the

evaporator is gradually transformed into potential energy respectively in pressure. Both vapor streams are liquefied in the condenser. The condenser pressure represents the back pressure of the ejector and is related to the cooling water temperature. If the temperature of the cooling water decreases the condenser pressure decreases, too. Lower condenser pressure leads to a lower necessary motive steam pressure, which reduce the motive steam consumption. This improves the thermal coefficient of performance (COP) of the refrigeration process. The steam to run the steam jet ejector can be generated by e. g. waste heat, renewable sources or be provided from district heating systems. Electric power is only used for auxiliary drives such as pumps, fans etc. Therefore the power consumption is reduced to a minimum and makes an all-weather snow machine without using an electric driven compressor an ecologically friendly concept of snow supply. The development of the snow machine started in 2012 thanks to a regional grant which financed the development of the first test rig. The snow machine was commissioned in October 2014 in Val di Fiemme at the Nordic Ski stadium. Within an EU-project, which started in 2017, a first prototype has been developed with a snow production capacity of approx. 2 m³/h. Furthermore, it is planned to realize two demonstration plants with a snow production capacity of 4 m³/h, one with biomass and one with solar energy as heat source. The foreseen location to erect the solar driven one is a ski dome in the Netherlands and the biomass driven one in a ski resort in Italy. This paper presents first operational experience as well as performance figures of the prototype, which is electric driven. The prototype has been presented on the Interalpin trade fair in 2017.

2. Design and test operation of the prototype

The prototype of the snow machine consists of a single-stage steam jet ejector chiller (SJEC) with a snow production rate of approx. 2 m³/h. The thermal power for the steam supply is nowadays provided by an electric boiler for testing the technology. The mass flow of the steam is approx. 240 kg/h and the steam is provided at a pressure of 4.5 bar(abs). A plate heat exchanger is used as condenser, which is cooled via a secondary cooling water loop connected to a wet cooling tower. Two pictures of the prototype are shown in Fig. 2. The left picture shows the installation at the Interalpin trade fair in Innsbruck in April 2017 and the right picture shows the installation at the test site in Bolbeno, Italy, in July 2017. The system is integrated into a 20 ft container. The hydraulic scheme of the snow machine with the main process data is depicted in Fig. 3. The steam jet ejector is designed for a back pressure of approx. 40 mbar. According to the design of the cooling water circuit, this design point corresponds to a maximum temperature of 20 °C (e.g. wet bulb temperature t_{WB} of 15 °C with 60 % rel. humidity).

Fig. 2: Pictures of the prototype (left: trade fair installation at Interalpin 2017; right: installation at test side in Bolbeno, Italy)

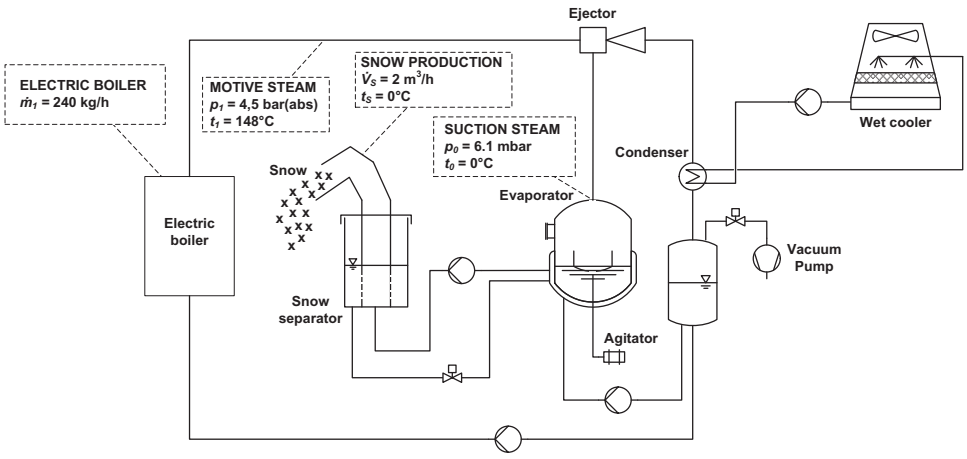

Fig. 3: Process scheme of the prototype

The prototype has been tested on 28. July 2017 in Bolbeno, Italy. At the test site well water with a constant supply temperature of approx. 10 °C was used for the heat rejection. Fig. 4 depicts the system temperatures and Fig. 5 the system pressures during the operation time from 16:10 – 17:40. The diagram in Fig. 6 depicts the heating and cooling capacity, the evaporator temperature and the thermal COP of the SJEC from 16:55 – 17:40. The SJEC was in operation from 16:22 – 16:40, from 16:43 – 17:08, from 17:15 – 17:31 and from 17:32 – 17:39. The evaporator temperature and pressure decreases during the SJEC operation. During the short operation breaks the evaporator was heated up with hot steam from the boiler (at 16:40 from 5 – 10 °C and at 17:07 from 0 – 15 °C).

The cooling water spreading was approx. 7.5 °C and larger than the designed 4 °C due to a lower flow rate of the cooling water pump. However, the SJEC was running close to the design point of the SJEC of 40 mbar back pressure. The condenser pressure was ranging between 32 – 41 mbar (see p_2 in Fig. 5). The cooling capacity plotted in Fig. 6 is calculated related to the evaporator water level and the temperature decrease of the evaporator during the operation of the SJEC. The cooling capacity is underestimated as no heat input from the ambience as well as from the ice slurry pump is considered. The heat consumption has been calculated to determine the thermal COP. The steam consumption was calculated according to (DIN 28430) and (GEA Wiegand 2017). The product of nozzle loss coefficient and outflow function is according to (Loschge 1914) constant for water vapor with a value of 0.459. The calculated value was crosschecked with the electricity consumption, which was measured by a current clamp.

$$\dot{m}_1 = \alpha \cdot \psi_{crit} \cdot A_1 \cdot \sqrt{2 \cdot p_1 \cdot \rho_1} \qquad \text{(eq. 1)}$$

with:

α	–	Nozzle loss coefficient [-]
ψ_{crit}	–	Outflow function [-]
A_1	–	Nozzle cross-section [m²]
p_1	–	Inlet pressure [Pa]
ρ_1	–	Density of water vapor [kg/m³]

In Fig. 6 the thermal COP ranges between 0.1 and 0.9 and is decreasing with declining evaporator temperature. At a temperature close to 0 °C (time span after 17:30) the thermal COP is between 0.1 and 0.4. The calculation of the cooling capacity does not consider the freezing of the water in the evaporator, so that the thermal COP is underestimated in the temperature range close to 0 °C. Actually there is no possibility to directly measure the cooling capacity while water freezes in the evaporator and thus to calculate a more accurate thermal COP value.

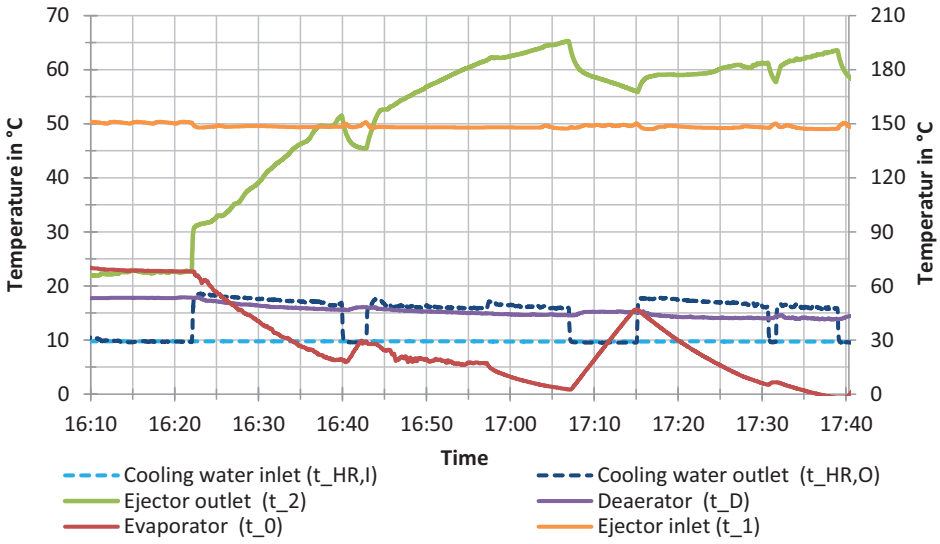

Fig. 4: Exemplary measurement data of the prototype: System temperatures (read ejector motive steam inlet temperature t_1 on right ordinate)

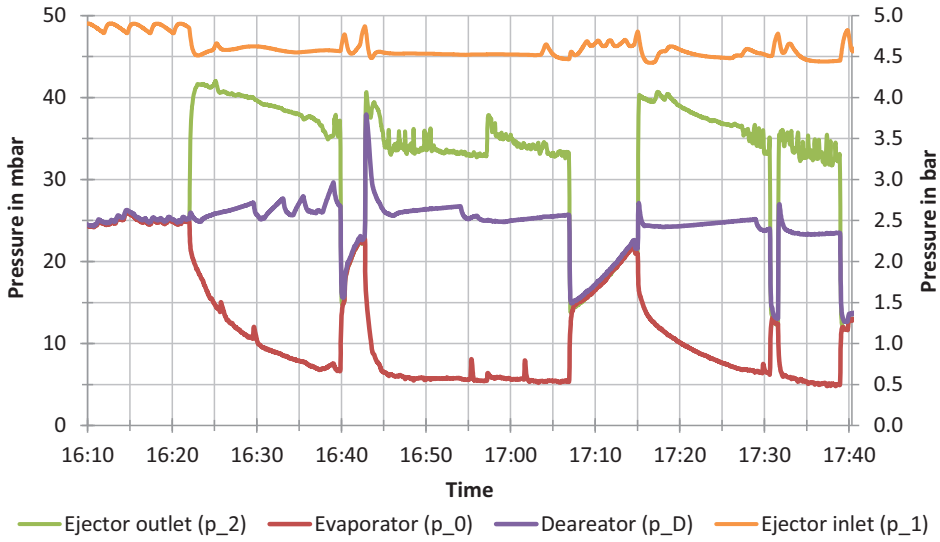

Fig. 5: Exemplary measurement data of the prototype: System pressures (read ejector motive steam inlet pressure p_1 on right ordinate)

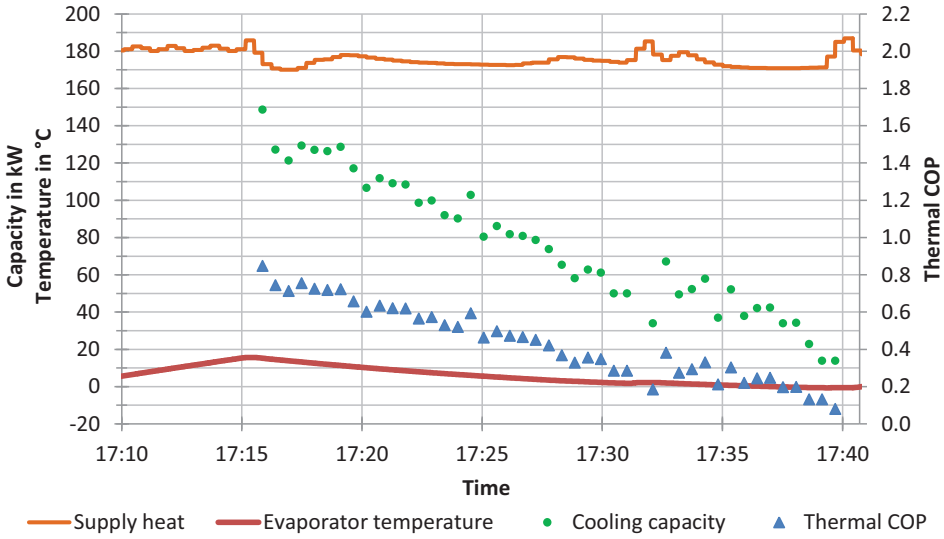

Fig. 6: Exemplary measurement data of the prototype: Heating and cooling capacity, evaporator temperature & thermal COP

3. Solar-assisted snow machine

3.1. Solar steam generation

There are parabolic troughs and Fresnel collectors, innovative evacuated tube and high-vacuum flat plate collectors available for the temperature range up to 250 °C. The collector types can be distinguished between concentrating and non-concentrating systems. The usable irradiation of concentrating collectors is often significantly lower compared to non-concentrating collectors. In case of 50 % lower irradiation the efficiency of the concentrating collector has to be twice as high to reach the same yield. Hence, important selection criteria for the choice of a suitable collector type are the solar profile at the system site and the required temperature.

Generally, there are two fundamental manners in which solar heat can be transferred to the ejector chiller system: direct steam generation (DSG) and indirect steam generation with pressurized water loop and steam drum. With DSG systems the motive steam is directly generated within the collector field and transported to the ejector. However, an intermediate steam drum, which can be bypassed, can be useful as an additional heat capacity to smooth the operation of the SJEC. In addition, it could also serve as droplet separator. The DSG technologies can be realized with parabolic trough collectors or linear Fresnel collectors. In case of a direct solar steam generation in the collector field, thermodynamic losses can be reduced. The control of the resulting two-phase flow has been extensively researched and has been already demonstrated in first commercial pilot plants. Alternatively to the line-focusing collector systems, evacuated tube collectors (ETC) can be used for DSG, too. This possibility has

been investigated within the research project ProSolarDSKM (Joemann et al. 2016). However, until now there is no commercial ETC available, which is designed for DSG.

The second technical solution for the solar thermal steam generation is a pressurized water loop. This means, that boiling in the collector is inhibited by increasing the pressure in the solar collector. The water boils in a steam drum subsequent to the collector field at lower pressure. The advantages of this technical solution are an easier controllability of the solar thermal system as well as a more reliable operation condition of the collector field. The pressurized hot water loop can be realized in different manners, either by hydraulic separation (heat exchanger between solar loop and steam drum) or by applying a specially designed solar pump which maintains an overpressure in the solar circuit in combination with a throttle valve before expanding into the steam drum. If there is no hydraulic separation with a heat exchanger and thus no water-glycol mixture is used as heat transfer medium one has to consider antifreeze protection if the ambient temperature can drop below 0°C.

Fig. 7 provides an exemplary hydraulic scheme for a solar loop of the presented all-weather snow machine. However, there is a variety of possibilities. The following requirements have been defined for the system:

- Indirect steam generation with pressurized water loop and steam drum: ✓
- Solar storage: ✓
- Short start-up time of the SJEC (→ small volume/capacity of the steam drum): ✓
- Operation of SJEC only with heat from storage: ✓
- Backup heating system: ✓
- Reheating of solar fluid with backup system (prior to the steam drum): ✓
- Operation of SJEC only with heat from backup system ✓

To meet the various requirements of the solar loop, the system needs two pumps. One pump to feed the collector field and a second pump to enable the operation of the SJEC with the backup system without solar energy. The control throttle valve VRM-S1 is used to maintain the required overpressure in the system to inhibit boiling in the solar loop. In case that the solar loop is not in operation, the valves VAM-S1 and VRM-S1 are closed. The main operation modes are: 1) solar heating of the steam drum, 2) charging of the solar heat storage (no operation of steam drum), 3) heating of the steam drum with heat from the storage (no operation of the solar field) and 4) backup heating mode.

1) In case of solar heating of the steam drum both pumps are in operation. The proportion of the flow rates of the pumps defines, whether the storage is simultaneously charged (P1>P2) or discharge (P1<P2). If both flow rates are equal, the storage is neither charged nor discharged. To disconnect the storage the valve VAM-S3 can also be closed. In this operation mode, the valve VAM-S4 is open and the valve VAM-S2 is closed. If the solar irradiance is not sufficient to reach the desired temperature, the backup system is used to heat the water up.
2) If solar heat is available, but not required from the SJEC, the heat can be used to heat up the solar storage. In that case, only P2 is in operation, VAM-S3 and S4 are open and VRM-S1, VAM-S1 and S2 are closed.
3) P1 is in operation, when heating the steam drum with heat from the storage. VAM-S3 is open and VAM-S2 and S4 are closed. The backup system can be used to increase the temperature level.
4) To heat up the steam drum with the backup system only P1 is in operation. The valve VAM-S2 in the bypass is open and the valves VAM-S3 to the solar storage and VAM-S4 to the solar field are closed.

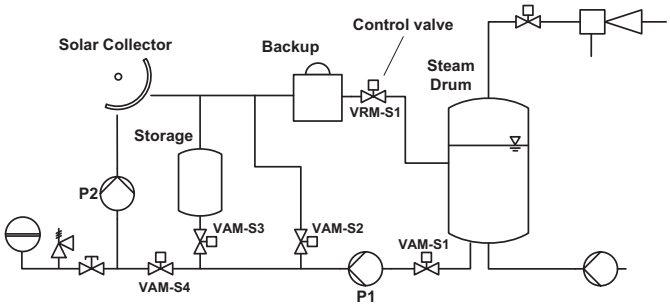

Fig. 7: Hydraulic scheme of the solar loop for a solar driven all-weather snow machine

3.2. Model of the snow machine

For the design of a solar-assisted snow machine, a calculation tool is required to evaluate different system designs and to investigate the operational behavior at varying climate conditions. Such a calculation tool has been developed based on a model of the system using mass and energy balances. The model describes the operational characteristic of the different components, e.g. solar collector, SJEC, pumps, fans, etc. It calculates the pumping power, pressure losses and flow rates of all hydraulic circuits for the determination of auxiliary power demand. Furthermore, the model enables to do year-round calculations on an hourly basis. Microsoft Excel with its spreadsheets in conjunction with VBA (Visual Basic for Applications) is used as software to compile parametric studies for different parameters such as solar field size, storage size or nominal motive steam temperature of the SJEC. Input data for the simulation are meteorological data, which are taken from Meteonorm database 4.0. Consumption and yield data for the components as well as various indicators, such as the solar fraction or the seasonal thermal and electrical efficiency of the system are calculated.

3.3. System design and system performance evaluation

In this chapter different aspects of the system design and system performance of a solar-assisted snow machine with SJEC will be discussed and evaluated. The application scenario is the snow production for an indoor ski dome. In order to assess the climatic influences on the system, three locations are considered (Doha in Qatar; Seville in Spain; Essen in Germany). Below, the reference scenario and design parameters are listed:

- Snow production rate: 4 m³/h (constant → additional heat provided by a backup system)
- Cooling capacity: 215.2 kW (snow density: 500 kg/m³)
- Operation time: 08:00 – 18:00; Season: all year round
- Condenser technology: mixing condenser; heat rejection: wet cooling tower
- Motive steam design temperature: optimized in dependence of system site (climatic conditions)
- Motive steam consumption at varying operating conditions:
  - Motive steam pressure p_1 increases/decreases by the ratio of the back pressure p_2 to nominal back pressure $p_{2,nom}$ (min: 80 % of $p_{1,nom}$; max: 115 % of $p_{1,nom}$)
- Nominal back pressure $p_{2,nom}$ of SJEC: selected in dependence of climatic conditions to be able to operate the SJEC ca. 95 % of the year (5 % no operation possible due to too high t_{WB})
  - Essen: $p_{2,nom}$ = 37.7 mbar (corresponds to t_{WB} of 15 °C + Δt 12 °C + $\Delta p_{Leakage\ Air}$ 2 mbar)
  - Seville: $p_{2,nom}$ = 48.3 mbar (corresponds to t_{WB} of 19.5 °C + Δt 12 °C + $\Delta p_{Leakage\ Air}$ 2 mbar)
  - Doha: $p_{2,nom}$ = 67.6 mbar (corresponds to t_{WB} of 25.8 °C + Δt 12 °C + $\Delta p_{Leakage\ Air}$ 2 mbar)
- Design of the internal and external cooling water loop and cooling tower
  - $\Delta t_{Cooling\ limit\ distance\ of\ wet\ cooler} = 3.0$ °C; $\Delta t_{Heat\ exchanger} = 5.0$ °C; $\Delta t_{Internal\ cooling\ water\ loop} = 4.0$ °C
- Collector field:
  - ETC (Paradigma AQUA PLASMA 15/27)
  - Fresnel (Industrial Solar LF-11)
  - Specific collector area: 7.5 m² per kW cooling capacity of SJEC (total collector area: ca. 1,600 m²)
  - Specific storage volume: 10 l per m² collector area (total storage volume: ca. 16 m³)
- Design data of auxiliaries
  - Nominal pump efficiency $\eta_P = 77.9$ % (efficiency varies with flow rate of the pump)
  - Nominal pump head H_P of the different pumps (pump head varies with flow rate of the pump):
    - Solar pump head $H_P = 6\ m$, storage pump head $H_P = 5\ m$, backup system pump $H_P = 5$ m, ice slurry pump $H_P = 15$ m, internal cooling water pump $H_P = 5$ m, external cooling water pump $H_P = 15$ m
      → to overcome pressure losses in the solar circuit a surcharge to avoid boiling in the collector has been considered for the solar pump, the storage pump and the backup system pump
- Nominal efficiency η_F and total pressure of the wet cooling tower fan p_F
  - Fan efficiency $\eta_F = 60$ %; total pressure p_F approx. 120 mbar

For the design of a solar-assisted snow machine based on SJEC technology, it is important to consider that the efficiency of the SJEC increases up to a certain level with increasing motive steam temperature, but contrary the solar collector efficiency decreases with increasing temperature, which governs the motive steam temperature. The design point is ought to be the optimum operation point taking both effects into account. Furthermore, each solar collector type has a specific decrease of the efficiency with temperature, thus the selection of the design point must be made in view of the selected solar collector type. Finally, it is an optimization problem, since both influence the system efficiency. In Fig. 8 (left part) the average annual thermal COP of the SJEC is plotted over the motive steam temperature for the three locations. For each location the respective dimensions of the SJEC (e. g. nozzle diameter) have been optimized for the motive steam temperature. The required motive steam temperature ranges between 140 and 160 °C to reach the highest possible efficiency. The comparison of the solar fraction for the different scenarios (see right diagram in Fig. 8) indicates that the highest solar fraction is reached at a lower temperature than the temperature level of the highest thermal COP. The reason for this is that the collector efficiency and hence the collector yield decreases with increasing temperature (see Fig. 9). Furthermore, the comparison points out that the ETC collector reaches the highest solar fraction (Essen ETC 100 °C; Seville ETC 120 °C; Doha ETC 140 °C).

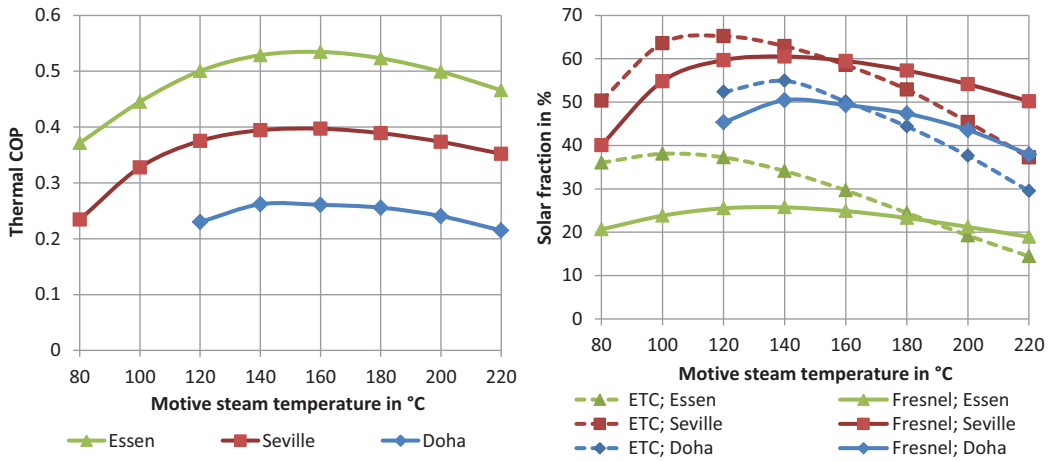

Fig. 8: Average annual thermal COP of the SJEC in dependence of motive steam temperature (left) and solar fraction (right) in dependence of motive steam temperature for ETC and Fresnel collector for the locations Essen, Seville and Doha

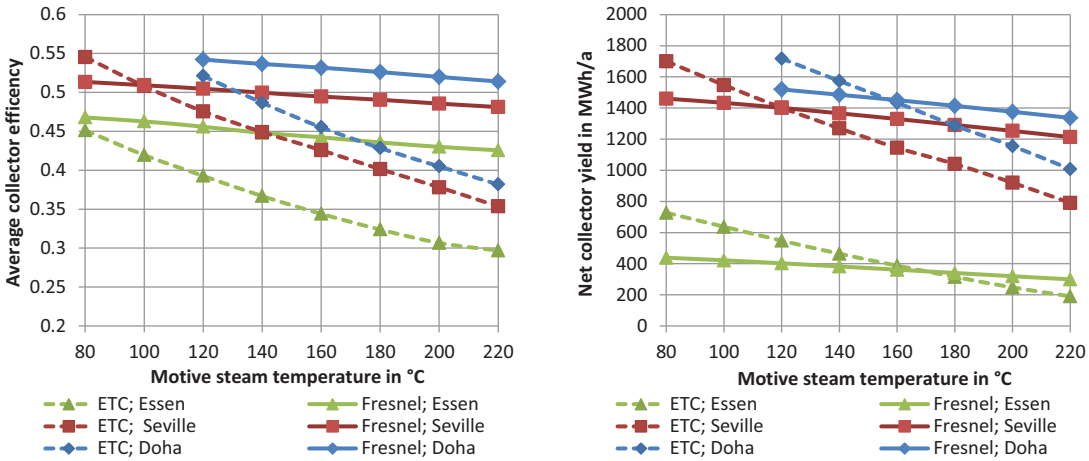

Fig. 9: Average collector efficiency (left) and net collector yield (right) in dependence of motive steam temperature for ETC and Fresnel collector for the locations Essen, Seville and Doha

The results of a parameter variation of the collector field and storage size for the location Seville are depicted in Fig. 10. For the reference scenario with a specific collector area of 7.5 m²/kW$_{Cooling}$ and a specific storage volume of 10 l/m² a solar fraction of approx. 67 % is reached. Small solar fields with a specific collector area of 2.5 – 5 m²/kW$_{Cooling}$ do not require heat storage. Larger solar fields require a storage size of 30 l/m², but not more. A further increase in storage volume would not result in a significant increase of the solar fraction. In comparison to solar driven cooling systems for comfort cooling, the required specific collector areas are significantly higher (cf. (Joemann 2015) page 118). This issue can be explained by different reasons. The cooling load profile of a

building is often dominated by the solar irradiation profile, thus the Solar-Load-Match is significantly higher. Another reason is that the thermal COP of the SJEC is much lower due to a lower evaporator temperature of 0 °C. Also the average solar field temperature to run the SJEC is higher than for a single stage absorption chiller which decreases the solar heat yield.

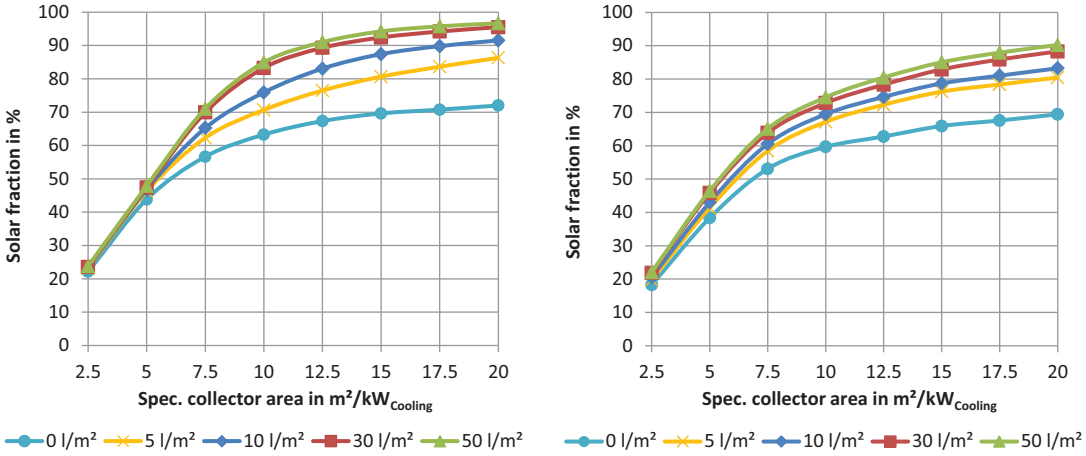

Fig. 10: Solar fraction in dependence of specific collector area and the specific heat storage volume for ETC (left) and Fresnel collector (right) for the location Seville; nominal system temperature: ETC = 120 °C, Fresnel = 140 °C

The annual sums of motive heat demand of the SJEC as well as gross and net heat supply are given by Fig. 11: monthly based (left diagram) and hourly based (right diagram) timeline. The data are given for ETC and Fresnel collector at the location Seville. The results prove that both collectors can provide the required motive heat to operate the SJEC in summer from May to August. The Fresnel collector even provides some surplus heat. From September to April, the backup heating system provides a significant amount of the heat to cover the demand. The data in the right diagram, which are the yield of heat energy and the demand of motive steam over the day, point out that the Fresnel collector provides the heat on a more constant level over daytime, whereby the solar heat provided by the ETC collector has a bell-shaped course so that some surplus heat is generated between 13:00 and 15:00.

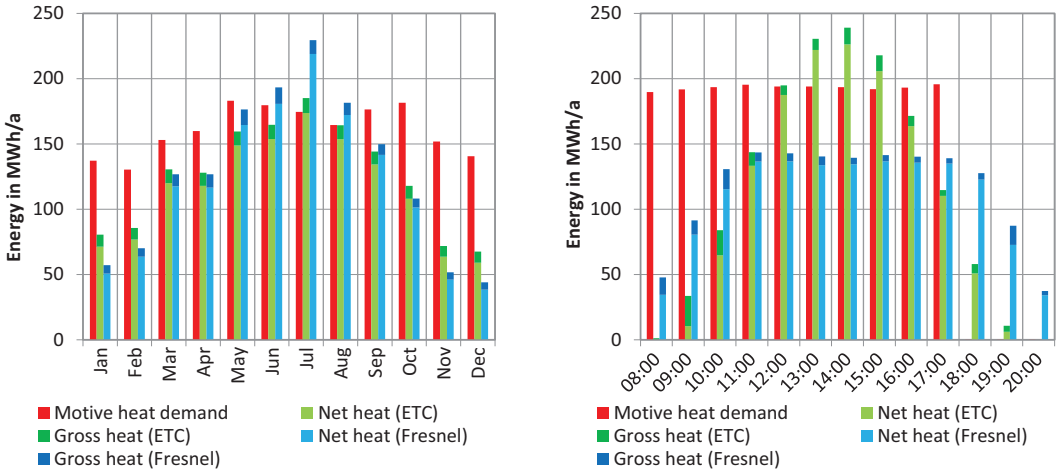

Fig. 11: Annual sums monthly for the year (left) and hourly for the day (right) of motive heat demand of the SJEC as well as gross and net heat supply of the ETC and Fresnel collector for the location Seville; nominal system temperature: ETC = 130 °C, Fresnel = 130 °C (same temperature to assure an identical motive heat demand of SJEC)

The electrical COP given in Fig. 12 is the ratio of the cooling capacity to the auxiliary power demand. The given data are average values for electrical COP monthly for the year (left) and hourly for the day (right) of systems with ETC collector. The nominal system temperature has been optimized to reach the highest possible solar fraction (see right diagram of Fig. 9). The values range between approx. 6 and 14. The annual average values are 10.5 for Essen, 8.8 for Seville and 7.1 for Doha. At the design point of the system, the nominal power consumption is 31.2 kW for Essen, 35.4 kW for Seville and 44.5 kW for Doha. At favorable ambient conditions, the power consumption is significantly lower due to the higher thermal COP of the SJEC. Thus the annual average values

for power consumption are 20.6 kW for Essen, 24.3 kW for Seville and 30.2 kW for Doha. However, it has to be mentioned that the power consumption of the control cabinet, of the drives of valves and of the vacuum pump is not considered, thus the electrical COP is slightly overestimated.

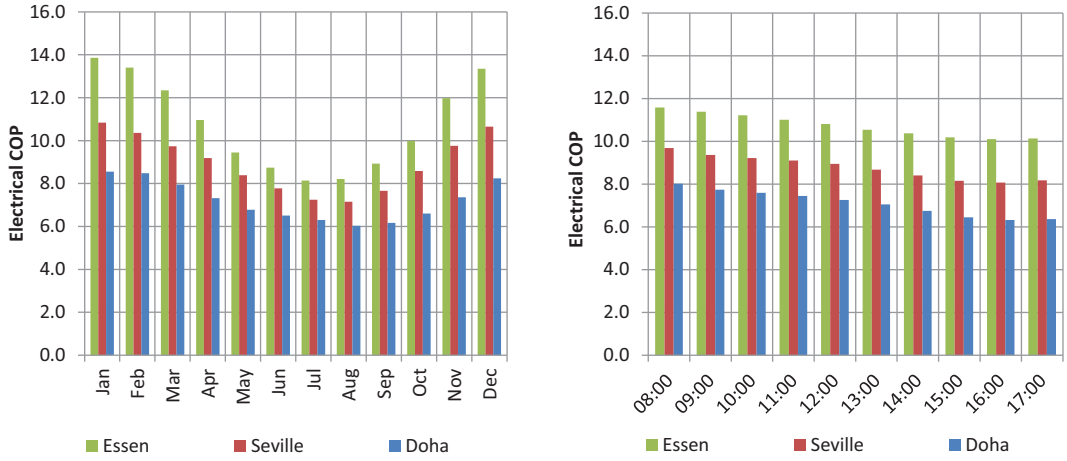

Fig. 12: Average electrical COP monthly for the year (left) and hourly for the day (right) for ETC and for the locations Essen, Seville and Doha; nominal system temperature: Essen = 100 °C, Seville = 120 °C, Doha = 140 °C

The average electrical energy consumption is depicted in Fig. 13 monthly for the year (left part) and hourly for the day (right part) of a system with ETC collector. The electrical energy consumption ranges between approx. 4 and 9 kWh/m³ depending on the climatic conditions. The annual average values are 5.1 kWh/m³ for Essen, 6.1 kWh/m³ for Seville and 7.6 kWh/m³ for Doha. In hot ambient climatic conditions the motive steam consumption of the SJEC increases and thus the power consumption increases, too. The reason is that higher amounts of heat have to be transported, mainly in the internal and external cooling water circuit. That also explains the higher values for electrical energy consumption in the summer time (compare for Essen) and for warmer regions like Doha. There is also a slight increase in power consumption throughout the day as the temperature increases over the day. Summarizing, a contrary behavior of the electrical COP (see Fig. 12) can be seen, which decreases while ambient temperature increases.

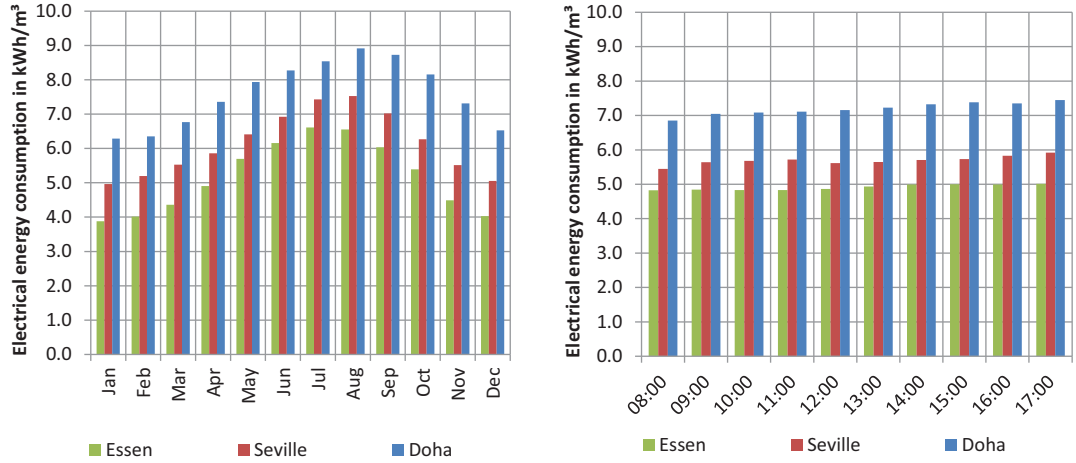

Fig. 13: Average electrical energy consumption monthly for the year (left) and hourly for the day (right) for ETC and for the locations Essen, Seville and Doha; nominal system temperature: Essen = 100 °C, Seville = 120 °C, Doha = 140 °C

The electrical energy consumption of the presented technology for snow production is about 2.7 to 6 times lower compared to other all-weather snow machines (cf. Tab. 1). Furthermore, it has to be highlighted that the presented values are seasonal values. The consumption data for all-weather snow machines from Tab. 1 are only given for the design point and are expected to be worse at a seasonal contemplation. Nevertheless, the snow machine based on SJEC technology needs thermal energy, too. This should come from renewable energy source to assure a sustainable system operation.

4. Conclusion

The developed pilot plant of the all-weather snow machine represents an innovative system for high quality snow generation at temperatures above 0 °C. The system is based on an ice slurry generator with vacuum freezing method and uses a steam jet ejector as thermal compressor for the refrigerant. Water is used as refrigerant in the process. The system can be operated with heat from renewable sources which enables a sustainable system operation. With the aid of the pilot plant it was possible to examine the performance system. The functionality of the system has been proven and the first measurement data of the pilot plant are giving a promising outlook.

Based on the experiences of the pilot plant, a concept for a solar-assisted snow machine has been developed. The development of the concept includes the determination of the design points and the evaluation of the system performance. Both have been realized by year-round calculation and simulating the operation of the system. The simulation proves that the electrical energy consumption of the presented technology for snow production is about 2.7 to 6 times lower compared to other all-weather snow machines, which are currently available.

5. References

Dieseth, J-B. R., 2016. Snow production equipment at ambient temperatures above zero degrees celsius. Master thesis, Norwegian University of Science and Technology, Trondheim.

Eikevik, T. M.,2017. Snow for the Future. Presentation at Holiday Club, Åre. Norwegian University of Science and Technology.

Fuhrmann, H., 1996. Basisschnee – basesnow, Einführung in die Nivologie, first edition VSI, Salzburg.

GEA Wiegand, 2017. Product Catalogue , Jet Pumps, Mixers, Heaters, Vacuum Systems.

IDE, 2017. VIM 100 All Weather Snowmaker. Product Data Sheet, IDE Technologies LTD.

Joemann, M., 2015. Evaluierung der Wettbewerbssituation solarthermischer und solarelektrischer Kühlsysteme hinsichtlich technischer, energetischer und ökonomischer Aspekte. Dissertation. Ruhr-Universität Bochum..

Joemann, M., Pollerberg, C., Kauffeld, M., Oezcan, T., Bauer, I., Grave, H., Dietzmann, T., 2016. ProSolarDSKM - Prozessdampf- und Kälteerzeugung mit Solarkollektoren, Dampfstrahlkältemaschine und latenten Wärmespeichern. Final report.

Kauffeld, M., Kawaji, M., Egolf, P. W., 2005. Handbook on Ice Slurries, Fundamentals and Engineering. Published by International Institute of Refrigeration.

Loschge, A., 1914. Über den Ausfluß von Dampf aus Mündungen (Emission of steam from orifices), Mitteilungen über Forschungsarbeiten auf dem Gebiet des Ingenieurwesens (Reports on research activities in the engineering field). 144. edition. Published by VDI. Berlin.

Mogilevsky, M., 2013. Heat exchanger for use in cooling liquids. Patent, application no: US 12/876,042, publication number: US 8479530 B2.

Timonen L., Ikkunassa Oy, V. 2010. Energy efficient ski resort. Published by Motiva Ltd.

Ophir, A., Rojanskiy, H., Siluk, R., Kanievski, A., 2011. Compact heat pump using water as refrigerant. Patent, publication number: US 7866179 B2.

Pierce, W. M., JR., 1954. Method for making and distributing snow. Publication number: US 2676471 A.

Rogstam, J.; Dahlberg, M., 2011. Energy usage for snowmaking, A review of the energy use of mobile snowmaking at Swedish ski resorts. Published by Energi & Kylanalys AB.

Smith, R., 2010. Next-Gen Snowmaking. Ski Area Management (49:3).

DIN 28430, 2016. Vakuumtechnik, Messregeln zur Ermittlung von Kenndaten für Dampfstrahlvakuumpumpen und Dampfstrahlkompressoren – Treibmittel: Wasserdampf. DIN Deutsches Institut für Normung e. V.

Infrared optical properties of doped and pure thermochromic coatings for solar thermal absorbers

Anna Krammer[1], Fabrice T. Demière[1] and Andreas Schüler[1]

[1] Solar Energy and Building Physics Laboratory, École Polytechnique Fédérale de Lausanne (EPFL), Lausanne (Switzerland)

Abstract

A new generation of solar collectors is based on thermochromic thin film technology, where the remarkable optical changes of vanadium dioxide, through its reversible semiconductor-to-metal phase transition, are exploited. This study reports on the infrared optical properties of VO_2 based coatings deposited on Al substrates by reactive magnetron sputtering. Fourier transform infrared (FTIR) spectroscopy is used to determine the emittance of a VO_2 coated sample before (ε = ~6%) and after (ε = ~33%) the phase transition. The angular dependence of the thermal emittance for such coating is investigated. It is found that the emittance increases with increasing the angle from normal incidence. In literature it is widely reported that the transition temperature of vanadium dioxide can be tuned by doping with different elements. An increase in the transition temperature is desired for solar thermal applications and it is reached with the addition of Ge into the VO_2 matrix. Here we show that through Ge doping, the emittance switch, especially the emittance in the high temperature state, can be optimized as well. An increase of ~10% in emittance is recorded.

Keywords: Solar thermal, thermochromic absorber coating, doped vanadium dioxide, overheating protection

1. Introduction

Due to their simple design and operation, solar thermal collectors for domestic hot water generation and space heating are one of the most common solar energy harvesting systems in use today. Such collectors are typically designed to cover between 50-80% of the annual domestic hot water demand. During cold periods all the absorbed energy is useful. During hot periods, however, when solar radiation is abundant and demand is low, stagnation occurs. Storage is limited and excess heat cannot be diverted. The heat transfer fluid evaporates and temperature of the solar absorber can exceed 200°C. A self-draining system and special valves are then necessary. At such temperatures, glycol degradation and further damage of the collector occurs. Frame, thermal insulation, selective absorber coating deteriorate and become less efficient.

A novel type of thermochromic solar collector has been proposed [1, 2, 3]. Recently, industry has demonstrated functional collectors on the real scale [4]. These new collectors are based on switchable selective absorber coatings that can change their optical properties in the infrared spectral region so that they can absorb and repel heat in a controlled manner. Thus, the stagnation temperature is limited and overheating of the system is avoided. Until recently, this was one of the main drawbacks of thermal collectors.

The “smart” thermochromic absorber coating exhibits good selectivity (high absorptance, low emittance) up to a given temperature and bad selectivity (high absorptance, high emittance) above that temperature in order to prevent overheating. Here the material of choice is vanadium dioxide.

It undergoes a reversible thermochromic transition, during which its switch in thermal emittance and subsequent heat dissipation to the surroundings at high temperatures is sufficient to limit the stagnation temperature. Evaporation of the transfer fluid is avoided and thermal charges on the system reduced.

doi:10.18086/swc.2017.17.04 Available at http://proceedings.ises.org

1.1 Vanadium dioxide

Vanadium dioxide is an emblematic thermochromic material. It undergoes an ultrafast and fully reversible first order semiconductor-to-metal (SMT) transition at 67°C.[5] Through the transition the crystal structure changes from the low temperature monoclinic (P21/c) to tetragonal rutile (P42/mnm) at high temperature and is accompanied by abrupt changes in electrical and optical properties.[6] A resistivity change of several orders of magnitude and significant changes in the optical constants – especially in the infrared range – occur at the transition. Due to these remarkable changes occurring close to room-temperature, vanadium dioxide has been the object of overwhelming fundamental and applied research. Vanadium dioxide shows potential in a wide range of applications ranging from smart windows[7] and radiators for space applications[8] to microelectronic and device applications such as steep-slope switches[9], tunable capacitors[10] etc. Meanwhile, the underlying mechanism – structural or charge driven transition – is still open to debate with recent studies [11] suggesting a correlation-assisted Peierls transition, stressing the joint effect of lattice symmetry breaking and Coulomb interactions. Additionally, discoveries of exotic VO_2 behaviors, such as the very recently reported one order-of magnitude breakdown of the Wiedermann-Franz law in the vicinity of the semiconductor-to-metal transition[12], push the fundamental research of VO_2 even further.

Through doping with different elements, the optical and electrical properties of vanadium dioxide can be tuned and, most importantly, its transition temperature can be tailored to suit various applications. W^{6+}, Mo^{6+} Ta^{5+} and Nb^{5+} have been widely reported as dopants decreasing the transition temperature[6]. Tungsten has been regarded as one of the most efficient in doing so, enabling a reduction of 49-55°C per at.% dopant[13]. Therefore, for room temperature applications such as smart windows, tungsten doping is well-established. On the other hand, increasing the transition temperature through doping has been less studied and the identified dopants proved less efficient. Aluminium doping has been reported as both increasing and decreasing the transition temperature. In [13], authors show that Al^{3+} induces gradual amorphization of the thin films without significant effect on the transition temperature. Cr^{3+} and Fe^{3+} were reported to increase the transition temperature with no more than 3°C [14]. Thermochromic VO_2 based solar absorber coatings, as discussed in the present work, or the recent developments at microelectronic device level (where the required switching temperatures are higher than the normal operating temperatures of the device), underline the importance of an efficient and reliable doping which allows for a range of elevated transition temperatures to be achieved.

Authors have recently showed that Ge doping is successful in increasing the transition temperature of vanadium dioxide sputtered thin films and a transition temperature of ~95°C has been reached [15]. In comparison, the currently available commercial products, based on Al doped (4 – 12 at.%) vanadium oxide films, transition at 70° - 75°C. Therefore, the above 20°C temperature rise constitutes a significant increase and an important step in establishing efficient vanadium dioxide based absorber coatings. In the present work, authors determine the effect of Ge addition to the vanadium dioxide lattice from the thermal emissivity point of view. First, the spectral reflectance and emissivity of a pure VO_2 film in the mid-infrared range (2-15μm) is measured. The sample is measured both below and above the switching temperature. Then, the angular dependence of the thermal emittance is discussed. Finally, the spectral emissivity in two differently doped samples is measured and compared with that of a pure VO_2 film. Thus, the influence of Ge doping on the IR optical properties of the coatings - specifically their thermal emissivity - is determined.

2. Experimental

Pure and doped vanadium dioxide thin films have been deposited by reactive magnetron co-sputtering in sputter-up configuration. A schema of the deposition chamber and the process is shown in Fig. 1.

The base pressure of the chamber was below $5 \cdot 10^{-8}$ mbar. The process gas is Ar (purity 99.999%) and O_2 (purity 99.995%) is the reactive gas for oxide formation. A mass flow controller regulates the Ar gas feed to the chamber and the Ar flow is set to 17.4 sccm. Inside the chamber, a lambda-probe (Zirox XS22) oxygen sensor is installed. Based on the pressure readings, a Proportional Integral Derivative (PID) feedback control regulates the oxygen flow such that a constant oxygen pressure is maintained. The oxygen partial pressure during depositions is $5.25 \pm 0.25 \cdot 10^{-4}$ mbar, while the working pressure is $\sim 7.1 \pm 0.1 \cdot 10^{-3}$ mbar.

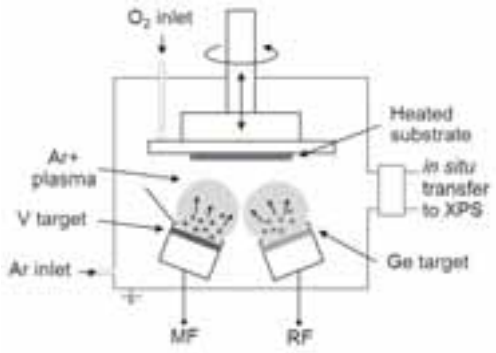

Fig. 1: Schematic representation of the sputtering chamber with targets, plasma glow and adjustable substrate holder

The magnetrons are run by DC power (MKS) for the vanadium target and radio frequency (RF) AC power (Advanced Energy) for the germanium target. The metallic target discs are provided by Testbourne Ltd. The purity of the 2" targets is guaranteed at 99.95% for the V and 99.999% for the Ge target. The power on the V target is set to 150 W, whereas for the Ge source, RF power (13.56 Mhz) of 8W and 12W are applied. To limit doping, magnets are removed from the magnetron, thus reducing the magnetic field and, subsequently, the plasma density.

The films are deposited on 0.5 mm thick, 50 mm x 50 mm sized Al foil (Goodfellow) for the Fourier transform infrared (FTIR) spectrometry, on stainless steel for the thermal imaging and on Si wafer for the angular dependence determination. The deposition takes place at high temperature – 600°C is measured by a stationary thermocouple above the rotating substrate holder. The thickness of the deposited films is estimated at ~320 – 340 nm.

A commercial thermographic camera (FLIR Systems, Inc.) is used to visualize the optical switch of VO_2 based coatings over the transition and to determine the angular dependence of the emissivity of these samples. The camera detects infrared radiation in the range of 7.5 - 13 μm.

The spectral reflectance is measured with a Bio-Rad FTS-175C Fourier transform infrared spectrometer equipped with a 3" golden integrating sphere and a high performance nitrogen-cooled MCT detector for the Mid-IR range (2-20 μm).

3. Results and discussion

3.1. Switching emittance

The optical switch of the thermochromic film in the infrared spectral region has been captured by thermal imaging (Fig.2). A VO_2 based coating has been deposited on reflecting stainless steel (SS) substrate. Below the transition temperature, the semiconducting VO_2 coating is transparent to the IR radiation and only the substrate is seen on the thermal image. However, above the transition temperature, the film - deposited in the middle of the SS sheet - appears on the thermal image as the VO_2 becomes opaque to the infrared radiation in its metallic state. Therefore, when deposited on a reflecting substrate such as stainless steel, copper or aluminium, the thermochromic coating has a low thermal emittance below and a high emittance above the transition temperature.

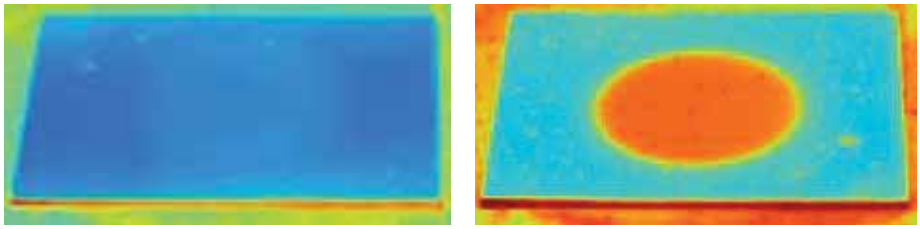

Fig. 2: Thermal image of the thermochromic absorber coating in the cold state with low emittance (left) and in the hot state with high emittance (right)

Then, with an FTIR spectrometer coupled with an integrating sphere and a Mid-IR MCT detector, the total reflectance spectra of a VO_2 coated aluminium sheet is determined. The measurement is done both below and above the transition temperature (T_C) of vanadium dioxide. Since the considered sample is opaque, from the measured reflectance spectra, the spectral emissivity can be determined and the results are displayed in Fig. 3. The thermal emittance of the thermochromic absorber in its two states considerably differs.

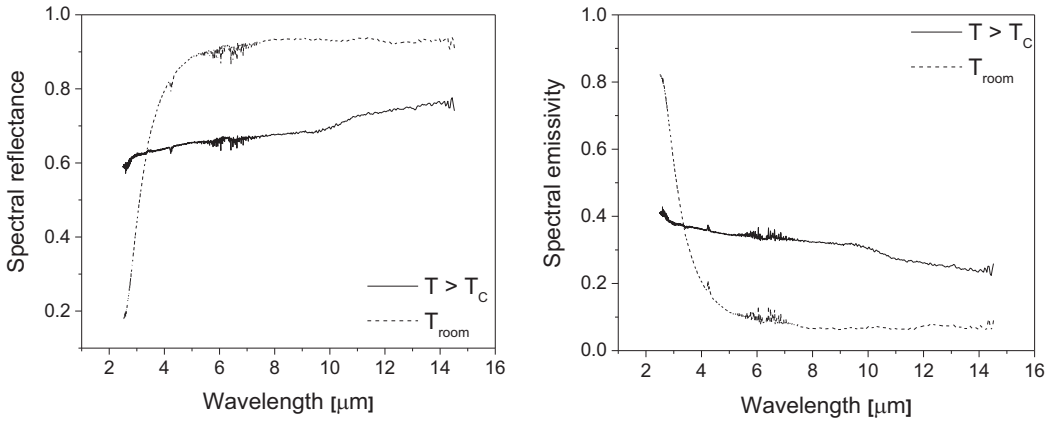

Fig. 3: Spectral reflectance and corresponding spectral emissivity of the thermochromic absorber both below and above the transition temperature of vanadium dioxide.

Above 100°C collector temperature, the operating temperature should be limited to avoid thermal stresses on the system. The spectral emittance of a blackbody at 100°C peaks at around 8 μm wavelength. Therefore, the emittance change in this spectral region is of special interest. In Fig. 3, at 8 μm, the emissivity changes markedly from ~6% below T_C to ~33% above T_C.

3.2. Angular dependence

The angular dependence of the emittance of a thermochromic VO_2 film deposited on Si wafer, above its critical transition temperature was determined. Since the coating is supposed to show metallic properties, the emittance versus angle for a rough oxidized aluminum plate was measured for comparison. The measurements were performed at 100°C for the VO_2 and aluminium samples. The results are shown in Fig. 4a. The curves are similar. The VO_2 coating in the metallic state follows the same trend of directional emissivity as the Al plate, whose values are similar to those given in tables. They are roughly constant from normal angles to about 60 degrees from the normal. At angles higher than 60 degrees the thermal emittance rises and reaches a maximum at grazing angles. The thermal emittance is expected to drop to 0 when parallel to the surface, but this measurement could not be made precisely with the experimental setup. This behavior is well described by the Fresnel's equation and typical results for metals are illustrated in Fig. 4b.

The emittance being higher at greater angles is beneficial as most thermal emittance measurements are done at normal angles. Therefore the thermochromic coating will be more efficient at dissipating heat via radiation than what normal measurements would predict.

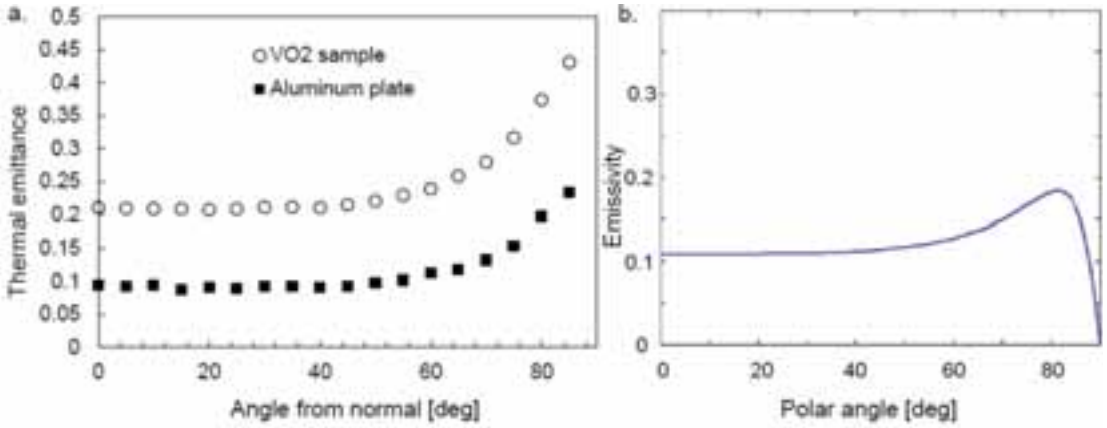

Fig. 4: a) Angular dependence of the thermal emittance of VO_2 and Al plate. b) Typical directional emissivity of a metal according to Fresnel's relation with n=1.5 and k=7 [16].

3.3. Thermal emittance of doped thermochromic samples

The transition from low to high emittance of the thermochromic absorber at a temperature of 67°C might be too low for solar thermal applications. Several elements have been reported to alter the phase transition temperature of vanadium dioxide. The authors have long studied dopants capable of increasing T_C to around 100°C. Recently [15], we have reported on the successful increase of the transition temperature to ~95°C. This has been reached with 5.9 at.% Ge doping. In the next step, our aim is to measure the effect of such doping on the thermal emittance of the samples. A pure and two Ge doped thermochromic coatings have been deposited on Al sheet. The Ge content in the doped samples has been varied by applying different power on the Ge target during deposition – 8W and 12W. This is calculated to correspond to 1.1 and 2.6 at.% Ge in the samples, leading to transition temperatures of ~75°C and ~77°C respectively. The three different samples have been compared and it is found that the emittance, notably in the hot state, is gradually increasing with doping. Roughly 10% increase in emittance between the pure and the strongly doped sample (with 12W applied on the Ge target) at 8 μm, is recorded. The results are shown in Fig. 5.

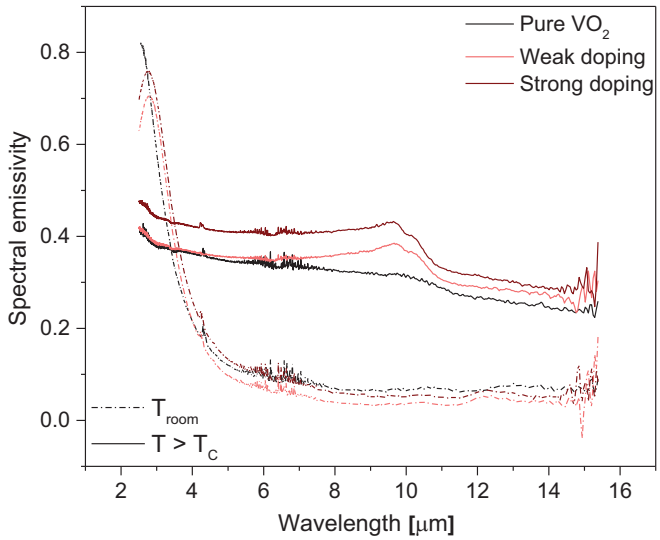

Fig. 5: Spectral emissivity change between the low (dashed line) and high temperature state (solid line) of three samples with different composition: pure VO_2, weakly doped and strongly doped coatings.

Using a simple model collector consisting of a glass cover, an air gap and a switchable absorber in thermal contact with the water pipes, *Baldi et al.*[17] calculated the stagnation temperature map plotted as a function of solar absorptance and thermal emittance. Based on this work and with the assumption that the switch only impacts the absorber emittance, while the solar absorptance remains relatively unchanged, the stagnation temperature is estimated to be lowered from ~195°C to ~150°C using pure VO_2 based absorbers and from ~185°C to ~140°C for Ge doped VO_2 based absorbers. At these reduced stagnation temperatures, the degradation of glycols is mostly prevented and, at the typical pressures present in the collector (3 bars), the evaporation of the heat transfer fluid is overcome.

4. Conclusions

Adding a thermochromic function to the currently available selective solar absorber coatings could bring forward a new generation of smart solar thermal collectors where the stagnation temperature is limited and overheating prevented. In this work, pure and Ge doped vanadium dioxide based thermochromic coatings have been deposited by reactive magnetron co-sputtering on highly reflective substrates. Their optical properties in the Mid-IR range have been determined. Pure VO_2 films show high potential as their emissivity changes significantly from 0.06 to 0.33 at the wavelength of interest of 8 μm. Moreover, the angular dependent emittance measurements show that the emittance of the coatings in the hot state (above the transition temperature of the thermochromic layer) is increasing with the angles from the normal. This suggests that normal emittance measurements underestimate the total emittance of the coatings. Finally, it is shown that, besides raising the phase transition temperature to 95°C, Ge doping has the additional advantage of increasing the emissivity of the thermochromic coating above T_C and, therefore, decreasing the stagnation temperature of the collector.

Acknowledgements

Authors are grateful to the Swiss Federal Office of Energy for the financial support under grant number 8100072.

5. References

[1] Huot G., Roecker C., Schüler A., 2008. Evaluation of the potential of optical switching materials for overheating protection of solar thermal collectors. Swiss Federal Office of Energy Report, Project-No. 102016.

[2] Paone A., 2013. Switchable Selective Absorber Coatings for Overheating Protection of Solar Thermal Collectors. EPFL Thesis 5878.

[3] Corvisier A., 2014. Elaboration par pulverisation magnetron reactive d'une couche thermochrome a base de dioxyde de vanadium. Application a la regulation passive de la temperature de panneaux solaires. Thesis Universite de Lorraine.

[4] http://www.viessmann.ch/de/presse/aktuelles/Viessmann-Vitosol-200-FM-und-100-FM.html last accessed on 23.03.2017.

[5] Morin F. J., 1959. Oxides which show a metal-to-insulator transition at the Neel temperature. Phys. Rev. Lett. 3, 34–36.

[6] Goodenough J. B., 1971. The two components of the crystallographic transition in VO_2. J. Solid State Chem. 3, 490–500.

[7] Granqvist C. G., 1990. Window coatings for the future. Thin Solid Films 193–194, 730–741.

[8] Benkahoul M., Chaker M., Margot J., Haddad E., Kruzelecky R., Wong B., Jamroz W., Poinas P., 2011. Thermochromic VO_2 film deposited on Al with tunable thermal emissivity for space applications . Sol. Energy Mater. Sol. Cells 95, 3504–3508 .

[9] Vitale W. A., Casu E.A., Biswas A., Rosca T., Alper C., Krammer A., Luong G.V., Zhao Q-T.,

Mantl S., Schüler A., Ionescu A.M., 2017. A Steep-Slope Transistor Combining Phase-Change and Band-to-Band- Tunneling to Achieve a sub-Unity Body Factor. Sci. Rep. 7, 355.

[10] Vitale W. A., Petit L., Moldovan C.F., Fernández-Bolanos M., Paone A., Schüler A., Ionescu A.M.,2016. Electrothermal actuation of vanadium dioxide for tunable capacitors and microwave filters with integrated microheaters. Sensors Actuators, A Phys. 241, 245–253.

[11] Biermann S., Poteryaev A., Lichtenstein A. I., Georges A., 2005. Dynamical Singlets and Correlation-Assisted Peierls Transition in VO_2. Phys. Rev. Lett. 94, 26404.

[12] Lee S., Hippalgaonkar K., Yang F., Hong J., Ko C., Suh J., Liu K., Wang K., Urban J.J., Zhang X., Dames C., Hartnoll S.A., Delaire O., Wu J., 2017. Anomalously low electronic thermal conductivity in metallic vanadium dioxide. Science 355, 371–374.

[13] Paone A., Sanjines R., Jeanneret P., Whitlow H.J., Guibert E., Guibert G., Bussy F., Scartezzini J.-L., Schüler A., *2015.* Influence of doping in thermochromic $V_{1-x}W_xO_2$ and $V_{1-x}Al_xO_2$ thin films: Twice improved doping efficiency in $V_{1-x}W_xO_2$. J. Alloys Compd. 621**,** 206–211.

[14] MacChesney J. B., Guggenheim H. J., 1969. Growth and electrical properties of vanadium dioxide single crystals containing selected impurity ions. J. Phys. Chem. Solids 30**,** 225–234.

[15] Krammer A., Magrez A., Vitale W.A., Mocny P., Jeanneret P., Guibert E., Whitlow H.J., Ionescu A.M., Schüler A., 2017. Elevated transition temperature in Ge doped VO_2 thin films. J. Appl. Phys. 122, 045304.

[16] Siegel R., Howell J., 2002. Thermal Radiation Heat Transfer, 4th edition, Taylor & Francis, New York.

[17] Baldi A., Borsa D.M., Schreuders H., Rector J.H., Atmakidis T., Bakker M., Zondag H.A., van Helden W.G.J., Dam B., Griessen R., 2008. Mg–Ti–H thin films as switchable solar absorbers. International Journal of Hydrogen Energy, 33 (12), 3188-3192.

Parametric analysis of a photonic radiative cooling system

Weimin Wang[1], Nick Fernandez[2] and Srinivas Katipamula[2]

[1] The University of North Carolina at Charlotte, Charlotte (USA)

[2] Pacific Northwest National Laboratory, Richland (USA)

Abstract

Spectrally selective materials show high technical potential for use as radiative cooling heat exchangers for buildings. Recent work by Stanford University has applied a photonic approach to tailor the optical properties of a coating material. In a prototype test, a radiative cooler based on that photonic material has demonstrated the ability to maintain radiator surfaces at below-ambient temperatures in the presence of intense, direct sunlight. This paper presents the simulation and parametric analysis of photonic radiative cooling system that integrates the use of the photonic radiative cooler and radiant floor cooling via the whole energy simulation program EnergyPlus. The simulation was made for a medium office building with three floors and a total floor area of 5,000 m^2. Three key design parameters including the radiator area, the storage tank volume to radiator area ratio, and the water flow rate to radiator area ratio, which are expected to have a large impact on system performance, were investigated in this paper. The results show that the percentage of cooling electricity savings from the photonic radiative cooling system relative to a reference variable-air-volume system has a linear relationship with the radiator area, and a quadratic correlation with the other two variables. The findings from this parametric analysis are valuable to understand how component sizing affects system performance.

Keywords: radiative cooling, parametric analysis, building simulation, nanomaterial

1. Introduction

Space cooling accounts for about 15% of the total primary energy consumed by all commercial buildings in the U.S. (DOE 2011). In the current practice, electricity-driven equipment such as room air conditioners, packaged air conditioners, and chillers are usually the source of mechanical cooling. Although the mechanical cooling equipment can operate reliably to maintain space thermal comfort, they are major energy consumers in buildings. To reduce energy consumption for space cooling, more efforts are needed to utilize passive cooling techniques to replace at least partially the mechanical cooling energy requirement. Possible passive cooling techniques fall into three broad categories (Geetha and Velraj 2012): 1) solar and heat protection techniques to reduce heat gains; 2) heat modulation or amortization techniques to modify heat gains; and 3) heat dissipation techniques to remove heat gains. Radiative cooling belongs to the third category because it uses natural heat sinks (the sky) for heat dissipation.

Radiative cooling refers to the physical process by which a body loses heat to another body of lower temperature via long-wave radiation. In the case of buildings, radiative cooling results from the thermal radiative heat transfer between building surfaces and the colder atmospheric layers in the sky. For a surface with high thermal emittance, the maximum radiative cooling power is about 100 W/m^2 for clear night sky and low ambient relative humidity (Meir et al. 2002). Because of the significant potential of radiative cooling, many studies have been conducted to design suitable materials and systems to make use of radiative exchange with the sky to condition buildings. In general, there are two methods of applying radiative cooling in buildings (Argiriou 2013): passive radiative cooling and active radiative cooling. With passive radiative cooling, the building roof radiates towards the sky and the cooled roof surface temperature then contributes to decreasing the conductive heat gains from the exterior. Representative design strategies of passive radiative cooling include moveable insulation and cool roofs (Al-Obaidi et al. 2014). With active radiative cooling, a heat carrier (air or water) is circulated between the interior spaces and radiative panels on the roof. Example studies on active radiative cooling can be found in (Eicker and

doi:10.18086/swc.2017.17.05 Available at http://proceedings.ises.org

Dalibard 2011, Mihalakakou et al. 1998, Parker 2005). These studies vary with respect to the characteristics of radiative panels, the heat transfer medium used, and the system design.

2. Photonic Radiative cooling

Spectrally selective materials have high technical potential for radiative cooling applications by tailoring the spectral optical properties (e.g., emissivity and reflectivity) of the surface in order to maximize thermal heat losses and minimize absorbed solar radiation. In the context of radiative cooling, heat losses occur in the infrared (IR) wavelength range, for which a 300 K blackbody radiation peaks at approximately 10 microns. The blackbody radiation peak shifts to shorter wavelengths with higher temperatures, but is still in this approximate range for most buildings applications. Spectrally selective materials can potentially offer the capability of daytime radiative cooling, which is highly sought after because of its potential to offset peak cooling loads. However, realizing daytime radiative cooling is severely complicated by both solar irradiance, which peaks at approximately 1,000 W/m^2 between 0.25 and 3 microns (Granqvist 2003), and atmospheric absorption. Without an effective solar irradiation heat shield in place, solar irradiance will easily swamp any radiative cooling effect during most of the day. Atmospheric absorption is problematic in that at many infrared wavelengths, the heat transfer phenomena at a conventional building surface or from radiative panels are closely coupled with the surrounding air (atmosphere is opaque to thermal radiation) and can be further complicated by sky conditions. There is however, a range between 8 to 14 microns where atmospheric absorption is negligible and the buildings thermal radiation can effectively be exchanged with the coldness of outer space. Thus, for optimal cooling, the spectral reflectivity of a building envelope coating would then be (Granqvist 2003):

- $R(\lambda) = 1$ for $0.3\ \mu m < \lambda < 3\ \mu m$ (Daytime radiation shield)
- $R(\lambda) = 0$ for $8\ \mu m < \lambda < 14\ \mu m$ (Thermal emission)

Much of the initial work [e.g., Eriksson and Granqvist 1986, Niklasson and Nilsson 1995) on spectrally selective materials focused on pigments (e.g., ZnS, and ZnO) and sputtered multilayer dielectric films (e.g., MgO, LiF, and oxynitride) on Aluminum backing (infrared reflective). Although such materials are relatively easy to fabricate and deposit, their solar reflectivity is only approximately 80-85%, which means that daytime radiative cooling is not possible, with the exception of early morning or late evening when the solar irradiance is low. Because of the inability of standard materials to meet the strict requirements for daytime radiative cooling, there has been recent research into advanced materials with tailored optical properties to fill the need. These advanced materials are primarily featured of nanomaterials or nanostructured and microstructured thin films (Gentle and Smith 2015, Raman et al. 2014).

The work presented in this paper is based on the nanostructured coatings developed by a research team at Stanford University (Raman et al. 2014). The advanced coatings are made up of seven one-dimensional photonic layers. The incorporation of the micro or nano photonic layers allows the tailoring of the optical properties of the coating in ways not possible with bulk materials. Such a photonic structure has achieved spectrally selective emittance: strongly reflective over visible and near-infrared wavelengths but strongly emissive between 8 and 14 μ (Fig. 1). When exposed to direct sunlight exceeding 850 W/m^2, the photonic radiative cooler maintained its surface temperature 4.9°C below the ambient air.

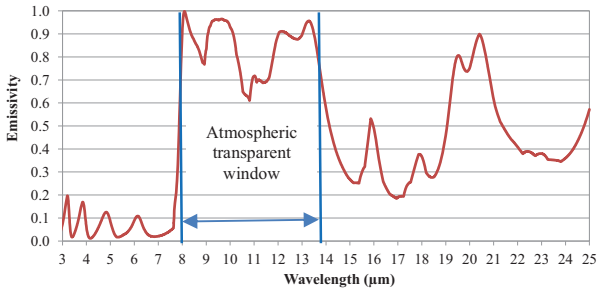

Fig. 1: Photonic material emissivity in the infrared range

3. Photonic radiative cooling System design

It must be noted that the nanostructured coating material studied in this paper is still at the very early research stages. No commercial photonic radiative cooling panels are available, let alone the application of photonic radiative cooling systems in buildings. Many materials presented in the following are more on the conceptual design than the real application design because the focus is to estimate the potential of energy savings from photonic radiative cooling and the associated impact of key design variables.

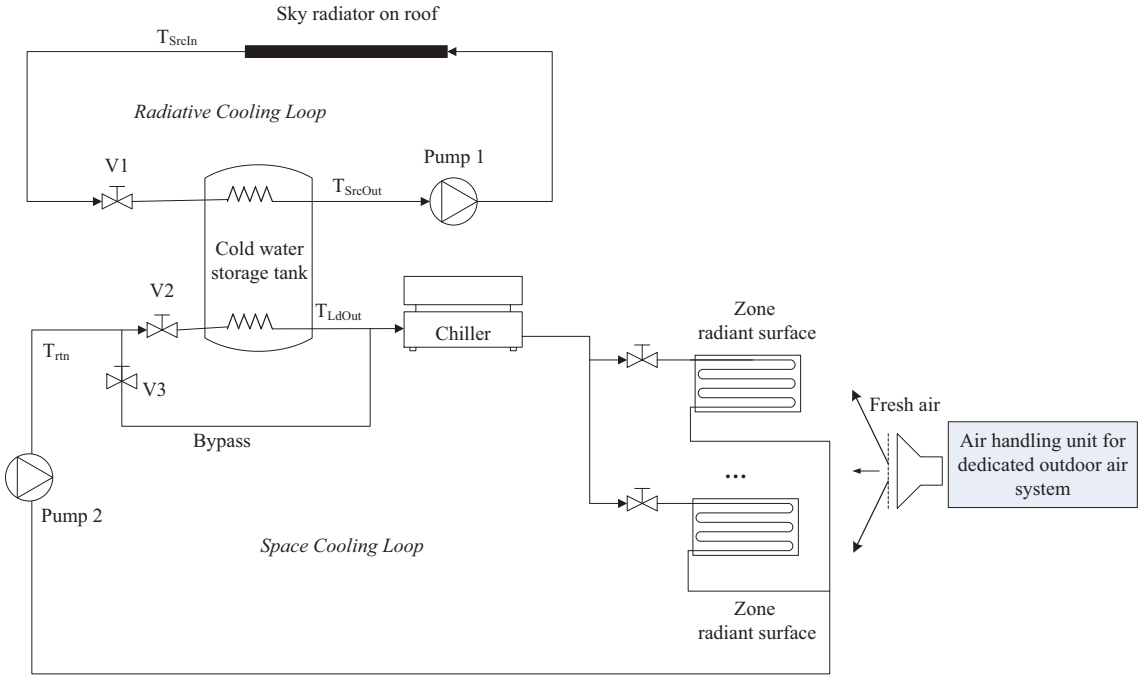

Fig. 2: Schematic diagram of the photonic radiative cooling system

Fig. 2 shows the schematic of the proposed radiative cooling system, which consists of two hydronic loops: a radiative cooling loop and a space-cooling loop. These two loops are coupled via a cold-water storage tank. The radiative cooling loop circulates water through a roof-mounted radiator via a constant-speed pump (Pump 1 in Fig. 2), which draws water from the storage tank and delivers cold water back to the tank. The pump is controlled to run whenever the temperature at the outlet of the radiator (T_{SrcIn}) is lower than the temperature of water at the outlet node of the tank (T_{SrcOut}), subject to the constraint that the loop will not run when the radiator temperature falls below 1°C. The space-cooling loop uses the water storage tank and a supplementary air-cooled chiller to provide cooling. A variable-speed pump (Pump 2 in Fig. 2) serves the space-cooling loop and adjusts the flow as necessary to provide sufficient cooling water to the space. If the outlet tank water temperature for the space cooling loop (T_{LdOut}) is colder than the chilled water temperature set point ($T_{chw,sp}$), i.e., $T_{LdOut} < T_{chw,sp}$, both valves V2 and V3 modulate open, mixing bypassed return water with cold water from the storage tank such that the desired water temperature set point is achieved. Under this scenario, the chiller is not used. If T_{LdOut} is higher than the chilled water return temperature (T_{rtn}), valve V2 closes, the water tank is bypassed, and only the chiller operates to address the cooling load. If $T_{chw,sp} < T_{LdOut} < T_{rtn}$, valve V3 closes and the chiller operates to address the remaining cooling load unmet by the tank.

Because radiative cooling generates cool water at a relatively higher temperature than the chilled water from conventional hydronic systems, it is favorable to employ a zone-level system design that makes use of high-temperature water for cooling. Therefore, as Fig. 2 shows, hydronic radiant floors are used to address the space sensible loads. In the radiant floor design, water tubes spaced at 150 mm are embedded in cement screed for sensible heat exchange with the space. The water tubes are separated from the concrete thermal mass by a 25-mm thick insulation layer (Raman et al. 2014).

To maximize the contribution of radiative cooling, the cold water supplied from the system should be controlled

to run at the highest possible temperature. This minimizes the use of the chiller by bringing the supply-water temperature set point closer to the tank water temperature. To achieve a balance between meeting the space cooling demand and maximizing radiative cooling, the supply-water temperature set point is reset according to the following strategy. If the average temperature for all thermal zones is above the space cooling set point more than 0.27°C, the supply-water temperature set point is decreased at a rate of 2°C per hour. On the other hand, if the average temperature is below the cooling set point more than 0.13°C, the supply-water temperature set point is increased at a rate of 2°C per hour. The supply-water temperature set point is limited to the range between 12.8°C and 18.3°C. Note that the above strategy supply-water temperature reset is based on our engineering experience for this simulation study oriented towards the dry climate in Las Vegas. Refinement and modifications may be needed for real implementations and for different climates.

As mentioned earlier, an air-cooled chiller is used in the photonic radiative cooling system to provide auxiliary cooling whenever the tank water temperature is higher than the supply-water temperature set point. Because of the high supply water temperature, it is desirable to use a low-lift chiller for supplemental cooling, such as that from Katipamula et al. (2010) to achieve superior performance at part load and "low lift" conditions (reduced difference between the entering condenser air temperature and the leaving chilled water temperature). These conditions are representative characteristics of hydronic radiant systems, which use much warmer chilled water temperatures (e.g. ~15°C) than conventional hydronic cooling systems.

A dedicated outdoor air system (DOAS) is used to provide ventilation air to the building in the absence of conventional air-handlers. The DOAS contains a constant volume fan, a hydronic heating coil and a direct-expansion cooling coil for air conditioning. The supply-air temperature set point of the DOAS is set at 12.8°C when the outdoor-air temperature is higher than 16°C, 18°C when the outdoor-air temperature is lower than 10°C, and linearly between the above boundary set points when the outdoor-air temperature lies in the range between 10°C and 16°C.

Regarding the sky radiator on roof (Fig. 3), it is conceptualized as a flat, metallic plate with its surface covered with the nanostructured, spectrally selective coating material as described in the previous section. Underlying the surface layer is an array of metallic piping, welded to the underside of the top plate. Each pipe runs parallel from an inlet manifold on one side of the radiator and returns to an outlet manifold on the other side of the radiator. The spacing between pipes is 150 mm (6 in.) and the pipe diameter is 19 mm (0.75 in.). Water pipes are located in-between the radiative cooler and a thin thermal conductive layer (e.g., aluminum plate). The sky radiator is integrated with the roof construction. To mitigate the convective heat gains from the surrounding, the photonic radiative cooler (Fig. 3) is covered with a 25-μm low-density polyethylene film and there is a 25 mm air space in between them. The use of polyethylene film follows the prototype design by the photonic radiative cooling material developer (Raman et al. 2014).

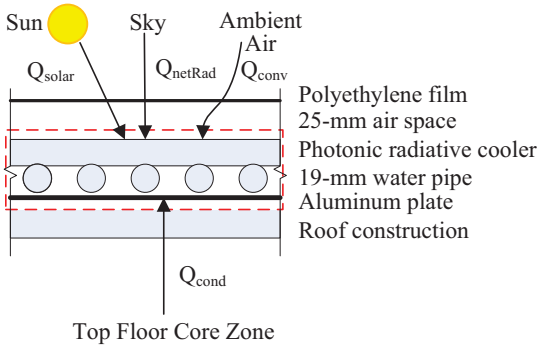

Fig. 3: Roof-integrated photonic radiator design

4. Building Model and Reference System

The building model originated from the Building Energy Codes Program (DOE 2015), which maintains a series of EnergyPlus models in compliance with different versions of commercial codes. A prototype medium-sized office building was used for the parametric analysis. The building (Fig. 4) has three floors and a total floor area of about 5000 m^2. The building has a rectangular shape with an aspect ratio of 1.5. Windows are distributed evenly

in continuous ribbons around the perimeter of the building. The window fraction of the overall façade area is 33%. The building construction includes steel-framed walls, a flat roof with insulation above the deck, and a slab-on-grade concrete floor. The performance values of the exterior envelope meet the minimum requirement of ASHRAE Standard 90.1-2013 (ASHRAE 2013). More detailed description about the building model including thermal zoning and internal loads can be referred to Thornton et al. (2011).

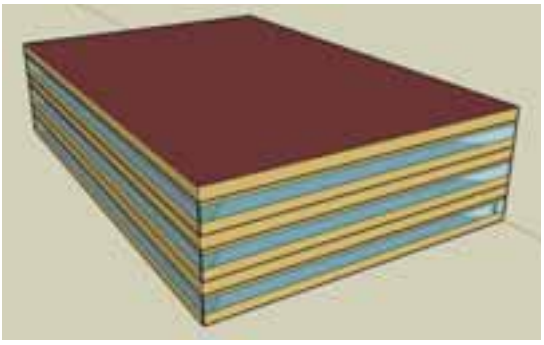

Fig. 4: Axonometric view of the medium office building

To investigate the impact of different design parameters of the photonic radiative cooling system on building energy consumption, we defined a reference system to represent the prevailing technology used to condition medium-sized office buildings. With a reference system, the potential of energy savings from different design scenarios of the photonic radiative cooling system can be conveniently derived and compared in a straightforward manner. The reference has an individual variable-air-volume (VAV) system for each floor (Fig. 5). All equipment types, efficiency, and system design features followed Standard ASHRAE 90.1-2013. The building model is essentially the same as the original source (DOE 2015) except for one change. The original source used the mean air temperature to define the heating and cooling set points at 21°C and 24°C, respectively. They were changed to use operative temperature for thermal comfort, with heating set point at 21.6°C and cooling set point at 25.7°C. Such a change is necessary to make a fair comparison between the VAV system and the photonic radiative cooling system. The use of hydronic radiant floors is favorable for occupant thermal comfort because of its higher floor temperature for heating and lower floor temperature for cooling relative to the VAV system.

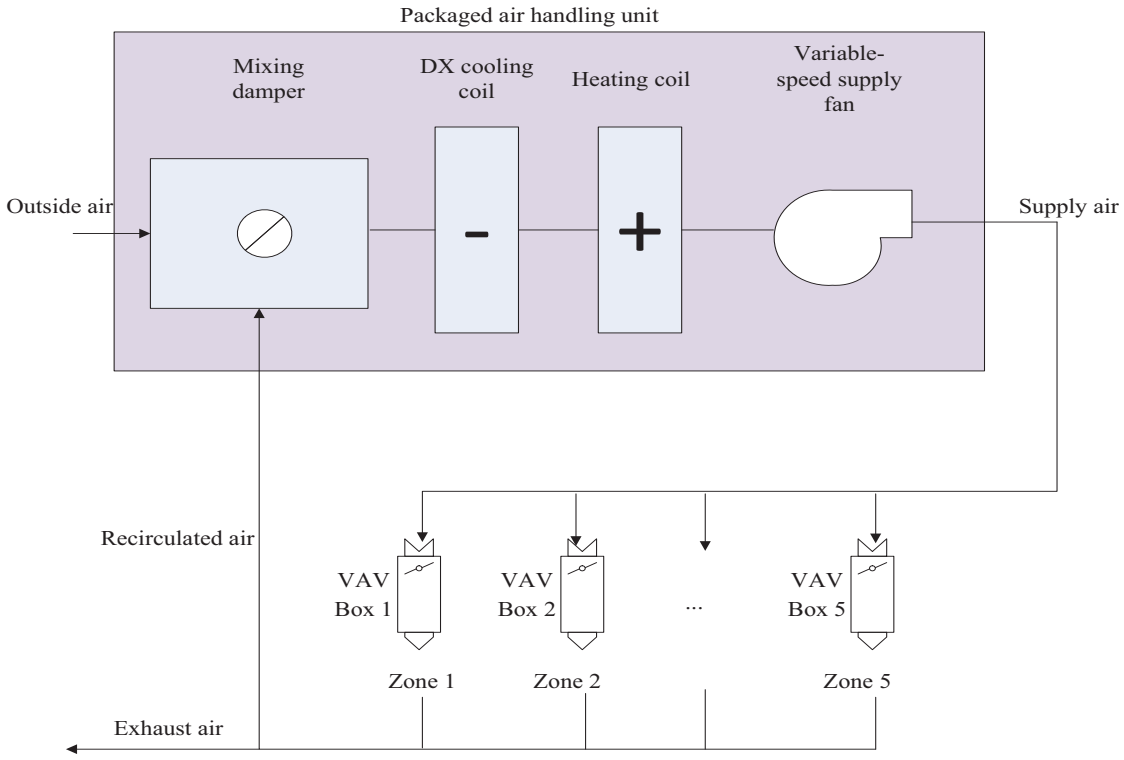

Fig. 5: Schematic diagram of the reference VAV system for each floor

5. System Modeling and Simulation Matrix

The photonic radiative cooling system, the reference VAV system, and the building were all simulated with EnergyPlus, a dynamic, whole building simulation program that supports a large variety of mechanical systems and components. Because there is no existing object in EnergyPlus for the novel photonic radiator, the energy management system (EMS) module in EnergyPlus was used to create a user-defined model of the radiator that is directly interfaced with the rest of the hydronic system specified in EnergyPlus. The EMS supports a simple programming language through which the user can construct new models and customize control sequences. To calculate the expected outlet temperature from the rooftop radiator and the average temperature of the radiator, the rooftop radiator was modeled in the EMS as a discretized heat exchanger by dividing the radiator into a discrete number of segments (Fig. 3 shows on segment as enclosed in the dashed lines). Heat transfer processes involved in the modeling of the photonic radiator includes the following:

- Absorbed solar radiation (Q_{solar}, W/m^2);
- Conduction (Q_{cond}, W/m^2) heat transfer between the underside of the radiator and the underlying building roof;
- Convection (Q_{conv}, W/m^2) heat transfer between the upper radiator surface and the ambient air; and
- Net longwave radiation (Q_{rad}, W/m^2) heat transfer between the upper radiator surface and the sky, which combines the outgoing longwave radiation emitted from the radiator minus the downward radiation from the sky absorbed by the radiator.

Detailed modeling of the photonic radiative cooler and the strategies used for the system simulation were reported in a previous paper (Wang et al. 2016) and are no longer repeated here.

Many design variables potentially affect the performance of the photonic radiative cooling system. Examples of those design variables include the sky radiator area, the tank size, the water flow rate in the radiative cooling loop, the system control variables (e.g., the supply water temperature), and building design variables (e.g., building location, area, and envelope thermal resistance). Recognizing that performing an exhaustive parametric analysis is resource-prohibitive, we decided to select the following three variables for further parametric analysis: the sky radiator area, the cold-water storage tank size, and the cold-water flow rate in the radiative cooling loop. These

three variables were thus selected because they are usually regarded as the key variables to be considered for a radiative cooling system design. Both the baseline values and the perturbed values of these three variables are discussed below.

The sky radiator area directly affects the amount of free cooling that the system can provide. A larger radiator area can generate more cooling but also implies a higher initial cost. In addition, practical constraints may apply for the area of roof-integrated radiators because the existence of mechanical equipment, ventilation and roof access infrastructure makes it unrealistic to cover the entire roof with the radiative panels. In the baseline mode, the sky radiator is assumed to occupy 50% (i.e., 830 m^2) of the roof area. Additional values studied for the parametric analysis include 30% (498 m^2), 40% (664 m^2), 60% (996 m^2), and 70% (1163 m^2) of the roof area.

The cold-water storage tank plays an important role in the system as the mismatch (temporal or magnitude) between radiative cooling capacity and space cooling load is common throughout the whole year. However, no practical design guide was found to determine the optimal size of tank storage. Eicker and Dalibard (2011) used a 1.2 m^3 storage tank for a net-zero home with a radiator area of 38 m^2. We simply scaled up the tank size following the same storage tank volume to radiator area ratio (i.e., 1200 L/38 m^2 = 31.6 L/m^2), which ends up with a tank volume of 26.2 m^3 in the baseline model. In the parametric analysis, the tank size was perturbed to take 50%, 75%, 125%, and 150% of the baseline value, which has the storage tank volume to radiator area ratio of 15.8 L/m^2, 23.7 L/m^2, 39.4 L/m^2, and 47.3 L/m^2, respectively.

The cold-water flow rate was also explored in the parametric analysis to investigate its impact on system performance. The baseline model had a cold-water flow rate at 26 kg/h per m^2 of radiator area. In the parametric analysis, the cold-water flow rate was perturbed to take 50%, 75%, 125%, and 150% of the baseline value, which respectively corresponds to 13.0 kg/h, 19.5 kg/h, 32.5 kg/h, and 39.0 kg/h per m^2 of the radiator area.

Tab. 1 summarizes the parameter values used in the baseline design as well as 12 other parametric models. It needs to be noted that in each run, a single variable was perturbed in the parametric analysis, relative to the baseline. Multi-variable parametric analysis is left for future work.

Tab. 1: Simulation runs for parametric analysis

Run	% of roof area used for radiator	Storage tank volume to radiator area ratio (L/m^2)	Water flow rate to radiator area ratio (kg/h/m^2)
1 (baseline)	50%	31.6	26.0
2	60%	31.6	26.0
3	70%	31.6	26.0
4	40%	31.6	26.0
5	30%	31.6	26.0
6	50%	15.8	26.0
7	50%	23.7	26.0
8	50%	39.4	26.0
9	50%	47.3	26.0
10	50%	31.6	13.0
11	50%	31.6	19.5
12	50%	31.6	32.5
13	50%	31.6	39.0

6. Simulation Results and discussion

All simulation runs shown in Table 1 were made for the location of Las Vegas, NV. Simulation results are discussed below.

As Fig. 2 shows, the sky radiator provides cooling and thereby reduces the time needed to run the electric chiller. Therefore, in comparison with the reference VAV system, the photonic radiative cooling system saves the

electricity for cooling, saves the fan energy, but also introduces additional pump energy as needed by the hydronic system. We will focus on the cooling electricity savings only because 1) fan energy savings is mainly due to the use of DOAS, which is not exclusive to photonic radiative cooling; and 2) the pump energy is negligible in comparison with cooling energy.

Fig. 6 shows the impact of sky radiator area on cooling electricity savings. The following can be seen from this figure:

- Relative to the reference VAV system, the photonic radiative cooling system saved 42% cooling electricity for the case of sky radiator occupying 50% of the roof area. The percentage of savings increased by 2% as the roof area used for the sky radiator increased by every 10%.
- There is a linear relationship between the percentage of cooling electricity savings and the percentage of roof area for radiative panels. Eq. 1 is the linear regression derived from the five sets of data with different radiator areas.

$$PerClgElec=0.204*PerRA+0.317 \quad \text{(eq. 1)}$$

where, $PerClgElec$ is the percentage of cooling electricity savings of the photonic radiative cooling system, and $PerRA$ is the percentage of roof area used for radiative panels.

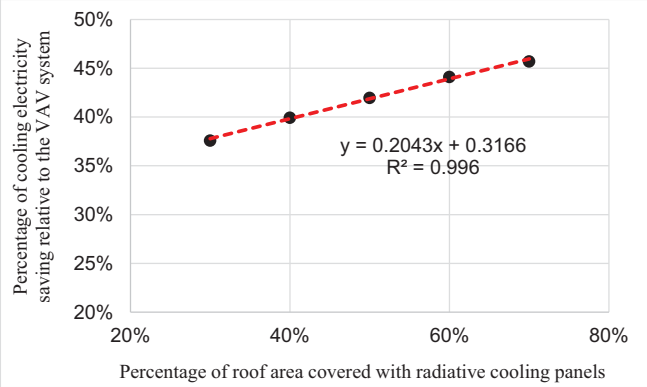

Fig. 6: Impact of radiator area on cooling electricity savings

Fig. 7 shows the impact of tank size on cooling electricity savings. This figure indicates that:

- Relative to the reference VAV system, the photonic radiative cooling system saved 42% cooling electricity for the case of baseline design of the cold-water storage tank size. The percentage of savings increased to 42.7% and 43.3% if the tank volume to radiator area ratio (VAR, L/m^2) was increased to 39.4 L/m^2 and 47.3 L/m^2. The percentage of savings decreased to 38.8% and 40.7% if the VAR was decreased to 15.8 L/m^2 and 23.7 L/m^2.
- The marginal benefit decreases with the increase of tank size. It is reasonable to expect that the cooling electricity savings will reach to a peak at certain value of VAR, beyond which no marginal benefit can be achieved.
- A quadratic correlation exists between the percentage of cooling electricity savings and the tank volume to radiator area ratio. Eq. 2 is the regression derived from the five sets of data with different values of VAR.

$$PerClgElec=-0.00004*VAR^2+0.0037*VAR+0.3394 \quad \textit{(eq. 2)}$$

Fig. 8 shows the impact of the water flow rate to radiator area ratio on cooling electricity savings. This figure shows that:

- The percentage of cooling electricity savings increased from 42% to 44% if the water flow rate to radiator area (FAR, kg/h/m^2) was decreased from 26 kg/h/m^2 for the baseline by half to 13 kg/h/m^2. No evident change of cooling electricity savings was observed if the FAR was increased from the baseline.

- A quadratic correlation also exists between the percentage of cooling electricity savings and the water flow rate to radiator area ratio. Eq. 3 is the regression derived from the five sets of data with different values of FAR.

$$PerClgElec=0.000005*FAR^2 - 0.0036*FAR+0.4753 \quad \text{(eq. 3)}$$

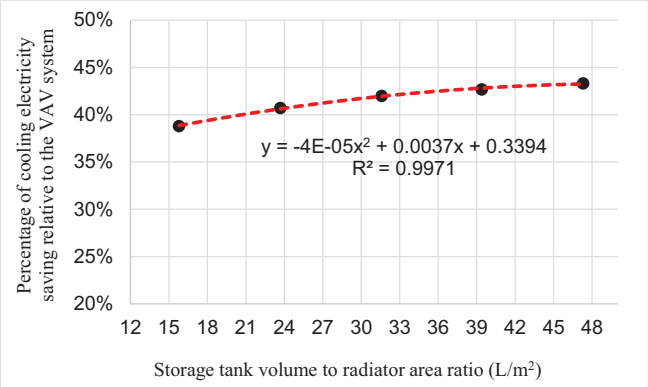

Fig. 7: Impact of storage tank volume to radiator area ratio on cooling electricity savings

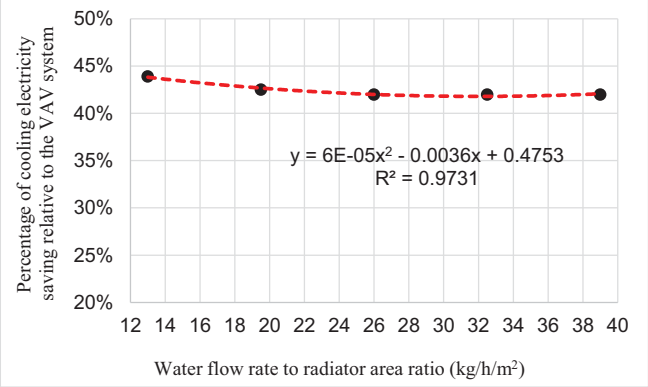

Fig. 8: Impact of water flow rate to radiator area ratio on cooling electricity savings

The difference of cooling electricity savings is attributable to the capacity of radiative cooling relative to the system cooling demand. As Fig. 2 shows, the water returned from radiant floors is cooled by the storage tank or the air-cooled chiller. The tank cooling energy is from the radiative cooler, so it can be regarded as "free" energy. For the photonic radiative cooling system, the percentage of free energy used to address the cooling load for each month is illustrated in Fig. 9 and Fig. 10, respectively illustrating the impact of radiator area and storage tank volume to radiator area ratio. The results for flow rate to radiator area ratio is not shown because of its minor impact on cooling electricity.

Fig. 9 and Fig. 10 show the following:

- For both cases, the percentage of "free" cooling from the sky radiator was the lowest in the summer months when there was a higher cooling load and a lower radiative cooling potential.
- As expected, the percentage of free radiative cooling increased with the sky radiator area (Fig. 9) and the tank size (Fig. 10).
- The percentage of free radiative cooling is less sensitive to the tank size than to the radiator area. Over all 12 months, the average difference of cooling electricity savings is 14% by changing the sky radiator area from 30% to 70% of roof area, while it is about 9% by changing the storage tank volume from 50% to 150% of its baseline design.

- For the baseline model, the free cooling from the sky radiator is can satisfy more than 90% of the entire building cooling load in January, February, March, November, and December. Such observation still holds true when the sky radiator area is reduced down to 30% of the roof area.

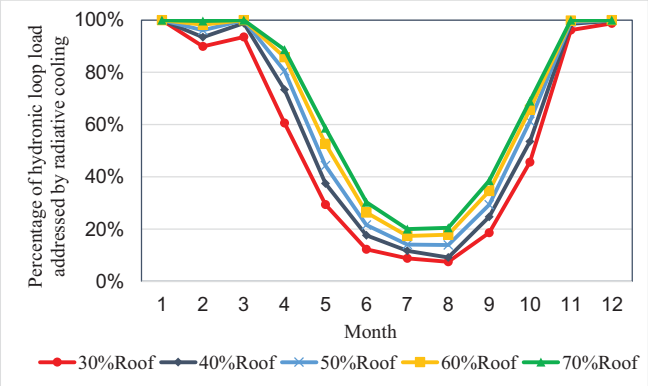

Fig. 9: Percentage of free cooling relative to radiator area

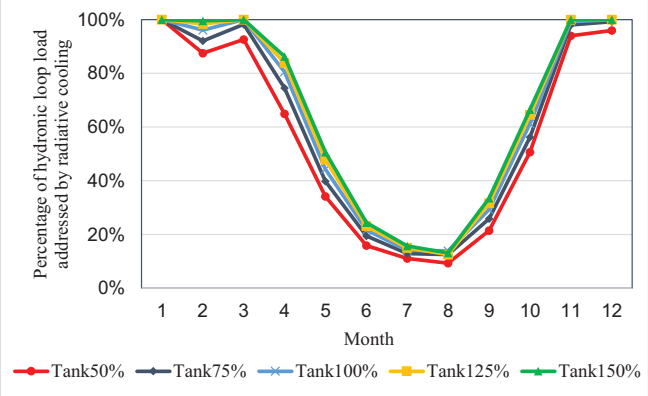

Fig. 10: Percentage of free cooling relative to tank volume to radiator area ratio

It needs to be noted that the electricity savings presented in this section should be interpreted as the outcome of system change, instead of the photonic radiative cooler only. The technical report (Fernandez et al. 2015) can be referred to for the benefits of the photonic radiative cooling system in comparison with other alternative systems (e.g., hydronic radiant systems and nighttime radiative cooling systems). In addition, using the regression equations to extrapolate results beyond the ranges investigated in this work may be questionable.

7. Conclusions

The photonic radiative cooling system has a great potential in building applications to save cooling electricity, compared to typical VAV systems for office buildings. The detailed energy simulation showed that for a three-floor medium office building located in Las Vegas, a baseline design of the photonic radiative cooling system with 50% of the roof area used for radiator and cold water storage tank sized at 31.6 L per m^2 of radiator area saved 42% cooling electricity relative to the reference VAV system. Based on a parametric analysis for three key design parameters, namely the radiator area, the storage tank volume to radiator area ratio (VAR), and the water flow rate to radiator area ratio (FAR), the simulation results revealed that the percentage of cooling electricity savings had a linear relationship with the radiator area, and a quadratic relationship with both VAR and FAR. The percentage of savings increased by 2% as the roof area used for the sky radiator increased every 10%. The marginal benefit decreased with the increase of storage tank volume to radiator area ratio. The cooling electricity savings decreased by if the flow rate to radiator area ratio was increased from 13 kg/h/m^2 to 26 kg/h/m^2, beyond which there is no change of electricity savings. The percentage of free radiative cooling increased with the sky radiator area and the tank size. The percentage of free radiative cooling is more sensitive to the radiator area than to the

storage tank volume to radiator area.

Further investigation can be made for other variables such as the radiator orientation if standalone sky radiator is used. Design optimization of multiple variables is also worth considering in future work.

ACKNOWLEDGMENTS
The work was funded by the Building Technologies Office of the U.S. Department of Energy.

REFERENCES

Al-Obaidi K.M., Ismail, M., Rahman, A.M.A., 2014. Passive cooling techniques through reflective and radiative roofs in tropical houses in Southeast Asia: A literature review. Frontiers of Architectural Research, 3(3), pp. 283-297

Argiriou A., 2013. Radiative cooling, in: Santamouris, M. and Asimakopoulos, D. (Eds.), Passive Cooling of Buildings, Earthscan New York, pp. 424-454.

ASHRAE, 2013, ANSI/ASHRAE Standard 90.1-2013: Energy Standard for Buildings Except Low-Rise Residential Buildings, American Society of Heating, Refrigerating and Air Conditioning Engineers, Inc., Atlanta, GA.

DOE, Department of Energy, U.S., 2011. Building Energy Data Book, http://buildingsdatabook.eren.doe.gov/, Accessed in June 2017

DOE, 2015. Commercial Prototype Building Models. Building Energy Codes Program, Department of Energy, https://www.energycodes.gov/commercial-prototype-building-models, Accessed in June 2017

Eicker U., and Dalibard, A., 2011. Photovoltaic-thermal collectors for night radiative cooling of buildings. Solar Energy, 85(7), pp.1322-1335.

Eriksson T.S., Granqvist, C.G., 1986. Infrared properties of Silicaon Oxynitride Filens: experimental data and theoretical interpretation. Journal of Applied Physics (60):2081.

Fernandez N., Wang, W., Alvine K.J., Katipamula, S. 2015. Energy Savings Potential of Radiative Cooling Technologies. PNNL-24904, Pacific Northwest National Laboratory, Richland, WA.

Geetha N.B., Velraj, R., 2012. Passive cooling methods for energy efficient buildings with and without thermal energy storage – A review. Energy Education Science and Technology Part A: Energy Science and Research, 29(2), pp. 913-946.

Gentle A.R., Smith, G.B., 2015. A subambient open roof surface under the mid-Summer sun. Advanced Science, 2(9):1500119. DOI: 10.1002/advs.201500119

Granqvist C.G., 2003. Solar energy materials. Advanced Materials 15(21):1789-1803.

Katipamula S., Armstrong, P., Wang, W., Fernandez, N., Cho, H., Goetzler, W., Burgos, J., Radhakrishnan, R., and Ahlfeldt, C., 2010. Development of High-Efficiency Low-Lift Vapor Compression System - Final Report. Technical Report PNNL-19227, Pacific Northwest National Laboratory, Richland, WA.

Meir M.G., Rekstad, J.B., Lovvik, M., 2002. A study of a polymer-based radiative cooling system. Solar Energy, 73(6), pp. 403-417.

Mihalakakou G., Ferrante, A., Lewis, J.O., 1998. The cooling potential of a metallic nocturnal radiator. Energy and Buildings, 28(3), pp. 251-256.

Niklasson G.A., Nilsson T.M.J., 1995. Radiative cooling during the day: simulations and experiments on pigmented polyethylene cover foils. Solar Energy Materials and Solar Cells 37(1): 93-118.

Parker D., 2005. Theoretical Evaluation of the NightCool Nocturnal Radiation Cooling Concept. Technical Report No. FSEC-CR-1502-05, Florida Solar Energy Center, Cocoa, FL.

Raman A.P., Anoma, M.A., Zhu L., Raphaeli E., Fan, S. 2014. Passive radiative cooling below ambient air temperature under direct sunlight. Nature (515):540-544.

Thornton B.A., Rosenberg, M.I., Richman, E.E., Wang, W., Xie, Y., Zhang, J, Cho, H., Mendon, V.V., Athalye, R.A., Liu, B., 2011. Achieving the 30% Goal: Energy and Cost Savings Analysis of ASHRAE Standard 90.1-2010. Technical Report PNNL-20405, Pacific Northwest National Laboratory, Richland, WA.

Wang W., Fernandez, N., Katipamula, K., 2016. Modeling and simulation of a photonic radiative cooling system. Proceedings of the ASHRAE and IBPSA-USA SimBuild Conference, Salt Lake City, UT.

The development of the Sunridge® ICS system: an orientation independent solar system

Aart de Geus[1] and Henk de Beijer[2]

[1] ArtEnergy, M. Trompstraat 6, 2628 RD Delft, The Netherlands

[2] Solabcool bv, Stenograaf 1, 6921 EX, Duiven, The Netherlands

Abstract

In order to realize Nearly Zero Energy Buildings and make the existing building stock energy efficient, the energy demand for heating and cooling and the electrical energy consumption needs to be reduced drastically. The next step in the so-called Trias Energetica is the local production of renewable energy, both electricity and thermal energy. A large (growing) part of the energy demand is related to hot water consumption. Here thermal solar energy can play an important role. Therefore, development of easy to integrate and install, efficient thermal solar systems is essential. Moreover, the main disadvantage of thermal solar energy systems, i.e. the required south orientation on z tilted roof and the competition with PV systems needs to be tackled to increase the applicability of such systems. In this paper the development of the Sunridge® system, a ridge integrated solar domestic hot water system, is described. A tube in tube concept as SDHW is developed and is placed on the ridge of the roof. The outer tube contains the spectral selective layer and the inner tube is the storage volume, a transparent cover is placed as outer layer. Heat is transferred from the outer tube to the inner tube by means of the effective boiling and condensation of water under low pressure between the two cylinders. The system will be inherent safe for overheating and freezing. The performance and end user price target is to be in the order of the price /performance of a standard SDHW system, nowadays on the market. The final design for the system is ready and pre-production takes place. In 2018 the first systems will go to the market.

Keywords: Integrated collector system, Solar domestic hot water, system, ridge integrated solar energy system,

1. Introduction

In order to realize Nearly Zero Energy buildings not only renewable electricity has to be produced, but also energy consumption needs to be reduced as well as renewable heat needs to be generated and used effectively. The heat demand of existing and new buildings is about 1.5 to 3 times higher than the electricity demand. A large part of the energy consumption in buildings is for space heating, space cooling and hot tap water production. The yearly energy needed for hot tap water is about the same as the yearly electricity demand for a household. In the next years the demand for electricity will increase, the demand for house heating will decrease but the energy needed for hot tap water will increase (comfort!). Better insulation of the buildings, energy efficient windows, and heat recovery results in a lower space heating demand in the building. For the reduction of the energy consumption for hot tap water production, new high efficient equipment such as HE gas burners and heat pumps offers possibilities, but still fossil energy is needed. For hot tap water production, the solar domestic hot water system is a good alternative. Thermal solar energy systems can reduce the heat demand and especially the heat demand for hot water production. However, thermal solar energy systems have some draw backs. These are among others:

- a required south orientation on z tilted roofs,
- competition for suited roofs space with PV systems,
- competition with windows in the roof

doi:10.18086/swc.2017.17.06 Available at http://proceedings.ises.org

- the space needed in the house for the water tank.
- an easy to integrate and install, efficient thermal solar system is under development.
- aesthetics

These main disadvantages are tackled through the development of the Sunridge® system. This development of a ridge integrated solar domestic hot water system, is in this paper further described. As ridge integrated system, the Sunridge® system is truly orientation independent. The system under development is a tube in tube concept placed on the ridge of the roof (see fig 1) . The ridge integrated solar energy system offers the integration of a solar product at a place of the building (the ridge) which has a low attention factor (aesthetics), is not in competition with other energy systems at that place, integrates also the water tank (no extra space in the building needed), is scalable to fit the ridge length and the Sunridge® product deviates not too much from ridge caps or upper roof tiles. From street level the system is almost invisible. For safety and health reasons the hot water temperature should be higher than ca. 60 °C. So the energy consumption in the built environment will be more and more dominated by the energy needed for the hot water production, at relative high temperature. A typical SDHW system reduces the conventional energy consumption by about 50%. Since the Sunridge® product will be very well suited for especially the existing one family buildings the market potential is huge (approx. 120 million existing dwellings across Europe are suited). The product is orientation independent, suited for both tilted roofs and flat roofs and modular adaptive to the length of the ridge. The calculated energy performance for 3 modules is that more than 50% of the energy consumption needed for hot water will be produced by the Sunridge® system. This performance will, of course, vary according to the climate, the number of modules and the hot water consumption. Higher contribution (>75%) in the South of Europe and lower contribution in the Northern countries of Europe (approx. 40%).

Fig 1 Artist impression of the. Sunridge® system on the ridge of a dwelling.

2. Technology of the Sunridge® system.

The Sunridge® product is a solar system in which the absorber for solar energy and the storage tank, for the hot water, have been merged into one unit.(see figure 2). The product consists of two tubes whereby one tube is assembled into the other. The inner tube is the container for (hot) tap water. The outer tube (copper) will be provided with a special layer with which the absorbed solar energy is efficiently transferred into heat. Water is placed in the space under low pressure between the inner and outer tube in order to transport the solar heat form the outer tube to the inner tube. When the outer tube is heated by solar energy, the water evaporates. The evaporated water condenses at the inner tube and transfers in this way the heat from the outer tube

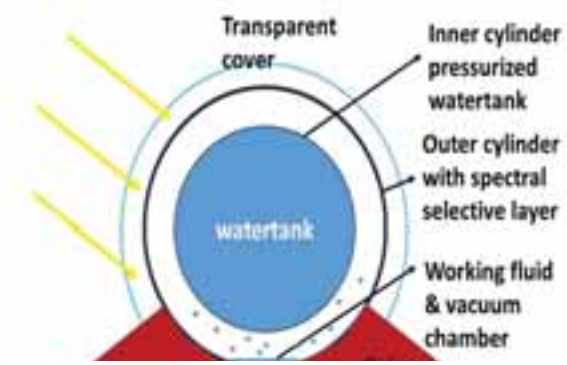

Fig 2. Scheme of the Sunridge® system.

to the inner tube. The condensed water drips of the inner tube and the whole process of evaporation and condensing starts again. In case of absence of solar energy, the heat transfer from the inner tube to the outer tube is only possible through radiation because the inner tube does not come direct into contact with water.

The inner tube serves as storage tank for the hot water. When the outer tube is heated, this water evaporates and consequently condenses on the colder side of the inner tube. In this way the solar heat is efficiently transported to the storage tank. Because the space between the inner and the outer tube is vacuumed, as a result of which the storage tank works as a thermos flask.

In figure 3 the physical process, used in the modelling are shown. The solar irradiation passes the outer transparent cover. For the largest part of the solar radiation passes heats the first copper cylinder. heats the outer surface of the outer tube. Heat losses are occurring due to re-radiation and convection. The first cylinder is equipped with the spectral selective layer. The radiation losses are low due to the low emissivity of the layer. The space between the tubes is under very low pressure enabling the water to evaporate and condensate to the inner tube, filled with tap water. In this way the solar heat is transferred to the inner tube and heats the tap water storage tank.

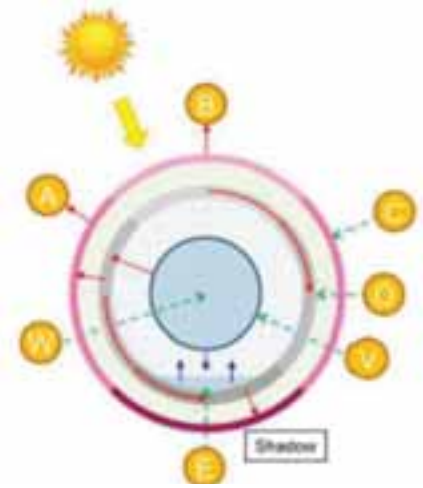

Fig. 3 Energy flows in the Sunridge® System

The Sunridge® product is placed on the ridge of the dwelling and placed in series of modules in order to reach the required volume for storing the hot water. Dependent on the number of modules connected the volume can go up to 130 liters, for a typical Dutch one family house. Due to the characteristic of the tubular SUnridge® system and the placement of the system at the ridge of the roof, the system performance is now almost independent of the orientation of the dwelling. Another advantage of the integrated system is the fact that in this concept an extra storage tank for hot water is not needed inside the dwelling, but is integrated at the roof. In this way a large market for SDHW systems now becomes available especially in refurbishment sector.

3. Experience with previous system

The first development of the Sunridge® system (Ekonok system) started some years ago. The manufacturing of tube in tube construction with vacuum has been carried out successfully. The principle of heat transport and diode function through the water/vapor under low pressure was tested and the performance is designed. The long-term performance and durability of the system was demonstrated in a field test over more than 10 years. After first market introduction, the market development stagnated at that time. The overall system concept had some drawbacks. These were:

- Installing the system on the roof and the connection to the tap water circuits was too complex, due to the connection of the modules connection under the roof.
- Deterioration of the transparent polymeric cover was going too quick
- The heat losses were high, for reasons of not having a spectral selective layer
- Industrial redesign of the system and production process was delayed

The system concept has been proven over the years. Therefor the redevelopment of the Sunridge system started with the help of the InnoEnergy innovation project. In order to get a good starting point for this development a module of the old system was tested at IREC.

In Figure 4 the calculated output of the DST test is presented. Under Dutch conditions the Sunridge system (consisting of 3 elements) had a performance of 2.6 GJ based on 100 L/day from 10°C to 65°C, preheated by the system, tested outdoors according to the DST test method in 2002. Since than the DST method is using other climatic conditions and is using other testing parameters. Nowadays the performance would be in the order of about 2.75 GJ.

A module of the old system has been tested at IREC. In figure 4 is shown that the module produced in 2015 without spectral selective layer gives the performance comparable to the old system.

The new design of the Sunridge system is based on spectral selective layer and new other materials is opting for 3. GJ for the Dutch conditions.

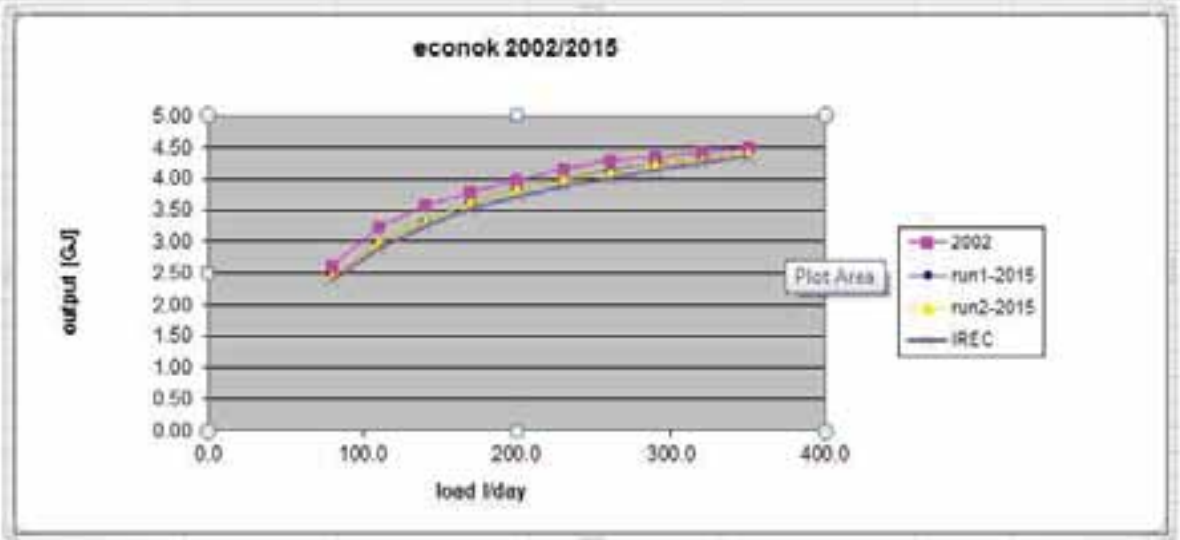

Fig 4. The output of the old Sunridge® system based on the DST test.

4. The Industrial Design.

As described in chapter 3 the old system had some drawbacks, reasons why parties in the market could not enter the market well enough. Some developments were needed and at that point of time this investment could not be made.

Since InnoEnergy (Knowledge Innovation Community of European Institute of Technology) started in 2010, a new vehicle became available supporting the further developments of products with a relative high TRL(technology readiness level) level from about TRL=6. This opportunity was used to develop a KIC InnoEnergy innovation project [1]. The Sunridge® product is since end 2014 under development to realize a competitive product for the market by 2018. The following aspects are under development:

- improve the performance of the systems (higher solar absorption and lower heat losses);
- make an inherent safe product for overheating and freezing;
- an esthetic, simple and scalable ridge integration for new and existing dwellings;
- Easy to be installed by roofers and installers
- Robust and quick connection for the modules;

Furthermore, the goal of the development in this InnoEnergy innovation project is to develop the pilot prototype production line, showing the manufacturing process at small scale, proving the realistic end price of the system and showing the high performance under realistic conditions.

The program of requirements was made with the following main aspects:

- The product has to withstand all the tests according to the standard and internal Monier standards for roofing product, such as wind, ventilation, hail, durability and safety.
- The product must be easy adaptable to different widths of the roof.
- Product should be easy to install by roofing companies
- Installation connections: only at one place of the roof connection through the roof for connection the water pipes to the aux and mains water supply.
- Inherent safe overheating and freezing protection.

Based on these requirements the industrial design of the Sunridge system was made, leading to the following important systems parts to be further developed and tested. These are

- The transparent outer cover. The choice has been made to use glass tubes.
- Stainless steel as the material for the inner tank containing the drinking water. Copper as material for the outer tank with water under very low pressure for the heat transfer between the outer and the inner tube.
- Spectral selective layer applied on the outer copper tank.
- Supporting construction for quick installation between the ridge and the system, in the form of dedicated aluminum profiles.

In the following figures 5 to 9 the results of the industrial design are showed.

Besides the solar and thermal performance, the durability, safety and ecological performance must be excellent. And of course, last but not least the price performance ratio must be competing with normal solar domestic hot water system.

The roofing company Monier is participant in this project and has the rights for the first market introduction. For this reason, the systems overall performance and the integration in the roof should fulfill all the requirement of the quality of products which are standard at Monier. For this reason, the durability and safety tests will be performed by Monier in their roof testing Centre in Heusenstamm, Germany.

Fig 5. Spectral layer on copper tube

Fig 6. Mock-up of the Sunridge®

Fig 7. Ridge profile, upper for the system, under profile to the beam of the ridge

Fig 8. End cap for the module

Fig 9. Detail of the tube on the aluminium profile

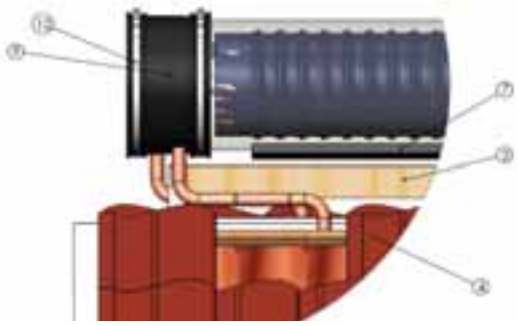

Fig 10. Inlet-outlet connection to the module Spectral layer on copper tube

Fig 11. **Connenction between the modules**

5. Testing the new Sunrise system

In the spring 2017 one module for the Sunridge system consisting of the spectral selective layer and glass transparent layer was delivered at IREC, for outdoor performance testing. In figure 12 the system placed at the testing roof at IREC is shown.

Fig. 12. The Sunrise system at test facility at IREC(Taragona Spain)

During summer 2017 one module of the Sunridge system was tested. This module was 1.4 m long and had a tap water content of 35 l.

5.1 Performance testing

The system was tested according to the DST test method described in the EN 12976. The performance of the new Sunridge module is compared to the old Econok system. Based on the test results obtained in summer 2017 the DST parameters were established. These parameters are used for the long term performance calculations for various climatic conditions and tap water consumptions. In figure 13 the outcome of the new module is presented and compared to the old module. The results shown are for one module. For typical one family conditions about 3-4 modules will be used.

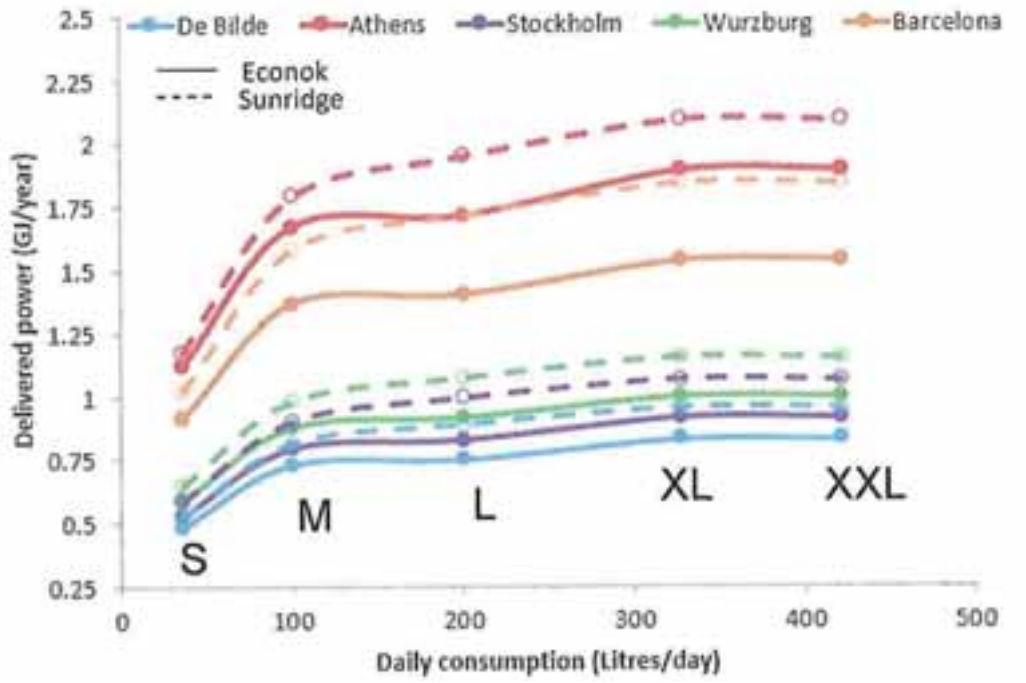

Fig. 13. Results from the DST test. Yearly energy output for one module for various climatic zones and different daily hot water consumptions. Comparison between the old Eocnok module and the new Sunrise module

From the testing the following conclusions for the Sunridge system under development were drawn, incomparison to the previous (Ekonk) system:

- The DST model parameters points at lower storage losses
- The DST parameters point sat significant mixing during draw-off
- The performance increase is in the order of 10 to 25%

Based on the test results for only one module it is shown that the goal set for the performance improvement of at least 10% for Dutch conditions is clearly met. Complete Sunrise® system, consisting of 3 modules, will be demonstrated end 2017 and beginning 2018 in The Netherlands. Moreover, in April 2018 the solar key mark testing for the complete system will start.
Based on the tests at IREC summer 2017 the design model of the system is validated. This design model is a dedicated TRNSYS model for the Sunrise system. Moreover, a detailed model for the Sunrise system has been developed at TNO. With this model the effective collector efficiency curve can be calculated. This effective collector curve is used in the design model. W
With the design model the lay-out of the system can be calculated based on the climate and predicted hot water consumption. The result is a predicted performance, energy savings and number of modules needed.

5.2 Outdoor Shock test

As part of the testing at IREC, internal and external shock test have taken place and the stagnation temperature has been characterized. These tests have been performed according to the EN12975-2 standards.

Fig. 14. Condensation after the first external shock test.

The stagnation temperature measured for the system fully filled with tap water reached a value of 63,4 °C. using the standard conditions of the EN 12975-2 means that this a value is 67,7 °C.

The internal and external thermal shock tests were performed and the results showed no damages or leakage. Moreover, the vapor pressure of the vacuum space between the tubes showed no significant changes. At the first external shock test significant condensation at the glass tube was detected visually (see fig 14).

5.3 Overheating and freezing test

As discussed in 5.2 the stagnation temperature of the system has been measured. In the case of long period of absence (holiday) and high solar radiation the temperature in the tank of the Sunridge system can be very high, even higher than 100 ℃. for this reason a well-known safety control will always be a part of the installed installation.

Since the complete system is place outside freezing during winter conditions can occur. For this reason, the Sunridge will be equipped with an electrical tracer. The typical vulnerable aspects in the design are in the inlet and outlet tap water piping and the connecting pipes between the modules (see fig 14 and 15).

Fig. 15. Tracer on the connection pipe between the modules

Fig. 16. Electrical tracer to the inlet and outlet pipe of the module.

In a freezing cabinet at TNO the Sunridge system including the installed electrical tracers were tested according the requirements of EN 12976-2. The complete system has to withstand an outdoor temperature of -20°C during a period of 12 hours with a start temperature of the tap water of 5 °C In fig. 17 the test results are shown.

The system was tested under -20°C for more than 30 hours. The temperatures of T203, T204 and T205 are around 0°C, but the more critical temperatures of the connecting pipes are above 15°C. The temperatures T deep and T shallow drop to a still safe level of slightly below 3°C.

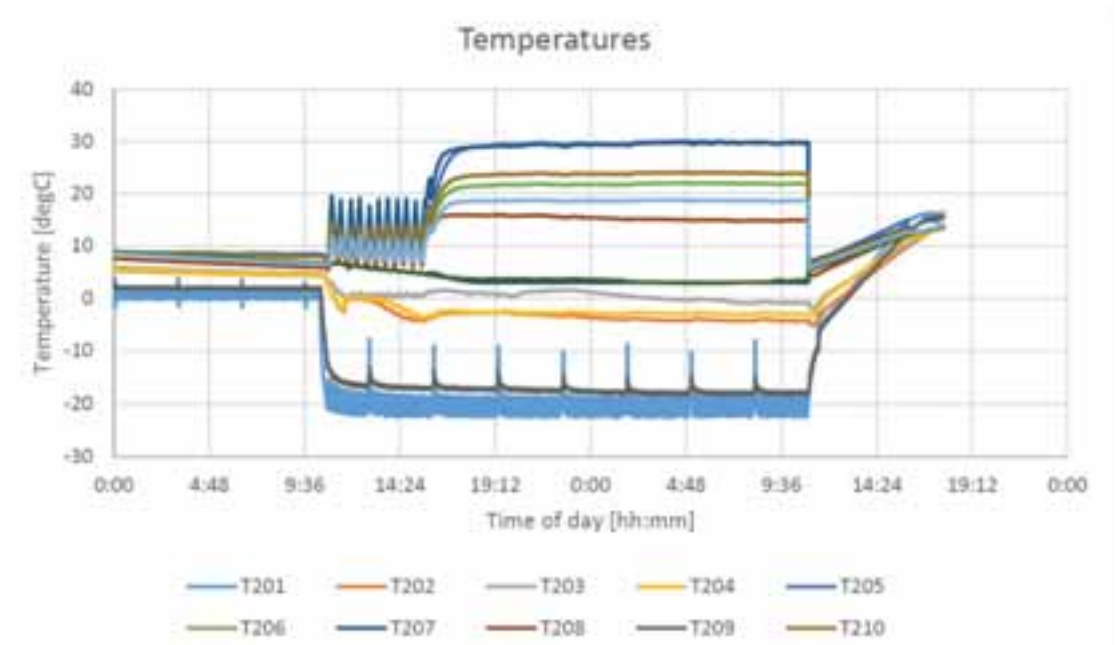

Fig. 17. Temperatures in the and around the Sunridge®water tank during the freeze testing

The conclusion from the test was that the Sunridge® system equipped with the electrical traces and the clckon sensor placed on the right position, fulfills the EN12975-2 requirements with respect to withstanding freezing.

5.4 Wind load design

Fig 18. The aluminum profile connected to the beam and the clamp for holding the wooden beam for connection to the roof plates.

The Sunridge® system is mounted on an aluminum profile. This profile clicks in to a profile that is connected to the ridge. The wooden beam for the ridge is connected to the roof plates by means of a number of clamps. Wind loads will come on the glass tube of the Sunridge® system. These forces will generate momentum to the roof. The connection from the system to the roof plates have to withstand severe wind loads. For this the most severe conditions from the standards are taken. In this case that is the British Standard for wind loads on roofs. The glass tube is mounted on the aluminum support profile. The profile is screwed on the beam of the ridge. This is a new wooden beam mounted with ridge batten holders on the roof plates. A dedicated design has been made for the ridge batten because they form a constructive unit with profiles. In order to with stand the wind load, the place and thickness of the screws was calculated. Moreover, this was also carried out for the clamps and ridge batten holder. Hereafter this was manually tested at the test roof set-up at Monier. A first quite simple tests showed that the steel support for the beam were not strong enough. Redesign was carried out and this ended up with thicker clamps. In figure 19 the testing of the system and forces are shown.

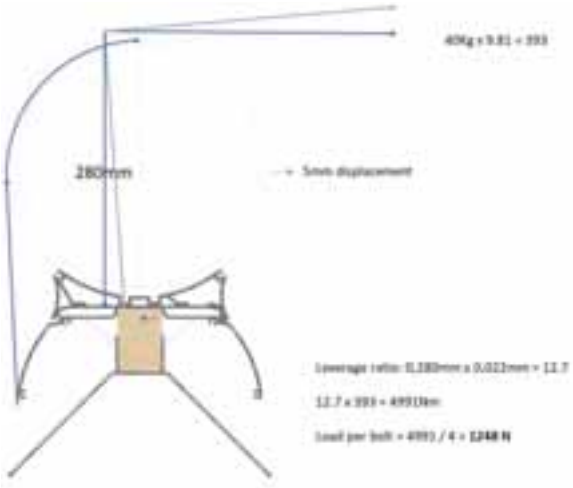

Fig. 19 Forces on the Sunridge system

6. .Production

An important aspect of the project is the cost price of the Sunrise® product. The cost price is among others determined by the bill of materials, bill of labor and the production process.
The flow chart for the production process is developed. A very import step in the production is the welding process of the end caps for the tubes with the tap water connections. Since the pressure between the copper outer and stainless steel inner tube is very low, leakage can occur. For the welding process an excellent supplier has been selected. The welding of the copper tube and the stainless steel tube is performed at a manufacturing plant with an automated rolling and welding process. The next step is the welding of the end caps first to the stainless-steel tanks. Here the connecting pipes for inlet and outlet tap water are welded to the caps.
Then stainless-steel end caps are welded to the copper tube with connecting water pipes through this end caps. This welding of the end caps is a very critical production step. The welding has to be airtight since a very low pressure between the tubes is needed for the working of the Sunridge® system.

Fig. 20: Industrially designed module complete with caps and the tap water connections between the modules.

Fig. 21 Welding of the copper tube.

In figure 20 the industrial design of a module is presented. In the figures 21-24 the welding process is shown.
The field demo modules are produced in March 2017. About 25 modules will be produced. From this demo modules a number of about 15 modules will be used for performance testing and testing as demo in the field. Other modules will be used for risk assessment test at Monier test Center in Heusenstamm.
Based on the test results for the performance, installing in the demo, risk assessment testing and other new information the final design will be made during 2017/2018. This also will lead to a final production plan with bill of materials and bill of labor. In the end the cost price will be determined. During 2018 first modules will be sold to the market through the channels of Monier.

Fig.22. The end cap with tap water connection. Welding of copper tube, stainless steel cap and copper water tube.

Fig.22. The longitudinal automatic welding machine.

7. Conclusions

In this paper the development of the ridge integrated solar water heating system, Sunridge® is described. The Sunridge system consist of a number of modules coupled and placed on the ridge of the roof. With this flexible design for the system, the solar energy contribution to the hot tap water can be tuned to the demand, the climate and the dwelling. The energy performance of the ridge integrated system can be about 50% of the energy demand for hot tap water and most important this is orientation independent. Moreover, the ridge integration enables the roof of the dwelling being used for other purposes, such as photo voltaic panels and/or roof windows.

The Sunridge system is a preheater for hot tap water with the tap water storage tank placed outside the dwelling, on the roof. The design of the system enables an inherent safe product, easy to install and to connect to the hot water system in the dwelling.

The industrial production process is designed in order to produce the system at high quality in a professional way. The overall cost price including installing the system is expected to be competitive the standard solar thermal domestic hot water systems. The production process can be up scaled to large numbers in a due time, due to the modular set-up of the system and production. In 2018 the Sunridge® product will be introduced in the market in The Netherlands.

8. Acknowledgements

This development is supported by InnoEnergy a Knowledge Innovation Community through the funding of the Sunridge® project. InnoEnergy is supported financially by European Institute of Technology. In this project the following parties are cooperating:

- Monier roof and tiles manufacturer,
- TNO research Institute in The Netherlands,
- IREC Renewable Energy laboratories,
- RTB de Beijer innovative SME company
- ArtEnergy bv SME company

References

[1] KIC InnoEnergy, sun-RISE, Ridge Integrated Solar Energy system, project proposal 2014.

PVT Systems

Analytical Study on The Effect of Optical Filtration and Nano-PCM on The Performance of PV/T Solar Collectors

Ahmed S. Abd-Elrazik [1,4], FA Al-Sulaiman[1,2 *], Saidur R. [2,3], and R Ben-Mansour [1]

[1] Mechanical Engineering Department, King Fahd University of Petroleum and Minerals, Dhahran, Saudi Arabia

[2] Center of Research Excellence in Renewable Energy (CoRERE), King Fahd University of Petroleum and Minerals, Dhahran, Saudi Arabia

[3] Research Centre for Nano-Materials and Energy Technology (RCNMET), School of Science and Technology, Sunway University, Malaysia

[3] Mechanical Power Engineering Department, Ain Shams University, Cairo (Egypt)

*Corresponding Author: fahadas@kfupm.edu.sa, Tel: +966 (13) 860-4628.

Abstract

High temperature is a challenging problem with all solar collectors that are using PV panels for electricity production. Cooling of PV panels using traditional fluids become not effective as for the poor thermal properties of these fluids. Dispersion of nanoparticles with different liquid was found to enhance the thermal properties of these liquids. Nanofluids and Nano-Phase Change Materials (Nano-PCMs) were considered as promising solutions to enhance the performance of PV/Thermal (PV/T) systems. Nanofluids can be used beneath the PV for cooling or above it for optical filtration. In addition, Nano-PCM can be used beneath the PV for cooling and storage. In this study, an analytical solution was developed to evaluate the effect of using nanofluid filtration and nano-PCM on the overall performance of the PV/T solar collector. Four models were examined alternating between the presence and absence of optical filtration and lower nano-PCM layer. Neglecting the storage side, it was found that without optical filtration, presence of nano-PCM below the PV module decreases the overall efficiency (thermal + electrical) by around 6.7%. In contrast, presence of optical filtration decreases this percentage to be less than 1%. Moreover, using the optical filtration alone improves the overall efficiency by 6-12%.

Keywords: Nanofluid, PCM, PV/Thermal, PV cooling, Optical filteration

1. Introduction

Solar energy is considered one of the most promising sources of renewable energies that should be used efficiently to be able to completely replace the fossil fuel energy very soon. Many devices are used for the collection process of solar radiation. Hybrid Photovoltaic/Thermal collectors are found to combine the advantages of electrical and thermal energy generation as well as solving the problem of performance degradation of PV cells because of high temperature by cooling the PV panels. In this demand, many researches had been made alternating from changing the design of the collector to using different cooling fluids to attain the highest possible overall efficiency.

Hussain et al. (2013) studied the efficiency of using honeycomb channels beneath the PV in enhancing the thermal efficiency of hybrid PV/T collector cooled by air. They examined the enhancement under different flow rates. It was found the thermal efficiency enhanced from 27% to 87% when using honeycomb channels with air mass flow rate of 0.11 kg/s. Fudholi et al. (2014) investigated a study for different configurations of water cooled PV/T under different mass flow rates and solar irradiation levels. Three different new absorber channels were proposed; web flow absorber, direct flow absorber, and spiral flow absorber. They found that as the mass flow rate increases, the PV temperature decreases and the electrical efficiency increases. Also, increasing the solar radiation level increases the PV temperature and the generated electrical efficiency. They ended up with that the spiral flow absorber presented

doi:10.18086/swc.2017.18.01 Available at http://proceedings.ises.org

the highest overall performance at solar incident radiation of 800 W/m2, with overall, thermal, and electrical efficiencies of 68.4, 54.6, and 13.8% respectively.

Nanofluids, which was first proposed by Choi and Eastman (1995), for enhancing the thermal properties of different fluids were used for the cooling purposes of the PV module as well as collecting the large possible amount of heat from solar radiation. Nanofluids were used in channels below the PV module (H Zhu and C Zhang, 2006; A Kasaeian et al., 2015; W I.A.Aly, 2014) and were recently used to flow in the front of the PV module for optical filtration (N. E. Hjerrild et al., 2016) beside the cooling objective. Vakili et al. (2016) examined the effect of using graphene nanoplatelets in enhancing the heat transfer in solar collectors as it is dispersed in a deionized water as a base fluid. The authors tried different concentration in weight fractions of 0.0005, 0.001, and 0.005, and different mass flow rates of 0.0075, 0.015, and 0.225 kg/s. Maximum efficiency was obtained at mass flow rate of 0.015 kg/s and there was an enhancement in the thermal efficiency with increasing the concentration of the nanoparticles. Hajjar et al. (2014) proposed a study on the thermal conductivity enhancement as a result of using graphene oxide nanofluids. Through all types of GO/water nanofluids, GO 5 had the best enhancement in thermal conductivity relative to that of water (about 47.54% more than water at 40°C). In addition, regarding its optical properties, they examined high absorptance for the graphene oxide nanofluid in the spectral range of solar radiation. Hassani et al. (2016a, 2016b) used nanofluid as spectrally-selective material for the solar irradiation. They found that the nanofluid-optical filter did not prevent solar radiation from reaching the PV panels, and at the same time, it gets the most benefit from the solar thermal energy. Moreover, silver/water nanofluid was found to be better than only water, as water alone is not capable of absorbing except the IR spectra.

As the solar radiation is not constant throughout the day and the need for the availability of energy in the night time, it became necessary to have storage for the absorbed solar radiation. Phase Change Materials (PCMs) were found to be the best storage idea with solar collectors, as it has very high capacity and it makes cooling as well. In contrast, low thermal conductivity of PCM causes a resistance for heat transfer so dispersing some nanoparticles for enhancement of thermal conductivity was proposed reaching the Nano-PCMs concept. Colla et al. (2017) discussed the feasibility of using alumina and carbon black nanoparticles with pure paraffin waxes PCM. Two PCM materials were examined (RT20 and RT25) with the addition of nanoparticles (Carbon black and Aluminum oxide). They ended up with that the addition of alumina can make an enhancement in the latent heat while CB will be able to make an enhancement in the thermal conductivity that is required. Su et al. (2017) investigated a comparative study on the benefits behind using PCM in cooling the hybrid PV/T solar collectors. The effect of PCM position relative to the cooling channels on the surface temperature, outlet temperature and the efficiencies were studied as well as the effect of the thickness of the PCM layer. It was found that putting the PCM on the upper side of the duct with 3 cm thickness gives higher overall efficiency.

The current paper studies the effect of existence of optical filtration above the PV and PCM beneath the PV in enhancing the overall efficiency of the PV/T solar collector by studying four different models alternating between existence and absence of optical filtration and PCM layer. It was found that existence of optical filtration above the PV and absence of PCM layer beneath the PV will result in the best performance.

2. Method:

The analytical equations governing the energy transfer through the PV/T were developed. These equations included all the physical, optical, thermal, and electrical contributions of the system. A systematic study for the governing equations was studied under reasonable assumptions to examine the thermal and electrical performance of the PV/T under different configurations.

2.1. The physical model:

In this part, the physical descriptions of the different provided configurations (M-1 to M-4) are discussed. Model-1 consists of one PV module, one thermal unit below the PV for the cooling purposes at which water/graphene nanofluid is used, and one thermal above the PV for the optical filtration purposes at which water/silver is used. Also, single PCM layer under the PV with graphene nanoparticles for storage and cooling as well. Model-2 is the same as Model-1 but without nano-PCM layer at the bottom of PV. Model-3 is slightly different from Model-1 that the optical filtration was removed and a vacuum channel was added at the bottom of the cooling channels. Model-4 is exactly like Model-3 but also without using nano-PCM layer at the bottom of the PV panels. Figure 1 shows schematic

diagrams for the proposed designs for the PV/T solar collector.

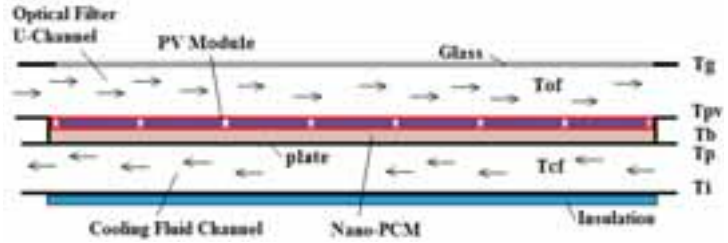

(a) M-1

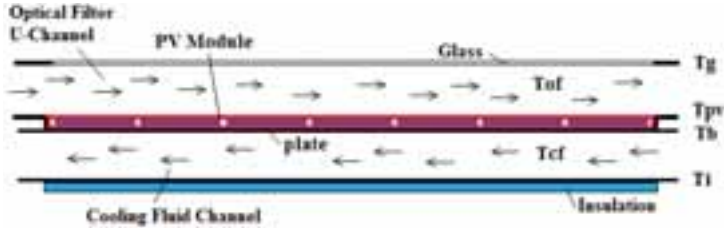

(b) M-2

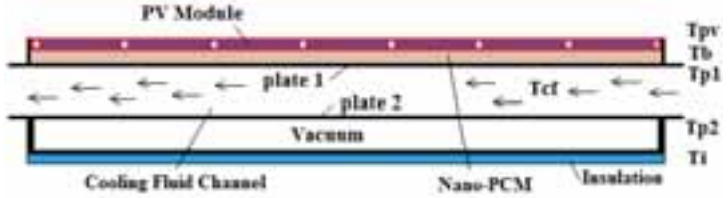

(c) M-3

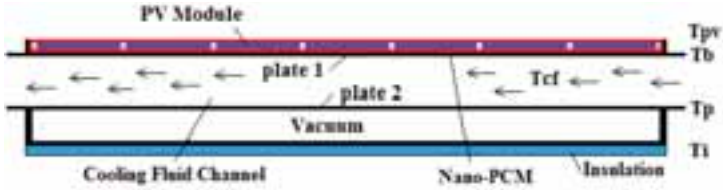

(d) M-4

Figure 1 Numerical solution models

2.2. *Working principles of PV/T configurations:*

Figure 1-(a) shows the configuration of the first model M-1. In M-1, the incident solar radiation reaches the PV cells after passing through the first cover glass, then through the optical filtration fluid channel through. The optical filtration fluid is responsible for allowing the solar radiation within the useful spectral range for electricity production only to pass through. The nano-PCM layer at the bottom of the PV is responsible for storing heat as well as transferring heat to the cooling fluid beneath the PV module. Nanoparticles were added to the PCM layer to enhance its thermal conductivity. It was guessed that the nano-PCM layer may resist the heat transfer to the cooling fluid and that's why it was removed in M-2. In Model-3, the optical filtration was removed totally and the solar radiation reached the PV cells directly. In M-4 the nano-PCM layer was also removed.

2.3. *Mathematical model:*

The simple general numerical models presented later were used to evaluate the performance of the PV/T collector through the calculation of the different temperatures, thermal, and electrical efficiencies using previously calculated optical and thermal properties. Table 1 shows the governing equations for the four proposed models. The assumptions that were used in this study are listed in Table 2. In addition, the technical data of the proposed models are available

at Table 3. The optical properties for the optical filter were taken from literature [10,11]. Table 4 summarize the thermal and rheological properties of the main substances used in the models.

Table 1 Governing equations for the proposed Models

M- #	Balance	Governing Equations	Equation no.
1	Glass cover	$\alpha_g G = h_{g-am}(T_g - T_{am}) + h_{g-of}(T_g - \bar{T}_{of})$	(eq. 1)
	Optical fluid	$\tau_g \alpha_{of} G = h_{of-g}(\bar{T}_{of} - T_g) + h_{of-pv}(\bar{T}_{of} - T_{pv}) + \frac{m^o{}_{of} cp_{of}}{W} \frac{dT_{of}}{dx_1}$	(eq. 2)
	PV panel	$\alpha_{pv} \tau_g \tau_{of} G = h_{pv-of}(T_{pv} - \bar{T}_{of}) + \frac{T_{pv} - T_b}{R_b} + \eta_c \alpha_{pv} \tau_g \tau_{of} G$	(eq. 3)
	Back plate	$\frac{T_{pv} - T_b}{R_b} = k_{PCM} \frac{T_b - T_{p1}}{\Delta t_{PCM}}$	(eq. 4)
	Plate 1	$k_{PCM} \frac{T_b - T_p}{\Delta t_{PCM}} = h_{p-cf}(T_p - \bar{T}_{cf})$	(eq. 5)
	Cooling fluid	$h_{p-cf}(T_p - \bar{T}_{cf}) = h_{cf-I}(\bar{T}_{cf} - T_I) + \frac{m^o{}_{cf} cp_{cf}}{L} \frac{dT_{cf}}{dx_2}$	(eq. 6)
	Insulation	$h_{cf-I}(\bar{T}_{cf} - T_I) = h_{I-am}(T_I - T_{am})$	(eq. 7)
	Efficiency	$\eta_c = \eta_{ref}[1 - \beta_{ref}(T_c - T_{ref})]$	(eq. 8)
2	Glass cover	$\alpha_g G = h_{g-am}(T_g - T_{am}) + h_{g-of}(T_g - \bar{T}_{of})$	(eq. 9)
	Optical fluid	$\tau_g \alpha_{of} G = h_{of-g}(\bar{T}_{of} - T_g) + h_{of-pv}(\bar{T}_{of} - T_{pv}) + \frac{m^o{}_{of} cp_{of}}{W} \frac{dT_{of}}{dx_1}$	(eq. 10)
	PV panel	$\alpha_{pv} \tau_g \tau_{of} G = h_{pv-of}(T_{pv} - \bar{T}_{of}) + \frac{T_{pv} - T_b}{R_b} + \eta_c \alpha_{pv} \tau_g \tau_{of} G$	(eq. 11)
	Back plate	$\frac{T_{pv} - T_b}{R_b} = h_{p-cf}(T_b - \bar{T}_{cf})$	(eq. 12)
	Cooling fluid	$h_{p-cf}(T_b - \bar{T}_{cf}) = h_{cf-I}(\bar{T}_{cf} - T_I) + \frac{m^o{}_{cf} cp_{cf}}{L} \frac{dT_{cf}}{dx_2}$	(eq. 13)
	Insulation	$h_{cf-I}(\bar{T}_{cf} - T_I) = h_{I-am}(T_I - T_{am})$	(eq. 14)
	Efficiency	$\eta_c = \eta_{ref}[1 - \beta_{ref}(T_c - T_{ref})]$	(eq. 15)
3	PV panel	$\alpha_g G = h_{pv-am}(T_{pv} - T_{am}) + \frac{T_{pv} - T_b}{R_b} + \eta_c \alpha_g G$	(eq. 16)
	Back plate	$\frac{T_{pv} - T_b}{R_b} = k_{PCM} \frac{T_b - T_{p1}}{\Delta t_{PCM}}$	(eq. 17)
	Plate 1	$k_{PCM} \frac{T_b - T_{p1}}{\Delta t_{PCM}} = h_{p1-cf}(T_{p1} - \bar{T}_{cf})$	(eq. 18)
	Cooling fluid	$h_{p1-cf}(T_{p1} - \bar{T}_{cf}) = h_{cf-p}(\bar{T}_{cf} - T_{p2}) + \frac{m^o{}_{cf} cp_{cf}}{L} \frac{dT_{cf}}{dx_2}$	(eq. 19)
	Plate 2	$h_{cf-p2}(\bar{T}_{cf} - T_{p2}) = h_{r,p2-I}(T_{p2} - T_I)$	(eq. 20)
	Insulation	$h_{r,p2-I}(T_{p2} - T_I) = h_{I-am}(T_I - T_{am})$	(eq. 21)
	Efficiency	$\eta_c = \eta_{ref}[1 - \beta_{ref}(T_c - T_{ref})]$	(eq. 22)
4	PV panel	$\alpha_g G = h_{pv-am}(T_{pv} - T_{am}) + \frac{T_{pv} - T_b}{R_b} + \eta_c \alpha_g G$	(eq. 23)
	Back plate	$\frac{T_{pv} - T_b}{R_b} = h_{b-cf}(T_b - \bar{T}_{cf})$	(eq. 24)
	Cooling fluid	$h_{b-cf}(T_b - \bar{T}_{cf}) = h_{cf-p}(\bar{T}_{cf} - T_p) + \frac{m^o{}_{cf} cp_{cf}}{L} \frac{dT_{cf}}{dx_2}$	(eq. 25)
	Plate	$h_{cf-p}(\bar{T}_{cf} - T_p) = h_{r,p-I}(T_p - T_I)$	(eq. 26)

	Insulation	$h_{r,p-I}(T_p - T_I) = h_{I-am}(T_I - T_{am})$	(eq. 27)
	Efficiency	$\eta_c = \eta_{ref}[1 - \beta_{ref}(T_c - T_{ref})]$	(eq. 28)

Table 2 Assumptions considered in the present study

	Assumptions
1	Steady state
2	Normal incident radiation
3	Radiation losses from glass cover or insulation to atmosphere were neglected
4	Very thin glass covers, plates, and insulation so conduction was neglected
5	Working fluid is flowing through a rectangular channel
6	Heat transfer was only considered in one dimension
7	All fluids remain liquids through the operation of the system
8	Thermal properties were calculated at an average temperature of 30°C
9	Negligible pumping power due to very low mass flow rate
10	Reference electrical efficiency of 12%

Table 3 Technical design data of the different solar collectors investigated in the present study

Item	Specifications	M-1	M-2	M-3	M-4
Glass cover-1	$\tau_g = 0.9$ $\alpha_g = 0.05$	√	√	√	√
Optical filter	Nanofluid, water/silver [11] $\tau_{of} = 0.62$ $\alpha_{of} = 0.38$	√	√		
Glass cover-2	$\tau_g = 0.9$ $\alpha_g = 0.05$	√	√		
PV cell	Multi-crystalline $\alpha_g = 0.945$	√	√	√	√
Back-plate		√	√	√	√
Nano-PCM	PCM/graphene	√		√	
Plate-1		√		√	
Working fluid	Nanofluid, water/graphene	√	√	√	√
Plate-2	$\varepsilon_p = 0.9$	√	√	√	√
Vacuum				√	√
Insulation		√	√	√	√

Table 4 Thermal and rheological properties

Substance/Property	k	μ	ρ	C_p
Air	0.026424	18.718×10^{-6}	1.165285	1007.22
Water	0.615504	0.000797345	995.65	4180.02
PCM	0.195	0.01145	820	2500
Graphene	5000	-	1000	15
Silver	429	-	10500	235

2.4. Thermal and rheological properties of nanofluids and nano-PCM:

The equivalent thermal properties for the nanofluids and nano-PCM were calculated based on the formulas that are available in the literature.

Thermal conductivity:

$$k_{nf} = \left[\frac{k_p+2k_f-2\emptyset(k_f-k_p)}{k_p+2k_f+\emptyset(k_f-k_p)}\right] k_f \qquad \text{(eq. 29)}$$

Dynamic viscosity:

$$\mu_{nf} = \frac{1}{(1-\emptyset)^{2.5}}\mu_f \qquad \text{(eq. 30)}$$

Density:

$$\rho_{nf} = \emptyset\rho_p + (1-\emptyset)\rho_f \qquad \text{(eq. 31)}$$

Specific heat:

$$(\rho c_p)_{nf} = \emptyset(\rho c_p)_p + (1-\emptyset)(\rho c_p)_f \qquad \text{(eq. 32)}$$

Table 5 shows the thermal and rheological properties of the nanofluids and nano-PCM used in the present study.

Table 5 Properties of Nanofluids and nano-PCM

	∅	μ	ρ	c_p	k
Optical filter	0.001	0.0008	1005.1543	4138.8	0.61734
Working fluid	0.001	0.0008	995.65	4175.855	0.61735
Nano-PCM	0.001	-	820.18	-	0.19558

2.5. Temperature distribution::

In the current section, the equations describing the temperature distribution throughout the optical filtration and cooling nanofluids used with M-1 were formulated. The energy equations that communicate between the fluids temperatures and its surroundings were used.

The working fluid:

From eq. 6:

$$h_{p-cf}(T_p - \bar{T}_{cf}) = h_{cf-I}(\bar{T}_{cf} - T_I) + \frac{m^o{}_{cf} cp_{cf}}{L}\frac{dT_{cf}}{dx_2}$$

By rearranging,

$$\therefore \frac{dT_{cf}}{dx_2} = \frac{L}{m^o{}_{cf} cp_{cf}}\left[h_{p-cf}(T_p - T_{cf}) - h_{cf-I}(T_{cf} - T_I)\right]$$

$$\therefore \frac{dT_{cf}}{dx_2} = \frac{L}{m^o{}_{cf} cp_{cf}}\left[h_{p-cf}T_p + h_{cf-I}T_I - T_{cf}(h_{p-cf} + h_{cf-I})\right]$$

Take $A = \frac{L}{m^o{}_{cf} cp_{cf}}(h_{p-cf}T_p + h_{cf-I}T_I)$, $B = \frac{L}{m^o{}_{cf} cp_{cf}}(h_{p-cf} + h_{cf-I})$

$$\therefore \frac{dT_{cf}}{dx_2} = A - BT_{cf}$$

$$\int_{T_{cf,in}}^{T_{cf,x2}} \frac{dT_{cf}}{A - BT_{cf}} = \int_0^{x_2} dx_2$$

$$\therefore T_{cf}(x_2) = \frac{A}{B} - \left[\frac{A}{B} - T_{cf,in}\right] exp(-Bx_2) \quad \text{(eq. 33)}$$

$$T_{cf}(W) = \frac{A}{B} - \left[\frac{A}{B} - T_{cf,in}\right] exp(-BW) \quad \text{(eq. 34)}$$

$$\bar{T}_{cf} = \frac{1}{W}\int_0^W T_{cf}(x_2)dx_2 = \frac{1}{W}\int_0^W \left[\frac{A}{B} - \left[\frac{A}{B} - T_{cf,in}\right] exp(-Bx_2)\right] dx_2$$

$$\therefore \bar{T}_{cf} = \frac{A}{B} - \frac{1}{B^2W}\left[A - BT_{cf,in}\right][exp(-BW) - 1] \quad \text{(eq. 35)}$$

The optical filter channel:

From eq. 2:

$$\tau_g \alpha_{of} G = h_{of-g}\left(\bar{T}_{of} - T_g\right) + h_{of-pv}\left(\bar{T}_{of} - T_{pv}\right) + \frac{m^o{}_{of} cp_{of}}{W} \frac{dT_{of}}{dx_1}$$

By rearranging,

$$\therefore \frac{dT_{of}}{dx_1} = \frac{W}{m^o{}_{of} cp_{of}}\left[\tau_g \alpha_{of} G - h_{of-g}\left(T_{of} - T_g\right) - h_{of-pv}\left(T_{of} - T_{pv}\right)\right]$$

$$\therefore \frac{dT_{of}}{dx_1} = \frac{W}{m^o{}_{of} cp_{of}}\left[\tau_g \alpha_{of} G + h_{of-g} T_g + h_{of-pv} T_{pv} - T_{of}\left(h_{of-g} + h_{of-pv}\right)\right]$$

Take $C = \frac{W}{m^o{}_{of} cp_{of}}\left[\tau_g \alpha_{of} G + h_{of-g} T_g + h_{of-pv} T_{pv}\right]$, $D = \frac{W}{m^o{}_{of} cp_{of}}\left(h_{of-g} + h_{of-pv}\right)$

$$\therefore \frac{dT_{of}}{dx_1} = C - DT_{of}$$

$$\int_{T_{of,in}}^{T_{of,x1}} \frac{dT_{of}}{C - DT_{of}} = \int_0^{x_1} dx_1$$

$$\therefore T_{of}(x_1) = \frac{C}{D} - \left[\frac{C}{D} - T_{of,in}\right] exp(-Dx_1) \quad \text{(eq. 36)}$$

$$T_{of}(L) = \frac{C}{D} - \left[\frac{C}{D} - T_{of,in}\right] exp(-DL) \quad \text{(eq. 37)}$$

$$\bar{T}_{of} = \frac{1}{L}\int_0^L T_{of}(x_1)dx_1 = \frac{1}{L}\int_0^L \left[\frac{C}{D} - \left[\frac{C}{D} - T_{of,in}\right] exp(-Dx_1)\right] dx_1$$

$$\therefore \bar{T}_{of} = \frac{C}{D} - \frac{1}{D^2L}\left[C - DT_{of,in}\right][exp(-DL) - 1] \quad \text{(eq. 38)}$$

Table 6 Reference values used

L (cm)	103.5	**$T_{wf,\,in}$ (K)**	298
W (cm)	100	**$T_{of,\,in}$ (K)**	298
L_c (cm)	100	**V_{am} (m/s)**	1
Δt_{PCM} (cm)	0.5	**m^o (kg/s)**	0.0104
Working fluid channel width (cm)	4	**η_{ref} (%)**	12
Optical filter channel width (cm)	2	**β**	0.0045
T_{am} (K)	298		

2.6. Calculation of heat transfer coefficients for M-1:

For flow over flat plate surfaces, $Nu = 0.86Re^{1/3}Pr^{1/2}$, $Re = \frac{\rho v L_c}{\mu}\Big|_{am}$, $Pr = \frac{\mu c_p}{k}\Big|_{am}$

Using the properties of air mentioned before and that $h = \frac{Nuk_{am}}{L_c}$

$$h_{g-am} = h_{l-am} = 5.065\ W/m.K$$

For internal laminar flow with constant heat flux inside rectangular channels, and with height to width>8, Nu=8.24,

Then for the optical filter fluid, $h = \frac{Nuk_{of}}{D_{h,of}}$

With $D_{h,\,of}$ = 3.92 cm, and the properties of the optical filter nanofluid,

$$h_{g1-of} = h_{g2-of} = h_{p2-of'} = h_{l-of'} = 129.715\ W/m.K$$

And for the working fluid, $h = \frac{Nuk_{wf}}{D_{h,wf}}$

With $D_{h,\,wf}$ = 7.69 cm, and the properties of the working fluid nanofluid,

$$h_{p1-wf} = h_{p2-wf} = 66.13\ W/m.K$$

3. Analytical results and discussion

The governing equations were solved separately for each model and the results are shown in Figure 2, Figure 3, Figure 4, and Figure 5. In addition, the results for solving the governing equations for conventional PV module were also discussed.

Studying the effect of existence of optical filtration, a comparison were held between the performance of models 1 and 2 versus that for models 3 and 4, it can be seen clearly that the existence of the optical filtration helped in enhancing the overall performance of the PV/T system. Comparing the models with optical filtration to the models without optical filtration, it was found that the PV temperature has decreased by 16-27.6 ˚C (Figure 2), electrical efficiency increased by 0.87-1.49% (Figure 3), and thermal efficiency increased by 11.7-17.4% (Figure 4).

The effect of the existence of the nano-PCM layer below the PV module can be distinguished by comparing the performance of M-1 with M-2 and M-3 with M-4. It was found that treating the nano-PCM on its thermal conductivity and neglecting its storage effects will end up with the result that existence of nano-PCM will decrease the performance due to low thermal conductivity and as a result resistance to heat transfer from the bottom side of the PV to the cooling fluid. Figure 2 to Figure 5 show that the effect of nano-PCM existence is not significant in the models that deal with optical filtration fluid; M-1 and M-2, M-3. In contrast, the effect of existence of nano-PCM layer in resisting the heat flow is very clear when comparing the performance of M-3 to M-4.

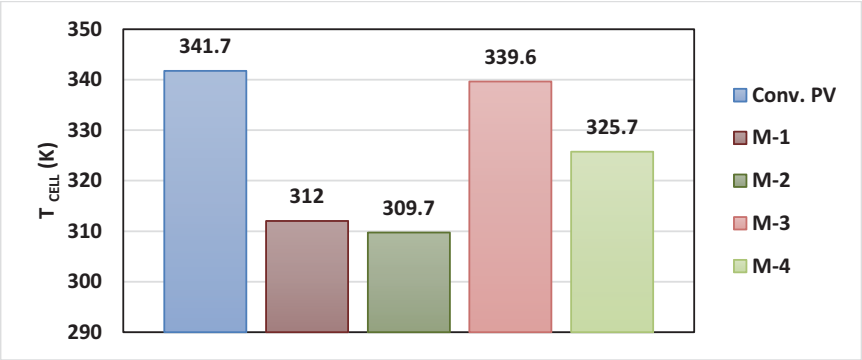

Figure 2 PV cell temperature for different models

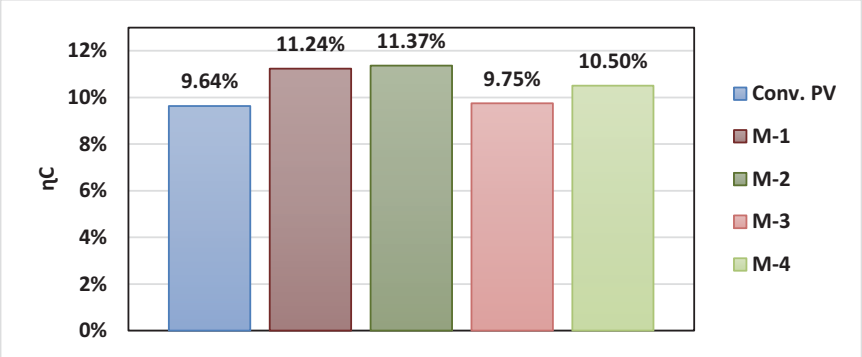

Figure 3 Electrical efficiency for different models

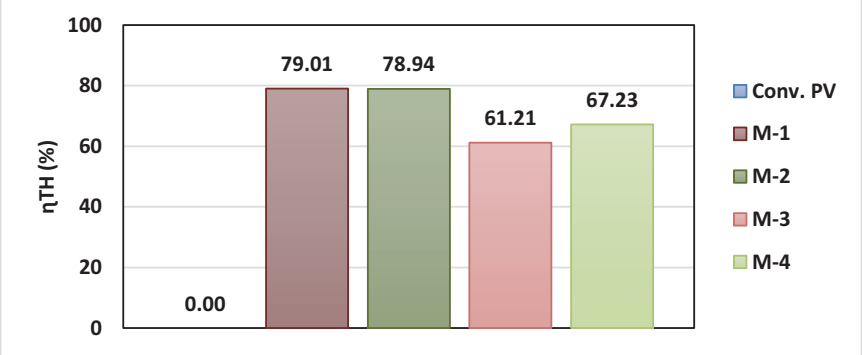

Figure 4 Thermal efficiency for different configurations

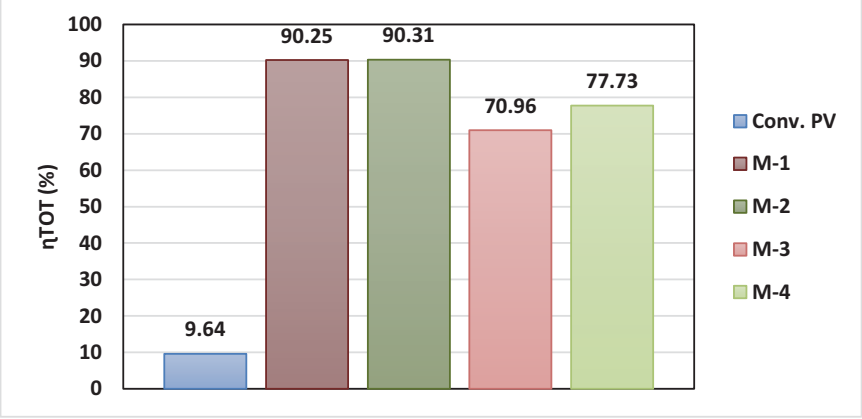

Figure 5 Total efficiency for different configurations

4. Conclusions

In the current paper, an analytical solution based on steady state assumption was developed. Four different models of hybrid PV/T solar systems studying the effect of optical filtration and nano-PCM technologies were studied. The governing energy equations for the heat transfer throughout the four models were solved to evaluate the solar utilization performance. From the discussion of the results, different conclusions were attained and can be summarized in:

- Using optical filtration is highly beneficial in enhancing the overall performance of PV/T systems.
- Neglecting the storage effect of the nano-PCM, existence of nano-PCM layer below the PV cells resists heat transfer to working fluid and thus increase the temperature of PV cells and decrease the performance of PV/T.

5. Additional work:

- Considering the honeycomb channels during analysis should end up with more enhancement in the performance of the PV/T.
- Using only one channel for optical filtration may increase or decrease the performance, so it needs to be studied.

6. References:

Aly WI ,2014. Numerical study on turbulent heat transfer and pressure drop of nanofluid in coiled tube-in-tube heat exchangers. Energy Convers Manage;79:304–16.

Choi SUS, Eastman JA, 1995. Enhancing thermal conductivity of fluids with nanoparticles. ASME Int Mech Eng Congr Expo;66:99–105.

Colla L, Fedele L, Mancin S, Danza L, Manca O, 2017. Nano-PCMs for enhanced energy storage and passive cooling applications. Appl Therm Eng;110:584–9.

Fudholi A, Sopian K, Yazdi MH, Hafidz M, Ibrahim A, Kazem HA, 2014. Performance analysis of photovoltaic thermal (PVT) water collectors. Energy Convers Manag;78:641–51.

Haitao Zhua and Canying Zhang, 2006. Effects of nanoparticle clustering and alignment on thermal conductivities of Fe3O4 aqueous nanofluids n.d. Appl. Phys. Lett. 89, 023123

Hajjar Z, Rashidi A, Ghozatloo A, 2014. Enhanced thermal conductivities of graphene oxide nano fluids. Int Commun Heat Mass Transf;57:128–31.

Hjerrild NE, Mesgari S, Crisostomo F, Scott JA, Amal R, Taylor RA, 2016. Hybrid PV/T enhancement using selectively absorbing Ag-SiO2/carbon nanofluids. Sol Energy Mater Sol Cells;147:281–7.

Hussain F, Othman MYH, Yatim B, Ruslan H, Sopian K, Ibarahim Z, 2013. A study of PV/T collector with honeycomb heat exchanger. AIP Conf Proc;1571:10–6.

Kasaeian A, Daviran S, Azarian RD, Rashidi A, 2015. Performance evaluation and nanofluid using capability study of a solar parabolic trough collector. Energy Convers Manage;89:368–75.

Samir Hassani, Robert A. Taylor, Saad Mekhilef, R. Saidur, 2016a. A cascade nanofluid-based PV/T system with optimized optical and thermal properties. Energy;112:963–75.

Samir Hassani, R. Saidur, Saad Mekhilef, Robert A. Taylor, 2016b. Environmental and exergy benefit of nanofluid-based hybrid PV/T systems. Energy Convers Manag;123:431–44.

Su D, Jia Y, Alva G, Liu L, Fang G, 2017. Comparative analyses on dynamic performances of photovoltaic – thermal solar collectors integrated with phase change materials;131:79–89.

Vakili M, Hosseinalipour SM, Delfani S, Khosrojerdi S, Karami M, 2016. Experimental investigation of graphene nanoplatelets nanofluid-based volumetric solar collector for domestic hot water systems. Sol Energy;131:119–30.

A Simulation Analysis on Thermal Performance of Air-type PVT Collector with Diversity of Baffles

Jong-Gwon Ahn[1], Ji-Suk Yu[1], Jin-Hee Kim[2], and Jun-Tae Kim[3*]

[1] Dept. of Energy systems Engineering, Kongju National University, Cheonan (South Korea)

[2] Green Energy Research Center, Kongju National University, Cheonan (South Korea)

[3] Dept. of Architectural Engineering, Kongju National University, Cheonan (South Korea)

Abstract

Photovoltaic Thermal (PVT) collector is a type of solar collector that produces electricity and uses heat from the backside of PV simultaneously for space heating. In particular, air type PVT has the benefit of being easily managed and can be used directly for heating in buildings. Baffle is installed in the heat-collecting layer of the PVT collector to increase the velocity and flow path of air inside the collector. As a result, it can be used to improve the performance of the PVT collector. In this study, effect of different baffle types on thermal performance of air type PVT collector was analyzed using NX simulation program. The design variables used for analysis were square, triangle, and bent (using absorb plate) type of baffles of collector. The outlet temperature rose by 3-6^{o}C when the shape of the baffles changed from square to triangular to bent type. Also, the thermal efficiency of the collector with the absorber plate increased by 11.3% compared to the collector without baffle..

Keywords: Air-type PVT Collector, Thermal efficiency, Baffle design, CFD analysis

1. Introduction

Photovoltaic Thermal (PVT) collector is a type of solar collector that produces electricity and uses heat from the backside of PV for space heating simultaneously. In particular, air type PVT has the benefit of being easily managed and can be used directly for heating in buildings as compared to water-type PVT collector. Baffle is installed in the heat-collecting layer of the PVT collector to increase the velocity and flow path of air inside the collector. As a result, it can be used to improve the performance of the PVT collector.

In this study, effect of baffle on thermal performance of air type PVT collector was analyzed. For this purpose, collectors with different types of baffles were designed and analyzed using NX simulation program.

2. Air-type PVT Collector with Baffles

2.1. Air-type PVT collector with various baffle types

Air-type PVT Collector has been developed with lots of space types, materials, and flow path to improve thermal efficiency. The space consists of various types of air space layer such as applying fins, aluminum sheet and steel absorber. Inside structure of air-type PVT collector can highly affect the thermal efficiency and electrical efficiency as well. Especially, Baffles which is installed in surface on air space have merits for air uniformity and heat absorption. Currently, many type of baffles has been developed and analyzed (Fig. 1) [2]. Square baffle design is a basic type and other shapes are analyzed with different baffle sizes and installation positions. Particularly, minimizing vortices and dead zone has been more important and focused on the research field (Fig. 2).

doi:10.18086/swc.2017.18.02 Available at http://proceedings.ises.org

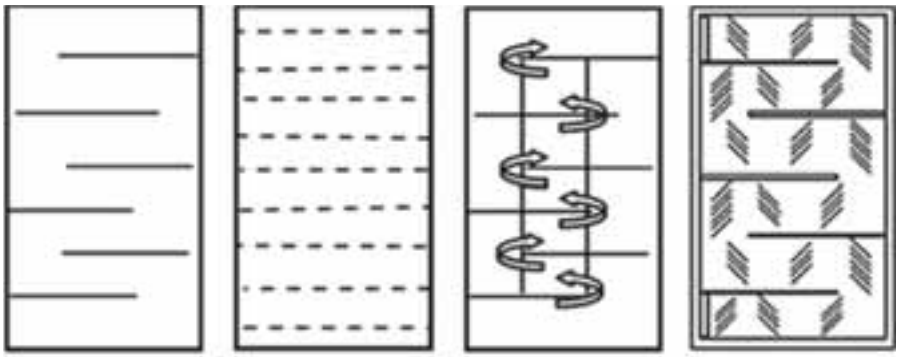

Fig. 1: Various baffle designs inside collector

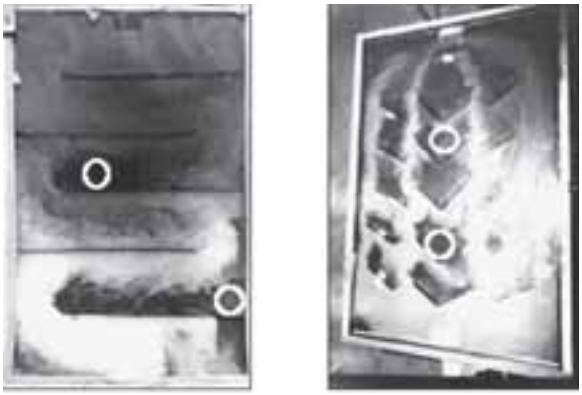

Fig. 2: Vortices and Dead zone inside collector

3. Methodology

3.1. Modelling of Air-type PVT collector with baffle designs

In this study, general PVT collector without baffle and with different shape of baffles were designed. The shapes of baffle used were square, triangle and bent (using absorber plate) type as shown in Fig. 3. For comparison, a collector without baffle was added, and other variables such as the shape and size of inlet/outlet for each condition were set to be same. The square baffle type was designed in an intercrossed placement with spacing between the baffles to increase the flow rate of the air. The top surface of triangle baffle was made streamlined so that the air passes smoothly through the PV back surface to improve thermal absorption. The bent type baffle was designed with different PV arrangement so that solar radiation directly reaches the absorber plate inside the collector. And the plate was designed to receive more solar radiation with the form of curves. The 3 types of air-type PVT collectors with different baffles were modeled with NX simulation program.

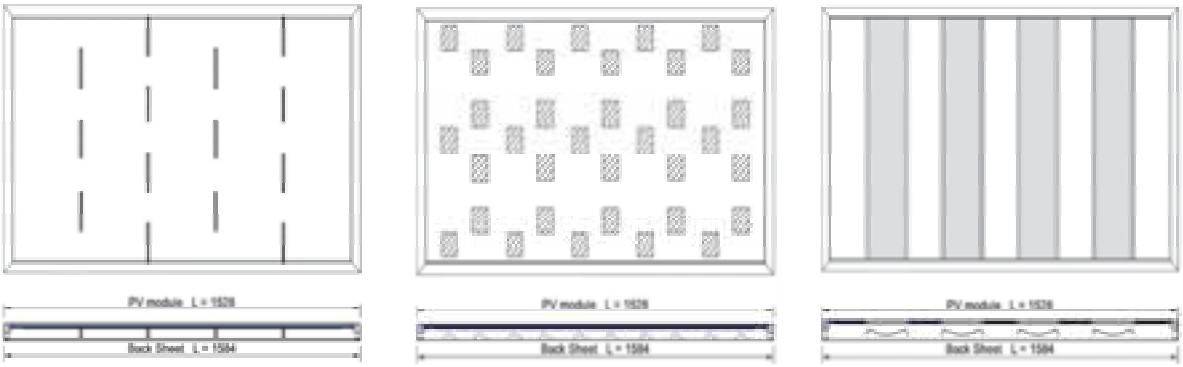

Fig. 3: Baffle designs inside of the collectors(from left; square, triangle bent types)

3.2. Simulation Properties

Modelled Air-type PVT collector size is 1.63m^2 (height 42.5mm), and supplied thermal energy 780W/m^2 that is supposing 15% of solar radiation reached the PV surface. Ambient temperature was 20^{o}C for heat loss calculation, and the air density was decided by each air temperature value such as 1.225kg/m^3 when the air temperature was 25^{o}C. K-epsilon model was applied for turbulence expectation, and inlet, outlet and heat flux area of all collector types were equivalent for comparison. Input difference was air flow rate (30, 60, 100 CMH) and baffle designs. The parameters are summarized Table 1.

Table 1: CFD Simulation parameters

Input	Elements	Unit
Collector size	1.6	m^2
Collector height	42.5	mm
Supplied thermal energy	780	w/m^2
Ambient temperature	25	^{o}C
Air density	1.225(25^{o}C)	kg/m^3
Air flow rate	30, 60, 100	m^3/h(CMH)
Turbulence model	K-epsilon	-

4. Results and Discussion

4.1. Air uniformity distribution

As a result, partial congestion of temperature was observed inside the collector depending on the shape of the baffles. Turbulence and dead zone was found in Square type, on back side surface of the installed baffles against air flow pathway (Fig 4). Triangle type was improved compared with square type. However, lots of Dead zone were caused. Unlike the triangle and square baffles, air uniformity and collector temperature of the bent baffle was uniformly distributed. The average flow rate of collector increased to 19% with square baffle. Also, the temperature distribution in the collector was relatively uniform according to the installation of the baffles.

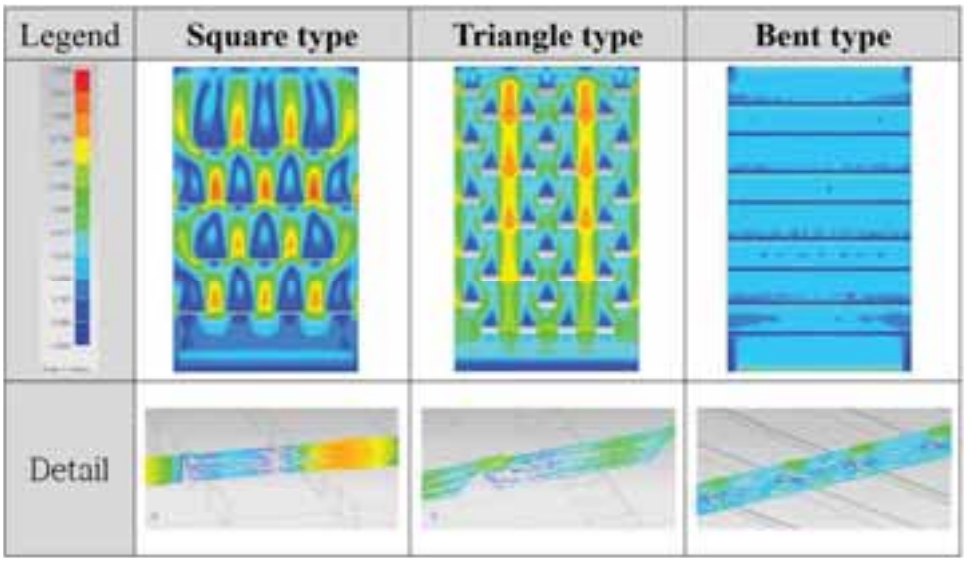

Fig. 4: air flow pathway with velocity in different baffle types of the collector

4.2. Temperature characterization of the Air-type PVT collector

Fig. 5 displays the air temperature inside collector according to different baffles. Square type had lots of air stagnant behind baffles against air movement. Triangle type improved the uniformity of the air and velocity especially between baffles. Bent type showed better air uniformity and movement. The air moved to whole surface of the collector and efficiently took heat from the space.

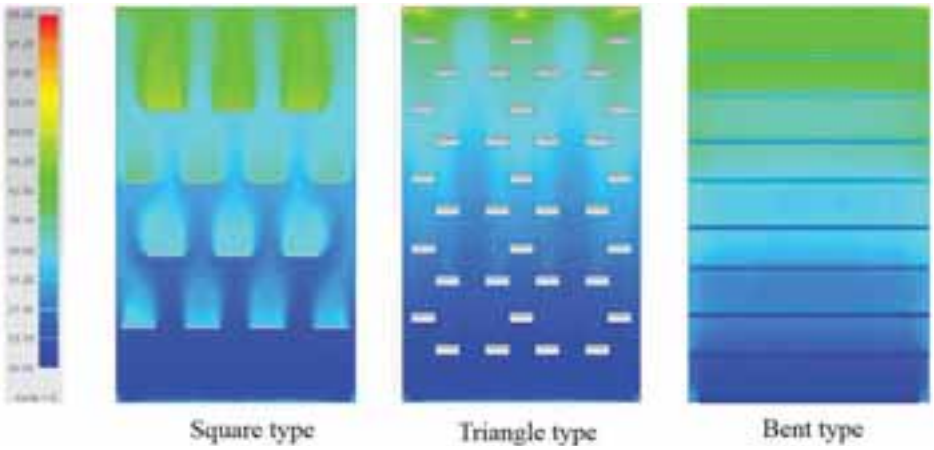

Fig. 5: air flow pathway with velocity in different baffle types of the collector

4.3. Thermal performance

Thermal efficiency are presented in Fig. 6. The results were calculated by equation 1.

$$\eta_{th} = \frac{\dot{m} C_p (T_o - T_i)}{A_{pvt} G} \qquad \text{(equation. 1)}$$

η_{th} thermal efficiency [-]
A_{pvt} collector area [m^2]
T_o collector outlet air temperature [$^{\circ}C$]
T_i collector inlet air temperature [$^{\circ}C$]
$\dot{m}$ air flow rate [$m^3 h^{-1}$]
C_p specific heat [$J kg^{-1} K^{-1}$]
G irradiance on the collector surface [$W m^{-2}$]

According to the shape of the baffle, the outlet temperatures were varied by 3-6 degrees. With the outlet temperature difference, thermal efficiency of the air-type PVT collector without baffles was 31.3%. The collector with square and triangle type showed improved thermal efficiency of 32.5% and 33.1% respectably. Bent type had 35.3% with minimized turbulence and dead zone inside collector. Consequently the thermal efficiency of PVT collector with baffle increased by 11.3% than the collector without baffle.

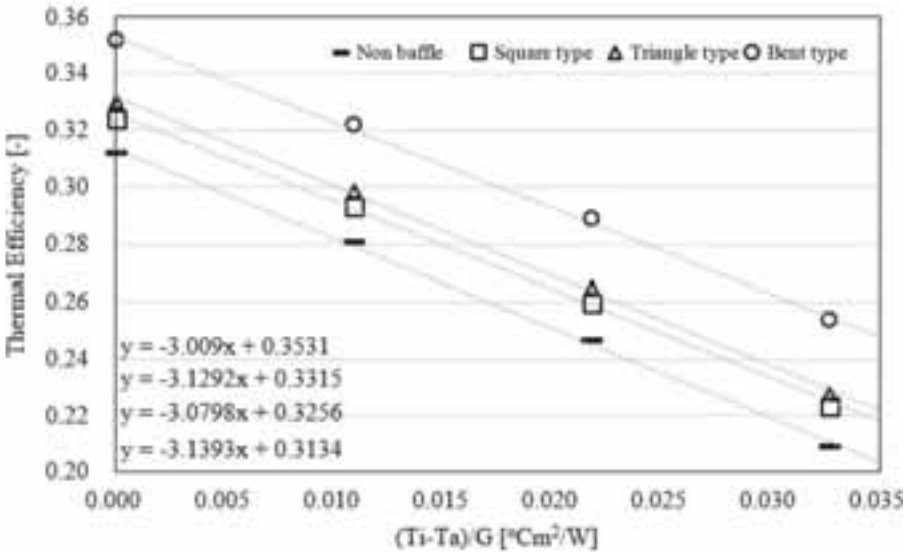

Fig. 6: Thermal efficiency graph of the different baffle type collectors

5. Conclusion

In this research, Air-type PVT Collector with various baffle types was analyzed with CFD simulation. Results showed that partial air statement was caused with baffle types except for bent type. Also, air uniformity of bent type was improved compared with square and triangular baffles. Outlet air temperature varied by 3-6°C according to baffle type. Air flow velocity of square type baffle improved 19% compared with basic baffle type. Dead zone was minimized for bent baffle type than square and triangular types by baffle shapes. Furthermore, thermal efficiency of the air-type PVT Collector with bent type improved 11.3% compared with basic (Non baffle) type.

Acknowledgments: This paper was supported by an International Cooperation grant (No. 20148520011270) from the Korea Institute of Energy Technology Evaluation and Planning (KETEP), funded by the Ministry of Trade, Industry and Energy of the Korean government, and the Leading Human Resource Training Program of Regional Neo industry through the National Research Foundation of Korea (NRF) funded by the Ministry of Science, ICT and future Planning (2016H1D5A1910875).

Nomenclature

A_{pvt}	Surface area of the collector	m^2
C_p	Specific heat of air at a constant pressure	$J\ kg^{-1} \cdot K^{-1}$
G	Solar radiation	$W\ m^{-2}$
$\dot{m}$	Mass flow rate	$m^3\ h^{-1}$
T_a	Ambient air temperature	°C
T_o	Outlet air temperature of PVT	°C
T_i	Inlet air temperature of PVT	°C
η_{th}	Thermal efficiency	-

6. Reference

1. Jin-Hee Kim, Jong-Gwon Ahn, Jun-Tae Kim, 2016, Demonstration of the performance of an Air-Type Photovoltaic Thermal (PVT) System Coupled with a Heat-Recovery Ventilator, 728, 1-9.

2. Romdhane B.S, 2006, The air solar collectors: Comparative study, introduction of baffles to favor the heat transfer, Solar Energy, pp.139-149

3. Zondag H, Van der Borg N, Eisenmann W., 2005, D8-6: PVT Performance measurement guidelines, ECN Editor, Petten, The Netherlands.

Modelling approach for hybrid solar photovoltaic-thermal (PV/T) panels with an integrated phase change material (PCM) layer

Manuel Andrés[1], Luis A. Bujedo[1], Roberto Sanz[1], Jesús Samaniego[1] and José C. Esteban[2]

[1] CARTIF Technology Centre, Parque Tecn. de Boecillo, 205, 47151, Boecillo, Valladolid (Spain)

[2] ACCIONA Construcción S.A. R&D Centre, C/Valportillo II, 8, 28108, Alcobendas, Madrid (Spain)

Abstract

This work, performed in the context of the LowUP H2020 European project, presents a modelling approach for innovative renewable technology consisting of a hybrid solar photovoltaic-thermal (PV/T) collector system that includes Phase Change Material in its back layer. The whole model is described focusing on the mathematical representation of the PCM layer and its associated non-linear behaviour. Main modelling assumptions are based on an energy balance for the PCM and a simple representation of the phase change process through the parametrization of the h-T curve. The thermal resistance between the absorber and the PCM layer is identified as a key model parameter, and its influence is demonstrated in a preliminary simulation analysis of different designs. Thus, the model developed within this work provides interesting for integration into energy simulations, enabling contributions to the design and smart operation of sustainable heating and power systems.

Keywords: PV/T solar panels, Phase Change Materials (PCM), mathematical model, TRNSYS

1. Introduction

Hybrid PV/T solar collectors have been widely studied and developed in the past years (Chow 2010, IEA-SHC 2005). They increase global system's efficiency and enables that the amount of low-grade heat dissipated by PV cells (that will be otherwise rejected to the ambient) can be used to meet thermal energy demands (DHW or space heating) through the application of low exergy concepts in heating facilities. Indeed, this idea is being investigated within the LowUP European project (LowUP 2017), aimed at integrating different low-grade energy sources for innovative, efficient heating solutions.

LowUP works to improve the design and operating performance of this technology, particularly addressing the demonstration of a novel PV/T system that includes a Phase Change Material (PCM) in the back layer of the panels. Positive effects of the hybrid PV/T concept are expected to be enhanced. PCM will act as a thermal storage able to limit the operating cell temperature (increasing the electrical efficiency). Besides, it can be able to extend the availability of the thermal resource beyond the periods of relevant solar radiation at the end of the day.

The particular purpose of this work is to present a mathematical model for this PV/T-PCM innovative configuration. So far, some references from literature address the use of PCM to cool down PV cells and improve their efficiency (Smith et al. 2014). However, very little experience on the proposed hybrid PV/T-PCM concept has been previously reported (Browne et al. 2015) and no existing specific models are known. The proposed model will facilitate the estimation of systems' behaviour and help the design process for later implementation.

2. Description of the modelling approach

The selected modelling approach for the PV/T-PCM panel intends to account for the original PV/T geometry together with those modifications involved by the PCM layer. To this end, TRNSYS Type560 (TESS 2012) was used as the basis to account for hybrid PV/T characteristics and a self-developed PCM layer model was integrated with consistent modifications on several parameters and the original back insulation.

2.1 PV/T reference model

Type560 PV/T thermal model relies on algorithms from the classic work by Duffie and Beckmann (2013)

doi:10.18086/swc.2017.18.03 Available at http://proceedings.ises.org

and is based on the following main considerations:

- Linear relation between PV efficiency (η_{PV}), cell temperature (T_{PV}) and incident solar radiation (G_T)
  $\eta_{PV} = \eta_{nom}\chi_T\chi_G = \eta_{nom}\left(1 + eff_T\left(T_{PV} - T_{ref}\right)\right)\left(1 + eff_G\left(G_T - G_{ref}\right)\right)$ (eq.1)
  where eff_T and eff_G are constant factors.
- PV cells are assumed to be operating at their maximum power condition.
- Energy balance equation for the PV cell surface neglecting conduction effects along the surface
- Classical considerations on absorbed solar radiation based on transmittance, absorptance and incident angles.
- Energy balance equation for the absorber surface, which is addressed as a classical fin problem to derive absorber plate temperature distribution
- Energy balance equation to the base area of the absorber in contact with the fluid tubes (see Figure 1)

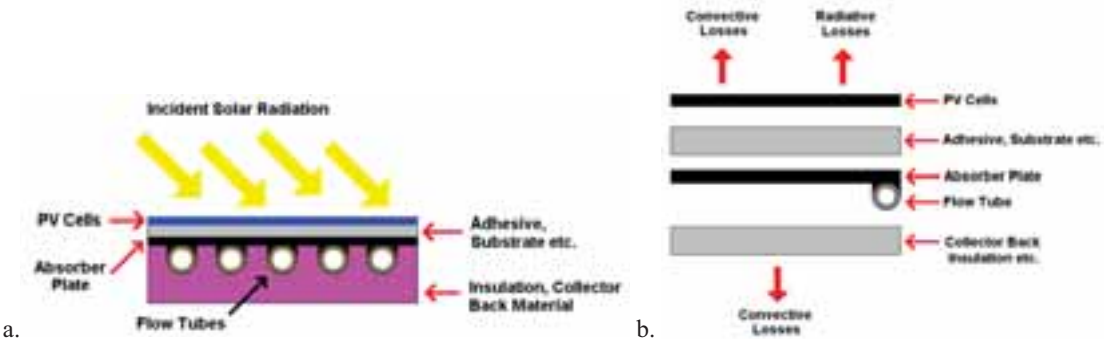

Figure 1. . (a) Schematic solar panel configuration and (b) relevant component definitions for TRNSYS Type560 PV/T model Source: (TESS 2012)

This mathematical representation allows deriving the temperature values of the different PV/T components as well as relevant output variables (both thermal and electrical). Yet, the current model does not account for the possibility of including the PCM, which requires the integration of a completely new layer with non-linear behaviour.

2.2 PCM modelling and integration

The novel PV/T-PCM system implies that the back layer (adjacent to the absorber plate) is now able to store the dissipated heat while keeping constant temperature along the phase change process. Back surface is still considered to be in contact with ambient temperature. The existence of this PCM layer involves a non-linear behaviour that cannot be modelled with a simple additional thermal resistance. Therefore, this work proposes a simple model that treats the PCM layer as a thermal storage with homogeneous temperature and is based on the energy balance equation and a simple parametrization of the enthalpy-temperature (h-T) behaviour of the Phase Change Material.

PCM temperature is affected by the heat transfer received from the collector, and simultaneously this temperature (as a boundary condition for the PV/T collector) influences the aforementioned heat transfer. Based on this, the energy balance to the PCM 'storage' layer provides its energy content at every timestep.

$$E_{i+1} = E_i + \Delta t \cdot \left(\dot{Q}_{PV/T,i} - \dot{Q}_{loss,i}\right) \qquad \text{(eq.2)}$$

Then, from the h-T curve of the material and the energy content, the PCM layer temperature is obtained. The parametrization of this h-T behaviour is described next. Figure 2 represents the h-T curves corresponding to different real heating and cooling processes of a given PCM (Belmonte et al. 2016). Although an idealized thermal behaviour with constant melting temperature is often considered when analysing Phase Change Materials, deviations associated to three main different effects can be observed:

- Variable temperature along the phase change process (temperature range)
- Different h-T curves (within the phase change range) for cooling and heating evolutions (i.e. hysteresis effects)
- Sub-cooling effects that makes the PCM requiring to achieve colder temperatures than the 'normal'

melting temperature range in order to start solidification (therefore, once the freezing process starts, the temperature increases slightly).

The present PCM model defines 3 parameters: melting temperature (T_{melt}), melting range ($range_{PCM}$) and melting hysteresis ($hyst_{PCM}$), which allows accounting for most of common h-T behaviours with reasonable accuracy (see Figure 2). Sub-cooling effects are neglected by this model.

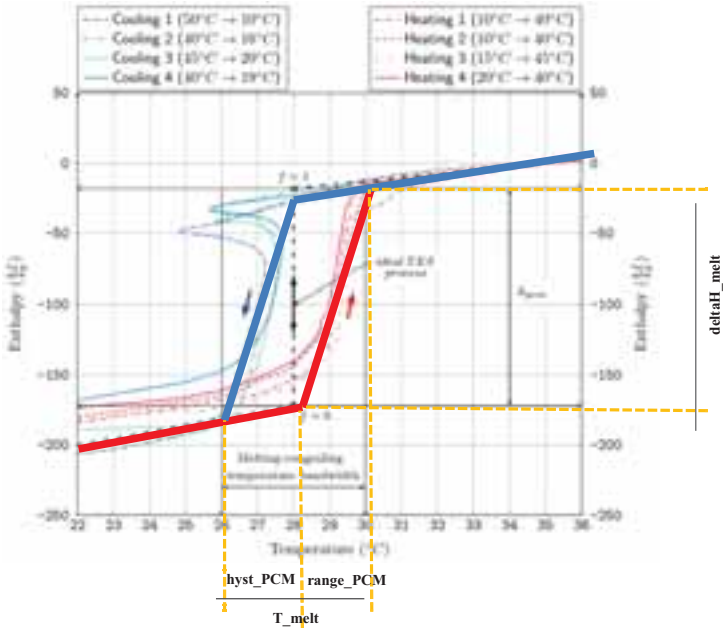

Figure 2. h-T behaviour of a particular PCM (Source: Belmonte et al. 2016) and definition of related model parameters

The PCM layer model was developed in C++ and integrated in the corresponding new TRNSYS type (Type261). Model inputs and outputs (required to connect the new type to other modelling components) as well as internal model parameters are collected in Table 1.

Table 1. Inputs, outputs and internal parameters for the PCM layer model

Model Inputs	
T_ini_PCM	Initial temperature of the PCM
A_coll	Area of collector surface
ePCM	Thickness of the PCM layer
Q_PVT	Heat transfer from the absorber to the PCM layer
T_ext	External (ambient) temperature
Model Outputs	
T_PCM	Temperature of the PCM layer
E_PCM	Energy level of the PCM layer
Q_loss	Heat transfer losses from the back surface of the PCM layer
f	Melted fraction of PCM (0 = completely solid; 1 = completely liquid)
Internal Parameters	
U_loss	Overall heat transfer coefficient from the PCM layer to the ambient temperature (including insulation and convective/radiant external thermal resistance)
Rho_PCM_liq	Density of the PCM liquid phase
Rho_PCM_sol	Density of the PCM solid phase
Cp_PCM_liq	Specific heat capacity of the PCM liquid phase
Cp_PCM_sol	Specific heat capacity of the PCM solid phase
T_melt	Melting temperature of the PCM
deltaH_melt	Specific enthalpy
Range_PCM	Characteristic temperature range for the phase change process (see Figure 2)
Hyst_PCM	Characteristic temperature hysteresis for the phase change process (see Figure 2)

Finally, in order to enable the integration of the proposed model, the thermal resistance of the Type560's back layer was modified and new connections between both TRNSYS components (560 for PV/T and 261 for PCM) were defined:

- PCM temperature is given to the PV/T model as the back surface environment boundary condition.
- Heat transfer through the PV/T back surface is given to the PCM model as an input.

It should be remarked that the thermal resistance between the absorber and the PCM layer is one of the key parameters of the proposed model. Theoretical derivation of this parameter is not evident, so its value should be calibrated with experimental data from manufacturer tests or real operation monitoring data.

3. Results and discussion

To explore the behaviour of the proposed modelling approach and demonstrate the influence of the above-mentioned thermal resistance some simulations were conducted for the first week of January in Seville (Spain). The TRNSYS simulation setup showed in Figure 3 was devised based on the following conditions and simulation hypotheses:

- Two solar systems with the same dimensions and configuration, except the back layer : PV/T panel with conventional back insulation, and PV/T panel with integrated PCM layer (3 cm-thick)
- PCM melting temperature of 30 ºC.
- Ideal energy demands able to return 25 ºC to the panels.
- Simple control strategy with pump operation turned on if minimum solar radiation is available or if outlet water temperature above 25 ºC can be achieved (even without solar radiation).

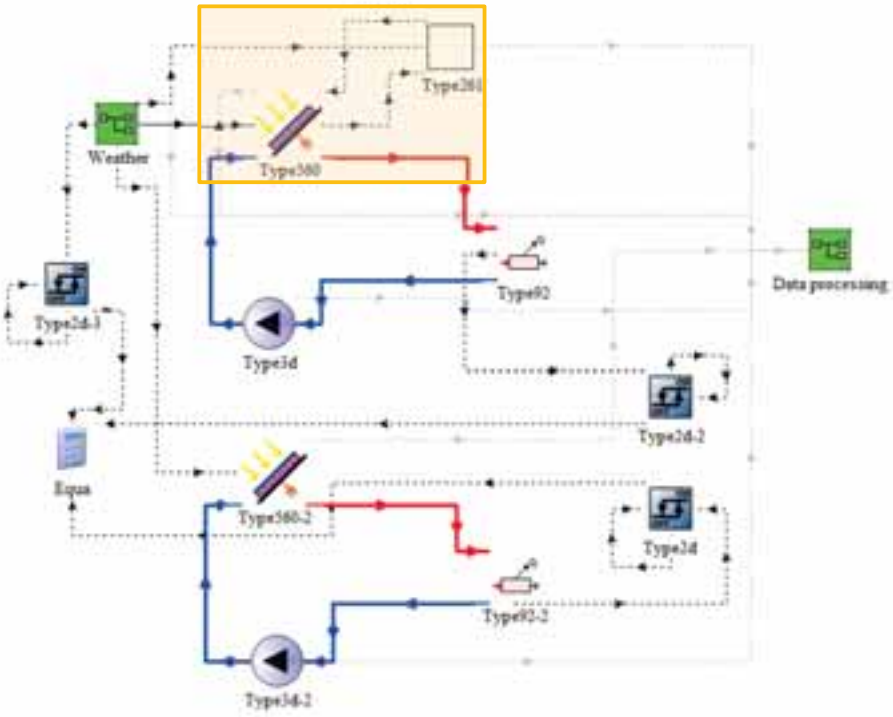

Figure 3. TRNSYS simulation setup for PV/T-PCM model analysis

A preliminary sensitivity analysis was done by modifying the thermal resistance (R) between the absorber and the PCM layer in the PV/T-PCM system: a) R = 0.07 $m^2 \cdot K \cdot W^{-1}$, b) R= 0.0007 $m^2 \cdot K \cdot W^{-1}$ and c) R= 0.00007 $m^2 \cdot K \cdot W^{-1}$. Figure 4 shows the obtained results.

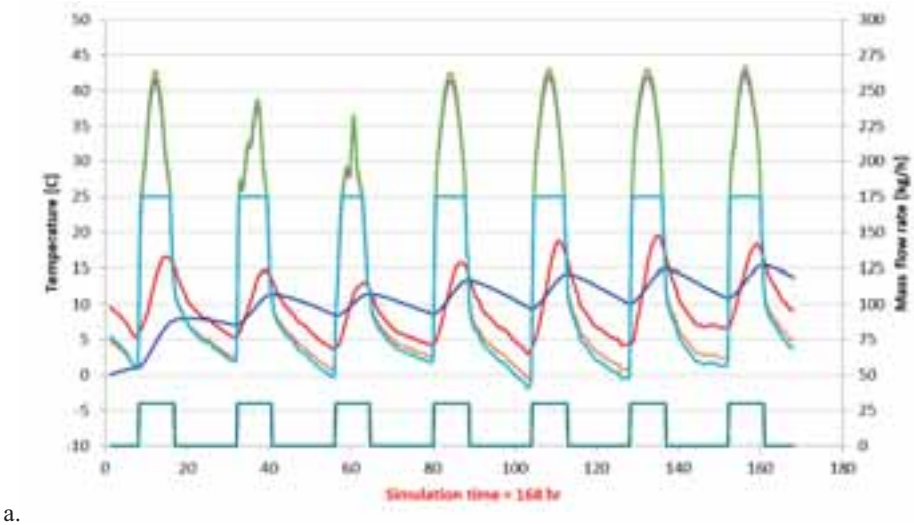

a.

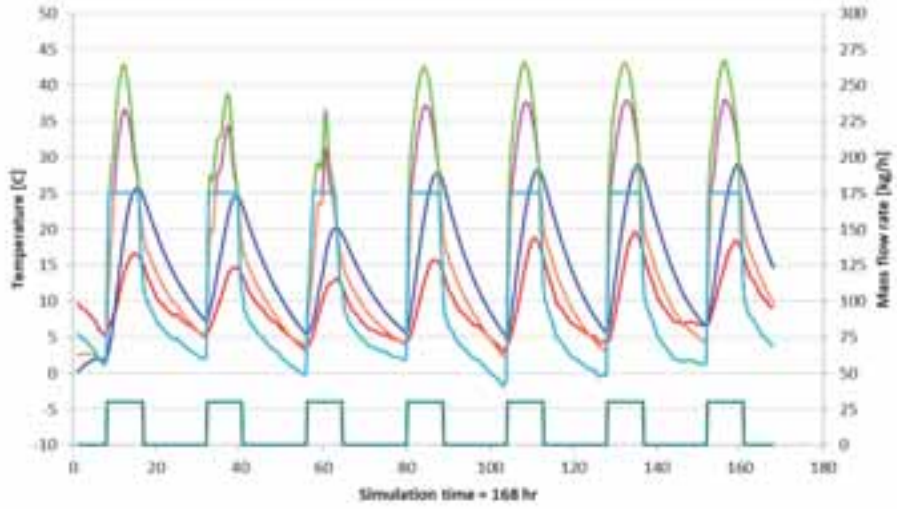

b.

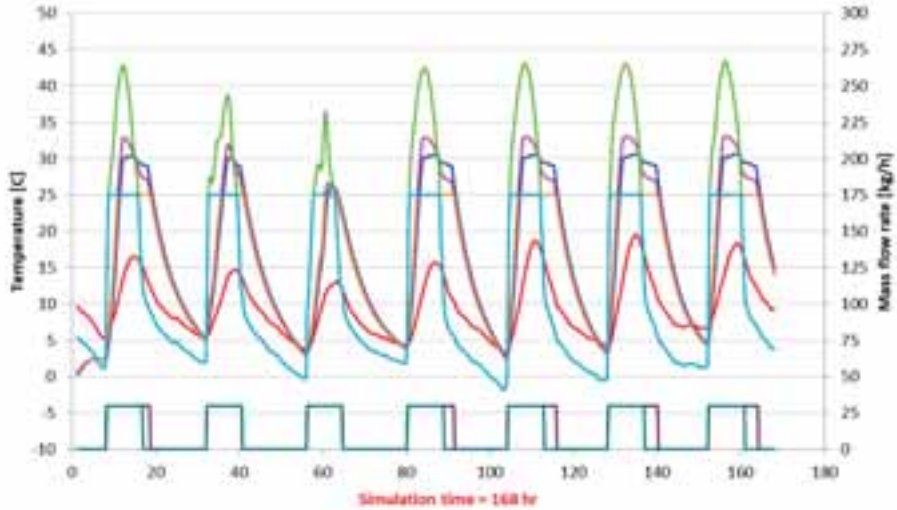

c.

Legend:
Left axis – Temperatures (ºC):
T_ext (red), T_PCM (dark blue), Tfluid,out_wPCM (pink), Tfluid,out_woPCM (green), Tfluid,in_wPCM (orange), Tfluid,in_woPCM (light blue)
Right axis – Mass flow rates (kg/h):
m_woPCM (dark green), m_wPCM (purple)

Figure 4. Temperature evolutions for PV/T system with and without PCM considering different values of the characteristic thermal resistance between the absorber and PCM layer (R in m2·K·W-1): (a) R = 0.07, (b) R= 0.0007, (c) R= 0.00007

One can observe clearly different behaviours of the PCM and fluid outlet temperatures depending on the R-values. If the R-value is high enough, the model reflects a decoupling effect between the thermal responses of the fluid and the PCM layer. In such case, the PV/T-PCM behaviour is very similar to the original PV/T system.

However, as the considered R-value is reduced, the PCM layer plays a relevant role in the overall thermal behaviour of the panel. The PCM layer absorbs enough heat from the PV/T configuration to reach its melting point. Then, less heat transfer to the fluid takes place and the outlet fluid temperature is clearly lower than that from the PV/T system.

Additionally, at the end of the day that heat stored into the PCM layer enables panel temperatures to decrease slowly and daily system operation to be extended beyond the solar radiation availability schedule. It is difficult to say how close to the first or the second option will be. Then, within the proposed model, the R-value will be a characteristic parameter of a given PV/T-PCM panel product that requires to be calibrated with experimental data.

4. Conclusions

This work presented the development of a mathematical model for innovative renewable technology consisting of a hybrid photovoltaic-thermal (PV/T) solar panel integrating a PCM-based thermal storage in its rear side. This simple approach, with a few input parameters, provides interesting potential for integration into energy simulations, enabling contributions to the design and smart operation of sustainable heating and power systems.

The key point of the proposed model is the definition of a simple representation for the h-T behavior of the PCM in the phase change temperature range. Then, a reasoned integration of the PCM behavior together with heat transfer from the PV/T system was analyzed in terms of a characteristic thermal resistance.

Moreover, a calibration procedure was envisaged focusing on the adjustment of this thermal resistance allowing to model different PV/T-PCM systems with different designs of the coupling between the absorber (heat recovery component) and the PCM layer.

Finally, it should be noted that this model is the result of tasks developed within the LowUP European project and detailed validation of the obtained results will be accomplished in the very next steps of the project based on actual monitoring data.

5. Acknowledgements

This work has been developed within the LowUP ('Low valued energy sources Upgrading for buildings and industry uses') project, which has received funding from the EU's Horizon 2020 Research and Innovation Programme under Grant Agreement n°723930.

6. References

Belmonte, J.F., Eguía, P., Molina, A.E., Almendros-Ibáñez, J.A., Salgado, R. 2016. A simplified method for modelling the thermal performance of storage tanks containing PCMs. Applied Thermal Engineering, 95, 394-410

Browne, M. C., Lawlor, K., Kelly, A., Norton, B., Mc Cormack, S. J. 2015. Indoor characterization of a photovoltaic/thermal phase change material system. Energy Procedia, 70, 163-171.

Chow, T. T. 2010. A review on photovoltaic/thermal hybrid solar technology. Applied energy, 87, 365-379

Duffie, J. A., Beckman, W. A. 2013. Solar engineering of thermal processes. John Wiley & Sons.

IEA-SHC Task 35 PV/Thermal Solar Systems. 2005. International Energy Agency (IEA) Solar Heating and Cooling (SHC) Programme. Available at: http://archive.iea-shc.org/task35/ (Last accessed: March 23rd, 2017).

LowUP: Low valued energy sources Upgrading for buildings and industry uses. LowUP project. EU's

Horizon 2020 R&I Programme. GA n°723930. Available at: http://lowup-h2020.eu/ (Last accessed: March 23rd, 2017)

Smith, C. J., Forster, P. M., Crook, R. 2014. Global analysis of photovoltaic energy output enhanced by phase change material cooling. Applied Energy, 126, 21-28.

TESS Thermal Energy Systems Specialists, 2012. TESSLibs 17 Component Libraries for the TRNSYS Simulation Environment, Volume 03: Electrical Library Mathematical Reference. LLC of Madison, WI (USA).

7. Nomenclature and symbols

Table 2. List of symbols (not detailed along the text)

Magnitude	Symbol	Units
Enthalpy	h	J/kg
Temperature	T	C
Efficiency	η	Dimensionless
Efficiency modifier group	χ	Dimensionless
Efficiency modifier constant	*eff*	C^{-1}
Solar irradiation	G	W/m^2
Energy	E	J

Table 3. List of sub-indexes (not detailed along the text)

Sub-index	Meaning
i	Time instant 'i'
G	Solar radiation
loss	Back heat losses
PV	Photovoltaic panel
PV/T	Photovoltaic-thermal panel
nom	Nominal
ref	Reference
T	Cell temperature

Experimental Validation of 1D model for photovoltaic/ thermal (PV/T) modules

Laetitia Brottier[1,3], David Cheze[2], Mathieu Mariotto[2], Franck Medlege[2], Guillaume Razongles[2] and Rachid Bennacer[3]

[1] DualSun, Marseille (France)

[2] CEA, Le Bourget-du-Lac (France)

[3] LMT/ENS-Cachan/CNRS/Université Paris Saclay, Cachan (France)

Abstract

To understand specific performance characteristics of a flat photovoltaic thermal (PV/T) module, a general simplified model (1D) has been performed, leading to an exponential equation for output temperature when weather and input fluid characteristics are known. To validate the model, a unique parametrical experimental validation was performed and is the focus of this paper. The present work includes nine prototypes built and monitored with the normative Solar Keymark approach.

The model exhibit a good fit with the experimental results. This conclusion has to be confirmed for future prototypes based on a polymeric heat exchanger.

Keywords: Photovoltaic thermal (PV/T) collector; Experimental validation; Energy performance

1. PV/T context and propose of the work

Since 2015, solar power is the number one energy source in terms of new capacities of electricity production ahead of coal, and the IEA published in Renewable 2017 (Renewable 2017, IEA) that the share of renewables for electrical needs will be 30% in 2022.

UNEP estimates that the buildings sector represent 30% of total energy consumption in the world (Global Status Report 2016, UNEP). Photovoltaics (PV) on buildings is ineluctable and the European Energy Performance of Buildings Directive requires all new buildings to be Nearly Zero-Energy (NZEBs) by the end of 2020. This directive is one of the political initiatives that gives a frame for its massive development.

But heat will certainly be the issue of the 21st century for Buildings. Almost 80% of energy demand in the buildings sector is for heat according to the IEA's article (Renewable energy's next frontier: heat, 6/12/2016).

Even with a strongly insulated building, the need for domestic hot water (DHW) is still here, and the space on the buildings' rooftops is not infinite. That is why the "2-in-1" PV/T technology a key solution to meeting energy needs of highly energy-efficient buildings. PV/T modules enable to produce DHW and photovoltaic with the same module, and make buildings more and more autonomous in heat and electricity using solar power.

Additionally, building-integrated PV (BIPV) may lead to a decrease in electrical performance of photovoltaic cells due to an increase in operating cell temperature (0.5%/K for mono-crystalline technology). In this context, the design of hybrid Photovoltaic-Thermal (PV-T) collectors, which recover wasted heat from the photovoltaic panel and in effect reduce cell temperature, offer an innovative solution for BIPV.

A review of PV/T technologies has been done by Zhang *et al.* (2012) and Good *et al.* (2015). The DualSun PV/T module in the study (Fig. 1) is based on the unglazed flat-plate liquid design described in these reviews. It has 60 monocrystalline cells for a nominal power of 250 Wp (PV) and 912Wth (Thermal).

doi:10.18086/swc.2017.18.04 Available at http://proceedings.ises.org

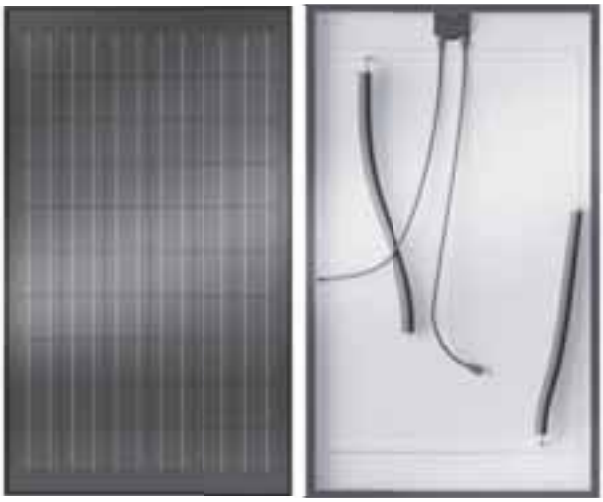

Fig. 1: DualSun PV/T module, 60 cells 250Wp, direct lamination of a stainless steel heat exchanger 912Wth

As reported by Zondag, H.A., 2008 in his review on flat-plate PV-T collectors, one key point for the development of PV-T collectors concerns the heat transfer between PV cells and fluid. That is why DualSun focused during their PV/T module developments on heat transfer between PV cells and fluid. Thermal resistance has been minimized by direct lamination of the specific heat exchanger. Direct lamination is possible due to a pertinent material choice, which prevents delamination due to differential dilatation in the long term.

As Dupeyrat, P., et al., 2009 pointed out, glazed PV-T modules lead to a better overall energy conversion. But DualSun has made the choice of an unglazed collector to keep a low stagnation temperature, and thus prevent overheating. The PV encapsulant is very sensitive to high temperature, which could irreversibly destruct the laminate. Furthermore, the residential sector, stagnation will often occur during summer months when families have left on vacation, and thus when solar irradiation is important.

The original concept of the DualSun module is different from what can be observed in existing literature. In order to simulate the energetic performances of the DualSun module, a numerical 1D model was developed. To validate the 1D model, the layers of the module have been changed in this study and tested.

2. Numerical model

An energy balance of the module leads to a quasi 1D simplified model, a methodology which has been previously used by many authors (Chow et al. 2008, Duffie and Beckman 1991, Fraisse et al. 2017, Tess library). The model input values include weather entries (ambient temperature T_A, insulation, wind velocity V_{WIND}) and solar domestic hot water load parameters (stock bottom temperature $T_{F,IN}$, flow rate $\dot{m}$). Thanks to an energy balance (Fig.2) on photovoltaic cells and on a fluid slice (eq. 1), we deduce an exponential behavior of fluid temperature along the path (eq. 2).

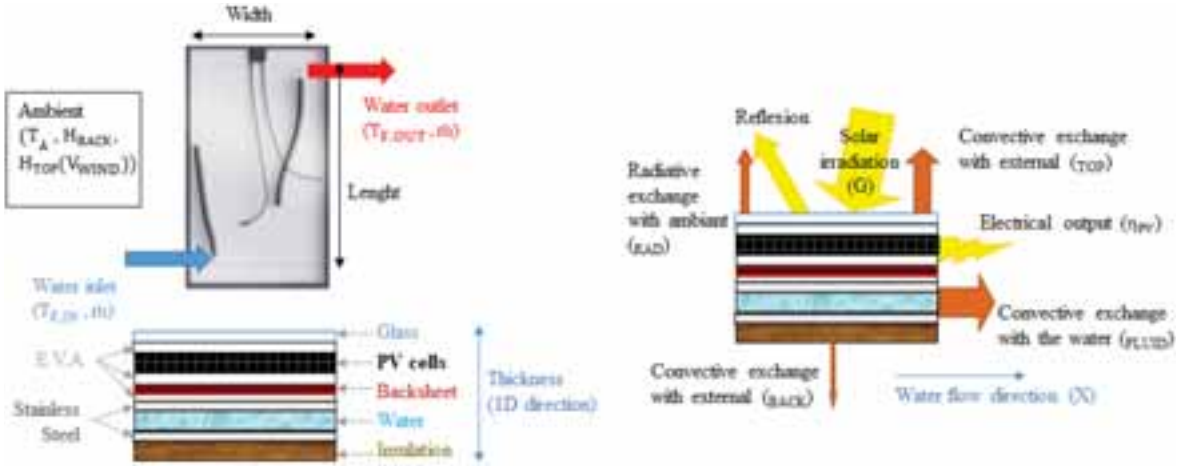

Fig. 2: Description of the studied system

Module output temperature and electrical power are then deduced thanks to an iterative approach on photovoltaic temperature (T_{PV}). The definitions of the symbols are given in Tab. 1 and subscript in Tab. 2.

$$\underbrace{(\tau_\alpha).G.\left(1-\eta_{PV}(G,T_{PV})\right)}_{\textit{Solar Recovered energy}} = \underbrace{h_{RAD}(T_{PV}).(T_{PV}(x)-T_{SKY})}_{\textit{Radiative exchange with ambiant}} + \underbrace{H_{TOP}(V_{WIND}).(T_{PV}(x)-T_A)}_{\textit{Convective exchange with external}} + \underbrace{H_{FLUID}.\left(T_{PV}(x)-T_F(x)\right)}_{\textit{Convective exchange with the water}} \quad \text{(eq.1)}$$

$$\underbrace{H_{FLUID}.\left(T_{PV}(x)-T_F(x)\right)}_{\textit{Convective exchange with the water}} = \underbrace{H_{BACK}.(T_F(x)-T_{BACK})}_{\textit{Convective exchange with external}} + \dot{m}.Cp.\frac{dT_F}{dx} \quad \text{(eq.2)}$$

Module outlet temperature and electrical power are then deduced thanks to an iterative approach on photovoltaic temperature (T_{PV}).

$$T_{F,OUT} = \left(T_{F,IN} - C\right).\, e^{-D.Width} + C \quad \text{(eq.3)}$$

$$T_{PV} = A\,.\,T_{F,MEAN} + B \quad \text{(eq.4)}$$

In non-null flow rate cases, equations were simplified to follow Solar Keymark standard directives (eq. 5).

$$\eta_{TH} = a_0 - a_1\,.\left(\frac{T_{F,MEAN}-T_A}{G}\right) \quad \text{(eq.5)}$$

Relations between the 1D-model and the linear formula are given by Eqs. 6 and 7.

$$a_0 = \frac{\dot{m}\cdot Cp\cdot D\cdot Width\cdot(C-T_A)}{G\cdot Area} \quad \text{(eq. 6)}$$

$$a_1 = \frac{\dot{m}\cdot Cp\cdot D\cdot Width}{Area} \quad \text{(eq. 7)}$$

Tab. 1: Meaning and units for symbols

Symbol	Meaning	Units
A,B,C and D	Coefficients depending on module characteristics	
Cp	Heat capacity	W/kg/K
G	Solar irradiation	W/m²
H	Global coefficient	W/m²/K
h_{RAD}	Radiative coefficient	W/m²/K
H_{WIND}	Convective coefficient on top plate due to the wind	W/m²/K
H_{FLUID}	Convective coefficient on the plate due to the water	W/m²/K
$\dot{m}$	Water Flow rate	L/s
T	Temperature	K
V_{WIND}	Wind velocity	m/s
Width	Width of solar collector	m
X	Water flow direction	
Tα	Transmitto-absorption depending on diffuse, direct and horizontal irradiation	-
η_{PV}	Electrical efficiency	-
η_{TH}	Thermal efficiency	-

Tab. 2: Meaning for subscripts

Subscript	Meaning
A	Ambient
BACK	Between fluid and back ambient
F	Fluid
FLUID	Between PV cells and fluid
PV	Photovoltaic cells
TOP	Between cells and ambient

3. Prototypes and testing

Some experimental validations at the module level were proposed but only with specific heat exchanger (Ben Cheikh et al. 2015, Rejeb et al. 2016). The aim of this paper is to do a complete parametric validation with a basic shape for the integrated heat exchanger with a full water slice (no tubes).

In order to validate the proposed simplified model, 9 prototypes were build and monitored according to the Solar Keymark approach in a sunlight test bench. All prototypes size 1669 x 982mm², except n°8 and 9, which were smaller (1365 x 886mm²). All integrated heat exchangers are directly laminated with the cells with an Ethylene Vinyl Acetate layer (EVA) under the BackSheet (BS) during a unique lamination step. Such manufactured heat exchanger (0.6mm stainless steel plates) allow a 2mm water gap to cool the photovoltaic part and have a 15mm non-irrigated border.

The description of the constitutive layers for the 9 prototypes tested are summarized in Tab. 3.

Tab. 3: description of the 9 prototypes tested

	Glass (mm)	EVA (mm)	Cells	EVA (mm)	BS (mm)	Fixation (mm)	Stainless Steel Heat exchanger / PV surface	Insulation equivalent thickness (k=0.033 W/(m.K))
1	2	0.6	60 (MPPT)	1.2	0.4	1.2	74%	NO
2	2	0.6	60 (OC)	1.2	0.4	1.2	74%	NO
3	2	0.6	60 (MPPT)	1.2	0.4	1.2	74%	39.6mm
4	2	0.6	60 (MPPT)	1.2	0.4	1.2	74%	24.8mm
5	2	0.6	60 (MPPT)	0.6	0.4	0.6	74%	NO
6	4 Low E	0.6	60 (MPPT)	1.2	0.4	1.2	74%	NO
7	2	-	-	0.6	0.4	0.6	74%	NO
8	-	-	-	-	-	-	exch only	NO
9	2	0.6	40 (OC)	1.2	0.4	1.2	100%	NO

The bench of artificial sunlight consists of two independent parts: the lamp holder and the sensor holder. The simulator is class BBB (Fig. 2). For the characterization of the PV/T module, an irradiant flux of 1000W / m² is adjusted at the level of the lamps.

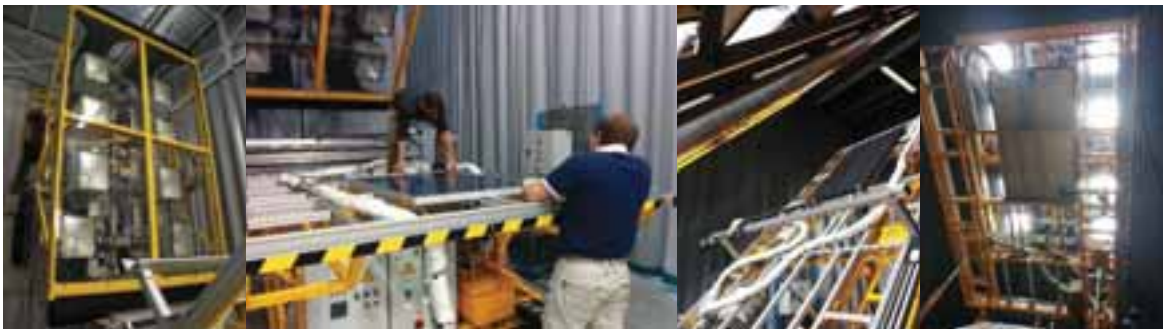

Fig. 2: Pictures of the artificial sunlight test bench

A mapping of the flux measurements is carried out in order to check a homogeneity on the surface of the sensor of plus or minus 5% on the mean value of the flux (Fig. 3). This mapping is carried out with each new characterization and it is obvious that the flux homogeneity is within ±1.5%.

Height [mm]	G = Irradiation [W/m²] - Average = 1006.36W/m²							
1590	942,0	956,4	960,4	971,0	964,1	961,1	962,6	944,0
1440	974,7	986,8	988,3	997,3	985,5	982,8	986,2	96[illegible],5
1290	998,9	1006,4	1006,7	1010,7	997,7	993,6	997,5	98[illegible],0
1140	1036,9	1046,7	1041,6	1038,3	1026,8	1021,7	1021,1	10[illegible],4
990	1044,8	1056,7	1053,5	1056,5	1040,8	1035,6	1039,9	10[illegible],2
840	1049,9	1061,3	1061,3	1063,5	1050,3	1047,0	1048,7	10[illegible],2
690	1044,9	1056,1	1056,9	1059,5	1049,6	1045,9	1048,4	10[illegible],2
540	1017,0	1031,2	1032,7	1037,4	1029,6	1027,9	1029,2	10[illegible],8
390	[illegible]	997,7	997,3	1003,6	996,9	996,9	998,6	98[illegible],0
240	980,8	993,4	991,5	991,1	988,4	986,3	987,8	97[illegible],9
90	972,1	977,9	980,6	984,3	974,7	976,0	981,3	96[illegible],4
-60	970,9	976,5	978,1	984,3	974,7	974,6	980,1	962,9
Width [mm]	-700	-550	-400	-250	-100	50	200	350

Fig. 3: Mapping measurements of the irradiation [W/m²]

Fans are used to generate a wind parallel to the top of the analysed system. A mapping of the air flow velocity measurements is carried out by means of a mobile hot wire sensor (Fig. 4). A speed around 1.5m / s is targeted.

Height [mm]	Air speed [m/s] - Average = 1.63m/s							
1590	1,12	1,35	1,45	1,48	1,63	1,61	1,50	1,34
1440	1,26	1,42	1,40	1,64	1,62	1,70	1,44	1,48
1290	1,46	1,43	1,52	1,64	1,57	1,73	1,67	1,39
1140	1,30	1,40	1,53	1,57	1,65	1,68	1,77	1,39
990	1,28	1,53	1,61	1,76	1,77	1,62	1,71	1,39
840	1,38	1,34	1,62	1,60	1,70	1,62	1,74	1,43
690	1,05	1,62	1,74	1,68	1,61	1,66	1,66	1,39
540	1,41	1,64	1,63	1,85	1,88	1,79	1,69	1,59
390	1,44	1,61	1,71	1,85	1,83	1,75	1,73	1,51
240	1,89	1,76	1,76	1,73	1,82	1,91	1,78	1,53
90	1,83	1,94	1,87	1,89	1,73	2,02	1,84	1,47
-60	2,00	2,00	1,95	2,00	1,69	1,90	1,97	1,46
Width [mm]	-700	-550	-400	-250	-100	50	200	350

Fig. 4: Mapping measurements of the wind speed [m/s]

A thermal regulation ensures the conditioning of the fluid (water), in order to generate a regulated inlet temperature in the module and to ensure good circulation in the exchanger. Six input temperature steps from 20 ° C to 70 ° C are programmed to scan the operating range of the module.

Local input / output temperature measurements and fluid flow measurements make it possible to draw up the appropriate thermal balances and determine the powers involved for each thermally stabilized operating point.

The measuring instrument I (V) plots the curves and extracts the important photovoltaic values. The red rectangle shows the location of the reference cell for the instrument which plots the I (V) curves, and the blue rectangle the module location (Fig. 3). The power of the module is limited by the current of the least photo-generating cell, which depends mainly on the minimum irradiance that the surface of the module receives (the limiting cell). In practice, the power value "equivalent to 1000 W / m²" is obtained from the reference cell (approx. -5% deviation).

Results are given in Tab.4.

Tab. 4: Thermal and photovoltaic results for the 9 prototypes

	a_0 (%)	a_1 (W/K/m²)	Wp *	β (%/°C)
1	50.2	12.8	238	-0.048
2	59.9	13.1	-	-
3	49.6	10.6	238	-0.050
4	49.8	11.4	238	-0.050
5	52.8	13.1	245	-0.055
6	49.8	13.0	225	-0.050
7	66.1	13.3	-	-
8	39.8	11.3	-	-
9	75.7	17.9	-	-

*limiting cell equivalent power at 1000W/m² and 25°C

4. Model validation

Two parameters were introduced to take better into account for the specific behavior of the Dualsun stainless steel heat exchanger. The first was the ratio Stainless Steel Heat exchanger over PV surface for the effect of the fin. Additionally, the heat exchange between the fluid and the stainless steel was supposed fixed at 800 W/(m².K) but is unknown. The second parameter was length of exchange.

Both parameter have been deduced from numerical optimization. The ratio Stainless Steel Heat exchanger over PV surface has been raised from a numerical optimization to 82% instead of 74%. The length of exchange has been optimized to fit with the experimental results to 770mm instead of 856mm.The model fit the experimental data very well as shown in Tab. 5 and Fig. 5 with a maximum root-mean-square error (RMSE) inferior of 67 to compare with the 1000Wth. The quality of the direct lamination for the 9th prototype was harder to achieve with the unusual size, which certainly explains the higher error with the theory.

These results seems to confirm that the 3D design could be neglect to predict performances, but this analyze could not be directly use for non-conductive material for the heat exchanger, as it could be an effect of the high homogenization of the temperature in the heat exchanger due to the relatively high conduction in the stainless steel. So it would be interested to continue this study with a polymeric heat exchanger.

Tab. 5: Root-mean-square error for each model/ test fitting

Test	1	2	3	4	5	6	7	8	9
RMSE	8.74	17.14	26.39	15.09	29.98	20.33	28.35	25.42	66.98

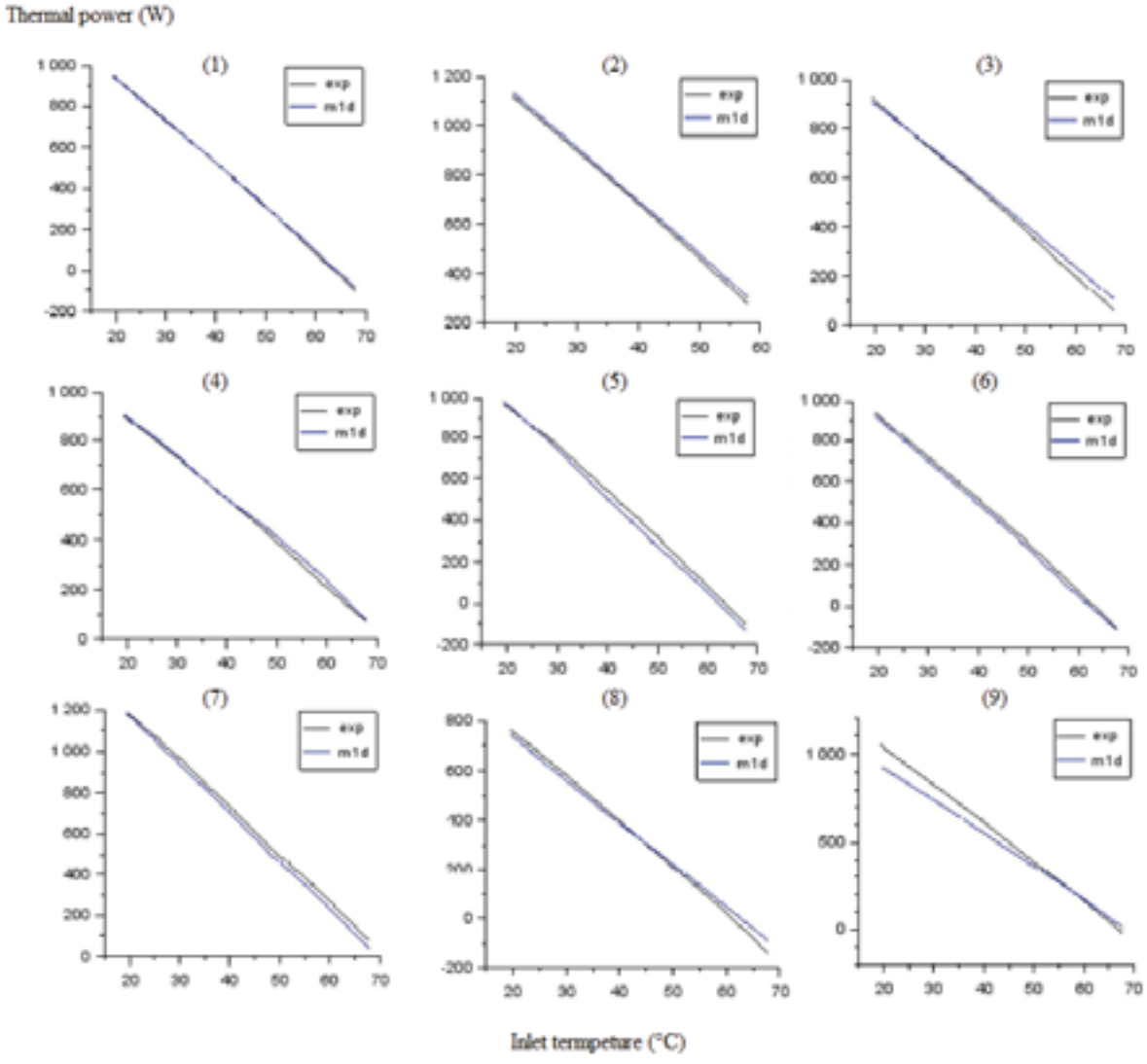

Fig. 5: Experimental and theorical thermal performance curves for the 9 prototypes

5. Conclusion

In this study, a general simplified model (1D) of PV/T module was proposed leading to an exponential equation for output temperature when weather and input fluid characteristics are known.

To challenge this model, the layers properties have been changed in 9 prototypes. The electrical and thermal performances of these 9 prototypes has been experimentally monitored with the normative Solar Keymark approach, and then compared with the performance outputs of the model.

The 9 first prototypes performance results have a good fit with the 1D model. These encouraging results must be confirmed with further tests with a polymeric heat exchanger.

6. References

Ben Cheikh El Hocine, et al., 2015, Model Validation of an Empirical Photovoltaic Thermal (PV/T) Collector, Energy Procedia. 74. 1090-1099

Chow, T.T., et al., 2008, Computer modeling and experimental validation of a building-integrated photovoltaic and water heating system, Applied Thermal Engineering 28, 1356–1364

Duffie, J.A., Beckman, W.A., 1991. Solar Engineering of Thermal Processes, second ed. Wiley Interscience, New York, 919p.

Dupeyrat, P., et al., 2009, International Scientific Conference - Renewables in a changing climate - From Nano to Urban Scale - CISBAT, Lausanne : Suisse

European Directive, Energy Performance of Buildings : 2010/31/UE, 19/05/2010

Fraisse, G., et al., 2007, Energy performance of water hybrid PV/T collectors applied to combisystems of Direct Solar Floor type. Solar Energy 81, 1426–1438

Good, C., et al., 2015. Hybrid photovoltaic-thermal systems in buildings – a review. Energy Procedia. 70, 683 – 690

IEA, Renewable 2017

IEA, Article, Renewable energy's next frontier: heat, 6/12/2016

Rejeb, O., et al., 2016, Numerical and model validation of uncovered nanofluid sheet and tube type photovoltaic thermal solar system, Energy Conversion and Management, 110. 367-377

Solar Keymark certification: http://www.estif.org/solarkeymarknew/index.php

TRNSYS - TESS libraries; library 17; TYPE 560: Fin Tube PV/T Solar Collector

UNEP, Global Status Report 2016

Zhang X., et al., 2012, Review of R&D progress and practical application of the solar photovoltaic/thermal (PV/T) technologies. Renewable and Sustainable Energy Reviews; Vol 16, Issue 1, p. 599–617

Zondag, H.A., 2008, Flat-plate PV-Thermal collectors and systems: A review. Renewable and Sustainable Energy Reviews. Volume 12, Issue 4, Pages 891-959.

Ray Tracing Simulations of a Novel Low Concentrator PVT Solar Collector for Low Latitudes

Diogo Cabral[1], João Gomes[1,2], Paul-Antoine Dostie-Guindon[3], Björn Karlsson[1]

[1] University of Gävle, Gävle (Sweden)

[2] Solarus Sunpower Sweden AB, Gävle (Sweden)

[3] Ecole Polytechnique Montréal, Montréal (Canada)

Abstract

One way to reduce solar collector's production costs is to use concentrators that increase the output per photovoltaic cell. Concentrating collectors re-direct solar radiation that passes through an aperture into an absorber. The current study evaluates electrical performance of symmetric C-PVT solar collectors with a vertical bifacial receiver, through a numerical ray tracing model software, Tonatiuh. Several designs have been analysed, such as the Pure Parabola (PP) and MaReCo CPC geometries, both symmetric. Parameters such as concentration factor, electrical performance, transversal and longitudinal IAM (Incidence Angle Modifier), the influence of optical elements and influence of the length of the reflector in the shadow effect have been studied for different geometries. The simulations were performed for Mogadishu, Somalia and showed good results for the Pure Parabola collector (PPc) annual received energy, 379 and 317 kWh/m^2/year for a focal length of 15 e 30 mm, respectively. A symmetrical double MaReCo CPC collector has been simulated with the annual received energy of 315 kWh/m^2/year. The addition of the optical elements will decrease the annual received energy of the PPc by around 11.5%, where the optical properties (7.1%) and glass (4.1%) have the biggest impact in the annual received energy. Overall, symmetric geometries proved to be the most suitable geometries for low latitudes applications, being the geometry *f1* (focal length of 15 mm) the best one.

Keywords: Symmetric C-PVT, Pure Parabola collector, MaReCo CPC geometry, Tonatiuh.

Quantity	Symbol	Unit
Acceptance angle	θ_c	degrees
Incidence angle	θ_i	degrees
Focal length	f	mm
Receiver height	Hr	mm
Aperture	$x_{máx}$	mm
Reflector height	z	mm
Aperture area	Apt_{area}	m^2
Solar irradiance	I_a	W/m^2
Concentration factor	Ci	-

1. Introduction

PVT systems can be based on Compound Parabolic Collector (CPC) (C-PVT) or on flat plate solar thermal collectors (PVT's) [1]. PVT collectors are hybrid solar collectors that simultaneously generate electrical (through PV cells) and thermal energy (through the solar radiation absorbed by the PV cells that is not converted into electricity). Since the efficiency of PV cells is temperature dependent, it is necessary to remove the excess heat. Previous studies showed that for every degree increase in temperature, the PV cell decreases around 0.45% [2]. This leads to a significant efficiency drop since PV cells can reach very high temperatures in summer [3], [4].

In order to carry the excess thermal energy generated by the PV cells, a cooling fluid is used (generally water), which leads to a decrease of the temperature of the solar cells, 'increasing' their overall efficiency. The waste heat harvested by the cooling fluid can be used as a cogenerated product and for heating applications [3]. This study will address different sets of simulations on symmetric low concentrator PVT geometries (with a vertical bifacial receiver), namely Pure Parabola (*f1* and *f2* geometry) and MaReCo CPC. Table 1.1 shows the main characteristics of the simulated reflector geometries, where the concentration factor, reflector height and focal length are shown.

doi:10.18086/swc.2017.18.05 Available at http://proceedings.ises.org

Table 1.1. Geometry characteristics.

		Concentration factor (C_i)	Reflector height (z) [mm]	Focal length (f) [mm]
f1		1.2	75	15
f2	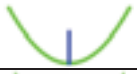	1.7	75	30
MaReCo CPC[1]	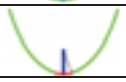	1.6	75	30

[1]The MaReCo CPC geometry has an arc circle angle of 20° and a parabolic section with a focal length of 30 mm.

1.1 Concentrator Solar Panels

Solar energy technologies, just like any energy technologies, aim at providing energy at the lowest possible cost. This can be reached by increasing the efficiency or decreasing the investment cost. Concentrating collectors re-direct solar radiation that passes through an aperture into the receiver or absorber. These type of systems usually have a tracking system in order to maximize the energy yield [5]. Concentrating collectors are normally categorized on the field technology used, high or low concentration. The low concentration is categorized in three different categories such as (i) Booster reflector; (ii) Compound Parabolic Concentrator; (iii) Luminescent Concentrator. The high concentration technologies currently available are (i) parabolic trough collector; (ii) Linear Fresnel reflector; (iii) Central receiver (Tower); (iv) Parabolic Dish [6]-[8].

1.2 Compound Parabolic Collectors

CPC (Compound Parabolic Collectors) are non-imaging concentrators that do not require tracking system due to the ability to reflect all available beam radiation to the receiver. The incidence angle for these concentrators makes them very attractive from the point of view of system simplicity, flexibility and cost-effectiveness [9]. CPCs combine two parabolic reflectors (symmetric or asymmetric), each one of them with its own focus length (F, the focus of the right-hand parabola in Figure 1.1) at the lower edge of the other parabola [10], shown in Figure 1.1. The angle between the axis of the collector and the line connecting the focus of one of the parabolas with the opposite edge of the aperture is called acceptance half-angle (θ_c) [14].

The relationship between the size of the aperture (2a), the size of the receiver (2a') and the acceptance half-angle is expressed through the following Equation 1.1 [10]:

$$2a' = 2a \sin\theta_c \qquad \text{(eq. 1.1)}$$

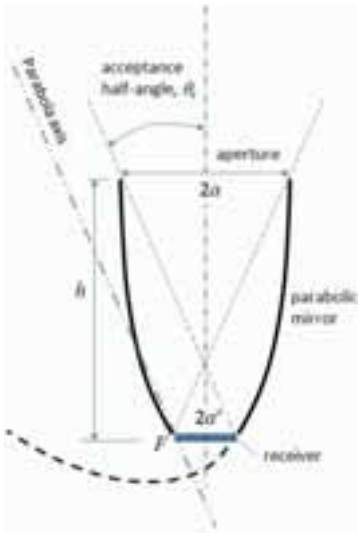

Figure 1.1. Cross section of a symmetrical non-truncated CPC [10].

Knowing the concentration ratio is possible to obtain the relationship between the concentration ratio and the acceptance angle [10]:

$$C_i = \frac{2a}{2a'} = \frac{1}{\sin\theta_c} \qquad \text{(eq. 1.2)}$$

Other useful equations that describe the design of CPC concentrators are shown below. The following equations relate the focal distance of the side parabola to the acceptance half-angle (θ_c), receiver size, and height of the collector (h) [10]:

$$f = a'(1 + \sin\theta_c) \qquad \text{(eq. 1.3)}$$

$$h = \frac{f\cos\theta_c}{\sin^2\theta_c} \qquad \text{(eq. 1.4)}$$

These types of concentrators are made for each ray with an angle θ that comes into the CPC aperture with an angle smaller than θ_c to be reflected to the receiver at the base of the collector. The ray will be reflected back to the atmosphere, if the angle θ is greater than θ_c, as shown in Figure 1.2 [10].

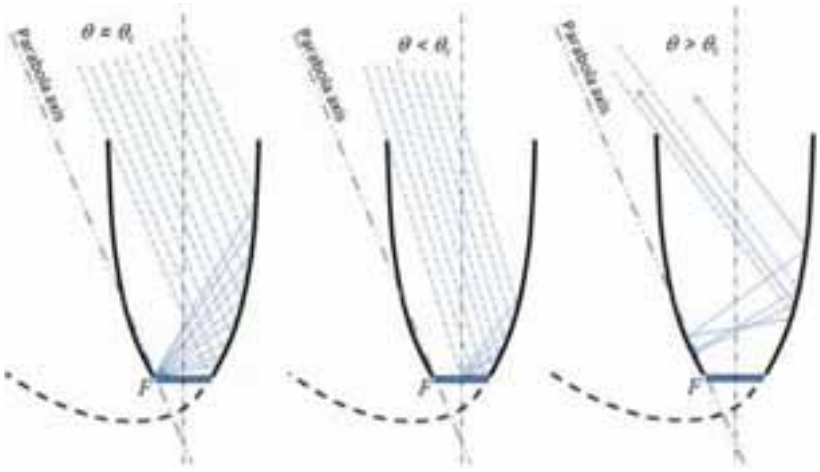

Figure 1.2. Reflection of the light rays directed to the CPC concentrator, at different angles [10].

1.3 Concentration with parabolic reflector

Different reflector geometries (symmetric) have been simulated in a ray tracing software, Tonatiuh. The simulated geometries are composed of either a full parabolic section or an arc circle with a parabolic section, thus, the importance of analysing the geometrical shape of these reflectors. For each point of the parabola, the distance between DR and RF is the same. Figure 1.3 shows the distance (VF) between the vertex and the focus of the parabola, known as focal length (*f*). The parabola axis intercepts the directrix and the focus, dividing the parabola into two symmetrical parts.

The following Equation 1.5 allows the calculation of the half aperture (x) in function of the reflector height (z) and the focal length (f) [4], [13].

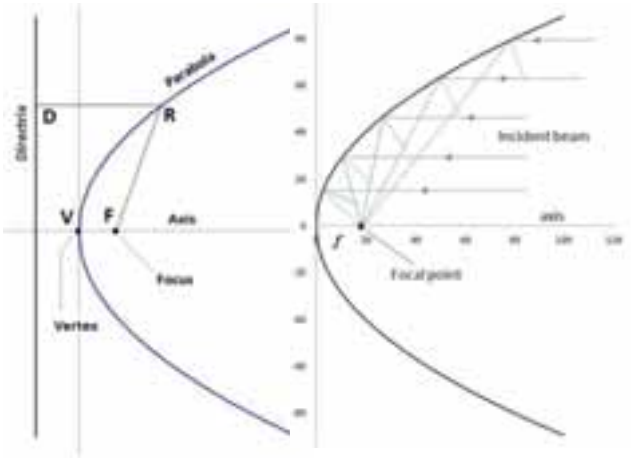

Figure 1.3. Parabola's geometry shape (left) and parallel incident beam rays (right) [11].

$$x = \sqrt{f \times 4 \times z} \qquad \text{(eq. 1.5)}$$

All incoming light rays parallel to the axis of the parabola will be reflected the focus area, by definition of the focal point of the parabola. The ideal location of the receiver can be given as the focal point position, assuming that the light rays that arrive at the reflector surface are essentially parallel light rays, as shown previously in Figure 1.3.

2. Methods

A thorough literature review in the field on reflector geometries and PVT technologies was carried out. Several sets of ray tracing simulations have been performed and posteriorly analyzed in Matlab. Below a short description of the procedure is presented.

- Literature review on symmetric and asymmetric reflector geometries and PVT technologies.
- Based on the literature review, two symmetric reflector geometries, Pure Parabola (PP) and MaReCo CPC geometries with a vertical bifacial receiver were selected:
  - Pure Parabola *f1* [focal length of 15 mm].
  - Pure Parabola *f2* [focal length of 30 mm].
  - MaReCo CPC [arc angle: 20°; focal length of 30 mm].
- Ray tracing simulations were performed for Mogadishu, Somalia (Latitude 2.04°, Longitude 45.31°) using a ray tracing software called Tonatiuh. The goal was to obtain the concentration factor, annual energy output, IAM (both transversal and longitudinal), the influence of optical elements (geometry *f2*), shadow effect (geometry *f1* and *f2*) and non-electrical area of the receiver.
- Analysis of the results was performed in a multi-paradigm numerical computing environment software, called Matlab.
- A comparison between the different geometries was established.

The ray tracing simulations were set for a location near the equator (low latitudes), Mogadishu, Somalia (Latitude 2.04°, Longitude 45.31°) in order to study different geometries that work at these latitudes. No meteorological files or historical years were used during the simulations.

2.1 Tonatiuh

For the analysis and design of solar concentrating systems, a Monte Carlo ray tracer software was used. Principles of geometrical optics are used as a statistical method to get a complete and statistically analysis of an optical system, studying the route of a ray of light as it passes through the optical system. It creates an accurate and easy use of Monte Carlo ray tracer, simplifying the optical simulation of almost any type of solar reflector system. The rays are generated in a light source that simulates the sun and then these ray's intersections with system surfaces are calculated. The sunlight is defined by the sun position, i.e. the elevation and the azimuth. These two parameters can also be calculated as a function of the day, the hour, the latitude and the longitude. In order to simulate an entire year, the program has the possibility to input a script for parametrical simulations allowing to launch several simulations by means of a few loops in a script file that was created in Matlab (a multi-paradigm numerical computing environment software). After the simulations, the data is exported to Matlab in order to analyze the data.
The optical properties of the different collector elements were considered non-ideal (losses were taken into account), that is, the different characteristics of the materials, such as reflector reflectivity (92%), glass and gable transmittance (96% and 90%, respectively) were introduced in the software. Each simulation had 10 000 rays and the direct irradiation set as 1 000 W/m².

2.2 Software and simulation limitations

Regarding the software used for the sets of simulations, some limitations were found while the simulations were being performed, such as:

- Tonatiuh simulates the rotation of the 'sun' around the collector as 360° in longitudinal and transversal directions over a day. This meant that is needed to set the sunrise and sunset to 6 am to 6 pm, respectively in order not to have night output. The sunset and sunrise differ from day to day around 30 minutes throughout the year in Mogadishu. Tonatiuh can only store 24 cells (corresponding to 24 hours per day), therefore it was necessary to select by hours, leading to a slight inaccuracy. The error is not relevant since the annual received energy at low angles is significantly lower.
- No meteorological data has been inserted in the ray tracing simulation tool.
- The software does not take into account the cooling factor of solar cells from the working fluid (PV cell temperature dependence).
- PVT system losses and cell efficiency are not taken into account in Tonatiuh.

2.3 Reflector shape selection

Regarding the Pure Parabola geometries, each set of simulations, the reflector height (z) was fixed at 75 mm and the focus length (f) varied between 15 and 30 mm. After the first set of simulations (with a focal length of 15 mm and reflector height of 75 mm), the focus length was increased to 30 mm and fixed (being the reflector height constant during the whole simulation). This procedure was made for reflector height of 75 mm, and for a focal length of 15 and 30 mm [12]. The simulations were performed for Mogadishu, Somalia (Latitude 2.04°, Longitude 45.31°). The geometry (*f1*) is composed of a focal length (f) of 15 mm, reflector height (z) of 75 mm and a low concentration factor (C_i= 1.2). The additional geometry (*f2*) has a C_i= 1.7, f = 30 mm and z = 75 mm.

In order to get a good perspective of how the PPg (Pure Parabola geometry) performs, a different geometry has been simulated. The simulation was performed for a symmetrical MaReCo CPC with a concentration factor of 1.6, an arc circle angle of 20° and a reflector height of 75 mm. The focal length of the parabola section and the reflector height were set in line with the *f2* geometry. Figure 2.1 shows a symmetrical MaReCo CPC geometry based on the MaReCo geometry. The receiver dimensions were set to fit this geometry (QQ'). The section of the concentrator between P_O and P'_O (red section in Figure 2.1) is an arc of a circle centred on Q. Section $A'P'_O$ and AP_O (green section in Figure 2.1) is a parabola with focus at Q and axis QP'_O. θ_i is the half-acceptance angle and θ_c is the arc circle angle.

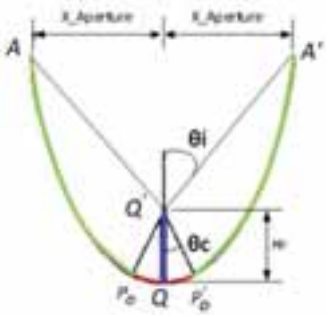

Figure 2.1. The optimum symmetrical MaReCo CPC.

2.4 IAM

The Incidence Angle Modifier (IAM) is the variance in output performance of a solar collector as the angle of the sun changes in relation to the surface of the collector. The longitudinal and transversal IAM can be obtained through the overall and optical efficiency, and aperture area (Apt_{area}). These values were collected from a Matlab script. The aperture area for receiver side is given by the following Equation 2.1.

$$\mathrm{Apt_{area}} = \left(\sqrt{z \times 4 \times f} - \frac{\mathrm{thickness_{receiver}}}{2}\right) \times \mathrm{Length_{receiver}} \qquad \text{(eq. 2.1)}$$

The aperture area allows the calculation of the overall efficiency of the collector [4].

$$\mathrm{Eff}(\theta_i) = \frac{\mathrm{Power}\ (\theta_i)\ [\mathrm{W}]}{\mathrm{I_a}\ [\mathrm{W/m^2}] \times Apt_{area}\ [\mathrm{m^2}]} \qquad \text{(eq. 2.2)}$$

Where the Power (θ_i) is given by Tonatiuh and I_a is the solar irradiance that passes through the collector aperture, with a value of 1 000 [W/m²].

The optical efficiency (η_{opt}) is given by the maximum value of Equation 2.3.

$$\eta_{opt} = \max(\mathrm{Eff}(\theta_i)) \qquad \text{(eq. 2.3)}$$

With all the parameters obtained, the transversal and longitudinal IAM is obtained using Equation 2.4.

$$\mathrm{IAM}(\theta_i) = \frac{\mathrm{Eff}\ (\theta_i)}{\cos(\theta_i) \times \eta_{opt}} \qquad \text{(eq. 2.4)}$$

Where θ_i are the angles [-90°, -89°, -88°, -87°, -86°, 85°, .. 0 .. , 85°, 86°, 87°, 88°, 89°, 90°]. The interval between angles was set in order to achieve a more accurate data.

2.5 Influence of the optical elements

In order to get a more precise knowledge of how the different elements affect the annual received energy of these kind of collectors, the influence of the optical elements such as (i) frame; (ii) glass; (iii) gables; (iv) receiver thickness; (v) optical properties were studied. The simulations consisted by adding the different elements to geometry *f2* and visualize their influence in the annual received energy.

2.6 Shadow effect

The effect of the shadow in the annual received energy was studied, by increasing the reflector length. Consisted by adding progressively length to the reflector, in order to reduce the shadow on the receiver. The receiver length was set as constant and the reflector area was gradually increased by 0.02, 0.04 and 0.06 m^2.

2.7 Electrical non-active area

The electrical non-active area gives the percentage of receiver area that does not produce electricity. In order to improve the performance of the collector, it is necessary to improve the performance of the receiver, by reducing the electrical non-active area. A study has been conducted in order to find the electrical non-active area of the selected receiver. The electrical non-active area was removed and after the annual received energy has been updated.

3. Results

3.1 Maximum efficiency and yearly energy output

This section presents the main results for an annual receive energy and a 3D view of the maximum efficiency at each angle. The vertical bifacial receiver is composed of side A (receiver side facing north) and side B (receiver side facing south).

3.1.1 Pure Parabola f1 collector

From the ray-tracing software, it was possible to extract the data to a Matlab script and run it, in order to get the annual received energy from both receivers A and B. This geometry receives an annual received energy of 2 186 kWh/m^2/year. The presented value is obtained by using a scale factor of 3.2, due to the fact that the simulated collector has 0.31 m^2.

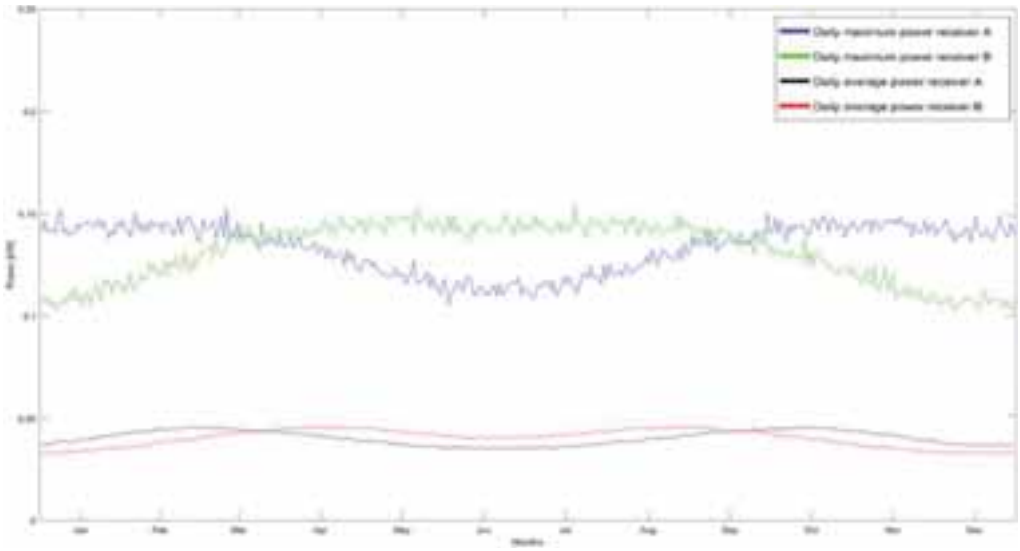

Figure 3.1. Daily maximum and average power output for the *f1* collector.

The receiver B will have higher annual received energy during the months of March-September, due to the fact that the sun will be on the north side of the collector. On the remaining months, the receiver A will have a higher annual received energy from September-March, when the sun is on the south side of the collector.

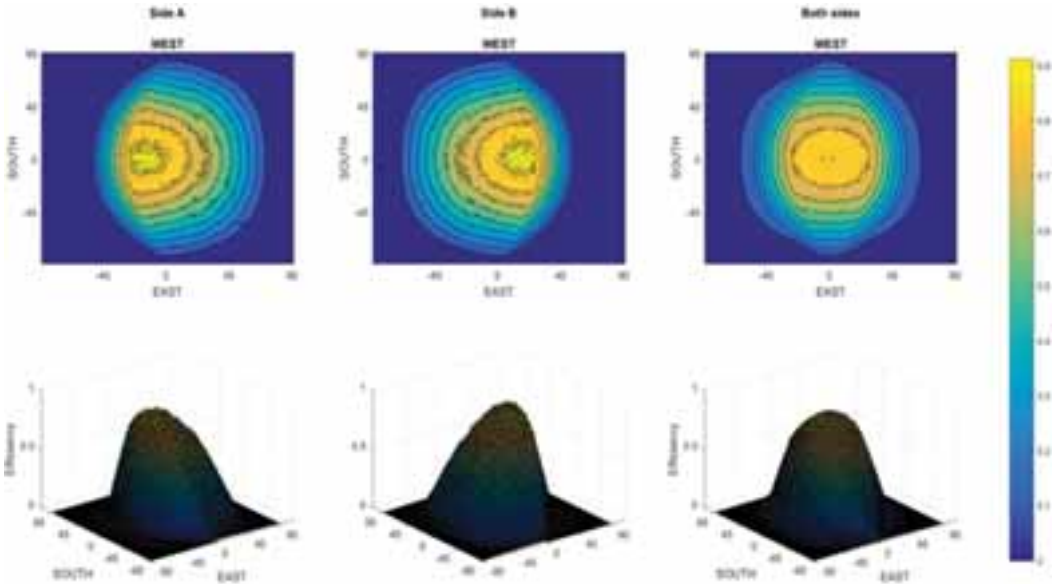

Figure 3.2. 3D view of the maximum efficiency at each angle (transversal and longitudinal) for the *f1* collector.

The distribution of the solar radiation is more evenly distributed across both receivers since they produce around the same. The maximum efficiency value is slightly above 90%. The collector performance (daily average power) throughout the year is in line with the average seasonal variation of the daily extra-terrestrial solar radiation for horizontal surfaces at low latitudes.

3.1.2 Pure Parabola f2 collector

This geometry receives an annual received energy of 1 831 kWh/m^2/year, with a scale factor of 2.3, for a simulated collector area of 0.44 m^2. Due to its concentration factor (bigger aperture), this geometry does not have the same properties as the one described above, since it has a different capacity to reflect the rays with the same accuracy as the geometry presented previously (*f1* geometry).

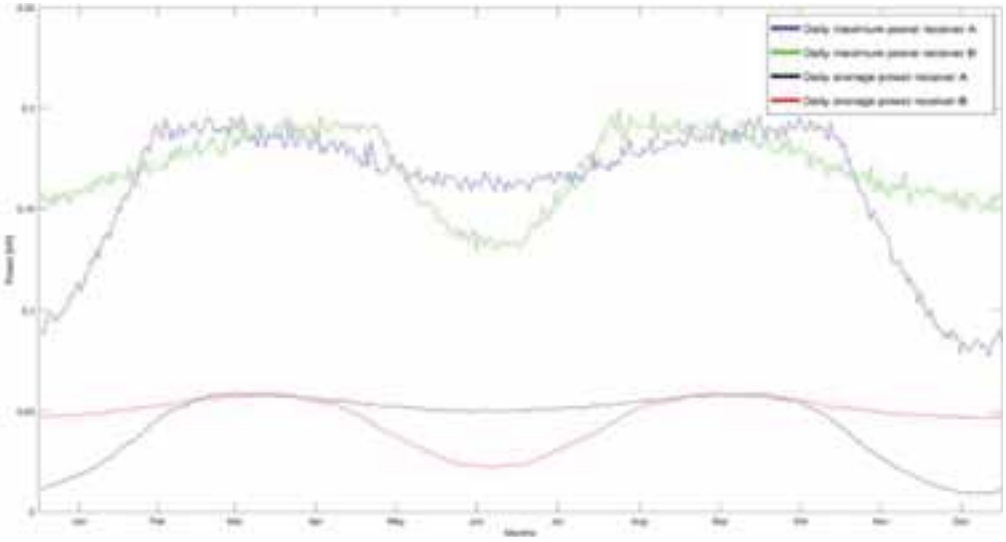

Figure 3.3. Daily maximum and average power output for the *f2* collector.

The receiver B has a higher annual received energy during the months of November-February, March-May and July-September, due to the fact that the sun is on the north side of the collector. On the other hand, the receiver A has a higher annual received energy during the months of February-March, May-July and September-November when the sun is on the south side of the collector.

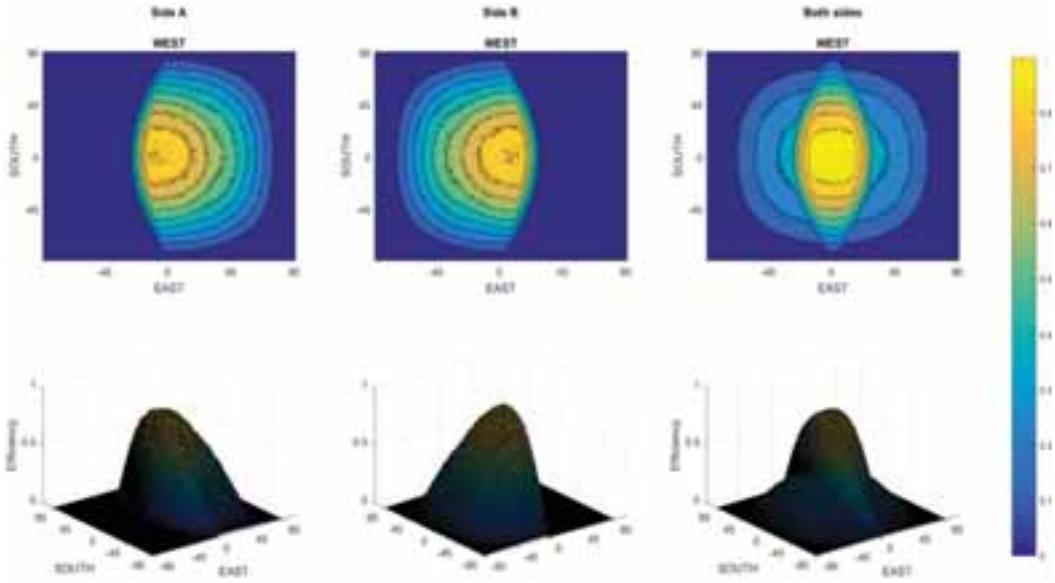

Figure 3.4. 3D view of the maximum efficiency at each angle (transversal and longitudinal) for the *f2* collector.

The maximum efficiency value is slightly below 90%. As *f1* geometry, this collector performance (daily average power) throughout the year is in line with the average seasonal variation of the daily extra-terrestrial solar radiation for horizontal surfaces at low latitudes.

3.1.3 MaReCo CPC geometry

A value of 1 819 kWh/m^2/year was obtained for this reflector shape, by using a scale factor of 2.4, due to the fact that the simulated collector has 0.42 m^2.

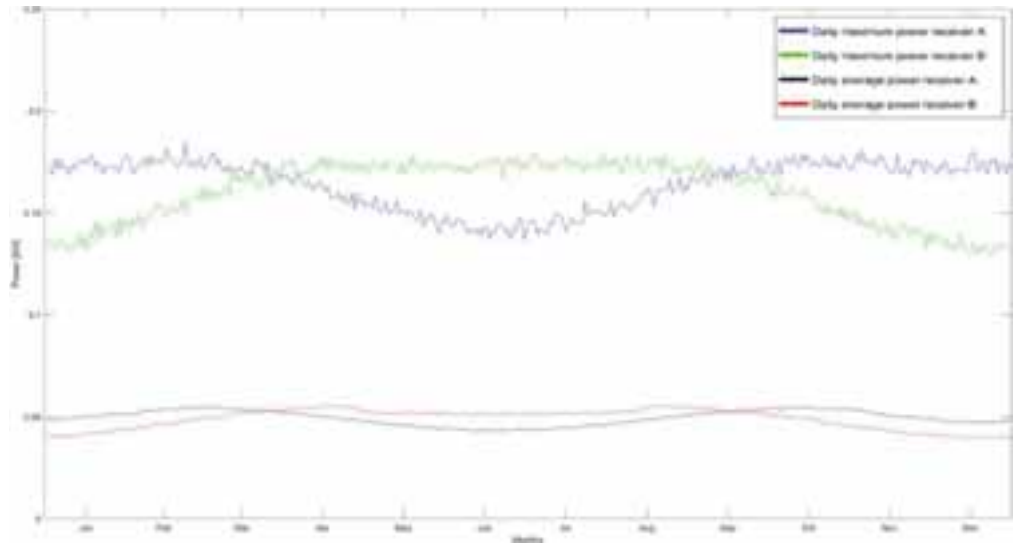

Figure 3.5. Daily maximum and average power output for the MaReCo CPC geometry.

The receiver B will have higher annual received energy during the months of March-September, due to the fact that the sun will be on the north side of the collector. On the remaining months, the receiver A will have a higher annual received energy from September-March, when the sun is on the south side of the collector.

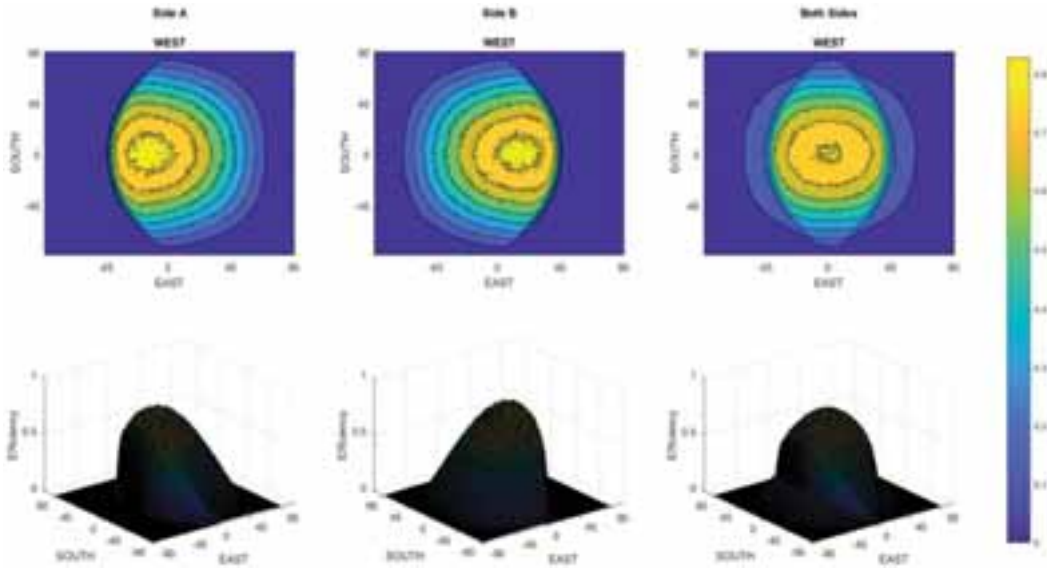

Figure 3.6. 3D view of the maximum efficiency at each angle (transversal and longitudinal) for the MaReCo CPC geometry.

Despite having a similar annual received energy as geometry *f2*, the maximum efficiency range of this geometry is bigger than in geometry *f2,* with a value slightly above 80%.

3.2 IAM

3.2.1 Pure Parabola f1 collector

Figure 3.7 shows the normalized maximum efficiency working range for the PPc *f1*, around [-30°S, 30°N].

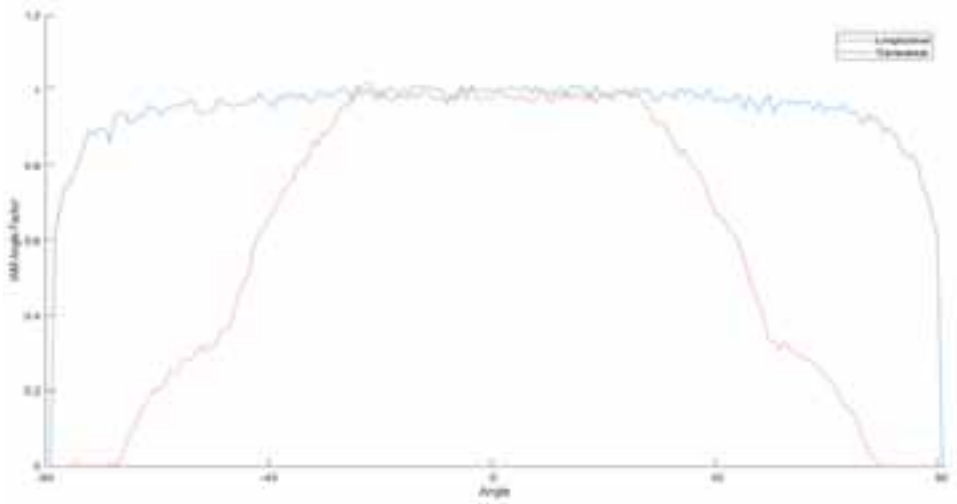

Figure 3.7. IAM transversal and longitudinal for both receiver sides, *f1* collector.

This geometry has the ability to re-direct efficiently the sun rays towards the receiver, due to the fact that the angles θ that comes into the CPC aperture with an angle smaller than θ_c (acceptance half-angle) will be reflected more efficiently into the receiver.

3.2.2 Pure Parabola f2 collector

Figure 3.8 shows the normalized maximum efficiency working range for the PPc *f2*, around [-15°S, 15°N].

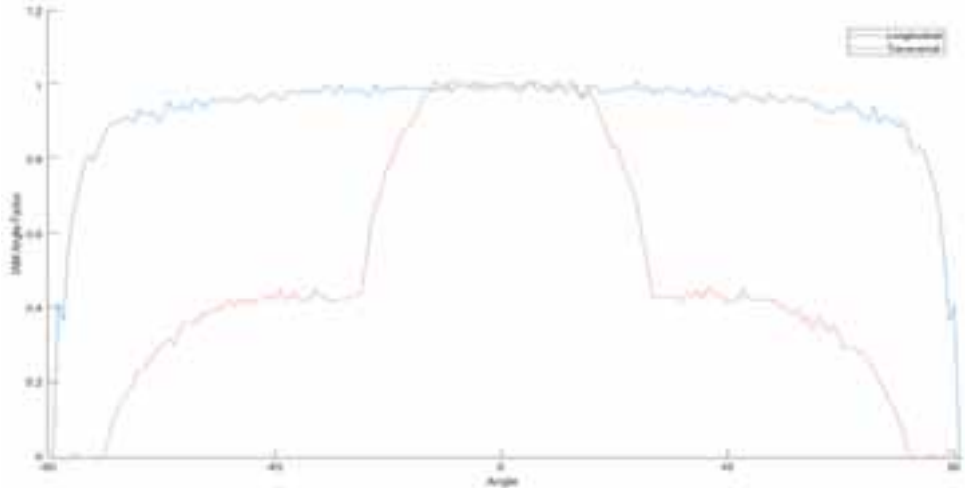

Figure 3.8. IAM transversal and longitudinal for both receiver sides, *f2* collector.

Comparing geometry *f2* with *f1*, it is possible to verify that at some angles, geometry *f2* has no ability to re-direct the incident rays to the receiver efficiently (steeper curve from [-30°S, -15°N] and [15°S, 30°N]), since the angle θ is bigger (for a longer period than for geometry *f1*) than θ_c, thus lowering the maximum efficiency range. A narrower maximum efficiency range and lower maximum efficiency led to a lower annual received energy when compared with geometry *f1*.

3.2.3 MaReCo CPC collector

Figure 3.9 shows the normalized maximum efficiency working range for the symmetrical MaReCo CPC collector, around [-40°S, 40°N].

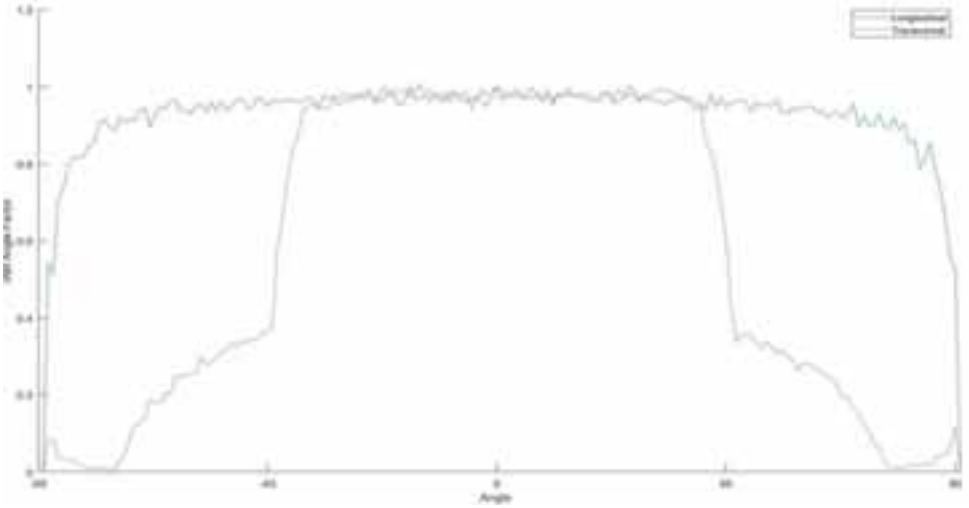

Figure 3.9. IAM transversal and longitudinal for both receiver sides, MaReCo CPC geometry.

The lower maximum efficiency value of this geometry is compensated by a wider maximum efficiency working range, when compared with geometry *f2*.

3.3 Influence of the optical elements in geometry f2

The PPg corresponds to the PPc without a frame, gable, glass, optical properties and a 2 mm receiver thickness.

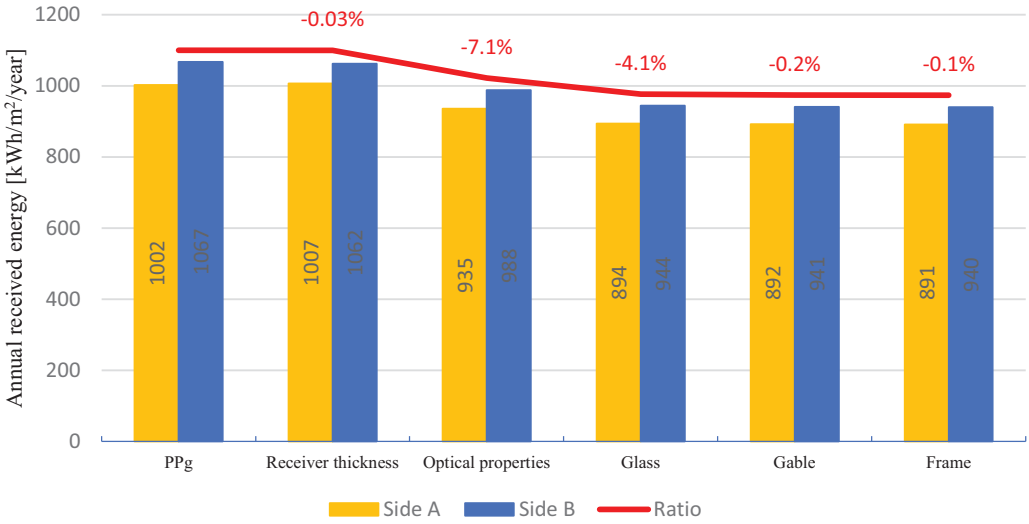

Figure 3.10. Results of the influence of the optical elements and properties in the geometry *f2*.

Figure 3.10 shows that the optical properties and glass have the biggest impact on the electrical performance of the collector. On the other hand the receiver thickness, gable and frame almost have no influence in the results, accounting for 0.3%. Overall, the difference between the geometry and the collector is around 11.5%. The energy production ratio between receiver sides decreases with the influence of the optical properties of the materials. Since the value of reflectivity was considered constant (normal to the collector) regardless the suns' altitude, the influence of the glass is lower. It is expected that the glass will have a bigger influence if this parameter is taken into account.

3.4 Shadow effect (Pure Parabola f1 collector)

Electricity costs were set as 0.211 €/kWh for households [12] and the reflector price was taken from a standard reflector with reflectivity of 98%. Table 3.1 shows the payback time for an increased reflector length.

Table 3.1. Payback time for an increased reflector length, geometry *f1*.

Additional area [m²]	Additional reflector price [€]	Production surplus [kWh/m²]	Payback [years]
+ 0.02	0.7	18	9.2
+ 0.04	1.5	20	8.9
+ 0.06	2.2	22	7.9

The payback time goes from 7.9 up to 9.2 years to start to pay off (breakeven point), showing that is not effective since the payback time is too big for such a small area. The presented values show that a longer reflector reduces the shadow effect, increasing the annual received energy.

3.5 Electrical non-active area

The electrical non-active area accounts for 12.1 % and the cell efficiency for 19.7%. The updated values for each collector are given in the following Table 3.2.

Table 3.2. Updated annual received energy per collector.

Annual received energy [kWh/m²/year]		
	Tonatiuh	**Updated**
PP *f1*	2 186	379
PP *f2*	1 831	317
MaReCo CPC	1 819	315

4. Discussion

As expected, the *f1* geometry has a wider transversal maximum efficiency working range as a result of its narrow aperture, when compared with *f2* geometry. This geometry has the ability to re-direct more efficiently the sun rays towards the receiver. The transversal maximum efficiency working range of the PPc is around [-30°, 30°] and [-15°, 15°] for a focal length of 15 and 30 mm, respectively. On the other hand, the MaReCo CPC collector has a maximum efficiency working range around [-40°S, 40°N].

The values for the annual received energy are, as expected, higher for the *f1* collector (2 186 kWh/m^2/year) than for the *f2* collector (1 831 kWh/m^2/year), especially as a result of its geometrical characteristics (lower concentration factor). Regarding the symmetric MaReCo CPC collector, the results show that this geometry has a slightly lower annual received energy than the *f2* geometry. It was expected that this geometry would perform better than the *f2* geometry, due to its lower concentration factor (fewer reflection losses). The MaReCo CPC collector has an annual received energy around 1 819 kWh/m^2/year. Lower concentration means higher annual received energy, due to lower reflection losses.

Figure 3.10 shows that the glass and the optical properties have the biggest impact in the annual received energy of the *f2* collector. The annual received energy for the symmetrical geometries can go up to 11.5%, showing that the optical properties of the different elements affect significantly the performance of these geometries.

Table 3.2 shows the annual received energy, considering a non-electrical area of 12.1% and a cell efficiency of 19.7%. The addition of these parameter led to an annual received energy of 379, 317 and 315 kWh/m^2/year for the collector *f1*, *f2* and MaReCo CPC, respectively.

Regarding the shadow effect, it is possible to acknowledge that increasing the reflector length is not effective, not only because at low angles (sunrise and sunset) the reflected sun rays will be reflected back to the atmosphere (the receiver is not long enough to collect the sun rays), but also due to the fact that the payback time for such small area can go from 8 to 9 years for such small area.

Overall, the simulated geometries showed potential for low latitudes applications, being the geometry *f1* the best one. A way to validate the simulations would be the construction of a prototype and to perform CFD simulations in order to study the thermal potential of a C-PVT with these geometries.

5. References

[1] O. Z. Sharaf and M. F. Orhan, "Concentrated photovoltaic thermal (CPVT) solar collector systems: Part I – Fundamentals, design considerations and current technologies," *Renewable and Sustainable Energy Reviews,* vol. 50, pp. 1500-1565, 10, 2015.

[2] A. H. Jaaz *et al*, "Design and development of compound parabolic concentrating for photovoltaic solar collector: Review," *Renewable and Sustainable Energy Reviews,* vol. 76, pp. 1108-1121, 9, 2017.

[3] S. A. Kalogirou and Y. Tripanagnostopoulos, "Hybrid PV/T solar systems for domestic hot water and electricity production," *Energy Conversion and Management,* vol. 47, *(18–19),* pp. 3368-3382, 11, 2006.

[4] S. R. Reddy, M. A. Ebadian and C. Lin, "A review of PV–T systems: Thermal management and efficiency with single phase cooling," *Int. J. Heat Mass Transfer,* vol. 91, pp. 861-871, 12, 2015.

[5] William B Stine and Michael Geyer, Eds., *Power from the Sun.* (2001st ed.) 2009.

[6] V. V. Tyagi, S. C. Kaushik and S. K. Tyagi, "Advancement in solar photovoltaic/thermal (PV/T) hybrid collector technology," *Renewable and Sustainable Energy Reviews,* vol. 16, *(3),* pp. 1383-1398, 4, 2012.

[7] R. Abbas *et al*, "Parabolic trough collector or linear Fresnel collector? A comparison of optical features including thermal quality based on commercial solutions," *Solar Energy,* vol. 124, pp. 198-215, 2, 2016.

[8] R. Pujol-Nadal *et al*, "Optical and thermal characterization of a variable geometry concentrator using ray-tracing tools and experimental data," *Appl. Energy,* vol. 155, pp. 110-119, 10/1, 2015.

[9] L.A. Diwan, "Study of Optimizations in a Novel Asymmetric Photovoltaic/Thermal Hybrid Solar Collector", 2013.

[10] M. Fedkin and A. Dutton, "CPC Collectors - concentration of diffuse radiation," 2015.

[11] M. Fedkin and A. Dutton, "Concentration with a parabolic reflector," vol. 2017, *(19 March),* 2015.

[12] 'Electricity and gas prices, second half of the year', 2013-15 (EUR per kWh), 2017.

[13] R. Winston, R. Finkler and J. Shamir, "High Collection Nonimaging Optics," *6th Mtg in Israel on Optical Engineering,* vol. 1038, pp. 590-598, Dec-7, 1988.

[14] W. T. Welford and R. Winston, "Chapter 4 - nonimaging concentrators: The compound parabolic concentrator," in *High Collection Nonimaging Optics*, W. T. WELFORD and R. WINSTON, Eds. Academic Press, 1989, pp. 53-76.

Characterization of Two Secondary Optics for a Fresnel Mirror

Daniela Fontani, David Jafrancesco, Franco Francini, Paola Sansoni
CNR-INO Istituto Nazionale di Ottica, Largo E. Fermi, 6 – Firenze - 50125 – Italy
Phone: +39-055-23081; Fax: +39-055-2337755; Email: daniela.fontani@ino.it

Abstract

The advantage of this laboratory optical characterization is to reproduce under controlled conditions an existing solar plant of Fresnel mirror type. The plant has 20 identical plane mirrors that concentrate the sunlight toward the secondary optics, which focuses it on the receiver. The procedure consists in performing the tests separately simulating the illumination of each plane mirror, finally combining the measured results to obtain collection efficiency and concentration factor of the entire solar plant. Two alternative secondary optics, a prismatic lens and a reflective concentrator, were optically tested to compare their behaviour. The total collection efficiency is similar, while the concentration factor is higher for the prismatic lens. Since the receiver is a photovoltaic device, a key aspect to be studied is the uniformity of receiver lighting: the power density measured in the image plane of the secondary optics evidences lateral zones of uneven lighting.

Keywords: secondary optics, Fresnel mirror, optical measurement, solar concentration

1. Analysis of the system

Two secondary concentrators were designed and realized for an actual solar concentration plant based on the principle of the Fresnel mirror [Abbas et al. 2012a, 2012b; El Gharbi et al. 2011; Fernandez-Garcıa et al. 2010; Kalogirou, 2004; Mills and Morrison, 2000; Singh et al. 1999; Winston et al. 2005]. The optical component is illuminated by 20 plane mirrors of equal size (50 mm x 1000 mm) that reflect the solar rays under various angles depending on the sunrays' inclination and on the relative positions of mirror and receiver [Fontani et al. 2015]. The secondary collector should then concentrate the solar light on a rectangular receiver of dimensions 50 mm x 10 mm [Fontani et al. 2015]. The secondary optics is placed as near as possible to the receiver to improve the collection efficiency, reduce the dimensions and avoid undesired shadow effects.

Several optical measurements and tests were effectuated on the implemented secondary concentrators. The tested optical components are a prismatic lens and a reflective concentrator [Abbas et al. 2012a, 2012b; El Gharbi et al. 2011; Fernandez-Garcıa et al. 2010; Kalogirou, 2004; Mills and Morrison, 2000; Singh et al. 1999]. The two elements are quite different because the working principle of the prismatic lens is based on refraction, while the other optics is based on reflection. The purpose of the laboratory tests is to study and characterize the optical properties and behaviour of the secondary optics in order to decide which is more suitable for improving the performance of the system. The two optical systems are compared in terms of collection efficiency and concentration factor, simulating the illumination arriving from the 20 mirrors at noon. In addition some image acquisitions are effectuated on the plane where the receiver will be placed, for a qualitative analysis of the illumination produced by the secondary optics on the receiver.

Tests and measurements are performed separately simulating the illumination of each plane mirror, being impossible to illuminate the samples in laboratory utilising 20 sources from different directions. The next phase is the data elaboration, for which it was chosen to perform the analysis at noon (as representative position, but the mirrors constantly move during the day). At noon the study can consider only 10 mirrors, exploiting the symmetry of the plant, and at noon there should be the maximum output of the solar plant. Hence it is interesting to compare the secondary optics behaviour in this particular moment of the day.

Angular aperture and incidence angle of the beam are the main factors that influence the collection efficiency of the secondary concentrator [Fontani et al. 2015]. Referring to Fig. 1, for the i-th mirror, the relevant parameters

doi:10.18086/swc.2017.18.06 Available at http://proceedings.ises.org

are:

- d: distance between mirrors line and receiver input (1000 mm).
- x_i: mirror position relative to the origin (fixed at the junction between the receiver normal passing through its centre and the mirrors line); measured positive to the right and negative to the left.
- D_i: distance between receiver centre and mirror centre.
- $\theta(t)$: sunlight incidence angle; measured from the normal to the mirrors line.
- $i_i(t)$: incidence angle of sunlight on the mirror; measured from the normal to the mirror.
- $\beta_i(t)$: tilt of the mirror; measured relative to the mirrors line.
- α_i: angle of the reflected beam; measured from the line of the mirrors.
- α'_i: incidence angle of the beam reflected on the receiver.

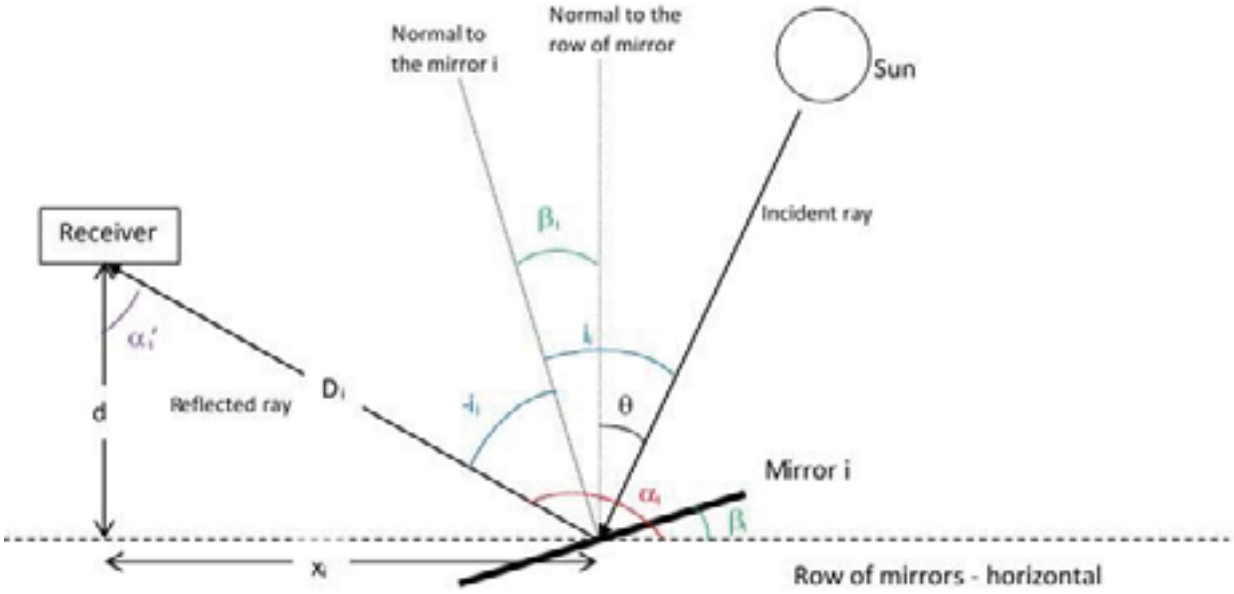

Fig. 1 – How the sunray is reflected by the primary system.

The sign of the angles is positive measuring counter-clockwise and negative measuring them clockwise.

For a given mirror, the angles i, β_i and θ are time dependent, while α_i must be constant to direct the beam toward the receiver. Referring to Fig. 1, the angles $i_i(t)$, $\theta(t)$, $\beta_i(t)$ and α_i are linked by 4 equations; so knowing α'_i (from the system geometry) and $\theta(t)$ (from the time of the day) α_i, $i_i(t)$, $\beta_i(t)$ can be derived [Fontani et al. 2015].

The collection efficiency of the receiver depends on how it is illuminated. For a single mirror the collection efficiency is defined as:

$$\eta_i\left(\alpha'_i, A_{eff,i}\right) = \frac{P_{out,i}(t)}{P_{in,i}(t)} \quad (1)$$

where $P_{out,i}(t)$ is the output power exiting from the receiver, and $P_{in,i}(t)$ the input power; α'_i is the entrance angle and $A_{eff,i}$ is the effective area of the beam entering into it. The input power is given by

$$P_{in,i}(t) = \bar{p}_i(t) \cdot A_{eff,i}(t) \quad (2)$$

where $\bar{p}_i(t)$ is the average power density of the beam at the receiver input.

The total collection efficiency (considering the contributions of all the mirrors) is

$$\eta = \frac{\sum_{i=1}^{20} P_{out,i}(t)}{\sum_{i=1}^{20} P_{in,i}(t)} \quad (3)$$

The concentration factor C_i for the i-th mirror is defined as:

$$C_i = \eta_i \frac{A_{in}^R}{A_{out}^R} \quad (4)$$

where A_{in}^{R} and A_{out}^{R} are respectively the physical area of receiver input and of receiver output.

Finally the total concentration factor C is given by:

$$C = \eta \frac{A_{in}^{R}}{A_{out}^{R}} \quad (5)$$

2. Measurement setup and procedure

The optical measurements are performed in a laboratory setup based on a solar divergence collimator, which produces a beam with solar divergence [Fontani et al. 2013]. Source, test sample and sensor are the principal components of the measurement system employed to optically characterize the samples of secondary collector. The scheme of the measurement set-up is reported in Fig. 2, with the pictures of the actual components as they are mounted on the optical table in laboratory.

The white beam emitted by the illuminator is angularly homogenized in the integrating sphere and comes out from the exit aperture of the sphere. Then the light is reflected by the collimation mirror, which generates a solar divergence beam. Suitable screens, to obtain a beam with dimensions adapted to illuminate the sample under test, finally cut this beam. The combination of the size of the sphere aperture with the focal length of the spherical mirror (collimation mirror) produces a uniform beam with solar divergence [Fontani et al. 2013].

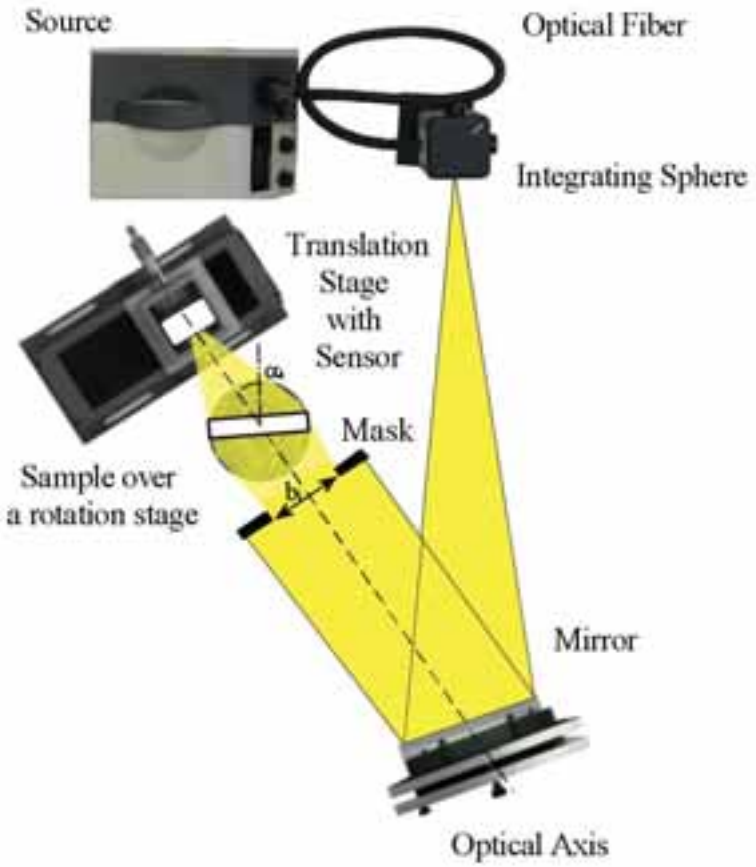

Fig. 2 – The optical system to test the secondary collectors.

The two secondary collectors examined are a prismatic lens and a reflective concentrator, specifically designed for the solar collection system of Fresnel mirror type.

The optical tests are executed with a reproducible procedure, identical for the two types of secondary optics. The final aim of this procedure of sample alignment and displacements is to reproduce the working conditions at noon

of the actual solar plant for which the secondary optics was developed.

Each examined sample is placed on a platform allowing rotation and translation with elevated precision and stability. The rotator has sensitivity of 0.025° and it permits to vary the incidence angle of the beam coming from the mirror. The micrometric translator allows to correct for the small difference between the rotation axis and the entrance of the secondary optics, so that the latter is always at the centre of the beam.

The acquisitions are of two types: photodiode measurements to obtain the collection efficiency or image acquisitions with a CMOS camera to know the light distribution in the image plane. The photodiode scan is a quantitative assessment, while the CMOS camera acquisition gives only qualitative information.

The main sensor is a photodiode with squared sensitive area of sizes 1 mm x 1 mm. The detector is mounted on a micrometric XY translating system, which allows to perform two-dimensional scans in a vertical plane (perpendicular to the optical axis, indicated in Fig. 2). Typically the examined vertical plane is the image plane of the secondary optics, where the optical design foresees that the collector creates its image. For these concentrators the photovoltaic (PV) receiver is placed in this plane and obviously the region of interest corresponds to the area of the receiver. The photodiode is connected to an amplifier, and the total amount of focused light, obtained by photodiode measurements, is used to calculate collection efficiency and concentration factor.

In addition to the photodiode scans, some image acquisitions are performed using a CMOS camera to know the light distribution in the image plane examined by the photodiode scans. The CMOS camera has sensitive area of size 7.74 mm x 10.51 mm. The camera is displaced with the same translation system used with the photodiode. The purpose is to assess the power density of the light focused on the receiver plane. This measurement gives information about uniformity of receiver illumination, which is a key parameter for obtaining the maximum conversion by the PV receiver.

A devoted LabVIEW program manages scansion and elaboration of measured signals for both sensors, allowing to select area and pitch of the scan. The mapping of the region of interest is automatically handled by this LabVIEW program that provides to move the shifters and to acquire the signal of the used sensor.

For the collection efficiency assessment with photodiode the procedure steps are listed below.

1) For a given time *t* the mirrors inclinations β_i for $\theta(t) = 0$ are known, consequently are obtained the angles α'_i of beam incidence on the receiver (10 in total, the other 10 correspond to $-\alpha'_i$), and the beam limiter widths.

2) Firstly a reference measurement is executed: the photodiode axis is aligned with the direction of the incident beam. It is performed a mapping of the beam incident on the receiver. The scanning is made on a plane perpendicular to the beam direction without the secondary optics.

3) The secondary optics is mounted, it is rotated up to the angle α'_i and the limiter opening is regulated.

4) Placing the photodiode in the measurement plane, the illuminated area is scanned to obtain a map, aligning the scan plane with the hypothetical plane of the PV cell. For the reflection concentrator, the detector is placed in the vicinity of the exit aperture. For the lenses, the detector is placed on the working plane, 50 mm from the rear surface of the lens. The shifters are moved with steps of 1 mm x 1 mm, in this way a direct and complete mapping of the image, with resolution limited by the detector size, is obtained.

5) steps 3) and 4) of the measurement procedure are repeated for all α'_i.

For the acquisition of images with CMOS camera the procedure is identical to the previous one, with the exclusion of the reference measurement, which is not needed in this type of acquisition since it is not a quantitative measurement. The scanning steps are in agreement with the CMOS sensor dimensions.

3. Data elaboration and results

The photodiode acquisitions are elaborated to calculate collection efficiency and concentration factor of the examined optical component.

The result of a scan with the photodiode is a two-dimensional matrix with dimension corresponding to the number of sampled points, and whose elements are the photodiode output current, which is proportional to the incident power. Since the sensitive area of the photodiode is 1 mm^2, these values can be considered as the power density

per mm^2.

The collection efficiency of the receiver is calculated using equations Eq. (1), Eq. (2) and Eq. (3). $P_{in,i}$ is given by Eq. (2), in which $\bar{p}$ is calculated by averaging the values of the scan on the incident beam. The effective area is rectangular: $A_{eff,i} = a \cdot b_i$. The receiver is always fully illuminated in the vertical direction, so a is constant for each measurement. The horizontal dimension (b_i) must be accurately calculated considering the projection (of length $l_{eff,i}$) of the receiver side (of length L_R) on the plane orthogonal to the beam axis [Fontani et al. 2015]. Each plane mirror (of length L_M) in the horizontal direction is seen with a length $L'_{eff,i}$, obtainable considering the projection effect and the beam divergence enlargement [Fontani et al. 2015].

Hence there are different situations of illumination. The receiver is fully illuminated (b_i data in bold in Tables 1-2) or it is partially illumined (b_i data in italics in Table 1). When it is entirely lighted $L'_{eff,i} > l_{eff,i}$ and $b_i = l_{eff,i}$, while in case of partial illumination $L'_{eff,i} < l_{eff,i}$ and $b_i = L'_{eff,i}$ [Fontani et al. 2015]. These quantities are visualized in Fig. 3.

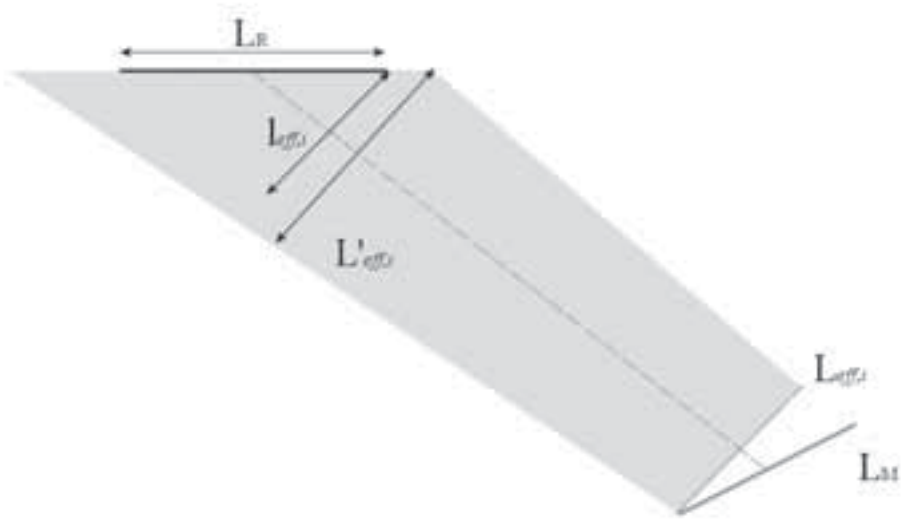

Fig. 3 – Effects on the beam.

Table 1 presents the measurement results for a reflection concentrator; whilst Table 2 reports the results measured on two samples of prismatic lens (denominated Lens1 and Lens2). The columns refer to: mirror tilt with respect to the mirrors line (β_i), incidence angle of the beam reflected on the receiver (α_i'), horizontal size of the effective area (b_i), and effective area ($A_{eff,i}$). The vertical size of the effective area is a.

From Table 1 it is clear that for the reflection concentrator there are some angles for which the beam does not completely enter in the receiver; in these cases the light collection is limited by the size of the receiver and not by the beam itself.

β_i (°)	α_i' (°)	b_i (mm)	$A_{eff,i}$ (mm^2)
0.759	1.518	**58.72**	2819
2.273	4.546	**58.69**	2817
3.774	7.548	**58.62**	2814
5.254	10.508	**58.52**	2809
6.707	13.414	*58.36*	2801
8.126	16.252	*57.60*	2765
9.504	19.008	*56.73*	2723
10.839	21.678	*55.76*	2676
12.126	24.252	*54.70*	2626
13.363	26.726	*53.59*	2572

Table – Effective area of the beam entering in the reflection concentrator as a function of the entrance angle, for a = 48 mm.

β_i (°)	α_i' (°)	b_i (mm)	$A_{i,eff}$ (mm^2)
0.759	1.518	**58.72**	2936
2.273	4.546	**58.69**	2934
3.774	7.548	**58.62**	2931
5.254	10.508	**58.52**	2926
6.707	13.414	**58.38**	2919
8.126	16.252	**58.22**	2911
9.504	19.008	**58.04**	2902
10.839	21.678	**57.83**	2892
12.126	24.252	**57.61**	2881
13.363	26.726	**57.37**	2869

Table 2 – Effective area of the beam entering in the prismatic lens as a function of the entrance angle, with a = 50 mm.

For the determination of P_{out} it is necessary to distinguish the two types of secondary optics.

For the reflection concentrator, the PV receiver is placed on the exit aperture and it collects all the light coming from it. Therefore, in this case P_{out} is obtained by integrating all the radiation collected in the scan.

For the lens, the PV receiver is placed at 5 cm distance. It will collect the light that falls directly on it and that is reflected from the lateral flaps. P_{out} is then obtained as the sum of these two contributions. The situation is illustrated in Figures 5 and 6. The radiation within the red rectangle is coming directly from the lens, while the radiation inside the yellow rectangles is reflected by the flaps. In any case, from the pictures of focused beam it can be noted that the light falls predominantly within the central band.

It is interesting to examine the values of efficiency and concentration obtained for the individual angles. The collection efficiency η_i is calculated using Eq. (1) while the concentration factor C_i is obtained from Eq. (4). Tables 3, 4 and 5 illustrate the results corresponding to each angle β_i (mirror tilt from the mirrors line); the columns report entrance angle α_i', collection efficiency η_i and concentration factor C_i.

β_i (°)	α_i' (°)	η_i	C_i
0.759	1.518	0.717	3.75
2.273	4.546	0.708	3.71
3.774	7.548	0.701	3.67
5.254	10.508	0.695	3.64
6.707	13.414	0.674	3.53
8.126	16.252	0.657	3.44
9.504	19.008	0.638	3.34
10.839	21.678	0.613	3.21
12.126	24.252	0.589	3.08
13.363	26.726	0.548	2.87

Table 3 – Collection efficiency and concentration factor varying the tilt angle, for the reflection concentrator.

β_i (°)	α_i' (°)	η_i	C_i
0.759	1.518	0.749	5.25
2.273	4.546	0.752	5.26
3.774	7.548	0.745	5.21
5.254	10.508	0.744	5.21
6.707	13.414	0.750	5.25
8.126	16.252	0.740	5.18
9.504	19.008	0.712	4.99
10.839	21.678	0.697	4.88
12.126	24.252	0.667	4.67
13.363	26.726	0.614	4.29

Table 4 – Collection efficiency and concentration factor varying the tilt angle, for the first sample of prismatic lens (Lens1).

β_i (°)	α_i' (°)	η_i	C_i
0.759	1.518	0.744	5.21
2.273	4.546	0.753	5.27
3.774	7.548	0.756	5.29
5.254	10.508	0.755	5.29
6.707	13.414	0.739	5.17
8.126	16.252	0.736	5.16
9.504	19.008	0.728	5.10
10.839	21.678	0.699	4.89
12.126	24.252	0.686	4.80
13.363	26.726	0.593	4.15

Table 5 – Collection efficiency and concentration factor varying the tilt angle, for the second sample of prismatic lens (Lens2).

Finally the total values are obtained by summing the contributions of all the examined angles, as Eq. (3) and Eq. (5) indicate.

Tables 6 summarizes the values of total collection efficiency and total concentration factor for all the examined samples of secondary optics designed for the solar plant with Fresnel mirror configuration. For the prismatic lenses two situations are considered, assuming that the reflectance of the lateral flaps could be equal to 90% or 75%, for helping to understand the influence of the flaps in the resulting performance of the component.

Secondary collector	Reflection of the flaps R (%)	total collection efficiency η	total concentration factor C
Reflection concentrator		0.656	3.43
Lens1	90	0.695	4.87
Lens1	75	0.663	4.64
Lens2	90	0.696	4.87
Lens2	75	0.664	4.65

Table 6 – Total values of collection efficiency and concentration factor for all the examined secondary optics.

1. Analysis in the image plane

The distribution of the radiation concentrated on the image plane of the secondary collector is accurately analysed to assess the level of uniformity of receiver illumination. The images in Figures 4-6 are obtained elaborating the measurements with the photodiode, and provide a schematic representation of the illumination produced by the 20 mirrors. The contributions of the various mirrors are calculated by summing the acquired maps and their specular copies (added in the elaboration phase).

The image of the reflection concentrator (Fig. 4) is simply obtained by summing the contributions of the various angles, given that it was possible to align the photodiode with the exit aperture of the reflection concentrator, and thus the analysed area was always the same.

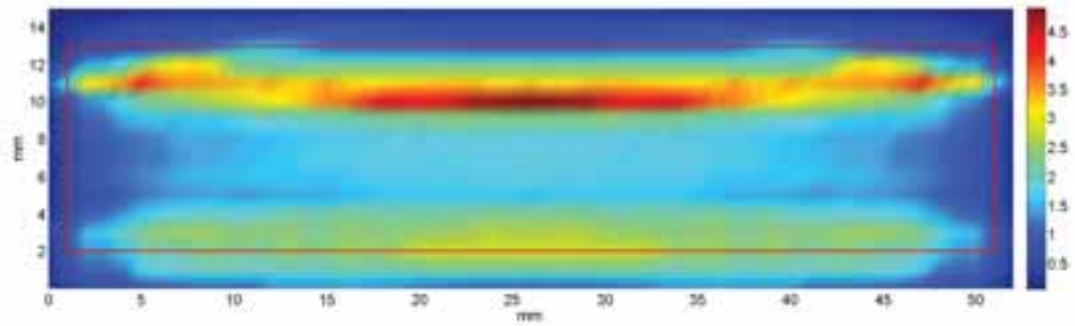

Fig. 4 – Elaboration in false colour of the power density (arbitrary units) on the image plane for the reflection concentrator.

The red rectangle in Fig. 4 denotes the area covered by the PV cell. It must be noted that this is not exactly the map of power density on the cell plane, because the measurement plane for Fig. 4 is about 2 mm behind it. Even

the light external to the rectangle is actually captured by the cell and contributes to the collection efficiency. The difference in intensity of the two horizontal bands at the edges of the rectangle can be attributed to a small vertical misalignment.

In Figures 5 and 6, in addition to the red rectangle of the cell, two side areas bounded by yellow lines are highlighted. The light that falls within these zones interacts with the lateral flaps of the collector and falls (attenuated) within the cell. For the evaluation of the collection efficiency it has been considered the contribution of the entire central band (with red zone and yellow zones). How the yellow zones contribute to the uniformity of illumination, however, depends on the interaction of the radiation with the flaps.

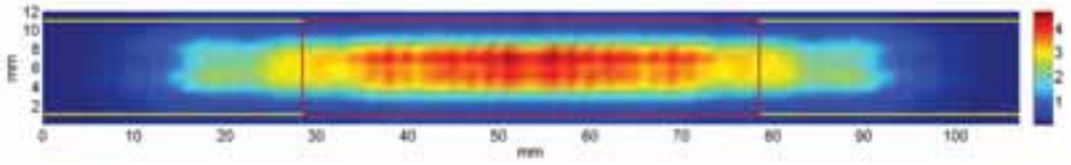

Fig. 5 – Elaboration in false colour of the power density (arbitrary units) on the image plane for Lens1.

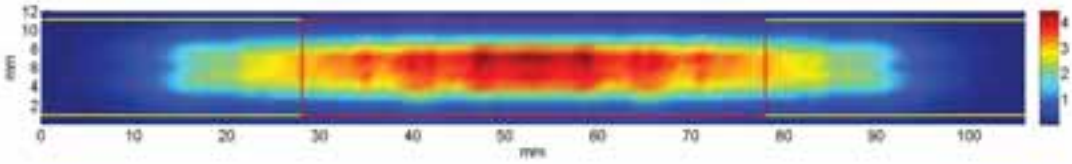

Fig. 6 – Elaboration in false colour of the power density (arbitrary units) on the image plane for Lens2.

The analysis is completed by the elaboration of the CMOS camera acquisitions. Due to the large size, the acquired images must be numerous and they must be accurately combined in order to obtain a final view of the illumination distribution.

As qualitative estimation, Figures 7 and 8 show the reconstructed images for reflection concentrator and prismatic lenses, respectively. Since fundamentally both lenses generate similar images, Fig. 8 shows only one image. It can be noted that the obtained images are in agreement with the results found with the photodiode.

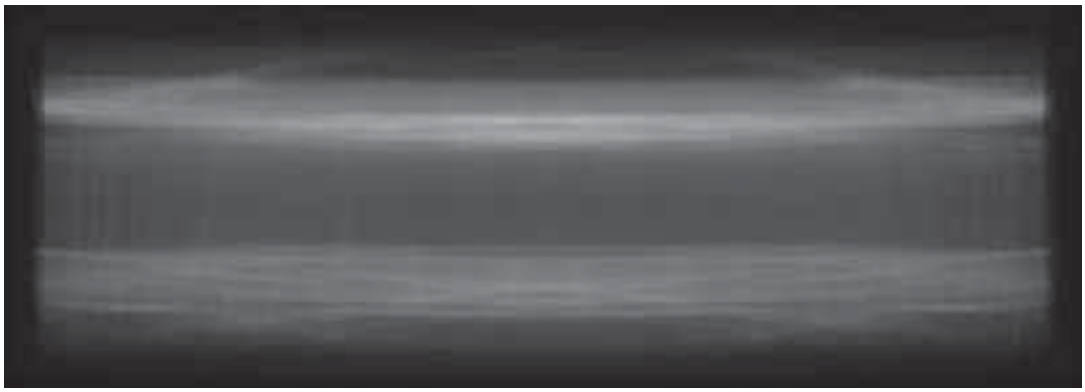

Fig. 7 – Image reconstructed for the reflection concentrator.

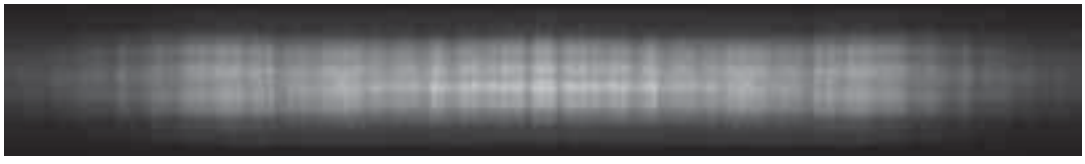

Fig. 8 – Image reconstructed for the prismatic lenses.

These reconstructed images serve only to have an idea of the distribution of the concentrated beam, which as it

can be seen in both cases is not homogeneous.

2. Conclusion

The purpose of this experimental work is to analyse the behaviour of two different secondary optics mounted near the focus of a solar collection system with a Fresnel mirror. An accurate analysis of the concentration layout and of the behaviour of the components inside the plant offered the possibility of performing in laboratory all the measurements simulating the behaviour of the single parts of the system. The contributions are then suitably combined to obtain collection efficiency and concentration factor of the entire solar plant.

The examined secondary optics are a prismatic lens and a reflection concentrator. These two types of secondary collector were optically designed for this solar plant, and samples of them were implemented. The tested secondary collectors are compared on the basis of their optical characteristics. The entrance area of the prismatic lens is larger than that of the reflective concentrator. The main comparison concerns total collection efficiency and total concentration factor of the secondary collector. These quantities are fundamental to understand the operation of the optical component and of the whole system for sunlight collection. The collection configuration is quite complicated and contains a large number of optical elements; therefore it was necessary to develop a special system for the calculation of collection efficiency and concentration factor. Another essential quantity to be analysed is the light distribution in the image plane of the secondary optics, because the level of uniformity of receiver illumination influences the photovoltaic conversion.

A specific experimental set-up was optically designed, implemented and aligned to perform the optical tests simulating the collection geometry of the existent plant. Having chosen to study the system at noon, there is symmetry with respect to the central axis of the system, so only half of the 20 mirrors were reproduced in laboratory. The procedure consists in performing the tests separately simulating the illumination of each mirror, finally combining the measured results. It was decided to perform the analysis at noon, considering that this hour usually corresponds to the maximum solar irradiation. In the actual plant the mirrors move during the day, thus for examining other day times 20 measurements are required and the inclination angles must be properly selected.

Two samples of prismatic lens and one sample of reflection concentrator are compared with an optical characterisation considering the inclinations of the mirrors at noon. The values of total collection efficiency (η) are very similar for all examined samples and they are around 0.66 – 0.69. The total concentration factor (C) is 4.6 – 4.9 for the prismatic lenses and 3.4 for the reflection concentrator. The higher value of C measured on the lenses is probably due to a larger entrance area of the prismatic lens with respect the other optics. In particular, specific tests verified that for some angles the beam does not completely enter into the reflective concentrator. To study the lighting distribution in the image plane of the secondary collector, the power density was computed from the photodiode measurements and some image reconstructions were obtained from the CMOS acquisitions. All these pictures evidence a quite uniform illumination of the receiver; only the two horizontal extremes show lower illumination levels.

The final results of this optical comparison are that the collection efficiency is comparable among all examined samples, while the concentration factor is higher for the prismatic lenses. Therefore, taking into account also that the entrance aperture of the prismatic lenses is larger with respect to the other, it can be concluded that the prismatic lens is a better performing secondary optics than the reflective concentrator. The characteristics of receiver illumination uniformity are analogous for both secondary collectors, which provide a focused image with elevated uniformity in the centre and some inferior light levels towards the right and left extremes.

Reminding that the presented study was carried out at noon, a more complete analysis should examine other hours of the day. Another interesting investigation could consider the angular limitations in order to control the losses, because the experimentation evidenced that there are some cases in which the reflection concentrator is not entirely illuminated.

3. References

Abbas, R., Montes, M.J., Piera, M., Martinez-Val, J.M., 2012. Solar radiation concentration features in Linear Fresnel Reflector arrays. Energy Conversion and Management 54, 133-144. (a)

Abbas, R., Muñoz, J., Martínez-Val, J.M., 2012. Steady-state thermal analysis of an innovative receiver for linear Fresnel reflectors. Applied Energy 92, 503-515. (b)

El Gharbi, N., Derbal, H., Bouaichaoui, S., Said, N., 2011. A comparative study between parabolic trough collector and linear Fresnel reflector technologies. Energy Procedia 6, 565-572.

Fernandez-Garcıa, A., Zarza, E., Valenzuela, L., Perez, M., 2010. Parabolic-trough solar collectors and their applications. Renewable and Sustainable Energy Reviews 14, 1695-1721.

Fontani, D., Sansoni, P., Sani, E., Coraggia, S., Jafrancesco, D., Mercatelli, L., 2013. Solar divergence collimators for optical characterisation of solar components. International Journal of Photoenergy 2013, 610173, 1-10.

Fontani, D., Sansoni, P., Francini, F., Jafrancesco, D., 2015. Comparison of two secondary optics for a Fresnel mirror. Proceedings of SolarPaces2015 – Cape Town, South Africa.

Kalogirou, S.A., 2004. Solar thermal collectors and applications. Progress in Energy and Combustion Science 30, 231-295.

Mills, D.R., Morrison, G.L., 2000. Compact linear Fresnel reflector solar thermal powerplants. Solar Energy 68, 3, 263-283.

Singh, P.L., Ganesan, S., Yadav, G.C., 1999. Performance study of a linear Fresnel concentrating solar device. Renewable Energy 18, 409-416.

Winston, R., Miñano, J.C., Benítez, P., Shatz, N., Bortz, J.C., 2005. Nonimaging Optics. Elsevier Academic Press, Amsterdam.

Energy Performance of a Solar Trigeneration System Based on a Novel Hybrid PVT Panel for Residential Applications

María Herrando[1], Alba Ramos[1], Ignacio Zabalza[2] and Christos N. Markides[1]

[1] Clean Energy Processes (CEP) Laboratory, Department of Chemical Engineering, Imperial College London, London (United Kingdom)

[2] School of Engineering and Architecture, University of Zaragoza, Zaragoza (Spain)

Abstract

The overall aim of this work is to assess the performance of high-efficiency solar trigeneration systems based on a novel hybrid photovoltaic-thermal (PVT) collector for the provision of domestic hot water (DHW), space heating (SH), cooling and electricity to residential single-family households. To this end, a TRNSYS model is developed featuring a novel hybrid PVT panel based on a new absorber-exchanger configuration coupled via a thermal store to two alternative small-scale solar heating and cooling configurations, one based on an electrically-driven vapour-compression heat pump (PVT+HP) and one on a thermally-driven absorption refrigeration unit (PVT+AR). The energy demands of a single-family house located in three different climates, namely Seville (Spain), Rome (Italy) and Paris (France), are estimated using EnergyPlus. Hourly transient simulations of the complete systems considering real weather data and reasonable areas for collector installation (< 30 m^2) are conducted over a year. The household energy demands covered by the two systems indicate that the PVT+HP configuration is the most promising for the locations of Rome and Paris, covering more than 74% the DHW demand, 100% of the space heating and cooling demands, as well as an important share of the electricity demand. Meanwhile, for Seville, the PVT+AR configuration appears as a promising alternative, covering more than 80% of the DHW, around 70% of the cooling and electricity, and 54% of the space heating demands.

Keywords: solar energy, hybrid PVT, heat pump, absorption cooling, residential energy, energy modelling

1. Introduction

The EU low-carbon economy roadmap (European Commission, 2011) concludes that it is possible to reduce the emissions in the build environment by around 90%, and that this would be a significant contribution towards achieving the 80% total emissions reductions relative to 1990 levels by 2050 without disrupting energy supplies. Meeting this commitment requires an increased generation of renewable energy in the built environment by clean and affordable technologies. Solar energy has the potential to play a leading role in delivering such a high-efficiency sustainable energy future, and is quickly approaching grid parity in high-irradiation regions. In addition, it is capable of satisfying both the electrical and thermal needs of buildings, by means of photovoltaic (PV) and solar thermal (ST) technologies, respectively. Especially where there are space constraints, hybrid photovoltaic-thermal (PVT) panels appear as highly suitable solutions, as these units combine the advantages of PV and ST systems while generating both electricity and a useful thermal output simultaneously from the same aperture area, and with a higher overall efficiency than separate stand-alone systems (Guarracino et al., 2016). Nevertheless, the wider use of PVT technology currently remains limited (Herrando et al., 2014), and it is of interest to consider and to improve aspects of this technology that would enable its further deployment.

Interestingly, PVT-water systems can have higher efficiencies by up to ~15% compared to PV while generating hot water suitable for domestic use (DHW) or for space heating (SH), and it is believed that this technology has an important potential in the residential sector (Affolter et al., 2005) that accounts for 25% of the total electricity and 30% of the total final energy consumption in the EU (Antonanzas et al., 2015), and where the heat demand accounts for 60-90% of the energy demand in buildings in cold climates, and 30-40% in warmer climates (Kempener et al., 2015). However, despite its potential, there are still very few companies worldwide commercialising this technology (Herrando and Markides, 2016), with most of the products available on the market not having optimised designs for PVT applications. In an attempt to overcome this barrier, previous work

doi:10.18086/swc.2017.18.07 Available at http://proceedings.ises.org

focused on the design and characterisation of novel absorber-exchanger configurations for flat-plate PVT collectors based on a flat-box structure (Herrando et al., 2016, 2017), which demonstrated promising results, specifically a ~4% higher optical efficiency and a ~16% lower heat-loss coefficient than an equivalent commercial sheet-and-tube PVT panel, also with a lower weight (close to 10%) and capital cost (about 20%). This novel PVT panel configuration is the one selected in the present work for further research.

One of the limitations of the integration of hybrid PVT systems in buildings for power and heating provision, especially in the residential sector, arises from the annual heat demand variations of these buildings, which in temperate climates such as in Mediterranean countries splits into an 75-80% demand for space heating and a remaining 20-25% for DHW, with the minimum demand being in summertime when the irradiation levels are high. To avoid oversizing/generation, an installation is typically sized to cover about 50% of the DHW load, such that the generated solar-thermal energy can only cover 10% of the total heating load of the building (del Amo, 2015). To avoid this limitation and use the surplus heat provided by the PVT panels for other building energy needs, the present work proposes integrating PVT panels with thermal storage and heat pumps (HPs) or absorption refrigeration (ARs) units, thereby allowing the generation of heating (SH and DHW), cooling and electricity from a single, affordable solar-energy system (IEA, 2012).

Solar cooling, in particular in domestic applications, is considered attractive because high solar irradiance levels are typically in phase with high building cooling demands, which have been and are projected to continue growing on a worldwide basis (Montagnino, 2017). Previous research has highlighted the fact that the relationship between the solar resource availability and the cooling demand is of key importance in obtaining accurate estimations of the potential of solar-cooling technologies (Mokhtar et al., 2010). At the same time, other recent studies have indicated that suitable solar-cooling technologies are currently associated with noteworthy challenges, including their limited performance and high cost (Bataineh and Taamneh, 2016). Ongoing research on a range of solar-cooling technologies has focussed on overcome these challenges.

Most studies found in literature propose the integration of heating/cooling technologies with concentrated PVT (Mittelman et al., 2007), or PVT-air systems (Eicker and Dalibard, 2011; Kamel and Fung, 2014). Instead, in the few studies found to date on PVT-water panels integrated thermally with AR units, the hot water generated by flat-plate PVT-water collector designs (which can reach around 80-90 °C), can be utilized as a heat source for the generator of the absorption unit, thus providing cooling to the household. Recent studies have shown that coefficients of performance (COPs) of up to 0.8 can be achieved by solar-driven single-stage LiBr-water absorption chillers (Bellos et al., 2016). Some authors (e.g., Calise et al., 2012; del Amo, 2014; Ramos et al., 2017) considered the integration of PVT-water collectors with AR units, and concluded that this combination has an important potential for energy savings owing to the generated heating, cooling and electricity.

Alternatively, vapour-compression heat pumps (HP) driven by the electrical output of PVT-water collectors can also be integrated with the thermal output of the same collectors, increasing the COP of this configuration in winter “heating mode”, while in summer the electrical output generated by PVT units can be used to run the HP unit to provide cooling. Most of the approaches for the hybridisation of HPs with solar collectors involve a simple combination of ST and PV conventional systems. The ST+HP combination was the first the concept developed as a parallel source for minimising the HP operation or with more complex architectures in order to take advantage of higher source temperatures for enhancing the HP performance. Examples are solar air heaters coupled with air-air HP or ST collectors coupled with water-water HPs. The higher potential of heat source side solutions requires sophisticated, robust and well-tuned control systems to achieve high solar fraction for annual basis figures (Drosou et al., 2014). Further, Xu et al. (2009) developed a photovoltaic-thermal heat pump (PVT-HP) system model, from which they concluded that almost all of the required heating load in winter months in Nanjing and Hong Kong (China) can be covered by using a variable compressor for the HP. Similarly, Kamel and Fung (2014) studied an air-PVT collector integrated in a roof and coupled with air source HP, where the warm air generated in the air-PVT acted as the source for heat production. These authors concluded that an important reduction in electricity costs to run the HP can be achieved when it is connected with PVT systems. The economic performance of a solar photovoltaic/loop-heat-pipe (PV/LHP) and HP system for domestic heating applications has also been studied, e.g., by Zhang et al. (2014), who identified local utility prices and renewable incentives to be critical for the implementation of these systems.

The interest in the PV+HP combination is a more recent development, mainly driven by the cost reduction of PV modules in the last years; boosted also by the power-to-heat trends, the combination of these electricity-based

technologies seems promising. A theoretical and experimental study of PV modules coupled with a solar assisted HP (SAHP) showed higher values of the HP COP as well as higher averaged PV efficiencies than separated units (Ji et al., 2008). However, the weakly coupled profiles of PV generation and HP consumption lead to an important distribution grid impact if they are not properly managed (i.e., through electrical storage), and thus in a high penetration scenario the ideal grid storage solution is not feasible (Protopapadaki and Saelens, 2017) due to grid operation and infrastructure oversizing needs.

This research aims to investigate the potential of domestic solar trigeneration systems based on hybrid PVT-water collectors for the provision of DHW, SH, cooling and electricity in residential single-family households.

2. Methodology

The most promising PVT panel identified in previous research (Herrando et al., 2016), based on a polycarbonate flat-box structure design, is connected to a HP or AR unit and a suitable thermal store, within a combined heating-cooling-electricity (trigeneration) system model in TRNSYS (Klein, 2016) (see Fig. 1). Two alternative system configurations are considered: 1) PVT integrated with a water-to-water reversible heat-pump/refrigeration unit fed by the electrical and/or thermal output of the PVT panel to provide heating/cooling; and 2) PVT integrated with a thermal absorption refrigeration unit (single-stage LiBr-water) fed by the thermal output of the PVT panel to satisfy the cooling demand in summer, plus a suitable thermal store. Innovative approaches in the PVT+HP configuration are studied such as the integration of the PVT thermal output with a water-to-water HP unit to increase its COP (see Fig. 1 left), and the optimisation of the tank size.

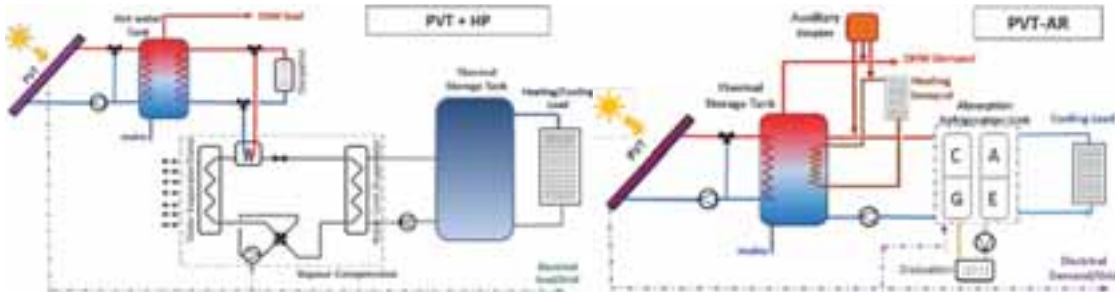

Fig. 1: Schematic diagrams of solar PVT panels integrated with (left) heat pumps, Configuration 1, and (right) absorption refrigeration units, Configuration 2.

2.1. Solar trigeneration system models

The core components of the solar trigeneration systems studied and modelled in this work are: i) the PVT collector, ii) a stratified water storage tank, iii) a closed loop with a water circulator pump that connects the PVT collector with the storage tank through an internal heat exchanger, iv) a HP unit (Configuration 1), v) an auxiliary heater, and vi) an AR unit (Configuration 2). The PVT collector, the stratified water storage tank, the HP and the AR unit models are described in detail below.

PVT collector

The novel PVT collector proposed and investigated in this work is based on a polycarbonate flat-box structure, which improves the heat transfer from the absorber to the fluid by means of 2×3 mm channels (Herrando et al., 2016). This main design features of this PVT collector are presented in Fig. 2.

Fig. 2: Schematic diagram of the novel PVT collector proposed in this work, based on a polycarbonate flat-box structure.

In order to model the proposed PVT collector, an existing PVT unit in TRNSYS (Type 560) is modified accordingly and the adjusted PVT model is validated against experimental data (Herrando, 2017). The PVT

collector has a nominal electrical power of 240 W_p and an aperture area of 1.55 m^2. The nominal electrical efficiency (η_{el}) of the PVT collector is 14.7%, and the temperature coefficient of the PV cells is 0.45 %/K. The thermal performance (η_{th}) of the collector is described by Eqs. 1 and 2 as follows,

$$\eta_{th} = 0.726 - 3.325 \cdot T_r - 0.0176 \cdot G \cdot {T_r}^2 \quad \text{(eq. 1)}$$

$$T_r = \frac{(T_{fm} - T_a)}{G} \quad \text{(eq. 2)}$$

where G is the total global solar irradiance on the surface at tilted angle (in W/m^2), T_{fm} is the mean fluid temperature and T_a is the ambient temperature.

Stratified water storage tank

A one-dimensional (1-D) model is used for the hot water storage tank (Type 534). The tank is assumed to consist of 6 fully mixed equal-volume segments that divide the cylinder along its vertical axis. The total mass of fluid in the tank is assumed constant, therefore the total mass flow-rate entering the tank through the inlet port must equal the total mass exiting the tank from the outlet port. For the stratification, a temperature gradient is preserved in the tank by ensuring that the hot water for DHW demand is supplied via a port at the top of the tank (at node n = 1), while replacement cold water from mains is introduced at the bottom (n = 6). The tank also has two immersed heat exchangers (HX): one connected to the PVT collector and another one to provide hot water to satisfy the SH demand (via radiant underfloor heating, UFH) to the household. In this second HX, water flowing in a separate closed loop circuit enters the heat exchanger coil (at node n = 4) at the UFH return temperature of 35 °C and is heated to a target supply temperature of 45 °C. This closed loop exits the tank at node n = 2. A bypass is included, to avoid sending fluid to the heat exchanger when the tank temperature is lower than 35 °C. In Configuration 1, the outlet of this second HX is connected to the HP to provide the target supply temperature when it is not reached within the tank, while in Configuration 2, a (gas-fired) auxiliary heater (nominal efficiency of 90.1% (BRE, 2014) is used. To satisfy the cooling demand, the reversible HP is used in Configuration 1, whereas in Configuration 2 the AR unit generator is connected to a second port leaving the tank at the top (n = 1) and entering at the bottom node (n = 6).

The storage tank volume is varied through the variation of the V_t/A_{cT} ratio, where V_t is the tank volume in litres and A_{cT} is the total PVT collector area in square meters. According to the Ministry of Housing of the Spanish Government (Gobierno de España, 2013), for solar thermal installations in households this range should be kept between $50 < V_t/A_{cT} < 180$. In this work, this recommendation has been considered for the 3 different locations under study. The size of the solar immersed heat exchanger coil also varies with the tank size, through the variation of the tank height, such that the ratio between the coil heat transfer area, and the total PVT collector area, is not lower than 0.15 (IDAE and CENSOLAR, 2009) to ensure adequate heat transfer. This HX enters the tank at the top (n = 1) and exits it at the bottom (n = 6).

Heat pump unit

In Configuration 1 (PVT-HP system), the PVT collector and the water storage tank are coupled with a single-stage water-to-water heat pump (HP) unit (Type 927). The heat pump conditions a liquid stream by rejecting energy to (cooling mode) or absorbing energy from a second liquid stream (heating mode). In heating mode, as detailed above, the inlet of the hot side of the HP is connected to the HX outlet of the water storage tank to raise the water temperature up to 45 ºC when required, while the inlet of the cold side of the HP is fed with water from mains, which is cooled down to absorb the energy required and transfer it to the hot side. In cooling mode, the cold side is cooling water from the mains to serve the cooling demand, while the hot side heats up the water from the bottom part of the tank to compensate the heat rejection on the cooling side; then the warm water is returned to the tank. Performance modelling of this HP unit is based on user-supplied data files containing catalogue-data for the normalised capacity and power draw, based on the entering load and source temperatures and the normalized source and load flow-rates (Klein, 2016).

Absorption refrigeration unit

In Configuration 2 (PVT-AR system), the PVT collector and the water storage tank are coupled with a single-effect absorption refrigeration (AR) unit (Type 107). The refrigeration cycle starts with LiBr-water pumped to the generator to be heated (using hot water from the top of the storage tank), as a result water is desorbed from this solution to vapour form as it is heated. Water vapour then flows to the condenser (cooling tower) where it is

condensed and rejects heat to the ambient. Condensed fluid then flows through an expansion device where the pressure is reduced and evaporated for the cooling effect (refrigeration or space cooling). The evaporated water is then absorbed into a strong LiBr solution in the absorber and the cycle is repeated. When the water exiting the top of the storage tank is lower than 65 ºC, an auxiliary (gas-fired) heater heats it up to ensure that it enters the AR unit at a temperature above 60 ºC (minimum temperature to start the cycle). Performance data of a commercial AR unit, Sonnen Klima-10 kW, is considered for the modelling of this unit (Mugnier and Sire, 2009). In addition, the data files are normalised so different AR unit sizes can be modelled.

2.2. Reference family house

To simulate the performance of the solar trigeneration system for domestic applications, a reference house is modelled in EnergyPlus (EnergyPlus, 2017) using real hourly weather data to estimate the energy demand in different months, including the thermal energy for space heating and DHW, the cooling demand, and electricity for lighting and other household appliances. The reference house is a semi-detached household with 2 floors with an area of ~58 m^2 each, a façade U-value of 0.26 W/(m^2·K), a roof U-value of 0.18 W/(m^2·K), and double-glazed windows. Typical occupancy profiles of a 4-inhabitant house (2 adults, 2 children) are considered, following the guidelines provided in the Spanish Building Code (Código Técnico de la Edificación) (Gobierno de España, 2013), which differentiates between working and non-working day, and provides loads and schedules for lighting and home appliances, as well as for occupancy, and the air renovations in the different months. Based on the aforementioned normative, the following temperature set-points are set: 20 °C primary and 17 °C secondary for space heating (January to May and October to December) and 25 °C primary and 27 °C secondary for air conditioning (June to September). As shown in Table 1, even though the same set-points and occupancy profiles are considered, due to the different weather conditions of the locations under analysis, considerably different space heating and cooling demands are estimated. The electricity demand (lighting and other household appliances) is relative similar between these three locations, and the small differences found are due to the lower lighting necessities while moving towards southern latitudes.

Tab. 1: Annual energy demand breakdown of the reference single-family house in the three different locations under analysis.

Location	DHW		Space Heating		Cooling		Electricity	
	kWh/year	kWh/m^2-year	kWh/year	kWh/m^2-year	kWh/year	kWh/m^2-year	kWh/year	kWh/m^2-year
Seville	942	8.19	668	5.81	2762	24.02	2603	22.63
Rome	942	8.19	2527	21.97	1327	11.54	2669	23.21
Paris	942	8.19	5373	46.72	529	4.60	2659	23.12

2.3. Methodology approach

The objective of the work presented in this paper is to analyse the performance of a solar trigeneration system based on the novel hybrid PVT panel described above. Two different configurations (PVT-HP and PVT-AR) are studied in three different climates: Seville (Spain), Rome (Italy) and Paris (France). For each of the former locations and for each different configuration, the sizing of the systems is undertaken as follows: i) the number of PVT collectors is selected after a parametric analysis to cover as much energy demand as possible (including DHW, SH, cooling and electricity), while minimising the excess of thermal energy and using reasonable areas (up to 29 m^2 area is considered available for the PVT collectors, which is half of the floor area of the reference house); ii) the tank size is selected as a trade-off to minimise the thermal energy excess while maintaining appropriate temperatures through the different nodes to satisfy the demand; iii) the PVT collector flow-rate selected for each location is that resulting in the highest percentage of the domestic energy demand covered from a previous parametric analysis, and in this analysis is kept constant over the year following previous conclusions (Herrando, 2017); iv) for the PVT-HP configuration, the size (nominal power) of the HP unit corresponds to maximum peak power required over the year (for both heating and cooling modes); this varies for each studied location; and v) and for the PVT-AR system the size of the AR unit corresponds to the peak cooling power required instantaneously, which also varies depending on the location.

The model for the PVT+AR configuration built in TRNSYS environment is presented in Fig. 3, with the element types indicated. The diagram presented in this figure has been simplified for clarity purposes. The main elements are the PVT panel, the water tank (thermal storage), the pumping system, the controller, the auxiliary heater and the AR unit. As it can be observed, DHW, SH, cooling and electricity demands are inputs to the model, as well as

the weather data. The main outputs are the electricity and thermal energy generated by the PVT panels, and the percentages of the household energy demands covered. The equivalent model built for the PVT+HP configuration is not presented here due to space constraints. Briefly, the PVT+HP model is built removing the AR unit, and its corresponding connections from the TRNSYS model presented in Fig. 3, and connecting the outlets of the two tee piece units in Fig. 3 with a new element, the HP unit (Type 927), which also needs a second controller unit (Type 2b) and second water tank (Type 4b), as indicated in Fig. 1.

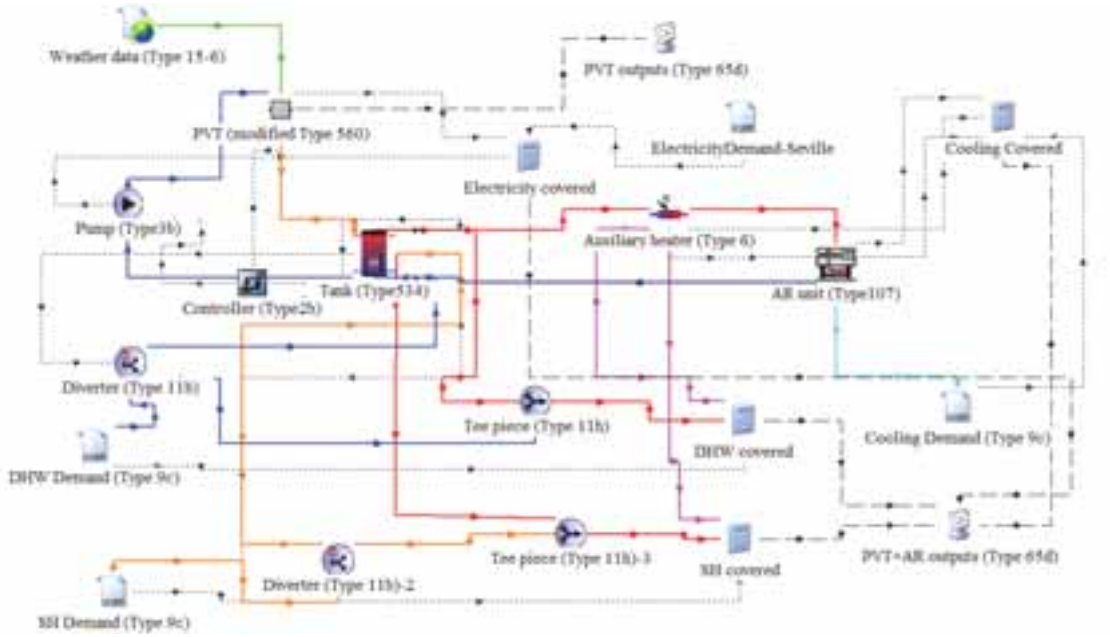

Fig. 3: Simplified model of the PVT+AR configuration built in TRNSYS environment.

Once each solar trigeneration system is sized for each of the aforementioned locations, an hourly transient simulation considering real weather data (Meteonorm Data Base, 2017) is conducted over a year, and the percentages of DHW, space heating, cooling and electricity demands covered are estimated. The modelled system, in all the locations and for both configurations, prioritises first of all DHW and SH demand, then cooling demand, and finally the electricity demand (corresponding to lighting and home appliances). For the results presented below, the family house is assumed to be connected to the electricity grid allowing the continuous exchange of electricity: i.e., electricity generation surplus is fed to the grid and when the PVT electricity generation is not enough to cover the instantaneous demand (deficit), this can be taken from the grid. However, this electricity exchange is only allowed until the electricity balance over a year is reached, that is, when the total annual electricity exported equals the total annual electricity imported to/from the grid.

3. Results and discussion

3.1 Solar trigeneration system configurations

For each of the selected locations and the two different configurations considered (PVT+HP and PVT+AR) a preliminary analysis is conducted, as indicated in the Methodology section, to size each system. In Table 2, the selected size of the storage tank together with the corresponding number of PVT collectors for each solar trigeneration system, based on an innovative polycarbonate flat-box PVT panel, are presented for Seville (Spain), Rome (Italy) and Paris (France). In addition, within the ranges of inlet and outlet temperatures considered for the HP and AR units, in the PVT+HP configuration an annual averaged COP of 4/5 is obtained in heating/cooling modes respectively; while for the PVT+AR configuration the annual averaged COP is 0.78.

On the basis of the solar trigeneration systems size presented in Tab. 2, hourly transient simulations over a year are conducted in TRNSYS software, and results and percentages of the energy demand (DHW, space heating, cooling and electricity) covered are discussed in the following subsections.

Tab. 2: Solar trigeneration systems size based on an innovative PVT collector for each particular location under analysis.

Location	Total PVT collector number / area	PVT collector flow-rate	Water storage tank volume	Peak heating/cooling power
Seville	6 / 9.3 m^2	50 L/h	0.54 m^3	3.9 kW/ 11.9 kW
Rome	12 / 18.6 m^2	50 L/h	1.08 m^3	4.6 kW/ 7.3 kW
Paris	18 / 27.9 m^2	30 L/h	1.08 m^3	5.2 kW/ 5.8 kW

3.2 Annually-integrated results in the selected locations

Annual results for the two solar trigeneration configurations, including the single-family house DHW, space heating (SH), cooling and electricity demand fractions covered in Seville, Rome and Paris are presented in Table 3. It is worth mentioning that the breakdown of the energy demand varies significantly from one location to another, as previously shown in Table 1; i.e., while the DHW demand is virtually the same in all the selected locations, it represents 1.4, 0.37 and 0.17 of the annual SH demand in Seville, Rome and Paris, respectively. Significant differences can also be found in the annual cooling/SH demand ratios between the mentioned locations, which take values of 4.13, 0.53 and 0.10, for Seville, Rome and Paris, respectively.

Tab. 3: Annual results for the two different solar trigeneration configurations, including percentages of DHW, space heating (SH), cooling and electricity demands covered of a reference single family house in three different locations.

Location	Configurations	DHW covered	SH covered		Cooling covered	Electricity Covered	
			PVT	HP$^+$		Inst.*	with excess$^+$
Seville	PVT+HP	90.0%	53.7%	100%	100%$^+$	24.5%	35%
	PVT+AR	81.9%	53.7%	-	71.4%	29.8%	70%
Rome	PVT+HP	87.7%	44.1%	100%	100%$^+$	27.2%	81%
	PVT+AR	86.9%	44.1%	-	96.9%	30.9%	126%
Paris	PVT+HP	74.3%	18.7%	100%	100%$^+$	25.1%	37%
	PVT+AR	73.4%	18.7%	-	85.8%	31.6%	124%

**Percentage of demand covered instantaneously at each time step, without grid interaction.*

$^+$*Percentage of demand covered considering that instantaneous surpluses of electricity exported to the grid can be used at other time step to cover a deficit of electricity.*

From the results summarised in Table 3, Configuration 1 (PVT+HP) appears as the most promising alternative in two of the locations (Rome and Paris), since percentages above 74% of DHW and 100% of the SH and cooling demand are covered; while with Configuration 2 (PVT+AR), similar percentages for DHW and slightly lower for cooling demand are covered, but instead less than 45% and 20% of the SH demand are covered in Rome and Paris, respectively. The case of Seville is significantly different, mainly due to the higher solar irradiance levels, thus the household has very small SH demand and quite high cooling demand. Therefore, in this location, the integration of the PVT collectors with an AR unit appears as a promising alternative because, although only around 54% of the SH demand is covered, the remaining percentage corresponds to a small amount of energy in absolute numbers (332 kWh/year), while the electricity covered with the PVT+AR is twice than the one covered with the PVT+HP configuration (1826 kWh/year *vs*. 915 kWh/year respectively).

3.2 Time-resolved weekly analysis of the systems in the selected locations

In this section, detailed results (weekly results on an hourly basis) are presented with the aim of understanding of the annual data presented in Table 3. A more detailed description of the energy performance of the most promising solar configuration at each of the selected locations is also included.

Solar trigeneration (PVT+AR) system integrated in the household located in Seville (Spain)

As shown in Table 3, the integration of the PVT collectors with an AR unit appears to be a promising alternative in Seville (Spain), as the AR unit uses the hot water generated by the PVT collectors in the summer months to satisfy the cooling demand, leaving a significant amount of electricity generated by the PVT collectors to satisfy the rest of the household's electricity demand. The later observation may seem not clear from the annual results presented in Table 3, where higher percentages of space heating and cooling are covered with the PVT+HP configuration. However, the PVT+AR configuration presents the additional advantage of covering double of the electricity domestic demand, since most of the cooling demand is covered by means of the PVT thermal output, thus avoiding excess of thermal energy that would be otherwise dumped to the ambient.

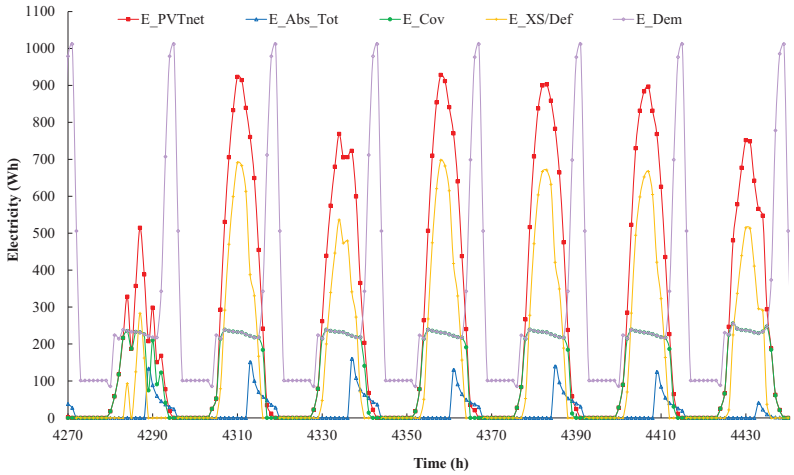

Fig. 4: Electricity generated by the PVT collectors (E_{PVTnet}), electricity consumed by the AR unit ($E_{Abs,Tot}$), electricity demand covered (E_{Cov}), electricity demand (E_{Dem}) and electricity excess/deficit ($E_{XS/Def}$) for the PVT+AR system located in Seville (Spain) during a summer week (28th June - 4th July).

Figures 4 and 5 show the hourly results of the PVT+AR system located in Seville detailed in Table 3 during a representative summer week (28th June - 4th July). It is observed that there is a clear mismatch between the profile of electricity generation (E_{PVTnet}) and that of the electricity demand (E_{Dem}), which implies that during the day all or most of the electricity demand is covered by the PVT+AR system (green circles in Fig. 4), with also an important excess of electricity (yellow pluses) that is exported to the grid. Meanwhile, at night the peak electricity demand (purple diamonds) is not covered. This gives rise to the difference in the percentage of electricity covered in Table 3, depending on whether only the electricity generated at each time step is considered ('Inst.' Column in Table 3) or whether it is assumed that the electricity exported to the grid at any time step can be used at other time step to satisfy the demand ('with excess' Column in Table 3).

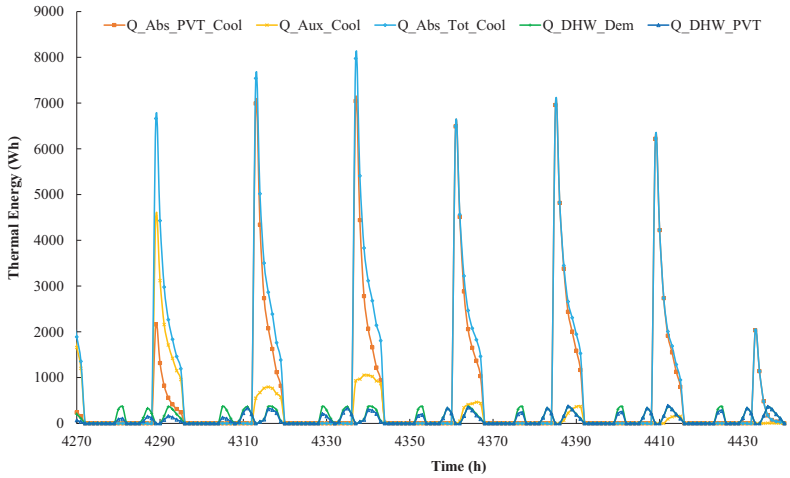

Fig. 5: DHW demand ($Q_{DHW,Dem}$), DHW demand covered by the proposed PVT+AR system ($Q_{DHW,PVT}$), thermal energy required by the AR unit to satisfy the cooling demand ($Q_{Abs,Tot,Cool}$), thermal energy provided by the proposed PVT+AR system to satisfy the cooling demand ($Q_{Abs,PVT,Cool}$) and auxiliary energy required to satisfy the cooling demand ($Q_{Aux,Cool}$) for the PVT+AR system located in Seville (Spain) over a summer week (28th June - 4th July).

In Fig. 5 we consider the thermal energy generation/consumption. From this figure, it can be seen that in the selected summer week most of the DHW demand can be covered by the proposed PVT+AR system (dark blue triangles and green pluses), as well as a significant part of the cooling demand (light blue diamonds and orange squares). It is observed that on the first day, due to the lower solar irradiance (which can be inferred from the electricity generated by the PVT panels in Fig. 4), the temperature reached at the top of the tank is not enough to feed the AR unit and to satisfy the cooling demand, so an important amount of auxiliary heat is need (yellow crosses). Conversely, later in the week, thanks to the increase in solar irradiance, more thermal energy is collected by the PVT collector array, leading to an increase in the storage tank temperature and thus a reduction in the

auxiliary energy required to heat the water that feeds the AR unit.

Solar trigeneration (PVT+HP) system integrated in the household located in Rome (Italy)

In the case of the household located in Rome (Italy), the results indicate that it is more appropriate to integrate the PVT collectors with a HP instead of with an AR unit, as this allows the system to cover all the space heating and cooling demands while also covering most of the DHW and an important fraction of the electricity demands, when the electricity excess at different time steps is considered ('with excess' Column in Table 3).

To compare the energy performance of the PVT+HP system with the PVT+AR system, the same summer week as in the case of Seville is shown in Fig. 6 below. In this case, only the electrical results are shown as the thermal outputs are the ones corresponding to the DHW demand and are very similar to those shown in Fig. 5. As before (in Seville, Fig. 5), a mismatch is observed between the electricity generated by the PVT panels and the household electricity demand. However, here, the cooling demand is satisfied by the HP, consuming electricity (see dark blue triangles), so there is less excess of electricity during the main cooling hours (early afternoon), while when the electricity generation decreases later in the day (red squares), there is a deficit of electricity (yellow crosses) that should be bought from the grid to cover the HP electricity consumption.

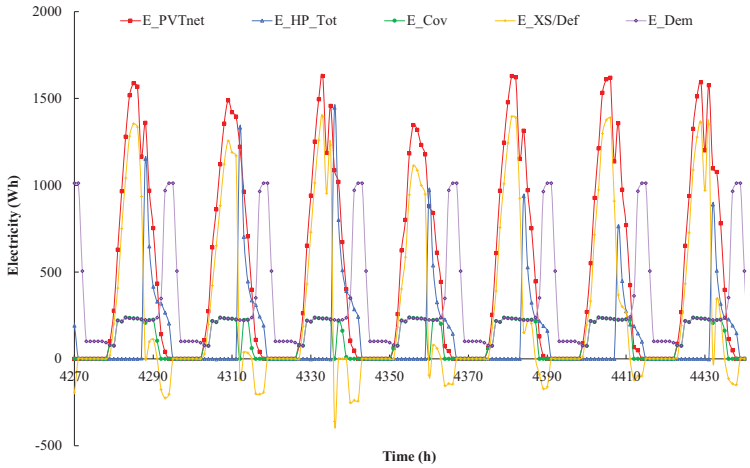

Fig. 6: Electricity generated by the PVT collectors (E_{PVTnet}), electricity consumed by the HP unit ($E_{HP,Tot}$), electricity demand covered (E_{Cov}), electricity demand (E_{Dem}) and electricity excess/deficit ($E_{XS/Def}$) for the PVT+HP system located in Rome (Italy) over a summer week (28 June - 4 July).

Solar trigeneration (PVT+HP) system integrated in the household located in Paris (France)

For the case of the household located in Paris (France), the results show once again that the most appropriate system configuration is the one that integrates the PVT collectors with a HP instead of an AR unit, which in this case allows the system to cover up to 100% of the space heating and cooling demands, while also covering most of the DHW demand; on the other hand, only 37% of the electricity demand is covered (see Table 3).

In this case, it is considered more relevant to show a representative winter week (27th January to 2nd February) since the cooling demand in Paris is small compared to that for space heating. In Fig. 7 one can clearly observe the mismatch between the profiles of the electricity generated by the PVT panels and that of the household electricity demand, while it can also be seen that the electricity demand (purple diamonds) is lower than the electricity needed by the HP to cover the SH demand (blue triangles) from morning to evening. In addition, despite the fact that the amount of electricity covered seems quite small (green circles), on an annual basis the instantaneous energy covered is around 668 kWh/year which, together with the annual excess of electricity (310 kWh/year), allows the system to cover 37% of the total domestic electricity need (assuming that the electricity exported to the grid at any time step can be used at other time step to satisfy the electricity demand).

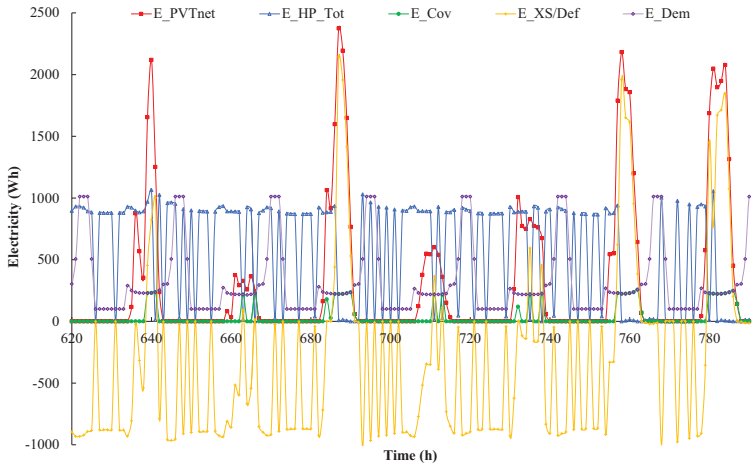

Fig. 7: Electricity generated by the PVT collectors (E_{PVTnet}), electricity consumed by the HP unit ($E_{HP,Tot}$), electricity demand covered (E_{Cov}), electricity demand (E_{Dem}) and electricity excess/deficit ($E_{XS/Def}$) for the PVT+HP system located in Paris (France) during a winter week (27 Jan. - 2 Feb.).

The total heating demand, including both DHW and SH, is presented in Fig. 8, together with the part of these demands covered directly by the PVT thermal-energy generation. From Fig. 7, the 4 days of the selected week that have relevant irradiance levels can be inferred (red squares), which allows the system to cover some percentage of the SH demand with the thermal PVT output on those days, especially in the evening (red squares on Fig 8). However, when the electricity generated by the PVT is used by the HP to cover the remaining SH needs (blue triangles in Fig. 7), 100% of the SH demand is covered (see Table 3).

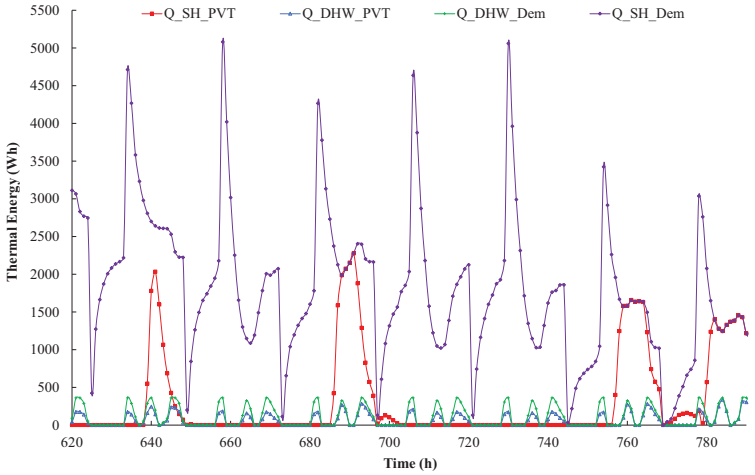

Fig. 8: Space heating demand ($Q_{SH,Dem}$), Space heating demand covered by the thermal output (hot water) of the proposed PVT+HP system ($Q_{SH,PVT}$), DHW demand ($Q_{DHW,Dem}$), DHW demand covered by the thermal output (hot water) of the proposed PVT+HP system ($Q_{H,PVT}$) for the PVT+HP system located in Paris (France) over a winter week (27 Jan. - 2 Feb.).

4. Conclusions

In this paper, the performance of high-efficiency solar trigeneration systems based on a novel hybrid photovoltaic-thermal (PVT) collector based on a flat-box structure for the provision of domestic how water (DHW), space heating (SH), cooling and electricity to residential single-family households is assessed. To this end, the energy demands of single-family houses located in three different climates, namely Seville (Spain), Rome (Italy) and Paris (France), are estimated using the engine tool EnergyPlus, and a TRNSYS model is developed featuring the hybrid PVT panel coupled via a thermal store in two alternative small-scale solar heating and cooling configurations to: 1) an electrically-driven vapour-compression heat pump (PVT+HP), or 2) a thermally-driven absorption refrigeration unit (PVT+AR).

Based on transient simulations over a full year on an hourly basis, it can be concluded that the proposed solar

configurations, PVT+HP or PVT+AR depending on the location, appear as an interesting solutions for the provision of solar DHW, SH, cooling, and electricity in residential buildings. Significant fractions of domestic energy demands can be covered with reasonable PVT collector-array areas. It is also concluded that the most promising solar trigeneration configuration for each location depends on the weather conditions (in particular solar irradiance levels) and the household energy demand profiles. The percentages of the different energy demands covered indicate that the PVT+HP configuration is the most promising alternative for the locations of Rome and Paris, covering 87.7% and 74.3% of the DHW respectively, 100% of the space heating and cooling demands in both locations, as well as 81% and 37% of the electricity demand, respectively. This is achieved with a PVT panels installed area of 18.6 m^2 in Rome and 28.9 m^2 in Paris. For the case of Seville, due to the higher solar irradiance levels and the significant cooling demand, the PVT+AR configuration arises as a promising alternative, with which it is possible to cover 81.9% of the DHW, 53.8% of the space heating, 71.4% of the cooling and 70% of the electricity demands, with a PVT panels installed area of 9.3 m^2. In this case, the PVT+AR configuration presents the advantage of covering double of the domestic electricity demand compared to the PVT+HP system, since most of the cooling demand is covered by means of the PVT thermal output, thus making more electricity available for other purposes that would otherwise have been required to run the HP. Furthermore, the use of the PVT thermal output in summer helps reducing the high temperatures that would be otherwise reached in the storage tank and would lead to heat being dumped to the ambient.

This work suggests that PVT trigeneration systems have an important potential in domestic applications, in particular in urban areas where space is at a premium, since both electrical and thermal outputs are generated from the same area. Still, for the benefits of this technology to be realised and for it to contribute meaningfully towards the envisaged renewable energy generation in the built environment, additional research on solar heating and cooling technologies is required into enhancing efficiency, solar resource use, and reducing costs.

Acknowledgements

This work was supported by the UK Engineering and Physical Sciences Research Council (EPSRC) [grant number EP/M025012/1]. Data supporting this publication can be obtained on request from cep-lab@imperial.ac.uk.

5. References

Affolter, P., Eisenmann, W., Fechner, H., Rommel, M., Schaap, A., Sorensen, H., Tripanagnostopoulos, Y., 2005. PVT roadmap: A European guide for the development and market introduction of PV-Thermal technology. Present. 20th Eur. Photovolt. Sol. Energy Conf. Exhib. 6, 10.

Antonanzas, J., del Amo, A., Martinez-Gracia, A., Bayod-Rujula, A.A., Antonanzas-Torres, F., 2015. Towards the optimization of convective losses in photovoltaic–thermal panels. Sol. Energy 116, 323-336. doi:10.1016/j.solener.2015.04.013

Bataineh, K., Taamneh, Y., 2016. Review and recent improvements of solar sorption cooling systems. Energy Build. 128, 22-37. doi:10.1016/j.enbuild.2016.06.075

Bellos, E., Tzivanidis, C., Antonopoulos, K.A., 2016. Exergetic and energetic comparison of LiCl-H2O and LiBr-H2O working pairs in a solar absorption cooling system. Energy Convers. Manag. 123, 453-461. doi:10.1016/j.enconman.2016.06.068

BRE, 2014. SAP 2012 The Government's Standard Assessment Procedure for Energy Rating of Dwellings. doi:10.1007/s13398-014-0173-7.2

Calise, F., D'Accadia, M.D., Vanoli, L., 2012. Design and dynamic simulation of a novel solar trigeneration system based on hybrid photovoltaic/thermal collectors (PVT). Energy Convers. Manag. 60, 214-225. doi:10.1016/j.enconman.2012.01.025

del Amo, A., 2015. Estudio, modelado y simulación de paneles solares híbridos con Cubierta Transparente y Aislante y validación experimental para su aplicación en sistemas de trigeneración. University of Zaragoza.

del Amo, A., 2014. Solar Trigeneration: a Transitory Simulation of HVAC Systems Using Different Typologies of Hybrid Panels. J. Sustain. Dev. Energy, Water Environ. Syst. 2, 1-14. doi:10.13044/j.sdewes.2014.02.0001

Drosou, V.N., Tsekouras, P.D., Oikonomou, T.I., Kosmopoulos, P.I., Karytsas, C.S., 2014. The High-Combi project: High solar fraction heating and cooling systems with combination of innovative components and methods. Renew. Sustain. Energy Rev. 29, 463-472. doi:10.1016/j.rser.2013.08.019

Eicker, U., Dalibard, A., 2011. Photovoltaic-thermal collectors for night radiative cooling of buildings. Sol.

Energy 85, 1322-1335. doi:10.1016/j.solener.2011.03.015
EnergyPlus, 2017. EnergyPlus software. URL: https://energyplus.net/ (accessed: 27.09.2017)
European Commission, 2011. Communication form the Commision: A Roadmap for moving to a competitive low carbon economy in 2050. COM(2011) 112 Final 34, 1-34. doi:10.1002/jsc.572
Gobierno de España, 2013. Orden FOM/1635/2013, Documento Básico DB-HE «Ahorro de Energía», del Código Técnico de la Edificación, Real Decreto 314/2006, Boletín Oficial del Estado.
Guarracino, I., Mellor, A., Ekins-Daukes, N.J., Markides, C.N., 2016. Dynamic coupled thermal-and-electrical modelling of sheet-and-tube hybrid photovoltaic / thermal (PVT) collectors. Appl. Th. Eng. 101, 778–795. doi:10.1016/j.applthermaleng.2016.02.056
Herrando, M., 2017. Analysis of Solar Hybrid PV-Thermal (PVT) Systems for Heat and Power Supply in Buildings. PhD Thesis. University of Zaragoza.
Herrando, M., Guarracino, I., del Amo, A., Zabalza, I., Markides, C.N., 2016. Energy Characterization and Optimization of New Heat Recovery Configurations in Hybrid PVT Systems, in Proceedings of: EuroSun 2016 International Conference on Solar Energy and Buildings, Palma de Mallorca, Spain.
Herrando, M., Markides, C.N., 2016. Hybrid PV and solar-thermal systems for domestic heat and power provision in the UK: Techno-economic considerations. Appl. Energy 161, 512-532. doi:10.1016/j.apenergy.2015.09.025
Herrando, M., Markides, C.N., Hellgardt, K., 2014. A UK-based assessment of hybrid PV and solar-thermal systems for domestic heating and power: System performance. Appl. Energy 122, 288-309. doi:10.1016/j.apenergy.2014.01.061
Herrando, M., Ramos, A., Zabalza, I., Markides, C.N., 2017. Structural characterization and energy performance of novel hybrid PVT solar-panels through 3-D FEM and CFD simulations, in Proceedings of: ECOS 2016 30th International Conference on Efficiency, Cost, Optimization, Simulation and Environmental Impact of Energy Systems, San Diego, California, pp. 1-12.
IDAE and CENSOLAR, 2009. Solar Thermal Energy Installations. Technical Specifications Document of Low Temperature Installations, IDAE.
IEA, 2012. Technology Roadmap: Solar Heating and Cooling. Paris (France).
Ji, J., Liu, K., Chow, T.T., Pei, G., He, W., He, H., 2008. Performance analysis of a photovoltaic heat pump. Appl. Energy 85, 680-693. doi:10.1016/j.apenergy.2008.01.003
Kamel, R.S., Fung, A.S., 2014. Modeling, simulation and feasibility analysis of residential BIPV/T+ASHP system in cold climate-Canada. Energy Build. 82, 758-770. doi:10.1016/j.enbuild.2014.07.081
Kempener, R., Burch, J., Navntoft, C., Mugnier, D., Nielsen, J.E., Weiss, W., 2015. Solar Heating and Cooling for Residential Applications. IEA-ETSAP and IRENA.
Klein, S.A., 2016. TRNSYS 17: A Transient System Simulation Program.
Meteonorm Data, 2017. Meteonorm Data Base. URL: http://www.meteonorm.com (accessed 20/7/09).
Mittelman, G., Kribus, A., Dayan, A., 2007. Solar cooling with concentrating photovoltaic/thermal (CPVT) systems. Energy Convers. Manag. 48, 2481-2490. doi:10.1016/j.enconman.2007.04.004
Mokhtar, M., Ali, M.T., Bräuniger, S., Afshari, A., Sgouridis, S., Armstrong, P., Chiesa, M., 2010. Systematic comprehensive techno-economic assessment of solar cooling technologies using location-specific climate data. Appl. Energy 87, 3766-3778. doi:10.1016/j.apenergy.2010.06.026
Montagnino, F.M., 2017. Solar cooling technologies. Design, application and performance of existing projects. Sol. Energy 1-14. doi:10.1016/j.solener.2017.01.033
Mugnier, D., Sire, R., 2009. SONNEN KLIMA package solution description. Solar Combi Plus.
Protopapadaki, C., Saelens, D., 2017. Heat pump and PV impact on residential low-voltage distribution grids as a function of building and district properties. Appl. Energy 192, 268–281. doi:10.1016/j.apenergy.2016.11.103
Ramos, A., Chatzopoulou, M.A., Guarracino, I., Freeman, J., Markides, C.N., 2017. Hybrid photovoltaic-thermal solar systems for combined heating, cooling and power provision in the urban environment. Energy Convers. Manag. doi:dx.doi.org/10.1016/j.enconman.2017.03.024
Xu, G., Deng, S., Zhang, X., Yang, L., Zhang, Y., 2009. Simulation of a photovoltaic/thermal heat pump system having a modified collector/evaporator. Sol. Energy 83, 1967–1976. doi:10.1016/j.solener.2009.07.008
Zhang, X., Shen, J., Xu, P., Zhao, X., Xu, Y., 2014. Socio-economic performance of a novel solar photovoltaic/loop-heat-pipe heat pump water heating system in three different climatic regions. Appl. Energy 135, 20–34. doi:10.1016/j.apenergy.2014.08.074

Mathematical Modeling of a Nano-Engineered Photovoltaic/Thermal (PV/T) System

M. Imtiaz Hussain[1] and Jun-Tae Kim[2,*]

[1] Green Energy Technology Research Center, Kongju National University, Cheonan (South Korea)

[2] Department of Architectural Engineering, Kongju National University, Cheonan (South Korea)

Abstract

Integrating photovoltaic (PV) cells with the solar thermal collector is found beneficial and attractive in the context of the simultaneous production of electricity and heat. Using nanofluid and air as the coolants, a transient mathematical model of a bi-fluid photovoltaic/thermal (PV/T) is developed. Experimental validation of the mathematical model is performed using results from the published work. For nanofluid, aluminum oxide (Al_2O_3) nanoparticles with different concentrations of 0.15 wt%, 0.3 wt%, 0.45 wt%, and 0.6 wt% were dispersed in a base fluid (pure water). The interdependence transient temperature responses of the PV/T collector components are simulated using MATLAB® software. The overall collector performance is predicted and compared when both fluids are to be operated independently and simultaneously. The simulation results indicate that when the fluids are operated simultaneously, the collector performance is better than the independent mode. It is observed that nanofluid & air based PV/T collector provides a higher performance in comparison with conventional heat exchanger systems used in this study.

Keywords: *Mathematical model, Bi-fluid PV/T, Nano-engineered, Model validation*

1. Introduction

A photovoltaic/thermal (PV/T) system possesses better solar harvesting ability in comparison with an individual solar thermal collector or Photovoltaic (PV) system (Hussain and Lee, 2015). Therefore, the PV/T collectors can generate more energy per unit surface area than that of conventional collectors. In a hybrid-PV system, the PV cells performance can be further improved by circulating appropriate heat transfer fluid across its surface. By considering this fact various types of heat transfer fluids having different thermophysical properties have been studied for the PV/T systems (Bhattarai et al., 2012; Rejeb et al., 2016). Water and air among them were the most frequently used cooling fluids (Imtiaz Hussain et al., 2015; Kim et al., 2014). Furthermore, the literature review shows that the rate of heat transfer between the absorber and circulating fluid can be enhanced by increasing the thermal conductivity of the base fluid. The thermal conductivity of the coolant is improved by dispersing nano-sized metallic, metal oxides and nanotube particles in the base fluid. Therefore, application of nanofluid as a coolant for the PV/T system seems to be more promising.

Since the mid-1970s, when the research on the PV/T system started many researchers focused their efforts to improve its performance to get maximum possible thermal and overall efficiency. Chow (2003) proposed an explicit dynamic model that can predict the PV module and circulating fluid temperatures even under rapidly fluctuating solar radiation. Rejeb et al. (2016) evaluated the effect of nanofluid as a heat transfer fluid on the performance of the PV/T system. Among various colloidal solutions, the suspension of copper nanoparticles in pure water provided higher overall energy efficiency compared to alumina. Simultaneous application of two fluids as the heat transfer fluids for the PV/T system offer a great range of benefits in terms of a higher thermal and electrical output. As mentioned by Abu Bakar et al. (2014), the dual fluids based PV/T system was first built and tested by Tripanagnostopoulos (2007). For the purpose of heat extraction improvement, the PV module was integrated with water or air heat extraction elements. Thenceforward, further studies on the effectiveness of the bi-fluid PV/T design was carried out by applying low cost modifications such as introducing serpentine-shaped copper tube as the water heat extraction element transverse to the air flow and fins in the air channel parallel to the air flow direction (Abu Bakar et al., 2014; Jarimi et al., 2016). According to published literature, no previous study using nanofluid and air as the heat extraction fluids for PV/T system has been reported.

doi:10.18086/swc.2017.18.08 Available at http://proceedings.ises.org

This study suggests a transient mathematical model of a bi-fluid PV/T system with the novelty lies in design and the heat extraction components in which nanofluid along with air is introduced. This research seeks to overcome the challenges and gaps to develop a bi-fluid based PV/T system which can significantly decrease PV cells temperature and increase the overall performance of the system.

2. Design concept

A novel bi-fluid PV/T system mainly consisted of standard off the shelf mono-crystalline PV module, copper pipes as the nanofluid heating component, and a single pass air duct as the air heating component. Schematic diagram of the nano-engineered bi-fluid PV/T system is shown in Fig. 1. The flow paths for the nanofluid and air are designed in such a way that there is no physical interaction between two fluids. However, interdependence heat exchange occurs across both heat exchanger components. In order to improve heat transfer rate to the flowing air, the surfaces of the nanofluid carrier pipe and the PV panel are taken as matt black. To heat transfer improvement, a set of baffles is introduced transverse to the direction of airflow. The parallel-arranged fluid carrier pipes are attached directly to the PV module back surface instead of using absorber plate. This direct coupling of PV module with nanofluid heating component results in a decrease of thermal resistance and an increase of heat transfer rate between the PV surface and circulating fluids.

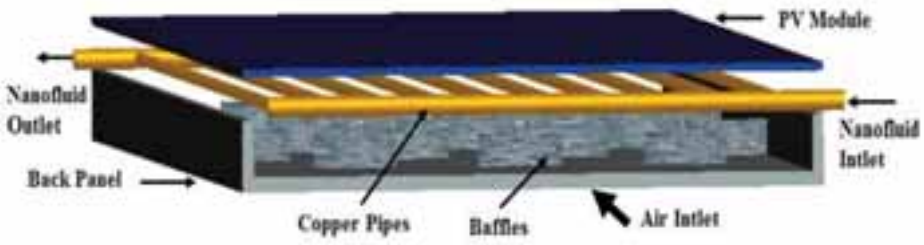

(a)

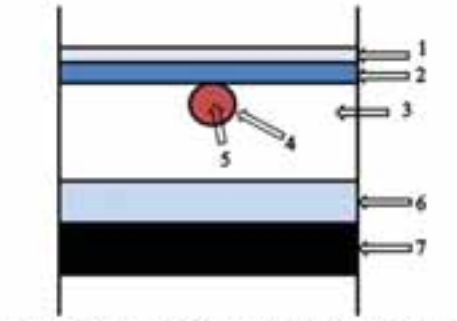

(b)

Fig. 1: (a) Three dimensional view (b) Cross-section view of the bi-fluid PV/T system.

Tab. 1: Parameters for simulation

Description		Value	Description		Value
PV module (length & width)	L & W	1.62 m & 0.98 m	Pipe Density	ρ_t	2702 kg/m^3
PV absorptivity	α_p	0.9	No. of tubes	-	9
PV emissivity	ε_p	0.88	Pipe spacing	-	0.11m
PV specific heat	C_p	900 J/kgK	Back panel Density	ρ_b	20 kg/m^3
PV reference efficiency (%)	η_r	17.3	- Panel Specific heat	C_b	670 J/kg K
Packing factor	P	-	- Panel Thermal conductivity	K_b	0.034 W/m K
Temperature coefficient	β_r	0.0045/°C	Aluminum oxide	Al_2O_3	-

Pipe inner diameter	D_i	0.008 m	Al_2O_3 Thermal conductivity	-	30 W/m K
Pipe thickness	δ_t	0.0012 m	Al_2O_3 Specific heat	-	773 J/kg K
Pipe Specific heat	C_t	903 J/kgK	Al_2O_3 Density	-	3890 kg/m^3

3. Mathematical model

A model based on conservation of energy of bi-fluid PV/T system components is developed and analyzed in transient conditions using ODE solver in MATLAB®. Details of simulation parameters and thermo-physical properties are presented in Table 1. To evaluate the electrical and thermal performances of a bi-fluid PV/T system, heat balance equations for different components such as PV module, copper pipes, nanofluid, circulating air, and back panel are presented as follows:

For PV

$$M_pC_p(dT_p/dt) = G\alpha_p - E - h_{wind}A_{p\infty}(T_p - T_\infty) - h_{p\infty}A_{p\infty}(T_p - T_\infty) - h_{pt}A_{pt}(T_p - T_t) - A_{pa}\,h_{pa}(T_p - T_a) - h_{pb}A_{pb}(T_p - T_b) \quad \text{(eq. 1)}$$

$$E = GP\eta_e \quad \text{(eq. 2)}$$

For copper pipe

$$M_tC_t(dT_t/dt) = h_{pt}A_{pt}(T_p - T_t) - A_{tn}\,h_{tn}(T_t - T_n) - A_{ta}\,h_{ta}(T_t - T_a) - h_{tb}A_{tb}(T_t - T_b) \quad \text{(eq. 3)}$$

For nanofluid in pipe

$$M_nC_n(dT_n/dt) = \dot{m}_nC_n\,(T_{n,o} - T_{n,in}) + A_{tn}\,h_{tn}(T_t - T_n) \quad \text{(eq. 4)}$$

For inside air

$$M_aC_a(dT_a/dt) = \dot{m}_aC_a\,(T_{a,o} - T_{a,in}) + A_{pa}\,h_{pa}(T_p - T_a) + A_{ta}\,h_{ta}(T_t - T_a) + h_{ab}A_{ab}(T_a - T_b) \quad \text{(eq. 5)}$$

For back panel

$$M_bC_b(\partial T_b/\partial t) = h_{tb}A_{tb}(T_t - T_b) + h_{pb}A_{pb}(T_p - T_b) + h_{ab}A_{ab}(T_a - T_b) - h_{b\infty}A_{b\infty}(T_b - T_\infty) \quad \text{(eq. 6)}$$

where, G, α_p, E, and P are the solar radiation, the absorptivity of PV cells, electrical power and packing factor, respectively. M, C, T, A, $\dot{m}$, and h are the mass, specific heat, temperature, surface area, mass flow rate and heat transfer coefficient, respectively. The subscripts p, t, n, a, b, and ∞ are denoted the PV, copper pipe, nanofluid, inside air, back panel insulation and ambient air, respectively. The subscripts p∞, pt, pa, tn, ta, ab, tb, pb, and b∞ are denoted the heat transfer contacts between the PV and ambient air, PV and pipe, PV and inside air, pipe and nanofluid, pipe and inside air, back panel and inside air, back panel and pipe, back panel and PV, and back panel and ambient air, respectively. The subscripts in and o are denoted fluid inlet and outlet, respectively. The electrical, thermal and primary energy saving efficiencies of dual-fluid PV/T systems are calculated using following expressions (Baljit et al., 2017):

$$\eta_e = \eta_r[1 - \beta_r(T_p - T_r)] \quad \text{(eq. 7)}$$

$$\eta_{th} = \frac{\dot{m}_nC_n\,(T_{n,o} - T_{n,in}) + \dot{m}_aC_a\,(T_{a,o} - T_{a,in})}{A_cG} \quad \text{(eq. 8)}$$

$$\eta_{PVT} = \eta_{th} + \eta_e/\eta_{pp} \quad \text{(eq. 9)}$$

where, β_r and A_c are the solar cells temperature coefficient and collector area, respectively. η_r is the efficiency of the solar cells at a reference temperature (T_r). η_e, η_{th} and η_{PVT} are the electrical, thermal and primary energy saving efficiencies, respectively. η_{pp} is the power generation efficiency of the conventional power plant.

4. Results and discussions

4.1. Model validation

Model validation of a proposed PV/T system is performed in two steps, at first the nominal operating cell

temperature (NOCT) of the PV module is predicted using model and then validated against NOCT value obtained from manufacturer's datasheet e.g. 47 °C (PV-MJU240GB). The percentage difference between predicted and datasheet value is less than 1.8%. Second step is a validation of thermal component of air heating against the experimental data (Table 2) for unglazed PV/T air heating system presented by Joshi et al. (2009). To ease the comparison, the nanofluid flow rate is set to be zero. During simulation, similar design and environmental conditions are considered, as presented in (Joshi et al., 2009), other information which is not given in this research were taken from the study by Abu Bakar et al. (2014).

Tab. 2: Simulated values by model against experimentally measured data by (Joshi et al., 2009)

Time (hour)		8	9	10	11	12	13	14	15	16	17
PV cells temperature (°C)	Exp	37.60	41.40	47.90	50.40	54.90	54.70	52.90	50.70	47.20	42.30
	Sim	38.01	41.65	48.52	50.85	55.70	55.50	53.58	51.32	47.79	42.66
Outlet air temperature (°C)	Exp	33.20	36.30	38.90	41.70	46.10	41.50	46.40	44.50	43.00	40.30
	Sim	33.59	36.71	39.33	42.21	46.69	42.11	46.91	44.12	43.49	40.77

Using validated model, the overall performance of a bi-fluid PV/T system is evaluated under different modes of fluid operation. During independent mode, one of the heat extraction fluids is kept stagnant, while other fluid is operated at a designated flow rate. For the simultaneous mode of fluids operation, both fluids are operated at the same time. During simulation, all heat transfer coefficients were calculated in real time.

4.2. Simulation results

To locate the best concentration, different weight fractions of Al_2O_3 nanoparticles in a base fluid have been considered. Generally, a variation of nanoparticles concentration affects directly the thermo-physical properties (thermal conductivity and specific heat in particular) of the colloidal solution, and hence the heat transfer rate. Variation of daily solar radiation and ambient temperature are shown in Fig. 2. Influence of Al_2O_3 nanoparticles concentration on the thermal conductivity ratio and specific heat ratio is shown in Fig. 3. Increasing the nanoparticles (np) concentration in the base fluid (bf) increases the thermal conductivity and decreases the specific heat of the Al_2O_3 nanofluid. It is observed that the thermal conductivity ratio (knp/kbf)) increased to 1.162 and the specific heat ratio (Cnp/Cbf) decreased to 0.954 when the Al_2O_3 weight fraction increased from 0 to 0.75 (wt%). This can be attributed to the higher thermal conductivity and lower specific heat of the Al_2O_3 nanoparticles compared to water as the base fluid.

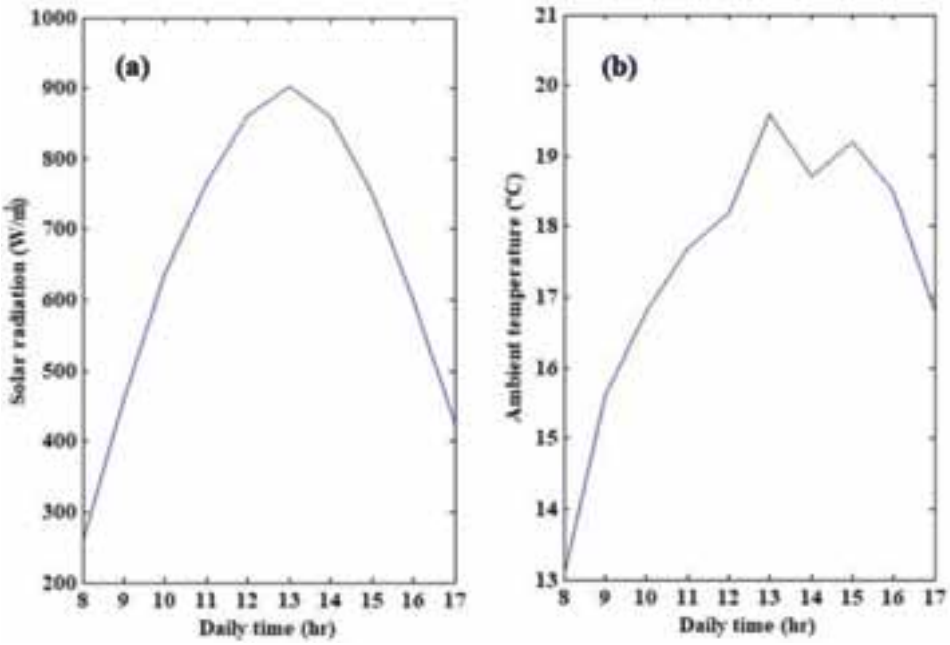

Fig. 2: Daily variation of (a) solar radiation (b) ambient temperature

The PV cells temperature has been predicted using different working fluids both simultaneously and independently. Fig. 4 depicts the PV cells temperature under different modes of fluid operation namely: Al_2O_3/air, water/air, nanofluid, air, and without the heat transfer fluid. Compared to the PV temperature obtained without working fluid (69.4 °C), the average PV temperature drop by 7.8, 9.2, 11.3, and 13.6 °C when either one or two fluids are operated such as air, Al_2O_3 nanofluid, water/air, and Al_2O_3/air, respectively. It is worth to note that introducing bi-fluid heat extraction component, in particular, Al_2O_3/air, underneath the PV module increases not only its electrical efficiency but also produces high-temperature heat at the same time.

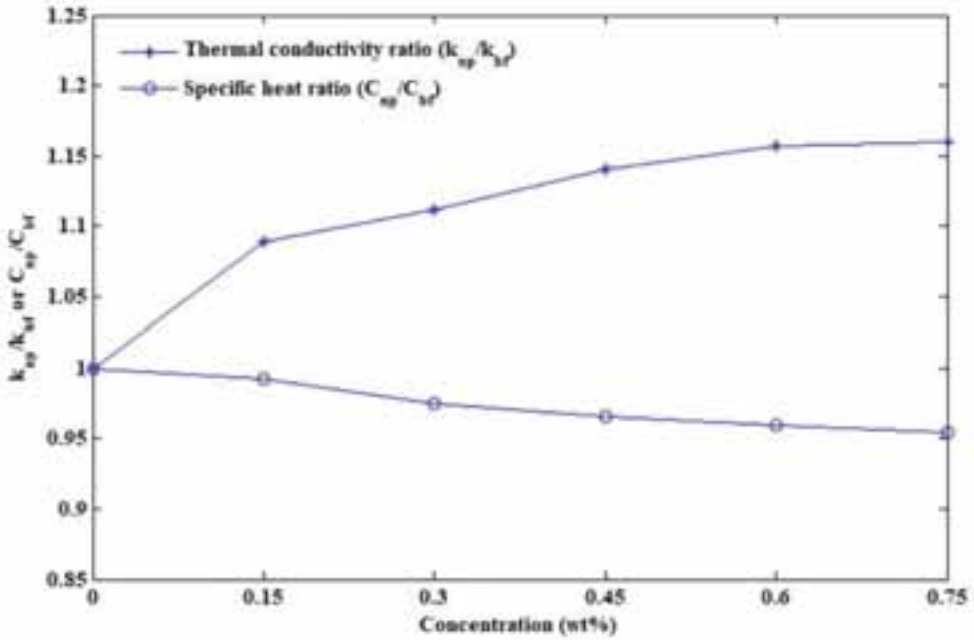

Fig. 3: Variation of thermal conductivity ratio and specific heat ratio of Al_2O_3 with concentration (wt%).

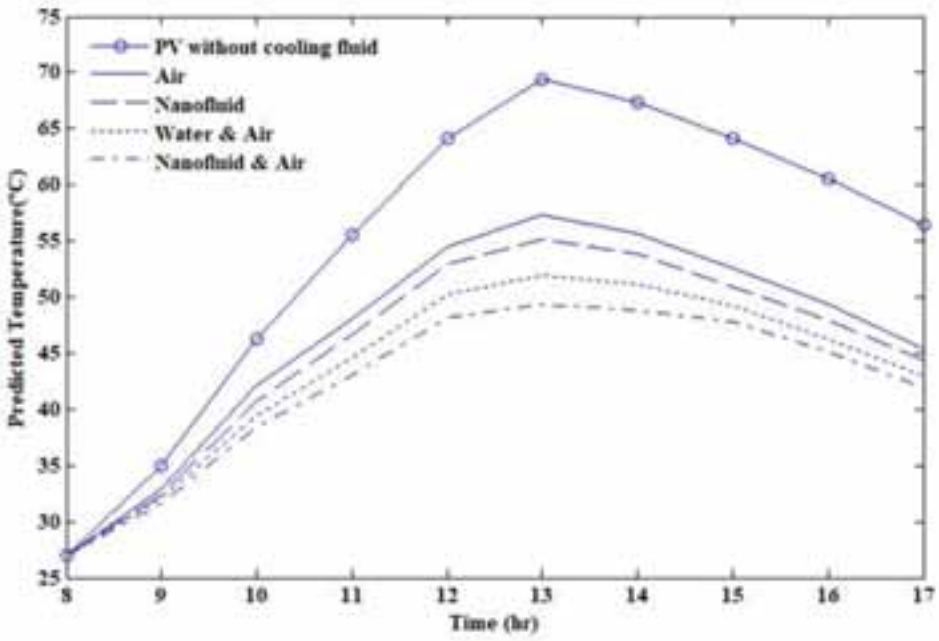

Fig. 4: Predicted PV temperature using different coolant fluids and modes of fluid operations.

The effect of different modes of fluid operation on the daily total efficiency of a PV/T system is observed by varying nanofluid or water flow rate at a fixed air flow rate of 0.05 kg/s (Fig. 5). The total efficiency of the bi-fluid PV/T system is considerably higher than the system with a single heating component. The simulation results show that the overall energy efficiency of a Al_2O_3/air based PVT was found significantly higher than that

of the cases with water/air and nanofluid heat exchanger systems, owing to additional thermal and electrical energy produced. The use of nanofluid as a heat extraction component for PV/T system provides excellent overall energy performance in comparison with either water or air.

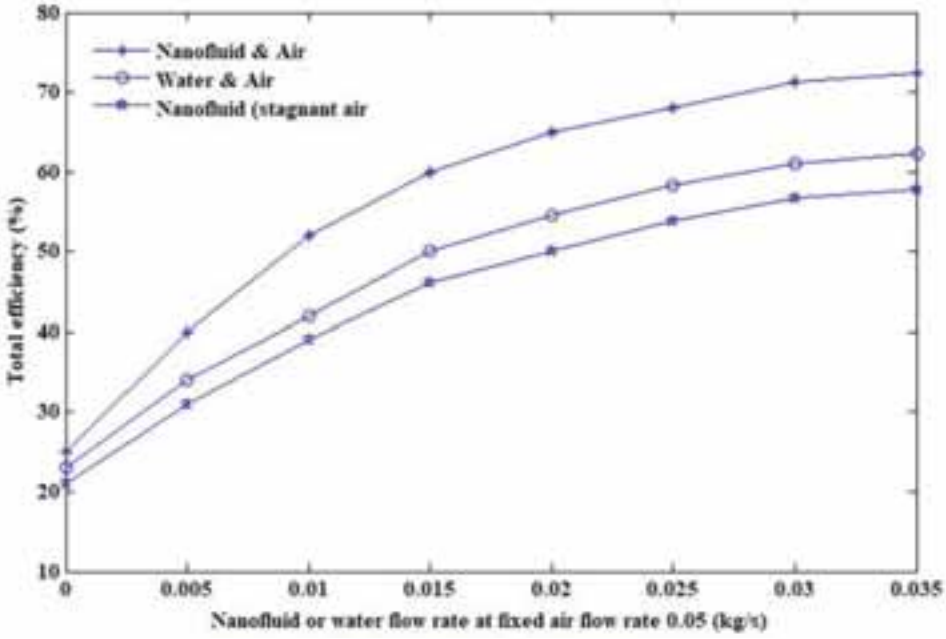

Fig. 5: Total PV/T efficiency with varying nanofluid or water flow rate at fixed air flow rate of 0.05 kg/s.

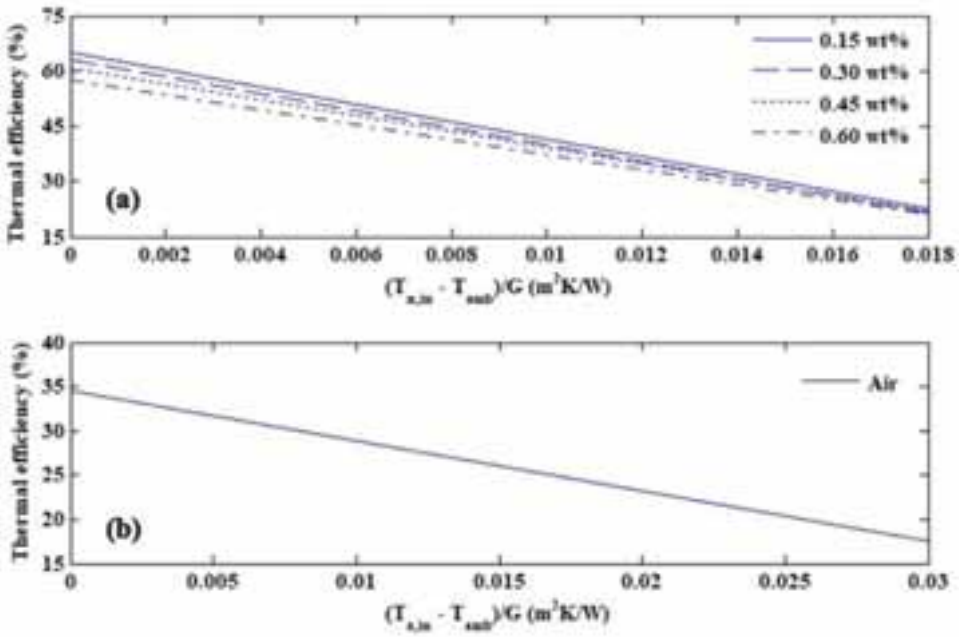

Fig. 6: PV/T thermal efficiency (a) with different concentration of Al_2O_3 at stagnant air (b) with varying air flow rate at stagnant nanofluid.

Even though the model is developed considering dual-fluid heat exchangers for the dual-fluid PV/T system. However, by setting one of the fluids in stagnant mode, the given model can also be used for a single fluid operation. Fig. 6 compares the thermal efficiency of the PV/T system with Al_2O_3 nanofluid and air at zero reduced temperature. In addition, the influence of nanoparticle concentrations on the collector performance is also investigated, as shown in Fig. 6a. In this paper, four nanofluid concentrations (0.15 wt%, 0.3 wt%, 0.45 wt%, 0.6 wt%) were selected to investigate. It is observed that the zero-loss thermal efficiencies of the PV/T system with Al_2O_3 nanofluid and air were found to be 65.3% and 34.5%, respectively. Furthermore, the thermal

efficiency of the PV/T system increases with increasing the weight fraction of Al_2O_3 nanoparticles in the base fluid. It should be noted that changing the nanoparticles concentration from 0.15 to 0.6 wt% results in a thermal efficiency enhancement from 58% to 65.3%, respectively. The higher thermal efficiency of PV/T system with nanofluid as a coolant can be explained by an improvement of thermal conductivity of the base fluid by dispersing nanoparticles (Sharma et al., 2017). Thus, enhancement of heat transfer coefficient between the absorber and circulating fluid is observed.

In order to evaluate the overall performance of a nano-engineered dual-fluid PV/T system, it is important to investigate the effects of the simultaneous fluid operation on primary energy saving efficiency. Influence of variable mass flow rate of Al_2O_3 nanofluid (at fixed air flow rate) and air (at a fixed nanofluid flow rate) on the primary energy saving efficiency is shown in Fig. 7. Increasing the nanofluid flow rate from 0.005 to 0.03 kg/s with fixed air flow rate at 0.015 kg/s, 0.035 kg/s, and 0.055 kg/s the maximum primary energy saving efficiency were 88.6%, 89.3% and 90.2%, respectively. Whereas, increasing air flow rate from 0.02 to 0.12 kg/s with fixed nanofluid flow rates at 0.008 kg/s, 0.013 kg/s, and 0.018 kg/s these values were found to be 78.9% to 79.3% and 79.8%, respectively. It is important to note that the percentage increase in the primary energy saving efficiency with the variable nanofluid flow rate is considerably higher than the variable air flow rate. This can be explained by the fact that nanofluid has higher average thermal conductivity than water and air. Therefore, the solar heat being sufficiently absorbed from the PV panel by the circulating nanofluid when the flow rate of air is kept constant.

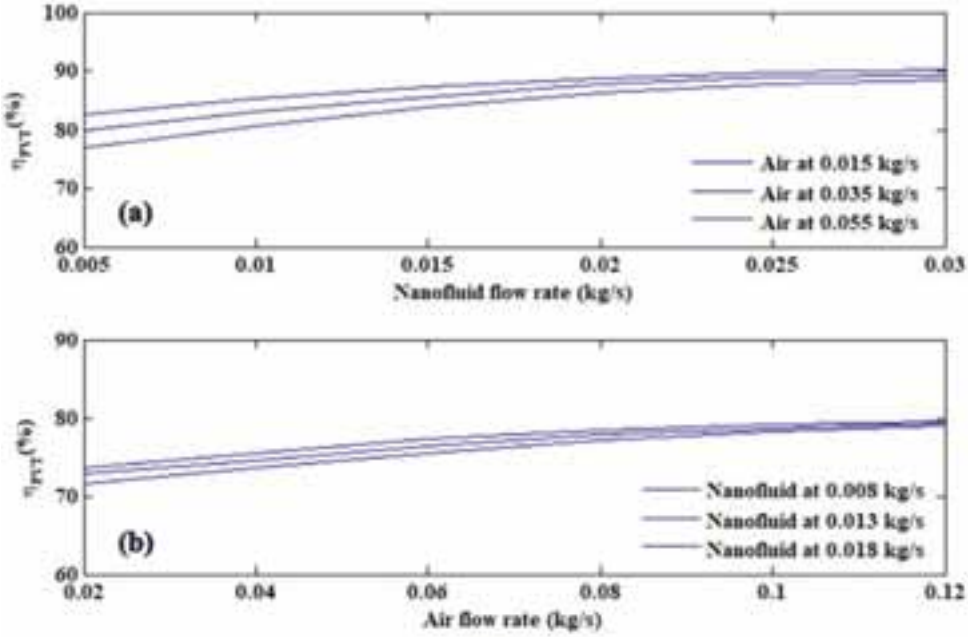

Fig. 7: Primary energy saving efficiency (a) variable nanofluid flow rate at fixed air flow rate (b) variable air flow rate at fixed nanofluid flow rate.

5. Conclusion

The transient numerical analysis of a bi-fluid PV/T system which incorporates the simultaneous application of Al_2O_3 nanofluid and air heat extraction components is performed. The developed transient model can be used to predict the PV/T system's performance for both independent and simultaneous modes of fluid operation. All heat transfer coefficients were calculated in real time during the simulation. The heat transfer rate to the flowing air is improved by introducing a set of baffles transverse to the air flow. The model of a nano-engineered dual-fluid PV/T system is developed and validated against the experimental data given in the literature. The use of Al_2O_3 nanofluid plus air as the dual heat exchanger system provides excellent overall energy performance for the PV/T system in comparison with water plus air and other conventional heat transfer fluids. The developed transient mathematical model can able to accurately predict and optimize the collector performance under a

wide range of varied operating and climatic conditions.

6. Acknowledgements

This work was supported by Korea Research Fellowship Program through the National Research Foundation of Korea (NRF) funded by the Ministry of Science and ICT (2016H1D3A1938222); International Cooperation grant (No. 20148520011270) from the Korea Institute of Energy Technology Evaluation and Planning (KETEP), funded by the Ministry of Trade, Industry and Energy of the Korean government.

7. References

Abu Bakar, M.N., Othman, M., Hj Din, M., Manaf, N.A., Jarimi, H., 2014. Design concept and mathematical model of a bi-fluid photovoltaic/thermal (PV/T) solar collector. Renewable Energy 67, 153-164.

Baljit, S.S.S., Chan, H.Y., Audwinto, V.A., Hamid, S.A., Fudholi, A., Zaidi, S.H., Othman, M.Y., Sopian, K., 2017. Mathematical modelling of a dual-fluid concentrating photovoltaic-thermal (PV-T) solar collector. Renewable Energy 114(Part B), 1258-1271.

Bhattarai, S., Oh, J.-H., Euh, S.-H., Krishna Kafle, G., Hyun Kim, D., 2012. Simulation and model validation of sheet and tube type photovoltaic thermal solar system and conventional solar collecting system in transient states. Solar Energy Materials and Solar Cells 103, 184-193.

Chow, T., 2003. Performance analysis of photovoltaic-thermal collector by explicit dynamic model. Solar Energy 75(2), 143-152.

Hussain, M.I., Lee, G.H., 2015. Parametric performance analysis of a concentrated photovoltaic co-generation system equipped with a thermal storage tank. Energy Conversion and Management 92, 215-222.

Imtiaz Hussain, M., Ali, A., Lee, G.H., 2015. Performance and economic analyses of linear and spot Fresnel lens solar collectors used for greenhouse heating in South Korea. Energy 90, Part 2, 1522-1531.

Jarimi, H., Bakar, M.N.A., Othman, M., Din, M.H., 2016. Bi-fluid photovoltaic/thermal (PV/T) solar collector: Experimental validation of a 2-D theoretical model. Renewable Energy 85, 1052-1067.

Joshi, A., Tiwari, A., Tiwari, G., Dincer, I., Reddy, B., 2009. Performance evaluation of a hybrid photovoltaic thermal (PV/T)(glass-to-glass) system. International Journal of Thermal Sciences 48(1), 154-164.

Kim, J.-H., Park, S.-H., Kim, J.-T., 2014. Experimental Performance of a Photovoltaic-thermal Air Collector. Energy Procedia 48, 888-894.

PV-MJU240GB,
http://www.mitsubishielectricsolar.com/images/uploads/documents/specs/MJU_spec_sheet_240W.pdf.
(Accessed March 10 2017).

Rejeb, O., Sardarabadi, M., Ménézo, C., Passandideh-Fard, M., Dhaou, M.H., Jemni, A., 2016. Numerical and model validation of uncovered nanofluid sheet and tube type photovoltaic thermal solar system. Energy Conversion and Management 110, 367-377.

Sharma, K., Suleiman, A., Hassan, H.S.B., Hegde, G., 2017. Considerations on the Thermophysical Properties of Nanofluids, Engineering Applications of Nanotechnology. Springer, pp. 33-70.

Tripanagnostopoulos, Y., 2007. Aspects and improvements of hybrid photovoltaic/thermal solar energy systems. Solar Energy 81(9), 1117-1131.

Experimental Performance of an Advanced Air-type Photovoltaic-Thermal(PVT/a) Collector

Jin-Hee Kim[1], Jong-Gwon Ahn[2], Sang-Myung[2] and Jun-Tae Kim[3]

[1] Green Energy Research Center, Kongju National University, Cheonan (South Korea)

[2] Graduate School, Kongju National University, Cheonan (South Korea)

[3] Department of Architectural Engineering, Kongju National University, Cheonan (South Korea)

Abstract

A photovoltaic-thermal (PVT) collector is a solar collector that combines a photovoltaic module with a solar thermal collector, which produces electricity and heat at the same time. Depending on the medium used for collecting thermal energy, there are two types of PVT collectors: air-type and water-type. The integration of PV modules with a thermal collector can cause a temperature rise of the PV module, which in turn decreases the efficiency of the PVT collector. In order to obtain better performance of air-type PVT (PVT/a) collectors, it is necessary to extract the heat, in the form of hot/warm air, from the PV module, which then decreases its temperature. This article presents the performance of a new design of a PVT/a collector that uses air as the heat recovery fluid. In this study, an advanced PVT/a collector were newly developed, and its electrical and thermal performance was analyzed from experimental results in outdoor conditions. The results indicated that the thermal and electrical efficiencies of the PVT/a collector were, on average, approximately 30 % and 7 %, respectively.

Keywords: Air-type PVT collector, advanced design, baffle absorber plate, Thermal efficiency, Electrical efficiency

1. Introduction

A photovoltaic-thermal (PVT) collector is a solar collector that combines a photovoltaic module with a solar thermal collector, which produces electricity and heat at the same time. Depending on the medium used for collecting thermal energy, there are two types of PVT collectors: air-type and water-type. The integration of PV modules with a thermal collector can cause a temperature rise of PV the module, which in turn decreases the efficiency of the PVT collector. Ooshaksaraei et al. (2017) investigated four types of air-based bifacial PVT collectors by experimental and analytical methods under steady-state conditions [1]. Tomar et al. (2017) studied analytical models for four PVT/a collectors with different layers. The electrical and thermal efficiency were compared under outdoor condition [2]. Jaaz et al. (2018) experimentally tested a compound parabolic concentrator (CPC) along with PVT/w where the cooling process of the CPC was conducted using water jet impingement technique [3]. Tomar et al. (2018) made five PVT/w collectors with different cell types, namely mono-crystalline (m-Si), polycrystalline (p-Si), amorphous silicon thin film (a-Si), cadmium telluride thin film (CdTe) and copper indium gallium selenide (CIGS) photovoltaic modules. In the paper, theoretically calculated results were experimentally validated in outdoor ambient environment [4]. In order to obtain better performance of air-type PVT (PVT/a) collectors, it is necessary to extract the heat, in the form of hot/warm air, from the PV module, which decreases its temperature. The thermal and electrical performance of a PVT/a collector depends on their design affected airflow and heat transfer. In this light, there is need for an advanced design of PVT/a collector to improve the uniformity of the air flow and the heat transfer. This article presents the performance of a new design of a PVT/a collector that uses air as the heat recovery fluid.

In this study an advanced PVT/a collector was newly designed and made, and their performance was analyzed

doi:10.18086/swc.2017.18.09 Available at http://proceedings.ises.org

through experimental results. The aim of this study is to characterize the thermal and electrical performance of a new collector design of a PVT/a collector under both steady-state conditions.

2. Advanced Air-Type PVT(PVT/a) Collector Design and Experiment

2.1. Advanced Air-Type PVT (PVT/a) prototype

For this study, a prototype of an advanced air-type PVT (PVT/a) collector was developed, as shown in Fig.1. The PVT/a collector consists of a special PV module and absorber plates as a baffle for uniform of air flow; it has a 0.7m^2 PV area and an air layer of 80mm for collecting hot air. The glass to glass type (G/G) PV module was designed with 123W$_p$ mono-crystalline silicon PV for the advanced PVT/a prototype. PVT/a prototype were developed as shown in Fig.1. It has an absorber consisting of both photovoltaic (PV) cells and thermal absorbers in alternate rows. There are four thermal absorbers equally spaced in the PVT/a collector. They are located in the air cavity behind the glass PV glass assembly such that air can circulate above and below the thermal absorbers. The thermal absorber is made out of a thin metal sheet with highly selective blue coating. The PVT/a prototype have a gross are of 1.63m^2, and the PV modules' efficiency used for the collectors was 7.6% under standard test conditions (STC).

In outdoor experiment, the PVT/a prototype were tested. The back surface temperature of the glass-PV-glass assembly was measured with 5 surface thermocouples located in the middle of each PV row along the collector length; that is thermocouples referred to as Td1, Td2, Td3, Td4 and Td5 were arranged from the bottom to the top of PVT/a collector equidistantly. In addition, a distribution box was added at the second module outlet to promote flow uniformity across the cavity.

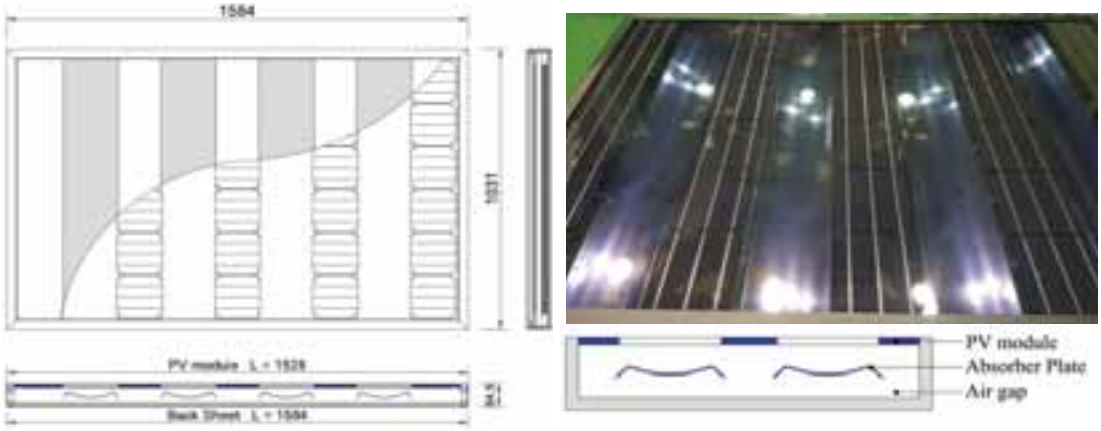

Fig. 1: Prototype design of the advanced PVT/a collector

The advanced PVT/a collector were also tested under outdoor conditions based on the ASHRAE 93-2013 [1] and ISO 9806 standards [2]. Several experimental devices were installed to measure the temperature of the PV laminate backside, the air layer, and the exhausted air, as well as the electrical power of the PVT/a collector. A T-type thermocouple was used to measure the temperature and an I-V curve tracer with Maximum Power Point Tracking (MPPT) was installed for measuring the electrical performance. For the measurement of the air flow rate, flow meters were installed inside the pipes of the inlet and outlet of the PVT/a collector. A data acquisition instrument was also connected to record all of the data related to the thermal and electrical performance of the PVT/a collector and the outdoor conditions.

The PVT/a Testing facility is an open-loop air circulation system. It includes the equipment required to circulate and control the amount of air entering and leaving the PVT/a collector as well as the sensors providing the information required for quantifying the amount of thermal energy that is being recovered. It is an open-loop system because the air heated by the collector is not recirculated in the loop, but rejected outdoors. However, ambient air is preheated in a chamber to temperature of 35 ^{o}C before being supplied to PVT/a collector. Some components for the thermal characterization are located in the air-loop chamber while some others are mounted directly on the multi-functional grid. The air-loop chamber sits separately with system and is connected to the

PVT/a collector on the multi-functional grid with two flexible ducts, one for the inlet and one for the outlet. To control the pressure inside the collector, the PVT/a testing facility uses two blowers to circulate air in the PVT/a collector. The blower located upstream of the collector, the inlet blower, operates in positive pressure and the blower located downstream of the collector operates in negative pressure (see Figure 2). For the experiment, air flowrate of 120kg/h was settled in a PVT testing facility. The experiment was carried out on September 2017. Fig. 2 shows the advanced PVT/a collector and the experiment setup.

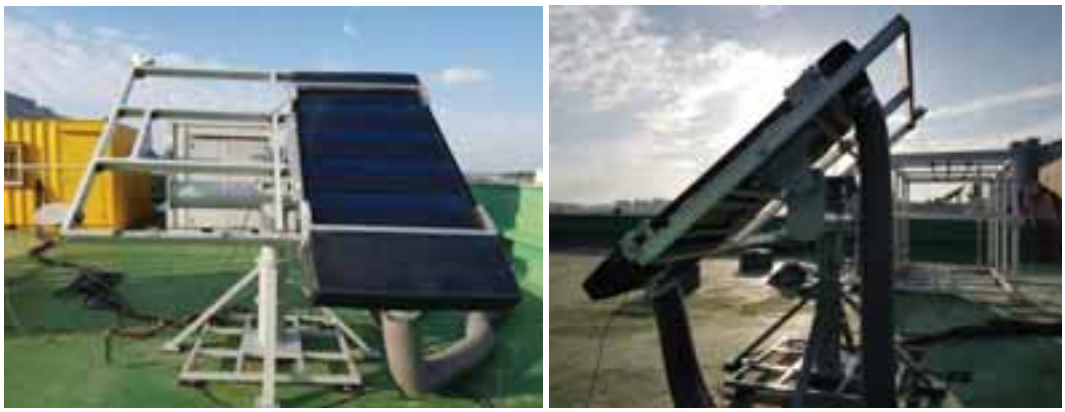

Fig. 2: Outdoor experiment setup

3. Results and Discussion

3.1. Temperature characterization

On the basis of the experimental results, the temperature characterization of the advanced PVT/a collector is presented in figure 3, 4. In Fig. 3, it was found that the advanced PVT/a collector has a temperature gradient, as the temperature of the PV laminate backside is 50~64℃ at ambient of 29℃ and average irradiance of 870 Wm^{-2}. The temperatures at bottom and top part of PV backside are 50~53℃, 62~64℃, respectively.

Fig. 4 presents the inlet and outlet air temperature of PVT/a at the steady-state conditions. This graph show that the air temperature rise of the inlet and outlet of the PVT/a where a difference of 17 °C can be observed at the outdoor condition at ambient of 29 ℃ and irradiance levels of 870 Wm^{-2} with a flowrate of 120 kg/h.

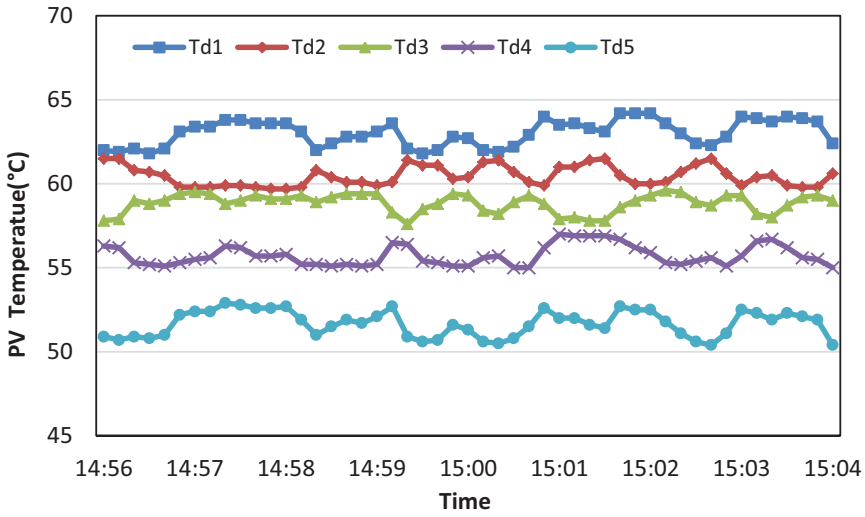

Fig. 3: PV backside (five points) temperatures of the PVT/a collector

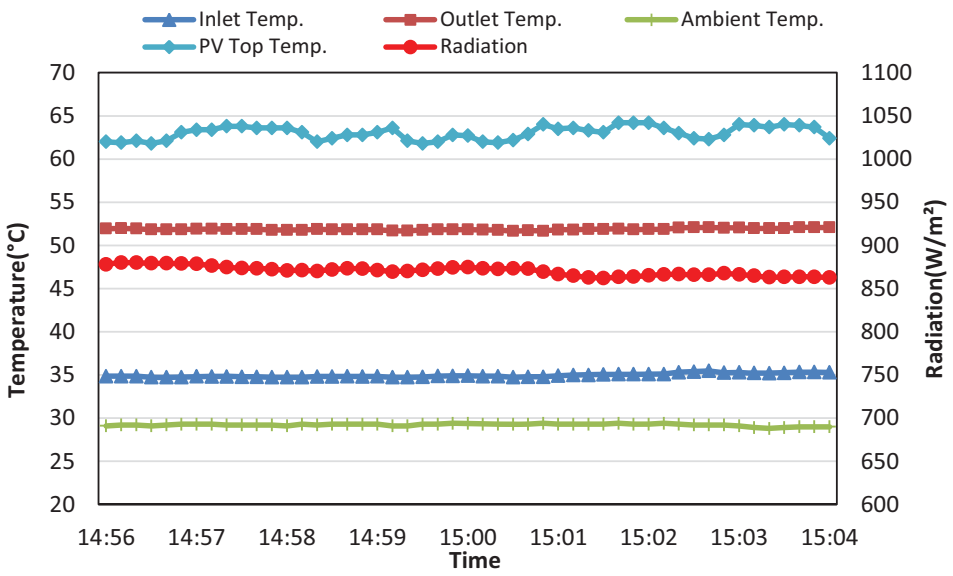

Fig. 4: The air temperature of inlet and outlet of PVT/a collector at the outdoor of steady-state condition

3.2. Thermal and Electrical performance

The thermal performance of PVT/a collector can be characterized by the air temperature difference of the PVT/a collector. On this basis, the thermal efficiency is determined as a function of the solar radiation (G), the mean fluid temperature (T_m) and the ambient temperature (T_a). The steady-state efficiency is calculated by the following equation [7]:

$$\eta_{th} = \frac{\dot{m}\, C_p\, (T_o - T_i)}{A_{pvt}\, G} \qquad \text{(eq. 1)}$$

η_{th} thermal efficiency [-]
A_{pvt} collector area [m^2]
T_o collector outlet air temperature [$^{\circ}$C]
T_i collector inlet air temperature [$^{\circ}$C]
$\dot{m}$ mass flow rate [$m^3\ h^{-1}$]
C_p specific heat [$J\ kg^{-1}\ K^{-1}$]
G irradiance on the collector surface [$W\ m^{-2}$]

The thermal efficiency of the PVT collectors was conventionally calculated as a function of the ratio $\Delta T/G$, where $\Delta T = T_m - T_a$. Here, T_m and T_a are the PVT collector's mean fluid temperature and the ambient temperature, respectively, and G is the solar radiation at the collector surface. Hence, ΔT denotes the measurement of the temperature difference between the inlet fluid and ambient air relative to the solar radiation. The thermal efficiency, η_{th}, is expressed as

$$\eta_{th} = \eta_0 - \alpha_1 \frac{\Delta T}{G}$$

where η_o is the thermal efficiency at zero reduced temperature, and α_1 is the heat loss coefficient.

The thermal efficiency as a function of the ratio $\Delta T/G$ is shown in Fig. 5. As it can be observed, the thermal efficiency decreases with ratio $\Delta T/G$. This thermal performance dependency to ratio ΔT/G indicates that the prototype behaves like conventional solar thermal collector.
From the measurement results for the advanced PVT/a collector, it can be seen that the thermal performance can be expressed as in Fig. 5. The thermal efficiency of the PVT/a collector can be therefore be described by the relational expression, $\eta_{th} = 0.3709 - 5.5371(\Delta T/G)$. Thus, the collector thermal efficiency (η_0) at zero reduced

temperature is 37%, which indicates relatively high performance. The heat loss coefficient (α_1), which can have an effect on reduction of thermal efficiency was 5.54 (℃ $m^2 W^{-1}$), which is can be observe low heat loss ratio. The average thermal efficiency of the PVT/a collector is about 30% under outdoor test conditions and with the given X axis coefficients ($\Delta T/G$).

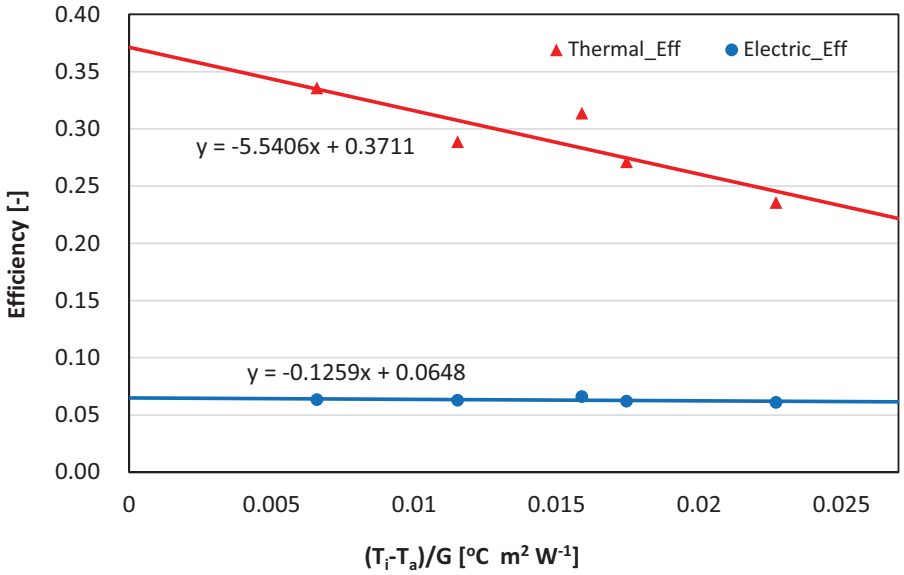

Fig. 5: Thermal and electrical efficiencies of the PVT/a collector

The electrical efficiency depends mainly on the incoming solar radiation and the PV module temperature. It is calculated with the following equation:

$$\eta_{el} = \frac{I_m V_m}{A_{pvt} G} \qquad \text{(eq. 2)}$$

where, I_m and V_m are the current and the voltage of the PV module operating under a maximum power.

The electrical efficiency of the PVT/a collector can be expressed with the following relational expression: η_{el} = 0.0648-0.1259(ΔT/G). The highest electrical efficiency of the PVT collector is 6.5% with the given X axis coefficients ($\Delta T/G$). As shown in Figure 5, the electrical efficiency is positive with regard to the X axis coefficients, as compared to the thermal efficiency. This occurs because, in spite of identical test conditions of the X axis coefficients, the electrical performance of the PVT/a collector was affected immediately by the PV temperature in addition to the X axis coefficients ($\Delta T/G$), i.e., ambient temperature, mean fluid temperature and solar radiation.

4. Conclusion

This paper presented the steady-state thermal and electrical performance of a new prototype of an advanced PVT/a collector. The design of this prototype is unique because its absorber consists of a combination of both photovoltaic cells and thermal absorbers in alternate rows. Experimental measurements were taken in outdoor conditions one PVT/a collector operated in open-loop.

Experimental results performed outdoors at the steady-state showed that at a flowrate of 120 kg/h and an irradiance level of 870 W/m², a temperature rise of 17°C.

The results show that at zero reduced temperature, the thermal and electrical efficiency levels of an advanced

PVT/a collector are 37% and 7%, respectively. Due to the unique design, the power generation is relatively low. Therefore, the advanced PVT/a collector had better thermal performance than the electrical performance.

Acknowledgments: This paper was supported by a Korea Energy Agency (No. 71000149) and an International Cooperation grant (No. 20148520011270) from the Korea Institute of Energy Technology Evaluation and Planning (KETEP), funded by the Ministry of Trade, Industry and Energy of the Korean government.

Nomenclature

A_{pvt}	Surface area of the collector	m^2
C_p	Specific heat of air at a constant pressure	$J\ kg^{-1}\ K^{-1}$
G	Solar radiation	$W\ m^{-2}$
$\dot{m}$	Mass flow rate	$kg\ h^{-1}$
T_a	Ambient air temperature	°C
T_o	Outlet air temperature of PVT	°C
T_i	Inlet air temperature of PVT	°C
η_{th}	Thermal efficiency	-
η_{el}	Electrical efficiency	-
I_m	Maximum current	A
V_m	Maximum voltage	V
P_{max}	Maximum power	W
FR(τα)	Thermal efficiency coefficient	-
FRUL	Heat loss coefficient	$^oC\ m^2\ W^{-1}$

5. References

1. P. Ooshaksaraei, K. Sopian, S. H. Zaidei, R. Zulkifli, 2017, Performance of four air-based photovoltaic thermal collectors configurations with bifacial solar cells, Renewable Energy, 102, 279-293.

2. V. Tomar, G. N. Tiwari, T. S. Bhatti, 2017, Performance of different photovoltaic-thermal (PVT) configurations integrated on prototype test cells: An experimental approach, Energy Conversion and Management, 154, 394-419.

3. A. H. Jaaz, K. Sopian, T. S. Gaaz, 2018, Study of the electrical and thermal performances of photovoltaic thermal collector-compound parabolic concentrated, Results in Physics, 9, 500-510.

4. V. Tomar, G. N. Tiwari, T. S. Bhatti, B. Norton, 2018, Thermal modeling and experimental evaluation of five different photovoltaic modules integrated on prototype test cells with and without water flow, Energy Conversion and Management, 165, 219-235.

5. Jin-Hee Kim, Jong-Gwon Ahn, Jun-Tae Kim, 2016, Demonstration of the performance of an Air-Type Photovoltaic Thermal (PVT) System Coupled with a Heat-Recovery Ventilator, Energies, 728, 1-9.

6. ASHRAE Standard Committee, 2010. Standard 93-2010-Methods of Testing to Determine the Thermal Performance of Solar Collectors, American Society of Heating, Refrigerating and Air Conditioning Engineers, Inc., Atlanta.

7. International Organization for Standardization, 2013. ISO 9806 - Solar Energy - Solar thermal collectors - Test methods, International Organization for Standardization, Geneva.

Assessing suitable fields of application for PVT collectors with the characteristic temperature approach

Manuel Lämmle, Korbinian Kramer, Michael Hermann
Fraunhofer Institute for Solar Energy Systems ISE, 79110 Freiburg, Germany

Abstract

PVT collectors co-generate heat and electricity and a single component. There are various PVT collector technologies available, with varying efficiencies and thus varying fields of application. But which PVT collector technologies are suitable for which fields of application?

The characteristic temperature approach is a novel method, which correlates the electrical and thermal yield with the mean operating temperatures T_{char}. Thus, the complexity of the system is reduced to a single temperature. T_{char} is therefore an apt indicator to assess suitable fields of applications for PVT collectors and select the most suitable collector technology. Moreover, the characteristic temperature approach allows a preliminary dimensioning of a PVT system and estimate yields of different technologies.

Keywords: PVT system; system simulations, Hybrid PV/Thermal collector; yield assessment

1. Introduction

PVT collectors can be classified according to their design (unglazed, glazed, concentrating), their heat transfer medium (water, air), and their PV cell technology (Zondag 2008). In Europe, unglazed PVT collectors have the highest market share, but their application is limited to low temperature systems due to high collector heat losses. Glazed PVT collectors offer an enhanced thermal efficiency owing to reduced thermal losses by a transparent front cover. Spectrally selective low-emissivity (low-e) coatings in glazed PVT collectors reduce infrared radiative heat losses, yet at the cost of a drop of electrical efficiency (Lämmle et al. 2016). Concentrating PVT collectors can be realized out from low to high concentration ratios, with the possibility of both stationary and tracked operation. Concentrating PVT collectors potentially achieve very low heat losses and high temperature levels (Chow 2010).

These considerations demonstrate that each collector technology has its specific temperature levels and accordingly suitable applications. From an energetic point of view, the annual electrical and thermal yields of PVT collectors in typical system installations are of major interest.

2. Characteristic temperature approach

2.1. Definition of the characteristic temperature T_{char}

As is generally known, the fluid temperatures have a strong influence on the instantaneous performance of PVT collectors. The electrical efficiency of silicon PV cells drops by approximately 0.4 % per Kelvin of increased cell temperature owing to the negative power temperature coefficient γ. Also the thermal efficiency drops due to higher heat losses at higher absorber temperatures.

To investigate the influence of the annual operating temperatures, a new system indicator was introduced in Lämmle et al. (2017), which characterizes a PVT system based on its mean operating temperatures. The characteristic operating temperature T_{char} is defined as the annual, irradiance-weighted, mean fluid temperature in the collector:

$$T_{char} = \frac{\int G\, T_m dt}{\int G\, dt} \qquad \text{(eq. 1)}$$

with the instantaneous irradiance in the collector plane G, and the mean fluid temperature T_m.

doi:10.18086/swc.2017.18.10 Available at http://proceedings.ises.org

2.2. Comparison of PVT collector technologies

Different flat plate, water-type PVT collector technologies are included in the assessment:

- a commercially available unglazed PVT collector without rear insulation,

- a glazed PVT collector with an anti-reflectance coated front cover

- a glazed PVT with a low-emissivity coating on the PVT absorber (Lämmle et al. 2016)

- a conventional PV module and a flat plate collector for comparison purposes

Concentrating PVT collector technologies are not included in this analysis. An initial comparison of energy yields revealed no energetic benefit of applying currently available concentrating PVT collector technologies in the central European climate.

Fig. 1 compares the electrical efficiency at standard test conditions and the thermal efficiency curves of the investigated technologies. The detailed efficiency parameters can be found in Lämmle et al. (2017).

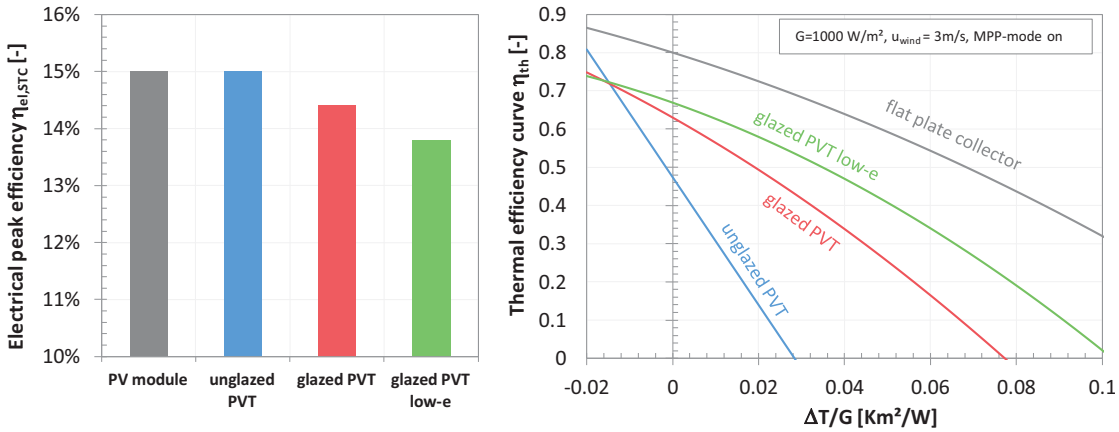

Fig. 1: Comparison of the standard efficiency of PVT collector technologies.

A conflict of interest between a high electrical vs. a high thermal efficiency can be observed, which results from the trade-off between a good optical performance vs. thermal insulation.

2.3. Analysis of correlation between yields and T_{char}

System simulations were carried out to analyze the correlation between collector yields and the characteristic temperature. For this purpose, several different types of PVT systems were analyzed, including systems for domestic hot water (DHW) heating in single and multi-family-homes, as well as combined DHW and space heating systems with and without heat pump. To achieve a wide variation of operating temperatures, the key system parameters of collector area and storage volume were varied. Simulations were carried out for the German location of Würzburg, and the detailed assumptions and results can be found in (Lämmle et al. 2017).

Analyzing the correlation between the characteristic temperature T_{char} and electrical and thermal yields, characteristic curves for each collector technology are found (Fig. 2). In the diagrams, each point represents results of a specific annual system simulation run and different types of PVT systems with varying system dimensions are included therein.

Due to the observed strong correlation between yields and T_{char}, the characteristic temperature describes the effect of the PVT system on yields independent from the system type. T_{char} is therefore a suitable indicator to characterize the thermal operating conditions of PVT systems. Depending on T_{char}, different PVT collector technologies can exploit their specific strengths. Therefore, the most suitable PVT collector technology has to be selected to match the given T_{char} of the PVT system.

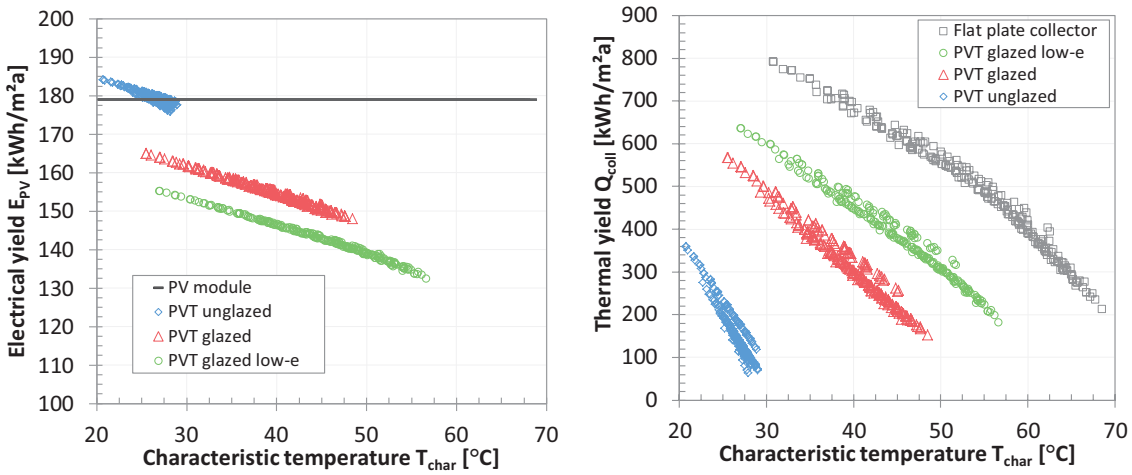

Fig. 2: Characteristic curves of the electrical and thermal collector yield of different PVT technologies as function of the characteristic temperature T_{char} (Lämmle et al. 2017).

2.4. Exemplary application of the characteristic temperature approach

To assess the applicability of PVT collectors in specific systems the following schematic procedure can be applied:

1. Identify T_{char} for the present application. This can be either done by a single annual simulation run or T_{char} can be estimated from operating temperatures of known systems
2. Read specific yields from Fig. 2
3. Size collector field to achieve the required electrical or thermal target output
4. Calculate the total electrical and thermal output of the PVT system

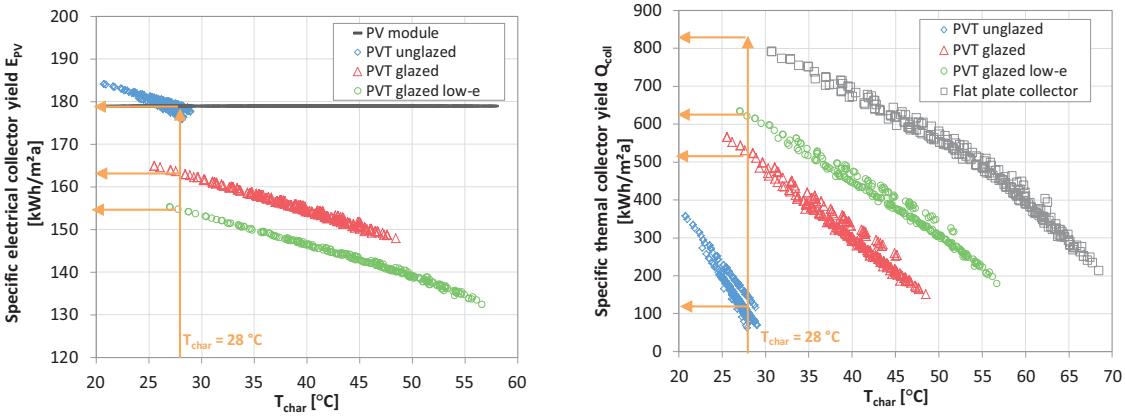

Fig. 3: Exemplary application of the characteristic temperature approach for the preliminary design of a PVT system with a characteristic temperature T_{char} = 28 °C at the location of Würzburg, Germany

Fig. shows the exemplary application of this procedure for a hot water system in an office building with a characteristic temperature of T_{char} = 28.0 °C. With the knowledge of T_{char}, the electric and thermal yields can be read from the graph. While the unglazed PVT collector reaches the highest electrical yields, the glazed PVT collector with low-e coating reaches the highest thermal yields.

Depending on the local energy demand, priority is either given to high electrical or high thermal yields. Typical energetic evaluation criteria include, amongst others, the specific yields per square meter of collector area, the roof area required to meet the required local solar energy demand, or the maximum energetic electricity and heat output a specific roof area can reach. If cost functions are supplied, also levelized costs of electricity and heat can be calculated. All these evaluation criteria can be preliminarily assessed by means of the characteristic temperature approach.

3. Assessing suitable fields of applications for PVT collectors

A central motivation for PVT collectors is the optimization of the overall combined electricity and heat output. As PVT collectors co-generate solar electricity and heat from the same area, potentially highest overall yields can be achieved. To quantify the combined electricity and heat output as a single value, primary energy yields are used. The primary energy yield per square meter of collector area is given by:

$$Q_{PE} = f_{PE,el}\, E_{PV} + f_{PE,heat}\, Q_{coll} \qquad \text{(eq. 2)}$$

with the primary energy factors for electricity $f_{PE,el}$ = 2.0 and for heat $f_{PE,heat}$ = 1.1 (DIN V 18599-1:2013-05), and the specific electrical and thermal yield E_{PV} and Q_{coll}.

Fig. 4 plots the primary energy yield Q_{PE} as function of the characteristic temperature T_{char} for the previously mentioned PVT systems. On account of the dependence of electrical and thermal yields from T_{char}, a strong correlation is also observed between T_{char} and primary energy yields, resulting in characteristic curves for each collector technology.

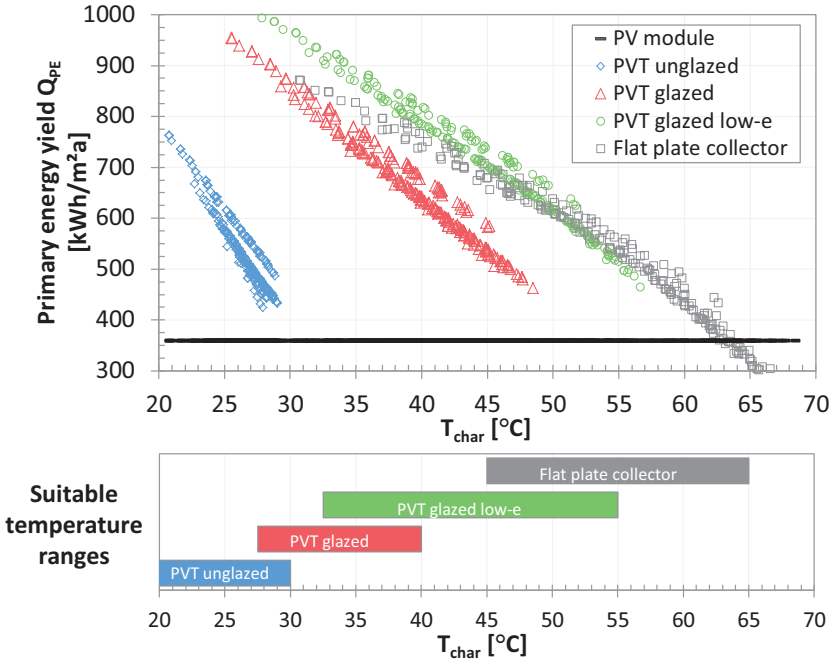

Fig. 4: Primary energy yields and derived suitable temperature ranges per PVT collector technology.

For an optimized utilization of available solar areas, the primary energy yield needs to be maximized.

Firstly, this can be achieved by reducing $T_{char.}$ As both the electrical and thermal efficiency benefit from low operating temperatures, a reduction of the fluid temperatures affects an increase of both electrical and thermal yields. For instance, low characteristic temperatures are achieved by smaller dimensions of the PVT array, larger storage volumes, and lower storage temperatures.

Secondly, the primary energy yields can be maximized by an adequate selection of a suitable collector technology, which matches the characteristic temperature. From Fig. 4, suitable temperature ranges can be derived for each collector technology. The following temperature ranges, and accordingly suitable fields of application, seem recommendable:

- **Unglazed PVT collectors** for very low operating temperatures near or below ambient of T_{char} < 30 °C.
- **Glazed PVT collectors** for low to medium operating temperatures of T_{char} < 40 °C.
- **Glazed PVT collectors with low-e** for medium operating temperatures of T_{char} < 55 °C.
- For higher temperatures, **concentrating PVT collectors** or a side-by-side installation of **flat plate collectors and PV modules** might achieve an optimized primary energy yield.

4. Conclusion

The operating temperatures in PVT systems are of pivotal importance, since both the electrical and thermal performance depend on it. The characteristic temperature approach puts these operating temperatures into the focus by introducing the new indicator T_{char}, which specifies the mean annual operating temperatures of the PVT system.

The characteristic temperature approach can be used to preliminarily design a PVT system and evaluate the technical and economic feasibility. Depending on the temperature level T_{char} of a specific PVT system, the most suitable collector technology can be selected. T_{char} is therefore a good indicator to assess the applicability of different PVT technologies in different PVT systems with varying temperature levels.

References

Chow, T. T. (2010): A review on photovoltaic/thermal hybrid solar technology. *Applied Energy* 87 (2), pp. 365–379. DOI: 10.1016/j.apenergy.2009.06.037.

DIN V 18599-1, 2013: DIN V 18599-1 Berichtigung 1:2013-05 Titel (deutsch): Energetische Bewertung von Gebäuden - Berechnung des Nutz-, End- und Primärenergiebedarfs für Heizung, Kühlung, Lüftung, Trinkwarmwasser und Beleuchtung - Teil 1: Allgemeine Bilanzierungsverfahren, Begriffe, Zonierung und Bewertung der Energieträger, Berichtigung zu DIN V 18599-1:2011-12.

Lämmle, Manuel; Kroyer, Thomas; Fortuin, Stefan; Wiese, Martin; Hermann, Michael (2016): Development and modelling of highly-efficient PVT collectors with low-emissivity coatings. *Solar Energy* (130), pp. 161–173. DOI: 10.1016/j.solener.2016.02.007.

Lämmle, Manuel; Oliva, Axel; Hermann, Michael; Kramer, Korbinian (2017): PVT collector technologies in solar thermal systems: a systematic assessment of electrical and thermal yields with the novel characteristic temperature approach. *Solar Energy* (155), pp. 867–879. DOI: 10.1016/j.solener.2017.07.015.

Zondag, H.A. (2008): Flat-plate PV-Thermal collectors and systems: A review. *Renewable and Sustainable Energy Reviews* 12 (4), pp. 891–959.

Reverse Engineering Prototype Solar PV/Thermal Collector Properties from Empirical Data for Use in TRNSYS Type 560

Nelson Sommerfeldt[1] and Patrik Ollas[2]

[1] KTH Royal Institute of Technology, Dept. of Energy Technology, Stockholm (Sweden)

[2] RISE Research Institutes of Sweden, Built Environment Division, Borås (Sweden)

Abstract

Using the known physical characteristics of a prototype photovoltaic-thermal (PVT) collector components and raw test data from a prematurely terminated ISO 9806 test, the objective of this study is to reverse engineer a thermal resistance value for the heat exchanger assembly for use in the theoretical TRNSYS model Type 560. Modeling is done using both TRNSYS as well as commercial heat transfer software TAITherm. Performance is measured by the mean absolute error and correlation of the outlet temperature and thermal power, as well as the differences in total thermal energy generated. The results show a thermal resistance of 0.005 to 0.010 m^2 K W^{-1} in TAITherm and 0.010 to 0.040 m^2 K W^{-1} in Type 560. TAITherm gives better statistical indicators which is likely due to the inclusion of thermal mass in the model. The results have informed prototype development and can be used in further systems modeling.

Keywords: PVT, Prototype, Testing, Simulation, TAITherm, TRNSYS, Validation

1. Introduction

Photovoltaic-thermal (PVT) hybrid modules absorb solar radiation and can convert it into electricity and heated fluids. There is a broad range of design concepts, however the most feasible solution for building applied or integrated products is a flat plate collector (Michael et al., 2015). In this arrangement, PV cells are mounted to a flat plate heat exchanger with cooling channels on the opposite side. With a glass front, this hybrid absorber can be used directly, known as an unglazed collector, or insulated from the environment with the glazing separated by an air gap over the PV. Insulation is most commonly added to the rear of the panel as well, but is not necessary.

PVT collectors are predominantly used for direct domestic hot water or space heating, and recently there has been growing interest in combining them with heat pumps (Hardorn, 2015). There are numerous potential system configurations, and one such configuration with relevance for Sweden is PVT in conjunction with ground source heat pumps (GSHP) (Sommerfeldt and Madani, 2016). If placed on the cold side of the heat pump, there are mutual benefits for each component; there is more energy captured from the solar collectors, the heat pump can receive a higher inlet temperature that improves the coefficient of performance (COP), and excess heat can be delivered to the borehole(s) for long-term storage.

A Swedish startup company is developing a system solution for integrating PVT collectors with GSHP. Unsatisfied with existing PVT products, they have decided to develop their own specifically designed for a GSHP application. Laminating PV cells directly to the absorber plate is difficult due

doi:10.18086/swc.2017.18.11 Available at http://proceedings.ises.org

to the need of a clean environment while also maintaining good electrical insulation between the absorber and PV cells (Zondag, 2008). PV manufacturing has matured to where the lamination process occurs with very high quality and low cost due to automation and economies of scale. This scale has yet to reach PVT collectors, which can be three to five times more expensive than a PV module due to the additional materials and complexity.

It is much simpler to take an off-the-shelf PV module and affix a heat exchanger to the rear side, either mechanically or with an adhesive. The greatest drawback of this approach is the reduced heat transfer between the PV cells and working fluid, thus reducing the electrical and thermal efficiencies (Zondag, 2008). However, if the cost of creating the heat exchanger can be substantially reduced, the loss of performance may be acceptable. This may be particularly so for PVT collectors in combination with heat pumps, where operating temperatures are much lower than most previous applications, thus removing the need for glazing and insulation due to lower losses (and potential gains) from the ambient air.

The Startup has gone through several prototype rounds tested in multiple installations, and has settled on a glass-glass PV module with an aluminum manifold mechanically pressed against the back. Using a glass backer allows greater contact with the heat exchanger and increases durability at the expense of increased thermal resistance. Opposite the PV module, the manifold has a trough to fit a 12 mm copper pipe, which is also mechanically fixed. Both interfaces are lined with thermal grease to encourage heat transfer. A cross section of the design is given in Figure 1 where it is compared with the models used in this study.

Two prototypes were tested according to ISO9806:2013 parameters during the autumn of 2016 at the RISE facility in Borås, Sweden with the goal of determining thermal performance coefficients of the empirical model described by Perers et al. (2012). However, issues with pressure drop and an unbalance flow were found late in the test cycle and were unable to be corrected before outdoor testing was forced to end for the winter. The result was a lack of data for making the necessary regressions, however there is enough raw data available to perform an empirical confirmation of theoretical models.

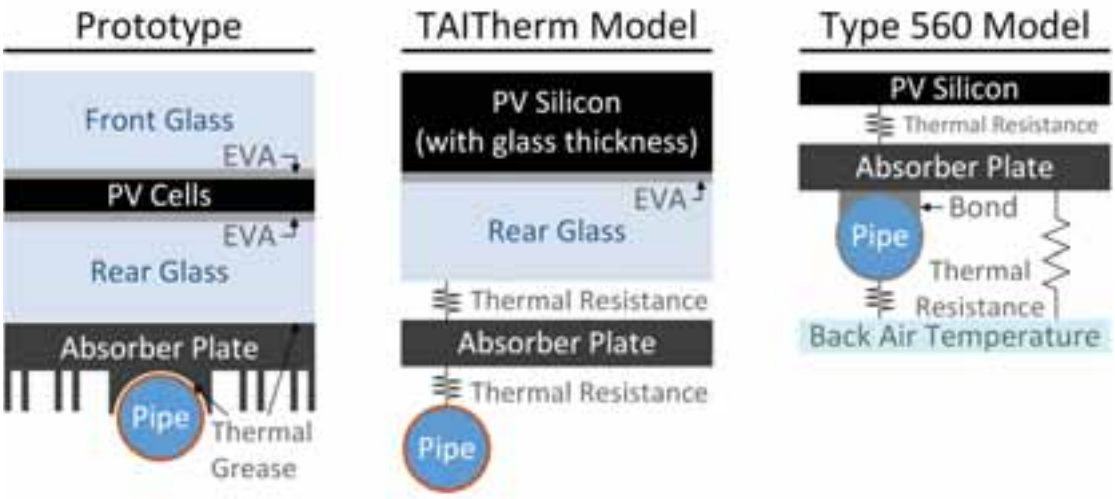

Figure 1 - Cross sectional representations of the PVT prototype, TAITherm, and Type 560 models (not to scale)

2. Objective and Methodology

With what is known about the PV module and heat exchanger construction, most of the collector's physical properties are fixed. The most critical missing characteristic is the conductive heat transfer behavior between the PV module and the pipes carrying the heat transfer fluid. Therefore, the primary objective is to determine a thermal resistance value between the PV module and the heat exchanger assembly to better understand the efficiency penalty of the design over dedicated PVT modules. This is done using the commercial heat transfer software TAITherm (ThermoAnalytics, 2016), which uses a numerical, finite volume approach. The motivation for using this modeling approach is twofold, 1) to capture the unconventional geometry of the heat exchanger, and 2) to independently control fluid streams for recreating the imbalanced flow observed during testing.

Collector development is just one part of a larger goal of PVT plus GSHP systems modeling, which is being done using the well-known tool TRNSYS (Klein et al., 2009). Therefore, the results from TAITherm need to be transferred into TRNSYS, which is most easily done using Type 560 whose theoretical model construction is most similar to TAITherm and the prototype. Given the differences between models, it is unlikely that the parameters will transfer directly, therefore the tuning process will be performed for TRNSYS as well. The results will also give a better understanding of the behavior of Type 560 which may be accounted for in systems models.

3. Method

Meeting the objectives involves a multistep process of constructing the model in TAITherm, manually tuning unknown parameters to achieve a best possible fit to empirical data, transfer of model settings into TRNSYS, and a manual re-tuning of parameters. The unknown parameters tuned with thermal resistance include; flow rates in each collector, absorptance and emittance of the PV module, and convection coefficients on the front and rear.

The mixed outlet temperature of the heat transfer fluid is used as the primary calibration measurement and thermal power used as a secondary indicator. In the TAITherm model, thermal power is calculated using the volumetric flow rate, fluid density, and inlet temperature measurements with modeled outlet temperature. In Type 560, thermal power is output directly from the model. Performance is measured using differences in total thermal energy generated as well as mean absolute error (MAE) and correlation of the outlet temperature and thermal power time series.

3.1 TAITherm Model Description

The TAITherm geometry is a 2.5 dimension mesh, meaning that the components are represented with surfaces and assigned multiple layers with individual properties. The PV module is represented by a 1.658 m by 0.992 m flat plate with 60 elements (10 x 6). The plate has three layers; the PV cells, plastic EVA encapsulate, and the rear glass as shown in Figure 1. A notable omission is the front glass layer. This is due to TAITherm's inability to model transparent and opaque layers together in a single part. The density of the glass and silicon are similar, so to adjust for the missing mass the thickness of the PV layer is made to encompass both the PV and glass. The layer thicknesses and material properties are given in Table 1. The primary sources for the physical characteristics of the module are the PV module spec sheet (Perlight PLM-260M) and from Armstrong and Hurley (2010).

Table 1 - Material properties of the TAITherm model

Layer	Material	Thickness	Density	Conductivity	Specific Heat
-	-	*mm*	*kg m^{-3}*	*W m^{-1} K^{-1}*	*J kg^{-1} K^{-1}*
PV	Silicon	0.225 + 2.5	2330	148	677
EVA	EVA	0.5	960	0.7	2090
Rear Glass	Glass	2.5	2530	1.8	500
Tube	Copper	1	8954	390	383
Fluid	Water	-	Vary w/ temp	0.6	4186

The heat exchanger is represented by flat plat and a collection of six tubes, each a single layer part. As can be seen from the screen shot in Figure 2, the parts are not physically connected, but manually using a conduction link with a user input thermal resistance parameter. Both links are given the same thermal resistance since they are both mechanically pressed and have thermal grease between the parts. Inside the tubes are 1-D fluid streams that have convective heat transfer with a coefficient calculated using the pipe geometry, fluid velocity, and duct flow models incorporated into TAITherm. There are six pipes with corresponding fluid streams for each module, and the flow rates of each can be set independently. The streams all stem from a single fluid node and recombine into a single fluid node, which represent the measured inlet and outlet temperatures.

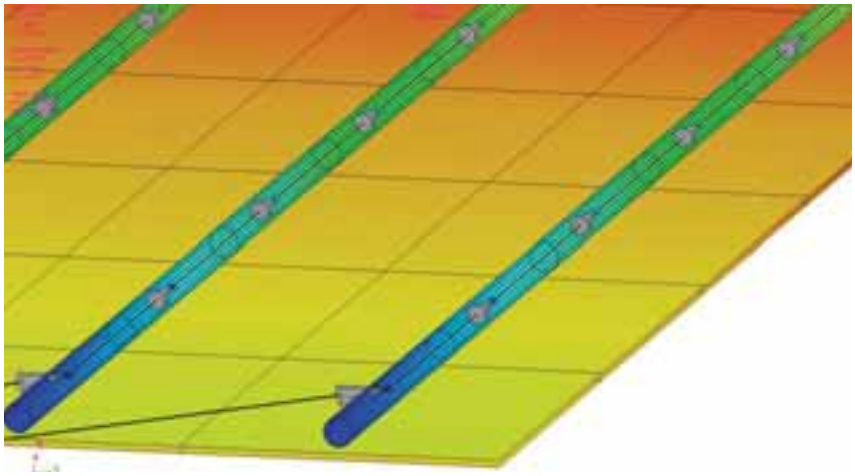

Figure 2 - Detailed view of the TAITherm model backside, showing the PV and heat exchanger parts

The internal heat transfer model within TAITherm is a dynamic, numerical solver based on first principle physics and has highly flexible inputs for boundary conditions. The measured irradiance is imposed directly on the front PV surface. PV generation is not modeled but instead the measured power is removed as heat from the back PV surface. Long wave infrared radiation was measured during testing and converted into sky temperature (T_s) using Equation 1 (Gliah et al., 2011), which is then used for radiant exchange. The collectors are mounted parallel with an asphalt roof within 15 cm, therefore the roof is the only rear view factor and is assumed to be the air temperature.

$$T_s = \left(\frac{Q_{lw}}{\sigma}\right)^{1/4} \qquad \text{Eq. 1}$$

$Q_{lw} = Long\ wave\ infrared\ irradiance\ (W\ m^{-2})$
$\sigma = 5.670\ x10^{-8}\ W\ m^{-2}\ K^{-4}$ (Stefan-Boltzmann constant)

3.2 Type 560 Model Description

Type 560 is one of two PVT models available from TESS, the makers of TRNSYS, and is based on the Hottel and Whillier model, later modified by Florschuetz, and described by Duffie and Beckman (2013). A full derivation and description is also available in the TESS library documentation and therefore will only be briefly reviewed here. The thermal model is the same as a standard solar thermal collector with fin-and-tube construction as shown in Figure 1. The primary modification is that the glazing has been removed and a PV model has been added on top of the absorber plate. One improvement of Type 560 over previous models is the inclusion of a thermal barrier between the PV cells and the absorber plate, a notable point of inefficiency in a PVT collector (Zondag, 2008). The calculation comprises of a set of 10 analytical equations are that solved iteratively since the power output of the PV cells is dependent on their temperature, which is also a function of the thermal collector.

The geometry and model construction of Type 560 and the TAITherm model are similar in several ways; the front glass of the PV module has been omitted, the thermal resistance between the PV cells and absorber plate can be set directly, and dynamic convection coefficients can be applied to front and back surfaces and to the working fluid. Major differences in 560 include modeled PV generation, rear insulation by default (represented by a thermal resistance input), the conduction between the absorber plate and tubes is defined with conductivity rather than thermal resistance, and there is no consideration for the collector's thermal mass.

3.3 Testing Conditions

Testing was performed on two prototype collectors, plumbed in parallel, and mounted on a south-facing roof at a 45° slope. Data was collected between September 19th and October 6th, 2016 using a five-minute time step. Three distinct periods are used in this study and are chosen due to the variation in inlet temperatures and their relatively long, continuous duration. The nominal volumetric flow rate in all of the testing is 240 l/h, equivalent to 0.02 l/s-m^2.

Test One occurs on September 19th, which was a warm and partly cloudy day, using a 10°C target inlet temperature. There are 9.5 hours of data total between 10:11 and 19:46, and Figure 3 shows the ambient air temperature, calculated sky temperature, total irradiance (measured in the collector plane), and wind speed.

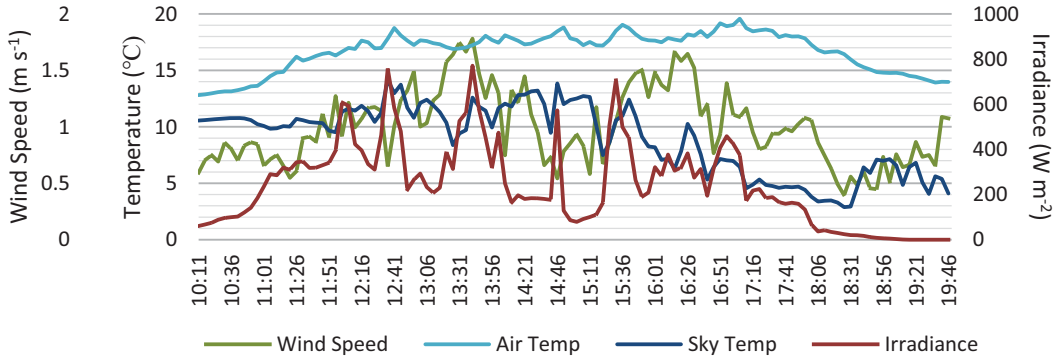

Figure 3 - Measured climate data for Test One

Test Two begins in the morning of October 5th and ends in the early afternoon on October 6th. During the mornings, there are some clouds but otherwise the skies are mostly clear with little wind as shown by the climate data in Figure 4. The inlet temperature target was 20°C, however the actual values are closer to 19°C.

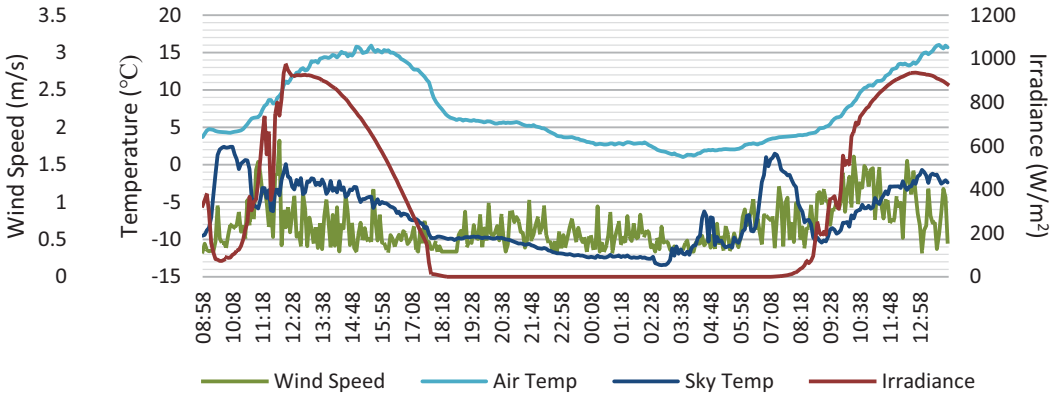

Figure 4 - Measured climate data for Test Two

Test Three is the longest at just over 46 hours, beginning the morning of September 24th and concluding in the morning of September 26th. During the majority of the test there were partly cloudy skies with little wind at night and a gentle breeze during the day, shown in Figure 5. The target inlet temperature here is 30°C, however most of the test has temperatures between 28°C and 29°C.

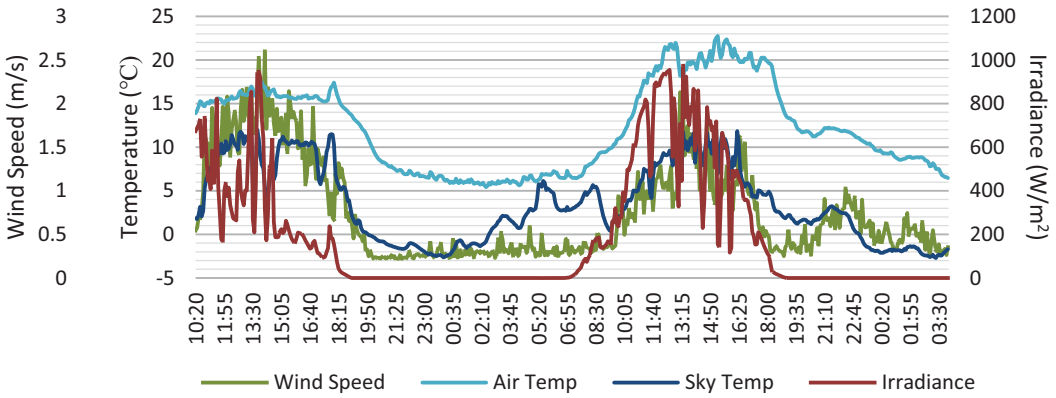

Figure 5 - Measured climate data for Test Three

4. Results

The first step in the tuning process is to determine the flow rates in each collector. An IR image taken during testing discovered the flow imbalance and is used here to compare with TAITherm results, shown in Figure 6. The post-processor in TAITherm allows the visualization of thermal gradients, however only the thermal patterns are considered and not the absolute temperature values. The image suggests that the majority of flow is through the right collector and several flow distributions (2%/98%, 1%/99%, 0%/100%) tested have determined that effectively all of the working fluid is passing through the right collector. Passing any significant amount of fluid through the left collector leads to a much less pronounced thermal gradient, however a negligible flow of 0.6 l/h is passed through the left collector for solver stability.

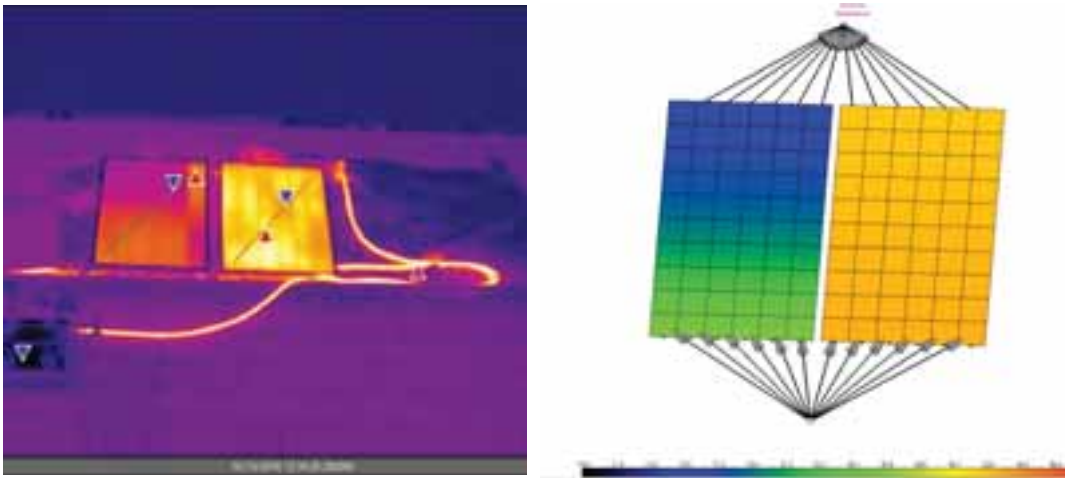

Figure 6 - IR image (left) during testing and TAITherm model (right) with 100% flow in the right collector

Convection on the front side is assumed to be wind dominated and several coefficient models have been tested, including; McAdams (1954), Test et al. (1981), and custom coefficients during the tuning process. Convection coefficients include a high degree of uncertainty (Mirsadeghi et al., 2013), and wind direction was not measured during testing which limits the ability to adjust the model for specific conditions. The commonly used McAdams model is found to be acceptable and is used on the front surface in all cases. The rear side of the collector was tested with both variable and constant convection coefficient models. All external convective heat transfer is modeled with the ambient air temperature.

Time series results are presented for each test in the following sections, while Table 2 with the statistical indicator results for all tests is given at the end of the section. Other common parameters include absorptance and emittance, which is found to be acceptable in all models at 0.85 and 0.90, respectively. It should also be noted that the range of plausible bond conductivities had an insignificant effect on the results for Type 560, meaning the primary tuning parameters are limited to the resistance between PV cells and absorber plate, rear convection coefficient, and the working fluid coefficient.

4.1 Test One

The thermal resistance discovered in TAITherm for Test One is 0.005 m^2 K W^{-1}, which applies to both the PV-absorber and absorber-tube interfaces. In Type 560, a resistance of 0.015 m^2 K W^{-1} is found to be a better fit. This only applies to the PV-absorber interface but includes the EVA and glass not included in the TAITherm value. The McAdams convection model is also an improvement for Type 560 where a fixed convection coefficient of 5 W m^{-2} K^{-1} is more suitable in TAITherm.

The time series results for temperature and power (both thermal and electric) are shown in Figure 7 and Figure 8, respectively. In these figures, it can be seen that the TAITherm model tracks the measured data more consistently than Type 560, with less pronounced peaks and valleys during strong irradiation events. This is confirmed with the performance indicators given in Table 2, where the TAITherm model is shown to have a lower MAE and higher correlation.

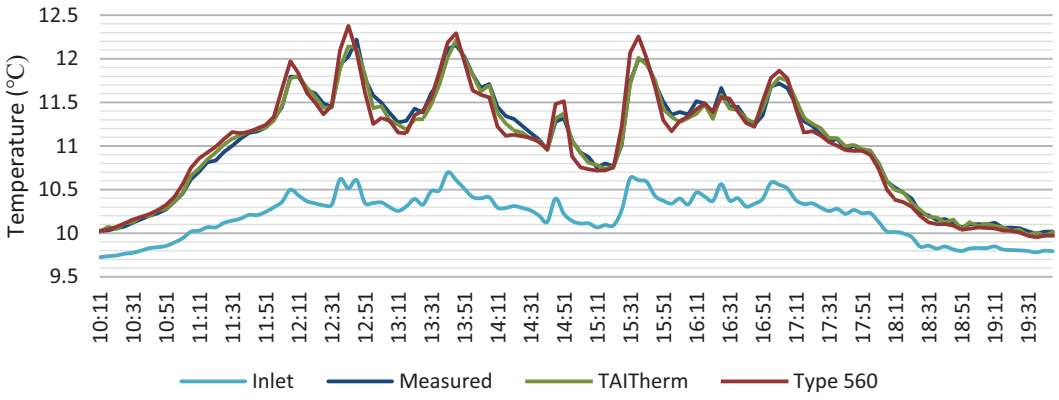

Figure 7 - Measured and model fluid outlet temperatures for Test One

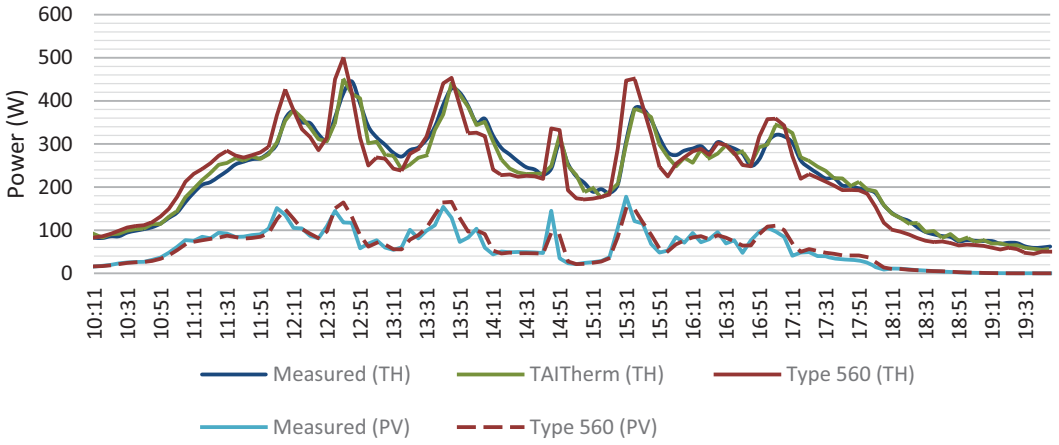

Figure 8 - Thermal and electrical power results for Test One

4.2 Test Two

The thermal resistance in Test Two for TAITherm is again 0.005 m^2 K W^{-1} while in Type 560 0.010 m^2 K W^{-1} is found to be a better fit. Once again the McAdams convection model is an improvement for Type 560 while a fixed coefficient of 5 W m^{-2} K^{-1} works better in TAITherm. The time series results shown in Figure 9 and Figure 10 show that Type 560 is tracking the measured data more closely when the irradiance is steadier with the clear skies. The performance indicators in Table 2 show a worse performance for TAITherm but approximately the same for Type 560 as in Test One.

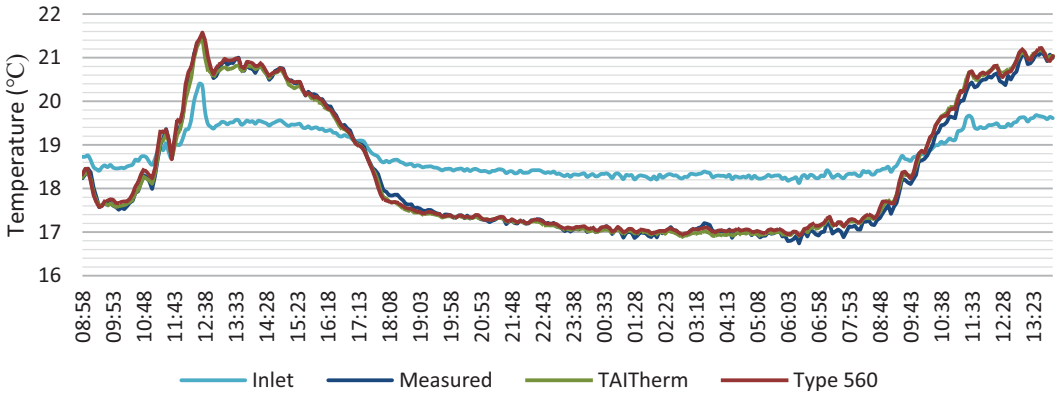

Figure 9 - Measured and model fluid outlet temperatures for Test Two

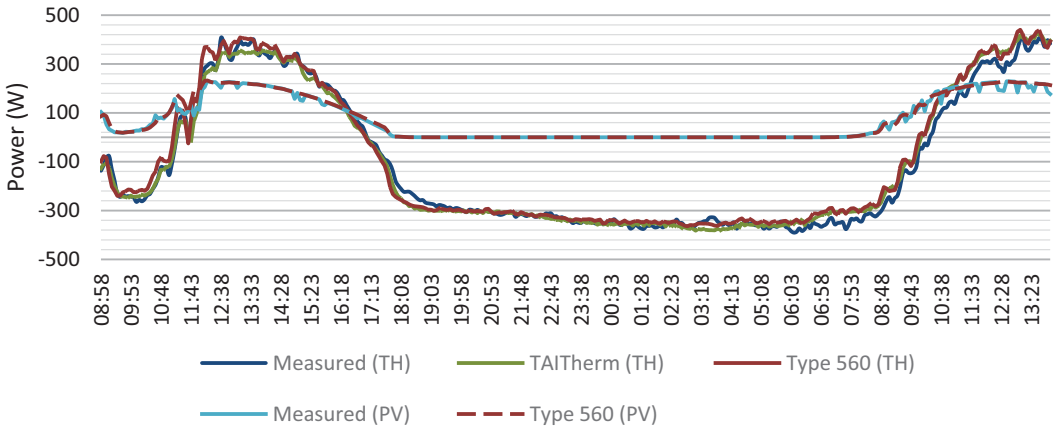

Figure 10 - Thermal and electrical power results for Test Two

4.2 Test Three

The thermal resistance in Test Three for TAITherm is increased to 0.010 m^2 K W^{-1} and 0.040 m^2 K W^{-1} for Type 560. In this test a static rear convection coefficient is best for both models and is the same in each at 6 W m^{-2} K^{-1}. The time series results shown in Figure 11 and Figure 12 are more difficult to interpret due to the longer timespan, however fluctuating irradiance again leads to a lower correlation for Type 560 during the daytime. The statistical indicators are notably worse for both models for this test as compared to the others.

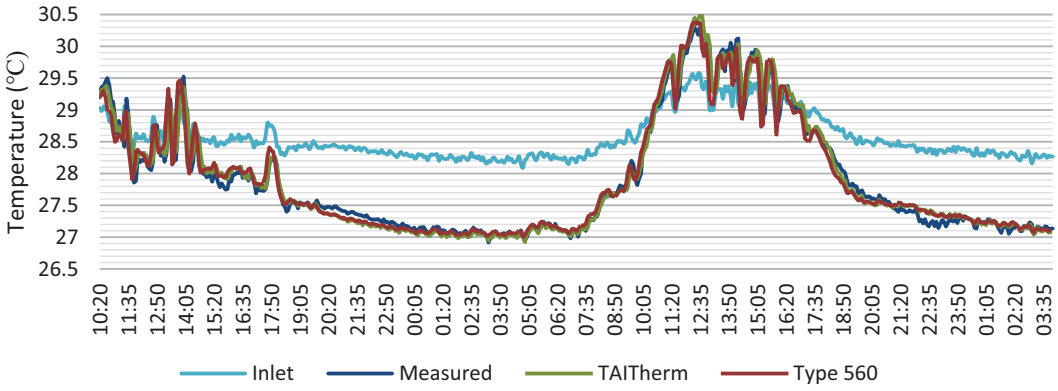

Figure 11 - Measured and model fluid outlet temperatures for Test Two

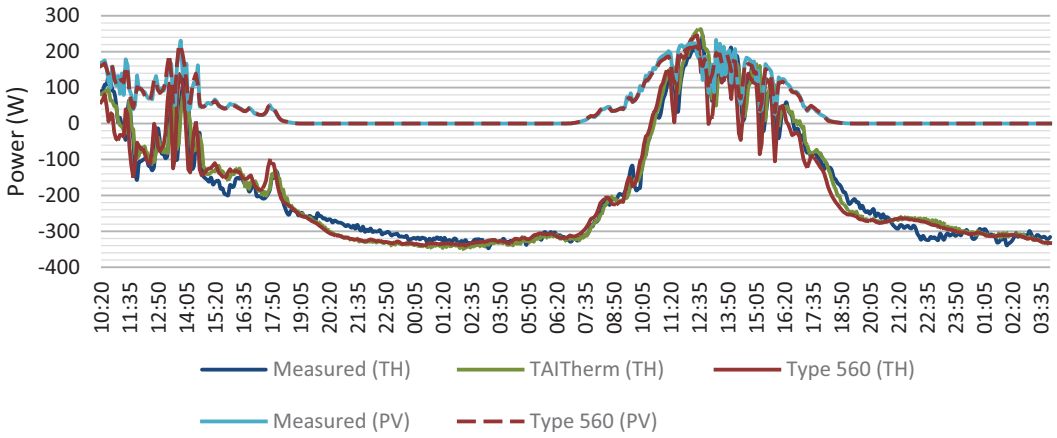

Figure 12 - Thermal and electrical power results for Test Two

Table 2 - Statistical performance indicators for all tests

Thermal Generation	Test One			Test Two			Test Three		
	Meas.	TAI	560	Meas.	TAI	560	Meas.	TAI	560
Total (kWh)	2.24	2.22	2.21	-3.24	-3.12	-2.74	-7.55	-7.52	-7.73
Diff. (kWh)	-	-0.02	-0.03	-	0.12	0.50	-	0.02	-0.19
Diff. (%)	-	-1.06%	-1.40%	-	-3.66%	-15.4%	-	-0.30%	2.46%

Electric Generation	Test One			Test Two			Test Three		
	Meas.	TAI	560	Meas.	TAI	560	Meas.	TAI	560
Total (kWh)	0.56	N/A	0.59	2.05	N/A	2.13	1.85	N/A	1.83
Diff. (kWh)	-	N/A	0.03	-	N/A	0.08	-	N/A	-0.02
Diff. (%)	-	N/A	4.86%	-	N/A	3.97%	-	N/A	-1.12%

	Test One		Test Two		Test Three	
Temp (K)	TAI	560	TAI	560	TAI	560
MAE	0.041	0.093	0.084	0.093	0.071	0.122
Correlation	0.997	0.983	0.997	0.998	0.996	0.979
Power (W_{th})	TAI	560	TAI	560	TAI	560
MAE	11.31	29.35	21.30	27.35	11.31	30.37
Correlation	0.989	0.939	0.996	0.994	0.989	0.961
Power (W_{el})	TAI	560	TAI	560	TAI	560
MAE	-	8.93	-	5.27	-	5.03
Correlation	-	0.945	-	0.990	-	0.984

5. Discussion and Conclusion

The tuning process is slow and tedious, however here it has produced two well performing models. The absolute uncertainty of the temperature probes is 0.1 K, therefore it is encouraging that MAE values are consistently below this. Besides uncertainty, the errors that remain are likely due to variations in the convection coefficients. Without knowledge of wind direction, it is difficult to know air speeds underneath the collectors. This is an addtional challenge with this type of PVT collector since the lack of insulation on the rear results in more sensitive convection gains or losses. In an actual installation, it is common to have skirting around the array such that air is not likely to pass underneath, which suggests a fixed coefficient will be more useful in systems modeling. Nevertheless, within this study the errors remain acceptably small particularly when considering larger systems models and annual simulations.

TAITherm produces results that are consistently better than Type 560, which is likely due to the modeling of thermal mass. With its glass-glass construction and thick aluminum extrusions, the PVT collector is approximately 35 kg, which is enough to potentially slow the response time of the heat transfer to the working fluid. This is seen in the time series data where there are rapid fluctuations in irradiance. It also appears in the Test Two statistical results, which had the most steady outdoor conditions and Type 560 performed the best. Adding thermal mass with other TRNSYS models in the system (e.g. pipes) could be a method to slow the thermal response. It is worth noting that this issue largely applies to studies where short time steps are critical. The energy generation values are within acceptable tolerances such that daily, monthly, or annual production is likely to be

reliable. This study does not quality as a full validation, however, and making these claims with certainty will require additional testing of the models against other data sets.

The modeling performed in this study has been valuable for several reasons. First, the thermal resistance values, summarized in Table 3, help place the performance of the prototype within other designs and/or products. Chow describes the thermal resistance between the PV cells and absorbers as being perfect when equal to 0.0001 m^2 K W^{-1}, and defective at 0.040 m^2 K W^{-1} (Chow, 2003). In this context, the 0.010 to 0.015 m^2 K W^{-1} values found with Type 560 in the first two test is relatively good, however the significantly higher value in Test Three is a cause for concern. A sensitivity analysis of this input is worthwhile when doing annual systems modeling, and the results here now provide a plausible range of values.

Table 3 - Thermal resistance parameters for each test and model (in m^2 K W^{-1})

	Test One	Test Two	Test Three
TAITherm	0.005	0.005	0.010
Type 560	0.015	0.010	0.040

Secondly, most solar thermal collector studies use the quadratic efficiency model. Having a theoretical PVT model is beneficial in that new designs without known efficiency coefficients can be modeled within systems, but it is important to have appropriate characteristics. The comparison between TAITherm and TRNSYS is useful because it validates the tuning process by having a second, fundamentally different model with similar results and it highlights the impact of the model structure on input parameters and the particular behavior of Type 560.

6. Acknowledgement

This research is funded by the Swedish Energy Agency under the Effsys Expand program, project number 40936-1.

7. References

Armstrong, S., Hurley, W.G., 2010. A thermal model for photovoltaic panels under varying atmospheric conditions. Appl. Therm. Eng. 30, 1488–1495. doi:10.1016/j.applthermaleng.2010.03.012

Chow, T.T., 2003. Performance analysis of photovoltaic-thermal collector by explicit dynamic model. Sol. Energy 75, 143–152. doi:10.1016/j.solener.2003.07.001

Duffie, J.A., Beckman, W.A., 2013. Solar Engineering of Thermal Processes, Fourth. ed. John Wiley & Sons, Inc., Hoboken, NJ.

Gliah, O., Kruczek, B., Etemad, S.G., Thibault, J., 2011. The effective sky temperature: An enigmatic concept. Heat Mass Transf. 47, 1171–1180. doi:10.1007/s00231-011-0780-1

Hardorn, J.-C. (Editor), 2015. Solar and Heat Pump Systems for Residential Buildings, First. ed. Ernst & Sohn GmbH & Co., Berlin.

Klein, S., Beckman, W.A., Mitchell, J., Duffie, J.A., Freeman, T., 2009. TRNSYS 17, A Transient System Simulation Program.

McAdams, W.H., 1954. Heat Transmission, Third. ed. McGraw-Hill, New York.

Michael, J.J., Iniyan, S., Goic, R., 2015. Flat plate solar photovoltaic – thermal (PV / T) systems : A reference guide. Renew. Sustain. Energy Rev. 51, 62–88. doi:10.1016/j.rser.2015.06.022

Mirsadeghi, M., Cóstola, D., Blocken, B., Hensen, J.L.M., 2013. Review of external convective heat transfer coefficient models in building energy simulation programs: Implementation and uncertainty. Appl. Therm. Eng. 56, 134–151. doi:10.1016/j.applthermaleng.2013.03.003

Perers, B., Kovacs, P., Olsson, M., Persson, M., Pettersson, U., 2012. A tool for standardized collector performance calculations including PVT. Energy Procedia 30, 1354–1364. doi:10.1016/j.egypro.2012.11.149

Pressiani, M., 2016. Photovoltaic/thermal hybrid solar collectors: TRNSYS analysis and possible improvements. Politecnico Milano.

Sommerfeldt, N., Madani, H., 2016. Review of Solar PV/Thermal Plus Ground Source Heat Pump Systems for European Multi-Family Houses, in: 11th ISES Eurosun Conference. Palma de Mallorca, Spain.

Test, F.L., Lessmann, R.C., Johary, a., 1981. Heat Transfer During Wind Flow over Rectangular Bodies in the Natural Environment. J. Heat Transfer 103, 262. doi:10.1115/1.3244451

ThermoAnalytics, 2016. TAITherm [WWW Document]. URL http://www.thermoanalytics.com/products/taitherm

Zondag, H., 2008. Flat-plate PV-Thermal collectors and systems: A review. Renew. Sustain. Energy Rev. 12, 891–959. doi:10.1016/j.rser.2005.12.012

PVT Wrap-Up:
Energy Systems with Photovoltaic-Thermal Solar Collectors
-
Technology, Market, Experiences

Daniel Zenhäusern, Evelyn Bamberger, Aleksis Baggenstos and Andreas Häberle

SPF Institute for Solar Technology, HSR University of Applied Sciences, Rapperswil (Switzerland)

Abstract

While the interest in Photovoltaic Thermal (PVT) solar collectors is growing, the related practical knowhow and experience are still rather sparse. In this context, a review study on PVT was carried out, focusing on three main aspects: 1) Technology : different types of collectors, different ways of integrating PVT into energy systems, energetic yields of different system configurations, 2) Market overview : PVT industry, available products, principle fields of application, 3) Experiences : experiences from 7 pilot plants with collector areas between 50 m^2 and 3500 m^2, additional PVT plants in operation, points of view of different actors involved in the planning, construction and operation of PVT systems. In this article, we present the key outcomes of the study.

Keywords: Photovoltaic-Thermal Collectors, PVT Collectors, PVT Review

1. Introduction

PVT collectors integrate photovoltaic and thermal solar energy conversion in a single device and thereby reach high yields per area. In situations where roof area is limited, and particularly in the light of new regulations requiring a part of the energy demand of buildings to be produced on site, PVT collectors provide an attractive option. In order to answer the growing interest in PVT, in particular from house builders and installation companies, the presented wrap-up study, mandated by the Swiss Federal Office of Energy, aims to give a concise overview of the PVT technology, the PVT market, and the experiences made with PVT in real system operation. Besides a thorough literature research, a survey as well as a number of interviews were carried out among the different actors related to PVT, such as manufacturers, distributors, planners and installers. The study further included several case studies, based on data acquired by different research groups. The full report of the study was published in german in Ref. (Zenhäusern, et al., 2017). The present article summarizes its key results.

2. Technology and Market

Different concepts of PVT collectors have been considered in applied research for about 40 years. Extensive reviews of the diverse developments, as well as entry points to the relevant literature are provided by Refs. (Zondag, 2008; Michael, et al., 2015). Numerous manufacturers have brought PVT products to the market. However, while new products regularly enter the market, other manufacturers withdraw from the PVT sector. Earlier market-related review studies were presented in Refs. (Adam, et al., 2014; Cremers, et al., 2015; UK Department for Business, Energy & Industrial Strategy, 2016). The PVT sector has gained interest in recent years. Among the reasons for this upsurge are the increased spread and the price drop of photovoltaic modules, as many PVT products are extensions of standard PV modules. In the case of Switzerland, the rise of interest in PVT collectors was particularly triggered by the increasing need of low-temperature heat for the regeneration of ground heat sources in heat pump systems.

doi:10.18086/swc.2017.18.12 Available at http://proceedings.ises.org

For the market survey in the present study, PVT collectors were grouped in three categories: collectors working with a liquid heat carrier medium divided into products with and without cover (transparent cover to reduce convective heat losses) and air-based collectors (typically without cover).[1] The survey with main focus on Switzerland and neighbouring countries revealed 53 PVT collector manufactures in 17 countries (Figure 1). The large majority of products (38) corresponds to liquid-cooled uncovered PVT collectors with or without heat insulation on their backside. 6 products are covered liquid-cooled collectors, and 9 products are uncovered air-cooled PVT collectors.

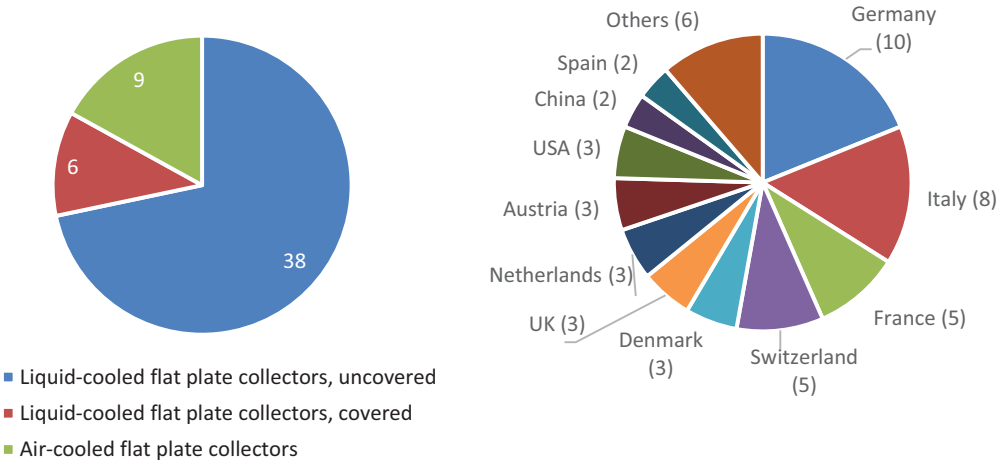

Figure 1: PVT products grouped in collector type categories (left) and number of manufacturers in the different countries (right).

3. System integration of PVT collectors

Like in the case of conventional solar thermal collectors, the thermal efficiency of the different types of PVT collectors strongly depends on their operating temperature. Thermal power curves for typical market-available products of the different categories are shown in Figure 2.

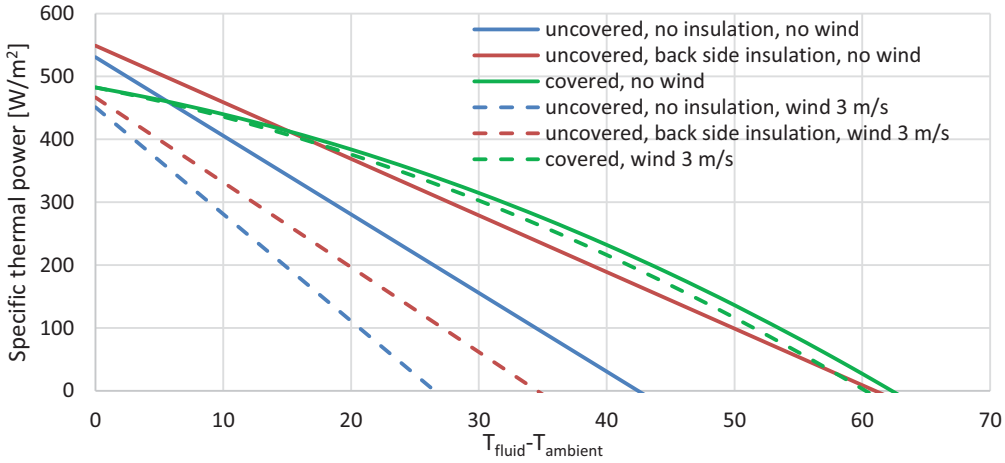

Figure 2: Thermal power of typical liquid-cooled PVT collectors at maximum electrical power point (MPP), related to the gross collector area and for a global solar irradiance of G=1000 W/m².

Expectable annual gross heat and electricity gains as well as differences in electricity gain compared to pure PV modules were calculated with the software Polysun, for different liquid-cooled PVT collectors and different operating temperatures. The gross heat and electricity gains correspond to the heat and electricity yields one would obtain, if the thermal circuit was turned on and operated at the specified temperature, whenever the thermal efficiency of the collector at this temperature is positive. Figure 3 shows the results for the climate of Zürich (CH) with a yearly solar irradiation on the horizontal plane of 1109 kWh/m² and a mean ambient temperature of 9.9 °C.

[1] Concentrating PVT collectors were not considered in this survey.

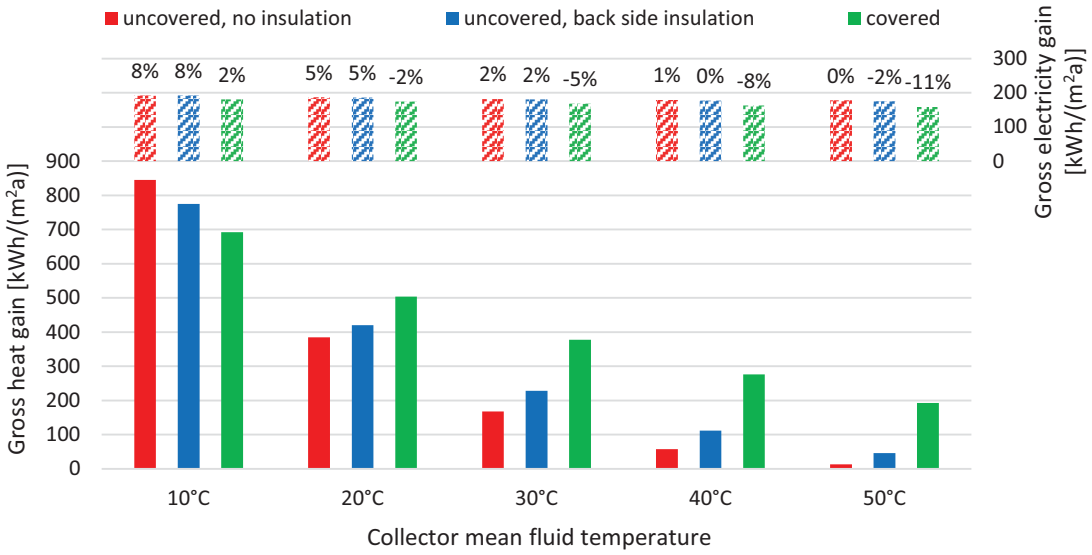

Figure 3: Gross heat and electricity gains for different liquid-cooled PVT collector types, climate of Zürich (CH), collector orientation south, inclination 45°. Percentages correspond to the difference in electrical yield compared to pure PV modules.

For low operating temperatures, the heat gains include converted solar irradiation as well as ambient heat collected in periods where the collector is operated below ambient temperature. Therefore, for low operating temperatures, uncovered collectors and collectors without back side heat insulation have an advantage. For higher operating temperatures, i.e. which over the year predominantly lie above ambient temperature, heat insulation and transparent covers are advantageous. In systems where the heat is always needed at temperatures above 50 °C, only covered collectors can contribute a notable amount of heat.

The lower the operating temperatures, the higher are the electrical yields. The percentage values in Figure 3 indicate the additional electrical yield compared to a standard PV module with average ventilation on the rear side. *Uncovered PVT modules without rear insulation* achieve the highest additional electricity yields. Their maximum (stagnation) temperatures correspond to the temperatures of pure PV modules. When no heat is extracted, they have the same electrical yield. *Uncovered PVT collectors with rear insulation* achieve similar additional electrical yields at low temperatures. As they can reach higher temperatures, their electrical yield at high temperatures is somewhat below the yield of PV modules. *Covered PVT collectors* generally reach lower electricity yields compared to uncovered ones. This is due to higher reflection losses at the transparent cover and due to longer periods of operation at higher temperatures. Compared to pure PV modules, a slight increase of electricity production can be achieved at low operating temperatures, in spite of the additional reflexion losses. At higher operating temperatures, however, their electrical yield can lie considerably below the one of PV modules. Therefore, in systems with covered PVT collectors, it is important to avoid long periods without heat consumption (stagnation).

Systems with uncovered liquid-cooled PVT collectors

From the above discussion, it is clear that uncovered PVT collectors are most suited for low-temperature applications. An important field of use is their integration in heat pump systems, where the low-temperature heat most commonly serves the following purposes: a) regeneration of a ground heat source, b) regeneration of a latent heat (ice) storage, c) regeneration of a cold sensible heat storage, d) pre-heating of a groundwater storage, and e) direct heat source of the heat pump (Figure 4). Variants a)-d) can all be combined with variant e). Further, all variants can be supplemented with the option to directly deliver solar heat to the secondary side of the heat pump, i.e. for example to a hot water or a space heating storage tank. This option is profitable to the energetic efficiency of the system. The quantitative benefit depends on storage temperatures and volumes. Further, one has to consider the additional complexity of the system.

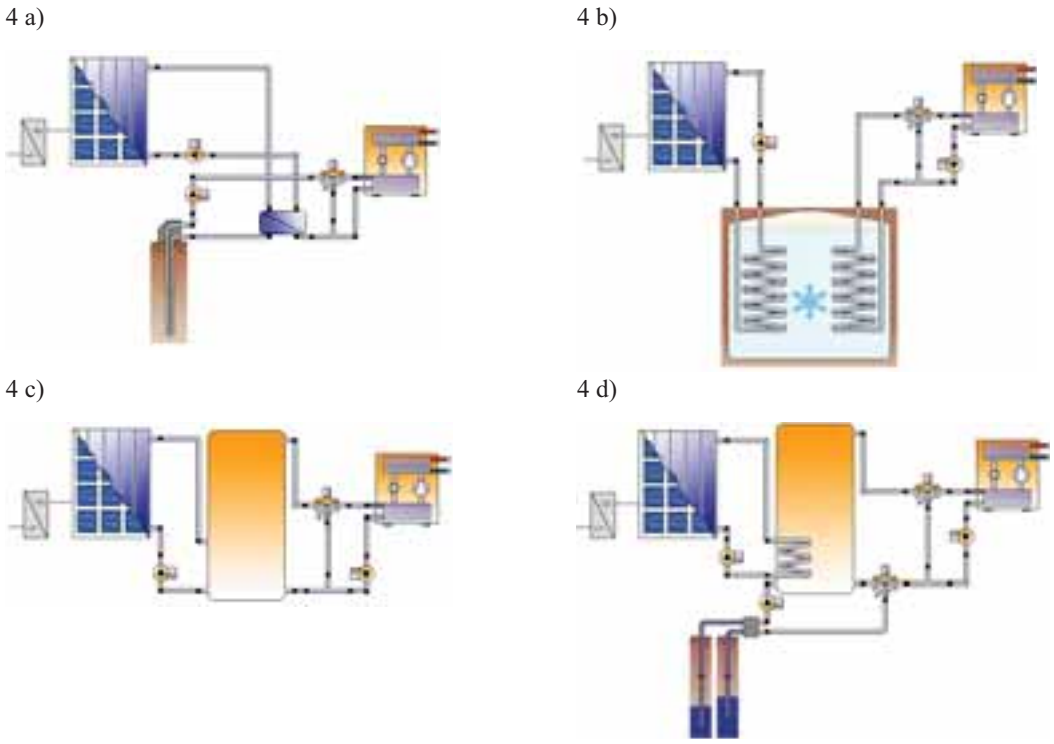

Figure 4: Schematics of different variants for integrating uncovered PVT collectors on the primary (source) side of a brine/water- or water/water-heat pump system. The heat sinks, which would be on the right side of the heat pump, are not depicted. (Schematics were made with the Software Polysun.)

Besides being integrated on the primary (source) side of heat pump systems, uncovered liquid-cooled collectors are also used in systems where they directly provide useful heat at the required temperature level. The applications basically correspond to the classical variants of solar thermal systems, such as: a) domestic hot water (pre-)heating, b) pool heating, and c) domestic hot water heating plus space heating (Figure 5).[1]

Systems with covered liquid-cooled PVT collectors

Regarding only the thermal part, covered PVT collectors can essentially be used like covered (glazed) solar thermal flat plate collectors. Most common is their application in systems for domestic hot water preparation with or without solar assisted space heating (Figure 5). A major difference to systems with pure thermal collectors lies in the handling of stagnation situations. In fact, several market-available covered PVT collectors must not be exposed to extended periods of stagnation at high temperatures, due to the low temperature resistance of the involved materials. Hence, the use of such products requires a fail save stagnation prevention on the system level, such as an additional heat dump (e.g. heat exchanger to ambient air) together with an appropriate system control.

Systems with air-cooled PVT collectors

Air-cooled PVT collectors are predominantly used in open systems. Ambient air is aspirated by a ventilator and guided behind the PV cells. The warmed-up air is often used for direct space heating or ventilation (Figure 6 a). The same configuration can serve be used for space cooling. An additional application is the use of the pre-heated air on the source side of an air/water-heat pump, for hot water preparation or space heating, permitting a rise of the performance factor of the heat pump (Figure 6 b). Further interesting applications of air-based PVT collectors include drying plants (e.g. for agricultural products or wood) and the ventilation of indoor swimming pools or enamelling plants.

[1] For the case of domestic hot water (DHW) preparation, a “pre-heating” system is dimensioned such that it reaches a solar fraction around 20 %, while a standard solar DHW system reaches a solar fraction around 50 %.

5 a)

5 b)

5 c)

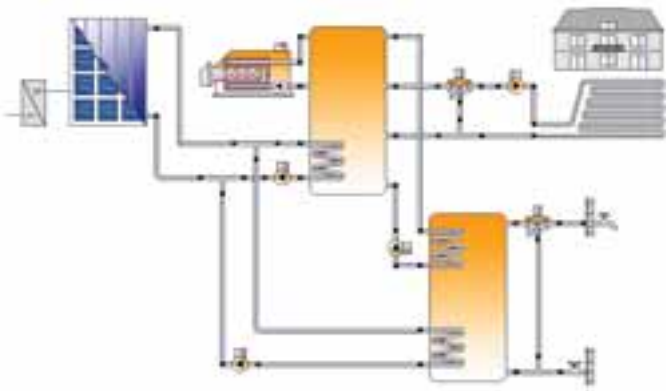

Figure 5: Schematics of system variants with PVT collectors directly providing useful heat at required temperature level.

6 a)

6 b)

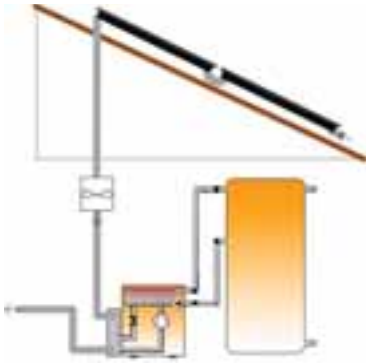

Figure 6: Schematics of system integrations of air-cooled PVT collectors: a) direct room heating or cooling, b) pre-heating of ambient air on the source side of an air/water heat pump.

Systems installed

In Switzerland, there are at present about 300 PVT systems in operation, with an estimated total area of 15'000 m^2. The vast majority of the plants uses liquid-cooled uncovered PVT collectors. According to the interviewed companies, in almost 50 % of the systems the PVT heat serves the (pre-)heating of domestic hot water (DHW), sometimes in a combination with space heating. In more than 40 % of the systems, the collectors are combined with heat pumps, where the solar heat is most commonly used for the regeneration of ground heat sources. A smaller share of the systems (< 10 %) uses PVT for pool heating. Given the generally large size of installations for ground source regeneration, this application makes for the largest part of the total installed collector area.

4. Survey results

A survey was conducted among two groups, manufacturers of PVT modules on one hand and planners/distributors/installers of PV, PVT and solar thermal systems on the other hand. Besides a number of other questions, participants of the survey were asked about the motivation of house builders for choosing PVT. The corresponding answers are shown in Figure 7.

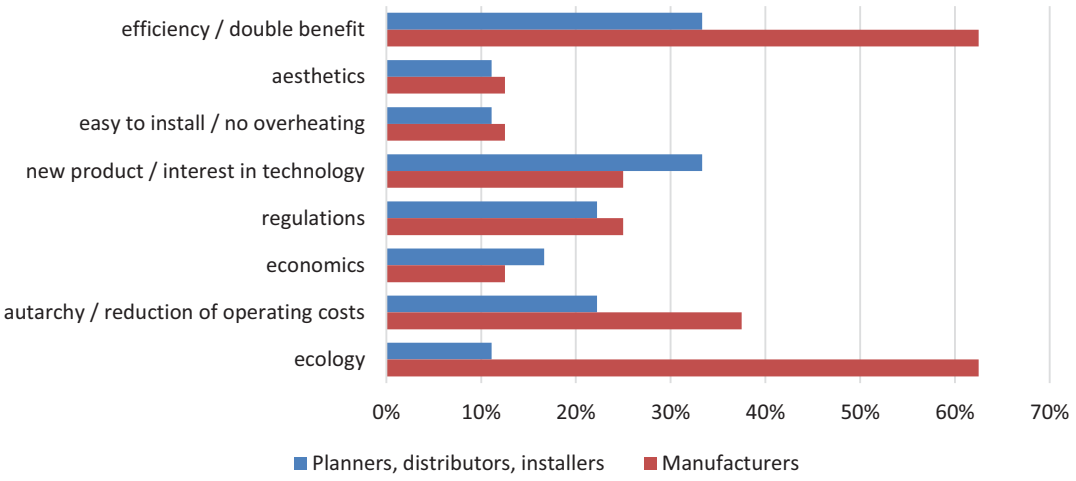

Figure 7: Motivations of house builders for choosing PVT collectors, as seen by manufactures and planners/distributors/installers respectively. The bars show the percentage of answering companies, which mentioned the corresponding argument.

Answers to the question about what should change in order to foster the deployment of PVT are shown in Figure 8. “high costs” and “sparse know-how” are raised as important aspects by both groups, manufacturers of PVT as well as distributors/planners/installers. It is interesting to notice that only the latter group mentions that product design and efficiency of PVT collectors should be improved.

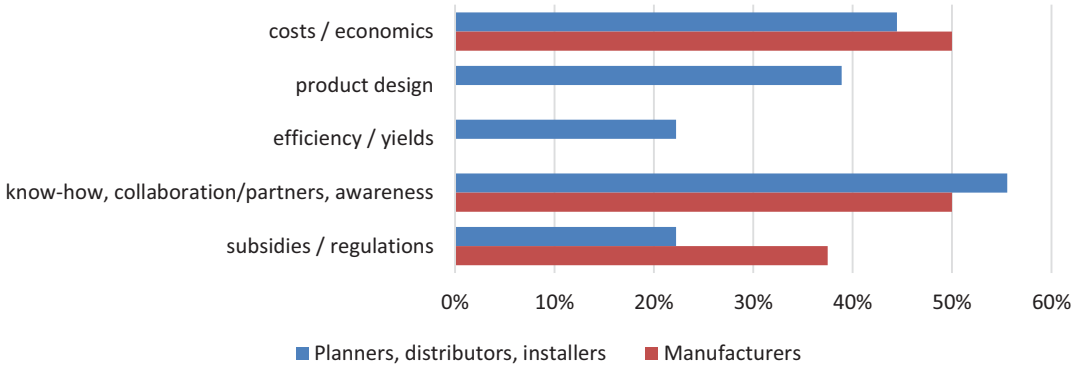

Figure 8: Survey results to the question about what should change, in order to foster the deployment of PVT.

5. Case studies

In Switzerland, 7 large PVT plants with collector field areas between 50 m^2 and 3500 m^2 were built in connection with so-called Pilot and Demonstration (P&D) projects, which received public financial support. In these installations, PVT is used for ground source regeneration, pre-heating of ground water providing heat to a heat pump, and in connection with a low-temperature heat distribution network, respectively. All installations are equipped with detailed monitoring and data acquisition systems and their performance is analysed by different research groups. In the full report of the presented review study, all these projects are briefly presented together with the main results obtained by the respective groups and references to further information (Zenhäusern, et al., 2017). Two examples of pilot plants are shown in Figure 9 and Figure 10. Based on measurement data of various projects (P&D and other), one can state that standard uncovered liquid-cooled PVT collectors in a typical Swiss climate reach an electrical yield of ~ 170 kWh m^{-2} a^{-1} plus a thermal yield of ~ 150 kWh m^{-2} a^{-1} (DHW), ~ 250 kWh m^{-2} a^{-1} (DHW pre-heating), 300 – 400 kWh m^{-2} a^{-1} (regeneration of ground source), and > 400 kWh m^{-2} a^{-1} (pre-heating of ground water at the source of a heat pump), respectively.

Figure 9: P&D project Sotchà in Scuol (CH). Roof-integrated PVT plant for the regeneration of boreholes (Vassella & Baggenstos, 2015).

Figure 10: P&D project Lintharena in Näfels (CH). Uncovered PVT collectors for the pre-heating of groundwater providing heat to a heat pump (Rohrer, 2016).

Acknowledgements

This article is based upon work financed by EnergieSchweiz, a programme by the Swiss Federal Office of Energy (SFOE). The authors gratefully acknowledge the financial support.

References

Adam, M., Wirth, H. P. & Radosavljevic, R., 2014. *Verbundprojekt: Standardisierung und Normung von multifunktionalen PVT Solarkollektoren (PVT-Norm), Teilvorhaben: PVT-Systemanwendungen und Simulationen,* Düsseldorf.

Cremers, J. et al., 2015. *Multivalente photovoltaisch-thermische Kollektoren zur Kälte-, Wärme- und Stromerzeugung und Szenarien für die Gebäudeintegration [PVTintegral],* Stuttgart.

Michael, J. J., Iniyan, S. & Goic, R., 2015. Flat plate solar photovoltaic–thermal (PV/T) systems: A reference guide. *Renewable and Sustainable Energy Reviews,* Vol. 51.

Rohrer, J., 2016. *PVT-Solarkraftwerk linth-arena sgu: Strom und Wärme vom Dach,* Bern: Projekt Nr. SI/501095, Jahresbericht 2016 an BFE, Bundesamt für Energie.

UK Department for Business, Energy & Industrial Strategy, 2016. *Evidence Gathering - Low Carbon Heating Technologies, Hybrid Solar Photovoltaic Thermal Panels,* London.

Vassella, C. & Baggenstos, A., 2015. *Drei unterschiedliche innovative solarunterstützte Wärmeerzuegungssysteme für drei identische Minergie-A-Gebäude,* Bern: Projekt Nr. SI/501244-01, Jahresbericht 2015 an BFE, Bundesamt für Energie.

Zenhäusern, D., Bamberger, E. & Baggenstos, A., 2017. *PVT Wrap-Up, Energiesysteme mit Photovoltaisch-Thermischen Solarkollektoren,* Bern: EnergieSchweiz.

Zondag, H. A., 2008. Flat-plate PV-Thermal collectors and systems: A review. *Renewable and Sustainable Energy Reviews,* Vol. 12.

Paper formatting

The manuscript must be written in English. The paper title should be written in Arial, 14 point, bold. The section headings should be numbered, in **Arial 12 pt bold**, the sub-sections in *Arial 11 pt italic*. The standard font for the manuscript is Times New Roman for the text and Symbol for special characters. Body text should be justified as block, 10 pt, in single column format. Line spacing is at multiple of 1.15

The paper size is A4 (210 mm x 297 mm). Margins are 19.0 mm top; 25.4 mm right and bottom and 30.0 mm left. Do not change the paper formatting and do not insert page numbers, headers or footers! Papers using incorrect formatting may be rejected for publication in the proceedings if the author does not make corrections. Insert the lead author name in header starting on the second page. References must be formatted exactly as shown in the examples given below. The sections and sub-sections must be numbered by the author(s); do not use automatic paragraph numbering.

Please use the styles that are defines in the Word Document (under the Style Menu) to format the text instead of directly setting the fonts. The styles are

- *SWC_heading1* for first level section headers
- *SWC_heading1.1* for second leven section headers
- *SWC_text* for the body
- Styles for table and figure captions.

This will ensure that the margins for the sections are also correct and will result in less work for you and a consistent layout for our conference proceedings

Tables, figures, equations, and lists

3.1. Tables

All figures and tables must be cited in the text, numbered in order of appearance and followed by a centered title. Each table column should contain a brief explanatory heading.

Tab. 1: Table captions (8 pt) should be justified as block and placed above the table

Table Header	Header	Header
Tables	Text	Text

3.2. Figures

Figures should be submitted with a resolution of minimum 300 dots per inch and followed by a figure caption, justified as block. Please make sure that the axes and any text within the figure are legible with a minimum font size of 8.

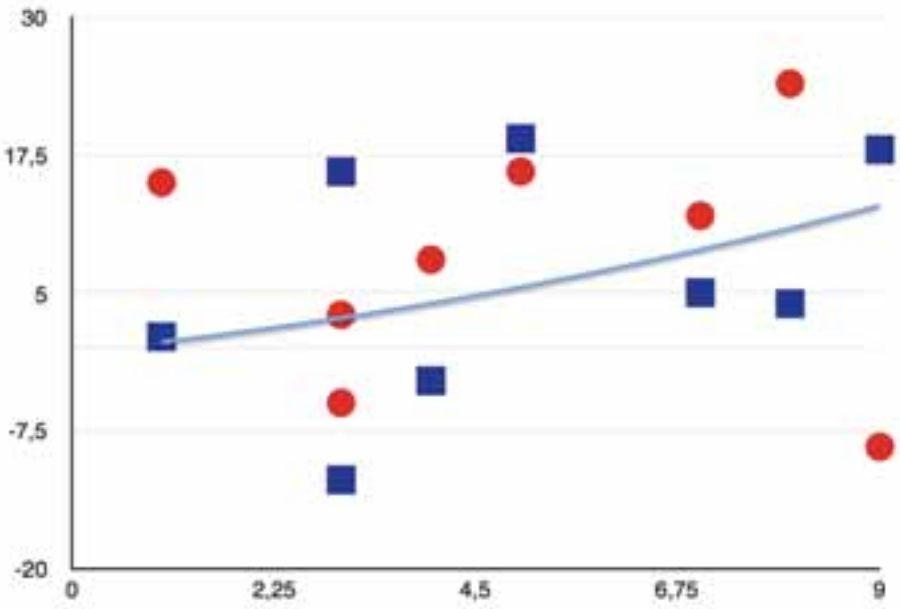

Fig. 1: Figure captions (8 pt) should be justified as block and placed below the figure

3.3 Equations

Equations should be arranged to the left, with characters similar to that of the body text and should be numbered.

$$\frac{1}{2\pi}\int_0^{2\pi}\frac{d\theta}{a+b\sin\theta}=\frac{1}{\sqrt{a^2-b^2}} \qquad \text{(eq. 1)}$$

$$\sin\alpha\pm\sin\beta=2\sin\tfrac{1}{2}(\alpha\pm\beta)\cos\tfrac{1}{2}(\alpha\mp\beta) \qquad \text{(eq. 2)}$$

3.4 Lists

- Bulleted lists can be used to arrange information more clearly in the text.

References

All references should be made according to the guidelines, as shown below.

Please ensure that each reference cited in the text is also present in the reference list (and vice versa). Any references cited in the abstract must be indicated completely. Unpublished results and personal communications are not recommended in the reference list, but may be mentioned in the text.

For web references, at least the full URL should be given and the date when the reference was last accessed. Any further information, if known (DOI, author names, dates, reference to a source publication, etc.), must also be given. Web references can be listed separately (e.g., after the reference list) under a different heading if desired, or can be included in the reference list. DOI must be included if available.

4.1 Text

All citations in the text should refer to:

1. *Single author*: the author's name (without initials, unless there is ambiguity) and the year of publication;

2. *Two authors*: both authors' names and the year of publication;

3. *Three or more authors*: first author's name followed by "et al." and the year of publication. Citations may be made directly (or parenthetically). Groups of references should be listed first alphabetically, then chronologically.

Example: "as demonstrated (Allan, 1996a, 1996b, 1999; Allan and Jones, 1995). Kramer et al. (2000) have recently shown ...."

List:

References should be arranged first alphabetically and then further sorted chronologically if necessary. More than one reference from the same author(s) in the same year must be identified by the letters "a", "b", "c", etc., placed after the year of publication.

Examples for references:

Reference to a journal publication:

Van der Geer, J., Hanraads, J.A.J., Lupton, R.A., 2000. The art of writing a scientific article. J. Sci. Commun. 163, 51-59.

Reference to a book: Strunk Jr., W., White, E.B., 1979. The Elements of Style, third ed. Macmillan, New York.

Reference to a chapter in an edited book: Mettam, G.R., Adams, L.B., 1999. How to prepare an electronic version of your article, in: Jones, B.S., Smith, R.Z. (Eds.), Introduction to the Electronic Age. E-Publishing Inc., New York, pp. 281-304.

Use of units and symbols:

For the use of units and symbols, please see the appendix below.

Appendix: Unites and Symbols

1. Units

The use of S.I. (Système International d'unités) in papers is mandatory. The following is a discussion of the various S.I. units relevant to solar energy applications.

Energy
The S.I. unit is the joule (J ≡ kg m^2 s^{-2}). The calorie and derivatives, such as the langley (cal cm^{-2}), are not acceptable. No distinction is made between different forms of energy in the S.I. system so that mechanical, electrical and heat energy are all measured in joules. Because the watt-hour is used in many countries for commercial metering of electrical energy, its use is tolerated here as well.

Power
The S.I. unit is the watt (W ≡ kg m^2 s^{-3} ≡ J s^{-1}). The watt will be used to measure power or energy rate for all forms of energy and should be used wherever instantaneous values of energy flow rate are involved. Thus, energy flux density will be expressed as W m^{-2} and heat transfer coefficient as W m^{-2} K^{-1}. Energy rate should not be expressed as J h^{-1}.
When power is integrated for a time period, the result is energy that should be expressed in joules, e.g. an energy rate of 1.2 kW would produce 1.2 kW x 3600 s = 4.3 MJ if maintained for 1 h. It is preferable to say that

Hourly energy = 4.3 MJ

rather than

Energy=4.3 MJ h^{-1}.

Force
The S.I. unit is the Newton (N ≡ kg m s^{-2}). The kilogram weight is not acceptable.

Pressure
The S.I. unit is the Pascal (Pa ≡ N m^{-2} ≡ k^2 m^{-1} s^{-2}). The unit kg cm^{-2} should not be used. It is sometimes practical to use 10^5 Pa = 1 bar = 0.1 MPa. The atmosphere (1 atm = 101.325 kPa) and the bar, if used, should be in parenthesis, after the unit has been first expressed in Pascals. e.g. 1.23 x 10^6 Pa (12.3 atm). Manometric pressures in meters or millimeters are acceptable if one is reporting raw experimental results. Otherwise they should be convened to Pa.

Velocity
Velocity is measured in m s^{-1}. Popular units such as km h^{-1} may be in parentheses afterward.

Volume
Volumes are measured in m^3 or litres (1 litre = 10^{-3} m^3). Abbreviations should not be used for the litre.

2. Flow

In S.I. units, flow should be expressed in kg s^{-1}, m^3 s^{-1}, litre s^{-1}. If non-standard units such as litre min^{-1} or kg h^{-1} must be used, they should be in parentheses afterward.

Temperature
The S.I. unit is the degree Kelvin (K). However, it is also permissible to express temperatures in the degree Celsius (°C). Temperature differences are best expressed in Kelvin (K).
When compound units involving temperature are used, they should be expressed in terms of Kelvin, e.g. specific heat J kg^{-1} K^{-1}.

3. Nomenclature and Symbols

Tables 1-5 list recommended symbols for physical quantities. Obviously, historical usage is of considerable importance in the choice of names and symbols and attempts have been made to reflect this fact in the tables. But conflicts do arise between lists that are derived from different disciplines. Generally, a firm recommendation has been made for each quantity, except for radiation where two options are given in Table 5.
In the recommendations for *material properties* (see Table 1), the emission, absorption, reflection, and transmission of radiation by materials have been described in terms of quantities with suffixes 'ance' rather than 'ivity', which is also sometimes used, depending on the discipline. It is recommended that the suffix 'ance' be used for the following four quantities:

$$\text{emittance } \varepsilon = \frac{E}{E_b}\left(or \frac{M_s}{M_{sb}} \right)$$

$$\text{absorptance } \alpha = \frac{\Phi}{\Phi_i}$$

$$\text{reflectance } \rho = \frac{\Phi}{\Phi_i}$$

$$\text{transmittance } \tau = \frac{\Phi}{\Phi_i}$$

where E and ϕ is the radiant flux density that is involved in the particular process. The double use of α for both absorptance and thermal diffusivity is usual, as is the double use of ρ for both reflectance and density. Neither double use should give much concern in practice.

Table 1: Recommended symbols for materials properties

Quantity	Symbol	Unit
Specific heat	c	J kg^{-1} K^{-1}
Thermal conductivity	k	W m^{-1} K^{-1}
Extinction coefficient^{+}	K	m^{-1}
Index of refraction	n	
Absorptance	α	
Thermal diffusivity	α	m^2 s^{-1}
Specific heat ratio	γ	
Emittance	ε	
Reflectance	ρ	
Density	ρ	kg m^{-3}
Transmittance	τ	

$^{+}$ In meteorology, the *extinction coefficient* is the product of K and the path length and is thus dimensionless.

Table 2: Recommended symbols and sign convention for sun and related angles

Quantity	Symbol	Range and sign convention
Altitude	α	0 to ± 90°
Surface tilt	β	0 to ± 90°; toward the equator is +ive
Azimuth (of surface)	γ	0 to 360°; clockwise from North is +ive
Declination	δ	0 to ± 23.45°
Incidence (on surface)	Θ, i	0 to + 90°
Zenith angle	Θ_z	0 to + 90°
Latitude	Φ	0 to ± 90°; North is +ive
Hour angle	ω	-180° to +180°; solar noon is 0°, afternoon is +ive
Reflection (from surface)	r	0 to + 90°

Table 3: Recommended symbols for miscellaneous quantities

Quantity	Symbol	Unit
Area	A	m^2
Heat transfer coefficient	h	W m^{-2} K^{-1}
System mass	m	kg
Air mass (or air mass factor)	M	
Mass flow rate	$\dot{m}$	kg s^{-1}
Heat	Q	J
Heat flow rate	$\dot{Q}$	W
Heat flux	q	W m^{-2}
Temperature	T	K
Overall heat transfer coefficient	U	W m^{-2} K^{-1}
Efficiency	η	
Wavelength	λ	m
Frequency	ν	s^{-1}
Stefan-Boltzmann constant	σ	W m^{-2} K^{-4}
Time	t, τ, Θ	s

Table 4: Recommended subscripts

Quantity	Symbol
Ambient	a
Black-body	b
Beam (direct)	b
Diffuse (scattered)	d
Horizontal	h
Incident	i
Normal	n
Outside atmosphere	o
Reflected	r
Solar	s
Solar constant	sc
Sunrise (sunset)	sr, (ss)
Total of global	t
Thermal	t, th
Useful	u
Spectral	λ

Table 5: Recommended symbols for radiation quantities

	Preferred name	Symbol	Unit
a)	Nonsolar radiation		
	Radiant energy	Q	J
	Radiant flux	Φ	W
	Radiant flux density	Φ	W m^{-2}
	Irradiance	E, H	W m^{-2}
	Radiosity or Radiant exitance	M, J	W m^{-2}
	Radiant emissive power (radiant self-exitance)	Ms, E	W m^{-2}
	Radiant intensity (radiance)	L	W m^{-2} sr^{-1}
	Irradiation or radiant exposure	H	J m^{-2}
b)	Solar radiation		
	Global irradiance or solar flux density	G	W m^{-2}
	Beam irradiance	G_b	W m^{-2}
	Diffuse irradiance	G_d	W m^{-2}
	Global irradiation	H	J m^{-2}
	Beam irradiation	H_b	J m^{-2}
	Diffuse irradiation	H_d	J m^{-2}
c)	Atmospheric radiation		
	Irradiation	$\Phi\downarrow$	W m^{-2}
	Radiosity	$\Phi\uparrow$	W m^{-2}
	Exchange	Φ_N	W m^{-2}

Performance Measurement, Durability and Reliability

Advanced Testing and Quality Assurance Methods for Solar Thermal Systems and Components

Dominik Bestenlehner, Harald Drück and Stephan Fischer

Solar and Heat Technology Stuttgart (SWT)

Pfaffenwaldring 6, 70569 Stuttgart, Germany

bestenlehner@swt-stuttgart.de, www.swt-technologie.de

Abstract

Reducing costs and increasing efficiency is important for solar thermal test laboratories. However, this aspect is in contrast to the requirements for high quality and reproducible tests. To overcome this problem the present publication shows methods and procedures in combination with an "all-in-one test facility" to provide both, high quality and reproducible test results within shortest time requiring as less human resources as possible. Furthermore, the reliability of the test methods in combination with the described test facilities is shown by means of .validation measurements.

Keywords: solar thermal, test facility, performance testing, durability and reliability testing, quality assurance, test procedures, standards, certification

1. Introduction

Testing of solar thermal systems and components is mandatory for quality assurance. Furthermore, detailed tests and reproducible test methods ensure the conformity of related products with requirements of certification schemes.

Most certification schemes such as Solar Keymark in Europe, SRCC in the US, Golden Sun in China and SHAMCI in the Arab region require several tests, both for durability and reliability as well as tests for the thermal performance of the related products. To perform all required tests in an accurate and reproducible way, appropriated test facilities are needed by the testing laboratories. These test facilities usually absorb both, a high financial investment and huge amounts of man power to operate the test facilities. To overcome this problem an all-in-one test facility for solar thermal collectors, stores and systems was developed a few years ago. As the regulations and standards have now changed, the "all-in-one test facility" was redesigned, further developed and improved to fulfill the latest state of the art technology for testing solar thermal products.

2. Durability and reliability testing

For testing the performance, reliability, durability and safety solar thermal collectors according to the standard ISO 9806:2017 several tests and therefore various test facilities are necessary.

Besides the test for the determination of the thermal performance the most complex test procedures related to durability and reliability are the following six tests:

- the high-temperature resistance test,
- the determination of the standard stagnation temperature,
- the exposure and pre-exposure test,
- the external and internal thermal shock test,
- the rain penetration test.

Beside these tests the following, minor challenging tests are required:

doi:10.18086/swc.2017.19.01 Available at http://proceedings.ises.org

- Internal pressure tests of fluid channels,
- Freeze resistance test
- Mechanical load test with positive and negative pressure
- Impact resistance test

Usually, for each of those test procedures a single test facility is required comprising a test stand and measuring equipment. Furthermore, for the operation of the test facility qualified test engineers are necessary.
For example, the **exposure test** requires a test stand for the solar thermal collector, a data logger, temperature sensors and a pyranometer. The **external thermal shock test** requires also temperature sensors, a data logger and a flow rate measuring device. A smart combination of the different test facilities and a clever arrangement of the order the tests are performed reduces not only the measuring equipment and the number of test facilities itself, but also the personal's workload. Furthermore, the time required for testing can be reduced remarkable

E.g. on a sunny day during that the exposure test is carried out, also the external thermal shock test can be performed. Using such kinds of synergy effects requires that the facility for the exposure test additionally fulfills the requirements of the external thermal shock test. In this case, several tests of the test sample can be performed without remarkable additional effort.
If the rain penetration is also performed directly after the exposure test and on the same test facility, the measuring equipment such as the flow rate measuring equipment can be used twice as well.

To reduce the required financial effort and the human resources six test procedures of the above mentioned standard have been combined into one single test facility. So the smart combination of the individual tests related to the test sequence but also related to the test facility itself allows for an effective use of resources.

The above mentioned tests have to be performed consecutive but the test sample can be mounted during the entire test sequence on the same test facility. Even for the external and internal thermal shock test as well as for the rain penetration tests it is not necessary to install the collector to be tested on a different test facility. Fig 1 shows a schematic of the test facility during the exposure test (left) and the rain penetration test (right).

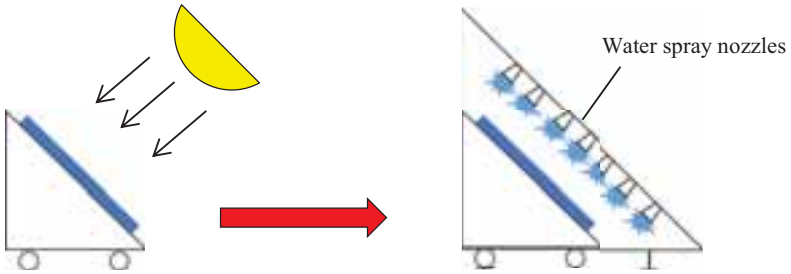

Fig. 1: Test facility for combining the exposure test facility (left) and the rain penetration test facility (right); for performing the rain penetration test the exposure test facility is removed under the water spray nozzles for the rain penetration test facility – or vice versa

For situations and countries where water shall not be drained after spraying it on the collector, a new rain penetration test facility with water recycling was designed. After spraying onto the collector, the water is collected and flows via a channel into a bucket. From there a pump transports the collected water into a store. A second pump transports the water from the store again through the spray nozzles onto the collector. Self-evident, the inclination angle of this test facility is variable and can be adjusted infinitely. Fig. 2 shows a rendering of the new designed rain penetration test facility. A mounted splash guard avoids the waste of water.

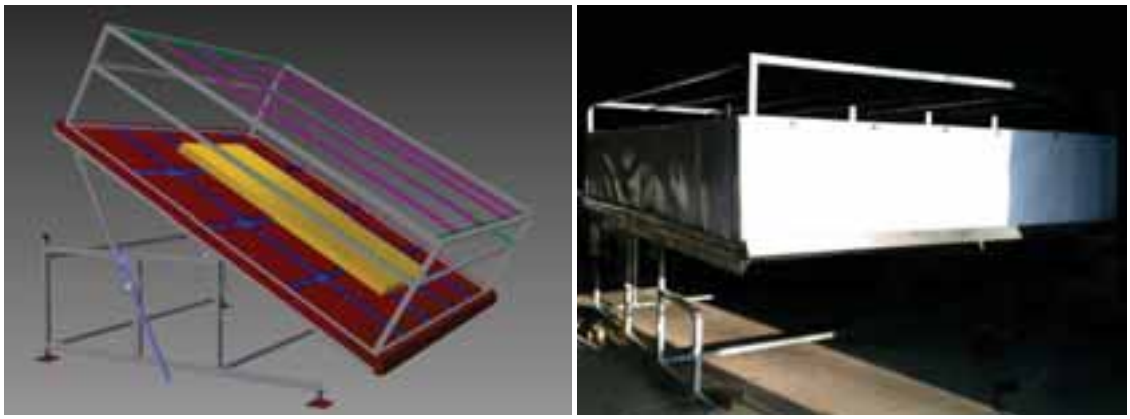

Fig. 2: Rendering (left) and picture (right) of the newly developed rain penetration test facility, which allows water recycling

3. Thermal performance testing of solar thermal systems and solar collectors

The combination of test procedures for testing the thermal performance of solar domestic hot water systems according to ISO 9459-2 and -5 together with the one of solar collectors according to EN 12975 have been already published (Bestenlehner). Due to the replacement of the EN 12975-2 by ISO 9806 some minor changes related to the hydraulics and the measuring equipment have been realized.

However, the test rig for thermal performance testing has been revised significantly to allow a more flexible and multifunctional use. The inclination angel is now adjustable to every desired angle between 0° (horizontal) and 90° (vertical). On the one hand, adjusted to the horizontal, it allows for an easy installation of the test sample. On the other hand, façade collectors intended to be mounted vertically can be tested as well. Additionally the horizontal position of the test rig allows even for testing of solar thermal systems equipped with a self-supporting frame such as e.g. non-pressurized thermosiphon systems mainly produced in Asia. Fig 3 shows renderings and Fig. 4 a picture of the newly designed test rig for performing thermal performance test of solar thermal systems and collectors.

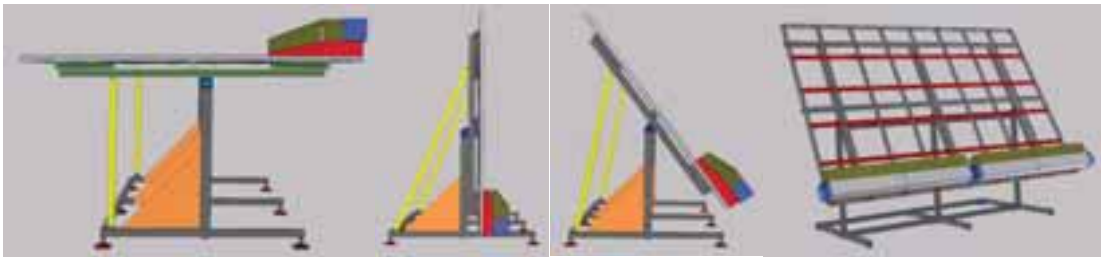

Fig. 3: Renderings of the newly designed test rig for thermal performance tests of solar thermal systems and collectors

Fig. 4: Picture of the newly designed test rig for thermal performance tests of solar thermal systems and collectors

4. Thermal performance testing of thermal energy stores

A third issue for the update of the test facility was the aim to combine the capability of performing tests according to four different test procedures in one test facility in order to determine also the thermal performance of hot water stores using the same test facility. With regard to hot water stores, the test methods of the following standards have been implemented: EN 12977-3, -4, EN 12897, EN 15332. Whereas the test methods defined in the EN 12977 part 3 and 4 are detailed procedures to determine the characteristics of hot water stores and combistores, the test methods described in EN 12897 and EN 15332 are procedures to determine predominantly the heat losses of the store.

Since it is not everywhere possible to install such an all-in-one test facility for testing up to 4 solar thermal collectors, systems and hot water stores in parallel, a small and handy test facility was developed. This test facility is designed for performing tests for the determination of the heat losses of hot water stores according to the above-mentioned standards. Fig. 5 shows a picture of such a test facility.

Fig. 5: Picture of the handy and mobile test facility for the determination of the heat loss rate of hot water stores

5. Validation measurements

To ensure the reliable and reproducible operation of the updated “all-in-one” test facility, validation measurements concerning thermal performance testing have been performed successfully. Exemplarily, the results of the validation measurement of a solar thermal system are presented and discussed in the following. The system under investigation was a thermosiphon system with 1.98 m² solar collector area and a hot water store with 180 L and a jacket heat exchanger. Fig 6 shows the solar thermal fraction of the related solar thermal system at different locations calculated on the basis of the determined test results. The hot water load plotted as tapped hot water volume is varied between 80 L/d and 600 L/d. The results show a decreasing solar thermal fraction with increasing daily load volume, which is quite obvious. The deviation was calculated between the reference measurements and the measurements performed with the updated test facility. All measurements have been performed using the same test samples or solar thermal system respectively. The deviation in the solar fraction is for all measurements below ±2 % (relative).

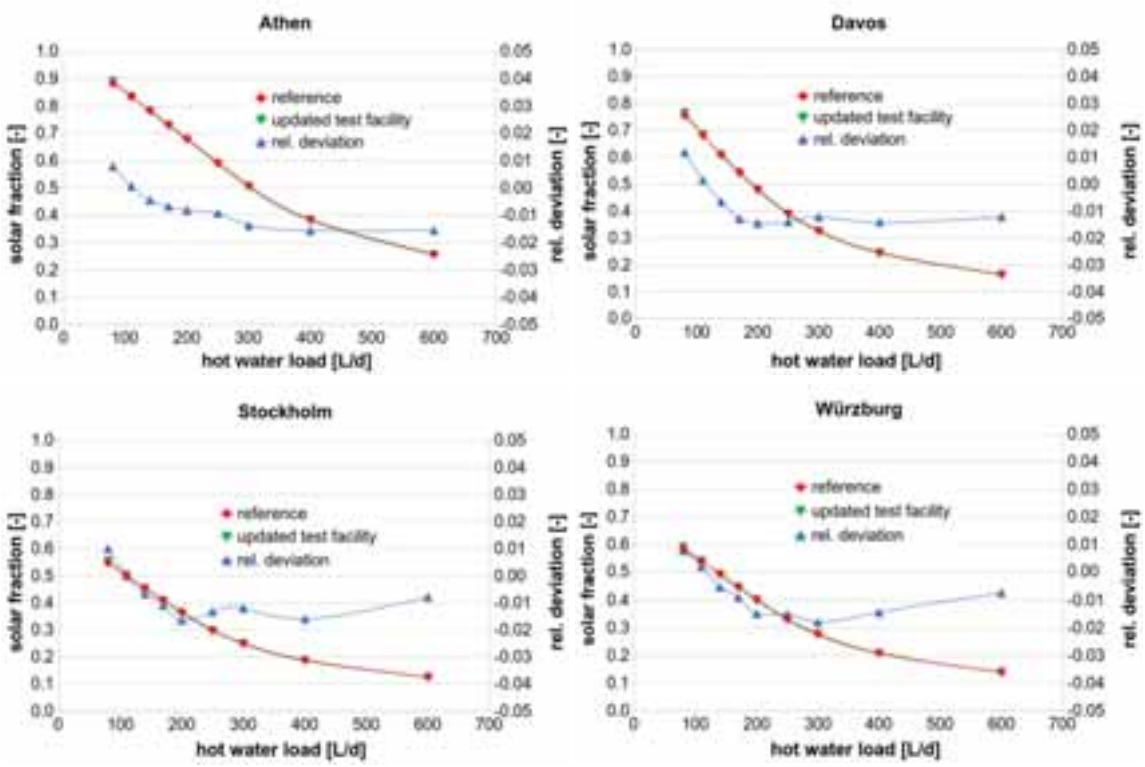

Fig. 6: Presentation of the validation measurements; solar fraction (left ordinate) and deviation (right ordinate) between tests performed with the original and the updated test facility versus tapped hot water volume

6. Summry

The results of the evaluated solar thermal system show that the updated all-in-one test facility enables reliable and cost effective testing. The relative deviation of 2 % of the test results referring to the solar fraction is far below the required limits. The mandatory tests according to the new international standard ISO 9806:2017 the high-temperature resistance test, the determination of the standard stagnation temperature, the exposure and pre-exposure test, the external and internal thermal shock test, and the rain penetration test can be reliable and cost-effective performed with the updated all-in-one test facility.

7. References

[1] D. Bestenlehner, H. Drück, S. Fischer, H. Müller-Steinhagen, Development of a mobile, stand-alone test facility for solar thermal collectors and systems; Proceedings of ISES 2007 Solar World Congress, September 18 to 21, 2007, Beijing, China, ISBN 978-7-302-16146-2, Tsinghua University Press, Beijing and Springer-Verlag GmbH Berlin Heidelberg, CD: ISBN 978-7-89486-623-3

[2] D. Bestenlehner, H. Drück, H. Müller-Steinhagen, D. Qually, K. Deist, C. van Hoewe, Experiences with a mobile stand-alone test facility for solar thermal collectors and systems, HEFAT 6th Conference on Heat Transfer, Fluid Mechanics and Thermodynamics, 30.06.-02.07.08, Pretoria, South Africa

[3] D. Bestenlehner, H. Widlroither, H. Drück, S. Fischer, Müller-Steinhagen, Development of Test Facilities for Solar Thermal Collectors and Systems, Conference Proceeding of Euro Sun 2008, 7 - 10 October 2008, Lisbon, Portugal, S. 384 – 385, ISBN 978-972-95854-7-0

[4] D. Bestenlehner, H. Drück, S. Fischer, H. Müller-Steinhagen, Complete Test Facility for Solar Thermal Collectors and Systems, RIO 9 – March 17 - 19, 2009 - Rio de Janeiro, Brazil

SOLAR THERMAL COLLECTOR'S DEGRADATION – INFLUENCE OF CORROSIVITY INSIDE AND OUTSIDE THE COLLECTORS

M.J. Carvalho[1], S. Páscoa[1], N. Mexa[1], R. Gonçalves[1], J. Correia[1], A. Gano[1], T. Diamantino[1]

[1] LNEG - Laboratório Nacional de Energia e Geologia I.P., Lisboa (Portugal)

Abstract

Influence of atmospheric corrosivity on solar thermal collector's degradation was studied by exposure of flat plate collectors to two different corrosivity environments, one urban Outdoor Exposure Testing (OET) site with medium corrosivity (C2-C3) and a very high/extreme corrosivity (industrial and marine) (C5-CX) atmosphere highly polluted and simultaneously with highly airborne salinity. Results of thermal performance measurements after two years of exposure in the two OET sites are presented, as well as the evaluation of the corrosion rate inside the collectors, with zinc as reference material, atmospheric contaminants, temperature and relative humidity. For the measurement of temperature and relative humidity inside the collectors, in house produced data acquisition system and sensors were used and are shortly described. Collectors were dismantled and optical properties of the absorbers were measured.

Keywords: *Solar thermal collectors, atmospheric corrosivity, thermal performance degradation*

1. Introduction

Solar thermal collectors (STC) have to withstand stress conditions like high temperatures, high humidity, ultraviolet irradiance or wind and snow loads depending on the geographic location. Literature points out to dependence on other influences like prevailing wind conditions, contaminants like chlorides, SO_2 and NO_x, global solar irradiation, wetness time and precipitation (Köhl et al., 2004; Slamova et al., 2016).

Although for certification of solar thermal collector (e.g. Solar Keymark, SRCC), the testing standards applied, namely ISO 9806:2013, consider a set of tests which address testing of collector resistance to most common adverse conditions when collectors are in use, these tests do not address long term collector durability.

In order to better know how different environmental conditions influence STC, as well as collector components, two OET (Outdoor Exposure Testing) sites were used to expose collectors and collector components. The two OET sites represent an urban climate (Lumiar-Lisboa) and a maritime climate with industrial influence (Sines) (Diamantino et al., 2017). The results of collector exposure will be presented in this work for the two OET sites after two years of exposure. Corrosion rate for zinc, atmospheric contaminants, temperature and relative humidity inside de collectors are also presented. Collectors were dismantled and absorber optical properties measured.

2. Materials and methods

2.1. Exposure of STC at OET sites

STC studied were Flat Plate Collectors with tempered glass cover, commercially available. Their main characteristics are described in Table 1.

For each collector model, two samples were exposed in each OET sites (see Figure 1). Thermal performance was measured before exposure for each collector model. For three of the models, zinc standard specimens were installed inside one of the collector samples. After two years exposure, thermal performance was measured. Preliminary results for one of the OET sites were presented in (Carvalho et al., 2016). Summary of all thermal performance results are presented in this work, in section 3.2.

doi:10.18086/swc.2017.19.02 Available at http://proceedings.ises.org

Tab. 1: Main collector characteristics

Collector reference	Type of collector
A *	Aluminum absorber surface with PVD coating (Mirotherm ®); Aluminum box
C *	Aluminum absorber surface with PVD coating (Eta plus ®); Aluminum box.
D *	Copper absorber surface with selective paint coating (SUNCOLOR TS S Black); Stainless steel box.
*1 replicate with zinc standard specimens	

Fig. 1: Installation of collectors in OET sites - Urban (left); Maritime/Industrial (right)

2.2. STC thermal performance evaluation method

Thermal performance tests of solar thermal collectors were performed according to ISO 9806:2013, using quasi-dynamic test method. The comparison is made based on the power curve as defined in ISO 9806:2013 for normal incident irradiance of 1000 W m^{-2} (Direct irradiance = 850 W m^{-2}; Diffuse irradiance = 150 W m^{-2}).

Initial thermal performance was measured only in one collector of each reference. Final results of thermal performance were measured for all collector models exposed. The collectors with installed reference materials were dismantled for inspection and for evaluation of the corrosion rate in zinc samples as well as atmospheric contaminants (chlorides, nitrates and sulphates).

2.3. Optical properties of absorbers

Optical properties of absorbers were also measured. Information on optical properties of absorbers used in each collector exists and will also be presented (initial values) and compared with the performed measurements of the absorber samples extracted from collectors, after two years exposure.

The measured optical properties were solar absorptance (α_s) and thermal emittance (ε_t). The solar absorption (α_s) was measured using a Perkin Elmer's Spectrophotometer Lambda 950 UV/VIS/NIR with a 150 mm integrating sphere.

The thermal emittance (ε_t) was initially determined with a portable emissometer, Devices & Service Company model AE-AD3, which measures a surface emittance at 80 °C of temperature and corrected for a temperature of 100 ºC based on later measurements using a Spectrophotometer Frontier IR/NIR of Perkin Elmer, with integrating sphere.

2.4. Zinc corrosion rate inside STC and atmospheric contaminants evaluation

In each of the collectors referenced in Table 1 with *, five (5) replicates of zinc metal samples were put in the air gap between absorber and glazing (Carvalho, et al, 2016), to evaluate the corrosivity of the microclimate after approximately two years exposure. Zinc samples inside the collectors are equal to the zinc samples placed outdoors to comparatively evaluate the atmospheric corrosivity. The corrosion categories of outdoor exposure test sites were obtained by determination of the corrosivity based on corrosion rate measurement of standard specimens (carbon steel, zinc, copper and aluminum) according to ISO 9223: 2012 and ISO 9226:2012 during

main period of STC exposure.

The atmospheric contaminants present in the solar absorber surfaces, inside the collectors, were also collected by Bresle method (ISO 8502-6, 2006) and analyzed by Ion chromatography. Atmospheric contaminants were analyzed in three different parts of the collectors (1, 2 and 3). In Figure 2 is possible to see the zinc reference materials (5 samples) and where environmental contaminants were collected (1, 2 and 3),

Fig. 2: STC with zinc reference materials and the indication where environmental contaminants were collected after dismantling of collectors

2.5. Measurement of STC inside temperature and relative humidity

Aiming STC's internal temperature and relative humidity measurement and analysis over a predefined period under real working conditions, a custom real-time monitoring and data-logging programmable smart data acquisition system was developed and prototypes were implemented for 'in-situ' data collection in the two OET sites.

Due to the internal ambient working STC conditions, with peak temperatures exceeding 120 ºC, most commercial relative humidity (RH) measuring and logging equipment do not comply with these specifications, mainly due to temperature restrictions of most of the relative humidity electronic sensors available in the market.

The developed system has the following specifications:

- two custom sensor probes for insertion in two STC's, each with one resistive thermal platinum sensor (Pt_{100}) and one high temperature capacitive relative humidity sensor (see Figure 3a):
  - temperature measuring range: -10 to 150 ºC with ±0.1 ºC resolution;
  - relative humidity range: 0 to 100% (non condensing) with ±5 % resolution, with [-10 ºC, +150 ºC] working temperature range;
- programmable sampling periods sets, ranging from 1 sample/min (1440 Samples/Day), as maximum sample rate, to 1 sample/ 4 Hours (6 Samples/Day) as minimum sampling rate;
- system power autonomy of at least one year, for a full set of variables data logging with a sampling period greater than 15 min;
- local data logging of the acquired data using internal non-volatile flash memory;
- data communication with an external computer for system configuration and data gathering using a standard USB2.0 interface;

This custom smart data acquisition and processing unit (see Figure 3b) enables the simultaneous monitoring and data logging of two separate, but adjacent, solar thermal collectors, being its hardware based on a low power, high performance 16-bit microcontroller. This custom unit includes extra functionalities for increased flexibility in signal acquisition, local data processing and external data communication, without compromising system's energy autonomy. Special attention was paid to the system's power consumption in order to keep the intended system's autonomy, being used ultra-low power electronic circuits whenever possible.

The system was developed having in mind an high configurability and flexibility in data acquisition and logging, in order to perform internally all data processing for an 'all digital' information output, along with optimized algorithms to minimize the system's power consumption when active.

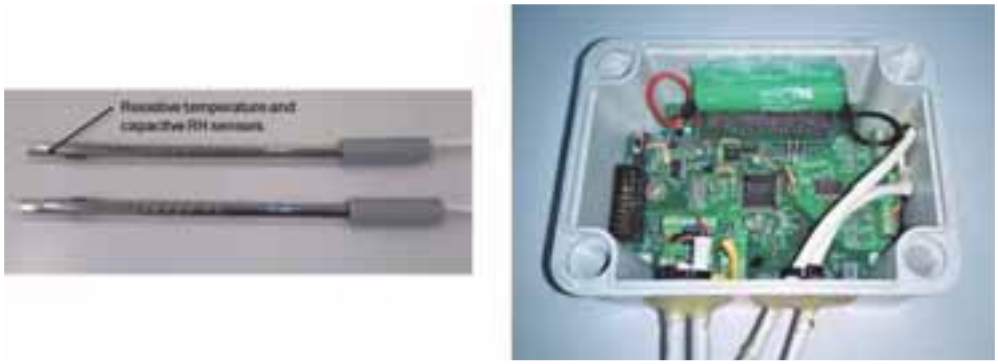

Fig. 3: Collector's internal sensor probes with resistive platinum Pt100 temperature sensor and a high temperature capacitive sensor for relative humidity (Left); b) Custom smart data acquisition and processing unit (right).

A custom user interface software (see Figure 4) was also developed for system's configuration and logged data gathering. The software application runs under Windows environment, allowing an easy system's operation. The logged data can directly be imported into Excel datasheets using a standard text file with CSV format, being each recorded sample stamped with Date/Time information from the system's internal real-time clock, synchronized with the computer's clock when the system is initially configured to start acquisition.

This smart monitoring system is presently being enhanced to include, in the near future, new sensors for other collector's physical environmental variables, like ambient temperature and relative humidity, internal absorber working temperature, UV irradiation, etc,

Fig 4. System's user interface for configuration and data gathering

2.6. Scanning Electron Microscopy (SEM) with Energy Dispersive X-ray Spectroscopy (EDS)

The morphology of solar absorber surfaces (after two year of exposure in Sines OET sites) were examined using a Philips Scanning Electron Microscope, Model XL30 FEG with Energy Dispersive X-ray Spectroscopy (EDS) associated. Before observation, the samples were cut in a cut-off machine to a 1.0 cm X 2.0 cm size. After that, for better conduction, samples were gold coated in the Emitech K575X turbo sputter coater, for 5 seconds.

3. Results and Discussion

3.1. OET sites characterisation

The characterization of Sines and Lumiar-Lisboa OET sites is presented in Table 2 with indication of yearly values in terms of main climatic parameters. A more detailed presentation of ambient temperature and global irradiance can be seen in Fig. 5. Table 3 and 4 present the corrosion rates and atmospheric corrosion categories for Sines and Lumiar-Lisboa OET site, respectively.

These results show the different environmental parameters and corrosivities of Sines and Lumiar-Lisboa OET sites. Both have similar temperature and relative humidity mean values, although Sines with slightly higher mean values. The differences lie in atmospheric contaminants (chlorides and sulphur dioxide deposition values) with much higher values in Sines. In terms of corrosivity, Sines has a high corrosivity for aluminum (category C4), very high for steel and zinc (category C5) and extreme for copper category CX. Lumiar-Lisboa with low corrosivity for aluminum and steel (category C2), medium for zinc (category C3) and medium-high for copper (category C3-C4).

Tab. 2: Climate characterization in the two OET sites (2014-2015) (Sines and Lumiar-Lisboa)

Location	Latitude	Longitude	Altitude	Year	Average ambient temperature [°C]	Average relative humidity [%]	Cl^- [mg day^{-1} m^{-2}]	SO_2 [mg day^{-1} m^{-2}]
Sines	37.95°N	-8.88°W	17 m	2014	16.9	78.7	191.8	139.1
				2015	17.9	81.2	89.5	93.4
Lumiar Lisboa	38.77°N	-9.17°W	116 m	2014	16.6	76.9	15.4	10.8
				2015	17.2	77.6	16.9	33.0

Tab. 3: Corrosion rates of carbon steel, copper, zinc and aluminum and corrosion categories measured in Sines OET site

Sines OET site				
Reference materials	**Carbon steel**	**Copper**	**Zinc**	**Aluminum**
Corrosion rate (g m^{-2} y^{-1})* (2014)	1346.01	64.33	59.16	3.98
Corrosion rate (g m^{-2} y^{-1})* (2015)	981.11	52.01	44.08	2.21
Category/corrosivity (Year)	**C5 / Very High (2014)**	**CX / Extreme (2014)**	**C5 / Very High (2014)**	**C4 / High (2014)**
Category/corrosivity (Year)	**C5 / Very High (2015)**	**CX / Extreme (2015)**	**C5 / Very High (2015)**	**C4 / High (2015)**

*corrosion rates expressed in grams per square meter per year

Tab. 4: Corrosion rates of carbon steel, copper, zinc and aluminum and corrosion categories measured in Lumiar-Lisboa OET site

Lumiar-Lisboa OET site				
Reference materials	**Carbon steel**	**Copper**	**Zinc**	**Aluminum**
Corrosion rate (g m^{-2} y^{-1})* (2014)	163.29	11.51	9.85	0.25
Corrosion rate (g m^{-2} y^{-1})* (2015)	194.35	16.76	6.69	0.20
Category/corrosivity (Year)	**C2 / Low (2014)**	**C3 / Medium (2014)**	**C3 / Medium (2014)**	**C2 / Low (2014)**
Category/corrosivity (Year)	**C2 / Low (2015)**	**C4 / High (2015)**	**C3 / Medium (2015)**	**C2 / Low (2015)**

*corrosion rates expressed in grams per square meter per year

In Figure 5 it is represented the frequency distribution of irradiance and ambient temperature of both OET sites (September 2016 to August 2017). Although ambient temperature average values are slightly higher in Sines, Lumiar-Lisboa has higher ambient temperature amplitudes. The irradiance behavior is similar in both OET sites although with higher irradiance values for Sines.

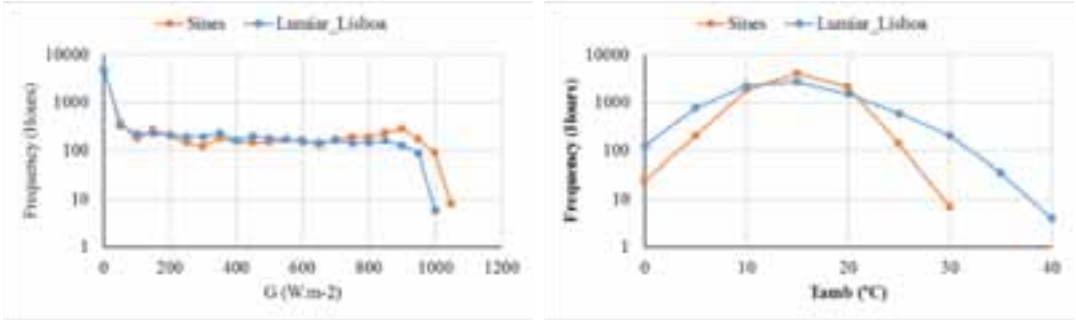

Fig. 5: Irradiance (global) (Left): Ambient temperature (right)

3.2. STC thermal performance and optical properties after approximately two years exposure

In a previous paper (Carvalho, et al, 2016) the thermal performance evaluation for collectors exposed in Sines after one and two years exposure was presented. In this work, only results with two years exposure, both for Sines and Lumiar-Lisboa, are presented. In Table 5 the periods of exposure of these collectors are listed.

Tab: 5 – Exposure dates of STC in Sines and Lumiar-Lisboa OET sites

	Model (Ref.)	Installation date	Uninstallation data	Exposure time (month)
Sines	S_A2 *(**)	11-04-2014	01-06-2016	26
	S_C2 * (**)	09-05-2014	01-06-2016	25
	S_D2 *	11-04-2014	01-06-2016	26
Lumiar-Lisboa	L_A2 * (**)	23-06-2014	11-11-2016	30
	L_C2 * (**)	19-09-2014	11-11-2016	27
	L_D2 *	19-09-2014	11-11-2016	27

*one (1) replicate with zinc metal samples; ** Temperature and humidity measurements inside the collector

After approximately two years of exposure (see Exposure time in Table 5), the collectors with zinc samples were tested for thermal performance and dismantled after. Measurement of optical properties was performed in different points of the absorber. These results also presented in this section.

Fig. 6 to 8 show the collector's power curve according to the definition of ISO 9806:2013, comparing the thermal performances after exposure with the initial thermal performance, measured in collectors of the same type before exposure.

In Table 6 the average relative difference between the power curves is presented.

Fig. 6 and 7 show the thermal performance after two years of exposure in Sines and Lumiar-Lisboa OET sites for collectors with aluminum absorbers and PVD coatings (Mirotherm ® and Eta plus ®, respectively) (models A and C). After two years exposure in Sines and Lumiar-Lisboa, collector A does not show significant degradation – average power difference of -0.9% and -1.8%, respectively. Collector model C exposed in Sines shows degradation – average power difference of -6.2%. After two years in Lumiar-Lisboa no significative difference is observed in this collector (model C) – average power difference of -1.1%.

Fig. 8 shows the impact of two years of exposure of collectors with copper absorber and paint coating SUNCOLOR TS S Black (Model D). The collector exposed in Sines shows sixthly lower power curve while in Lumiar-Lisboa the collector exposed after two years shows higher thermal performance – average power difference of +3.0%.

Tab. 6: Average difference of power curve relative to initial peak power (%) in the temperature range 0-90 K

Collector sample	Exposure time (month)	Average difference of power curve relative to initial peak power (%) in the temperature range 0-80 K
S_A2 * (**)	26	-0.9
S_C2 * (**)	25	-6.2
S_D2 *	26	-0,9
L_A2 * (**)	30	-1.8
L_C2 * (**)	27	-1.1
L_D2 *	27	3.0

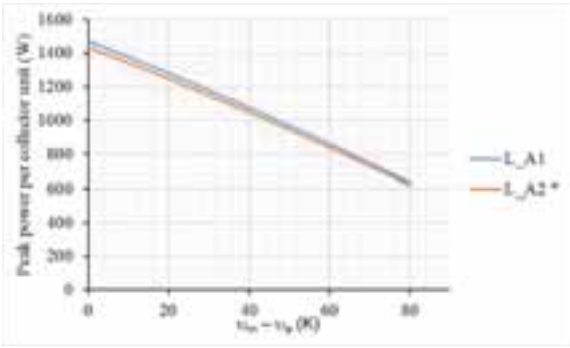

Fig. 6a): Power curves of collector model A (L_A1 – initial measurement: L_A2 * – measurement after two years).

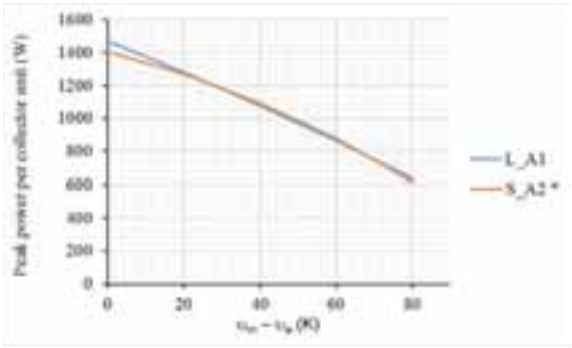

Fig. 6b): Power curves of collector model A (L_A1 – initial measurement: S_A2 * – measurement after two years).

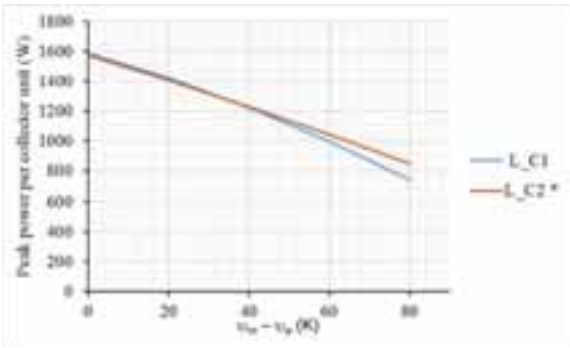

Fig. 7a): Power curves of collector model C (L_C1 – initial measurement: L_C2 * – measurement after two years).

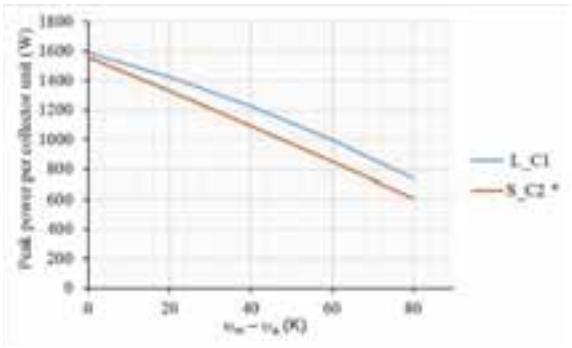

Fig. 7b): Power curves of collector model C (L_C1 – initial measurement: S_C2 * – measurement after two years).

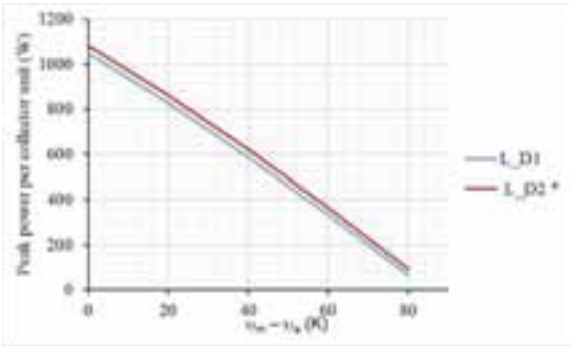

Fig. 8a): Power curves of collector model D (L_D1 – initial measurement: L_D2 * – measurement after two years).

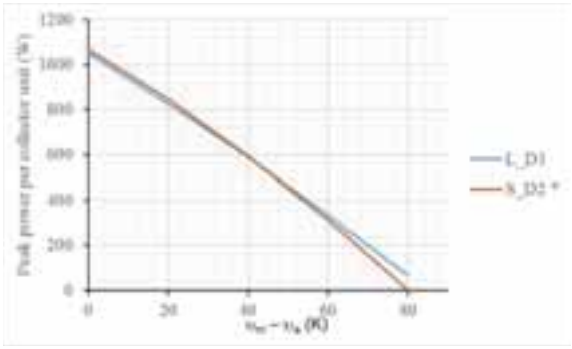

Fig. 8b): Power curves of collector model D (L_D1 – initial measurement: S_D2 * – measurement after two years).

In Table 7 the optical properties of the absorbers of the three collector models are listed. Initial values were obtained from measurement of thirty samples of the absorber used in each collector. The values after two years of exposure were measured in different sections of the collector's absorber after dismantling.

The initial values of the optical properties correspond to average values of thirty samples with corresponding standard deviation. The values after approximately two years correspond to values of measurements made on two or three different samples of the absorber (top, center and bottom) and, when more than one measurement was made, the standard deviation is given.

For collectors A with aluminum substrate and PVD coating, the variation in the solar absorptance is in agreement with the change in peak power (see Fig. 6) for both Sines and Lumiar-Lisboa. The thermal emittance shows a

higher change in Lumiar-Lisboa than in Sines. There are no significant differences between values in the center and bottom of the collector.

For collectors C the solar absorptance does not show significant difference although some change in peak power measured (see Figure 7) is observed. A change in glass transparency may be the reason for this. For Lumiar-Lisboa a higher change in thermal emittance is also observed and this change is not uniform. In Sines, the bottom part of the absorber shows higher thermal emittance values while in Lumiar-Lisboa the center part of the absorber shows higher thermal emittance values.

Tab. 7: Optical properties of collector absorber coatings

Note: Figures in parentheses indicate that the standard deviation observed is lower than the measurement uncertainty.

Collector sample	Exposure time (month)	Location inside collector	α	σ_α	ε	σ_ε
	Initial	**---**	**0.96**	**0.00(1)**	**0.11**	**0.00(2)**
S_A2 *	26	center	0.94	0.00(1)	0.13	0.01
		bottom	0.94	0.00(1)	0.12	0.0(0)
L_A2 *	30	center	0.94	0.00(1)	0.16	0.01(2)
		botom	0.94	0.00(2)	0.15	0.00(9)
	Initial	**---**	**0.96**	**0.00(0)**	**0.11**	**0.00(3)**
S_C2 *	25	center	0.95	--	0.11	--
		bottom	0.95	--	0.14	--
L_C2 *	27	top	0.94	0.00(2)	0.15	0.02
		center	0.94	0.00(2)	0.18	0.02
		bottom	0.94	0.00(2)	0.16	0.01
	Initial	**---**	**0.95**	**0.00(1)**	**0.72**	**0.02**
S_D2 *	26	center	0.93	--	0.56	--
		bottom	0.93	0.00(1)	0.56	0.00(4)
L_D2 *	27	top	0.93	0.00(1)	0.55	0.01
		center	0.93	0.00(1)	0.57	0.01
		bottom	0.93	0.0005	0.58	0.006

3.3. Zinc corrosion rate inside STC and atmospheric contaminants evaluation

Table 8 and 9 present the results of zinc corrosion rate and results of chemical analysis inside the STC in Sines and Lumiar-Lisboa OET site, respectively.

Tab. 8: Zinc corrosion rate and results of chemical analysis inside the STC in Sines OET site.

STC	Position inside collector	Chlorides (mg L^{-1})	Nitrates (mg L^{-1})	Sulfates (mg L^{-1})	Zinc corrosion rate inside collectors r_{corr} (g m^{-2} y^{-1}) (SD)	Corrosion category according to ISO 9223:2012
A	1	0.8	<1	<1	90.31 (9.53)	CX
	2	0.7	<1	<1		
	3	1.7	1.6	<1		
C	1	0.7	<1	<1	99.91 (10.63)	CX
	2	1.0	<1	<1		
	3	4.1	1.8	<1		
D	1	1.5	<1	<1	4.56 (0.55)	C2
	2	1.0	<1	<1		
	3	8.0	2.0	<1		

Tab. 9: Zinc corrosion rate and results of chemical analysis inside the STC in Lumiar-Lisboa OET site.

STC	Position inside collector	Chlorides (mg L^{-1})	Nitrates (mg L^{-1})	Sulfates (mg L^{-1})	Zinc corrosion rate inside collectors r_{corr} (g m^{-2} y^{-1}) (SD)	Corrosion category according to ISO 9223:2012
A	1	<0.5 (QL)	<0.5 (QL)	<0.5 (QL)	47.76 (3.12)	C5
	2	0.74	<0.5 (QL)	<0.5 (QL)		
	3	<0.5 (QL)	<0.5 (QL)	<0.5 (QL)		
C	1	0.5	<0.5 (QL)	<0.5 (QL)	- (*)	-
	2	0.7	<0.5 (QL)	<0.5 (QL)		
	3	1.4	<0.5 (QL)	<0.5 (QL)		
D	1	0.53	<0.5 (QL)	<0.5 (QL)	6.84 (0.24)	C3
	2	1.0	1.0	<0.5 (QL)		
	3	1.1	<0.5	<0.5 (QL)		

(QL) - Quantification limit; (*) It was not possible to evaluate the zinc corrosion rate because the reference materials fell due to the degradation of the polymeric screws that held them.

From the presented results, it is possible to see that the concentration of contaminants is higher at the base of the collectors relative to the top and to the middle. The concentration of contaminants in the absorber surfaces is highest for collector D and lowest for collector A in Sines OET site. The collectors in Sines show higher contaminants concentration than in Lumiar-Lisboa.

It is also possible to see that in Sines, collector D has, for zinc a lower corrosivity than collectors A and C. Between collectors A and C, the corrosivity inside collector C is higher than in collector A. This can be related to the fact that collector C showed a higher concentration of contaminants and reaches higher internal temperatures (Figure 9).

Although temperature and humidity inside collector D was not monitored, its thermal performance clearly indicates that the collector has lower stagnation temperature than collectors A and C. The tightness also seems to be smaller with respect to the collectors A and C.

In Sines the zinc corrosion rate inside the collectors can be associated with the contaminants but the temperature seems to be a determining factor.

The corrosivity inside the collector A is lower in Lumiar-Lisboa than in Sines. However, for the collector D the zinc corrosion rate in Lumiar-Lisboa collector is a little higher than in Sines. Although the concentration of contaminants is lower in Lumiar-Lisboa than in Sines, this may be justified by the fact that a great condensation has been observed in the case of this collector in Lumiar-Lisboa, much higher than in the collector exposed in Sines. Taking into account that zinc reaches in air-saturated water the higher corrosion rate between 60-80ºC (X. G. Zhang, 2011), it can justify the little higher corrosion rate observed in Lumiar-Lisboa. The greater condensation in Lumiar's collector may have contributed more to zinc corrosion than the higher concentration of contaminants in Sines.

3.4. Environmental characterisation of collectors inlet

Figure 9 shows the maximum measured values of temperature in collector models A and C, in Sines and Lumiar-Lisboa, respectively. Figure 10 shows the average measured values of humidity in collector models A and C, in Sines and Lumiar-Lisboa respectively.

The measurement period is different in Sines and Lumiar-Lisboa but it covers in both cases almost one year. In Sines measurements where made between June 2015 to April 2016 and in Lumiar-Lisbooa between December 2014 to October 2015.

The sensors were placed in the upper left or right corner of the collectors.

The measurements show higher temperatures in collector C then in collector A. This is coherent with the relative humidity values that are higher in collector A then in collector C, although results for Lumiar-Lisboa in February and March are not in agreement with this tendency.

On a daily bases the evolution of temperature and relative humidity can be seen in Figure 11.

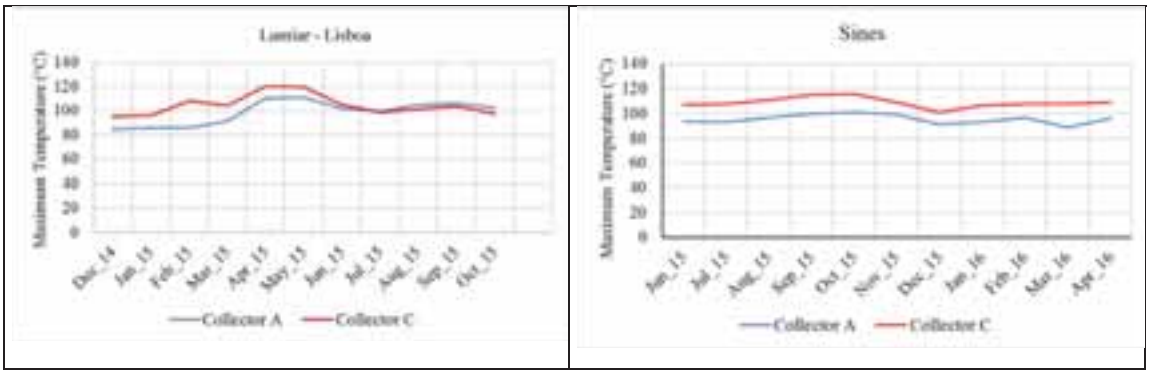

Fig. 9: Maximum measured values of temperature in collector models A and C

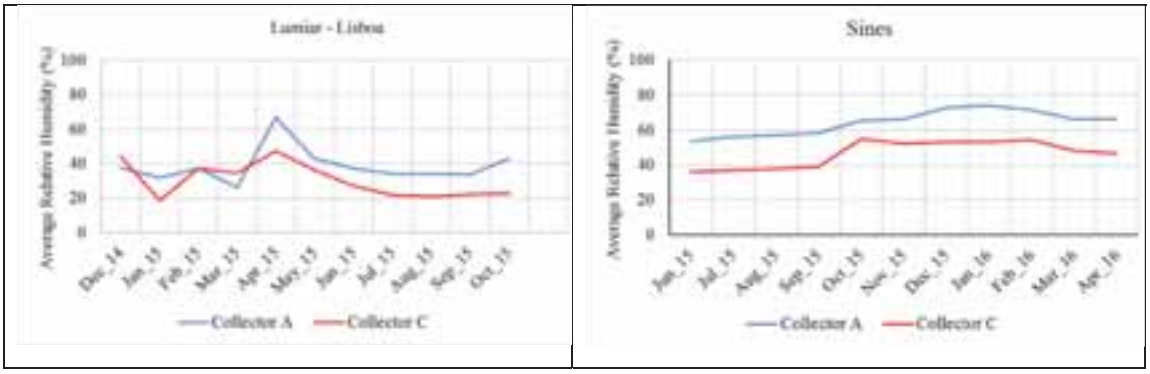

Fig. 10: Average measured values of humidity in collector models A and C

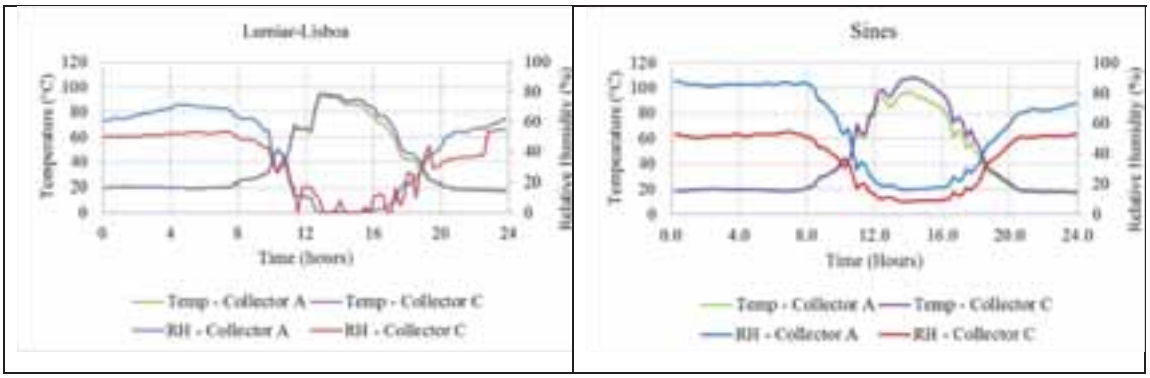

Fig. 11: Representation of one day data (Temperature and relative humidity for collector models A and C) in Lumiar-Lisboa (left) and Sines (right).

3.5. Scanning Electron Microscopy (SEM) with Energy Dispersive X-ray Spectroscopy (EDS)

Table 10 presents SEM micrographs and EDS spectra obtained on solar absorber surfaces inside STC after two years of exposure in Sines OET site.

By SEM was possible to observe the selective surfaces from the three STC and to verified that the surface where there are major changes due to corrosion is on the surface of the collector C, where the chlorine and sulfur elements are present in the corrosion products.

In collector A sodium chloride deposits are observed on the surface but no corrosion products are detected by SEM on the surface.

On the surface of collector D are also visible atmospheric contaminants and some coating cracking / degradation, as well as sodium chloride deposits. Considering that this coating initially had some application defects, it is not possible to distinguish if these observed changes are due to initial corrosion process or to the initial defects of the application.

Tab. 10: SEM micrographs and EDS results of the chemical elements identified on solar absorber surfaces inside STC in Sines OET site after two years

STC	SEM micrographs	EDS spectrum of chemical elements detected
A	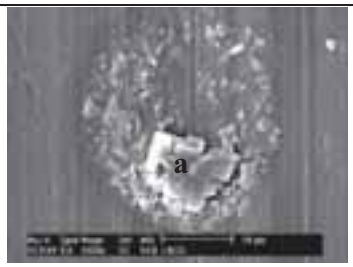	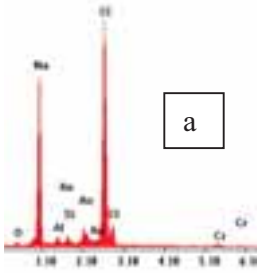
C	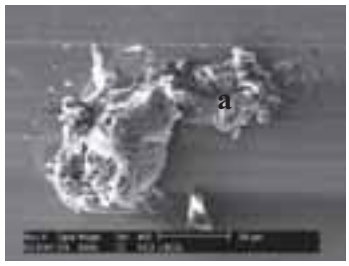	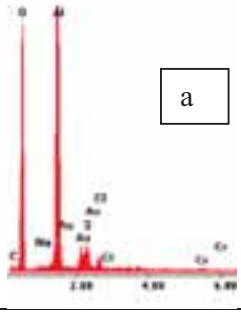
D	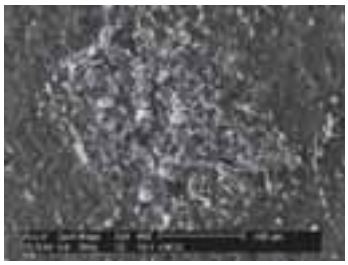	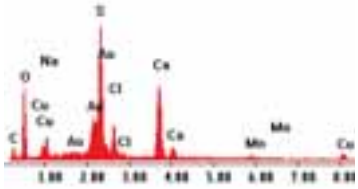

4. Conclusions

After two years exposure, the measurement of thermal performance of the STC shows higher decrease in Sines than in Lumiar-Lisboa for collectors A and C. The decrease in thermal performance is higher for collector C than collector A, especially in Sines. These results are in agreement with higher level of contaminants, especially chlorides, and also in line with the corrosion rates for zinc measured in Sines and Lumiar-Lisboa for collectors A and C.

In the case of collector D, the variation of the thermal performance does not show a clear relation to the location. This may be because the manufacturing process of the collector is not completely controlled. Differences in initial thermal performance of each collector were not detected since the initial measurement was done in only one collector of model D. The low corrosion rates for zinc in this case may be a result of much lower temperature levels in this collector. Although the temperature and humidity was not monitored in this case, the thermal performance of the collector indicates a lower stagnation temperature than in collectors A and C.

The contaminants present on the different solar absorber surfaces were also different depending on the type of collector. Different ventilation rates and higher temperatures in collectors A and C may explain these differences in terms of contaminants and zinc corrosion rate.

The contaminants detected on the absorbers are mainly chlorides in all collectors and nitrates (Sines OET). The concentration of sulfates and nitrates are low and in some cases below the limits of quantification. From the observations by SEM made for the absorbers of collectors exposed in Sines, we may correlate changes due to

corrosion in collector C to the presence of contaminants. In the case of collector A, although chlorine was present on the surface, no corrosion was observed. The high corrosion resistance of PVD present in collector A relatively to collector C is in agreement with the results presented for these selective surfaces exposed in OET sites (Diamantino et al. 2017) and in accelerated aging tests (Diamantino et al, 2016).

Two years exposure is still a short period to correlate thermal performance decrease with corrosion due to atmospheric contaminants but it is possible to identify the importance of chloride for locations like Sines and the need to introduce this contaminant in the accelerated aging tests for qualification of absorber surfaces. ISO 22975-3:2014 only considers sulfur as contaminant.

5. Acknowledgements

This work is a result of the project FCOMP-01-0124-FEDER-027507 (Refª FCT RECI/EMS-ENE/0170/2012) supported by Operational Competitiveness Programme (COMPETE) through the European Regional Development Fund (ERDF) and supported by FCT- Fundação para a Ciência e a Tecnologia, I.P. through National Funds and the project POCI-01-0145-FEDER-016709 (Refª FCT PTDC/EMS-ENE/0578/2014) supported by COMPETE 2020 and LISBOA 2020 under the PORTUGAL 2020 Partnership Agreement through the European Regional Development Fund (ERDF) and supported by FCT through National Funds.

The authors would like to thank to industrial partners (FogãoSol, Hempel, OpenPlus and Permasolaris), by the supply of samples and the means for performing this work.

6. References

Carvalho, M. J., Páscoa, S., Gonçalves, R., Mexa, N., Diamantino, T. C., 2016, Influence of maritime/industrial atmosphere on solar thermal collector's degradation, Comunication to Eurosun 2016, Palma de Maiorca, Spain doi:10.18086/eurosun.2016.07.04 (http://proceedings.ises.org/?mode=list&conference=eurosun2016)

Diamantino, T. C., Gonçalves, R., Nunes, A., Páscoa, S., Carvalho, M. J., 2017. Durability of different selective solar absorber coatings in environments with different corrosivity. Solar Energy Materials & Solar Cells Vol. 166, July 2017, Pages 27–38 (http://dx.doi.org/10.1016/j.solmat.2017.03.004)

Diamantino, T. C., A. Nunes, R. Gonçalves, S. Páscoa, T. Chambino and M. J. Carvalho., 2016 Selective Absorber Coatings Qualification - ISO 22975-3:2014. Full Application. Comunication to Eurosun 2016, Palma de Maiorca, Spain. doi:10.18086/eurosun.2016.06.01 (http://proceedings.ises.org/?mode=list&conference=eurosun2016)

Köhl, M., B. Carlsson, G.J. Jorgensen, A.W. Czanderna (Eds.), Performance and Durability Assessment. Optical Materials for Solar Thermal Systems, Elsevier, Oxford, 2004.

ISO 8502-6:2006 Preparation of steel substrates before application of paints and related products. Tests for assessment of surface cleanliness. Part 6: Extraction of soluble contaminants for analysis. The Bresle method

ISO 9223:2012 Corrosion of metals and alloys - Corrosivity of atmospheres - Classification, determination and estimation. 2012

ISO 9226:2012 Corrosion of metals and alloys - Corrosivity of atmospheres - Determination of corrosion rate of standard specimens for the evaluation of corrosivity. 2012

ISO 9806:2013(E), Solar Energy – Solar Thermal Collectors – Test Methods

ISO 22975-3:2014 Solar energy -- Collector components and materials -- Part 3: Absorber surface durability, 2014

Slamova, K., Duerr, I., Kaltenbach, T., Köhl, M., 2016. Degradation effects of maritime atmosphere on metallic components of solar collectors. Solar Energy Materials & Solar Cells 147, 246–254 (http://dx.doi.org/10.1016/j.solmat.2015.12.011)

Zhang, X. G., Uhlig's Corrosion Handbook, R. Winston Revie (editor). 3rd Edition; New Jersey: Wiley, (2011) (pp879-892) ISBN: 978-0-470-08032-0,

Test Procedure for Accelerating Aging of Solar Thermal Collectors

Stephan Fischer[1]

[1]Research and testing center for solar thermal systems (TZS), Institute of Thermodynamics and Heat Transfer, University of Stuttgart (ITW), Pfaffenwaldring 6, 70550 Stuttgart, Germany

Abstract

Based on the experience and data gained during a 3 year exposure of different solar thermal collectors under different climate conditions (tropical, arid, arid maritime, moderate and cold alpine) and system simulations using TRNSYS a test procedure for accelerating aging of solar thermal collectors has been developed and exemplary conducted on flat plate collectors. The overall test procedure which comprises a UV resistance test, a salt mist test, a humidity test, a temperature cycle test and an extended high temperature test is introduced and described in detail.

Key-words: collector test, accelerated aging test, lifetime prediction

1. Introduction

During their lifetime solar thermal collectors are exposed to a variety of partially overlapping aging effects. These are introduced on the one hand from the system type and the mode of operation resulting in different inlet temperatures of the heat transfer fluid. On the other hand site-specific climatic conditions have an important impact on the aging process as shown by B. Traub et al. (2012) and P. Kofler et al. (2013).

To assess and judge the durability and reliability of solar thermal collectors for different system types and different locations a test procedure which takes into account these different ageing processes is needed which goes far beyond the existing durability and reliability test sequences which are documented in the ISO 9806 (2013) testing standard. Thus a test sequence was developed within the German project *Speed*Coll taking into account all relevant kinds of different ageing processes a solar thermal collector is exposed during its lifetime. The test sequence comprises the following tests:

- Initial test
- UV resistance test
- Salt mist test
- Humidity test
- Temperature cycle test
- Extended high temperature test
- Final assessment

The test conditions of each single test can be chosen according to the desired climate and system type the collector will be used for. The different test conditions were derived from a three year long outdoor exposure and monitoring at 6 different test sites (Stuttgart (Germany), Freiburg (Germany), Zugspitze (Germany), Gran Canaria (Spain), Sede Boker (Israel) and Cochi (India)) and from the results of simulations using TRNSYS. Table 1 shows the different climates of the exposure sites.

The data monitored included besides the weather data also the measurement of different temperatures within the collectors as the absorber temperature and the temperature with in the glue joint between the glass cover and the frame and the humidity in the collector between the absorber and the glass cover. The resistance of the tested collectors against the single tests is rated by different criteria. These criteria include lasting and the function of the collector or single components influencing changes and include incidences like brakeage of the glass cover or frame, fogging and a reduction of thermal performance.

doi:10.18086/swc.2017.19.03 Available at http://proceedings.ises.org

Tab. 1: Climates and exposure sites

Climate	Exposure site	Remarks
Tropical climate	Cochi (India)	Hot, humid and wet (Monsun) conditions
Arid climate	Sede Boqer (Israel)	Hot, dry and sandy
Arid maritime climate	Gran Canaria (Spain)	Saline atmosphere
Moderate climate	Stuttgart (Germany)	-
Moderate climate	Freiburg (Germany)	-
Cold alpine climate	Zugspitze (Germany)	High mechanical load through wind and snow loads

2. Initial test

Before the collector will go through the actual aging tests the following initial tests will be carried out

1. Thermal performance test according to ISO 9806, section 20 "Performance testing of fluid heating collectors" to assess the thermal performance prior to aging testing.
2. Mechanical load tests according to ISO 9806, section 16 "Mechanical load test with positive or negative pressure" with a load (positive and negative) of 2400 Pa to ensure a minimum resistance against wind and snow loads. The load (positive and negative) of 2400 Pa is applied 10 times.

3. UV resistance test

To pre-age the collector and to assess the ability of the collector construction including collector parts as polymeric sealing, transparent covers, adhesives and other potential parts sensitive to ultraviolet (UV) radiation the collector is tested using an artificial UV source.

The test setup consists of a climate chamber, light sources and instrumentation with the following specifications:

- Maximum UV radiation (280 nm – 400 nm) shall not exceed 230 W/m² at any location in the collector plane
- The homogeneity of the UV-radiation shall be in the range of ± 15 %. Homogeneity shall be measured at least at 6 locations, evenly distributed over the collector plane.
- Relative humidity in the climate chamber shall be in the range of 15 % ± 5 %
- The temperature in the climate chamber shall be controlled to a value which results in a surface temperature of the collector frame of 80 °C ± 2 °C, measured at location of frame at the top of the collector in an area which is not directly irradiated.
- All temperatures are measured with a standard uncertainty of ± 1 K.

The collector is placed in the climate chamber at a tilt angle of at least 60° and parallel to the light source. The light source is turned on and the climate chamber is set to 15 % relative humidity. Afterwards the temperature within the climate chamber is adjusted such that the surface temperature of at the location of the collector frame at the top of the collector in an area which is not directly irradiated reaches 80 °C ± 2 °C. When this temperature is reached the test begins. During the test ambient temperature, frame temperature and UV irradiance (280 nm – 400 nm) is measured and recorded. The test is completed after an UV irradiation of 280 kWh/m² is reached.

After the test the collector is visually examined and obvious changes or damages like decolouring, changes in structure or surface are documented.

4. Salt mist test

Collectors are often installed close to the sea side and are exposed to significant loads of salt in the air. The test is intended to assess if and to what extend salt will enter the collector and deposit on the absorber and other parts of the collector.

The test setup consists of a salt mist chamber according to EN 60068-2-52:1996 (EN 1996), section 4. A natrium chloride (NaCl) solution of 3 % ± 0.5 % is used. The pH-value of the solution is in the range of 6.5 to 7.2. The salt mist chamber is qualified for the measurement using working standards according to EN ISO 9227:2012 (EN 2012). The working standard is placed in the salt mist chamber at a tilt angle of 70° and is exposed for 48 h a salt mist spray at an ambient temperature of 35 °C ± 2 °C and a relative humidity of more than 90 %. The removal of the working standard shall be 85 g/m² ± 20 g/m²after the test. A pumped heat transfer loop using a suitable heat transfer liquid, with the collector forming part of the loop.

The collector is placed in the salt mist chamber at a tilt angle between 30° and 60° and connected to the heat transfer loop. Afterwards the test cycle as shown in Table 2 is performed on the collector.

During the test the relative humidity and the temperature with in the salt mist chamber shall be measured and recorded. The test is completed when altogether 22 cycles (see Table 2 and Figure 1 are completed.

Tab. 2: Test cycle salt mist test

Phase (duration)	Description
Humid phase (5 h)	Heat transfer loop on, mean heat transfer fluid temperature ϑ_m = 60 °C ± 2 °C. Ambient temperature with in the salt mist chamber ϑ_a = 40 °C ± 2 °C. Relative humidity φ > 90 %
Salt mist phase (2 h)	Heat transfer loop on, mean heat transfer fluid temperature ϑ_m = 60 °C ± 2 °C. Ambient temperature with in the salt mist chamber ϑ_a = 35 °C ± 2 °C. Relative humidity φ > 90 %
Humid phase (10 h)	Heat transfer loop off, ambient temperature with in the salt mist chamber ϑ_a = 40 °C ± 2 °C. Relative humidity φ > 90 %
Salt mist phase (2 h)	Heat transfer loop off, ambient temperature with in the salt mist chamber ϑ_a = 35 °C ± 2 °C. Relative humidity φ > 90 %
Humid phase (5 h)	Heat transfer loop off, ambient temperature with in the salt mist chamber ϑ_a = 40 °C ± 2 °C. Relative humidity φ > 90 %
Drying phase (24 h)	Heat transfer loop on, mean heat transfer fluid temperature ϑ_m = 60 °C ± 2 °C. Ambient temperature with in the salt mist chamber ϑ_a = 23 °C ± 2 °C. Relative humidity in the range of 30 < φ < 70 %

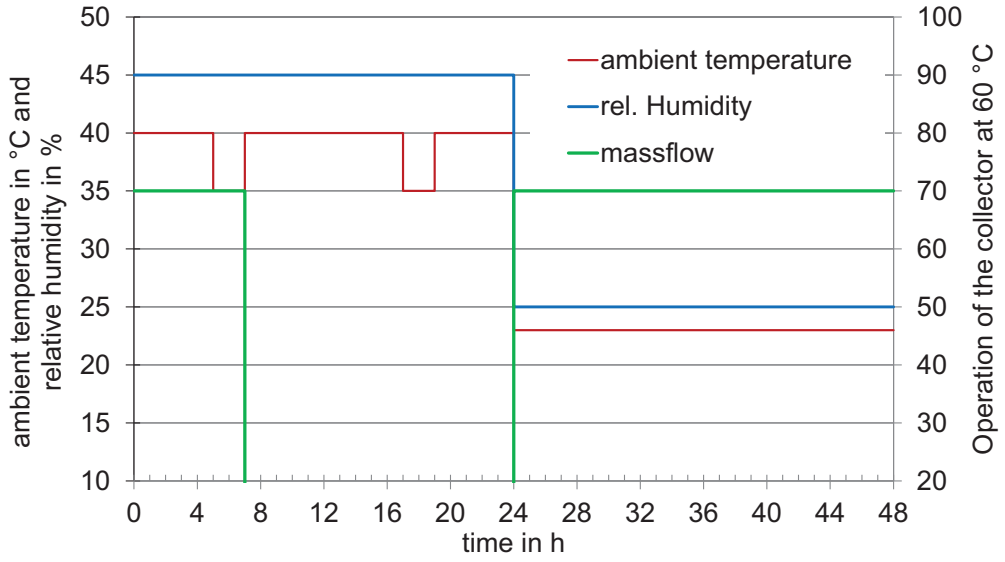

Fig. 1: Schematic test cycle salt mist test

5. Humidity test

The humidity test is designed to test the durability of the collectors against high humidity and is realized by the accelerated simulation of the day night cycle within a climate chamber. Figure 2 shows the graphs of temperature and relative humidity within the climate chamber as well as the switching points for turning on and off of the irradiance and the mass flow. Figure 3 shows the resulting graphs of the temperature and the relative and absolute humidity within the air gap between the absorber and glass cover of a tested collector. The graphs during the humidity test are very close to the data recorded during the real exposure as shown by Fischer et al. (2016).

This test cycle accelerates the outdoor exposure by the factor of 4. The boundary conditions like ambient temperature relative humidity as well as the hemispherical irradiance can be adjusted when required.

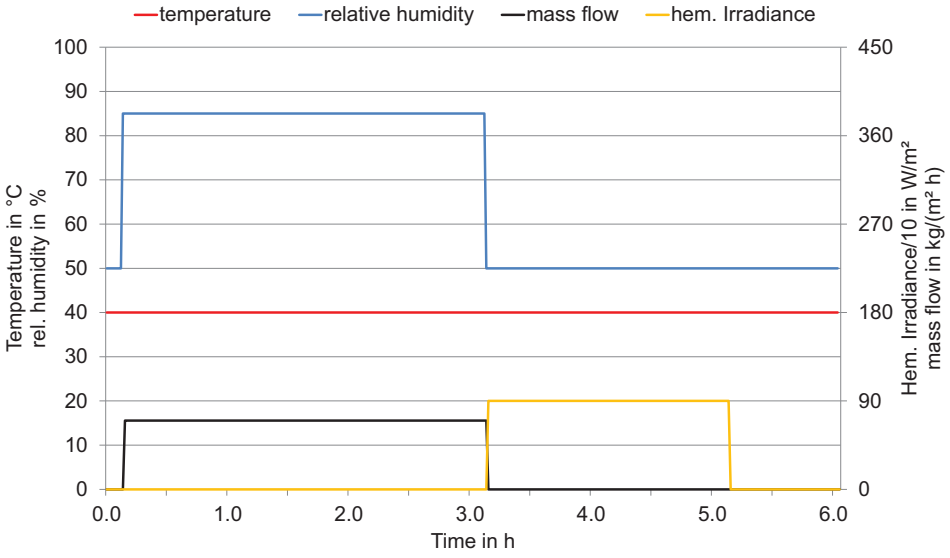

Fig. 2: Temperature, relative humidity, hemispherical irradiance and mass flow during the humidity test cycle

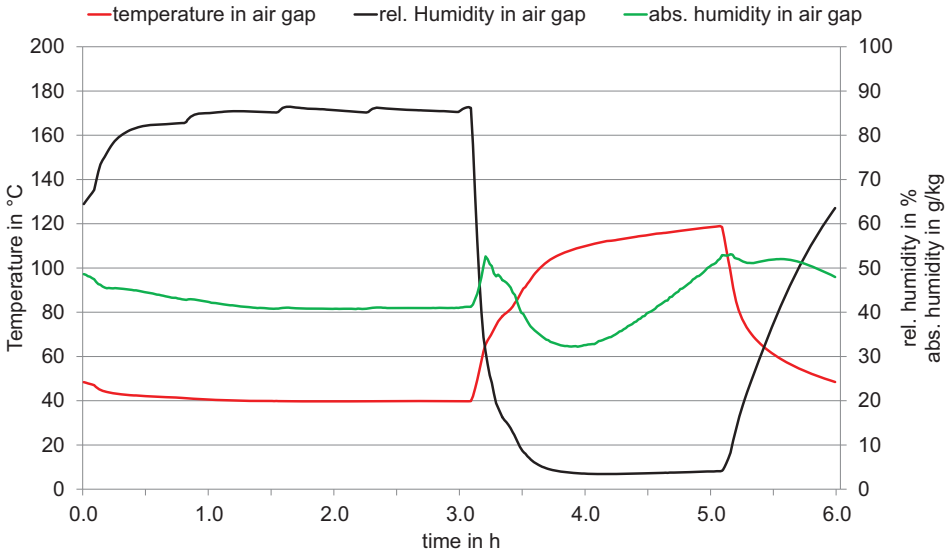

Fig. 3: Temperature, relative and absolute humidity within the air gap between absorber and glass cover of a tested collector during the humidity test

6. Temperature cycle test

During operation a collector and its components will undergo numerous temperature cycles during its lifetime. This test is intended to assess the ability of the collector design to withstand these temperature cycles without damage.

The test setup consists of a climate chamber and instrumentation with the following specifications:

- A climate chamber suitable for the operation in the range of -45 °C to + 95 °C
- The temperature in the climate chamber at quasi-stationary conditions is controlled to a value which results in a surface temperature of -40 °C ± 2 °C and +90 °C ± 2 °C respectively at the top of frame of the collector.
- Instrumentation for the measurement of the relative humidity.
- All temperatures are measured with a standard uncertainty of ± 1 K.

The collector is placed in the climate chamber at ambient conditions (room temperature and corresponding relative humidity). The air in the climate chamber is cooled down to a temperature leading to a temperature at the surface of the frame at the top of the collector of -40 °C ± 2 °C and held at this temperature for 1 h. Afterwards the climate chamber is set to a temperature leading to a temperature at the surface of the frame at the top of the collector reaches +90 °C ± 2 °C and held for 1 h, see Figure 4. During the whole test the temperature and relative humidity within the climate chamber as well as the frame temperature at the top of the collector are measured and recorded. The test is completed when altogether 200 temperature cycles are completed.

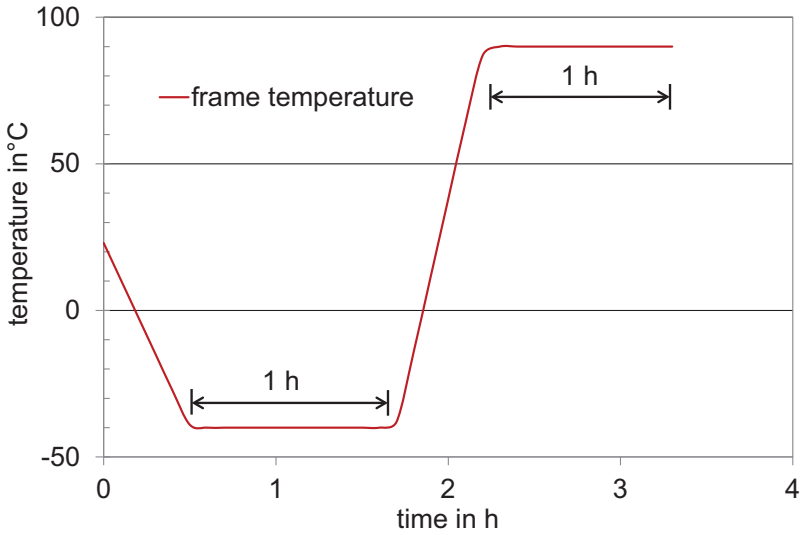

Fig. 4: Schematic test cycle of temperature cycle test

7. Extended high temperature test

This test assesses the ability of the collector to withstand high temperatures during operation and lifetime like they may occur during times with high solar irradiance and high ambient temperature while no heat is removed by circulating the heat transfer fluid (stagnation). Times when the collector needs to withstand these high temperatures are:

- When empty during installation.
- When empty during any period of maintenance.
- When filled with heat transfer fluid or steam at stagnation conditions.

The absorber temperature ϑ_{abs} used for the test is the absorber temperature which will be reached at hemispherical radiation G of 1100 W/m² and an ambient temperature ϑ_a of 50 °C and shall be calculated

according to the following equation (1)

$$\vartheta_{abs} = 50°C + \frac{-a_1 + \left(a_1^2 + 4\eta_0 a_2 1100W/m^2\right)^{0.5}}{2a_2} + 20°C \quad \text{(eq. 1)}$$

The collector parameters η_0, a_1 and a_2 are taken from thermal performance measurement during the initial test.

7.1 Method 1: Test setup, conditions and procedure

The test setup of Method 1 consists of a climate chamber, solar simulator and instrumentation with the following specifications:

- A combination of climate chamber and solar simulator which allows to heat the absorber to the required test temperature ϑ_{abs} and to keep this temperature constant to ± 2 K. The irradiance level in the collector plane shall be between 900 W/m² and 1200 W/m².
- A temperature sensor to measure the absorber temperature ϑ_{abs} is positioned at two-thirds of the absorber height and half the absorber width. It is fixed firmly in a position to ensure good thermal contact with the absorber. The sensor shall be shielded from solar radiation.
- A temperature sensor is positioned on the frame at the top of the collector. The sensor shall be shielded from solar radiation.
- Instrumentation for the measurement of the relative humidity.
- All temperatures shall be measured with a standard uncertainty of ± 1 K.

The collector is placed in the climate chamber at a tilt angle of at least 60° and parallel to the solar simulator. All but one of the fluid pipes are sealed to prevent cooling by natural circulation of air. The climate chamber is set to 50 % relative humidity. Solar simulator and climate chamber are set to an irradiance and temperature that the absorber temperature according to equation 1 ± 2 °C is reached. At this stage the test begins and runs for 8 h. Afterwards the solar simulator is shut down and the ambient temperature is set to 25 °C. After 4 h the solar simulator and climate chamber are turned on again until the absorber temperature has stayed another 8 hour time period at the test temperature ± 2 °C. The collector should be visually inspected daily during the cooling phase and any it´s appearance shall be reported. During the whole test the relative humidity and the temperatures of the absorber, the collector frame and of the ambient are measured and recorded. The test is completed when altogether 15 temperature cycles (see Figure 3) are completed.

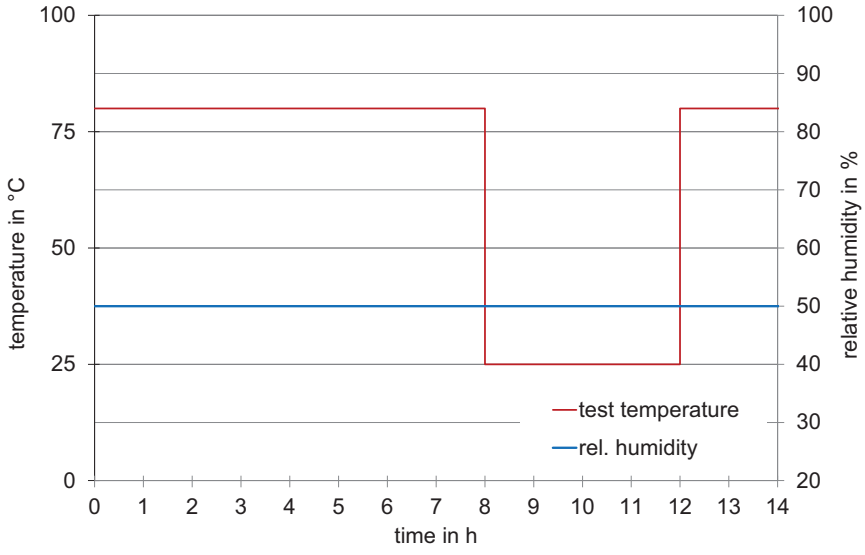

Fig. 5: Schematic test cycle of extended high temperature test

7.2 Method 2: Test setup, conditions and procedure

- A pumped heat transfer loop using a suitable heat transfer liquid, with the collector being part of the loop. A suitable heat transfer fluid is one that will remain in its liquid state at the test temperature and the maximum operating pressure of the collector.
- A temperature sensor to measure the absorber temperature ϑ_{abs} is positioned at two-thirds of the absorber height and half the absorber width. It is fixed firmly to ensure good thermal contact with the absorber. The sensor is shielded from solar radiation.
- A temperature sensor is positioned on the frame at the top of the collector. The sensor shall be shielded from solar radiation.
- Instrumentation for the measurement of the relative humidity.
- All temperatures shall be measured with a standard uncertainty of ± 1 K.

The collector is mounted at a tilt angle of at least 60° and connected to the heat transfer loop. The climate chamber is set to 50 % relative humidity. Heat transfer loop and climate chamber are set to temperatures that the absorber temperature according to equation 1 ± 2 °C is reached. The mass flow rate shall be adjusted in a way that the heat transfer fluid will not lose more than 2 K while passing through the collector. At this stage the test begins and runs for 8 h. Afterwards the heat transfer loop is shut down and the ambient temperature is set to 25 °C. After 4 h the heat transfer loop and climate chamber are turned on again until the absorber temperature has stayed another 8 hour time period at the test temperature ± 2 °C. The test is completed when altogether 15 temperature cycles (see Figure 5) are completed.

7.3 Inspection

After the test the collector is visually inspected for any changes or damages like permanent deformation, glass or adhesive brakeage any structural failure, any burning, scorching, or heat shrinkage, outgassing and any effect likely to impair the serviceability of the collector.

8. Final assessment

After the collector went through all accelerating aging tests the following final tests will be carried out to assess the impact of the previous test on the performance of the collector:

1. Thermal performance test according to ISO 9806, section 20 "Performance testing of fluid heating collectors" to assess the thermal performance prior to aging testing.
2. Mechanical load tests according to ISO 9806, section 16 "Mechanical load test with positive or negative pressure" with a load (positive and negative) of 2400 Pa to ensure a minimum resistance against wind and snow loads. The load (positive and negative) of 2400 Pa is applied 10 times.

When the tests have been completed the collector used for the tests is dismantled and inspected. All abnormalities shall be documented and accompanied by photographs. The collector and all of its components shall be described and should be photographed (glazing, absorber, absorber coating, insulation, housing, inlet and outlet ports, glazing supports and retainers, seals, gaskets, back sheet, etc.).

9. Summary and outlook

In the framework of the German research project *Speed*Coll " Development of Accelerated Ageing Tests for Solar Thermal Collectors and their Components" a test procedure for the accelerated aging of collectors has been developed and was carried out. The proposed test conditions of the single tests can be adopted according to specific climatic and operational requirements. Thus the proposed test procedures allow an assessment of the impact of the operation and climatic conditions during the lifetime of the collector.

Currently the test sequences are further developed with in the follow-up research project *Speed*Coll2 "Estimation of the service life of solar collectors and its components". The aim of the project are accelerated aging tests which allow the estimation of the service life of solar collectors and its components depending on the climate and the operation conditions the collectors will be used at.

10. References

EN, 1996. European Standard, EN 60068-2-52:1996, Environmental testing - Part 2: Tests, Test Kb: Salt mist, cyclic (sodium chloride solution), Brussels, Belgium

EN, 2012. European Standard, EN ISO 9227:2012, Corrosion tests in artificial atmospheres - Salt spray tests, Brussels, Belgium

Fischer, S., Kofler,P., Traub, B., Drück, H., 2016. Untersuchungen zur Feuchtebelastung im Inneren von solarthermischen Flachkollektoren, Tagungsband zum 26. Symposium Thermische Solaranlagen (Kurzfassung), Kloster Banz, Bad Staffelstein, 20. – 22.04.16, ISBN 978-3-943891-65-2

ISO, 2013. International Standard ISO9806:2013, Solar energy – Solar thermal collectors –Test methods, Geneva, Switzerland

Kofler, P., Traub, B., Fischer, S., Drück, H., 2013. Alterungseinflüsse auf Sonnenkollektoren in gemäßigten und tropischen Klimazonen, Tagungsband zum 23. Symposium Thermische Solaranlagen, Seiten 138-139 (Kurzfassung), Kloster Banz, Bad Staffelstein, 24. – 26.04.13, ISBN 978-3-943891-10-2

Traub, B., Kofler, P., Fischer, S., Drück, H., 2012. Beanspruchung von Sonnenkollektoren unter Berücksichtigung unterschiedlicher Klimazonen und Anwendungen, Tagungsband zum 22. Symposium Thermische Solaranlagen, Seiten 154-155 (Kurzfassung), Kloster Banz, Bad Staffelstein, 09.05. – 11.05.12, ISBN 978-3-941785-89-2

11. Acknowledgements

The research projects “Development of Accelerated Ageing Tests for Solar Thermal Collectors and their Components”, acronym “*Speed*Coll”, and "Estimation of the service life of solar collectors and its components", acronym “*Speed*Coll2”, are funded by the German Federal Ministry for Economic Affairs and Energy by resolution of the German Parliament and managed by Project Management Jülich (PTJ) under grant numbers 0325969B and 0325865B. The author gratefully acknowledges this support and take the responsibility for the contents of this publication.

PVT Performance Prediction

Ulrich Fritzsche, Markus Schweiger, Florian Reil
TÜV Rheinland Energy GmbH, Cologne (Germany)

Abstract

Photovoltaic Thermal (PVT) hybrid modules producing electricity and heat in parallel are becoming more relevant in the Solar Thermal market. Especially PVT modules in combination with heat sinks operating in low temperature ranges like heat pumps are showing perfect conditions for that kind of combination. One important topic for a broader market implementation and distribution will be a clear and overall performance characterization with respect to electrical and thermal power measurements and their interaction.

The presented project has validated a method for a junction (module) temperature forecast based on the thermal behavior of PVT's under consideration of mean fluid temperature, ambient temperature and wind speed. This approach will give the required link between thermal collector testing and electrical PV module characterization and provide a clear distinction of responsibilities for the thermal and PV experts and laboratories.

Keywords: PVT, Performance prediction, junction temperature, module temperature

1. Motivation

As for most PVT applications it is not possible to use temperature probes for direct measurement of the cell temperature, a new approach without additional sensors inside the PVT construction was developed.

Based on the method of the equivalent cell temperature ECT [IEC 60904-5:2011] it is possible to receive all required information for a detailed description of the overall thermal behavior including the cell/ junction temperature.

$$ECT = 25°C + \frac{1}{\beta}\left[\frac{U_{OC2}}{U_{OC,STC}} - 1 - \alpha\ ln\left(\frac{G_2}{1000}\right)\right] \qquad \text{(eq. 1)}$$

A general equation to estimate the module temperature by field measurements is described in IEC 61853-2:2016:

$$T_m - T_{amb} = G/ (u_0 - u_1 * v) \qquad \text{(eq. 2)}$$

As this approach is not covering the main influence of PVT's, the fluid temperature dependency, it is not applicable for modules combined with a thermal heat absorber. Therefore, a new model or equation was developed to cover also this influence.

This new approach which will be presented in the next clause was already introduced before in the project report "Harmonization and Standardization of multi-functional PVT Solar Collectors (PVT-Norm)" Fritzsche et al. (2016). The current work should validate the indoor steady state results with dynamic outdoor field results. A detailed field test of two similar PVT modules with (PVT 1) and without thermal back-side insulation (PVT 2) was performed over several months to provide a large set of data with a wide range of environmental conditions.

doi:10.18086/swc.2017.19.04 Available at http://proceedings.ises.org

2. Procedure

Based on the long experience of performance testing of PVT's and the results of absorber temperature estimation right from the beginning of our testing it was obvious, that the behavior of the module resp. cell temperature could be described similar to that of the thermal performance, but with an opposite sign as the temperature is rising and not decreasing with higher fluid temperatures. Figure 1 is showing an excellent example, how the measurement points from the steady state indoor test are distributed and how the resulting curves will look like.

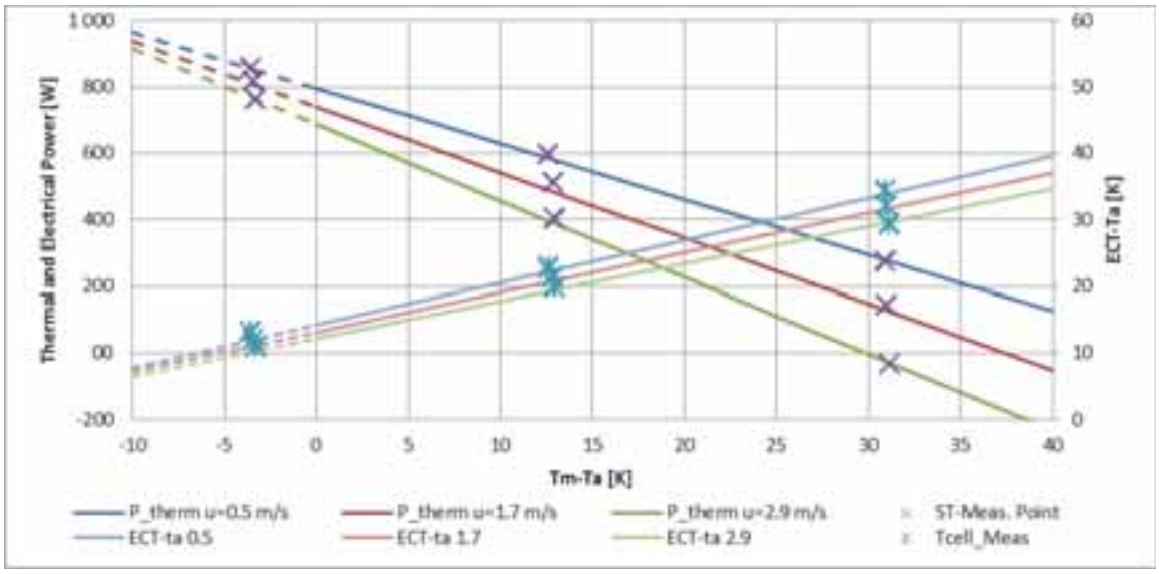

Fig. 1: Example of thermal performance and cell over temperature measurement points and resulting curves

EN ISO 9806:2013 is giving the following equation 3 for the steady state testing of "uncovered" collectors.

$$\dot{Q} = \dot{A}_G \cdot G'' \left(\eta_{0,hem}(1 - b_u u) - (b_1 + b_2 u) \frac{\vartheta_m - \vartheta_a}{G''} \right) \qquad \text{(eq. 3)}$$

The new equation describing the cell over temperature is based on the regular equation for thermal performance of unglazed collectors. By changing the sign, the gradient of the cell (absorber) over temperature could be described as seen in equation 4. It was evaluated, if the global irradiance has to be taken into account, but the influence of wind and fluid temperature was dominating, that the global irradiance was finally neglected.

$$\vartheta_{cell} - \vartheta_a = \vartheta_{cell,0}(1 - d_u u) + (d_1 + d_2 u)\,(\vartheta_m - \vartheta_a) \qquad \text{(eq. 4)}$$

With:

ϑ_{cell} = cell (absorber) temperature

$\vartheta_{cell,0}$ = cell (absorber) temperature conversion point

d_u = wind dependence of the conversion point

d_1 = heat „gain" coefficient

d_2 = wind dependence of heat gain coefficient

The units are currently following the EN ISO systematic. The nomenclature itself is open for discussion, but describes the different coefficient in the best way.

3. Test sequences

As mentioned before, two similar PVT modules with and without a thermal insulation were used for the validation of the procedure. After an initial indoor test of electrical and thermal properties, the modules had performed an outdoor field test over several months.

3.1. Initial steady state testing

Beside a characterization of the electrical performance according to standard test conditions STC, a detailed indoor performance test was. The collectors were tested according to EN ISO 9806:2013 with the steady state test method for uncovered collectors. This method requires a constant high irradiance level and three different inlet temperatures with three different wind speed ranges.

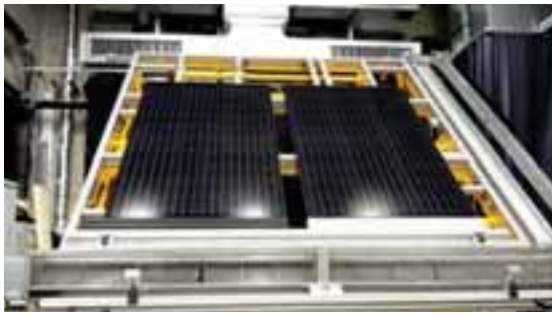

Fig. 2: Indoor steady state test set up

It is obvious, that those requirements are really hard to fulfill, if this procedure should be applied outdoors. As the boundary conditions within a sun simulator are stable and highly reproducible, it was always the preferred method at TÜV to test this wind dependent collector types.

During thermal performance testing, the electrical part of the PVT was operating in the so called MPP Maximum Power Point controlled by an electronic load. In addition to that, the load was measuring the PV module IV curve every five minutes. Even, if not the full IV curve is necessary for the ECT method; at least the open circuit voltage signal has to be detected regularly.

The parameter sets describing the thermal performance according to equation (3) as well as the cell temperature above ambient (4) were determined for the two used test samples are described in table 1 and 2.

Tab. 1: Data set for prediction of the thermal performance of the two test samples

	PVT 1 with back side insulation		PVT 2 without back side insulation	
	Value	**Standard deviation [%]**	**Value**	**Standard deviation [%]**
$\eta_{0,hem}$ [ ]	0.490	0.9	0.538	1.6
b_u [s/m]	0.055	8.3	0.048	14.6
b_1 [W/(m²K)]	9.336	2.5	13.805	3.4
b_2 [J/(m³K)]	1.574	7.5	1.905	10.4

Tab. 2: Data set for prediction of the module (cell) temperature above ambient

	PVT 1		PVT 2	
	Value	**Standard deviation [%]**	**Value**	**Standard deviation [%]**
$\vartheta_{cell,0}$ [°C]	19.82	1.12	14.65	1.11
d_u [s/m]	-0.047	10.3	-0.058	9.79
d_1 [ ]	0.651	1.80	0.653	1.29
d_2 [s/m]	-0.030	16.6	-0.032	13.3

3.2. Field Test

As described before, the two samples had been sent to our outdoor test field in Italy after initial indoor testing. There we've extended the already existing infra structure to monitor not only the electrical the PV long term performance, but also the thermal behavior of PVT modules.

Beside additional sensors as Pyrgeometer for long wave irradiation detection or wind speed sensors to measure the wind speed in the aperture area, a thermal testing loop for two samples had been realized.

Fig. 3: Field test set up

Delayed tests for certification of the products are the reason, that only about four month from October to January had been available for the final validation of this procedure. The initial plan was at least half a year including the summer and autumn.

3.3. Final steady state testing

After that outdoor field test, the samples had been sent back to Cologne to undergo a final test under the sun simulator. As this test was showing performance degradation, these values had not been used for the final validation. As the field measurement didn't show any degradation over time, the vertical transport of the samples might be the reason for that minor degradation.

Nevertheless, the final tests had been used to perform the tests not only according to the "old" method described in EN ISO 9806:2013, but also according to the new method described in the 2017 release of the standard. The comparison of both methods didn't show significant deviations, that the applicability of this new equation for so called WISC collectors under the sun simulator was confirmed.

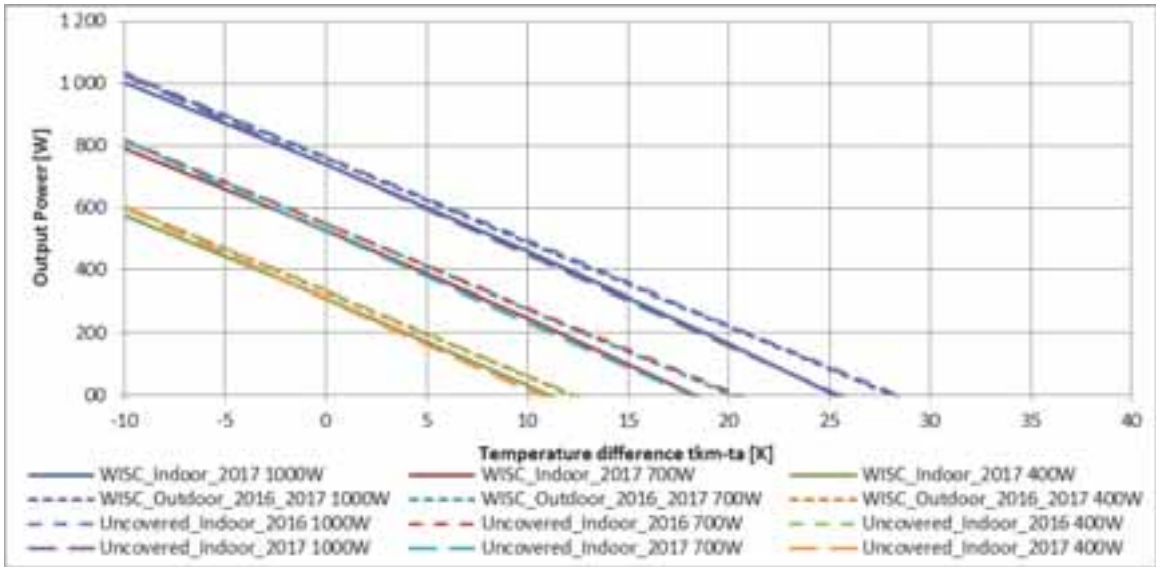

Fig. 4: Comparison of initial and final test performance tests for the PVT 2 collector without thermal insulation

4. Validation

The validation of the new model was made on the basis of the resulting electrical performance. Even, if the model itself gives only the module temperature above ambient, the final aim is a precise prediction of the electrical output. This approach was also necessary, as the electrical output was measured with a much higher resolution than the open circuit voltage signal during the IV-Curve measurement.

The limit for the minimum irradiance level was set to 200 W/m² not only because of spectral response of the cells, but also because of higher uncertainties during this low irradiance performance.

4.1 PVT 2 without thermal insulation

In figure 5, you will find the comparison results between measured and calculated electrical output for the PVT without thermal insulation.

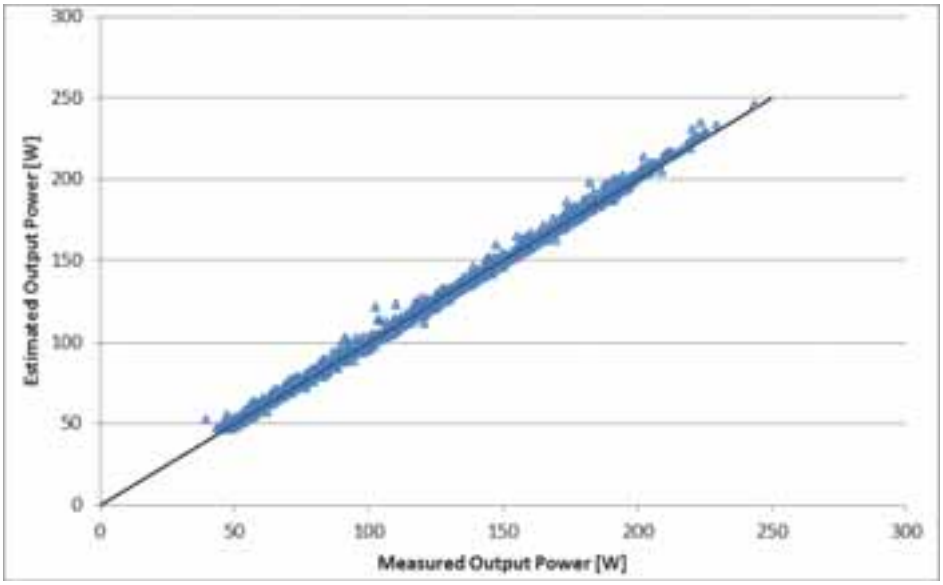

Fig. 5: Precision of measured and calculated electrical performance

In general, the comparison of simulated and measured output power fits quite well as shown in figure 5. The energy difference during irradiance levels above 200 W/m² over the complete test period is about 0.14%. The used quality figure described as the integral of the absolute deviation (energy of deviation) divided by the measured energy is only 1.3 %.

The following figures 6 & 7 are showing representative days and the resulting deviation of measured and estimated electrical output. For a long term prediction, these short time depending deviations up to a few percentages are not relevant and could be neglected.

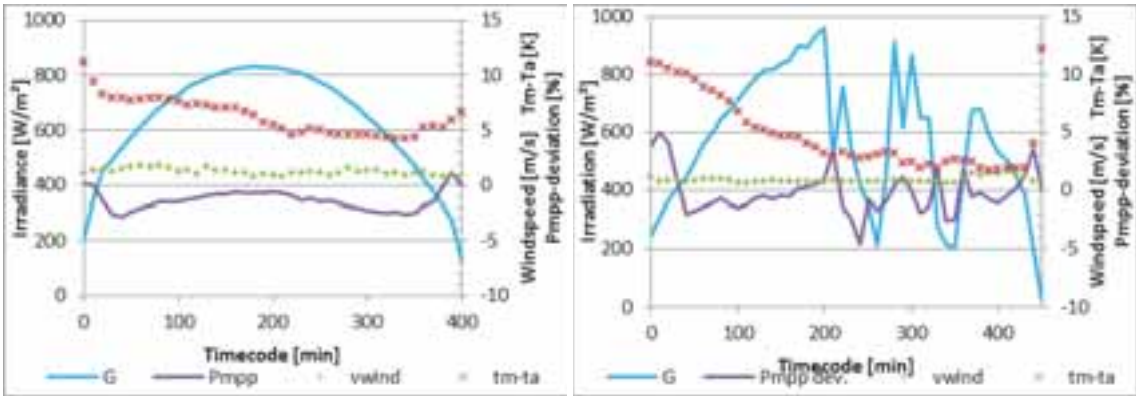

Fig. 6 & 7: Representative days for clear sky and partly cloudy days

4.2 PVT 1 with thermal Insulation

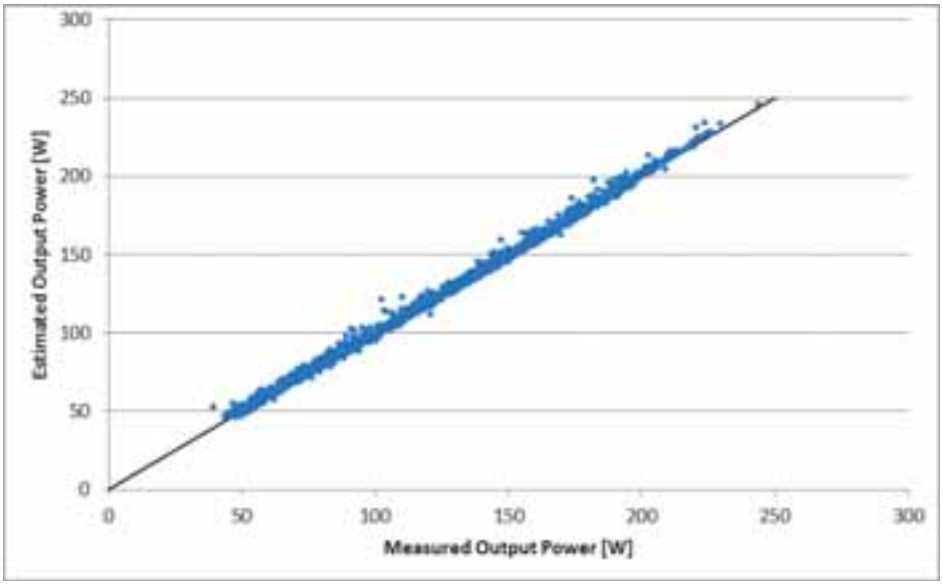

Fig. 8: Precision of measured and calculated electrical performance

In general, the comparison of simulated and measured output power fits quite well as shown in Fig. 8. The energy difference during irradiance levels above 200 W/m² over the complete test period is about 0.24 %. The used quality figure described as the integral of the absolute deviation (energy of deviation) divided by the measured energy is only 1.8 %.

The following figures 9 & 10 are again showing representative days and the resulting deviation of measured and estimated electrical output for the sample with thermal insulation.

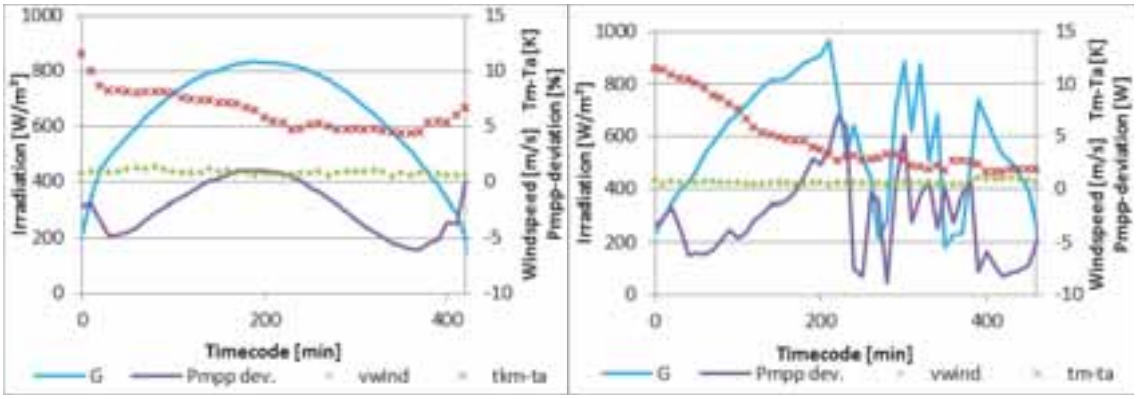

Fig. 9 & 10: Representative days for clear sky and partly cloudy days

The resulting deviation between measured and calculated output power and energy is slightly higher than for PVT 2. But even this higher deviation is still more than appropriate for a long term energy yield.

5. Conclusion

5.1 Model for estimation of cell temperature of PVT's

This model is showing promising results with an appropriate accuracy. As you can see below in Fig. 6, 7, 9, 10, there is still a daytime depending deviation as well as deviations based on quick irradiance changes, but this is not relevant for long time or annual performance prediction. From current perspective, this might be solved by using a 2-node model, where the cell is the first and the fluid the second note. As this model is not referred in the collector standard or necessary for the described purposes, this might be a solution for R&D, but not for certification and general performance indication.

Beside the accuracy, a clear distinction of the different responsibilities is given. Beside a regular determination of the open voltage signal and the already required performance under MPP, no additional electrical measurements are necessary.

An accurate measurement of the wind speed over aperture will be the main challenge for outdoor measurements.

5.2 Performance Indicator for PVT collectors based on NMOT conditions

A harmonized and realistic presentation of the electrical as well as thermal performance of PVT's is a main requirement for a broader distribution and acceptance of this technology. Currently, there's no harmonized way to present these results and a direct comparison of the performance of different PVT's is nearly impossible. Furthermore, the partly used unrealistic presentation based on reference conditions, which will never occur at the same time will result in unrealistic expectation and disappointed owner or user.

The performance indication based on standard test conditions, which will usually be used for PV modules are not applicable for PVT. These conditions are fixed to a cell temperature of 25°C and could never consider the thermal behavior in an appropriate way. One opportunity for PVT's is a performance indication based on Nominal Module Operation Temperature conditions, as these are considering a realistic module temperature in the field as basis. Not only for PVT, but also for standard PV modules, the performance at NMOT as described in IEC 61215-2:2016 is a much more realistic performance indicator than the performance at a fixed cell temperature of 25°C and 1000 W/m² irradiance.

Beside the conditions at NMOT, additional reference conditions for the collector inlet temperature or the mean collector fluid temperature has to be defined. To distinguish between different applications of PVT's as combined with heat pipes, pools or as pre-heater, there should be a set of different inlet temperatures available.

To cover the main fields of application the inlet temperature levels 10 K below ambient, ambient and 10 K above ambient might be a reasonable range. Considering the ambient temperature of 20°C for NMOT, this would result in mean fluid temperatures of 10, 20 and 30°C. A possible nomenclature would be $NMOT_{PVT10}$.

Table 3 is showing exemplary results for the PVT 1 with thermal insulation.

Table 3: Performance indication based on NMOT conditions with a global irradiance of 800W/m², 20°C ambient temperature and a wind speed of 1 m/s

	Mean Fluid Temperature [°C]	Equivalent Cell Temperature @ NMOT [°C]	Electrical Power @ NMOT [W]	Electrical power gain [%]	Thermal Power @ NMOT [W]
$NMOT_{PVT10}$	10	29.5	197.7	8.2	747
$NMOT_{PVT20}$	20	35.8	192.3	5.2	567
$NMOT_{PVT30}$	30	42.0	187.0	2.3	476
NMOT	PV module	46.9	182.8	-	-

If the mean fluid or the inlet temperature should be used need to be discussed. The use of the mean fluid temperature would be much easier, but if we think about an overall indication as used in the Solar Keymark data sheets and calculated also of the electrical energy yield in the future, it might be worse to start directly with fixed defined inlet temperatures. This would be applicable, if the resulting means fluid temperature for these fixed inlet temperatures will be calculated in advance.

6. Outlook

In the framework of this small project PVT Field evaluation, a new approach to estimate the cell temperature of PVT collectors under consideration of the thermal working point was developed. This model is independent from the chosen collector model and could be used for indoor and outdoor measurements.

To reach more confident, further validations with additional PVT collectors should be performed. Therefore, existing monitoring results might be used or new field measurements need to be performed.

As a final step, a technical specification out of an IEC or ISO work item may be published. In the meantime, certification schemes like Solar Kemyark or SRCC might consider this model for an appropriate performance indication in the frame of their individual data sheets.

7. Reference

EN ISO 9806:2013, Solar Energy – Solar thermal collectors – Test methods

IEC 60904-5:2011, Photovoltaic devices – Part 5: Determination of the equivalent cell temperature (ECT) of photovoltaic (PV) devices by the open-circuit voltage method

IEC 61853-2:2016, Photovoltaic (PV) module performance testing and energy rating – Part 2: Spectral responsivity, incidence angle and module operation temperature measurement

IEC 61215-2:2016, Terrestrial photovoltaic (PV) modules - Design qualification and type approval - Part 2: Test procedures

“Harmonization and Standardization of multi-functional PVT Solar Collectors (PVT-Norm)” Fritzsche et. al. (2016).

Symbols

IEC 60904-5:2011

α	Temperature coefficient of the short circuit current	%/°C
β	Temperature coefficient of the open circuit voltage	%/°C
U_{OC}	Open circuit voltage	V
$U_{OC,STC}$	Open circuit voltage at standard test conditions	V
G	Global irradiance	W/m²

IEC 61853-2:2016

T_m	Module temperature	°C
T_{amb}	Ambient temperature	°C
u_0	Irradiance depending correction factor	
u_1	Wind depending correction factor	
v	Wind speed	m/s

EN ISO 9806:2013

Q	Useful power extracted from collector	W
A_G	Gross area of collector as defined in the ISO 9488	m²
G“	Net irradiance	W/m²
G_{hem}	Hemispherical solar irradiance	W/m²
$\eta_{0,hem}$	Collector efficiency based on hemispherical irradiance G_{hem}	-
b_u	Collector efficiency coefficient (wind dependence)	s/m
b_1	Heat loss coefficient at $(\vartheta_m - \vartheta_a) = 0$	W/(m2·K)
b_2	Wind dependence of the heat loss coefficient	Ws/ (m3·K)
ϑ_m	Mean temperature of heat transfer fluid	°C
ϑ_a	Ambient air temperature	°C
u	Surrounding air speed	m/s

A flexible software framework for self-adapting algorithm-based fault detection and diagnosis in solar heating systems

Matthias Georgii, Christoph Schmelzer, Hagen Braas, Janybek Orozaliev and Klaus Vajen

Institute of Thermal Engineering, University of Kassel (Germany)

Abstract

A software framework for algorithm-based fault detection in solar heating systems is described. It automatically links modular algorithms in order to perform the best applicable fault detection methods considering the data available for each monitored system. It follows an object-oriented design, where algorithm objects communicate their needed data and parameter inputs, offered outputs as well as constraints via corresponding objects to a path finder. Special effort is made to enable the creation of flexible measurement data requests that do not need to know sensor names in advance. In this paper the basic concepts and implementation approaches to achieve this flexibility in the software framework are described. Finally, exemplary results are shown for a set of algorithms that were implemented in the software framework to determine gradual leakage in a monitored system and bring the capabilities of the framework to life.

Keywords: Solar heating, fault detection, function control, monitoring

1. Introduction

Solar heating systems for moderate climates are equipped with an auxiliary heater which is able to cover the whole heat demand on its own. Hence, faulty behavior of the solar part of the heating system often remains undetected by the end user, at least for a longer period. Higher fossil energy consumption and increased degradation of installed components may be the consequence. But the complexity of these systems can make it time-consuming (and thus expensive) even for an expert to assess the functioning or to detect faults of the solar heating system. Moreover, several faults may only occur temporarily under certain circumstances and remain hidden during an inspection. Therefore, automatic function control of solar heating systems is preferable.

However, the possibilities to automatically detect (and localize) faults depend on the system type, the underlying hydraulics, available measurement instrumentation and known system parameters. So, different approaches, additional assumptions or conditions may be necessary to detect a certain fault for different systems, implying different levels of accuracy that can be reached. Hence, it was the aim to design a FDD software package which can automatically adapt itself to such boundary conditions of each system (i.e. the available data basis) and subsequently perform the best applicable FDD algorithms.

To enhance automated fault detection for solar heating systems, ongoing research is important and necessary. This includes identifying relevant and observable symptoms of different faults for different systems and operation conditions, deriving algorithmic descriptions to check for these symptoms and faults, and -even more challenging- finding acceptable threshold values that differentiate between faulty and normal operation. Besides that, constant questioning and advancement of the best ways to implement and structure fault detection systems is important. One approach for a self-adapting fault detection system is presented here.

2. Basic concept

Since network-connectable data loggers and controllers get more common, a server-based approach for fault detection and diagnosis (FDD) of solar thermal systems (STS) is considered here. This means that measured data will be transferred from local data loggers to central servers which are tasked to monitor many solar thermal systems simultaneously. The local controller will only perform function control routines which either can be implemented easily without extra cost, or which check for conditions that require immediate response from the controller, e.g. to avoid damages in the STS. On the central server, the FDD analysis is performed and the results

doi:10.18086/swc.2017.19.05 Available at http://proceedings.ises.org

are passed to some "action module" which decides how to proceed (e.g. store to some database, write alarm messages, communicate with the controller, …). Such a centralized server-based solution allows for easy maintenance and continuous improvements of the FDD analysis routines that immediately benefit the whole user base. Furthermore, it does not require more powerful (and thus expensive) controllers in order to perform increasingly complex algorithms which are not part of the intrinsic control task. The software framework described here focuses on the part of the FDD analysis, i.e. how to extract faults and malfunctions in the STS from the available measurement data which is accessible in databases.

To achieve a FDD software package that can flexibly adapt itself to the available data basis, the whole procedure of fault detection and diagnosis is split into small subtasks which then will be managed automatically. This modular approach starts with the underlying FDD method which is described in Isermann (2006) and was also used by Küthe et. al (2011). It features several levels that are passed consecutively, as shown in fig. 1. Starting from measured values (e.g. the collector temperature), features are generated via appropriate feature algorithms. Features are (combined) properties of measured signals or some information derived thereof (e.g. nonzero flow rate in solar loop). Symptom algorithms then check related features for exceptional values to generate symptoms. Symptoms specify unusual or undesired states in the STS (e.g. unwanted cooling through collector during night). In the last step, fault algorithms usually combine several symptoms to identify the fault(s) which might cause the observed symptoms (e.g. malfunctioning check valve). Note that the outputs of symptom and fault algorithms are "statements about" symptoms and faults, since the result may also be their nonexistence. Hence, it is possible to differentiate whether a symptom or fault was checked for at all, and to make use of a "confirmed nonexistence".

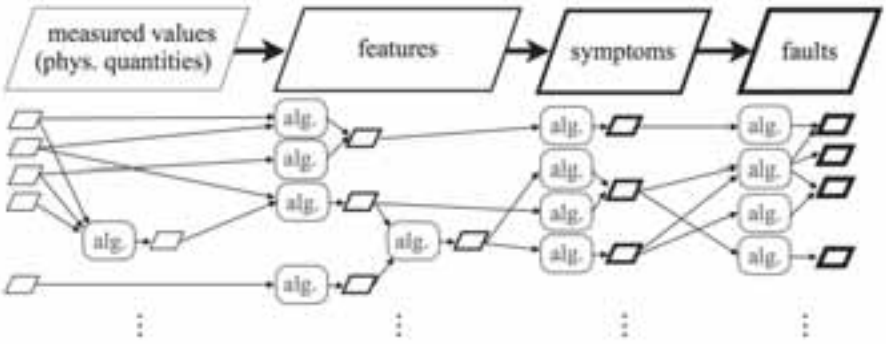

Fig. 1: Levels of the FDD method and exemplary algorithms of each level with their links. Each rhomboid denotes a specific quantity (i.e. a certain sensor/measuring point, feature, symptom, fault)

The FDD algorithms described in the previous section can be considered as "special knowledge" solving a small subtask under certain prerequisites and hence are part of a "knowledge base". Also, all information available about hydraulic schemes, each system's installed sensors as well as properties (called parameters here) of those sensors and of other installed hydraulic components contribute to the knowledge base. The software framework described here can access the knowledge base and then automatically link the knowledge found in order to apply it to a specific STS. The knowledge base can be extended easily over time, and every new piece of information will automatically be used wherever applicable. This distinction between knowledge base and automated knowledge linking is also indicated in fig. 2 where important software elements are depicted along with the interconnecting information flow.

3. Main software elements

In this section, first the structure of the knowledge base is described, on top of which the software framework will work. After that, the mechanism needed to communicate inputs, outputs and constraints between algorithms and the framework is presented. In the third subsection, the process of knowledge linking utilizing the communication mechanism is explained. The next subsection then sketches how the single parts are put together and which steps are performed during a particular investigation of a STS. The last subsection summarizes how data can be accessed and manipulated within an algorithm.

3.1 Knowledge base

As mentioned above, the knowledge base holds all FDD algorithms and known properties of STS, their

components and measurement equipment. Two things are essential for every FDD analysis: what is the type/ hydraulic design of the STS, and what sensors are intended to measure which quantity. Also, the names for sensors and components have to be defined. For this purpose, each STS that is to be investigated by the FDD software must be assigned to both a hydraulic scheme and a sensor scheme. The hydraulic scheme is – in the easiest case – a name that uniquely identifies the hydraulic layout of a STS. The possibility to compose a hydraulic scheme from several hydraulic modules as described in (Dröscher et al., 2009) will also be implemented in future. Moreover, for a given hydraulic scheme, names can be defined for components (except sensors) in the STS layout (e.g. "primary solar pump"), along with their types (e.g. "pump"). Also default parameters for the components of the hydraulic

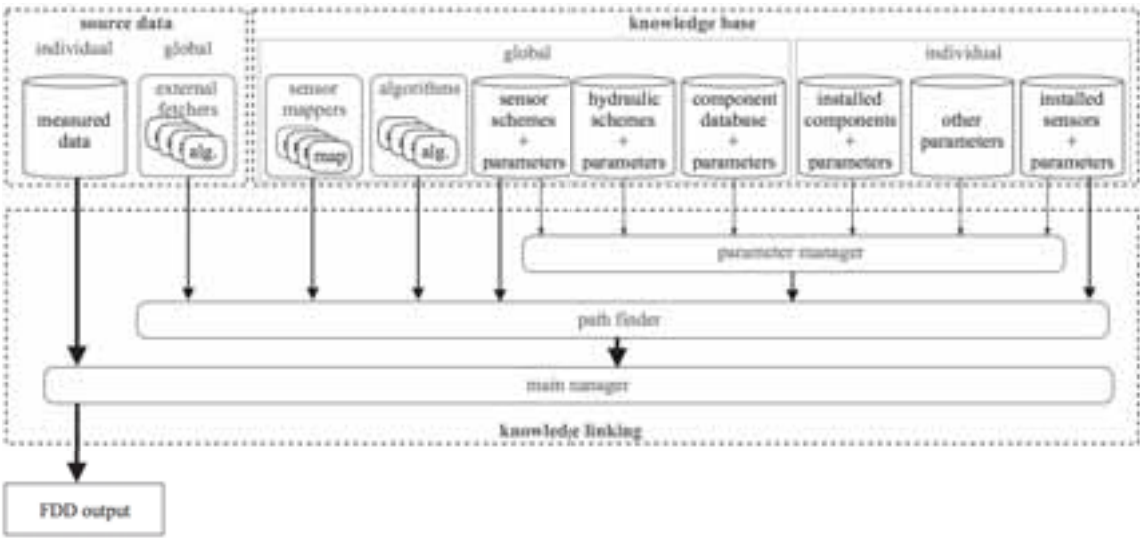

Fig. 2: Main software elements and the information flow

scheme may be provided if reasonable. All these component names and their default parameters are stored in a central hydraulic schemes database.

For each hydraulic scheme, one or several sensor schemes can be defined. The sensor scheme uniquely identifies the set of possible sensor names, where each sensor name is unambiguously linked to the measured quantity and a measuring location. Again, for each sensor also default parameters may be stored here (e.g. typical maximal flow rates or temperatures). By specifying the hydraulic scheme and the sensor scheme for each STS, the software framework knows the namespaces that are used to identify sensors and components in its data tables. A STS may also provide an *individual* installed sensors and installed components table, where individual parameters can be stored and override the default values in the scheme tables.

Moreover, a central component and sensor database is available. Here, for each component/sensor type, specific products can be registered along with known parameter values. Reversely, component or sensor parameters (e.g. collector efficiency, or measurement uncertainties) can be retrieved when type, manufacturer id, product id and parameter name are known.

Algorithms can be added by simply copying the corresponding python module file(s) into a specified directory. To be recognized by the framework, the module files must contain algorithm objects which are created by invoking a central factory function offered by the framework.

3.2 Communication mechanism

Each algorithm is confined to a small subtask and is valid under certain premises. For automatic linking, the surrounding management framework has to know the output of each algorithm as well as the required input quantities. In the design used by the framework, algorithms are objects which communicate their output quantity and input quantities via so-called "label" objects. Normally, each algorithm defines exactly one output label, only fault algorithms may have several fault labels as output. Besides these requested input labels, an algorithm can also request parameters and set up constraints that must be fulfilled in case of execution. Parameter requests and constraints are also objects. Parameters in this context are defined as fixed values that are looked up in the corresponding databases in the knowledge base (they might have been stored there by parameter identification algorithms, but the latter will not be integrated in regular FDD investigations). The most common constraints limit

an algorithm to a set of valid hydraulic schemes. But also parameter constraints can be created, demanding that the parameter could be looked up and has the required value. Algorithm objects, label objects, parameter objects and constraint objects are generated in a module file by calling the corresponding central factory functions offered by the framework. The factory functions make sure that objects of the correct types are used.

The label objects describe a certain input or output quantity, but hold in their attributes much more information than a simple name: For instance, whether it is an offer or a request, what kind of data it is associated with (just a single value, or multiple values linked to points in time, etc.), the dimension and unit for the offered or requested data, and so on. Label objects provide methods to check whether they match each other to allow for comparisons. For the simplest class of labels, the matching rule looks for equality of the relevant attributes. Some attributes like "unit" are always irrelevant and never influence matching, since two data sets containing the same quantity in different units are equivalent in view of the information content. Such standard labels can have only one match or none. But also label classes with more sophisticated matching rules exist (see below). However, such labels can encounter multiple matches. In that case, the best or preferred match has to be selected.

While features, symptoms and faults can simply be labeled with meaningful unique names to link offers and requests, the situation is somewhat more difficult for measurement data, as will be explained in the following. In order to request measured data, an algorithm needs to specify it (or the corresponding sensor) in a well-defined way. An obvious approach would be to set up a universal naming scheme, according to which each sensor of each STS gets an unambiguous name, in the sense that equivalent sensors in different STS get the same name. Such a naming scheme should include all aspects that might be needed for differentiation (e.g. quantity and some hierarchical description of position, like "T_solarloop_primary_return"). But this results in sensor names that are cumbersome in simple setups, while the naming scheme still may fail in cases where an unforeseen degree of distinction is needed. It also doesn't account for the fact that differently named sensors of different systems may serve the same purpose in some context, thus necessitating several algorithms, with their only difference being the sensor name requested. For instance, an algorithm needing the flow temperature coming to a heat storage from the solar loop might have to request "T_solarloop_secondary_supply" (supposing an according naming scheme) in case of the solar loop being connected via an external heat exchanger, but "T_solarloop_primary_supply" in case of an internal heat exchanger. Therefore, we take a more flexible approach by including an additional layer: the "PHYSICALQTY" label objects that describe a measurement data request in general terms, i.e. without knowing hydraulic details and from the perspective of measurement purpose. While PHYSICALQTY labels describe sensor requests, offered sensors are still identified via sensor names which are contained in the sensor label objects. But in contrast to a universal naming scheme, these sensor names can be chosen freely within the sensor schemes that were introduced in the previous subsection. Hence, the sensor names can be adapted to the needs of the hydraulic layout. To link PHYSICALQTY requests and offered sensor labels, sensor mappers (compare fig. 2) must be provided for each sensor scheme.

In the context of PHYSICALQTY labels, also the advanced label matching methods come into play. In principle, PHYSICALQTY labels have several attributes that hierarchically narrow down the requested measuring purpose. Here matching rules can be implemented that only check the equality up to the level of detail that is demanded by the request label. For instance, it is possible to generate labels that request the flow temperature in the solar loop, but do not care whether it is measured close to the collector or close to the heat sink. Due to the advanced matching rule, there is no need to create a mapping link just for this request variant. It is sufficient if the PHYSICALQTY label with highest level of detail was linked, easing the mapping effort.

Hence, to request measured data for an algorithm, one still can use the corresponding sensor name via a sensor label object. This leads to the implicit constraint, that the algorithm can only be applicable if the investigated STS also refers to the hydraulic scheme and sensor scheme where the sensor name is defined. This is welcome for algorithms which are valid for only one hydraulic scheme. For algorithms applicable to several hydraulic schemes resp. sensor schemes, the requested measured quantity is specified in general terms via corresponding PHYSICALQTY labels.

To summarize, we want to emphasize four advantages of PHYSICALQTY labels when compared to the utilization of a universal sensor naming scheme: Firstly, these are objects and not strings that are composed in a fixed pattern, making it easier to access the contained information and to alter the constituent parts in future. Secondly, the description of a measuring point does not need to include every aspect that might play a role in some special contexts. Instead, only measuring points which are quite common on many hydraulics need to be addressable with sufficient precision by PHYSICALQTY labels, since only those might be used in universal algorithms which do not depend on the peculiarities of the hydraulic scheme. Thirdly, a universal naming scheme starts from possible

measurement points in hydraulic layouts and makes sure to assign each one a unique name, meaning each "offer" is identified unambiguously. The PHYSICALQTY labels reversely describe sensors from the perspective of requests (which are unaware of hydraulic details), so not each offered, but each requested quantity is uniquely identified. This means that different PHYSICALQTY labels may point to to two different sensors in one hydraulic scheme, but to just a single sensor in another hydraulic scheme. To illustrate this, let one request be the sensor that measures the temperature of the heat carrier coming from the solar loop to the heat storage, and the other request the sensor measuring the flow temperature in the main (primary) solar loop before the heat sink. These are two different measuring points when an external heat exchanger is present (primary and secondary supply temperature), but a single one for an internal heat exchanger. Fourthly, with PHYSICALQTY labels, also requests of sensor collections can be defined, like "all available storage temperature sensors" or "all available output temperature sensors for parallel collector fields". To translate PHYSICALQTY labels to the delivering sensor labels, corresponding sensor maps are provided in the knowledge base for each sensor scheme (compare fig. 2).

3.3 Linking process (path finder)

To make use of the gradually growing knowledge base for a particular investigation, you need to check the applicability of all known algorithms, find linking possibilities and select the best ones. This is the task of the surrounding management framework, specifically the "path finder" (see fig. 2).

The path finder will search for known algorithms starting in a configurable root directory, but can be told to import just certain types of algorithms. For instance, for each algorithm a maximum automated execution frequency/minimum time interval can be specified, since some algorithms may need to look at larger timescales to work properly, meaning it also makes no sense to call them too often. The path finder is also given a threshold time interval, making it ignore all algorithms that have higher minimum time intervals. Hence, a path finder for daily evaluations will omit algorithms that do not add value if called more often than once a month, but monthly path finder will import them as well as daily algorithms.

To start the path search, the path finder fetches the set of installed sensors at the STS. It uses the sensor mappers from the knowledge base to determine the set of deliverable PHYSICALQTY labels. For every algorithm imported, it is checked if required input data can be supplied, if requested parameters could be looked up successfully by the parameter manager (compare fig. 2) and if all constraints are fulfilled. The parameter manager knows how to access all parameter tables and will look for a parameter at all relevant places. For instance, an equipment-dependent sensor parameter will first be searched in the individual installed sensors table. If not successful, it will try to retrieve manufacturer id and model id (first individual, then default) and use them to search for the parameter in the central component database. A specially treated kind of algorithms are external fetchers which may deliver data from external weather databases. These external fetchers normally are only activated by the path finder, if the data cannot be provided by sensors installed at the heating system.

As illustrated in fig. 1, several applicable algorithms providing the same output quantity may exist. For instance, the simple feature "it is night" could be calculated more accurately, if the zip code of the STS is known, but can also be given, if only the country is known. Thus, the algorithms are branded with a ranking score which rates the reliability and accuracy of an algorithm under the prerequisite of accurate input data. If several algorithms delivering the same output are applicable, the situation is resolved depending on the configuration of the path finder. It can be configured to choose the best algorithm a priori, based on the ranking score of the algorithm. Alternatively, each of those algorithms is added to the execution list to calculate the output quantity. Then the result data set with the highest reliability score will be chosen for further use. The reliability score of the output data will be calculated via the reliability scores of the inputs and the ranking of the algorithm.

Algorithms can not only have inputs of the lower level, but also of the same level (compare fig. 1). This allows for "virtual" sensors (e.g. calculating heat sums) as well as sophisticated features derived from other features. To make sure to detect all linking possibilities, the path finder iteratively checks the applicability of algorithms with inputs of the same level. It will adjust the execution order automatically, but avoid creating circular references.

At the end of the path search, when no algorithms can be added any more, the path finder removes all algorithms from the execution list that are placed on dead end execution paths. Dead ends are defined by giving a threshold target level to the path finder, usually being the symptom level. In that case, only algorithms that contribute to at least one symptom generation would be executed. However, also symptoms that are not used by any operable fault algorithm would be generated, as they might be of interest when post-processing the FDD results.

Because many comparisons of label objects have to be made during a path search, the path finder uses data structures for its internal input/output registries that on the one hand utilize fast membership testing via hashing methods, on the other hand also minimize the number of unavoidable matching comparisons. This means the comparison effort for the path search shows rather linear than quadratic growth with increasing number of algorithms.

3.4 Main manager

The main manager is responsible for performing all steps that are necessary to perform an FDD analysis for a given STS and time range. Based on provided configuration parameters, the main manager creates instances of the pathfinder and the parameter manager. Also, all necessary fetchers are initialized. Each fetcher knows how to look up certain kind of information in a certain database table. Now the path finder imports the algorithms and sensor mappers and determines the set and order of algorithms to execute. After that, the set of sensors needed as inputs is determined. Their measurement data are fetched from the database and packed into a data collection object, where they can be preprocessed. The data series can be checked for boundary values and/or plausibility, where the preprocessing parameters are gathered from individual installed sensor or sensor scheme table. Invalid values are registered and considered as data gap. Small data gaps may be interpolated (depending on the sensor's preprocessing parameter), larger data gaps are retained and registered. Also, a reliability score may be computed. Optionally, a sensor may be totally removed from the list of available sensors, necessitating a new path search. Of course, it is also possible to skip the preprocessing procedure here and perform it already before inserting new measurement data into a database holding sanitized data. In any case, it is ensured that in the end all measured data arrays are synchronized with one equidistant gapless timeline determining the fundamental time resolution of all subsequent calculations. If necessary, data points are mapped or interpolated accordingly.

When the data collection of all needed preprocessed measurement data is created, it is passed from one algorithm to the next. Each algorithm retrieves the requested input data from the collection via its input label objects. Thereby, the label request is first mapped to the right offer in the data collection (e.g. a PHYSICALQTY to the real sensor data), if necessary. Furthermore, the data is automatically converted to the requested unit as needed. Finally, the result data is added to the data collection, where it gets labeled automatically. After the execution of the last algorithm, the data collection can be passed to some "action" module responsible for final processing, which is not in the focus here. Commonly the results would be stored in some database where they can be accessed later, but also immediate triggering of alarm messages could be implemented here. For the algorithm development and testing tasks, the data collection is passed to our result visualization and evaluation tool.

3.5 Data sets

The core of each algorithm object is its method where real processing takes place. When an algorithm retrieves input data from the data collection via the request label, the data is returned as data set object. Different kinds of data set types exist, with continuous data sets being the most common one. They contain the data as array and a corresponding timeline object. The timeline object provides many convenient methods e.g. to locate days, weeks, months and so on, or to determine the day of the week for each point. Also, sub-timelines can be created easily. Likewise, especially the continuous data sets offer convenient methods of often needed operations. For instance, time averages over a specified time interval, daily/weekly/monthly sums, shifting data by a specified time range, determining start or end points in mask arrays, and other signal processing methods or filters like smoothing will be added. This makes it easier to write the processing steps in a few lines of codes for many algorithms.

4. Validation

The software framework is developed and employed in our academic environment where a few STS are monitored. In particular, two STS for domestic hot water preparation in multi-family houses (MFH) are available that serve as regular heat sources under real use conditions, but may be used for experiments as well. Since they are equipped with an extensive measurement instrumentation, these systems allow to generate real life data of the STS when a deliberately induced fault is present. More information regarding the MFH STS can be found in (Schmelzer et al., 2015).

Dozens of algorithms for features, symptoms and faults are already implemented in the knowledge base of the

software framework. They were checked against measurement data from the MFH STS as far as possible, or adopted from previous projects. Of course, the correct operation of the software framework including path finder and all implemented mapping and matching functionalities were checked with dedicated test algorithms and test cases, but also confirmed when used for the algorithm development and validation.

To bring the capabilities of the framework to life, exemplary results of a set of advanced algorithms are shown. They were implemented in the software framework, aiming to detect gradual leakage in the solar loop when a pressure sensor is available. Based on a validated physical model of the temperature-dependent pressure in the solar loop and related sensitivity analysis studies, the expected pressure signal and uncertainty margins are calculated as features with help of several temperature signals from the STS. The model only considers states when the pump is off and no stagnation occurs. Hence, according features provided by other algorithms are used as input, too. From a first version of algorithms which used several sensors that are only available at the MFH STS, a more

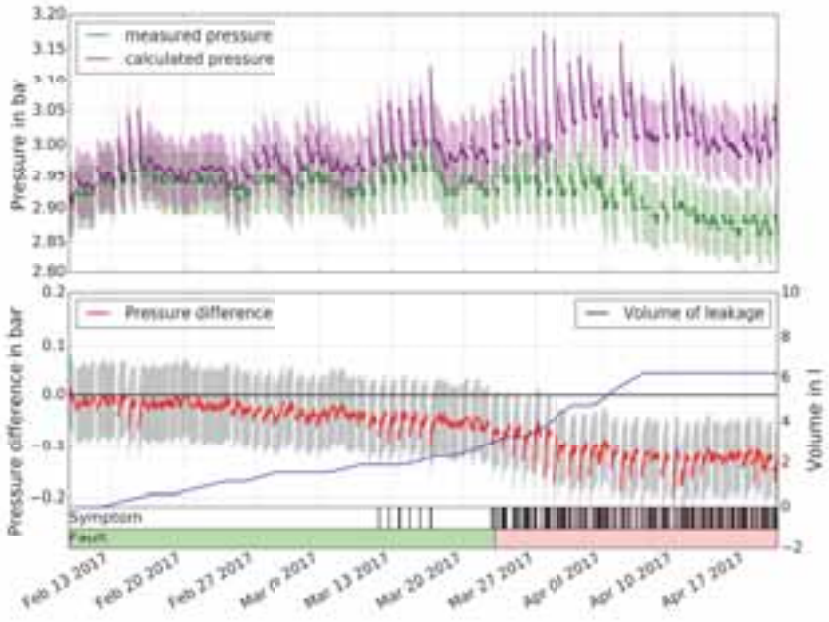

Fig. 3: Measured (green) and calculated (violet) pressure signals incl. their uncertainties, their difference (red) incl. uncertainty (gray), the cumulated leakage volume (blue) and the times where the corresponding symptom and fault are recognized.

simplified version using more common sensors was developed. They both performed similar well and were able to detect the gradual leakage quite soon. The results of the simplified set of algorithms are shown in fig. 3. On the MFH STS, a gradual leakage was initiated on purpose and the total leakage volume measured (blue line fig. 3). Fig. 3 shows the calculated and measured pressure signals and their difference including the corresponding calculated uncertainties. At the bottom it is indicated where symptoms are recognized and for which days faults are reported. Although only 3 liter (<5% of fluid in collectors and supply/return pipes, <2% of expansion vessel volume) were lost in total, and although the measured pressure stayed on the same level, the leakage was detected correctly by the algorithms. While a detection approach looking only at absolute pressure drops would have failed, the implemented algorithms could derive that the pressure should have increased in normal operation. Reversely, no leakage was detected in the leakage-free operation times. However, in order to be applicable, a pressure sensor as well as several parameters like size of the expansion vessel and the (rough) fluid volume must be available. Hence, it is useful for medium to large STS. Algorithms that require fewer parameters, yielding in higher uncertainties, will be derived, too. Thanks to the path finder of the software framework, the best applicable algorithms of these variants will be chosen automatically.

5. Summary

A flexible software framework for fault detection and diagnosis was presented. It automatically links modular algorithms and other information from the knowledge base to flexibly adapt itself to the boundary conditions of each solar thermal system. Hence, it can perform the best faults detection methods in dependence of the information available. In this paper, the underlying concepts and implementation approaches to achieve this flexibility were introduced. The usefulness and interaction of offer and request label objects, data set and algorithm

objects and the functioning of the path finder and the overall procedure were described. Exemplary results for algorithms detecting a gradual leakage were also shown. The FDD software framework and the corresponding algorithms currently are developed and tested in an academic environment where a few well known systems are monitored.

6. References

Dröscher, A., Ohnewein, P., Haller, M. Y., Heimrath, R., 2009. Modular specification of large-scale solar thermal systems for the implementation of an intelligent monitoring system, Proceedings of the ISES Solar World Congress 2009, pp. 683-688

Isermann, R., 2006. Fault-Diagnosis Systems: An Introduction from Fault Detection to Fault Tolerance, Springer, Berlin.

Küthe, S., de Keizer, C., Shahbazfar, R., Vajen, K., 2011. Implementation of Data Processing and Automated Algorithm Based Fault Detection for Solar Thermal Systems, Proceedings of the ISES Solar World Congress 2011, doi: 10.18086/swc.2011.28.16

Schmelzer C., Georgii M., Vajen K., 2015. Entwicklung, Untersuchung und Anwendung von Methoden zur Langzeitüberwachung und automatisierter Fehlerdetektion großer, solarunterstützter Wärmeversorgungs-systeme, final report of the FeDet project FKZ-0325975A, funded by the German Federal Ministry for Economic Affairs and Energy

7. Acknowledgements

The software development was supported by the German Federal Ministry for Economic Affairs and Energy within the project FKZ-0325975A.

ABSORBER SURFACE DURABILITY STANDARD TESTING ISO 22975-3 VS. MEASURED THERMAL STRESS AT EXTREME TEST SITE

Thomas Kaltenbach[1], Markus Heck[1] and Karl-Anders Weiß[1]

[1] Fraunhofer-Institute for Solar-Energy-Systems ISE
Heidenhofstr. 2, 79110 Freiburg, Germany

Abstract

Solar absorbers, as a key component in solar thermal collectors, are in the focus of this paper. A well introduced durability testing method for the solar absorber is the testing procedure described in ISO 22975-3 [1]. This standard testing procedure is applicable to the determination of the long term behavior and service life of selective solar absorbers for use in vented flat plate solar collectors.

Different samples of solar absorbers on aluminum and copper substrates are characterized before, during and after the accelerated ageing tests and outdoor exposure with various methods, including FT-IR spectroscopy and microscopic technologies like AFM microscopy to measure the degradation on different scales.

It turned out, that the corresponding testing time of the procedure for high temperature test was less than in the standard ISO 22975-3. Therefore, the standard testing procedure is testing at higher thermal loads then the extreme test sites with high absorber temperature in constant stagnation mode.

Keywords: *Solar absorber, components for collectors, durability, accelerated ageing, optical characterization*

1. Introduction

Depending on their location and prevalent climatic conditions, the components of solar thermal collectors have to bear high climatic and mechanical stresses. Besides high temperatures, UV-light, wind, snow, humidity or saline and corrosive atmospheres can be causes for a rapid degradation of materials and components.

Despite these well-known obstacles for solar thermal installations in extreme climates, the aging processes with regard to different climatic and operational conditions are only partially analyzed. To qualify and enhance the durability of solar thermal systems and improve the opportunities on a world-wide scale, the development of suitable accelerated aging tests is necessary. The project “SpeedColl”[2] is dedicated to the research on these issues.

The aging effects occurring in solar collectors with glass covers are determined primarily by the temperature level in the collector. This temperature level has significantly increased during the last years due to the enhancement of the collector efficiency and the trend towards systems with higher solar fractions with the resulting increase in stagnation times and temperatures. Furthermore, durability analyses of new products on the market such as spectrally selective absorber layers are needed, since only little is known about their long-term behavior.

Next to the influence of increased temperatures, other causes for aging have to be analyzed too, especially UV-radiation, moisture and the influence of saline atmospheres. Furthermore the frequent use of solar thermal collectors in Mediterranean regions for the preparation of domestic hot water generation and solar cooling, a quality check regarding the impact of the saline atmosphere predominating close to the sea-shore in these countries is necessary. This will be emphasized in detail in the “SpeedColl” project. This paper will focus on the influence of the stress factor temperature on the absorber. The samples are provided by the industrial project partners.

Of all components in solar thermal systems, solar collectors experience the highest climatic and mechanical stress. They are subjected to high temperatures and, depending on the location, variable and extreme weather conditions. Just as coastal and sun-rich regions offer large potential for solar energy use; the systems installed in these areas

doi:10.18086/swc.2017.19.06 Available at http://proceedings.ises.org

are exposed to especially high levels of UV radiation, humidity and salt air. As a result, the collectors often age and degrade faster.

In "SpeedColl" actual environmental stress data such as humidity, UV radiation, temperature and salt concentration are determined. The data collection varies from tests carried out in alpine, moderate and maritime locations through to measurements in arid and tropical regions. Test stands are installed on the Zugspitze, the highest mountain in Germany, as well as in Freiburg, Stuttgart, Gran Canaria, the Negev Desert and in India. Additionally the solar collectors and components undergo accelerated aging tests in the laboratory. Using the collected data, the researchers validate the procedures of the aging tests, which provide information about the collector's thermal performance over its entire lifetime. The results also serve as a basis for standardization.

2. Absorber surface durability testing

The absorber surface durability testing specifies a failure criterion of a solar absorber based on changes in optical performance of the absorber. The optical properties of interest are the solar absorptance α and the thermal emittance ε. The testing according to ISO 22975-3 specifies durability testing procedures focused on resistance to high temperatures and condensation of water on the absorber surface as well as high humidity.

Within the test procedure, the reference of the thermal load for the assessment of the thermal stability of the absorber coating was measured in a flat plate collector. The collector was exposed in Freiburg, Germany. The absorber temperature was measured in stagnation over one day of clear conditions with a maximum global irradiation of 930 W/m². The total annual load assumed 30 days of stagnation. The maximum stagnation temperature was 184°C. [3].

In the "SpeedColl" project, the absorber samples are exposed to outdoor weathering at five test sites with different climatic conditions with continuous monitoring of the micro and macro climatic conditions. Since a direct exposure of absorbers is not adequate to the real situation of the solar absorbers in solar thermal collectors, the test samples were mounted above the solar absorber with purpose-built galvanically insulated spacers in a commercial solar thermal collector. The absorber temperature is continuously monitored. To receive also information of the corrosivity of the micro climate inside the collector, test coupons of four different metals are placed inside the collector, too. The ambient climatic conditions in terms of corrosivity are also measured as a reference next to the test collector [4].

The temperature of the solar absorber inside the test collector is measured continuously during exposure in order to set up a data base for the development of suitable accelerated lifetime tests.

Accelerated ageing tests with a variation of the relevant parameters, temperature and condensed water on the absorber surface are performed in climatic cabinets. Especially tests with condensed water at high temperature levels are used for the qualification of the materials since this is seen as the most demanding factor and relevant for the application of solar thermal systems in sunny regions.

For collectors placed in marine environments chloride ions from sodium chloride are considered to be major corrosion agent in these regions [5].

3. Characterization methods

The spectral measurements were carried out with a Fourier transform spectrometer Bruker Vertrex70 equipped with two integrating spheres (a PTFE coated sphere for the shorter wavelength-range ($\lambda < 2{,}0$ µm) and a diffuse-gold coated sphere for the IR ($\lambda > 1{,}7$ µm) in order to measure both the directly reflected and the scattered radiation. The diffuse part of the reflectance was calibrated with a PTFE standard from National Institute of Standards and Technology (NIST) for the solar range and from National Physical Laboratory (NPL) for the thermal range. The specular part in the solar and the infrared ranges was calibrated with an aluminum mirror from NPL. The accuracy of the reflectance data was better than 1 % in the solar range and better than 2 % in the IR. The solar absorptance/reflectance was calculated by weighted integration of the spectral reflectance with the solar spectrum AM 1.5 according to ISO 9845-1. The thermal emittance was calculated by weighted integration of the spectral reflectance with the Planck Black Body radiation distribution at a temperature of 373 K.

4. Weathering tests

The samples are exposed to outdoor weathering at five test sites with different climatic conditions under continuous monitoring of the climatic conditions (temperature, humidity, wind, precipitation, UV) and the collector micro climate (temperature and humidity inside the collector). In order to gain worst-case-data some of the test sites are positioned in extreme climates with very harsh conditions (Table 1).

Tab. 1: Exposition of collectors at locations with extreme climates

Climates	**Location**
Tropical	Kochi, India
Alpine	Schneefernerhaus, Zugspitze, Germany
Aride	Sede Boker, Negev Dessert, Israel
Maritime	Pozo Izquierdo, Gran Canaria, Spain
Moderate	Stuttgart and Freiburg, Germany

Figure 1 shows the temperature distribution of the same commercial vented flat plate solar collector type at the 5 different explosion sits within the “SpeedColl” project. The collectors were not actively cooled; therefore they were in constant stagnation mode.

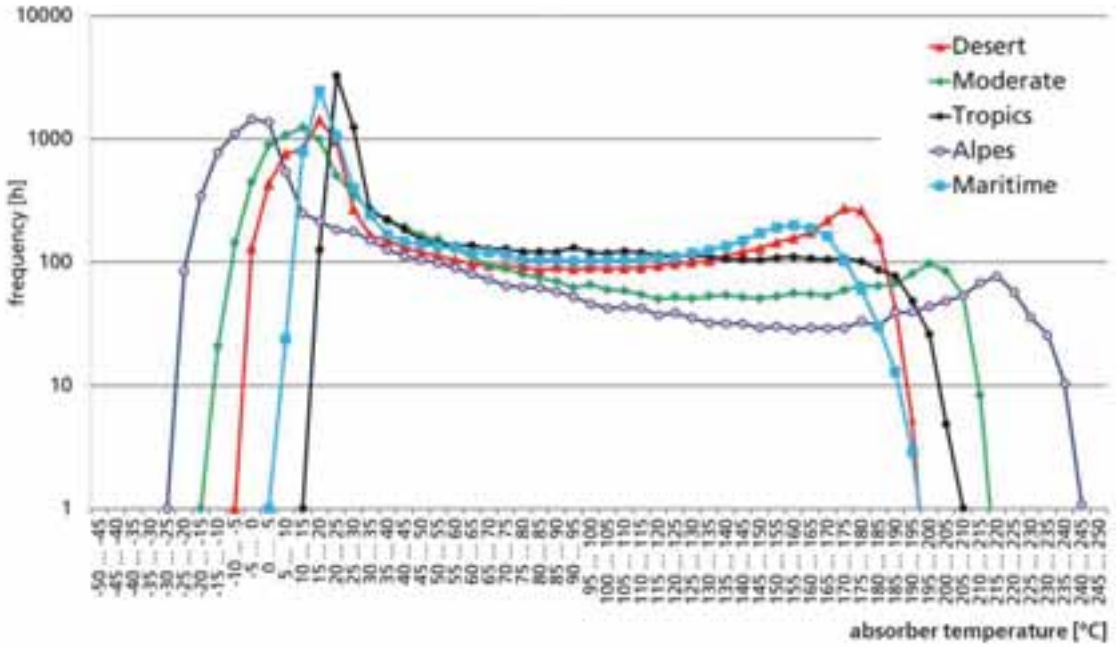

Fig. 1: Histogram of the absorber temperatures [°C] at different exposition sites, measured period from 12/2013 to 11/2014, Negev desert (arid) in Israel; Freiburg (moderate) in Germany; Kochi (tropical) in India; Zugspitze (alpine) in the German Alps and Gran Canaria (maritime) in Spain

The alpine exposition site reached the biggest temperature spread of the absorber temperature with minimum temperature of -30°C and maximum temperature of 245°C.

5. Service life testing

To measure the load during an operating time of one year of the absorber coating the effective mean temperature T_{eff} turns out to be a suitable parameter. It is defined in equation 1.

$$\exp\left(-\frac{E_T}{R}\cdot T_{eff}^{-1}\right)=\int_{T_{min}}^{T_{max}}\exp\left(-\frac{E_T}{R}\cdot T^{-1}\right)\cdot f(T)\cdot dT \qquad \text{(eq. 1) [6]}$$

with

f(T)	the temperature frequency function for the observed load over one year
T_{max}, T_{min}	maximum or minimum absorber temperature of the load
E_T	activation energy

For thermal degradation f(T) is the time in one year, during which the absorber temperature lies between T and T+dT. For degradation by condensation and high humidity, f(T) is the time in one year, during which the absorber temperature lies between T and T+dT, and the relative humidity in the collector exceeds 99% or condensation takes place on the absorber.

The effective mean temperatures of the same commercial vented flat plate solar collector type with a chosen activation energy of 50 kJ/mol as a lower estimate at the 5 different explosion sits within the “SpeedColl” project are shown in figure 2.

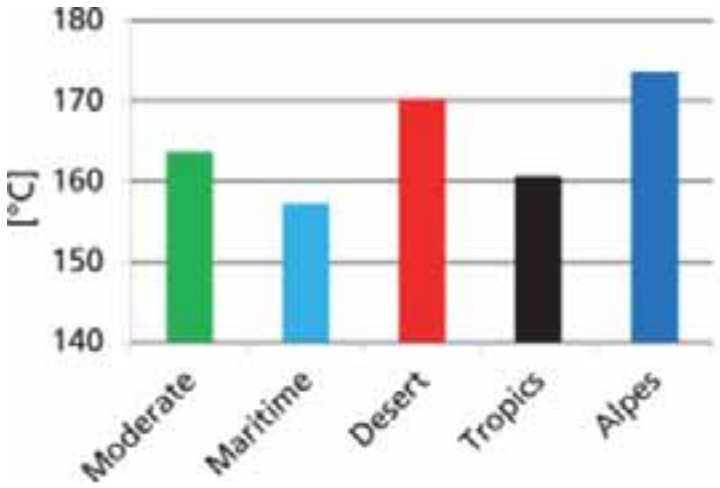

Fig. 2: Effective mean absorber temperature [°C] at different exposition sites, measured period from 12/2013 to 11/2014 with an activation energy of 50 kJ/mol, Freiburg (moderate) in Germany; Gran Canaria (maritime) in Spain; Negev desert (arid) in Israel; Kochi (tropical) in India and Zugspitze (alpine) in the German Alps

The alpine exposition site led to the highest effective mean temperature of 174°C. With this measured thermal load we used the same time transformation function for the assessment of the thermal stability of the absorber coating like it was done in the standard testing procedure ISO 22975-3.

The corresponding testing time for the procedure for the execution of the high temperature testing to 25 years lifetime based on the Arrhenius relationship is shown in figure 3 for three different testing temperatures as a function of the activation energy.

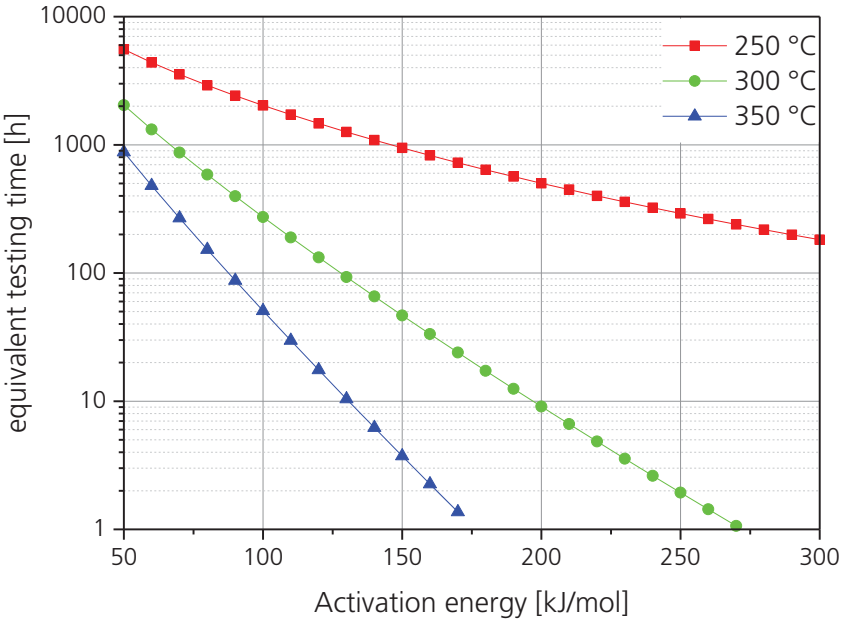

Fig. 3: Testing time equivalent to 25 years lifetime with measured thermal load of Zugspitze (alpine) in the German Alps for 250°C, 300°C and 350°C testing temperature as function of the activation energy

In figure 4 the corresponding testing time for the procedure for the execution of the high temperature to 25 years lifetime according to ISO 22975-3 is shown for three different testing temperatures as a function of the activation energy.

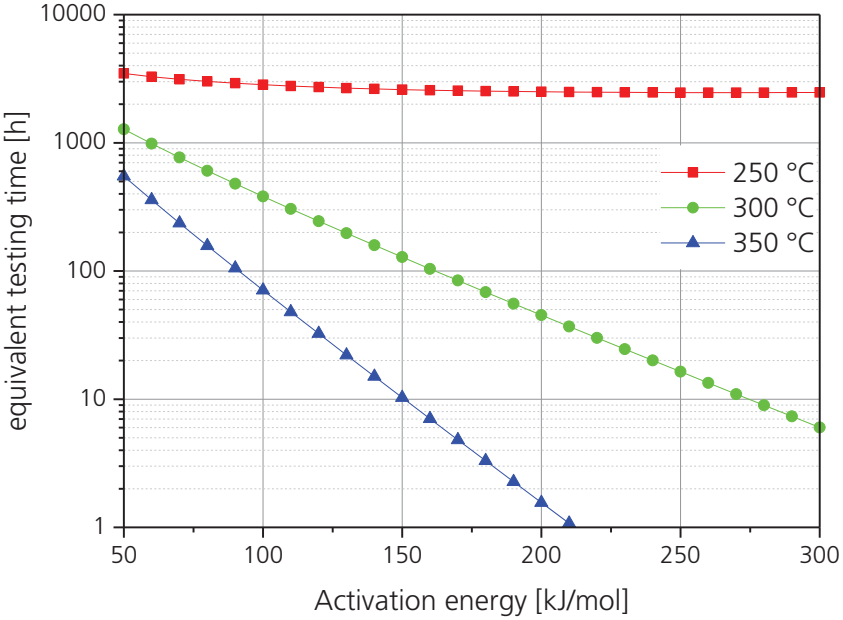

Fig. 4: Testing time equivalent to 25 years lifetime according to ISO 22975-3 with thermal load of Zugspitze (alpine) in the German Alps for 250°C, 300°C and 350°C testing temperature as function of the activation energy

It turns out, that the corresponding testing time for the procedure for the execution of the high temperature test determined in the project was less than the testing time in the standard. For example with an assumed activation Energy E_T of 100 kJ/mol the testing time equivalent at a testing temperature of 300°C is 273 h and for ISO 22975-3 the testing time equivalent is 381 h.

Therefore, the standard testing procedure is testing at approx. 40% higher thermal loads then the extreme alpine test site with high absorber temperature in constant stagnation mode.

6. Conclusion and outlook

The relevant physical properties of the material samples were measured before and after the exposure to accelerated ageing tests and outdoor weathering. The results of the initial optical characterization of the test-samples proved a very good homogeneity. The standard deviation out of 21 test panels for the solar absorptance value α is 0,001 and for the thermal emittance value ε the standard deviation is 0.003. This assumes an excellent production quality

It turned out, that the corresponding testing time of the procedure for high temperature test for the alpine test site was less than in the standard. Therefore, the standard testing procedure is testing at higher thermal loads then the extreme alpine test site with high absorber temperature in constant stagnation mode.

Thus the standard testing procedure ISO 22975-3 fully covers the aging behavior of absorbers in terms of high temperature loads even at the condition measured at the extreme alpine test site, where the highest absorber temperatures within the “SpeedColl” project were measured.

The effects of high humidity and condensed water in terms of the stability of the absorber coating will be addressed in the current “SpeedColl2” project.

7. Acknowledgements

The authors would like to thank the industrial partners and the German Federal Ministry for Economic Affairs and Energy (FKz. 0325969A) for their support and funding.

8. References

[1] ISO 22975 Part 3:2013, Solar Energy-Collector components and materials, Absorber surface durability

[2] Development of Accelerated Aging Tests for Solar Thermal Collectors and their Components, www.speedcoll2.de

[3] Accelerated Life Testing of Solar Energy Materials – Case study of some selective solar absorber for DHW systems. A Technical report of Task X Solar Materials Research and Development of the International Energy Agency Solar heating and Cooling Program; B. Carlsson, U. Frei, M. Köhl, K. Möller; SP-Report 1994:13, ISBN 91-7848-472-3

[4] ISO 9226:1992 Corrosion of metals and alloys - Corrosivity of atmospheres- Determination of corrosion rate of standard specimens for the evaluation of corrosivity

[5].Slamova, K., I. Duerr, T. Kaltenbach, M. Köhl, 2016. Degradation effects of maritime atmosphere on metallic components of solar collectors. Solar Energy Materials & Solar Cells 147, 246–254

[6] ADVANCED PROCEDURE FOR THE ASSESSMENT OF THE LIFETIME OF SOLAR ABSORBER COATINGS; Köhl, M.; Heck, M.; Brunold, S.; Frei, U.; Carlsson, B.; Möller, K.: Advanced Procedure for the assessment of the lifetime of solar absorber coatings. Solar Energy Merials and Solar Cells, Volume 84, Issues 1-4 , October 2004, Pages 275-289

Development of Solar Thermal Appliances Using Building Materials

Sunita Mahavar[1], Ramchandra Punia[2] and Prabha Dashora[1]

[1]Department of Physics, University of Rajasthan, JLN Road, Jaipur (India)

[2]Govt. Polytechnic College, Sikar (India)

Abstract

Solar thermal appliances (STAs) can be made as an integrated part of the building/housing using building material housings (BMH), which ultimately make these appliances more user friendly, durable and weather resistance. This paper presents fabrication and testing of three different solar thermal appliances. Appliances are developed for water heating and cooking purposes, these are: Building material housing solar water heater (BMSWH), Fixed structure solar concentrator (FSSC), Community size solar cooker (CSSC). According to the test results, the thermal performances of CSSC and BMSWH are found satisfactory even after 2 and 10 years, respectively. Two meals cooking for 8 to 10 persons can be done in CSSC on a sunny day and in BMSWH (62 liter) water can be stored near 60 ºC. Due to building material housing, systems have good durability and high weather resistance. For FSSC thermal profile and cooking test show it's cooking ability (100-200 gm rice within 45 minutes to 1.5h) in peak sunny hours in lesser time than box type solar cooking. Fix structure makes the system user friendly and building material structure decreases payback period of the system.

Keywords: solar water heater, solar cooker, solar concentrator, building material

1. Introduction

Human civilization has been witnessing a gradual shift towards cleaner fuels- from wood to coal, from coal to oil, from oil to natural gas; renewable is the present demand. It is quite obvious that solar energy is the most promising current and future option among all non-renewable and renewable energy resources used currently across the globe. Energy form the sun can be utilized in two ways: (i) in the form of heat or thermal energy called solar thermal applications and (ii) in the form of electrical energy called solar photovoltaic applications. In all nations, a major share of total energy consumption is utilized by the household sector for water heating and cooking purpose. Solar thermal applications have immense potential especially in domestic and industrial sector to meet thermal energy demand of the world (Dzioubinski and Chipman, 1999; Sen, 2004; Thirugnanasambandam et al., 2010; Mahavar et al., 2012a, 2012b; Mahavar, 2015).Therefore, in the present research work our interest have been to provide cost effective, user friendly and durable solar thermal appliances for the domestic or small industries.

Solar thermal appliances (STAs) e.g. water heater, solar concentrator, box–type solar cookers, solar stills and dryers work on direct application of solar power. These all appliances have some common components: (i) absorber/receiver, (ii) glaze, (iii) insulation, (iv) casing and (v) reflector. In the present piece of work we have focused our attention on building materials (bricks, cement and their composite) to use as casing material of different solar thermal appliances (Sukhatme, 2007).

With building material housing (BMH) STAs can be made as an integrated part of the building, which ultimately make this appliances more user friendly and durable. BMH casing is highly weather resistant hence increase the life time of the appliance and decreases payback period of the appliance. This casing also favorable to increase thermal performance of appliances as it has low thermal conductivity. In order to test building material as casing in STAs we have fabricated different solar thermal appliances viz. community size solar cooker, fixed structure solar concentrator and solar water heater. The experimental studies of fabricated appliances have been done as per Indian and international standard (Nayak, 2000; BIS, 2000; Belusko, 2004; Sukhatme, 2007; Hossainb, 2011). The thermal performances of appliances are found quite satisfactory even for long time duration of 2 to 10 years. It reveals that building material casing can makes STAs more convenient to use (due to fix structure), increase durability and weather resistance.

doi:10.18086/swc.2017.19.07 Available at http://proceedings.ises.org

2. Literature review

In a small capacity domestic solar water heater (SWH) a closed shallow rectangular box made of metal sheet (absorber) is contained in a housing which supports a glass cover on the top and, insulation material that surrounds the bottom and sides of the absorber tray. In a close-coupled SWH system the storage tank is horizontally mounted above the solar collectors on the roof and the hot water naturally rises into the tank through thermosyphon flow (Sukhatme, 2007; Mahavar , 2015). Different type of solar water heaters have been developed and tested by several researchers (Hossainb, 2011; 5, Mahavar, 2015). This literature also reveals that a few researches have been done to make solar water heaters as integrated part of housing by use of building material casing (Sengar, 2007; Marwal, 2012). As far as solar concentrators concern, these are the most effective for collecting solar radiations. This is due to high concentration ratio and high thermal energy collection ability (Mahavar et al., 2016). Five main solar concentrator technologies can be identified: (i) compound parabolic concentrator (CPC) (ii) parabolic trough concentrator (PTC) (iii) linear fresnel reflector (LFR) (iv) parabolic dish with fixed focus (e.g. Scheffler) (v) parabolic dish with moving focus. A number of solar concentrator has been developed from very large to small scale for a wide range of applications viz. power generation, thermochemical reactions that involve production of synthetic gas and hydrogen, production of hybrid solar-fossil fuel and solar thermal detoxification and recycling of waste materials (Kaushika and Reddy, 2000; Sonune and Philip, 2003; Lovegrove, 2011; Reddy, 2013). Besides these applications these systems are also used for solar cooking. Considering above aspects a parabolidal dish solar concentrator has been fabricated for cooking in peak sunny hours. A parabolidal dish solar concentrator is a point focal collector that requires dual axes sun tracking to concentrate solar energy onto a receiver located at the focal point. Instead for tracking keeping the structure fix cooking can also be performed in short duration at local noon. This cooking time is lesser than the box type solar cookers and as system does not require tracking so it is also easy to handle by users. Use of building material housing for structure of concentrator makes the system more durable and weather resistance. Concentrating on this, fixed structure solar concentrator (FSSC) is consisted of building material.

The other solar thermal appliance i.e. box type solar cooker consists of a rectangular enclosure insulated on the bottom and sides, and having one or two transparent covers on the top called glazes. Solar radiation enters through the upper glaze and heats up the absorber and container containing food stuff. Different types of solar cookers (box type , focusing type and advanced or indirect type) have been developed by many researchers (Panwara, 2012; Mahavar et al., 2012a, 2012b, 2013, 2015, 2017; Cuce and Cuce, 2013; Punia, 2013) using different kind of materials for different components. A considerable work has also been done for development of community size solar cooker (Nahar, 1993; Piroschka, 2014) i.e. a cooker which serve cooking for 8 to 20 persons. Senger.et al. (2011) have developed a building material housing solar cooker for cooking need of 2 to 4 persons. Fabrication of community size solar cooker using building material has not been done yet (Punia, 2013).

Hence, building material casing has been used for fabrication of various solar thermal appliances and its long term effect has also been tested for these appliances.

3. Fabrication of appliances

All the systems are installed (facing south) at open rooftop of Department of Physics, University of Rajasthan, Jaipur (26.92ºN, 75.87ºE). Building material housing solar water heater (BMSWH): This system is shown in Fig. 1. Mainly system consists of a solar collector and a storage tank. The details of these components are given in Table 1. Fixed structure solar concentrator (FSSC): This system is shown in Fig. 2. The dimensions of system are: 0.7 m diameter, 0.2 m height and 0.15 m focal length. An aluminum sheet of diameter 0.09 m, 0.3 mm thick and 0.013 kg mass is used as receiver for measurement of thermal profile. A steel pot (coated with thin black coat) of diameter 0.1 m is used for cooking placing at focal length distance. Community size solar cooker (CSSC): The cooker has been designed in such a way that length to width ratio is about four, so maximum radiation reflected from the reflector falls on the glass cover. Since aperture of the system is very large, the glaze has been designed in two pieces, each of dimension 100×60 cm^2. The lid is hinged at the top of the cooker and is used to reflect the solar radiation onto the cooker aperture. The cooker size is sufficient to cook two meals per day for 8 to 10 persons. System is shown in figure 3 and 4, and the component details are given in Table 2.

Table 1: Design details of building material housing solar water heater (BMSWH)

S. No	Parameters	Details
	Solar collector	
1.	Casing (i)Dimension (ii) Material (iii) Thickness (iv) Inclination (tilt angle)	 144×140×37 cm^3(outer), 122×112×23 cm^3 (inner) RCC, tile bricks and cement 11 cm (upper and lower walls),14 cm (side walls) 45° (facing due south)
2.	Absorber tray (i)Dimension (ii) Shape Collector tube (i) Shape (ii) Diameter (iii) Length (iv) Material (iv) Coating	 110×100× 6 cm^3(aperture) Trapezoidal Spiral 1.15 cm 15.24 m Copper (both) Black matt paint (both)
3.	Glaze (i) No. of glaze (ii) Material (iii) Thickness (iv) Spacing between glaze	 2 Transparent acrylic (PMMA) 2.75 mm 10 mm
4.	Insulation (i) Material (ii) Thickness	 Mineral wool 6 cm (bottom and all sides)
	Storage tank	
1.	(i) Shape (ii)Dimension(outer) (iii) Material (iv) Insulation thickness (v) Storage capacity	Cylindrical 0.45 m (diameter), 0.66 m height Stainless Steel 0.04 m 62 liter

Fig. 1: Building material housing solar water heater (BMSWH)

Fig. 2: Fixed structure solar concentrator (FSSC)

Table 2: Design details of community size solar cooker (CSSC)

S. No.	Parameters	Details
1.	Casing (i)Dimension (ii) Material (iii) Thickness (iv) Orientation	 $210\times67.5\times17cm^3$ Bricks and cement 15 cm Facing due south
2.	Absorber tray (i)Dimension (ii) Shape (iii) Material (iv) Thickness (v) Coating (vi) Absorptivity	 185×47 cm^2(Bottom) Trapezoidal Aluminum 0.35mm Black board paint 0.9
3.	Glaze (i) No. of glaze (ii) Material (iii) Thickness (iv) Spacing between glaze	 2 Glass Lower 5 mm and upper 4 mm 13 mm
4.	Insulation (i) Material (ii) Thickness	 Glass wool 5 cm (all sides)
5.	Containers (i) Shape (ii) Dimension (iii) Material (iv) No. of pots (v) Coating	 Cylindrical Diameter 19 cm, height 7 cm Stainless steel 16 Black matt paint
6.	Reflector (i) Number (ii)Dimension (iii) Thickness (iv) Material	 1(Three parts) $70\times74cm^2$(each) 4 mm Silicate glass

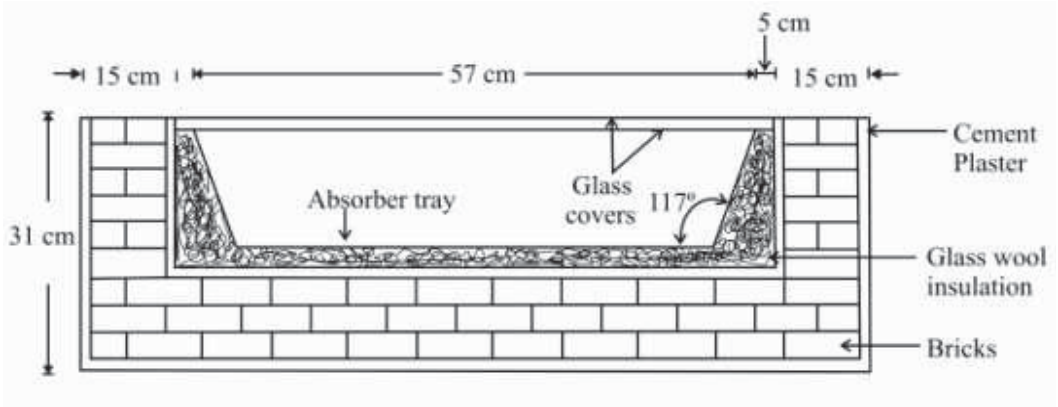

Fig. 3: Schematic view of developed community size solar cooker (CSSC)

Fig. 4: Community size solar cooker (CSSC)

4. Experimental study of appliances

4.1. Experimental set-up

On a number of days the experimental studies of all the systems have been conducted at the University of Rajasthan, Jaipur (26.92˚N, 75.87˚E). In these experiments, the solar radiation intensity (I_s) on a horizontal surface was measured using a pyranometer (Nation Instruments Ltd. Calcutta, instrument no. 0068). CIE-305 thermometer with point contact thermocouples (accuracy 0.1 ºC) was used to measure the temperatures at different locations of the CSSC and FSSC; viz. the water load (T_w), and the absorber plate (T_P). For BMSWH eight channel MS 1208 Multispan thermometer (accuracy 1 ºC) is used with J-type thermocouple to measure temperature of inlet (T_{in}), outlet (T_{out}) and storage tank (T_s) temperature. Ambient temperature (T_a) was measured using a mercury thermometer (accuracy 0.1ºC) placed in an ambient chamber. The measurements of temperatures of different regions were carried out on clear sunny days at every 10 minutes interval for the duration of 10:00 to 16:00 Indian Standard Time (IST) for CSSC and BMSWH. For FSSC this time interval is 5 minute and experimental time period is around local noon. The experimental arrangement of temperature measurements is shown in Fig. 4 for CSSC. Other instruments namely pyranometer and mercury thermometer were situated within 5 meter distance of this arrangement during testing.

4.2. Thermal Profiles

For solar water heater temperature of inlet (T_{in}), outlet (T_{out}) and storage tank temperature (T_s) are measured and reported in Fig. 5. Sengar, (2007) and Marwal, (2012) have also studied the system with different other components. For the reference thermal profiles of system measured in 2006 is also shown in Fig. 6 and 7 (Sengar, 2007). Fig. 8 shows the temperature profile of FSSC. The thermal performance of CSSC has been measured without load and with load. These are depicted in Fig. 9 and 10.

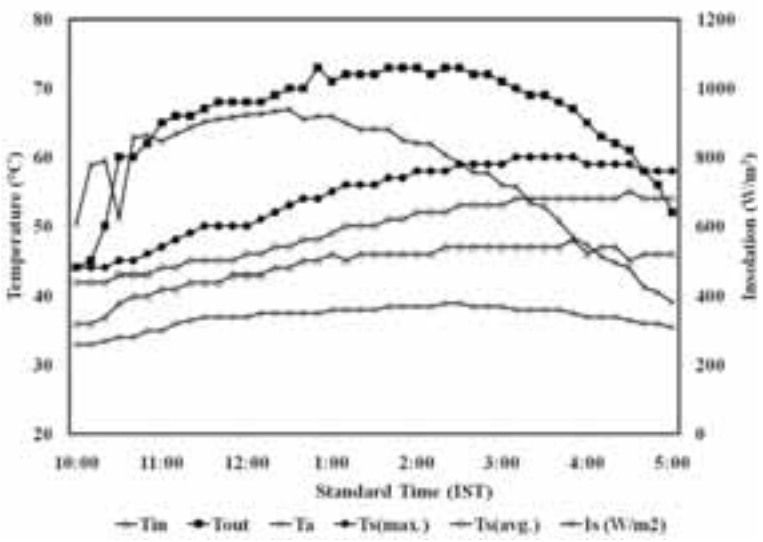

Fig. 5: Thermal profile of BMSWH (close loop) on 21 June 2017 with PMMA double glaze (T_a, T_{in}, T_{out} and T_s are ambient, inlet water, output water and storage tank water temperatures, I_S is solar insolation).

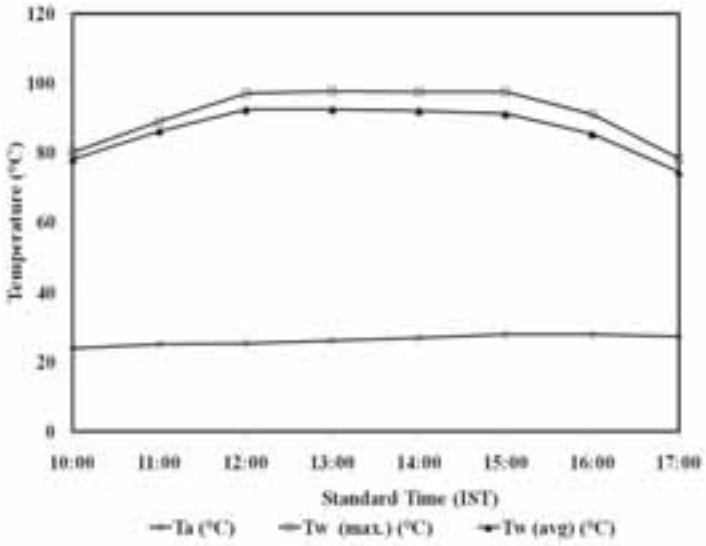

Fig. 6: Thermal profile of BMSWH (open loop) on 25th Nov. 2006 with single glass glaze (T_a and T_w are ambient and output water temperatures) (Sengar, 2007).

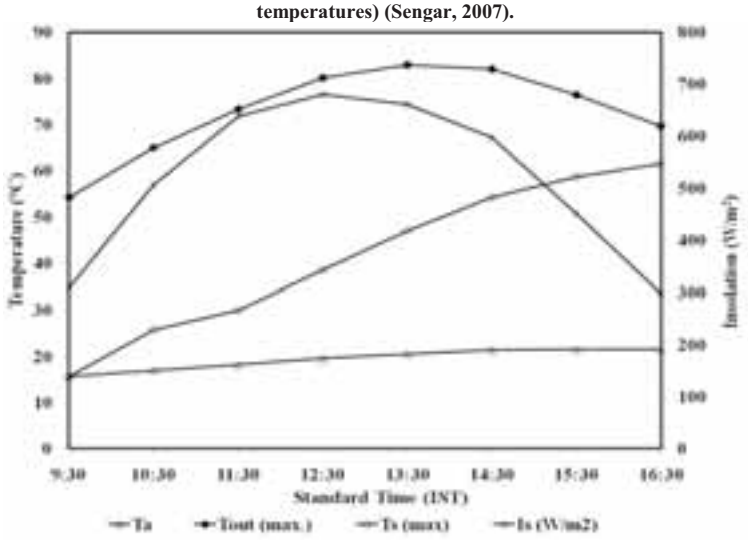

Fig. 7: Thermal profile of BMSWH (close loop) on 21 Dec. 2006 with single glass glaze (T_a, T_{out} and T_s are ambient, output water and storage tank water temperatures, I_S is solar insolation) (Sengar, 2007).

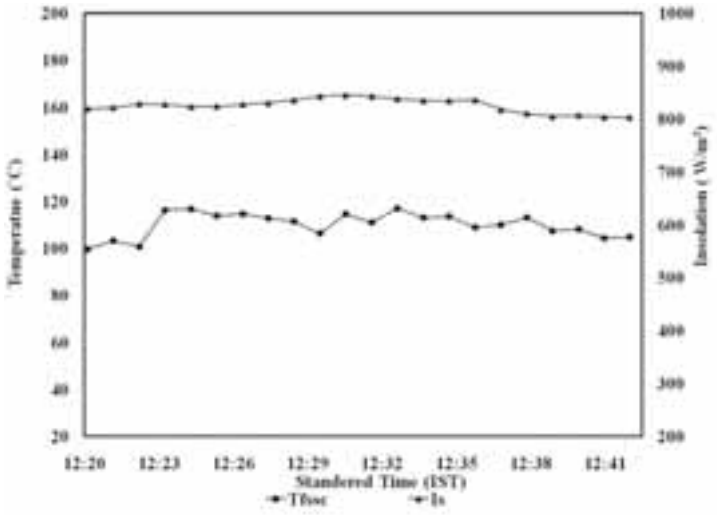

Fig. 8: Temperature profile of FSSC on 20 Jun 2015 (T_{fssc} is receiver temperature and I_S is solar insolation).

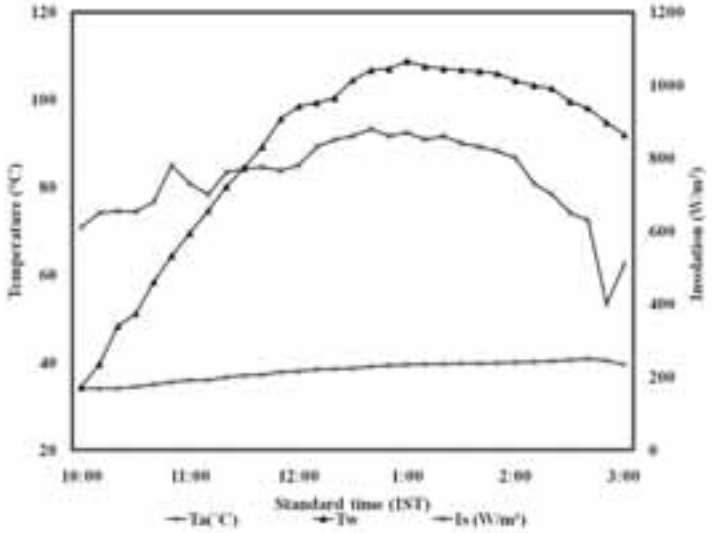

Fig.9: Measured temperature profiles and radiation intensity during sensible heating test of CSSC (8 kg water load) on 08 April 2012 (T_a and T_w are ambient and load water temperatures, I_S is solar insolation).

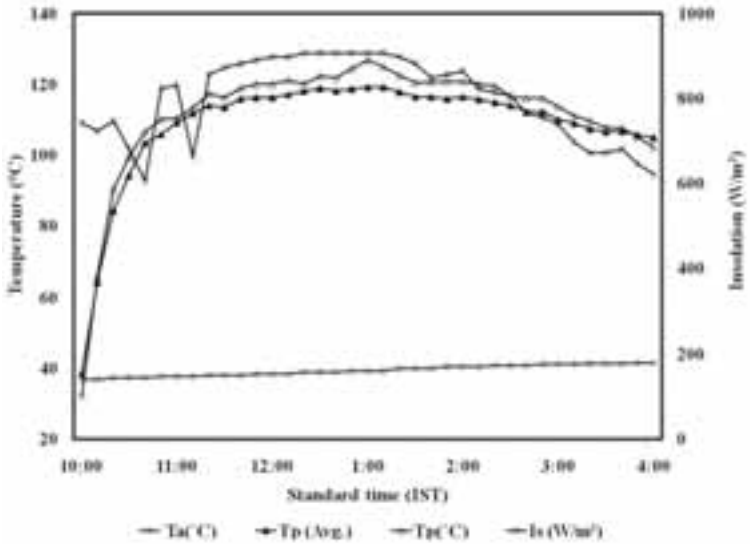

Fig. 10: Temperature profile of the different components (T_p- base plate, T_a-ambient, T_p (avg.)- average plate) of CSSC and variation of solar insoltion (I_s) with the standard time on 12 July 2014.

5. Results and discussion

Building material housing solar water heater: Initial experimental studies (in year 2017) are performed with PMMA glaze for BMSWH. The representative experimental observations for close loop cycle are plotted in Fig. 5. The maximum outlet water temperature is about 74 ºC and storage tank temperature reaches around 60 ºC. System thermal performance has also studied by Sengar; (2007) and Marwal; (2012). This is shown in Fig. 6 and 7. For slow mass flow rate in open loop cycle the maximum outlet temperature was recorded about 90 ºC in 2006 (Fig. 6). These tests were conducted with single glass glaze and hybrid insulation. A comparison of Fig. 5 with reference thermal profile Fig. 7 reveals that system thermal performance is quite good (storage temperature 60 ºC) even after more than 10 years. Although components of system (glaze, insulation, storage tank etc.) have been changed yet the casing is same. It indicates building material casing makes the system good weather resistance and increases the durability. System is still under the testing for determination of different characteristic parameters of a solar water heater.

Fixed structure solar concentrator: Fig. 8 shows that FSSC receiver attained a maximum temperature of 117 ºC at local noon and remains above 100ºC for about 20 minutes for insolation around 800 W/m^2. In FSSC cooking of rice is also done in a pot of diameter 10 cm and height 6 cm. The observed cooking time is 45 min. for 100 gm rice cooking which required 200 gm of water to cook. Hence, FSSC is suitable for cooking of boiling type food in peak sunny hours.

Community size solar cooker: The diurnal variation of water load temperature, solar insulation and ambient temperature for 8kg water load are depicted in Fig. 9.The results of these figures are used to calculate the second figure of merit. Figure shows that in 1 h 30 min water load attained temperature about 80 ºC and it is sustained for more than 3 h. This reveals that two meals cooking for 8 to 10 persons can be done in this cooker as per ref. (Mahavar et al., 2015). The value of second figure of merit (F_2) (using T_{w1}=63.8ºC,T_{w2}=95.1ºC, τ=5400 sec. , average values for the ambient temperature 39.2ºC insulation is 806 W/m^2) calculated as per ref. (Mahavar et al., 2012a) is found to be 0.416 . Fig. 10 represents the diurnal variation of solar insolation, absorber plate and ambient temperature of CSSC under no lad condition. The temperature of the absorber plate increases with time until it achieves the maximum values around 1:00 p.m. The maximum temperature of the absorber plate T_p is recorded to be 126.9ºC. The absorber plate temperature remains above 100ºC for most of the time. This stagnation test as per ref. (BIS, 2000) assures the satisfactory thermal performance of community size solar cooker. This test is conducted after more than two years in 2014 with same components and still the thermal performance of the system is found satisfactory, it indicates the good weather resistance and durability of the system due to the building material casing.

Hence, building material housing can serve as good casing material for solar thermal appliances and using this casing these appliances can be made an integrated part of the building/housing.

6. Conclusion

Solar thermal applications (STAs) have immense potential especially in domestic and industrial sector to meet thermal energy demand of the world. Beside all the development of STAs, there is still need of user friendly, more durable and weather resistant appliances with good thermal performance. Paper concludes that the appliances (water heater, solar concentrator and solar cooker) developed using building material housing have good thermal performance for long duration of 2 to 10 years or even more years. Hence, with building material casing STAs can be developed as integrated part of the housing or small industries and can be more popularized for hot water and cooking need of individual houses in effective way.

7. Acknowledgment

Authors are thankful to UGC (New Delhi) and DST (New Delhi) to provide fund to conduct experimental study.

8. References

- Bureau of Indian Standards (BIS) IS 13429. 2000.
- Belusko, M., , Saman W., Bruno F., 2004. Roof integrated solar heating system with glazed collector. Solar Energy. 76, 61-69.
- Cuce, E., and Cuce, P.M., 2013. A comprehensive review on solar cookers. Applied Energy. 102, 1399–1421.
- Dzioubinski, O., and Chipman, R., 1999. Trends in Consumption and Production: Household Energy Consumption. Discussion Paper of the United Nations, Department of Economic and Social Affairs. P. No. 6.
- Hossainb, M.S., Saidura, R.,Fayazb, H., Rahimb, N.A., Islama, M.R., Ahameda, J.U., Rahmanb, M.M., 2011. Review on solar water heater collector and thermal energy performance of circulating pipe. Renewable and Sustainable Energy Reviews. 15, 3801–3812
- Kaushika, N.D., and Reddy, K.S., 2000. Performance of a low cost solar paraboloidal dish steam generating system. Energy Conversion and Management. 41, 713–726.
- Lovegrove, K., Burgess, G., Pye, J., 2011. A new 500 m^2 paraboloidal dish solar concentrator. Solar Energy. 85, 620–26.
- Mahavar, S., Sengar, N., Rajawat, P., Verma, M., Dashora, P., 2012. Design development and performance studies of a novel Single Family Solar Cooker. Renew Energ. 47, 67-76.
- Mahavar, S., Rajawat, P., Marwal, V.K., Punia, R.C., Dashora, P., 2012. Modeling and on-field testing of a Solar Rice Cooker. Energy. 49, 404-12.
- Marwal, V., 2012. Study of solar radiation and novel building material housing flat-plate solar collector for hybrid applications. Thesis submitted to University of Rajasthan, Jaipur, India.
- Mahavar, S., Verma, M., Rajawat, P., Sengar, N., Dashora, P., 2013. Novel solar cookers: suitable for single families. International Journal of Sustainable Energy. 32(6),574-586.
- Mahavar , S., Punia, R.C., Verma, M., Rajawat, P., Dashora, P., 2015. Evaluating the optimum load range for box-type solar cookers. Renew Energ. 74, 187-94.
- Mahavar, S., 2015. Solar Engineering-I (Applications) Vol. 5 (Chapter 6), USA: Studium Press LLC.
- Mahavar, S., Bhardwaj, A., Dashora, P., 2016. Fabrication and testing of a light weight solar concentrator. In Proceeding of National conference on renewable energy and energy conservation, Poornima University, Jaipur.
- Mahavar , S., Sengar, N., Dashora, P., 2017. Analytical model for electric back up power estimation of solar box type cookers., Energy. 134, 871-881.
- Nayak, J.K., Sukhatme, S.P., Limaye, R.G., Bopshetty, S.V., 1989. Performance studies on solar concrete collectors. Solar energy. 42, 45-56.
- Nahar, N.M., Gupta, J.P., Sharma, P., 1993. Performance and *testing of an improved community size solar cooker*. *Energy Conversion and Management*. *34* (*4*), 327-333.
- Otte, P.P., 2014. Warming Up to Solar Cooking – A Comparative Study on Motivations and the Adoption of Institutional Solar Cookers in Developing Countries. Energy Prodedia. 57, 1632-41.
- Panwara, N.L., Kaushika, S.C., Kotharib, S., 2012. State of the art of solar cooking: An overview. Renewable and Sustainable Energy Reviews. 16, 3776– 85.
- Punia, R.C., 2013. Thesis: Modelling, Design Development and Study of Some Non-Concentrating Community Solar Thermal Appliances, Thesis submitted to University of Rajasthan, Jaipur, India.
- Reddy, V.S., Kaushik, S.C., Ranjan, K.R., Tyagi, S.K., 2013. State-of-the-art of solar thermal power plants—A review. Renewable and Sustainable Energy Reviews. 2, 258–273.
- Sonune, A., and Philip, S., 2003. Development of a domestic concentrating cooker. Renew Energy.28,1225–34.
- Sen., Z., 2004. Solar Energy in Progress and Future Research Trends. Progress in Energy and Combustion Science. 30, 367-416.
- Sukhatme, S.P., 2007. Solar energy: Principles of thermal collection and storage, New Delhi: Tata McGraw-Hill Book Co.
- Sengar, N., 2007. Utilization of solar energy in low grade energy applications. Thesis submitted to University of Rajasthan, Jaipur, India.
- Sengar, N., Dashora, P., Gupta, M., Mahavar, S., 2011. Experimental Studies, Energy Savings and Payback Periods of a Cylindrical Building-Material-Housing Solar Cooker. International Journal of Energy Information and Communications. 2(3), 75-84.
- Thirugnanasambandam, M., Iniyan, S., Goic, R., 2010. A review of solar thermal technologies. Renewable and Sustainable Energy Reviews. 14, 312–322.

Photovoltaics

Study on Crawler-Type Solar EV

Toru Fujisawa[1], Yuki Nemoto[1], and Takashi Kawaguchi[1]

[1] Kanagawa Institute of Technology, Atsugi (Japan)

Abstract

In this study, a photovoltaic module was installed on the rooftop of a crawler vehicle. If the power grid is unable to supply electricity, the crawler-type solar electric vehicle (solar EV) is able to travel on rough ground and has a self-charging function owing to solar energy absorption. The crawler can move in various ground conditions, such as asphalt, soil, grass, and gravel. Driving experiments were performed under different conditions, and we measured the photovoltaic current, voltage, acceleration, and power consumption. As a result, the solar fraction is compared with the vibration, it was found that solar fraction of the crawler-type solar EV was achieved 40-44 % on a winter clear day, power consumption of the motor was not proportional to z-axis acceleration. For specified solar fraction, ratio between PV and motor ratings was around 30 %, it is larger than scooter-type solar EV.

Keywords: Crawler, Solar EV, PV System, Solar Fraction, Farm Car

1. Introduction

After the Great East Japan Earthquake of 2011, as damaged infrastructure needed a longer time to return to a normal state, many Japanese people considered harvesting solar energy for daily life, and also for automobile use. Solar EV is a unique name proposed by the regulation of the World Solar Challenge (WSC 2012). In Japan, a company (Fukuzawa-Oder, 2015) produced a crawler-type solar-power-driven planter for Chinese yams (*Dioscorea batatas*). In recent years, we found the motivation for this study from our university students, aiming at developing sustainable solar-powered EV. It is a low-cost and reusable vehicle with potential applications in areas such as agriculture, delivery use (Toru Fujisawa and Takashi Kawaguchi, 2016), on uneven surfaces, or in rural areas with a stand-alone photovoltaic system.

2. EV conversion

The solar EV is converted from an old grain thresher, OSHIMA Harvester MK-100 (fabricated by Oshimanoki, 1983–1986), as shown in Fig. 1. Its driving seat and photovoltaic module are reused components. The aluminum frame, synchronous motor, lead-acid battery, inverter, and boost-type maximum power point tracker (MPPT) are new components needed for conversion to a solar EV. Tab. 1 gives the specifications of the grain threshing machine. Tab. 2 lists the major components of the converted crawler-type solar EV. Fig. 2 shows a side view of the crawler-type solar EV. In the figure, each major component is indicated. The electrical system of the crawler-type solar EV is shown in Fig. 3.

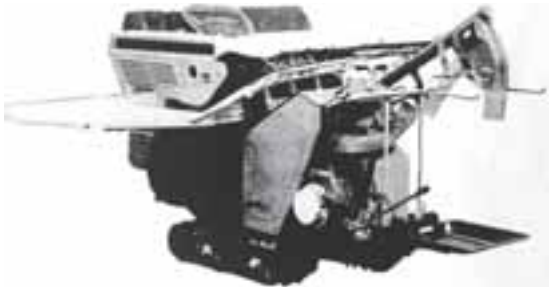

Fig. 1: Oshima MK-100 thresher

doi:10.18086/swc.2017.20.01 Available at http://proceedings.ises.org

Tab. 1: Specifications of the grain thresher

Length	Width	Height	Tread	Mass
1,743 mm	878 mm	1,586 mm	635 mm	181 kg
Max speed of powertrain	**Max Engine Power**	**Engine**	**Compression Ratio**	**Fuel**
1,800 rpm	3.5 PS	G510L NA 192 cc	6.2	Unleaded petrol

The traveling speed of the thresher can be selected, at 0.38 m/s, 0.43 m/s, and 0.91 m/s, using its transmission gear. We considered traveling safety and decided to avoid using a highest-speed gear. When the engine pulley rotates 10 rounds in the lowest gear, the crawler travels 1.2 m on the road. This means that the vehicle speed can be calculated from the rpm of the driving unit.

Tab. 2: Specifications of major components for converted crawler-type Solar EV

Battery	Motor	Inverter	PV module	Tracker	Pyranometer
VRLA 12 V × 4, 20 Ah	FBLM86 PMSM 660 W	BLD4820 ≤ 1200 W	MD-HH210T 210 W	Boost PT-209U	Silicon sensor ML-020VM

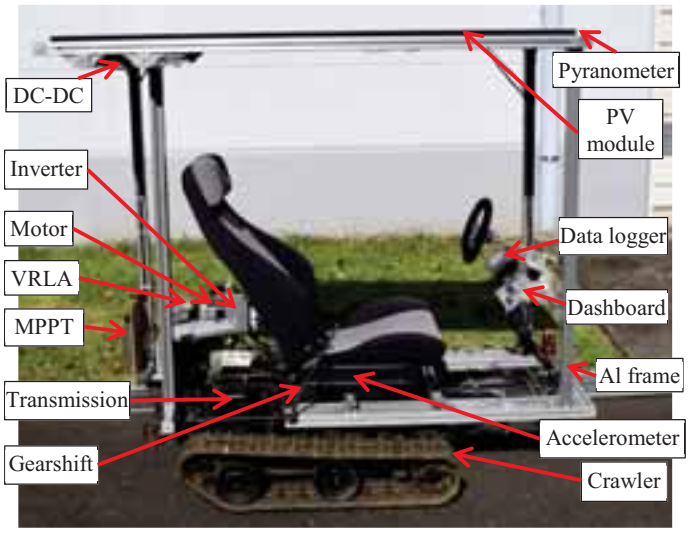

Fig. 2: Crawler-type Solar EV

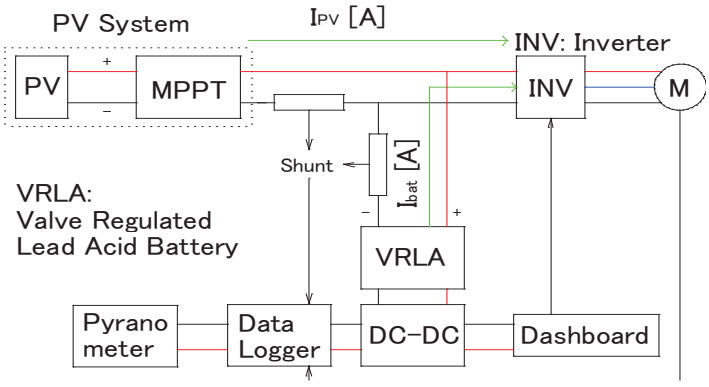

Fig. 3: Block diagram of electrical system

Fig. 4 shows outdoor solar charging in summer and an indoor garage view with undergraduate students in winter. Fig. 5 represents the PV system output current, valve regulated lead acid (VRLA) battery current, and motor current while climbing backward a step from asphalt to greenbelt ground, as in Fig. 4.

Fig. 4: Converted crawler-type solar EV (Left: outdoor charging in summer, Right: in a garage in winter)

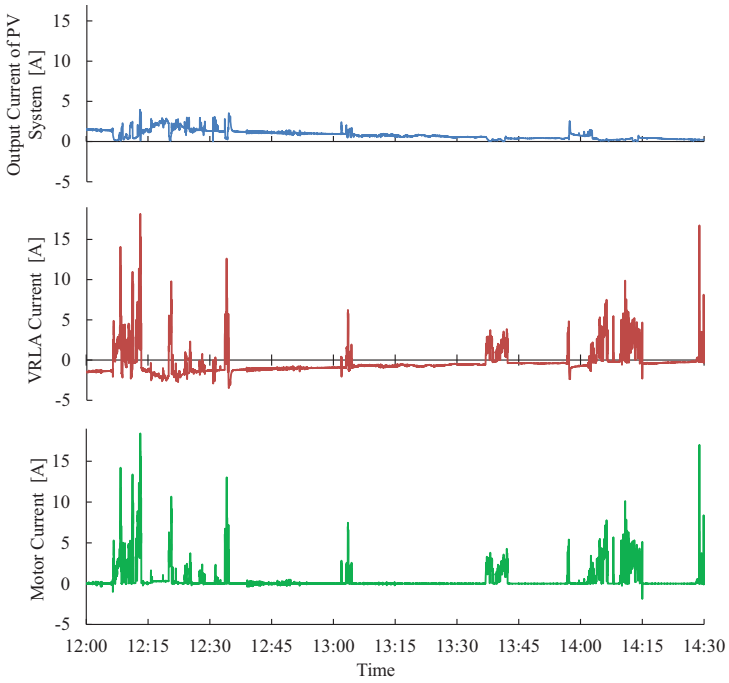

Fig. 5: Motor current and PV system output current in summer (climbing backward a step from asphalt to greenbelt ground)

3. Evaluations

3.1. Solar Fraction

The solar fraction (F_s) was calculated using the output PV power (P_{pv}) and consumed power using load (P_{load}).

$$F_s = \frac{\int P_{pv} dt}{\int P_{load} dt} \qquad \text{(eq. 1)}$$

$$P_{pv} = I_{pv} V_{bat} \qquad \text{(eq. 2)}$$

$$P_{load} = I_{bat}V_{bat}, \qquad \text{(eq. 3)}$$

Here, I_{pv} is the output current of the peak power tracker, V_{bat} is the voltage of the lead-acid battery (same as the load voltage), and I_{bat} is the current of the battery. These data, along with the irradiance, accelerometer output, and revolution speed (12 pulses per revolution) of the motor are recorded by a 10-channel data-logger (GRAPHTECH GL220A) every 100 ms.

A three-axis accelerometer, Kionix KXSC7-2050, was installed under the driving seat near the center of mass, as shown in Fig. 6. The output from this sensor is also recorded simultaneously in the same interval by the logger. To evaluate the vibration of the vehicle, the root mean square (RMS) value of the z-axis acceleration a_z is calculated as

$$RMSA = \sqrt{\frac{\sum_{i=1}^{n} {a_z}_i^{\,2}}{n}}. \qquad \text{(eq. 4)}$$

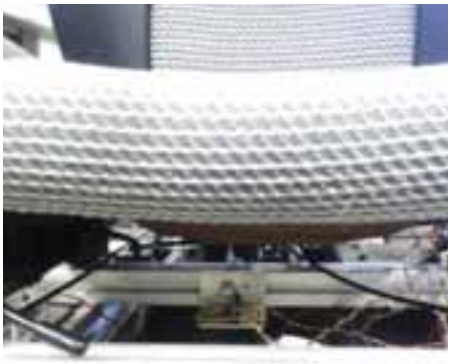

Fig. 6: Installation position of three-axis accelerometer

3.2. Experiments

Three different experimental surfaces are shown in Fig. 7. The grain diameter of gravel was ~15–40 mm, and the glass depth was ~20–40 mm. The experimental results of speed vs. power consumption on the three different surfaces, gravel, grass, and asphalt, are shown in Fig. 8. Fig. 9 shows the z-axis acceleration for the RMS value vs. vehicle speed. From this figure and the previous one, it can be observed that the z-axis acceleration does not always directly affect the power consumption of the driving load.

(a) gravel **(b) glass** **(c) asphalt**

Fig. 7: Ground surface conditions

As a result, the power consumption was greater on gravel and glass than on asphalt. On the other hand, the RMS value of the z-axis acceleration is smaller on grass and on asphalt than that on gravel. The solar fraction for each

condition is calculated using eq. 1 and listed in Tab. 3.

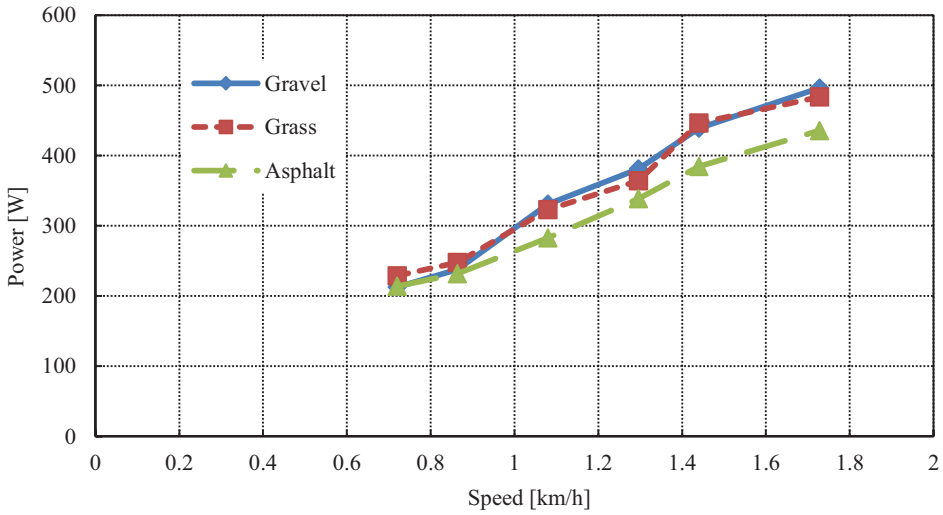

Fig. 8: Speed vs. average power consumption for three different roads

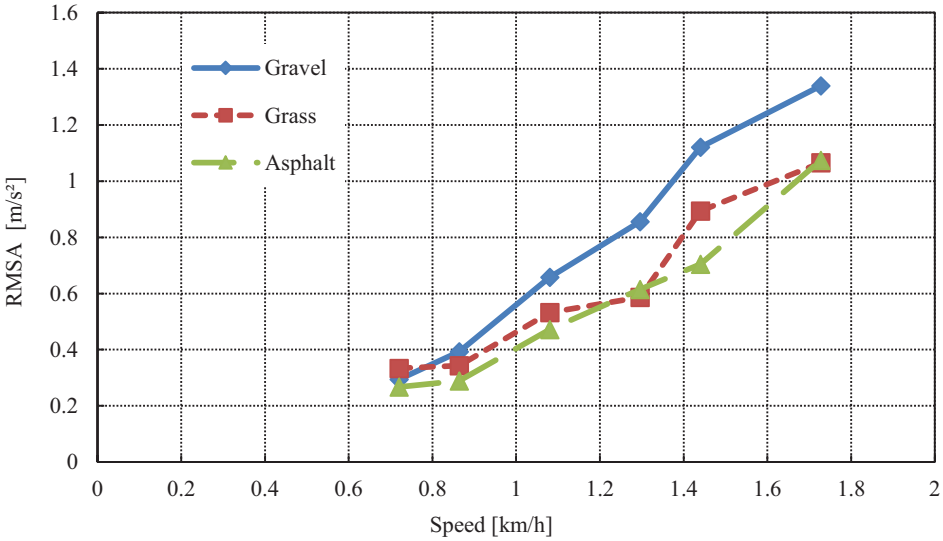

Fig. 9: RMS acceleration of vertical direction (z-axis) vs. vehicle speed

Tab. 3: Solar fraction of crawler-type solar EV on different flat surfaces on a clear winter day

Motor Speed	Gear	Speed [km h^{-1}]	Gravel 15th Dec 17	Grass 26th Jan 17	Asphalt 21st Jan 17
1000 [rpm]	First	0.720	60.9 %	56.6 %	60.6 %
	Second	0.864	54.5 %	52.3 %	55.9 %
1500 [rpm]	First	1.08	39.2 %	40.1 %	45.8 %
	Second	1.30	34.0 %	35.6 %	38.3 %
2000 [rpm]	First	1.44	29.5 %	29.0 %	33.7 %
	Second	1.73	26.1 %	26.8 %	29.7 %
Average			40.7 %	40.1 %	44.0 %
Peak Irradiance [W/m^2]			645	527	637
Solar Altitude [deg.]			30.9	25.9	34.8

4. Discussions

Tab. 4 presents the comparison between various solar EVs. The power unit, mass, PV rating, battery capability, travel distance per charge, and solar mileage are discussed. Fig. 10 shows the ratio between the PV and power unit ratings in terms of the specified solar fraction for comparison. Spirit is the name of the racing solar car that participated in the WSC 2013 Adventure class, the Gyro Canopy is a converted solar EV scooter, and the Prius PHV is TOYOTA's first commercial solar EV that can incorporate electric power into its power battery storage while driving.

Tab. 4: Three different types of Solar EV and plug-in HEV with photovoltaic roof (including 60-kg driver)

	Motor	Mass	PV	Motor / Mass	Battery	PV / Motor	Distance	Solar mileage	Duration
	[kW]	[kg]	[kW]	[W/kg]	[kWh]	[-]	[km/charge]	[km/day]	[h]
Racing solar car KAIT Spirit	2.0	220	1.3	9.52	5.0	0.65	350	300	4.3
Crawler solar EV	0.66	245	0.21	2.69	0.6	0.32	1.5	0.6	0.6
Gyro canopy converted solar EV	1.5	210	0.13	7.14	1.3	0.87	19.5	2.4	0.2
Prius PHV	80	1810	0.2	44.2	10	0.0025	60	6	0.1

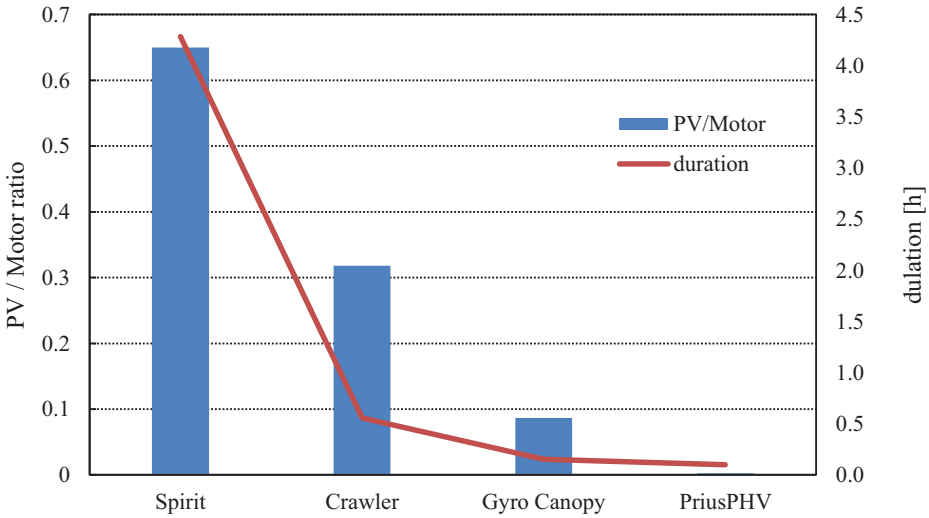

Fig. 10: The ratio between PV and power ratings

5. Conclusions

From the outdoor driving experiments with the converted crawler-type solar EV, the following conclusions were drawn:

- The solar fraction was 44% on the asphalt road on a sunny winter day.
- The consumed power was proportional to the vehicle speed, and the lowest curve was obtained on an asphalt road.
- The crawler-type solar EV is affordable with a 660-W synchronous motor and a VRLA battery with a nominal power of 48 V.
- The highest power consumption rate was obtained on asphalt, achieving 10 km/kWh in the lowest gear.
- The rating power ratio of PV/Motor for the crawler-type solar EV was 0.32.

Farm-use cars or robotic vehicles are necessary for Japanese rural agriculture, as the rapidly aging society with

fewer children has become the largest problem for Japan's future.

6. References

Fukuzawa-Order, 2015, Solar Nagaimo Planter, fukuzawa-order.com (last access: 14 OCT 2017)

Oshimanoki, 1983, MK-100 User's manual, www.oshimanoki.com (last access: 14 OCT 2017)

Toru Fujisawa and Takashi Kawaguchi, EuroSun 2016, Performance Evaluation and Trial Making of a Compact Solar EV, No. 0134, ISES Conference Proceedings, DOI:10.18086/eurosun.2016.08.05

World Solar Challenge, 2012, World Solar Challenge Regulations, www.worldsolarchallenge.org (last access: 19 JUN 2012).

Beam Splitting with a Luminescent Solar Concentrator in a Hybrid Photovoltaic/Thermal Collector

Maja Gajic[1], David Rodriguez-Sanchez[1] and Gary Rosengarten[1]

[1] RMIT University, School of Engineering, Melbourne (Australia)

Abstract

This work investigates the combination of two non-imaging types of concentrating solar technologies: the luminescent solar concentrator, that generates electricity via photovoltaic cells and the compound parabolic concentrator, used normally with a thermal receiver. The luminescent solar concentrator in this new application is used as a cover for the solar thermal collector (the CPC) whilst at the same time concentrating a specific wavelength band of light to its edges where solar PV cells convert photons to electricity. Absorption of a part of the solar spectrum occurs in the LSC, whilst the rest of the solar spectrum can be captured as thermal energy in the CPC, essentially forming a new type of spectral splitting hybrid solar collector that can produce electricity and medium temperature heat. A small prototype hybrid CPC and LSC collector was tested in the lab using a solar simulator. This proof of concept device compared a high transmission and low transmission LSC and demonstrated the experimental basis of the new type of PV-T collector. An outdoors flow experiment was undertaken, measuring instantaneous thermal efficiency and electrical output.

Keywords: solar photovoltaic, solar thermal, hybrid

1. Introduction

The sun is the world's most abundant energy source and means of harvesting it include photovoltaic cells to create electricity and solar thermal collectors to generate heat. Low temperature heat can be used for domestic applications where in urban environments available space is often limited. By combining solar thermal and photovoltaics in one system, roof space can be saved and potentially efficiency can be increased. Photovoltaic technologies can only convert photons with energies above their bandgap to electricity, with the remainder of the solar spectrum wastefully generating heat. In a hybrid configuration that heat is not wasted but collected instead.

This work combines for the first time two types of non-imaging solar concentrators, the luminescent solar concentrator (LSC) and the compound parabolic solar thermal collector in a hybrid configuration as shown in Fig. 1. The LSC cover acts as a beam splitter of solar radiation. The absorption and emission spectra of the fluorescent molecules within the LSC device select a part of the spectrum, where ideally it is totally internally reflected to the solar PV cells attached to the edges of the LSC. The rest of the solar spectrum is transmitted through the LSC cover to the solar thermal collector.

There are many potential applications for such a technology depending on what the desired outcome is. The CPC solar thermal collector can be designed for domestic applications requiring low temperature heat or for commercial applications where medium temperature heat is required (up to approximately 200 °C). Currently the LSC can generate modest amounts of electricity that could potentially power peripheral devices or sensors. This is due to the low power conversion efficiencies of the device, with the world record device achieving 7.1 % with expensive gallium arsenide PV cells (Slooff et al., 2008).

There is of course a trade-off between electricity generated and thermal energy collected and one or the other could be prioritised depending on loads and needs. The potential applications for hybrid photovoltaic and thermal (PV-T) collectors are more numerous in urban environments where roof space is often limited (Ramos et al., 2017). By making better use of the solar source, PV-T collectors can save on space and improve energy collection efficiency.

doi:10.18086/swc.2017.20.02 Available at http://proceedings.ises.org

2. Hybrid CPC and LSC Collector

2.1 Luminescent solar concentrator

Luminescent solar concentrators consist of a fluorescent material embedded in a waveguide such as poly methyl methacrylate (PMMA). Photons that fall within the absorption spectrum of the fluorescent material can be absorbed and then isotropically emitted at a longer wavelength. Ideally these re-emitted photons are propagated to the edge of the waveguide via total internal reflection (Debije and Verbunt, 2012). Solar PV cells (or other absorbers) can then be attached to the edges of the device to convert photons to electricity. An important benefit of LSCs is that they can concentrate both diffuse and beam radiation (Smestad et al., 1990) and they have a wide acceptance angle, which allows them to function without tracking. The acceptance angle is defined as the maximum angular deviation of a ray with respect to the normal to the aperture plane, which allows the ray to be intercepted by the receiver. Additionally, the fluorescent dye can be chosen to emit photons that the solar PV cells can convert with higher efficiency. Conventionally their use has been envisaged to be in the urban environment to reduce the environmental impact of buildings (Gajic et al., 2017; Kanellis et al., 2017).

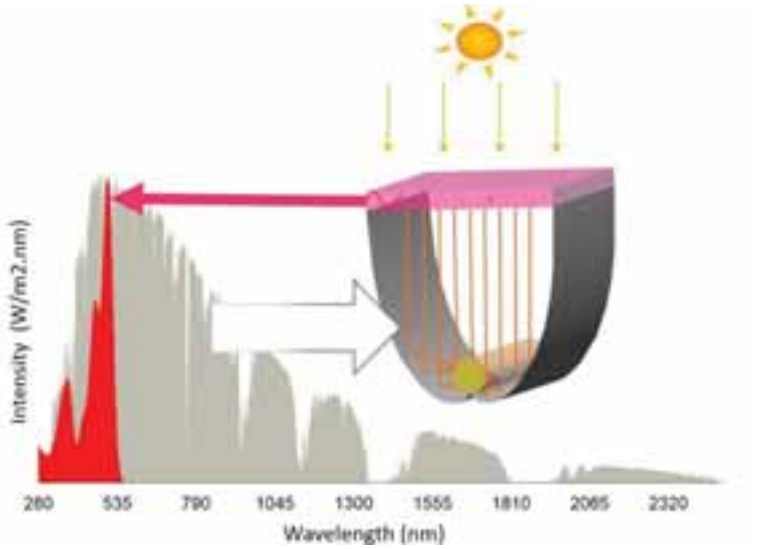

Fig. 1: Schematic of LSC and CPC hybrid collector overlaid with solar AM 1.5 spectrum (grey) and Lumogen Red 3505 fluorescent dye absorption spectrum (red)

2.2 LSC design and fabrication

For the small-scale prototype hybrid CPC and LSC, two LSCs were fabricated from commercially available fluorescent sheets as shown in Fig. 2. A pink sheet, commercially manufactured by Evonik ("Evonik Industries," 2017) and a red sheet named Mars Red 4t56 available from online retailers. The properties of the LSCs are summarised in Table 1. Since these fluorescent sheets were commercially procured, it was not possible to determine the exact concentration of fluorescent dye or even confirm the fluorescent material. The pink sheet is assumed to contain the dye Lumogen Red 305, estimated from spectroscopic properties. The solar AM 1.5 averaged absorption was measured for the pink sheet to be 8.6 % and red sheet to be 32.8 %. The high transparency of the pink sheet is useful for collecting most of the energy as heat in the solar thermal collector while the higher absorbing red sheet transmits more energy to the PV cells. The absorption spectra of the two LSCs and the AM 1.5 spectrum is shown in Fig. 3. The figure shows how that the red sheet absorbs much more of the visible spectrum than the pink sheet, which will enhance transmission to the PV cells. The fluorescent sheets were cut to size and the edges were optically polished with very fine sand paper and polishing oil. Sunpower high efficiency back contact PV cells were diced and cut to fit the edge of the LSC. These cells are very well suited to LSC applications as they have all the wiring on the back. The thickness of the cells is 3 mm and for the prototype LSCs, cells of length 9.5 cm and 5 cm were fabricated. The pink and red LSCs have the 9.5 cm cells placed along the 10 cm edge of the LSC and along the 15 cm length both 9.5 cm and 5 cm cells were attached. Each had attached wiring that was connected in parallel externally.

Tab. 1: LSC prototype specifications

LSC specifications	Value
Size	10 x 15 x 0.3 cm
Geometric concentration ratio	15
Optical coupling	Silicone Elastosil Solar 2202
Red fluorescent material	Unknown
Pink fluorescent material	Lumogen Red 305
LSC waveguide	Perspex
Fluorescent dye concentration	Unknown
Solar PV cells	Sunpower PV cell cut to 3 mm thick, edge coupled

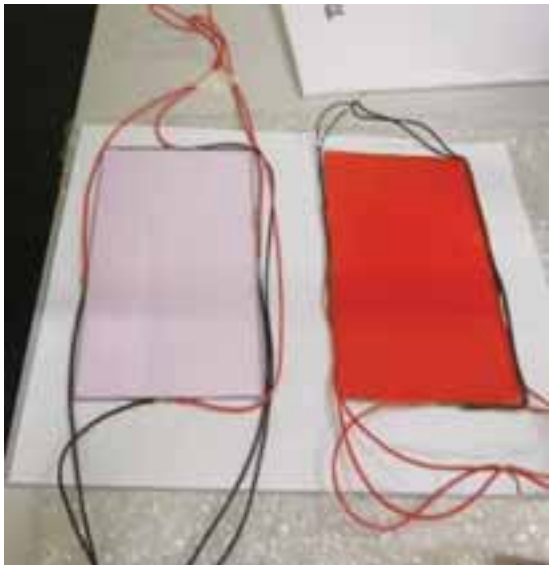

Fig. 2: Pink LSC (left) and red LSC (right)

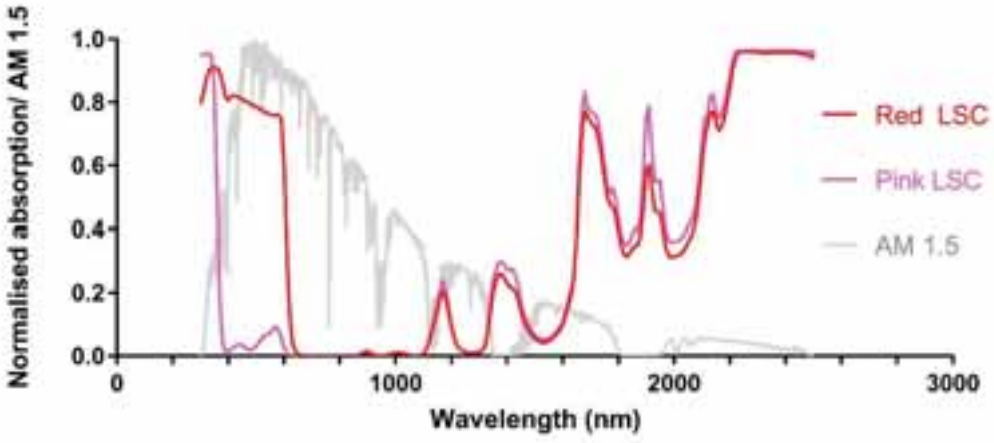

Fig. 3: AM 1.5 solar spectrum (grey) overlaid with the pink LSC absorption spectrum and red LSC absorption

2.3 Compound parabolic concentrator

The compound parabolic concentrator was developed by Roland Winston when he was investigating means of efficiently detecting Cherenkov radiation (Hinterberger, 1966). The discovery of the CPC led to the development of the field of non-imaging optics, whose designs approach and even realise the maximum concentration allowable for a given acceptance angle, due to removing the need for point to point mapping required by conventional optics (Rabl and Winston, 1976; Winston, 1970; Winston et al., 2009; Winston and Welford, 1978).

Ideally, the CPC concentrates all rays that fall within its acceptance half angle, Θ_A. The acceptance angle will determine the hours of light that can be collected as CPC designs are almost always non-tracking. The concentration ratio C of a two-dimensional CPC is determined by the ratio of the aperture area to the area of the receiver and quantifies the increase of solar flux on the receiver. C is inversely related to the acceptance angle and this means we can achieve higher concentration ratios, but at the expense of hours of sunlight that can be concentrated. A two-dimensional CPC can be considered as trough like and this shape is ideal for thermal applications where a cylindrical receiver such as an evacuated tube can be placed along the focal length of the collector (Herrick, 1982; Karwa et al., 2015). A cross sectional view is shown in Fig. 4. An involute shape CPC with an entrance aperture, d_1, and receiver radius, r, has a concentration ratio as shown in eq. 1. Θ_A is the acceptance half angle and ideally all incident rays at and below this angle will be transmitted to the receiver.

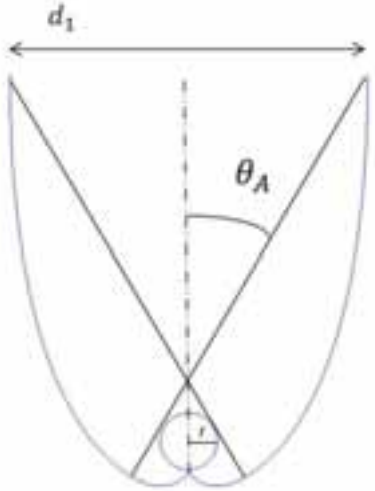

Fig. 4: Involute shaped compound parabolic concentrator

$$\text{Concentration ratio} = \frac{1}{\sin(\theta_A)} = \frac{d_1}{2\pi r} \qquad \text{(eq. 1)}$$

There is a large potential for solar technologies to meet industrial process heat needs, where medium temperatures are required (90 - 250 ˚C). CPCs offer a simple robust solution that has the potential to meet these needs. It has also been shown that CPCs can perform better than other solar collectors over a wide range of temperatures and without tracking (Brunold et al., 1994; Carvalho et al., 1995; Gallagher et al., 1993; Gu et al., 2014). As CPCs can reach the maximum allowed concentration for a given acceptance angle they are the best choice for a proof of concept collector that utilises a cover made up of a luminescent solar concentrator.

2.4 Compound parabolic concentrator for proof of concept hybrid collector

A small proof of concept prototype CPC and LSC hybrid was developed in this work. The CPC is designed with an aperture area of 15 cm and an absorber of radius 0.87 cm, giving a concentration ratio on the absorber of 2.74. An extruded profile of length 10 cm was generated and using CAD software, a profile was created as shown in Fig. 5 (right). The height was truncated by 70 % to save on material costs and to allow for a thinner collector

profile. The profile was then 3D printed with ABS polymer, and coated with highly reflective sputtered aluminium. The properties of the CPC are summarised in Table. 2. The involute compound parabolic shape was designed to be combined with a cylindrical receiver made up of an absorber within an evacuated tube and a 3 mm clearance gap between absorber and glass envelope. The evacuated receiver was supplied by commercial suppliers. However, the datasheet of the selective surface was not provided. The hybrid prototype under test conditions is shown in Fig. 5 (left).

Tab.2: CPC specifications and values

CPC specifications	Value
Radius absorber	0.87 cm
Gap between absorber and glass	3 mm
Aperture	15 cm
Concentration ratio	2.74
Acceptance angle	21.4 °
Mirror reflectance	AM 1.5 averaged 91 %
Truncation of height	70 %
Cost to 3D manufacture	$ 200 (material cost only)

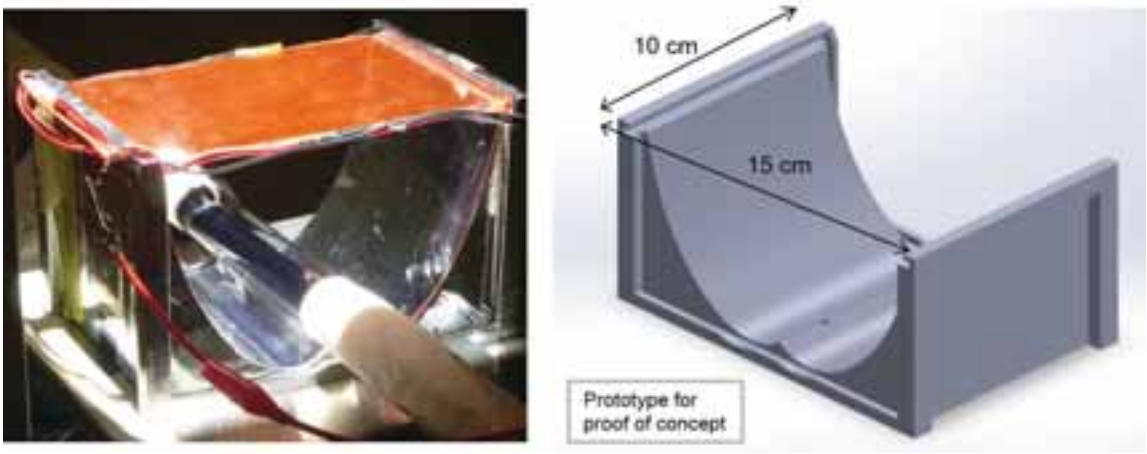

Fig. 5: Prototype hybrid under indoor test conditions (left), image of 3D printed prototype CPC (right)

4.2 Experimental setup

Indoor performance testing of the hybrid collector was analysed under a triple-A rated solar simulator. A 1000 W/m^2 radiation flux at the aperture plane of the CPC was set up using a calibrated pyranometer. To measure electrical performance of the LSC cover, I-V curves were taken with a Keithley 2400 source measuring unit. The indoor experimental set up is shown below in Fig. 6. The experiment compared both the pink and red LSC covers. I-V curves were measured under three different conditions shown below.

- LSC only (without the CPC) placed onto an absorbing material (TiNOX). This is necessary to stop reflected photons passing back into the LSC.
- LSC coupled with the CPC collector at the start of illumination (cold).
- LSC coupled with the CPC collector and after three hours of illumination (after 3 hours).

Thermal performance was characterised by measuring the stagnation temperature of various configurations of the device. Performance testing of solar collectors describes stagnation temperature as maximum achievable collector temperature. This occurs at zero flow conditions where the heat input is equal to the heat loss. The collector is illuminated at a constant radiation until this maximum temperature is reached, providing a useful comparison of the different configurations.

The thermal receiver used in the experiment is shown in Fig. 7. The 10 cm length required was left bare while the remainder of the tube was wrapped in foil and the ends were insulated. The tube is comprised of a selective surface absorber in an evacuated tube. To measure the stagnation temperature three k-type thermocouples were placed in the tube - one at the far end, one in the middle in the active area and one at the near end of the entrance.

A data logger is used to measure the temperature and the hybrid configuration was left to stagnate under the solar simulator for up to 3 or more hours, with at least 5 measurements made of each configuration.

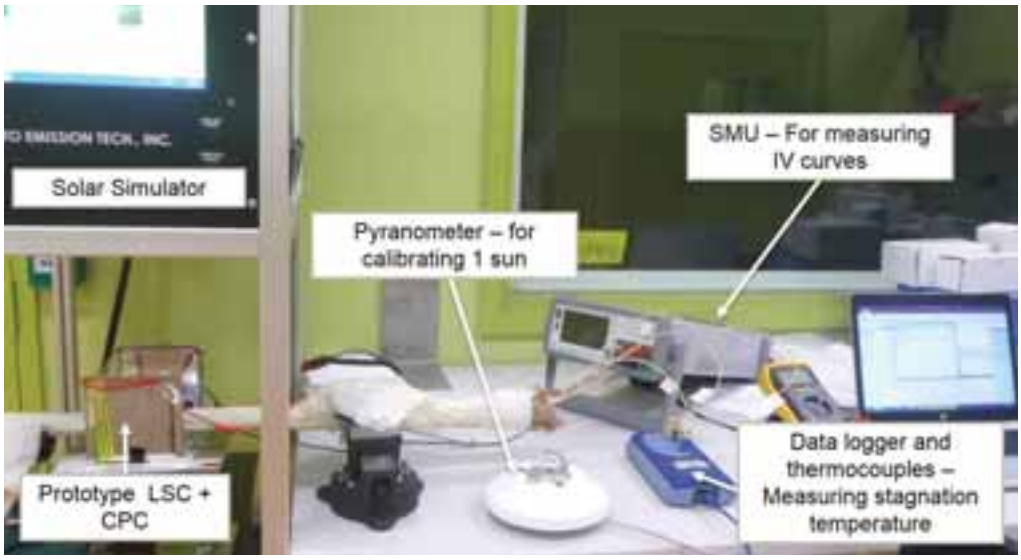

Fig. 6: Indoor experimental test setup

Fig. 7: Evacuated thermal receiver used in the stagnation tests

4.3 Results

The stagnation temperature test results on various configurations of the hybrid CPC and LSC are shown in Fig. 8. The stagnation temperatures reached for the different configurations (ambient subtracted) were: 208 ˚C for the CPC without an LSC cover, 192 ˚C for the CPC with the pink LSC cover, 150 ˚C for the CPC with the red LSC cover and 77 ˚C for the tube on its own under one sun illumination. This value is representative of the poor quality of these tubes we received from the manufacturer, an evacuated tube with a proper vacuum and a good selective surface should be able to stagnate at over 200 ˚C without concentration.

Pink and red LSC I-V curves were measured twice during the stagnation experiment; at the beginning of the experiment, and after three hours of continuous illumination under the solar simulator. The performance of both LSCs decreased after three hours, the pink LSC short circuit current reduced by 40 % and the red LSC short circuit current reduced by 16 % (results are summarised in Table 3). This is an interesting result considering LSCs are claimed to decouple the heat generating area, since it's the LSC that receives light and heats up and is thought not to transmit much heat to the solar PV cells around the edge. It remains unclear however if it is the PV cell around the edge of the device that is heating up, if the performance of the polymer itself is degrading or even if the behaviour of the fluorescent material changes with temperature. When the temperature of a polymer such as PMMA is increased its refractive index changes due to a change in its thermo-optic coefficient (Zhang et al., 2006). This behaviour has received little attention in LSC literature. An analysis of thermal performance of LSCs was completed by (Rajkumar et al., 2015), who studied the temperature of LSCs under illumination. The authors found the surface of the LSC reached a temperature of 50 ˚C after one hour and the edge mounted PV cells remained 10 ˚C cooler (the ambient temperature recorded in their lab was 21.5 ˚C and under the solar simulator was 34.5 ˚C). All these effects come into play as well as ambient temperature and presence of heat transfer due to convection (higher convective heat transfer coefficients outside than inside the lab).

Measurements were also taken by placing the LSC only, on a highly absorbent “black” material TiNOX that does not reflect any photons back into the LSC. The I-V curves under the various conditions are summarised in Fig. 9. It can be seen that simply placing the LSC on the CPC improves performance due to reflected photons from within the collector getting a chance to be captured by the LSC, that is the performance of the LSCs improves compared with simply measuring on a black absorber TiNOX. The reason for this is that some isotropically emitted photons from within the LSC are emitted into the CPC at angles that do not result in them being transmitted to the receiver and hence reflect back into the LSC. This is an interesting result showing LSCs perform better in this new application than on their own.

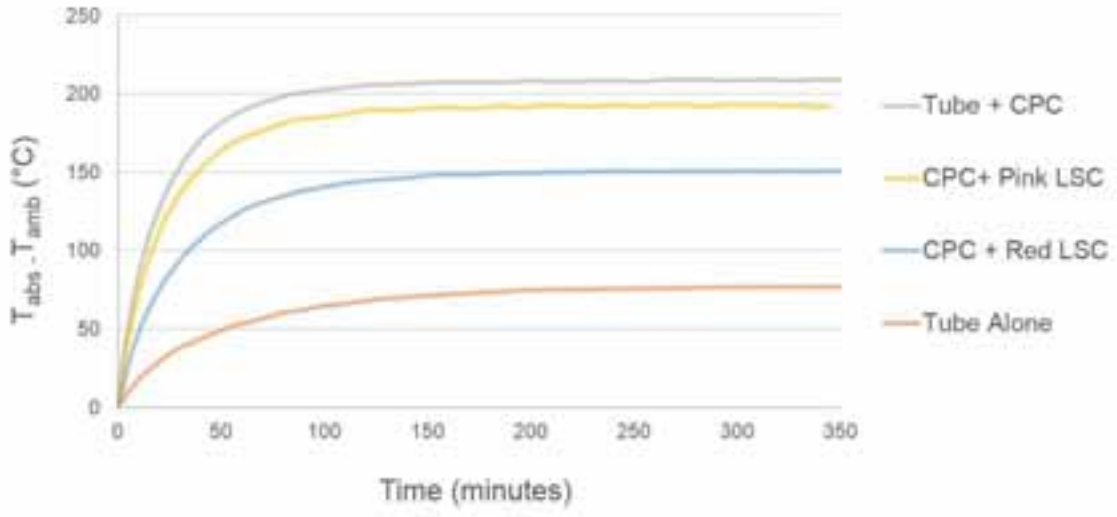

Fig. 8: Results of stagnation temperature test of hybrid CPC and LSC collector

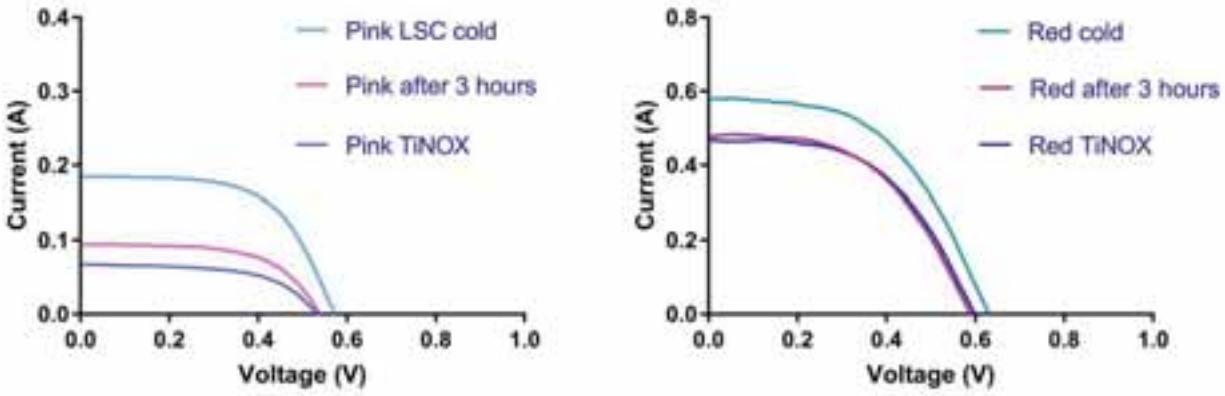

Fig. 1: I-V curves under different configurations of the hybrid prototype with the pink LSC (left) cover and red LSC cover (right)

Tab. 3: Summary of results

Hybrid prototype configuration	Short circuit current of LSC	Power conversion efficiency of LSC	Stagnation temperature (T_{abs}-T_{amb}) ˚C
Red LSC on CPC After 3 hours	485 mA	0.98 %	150 ˚C
Red LSC on CPC	578 mA	1.3 %	
Red LSC on TiNOX	473 mA	0.99 %	
Pink LSC on CPC After 3 hours	111 mA	0.2 %	191 ˚C
Pink LSC on CPC	185 mA	0.43 %	
Pink LSC on TiNOX	68 mA	0.14 %	
Evacuated tube on its own			77 ˚C

3. Full Scale Roof Experiment

3.1 Introduction

In the previous section a small prototype hybrid CPC and LSC was shown to reach high stagnation temperatures even with the LSC cover that absorbs a small proportion of the solar spectrum. In this section we extend this work to investigate a full length, 1-meter long CPC. This full-length collector was connected to a solar test rig on a rooftop facility at RMIT University in Melbourne as shown in Fig. 10. The collector was mounted in the east-west direction on the test rig and connected to a high temperature fluid delivery system. The CPC was covered with LSCs and flow experiments were performed whilst I-V measurements were made of the LSCs that had been wired together. This work demonstrates the benefits of using this system as a decoupled photovoltaic and thermal collector capable of delivering medium temperature heat and electricity.

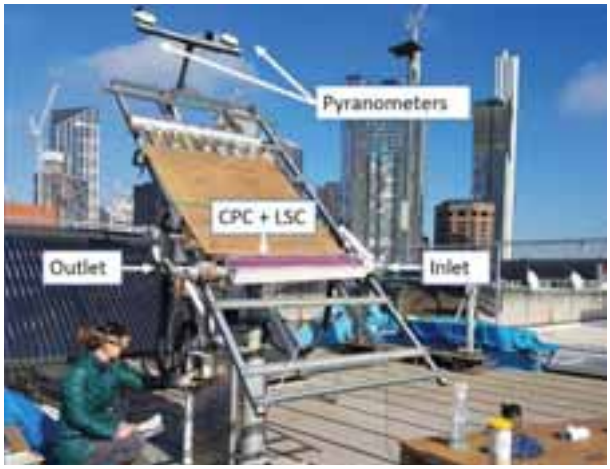

Fig. 10: Experimental setup for full length CPC and LSC collector mounted on two axis tracker

3.2 LSC design

A large sheet of Evonik PLEXIGLASS Red 3C50 GT was cut into four modules to cover the 1 m length CPC collector. Four modules of 25 cm length x 12 cm width were fabricated to cover the CPC collector. The thickness of the sheet was 3 mm and the edges were all polished until they became optically smooth using sandpaper and polishing oil. Sunpower back contact PV cells were coupled with silicone gel along the top edge and bottom edge but not sandwiched in between modules as they would heat up too much and it would be difficult to seal the collector.

3.3 CPC design

A one-meter length CPC was fabricated out of timber in the workshop using a CNC router. The specifications of the CPC are slightly different to section 2 of this paper, the properties of the receiver remain the same but the aperture is reduced to 11 cm. The CPC was sanded smooth and then coated with high gloss polyurethane ready for the reflective foil to be laid down. The reflective film, purchased from an online retailer was found to have a solar weighted reflectivity of 90 %. The receiver consisted of an evacuated tube with a selective surface absorber purchased from commercial suppliers, a second batch with the same specifications as the tube used in the indoor experiments.

3.4 Experimental setup

The CPC and LSC hybrid collector was mounted east-west orientation onto a test rig that also performs two-dimensional solar tracking. Tracking was used to keep the collector normal to the sun for performance measurements, to minimise as much as possible non-normal incidence angle effects. This is a standard method for testing solar collectors as found in the AS/NZS 2535.1:1999 standards. The hybrid collector is connected to the closed loop fluid delivery system that is composed of a heater and cooling fan that can control the input temperature of the collector via a PID controller and thermocouple at the heater outlet (not shown in Figures). To determine the collector efficiency several measurements need to be made: the fluid temperature at the collector inlet, T_{in}, the fluid temperature at the collector outlet $T_{out,}$ mass flow rate, irradiance incident on the collector and collector area. In this way the useful energy absorbed in the fluid (Therminol 66) can be calculated as shown in eq. 2.

$$Q = \dot{m}\, C_p\, (\mathrm{T_{out}} - T_{in}) \qquad \text{(eq. 2)}$$

Then the instantaneous thermal efficiency of the collector can be calculated as shown in eq. 3.

$$\eta = \frac{\dot{m}\, C_p\, (\mathrm{T_{out}} - T_{in})}{A\, G} \qquad \text{(eq. 3)}$$

Where A is the collector area and G is the global irradiance on the collector (measured with the pyranometer). The measurements were made after waiting for the inlet temperature and mass flow rate to stabilise, then the values were recorded for at least 10 minutes at a rate of one measurement per second. Then the inlet temperature

was increased again and the process repeated. The efficiency was calculated for each sample and then averaged. To maximise ΔT, the temperature increase in the collector it was necessary to aim for as low mass flow rate as practical whilst maintaining flow in the turbulent regime.

3.5 Results – electrical output

The LSC cover was made up of four LSC modules with Sunpower solar PV cells along the two long edges. All the cells along the top of the LSC and all the cells along the bottom of the LSC are connected in parallel as shown in Fig. 11, these form two outputs at both the top and the bottom of the collector. The I-V curve measurements were taken with a laptop and Ketithley source measuring unit that were brought to the roof and connected to the LSC for measurement. Several measurements were taken, initially and after several hours of tracking. At least four measurements were taken at a time and averaged.

Fig. 12 left shows the I-V characteristics when the top row and bottom row were connected together in series. Fig. 12 right shows the P-V curves comparing top/bottom outputs connected in series (purple) and parallel (pink). The series connected output in pink has a maximum power of .220 W and performs better than the parallel connected output achieving only 0.167 W. With a power input on to the LSC area of 120 W gives an overall LSC cover efficiency of 0.183 %. This is an efficiency based on the AM 1.5 solar spectrum. The low power conversion efficiency can be explained by the low initial absorption of highly transparent pink Evonik sheet that initially only absorbs 8.6 % of the solar AM 1.5 spectrum, making this type of LSC suitable for generating modest amounts of power and transferring most of the solar energy to the thermal receiver.

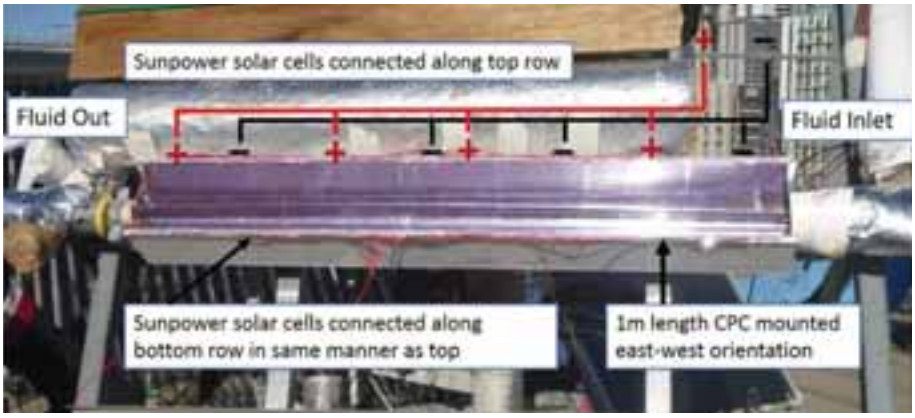

Fig. 2: LSC wiring for full length module

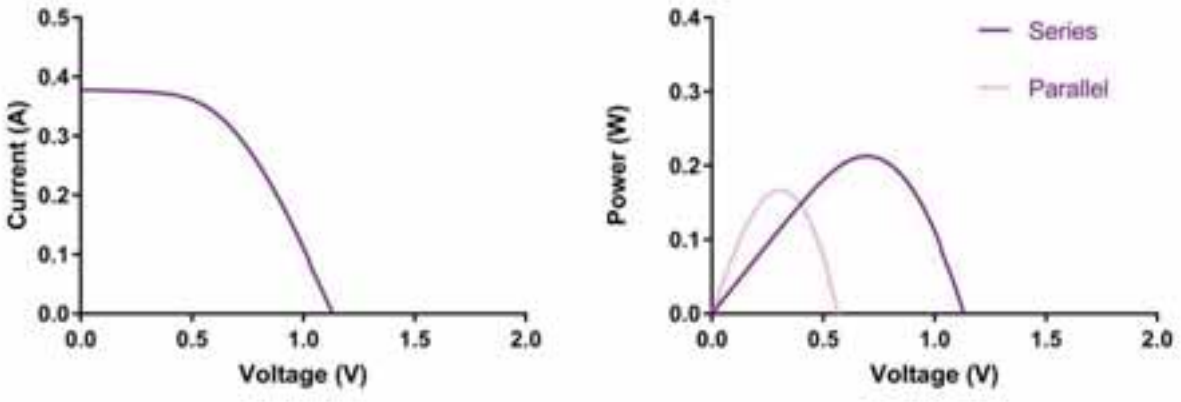

Fig. 12: I-V curve showing top and bottom output connected in series (left), P-V curve comparing top and bottom connected in series and in parallel (right)

3.5 Results – instantaneous thermal efficiency

The thermal performance of the collector was determined by obtaining values of instantaneous efficiency for combination of measured incident radiation, inlet/outlet temperatures and flow rate in a steady or quasi steady state. The useful power extracted is determined by eq. 3 and the thermal efficiency as a function of fluid inlet temperature is shown in Fig. 13. An uncertainty analysis was completed and the reason for the large error bars is due to the small ΔT across a single tube. While each RTD that measures inlet and outlet temperature has an uncertainty of +/- 0.082 ˚C when uncertainties are propagated due to taking a difference between the two measurements the uncertainty of ΔT becomes +/- 0.117 ˚C. Due to the high viscosity of the thermal fluid employed during the tests, a high flow rate had to be set in the experimental rig to assure turbulent flow and enhance heat transfer. This high flow rate decreases proportionally ΔT as shown in eq 2. In future work, a different heat transfer fluid which allows operating at lower flow rates or a longer receiver may be considered to increase the temperature at the outlet and minimise uncertainties in the measurements.

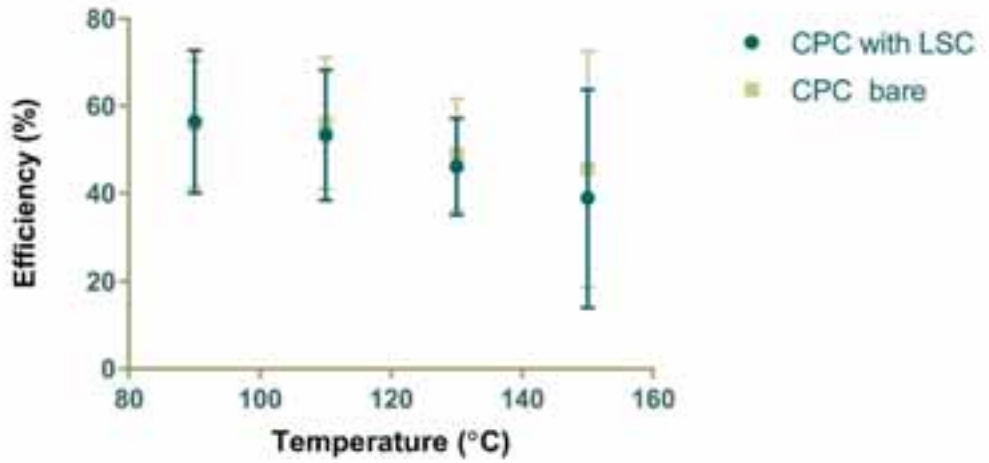

Fig. 3: Instantaneous thermal efficiency measured at different inlet temperatures

4. Conclusion

We successfully demonstrated the experimental basis for a new type of hybrid photovoltaic and thermal concentrator based on two non-imaging technologies, the CPC and the LSC. As a solar thermal collector requires a cover we have demonstrated a new type that generates electricity with LSCs. Utilising commercially available large area fluorescent sheets we demonstrated experimentally with a small prototype that a photovoltaic-thermal collector can work well when an LSC is used as a cover for a CPC. A small 10 cm x 15 cm prototype was stagnated in indoor test conditions and found to reach temperatures of up to 208 ˚C without an LSC and 191˚C with an LSC with a high transmission. In this configuration a small amount of thermal energy is sacrificed for a modest gain in electricity generation. Outdoor testing was completed on a full-length CPC and LSC hybrid collector with four LSC modules. It was found that less losses occurred (noticed by a much better fill factor) when the two sides of cells were connected in series, producing over 220 mW compared to parallel. I-V measurements were taken again after several hours of operation and it was found the performance of the LSCs did not decrease. This was most likely due to the experiment being run during cold days when ambient temperature was around 10-12 ˚C. The thermal efficiency was measured for a variety of temperatures and varied between 55 % and 40 % but with a high uncertainty. We demonstrated an LSC works well as a cover for a solar thermal receiver, although only generating modest amounts of power. The near future holds exciting possibilities of precisely engineering optical properties of LSCs. Perhaps one day we will be able to fabricate LSCs bottom up, molecule by molecule similar to 3D printing and once materials breakthroughs occur and LSCs can be engineering with tightly controlled optical properties, allowing for better performance of this type of PV-T collector.

5. References

Brunold, S., Frey, R., Frei, U., 1994. Comparison of three different collectors for process heat applications. SPIE 2255, Opt. Mater. Technol. Energy Effic. Sol. Energy Convers. XIII 2255, 107–118. doi:10.1117/12.185361

Carvalho, M.J., Collares-Pereira, M., Oliveira, J.C. De, Mendes, J.F., Haberle, A., Wittier, V., 1995. Optical and thermal testing of a new 1.2X CPC solar collector. Sol. Energy Mater. Sol. Cells 37, 175–190.

Debije, M.G., Verbunt, P.P.C., 2012. Thirty Years of Luminescent Solar Concentrator Research: Solar Energy for the Built Environment. Adv. Energy Mater. 2, 12–35. doi:10.1002/aenm.201100554

Evonik Industries [WWW Document], 2017. URL https://www.plexiglas-shop.cn/CN/en/category.htm?$category=9qlreq6bvlw (accessed 10.13.17).

Gajic, M., Lisi, F., Kirkwood, N., Smith, T.A., Mulvaney, P., Rosengarten, G., 2017. Circular luminescent solar concentrators. Sol. Energy 150, 30–37. doi:10.1016/j.solener.2017.04.034

Gallagher, J.. ., Winston, R., Duff, W.., 1993. Non imaging integrated evacuated solar collector. Int. Symp. Opt. Imaging, Instrum. 2016, 128–136.

Gu, X., Taylor, R.A., Morrison, G., Rosengarten, G., 2014. Theoretical analysis of a novel, portable, CPC-based solar thermal collector for methanol reforming. Appl. Energy 119, 467–475. doi:10.1016/j.apenergy.2014.01.033

Herrick, C.S., 1982. Optical transmittance measurements on a solar collector cover of cylindrical glass tubes. Sol. Energy 28, 5–11.

Hinterberger, H., 1966. Efficient Light Coupler for Threshold Cherenkov Counters. Rev. Sci. Instrum. 37, 1094. doi:10.1063/1.1720428

Kanellis, M., de Jong, M.M., Slooff, L., Debije, M.G., 2017. The solar noise barrier project: 1. Effect of incident light orientation on the performance of a large-scale luminescent solar concentrator noise barrier. Renew. Energy 103, 4–9. doi:10.1016/j.renene.2016.10.078

Karwa, N., Jiang, L., Winston, R., Rosengarten, G., 2015. Receiver shape optimization for maximizing medium temperature CPC collector efficiency. Sol. Energy 122, 529–546. doi:10.1016/j.solener.2015.08.039

Rabl, A., Winston, R., 1976. Ideal concentrators for finite sources and restricted exit angles. Appl. Opt. 15, 2880–3.

Rajkumar, V. a., Weijers, C., Debije, M.G., 2015. Distribution of absorbed heat in luminescent solar concentrator lightguides and effect on temperatures of mounted photovoltaic cells. Renew. Energy 80, 308–315. doi:10.1016/j.renene.2015.02.003

Ramos, A., Chatzopoulou, M.A., Guarracino, I., Freeman, J., Markides, C.N., 2017. Hybrid photovoltaic-thermal solar systems for combined heating, cooling and power provision in the urban environment. Energy Convers. Manag. doi:10.1016/j.enconman.2017.03.024

Slooff, L.H., Bende, E.E., Burgers, a. R., Budel, T., Pravettoni, M., Kenny, R.P., Dunlop, E.D., Büchtemann, A., 2008. A luminescent solar concentrator with 7.1% power conversion efficiency. Phys. status solidi - Rapid Res. Lett. 2, 257–259. doi:10.1002/pssr.200802186

Smestad, G., Ries, H., Winston, R., Yablonovitch, E., 1990. The thermodynamic limits of light concentrators. Sol. Energy Mater. 21, 99–111. doi:10.1016/0165-1633(90)90047-5

Winston, R., 1970. Light Collection within the Framework of Geometrical Optics. J. Opt. Soc. Am. 60, 245–247.

Winston, R., Wang, C., Zhang, W., 2009. Beating the optical Liouville theorem: How does geometrical optics know the second law of thermodynamics? Opt. Express 20, A622–A629. doi:10.1117/12.836029

Winston, R., Welford, W.T., 1978. Two-dimensional concentrators for inhomogeneous media. J. Opt. Soc. Am. 68, 289. doi:10.1364/JOSA.68.000289

Zhang, Z., Zhao, P., Lin, P., Sun, F., 2006. Thermo-optic coefficients of polymers for optical waveguide applications. Polymer (Guildf). 47, 4893–4896. doi:10.1016/j.polymer.2006.05.035

Aerial thermographic inspection of photovoltaic plants: analysis and selection of the equipment

Sara Gallardo-Saavedra[1], Estefanía Alfaro-Mejia[2] Luis Hernández-Callejo[1], Óscar Duque-Pérez[3], Humberto Loaiza-Correa[2] and Edinson Franco-Mejia[2]

[1] Universidad de Valladolid (UVa), School of Forestry, Agronomic and Bioenergy Industry Engineering (EIFAB), Department of Agricultural and Forestry Engineering, Soria (Spain)

[2] Universidad del Valle, Escuela de Ingeniería Eléctrica y Electrónica, Santiago de Cali (Colombia)

[3] Universidad de Valladolid (UVa), Industrial Engineering School, Department of Electrical Engineering, Valladolid (Spain)

Abstract

In recent times, more and more countries are choosing the alternative of generating clean energy. The photovoltaic (PV) energy installed is rapidly increasing around the World. PV cells are made with semiconductor materials such as Si, GaAs, among others. Despite the quality controls in the manufacture and manipulation of the panels, damages occur during their manufacturing, installation, use or of wear due to environmental factors, doing it necessary a periodic review. Manual inspections become expensive and largely inefficient due to the big extensions of PV plants. For this reason, it is necessary to automate the inspection task. This paper presents a methodology for the selection of equipment used to make inspections of faults in solar panels using aerial thermography, based on the review of the state of the art and the latest equipment technology available.

Keywords: Aerial thermography, photovoltaic inspection, photovoltaic thermography, faults diagnosis

1. Introduction

Renewable energies are an adequate answer to the actual problems of energy deficit. The negative effects caused by fossil fuels are disheartening due to their harmful impact on climate change, marine and terrestrial ecosystems. The impact generated is so big that there have been appreciable increases in the expected extinction rates.

Nowadays, more countries are choosing the alternative of generating clean energy. An example of this is Portugal, which used solar, wind and hydroelectric energy during four days, supplying the entire country network using natural sources of energy generating zero carbon emissions.

It is therefore necessary to be aware of the current environmental situation by promoting the use of clean energy. Solar radiation is a renewable source harnessed from photovoltaic cells, which are made with semiconductor materials such as Si, GaAs, among others. Despite the quality controls in the manufacture and manipulation of the panels, damages occur during their installation, their use or of wear due to environmental factors. The environmental exposure is one of the factors that most contributes to the underproduction of the modules. Optical degradation is a common effect produced as a consequence of a prolonged sun exposure, generating a discolored appearance and favoring the increment of temperature and humidity in the module. This affects electrical characteristics of the module and produces electrical mismatches which can lead to fractured cells that generate remarkable power losses (Tsanakas et al., 2016), doing it necessary a periodic review.

Also, due to the big extensions that modules cover, manual inspections become expensive and largely inefficient as a result of the capture conditions such as solar angle, irradiance levels, among other factors, which must be taken into account. For this reason, it is necessary to automate the inspection task. An alternative technique often used today, is to perform a photogrammetric flight with Unmanned Aerial Vehicles (UAVs), considering parameters such as the area covered by each photograph, separation between flight lines, among others.

doi:10.18086/swc.2017.20.03 Available at http://proceedings.ises.org

The inspection of solar panels using aerial thermography with UAVs is a topical issue. During the years 2015, 2016 and 2017 it has had 6, 9 and 13 publications respectively in high impact magazines, which confirms that aerial thermography is a very active area of research at the present time.

Different methodologies have been explored for the detection of faults in solar panels, some of them are: the analysis of electrical measurements to classify abnormal behavior in the characteristic curve IV, infrared thermography (IRT) and electroluminescence (El). The first alternative can be impractical and costly since it requires that each module must be monitored. Alternatively, IRT and EL allow non-invasive quantification of the damage presented by the photovoltaic module.

The main objective of this paper is to study the equipment that has been used in the researched presented up to now, with the objective of proposing a methodology for the selection of equipment for fault detection with thermography applied to photovoltaic plants and considering the requirements for the protocol of image capture. To achieve that goal, a comprehensive review of the equipment used for fault inspection in solar panels using thermography is accomplished and a methodology for the selection of equipment is proposed, highlighting relevant aspects in thermographic cameras and UAVs.

2. Method

The applied methodology used to fulfil the objectives of this paper has been the research on the necessities and aspects involved in thermographic inspections of PV plants, the key characteristic of sensors and platforms and the current technologies available in the market. The results have been obtained by means of reviewing the current literature in relation with this topic; investigating the available technology in the market contacting manufacturers and distributors of this instrumentation and by the internet and collecting information about the most important aspects with the aid of professional operators. More than thirty different parties have been contacted, from which relevant information and key points have been obtained.

3. Results and discussion

Nowadays, 80% of the energy produced worldwide is produced from fossil fuels, generating therefore a negative impact on the environment and increasing the CO_2 emissions and increasing the global warming. Consequently, it is necessary to change to renewable alternatives that replace non-renewable energy sources. A clean alternative is the solar energy, which is produced from photovoltaic modules manufactured with GaAs and monocrystalline and polycrystalline Si, being more efficient in the monocrystalline configuration. Each kW produced by photovoltaic systems reduces 0.6 kg the CO_2 emissions (Elibol et al., 2017).

Photovoltaic modules present faults throughout different stages, being the environmental exposure the one that most contributes to the underproduction of the modules. Optical degradation is a common effect produced as a consequence of a prolonged sun exposure, generating a discolored appearance and favoring the increment of the modules temperature and humidity. This affects electrical characteristics of modules and produces electrical mismatches which can lead to fractured cells, generating remarkable power losses (Tsanakas et al., 2016).

Different methodologies have been explored for the detection of faults in solar panels, some of them are: the analysis of electrical measurements to classify abnormal behavior in the characteristic curve IV, IRT and El. The first alternative can be impractical and costly since it requires that each module must be monitored. Alternatively, IRT and EL allow non-invasive quantification of the damage presented by the photovoltaic module, measuring the temperature difference that the faulty modules present. Due to the large area that current photovoltaic sites take up, an adequate way to carry out the inspection is using UAV, where the photogrammetric routes are plotted, considering times to cover the total area and the amount of frames per second or overlap of images

The research on this topic has had an important impact since the year 2015, when the use of UAVs and portable thermographic cameras in aerial vehicles was integrated to the inspection and diagnosis of photovoltaic modules. This impact can be shown in Fig. 1 which has been obtained by examining the bibliography Scopus database for the last years, using the following search equation: PV AND UAV AND THERMOGRAPHY AND PUBYEAR > 2014 AND PUBYEAR < 2018 AND (LIMIT-TO (PUBYEAR,2017) OR LIMIT-TO (PUBYEAR,2016) OR LIMIT-TO (PUBYEAR,2015)). This figure represents the high impact of this topic, in

which the number of published articles has increased from 6 articles in 2015, to 9 in 2016 and 12 articles so far this year. The research centers and universities that lead this research at to now are: Universia degli Studi di Napoli Federico II, Politecnico di Milano, Korea Institute of Civil Engineering and Building Technology.

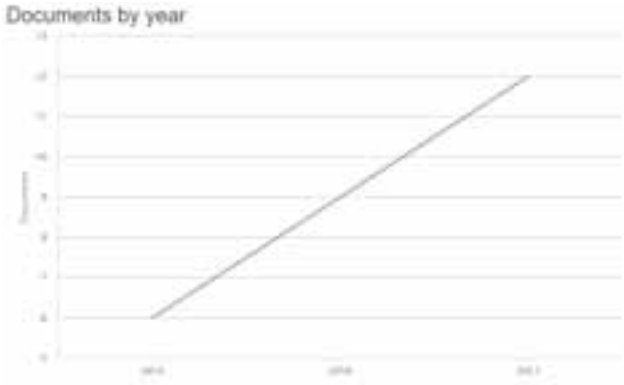

Fig. 1 EB1 impact of the theme between 2015-2017

The results obtained regarding the characteristics of the instrumentation used in the research reported so far are presented throughout the following paragraphs. Different offline processing techniques are introduced and analyzed.

There are different manufacturers which offer alternatives for the inspection and diagnosis of defects in PV plants. One example of this is the manufacturer Workswell, which proposes the use of its thermographic cameras in different applications, as the building diagnosis, roofs and high voltage lines inspections. This manufacturer has developed high spectral range thermographic cameras that combine the thermographic and visual images, as they incorporate a RGB camera. Additionally, there are some tier one brands which are starting to offer ready-to-flight products for the inspection of PV plants, as for example DJI and Workswell. These brands offer the possibility of using a DJI S900 with a Workswell thermographic camera and the software Workswell CorePlayer for the image post-processing. This software has different functionalities, as modifying the emissivity or the reflection temperature values, obtaining thermal curves, geometrical delimitation of relevant areas using dots or rectangles or generating reports. The equipment reported in (Wiris, n.d.) is summarized in Tab. 1.

Tab. 1: UAV and Thermographic camera characteristics reported in (Wiris, n.d.)

UAV	**Characteristics**		**Thermographic camera**	**Characteristics**	
DJI S900	**Flight controller**	A2	Worskswell Wiris (integrated RGB camera)	**Resolution (pixels)**	640x512 - 336x256
	Total Weight (kg)	3,3		**Temperature sensitivity (mK)**	50 to 30
	Power Battery	LiPo (6s 10000 mAh)		**Spectral range (um)**	7,5 to 13
	Max Power consumption (W)	3000		**Weight (g)**	<400
	Hover time (min)	18		**Memory**	32 GB
	Hover environment temperature (°C)	-10 to 40		**Temperature ranges (°C)**	25 to 150
	Takeoff Weight (kg)	4,7-8,2		**Accuracy**	+-2% or +- 2 °C
	Dimensions (mm)	460x450x360		**IR Color Palettes**	19 interchangeable in real time
	Type	Hexacopter		**Emissivity**	Adjustable

The main equipment used in (Addabbo et al., 2017) is an UAV Matrice 100 of DJI and a thermographic camera Flir Tau 2. Their main characteristics are summarized in Tab. 2. Additionally, it is used a RGB DJI Zenmuse X3 camera to obtain visual images. In this research, the UAV performs a defined flight plan over the modules to capture the thermographic and visual images separately.

Tab. 2: UAV and Thermographic camera characteristics reported in (Addabbo et al., 2017)

UAV	Characteristics		Thermographic camera	Characteristics	
DJI Matrice 100	**Flight controller**	N1	Flir Tau 2	**Resolution (pixels)**	640x512 - 336x256
	Total Weight (kg)	2,3		**Temperature sensitivity (mK)**	50 to 30
	Power Battery	LiPo (6s 10000 mAh)		**Spectral range (um)**	7,5 to 13
	Max Power consumption (W)	3000		**Weight (g)**	112
	Hover time (min)	18		**Memory**	32 GB
	Hover environment temperature (°C)	-10 to 40		**Temperature ranges (°C)**	-25 to -135, -25 to -100
	Takeoff Weight (kg)	3,6		**Accuracy**	+-5% or +- 5 °C
	Dimensions (mm)	650		**IR Color Palettes**	15 interchangeable in real time
	Type	Quadcopter		**Emissivity**	Adjustable

The data taken by the optical RGB sensor is communicated through one of the drone buses with the embedded system equipped on board the UAV, called the Intel Joule 570X quad-core, where some processes are carried out, such as management of sensor acquisition, the storage of the acquired images and the detection algorithm, in which a task of labeling and identification of the panels is executed. The input data for the tracking and geo referencing algorithms require altitude data and GPS, which are extracted from the DJI on board SDK. The SDK can be modified using programming languages such as C or C ++.

For the definition of the thermographic images capturing protocol, a video/C&C port (GPIO) of the drone is used. This port is connected with the embedded system Joule 570X, which allows the control of the Gimbal by a serial port. Subsequently, the processing of the thermographic images is done offline.

In (Kauppinen et al., 2015) it is used a quadcopter Walkera QR X800 a thermographic camera Flir Tau 2 and a RGB camera GoPro Hero 3. As embedded system it is used a Raspberry Pi on board, which is connected with the terrestrial station through WLAN connection.

In order to perform the image acquisition protocol, they consider the meteorological conditions, such as measurements of air temperature, relative humidity using a Vaisala HM34C sensor and irradiance levels on the photovoltaic system with the Ophir PD-300-3W sensor.

The captures of the thermal images are obtained by operating the UAV manually, monitoring the live image from the terrestrial web browser and taking the images, only when they have the right scene. In this way it is eliminated the possibility that the UAV shadow projection interferes with the measurement. The images are stored in the memory of the Flir Tau 2 camera. On the other hand, the acquisition of RGB images is done automatically using the APM flight controller planner2. The resultant images are stored in the Raspberry Pi. In addition, in this research it is performed manual inspection of the site with a FLIR E300 thermal camera.

Tab. 3: UAV and Thermographic camera characteristics reported in (Kauppinen et al., 2015)

UAV	Characteristics		Thermographic camera	Characteristics	
Walkera QR X800	**Flight controller**	Walkera FCS800	Flir Tau 2	**Resolution (pixels)**	640x512 - 336x256
	Total Weight (kg)	3,9		**Temperature sensitivity (mK)**	50 to 30
	Power Battery	LiPo (6s 10000 mAh)		**Spectral range (um)**	7,5 to 13
	Max Power consumption (W)	-		**Weight (g)**	112g
	Hover time (min)	40		**Memory**	32 GB
	Hover environment temperature (°C)	-15 to 65		**Temperature ranges (°C)**	-25 to 135°C, -25 to-100
	Takeoff Weight (kg)	3		**Accuracy**	+-5% or +-5 °C
	Dimensions (mm)	620x620x460		**IR Color Palettes**	15interchangeable in real time
	Type	Quadcopter		**Emissivity**	Adjustable

In (Aghaei et al., 2015) it is used a UAV PLP-610 Nimbus Platform and a Flir A35 thermographic camera, which main features are summarized in Tab. 4. Some of the most relevant issues to be considered while performing a flight plan and capturing the images are described in the paper, as reflections or shadows produced by the surrounded vegetation, clouds, other module structures or by the own drone. The geo referencing data is not considered in this study.

The thermographic image processing is done offline using Matlab. The flow diagram of the algorithm goes from the conversion of the IR image to RGB, later to grayscale to perform a Gaussian type filtering. To the resultant image is applied Laplace algorithm and a diagnosis is issued. If the panel is healthy, the post processing is finished, otherwise, in case of detecting a defect in the module, it is established the degradation percentage of the photovoltaic module.

Tab. 4: UAV and Thermographic camera characteristics reported in (Aghaei et al., 2015)

UAV	Characteristics		Thermographic camera	Characteristics	
PLP 610 Nimbus Plataform	**Cruise Speed (kts)**	0-20	Flir A35	**Resolution (pixels)**	320x256
	Operational range (km)	0.25		**Temperature sensitivity (mK)**	50 to 30
	Max Altitude (m)	150		**Spectral range (um)**	7,5 to 13
	Hover time (min)	25		**Weight (g)**	112g
	Weight (kg)	2,8		**Memory**	32 GB
	Dimensions (mm)	300x980		**IR Color Palettes**	15interchangeable in real time
	Type	Hexacopter		**Emissivity**	Adjustable

In (Tsanakas et al., 2017) it is used a hexacopter Condor AY-704 with an Optris PI450 on board and a conventional Single Les Reflex (SLR) connected to the UAV. The embedded system is not described in the paper. The image capturing conditions complied with IEC 62446-3 TS first edition standard in relation with the minimum irradiance, soft clouds and maximum wind speed. The resultant images are represented in an

interactive map without connection, similar to Google Earth. The fault processing algorithm is implemented on the ortomosaic in Matlab. Additionally, when an anomaly is found in the image, a manual inspection and I-V electrical characterization curve are performed on site, as validation of results.

Tab. 5: UAV and Thermographic camera characteristics reported in (Tsanakas et al., 2017)

UAV	Characteristics		Thermographic camera	Characteristics	
Condor AY 704	**Flight controller**	-	Optris PI450+lightweight mini PC	**Resolution (pixels)**	382x288
	Total Weight (kg)	-		**Temperature sensitivity (mK)**	50 to 30
	Power Battery	LiPo (6800 mAh)		**Spectral range (um)**	7,5 to 13
	Max Power consumption (W)	-		**Weight (g)**	380
	Hover time (min)	20		**Memory**	32 GB
	Hover environment temperature (°C)	-10 to 50		**Temperature ranges (°C)**	-25 to 135, -25 to 100
	Takeoff Weight (kg)	-		**Accuracy**	+-2% or +- 2 °C
	Dimensions (mm)	1,7		**IR Color Palettes**	15 interchangeable in real time
	Type	Hexacopter		**Emissivity**	Adjustable

In (Zhang et al., 2017) it is used an octocopter DJI Spreading Wings S100 with a Flir Tau 2 on board. Additionally, it includes an image storage module that allows saving image and positioning data at the same time. The image acquisition is performed with flight speed of 2 m/s and flight height of 20 and 40 meters with respect to the module. The image capture schedule corresponds to the time period between 10:00 am and 12:00 pm, corresponding with the maximum irradiance. Image processing is offline; the flowchart of the algorithm developed includes a preprocessing stage, recognition of each individual module and detection of the anomaly.

Tab. 6: UAV and Thermographic camera characteristics reported in (Zhang et al., 2017)

UAV	Characteristics		Thermographic camera	Characteristics	
DJI S1000	**Flight controller**	A2	Flir Tau 2	**Resolution (pixels)**	640x512 - 336x256
	Total Weight (kg)	4,2		**Temperature sensitivity (mK)**	50 to 30
	Power Battery	LiPo (6s 10000 mAh, to 20000 mAh)		**Spectral range (um)**	7,5 to 13
	Max Power consumption (W)	4000		**Weight (g)**	112g
	Hover time (min)	15		**Memory**	32 GB
	Hover environment temperature (°C)	-10 to 40		**Temperature ranges (°C)**	-25 to 135°C, -25 to-100
	Takeoff Weight (kg)	6,0 to 11		**Accuracy**	+-5% or +-5 °C
	Dimensions (mm)	460x511x305		**IR Color Palettes**	15interchangeable in real time
	Type	Octocopter		**Emissivity**	Adjustable

In (Dotenco et al., 2016) it is used a Da Vinci Scara Bot X8 with a thermographic camera Optris PI450 and a RGB GoPro Hero3+. The inspection was always performed with a minimum irradiance of 600W/m^2 and a maximum of 1000W/m^2.

The processing of the thermographic images is done by means of a segmentation that allows identifying the region of interest, in this case the photovoltaic modules, from the information that does not contribute to the analysis, as the background.

The implemented algorithm is described in four stages: normalization, thresholding, orientation of photovoltaic modules estimation and correction and refinement. The first stage proposed, corresponds to thermal contrast. This procedure allows dismissing temperature values below a defined threshold. In the following stages it is done the automatic selection of thresholds in order to separate the solar panels from the background, using combinations of Gaussian models (GMMs).

Subsequent to the segmentation stage, it is proposed the extraction of information obtained from the average temperature values of each solar module and its cells. Additionally, the asymmetry measures of the histograms are used to provide information about the distribution of the temperature in the picture

Tab. 7: UAV and Thermographic camera characteristics reported in (Dotenco et al., 2016)

UAV	Characteristics		Thermographic camera	Characteristics	
Da Vinci Copters ScaraBot X8	**Flight controller**	Pixhawk	Optris PI450	**Resolution (pixels)**	382x288
	Total Weight (kg)	2,15		**Temperature sensitivity (mK)**	50 to 30
	Power Battery	6S Li-ion 15Ah		**Spectral range (um)**	7,5 to 13
	Max Power consumption (W)	4000		**Weight (g)**	380
	Hover time (min) payload 2400g	24		**Memory**	32 GB
	Hover environment temperature (°C)	-10 to 40		**Temperature ranges (°C)**	-25 to 135, -25 to 100
	Takeoff Weight (kg)	5.0		**Accuracy**	+-2% or +- 2 °C
	Dimensions (mm)	545x545x402		**IR Color Palettes**	15interchangeable in real time
	Type	Octocopter		**Emissivity**	Adjustable

In (Leva et al., 2015) it is used an UAV Nimbus PLP-610, as in (Aghaei et al., 2015), with a visible spectrum camera Nikon 1-v1.

In the article, it is developed a protocol for the acquisition of the images, which describes the characteristics and conditions of flight as altitude, and angles of capture, to detect faults and defects on the photovoltaic modules using only an RGB camera. The obtained results, allow establishing the relations on the flight height at which the acquisition of the images is done and the type of faults detected. The paper does not have a diagnosis that identifies the severity of the faults as they do not use thermographic images.

In order to properly evaluating the features of the instrumentation required in aerial thermography of PV plants it is necessary to consider some relevant aspects about the image capturing conditions that are analyzed throughout this paragraphs. These capturing conditions restrict the platform and sensors characteristics that can be used to obtain usable results. According to the review of the state of the art some of the most relevant characteristics for the selection of cameras correspond to the following items: resolution, ranges of temperature, sensitivity, precision, spectral range, calibration, memory, file transfer, interface, video resolution, weight, FOV, spatial resolution.

Tab. 8: UAV and Thermographic camera characteristics reported in (Leva et al., 2015)

UAV	Characteristics		Thermographic camera	Characteristics	
PLP 610 Nimbus Plataform	**Cruise Speed (kts)**	0-20	Flir A35	**Resolution (pixels)**	3906x2606
	Operational range (km)	0.25		**Dimensions (m)**	113x76x43.5
	Max Altitude (m)	150		**Lens focal length (mm)**	35
	Hover time (min)	25		**Weight (g)**	294g
	Weight (kg)	2,8		**Battery**	Nikon EN-El 15 Lithium-Ion
	Dimensions (mm)	300x980			
	Type	Hexacopter			

In order to obtain accurate and usable images, the camera should be on-board of a stable gimbal and the platform should be able to hover for obtaining detailed information. In this regard, the most appropriate platform to perform aerial thermography for PV plants inspections are the multirotor, also known as multirotor. There are different multirotor kinds generally classified in terms of the number of rotors that the UAVs have.

Additionally, the platform should have the capacity of carrying at least two different sensors, the thermographic and the visual camera. A visual image along with a thermographic image facilitates the identification of the defect mode, the detection of false hot spots, as bird drops or shadows and makes it easy to determine the exact location of the defect module in the PV plant.

Nowadays multirotor allow the autonomous operation mode by waypoints, which is a desirable option to avoid human errors that can be produced during the manual flight. In this case, it is necessary to have cartographic information of the site and if not, performing a flight previously to the inspection to feed the platform software.

The UAV batteries should be as long as possible to maximize the producing time and to optimize the inspection performance. There are different batteries options and several researches are being done in this respect during the last years. UAVs with Lithium Polymer (Li-Po) batteries can fly approximately from 10 to 40 minutes. A battery recharge cycle takes one hour and a half approximately. In order to perform an efficient inspection, it is convenient to have various batteries not to be recharging them during the inspection. There are several researches on innovative batteries that offer a greater energy density and reduce charge time, weight and volume, as graphene batteries.

The flight height of the UAV delimits the resolution that the sensors must have so as to acquire acceptable results. If the pixel size is higher than the cell size, the accuracy of the resultant images is not acceptable as smaller defect will not be properly identified. Therefore, the flight height restrings the sensor resolution required, considering also the lens used and the consequent field of view.

4. Conclusions

Although some authors mention the equipment used in their researches there is not a convenient study which compiles other available alternatives that meet the requisites established and their most relevant characteristics.

A procedure to indicate a review of the available equipment used in aerial inspection of photovoltaic plants was presented, in order to determinate and to analyze the key aspects that have to be considered to properly select the equipment to be used. The results are obtained by means of the examination all the information in relation to the characteristics of the instrumentation involved and the compilation of the UAVs and thermographic sensors alternatives with their available characteristics.

The necessary equipment consists mainly of a thermographic camera and an Unmanned Aerial Vehicle. In the case of UAVs, full compatibility with the camera must be guaranteed and factors such as maximum operating

temperature, flight controller, and flight autonomy are necessary characteristics for the selection of the equipment. According to the review of the state of the art, some of the most relevant characteristics for the selection of cameras correspond to the following items: resolution, ranges of temperature, sensitivity, precision, spectral range, calibration, memory, file transfer, interface, video resolution, weight, FOV, spatial resolution. These respects have been analyzed with the aim of informing about the essential aspects to consider while selecting the equipment for this application and of facilitating this selection to researchers. It is important to understand that the utility of the equipment is in many cases directly linked to the available budget, as the improvement of the features is usually associated with a notable increase in the price.

5. Bibliography

Addabbo, P., Angrisano, A., Bernardi, M. L., Gagliarde, G., Mennella, A., Nisi, M., Ullo, S., 2017. A UAV infrared measurement approach for defect detection in photovoltaic plants. IEEE International Workshop on Metrology for AeroSpace 2017 (MetroAeroSpace). 345–350.

Aghaei, M., Gandelli, A., Grimaccia, F., Leva, S., Zich, R. E., 2015. IR real-time analyses for PV system monitoring by digital image processing techniques. International Conference on Event-based Control, Communication, and Signal Processing 2015 (EBCCSP). 1–6.

Dotenco, S., Dalsass, M., Winkler, L., Wurzner, T., Brabec, C., Maier, A., Gallwitz, F., 2016. Automatic detection and analysis of photovoltaic modules in aerial infrared imagery. IEEE Winter Conference on Applications of Computer Vision (WACV). 1–9.

Elibol, E., Tüzün Özmen, Ö., Tutkun, N., Köysal, O., 2017. Outdoor performance analysis of different PV panel types. Renewable and Sustainable Energy Reviews. 67, 651–661.

Kauppinen, T., Panouillot, P.-E., Siikanen, S., Athanasakou, E., Baltas, P., Nikopoulos, B., 2015. About infrared scanning of photovoltaic solar plant. THERMOSENSE: THERMAL INFRARED APPLICATIONS XXXVII. 9485, 948517 1-14.

Leva, S., Aghaei, M., Grimaccia, F., 2015. PV power plant inspection by UAS: Correlation between altitude and detection of defects on PV modules. IEEE 15th International Conference on Environment and Electrical Engineering, EEEIC 2015. 1921–1926.

Tsanakas, J. A., Ha, L., Buerhop, C., 2016. Faults and infrared thermographic diagnosis in operating c-Si photovoltaic modules: A review of research and future challenges. Renewable and Sustainable Energy Reviews. 62, 695–709.

Tsanakas, J. A., Ha, L. D., Shakarchi, F. Al., 2017. Advanced inspection of photovoltaic installations by aerial triangulation and terrestrial georeferencing of thermal/visual imagery. Renewable Energy. 102, 224–233.

Wiris, W. (n.d.). Thermo diagnosis of photovoltaic power plants. Retrieved October 2, 2017, from https://www.drone-thermal-camera.com/wp-content/uploads/Workswell-WIRIS_photovoltaic.pdf

Zhang, P., Zhang, L., Wu, T., Zhang, H., Sun, X., 2017. Detection and location of fouling on photovoltaic panels using a drone- mounted infrared thermography system. Applied Remote Sensing, 11(1), 016026 1-11.

Failure rate determination and Failure Mode, Effect and Criticality Analysis (FMECA) based on historical data for photovoltaic plants

Sara Gallardo-Saavedra[1,2], Javier Pérez-Moreno[2], Luis Hernández-Callejo[1] and Óscar Duque-Pérez[3]

[1] Universidad de Valladolid (UVa), School of Forestry, Agronomic and Bioenergy Industry Engineering (EIFAB), Department of Agricultural and Forestry Engineering, Soria (Spain)

[2] Solarig, Soria (Spain)

[3] Universidad de Valladolid (UVa), Industrial Engineering School, Department of Electrical Engineering, Valladolid (Spain)

Abstract

It is essential for photovoltaic plants investors, operators and equipment manufacturers to identify the failure modes and rates of the system in order to reduce investment risk, to focus their maintenance efforts on preventing those failures and to improve longevity and performance of the PV Plant. In this paper, it is assessed the importance of the Failure Modes within a real existing portfolio in Spain and Italy of continuous operation since 2008 and it is identified the module level failure modes, which are imperceptible in the standard monitoring systems, through the application of thermographic inspection. The experimental Mean Time Between Failures (MTBF) and the failure rates are calculated and these ratios are used to define the ranking criterion to perform the Failure Mode, Effect and Criticality Analysis (FMECA) and to focus on the module level analysis. The conclusions highlight the most critical sub-system and failure modes within a photovoltaic PV plant.

Keywords: Failure Rate, FMECA, Photovoltaic reliability, PV Module Thermography

1. Introduction

It is essential for photovoltaic (PV) plants investors, operators and equipment manufacturers to identify the failure modes and rates that the main equipment experiences in order to reduce investment risk, to focus their maintenance efforts on preventing those failures and to improve longevity and performance of the PV Plant. The reliability is defined as the capacity of a component to maintain its functionality over the years.

The Failure Mode, Effects and Criticality Analysis (FMECA) is an inductive analytical method in which the results present the failure modes and the severity of the consequences with relatively high probability. The main objective is to identify the failure modes that have a relevant combined occurrence, severity and non-detection probability in order to set the preventive actions accordingly. Equipment manufacturers try to identify all the failure modes of its products in order to increase reliability and reduce warranty cost, by researching and emulating different situations using mathematical models and experimental Highly Accelerated Life Test (HALT) (Moorthy and Tamizhmani, 2016). Resulting from the analysis, a battery of measures is implemented to reduce the key factors occurrence, severity or non-detection probability. The FMECA is a broadly used technique to assess the quality being applied on the elaboration and/or definition of, for example, safety analysis, quality control points, high standard requirements, quality procedures, working instructions, or resources distribution (Colli, 2015). The failure mode analysis also justifies the importance of maintenance activities and the associated cost on PV Plants to prevent premature failure and relevant catastrophic problems.

The greater challenge that researchers address and indicate while investigating about PV systems failures is the lack of reliable real quantitative data since most of the operators are private and do not disclose the data

doi:10.18086/swc.2017.20.04 Available at http://proceedings.ises.org

or either they do not have enough capabilities to record the data (Colli, 2012).The existing publications base their studies on the few available open-access data and subjective evaluations from experts' opinions with limited experimental and scientific base. Through the implementation of advanced PV plant monitoring systems (Cristaldi et al., 2015), the implementation of Computerized Maintenance Management Systems (CMMS) and the feedback of the field technicians, it is possible to have an experimental database to assess the failure rate and the FMECA of the PV plants (Colli, 2012).This fact is one of the greater strengths of this paper, in which the information from the historical data of fifty-eight PV plants portfolio in Italy and Spain of a well-known photovoltaic operator since 2008 has been accessible.

Monitoring of the different system components that constitute the PV plant facilitates the detection of failures and, from the reliability point of view, allows the operator to improve the plant performance (Cristaldi et al., 2015). Nevertheless, in utility scale PV plants, typically the monitoring system trails the string series current of multiple modules connected and does not track the performance of the individual PV modules, which is the key element on a photovoltaic system. Therefore, it is specially complicated the detection of failures at this level and, even more difficult, the recognition of the failure cause and mode. Because of this reason, during the last years additional tests have been required by solar PV investors at the PV module level with the aim of controlling the individual module performance, for example, IV curves tracing, electroluminescence test and thermographic test. To complete the FMECA analysis of this paper, it has been considered that other source of information is needed for the module level assessment. Aerial thermographic inspections, in which an Unmanned Aerial Vehicle (UAV) carries a thermographic sensor, are recently becoming popular because it reduces the inspection cost and it is less time consuming than manual thermographic inspections and/or IV curve tracing. Thermographic tests have been applied at a module level to a sample of the base data to complete the FMECA of the whole PV Plant.

The main objective of the paper is to assess the importance of the Failure Modes in PV plants considering the information taken within a real existing portfolio in Spain and Italy of continuous operation since 2008, and the application of thermographic inspection to identify the module level failure modes. This goal is achieved by means of calculating the experimental failure rates and the Mean Time Between Failures (MTBF) of the systems of a sample of PV plants during a relevant time using the historical database facilitated by Solarig, a worldwide PV operator. Based on the results, it will be applied the FMECA technique to the system elements. Once the different Failure Mode in the field are identified, the analysis is focused in the Module level related failures by cataloging the root cause analysis and the identification process through drone or manual thermographic inspection.

2. Method

In this section, it is summarized the different steps that have being followed to accomplish the analysis and to get the desired results.

The first step lies in identifying all the system components that can be affected and can produce a failure mode within the PV plant (Tab. 1).

In the current research, the PV system has been simplified in eight possible affected elements and for each of these elements, it has been identified the possible sub-element originating the failure. These elements are: PV generator, inverter, MV transformer station, meter, security systems, communication systems, monitoring systems and civil works.

After that, it has been analyzed all the available historical data and defined the sample that has been used for each of the calculations. These calculations are performed for different PV plants with the historical data available. With this selected data, the failure rates and the MTBF are calculated for the whole system and each sub-system. The failure rate is calculated as the number of failure per PV plant per unit year and the MTBF as the inverse of the failure rate.

These ratios are used to define the ranking criterion, to perform the FMECA analysis and to focus on the module level analysis. Finally, thermographic tests have been applied at a module level to complete the FMECA of the whole PV Plant. The results obtained throughout this analysis are presented in the results section.

Tab. 1: Affected elements and possible causes analyzed

Affected Element	Sub-element / Cause	Affected Element	Sub-element / Cause
Photovoltaic generator	Modules	Security System	Control Unit
	Cable		Cameras
	Fuse		Sensors
	Structure		Cabling
	Others		UPS
Inverter	Control Board		Others
	Communication Boards	Communications System	Router
	Protections		Satellite/LAN connect.
	Display		Others
	Power Block	Monitoring system	Control Unit
	Contactors		UPS
	Others		Fiber Optics/ Cabling
MV Transformer Station	Transformer		Others
	MV Switchgear	Civil works	Manhole
	Auxiliary System		Roads
	Others		Fence
Meter	Meter		Others
	Current /Voltage transformers		
	Others		

3. Results and discussion

The scoring system to define the ranking criterion has been defined considering the available data and the subjective evaluations of solar experts with more than a decade experience. Three different ranking criteria have been developed, for the severity, detection and occurrence respectively. Each ranking follows a scale from 1 to 5, in which 1 denotes the best situation while 5 denotes the worst. As a result, the Risk Priority Number (RPN) goes from 1 to 125, where a highest value of RPN indicates a most risky situation.

For the definition of the Severity ranking criteria, it has been considered the cost of fixing the failure (spare parts and workforce) and the Loss of Profit (LOP) that the failure generates due to the reduction of energy production (in case it is necessary to shut down the plant or part of it). The fixing price has been considered in an interval from 0 €, in case the failure does not involve a fixing cost or it is negligible, as a wire that is not well fastened, an equipment badly labelled or a communication failure due to the operator, to 60,000 € in case of an extremely high fixing cost, as the fixing cost resulting from a fire. On the other hand, the loss of profit that has been considered is the following: 0 € when the failure does not produce disconnection of the PV site, 190 € when the failure produces a disconnection of approximately 1 hour, 950 € in case of half a day disconnection, 13,300 € in case of one week disconnection and 57,000 € in case of one month disconnection. With the combination of these two factors, it is obtained the Severity ranking criteria, showed in Tab. 2 and Tab. 3.

Finally, the Occurrence ranking criteria has been calculated based on the failure rates obtained for each failure mode in the portfolio analyzed and following the subjective evaluation of this data by photovoltaic experts with more than ten years of experience in this sector. The Occurrence based on the failure rates calculated is classified following this criterion: 1 for unlikely failures, 2 for remote probability, 3 for occasional probability, 4 for moderate probability and 5 for high probability.

Tab. 2: Severity ranking intervals calculated from the fixing price and the loss of profit that a failure produces

		Loss of Profit (LOP)				
		57.000 €	**13.300 €**	**950 €**	**190 €**	**- €**
Fixing Price (Spares and Workforce)	**60.000 €**	117,000 €	73,300 €	60,950 €	60,190 €	60,000 €
	15.000 €	72,000 €	28,300 €	15,950 €	15,190 €	15,000 €
	1.000 €	58,000 €	14,300 €	1,950 €	1,190 €	1,000 €
	500 €	57,500 €	13,800 €	1,450 €	690 €	500 €
	- €	57,000 €	13,300 €	950 €	190 €	0 €

Tab. 3: Severity ranking criteria

Rank	**X (Fixing Cost + LOP)**	**Description**
1	X <690 €	Minor failure with almost no influence in the performance of the plant and insignificant parts deterioration
2	1,950 €>X>690 €	Failure with low influence in the performance of the plant and parts deterioration
3	28,300 €>X>1,950 €	Failure with quite important influence in the performance of the plant and parts deterioration
4	60,950 €>X> 28,300 €	Failure with important influence in the performance of the plant and parts deterioration
5	X >117,000 €	Major failure with extreme influence in the performance of the plant and parts deterioration

The Detection criteria has been obtained following (Colli, 2015), and it is expressed in Tab. 4.

Tab. 4: Detection ranking criteria

Rank	**Description**
1	Almost certain that the problem will be detected (chance 81–100%)
2	High probability that the problem will be detected (chance 61–80%)
3	Moderate probability that the problem will be detected (chance 41–60%)
4	Low probability that the problem will be detected (chance 21–40%)
5	None/minimal probability that the problem will be detected (chance 0–20%)

Throughout analyzing the corrective maintenance reports that the plant technicians of the analyzed portfolio have uploaded to the CMMS during the last years, it has been identified 168 failures modes that appears in the operation of PV plants. Considering the previous detailed ranking criteria, it has been attributed a Severity, non-Detection and Occurrence number to each of the failure modes detected. Multiplying these three numbers it is obtained a Risk Priority Number for each of the failures. An extract of some of the main failure modes detected in the analysis is detailed in Tab. 5.

Tab. 5: Failure mode analysis table with the Severity, Detection, Occurrence and Risk Priority Number for some of the main failure modes identified in the analyzed portfolio of PV plants

Group	Element	Description Failure	S	D	O	RPN
Security syst.	CCTV	Camera/videorecorder/barrier/Sensor failure	1	3	5	15
Security syst.	CCTV	Communications failure	1	1	5	5
Meters	Meters	Erroneous meter configuration	1	3	3	9
Meters	Meters	Meter burnt	2	2	3	12
Meters	Meters	Communications failure	1	1	4	4
Grid	Grid	Overvoltage	3	1	3	9
Grid	Grid	Overcurrent	3	1	3	9
Grid	Grid	Disconnection	4	1	3	12
Civil Work	Perimeter	Fence damaged	2	4	2	16
Civil Work	Roads	Road damaged	2	3	2	12
UPS	UPS	Damaged battery	1	4	4	16
PV modules	Modules	Junction box detached	1	3	2	6
PV modules	Modules	Module damaged: degraded, hot spot, yellowing, diode, connection.	2	5	2	20
PV modules	Structure	Galvanizing damaged	3	3	2	18
PV modules	Structure	Structure bent/rusted	3	2	2	12
PV modules	Structure	Structure not grounded	2	4	2	16
DC wiring	DC wiring	Cable damaged	2	4	2	16
DC wiring	DC wiring	Cable unfastened	1	4	4	16
Combiner box	Breakers	Circuit breaker broken	2	4	4	32
Combiner box	Cabinet	Cover damaged	1	3	4	12
Combiner box	Cabinet	Deficient ground connection	3	4	4	48
Combiner box	Communic.	Communications failure	1	1	5	5
Inverter	Inverter	High temperature	2	2	5	20
Inverter	Inverter	Display failure	2	2	3	12
Inverter	Inverter	IGBT failure	4	2	4	32
Inverter	Inverter	Communications lost	1	1	5	5
Inverter	Inverter	DC/AC fuse damaged, broken, switch off	2	4	5	40
Inverter	Inverter	Earth or insultaion fault	2	4	4	32
AC wiring	LV wiring	Cable damaged	3	4	3	36
AC wiring	LV wiring	Cable unfastened	1	4	5	20
Monitor.syst.	Monitoring	Communications card failure	1	3	4	12
Monitor.syst.	Monitoring	Power source broken	1	3	4	12
Monitor.syst.	Monitoring	Local/Remote access not allowed	1	3	4	12
Monitor.syst.	Weather Station	Weather station broken	2	3	5	30
MV	Transformer	Oil temperature alarm	3	2	4	24
MV	Transformer	Windings temperature alarm	3	2	4	24
MV	Transformer	Oil leak	4	4	2	32
MV	Transformer	Fire	5	3	2	30
MV	Transformer	Deficient transformer tank ground connection	3	4	3	36

The reported failure modes are further analyzed throughout these paragraphs, in order to identify the ones that present a higher RPN and their possible causes and effects to be considered by operators. In Fig. 1 it is shown the sum of the RPN for each of the groups of elements under study and the accumulated RPN sum.

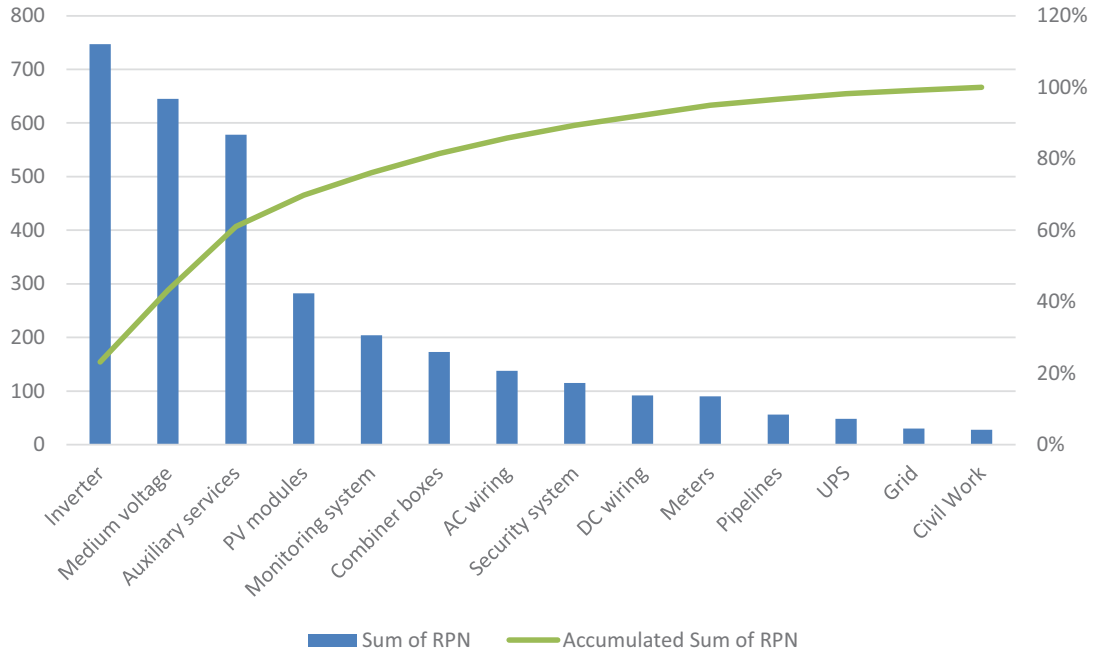

Fig. 1: Sum of RPN per group - FULL O&M

It can be seen that the inverter presents the higher RPN sum for the identified failure modes, followed by the medium voltage and the auxiliary services. Due to the fact that not all the groups present the same number of failure modes identified, it is necessary to know the average RPN in each of the groups. This analysis can be seen in Fig. 2. It can be seen that in this case, the groups that present a higher RPN in average are the medium voltage and the inverters, followed by AC wiring, combiner boxes, pipelines and PV modules.

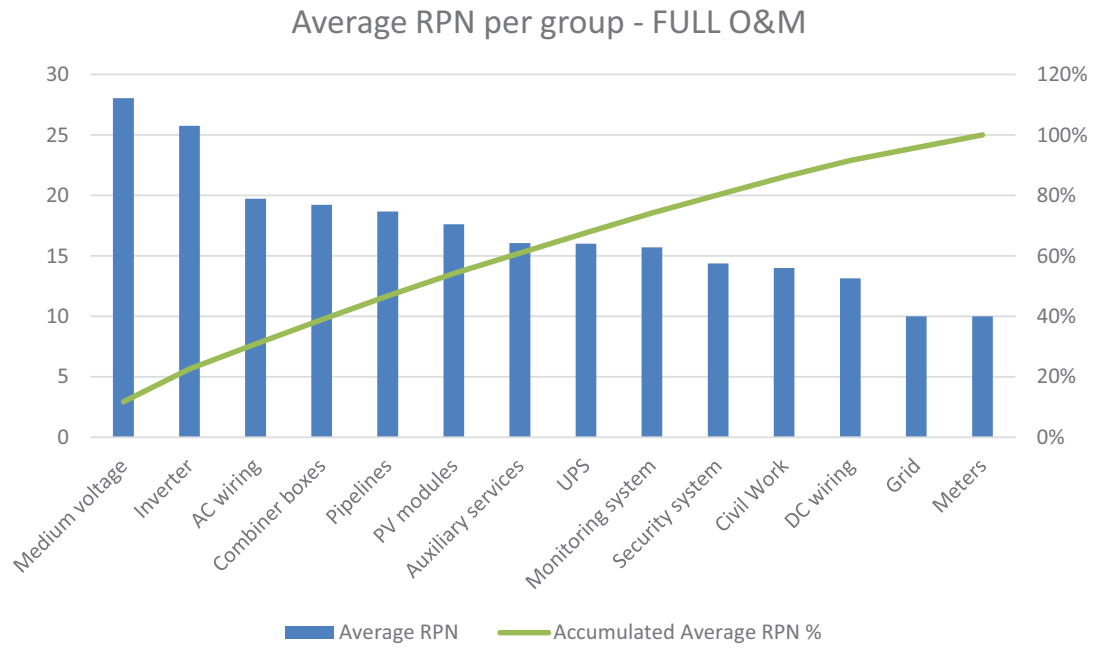

Fig. 2: Average of RPN per group - FULL O&M

As it has been previously mentioned, monitoring the different system components that constitute the PV plant facilitates the detection of failures and from the reliability point of view allows the operator to improve the plant performance (Cristaldi et al., 2015). Nevertheless, in utility scale PV plants, typically the monitoring system trails the string series current of multiple modules connected, or even the inverter current, which is the sum of the parallel string current, and does not track the performance of the individual PV modules, which is the key element on a PV system as it converts the incident irradiance into electric power and module's cost is commonly upon 50% of the total PV installations cost (Agroui, 2012). Therefore, it is specially complicated the detection of failures at this level and even more difficult the recognition of the failure cause and mode. To complete the FMECA analysis of this paper it has been considered that other source of information is needed for the module level assessment and that is why the final point of this research is in the way of studying the current possibilities for operators to detect module failures and therefore, increasing the energy output of the PV plant

During the last years, additional tests are required by solar PV investors at the PV module level with the aim of controlling the individual module performance, for example, electrical test, electroluminescence test and thermographic test.

Electrical test, as IV curves tracing, allow the detection of abnormal underperforming situations but do not allow identifying the cause neither location of the defective cell. Additionally, to perform these tests it is necessary to shut down the plant during the electrical inspection, which involves an important energy output reduction. Electroluminescence (EL) imaging is a non-invasive technique developed to detect the radiative recombination of charge carriers excited under forward bias in which the resultant light intensity is proportional to the voltage. Therefore any electrically inactive parts of the module or cell are represented as dark areas, as micro-cracks that are not visible, as well as broken contact fingers, which can be identified. Although improvements in EL imaging equipment, involving InGaAs uncooled detectors and InSb cooled ones, have encompassed the first steps for reliable outdoor measurements and fault diagnosis in PV sites, electroluminescence is typically performed in indoor laboratories following strict indoor conditions.

On the other hand, thermographic inspection is fast and simple to implement and giving results in real time, not being necessary to shut down the plant during the inspection. It is non-destructive, contact-less and allows the identification of defects and their exact location with great accuracy, representing a temperature distribution of the surface of the modules which discloses the defects. Nonetheless, despite being a reliable method, manual thermography presents some relevant drawbacks. It is a costly and time-consuming technique and there are some situations in which it is hard to detect the defective cells using manual thermography, as in locations in which the inclination of modules is too low or during the middle hours of the day in PV plants with trackers. That is why aerial thermographic inspections, in which an UAV carries a thermographic sensor, is recently becoming most popular because it reduces the inspection cost and it is less time consuming than manual thermographic inspections and/or IV curve tracing.

Thermographic tests have been applied at a module level to a sample of the base data to complete the FMECA of the whole PV Plant. Some of the module failures that generate a difference in the temperature are experimentally identified by thermographic techniques and their criticality is analyze, as the overheating in multiple or one cell, connection point, module box, whole module and one row or bypass circuit. The thermographic images obtained performing on-site manual thermographic inspection are presented in Fig. 3.

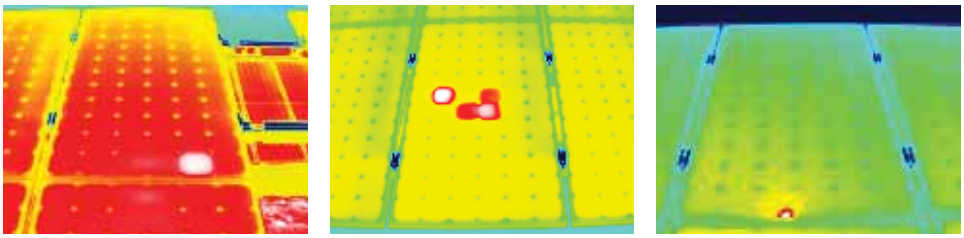

(a) **(b)** **(c)**

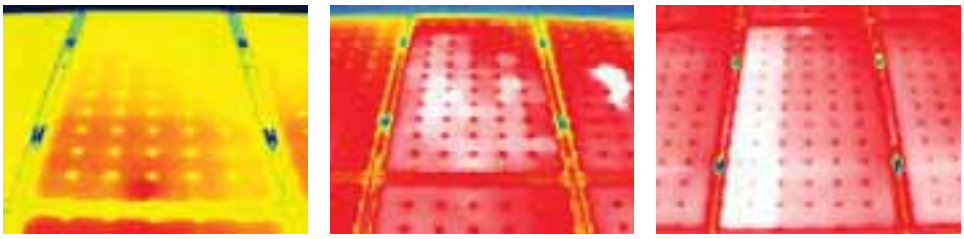

(d) (e) (f)

Fig. 3: Thermographic image of PV modules taken on-site with a manual thermographic camera whic presents different defects (a) hot spot, (b) multiple cells hot spot, (c) connection overheated (d) module box overheated, (e) whole module overheated, (f) bypass circuit overheated.

4. Conclusions

This paper presents a failure mode analysis of PV plants based on the analyses performed to the available data of a real existing portfolio in Spain and Italy of continuous operation since 2008. Throughout the paper, it has been analyzed which are the most critical sub-system and failure modes within a photovoltaic PV plant, resulting that inverters presents the higher RPN sum for the identified failure modes, followed by the medium voltage and the auxiliary services. On the other hand, it has been proved that the groups that present a higher average RPN are the medium voltage and the inverters, followed by AC wiring, combiner boxes, pipelines and PV modules.

This information is essential for PV operators and manufacturers to focus their efforts on preventing those failures and to contribute to the improvement of the reliability in PV installations.

Additionally, it has been performed a manual thermographic inspection to a PV plant to identify the module level failure modes, as typically in utility scale PV plants the monitoring system does not track the performance of the individual PV modules, which is the key element on a PV system as it converts the incident irradiance into electric power and module's cost is commonly upon 50% of the total PV installations cost. Some of the module failures that generate a difference in the temperature have been experimentally identified, as the overheating in multiple or one cell, connection point, module box, whole module and one row or bypass circuit.

5. References

Agroui, K., 2012. Indoor and Outdoor Characterizations of Photovoltaic Module Based on Mulicrystalline Solar Cells. Energy Procedia, 18, 857–866.

Colli, A., 2012. Extending performance and evaluating risks of PV systems failure using a fault tree and event tree approach: Analysis of the possible application. 38th IEEE Photovoltaics Specialists Conference, 2922–2926.

Colli, A., 2015. Failure mode and effect analysis for photovoltaic systems. Renewable and Sustainable Energy Reviews, 50, 804–809.

Cristaldi, L., Faifer, M., Lazzaroni, M., Khalil, M.M.A.F., Catelani, M., Ciani, L., 2015. Diagnostic architecture: A procedure based on the analysis of the failure causes applied to photovoltaic plants. Measurement, 67, 99–107.

Moorthy, M.K., Tamizhmani, G., 2016. Automation of Risk Priority Number Calculation of Photovoltaic Modules. IEEE 43rd Photovoltaic Specialists Conference (PVSC), 1730–1735.

Decoupling Crystallinity and Size of TiO2 Nanoparticles of TiO2: Application in Large Area Dye-Sensitized Solar Cells

Aiat Hegazy[1], Essam El-Shenawy[1] and Mohamed Abdelatef[1]

[1] National Research Centre, Cairo (Egypt)

Abstract

Dye-sensitized solar cells (DSSCs) have attracted great attention in recent years as a potential alternative to conventional silicon solar cells. However, a lot of current research is still focusing on enhancing their efficiency through the individual improvement of the DSSCs components, as well as their integration. Among these components, mesoporous TiO_2 plays an important role in the cell photoanode. Achieving well-crystallized small nanoparticles usually requires a room temperature synthesis, giving very small crystallites (4-10 nm) of TiO_2 anatase. As as-synthesized materials contain hydration water, a major drawback in DSSCs, we report how dehydration and crystallinity can be improved by annealing at a moderate temperature, without any sintering or significant particle coarsening. We report in this study a comprehensive study of the cell assembling, and its efficiency, characterized under AM 1.5 illumination with 100 mw/cm^2 light intensity.

Keywords: DSSC,TiO_2, nanoparticle, photovoltaic, anatase, solar cell, solar energy.

1. Introduction

Since their initial discovery (O'regan and Gratzel, 1991; Gratzel 2001) liquid-based dye-sensitized solar cells (DSSCs) are known as alternatives to conventional silicon-based photovoltaic devices. The first generation of liquid electrolyte-containing DSSCs display significant Power Conversion Efficiencies (PCE) > 14% (Mathew et al. 2014; Kakiage et al. 2015) at lab scale and 10% in module (Kazim et al. 2014), but the use of a liquid electrolyte becomes a burden for large-scale developments. Therefore, research on solid-state DSSCs (ss-DSSCs) has significantly increased over the last years reaching up 8.2% (Freitag et al. 2015) with the recent breakthrough of perovskites, especially organic-inorganic perovskites, which act as light harvester in place of organic dyes, and Hole Transporting Material (HTM)(Kazim et al. 2014). Nevertheless, TiO_2 anatase remains an important component in both types of DSSCs, as an electron collector. The reduction of interface transport resistance between all components is also a major requirement, which requires a high interfacial intimacy between components.

The electronic conduction in the protonated TiO_2 film, usually made of 20 nm TiO_2 particles, is the result of a complex mechanism in liquid DSSCs. First, the presence of both dye cations and iodine species, with the resulting formation of a positive layer on the surface of titania, create a Helmholtz double layer screening shell around the particles, which contributes to the reduction of the electron-hole recombination in TiO_2 (Cahen et al. 2000). It is also stated that the electrons are diffusing along the surface of the particles, as a result of a short screening Debye length (1.5 nm) (Cahen et al. 2000). If this limits the electron diffusion to a surface process for particles larger than 10 nm, we could wonder the effect of using smaller (sub-10 nm) nanoparticles, and if the whole volume will be used for conduction.

A major contributing factor to the efficiency of the titania-based photoanode is its structure, especially, the size of TiO_2 crystals. Although the reduction in crystal size influences positively the amount of dye adsorbed onto the surface and the dye-to-TiO_2 charge transfer, it affects negatively the total internal resistance of the cell as more grain boundaries are created per unit volume, reducing the light internal reflection. For example, it was demonstrated that mesoporous TiO_2 single crystals can deliver an enhanced mobility, good optoelectronic performances, and high material intimacy (Crossland et al. 2013).

doi:10.18086/swc.2017.20.05 Available at http://proceedings.ises.org

We prepared previously anatase nanocrystals at room temperature, as a result of synthesis parameters being finely optimized via a mixture design method (Hegazy and Prouzet, 2012). This nanopowder, already successfully tested for their photocatalytic properties, (Hegazy and Prouzet, 2013) could become the raw material for future roll-to-roll manufacturing of large-scale DSSCs, if the nanostructure can be dehydrated with thermal annealing without particle sintering or coarsening. As we demonstrated previously that the initial particle size can be preserved up to ≈ 400°C, (Hegazy and Prouzet, 2012) we decided to verify the efficiency of a dehydration treatment in this temperature range, and assess the photovoltaic properties of a DSSC assembled with this material. Different parameters in cell assembly were tested in order to improve the final structure and connectivity of the final TiO_2 photoanode. The influence of these parameters is reported in the present study, along with the assessment of our materials, in comparison with commercially available compounds assembled with the same method.

2. Experimental

2.1. Synthesis of TiO_2 nanoparticles

We reported the detailed study of this synthesis previously (Hegazy and Prouzet, 2012). This study allowed us to extrapolate the best composition, which would give both small nanocrystallites, and a pure anatase phase. This specific composition was chosen inside the composition mixture diagram giving the pure TiO_2 anatase phase. It corresponds to a composition between the (A) and (J) data points in the mixture phase diagram of our previous study (Hegazy and Prouzet, 2012).

2.2. Synthesis of the TiO_2 paste

The paste was prepared by mixing the TiO_2 nanopowder, with different organic additives used as plasticizers. Depending on their nature, we proceeded differently for their addition. In method 1, 0.35 g Pluronic™ P123, was dissolved into 5 mL EtOH, and then mixed with a suspension of 1.0 g of TiO_2 dispersed into 10 mL of EtOH. The resulting mixture was left at 100°C for 24 h, in a sealed vial. The vial was further cooled down before using the paste. In method 2, a mixture of Span™80/Tween™80 was prepared with the aim to obtain a final Hydrophilic Lipophilic Balance (HLB) of 13.6, (Hessien et al. 2012) and 0.035g of this mixture (equiv. one to two drops) was directly added into a suspension of 1g TiO2 in 10 mL acetic acid (N). The resulting paste was ground in a mortar to ensure good dispersion of the organics among the solid phase before being pasted.

2.3. Preparation of the TiO_2 film

The film was coated onto a FTO glass substrate, with doctor-blade method. The film thickness was controlled by the thickness of a 17 µm 3M adhesive tape, and the paste was spread with a glass rod over the space between the tape strips. The electrode was left to dry at 80°C for 3 hours. We cured organics used as plasticizers by either a thermal, or UV treatment. With the thermal treatment, the electrode was heated at 450°C for 30min, cooled down, and immersed into a 0.1M HCl aqueous solution for 2 hours. With UV treatment, the electrodes were exposed to an intense curing (300 W.inch^2) UV radiation for 20 min, before being immersed in the HCl solution. After analysis, we decided to combine both methods, and all electrodes used for the cell assembly, were made out of the TiO_2nanopowder, first annealed at 350°C for 4 hours, then cured at 450°C for 30 min, and exposed to UV. All electrodes were further grafted with the Z907 dye molecule. Adsorption of the dye was undertaken by immersing the TiO_2 electrode overnight in a 0.4 mM dye in 50:50 vol. t-butanol:acetronitrile solution. The grafted electrodes were finally washed with acetone to remove the excess of dye.

2.4. Counter electrode preparation

The presence of Pt nanoparticles at the surface of the counter-electrode is mandatory to achieve the reduction of the iodide/triiodide couple (Bonnemann et al. 2007). A commercial platinum paste (Platisol-T, Solaronix) was used as received and fired at 450°C for 30 min in order to remove organic binders. The electrode was immersed in DI water, before being sonicated for 20 minutes in ethanol, without any noticeable wrenching of the Pt layer from the substrate.

2.5. Cell assembly

The Pt electrode and the dye-adsorbed TiO_2 electrode were assembled as a sandwich-type, leading to a 5 cm^2 photoactive surface. The redox electrolyte was introduced to the cell by capillary action.

3. Results and discussions

3.1 Influence of treatment on structure of TiO_2

3.1.1 Thermal annealing

We have demonstrated in a previous study, that the crystallinity of as-synthesized TiO_2 anatase could be improved by a moderate thermal treatment without any dramatic change in the crystal size if the maximum temperature remained below 450°C (Hegazy and Prouzet, 2012). A fully dehydrated material is a compulsory requirement for use in DSSCs.

We analyzed by TEM the influence of annealing on the crystalline and particle structure for nanopowders annealed for 4 hours at 350 °C (Figure 1.a), 450°C (Figure 1.b), and 500°C (Figure 1.c). TEM diffraction reveals an improved crystallinity from 350 to 450°C (see figures inset), without drastic change in crystal size. HR-TEM investigation of the sample annealed at 450°C (Figure 1.d) confirms the formation of 10 nm average single crystal particles with high crystallinity. The inter-reticular distances of 3.62 Å and 2.1 Å correspond to the (101), and (200) planes, respectively. They are in the usual value range reported in literature for nanocrystalline TiO_2. The crystal size increases at 500°C (Figure 1.c), leading to well-defined diffraction patterns, which result from this size increasing.

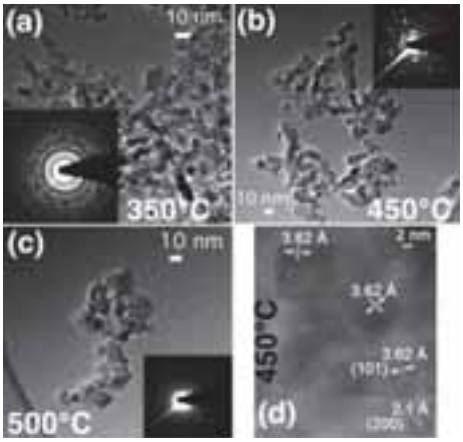

Figure 1: TEM micrographs and the corresponding diffraction patterns of nanocrystalline anatase TiO2 nanoparticles annealed at (a) 350 °C, (b) 450 °C, and (c) 500°C. (d) HR-TEM of TiO2

3.1.2 Organic additives

A TiO_2 paste was prepared with the addition of various organic additives used as binders: (i) Pluronic P123, (ii) PEG 12,000, or (iii) Span80/Tween20/acetic acid. These organics were chosen as plasticizers for facilitating the film formation. They were added to the anatase nanoparticles previously annealed at 350°C for 4 hours. As these organics must be removed after the film formation, we tested two types of curing, with a short thermal treatment (450°C, 30 min), or high intensity UV (300 W/in^2, 15 min). An observation by TEM (not shown) did not reveal any drastic change in the structure of titania particles, after either thermal or UV curing, irrespective of the type of additive.

Both surface area and porosity of the film are two important parameters in performance of DSSC, and porosity should be typically in the 50%-65% range (van de Lagemaat et al. 2001). Previous analyses showed that the small size of these nanoparticles create a significant textural porosity in the mesoporous range, with both specific surface area and porous volume changing with the thermal treatment (Hegazy and Prouzet 2012). We report in Figure 2, the N2 adsorption/desorption isotherms for the powder annealed at 350°C, and

the same powder prepared with the Span/Tween mixture plasticizing additive and cured either at 450°C, or under UV. Figure 3.a shows that all isotherms are rather similar (Type IV isotherms), with a steep adsorption between 0.6 and 0.9 of partial pressure. The specific surface area calculated via the multipoint BET model, gives values of 130, 160, and 200 $m^2.g^{-1}$ for the annealed, thermally cured, and UV cured samples, respectively. Their respective porous volume is 58% for the annealed powder, and 63% for both cured samples. The modeling of the pore size distribution (PSD), using the desorption isotherm, (Figure 2.b) allowed us to assess the possible influence of curing on the material porous structure. The initial PSD lies between 8 and 13 nm, and both materials after either thermal or UV curing, show only a slight broadening of PSD toward larger pores (8 – 18 nm range). We assign this PSD shift toward larger values, as a result of the organic additive that acts as a pore promoter and contributes to create some larger pores in addition to the initial PSD (the PSD is only broadened toward larger values, not fully shifted).

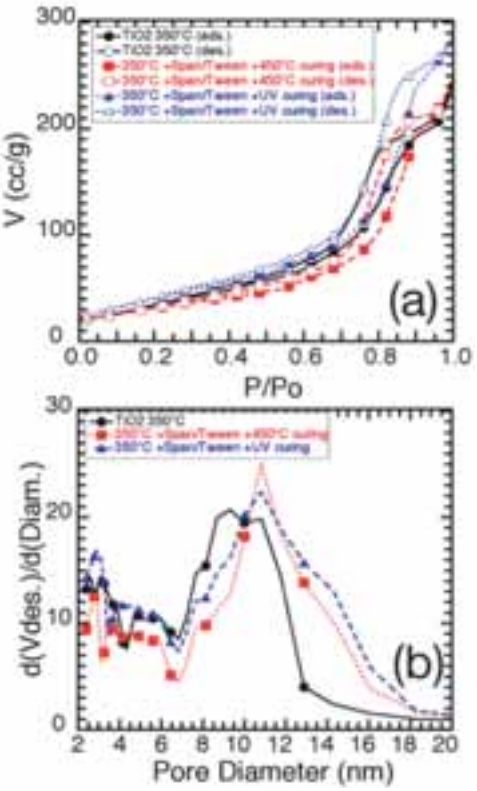

Figure 2: Nitrogen adsorption isotherms for the nanopowder after thermal annealing (350°C, 4h), and the same material after addition of the Span/Tween mixture additive, and either thermal (450°C, 30 min.) or UV (15 min) curing: (a) ads

3.2. Effect of dye absorption and photoelectronic properties onTiO_2 film

The cell performance is strongly affected by the efficiency of injected electrons from the dye to the conduction band of the TiO_2, which reflects the importance of the way the dye anchored to TiO_2 surface. As it has been demonstrated that both UV exposure and HCl treatment improve the photoanode properties, (Lee at al. 213; Hao et al. 2004). The thermally cured TiO_2 film was additionally activated under UV (10 min) and immersed into a 0.1 M hydrochloric aqueous solution for two hours, then rinsed with DI water until no acid trace could be found in washing water. The major effect of UV exposure is to reversibly create a high concentration of photoactive surface states, which were described as being continuously distributed below the conduction-band edge as shallow electron traps that would be beneficial for electron injection from the dye and transport by thermally activated detrapping (Lee at al.213; Hao et al. 2004; Tebby et al. 2009). The major effect of acid treatment is to increase the density of protonated sites, which favors multidentate dye adsorption. The actual influence of this HCl treatment is illustrated by comparing the UV-Vis spectra for both films prepared according to the procedure (thermally annealed and cured), and exposed to UV: adding an HCl treatment before dye adsorption, increases in the absorbance. A similar blue shift was observed for

all samples, which reveals a change in the electronic structure of the thin films surface, probably due to surface hydroxylation (Hao et al. 2004).

Figure 3 shows the J -V characteristics of the solar cell device made using thermally treated TiO_2/ plutonic P123 films at 450°C, the TiO_2 nanoparticles were preheated at 350°C. The photovoltaic parameters of the devices made using initially treated nanoparticles at 350°C and 450°C with and without HCl treatment. The short-circuit photocurrent density (Jsc) and the photoconversion efficiency (η) of the treated TiO_2 films are higher than those of the untreated counterparts, the active surface area was 5 cm^2 for all samples. After HCl treatment of the 350°C sample, the Jsc and η were increased by 28.4% and 4.5%, respectively. However, the open circuit voltage (Voc) was slightly changed and the fill factor (FF) was decreased. Whereas, for the sample prepared at 450°C, J_{sc} was increased by 36.3%, η by 37.2% and Voc by 8.6%. The poor FF is a result of a combination of the high series resistance (Rseries) and low shunt resistance (Rshunt). Figure 4 demonstrates that both devices made using our synthesized TiO_2 exhibit higher cell performance compared to the commercial ones. Although the sample prepared by surfactant and acetic acid displays higher efficiency than that made using pluronic, the later provides higher shunt resistance, Table 2.

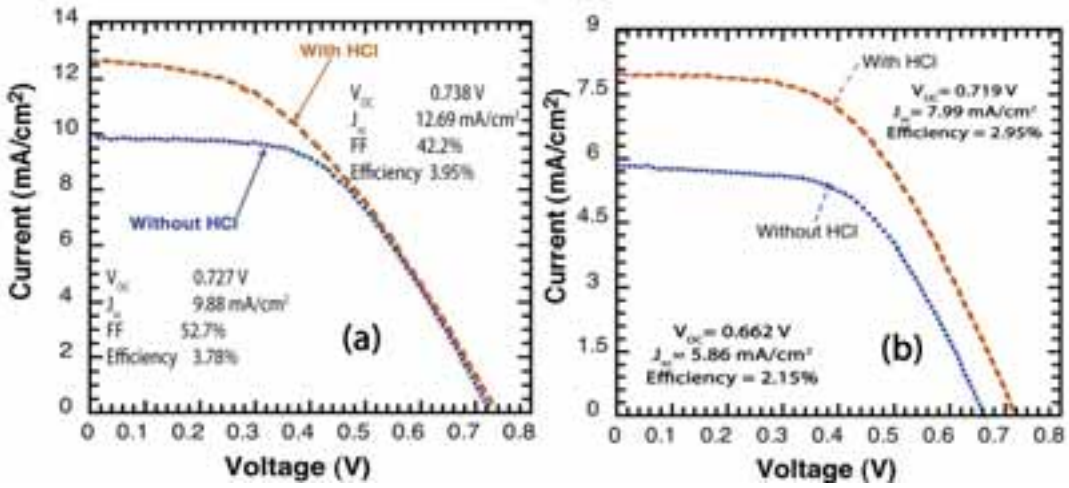

Figure 3: J-V curves for the comparison of the thermal and UV organic curing for nano powders being annealed beforehand at (a) 350°C, or (b) 450°C.

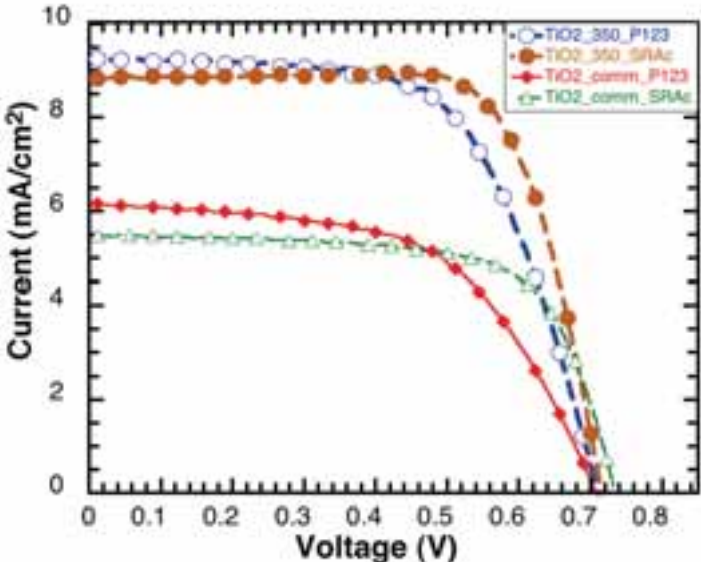

Figure 4: J-V curves of dye-sensitized TiO_2 films prepared on FTO/glass: with different organic additives to our nanopowder and the commercial one(active area=5 cm^2)

Table 1: Comparison between photovoltaic parameters of DSSCs prepared by the synthesized TiO_2 nanoparticles and the commercial TiO_2 counterparts.

Sample	V_{oc} (V)	J_{sc} (mA/cm^2)	*FF*	Efficiency %	R_s (Ω)	R_{sh} (Ω)
TiO_2_350°C_P123	0.713	9.43	62.6	4.21	16.6	1392
TiO_2_Degussa_P123	0.707	6.16	56.7	2.47	15.72	462
TiO_2_350°C_SRAc	0.72	8.41	77.1	4.67	2.21	324
TiO_2_Degussa_SRAc	0.734	5.47	68.9	2.77	4.12	606

Several DSSC devices were fabricated based on the TiO_2 films treated under different conditions. Unlike usual testing cells with an active surface area close to 1 cm^2, our cells were assembled with an active surface area of 5 cm^2, Fig.5 represents a picture of the tested cell. Therefore, the performances of the cells can hardly be compared to literature, and they were initially used as comparative within this study.

Figure 5 Picture of the full-assembled cell

The adsorption of Z907 Dye on the TiO_2 surface was characterized by ATR-FTIR spectroscopy. Figure 4 shows the ATR-FTIR absorption spectra of the Z907 dye adsorbed onto the TiO_2 surface. Many studies have shown that the dye anchors to the TiO_2 surface through different carboxylate anchoring modes, like physisorbed through hydrogen bonding, or chemisorbed via various types of chemical bonds (unidentate, bidentate, and bridging), with bridging and bidentate being the most stable ones (Lee et al. 2011; Leon et al. 2006; Wang et al. 2004).

Strong peaks were observed at 1,380 cm^{-1} and 1,613 cm^{-1} characteristics of the vsym (COO-) and vasym (COO-), respectively (Finnie et al.1998; Agrell et al. 2004). There is no indication of the presence of carboxylic bond at 1,716 cm-1. This indicates that the dye is anchored to the TiO_2 surface via bidentate or bridging not via unidentate mode. The saturated hydrocarbon chains are identified by the C-H stretch modes in the 2,800-3,000 cm^{-1} region with vibration modes of 2,852 cm^{-1} and 2,924 cm^{-1} for symmetric and asymmetric -CH_2-, respectively. The corresponding CH_3– peak is observed at 2,956 cm^{-1}. A broad absorption

peak is observed between 3,200-3,400 cm^{-1} (not displayed), corresponding to the –OH stretching modes of hydroxo and aquo ligands.

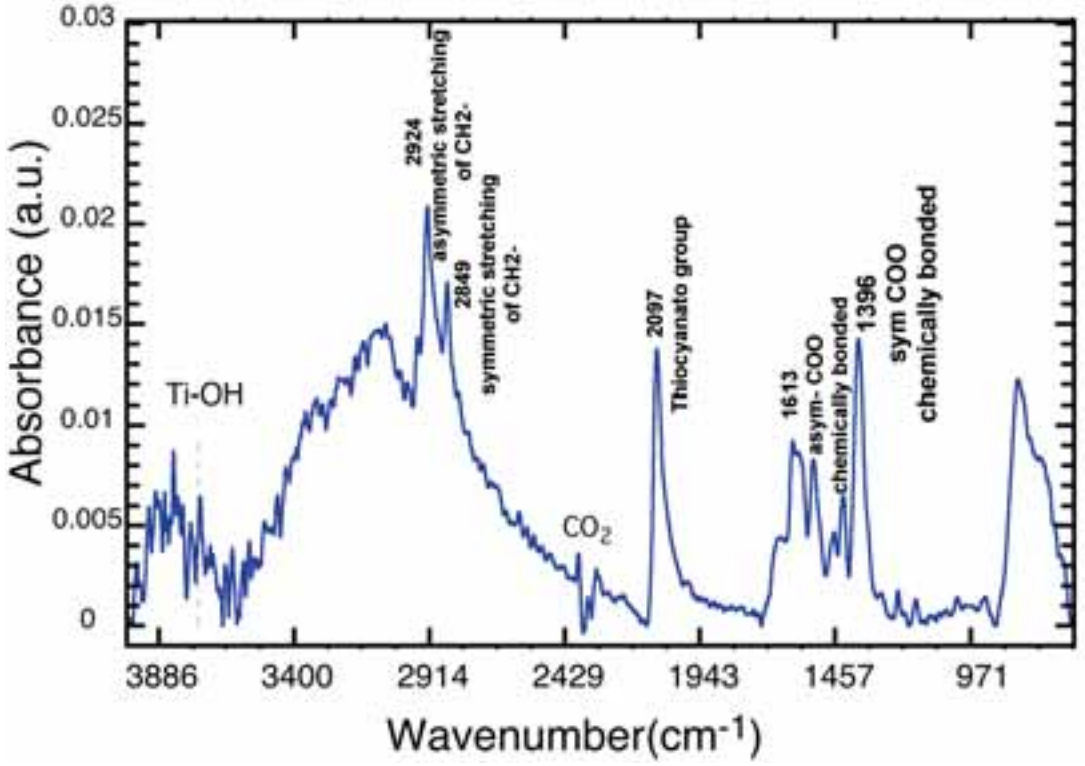

Figure5: FTIR spectrum of the TiO2- thin film after dye adsorption.

Another significant difference between our nanopowder and the commercial one is the strength of the dye adsorption. The samples prepared with Span/Tween show higher absorbance, which is consistent with the overall cell efficiency. All the reference cells made from the commercial TiO_2 exhibit lower absorbance, as a result of the dye being less adsorbed or easily removed before measurements. Our nanoparticles have the ability to keep 7 times more of dye after this process, than the commercial powder.

We performed an EIS analysis on different configurations to get more insights into the effect of resistances on the cell performance. We display the results obtained with TiO_2 films prepared with Span/Tween (Figure 5.a) or Pluronic P123 (Figure 5.b). A large semicircle can be observed in the Nyquist plot, which corresponds to the TiO2/dye/electrolyte triple interface. The interface between the high–frequency semicircle and the intermediate–frequency semicircle is difficult to distinguish due to the strong overlap of the charge transfer resistance on the TiO_2 surface and that on the Pt surface. A sub-circle in the low-frequency response is observed, which accounts for the contribution of the diffusion of the electro-active species in the liquid electrolyte (Longo et al. 2004). In the dark, the solar cells showed high impedance and the time constants are not well defined. For all devices testes (see Table 2), almost all the impedance parameters show a difference between illuminated and non-illuminated cells. The response at the intermediate interface under dark condition is much higher than the one under illumination, which corresponds to a high capacitance because of the expected accumulation of electrons and redox species at this interface (Nogeira et al.2004). From our results, it appears that the cells prepared with span/Tween exhibit a longer electron lifetime than those prepared with Pluronic(P123). The reference cells (commercial TiO_2 powder) showed an electron lifetime half times shorter electrons for recombination under illumination compared to the cells made with our

nanocrystalline TiO_2 material. Higher electron lifetime leads to significant electron transfer, and thus, an improved Jsc. Therefore, EIS analysis confirms the promising results obtained with cells assembled with our synthesized nanocrystalline material.

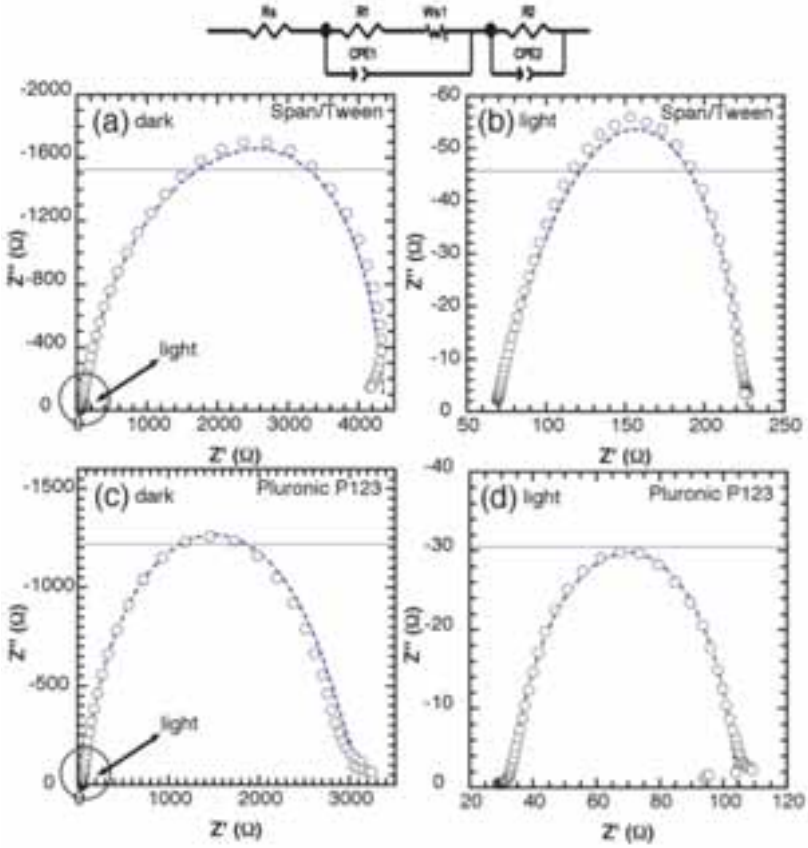

Figure 5: Nyquist representation of the impedance data obtained for Z907 dye–sensitized TiO2 solar cells prepared with preheated nanoparticles at 350oC mixed with (a,b) Span/Tween, (c,d) Pluronic P123, measured in the dark (a,c) or under light (b,d). The symbols represent the experimental data and the dashed lines correspond to the fitting obtained with View software using the displayed equivalent circuit displayed.

Sample	Area (cm^2)	R_s, Ωcm^{-2}	$R_{1(CE)}$, Ωcm^{-2}	T_1*10^6	P_1	$R_{2(REC)}$, Ωcm^{-2}	T_2*10^5	P_2	*Ws*, Ωcm^{-2}	τ_r/ms
AP_light	1	23.53	2.266	9.831	0.862	39.97	0.269	0.985	*39.35*	63
AP_light	1.5	48.45	1.908	0.405	1.023	23.48	1.893	1.043	47.27	35
AS_light	2.5	67.95	$1.7*10^{-7}$	0.195	0.6117	79.21	6.14	.9174	81.2	189

RP_light	1.2	37.4	0.586	3.041	0.966	59.31	1.034	.985	27.37	35

Table 2: Electrochemical parameters of DSSC prepared with different TiO2 films and organic additives. 'A' refers to the synthesized TiO2 nanoparticles prepared with S (Span/Tween) or P (Pluronic) additives, 'R' refers to reference electrodes prepared with TiO2 Degussa with S or P additives

4. Summary

In summary, we have successfully synthesized small crystalline TiO_2 nanoparticles by a novel soft chemistry method and investigated their properties in dye–sensitized solar cells. We also demonstrated that different organic additives can be used to prepare the photoanode and obtain the well defined working range of the porosity. The effect of UV exposure on the structure and crystal size of as-synthesized TiO_2 nanoparticles was tested through the XRD and N_2 isotherm characterization, which indicates no change in the crystal size and a higher surface area, respectively. Furthermore, various treatment methods (UV alone, thermal treatment alone, and combination of both) were applied. Although, UV treatment is able to clean the TiO_2 surface from organic contaminates, it is less efficient to be used alone, and leads to lower performance of solar cells, compared to thermal treatment. Interestingly, when it is used after the thermal treatment, the cells seem to show better efficiency, which will have to be confirmed in the future with more tests. The HCl treatment increases the cell efficiency by almost one to three. The enhancement was attributed to the increase of the amount of the dye. An intensive investigation on the effect of HCl on the adsorbed dye was done by the FTIR analysis. More investigation on the dye by the FTIR, demonstrates that the dye anchored chemically to TiO_2 surface. The amount of adsorbed dye for our TiO_2 films was 6 times compared to the amount of the commercial ones. The internal resistance of the cells were checked with EIS analysis, which shows higher electron lifetime, smaller charge transfer resistance for counter electrode and high recombination resistance compared to the commercial cells.

5. References

[1] Agrell, H. G., J. Lindgren, A. Hagfeldt, 2004. Coordinative interactions in a dye-sensitized solar cell, Journal of Photochemistry and Photobiology A: Chemistry, 164, 23-27.

[2] Bonnemann, H., G. Khelashvili, S. Behrens, A. Hinsch, K. R. Skupien, E. Dinjus, 2007. Role of the platinum nanoclusters in the iodide/triiodide redox system of dye solar cells, Journal of Cluster Science, 18, 141-155.

[3] Broekhoff, J. C. P., J. H. De Boer, 1968. Studies on pore systems in catalysts. Xiii. Pore distributions from the desorption branch of a nitrogen sorption isotherm in the case of cylindrical pores. B. Applications, Journal of Catalysis, 10, 377-390.

[4] Broekhoff, J. C. P., J. H. De Boer, 1968. Studies on pore systems in catalysts. Xii. Pore distributions from the desorption branch of a nitrogen sorption isotherm in the case of cylindrical pores. A. An analysis of the capillary evaporation process, Journal of Catalysis, 10, 368-374.

[5] Cahen, D., G. Hodes, M. Gratzel, J.-F. Guillemoles, I. Riess, 2000. Nature of photovoltaic action in dye-sensitized solar cells, J. Phys. Chem. B, 104, 2053-2059.

[6] Crossland, E. J. W., N. Noel, V. Sivaram, T. Leijtens, J. A. Alexander-Webber, H. J. Snaith, 2013. Mesoporous tio2 single crystals delivering enhanced mobility and optoelectronic device performance, Nature, 495, 215-219.

[7] Fang, X., T. Ma, G. Guan, M. Akiyama, E. Abe, 2004. Performances characteristics of dye-sensitized solar cells based on counter electrodes with pt films of different thickness, Journal of Photochemistry and

Photobiology a-Chemistry, 164, 179-182.

[8] Finnie, K. S., J. R. Bartlett, J. L. Woolfrey, 1998. Vibrational spectroscopic study of the coordination of (2,2 '-bipyridyl-4,4 '-dicarboxylic acid)ruthenium(ii) complexes to the surface of nanocrystalline titania, Langmuir, 14, 2744-2749.

[9] Freitag, M., Q. Daniel, M. Pazoki, K. Sveinbjörnsson, J. Zhang, L. Sun, A. Hagfeldt, G. Boschloo, 2015. High-efficiency dye-sensitized solar cells with molecular copper phenanthroline as solid hole conductor, Energy & Environmental Science, 8, 2634-2637.

[10] Gratzel, M., 2001. Photoelectrochemical cells, Nature, 414, 338-344.

[11] Hao, S., J. Wu, L. Fan, Y. Huang, J. Lin, Y. Wei, 2004. The influence of acid treatment of tio 2 porous film electrode on photoelectric performance of dye-sensitized solar cell, Solar Energy, 76, 745-750.

[12] Hegazy, A., E. Prouzet, 2012. Room temperature synthesis and thermal evolution of porous nanocrystalline TiO_2 anatase, Chemistry of Materials, 24, 245-254.

[13] Hegazy, A., E. Prouzet, 2013. Effect of physical chemistry parameters in photocatalytic properties of TiO_2 nanocrystals, Comptes Rendus Chimie, 16, 651-659.

[14] Hessien, M., N. Singh, C. Kim, E. Prouzet, 2011. Stability and tunability of o/w nanoemulsions prepared by phase inversion composition, Langmuir, 27, 2299-2307.

[15] Hirose, F., K. Kuribayashi, M. Shikaku, Y. Narita, Y. Takahashi, Y. Kimura, M. Niwano, 2009. Adsorption density control of n719 on TiO_2 electrodes for highly efficient dye-sensitized solar cells, J. Electrochem. Soc., 156, B987-B990.

[16] Jaroniec, M., 1995. Evaluation of the fractal dimension from a single adsorption isotherm, Langmuir, 11, 2316-2317.

[17] Kakiage, K., Y. Aoyama, T. Yano, K. Oya, J.-I. Fujisawa, M. Hanaya, 2015. Highly-efficient dye-sensitized solar cells with collaborative sensitization by silyl-anchor and carboxy-anchor dyes, Chemical Communications, 51, 15894-15897.

[18] Kang, S. H., J.-Y. Kim, H. S. Kim, H.-D. Koh, J.-S. Lee, Y.-E. Sung, 2008. Influence of light scattering particles in the TiO_2 photoelectrode for solid-state dye-sensitized solar cell, Journal of Photochemistry and Photobiology A: Chemistry, 200, 294-300.

[19] Kazim, S., M. K. Nazeeruddin, M. Gratzel, S. Ahmad, 2014. Perovskite as light harvester: A game changer in photovoltaics, Angew. Chem.-Int. Edit., 53, 2812-2824.

[20] Kopidakis, N., K. D. Benkstein, J. Van De Lagemaat, A. J. Frank, 2003. Transport-limited recombination of photocarriers in dye-sensitized nanocrystalline tio2 solar cells, J. Phys. Chem. B, 107, 11307-11315.

[21] Lee, M.-K., H. Yen, C.-C. Hsiao, 2011. Efficiency improvement of dye-sensitized solar cell with ultraviolet and hydrogen chloride treatments, J. Electrochem. Soc., 158, K136-K139.

[22] Leon, C. P., L. Kador, B. Peng, M. Thelakkat, 2006. Characterization of the adsorption of ru-bpy dyes on mesoporous TiO_2 films with uv-vis, raman, and ftir spectroscopies, Journal of Physical Chemistry B, 110, 8723-8730.

[23] Longo, C., M.-A. De Paoli, 2003. Dye-sensitized solar cells: A successful combination of materials, J. Braz. Chem. Soc., 14, 889-901.

[24] Mathew, S., A. Yella, P. Gao, R. Humphry-Baker, B. F. Curchod, N. Ashari-Astani, I. Tavernelli, U. Rothlisberger, M. K. Nazeeruddin, M. Grätzel, 2014. Dye-sensitized solar cells with 13% efficiency achieved through the molecular engineering of porphyrin sensitizers, Nature Chemistry, 6, 242-247.

[25] Hara, K. and Arakawa, H. (2003) Dye-Sensitized Solar Cells, in Handbook of Photovoltaic Science and Engineering (eds A. Luque and S. Hegedus), John Wiley & Sons, Ltd, Chichester, UK. doi: 10.1002/0470014008.ch15

[26] Nogueira, A. F., C. Longo, M. A. De Paoli, 2004. Polymers in dye sensitized solar cells: Overview and perspectives, Coordination Chemistry Reviews, 248, 1455-1468.

[27] O'regan, B., M. Gratzel, 1991. A low-cost, high-efficency solar-cell based on dye-sensitized colloidal tio2 films, Nature, 353, 737-740.

[28] Prouzet, E., C. Boissière, S. S. Kim, T. J. Pinnavaia, 2009. Roughness of mesoporous silica surfaces deduced from adsorption measurements, Microporous Mesoporous Mat., 119, 9-17.

[29] Prouzet, E., F. Cot, G. Nabias, A. Larbot, P. J. Kooyman, T. J. Pinnavaia, 1999. Assembly of mesoporous silica molecular sieves based on nonionic ethoxylated sorbitan esters as structure directors, Chemistry of Materials, 11, 1498-1503.

[30] Shao, W., F. Gu, C. Li, M. Lu, 2010. Interfacial confined formation of mesoporous spherical tio2 nanostructures with improved photoelectric conversion efficiency, Inorg. Chem., 49, 5453-5459.

[31] Tebby, Z., O. Babot, D. Michau, L. Hirsch, L. Carlos, T. Toupance, 2009. A simple route towards low-temperature processing of nanoporous thin films using uv-irradiation: Application for dye solar cells, Journal of Photochemistry and Photobiology a-Chemistry, 205, 70-76.

[32] Van De Lagemaat, J., K. D. Benkstein, A. J. Frank, 2001. Relation between particle coordination number and porosity in nanoparticle films: Implications to dye-sensitized solar cells, J. Phys. Chem. B, 105, 12433-12436.

[33] Wang, P., S. M. Zakeeruddin, J. E. Moser, R. Humphry-Baker, P. Comte, V. Aranyos, A. Hagfeldt, M. K. Nazeeruddin, M. Gratzel, 2004. Stable new sensitizer with improved light harvesting for nanocrystalline dye-sensitized solar cells, Advanced Materials, 16, 1806.

Wavelength Dependent Optical Characteristics: Intensity Distribution in Flat Silicon and Silicon Nanowire Used as Absorber in Solar Cell

Mohammad K. Hossain[1,*], Billel Salhi[1] and Ayman W. Mukhaimer[2]

[1] Center of Research Excellence in Renewable Energy (CoRERE), King Fahd University of Petroleum and Minerals (KFUPM), Dhahran 31261, Dhahran (Kingdom of Saudi Arabia)

[2] Department of Mechanical Engineering, King Fahd University of Petroleum and Minerals (KFUPM), Dhahran 31261, Dhahran (Kingdom of Saudi Arabia)

[*]Correspondence to: kamalhossain@kfupm.edu.sa

Abstract

Solar cells utilize a small portion of solar spectrum depending on the technology while solar radiation being a full of UV-VIS-IR wavelengths does not leave absorbing and other layers unaffected. Only the photon energy that matches with absorber layer contributes to effective power generation of solar cell. Higher and lower energy wavelengths induce thermalization and absorption losses which in turn introduce several consequences including heating and degradation in the cell level. Therefore engineered absorbing layer such as nanowire based solar cell holds huge potential. Here in this work, we have investigated and simulated four deterministic characteristics, *viz*, absorption depth profile, electromagnetic field, Poynting vector and exciton generation rate distribution at different incidents. Flat silicon and silicon nanowire were considered as examples along with a comparative outlook. Such predictive studies facilitate the choice of technology and how to improve the cell efficiency using light trapping technique.

Key-words: Optical characteristics, Silicon nanowire, FDTD simulation, Optical confinement.

1. Introduction

Solar radiation per second (i.e. 1.74×10^5 TW) is more than sufficient to provide all the energy demands needed to facilitate entire world population in a year. Unfortunately it has been impractical because of technological challenges. Silicon (Si)-based solar panel is the most popular one in this regard and holds more than 90% of current photovoltaic (PV) market

doi:10.18086/swc.2017.20.06 Available at http://proceedings.ises.org

(Sachs 2011). Although Si is abundant and superior in stability and non-toxicity, the Shockley and Queisser efficiency limit (i.e. ~31%) for a single band gap Si-based solar cell has become an issue and a matter of challenge for current research community. A small portion of solar spectrum contribute to solar cells performances, whereas solar radiation being a full of other wavelengths does not leave the associate layers unaffected. The photon energy that matches with absorber layer contributes to effective power generation of solar cell. Higher and lower energy wavelengths induce thermalization and absorption losses respectively which in turn introduce several subsequent problems including heating and degradation in the cell level. These additional consequences add up extra cost whereas current technology is already facing various challenges to limit the cost below 1¢ per kWh. Therefore, it is important to increase the cell efficiency at low cost to bring this technology within afford and reach.

Si nanowires (Si-NWs) have been considered potential to face the efficiency constrain because of nanometric features led unique properties (Kelzenberg et al. 2010; Polman and Atwater 2012; Zhao at al. 2004; Krogstrup et al. 2013; Yu et al. 2014). Si-NWs have strong optical absorption compared to that of flat silicon along with many other electrical characteristics that lead to reduced production cost (Salhi et al. 2016). The efficiency can be further improved by optimizing and tuning incident solar spectrum that is useful in efficient solar cell system. A predictive analysis of inherent optical characteristics of such nanowire based system indeed facilitates to determine and improve other associate layers of the solar cell. Previously we have reported absorption profile, energy flow, EM field distribution and exciton generation rate at 740 nm in addition to spectral analysis of absorption depth profile for Si-NW system (Hossain 2016a, 2016b). Nevertheless, further correlated spectral analysis on absorption profile, energy flow, EM field distribution and exciton generation rate distributions is indispensable.

Two key challenges, low cost materials as well as higher efficiency, are immensely needed at this moment to accelerate mass-production and utilization of PV technology. PV solar cell based on nanometric Si-NW-based possess huge potential in this regard. Apart from optical characteristics, short collection length for charge carriers in Si-NWs boosts up efficiency and allows to use down grade absorbing materials. First ever PIN configured solar cells based on Si-NWs was presented by Tian group in 2007 (Tian et al., 2007). The Si-NWs were grown by vapor-liquid-vapor process. Since then, a variety of methods have been reported to obtain Si-NW such as high temperature evaporation of silicon powder in furnace (Cui et al., 2001,

2000; Wu et al., 2004), vapor-liquid-solid process (Wang et al., 1999; Westwater, et al 1997), laser ablation (Zhang et al., 1999), liquid solution solid process (Davidson et al., 2004), solid liquid solid process (Yan et al., 2000), metal catalyst assisted electroless etching (Peng et al., 2009, 2006a. 2006b, 2005, 2002), etc. There are huge and extensive studies on conventional flat panel, although 3rd generation solar cell especially nanostructured materials based photovoltaic solar cell is not well understood. Numerical studies always support to implement the proof-of-concept into prototype that ultimately ends up with a suitable product. The studies also open up new avenue and in-depth understanding of the technology. Therefore, an correlated and simulative study, such as absorption profile, electromagnetic (EM) field, Poynting vector, excitation generation rate distribution, etc. are inevitable.

Here in this work, we have investigated and simulated four deterministic characteristics, *viz*, spectral absorption depth profile, electromagnetic field, Poynting vector and exciton generation rate distribution. Two Si-based absorbing layers generally used in thin film solar cell, such as flat silicon and silicon nanowire, were considered as examples. A comparative study has been carried out to illustrate how an efficient light management can be obtained in silicon nanowire based solar cell.

2. Method and materials

c-Si slab and Si-NW on c-Si wafer were modeled in FDTD package of Lumerical Solution (ver 8.6) and a three-dimensional (3D) analysis was carried out to obtain and compare optical characteristics of such systems. The model geometry was selected in such a way so that the parameters can be as close as of those reported previously (Hossain et al. 2016). Absorption profile, Poynting vector, EM field distribution, and generation rate distributions at different wavelengths ranging from UV to NIR region were extracted. Unpolarized plane wave as illumination source was set as incident to the vertically modelled Si-NW. The characteristics of Si-NW system were compared with that of c-Si slab only. Intensities of absorption profile, Poynting vector, EM field and exciton generation rate distributions were obtained slice by slice at different incident wavelengths.

3. Results and discussion

Solar cell internal quantum efficiency is known to be directly related to the photon absorption profile of the absorbing layer. Such photon absorption can be confined and enhanced depending on the geometry of absorbing layer in solar cell. Absorption profile, EM field distribution, Poynting energy and excitation generation rate distribution are inter-related and

deterministic factor to efficient solar cell. We have extracted aforementioned characteristics at different wavelength ranging from UV to NIR region (i.e. at 300, 500, 700, 900, and 1100 nm). Figure1a–c and Fig. 2a-c show absorption profiles and electromagnetic field distribution

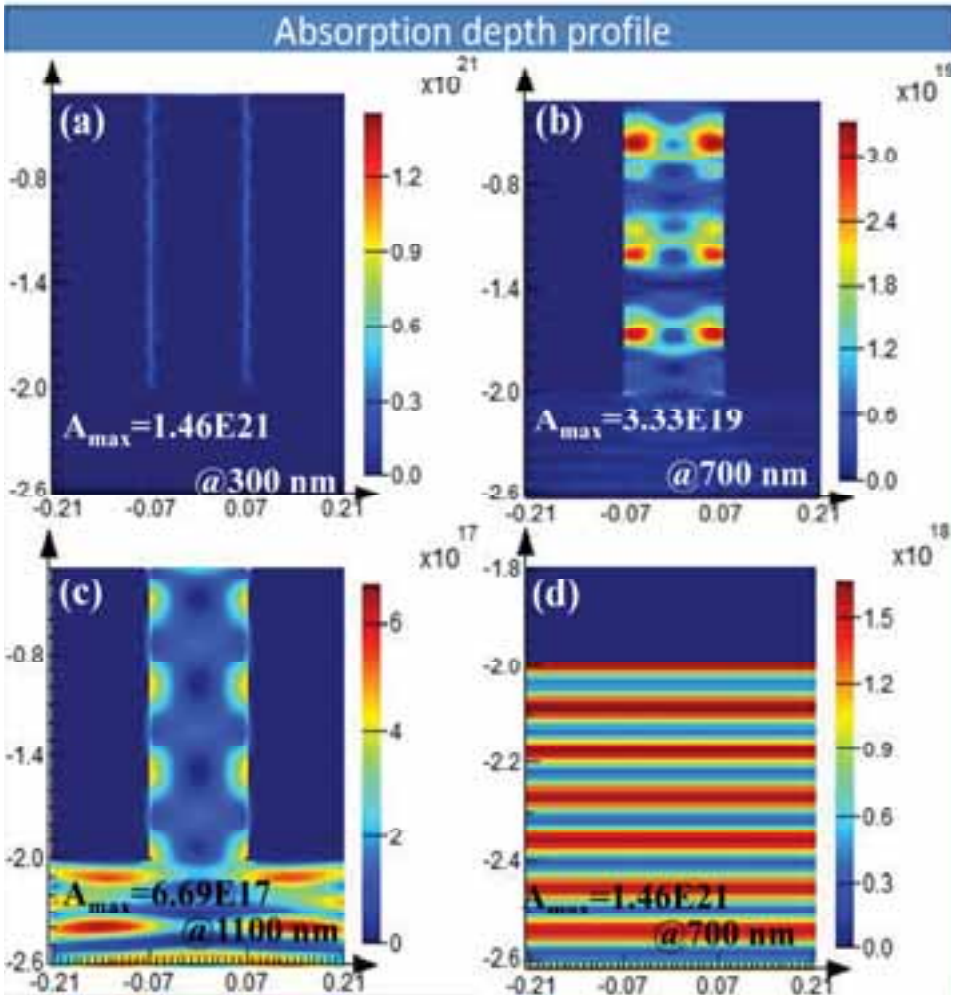

Fig. 1: (a)-(c) Spectral absorption depth profile of Si-NW model system at 300, 700 and 1100 nm wavelengths respectively, and (d) that of flat c-Si slab at 700 nm wavelength.

of nanowire model system at 300, 700, and 1100 nm wavelength respectively. Absorption profile and electromagnetic field distribution of c-Si slab only at 700 nm wavelength of solar spectrum was shown in Fig. 1.d and Fig. 2d respectively as references. For shorter wavelength with higher energy, such as at 300 nm, almost no absorption and EM field distribution was observed. On the other hand, for longer wavelengths, such as at 1100 nm, slight distribution was observed near the edge and started to reduce within the absorbing layer. At 700 nm wavelength of solar spectrum, the intensity distribution was confined within

the nanowire model system. For conventional flat panel Si-based solar cell, single band gap material (E_g= 1.8 eV or 700 nm) utilizes the solar spectrum at around 700 nm.

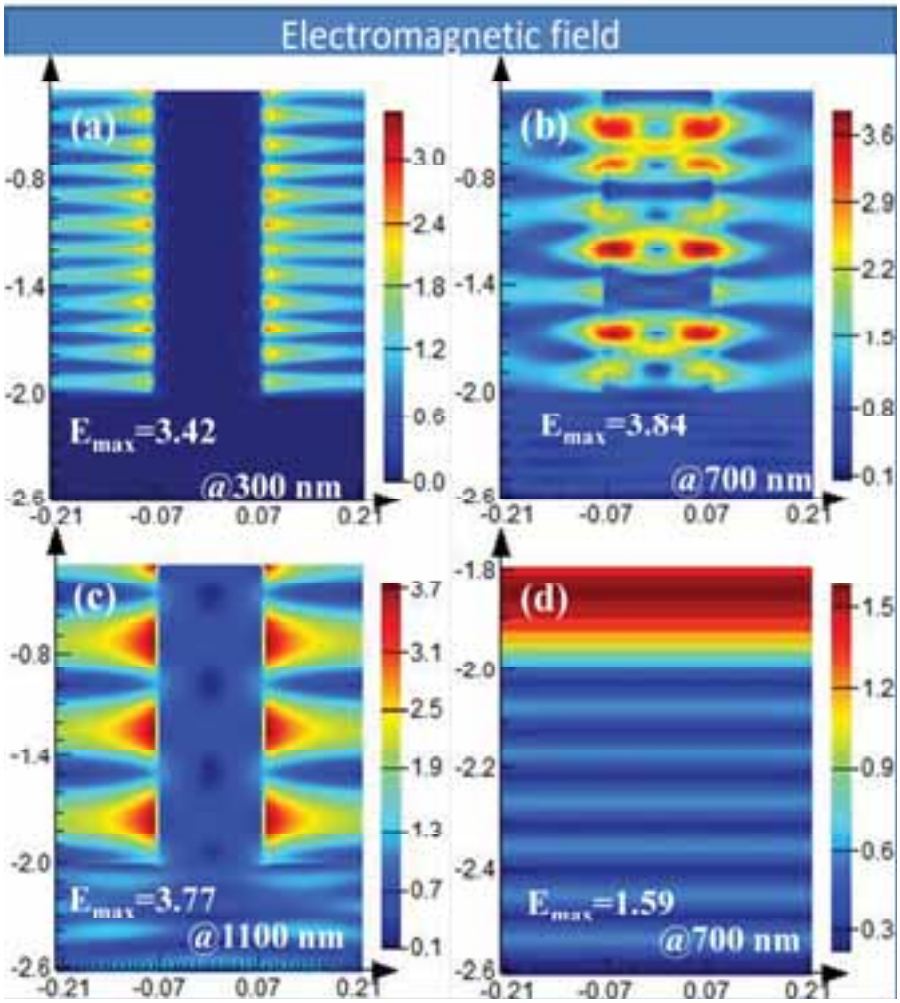

Fig. 2: (a)-(c) spectral EM field distribution for Si-NW model system at 300, 700 and 1100 nm wavelengths respectively and (d) that of flat c-Si slab at 700 nm wavelength.

In photovoltaics, excitation generation rate defines how many of excess excitons (i.e., excited electrons and holes) are available to collect. Number of useful excitons per incident photon is very crucial in designing efficient solar cell. Current (i.e. rate of charge flow) in solar cell depends on the concentration of such excitons. Therefore, generation rate is calculated by taking divergence of Poynting vector considering a zero recombination loss. Therefore, understanding of spectral distribution of Poynting vector and excitation generation rate within flat silicon as well as Si-NW system is very important. Energy flow distribution throughout a

single Si-NW from top to the bottom are shown in Fig. 3a–c at different wavelength such as 300, 700, and 1100 nm wavelength respectively. At shorter wavelength, such as at 300 nm, distributions were found intense near the edge and there was almost no distribution within the nanowire model system. For longer wavelengths with lower energy, such as at 1100 nm, there was slight confined distribution but that started to reduce within the absorbing layer. At 700 nm wavelength of solar spectrum, the intensity distribution was observed to be confine and well distributed. Confined energy flow distribution was observed within the nanowire model system. Figure 3d shows the Poynting vector profile obtained in flat c-Si slab at 700 nm wavelength as reference.

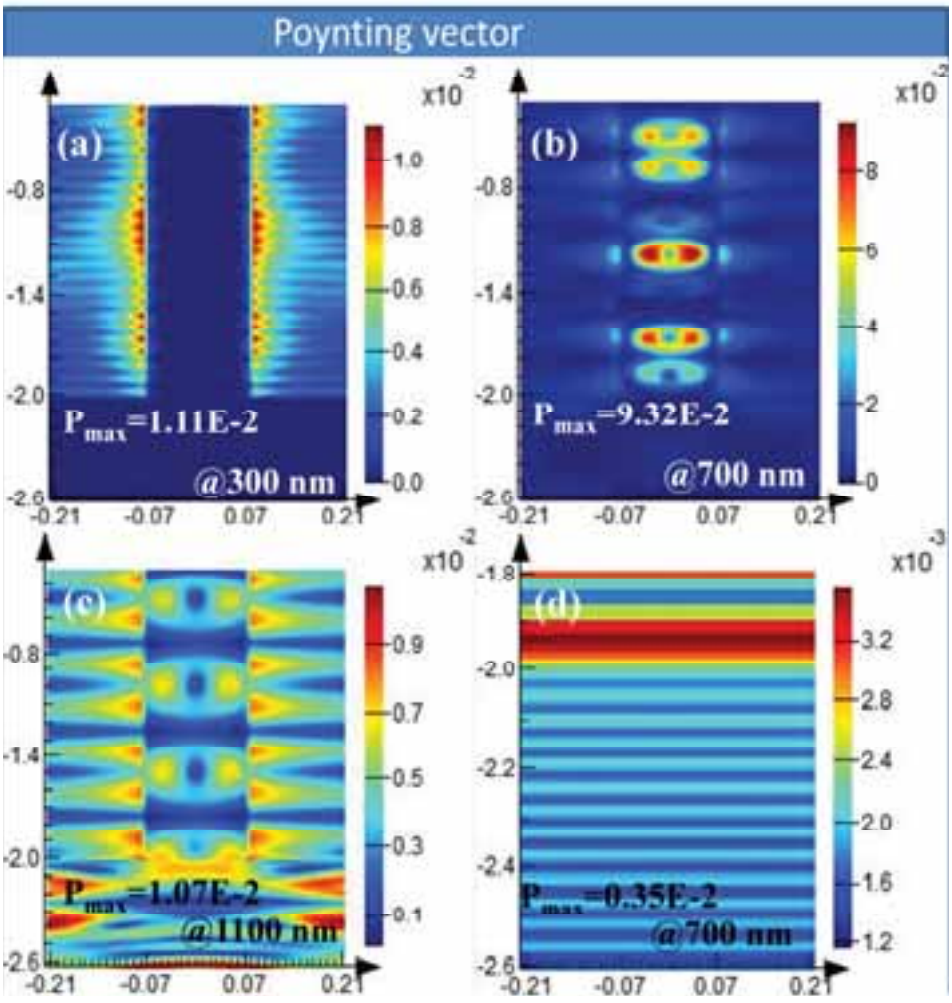

Fig. 3: (a)-(c) Spectral Poynting vector profile of Si-NW model system at 300, 700 and 1100 nm wavelengths respectively, and (d) that of flat c-Si slab at 700 nm wavelength.

Figure 4a-c show excitation generation rate distribution of nanowire model at 300, 700, and

1100 nm wavelength, respectively. At shorter wavelength with higher energy, no excitation generation rate distribution was observed. For longer wavelengths, such as at 1100 nm, slight distribution near the edge was observed. At 700 nm wavelength of solar spectrum, most of the exciton generation rate distribution was confined within the nanowire model system and the intensity distribution was well distributed. Excitation generation rate distribution of c-Si slab only at 700 nm wavelength of solar spectrum was shown in Fig. 4d as references.

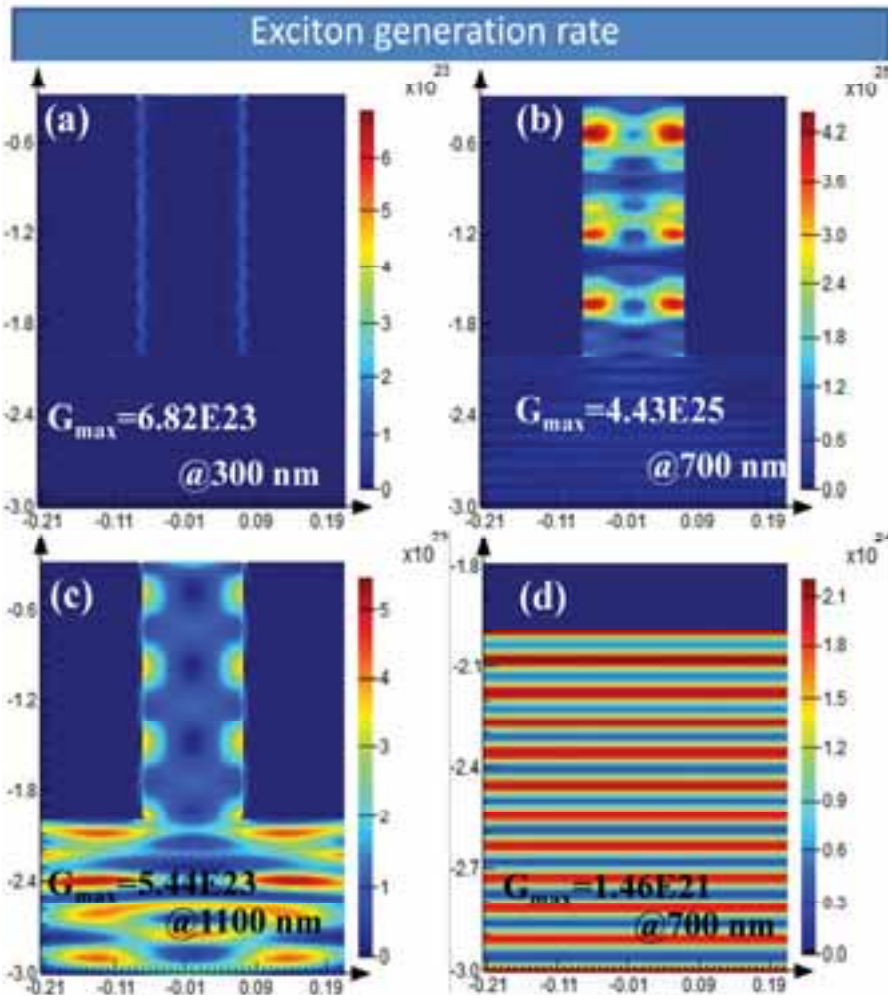

Fig. 4: (a)-(c) spectral exciton generation rate distribution for Si-NW model system at 300, 700 and 1100 nm wavelengths respectively and (d) that of flat c-Si slab at 700 nm wavelength.

4. Conclusion

Absorption depth profile, electromagnetic field, Poynting vector, and excitation generation rate distribution of two typical model systems, flat silicon and nanowire model systems, were observed at different wavelengths. At around 700 nm (band gap, E_g= 1.8 eV), intensity distributions were found confined and well distributed within the Si-NW model system with reference to those obtained at other wavelengths. Exciton generation rate was available and well distributed all the way down to the bottom of the wire. Lower wavelength with higher energy solar spectrum was not found to be efficient for Si-NW model system.

5. Acknowledgment

Authors like to thank Center of Research Excellence in Renewable Energy (CoRERE), King Fahd University of Petroleum and Minerals (KFUPM) for the support in this work.

6. References

Kelzenberg, M.D., Boettcher S.W., Petykiewicz J.A., Turner-Evans D.B., Putnam M.C., Warren E.L., Spurgeon J.M., Briggs R.M., Lewis N.S., Atwater H.A., 2010. Enhanced absorption and carrier collection in Si wire arrays for photovoltaic applications. Nat Mater. 9, 239–244.

Polman A., Atwater H.A., 2012. Photonic design principles for ultrahigh-efficiency photovoltaics. Nat Mater. 11, 174–177.

Yu L.W., Misra S., Wang J.Z., Qian S.Y., Foldyna M., Xu J., Shi Y., Johnson E., Cabarrocas P.R., 2014. Understanding light harvesting in radial junction amorphous silicon thin film solar cells. Sci Rep. 4, 4357–4363.

Krogstrup P., Jorgensen H.I., Heiss M., Demichel O., Holm J.V., Aagesen M., Nygard J., Morral A.F., 2013. Single-nanowire solar cells beyond the Shockley-Queisser limit. Nat Photonics. 7, 306–310.

Salhi B., Hossain M.K., Mukhaimer, A.W., AlSulaiman, F.A., 2016. Nanowires: A New Pathway to Nanotechnology-based Applications. J Electrocer. 37, 34–49.

Hossain M.K., Salhi B., Mukhaimer A.W., 2016. Optical confinements in correlated spectral characteristics of vertically aligned silicon nanometric wires followed by a facile fabrication thereof. Plasmonics. 1–8 (10.1007/s11468-016-0387-y).

Hossain M.K., Salhi B., Mukhaimer A.W., Al-Sulaiman F.A., 2016. Fabrication and optical

simulation of vertically aligned silicon nanowires. Appl Nanosci. 6, 1031–1036.

Tian, B., Zheng, X., Kempa, T.J., Fang, Y., Yu, N., Yu, G., Huang, J., Lieber, C.M., 2007. Coaxial silicon nanowires as solar cells and nanoelectronic power sources. Nature, 449, 885–889.

Cui, Y., Duan, X., Hu, J., Lieber, C.M., 2000. Doping and Electrical Transport in Silicon Nanowires. J. Phys. Chem. B. 104, 5213–5216.

Cui, Y., Lauhon, L.J., Gudiksen, M.S., Wang, J.F., Lieber, C.M., 2001. Diameter-controlled synthesis of single-crystal silicon nanowires. Appl. Phys. Lett. 78, 2214–2216.

Wu, Y., Cui, Y., Huynh, L., Barrelet, C.J., Bell, D.C., Lieber, C.M., 2004. Controlled growth and structures of molecular-scale silicon nanowires. Nano Lett. 4, 433–436.

Wang, N., Tang, Y.H., Zhang, Y.F., Lee, C.S., Bello, I., Lee, S.T., 1999. Si nanowires grown from silicon oxide. Chem. Phys. Lett. 299, 237–242.

Westwater, J., Gosain, D.P., Usui, S., 1997. Control of the size and position of silicon nanowires grown via the vapor-liquid-solid technique. Japanese J. Appl. Phys. Part 1-Regular Pap. Short Notes Rev. Pap. 36, 6204–6209.

Zhang, Y.F., Tang, Y.H., Peng, H.Y., Wang, N., Lee, C.S., Bello, I., Lee, S.T., 1999. Diameter modification of silicon nanowires by ambient gas. Appl. Phys. Lett. 75, 1842.

Davidson, F.M., Schricker, A.D., Wiacek, R.J., Korgel, B. a, 2004. Supercritical fluid-liquid-solid synthesis of gallium arsenide nanowires seeded by alkanethiol-stabilized gold nanocrystals. Adv. Mater. (Weinheim, Ger.) 16, 646–649. doi:10.1002/adma.200306284.

Yan, H., Xing, Y., Hang, Q., Yu, D., Wang, Y., Xu, J., Xi, Z.., Feng, S., 2000. Growth of amorphous silicon nanowires via a solid–liquid–solid mechanism. Chem. Phys. Lett. 323, 224–228. d

Peng, K., Fang, H., Hu, J., Wu, Y., Zhu, J., Yan, Y., Lee, S., 2006a. Metal-particle-induced, highly localized site-specific etching of Si and formation of single-crystalline Si nanowires in aqueous fluoride solution. Chem. Eur. J. 12, 7942–7947.

Peng, K., Hu, J., Yan, Y., Wu, Y., Fang, H., Xu, Y., Lee, S., Zhu, J., 2006b. Fabrication of single-crystalline silicon nanowires by scratching a silicon surface with catalytic metal particles. Adv. Funct. Mater. 16, 387–394.

Peng, K., Xu, Y., Wu, Y., Yan, Y., Lee, S.T., Zhu, J., 2005. Aligned single-crystalline Si

nanowire arrays for photovoltaic applications. Small 1, 1062–1067.

Peng, K.-Q., Wang, X., Wu, X., Lee, S.-T., 2009. Fabrication and photovoltaic property of ordered macroporous silicon. Appl. Phys. Lett. 95, 143119.

Peng, K.-Q., Yan, Y.-J., Gao, S.-P., Zhu, J., 2002. Synthesis of Large-Area Silicon Nanowire Arrays. Adv. Mater. 14, 1164–1167.

Performance and economic optimization of hybrid solar thermal and photovoltaic power plants with dynamic simulation

Hannah O'Hern[1], Todd Otanicar[1] and Matthew Orosz[1]

[1] The University of Tulsa, Tulsa (USA)

Abstract

Energy storage is a critical determinant of grid stability under scenarios with a high percentage of renewables in the generation portfolio. Concentrating solar thermal power traditionally offers high capacity thermal energy storage (TES) on timescales up to 24 hours, while photovoltaics operate with comparatively better economy but are limited to direct injection into the grid during the daytime in the absence of mature, high throughput battery storage technology. Obtaining the advantages of both systems through hybridization has been proposed in the ARPA-E FOCUS program, and this work investigates the performance and cost trade-offs of updating existing CSP infrastructure to include superimposed spectral filtering and concentrating photovoltaics in a linear optical configuration. A numerical energy balance model for a retrofit parabolic trough collector is deployed in an hourly simulation using plant characteristics and typical meteorological year (TMY) data for a location of interest. Design features including PV band pass filtering, operating temperature, and primary optics intercept are varied for an optimization of levelized cost of electricity. A case study for the US southwest illustrates the potential for performance enhancement relative to a CSP baseline via increased photovoltaic output (>30%), and favourable financial returns in comparison to greenfield PV plant development (with installed specific costs <1.5 USD/W), that preserves the advantages for grid operators of maintaining the dispatchability of TES.

Keywords: Solar thermal, concentrating photovoltaics, energy storage, dynamic simulation, hybrid system, CSP, CPV

1. Introduction

The hybridization of CSP and concentrated photovoltaics (CPV) technologies combines the energy storage capabilities of CSP with the economy of PV conversion. Retrofitting an existing parabolic trough collector CSP plant with a spectral splitting filter reflecting optimal wavelengths to a CPV receiver is expected to increase the annual power output of a traditionally configured CSP plant using linear Parabolic Trough Collectors (PTCs). This is due to the relatively higher in-band efficiency of PV cells compared to the output of a steam Rankine cycle after accounting for optical and thermal losses in the CSP array. The concept of interposed secondary optics has been considered previously as means to increase the concentration ratio onto the PV cell, however, in this study we take advantage of an existing as-built CSP array, with its energy storage benefits, and add secondary optics to redirect specific wavelengths of light to a CPV receiver. The key advantage of the hybrid CSP-CPV system is that the filter can be designed to reflect wavelengths optimal for conversion in the PV cell, while passing the poorly utilized wavelengths through to the CSP, thus allowing the PV cell to operate effectively while ensuring that light wavelengths that would otherwise go to waste are exploited (Orosz 2015). The hybrid CPV retrofit of a CSP plant would be an economical option to increase the annual power output, while still utilizing the energy storage capabilities of CSP.

The secondary optic consists of a dichroic filter attached in plane intermediate between the primary mirror and the focal line of the parabolic trough mirror, with the CSP heat collection element (HCE) above it and the CPV receiver below, as shown in Figure 1. The filter splits the spectrum such that ultraviolet and infrared wavelengths pass through the dichroic mirror to the HCE while wavelengths that are efficiently used by the CPV cell are reflected down to the CPV receiver. The diversion of part of the solar spectrum results in reduced CSP power output, however, the CPV power output increases the net output of the plant due to its higher in-band conversion efficiency.

doi:10.18086/swc.2017.20.07 Available at http://proceedings.ises.org

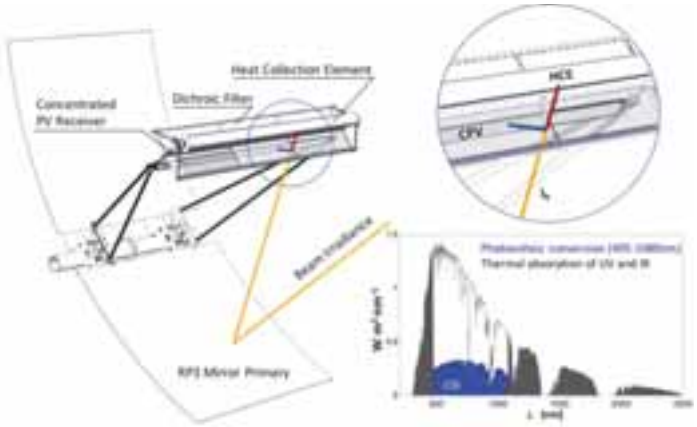

Figure 1: A CPV retrofit attaches to and operates with an existing standard parabolic trough collector (RP3 outer mirrors not shown). Inset shows a detail of the beam splitting secondary optics, the respective CSP and CPV targets, and the AM1.5 band of photovoltaic conversion (lower right) where the right band edge is set to the cSi band gap and the left band edge is tuned to maximize combined CSP and CPV output.

2. Annual Performance Model

Probabilistic yield estimation (monthly and annual energy output) based on design and location is an important input in the development cycle of solar energy projects and critically determines the financial merit of a proposed solar plant. There are many commercial software packages (PVSyst, Helioscope, etc.) in use for determining the annual yield of a solar PV power plant. The System Advisor Model (SAM) is a free software developed by NREL (National Renewable Energy Laboratory 2016) that is utilized for both performance and detailed financial modelling. While SAM and other specialized tools are capable of modelling PV, parabolic trough CSP and CPV plants, there is no commercially available platform that can simulate a hybrid of both CSP and CPV, and in particular with reference to spectral dependencies e.g. the secondary optics used in the retrofit which our team is developing with support from the U.S. Department of Energy (DOE) Advanced Research Projects Agency (ARPA-E) FOCUS program (ARPA-E n.d.). To address this observed gap in performance prediction tools, a dynamic simulation was created in Python which embeds a previously developed detailed steady-state model of the energy balance of a parabolic trough CSP plant with a coupled spectrum-splitting filter and CPV cell retrofit (Orosz et al. 2016).

2.1. Steady-State Energy Balance Model

A steady-state physics based energy balance model was developed in Python, based on the Forristall energy balance model (Forristall 2003). The heat transfer equations of the Forristall model are combined with the necessary equations to determine PV power generation, in order to determine the net generation of a retrofitted plant. Inputs into the model include collector and HCE geometry, heat transfer fluid (HTF) properties, inlet temperature, and flow rate, optical properties, and ambient weather conditions. In addition to CSP generation, with and without the retrofit and CPV generation, the model also determines HTF outlet temperature, necessary pumping power, and thermal and optical losses.
The HCE is comprised of a stainless steel tube with a selective coating inside a glass envelope, with an evacuated annulus. The model assumes all temperatures, heat fluxes, and thermodynamic properties are uniform around the circumference of the HCE, and that the only heat transfer in the axial direction along the length of the trough is via the HTF. The effective incoming energy is the solar beam irradiance reduced by optical losses incurred through the dichroic filter. The incoming irradiance is predominantly transmitted through the glass jacket, absorbed and conducted through stainless steel absorber, and finally transferred to the HTF by convection. Residual energy is lost to the environment via convection and radiation. The beam irradiance that is reflected by the dichroic filter is converted to electricity directly by the CPV reciever. These energy losses and gains are calculated along the length of the trough.

2.2 Model Reduction and Annual Simulation

A meaningful comparison between a CSP plant and hybrid retrofitted plant would need to be done on at least an annual scale to determine how the plants differ throughout a year. The computational effort associated with running the steady-state model at every hourly time step for a year to build up an annual generation profile would be extensive. In order to reduce this computational effort a model reduction strategy was implemented by means of a parametric sweep, varying dry bulb temperature and direct normal irradiance. The resulting dataset was subjected to a symbolic regression algorithm (Schmidt and Lipson 2009) to simultaneously search the parameter and form space for highly fitted equations representing the steady-state model's prediction for CSP and CPV yields of the retrofit.

Equation 1:

$$\eta_{CSP} = a_0 + a_1 * T_{amb} + \frac{a_2}{I_b}$$
$$R^2 = 0.99783307$$

Equation 2 (Curzon and Ahlborn 1975):

$$\eta_{carnot} = 1 - \sqrt{\frac{T_{amb} + 273}{663}}$$

Equation 3:

$$CSP\ (MW) = \frac{\eta_{CSP} * \eta_{carnot} * I_b * A}{1000000}$$

Equation 4:

$$CPV\ (MW) = \frac{A * ((b_0 * I_b) - b_1 - (b_2 * T_{amb} * I_b) - (b_3 * {I_b}^2))/32}{1000000}$$
$$R^2 = 0.99999724$$

TABLE 1: Values of coefficients for dynamic simulation calculations

Coefficient	Value
a_0	0.81123
a_1	0.000133
a_2	-34.4304
b_0	5.644508
b_1	7.367557
b_2	0.000626
b_3	0.000269
c1	0.000831
c2	3.498752
c3	2.055137
c4	0.001483
c5	4.371873
c6	7.378e-6
c7	2.141e-9

TABLE 2: Parameters used for dynamic simulation calculations

Parameter	Value
A	Aperture Area (190,338 m^2)
T_{amb}	Ambient Dry Bulb Temperature
I_b	Beam Irradiance
$TES_{SOC\ IN}$	Thermal Energy Storage state of charge from previous time step

To initialize the annual simulation model, typical meteorological year (TMY) data (National Renewable Energy Laboratory 2003), consisting of 8760 hourly values for ambient conditions, is read into the model. The correlation equations, from the symbolic regression, that make up the annual simulation model are shown in equations 1-4, with coefficients in Table 1, and parameters in Table 2. The ambient dry bulb temperature and direct normal irradiance is applied to these equations at each hourly time step for a year. The model calculates the CSP yield before the retrofit, as well as the CSP and CPV yields with the retrofit. This simulation can be applied to any plant as long at the aperture area and TMY data is available. After the model calculates the yields of the plant, the CSP yields are compared to the nameplate capacity of the power block to ensure the power block is not being overloaded. If the CSP load is greater than the nameplate capacity, the model assumes that collectors will be defocused to avoid this overload and therefore the CSP yield is set equal to the nameplate capacity of the power block, as shown in Figure 2. The model also assumes that there will be no yield of any kind if the sun is not shining, e.g. direct normal irradiance is less than 200 W/m^2.

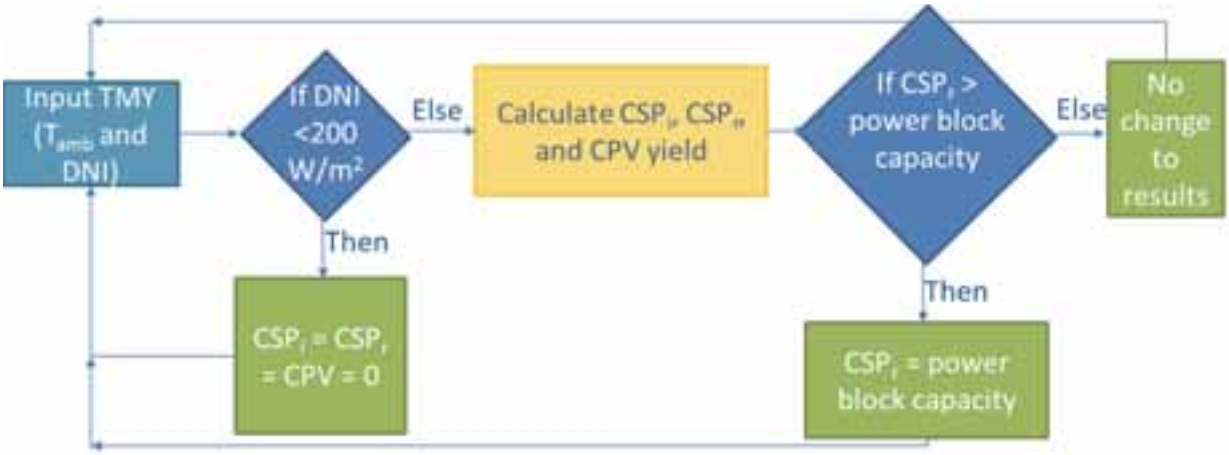

Figure 2: Annual performance model block diagram

3. Case Study

For this study the CPV retrofit of the Genesis solar trough plant in the Mojave Desert near Blythe, California (33.6650°N, 114.9948°W) is investigated. The Genesis CSP plant features linear parabolic trough collectors in a solar field with an aperture area of 1,928,320 m^2 and average annual power block output of 580,000 MWh (National Renewable Energy Laboratory 2014). This facility has a steam Rankine power block of 250 MW net capacity and no Thermal Energy Storage (TES)(U.S. Department of the Interior Bureau of Land Management 2016), consequently the CSP electricity power output in the model was capped at 250 MW. The model assumes that the entire solar field aperture area is retrofitted with the hybrid CPV system.

The Genesis plant's first full year of operation was 2014 and monthly data for the energy output in MWh is published online (National Renewable Energy Laboratory 2014). Actual meteorological data for Blythe, CA for 2014, 2015, and 2016 was obtained to initialize the dynamic simulation; the dry bulb temperatures and irradiances for every hour of those years are shown in Figure 3. The measured data provides direct normal irradiance, which does not account for the cosine losses of a single axis tracking plane. To increase the accuracy of the dynamic simulation, the direct normal irradiance is multiplied by the plane of array cosine loss factor for each hour, using a method adapted from (Duffie, Beckman, and Worek 1994).

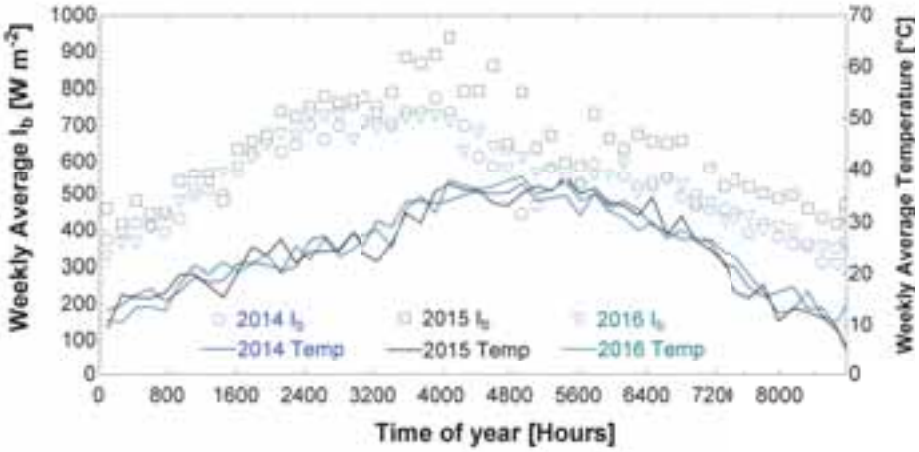

Figure 3: Beam Irradiance and Dry Bulb Temperature for 2014, 2015, and 2016 in Blythe, CA. The beam irradiance is a modification of the direct normal irradiance considering cosine losses of a single axis tracking plane.

4. Results

4.1. Model Validation

The optical and thermal validation and parametric tuning of the dynamic simulation is achieved through comparison of the predicted output of the CSP component (without the retrofit) to the published output data for the Genesis plant. The model calculates the output for every hour. These were summed into each month for comparison to the measured

data. Each of the modelled months was then compared to the measured data. A relationship is found to improve the closeness of fit between the results of physical modeling and the published output of the genesis plant:
Equation 5:

$$Model_2 = c_1 * I_b + c_2 * CSP * T_{amb} + \frac{c_3 * \tan\left({}^{c_4}/_{I_b}\right)}{{T_{amb}}^2} + \tan(c_5 * I_b + c_6 * CSP * T_{amb}) - c_7 * CSP - c_8 * T_{amb} * I_b - c_9 * \sin(c_{10} * I_b)$$

Table 3: Values of coefficients for tuned model simulation

Coefficient	Value
c_1	329.1380845
c_2	0.168203567
c_3	332684.8232
c_4	367.1260423
c_5	329.1380845
c_6	0.168203567
c_7	3.462152074
c_8	12.08652194
c_9	5303.369644
c_{10}	13796.71749

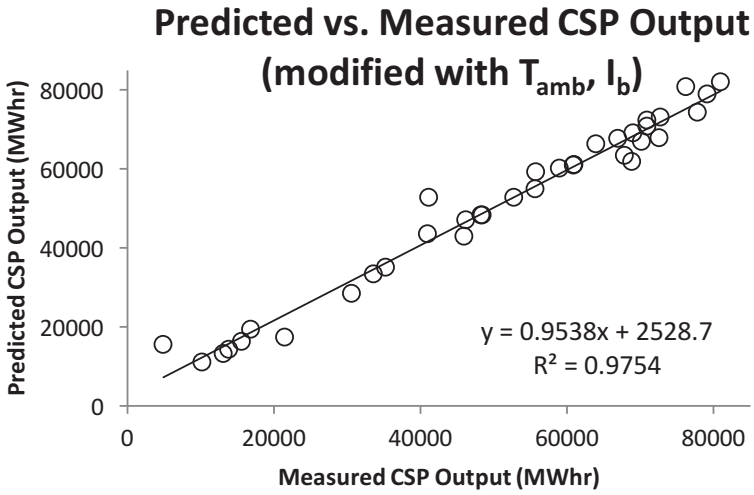

Figure 4: Predicted vs. measured CSP output modified by equation 5 with temperature and irradiance dependencies

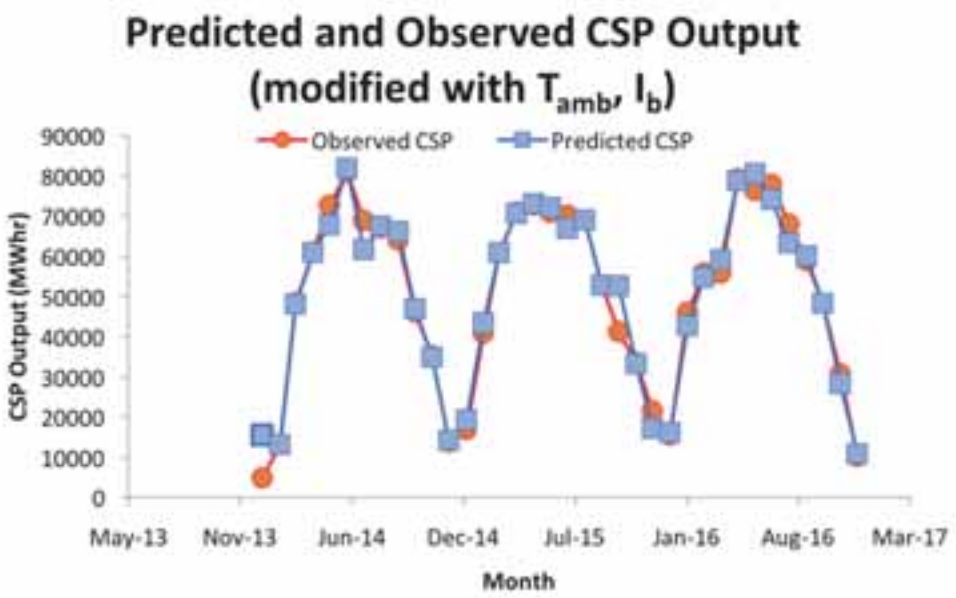

Figure 5: Modelled and Actual CSP Output (MWhr) for each month of the years of operation, modified equation 5.

As shown in **Figure 4**, using average temperature and daytime irradiance the predicted data matches closely with the measured data, with an R^2 value of 0.9754. Accuracy can be improved in sub-annual time periods by using the average data. The predicted CSP output matches the observed data well for each month, as shown in Figure 5.

4.2. Retrofit Yield Estimate

The overall yield of the plant with the retrofit, as well as the baseline measured CSP yield for the three years of operation is shown in Figure 6. The total yield of the plant is increased by 25%.

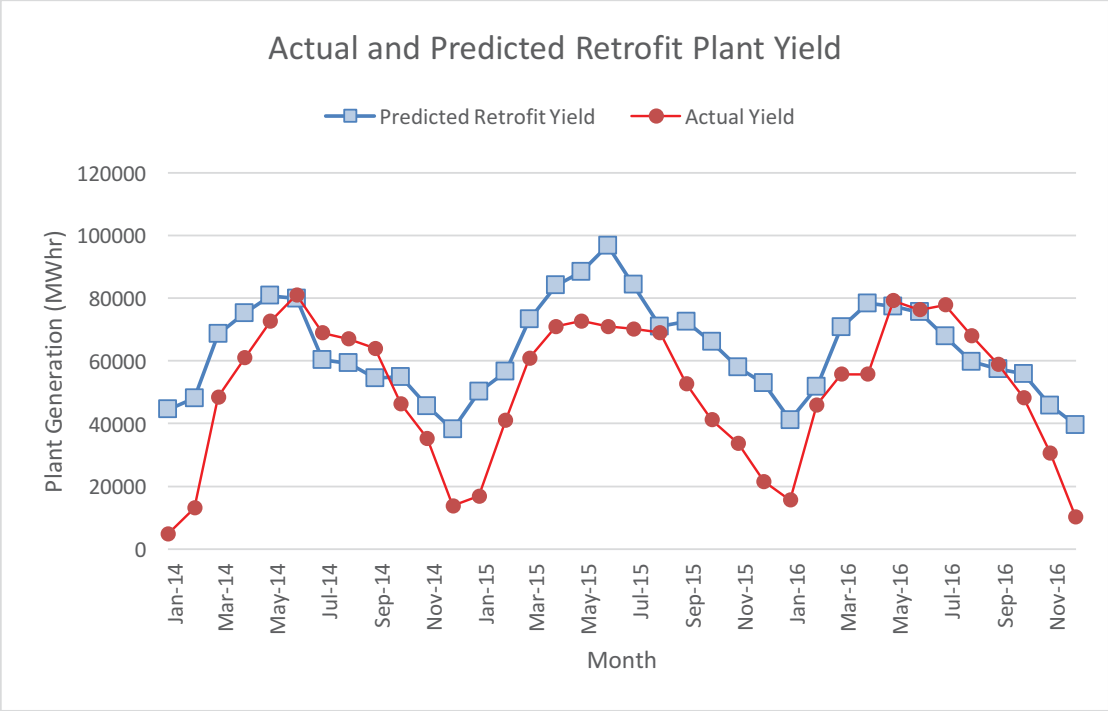

Figure 6: Actual and predicted retrofit(modelled) annual yield of Genesis plant.

5. Conclusions

The addition of a dichroic filter as a secondary optic in a Parabolic Trough Collector allows for the concentration of selected bands of the solar spectrum onto two physically and thermally decoupled receiver targets. This approach is proposed as a retrofit to existing CSP plants using the PTC format, whereby the second receiver is a solar panel. To characterize the performance of this hybrid retrofit, a dynamic simulation model is developed using correlation equations derived from a detailed steady state energy balance model, as a tool to facilitate the calculation of the change in yield of an existing CSP plant with the addition of a CPV retrofit. The overall yield of the plant with the retrofit, as well as the baseline measured CSP yield for the three years of operation is evaluated for a case study CSP plant (Genesis) located in California in the USA, and the results of this analysis indicate that the total yield of the plant is increased by 25%. The magnitude of the performance increase and the comparatively minor equipment investment supports further investigation of this technology as a retrofit to the currently operating fleet of PTC plants, and future work includes experimental validation of a prototype retrofit in a controlled environment in operating solar fields.

6. Acknowledgements

The information, data, or work presented herein was funded in part by the Advanced Research Projects Agency-Energy (ARPA-E), U.S. Department of Energy, under Award Number DE-AR0000729

7. References

ARPA-E. n.d. “Hybrid Solar Converter with Light-Filtering Mirror.”

Curzon, F. L. and B. Ahlborn. 1975. “Efficiency of a Carnot Engine at Maximum Power Output.” *American Journal of Physics* 43(1):22.

Duffie, J. A., William A. Beckman, and W. M. Worek. 1994. *Solar Engineering of Thermal Processes, 2nd Ed.* Wiley.

Forristall, R. 2003. “Heat Transfer Analysis and Modeling of a Parabolic Trough Solar Receiver Implemented in Engineering Equation Solver.” (October):164.

National Renewable Energy Laboratory. 2003. “National Renewable Energy Laboratory. NREL—National Solar Radiation Database.” *National Renewable Energy Laboratory*. Retrieved September 2, 2017 (http://rredc.nrel.gov/solar/old_data/nsrdb/1991-2005/tmy3/by_state_and_city.html).

National Renewable Energy Laboratory. 2014. “Genesis Solar Energy Project.” *National*

Renewable Energy Laboratory. Retrieved September 2, 2017 (https://www.nrel.gov/csp/solarpaces/project_detail.cfm/projectID=54).

National Renewable Energy Laboratory. 2016. "System Advisor Model Version 2016.3.14 (SAM 2016.3.14). National Renewable Energy Laboratory." Retrieved (https://sam.nrel.gov/content/downloads).

Orosz, Matt. 2015. "Photovoltaics and Concentrating Solar Power : Why Hybridization Makes Sense." *SPIE Newsroom* 1–4.

Orosz, Matthew, Nicolas Zweibaum, Tamir Lance, Maritza Ruiz, and Ratson Morad. 2016. "Spectrum-Splitting Hybrid CSP-CPV Solar Energy System with Standalone and Parabolic Trough Plant Retrofit Applications." *AIP Conference Proceedings* 1734.

Schmidt, Michael and Hod Lipson. 2009. "Distilling Free-Form Natural Laws from Experimental Data." *Science* 324(5923):81–85.

U.S. Department of the Interior Bureau of Land Management. 2016. "Renewable Energy Projects Approved since 2009." *U.S. Department of the Interior Bureau of Land Management*. Retrieved February 27, 2017 (https://www.blm.gov/wo/st/en/prog/energy/renewable_energy/Renewable_Energy_Projects_Approved_to_Date.html).

The Back Contact in CdTe/CdS Thin Film Solar Cells

Nicola Romeo, Alessio Bosio, Greta Rosa

University of Parma, Viale delle Scienze 7/A, 43124 - Parma

Summary

A barrier-free back contact in CdTe/CdS solar cells is fundamental for obtaining high-efficiency devices. Generally, the back contact is made by depositing a few nanometres of copper onto an etched CdTe surface, where a thin layer of tellurium is formed. In this way, a Cu_xTe film is obtained forming an ohmic contact with CdTe. However, if x exceeds 0.4 the contact is not stable and the solar cell degrades. Several attempts were made to make a barrier-free contact by using low-resistivity p-type materials such as: Sb_2Te_3, As_2Te_3, Bi_2Te_3, MoO_x and ZnTe but the results were not definitive. Still some copper seems to be needed. We used As_2Te_3, Bi_2Te_3 and ZnTe as buffers covered by ~10 nm of copper deposited at 520 K substrate temperature. This kind of contact works very well but only if the final contact is made of a thin layer of platinum covered by a thicker layer of molybdenum. Platinum exhibits a high work function (5.8 eV) and it is thus suitable to make an ohmic contact to the p-type high-conductivity buffer layers. Keywords: CdTe, Back Contact

1. Introduction

The CdTe/CdS solar cell has reached an efficiency of 22.1% [1] which, together with $CuInGaSe_2$ (CIGS), is the highest efficiency obtained for thin film solar cells. This efficiency is comparable with that of the best crystalline silcon solar cells. However, there is something which has not been completely clarified. That is, how to make an ohmic and stable contact to CdTe? Is it necessary to use copper? If yes, how to limit the copper diffusion into CdTe? It is known that, if copper reaches the junction, it can cause short-circuits or it can dope CdS, which becomes insulating. Several attempts have been made in order to avoid the use of copper in the back contact. For example, Lin et al. [2] and Drayton et al. [3] used MoO_3 thermally evaporated onto the CdTe surface as back contact. They find that this kind of contact works well on CdTe made both by closed-space sublimation (CSS) or R.F. sputtering. However, this contact works well if MoO_3 exhibits the right stoichiometry, which is not so simple to be obtained. Another promising material to be used as a Cu-free back contact is iron pyrite [4] but the obtained results are not definitive. In the past, we reported the preparation of a copper-free back-contact to CdTe by using a low resistivity p-type material such as Sb_2Te_3 [5] covered by molybdenum. Despite a high efficiency (~15%) was obtained, we found out that a roll-over is present in the J-V characteristics which is an indication that some barrier still exists at the back-contact. More recently, we used other buffers such as As_2Te_3 and Bi_2Te_3 covered by 5 – 10 nm of copper and we have demonstrated that an annealing at 520 K in air frees tellurium which combines with copper that, diffusing through the buffer, forms a thin layer of Cu_xTe on the CdTe surface [6-7]. If the Cu-diffusion is controlled in order that the x in the Cu_xTe is less than 0.4, then the contact is quite stable over time. It seems that a Cu_xTe (with $x \leq 0.4$) film is necessary to form a good contact with CdTe. In theory, the most suitable contact should be ZnTe since it is p-type, it does not exhibit any lattice mismatch with CdTe and its valence band is aligned to that of CdTe. However, ZnTe thin films generally exhibit high resistivity. We found out that, if ZnTe thin films are grown by radio frequency (R.F.) magnetron sputtering at 300 K substrate temperature and then annealed at 520 K for 20 minutes, their resistivity is lowered from 10^5 Ω cm to 2 Ω cm. In these conditions, ZnTe is suitable to be used as a back contact for CdTe. In any case, in order to make a good contact, a few nanometers of copper (~ 10 nm) on top of ZnTe are necessary in order to form, through Cu-diffusion, a Cu_xTe layer in the CdTe surface. Finally, the last contact on the buffer layer must be a metal which must form an ohmic contact with the buffer layer. We found out that, in order to avoid any roll-over and to have always a fill factor (F.F.) greater than 0.7, we had to use a few nanometers of platinum covered by molybdenum, that is, only platinum which exhibits a work function of 5.8 eV makes an ohmic contact with ZnTe. The same results are obtained if As_2Te_3 or Bi_2Te_3 are used as buffer layers.

2. Experimental

As shown in figure 1, CdTe/CdS solar cells are made up of 4 main layers. As a substrate, a 1 inch square soda lime glass is used. The front contact is prepared by depositing in sequence on the glass 500 nm of indium tin oxide (ITO) and 150 nm of pure ZnO at a substrate temperature of ~ 670 K. ITO is prepared by direct current (D.C.) pulsed magnetron sputtering in an atmosphere of Ar + 2% of O_2, while ZnO is prepared by R.F. magnetron sputtering from a target of pure Zn in an atmosphere of Ar + 10% of O_2. In both cases O_2 has to be minimized in order to avoid any excess of oxygen in the films. CdS is also prepared by R.F. magnetron

doi:10.18086/swc.2017.20.08 Available at http://proceedings.ises.org

sputtering in an atmosphere of Ar + 6% Trifluorometane (CHF_3). This gas contains F, which is freed in the sputtering discharge and, being electronegative, bombards the substrate during the growth of the CdS film. In this way, any excess of Cd or S are removed from CdS during its growth and the film results stoichiometric with a forbidden gap a little higher than that of the film grown without CHF_3 [8]. CdTe is prepared by CSS at a substrate temperature of 773 K. Typical thickness of CdS is 100 nm while CdTe thickness is 6 μm. Before making the back-contact CdTe is treated for 20 – 30 minutes at 690 K in an atmosphere containing 2 x 10^3 Pa of Freon R22, whose formula is $CHClF_3$, and 5 x 10^4 Pa of argon.

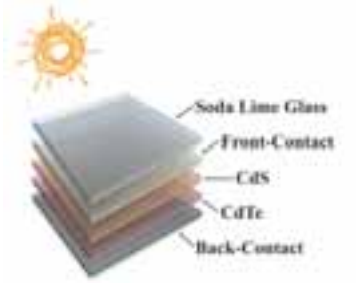

Fig. 1: Outline of CdTe/CdS solar cell.

For the back-contact we experimented four buffer layers namely: Sb_2Te_3, As_2Te_3, Bi_2Te_3 and ZnTe. Those buffer layers are generally covered by 10 nm of copper and the external layer is made by depositing in sequence 10 nm of platinum and 200 nm of molybdenum (as shown in figure 2).

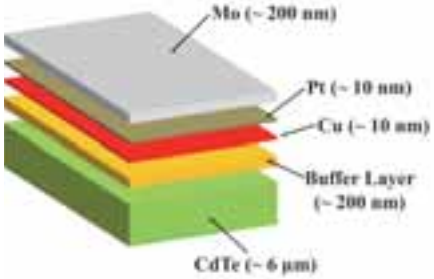

Fig. 2: Scheme of back-contact structure.

Sb_2Te_3, As_2Te_3, Bi_2Te_3 all exhibit a low resistivity on the order of 10^{-2} – 10^{-3} Ω cm but ZnTe exhibits a high resistivity. The lowest resistivity observed on ZnTe is about 10^5 Ω cm, when it is deposited by R.F. sputtering with the substrate kept at room temperature. But, it is enough a 20 minutes annealing made at 520 K in vacuum to lower the resistivity to 2 Ω cm. At higher annealing temperatures the resistivity tends to increase again. The results obtained with As_2Te_3, Bi_2Te_3 and ZnTe are very similar while the efficiency obtained with Sb_2Te_3 is a little smaller. Efficiency for these cells is on the order of 15 - 16% with a fill factor of 0.7 - 0.72. Figure 3 shows the J-V characteristics of the solar cell with a buffer layer of ZnTe and the external contact made with or without platinum. While the short-circuit current density (J_{SC}), open-circuit voltage (V_{OC}) and F.F. are almost the same, a roll-over appears in the J-V characteristic when platinum is not used. From these results it comes out that in order to get CdS/CdTe solar cells with high efficiency without any roll-over:

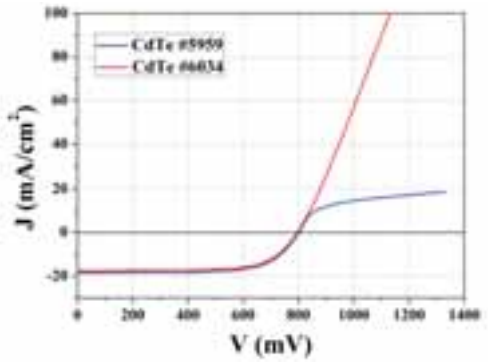

Fig. 3: Sample CdTe #5959: external contact is made without platinum. Sample CdTe #6034: external contact is made with platinum.

1 - Copper is necessary in order that a Cu_xTe layer is formed on top of CdTe. 2 - The diffusion of copper has to be controlled in order to form a Cu_xTe layer with $x \leq 0.4$. 3 - A buffer layer is needed in order to control the Cu-diffusion. 4 - A contact with a high work function, such as platinum (with a work function of 5.8 eV) is needed in order to make an ohmic contact to the buffer layer.

3. Stability tests

Accelerated lifetime tests have been done on solar cells with different buffer layers. Typically, the tests are made by keeping the devices in a box in which the temperature is controlled at 350 K. During the tests the solar cells are exposed to one sun light for about 1200 hours. Almost no efficiency degradation is observed on solar cells with ZnTe buffer layers. There is an initial increase in the efficiency which then stabilizes at values close to the initial value. For the other buffer layers the efficiency decrease from 5% to 10% after 1200 hours of light soaking at 350 K.

4. Conclusion

Here we described a way to make a non-rectifying back-contact to CdS/CdTe solar cells. We found out that the back-contact can contain copper whose diffusion must be controlled by a buffer layer. Finally, we would like to put in evidence that, in order to avoid any roll-over in the J-V characteristic, the contact on the buffer layer has to be made with a high work function metal such as platinum.

5. References

[1]. https://upload.wikimedia.org/wikipedia/commons/3/35/Best_Research-Cell_Efficiencies.png (accessed on 06 03 2017).

[2]. Lin, H., Xia, W., Wu, H. N., Tang, C. W., 2010. CdS/CdTe solar cells with MoO_x as back contact buffers. Applied Physics Letters, 97(12), 123504.

[3]. Drayton, J. A., Williams, D. D., Geisthardt, R. M., Cramer, C. L., Williams, J. D., Sites, J. R., 2015. Molybdenum oxide and molybdenum oxide-nitride back contacts for CdTe solar cells. Journal of Vacuum Science & Technology A: Vacuum, Surfaces, and Films, 33(4), 041201.

[4]. Bhandari, K. P., Koirala, P., Paudel, N. R., Khanal, R. R., Phillips, A. B., Yan, Y., Ellingson, R. J., 2015. Iron pyrite nanocrystal film serves as a copper-free back contact for polycrystalline CdTe thin film solar cells. Solar Energy Materials and Solar Cells, 140, 108-114.

[5]. Romeo, N., Bosio, A., Tedeschi, R., Canevari, V., 1998. High efficiency and stable CdTe/CdS thin film solar cells on soda-lime glass. 2nd World Conference on Photovoltaich Solar Energy Conversion. 88, 446-447.

[6]. Romeo, N., Bosio, A., Mazzamuto, S., Romeo, A., Vaillant-Rocac, L., 2007. High efficiency CdTe/CdS thin film solar cells with a novel back-contact. 22nd European Photovoltaic Solar Energy Conference. 1919-1921.

[7]. Wu, X., Zhou, J., Duda, A., Yan, Y., Teeter, G., Asher, S., Metzger, W.K., Demtsu, S., Wie, S.H., Noufi, R., 2007. Phase control of Cu_xTe film and its effects on CdS/CdTe solar cell. Thin Solid Films. 515, 5798-5803.

[8]. Romeo, N., Bosio, A., & Canevari, V., 2003. The role of CdS preparation method in the performance of CdTe/CdS thin film solar cell. In: Photovoltaic Energy Conversion 2003, Proceedings of 3rd World Conference on, 1, 469-470.

Advantages and Limitations of Thermography in Utility Scale Solar PV Plants

Rajat Sethi[1] and Pankaj Kumar[2]

Tata Power Solar Systems Ltd, Bangalore (India)

Abstract

Thermal Imaging has always been used in military applications along with night vision, when there is no sun. Now is the time we need thermal imaging technology to check the performance and find out abnormalities/underperforming areas in Solar PV power plant. While the advantages of thermal imaging are large in number, but it comes with a need of awareness of the concepts of heat transfer and fundamentals of measurement. A lot of research has been done, on how to do the thermal imaging of various type of surfaces, which have glazing or some type of coating over them. This paper tries to summarize the knowledge gained in the field of heat transfer along with the application areas where Infrared (IR) thermography can help us track down high temperature regions (hot spots) in a Utility Scale Solar PV Plant. This paper will also serve as a quick reference guide for the Solar industry engineers for a fast set up, measurement and understanding of Thermographic Instruments. For the analysis purpose, a 100MW Utility scale solar site and few rooftop solar projects in India were chosen to collect the data and for taking the measurements.

Keywords: Thermal Imaging, Performance of PV plant, Hot Spot, Heat Transfer, IR Thermography, Reference guide

1. Introduction

Numerous techniques are being used to measure the performance of components in a PV plant. Monitoring systems come into play, starting from the string level/array level data and it goes till current reaches the grid. Sensors are used to measure temperature of modules, ambient temperature, Irradiance, wind speed, wind direction and also in the electrical and electronic equipment to keep a check on the performance and operation. The solar industry has started using Infrared thermography for finding the underperformance in their modules and to narrow down the faults to specific cells (Hot Spots). It is also being used for checking the uniform oil flow in heat exchangers of transformers and check whether the oil is circulating as expected or there are regions of blockage by seeing the thermal image of the equipment. Similarly, this can be used to check spark or loose contacts at isolator or evacuations points or substation level of a solar power plant. So, a lot of early failures can be detected.

To check the performance of the components, one needs a good understanding of materials, their glazing behavior as well as knowledge of heat transfer subject. Every object can emit, reflect and transmit radiations in different band of the electromagnetic spectrum, depending on the properties of the material and the temperature of the object. Sun is emitting electromagnetic (EM) radiations in a broad range of Infrared (IR), Visible, UV and X-ray, etc. Every object above 0 K (Kelvin) emits and receives energy (Plank's Law). In IR thermography, we use the infrared emitting capacity of a body which most of the time is a strong function of temperature (Stefan-Boltzmann law). A thermal imager can capture the IR radiations emitted and can convert the IR data in high and low temperature regions using visible spectrum on our display screen.

2. Working of Thermal Imaging Technology:

2.1 Background

In the last 50 years, there have been three major developments in area of thermal imaging and these are: (1) Scanners or Scanning Systems, (2) Pyroelectric Videocon's (PEVs), and (3) Focal Plane Arrays (FPAs). FPA technology is more popular these days due to advancement in semiconductor industry and because of the accuracy possible with them. The function of the equipment is to detect the infrared radiations emitted by

doi:10.18086/swc.2017.20.09 Available at http://proceedings.ises.org

an object or equipment (known as Target). Corresponding to the Radiosity (sum of radiations, emitted, reflected and transmitted per unit surface area) of the object, there is induced voltage or change in resistance of semiconductor array. These signals are then read by the electronic circuits present in the equipment and a thermogram is created which is visible to us on the display screen of equipment (Fig. 1). Each pixel of thermogram inherits the point to point temperature measurement on the surface of the object. This is done by an array of semiconductor detectors, which are placed on a plane and are highly sensitive to temperature. More is the density of plane of the array; more will be the resolution of the thermal image and hence higher accuracy of measurement. Typical arrays used are 256x256, 320x240, etc. For the current analysis, we have used thermal equipment of Testo and Fluke companies, and used their respective software for the analysis.

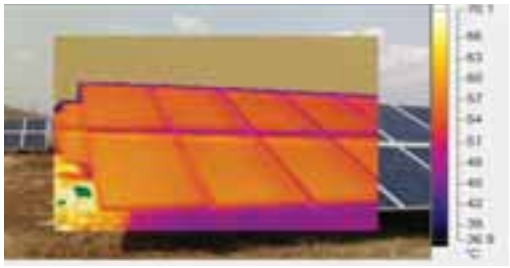

Fig.1: Thermal image distinguishing the high and low temperature regions with the help of the visible spectrum, white and yellow being the highest temperature region while black and blue indicating a lower temperature range. (Image taken at one of the megawatt scale solar plant in India)

2.2 Sun's Spectrum

Sun has always been the source of energy for earth. From photosynthesis to blowing wind, it is all because of the sun. In recent years, we have learnt the importance of using sun's energy directly instead of stored forms like fossil fuels, as we don't have to spend extra money for their extraction and purification. We just need technology, which can convert Sun energy directly to electricity. Solar PV technology is at the forefront of all renewable energy sources. As per International Energy Outlook 2016 by the IEA, around 30% of total electricity generation in 2040 will be from Renewable sources of energy (International Energy Outlook, 2016). In another Annual Energy Outlook report 2017 of the IEA, solar capacity addition is projected to be the primary replacement of retiring coal power plants between 2030 and 2040 (Annual Energy Outlook, 2017). Utilizing sun's energy will be the most economical and most sustainable option in coming years. The more we know about the sun and the ways to utilize its energy, the better it will be for us.

The photons coming from the sun, carrying this energy, have a wavelength varying from high energy X-rays and gamma rays to visible light to the infrared and radio. However, here on earth, we receive only a certain portion of the spectrum. Sun's spectrum (shown in Fig.2) is similar to that of a spectrum of black body at 5800K as mentioned by Duffie and Beckman (Duffie and Beckman, 2013). Out of these radiations, around 44% of radiation are in visible range, i.e. 400-700 nm or 0.4-0.7 μm and 49% in the infrared region.

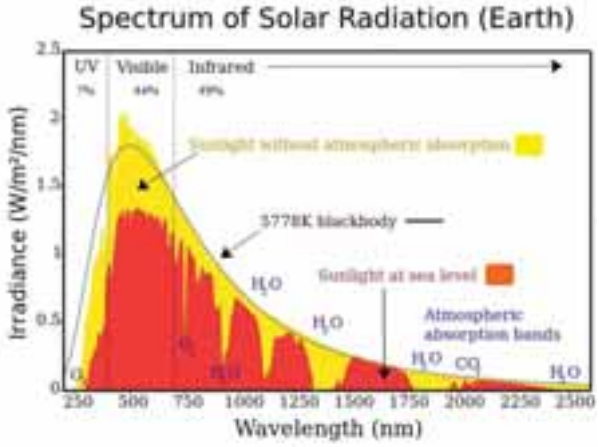

Figure 2: Sun's Electromagnetic Spectrum (Nick, wikipedia)
Image credits: Nick84 http://commons.wikimedia.org/wiki/File:Solar_spectrum_ita.svg, CC BY-SA 3.0,

2.3 Infrared Radiations (IR)

Any Radiation falling on any object is never perfectly absorbed, transmitted or reflected. Always, two or all three of these phenomena happen at once. For a typical transparent glass, 92% of the radiation are transmitted, 6% are reflected at the glass surface and 2% are absorbed. In the solar PV modules, the glass used is extra clear glass with low iron oxide content, which helps in less absorption of light. The transmission curve of glass also shows us that the glass is somewhat transparent in the short waveband and opaque in the long waveband. All these phenomena are also true for IR falling/transmitting through the glass surface.

When we see a surface, we can see the radaitions being absorbed by it along with the radiations reflected or transmitted by it. Neither the reflected nor the transmitted radiations, provide any details about the temperature of the object. Only emitted radiation coming out of a body give us a sense of temperature. This radiation being emitted by a body is directly dependent on the emissivity of the surface.

In thermography, the biggest task for a professional is to separate the reflected and transmitted part of radiation from the emitted radiations. Glasses are typically transparent to short IR wavelengths and opaque to long IR wavelengths. Our atmosphere is transparent in two regions of wave i.e. visble, infared and radio wave bands, rest of thermal spectrum is absorbed by water vapors, carbon dioxide and other gases (Fig.3).

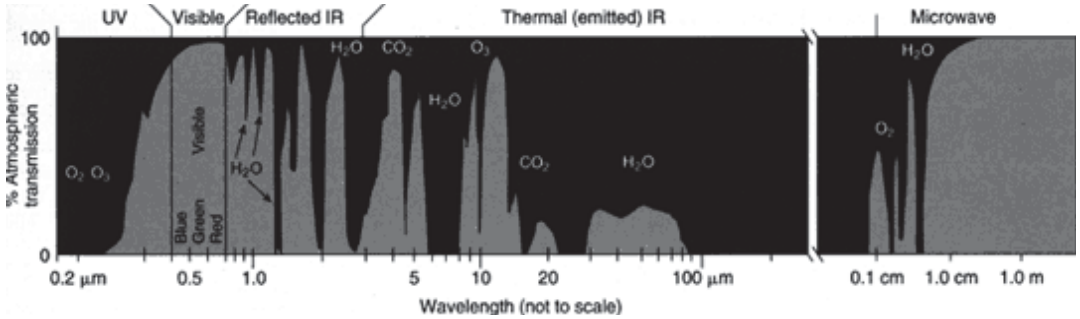

Fig.3: Absoption spectrum of earth's atmosphere. Chemical notation (CO2, O3) indicates the gas responsible for blocking sunlight at a particular wavelength. (Earth observatory, NASA)

2.4 Materials and Emissivity measurement

A black body is a perfect absorber and emitter of radiation. The emissivity of a surface represents the ratio of the radiation emitted by the surface at a given temperature to the radiation emitted by a blackbody at the same temperature. The emissivity of a surface is denoted by ε, and it varies between zero and one, $0< \varepsilon<1$. Emissivity is a measure of how closely a surface approximates a black body, for which $\varepsilon=1$ (Yunus A. Çengel, 2002).

For better measurements, we also need to know about the absorption property of a body. Absorptivity is a measure of how much fraction of the radiation falling on the object/medium is absorbed by it. Radiation falling on a surface/medium could have encountered three phenomena (a.) Absorption (b.) Reflection (c.) Transmission (explained in eq.1). The fraction of these will vary depending on property of the object/medium.

From the first law of thermodynamics we can say that,

Energy Incident = Energy Absorbed + Energy Reflected + Energy Transmitted

1 = (Energy Absorbed + Energy Reflected + Energy Transmitted) / (Energy Incident)

Or, $1 = \alpha + \rho + \tau$ (eq. 1)

Where, α is Absorptivity, ρ is Reflectivity and τ is Transmissivity of the material.

For finding the temperature of any object, there are equipment available. There are Infrared thermometers, which can give us point-to-point temperature readings and there are thermal imagers, which gives us the 2D image of the surface showing hot and cold regions with different colors/contrast. Many Instruments from various manufacturers like Fluke, Meco, Testo etc. have come into the market. But, measurements made by these instruments do not make sense till accurate values of material/media properties, external factors are given as input first.

For example: To find out any hotspot in a string or array we need to have knowledge of emissivity of silicon material (assuming multi crystalline silicon solar cells) and how the upper glazing is affecting the measurement. All the metals are good conductors of heat and electricity, so they don't emit a lot of radiation

in IR region and also they don't emit the radiation from the same place where radiation has fallen. Inside metals molecules vibrate quickly and energy gets conducted to all surrounding molecules, which results in lesser values of emittance. Metals also reflect a part of incoming energy/light falling on it. This kind of behavior is not shown by semiconductor materials. They absorb the radiation and emit it in the IR region. Most of the radiation is emitted from the same place where incident radiations fell. So, most of the time Semiconductors and insulators have higher emissive values. Table 1 lists the common materials encountered while doing thermal imaging along with their emmissivity values.

Tab 1: List of common materials and their emissivity.
(Fluke, Emissivity of materials), (Transmetra, Emissivity for various surfaces)

Sr. No.	Material	Emissivity	Sr. No.	Material	Emissivity
1	Aluminum Foil	0.04	26	Mild Steel	0.20 0.32
2	Aluminum Highly Polished	0.039-0.057	27	Paper	0.93
3	Aluminum Heavily Oxidized	0.2-0.31	28	Plastics	0.90-0.97
4	Asbestos board	0.96	29	PVC	0.91-0.93
5	Asphalt	0.93	30	Silica	0.79-0.85
6	Brick, red rough	0.93	31	Soil	0.79
7	Brick, fireclay	0.75	32	Steel Polished	0.07
8	Cast Iron, newly turned	0.44	33	Steel Galvenized old	0.88
9	Cast Iron, turned and heated	0.60 0.70	34	Steel Galvenized new	0.23
10	Cement	0.54	35	Tin unoxidized	0.04
11	Clay	0.91	36	Titanium polished	0.19
12	Coal	0.8	37	Tungsten polished	0.04
13	Concrete	0.85	38	Water 0.95 0.963	0.95 0.963
14	Cotton cloth	0.77	39	Wood Beech, planned	0.935
15	Copper electroplated	0.03	40	Wood Oak, planned	0.885
16	Copper heated and covered with thick oxide layer	0.78	41	Wood, Pine	0.95
17	Copper Polished	0.023-0.052	42	Wrought Iron	0.94
18	Copper Nickel Alloy, polished	0.059	43	Zink Tarnished	0.25
19	Glass smooth	0.92 0.94	44	Zink polished	0.045
20	Human Skin	0.985	45		
21	Ice smooth	0.966	46		
22	Ice rough	0.985	47		
23	Iron polished	0.14 0.38	48		
24	Iron, plate rusted red	0.61	49		
25	Mercury liquid	0.1	50		

Note: As we know, emissivity of a given material will vary with temperature and surface finish, the value in these tables should be used only as a guide for relative or differential temperature measurements. The exact emissivity of a material should be determined when high accuracy is required.

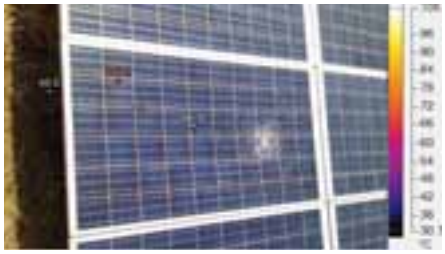

Fig. 4: Optical Image of a damaged module.

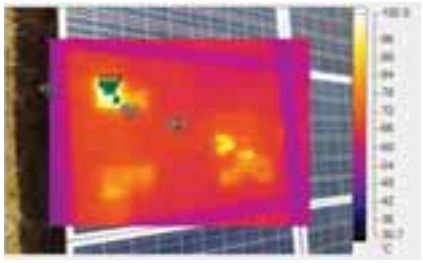

Fig. 5: IR Image for damaged module (fig.4) with hot spot and high temperature region.

In IR thermography, camera sensor takes the IR radiations emitted by a body as its input to calculate the temperature of the body. These instruments most often need the ambient temperature values for reference temperature and then calculate the temperature of materials/medium accordingly. For silicon, two values of emissivity are given in standards 0.8 and 0.9, depending on glazing. Assuming the value of emissivity as 0.8 and setting the measurement range at 35 to 75 degree centigrade in the equipment, we were able to get better results. For cross checking our measurement, we had used a thermocouple at the back of one of the solar modules.

3. Application of Thermography in Solar PV Plants

Thermal imagers will pin point us in the direction where fault/abnormality is present. By using electrical instruments like Multimeter, Clampmeter and Resistance measuring units, we can get into the root cause of an issue. Suppose there is an extra heating in one phase out of the three, thermal imager will direct us to that phase, now to find out the reason for heating, we need to check the amount of current flowing as well as the resistance in the circuit. A list of solar plant areas, where thermal imaging is used, is mentioned below:

3.1 Application area: To check underperforming solar strings and arrays:

Solar modules are the main component of energy conversion. The plant‘s efficiency depends primarily on this conversion process. We can also calculate overall solar plant efficiency as the product of all the efficiency in the process (as shown in eq. 2). For the efficiency calculation, we must know the losses in each step of conversion.

The losses in a solar plant are as follow:

1. Loss due to temperature (The rated power of modules is calculated at 25°C) = L1
2. Dirt or soiling on face of solar module (Often, Dirt loss=5-10% or 0.05) = L2
3. Manufacturer's tolerance (3-4% or 0.03, given by the manufacturer) = L3
4. Voltage drop through AC and DC cabling = L4
5. Inverter efficiency/loss = L5
6. Shading = L6
7. Tilt angle of the solar modules = L7
8. Orientation of solar modules = L8

Overall efficiency= (1-L1) x (1-L2) x (1-L3) x (1-L4) x (1-L5) x (1-L6) x (1-L7) x (1-L8) (eq. 2) (GSES,2013)

Using this only, we also calculate the Energy yield of the plant,

Energy Yield = Irradiation x Module rated power x Losses (as efficiencies)

Using a thermal imager, we can calculate the thermal loss of the module and if there is any hotspot areas on the panel.

In a solar panel, generally the cell temperature is 20-25°C higher than the ambient temperature because of continuous heat generation at cell level. So, in the countries, which lie in between the tropic of cancer and the tropic of capricon, this thermal loss can reach upto 20% (considering ambient temperature can go upto 50°C). The performance of these semiconductor solar cells is highest when the temperature is 0 degree C,

which is not usually the case. This is one of the reasons that a place with high radiation need not be generating the most amount of energy, compared to a place with low irradiance and low temperature.

So, thermal cameras can be used to check the healthiness of modules and for each degree higher temperature, we lose roughly 0.3-0.5% of power output of cells. The Supervisory control and data acquisition (SCADA) systems used currently will tell us the strings which are not giving full output and combined with thermal cameras we can easily distinguish the faulty or damaged module which are making the loss.

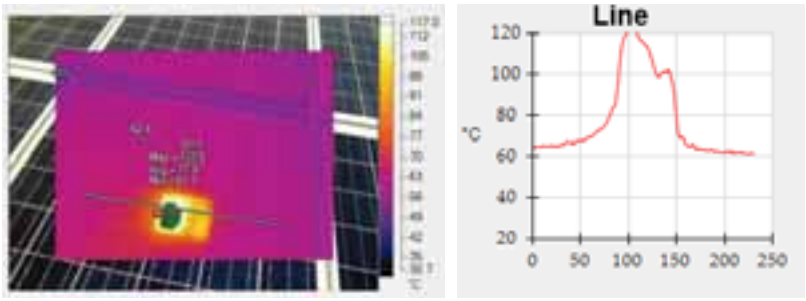

Fig 6: The image on left shows the hot spot on a module and the damaged cell with temperatre going upto 120°C (Shown in right side figure with line graph)

3.2 Application Area: String Monitoring Unit (SMU)/ String Combinor Box Monitoring (SCB)

These days SCADA systems are primarily used to check the string current in a large solar plant. Burning issues in SCB/SMU are also common. At places around the world, fire incidents have also occurred because of overheating issues at the terminal inside the SCB. On many occasions, it is found that connecting terminals/joints are getting heated, but the temperature is not high enough that they will glow brightly and it will become visible to the naked eye. The temperatures will go upto 200-250°C before the melting and burning of plastics/rubber happen on wire insulation. Most plastics used are fire retardant but not fire proof, so till date, early detection is the only key to avoid these accidents. Thermography being a non-contact type technique, we can easily distinguish the overheated points, which may be because of any of the reasons like, loose connection, dust in between the joints, some malfunctioning etc. The same is true for isolator panel boxes also on AC and DC sides.

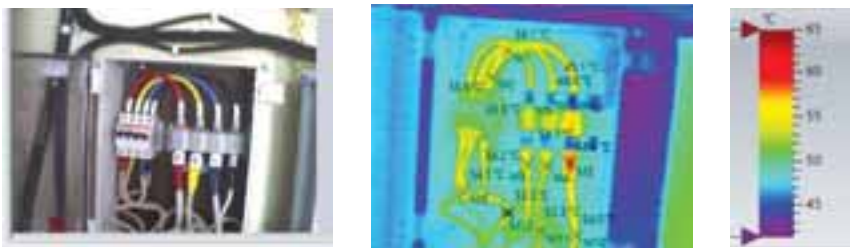

Fig 7: Normal and Thermal image of a typical Isolator Panel of a rooftop solar plant. In centre image we see that blue phase wire temperature is roughly 5°C higher than wires of remaining two phases.

Action plan for relative temperature difference between phase connections:

40°C or more : Failure can happen at any time and corrective measure should be taken immediately

20°C-40°C : Corrective measures to be taken at earliest to avoid failure in coming hours/days

20°C : Corrective measure required to prevent from failure in coming weeks

Below 20°C : Chance of failure; measure should be taken in next scheduled maintenance activity

3.3 Application Area 3: Power Conditioning Unit (PCU) / Inverter Level Inspection:

Inverters available in the market now (2016 onwards) have efficiencies of 95-98%. The remaining are the conversion losses which happen in electrical and electronic components of the inverter. High quantity of current coming from PV panels enters the inverter as Direct Current (DC) and we get 3-phase Alternating

Current (AC) at the output. In recent inverter models, it is hard to see insulated-gate bipolar transistor (IGBT) from outside, which is responsible for DC to AC conversion. This is adopted because of safety features and Ingression protection standards like IP 65, IP 66 etc. In some older Inverter models (prior to 2014-15), checking healthiness of IGBT's against overheating was possible with thermal cameras. We can also check the heat emitted by bus bars, circuit breakers and at other connection points and can tell whether there is something abnormal or not. In some cases, because of less space below Inverters and Junction boxes, wires are bent in 'U' shape, This causes a lot of resistance to current flow and hence heating of wires. We can inspect such areas with thermal cameras.

3.4 Application Area: Switchyard and Substation Area:

Switch yard is the area, where the same power, which is generated by a solar plant, is transmitted to the state electricity board substation or transmission company. Substation steps up or steps down the voltages coming from the generating station. In both substation and Switch yard areas, thermography has huge application because of the criticality of the equipments used. The components include circuit breakers of various types, isolators, isolated phase buses, T joints, straight joints, bolts on bus bars, various fuses, transformers, etc. Heating of bolts, moving contact parts, etc. in substation are often checked with thermal cameras. The fault or failure of any of the components can lead to significant breakdown and hence loss of power. To confirm the healthy functioning of these areas, in terms of smooth power evacuation without excessive heat being generated on isolators, at bus bar connection points, we use thermal cameras. Depending on the material used like bus bars are generally aluminium rods; we can set our instrument for the measurement. For high voltages, aluminium is the most preferred choice because of conductivity, strength and corrosion resistance.

This not only saves time but also gives us confidence about the smooth operation of the plant.

Fig 8: Visible and infrared image of isolator and bus bars.

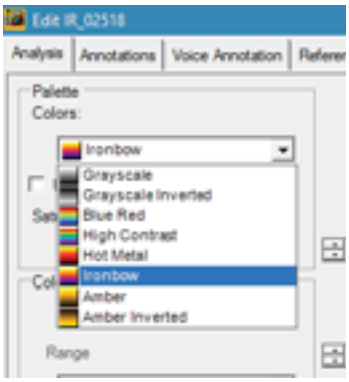

Fig 9: Palette options available in softwares to have better visual effect. (Screen: Fluke smart view software)

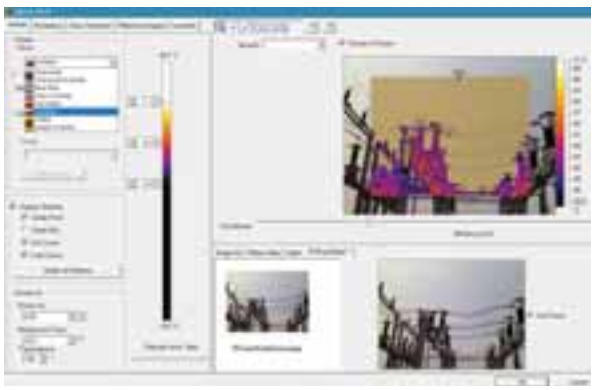

Fig 10: Fluke Smart view software window with image of a typical isolation yard.

Note: When using the software for analysis, we need to put correct emissivity one by one for materials under observation to see correct values of temperature. One should not conclude on basis of half-baked information. One can also choose different kind of palettes as per one's ease and visual advantage (Fig 9).

4. Advantages and Limitations of IR Thermography

4.1 Advantages of Thermography (Tequipments.net)

- It uses non-contact type of measuring technique, which makes it safe.
- It is fast, accurate and easy to use.
- It helps in detecting situations of electrical unbalance or overloads.
- It can be used for electrical, mechanical and other building envelope related work.
- It helps in fast identification of loose, corroded connections even if they are not visible to naked eye.
- It helps in developing the Inspection program for various equipment and machineries.
- It can be driver in making predictive and preventive maintenance schedules.
- It can be used to check, heating in electronic circuit board and narrowing down to faulty area.

4.2 Limitation of Thermography

- High reflecting metals: Using thermal imaging becomes tricky, when one takes measurement of isolation yard on a sunny day. Unlike coal thermal stations or other energy generating stations, in solar plants peak generation is in the hours, when the sun is shining bright. At this point of time, the metals also reflect a lot of visible light. The expert has to carefully choose an angle, where sun interferes least and try to get more radiations, which are emitted by the target equipment under consideration. This can be done by varying the emissivity value or using some correction factor.
- Trapping of IR radiation inside glass enclosures: Most of the thermal cameras available today can take the measurement in short and medium infrared region. Filters are available to take care of interference by glazing and other radiations.
- Weather dependence in solar plant also plays a role. Recommended time for taking measurement is peak sunshine hours. (between 11 am -2 pm in India)
- Significant change in readings, when angle of measurement change. The recommended practice is to take the measurement at an angle of 90 degree (normal) to the surface of object. If we take the image at acute angles, then, the measurement will be incorrect.
- When wind blows over a surface, a boundary layer is formed which effects the heat transfer. Recommended practice is to take the measurement in still air conditions and at steady state conditions.
- IR themography takes the instantaneous measurement and not the gradient. In some cases, when temperature is rising and falling with time, we cannot find the rate of change of temperature directly. In those areas, thermocouples are best suited to analyze the trend with time.
- For small rooftop solar plants, the cost of thermal equipment is high in comparison to the investment one has done. So, it is common practice to ask an O&M company, which has taken annual maintenance contract to do the themographic exercise once a year. This has more application in large scale utility solar plants, where electricity is directly going to national grid and one can not afford any failure in any components.

4.3 Other Application Areas:

- Used commonly by Energy Auditors to find the areas of heat loss and poor insulation in processing industry and manufacturing industry.
- Used to find oil/gas leakages from the vessels.
- Used by civil work departments and building professionals to check the structural integrity and sometimes the moisture inside the roof/wall etc.
- Military use this technology along with night vision cameras in aircraft and auto guided missile systems.
- Used oftenly, in industries where lot of motors and rolling machines are present. This technology helps in planning their maintenance schedules.

5. Conclusion

As solar energy sector has shown its dominance in last few years, with accelerated growth rates; in coming years, our life will be surrounded by equipment, machines and homes, running completely on solar energy. This paper has tried to summarize the learning from megawatt scale solar plants in India, along with the general understanding about IR thermal imaging technology. Most suitable person for thermal inspection activity will be an engineer with basic understanding of concepts of heat transfer like radiosity, boundary layer along with some knowledge of material science. The awareness of parameters like background temperature, ambient air temperature, relative humidity, information on effect of wind or convection heat transfer, emissivity properties, effect of sun, ideal distance of target, angle of incidence, will make the measurement highly accurate. This paper has tried to touch upon these above parameters with field examples and learnings from the SPV power plant. Few general thumb rules are also suggested, on the how to decide the criticality and frequency of maintenance activity, based on the temperature readings (sub-section 3.2). This paper will also serve as a reference guide, for using thermal imaging in different solar power plants and other areas of energy efficiency.

6. References:

Annual Energy Outlook 2017 with projections to 2050, U.S. Energy Information Administration, https://www.eia.gov/outlooks/aeo/

Fluke, Emissivity values of common materials, Fluke Corporation, http://support.fluke.com/find-sales/Download/Asset/3038318_6251_ENG_A_W.PDF as accessed on 23.09.17

GSES, Grid Connected PV Systems: Design and Installation, 2013. First Ed. GSES Pty. Ltd., New Delhi.

Tequiment.net Education series, http://assets.tequipment.net/assets/1/26/Documents/thermalapplication_edu-series.pdf as acceessd on 10.08.2017

International Energy Outlook 2016, U.S. Energy Information Administration, https://www.eia.gov/outlooks/ieo/

John A. Duffie, William A. Beckman, 2013. Solar Engineering of Thermal Processes, Fourth Ed. John Wiley & Sons, New Jersey

Earth Observatory NASA https://earthobservatory.nasa.gov/Features/RemoteSensing/remote_04.php as accessed on 08.10.2017

Nick84 - http://commons.wikimedia.org/wiki/File:Solar_spectrum_ita.svg, CC BY-SA 3.0, https://commons.wikimedia.org/w/index.php?curid=24648395

Transmetra, Table of Emissivity of various surfaces, www.transmetra.ch https://transmetra.ch/dokumentation/dokumentation-publikationen/category/123-pyrometrie-thermografie as accessed on 23.09.17

Yunus A. Çengel, 2002. Heat and Mass Transfer- A Practical Approach, Second Ed. Mcgraw-Hill, New York.

Correlation of Leakage Current Pathways and Potential Induced Degradation of CIGS Thin Film Solar Modules

Sebastian Voswinckel, Viktor Wesselak, Sven Münter, Lukas Gerstenberg
Institute for Renewable Energy Technologies/ University of Applied Sciences Nordhausen (Germany)

Abstract

The life time of over 20 years is a unique feature of PV modules. Because of weather exposition and the system design of PV power plants system induced degradation can occur. In case of CIGS PV modules it is called Potential Induced Degradation (PID). The rate of degradation depends on the transferred charge, which can be determined by measuring the leakage currents because of the potential between module connectors and ground. Thereby only the sum of the leakage current can be measured, but there are different leakage current pathways. The main pathways are through the cover glass and the back glass/ material. For a real lifetime prediction the correlation of climate chamber tests and outdoor conditions is necessary. A method for measuring the exclusive leakage current pathway through the cover or the back glass was developed. The encapsulation foil enables the possibility to deactivate the leakage current pathways which is more harmful in relation to PID of CIGS PV modules.

Keywords: CIGS, Potential Induced Degradation, leakage current, transferred charge

1. Introduction

Like all other module technologies, thin film solar modules (TFSM) are exposed to the environmental conditions during lifetime. Because of the repeated long term environmental stress (e.g. temperature changes, UV radiation, moisture ingress, mechanical stress etc.) the material properties may change and loss their functionality. Furthermore, the environmental stress can accelerate the movement of volatile components of materials or semiconductor layers. Especially reactive sodium ions are suspected to move into the semiconductor layers. This can be lead to reversible or irreversible degradation of thin film solar cells (Osterwald et al., 2003). However, because of the module wiring and the inverter concept a potential between module connectors and ground can occur (Schmidt, 2009). The result is a leakage current between these two connection points. In principle this effect can be observed for all module technologies. In this context, the specific effects, strategies for prevention and notations are different for each technology. In case of crystalline silicon the term used is Potential Induced Degradation (PID). In case of TFSM TCO corrosion occurs for superstrate modules and PID can be observed for CIGS modules (substrate modules). Note, the PID effect for CIGS modules differs from the PID effect for cSi modules. In both cases a sodium ion diffusion is suggested to reduce the efficiency. But for CIGS modules a diffusion into the CdS/CIGS interface is supposed (Fjällström et al., 2013) whereas for cSi modules the anti-reflection coating plays the main role (Naumann et al., 2012).

1.1 Module Technology

Thin film solar modules (TFSM) represent a young technology in comparison to crystalline silicon solar modules. There are two main production technologies for TFSM: Superstrate and substrate modules. As shown in Fig. 1, the layer deposition of superstrate modules starts with the front contact on the cover glass. CIGS thin film solar modules are produced in substrate technology. The layer deposition starts with the back contact on the back glass. The CIGS absorber will be deposited by co-evaporation, where the CIGS is formed during the deposition or by a deposition reaction, where a precursor will be deposited and the CIGS formation occurs during a second step (Scheer and Schock, 2011). On top of the CIGS layer a CdS buffer layer will avoid

doi:10.18086/swc.2017.20.10 Available at http://proceedings.ises.org

shunting paths followed by transparent intrinsic ZnO (i-ZnO) and an aluminum doped ZnO (ZnO:Al) layer as front contact. Because of the material consumption of the CIGS the absorber is p-type whereas CdS and the

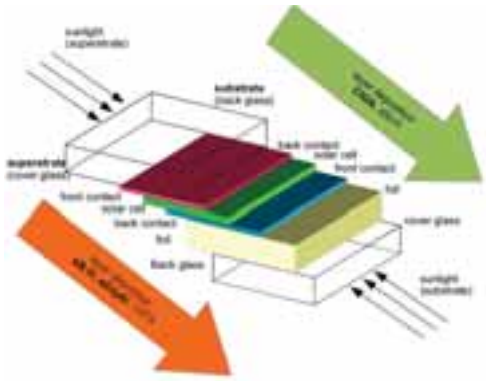

Fig. 1: Order of layer deposition for substrate and superstrate thin film solar modules.

ZnO layers are n-type.

Between the single deposition steps a structuring via mechanical tools or laser will separate the homogeneous layers into single cells. Because of the structuring between the single deposition steps a monolithical series connections as shown in Fig. 2 will occur. These created scribes are specified in order of the structuring step as scribe P1 to P3. The first scribe separates the back contact, P2 the CIGS/ CdS/ i-ZnO layer and P3 the separate the front contact and the CIGS layer again. Following by this a series connection of the solar cells is realized. However, scribe P1 leads to direct connection between CIGS and back glass. For the substrate soda lime glass with a high content of earth alkali ions is used. As indicated in Fig. 2, a fraction of selenium which is part of the absorber formation reacts with the molybdenum back contact to $MoSe_2$. This is the precondition for a low resistant contact on the back side of the cell.

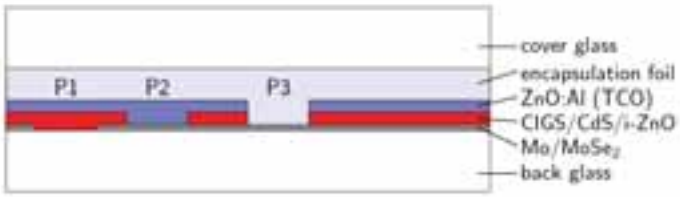

Fig. 2: Simplified illustration of layer order and solar cell connection.

1.2 Potential Induced Degradation of CIGS thin film solar modules

In PV power plants a series connection of PV modules is called module string. The aim of the series connection is to scale up the power of the PV system with ohmic losses as small as possible. This is realized by high system voltages. The system voltage V_{sys} can be measured between the first and the last module in a module string, as shown in Fig. 3. Typical system voltages in Europe achieve up to 1000 V DC, in some cases up to 1500 V DC.

In addition, a voltage between the positive and negative pole of the module string occur. The grounding situation of the module string and the type of inverter influence the amount and sign of this voltage (Schmidt, 2009). For ungrounded systems a voltage of -½ V_{sys} can be measured between the negative pole and ground. In case of the positive pole + ½ V_{sys} can be measured. In dependency of the type of inverter the amount of this voltage can be shifted to higher negative voltages and lower positive voltages or vice versa. Normally only in case of inverters with transformers an external grounding of the module string is possible. For the grounding of the negative pole a voltage of $+V_{sys}$ can be measured between the positive pole and ground, and no voltage between the negative pole occurs. For the grounding of the positive pole the opposite is the case. This voltage is

the reason for an accelerated migration of alkali ions and lead to PID. Furthermore, because of this voltage a current flow between module connector and ground can arise, the so called leakage current. The amount of the leakage current depends on the potential between the module connectors and ground. The leakage current is suspected to be an indicator of the progress of PID. However, the conductivity of the module is influenced by temperature and humidity. Following by this, the influence of environmental conditions in relation to PID has to be taken into account.

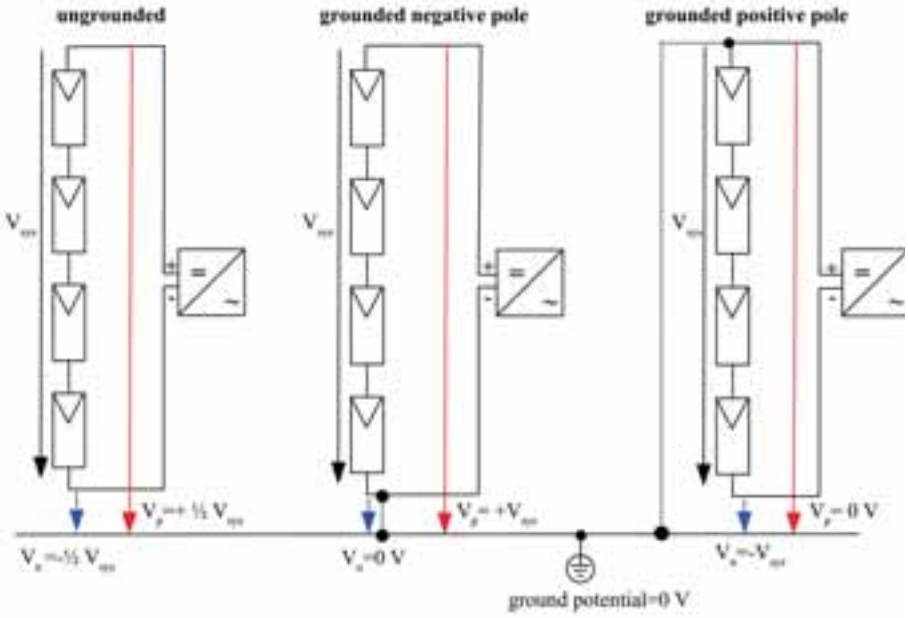

Fig. 3: Potential against ground for different grounding situations.

There are mainly four leakage current pathways in a module. The leakage current from the solar cell through the encapsulation foil and the cover glass is called I_1. The leakage current through the encapsulation foil, the edge sealing and the frame is called I_2. If the leakage current flows through the interface of the encapsulation foil and back glass and the edge sealing it is called I_3. Leakage current I_4 flows from the solar cell through the back glass. From Ohm's law it is known that the current takes the path of least resistance. This depends on the conductivity of the materials and the influence of humidity and temperature. So this lead to the question weather the current through the cover glass is most harmful or one of the others.

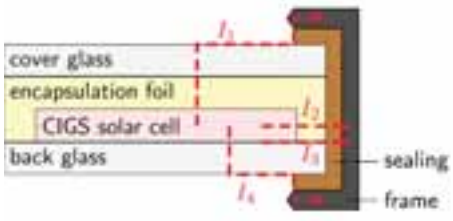

Fig. 4: Simplified illustration of the main leakage current pathways of a CIGS thin film solar module.

The aim of this study is to prove the origin of the leakage current for CIGS photovoltaic modules. The leakage current can take several different pathways. Fig. 1 shows the four main pathways for a CIGS thin film solar module. Especially the leakage current through the cover glass and through the back glass are from special interest. For a correlation of accelerated aging tests in climate chambers with outdoor exposure in the field the knowledge of active leakage current pathway is necessary. Thereby, the path activation depends on the surface

and the volume conductivity of the cover and back glass as well on the encapsulation foil. Especially the surface conductivity is influenced by the environmental conditions. Consequently, a method for modeling the active leakage current as a function of environmental conditions will be shown. Therefore, lab tests are performed to correlate the outdoor measured leakage current to indoor measurements.

2. Experimental

2.1 Outdoor Test Facility

On an outdoor test facility six CIGS TFSM with two different encapsulation foils are mounted on individually insulated racks. The semiconductor device of the modules is identical. These are framed glass glass modules. However, for each foil type one module is connected with an external applied voltage of -500 V and -1000 V between module connectors and ground. The remaining two modules are mounted as reference modules, without any applied external voltage. So degradation effects because of metastable defects can be detected and differentiated from the degradation which are investigated in this study. Every ten seconds the leakage current is measured through a shunt resistant. The schematic circuit diagram of the test setup is shown in Fig. 5. Thereby,

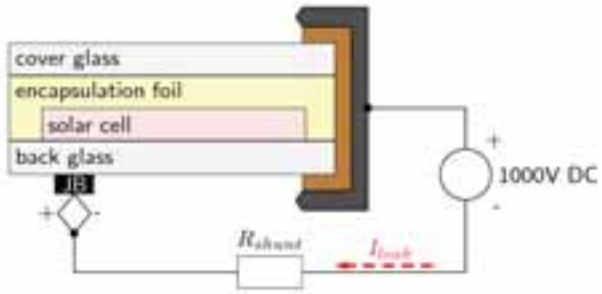

Fig. 5: Standard test setup for accelerated aging tests.

the problem that only the sum of all leakage currents can be measured occurs. But depending on the surface humidity the main leakage current pathway will change. Therefore, in addition climate chamber and water basin tests has to be done to assess the actual pathway. In order to simulate real operating conditions the external applied voltage is switched off during night and irradiations below 50 W/m^2. During the test, the modules are operated near their maximum power points. The climate conditions are measured directly adjacent to the test rack by a weather station. So at the end of the tests for each climate condition the leakage current and the pathway can be classified.

2.2 Water basin tests

For analyzing typical leakage current magnitudes depending on the leakage current pathway three different contacting methods are realized. To measure current I_1 only the cover glass is connected with an external voltage supply. In this case the current has to be overcome the resistant of the encapsulation foil and of the cover glass. However, this electrical contacting method corresponds with a wet surface of the cover glass in the field and a dry back glass surface. This can occur if it starts to rain.

In principle the same method is used to measure exclusively the current I_4 through the back glass. For this purpose only the back glass is connected. In the field this condition arise if there is dew on both sides of the module and sun is rising. The sun is drying the cover glass where the back glass is still wet. Consequently, in the third case both sides are connected to the voltage source.

All setups are realized in a water basin, as shown in Fig. 6. In the first case only the cover glass is wetted, in the second case only the back glass is wetted and for the sum of the currents the whole module is submerged in water. Furthermore, in the field a wide range of temperature for different moisture rates on the module can be

observed. So the water basin is heated during the tests. The result is a temperature dependent leakage current, which can be clearly attributed to one leakage current pathway.

Water basin tests are suitable to realize a homogeneous contact on the cover or back glass as well as for the hole module. In climatic chamber tests the contact is often realized by metal plate. A gap between plate and glass can occur. In the gap water vapor can condensate and lead to local reduction of conductivity (Voswinckel et. al., 2015). With a homogeneous water film the contact can be improved and local reductions of conductivity can be neglected. With an external heat source the water can be tempered. Following by this the leakage current behavior for different conditions which correspondent with real operating conditions and accelerated aging tests can be simulated and verified. For accelerated aging tests high temperatures are needed. This leads to evaporation of the water in the basin and to reduction of the water level, which can lead to a lack on electrical conduction. So it is obvious that this test setup is only appropriate for short testing times and the analysis of special operating points. For the analysis of the aging behavior accelerated aging tests in climate chambers are necessary. Note, the typical test duration of an accelerated aging test is between one and four weeks.

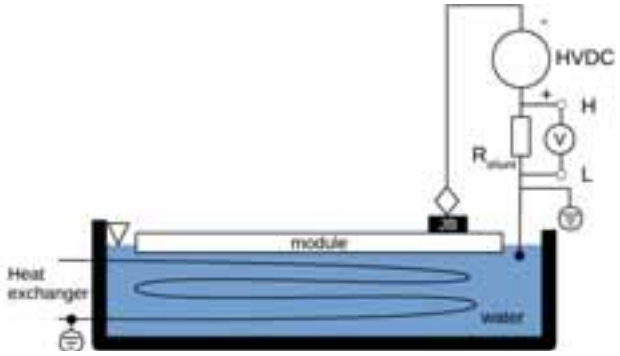

Fig. 6: Water basin test for a separate activation of one leakage current pathway.

2.3 climate chamber tests

According to the outdoor tests the climate chamber tests include two different potentials. In a first step two modules for each encapsulation foil are applied with an external voltage about -500 V. Thereby, one module is connected to module frame and the other is connected over the entire area of the cover glass. Differently from the outdoor tests, the modules are short circuited. This is done, because no irradiation is applied to the modules and no illuminated operation point can be chosen. The climate conditions during this tests are kept constant to 85°C and 85 percent relative humidity. Before and after 500 hour testing the I-V-curves are measured before and after a light soaking for four hours. The light soaking is used to stabilize the module performance before the test and to determine any regeneration effects after the tests. During the climate chamber tests the leakage currents between module connectors and frame respectively the cover glass contact are measured in a ten second interval. Furthermore, before and after the tests electroluminescence images are recorded. The influence of dark soaking in accordance to a possible regeneration or further degradation is measured in a monthly interval after the climate chamber tests. After the first experiment run the tests will be repeated with an external applied voltage of -1000 V.

For verifying the results of the water basin tests climate chamber tests with fluctuating climate conditions are performed. So, modules are connected to an external voltage supply for a bias damp heat test. However, several states of temperature in a range of -5°C and 90°C and relative humidity between 10 and 95 percent are realized. The modules are connected by metal plates on the cover glass and on the back glass. The result is a map of leakage currents for a wide range of temperature and humidity states as well as for different contacting methods.

3. Results

2.1 Degradation rate

Different climatic chamber tests are performed to analyze the degradation behavior regarding PID of CIGS TFSM. On the left side in Fig. 7 the power loss depending different contacting methods and different voltage levels is shown. One module group was contacted with metals blade on the cover glass (front) and the other group on the back glass (back). The encapsulation foil of this test run consist of PVB. The aging time was about 500 h with interruptions for measuring the I-V vurve of the modules. The results are shown for -500 V and -1000 V. It is clear visible that a higher voltage amount leads to a faster transferred charge and a faster degradation rate. However, there is a clear difference between the degradation rate of the front contacted and the back contacted modules. For the back contacted modules less transferred charge is needed to induce a power loss regarding to the front contact. The back contact corespondent with water on the backside of the module. This can occur in case of dew, if the dew on the front side is dried because of sunshine, or rain.

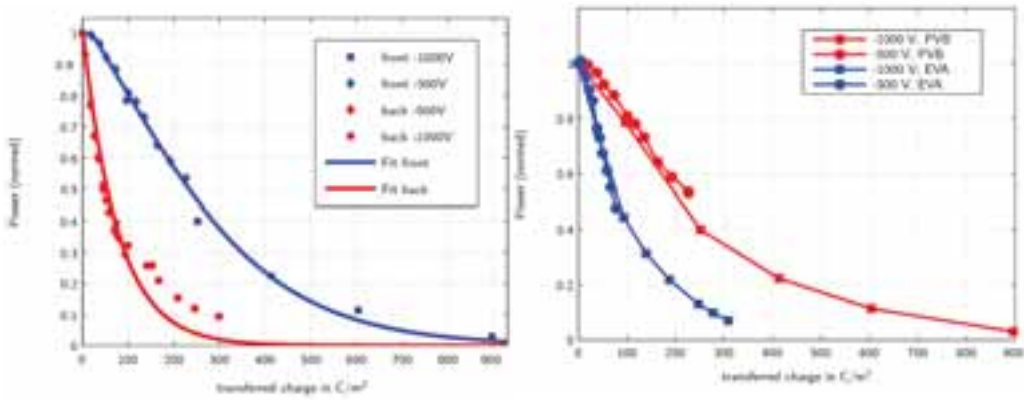

Fig. 7: Power loss as a function of transferred charge for different contact methods (left) and encapsulation foils (right).

The power loss depending on the transferred charge for different evaluated foil types is shown in Fig. 7 (right). Modules with a PVB and a EVA encapsulation foil are tested with an external voltage about -500 V and -1000 V. For the same test conditions and voltages there are clear differences regarding to power loss and transferred charge between these foil types. This indicates that there are differences in conductivity. The Foil EVA shows a faster degradation rate with higher power losses at lower transferred charges. The results show that there is a clear dependency if the leakage current flows through the back or the cover glass. The current through the back glass is more harmful than his counterpart through the cover glass. Furthermore, a clear dependency of the used encapsulation foil exists. The degradation rate can be reduced by a decrease of the conductivity of the encapsulation foil. This leads to less transferred charge and less power loss.

2.2 Leakage current pathway

Two module types with different encapsulation foils are tested. The first one is standard PVB and the second one is an EVA foil. The results of the water basin tests confirm the result of the climatic chamber tests.There is a clear difference depending on the encapsulation foil. The measured and modeled leakage current values are shown in Fig. 8. It is clear visible, that the leakage current I_1 through the cover glass for PVB is more dominant than I_4 through the back glass. In contrast, for EVA I_4 is more dominant. Nevertheless, the magnitude of I_4 for both modules is in the same range. In addition, the activation energy of the currents through the back glass is also the same for both foils, for the cover glass it is quite different. This fact is no surprise, because for both modules the same back glass is used. Whereas, in case of I_1 the material properties of the different encapsulation foils has been taken into account. Additionally, climate chamber tests are performed. Therefore, the modules are connected by a metal plate on the back glass. The results of the leakage currents measured in the water basin correspond with leakage currents in climate chamber well. However, there are some states in the climate chamber with dew on the module. In that case, the main current flow through the cover glass for PVB. In

contrast to that, for EVA the main current flow through the back glass at the same condition (water on the cover glass). A comparison with former bias damp heat tests show qualitatively comparable results. In a first approach, outdoor measured leakage currents can be correlate qualitative to these results.

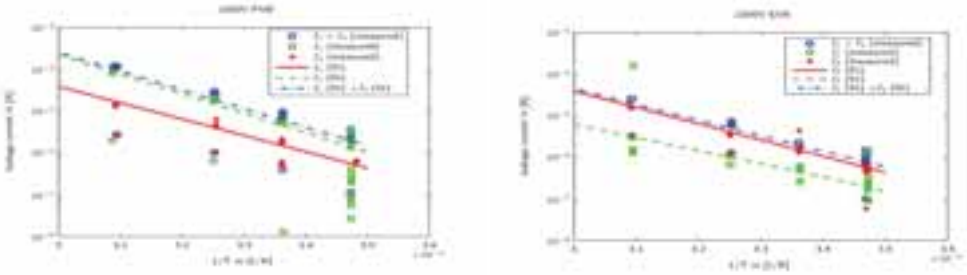

Fig. 8: Measured and modeled leakage currents through the cover glass (I_1) and the back glass (I_4) of a CIGS module with PVB (left) and EVA (right) encapsulation foil.

The Arrhenius plots in Fig. 8 can be used to extract the activation energy. The results are shown in Tab. 1. For the leakage current pathway I_4 through the back glass the same activation energy occur. The lack of differences between the two module types is because of the use of the same type of back glass. However, the estimated activation energy is typicall for soda lime glass. Regarding the leakage current pathway through the cover glass clear differences occur. The activation energy for the module with a EVA encapsulation foil is lower than for the module with PVB foil. For the latter the activation energy is also in the typicall range as for soda lime glass. This indicates, that in case of EVA the encapsulation foil limit the activation energy whereas in case of PVB the cover glass is the limiting factor.

Tab. 1: Activation energy for the leakage current pathways (Manz, 2015)

Leakage current pathway	$I_{1,\,EVA}$	$I_{1,\,PVB}$	I_4
Activation energy	0,63 eV	0,82 eV	0,78 eV

2.3 Outdoor relevance

Considering the Arrhenius equation, high temperatures lead to high degradation rates. Following by this, also

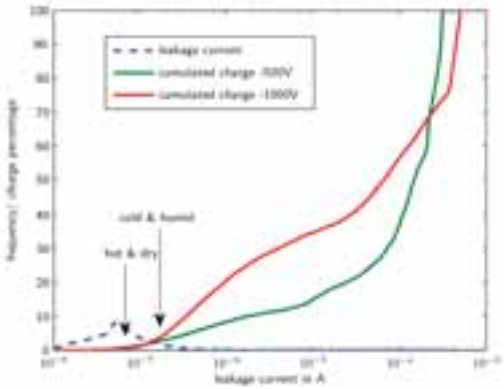

Fig. 9: .Leakage current frequency (dashed) and cumulated transferred charge (solid) in dependency of leakage current.

high leakage currents must occur. This relation is well proven by climatic chamber and water basin tests (Manz, 2015). It seems reasonable to suppose that especially the hot and humid climate regime has to considered to prevent PID of CIGS TFSM. This assumption could be true for tropic climatic regions. But for

moderate climates like in central Europe the opposite is the case. Fig. 9 shows the frequency of the leakage currents (dashed) and the cumulated transferred charge (solid) for the corresponding leakage current amount over one year in Nordhausen/ Germany. Most leakage currents occur for hot and dry conditions up to leakage currents amounts in the range of 10^{-7} A. But this lead only to a transferred charge less than one percent of the hole year. Also the cold and humid regime shows a high frequency of leakage currents. The cumulation of the transferred charge to the hot and dry regime leads to three percent of the hole transferred charge. Nearly 96 percent of the transferred charge occurs during dew and rain. This conditions are infrequent but the leakage current arise up to two or three magnitudes of orders in comparison to hot and dry and cold and humid states.

4. Summary

Accelerated aging tests regarding PID observe normaly only one leakage current path. Uncontrolled condensation can occur and can falsify the measurement. The results show that for realistic life time predictions the knowledge of the active leakage current pathway for the whole operating time is necessary. So in case of CIGS thin film solar modules more than simple climatic chamber tests are necessary to predict their lifetime.

Leakage current pathways for two different encapsulation foils of CIGS thin film solar modules are investigated. The results show that there is a difference of the dominating pathway if the glass surface is wet. For PVB a wet cover glass surface leads to a dominating current through this part of the modules. Whereas for EVA a wet cover glass surface do not lead to a dominating leakage current through it. As expected, for both encapsulation materials the leakage through the back glass shows a comparable magnitude. However, the results are compliant to climate chamber and outdoor measurements. As a result, these measurements can be used to identify the active leakage current pathway in the field. In combination with weather measurements this will enable a correlation of accelerated aging tests and outdoor measurements regarding the transferred charge. Last but not least, the encapsulation foil is generally suitable to influence the active leakage current pathway.

There is a clear difference regarding the amount and the consequences of the leakage currents through the cover and the back glass. The leakage current of the back glass can be over a magnitude lower than the current through the cover glass. But the power loss followed by the leakage current through the back glass needs much less transferred charge. There is a factor of up to 20 between the relevant charge which is needed to damage the module. To carry out the relevant active leakage current pathway a homogeneous contact of the glass plates is necessary (Voswinckel et al., 2015). For analyzing the amount of the leakage current a water basin is suitable. For climatic chamber tests at high temperatures metal plates are more suitable. However, this can lead to non connected areas.

5. References

Osterwald, C. R., Mcmahon, T. J., Adelstein, J., and J. Pruett, 2003. Accelerated Stress Testing of Thin-Film Modules with SnO_2:F Transparent Conductors. National Center for Photovoltaics and Solar Program Review Meeting Colorado.

Fjällström, V., Salom, P. M. P., Hultquist, A., Edoff, M., Jarmar, T., Aitken,B. G., Zhang, K., Fuller, K., Kosik Williams, C., 2013. Potential-induced degradation of $CuIn_{1-x}Ga_xSe_2$ thin film solar cells," IEEE J. PV, Vol. 3, No. 3, pp. 1090–1094.

Scheer, R. and Schock, H.-W., 2011. Chalcogenide Photovoltaics, Wiley-VCH, Weinheim.

Schmidt, H., 2009. Do Thin-Film Modules need special Inverters? 5th User Forum Thin Film Photovoltaics, Würzburg.

Naumann, V., Hagendorf, C., Grosser, S., Werner, M., Bagdahn, J., 2012. Micro structural root cause analysis of potential induced degradation in c-Si solar cells. Energy Procedia, Vol. 27, pp. 1–6.

Manz, P., 2015. "Investigation of Leakage Currents as an indicator of ageing effects (PID) occuring at CIGS photovoltaic modules," Master's thesis, University of Applied Sciences Nordhausen.

Voswinckel, S., Wesselak, V., Fokuhl, E., Schmidt, C., Watzlawik, K., 2015, Dos and Don'ts of Leakage Current Measurement. EU PVSEC, Hamburg.

Structural and Optical Characterization of Polymer based TiO_2 films for Photovoltaic Applications

Sebastian Waita* and Bernard Aduda

Condensed Matter Group, Department of Physics, University of Nairobi, P.O BOX 30197-00100, Nairobi, Kenya.

Abstract

The demand for energy worldwide is rising almost on a daily basis. There is need to research on new materials and ways to provide energy. In this preliminary study, we explore the properties of polymer based TiO_2 films for possible photovoltaic applications. TiO_2 films incorporating Polyvinylidene Fluoride-Co-Hexa fluoropropylene (PVDF-HFP) as the structure directing polymer and using Titanium Isopropoxide as the precursor were deposited by both dipping and spin coating techniques. The films were optimized with respect to solution concentration, and spin coater speeds as well as dip coating with drawl speed. X-Ray diffraction (XRD) structural, as well as transmittance studies were carried out. XRD spectra showed crystalline anatase films with crystal sizes of about 18-24 nm after annealing at about 430±50 ^oC for 30 minutes. The as deposited films were amorphous. For spin coated films, the films uniformity became better with spin speed. However, the optimum speed that ensures uniformity and lack of pin holes was found to be about 3000 RPM. The transmittance of the films decreased with the coater speed. As for the dip coated films the concentration of the solution and the withdrawal speed affect the film thickness and therefore the transmittance of the films. Thicker films were obtained from more concentrated solutions. Decrease in concentration of the solution tended to produce a minimum thickness at some withdrawal speed. It was found that higher withdrawal speeds led to lower transmittance due to thicker films.

Key words: TiO_2, Anatase, Polymer, Dip coating, spin coating, transmittance, thickness, structural, Optical, photovoltaic

*Corresponding author: swaita@uonbi.ac.ke

doi:10.18086/swc.2017.20.11 Available at http://proceedings.ises.org

SEBASTIAN WAITA

1.0 Introduction

With almost no exception, the current generation has assumed a lifestyle of using gadgets that need to be powered. Current estimates for the power needs of the roughly 7 Billion people worldwide are as high as 13 Terrawatts (TW) and it is estimated that in less than half a century, the demand will peak to about 23 Terrawatts (TW) (Kalyanasundaram, 2010). There is, therefore concerted effort in search for alternative energy sources to supplement the current sources. Fossil fuels, nuclear power and renewable energy (solar, wind, hydro etc.) are the key options. Of the three options, renewable energy based on solar resource could be the most appealing and promising since it is free, abundant and free from pollution.

Since the break through work on the possibility of generating electricity by applying the photosynthesis principle, a lot of research has gone in to this area due to its potential to offer cheaper power compared to conventional solar cell (Brain O'Regan and Michael Gratzel, 1991). This type of solar cell device is referred to as the Dye Sensitized Solar Cell (DSSC). In brief, a DSSC is composed of a nanocrystalline

semiconducting film sand winched between two photo electrodes; a photo electrode and a counter electrode. The nanocrystalline semiconducting film has a monolayer of a dye to enhance the absorption of incident photons. On illumination, the absorption of the radiation excites an electron from the dye which is conducted through the back contact of the photo electrode and regenerated through the counter electrode which is usually coated with an electron regeneration catalyst like platinic acid. The electron generated by irradiation on the dye is finally recovered at the counter electrode. Therefore, there is no electron loss.

The DSSC technology however has to overcome a number of bottlenecks before it is competitive enough with the conventional solar cell technology-the p-n junction. Research is ongoing to overcome shortcomings like electron loss through the back contact (Petra and Peter 2003; Waita et al., 2007), improving on the dyes (Kohjiro H. and Nagatoshi K., 2009), increasing porosity of the semi conducting film, (Waita et al., 2006, 2007, Kiema et al., 2005), use of other counter electrodes (Kim et al., 2012) among other approaches.

A number of techniques have been used in depositing the semiconducting film: Sputtering (Waita et al., 2007; J. Rodri´guez et al., 2000; M. Go´mez , et al., 2000), Screen printing (S. Burnside et al., 2000), Spray pyrolysis (A.Conde-Gallardo et al., 2005,),hydrolysis of TiCL4 (Kristel Möldre, et al., 2015), and sol-gel dip coating (Jan Prochazka et al., 2013). In their work, Jan Prochazka et al., (2013) incorporated the use of a polymer (poly (Hexafluorobutyl Methacrylate)) as the structure directing agent and titanium ethoxide as the precursor using the dip coating techniques. The films were found to be dense and promoted thixotropic properties. We would like, in this work try a different polymer and determine the properties of the film so obtained. Furthermore, we use two deposition techniques and compare the film properties.

In this paper therefore, we report the structural and optical properties of TiO_2 films that use Titanium Isopropoxide as the precursor and incorporating Polyvinylidene Fluoride-Co-Hexa fluoropropylene (PVDF-HFP) as the structure directing polymer deposited by the dipping and spin coating techniques.

2.0 Experimental Techniques

2.1 Solution Preparation

Two solutions, herein referred to as solution 1 and 2 were separately prepared at room temperature and then mixed together under magnetic stirring. Solution 1 was made by mixing ≈2.2 ml of Hydrochloric Acid (HCl) (Aq) (Aldrich) (37%) and ≈2.55 g of Titanium Isopropoxide (Aq) (Aldrich) with magnetic stirring and stirred until the solution was homogeneous (≈ 30 minutes). This formed the precursor solution. Solution 2 was also made under stirring and composed of ≈ 0.55 g (11-12 pellets) of Polyvinylidene Fluoride-Co-Hexa fluoropropylene (PVDF-HFP) (Aldrich) in a mixture of Acetone and N-Methyl-2-Pyrrolidone (NMP) (Aldrich) in the ratio of 2:3, Acetone to NMP, total volume of mixture, 60 ml. Magnetic Stirring was done until all polymer was dissolved (≈ 90 minutes). Solution 1 was then mixed with solution 2 under constant stirring which continued until the solution became homogeneous (≈ 2 hrs). All solutions were prepared at room temperature and kept covered thereafter.

2.2 Substrate cleaning

Both plain glass and Fluorine Doped Tin Oxide (FT0) (15 Ω/m^2) (Hartford) substrates were used for film deposition after cleaning. The substrates were cleaned by ultra-sonicating (about 30 minutes) in deionized soapy water, then in pure deionized water for about 10 minutes. Thereafter, the substrates were ultrasonically cleaned in ethanol which had 2-3 drops Hydrochloric Acid (HCl) added for about 30 minutes followed by 30 minutes in Acetone and 30 minutes in Ethanol. Finally, the substrates were rinsed with deionized water and dried by blowing with nitrogen gas.

2.3 Film deposition for Structural studies

Two films (4(a) and 4 (b)) were deposited on FTO glass substrates and allowed to dry at room temperature. 4(a) was used as deposited while 4 (b) was heat treated in a programmable oven (Nabertherm) for ≈ 30 mins at ≈ 430 ±50 ^oC and allowed to cool down to room temperature.

2.3 Film deposition and heat treatment

Pre-cleaned Flourine Doped Tin Oxide (FTO) glass substrates where used as substrates and the films were coated by simple hand dipping. For each solution, two films were made: 4a and 4b. 4a deposited and allowed to dry at room temperature (as deposited) while 4b was heat treated in open air for ≈ 30 minutes at ≈ 430 ±50 ^oC after coating and allowed to cool down to room temperature.

2.4 Thickness optimization

The amounts of Acetone and NMP were varied in order to vary the film thickness. The solution with concentration 1 (conc 1) was, 12 ml of Acetone and 18 ml of NMP. Two more dilute solutions were made: concentration 2 and 3 (conc 2 and conc 3). These concentrations were made by reducing the amount of polymer in the solvent in conc 1 while maintaining all else constant. The film thickness was measured using a Dektak 3 surface profilometer (Sloan Technology).

2.5 Film deposition by spin coater

The spin coater used was a KW-4A Model (CHETMAT Technology) and was first calibrated to create a correlation between the knob setting and the digital display. Film deposition using the spin coater was done on pre cleaned glass substrates masked at one end using a scotch tape to create a step for thickness measurements. The substrates were kept fixed on the coater using a double sided tape. About 500 µl of the solution was then carefully spread on the substrate using a calibrated pipette. Depositions were done at various digital speeds.

2.6 Film deposition by Dip coating

Dip coating was done using an automated, computer controlled Dip coater Robot (R & K Germany). Two solutions were made and added together making a total volume of 60 ml and were used immediately after preparation (concentration 1, (conc 1) . Different coatings on plain glass substrates were deposited by varying the withdrawal speed of the substrate. After deposition, the films were kept at room temperature until they were dry before heat treatment at ≈ 450 ^oC for ≈ 30 minutes in a programmable furnace.

2.7 Structural studies

X-ray diffraction (XRD) of the deposited films was done using a computer controlled Siemens Diffractometer at a voltage of 45 KV and current 40 mA. The diffraction angle was varied from 20^o to 60^o.

SEBASTIAN WAITA

2.8 Optical measurements

Optical measurements were done using both a computer controlled single beam UV-VIS-NIR High Resolution Spectacular HR 2000 Light Source Spectrometer (Ocean Optics Inc.) which was equipped with Halogen and Deuterium lamps..

3.0 Results and Discussion

3.1 Structural characterization of the coated films

The XRD patterns for the films is displayed in fig 1 below. Film 4a was found to be amorphous while 4b was found to be crystalline with Anatase phase. The average crystal size estimated from Scherer's formula was ~ 18-24 nm. The crystal size is critical in photovoltaics for it affects both the electron mobility as well as light harvesting. Small crystal sizes (< 20 nm) reduce the space charge area leading to electron recombination due to lack of electron /electron interface energy barrier as well as low conduction (Zaban et al., 2000, Gratzel, 2000). On the hand, large crystals create large surface area for more dye anchoring increasing electron generation rate, faster electron transport as well as slower recombination rate (S. Nakade et al., 2003).

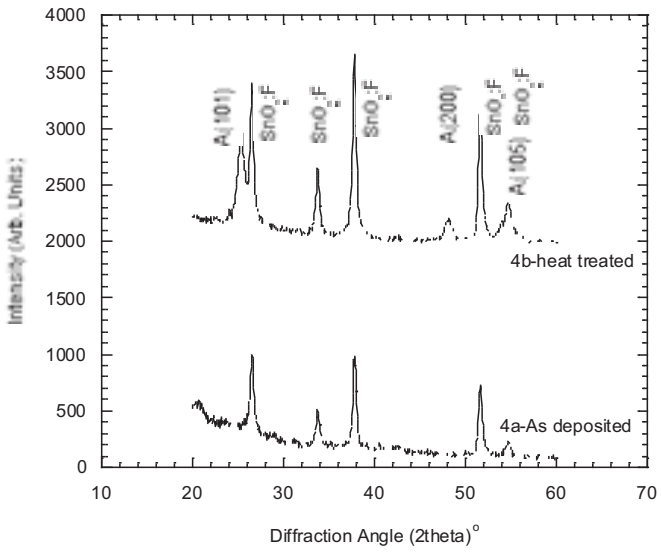

Fig 1. XRD patterns for the deposited films on FTO substrates

3.2 Spin coating

3.2.1 Spin Coater Calibration

The spin coater was calibrated and fig 2 below shows the variation of digital spin coater display with the position of the spin coater knob. As can be observed, there is a direct correlation between the two. This enabled us to determine the speed of the coater at various knob settings.

SEBASTIAN WAITA

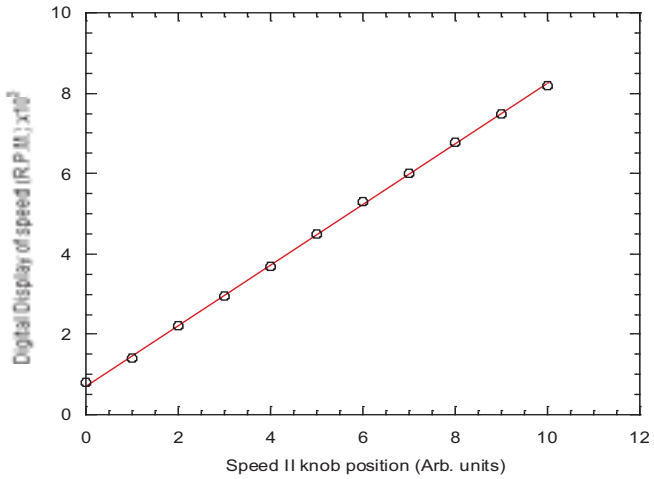

Fig 2. The spin coater calibration: Digital speed display versus the speed knob position

Fig 3 below shows the variation of film thickness with speed of the spin coater. The film thickness was measured using a Dektak 3 surface profilometer (Sloan Technology). Visual inspection was used to gauge how uniform the films were. The films deposited at 800 and 1400 R.P.M. 470 nm and 297 nm thick respectively (first two data points below)and did not appear very uniform. On the other hand, the films deposited at speeds of about 3000 R.P.M and above appeared uniform with the uniformity getting better with increase in speed but tended to lose continuity as the speed increased. The thickness of the films were measured for the various increasing spin speeds. Pinholes were visible in some of the films. The general trend observed is a decrease of the film thickness with the coater speed. Increased speeds increases also the centrifugal force accelerating the solution to the edges of the substrate. The solution spreads more and the film thickness therefore decreases.

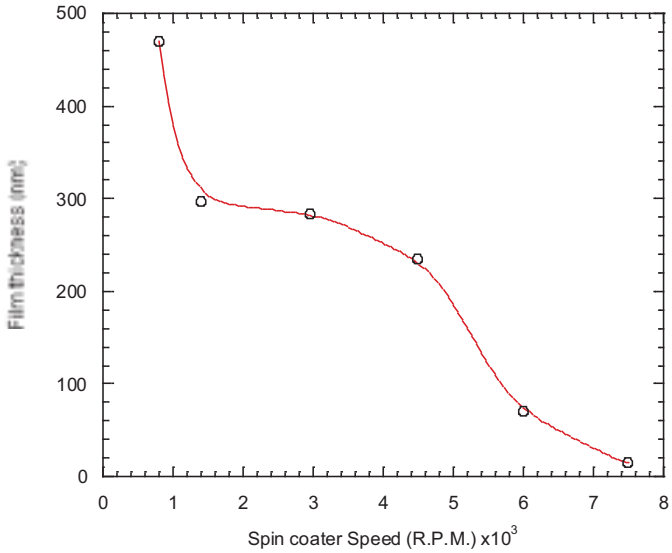

Fig. 3 . The Spin coater calibration: variation of film thickness with spin coater speed

SEBASTIAN WAITA

3.2.2 Optical measurements

The variation of transmittance and spin coater speed is displayed in figure 4 below. The transmittance of the films tend to increase with the spin coater speed. This observation is in agreement with the observation discussed above on speed variation with film thickness. This is because as the film thickness decreases due to higher speeds, the film will become more transparent. From our data, it appears that speeds of about 3000 and above would give us films with above 60 % transmittance for most of the wavelength and the film thickness can be carefully monitored so that it does not become too thin to create pin hole and no uniformity. Lower speeds produced films that seem to compromise the film's transmittance.It is also noted that at higher speeds, transmittance of the coated films and that of the plain glass tend to be close, a possible indication of pinholes in the coated films. However, we did not do further study to confirm this although it is needed.

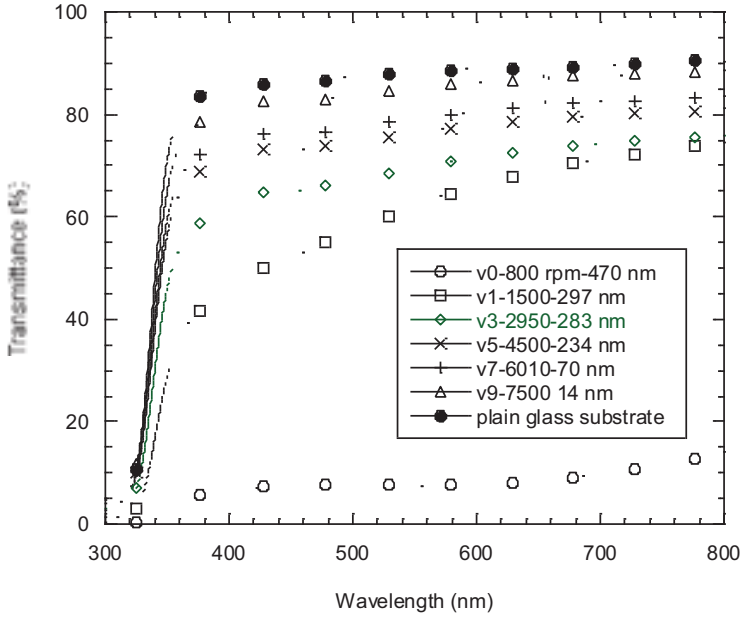

Fig 4. Transmittance of the films deposited at various spin coater speeds

3.3 DIP COATING

3.3.1 Film thickness variation with withdrawal speed

A plot of film thickness against withdrawal speed for the three concentrations is as displayed below in figure 5. The spectra for concentration 1 (conc 1) appears like a smooth tick/right (√) changing shape to more of a bowel as the solution concentration reduces. Thus, as the solution concentration reduces, the film thickness variation at low and high speeds becomes less significant. In other words, the withdrawal speed does not lead to large differences in the film thickness at low and high with drawal speeds. We explain the observation as follows: At low withdrawal speeds, evaporation as well as convection effects determine the film deposition rate. Due to the slow withdrawal speeds, these two effects create a low film deposition rate leading to thin films. As the withdrawal speed increases, gravity related viscous drag force dominates leading to increase in film thickness. This effect seems to become more prominent as the concentration of the solution increase. According to David Grosso (2011), the dip coating technique has three regimes: Capillary at low withdrawal speeds, draining at high withdrawal speeds and Intermediate which is an overlap of the two regimes and his observation of dip coating concurs with ours.

SEBASTIAN WAITA

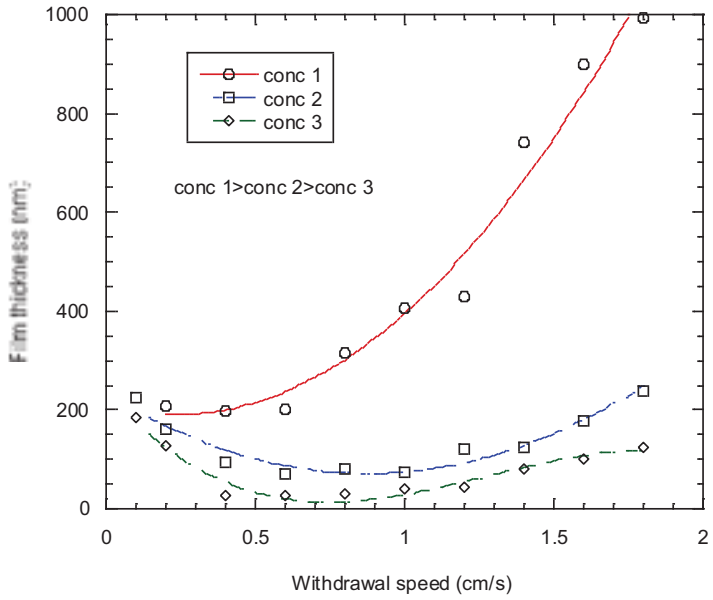

Fig 5. Film thickness variation with withdrawal speed for various concentrations of the solution

3.3.2 Transmittance of the films

The transmittance of the films deposited using the three different concentrations showed the same trend and behavior. The only difference was the level of transmittance which decreased as the concentration increased. Due to this, we present the transmittance spectra for the films deposited using concentration 1 only, as in figure 6 below. The observation below is that the higher the withdrawal speed, the lower the transmittance. This behavior has a direct correlation to film thickness because concentrated solutions produced thicker films. As a matter of fact, the transmittance of such films would be lower compared to less concentrated solutions. For films meant to have high transparency to radiation in the visible range, low withdrawal speeds are therefore recommended although that has to be balanced with the film thickness required.

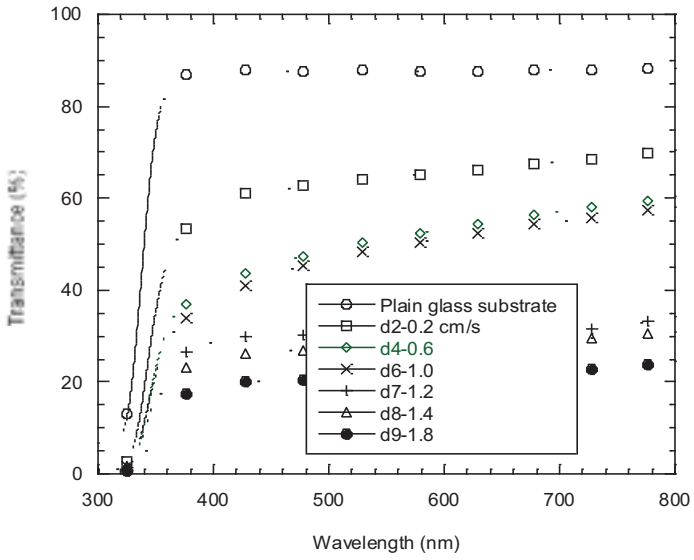

Fig 6. Transmittance versus wavelength for the films deposited at various withdrawal speeds. The films were made through solution of concentration 1 (conc 1).

3. 4 Conclusion

The structural and transmittance properties of TiO_2 incorporating Polyvinylidene Fluoride-Co-Hexa fluoropropylene (PVDF-HFP) as the structure directing polymer and using Titanium Isopropoxide as the precursor have been deposited by both dipping and spin coating techniques.

XRD structural studies revealed that as deposited films were amorphous but heat treated films at about 450±50 ^oC exhibited crystalline nature while revealing the Anatase phase of TiO_2 considered better for photovoltaic application than the other phases of TiO_2. The average crystal size estimated from Scherer's formula was ~ 18-24 nm.

Films deposited by spin coating showed better uniformity of thickness as the speed increased, although at very high spin speeds, the films showed some pin holes. The thickness also decreased with the spin coater speed. The optimum speed that ensures uniformity and lack of pin holes was found to be about 3000 RPM. Since the film thickness decreases with spin coater speed, it is expected that the transmittance of the films decreases with the coater speed. This was confirmed through our measurements.

As for the dip coated films, it was observed that the concentration of the solution as well as the withdrawal speed both affect the film thickness and therefore the transmittance of the films. More concentrated solutions had thicker films. The difference in thickness of the films at low and high speeds was also bigger as the solution concentration increased. Low concentrations had speeds where the film thickness was minimum.

The transmittance of the films deposited using the three different concentrations had the same trend. It was found that higher withdrawal speeds led to lower transmittance due to thicker films.

In order to complete our optimization of the films, we shall, in our next communication report on more optical parameters of the films as well as the performance of the solar cells fabricated using these films.

3.5 Acknowledgement

The Authors thank ISP, Sweden for support to carry out this work.

3.6 References

A.Conde-Gallardo, M.Guerrero, N.Castillo, A.B.Soto, R.Fragoso, J.G.Cabañas-Moreno, 2005. TiO_2 anatase thin films deposited by spray pyrolysis of an aerosol of titanium diisopropoxide, Thin Solid Films. Volume 473, Issue 1, 2005, 68-73.

Brain O'Regan and Michael Gratzel, 1991. A low cost, high –effficiency solar cell based on dye-sensitized colloidal TiO_2 films. Nature, Vol. 353, 737-739.

David Grosso, 2011. How to exploit the full potential of the dip-coating process to better control film Formation. J. Mater. Chem., 2011, 21, 17033–17038.

G.K. Kiema, M.J. Colgan, M.J. Brett, 2005. Dye sensitized solar cells incorporating obliquely deposited titanium oxide layers. Sol. Energy Mater. Sol. Cells, 85, 321.-331.

Jan Prochazka, Ladislav Kavan, Marketa Zukalova, Pavel Janda, Jaromir Jirkovsky, Zuzana Vlckova Zivcova,J. Heyrovsky, Ales Poruba, Solartec s.r.o, Mélanie Bedu, Solvionic S.A, .
Markus Döbbelin and Ramón Tena-Zaera, 2013. Dense TiO_2 films grown by sol–gel dip coating on glass,F-doped SnO_2, and silicon substrates. J. Mater. Res., Vol. 28, No. 3, 385-393.

J. Rodri´guez, M. Go´mez, J. Lu, E. Olsson, C.G. Granqvist, 2000. Reactively Sputter-Deposited Titanium Oxide Coatings with Parallel Penniform Microstructure.
Adv. Mater. 12, 341. Volume 12, Issue 5, 2000, 341–343.

SEBASTIAN WAITA

K. Kalyanasundaram, 2010. Photochemical and Photoelectrochemical Approaches to Energy Conversion, in: K. Kalyanasundaram, Dye sensitized solar cells, 1st Ed., EPFL Press, Switzerland, pp 1-2.

Kohjiro Hara and Nagatoshi Koumura, 2009. Organic Dyes for Efficient and Stable Dye-Sensitized Solar Cells. Material Matters, 4.4, 92.

M. Go´mez, J. Lu, J.L. Solis, E. Olsson, A. Hagfeldt, C.G. Granqvist, 2000. Dye-Sensitized Nanocrystalline Titanium-Oxide-Based Solar Cells Prepared by Sputtering: Influence of the Substrate Temperature During Deposition.J. Phys. Chem. B 104, 8712-8718.

Sebastian M. Waita, Bernard O. Aduda, Julius M. Mwabora, Gunnar A. Niklasson, Claes G. Granqvist, Gerrit Boschloo, 2009. Electrochemical characterization of TiO2 blocking layers prepared by reactive DC magnetron sputtering, Journal of Electroanalytical Chemistry 637, 79–83.

Hyunkook Kim, Hyonkwang Choi, Sookhyun Hwang, Youngjoo Kim and Minhyon Jeon, 2012. Fabrication and characterization of carbon-based counter electrodes prepared by electrophoretic deposition for dye-sensitized solar cells. Nanoscale Research Letters,1-4.
.
S. Burnside, S. Winkel, K. Brooks, V. Shklover, M. Gratzel, A. Hinsch, R. Kinderman, C. Bradbury, A. Hagfeldt, H. Pettersson, 2000. Deposition and characterization of screen-printed porous multi-layer thick Ælm structures from semiconducting and conducting nanomaterials for use in photovoltaic devices. Journal of Materials Science: Materials in Electronics, 11, 355-362.

Kristel Möldre, Lauri Aarik, Hugo Mända, rAhti Niilisk, Raul Rammula, Aivar Tarre, Jaan Aarik, 2015. Atomic layer deposition of rutile and TiO_2-II from $TiCl_4$ and O_3 on sapphire: Influence of substrate orientation on thin film structure, Journal of Crystal Growth.
Volume 428, 2015, 86-92.

M. Grätzel, 2000. Perspectives for Dye –Sensitized Nanocrystalline Solar Cells,. Progress in Photovoltaics : Research and Applications, Prog. Photovolt. Res. Appl. 8, 171-185.

Petra J. Cameron and Laurence M. Peter, 2003. Characterization of Titanium Dioxide Blocking Layers in Dye-Sensitized Nanocrystalline Solar Cells. *J. Phys. Chem. B*, 2003, 107 (51), 14394–14400.

S. Nakade, Y. Saito, W. Kubo, T. Kitamura, Y. Wada, S. Yanagida, 2003. Influence of TiO_2 Nanoparticle Size on Electron Diffusion and Recombination in Dye-Sensitized TiO_2 Solar Cells.
J. Phys. Chem. B 107, 8607—8611.

Sebastian M. Waita,Sten-Eric Lindquist, Bernard O. Aduda,, Julius M. Mwabora,, Claes G. Granqvist,, Gunnar A. Niklasson, Anders Hagfeldt, Gerrit Boschloo, 2007. Electron transport and recombination in dye sensitized solar cells fabricated from obliquely sputter deposited
and thermally annealed TiO_2 films. aJournal of Electroanalytical Chemistry 605, 151–156.

Waita, S. M., , Mwabora, J. M. , Aduda, B. O. , Niklasson, G. A. Sten-Eric Lindquist and Claes-Goran Granqvist, 2006. Performance of Dye Sensitized Solar Cells Fabricated from Obliquely DC Sputtered TiO_2 Films. African Journal of Science and Technology (AJST), Science and Engineering Series Vol. 7, No. 2, 106 – 119.

Zaban A., Chen S., Chapel S., Gregg B., 2000. Bilayer nanoporous electrodes for dye sensitized solar cells. Chem.Commun., 2231-2232.

A Transfer Matrix Approach to Aid in The Design and Optimization of Hybrid Advanced Passive Structures for Enhancing Photovoltaic Efficiency

James Walshe[1], Sarah. J Mc Cormack[2], Hind Ahmed[2], John Doran[1]

[1] Dublin Institute of Technology, Dublin (Ireland)

[2] Trinity College Dublin, Dublin (Ireland)

Abstract

The addition of a luminescent down-shifting (LDS) layer directly onto a photovoltaic (PV) cell introduces additional loss mechanisms within the system. The combination of non-ideal photo-luminescent materials encapsulated within a limited range of viable host materials, with the increased reflection losses arising from the newly created interface represent losses which must be overcome for LDS to offer an enhancement to the underlying cells efficiency. Exploiting the interaction between the highly enhanced electric fields established close to a metal nanoparticles (MNP's) surface is one route aimed at mitigating the poor optical properties of the luminophore-host combinations available. Alternative approaches, aimed at addressing the other loss mechanisms within such a system have gone relatively unexplored. Exploiting the non-ideal nature of the photo-luminescent materials available, offers a possibility of recycling the photons which previously did not undergo photoluminescence while also addressing the reflection losses through the inclusion of selectively reflecting optical structures. The hybrid device designs, incorporating single- and double layer- antireflection coatings composed of commonly available materials offer enhancements in the underlying PV cells performance of 8% - 30% depending upon the design criteria established. The transfer matrix approach adopted allowed the impact of individual design considerations on the reflection suppression capabilities of the structure, as well as their impact on the underlying cells efficiency to be readily determined.

Keywords: Spectral losses, Photovoltaics, Photoluminescence, Plasmonics, Nanophotonic's, Optical modelling

1. Introduction

Using luminescent materials to capture high energy photons, previously poorly utilized by a cell, and re-emit the energy at a longer wavelength, where a cell is more efficient, led to the development of luminescent down-shifting (LDS) layers as a potential solution to increase the efficiencies achievable by PVs (Strümpel et al. 2007; Klampaftis et al. 2009; Thomas, Wedding, and Martin 2012; Ahmed et al. 2013; Ahmed, Doran, and McCormack 2016; Ahmed, McCormack, and Doran 2016; de la Mora et al. 2017). The enhancement offered by LDS is limited by the optical properties (low luminescent quantum yield, re-absorption losses, fluorescent quenching, etc.) of the luminescent and encapsulating materials (Klampaftis et al. 2009; Rothemund 2014; Ahmed, McCormack, and Doran 2016; Ahmed et al. 2013; de la Mora et al. 2017).

Further enhancements in the short wavelength response of PV technologies can be enabled by exploiting the plasmonic interaction between a specific combination of metal (e.g. Ag) nanoparticles (NPs) and luminescent species. The highly localized electromagnetic fields established on a nanostructures surface, tailored through the structures morphology and size, allow the optical properties of luminescent species within the near fields to be augmented. Enhancements in the optical properties of luminescent materials, previously deemed non-viable for their inclusion in an LDS device due to their poor optical characteristics, has showcased the merits of including nanostructures within the encapsulating material (Smitha et al. 2008; Shen et al. 2009; Power 2011; Chen et al. 2013; Ahmed, McCormack, and Doran 2017; Rothemund et al. 2011). The wide range of synthesis routes, structure morphologies, and material combinations possible allows the optimization of such plasmonic enhanced luminescent down shifting (PLDS) designs.

doi:10.18086/swc.2017.20.12 Available at http://proceedings.ises.org

The premise of using additional optical structures, which are selectively reflecting, would allow recycling the photons that did not previously interact with the luminescent species present within a PLDS layer. Increasing the probability of a photoluminescence event, mitigating some of the losses associated with the non-unity luminescent quantum yield of the luminophore, through the recycling of these photons. Exploiting the Stokes shift between absorption and emission peaks of a luminescent species pushes the boundaries of the enhancement attainable with a conventional PLDS approach. The optical structures consisting of a series of 'anti-reflection' type coatings would permit a high reflectivity of photons within a luminophores absorption range, a moderately low reflectivity across the remaining the response range being still present (Walshe et al. 2016).

The effect of the design of single- and double-layer reflecting structures, constructed using materials commonly used in the fabrication of antireflection coatings, on the performance of a mono-crystalline silicon (mc-Si) solar cell was theoretically evaluated. By adopting a transfer matrix approach, the effect of each design parameter was evaluated in terms of its impact on the underlying solar cells performance. The aim is to establish a set of initial design considerations that will allow for both the development of a prototype device and further refinement in the design of such devices. This can be achieved by employing the model developed i.e. using more complex structure designs, different luminescent species, different nanoparticle morphologies or a different underlying PV cell type.

2. Structure Enhanced Luminescent Down-Shifting (SE-LDS)

The addition of an LDS layer directly on top of a PV cell increases the number of loss mechanisms available within the system (Klampaftis et al. 2009; Rothemund 2014). The non-ideal optical properties of the luminescent materials available, coupled with losses introduced through the parasitic absorption and poor photo-stability of the encapsulating materials, will allow further design revisions (McKenna and Evans 2017; de la Mora et al. 2017; Mayr 2016; Klampaftis et al. 2009). The typically low refractive index (n = 1.5 – 2.2) of the host materials employed in LDS devices to date is introducing reflection losses from the LDS layers front surface (McKenna and Evans 2017). Structure-enhanced LDS (SE-LDS) devices (figure 1A) could be one such design option as it is allowing to recycle photons and, also, minimizing the surface reflection losses introduced through the addition of the LDS layer.

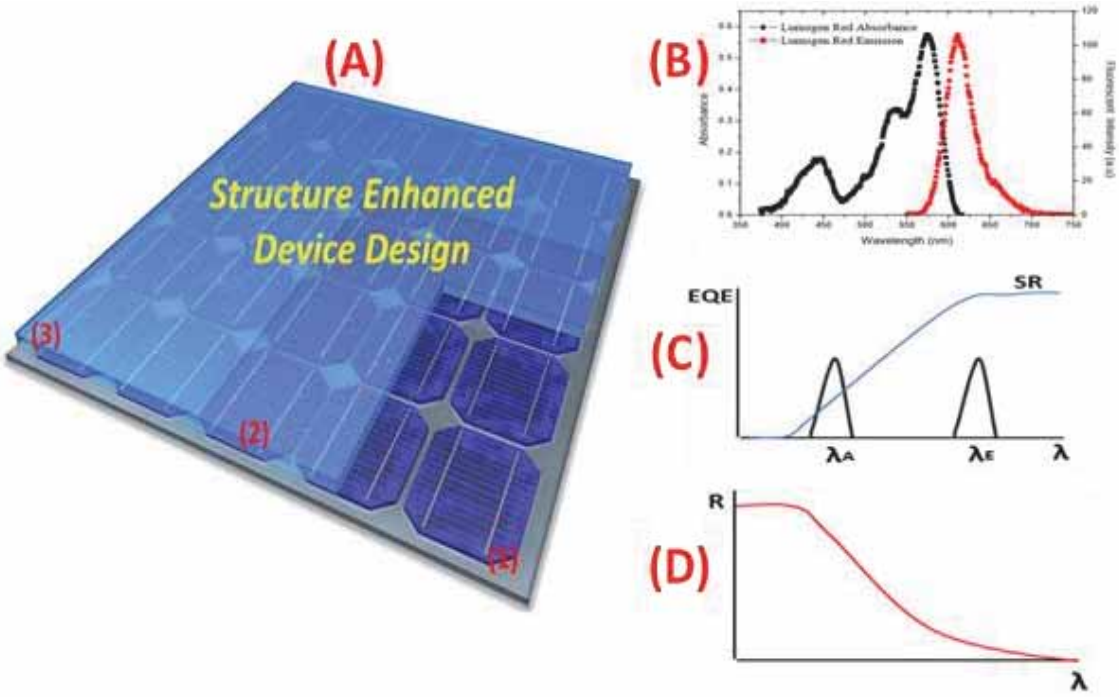

Figure 1: (A) Structure-enhanced (SE) device design concept consisting of three primary components (1) a photovoltaic cell, (2) a transparent matrix encapsulating either a luminescent material (B) or a combination of a luminescent material and metal nanoparticle and (3) a selectively reflecting coating with a reflection profile similar to that presented in (D). The selectivity of the reflecting structures can allows for recycling the photons lying within the encapsulated luminophore's absorption band (λ_A). This allows more photons to be shifted to higher wavelengths (λ_A) where the cells spectral response (SR) is greater (C)

The combination of a relatively small Stokes shift and the sub-unitary LQY are pushing for exploring more energy efficient architectures and novel design considerations. Through selectively designing the reflecting structures (similar to ARC's) a graded reflectivity profile (figure 1D) can be generated allowing for the recylcing of photons, which previously did not get a chance to undergo photoluminescence.

Utilising the formation of highly localized electromagnetic (EM) fields established within metal nanostructure vicinity further mitigates the loss mechanisms inherent within their electronic structure. Incorporating metal nanostructures within the transparent host media offers the capability of augmenting the luminophores optical properties through careful control of the nanostructures composition, morphology, physiochemical characteristics and size (Stalmashonak, Seifert, and Abdolvand 2013; Wiley et al. 2006; Ahmed, McCormack, and Doran 2017; Ahmed, Doran, and McCormack 2016; Zimbone et al. 2015; Power 2011; Smitha et al. 2008). Combining the PLDS approach with the structural enhanced element proposed here could allow for further enhancements in the cell performance.

3. Transfer Matrix Model

The propagation of light through a multi-layered structure, consisting of a series of thin dielectric media, with the variation between the refractive indices of subsequent layers varying significantly can be evaluated using a Transfer matrix model (TMM)(L, Matthew, and S 2007; Sánchez-Soto et al. 2012; Sahouane and Zerga 2014; Shabat and Ubeid 2014; Saylan et al. 2015; Shabat, El-Amassi, and Schaadt 2016; Sikder and Zaman 2016; Hamouche, Shabat, and Schaadt 2017). The TMM utilizes Maxwell's equations to connect the electric and magnetic field components across an existing boundary between two different isotropic dielectric media, allowing the interaction of the incident light with a single layer to be represented as a 2x2 transfer matrix (L, Matthew, and S 2007; Sánchez-Soto et al. 2012; Sahouane and Zerga 2014; Shabat and Ubeid 2014; Saylan et al. 2015; Shabat, El-Amassi, and Schaadt 2016; Sikder and Zaman 2016; Hamouche, Shabat, and Schaadt 2017). Extending this process to a multilayer structure is carried out through the determination of the matrix of each individual layer, with the overall systems matrix being the product of the individual layers matrices. The overall structures matrix is then converted back into transmission and reflection amplitude coefficients, allowing the resulting reflection, absorption and transmission spectra for complex multilayer structures to be readily determined.

4. Design Considerations

The wide range of ARC architectures, the different types of luminophore available and the tuneability of nanostructures granted by the numerous synthesis routes available allows for a large number of design considerations. To prove the viability of the SE-LDS concept only the simplest of structure designs were considered, consisting of single- and two-layer 'Bragg' structures. Here, the effect of the structures design and the numerous design parameters that are available were investigated using the transfer matrix approach. Two initial designs were selected for SE-LDS mc-Si devices (figure 2).

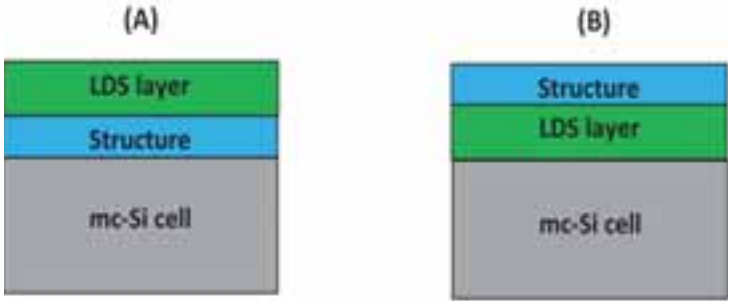

Figure 2: Initial designs for a structure-enhanced luminescent down-shifting (SE-LDS) mc-Si device with the selectively reflecting 'Bragg' structure situated (A) below the LDS layer and (B) above the LDS layer

Anti-reflection coatings (ARC's) can consist of a single layer or multilayer structure, with multilayer coatings offering the possibility of a greatly reduced broadband reflectance at one or more reflectance minima. Selectively reflecting structures were designed using both single and two layer ARC's to produce maximum reflection suppression at a series of wavelengths across the spectral range investigated (300nm – 1100nm), allowing the optimal materials and corresponding thicknesses to be determined for each structure investigated. Based upon the idealised refractive indices for both single and two layer ARC type structures, a range of suitable materials whose refractive indices lay both above and below the ideal values were considered. The materials utilized in the study outlined in table 1.

Table 1: List of the materials used to design structure enhanced elements (Green and Keevers 1995; Raut et al. 2011; 'SOPRA materials database' 2017; Polyanskiy 2017)

Single layer	Two layers
MgF_2	MgF_2-SiO
SiO	MgF_2-CeO_2
CeO_2	MgF_2-ZnS
ZnS	SiO_2-Si_3N_4
Ideal	MgF_2-Ta_2O_5
	MgF_2-TiO_2
	Ideal

To develop a deep understanding of the effect of the individual optical parameters (structure composition and design, dispersive media, optically thick layers, non-homogenous media etc.) of the system, the study was separated into components of increasing complexity. Adding each new element individually allowed monitoring the effect of the reflection suppression capabilities of an array of different structure enahcned (SE) designs and the impact of SE when are incorporated in the architecture of a silicon based device. Refining the optical properties of such structures can lead to viable structural and material configurations for the architectures of the SE-LDS (or PLDS) devices. As an initial approximation, all media are represented as being non-dispersive and homogeneous, with the optical properties of a layer being quantified by a single value of the refractive index and of the thickness.

5. Structure Enhanced (SE) Luminescent Down-Shifting (LDS) Devices

The single layer (SL) antireflection (AR) structures, comprising of the materials previously employed in two different design configurations, highlighted the ability of such simple structures to offer significant enhancements in the underlying cells performance (figure 3). Placing the AR structures below an LDS layer resulted in the greatest enhancement in device performance, with an 8% - 18% improvement in overall device achieved performance (figure 3A). The only instance in which a decrease in performance was observed was when the design included MgF_2. The MgF_2 refractive index is lower than the represented LDS layer, mitigating the π phase shift occurring when the $n1 < n2 < n3$ condition if fulfilled.

Through careful control of the AR structures composition and design, the enhancement factor can be maximised, with the maximum performance occurring for structures designed to suppress reflections at 600 nm - 650 nm. Reducing the thickness of the LDS had little effect on the enhancement offered by the addition of such structures to a LDS equipped device, leading to a 0.1% - 0.4% variation in the enhancement.

Considering the AR structure above an LDS layer resulted in a decrease in the overall device performance (figure 3B). As the light propagates from a media of lower refractive index to one with a higher index, it undergoes an 180^0 phase shift at the interface. This condition is only fulfilled for the structure design incorporating the material MgF_2 (figure 3B). Without the fulfilment of this condition the waves reflected from the two interfaces within such a system don't produce destructive interference but rather a collective of both constructive and destructive interference. The remaining materials employed possessed a refractive index larger than the polymer (PMMA) used to represent the LDS layer throughout the study. Decreasing the thickness of the LDS layer from 90 μm to 9 μm reduced the decrease in device performance for the majority of designs investigated (figure 3B) with values between 1% and 3%.

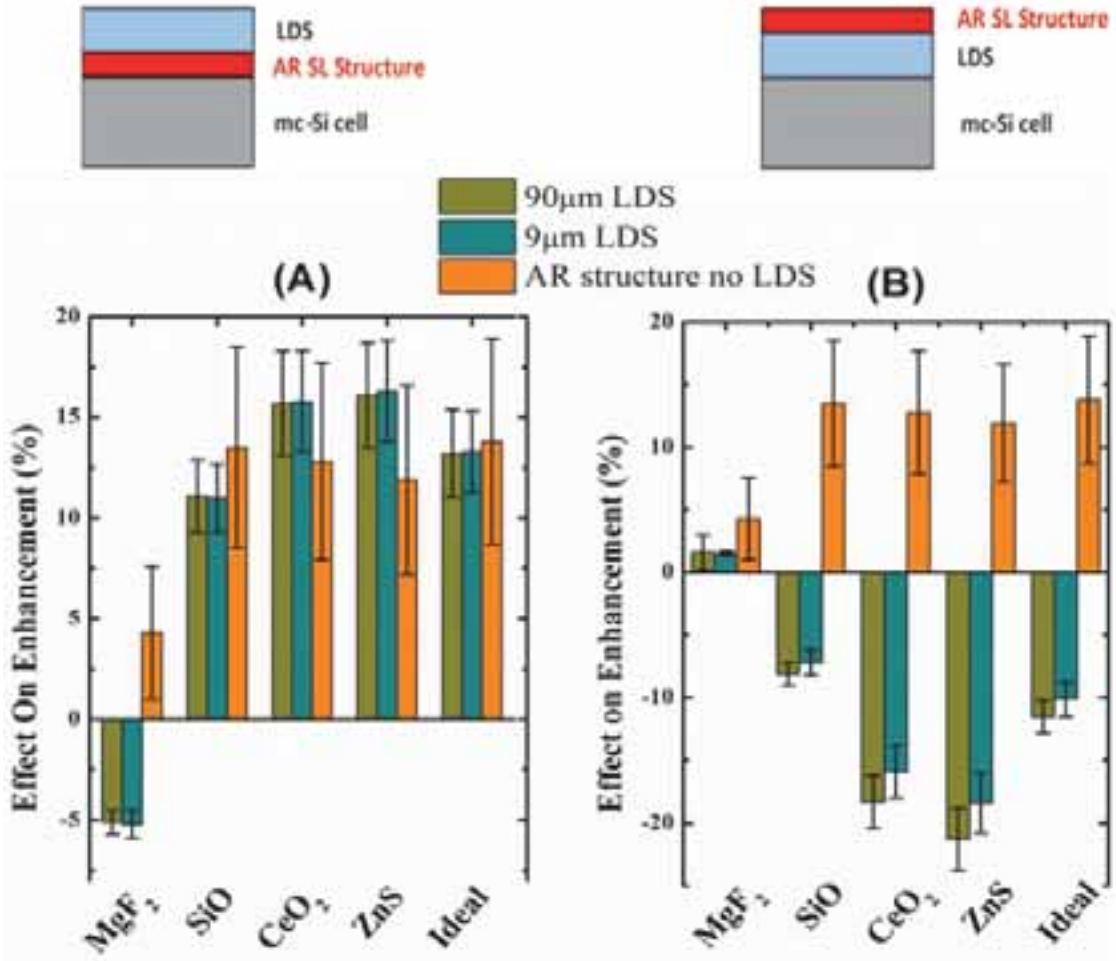

Figure 3: Average percentage (%) increase in the performance of mc-Si when fitted with two different structure enhanced LDS designs: (A)antireflection single-layer structure deposited directly below an LDS layer and (B) the antireflection single-layer structure deposited above. In all cases, the optical properties of the LDS layer were considered to be the optical properties of the polymer matrix material (PMMA), with two different layer thicknesses (90 μm and 9 μm). The variation in the levels of enhancement reported for each material is due to the variation in the wavelength at which the structures were designed to suppress reflection (λ0). Schematics of the design under consideration are included in the figure for each case.

Increasing to two the number of layers comprising the AR structure offered an even greater degree of enhancement in device performance (figure 4). The same trend for both initial outlined designs was reported. Placing the AR structure above the LDS layer results in a decrease in the mc-Si performance with values between 5% and 20% (figure 4). Initially, the SE devices designs that incorporated a selectively reflecting structure directly above the LDS layer (figure 3B and figure 4B) have shown no merit in enhancing the mc-Si cells performance and, consequently, they could be non-viable options.

Housing the AR structure between the LDS layer and mc-Si cell led to enhancements of 10% -24% in the cells energy conversion efficiency (figure 4A). Irrespective of the material combination employed in the device design, the cells performance was increased by 10% (figure 4). Fine-tuning of the design parameters facilitates enhancements on the order of 24%, a slight increase from the increase in performance being reported for single-layer structure designs (figure 3). Reducing the LDS layers thickness produces an increase in the enhancement offered by the structures in figure 24A with values between 2% - 4%.

Fabricating a SE device such that the AR component is located between the LDS layer and underlying PV cell shows the premise to deliver a significant enhancement to the PV cells conversion efficiency (figures 3A & 4A). In reality, the design process of the AR structures should contain a cost analysis element, whereby the

advancement in the performance enhancement will need to be weighed against the cost of increasing the structures complexity.

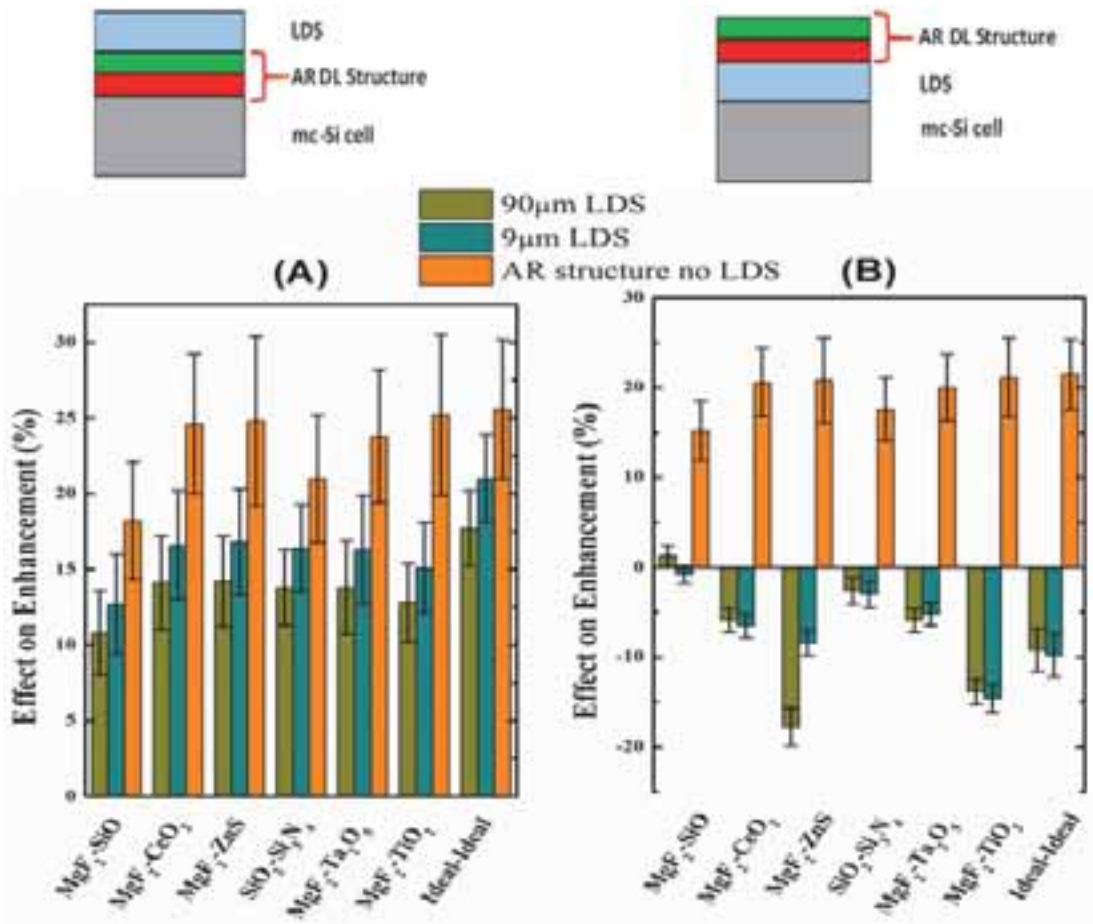

Figure 4: Average percentage (%) increase in the performance of mc-Si when fitted with two different structure-enhanced LDS designs: (A) antireflection bi-layer structure deposited directly below an LDS layer and (B) the antireflection bi-layer structure deposited above. The LDS layer in all cases have the optical properties of the commonly used polymer matrix material (PMMA) with two different layer thickness (90 μm and 9 μm). The variation in the levels of enhancement reported for each material is due to the variation in the wavelength at which the structures were designed to suppress reflection (λ_0). Schematics of the design under consideration are included in the figure for each case.

6. Conclusion

The premise of exploiting the incorporation of novel optical structures into the architecture of a mc-Si solar cell has been established using a TMM model. The structure designs considered highlighted their capacity to mitigate some of the loss mechanisms inherent in LDS and PLDS device designs. By careful selection of the design materials and the tolerance granted over their fabrication, the structures could offer potential device enhancements of 8% - 30% irrespective of photo-luminescent or metal nanostructure interactions. The transfer matrix approach adopted could potentially allow the design process to be automated and optimized for a given set of input criteria i.e. structure architecture, nanostructure and luminophore combination, as well as for the photovoltaic generation upon which the architecture is based. Refinements in the model investigated through experimental fabrication and characterization of such devices would help to establish a deeper understanding of the optical interactions within each component of the design.

7. Acknowledgements

The authors would like to acknowledge the support of Dublin Institute of Technology for the funding received under the Fiosragih scholarship program and the availability of their support and facilities during the course of the research. This research was carried out as a collaborative effort between DIT and Trinity Colleague Dublin, under the solar energy applications group (SEAG).

8. References

Ahmed, H., J. Doran, and S. J. McCormack. 2016. 'Increased short-circuit current density and external quantum efficiency of silicon and dye sensitised solar cells through plasmonic luminescent down-shifting layers', *Solar Energy*, 126: 146-55.

Ahmed, H., S. J. McCormack, and J. Doran. 2016. 'External Quantum Efficiency Improvement with Luminescent Downshifting Layers: Experimental and Modelling', *International Journal of Spectroscopy*: 7.

Ahmed, H. et al 2017. 'Plasmonic luminescent down shifting layers for the enhancement of CdTe mini modules performance', *Solar Energy*, 141: 242-48.

Ahmed, Hind A., James Walshe, Manus Kennedy, Thomas Confrey, John Doran, and Sarah J. McCormack. 2013. 'Enhancement in solar cell efficiency by luminescent down-shifting layers', *Advances in Energy Research*, 1: 117-26.

Chen, Jiao, Yuhui Jin, Nenny Fahruddin, and Julia Xiaojun Zhao. 2013. 'Development of Gold Nanoparticle-Enhanced Fluorescent Nanocomposites', *Langmuir*, 29: 1584-91.

de la Mora, M. B., O. Amelines-Sarria, B. M. Monroy, C. D. Hernandez-Perez, and J. E. Lugo. 2017. 'Materials for downconversion in solar cells: Perspectives and challenges', *Solar Energy Materials and Solar Cells*, 165: 59-71.

Green, M. A., and M. J. Keevers. 1995. 'OPTICAL-PROPERTIES OF INTRINSIC SILICON AT 300 K', *Progress in Photovoltaics*, 3: 189-92.

Hamouche, Houria, Mohammed M. Shabat, and Daniel M. Schaadt. 2017. 'Multilayer solar cell waveguide structures containing metamaterials', *Superlattices and Microstructures*, 101: 633-40.

Klampaftis, Efthymios, David Ross, Keith R. McIntosh, and Bryce S. Richards. 2009. 'Enhancing the performance of solar cells via luminescent down-shifting of the incident spectrum: A review', *Solar Energy Materials and Solar Cells*, 93: 1182-94.

L, Frank, Leno Matthew, and Leno S. 2007. *Introduction to optics* (Pearson Prentice Hall: Upper Saddle River, N.J).

Mayr, Torsten. 2016. 'Fluorescent Material Properites and Spectra. ', Applied Sensor Group: Institute of Analytical Chemistry at the Graz University of Technology in Austria, Accessed 2/6/17. http://www.fluorophores.tugraz.at/substance/868.

McKenna, Barry, and Rachel C. Evans. 2017. 'Towards Efficient Spectral Converters through Materials Design for Luminescent Solar Devices', *Advanced Materials*, 29: 1606491-n/a.

Polyanskiy, M. N. 2017. 'Refractive index database', Accessed 20/7/17. https://refractiveindex.info/cite.php.

Power, Aoife. 2011. 'The Preparation and Characterisation of Silver Nanomaterials and Their Application in Sensing Technique', Dublin Institute of Technology.

Raut, H. K., V. A. Ganesh, A. S. Nair, and S. Ramakrishna. 2011. 'Anti-reflective coatings: A critical, in-depth review', *Energy & Environmental Science*, 4: 3779-804.

Rothemund, R. 2014. 'Optical modelling of the external quantum efficiency of solar cells with luminescent down-shifting layers', *Solar Energy Materials and Solar Cells*, 120, Part B: 616-21.

Rothemund, R., S. Kreuzer, T. Umundum, G. Meinhardt, T. Fromherz, and W. Jantsch. 2011. 'External quantum efficiency analysis of Si solar cells with II-VI nanocrystal luminescent down-shifting layers', *Energy Procedia*, 10: 83-87.

Sahouane, Nordine, and Abdellatif Zerga. 2014. 'Optimization of Antireflection Multilayer for Industrial Crystalline Silicon Solar Cells', *Energy Procedia*, 44: 118-25.

Sánchez-Soto, Luis L., Juan J. Monzón, Alberto G. Barriuso, and José F. Cariñena. 2012. 'The transfer matrix: A geometrical perspective', *Physics Reports*, 513: 191-227.

Saylan, Sueda, Timothy Milakovich, Sabina Abdul Hadi, Ammar Nayfeh, Eugene A. Fitzgerald, and Marcus S. Dahlem. 2015. 'Multilayer antireflection coating design for GaAs0.69P0.31/Si dual-junction solar cells', *Solar Energy*, 122: 76-86.

Shabat, Mohammed M., Dena M. El-Amassi, and Daniel M. Schaadt. 2016. 'Design and analysis of multilayer waveguides containing nanoparticles for solar cells', *Solar Energy*, 137: 409-12.

Shabat, Mohammed M., and Muin F. Ubeid. 2014. 'Antireflection Coating at Metamaterial Waveguide Structures for Solar Energy Applications', *Energy Procedia*, 50: 314-21.

Shen, Xiao Shuang, Guan Zhong Wang, Xun Hong, and Wei Zhu. 2009. 'Nanospheres of silver nanoparticles: agglomeration, surface morphology control and application as SERS substrates', *Physical Chemistry Chemical Physics*, 11: 7450-54.

Sikder, Urmita, and Mohammad Asif Zaman. 2016. 'Optimization of multilayer antireflection coating for photovoltaic applications', *Optics & Laser Technology*, 79: 88-94.

Smitha, S. L., K. M. Nissamudeen, Daizy Philip, and K. G. Gopchandran. 2008. 'Studies on surface plasmon resonance and photoluminescence of silver nanoparticles', *Spectrochimica Acta Part A: Molecular and Biomolecular Spectroscopy*, 71: 186-90.

'SOPRA materials database'. 2017. Accessed 20/7/17. http://www.sspectra.com/sopra.html.

Stalmashonak, Andrei, Gerhard Seifert, and Amin Abdolvand. 2013. 'Optical Properties of Nanocomposites Containing Metal Nanoparticles.' in, *Ultra-Short Pulsed Laser Engineered Metal-Glass Nanocomposites* (Springer International Publishing: Heidelberg).

Strümpel, C., M. McCann, G. Beaucarne, V. Arkhipov, A. Slaoui, V. Švrček, C. del Cañizo, and I. Tobias. 2007. 'Modifying the solar spectrum to enhance silicon solar cell efficiency—An overview of available materials', *Solar Energy Materials and Solar Cells*, 91: 238-49.

Thomas, C. P., A. B. Wedding, and S. O. Martin. 2012. 'Theoretical enhancement of solar cell efficiency by the application of an ideal ‘down-shifting’ thin film', *Solar Energy Materials and Solar Cells*, 98: 455-64.

Walshe, J. , H Ahmed, S.J McCormack, and J Doran. 2016. "BRAGG ENHANCED PLASMONIC LUMINESCENT DOWNSHIFTING FOR PV DEVICES." In *EUPVSEC*. Munich Germany.

Wiley, Benjamin J., Sang Hyuk Im, Zhi-Yuan Li, Joeseph McLellan, Andrew Siekkinen, and Younan Xia. 2006. 'Maneuvering the Surface Plasmon Resonance of Silver Nanostructures through Shape-Controlled Synthesis', *The Journal of Physical Chemistry B*, 110: 15666-75.

Zimbone, M., E. Messina, G. Compagnini, M. E. Fragala, and L. Calcagno. 2015. 'Resonant depolarized dynamic light scattering of silver nanoplatelets', *Journal of Nanoparticle Research*, 17: 8.

Performance analysis of one-axis tracking photovoltaic system with flat planar reflectors

Ryoma Yoshimori*, **Masayuki Nakayama***, **Atsushi Akisawa***
*Tokyo University Agriculture and Technology, Tokyo (Japan)

Abstract

This study examined the performance of a photovoltaic system with flat planar reflectors and south-to-north direction sun tracking system. In order to enhance sunlight collection with simple mechanism, the flat planar reflectors are connected to the solar cells alternately, which can track the sun by expansion and contraction of the system. The objectives are to find out the optimum operation of the inclination angle of the solar cell and to design the ratio of the length of the flat planar reflector and the solar cell by ray-tracing simulations. According to the simulation results, the larger the reflector is the more sunlight is collected in winter. On the other hand, in summer the shorter reflector is effective. The system with short reflector collects more sunlight and less area for installation than conventional PV system. Simulations show that the system with reflectors, which is 1.5 times longer than solar cell is the best in consideration of both concentration performance and area for installation. Its annual sunlight collection is 41 % higher and area for installation is 19 % smaller than those of conventional PV system. The experiments were conducted outside in August and September. The solar radiation intesity on the solar cell of the system was higher than that of conventional PV system throughout the experiment period by 40 - 50 %. Power output of the system was larger than that of conventional PV system by at most 50 % on August 24th and 20 % on September 14th. Non-uniformity of the reflected sunlight affects the output of the system.

Keywords: Low concentrating PV system, Flat-planar mirrors, One-axis tracking, Ray-tracing simulation

1. Introduction

Renewable energies are expected to increase the installation to reduce the consumption of fossil fuels. Photovoltaic (PV) system is the most widely spread energy source using renewable energy all over the world. The main problem of the PV system is still more expensive than conventional electricity. This is caused by the cost of semi-conductors which is the most expensive part in the PV system, and low conversion efficiency. Conventional Si-based PV cells convert approximately 20 % of sunlight into electricity [1–3].

One of the effective measures to reduce the cost is concentrating photovoltaic (CPV) system, which enhance the sunlight on the PV cells. The CPV system reduces the use of PV cells for given power demand. Inexpensive optical devices such as lenses and mirrors are used for concentrator of the CPV system. Sunlight hits the earth surface in the forms of direct and diffuse radiations and their share in total received sunlight depends on the local climate, weather and sky conditions such as pollutants in the air and clouds. Sun tracking is required as concentrators only respond to direct radiation [4].

CPV systems are crassified with their concentrating ratio namely high and low concentration PV systems [5, 6].

High concentration PV (HCPV) system concentrates 500 suns or higher and it is usually constituted by multi-junction cells, which efficiency is reported over 40 % [7, 8]. Yuan-Hsiang Zou obtained effciency of 28.6 % with 800 suns concentrator and PV cell with the effciency of 35.5 % [10]. One of the disadvantages of this technology is the system needs highly accurate tracking system. The optical efficiency of HCPV system using Fresnel lenses, which concentrate approximately 150 suns, is about 20 % lower than its peak when the incident angle is 0.5 degree, reported by Dianhong Li [11]. The other disadvantage is that concentrators only respond to the direct sunlight. When the weather conditon changes from sunny to cloudy, the energy yield significantly decreases. HCPV system is suitable for the places like desert area, where almost all the days are sunny for whole year.

On the other hand, low concentration PV (LCPV) system concentrates up to 40 suns. The concentrating ratio is lower than HCPV system, however conventional silicon solar cells, which made for 1 sun, can be used for LCPV systems. The sollar cells are used under the concentration of 10 suns or below [5, 7, 12]. LCPV systems have less demand on tracking accuracy than HCPV systems. In the Giorgio Grasso's report [13], the prism-coupled compound parabola system is designed with 5 suns concentration. The optical efficiency

doi:10.18086/swc.2017.20.13 Available at http://proceedings.ises.org

does not decrease until incident angle is changed 15 degree in north and south direction. Consequently, LCPV system can be a low-cost solution to increase the density of the sunlight and to reduce the use of solar cells. For LCPV systems, compound parabolic reflectors, V-trough reflectors or flat planar reflectors are used [14–16]. In particular, the flat planar reflectors have the advantage of being inexpensive compared with both V-trough and parabolic reflectors [17].

The sun always changes its position in the sky. The location depends on the longtitude and the latitude, the date and the time. To harvest energy effectively PV modules and mirrors should be placed on the solar tracker. However this two-axis tracking system could be complicated in terms of structure and causes to be expensive. One-axis tracking systems, which moves north-south direction or west-east direction, can have more simple structure.

In this paper, a one-axis tracking LCPV system with flat planar reflectors is proposed. The flat planar reflectors are connected to solar cells alternately. This system enhances the sunlight to the solar cells by the reflectors and tracking when the system expands or contracts to control the inclination angles. Two main activities were conducted in this study. One is ray-tracing simulation described in section 3 which predicts the energy yield and evaluates the performance of the systems with different length of reflectors. It is one of the objectives to find out the optimum operation of the inclination angles of the solar cells and the flat planar reflectors. The other objective is the experiment investigation for confirming the performance under the real sunlight which is described in section 4. The optimum system model and the operation derived in section 3 was used in the experiments.

2. One-axis tracking LCPV system with flat planar reflectors

The one-axis tracking LCPV system with flat planar reflectors is represented by Fig.1 where solar cells are inclined at angle θ and the flat planar reflectors are declined at angle ϕ. The solar cells and the flat planar reflectors are connected each other in north and south direction. The inclination angle of the flat planar reflectors move in response to that of the solar cells. The equation of the relation of both angles is defined by Eq.(1). In this study, the inclination angle of the solar cells is controlled. This structure allows one driving source to controll multiple units. A unit means a combination of one solar cell and one flat planar reflector. There is a design parameter R which is the ratio of the length of the solar cell L_{PV} and the flat planar reflector L_m as defined by Eq.(2).

$$L_{PV} \cdot sin\theta = L_m \cdot sin\phi \tag{1}$$

$$R = L_m / L_{PV} \tag{2}$$

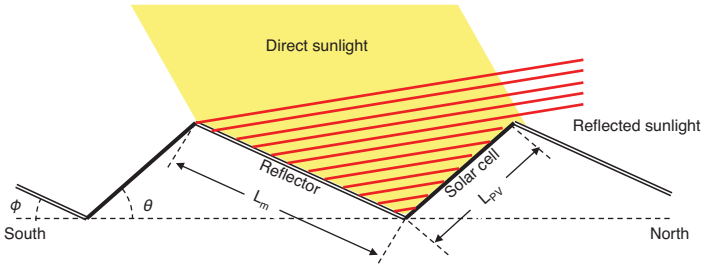

Fig. 1: Geometric scheme of the one-axis tracking LCPV system with flat planar reflectors

3. Ray-tracing simulaion for estimating sunlight intake

3. 1. Simulation conditions

Ray-tracing simulation was conducted as Fig.2 using *Solar Emulator* of *Tracepro* [18]. The sun positions were calculated automatically from the latitude and the longtitude of the system placed, date and time. To model the sunlight parallel light source is assumed. The power flux is set to 1067 W/m^2 considering atmospheric transmittance of whole year average. The weather in the simulation is all cloudlessness and direct radiation was considered while scattered radiation was neglected. The wavelength of sunlight spectrum was set to 550 nm since the software does not provide a continuous sunlight spectrum. The hourly data of solar

radiation from 6:00 to 18:00 in Tokyo were used in the simulations.

The solar cell was set to perfect absorber to evaluate the sunlight intake of the system that is the amount of the solar radiation collected on the solar cell. The reflection ratio of flat planar reflector was set to 0.95. The resolution of inclination angle was set to 10 degree from 10 degree to 80 degree and it was adjusted to optimum angle every one hour. The parameter R was selected from 1.0 to 3.5.

The concentration performances were calculated in the simulations. The monthly and annual concentration are expressed by the ratio of the proposed system to the conventional PV system of which PV system cells are fixed with the inclination angle of 35 degree. The seasonal, monthly annual concentration performances are reported in the following subsections. Moreover the areas of solar cells, mirrors and the land for the installation are also discussed to compare the performances.

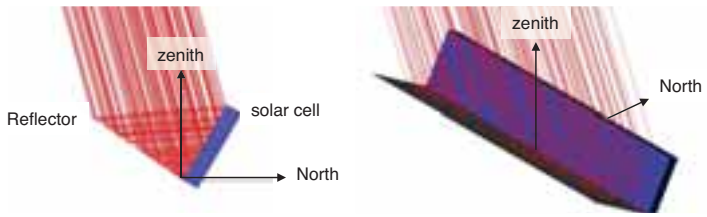

Fig. 2: Example of the ray-tracing simulation of the one-axis tracking LCPV system with the R = 1.5, θ = 60 degree on June 20th

3. 2. Seasonal concentration performance

The seasonal optimum inclination angle θ and concetration performances are represented in Fig.3. The representative dates of the seasons were selected as June 20th for summer, September 20th for fall and December 20th for winter. The optimum inclination angles and concentration performance of March 20th are similar to those of September 20th therefore they are left out on this paper.

In summer when the sun height is high, the systems with smaller R obtained high concentration performance ratios as Fig.4(a) shows. The system with R = 1.0 has the highest concentration performance. It is about 60 % higher than that of conventional system named as *std* in the graphs. The angles of the PV cells and the reflectors are relatively large. The more reflected sunlight hits the solar cells. On the other hand, The systems with large R such as R =3.0 and 3.5 give low concentration performance. The angles of the PV cells and the reflectors are small. Since most of reflected sunlight goes to the sky, the concentration performance of the systems with large R are low.

In middle season such as spring and fall show similar results. The results of fall are shown in Fig.3(b) and Fig.4(b). The concentration performance of each system is higher than the conventional system by 40 % to 60 %. All systems obtained reflected sunlight compared with the case of summer.

In winter when the sun height is low, the systems with larger R obtain high concentration performance as Fig.4(c) shows. The system with R = 3.5 has the highest concentration performance. It was twice as high as that of the conventional system. The larger area of the reflectors is advantageous to collect sunlight with low incident angle in winter. On the other hand, inclination angle of the PV cells with smaller R can not be large because there is a risk that the system makes the shade on the solar cells. Since the system with R = 1.0 makes shade on the solar cells, the concentration performance is lower than that of the conventional system.

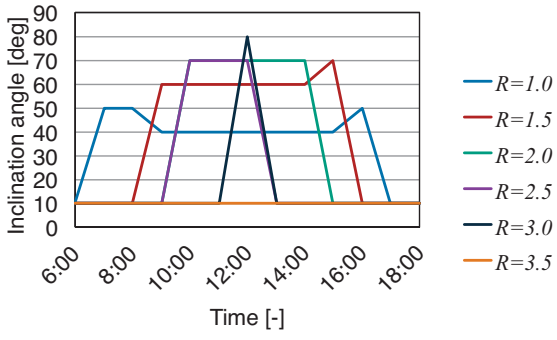

(a) June 20th

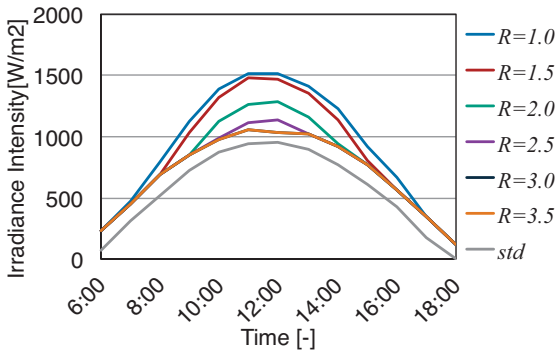

(a) June 20th

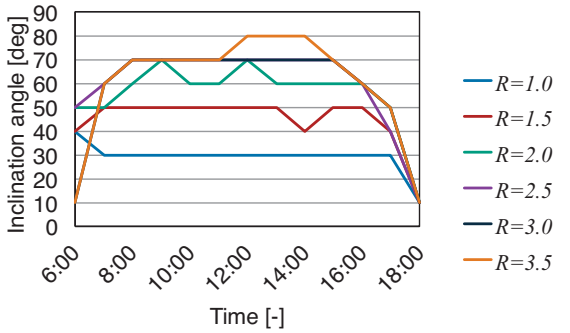

(b) September 20th

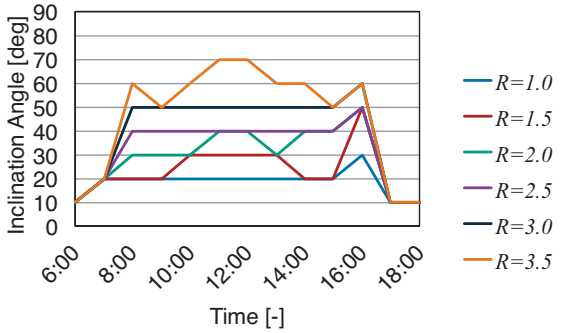

(c) December 20th

Fig. 3: Optimum angle of PV cells

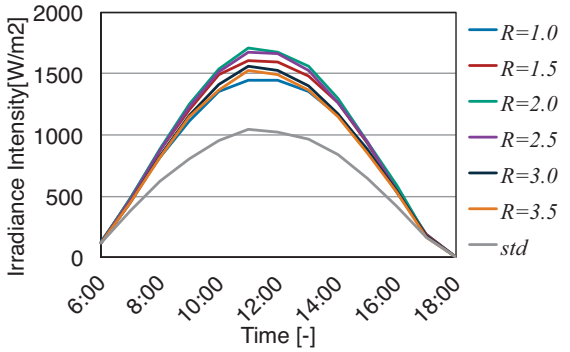

(b) September 20th

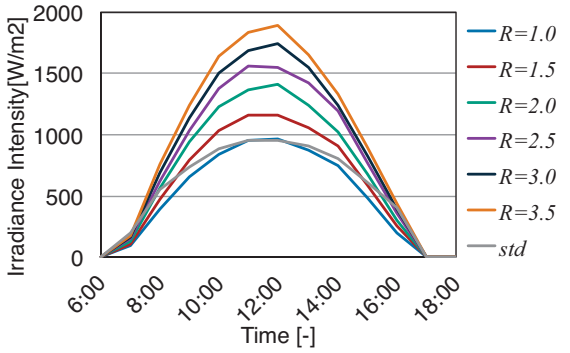

(c) December 20th

Fig. 4: Concentration performance

3. 3. Monthly and annual concentration performance

Monthly concentration performances of the proposed system with various R are represented in Fig.5. Here the improvement ratio is defined so that the performance of the proposed system is normalized with that of the conventional system. When the ratio is higher than 1.0, the proposed system works better. The ratios were calculated using total collected sunlight when the hourly inclination angle of the solar cells was operated optimally. In summer season, the concentration performance ratios of the systems with smaller R are higher. The system with R = 1.0 is the highest in June by 60 % higher than the conventional system. The system with R = 1.5 shows good performance from April to September by 50 % or higher than the conventional system. In winter season, the systems with larger R work effectively. The system with R = 3.5 shows relatively high performance from November to January by about 70 % as high as the conventional system. In December, the concentration performance ratio of the system with R = 1.0 is lower than that of the conventional PV system. As already mentioned in the previous subsection, the system makes shade on the solar cells.

Annual concentration performance ratios of the proposed system are represented in Fig.6. The system with R = 2.5 shows the highest performance by 44 % higher than the conventional PV system. When R is above 1.5, the system has stably high performance than the conventional PV system by 40 to 44 %. The system with R = 1.0 decreases the improvement. The result implies that the system should be designed with R more than 1.5.

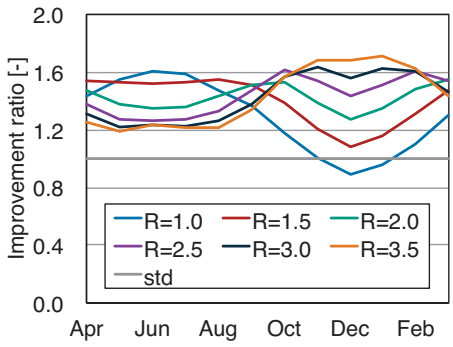

Fig. 5: Monthly concentration performance of the proposed system with various R normalized with the performance of the conventional PV system

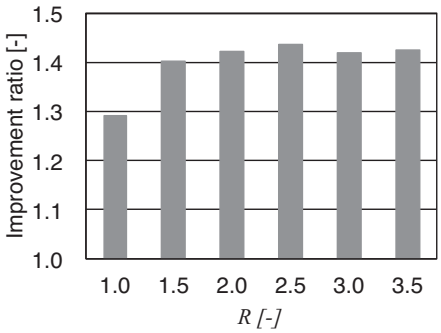

Fig. 6: Effect of R on the annual concentration performance of the proposed system compared with the conventional PV system

3. 4. Efficiency of land use of the installation

The comparison of land use for the systems is disscussed in this subsection. The size of the proposed system can be bigger than the conventional PV system because of additional reflectors. The conventional PV system is installed with a rule that is avoiding the PV array making shade on the other PV array behind [19]. It means avoiding shade when between 9 a.m. and 15 p.m. in Japan. For example, PV array with 1 m in length at 35 degree of inclination angle needs 2.2 m of distance including the gap between 2 arrays. On the other hand, the length of the land use for installation the proposed system is simply the sum of PV cell and the reflector, where the system is flat. For example, one unit of the system with R = 1.5 needs 2.5 m, where 1.0 m is for solar cell and 1.5 m for the reflector.

Here the efficiency of land use was defined as the land area needed to capture a given amount of solar irradiation for one year. The comaprison index was made so that the land area for the proposed system was divided by that of the conventional system. The conventional system uses 45 % of the land area for the solar cells. The system with R = 1.0 needs the smallest land area. It is 30 % smaller than that of the conventional PV system. The area of solar cells is 23 % as small as that of the conventional system. The system with R = 1.5 can make the land area smaller than conventional PV system by 20 %. Moreover the area of solar cells is smaller than that of conventional system by 30 % as shown in Fig.8. It is obvious that the wider the reflectors are the larger becomes the land area for the proposed systems. The systems with R over 1.5 use almost the same area of the solar cells while the area of the reflctors increases gradually.

In regard to the area of land, the systems with R = 1.0 and 1.5 have advantage. However, it should be noted that the performance of the system with R = 1.0 in winter is less than that of the conventional system due to the shade. From the viewpoints of monthly and annual performance, the system with R = 1.5 will be the best choice. As Fig.8 the area for system installation was 20 % smaller than the conventional PV system and cell area was 30 % smaller.

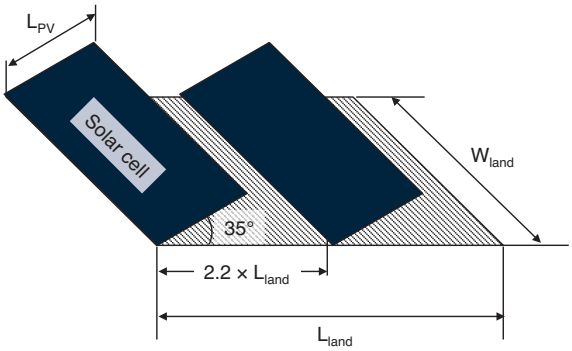

(a) Conventional system

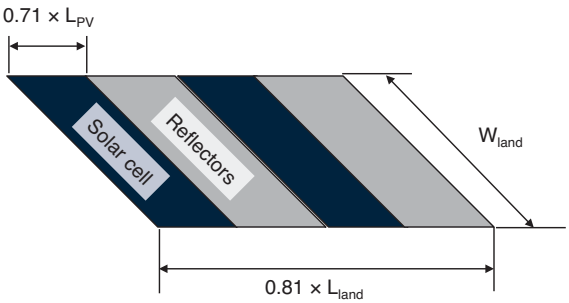

(b) One-axis tracking LCPV system with flat planar reflectors R = 1.5

Fig. 7: View of the land area

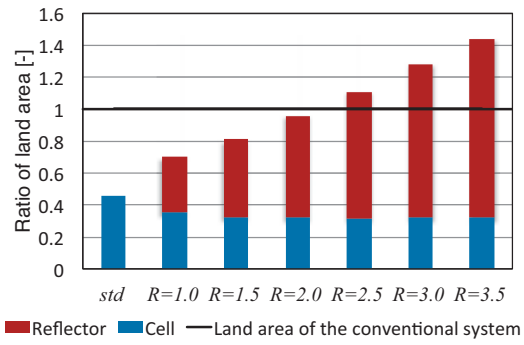

Fig. 8: The areas of solar cells, reflectors and land use for system instllation with a given intake of solar irradiation

4. Experiments for evaluating system performance

4. 1. Experimental setup

Based on simulation analysis, the system with R = 1.5 was selected to be build for the actual measurement of the perfromance by experiments. Figure 9 shows the experimental setup of the system with R = 1.5 which connects 2 solar panels and 2 reflectors. These solar panels and the reflectors can change their inclination angles at the same time by linear guide. The solar panels consist of single crystalline silicon. The single panel has the nominal maximun output of 5.5 W. The length of the solar panel is 100 mm and the width is 500 mm. The length of the mirror is 150 mm and the width is 500 mm. Cell A in Fig.9 measures the output of the conventional PV system by setting the inclination angle of Cell A to 35 degree while Cell B measures the output of the system with R = 1.5 by operating optimum angles calculated by the simulations. The solar radiation intensity on the solar panels was measured by a pyranometer. The pyranometer changed its position depending on the measurement. When measuring the solar radiation intensity of the conventional PV system, the pyranometer is set in front of the Cell A. On the other hand, when measuring the system with R = 1.5, the pyranometer is set behind the rear reflector as shown Fig.9. The output of the solar panels are measured by an I-V checker (EKO INSTRUMENTS CO., LTD, MP-170).

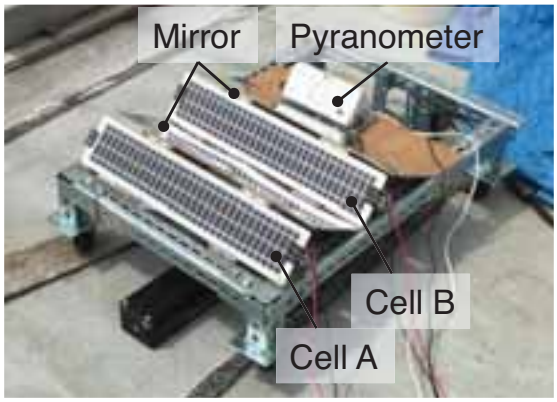

Fig. 9: The experimental setup of the system with R = 1.5

4. 2. Methods of experiment

Experiments were held with the following procedure. The weather conditions were sunny or partly cloudy.

Measurement of conventional PV system

1) Setting the inclination angle of Cell A to 35 degree and locating the pyranometer in front of the Cell A.

2) Measuring the solar radiation intensity by the pyranometer and the output by the I-V checker.

Measurement of the proposed system

3) Setting the inclination angle of Cell B to a specified degree and locating the pyranometer behind the rear reflector.

4) Measuring the radiation intensity by the pyranometer and the output by the I-V checker. The pyranometer detects the direct sunlight from the sun and reflected sunlight from the reflector.

This procedure was repeated every 20 minutes during the measurement period. Time lags occurred the measurements of Cell A and Cell B. The solar radiation intensity sometimes changes suddenly during the time lag.

The performances of partly cloudy day and sunny day were observed. The optimum angle of the system on these dates are shown in Table.1.

Table. 1: Operation of the inclination angles of the system with R =1.5

Weather	Time	9:00	10:00	11:00	12:00	13:00	14:00	15:00
Partly cloudy	Aug 24th	60 °	60 °	50 °	50 °	50 °	60 °	60 °
Sunny	Sep 14th	50 °	50 °	50 °	50 °	50 °	50 °	50 °

4. 3. Results of the experiments

The experiments were conducted outside in August and September. The results of August 24th, which was partly cloudy and September 14th, which was sunny, are reported in this paper.

Figure 10 (a) represents the solar radiation intensity on each of the solar panels on the 24th of August. The weather condition was partly cloudy therefore global solar radiation intensity was up and down with short steps. The solar radiation intensity on the solar cell of the system with R = 1.5 was higher than that of the conventional PV system almost every time, especially it was about 50 % higher around noon. As seen in Fig.10 (b), the output of the solar panels were in accordance with the solar radiation intensity from 11:00 until 13:00. In contrast the effect was not significant after 13:00.

Figure 11 represents the measurement results on the 14th of September which was sunny day. The solar radiation intensity on the solar panel of the system with R = 1.5 was about 50 % higher than that of the conventional PV system every time. However the output of the system with R = 1.5 was higher than that of conventional PV system only by 10 to 20 % around noon. It was found that the solar concentration did not enhance the power generation significantly.

In order to understand what caused the insufficient performance of the proposed system, it was observed how the mirror concentrated the irradiation on the solar panel. Fig.12 (a) to (e) show the reflected sunlight distribution on the solar panel of the system with R = 1.5. As can be seen in the graphs, there existed non-uniform distribution which changed time to time. Fig.12 (c) shows that the illuminated area was largest among the samples. The non-uniformity is considered to degrade the power generation as discussed by Hasan et al. [20]. The results suggest that the proposed system needs to employ suitable PV panels which can work even with non-uniform irradiation on it. The pyranometer measures the solar radiation intensity of the area the reflected sunlight hit.

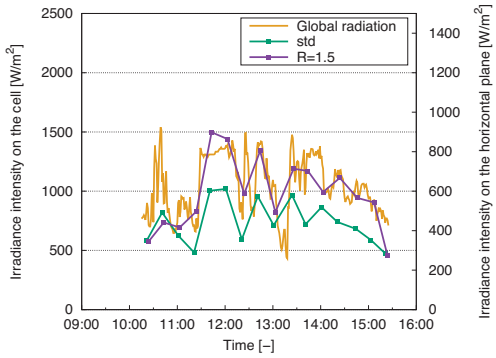

(a) Solar radiation intensity of two PV panels

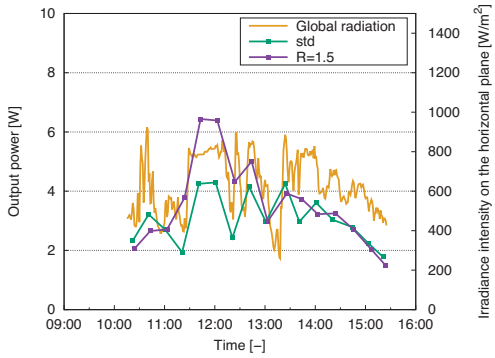

(b) Output of two PV panels

Fig. 10: Measurements on August 24th

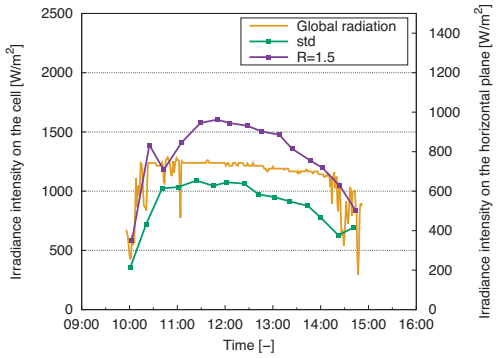

(a) Solar radiation intensity of two PV panels

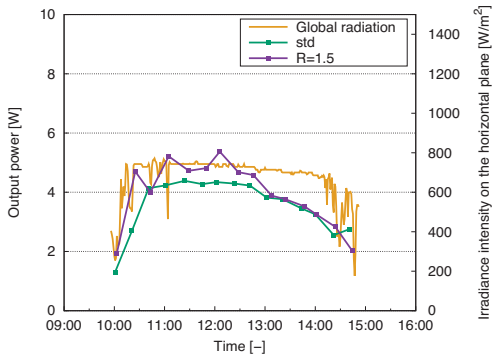

(b) Output of two PV panels

Fig. 11: Measurements on September 14th

(a) 10:00

(b) 11:00

(c) 12:00

(d) 13:00

(e) 14:00

Fig. 12: Sunlight distribution on the solar panel of the system with $R = 1.5$ on September 14th

5. Conclusion

The one-axis tracking LCPV system with flat planar reflectors was examined in this study. The performance was analysed by ray-tracing simulations and also investigated by experiments.

It was found from the simulations that the length of the reflector would affect the seasonal concentration performance of the proposed systems. The system with small reflectors shows high concentration performance in summer while the system with large reflectors gives high concentration performance in winter. The system with $R = 2.5$ showed the heighest annual concentraion performance, which is 44 % higher than that of the conventional PV system. The system with $R = 1.5$ gives similar performance of 41 % even though the area of the reflectors are three-fifth of the system with $R = 2.5$.

Regarding the area for system installation, the systems with $R = 1.0$, 1.5 or 2.0 need smaller area than the conventional PV system. Although the system with $R = 1.0$ shows the best result, its concentration performance is lower than the conventional PV system in winter. Consequently the system with $R = 1.5$ is considered the best design under the assumed operating conditions. The area of the installation and the solar panels of the system are 20 % and 30 % smaller than the conventional PV system respectively.

The system with $R = 1.5$ was built as an experiment setup. Experiments were conducted under the weather of partly cloudy and sunny in August and September. The solar radiation intesity on the solar panel of the system with $R = 1.5$ was successfully enhanced by the reflector up to 50 % at the maximum. In contrast, the

output power was not improved so much as the concentration. It was considered to be caused by the non-uniform distribution of the solar illumination on the solar panel. The results suggest that suitable PV panels are necessary to boost the output even with non-uniform illumination.

Nomenclature

L_m	The length of the flat planar reflrctor
L_{land}	The length of the land for installation of the conventional PV system
L_{PV}	The length of the solar cell
R	The ratio of the length of the solar cell and flat planar
W_{land}	The width of the land for installation of the conventional PV system
θ	The inclination angle of the solar cell
ϕ	The inclination angle of the flat planar reflector reflector

References

[1] Atsushi Akisawa, Masao Hiramatsu, Kouki Ozaki, Design of dome-shaped non-imaging Fresnel lenses taking chromatic aberration into account, Solar Energy, vol. 86 (2012), pp.877-885

[2] Priscila Goncalves Vasconcelos Sampaio, Mario Orestes Aguirre Gonzalez, Photovoltaic solar energy: Conceptual framework, Renewable and Sustainable Energy Reviews, vol. 74 (2017), pp.590-601.

[3] B. Fortunato et al., Modeling, performance analysis and economic feasibility of a mirror-augmented photovoltaic system, Energy Conversion and Management, vol. 80 (2014), pp. 276-286.

[4] Muhammad Burthan, Muhammad Shahzad, Ng Kim Choon, Long-term performance potential of concentrated photovoltaic (CPV) systems, Energy Conversion and Management, vol.148 (2017), pp. 90-99

[5] Yasaman Amanlou et al., A comprehensive review of Uniform Solar Illumination at Low Concentration Photovoltaic (LCPV) Systems, Renewable and Sustainable Energy Review, vol. 60 (2016), pp. 1430-1441

[6] Florencia Almonacid et al., Review of techniques based on artificial neutral networks for the electrical characterization of concentrator photovoltaic technology, Renewable and Sustanable Energy Reviews, vol. 75 (2017), pp. 938-953

[7] Ghassan Zubi, Jose L. Bernal-Agustin, Gian Vincenzo Fracastoro, High concentration photovoltaic systems applying III-V cells, Renewable and Sustainable Energy Reviews, vol.13 (2009), pp. 2645-2652

[8] Marios Theristis et al., Multiphysics modelling and experimantal validation of high concentration photovoltaic modules, Energy Conversion and Management, vol. 139 (2017), pp. 122-134

[9] D.L. Talavera et al., A worldwide assessment of economic feasibility of HCPV power plants: Profitability and competitiveness, Energy, vol. 119 (2017), pp. 408-424

[10] Yuan-Hsiang Zou, Tian-Shiang Yang, Optical performance analysis of HCPV solar concentrator yielding highly uniform cell irradiance, Solar Energy, vol. 107 (2014), pp. 1-11

[11] Dianhong Li, Yimin Xuan, Concept design and simulation of a concentration lens with uniform square irradiance, Optics Communications, vol. 400 (2017), pp. 9-19

[12] Fabio Famaso et al., Performance comparison between Low Concentration Photovoltaic and fixed angle PV systems, Energy Procedia, Vol. 81 (2015), pp. 516-525

[13] Giorgio Grasso et al., Competitiveness of stationary planar low concentration photovoltaic modules using silicon cells: A focus on concentrating optics, Solar Energy, vol. 86 (2012), pp 1725-1732

[14] Heng Zhang et al., Experimental and simulation studies on a novel compound parabolic concentrator, Renewable Energy, vol. 113 (2017), pp. 784-794

[15] Wisam A.M. Al-Shohani et al., Optimum design of V-trough concentrator for photovoltaic applications, Solar Energy, vol. 140 (2016), pp. 241-254

[16] Hiroshi Tanaka, Solar thermal collector augmented by flat plate booster reflector: Optimum inclination of collector and reflector, Applied Energy, vol. 88 (2011), pp. 1395-1404

[17] G. M. Tina, C. Ventura, Energy assessment of enhanced fixed low concentration photovoltaic systems, Solar Energy, vol. 119 (2015), pp. 68-82

[18] LAMBDA RESEARCH CORPORATION, Solar Collector Design and Analysis using TracePro, https://www.lambdares.com/wp-content/uploads/2017/02/Lambda-Solar-Collector-Data-Sheet.pdf

[19] Nuria Martin-Chivelet, Photovoltaic potential and land-use estimation, Energy, vol. 94 (2016), pp. 233-242

[20] Hasan Baig et al., Non-uniform illumination in concentrating solar cells, Renewable and Sustainable Energy Reviews, vol. 16 (2012), pp. 5890-5909

Renewable Resource Assessment and Applications

Photovoltaic Power Curtailment with Forecasting and Unit Commitment Scheduling: A Study on the Kanto Region in Japan

Joao Gari da Silva Fonseca Junior[1], Yuki Nishitsuji[1], Yusuke Udagawa[1], Takashi Oozeki[2], and Kazuhiko Ogimoto[1]

[1] Institute of Industrial Science, The University of Tokyo, Tokyo (Japan)

[2] National Institute of Advanced Industrial Science and Technology, Tsukuba (Japan)

Abstract

Photovoltaic, PV, power generation is reaching unprecedented levels of penetration in many power grids around the world. Such trend is forcing utilities and transmission system operators to rethink the traditional ways to schedule the operation of their power generators. In this study we investigate the impact of day-ahead forecasts of PV power on the unit commitment scheduling of a regional power system. To do that we assumed a scenario of 33 GW of PV installed in the Kanto region in Japan, and that PV power can be curtailed. Using day-ahead forecasts of PV power, we generated daily unit commitment scheduling for one year, and compared them with those generated with a forecast without error. Annually, the amount of power curtailed based on the day-ahead forecasts differed in 1% of the amount required when a perfect forecast was used. Nevertheless, day-ahead forecast errors caused an increase 1.7% of the generators fuel costs (a significant value for cost). Day-ahead forecast errors also caused a need of curtailment in months when the relation between power demand and PV power generation by itself would not require it, such as June and July. Finally, the detection of PV curtailment based on day-ahead forecasts had a positive predictive value (precision) of 73%, but a true positive rate (hit rate) of 32%. Such results are mainly explained by the poor performance of the forecasts on spring and summer in Kanto, indicating a specific period when the forecast error should be improved.

Keywords: Photovoltaic Power, Day-ahead Forecasting, Power System Simulation, Curtailment of Power.

1. Introduction

Scenarios of high penetration of photovoltaic, PV, power generation on power grids are becoming reality in many places around the world. Such growth is causing transmission system operators (system operators hereinafter) to search for new ways to operate their systems so that PV, and renewable energy systems in general, can be smoothly integrated with conventional power generators. To support such integration process, measures such as construction of better transmission lines, storage solutions, demand response measures, etc., should also be taken to prepare power grids and power systems to high levels of renewable energy penetration. The implementation of such measures, however, require considerable investments, and long periods. Thus, in markets where the penetration of renewable energy is growing sharply short-term measures must be taken to support renewable while long-term measures are being implemented. One of such short-term measures is curtailment of renewable power generation.

In Japan, a rapid growth of PV systems associated with limited interconnection capacity between balancing areas caused the government to authorize, since April of 2016, utilities to curtail PV power without quantity or period limitation whenever they judge its generation will affect the stability of the power grid. However, to do that the utilities must inform PV systems owners one day ahead of the time that their PV system's power generation should be curtailed. This rule makes the use of day-ahead forecasts of PV power an essential condition in the operation of PV systems in Japan. Unfortunately, day-ahead forecasts of PV power are not always accurate. Thus, it is necessary to evaluate the impact that forecast errors will have on the effective curtailment of PV power, and on the overall operation of power systems. In technical literature many studies focus on the unit commitment side of the problem, including the development of stochastic of probabilistic unit commitment planning that can integrate uncertainty of renewable energy system's power forecasts (Lowery and O'Malley, 2012), (Wang et al, 2011), (Peng and Jirutitijaroen, 2009), (Ikeda et al, 2012). Nevertheless, studies that evaluate directly the impact of forecast errors of PV system's power generation on its curtailment and on unit commitment planning are still scarce.

doi:10.18086/swc.2017.21.01 Available at http://proceedings.ises.org

Our research group has been investigating the general effects of different kind of PV and wind power forecasts and the use uncertainty information regarding such forecasts in modeling the operation of power grids (Udagawa et al, 2016, 2017a, 2017b). In this study our objective is to clarify the direct relation between day-ahead forecast inaccuracies and errors on curtailment of PV power. Specifically, we investigate such relation in a scenario of high penetration of PV power and when its curtailment is regarded as a routine to deal with PV power fluctuations. To provide realistic results, 30-minute UC scheduling for the region of Kanto in Japan, considering also a scenario for the distribution of power generators installed in the area by 2030, was done for a period of one year. The UC scheduling used day-ahead forecasts of PV power and the expected power demand for each day of the period studied. The impact of the forecast error on curtailment of PV, was also evaluated using as reference a second UC scheduling done with PV forecasts without errors. Such scheduling represents an ideal or perfect one as it is based on zero errors forecasts. Comparing both UC scheduling we analyze how forecasts affect the annual amount of power curtailed, if it is properly detected one day ahead of time, the annual running costs of the power generators, and other characteristics of the regional power system in different time scales.

2. PV Power Forecasting and Uncertainty Estimation

To forecast regional PV power generation a method developed by Fonseca et al., 2015a was used. With this method first insolation in 6 points locations within the Kanto area were forecasted hourly one day ahead of time. Point insolation values were used to obtain the regional yield, which then was converted to regional PV power generation. This calculation procedure was repeated for each targeted hour within the period studied. A brief description of the data and methods used are described in the following paragraphs.

The forecasts of insolation were done for each hour using as input data numerical weather prediction data of the Japan Meteorological Agency. Namely, data from the grid-point value meso-scale model, GPV-MSM, developed by Saito et al., 2006, were used. From the data set related with this model, air temperature, relative humidity and cloudiness in 3 levels were retrieved and used as input data of the forecasts of insolation. In its most recent version the GPV-MSM provides data with a lead time of up to 39 hours ahead of time, with a spatial resolution of 5 km by 5 km in Japan and surroundings. For the day-ahead forecasts data released at 12 h, Japan Standard Time, of the day preceding each targeted day were used as input. The targeted hours to be forecasted were within 5 h and 20 h of each day. Thus, the insolation and PV power forecasts were done one day ahead of time with a lead time varying from 17 hours to 33 hours. Besides the GPV-MSM variables the theoretical horizontal plane extraterrestrial insolation of each hour targeted was also used as input data of the forecasts. Finally, regarding the data used in the PV forecasts, they correspond to the fiscal year of 2013, April to March, and the forecasts were interpolated to 30-minute values to perform the UC scheduling calculations.

To make the forecasts a machine learning technique known as support vector regression was used. The support vector regression technique converts the learning problem as an optimization procedure, and the relation between the input and output variables is modeled through a linear fit in a high-dimensional space. The original problem is mapped to a high-dimensional space with kernels. Thus a kernel function has to be chosen and set as part of the problem. In this study the Gaussian kernel was used. The specific support vector regression technique used was the ν-support vector regression, which was developed by Schölkopf et al., 1998, implemented in port of the LibSVM library (Chang et al., 2001) for the R language.

Before being used in the training stage, the support vector regression algorithm has to have its configuration parameters set. The configuration parameters in this case were set with an ensemble based approach also described in Fonseca el al., 2015a. Regarding the training data, each set of 16 hours characterizing one day-ahead forecasts was done with a support vector regression model trained with data of the 60 days preceding the targeted day of the forecasts. Thus a unique forecast model for each day forecasted was developed.

Once an insolation forecast for a given hour and day is done for each of the 6 point locations within Kanto area, the regional value was obtained with an upscaling procedure, regarding the regional yield as the average value of the 6 point forecasts as showed in Eq. 1. Once the regional insolation forecast is obtained for a given hour, its value is converted to regional PV power following the formulation suggested by JISC8907 standard to calculate PV power from insolation. In this formulation all non-linearities and losses involved in insolation to PV power power are represented by a performance ratio factor as showed in Eq. 2.

$$H_{rj} = \frac{1}{N} \sum_{n=1}^{N} H_{p(n)} \quad (1)$$

$$P_{rf} = P_{ins} \cdot \frac{H_{rf}}{G_s} \cdot K \quad (2)$$

In Eq. 1 H_{rf} is the regional insolation forecasts, in kW/m^2, calculated for a given hour based on the insolation forecast H_p of N points within the target region. This regional insolation forecast is used in Eq. 2 with the PV installed capacity P_{ins}, in kW, the insolation in standard conditions G_s, regarded as 1 kW/m^2, and a performance ratio K, set as 0.8, to calculate the PV power forecast.

To make the UC scheduling with the model described in section 3, besides the deterministic forecast of PV power generation at a given time, it is also necessary to have information about the uncertainty of such forecast. If such information is not available, uncertainty could be represented by a margin of variation from the forecasted value, such as 10% or 20% of it. In this study, for each forecast value of day-ahead regional PV power generation, the uncertainty of it was estimated via prediction intervals. The prediction intervals for the forecasts of PV were calculated using a method we proposed in Fonseca et al, 2015b. In this method, past forecasts are used to estimate the prediction intervals of a target forecast. Basically, this is done in 3 steps. First, past forecasts are selected from a database of forecasts for the region based on how similar their input data are to those of the target hour. Once a set of past forecast is formed, their error is calculated and it is assumed that its distribution follows a Laplacian distribution. Finally, through the maximum likelihood method the best Laplacian distribution that fits the data is selected. Prediction intervals for any forecast are then calculated using the selected distribution. Details about the calculation of prediction intervals for PV forecasts are in Fonseca et al., 2015b. Prediction intervals for the PV forecasts with confidence level of 90% were used in the UC scheduling.

3. Power System Scheduling Model

The operation of power systems in Japan is executed by different system operators depending on the region of the country. Each system operator must schedule the use of their power generators in different time frames so that power demand is always properly and timely supplied. At the day-ahead time frame, the use of power generators available to the operator is planned so that total operational costs required to supply demand of power are minimized under constraints that guarantee all security of supply requirements and the balance between supply and demand of power are met. After that, in intra-day and real-time operation the use of the generators follow dispatch strategies with the similar objectives.

At day-ahead level, one way of scheduling power generators of a region is known as unit commitment, UC, scheduling. In this study we used an UC scheduling model developed by Udagawa et al, 2016. This model minimizes the fuel, *CF*, and start-up, *CS*, costs of a set of *n* thermal power generators in a given area necessary to meet the expected power demand of the 24 hours of the next day in each *t*, 30-minute intervals (Eq. 3). In Eq. 3 *pSt* is a binary variable (0 or 1) indicating if generator *n* is going to be started or not at time *t*. The fuel costs are calculated based on the power output of each power generator considering partial load efficiency and series of constraints that ensure that power demand will be met and that secondary regulation control reserves of power will be available in real time operation of the power system.

Detailed description of the basic model and its constraints are available at Udagawa, 2016. The development of specific constraint conditions model PV curtailment was presented in Udagawa, 2017b. In this section only the main constraints are presented. The constraint in Eq. 4 ensure that power demand forecast $d_t^{(f)}$, in MW, is met by power provided by *n* thermal power generators $p_{n,t}$, by *m* hydro-pumped power generators ($g_{m,t}$ for generated power and $h_{m,t}$ for consumed power) and by PV power after curtailment, pv_t. The constraint in Eq. 5, guarantees that PV power after curtailment is always equal to or smaller than the amount forecasted, $pv_t^{(f)}$, (as it is a day-ahead scheduling). Constraints in Eq. 6 to Eq. 11, ensure that the thermal generators operate within their maximum and minimum operation loads at any time, mxT_n, mnT_n, allowing for reserves of secondary regulation control, for each power generator. For example, the constraint in Eq. 6 controls the upward spinning reserves, Eq. 7 the downward spinning reserves, and Eq. 8 controls the maximum amount allowed for upward secondary control regulation reserve. Finally, Eq. 9 guarantees that the operation of the power generator does not exceed its maximum capacity and E.q 10 and Eq. 11 control downward secondary control regulation reserves. These constraints also ensure that at any given time there will be always power reserve available to deal with the forecast error up to a margin given by the superior and inferior prediction intervals, pv_t^{fu} and pv_t^{fd} provided with the forecasts.

Minimize $\sum_{t=1}^{T}\sum_{n=1}^{N}(CF_{n,t} + CS_{n,t} \cdot pSt_{n,t})$ (3)

Subject to

$$\sum_{n=1}^{N} p_{n,t} + \sum_{m=1}^{M} (g_{m,t} - h_{m,t}) + pv_t \geq d_t^l, \forall t \quad (4)$$

$$pv_t \leq pv_t^f \forall t \quad (5)$$

$$\sum_{n=1}^{N} (p_{n,t} - p_{n,t-1}) \geq 0.05 d_{t,max}^l + \max(pv_t - (pv_t)^f, 0), \forall t \quad (6)$$

$$\sum_{n=1}^{N} (p_{n,t} - p_{n,t-1}) \geq 0.05 d_{t,max}^l, \forall t \quad (7)$$

$$pWk_{n,t} \cdot mxT_n \cdot (1 - blT_n) \leq p_{n,t}, \forall t, \forall n \quad (8)$$

$$p_{n,t} \leq pWk_{n,t} \cdot mxT_n, \forall t, \forall n \quad (9)$$

$$pWk_{n,t} \cdot (mnT_n + mxT_n) - p_{n,t} \leq p_{n,t}, \forall t, \forall n \quad (10)$$

$$p_{n,t} \leq \bar{p}_{n,t}, \forall t, \forall n \quad (11)$$

In Eq. 5, Eq. 6, Eq. 7, Eq. 8, Eq. 9, Eq. 10 and Eq. 11, $\dot{p}_{n,t\ t}$ is the maximum power output of a thermal generator *n* at time *t* discounting its secondary regulation control reserve margin. The symbol $\underline{p_{n,t}}$ is the minimal power output of a thermal generator *n* at time *t*, discounting its secondary regulation. In Eq. 6 $pWk_{n,t}$ is a binary decision variable indicating if thermal generator *n* is online or not at time *t*, and blT_n is the maximum amount of secondary regulation reserve that can be provided by a thermal generator, and it is expressed as a ratio of the generator's maximum power output. Constraints that allow for the determination of the optimum number of power generator needed to provide necessary secondary regulation reserve are also inserted in the optimization model. They are described in in Udagawa et al, 2016.

It was assumed in this model that up to 5% of the maximum operation loads of online thermal generators are regarded as reserve for secondary regulation control reserves. For pumped hydro power the maximum values were 16.5% when generating power and 10% when pumping up water to the reservoir. Moreover, only 11 pumped hydro-power plants were regarded as capable to provide LFC reserve in pumping mode as not all of them have this capability. Pumped hydro power efficiency values were set with values from 60% to 70% depending of the plant. These values are regarded as typical values for the area studied and are also based on Udagawa et al, 2016.

In the UC scheduling calculation, PV power generation is used also to determine the necessary power reserve to deal fluctuations of power in real-time operations. Curtailment of PV will be scheduled then, whenever it is not possible to allocate enough power reserve to deal with PV power fluctuations at a feasible cost. The required reserve of power as having the magnitude of the prediction intervals of the forecasts of PV with a confidence level of 90% plus the power demand fluctuation. Every time, for any given operation time, power reserve required to cover forecasted PV and associated prediction intervals reach physically unfeasible values or has cost beyond acceptable values, curtailment of PV is scheduled.

Depending on how curtailment is applied in practice, different interpretations of the effects of the forecast errors can be done. We assumed, that when curtailment request signal is sent one day ahead of the time to a PV system owner, it sets in the power conditioning system, PCS, of the PV system a maximum output value allowed at a given hour. This value is fixed and based on the capacity of the PCS. Thus, if a curtailment request is issued at a given hour, and less insolation than forecasted is realized (yielding less PV than the maximum allowed), no curtailment of PV is done.

4. Target Region and Simulated Scenario Description

The Kanto region in Japan was the target area of the study. It is where Tokyo is located. It is the region with the highest regional power demand in Japan. The regional power system comprising power generation, transmission, distribution is operated by TEPCO power utility, although the market is currently in the process of being liberalized. Besides Kanto area, TEPCO operates also in parts of the prefecture of Shizuoka and Yamanashi. In this study we considered the whole area operated by TEPCO as Kanto area, so that the real balancing area could be better simulated. Regarding power generators installed in Kanto region, a scenario for 2030 regarding their configuration and installed capacity based on the study of Ogimoto et al., 2012 was used. The assumed values for number of generators, their type and capacity are in Table 1.

Tab. 1: Characteristics of the power plants simulated for Kanto region power system.

Type of Generator	Number of Generators	Installed Capacity (GW)
Coal	15	9.6
LNG	57	22.1
Oil	20	10.8
Hydro Pump Storage	52	13.68
Nuclear and Hydro	Assumed as providers of base load	13.1

A scenario of high penetration of PV was also assumed. Such scenario is based on a study published by New Energy and Industrial Technology Development Organization, NEDO (2010), investigating the possibility of 100 GW of PV power penetration in Japan by 2030 (NEDO, 2014). Based on this value, we considered PV installed capacity as following the ratio between each region and the national annual power demand. Doing that, in a scenario of 100 GW for Japan and if PV is deployed proportionally to the area power demand, Kanto area should have 33.1 GW of PV power installed, which was the scenario simulated.

To simulate real operation conditions of the power system in Kanto, power demand and weather forecast data of the region were used. Power demand data for 1 year, from April 2013 to March 2014, for Kanto region, with a temporal resolution of 30 minutes were used. Accordingly, weather data of the same period was used to yield the insolation and PV power forecasts. Forecast of insolation for 6 points within Kanto area were done one-day ahead of time, from 5h to 20h of each target day. The insolation forecasts were done hourly due to the temporal resolution of the weather data used as input of the forecasts. Thus a simple interpolation procedure was applied using values of two consecutive hours to obtain 30 minute forecasts. This procedure was only applied after the regional forecast of PV power was calculated. The names and approximate location of the 6 places within Kanto for which insolation forecasts were done and, from which the regional yield was estimated, are in Table 2. In each location there is a weather measurement station of the Japan Meteorological Agency.

Tab. 2: Location of the 6 points within Kanto for which forecasts of insolation were done.

Location	Utsunomiya	Maebashi	Kofu	Tsukuba	Choshi	Tokyo
Latitude	36.54 N	36.40 N	35.66 N	36.05 N	35.73 N	35.68 N
Longitude	139.87 E	139.06 E	138.55 E	140.13 E	140.85 E	139.76 E

5. Results

In Fig. 1 four annual values of the day-ahead forecast errors are presented. The root mean square error, $RMSE_n$, mean absolute error, MAE_n and mean bias, $Mbias_n$, were calculated hourly and normalized by the total rated PV power assumed to be installed in the region. To offer a extra measurement of the accuracy of the forecasts the mean absolute percent error $MAPE_n$ is also provided. In this case, it was calculated in daily fashion and normalized by average PV power generation (also daily). The values in Fig. 1 indicate that the accuracy of the regional day-ahead forecasts for Kanto had usual values found for this kind of forecast in Japan (Fonseca et al, 2014).

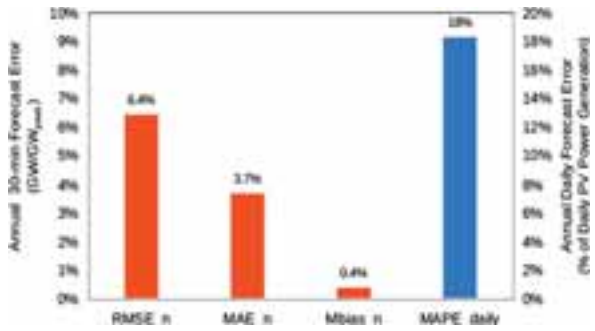

Figure 1: Regional PV Power Forecast Errors for Kanto.

One way to assess the impact of the day-ahead forecast errors showed in Fig. 1 on the UC scheduling of Kanto's power system is to compare the performance of a UC scheduling based on such forecasts with the performance of one based on a forecast without error (a perfect forecast). In Table 3, we present the annual amount of PV curtailed, fuel cost and curtailment period that both kinds of UC scheduling would yield. The results in Table 3 indicate that annually the total amount of PV curtailed, when each kind of forecasts was used, was near to 5% of total PV generated.

Tab. 3: Scheduling of PV curtailment and Running Cost of Kanto Power System in 1 Year based on a UC using day-ahead forecasts, and a UC using a perfect forecast (without forecast errors).

Forecast	PV curtailment scheduled (% of total PV power generated)	Generators' Fuel Cost (10^9 JPY)	Curtailment Period (% of total 30m intervals*)	PV Curtailment MAE_n (scheduled vs. total PV surplus) (% of average PV Power generated*)
Day-ahead	4.90	715.7	18.3	7.2
Perfect	4.96	703.7	13.0	--
Variation	-1.2%	+1.7%	+41%	--

*Within the period of PV forecasts (1 year from 5h to 20h).

Regarding the forecast error, its impact in the annual PV curtailed was relatively small; when day-ahead forecasts were used in the UC the annual PV scheduled to be curtailed was 1.2% lower than the amount that would be curtailed if perfect forecasts were used. On the other hand, looking at the curtailment period at Table 3, when day-ahead forecasts were used, curtailment was scheduled to happen for a longer period than it should reaching 18.3% of the time in the year studied (against 13% of the case when perfect forecasts were used). Thus, the forecast error caused scheduling of PV curtailment in hours when it was not necessary, and also insufficient scheduling of curtailment in the hours when it was necessary. The impact of the forecast error also caused an increase of 1.7% of the power systems fuel cost. Although this value seems small, as its unit is 10^9 JPY it has considerable impact in the operation cost of the system. Such increase of the operation cost is related with how the thermal and hydro pump power generators are used to satisfy the residual power demand in the day-ahead forecast based and perfect forecast based UC. It represents the impact of having to maintain reserve power to deal with the forecast error.

Finally, the cost of the forecast error can be expressed as the mean absolute error of PV power scheduled to be curtailed when compared with the total PV power surplus at each hour. Table 3 shows that, in average, 7.2% of the average annual PV power generated (in GW) was wrongly curtailed. In the cases that PV curtailment errors were negative, more PV than scheduled was curtailed, yielding higher economic and energy losses to owners of PV systems than expected. When the error was positive less PV than scheduled was curtailed (due to less PV generation than forecasted). Although, in this case some PV systems' owners will have less economic losses than expected, there will be losses due to issuing unnecessary PV curtailment requests.

In Fig. 2 the amounts of PV scheduled to be curtailed monthly with the the real forecast based UC and with the one based on a perfect forecast are presented. Because the day-ahead forecasts contain errors, when using them to curtail PV power, two other quantities will appear besides the scheduled PV curtailment. The first one is the actual curtailment of PV power, and it is a direct consequence of the way curtailment was applied (section 3). It represents the difference between actual PV power surplus and PV power scheduled to be used in the power grid, when curtailment was scheduled to happen. The second quantity is the required curtailment of PV. It represents the actual PV curtailment (black dotted line in Fig. 2) plus the PV surplus that must be curtailed but it was outside the hours in which PV curtailment was scheduled to happen. In the case of a perfect forecast both quantities disappear.

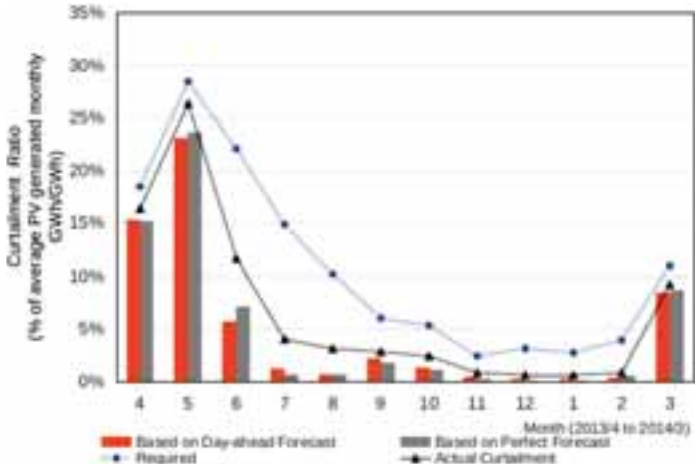

Figure 2: Monthly PV power curtailment ratio in Kanto using real day-ahead forecasts and perfect ones.

The results in Fig. 2 show that if there were no forecast errors, the months when PV would be strongly curtailed would be April and May, and at a lower level March and June. In spring in Kanto, insolation is almost as high as summer but power demand is lower than in winter and summer. In such conditions even using the conventional

power generators at their minimum loads would not be enough to prevent considerable curtailment of PV for the scenario studied. On summer, higher power demand reduces considerably the need for curtailment of PV. The result would be July and August with low PV curtailment as showed by day-ahead and perfect forecast based UC scheduling results in Fig. 2. Nevertheless, what happens is different due to the forecast error. The curtailment required item in Fig. 2 indicates that from June to August between 10% to 25% of the average PV generated in these months should be curtailed if day-ahead forecasts with errors were used. Moreover, in June the required curtailment was more than 2 times higher than the actual one. That result indicates that in June there were many hours in which there was surplus of PV power but there was no scheduling for its curtailment. These hours, in which curtailment happened, were not regarded as such one day ahead of the time.

A forecast error of the PV generation expected at a given hour can cause a difference between PV scheduled to be curtailed, the actual amount curtailed and the required amount to be curtailed. If such PV generation is underestimated, for example, the required curtailment of PV will be higher than the scheduled and the actually curtailed PV power. The result will be an unexpected surplus of PV that the power utility will have to deal with in a short period of time during the operation day. The results in Fig. 2, show that such unexpected surpluses of PV can occur even in months with high demand of power such as July and August.

To better understand the relation between the day-ahead PV power forecast error and the difference between actual PV curtailed and required curtailment in Fig. 2, in Fig. 3 we plotted the monthly PV forecast mean absolute errors and their respective mean biases.

Figure 3: Monthly day-ahead PV power .forecast mean absolute errors and mean biases of Kanto region.

The results in Fig. 3 show that June and July had the PV power forecasts with the highest mean absolute errors of the period studied. Furthermore, these two months also had not only negative biases but also the lowest ones of the period. These two characteristics indicate that in many hours in those months, the PV forecasts underestimated significantly the PV generated. As a consequence, the associated UC scheduling in this period did not curtail enough PV, yielding the behavior presented in Fig. 2.

Continuing the comparison between the curtailment of PV scheduled with day-ahead forecasts with the one curtailed with a perfect forecast, Fig. 4 shows the direct relation between both curtailment values throughout the period studied. A linear fitting is also plotted with the respective coefficient of determination. The value of coefficient of determination indicates that in general there was good agreement between both variables. It shows that 83% of the variance of the curtailment scheduled with a perfect forecast was explained by the curtailment scheduled with the day-ahead forecast. A particularly good relation between both variables is observed when curtailment of PV was higher than 10 GW. In this range, scheduled curtailment based on day-ahead forecasts of PV was usually similar to the one based on a perfect PV forecast. The lower the curtailment of PV based on day-ahead forecasts, the higher was the largest deviation from the curtailment value based on perfect

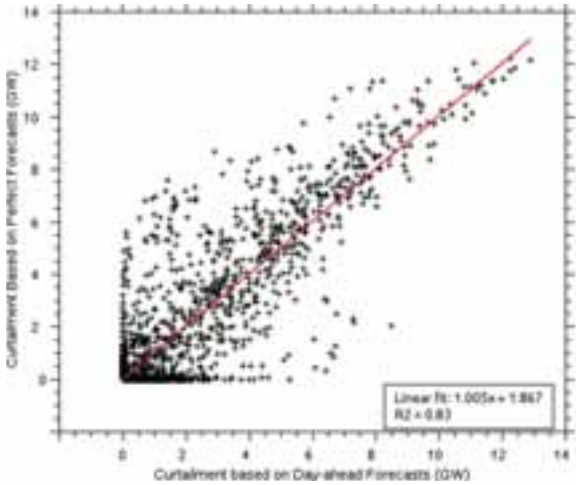

Figure 4: Curtailment of PV based on a perfect forecast versus curtailment of PV based on day-ahead forecasts for Kanto region.

forecasts. For example, when 2 GW of PV were scheduled to be curtailed with day-ahead forecasts, their errors caused a deviation of almost 6 GW from the value that would be curtailed if perfect forecasts were available. For this specific hour, the forecast of PV power generation greatly underestimated the amount actually of PV generated.

Besides the fuel cost of the power system and the error of the amount of PV curtailed, another effect of the day-ahead PV power forecast error on PV curtailment, regards the identification of the hours in a day when curtailment of PV should be applied. If PV curtailment is scheduled to happen at a given hour and due to the real amount generated, it is found that such curtailment was not necessary, this is an hour when curtailment was wrongly scheduled. The opposite, no curtailment scheduled but actually required, is also a scheduling error. To verify the effects of the forecast error from this point of view, Table 4 contains a contingency table of the hours (counted as two 30m time intervals) of the period studied with and without curtailment; the precision and hit rate achieved in the same table.

Table. 4: Hours with PV curtailment based on day-ahead forecasts of PV for Kanto region in 1 year.

		Required		Precision (AC/(AC+AB))
		Yes (A)	No (B)	
Based on day-ahead Forecasts	Yes (C)	1517	552	73.3%
	No (D)	3161	6085	
Hit rate (AC/(AC+AD))		32.4%		

The precision indicates how reliable was the PV curtailment scheduling based on day-ahead PV forecasts, when it indicates that in given hour curtailment will happen. According to this parameter, curtailment scheduling based on day-ahead forecasts had a good level of reliability; in 73% of the hours that curtailment was forecasted, it was actually required. The accuracy (ability to identify correctly the hour with and without PV curtailment) of the scheduling based on day-ahead forecasts was slightly lower than its precision, reaching 67.1%. Nonetheless, the corresponding hit rate was low, indicating that most of the hours of the period studied in which curtailment was required, it was not detected. The low detection of curtailment hours is associated with forecasting less PV power than the actual value. Additionally, in months with negative bias the difference between scheduled curtailment and required one was considerable. We infer from these results that, even though the bias of the day-ahead forecasts, in Fig. 1 and Fig. 3, were not particularly high, reducing even further the forecasts' bias may improve PV curtailment scheduling.

Comparing with a perfect forecast, the curtailment scheduling based on day-ahead forecasts actually yielded more hours of curtailment, Table 3. This result seem to contradict the results of low hit rate in Table 4. However, when should keep mind that the day-ahead error affected the occurrence of curtailment itself, by scheduling curtailment in the wrong hours and by not scheduling it in the right ones. This wrong scheduling generated a need for curtailment that would not exist if a perfect forecasts were used. Therefore, reducing the day-ahead error of the forecasts should cause a reduction of item AD and BC in Table 4, and a proportional increase on item BD.

Besides the error regarding the amount and hours of PV curtailed, the error and uncertainty of the day-ahead forecasts also have an important effect on the way different conventional power generators are scheduled to be used. To show this effect, in Fig. 5 we plotted the UC scheduling with day-ahead forecast and with a perfect forecast. The plots represent the respective UC scheduling in a day in which the forecast of PV power strongly underestimated the the actual PV generation.

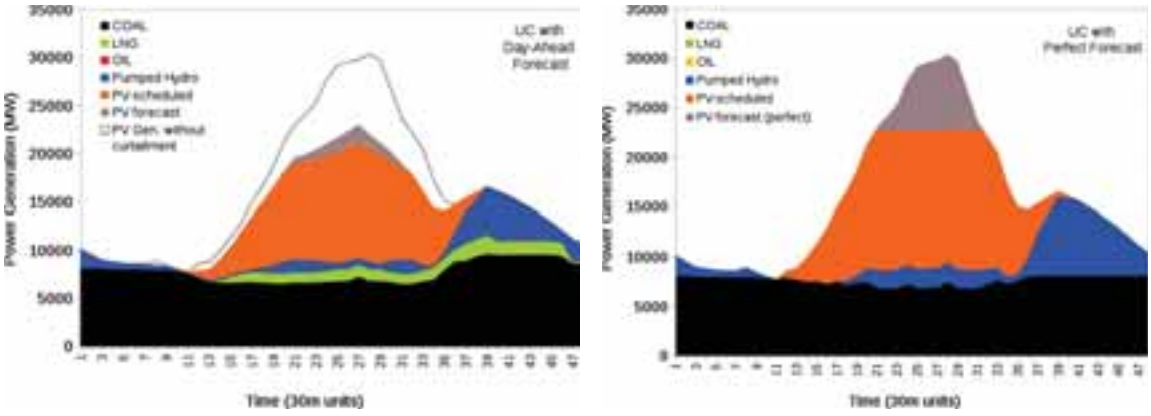

(a) (b)

Figure 5: UC scheduling of a day (June 2nd) based on day-ahead (a) and on perfect (b) forecasts of PV power generation for Kanto.

The UC scheduling based on day-ahead forecasts, in Fig. 5(a), shows that almost all of the PV generation forecasted was scheduled to be used, with small amounts pumped hydro and LNG, which are used to provide secondary regulation frequency control and to compensate for the uncertainty associated with the forecasts. Coal provides the remaining amount of power to meet the demand. Still, looking at the PV power generated in Fig. 5(a) one see that PV power generation greatly exceeded the forecasted amount even with the part scheduled to be curtailed. For example, looking at the dotted line in Fig. 5(a) at 13h30 (point 27 in the plot), 21 GW of PV were scheduled to be used from a forecast of 23 GW.The amount generated after curtailment was 27 GW, resulting in extra 6 GW of unscheduled PV power that will be curtailed. The economic loss for PV systems' owners will be in this case considerably higher than expected. On the other hand from point 11 to 20 and from point 32 to 35 no PV was scheduled to be curtailed and thus the surpluses generated at those hours will have to be dealt with in the intra-day operation to avoid frequency and instability problems on the power grid. In these hours unscheduled PV power curtailment occurs, something that could be avoided reducing the error of the forecast used.

In the UC scheduling based on a perfect forecast, the power generators are used differently. First, due to the lack of uncertainty of the perfect forecast and high amounts of PV power, LNG generators do not need to be used at all and pumped hydro increase its contribution on the total power generated. Moreover, in this case, from 9h to 16h, the maximum amount of PV the grid can absorb is scheduled, near to 22.5 GW, and the remaining PV generation is curtailed. The total amount scheduled to be curtailed in this day with the perfect forecast use was near to 50 GWh against 14 GWh with the day-ahead forecast. Although more PV is scheduled to be curtailed with the perfect forecast, considerably more PV is also used compared with the curve in Fig. 5(a) and no surplus of PV will have to be dealt with in intra-day operations. Moreover, although only 14 GWh of PV were scheduled to curtailed with the day-ahead forecast, in reality the actual curtailment reached by using the respective UC scheduling 94.7 GWh, considerably higher than what would be curtailed with a perfect forecast.

6. Conclusions

The objective of this study was to investigate the use of day-ahead forecasts of PV power in the unit commitment scheduling of a regional power system, and its effects of the scheduling of PV power curtailment. A comparison with a UC scheduling based on perfect forecasts showed that monthly, the use of the day-ahead approximates well the amount of PV power that should be curtailed with a perfect forecast.

Nevertheless, the day-ahead forecast errors had some important effects on UC scheduling and PV power curtailment. Annually, it caused a more expensive scheduling of power generators, and curtailment for longer periods than necessary and in the wrong hours. Additionally, although the monthly PV scheduled to be curtailed based on both UC scheduling were similar, the day-ahead forecast error caused a surplus of PV power generation that has to be curtailed in situations when insolation and power demand conditions would not justify curtailment. June and July were examples of when such cases occurred. In those months there was a negative bias of the day-ahead forecasts, which explain in part the poor detection of the hours when PV curtailment should happen. Thus, one potential measure to reduce such poor detection of curtailment is to further reduce the day-ahead forecast bias, particularly in spring and summer and in the hours when PV should be curtailed.

From the results we conclude that when using day-ahead forecasts of PV in the UC scheduling problem, the forecast error will cause not only affect the fuel cost of the power generators, but it will also yield a considerable

amount the PV surplus that will have to be dispatched or curtailed in intra-day operations. Thus, further measures to improve day-ahead forecast accuracy and to integrate PV forecast error in the UC modeling should be investigated to reduce PV curtailment and to support higher penetration of PV power in the power grid in Japan.

Finally, It should be mentioned that improvements on forecasting techniques are not the only way to deal with the problem of curtailment. Unoptimizing the tilt of PV panels, improved interconnections, demand response, and other measures can be applied together to reduce the need for curtailment of PV in a scenario of high penetration. The compound effect of all these measures together is an interesting topic that also should be investigated in further studies.

Acknowledgment

This study was funded by the New Energy and Industrial Technology Development Organization in the Project Mitigation Technologies on Output Fluctuations of Renewable Energy Generations in Power Grid.

References

Chang, C.-C., and Lin, C.-J., 2001, LIBSVM : a library for support vector machines.

Fonseca Jr., J.G.S., Oozeki, T., Ohtake, H., Shimose, K., Takashima, T., Ogimoto, K., 2014. Characterizing the Regional Photovoltaic Power Forecast Error in Japan: A Study of 5 Regions. IEEJ Transactions on Power and Energy 134.

Fonseca Junior, J.G.S., Oozeki, T., Ohtake, H., Takashima, T., Ogimoto, K., 2015a. Regional forecasts of photovoltaic power generation according to different data availability scenarios: a study of four methods. Prog. Photovolt: Res. Appl. 23, 1203–1218. doi:10.1002/pip.2528

Fonseca Jr., J.G.S., Oozeki, T., Ohtake, H., Takashima, T., Kazuhiko, O., 2015b. On the Use of Maximum Likelihood and Input Data Similarity to Obtain Prediction Intervals for Forecasts of Photovoltaic Power Generation. Journal of Electrical Engineering & Technology 10, 1342–1348.

Ikeda, Y., Ikegami, T., Kataoka, K., Ogimoto, K., 2012. A unit commitment model with demand response for the integration of renewable energies, in: 2012 IEEE Power and Energy Society General Meeting. Presented at the 2012 IEEE Power and Energy Society General Meeting, pp. 1–7. doi:10.1109/PESGM.2012.6344788

Lowery, C., O'Malley, M., 2012. Impact of Wind Forecast Error Statistics Upon Unit Commitment. IEEE Transactions on Sustainable Energy 3, 760–768. doi:10.1109/TSTE.2012.2210150

NEDO, 2014. White Paper on Renewable Energy Technologies - 2nd Edition, 'in Japanese'.

Ogimoto, K., Ikeda, Y., Kataoka, K., Ikegami, T., Oozeki, T., 2012. Flexibility of Japan's Power System to Accommodate PV Penetration in 2030, 27th European Photovoltaic Solar Energy Conference and Exhibition.

Peng, X., Jirutitijaroen, P., 2009. A probabilistic unit commitment problem with photovoltaic generation system, in: TENCON 2009 - 2009 IEEE Region 10 Conference. Presented at the TENCON 2009 - 2009 IEEE Region 10 Conference, pp. 1–6. doi:10.1109/TENCON.2009.5396186

Saito, K., Fujita, T., Yamada, Y., Ishida, J., Kumagai, Y., Aranami, K., Ohmori, S., Nagasawa, R., Kumagai, S., Muroi, C., Kato, T., Eito, H., Yamazaki, Y., 2006. The Operational JMA Nonhydrostatic Mesoscale Model. Monthly Weather Review 134, 1266–1298. doi:10.1175/MWR3120.1

Schölkopf, B., Bartlett, P., Smola, A., and Williamson, R., 1998, Support Vector Regression with Automatic Accuracy Control, Proc. ICANN98 Perspect. Neural Comput., pp. 111–116.

Udagawa, Y., Ogimoto, K., Oozeki, T., Ohtake, H., Ikegami, T., Fukutome, S., 2016. Development of Unit Commitment Model Considering Confidence Intervals of Photovoltaics Forecast and Analysis of a Large Scale Power System. IEEJ Transactions on Power and Energy 136, 484–496. doi:10.1541/ieejpes.136.484

Udagawa, Y., Ogimoto, K., Fonseca Junior, J. G. S., Ohtake, H., Fukutome, S., 2017, Economic Impact of Photovoltaic Power Forecast Error on Power System Operation in Japan, in: 12th IEEE PowerTech Conference. Presented at 12th IEEE PowerTech Conference, Manchester, UK.

Udagawa, Y., Ogimoto, K., Fonseca Junior, J. G. S., Ohtake, H., Fukutome, S., 2017, Analysis of Photovoltaic

Power Yield Curtailment in Day-ahead Unit Commitment, in: IEEJ Transactions on Power and Energy, 137, 7, pp. 1-10. doi:10.1541/ieejpes.137.1

Wang, J., Botterud, A., Bessa, R., Keko, H., Carvalho, L., Issicaba, D., Sumaili, J., Miranda, V., 2011. Wind power forecasting uncertainty and unit commitment. Applied Energy 88, 4014–4023. doi:10.1016/j.apenergy.2011.04.011.

Analysis of Daylight Availability in Italy trough different Luminous Efficacy Models

Francesco Spinelli, Domenico Iatauro, Paolo Signoretti, Luciano Terrinoni, Michele Zinzi

ENEA

(*Italian National Agency for New Technologies, Energy and Sustainable Economic Development)*
Via Anguillarese 301, 00123 Rome, Italy

Abstract

This paper presents the results of a study aimed at developing an Italian database of Typical Meteorological Year (TMY) for the global and diffuse outdoor illuminance, starting from solar irradiation measurements and luminous efficacy models. The main objective is to provide reliable climatic data to be used for the estimation of the daylight availability in buildings and predict the energy requirements for electric lighting with higher accuracy than the actual relevant standard. ENEA developed the national solar radiation atlas during the past years, implementing validated models to predict the global, direct and diffuse irradiation, starting from satellite remote sensing. For this study, the most relevant luminous efficacy models were applied to develop illuminance TMY starting from solar irradiation data. Illuminance availability curves were developed for three reference localities of the Italian territory (Milan, Rome, Palermo), highlighting how results can be used to derive the potential contribution of daylight for buildings energy applications. In order to verify the results obtained, a ground measurements compaign of the outdoor illuminance, was started to test the effectiveness of model. The first data processed, show low differences between estimated values and measured data, confirming the validity of selected model.

Keywords: Daylight availability; luminous efficacy; outdoor illuminance, TMY,

1. Introduction

The building sector is responsible for more than 40% of the energy end uses in Europe and plays a relevant role to reach the environmental and energy targets, in national and European policies [1,2,3]. It is also recognized that the energy performances of building should be addressed to the whole energy services, and not only the space heating as happened in the past decades [4]. Relevant studies carried out during the past years demonstrated the impact of the electric lighting on the energy uses in buildings. The figures are particularly relevant for the not residential buildings: 14% of the total consumption in EU, 26% in USA [5,6]. A study carried out recently in Spain set in 31% the share of the electricity uses on the total final demand in commercial buildings [7]. As a consequence, the energy savings in this energy service are found to be highly competitive in technical and economical perspective [8]. A relevant potential hence exist to improve the performance of existing and new building in terms of lighting energy uses.

It has to be noted that potential energy savings are often estimated in terms of higher efficiency of the electrical devices (lamps, luminaries, control sensors and systems) more than exploiting the daylighting potentialities by the implementation of advanced strategy and solutions. The reference document in EU for the assessment of lighting requirements in building is the EN standard Energy performance of Buildings. Energy requirements for lighting, which provides an operational method and two calculation methods, different in accuracy and complexity [9]. However, the reliability of the prediction methods needs to be carefully addressed, since the over/underestimation of the consumption respect to the practice is an obstacle to the technology spread, especially in the nearly zero energy building (nZEB) vision.

A critical issue is the assessment of the daylight contribution, which does not take into account the climatic conditions of the investigated locality. The Daylight Autonomy concept emerged in the past years as relevant metric to assess the daylighting contribution and, as a consequence, potential energy savings that can be achieved in buildings for the electric lighting service [10, 11]. Climate based approaches are getting interest for

doi:10.18086/swc.2017.21.02 Available at http://proceedings.ises.org

daylighting design methods, as described in [12]. The approach is also adopted in the implementation of an Italian alternative method is currently on going [13], whose main objective is merging the climate based daylighting with the calculation flux defined in [9].

The alternative method evidences the importance of robust and reliable climatic data, in this case global, direct and diffuse illuminance. This paper presents the first results of a review work aimed at developing an national atlas for outdoor illuminance data for building applications.

2. Objective and method

ENEA has defined an extensive database of hourly values of radiometric quantities: global horizontal irradiance (Igh), diffuse horizontal irradiance (Idh) and Direct Normal Irradiance (Idn) for any Italian site, have been derived by processing satellite data [14,15,16,17] provided by the EUMETSAT [18]. Advantages of satellite based data respect to ground measurements mainly depend of the fact that the latter are taken on a limited number of stations, while the former can be derived, if accurately geo-referenced, for any locality on the earth surface. Satellite images provide a measure of the reflection coefficient (albedo) of the planet surface at the switch instant. The algorithms developed by ENEA, based on the original idea of D. Cano et al. [19], compare the actual albedo with a reference one and convert the difference into a clearness index, used to derive the Igh. The application of additional empirical models of the atmosphere [20,21] allows to split Igh in its components: direct and diffuse. The results of the zoning of the solar radiation in Italy are published in the solar radiation atlas published by ENEA [14], which is going to be updated so to cover a 10 years observation period (2006-2015).

Core of this study is the use of radiometric quantities to derive correspondent photometric quantities, in order to build illuminance typical reference years to be used to assess the lighting performance of buildings. It has to be noted that radiometric and the photometric quantities are closely related, as the former measure the energy and the power of electromagnetic radiations, while latter translate the same energy or power in terms of visible light, linked to the physiological ability of the human eye. Since very few data, based either on ground or satellite measurements, are available to build illuminance reference years, empirical models were implemented. These models express the luminous efficacy of the solar radiation (ratio of the illuminance on the irradiance) as a function of variables that describe the sky conditions and the and the solar zenithal angle θz, clearness index KT, diffuse to global radiation ratio k, "clearness" and/or "brightness" indexes. Non general models, as those not implementing all the radiation components or those implemented for specific orientations, were not taken into account. In the this study some of most relevant models were taken into account and from in [22,23,24,25,26,27]. From now on selected models will be identified by the main author of the above listed references.

- Cucumo model, calibrated by irradiance and illuminance measurements at Arcavacata di Rende (CS), Italy [22].It is the simplest model of correlation, based on the direct proportionality between outdoor illuminance and irradiances.
- Muneer model, based in measurements taken in five UK localities, taken in the last decade of the previous century [23]. It is a
- relatively simple model that doesn't consider the current position of the sun and assumes the luminous efficacy expressed by polynomial equation linked to the only global transmission and the poliynomial coefficients derived by statistical regression.
- Perez model. Based on measurements taken in 10 USA and 3 European localities for periods ranging from few months up to 3 years. The model takes into account also the atmospheric precipitable water or, alternatively, the dew point temperature [24]. The irradiance not directly appear in the model expressions, but are combined with extra atmospheric irradiance, in specific indices: Perez's sky clearness index and Perez sky's brightness index. The model also takes into account the position of the sun through the zenithal angle. In the Perez simplified model, the hourly data of dew points are replaced with a daily mean value, constant for all the year. This simplification was introduced to test the impact of the parameter on the model accuracy, being often the dew point data of difficult availability

- Robledo models, based on historical series of data measured in 1994/95 in Madrid, Spain [25,26,27].

The Robledo and Soler models are as accurate as the Perez one, since they take into account the sun position and the sky's brightness and, at the same time, they only need few coefficients. Several models were developed as a function of different sky conditions: clear sky, partly cloudy and overcast sky. Furthermore simplified models are available to consider any weather conditions.

Outdoor illuminance time series database were thus built starting from an extensive solar irradiation time series database and luminous efficacy models. The time series were, next, used to develop a hourly based TMY (Typical Meteorological Year). The adopted criteria was to select, for each month of the year, a real complete month, among those available in the multi-year series, which best fitted the average of the multi-year datasets related to the specific month. This approach allows keeping the average values on the long term and catching the short term variability of the analyzed quantity, as it takes place in the reality. Reference months were selected using GHI as driving parameter, being the quantity directly derived from the satellite image.

TMYs were implemented for the following quantities: global horizontal (Egh), diffuse horizontal (Edh) and direct-normal illuminance (Edn), as done in the past for the solar irradiation. The TMY were developed for three reference localities:

- Milan, latitude 45°N, climatic conditions characteristics of the northern Italian regions.
- Rome, Latitude 41°N, climatic conditions characteristics of the central Italian regions.
- Palermo, 38°N, climatic conditions characteristics of the southern Italian regions.

This preliminary exercise has also the objective of model calibration and/or adjustment by comparison with ground measured data as next step. A total of 15 TMYs was developed, including 3 localities and 5 different luminous efficacy models, having introduced a sensitivity test on water content in model [22]. The TMYs, implemented with the different models, were compared to assess coherence among them and their suitability in providing reliable data to predict energy requirement for lighting in buildings.

The comparisons were made for all models, with reference to the three locations and two lighting quantities (global and diffuse illuminance). The diagrams analyses and the approach indices show minimal differences of each model compared to any other. It is worth noting that for each model a very good agreement was found for the global luminous efficacy, while higher discrepancies were found for the diffuse luminous efficacy. This topic, which needs deeper analyses, might be related to selective phenomena related to the spectral distribution of the solar radiation under variable sky conditions

3. Calculation

Once the TMYs were developed, calculations were carried out to check and compare the different luminous efficacy models. A preliminary check was carried out for the Perez model, with the objective of quantify the impact of the simplification introduced in the previous section. The TMYs of the three localities for the simplified Perez model were implemented taking into account a constant dew point temperature Td (10.3 °C for Rome, 9.4 °C for Milan, 11.4 °C for Palermo). Relevant statistical parameters were calculated to quantify this assumption, namely: the Bias (or Mean Bias Error, MBE), the Mean Bias Error Percent (MBE%) and Root Mean Squared Error Percent (RMSE%), defined as follow:

$$MBE\% = \frac{MBE}{Mean\ of\ observations} x100 \qquad RMSE\% = \frac{RMSE}{Mean\ of\ observations} x100$$

in this case the "*observations*" are the Perez standard model values, considered as benchmark.

Calculation were carried out for the three localities, as an example for Rome (Tab. 1). It resulted: MBE = -155 lx; MBE% = –0.4 % e RMSE% = 1.3 %. The test was carried out for Rome also using extreme dew point values (Tab. 2), -13 °C and +22 °C. Negligible differences were found, in relation to the accuracy required for the purpose of the study.

Tab. 1: Comparisons simplified (max, min and average dew point) and standard Perez model. City: Rome

Model	Illum.	MBE [lx]	MBE %	RMSE [lx]	RMSE %	Mean [lx]
Perez with Dew point average = 10.3 °C	Global	-155	-0.4	531	1.3	42410
	Diffuse	-52	-0.3	297	1.8	16645
	Direct	-33	-0.1	627	1.5	40889
Perez with Dew point min = –13.3 °C	Global	-928	-2.2	1444	3.4	42410
	Diffuse	-519	-3.1	770	4.6	16645
	Direct	938	1.0	1608	3.9	40889
Perez with Dew point max = 22 °C	Global	1062	2.5	1529	3.6	42410
	Diffuse	683	4.1	970	5.8	16645
	Direct	-724	-1.8	2051	5.0	40889

Tab. 2 : Comparisons of simplified (average Dew Point) Perez model for different cities

Model	Illum.	MBE [lx]	MBE %	RMSE [lx]	RMSE %	Mean [lx]
Milan Perez with Dew point average = 9.4 °C	Global	-223	-0.6	601	1.6	37657
	Diffuse	-136	-0.8	397	2.5	16151
	Direct	87	0.3	762	2.2	34525
Rome Perez with Dew point average = 10.3 °C	Global	-155	-0.4	531	1.3	42410
	Diffuse	-52	-0.3	297	1.8	16645
	Direct	-33	-0.1	627	1.5	40889
Palermo Perez with Dew point average = 11.4 °C	Global	-175	-0.4	618	1.4	45653
	Diffuse	-77	-0.4	373	2.1	17963
	Direct	19	0.0	745	1.8	41779

According to the above tables it can be inferred the slight impact of the hourly dew point data on the final form of the luminous efficacy model, thus the simplified model was selected for the final comparison. Each model was compared versus the other three ones in the next step. An example is provided in figure 1, where a graphical comparison between two models is promptly achieved by scatter plots.

According to the approach index calculated for all the comparisons, it was found that differences among models are small. The calculation exercise led to the final decision of applying the Robledo model to build the Italian TMY illuminance database. In table 3 the comparison of the TMYs built using Robledo versus the TMYs based on the other model is presents by means of relevant statistic indicators

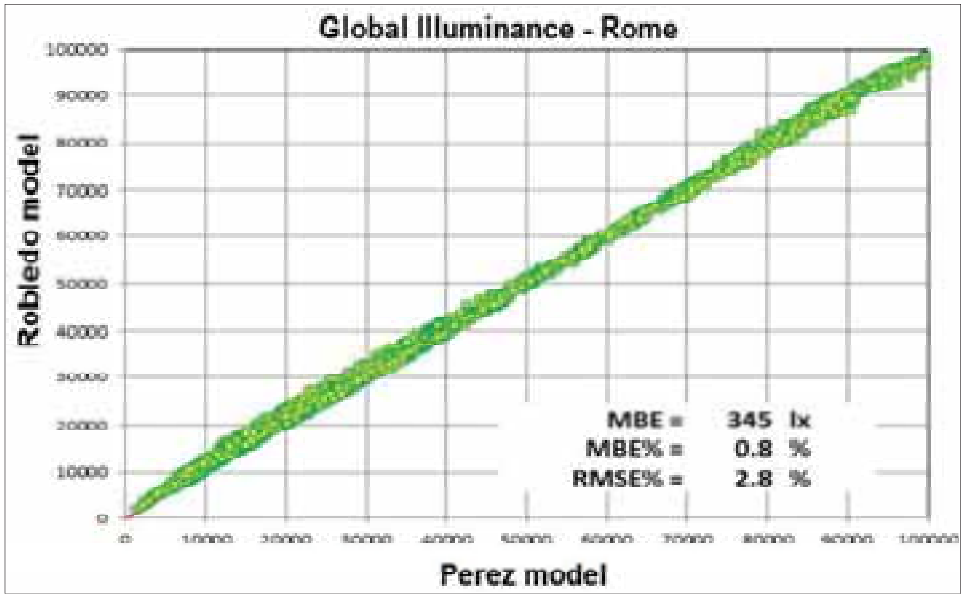

Fig. 1 Global illuminance values (Egh, in lx) of a typical year -town of Rome -comparison between two models

Tab.3 Comparisons with the Robledo model. City Rome

Model	Illum.	MBE [lx]	MBE %	RMSE [lx]	RMSE %	Mean [lx]
Perez standard	Global	-345	-0.8	1183	2.8	42770
	Diffuse	-1052	-5.9	1811	10.2	17700
	Direct	788	2.0	2192	5.5	40115
Perez with Dew point average = 10.3 °C	Global	-500	-1.2	1095	2.6	42770
	Diffuse	-1104	-6.2	1830	10.3	17700
	Direct	755	1.9	1965	4.9	40115
Cucumo	Global	-492	-1.2	1348	3.2	42770
	Diffuse	-3117	-17.6	3540	20.0	17700
	Direct	5007	12.5	5878	14.4	40115
Muneer	Global	1295	3.0	2160	5.0	42770
	Diffuse	-1606	-9.1	2143	12.1	17700
	Direct	4989	12.4	6380	15.9	40115

The Robledo model takes into account the sun position and the sky brightness, factors influencing the luminous efficacy, however the model is expressed in a compact form and do not takes into account the dew point temperature, figure of difficult availability. The Robledo model, here reported for clarity, is based upon the following equation set [25,26,27] :

$$\begin{cases} \eta_{dh} = \left(91.07 \cdot \Delta^{-0.254}\right) \ lm \ W^{-1} \\ \eta_{bn} = \left(134.27 \cdot \left(\cos \vartheta_z\right)^{0.269} \cdot \exp\left(-0.0045 \cdot \left(90° - \vartheta_z\right)\right) \cdot \left(1.045 - 0.427 \cdot \Delta\right)\right) \ lm \ W^{-1} \\ \eta_{gh} = \eta_{bn}\left(1-k\right) + \eta_{dh} k \end{cases} \quad \text{(eq. 1)}$$

Where:

Ƞ	luminous efficacy;
θz	zenith angle
Δ	sky brightness index:
dh	diffuse horizontal
bn	direct normal
gh	global horizontal

4. Results and Applications

The results following presented refer to the TMYs implementing the Robledo model. Figure 2 and 3 present the results of irradiance and illuminance availability for the global and diffuse quantities. The curves refer to the city of Rome, selected as exemplary locality for brevity, nevertheless similar results were found for Palermo and Milano. The radiometric and photometric quantities are expressed in relative figure (%) respect to the peak value to get rid of the different units and compare the profiles on the same graph.

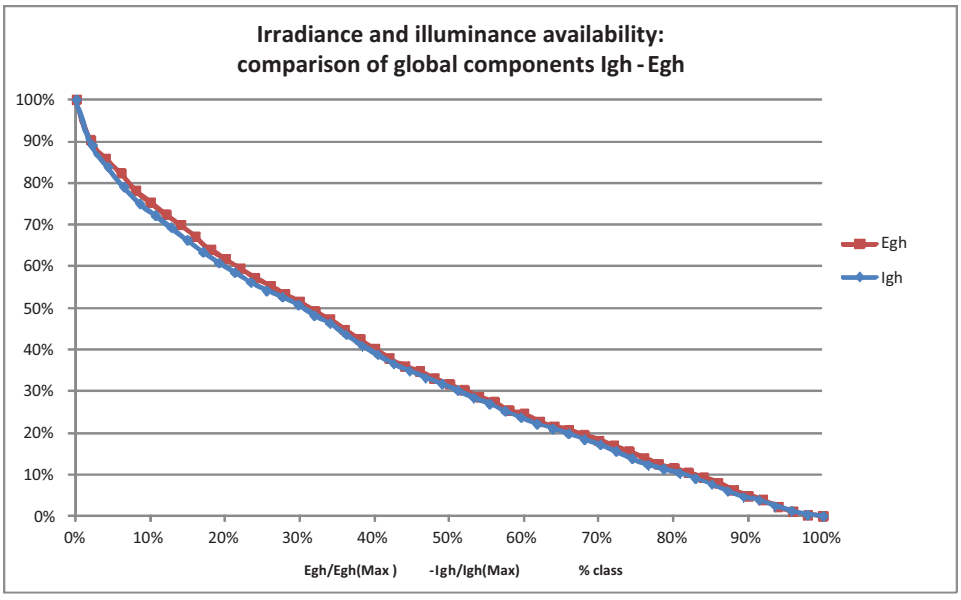

Fig. 2. Comparison of global irradiance Igh and global illuminance Egh

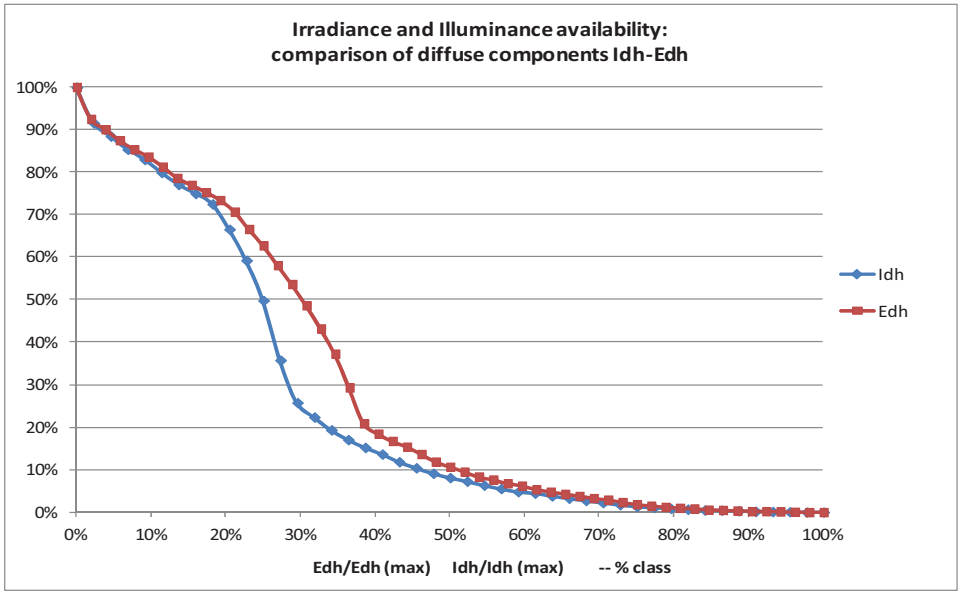

Fig. 3. Comparison of diffuse irradiance Idh and diffuse illuminance Edh

It is interesting to note that global quantities show similar trends, conversely corresponding diffuse components present a different behavior: trends are similar at high and very low relative values, but they show a significant deviation between 20% and 40% of such values.
This behavior evidences luminous efficacy variations, which needs further investigation. At the present stage, it can be noted that the luminous efficacy models takes into account the total solar irradiation, without considering changes in the spectral distribution arising from different sky conditions. Since daylighting metrics use the diffuse illuminance as driving climatic parameter, the latter is following used to present some results potentially relevant for building applications. Figure 3 presents an application of the implemented TMYs: the diffuse illuminance availability in the three reference localities considering the hours from dawn to dusk.

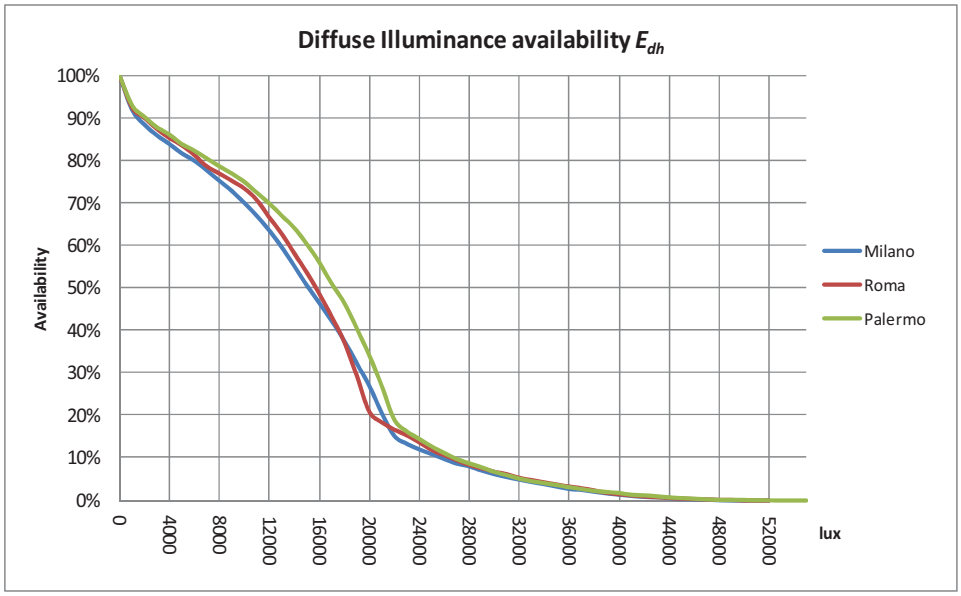

Fig. 4. Diffuse Illuminance availability MI-RM-PA -dawn to dusk-

As expected due its lower latitude, Palermo, have the greater outdoor illuminance availability. The latitude, on the other side, does not explain the result achieved for Rome and Milan. The two curves are very close, despite a latitude difference of about 4°, intersections at about 18000 and 21000 lux. This behaviour, which has a typical summer occurrence, is mainly due to the other higher water and aerosol content in the Milan region, which increases the diffuse components of the solar irradiation respect to the direct one.

Other operative results, derived by the illuminance TMYs, are presented in figures 4 and 5. The former presents the monthly mean diffuse illuminance for the three selected zones, these results are useful to analyze the seasonal variations of the daylight availability and address lighting solution for new and existing buildings, once operation times (8-18 in the example in figure) and indoor visual tasks are defined. Figure 5 presents possible manipulations of the TMYs to provide data tailored to the building needs. The two plots report the diffuse illuminance availability for the case of Rome for two different time usage: from dawn to dusk and for the 08:00-16:00 schedule, which is typical as an example for Italian schools. Holidays and festivities are excluded in the working hours count.

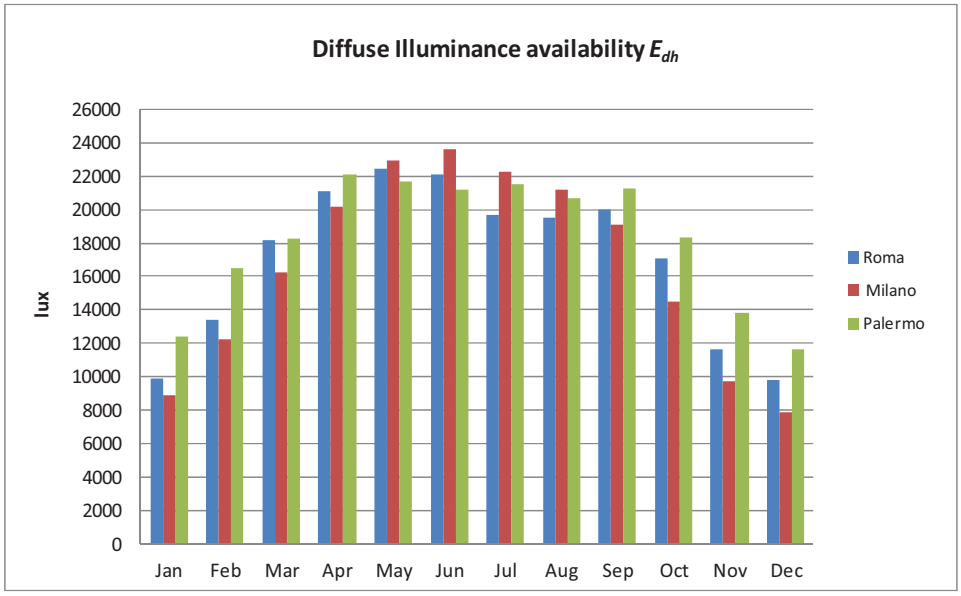

Fig. 5. Edh monthly average values MI-RM-PA operating time 8-18

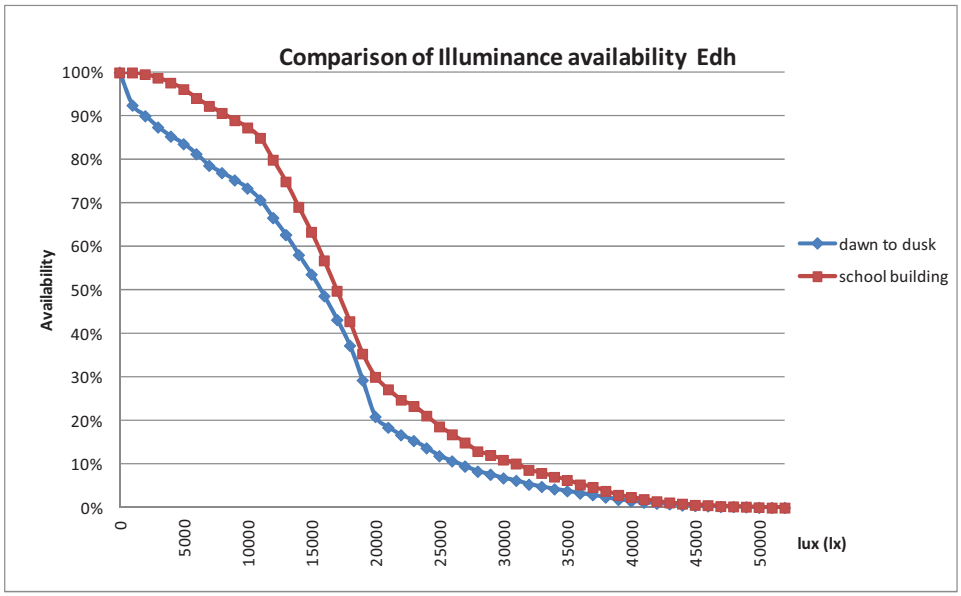

Fig. 5. Edh availability in Rome. Comparison: dawn to dusk and school building with operating time 8-16

5. Validation of model

In order to verify the results obtained, a ground measurements campaign was started in three different Italian sites, Milan, Rome and Lampedusa, to test the effectiveness of model, taking into account different latitudes of Italian territory (Tab 4). The scatter plots are reported figs. 6-7

Tab. 4: Measurements station sites

Site	Coordinates	Measurement [lx]	Sampling time [s]
Lampedusa island	35° 30.0' N 12° 36.5' E	Egh	10
Rome	42° 02.5' N 12° 18.4' E	Egh, Edh	10
Milan	45° 27.9' N 9° 11.3' E	Egh, Edh	10

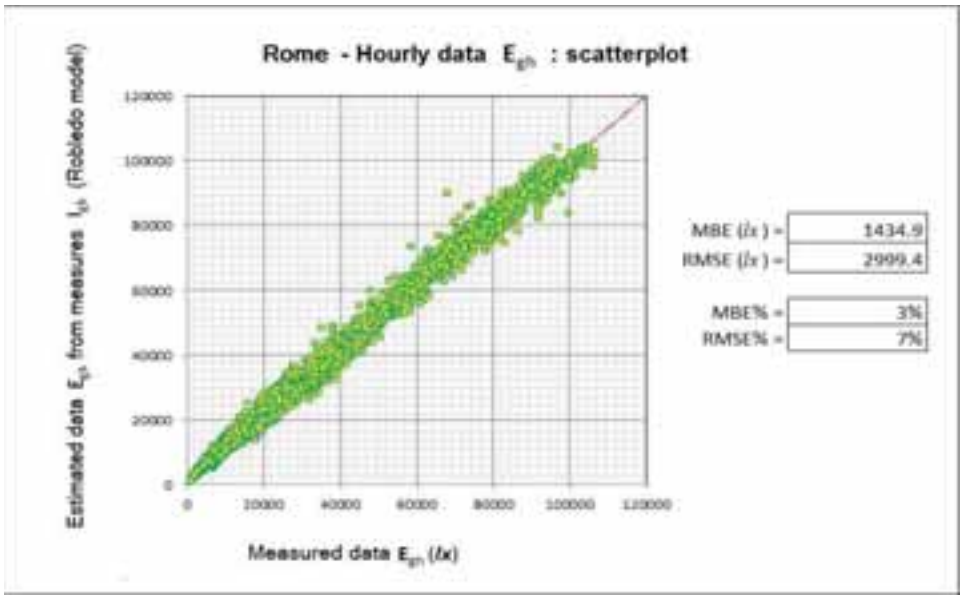

Fig. 6. Comparison: estimated (Robledo model) and measured data for Egh , Rome

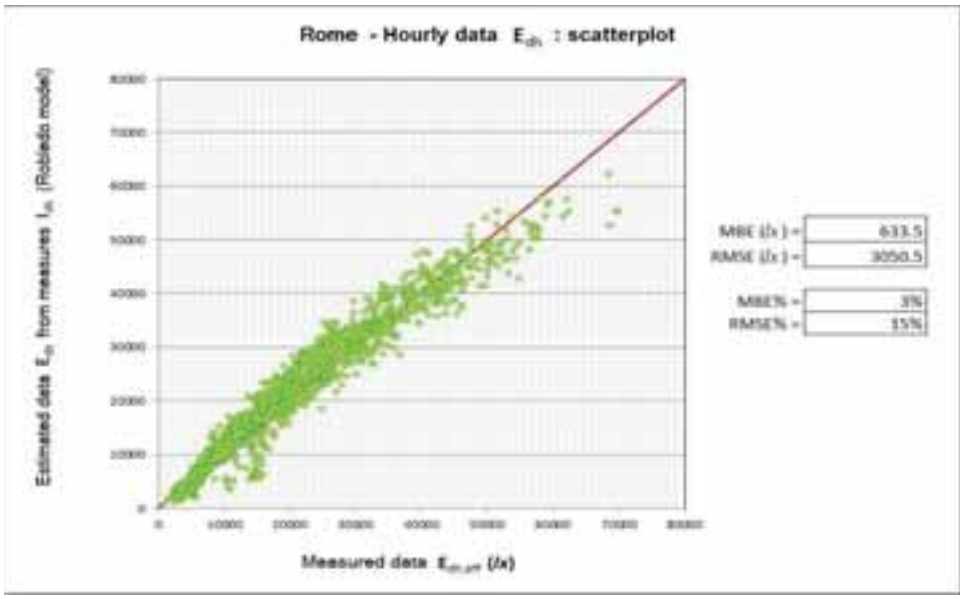

Fig. 7. Comparison: estimated (Robledo model) and measured data for Edh , Rome

The first data processed, for Rome (figs. 6-7), showed low differences between estimated values (R&S model) for Global (Egh) and Diffuse (Edh) illuminance and measured data. The findings have been confirmed by values of statistical indicators, MBE and RMSE, evaluated for both components. The measurements campaign is still ongoing and the further data, related to the other sites selected (Milan and Lampedusa) will allow to get an overall validation of model for Italian territory.

6. Conclusions

This paper presented preliminary studies for the preparation of a national atlas of illuminance data for building applications. Relevant models of luminous efficacy starting from solar radiation data were screened, in order to find the most suitable solution, in terms of accuracy and availability of the relevant input parameters.

Different illuminance hourly TMYs where hence built and comparisons were carried out in terms of daylight availability and autonomy. Discrepancies of the models in reproducing the diffuse component of the photometric quantities were highlighted. A reference model for the future national database was selected and compared with first land measurements data.

Preliminary results were presented to show how the data could be used for building applications. Further tests are ongoing to check, with ground measurements, the accuracy of the luminous efficacy models and eventually introduce refinements and adjustments. Final steps are: establish outdoor illuminance availability diagrams for main Italian towns for different operating times and plot Italian Daylight maps.

References

[1] Communication from the Commission of 3 March 2010 - Europe 2020. A strategy for smart, sustainable and inclusive growth [COM(2010) 2020 final – Not published in the Official Journal].

[2] Communication from the Commission to the European Parliament, the Council, the Economic and Social Committee and the Committee of the Regions of 8 March 2011 – Energy Efficiency Plan 2011 [COM(2011) 109 final – Not published in the Official Journal].

[3] Piano d'Azione Italiano per l'Efficienza Energetica (2013).

[4] Energy performance of buildings EU Directive (EPBD2) 2010/21/EU.

[5] EC (European Commission), www.ec.europa.eu/comm/energy_transport/atlas/html/buildings.html, 2007.

[6] DOE (U.S. Department of Energy). Building Energy Data Book available from: http://buildingsdatabook.eren.doe.gov/, 2009.

[7] IDEA (Instituto para la Diversificación y Ahorro de la Energia). Plan de Ación de Ahorro y Eficiencia Energética 2011–2020 – Annexo. Action Plan From the Spanish Government, Madrid, Spain, 2011.

[8] P.A. Enkvist, T. Nauclér and J. Rosander. A cost curve for greenhouse gas reduction: a global study of size and cost of measures to reduce greenhouse gas emissions yields important insights for businesses and policy makers, McKinsey Quarterly: the online journal of McKinsey & Co 1, 2007.

[9] EN 15193:2007. Energy performance of Buildings. Energy requirements for lighting. Eason, B. Noble, and I.N. Sneddon, "On certain integrals of Lipschitz-Hankel type involving products of Bessel functions," Phil. Trans. Roy. Soc. London, vol. A247, pp. 529-551, April 1955.

[10] C.F. Reinhart and O. Walkenhorst. Validation of dynamic RADIANCE-based daylight simulations for a test offi ce with external blinds. Energy and Buildings Vol. 33 (2001), 683–697

[11] C.F. Reinhart and D.A. Weissman. The daylight area – correlating architectural student assessments with current and emerging daylight availability metrics. Building and Environment, Vol. 50 (2012), 155–164.

[12] S. Wittkopf and L.O. Grobe, (2013). Climate-based daylight simulation as a planning aid for the design of solar façades. Proceedings of Energy Forum Building Skins (153-157). Brixen, Italy: Energy Forum.

[13] M. Zinzi and A. Mangione, The Daylighting Contribution in the Electric Lighting Energy Uses: EN Standard and Alternative Method Comparison, Energy Procedia, Volume 78, November 2015, Pages 2663-2668

[14] SolarItaly – Atlante italiano della radiazione solare, http://www.solaritaly.enea.it.

[15] Clisun - Archivio Climatico ENEA-DBT, http://clisun.casaccia.enea.it.

[16] S. Petrarca, E. Cogliani and F. Spinelli (2000), La radiazione solare globale al suolo in Italia. Anni 1998 e 1999 e media 1994-1999, ENEA, Roma.

[17] F. Spinelli, E. Cogliani, A. Maccari and M. Milone (2007), La misura e la stima della radiazione solare:

l'archivio dell'ENEA e il sito Internet dell'Atlante italiano della radiazione solare per la pubblicazione dei dati, Rapporto tecnico ENEA SOL/RS/2007/21, Roma.
http://www.solaritaly.enea.it/Documentazione/ArchivioRadiazioneSolaritaly.pdf

[18] European Organisation for the Exploitation of Meteorological Satellites (EUMETSAT), http://www.eumetsat.int.

[19] D. Cano, J.M. Monget, M. Albuisson, H. Guillard, N. Regas and L. Wald (1986), "A method for the determination of the global solar radiation from meteorological satellite data", Solar Energy, 37, 31–39, Elsevier.

[20] J. Boland and B. Ridley (2008), Models of Diffuse Solar Fraction, in Modeling Solar Radiation at the Earth's Surface, Springer-Verlag Berlin Heidelberg, cap. 8, p. 193-219.

[21] D.G. Erbs, S.A. Klein and J.A. Duffie (1982), Estimation of the Diffuse Radiation Fraction for Hourly, Daily, and Monthly-Average Global Radiation, Solar Energy, vol. 28, 1982, p.13

[22] M. Cucumo, A. De Rosa, V. Ferrero, D. Kaliakatsos and V. Marinelli (2004), Correlazioni sperimentali dell'efficacia luminosa della radiazione globale, diretta e diffusa, 59° Congresso ATI, Genova, Settembre 2004.

[23] T. Muneer and D. Kinghorn (1998), Luminous efficacy models: evaluation against UK data, Journal of the IES 1998; 27(1):163-70.

[24] R.R. Perez, P. Ineichen, R. Seals, J. Michalsky and R. Stewart (1990), Modeling daylight availability and irradiance components from direct and global irradiance, Solar Energy 44, 5 (1990), pp. 271-289.

[25] L. Robledo and A. Soler (2000), Luminous efficacy of global solar radiation for clear skies, Energy Conversion & Management, 41 (2000):1769-1779.

[26] L. Robledo and A. Soler (2001), Luminous efficacy of direct solar radiation for all sky types, Energy, 26 (2001):669-677.

[27] L. Robledo and A. Soler (2001), On the luminous efficacy of diffuse solar radiation, Energy Conversion & Management, 42 (2001):1181-11

Towards a Tuning Method of PV Power Measurements to Balance Systematic Influences

Sven Killinger[1], Jamie M. Bright[1], David Lingfors[2], and Nicholas A. Engerer[1,3]

[1]Fenner School of Environment and Society, The Australian National University, Canberra, Australia
[2]Department of Engineering Sciences, Uppsala University, Lägerhyddsvägen 1, 752 37 Uppsala, Sweden
[3]Corresponding author: nicholas.engerer@anu.edu.au, http://nickengerer.org

Abstract

With rapid deployment and penetration rates of residential photovoltaic (PV) systems in the distribution grid, there is growing need for accurate assessment of the real-time power generation for grid management and energy market operations. Many of these installed PV systems report their live power generation to online databases and can be used as references to estimate the power generation of neighbouring systems. Upscaling approaches have demonstrated their capability of using the data from these reference PV systems to estimate the power output of target PV systems that do not report their power generation data. However, there is an inherent issue with the representativeness of these reference PV systems power data, e.g. due to quality issues or system specific influences such as shading. Three methods were developed by the authors in earlier work: (1) a parametrisation of PV system metadata and quality control of the measured power, (2) a tuning routine that detects diurnal influences from shading and tunes the PV power in order to reach the expected generation without any shading. And (3) a method which eliminates high variances in k_{pv} based upscaling. An extensive cross-validation with 308 systems in Canberra, Australia in this paper shows significant improvements as a direct result of the application of these three methods. Furthermore, we present the preliminary findings for developments in: the parametrisation of shaded/multi-azimuth reference PV systems, as well as a method to reduce inertia in the shade detection and tuning. Overall, we successfully improve the management of reference PV system power data for use in upscaling.

Keywords – Upscaling, Parametrisation, Quality Control, Tuning, PV power

1. Introduction

In recent years, there has been worldwide growth in the total installed capacity of photovoltaic (PV) systems from 5.1 GWp to 300 GWp between 2005 and 2016 (REN21, 2016; Wedepohl, 2017). For operational control of the electricity grid and for economic trading in the electricity generation market, the precise knowledge of the current PV power generation is of increasingly high value (ENA, 2017).

A growing number of PV systems continuously report their power generation, enabling their data to be taken as a reference. These so called "reference PV systems" can be used to estimate the power of the remaining target PV systems through "upscaling" approaches. An extensive literature review covering upscaling approaches is provided by Bright et al. (2017). Upscaling approaches are impacted influences such as individual characteristics of the PV systems, their spatial distribution, the temporal and spatial aggregation level, interaction of individual and collective system behaviour and module orientation, as well as how variable small-scale weather conditions overlay each other in complex ways.

It is a direct consequence of these influences that not all reference PV systems reflect the power generation of neighboured systems. Earlier research present methods that improve upscaling approaches by increasing the representativeness of reference PV systems:

In Killinger et al. (2017b), a twofold routine is presented that parametrises metadata of reference PV systems (tilt β, azimuth γ and loss factor LF) and then quality controls their PV power output measurements. By eliminating measurement errors and other atypical data from the pool of reference PV systems, the representativeness can be increased. Killinger et al. (2017a) extends the concept of making refrernce PV systems appropriate for upscaling through the development of a tuning routine that can detect and balance diurnal patterns in PV power generation due to shading. The outcome of the tuning routine is an increase in representativeness of reference PV systems. This is because tuned reference PV systems better describe the current meteorological conditions and are a better source to estimate the power generation of other neighboured systems. Such is the success of reference PV system tuning, commercial solar forecasting company Solcast (2017); Engerer et al. (2017) are adopting the approach to drastically improve their forecasts. The preliminary use case for the tuning is demonstrated in Bright et al. (2017).

doi:10.18086/swc.2017.21.03 Available at http://proceedings.ises.org

Lingfors et al. (2017b) evaluated the tuning approach's capability at correctly detecting shading events and compared it with a LiDAR based approach (Lingfors et al., 2017a). The comparison highlighted important features in the tuning that had room for improvement, thus these improvements are the feature of this paper.

This paper has two main objectives. Firstly, the latest advancements in upscaling shall be evaluated in an extensive cross-validation with 308 systems in Canberra, Australia. These methods are briefly presented in section 2. In section 3, important data sources and models are announced. The evaluation is finally realised and discussed in section 4. Secondly, preliminary methods to further improve upscaling are developed and tested in section 5. The paper ends with a short conclusion in section 6.

2. Methodology

The methodological steps are presented in this section. An overview is illustrated in the flow chart of Fig. 1.

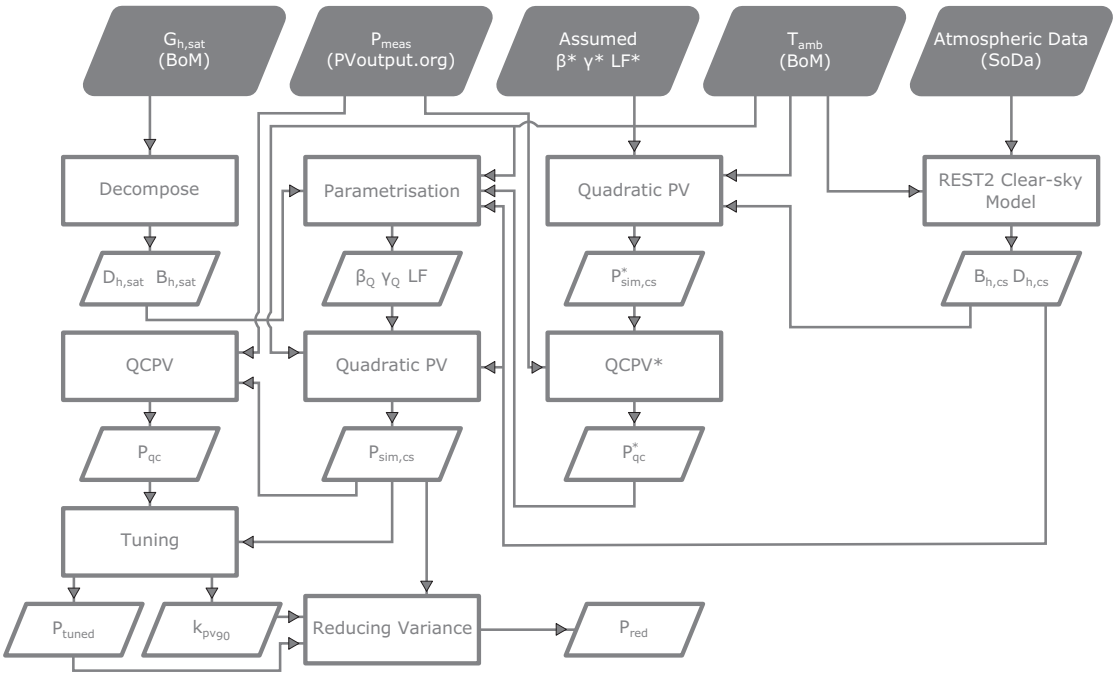

Fig. 1: Flow chart of the proposed methodology. Input data are in grey skewed boxes with data source provider in brackets. Model process steps are in rectangles and intermediate/final outputs are in white parallelograms.

2.1. Parametrisation and QCPV routine

An approach to parametrise the reference PV system metadata (tilt β, azimuth γ and loss factor LF) and to quality control the PV power measurements (QCPV routine) is presented by Killinger et al. (2017b). Both the parametrisation and QCPV routine were improved in Killinger et al. (2017a) and briefly summarised by Bright et al. (2017) and Lingfors et al. (2017b) Hence, only the basic principles of the methodology are detailed within this section.

1. To eliminate critical measurement errors from the parametrisation of the metadata, a modified version of the QCPV routine is applied to the measured power, P_{meas}, to find P^*_{qc} (Killinger et al., 2017a). All intermediate steps of the modified QCPV routine are marked with a * in Fig. 1. A central element in the routine to detect atypical behaviour is the simulation of the clear-sky power $P^*_{sim,cs}$. For the modified version of the quality control of PV power measurements (QCPV*), we assume the same metadata for all systems; north-facing azimuth (Canberra lies on the southern hemisphere), a tilt of 30°, and LF of 1. Two tests, the "maximum k_{pv}" and "cloud enhancements" criteria (section 5.1.3. and 5.2.1. in Killinger et al. (2017b), respectively) are excluded from the modified version QCPV*, as more detailed metadata would be required.

2. In the second step, the parametrisation of metadata is realised. The Non-linear Least-Square (NLS) solver takes satellite-derived beam ($B_{h,sat}$) and diffuse ($D_{h,sat}$) irradiance subcomponents (decomposed with

the Reindl decomposition model as inputs (Reindl et al., 1990a)), along with the ambient temperature (T_{amb}). These inputs are used to simulate PV power depending on the tilt, azimuth and LF. The three latter parameters are varied within the NLS solver until the squared error between the simulated power and the quality controlled measured power is minimal. Within the simulation chain, a quadratic PV power model (Killinger et al., 2017b) and transposition model (Reindl et al., 1990b) are applied. In a second step of the parametrisation, the derived LF is precisely adjusted based on detected clear-sky periods (see Killinger et al. (2017b) and Killinger et al. (2017a)).

3. Based on the parametrised metadata (tilt β_Q, azimuth γ_Q and loss factor LF), the PV power measurements are finally quality controlled. All tests are applied in this second run of the QCPV routine and atypical power values are set to NaN (not a number).

2.2. Tuning

The method for identification and correction of systematic influences that affect PV power output (particularly shading) at various time-steps throughout the day is known as the tuning routine, and is presented in detail by Killinger et al. (2017a). With the completion of parametrisation and QCPV routine, the quality controlled power output P_{qc} and the clear-sky power output at a reference PV system $P_{sim,cs}$ are used to calculate the clear-sky index for photovoltaics k_{pv} (Engerer and Mills, 2014):

$$k_{pv} = \frac{P_{qc}}{P_{sim,cs}}. \qquad \text{(Eq. 1)}$$

In theory, k_{pv} achieves a value of 1 when subjected to clear-sky conditions and higher values only when subjected to cloud enhancement events (Engerer, 2015; Killinger et al., 2017b). Low values of k_{pv} occur due to either increased thickness of cloud cover or reduced system performance. Conversely, in a case where a PV system never achieves clear-sky conditions in the form of $k_{pv} = 1$ for repeated particular time-steps in the course of the day, these periods can be considered to be influenced by systematic reduction, which is most predominantly caused by shading. For the reliable detection of shading, the k_{pv} values are analysed for a running window of time over 30 days. The 90$^{\text{th}}$ percentile ($k_{pv_{90}}$) is derived for each 10-min time-step of the day through an approach described by Lonij et al. (2012). The selection of the 90$^{\text{th}}$ percentile instead of other percentiles was a result of our analysis indicating it delivered a robust limit for representing clear-sky operations; in theory, k_{pv} values within the 90$^{\text{th}}$ are most likely to be clear-sky time periods. With the derivation of $k_{pv_{90}}$ and after the application of logical constraints, the tuning factor X can be calculated and allows for the tuning requirement of a system to be calculated for each time-step according to:

$$P_{tuned} = \frac{P_{qc}}{X}, \qquad \text{(Eq. 2)}$$

where P_{tuned} is the tuned power in $\mathrm{W/W_p}$ for a given system.

In essence, P_{tuned} represents the power profile of a reference PV system with all the systematic influences removed. By using P_{tuned} as opposed to P_{meas} or P_{qc} in the upscaling approach, power measurements recorded under shading of the reference PV system are corrected by balancing systematic influences (or tuned) before being used to estimate an unshaded neighbour.

2.3. Reducing k_{pv} related variance

Variances in k_{pv} are mainly due to cloud cover changes, systematic influences (e.g. shading), or inaccurate simulation of $P_{sim,cs}$. The latter two reasons are reference PV system specific and the influence of their probability and magnitude grows with increasing zenith angles θ_z. These reasons are increasingly important to consider when performing upscaling approaches as filtering system specific systematic influences in order to improve the representativeness of the reference PV systems. Systematic influences (such as shading) are already balanced with the tuning approach, and small inaccuracies in the simulation of $P_{sim,cs}$ can hardly be avoided. For example, if $P_{sim,cs}$ is slightly underestimated for small power measurements occurring during high zenith angles θ_z (0.005 $\mathrm{W/W_p}$ instead of 0.01 $\mathrm{W/W_p}$), the resultant k_{pv} factor would be twice as high; the same is applicable to overestimations in $P_{sim,cs}$. Should the same inaccuracy occur at midday (0.5 $\mathrm{W/W_p}$ instead of 0.505 $\mathrm{W/W_p}$), the effect on the k_{pv} value would be relatively insignificant. Consequently, the impact of such inaccuracies is limited by removing power measurements P_{tuned} from reference PV systems where time-steps exhibit high k_{pv}-related variances. This filter is realised by analysing the standard deviation of $k_{pv_{90}}$ in parallel to k_{pv}, detailed by Killinger et al. (2017a). With the removal of particularly large variances in the morning or evening by setting atypical values NaN, PV power with reduced variances (P_{red}) is derived from P_{tuned}.

3. Data

The data sources and models used within this paper are mostly identical with the ones described in Killinger et al. (2017a) and are mentioned in Fig. 1. Power output data is significantly extended in this paper covering 308 PV installations in Canberra, Australia, where previously only 78 were considered. The power measurements P_{meas} are extracted from http://pvoutput.org and subsequently normalised by their reported installed capacity. The collected power output data comprises a total period spanning from 7th September 2016 till 31st July 2017 with missing data from 25th March 2017 till 22nd April 2017. In contrary to Killinger et al. (2017a), multi-azimuth systems are considered within this work. Ambient temperature T_{amb} values are obtained from the Canberra airport (Australian Bureau of Meteorology station 070351) and missing data replaced by values from the numeric weather model MERRA, derived from http://www.soda-pro.com.

Climatological atmospheric parameters of ozone, water vapour, aerosol optical depth and Linke turbidity for the clear-sky irradiance modelling are retrieved from the SoDa database as described in Engerer and Mills (2015); Killinger et al. (2017b). These parameters are used to derive the beam ($B_{h,cs}$) and diffuse ($D_{h,cs}$) horizontal clear-sky irradiance via the REST2 model by Gueymard (2008). The derivation of the satellite based irradiance is described in detail in Engerer et al. (2017).

As the satellite based irradiance has a temporal resolution of 10-mins, all datasets used within this paper (e.g. the PV power measurements, ambient temperature, etc.) are aggregated to a resolution of 10 minutes in order to correspond.

4. Results and discussion

This section will firstly define the procedure of the cross-validations, and subsequently present and discuss the results.

4.1. Definition of the cross-validations

In this section, four different cross-validations (CV) labelled $k = 1, 2, 3, 4$ are realised. Within these cross-validations, the estimated power output of target PV systems P_{est,CV_k} is simulated using k_{pv}-based upscaling techniques (see Engerer and Mills (2014), Killinger et al. (2017a) and Bright et al. (2017)). k_{pv} based upscaling estimates the k_{pv} value at a target PV system's location using a geospatial interpolation approach called Inverse Distance Weighting (IDW, defined in Shepard (1968) and using the recommended factor of 2) and weights the influence of a reference PV system as a function of its distance to a target PV system; the closer a reference PV system is to the target, the more influence it has. With the interpolated k_{pv} value at a target PV system's location alongside its simulated clear-sky power $P_{sim,cs}$, the power output can now be estimated following the principle of Eq. 1.

Detailed assumptions of the cross-validations are provided in Tab. 1. CV1 is the baseline scenario without any data processing that uses metadata directly from http://pvoutput.org. Should metadata be missing, a north-facing azimuth and a tilt of 30° are assumed (P_{meas}). For all other validations (CV2-CV4), the parametrised metadata of both the reference and target PV systems as well as quality controlled power data from the methodology described in section 2.1 are used. In CV2, only the QCPV methodology from section 2.1 is applied (P_{qc}). In CV3, the additional inclusion of the tuning routine from section 2.2 is applied (P_{tuned}). Lastly, CV4 extends the tuning routine through application of the variance reduction routine (P_{red}) from section 2.3.

Estimates from each cross-validation are compared to the quality controlled version of the measured power P_{qc} in order to have a common dataset that is (mostly) free of measurement errors; using P_{meas} holds no value as there exists unquestionably erroneous data prevalent throughout the dataset. The simulated power estimates and number of NaN values are different in CV1-4 due to increased strictness of filtering with each methodology. If simulated or measured data registers a NaN, it is excluded from the evaluation.

Tab. 1: Definition for different cross-validations (CV).

	CV1	CV2	CV3	CV4
QCPV Routine		✓	✓	✓
Tuning			✓	✓
Reducing Variance				✓
Module Orientation	pvoutput.org	Simulated	Simulated	Simulated
Loss Factor LF	0.9	Simulated	Simulated	Simulated
P_{tar}	P_{qc}	P_{qc}	P_{qc}	P_{qc}

The cross-validations are conducted for an increasing number of reference PV systems I (2, 5, 10, 20, 30, 40, 50) and a fixed number of $J = 250$ target PV systems are simulated. The purpose is to explore the impact that number of available reference PV systems has on the accuracy of power estimate. For each value of I, simulations are repeated 100 times in order to obtain a representative distribution of error metrics and test reproducibility. With each test, the reference and target PV systems are randomly re-assigned each time while maintaining I and J allowing for a rich number of combinations per CV. The comparisons explore the performance of all the power estimates P_{est,CV_k} from each cross-validation $k = 1, 2, 3, 4$ against the actual power output from the target PV systems P_{tar}. Estimated and quality controlled measured target PV system power values are aggregated at each time-step t and normalised by J. P_{est,CV_k} and P_{tar} are, therefore, time series of aggregated power output for all J target PV systems.

An example test (1 of 100) to derive results is described:

1. $J = 250$ target PV systems randomly selected
2. I number of reference PV systems randomly selected from the remaining 58 systems
3. Aggregated P_{est,CV_k} calculated for each cross-validation $k = 1, 2, 3, 4$
4. Aggregated P_{tar} calculated
5. Compare power aggregate time series using different error metrics

Steps 1 to 5 are repeated 100 times before changing the value of I.

In the following evaluations, all results are restricted to time-steps fulfilling the zenith angle $\theta_z < 85°$ for the same reasons as mentioned in section 4.1. in Killinger et al. (2017a). Furthermore, all k_{pv} values used within the CV evaluations that are greater than 2 are excluded from the examinations as they represent an unrealistic magnitude.

4.2. Evaluation of the cross-validations

Results of the cross-validations are shown in Fig. 2. Each boxplot contains a distribution of results from the 100 different simulations, each with a unique combination of reference and target PV systems. The boxplots of the relative root mean square error ($rRMSE$, top plot in Fig. 2) indicate how each additional method presented in this paper further improves the estimated power outputs from the reference PV systems. The largest improvements are reached between CV1 and CV2 with the inclusion of QCPV. Although $rRMSE$ values further improve with CV3 and CV4, a decreasing marginal utility is visible.

Results in the $rRMSE$ also improve for an increasing number of reference PV systems with CV2-4. A similar improvement for an increasing number of reference PV systems can be seen for the baseline scenario CV1. An exception from this tendency occurs for a small number of reference PV systems in CV1 with $I = 2$ refrence PV systems, which is lower in $rRMSE$ than for $I = 5$; it is expected that this is a statistical coincidence which would disappear for a higher number of samples. Please also note that the ranges of the boxplots and outliers decrease for a greater number of reference PV systems; a balancing impact occurs with more reference PV systems and reduces uncertainty in the power estimation.

The uncertainty in the power simulation is not only reduced by an increasing number of reference PV systems, but also for the methods presented in this paper. This can be seen through analysis of the boxplots of the relative mean bias error ($rMBE$, middle plot in Fig. 2). The smallest ranges of $rMBE$ occur for CV3 and CV4 with a tendency towards overestimations. This can be explained with the tuning routine that increases the power magnitude of reference PV systems, however at present, this increase is applied to target PV systems that may also be shaded, resulting in an overestimation. These overestimations are not constant as shading only occurs for some systems at unique time-steps. In order to reduce such an estimation, future versions of the tuning must consider shading, perhaps by statistical diurnal consideration of typical shading events that can be probabilistically applied. This bias is rather dynamic and is different for each time-step of the day, making correction difficult.

Through the careful selection of time periods in the QCPV routine, as well as the constraints in the tuning and reduction of the variance, the number of NaN values in the time series of the reference PV systems increases. In the lower plot of Fig. 2 the time-steps excluded for the cross-validations are visualised. A time-step is excluded if either P_{est_k} or P_{tar} are NaN. While CV1 shows a rather consistent share of less than 25%, CV2-4 are greater for a small number of reference PV systems. The share slightly increases in CV4 due to the additional filters. At time-steps when a reference PV system registers a NaN value, it is obviously no longer able to estimate the power of other systems. Hence, for a very small number of reference PV systems, there can be individual time-steps in which it might be necessary to renounce the use of one of the methods or better use alternative data to estimate the power of the target PV systems. For all other time-steps, it is strongly recommended to use all the methods presented in this paper.

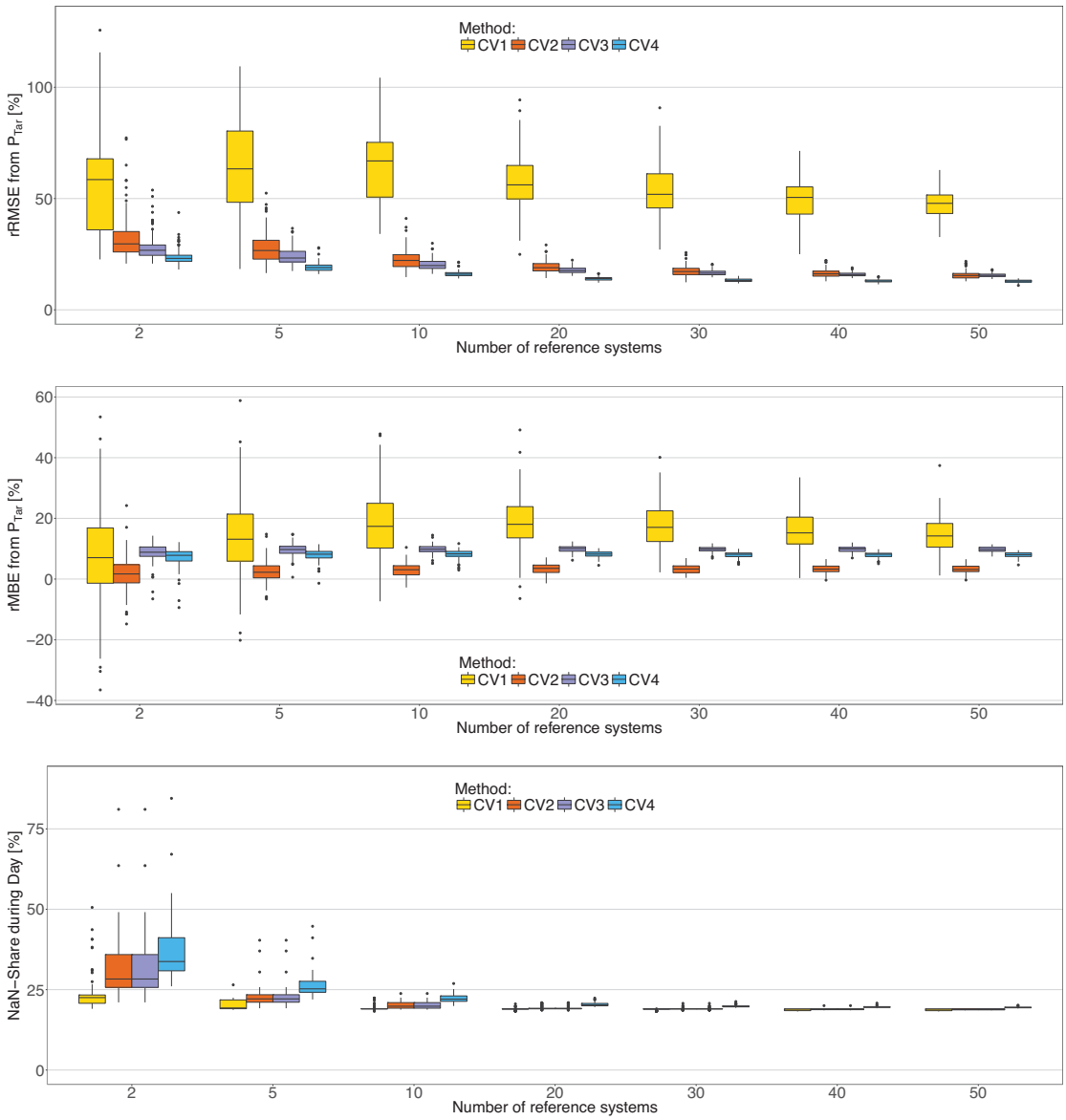

Fig. 2: Box plots indicating the four quartiles of error distributions. The lower, middle and upper lines of each box indicates the 25%, 50%/median, and 75% quartiles, respectively. Whiskers indicate the minimum and maximum values of the distribution. Outliers are represented as points and are defined as existing 1.5 times outside the inter-quartile range of the 25% and 75% quartiles. Each box plot represents the resulting error metric on the y-axis derived when comparing the estimate power value of a cross-validation $k = 1, 2, 3, 4$ (P_{est,CV_k}) against the target power value (P_{tar}). The error is plotted against the number of reference PV systems I. The colours represent the different cross-validations CV1-4. The top, middle and bottom plots indicate the relative root mean square error (rRMSE), the relative mean bias error (rMBE), and the fractional NaN-share, respectively.

5. Preliminary advancements

The analysis in the previous section showed that the strongest relative improvements are possible for a small number of available reference PV systems. Particularly for a small number of reference PV systems, it is important to better understand their individual behaviours. Hence, three different and preliminary methods are presented and evaluated within this section:

- The parametrisation of shaded systems in section 5.1
- The consideration of multi-azimuth systems in the parametrisation stage in section 5.2
- The reduction of the inertia in the tuning routine in section 5.3

The development of these methods are based on findings by Killinger et al. (2017a), Lingfors et al. (2017b), Bright et al. (2017) and from within this paper.

5.1. Parametrisation of shaded systems

Diurnal shading events can strongly influence the daily power profile of a PV system. Especially in case of strong shading in the morning or evening, it can be difficult for an observer to distinguish between shading events or a normal behaviour caused by an (extreme) azimuth angle of a system facing east or west. The parametrisation approach described in section 2.1 is facing exactly this challenge. Four PV systems are discussed in Lingfors et al. (2017b), which show significant errors in the parametrisation of the azimuth angles and strong influences of shading in the morning (see Lingfors et al. (2017b) ID 135, 157) or evening (ID 44, 67). The problem lies in the procedure of the NLS solver, which tries to find a combination of tilt (β_Q), azimuth (γ_Q) and loss factor (LF) leading to the smallest least square error. Even though this procedure hast a high rate of success for unshaded systems, there is a certain risk for erroneous parametrisation for shaded systems. As a consequence, all subsequent steps such as the QCPV and tuning routine are negatively influenced. Motivated by this challenge, an alternative procedure was developed and is presented next. The hypothesis behind this approach is that, should a system be shaded in the morning, the afternoon hours are more suitable to derive the correct module orientation, and vice versa. Hence, the approach uses different time periods throughout the days to run the parametrisation routine.

1. 00:00 - 23:55 ($\widehat{=}$ old procedure described in section 2.1)
2. 10:00 - 23:55 (if shaded in the early morning hours)
3. 12:00 - 23:55 (if shaded in the morning hours)
4. 00:00 - 13:00 (if shaded in the afternoon hours)
5. 00:00 - 15:00 (if shaded in the late afternoon hours)
6. 08:00 - 17:00 (if shaded in the early morning and late afternoon hours)
7. 10:00 - 14:00 (if shaded in the morning and afternoon hours)

The PV power is simulated with the derived parametrisation for each of the seven time periods. Then, the Mean Absolute Percentage Error (MAPE) is calculated between the simulated power and the quality controlled version of the measured power P^*_{qc}. The parametrisation leading to the smallest MAPE is then chosen.

Tab. 2: Tilt and azimuth of the studied PV systems identified by the old and new parametrisation approach. As a reference, reported tilt from SolarHub (SH, a reputable local solar installer in Canberra) and azimuths derived by inspecting aerial images (AI). The table includes in the last two columns the angle θ_n between the normal vector of the PV module (as derived from SH/AI) and the normal vector of the old and new parametrisation approach, respectively. The building ID corresponds to the study by Lingfors et al. (2017b).

ID	Tilt			Azimuth			θ_n	
	SH [°]	old [°]	new [°]	AI [°]	old [°]	new [°]	old [°]	new [°]
44	25	23	17	-57	-95	-83	18.9	12.1
67	20	28	17	55	10	70	18.6	5.5
135	22	22	9	5	46	1	16.9	12.5
157	18	30	15	-70	-18	-63	23.4	3.9

Tilt and azimuth of the studied PV systems identified by the old and new parametrisation approach are provided in Fig. 5. The tilt reported by SolarHub (SH) and the azimuth from an aerial inspection (AI) are given as references. It can be seen that the azimuth angles strongly improved with the new approach. This is also confirmed by smaller angles between the normal vector of the parametrised module orientation and the orientation from SH/AI. Presented in the table is θ_n, which is the angle between the normal vector of the reference PV system (calculated from from SH/AI metadata) and the parametrised-derived normal vector; an angle of $0°$ is an exact estimation. The use of θ_n is a better representation of the differences of orientation discrepancies than considering the azimuth and tilt separately. The new developments to the parametrisation routine show significant improvement for the four reference PV systems analysed with a 36%, 70%, 26% and 83% reduction in absolute deviation away from the normal for PV system IDs 44, 67, 135 and 157, respectively.

In Fig. 5 the simulated clear-sky curve with the old ($P_{cs,old}$) and new ($P_{cs,new}$) parametrisation method is visualised together with the measured power P_{meas} for an exemplary day. Both systems are facing strong shading events in the morning. As a consequence, the azimuth is overestimated by the old parametrisation, whereas the new method leads to a much more realistic clear-sky curve.

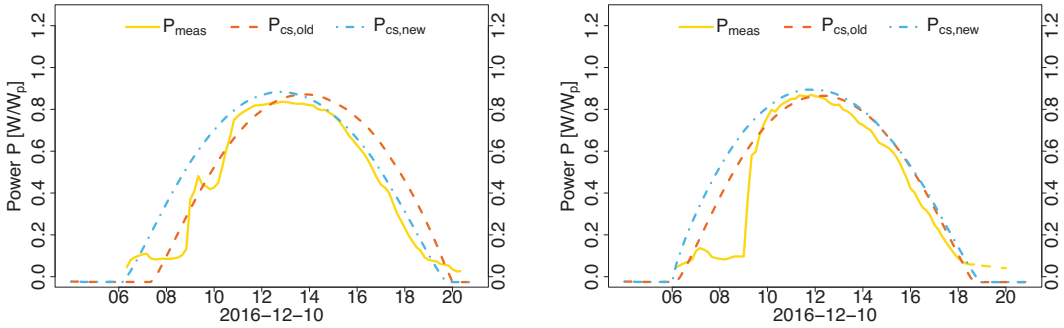

Fig. 3: PV systems (ID 135, left and ID 157, right) being influenced by strong shading events in the morning. Visualized is the measured power P_{meas} (yellow), the simulated clear-sky curve with the old parametrisation method from section 2.1 $P_{cs,old}$ (red) and the new approach from this section $P_{cs,new}$ (blue).

Even though the presented advancement of the parametrisation shows strong improvements for the four studied systems, first tests show problems for unshaded systems, leading sometimes to worsened results than the old parametrisation. Hence, the current challenge is to develop a method that helps to better decide which derived parametrisation option to use. Different error metrics were applied besides the MAPE, but no convincing strategy was found yet and is reserved to be the focus of future work.

5.2. Considering multi-azimuth systems

An additional challenge for the parametrisation approach are PV systems with modules facing different azimuth angles. Such multi-azimuth systems were not considered in Killinger et al. (2017b) and Killinger et al. (2017a) but included in this paper. The parametrisation approach was not adjusted in order to deal with PV power profile of such multi-azimuth systems. The NLS solver in this paper (see Eq. (1) in Killinger et al. (2017b)) estimates the parameters (tilt β_Q, azimuth γ_Q and loss factor LF) by minimising the least squares between the quality controlled version of the measured power P^*_{qc} and the simulated power based on the satellite derived irradiance $P_{sim,sat}$:

$$P^*_{qc} \sim P_{sim,sat}(\beta_Q, \gamma_Q, LF). \qquad \text{(Eq. 3)}$$

In order to deal with multi-azimuth systems, an alternative formulation was developed that allows the parametrisation of two different tilt and azimuth angles:

$$P^*_{qc} \sim \alpha \cdot P_{sim,sat,1}(\beta_{Q1}, \gamma_{Q1}, LF) + (1-\alpha) \cdot P_{sim,sat,2}(\beta_{Q2}, \gamma_{Q2}, LF) \qquad \text{(Eq. 4)}$$

The influence of the different module orientations is controlled by a factor α, being limited to a range between 0 and 1. In order to reduce the complexity, only one common loss factor LF is parametrised. To exclude other (disturbing) influences, this concept was tested based on simulated PV profiles. The findings from a multi and single azimuth system are presented next.

1. A multi-azimuth system (Tilt angles: $50°$ and $30°$; azimuth angles: $-45°$ and $90°$, $LF = 1$ and an $\alpha = 0.25$) was simulated with the transposition model from Reindl et al. (1990b) and the quadratic PV model from Killinger et al. (2017b). Then the NLS solver tried to derive the module orientation with Eq. 3 and alternatively with Eq. 4 based on the same irradiance and temperature data as input. The single azimuth approach lead to a tilt angle of $16°$, an azimuth of $68°$ and a $LF = 1$. Considering Fig. 4, the old parametrisation power estimate (P_{sing}, blue) seems to be a fair compromise for the multi-azimuth system and approximates the simulated PV profile (P_{sim}, yellow) well except for the early morning. The multi-azimuth approach from Eq. 4 (P_{multi}, red) is much more appropriate to approximate the simulated profile, as the morning pattern is excellently captured. The derived parametrisation was almost correct with tilt angles of $50°$ and $31°$; azimuth angles of $-47°$ and $90°$, $LF = 1$ and an $\alpha = 0.25$.

2. A single azimuth system (Tilt angle: 30°; azimuth angle: 0°, $LF = 1$) was simulated with the same models as above. This time the single azimuth approach from Eq. 3 finds the correct parametrisation and is able to perfectly approximate the simulated PV profile (P_{sim}, yellow), as is shown in the right plot of Fig. 4. However, the multi-azimuth approach from Eq. 4 shows small deviations in the late evening. The derived parametrisation in this scenario provides tilt angles of 35° and 17°; azimuth angles of −5° and 33°, $LF = 1$ and an $\alpha = 0.76$. The multi-azimuth approach obviously tried to find a combination of two module orientations describing the profile in the best way in order to satisfy Eq. 4.

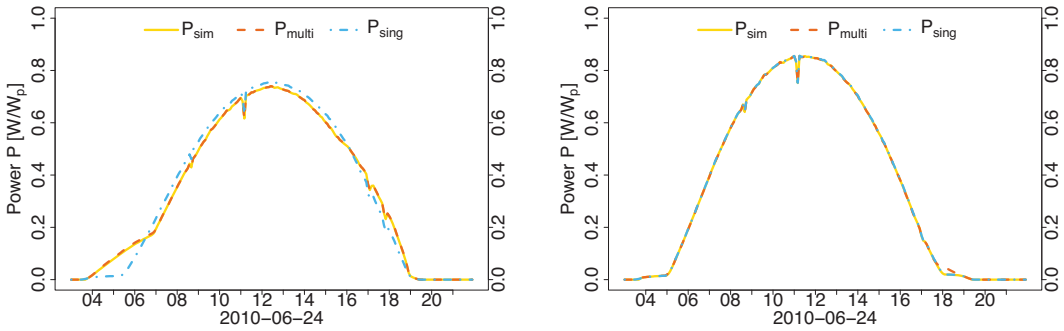

Fig. 4: Exemplary parametrisation for two different PV systems. In the left plot a multi-azimuth system (Tilt angles: 50° and 30°; azimuth angles: −45° and 90°, $LF = 1$ and an $\alpha = 0.25$) was simulated. In the right plot a single azimuth system (Tilt angle: 30°; azimuth angle: 0°, $LF = 1$) was simulated. The plots show the simulated profile (P_{sim}, yellow), the profile approximated by the multi-azimuth solver (P_{multi}, red) from Eq. 4 and the profile approximated by the single azimuth solver (P_{sing}, blue) from Eq. 3.

The above evaluations show that both the single and the multi-azimuth approach have their value and differences between the approaches are smaller than expected. Hence, future work is needed to quantify potential improvements of a multi-azimuth systems by analysing the presence and probability of such systems in reality. Similar to the approach in the last section, another challenge is when to use which approach without knowing if the parametrised system has a single or multi-azimuth angle. A selection based on error metrics between the actual (here: P_{sim}) and approximated (here: P_{sing} or P_{multi}) profiles were tested for some systems, but differences were insignificant. Further research is therefore needed to develop other selection criteria.

5.3. Reducing the inertia in the tuning routine

The discussion in Killinger et al. (2017a) revealed an inertia in the tuning approach that is mainly caused by the determination of $k_{pv_{90}}$ with a rolling window of time over 30 days (see section 2.2). As a consequence, time periods with shading cannot be completely compensated by the tuning approach as can be seen in the left plot in Fig. 5. Different approaches were developed and tested to overcome the inertia. One promising method considered $k_{pv_{90}}$ depending on the sun position as opposed to the time. However, the inertia still persisted. This is because the analysis had to be realised over a longer time period in order to differ between cycling shading influences and meteorological influences. Hence, the following advancement was developed and works in addition to the previous tuning routine.

1. For each time-step t within the time series of a PV system, the mean $k_{pv_{90}}$ values for the 30 minutes before and after the considered time-step are calculated. If one (or both) mean values are < 0.8, shading occurs during the 30 minute time period and criteria 1 is fulfilled. The idea behind this criteria is that, if shading occurs before or after a time-step t, the probability is increased that the current time-step is also affected. To further check if this is the case, two other criteria were developed.

2. Criteria 2 checks if the k_{pv} value of a system at time-step t is < 0.8. If this is the case, criteria 2 is fulfilled and an indication provided, that the system is influenced by shading.

3. In criteria 3, the mean k_{pv} value over all reference PV systems is calculated for time-step t and compared to the k_{pv} value of the analysed system at the same time-step. In case the k_{pv} value of the analysed system is no less than 0.2 smaller than the mean value, criteria 3 is fulfilled.

If criteria 1, 2 and 3 are all fulfilled, the $k_{pv_{90}}$ value is lowered for the analysed time-step t and the system is assigned the smallest mean $k_{pv_{90}}$ value from the 30 minutes before and after. The procedure with its three

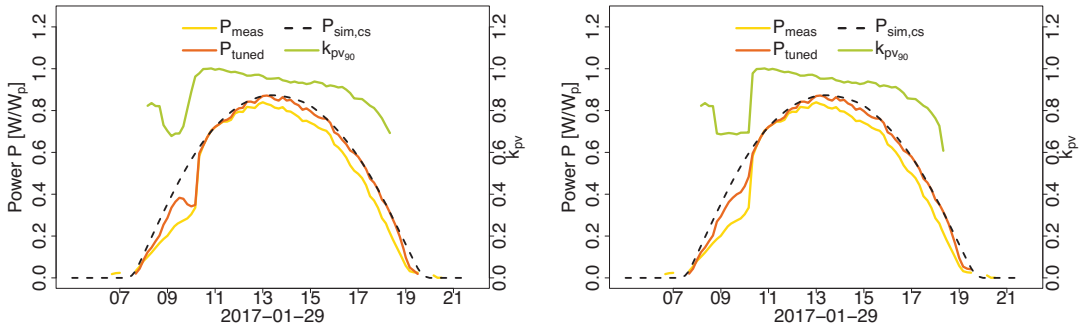

Fig. 5: Outputs for PV site 32 with the tuning method being described in section 2.2 in the left and an alternative approach being presented in section 5.3 in the right plot. The different series represent measured power output (yellow), tuned power output (orange), unsoiled clear-sky power output (black dashed line) and the running 90$^{\text{th}}$ percentile k_{pv} value $k_{pv_{90}}$ (green).

criteria is very cautious and tries to avoid an erroneous tuning. Results are promising as can be seen in the left plot in Fig. 5. The tuning method loses its inertia and is much more capable to balance the influence of shading. In future work this approach will be applied to more systems and carefully examined if the criteria are well suited.

Whilst the main objective of the three criteria was to find quantitative evidence that a time-step is subjected to shading, criteria 3 has an additional positive aspect. The across system analysis helps to consider the power generation of neighboured systems. If the power generation of these systems is reduced, e.g. due to the influence of an overcast sky, the calculated deviation to the analysed system is rather small and criteria 3 not satisfied. In cases where the analysed system is also under overcast skies, the procedure is advantageous because shading would be strongly reduced for an overcast sky. Hence, the consideration of across system analysis is an interesting feature for future developments of the tuning approach. However, there are also indisputable risks that some systems would be adjusted incorrectly by such an across system tuning routine and further developments would be necessary to handle them.

6. Conclusions

This paper aimed to address the latest suggestions and developments to the handling of reported power data from reference PV systems in the context of upscaling approaches. A central element of these upscaling approaches is the clear-sky index of photovoltaics k_{pv}, defined as the ratio between the current power generation of a system and its generation under clear-sky conditions. The key developments are (1) a parametrisation method to derive the module orientation (tilt and azimuth) as well as a loss factor for each system. This method is completed by a quality control routine to detect erroneous and atypical time-steps in PV power measurements. (2) a tuning routine that detects diurnal influences from shading and tunes the PV power in order to reach the expected generation without any shading. And (3) a method which eliminates high variances in k_{pv} based upscaling.

The application of these three advancements was evaluated based on power measurements of 308 PV systems in the region of Canberra, Australia, with data spanning almost one year of data. 250 of these systems are chosen as target PV systems, whereas a changing number systems are used as reference PV systems (2–50). Throughout many simulations, significant improvements were found as a direct result of the application of these three methods. Further improvements are possible when the number of reference PV systems is small, demonstrating the need to further consider individual characteristics of the reference PV systems. This reasoning provided the motivation for the development of three methods firstly presented in preliminary format within paper. These methods focus on (1) the parametrisation of shaded systems, (2) the consideration of multi-azimuth systems in the parametrisation, and (3) the reduction of the inertia in the tuning routine. These methods show preliminary merit in their application, however, have substantial potential for further improvements before they are of operational quality.

7. Conflict of interest

The authors declare no conflicts of interest.

Acknowledgement

The authors would like to thank the Australian Renewable Energy Agency (ARENA) for supporting this work (Research and Development Programme Funding G00854).

References

Bright, J.M., Killinger, S., Engerer, N.A., Lingfors, D., 2017. Improved satellite-derived PV power nowcasting using power data from real-time reference PV systems. Submitted to the special issue of Progress in Solar Energy .

ENA, 2017. Electricity network transformation roadmap: final report. Technical Report. Energy Networks Australia. URL: www.energynetworks.com.au/electricity-network-transformation-roadmap.

Engerer, N.A., 2015. Minute resolution estimates of the diffuse fraction of global irradiance for southeastern Australia. Solar Energy 116, 215–237. doi:10.1016/j.solener.2015.04.012.

Engerer, N.A., Bright, J.M., Killinger, S., 2017. Himawari-8 enabled real-time distributed PV simulations for distribution networks, in: 44th IEEE Photovoltaic Specialists Conference (PVSC), Washington D.C., USA.

Engerer, N.A., Mills, F.P., 2014. KPV: A clear-sky index for photovoltaics. Solar Energy 105, 679–693. doi:10.1016/j.solener.2014.04.019.

Engerer, N.A., Mills, F.P., 2015. Validating nine clear sky radiation models in Australia. Solar Energy 120, 9–24. doi:10.1016/j.solener.2015.06.044.

Gueymard, C.A., 2008. REST2: High-performance solar radiation model for cloudless-sky irradiance, illuminance, and photosynthetically active radiation – Validation with a benchmark dataset. Solar Energy 82, 272–285. doi:10.1016/j.solener.2007.04.008.

Killinger, S., Bright, J.M., Lingfors, D., Engerer, N.A., 2017a. A tuning routine to correct systematic influences in reference PV systems' power outputs. Solar Energy 157C, 1082–1094.

Killinger, S., Engerer, N., Müller, B., 2017b. QCPV: A quality control algorithm for distributed photovoltaic array power output. Solar Energy 143, 120–131. doi:10.1016/j.solener.2016.12.053.

Lingfors, D., Bright, J.M., Engerer, N.A., Ahlberg, J., Killinger, S., Widén, J., 2017a. Comparing the capability of low- and high-resolution LiDAR data with application to solar resource assessment, roof type classification and shading analysis. Applied Energy 205, 1216–1230. doi:10.1016/j.apenergy.2017.08.045.

Lingfors, D., Killinger, S., Engerer, N.A., Widén, J., Bright, J.M., 2017b. Identification of PV system shading using a LiDAR-based solar resource assessment model: an evaluation and cross-validation Submitted to Solar Energy.

Lonij, V.P., Brooks, A.E., Koch, K., Cronin, A.D., 2012. Analysis of 80 rooftop PV systems in the Tucson, AZ area, in: 38th IEEE Photovoltaic Specialists Conference (PVSC), Austin, USA. pp. 549–553. doi:10.1109/PVSC.2012.6317674.

Reindl, D.T., Beckman, W.A., Duffie, J.A., 1990a. Diffuse fraction correlations. Solar Energy 45, 1–7. doi:10.1016/0038-092X(90)90060-P.

Reindl, D.T., Beckman, W.A., Duffie, J.A., 1990b. Evaluation of hourly tilted surface radiation models. Solar Energy 45, 9–17. doi:10.1016/0038-092X(90)90061-G.

REN21, 2016. Renewables 2016 - global status report: Key findings. URL: http://www.ren21.net/wp-content/uploads/2016/10/REN21_GSR2016_KeyFindings_en_10.pdf.

Shepard, D., 1968. A two-dimensional interpolation function for irregularly-spaced data, in: 23rd ACM National Conference, Las Vegas, USA. pp. 517–524. doi:10.1145/800186.810616.

Solcast, 2017. Satellite Irradiance estimates from the Himawari-8 meteorological. URL: solcast.com.au.

Wedepohl, D., 2017. Photovoltaik-Meilenstein: weltweit 300 Gigawatt installiert. URL: https://www.solarwirtschaft.de/presse/pressemeldungen/pressemeldungen-im-detail/news/photovoltaik-meilenstein-weltweit-300-gigawatt-installiert.html.

BcChart v2.0 – a tool for bioclimatic potential evaluation

Mitja Košir[1] and Luka Pajek[1]

[1] University of Ljubljana, Faculty of Civil and Geodetic Engineering, Ljubljana (Slovenia)

Abstract

As bioclimatic design is becoming increasingly important in contemporary buildings, various analytical tools must be developed and introduced to the designers in order to guide them through the design process. Therefore, the BcChart v2.0 software was developed. It executes bioclimatic potential analysis of a location based on the theory of Olgyay's bioclimatic chart. The main advantage of the introduced tool, in contrast to other bioclimatic analysis tools, is that it directly considers the influence of solar radiation, which is factored through substitutive daily comfortable dry-bulb air temperature. The paper presents the theoretical background of the tool. Additionally, the capabilities and functionality of the software are demonstrated through bioclimatic analysis of two different locations with contrasting climates (i.e. Ljubljana, Slovenia and Abu Dhabi, UAE). The conclusions highlight the importance of considering solar radiation when performing bioclimatic analysis of a location in order to thoughtfully design bioclimatic buildings.

Keywords: bioclimatic analysis, climate analysis, bioclimatic potential, bioclimatic chart, solar radiation, sustainable building

1. Introduction

Bioclimatic building design is one of the key approaches to the design of buildings of the future. A building can be declared bioclimatic when it efficiently uses climatic resources of its location (Krainer, 2008). An aforementioned adapted building simultaneously provides comfortable indoor environment and efficiently uses energy sources, primarily with the help of building envelope elements. Although the use of bioclimatic design in architecture and construction industry was introduced decades ago by Victor Olgyay (1963), it was in some way overlooked by the designers and researchers. However, in recent years, research in the field of bioclimatic design is on the rise, as living comfort, energy use and climate change have been brought into the spotlight. Thus, several studies have been made encouraging the bioclimatic approach to building design. The most recent research by Pajek and Košir (2017), by Khambadkone and Jain (2017), or the one by Manzano-Agugliaro et al. (2015) highlighted the importance of bioclimatic analysis of a specific location in order to define the most efficient bioclimatic design strategies to be integrated into buildings.

Several tools can be used to bioclimatically asses a location. In this respect, the most elementary bioclimatic chart was developed by Olgyay (1963) or in a different form by Givoni (1969). Furthermore, new tools for bioclimatic analysis have been made by several other authors (Rohles et al., 1975; Arens et al., 1980; Al-Azri et al., 2013; Martínez and Freixanet, 2014; University of California, 2017). Martínez and Freixanet (2014) presented a comprehensive bioclimatic analysis tool, named BAT. It enables plotting of bioclimatic charts and several other graphs on the basis of climate data imputed by the user. Nonetheless, too many items of information given by BAT can disorient the user, thus lowering the user-friendliness of this tool. Furthermore, the main deficiency of the BAT tool is that the impact of solar radiation is not directly incorporated into the main bioclimatic analysis but is rather presented in a separate section. Another example of a broadly used bioclimatic analysis tool is also Climate Consultant software designed at the University of California, USA (University of California, 2017). The results of climate analysis performed by the Climate Consultant tool give its users an insight into climate specifics of a certain location. The tool also guides the user towards appropriate building design through a set of design strategies necessary to achieve human comfort with either passive or active solutions. However, similar as the BAT tool, Climate Consultant does not directly consider solar radiation in the determination of comfort conditions.

doi:10.18086/swc.2017.21.04 Available at http://proceedings.ises.org

To summarise, there exist several tools that can be used for a bioclimatic analysis in order to define possible passive building design measures. However, the above referenced tools do not sufficiently consolidate the influence of solar radiation into the calculations and consequential bioclimatic potential of a given location. This is of special interest in the case of locations with temperate and cold climatic characteristics. Although solar radiation is mostly presented as one of the decisive factors influencing bioclimatic potential, its influence is never directly incorporated into bioclimatic potential calculations. It is rather used comparatively as a separate quantity detached from the external air temperature and relative humidity. Such comparison between the two is relevant, but it is also likely prone to human errors. Bioclimatic location analysis is one of the most important initial steps when designing buildings. Thus, a tool used for the analysis must be on one hand very precise and user-friendly on the other. Nonetheless, it is crucial that bioclimatic analysis tool is freely available to the interested audience, as this will widen the number of designers applying bioclimatic solutions to their projects. All mentioned above is taken into account with BcChart v2.0 – a bioclimatic potential analysis tool, developed by the authors and presented in this paper.

2. Description of applied methodology

2.1 BcChart software and bioclimatic charts

The BcChart v2.0 software was developed at the University of Ljubljana, Slovenia, and has been validated and evaluated through the educational process at the Faculty of Civil and Geodetic Engineering. It can be used for the calculations of bioclimatic potential based on the theory of Olgyay's bioclimatic chart (Olgyay, 1963). Bioclimatic charts are initiated with human comfort, which is calculated for an average person. The basic input climate parameters are average minimum and maximum daily air temperature (T) and relative humidity (RH). However, in addition to the basic bioclimatic chart input data, the mean and maximum daily solar irradiation is also factored in, resulting in modifications of Olgyay's bioclimatic chart plots. Nonetheless, it has to be noted that the modifications of bioclimatic charts are made only when additional influence of solar irradiation does not cause overheating. In other words, it is presumed that whenever the solar irradiation could cause overheating, effective shading will be used (i.e. when ambient temperatures on the bioclimatic chart are above shading line). Thus, the substitutive daily comfortable dry-bulb air temperature for month i, $T_{sub,i}$ is introduced (Equation 1). The derivation of the calculations made with BcChart v2.0 is Equation 1, based on the equation for human body thermal equilibrium, presented by Olgyay (1963). Equation 2 is introduced to describe the influence of actually received solar irradiation.

$$T_{sub,i} = \frac{T_s-(M_m-E+R_i)\times(Clo/c+V.Clo/c)}{S\times S_c} \qquad \text{(eq. 1)}$$

$$R_i = G_i \times S_e \times \alpha \qquad \text{(eq. 2)}$$

Where R_i is radiation in W for month i, G_i is the mean daily global solar irradiance in W/m^2 for month i, S_e is the effective radiation area for a given subject in a given position and it is assumed as 0.5 m^2, and α = 0.4 is the absorptivity of the radiated surface of a clothed man. T_s is comfortable skin temperature, presumed as 33.9°C, M_m is the observed rate of metabolism 126 W, E is the rate of cooling due to perspiration actually evaporated 38 W, $Clo/c + V.Clo/c$ is clothing insulation and air effect on clothing coefficient (= 0.28) as defined by Olgyay (1963) and adapted to be expressed in m^{2}K/W. S is the mean body surface area of clothed man, assumed as 2.14 m^2 and S_c is the fraction of surface areas exposed to radiation and convection (= 0.9). Furthermore, the dry-bulb air temperature at which the passive solar heating (PSH) is still possible ($T_{PSH,i}$) was calculated using maximal daily global horizontal solar irradiance for each month ($G_{max,i}$). The plotted parts on bioclimatic chart, which are below this temperature, represent the part of each month, when passive solar heating cannot be used as an efficient passive strategy, because there is not enough solar energy available at a given location. Therefore, instead of the mean daily global solar irradiance (G_i) in Equations 1 and 2, the maximal values of solar radiation were used ($G_{max,i}$). T_{sub} and T_{PSH} were used only when modified bioclimatic charts were plotted, i.e. the solar radiation was directly incorporated into calculations. The main output of the BcChart v2.0 software is bioclimatic potential of the analysed location. It represents the time, expressed in % and presented either on yearly or monthly level, when the plotted combinations of temperature, relative humidity and solar irradiance fall either in or out of the comfort zone.

Tab. 1. Bioclimatic potential segments as calculated by BcChart.

Label	Colour	Bioclimatic potential	Suggested bioclimatic strategy
Q		mechanical cooling and/or dehumidification needed	
A		potential for passive solutions for hot arid climates	
V		natural ventilation needed	
M		natural ventilation and/or high thermal mass needed	
C_{sh}		comfort achieved with shading	
C_{sn}		comfort achieved with solar irradiation	
R		potential for passive solar heating	
H		no potential for passive solar heating	
S_h		shading needed ($S_h = Q + A + M + V + C_{sh}$)	

The described segments in Table 1 were calculated for every distinct month according to the length of the line plotted by using combinations of monthly average input climate data (Equation 3–14).

$$Q = \sum \frac{x_{q_j}}{l_j} \times \frac{100}{12} \quad \text{(eq. 3)}$$

$$A = \sum \frac{x_{a_j}}{l_j} \times \frac{100}{12} \quad \text{(eq. 4)}$$

$$V = \sum \frac{x_{v_j}}{l_j} \times \frac{100}{12} \quad \text{(eq. 5)}$$

$$M = \sum \frac{x_{m_j}}{l_j} \times \frac{100}{12} \quad \text{(eq. 6)}$$

$$C_{sh} = \sum \frac{x_{c_j}}{l_j} \times \frac{100}{12} \quad \text{(eq. 7)}$$

$$C_{sn} = \sum \frac{x'_{c_j}}{l'_j} \times \frac{100}{12} - C_{sh} \quad \text{(eq. 8)}$$

$$R = \sum \frac{x_{r_j}}{l_j} \times \frac{100}{12} \quad \text{(eq. 9)}$$

$$R' = \sum \frac{x'_{r_j}}{l'_j} \times \frac{100}{12} \quad \text{(eq. 10)}$$

$$H = \sum \frac{x_{h_j}}{l_j} \times \frac{100}{12} \quad \text{(eq. 11)}$$

$$H' = \sum \frac{x'_{h_j}}{l'_j} \times \frac{100}{12} \quad \text{(eq. 12)}$$

$$l_j = \sum x_{ij} \quad \text{(eq. 13)}$$

$$l'_j = \sum x'_{ij} \quad \text{(eq. 14)}$$

Where j = 1–12 or January–December and $i = q, a, m, v, c, c', r, r', h$ or h'. l_j is the total period of the month (i.e. the sum of x_{qj}, x_{aj}, x_{mj}, x_{vj}, x_{cj}, x_{rj} and x_{hj}). l'_j is the total period of the month considering solar irradiance, which is

different from l_j because of the consideration of solar radiation, thus the lengths of x_{ci}, x_{ri} and x_{hi} change. x_{ci} is the period of month (i.e. the length of the plotted line) inside the comfort zone when shading is needed, x'_{ci} is the period of month inside the comfort zone utilizing solar irradiance, x_{vi} is the period of month when ventilation in combination with shading is needed, etc. Definition of each calculated segment and the corresponding suggested bioclimatic strategy are explained in Table 1.

In the cases where the plotted lines fall inside the comfort zone, the achieving of comfort is defined as achieved by shading (C_{sh}) or by the use of solar energy (C_{sn}) (Table 1). Further on, the segments presented in Table 1 may also be combined into three main categories: shading needed ($S_h = Q + A + M + V + C_{sh}$), sun needed ($S_n = C_{sn} + R + H$) and comfort zone ($C_z = C_{sh} + C_{sn}$).

2.2 Limitations

The use of the bioclimatic chart used in the BcChart software is directly applicable only to inhabitants wearing customary indoor clothing, engaged in sedentary or light muscular work, at elevations not in excess of 300 m above sea level. The impact of sun radiation is calculated on the basis of Olgyay (1963), assuming the effective area of human body of 0.5 m^2. Internal heat gains cannot be considered when calculating bioclimatic potential, which can be determined as a limitation of the methodology. Another limitation of the BcChart software is that the borders of comfort zone, which is roughly between 21 and 27°C, cannot be manually modified in order to adapt it to different human comfort conditions.

3. BcChart v2.0 – user interface and functionality

The interface of the BcChart v2.0 software was created in MS Excel environment. It consists of 4 consecutive spreadsheets (see Fig. 1 and Fig. 2) guiding the user from input data to the result interpretation:

- Input data (climatological data and basic information about for the analysed location).
- Bioclimatic chart (plot of basic bioclimatic chart w/o the influence of solar radiation and modified bioclimatic chart w/ solar radiation).
- Bioclimatic potential analysis (interpretation of analysed data through yearly and monthly bioclimatic potential of the location).
- About (theoretical background explanation, copyright and terms of use and author contacts).

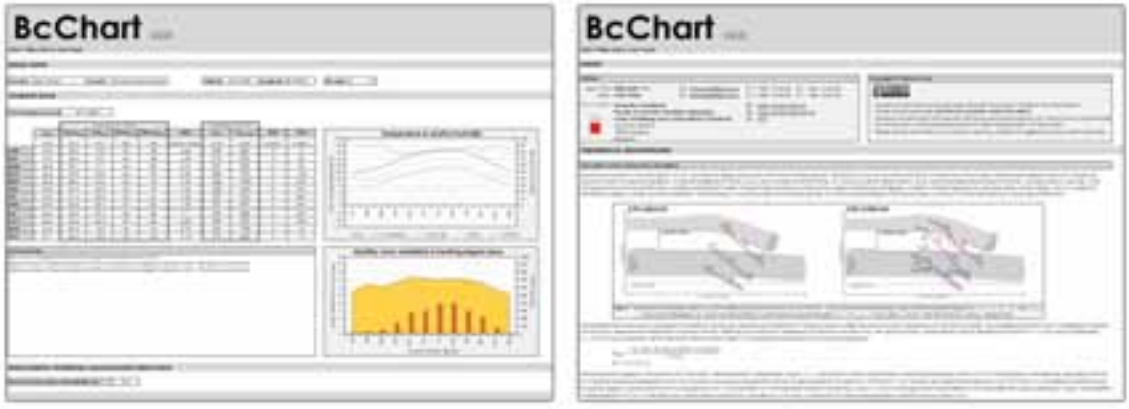

Fig. 1: BcChart v2.0 user interface screen shots: left – Input data (monthly average climatological data), right – About (explanation of calculation background).

In the first spreadsheet named Input data (Fig. 1, left), the user must input the location information data and key climate data used for the calculation of bioclimatic potential. The mandatory data are: average daily maximum ($Tmax_{avg}$) and minimum ($Tmin_{avg}$) dry bulb temperature (°C), average daily maximum ($RHmax_{avg}$) and minimum ($RHmin_{avg}$) relative humidity (%), average (G_{rad}) and maximum ($G_{rad,max}$) global daily irradiance (W/m^2) on the horizontal plane. In addition to the mandatory data necessary for the bioclimatic potential calculation, supplementary climatic characteristics can be entered as well. These are the following: average daily (T_{avg}) dry bulb temperature (°C), average sum of global irradiation ($IRAD$) on the horizontal plane (kWh/m^2) and heating

(*HDD*) and cooling (*CDD*) degree-days (Kday). However, these additional climate data do not influence the bioclimatic potential calculation and are only used in order to enable better interpretation of the bioclimatic analysis. Supplementary data are presented together with the mandatory data through diagrams (Fig. 1, left).

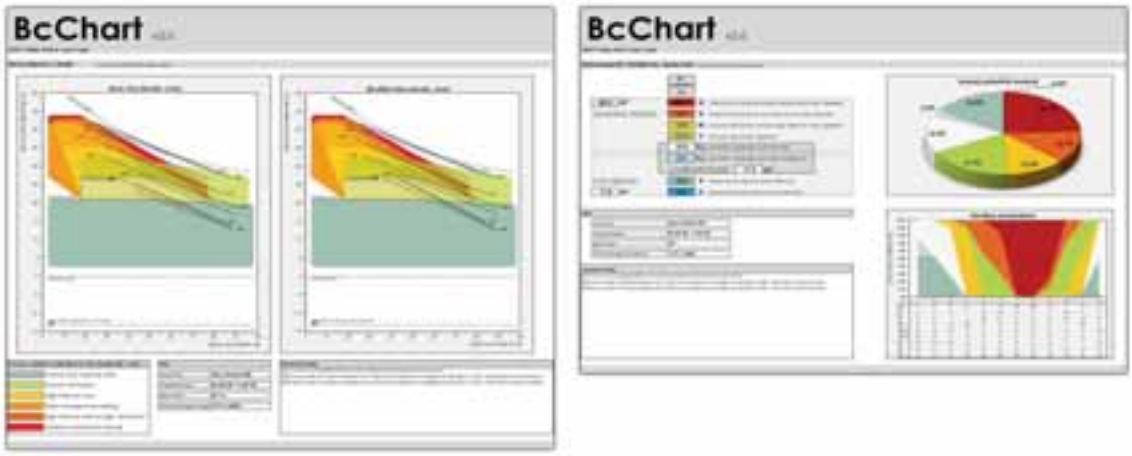

Fig. 2: BcChart v2.0 user interface screen shots: left – Bioclimatic chart (basic and modified bioclimatic chats), right – Bioclimatic potential analysis (yearly cumulative and monthly values of bioclimatic potential).

In the second spreadsheet (i.e. Bioclimatic chart) the basic and modified bioclimatic charts are plotted (Fig. 2, left). In the third spreadsheet (i.e. Bioclimatic potential analysis) the results of the bioclimatic interpretation are given (Fig. 2, right), while the fourth spreadsheet (i.e. About) gives information about the authors, copyright and basic information about used calculation methodology (Fig. 1, right). The results of the bioclimatic analysis can be interpreted directly through the evaluation of bioclimatic chart (Fig. 2, left) and the corresponding passive strategies marked on them, or by the results of yearly and monthly bioclimatic potential calculation (Fig. 2, right), which assist the user in the interpretation of the charts. It must be stressed that the calculated bioclimatic potential with its corresponding evaluation of the most important bioclimatic strategies for the analysed location is only a generic recommendation. Therefore, is up to the user of the software to appropriately apply the proposed solutions to a specific project.

4. Example of performed analysis and discussion

Functionality of the BcChart v2.0 software is presented through the evaluation and determination of bioclimatic potential at two selected characteristic locations. These were chosen in order to demonstrate how the bioclimatic potential analysis is performed with the BcChart v2.0 software. The chosen locations were the following:

- **Ljubljana, Slovenia, Europe** (46.22° N, 14.48°E); Köppen-Geiger climate classification: Cfb (temperate, without dry season, warm summer). In Ljubljana, the minimum average daily dry bulb temperature of –4.9°C occurs in January and the maximum of 26.4°C in July. The lowest average daily minimum *RH* of 43% occurs in July, while the maximum of 98% occurs in October. The lowest average daily global horizontal solar radiation of 17 Wh/m^2 occurs in December and the highest of 687 Wh/m^2 in July.
- **Abu Dhabi, UAE, Middle East** (24.43° N, 54.65°E); Köppen-Geiger climate classification: BWh (arid, desert, hot). In Abu Dhabi, the minimum average daily dry bulb temperature of 13.0°C occurs in January and the maximum of 42.0°C in August. The lowest average daily minimum *RH* of 22% occurs in May, while the maximum of 90% occurs in November. The lowest average daily global horizontal solar radiation of 140 Wh/m^2 occurs in December and the highest of 1020 Wh/m^2 in May.

Firstly, the results of the basic bioclimatic chart analysis (i.e. without considering the influence of solar radiation) are compared with those obtained by Climate Consultant software v6.0 (University of California, 2017) in the section 4.1. Secondly, the results without and with the influence of solar radiation (i.e. basic vs modified bioclimatic chart) are presented in section 4.2. Comparison of the basic and modified bioclimatic potential results will demonstrate the importance and impact of solar radiation on the prevalence of the determined bioclimatic design strategies.

4.1 BcChart vs Climate Consultant

In order to be able to compare the results obtained from both analyses (i.e. BcChart v2.0 and Climate Consultant v6.0), the boundary conditions were equalled as much as possible. Accordingly, the same input climatological data were used, namely the EPW weather data files for Ljubljana and Abu Dhabi (EnergyPlus, 2017). The calculation and the plot of psychrometric chart within Climate Consultant was made according to the ASHRAE Handbook of Fundamentals Comfort Model (up through 2005). Boundaries of comfort zone in the Climate Consultant were set in order to reflect those used by BcChart, i.e. comfort low temperature at 50% *RH* was set to 21°C and comfort high at 50% *RH* was set to 27°C. Minimal dry-bulb temperature when need for shading begins was set to 21°C.

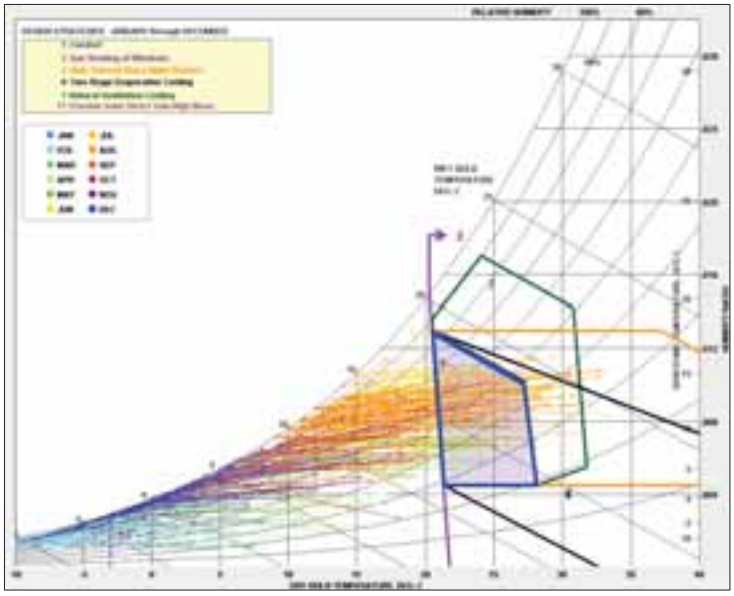

Fig. 3: Bioclimatic analysis for the location of Ljubljana created using Climate Consultant v6.0. Climate data are plotted as daily minimums and maximums in respect to the selected design strategies.

It has to be noted that the results obtained with Climate Consultant are calculated on the basis of hourly climate data, whereas the results obtained with BcChart are calculated using monthly daily averages. Recommended or effective passive measures, displayed on each of the two charts (bioclimatic chart in BcChart and psychrometric chart in Climate Consultant) are comparable but not equivalent. Therefore, a complete equivalency cannot be expected between the results of both tools. Correspondingly, in comparison to BcChart a broader set of passive and active measures is presented and proposed within Climate Consultant. Nevertheless, the results can be to some degree interpreted in such a way to enable the assessment of results between the two applications. For example, value *R* (for the explanation see Table 1) in BcChart can be compared to design strategy number 11 (i.e. passive solar direct gain, high mass) in Climate Consultant. Similarly, value C_z in BcChart is comparable to design strategy number 1 (i.e. comfort), value *V* to design strategy number 7 (i.e. natural ventilation), value *M* to design strategy number 4 (i.e. high thermal mass night flushed) and value *A* in BcChart to Climate Consultant design strategy number 6 (i.e. two-stage evaporative cooling). Other values found in BcChart (*H*, *Q*, C_{sn}, C_{sh}) cannot be directly paired with corresponding strategies proposed by Climate Consultant. All the described passive strategies can be observed and graphically compared in Figures 3 and 4, where the results for Ljubljana calculated with Climate Consultant and BcChart, respectively, are presented.

Because of the different methodology used in each of the selected software and the corresponding results, which cannot be directly compared, the results obtained by BcChart were compared by the Climate Consultant results only through the following three parameters: S_n – sun needed, C_z – comfort zone, S_h – shading needed. These results are presented in Table 2. Value S_n obtained by BcChart can be compared to design strategy number 11 (i.e. passive solar direct gain high mass) in Climate Consultant. Similarly, value S_h can be compared to a sum of design strategies number 1, 13, 14 and 15 in Climate Consultant (i.e. comfort, humidification only, dehumidification only and cooling, add dehumidification if needed). C_z is comparable to design strategy number 1 (i.e. comfort). In order to graphically compare the results, the psychrometric chart from Climate Consultant (Fig. 3) and bioclimatic chart

from BcChart (Fig. 4) were plotted for the city of Ljubljana. It can be noted from the results presented in Table 2 that the total sum of all three analysed parameters (S_n, C_z and S_h) is larger than 100%; the reason is that when comfort is achieved, also shading is needed (i.e. the lower boundary of comfort zone overlaps with the shading line – see Fig. 2 and 3). Although the described suggested passive strategies obtained by each of the considered tools are not completely equivalent, a correlation between the results is evident (Tab. 2, Fig. 3 and 4).

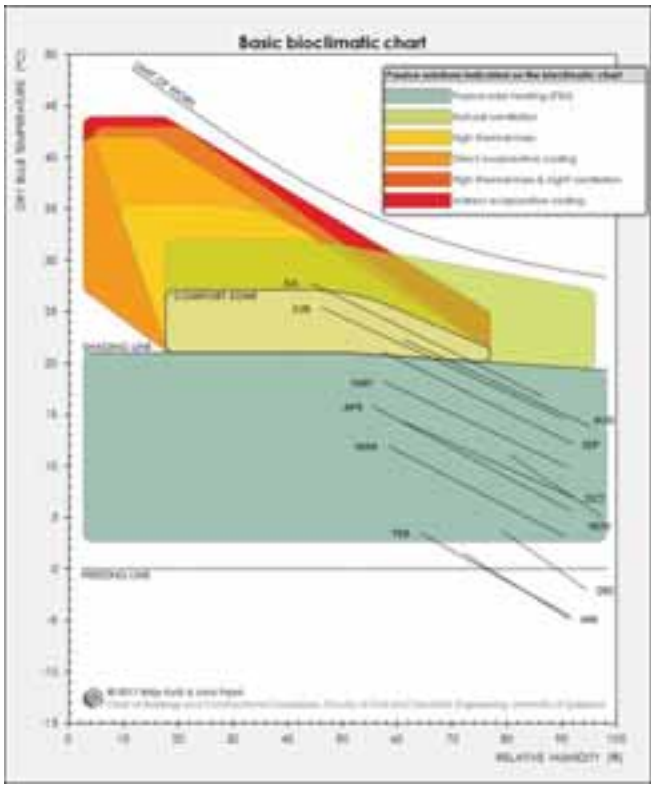

Fig. 4: Basic bioclimatic analysis for the location of Ljubljana created using BcChart v2.0. Climate data is plotted as monthly daily average minimum and maximum in respect to the selected passive solutions.

Observing Table 2 it can be concluded that the values of S_n, C_z and S_h, obtained by either BcChart or Climate Consultant are closer together in the case of Ljubljana. The latter was expected since the methodology, which runs in the background of the BcChart software, is more appropriate for the analysis of locations with temperate climate, rather than for locations with hot-arid, hot-humid or polar climate. The differences between the results obtained by BcChart and Climate Consultant in the case of the two selected locations range from 1.3 percentage points (pp) in the case of S_h and 3.9 pp for value C_z, both in Ljubljana (Tab. 2). The observed differences are most probably the consequence of differently processed climate data – Climate Consultant uses hourly, while BcChart uses monthly climate data. Additionally, dissimilarities in the results could also stem from different boundaries of passive (bioclimatic) strategies in both tools (i.e. the "areas of specific passive strategies" in the charts are not equivalent). Nonetheless, the obtained results in both applications can be considered as equivalent. Especially, if a substantial difference in the inputted climatic data is taken into account.

Tab. 2. The selected comparable parameters obtained by bioclimatic analysis using BcChart and Climate Consultant and their absolute differences.

	Abu Dhabi			**Ljubljana**		
	S_n	C_z	S_h	S_n	C_z	S_h
BcChart	17.8%	15.0%	82.2%	87.9%	11.5%	12.1%
Climate Consultant	21.2%	11.3%	78.8%	89.2%	7.6%	10.8%
|Δ|	3.4 pp	3.7 pp	3.4 pp	1.3 pp	3.9 pp	1.3 pp

4.2 Consideration of solar radiation and its effect on BcChart results

In order to assess the influence of the considered solar radiation influence on the BcChart tool results, this section studies monthly breakdown of bioclimatic potential with basic (i.e. original method – no direct consideration of solar radiation) and modified analysis (i.e. actually received solar radiation is included into the calculation) for both locations (i.e. Ljubljana and Abu Dhabi). Figures 5 and 6 represent basic and modified bioclimatic potential for Ljubljana and Abu Dhabi, respectively.

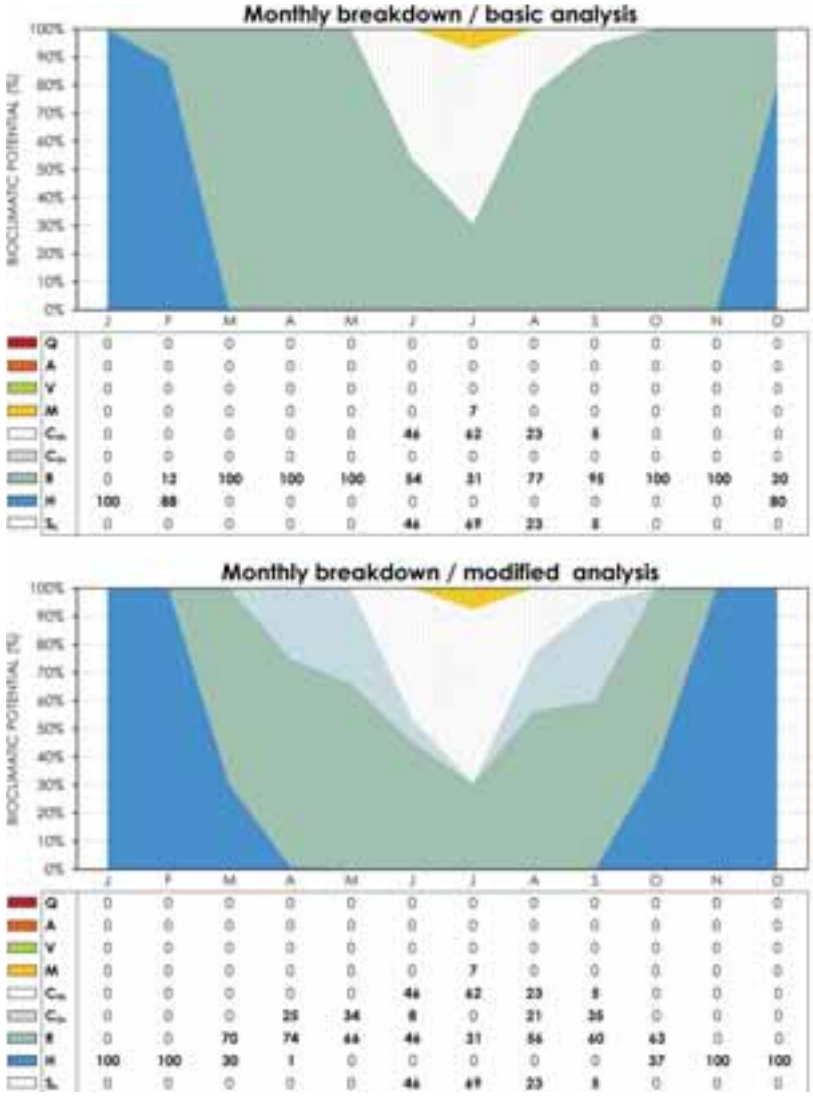

Fig. 5: Monthly breakdown of bioclimatic potential for Ljubljana using basic (top) or modified (bottom) method.

Observing Fig. 5 it can be seen that in Ljubljana, a location with temperate climate, solar radiation has a substantial effect on values C_{sn}, R and H. For example, in February value R changes from 12 to 0% and value H from 88 to 100%, while in April value R drops from 100 to 74%, value H increases from 0 to 1% and value C_{sn} increases to 25% as a consequence of solar energy utilization. The described phenomenon is expected, because values C_{sn} and R represent passive (bioclimatic) strategies, which utilize solar energy (Tab. 1), while value H is reciprocally connected with them. As expected, the modified analysis gives the same results as basic for hot (i.e. summer) months, where shading is needed and the excessive solar radiation is unwanted most of the time (i.e. shading is necessary). If bioclimatic potential in Ljubljana is observed on yearly level, the differences, which occur due to the solar energy consideration, are noteworthy. On yearly level value R decreases from 65.9 to 39.1% and value H increases from 22 to 38.6%, while the overall comfort zone increases by 10.2 pp from 11.5% (basic analysis) to 21.7% (modified analysis) due to the appearance of value C_{sn}. The latter means that in approximately 10% of the year, thermal comfort in Ljubljana can be achieved by utilizing solar energy.

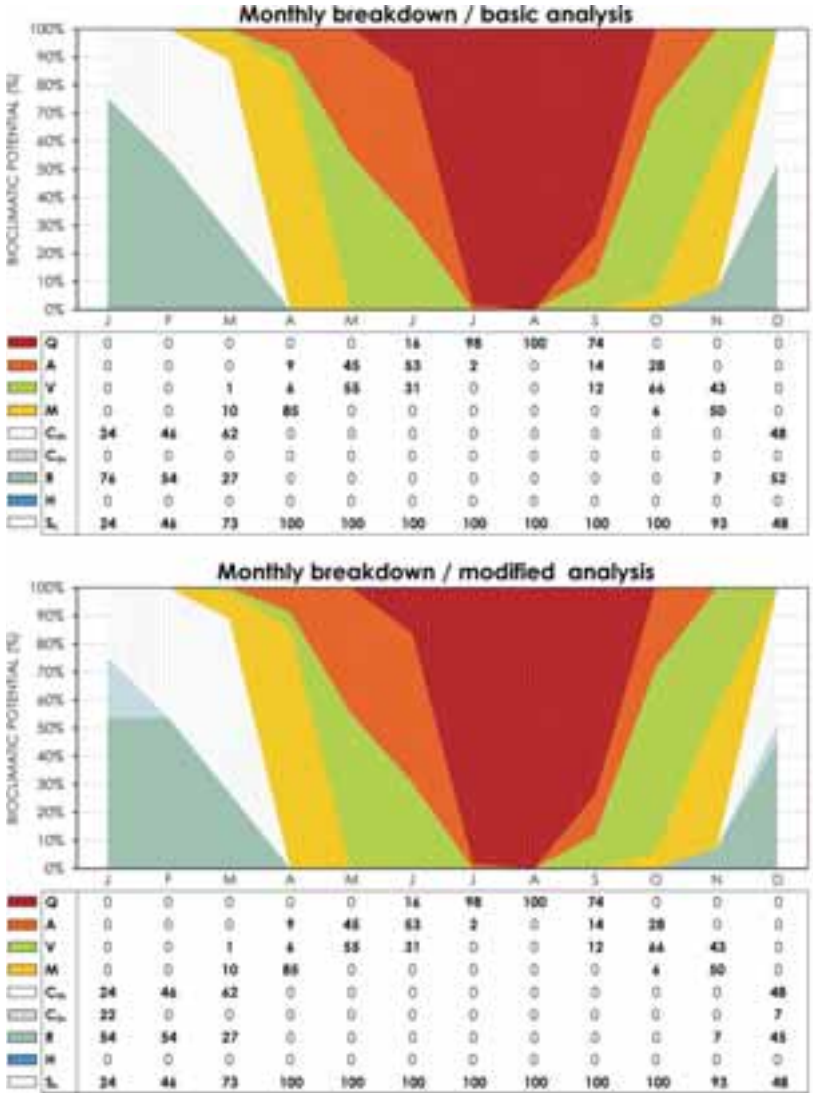

Fig. 6: Monthly breakdown of bioclimatic potential for Abu Dhabi using basic (top) or modified (bottom) method.

Observation of bioclimatic analysis for the location of Abu Dhabi with hot-arid climate in Fig. 6 gives completely different conclusions than in the case of Ljubljana. In Abu Dhabi the consideration of solar radiation has only minor effect on values C_{sn}, R and H. For example, the differences between basic and modified analysis appear only in January and December (Fig. 6), where value R changes from 76 to 54% and 52 to 45%, respectively. Consequentially, value C_{sn} appears only during these two months and amounts to 22 and 7% for January and December, respectively. The influence of solar radiation on bioclimatic potential calculation with BcChart in Abu Dhabi is of minor importance because, as mentioned before, solar radiation affects only values C_{sn}, R and H, which are in Abu Dhabi represented to a lesser extent. If these three values are compared on yearly level, value R decreases by 2.5 pp with a correspondingly equivalent increase of C_{sn}. Value H remains at 0%, as there is always enough solar energy and/or the ambient temperatures are high enough to heat up the living environment to comfortable temperatures.

4.3 Discussion

It is crucial to remember that the presented approach of solar energy inclusion into the bioclimatic analysis is extremely important, because such approach gives more precise results of locations' bioclimatic potential. Thus, the appropriate and most efficient bioclimatic strategies can be more accurately identified. However, the approach used by BcChart is far more useful in temperate, Mediterranean and cold climatic zones and less for the polar and hot-dry and hot-humid climatic zones, which was demonstrated in previous section. The main reason for this is that the relative importance of bioclimatic strategy for solar radiation harvesting is the greatest in the stated

climates. Another key note is that this theory used by BcChart applies only, when the actually received solar radiation is considered with a concurrent attention given to shading of transparent part of building envelope.

Further improvements of the BcChart tool are possible. It would be interesting to include in bioclimatic potential calculation the influence of actual wind speed at the analysed location, the same as it was done for solar radiation. However, it is questionable if such improvement would be reasonable, because air movement in buildings is a far more complex issue than solar energy utilization. In particular, air movement is harder to control and predict, due to various influential parameters, such as degree of urbanization, building aerodynamics, stack effect, etc. Additionally, with too many variables the tool would lose its simplicity and the results their universality. For such complex evaluations more sophisticated whole building simulation tools would be far better alternatives. Nonetheless, when quick and basic evaluations of applicable bioclimatic strategies in a specific location are needed, the BcChart tool represents the right choice in the early phases of building design.

5. Conclusions

As has been noted, the main advantage of the bioclimatic analysis using the BcChart v2.0 software is that it is simple and quick. The originality of the presented approach to bioclimatic potential analysis is expressed through the consideration of the actually received solar radiation with the introduction of T_{sub}. For instance, the performed analyses showed that solar radiation essentially influences the results of bioclimatic potential analysis, especially in temperate and cold climates, which was also highlighted by Pajek and Košir (2017). The analysis of the two selected locations determined the importance and usefulness of the approach incorporated in the BcChart v2.0. The indicated is certainly relevant when using climate data for the determination of relative importance of different bioclimatic design strategies.

References

Al-Azri, N.A., Zurigat, Y.H., Al-Rawahi, N.Z., 2013. Development of bioclimatic chart for passive building design. Int. J. Sustain. Energy 32, 713–723. doi:10.1080/14786451.2013.813026

Arens, E., Zeren, L., Gonzales, R., Berglund, L., McNall, P.E., 1980. A new bioclimatic chart for environmental design. Presented at the Proc. Building Energy Management conference (ICBEM), Pergamon, Pavoa de Varzim.

EnergyPlus, 2017. Weather Data [WWW Document]. URL energyplus.net/weather (accessed 8.2.17).

Givoni, B., 1969. Man, climate, and architecture, Elsevier architectural science series. Elsevier, Amsterdam, New York.

Khambadkone, N.K., Jain, R., 2017. A bioclimatic analysis tool for investigation of the potential of passive cooling and heating strategies in a composite Indian climate. Build. Environ. 123, 469–493. doi:10.1016/j.buildenv.2017.07.023

Krainer, A., 2008. Passivhaus contra bioclimatic design = Dedicated to em. Univ.-Prof. Dr. Ing. habil. Dr.h.c. mult. Karl Gertis on the occasion of his 70th birthday. Bauphysik 393–404. doi:10.1002/bapi.200810051

Manzano-Agugliaro, F., Montoya, F.G., Sabio-Ortega, A., García-Cruz, A., 2015. Review of bioclimatic architecture strategies for achieving thermal comfort. Renew. Sustain. Energy Rev. 49, 736–755. doi:10.1016/j.rser.2015.04.095

Martínez, J.C.R., Freixanet, V.A.F., 2014. Bioclimatic Analysis Tool: An Alternative to Facilitate and Streamline Preliminary Studies. Energy Procedia, 2013 ISES Solar World Congress 57, 1374–1382. doi:10.1016/j.egypro.2014.10.128

Olgyay, V., 1963. Design with climate. Princeton Univ Press, New Jersey, USA.

Pajek, L., Košir, M., 2017. Can building energy performance be predicted by a bioclimatic potential analysis? Case study of the Alpine-Adriatic region. Energy Build. 139, 160–173. doi:10.1016/j.enbuild.2017.01.035

Rohles, F.H., Hayter, R.B., Milliken, G., 1975. Effective temperature (ET*) as a predictor of thermal comfort. Presented at the ASHRAE Transactions, Boston, USA.

University of California, 2017. Energy design tool: Climate Consultant software [WWW Document]. URL http://www.energy-design-tools.aud.ucla.edu/climate-consultant/ (accessed 12.20.16).

Clear-Sky Broadband Irradiance: First Model Assessment in Uruguay

Agustín Laguarda[1,2], Gonzalo Abal[1,2]

1 Laboratorio de Energía Solar/CENUR LN, UDELAR, Salto (Uruguay)

2 Instituto de Física/Facultad de Ingeniería, UDELAR, Montevideo (Uruguay)

Summary

Three simple clear-sky models using easily available mean average atmospheric data are evaluated against hourly ground data for five sites in Uruguay. The ESRA model, based on a mean daily cycle Linke Turbidity calculated from independent GHI ground data, is the best model. It predicts hourly clear-sky irradiancie with typical uncertainties under 5 % and bias under 1 % of the average GHI for all sites considered. This is low enough for it to be useful in automatic quality check procedures for ground data and also as a basis for all-sky irradiance estimation based on satellite information.

Key-words: clear-sky irradiance, GHI, Linke Turbidity

1. Introduction

An accurate determination of clear-sky Global Horizontal Irradiation (GHI) is important both as a basis for satellite-based GHI estimation (Cano et al. 1986, Pérez et al. 2002, Rigollier et al. 2004, Pérez et al. 2015) and for automatized data quality assessment. Detailed clear-sky models, such as REST2 (Gueymard, 2008), require accurate data on the state of the atmosphere to achieve their full potential. This information has a local character and is not available at most locations worldwide. Broadband clear-sky models that can perform well using easily available average information, obtained either from ground data or from satellite-based estimates, are considered and evaluated here.

Comparisons between clear-sky models have been performed for several locations worldwide (Gueymard 2012, Reno et al., 2012, Inechien 2006). However, since both the quality of the available data and the climatic tendencies are location-dependent, the problem of choosing the best clear-sky model must be locally addressed. The review by (Gueymard 2012) provides a useful listing of eighteen clear-sky models with their inputs explicitly listed. They range form zero to eight inputs in the case of REST2, one the most sophisticated models. Acceptable models for clear-sky GHI have deviations under 6 % of the mean irradiation, the exact figure depending also on the quality of the data and the input parameters. In this work, we present a first inter-comparison between three simple hourly clear-sky models with a few daily-averaged inputs tested against quality-controlled hourly ground data from several sites in the territory of Uruguay, South America.

2. Models, methodology and data

2.1 Clear-sky models

Three models whose input parameters can be determined either from ground-based global horizontal irradiance (GHI) measurements or from reliable satellite-based estimates are considered: (i) the clear sky model used in the European Solar Radiation Atlas, ESRA (Rigollier et al., 2000), (ii) the model proposed in (Ineichen and Perez 2002) based on Kasten's pirheliometric formula (Kasten 1996) and (iii) the simplified version of the SOLIS model proposed in (Inechien, 2008). The first two rely on a single dimensionless parameter, the Linke Turbidity (TL) for air mass 2 and the third requires mean water vapor density (w) and mean Aerosol Optical Depth at 700 nm (aod700). In this work, we refer to these models as ESRA, KIP and

doi:10.18086/swc.2017.21.05 Available at http://proceedings.ises.org

sSOLIS, respectively. In all cases, the corrected air mass *m* (considering diffraction and altitude effects) and the solar zenith angle are calculated for the mid-point of each hour. The parametrization in (Kasten y Young, 1989) is used for the corrected air mass. A brief description of each of these models is provided here for completeness.

ESRA model: This model (Rigollier et al. 2000) estimates the direct and diffuse irradiance over an horizontal plane, and then adds them to obtain GHI. The Linke Turbidity for an air mass equal to 2 is its single parameter. In its hourly version, the beam component is given by

$$I_{bh}^{ESRA} = I_0 f_n \cos\theta_z e^{-0.8662 m \delta_R T_L} \quad (1)$$

where I_0 = 1367 Wh/m² is the hourly solar constant, $f_n = (r_0/r)^2$ is the orbital eccentricity factor parametrized in (Spencer 1971), and δ_R is the Rayleigh optical thickness (Kasten, 1996). The solar zenith angle, θ_z, is calculated at the midpoint of each hour from location and time information, in the usual form. Further corrections regarding altitude effects according to (Remund, 2003) are not implemented, since all the locations considered are in altitudes over the sea level below 140 meters, and these effects are negligible. The numerical factor *0.8662* in eq. (1) has an historical origin, associated to changes in the parametrization of δ_R. In early work, the Rayleigh optical thickness parametrization did not include absortion by permanent gases in the atmosphere and these effects appeared incorrectly as an increased effective turbidity (Inechien y Perez, 2002; Mavromatakis y Franghiadakis, 2007). In later work (Louche et al., 1986; Grenier et al., 1994; Kasten, 1996) the parametrization of δ_R was modified to include these effects and consequently, the turbidity T_L(m) was adjusted, since the product $\delta_R(m)\cdot T_L(m)$ is independent of air mass. The ratio of Linke Turbidity (new/old) at *m=2* gives rise to the *0.8662* factor in eq. (1) (Kasten, 1996). The Linke Turbidity coefficient takes into account the effects due to water vapor and aerosols and it is frequently interpreted as the number of clear, dry atmospheres which would produce the same effect on solar radiation as the actual atmosphere.

Diffuse irradiation on a horizontal plane is estimated as the product of the extraterrestrial irradiation times a diffuse transmitance factor on a vertical path (T_z) multiplied by a difuse angular modificator F_d,

$$I_{dh}^{ESRA} = I_0 f_n T_z(T_L) F_d(\theta_z, T_L) \quad . \quad (2)$$

The T_z and F_d expressions proposed in (Rigollier, 2000) are used here. Localization of this part of the model can be done with diffuse irradiation data. However, under clear sky conditions the diffuse fraction in the region of interest is about 10% (Abal et al. 2017), so small deviations due to the diffuse parametrization are expected to have little impact on model performance. The sum of eq. (1) and eq. (2) then provide the global irradiation on a horizontal surface.

KIP model: A second clear-sky model based on Linke Turbidity is described in (Kasten, 1984). Inechien and Perez observed a solar zenith angle and altitude dependence in its performance and introduced a correction (Inechien and Perez, 2002) which implies the inclusion of two altitude-dependent parameters a_1 and a_2 and the parametrization of global horizontal irradiation as ,

$$I_h^{KIP} = a_1 I_0 f_n \cos\theta_z e^{-a_2 m [f_{h1} + f_{h2}(T_L - 1)]} \quad . \quad (3)$$

Here $f_{h1} = \exp(-h/8000)$ and $f_{h2} = \exp(-h/1250)$ are coefficients that depend on the site altitude above sea level (*h)* in meters. The KIP model introduces a_1 and a_2 as linear functions of the altitude (Inechien and Perez, 2002) so that at sea level *(h=0)* a version of Kasten's original model is obtained. However in this formulation T_L is the main parameter used to describe the atmosphere.

sSOLIS Model: This simplified version of the SOLIS model, adequate for real-time use, has been proposed by (Inechien, 2008). The original SOLIS model is a spectrally resolved physical model based on radiative transfer model (RTM) calculations. The empirical equation is adopted as a good approximation for GHI,

$$I_h^{sSOLIS} = I_0' f_n \cos\theta_z e^{-\frac{\tau_g}{\cos^g \theta_z}} \quad (4)$$

Similar expression are used for beam and diffuse irradiance. I_0' is an enhanced extraterrestrial irradiance. In the original SOLIS model (Mueller, 2004) the optical depth τ_g and the parameter g are calculated from a RTM for different sun elevation angles, which limits the real-time applicability of this model. To solve this problem, Ineichen fitted analytical expressions for the parameters involved. Explicit expressions for I_o', τ_g and g as functions of aod700, water vapor *(w)* and atmospheric pressure *(p)* are provided in (Inechien 2008). According to this author, the simplification implies a negligible bias and standard deviation of 3 W/m^2 when compared with the results of the original RTM calculation.

2.2 Amospheric data

Three atmospheric variables (T_L, aod700 and w) are used as input for the models described above. For the region of interest in this work ground-based measurements are not available for any of them. However, as the are expected to vary slowly, yearly cicles of daily information based on satellite and ancialliary ground data can be used. In the following, this metodology is explained in further detail.

Linke Turbidity

As mentioned before, T_L includes in an effective way information on water vapor content and aerosols in the atmosphere. T_L can be estimated either from (i) watervapor and aerosol optical thickness at different wavelengths (Remund et al., 2003), (ii) from ground-based clear-sky DNI mesurements and eq. (1) or (iii) from clear-sky GHI measurements and eqs. (1) and (2) (Diabaté et al., 2003; Raichijk, 2009). When clear-sky DNI is avialable, (ii) is the preferred method (Pedros et al., 1999; Raichijk and Fasulo, 2010; Remund et al., 2003). For the region of interest in this work, this is not the case and it is necessary to resort to methods based on GHI data. The alternative of using parametric models to estimate the diffuse fraction from GHI and then use method (ii) mentioned above to obtain T_L from DNI has been used by (Cucumo et al., 2000) but the high uncertainty introduced by the DNI estimation procedure (Abal, 2017) render this method unreliable.

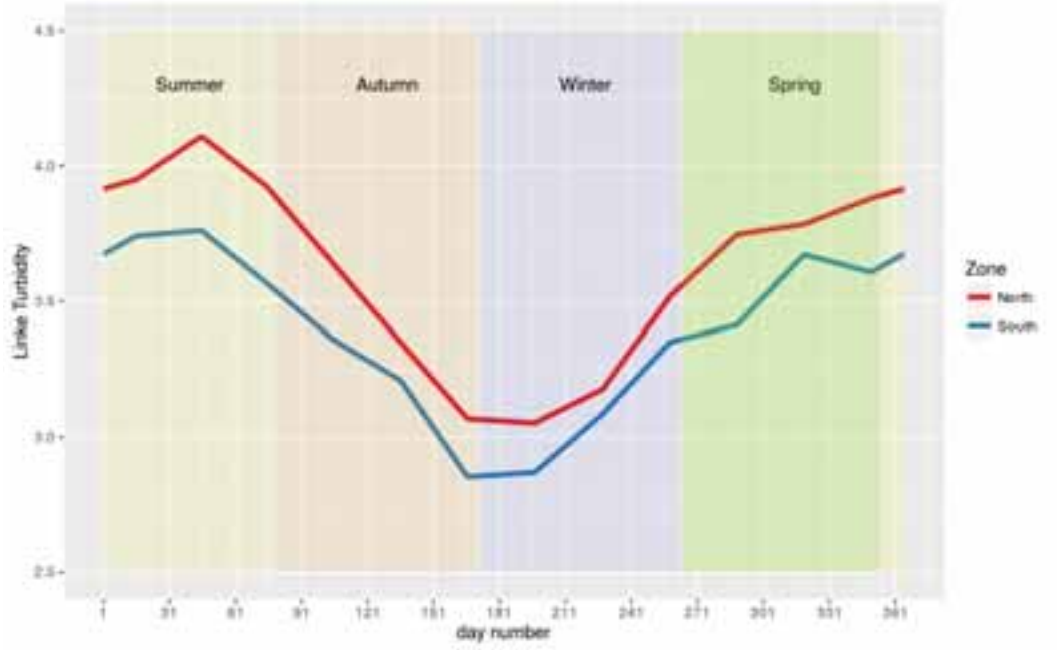

Fig. 1: Early cycle for Linke's Turbidity Parameter for Northern and Southern regions of Uruguay

In this work, we use the method (iii), to estimate daily T_L at several locations in the region of interest. T_L is determined in order to get the best fit of the ESRA model against clear-sky GHI ground data for ten different locations in the region that includes Uruguay and neighboring areas (Laguarda and Abal,

2016). Clear sky hourly data were selected from the 2010-2015 period using the procedure described in (Remund et al., 2003). Then, the monthly-averaged T_L was chosen in order to minimize a statistical indicator Kolmogorov Smirnoff Index (KSI), defined in Appendix A. The monthly values of T_L and their uncertainty was determined using a standard 10-fold cross validation technique. The data set used to obtain the T_L cycles is independent of the data used in this work for the evaluation of the clear sky models. This method was validated against the DNI-based method for a few locations where DNI measurements were available, for details we refer to (Laguarda and Abal, 2016). A daily T_L cycle is constructed by linear interpolation of the monthly mean values. Since the observed spatial dependence of this cycle is weak, just three daily-interpolated cycles (for the northern (N), center (C) and southern (S) parts of the country) adequately describe average atmospheric conditions at all sites. The T_L cycles used in this work (Northern and Southern regions) are shown in Fig. 1.

Aerosol Optical Depth and Water Vapor

The sSOLIS model describes the atmosphere using only aod700 and water vapor density as required information. Since there are no AeroNet or similar specialized measuring sites for these magnitudes in Uruguay, MODIS daily satellite estimates for water vapor column, Angstrom exponent and aod550 for 15 years (2/2002 to 12/2016) were used to estimate yearly cycles of the atmospheric variables. The Angstrom relation is used to obtain aod700 from aod550,

$$\tau_{700} = \tau_{550} \left(\frac{700}{550} \right)^{\alpha} \tag{5}$$

where α is the Angstrom exponent. Yearly cycles of average water vapor and aod700 were generated to be used as input for the sSOLIS model. The long term Aqua-MODIS satellite time series (area-averaged) data was used. The data is downloaded from the NASA site https://giovanni.gsfc.nasa.gov/giovanni/, and belongs to the level 3 series (highest quality available).

Specifically, daily information of Aerosol Angstrom coefficient (α), aod550, and precipitable water vapor column (w) from 2002 to 2015 were used for each site of interest. Using eq. (5), a series for aod700 series was obtained for each site. The final smoothed aod700 and *w* yearly cycles are obtained by averaging the series for each day of the year, and then taking a 25-day moving average and excluding data that exceeds 2 times the standard deviation for each day. The resulting smoothed cycles and the 15-year average cycles for w and aod700 at a given site are shown in Figs. 2 and 3, respectively.

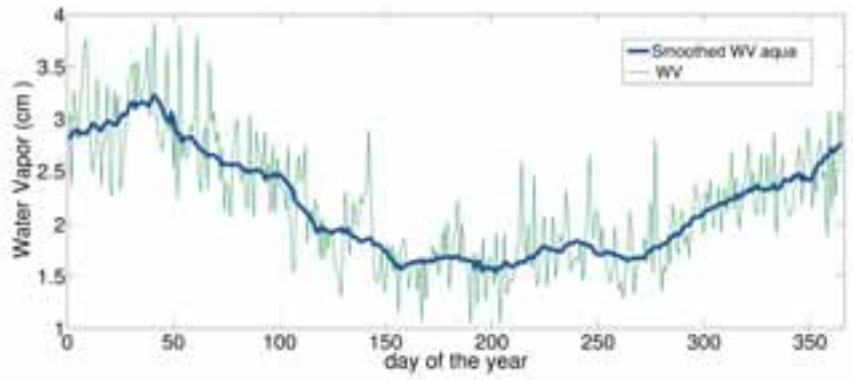

Fig. 2: Water vapor column cycle (in cm) from Aqua MODIS for the LE site, averaged by a 25-day moving window. The thin line shows the 15-year average cycle without smoothing.

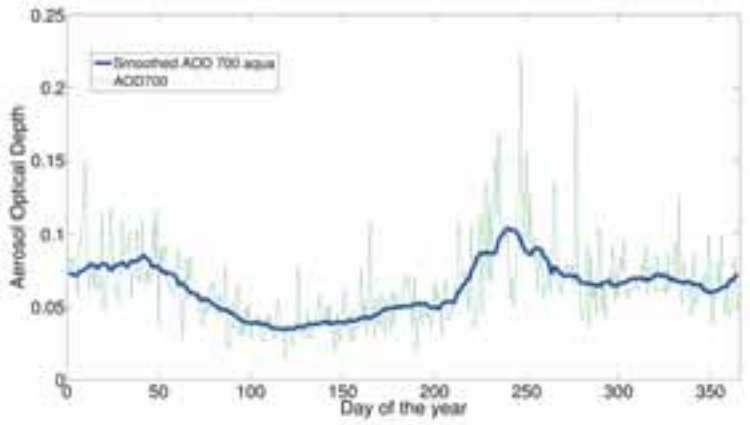

Fig. 3: Aerosol Optical Depth (dimensionless) yearly cycle from Aqua MODIS for the LE, averaged by a 25-day moving window. The thin line shows the 15-year average aod700 without smooting.

2.3 Ground solar irradiance data

The hourly irradiance predicted by these three models are compared with more than two years (January 2015 – March 2017) of GHI ground data from five sites from the continuous solar irradiance monitoring network run by our laboratory (see Table 1 and Fig. 4) GHI is registered each minute with first class or better pyranometers which are calibrated every two years at our laboratory against a Kipp & Zonen CMP22 secondary standard. This calibration is traceable to the PMOD World Radiation Center primary standard and to the World Radiometric Reference. All sites are in rural or semi-rural areas at low altitudes (less than 140 meters above the sea level) in a temperate climate.

Table 1: Details for the ground stations. The clear sky hours correspond to the data filtered and selected in the period january 2015 - March 2017 in all locations.

Site Code	Zone code	Latitude South degrees	Longitude West degrees	Altitude (m. a. s. l.)	Valid daytime hours	Clear Sky hours
LB	S	34.67	56.34	37	8985	3105
AR	N	30.40	56.51	136	9832	3218
LE	N	31.27	57.89	50	6147	1958
TT	S	33.28	54.17	35	6854	1840
RC	S	34.49	54.31	20	8676	2496
Total	-	-	-	-	40494	12617

Clear-sky filtering procedure

The ground data is filtered for basic quality control and integrated to obtain 40494 (daytime) valid hourly records. In order to obtain data associated to clear sky conditions, the algorithm in (Remund et al. 2003) is used to select 12617 (mostly) clear-sky hours. This algorithm is based in apply five consecutive filters to GHI hourly data.

1. DNI > 200 W/m^2. If DNI simultaneous information isn't available, it is estimated using Erbs correlation (Erbs et al., 1982). This procedure is only approximate, but it is sufficient to discriminate low direct radiation hours.
2. The hourly modified clearness index k_t' (Perez et al., 1990), Ec. (6), must be bigger than 0.7 (Molineaux and Delaunay, 1995).

$$k_t' = \frac{k_t}{0.1 + 1.031\, e^{-\frac{1.4m}{9.4+0.9m}}} \qquad (6)$$

where $k_t = I_h / I_0$ is the usual clearness index, and m is the air mass.

3. The daily clearness index ($K_t = H_h / H_0$) must be over 0.4.
4. For a given day if the clear sky hours are less than the 40% of the valid hours, then the whole day is discarded.
5. Data with solar altitude below 10 degrees is discarded.

After this set of five filters is applied, a set of clear sky hours is obtained for each site. The last column of Table 1 shows the number of hours for each site. These data was used as indicated in Section 2.2 to obtain monthly averaged T_L values for each site. Since site-to-site variability is low, data was grouped in three regions (North, Middle and South) and monthly T_L cycles for each region were obtained. These average cycles were interpolated linearly to obtain daily data and avoid abrupt changes across consecutive months.

Fig. 4: The area of interest in this paper includes the whole Uruguayan territory (located in the southeastern of South America). The blue dots show the sites that recorded the ground GHI data used in this work.

In (Laguarda and Abal, 2016) the ESRA model with these T_L cycles was compared to hourly clear sky data from 8 sites and the relative Root Mean Square Deviation (RMSD) was between 4.1 % and 5.1 % for all sites. These results show that clear-sky GHI can be estimated in this region by the ESRA model with uncertainty under 5 % using the mean T_L cycle determined for a broad region from long-term data. Marginal

improvements (under 1 %) can be obtained by using specific T_L cycles for each site.

3. Model performance

Three indicators used to evaluate model performance are Mean Bias Deviation (MBD), Root Mean Square Deviation (RMSD) and the Kolmogorov-Smirnov Integral (KSI). They measure bias, spread and distance between statistical distributions, respectively. Their definitions are standard and can be found in Appendix A. Table 2 lists these indicators for each clear-sky model and site. All models have small negative bias (indicating a tendency to underestimate GHI). Typical RMSD value range between 4 % and 7 %, depending on site and model.

Table 2: Relative performance indicators (in % of mean GHI) for each model and site.

Site	Mean	ESRA			KIP			sSOLIS		
Code	**Wh/m2**	**MBD**	**RMSD**	**KSI**	**MBD**	**RMSD**	**KSI**	**MBD**	**RMSD**	**KSI**
LB	615	0.0	4.3	1.1	-4.4	6.1	4.4	-2.3	6.0	2.7
AR	629	-0.6	4.3	1.1	-5.0	6.5	5.0	-2.1	5.5	2.1
LE	662	-0.3	3.8	0.9	-4.5	5.9	4.5	-3.4	5.9	3.4
TT	589	-0.8	4.8	1.0	-5.2	7.0	5.2	-2.0	6.2	2.4
RC	616	-1.0	4.7	1.2	-5.3	7.0	5.3	-2.3	6.2	2.8
ALL	**622**	**-0.5**	**4.4**	**1.1**	**-4.9**	**6.5**	**4.9**	**-2.4**	**6.0**	**2.7**

A simple global indicator C can be constructed for each model by averaging the absolute bias with RMSD and KSI (Gueymard 2014, Abal et al, 2017). This indicator, shown in Table 3, suggests that ESRA is the best model, followed by sSOLIS.

Tab. 3: Global indicator for each model

Model	C = (|MBD|+RMSD+KSI)/3
ESRA	2.0
KIP	5.4
sSOLIS	3.7

Fig. 5 shows detailed results for the LE site. The Left panel compares model prediction with grouind measurments. The small negative bias (underestimation) is associated to high irradiance (> 700 W/m^2) conditions. The right panel shows relative differences vs cosine of zenith angle. For low cosine values (low solar altitude) the biases increase as expected. The KIP model has a particularly large bias under this conditions. Fig. 6 shows the absolute difference between the ESRA model prediction and the ground truth vs Irradiation value. GHI values where classified into 11 bins, and average and standard deviation for each bin was calculated. This shows that bias is under 25 W/m^2 in all cases. For this model, negative biases come mainly from low irradiance (< 400 W/m^2) values. Since we are considering clear-sky data, these values are associated to low solar altitudes for which measurements are most uncertain.
Part of the observed deviations may be due to error in measurement or to errors in the automated clear-sky algorithm classification (i.e. mostly clear hours classified as cloudy or partly cloudy hours classified as

clear). This can only be assessed by a manual selection of the clear sky hours, a daunting task for the amount of data considered in this work.

Fig. 5: LB site. (left) Model predictions of clear sky GHI vs ground measurements and (right) relative difference between predictions and measurements vs cosine of the solar zenith angle z.

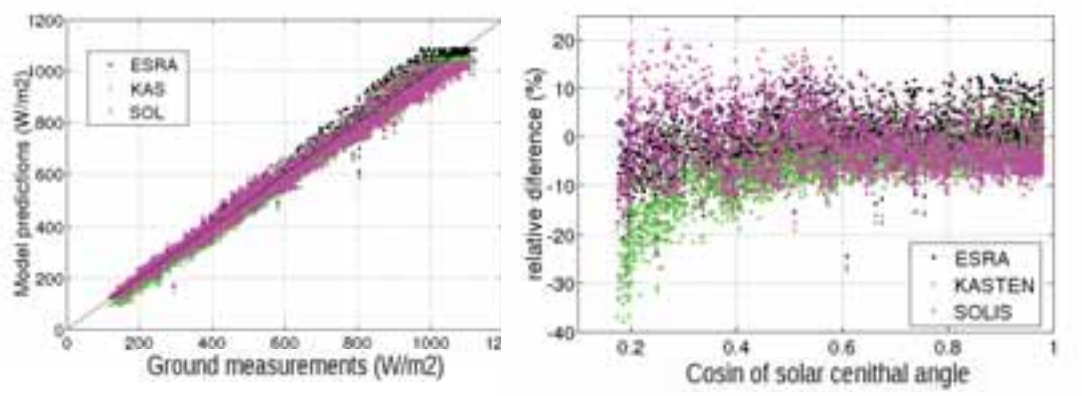

These results are similar to those found in the literature for these models. In (Ineichen, 2006) data from 16 sites in the Northern Hemisphere (with latitudes ranging between 30 and 48 degrees) was used to compare the performance of eight clear-sky models. Among them, the SOLIS model (the simplified model was not introduced until 2008), the ESRA and the KIP models. The SOLIS model was found to be one of the best among the models considered. Another comprehensive comparison was performed in (Gueymard, 2012) using high quality data from five sites in the Northern Hemisphere (latitudes between 19.5 and 40 degrees).

Fig. 6: Differences between ground data and ESRA model Predictions in LE station. Means are showed in black for different regions. The black bars represent the standard deviation in each region.

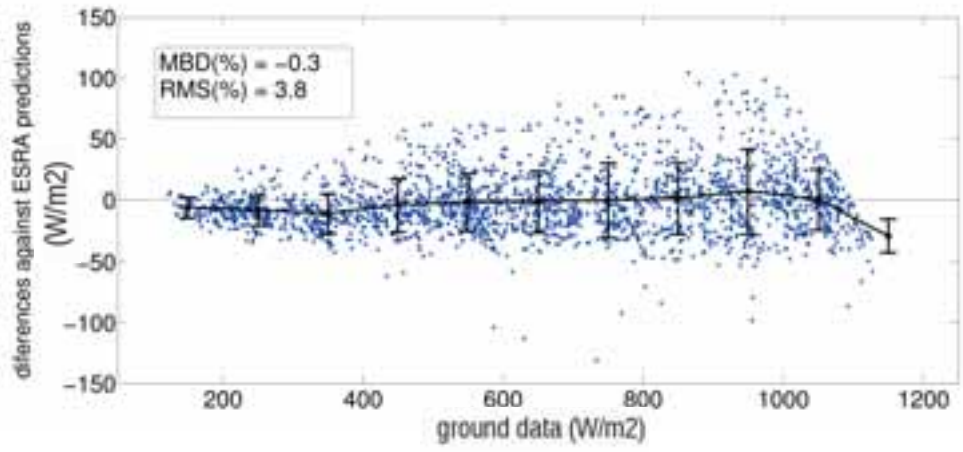

Tab. 4: A comparison of indicators for the selected models

Model	Indicator	(Gueymard, 2012)	(Ineichen, 2006)	This work
ESRA	MBD (%)	3.1	4.0	-0.5
	RMSD (%)	4.5	6.0	4.4
KIP	MBD (%)	not tested	-0.2	-4.9
	RMSD (%)	not tested	4.6	6.5
sSOLIS	MBD (%)	-1.6	(*) 1.8	-2.4
	RMSD (%)	2.8	(*) 4.9	6.0
Mean GHI(W/m^2)		675.6	547.0	622.0

(*) indicators are for the original SOLIS model.

In this comprehensive comparison, 18 clear-sky models where considered (the KIP model was not among them). The ESRA and simplified SOLIS where included and in fact, the sSOLIS was found to be the second best model, after the REST2 model.

It is not always possible to compare results from different authors, but in these cases, enough information is given so that results for all sites can be reduced to the same form and their averages are compared in Table 4. The relative RMSD indicators are similar in the three studies, ranging between 3% and 6% of the mean. As noted in (Ineichen, 2006) since there are no large differences in performance, the best clear sky model for a given region and application should be chosen with consideration to implementation simplicity and with regard to the quality and availability of its input data. For instance, in this study ESRA outperforms the sSOLIS model, which was found to be the second best among 18 other models in (Gueymard 2012). However, this study used the best available data for water vapor and aod, while in our implementation we have used daily averages based on satellite retrievals, which is available for this region. So, model rankings should not be read as ranking models according to their accuracy, but rather as ranking local model implementations (which include the quality of their input data).

4. Summary and conclusions

Three simple clear sky models (ESRA, Simplified SOLIS (sSOLIS) and Kasten (KIP)), are considered and evaluated using data for the region of Uruguay and neighboring areas (southeastern South America). These models have been selected taking into account the availability of the required input information for this area. Two of them use Linke Turbidity as their single parameter and sSOLIS uses water vapor density and Aerosol Optical Depth at 700 nm. This information was obtained from the MODIS satelite database on a daily basis and averaged over 15 years. The average Linke Turbidity was obtained from a large set of clear-sky GHI data for 10 sites on the region of interest by minimization of the KSI index.

The models are evaluated against an independent data set (i.e. not used to determine the TL cycles) from five sites in the region of interest. Clear sky conditions are automatically selected based on a set of criteria suggested by Remund, in which the Perez modified clearness index plays an important role. Results show that all models have RMSD between 4.3 % and 7 % of the mean value of GHI. Mean Bias is mostly negative for all models and sites, reaching -5.3%.

Our first conclusion is that our implementation of the ESRA model has the best indicators over all sites considered in this work. A combined indicator selects this model as the best alternative to estimate clear-sky GHI in this region. Clear-sky GHI can be estimated with bias under 1% and Root Mean Square Deviations under 5 % of the mean. In absolute terms, averaged over sites, the bias is MBD = -3 W/m^2 and the RMSD = 27 W/m^2. These indicators can be improved if T_L information for specific sites is used in the ESRA model.

However, the implementation based on the average cycle has indicators that are low enough to allow the use of the ESRA model in automated quality-check procedures for the ground GHI data. Furthermore, it is an adequate starting point for a physically motivated all sky irradiation model in which information about cloudiness is obtained from satellite images.

A second conclusion is that, since there are no drastic variations in performance, the selection of a clear sky model should take into account its ease of implementation and the quality and availability of its input data.

5. References

Abal, G., Aicardi, D., Alonso-Suárez, R., Laguarda, A.,2017. Performance of empirical models for diffuse fraction in Uruguay. Solar Energy, 141, 166-181.

Cano, D. Et al.1986. A method for the determination of the global solar radiation from meteorological satellite data, Solar Energy, 37, 31–39.

Cucumo, M., Kaliakatsos, D., Marinelli, V., 2000. A calculation method for the estimation of the Linke turbidity factor, Solar Energy 19, 249-258.

Diabaté, L., Remund, J., Wald, L., 2003. Linke turbidity factors for several sites in Africa. Solar Energy 75, 111-119.

Erbs, D., Klein, S., Duffie, J., 1982. Estimation of the diffuse radiation fraction for hourly, daily and monthly average global radiation. Sol. Energy 28, 293.

Grenier, J.C. et al., 1994. A spectral model of Linke‘s rurbidity factor and its experimental implications. Solar Energy, 52, 303-313.

Gueymard, C.A., 2008. REST2: High-performance solar radiation model for cloudless-sky irradiance, illuminance, and photosynthetically active radiation, Solar Energy 82, 272–285.

Gueymard, C. 2012. Clear-sky irradiance predictions for solar resource mapping and large-scale applications: imporved validation methodology and detailed performance analysis of 18 broadband radiative models. Solar Energy 86, 2145-2169.

Gueymard, C., 2014. Renew. Sustain. Energy Rev. 39, 1024.

Ineichen, P., 2008. A broadband simplified version of the Solis clear sky model. Solar Energy 82, 758–762.

Ineichen, P., Perez, R., 2002. A new airmass indpendent formulation for the Linke Turbidity coefficient, Solar Energy 73, 151-157.

Inechien, P. 2006. Comparison of eight clear sky broadband models against 16 independent data banks. Solar Energy 80, 468-478.

Kasten, F., 1996. The linke turbidity factor based on improved values of the integral rayleigh optical thickness. Sol. Energy 56, 239–244.

Laguarda, A., Abal,G., 2016.Índice de Turbidez de Linke a partir de irradiación global en Uruguay. Avances en Energías Renovables y Medio Ambiente Vol.20,11.35-11.46.

Louche, A. et al. 1986. An analysis of the Linke turbidity factor. Solar Energy 37, 393-396.

Mavromatakis F. and Franghiadakis, Y., 2007. Direct and indirect determination of the Linke turbidity coefficient. Solar Energy 81, 896-903.

Molineaux, B., Delaunay, J.J., 1995. Direct luminous efficacy and atmospheric improving model performance 55, 125–137.

Mueller, R. et al., 2004. Rethinking satellite based solar irradiance modelling – the SOLIS clear-sky module. Remote Sens. Environ. 91, 160-174.

Pedrós, R., Utrillas, M.P., Martinez-Lozano, J.A., Tena, F., 1999. Values Of Broad Band Turbidity Coefficients In A Mediterranean Coastal Site, Solar Energy 66, 11-20.

Perez, R., Schlemmer, J., Hemker, K., Kivalov, S., Kankiewicz, A., and Gueymard, C. (2015). Satellite-to-irradiance modeling - a new version of the SUNY model. IEEE 42nd Photovoltaic Specialist Conference (PVSC), pages 1–7.

Perez, R., Ineichen, P., Moore, K., Kmiecik, M., Chain, C., George, R., and Vignola, F. (2002). A new operational model for satellite-derived irradiances: description and validation. Solar Energy, 73, 307–317.

Perez, R., Ineichen, P., Seals, R., Zelenka, A., 1990. Making full use of the clearness index for parameterizing hourly insolation conditions. Sol. Energy 1, 3–6.

Raichijk, C., (2009). Estimación del índice de turbidez de linke para distintas localidades de Argentina, Avances en Energías Renovables y Medio Ambiente (AVERMA), 13, pp. 11-16.

Raichijk, C., Fasulo, A., (2010). Estudio de la turbidez atmosférica en la ciudad de San Luis, Avances en Energías Renovables y Medio Ambiente (AVERMA), vol. 25.

Remund, J., et al., 2003. Worldwide Linke turbidity information. In: Proceedings of ISES Conference. Stockholm, Sweden, International Solar Energy Society.

Reno, M.J., Hansen, C.W., Stein, J.S., 2012, Global Horizontal Clear Sky Irradiance: implementation and analysis. SANDIA REPORT SAND2012-2389.

Rigollier, C., Lefevre, M., and Wald, L. (2004). The method Heliosat-2 for deriving shortwave solar radiation from satellite images. Solar Energy, 77, 159–169.

Rigollier, C., Bauer, O., Wald, L., 2000. On the clearsky model of the 4th ESRA with respect to the heliosat method. Solar Energy 68, 33-48.

Spencer, J.W (1971). Fourier series representation of the position of the sun. Search, 2:172, 1971.

6. Appendix: Statistical indicators

There are several concordance indicators between measurements $\hat{Y}_i$, and n estimates Y_i of a variable. In this section RMSD, MBD, and KSI are defined.
The root mean square deviation (RMSD), and de Mean Bias Deviation (MBD) are defined as

$$RMSD=\sqrt{\frac{1}{n}\sum_{i=1}^{n}(\hat{Y}_i-Y_i)^2}$$

$$MBD=\frac{1}{n}\sum_{i=1}^{n}\hat{Y}_i-Y_i$$

For a variable z, the the Kolmogorov-Smirnov Integral indicator (KSI) is defined as

$$KSI=\int_{z_{min}}^{z_{max}} D(z)\,dz \quad ,$$

where

$$D(z)=\left|F_{\hat{Y}}(z)-F_Y(z)\right|$$

Here F_Y ($F_{\hat{Y}}$) is the empirical cumulative distribution function (CDF) for the variable Y ($\hat{Y}$), were Y and $\hat{Y}$ the measuements and model estimated data vectors of GHI, z is variable in the range of GHI. In this case, KSI (same units as GHI, W/m^2) is a measurements of the absolute difference between the CDFs.

Each statistical indicator can be expresed in a dimentionless way as

$$rMBD=\frac{RMBD}{mean(\hat{Y})}$$

and similar relations for the other indicators.

Proposal and Evaluation of Subordinate Standard Solar Irradiance Spectra with a Focus on Air Mass Effects

Stefan Wilbert[1], Wilko Jessen[1], Chris Gueymard[2], Jesús Polo[3], Zeqiang Bian[4], Anton Driesse[5], Aron Habte[6], Aitor Marzo[7], Peter Armstrong[8], Frank Vignola[9], Lourdes Ramírez[3]

[1]DLR, German Aerospace Center, Ctra de Senes s/n km4 04200 Tabernas, Spain. Stefan.Wilbert@dlr.de

[2]Solar Consulting Services, P.O. Box 392 Colebrook, NH 03576, USA

[3]CIEMAT, Avda Complutense, 40 Madrid 28040 Spain

[4]China Meteorological Administration No.46 Zhonguancun Nandajie Bejing 100081China

[5]Photovoltaic Performance Labs, Emmy-Noether-Str. 2 Freiburg 79110 Germany

[6]NREL 15013 Denver West Parkway Golden 80401 USA CO

[7]Centro de Desarrollo Energético Antofagasta (CDEA), University of Antofagasta Av. Angamos, 601 Antofagasta 1270300 Chile

[8]Masdar Institute, Khalifa University of Science & Technology, PO Box 54224 Abu Dhabi, United Arab Emirates

[9]Univ. of Oregon, 1274 Univ. of Oregon Eugene OR 97403-1274, USA

Abstract

This paper introduces a concept for global tilted irradiance (GTI) subordinate standard spectra to supplement the current standard spectra used in solar photovoltaic applications, as defined in ASTM G173 and IEC60904. The proposed subordinate standard spectra correspond to atmospheric conditions and tilt angles that depart significantly from the main standard spectrum, and can be used to more accurately represent various local conditions. For the definition of subordinate standard spectra cases with an elevation of 1.5 km above sea level the question arises whether the air mass should be calculated including a pressure correction or not. This study focuses on the impact of air mass used in standard spectra, and uses data from 29 locations to examine which air mass is most appropriate for GTI and direct normal irradiance (DNI) spectra. Overall, it is found that the pressure corrected air mass of 1.5 is most appropriate for DNI spectra. For GTI a non-pressure-corrected air mass of 1.5 was found to be more appropriate. The suitability of this selection for a given site is best for mid latitudes (~35°) and elevations below 1 km. It also depends on the vertical distributions of aerosols and water vapor.

Keywords: solar spectra, efficiency rating, spectral response, standardization, air mass

1. Introduction

Standard solar irradiance spectra are required to compare and specify key parameters of solar technologies, such as the efficiency of photovoltaic (PV) cells. In particular, the recent IEC standard 60904-3 prescribes a Direct Normal Irradiance (DNI) spectrum and a Global Tilted Irradiance (GTI) spectrum for a 37° tilted sun-facing surface, both defined for a clear-sky condition with air mass 1.5 (AM1.5) and low aerosol content. The IEC spectra are identical to the ASTM G173 spectra when scaled by a factor of 0.99708. These reference spectra are widely used for rating purposes when different products, such as PV cells, have to be compared under Standard Test Conditions (STC), as discussed by, e.g., Gueymard et al. (2002). To maintain comparability of results, it is important that a single standard spectrum for either GTI or DNI be used for the purpose. The present authors are also working towards replacing the current (but outdated) ISO 9845 spectra by the IEC spectra just mentioned within the ongoing update of the ISO standard.

The unique importance of the IEC (or ASTM) spectra is not at all called into question in this work. However, these reference spectra may differ strongly from realistic average spectra at sites with different atmospheric

doi:10.18086/swc.2017.21.06 Available at http://proceedings.ises.org

conditions or for tilt angles that are different from 37°. For such cases, it is useful to compare products using both the standard spectra and additional subordinate reference spectra that correspond better to specific local atmospheric conditions and sun-receiver geometries than the standard spectra. In particular, it should be noted that the current standards only represent sea-level conditions. High-elevation sites tend to have higher solar resource, which attracts many solar energy projects. In the case of small installations, for instance, such a rough comparison can be helpful as a simple product pre-selection tool when sophisticated performance evaluation is not feasible. For larger installations requiring more sophisticated evaluations, this kind of comparison may reduce the effort by decreasing the number of initial product candidates.

The impacts of the incident spectrum on the performance of different PV cell technologies have been studied using both measured and modeled solar spectra (Fernandez et al., 2014; Nofuentes et al., 2017; Dirnberger et al., 2015; Polo et al., 2017). These publications show the importance of atmospheric conditions on the magnitude and shape of incident spectra and underline the need for specific methods to evaluate spectral effects in yield analyses. One way to improve the state-of-the-art in PV modeling is to provide subordinate standard spectra that cover situations beyond what the ASTM G173/IEC 60904-3 standards are meant to address.

Section 2 below briefly presents suggestions for subordinate standard spectra corresponding to eight sets of atmospheric conditions and a range of tilt angles that are currently considered within the ISO working group. High-elevation locations (1.5 km above sea level) are included as well. Section 3 discusses the proper definition of air mass in the case of elevated sites. To this end, the cumulative annual direct normal and global tilted irradiations are analyzed as a function of air mass, based on irradiance measurements at 29 sites. Furthermore, the average solar spectra for two elevated sites are analyzed to establish which definition of air mass to use. Finally, a conclusion and an outlook are presented.

2. Proposed subordinate standard spectra

Subordinate GTI spectra are proposed for nine atmospheric conditions defined in terms of aerosol optical depth at 500 nm (AOD500), precipitable water vapor (PW), and elevation, as given in Table 1. The suggested tilt angles are from 0° to 90° in increments of 5°. To limit the number of subordinate spectra other parameters such as the azimuth orientation of the surface are not varied. Exemplary spectra for a tilt angle of 20° are shown in Fig. 1. As in the existing standards, AM1.5 is used. Why this specific air-mass value was selected originally is discussed elsewhere (Ross and Gonzalez, 1980; Gueymard et al., 2002). To be clear, the air mass indicates the *relative* (non-pressure corrected) air mass value M_{npc}. A discussion on various definitions of air mass appears in the next section. Additionally, DNI spectra for the same atmospheric conditions are also investigated, but are not shown graphically since they are not recommended as subordinate standard spectra. However, the air mass selection for DNI spectra is specifically discussed in what follows.

Tab. 1: Suggested conditions for the GTI subordinate standard spectra, below those used in (IEC, 2016). All cases use the aerosol type "rural" and the albedo "light sandy soil" except for DustyMedHum, for which "Desert_Max" and "dune sand" are used. The abbreviations used to describe the atmosphere are defined in (Gueymard, 2005).

Short name	Description	Elev. (km)	AOD@ 500nm	PW (cm)	Representative Atmosphere
IEC 60904	Reference (IEC 60904-3)	0	0.084	1.416	USSA
SemClmedHum	Semi-clean, medium humidity, sea level	0	0.27	1.416	USSA
SemClHum	Semi-clean, humid, sea level	0	0.27	4.115	TRL
HazMedHum	Hazy, medium humidity, sea level	0	0.54	1.416	USSA
DustyMedHum	Dusty, medium humidity, sea level	0	0.54	1.416	STS
HazHum	Hazy, humid, sea level	0	0.54	4.115	TRL
ClDryHi	Clean, dry, high elevation	1.5	0.084	0.708	MLW
SemClDryHi	Semi-clean, dry, high elevation	1.5	0.27	0.708	MLW
HazDryHi	Hazy, dry, high elevation	1.5	0.54	0.708	STW

Some aspects of the existing IEC/G173 standard spectra that can be considered outdated are modified here for creation of the proposed subordinate spectra. The first of these aspects is related to circumsolar radiation. DNI is defined in terms of the viewing geometry of a pyrheliometer following the WMO recommendations for a slope angle of 1° and an opening angle of 2.5° (WMO, 2014). In IEC/G173 this opening angle was slightly larger (2.9°).Second, the newer SMARTS version 2.9.5 (Gueymard, 2001, 2005) is used here to construct the proposed subordinate spectra as opposed to v2.9.2 that was used for the current standards. Third, the solar constant of 1361.2 W/m² (Gueymard, 2012) replaces the outdated historical value of 1367 W/m² (see justification in Kopp and Lean, 2011). The extraterrestrial spectrum (ETR) selected within SMARTS is still "Gueymard, synthetic" (as was used in the current standards) but multiplied by 1361.2/1367. Spectral changes resulting from all of the above relative to G173 are minor, as shown in Fig. 2.

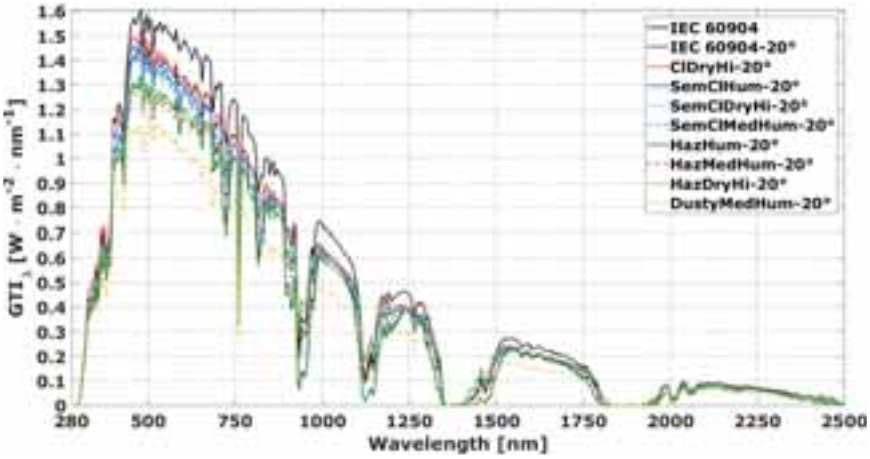

Fig. 1: Proposed subordinate standard spectra for GTI on a surface tilted 20° toward the equator.

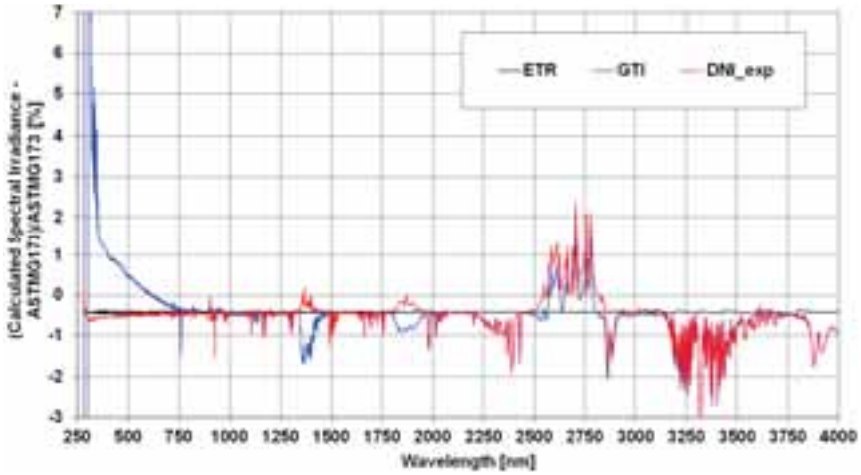

Fig. 2: Effect of changed circumsolar radiation settings, solar constant and SMARTS version, relative to the corresponding DNI and GTI spectra promulgated in G173 (red and blue line). The change of the extraterrestrial spectrum is shown in black.

The responsivity of a PV cell relative to an incident broadband solar irradiance, is obtained by multiplying its spectral responsivity, R_λ, with the solar irradiance spectrum, E_λ, according to

$$R_S = \frac{\sum_{j=1}^{N} R_\lambda(\lambda_j) \cdot E_\lambda(\lambda_j) \cdot \Delta\lambda_j}{\sum_{j=1}^{N} E_\lambda(\lambda_j) \cdot \Delta\lambda_j} \qquad \text{(eq. 1)}$$

where λ_j is the *j*th wavelength in the series 1–*N*. The relative deviation between the R_S value for a test spectrum and that for a reference spectrum is the spectral mismatch δ_{RS}. It can refer to a spectral gain or a spectral loss.

In a related study (Jessen et al., 2018), the proposed subordinate GTI spectra are compared to each other in terms of irradiance and PV device efficiency, using the spectral responsivities of exemplary solar cells from Winter et al. (2009), with or without concentration. The results show that the proposed subordinate spectra generate significant spectral mismatches compared to the IEC spectra (up to 6.5 %, for PV cells at a 37° tilt). Such mismatches indicate potential accuracy improvements that become possible by applying the subordinate standard spectra rather than the IEC spectra for a quick estimation of the *average* device efficiency.

To apply the subordinate standard spectra, manufacturers of solar devices could include PV module efficiencies for the different subordinate spectra in their data sheets. Alternatively, the spectral mismatches between using the IEC/G173 spectra and the subordinate spectra could be stated. A potential customer could then identify the potential change in efficiency based on a site's average AOD500, PW, elevation, and tilt angle. Consideration of all combinations of the aforementioned parameters with a tilt angle step of 5° would result in 171 efficiency values for PV panels, which could be conveniently presented by plotting the efficiency as a function of tilt angle. In case the manufacturer provides the spectral response rather than these values, a potential customer could independently calculate the specific mismatch between results based on either the IEC/G173 spectrum or the relevant subordinate spectrum, and thus estimate the changes in efficiency. Another advantage of these subordinate spectra is that they can assist in characterizing the durability of PV, CPV and CSP materials ex-

posed to natural weathering at a site.

A simple procedure to select subordinate standard spectra based on a site's average AOD500, PW, elevation and tilt angle was tested by Jessen, et al, (2018) at five exemplary sites [Tamanrasset, Sede Boker and Boulder (Baseline Surface Radiation Network, BSRN, König-Langlo et al., 2013), Plataforma Solar de Almería (PSA, Wilbert et al., 2013, Pozo et al., 2011), and Masdar (Kalapatapu et al., 2012)]. Two of these test sites, Tamanrasset and Boulder, are also used in this study. In Fig. 3, the average AOD500 and PW values for the annual data sets that were evaluated at these sites are shown next to the available AOD500 and PW values from the nine suggested atmospheric conditions. At all five test sites, complete time series of spectra (including both clear and cloudy periods) are determined using a combination of the SMARTS model and SEDES2 cloud modifiers (Nann and Riordan, 1991), with inputs based on site-specific sun-photometer and shortwave irradiance measurements. From all these all-sky spectra a site-specific annual-average spectrum is derived as a reference for the applicability test. In these reference spectra the impact of clouds is introduced through the use of SEDES2 in order to obtain realistic average spectra including the effect of clouds. For the subordinate standard spectra we propose only clear-sky spectra because clear sky conditions contribute stronger to the yield than most cloudy conditions and for simplicity. The resulting site-specific spectral mismatch values for the subordinate standard spectra and the IEC spectrum with respect to the site's average spectrum were derived. The subordinate spectrum with the most similar conditions to the site average results in a much lower spectral mismatch than the G173 spectrum (Jessen et al., 2018). Therefore, the proposed GTI spectra are applicable to the five test cases. Tests with other sites, for example with higher PW are of interest. For CSP and CPV applications, however, the suggested atmospheric conditions are found insufficient, due to the strong effects of AOD and Ångström exponent on DNI (Jessen et al., 2018). Hence, it is not intuitively possible to pick the most appropriate DNI spectrum from the subordinate spectra. Many more sets of atmospheric conditions would be required to allow the intuitive selection of a representative spectrum for the five test sites, let alone any other site. Hence, only GTI spectra with tilt variation are suggested for implementation in future standards.

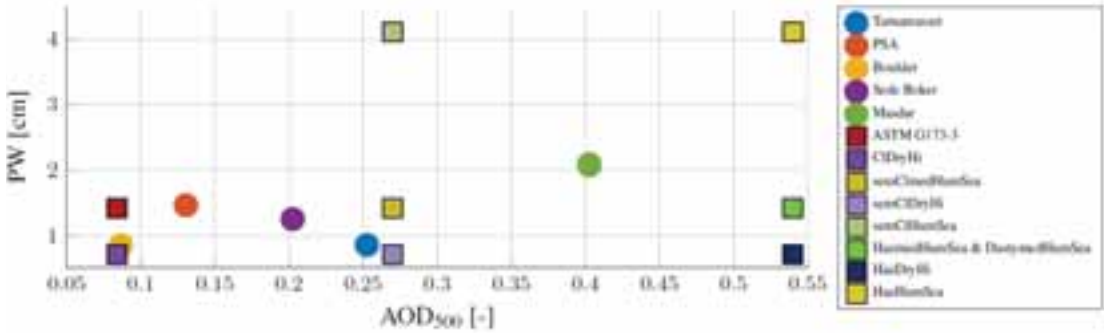

Fig. 3: AOD500 and PW for subordinate standard spectra (squares) and their averages for the sites (circles) that are used to test the intuitive selection of an appropriate reference spectrum. Matching colors mark the specific reference spectrum that would be selected based on a site's AOD500, PW and elevation.

3. Selection of air mass for the subordinate standard spectra

Besides the three AOD500 and three PW categories, an additional site elevation category of 1.5 km is suggested in Table 1 to extend the applicability of subordinate standard spectra. Introduction of high-elevation subordinate spectra raise the question of whether a pressure-corrected (absolute) or non-corrected (relative) definition of air mass is preferable. Note first that "air mass" itself is an ambiguous term. The *relative air mass* is a quantity that would be better called "optical mass for air molecules", since it corresponds to the geometric path length of the sun rays traversing the atmosphere relative to the vertical path length, and is a function only of the sun's zenith angle, Z. This quantity takes atmospheric refraction and Earth sphericity into account, and is thus more appropriate than the conventional $1/\cos Z$ factor used in the plane-parallel approximation that is typical in radiative transfer. Optical masses for aerosols, water vapor or ozone differ from the optical air mass because their concentrations have different vertical profiles. SMARTS, for instance, uses 15 different optical masses, corresponding to as many atmospheric species (or groups of species), because they have different vertical profiles. In contrast, the *absolute air mass* is pressure-corrected to reflect the actual slant "optical mass of air molecules" at higher elevations. At the top of atmosphere, this absolute mass becomes 0, and is conventionally noted AM0. The optical depth due to Rayleigh scattering by air molecules decreases with elevation as a direct function of pressure, whereas optical depths of aerosols and water vapor have a different dependence on pressure, which is moreover highly variable over space and time. All this makes the use of air mass and pressure suscep-

tible to misinterpretation and confusion.

The choice of air mass has a direct impact on the resulting spectrum and needs to be considered carefully. If a high-elevation subordinate standard DNI spectra had to be defined with a pressure-corrected (PC) air mass, M_{pc}, of 1.5, the SMARTS input value for the *air mass* would need to be adjusted accordingly, since the SMARTS input must be a non-pressure corrected (NPC) value. The needed air mass input value for M_{pc} = 1.5 is M_{npc} ≈1.8, considering the ratio between the ambient pressure at 1500 m elevation (≈840 hPa) and 1013.25 hPa. The choice of input value leads to noticeably different solar zenith angles of 48.236° (for M_{npc} = 1.5) and 56.267° (for M_{npc} = 1.8). SMARTS does not actually consider any pressure correction for its optical masses. Instead, the optical depths related to Rayleigh scattering and uniformly-mixed gases are scaled by the pressure ratio. All other optical depths, including those for aerosols and water vapor, are independent from site pressure, because they are defined as column quantities between the surface (at any elevation) and the top of atmosphere. Hence, site elevation and pressure are already accounted for in the inputs for PW and AOD. Changing the relative air mass M_{npc} from 1.5 to 1.8, the pressure from 1013.25 hPa to 840 hPa, and the input elevation from 0 to 1500 m, while maintaining the same AOD input value, results in a noticeable change in the DNI spectrum, so this distinction is important.

In what follows, the air mass effect is investigated by two methods. First, the cumulative relative fraction of annual irradiation is calculated as a function of air mass to determine a characteristic air mass. Based on this, specific air mass values are recommended for the determination of DNI and GTI spectra. Then, for further analysis, the spectral mismatch is evaluated for a number of spectra derived with different air mass options.

3.1 Cumulative relative fraction of annual irradiation as a function of air mass

An appropriate air mass needs to be selected for each subordinate standard spectrum. To that effect, the distribution of annual irradiation over many sites is analyzed as a function of air mass. In the late 1970s, the NASA-recommended terrestrial PV measurement procedures already stipulated an air mass value of 1.5 for reference measurements. This AM1.5 "optimal" value was confirmed in interrelated studies (Gonzalez and Ross, 1980; Ross, 1980; Ross and Gonzalez, 1980) as most representative for performance evaluation of PV concentrators using DNI, but not for fixed-tilt flat-plate PV, based on conditions pertaining only to the continental United States. This was later confirmed by Emery et al. (2002) for DNI, still under U.S. conditions only. These results provide an argument for working with a pressure-corrected M_{pc} =1.5 for standard spectra in the case of DNI. The "pressure-corrected" adjective is emphasized. Assuming equivalence between a spectrum obtained for M_{npc} =1.5 at sea level and another one for M_{npc} =1.8 (or M_{pc} =1.5) at 1500 m would imply that the effects of AOD and PW on DNI decrease the same way as those of air molecules when elevation increases. Based on the discussion above, this might not be the general rule. Hence, further scrutiny will have to be given to this important topic, since it conditions the desirable generalization to any world location.

To determine the appropriate air mass for the subordinate standard spectra, the method used by Emery et al. (2002) is applied to a total of 29 sites from BSRN and enerMENA (Schüler et al., 2016) at latitudes from 30°S to 52°N, including five sites close to the equator (between 16°N and 16°S). Both DNI and GTI are investigated. Since GTI measurements are rare, the model from Skartveit and Olseth (1986) is used to estimate GTI on tilted surfaces oriented towards the equator and with tilt angles equal to each site's latitude. The model uses the measured DNI and GHI along with inputs including solar position, tilt angle, and surface albedo. The latter is set to 0.3 for all sites, which roughly corresponds to the albedo option "light sand" used in G173. Eighteen of the sites are below 750 m elevation while eleven are at higher elevations. With regard to the proposed subordinate standard spectra, a site above 750 m would be considered a high-elevation site.

Figure 4 presents the cumulative relative fraction of annual global tilted irradiation, H_{tilt}, in relation to two alternate definitions of air mass for sites below 750 m elevation. On the left side of Fig. 4, the Y-axis corresponds to the fraction of the annual global tilted irradiation that is received for pressure corrected air masses below the PC air mass given on the X-axis. The right hand side of Fig. 4 uses the NPC air mass. Interestingly, the intersection of some curves with the Y-axis corresponds to a cumulative H_{tilt} strictly positive (and up to 0.18) for the PC air mass. This is because PC air masses below 1 occur for elevated sites due to the pressure correction. On the other hand, some curves cross the X-axis at air masses greater than 1. These curves belong to sites far away from the equator (e.g., Regina, Canada) where the zenith angle is much larger than 0° even at solar noon in summer, so that the air mass never reaches values close to 1. Similarly to Fig. 4, Fig. 5 shows the cumulative H_{tilt} as a function of air mass for sites above 750 m. The difference between the two air-mass cases is much more pronounced here, since the pressure correction is more intense. As in Fig. 4, the PC curves are shifted

towards the left relative to the NPC curves.

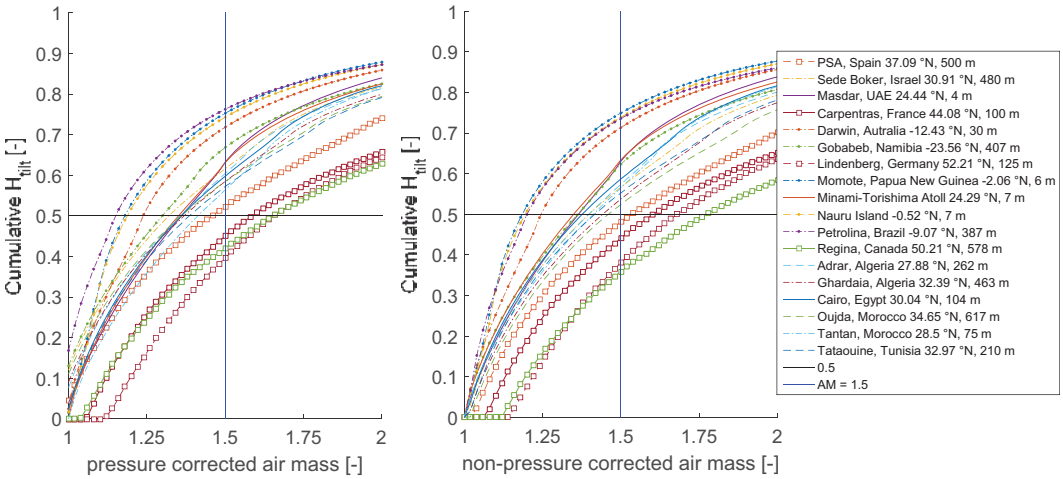

Fig. 4: Cumulative H_{tilt} over the air mass for sites below 750 m above mean sea level. Left: with pressure correction, right: without pressure correction. Sites less than 16° from the equator are marked with dots; sites at latitudes above 37° by squares.

To evaluate the effects of pressure correction and latitude in more detail, the results above are analyzed in terms of the threshold air mass, M_{half}, below which half of a site's total irradiation is received. M_{half} is indicated in Figs. 4 and 5 as the intersection of a site's curve and the horizontal line corresponding to a value of 0.5 on the Y-axis. Four different M_{half} values are derived for each site using PC and NPC air mass for GTI and using PC and NPC air mass for DNI. All M_{half} values for GTI are shown in Fig. 6 as a function of elevation (X-axis) and latitude (color bar). For both definitions of air mass, strong scatter is obvious. It is clear that an air mass value of 1.5 (or of any other fixed value) cannot accurately represent M_{half} at all investigated sites, irrespective of pressure correction. This shows a serious limitation of the approach considered in earlier studies (e.g., Emery et al., 2002), as well as the intrinsic limitation of reference spectra (standard or subordinate) that refer to a single air mass. However, for the simplification implied by the construction of the proposed subordinate spectra, this limitation must be acknowledged and accepted. Its effect, in terms of spectral mismatch, will be evaluated later after selecting single air mass values.

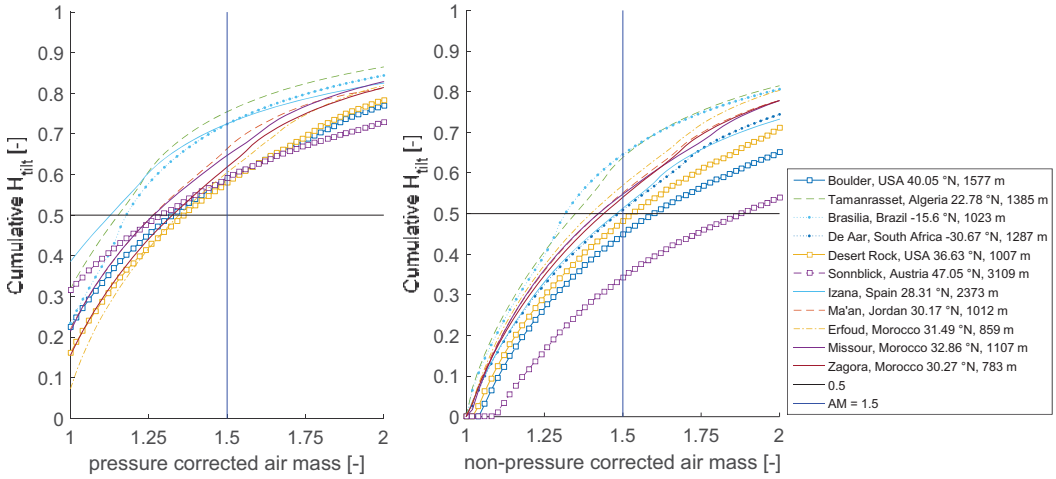

Fig. 5: Cumulative H_{tilt} as a function of the air mass for sites at elevations above 750 m. Left: with pressure correction, right: without pressure correction. Sites less than 16° from the equator are marked with dots; sites at latitudes above 37° by squares.

The spread of M_{half} values found for any small elevation range is related to latitude. Due to the higher solar elevation angles, proximity to the equator is associated with a smaller M_{half} value than higher latitudes. In the PC case, it is found that M_{half} decreases with elevation, so that in general lower M_{half} values are obtained. The elevation dependence is less pronounced in the case of the NPC air mass, whereas the latitude dependence is slightly higher. The latter finding could be expected, since the pressure correction reduces air mass, and hence also the latitude-dependent spread. At more than 3100 m, Sonnblick stands out for the NPC air mass case with a M_{half} value close to 1.9. This is mainly due to latitude (47.05°N). In the PC case, this particular site is much closer to 1.5 since M_{half} is now 1.3. This suggests that the deviations caused by high elevation and high latitude partly compensate each other. For the second highest site, Izaña (2373 m), M_{half} is close to 1.5 in the NPC case,

and ≈1.1 in the PC case, i.e., at the opposite extreme. This also shows that there is strong variability among sites, which cannot be explained by elevation or latitude alone. Typically, commercial PV plants are located below 3000 m due to the unavailability of higher sites, low population density, or other reasons. Therefore, the Sonnblick results are considered marginal, and removed from further analysis.

As stated before, the PC results show a noticeable elevation dependence. Moreover, M_{half} is then always below 1.5. This indicates that the selection of M_{pc} = 1.5 would not be ideal to construct GTI reference spectra, as was also stated early on (Gonzalez and Ross, 1980; Ross, 1980; Ross and Gonzalez, 1980). Using an NPC air mass of 1.5 is not ideal either. Nevertheless, a rather symmetrical spread around M_{npc} = 1.5 and a lower elevation dependence are found. Furthermore, use of the NPC air mass of 1.5 results in the same zenith angle for sea level and any elevation, which is advantageous for application of the spectra. Therefore, an NPC air mass of 1.5 is used for high-elevation subordinate GTI reference spectra in what follows. This result underlines that, in the case of GTI, the appropriate PC air mass is lower for sites with higher elevation.

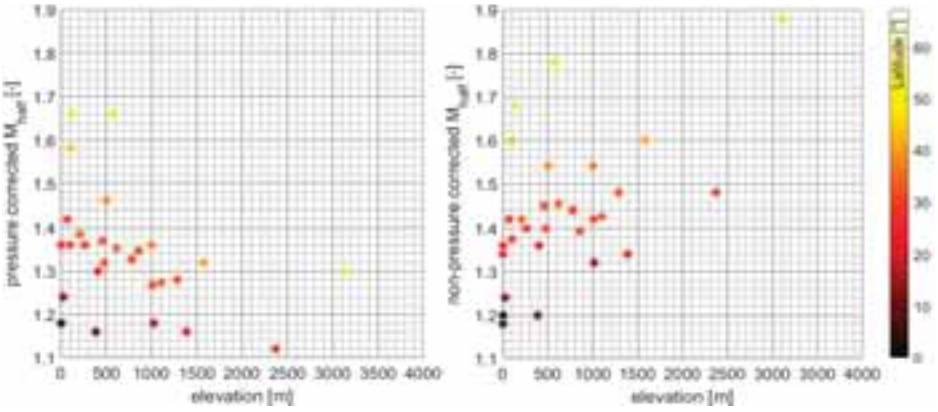

Fig. 6: M_{half} found for 29 sites for latitude-tilt GTI as a function of elevation and latitude (color bar). In the left plot two points are overlapping at elevation close to 0 m and M_{half} =1.18. This is also the case at elevation close to 0 and M_{half} =1.36.

Similar calculations are performed for DNI. Figure 7 presents the cumulative relative fraction of annual H_{b} as a function of air mass for sites below 750 m elevation. The differences between the plots for both air mass definitions are small, due to the low elevation of the sites. For the high-elevation sites in Fig. 8, the differences resulting from using pressure corrected or NPC air mass are clearly visible, due to the low atmospheric pressure at high elevation. The M_{half} values for DNI are shown in Fig. 9.

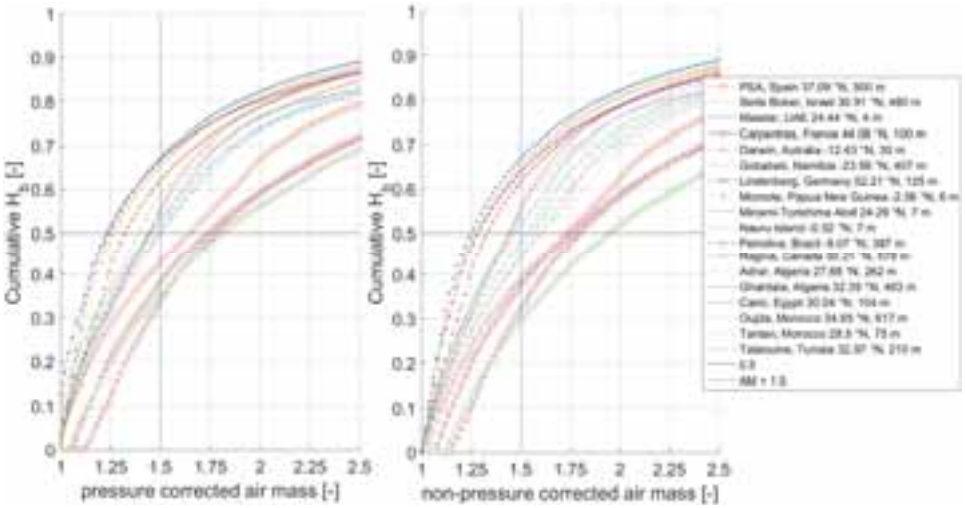

Fig. 7: Cumulative H_b over the air mass for sites below 750 m above mean sea level. Left: with pressure correction, right: without pressure correction. Sites less than 16° from the equator are marked with dots, sites with 37° or more by squares.

In addition to the sites discussed above for GTI, other sites analyzed by Emery et al. (2002) are presented. The latitude dependence is found similar to the case of GTI, albeit even more pronounced. Again, it is clear that the selection of a specific air mass value is not easy, or independent from the pressure-correction issue. Moreover, the highest sites (Sonnblick and Izaña) behave similarly for DNI and GTI. For the NPC air mass, Sonnblick has an M_{half} of 2.25, whereas M_{half} is only 1.52 for the PC case. In both cases, the 1.5 value is approximately midway between what is obtained for sites at high latitudes and sites near the equator, which supports the choice of

that value in the IEC/G173 standard spectrum. However, the elevation dependence of the PC cases is less pronounced for DNI than for GTI. The reverse is true in the NPC cases. The PC results also exhibit a smaller spread of M_{half} than those pertaining to the NPC air mass. This suggests a weak advantage of using the PC air mass definition for DNI. Hence, for DNI, these results are in relative agreement with previous studies (Emery et al., 2002; Gonzalez and Ross, 1980). Consequently, the application of a pressure-corrected air mass of 1.5 is selected here to evaluate the impact of using DNI spectra in spectral mismatch studies. Still, it is stressed that the approach described above and the resulting selection are not entirely satisfying in the case of DNI. Selection of a PC air mass of 1.5 means that higher zenith angles are representative at higher sites, a surprising result possibly explained in terms of Rayleigh transmittance as a function of site elevation. When the sun is at the zenith, the Rayleigh transmittances at 0-m and 1.5-km elevation are nearly identical. For a zenith angle of 80° the Rayleigh transmittance is noticeably lower at sea level due to the exponential behavior of transmittance (0.72 at sea level compared to 0.76 at 1.5 km for a Rayleigh OD of 0.05). Therefore, it could be true that lower air masses contribute more to H_b at higher elevations which means that greater zenith angles are more appropriate at higher elevations. However, both AOD and PW actually decrease with elevation in most cases. A typical scale height for them is 2.1 km, with large spatio-temporal variability, whereas that scale height is fixed at 8.43 km for both Rayleigh scattering and pressure. Therefore, the NPC air mass of 1.5 should also be considered for the DNI spectra. Since it is found problematic and potentially misleading to define subordinate DNI spectra (Jessen et al., 2018), the selection of the correct air mass is of low relevance in that case.

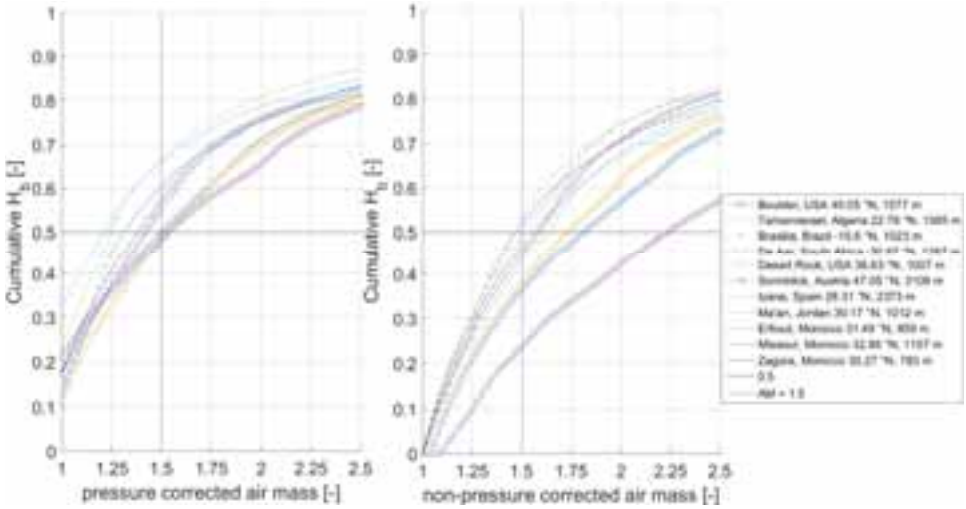

Fig. 8: Cumulative DNI over the air mass for sites at elevations above 750 m above mean sea level. Left: with pressure correction, right: without pressure correction. Sites less than 16° from the equator are marked with dots, sites with 37° or more by squares.

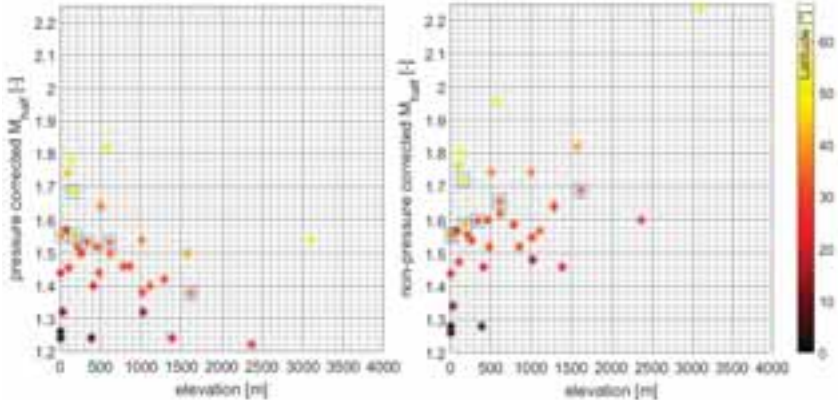

Fig. 9: M_{half} found for 36 sites for DNI as a function of the elevation and the latitude (color bar). Open blue squares mark additional sites from (Emery et al., 2002) (Albuquerque: 35.0853°N, 1619 m; Daggett: 34.8640°N, 610 m; Phoenix: 33.4484°N, 331 m; Tampa: 27.9506°N, 15 m; Sacramento: 38.5816°N, 9 m; Buffalo: 42.8864°N, 183 m; Seattle: 47.6062°N, 158 m).

3.2 Evaluation of air mass selection in terms of spectral mismatches

In order to test the two selections of the PC air mass of 1.5 for DNI and the NPC air mass of 1.5 for GTI, the effect of test spectra on the spectral mismatch is evaluated with different air masses. Two of the five aforementioned sites above 1-km elevation (Tamanrasset and Boulder) are useful to test the air mass specification. For this evaluation, the spectral mismatch values obtained with seven different spectra are compared for each site

and component (DNI or GTI). The reference spectrum in each case is the average spectrum for the site and component (see section 2). The spectral mismatch is calculated for these spectra:

1. ASTM G173/IEC 60904-3
2. The test spectrum for the atmospheric conditions in Tab. 1 that best match the average atmospheric conditions at the site, but for PC air mass M_{pc}=1.5
3. The test spectrum for the atmospheric conditions in Tab. 1that best matches the average atmospheric conditions at the site for NPC air mass M_{npc}=1.5
4. An ad-hoc spectrum specially developed for the site's average AOD, PW, elevation, and the M_{half} value for PC air mass $M_{half.pc}$ that is found for this specific site
5. An ad-hoc spectrum specially developed for the site's average AOD, PW, elevation, and the M_{half} value for NPC air mass $M_{half.npc}$ that is found for this specific site
6. An ad-hoc spectrum specially developed for the site's average AOD, PW, elevation, and M_{pc} = 1.5
7. An ad-hoc spectrum specially developed for the site's average AOD, PW, elevation, and M_{npc} = 1.5.

Moreover, for GTI the tilt angle is adjusted to the site's latitude in cases 4 to 7 just described. In cases 2 to 3 the closest available tilt angle (in 5° steps from 0 to 90°) is selected. For DNI, additionally, the two Ångström exponents for wavelength intervals below and above 0.5 µm are site-adapted in cases 4–7. Table 2 provides the values of M_{half} with and without pressure correction for GTI and DNI.

Tab. 2: M_{half} derived for Tamanrasset and Boulder from Fig. 5 and 8 with and without pressure correction for DNI and GTI.

Site	Component	$M_{half.pc}$, corresponding M_{npc} and standard conditions	$M_{half.npc}$
Boulder	GTI	1.325, corresponding to M_{npc} = 1.6 for ClDryHi	1.6
	DNI	1.5, corresponding M_{npc} = 1.81 for ClDryHi	1.82
Tamanrasset	GTI	1.15, corresponding to M_{npc} = 1.38 for SemClDryHi	1.35
	DNI	1.245, corresponding to M_{npc} = 1.5 for SemClDryHi	1.455

Figure 10 shows the seven DNI spectral mismatches for four CPV cell types under the seven DNI spectra at Tamanrasset. The different spectra are shown on the Y-axis, and mismatches for different PV cell types are shown by the marker type. The markers are connected to each other to increase readability. When using the base case of G173/IEC, deviations up to 4% are found. SemClDryHi behaves even worse than G173 in that case, so that if no pressure correction is applied even higher mismatch values are found. These deviations are mainly caused by Tamanrasset's average Ångström exponent that deviates strongly from that of SemClDryHi. Adjusting all atmospheric inputs to the site's averages reduces the mismatches noticeably for M_{npc} = 1.5, as well as the site's $M_{half,npc}$ and $M_{half,pc}$ (since all three cases result in the same input air mass). The spectrum for these site averages and M_{pc} = 1.5 results in the lowest spectral mismatch. This is surprising because the M_{half} values indicate that M_{npc} = 1.5 is more appropriate. The low spectral mismatches in this case are apparently caused by a compensation of errors. The average site spectrum also contains cloud effects and variations of the atmospheric properties that cannot be considered accurately when dealing with just a single spectrum. The approach using M_{half} is also only an approximation, as mentioned above.

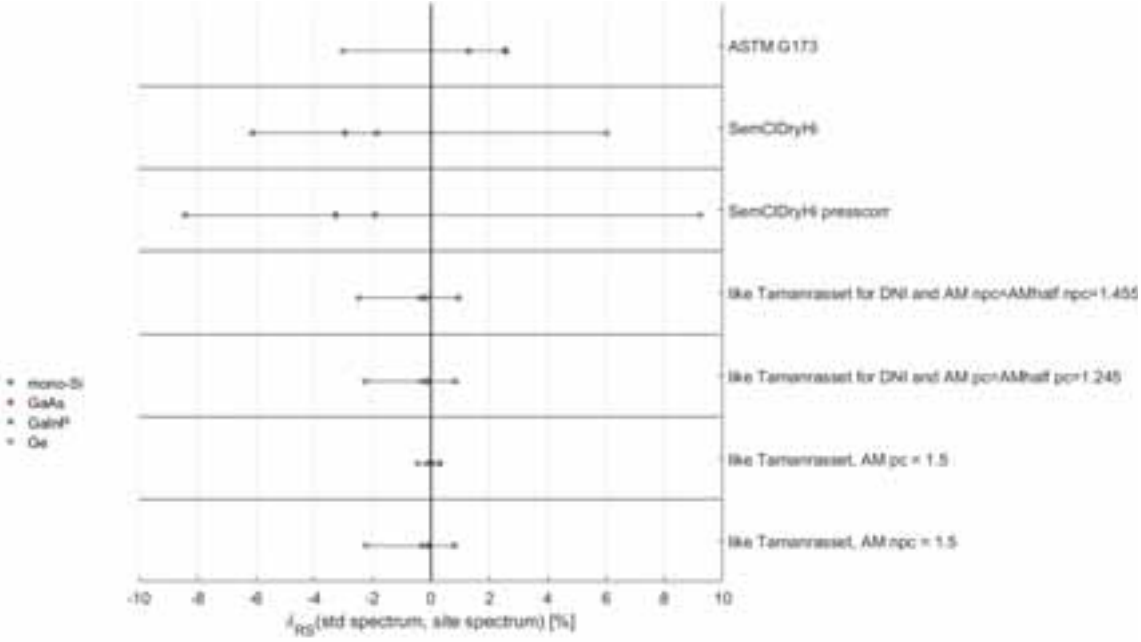

Fig. 10: ***Spectral mismatches for different spectra and CPV cell types for DNI at Tamanrasset.***

The results for Tamanrasset and DNI are summarized in Tab. 3 next to the other three cases, which are also shown in Figs. 11–13. The observations that do not correspond to expectations are marked in bold and underlined letters. The cases with more positive results than expected can be explained by the fact that several approximations and sources of error are included in the approach, and that different errors can compensate each other. The unexpected cases leading to worse results than G173 are marked with a minus sign. They are only found for DNI at Tamanrasset and have been explained above. Overall, it is found that the concept of using M_{half} is helpful, even though other air masses than those selected from M_{half} may perform better. This is interpreted as an effect of mutually compensating errors, too. The results confirm the expectation from section 3.1 that, for GTI, the NPC air mass of 1.5 can be used.

The results from Tab. 3 and Figs. 10 and 12 also show the aforementioned issues in the case of DNI. For Tamanrasset the Ångström exponent is found highly relevant. It can be concluded from this example that, due to the impact and variability of the Ångström exponent, a large number of subordinate DNI standard spectra would be needed to allow the selection of a subordinate spectrum that would be more representative than G173. Since this appears impractical, no subordinate standard spectrum is recommended here for DNI.

For DNI at Boulder, the actual Ångström exponent is similar to that characterizing all 7 test spectra. If site averages of the Ångström exponents, AOD and PW are used, the PC air mass of 1.5 delivers better results than the NPC value of 1.5, as expected. Even if the site averages for all significant inputs are used, greater deviations are found in comparison to GTI due to the high sensitivity of the DNI spectrum to air mass and atmospheric conditions, again as expected.

Tab. 3: Results of the evaluation of spectral mismatch based on air-mass selection. The + sign means improvement compared to G173/IEC, and the – sign means greater spectral errors than G173/IEC. Brackets refer to lower tendency than a sign without brackets, and various signs refer to higher differences. The * symbol means that a low spectral mismatch is found due to mutual compensation of errors. Cases with deviations from the expected behavior are underlined.

Spectrum	Tamanrasset DNI	Tamanrasset GTI	Boulder DNI	Boulder GTI
1. IEC/G173	-4 – 3 %	0.5% - 4.5 %	-7.5 % - 7 %	2 -5 %
2. test M_{pc}=1.5	**-**	+, for a-Si1 worse than G173	**(+)**	((+))
3. test M_{npc}=1.5	**-**	**++, ***	((+))	**++, ***
4. site's average parameters $M_{half,pc}$	+, same as 5 and 7	+(+), same as 5	((+)), same as 5 and 6	+(+), same as 5
5. site's average parameters $M_{half,npc}$	+, same as 4 and 7	+(+), same as 4	((+)), same as 4 and 6	+(+), same as 4
6. site's average parameters M_{pc} = 1.5	**++, ***	(+)	((+)), same as 4 and 5	(+)
7. site's average parameters M_{npc} = 1.5	+, same as 4 and 5	+ only for a-Si2 worse than case 6	(((+)))	**++**

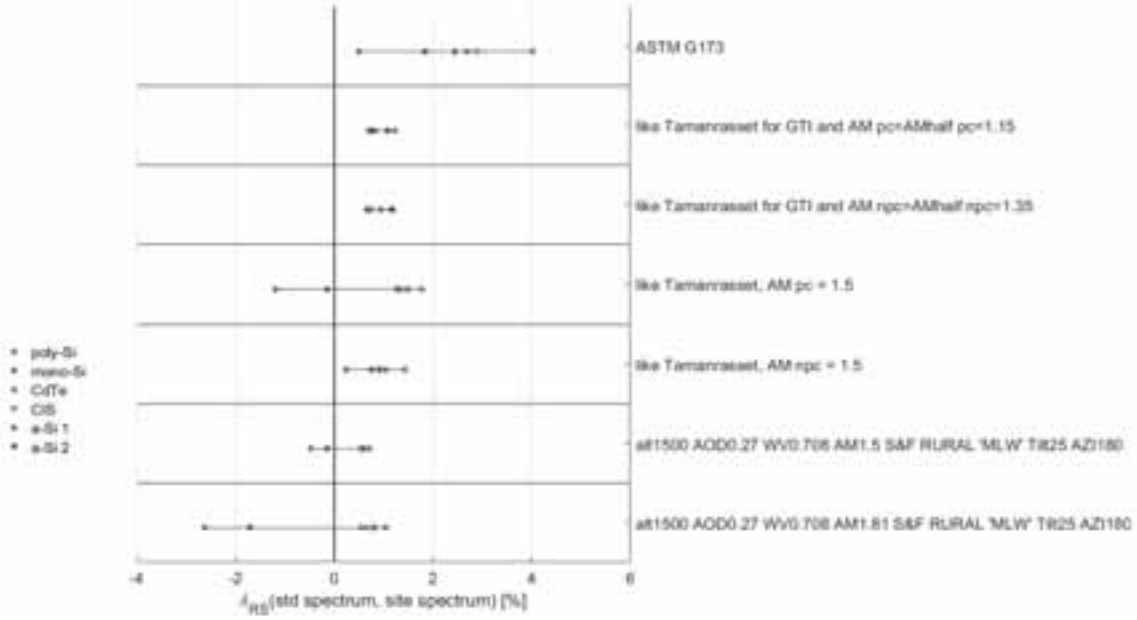

Fig. 11: ***Spectral mismatches for different spectra and PV cell types for GTI and Tamanrasset. The lower two spectra refer to SemCIDryHi for the tilt angle 25° with and without pressure correction.***

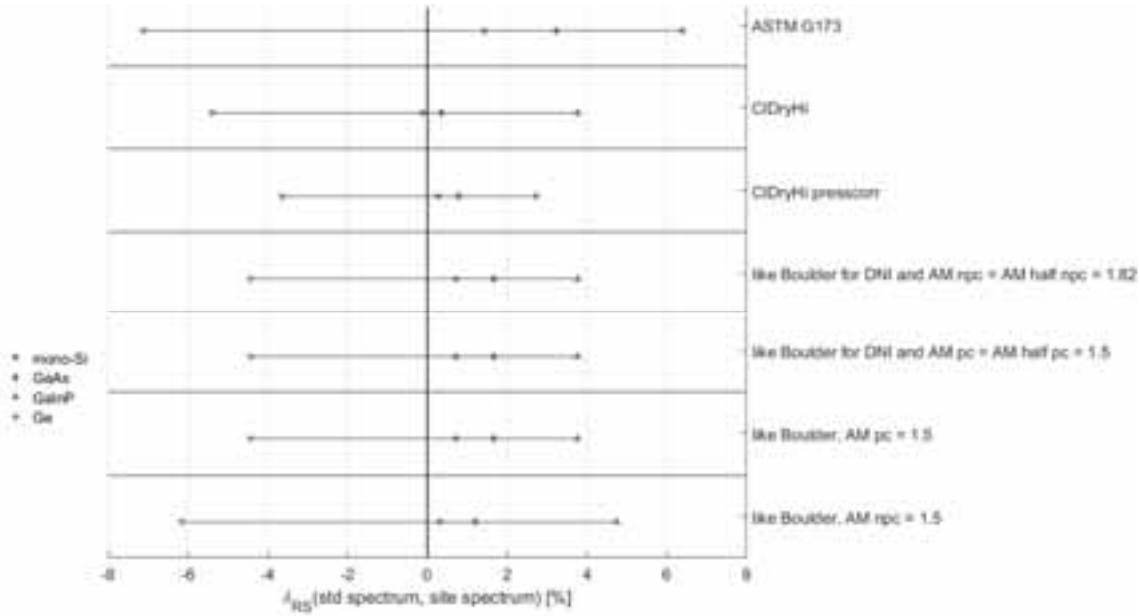

Fig. 12: ***Spectral mismatches for different spectra and CPV cell types for DNI and Boulder.***

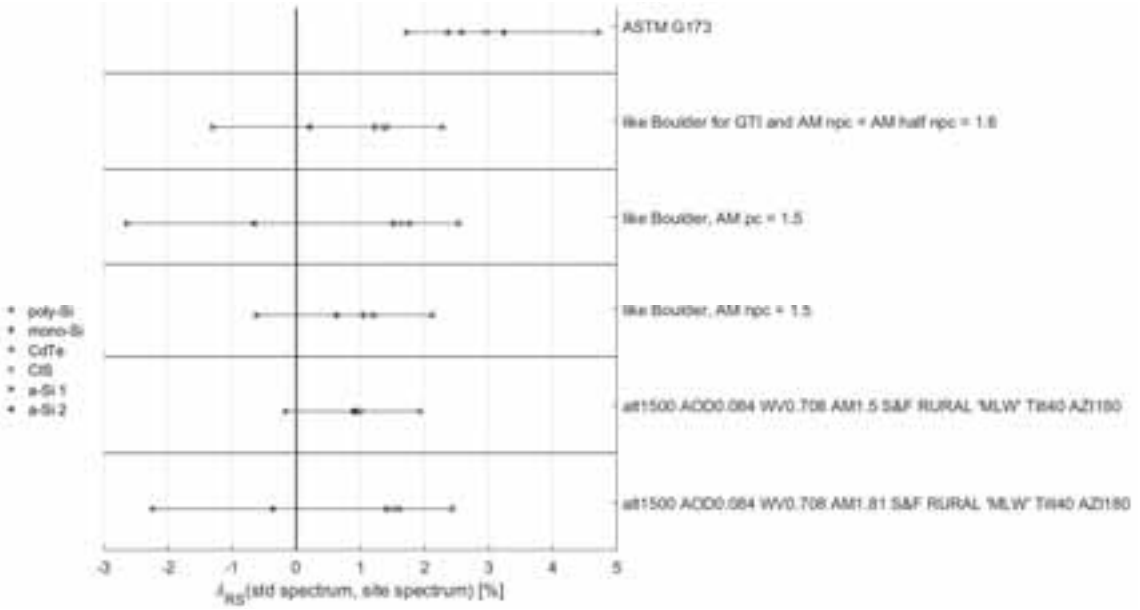

Fig. 13: ***Spectral mismatches for different spectra and PV cell types for GTI and Boulder. The lower two spectra refer to ClDryHi for the tilt angle 40° with and without pressure correction.***

4. Conclusion and outlook

The impact of different climatic conditions on the solar spectrum at the surface, and its consequences for solar energy system performance, reveals that the IEC/G173 standard spectra are far from representing the wide range of locally occurring conditions. Subordinate standard spectra are proposed here for solar energy applications utilizing GTI. They are meant to supplement the main standard spectra as defined in IEC/G173. These subordinate spectra represent atmospheric conditions and sun-receiver geometries that result in incident spectra departing significantly from the existing standard spectra. Some of the subordinate spectra correspond to site elevations of 1.5 km, since such higher-elevation sites are of interest in many solar energy applications. To apply the subordinate spectra, manufacturers could include PV module efficiencies for the different subordinate spectra in their data sheets. A potential customer could then identify the efficiency for the most appropriate subordinate spectra that is found using simple climate parameters, the site's elevation and the tilt angle.

The selection of the correct air mass to use in subordinate spectra is based on an analysis of the cumulative DNI and GTI for different air-mass ranges at 29 sites. A clear latitude dependence of the most appropriate air mass

for each site is found, so that using an air mass of 1.5 must be considered a crude approximation in any case. Overall, it is found that the pressure-corrected air mass value of 1.5 is more appropriate for DNI spectra, but not for GTI, thus confirming earlier studies. A non-pressure-corrected air mass of 1.5 is found more appropriate for GTI. Even though a pressure-corrected air mass is deemed preferable for DNI, the justification is weak. Physical explanations rather suggest that the pressure correction is actually not appropriate in that case. This is not an issue here, however, as we only recommend GTI subordinate spectra, but not DNI spectra. Indeed, it is found that there are no ideal subordinate spectra for DNI. Many subordinate DNI spectra for a large range of atmospheric conditions would be required to reduce the spectral mismatch compared to IEC/G173. It would thus be difficult to select the most appropriate spectrum, which is not practical. Hence, it is recommended not to include any subordinate DNI spectrum in the forthcoming ISO 9845 update.

The finding that a non-pressure corrected air mass of 1.5 is appropriate for GTI was confirmed by evaluating the spectral mismatch obtained for several PV cell types at the high-elevation sites of Boulder and Tamanrasset, using different test spectra. Hence, subordinate GTI spectra with the proposed atmospheric conditions, tilt angles, and non-pressure corrected air mass of 1.5, are recommended for inclusion in the update of ISO 9845, as an addition to the existing IEC or ASTM standard spectra. Comments on the proposed spectra are welcome and can be considered in the ISO and ASTM committees.

We thank the investigators and their support teams for the maintenance of the AERONET, enerMENA and BSRN stations used in this work. We thank the Actris and AERONET staff for their support with the operation, calibration and evaluation of PSA's and Masdar's sun photometer. This work was partly funded by the Helmholtz Association within the DESERGY Project. The financial support provided to the University of Antofagasta by the Chilean Economic Development Agency, CORFO, contract no. 17PTECES-75830 and the contract no.: 17BPE3-83761, and CONICYT/FONDAP/15110019 SERC-Chile is acknowledged.

5. References

Dirnberger, D., G. Blackburn, B. Müller, C. Reise, On the impact of solar spectral irradiance on the yield of different PV technologies, Solar Energy Materials and Solar Cells 132 (2015) 431–442.

Emery, K., Myers, D., and Kurtz, S., 2002. What is the appropriate reference spectrum for characterizing concentrator cells? 29th IEEE PV Specialists Conference, New Orleans, LA.

Fernández, E.F., F. Almonacid, J.A. Ruiz-Arias, A. Soria-Moya, Analysis of the spectral variations on the performance of high concentrator photovoltaic modules operating under different real climate conditions, Solar Energy Materials and Solar Cells. 127 (2014) 179–187. doi:10.1016/j.solmat.2014.04.026.

Gueymard, C., 2001. Parameterized transmittance model for direct beam and circumsolar spectral irradiance. Solar Energy 71 (5):325-346.

Gueymard, C.A., Myers, D., Emery, K., 2002. Proposed Reference Irradiance Spectra for Solar Energy Systems Testing. Solar Energy 73, 443-467.

Gueymard, C.A., 2005. SMARTS Code version 2.9.5 User's Manual. Solar Consulting Services.

Gueymard, C., 2012. Solar Radiation, Introduction, in: Meyers, R.A. (Ed.) Encyclopedia of Sustainability Science and Technology, Springer, pp. 608-633.

Gonzalez, C.C., Ross R.G., 1980. Performance Measurement Reference Conditions for Terrestrial Photovoltaics, Proc. Conf. American Section of the International Solar Energy Soc., Phoenix, Arizona, 1401–1405.

IEC 60904-3:2016 Photovoltaic devices - Part 3: Measurement principles for terrestrial photovoltaic (PV) solar devices with reference spectral irradiance data. Standard, Geneva, Switzerland.

Jessen, Wilko, Stefan Wilbert, Christian A. Gueymard, Jesús Polo, Zeqiang Bian, Anton Driesse, Aron Habte, Aitor Marzo, Peter R. Armstrong, Frank Vignola, and Lourdes Ramírez. 2018. "Proposal and evaluation of subordinate standard solar irradiance spectra for applications in solar energy systems." Solar Energy. https://doi.org/10.1016/j.solener.2018.03.043.

Kalapatapu, R. Chiesa, M., Armstrong, P., Wilbert, S., 2012. Measurement of DNI Angular Distribution with a Sunshape Profiling Irradiometer. SolarPACES Conf., Marrakesh, Morocco.

König-Langlo, G., Sieger, R., Schmithüsen, H., Bücker, A., Richter, F., Dutton, E.G. 2013. The Baseline Surface Radiation Network and its World Radiation Monitoring Centre at the Alfred Wegener Institute. GCOS - 174, WCRP Report 24/2013.

Kopp, G., and J. L. Lean, 2011. A new, lower value of total solar irradiance: Evidence and climate significance, Geophys. Res. Lett., 38, L01706, doi:10.1029/2010GL045777.

Nann, S. and Riordan, C., 1991. Solar spectral irradiance under clear and cloudy skies: Measurements and a

semiempirical model. J. Appl. Meteorol. 30, 447–462.

Nofuentes, G., Gueymard, C.A., Aguilera, J., Pérez-Godoy, M.D., Charte, F., 2017. Is the average photon energy a unique characteristic of the spectral distribution of global irradiance? Solar Energy 149, 32–43.

Polo, J., M. Alonso-Abella, J.A. Ruiz-Arias, J.L. Balenzategui, Worldwide analysis of spectral factors for seven photovoltaic technologies, Solar Energy. 142 (2017) 194–203. doi:10.1016/j.solener.2016.12.024.

Pozo-Vázquez, D., S. Wilbert, C. Gueymard, L. Alados-Arboledas, F. J. Santos-Alamillos, and M.J. Granados-Muñoz. 2011. Interannual Variability of Long Time Series of DNI and GHI at PSA, Spain. Paper read at SolarPACES Conference, at Granada, Spain.

Ross, C.C., 1980. Terrestrial Photovoltaic Performance Reference Conditions. Proc. Photovoltaic Solar Energy Conf., Cannes, France, 731–735.

Ross, R.G. and Gonzalez, C.C., 1980. Reference conditions for reporting terrestrial photovoltaic performance. Proc. AS/ISES Annual Conf., 1091–1097.

Schüler, D., Wilbert S., Geuder N., Affolter R., Wolfertstetter F., Prahl C., Röger M., Schroedter-Homscheidt M., Abdellatif G., Allah Guizani A., Balghouthi M., Khalil A., Mezrhab A., Al-Salaymeh A., Yassaa N., Chellali F., Draou D., Blanc P., Dubranna J., Sabry O. M. K., 2016. The enerMENA meteorological network – Solar radiation measurements in the MENA region. AIP Conference Proceedings no. 1734 (1):150008.

Wilbert, S., B. Reinhardt, J. DeVore, M. Röger, R. Pitz-Paal, C. Gueymard, and R. Buras, 2013. Measurement of solar radiance profiles with the Sun and Aureole Measurement system. J. Solar Energy Engineering 135 (4):041002-041002. doi: 10.1115/1.4024244.

Skartveit, A., Olseth, J.A., 1986. Modelling slope irradiance at high latitudes. Solar Energy 36, 333–344.

Winter, S., Friedrich, D., and Sperling, A., 2009. Effects of the new standard IEC 60904 3:2008 on the calibration results of common solar cell types. 24th European Photovoltaic Solar Energy Conf., Hamburg, Germany.

WMO, 2014. Guide to Meteorological Instruments and Methods of Observation. WMO-No. 8, 2014 Update.

Survey Research on Integrating Renewable Energy into the Mining Industry

Kateryna Zharan[1], Jan C. Bongaerts[2]

[1 and 2]TU Bergakademie Freiberg, 09599 Freiberg (Germany)

Abstract

Mining operations are energy intensive. The share of energy costs in total share is often reported to be in the range of 30 %. Saving energy costs is therefore an economical key element of any mine operator. With the improving reliability and security of renewable energy (RE) sources, and the requirements to reduce carbon dioxide emissions, perspectives for using RE in mining operations emerge. In fact, these aspects are stimulating the mining companies to search for ways to substitute fossil energy with RE. Survey research is novel on this topic. Hereby, this paper estimates the data of a survey conducted among mining and renewable energy experts. Towards the data estimation, this study applies the following methods. Here, first, to develop the survey we summarized and reviewed the findings from the previous literature review. Secondly, using these literature review three hypotheses have been developed. Thirdly, to compare outcomes of the survey with literature review the evaluating frequencies method has been developed and applied. Consequently, the results gather the expert's knowledge and opinions on incentives for mining operators to turn to RE, barriers and challenges to be expected, environmental effects, appropriate business models and the overall impact of RE on mining operations. In addition, the outcomes of the survey allow for identifying the factors that favor and disfavor decision-making on the use of RE in mining operations.

Keywords: Carbon dioxide emissions, mining industry, photovoltaic, renewable energy, survey research, wind generation.

Introduction

The mining industry still strong depends on conventional energy sources providing for its continuous and stable operations. In addition, energy costs accounts for 30 % of all operating costs in mining operations (Slavin 2017). RE technologies do not require such fossil fuels and have become mature and reliable, in particular for wind and solar power applications. Hence, they become attractive to mining operations, especially in hybrid systems. In this way, combining these sources like solar and wind with backup units provides more reliable, economic load supply and environment-friendly compared to a single source (Talaria, et al. 2017). Usually the cost reduction potential from implementation of the hybrid-energy system in mining operations is in the range of 25%–30%, and sometimes well above (Solar projects, energy efficiency and load shifting for an optimized energy management in the mining industry 2015). They also allow for lower carbon dioxide emissions giving mine operators a possibility to contribute to national and global climate policy agreements. For instance, the Kioto Protocol (United Nations Framework Convention on Climate Change 1997), the Fifth Carbon Budget (Committee on Climate Change 2015), and the Paris Agreement (UNFCCC 2015).

Because of such policies, the installed renewable electricity generation capacity and the rate of diffusion of RE technologies has increased rapidly (Bergek and Mignon 2017). Tab. 1 contains an overview of installed RE capacity in mining operations in particular.

Tab. 1: Installed capacity of renewables powering the mining industry

RE source	Installed capacity, MW
Wind	552
Solar PV	352
Solar thermal	39
Total	943

The energy and mining global ranking report (World Congress 2016) demonstrates the installed capacity of renewables powering the mining industry, which was 943 MW in total until 2016. It breaks down to 552 MW of wind power, 39 MW of solar thermal, and 352 MW of solar photovoltaic (PV). This integration could be

doi:10.18086/swc.2017.21.07 Available at http://proceedings.ises.org

possible because storage technologies become more accessible together with micro-grid integration. Moreover, hybrid energy solutions ensure to have a reliable energy system for mining processing.

Given several pilot projects of RE in mining in the countries such as Australia, Canada, and South Africa (Zharan and Bongaerts 2016) there is no comprehensive approach towards establishing RE into the mining industry as a global priority. This has inspired the authors of this paper to conduct a 31 question survey among experts in mining and in RE technologies about the implementation of RE into the mining industry. The survey captures the experts' assessment of economic, technological, social, and environmental aspects of a replacement of fossil fuel technologies with RE technologies. Furthermore, this survey defines the key factors leading to appropriate decision-making frameworks for energy managers and policy-makers.

The research objectives of this paper are to carry out the Literature Review (LR) in order to develop three hypotheses (H1, H2, H3), to compare the survey results with these hypotheses, to draw conclusions on using RE into the mining industry. Reaching these objectives will provide energy managers, decision-makers, and policy-makers with the expert's perception about implementing RE into the mining processing. That identifies vulnerable and strong priorities towards RE penetration. Therefore, the main purpose of this paper is to recognize the motives leading the experts to use RE for mining operations. Those motives could influence on investment choices (Lillemo, et al. 2013).

To our knowledge, there is no survey completed within this topic. Therefore, this study has a novelty and scientific relevance. Additionally, there is a lack of literature so far with focus on RE penetration into the mining industry.

Methodology

2. 1. Structure of the paper

This paper consists of four sections, and one appendix. Section 1 comprises the relevance of this topic, purpose of this paper, research objectives, and literature review. Section 2 includes the chosen methods developed to reach the purpose of this paper.

In Section 3, the evaluation of the survey's results has been accomplished in two steps. The Step 1 covers the demographic information of experts. Step 2 compares of the frequencies with the LR and demonstrates the Standard errors of the survey data. Section 4 contains the conclusions of this study.

This study has been written in a following order: (i) the survey has been developed based on the literature review. (ii) We choose stratified sampling method as our sampling technique to identify the RE and mining experts who can contribute to the study. (iii) All questions and the response items completed by the experts have been coded. (iv) Three hypotheses have been developed using the Literature Review (LR) method. (v) To evaluate the survey results we used the mean, and standard deviation (Std) criteria, maximum response item, percentage, evaluating frequencies method and standard errors analysis. (vi) Comparative analysis of three hypotheses with the survey results has been established. (vii) We drew the conclusions about the key findings of this study.

2.2. Survey administration

This survey was integrated between November 2016 and January 2017 within RE and mining experts all over the world via personal interview using the conference's platform 6th Solar Integration Workshop, and 15th Wind Integration Workshop in Vienna, Austria, and via email correspondence.

2.3. Research questionnaire and method

We assume that all questions are specific related only to the mining industry. This questionnaire contains two parts. In Part 1, we asked RE and mining experts about perspectives and relevance of the topic, necessity, incentives, barriers, government's support mechanisms, effects with respect to the integration of RE into the mining industry, as well as a significance of the environmental issues for industrial processing. In Part 2, we collected the experts personal information such as gender, age, level of education, working field, and working experience in the field. Tab. 2 shows the codes and scale each of the statements of the survey using the closed ended method of collecting information.

Tab. 2: Codes and scale of the survey

Statement	Code	Scale
1	Q1	two-point scale
2	Q2	three-point scale
3	Q3	five-point scale
4.1 - 6.5; 8 - 9.5	Q4-Q18; Q25 - Q30	six-point scale
7.1 - 7.6	Q19 - Q24	five-point scale
10	Q31	two-point scale

To evaluate the survey results first, the LR method has been chosen to develop three hypotheses. These hypothesis are shown in Appendix A, Tab. A.11. Main goal of this method is to provide complete summery of literature related to the survey questions. Second, three hypotheses have been assessing using the evaluating hypotheses method developed by the authors of this paper. The results of the survey are compared with three hypotheses in order to indicate whether they are true or false.

2.4. Evaluating frequencies method

The interpretations of evaluating frequencies method are as follows:

$$\begin{cases} c \leq a + b \geq d + \mathrm{e} \\ \mathrm{a} + \mathrm{b} \geq 0.33. \end{cases} \quad \text{(eq. 1)}$$

Eq. 1: the frequency of "a and b" is at least 33% and, overall, the ratings of "very important" plus "important" are more frequent than the ratings of "neutral" and of "less important" plus "not important", respectively.

$$\begin{cases} a + b \leq c \geq d + e \\ \mathrm{c} \geq 0.33 \end{cases} \quad \text{(eq. 2)}$$

Eq. 2: the frequency of "c" is at least 33% and, overall, the ratings of "neutral" are more frequent than the ratings of "very important" plus "important" and of "less important" plus "not important", respectively.

$$\begin{cases} c \leq d + \mathrm{e} \geq a + b \\ \mathrm{d} + \mathrm{e} \geq 0.33 \end{cases} \quad \text{(eq. 3)}$$

Eq. 3: the frequency of "d and e" is at least 33% and, overall, the ratings of "less important" plus "not important" are more frequent than the ratings of "neutral" and of "very important" plus "important", respectively.

$$\mathrm{f} \geq \mathrm{B} \; \forall \; \mathrm{f} \in [(\mathrm{a} + \mathrm{b}), \mathrm{c}, (\mathrm{d} + \mathrm{e})] \quad \text{(eq. 4)}$$

Eq. 4: the frequencies of "a and b", of "c" and of "d and e", respectively are all three larger than 33% (B).

Appendix A (Tab. A.11) demonstrates the LR. Based on the LR it assumes, that the Hypothesis 1 (H1) corresponds to the Eq. 1 and carries out for the Q3, Q4, Q5, Q7, Q8, Q9, Q11, Q12, Q15, Q16, Q18, Q19, Q22, Q24, Q25, Q26, Q27, Q28, Q29, Q30 questions. The Hypothesis 2 (H2) corresponds to the Eq. 2 and carries out for the Q6, Q14, Q20 questions. Finally, the Hypothesis 3 (H3) corresponds to the Eq. 3 and obtains for the Q10, Q13, Q17, Q21, Q23 questions.

Results

3.1 Demographic information of experts

This survey sample contained 30 observations, so called a sample size. We take this sample size as the representative sample. All the participants were male. Participants decided themselves either they are experts in the RE or mining industry, and educational institution or not. All experts had an education background starting from bachelor – a university education level. Tab. 3 shows the data of working experience and education level of the survey's participants..

Tab. 3: Working experience and educational level

Work experience in the field	Frequency	Percent	Education level	Frequency	Percent
1-5 years	7	25%	Bachelor	5	17%
5-10 years	9	32%	Master	14	47%
more than 10 years	12	43%	PhD	11	37%
Total	28	100%		30	100%

Furthermore, the surveyed sample contains engineers from either industrial companies or consulting, and researchers from educational institutions. The majority of experts 52 % are involved in the renewable energy industry.

The age of majority of experts 50 % is between 30 and 40 year. Tab. 4 shows the age and working field of the experts.

Tab. 4: Age and working field

Age	Frequency	Percent	Working field	Frequency	Percent
25 – 30 years	5	17%	mining industry	1	4%
30 – 40 years	15	50%	mining + renewable	1	4%
40 – 50 years	6	20%	renewable industry	13	48%
50 – 65 years	3	10%	renewable + education	2	7%
more than 65 years	1	3%	educational institution	10	37%
Total	30	100%		27	100%

The experts represented in this survey research are from 14 countries such as Germany – 9, Denmark – 3, Canada – 3, Finland – 3, Sweden – 2, Australia – 2, USA – 1, Austria – 1, New Zealand – 1, Mexico – 1, Ukraine – 1, France – 1, United Kingdom – 1, Chile – 1.

Tab. 5 shows the description of the survey sample..

Tab. 5: Description of the survey sample

Variables	Measurement	Mean	Std
Gender	Female/Male	1,00	0,00
Age	Six-point scale	3,33	0,96
Education level	Four-point scale	3,20	0,69
Working field	Five-point scale	2,35	0,55
Working experience in the field	Four-point scale	3,18	0,79
Sample size		30	
Response rate	Percent	96,67	

3.2 Comparing of the frequencies with the LR

In this survey research, answers of the experts were categorized in the sense that frequencies of their scale ratings were constructed. For example, if twenty percent of respondents give a rating of “very important” as answers to a specific question, that frequency is 20%.

Characterization refers to the frequency just described, e.g. characterization “a” would be 20 % as explained in Section 2.4. After, these frequencies have been compared with the hypotheses represented in Appendix A. The

results of this survey conforming the frequencies for the Eq.1, Eq.2, and Eq.3 have been shown in the Tab. 6, Tab. 7, and Tab. 8 correspondingly.

Tab. 6: Survey results corresponding to Eq.1

Code	Majority of responces	Number	Frequency	Eq.1
Q3	important	11	39%	64%
Q4	very important	12	40%	70%
Q5	very important	11	37%	70%
Q7	important	11	37%	53%
Q9	very important	11	37%	60%
Q10	important	9	30%	57%
Q12	neutral	8	27%	47%
Q14	important	11	39%	54%
Q15	very important	8	29%	50%
	neutral	8	29%	
Q16	very important	8	29%	57%
	important	8	29%	
	neutral	8	29%	
Q18	important	7	25%	46%
Q19	very important	18	60%	77%
Q20	important	8	27%	43%
Q21	neutral	10	33%	43%
Q22	important	18	60%	73%
Q24	very important	8	28%	48%
Q25	important	13	50%	92%
Q26	important	15	54%	75%
Q27	important	10	36%	50%
Q28	very important	11	39%	68%
Q29	important	7	25%	46%
	neutral	7	25%	
Q30	important	10	36%	68%

According to Table 6, not all results reported by the majority of responses correspond to the Eq. 1. For instance, for the Q21 the majority of experts gave the answer “neutral”, however, based on the evaluating frequency method the result of the Q21 corresponds to the Eq. 1. In this paper, we take the frequency evaluation as the main result to take a decision.

Tab. 7 shows the survey results corresponding to Eq.2.

Tab. 7: The survey results corresponding to Eq.2

Code	Majority of responces	Number	Frequency	Eq.2
Q8	neutral	12	40%	40%
Q17	neutral	11	39%	39%

Tab. 8 demonstrates the survey results corresponding to Eq.3.

Tab. 8: The survey results corresponding to Eq.3

Code	Majority of responces	Number	Frequency	Eq.3
Q6	neutral	8	27%	40%
Q11	less important	9	30%	40%
Q13	important	8	28%	45%
	less important	8	28%	
Q23	less important	10	34%	59%

According to the survey results, the hypotheses 1 (H1) is accepted for the Q3, Q4, Q5, Q7, Q9, Q12, Q14, Q15, Q16, Q18, Q19, Q22, Q24, Q25, Q26, Q27, Q28, Q29, Q30 and is rejected for the Q8, Q11 questions. To explain more precisely, government support mechanism has a "neutral" value, and connection mining to the grid has a "less important" value for experts. The H2 is rejected completely. There are not answers with the "neutral" value for experts. Eventually, the H3 is accepted for the Q13 and Q23 questions and rejected for the Q10, Q17, Q21 questions. In addition, it is confirmed that a lack of business models and development of domestic renewable energy market have "less important" value for experts.

According to the survey results, there are however, the questions which do not account the H1, H2, H3 but they have been identified by surveying. Such as, Q14, Q20, Q21 for the H1 and Q8, Q18 for the H2. For these questions, we accept that the response items are inconsistent and thereby require more detailed study integrating the second round of the survey.

Tab. 9: Comparative analysis of three hypotheses with the survey results

Hypothesis 1			Hypothesis 2			Hypothesis 3		
Important			Neutral			Less important		
LR	Results	Survey	LR	Results	Survey	LR	Results	Survey
Q3	TRUE	Q3	Q6	FALSE	Q8	Q10	FALSE	Q6
Q4	TRUE	Q4	Q14	FALSE	Q17	Q13	TRUE	Q11
Q5	TRUE	Q5	Q20	FALSE		Q17	FALSE	Q13
Q7	TRUE	Q7				Q23	TRUE	Q23
Q8	FALSE					Q21	FALSE	
Q9	TRUE	Q9						
Q11	FALSE	Q10						
Q12	TRUE	Q12						
	FALSE	Q14						
Q15	TRUE	Q15						
Q16	TRUE	Q16						
Q18	TRUE	Q18						
Q19	TRUE	Q19						
	FALSE	Q20						
	FALSE	Q21						
Q22	TRUE	Q22						
Q24	TRUE	Q24						
Q25	TRUE	Q25						
Q26	TRUE	Q26						
Q27	TRUE	Q27						

Q28	TRUE	Q28						
Q29	TRUE	Q29						
Q30	TRUE	Q30						

Identifying of standard error (SE), which refers to standard deviation of different sample statistics, establishes a data accuracy. The standard errors of each question of the survey is shown in Tab. 10. According to the survey results, the SE of the data is between 0.09 and 0.28.

Tab. 10: Standard errors of the survey data

Code	SE	Code	SE	Code	SE	Code	SE
Q1	0.09	Q9	0.25	Q17	0.26	Q25	0.14
Q2	0.13	Q10	0.22	Q18	0.28	Q26	0.20
Q3	0.17	Q11	0.24	Q19	0.23	Q27	0.23
Q4	0.22	Q12	0.25	Q20	0.25	Q28	0.23
Q5	0.24	Q13	0.24	Q21	0.20	Q29	0.26
Q6	0.23	Q14	0.22	Q22	0.12	Q30	0.22
Q7	0.22	Q15	0.25	Q23	0.24	Q31	0.08
Q8	0.20	Q16	0.22	Q24	0.25		

Conclusions

Summing up the survey research, the results are following:

- Using the LR three hypotheses have been developed.
- Demographic information of experts has been evaluated.
- *Evaluating hypotheses method* has been developed by authors to compare these hypotheses with the survey results.
- Standard errors of the survey data are between 0.09 and 0.28.

The results of this survey show that the integration of RE into the mining industry has perspectives and relevance for 24 experts (80%), with 2 experts (7%) opposing this idea and 4 experts (13%) remaining without an opinion. Decreasing costs of RE generation, off-grid location of a mine, and increasing prices of fossil energy are the main factors towards RE penetration. Volatility of RE technologies and costs of RE generation are the main barriers. Subsidies, establishing a policy, and a carbon tax might be the most efficient government support mechanisms. Reduction in fuel and electricity costs, including transportation costs, predictable energy costs; lower risk from volatile and rising diesel prices; and decreasing carbon emissions are seen as the key effects from RE implementation. All environmental issues such as low-carbon supply chain, recycling programs, using of RE, integrated waste management, and sustainable development are important for industrial companies.

In contrast, a lack of business models and the development of domestic renewable energy market are not important factors towards integrating RE into the mining industry

References

ABB. n.d. "Reducing energy costs and environmental impacts of off-grid mines." ABB Microgrid Business Case. Accessed 10 11, 2017. http://register.e.abb.com/ABBMicrogridBusinessCaseforMining.

Bergek, A., and I. Mignon. 2017. "Motives to adopt renewable electricity technologies: Evidence from Sweden." Energy Policy, 547–559.

Boyse, F., and A. Causevic., 2014. Sunshine for Miner: Implementing Renewable Energy for Off-Grid Operations. Carbon War Room, 34. Accessed 10 12, 2017. http://www.crm-ps.com/upload/files/CWR14_MinesReport_singles.pdf.

n.d. Business models for renewable energy applications at mines. Accessed 10 12, 2017. https://www.th-energy.net/english/platform-renewable-energy-and-mining/business-models/.

Choi, Y., and J. Song., 2016. "Review of photovoltaic and wind power systems utilized in the mining." Renewable and Sustainable Energy Reviews, 10 16: 1386–1391.

Committee on Climate Change., 2015. “The fifth carbon budget, the next step towards a low-carbon economy.” november. Accessed 08 04, 2017. https://www.theccc.org.uk/wp-content/uploads/2015/11/Committee-on-Climate-Change-Fifth-Carbon-Budget-Report.pdf.

Danvest and THEnergy study., 2015. "Low-load Gensets for Solar–Diesel Hybrid Plants in the Mining Industry." 13. Accessed 10 12, 2017. file:///C:/Users/fols/Desktop/2015OCT_STUDY_Danvest-THEnergy.pdf.

Dougherty, K., 2017. Rio Tinto boss lauds B.C.’s clean energy as trade advantage. Energy and Mines. 29 09. Accessed 10 11, 2017. http://energyandmines.com/2017/09/rio-tinto-boss-lauds-b-c-s-clean-energy-as-trade-advantage/.

Earopean Environment Agency., 2017. "Renewable energy in Europe 2017." Copenhagen, 65. Accessed 10 12, 2017. doi:10.2800/75442.

Fraser Institute., 2012. "How are waste materials managed at mine sites?" miningfacts.org. Accessed 10 12, 2017. http://www.miningfacts.org/Environment/How-are-waste-materials-managed-at-mine-sites/.

Hillig, T., and J. Watson., 2016. "Solar, storage and mining: New opportunities for solar power development." 6. Accessed 10 12, 2017. file:///C:/Users/fols/Desktop/20160126_Solar__storage_and_mining_final_1.pdf.

Huisman, L., 2014. "The potential impact of carbon missions tax on the South African mining industry." 115. Accessed 10 12, 2017. http://dspace.nwu.ac.za/bitstream/handle/10394/11725/Huisman_L.pdf?sequence=1.

Lillemo, S. C, F. Alfnes, B Halvorsen, and M. Wik., 2013. "Households’ heating investments: The effect of motives and attitudes on choice of equipment." Biomass and Bioenergy, Feb 27: 4-12.

2017. Mining Sector Embracing Microgrids: Hybrid Systems Reduce Energy Costs & Environmental Impact. The Beam. Accessed 10 11, 2017. https://cleantechnica.com/2017/09/25/mining-sector-embracing-microgrids-hybrid-systems-reduce-energy-costs-environmental-impact/.

Mitimingi, T.C., and M. Hill., 2017. Glencore Zambia Unit May Fire 4,700 Workers. 08 23. Accessed 10 11, 2017. https://www.bloomberg.com/news/articles/2017-08-22/glencore-says-zambia-power-dispute-could-impact-4-700-workers.

2016. Mobile Solar- and Wind Diesel Hybrid. PFISTERER/THEnergy, 13. Accessed 10 12, 2017. file:///C:/Users/fols/Desktop/2016OCT_Study_Pfisterer_THEnergy-mobile-microgrids-exploration_V5.pdf.

Moran, C.J., C. Lodhia, N. Kunz, and D. Huisingh., 2014. "Sustainability in mining, minerals and energy: new processes, pathways and human interactions for a cautiously optimistic future." Journal of Cleaner Production 84: 1-15.

Ram, M., M. Child, A Aghahosseini, D. Bogdanov, and A. Poleva., 2017. Comparing electricity production costs of renewables to fossil and nuclear power plants in G20 countries. Hamburg: Greenpeace, 66.

Ranangen, H., and A. Lindman., 2017. "path towards sustainability for the Nordic mining industry." Journal of Cleaner Production 151: 43-52.

Ripasso Energy and THEnergy study., 2016. "A hybrid solution with concentrated solar power (CSP) and fuel for baseload mining operations." 13. Accessed 10 12, 2017. https://www.th-energy.net/english/platform-renewable-energy-and-mining/reports-and-white-papers/.

Slavin, A., 2017. "New renewable energy for mine project - LAMGOLD Essakane to benefit from largest hybrid plant in Africa (Case Study)." Energy and Mines, 03 06: 547-559. Accessed 05 15, 2017. http://energyandmines.com/2017/03/new-renewable-energy-for-mine-project-iamgold-essakane-to-benefit-from-largest-hybrid-plant-in-africa/.

2015. Solar projects, energy efficiency and load shifting for an optimized energy management in the mining industry. CRONIMET/THEnergy study, 16. Accessed 10 12, 2017. file:///C:/Users/fols/Desktop/2015SEP_Study_Solar_EnergyEfficiency_LoadShifting.pdf.

Solomons, I., 2017. Carbon tax would have costly implications for mines – Accenture. Mining Weekly. 01 27. Accessed 10 12, 2017. http://www.miningweekly.com/print-version/accenture-warns-implementation-of-carbon-tax-would-have-costly-implications-for-mines-2017-01-27.

Talaria, S., M. Shafie-khaha, G.J. Osório, J. Aghaei, and J. P.S. Catalão., 2017. "Stochastic modelling of renewable energy sources from operators' point-of view: A survey." Renewable and Sustainable Energy Reviews.

UNFCCC., 2015. “Adoption of the Paris Agreement, proposal by the President, Draft decision -/CP.21.” United Nations Framework Convention on Climate Change (UNFCCC), FCCC/CP/2015/L.9/Rev.1, 12 12. Accessed 08 03, 2017. https://unfccc.int/resource/docs/2015/cop21/eng/l09.pdf.

United Nations Framework Convention on Climate Change., 1997. “Kyoto Protocol to the United Nations Framework Convention on Climate Change.” 11 12: 21. Accessed 08 04, 2017. http://www.bmub.bund.de/fileadmin/bmu-import/files/pdfs/allgemein/application/pdf/kpeng1.pdf.

World Congress., 2016. "943 MW of renewables currently powering mines with more on the way, experts say." Energy and Mines, 21-22 november: 4. Accessed 08 04, 2017. http://www.redaviasolar.com/wp-content/uploads/2016/10/EMWC-2016-Ranking-Feature-v4.pdf.

Zharan, K., and J.C. Bongaerts., 2016. "Case studies analysis of renewable energy implementation into the mining industry." 6th Solar Integration Workshop. Vienna. 481-486.

Appendix A

Tab. A.11: Systematic literature review on implementing RE into the mining industry

No.	Hypothesis	Literature source
Q3	H1	(Moran, et al. 2014), (Mobile Solar- and Wind Diesel Hybrid 2016), (Hillig and Watson 2016)
Q4	H1	(Mining Sector Embracing Microgrids: Hybrid Systems Reduce Energy Costs & Environmental Impact 2017), (Bergek and Mignon 2017), (Ripasso Energy and THEnergy study 2016), (Ram, et al. 2017)
Q5	H1	(Mining Sector Embracing Microgrids: Hybrid Systems Reduce Energy Costs & Environmental Impact 2017), (ABB n.d.), (Choi and Song 2016), (Mobile Solar- and Wind Diesel Hybrid 2016), (Ripasso Energy and THEnergy study 2016), (Solar projects, energy efficiency and load shifting for an optimized energy management in the mining industry 2015)
Q6	H2	(Mobile Solar- and Wind Diesel Hybrid 2016), (Solar projects, energy efficiency and load shifting for an optimized energy management in the mining industry 2015)
Q7	H1	(Mitimingi and Hill 2017)
Q8	H1	(Mobile Solar- and Wind Diesel Hybrid 2016), (Hillig and Watson 2016)
Q9	H1	(Ripasso Energy and THEnergy study 2016), (Ram, et al. 2017)
Q10	H3	(Mobile Solar- and Wind Diesel Hybrid 2016)
Q11	H1	(Danvest and THEnergy study 2015)
Q12	H1	(Danvest and THEnergy study 2015), (Mobile Solar- and Wind Diesel Hybrid 2016)
Q13	H3	(Business models for renewable energy applications at mines n.d.)
Q14	H2	(Mobile Solar- and Wind Diesel Hybrid 2016)
Q15	H1	(Mobile Solar- and Wind Diesel Hybrid 2016)
Q16	H1	(Moran, et al. 2014)
Q17	H3	-
Q18	H1	(Mining Sector Embracing Microgrids: Hybrid Systems Reduce Energy Costs & Environmental Impact 2017), (Solomons 2017), (Huisman 2014)
Q19	H1	(Mobile Solar- and Wind Diesel Hybrid 2016), (Ripasso Energy and THEnergy study 2016), (Hillig and Watson 2016), (Danvest and THEnergy study 2015)
Q20	H2	(Boyse and Causevic 2014)
Q21	H3	-
Q22	H1	(Mining Sector Embracing Microgrids: Hybrid Systems Reduce Energy Costs & Environmental Impact 2017)
Q23	H3	(Earopean Environment Agency 2017)
Q24	H1	(Ranangen and Lindman 2017), (Mining Sector Embracing Microgrids: Hybrid Systems Reduce Energy Costs & Environmental Impact 2017), (Choi and Song 2016), (Ripasso Energy and THEnergy study 2016), (Ram, et al. 2017)
Q25	H1	(Ranangen and Lindman 2017), (Choi and Song 2016), (Ripasso Energy and THEnergy study 2016)
Q26	H1	(Moran, et al. 2014) (Dougherty 2017)

Q27	H1	(Moran, et al. 2014)
Q28	H1	(Earopean Environment Agency 2017), (Ram, et al. 2017)
Q29	H1	(Fraser Institute 2012)
Q30	H1	(Ranangen and Lindman 2017), (Moran, et al. 2014)

Tab. A.12. Sample of the questionnaire

Code No.	Number	Question
Q1	1	Have you ever heard about implementation of renewable energy (RE) into the mining industry?
Q2	2	In your opinion, do RE have perspectives and relevance to be considered as an energy source for the mining industry?
Q3	3	How can you evaluate an integration of RE into the mining industry?
	4	The following are incentives to integrate of RE into the mining industry. Please, grade them using the scale from 1 to 5. You can use one number several times
Q4	4.1	Decreasing costs of RE generation
Q5	4.2	Off-grid location of a mine
Q6	4.3	Reliability and security of RE sources
Q7	4.4	Increasing prices of fossil energy
Q8	4.5	Government support
	5	The following are barriers in matter of RE integration into the mining industry
Q9	5.1	Volatility of RE sources
Q10	5.2	High investments in RE technologies
Q11	5.3	Connection of a mine to the grid
Q12	5.4	Costs of RE generation
Q13	5.5	Lack of business models
	6	The following are government's support mechanisms in order to integrate of RE into the mining industry
Q14	6.1	Tax breaks
Q15	6.2	Subsidies
Q16	6.3	Establishing a policy
Q17	6.4	Feed-in tariff
Q18	6.5	Carbon tax
	7	Please, evaluate the following effects from RE integration into the mining industry using the scale from 1 to 5
Q19	7.1	Reduction in fuel and electricity costs, including transportation costs
Q20	7.2	Reduction risk of power loss from supply disruptions
Q21	7.3	Predictable energy costs
Q22	7.4	Lower risk from volatile and rising diesel prices
Q23	7.5	Development of domestic renewable energy market
Q24	7.6	Decreasing of carbon emissions
Q25	8	How important is for your company (institution) making the industrial processing more environmental friendly?
	9	Evaluate, please, the following environmental issues for industrial processing using the scale from 1 to 5
Q26	9.1	Low-carbon supply chain
Q27	9.2	Recycling programs

Q28	9.3	Using of RE
Q29	9.4	Integrated waste management
Q30	9.5	Sustainable development
Q31	10	Have you ever been involved in a project for implementation of RE into the mining industry?

Resource Forecasting

The local climate impact of photovoltaic solar farms ——Results from a field observation campaign in gobi desert

Xiaoqing Gao, Liwei Yang, Xuhong Hou and Xiaoying Hui

Key Laboratory of Land Surface Process and Climate Change in Cold and Arid Regions, Northwest Institute of Eco-Environment and Resources, CAS, Lanzhou, Gansu (China)

Abstract

Large-scale solar power farms are rapidly increasing in size and number across the world. However, the surface heat balance is altered when a photovoltaic (PV) power plant is deployed. Modifications to the surface albedo through the deployment of photovoltaic arrays have the potential to change radiative forcing, surface temperatures and local weather patterns. In this work, the field observation data from a large solar farm and a region without PV array in Golmud are used to study the impact of large solar farms in desert areas on the local climate. The results show the mean daily albedo in the solar farm is 0.19, while it is 0.26 in the region without PV. The annual mean net radiation in the solar farm is evidently higher than that of the region without PV. The annual range of soil temperatures at depths of 5–180 cm in the solar farm is bigger than that in the region without PV. The soil temperatures at different depths in winter in the solar farm are clearly lower than those in the region without PV. The 2-m daytime air temperature in the two sites is essentially the same during winter, while during the other seasons, the daytime air temperature in the PV farm is higher than that in the region without PV, with the maximum difference appearing in summer. The nighttime air temperatures at the height of 2 m during the four seasons in the solar farm are higher than those in the region without PV.

Keywords: meteorological observation, photovoltaic farm, desert areas, local climatic effect

1. Introduction

Renewable energy is considered an important solution for mitigating global warming, energy crisis and environmental pollution. The predominant renewable energy sources include wind, solar, biomass, hydropower and geothermal. Photovoltaic solar power systems have drawn tremendous attention from government sectors, researchers and the industry over the past several decades (Gagnon et al., 2002; Liu et al., 2015).

Large-scale solar power plants are rapidly increasing in size and number in China, as well as in other parts of the world. Photovoltaic (PV) power plants in desert regions have a promising future in China, considering the intense radiation received in large areas in China. However, the surface heat balance is altered when a photovoltaic power plant is operating. Modifications to the surface albedo through the deployment of photovoltaic arrays have the potential to change radiative forcing, surface temperatures and local weather patterns. Nemet (2009) investigated the net radiative forcing from the widespread installation of photovoltaics on the earth's surface. However, Nemet did not consider local microclimates, nor have his analytical results been verified with any field data. Genchi et al. (2002) estimated the impact of large-scale installation of PV systems in Tokyo on the urban heat island effect. The simulation results showed that it would be negligible. Tian et al. (2007) analyzed the effect of the PV module on the microclimate of the urban canopy layer, with the simulation results showing that the urban canopy air temperature alters little and the increase in the PV conversion efficiency can reduce the urban canopy air temperature. Taha (2013) evaluated the potential atmospheric effects of PV deployment in urban areas and the simulation results showed a 1–2 ℃ decrease in peak urban temperatures at six locations across California. Turney and Fthenakis (2011) identified 32 categories of impacts from the installation and operation of large-scale solar power plants. They found the impacts were either beneficial or neutral, except the local climate effect, for which they concluded that research and observations were needed.

The potential effects of the deployment of PV panels on climate have been discussed in previous studies. However, most of these studies focus on urban areas and use simulation methods. In this work, the impact of solar farms on the local meteorology in desert areas is assessed with observational data. It is believed that the results from this research can provide basic data support for the simulation of the local climate effect of a photovoltaic power station.

doi:10.18086/swc.2017.22.01 Available at http://proceedings.ises.org

Moreover, it may be useful for guiding the development and appropriate utilization of solar energy.

2. Materials and methods

2.1. Study area and field experiment description

The observation data is taken from Golmud (36°21′55′′N; 95°06′48′′E; a.s. 2868 m), Qinghai Province. After Tibet, the solar radiation in Golmud is the highest in China. Located at the south edge of the Qaidam Basin, the solar farm covers an area of 2.37 square kilometers, measuring 2296 meters from east to west and 1271 meters from north to south. The type of landform is Gobi Desert, with a continental plateau climate. The dominant wind direction in Golmud is the westerly wind.

Photovoltaic arrays are fixed. The azimuth of a PV array is south, with a tilt angle of 36°, a height of 2.5 m, and a spacing between each PV row in the solar farm of 6 m. The solar conversion efficiency of the solar panels is 15%. There are two observation points in this test; one is in the photovoltaic power station (site A), located at 36˚20.128' N, 95˚13.372' E at an altitude of 2927 m. The underlying surface is the Gobi. Detailed measurements taken at a height of 10 m were wind speed, wind direction, air temperature, humidity and solar radiation, while measurements taken at a height of 2 m were wind speed, wind direction, air temperature and humidity. The measurement taken at a height of 1.5 m was solar radiation. Soil temperatures at 5, 10, 20, 40, 80, and 180 cm were recorded in the solar farm. The other measurement point was outside the photovoltaic power station (site B), to be used as a reference point indicating ambient conditions. It was to the southwest of site A, located at 36˚19.975' N and 95˚12.985' E, at an altitude of 2933 m, with the underlying surface being Gobi with sparse vegetation. Detailed measurements taken at a height of 3 m were wind speed and wind direction, while measurements taken at a height of 2 m were air temperature and humidity. The measurement taken at a height of 1.5 m was solar radiation. Soil temperatures at 5, 10, 20, 40, 80, and 180 cm were recorded in the region without a PV array. The two observation sites were 645 meters apart. The characteristics of the sensors can be found in Table 1. Figure 1 shows an illustration of the solar farm and the locations where the field measurements were taken.

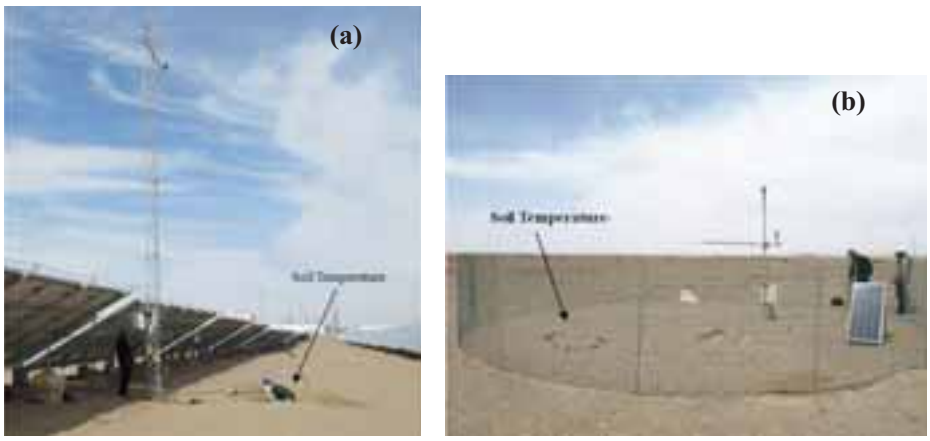

Fig. 1: The illustrations of the two sites in Golmud: (a) in the solar farm (Site A) and (b) in the region without PV (Site B).

2.2. Data and methods

The present work is based on data acquired at a 10-min step since October 2012. All the data have been passed through data quality control. All of the observation times are recorded in Beijing time. NR is deduced from the energy budget equation:

$$NR = (DSR - USR) + (DLR - ULR) \quad \text{(eq. 1)}$$

$$A = USR / DSR \quad \text{(eq. 2)}$$

where NR, DSR, USR, DLR and ULR are net radiation, downward and upward shortwave radiation and downward and upward long wave radiation (W/m^2), respectively. A is albedo (Tyagi et al., 2012). The energy balance equation is:

$$NR = H + LE + G + S_e \quad \text{(eq. 3)}$$

where H is the sensible heat flux, LE is the latent heat flux, G is the soil heat flux, S_e is the

solar panel electricity (Fig. 2). Due to the minimal precipitation in the Gobi area, the latent heat exchange is negligible. The land surface temperature (ST) is related to the surface long wave radiation by the Stefan-Boltzmann law (Wang and Liang, 2009):

$$ULR = \varepsilon_s \cdot \sigma \cdot ST^4 + (1-\varepsilon_s) \cdot DLR \qquad \text{(eq. 4)}$$

where ε_s is the broadband emissivity over the entire infrared region and σ is the Stefan-Boltzmann's constant (5.67×10^{-8} W· m^{-2}· K^{-4}). In the PV farm, 80% of the underlying surface is the ground, due to which, the emissivity ε_s is approximately 0.95. Therefore, ST can be estimated from Eq. (4). Soil thermal conductivity is calculated by the Harmonic method (Gao et al., 2009) as shown below.

The heat conduction equation (Horton et al., 1983) is:

$$\frac{\partial T}{\partial t} = k\frac{\partial^2 T}{\partial z^2} \qquad \text{(eq. 5)}$$

where T is the soil temperature (℃), t is the time (s), z is the depth (m), k is the thermal diffusivity, $k = \lambda / C_p$, λ is the thermal conductivity ($W\cdot m^{-1}\cdot ℃^{-1}$), and C_p is the volumetric heat capacity. The C_p and λ are assumed to be independent of depth and time.

For the Eq. (5), it can be solved without initial conditions in semi-infinite space, and its upper boundary condition is assumed as Fourier series:

$$T(0,t) = \overline{T}(0) + \sum_{i=1}^{n} A_i \sin(i\omega t + \Phi_i) \qquad \text{(eq. 6)}$$

The solution to Eq. (5) using superposition is:

$$T(z,t) = \overline{T}(z) + \sum_{i=1}^{n} A_i \exp(-B_i z) \times \sin(i\omega t + \Phi_i - B_i z) \qquad \text{(eq. 7)}$$

where $\overline{T}$ is the mean soil surface temperature, A is the amplitude of the diurnal soil surface temperature wave, Φ is the phase, n is the number of harmonics, $B_i = \sqrt{i\omega/(2k)}$ is the damping depth of the diurnal temperature wave. If the soil temperature at a depth of z_1 is the upper boundary, the formula for calculating the temperature of soil at any depth by the method of harmonic is:

$$T(z,t) = \overline{T}(z) + \sum_{i=1}^{n} A_i \exp(-B_i(z-z_1) \times \sin(i\omega t + \phi_i - B_i(z-z_1)) \qquad \text{(eq. 8)}$$

In the concrete calculation, the observed data of the two layers of soil temperature can be used to calculate the optimal estimation of the parameters (A_i, Φ_i) in Eq. (6), as well as the parameter (B) in Eq. (8) by using the least square method, thus obtaining the estimated value of soil thermal diffusivity (Horton et al., 1983). Taking the 5-cm soil temperature as the upper boundary (Eq. (6)), the least square method is used to fit different harmonic order numbers, with the second-order harmonic model having a high precision (correlation coefficient r = 0.998). Considering the simplification and precision of the model, the second-order harmonic model (n=2) is used as the model of the harmonic method, C_p =1.47×10^6 $J\cdot m^{-3}\cdot K^{-1}$, in this paper. Therefore, soil thermal conductivity can be estimated using Eq. (8).

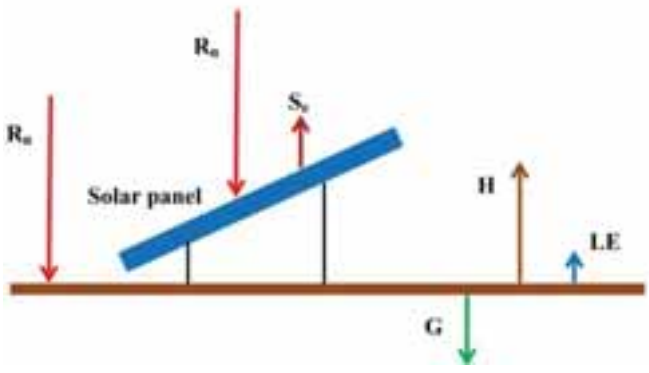

Fig. 2: The conceptual model of the heat balance near the surface in the solar farm

Tab.1: Summary of the instrumentations of sites A and B for the measurement presented in this paper.

Parameter (unit)	Sensor	Height above ground level	Accuracy	Sampling rate (min)	Averaging interval (min)
Air temperature (°C)	Vaisala HMP155A	2, 10 m in Site A; 2 m in Site B	±0.12°C (20℃)	1	10
Relative humidity (%)	Vaisala HMP155A	2, 10 m in Site A; 2 m in Site B	±1% (0~90% RH)	1	10
Short wave radiation incoming and outgoing ($W \cdot m^{-2}$)	Kipp and Zonen CNR 4 $0.31 < \lambda < 2.8$ μm	1.5, 10 m in Site A; 2 m in Site B	<1% (0~1000 W/m^2)	1	10
Long wave radiation incoming and outgoing ($W \cdot m^{-2}$)	Kipp and Zonen CNR 4 $4.5 < \lambda < 42$ μm	1.5, 10 m in Site A; 2 m in Site B	<1% (-250~250 W/m^2)	1	10
Soil temperature (°C)	Campbell 109SS-L	-5, -10, -20, -40, -80, -180 cm in Site A and B	±0.2℃ (0~70℃), ± 0.5℃ (-50℃)	1	10
Wind speed ($m \cdot s^{-1}$)	Gill WINDSONIC	2, 10 m in Site A; 3 m in Site B	±2%	1	10
Wind direction (°)	Gill WINDSONIC	2, 10 m in Site A; 3 m in Site B	±3°	1	10

3. Results and discussion

3.1. Comparison of the radiation field in the two sites

The surface radiation budget plays an important role in regional climate (Li et al., 2009). The intensity of incoming and outgoing radiative fluxes at the surface in the PV farm depends on the angle of inclination of the PV arrays and their exposure relative to the direction of the incoming solar beam, as well as on the PV system efficiency and the characteristics of the surrounding terrain (Matzinger et al., 2002; Kämpf et al., 2010; Zhang et al., 2016).

The observational data used in this study are from October 2012 to September 2013. The observations at a height of 10 m in the solar farm are 7.5 m higher than the perpendicular height of the PV array. The angle of the upward radiation sensor is 150°, with the field of view of the radiation sensor being the mixed underlying surface area with a 56-m diameter, due to which the radiation data at a height of 10 m is used to discuss the influence of PV array on the radiation field. Figure 3 shows the annual averaged diurnal variations of each component of the radiation budget and surface temperature at the two sites. Figure 4 shows the annual variation in radiation flux at the two sites, each black dot represents 10-min averaged value and Fig. 5 shows the annual variation in the monthly averaged albedo at the two sites.

There is no difference in the downward shortwave radiation (DSR) and the downward longwave radiation (DLR) between the two sites. Therefore, they are not analyzed.

The upward shortwave radiation (USR) reached a peak of approximately 128.8 $W \cdot m^{-2}$ at 14:00 in the annual averaged diurnal variations at site A, and 193.7 $W \cdot m^{-2}$ at 14:00 at site B, as shown in Fig. 3(a). The daily cumulative value of the USR at site A is 3.54 $MJ \cdot m^{-2}$, while it is 5.02 $MJ \cdot m^{-2}$ at site B. The value in the solar farm is 1.48 $MJ \cdot m^{-2}$ lower than that in the region without PV, with the difference between the two sites being large. Due to the snow cover during November and December, the surface albedo is higher, which makes the USR on sunny days abnormally high (Fig. 4(a) and (a1)). The monthly averaged USR reached a maximum in June and a minimum in December at site A, while it reached a maximum in April and a minimum in January at site B (Fig. 4(a) and (a1)). The solar conversion efficiency of the solar panels is related to meteorological factors, mainly ambient temperature, dust, wind speed and relative humidity. This causes the peaks and valleys of USR to appear during different months for the two sites. The difference in the values of USR between the two sites is negative during the year, which is evident in Fig. 4(d). The ratio of the average annual USR at site A to that at site B is 0.7 (Table 2), indicating that the response of the PV array to the radiation fields is mainly to enhance the absorption of the downward shortwave radiation, leading to a significant reduction in the upward short wave radiation, with an influence of up to 30%. The difference in the USR at the two sites reached the maximum in March–April (spring), with a value of -20.7 $W \cdot m^{-2}$, while it reached the minimum in December–January of the following year (winter), with a value of -11.6 $W \cdot m^{-2}$ (Fig. 4(d)).

The upward longwave radiation (ULR) depends on the surface temperature raised to the power of four (Eq. (4)).

The ULR has diurnal variation with the surface temperature (Li et al., 2009). The ULR reached a peak of approximately 443.0 $W \cdot m^{-2}$ at 15:00 at site A, and 471.5 $W \cdot m^{-2}$ at 15:00 at site B in Fig. 3(b). The ULR at site A is clearly lower than that at site B during 11:00–18:00, while it is higher during 00:00–9:00, which is mainly due to the change in surface temperature, as shown in Fig. 3(e). The daily cumulative value of the ULR at site A is lower than that at site B, while the cumulative value of the ULR in the daytime at site A is lower than that at site B. The difference is 0.62 $MJ \cdot m^{-2}$. The cumulative value of the ULR at night is 0.12 $MJ \cdot m^{-2}$ higher than that at site B, since the PV plants have an insulating effect at night and a cooling effect during daytime. The cooling effect is more noticeable. The monthly average ULR reached a maximum in July and a minimum in January at the two sites, as shown in Fig. 4(b) and (b1). The difference in the values of the ULR between the two sites is negative over a period of one year. The difference in the ULR at the two sites reached the maximum in October, with a value of -8 $W \cdot m^{-2}$. The average annual ULR changed slightly, compared to that at site B. The impact of the PV array on the ULR is no more than 2% (see table 2).

The net radiation (NR) is a measure of the incoming radiation incident on the earth's surface, minus the outgoing energy radiated by the Earth itself. It is related to the four radiation components (Pessacg et al., 2013). The NR reached a peak of approximately 438.0 $W \cdot m^{-2}$ at 14:00 at site A, and 366.8 $W \cdot m^{-2}$ at 14:00 at site B, as shown in Fig. 3(c). The daily cumulative value of the NR at site A is 8.30 $MJ \cdot m^{-2}$, and 6.34 $MJ \cdot m^{-2}$ at site B. The cumulative value of the NR during the daytime at site A is 1.98 $MJ \cdot m^{-2}$ higher than that at site B and 0.02 $MJ \cdot m^{-2}$ little lower at night. Therefore, the impact of a photovoltaic array on net radiation is mainly during the daytime, which is the photovoltaic power station's main working time. The monthly averaged NR reached a maximum in June and a minimum in December in the two sites, as shown in Fig. 4(c) and (c1). The difference in the values of the NR between the two sites is positive over the entire year, with the difference being evident. The ratio of the average annual NR at site A to that at site B is 1.32, which indicates that the solar farm has been collecting energy. The difference of the NR at the two sites reached the maximum in August, with a value of 33.0 $W \cdot m^{-2}$, while it reached the minimum in December, with a value of 13.2 $W \cdot m^{-2}$.

Surface albedo is the most important parameter affecting the surface radiation budget. As seen from Fig. 3(d), the distribution of the albedos from the two sites are U-shaped, being higher in the morning and evening and lower at noon. When the solar elevation is low, the surface albedo varies greatly. However, with the increase in the solar elevation, the surface albedo decreases and tends to be stable. A large number of photovoltaic devices in the solar farm have a greater capacity to absorb the solar radiation, resulting in lower albedo. The daily average values of surface albedo in the PV farm and without the PV panel are 0.19 and 0.26, respectively. As shown in Fig. 5, the albedos change significantly with the seasons, being lower in summer and higher in autumn and winter. Each seasonal average of the surface albedo at site A is higher than that at site B. The monthly average albedo reached a maximum in November and a minimum in September in the PV area, while it reached a maximum in November and a minimum in July in the region without PV. The difference between the two sites was larger in November 2012 and March 2013, when the average value was 0.11, while it was smaller in May–July, when the average value was 0.05. The annual average values of albedo in the PV farm and the area without the PV panel are 0.19 and 0.27, respectively.

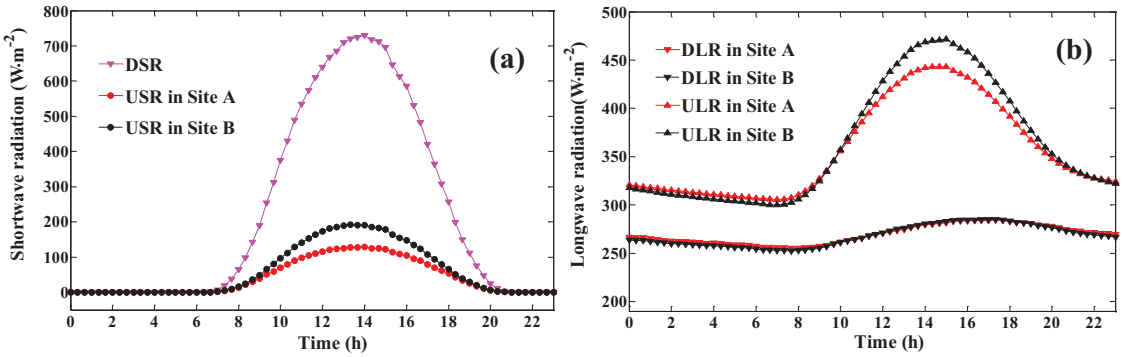

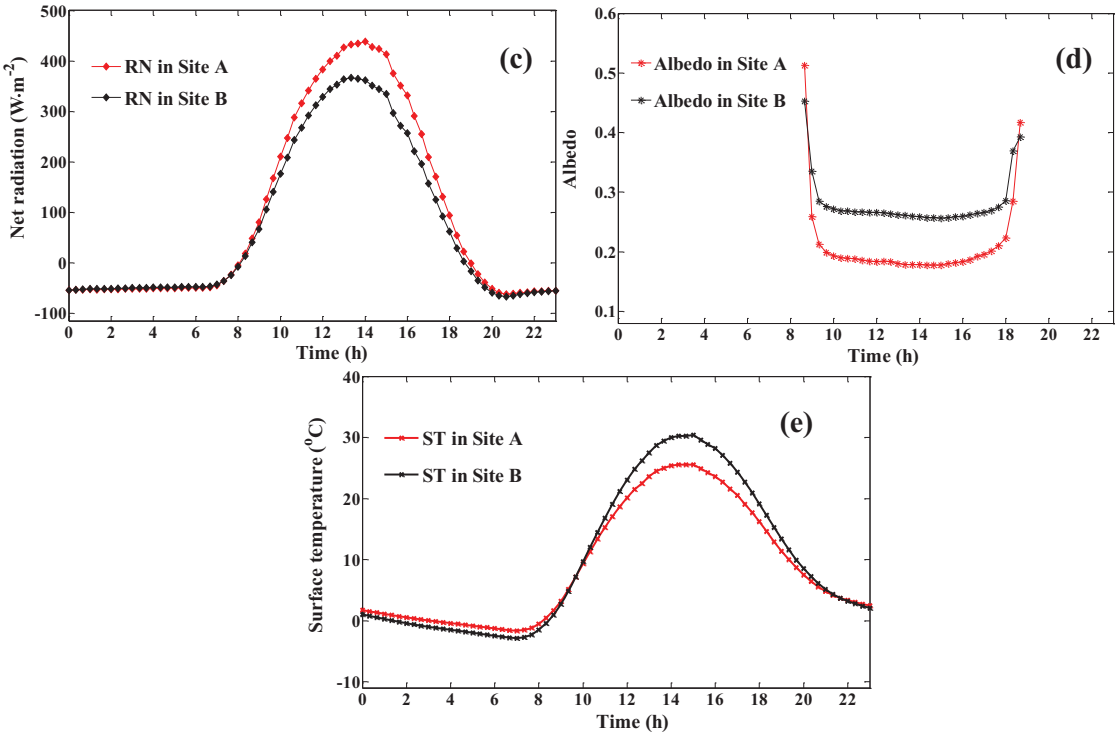

Fig. 3: Annual averaged diurnal variations of radiation components: (a) shortwave radiation, (b) longwave radiation, (c) net radiation, (d) albedo; and (e) surface temperature in the solar farm (Site A) and in the region without PV (Site B) in Golmud.

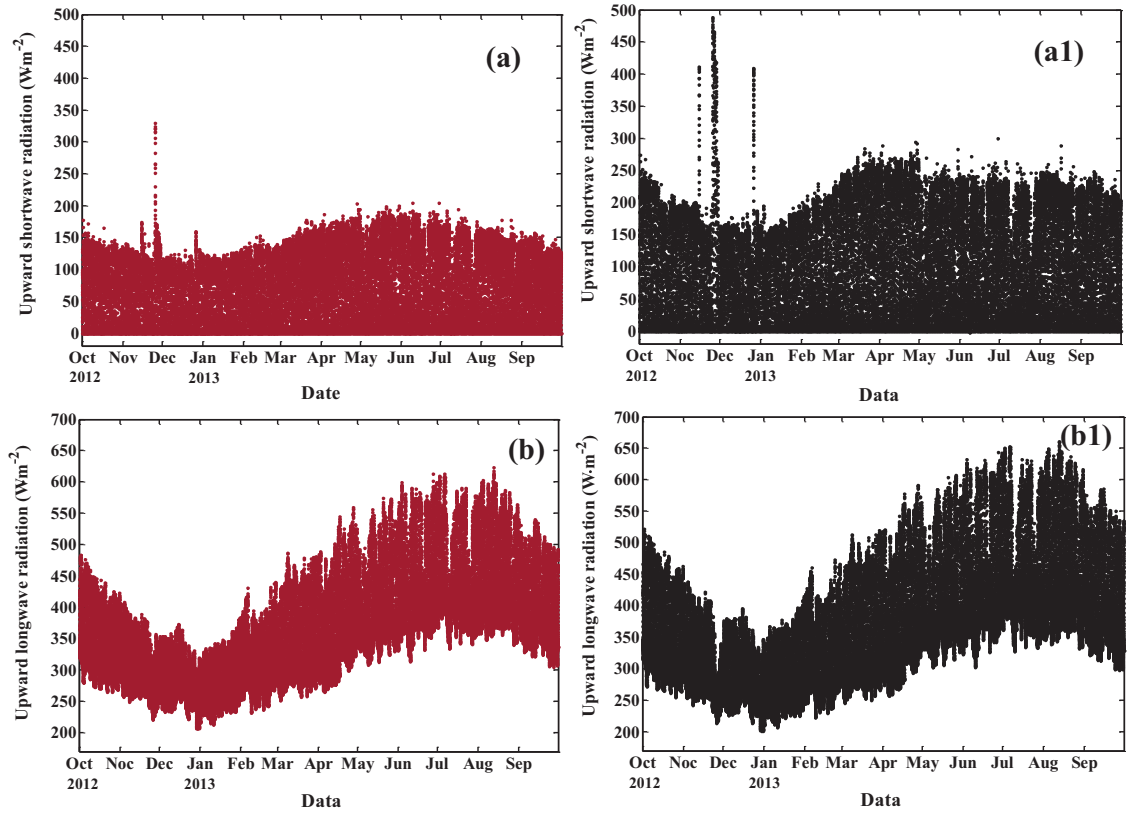

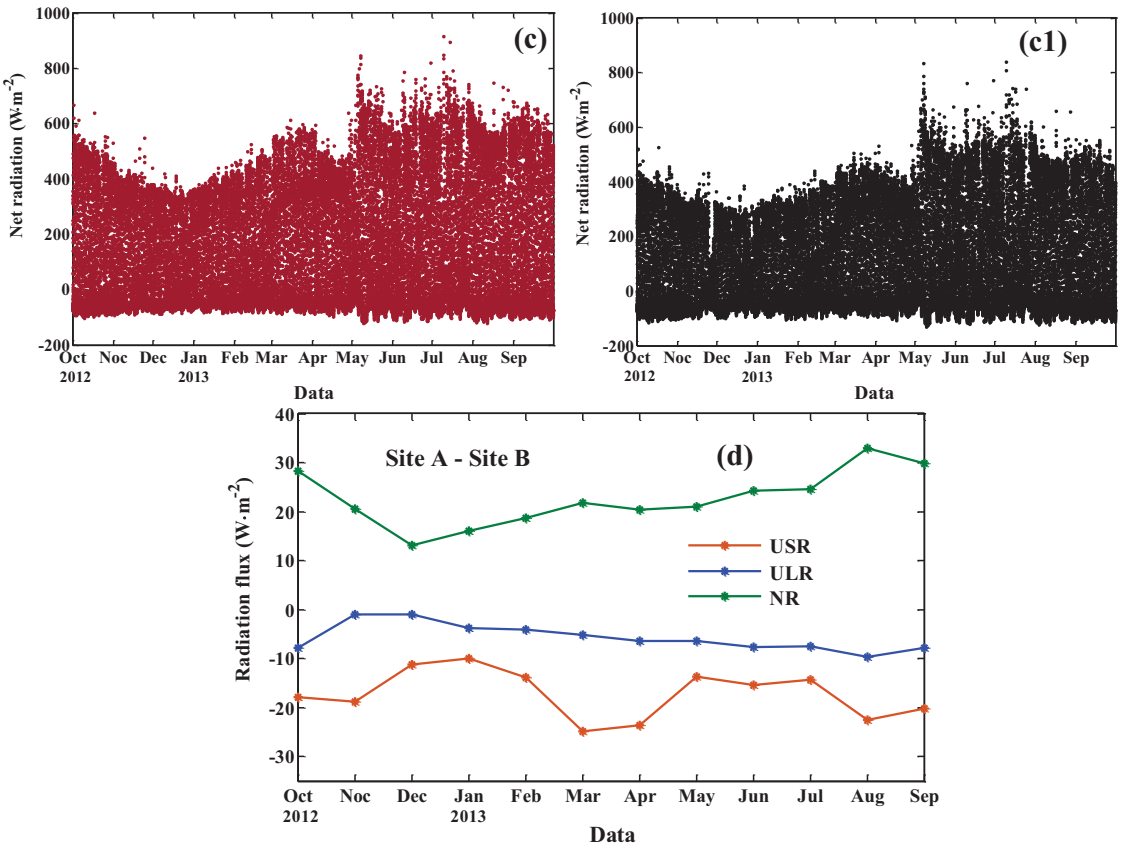

Fig. 4: Annual variation of radiation flux in the solar farm (Site A) and in the region without PV (Site B) in Golmud, where (a), (b) and (c) are the annual variations of USR, ULR and NR in Site A, respectively; (a1), (b1) and (c1) are the annual variations of USR, ULR and NR in Site B, respectively; (d) is the difference of monthly averaged radiation flux between the two sites.

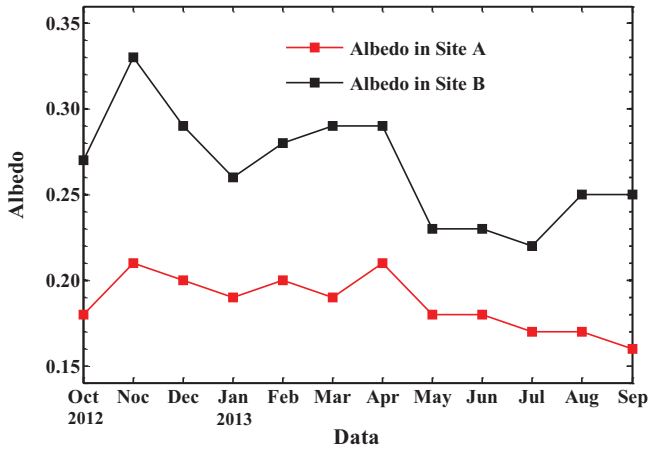

Fig. 5: Annual variation in the monthly averaged albedo in the solar farm (Site A) and in the region without PV (Site B) in Golmud

Tab.2 : Annual mean of the radiation components in the solar farm (Site A) and in the region without PV (Site B) in Golmud

	DSR (W·m^{-2})	USR (W·m^{-2})	DLR (W·m^{-2})	ULR (W·m^{-2})	NR (W·m^{-2})
Site A	221.83	40.97	269.13	356.17	93.81
Site B	223.37	58.15	267.81	361.87	71.16
Relative difference/%	0.69	29.54	0.49	1.58	31.83

3.2. Comparison of the soil temperatures at the two sites

Soil temperature is one of the most important physical properties in determining the rates and directions of physical

processes of the soil, including energy and mass exchange, evaporation and aeration (Gulser and Ekberli, 2004). However, very few studies have focused on the relationship between the soil temperature and a PV farm. In the present study, the soil temperature data obtained continuously at different depths and at different times of the day from the two sites, from October 2012 to September 2013, were analyzed to reveal the effects of PV arrays on soil temperature in Golmud.

Figure 6 shows the amplitude of the monthly averaged diurnal variation of the soil temperature at the two sites. It shows that the amplitude of the diurnal variation of the soil temperature at the two sites gradually decrease with an increase in soil depth. Moreover, the diurnal variation of the soil temperature at a depth of 5 cm is larger, while the change in the diurnal variation of the soil temperature below the depth of 80 cm does not exceed 0.3℃. The diurnal variation in temperature of each layer of soil between 5 and 40 cm in winter is significantly lower than that in spring, summer and autumn. The maximum value of the amplitude of diurnal variation at a depth of 5 cm at the two sites appeared in August, at 20.8℃ at site A, and at 31.7℃ at site B. The minimum value at site A appeared in January, at 4.6℃, while the minimum value at site B appeared in December, at 18.9℃.

The amplitude of the monthly averaged diurnal variation of the soil temperature at site A is significantly lower than that at site B in the shallow soil layer (5, 10 cm), which is mainly due to the existence of a large number of photovoltaic arrays in the solar farm, making it difficult for the solar radiation to spread in the soil during the daytime, with the soil heat not being able to spread outward easily during the night, resulting in a reduction of the diurnal variation of soil temperature in the solar farm. The thermal insulation effect of the photovoltaic array is particularly evident in the shallow layer of soil.

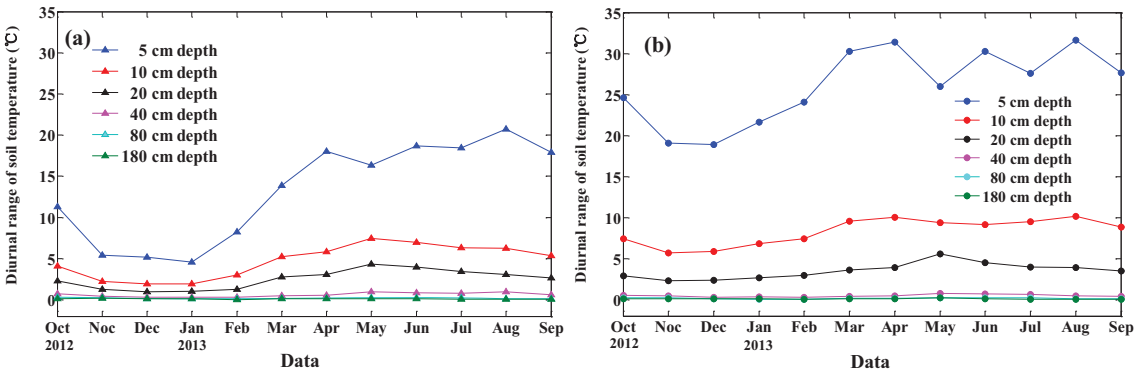

Fig. 6: The amplitude of the monthly averaged diurnal variation of the soil temperature: (a) in the solar farm (Site A) and (b) in the region without PV (Site B).

Figure 7 shows the annual variations of soil temperature at the two sites. As shown in Fig. 7, the changing trend of the annual variations at the two sites is accordant, showing waveform changes. The maximum average soil temperature values at depths of 5–80 cm at the two sites appear in August, while the minimum value appears in January. The maximum average soil temperature values at a depth of 180 cm at the two sites appears in September, while the minimum value appears in February. The average annual soil temperature values at depths of 5–180 cm at site A are 7.5, 7.5, 7.4, 7.6, 7.7, and 7.8℃, respectively, while those at site B are 9.5, 9.4, 9.5, 9.3, 9.4, and 8.9℃, respectively. In winter (December–February), the shadow area of the solar panels reached the maximum, falling onto the site where the soil temperature probes were buried, thus significantly reducing the soil temperature in the solar farm. In winter, the average soil temperature values at depths of 5–180 cm at site A were -10.8, -9.7, -9.1, -7.8, -5.0, and 0.2℃, respectively, while those at site B were -6.2, -5.4, -4.7, -3.2, -0.7, and 3.7℃, respectively. The soil temperatures at different depths in winter in the PV farm were evidently lower than those without PV. Hence, it can be said that the PV farm is a cooling system.

The annual range (annual variation amplitude) of soil temperature at a depth of 5 cm was the largest, with the annual range of soil temperature decreasing gradually, depending on the depth. The annual ranges of soil temperatures at depths of 5–180 cm at site A were 40.4, 37.8, 35.9, 33.4, 27.7, and 19.3℃, respectively, while those at site B were 35.3, 33.2, 31.8, 27.4, 22.1, and 13.6℃, respectively. The annual ranges of soil temperatures at different depths in the solar farm are higher than those in the region without PV.

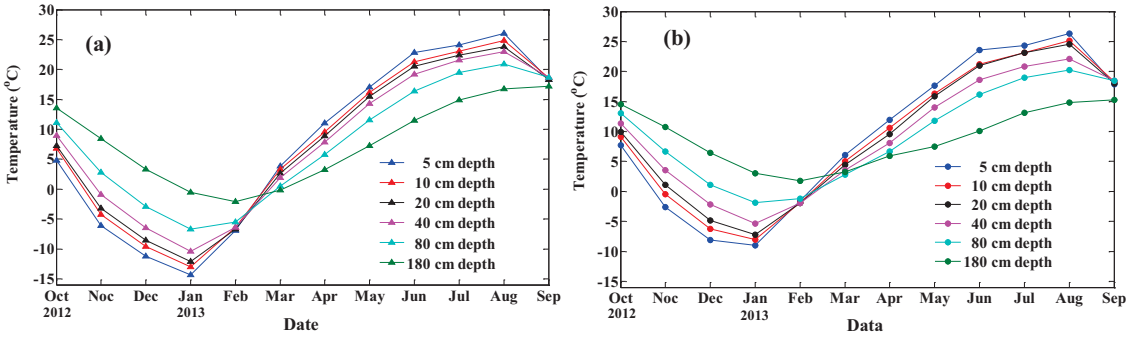

Fig. 7: Seasonal variations in soil temperature: (a) in the solar farm (Site A) and (b) in the region without PV (Site B) in Golmud.

In the PV farm, the presence of the photovoltaic array will affect the solar radiation received on the ground surface, as well as the heat radiating to the atmosphere, thus affecting the soil temperature. A T test was carried out for the daily mean soil temperature at the same depth at the two sites from October 2012 to September 2013 to analyze the influence of the PV array on soil temperature over a year. As shown in Table 3, the data are the P (Probability) values for the T Test (Huang, 1990) at the same depth at the two sites. There are significant differences in the soil temperature at different depths at the two sites from October to March of the following year at the level of 0.05. In addition, there are significant differences at a depth of 80 cm in April and July and at depths of 20 80 cm in August.

The difference between site A and site B at the different depths (the average daily soil temperature at site A, minus the average daily soil temperature at site B) is shown in Fig. 8, hereinafter referred to as the difference. As shown in Fig. 8, the difference in value at the different depths at the two sites from October to March of the following year is mostly below 0℃. Therefore, the average daily soil temperature value in the solar farm is smaller. The average difference in the values at depths of 5 80cm from October to March of the following year were -3.7, -3.4, -3.7, -3.7, and -3.5℃, respectively.

There is a notable feature, which can be seen in Fig. 8. The difference is very less between the two sites in summer. The possible reason is that the instability of atmospheric stratification of the surface layer and the surface turbulence is strong during summer daytime, resulting in a small temperature difference between the two sites. At the same time, the photovoltaic panels generate heat when they generate electricity during the day, causing the photovoltaic cell panels to have a heating effect on the air temperature of the surface layer, which is stronger in the summer than in the winter. It can also result in a smaller difference of soil temperature between the two sites.

Tab. 3 : The P values for the *T* –Test of the same depth of the two sites

	month											
Depth (cm)	**2012/ 10**	**11**	**12**	**2013/ 1**	**2**	**3**	**4**	**5**	**6**	**7**	**8**	**9**
5	0.018	0.000	0.000	0.000	0.000	0.002	0.393	0.564	0.464	0.901	0.665	0.575
10	0.021	0.000	0.000	0.000	0.000	0.004	0.239	0.825	0.898	0.998	0.433	0.570
20	0.005	0.000	0.000	0.000	0.000	0.002	0.375	0.590	0.418	0.191	0.016	0.593
40	0.005	0.000	0.000	0.000	0.000	0.003	0.707	0.600	0.116	0.070	0.000	0.594
80	0.003	0.000	0.000	0.000	0.000	0.000	0.025	0.568	0.495	0.001	0.000	0.425

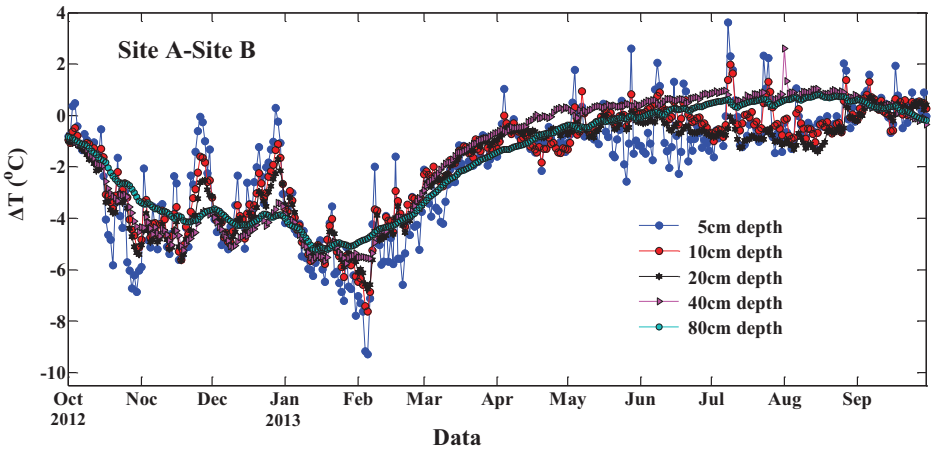

Fig. 8: Annual variations of difference value of different layers of soil temperature between the two sites

Figure 9 shows the annual variations of thermal conductivity at 5–20 cm depths at the two sites. Thermal conductivity in the soil may be explained as the quantity of heat flow through an area of soil per unit time and temperature gradient. The existing research shows that soil thermal conductivity is mainly influenced by soil texture and moisture content (Peterslidard et al., 1998). The soil texture of the two sites is the same; thus, thermal conductivity is mainly affected by the soil moisture content.

As shown in Fig. 9, the monthly mean thermal conductivity reached a maximum in May and a minimum in September at the two sites. Each monthly mean thermal conductivity at the PV farm is higher than that in the region without PV, with the difference being evident. The main reason could be the higher soil moisture in the solar farm. The photovoltaic panels increase the roughness, playing an important role in weakening the wind velocity. At the same time, solar radiation received by the surface in the solar farm is less than that in the region without PV. These factors decrease the evaporation of soil in the solar farm, thus increasing the soil moisture.

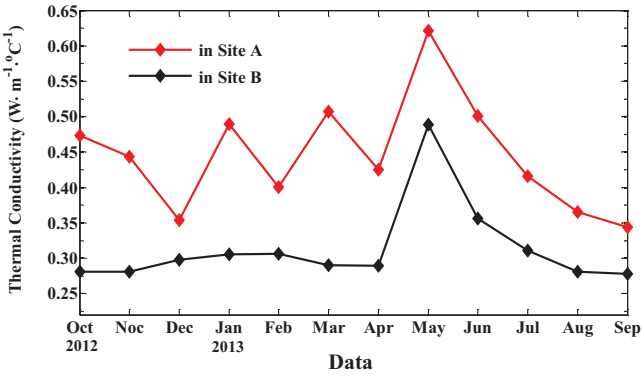

Fig. 9: Annual variation in the monthly mean thermal conductivity in the solar farm (Site A) and in the region without PV (Site B) in Golmud

3.3. Comparison of air temperatures at the two sites

The observational data we used are from May 2013 to April 2014. Figure 10 shows the diurnal variations of the 2-m air temperature and the differences (site A to site B) during the four seasons. July, October, January and April were selected to represent the four seasons of the year. The results show that the air temperature at a height of 2 m at the two sites is essentially the same during winter daytime, but in the other seasons, the daytime air temperature at the PV farm is higher than that in the region without PV. The maximum difference appears during the summer daytime, with a value of 0.7℃ (the summer daytime averaged value). This is because the solar panels enhance the local atmospheric turbulence flow and the heat transfer, as well as radiate heat during the day. Moreover, its effect of heating the air is greater during summer, when the irradiance is higher. As Fthenakis et al. (2013) observed, the PV module temperatures were consistently higher than those of the surrounding air during the day. The nighttime air temperature at a height of 2 m during the four seasons at the solar farm was higher than that in the region without PV arrays, since the solar panels have a heat preservation effect near the ground. The differences in values between the two sites were 0.1, 0.3, 0.2, and 0.1℃ in summer, autumn, winter and spring, respectively.

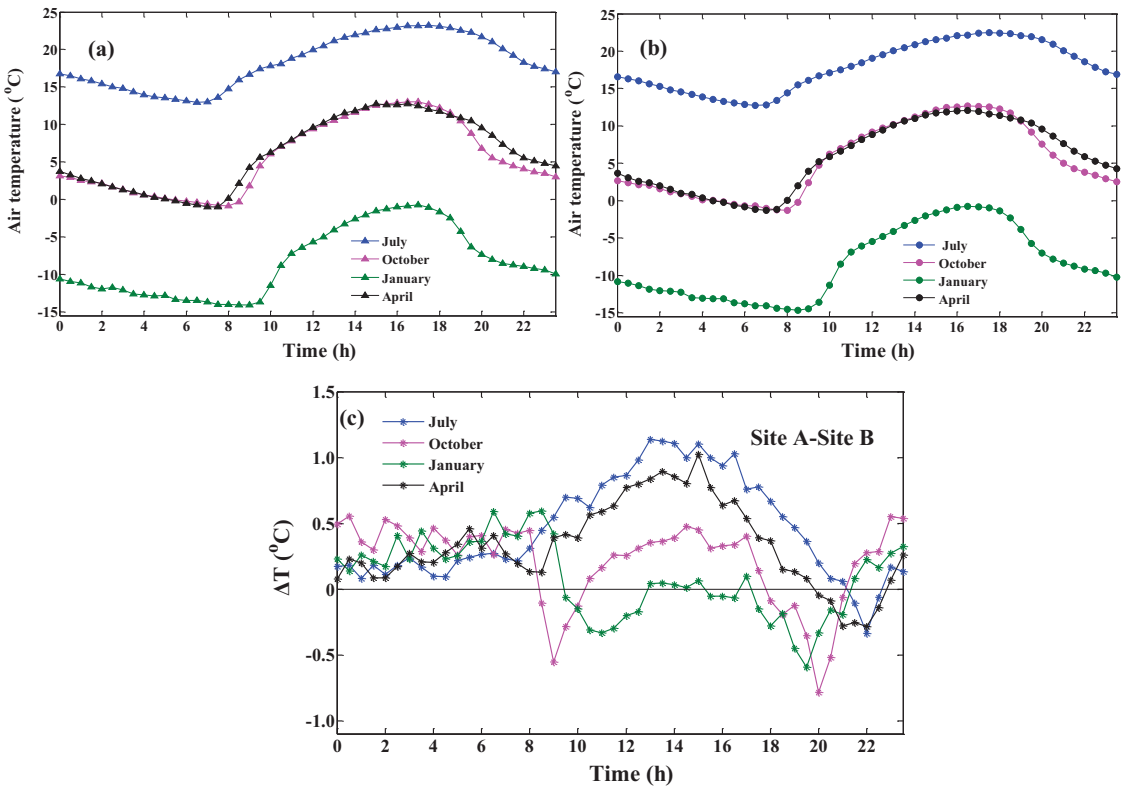

Fig. 10: Diurnal variations of 2 m- air temperature in the four seasons: (a) in the solar farm (Site A), (b) in the region without PV (Site B) and (c) difference between the two sites.

4. Conclusion

Based on the field observation data from the large solar farm and the region without a PV array in Golmud, the characteristics of surface radiation were analyzed. The results show that the total daily values of upward shortwave radiation and net radiation at the two sites are significantly different. The mean daily albedo at the solar farm is 0.19, while it is 0.26 in the region without PV. The annual mean of net radiation at the solar farm is evidently higher than in the region without PV, indicating that the solar farm is collecting energy. However, the PV array converts a part of the radiation energy to electrical energy for output, which can cause the surface layer temperature at the solar farm to be lower.

The characteristics of soil temperature were also analyzed. The results show that the daily range of soil temperature at a depth of 5–10 cm at the solar farm is lower than that in the region without PV farm. Therefore, the solar photovoltaic arrays demonstrated thermal insulation performance. The annual range of soil temperature at a depth of 5–180 cm at the solar farm was larger than that in the region without PV. The soil temperature at different depths during winter at the solar farm was clearly lower than that in the region without PV, indicating that the PV farm is a cooling system. The daily mean of the soil temperature at a depth of 5–80 cm from October 2012 to March 2013 was evidently lower than that in the region without PV array.

The characteristics of diurnal and annual variation features of the 2-m air temperature were analyzed at the two sites. The results show that the air temperature at a height of 2 m at the two sites is essentially the same during winter daytime, while during the other seasons, the daytime air temperature at the PV farm is higher than that in the region without PV. The maximum difference appears during the summer daytime, as the solar panels radiate heat during the daytime. This effect of heating the air is greater in summer. The nighttime air temperature at a height of 2 m during the four seasons at the solar farm is higher than that in the region without PV arrays, since the solar panels exhibit heat preservation effect near the ground.

5. References

Fthenakis, V., Yu, Y., 2013. Analysis of the potential for a heat island effect in large solar farms. IEEE, Photovoltaic Specialists Conference. 2, 3362-3366.

Gagnon, L., Belanger, C., Uchiyama, Y., 2002. Life-cycle assessment of electricity generation options: the status of research in year 2001. Energy Policy. 30, 1267-1278.

Gao, Z., Wang, L., Horton, R., 2009. Comparison of six algorithms to determine the soil thermal diffusivity at a site in the loess plateau of China. Hydrol. Earth Syst. Sci. Discuss. 6, 51-60.

Genchi, Y., Sugawara, Y., Ohtomo, J., Wen, C., Takahashi, H., Inaba, A., 2002. Development of a heat balance model of photovoltaic cells to assess PV installation impacts on the urban heat island effect. Environ. Syst. Res. 30, 271-276.

Gulser, C., Ekberli, I., 2004. A comparison of estimated and measured diurnal soil temperature through a clay soil depth. J. Appl. Sci. 4, 418-423.

Horton, R., Wierenga, P. J., Nielsen, D. R., 1983. Evaluation of methods for determining the apparent thermal diffusivity of soil near the surface. Soil Sci. Soc. Am. J. 47, 25-32.

Huang, J., 1990. Meteorological statistical analysis and forecast method. Beijing: China Meteorological Press. 18-27.

Kämpf, J. H., Montavon, M., Bunyesc, J., Bolliger, R., Robinson, D., 2010. Optimisation of buildings' solar irradiation availability. Sol. Energy. 84, 596-603.

Li, S., Lü, S., Ao, Y., Shang, L., 2009. Annual variations in the surface radiation budget and soil water and heat content in the upper yellow river area. Environ. Geol. 57, 389-395.

Liu, X., Hoekman, S.K., Robbins, C., Ross, P., 2015. Lifecycle climate impacts and economic performance of commercial-scale solar PV systems: A study of PV systems at Nevada's Desert Research Institute (DRI). Sol. Energy. 119, 561-572.

Matzinger, N., Andretta, M., Gorsel, E. V., Vogt, R., Ohmura, A., Rotach, M. W., 2002. Surface radiation budget in an alpine valley. Q. J. Roy. Meteor. Soc. 129, 877-895.

Nemet, G.F., 2009. Net radiative forcing from widespread deployment of photovoltaics. Environ. Sci. Technol. 43, 2173-2178.

Pessacg, N.L., Solman, S. A., Samuelsson, P., Sanchez, E., Marengo, J., Li, L., et al., 2013. The surface radiation budget over South America in a set of regional climate models from the Claris-Lpb project. Clim. Dyn. 43, 1221-1239.

Peterslidard, C.D, Blackburn, E., Liang, X., Wood, E.F., 1998. The Effect of Soil Thermal Conductivity Parameterization on Surface Energy Fluxes and Temperatures. J. Atmos. Sci. 55, 1209-1224.

Taha, H., 2013. The potential for air-temperature impact from large-scale deployment of solar photovoltaic arrays in urban areas. Sol. Energy. 91, 358-367.

Tian, W., Wang, Y., Xie, Y., Wu, D., Zhu, L., Ren, J., 2007. Effect of building integrated photovoltaics on microclimate of urban canopy layer. Build. Environ. 42, 1891-1901.

Turney, D., Fthenakis, V., 2011. Environmental impacts from the installation and operation of large-scale solar power plants. Renew. Sustain. Energy Rev. 15, 3261-3270.

Tyagi, B., Satyanarayana, A. N. V., Kumar, M., Mahanti, N. C., 2012. Surface energy and radiation budget over a tropical station: an observational study. Asia.-Pacific. J. Atmos. Sci. 48, 411-421.

Wang, K., Liang, S., 2009. Evaluation of aster and modis land surface temperature and emissivity products using long-term surface longwave radiation observations at surfrad sites. Remote Sens. Environ. 113, 1556-1565.

Zhang, L., Zhang, L., Wang, Y., 2016. Shape optimization of free-form buildings based on solar radiation gain and space efficiency using a multi-objective genetic algorithm in the severe cold zones of China. Sol. Energy. 132, 38-50.

A WAVELET DECOMPOSITION APPROACH TO IMPROVE MODELLING PERFORMANCE OF ARTIFICIAL NEURAL NETWORKS IN SOLAR ENERGY RESEARCH

Sajid Hussain and Ali Al Alili*

Department of Mechanical Engineering, Khalifa University of Science and Technology, Petroleum Institute, P.O.Box 2533, Abu Dhabi, the United Arab Emirates

Abstract

In solar energy research, estimating solar potential over a location of interest is an important step towards the successful planning of renewable energy projects. However, solar data are not available for every point of interest due to the absence of meteorological stations and sophisticated solar sensors. Therefore, the solar radiation has to be estimated with accurate solar radiation models. This paper presents a hybrid technique to increase the modeling performance of artificial neural networks (ANN), commonly used in solar radiation applications. A wavelet multiresolution is performed to decompose the meteorological data into different time and frequency scales before it is presented to the ANN models. As a result, improving the learning process of the ANN models. The proposed approach is compared to traditional ANN model and validated using well-known statistical validation metrics including coefficient of determination (R^2) and root mean square error (RMSE), mean bias error (MBE), mean absolute percentage error (MAPE), and t-statistics. In addition, wavelet cross spectrum (WCS) is used as a visual indicator of the model performance in time, frequency, and phase domains. The results show that the modeling performance of the ANNs is considerably improved from R^2 of 89.21% to 96.34%.

Keywords: *Solar radiation model, artificial neural network, wavelet analysis*

1. Introduction

There is an increasing concern over global warming, emission of greenhouse gases and climate change. This has encouraged the use of renewable energy sources as replacements to coal and oil fired electricity generation processes. Wind, hydro, solar, and geothermal are main sources of renewable energy. The United Arab Emirates, strategically located in the solar belt, has abundance of sunshine throughout the year where the yearly averaged GHI reaches around 6kWh/day (Islam et al. 2009). This gives the UAE an opportunity to harness solar energy and promote clean and green environment. Therefore, accurate solar resource assessment is an inseparable part of an efficient energy planning in the region. Solar radiation reaching the earth's surface are normally measured using different ground based sensors like pyroheliometers, pyranometers and radiometers. However, this process is expensive and cannot be implemented for every geographical region of interest. An alternate way is to model and predict the solar radiations using readily available economical measurements like T, RH, WS, and SSD. Models are trained and validated on historical data collected from ground based sensors at one particular geographical location and used to estimate the solar radiations at nearby locations. This highlights the importance of solar radiation models, their efficiency and accuracy.

Different statistically based (Hassan 2014), (Voyant et al. 2014), (Mohammadi et al. 2015), biologically inspired (Mohandes 2012), (Behrang et al. 2011), (İzgi et al. 2012) and hybrid (Salcedo-Sanz et al. 2014), (Babu and Reddy 2014), (Olatomiwa et al. 2015) models are used for solar radiation modeling. Artificial neural network (ANN) techniques are very common among biologically inspired models. ANN is used to model solar radiation either by using meteorological parameters (Cornaro et al. 2015), (Yacef et al. 2012) or satellite images (Lu et al. 2011), (Linares-Rodriguez et al. 2013).

Often, the modeling performance of the ANN is improved through hybrid techniques (Salcedo-Sanz et al. 2014) or different ANNs are used to model different seasons of the year or more specifically, to cater for temporal nonlinearities in the data. However, none of the considerations is given to spectral non-linearities present in solar and weather time series.

This paper proposes a relatively very simple technique based on wavelet multiresolution analysis. The novelty

doi:10.18086/swc.2017.22.02 Available at http://proceedings.ises.org

of this study is to analyze the time series, both in temporal and spectral domains. A wavelet multiresolution analysis is performed on the signals that decomposes the signals into different frequency and time resolutions, and different ANNs are trained accordingly. Other than modelling, the process filters out the noise present in the signal as noise can degrade the modeling performance of the ANN. This is reflected in the model performance indicators which penalize the model for not correctly modeling the noise components.

The rest of the paper is organized as follows. Section 2 introduces the methodology followed by simulations and discussions in section 3 and conclusions in section 4.

2. Wavelet Decomposition Combined with Artificial Neural Networks

2.1. Wavelet Multiresolution Analysis

In this section, complex time signals are decomposed or transformed into relatively simple parts through wavelet decomposition. Then modeling algorithms are applied on each decomposed part. In the end, all the parts are combined to construct the original signal. A time domain signal can be transformed into frequency domain signal by using the fast Fourier transform (FFT). Although, the frequency domain analysis offers excellent frequency resolution but no time resolution. This problem can be solved by using joint time–frequency analysis (JTFA) techniques like short-time Fourier transform (STFT) and wavelet transform (WT).

The WT applies a strategy where the decomposition of a complex signal is performed using varying time and frequency resolutions. WT is a convolution of a signal with a basis function $\Psi(t)$, called mother wavelet, and its dilated and translated components $\Psi_{d,s}(t)$, called daughter wavelets. Let us denote a time signal as $x(t)$ at time t, the continuous wavelet transform (CWT) of $x(t)$ is $W_x(d,s) = \int_{-\infty}^{+\infty} x(t)\,\Psi^*_{d,s}(t)dt$, where the operator * is a complex conjugate, and $\Psi_{d,s}(t) = \frac{1}{\sqrt{s}}\Psi\left(\frac{t-d}{s}\right)$, where d is translation in time, and s is dilation or scale operator. A discrete wavelet transform (DWT) of a discrete version $x(n)$ of the signal $x(t)$ is computed through a series of high-pass (`h[n]`) and low-pass (`g[n]`) filters, where an n level decomposition of the signal $x(n)$ is computed. This step decomposes the original signal into its detailed (D_1, D_2, …, D_n) and approximation (A_1, A_2, …, A_n) wavelet coefficients. A reconstruction step or inverse discrete wavelet transform (IDWT) with high-pass (`H[n]`) and low-pass (`G[n]`) filters is performed to get the original signal back as shown in Fig.1.

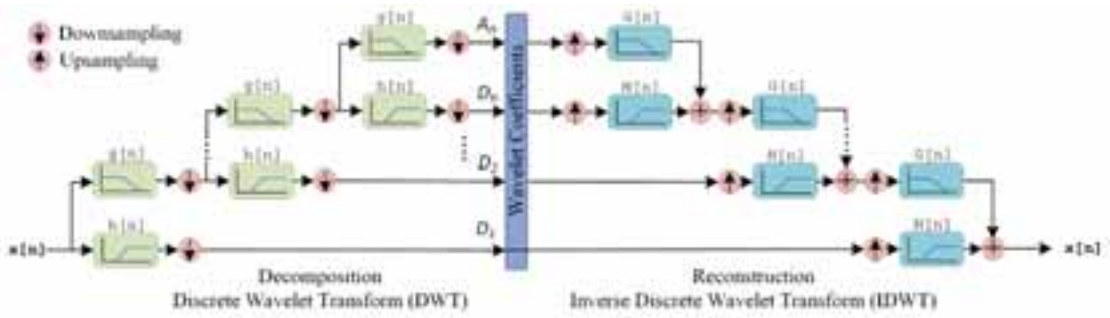

Fig. 1. Decomposition and reconstruction, DWT

The wavelet multiresolution analysis can be combined with ANNs to improve the modeling performance of traditional ANN. Each input variable $x(n)$ and output variable $y(n)$ are decomposed into their detailed and approximation wavelet coefficients through DWT. The decomposition process is stopped where R^2 is maximized. First level detailed coefficients of each input variable are used as input to an ANN to estimate first level detailed coefficient of the output. Similarly, second level detailed coefficients of the input variables are used as input to an ANN to estimate second level detailed coefficient of the output and so on. On the other hand, only n^{th} level approximation coefficients of each input variables are used to estimate n^{th} level approximation coefficient of the output variable. At the end, all estimated detailed and approximation coefficients of the output variable are combined through IDWT to construct an estimation of the original output signal. Figure 2 shows the process.

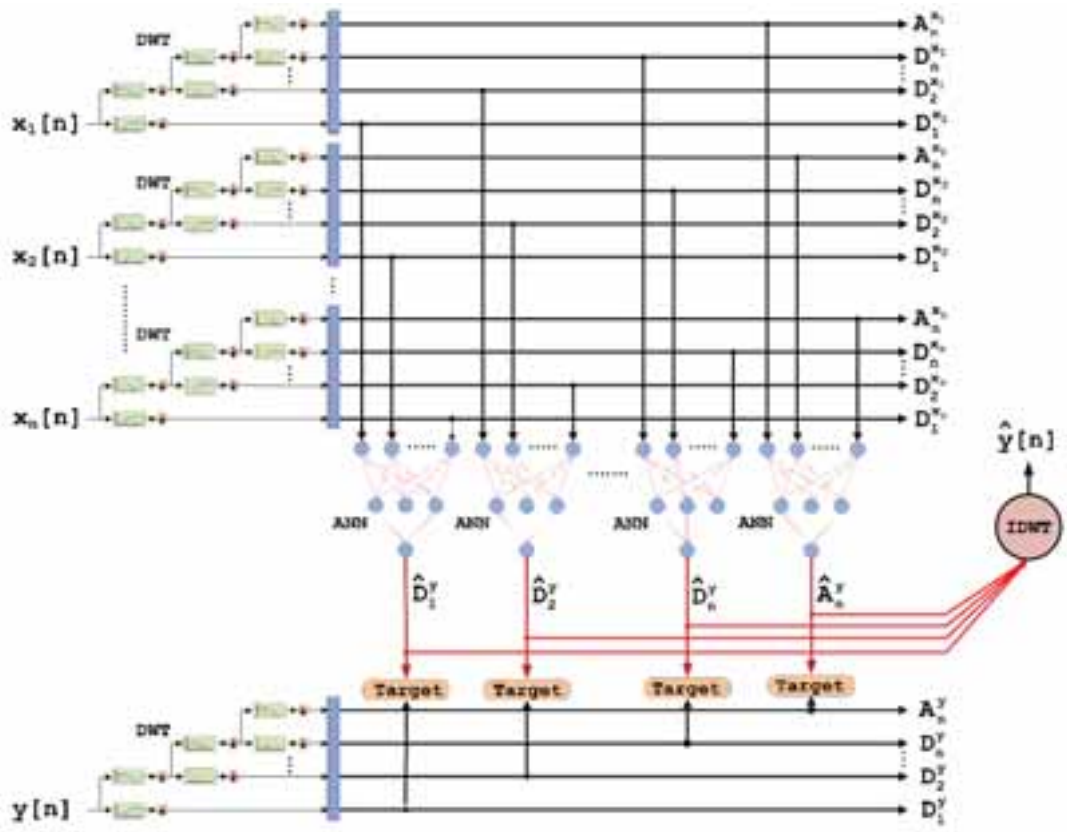

Fig. 2: Wavelet decomposition combined with ANN

2.2. Artificial Neural Network (ANN)

ANN simulates biological nervous systems and tries to mimic information processing capabilities of human brain. ANNs are successfully used in many real-world problems including non-linear function estimation, pattern identification, classification, regression, and forecasting. One of the most common ANN architecture used in research is Multi-layer perception (MLP). Among MLP, the widely used network architecture is feed-forward network with one hidden layer as shown in Fig. 3.

The input–output equations of the k^{th} neuron are as follows (Haykin 1994):

$$y_k = \Phi\left(u_k - \theta_k\right), \qquad u_k = \sum_{j=1}^{n} w_{kj} x_j \,. \qquad \text{(eq. 1)}$$

The input elements of the ANN are $x_1, x_2, ...x_n$ as shown in 3, the output of the summation is u_k , θ_k is a threshold, $w_1, w_2, ...w_n$ are the neuron's synaptic weights and $\Phi(.)$ is an activation function. The neural network has the ability to learn from its environment. In the learning process, synaptic weights of the ANN are updated through enforcement applied to the ANN from the environment. The learning rule has the following form

$$w_{kj}\left(n+1\right) = w_{kj}\left(n\right) + \Delta w_{kj}\left(n\right), \qquad \text{(eq. 2)}$$

where $\Delta w_{kj}\left(n\right)$ is the adjustment of the weight $w_{kj}\left(n\right)$ at n^{th} time-step. The computation of $\Delta w_{kj}\left(n\right)$ is performed through well-known back propagation algorithms including Levenberg-Marquardt optimization, steepest decent techniques and quasi-Newton methods (Haykin 1994).

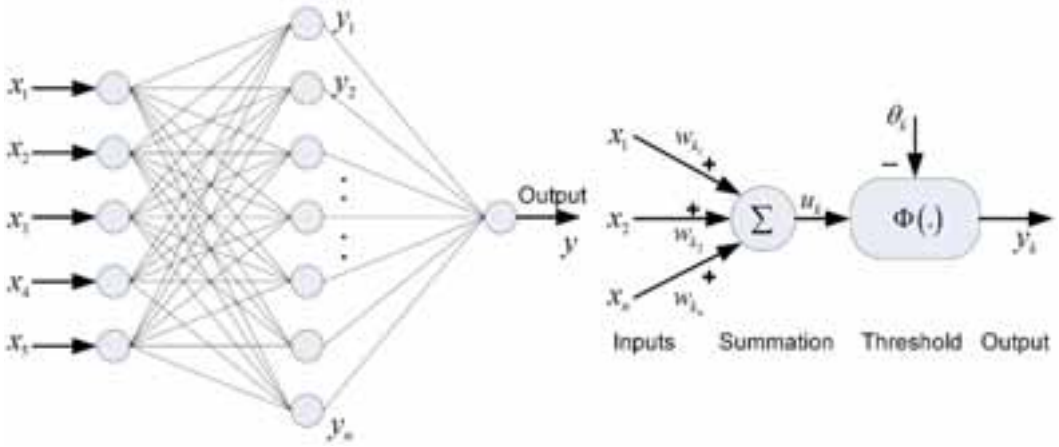

Fig. 3: Feed Forward Artificial Neural Network

2.3. Statistical Evaluation Metrics

The following statistical metrics are used to evaluate the model performance.

$$RMSE = 100\left(\frac{\sqrt{\sum_{n=1}^{N_t}\frac{(GHI-\widehat{GHI})^2}{N_t}}}{\sum_{n=1}^{N_t}\frac{GHI}{N_t}}\right)\%, \quad \text{(eq. 3)}$$

$$MAPE = 100\left(\frac{1}{N_t}\sum_{n=1}^{N_t}\frac{|GHI-\widehat{GHI}|}{|GHI|}\right)\%, \quad \text{(eq. 4)}$$

$$MBE = 100\left(\frac{\sum_{n=1}^{N_t} GHI-\widehat{GHI}}{\sum_{n=1}^{N_t} GHI}\right)\%, \quad \text{(eq. 5)}$$

$$R^2 = 100\left(1-\frac{\sum_{n=1}^{N_t}(GHI-\widehat{GHI})^2}{\sum_{n=1}^{N_t}(GHI-\overline{GHI})^2}\right)\%, \quad \text{(eq. 6)}$$

where root mean square error is RMSE, mean absolute percentage error is MAPE, mean bias error is MBE, and coefficient of determination is R^2. The terms $GHI, \widehat{GHI},$ and $\overline{GHI}$ are original, estimated and mean global horizontal irradiances. The total number of samples in the test data is N_t. In addition, *t*-statistics is performed where it is objectively determined whether a model's estimates are statistically significant. The *t*-statistics is calculated from RMSE and MBE as

$$t = \sqrt{\left(\frac{(N_t-1)MBE^2}{RMSE^2-MBE^2}\right)}. \quad \text{(eq. 7)}$$

The model's performance is better for smaller values of the t-statistics. In order to determine the statistical significance of the model's estimate, a critical t value from standard statistical tables has to be obtained for $\mathbf{1-\alpha}$ confidence level and $\boldsymbol{N_t-1}$ degrees of freedom (DoF).

3. Simulations and Discussions

3.1. Data Collection and Quality Control

Daily averaged data for ten years (2004 – 2013: 3650 samples), collected from Abu Dhabi international airport, UAE at Latitude of 24.22° N and Longitude of 54.65° E are used in this study. The data includes temperature (T : °C), relative humidity (RH : %), wind speed (WS : knots), sunshine duration (SSD : hours), and global horizontal irradiance (GHI : Wh/m^2). The data are checked for missing values by visual inspection. In addition, a multivariate statistical outlier detection using squared Mahalanobis distance is performed. A total of 109 (3%) samples are discarded as being outliers. This leaves a valid data of 3541 samples. Fig. 3 shows the time history of the cleaned data. The data are further normalized in the range of [-1 1], to be used for ANN training.

3.2. ANN Implementation

An MLP is initialized with four input neurons, ten hidden neurons, and one output neuron. The synaptic weights of the MLP are initialized randomly, and Levenberg–Marquardt algorithm is used for training. The stopping criteria are either maximum generations of 300 or MSE value of ≤ 0.02. The number of hidden layer neurons is an important parameter in the modeling process, and in this particular work, an MLP with ten neurons in the hidden layer is found reasonable. This number is found by a simulation experiment where an MLP is initialized with varying number of hidden layer neurons from 1 to 30, and for each MLP, the process of training, validation, and testing is repeated 30 times and the values of RMSE are recorded.

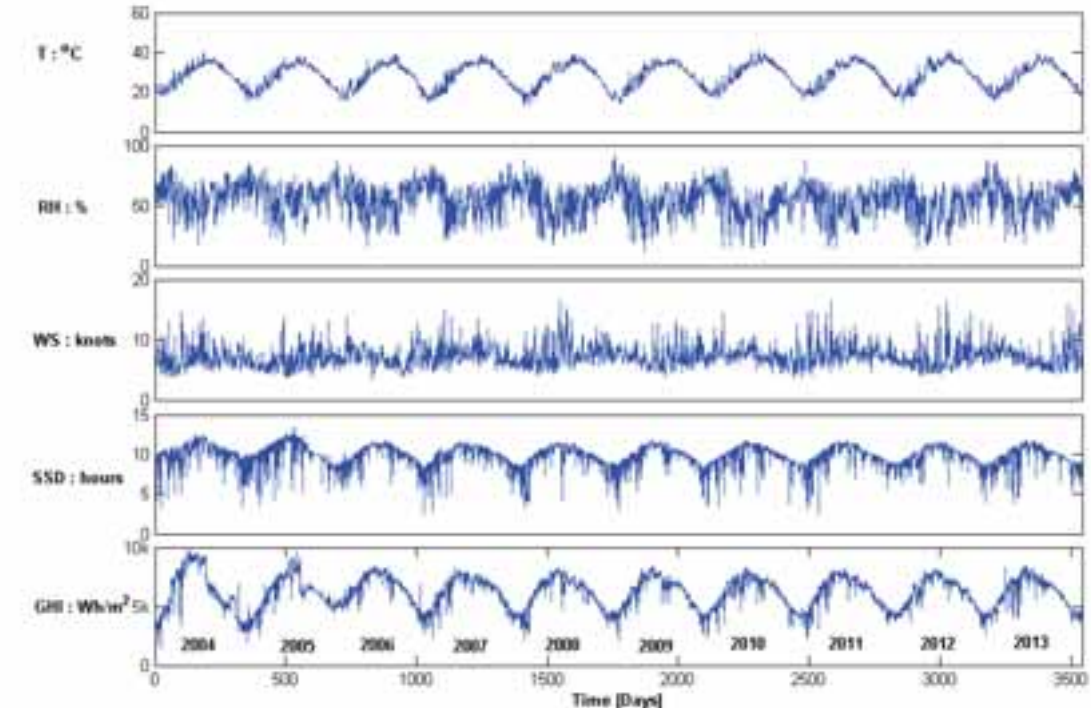

Fig. 4: Time history of the collected data

The MLP with low RMSE is selected for further modeling. The data are divided into training, validation and testing data sets of 2480 (70%), 530 (15%) and 530 (15%) data points, respectively. Fig. 5 shows the results with Fig.5 (a) plotting the time histories of measured and estimated GHIs without wavelet decomposition, using only standalone-MLP. Fig. 5 (d) shows time histories of measured and estimated GHIs with wavelet decomposition, the wavelet approach. Fig. 5 (b) and Fig. 5 (e) plots the results of regression analysis for both the standalone and wavelet approaches, respectively. Fig. 5(c) and Fig. 5 (f) plots the wavelet cross spectrum (WCS) analysis for both approaches. Further analysis of Fig. 5 reveals that wavelet-MLP approach improves the modeling performance of the MLP with R^2 of 96.34% and RMSE of 235.25 Wh m^{-2} day^{-1} (3.88%) as compared to the standalone-MLP approach with R^2 of 89.21% and RMSE of 415.54 Wh m^{-2} day^{-1} (6.83%). A WCS plot in Fig. 5 (c) reveals that in the case of standalone-MLP approach, a frequency component of 0.07×10^{-6} Hz (6-month on the frequency axis or y-axis) is not correctly modeled. A relative phase difference of 45° to 95° (direction of small black arrows inside the WCS plot) between measured and estimated GHIs is observed from the time stamp of 3200 to 3325 days on the time axis (see the red colored arrows indicated on the time axis or x-axis). On the other hand, this is not the problem with the wavelet-MLP approach and the relative phase difference is corrected as shown in Fig. 5 (f). The direction of small black arrows in the WCS plot is towards right most of the time. This concludes that standalone-MLP approach could not model the frequency contents of the GHI signal related to 6-month. However, when the signal is decomposed, with wavelet decomposition, into relatively simple parts, the problem vanishes. The value of R^2 is improved by 6.85%. In addition, looking closely at the time histories in Fig.5 (a), we clearly see the poor modeling performance of the standalone-MLP around time stamps of 3200 to 3325 days at time axis. This corresponds to the months of February, March, and April in the test year of 2013. The regression plot in Fig. 5 (b) reveals that the standalone-MLP model slightly overpredicts the values of GHI in the lower region on 3000 to 5000 Wh m^{-2} day^{-1}. However, this problem is improved in wavelet-MLP regression plot of Fig. 5 (e) because of the removal of

unwanted noise components. Overall, the modeling performance of the wavelet-MLP outperforms the standalone-MLP approach. The optimum wavelet decomposition level where R^2 is maximized is 6.

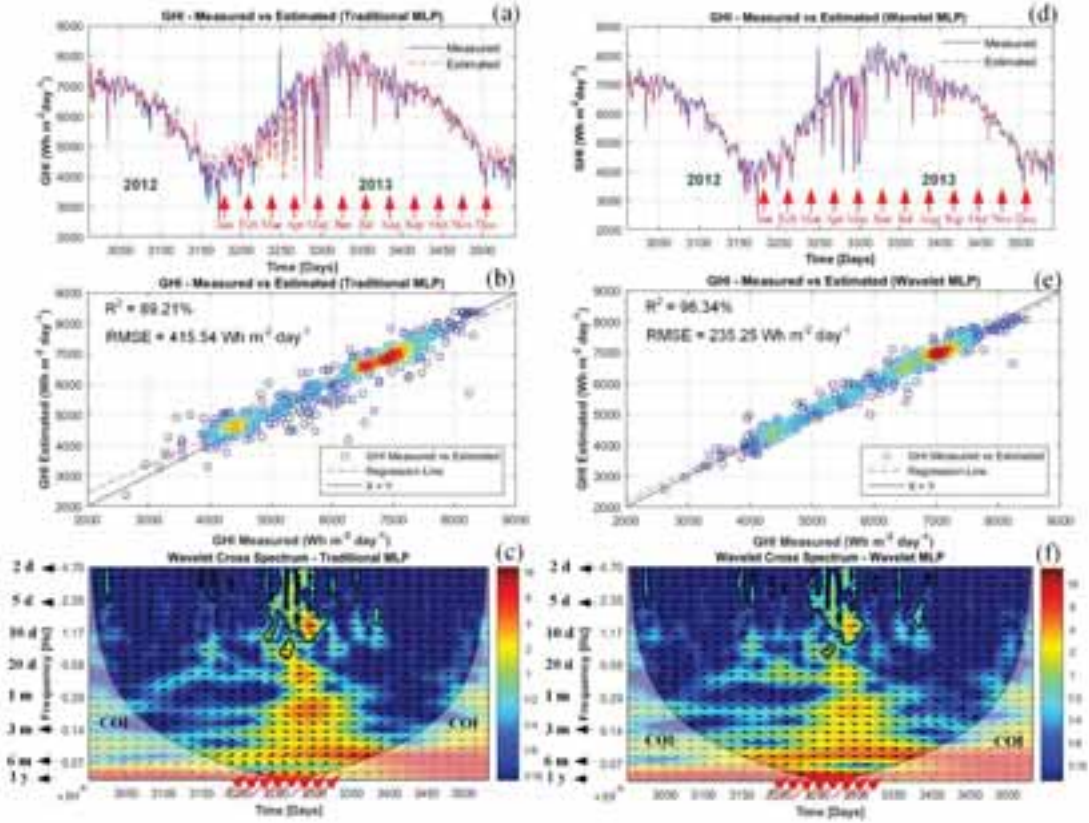

Fig. 5: ANN results (a) measured and simulated GHI, standalone-MLP (b) regression analysis, standalone-MLP (c) Wavelet cross spectrum, standalone-MLP, where relative phase arrows point right for in-phase and left for anti-phase coherence (d) measured and simulated GHI, wavelet-MLP (e) regression analysis, wavelet-MLP (f) Wavelet cross spectrum, wavelet-MLP, where relative phase arrows point right for in-phase and left for anti-phase coherence.

Table1. Model Comparisons

Model	Standalone approach					Wavelet approach				
	R^2 (%) [95% CI]	RMSE (%)	MAPE (%)	MBE (%)	*t*- stat	R^2 (%) [95% CI]	RMSE (%)	MAPE (%)	MBE (%)	*t*-stat
MLP	89.21 [0.87- 0.911]	6.82	5.15	-0.53	1.79	96.34 [0.959- 0.97]	3.89	2.98	0.11	0.59

4. Conclusion

This study models global horizontal irradiation (GHI) over Abu Dhabi, the United Arab Emirates using a widely used soft-computing algorithm in this domain, the artificial neural network (ANN). The suggested model use four sets of inputs: temperature (T), relative humidity (RH), wind speed (WS), and sunshine duration (SSD). The traditional ANN modeling approaches lack the ability to capture temporal and spectral dynamics present in the signals. In this paper, the complex input signals are decomposed into relatively simple time series with varying time and frequency resolutions using wavelet decomposition. ANN modeling is applied to these simple time series, and the modeled time series are combined to form an estimate of the final complex signal. The results show that the proposed strategy significantly improves the performance of traditional ANN. The maximum improvement is observed where the R^2 is improved by 6.83%. In addition, this paper presents a critical analysis of the results in time, frequency and phase domains. It is evident from the analysis that models work better when signals are de-noised, and frequency and phase coherence are achieved between measured and estimated solar radiations for critical and representative frequencies.

This study demonstrates the merits of wavelet-ANN models for solar radiations. However, further testing is required before the suggested techniques are applied to real-life applications. Tests are required for high-resolution data with quantification of potential uncertainties. There need to be rigorous tests at other geographical locations to assess the wider potential and versatility of the proposed wavelet-ANN models for solar energy applications.

5. References

Babu, C. N. and B. E. Reddy (2014). "A moving-average filter based hybrid ARIMA–ANN model for forecasting time series data." Applied Soft Computing **23**: 27-38.

Behrang, M. A., E. Assareh, A. R. Noghrehabadi and A. Ghanbarzadeh (2011). "New sunshine-based models for predicting global solar radiation using PSO (particle swarm optimization) technique." Energy **36**(5): 3036-3049.

Cornaro, C., M. Pierro and F. Bucci (2015). "Master optimization process based on neural networks ensemble for 24-h solar irradiance forecast." Solar Energy **111**: 297-312.

Hassan, J. (2014). "ARIMA and regression models for prediction of daily and monthly clearness index." Renewable Energy **68**: 421-427.

Haykin, S. (1994). Neural Networks: A Comprehensive Foundation. MacMillan, New York.

Islam, M. D., I. Kubo, M. Ohadi and A. A. Alili (2009). "Measurement of solar energy radiation in Abu Dhabi, UAE." Applied Energy **86**(4): 511-515.

İzgi, E., A. Öztopal, B. Yerli, M. K. Kaymak and A. D. Şahin (2012). "Short–mid-term solar power prediction by using artificial neural networks." Solar Energy **86**(2): 725-733.

Linares-Rodriguez, A., J. A. Ruiz-Arias, D. Pozo-Vazquez and J. Tovar-Pescador (2013). "An artificial neural network ensemble model for estimating global solar radiation from Meteosat satellite images." Energy **61**: 636-645.

Lu, N., J. Qin, K. Yang and J. Sun (2011). "A simple and efficient algorithm to estimate daily global solar radiation from geostationary satellite data." Energy **36**(5): 3179-3188.

Mohammadi, K., S. Shamshirband, M. H. Anisi, K. A. Alam and D. Petković (2015). "Support vector regression based prediction of global solar radiation on a horizontal surface." Energy Conversion and Management **91**: 433-441.

Mohandes, M. A. (2012). "Modeling global solar radiation using Particle Swarm Optimization (PSO)." Solar Energy **86**(11): 3137-3145.

Olatomiwa, L., S. Mekhilef, S. Shamshirband, K. Mohammadi, D. Petković and C. Sudheer (2015). "A support vector machine–firefly algorithm-based model for global solar radiation prediction." Solar Energy **115**: 632-644.

Salcedo-Sanz, S., C. Casanova-Mateo, A. Pastor-Sánchez and M. Sánchez-Girón (2014). "Daily global solar radiation prediction based on a hybrid Coral Reefs Optimization – Extreme Learning Machine approach." Solar Energy **105**: 91-98.

Voyant, C., C. Darras, M. Muselli, C. Paoli, M.-L. Nivet and P. Poggi (2014). "Bayesian rules and stochastic models for high accuracy prediction of solar radiation." Applied Energy **114**: 218-226.

Yacef, R., M. Benghanem and A. Mellit (2012). "Prediction of daily global solar irradiation data using Bayesian neural network: A comparative study." Renewable Energy **48**: 146-154.

Artificial Neural Networks (ANN) for the Prediction of Local Outside Temperatures and Solar Yields

Wolfgang Kramer, Moritz Bitterling

Fraunhofer Institute for Solar Energy Systems (Germany)

Abstract

Artificial Neural Networks (ANN) are the basis of a new intelligent control concept for residential heating systems developed at Fraunhofer ISE. This artificial intelligence based concept is able to predict data like local outside temperature, solar thermal yield, thermal behavior of a building and capacity level of a thermal storage based on measured data without using any physical model based simulation tool. This allows to improve energy efficiency and simplicity of control devices at the same time by considering the above mentioned predicted data. The current paper shows results of prediction by ANN for local outside temperature and solar yields of a solar thermal installation. The focus of the prediction method is not highest accuracy but simplicity of application, enabling low cost model predictive control. Accuracy of the local outside temperature prediction is doubled compared to a pure weather forecast data for the tested location. Solar yield prediction is also quite in line with real measurement data at the location investigated. The achieved prediction quality is reasonable and promising for improved heating system control.

Keywords: Artificial Neural Networks, Artificial Intelligence, Solar Thermal, Control, Prediction of Temperature, Prediction of Solar Yield, Heating System

1. Introduction

Similar to biological Neural Networks (brains), Artificial Neural Networks (ANN) are able to automatically develop strategies of operation based on experience in the past. The structure of ANN is motivated by the knowledge of research in Neural Science. For an introduction to Neural Networks see for example Gurney, 1997. It is obvious that such structures could be very beneficial for technical control tasks. For solar thermal heating applications ANNs seem to be useful for learning the individual thermal dynamics of a building including fossil fuel heating, the effects of passive solar heating (i.e. heating by sunlight hitting the building surface and passing window surfaces), shading and heat losses to the ambient, thus enabling the prediction of future temperature development in the building. Other applications are the prediction of storage temperature distribution and solar thermal yields of the installation. All these predictions do not need any physical model based simulation. The ANN is able to perform these predictions based on training from past measurement data, only. It is able to handle non-linear static and dynamic systems.

Thus, ANNs provide the back bone of a new self-learning control concept for solar thermal systems based on simple and cheap prediction methods. Local climate data, individual thermal behavior of buildings, solar passive and active gains can easily be forecasted without costly and tedious simulation. This allows not only a significant improvement of energy efficiency but also cost reduction installation and set-up of controllers.

This paper presents the description of the ANN method for the prediction of local outside temperatures and solar yields on a real building equipped with a solar thermal supported heating system. First prediction results are shown and discussed.

doi:10.18086/swc.2017.22.03 Available at http://proceedings.ises.org

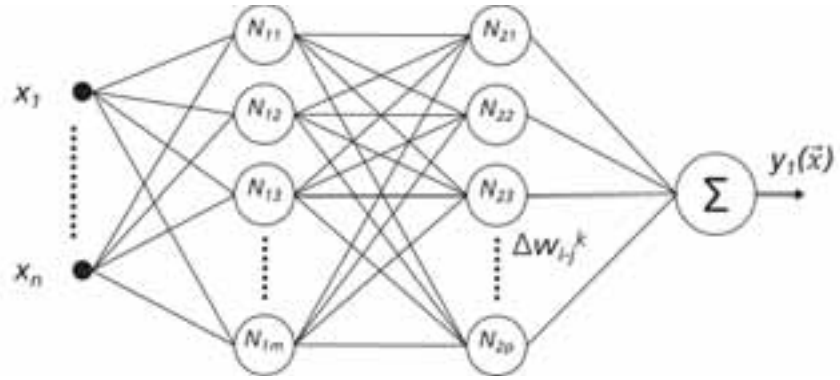

Fig. 1: 4-layer ANN Network with one input layer, 2 hidden layers and one output layer

2. Prediction using ANN Structures

ANN structures for the prediction of local outside temperatures and solar yields of a solar thermal installation have been developed at the authors' institution. The ANN models consist of a 4-layer ANN structure (figure 1) including one input layer, two hidden layers and one output. Input data x_1-x_m is normalized to +/- 1 before being transferred to the first hidden layer N_{11}-N_{1n}. The calculation procedure in each neuron N is presented in figure 2. Each normalized input value is multiplied by a weight W_i and summed up. An offset is added and the sum is passed through a transfer function. In our case this is hyperbolic tangent (*tanh*). The calculation scheme for the second layer is identical. In the last layer, which is the output layer, the output of the second hidden layer N_{21}-N_{2p} is summed up and extended in order to get the output value $y_1(\vec{x})$. Figure 1 shows the ANN.

A program code was developed to do training of the ANN. This means to determine the most suitable values of W_i for each neuron in order to get the best fit between measured input and output training data of the ANN. Main challenges of the training process are overfitting, convergence, termination method, being trapped in local minima, required processing power to perform an epoch of training and required RAM to perform an epoch of training.

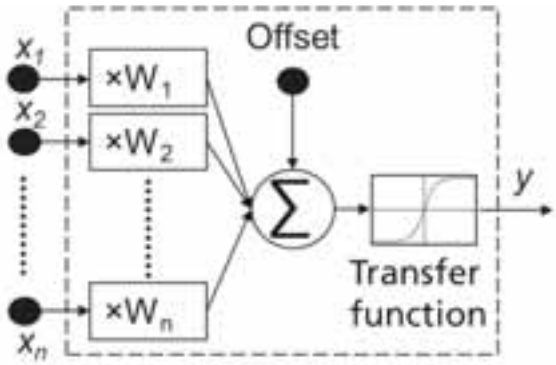

Fig. 2: Mathematical description of a neuron N_{ij}

Based the local conditions of weather data and a real individual building construction a trial and error approach was used to choose the most suitable topology. The most important criteria were accuracy of prediction, robustness of the training result and computation time. Overfitting can be avoided by minimizing the size of the ANN. A maximum of 2 hidden layers with not more than 15 neurons each proved to be appropriate for the application presented in this paper. The trials carried out showed that at least for the data that was available a simple termination rule could be defined by stopping the training after a fixed number of training epochs. The developed algorithm follows a supervised training approach and incorporates several training features including weight correction, momentum modification and temperature as described by Haykin 2005 in order to avoid being trapped in local minima. Required processing power and RAM does not seem to be a problem for the presented static ANNs. However, this has to be reevaluated for dynamic ANNs that will be used in further steps of the current work.

Training was based on measured training data from a real solar thermal heating installation, which was available for a complete year (2016) for the location of Marburg, Germany.

2.1. Prediction of Local Outside Temperature

Control of the heating system of a building is normally based on the measurement of the local temperature outside the building. Local outside temperature of a real building that is measured by a sensor mounted directly on the wall of the building differs obviously from reference temperature data of meteorological stations. When compared to local meteorological prediction, differences are expected to be even more important. On the one hand, this is due to inaccuracy in forecasting for a special location. In general, weather forecast does not account for very individual small scale local impacts on temperature. On the other hand, the local conditions of the mounting situation of the temperature sensor are not considered. This includes effects of wind, temporary exposure to irradiation, infrared cooling to the sky, heating by the wall of the building and error of local temperature measurement.

Thus, when trying to improve efficiency of a heating control system by considering future outside temperature development, it seems reasonable to use a more precise method of forecasting the local temperature. Instead of relying on weather forecast temperature only, ANN is able to deliver more precise information on future local temperature development. The big advantage of ANN is its self-learning capability. Just by automatically analyzing local measurement data such a system is able to predict local temperature development without any physical simulation model behind. The complex non-linear characteristics of the local climate is taken into account with this simple approach.

Such an ANN correlates real measured temperature and data from a weather forecast. Apart from the temperature data itself more variables like solar irradiation, wind speed and direction, hour of the day and day of the year are taken into account. This additional data deliver implicitly important information on the position of the sun, local shading, and heating by irradiation. The ANN is trained by combining historical locally measured temperature data and collected historical weather forecast data provided by meteoblue 2017.

Figure 3 shows the capability of an ANN to perform such a prediction. An ANN has been trained to predict the local outside temperature with a forecast horizon of one hour, based on historical data from a regional weather forecast provided by meteoblue and measurement data. The static ANN consisted of 4 inputs (temperature forecast one hour ahead (1), time (2), date (3) and current local temperature (4)), 2 hidden layers of 10 neurons each and one output (local temperature one hour ahead). Wind and irradiation data did not further improve the forecast. This is due to the fact that the sensor in this case never sees solar irradiation and is well protect from wind effects.

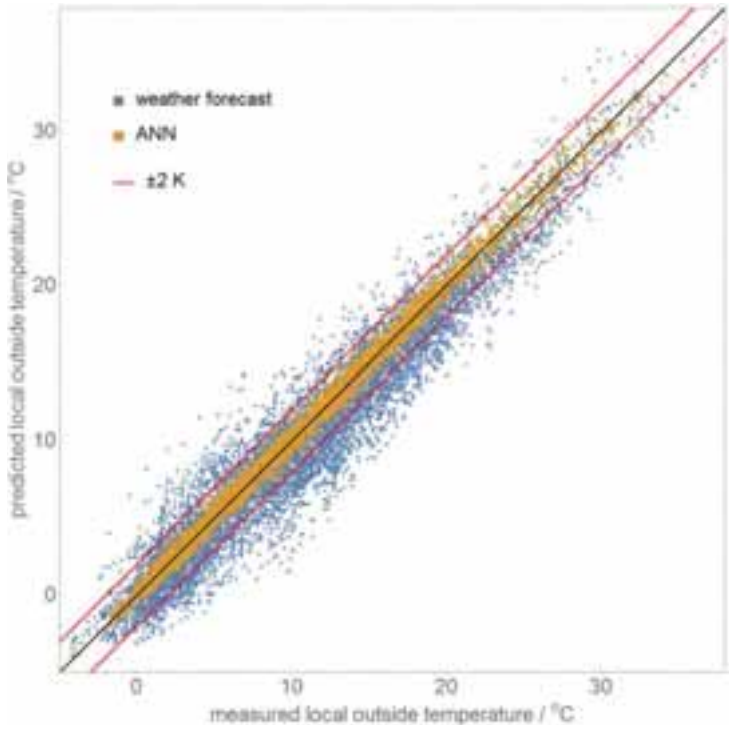

Fig. 3: Prediction of local outside temperature of a building

The results show an improvement in standard deviation from 1.9 K to 1.1 K when comparing pure weather forecast temperature data and ANN prediction with the real locally measured outside temperature. The mean deviation is corrected from 0.9 K to 0 K. At first glance this seems possibly disappointing. However, it has to be stressed that this improvement could be automatically generated in a real application without dealing with any tedious parameterization. Compared to many other prediction methods, it is somehow "for free".

2.2. Prediction of Solar Yield of a Solar Thermal Installation

A second ANN has been used to do a one-hour prediction of the solar yield. The product of temperature difference between collector inlet and outlet and the rotation speed of the pump was taken as an indicator of solar yield. The reason for using such an indicator instead of real yield data is the availability of data. In a future commercial application, data of real solar yield is not always available. Therefore, a control system has to work with such an indicator.

Training of the network has been performed with historical weather forecast data and measured data from one year. The appropriate ANN consists of two hidden layers with 12 neurons each. The input data given to the network were date (1), time (2), storage tank temperatures at top (3) and bottom (4) and predicted data from a weather forecast for radiation (5), ambient temperature (6) and cloud cover (7) as well as the measured solar heat input during the previous hour (8). The data was split into a training set and a validation set. Figure 4 shows quite reasonable agreement between prediction and measurement.

The accuracy of the predicted total daily solar yield is shown in figure 5. 80% of the daily solar yield data is predicted with an accuracy better than 15.2 % when compared to the average daily solar yield.

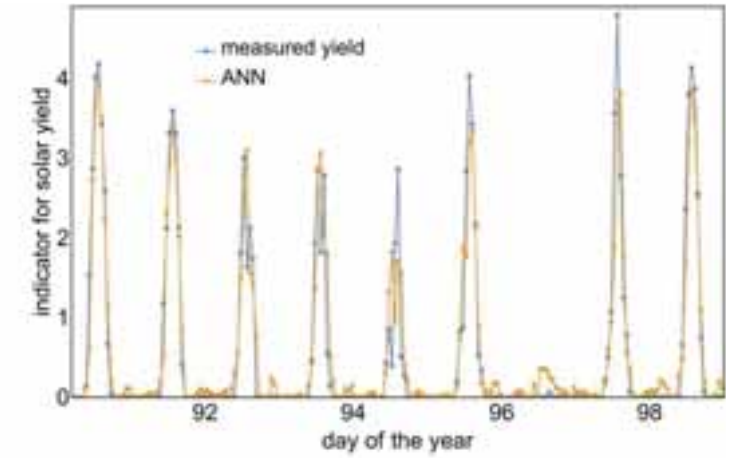

Fig. 4: Prediction of hourly mean solar yield indicator and comparison with measured data

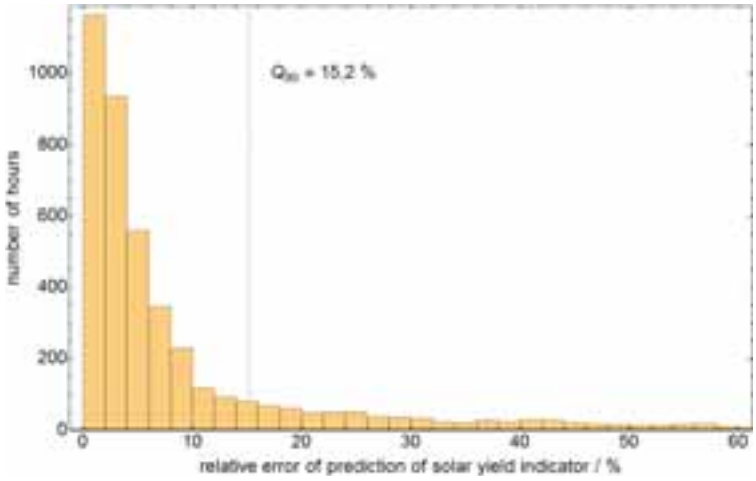

Fig. 5: Accuracy of prediction of solar yield indicator

3. Discussion of the Results

The results shown in this paper have been created by training ANNs for one single local site for one individual building in an urban environment in the city of Marburg, Germany based on real measured data and historical weather forecast data. The accuracy communicated is only valid for these individual conditions. Accuracy under different conditions is expected to be of similar magnitudes but have to be checked. In the case of the black box model ANN, this can only be done by statistical methods. A limited comparison of the ANN method presented with other statistical approaches for different sites and different types of training data showed comparable accuracy, though.

Answering the question of “How accurate is the ANN approach?” in a general sense is not possible. The ANN training approach can be regarded as a sort of sophisticated non-linear regression of input and output data. It is the same as asking how precise is a least-square method for linear correlation of data. This depends on the data, not on the method itself.

Unlike in simulations based on physical models, each site and building needs a new creation of an ANN model by training with individual data. The advantage of ANN is, that this model building procedure can be realized in an automatic way, whereas physical models often need tedious parameter identification for adjusting the model to individual conditions.

An important feature of ANN is that inaccurate input data is less of a problem than for other approaches, since

systematic inaccuracy is automatically compensated by the self-learning feature. The same holds for missing data or physically incomplete data with regard to the physical model. Simple weather forecast data, which is easily available for almost every place on earth, is sufficient to make the ANN approach work. For example calculating the solar yield of a solar thermal installation by a physical model needs a precise array of irradiation at any time. Such irradiation data is not easily available from simple weather forecast data. However, the ANN approach is able to process successfully such simple data. By feeding not only the ANN with the irradiation data from the weather forecast but also other inputs like time of the day, month, forecast of cloudiness, current outside temperature, temperatures of the thermal storage and others if necessary (i.e. barometric pressure, wind speed and direction, humidity etc.) the ANN is able to correlate these values with the individual output of the installation. This correlation inherently includes technical characteristics of the heating installation, thermo-physical properties of the building, passive heating, shading effects and others. As long as there is a systematic correlation of input data and the desired output (solar yield in this case), the system is able to generate a black box model describing this dependence. Accuracy depends on careful selection of input data, accuracy of input data, ANN topology and training method, of course.

4. Conclusion and Outlook

A new control approach using Artificial Neural Networks provide a powerful concept that could significantly improve energy efficiency and reduce cost at the same time. It is not expected, that ANN is more precise than other modelling approaches. Its strength is its simplicity in application by relying on local measured and simple weather forecast data, only. Parametrization as needed in physical models is not necessary. The ANN model describing individual characteristics of the building and the heating installation under local weather conditions can be created automatically. First results of using an ANN approach for predicting local outside temperatures and solar yields of a real installation show, that it is possible to use such an approach in order to avoid costly simulation methods. Future improvement is expected after more work on optimum ANN structures and training methods. Current work on ANNs with back propagation shows that dynamic ANN structures are even more appropriate for predicting future status several hours in advance. However, computational requirements and calculation speed have to be carefully monitored.

Further steps will include the prediction of inside room temperatures of a building and the development of the level of charge capacity in the thermal storage using the ANN approach and the implementation of complete control algorithm for a solar thermal heating installation. First results on the prediction of the stratification in thermal storage are also very promising (Kramer et al. 2017).

Further validation in order to provide information of the general applicability and limitations on different sites and in different buildings is needed.

5. Acknowledgment

This research was conducted within the project „Neuronale Netzwerke für die Anwendung in der Solarthermie“ (Neural Networks for the application in solar Thermal)(ANNsolar) and is supported by the German Ministry of Economics (Bundesministerium für Wirtschaft, BMWi) under the grant number FKZ 325548 and supported by the project executing organization PTJ Jülich. The responsibility for the content of this paper lies completely with the authors.

6. References

Gurney, K., 1979. An Introduction to Neural Networks, UCL Press Limited, London

Haykin,S., 2005. “Neural Networks – A Comprehensive foundation”, Pearson Prentice Hall, 2nd Edition

Kramer, W., Bohrer, J., Bitterling, M., 2017. Künstliche Neuronale Netzwerke für die Anwendung in der Solarthermie, Poster, in Ostbayerisches Technologie-Transfer-Institut e.V. -OTTI-, Regensburg, 27. Symposium Thermische Solarenergie, Bad Staffelstein, p.p. 36-37, 2017

Meteoblue. „http://www.meteoblue.com,“ 16 01 2017. [Online].

Resource Measurement and Instrumentation

COMPARISON BETWEEN LEBARON-PEREZ AND DAL PAI-ESCOBEDO CORRECTION METHODS FOR DIFFUSE IRRADIANCE MEASURED BY THE *MEO* SHADOWRING METHOD

Alexandre Dal Pai[1], João Francisco Escobedo[1] and Enzo Dal Pai[1]

[1] São Paulo State University, School of Agricultural Sciences/UNESP, Botucatu (Brazil)

Abstract

This study aims to determine the effectiveness of two methods of correction of diffuse irradiance measured with shadowbands: LeBaron-Perez method and Dal Pai-Escobedo method. For the LeBaron-Perez method, we use the original coefficients and adjusted coefficients for the atmospheric conditions of Botucatu. Global, direct and diffuse solar irradiances were supplied by the Laboratory of Solar Radiometry of Botucatu. The period assigned for the study comprised the years 1996 to 2005. The results showed that the LeBaron-Perez correction model with the original coefficients are not suitable for correction of diffuse irradiance in Botucatu. Otherwise, the LeBaron-Perez model with adjusted coefficients and Dal Pai-Escobedo model are indicated for the correction of diffuse irradiance in Botucatu measured by shading ring with accuracy of 0.5%.

Keywords: Shading ring, diffuse irradiance, Correction Factors, anisotropy, Measurement Methods.

1. Introduction

Information of the solar potential are required in various industries and areas of society, with applications in climatology, architecture, agriculture, passive lighting, satellite studies, among others. In general, the information serves to supply solar energy conversion models, thermal comfort and energy balance.

Several weather stations, for practical reasons, measure, routinely, only the global radiation. Measures of direct and diffuse radiation are less frequent due to the high financial costs. However, it is possible to establish a database of global, diffuse and direct radiation with low financial investment. In this case, the global component is monitored by a pyranometer positioned in the horizontal plane of the locality, the diffuse component is monitored by a pyranometer placed under the shade of a shading ring and the direct component is obtained by the difference between the global and diffuse components.

This method of measuring diffuse radiation is known as shading ring method. Different assemblies are described in the literature and best known is the Drummond´s assembly (1956) (Fig. 1). In Drummond assembly, the pyranometer remains fixed and the shading ring moves parallel to the polar axis to compensate the variations in the solar declination. The Drummond assembly is currently the most widely used. An alternative assembly with low cost, easy operation and maintenance, was proposed by Melo and Escobedo (1994) - *MEO* assembly (Fig. 1). In this system, the shading ring is fixed with an inclined angle equal to the local latitude, and to compensate the solar declination, the pyranometer moves parallel to the local horizon plane on a moving base to stay under the shadow produced by the ring.

Despite having operational and financial advantage, shading ring method has the disadvantage of correction factors (CF) to offset the portion (LF) of diffuse irradiance barred by shading ring (Drummond, 1956; Kasten et al, 1983; Stanhill, 1985). 5% errors in the measurement of diffuse radiation can propagate up to 20% uncertainty in the estimate of direct radiation to high zenith angles (Lebaron et al, 1990). Correction factors are based on isotropic radiation, and consider only the use of geometric factors (radius and ring width) and geographic (latitude and solar declination).

doi:10.18086/swc.2017.23.01 Available at http://proceedings.ises.org

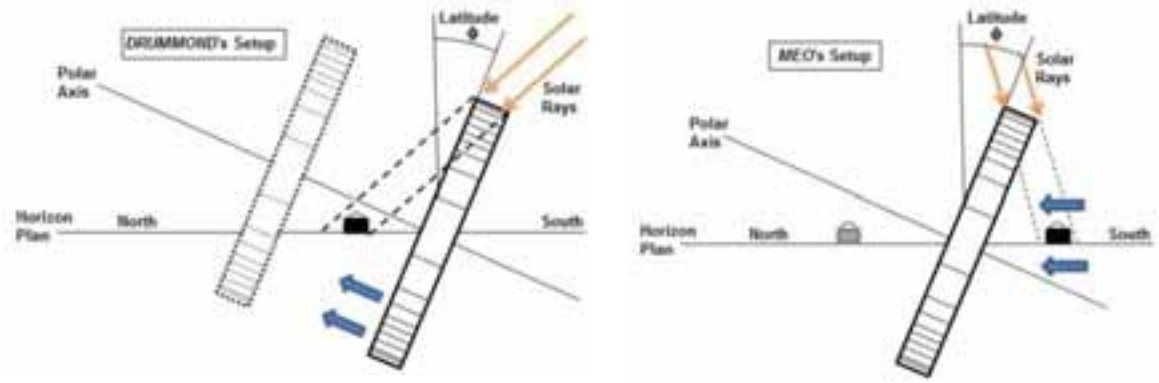

Figure 1 - Shading ring assembly: Drummond and MEO.

Several researchers have shown that the application of isotropic correction does not include atmospheric effects (turbidity, cloudiness, pollution, water vapor) that are responsible for anisotropy in the diffuse radiation. Kasten et al. (1983) and Pollard and Langevine (1988) introduced corrections based on anisotropic parameters such as K_T clearness index (ratio between the global irradiance I_G by the extraterrestrial irradiance I_O), zenith angle and atmospheric turbidity associated with isotropic correction to improve the accuracy of the measurement of diffuse irradiance by Drummond shading ring. Stanhill (1985) found that the anisotropic corrections showed spatial and temporal dependence, caused mainly by the different sizes and concentration levels of aerosols in the atmosphere. LeBaron et al (1990) proposed anisotropic correction models by combining three anisotropic parameters (zenith angle and brightness index) and an isotropic parameter (geometric and geographic), highlighting the K_T clearness index as the most significant parameter in the representation of anisotropic conditions. In this way, Iqbal (1983) recommends different anisotropic corrections to the ring as a function of K_T clearness index (3% to $0 < K_T < 0.30$; 5% to $0.30 < K_T < 0.65$ and 7% to $0.65 < K_T < 1$). Battles et al (1995) used the same parameters of LeBaron and developed two numerical correction methods through multiple linear regression: the first method uses all the parameters in a single equation, whereas the second uses geometric parameters, brightness and solar zenith angle grouped by four intervals of the K_T clearness index, a total of four numeric correction equations.

In this sense, the objective is to compare the efficiency of Lebaron-Perez and Dal Pai-Escobedo methods for correction of diffuse solar irradiance measured by the *MEO* shading ring assembly.

2. Materials and Methods

The study is based on global, direct and diffuse irradiance measurements provided by the Laboratory of Solar Radiometry, located at the Department of Bioprocess and Biotechnology, School of Agricultural Sciences / UNESP / SP (latitude 22º 54 'S, longitude 48º 27' W and altitude 716 m). There were used 10-years data (1996-2005), 75% intended for modeling and 25% for validation purposes. A computational routine was developed to separate the data, being three lines for modeling and 1 line for validation..

The city of Botucatu (Fig. 2) lies in a region of planting sugarcane and eucalyptus. It has about 130,000 inhabitants and is surrounded by an asymmetric embossing called Cuesta de Botucatu and the watersheds of the Tietê and Paranapanema. It has few industries and its economy is based on service delivery.

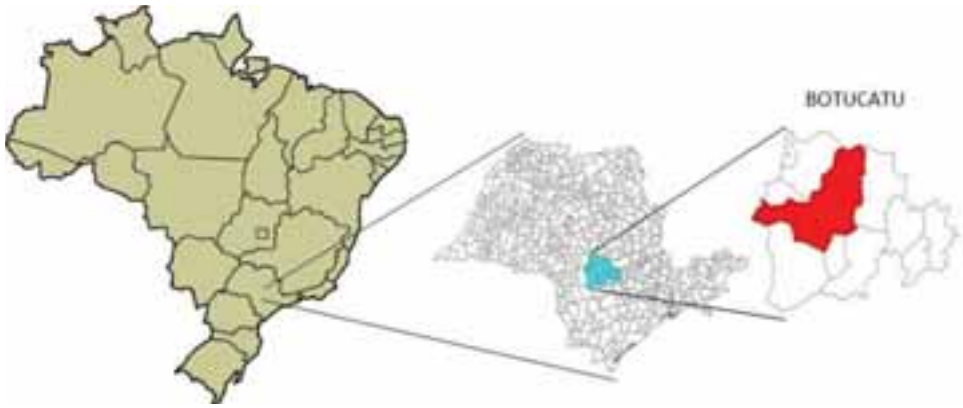

Figure 2 - Map of Brazil with state divisions showing the location of the study (Botucatu in the state of São Paulo)

According to the Köppen climate classification, the local climate is Cwa (humid subtropical climate), with hot, humid and rainy summers and dry winters and mild temperatures. The temperature and relative humidity values follow the astronomical variations, with maximum values of temperature and relative humidity in February (23.12 ° C and 78.25% respectively) and minimum temperature values in July (17.10 ° C) and relative humidity in August (63.97%). The rainy season occurs in the summer and spring, accompanied by high cloudiness. About 80% of the annual rainfall occurs during this period, with a maximum in January (246.2 mm). In the winter and fall seasons, the average rainfall is less than 100 mm per month, and minimum in August (36.1 mm). Regarding aerosols, industrial activity and motor vehicles are the largest emitters of aerosols in the atmosphere. However, as the Botucatu is full of sugarcane crops, the practice of harvest burning can emit large amounts of particulate matter in the atmosphere, especially in winter, where the removal by rain is minimal (Codato et al, 2008).

The global solar irradiance I_G was measured by an Eppley PSP pyranometer; the direct solar irradiance by an Eppley NIP pyrheliometer equipped with a ST-3 solar tracking device; and diffuse solar irradiance by an Eppley PSP pyranometer under the *MEO* shading ring (radius of 0.40 m width 0.10 m). Tab. 1 shows the operating characteristics of the measurement devices.

Table 1 - Operational characteristics of the global, direct and diffuse solar irradiance measurements.

Irradiance	**Global**	**Direct**	**Diffuse**
Sensor-brand	Eppley Precision Spectral Pyranometer	Eppley Normal Incidence Pyrheliometer	Eppley Precision Spectral Pyranometer
Sensibility	±7,45 µV/Wm²	7,59 µV/Wm²	±7,47 µV/Wm²
Spectral Range	295 – 2800 nm	295 – 2800 nm	295 – 2800 nm
Response time	1 s	1 s	1 s
Linearity	±0,5% (from 0 to 2800 W/m²)	±0,5% (from 0 to 1400 W/m²)	±0,5% (from 0 to 2800 W/m²)
Cosine effect	±1% (0º<Z<70º) ±3% (70º≤Z<80º)	–	±1% (0º<Z<70º) ±3% (70º≤Z<80º)
Temperature Dependence	±1% (from -20ºC to +40ºC)	±1% (from -20ºC to +40ºC)	±1% (from -20ºC to +40ºC)



Figure 3 – Global, diffuse and direct solar irradiance measurements.

The values of solar irradiance were monitored by an automatic data acquisition system model Datalogger 23X Campbell Scientific Inc with a 0.2 Hz frequency. Mean values were calculated every 5 minutes and stored in W/m^2 format.

The diffuse irradiance data measured by the MEO shading ring (Id_{ANEL}) were corrected using the geometric correction factors proposed by Oliveira et al (2002). True diffuse irradiance, called reference diffuse irradiance (Id_{REF}) was calculated as the difference between the global and direct irradiance. Of the 525 592 available data on ten years of monitoring, 47725 (representing 9.09% of total) were removed due to the application of filters shown in Tab. 2 (Kudish and Evseev, 2008). The cutoff values are due to misalignment, lack of electricity and internal reflections occurred in the shading ring caused by low solar altitude.

Table 2 - Quality control filters and results (Kudish and Evseev, 2008).

Solar Irradiance	Filter
Global	$I_G < I_O$
Direct	$I_b \leq Io$
Diffuse	$0{,}1\ I_G \leq Id_{ANEL} < I_G$
Diffuse Reference	$0 \leq Id_{REF} \leq I_o$

For LeBaron-Perez correction method (Lebaron et al, 1990), we calculated the zenith angle (Z), the clarity index Epsilon (ε) and the brightness index (Δ).

$$Z = \cos^{-1}[\sin\phi \sin\delta + \cos\phi \cos\delta \cos\omega] \quad (1)$$

$$\varepsilon = \frac{I_G - I_d}{I_d \cos Z} + 1 \quad (2)$$

$$\Delta = \frac{I_d . m}{I_o} \quad (3)$$

where ϕ is the local latitude, δ the solar declination, ω the hour angle, I_G the global irradiance I_d the diffuse irradiance uncorrected measured by the shading ring, m the optic mass and Io the extraterrestrial irradiance mass. The Dal Pai-Escobedo correction method (Dal Pai et al, 2011) uses the atmospheric transmissivity parameter K_T.

$$K_T = \frac{I_G}{I_o} \quad (4)$$

The original method of LeBaron-Perez used the geometric correction factors for Drummond assembly. As in Botucatu the diffuse irradiance measurement method uses the MEO assembly, the geometric correction factors were adjusted for such assembly. Equations (5) and (6) show the loss of fractions of assemblies Drummond (Drummond, 1956) and MEO (Oliveira et al, 2002), respectively, and the equation (7) the calculation of the geometric correction factors.

$$F_{lost-D} = \left(\frac{2b}{\pi R}\right).cos^3\,\delta \int_0^{w_z} \cos Z\, d\omega \tag{5}$$

$$F_{lost-MEO} = \left(\frac{2b}{\pi R}\right).\cos\delta.\left[\frac{\cos(\phi+\delta)}{\cos\phi}\right]^2 \int_0^{w_z} \cos Z\, d\omega \tag{6}$$

$$F_G = \frac{1}{1-F_{lost}} \tag{7}$$

where b is the width of the ring and R the radius of the ring. The evaluation of the correction model is based on MBE and RMSE statistical indicative (Stone, 1993) given by Eq. (8) and Eq. (9), respectively.

$$MBE = \left(\sum_i^N (y_i - x_i) \Big/ N\right) \tag{8}$$

$$RMSE = \left(\sum_i^N (y_i - x_i)^2 \Big/ N\right)^{1/2} \tag{9}$$

where y_i represents the ring diffuse irradiance, x_i the reference diffuse irradiance and N is the number of observations. The MBE is the simple deviation and a positive value indicates an overestimate, while a negative value indicates an underestimate. The RMSE is the standard deviation and is related to the dispersal of values from the average.

3. Results and Discussions

In this section are compared two methods of correction of diffuse solar irradiance measured by the shading ring. The first method used is based on LeBaron-Perez correction method (Lebaron et al, 1990), using four parameters for a sky conditions description (geometrical factor, zenith angle, clarity index and brightness index). The second methodology is based on the correction method of DalPai-Escobedo (Dal Pai et al, 2011), and used two parameters for description of sky conditions (geometric factor and atmospheric transmissivity).

The LeBaron-Perez correction model considers both isotropy and anisotropy conditions of the radiation. A geometric factor was proposed for isotropy conditions based on construction features of the ring, while zenith angle, clarity index and brightness index was assigned for anisotropy conditions. In this case, while zenith angle is responsible for the position of the sun in the celestial hemisphere and the optical path taken by the sun's rays, clarity index and brightness index are linked to measurements performed on surface and reflect the interaction of radiation with the atmosphere. Tab. (3) shows the parameter values used in the LeBaron Perez-correction model divided into four sets, which result in 256 sky categories. Two situations were present for geometric factors: one containing the values of the original model for Drummond assembly and one adjusted for *MEO* assembly at Botucatu.

Table 3 - Limit values used for the four parameters chosen to describe the corrections applied to the diffuse irradiance measured by the shading ring. The combination of these parameters allow 256 sky coverage categories.

Parameters			Groups			
			1	**2**	**3**	**4**
i	Zenith angle		0 to 35	35 to 50	50 to 60	60 to 90
j	Geometric factor	(*Original)*	1 to 1.068	1.068 to 1.100	1.100 to 1.132	1,132 to ---
		(*Adjusted*)	1 to 1.123	1.123 to 1.165	1.165 to 1.208	1,208 to ---
k	Epsilon		0 to 1,253	1.253 to 2.134	2.134 to 5.980	5.980 to ---
l	Delta		0 to 0,12	0.12 to 0.20	0.20 to 0.30	0.30 to ---

Once you have determined 256 categories of sky condition, corrections were calculated by the ratio of reference diffuse irradiance to not corrected diffuse irradiance. The advantage of Lebaron Perez-model is that these 256 classes represent a "scan" of more complex analytical formulas and, since these values are tabulated, the computational time in processing is more efficient. Tab. 4 and Tab. 5 show the correction factors obtained for Lebaron Perez-correction method. In Tab. 4 are shown the original coefficients developed using Drummond assembly. In Tab. 5 are shown the adjusted coefficients for Botucatu for *MEO* assembly.

Table 4 - Correction factors for each parameter category. (LeBaron-Perez model with original coefficients)

Categories (i j k l)

(i = zenith; j = geometric factor; k = epsilon; l = delta)

categ	**fc**	**categ**	**fc**	**categ**	**Fc**	**categ**	**fc**	**categ**	**fc**	**categ**	**fc**	**categ**	**Fc**	**categ**	**fc**
1111	1.051	*1311*	1.117	*2111*	1.051	*2311*	1.115	*3111*	1.069	*3311*	1.119	*4111*	1.047	*4311*	1.074
1112	1.051	*1312*	1.117	*2112*	1.051	*2312*	1.130	*3112*	1.073	*3312*	1.115	*4112*	1.058	*4312*	1.117
1113	1.051	*1313*	1.117	*2113*	1.051	*2313*	1.128	*3113*	1.076	*3313*	1.131	*4113*	1.060	*4313*	1.103
1114	1.051	*1314*	1.117	*2114*	1.051	*2314*	1.143	*3114*	1.085	*3314*	1.117	*4114*	1.069	*4314*	1.117
1121	1.051	*1321*	1.117	*2121*	1.051	*2321*	1.117	*3121*	1.161	*3321*	1.147	*4121*	1.076	*4321*	1.104
1122	1.051	*1322*	1.117	*2122*	1.051	*2322*	1.186	*3122*	1.086	*3322*	1.168	*4122*	1.074	*4322*	1.118
1123	1.051	*1323*	1.117	*2123*	1.051	*2323*	1.180	*3123*	1.135	*3323*	1.176	*4123*	1.092	*4323*	1.143
1124	1.051	*1324*	1.117	*2124*	1.051	*2324*	1.195	*3124*	1.132	*3324*	1.183	*4124*	1.118	*4324*	1.150
1131	1.051	*1331*	1.117	*2131*	1.051	*2331*	1.117	*3131*	1.051	*3331*	1.117	*4131*	1.187	*4331*	1.139
1132	1.051	*1332*	1.117	*2132*	1.051	*2332*	1.203	*3132*	1.080	*3332*	1.211	*4132*	1.140	*4332*	1.191
1133	1.051	*1333*	1.117	*2133*	1.051	*2333*	1.207	*3133*	1.169	*3333*	1.193	*4133*	1.150	*4333*	1.180
1134	1.051	*1334*	1.117	*2134*	1.051	*2334*	1.210	*3134*	1.144	*3334*	1.226	*4134*	1.117	*4334*	1.178
1141	1.051	*1341*	1.117	*2141*	1.051	*2341*	0.990	*3141*	1.015	*3341*	0.946	*4141*	0.925	*4341*	0.977
1142	1.051	*1342*	1.117	*2142*	1.051	*2342*	1.120	*3142*	1.182	*3342*	1.081	*4142*	1.057	*4342*	1.133
1143	1.051	*1343*	1.117	*2143*	1.051	*2343*	1.117	*3143*	1.051	*3343*	1.117	*4143*	1.089	*4343*	1.216
1144	1.051	*1344*	1.117	*2144*	1.051	*2344*	1.117	*3144*	1.051	*3344*	1.117	*4144*	1.024	*4344*	1.162
1211	1.082	*1411*	1.173	*2211*	1.104	*2411*	1.163	*3211*	1.082	*3411*	1.140	*4211*	1.063	*4411*	1.030
1212	1.082	*1412*	1.176	*2212*	1.095	*2412*	1.162	*3212*	1.089	*3412*	1.142	*4212*	1.076	*4412*	1.156
1213	1.082	*1413*	1.182	*2213*	1.082	*2413*	1.159	*3213*	1.088	*3413*	1.129	*4213*	1.085	*4413*	1.156
1214	1.082	*1414*	1.191	*2214*	1.105	*2414*	1.168	*3214*	1.093	*3414*	1.156	*4214*	1.082	*4414*	1.156
1221	1.082	*1421*	1.248	*2221*	1.082	*2421*	1.184	*3221*	1.161	*3421*	1.168	*4221*	1.078	*4421*	1.146
1222	1.082	*1422*	1.211	*2222*	1.082	*2422*	1.194	*3222*	1.130	*3422*	1.177	*4222*	1.102	*4422*	1.174

1223	1.082	*1423*	1.221	*2223*	1.171	*2423*	1.213	*3223*	1.148	*3423*	1.197	*4223*	1.119	*4423*	1.182
1224	1.082	*1424*	1.238	*2224*	1.148	*2424*	1.230	*3224*	1.160	*3424*	1.210	*4224*	1.116	*4424*	1.185
1231	1.082	*1431*	1.156	*2231*	1.082	*2431*	1.156	*3231*	1.082	*3431*	1.156	*4231*	1.167	*4431*	1.191
1232	1.082	*1432*	1.237	*2232*	1.082	*2432*	1.212	*3232*	1.195	*3432*	1.185	*4232*	1.098	*4432*	1.181
1233	1.082	*1433*	1.238	*2233*	1.160	*2433*	1.230	*3233*	1.191	*3433*	1.210	*4233*	1.133	*4433*	1.156
1234	1.082	*1434*	1.232	*2234*	1.206	*2434*	1.238	*3234*	1.178	*3434*	1.216	*4234*	1.155	*4434*	1.167
1241	1.082	*1441*	1.181	*2241*	1.082	*2441*	1.104	*3241*	1.016	*3441*	1.027	*4241*	0.967	*4441*	1.150
1242	1.042	*1442*	1.217	*2242*	1.082	*2442*	1.180	*3242*	1.115	*3442*	1.111	*4242*	1.119	*4442*	1.033
1243	1.082	*1443*	1.156	*2243*	1.082	*2443*	1.156	*3243*	1.082	*3443*	1.156	*4243*	1.194	*4443*	1.064
1244	1.082	*1444*	1.156	*2244*	1.082	*2444*	1.156	*3244*	1.082	*3444*	1.156	*4244*	1.025	*4444*	1.142

Table 5 - Correction factors for each parameter category. (LeBaron-Perez model with adjusted coefficients)

Categories (i j k l)

(i = zenith; j = geometric factor; k = epsilon; l = delta)

categ	**fc**	**categ**	**fc**	**categ**	**Fc**	**categ**	**fc**	**categ**	**fc**	**categ**	**fc**	**categ**	**Fc**	**categ**	**Fc**
1111	1.061	*1311*	1.137	*2111*	1.063	*2311*	1.103	*3111*	1.065	*3311*	1.100	*4111*	1.045	*4311*	1.062
1112	1.061	*1312*	1.138	*2112*	1.068	*2312*	1.132	*3112*	1.066	*3312*	1.108	*4112*	1.047	*4312*	1.068
1113	1.061	*1313*	1.148	*2113*	1.068	*2313*	1.137	*3113*	1.066	*3313*	1.121	*4113*	1.054	*4313*	1.060
1114	1.061	*1314*	1.159	*2114*	1.086	*2314*	1.141	*3114*	1.076	*3314*	1.109	*4114*	1.040	*4314*	0.934
1121	1.061	*1321*	1.249	*2121*	1.174	*2321*	1.208	*3121*	1.173	*3321*	1.170	*4121*	1.102	*4321*	1.159
1122	1.061	*1322*	1.249	*2122*	1.220	*2322*	1.233	*3122*	1.205	*3322*	1.165	*4122*	1.087	*4322*	1.151
1123	1.061	*1323*	1.250	*2123*	1.209	*2323*	1.225	*3123*	1.187	*3323*	1.190	*4123*	1.096	*4323*	1.142
1124	1.061	*1324*	1.257	*2124*	1.189	*2324*	1.232	*3124*	1.170	*3324*	1.204	*4124*	1.097	*4324*	1.150
1131	1.061	*1331*	1.470	*2131*	1.460	*2331*	1.479	*3131*	1.061	*3331*	1.187	*4131*	1.211	*4331*	1.241
1132	1.061	*1332*	1.338	*2132*	1.326	*2332*	1.342	*3132*	1.343	*3332*	1.320	*4132*	1.257	*4332*	1.224
1133	1.061	*1333*	1.314	*2133*	1.284	*2333*	1.306	*3133*	1.281	*3333*	1.299	*4133*	1.277	*4333*	1.292
1134	1.061	*1334*	1.318	*2134*	1.244	*2334*	1.295	*3134*	1.218	*3334*	1.261	*4134*	1.132	*4334*	1.172
1141	1.061	*1341*	1.384	*2141*	1.357	*2341*	1.394	*3141*	1.257	*3341*	1.290	*4141*	1.064	*4341*	1.055
1142	1.061	*1342*	1.372	*2142*	1.293	*2342*	1.371	*3142*	1.229	*3342*	1.309	*4142*	1.063	*4342*	1.110
1143	1.061	*1343*	1.187	*2143*	1.251	*2343*	1.328	*3143*	1.218	*3343*	1.292	*4143*	1.019	*4343*	1.142
1144	1.061	*1344*	1.187	*2144*	1.061	*2344*	1.187	*3144*	1.165	*3344*	1.304	*4144*	1.014	*4344*	1.145
1211	1.112	*1411*	1.185	*2211*	1.103	*2411*	1.151	*3211*	1.091	*3411*	1.109	*4211*	1.058	*4411*	1.039
1212	1.119	*1412*	1.183	*2212*	1.104	*2412*	1.162	*3212*	1.103	*3412*	1.122	*4212*	1.058	*4412*	1.041
1213	1.120	*1413*	1.186	*2213*	1.111	*2413*	1.163	*3213*	1.097	*3413*	1.125	*4213*	1.060	*4413*	1.045
1214	1.125	*1414*	1.193	*2214*	1.117	*2414*	1.160	*3214*	1.100	*3414*	1.133	*4214*	1.004	*4414*	1.005
1221	1.144	*1421*	1.245	*2221*	1.222	*2421*	1.212	*3221*	1.176	*3421*	1.202	*4221*	1.134	*4421*	1.187
1222	1.228	*1422*	1.267	*2222*	1.237	*2422*	1.219	*3222*	1.171	*3422*	1.202	*4222*	1.117	*4422*	1.188
1223	1.224	*1423*	1.284	*2223*	1.222	*2423*	1.230	*3223*	1.189	*3423*	1.204	*4223*	1.122	*4423*	1.189
1224	1.231	*1424*	1.292	*2224*	1.219	*2424*	1.257	*3224*	1.191	*3424*	1.232	*4224*	1.120	*4424*	1.190
1231	1.345	*1431*	1.445	*2231*	1.379	*2431*	1.420	*3231*	1.144	*3431*	1.240	*4231*	1.216	*4431*	1.254
1232	1.315	*1432*	1.362	*2232*	1.311	*2432*	1.349	*3232*	1.313	*3432*	1.321	*4232*	1.187	*4432*	1.229
1233	1.261	*1433*	1.360	*2233*	1.296	*2433*	1.344	*3233*	1.264	*3433*	1.317	*4233*	1.256	*4433*	1.246

1234	1.256	*1434*	1.344	*2234*	1.266	*2434*	1.337	*3234*	1.243	*3434*	1.316	*4234*	1.148	*4434*	1.207
1241	1.328	*1441*	1.426	*2241*	1.349	*2441*	1.405	*3241*	1.240	*3441*	1.312	*4241*	1.069	*4441*	1.177
1242	1.361	*1442*	1.355	*2242*	1.314	*2442*	1.360	*3242*	1.239	*3442*	1.310	*4242*	1.083	*4442*	1.161
1243	1.144	*1443*	1.230	*2243*	1.283	*2443*	1.322	*3243*	1.256	*3443*	1.305	*4243*	1.048	*4443*	1.155
1244	1.144	*1444*	1.230	*2244*	1.144	*2444*	1.230	*3244*	1.205	*3444*	1.287	*4244*	1.030	*4444*	1.169

The categories consist of the zenith angle parameters, geometrical factor, epsilon and delta, when combined, result in 256 categories. The groups was carried out by the indices "i", "j", "k" and "l", which represent, respectively, the zenith angle, geometrical factor, epsilon and delta, and each of these indices can take values from 1 to 4 depending on their range (Tab. 3). Thus, the cluster was determined by means of a number consisting of four digits in the format "ijkl". For example, the category 4321 describes a state with zenith angle ranging from 60 to 90, the geometrical factor of 1.100 to 1.132, epsilon 1.253 to 2.134 and delta 0 to 0.12. Some categories were not filled with solar irradiance data due to physical limitations of the parameters. In this case, the correction factor was adopted an average of the geometrical factor.

Tab. 4 shows the original correction factors proposed by LeBaron et al (1990), developed for the assembly of Drummond, ranging from 0.925 to 1.248. The largest corrections occurred for low cloudiness and high brightness index (delta), typical of the days of high solar declination. Minor corrections occurred for high cloudiness, wherein the isotropic behavior of the radiation is more evident.

We adjusted LeBaron-Perez's methodology for Botucatu atmospheric conditions and MEO shadow ring's assembly (LeBaron Perez-adjusted model). Tab. 5 shows the adjusted coefficients. Corrections ranged from 0.934 to 1.470. The largest correction also occurred for low cloudiness, showing great influence of the anisotropy. The lowest correction value occurred for high situation zenith angle and brightness index, probably linked to reflections inside the shading ring.

We also use the Dal Pai-Escobedo correction model, which is based on geometric factor (isotropy) and K_T atmospheric transmissivity (anisotropy). Tab. 6 shows the numerical factors used by the Dal Pai-Escobedo correction model for four K_T atmospheric transmissivity intervals.

Table 6 - Correction factors based on K_T atmospheric transmissivity intervals (*MEO* shading assembly).

K_T Interval	**Correction Factors**
$0 \leq K_T < 0.35$	0.975
$0.35 \leq K_T < 0.55$	1.034
$0.55 \leq K_T < 0.65$	1.083
$0.65 \leq K_T < 1$	1.108

To validate the correction models, corrected diffuse irradiance were compared with reference diffuse irradiance by means of MBE and RMSE statistical indicators. MBE shows the long-term model behavior, with an underestimating or overestimating by the model. RMSE shows the dispersion of the model around the measure. Tab. 7 shows MBE, RMSE and slope, while Fig. 4 shows the graphs between reference diffuse irradiance and corrected diffuse irradiance by the correction models (LeBaron-Perez (Original), LeBaron- Perez (Adjusted) and Dal Pai-Escobedo).

Table 7 - MBE, RMSE and slope for reference diffuse irradiance and corrected diffuse irradiance (LeBaron-Perez (Original), LeBaron-Perez (Adjusted) and Dal Pai-Escobedo).

Correction Model	**Statistical Indicators**				
	MBE (W/m^2)	**MBE (%)**	**RMSE (W/m^2)**	**RMSE (%)**	**Slope**

LeBaron-Perez - OR	-9,52	-5,93	22,87	14,24	1,053
LeBaron-Perez - AJ	-0,74	-0,46	17,32	10,79	1,005
Dal Pai-Escobedo	-0,02	-0,01	18,11	11,28	0,999

The worst performance was given to the model LeBaron-Perez correction with original coefficients, with an underestimation of 6% and dispersion of 14.3%. This result was expected, since the original model coefficients were developed for a different atmospheric condition of Botucatu, both aerosols, water vapor and clouds. This model was significantly improved when setting the coefficients for atmospheric situation of Botucatu, causing a reduction in MBE (~ 0.5%) and RMSE (~ 11%). A good performance was also attributed to Dal Pai-Escobedo correction model, with low values of MBE (- 0.01%) and RMSE (11.28%). With respect to slope, Lebaron-Perez adjusted and Dal Pai-Escobedo correction models had the same great performance, with slope closer to 1. Overall, LeBaron-Perez (Adjusted) and Dal Pai-Escobedo correction models exhibit the same order of accuracy in correction of diffuse irradiance measured by the shading ring. Dal Pai-Escobedo correction model takes a small advantage by presenting less parameters to classify the sky.

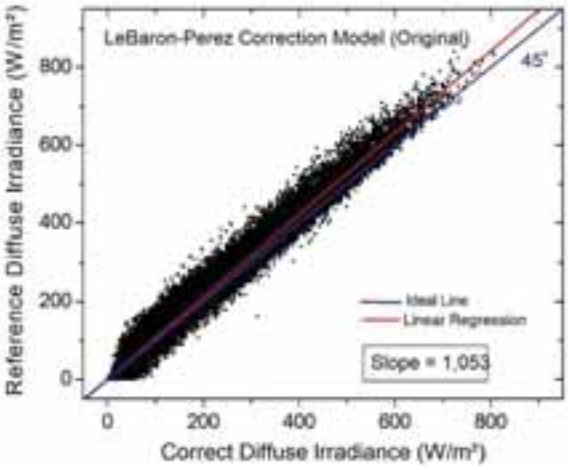

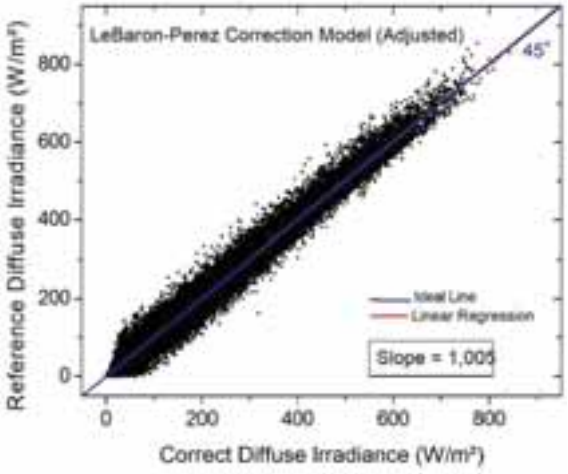

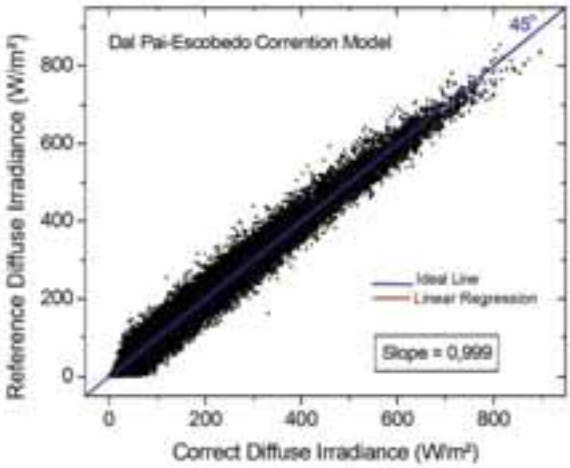

Figure 4 - Comparison between the diffuse irradiance reference and corrected diffuse irradiance by the correction models: a) LeBaron-Perez (Original). b) LeBaron-Perez (Adjusted). c) Dal Pai-Escobedo.

4. Conclusion

Our results allowed the following conclusions:

a) Lebaron-Perez correction model with the original coefficients, is not suitable to correct diffuse irradiance measured in Botucatu with the *MEO* shading ring method.

b) Lebaron-Perez correction model, when adjusted for Botucatu sky conditions, can be used to correct the diffuse irradiance measured by the *MEO* shading ring method.

c) Dal Pai-Escobedo correction model is suitable to correct diffuse irradiance measured by the *MEO* shading ring method.

d) Lebaron-Perez (Adjusted) and Dal Pai-Escobedo correction models has the same efficiency to correct diffuse irradiance.

e) We recommend Dal Pai-Escobedo correction model to correct diffuse irradiance because it uses fewer parameters.

5. References

Battles, F. J., Olmo, F. J., Alados-Arboledas, L., 1995. On shadowband correction methods for diffuse irradiance measurements. Solar Energy, v.54, n.2, p.105-114.

Codato, G, Oliveira, A P, Soares, J, Escobedo, J F, Gomes, E N, Dal Pai, A., 2008. Global and diffuse solar irradiances in urban and rural areas in southeast Brazil. Theor Appl Climatol, v 93, p 57-73.

Dal Pai, A., Escobedo, J. F., 2011. Numerical correction for the diffuse solar irradiance by the Melo-Escobedo shadowring measuring method, ISES SOLAR WORLD CONGRESS, Kassel, Germany.

Drummond, A. J., 1956. On the measurements of sky radiation. Archiv. fur Meteorologie. Geophysik Bioklimatologie, v.7, p.413-436.

Iqbal, M. An introduction to solar radiation. Nova Iorque, Academic Press, 1983. 390p.

Kasten, F., Dehne, K., Brettschneider, W. 1983. Improvement of measurement of diffuse solar radiation. Solar radiation data, série F, n.2, pp.221-225, D. Redel, Dordrecht.

Kudish, A I, Evseev, E G., 2008. The assessment of four different correction models applied to the diffuse radiation measured with a shadow ring using global and normal beam radiation measurements for Beer Sheva, Israel. Solar Energy, v.82, p.144-156.

Lebaron, B. A., Michalsky, J. J., Perez, R. 1990. A simple procedure for correcting shadowband data for all sky conditions. Solar Energy, v.44, n.5, pp.249-256.

Melo, J. M. D., Escobedo, J. F., 1994. Medida da radiação solar difusa. In: ENERGÍAS LÍMPIAS EN PROGRESO, VII CONGRESSO IBÉRICO DE ENERGIA SOLAR, Vigo, Espanha. Anais INTERNATIONAL SOLAR ENERGY SOCIETY, v. 1.

Oliveira, A. P., Escobedo, J. F., Machado, A. J., 2002. A new shadow-ring device for measuring diffuse solar radiation at surface. Journal of Atmospheric and Oceanic Technology, Boston, v. 19, p. 698-708.

Pollard, D. G. E Langevine, L. P., 1988. An anisotropic correction for diffuse irradiance measurements in Guyana. In: Proceeding of the 1988 Annual Meeting, M. J. Coleman (Ed.), p. 238-243, ASES Cambridge.

Stanhill, G. 1985. Observations of shadering correction factors for diffuse sky radiation measurements at the Dead Sea.Quarterly Journal of the Royal Meteorological Society, v.111, pp.1125- 30.

Stone, R. J. 1993. Improved statistical procedure for the evaluation of solar radiation estimation models. Solar Energy, v.51, n.4, pp.289-291.

Acknowledgements. The authors acknowledge the financial support from FAPESP.

Solis Clear Sky Scheme: Extension to High Turbidity, Development and Validation

Pierre Ineichen

University of Geneva, Institute for Environmental Sciences,
Department F.-A. Forel for environmental and aquatic sciences

Abstract

The Solis clear sky model is a spectral scheme based on radiative transfer calculations and the Lambert–Beer relation. Its broadband version is a simplified fast analytical version; it is limited to broadband aerosol optical depths at 700nm lower than 0.45, which is a weakness when applied in countries with very high turbidity such as China or India. This paper aims to extend the validity of the model to higher aerosol optical depth values. In 2014, Zhang published a modification of the scheme to extend its validity to aerosol optical depth values up to 6.5, but this extension is only applicable for the beam irradiance component and presents some weakness for very high turbidity values. In a first step, we tried to apply a correction to the Zhang adaptation. In order to extend the use of the original simplified version of Solis for high turbidity, we developed a new version of the broadband Solis, valid for the three components, global, beam and diffuse, and for the four aerosol types defined by Shettle and Fenn.

Keywords: Solis scheme, clear sky, radiation model, radiative transfer, high turbidity, water vapor

1. Introduction

The clear sky Solis scheme was first developed within the Mesor European program whose subject was the *management and exploitation of solar resource knowledge*. In 2008, Ineichen published a broadband analytical version of the Solis model for rural aerosol type, and in 2010 a version in the form of an excel tool for the four types of aerosols as defined by Shettle and Fenn. These versions were limited to aerosol optical depth values aod_{700} lower than 0.45. The anthropogenic heating and transportation activities conducted to a serious increase of the turbidity in countries like India or China. Looking into the limitations of the state of the art clear sky models, it appears that none is applicable for high turbidity. Indeed, for example, Gueymard CPCR2 model (Gueymard 1989) is limited to β turbidity values lower than 0.4 (which correspond to an aod_{700} of 0.64 for rural aerosol type, α = 1.3), Gueymard REST2 (Gueymard 2003) is limited to β = 1 (aod_{700} = 1.6, rural aerosol), Bird's model (Bird 1980) is defined for visibility values up to 23 km (which corresponds to an aod = 0.27) and the ESRA clear sky scheme (ESRA 2000, Rigollier 2000, Geiger 2002) was developed for Linke turbidity values T_L not exceeding a value of 7 (i.e. an aerosol optical depth aod_{700} = 0.44 for a 2 cm water vapor column). As the 2003 and 2008 versions of Solis diverge for high turbidity as shown by Zhang (2014), an extension of the model for higher turbidity values is needed.

This paper presents a validation and an adaptation of the model for the beam component extended by Zhang, and the development and validation of a new version of the analytical Solis scheme valid for the three radiation components, the global, the beam and the diffuse, and the four aerosol types, urban, rural, maritime and tropospheric.

2. The Solis scheme

The Solis scheme (Mueller 2004) is a model based on LibRadTran radiative transfer calculations (Mayer 2005, 2010). The basis of the model is the Lambert-Beer attenuation relation:

doi:10.18086/swc.2017.23.02 Available at http://proceedings.ises.org

$$I_{bn} = I_o \cdot \exp(-M \cdot \tau) \qquad \text{(eq. 1)}$$

where I_o is the extraterrestrial irradiance, I_{bn} the normal beam irradiance reaching the ground, M the optical air mass and τ the total atmospheric optical depth. This expression of the atmospheric transmittance is valid for monochromatic radiation, and the optical depth is then constant over the air mass range. Due to the non-linear nature of the exponential function, the Lambert-Beer relation has to be modified to extend the expression to wavelength bands; it takes then the following form:

$$I_{bn} = I_o \cdot \exp\left(-\frac{\tau}{\sin^b h}\right) \qquad \text{(eq. 2)}$$

where h is the solar elevation angle and b the fitting parameter obtained from RTM calculations at two different solar elevation angles.

When dealing with global irradiance, the Lambert-Beer relation is no longer applicable because of the back scatter effects, but remains a relatively good approximation, and

$$I_{gh} = I_o \cdot \exp\left(-\frac{\tau}{\sin^g h}\right) \cdot \sin h \qquad \text{(eq. 3)}$$

is a good fitting function for the horizontal global irradiance (Mueller 2004).

The source of the incoming diffuse irradiance is the attenuation of the beam radiation due to scattering process and it cannot be described in term of attenuation of the incoming radiation. Nevertheless, skipping the sin h term, the modified Lambert-Beer relation also works well:

$$I_{dh} = I_o \cdot \exp\left(-\frac{\tau}{\sin^d h}\right) \qquad \text{(eq. 4)}$$

At high aerosol load, *Io* has to be enhanced for the global and diffuse irradiance calculations, and a common modified *Io'* irradiance is defined for the three radiation components. The final expression of the model has then the following form:

$$I_{bn} = I'_o \cdot \exp\left(-\frac{\tau_b}{\sin^b h}\right) \quad I_{gh} = I'_o \cdot \exp\left(-\frac{\tau_g}{\sin^g h}\right) \cdot \sin h \quad I_{dh} = I'_o \cdot \exp\left(-\frac{\tau_d}{\sin^d h}\right) \qquad \text{(eq. 5)}$$

where τ_b, τ_g and τ_d are respectively the beam, global and diffuse total optical depths, and b, g and d the corresponding fitting parameters obtained from RTM calculations.

3. Zhang extension validation

To extend the range of the model application, Zhang added two terms in the extinction equation for the beam component, one for the aerosol optical depth K_{aod} , and one for the water vapor column K_w. These two terms are constant and defined in order to have a smooth behavior at $aod_{700} = 0.45$ which is the original Solis *aod* limitation (i.e. a null derivative for $aod_{700} = 0.45$).

We made a validation of the extended model against data evaluated with the Radiative Transfer Model (RTM) LibRadTran for a wide range of aerosol optical depths values, water vapor column and altitudes. As the Zhang extension shows slight deviations for low water vapor column and high turbidity values when plotting the modeled beam irradiance against the correspondent value calculated with the help of the LibRadTran radiation transfer model (see Fig. 1, left), we adapted the Zhang extension coefficient K_{aod} by making it *aod* dependent. This allowed to slightly better aligning the dots on the 1:1 diagonal as illustrated on the right graph of Fig. 1.

For altitudes from sea level to 7000 m, water vapor from 0.05 cm to 10 cm and *aod* from 0 to 7, and a solar elevation of 60°, the results are the following:

- Zhang extension $mbd = 0.2\%$ $sd = 4.7\%$
- Zhang + Ineichen $mbd = 0.2\%$ $sd = 2.8\%$.

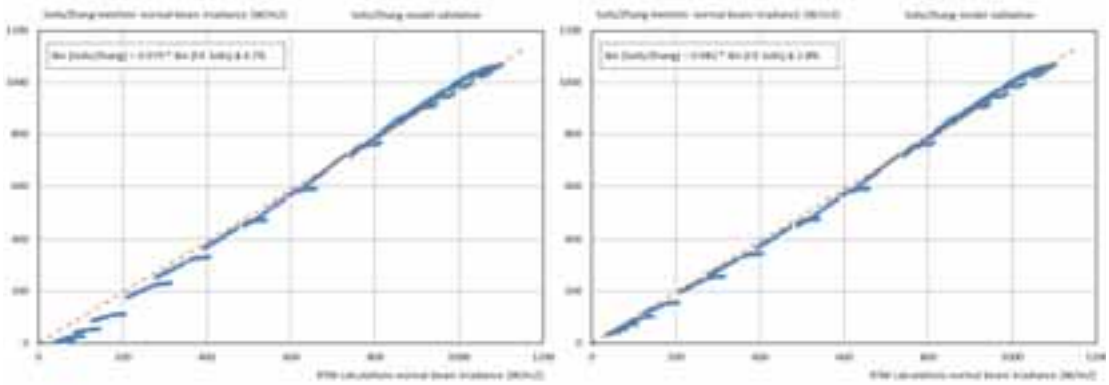

Fig. 1: Normal beam validation for the Zhang extension (left) and the Zhang-Ineichen correction (right)

4. Solis extension to high turbidity

The weakness of the Zhang extension is that it derives only the beam component. To circumvent this problem, we developed a Solis-2017 version that is applicable for values of *aod* up to 7. This means that the model goes up to very high atmospheric aerosol load, but one has to keep in mind that above *aod* = 2, it is not clear that the turbidity can be considered as an aerosol optical depth, but a turbidity due to bigger particles like sand, or in our countries, high altitude thin clouds. Nevertheless, it is important that in on-line automatic production processes, the model does not diverge and still derive coherent values, even with some discrepancies with ground measurements.

4.1. Model development

In a first step, we made spectral calculations with LibRadTran for the following parameters:

Tab. 1: aerosol types, altitudes, optical depths and water vapor columns values for the RTM calculations

aerosol type	altitude	aod_{550}	w [cm]
urban	sea level	0.01	0.01
rural	500m	0.03	0.03
maritime	1000m	0.05	0.05
tropospheric	2000m	0.1	1
	3000m	0.15	0.15
	4000m	0.2	0.2
	5000m	0.4	0.3
	6000m	0.7	0.5
	7000m	1	1
		1.5	1.5
		2	2
		3	3
		4	4
		5	6
		6	8
		7	10

These RTM calculations permit to generate the seven coefficients that drive the model: I_o', τ_b, b, τ_g, g, τ_d, and d. The next step is to develop an analytical formulation for these coefficients with the 4 input parameters given in Tab. 1.

The analysis of I_o', τ_b, and τ_g shows a similar behavior for these three parameters. The first analyzed dependence is with the aerosols optical depth *aod*. A third order polynomial model is applicable for the three parameters of the form:

$$I_o'/I_o = a \cdot aod^3 + b \cdot aod^2 + c \cdot aod + d \quad \text{(eq. 6)}$$

The behavior for I_o' and τ are represented on the Fig. 2 below.

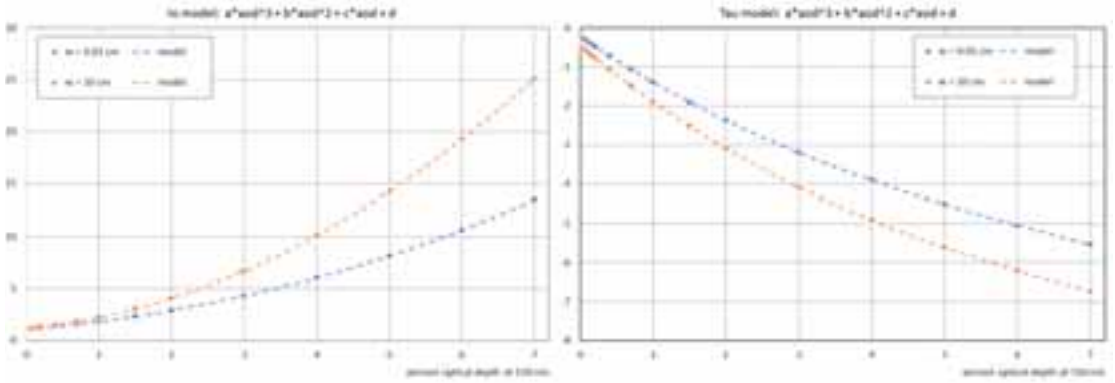

Fig. 2: Normal beam validation for the Zhang extension (left) and the Zhang-Ineichen correction (right)

We then analyzed the dependence of each of the a, b, c and d coefficient of equation 6 with the atmospheric water vapor content. The behavior of the four coefficients shows a water vapor dependence of the form:

$$n = n1 \cdot w^{0.5} + n2 \cdot \ln(w) + n3 \quad \text{(eq. 7)}$$

The best fits of two of these coefficients are given on the Fig. 3

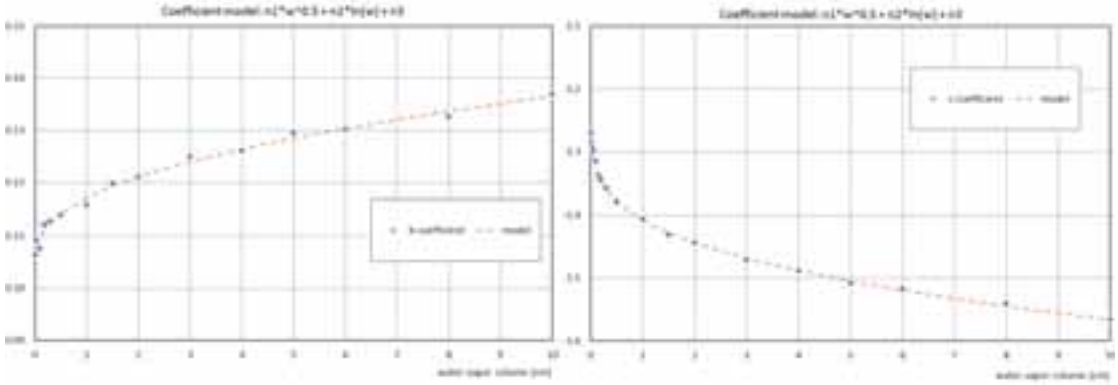

Fig. 3: Behavior of two of the cubic equation coefficients with the water vapor column

Finally, the dependence of the three above coefficients with the altitude, respectively the normalized atmospheric pressure p/p_o (the pressure p at a given altitude normalized by the corresponding sea level pressure p_o) is analyzed. It appears that a linear regression gives the best results.

The model has then the following form:

$$a = a_1 \cdot w^{0.5} + a_2 \cdot \ln(w) + a_3 \quad \text{(eq. 7a)}$$
$$b = b_1 \cdot w^{0.5} + b_2 \cdot \ln(w) + b_3 \quad \text{(eq. 7b)}$$
$$c = c_1 \cdot w^{0.5} + c_2 \cdot \ln(w) + c_3 \quad \text{(eq. 7c)}$$
$$d = d_1 \cdot w^{0.5} + d_2 \cdot \ln(w) + d_3 \quad \text{(eq. 7d)}$$

and each of the n_i coefficient is obtained with a linear function of p/p_o

$$n_i = n_{i1} \cdot p/p_o + n_{i2} \quad \text{(eq. 8)}$$

Finally, the inputs for the model for I_o', τ_b and τ_g, consist of the aerosol optical depth at 550 nm aod_{550}, the water vapor content of the atmosphere w and the relative atmospheric pressure p/p_o. The corresponding coefficient are given in a 3x3x2 matrix.

For τ_d, the best correlation we found is a relation with to τ_b and τ_g that has the form:

$$\tau_d = e + f \cdot \tau_g + g / \tau_b + h / \tau_g^2 + i \cdot \tau_g / \tau_b \quad \text{(eq. 9)}$$

The exponents of the sin (h) in the Lambert-Beer function are respectively best fitted as follow:

$$g = c_{a1} + c_{a2} \cdot \ln(w) + c_{a3} \cdot \ln(aod) + c_{a4} \cdot \ln(w)^2 + c_{a5} \cdot \ln(aod)^2 + c_{a6} \cdot \ln(w) \cdot \ln(aod) \qquad \text{(eq. 10)}$$

$$b = c_{b1} \cdot w^{\,cb2} \cdot c_{b3}^{\,aod} \qquad \text{(eq.11)}$$

$$d = c_{d1} + c_{d2} \cdot \ln(w) + c_{d3} \cdot aod + c_{d4} \cdot aod^2 + c_{d5} \cdot aod^3 + c_{d6} \cdot aod^4 + c_{d7} \cdot aod^5 \qquad \text{(eq. 12)}$$

4.2 Parameter validation

The validation of the seven parameters of the model is expressed as scatter plots between the modeled parameter and the corresponding LibRadTran calculated parameter. The validation points should be aligned on the 1:1 diagonal. On the graphs are also given the average parameter value, the mean bias difference *mbd*, the standard deviation *sd* and the correlation coefficient R^2. An illustration is given on Fig. 4 for I_o' and the *a* coefficient, urban aerosol type.

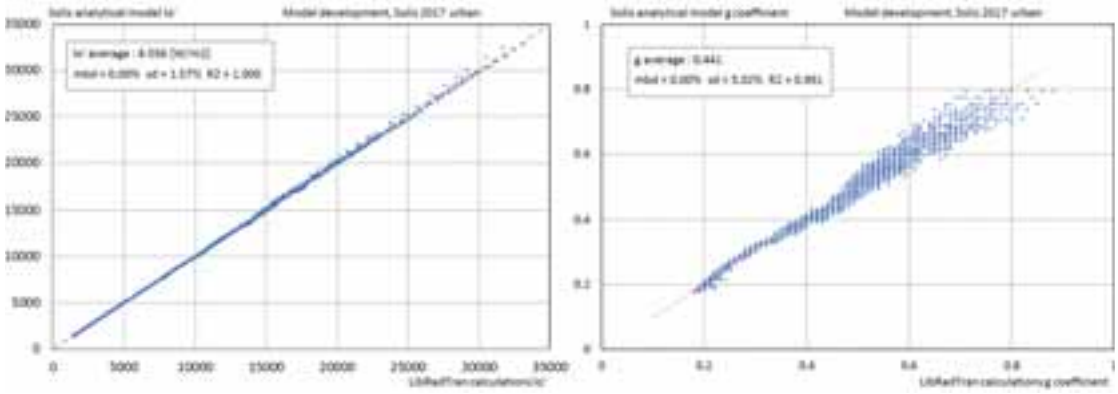

Fig. 4: I_o' and *g* coefficient validation

The average, *mbd* and *sd* values cannot be taken as an absolute validation of the precision as all the values calculated from the input matrix (altitude, *aod* and *w)* have the same weight. Nevertheless, it gives a good idea of the roughness of the parameter best fit. These values are given in Tab. 2.

Tab. 2: Average, *mbd*, *sd* and R^2 for the I_o', τ_b, *b*, τ_g, *g*, τ_d, and *d* model.

	Io'				τ_g				*g*			
aerosol type	average	mbd	sd	R2	average	mbd	sd	R2	average	mbd	sd	R2
rural	6284	-0.5	92.9	1.000	-1.49	0.00	0.01	1.000	0.41	0.00	0.02	0.993
urban	6036	0.0	94.7	1.000	-1.68	0.00	0.02	1.000	0.44	0.00	0.02	0.991
tropo	12210	-7.8	133.9	1.000	-1.89	0.00	0.01	1.000	0.39	0.00	0.02	0.994
maritime	5380	0.2	40.3	1.000	-1.40	0.00	0.01	1.000	0.41	0.00	0.02	0.992
					τ_b				*b*			
rural					-2.21	0.00	0.01	1.000	0.42	0.00	0.02	0.965
urban					-2.21	0.00	0.01	1.000	0.44	0.00	0.03	0.941
tropo					-2.68	0.00	0.01	1.000	0.45	0.00	0.02	0.912
maritime					-2.08	0.00	0.01	1.000	0.40	0.00	0.02	0.976
					τ_d				*c*			
rural					-2.75	0.01	0.04	0.998	0.32	0.00	0.01	0.995
urban					-3.08	0.01	0.05	0.999	0.29	0.00	0.01	0.995
tropo					-2.86	0.01	0.04	0.999	0.31	0.00	0.01	0.995
maritime					-2.67	0.01	0.04	0.998	0.33	0.00	0.01	0.995

4.3 Irradiance validation

In the same way, the validation of the irradiance components is expressed as scatter plots and the usual first order statistics. Here again, due to the unweighted input matrix, the validation values obtained give not an absolute precision of the model. The scatter plots given on Fig. 5 below illustrate the behavior of the model. They represent the modeled values plotted against the corresponding values evaluated from RTM calculations, urban type aerosols, for the three components.

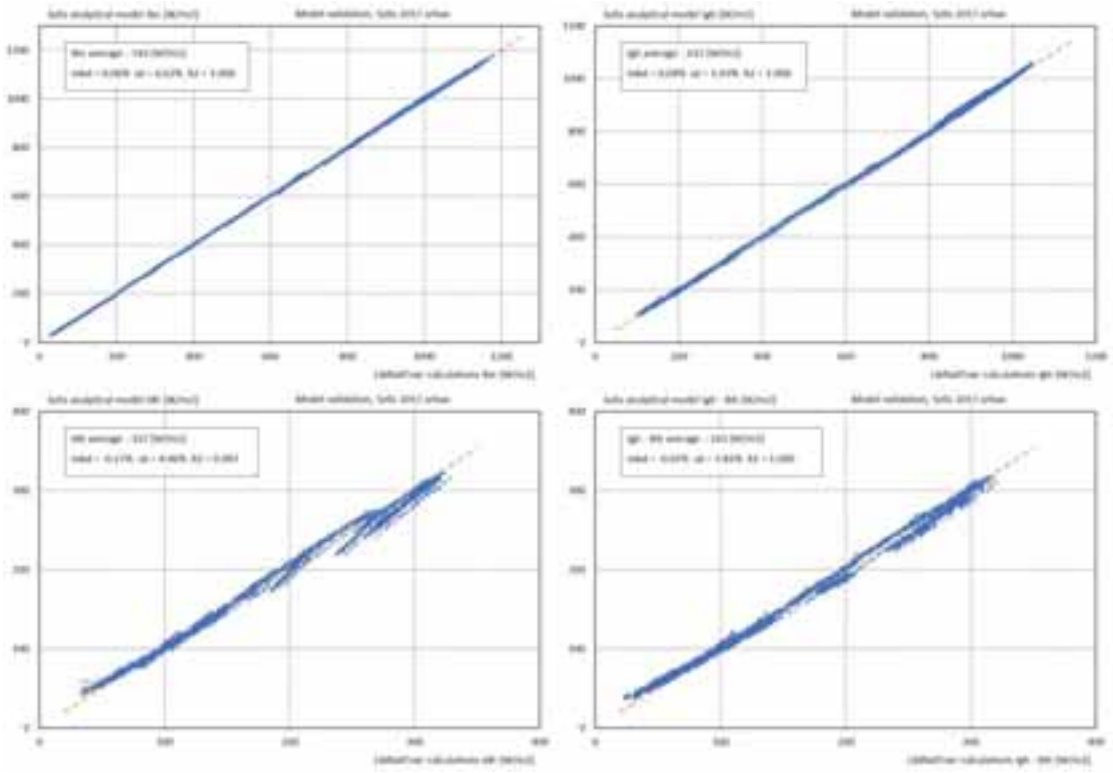

Fig. 5 Irradiance model validation

To obtain the diffuse component, there are two possibilities: the use of the model coefficients τ_d and d, or to evaluate it from the global and the beam components with the use of the closure equation $I_{dh} = I_{gh} - I_{gh}$. The diffuse obtained from the closure equation looks slightly better on Fig. 5, but it presents negative values for very low solar elevations.

The corresponding values are given in Tab. 3

Tab. 3: Average, *mbd*, *sd* and R^2 for the irradiance components.

	I_{gh}				I_{bn}				I_{dh}			
aerosol type	average	mbd	sd	R2	average	mbd	sd	R2	average	mbd	sd	R2
rural	727	0.4	3.9	1.000	549	0.0	4.7	1.000	223	0.5	7.3	0.998
urban	632	0.3	6.5	1.000	543	0.3	3.4	1.000	167	-0.3	6.8	0.997
tropo	740	0.2	4.7	1.000	559	-0.3	6.8	1.000	227	0.4	6.6	0.999
maritime	753	-1.3	16.7	0.997	519	-3.0	17.7	0.999	266	1.6	10.7	0.998

All the development and validation graphs for the urban aerosol type are given in the annex.

4.4 Components coherence

To visualize the behavior of the model and the coherence between the irradiance components, the model trends are represented for four typical values of aerosols optical depths *aod* (0.5, 0.9, 1.5 and 6) and a value of w = 1cm for the atmospheric water vapor column on Fig. 6. The ozone amount is taken constant at a value of 340 Dobson units, the aerosol characteristics is of urban type, and the albedo coefficient at 20%. On the left graph, the diffuse fraction I_{dh} / I_{gh} is represented versus the global clearness index K_t ($Kt = I_{gh} / I_o \sin h$), and on the right graph, the beam clearness index K_b ($K_b = I_{bn} / I_o$) versus the global clearness index. The Linke turbidity values T_L, evaluated from the aerosol optical depth and the water vapor column are also indicated on the graphs.

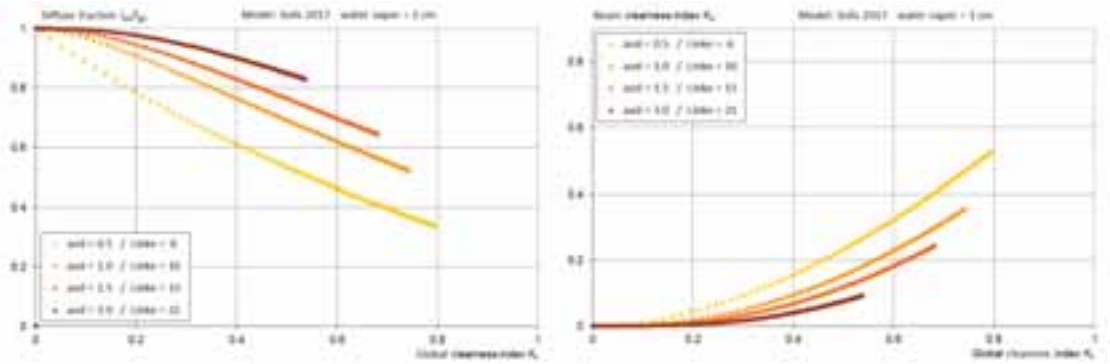

Fig. 6 Trends for the diffuse fraction and the beam clearness index versus the global clearness index

4.5 Validation on ground data from Geneva and Jaipur

The model should be validated against ground measurements acquired in highly polluted conditions. At this time, we had no access to such data (ground irradiances and *aod*); therefore, a preliminary validation is done on data acquired in Geneva for the years 2004 to 2011 where the *aod* is pretty low, and Jaipur with *aod* values up to 2.5 for 17 months in 2016 and 2017.

The average aerosol optical depth in Geneva is of order of 0.17 with a maximum of 0.5 during polluted episodes. As no specific aerosol optical depth values are measured in Geneva, we used one of the best state of the art model, REST2 (Gueymard 2004), to retrieve by retrofit the *aod* following the method described in Ineichen (2016). The clear sky condition selection is also described in Ineichen (2016). The results, illustrated on Fig. 7, are slightly better than for Solis 2008 (Ineichen 2016).

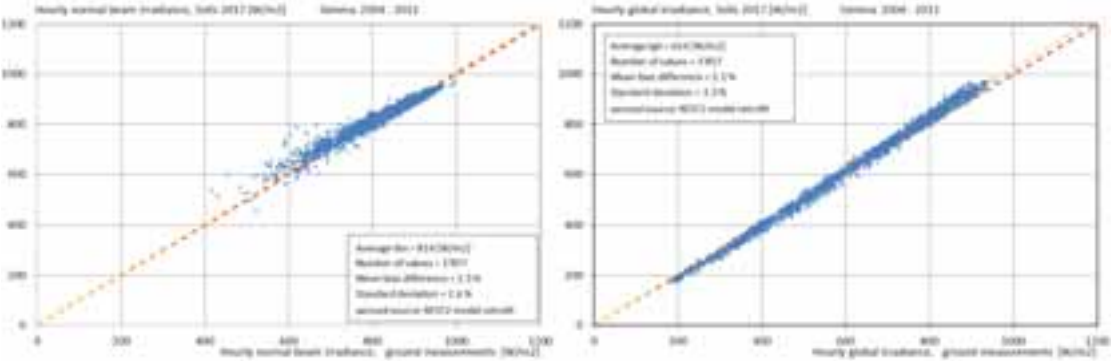

Fig. 7 Validation against ground data acquired in Geneva. The *aod* is retrofitted with REST2

For Jaipur, the aod_{550} values can reach 2.5, as this exceeds the REST2 limitations, we obtained values by retrofit with the use of Molineaux *bmpi* model (1998). The graphs are given on Fig. 8.

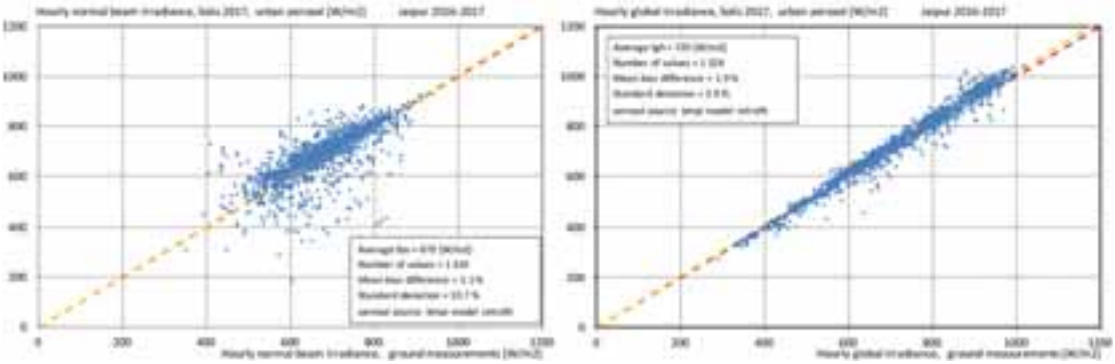

Fig. 8 Validation against ground data acquired in Jaipur. The *aod* is retrofitted with *bmpi* model.

It can be seen that the dispersion is higher, especially for the beam irradiance. This is due to the higher turbidity values, conditions for which it is difficult to determine the aerosol type. The extinction of the beam

irradiance can also be due to high altitude thin clouds or variability in the atmospheric water vapor column (evaluated from ground temperature and humidity).

5. Conclusion

When dealing with satellite images to derive the irradiance components on a wide space scale and every 15 minutes, the computer time should be as short as possible. The analytical Solis clear sky scheme was developed to fulfill this requirement but had the weakness to be limited to aerosol optical depth values lower than 0.45. The new analytical Solis scheme is valid for *aod* up to seven, even if very high values are not realistic as an optical depth; it is probably more due to bigger particles like sand, or in our countries, thin high altitude clouds. Nevertheless, in contrary to other clear sky models, this permit to produce coherent irradiance values, even with questionable input values.

The new Solis clear sky scheme is valid for aerosol optical depths values aod_{550} from 0.02 to 7, atmospheric water vapor w content from 0.01 to 10 cm, and altitude from sea level to 7000 m, and four aerosol types as defined by Shettle and Fenn. For the urban, rural and tropospheric aerosol types, the validation against the original RTM calculations presents no bias and a standard deviation lower than 1% for the global and the beam component, and 3% for the diffuse. When dealing with maritime aerosol type, the standard deviation is respectively 2.2%, 3.4% and 4% for the global, the beam and the diffuse components.

A preliminary validation against ground measurements acquired in Geneva and Jaipur gives a mean bias difference of 2%, a standard deviation of 3-4% for the global component, and a mean bias difference of 1.3% with a standard deviation of 2.6% and 10.7% for the beam component for respectively Geneva and Jaipur.

6. Nomenclature

I_{gh}	horizontal global irradiance	*aod*	aerosol optical depth
I_{bn}	normal beam irradiance	τ	total atmospheric optical depth
I_{dh}	horizontal diffuse irradiance	w	atmospheric water vapor column
I_o	sun-earth distance corrected solar constant	α	particle size exponent
K_t	global clearness index	β	turbidity coefficient
K_b	beam clearness index		
mbd	mean bias difference	M	optical air mass
sd	standart deviation	T_L	Linke turbidity
R^2	correlation coefficient	p	atmospheric pressure at the considered altitude
h	solar elevation	p_o	atmospheric pressure at sea level

7. References

ESRA, European Solar Radiation Atlas, 2000. Fourth edition, includ. CD-ROM. Edited by Greif J., Scharmer K.. Scientific advisors: Dogniaux R., Page J.K.. Authors: Wald L., Albuisson M., Czeplak G., Bourges B., Aguiar R., Lund H., Joukoff A., Terzenbach U., Beyer H.G., Borisenko E.P. Published for the Commission of the European Communities by Presses de l'Ecole, Ecole des Mines de Paris, France, France.

Geiger M., Diabaté L., Ménard L., Wald L., 2002. A web Service for Controlling the Quality of Measurements of Global Solar Irradiation. Solar Energy, 73 (6), 475-480.

Gueymard C., 1989. A two-band model for the calculation of clear Sky Solar Irradiance, Illuminance, and Photosynthetically Active Radiation at the Earth Surface. Solar Energy, Vol. 43, N° 5, 253-265

Gueymard C., 2003. Direct solar transmittance and irradiance predictions with broadband models. Part 1: Detailed theoretical performance assessment. Solar Energy 74, 355–379, Corrigendum: Solar Energy 76, 513.

Ineichen P., 2008. A broadband simplified version of the Solis clear sky model, Solar Energy, 82, 768-772. < http://archive-ouverte.unige.ch/unige:17186>

Ineichen P., 2010. A broadband simplified version of the Solis clear sky model, Excel tool. Available from: <http://www.unige.ch/energie/fr/equipe/ineichen/solis-tool/> (last access in Sept. 2017)

Ineichen P., 2016. Validation of models that estimate the clear sky global and beam solar irradiance. Solar Energy 132, 332–344 < http://archive-ouverte.unige.ch/unige:81856>

Mayer B. and Kylling A., 2005. Technical note: The LibRadTran software package for radiative transfer calculations – description and examples of use, Atmos. Chem. Phys., 5, 1855–1877, doi:10.5194/acp-5-1855-2005.

Mayer B., Kylling A., Emde C., Buras R., Hamann U., 2010. LibRadTran: library for radiative transfer calculations, Edition 1.0 for libRadtran version 1.5-beta, http://www.libradtran.org (last access in Sept. 2017).

Molineaux B., Ineichen P., O'Neill N., 1998. Equivalence of pyrheliometric and monochromatic aerosol optical depths at a single key wavelength. Applied Optics / Vol. 37, No. 30 < http://archive-ouverte.unige.ch/unige:17210>

Mueller R.W, Dagestad K.F., Ineichen P., Schroedter-Homscheidt M., Cros S., Dumortier D., Kuhlemann R., Olseth J.A., Piernavieja G., Reise C., Wald L., Heinemann D. 2004. Rethinking satellite based solar irradiance modelling - The SOLIS clear-sky module. Remote Sens. Environ. 91, 160-174

Rigollier C., Bauer O., Wald L., 2000. On the Clear Sky Model of the ESRA - European Solar Radiation Atlas - with Respect to the Heliosat Method. Solar Energy 68 (1), 33-48.

Shettle E.P, Fenn R.W., 1979. Models fort the aerosol of lower atmosphere and the effect of humidity variations on their optical properties.

Shettle E.P., 1989. Models of aerosols, clouds and precipitation for atmospheric propagation studies. AGARD Conference proceedings, Copenhagen, Denmark, 9-13 October

Zhang T., Stackhouse P.W., Chandler W.S., Westberg D.J., 2014. Application of a global-to-beam irradiance model to the NASA GEWEX SRB dataset: An extension of the NASA Surface meteorology and Solar Energy datasets. Solar Energy 110, 117–131

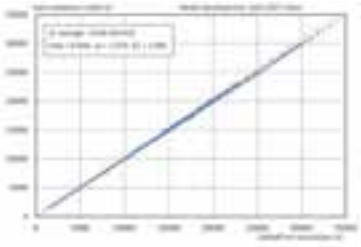

Annex

Development of the Solis 2017 model
Validation graphs and coefficients dependence for the urban type aerosol

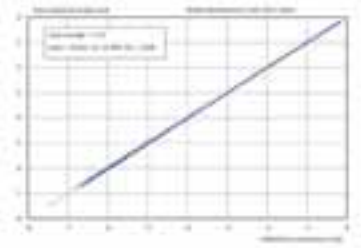
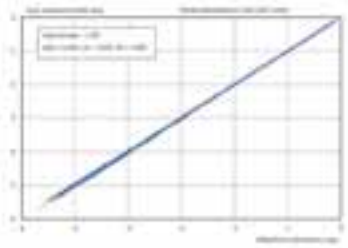
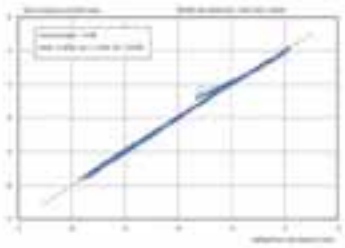
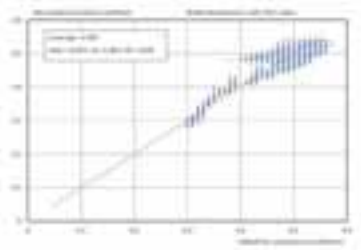
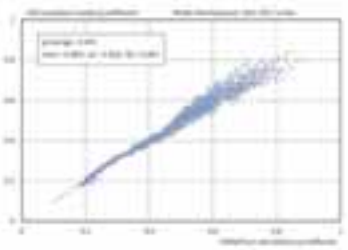
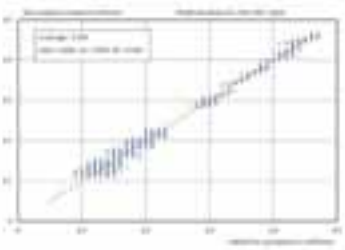
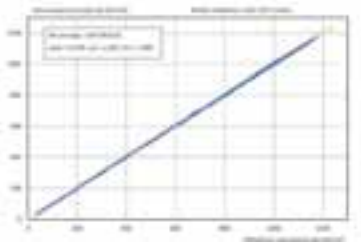
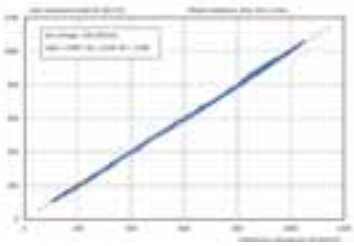
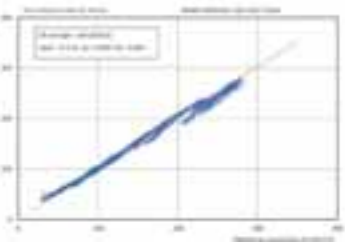
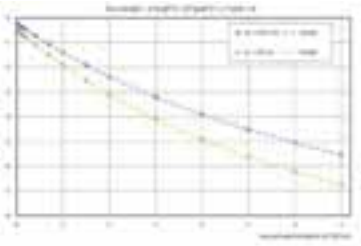
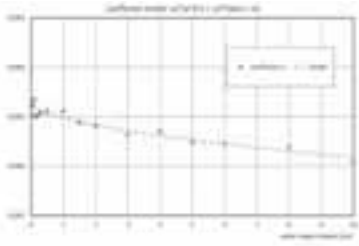
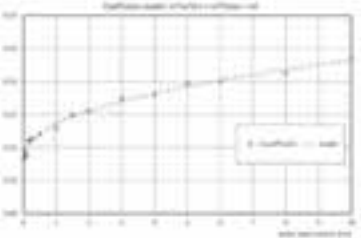
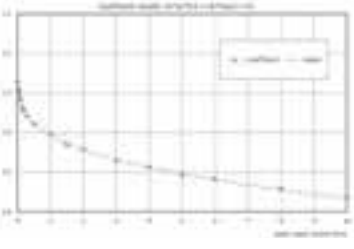
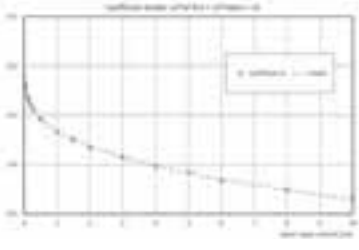

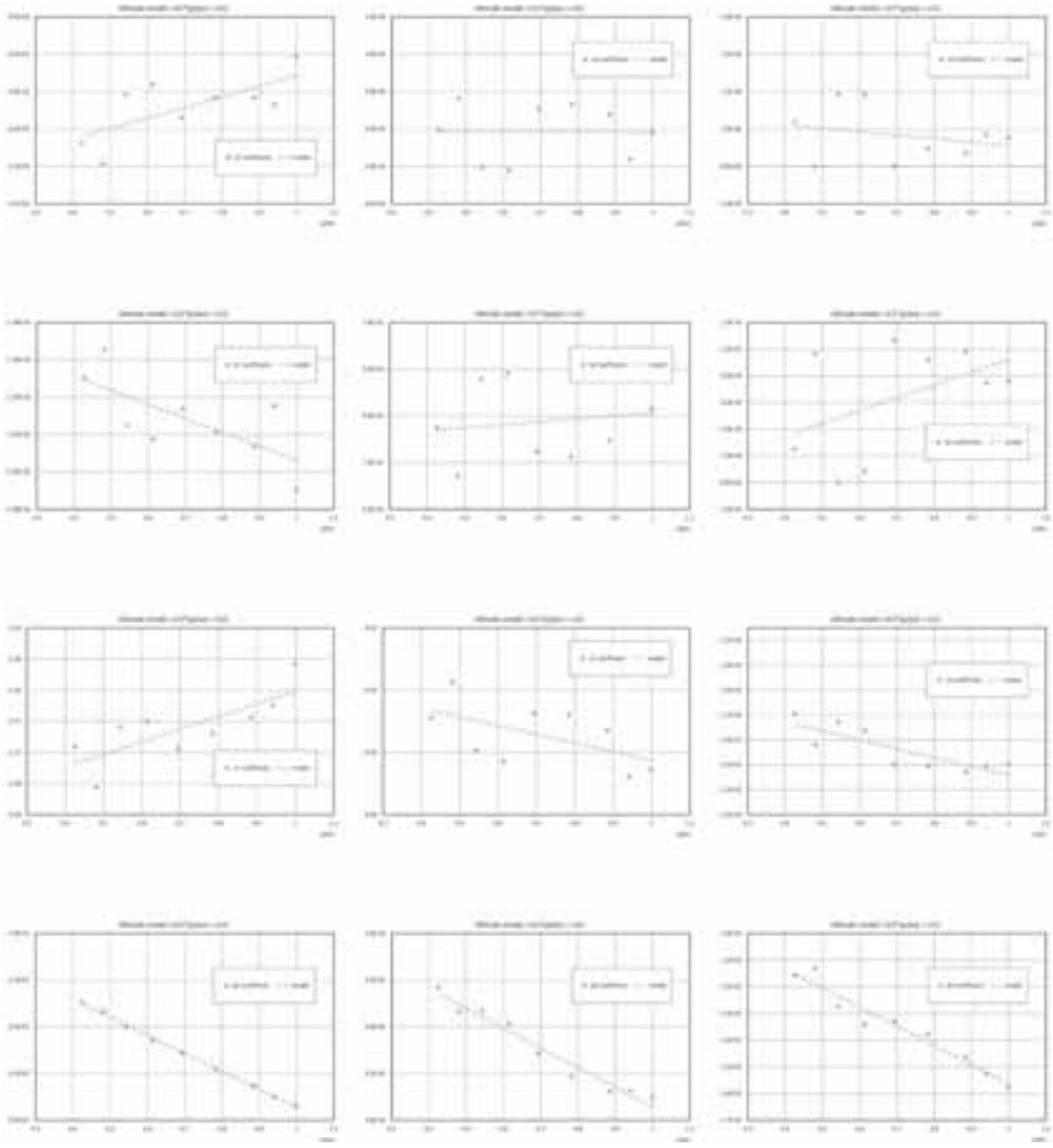

Evaluation of Solar Energy Losses for the Heliostat-to-Receiver Path of a Tower Solar Plant for Different Aerosol Models

Gabriel López[1], Christian A. Gueymard[2] and Juan Luis Bosch[1]

[1] Dpto. Ingeniería Eléctrica y Térmica, de Diseño y Proyectos, Universidad de Huelva, Huelva (Spain)

[2] Solar Consulting Services, Colebrook, NH (USA)

Abstract

The efficiency of solar tower plants is impacted twice by atmospheric aerosols. First, aerosols attenuate the direct solar irradiance reaching the heliostats, and then reduce the irradiance reflected by these heliostats while it propagates to the receiver. The aerosol transmittance from the top of atmosphere to the ground is well modeled by many radiative transfer codes, but its counterpart for the heliostat-to-receiver slant path has only been estimated for a very limited number of ideal atmospheric conditions. In this work, the solar losses for the heliostat-to-receiver slant paths are extensively analyzed for different aerosol models, atmospheric conditions, and mirror-to-tower geometries by performing detailed simulations with the MODTRAN radiative transfer code. Reductions up to 30% of the solar irradiance incident on distant heliostats can occur under moderately turbid situations, due to the concentration of aerosols near the ground. It is found that site elevation is not a significant factor, contrary to what was anticipated, according to an old empirical model of the literature.

Keywords: Solar tower plants, transmission losses, aerosol models, atmospheric attenuation, CSP.

1. Introduction

The accurate evaluation of the irradiance reaching the receiver of a Tower Solar Power plant (TSP) is of primary importance to prepare its design, and later evaluate its actual performance. The literature mentions numerous radiative transfer models (e.g., SMARTS, libRadtran, or MODTRAN) that can derive the spectral aerosol transmittance from the top of the atmosphere to the surface with sufficient accuracy for normal plant operation, provided that the bulk aerosol optical properties are known over the vertical column. Most of these models, however, are not suitable to easily predict the atmospheric radiation losses over the heliostat-to-receiver slant path. Such calculations are complex, time consuming, and require specific inputs (such as vertical aerosol profiles) that are usually not known. Moreover, most models (with the notable exception of MODTRAN, or its predecessor, LOWTRAN) are not designed to calculate the radiation transmission over short slant paths in any arbitrary direction. Some efforts were conducted several decades ago to derive simple empirical parameterizations from detailed modeling and obtain such results in a more accessible form. Examples include the empirical Pitman and Vant-Hull model (1981), as well as modules that are part of the DELSOL and MIRVAL CSP design codes, for instance. The main drawback of this approach is the extremely limited number of possible atmospheric conditions, i.e., lack of general validity. In this respect, the range of possible atmospheric conditions that these simplified models can handle is limited to a few visibility values only (typically 23 km and 5 km). Originally, such values were assumed to describe clear conditions and hazy conditions, respectively.

In recent years, this topic has gathered renewed interest, so that new studies have been conducted to improve this type of algorithm (Gueymard et al., 2017; Hanrieder et al., 2016, 2017; Sengupta and Wagner, 2012). Previous investigations by the authors have shown that the attenuation specifically caused by water vapor near the surface was significant, albeit small in comparison to that of aerosols (Gueymard et al., 2017; López et al., 2016). In addition, the measurement of horizontal visibility for the specific needs of the TSP industrial sector has progressed, with the development of several low-cost automatic devices, such as forward-scatter-based visibilimeters (Hanrieder et al., 2017). Some of the first studies using the latter technology report that visibility

doi:10.18086/swc.2017.23.03 Available at http://proceedings.ises.org

values are commonly much higher than 23 km (López et al., 2017). These results constitute a motivation to conduct more in-depth studies, with the goal of better understanding the effect of variable atmospheric conditions on the attenuation of solar radiation after reflection by heliostats.

In this work, an extensive and detailed analysis of the aerosol transmittance is undertaken with MODTRAN for heliostat-to-receiver slant paths of varied lengths. Five aerosol models are used along with four atmospheric profiles and two different ground elevations. The combination of these aerosol models with the water-temperature-pressure profiles at each ground level generates a total of 40 different model atmospheres. The resulting large range of atmospheric conditions is analyzed in this study, with the underlying goal of developing a general simplified model.

2. Methodology

2.1 Slant atmospheric attenuation

The aerosol-induced irradiance attenuation A taking place along the mirror-to-receiver slant path is evaluated (in percent) by means of the following expression:

$$A = 100\,\frac{G_{bT0}-G_{bT}}{G_{bM}} \qquad \text{(eq. 1)}$$

where G_{bT0} is the reflected direct normal irradiance (DNI) reaching the receiver at the top of the tower assuming no aerosol, G_{bT} is the reflected DNI reaching the receiver but assuming the presence of aerosol, and G_{bM} is the DNI incident on the mirror (Fig. 1). The atmospheric conditions are assumed identical for both G_{bM} and G_{bT}. In this way, eq. (1) represents the percent fraction of energy loss due exclusively to aerosol extinction along the slant range considered. Additional extinction is expected, and would be caused primarily by water vapor (Gueymard et al., 2017; López et al., 2016).

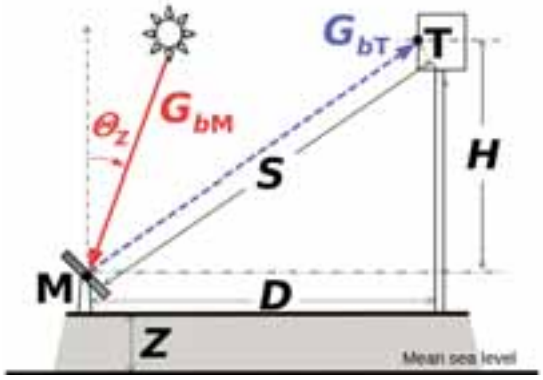

Fig. 1: Schematic description of a solar power tower plant, and nomenclature.

The irradiance incident on the mirror M, G_{bM}, and the irradiance reaching the tower receiver T reflected by the mirror (Fig. 1) may be obtained as:

$$G_{bM} = \int_{\lambda 1}^{\lambda 2} T_{\lambda M} G_{b\lambda 0}\,\mathrm{d}\lambda \qquad \text{(eq. 2)}$$

$$G_{bT} = \int_{\lambda 1}^{\lambda 2} \rho_{\lambda} T_{\lambda M-T} T_{\lambda M} G_{b\lambda 0}\,\mathrm{d}\lambda \qquad \text{(eq. 3)}$$

$$G_{bT0} = \int_{\lambda 1}^{\lambda 2} \rho_{\lambda} T_{\lambda M-T0} T_{\lambda M} G_{b\lambda 0}\,\mathrm{d}\lambda \qquad \text{(eq. 4)}$$

where $G_{b\lambda 0}$ is the extraterrestrial spectral irradiance, $T_{\lambda M}$ is the atmospheric spectral transmittance for the Sun-to-Mirror path (which depends on the abundance of various atmospheric constituents, and thus varies over time), $T_{\lambda M\text{-}T}$ is the spectral transmittance for the Mirror-to-Tower slant path taking into account the aerosol load, $T_{\lambda M\text{-}T0}$ is also the spectral transmittance for the Mirror-to-Tower slant path but considering no aerosols in the slant path, and ρ_λ is the mirror's spectral reflectance (set to 1 here for the sake of simplicity in this work). The integration limits are fixed to λ_1 = 0.28 μm and λ_2 = 10 μm. Following López et al. (2016), the solar zenith angle of the DNI incident on the mirror is varied incrementally from 0º to 89º, as shown in Table 1. Although TSP plants do not operate under large solar zenith angles, values higher than 80º are considered here in order to analyze the trend of transmission loss under these extreme limits.

Tab. 1: Values of the MODTRAN inputs used to obtain the simulated database.

Inputs to MODTRAN	Values
Θ_Z (degrees)	0, 10, 20, 30, 40, 50, 60, 70, 80, 85, 89
H (m)	100, 200, 250
D (km)	0.15, 0.5, 1, 2, 4
Z (km)	0, 1
Vis (km)	23, 50, 75
Aerosols Model	Rural, Maritime, Urban, Tropospheric, Desert
Atmospheric Model	MLW, MLS, Tropical, USSA

MODTRAN version 4v1r1 (Berk et al., 1989) is the radiative transfer code selected here for its remarkable capability of computing short-range transmittances. MODTRAN is the successor of LOWTRAN, which was used initially to demonstrate the impact of near-surface atmospheric constituents on the slant attenuation (Vittitoe and Biggs, 1978). MODTRAN is used parametrically to calculate each irradiance value in eqs. (2-4) for a number of specific atmospheric conditions. In particular, transmittances $T_{\lambda M\text{-}T}$ and $T_{\lambda M\text{-}T0}$ are obtained using MODTRAN's slant-path option, which evaluates the high-resolution spectral transmission between two points at finite distance—the mirror and the receiver, in the present case. MODTRAN considers the detailed effects of any vertical variation in atmospheric constituents, as well as the optical effects caused by atmospheric refraction and earth curvature..

2.2 Visibility and optical characteristics of aerosols

MODTRAN evaluates the radiative impact of aerosols as a function of their abundance. The latter is reported in terms of "visibility", whose definition needs to be clarified here. In meteorological terms, visibility is an old *subjective* estimation technique based on a human observer's evaluation of the maximum distance at which distant objects can be distinguished against a contrasting background, usually the sky. Modern instruments, like visibilimeters or transmissometers, now provide an *objective* evaluation of visibility, which is referred to as "meteorological optical range" (MOR), according to Koschmieder's law (Koschmieder, 1925):

$$MOR = \frac{\ln\left(1/\varepsilon\right)}{\sigma} \qquad \text{(eq. 5)}$$

where σ is the air extinction coefficient at 550 nm and ε is the threshold contrast between an object and the background. According to the World Meteorological Organization (WMO, 2014), ε must be set to 0.05 to obtain MOR. Another definition, referred to as "meteorological range" (MR) in MODTRAN, uses a more optimistic threshold contrast ε = 0.02:

$$MR = \frac{\ln\left(1/0.02\right)}{\sigma} \qquad \text{(eq. 6)}$$

It is straightforward to perform the conversion between these two definitions: MR = 1.306 MOR. The relationship given by eq. (5) or (6) may be deceptively simple, however, since its derivation depends on a number of serious assumptions (Middleton, 1952). Even though MODTRAN and its predecessor, LOWTRAN, use the term "visibility" to describe the aerosol input, what is actually meant is MR, which is highly confusing, since it is different from MOR. Kneizys et al (1980) acknowledged the difference between MR and observer (subjective) visibility, V_{obs}, and indicated that MR ≈ (1.3 ± 0.3) V_{obs}. (The coefficient 1.3 simply represents the ratio MR/MOR = ln(1/0.02)/ln(1/0.05).) Hence, MOR is just a technical term for what was previously known as "observer visibility", or V_{obs}. In what follows, the abbreviation VIS is used to conform to MODTRAN's usage, even though the intended variable name is MR.

One key issue of using VIS to describe the optical impact of aerosols is the limited number of monitoring sites, mostly at airports. Hence, access to actual local data is difficult in practice. In comparison, there are many more sources of data that provide the aerosol optical depth (AOD), based on ground measurements with sunphotometers, chemical transport models (and derived reanalysis models), or space borne remote-sensed observations. Additionally, visibilimeters installed at airports have a very limited range, typically 20 km (Gueymard, 2012), which is not enough to provide the precise inputs needed here. A relationship between VIS and AOD is thus desirable, so that VIS can be estimated from AOD observations, or vice versa. Experimental studies have shown that the two variables are only weakly correlated in practice, due to a number of difficulties (Wilson et al., 2015). For the present study, what is important is the theoretical correspondence between VIS and AOD, as specifically applicable to MODTRAN. This desired relationship is built in SMARTS (Gueymard, 2001) to allow the conversion of VIS to AOD or vice versa. Table 2 provides the needed information to allow comparisons between the results presented here (based on VIS) and those provided in other studies that are rather based on AOD (Sengupta et al., 2012).

Tab. 2: Approximate equivalence between Meteorological Range (as used in MODTRAN), Visibility, and Aerosol Optical Depth at 550 nm, based on SMARTS simulations.

Meteorological Range (km)	Observer/Subjective Visibility (km)	AOD at 550 nm
5	3.8	1.1730
10	7.7	0.6667
15	11.5	0.4744
20	15.4	0.3686
23	17.7	0.3251
25	19.2	0.3014
50	38.5	0.1596
75	57.7	0.1126
100	76.9	0.0901
150	115.4	0.0667
200	153.8	0.0549

Various aerosol loads are considered in this study by means of three surface visibility values: 23, 50 and 75 km (higher visibilities correspond to lower aerosol optical depths, as shown in Table 2). Various aerosol models are available in MODTRAN, and can be selected in order to analyze the effect of the optical properties of each possible aerosol type on transmission losses. Five common aerosol models are selected here: rural, maritime, urban, tropospheric, and desert (Tab. 1). The desert aerosol model is an important aerosol type since it is representative of arid and semiarid regions, which are favorite emplacements for TSP plants due to the high DNI resource there. The desert aerosol model is dependent on wind speed, leading to the expectation that the slant-path attenuation will increase with wind speed. This is mainly due to the hematite contained in sand particles, which leads to selective absorption at visible wavelengths, becoming more pronounced when it is entrained as wind speed increases (Longtin et al., 1988). In this first analysis, wind speed is fixed to 10 m s^{-1}, corresponding to the reference value given in MODTRAN.

2.3 Other variables

Since the concentration and mixture of aerosol particles have variable vertical profiles, the potential influence of ground elevation on transmission losses is explored by considering two site elevations, Z = 0 km and 1 km above mean sea level. For elevated sites (e.g., Z = 1 km), MODTRAN´s modeling is more elaborate than at sea

level. The aerosol densities below 6 km are subjected to vertical compression, in such a way that the aerosol sources are moved up to that altitude. Hence, the energy loss computation may be performed using visibility observations at the elevated site, which eliminates the need for additional calculation (scaling between sea level and the actual site elevation). In other words, MODTRAN transparently takes into account the fact that the aerosol concentration near the surface at an elevated site is normally larger than in the free atmosphere at the same altitude.

In addition to the above variables, which are explicitly related to the aerosol effect, the impact of different atmospheric water-temperature-pressure profiles on the transmission losses by aerosols is also analyzed by means of four built-in standard atmosphere models: Mid-Latitude Winter (MLW), Mid-Latitude Summer (MLS), Tropical, and U.S. Standard Atmosphere (USSA). The spectral distribution of DNI both at the mirror and at the receiver is modified according to the atmosphere model. Consequently, the transmission loss by aerosols can also be expected to differ. All the gaseous concentrations (such as water vapor) are set to the reference values imposed by the selected atmosphere model.

Finally, different slant ranges are considered between mirror and receiver. The geometries selected here attempt to mimic the typical configurations encountered in current or future TSP plants. Three tower heights, H, are used (100, 200 and 250 m), as well as five values for the horizontal mirror-to-tower distance D (0.15, 0.5, 1, 2 and 3 km). The resulting combinations of H and D represent a large range of possible geometries, which is needed to generalize the results.

3. Results

3.1 Effect of zenith angle

Figure 2 shows the transmission losses, A, or "energy losses" due to aerosols alone, as a fraction of G_{bM} for a set of atmospheric conditions: eleven zenith angles between 0º and 89°, three slant ranges, S, corresponding to the combination of a single tower height (H = 100 m) with three mirror-to-tower horizontal distances (D = 0.15, 1, and 4 km), ground at sea level (Z = 0 m), and three visibilities (23, 50, and 75 km). All five aerosols models are used here, combined with the MLS atmosphere.

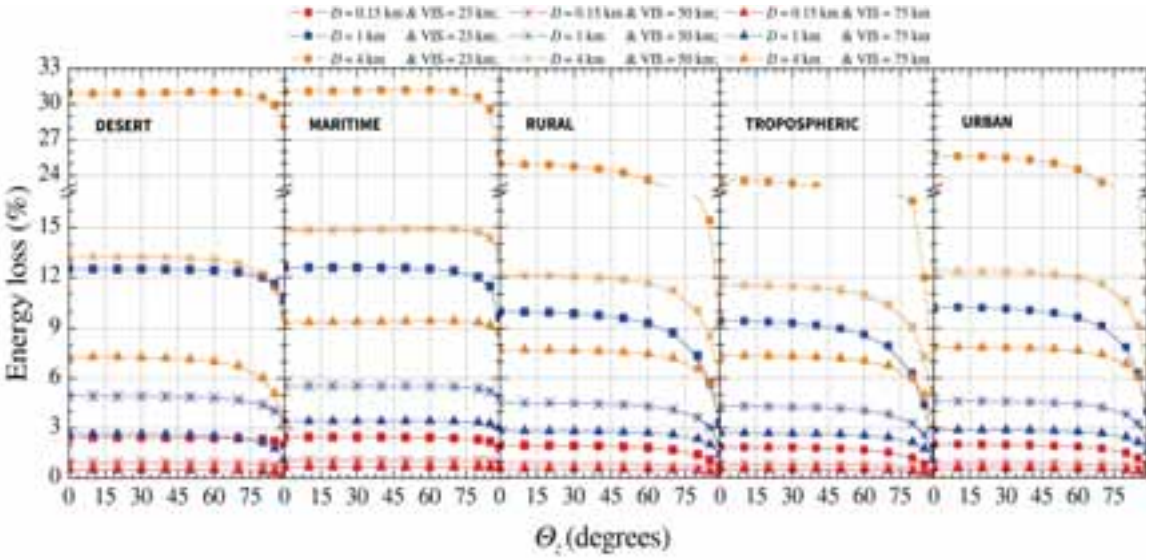

Fig 2. Energy losses in the mirror-to-receiver slant path versus zenith angle for five different types of aerosol, using the MLS Atmosphere, three visibilities (23, 50 and 75 km), a tower height of 100 m, three horizontal mirror-to-tower distance (D = 0.15, 1 and 4 km) and a site at sea level (Z = 0 m).

For short distances (D = 0.15 km), the energy losses are almost constant for any visibility and any aerosol model. The impact of zenith angle is also found negligible over the normal operation range of TSP plants. In contrast, when slant range increases (using D = 1 and 4 km), the energy losses corresponding to the rural, urban and tropospheric aerosol models show a higher dependence with zenith angle, and get stronger when D increases. When the sun rises and Θ_Z decreases from 75º to 30º, energy losses increase by 2% in the case of rural

and urban aerosols, and even more for tropospheric aerosols. This relationship with zenith angle is also observed for the energy losses that are specifically due to water vapor (López et al., 2016). The type of aerosol mixture is important here, since desert or maritime aerosols do not produce this marked zenith angle dependence, at least for $\Theta_Z < 80^o$. The results shown in Fig. 2 are representative of those corresponding to the other tower heights, horizontal mirror-to-tower distances, ground elevations and atmospheric profiles.

3.2 Effect of atmosphere model

Similar to Fig. 2, Fig. 3 shows the calculated energy losses as a function of zenith angle for a slant range corresponding to a tower height H = 100 m, a mirror-to-tower horizontal distance D = 1 km, ground at sea level (Z = 0 m), and two different visibilities, 23 and 75 km. The five aerosols models and all four atmosphere models are used here to evaluate their combined effects.

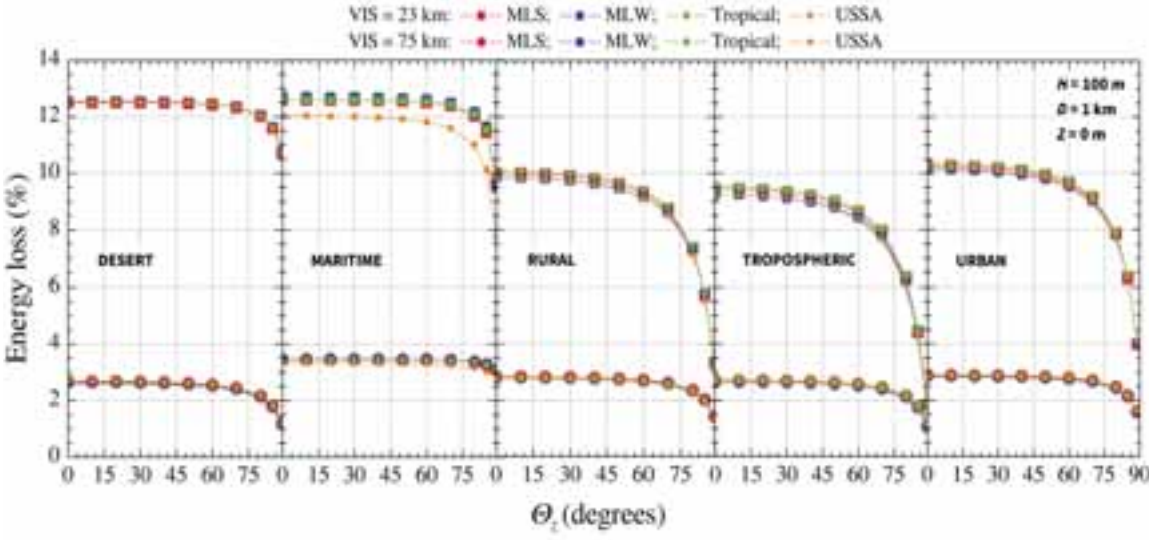

Fig 3. Energy losses in the mirror-to-receiver slant path versus zenith angle for five different types of aerosol and four atmosphere models, using two visibilities (23 and 75 km), a tower height of 100 m, a horizontal heliostat-to-tower distance D = 1 km, and a site at sea level.

In general, it is found that the atmosphere model has little impact, if not negligible. With the desert aerosol model, for instance, all four atmosphere models provide the same energy loss for each of the two visibilities (23 km and 75 km), with maximum energy losses of about 13% and 3%, respectively. This means that the desert aerosol model appears insensitive to changes in meteorological conditions such as temperature, pressure, relative humidity, or water vapor content. This tendency is also observed with the remaining four aerosol models when used under very clear conditions (VIS = 75 km). Moreover, under such ideal conditions, all types of aerosol mixtures yield a similar energy loss of ≈3%, except for the maritime aerosol (≈3.5%). When visibility reduces to 23 km, the energy losses exhibit a weak dependence on the type of atmosphere model, with differences lower than 0.5%. The only exception is when the USSA atmospheric model is used along with the maritime aerosol, which leads to energy losses lower than 1% compared to what is obtained with the MLS, MLW or Tropical atmospheres. This is likely caused by the high sensitivity of the optical properties of maritime aerosols to variations in relative humidity. As a matter of fact, the aerosol mixtures of oceanic origin have significantly different properties compared to continental aerosol types, in particular (Shettle and Fenn, 1979). In the lower atmosphere, the MLS, MLW and Tropical atmospheres have vertical profiles of relative humidity that are similar between each other, but significantly different from the USSA model.

3.3 Effect of ground elevation

Site elevation has been identified as a critical factor by Pitman and Vant Hull (1982), and thus deserves attention. Its effect is analyzed here by evaluating the energy losses for two surface elevations (Z = 0 and 1 km), while parametrically varying the sun's zenith angle and using the MLS atmosphere for various conditions: H = 100 m, D = 1 km, the five aerosol models, and two visibilities. The results appear in Fig. 4a for VIS = 23 km and Fig. 4b for VIS = 75 km. It is observed that the elevation effect seems negligible in all cases, since the energy losses are almost identical for any input configuration at a specified Z. This is contrary to the Pitman and

Vant-Hull (1982) conclusions, which was not expected. A likely explanation for this discrepancy is that MODTRAN (used here) and LOWTRAN (used by Pitman and Vant Hull, among others) differ on how they consider visibility at an elevated site. This is directly related to the vertical aerosol scaling that is performed transparently by MODTRAN (but not in LOWTRAN), as mentioned above. It is also possible that the assumptions and results provided here, which are relative to aerosol-induced losses only, are not exactly compatible with those of Pitman and Vant Hull. This will require further scrutiny.

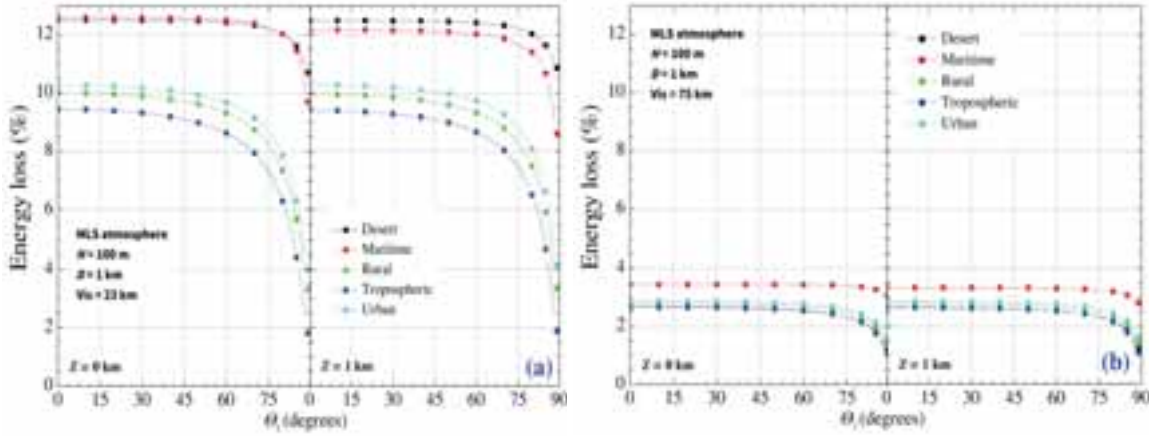

Fig 4. Energy losses versus zenith angle for five types of aerosol and two visibilities: (a) VIS = 23 km, and (b) VIS = 75 km. The MLS atmosphere, a tower height of 100 m, a horizontal mirror-to-tower distance *D* = 1 km, and two ground altitudes (*Z* = 0 and 1 km) are selected in both cases.

3.4 Effect of slant path range

The last parameters to be analyzed are those determining the length of the slant path *S* followed by the reflected sun rays from the mirror up to the receiver at the top of the tower: the horizontal mirror-to-tower distance *D* and the tower height *H*. Figure 5 displays the energy loss for a fixed zenith angle (Θ_z = 30º) and various combinations of *D* and *H*, per the values listed in Table 1. Under very clear conditions, corresponding to VIS = 75 km, the energy loss is not sensitive to variations in tower height, even though the aerosol concentration normally decreases with elevation in the free atmosphere. It is possible that this lack of sensitivity reflects the crude vertical resolution (1 km) of aerosol and atmosphere models in MODTRAN.

Desert, rural, tropospheric and urban aerosol determine similar energy losses, ranging from < 1% for *D* = 0.15 km, up to 7% for *D* = 4 km. The attenuation due to maritime aerosols is slightly higher, reaching a maximum of 9%. When a lower visibility (23 km) is considered, the influence of *H* on *A* is weak for large distances (*D* > 2 km), and becomes imperceptible for short distances (*D* < 2 km). Only the attenuation due to maritime aerosols shows any dependence on tower height. The results for the other atmospheres are similar to this.

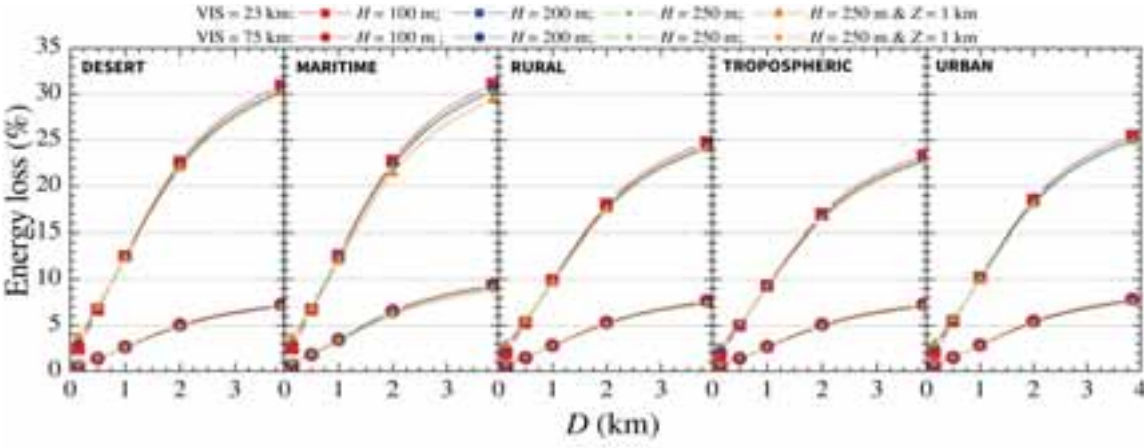

Fig 5. Energy losses vs. horizontal mirror-to-tower distance for five different types of aerosol. All cases use the MLS atmosphere, two visibilities (23 and 75 km) and three tower heights (*H* = 100, 200 and 250 m). In addition, the red, blue and green lines correspond to *Z* = 0 km, whereas the orange line is for *Z* = 1 km.

3.5 Generalized results

The results provided above show how energy losses depend on a number of variables. Some of these variables have more impact than others. Because of the intricacies of all the implied relationships, it is desirable to derive a simplified, generalized model. Results for the desert and maritime aerosols are similar, but differ from those obtained with the other three aerosol models. A simplification thus consists in considering only two distinct groups of possible aerosols: Either desert/maritime or rural/urban/tropospheric. In each group, the energy losses do not vary much with aerosol type, so that an aerosol-independent average can be used for simplification. Moreover, since tower height, atmosphere model, surface elevation and zenith angle have no significant effects, the only remaining critical factors are VIS and *D.* Plots providing the energy loss *A* as a function of VIS and *D* for each aerosol group appear in Fig. 6. As could be expected, *A* is a strong function of both VIS and *D*. *A* is also affected by the aerosol group, but to a lower extent—particularly for high visibilities. In theory, these plots can also be used to rather relate *A* to AOD and *D*, using the data in Tab. 2. As noted above, however, the relationship between VIS and AOD is not an exact one under real conditions. Hence, additional studies would be needed to better establish the relationship between *A* and on-site AOD observations, for instance.

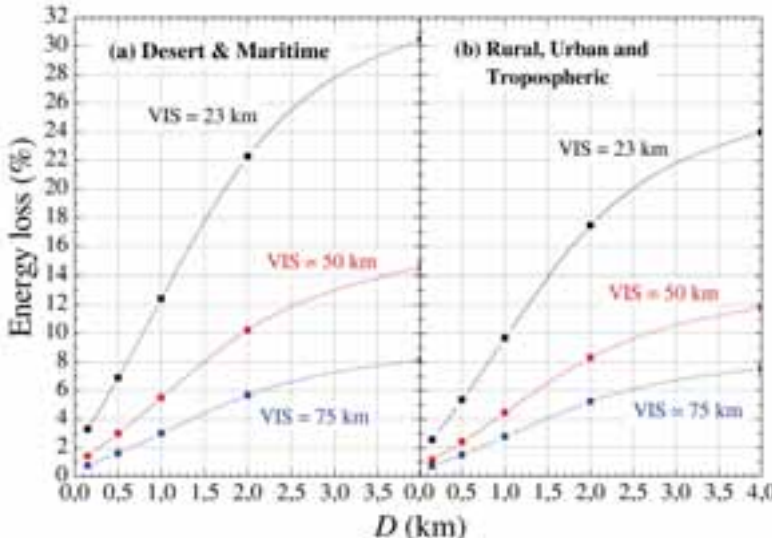

Fig. 6. Generalized results relating the energy lost between a mirror and the tower receiver to VIS and horizontal distance *D* for two distinct groups of aerosols.

4. Conclusions

For Tower Solar Plants (TSP), the energy losses for the mirror-to-tower slant path caused by the presence of aerosols near the ground have been analyzed as a fraction of the DNI incident on the mirror. Many different configurations of possible TSP geometries and atmospheric conditions were employed to generate the transmission losses, using the MODTRAN spectral atmospheric code with its slant-path option. A first result obtained here is that the energy loss does not appreciably depend on the specific atmosphere model that can be selected in MODTRAN (e.g., mid-latitude winter, mid-latitude summer, tropical or USSA). This leads to an important simplification, since the energy loss caused by aerosols can be properly calculated for any site using only one atmospheric profile. Similarly, the energy loss is virtually independent from the sun's zenith angle (up to ≈75°), and does neither depend on ground elevation, nor on the TSP's tower height. The main atmospheric variable driving the energy loss caused by aerosols is visibility (or more precisely, "meteorological range", per MODTRAN's definition). Selecting various types of aerosol (rural, urban, tropospheric, maritime, or desert) leads to different energy losses and different dependences on the sun's zenith angle. However, the five aerosol models may be reduced to only two categories: (i) 'optically thin aerosols', consisting of the rural, urban and tropospheric aerosols, which yield maximum energy losses lower than 25% for a 23-km visibility and 4-km horizontal distance; and (ii) 'optically thick aerosols' composed of the desert and maritime aerosols, generating maximum energy losses of 30% for the same visibility and distance.

Taking some possible simplifications into account, all results can be synthesized into two plots (one for each aerosol group) that provide the aerosol-induced energy losses at any site as a function of visibility and horizontal mirror-to-tower distance. A theoretical correspondence between visibility, as defined here, and aerosol optical depth is also provided, in case visibility measurements are not available. Finally, the present results will allow the development of future parameterizations of the transmission losses, based on only a limited number of essential variables. In addition, the proposed results can be used as benchmark values for assessing the performance of other models of the literature, such as those used in various CSP design codes.

5. Acknowledgments

The authors are grateful for the financial support provided by the Spanish Project "PRESOL" ENE2014-59454-C3-2-R, which is funded by the Ministerio de Economía y Competitividad and co-financed by the European Regional Development Fund (FEDER).

6. References

Berk, A., Bernstein, L.S., Robertson, D.C., 1989. MODTRAN: A Moderate Resolution Model forLOWTRAN7. Report GL-TR-89-0122, Air Force Geophysical Laboratory, Hanscom, MA.

Gueymard, C.A., 2001. Parameterized Transmittance Model for Direct Beam and Circumsolar Spectral Irradiance. Solar Energy 71, 325-346.

Gueymard, C.A., 2012. Visibility, aerosol conditions, and irradiance attenuation close to the ground. Solar Energy 86, 1667-1668.

Gueymard, C.A., López, G., Rapp-Arrarás, I., 2017. Atmospheric transmission loss in mirror-to-tower slant ranges due to water vapor. AIP Conference Proceedings, 1850, 140010; doi: 10.1063/1.4984518

Hanrieder, N., Sengupta, M., Xie, Y., Wilbert, S., Pitz-Paal, R., 2016. Modeling beam attenuation in solar tower plants using common DNI measurements. Solar Energy, 1529, 244–255.

Hanrieder, N., Wilbert, S. Mancera-Guevara, D., Buck,R., Giuliano, S., Pitz-Paal, R., 2017. Atmospheric extinction in solar tower plants – A review. Solar Energy, 152, 193-207.

Kneizys, F.X., Shettle, E.P., Gallery, W.O., Chetwynd, J.H., Abreu, L.W., Selby, J.E.A., Fenn, R.W., McClatchey, R.A., 1980. Atmospheric transmittance/radiance: Computer code LOWTRAN 5. Report AFGL-TR-80-067, Air Force Geophysics Lab., Hanscom AFB, MA.

Koschmieder, H., 1925. Theorie der horizontalen Sichtweite, Keim & Nemnich.

Longtin, D. R., Shettle, E. P., Hummel, J. R., Pryce, J.D., 1988. A Wind Dependent Desert Aerosol Model: RadiativeProperties, AFGL-TR-88-0112, Air Force Geophysics Laboratory, Hanscom AFB, MA.

López, G., Gueymard, C.A., Bosch, J.L., Rapp-Arrarás, I., Alonso-Montesinos, J., Ballestrín, J., Polo, J., Barbero, J., Pulido-Calvo, I., 2016. Modelling water vapor impact on the solar energy reaching the receiver of a solar tower plant by means of artificial neural networks. . Proc. 11th EuroSun Conference, Palma de Mallorca, Spain, International Solar Energy Soc.

López, G., Bosch, J.L., Pulido-Calvo, I., Gueymard, C.A., 2017. Visibility Estimates from Atmospheric and Radiometric Variables Using Artificial Neural Networks. Proc. Air Pollution XXV Conf., WIT Transactions on Ecology and The Environment, vol 211, 129-136; doi:10.2495/AIR170131.

Middleton, W.E.K., 1952. Vision through the atmosphere. Univ. Toronto Press.

Pitman, C.L., Vant-Hull, L.L., 1982. Atmospheric transmittance model for a solar beam propagating between a heliostat and a receiver. ASES Progress in Solar Energy, 1247–1251.

Sengupta, M., Wagner, M., 2012.Atmospheric attenuation in central receiver systems from DNI measurements. Proc. Solar 2012 Conf., Denver, CO, American Solar Energy Soc.

Shettle, E.P., Fenn, R.W., 1979. Models for the aerosols of the lower atmosphere and the effects of humidity variations on their optical properties. Report AFGL-TR-79-0214, Air Force Geophysics Lab., Hanscom AFB.

Vittitoe, C., Biggs, F, 1978. Terrestrial propagation loss. Proc. American Section of ISES annual meeting, Denver, CO, 664–668.

Wilson, R.T., Milton, E.J., Nield, J.M., 2015. Are visibility-derived AOT estimates suitable for parameterizing satellite data atmospheric correction algorithms? International Journal of Remote Sensing 36, 1675-1688, 10.1080/01431161.2015.1023558.

WMO, 2014. Measurement of Visibility, in WMO No-8 2014, Guide to Meteorological Instruments and Methods of Observation (CIMO guide). Geneva, Switzerland. https://library.wmo.int/opac/doc_num.php?explnum_id=3121.

Assessment of Hydrokinetic Potential in the Umbeluzi Basin, Mozambique

Summary

Hydrokinetic turbines can play a pivotal role in providing electricity access to remote areas in Mozambique, as stand-alone isolated mini-grids. However, the suitable sites for application of Hydrokinetic Turbines throughout the country are not known, hence the need for this research. The study was done to evaluate electricity generation based on hydrokinetic turbines in the Umbeluzi basin. For this purpose, the following methods have been applied: 1) Frequency analysis using historical data of river stream velocity to generate velocity duration curves (VDC); 2) comparison of stream flow velocity to the design velocity of the hydrokinetic turbine and comparison of the rotor diameter of hydrokinetic turbine to the depth of the river to enable the evaluation of the feasibility of installation of the turbine in the basin. The results show that low flow velocities characterize the Umbeluzi River, hence no considerable potential sites for installations of hydrokinetic turbine. However, 444 W can be extracted in station 638 using dual axial turbine (Under Water Electric kit).

Key-words: **Hydrokinetic Turbines, Resources, Assessment**

1. Introduction

Mozambique has 27.2 million inhabitants and only about 20.2 % have access to electricity. Almost 97% of the total household energy needs are still met by traditional biomass fuels (wood and charcoal). Biomass meets 78% of the country's energy needs, followed by hydro (13%), oil products (7%) and 2% from other resources (IRENA, 2012; Mahumane, G. & Mulder, P., Nadaud, 2012). Total installed hydropower capacity is 2187 MW of which 2075 MW is from Cahora Bassa hydropower plant (IHA, 2015). Hydropower generation potential is estimated at 12,000 MW of which only 2,200 MW (Uamusse, Tsamba, Matsinhe, & Persson, 2015) has been exploited. The potential of small hydropower plants (<10 MW) is 1000 MW (Klunne, 2013) of which only 2.63 MW has been exploited. In fact, small hydropower compares well with other supply technologies; however, over 36 years large-scale hydropower projects dominated Mozambique's energy plans targeting neighboring countries market, especially South Africa.

Mozambique is a large country with widely dispersed; mostly rural population (70%) and no ambitious grid extension plans can reach the entire country in the short and medium term (IRENA, 2012).Other options such as small hydro therefore have to be explored to increase access to electricity. One of the options for harnessing kinetic energy from river currents is by using hydrokinetic turbines. However, the suitable sites for application of Hydrokinetic Turbines throughout the country are not known, hence the need for this research.

Hydrokinetic systems harness energy from natural water movement (kinetic energy) to generate electricity or provide mechanical power. The systems have been successfully powering rural communities such as 1.2 kW in Brazil (Els, 2008; Souza, j., Els & Diniz, J. & Wehrman, 2008); 5 kW in Ruby(Sornes, 2010), 200 W in Peru(Sornes, 2010)and pumping water for irrigation system in Sudan (M. J. Khan, Bhuyan, Iqbal, & Quaicoe, 2009). In Mozambique, the potential of hydrokinetic turbines is being studied at Eduardo Mondlane University (UEM) in partnership with University of Brasilia (UnB).

Traditionally, one way to validate water resources as adequate energy alternative is to evaluate its power potential available at the sites. For the case of hydrokinetic systems, the important parameter for this evaluation are: flow velocity and water depth of the rivers. This is the basic information required for system design and energy planning, especially to ensure that energy supply and demand decisions are compatible with overall goals for national sustainable development while diversifying energy resources.

1.1 Principle of Hydrokinetic Power

Through conservation of energy, the power existing at a point in the cross-sectional area of a stream of water flowing at a given speed can be obtained using Equation 1.

doi:10.18086/swc.2017.23.04 Available at http://proceedings.ises.org

$$P_k = \frac{\rho}{2} A_c V^3 \quad \text{(eq. 1)}$$

Where P_k is available kinetic power, ρ is density of water (1000 kg/m^3), Ac is the cross-sectional area of the extraction and, V is the flow velocity (m/s). Hydrokinetic power is often reported as a power density, which is the power normalized to unit are:

$$\frac{P_k}{A_c} = \frac{\rho}{2} V^3 \quad \text{(eq. 2)}$$

Computation of the kinetic power depend on the cross-section area, which is either the river cross-sectional area for assessment of the total energy in then river, or the area of the device that will be used to extract the kinetic energy (NRC-CHC, 2010). For the purpose of this study, the cross-sectional area of the river is used to estimate power potential.

1.2 Extractable Hydrokinetic Power

When considering the use of a device to extract the available power, the cross-sectional area of the device that intersects the flow is taken as the area of interest and the total efficiency of the device and associated power system in converting the kinetic power into electrical power has to be considered. Thus, the generated power (Pg) given as:

$$P_g = Cp \frac{\rho}{2} A_s V^3 \quad \text{(eq. 3)}$$

Where Cp is power coefficient of the turbine and A_S is the swept rotor area of the turbine given as:

$$A_s = \pi \frac{D^2}{4} \quad \text{(eq. 4)}$$

Where D is the rotor diameter of the turbine, Л=3.14

Considering the Betz limits as the maximum turbine efficiency, the power extractable from a turbine is given as:

$$P_{g-Max} = 0.593 \frac{\rho}{2} A_s V^3 \quad \text{(eq. 5)}$$

1.3 Hydrokinetic technology and rural electrification

This section describes—in brief—the hydrokinetic turbines used for feasibility evaluation of hydrokinetic power with the river. Detailed technology review can be found in (Verdant Power Canada, 2006), (M. J. Khan et al., 2009)and (Lago, Ponta, & Chen, 2010).

The Amazon aquacharger shown in figure 1 has ability to charge up to five 12 V or 24 V batteries simultaneously (Anyi & Kirke, 2010). The EnCurrent turbine shown in Figure 2 is a vertical axis Darrieus cross-axis turbine available in both ducted and non-ducted. The non-ducted configuration uses a 1.6 m diameter and 0.8 m tall turbine, it requires a minimum water velocity of 2 m/s to provide effective power output. However, as stated by (J. Khan, 2006), the turbine has ability to generate 0.4 kW power output at 0.9 m/s. In their website, (New Energy Corporation, 2014)), announce the use of Encurrrent turbine in powering rural community in Ruby at central Alaska.

Figure 1: Amazon AquaCharger

Figure 2: EnCurrent HydroTurbine

The Axial flow turbine (figure 3) was designed by University of Brasilia to attend specific rural electrification projects with installed capacity from 300W up to 2000W(Els, R. & Junior, 2015) and was installed in Suriname village. The system provide power to school, health centre and hybrid solar dryer (Els, 2008). Under Water Electric Kit shown in figure 4, is designed to operate in river, tidal and ocean currents. The turbine with rotor ranging from 2 to 5 m operates in extremely low velocities of 0.20 m/s or less (Verdant Power Canada, 2006). However, Anyi & Kirke(2010) discuss that the axial flow turbine with diameter ranging from 0.8 – 2.7 m can be used to generate a practical amount of electrical power from water between 0.5 - 2 m/s up to 100 kW.

The Garlov-Darrieus Helical Turbine, shown in Figure 5 consists of a rotor with 2 to 4 blades, whose extremities are fixed to disks, forming only one set that rotates together with generator. The turbine is available in several diameters: 1.25 m, 1.5m, 2.5 m, 3.0 m, and 6.0 m. The smallest turbine developed by Alternative Hydro Solutions is 1.25 m diameter and 0.5 m height (Verdant Power Canada, 2006). The turbine starts producing power at approximately 0.60 m/s, according to studies done in 2004 (Sornes, 2010; Verdant Power Canada, 2006).

Figure 3: Axial Cross flow –UnB (Viana, 2014)

Figure 4: Under Water Electric

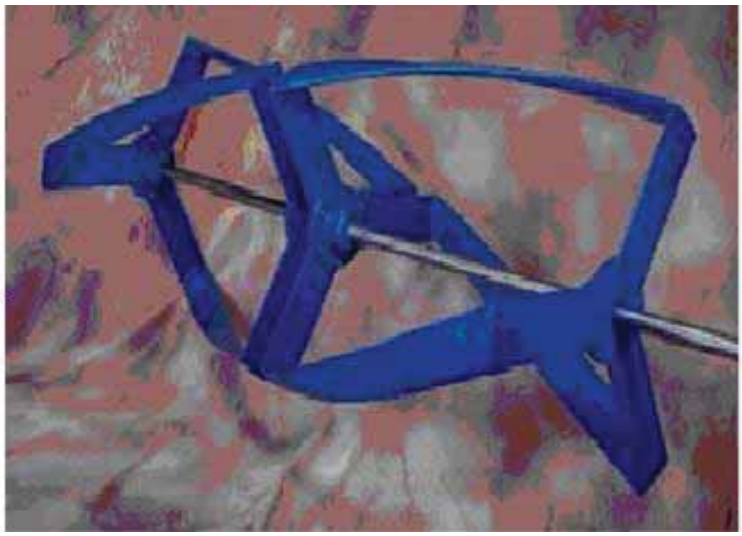

Figure 5: Garlov Helical Turbine

Turbines specification and their operation requirement are shown in table 1.

Table 1: Output Power of Axial and Cross-Flow Hydrokinetic Turbines

Device	Minimum River Depth requirement (m)	Stream Flow Velocity requirement range (m/s)	Rotor diameter (m)	Power Output Capacity
Amazon Aquacharger turbine	1.75	0.45- 1.5	1.8	500 W at 1.5 m/s
Under Water Electric Kit Turbine(twin unit)	2	0.20	2 - 5	100 kW
Garlov Helical Turbine	2.5	0.6-1.3		0.7 kW at 1.3 m/s
EnCurrent Hydro Turbine	0.8	1.5-2.5	1.6	10 kW at 1.5 m/s
Axial-Flow (UnB) Turbine	1	1.5	0.8	20 kW

2. Methodology

This study was based on frequency analysis of historical data, survey on hydrokinetic technologies for river application, hydrokinetic resources studies approaches and field survey. Preliminary data for desk analysis were collected from Department of Water Resources under National Directorate of Water in Mozambique.

2.1 Area of study

Umbeluzi is an international river shared by Swaziland, Mozambique and South Africa; it originates in Swaziland close to the border with Mozambique. It covers a total area of 5,400 km^2, of which 40% in Mozambican, 58% in Swaziland and the remaining 2% in South Africa (Joel das Neves Tembe and Aristides Baloi, 2001). The basin and Umbeluzi river main course are shown in Figure 6.

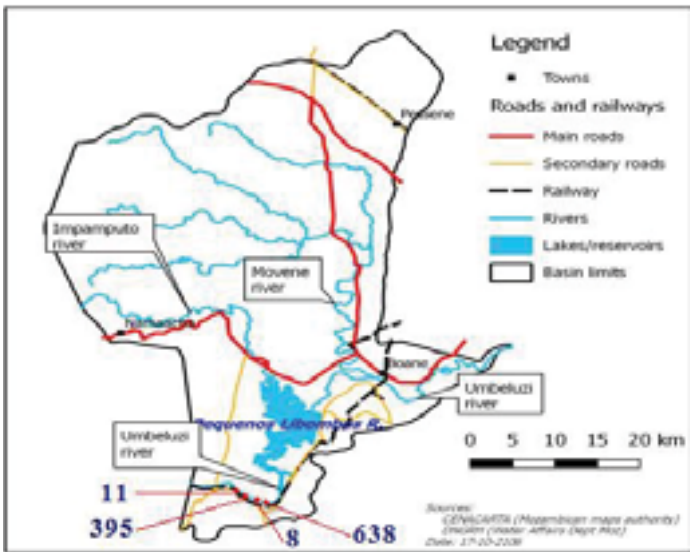

Figure 6: Umbeluzi Basin and its tributaries rivers. Source: CENACARTA (2016)

The main course of the Umbeluzi River runs in the East direction and discharges into Indian Ocean through Espirito Santo estuary at the southern Maputo bay. The main course consists of two tributaries, Mbuluzane River in Swaziland and Movene River in Mozambique (Juizo, D.,Liden, 2008). The table below indicates the sites (stations) were the study took place.

Table 2: Stations studied

Station number	Latitude	Longitude	Altitude
8	26:5:41 S	32:19:30 E	3
11	26:11:46 S	32:7:17 E	63
395	26:5:15 S	32:14:32 E	17
638	26:2:11 S	32:23:1 E	99

2.2 Stream Flow Velocity flow Characterization of the Main Maputo's Hydrological Basins

The study has used Frequency Analysis using historical data of velocity of river streams to generate velocity duration curves (VDC). VDC are graphical plot of stream velocity against the corresponding percent of time that the stream velocity is same or is exceeded. It describes the variability of the stream velocity. VDC were generated arranging velocity data in descending order and the percentage probability, Pp, of any magnitude, V, being exceeded calculated using Equation 6.

$$Pp = \frac{m}{N+1} \times 100\% \qquad \text{(eq. 6)}$$

Where P_P is percentage probability (%), m is number of the velocity (rank), N is number of the data in the list.

2.3 Evaluation of the feasibility for Installation of hydrokinetic turbines in the Umbeluzi main course

The evaluations of the feasibility for installation of hydrokinetic turbine in the Umbeluzi basin was done through comparison of the velocity of the stream versus the design velocity of the hydrokinetic turbines, and comparing the rotor diameter of the hydrokinetic turbines to the depth of the river, then evaluate the feasibility for installation of hydrokinetic turbines in the Umbeluzi River.

2.4 Hydrokinetic and Extractable Power

Assuming hydrokinetic turbines maximum efficiency 0.593 stated by Betz limit, extractable power was computed using Equation 5. However, this was done for stream section which equally had the minimum water

depth matched with the specific turbine requirement, such as station number 638. The turbines used for energy evaluation at these stream sections are respectively Under Water Electric kit (UEK), the ducted cross-axis by UnB and EnCurrent.

The energy evaluation was based on the stream flow velocities which is more than 90% of time available throughout the year.

2.5 Field Measurements and Equipment

River depth and flow velocity through main Umbeluzi channel was carried out at Goba and Mafavuca communities. The flow velocity of the river was directly measured using Gurley 572771 current meter shaft. Area of each sub-section was determined by directly measuring width and depth and computed using Equation 7.

$$A_i = W_i \times D_i \quad \text{(eq. 7)}$$

Where A_i is sub-sectional area, W_i, D_i area the correspondent width and depth of each subsection. The flow velocity in each sub-section was estimated at selected vertical locations in the water column.

3. Results and Discussion

3.1 Characterization of Umbeluzi River Flow Velocity

Umbeluzi basin consists of 37 hydrometric stations most of them built in 1950s. For the purpose of this study, four Gauging Stations have been used to characterize Umbeluzi River flow velocity. Figure 7 up to Figure 14 show Umbeluzi River Flow Velocity hydrographs and velocity duration curves from Goba Village (where the river enters Mozambique from) up to Boane Village.

The observations of stream flow of Umbeluzi at Station 11, downstream Goba Village is shown in figure7. The curve was plotted using monthly averaged values of 5 years (1981-1985).

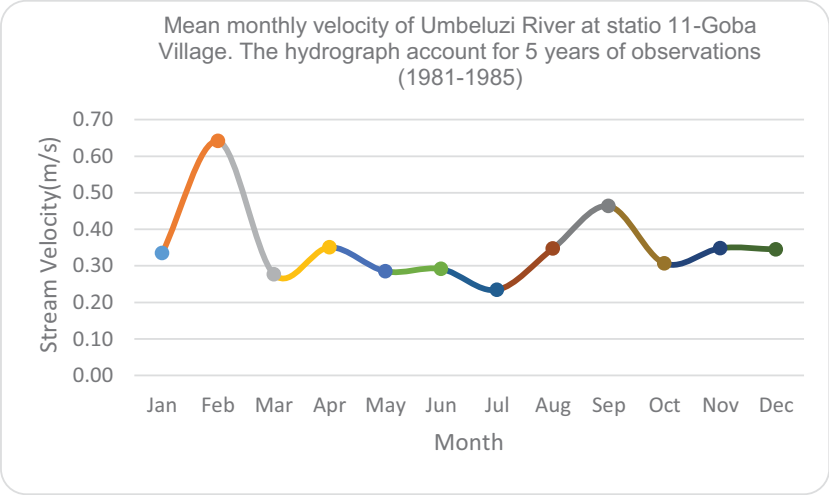

Figure 7: Umbeluzi Mean Monthly Velocity-Station 11 at Goba Village

From the hydrograph (mean monthly flow velocity variation) in figure 7, it can be noted that the maximum flow velocity of 0.64 m/s is reached in February. The minimum stream flow is 0.23 m/s observed in July However, with the exception of February, the stream flow velocity of Umbeluzi at this site is in the range of 0.23 m/s to 0.4 m/s. Figure 8 shows the time each stream flow is available throughout the year.

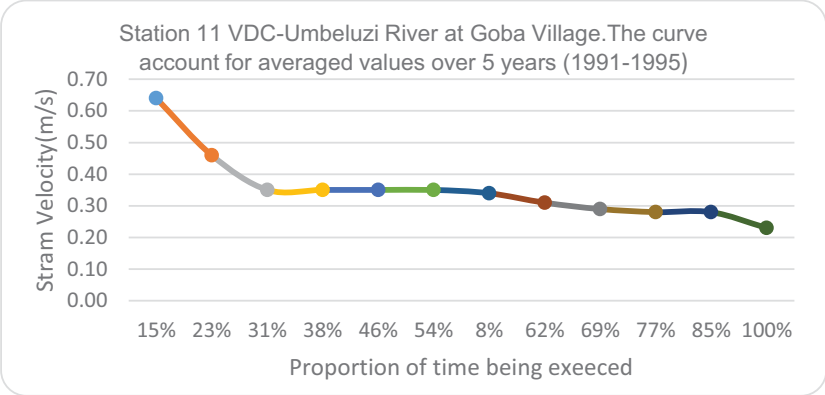

Figure 8: Umbeluzi Velocity Duration Curve-Station 11 at Goba Village

Looking at velocity duration curves (Figure 8) it can be drawn that (with reference to period 1981-1985), the stream velocity of 0.20 m/s is 92% of time available, and 0.64 m/s is 15% of time available throughout the year. However the firm velocity for energy generation should be available 100% of time all days of the months.

From 1982 to 1983, the river depth is in average of 0. 7 m. In 1984, the river reached 2.4 m of minimum water depth. At Station 638, the fluctuation of flows velocity through the years is very high. Such behaviour is shown in the hydrograph of figure 9.

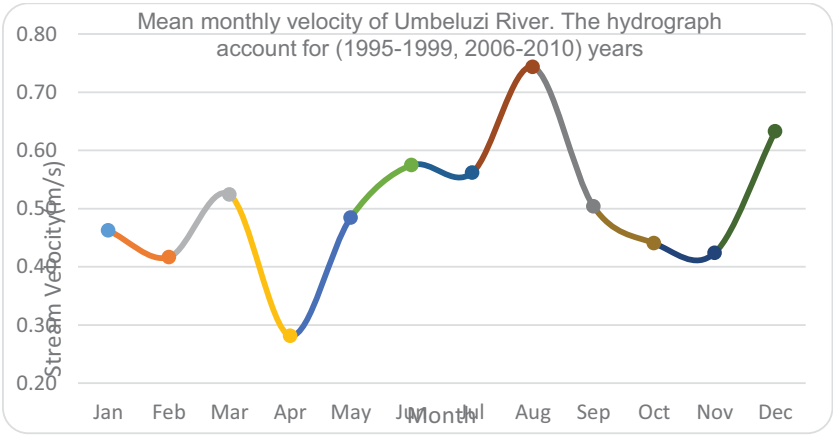

Figure 9: Umbeluzi Mean Monthly Velocity-Station 638

The Flow velocity data, taken as averages for the time in analysis (1995-1999, 2006-2010) show that the stream flow velocity ranges from 0.28 to 0.74 m/s where the maximum was registered in August.

The availability of firm velocity for hydrokinetic turbine installation in the last ten years (1995-1999, 2006-2010) of observation shows that 0.28 m/s is 92% of the time available, while above stream velocity of 0.6 m/s is only 8% time available (Figure 10). This means that, the river flows at 0.28 m/s from January to December and 0.6 m/s during less than one month.

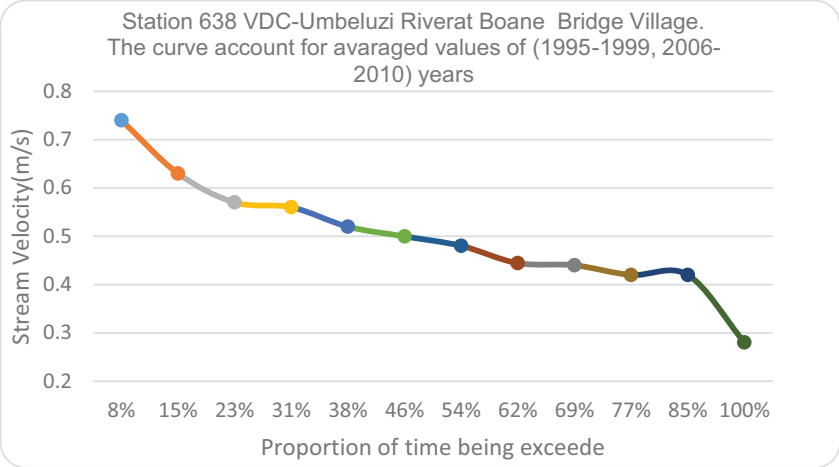

Figure 10: Umbeluzi Velocity Duration Curve-Station 638

According to figure 10, at this stream section 638, Umbeluzi registers 5.91 m and 2.64 m maximum and minimum water depth respectively.

Toward downstream, at Station 395, the maximum and minimum river depth of Umbeluzi are 1.0 and 0.55 m respectively. The stream velocity throughout the month can be seen from hydrograph curves of figure 11.

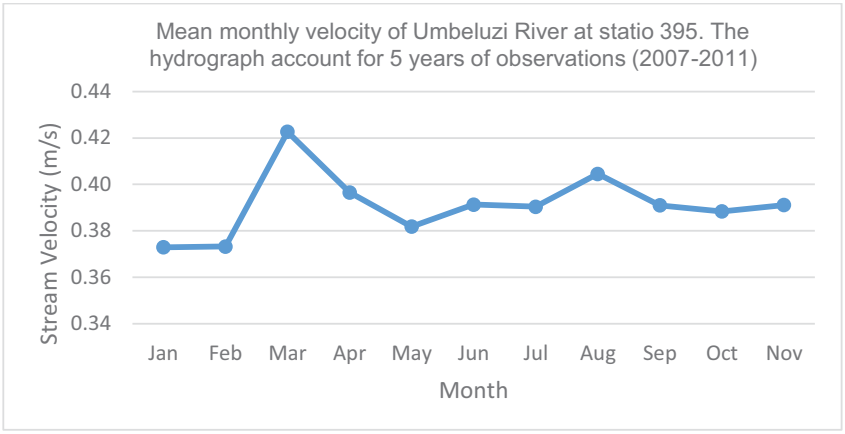

Figure 11: Mean Monthly Velocity Over Umbeluzi River-Station 395

During four years of observations (2007, 2008, 2009, 2010 and 2011 curves) Umbeluzi reached the maximum flow velocity during March and August being 0.42 m/s and 0.40 m/s respectively. The minimum stream flow velocities occurred in January and February. From May up to August, the stream flow increases from 0.38 m/s to from 0.40 m/s. From August to December, it drops from 0.40 m/s to 0.38 m/s. Figure 12 shows the time such range of stream flow can be harnessed for hydrokinetic application.

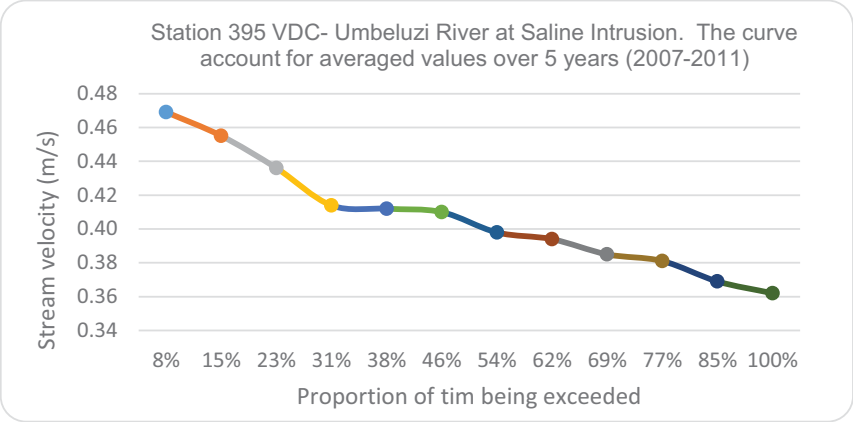

Figure 12: Umbeluzi Velocity Duration Curve-Station 395

As it can be seem from figure 12, Velocity Duration Curves above 0.36 m/s is 100% of time of the year available (From January to December) while 0.47 m/s is 8% of time available throughout the year. It means that the firm stream flow available for energy generation and provide power all months is 0.37 m/s.

The last stream flow observation was done at Station 8, whereby Umbeluzi River observes maximum and minimum water depth of 5.3 and 0.55 m respectively. Its mean monthly stream flow velocity it is shown in figure 13.

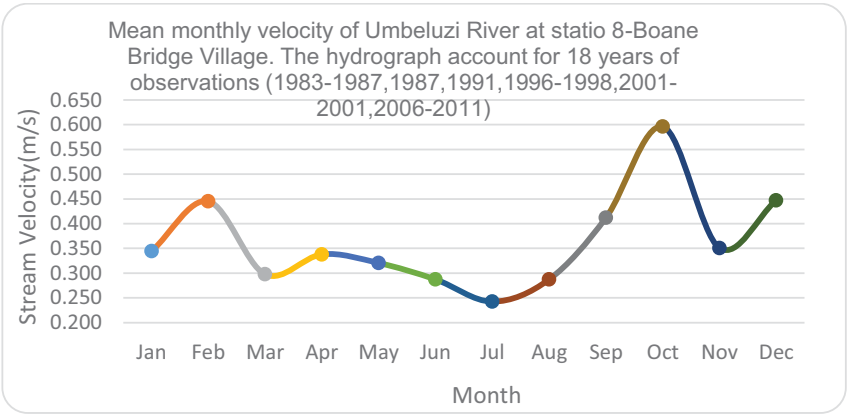

Figure 13: Mean Monthly Velocity over Umbeluzi Main Course-Station 8, Boane Village

The hydrograph curve of figure 13 shows that the stream velocity ranges from 0.3 m/s to 0.60 m/s from March to July. In February, has reached 0.44 m/s while October, Umbeluzi reaches 0.6 m/s. Figure 14 shows the analysis of stream flow velocity availability at station 8.

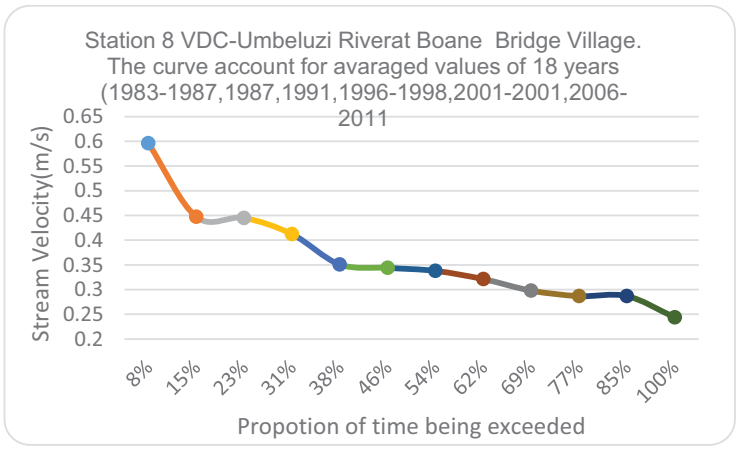

Figure 14: Umbeluzi Velocity Duration Curve-Station 8 at Boane Village

From Velocity Duration Curves shown in Figure 14, it is figured out that 0.244 m/s of flow velocity is 100% of time available throughout the year while 0.60 m/s is 8% of time available. Thus, similar to the station 395, 0.24m/s is the firm flow available for energy generation during all months at this section.

3.2 Feasibility for Installation of Hydrokinetic Turbines in the Umbeluzi River

The following analysis was done with reference to turbines operation requirements in natural current river flows provided in table 1. The parameters analyzed are: river flow velocity and river depth compared to operational flow velocity of the turbines and their rotor diameter (for axial type) or the height of the turbine (in case of cross-flow turbines type).

In Goba Village (station 11), the velocity duration curves plotted from 1981 to 1985 show that the river flow velocity of 0.20 m/s is 100% of time available (Figure 8). The minimum water depth observed from 1981 to 1985 is 0.69 m. In such flow velocity, Under Water Electric Kit (Figure 4), could be used to extract kinetic energy. However, the turbine requires 2 m of minimum river depth, which is not available at the site.

At Station 638, the last five years of observation (2007,2008, 2009, 2010 and 2011) show the stream velocity of 0.28 m/s is 100% of the time available and the stream velocity of 0.40 m/s is available 85% of the time throughout the year (see Figure 10). At this stream section, Umbeluzi River registered 5.9 m maximum and 2.64 m minimum of water depth.

The maximum and minimum river depth at Station 395 is 1.0 and 0.455 m. Stream flow velocity 100% of time available throughout the year is 0.36 m/s (see Figure 12).

At Station 8 located in Boane Village, Umbeluzi River observes a maximum and minimum water depth of 5.3 and 0.55 m respectively. Figure 14 shows that less than 0.244 m/s of flow velocity is 100% of time available throughout the year.

Looking at the turbines specification in table 1 and compared to the river flow velocity, it is found that the river meets operating flow velocity of Under Water Electric Kit at stations 11, 638 and 395. However, when the river depth is brought into comparison with the turbines specification, only Under Water Electric Kit could be used to extract kinetic energy at station 638, as the minimum river depth is 2.64 m, matched with 2 m rotor diameter.

3.3 Evaluating Extractable Power by Under Water Electric Kit Turbine

Under Water Electric Kit (UEK) is claimed to operate under extremely low velocities (Verdant Power, 2006). Therefore, it will be used to evaluate the hydrokinetic potential in station 638. At this section, the natural stream flow conditions are: 0.42 m/s is 85% of time available (see Figure 10); the stream cross-section area is 4.24 m^2 and minimum river depth of 2.64 m.

The hydrokinetic power available in the river computed using Equation 1 is 157.07 W and the extractable power by the turbine with 2 m rotor diameter computed by equation 5 results in 69.01 W (see Table 2). If the cross-section area of the river is strangulated from 4.24 m^2 to 2.12 m^2, the stream flow increased up to 0.84 m/s. The hydrokinetic power available in the river, calculated using equation 1 is 628.27 W and the extractable power by the turbine, using Equation 5 result in 552.09 W, which is enough to meet the basic needs of 10 households at World Bank standards for rural electrification using solar energy.

Table 3: Increased Flow Velocity and Output Power by the use of Under Water Electric Kit

Cross-section Area (m^2)		Flow Velocity (m/s)		Hydrokinetic Power (W)		Extractable Power (W)	
A_{c0}	4.24	V_0	0.42	P_{K0}	157.07	$P_{g\text{-}max0}$	69.01
A_{c1}	2.12	V_1	0.84	P_{K1}	628.27	$P_{g\text{-}max1}$	552.09

4. Conclusion

Hydrokinetic technology are designed to supply power for low demand communities living close to the rivers, hence increase the provision of energy services in rural areas. However, its exploration is dependent on availability of the water resources at the site, which are the river flow velocity and river depth. In that context:

Umbeluzi flows at 0.60 m/s maximum velocity, which is 8% of time available. Flow velocity ranging from 0.23 to 0.36 m/s is 100% of time available throughout the year. In addition, almost all stations have registered the minimum river depth in a range from 0.55 to 0.7 m.

Comparing the range of flow velocities to the turbines requirements, it is found that low flow velocities for hydrokinetic technology characterize Umbeluzi River. However, kinetic energy can be extracted at station 638 if augmentation device is used to strangulate the river channel. The river flow at 0.42 m/s is 100% of time available throughout the year in an average cross-section area of 4.24 m^2.

The extractable power using Under Water Electric Kit is 69.01 W. However, if the cross-section area is reduced from 4.24 to 2.12 m^2, the flow velocity increases from 0.42 to 0.84 m/s. The corresponding extractable power is 552.09 W, useful to charge some batteries.

5. References

Anyi, M., & Kirke, B. (2010). Evaluation of small axial fl ow hydrokinetic turbines for remote communities. *Energy for Sustainable Development*, *14*(2), 110–116. https://doi.org/10.1016/j.esd.2010.02.003

Els, R. & Junior, A. C. (2015). ELS nad JUNIOR- The Brazilian experience with hydrokinetic turbines. In *Energy Procedia* (pp. 259–264). Elsevier Ltd. Retrieved from http://ac.els-cdn.com/S1876610215010966/1-s2.0-S1876610215010966-main.pdf?_tid=558e3844-a0f3-11e6-9f48-00000aab0f01&acdnat=1478087946_c8617c3eafb511b58bf355447119d70f

Els, R. H. van. (2008). *Universidade de Brasília Centro de Desenvolvimento Sustentável Sustentabilidade de projetos de implementação de aproveitamentos hidroenergéticos em comunidades tradicionais na Amazônia : Casos no Suriname e Amapá Rudi Henri van Els Orientador : João Nildo*. Universidade de Brasília, Brasília.

IHA. (2015). Mozambique _ International Hydropower Association. Retrieved from http://www.hydropower.org/country-profiles/mozambique

IRENA. (2012). *Mozambique renewables readiness assessment 2012*.

Joel da s Ne ves Tembe and Ar ist ides Baloi. (2001). *Water Access , Policies and Irrigation Schemes Management in Mozambique*. Madison.

Juizo, D.,Liden, R. (2008). Modeling for transboundary water resources planning and allocation Modeling for transboundary water resources planning and allocation. *Hydrology and Earth System Sciences*, *5*(1), 475–509.

Khan, J. (2006). State of River Energy Technology. *In-Stream Hydrokinetic Turbines*, 1–6.

Khan, M. J., Bhuyan, G., Iqbal, M. T., & Quaicoe, J. E. (2009). Hydrokinetic energy conversion systems and assessment of horizontal and vertical axis turbines for river and tidal applications: A technology status review. *Applied Energy*, *86*(10), 1823–1835. https://doi.org/10.1016/j.apenergy.2009.02.017

Klunne, W. J. (2013). Small hydropower in Southern Africa – an overview of five countries in the region. *Journal of Energy in Southern Africa*, *24*(3), 14–25.

Lago, L. I., Ponta, F. L., & Chen, L. (2010). Energy for Sustainable Development Advances and trends in hydrokinetic turbine systems. *Energy for Sustainable Development*, *14*(4), 287–296. https://doi.org/10.1016/j.esd.2010.09.004

Mahumane, G., & Mulder, P., Nadaud, D. (2012). Energy outlook for Mozambique 2012- 2030 LEAP-based scenarios for energy demand and power generation. In *Iii Conferência Internacional Do Iese* (pp. 1–5). Retrieved from http://www.iese.ac.mz/lib/publication/III_Conf2012/IESE_IIIConf_Paper16.pdf

New Energy Corporation. (2014). Experience with EnCurrent Power Generation Systems. Retrieved from http://www.icoe2014canada.org/wp-content/uploads/2014/11/5-Clayton-ICOE-2014-Showcase1.pdf

NRC-CHC. (2010). *Assessment of Canada ' s Hydrokinetic Power Potential*.

Sornes, K. (2010). Small-scale Water Current Turbines for River Applications. *Zero Emission Resource Organization*, (January), 1–19. Retrieved from www.zero.no

Souza, j., Els, R., & Diniz, J. & Wehrman, M. (2008). Extensão multidisciplinar em uma comunidade de castanheiros no estado do Amapá.

Uamusse, M. M., Tsamba, A. J., Matsinhe, J., & Persson, K. M. (2015). Capacity Optimization Study of Chua Mini-Hydropower Plant at Chua River , (December), 604–612.

Verdant Power Canada. (2006). *Technology Evaluation of Existing and Emerging Technologies: Water Current Turbines for River Applications*. St. Catharine. Retrieved from http://www.akenergyauthority.org/Content/Programs/AEEE/OceanRiver/Documents/PDF/VRTurbinesRpt0627.pdf

Solar Cooking and Clean Cook Stoves

Towards a homogenous drying rate using a solar fruit dryer

Henrik Davidsson[1], Joakim Olsson[1] Randi Phinney[1], Ricardo Bernardo[1] Pia Otte[2] and Lucas D. Tivana[3]

[1] Lund University, Lund (Sweden)

[2] Centre for Rural Research, Trondheim (Norway)

[3] Eduardo Mondlane University, Maputo (Mozambique)

Abstract

Solar fruit drying has the potential to reduce food insecurity in developing nations. One possible technique for drying fruit is to use solar dryers. This technique is easy to use without requiring high investments. However, the drying technique can be challenging. One problem is that the drying rate could be different depending on where in the dryer the process takes place. At the beginning of the dryer, the air is dry and warm while at the exit it has picked up moisture from the products and has cooled down. This could result in severe problems for the user. One possible solution is to have an arrangement that inverts the direction of the airflow periodically. This means that the entrance and the exit of the air are shifted. Thus, the drying rate evens out. Results from the performed simulations shows that the difference in drying rate comparing the fastest with the slowest drying rate in the dryer can be reduced from approximately 110 % to 10 % with this approach. Furthermore, this paper also describes how weather condition for a design day was established. This weather condition can be used for more accurate estimates regarding drying rates and temperatures in the solar dryer.

Keywords: Solar drying, food processing

1. Introduction

Even though absolute/extreme poverty and starvation has decreased over the latest decades (UN 2010; The World Bank), there is still food shortage and malnutrition in many developing nations. This is despite a fast economic growth in some developing countries. One of these countries, Mozambique, had a Human Development Index (HDI) ranking of 180 out of 188 countries despite the HDI value being 75 % higher than in 1980 (UNDP, 2015). Food security is lowest in the south of the country where almost one third of the people suffers from food insecurity (World Food Programme, 2016). At first sight, this appears strange as there is plenty of food grown in the country. However, large amounts of the grown food are either not harvested or are lost after the harvest due to spoilage (FAO, 2011). As much as 25 % to 40 % of the harvested fruit is estimated to be lost, mainly due to a lack of small-scale preservation techniques that do not require infrastructure (Feed the Future, 2011).

Preservation techniques such as aseptic filling and canning would in principle be possible solutions, however, this would require large investments and infrastructure which are often not available in these areas today. Freezing and other techniques that require large amounts of electricity are not an option due to the lack of an electric grid in rural areas. In Mozambique, approximately 80 % of the population is not connected to the electric grid (SIDA 2014). Unfortunately this problem is the same for fruit drying using electrical heaters. Drying of, for instance, fruit is otherwise an attractive technique as it needs no energy after the actual drying. The fruit can also be stored for long periods of time ranging up to several years, depending on the type of fruit and final moisture content after drying (Rahman & Perera, 2007). Drying could become a viable solution in developing nations if the electricity problem could be overcome. Furthermore, in order to have a preservation technique that plays a role for a large part of the society, the technique must be scalable as well as easy to use, cheap and reliable.

doi:10.18086/swc.2017.24.01 Available at http://proceedings.ises.org

One possible solution for this is to use solar driven dryers. The technique uses little to no power to run, is cheap and is simple to use. The work presented in this paper is part of a larger project where an interdisciplinary research group is focusing on finding suitable technical and social solutions for this drying technology. The main objective in this project is to find solutions for drying fruit juices made from juicy fruits like tangerines and oranges that have high spoilage rates (Affognon et al., 2015). The technique that has been developed for drying juices is called Solar Assisted Pervaporation (SAP). It involves the use of semi-permeable membrane bags which are filled with juice, clamped shut and then placed horizontally in the sun to dry. With adequate solar irradiation and ventilation, water vapour is able to pass through the semi-permeable membrane layer of the bag resulting in a shelf-stable dried product after two to three days (Phinney et al., 2015). Solar drying has traditionally been seen as unhygienic since the product is fully exposed to the open air, but with the SAP technique, microorganisms and larger pests are not able to penetrate the bag which greatly reduces the food safety risk (Phinney et al., 2015). Earlier work within the project has shown that even if the bags are directly exposed to solar radiation, a cooler wind passing over the bags can drastically reduce the drying flux. This result supports the need of a solar dryer that can pre-heat the air that passes over the bags in order to maintain the highest drying flux possible. The pre-heat of air would increase the temperature to a level not favourable to microbial. In addition, not radiating the fruit directly could be beneficial as the sun light could activate the degradation of vitamin or pro-vitamin in the fruits. Direct irradiation could potentially also form a crust on the inside of the bags, which would then lead to lower drying rates (Mills-Gray, 2015). By using an indirect drying technique, the heating of the fruits become more adjustable and less fluctuating over time as the dimensions and materials of the solar collector will determine the drying conditions (Kumar et al., 2015).

The initial indirect solar dryer design that was developed for SAP is shown in Fig. 1. The air is heated in the solar collector and this hot air passes to the drying tower.

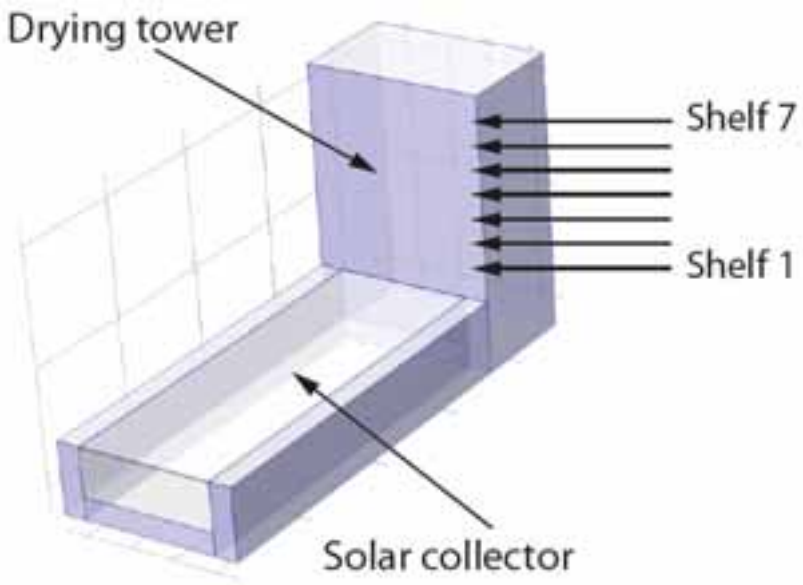

Fig. 1: The solar dryer with the solar collector and the drying tower.

Earlier reports have shown that the drying rate of the product (i.e. bag) is dependent on at least air temperature, air speed and the relative humidity of that air (Blanco-Cano et al., 2016; Phinney et al., 2015). Furthermore, Olsson (2016) showed that the drying rate in a passive drying tower, illustrated in Fig. 1, is strongly dependent on where the bag is placed in the drying cabinet. As the air is dryer and warmer at the entrance of the cabinet, the drying rate is also higher here. As the dry air picks up moisture from the bags at the entrance region, the relative humidity increases. Furthermore, as this process is energy demanding the temperature will also decrease. As a consequence of this, the drying rate is reduced for bags placed at the top of the cabinet. This is a serious problem for the successful implementation of this technique. The target group for the technique, i.e.

farmers in rural Mozambique, are too busy to spend time shifting bags around in the drying tower in order to reduce the uneven drying rates. Furthermore, keeping track of the time for when to shift the bags will also add problems for the user. A high drying rate reduces problems relating to mould growth and the evenness is important for a homogeneous quality of the dried products. It is therefore very important that the drying rate is both high and even.

Understanding the process of solar drying needs understanding of the physical boundaries and the driving forces, i.e. the weather conditions. Running simulations with full weather data is time consuming and often inconvenient during a development phase of a new collector type. In this type of process, rough estimates are often more suitable. In order to do this, a typical weather situation for the process is needed. This is not well established today. Earlier work presented is based on reasonable guesses for typical weather situations Olsson (2016).

Investigated problems:

Shifting the bags in the drying cabinet has the potential to increase the evenness in the drying rate. Furthermore, using real weather data rather than assumed values will affect the calculated drying rates in the cabinet. The research questions are therefore;

- To what extent can the evenness in drying rate be increased by either shifting the positions of the bags in the cabinet or reversing the flow in the dryer tower?
- To what extent is the drying rate affected by using real weather data? And, can a characteristic weather situation be identified?

The evenness is measured as a relative difference in drying rate between the bags that dry the fastest and the slowest.

2. Method

The performed simulations are based on a program described in Olsson (2016). The program is built in Maple 2015 (Maple) which is a software mainly used to analytically solve and evaluate mathematical problems, but can also be used as a programming tool. The model consists of two parts; the solar collector and the drying tower, see Fig. 1. The solar collector has a constant airflow going through it, user defined insulation on the sides and bottom and a single layer of glazing on the top which can let through sunlight. The absolute humidity and the air temperature calculated at the outlet of the collector will then act as input values for the drying tower and thus determine the initial drying conditions. The drying cabinet consists of four walls impermeable to sunlight and has an airflow going from its bottom to its top. Inside the cabinet, a certain amount of shelves are located on which SAP-bags can be placed. The drying rates of the SAP-bags are then calculated for each shelf depending on the air velocity and the relative humidity at each shelf.

The program was used in order to calculate the drying rate for bags placed at seven different shelves in the drying tower. The placement is indicated in Fig. 1. The drying rate was used in order to calculate the evenness depending on shelf position in the tower. Furthermore, the consequences of shifting around the bags in the drying tower were also calculated. For this shifting simulation: the bags placed on shelf 7 were shifted with the bags on shelf 1 after 30 minutes. Bags on shelf 6 were shifted with bags on shelf 2 and the bags on shelf 5 were shifted with the bags on shelf 3. The bags on shelf 4 were left without being shifted.

The characteristic weather for fruit drying in Mozambique was found by creating a constant weather condition that results in the same total drying over a three months period as would be the result using the real measured weather over the same three months. The point in doing this is mainly to have a typical design condition for the solar drying technology. Using the characteristic weather will result in better estimations for drying capacities. Included in the characteristic weather is radiation, temperature and relative humidity. As can be seen in Fig. 2 the temperature and the relative humidity varies considerably less than the irradiation. Therefore these two parameters where calculated to be the arithmetic mean value during the period. After these values

were established, the irradiation level for the characteristic weather situation was calculated. This was carried out by means of iteratively running simulations changing the characteristic radiation. When the total drying over the three month period was the same using the characteristic weather situation as using the real weather data the characteristic radiation was found. Fig. 2 shows a typical weather situation during two days. The black line shows the irradiation on a horizontal surface, the blue line shows the ambient temperature and the red line shows the relative humidity. The dashed blue and red lines are the arithmetic mean values of the temperature and the relative humidity during the active time of operation, in this case from 8:00 to 16:00. The dashed black line is the irradiation used in the calculation program in order to get the same total drying during operation (i.e. running a simulation using the fixed values shown with dashed lines or running a simulation using the weather data will produce the same total drying effect). The grey shaded area indicates the time that the solar dryer is assumed to be in operation. The figure is used only as an illustrative example of the method.

The drying of the SAP bags in not a linear function of the irradiation or the temperature or even the relative humidity Olsson (2016). Therefore, a change in for instance the relative humidity in the drying tower will lead to a compensation of the irradiation in the calculated characteristic weather. In order to evaluate how important this none linearity is the characteristic weather was calculated for two different versions of the solar dryer. The two different versions of solar dryers will create two different drying conditions and therefore two different characteristic weathers. One with a drying tower with a cross section measuring 0.2 m · 0.2 m with 2 SAP bags per shelf. The other tower with a cross section that measures 0.4 m · 0.4 m and has 10 SAP bags per shelf. Both cases use a 2.4 m² large solar collector unit. This creates two different conditions in the dryer. In the larger tower, the air will move with a lower speed and the air will also become more humid in the upper layer. Other details on the dryer are discussed in Olsson (2016). This test was carried out in order to see how sensitive the characteristic weather is to changes in the solar collector.

The simulations were performed assuming a horizontal collector. Furthermore, the characteristic weather was evaluated for two operation times, 8 hours per day and for 4 hours per day. Fig. 2 is an illustration of the characteristic weather for the 8 hour case.

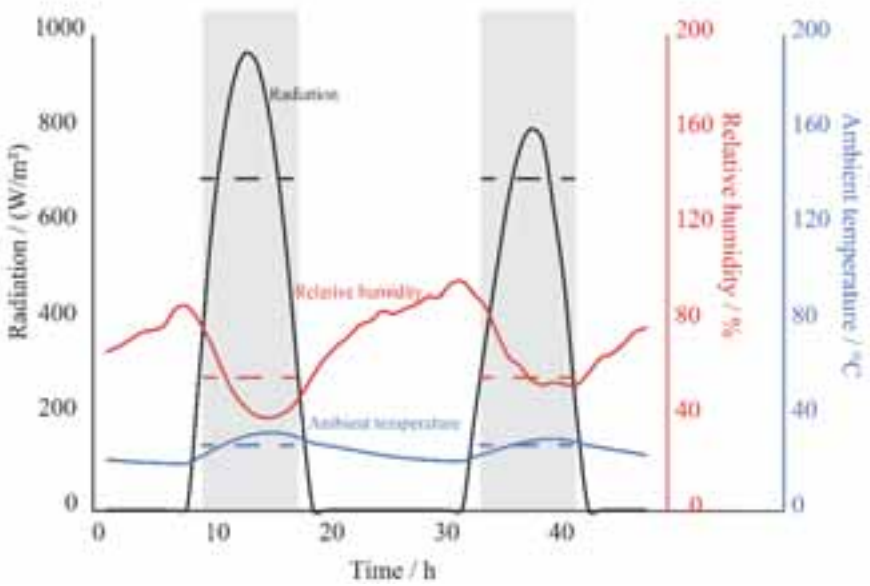

Fig. 2: Illustration of the characteristic weather for the 8 hour drying case during a two day period. The black line shows the radiation, the red line shows the relative humidity and the blue line shows the ambient temperature. The dashed lines shows the characteristic weather during this period.

Hourly weather data was obtained for Maputo, Mozambique using Meteonorm 7.0. Data was selected from beginning of May to end of July as this is the period for tangerines in Mozambique.

3. Results

Fig. 3 shows the results from a simulation where the drying rate per square metre of SAP-bag per hour was calculated over one week in the beginning of May. The results are based on a simulation that uses real weather data. The drying tower was set to be 0.4 m · 0.4 m and there was 10 bags placed per shelf. The left figure shows the drying rate for the SAP bags placed on the different shelves. The placement of the shelves is shown in Fig. 1. The results show the highest drying rate at the first shelf and a decreasing drying rate moving up in the tower. During the peak hour on the first day, the difference in drying rate between shelf 1 and shelf 7 is approximately 110 %, i.e. bags on shelf 1 dry more than twice the rate of bags placed on shelf 7. To the right is a calculation where the bags have been shifted every 30 minutes. The mixed mode, i.e. the right figure, shows that this difference in drying rate is reduced to 10 % between bags placed on shelf 4 and bags placed and shifted on shelf 1 and shelf 7.

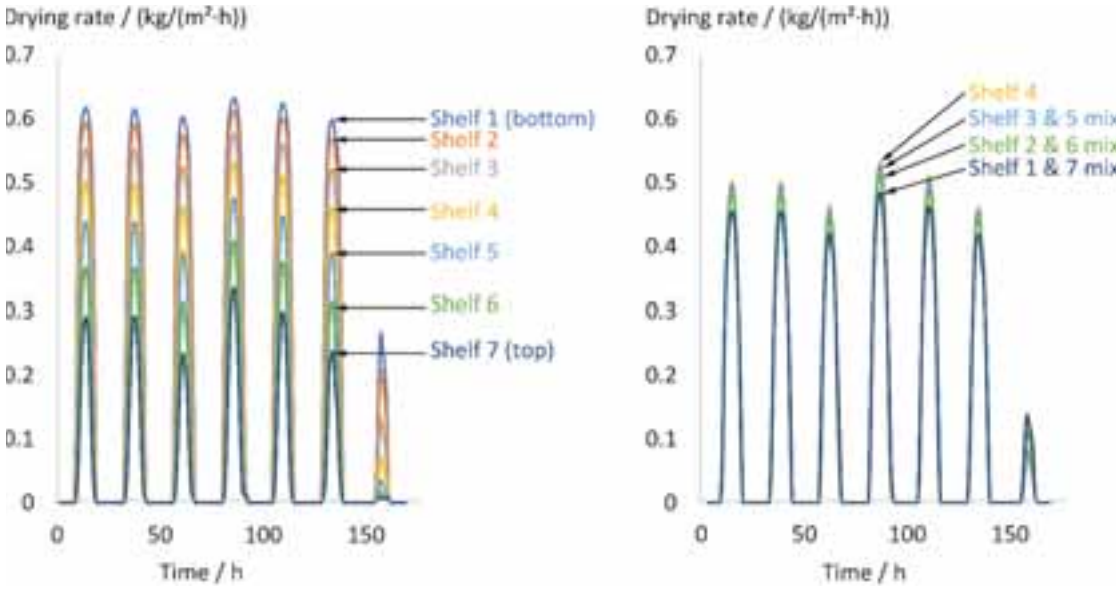

Fig. 3: The drying rate at different shelves during one week. The left figure shows constant position (shelf) for the bags. The right figure shows drying rate where the bags are shifted continuously over the week.

The characteristic weather found for the two different solar dryers using the 4 hour and the 8 hour daily drying period is presented in Table 1. By using the values presented in Table 1, the same total drying as using a full weather file in the simulation tool is obtained.

Tab. 1: Characteristic weather for two types of dryers and for two drying times

Calculated value	Low concentration of SAP bags in the dryer		High concentration of SAP bags in the dryer	
	4 hour period	8 hour period	4 hour period	8 hour period
Temperature / °C	25	25	25	25
Relative humidity / %	50	50	50	50
Irradiation / (W/m²)	700	530	740	575

4. Discussion

The calculations performed in order to evaluate the effects of shifting the positions on the bags in the dryer showed great potential in order to get a more even drying rate. However, shifting the bags manually will be

very time consuming and this will likely not be carried out by the user. This could lead to accidental spoilage of fruit. Instead, it would be preferable if the dryer was built in such way that this was carried out automatically. One alternative could be to build a collector that has double collectors, one before the drying section and one after the drying section. The airflow can then be controlled with a fan to change the direction of the flow every 30 minutes. Doing so will give the same result as continuously shifting the bags, i.e. shelf 1 will be shelf 7 as the airflow direction changes. The price for such a product will be higher but it will likely allow for operation without causing unnecessary work for the user. Alternatively, a small fan can be installed inside the drying tower in order to mix the air. Other techniques could be possible.

The characteristic weather was concluded from an analysis based on using all the days during May, June and July. Doing so also includes cloudy cold days. During such days the user is not as likely to start drying fruits. Therefore it might be more reasonable to establish a characteristic weather not based on days including such weather. Such selective picking of suitable drying days would lead to a higher characteristic radiation for the collector. However, if the drying process is longer, for instance a couple of days, then the cloudy day might come in the middle of the drying process and there is no chance to abort the drying and start over. Instead the cloudy days will be included. This analysis can be stretched further for a more complete conclusion. Furthermore, the analysed weather data comes from Maputo in the south of Mozambique. Using weather from the central or the northern parts might result in a different characteristic weather. Nevertheless, it was decided that the reached values are accurate enough for the purpose of preliminary design considerations.

However it is also important to understand that there are many characteristic weather situations that will result in a specific total drying over the three months. For instance reducing the temperature but increasing the solar radiation simultaneously will keep the drying constant. Therefore it's impossible to find one specific weather situation that is the only solution to the given problem.

There is a small difference in what characteristic weather should be used depending on the setting of the dryer. More SAP bags and thus higher relative humidity combined with a lower airflow in the tower results in a somewhat higher characteristic irradiation. However, this difference is very small, in the order of 5 % to 10 %. This is seen comparing the irradiation levels in Table 1, 700 W/m² compared to 740 W/m² and 530 W/m² compared to 575 W/m². Thus, this difference can be neglected.

5. Conclusion

The uneven drying rate can be drastically reduced if the SAP bags are shifted within the drying tower. Shifting the bags every 30 minutes, or more realistically changing the airflow direction, was shown to reduce the difference in drying rate from approximately 110 % to 10 % between the highest and lowest drying rates.

A characteristic weather could be determined and are presented in Table 1. For longer drying periods, i.e. longer than 8 hours, the characteristic weather is typically 25 °C a relative humidity of 50 % and approximately 550 W/m² of solar radiation. For shorter drying periods where only the peak hours of the day is used the solar radiation can be assumed to be somewhat more than 700 W/m². The none-linearity in the drying process discussed in the method section was indicated to have only small effects. Varying the drying tower cross sectional area and number of SAP bags per shelves within the above stated limits will not affect the characteristic weather to a significant degree and this effect can be ignored.

6. Acknowledgement

Erik Johansson at the division for HDM at Lund technical faculty, Lund University is acknowledged for assistance with weather data files.

7. References

UN 2010, Webpage http://www.un.org/esa/socdev/rwss/docs/2010/chapter2.pdf [Accessed 20 March 2017]

The World Bank, Webpage http://data.worldbank.org/topic/poverty [Accessed 20 March 2017]

UNDP. (2015). Briefing note for countries on the 2015 Human Development Report, Mozambique. New York: UNDP.

World Food Programme. (2016, February 20). Mozambique. Retrieved from World Food Programme: http://www.wfp.org/countries/mozambique

FAO (2011) http://www.fao.org/docrep/014/mb060e/mb060e00.pdf

Feed the Future Mozambique 2011 USDA, 30 June, 2011. Available: https://www.feedthefuture.gov/sites/default/files/resource/files/MozambiqueFeedtheFutureMultiYearStrategy_Public_FINAL.pdf [Accessed 20 March, 2017].

SIDA Swedish International Development Cooperation Agency (2014) , Published: 20 September 2011 Updated: 27 August 2014, http://www.sida.se/English/where-we-work/Africa/Mozambique/examples-of-results/Inacio-Yemusee-Dyaha-in-Mozambique/Facts-Rural-electrification-in-Mozambique/ [Accessed 16, March 2017]

Mohammad Shafiur Rahman, Conrad O. Perera, Chapter 18 Drying and Food Preservation, Handbook of Food Preservation 2nd Edition, Editbed by M. Shafiur Rahman, CRC Press 2007

Hippolyte Affognon, Christopher Mutungi, Pascal Sanginga, and Christian Borgemeister, Unpacking Postharvest Losses in Sub-Saharan Africa: A Meta-Analysis, http://dx.doi.org/10.1016/j.worlddev.2014.08.002 World Development Vol. 66, pp. 49–68, 2015

L. Blanco-Cano, A. Soria-Verdugo, L.M. Garcia-Gutierrez, U. Ruiz-Rivas, Modeling the thin-layer drying process of Granny Smith apples: Application in an indirect solar dryer. Applied Thermal Engineering Volume 108, 5 September 2016, Pages 1086–1094, Applied Thermal Engineering http://dx.doi.org/10.1016/j.applthermaleng.2016.08.001

Phinney, R., Rayner, M., Sjöholm, I., Tivana, L. and Dejmek, P. (2015). Solar assisted pervaporation (SAP) for preserving and utilizing fruits in developing countries. In: 3rd Southern African Solar Energy Conference (SASEC). [online] Kruger National Park: University of Pretoria, pp. 170-175. Available at: http://www.repository.up.ac.za/handle/2263/49551

Maple (2017). Homepage, http://www.maplesoft.com/ [Accessed 16, March 2017]

Susan Mills-Gray, Drying Foods (rev. 2015). Retrieved from University of Missouri Extension: http://extension.missouri.edu/p/GH1562

Mahesh Kumar, Sunil Kumar Sansaniwal, Pankaj Khatak, Progress in solar dryers for drying various commodities. Renewable and Sustainable Energy Reviews Volume 55, March 2016, Pages 346–360, http://dx.doi.org/10.1016/j.rser.2015.10.158

Joakim Olsson (2016) Modelling of a solar dryer for food preservation in developing countries, Master thesis Lund University, http://lup.lub.lu.se/luur/download?func=downloadFile&recordOId=8890943&fileOId=8890985

A DIRECT SOLAR FRYER FOR INJERA BAKING APPLICATION

Mesele H. Hailu[1, 2], Ole J. Nydal[1], Mulu B. Kahsay[2] and Asfafaw H. Tesfay[2]

[1] Department of Energy and Process Engineering of NTNU, Trondheim, Norway
[2] School of Mechanical & Industrial Engineering, EiT-M of Mekelle University, Mekelle, Ethiopia
Contact email: meseleha@yahoo.com, mesele.h.hailu@ntnu.no

Summary

Injera is a traditional staple pancake and it is part of the daily dish to most of the one hundred million population in Ethiopia and Eritrea. The conventional baking method uses either biomass in rural areas or Electricity in majority of urban areas. A direct solar fryer for Injera baking application is developed as an alternative to the conventional baking methods. The solar fryer system uses a 1.8m rim diameter dish covered with aluminum reflective sheet. The system employs an aluminum baking plate of 550 mm diameter, 12.5 mm thickness and is equipped with two axis manual tracking. The direct solar fryer model has two possible operational modes; the continuous heating-baking mode and the alternating heating-baking mode. The experimental result show that the initial heating up time in both modes was in the range of 30 to 45 minute and this initial heat up time was comparable to the conventional baking process. In the initial heat up period, the plate has reached an average temperature of 120 to 130 ℃ in the continuous type model and 160 to 180 ℃ in the alternating type model, which was sufficient surface temperature to initiate a baking activity. The baking process in the continuous type model has taken an average of 5 minutes while the subsequent additional heat up time was 2 minutes giving an average baking time of 7 minutes per Injera. The alternating type model has slower heating time at each consecutive baking activity. The direct solar fryer will provide a baking power of 563W with a system thermal efficiency, including the collector efficiency of 37 %.

Key words: Injera, solar baking, Solar Fryer, baking time, baking power, baking energy

1. Introduction

Injera also written as enjera is an endemic staple food in Ethiopia and Eritrea. Injera is made from the flour of tiny grain locally called teff (Eragrostis tef), a species of in the genus Eragrostis, native to Ethiopia and Eritrea [Mekonnen et al, 2014; Aptekar, 2013; Demissie, 2000]. The teff flour is mixed with water, on average of 30 % to 70 % proportion respectively on mass basis and a sourdough as starter. The mixture in the form of runny dough is left to ferment for few days, usually 3 to 5 days. The sourdough starter and the fermentation process makes the Injera to be mildly sour taste. The fermented dough is then baked into large flat pancake by pouring into a hot clay pan. The dough then stays in the hot clay until the water boiling temperature is reached and as a result, water bubbles scape the pancake forming thousands of tiny craters, traditionally referred as 'eyes' giving it spongy honeycomb like structure while the bottom surface, which comes in contact with the baking hot surface, is relatively smooth. The fully cooked injera then becomes thin, soft and slightly spongy.

Injera is part of the daily dish to most of the one hundred million population in Ethiopia and Eritrea. The Injera, placed on flat serving utensil, is consumed with different toppings or stews, traditionally called "wat". There are similar variants to Injera worldwide. Such variant include "*canjeero"* (also known as "*lahooh"* or "*lahoh"* in Somalia and Djibouti [Abdullahi et al, 2001], "*kisra*" in Sudan and South Sudan, "mandazi" in Kenya, "Lahuhua, pita and falafel" in Yemen and the middle east, "Baghrir" or "beghrir" in the Maghreb region, "chapatti" and "puri" in India, pan fried cakes, paratha, vada and mutuan in Asia and tortilla and navaho fry bread in North America [Gallagher, 2011].

Similar to the worldwide pancake frying process, Injera making process is an energy intensive activity. The household sector in Ethiopia accounts for about 89% of the total energy consumption and with 96% of this energy contributed from biomass (firewood, cow dung and agricultural residue) (Energypedia, 2017; Asfafaw et al, 2014; GiZ, 2011). Majority of the domestic energy requirements is for baking and cooking purposes, accounting for about 60% of energy consumption (Gebreegziabher, 2004, 2007; RPTC, 1998). This makes the injera making activity as the most energy-consuming process in every household in Ethiopia.

doi:10.18086/swc.2017.24.02 Available at http://proceedings.ises.org

Nomenclature

Q_{baking}	*Baking energy [kJ]*
m_{dough}	*Mass of dough [Kg]*
$C_{p,dough}$	*Specific heat capacity of the dough [kJ/(Kg. K)]*
T_{bt}	*Baking temperature [K)*
T_i	*Initial temperature of the dough [K]*
m_w	*Mass of the evaporated water [Kg]*
Δh_{ev}	*Enthalpy of vaporation of water [kJ/Kg]*
x_w	*Moisture content of the dough (water mass fraction) [ ]*
$C_{p,w}$	*Specific heat capacity of water [kJ/(Kg. K)]*
x_t	*Teff mass fraction in the dough [ ]*
$C_{p,t}$	*Specific heat capacity of teff [kJ/(Kg. K)]*
Q_{plate}	*Plate stored energy [kJ]*
P_{plate}	*Plate heating power [kW]*
$t_{process}$	*Time taken for the whole baking process [sec]*
q_s	*Heat flux supplied to the receiver [W/m^2]*
G_b	*Beam irradiance [W/m^2]*
ρ_c	*Reflectance of the concentrating dish [ ]*
$(\tau\alpha)_e$	*Effective transmittance and absorptance of the receiver surface [ ]*
γ_{rsf}	*Receiver shading factor [ ]*
C	*Area concentration ratio [ ]*
$\dot{Q}$	Heat supply to the receiver [W]
A_r	Receiver aperture area [m^2]
A_a	Concentrating satellite dish aperture area [m^2]
η_{opt}	Optical efficiency of the parabolic dish [ ]
Q_{in}	*Input solar energy [kJ]*
h_L	Overall heat transfer coefficient [W/M^2.K]
$\eta_{th,plate}$	Thermal efficiency of the receiver [ ]
$\eta_{th,baking}$	Thermal efficiency of the of the overall baking process [ ]

The conventional baking process mostly employs a traditional large size clay plate (locally called ‘mitad’) with 500 to 600 mm in diameter and 20mm thickness. This traditional baking clay has relatively low thermal property hence it requires higher amount of heat than for typical for boiling. The conventional baking method uses either biomass in rural areas or Electricity in majority of urban areas. Biomass based baking process is inefficient, poses pollution hazard and it is becoming expensive due to limited biomass resource in the country while electricity access is very low as majority of Ethiopians live off grid. Therefore, the development of alternative technology for Injera baking application will have significant contribution in the energy consumption profile and socio-economic aspect of the country.

From Ethiopian perspective, a solar energy-based technology is the most promising alternative to the existing energy resource for Injera baking application. Injera baking is high-energy intensity application. The baking process occurs in the temperature range of 130 ℃ to 220 ℃ at an energy consumption of approximately 1MJ/kg of Injera and with a baking time of 180 seconds to 240 seconds. Ethiopia is endowed with abundant solar energy, with daily average solar radiation of 5 kWh/m^2 [Anwar et al, 2014]. Solar energy can be converted into thermal energy as per the baking process energy consumption requirement more easily and in a sustainable way than other alternative energy sources such as biomass, wind, hydropower and geothermal energy.

Solar energy based Injera baking technology can be either a direct system [Gallagher, 2011] or an indirect system [Asfafaw et al, 2014; Maxime et al, 2013]. The direct system uses direct illumination of the solar radiation into the illumination surface (bottom surface) of a baking pan while the Injera is baked at its baking surface (the top surface). Such direct system is suitable for outdoor baking activity. The indirect system uses heat transfer fluid (HTF) to transport thermal energy from the solar energy collector and/or absorber to the application, in which case again the HTF may heat the baking plate directly or the thermal energy in the HTF

is transferred and stored in other thermal energy storage materials, such as solar salt or thermal oil. The direct system is simpler and cost effective while the indirect system will be more complicated and with high cost. The intention of this study is to develop simple and cost effective direct solar fryer for Injera baking application and analyze the performance of the solar thermal technology.

The Injera baking process would pose two main challenges for any type of solar energy based Injera baking technology. The first challenge is due to the size of the traditional Injera, which is about 50 to 60 cm in diameter. This implies that the baking process demands the provision of uniformly distributed heat on larger size baking pan. This would be a challenge as the solar radiation is reflected into a larger area baking pan while the radiation is being focused from the larger solar concentrators. Furthermore, while Injera is prepared softer and thinner, other variant of pancakes seems to be made thicker and taken drier at the end of the baking process. Due to that, Injera baking process will require relatively more uniformity in temperature distribution over the larger size baking plate. The second challenge is the requirement of high intensity of heating of the baking process. This challenge requires the availability of sufficient beam irradiance and an employment of an appropriate solar collector size.

While many designs of the direct system type exist for cooking application or baking of smaller size staple foods; a solar fryer of large size specifically for injera baking application is designed and reported by Gallagher [Gallagher, 2011]. In this system, a 1.2 m diameter solar collector with quasi focus is employed to heat a 0.46m diameter baking pan, which is designed for cooking 0.42 m diameter slices of injera bread. A mirror below the pan directs the radiation to the pan bottom, which is coated with a low-emissivity black absorber. The mirror uses flat, hexagonal panels of aluminized polyester (Mylar) to provide relatively uniform illumination across most of the pan bottom. The baking pan can be stationary at the quasi focus of the mirror assembly (i.e. simultaneous heating and baking) or it can be taken in or out of the dish in north-south direction while pouring the dough and while removing the baked injera and put back into the dish for heating in the remaining time of the baking process (i.e. discontinuity of heating during the baking process).

One of the main challenges in applying the Gallagher prototype to developing country like Ethiopia is the difficulty and challenge of making the quasi focus solar collector which is comprised of flat and hexagonal mirrors. Therefore, due to manufacturing difficulty, such collector will literally be subjected to significant radiation loss if adapted and redeveloped. In this regard, the core design condition of attaining relatively uniform illumination on the backside of the baking plate will be affected, if not it will be significantly expensive. The second challenge is the upscaling of any concept by itself. In upscaling, the challenge of attaining relatively uniform temperature distribution over the baking surface of the plate has to be addressed either by attaining uniform illumination or by employing baking plate material and optimized plate thickness that will ensure optimum conduction process, in turn that will lead to relatively uniform temperature distribution over the baking surface of the plate.

Traditionally, Ethiopia's Injera is with the size of 500 mm to 600mm in diameter. Therefore, the social acceptance of the traditional staple food demands the development of a solar fryer prototype that will enable to bake an Injera of the above size, while the Gallager prototype is designed for 420 mm slice of Injera. The work by Gallagher is used as a basis for the design and development of a direct solar fryer as reported in detail in this research. This newly developed system is an up scaled and an alternative version while addressing the possibility of conducting solar baking with larger size direct solar fryer. An extensive experimentation of baking process is also conducted and the performance of the system is evaluated. This direct solar fryer system for baking application is with the largest fryer size and no other such large area-frying panel has been reported so far.

2. Design of the direct solar fryer

2.1 Geometrical design of the solar fryer system

The solar fryer system uses a dish, cheap and widely available in the market with 1.8m rim diameter (focal length 0.684 m and dish depth 0.296 m) and by gluing aluminum reflective sheet (Miro high reflective 95) on the dish. The solar fryer is designed for an outdoor application, hence here called a "direct solar fryer". The direct solar fryer is made with a baking pan or plate made of aluminum (through casting process at local workshops). The optimum thickness and the high heat conductivity property of the Aluminum plate ensures

there exists relatively uniform temperature distribution on the baking surface of the plate.

The solar fryer model is designed with a baking pan size of 550 mm in diameter and 12.5 mm in thickness. The solar fryer has two possible operational modes. The first operational mode is the configuration that enables simultaneous heating and baking process here referred as "*solar fryer with continuous heating and baking mode*" while the second mode is the configuration that enables heating and baking to be conducted alternatively, here referred as the "*solar fryer with alternating heating and baking mode*". These two modes of the solar fryer are illustrated in figure 1 and figure 2 respectively.

The baking plate can be placed at a distance of 5 to 8 cm distance above or below the focal point, illuminating major part of the heating surface, about 40 to 70% of the plate surface, which gives 25 to 15 concentration ratio respectively. This focusing is done by using the telescopic adjustment structure on the dish support. The plate support structure is also provided with additional rotational motion to allow small inclination during initial heat up period and at consecutive heating and baking periods thus to increase the efficiency of the radiation absorption at the illumination surface of the plate. In the continuous type model, the telescopic adjustment will also help to compensate the seasonal declination of the sun, combined with seasonal translational adjustment of the plate support about orthogonal direction to the axis of rotation of the dish collector.

The system uses two axis manual tracking. The first manual tracking (i.e. the dish rotation about an axis of rotation which pass through the focal point of the dish coupled with the plate rotation during initial heating period) is intermittently adjusted throughout the day. The second manual tracking (i.e. the wheel rotation attained by the roller support coupled with the rotation at the bearing) needs to be adjusted at an average of 10 minutes or at the interval of every baking. In this model, the baking process is conducted under no shading, giving some level of discomfort to the user as a result of the radiation exposure while baking.

2.1.1 Continuous heating and baking mode

The solar fryer with continuous heating and baking mode is indicted in figure 1. In this solar fryer, the baking plate is heated from its bottom surface (i.e. the illumination surface) while baking is conducted at its top surface. The plate can be constantly placed near the focus, enabling simultaneous heating and baking or be moved in and out of the dish for short period during dough pouring and baked Injera removing activity, while in the remaining time the plate will be in heating and baking mode. The choice of these two modes basically depends if the user would like to access the baking plate inside the dish or by moving out of the dish for dough pouring and baked Injera removing activity.

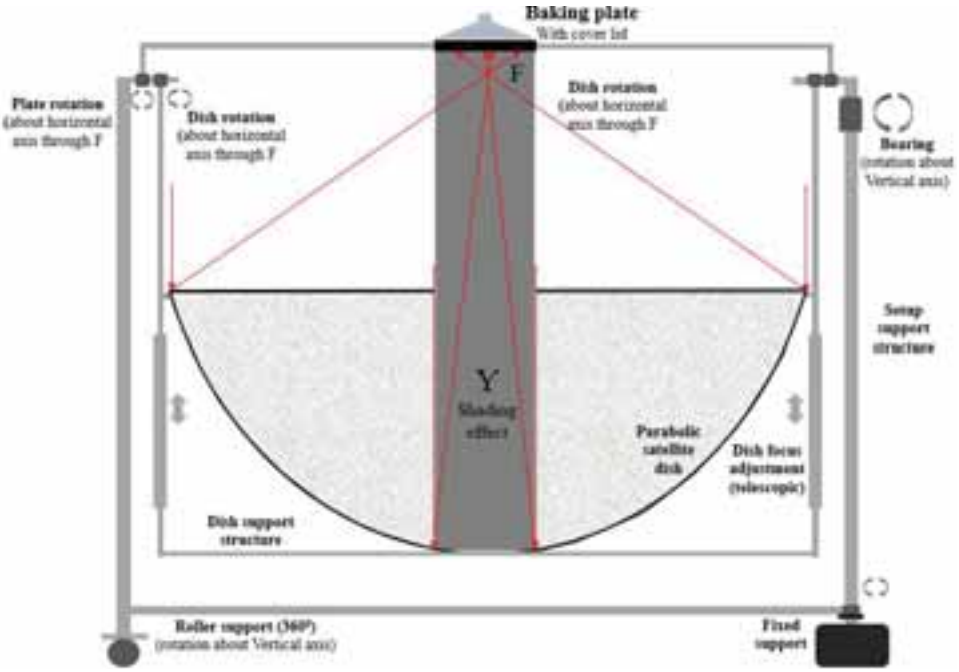

Figure 1: The direct solar fryer with continuous heating and baking mode

2.1.2 Alternative heating and baking mode

The solar fryer with alternative heating and baking mode is indicated in figure 2. In this *model*, heating and baking occurs alternately and on the same surface of the plate, while the backside of the plate is covered with insulation. The plate-dish assembly can easily be rotated at the rim of the dish, which is close to the mass center of the whole assembly. This system provides the baking process to be conducted under the shading of the dish, giving some comfort to the user. In this system, the baking energy requirement is obtained from the stored thermal energy of the plate.

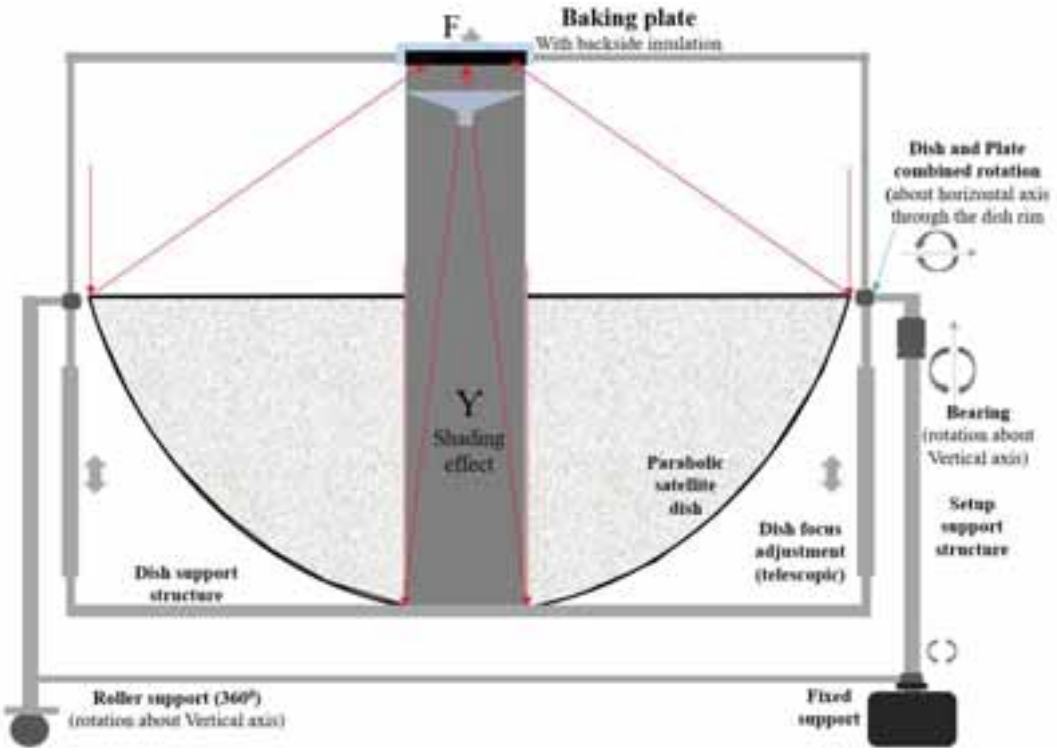

Figure 2: The direct solar fryer with alternative heating and baking mode

2.2 Thermal design of the system solar baking application

The thermal design of the solar fryer is based on the Injera baking energy requirement. An average Injera of 550 mm to 600 mm in diameter is made from 550 g dough, which in turn is made of 70% and 30% proportion (by mass) of water and teff flour respectively. Upon completion of the baking process, the dough is heated from room temperature 25 ℃ to water boiling temperature of 100 ℃ as a result about 25% of the moisture content of the dough is evaporated at the end of the baking process. The baking energy requirement is therefore the thermal energy consumed for raising the temperature of the dough and the latent heat of vaporization of the 25% water content. Mathematically, this baking energy [kJ] can be given by;

$$Q_{baking} = m_{dough}\, C_{p,dough}\, (T_{bt} - T_i) + m_w \Delta h_{ev} \qquad \textit{(Eq. 1)}$$

During the baking process, the mass (m_{dough}) and specific heat capacity ($C_{p,dough}$) of dough varies with time. Therefore an average value for the m_{dough} and $C_{p,dough}$ shall be taken, considering the value of these parameters at the beginning and end of the baking process. The average specific heat capacity of the dough can be given by;

$$C_{p,dough} = x_w\, C_{p,w} + x_t C_{p,t} \qquad \textit{(Eq. 2)}$$

The baking plate is a receiver or an absorber and it acts as a buffer storage during the baking process. This stored energy [KJ] is given by;

$$Q_{plate} = \left(mC_p\right)_{plate} \left(T_f - T_i\right) \qquad \textit{(Eq. 3)}$$

The solar fryer average capacity in terms of heating power can be given by

$$P_{plate} = \frac{Q_{plate}}{t_{process}} \quad \textit{(Eq. 4)}$$

The useful energy of the baking process is the thermal energy consumed for the baking activity, i.e. Q_{baking}. But sometimes, the stored thermal in the baking plate itself can be considered as part of the useful energy. In such case, the total thermal energy from the system will be the sum of the baking energy and the thermal energy stored in the baking plate.

$$Q_{thermal} = Q_{baking} + Q_{plate} \quad \textit{(Eq. 5)}$$

The input energy is the solar radiation falling on the collector. This solar radiation is reflected into the fryer, illuminating major part of the bottom surface of the aluminum plate. The heat is then transferred through conduction radially and vertically to the top surface of the baking plate (3D heat transfer). The optimum thickness and the high heat conductivity property of the Aluminum plate ensures there exists sufficiently uniform temperature distribution on the baking surface of the plate. The heat flux, q_s [W/m^2] and the heat flow rate, $\dot{Q}$ [W] supplied to (received by) the receiver surface is given by;

$$q_s = G_b \rho_c (\tau\alpha)_e \gamma_{rsf} C \quad \textit{(Eq. 6)}$$

$$\dot{Q} = q_s A_r = q_s \frac{A_a}{C} \quad \textit{(Eq. 7)}$$

The receiver shading factor, γ_{rsf} and the optical efficiency of the parabolic solar collector, $\boldsymbol{\eta}_{opt}$ are defined as;

$$\gamma_{rsf} = \frac{A_a}{A_r} = 1 - \frac{1}{C} \quad \textit{(Eq. 8)}$$

$$\eta_{opt} = \rho_c (\tau\alpha)_e \gamma_{rsf} \quad \textit{(Eq. 9)}$$

The thermal energy efficiency of the solar fryer is determined as a ratio of the useful energy to that of the input solar energy. Temperature measurement is taken on the heating and baking surface of the plate in order to determine the heat transfer of the overall baking process.

The input energy to the solar collector, Q_{in}, the useful energy delivered by the collector and gained in the receiver plate, Q_{plate} and the thermal efficiency of the receiver, $\boldsymbol{\eta}_{th,\,plate}$ and the thermal efficiency of the baking process, $\boldsymbol{\eta}_{th,\,baking}$ are given by;

$$Q_{in} = G_b A_a \gamma_{rsf} \quad \textit{(Eq. 10)}$$

$$Q_{plate} = q_s A_r - h_L A_r (T_r - T_a) = \left(mC_p\right)_{plate} \left(T_f - T_i\right) \quad \textit{(Eq. 11)}$$

$$\eta_{th,plate} = \frac{Q_{thermal}}{Q_{in}} \quad \textit{(Eq. 12)}$$

$$\eta_{th,baking} = \frac{Q_{baking}}{Q_{in}} \quad \textit{(Eq. 13)}$$

The *solar fryer mode with* continuous heating and baking mode will have lower heating and baking time hence relatively higher efficiency while in the alternative heating and baking mode the heating and baking time will be larger resulting reduced efficiency.

2.3 Solar tracking and application time

The solar fryer is designed and provided with two application modes. The continuous type model is more preferable for applications areas and time in which the sun is in relatively overhead position thus the dish inclination angle is in the range of $\pm 15^0$ from the vertical position. Such conditions can be easily obtained in Ethiopia when the local time is in the range of 10:00 to 15:00. The alternating type model provides more flexible in terms of solar inclination, as heating and baking are conducted alternatively. Therefore, while the alternatively type model is equally applicable in the above time, it is more preferable if an application is required for the remaining time of the day i.e. early morning and late afternoon, provided if there is sufficient solar radiation.

2.4 Injera quality assessment

The performance of the direct solar fryer is also determined qualitatively based on the quality of Injera as compared to quality of Injera baked by conventional baking process, such as electrical baking. The quality of the baked Injera is determined qualitatively by physical inspection of its size (thickness), colour, eye formation, underside appearance, texture and taste. This physical property is qualitatively evaluated with the respective physical property of Injera baked by conventional baking methods, such as electrical mitad.

3. Experimental methods and materials

A prototype developed for the direct solar fryer model is shown in figure 3, with the prototype in a) indicates for the continuous heating and baking mode of operation while the prototype in b) indicates for the alternative heating and baking mode of operation.

a) b)

Figure 3: the direct solar fryer model a) with continuous heating-baking mode b) with alternative heating-baking mode

Extensive experiments on the two models were carried out, thereby to evaluate the thermal performance of the system by conducting temperature measurement on the different points on the baking plate, mass and solar radiation measurement. The experimental setup is shown in figure 4.

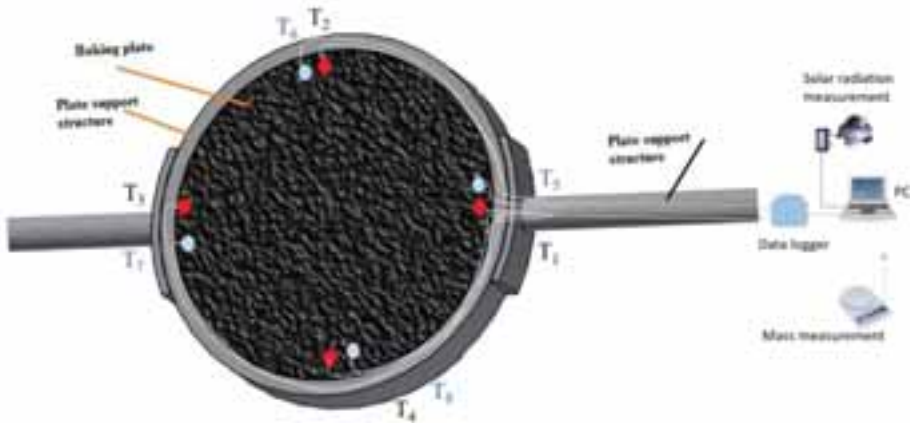

Figure 4: schematics of the experimental setup for temperature, solar radiation and mass measurement

Eight thermocouple (k type) were used to measure temperature at the surface of the baking plate. For the continuous mode, the temperature measurement on the illumination side is denoted as T_1, T_2, T_3 and T_4 and the baking surface as T_5, T_6, T_7 and T_8. Similarly, for the alternative mode, the temperature measurement on the illumination (or baking) side is denoted by T_1, T_2, T_3 and T_4 while the backside (insulated side) of the plate is denoted by T_5, T_6, T_7 and T_8. During the analysis, an average of these temperature measurements were calculated, indicated as $T_{av,\ baking\ surface}$, $T_{av,illumination\ surface}$ and $T_{av,\ plate.}$ Solar radiation measurement using the Delta T instrument (SP1 sunshine pyranometer) were conducted, measuring global (G) and diffuse irradiance (G_d). Mass measurement of the dough and the baked Injera were also taken.

4. Result and discussion

In this research, the thermal performance of the direct solar fryer with two mode of operation i.e. the continuous heating and baking mode and the alternative heating and baking mode is analyzed and presented. The performance of the direct solar fryer is presented in terms of heating-baking temperature profile, power, energy consumption and thermal efficiency, as discussed in the following sections.

4.1 Heating and Baking Temperature Profile

The temperature profile of the heating-baking process for the direct solar fryer model with continuous heating and baking mode is indicated in figure 5. The initial heating up of the plate has taken an average of 30 minutes until it reaches a baking temperature of 120 ℃ to 130 ℃, which was sufficient surface temperature to initiate the baking activity. The heat distribution was also relatively within acceptable uniformity, with an average temperature difference between the bottom illumination and upper baking surface of 3 ℃ while the instantaneous difference was between 0 to 10 ℃.

For the solar fryer with the alternating heating baking mode, the plate has reached an average temperature of 160 to 180 ℃, which was sufficient to initiate the baking process. The average temperature drop per each baking was about 40 ℃ (170-130 ℃), which indicated the thermal energy storage requirement of the baking plate.

In comparison to the conventional baking process, the temperature profile of the heating and baking process was similar as this temperature profile was independent of the type of energy utilized, rather the baking energy requirement of the process.

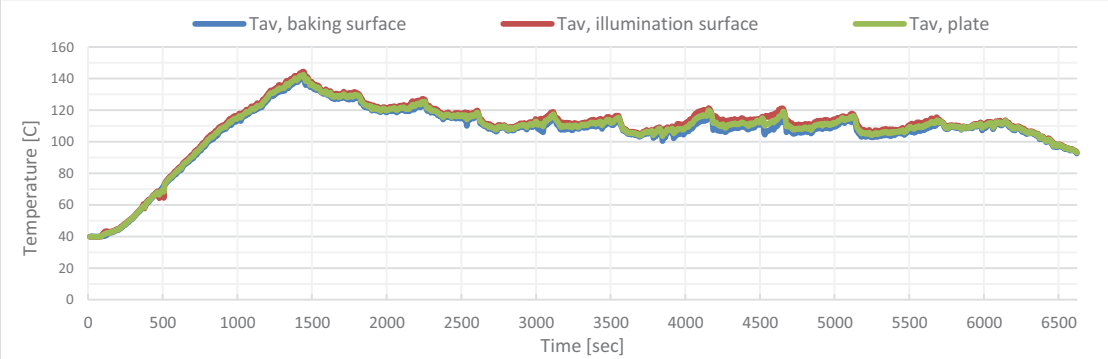

Figure 5: Heating and baking temperature profile for the alternative solar fryer model with continuous heating and baking mode
[Note: the result here is from an experiment taken on March 16, 2017 at Mekelle Ethiopia. Similar result has been obtained on experiments taken on 10th and 11th of February; 15th and 17th of March; 11th, 12th and 13th of May; 16th 17th and 19th of June 2017]

4.2 Heating and Baking Time

As indicated in figure 5, each baking activity using the continuous heating and baking mode fryer has taken an average of 5 minutes while the subsequent additional heat up time is 2 minutes, giving an average baking time of 7 minutes per Injera. The direct solar fryer with the alternating heating and baking mode requires larger heating time at each interval of baking process, as the plate needs to store thermal energy for the subsequent baking process.

In comparison to the conventional baking process, both modes of the direct solar fryer have the same degree of initial heating time. The subsequent heating-baking time for both models is slower than the conventional baking process while the solar fryer with the alternating heating-baking mode is even slower. The conventional baking process usually requires an initial heating time of about 30 minutes while the subsequent heating-baking time is about 3-5 minute per Injera.

4.3 Baking Power and Energy

The heating and baking power requirement for the direct solar fryer model with continuous heating and baking mode is indicated in figure 6. The area under the power curve in figure 6 will give the total thermal energy from the sun, the thermal energy stored in the baking plate and the energy consumption for the baking process. The average plate stored energy was about 153kJ per Injera and this was equivalent to 563W of baking plate power.

The average direct solar intensity has been 932W/m^2 and considering the collector size, this is equivalent to 2kW available energy from the solar radiation. Considering an aluminum material reflectivity of 95 % and other factors (i.e. pan surface reflectance, pan shading effect and dish estimated defect) combined effect of 72% will give 1538 W capacity of incoming radiation from the solar collector, thus about 37 % of the solar radiation reaching the illumination surface was converted into the baking plate power.

The overall energy consumption of the direct solar fryer model with continuous heating and baking mode is indicated in figure 7. The baking energy was determined to be 1150 kJ/Kg of Injera or 450 kJ per Injera. The solar fryer thermal efficiency ($\eta_{th,baking}$) including the solar collector efficiency, was determined to be 37 % while the thermal efficiency ($\eta_{th,plate}$), by including the plate stored energy as a useful energy was about 65%. The low thermal efficiency was attributed as the baking plate is very large (550 mm in diameter and 12.5mm thickness) in order to meet the traditional Injera size, prompting higher surface convective and radiative heat losses. The solar fryer would have been more efficient if it was smaller size but that will have social acceptance problem because of its smaller Injera size. Large size solar fryer compromises efficiency and baking time; the larger the size the less efficient and the larger baking time but it satisfies the traditional Injera size requirement.

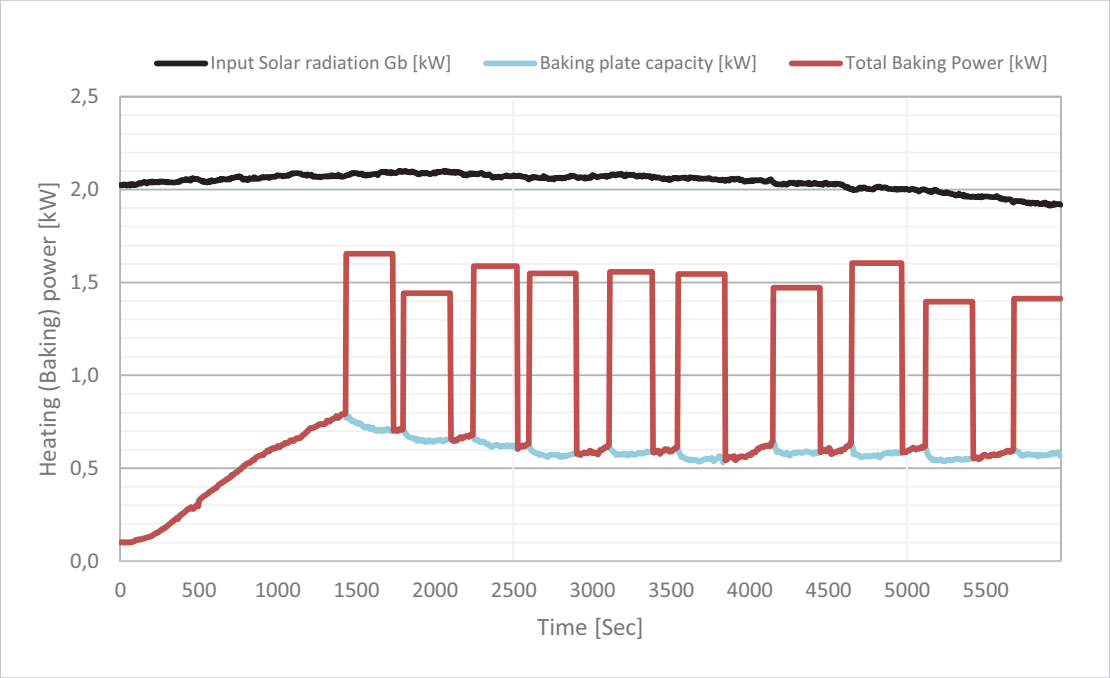

Figure 6: Heating and baking power for the direct solar fryer model with continuous heating and baking mode

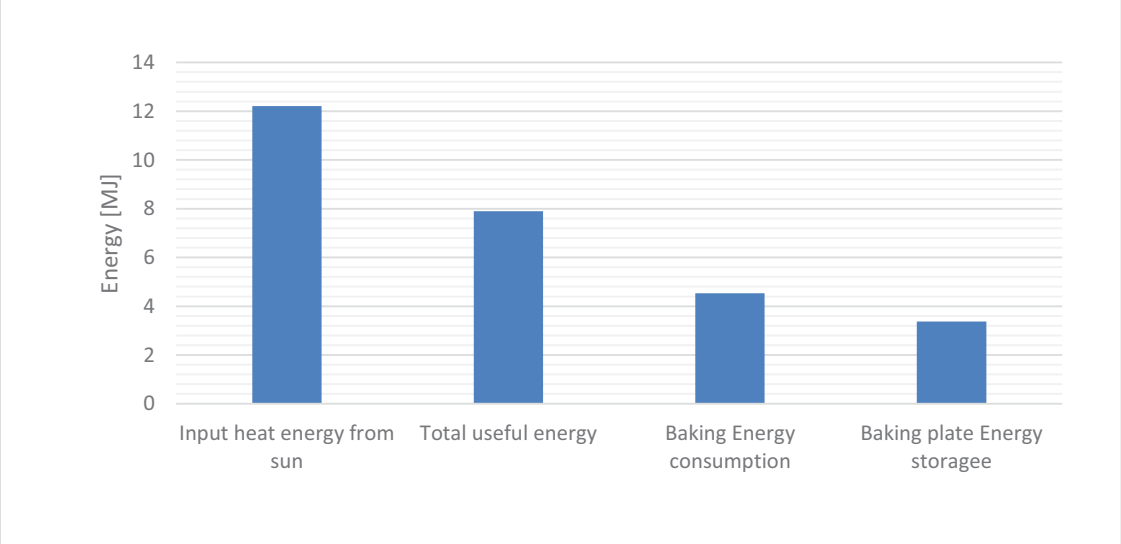

Figure 7: Overall energy consumption of the direct solar fryer with continuous heating and baking mode

4.4 Quality of the Injera

The quality of the baked Injera is as indicated in figure 8. It can be seen that the quality of the Injera with respect to the physical property of size (thickness), color, eye formation, underside appearance, texture and taste is very good and it is the same as any Injera baked with the conventional baking system.

Figure 8: quality of the Injera from the direct solar fryer with continuous heating and baking mode

5. Conclusion

This research has demonstrated solar injera baking using a large size direct solar fryer. The solar fryer was designed to address simplicity in the system and its application. The solar fryer is effective, with 37% thermal efficiency while enabling to harvest cost-free solar energy. The system can be used for injera baking application in a single household, small group rural households or small scale Injera baking business individuals or groups. The only limitation of the application is when there is no sufficient solar radiation such as in cloudy days or if a baking application is required during off sunshine hours, such as at night. For such cases, a backup alternatives should be provided.

References

Abdullahi, Mohamed Diriye, 2001, Culture and Customs of Somalia, Cultures and Customs of the World Series, Greenwood Press, p. 113.

Abdulkadir A. Hassen, Demiss A. Amibe, and Ole J. Nydal, Performance Investigation of Solar Powered Injera Baking Oven for Indoor Cooking, ISES solar world congress 2011 proceedings, 186-196.

Anwar Mustefa Mahmud, Mulu Bayray Kahsay, Asfafaw Hailesilasie, Ftwi Yohaness Hagos, Petros Gebray, Hailay Kiros Kelele, Kindeya Gebrehiwot, Hans Bauer, Seppe Deckers, Josse De Baerdemaeker, Johan Driesen; Solar Energy Resource Assessment of the Geba Catchment, Northern Ethiopia, 2013 ISES Solar World Congress, Energy Procedia, Volume 57 (2014) Pages 1266-1274

Aptekar, Lewis (2013). In the Lion's Mouth: Hope and Heartbreak in Humanitarian Assistance. XLibris LLC. p. 9. ISBN 978-1-4836-9519-8.

Asfafaw Haileselassie Tesfay, Mulu Bayray Kahsay, Ole Jørgen Nydal, Solar powered heat storage for Injera baking in Ethiopia, 2013 ISES Solar World Congress, Energy Procedia 57 (2014) 1603 – 1612

Badi, S. M., Bureng, P. L., and Monowar, L. Y. 1988. Commercial production: A breakthrough in kisra

technology. Pages 31-45 in: ICC 4th Quadrennial Symposium on Sorghum and Millets. D. A. V. Dendy, ed. International Association for Cereal Science and 250 Technology:Schwachet, Austria.

Demissie A. Teff genetic resources in Ethiopia. In: Tefera H, Belay G, Sorrells M, editors. Narrowing the rift: teff research and development. Ethiopia: Debrezeit; 2000. pp. 27–31

Ejeta, G. 1982. Kisra quality: Testing new sorghum varieties and hybrids. Pages 67- 261 72 in: Proceedings of the International Symposium on Sorghum Grain Quality. J. V. Mertin, ed. International Crops Research Institute for the Semi-Arid Tropics:Patancheru, India

Energypedia, Ethiopian Energy situation, https://energypedia.info/wiki/Ethiopia_Energy_Situation, March 2017

Gallagher Alan, A solar fryer. Science direct, Solar energy 85; 2011, p. 496–505

Gebreegziabher, Z., Urban Domestic Energy Problems in Ethiopia: An Overview. Addis Ababa, Ethiopia: EDRI (Ethiopian Development Research Institute), 2004

Gebreegziabher, Z.,. Household Fuel Consumption and Resource Use in Rural-Urban Ethiopia. PhD diss. Department of Social Sciences, Wageningen University, 2007.

GIZ, The Development Intervention in Ethiopia, GiZ Energy Coordination Office Ethiopia (GiZ ECO Ethiopia) Report, March 2011.

Maxime Mussard, Ole Jørgen Nydal; Charging of a heat storage coupled with a low-cost small-scale solar parabolic trough for cooking purposes; Science direct, Solar Energy Volume 95, September 2013, Pages 144-154

Maxime Mussard, Alexandre Gueno, Ole Jørgen Nydal; Experimental study of solar cooking using heat storage in comparison with direct heating; Science direct, Solar Energy Volume 98, Part C, December 2013, Pages 375-383

Mekonnen Melaku Gebremariam, Martin Zarnkow, and Thomas Becker; Teff (Eragrostis tef) as a raw material for malting, brewing and manufacturing of gluten-free foods and beverages: a review; Journal of Food Science Technology 2014 Volume 51 Issue 11 pp 2881–2895 https://doi.org/10.1007/s13197-012-0745-5

RTPC (Rural Technology Promotion Center), Biomass Stove (Mogogo Eton) Test Report; Mekelle, Ethiopia: RTPC, 1998.

Sustainability As A Characteristic Of Renewable Energy Systems In Remote Himalayan Villages

Rick Sturdivant[1], James Yeh[2], Mark Stambaugh[2], Alex Zahnd[3],

[1]Azusa Pacific University, Azusa, CA, USA

[2]RIDS-USA, [3]RIDS-Switzerland

Abstract

This work investigates sustainability as a characteristic of renewable energy systems with the goal of improving the rigor of how it is applied. This work is based upon 20 years of developing and deploying sustainable solutions to villages in the Nepal Himalayas and particular to the village of Moharigaun (near Jumla) since 2002. Sustainability has been used in at least four different ways when applied to renewable energy systems which are described and contrasted. In addition, sustainability is analyzed using a systems engineering approach so they are recognized as non-functional properties impacting stakeholder value. Stakeholders of these systems include users, system developers, various relevant government entities and investors. A set of more rigorous definitions are then given along with suggestions on how the definitions can be applied. The work concludes with suggestions for additional work on sustainability.

Keywords: Renewable, Pico Hydro, Sustainability, Energy Systems

1. Introduction

As described in [1,2,3], the Rural Integrated Development Services (RIDS) has been developing methods to enhance the living conditions of remote mountain communities in Nepal since 1996. The approach taken by RIDS is holistic and contextualised to geographical region, local cultural values and belief systems, meteorology and governmental policies. This approach improves the long term success of the deployed systems. Those solutions include:

1) Pit Latrines: Used for individuals and communities to improve overall village hygiene and sanitation.

2) Smokeless Metal Stoves: They are used for cooking the local available dishes, room heating and heating of water for tea and personal hygiene (through a separate attached stainless steel water tank).

3) Basic Indoor Lighting: Local energy resources such as water, solar energy or wind are used for pico-hydro power plants, solar photovoltaic systems based on the local context and small scale wind turbines, to generate electricity for basic access to indoor lighting with low wattage while LED lights.

4) Clean and sufficient Village Drinking Water Supply: Water supplies from the communities' owned water sources are designed and built for safe and sufficient drinking water for all.

The development of these four solutions, called the "Family of 4" (http://www.rids-nepal.org/index.php/Family_of_4.html) has resulted in a new understanding of sustainability that has important, synergistic benefits. This is due in part to a recognition that the needs of all stakeholders, especially of the end-users' expressed verbally, must be taken into account when considering sustainability.

Prior workers have investigated sustainability. In [4], for instance, the authors provide several examples of how sustainability is applied such as economic, energy, agriculture and then attempt a common definition. However, their definition does not account for long term continuance of systems and neglects critical stakeholders such as investors. In [5], the authors take a systems approach and investigate sustainability across multiple levels of complex systems. While this is a valuable contribution, the authors emphasize environmental engineering and focus only on systems themselves. As a result, they don't account for stakeholder needs.

doi:10.18086/swc.2017.24.03 Available at http://proceedings.ises.org

This work is a unique contribution since it recognizes sustainability of renewable energy as a non-functional system property, often called "quality attributes" of a system, of particular importance to stakeholders. As a result the needs of the stakeholders are paramount. This approach is critical for deployment of renewable energy solutions to remote villages since it allows other stakeholders to listen to their self-identified needs, enabling a better understanding of the local stakeholder essential requirements through long term local engagement. This work also considers other stakeholders such as financial backers of renewable energy solutions. This group of stakeholders is a critical partner required for long term success. However, financial stakeholders often have a different perspective and motivations for requiring "sustainable" solutions, though based on current and "ear tickling" development theories rather than on detailed baseline surveys and long term understanding of the end users' context and self-identified needs. In addition, this work proposes a sustainability measurement system so that it can be optimized. Emphasis upon sustainability as a non-functional system property and upon stakeholder needs is the focus of this work.

2. Sustainability as a Non-Functional Requirement

It is common in systems engineering to use 'ilities' to describe non-functional system properties. Examples are reliability, portability, quality, maintainability, and durability [6]. One benefit of using "ilities" is that they allow the system designer and user community to perform system architecting trade studies with a focus on a balanced solution with the potential to meet stakeholder needs [7]. From this perspective, sustainability is one of many different stakeholder needs that must be met to ensure value delivery over the life cycle of the system. Once a full set of "ilities" and their relative importance has been established, trade studies can be a useful tool for choosing the preferred system architecture as described in [8].

One trade study method is to use a quality function deployment matrix as described in [9]. This method uses criteria (ilities in this case) which are assigned a weighting, W_k. Each system architecture option is evaluated against the criteria (ilities) and assigned a value, V_k, which represents the capacity of the architecture to achieve the criteria. The score for each architecture option is then calculated using.

$$Score = \sum_{k=1}^{n} W_k V_k \tag{1}$$

The result of this approach is a system architecture baseline that can be further developed.

The importance of system architecting using "ilities" for this work is that shows that sustainability is one of many system level non-functional properties that must be considered when developing highly contextualized green energy solutions.

3. Four Uses of Sustainability In Highly Contextualized Renewable Energy Systems

There are at least four different uses of sustainability when applied to green electric power systems for remote villages. While each of the definitions may have common stakeholder interests as a concern, each of the definitions also address interest of specific stakeholders.

The first is Investor Centric Sustainability. The deployment of renewable energy solutions requires financial backing which is just as true for large multi-mega Watt solar power systems as it is for pico-hydro electric systems. Most financial backers want to supply a onetime investment (or investment over a fixed time frame) and after the investment period is over, they expect the system to continue without any further investment.

True enough that future expansion may require additional funding, but the goal of the financial backer is a system that continues to perform its function without additional investment. This is the case for investors in for-profit power generation ventures with an expectation of a return on their investment and it is true for financial backers in non-profit power generation systems. The investor in a non-profit power generation system expects their investment to continue to deliver value to the users after the investment period has ended.

Financial backers of non-profit power generation systems expect that the deployed system will continue well after they have invested. Moreover, non-profit power system investors will often expect the system the system to sustain expansion to new users without additional investment. This is due, in part, to the fact that some non-profit investors desire their investment to continue to deliver value as a personal legacy. Investor Centric

Sustainability is an important driver to proper system architecting since it can mean the difference between attracting and not attracting investment.

The second is Environmental Sustainability. This understanding is what most individuals think of when they hear the word sustainable. It means that the deployed system will deliver value to users with minimal or zero negative impact to the environment.

The third is Physical Sustainability. The concept is that the deploy system can be sustained and maintained by the resources gathered as revenue from the operation of the system. This requires a maintenance plan and financial plan (often user payment for energy services/units) which funds required maintenance as required.

The fourth is Growth Sustainability. This type of sustainability refers to the capacity of the system to sustain value delivery as the system itself grows and increases in scope. This requires a long term plan (≥20 years) for how the system will be expanded over time. Growth sustainability includes the idea that the solution can serve as an example for others to implement. In this case, the system is sustainable when its energy services can be delivered as the user community grows over the decades and when the system can be replicated by others.

4. Measurement of Sustainability

Sustainability can be measured. For instance, the long term financial sustainability of the system can be analyzed according to income sources once the system is deployed. Some percentage of the local population will be able to contribute to Maintenance Sustainability and some percentage of new residents will be able to contribute to Growth Sustainability. Contribution (financial, human resource, land, etc.) goals can be established and compared to actual levels to understand trends and lessons learned for future deployments.

5. Conclusions

Sustainability has been analyzed as a non-functional system property of rural green power systems. The method of using “ilities” to architect the solution was described. Four uses of sustainability were also described. Finally, a method for measurement of sustainability has been proposed.

6. References

[1] www.rids-switzerland.org

[2] R. Sturdivant, J. Yeh, M. Stambaugh, A. Zahnd, E.K.P. Chong, “Pico-hydro electric power in the Nepal Himalayas,” IEEE Green Technologies Conference, March 29-31, 2017, Denver, CO.

[3] A. Zahnd, M. Stambaugh, D. Jackson, T. Gross, C. Hugi, R. Sturdivant, J. Yeh, S. Sharma, “Modular Pico-Hydro Power System for Remote Himalayan Villages,” in World Renewable Energy Congress XVI, Feb 5-9, 2017.

[4] B. Brown, M. Hanson, D. Liverman, R. Merideth, “Global sustainability: toward definition,” Environmental Management, Vol. 11, No. 6, Nov. 1987 pp. 713-719.

[5] P. Glavic, R. Lukman, “Review of sustainability terms and their definitions,” Journal of Cleaner Production, Vol. 15, No. 18, Dec. 2007, pp. 1875-1885.

[6] O. de Weck, D. Roos, C. Magee, C. Vest, Engineering Systems (Cambridge, MA: The MIT Press, 2011), p. 67.

[7] A. Engel, T. Browning, “Designing systems for adaptability by means of architecture options,” Systems Engineering, Vol. 11, No. 2, Summer 2008, pp. 125-146.

[8] S. Corpino, F. Nichele, “An ilities-driven methodology for the analysis of gaps in stakeholder needs in space systems conceptual design,” IEEE Systems Journal, Vol. PP, No. 99, June 2016, pp. 1-10.

[9] R. Sturdivant, E.K.P. Chong, “Systems engineering of hybrid renewable electric power,” IEEE Green Technologies Conference, April 7-8, 2016, Kansas City, MO.All references should be made according to the guidelines, as shown below.

Solar Detoxification of Water

PULP AND PAPER SOLAR EFFLUENT TREATMENT AND DETOXIFICATION: PHOTO CATALYTIC DEGRADATION OF METHYLENE BLUE BY NATURAL ULTRA-VIOLET LIGHT CATALYSED BY TITANIUM OXIDE

Orori O. Bernard[1], Mwamburi M. Muindi[2], Odipo F. Osano[3] and Etiegni Lazare[1]

[1] Department of Forestry and Wood science/University of Eldoret, Eldoret (Kenya)

[2] Department of Physics / University of Eldoret, Eldoret (Kenya)

[3] School Environmental Studies/ University of Eldoret, Eldoret (Kenya)

Abstract

Pulp and paper mill effluent treatment and detoxification methods have been extensively investigated resulting to varying efficiencies and capital and operational costs. The main toxic component in the mills' effluent is modified lignin, which is difficult to degrade by convectional effluent treatment systems applied by most mills. This study aimed at using natural photo catalytic degradation of methylene blue using anodised pigmented and non-pigmented titanium plates to optimise anodising time and voltage. Titanium plates were anodised at varying voltages and times in a mixture of sulphuric and hydrofluoric acids. Irradiation of aqueous solution of methylene blue was done using varies anodised pigmented and non pigment plates in a batch reactor cell. Absorbance of each photo catalysed solution was determined every five minutes after a dark phase of fourteen minutes using a laser light source. Absorbance was then converted to transmittance, which gave photo catalytic reactivity of plates. The study revealed that photo catalytic reactivity of pigmented titanium plates was higher than non-pigmented. Photo catalytic reactivity also increased with increase in anodising time and voltage. Anodised plate at 200volts for 120 seconds and pigmented with photo catalytic reactivity of 62.325×10^{-3} was found to be the best to degrade methylene blue. Application of this optimised plate on Kraft Pulp mill effluent showed reduction in COD, BOD, turbidity, colour and total suspended solids. However effluent pH and electrical conductivity increased. COD, BOD, turbidity and colour removal efficiency improved on introduction of wood ash leachate (electrolyte) in photo catalytic activity. The study recommended the use anodised titanium plates using natural ultra violet energy aid by an electrolyte to treat Kraft pulp and paper mill effluent.

Keywords: pulp and paper, methylene blue, Photo-catalytic degradation, titanium oxide

1. Background

Pulp and paper industry started during ancient times and since then it has remained to be a very important industry in the development of many countries (Hossain and Rao, 2014; Raj *et al*., 2014). The pulp and paper industry is important as a result of its major roles of paper and paper products in many areas of human activities. It has contributed immensely to gross domestic products of both developing and developed economies over a long period time (FAO, 1998, Kamali and Khodaparast, 2015). The Pulp mill sector utilizes a huge amount of lignocellulosic materials and water during its operations and processes. In the recent past the sector has been faced with ever changing and stringent regulations of its effluent discharge standards with high possibilities for the same to continue in the future. Pulp and paper production has long been recognised as a significant point source of contaminants and toxic components to aquatic life (Gupta, 1994; Sumathi and Hung, 2006; Monte, *et al.,* 2009; Hossain, and Ismail, 2015). Several compounds with varying toxicological significance have been identified in pulp and paper liquid effluent. Effluent from the mills contain chlorinated lignosulphonic acids, chlorinated resin acids, chlorinated phenols and chlorinated hydrocarbon among others (Mahida, 1981; Thompson, *et al*, 2001; Chandra *et al*., 2007; Mehta, *et al.,* 2014; Barapatre and Jha, 2016).

doi:10.18086/swc.2017.25.01 Available at http://proceedings.ises.org

Treating and detoxifying effluent is a significant challenge to pulp and paper mills, and is an integral part of their operation in order to meet ever changing discharge standards for several pollutants and toxic materials (Kamali and Khodaparast, 2015). Several effluent treatment methods have been investigated extensively and they include use of activated carbon, membrane adsorption, cationic coagulation, polymer addition, ultrafiltration, biological and chemical oxidation, electrochemical, electro-coagulation, photo-catalysis among many more (Hilleke, 1991; Bellew, 1978; Orori, *et at*, 2007; Etiegni, *et al*, 2010; Chandra *et al.,* 2012; Cong,et. al., 2012; Chandra *et al*., 2013; Hossain and Ismail, 2015, Saez *et al.,* 2013; Zongo *et al.,* 2009; Barapatre and Jha, 2016).

2. Material and Methods

2.1. Study Area

Effluent samples for this study were obtained from Mufindi Paper Mills (MPM) situated in Mgololo valley close to Mafinga town in Mufindi District, Iringa province, in the United Republic of Tanzania. The mill is located about a latitude of 08º55'S and longitude of33º32'E on an altitude of1600 meters above sea level. The area has a mean temperature of 21-25^{o}C (Massawe, *et al,* 2016). MPM produces 35000 metric tonnes of pulp and 28000 metric tonnes of paper, with approximately 70 percent of its rated capacity. The main raw materials for the mill are from pine and eucalyptus plantations owned by company (Sutton and Olomi, 2012). MPM has three Kraft pulping digesters each with a capacity of 40m^3. MPM has two fourdrineer paper machines running on different revolutions per minute depending on the paper grade being manufactured. Its main products are packaging materials of various grades and specifications, including Kraft Liner, Sack Kraft, Bag Kraft, Deckle and Grammage (Sutton and Olomi, 2012)

MPM mill has instituted measures to reduce pollution to receiving water by chemical recovery system in which pulping chemicals are recovered through combustion of organics. The mill has not installed a closed white water system, which is very important in the reduction of fibers losses and chemicals. There is need for MPM to install micro-screens on paper machines to cut down fiber loss. The brown coloured combined mill effluent from pulp washing and papermaking sections is passed through trash screens to remove large suspended solids. The screens are designed with effluent volume of 1800m^3/hr of 50mm and 15mm manual and mechanical bars spacing respectively. The effluent is passed through a single primary clarifier (turbo circulator) employing an air flotation principle. The clarifier is designed with a flow of 1080 m^3/hr with a maximum flow of 1800 m^3/hr. The diameter of the clarifier is 43m and 4m peripheral water depth with inlet suspended solid load of 5500kg/day with a total suspended solid removal efficiency of 88-98% (Sutton and Olomi, 2012).

After clarification the supernatant effluent flows into specially designed aeration lagoon fitted with four of 45-watt electrically operated surface aerators. The detention time in the aeration lagoon is approximately 7 days. After aeration the supernant effluent flows to settling pond where it takes approximately 5 days. Thereafter the effluent drains slowly through a swamp into river Kigogo Ruaha. River Kigogo Ruaha drains into River Luhuji that drains into River Kilombero, which drains into River Rufiji that into Indian Ocean.

2.2 Anodising and pigmenting of titanium plates

Titanium grade two foil of 0.3mm thick (TiGr2-FL-230-01-02) was obtained from William Gregor Limited shop. The foil was cut into pieces measuring 20mm by 80mm (plates). The plates were degreased in acetone for five minutes and thereafter thoroughly rinsed in distilled water. Before anodizing, each plate was further cleaned by immersing it in a mixture of Nitric acid (1 molar), Hydrofluoric (1molar) and distilled water in a ratio of 13:1:7.5 for 15 seconds and quickly rinsed using a lot of distilled water. Anodizing of titanium was carried out in a one litre cell with varying times and voltages. Anodising time varied from 30, 60, 90 and 120 seconds Anodizing voltage also varied from 60, 80, 100, 120, 140, 160, 180 and 200 volts. Anodising electrolyte was made of double distilled water, sulphuric acidic (18M) and Hydrofluoric (1M) in the ratio of 972:27:1 respectively. The distance between the electrodes and anode was kept at 1cm and was held constant for all anodising reactions. The electrolyte was continuously stirred using a magnetic starrier. Anodized plates were

pigmented using 0.1M solution of copper (II) sulphate electrolyte at 12volts for 5 seconds. The anode was made of copper plate fixed at distance of 3cm from titanium cathode plate. Each plate was pigmented separately using a fresh electrolyte in orders to obtain similar pigmenting results. Annealing of titanium plates was accomplished in a furnace at a temperature of 450^{o}C ±5^{o}C for three hours.

2.3 Optimum anodizing conditions

Plate 1 show a fabricated reactor used in this study. Each of the plate was used at a time in the reactor with 60ml of 1.5×10^{-5}M of methylene blue. Optimization of anodizing variables was achieved through a fabricated cell reactor utilising the principle of laser light absorbance by methylene blue. Methylene blue was chosen because of its close chemical structure and bonding to that of lignin, which is the main component found in the pulp paper mill effluent. Two anodizing variables (anodizing voltage and time) were investigated that mainly affect catalytic efficiency of phenyl compounds. The reaction was run for 14 minutes of dark and 46 minutes of UV phase. Absorbance was measured at an interval of 2 minutes during dark phase and 5 minutes during UV phase. The dark phase was important to allow the solution to be homogenous and any adsorption to take place. Absorbance was used to determine the level of degradability of methylene during the experiment. Absorbance was obtained from the concept of laser light intensity before and after going through the solution.

Plate 1: Fabricated reactor unit for optimization of anodised titanium plates

Natural solar ultra violet was used with all experiments carried out between 11.30am and 2.30pm when the UV was between 360-400nm. Absorbance was then converted to transmittance using the Beer Lambert relationship. The best linear relationship between time and transmittance was then determined. The gradient of a linear relationship gave reactivity of each plate that was used to optimise the two variables of interest in the study. Optimised conditions were then used to prepare titanium plates that were used to treat effluent from Kraft mill of Mufindi Paper Mills.

2.4 Effluent treatment efficiency

Plate 2 shows a set-up of photo catalytic effluent treatment unit used in the study. A photo catalytic unit was fabricated with an equal width and length of 24cm and 20cm depth using 4mm clear transparent glass. Twenty four (24) optimized titanium plates measuring 30mm by 80mm were prepared and carefully stuck on a 4mm-thick glass substrate using silicon. Three litres of the effluent was used for each photo catalytic effluent treatment. One side of the stuck titanium plates were held 2cm above effluent surface with a gentle slope ending in the effluent to complete the current flow with the effluent. Using an electric pump (magi-200) a thin layer of effluent was continuously circulated over the plates while exposing it to direct natural ultra violet rays for 6

hours. Regularly the set up was tilted towards direct sun rays for higher light intensity. Effluent from the Kraft pulping mill was subjected to a combination of different photo catalytic effluent treatment combinations. Combined treatments included, photo catalytic alone (PHCALON) and photo catalytic with wood ash leachate as an electrolyte (PHCASH). A control effluent treatment was set by allowing the effluent to circulate over a plain transparent glass (PHOALON). Treated effluent samples were then allowed to settle overnight and the supernant was analysed for colour, turbidity, pH, biochemical oxygen demand, chemical oxygen demand, total solids, total suspended solids and electrical conductivity.

Plate 2: Fabricated photo catalytic effluent treatment unit

3. Results and Discussion

3.1 Methylene Blue Degradation

Rate of degradation, Absorbance, transmittance of methylene blue gave the reactivity varies titanium anodized pigmented and non pigmented titanium plates. The titanium plate with highest reactivity on methylene blue was then use in treatment of a Kraft pulp and paper mill effluent.

3.2 Absorbance of Methylene Blue

Plate 3, 4, 5, and 6 show selected absorbencies of methylene blue with time. Generally, absorbance decreased for all anodised titanium plates experimented in this study. Absorbance decreased but transmittance increased because some bonds causing colour may have been broken. When more bonds were broken then methylene blue underwent further decolourization. Decrease in methylene blue absorbance is attributed to its degradation by natural UV catalysed by anodised titanium plates, which consequently reduced the ability of the solution to absorb more UV light. The higher the rate of degradation the better the catalytic activity of anodised plates employed.

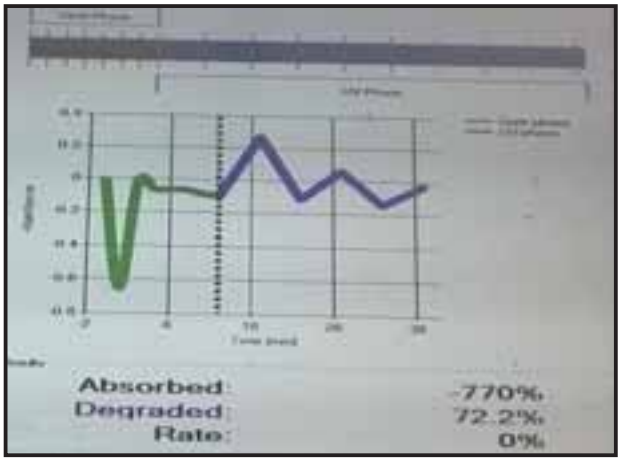

Plate3: Degradation of methylene Blue without titanium plate

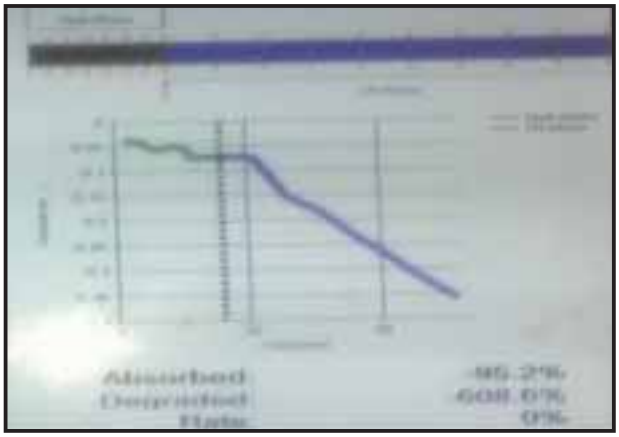

Plate 4: Degradation of methylene Blue with titanium plate anodised at 200 volts for 120 seconds and pigmented

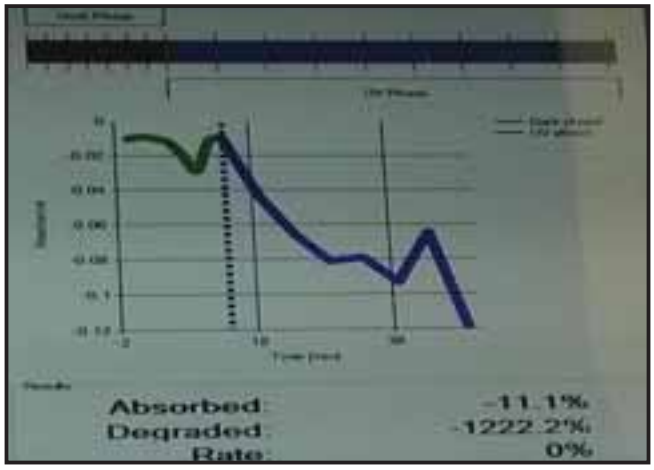

Plate 5: Degradation of methylene Blue with titanium plate anodised at 180 volts for 120 seconds and non-pigmented

Plate 6: Degradation of methylene Blue with titanium plate anodised at 180 volts for 120 seconds and pigmented

3.3 Transmittance of Methylene Blue

Figure 7 show selected transmittance during methylene blue degradation by natural UV catalyzed by anodized titanium and non pigmented plates. The best relationship between transmittance and degradation time of methylene blue for various plates were linear relationships with values for R-squared ranging from 0.9564 to 0.9802. R-squared values closer to one indicated a very good relationship between transmittance and degradation. The relationship takes the first order reaction equation in which the gradient is the rate of reactivity of anodized titanium plates while transmittance is the intercept and degradation time varying.

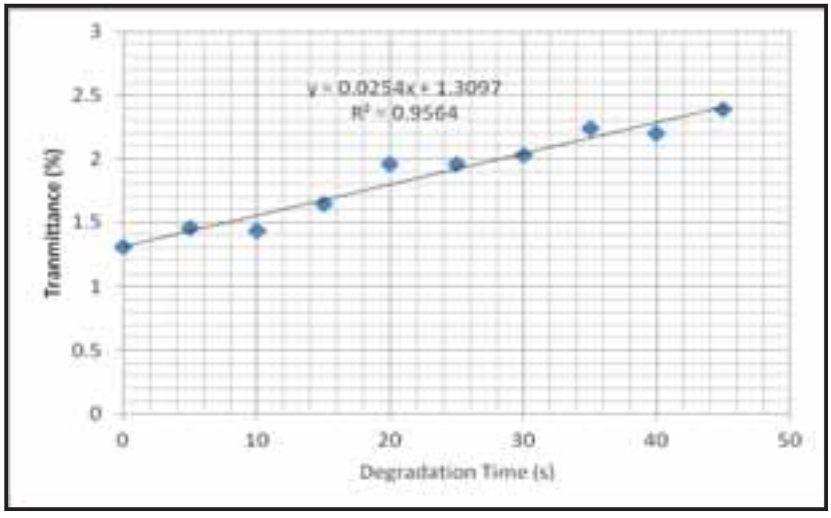

Figure 7: Transmittance of methylene blue using Natural UV catalysed by anodised titanium plate at 160 volts for 120 seconds and non-pigmented

3.4 Degradation Rate of Methylene Blue

Table 1 show means reactivaties of various anodised titanium plates during methylene blue degradation at different using natural Ultra Violet solar radiations. Highest degradation of methylene blue was noted with a plate that was anodised at 200volts for 120 seconds and pigmented using copper solution. The lowest reactivity was noted in non pigmented titanium plates anodised for 30 seconds. There was a significant difference

(P≤0.05) among reactivity of plates anodised at different voltages and times. Further there was a significant difference (P≤0.05) in reactivity between anodised pigmented and non pigmented plates. Furthermore, result indicted that there is significant (P≤0.05) interaction between anodising time and voltage.

Table 1: Mean Reactivity of titanium plates anodised at various voltages and time

	Reactivity × 10^{-3}							
Volts	**30SP**	**60SP**	**90SP**	**120SP**	**30S**	**60S**	**90S**	**120S**
60	2.646	7.291	8.624	9.800	3.170	5.636	6.630	7.800
80	3.873	9.675	14.528	16.100	3.920	7.870	8.670	10.200
100	4.799	13.960	23.954	28.890	4.055	9.908	12.600	15.600
120	6.324	21.765	31.896	39.500	6.332	13.923	17.470	19.200
140	9.858	24.997	37.320	45.950	8.656	15.389	18.105	21.300
160	14.285	31.857	42.979	54.840	9.649	16.265	22.135	25.500
180	16.893	35.786	47.328	58.100	13.796	19.363	22.780	26.800
200	19.896	38.379	51.936	62.300	12.879	19.703	27.180	29.800

3.5 Reactivity Trends of Anodized Titanium plates

Further analysis of relationship among reactivity, time and voltage for pigmented and non-pigmented plates is shown on figure 8 for selected plates. The best relationship of reactivity with voltage of titanium anodised and pigmented plates for degradation of methylene blue were logarithmic relationships apart from plated anodised for 30seconds. For all plates with logarithmic trends gave R-squared ranging from 0.9871 to 0.9565. These implied that rate of degradation of methylene blue increases with increase in anodising voltage and time but diminish for pigmented plates.

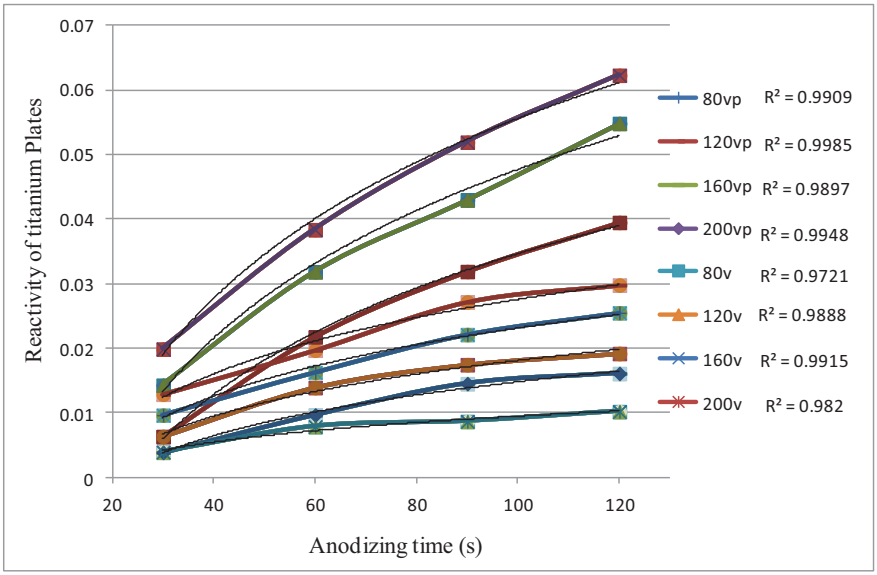

Figure 8: Reactivity trends of selected titanium plates

Only plates anodised for 30 seconds and pigmented showed that the best relationship was linear with R-squared being 0.9818. It therefore imply that better reactivity of plates can be achieved through longer anodizing times. It is also probable that reactivity rate for plates anodised at low voltage for instance that of 60, 80 and 100 volts might follow a logarithmic trend if anodising time was increased beyond the end point time (120 seconds) used

in this study. Reactivity increased with increase in anodising time but the rate slowed as anodising time increased. The best relationship between reactivity and time for non pigmented plates was logarithmic. Obtained R-squared values range between 0.9685 and 0.9685 for all plates tested, which indicates a good relationship. However, a good liner relationship (R-squared of 0.9822) was obtained for anodising time of 30 seconds.

3.5 Effluent Treatment Efficiency

Table 2 shows the treatment efficiency of optimised titanium plate applied in treatment of a pulp and paper mills effluent. Effluent COD reduced by 24.8%, 74.2% and 48.3% for PHOALON, PHCASH and PHCALONE respectively. The obtained COD final values were significantly different ($P \leq 0.05$) among all the treatment combinations. Effluent BOD was also reduced by all treatment combinations by 15.3%, 76.7% and 61.6% by PHOALON, PHCASH and PHCALONE respectively. Treated effluent colour increased for PHOALON (16.7%) but reduced by 80.7% and 58.5% for PHCASH and PHCALONE respectively. PHOALON does not involve titanium plates therefore is more of aeration of the effluent without degradation. Therefore, the probable reason for increase in colour for PHOALON could be that lignin compounds were oxidised resulting into more coloured compounds than before treatment. This finding conger with Haslam (1987) assertion that explained why biological degradation of the pulp mill effluent results in increase in effluent colour. Effluent turbidity reduced by over 23.8%, 82.7% and 86.5 by PHOALON, PHCASH and PHCALONE respectively. The final turbidity values for PHOALON, PHCASH and PHCALONE were significantly different ($P \leq 0.05$).electrical conductivity reduced of lecheate. PHALON and PHCALONE but increased for PHCASH. The increase in electrical conductivity increased for PHCASH because of dissolved mineral introduced to the effluent by the wood ash Total suspended solids (TSS) reduced by 34.4%, 70.8% and 45.5% for PHOALON, PHCASH and PHCALONE respectively. Total Dissolved Solids reduced for PHOALON (46.5%) and PHCALONE (8.5%) but increased by 19.5% for PHCASH. For PHCASH the increase might have been due to introduction of the wood ash leachate with more chemical constituents. Total Solids (TS) reduced for PHOALON (44.3%) and PHCALONE (15.4%) and increased for (PHCASH)

Table 2: Effluent treatment efficiency by PHOALON, PHCASH and PHCALONE

Properties	Original	PHOALON		PHCASH		PHCALONE	
		Final	Reduction %	Final	Reduction %	Final	Reduction %
COD(mg/l)	824.2	620	24.8	212.4	74.2	426.2	48.3
BOD(mg/l)	352	298	15.3	82	76.7	135	61.6
Colour (Pco)	1200	1400	16.7*	232	80.7	498	58.5
Turbidity(NTU)	63	48	23.8	11	82.5	8.5	86.5
EC (µS/cm)	1085	812	25.2	1420	30.9*	628	42.1
pH	7.06	7.02	0.6	8.2	16.1*	7.12	0.8*
TSS(mg/l)	154	101	34.4	45	70.8	84	45.5
TDS(mg/l)	673	360	46.5	804	19.5*	616	8.5
TS(mg/l)	827	461	44.3	849	2.7*	700	15.4

* Percent increase

4. Conclusions and Recommendations

The study revealed that photo catalytic reactivity of pigmented titanium plates was higher than non-pigmented titanium plates. Titanium plates anodised at various voltages and times had different photo catalytic reactivity. Reactivities of titanium plates anodised increased as anodising time and voltage increased. The study revealed that a pigmented plate and anodised at 200volts for 120 seconds with photo catalytic reactivity of 62.325×10^{-3} was the best to degrade methylene blue. The plate was then used to treat and detoxify Kraft pulp and paper mills

effluent. The study revealed that effluent treatment efficiency was higher for photo catalytic aided by wood ash leachate compared with photo catalytic alone using anodised pigmented titanium plates. However, effluent treatment efficiency was low for photo degradation alone for most physical chemical characteristics such as COD, BOD, colour and turbidity. Percent electrical conductivity, pH TDS and TS increased for photo catalytic aided by wood ash leachate. Therefore, it was recommended that application of photo catalytic aid by wood ash leachate in treatment of Kraft pulp and paper mill effluent is viable and can be applied.

5. References

Barapatre, A. and H. Jha 2016. Decolourization and Biological Treatment of Pulp and Paper Mill Effluent by Lignin-Degrading Fungus *Aspergillus flavus* Strain F10. *International Journal of Current Microbiology and Applied Sciences ISSN: 2319-7706* Volume 5 Number 5 (2016) pp. 19-32

Bellew, E. F., 1978. Comparing Chemical Precipitation Methods for Water Treatment, In: Chemical Engineering, March 13, 1978, Ecodye Corporation, New York.

Chandra, R. and R.N. Bharagava, 2013. Bacterial degradation of synthetic and kraft lignin by axenic and mixed culture and their metabolic products. J. Environ. Biol., 34: 991-999.

Chandra, R., A. Raj, H.J. Purohit and A. Kapley, 2007. Characterisation and optimisation of three potential aerobic bacterial strains for kraft lignin degradation from pulp paper waste. Chemosphere, 67: 839-846.

Chandra, R., Singh, R., 2012. Decolourisation and detoxification of rayon grade pulp paper mill effluent by mixed bacterial culture isolated from pulp paper mill effluent polluted site. Biochem. Eng. J. 61, 49–58.

Cong, Y., Z. Li, Y. Zhang, Q. Wang and Q. Xu, 2012. Synthesis of a-Fe2O3/TiO nanotube arrays for photoelectro-Fenton degradation of phenol. Chem. Eng. J., 191: 356-363.

Etiégni, L., K. Senelwa, B. K. Balozi, D. O. Oricho, K. Ofosu-Asiedu and B. O. Orori, 2010. Treatment of Wastewater by Electro-coagulation Method and the Effect of Low Cost Supporting Electrolytes, **in** "Fluid Waste Disposal": K. W. Canton (ed), Nova Science Publishers, New York USA. (Chapter One)

FAO. 1998, Pulp and Paper Capacities. FAO Publishers, Rome, Italy, 205p.

Gupta, P. K. 1994. Environmental Management in The Agro-Based Pulp and Paper Industry in India–a Holistic Approach. *Water Science and Technology*, *30*(3), 209-215.

Haslam, E. (1987). Twenty-second Procter Memorial Lecture: Vegetable Tannins - Renaissance and Reappraisal. Journal of the Society of Leader Technologists and Chemists, Vol. 72, pp. 45-64.

Hilleke, J. 1991. Industrial Environmental Control in Springer A. M., (ed) 2nd edn. TAPPI Press. Atlanta. pp. 305-343.

Hossain, K. and A. R. Rao 2014. Environmental change and its affect. European Journal of Sustainable Development. 3: 89-96 Raj *et al*., 2014

Hossain, K. and N. Ismail. 2015. Bioremediation and Detoxification of Pulp and Paper Mill Effluent: A Review. *In:* Research Journal of Environmental Toxicology 9 (3): 113-134, 2015

Hossain, K. and N. Ismail. 2015. Bioremediation and Detoxification of Pulp and Paper Mill Effluent: A Review. *In:* Research Journal of Environmental Toxicology 9 (3): 113-134, 2015

Kamali, M. and Z. Khodaparast, 2015. Review on recent developments on pulp and paper mill wastewater treatment. Ecotoxicol. Environ. Saf., 114: 326-342.

Mahida, U. N. (ed). 1981. Water pollution and disposal of wastewater on land. New Delhi, 335p.

Massawe S. B., Olorunnisola A. O., A. Adenikinju 2016. The Environmental Challenges of Biomass Utilisation for Combined Heat and Power Generation in a Paper Mill in Tanzania. J Fundam Renewable Energy Appl 6:202. doi:10.4172/2090-4541.1000202

Mehta, J., Sharma, P. and A.Yadav 2014. Screening and Identification of Bacterial Strains for Removal of COD from Pulp and Paper Mill Effluent. Advances In Life Sciences And Health Volume 1, Number 1, August 2014Barapatre and Jha, 2016

Orori, B. O., Etiégni, L., Rajab, M. S., Situma, L. M. and Ofosu-Asiedu, K., 2005. Decolorization of a Pulp and Paper Mill Effluent in Webuye by A Combination of Electrochemical and Coagulation Methods. In Pulp and Paper Canada 106:3 (2005) pp. 21 to pg. 26.

Saez, C., Canizares, P., Llanos, J., and M.A. Rodrigo. 2013. The Treatment of Actual Industrial Wastewaters Using Electrochemical Techniques, Electrocatalysis, 4, 252-258, DOI: 10.1007/s12678-013-0136-3

Sumathi, S. and Hung, Y.T. 2006. Treatment of pulp and paper mill wastes, In: *Waste treatment in the process industries.* (Eds: Wang, L.K., Hung, Y.T., Lo, H.H. and Yapijakis, C.) Taylor and Francis, USA, p. 453-497. Monte *et al.,* 2009;

Sutton, J. and D. Olomi, 2012. An Enterprise Map of Tanzania. London and Dar-esSalaam: International Growth Centre (IGC).

Thompson, G.; Swain, J.; Kay, M. and Forster, C. 2001. The treatment of pulp and paper mill effluent: a review. Bioresource Technology, Vol. 77, pp. 275–286.

UNEP. (1981). Environmental Management in the Pulp and Paper Industry, Vol. 1, 234p.

Zongo, I., Hama Maiga, A., Wéthé, J., Valentin, G., Leclerc, J-P., Paternotte, G., and F., Lapicque. 2009. Electrocoagulation for the treatment of textile wastewaters with Al or Fe electrodes: Compared variations of COD levels, turbidity and absorbance, Journal of Hazardous Materials, 169, 70-76, DOI: 10.1016/j.jhazmat.2009.03.072

Solar Heat for Industrial and Agricultural Processes

Medium temperature solar thermal installation for industrial thermal storage of bituminous

Mircea Bunea, Catherine Hildbrand, Sara Eicher, Alexis Duret, Stéphane Citherlet

HEIG-VD, LESBAT, Solar Energy and Building Physics Laboratory
Avenue des Sports 20, CH1400 Yverdon-les-Bains, Switzerland

Abstract

In this article, the performance analysis of a medium-temperature solar thermal installation integrated at the Colas Suisse SA industrial site in Yverdon-les-Bains (CH) is presented. The innovative collector system supplies energy for the temperature maintenance of bituminous products and provides part of the heating needs of the administrative building in the industrial site. The initial objective of Colas Suisse SA was to cover approximately 60% of the thermal energy demand of the site with solar energy. Field measurements provided an insight into the overall operation of the installation during 2015 to 2017. Despite improvement of the system, the performance of the collector field both in terms of energy and financial aspects was found below the expected values. On the other hand, simulations have shown the potential for improvement offered by the current installation. Despite non-optimal operation of the solar installation, a life cycle impact assessment have indicated interesting potential primary energy savings and greenhouse gas reductions.

Keywords: solar thermal, medium temperature collectors; industrial applications; bituminous storage; numerical simulation; measurements

1. Introduction

In Europe, the industrial sector accounts for one fourth of the total final energy consumption (Eurostat, 2015) of which more than two-thirds is used for heating purposes (IRENA, 2015). Moreover, 26% of these process heating concerns low temperatures (< 100°C) while 19% uses heat between 100 and 400°C (Krummenacher & Muster, 2015). A huge potential exists to provide low to medium temperature processes with heat from existing conventional and advanced collector technologies. It is, therefore, very important to capitalise on this technical potential as today solar energy is reported to cover less than 0.1% of current industrial heat demand (Mauthner et al., 2016).

In 2012, as part of its emission reduction plan, Colas Suisse, a Swiss subsidiary of Colas International, world leader in construction and maintenance of transport infrastructure, decided to overhaul the heating system of its industrial site in Yverdon-les-.Bains so that 60% of its thermal energy demand is met through solar energy. A real application of solar thermal integrated in the road construction industry is presented here, where heating needs for bitumen and emulsion storage can be met by temperatures below 200 °C. The thermal and environmental evaluation of this real solar thermal installation is described based on field measurements and numerical simulations.

Bitumen and emulsions are used in road construction, an industry largely relying on fossil fuels, to provide low to medium temperature heat demands. The operating temperature for bitumen emulsion ranges from 60 to 75°C while for bitumen it ranges from 160 to 200°C. These hot products must be stored, transported and used hot to maintain their workability. Conscious of the important potential of solar heating in the industrial context, but also of the economic and environmental issues related to fossil energy use, COLAS Switzerland, has implemented a medium temperature solar thermal system to maintain its bituminous products tanks at the required temperature. The objective was to maximise the share of heat provided by solar heating and optimise the overall energy system.

doi:10.18086/swc.2017.26.01 Available at http://proceedings.ises.org

2. System description

The industrial site located in Yverdon-les-Bains (CH) is composed of a building and the bituminous storage installation situated next to the building. The advantage of this sector is that road construction in Switzerland operates only in the summer season from April to September when solar energy is most available.

A solar collector field was integrated to this industrial site during 2012, but several problems related to wrong hydraulic setups and failures of the control system were identified and therefore important modifications of the installation were performed at the beginning of 2015. The new hydraulic scheme is shown in Fig.1.

Thirty-five solar collectors type C2 (175 m^2 aperture area) manufactured by SRB Energy were installed on the site to cover an important share of the thermal energy demand of the industrial site. These collectors are flat plate collectors placed in front of two cylindrical mirrors and requires no solar tracking device. They present a very high efficiency at temperatures above 200 °C due to the ultra-high vacuum inside the collector (10-8 mbar at ambient temperature). Thermal oil is used as heat transfer fluid for this system.

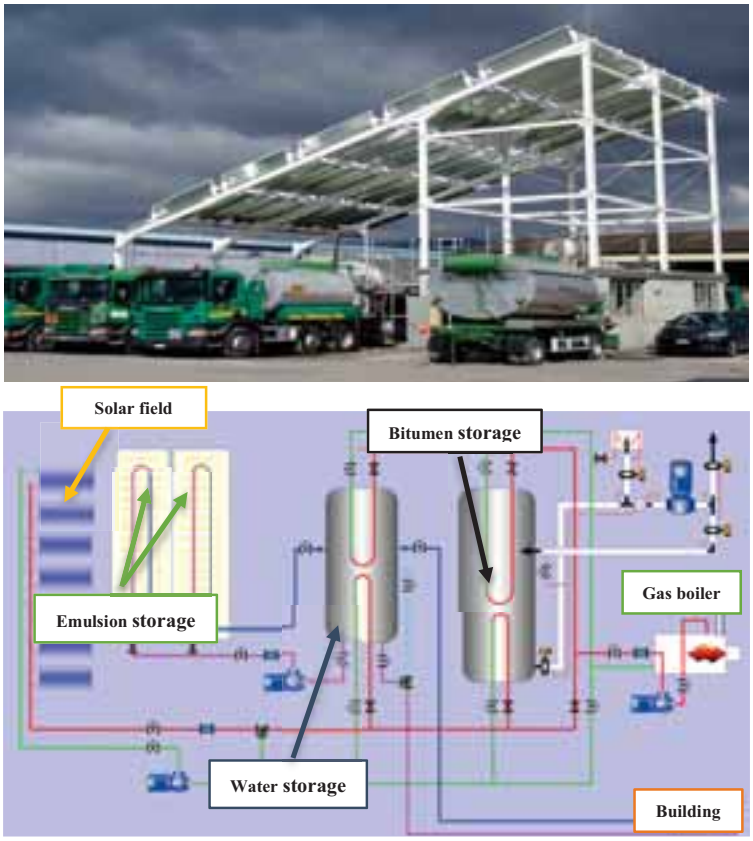

Fig. 1: Picture of the solar installation (up); Simplified representation of the solar thermal installation at COLAS SA after technical modifications (down)

For this particular site, energy is supplied at two different temperature levels:

- Between 50 and 90°C for space heating and domestic hot water for the building as well as to keep emulsions (mixture of water and bitumen) at a specific temperature.
- Between 160 and 190°C for bitumen storage, also depending on the bitumen's characteristics.

Four storage tanks are also present on the site (see Fig. 1): two 50 m^3 emulsion storages, one 70 m^3 bitumen storage and one 27 m^3 water storage. The latter is used for both building and emulsion heat demand. With the exception of the water storage tank, all other tanks have a variable filling level as the tanks are daily loaded and unloaded depending on the demand.

The solar energy deliver priority is to the water tank in order to lower the operating temperatures of the solar collector field and implicitly maximise collectors' efficiency. If this storage reaches the set point temperature,

solar energy is delivered to the bitumen storage at higher temperature level. Whenever solar energy is not available, a 250 kW back-up gas boiler supply the required energy. For further details on this solar thermal installation, please refer to Bunea et al. (2016).

3. Field measurements results

Follow-up field measurements and monitoring of the installation have shown the operation of the system as a whole from April 2015 to September 2017.

Bunea et al. (2016) have shown detailed analyse of the system for one year operation. It has been highlighted that the solar yield is strongly influenced by the overall system management. Therefore, it is very important to supply solar energy for low temperature applications (space heat and emulsion needs) in order to optimise collector's efficiency.

Measurement of the collectors' efficiency have shown an important discrepancy between the accredited test values and the measured ones, see Fig. 2. Differences observed for the optical efficiency (15%) can be partly explained by eventual dust or bituminous particles deposits on the collector glasses and mirrors. A thermographic analysis of the solar collectors' field has further suggested that the thermal insulation of the UHV is also not fully ensured for some collectors. Consequently, global efficiency of the collector field is compromised. Differences may also appear as the curve from the certification tests (blue) is given for a fixed irradiation of 800W/m^2 while the measurements are done considering real time fluctuating conditions.

For high operating temperatures, the difference with the theoretical efficiency of the collector exceeds 50%. This highlights the fact that extrapolation of certified tests results beyond 100°C is not appropriate for evaluating these solar thermal collectors.

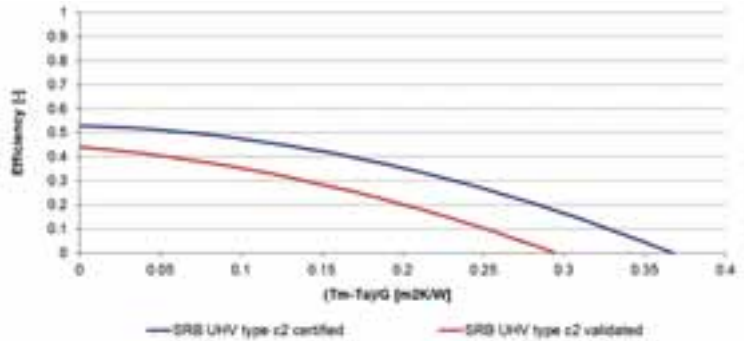

Fig. 2: Comparison of SRB type C2 collector efficiency from certification testing and field measurements

This section presents the evolution of the system operation during three full bitumen seasons from April 2015 to September 2017. Globally it can be seen that the bitumen loaded and unloaded activites in the tank are constantly decreasing every year, which means less activity for Colas and implicitly lower energy consumption, see Fig. 3. The reason for this low activity is the large number of roads built and/or repaired before 2015 that imply no important road work after that. This points out the strong irregularity of the consumption profile over the different years.

Fig. 3: Quantity of bitumen loaded and unloaded in the bitumen tank

This low activity has also an impact in the solar field production due to a decreasing energy demand, but Fig. 4 shows that the solar yield is relatively constant over the years. This happens because the control management gives priority to the low temperature heat demand and therefore most solar energy is delivered to the water storage with only 10 to 21% of solar energy delivered to the bitumen storage yearly.

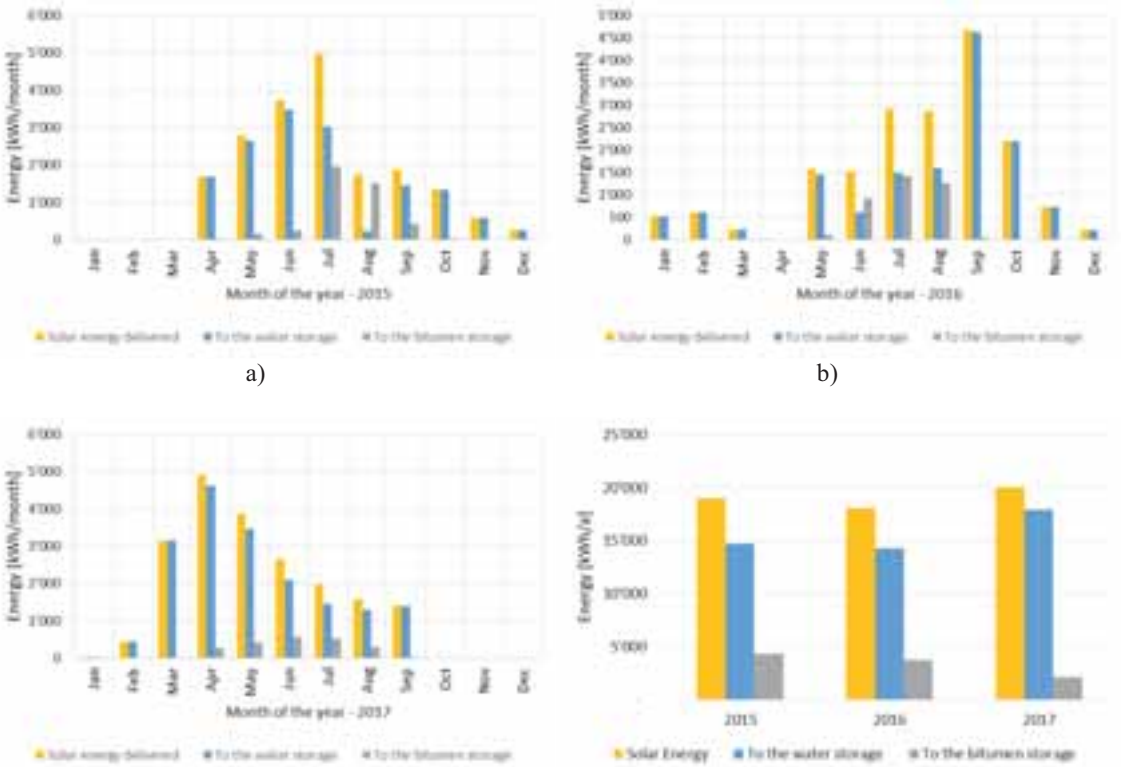

a) b)

c) d)

Fig. 4: Solar energy delivered to the system. a) in 2015, b) in 2016, c) in 2017 and d) yearly

Fig. 4 also indicates that the solar production profile over one year is also very different not only because weather conditions vary, but particularly because of the high irregularity of the demand profile due to the different construction sites and their specific demand for a given year. The control strategy and the eventual breakdowns occurred at different points of the system can also affect considerably the solar efficiency. For example, a breakdown in the emulsion system in August 2015 caused a drastic decrease in solar production, with sensibly the same weather conditions as July. Under this configuration, solar collectors delivered energy mainly to the bitumen storage, operating at higher temperatures, which greatly reduced the efficiency of the solar thermal system. Another breakdown of the system forced the operator to completely shut off the solar pump from March to early May 2016, reducing to 0 the solar energy delivered to the system during this period.

The year 2017 was characterised by the non-utilisation of the emulsion products stored on site, a strategic decision taken by Colas. Consequently, the reduction of the low temperature energy demand during the bitumen season decreased the solar yield during the summer of 2017. This points out, once again, the tremendous influence of the heat demand on the heat supply for low exergy production devices like solar thermal collectors.

As the solar collectors supply energy to the water tank, their performance changes from that when energy is delivered to the bitumen tank due to their different operating temperature. To illustrate this Fig. 5 shows a comparison of the performances under these two supply configurations against the daily radiation.

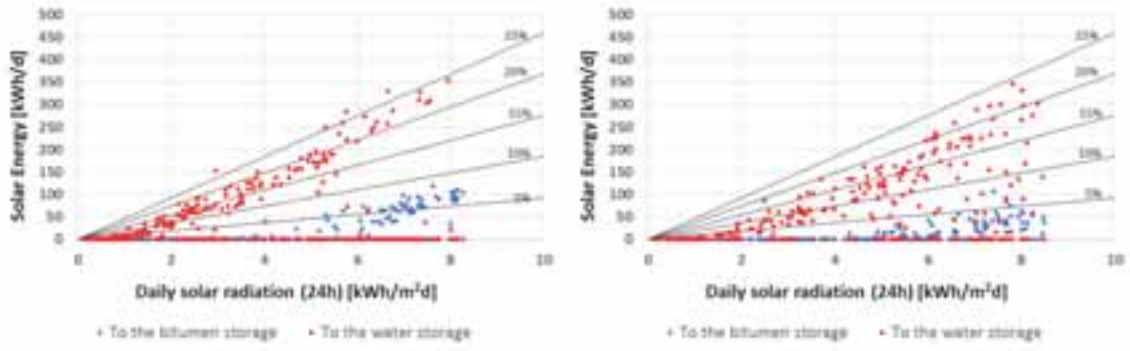

Fig. 5: Performance distribution of solar collectors. a) for 2016, b) for 2017

Overall, the performance is below expectations under all operating modes. The distributions indicate that the collectors' performance decrease when charging the bitumen tank (blue dots) with values below 10%. However, when delivering energy to the water tank (red dots) the performance is improved and could reach 25%. In this case, scattering of the data is more pronounced because of the different utilisation modes of the water tank. Data points at 0% performance correspond to days where the collectors' pump was operating but no heat was delivered to any of the two tanks. This happens because the operating temperature is lower than the storage tanks temperature. Consequently, 35% of the total energy used by the solar pump was spent for circulation only, clearly revealing a controller malfunction.

An evolution of collector's efficiency can be observed between the two years of operation and this for both operation modes. In 2016, when delivering energy to the water storage, the collector field operated with a mean efficiency around 20%, while in 2017 the efficiency decreases at around 15% for this application. Additionally, when delivering energy to the bitumen tank a decrease from ~7% in 2016 to less than 5% in 2017 is observed. The main reason for this decrease could be related to the vacuum loss inside the solar collectors, increasing the thermal losses of the collector itself.

Another point highlighted during this project was the important energy consumption needed for heating a few meters of hydraulic ducts used for loading and unloading the bitumen tank. These pipes are constantly maintained at 220°C to enable sufficient fluidity and proper workability of the bitumen. Fig. 6 shows that in the first years of operation the energy consumed for this circuit was in the range of the energy used for maintaining several tons of bitumen in temperature. Advised by LESBAT, different measures were applied in 2017 by Colas, acting both on the control management and on the thermal insulation of the pipes. These measures enabled a reduction of this consumption to less than 50% of the energy needed for bitumen maintain in temperature during 2017.

Fig. 6: Breakdown of energy delivered by the gas boiler

4. Numerical simulation results

Numerical simulations of the installation performed with Polysun, showed the potential for energy management improvement. A parametric study was carried out to study the effect of different operating and design parameters on the overall installation performance. For example, improving emulsions processing with heat provided by solar energy or gas boiler through the water storage could result in 25% increase of the annual solar production, see Fig.7. In addition, improvements of the collector efficiency could double the current annual solar production.

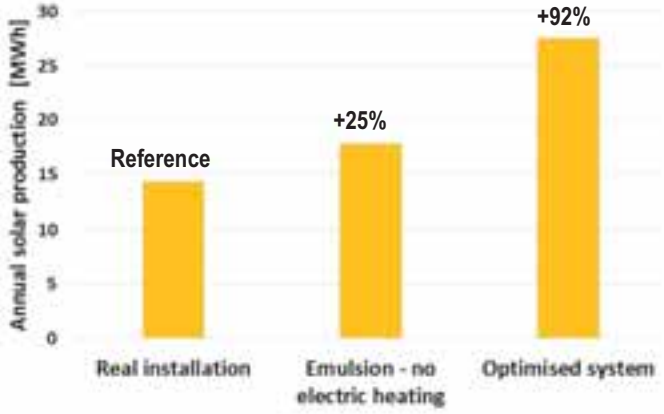

Fig. 7: Simulated annual solar production through system optimisation

Other simulations to predict the effect of other parameters such as collector surface area or type, on the annual solar production, demonstrate that the installation as a whole could absorb much more solar energy, see Fig. 8.

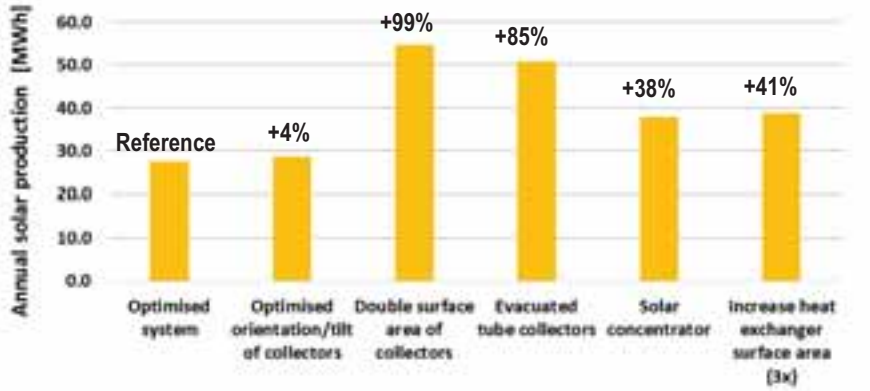

Fig. 8: Comparison of the predicted annual solar production for different configurations

It can be seen that optimisation of the orientation and tilt of current installed collectors do not significantly increase the annual solar production. However, doubling the collector surface area could potentially double this production mainly because the share of solar heating in the reference, optimised installation, is still minimal. Interesting to notice is the 85% increase in solar production by replacing the SRB collectors with evacuated tube collectors with equivalent aperture area. This type of collector is, nevertheless, not able to provide heat in the temperature range of bitumen processing, the primary reason for considering solar thermal integration in this industrial process.

The use of solar concentrators also indicates an increase in solar production (up to 38%). In all these simulations, most of the solar energy harvested is supplied to the water tank but solar heating of the bitumen tank presents a better efficiency when compared with the two other collectors. Disadvantages of this technology are the additional investment and operating costs as well as the increase of the effective space occupied by the system. Finally, following observations that the heat exchanger performance in the tanks was not optimal, simulations were used to investigate the effect of varying the heat exchanger surface area on the annual solar production. As the heat exchanger area is increased the solar production increases considerably, demonstrating that the actual heat exchange surface is largely undersized.

5. Financial analysis

In order to estimate the financial efficiency of the solar system installed by Colas in Yverdon-les-Bains and to evaluate the solar energy cost, a short financial analysis was conducted taking into consideration costs given by the industrial partner and measurements operated on site.

The total system investment cost was evaluated at 365 kCHF (1'984 CHF/m^2 – aperture area). Data and assumptions made for cost evaluations are given in Table 1 and the breakdown of these costs is given in Fig. 9 a). This shows the low share (39%) of the solar collector field compared to the system integration (60%). The imposing stainless steel structure designed to hold the collector field was very costly and significantly increases the overall system cost. Moreover, this structure required some modifications after its installation in order to meet local standards in terms of aesthetics.

Tab. 1 Financial analysis – Data and assumptions

Data/assumption	Value
Investment cost	380'200 CHF
Subsidies	15'000 CHF
Operation & Maintenance costs	8'000 CHF/y
System life span	20 years
Interest rate	3 %
Annuity factor	6.72 %

The price of this system is therefore much higher than conventional prices for solar thermal installations (Mauthner et al., 2016), but it must be considered that this was a pilot project, first of its kind, and almost everything was custom made. Of course, there is a lot of room for cost optimisation, starting with canceling the holding structure and improving the maintenance of the system. The solar collector manufacturer should also try to reduce the collector costs for a better competitiveness on the market.

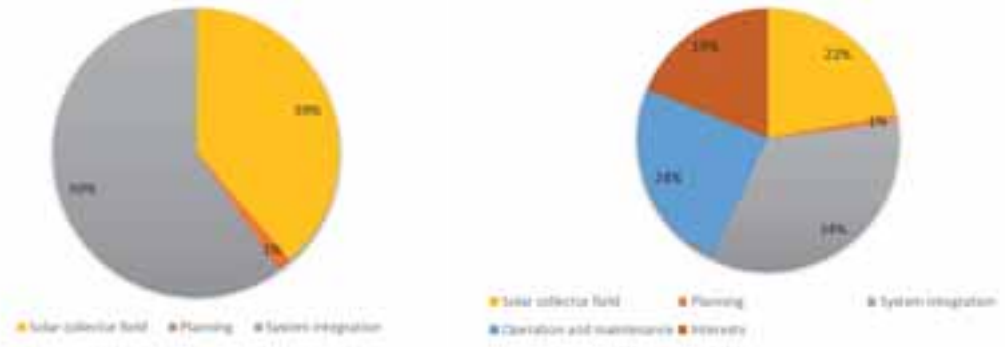

a) b)

Fig. 9: Solar system cost breakdown for the Colas industrial site: a) Investment costs, b) costs over the life span

Energy costs were evaluated using the uniform capital recovery method. By adding the operating and maintenance costs to the total investment cost and taking into account the interest rate, the cost of solar energy is obtained and can be compared to other conventional energy sources. These costs were calculated for both the real operation of the system and for an optimised system as presented in the previous section (numerical simulations).

The results give 1.80 CHF/kWh in the actual operation mode which is far from being satisfying and the reason for this high energy cost is mainly the investment cost, but also the non-optimal system operation. With an optimised system, the price is reduced to 1.18 CHF/kWh which is much better, but it is still 10 times higher than the actual price of natural gas paid on site. Therefore, an estimation of this price was calculated with an optimised investment cost, not taking into account the holding structure, and reducing by 50% the operating and maintenance spending. The result gives 0.47 CHF/kWh, which can be acceptable for this kind of pilot project.

Furthermore, if evacuated tube collectors were used instead of the SRB collectors the price could be reduced to 0.11 CHF/kWh considering an investment cost of 500 CHF/m^2. This price could be easily reached for important collector fields, without special holding structure (Mauthner et al., 2016). In this case, solar energy can be

considered as competitive with any other energy source, but once again, this system could only provide low temperature level energy demand and could not supply the bitumen storage tank.

6. Life cycle impact assessment results

A life cycle impact assessment was carried out to quantify the environmental impacts of the solar installation. Methodology details and indicators considered in this study have been described elsewhere; please refer to Bunea et al. 2016 for additional information.

5.1 Impact of the solar installation

The analysis aims to estimate the environmental impact of the solar installation (solar collectors, pipework components and supporting structure) to compare to the potential energy savings it could possibly bring. Energy consumption of the installation was defined based on monthly simulations. Fig. 10 shows that impacts from the supporting structure are the major contributor from the overall solar installation.

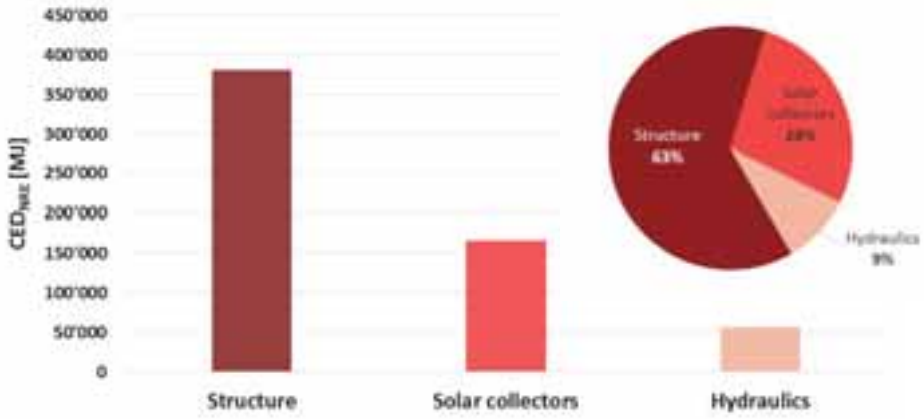

Fig. 10: Calculated environmental impacts of the solar installation, CED_{NRE}

5.2 Potential environmental savings

The potential environmental savings of using a solar thermal installation in this type of heating process are compared to a solar-free installation. Three installation configurations are considered:

- No solar thermal system
- Solar thermal system (current installation)
- Solar thermal system (optimised case)

The impacts related to energy use in the form of gas and electricity as well as impacts from material components of each configuration are presented in Fig. 11.

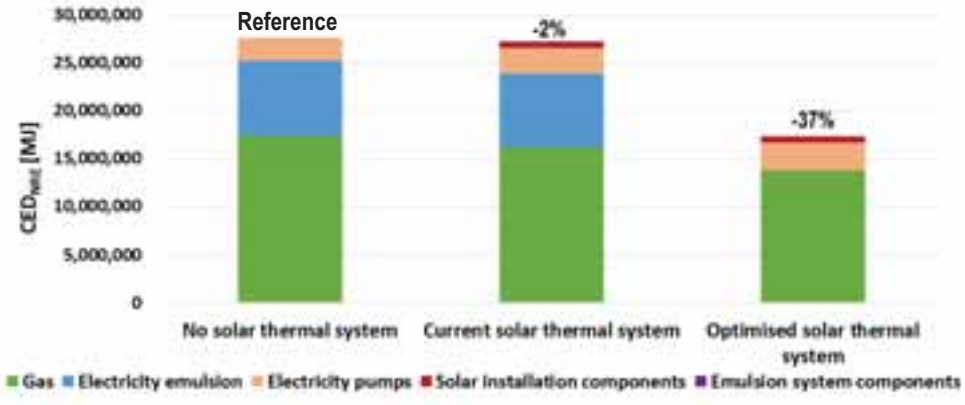

Fig. 11: Comparison of CED_{NRE} for different configurations

Integration of a solar thermal system in this type of industrial process potentially contributes to primary energy savings. This value is quite low for the case of an installation operated under current real conditions. The reasons are twofold: emulsion heating is primarily electric which greatly contributes to increase of the CED_{NRE}; secondly, under these conditions solar production is penalised because of the low water tank energy demand. In contrast, primary energy savings are more pronounced in the case of the optimised system since emulsion heating is now entirely supplied either with solar or gas. This configuration also results in an increase of the solar production, which directly affects gas consumption.

An environmental cost-benefit analysis showed that the energy savings brought by the solar installation could be compensated the additional material impacts within twelve years. This time is reduced to two years if the installation operates under optimal conditions, see Table 2.

Tab. 2 Payback time of the environmental cost of modifications

Configuration	CED_{NRE}
Current solar thermal system	11.5 ans
Optimised solar thermal system	1.2 ans

7. Conclusion

The behaviour and performance of a medium–temperature solar industrial process for bitumen storage was investigated based on measurements and simulations for subsequent optimisation of the process. Measurements over 30 months of operation revealed a very variable consumption profile over the year, but also from one year to another. Important differences, up to 50% at 220°C, between the certified performances of the solar thermal collectors and measured were observed during this project and consequently low specific solar production, around 100kWh/m2. The reason for this low productivity is not only the poor performances of the collector itself, but also the non-optimised control management of the system.

Simulations show that there is room for improvement and that the solar production could be roughly doubled if the system operates as designed. Furthermore, simulations prove that the heat exchangers designed for both thermal storages are undersized. Increasing solar collector area results in higher solar productivity, but still relatively low annual collector field efficiency. Evacuated tube collectors are shown to be a cost-effective configuration for this system, but these collectors could only supply energy at low temperature level and not to the bitumen tank, as the system was designed initially.

The financial analysis shows a cost of solar energy supplied to the system at 1.80 CHF/kWh. This value could be reduced to 1.18 CHF/kWh in the case of an optimised system, but it is still very high when compared to conventional energy prices. The highest share in the investment cost is not generated by the collector field, but by the system integration and mainly by the supporting structure. Therefore, with a lighter system integration and a better operation and maintenance management, the energy cost can achieve 0.47 CHF/kWh, which can be acceptable for a pilot project.

The life cycle impact assessment of the solar installation showed that, as for the investment cost, the infrastructure impacts predominate over the entire life cycle, accounting for over 60% of the total CED_{NRE}. Energy savings brought along by the solar installation more than compensate the additional material and energy related impact of integrating such a system. Less than 2 years environmental return on investment periods were found in the case of an optimised solar bitumen storage system.

8. References

Bunea, M., Hildbrand, C., Eicher, S., Duret, A. and Citherlet, S., 2016. Analysis of a Solar Thermal Installation for Medium Temperature Industrial Applications. Eurosun 2016 – ISES Conference Proceedings.

Eurostat. Energy, transport and environment indicators – 2016 edition

IRENA. Solar Heat for Industrial Processes. EA-ETSAP and IRENA 2015, in: Technology Brief E21.

Krummenacher, P., Muster, B., 2015. Methodologies and Software Tools for Integrating Solar Heat into Industrial Processes.

Mauthner, F., Weiss, W., Spörk-Dür, M., 2016. Solar Heat Worldwide. Markets and contribution to the Energy supply 2014

SIMULATION AND OPTIMIZATION STUDY ON A SOLAR HEATING HOUSEHOLD BIOGAS DIGESTER SYSTEM

Yaowen Chen, Yanfeng Liu, Dengjia Wang, Tao Li, Yong Zhou, Daokun Wang

Xi'an University Of Architecture and Technology

Abstract

A solar heating household biogas digester system (System C) coupled with auxiliary heating source and operational control system is proposed in this paper. The mathematical model and TRNSYS simulation model of the system were established. Firstly, the heating effect of System C was compared with that of System A (without auxiliary heating and temperature control system) and System B (with auxiliary heating system and without temperature control system). Secondly, the influence of the insulation thickness and the collector area on solar fraction was analyzed. The results show that System C could keep the temperature fluctuation range of manure at ±1°C under the setting condition. Besides, the solar fraction of the system C is higher than the system B, the daily energy net production of System C is higher than that of the system A and B with the value of 19.2 kWh. The solar fraction increased with the insulation thickness increased as logarithmic function, which has the most significant growth rate when the collector area is 14 m^2. In addition the solar fraction increases with the increase of the collector area in the form of sigmoid function. The research results provide a basis for the optimization design of solar heating household biogas digester system.

Keywords: Solar heating; Household biogas digester; TRNSYS simulation; Solar fraction

1. Introduction

The household biogas digesters can provide residents with the necessary energy (biogas) for cooking, lighting, heating and deal with the manure waste of people and livestock. Household biogas digesters are widely used all over the world, especially in developing countries such as China and India (Surendra, Takara, & Hashimoto, 2014). In recent years, the biogas industry of China has developed rapidly. China had possessed 41.93 million household biogas digesters by 2015 (Academy of state administration of grain, 2017).

Temperature has a significant influence on biogas production rate. Three fermentation processes exist, corresponding to different fermentation temperatures, namely, thermophilic fermentation (45-60 °C),mesophilic fermentation (25-40°C),and normal temperature fermentation (10-25 °C) (El-Mashad, Zeeman, & van Loon, 2004a).When the temperature of the manure is lower than 10°C, the biogas production of the digester is very little (Kocar and Eryasar, 2007). During the winter in northern of China, a large number of digesters have been idled due to less biogas production. However, the insufficient energy supplied by the biogas digester and the energy demand of heating and hot water in winter increases rapidly form a sharp contradiction with. Therefore, it is the key to solve this problem that increase the biogas production of the digester by improving the temperature of digester.

At present, many heating methods for the digester such as coal fired boiler heating, electro thermal membrane heating, biogas boiler heating, solar heating and heat pump heating were proposed (Li, Guo, & Qin, 2011). Some heating methods are not suitable for the household biogas digester due to the constraints of economical and environmental conditions. The solar heating for biogas digester has become the research focus with the advantages of less pollution, lower manufacture and operation cost. Hassanein et al. (2015) proposed a passive heating technique to increase the temperature of the biogas digesters using two solar greenhouses, one surrounding the digester and the other heating the digester inlet. The simulation results showed that the digester with the modifications could reach adequately high temperatures in the winter. Although the cost of solar passive warming technology is low, the range of manure temperature increasing is limited, so the biogas production of biogas digesters is still little, which can only meet the needs of cooking.

The system consists of high efficiency solar collectors and other equipment is also the main research direction of

doi:10.18086/swc.2017.26.02 Available at http://proceedings.ises.org

solar heating digesters. Axaopoulos, et, al. (2001), proposed an active solar heating biogas digester system, and established the corresponding system mathematical model. The performance of the system is studied both by simulation and experiment, and the results show that the system could efficiently increase the manure temperature and reduce the heat loss of the digester envelope at the same time. The energy required for the digester heating in the system is directly supplied by solar collectors, so that the temperature of the manure is subject to fluctuations in the solar radiation. However, the biogas production rate will decrease when the manure temperature changes more than 3 °C (Zhang, et al., 2016). El-Mashad et al. (2004b) and Pollard & Blanchard (2014) have designed a solar heating digester system with auxiliary heater. When the energy supplied by solar collector is insufficient, the auxiliary heat collector is worked to ensure that the digester runs under relatively stable conditions. But the system above may run abnormally for them without any monitor and control system of manure temperature, auxiliary heating source and the solar collector, which leads to the lower system efficiency and solar fraction and larger conventional energy consumption.

In this study, a solar heating digester system with auxiliary heater and heating control system is proposed. The heating effect for the biogas digester and net energy production performance of the system under different system forms were compared through TRNSYS simulation. Besides, the influence of the insulation thickness and the collector area on solar fraction was analyzed.

2. System description and Modelling

2.1 System description

As shown in Fig. 1, the solar heating household biogas digester system is composed of heating collection and heating utilization loop, the above loop were connected by heat storage water tank. The heating collection loop is consisted of flat plate collector, circulation pump-1, expansion tank and pipeline. The heating utilization loop is consisted of underground biogas digester, heating coil, heat storage tank and auxiliary heater. The energy collected from solar collector is used to heat the digester and the extra heat is storaged in the heat storage water tank in the day time. The heat in the water tank is transferred to heat the digester and the insufficient energy is supplied by the auxiliary heater in the nighttime. The control system automatically controls the opening and closing of the components according to the pre-set control strategy by monitoring the temperature parameters in the system loop.

2.2 Assumptions

There are several assumptions used for establishing mathematical model of the solar heating household biogas digester system:

(1) Physical properties of the soil, digester material, and insulation material are uniform (Perrigault, Weatherford, & Martí-Herrero, 2012).

(2) During biogas fermentation, microbial heat generation is neglected (Hashimoto, & Chen, 1979).

(3) The heat carried by the biogas flow during biogas fermentation is neglected.

(4) Liquid manure in the digester is assumed to be water.

(5) The temperature of the manure in the digester is uniform.

2.3 Mathematical model description

The mathematical model of the solar heating digester system consists of the system energy balance equation and the mathematical expressions of the subcomponent. The energy balance equation of the system could be written as:

$$\rho_m V_m c_m \frac{dT_m}{d\tau} = Q_{heating} - Q_{cover} - Q_{floor} - Q_{wall} - Q_{feed} \quad \text{(eq.1)}$$

$$Q_{heating} = Q_{col} + Q_{aux} - Q_{loss} \quad \text{(eq.2)}$$

$$Q_{loss} = Q_{loss,\,aux} + Q_{loss,\,tank} + Q_{loss,\,pipes} \quad \text{(eq.3)}$$

where; c_m is the manure specific heat capacity, J kg^{-1} K^{-1}; ρ_m is the manure density, kg m^{-3}; V_m is the manure volume, m^3; T_m is the manure temperature, °C; τ is the time, s; $Q_{heating}$ is the heat supplied by the heating system, W; Q_{cover} is the heat losses through the digester cover, W; Q_{wall} is the heat losses through the digester wall, W; Q_{floor} is the heat losses through digester floor, W; Q_{feed} is heat required to raise temperature of the influent manure to the operating

temperature, W; Q_{col} is the heat supplied by the solar collector, W; Q_{aux} is the heat supplied by the auxiliary heater, W; Q_{loss} is the total heat loss of the system, W; $Q_{loss,\ aux}$ is the heat loss from heater to environment, W; $Q_{loss,\ tank}$ is the heat loss from water tank to environment, W; $Q_{loss,\ pipes}$ is the heat loss from pipes to environment, W.

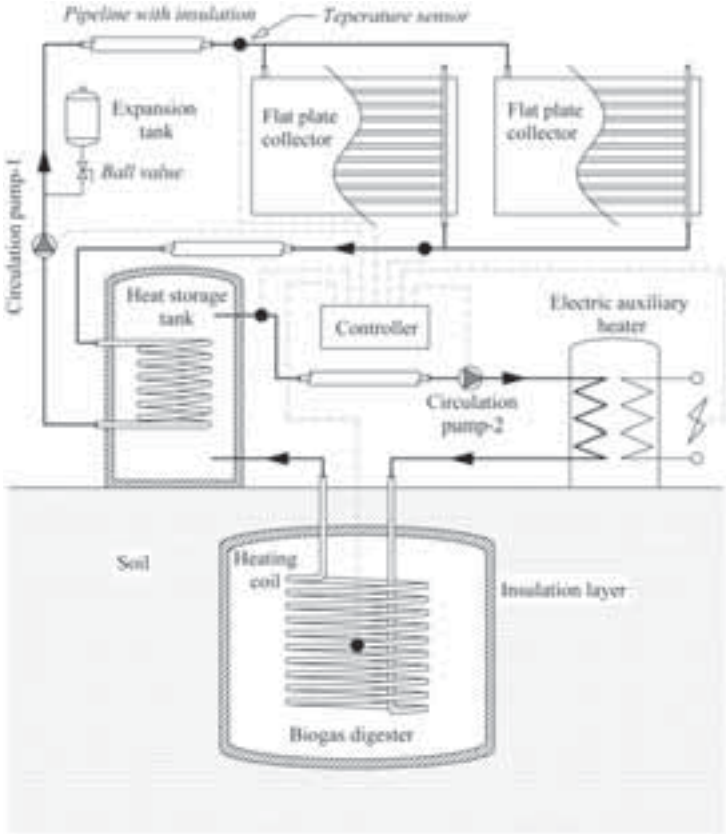

Fig 1. Schematic of the solar heating household biogas digester system

2.3.1 Energy delivered from solar collectors and auxiliary heater

The heat gain from the solar collector can be calculated using following equations (Duffie & Beckman, 1991):

$$Q_{col} = A_{col} I_T \eta_{col} = m_{hm} c_{hm} (T_{co} - T_{ci}) \quad \text{(eq.4)}$$

where A_{col} is the solar collector area, m^2; I_T is the solar radiation rate on the collector surface per unit area, W m^{-2}; η_{col} is the collector efficiency, dimensionless; m_{col} is the mass flow through the collector, kg s^{-1}; c_{hm} is the specific heat capacity of heat medium, J kg^{-1} K^{-1}; T_{co} is the temperature of the fluid flowing out of the collector, °C; T_{ci} is the temperature of the fluid flowing into the collector, °C.

$$\eta = F_R (\tau\alpha)_n - F_R U_{col} (T_{ci} - T_{amb}) \quad \text{(eq.5)}$$

where F_R is the overall collector heat removal efficiency factor, dimensionless; $(\tau\alpha)_n$ is the cover transmittance and the absorber absorptance of the collector at normal incidence, dimensionless; U_{col} is the overall thermal loss coefficient of the collector per unit area, W m^{-2} K^{-1}; T_{amb} is the ambient temperature, °C.

$$F_R = m_{hm} c_{hm} [1 - \exp(-A_{col} U_{col} F' / m_{hm} c_{hm})] / (A_{col} U_{col}) \quad \text{(eq.6)}$$

where F' is the collector fin efficiency factor, dimensionless.

The heat gain from the auxiliary heater can be calculated using following equations:

$$Q_{fluid} = m_w c_w (T_{set} - T_{ai}) \quad \text{(eq.7)}$$

$$Q_{loss,\ aux} = U_a (\bar{T} - T_{amb}) + (1 - \eta_{aux}) Q_{max} \quad \text{(eq.8)}$$

$$Q_{aux} = Q_{max} \quad \text{(eq.9)}$$

$$Q_{\text{aux}} = Q_{\text{fluid}} + Q_{\text{loss, aux}} = \frac{m_{\text{w}} c_{\text{w}} (T_{\text{set}} - T_{\text{ai}}) + U_{\text{a}} (\bar{T} - T_{\text{amb}})}{\eta_{\text{aux}}}$$

(eq.10)

where Q_{fluid} is the rate of heat addition to the water, W; m_{w} is the mass flow rate of water flowing into the auxiliary heater, kg s^{-1}; c_{w} is the water specific heat capacity, J kg^{-1} K^{-1}; T_{set} is the set temperature of heater internal thermostat, °C; T_{ai} is the inlet temperature of auxiliary heater, °C; U_{a} is the overall loss coefficient between the heater and its surroundings, W; $\bar{T}$ is the average temperature of fluid in heater, °C; η_{aux} is the efficiency of auxiliary heater, dimensionless; Q_{max} is the maximum heating rate of heater, W.

The solar fraction is calculated by (Deng et al. 2016):

$$f = \frac{Q_{\text{solar}}}{Q_{\text{solar}} + Q_{\text{auxiliary}}} \quad \text{(eq.11)}$$

where Q_{solar} is the heat supplied by the collector, W; $Q_{\text{auxiliary}}$ is the heat supplied by the auxiliary heater, W.

2.3.2 Heat transfer between digester and soil

Household biogas digesters are usually buried underground, and those heat transfer process are affected by the surrounding soil temperature and soil thermal properties. Therefore, the function of soil temperature field and soil physical parameters are needed to establishing the heat transfer model of the digester (Liu, Chen, & Li, 2017).

The soil initial temperature field can be calculated by (Zhang, Ren, & Mei, 2007):

$$T_{\text{s}}(z, \tau_0) = T_{\text{ave}} + A_{\text{w}} \exp\left(-z\sqrt{\frac{\pi}{ak}}\right)\cos\left(\frac{2\pi}{k}\tau_0 - z\sqrt{\frac{\pi}{ak}}\right) \quad \text{(eq.12)}$$

where T_{ave} is the annual average temperature of ground surface, °C; A_{w} is the annual temperature fluctuation of ground surface, °C; k is the annual fluctuation period, h; a is the soil thermal diffusivity, m^2 s^{-1}; and τ_0 is the initial time, s.

The amount of heat loss from digester to the soil can calculated by:

$$Q_{\text{cover}} = \frac{(T_{\text{m}} - T_{\text{s}}) A_{\text{cover}}}{\left(\frac{1}{h_1} + \frac{\delta_1}{\lambda_1} + \frac{\delta_2}{\lambda_2}\right)} \quad \text{(eq.13)}$$

$$Q_{\text{wall}} = \frac{(T_{\text{m}} - T_{\text{s}}) A_{\text{wall}}}{\left(\frac{1}{h_2 \pi d_1} + \frac{1}{2\pi\lambda}\ln\frac{d_2}{d_1} + \frac{1}{2\pi\lambda}\ln\frac{d_3}{d_2}\right) H} \quad \text{(eq.14)}$$

$$Q_{\text{floor}} = \frac{(T_{\text{m}} - T_{\text{s}}) A_{\text{floor}}}{\left(\frac{1}{h_3} + \frac{\delta_1}{\lambda_1} + \frac{\delta_2}{\lambda_2}\right)} \quad \text{(eq.15)}$$

where T_{s} is the soil temperature, °C; h_1, h_2, h_3 are the convective heat transfer coefficient of inner surface of cover, wall, floor, respectively, W m^{-2} K^{-1}; λ_1 is the thermal conductivity of digester, W m^{-1} K^{-1}; δ_1 is the wall thickness of digester, m; λ_2 is the thermal conductivity of insulating layer, W m^{-1} K^{-1}; δ_2 is the wall thickness of insulating layer, m.

The heat loss caused by manure feeding can be calculated by the formula:

$$Q_{\text{feed}} = m_{\text{f}} c_{\text{m}} (T_{\text{m}} - T_{\text{f}}) \quad \text{(eq.16)}$$

where m_{f} is mass flow rate of the feed liquid, kg day^{-1}; T_{f} is the temperature of the feed liquid, °C.

2.3.3 Biogas production rate

A methane production model was proposed during the anaerobic fermentation process, calculated as (Chen, & Hashimoto, 1978):

$$\gamma = \frac{B_0 S_0}{HRT\,\beta_{\text{methane}}}\left(1 - \frac{K}{HRT \cdot \mu_{\text{m}} - 1 + K}\right) \quad \text{(eq.17)}$$

where γ is volumetric biogas production rate, m^3 CH^4 m^{-3} digester day^{-1}; B_0 is biochemical methane potential, m^3 CH4 kg^{-1} VS; S_0 is influent VS concentration, kg m^{-3}; HRT is hydraulic retention time, days; K is the kinetic constant, dimensionless; and μ_{m} is maximum specific growth rate of micro-organisms, day^{-1} β_{methane} is percentage of methane content in biogas.

K is a kinetic parameter related to the influent VS concentration, and is expressed as:

$$K = 0.6 + 0.0206\text{e}^{0.051 S_0} \quad \text{(eq.18)}$$

Pham et al. (2014) predicted the dynamic methane production based on the Chen et al. (1978) model, making it available for the performance prediction of UHBD. Concurrently, Hashimoto (1982) proposed a relationship between the maximum specific growth rate of microorganisms and the temperature under mesophilic and thermophilic fermentation as:

$$\mu_{\text{m}} = \begin{cases} 0.0026\text{e}^{0.1319 T_{\text{m}}} & 15°\text{C} \le T_{\text{m}} \le 30°\text{C} \\ 0.013 T_{\text{m}} - 0.129 & 30°\text{C} < T_{\text{m}} \le 60°\text{C} \end{cases} \quad \text{(eq.19)}$$

2.3.4 Heat storage tank with immersed heat exchanger

$$\rho_{\text{w}} V_{\text{w}} c_{\text{w}} \frac{\text{d}T_{\text{w}}}{\text{d}\tau} = Q_{\text{hx}} - Q_{\text{in, out}} - Q_{\text{loss, tank}} \quad \text{(eq.20)}$$

Where ρ_{w} is the water density, kg m-3; V_{w} is the manure volume, m3; c_{w} is the water specific heat capacity, J kg^{-1} K^{-1}; T_{w} is the water temperature, °C; Q_{hx} is the heat transfer between the water and the heat exchanger, W; $Q_{\text{in, out}}$ is the heat taken by the hot water, W.

2.4 TRNSYS simulation model description

According to the system mathematical model established in the 2.3 section, the TRNSYS system simulation model (TRNSYS, 2012) is further established, and the details of the model are shown in Fig. 2. The meteorological parameters used in the system simulation are imported by Type 109, the solar collector adopts Type 73, and the auxiliary heat source adopts Type 2b. The coupled heat transfer model of digester and soil (J. Zhao et al., 2008) is consist of the ground coupling model (Type 707b) and thermal storage tank (Type 534) to calculate heat loss through the digester envelope to the ground and hourly manure temperature. The periodic manure feeding was imported into dates readers (Type9e) and New Equation to calculate heat transfer from manure inflow.

The biogas production model is embedded into the solar heating digester system model by using the New Equation to calculate the amount of biogas production during the operation of the system. The detailed TRNSYS components and parameters adopted were explained in Table 1.

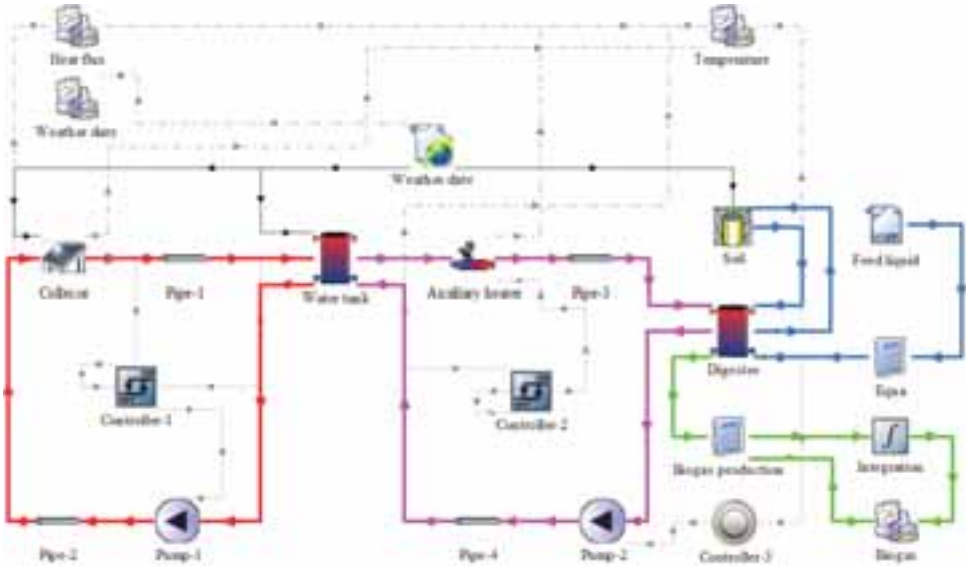

Fig 2. TRNSYS model of the solar heating digester system

Table 1. The main components of the TRNSYS simulation program

Components	Key parameter	Descriptions
Type 73 (flat-plate solar collector)	Collector area: 2, 8, 14, 20, 26 m^2; Bottom, edge loss coefficient: 0.56 W m^{-2} K^{-1}; Collector fin efficiency factor: 0.7;	Calculate the heat supplied by the solar collector
Type 707b (ground coupling model)	Mean surface temperature: 11.64 °C; Amplitude of surface temperature: 18.73 °C; Day of minimum surface temperature: 5 day; Soil column radius and height: 10, 10 m;	To calculate the energy exchange through the bottom, top, and sides of a digester that is entirely buried beneath the ground surface
Type 534 (biogas digester)	Digester radius and height: 1.3, 1.5 m; Thickness of insulation layer: 0, 30, 60, 90, 120, 150 mm; Number of tank nodes: 1 Length of coiled tubes: 32.68 m; Coiled tubes thermal conductivity: 0.33 W m^{-1} K^{-1}; Coil diameter: 1.3 m; Number of tubes: 8; Coil pitch: 0.1 m;	The hourly manure temperature is calculated by heat balance calculation。The gas production rate and total gas production of biogas digester are further calculated
Type 4c (heat storage tank)	Tank volume: 0.5 m^3; Tank heat loss coefficient: 0.5 W m^{-2} K;	The extra heat stored in the heat storage tank, which plays a role in peak shaving and valley filling
Type 6 (auxiliary heater)	Maximum heating rate: 3 kW; Efficiency of auxiliary heater: 0.95;	Added to supply heat when the collector heat is insufficient
Type 109 (TMY-2 weather data)	Import typical meteorological year weather date;	Used for the optimization analysis
Type 1502 (simple thermostat)	Setpoint temperature for stage: 35 °C; Temperature dead band: 1 °C;	Keep slurry temperature at 35±1 °C
Type 2b (controller)	Upper and Lower dead band dT: 1, 8 °C;	Control whether the heat medium flows through the collector
Type 2b (control auxiliary heater)	Upper input temperature Tl: 50 °C; Upper and Lower dead band dT: 0, 5°C;	Control the start-stop of the auxiliary heater
Type 3d (pump)	Flow rates of the solar system and the heat supply were 0.4, 0.4 m^3 h^{-1}, respectively;	Drive system to circulate
Type 31 (pipe)	Pipe length: 8 m; Inside diameter: 0.02 m; Loss coefficient: 0.14 0.5 W m^{-2} K^{-1};	Connect each equipment unit and calculate heat loss of pipeline

The control logical diagram of the solar heating digester system are shown in Fig 3. The control system consists of solar collector control, auxiliary heating control and biogas digesters heating control subsystem. As shown in Fig 1, Firstly, the solar collector inlet and outlet water temperature, heat storage tank outlet water temperature and the manure temperature were monitored by the control system. Secondly, the temperature above would be compared with the temperature or the temperature difference set before. Finally, the automatic control of the heating system were achieved by controlling on and off of the circulating pump and auxiliary heater. The control logic details are as follows:

- The control logical of heat collection system: Comparing the inlet and outlet temperature of the heat collector, the pump-1 opens at next moment when pump-1closes at present and the temperature difference ⩾8 °C, and

the pump-1 closes at next moment when pump-1opens at present and the temperature difference ⩽1 °C.

- The control logical of auxiliary heater: The auxiliary heater closes at next moment when the auxiliary heater opens at present and the outlet temperature of the heat storage tank ⩾ 50 °C, and the auxiliary heater opens at next moment when the auxiliary heater closes at present and the outlet temperature of the heat storage tank ⩽ 45 °C.
- The control logical of digester heating system: The pump-2 closes at next moment when pump-2 opens at present and the temperature difference ⩾1°C, and the pump-2 opens at next moment when pump-2 closes at present and the temperature difference ⩽-1°C.

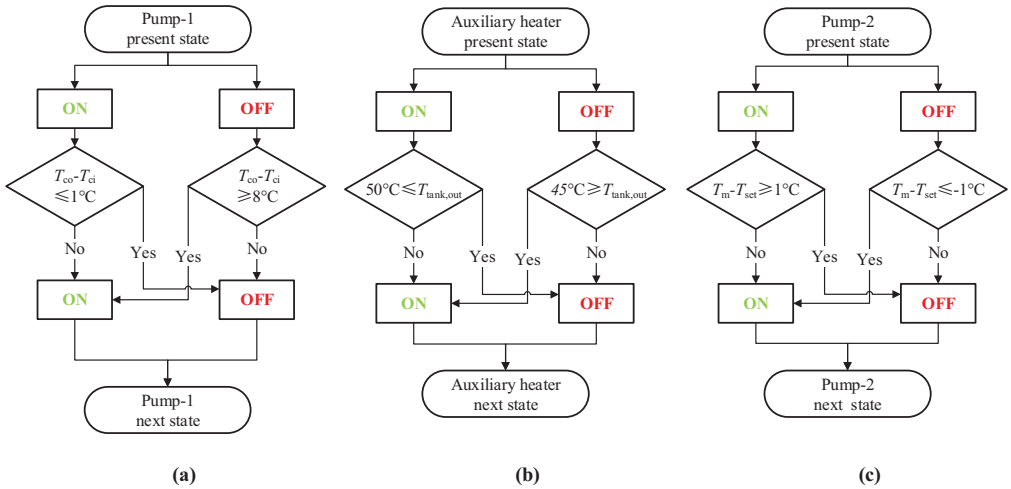

Fig 3. Control logical diagram of the solar heating digester system. (a) the control of heat collection system, (b) the control of the auxiliary heater, (c) the control of the digester heating system.

3. Results and discussion

3.1 Weather data

Lhasa (latitude 29 ° 36 'N, longitude 91 ° 06' E) is located in the Qinghai-Tibet Plateau, the solar energy in this region is abundant and suitable for solar heating digester system application. The weather parameters includes the hourly horizontal solar radiation intensity, the hourly outdoor dry bulb temperature and the underground 1m and 2m soil temperature derived from TRNSYS are shown in Fig 4. The difference of horizontal solar radiation intensity of Lhasa in different seasons is small, and the annual average solar radiation intensity is 227.4W m^{-2}. The outdoor air temperature difference between winter and summer is about 25 °C, and the lowest temperature in winter is about -10 °C. The soil temperature at underground 1m is greater than 0°C throughout the year, and the soil temperature at underground 2m is greater than 5°C throughout the year.

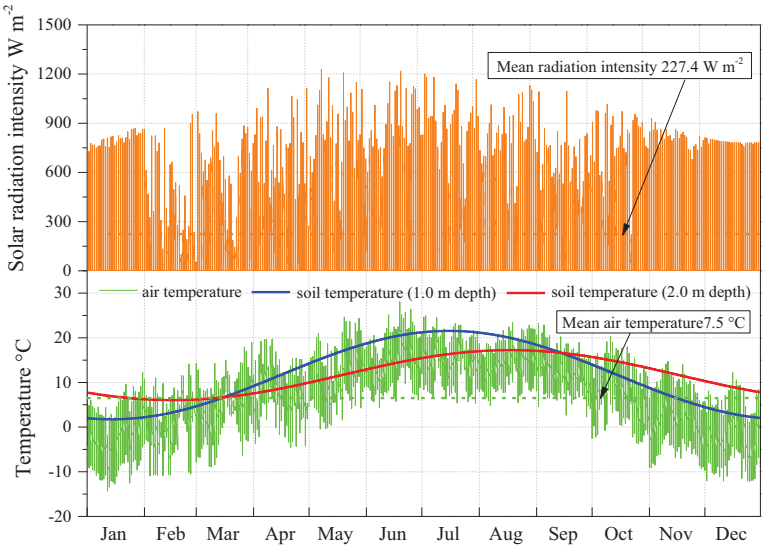

Fig. 4: Outdoor meteorological parameters in Lhasa

3.2 System form optimization analysis

The operation performance of three different forms of solar heating biogas digesters is compared and analyzed. The system A has no auxiliary heat source and no temperature control system, the system B has auxiliary heat source but no temperature control system, the system C has both auxiliary heat source and temperature control system. The polar temperature is 35 °C under the condition of medium temperature fermentation (Y. Lu et al., 2016), so the biogas fermentation temperature in system C is set to 35 °C. The simulated manure temperature under different system forms are shown in Fig5. As shown in Figure, The biogas digester keeps at 6-8°C when it without any heating system, and its biogas production can be basically ignored. The manure temperature of System A is significantly higher than the system without heating measures, the manure temperature can be increased to 25 °C before February, the manure temperature in February to March decreased significantly for cloudy days in February to March is larger than other months(Fig4).

The manure temperature in system B is the largest among three system forms, the manure temperature keeps at 50 °C before February, and the manure temperature decreased continually in February to March. The results shows that the auxiliary heater continually operated has consumed amounts of conventional energy, and the manure temperature fluctuates greatly when the solar radiation is insufficient. The manure temperature of the system C is basically the same as the design temperature, the manure temperature fluctuation is about ±1°C before February and increased slightly which is no more than 3 °C in February and March.

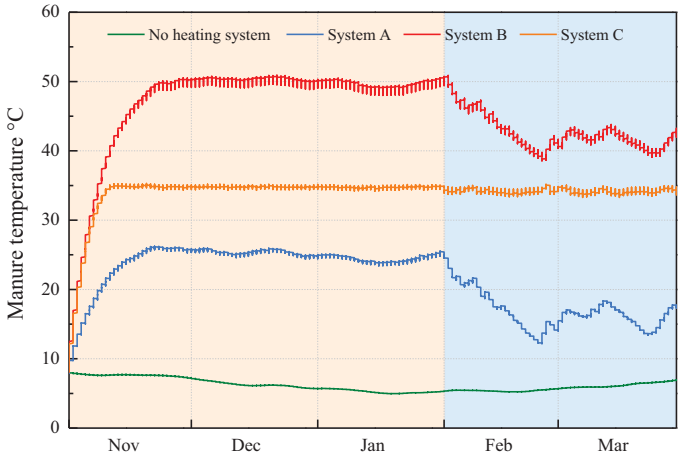

Fig. 5: The simulated manure temperatures under different system forms

Fig. 6 shows heat supply biogas production and the system net energy production of three system forms. As shown in figure, the heat supplied by System B to the digester is the most, followed by System C, and System A provide the least amount of heat. 71% of the heat provided by the auxiliary heater in System B, while 42% of the heat provided by the auxiliary heater and 58% is supplied by the collector in System C. The biogas production of the System B is the largest among three system due to its higher manure temperature. The daily biogas production of System B is 1.41m^3 larger than that of System C, and 4.35m^3 than that of System A. The daily net energy production refers to the converted heat of daily biogas production minus energy consumed by the auxiliary heater. The daily net energy production of System C is the largest (19.2kWh), and daily net energy of System B is the smallest (8.6kWh). The results showed that the performance of System C is better. However, the solar fraction of System C is not high, so it is better to improve the solar fraction of the system by optimizing the components in system.

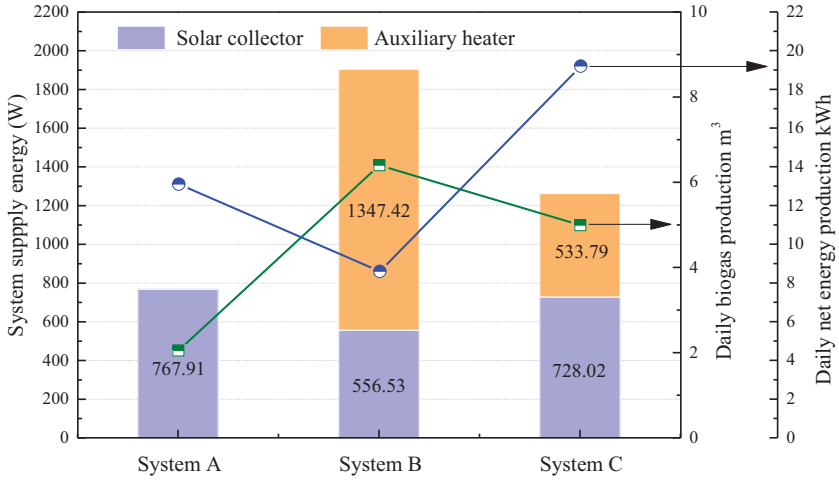

Fig. 6: System Heat supply, daily biogas production and daily net energy production under differant system forms

3.3 The influence of the thickness of insulation layer on solar fraction

The heat supply of the system could be reduced by decreasing digester heat loss. Therefore, the solar fraction can be improved by reducing the energy supply of auxiliary heater under the condition of solar collector area unchanged. Fig. 7 shows the variation of the solar fraction with the insulation thickness. The solar fraction increase logarithmically with the increases of insulation thickness, and the growth of solar fraction is not obvious when the thickness of insulation layer exceeds 120mm. Accordingly, it is necessary to comprehensively compare the increase of investment with the insulation thickness increase and the decrease of the operating cost caused by the reduction of the auxiliary energy to select the economical insulation thickness. Besides, the increase of insulation layer thickness is not significant to enhance solar fraction of the system when the collector area is larger or smaller. The solar fraction increased from 0.47 (no insulation) to 0.73 (150 mm insulation) when the collector area is set as 14 m^2.

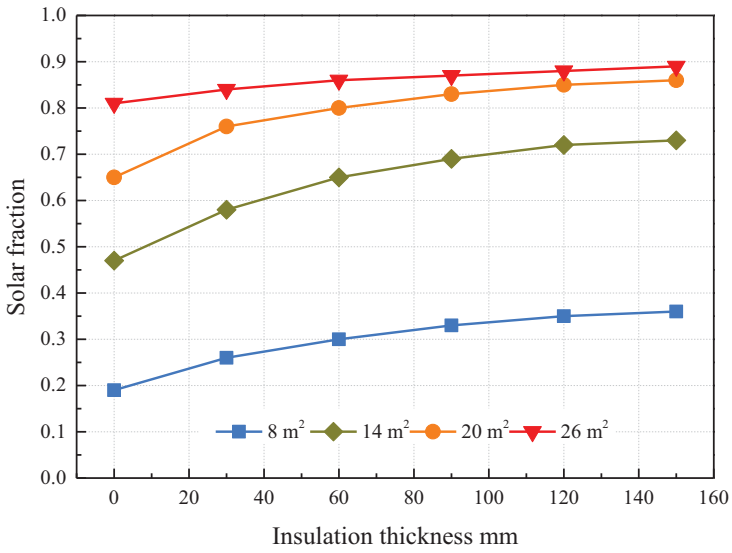

Fig. 7: The variation of the solar fraction with the insulation thickness

3.4 The influence of the collector area on solar fraction

The heat production of the heating collection loop can be directly improved with the increasing of the solar collector area, and then the solar fraction of system can be improved. Fig 8 shows the variation of the solar fraction with the collector area. The solar fraction increases with the increase of solar collector area in the form of the sigmoid function. The solar fraction increases most (from 0.33 to 0.69) when the collector area is increased from 8 m^2 to 14 m^2. Hence, it is also necessary to select the appropriate collector area in combination with economic factors.

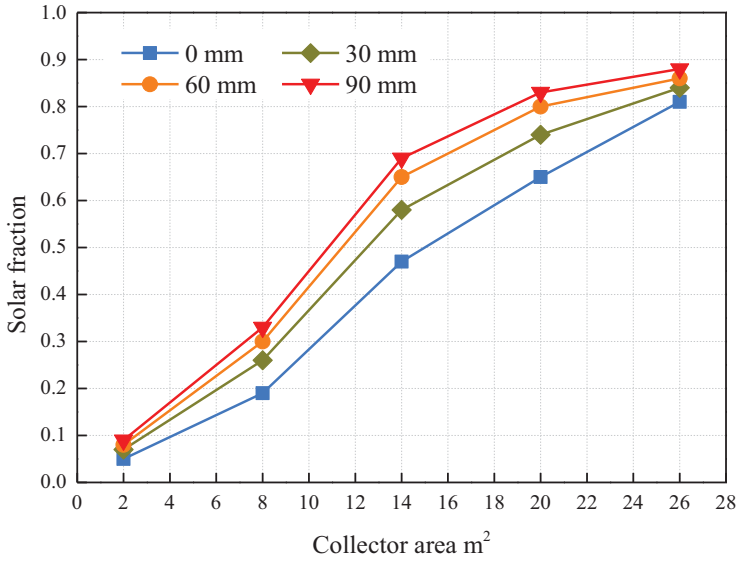

Fig. 8: The variation of the solar fraction with the solar collector area

4. Conclusion

In this study, the mathematical of the solar heating household biogas digester system and the simulation model based

on TRNSYS were established. The conclusions drawn from the results are stated as follows:

- System C could maintain the stable operation of the biogas digester under the designed conditions, and the range of temperature is about ±1 °C. Besides, the solar fraction of System C is higher than that of System B. The daily net energy production of System C is the highest among three system forms with the value of 19.2 kWh.
- The solar fraction increased with the insulation thickness increased as logarithmic function, which has the most significant growth rate when the collector area is 14 m^2.
- The solar fraction increases with the increase of the collector area in the form of sigmoid function. The solar fraction increases most (from 0.33 to 0.69) when the collector area is increased from 8 m^2 to 14 m^2.

Acknowledgements

This research was supported by the National Key Research projects (Nos.2016YFC0700400) and the National Natural Science Foundation of China (Grant Nos. 51378411, 51678468 and 51590911).

References

Surendra, K. C., Takara, D., Hashimoto, A. G., & Khanal, S. K., 2014. Biogas as a sustainable energy source for developing countries: opportunities and challenges. Renewable & Sustainable Energy Reviews, 31(2), 846-859.

Academy of state administration of grain, 2017. The National Rural Biogas Development Plan "In 13th Five-Year", http://www.chinagrain.org/sjkgx/fzghshjk/201702/t20170214_4794.html, (accessed 2017.02.14).

El-Mashad, H. M., Zeeman, G., van Loon, W. K., Bot, G. P., & Lettinga, G., 2004a. Effect of temperature and temperature fluctuation on thermophilic anaerobic digestion of cattle manure. Bioresource Technology, 95(2), 191-201.

G. Kocar, & A. Eryasar., 2007. An application of solar energy storage in the gas: solar heated biogas plants. Energy Sources Part A Recovery Utilization & Environmental Effects, 29(16), 1513-1520.

Li, L., Guo, Y., Qin, N., Huang, W., 2011. Progress in research on the biogas heating. Environmental Engineering, 29(4), 125-129.

Hassanein, A. A., Qiu, L., Junting, P., Yihong, G., & Witarsa, F., 2015. Simulation and validation of a model for heating underground biogas digesters by solar energy. Ecological Engineering, 82, 336-344.

Axaopoulos, P., Panagakis, P., Tsavdaris, A., & Georgakakis, D., 2001. Simulation and experimental performance of a solar-heated anaerobic digester. Solar Energy, 70(2), 155-164.

Zhang, T. T., Tan, Y.F., Zhang, X. D., 2016. Using a hybrid heating system to increase the biogas production of household digesters in cold areas of China: An experimental study. Applied Thermal Engineering. 103, 1299-1311.

El-Mashad, H. M., van Loon, W. K., Zeeman, G., Bot, G. P., & Lettinga, G., 2004b. Design of a solar thermophilic anaerobic reactor for small farms. Biosystems Engineering, 87(3), 345-353.

Pollard, A. M., & Blanchard, R. E., 2014. A hybrid biogas system for Kolkata. International Conference on Non-Conventional Energy IEEE, 111-116.

Perrigault, T., Weatherford, V., Martí-Herrero, J., & Poggio, D., 2012. Towards thermal design optimization of tubular digesters in cold climates: a heat transfer model. Bioresource Technology, 124(337), 259-268.

Hashimoto, A.G., & Chen, Y.R., 1979. The overall economics of anaerobic digestion. In: First International Symposium on Anaerobic Digestion, University College, Cardiff, Wales, England (September 17–21).

Duffie, J. A., Beckman, W. A., & Mcgowan, J., 1980. Solar engineering of thermal processes. Journal of Solar Energy Engineering, 116(1), 549.

J. Deng, Z. Y. Tian, J. H. Fan, M. Yang, S. Furbo, Z. F. Wang, 2016. Simulation and optimization study on a solar space heating system combined with a low temperature ASHP for single family rural residential houses in Beijing. Energy Build. 126, 2–13.

Y. F. Liu, Y, W. Chen, T, Li, D. J. Wang, D. K. Wang, 2017. Investigation on the heat loss characteristic of

underground household biogas digester using dynamic simulations and experiments. Biosystems Engineering, 163, 116-133.

Zhang, X. M., Ren, Z, P., & Mei, F. M., 2007. Heat transfer. (5th ed.). Beijing: China Building Industry Press, (Chapter 3).

Chen, Y. R., & Hashimoto, A. G., 1978. Kinetics of methane fermentation. Biotechnology & Bioengineering Symposium, 8(4), 503-511.

Pham, C. H., Jin, M. T., & Sommer, S. G., 2014. Predicting methane production in simple and unheated biogas digesters at low temperatures. Applied Energy, 136, 1-6.

Hashimoto, A. G., 1982. Methane from cattle waste: effects of temperature, hydraulic retention time, and influent substrate concentration on kinetic parameter (k). Biotechnology & Bioengineering, 24(9), 2039–2052.

TRNSYS. 2012. A Transient Simulation Program, Version 17.1. University of Wisconsin Solar Energy Laboratory, Madison, WI.

Lu, Y., Tian, Y., Lu, H., Wu, L., Li, X., 2015. Study of solar heated biogas fermentation system with a phase change thermal storage device. Applied Thermal Engineering, 88, 418-424.

A solar furnace for copper smelting in Chile: assessment of economic benefits and reductions in greenhouse gas emissions

Dimitrij Chudinzow[1, a)], Dirk Switon[1] and Ludger Eltrop[1]

[1] Institute of Energy Economics and Rational Energy Use (IER), University of Stuttgart, Heßbrühlstraße 49a, 70565 Stuttgart, Germany

[a)] Corresponding author: dimitrij.chudinzow@ier.uni-stuttgart.de

Abstract

This work investigates the integration of a solar furnace (SF) into the smelting processes of copper in a flash furnace under Chilean solar irradiation conditions. A computer model of a 1 MW_{th} solar furnace, inspired by the French solar furnace in Odeillo, with a total heliostat specular area of 2,835 m² was developed and the annual energy contribution of the SF for copper smelting in a flash furnace was simulated. Economic benefits through fossil fuel savings in three different flash furnaces were compared with the investment costs for a SF for a lifetime of 50 years. Furthermore, reductions in greenhouse gas emissions ($CO_{2\text{-eq}}$-emissions) through fuel saving were calculated. The results show that, depending on the fuel type used in the flash furnace, up to 24% in $CO_{2\text{-eq}}$-emissions and up to 10% of lifetime costs can be saved.

Keywords: Solar Furnace, Chile, Smelting, Copper, Greenhouse Gas Emissions

1. Introduction

Metal smelting requires huge amounts of thermal energy. Usually, this energy demand is covered by liquid fossil fuels or electricity. While the utilization of solar energy for electricity generation and medium temperature thermal applications is widespread, yet there is no commercial use of solar energy for high temperature applications like metal smelting.

Solar furnaces (SF), like the French solar furnace in Odeillo (Fig. 1), collect and reflect direct solar radiation

Fig. 1: French solar furnace in Odeillo (World's Largest Solar Furnace n.d.)

with 63 heliostats onto a parabolic shape (concentrator) which in turn is redirected into a receiver. In the focal point temperatures up to 3,800 °C can be reached (Trombe, Le Vinh 1973). Currently, solar furnaces are used in research institutions only, e.g. for high temperature calcium carbide (CaC_2) formation (Paizullakhanov, Faiziev 2006), for smelting (Abdurakhmanov et al. 2008a) or material testing (Neumann 2005), (PROMES b).

Chile's economically most important produced metal is copper, which contributed 88% to Chilean export shipment values from the mining sector in 2015 (Servicio Nacional de Geología y Minería 2016). The fossil fuel consumption for copper production amounted 21.9 TWh in 2014, of which 7% were needed for smelting (Fundación Chile n.d.). The use of solar energy for metal smelting might have the potential to reduce costs and

doi:10.18086/swc.2017.26.03 Available at http://proceedings.ises.org

greenhouse gas emissions through replacing fossil fuels. Therefore, this work investigates the technical and financial potential of the integration of solar furnaces into high temperature smelting of copper under Chilean conditions as well as possible reductions in $CO_{2\text{-eq}}$-emissions.

2. Previous Work

Funken et al., from the German Aerospace Center DLR, developed a mini-scale SF powered rotary kiln for smelting 1 kg of aluminum scrap (Funken et al. 2001). They report a duration for smelting in the range of 0.5 to 6 h, depending on irradiance conditions (Cologne, Germany) and the achieved temperature. Additionally, a large scale solar kiln (capacity: 8 t) was designed and the heliostat field was optimized. The benefit of the applied solar smelting was the reduced amount of resulting flue gas that had to be cleaned. Furthermore, cost savings due to avoided fuel consumption can be expected. This concept is further investigated in the SOLAM project, a German-South African research initiative (DLR 2015). Abdurakhmanov et al. investigated different types of smelting furnaces using the large solar furnace in Uzbekistan (Abdurakhmanov et al. 2008b).

3. Integration of a solar furnace into copper smelting

3.1 Weather data

The solar resource website *Explorador Solar* provides both typical meteorological years (TMY) data files in an hourly resolution and weather measurement datasets in a 10-minute resolution (Ministerio de Energía 2017). To achieve a higher accuracy, a TMY was developed based on the weather measurement datasets from *Crucero 2*, which is located 45 km from Chuquicamata, the world's largest open-pit copper mine (latitude: -22.1647°, longitude: -69.339777°). For the selection of representative months, the direct normal irradiation (DNI) was used as the only criterion, since this is the most influencing parameter on the performance of a SF. The DNI values from the developed TMY are shown in Fig. 2. Clearly this location exhibits exceptional high solar irradiation.

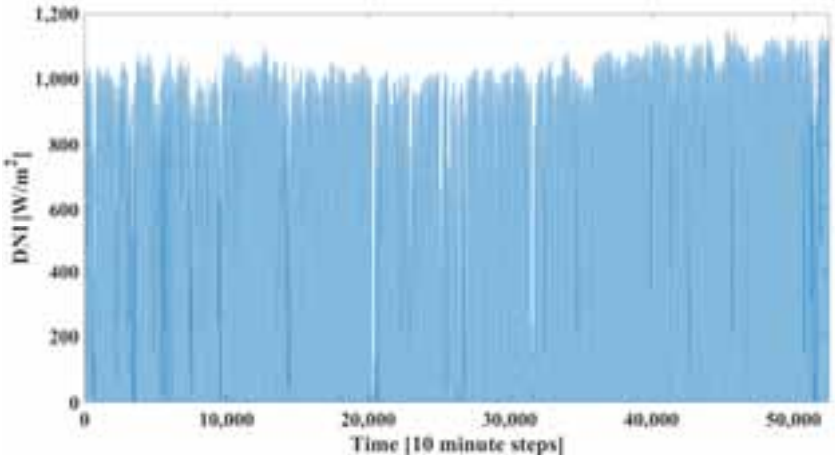

Fig. 2: DNI values from developed TMY based on *Crucero 2* measurements

3.2 Development of a solar furnace model in Matlab

Fig. 3 shows the subcomponents of the developed SF model. The layout of the heliostat field and the design of the concentrator is based on the French SF in Odeillo (PROMES a). The formulas to compute the time-variant cosine loss factor and the time-dependent orientation of each heliostat are taken from (Stine, Geyer 2001). The resulting total thermal power output of the SF system is calculated according to eq. (1).

$$P_{SF} = A_{Heliostat} \cdot DNI(t) \cdot \eta_{rh} \cdot \eta_{rc} \cdot \eta_{sbh} \cdot \eta_{sbc} \cdot \eta_{int} \cdot \eta_{aa} \cdot \eta_{circ} \sum^{n_{Heliostats}} \eta_{cos,i}(t) \qquad \text{eq. (1)}$$

The cosine loss factors were calculated for each heliostat separately to achieve more accurate results. The values from the other efficiencies are given in Appendix I.

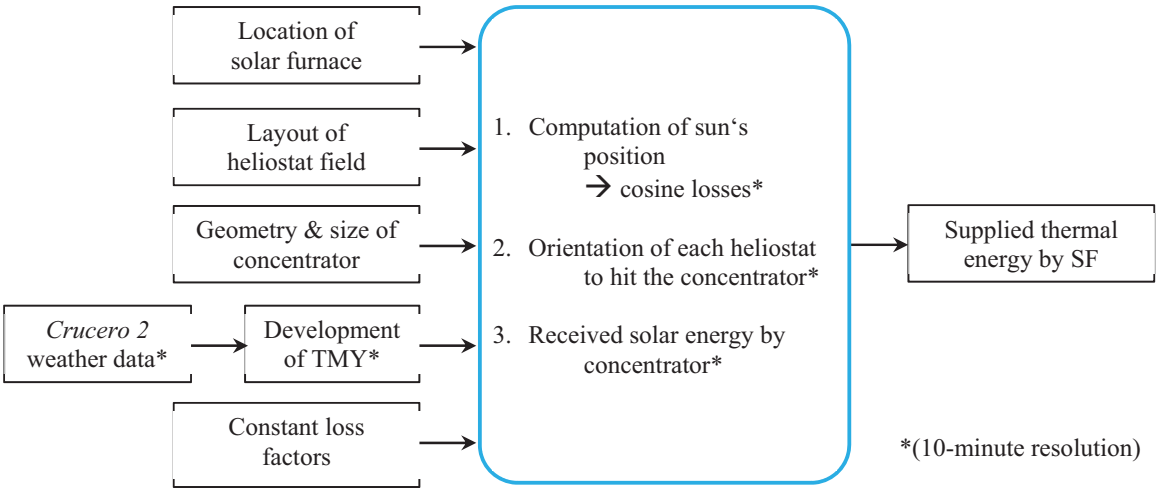

Fig. 3: Subcomponents of developed SF model

Fig. 4 shows a plot of the modelled SF in Chile.

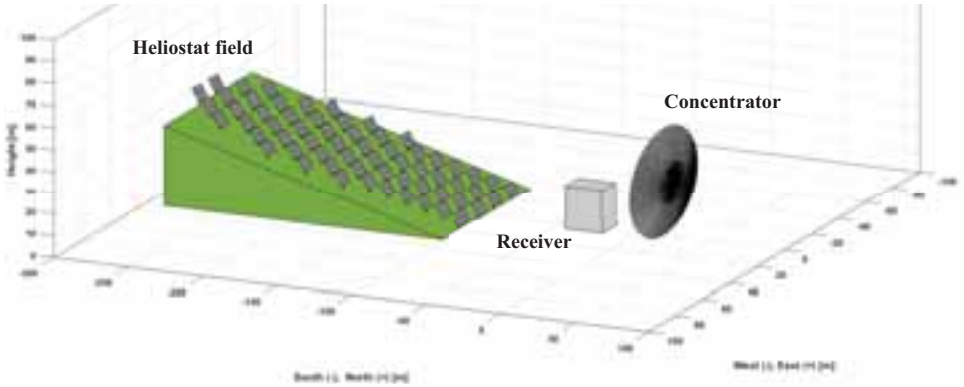

Fig. 4: Plot of the modelled SF and heliostat field located in Chile

In Fig. 5 the simulated thermal output of the SF is shown. We can clearly observe that most of the time the output of the SF exceeds the design point of 1 MW_{th}, due to high DNI irradiation found in northern Chile. It is

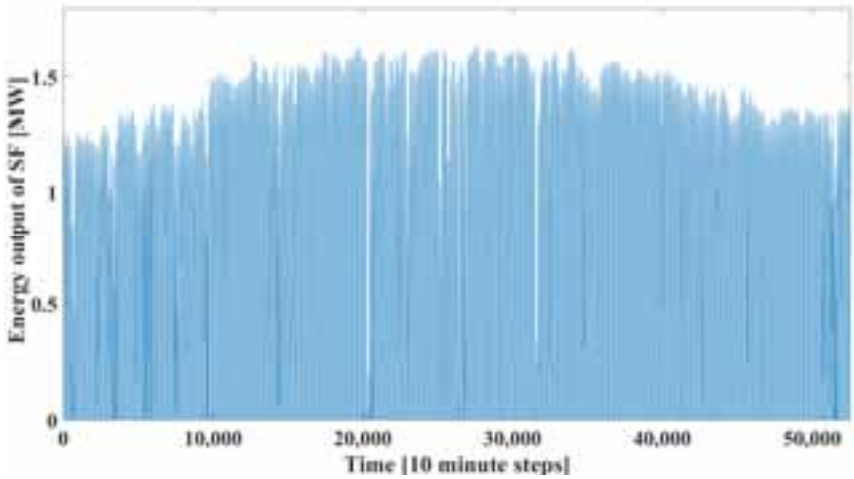

Fig. 5: Thermal output of the modelled SF, located in Chile

interesting to observe, that in winter time on the southern hemisphere the performance of the SF is higher than in summer. This can be explained by two factors: first, the DNI in northern Chile is constantly high throughout the whole year; secondly, the field performance of a point-focusing heliostat field is better in winter time when the sun hangs low in the sky.

3.3 Integration into copper smelting

The basic concept for the implementation of a SF into the copper smelting process is shown in Fig. 6. In this work we investigate three different flash furnaces, which need additional fuel for maintaining the thermal equilibrium. The thermal energy delivered by the SF contributes to the thermal equilibrium in a flash furnace and thus allows savings in fossil fuel consumption.

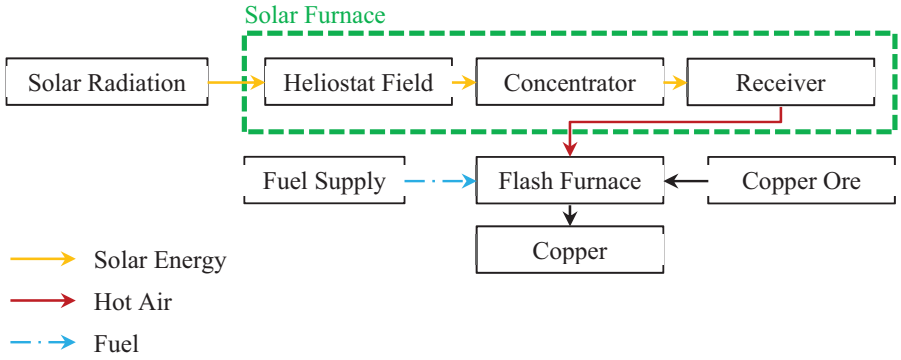

Fig. 6: Basic concept of the implementation of a solar furnace (SF) into the copper smelting process in a flash furnace

The properties of the investigated three flash furnaces are shown in Tab. 1, based on (Schlesinger 2011).

Tab. 1: Data of three flash furnaces used for cost analysis, based on (Schlesinger 2011)

	Flash furnace 1	**Flash furnace 2**	**Flash furnace 3**
Start of operation	1983	1972	1971
Concentrate feed [t/d]	2,000 (23-29% Cu)	2,241 (29.2% Cu)	3,830 (28.8% Cu)
Matte production [t/d]	1080 (54-56% Cu)	1129 (63.3% Cu)	1895 (64% Cu)
Fuel consumption [kg/h]	198.2 (Bunker C)	1,200 (Coal)	147 (Coal) + 404 (Diesel)
Fuel costs [USD$_{2017}$/h]	69	54	350
$\dot{m}_{Fuel}$·LHV [MW]	2.18	9.6	6.27

Since the fuel type varies among different flash furnaces, we took all three different fuels into account. Tab. 2 contains the characteristics of the fuel types.

Tab. 2: Lower heating values (LHV), specific $CO_{2\text{-eq}}$-emissions and costs of considered fuel types (Fürkus n.d.; Emission factors in kg CO2-eq per unit)

Fuel	**LHV [kWh/kg]**	**Specific $CO_{2\text{-eq}}$-emissions [kg$CO_{2\text{-eq}}$/kWh]**	**Costs [USD$_{2017}$/kg]**
Hard Coal	7.80	0.32	0.045
Diesel	11.83	0.3	0.85
Bunker C	11.00	0.29	0.35

3.4 Costs of the solar furnace

To estimate the costs of a SF, we adapted the specific costs for a heliostat from (new energy update 2017) and updated the figure to USD$_{2017}$, using an average inflation rate of 2%/a. This leads to specific heliostat costs of 147.9 USD$_{2017}$/m². Furthermore, we assume that heliostat costs constitute a share of 40% of total costs of a thermal CSP system (i.e. excluding “balance of plant”, “thermal energy storage” and “power block” from the cost components of a CSP power tower), based on the cost breakdown from (IRENA 2012). Finally, we assume annual operation and maintenance ($O\&M_{annual}$) costs as 5% of the initial investment. For the SF in Chile, a

heliostat field consisting of 63 heliostats (45 m² each) was designed (cf. Appendix II). With this information we calculate:

$$I_0 = \frac{147.89 \frac{USD_{2017}}{m^2} \cdot 63\ Heliostats \cdot \frac{45m^2}{Heliostat}}{40\%} = 1{,}048{,}170\ USD_{2017} \qquad \text{eq. (2)}$$

$$O\&M_{annual} = I_0 \cdot 5\% = 52{,}409\ USD_{2017} \qquad \text{eq. (3)}$$

Due to the fact that the French SF was completed in 1970 and is still in operation, a lifetime of T=50 years is assumed (Trombe, Le Vinh 1973). Taking into account an interest rate of *i*=2.5% (Chile Interest Rate 2017), we determine the present value PV_{SF} of the solar furnace as follows:

$$PV_{SF} = I_0 + O\&M_{annual} \cdot \frac{(1+i)^T - 1}{i \cdot (1+i)^T} = 2{,}534{,}597\ USD_{2017}$$

4. Results

The developed SF model calculated an annual thermal energy output of 4.66 GWh/a for the location in Northern Chile. To determine monetary savings, we assume that this energy output reduces the fossil fuel consumption of the flash furnaces each year. This gives us the net present values of the fuel costs of the three flash furnaces (FF1, FF2, FF3) without and with the integration of a SF for a lifetime of 50 a, as shown in Fig. 7. We can observe, that under the described assumptions, the integration of a SF is profitable for FF1 (-10%) and FF3 (-8%). Since in FF2 cheap coal is used, the integration of a SF is not profitable (+13%). "SF Costs" is the net present value of the SF, taking into account the investment costs I_0 and the annual O&M costs over the course of 50 a.

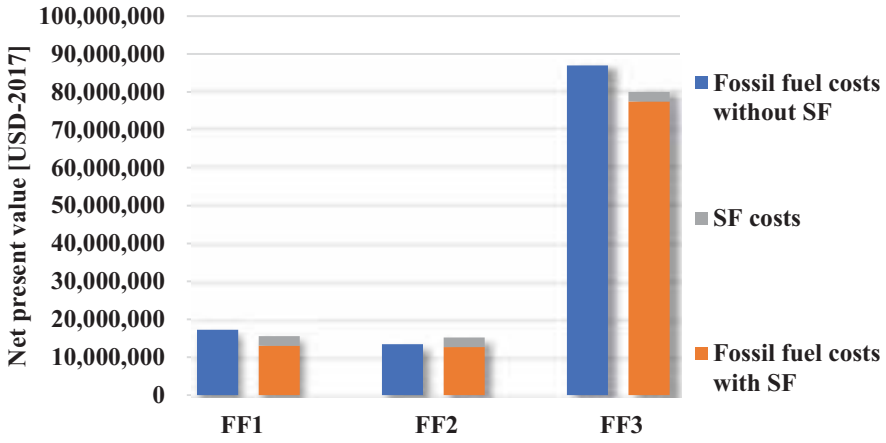

Fig. 7: Net present values of fuel costs for three flash furnaces, without and with the integration of a solar furnace

In Fig. 8 reductions in $CO_{2\text{-eq}}$-emissions through the integration of a SF are depicted. We can clearly see that the integration of a SF can reduce $CO_{2\text{-eq}}$-emissions. For FF1, FF2 and FF3 the savings are 24.4%, 5.6% and 8.9%, respectively.

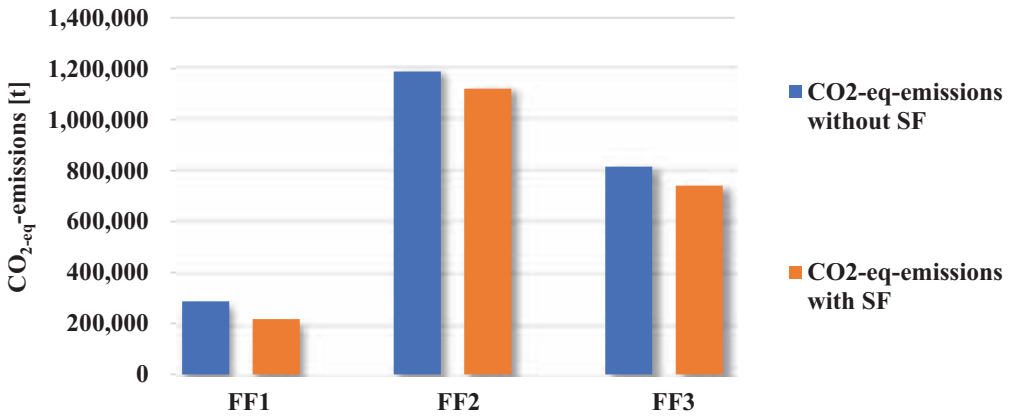

Fig. 8: CO_{2-eq}-emissions for three flash furnaces, without and with the integration of a solar furnace, after 50 a

5. Conclusion and outlook

In this work, we investigated the economic benefits as well as reductions in CO_{2-eq}-emissions through the integration of a solar furnace (SF) into copper smelting in Chile. A solar furnace was modelled in Matlab and the annual thermal energy production in the North of Chile was simulated. A SF with the same design as the French SF in Odeillo, located in Chile, would generate around 4.66 GWh/a. Depending on the type of fuel that is used in a flash furnace, up to 10% of fossil fuel costs and 24% in CO_{2-eq}-emissions could be saved. The results show, that it can be advantageous in economic and environmental terms to put more efforts in the research on solar aided metallurgy. Future research should focus on the concrete development of a solar aided flash furnace, taking into account specific metallurgical requirements during the smelting process.

6. Appendix

Appendix I – Values of efficiencies used in the developed SF model

References: (Stine, Geyer 2001; Téllez et al. 2014; Ewert, Fuentes n.d.; Segal 2012; The Circumsolar Radiation 2013):

η_{rh}:	Reflectivity of the heliostats, including the contamination with dust and the aging	= 0.94
η_{rc}:	Reflectivity of the concentrator, the same values as for the heliostats were selected	= 0.94
η_{sbh}:	Shading and blocking factor for the heliostat field	= 0.98
η_{sbc}:	Shading and blocking factor for the concentrator	= 0.98
η_{int}:	Factor for the interception of the solar rays	= 0.97
η_{aa}:	Atmospheric attenuation of the solar rays in the solar furnace system	= 0.97
η_{circ}:	Factor for the circumsolar radiation	= 0.8
$\eta_{cos,i}(t)$:	Cosine loss factor of each heliostat	Calculated in 10-minute steps

Appendix II – Parameters of the French solar furnace in Odeillo

Position	Concentrator	Heliostats	Heliostat field
Latitude: 42.2939° Longitude: 2.0145°	40 m height, 54 m width, focal length= 18 m	N=63, 7.5 m height, 6 m width	8 terraces, 16 heliostat rows in total

Reference (Centre National De La Recherche Scientifique (CNRS) n.d.)

7. Publication bibliography

Abdurakhmanov, A. A.; Akbarov, P. Yu.; Akhadov, Zh. Z.; Mamatkosimov, M. A.; Sobirov, Yu. B.; Turaeva, U. F. (2008a): Creating melting furnaces based on the large solar furnace. In *Appl. Sol. Energy* 44 (4), pp. 284–287. DOI: 10.3103/S0003701X08040129.

Abdurakhmanov, A. A.; Akbarov, R. Yu.; Sobirov, Yu. B. (2008b): Analysis of operating characteristics of various smelting furnaces on a Large Solar Furnace. In *Applied Solar Energy* 44 (1), pp. 24–27. DOI: 10.3103/S0003701X08010088.

Centre National De La Recherche Scientifique (CNRS) (n.d.): High Temperature Solar Energy. Odeillo. Available online at https://www.gtri.gatech.edu/history/files/media/other-publications/High_Temp_Solar_Energy_Pamphlet.pdf, checked on 7/19/2017.

Chile Interest Rate (2017). Available online at https://tradingeconomics.com/chile/interest-rate, checked on 9/1/2017.

DLR (2015): SOLAM - solar aluminium smelting in a directly irradiated rotary kiln. Available online at http://www.dlr.de/sf/en/desktopdefault.aspx/tabid-9315/16078_read-46207/, checked on 3/16/2017.

Emission factors in kg CO2-eq per unit. Available online at http://www.winnipeg.ca/finance/findata/matmgt/documents/2012/682-2012/682-2012_Appendix_H-WSTP_South_End_Plant_Process_Selection_Report/Appendix%207.pdf, checked on 10/10/2017.

Ewert, M.; Fuentes, Navarro (n.d.): Modelling and simulation of a solar tower power plant. RWTH Aachen University. Available online at http://www.mathcces.rwth-aachen.de/_media/5people/frank/solartower.pdf, checked on 9/14/2017.

Fundación Chile (n.d.): From copper to innovation. Mining technology roadmap 2035. Available online at http://programaaltaley.cl/archivo-publicaciones/hoja-de-ruta-tecnologica-para-la-mineria-en-ingles/, checked on 10/11/2017.

Funken, Karl-Heinz; Roeb, Martin; Schwarzboezl, Peter; Warnecke, Heiko (2001): Aluminum Remelting using Directly Solar-Heated Rotary Kilns. In *J. Sol. Energy Eng* 123 (2), pp. 117–124. DOI: 10.1115/1.1355242.

Fürkus, S. (n.d.): Heizkostenrechner. Available online at http://heizkostenrechner.eu/heizwert-brennwert-tabelle.html, checked on 10/10/2017.

IRENA (2012): Concentrating Solar Power.

Ministerio de Energía (2017): Explorador Solar. Available online at http://www.minenergia.cl/exploradorsolar/, checked on 9/14/2017.

Neumann, Andreas (2005): Solar Furnace Ten Years Old. DLR. Available online at http://www.dlr.de/en/Portaldata/1/Resources/kommunikation/publikationen/109_nachrichten/dlr-nari109_en_76-79.pdf, checked on 3/9/2017.

new energy update (2017). CSP tower installation costs drop on heliostat innovations, pre-assembly. Available online at http://analysis.newenergyupdate.com/csp-today/csp-tower-installation-costs-drop-heliostat-innovations-pre-assembly, checked on 10/12/2017.

Paizullakhanov, M. S.; Faiziev, Sh. A. (2006): Calcium carbide synthesis using a solar furnace. In *Tech. Phys. Lett.* 32 (3), pp. 211–212. DOI: 10.1134/S1063785006030102.

PROMES a. The solar furnace of Odeillo font romeu. Available online at https://www.promes.cnrs.fr/index.php?page=the-solar-furnace-of-odeillo-font-romeu, checked on 10/11/2017.

PROMES b. Available online at https://www.sollab.eu/promes.html, checked on 3/9/2017.

Schlesinger, Mark E. (2011): Extractive metallurgy of copper. Amsterdam, Boston: Elsevier.

Segal, A. (2012): Optimum layout of heliostat field when the tower-top receiver is provided with secondary concentrators. Available online at http://sfera.sollab.eu/downloads/JRA/WP13/R13.3b_SFERA_WP13T2_Opt_HelioField_Secondary_TopReceiver.pdf, checked on 10/1/2017.

Servicio Nacional de Geología y Minería (2016): Anuario de la Minería de Chile 2015. Available online at http://www.sernageomin.cl/pdf/mineria/estadisticas/anuario/Anuario-de-la-Mineria2015.pdf, updated on 3/17/2017.

Stine, B. William; Geyer, Michael (2001): Power From The Sun. Available online at http://www.powerfromthesun.net/book.html, checked on 9/14/2017.

Téllez, F.; Villasante, C.; Burisch, M. (2014): State of the Art in Heliostats and Definition of Specifications. Survey for a low cost heliostat development. Available online at https://www.stage-ste.eu/deliverables/STAGE_STE_Deliverable_12_1.pdf, checked on 9/15/2017.

The Circumsolar Radiation (2013). Available online at http://www.black-photon.de/products/circumsolar-radiation/71-measurement-principle-csr-sensor.html, checked on 10/12/2017.

Trombe, Felix; Le Vinh, Albert Phat (1973): Thousand kW solar furnace, built by the National Center of Scientific Research, in Odeillo (France). In *Solar Energy* 15 (1), pp. 57–61. DOI: 10.1016/0038-092X(73)90006-6.

World's Largest Solar Furnace (n.d.). Available online at http://www.atlasobscura.com/places/worlds-largest-solar-furnace, checked on 10/5/2017.

Thermal Model Development for Solar Greenhouse Considering Climate Condition

Homa Esmaeli[1], Ramin Roshandel[1]

[1] Sharif University of Technology, Department of Energy Engineering, Tehran (Iran)

Abstract

Water crisis in the Middle East, leads policy makers to consider development of greenhouses on large scale. Typical greenhouses usually use energy carriers like natural gas and gasoline to provide suitable microclimate for plants. The consequence of greenhouse development will be huge amount of fossil fuels consumption, producing CO_2 and forcing loads to gas, gasoline and electricity networks. Considering excellent solar energy potential in the Middle East, solar greenhouses seems to be an innovative solution.

In this research, after studying different solar greenhouse experiences around the world, a successful model has been chosen, redesigned and improved. Solar greenhouse is designed to utilize solar energy by its passive energy system and minimize external energy demand. In order to investigate its performance, a mathematical thermal model has been developed to predict inside air temperature, which is the most important parameter in greenhouse performance. Solar Greenhouse Thermal Model (SGTM) is based on solar collector analysis and trombe wall calculations in buildings, it receives hourly climate data (solar radiation, wind speed and ambient temperature) and calculate hourly solar greenhouse inside air temperature during the year. SGTM has been validated and can be used to predict solar greenhouse inside air temperature in any region.

Results of using SGTM show that solar greenhouse is suitable for Tehran climate condition, and it works passively without auxiliary heating system in the winter, but it needs auxiliary cooling system in the summer. Sensitivity analysis indicates that the greenhouse size play a vital role in its thermal performance. So, there is an optimal size for solar greenhouse in each climate condition.

Keywords: Solar Greenhouse, Thermal Model, Solar Energy, Water Crisis

1. Introduction

World is dealing with several concerns, Water-Food-Energy nexus is one of them that has great impacts on people life directly. However, the water nexus may be more important than the others in the Middle East. Agriculture sector uses 84 percent of total water usage in the MENA region (Statista (2015)), which indicate essential actions must have done. Development of Greenhouses in large scale is one of the solutions which has attracted the attention of policy makers and leads them to consider development of greenhouses on large scale.

Greenhouses are designed to provide suitable microclimate for growing plant efficiently. Higher production per area, less water consumption and higher production quality are the main advantages of greenhouses but greenhouses consume energy carriers like natural gas, gasoline and electricity to provide desired microclimate. So, the consequence of greenhouses large scale development will be huge amount of fossil fuels consumption, producing CO_2 and forcing loads to gas, gasoline and electricity networks.

The Brundtland Commission's report (1988) defined sustainable development as "development which provides the current generations needs without compromising the future generations ability to meet their own needs", which imposed the idea of limitations by the state of technology on the environment's ability to meet present and future needs. Sustainable development concept and great solar energy potential in Middle East make solar greenhouses to seem an interesting idea and an innovative solution.

Passive design of solar greenhouse is utilizing solar energy for heating without any additional heating system, specifically it supports the idea of maximizing solar gain and minimizing heat loss to eliminate the dependence of fossil fuels for heating/cooling (Schiller and Plink (2016)) . Santamouris et al. (1994) categorized solar greenhouses in passive solar greenhouses and active solar greenhouses. Passive solar greenhouses have an integrated design to collect heat or the greenhouse works as a solar collector, the design is based on maximizing the solar gains but active solar greenhouses have equipment separated from the greenhouse to utilize solar energy, and an independent heat storage system. Several passive heating and cooling systems have been used in solar

doi:10.18086/swc.2017.26.04 Available at http://proceedings.ises.org

greenhouses around the world, Sethi and Sharma (2007 and 2008) reviewed and evaluated them and discussed the representative application of each technology, also they studied several cases for each technology and drive experimental equations for evaluating these technologies. These researches focused on heating and cooling systems that used on different structure designs.

There is a kind of solar passive greenhouses mainly located in northern region of China (Wang et al. (2014)), they are used to grow vegetables in the winter without any auxiliary heating. The building parameters have an important impact on the solar energy utilization and temperature in the greenhouse (Tong et al. (2013)). Tong et al. (2013) reviewed all researches that discussed solar greenhouse building parameters, they concluded all the building parameters are related to each other and to the local climate condition in solar passive greenhouse system and they should be analyzed together.

In this study, in the first step after studying different solar greenhouse experiences around the world, a successful model has been chosen, redesigned and improved, considering principles of solar passive design. Secondly, an innovative mathematical thermal model has been developed to predict inside air temperature annually in any climate condition, in order to investigate its performance. Thirdly, sensitivity analysis has been done on structural parameters to investigate effect of structural parameters on thermal performance of solar greenhouse.

2. Methodology

2.1. Solar Greenhouse Design

In order to design a solar passive greenhouse, orientation toward sun, insulate the areas that do not collect solar energy and underground, maximizing the light and heat in winter and reduce it in summer, using thermal storage techniques and supplying sufficient ventilation are the main principles that should be considered (Schiller and Plink (2016)).

Also, van't Ooster et al. (2007) represent a systematic procedure to develop a zero fossil greenhouse concept for the Netherlands. This design procedure contains following steps:

- Step 0: Design objective definition
- Step 1: Brief of requirements definition
- Step 2: Required functions definition
- Step 3: Working principles definition
- Step 4: Conceptual designs derivation
- Step 5: Conceptual designs evaluation

A solar passive greenhouse is designed based on above design principles. This is a south oriented elliptic shape greenhouse, covered by transparent material and a thermal insulation cover to prevent heat loss at night, a thermal storage wall (layered) is installed in the north of the greenhouse (Fig.1). Solar radiation transmits into the greenhouse during the day, south oriented elliptic shape roof from east to west collect solar radiation from sunrise to sunset efficiently, then is absorbed by heat storage wall and soil of the ground, which increase their temperatures because absorbed solar radiation is converted to sensible heat. Temperature difference between the surfaces and inside air causes heat transfer via convection, into the thermal storage wall via conduction, to store heat in it and keeping greenhouse warm at night, and into the ground via conduction. Part of absorbed solar energy is transformed into the latent heat by crop transpiration and evaporation from wet surfaces.

Thermal insulation covers the elliptic shape roof to prevent heat loss during the night. Stored heat in thermal storage wall transfers through convection to keep inside air warm.

Solar photovoltaic panels and solar collectors can be installed in the roof to supply electricity demand of greenhouse (for irrigation, lightening, fans, motors, climate control system, etc.) and to supply additional heat demand.

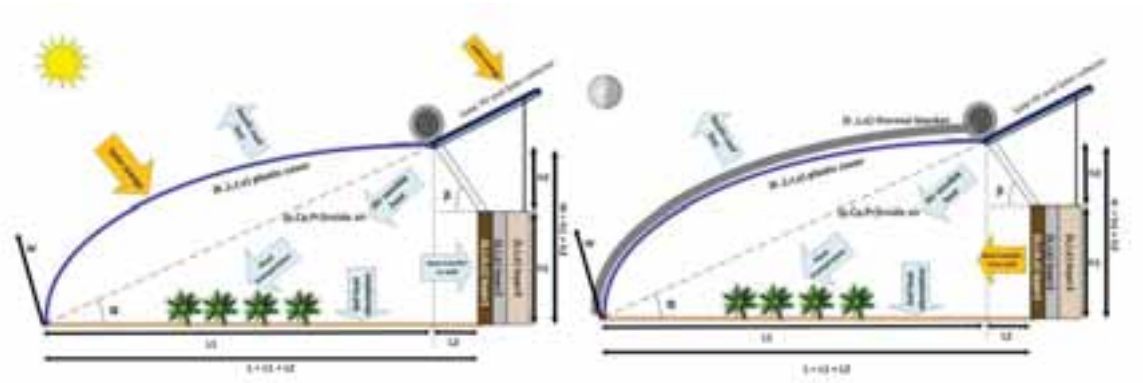

Figure 1: Cross sectional conceptual view, heat transfer mechanism and structural parameters of solar passive greenhouse at day and night

2.2. Thermal Model Description, Equations and Validation

The most important parameter in greenhouse performance is inside air temperature. Several energy analysis have been done to evaluate greenhouse performance. De Zwart (1996) developed a comprehensive greenhouse climate simulation model that included three sub models: CO_2, water vapor and thermal. The basis of equations was energy and mass balances and was developed for different temperature layers of greenhouse. Chen et al. (2015) developed a greenhouse energy demand model which was based on mass and energy balance considering physiological behavior of plants.

Thermal Model (SGTM) is based on solar collector analysis and trombe wall calculations in buildings (Duan et al. (2016)), it receives hourly climate data (solar radiation, wind speed and ambient temperature) and calculate hourly solar greenhouse inside air temperature during the year. Fig.2 shows how different parameters are connected in SGTM.

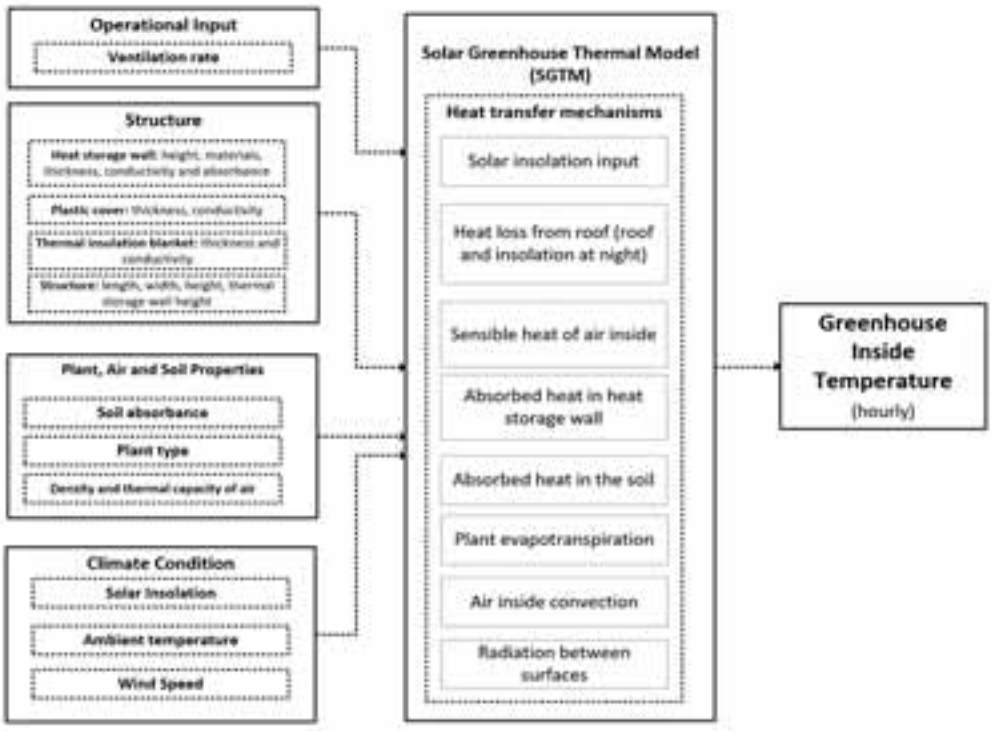

Figure 2: Data circulation diagram of SGTM

Seven surface of temperature has been considered (Fig.3) and for each surface energy balance equation has been developed. It is assumed that there is steady state condition, each surface has a constant temperature and air inside temperature is uniform.

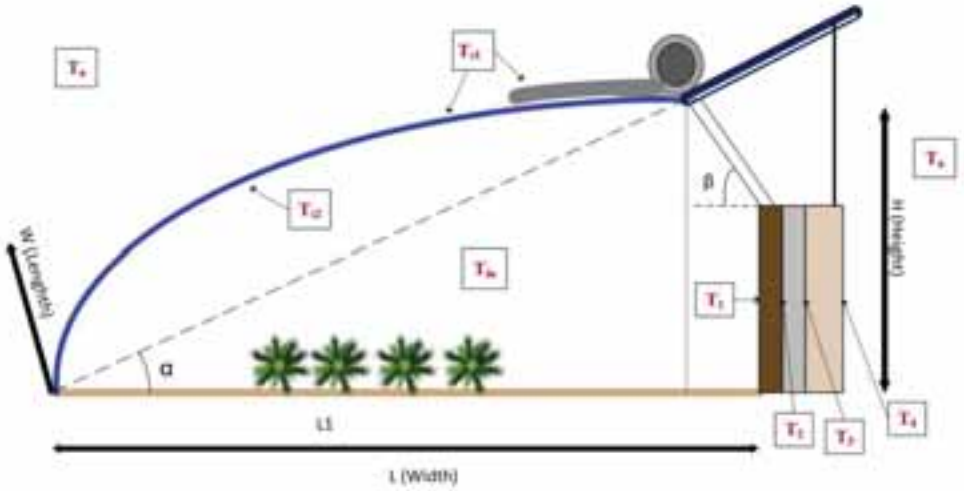

Figure 3: Temperature levels of SGTM

First level of equations belongs to the outer surface of plastic roof, equation 1 indicates the energy balance for it:

$$h_{c,cover-out}A_{cover}(T_{s1}-T_a)+h_{r,cover-out}A_{cover}(T_{s1}-T_a)+\frac{k_{cover}}{L_{cover}}A_{cover}(T_{s1}-T_{s2})=I\alpha_{cover}A_{cover} \quad \text{(eq. 1)}$$

$$h_{c,cover-out}=5.7+3.8u_w \quad \text{(eq. 2)}$$

$$h_{r,cover-out}=\varepsilon_{cover}\sigma(T_{s1}+T_s)(T_{s1}^2+T_s^2) \quad \text{(eq. 3)}$$

$$T_s=0.055T_a^{1.5} \quad \text{(eq. 4)}$$

Where T_{s1}, T_{s2}, T_s and T_a are respectively the temperature of outer surface of plastic roof, inner surface of plastic roof, sky temperature (equation 4) and ambient temperature, $h_{c,\text{ cover-out}}$ refers to convection heat transfer coefficient from plastic roof to out of greenhouse and calculate through equation 2, $h_{r,\text{ cover-out}}$ refers to radiation heat transfer coefficient from plastic roof to sky and calculate with equation 3.

Second level of equations belongs to internal surface of plastic roof and energy balance for it express as equation 5.

$$\left(h_{r,cover-wall}+\frac{k_{air,cover-wall}}{L_{air,cover-wall}}\right)A_{wall}(T_{s2}-T_1)+\frac{k_{cover}}{L_{cover}}A_{cover}(T_{s2}-T_{s1})+h_{c,cover-air}A_{cover}(T_{s2}-T_{in})=0 \quad \text{(eq. 5)}$$

$$h_{r,cover-wall}=\frac{\sigma(T_{s2}^2+T_1^2)(T_{s2}+T_1)}{\frac{1-\varepsilon_{cover}}{\varepsilon_{cover}A_{cover}}+\frac{1}{A_{cover}F_{cover-wall}}+\frac{1-\varepsilon_1}{\varepsilon_1 A_{wall}}} \quad \text{(eq. 6)}$$

$$h_{c,cover-air}=\frac{k_{air,cover-wall}Nu}{L_{air,cover-wall}} \quad \text{(eq. 7)}$$

Where T_1 and T_{in} are respectively temperature of inner surface of heat storage wall and inside air temperature.

Third level of equations belongs to internal surface of heat storage wall and energy balance for it express as eq. 8.

$$h_{c,wall-air}A_{wall}(T_1 - T_{in}) + \left(h_{r,wall-cover} + \frac{k_{air,wall-cover}}{L_{air,wall-cover}}\right)A_{wall}(T_1 - T_{s2}) + \frac{k_1}{L_1}A_{wall}(T_1 - T_2) + h_{r,L_1-L_2}A_{wall}(T_1 - T_2) = I\alpha_{wall}\tau_{cover}A_{wall} \quad \text{(eq. 8)}$$

$$h_{r,L_1-L_2} = \frac{\sigma(T_1^2+T_2^2)(T_1+T_2)}{\frac{1}{\varepsilon_1}+\frac{1}{\varepsilon_2}-1} \quad \text{(eq. 9)}$$

$$h_{c,wall-air} = \frac{k_{air,wall-cover}Nu}{L_{air,wall-cover}} \quad \text{(eq. 10)}$$

Where T_2 refers to the connection of first and second layers of heat storage wall temperature. Energy balance for connecting layers which express with T_2 and T_3 (connection of second and third layers of heat storage wall temperature) express with following equations:

$$\left(h_{r1} + \frac{k_1}{L_1}\right)A_{wall}(T_2 - T_1) + \left(h_{r2} + \frac{k_2}{L_2}\right)A_{wall}(T_2 - T_3) = 0 \quad \text{(eq. 11)}$$

$$h_{r1} = \frac{\sigma(T_1^2+T_2^2)(T_1+T_2)}{\frac{1}{\varepsilon_1}+\frac{1}{\varepsilon_2}-1} \quad \text{(eq. 12)}$$

$$h_{r2} = \frac{\sigma(T_2^2+T_3^2)(T_2+T_3)}{\frac{1}{\varepsilon_1}+\frac{1}{\varepsilon_2}-1} \quad \text{(eq.13)}$$

$$\left(h_{r3} + \frac{k_2}{L_2}\right)A_{wall}(T_3 - T_2) + \left(h_{r4} + \frac{k_3}{L_3}\right)A_{wall}(T_3 - T_4) = 0 \quad \text{(eq. 14)}$$

$$h_{r3} = \frac{\sigma(T_3^2+T_2^2)(T_3+T_2)}{\frac{1}{\varepsilon_3}+\frac{1}{\varepsilon_2}-1} \quad \text{(eq.15)}$$

$$h_{r4} = \frac{\sigma(T_4^2+T_3^2)(T_4+T_3)}{\frac{1}{\varepsilon_3}+\frac{1}{\varepsilon_2}-1} \quad \text{(eq.16)}$$

Sixth layer is outer surface of heat storage wall. Equation 17 refers to energy balance for this surface.

$$h_{c,wall-out}A_{wall}(T_4 - T_a) + \frac{k_3}{L_3}A_{wall}(T_4 - T_3) + h_{r4}A_{wall}(T_4 - T_3) + h_{r,wall-out}A_{wall}(T_4 - T_a) = 0 \quad \text{(eq. 17)}$$

$$h_{r,wall-out} = \varepsilon_3\sigma(T_4 + T_s)(T_4^2 + T_s^2) \quad \text{(eq. 18)}$$

Where T_4 is outer surface of heat storage wall temperature.

Last level is energy balance for greenhouse air inside control volume, assuming there is no temperature distribution and T_{in} as inside air temperature.

$$h_{c,cover-air}A_{cover}(T_{in} - T_{s2}) + h_{c,wall-air}A_{wall}(T_{in} - T_1) + \rho_{air}\dot{V}C_{p,air}(T_{in}(t) - T_{in}(t-1)) + ach\, V_{inside}\rho_{air}C_{p,air}\left(T_{in,h} - T_a\right) + A_{ground}\lambda E(t) + U_{cover}A_{cover}(T_{s2} - T_a) + I\tau_{cover}\alpha_{soil}A_{ground} = I\tau_{cover}A_{cover} \quad \text{(eq.19)}$$

Where λE(t) refers to the crop transpiration and expresses with Penma-Monteith formula (Chen et al. (2014)):

$$\lambda E(t) = \frac{I_a \tau_a \Delta + 2LAI(\frac{\rho c_a}{r_a})(e_s(t) - e_a(t))}{\Delta + \gamma(1 + \frac{r_c}{r_a})} \qquad \text{(eq. 20)}$$

$$\Delta = \frac{2504000}{(T_{in} - 35.6)^2} \exp(\frac{17.27(T_{in} - 273.16)}{T_{in} - 35.86}) \qquad \text{(eq. 21)}$$

Ventilation happens by using of fans which causes force convection. Nusselt number force convection in non-circular ducts can be calculated by circular ducts equations by substitution of hydraulic diameter (Bergman and Incropera (2011)).The distance between the wall and cover is also assumed hydraulic diameter.

$$D_h = \frac{4A_c}{P} \qquad \text{(eq. 22)}$$

Where A_c and P are respectively cross sectional area of duct and wetted environment. Nusselt number is calculated by Colburn equation (Bergman and Incropera (2011)):

$$Nu_D = 0.023 Re_D^{0.8} Pr^{1/3} \qquad \text{(eq. 23)}$$

Equations 1, 5, 8, 11, 14, 17 and 19 form a system of non-linear equations and the output will be temperature of greenhouse levels, the main result is inside air temperature.

In order to predict reliable results with SGTM, a validation has done. The best way to check the accuracy of model results is to compare them with experimental data. Tong et al. (2009) studied a similar solar greenhouse located in Shenyang, China (latitude: 41.8ºN, longitude 123.4ºE, altitude: 42 m). The greenhouse was 60 meter long and 12.6 meter wide with 5.5 meter ridge height, a 0.6 meter layered heat storage wall made of bricks and XPS foam as a thermal insulation material. The plastic roof was made of 0.12 mm PVC film, covered with a 20 mm thick cotton blanket during the night time. Other necessary data like solar insolation, ambient temperature, and physical properties, was reported in this paper as well. The typical weather file of Shenyang downloaded from the U.S. Department of Energy and used for wind speed data.

The highest temperature difference between SGTM model and experimental data is 2.8 Kelvin and the average of differences is 0.89. Figure 4 shows the model results compering to experimental data.

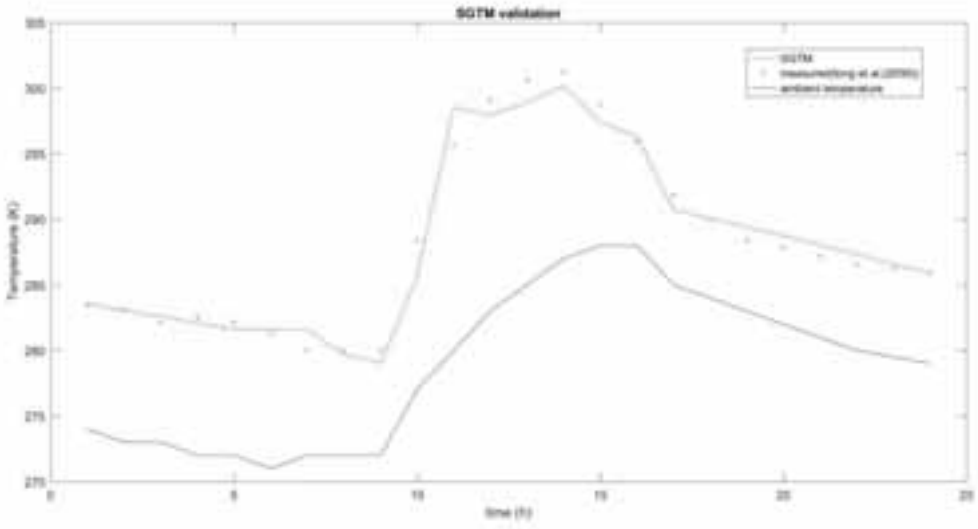

Figure 4: Validation of SGTM model for hourly greenhouse air inside temperature with experimental data in 20 February 2004 in Shenyang, China (Tong et al. (2009))

2.3. Simulation Outline

To investigate solar greenhouse performance in Tehran climate condition, a solar greenhouse is considered with 5.5 meter height, 12 meter width and 100 meter length and the 3 layered heat storage wall is 3 meter high and 0.6 meter thick.

Table 1: Natural and physical properties of solar greenhouse structure

Location	Thickness (m)	Thermal conductivity (W/m.K)	Emissivity ε	Absorptance α	Transmission τ
Plastic cover	0.00012	0.17	0.9	0.03	0.88
Thermal insulation	0.036	0.09	0.9	0.75	0
Heat storage wall inside layer	0.36	0.81	0.93	0.6	0
Heat storage wall middle layer	0.12	0.03	0.9	-	0
Heat storage wall outside layer	0.12	0.81	0.93	0.6	0

3. Results and Discussion

3.1. Solar Greenhouse Performance in Tehran

The aim of using solar greenhouse is to maximize solar energy utilization and minimize using of active energy systems to provide desirable micro-climate for plants. There are two extreme states to investigate greenhouse thermal performance in order to know if it will work properly in a specific climate, hottest and coldest months of the year. July and January are the hottest and coldest months in Tehran based on typical weather file downloaded from the U.S. Department of Energy.

Typical vegetable plants can tolerate temperature range 10 to 32, as it has shown in Figure 5, during the average day of July, greenhouse will be overheated, and it is caused of huge amount of solar radiation and high ambient temperature which means it is necessary to use a cooling system or some energy management solutions like shading and using an optical object to send excessive solar insolation to outside. Figure 6 shows solar greenhouse will work properly in winter and the inside temperature will not be less than 286 Kelvin although the ambient temperature is less than the minimum temperature all the time and it is near to 273 kelvin.

Solar greenhouse can be used in hot climates like Tehran without any auxiliary heating. To prevent overheating in summer a cooling system can be used or can be planned to operate greenhouse only in cold seasons, also some other passive systems can be designed to adjust inside air temperature in a better range like ground to air heat exchanger (Sethi and Sharma (2007 and 2008)).

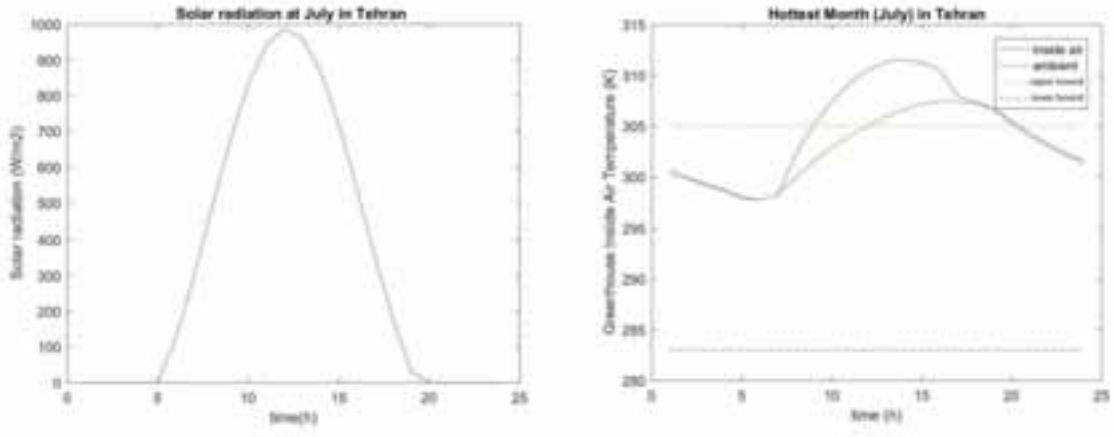

Figure 5: Solar insolation (left) and thermal performance of solar greenhouse (right) at July in Tehran

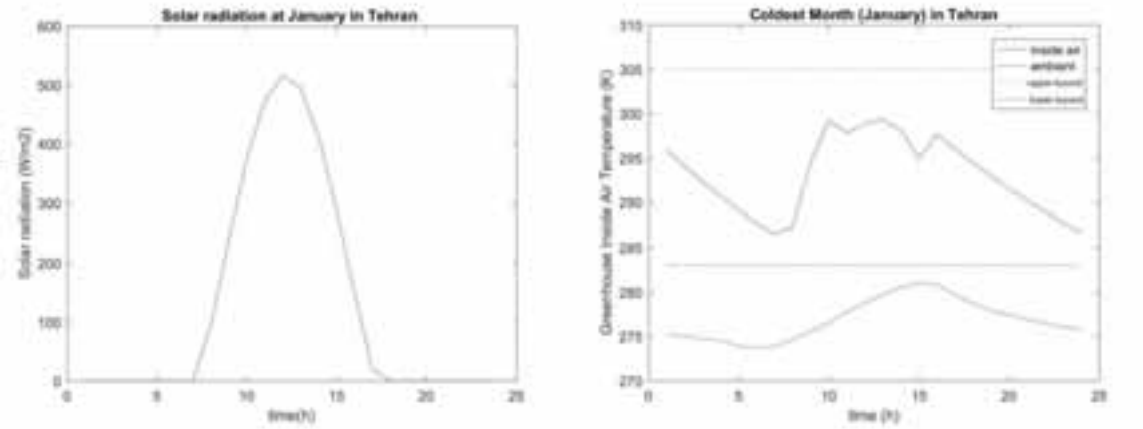

Figure 6: Solar insolation (left) and thermal performance of solar greenhouse (right) at January in Tehran

3.2. Sensitivity analysis

Passive solar greenhouse can be assumed as a solar collector. Like any kind of solar collector its sizing has an essential role in its performance that is determined based on climate condition, to investigate the effect of changing the structural parameters, three cases have been defined and studied. Size parameters of greenhouse structure are α and β which define the ratio of height to width and L and H which define the height and width.

- Case 1
  In this case, α and β remain constant and the total size of greenhouse is changed, which is equal to change the inside air volume. As it has shown in figure 7, the solar greenhouse thermal performance gets better by increasing the size of greenhouse in hottest month of year and it works well in all the cases in coldest month of year, so the bigger solar greenhouse works better in Tehran climate condition. Also bigger greenhouse has a better temperature distribution which is better for crop transpiration.

Table 2: Solar greenhouse structural parameters details for case 1

Number of the case	H (m)	L (m)	α	β
Case 1.1	4.58	10	30	45
Case 1.2	5.5	12	30	45
Case 1.3	6.42	14	30	45
Case 1.4	7.5	16	30	45

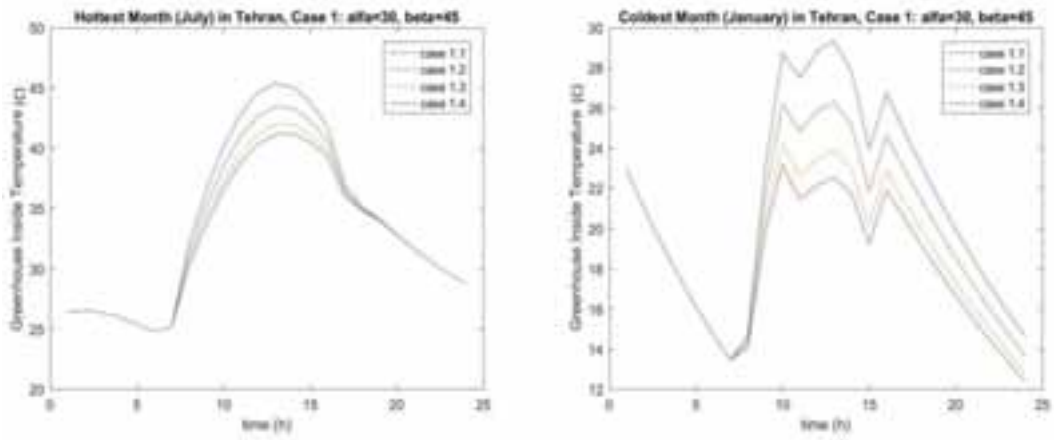

Figure 7: Solar greenhouse thermal performance in case 1

- Case 2

  In this case β and H are constant and α and L are changed to investigate the effect of α angle in thermal performance of solar greenhouse, α angle's function is like tilt angle function in solar collector, but in this case the best tilt angle for winter is important to keep greenhouse warm in winter.

  As it has shown in figure 8, case 2.1 (α=36) has the best performance in hottest month of year and the bigger α angles have better performance in coldest month of year.

Table 3: Solar greenhouse structural parameters details for case 2

Number of the case	H (m)	L (m)	α	β
Case 2.1	5.5	10	36	45
Case 2.2	5.5	12	30	45
Case 2.3	5.5	14	25	45
Case 2.4	5.5	16	22	45
Case 2.5	5.5	9	40	45

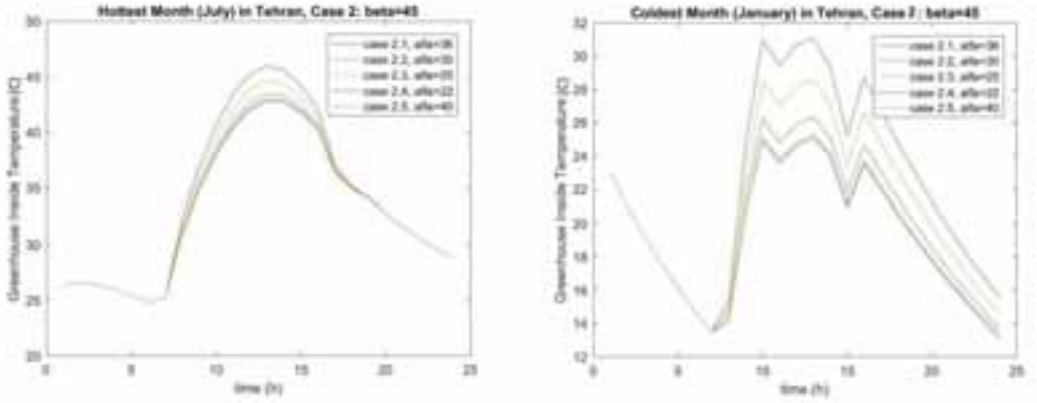

Figure 8: Solar greenhouse thermal performance in case 2

- Case 3

  In this case the effect of β angle and heat storage wall height are investigated. As it has shown in figure 9, bigger β has worse performance not only in summer but also in winter, because bigger beta equals to more area for plastic roof and more area to collect solar energy, in simpler words it leads to a bigger solar collector. The bigger heat storage wall also has overheating in both summer and winter, because of using more thermal mass to store heat.

  Bigger beta and heat storage wall values will effect positively on greenhouse performance in cold climates.

Table 4: Solar greenhouse structural parameters details for case 3

Number of the case	H (m)	L (m)	α	β	Heat storage wall height (m)
Case 3.1	5.5	10	30	45	5
Case 3.2	5.5	10	30	78	3
Case 3.3	5.5	12	30	45	3

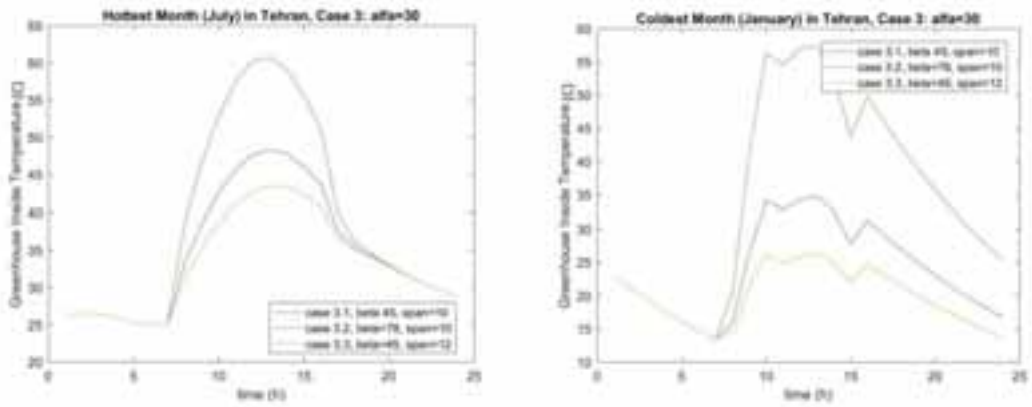

Figure 9: Solar greenhouse thermal performance in case 3

4. Conclusions

In this research a solar greenhouse is designed and its performance is evaluated by developing a thermal model in order to calculate inside air temperature. This study shows that:

- Solar greenhouse thermal model receives climate condition data, plant type, size and materials of structure and operational data and puts them in a system of non-linear equations to predict greenhouse air inside temperature in any region.
- Solar greenhouse can operate without auxiliary heating in winter in hot climates like Tehran, but there is necessary to use an active cooling system (like fan and pad) or use passive systems (shading, ground to air heat exchanger) to cool it in summer. The other solution is to plan greenhouse to operate seasonally.
- The sensitivity analysis has showed that the structural parameters of greenhouse have a great impact on greenhouse thermal performance. It can be concluded that the bigger greenhouse with α angle around 36 and beta angle around 45 is the best structure between the studied cases. It shows that there is an optimum structure for each climate.
- Although greenhouse inside air temperature stays in appropriate range most of the time, there is a specific temperature range for each plant. If the greenhouse keeps in that range, the production performance will be higher, so auxiliary heating and cooling systems can be designed and used. The energy demand of them will be much less than typical greenhouses.

5. Acknowledgment

This study has been done under the grant project number G941013 of Sharif University of Technology.

6. References

5.1. Journals and books

Bergman, T.L. and Incropera, F.P., 2011. Fundamentals of heat and mass transfer. John Wiley & Sons, United States of America.

Chen, J., Zhao, J., Xu, F., Hu, H., Ai, Q. and Yang, J., 2015. Modeling of energy demand in the greenhouse using PSO-GA hybrid algorithms. Mathematical Problems in Engineering, 2015.

De Zwart, H.F., 1996. Analyzing energy-saving options in greenhouse cultivation using a simulation model. Institute of agriculture and environmental engineering, Wageningen.

Duan, S., Jing, C. and Zhao, Z., 2016. Energy and exergy analysis of different Trombe walls. Energy and Buildings, 126, pp.517-523.

Keeble, B.R., 1988. The Brundtland report: 'Our common future'. Medicine and War, 4(1), pp.17-25.

Santamouris, M., Balaras, C.A., Dascalaki, E. and Vallindras, M., 1994. Passive solar agricultural greenhouses: a worldwide classification and evaluation of technologies and systems used for heating purposes. Solar Energy, 53(5), pp.411-426.

Schiller, Lindsey, Plink, Mark, 2016. The year round solar greenhouse. New society, Gabriola Island.

Sethi, V.P. and Sharma, S.K., 2007. Survey of cooling technologies for worldwide agricultural greenhouse applications. Solar Energy, 81(12), pp.1447-1459.

Sethi, V.P. and Sharma, S.K., 2008. Survey and evaluation of heating technologies for worldwide agricultural greenhouse applications. Solar energy, 82(9), pp.832-859.

Tong, G., Christopher, D.M. and Li, B., 2009. Numerical modelling of temperature variations in a Chinese solar greenhouse. Computers and electronics in agriculture, 68(1), pp.129-139.

Tong, G., Christopher, D.M., Li, T. and Wang, T., 2013. Passive solar energy utilization: A review of cross-section building parameter selection for Chinese solar greenhouses. Renewable and Sustainable Energy Reviews, 26, pp.540-548.

Van' t Ooster, A., Van Henten, E.J., Janssen, E.G.O.N., Bot, G.P.A. and Dekker, E., 2007, October. Development of concepts for a zero-fossil-energy greenhouse. In International Symposium on High Technology for Greenhouse System Management: Greensys2007 801 (pp. 725-732).

Wang, J., Li, S., Guo, S., Ma, C., Wang, J. and Jin, S., 2014. Simulation and optimization of solar greenhouses in Northern Jiangsu Province of China. Energy and Buildings, 78, pp.143-152.

5.2. Links

https://energyplus.net/weather, August 11, 2017.

https://www.statista.com/statistics/731451/mena-water-usage-by-sector/

7. Appendix: Unites and Symbols

Table 5: Symbols definition and units

Quantity	Symbol	Unit
Specific heat	C_p	J kg^{-1} K^{-1}
Thermal conductivity	k	W m^{-1} K^{-1}
Absorptance	α	
Emittance	ε	
Density	ρ	kg m^{-3}
Transmittance	τ	
Radiation heat transfer coefficient	h_r	W m^{-2} K^{-1}
Convection heat transfer coefficient	h_c	W m^{-2} K^{-1}
Area	A	m^2
Temperature	T	K
Solar radiation	I	W m^{-2}
Overall heat transfer coefficient	U	W m^{-2} K^{-1}
Stefan-Boltzmann constant	σ	W m^{-2} K^{-4}
View factor	F	
time	t	s
Wind speed	u_w	m s^{-1}
Thickness	L	m
Volumetric flow rate	$\dot{V}$	m^3 s^{-1}

Air change per hour	ach	
Nusselt number	Nu	
Reynolds number	Re	
Prandtl number	Pr	
Latent heat of vaporization	λ	kJ kg^{-1}
Plant canopy leaf area index	LAI	
Canopy transpiration rate	E(t)	Kg m^{-2} s^{-1}
Saturated vapour pressure of air	e_s	Pa
Water vapour pressure of air	e_a	Pa
leaf aerodynamic	r_c	s m^{-1}
Stomatal resistances of the leave	r_a	s m^{-1}
psychometric constant	γ	kPa K^{-1}
slope of the water vapor saturation curve	Δ	Pa K^{-1}
Hydraulic diameter	D_h	m
Environment	P	m

Use of Hydration Heat and Solar Energy in Prefabricated Concrete Production Lines

Hilbert Focke[1], Lukas Wimhofer[1], Bernhard Krug[2], Joachim Petz[2], Martin Peyerl[3] and Christian Dillig[3]

[1] FH- OÖ Forschungs & Entwicklungs GmbH, Wels (Austria)

[2] Franz Oberndorfer GmbH & Co KG, Gunskirchen (Austria)

[3] Smart Minerals GmbH, Wien (Austria)

Abstract

The paper analyses the thermal energy requirements of an industrial production line for prefabricated concrete parts using measurements and tests. The goal is to significantly reduce the energy demand and reduce the temperature level in order to be able to integrate solar thermal process heat, and the first-time use of the hydration heat. The final production line, optimized on the basis of the research results, is presented, as well as a simulation study, which shows, that economically interesting solar thermal process heat production costs can be achieved through an optimized overall concept. Regarding the export of this production technology to countries with hot and dry climates it is also aspired, to cover the additional required cooling load by means of solar thermal driven chillers. This option should also be examined by system simulations. These simulations put also emphasis on the development of cost- effective system concepts, which allow the integration of solar thermal process heat and/ or cold.

Keywords: Solar thermal process heat and/ or cold, prefabricated concrete parts, measurements and tests, heat production costs, optimized overall concept, solar thermal driven chillers, polysun system simulations

1. Introduction

The cooling, respectively heating during the production process of precast concrete parts is extremely important regarding quality. In Middle and Northern Europe concrete heating is more relevant, whereas, in Southern countries such as Turkey, United Arab Emirates a production of high quality concrete would hardly be possible without cooling.

The plants operated by the Austrian company Franz Oberndorfer GmbH & Co KG are producing prestressed hollow core slabs in various construction heights at the locations Wöllersdorf, Herzogenburg, Gunskirchen, Grosswilfersdorf, Radfeld and Völkermarkt. Through the restructuring of the production process in the plant Wöllerdorf the energy consumption shall be reduced by 90% in future. This target is a result of an ongoing company internal development process. The final target will be reached through the worldwide first time usage of the so called hydration heat (heat development through chemical reaction of water and cement) and the integration of solarthermal energy in the whole process. The use of hydration heat decreases the energy demand and necessitates changes in the heat distribution system towards lower temperatures. This modification on the other hand, approves the use of solar thermal energy in the production process.

The use of hydration heat insists a long-term comprehensive evaluation of the production data. In the end the heat shall be discharged by means of a heat transfer medium via the mold surface. Based on the results from the evaluation of the production data as well as a series of laboratory tests, the target is to develop a proven hydraulic concept and a control system for the recovery of hydration heat. Hence the achieved production data will be converted to load profiles. These load profiles serve as a basis for dynamic simulations in order to examine the integration of solar thermal energy in the production process. Regarding the export of this production technology to countries with hot and dry climates it is also aspired, to cover the additional required cooling load by means of solar thermal driven chillers. This option is examined also by system simulations.

doi:10.18086/swc.2017.26.05 Available at http://proceedings.ises.org

The project puts emphasis on the development of cost- effective system concepts, which allow the integration of solarthermal process heat and/ or cold. The lessons learned during the long-term comprehensive evaluation of the production data and the lab tests will be incorporated also into the redesign of the other production plants. It is planned to hand over the achieved conclusions to further application areas (precast concrete product range worldwide) by licenses to interested competitors.

2. Production data evaluation

The basis for the planned project objectives is a comprehensive, long-term production data analysis at the demonstration and test facility located in in Wöllersdorf, Austria.

Prestressed hollow core slabs are characterized by low overall height and minimum building material consumption. They belong to the group of full-surface ceilings without subdivision with subsequent grouting and are built according to ÖNORM EN 1168 at heights of 16 cm; 20 cm; 26 cm; 32 cm; 40 cm; 45 cm and 50 cm with a length of up to 22 meters [1]. Up to now, the elements have been produced on up to 150 m long lanes, which are heated by means of a thermo- oil heating system. The corresponding pipe system had to be heated to a temperature of approx. 150 ° C.

In Figure 1, the demonstration (right) system is compared to the previous heating system (left). By increasing the number of tubes, embedding them into a storage medium and connecting it to the steel plate, a better heat transfer is achieved. Therefore, the flow temperatures can be lowered, and water can be used as a heat transfer medium. Due to the novel hardening process, the required surface temperature of the floor panel of 35° C. is achieved with a substantially lower energy input. The temperature of the water circuit is now 50-60 °C.

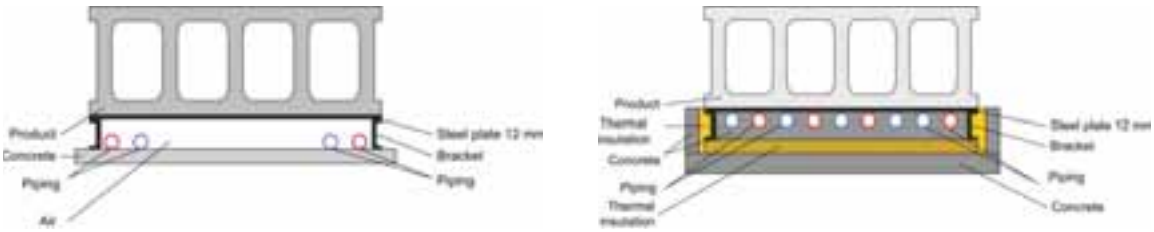

Fig. 1: Comparison old(left) and new (right) product heating system

Three heating circuits are designed hydraulically as parallel circuits with mixing control by three-way valves. A modulating 275 kW gas boiler is the heat source. A control system allows the presetting of a set flow temperature and the definition of heating times per circuit as well as the recording of measured data. The entire production process takes about 24 hours. This production process involves straining the steel ropes, extruding, (applying the concrete on the lane), curing, removing the slab and cleaning the lane.

Irregularities in the internal data collection as well as unexplained temperature gradients along the length of the lane led to the temporary installation of additional data loggers and to the analysis of thermographic images. Control measurements with mobile ultrasonic heat meters confirmed incorrectly closing control valves and showed conversion errors in the internal measurement data acquisition.

The annual energy balance in Figure 2 shows the enormous savings potential that can be achieved by really simple measures. Regarding domestic hot water production and building heating, further measurements are planned.

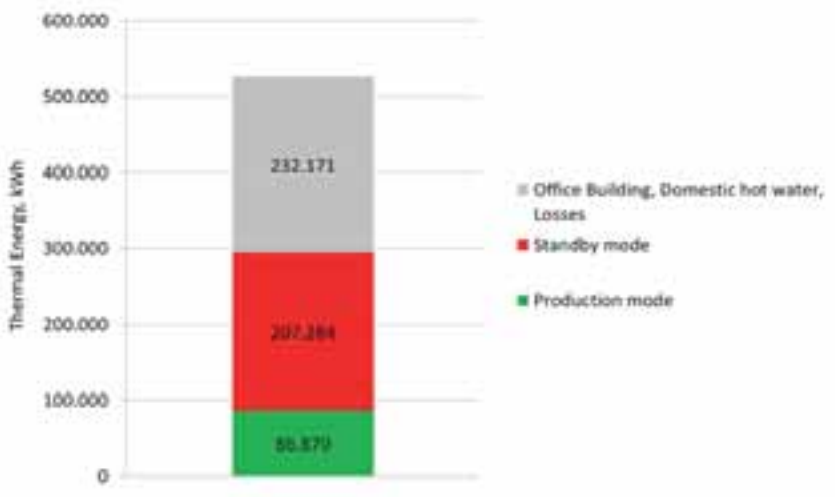

Fig. 2: Annual energy balance of a typical fabrication plant in Austria

3. Use of hydration heat

For the production of concrete, water, binders (e.g. cement), aggregate (e.g. sand/ gravel) and possibly additives (e.g. fluxes) are needed. The chemical- physical reaction of cement with water is called hydration. The heat evolution depends essentially on the amount of cement and the type of cement. The amount of heat developed up to the complete hydration does not differ significantly for the individual types of cement.

Depending on the application, different solutions for the prevention or reduction of hydration heat are sought. On the one hand, attempts are being made to accelerate the curing time of the concrete parts by supplying heat, but on the other hand, the concrete part temperature must not rise too much because of cracking and possible product damaging.

In this project, the heat of hydration is seen as an additional, previously unused energy or heat source, which can help to reduce production costs and increase product quality. The main challenge is posed in the fact that until now there was no way to control the heat of hydration or to offer any technical solutions for removing the heat of hydration. On the basis of temperature measurements and simulations with the software COMSOL® Heat, an attempt was made to document the temperatures occurring during a whole production cycle. Subsequently, a sample was taken to determine tensile and compressive strength. Figure 3 shows one time step of the occurring temperature profile.

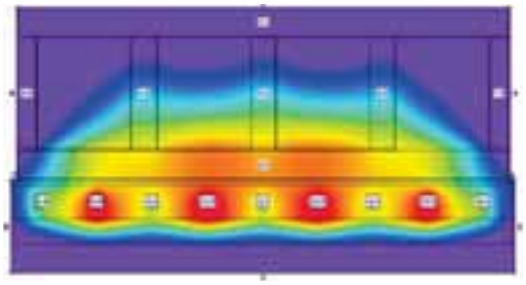

Fig. 3: Temperature profile during production

The high savings potential realized due to the production data analysis relativizes the expected savings of hydration heat recovery. The maximum surface temperature on the bottom side is max 5°C above the current heating return temperature of 45°C. The heat recovery potential is therefore low. For the quality of the products, however, the occurring temperature gradients are important, which should not exceed the maximum 0.3K per hour and 0.7 K/cm slab height.

4. Simulations

4.1 Location Austria, heating energy supply

The data collected during the evaluation over a year were used to create load profiles for the heating of the lanes. From the huge amount of production data and the production plan, the required heating energy quantities were analyzed at different fresh concrete temperatures. The production process consists of 3 parts. The preheating process is used to bring the massive flooring sheet to temperature. A required preheating time of 2 h was selected. The production process is characterized by different thickness of the slabs and therefore different production times. Thus, the thickest slab type is extruded in more than twice the time of the thinnest slab. Finally post heating is used for quality assurance and is necessary to prevent material stresses and to accelerate the hydration. The fresh concrete temperature was approximated with the outside temperature. The resulting energy need equals to 400- 450 kWh for the slight lanes (16-26 cm height) and 600-700 kWh for the massive lanes. (32- 50 cm height). In general, there is only a slight influence caused by the fresh concrete temperature.

The power consumption, the duration and the temperature profile of the production steps results in specific load profiles. These load profiles and the current production plan serves as a basis for the dynamic system simulations using the Vela Solaris software Polysun Designer. This results in a theoretical process heat energy consumption of 248.400 kWh. Figure 4 shows the corresponding plant concept.

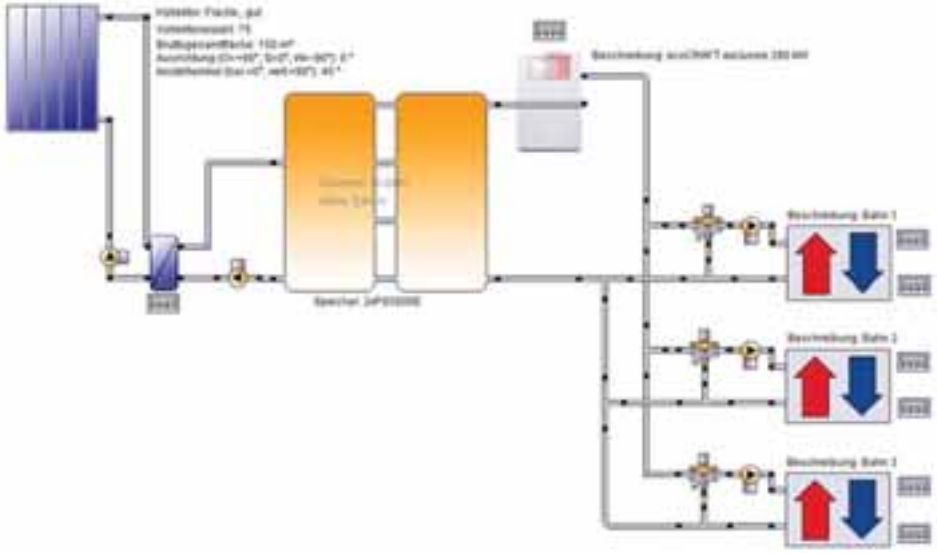

Fig. 4: System concept in the software Polysun Designer

The solar system is designed, that the process heat demand can be covered on a clear summer day. This is to avoid stagnation in summertime. High specific yields are the result, which are important for the profitability of the system. However, the achievable solar fraction is limited. In the industrial sector the aspect of economic efficiency plays an important role [2]. For the design of the hot water storage, it should be noted that the dimensioning depends strongly on the respective load profile. The specific storage volume is calculated by means of the return temperature.

Figure 5 shows the simulation results for flat plate collectors (tilt angle 45°) with optimum azimuth alignment using a 25m³ hot water storage. The plant performance ratio is 29% for a gross collector area of 200m², whereby 25m³ is the minimum storage size. As a result of an increase in the storage volume, the performance ratio increases only slightly.

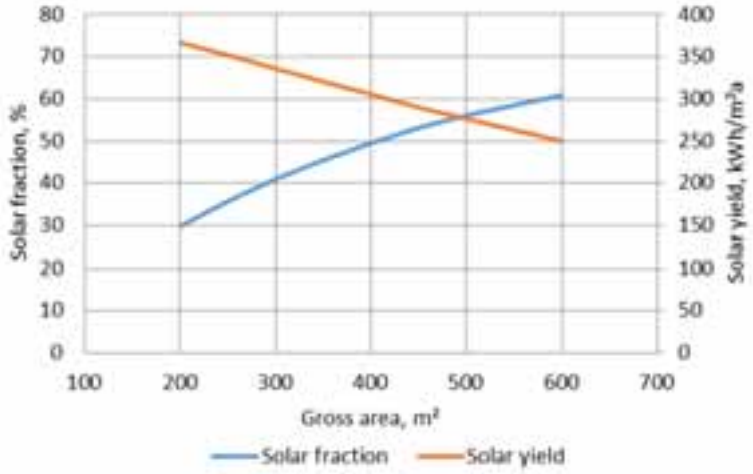

Fig. 5: Solar fraction and solar yield depending on gross area, 25m³ hot water storage

For economic considerations, the costs per kWh heat are used. The investment costs of the plant, an annuity factor, operating costs, consumption costs and the annual solar energy yield influence the costs per kWh heat [2]. For an accurate calculation of the investment costs, functions from a tool developed in IEA SHC Task 48 were used [3]. Since in this case no new additional heat source has to be installed, only the collectors, piping and storage has to be considered. In addition, an Austrian subsidy of 40% of the investment costs was taken into account [4].

At the location Austria,a solar thermal system with a total gross area of 200m² with a 25m² water storage tank for example, can supply 30% of the annual thermal energy demand at a price of 5.6 €cent per kWh heat. This value can be reduced by doubling the storage volume to 4.9 €cent / kWh.

4.2 Location United Arab Emirates, cooling energy supply

Regarding the export of this production technology to countries with hot and dry climates the power consumption load profiles were adapted for the climate in the United Arab Emirates. In these climate the production of high quality concrete is hardly possible without cooling. Therefore a cold supply temperature of 20°C for the lanes was chosen. This results in a theoretical process cold energy consumption of 426.280 kWh.

The system concept includes a single effect absorption chiller with a wet cooling tower, a hot water storage tank which is powered by flat plate solar collectors and a gas backup boiler. A solar thermal driven cooling system with a total gross area of 500m² with a 30m² hot water storage tank, can supply 53% of the annual thermal cooling energy demand. The price per kWh solar generated cold amounts however more than 15 €cent. The investment and operating costs for the backup system are not yet taken into account.

5. Results and conclusion

The detailed investigation of a production line for precast concrete parts in Austria showed that a reduction of the thermal energy requirement to one third is possible. The additional use of the hydration heat (heat development by chemical reaction of water and cement) in order to further reduce the energy requirement has a significant influence on product quality and production time. To ensure a consistent product quality, a massive covering (insulation) of the lanes after the extrusion process, or a heating of the production hall, appears to be more appropriate.

The optimized production line based on these results, was used as a basis to investigate the integration of solar thermal energy generation with simulations. A solar thermal system, located in central Europe, with a total gross area of 200m² with a 25m² water storage tank, can supply 30% of the annual thermal energy demand at a heat price of 5.6 €cent per kWh.

The analysis clearly shows that competitive heat prices can be achieved by the use of solar thermal heat on prefabricated concrete production lines. The precast concrete market or the construction industry represents a promising application for solar thermal process heat integration.

Regarding the export of this production technology to countries with hot and dry climates (e.g. United Arab Emirates), a solar thermal driven cooling system with a total gross area of 500m² with a 30m^3 hot water storage tank, can supply 53% of the annual thermal cooling energy demand. However, costs of 15 €cent/kWh cold must be applied.

6. References

[1] FRANZ OBERNDORFER GmbH & Co KG
http://www.oberndorfer.at/produkte/deckensysteme/vsdvorgespannte-hohldiele/ 2017

[2] Dr.-Ing. Bastian Schmitt, Dr.-Ing. Christoph Lauterbach, Prof. Dr. Klaus Vajen:
Leitfaden zur Vorplanung solarer Prozesswärme 201

[3] Daniel Neyer, Jacqueline Neyer, Alexander Thür, Roberto Fedrizzi, Alice Vittoriosi, Stephen White, Hilbert Focke: Collection of criteria to quantify the quality and cost competitiveness for solar cooling systems, 2015

[4] Leitfaden Solarthermie – Solare Großanlagen. 7. Ausschreibung, Mai 2016. Klima und Energiefonds der österreichischen Bundesregierung

7. Acknowledgment

The presented work refers to the project “Hydrasol”, which is funded by the Austrian Climate and Energy Fund and is carried out within the framework of the Energy Research Program 2014.

SAM PROCESS HEAT MODEL DEVELOPMENT AND VALIDATION: LIQUID-HTF TROUGH AND DIRECT STEAM GENERATION LINEAR FOCUS SYSTEMS

Parthiv Kurup[1], Abhishek Parikh[1], Jana Möllenkamp[2], Thomas Beikircher[3], Alexia Samoli[3], and Craig Turchi[1]

[1] National Renewable Energy Laboratory (NREL), Golden (USA)

[2] SPF Institute for Solar Technology, Rapperswil (Switzerland)

[3] Bavarian Center for Applied Energy Research (ZAE Bayern), Garching (Germany)

Abstract

Two new solar industrial process heat (SIPH) models have been added to the System Advisor Model (SAM) energy simulation tool. The two process heat models were: i) liquid-heat transfer fluid (HTF) parabolic troughs; and ii) direct steam generation (DSG) linear-focus collectors. The DSG model can simulate either DSG parabolic troughs (PT) or DSG Linear Fresnel (LF) fields, based on the optical characteristics supplied. These models help to meet the need for independent, validated tools that reliably simulate the effects of adding a solar field to provide heat for potential IPH applications. During the pre-validation of the liquid-HTF model, operational data was provided and preprocessed by SPF and evaluated at ZAE Bayern. The beta liquid-HTF model provided excellent agreement between the simulations and the operational data for the solar thermal yield generation on a yearly and monthly basis (4.4% difference). The final liquid-HTF process heat model has been further optimized with test users such as ZAE Bayern and SPF. Key improvements in the SIPH models to better model SIPH fields include the use of smaller piping systems and heat capacities, a single collector field, and a higher time-step resolution than for electricity generation (down to 10 minutes). Both the final liquid-HTF and DSG models were successfully validated against operational data for respective solar fields, and showed less than 5% deviation to actual results. A brief application where the liquid-HTF process heat model is used for a brewery in California and the value of reliably simulating a potential SIPH solar field are highlighted.

Keywords: Solar Industrial Process Heat (SIPH), Concentrating Solar Power (CSP), Parabolic Trough (PT), Linear Fresnel (LF), Direct Steam Generation (DSG),), System Advisor Model (SAM), Energy Modelling

1. Introduction

After significant interest during the 1970s, but relatively few deployments, the use of concentrating solar technologies for thermal and industrial applications, including solar enhanced oil recovery (solar EOR), thermally-driven desalination, and industrial process heat (IPH), are again receiving global interest (Kurup and Turchi 2015; IEA 2017; Frank et al. 2014). For larger scale adoption of both non-concentrating and concentrating solar power (CSP) technologies for SIPH, trusted, validated, and readily available thermal energy generation and simulation tools are needed. Free tools that can simulate the use of CSP technologies for SIPH now include the newly modified System Advisor Model (SAM) and the German Aerospace Center's Greenius software packages (NREL 2017b; Deutsches Zentrum für Luft und Raumfahrt (DLR) 2017).

This paper highlights the overall developments and validations to SAM's new process heat models for using concentrated solar thermal energy, made available from the 2017 release of SAM. The paper describes: the need for developing SIPH modules using CSP technologies; detailed model developments for both SIPH models; the differences between the thermal models and SAM's existing electricity generation models; and importantly, the validations of both models to real operational sites where the solar field provides heat. It is worth noting that the SIPH models have focused only on concentrating technologies, but non-concentrating technologies are also very suitable for lower-temperature hot water heating applications, as seen in the Solar Water Heating models in SAM (NREL 2017b). Two models have been developed for SIPH application, the first that utilizes a selectable liquid-HTF with parabolic troughs (e.g., pressurized water, glycol or a synthetic mineral oil), and the second, DSG systems using water in linear-focus collectors. It is important to highlight that the DSG SIPH model can model the parabolic trough (PT) and linear Fresnel (LF) systems, based on changing the optical characteristics, pumping power, and heat loss of the collector. The paper also highlights a utilization of the liquid-HTF model for a brewery in California that could potentially install a new parabolic trough solar field to provide heat.

doi:10.18086/swc.2017.26.06 Available at http://proceedings.ises.org

1.1 Motivation for the developing the SAM SIPH models due to the increasing global interest

Energy-generation and simulation tools such as Greenius and SAM provide a reputable, validated and "consistent framework for analyzing and comparing power system costs and performance across the range of solar technologies and markets" (Wagner and Gilman 2011). SAM's original solar-thermal models were specifically developed for the electricity sector. With growing interest in SIPH, it is important to develop energy-generation modelling tools also able to undertake thermal energy yield analysis. It is straightforward to provide IPH temperatures (e.g., >150°C) using the same CSP technologies as for electricity (e.g., liquid-HTF troughs or DSG collectors). However, there are differences in the solar field modelling used for electricity generation, and a SIPH field used for heat generation. In CSP electricity modelling, the solar field typically is coupled to an integrated steam-Rankine power block used for electricity generation (Wagner and Gilman 2011). It has been shown that when the SAM inputs and the SAM code were changed to minimize the power-cycle impacts (e.g., a constant solar field inlet temperature), the "power cycle caused a 6% underestimation of performance from what should have transpired had the model been freed of the power cycle constraints" (Turchi et al. 2016). Since the outlet of the power block serves as an inlet to the solar field, the state of operation of the power block has a direct impact on the solar field performance. Without the constraints (e.g., a variable solar field inlet temperature) and de-coupling of the power cycle, in attempting to model solar fields used for process heat applications, it was found the performance was underestimated by about 14% (Turchi et al. 2016).

A key project known as Solar Payback was initiated in October 2016 with support from the German Federal Environment Ministry and has partners including the Fraunhofer Institute for Solar Energy and the German bank KFW (German Solar Association 2017). This three-year project funded at nearly €3 million has the purpose of promoting the use of SIPH across four partner countries (Brazil, Mexico, India, and South Africa) to: 1) raise SIPH awareness; 2) highlight the technical merits and economic potential, to then 3) help increase commercial investment in all forms of SIPH (German Solar Association 2017). The first "Solar Heat for Industry" report has highlighted that 74% of the global energy consumed by industry was for heat, with only ~9% of that being provided by renewables rather than by conventional fuels (e.g., coal and natural gas) (German Solar Association 2017). With industrial heat demands expected to increase, SIPH could play an increasingly important role globally, particularly in decarbonizing the industrial sector. Real examples of installed CSP solar fields (e.g., PT or LF) for IPH have highlighted that up to 40% of a large industrial site's heat demand can be met with the CSP solar field. For example, at the Lechera Guadalajara plant the solar field installed in 2016 meets nearly 35% of the heat demand in the pasteurization process. In another example, at Ram Pharma's large pharmaceutical plant, between 30% and 40% of diesel demand is being met with the new solar field (German Solar Association 2017).

Within India, CSP has great potential for SIPH use at the small and industrial scale, with the prospect of fuel displacement in industry and rural areas. The United Nations International Development Organization (UNIDO) has estimated that a market potential of approximately 6.45 GW_{th} for concentrating solar thermal (CST) technologies could exist for Indian industrial applications (MNRE 2017). For example, at the SKF Technologies manufacturing plant in Mysore before solar integration, diesel was the prime fuel burnt to provide heat for the phosphating process. After the integration of the 256.4 m^2 parabolic trough solar field in 2013, the facility now obtains pressurized water from the solar field at 130°C for use in the phosphating processes (PWC India 2017). The solar field, which received a grant for the installation, has been found to reduce diesel consumption by approximately 14,000 liters annually, and the investment had a payback of 5.2 years (PWC India 2017).

India is also increasing investment significantly to meet the potential for SIPH using CST collectors and storage, which provide potential opportunity for technology developers. The SunFocus quarterly report highlights the use of CST (for both electricity and IPH) in India. There is significant developing interest for storage (e.g., phase-change materials [PCMs] and salts) as part of the SIPH integrated solution (MNRE 2017). The Indian Ministry of New and Renewable Energy (MNRE) and UNIDO are also working on a project to provide financial support to concentrating SIPH projects and are helping to create new business models for solar thermal heat to help adoption and deployment (MNRE 2017). With SIPH projects being developed both in the U.S. and globally, the value of independent and validated SIPH modelling tools is clear.

Without such freely available tools, the end-users/beneficiaries of such SIPH solar fields would find it difficult to gauge the value, thermal energy yield, and potential fuel savings from the new solar fields for their applications. The new SAM modules (liquid-HTF and DSG) were created to better understand thermal energy generation and the potential levelized cost of heat (LCOH) at global locations for SIPH applications.

2. Liquid-HTF and DSG Model Development

Various technologies such as non-concentrating collectors and concentrating systems (e.g., sensible liquid-HTF troughs and DSG systems) can be utilized for SIPH applications, depending on the temperatures required by the end-user and the industrial processes (Artic Solar Inc. 2017; IEA 2017). It is important to select the collector technology best suited to the irradiance and land conditions most suitable for the site. This paper considers only the modelling and validation for concentrating collectors, including collectors utilizing either liquid-HTF or DSG, but non-concentrating collectors for SIPH (e.g., flat plate) can also be modeled by SAM (NREL 2017b). Prior to 2017, older versions of SAM already employed robust models for CSP electricity generation systems. The steam power cycle added complexities to extract results relevant for the case where the solar field is only providing thermal energy, i.e., for SIPH. Also, many aspects of the model, such as the solar field layout and piping design, were not optimal for IPH application due to the coupled nature of the solar field and the power cycle. Hence, two new modules were developed to simplify access to SAM's solar thermal collector/receiver models and to simulate solar thermal systems for IPH. Here, we describe some of the development efforts.

2.1 Pre-validation of the liquid-HTF process heat model during model development

In 2016 before the final 2017 development and validation of the liquid-HTF process heat model, a pre-validation was undertaken of a beta SAM version that sought to test the process heat model using liquid-HTF. This work was conducted to isolate the CSP solar field operation, improve the liquid-HTF process heat model, identify bugs, and enhance the user interface. As part of the pre-validation efforts, operational data was provided by the Swiss Institute for Solar Technology (SPF), which highlighted the operations of a 627-m^2 parabolic trough solar field used for a Swiss dairy processing plant (Frank et al. 2014). SPF delivered high-quality operational data and, together with the Bavarian Center for Applied Science (ZAE Bayern), preprocessed and evaluated the operating data; both groups were test users for a beta version of the SAM liquid-HTF model. The Swiss SIPH site is in Saignelégier (northwest of Switzerland), has a 360-kW peak power, and the heat from the solar field is utilized as part of the milk processing. A pressurized water-glycol mixture is used as the HTF, and the required outlet temperature of the solar field is 120°C (Frank et al. 2014). The beta SAM model was used to compare the simulated results of the solar field to one year of operational data from the SIPH site. The SAM weather file for Saignelégier was developed using on-site measured direct normal irradiance (DNI), and ambient temperature.

The beta SAM process heat model already showed good agreement with the operational data from the Saignelégier SIPH site when the solar field was constrained from the power-cycle effects. This was the case especially for the monthly and annual comparison of results for the thermal energy generated. The Saignelégier SIPH site has a designed yearly heat production of 220 MWh. ZAE Bayern utilized beta versions of the SAM liquid-HTF model to validate and compare the modeled thermal output from the solar field to the real yearly experimental thermal yield of 203 MWh. In 2015 NREL provided recommendations for use of the existing CSP Physical Trough model that allowed ZAE Bayern to model the SIPH plant without the specific SAM thermal-application models that are currently available in SAM 2017. Fig. 1 shows the monthly thermal outputs of the simulated SAM Saignelégier solar field compared to the measured or real case. The cumulative yearly thermal energy yield of the solar field simulated through the beta SAM model was 194 MWh, corresponding to an underestimation of only 4.4% compared to the measured thermal output of 203 MWh. On monthly comparisons, the results of the beta version were similarly encouraging, see Fig. 1.

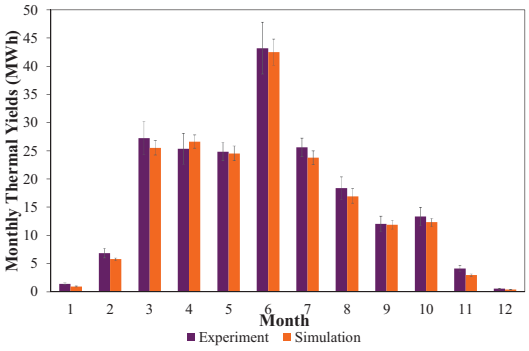

Fig. 1: Monthly comparison between modeled and real thermal outputs at Saignelégier PT-SIPH by ZAE Bayern (Samoli 2016)

The simulated results for the annual thermal energy generation between the real and the beta-version simulated Saignelégier case were within 5% of each other, though deviations in daily simulations could be identified compared to the real operational data. Especially for cloudy days, which do not have a large influence on the total monthly thermal energy generation, an underestimation between the simulated and experimental solar thermal energy generated on an hourly basis showed total daily deviations of up to 15% (Samoli 2016).

It is important to note that SAM typically can handle simulations in one-hour time steps, which were identified as too large for SIPH applications. A key issue in the beta SAM liquid-HTF process heat model was the restriction in using large piping diameters and pipe lengths (suited for power generation), which resulted in large thermal masses. Hence, longer heating periods for the solar field and consequently less thermal energy output was delivered from the solar field in the simulated results compared to the operational data. There were significant differences between the simulated and measured inlet and outlet temperatures, as well as for the volume flow in the main circuit of the solar field. Prior research has identified that the thermal masses play an important role for the prediction of the solar thermal energy generation, particularly for SIPH applications (Möllenkamp et al. 2016). As such, with discussions between NREL and SPF/ZAE Bayern, a more flexible field design as well as a higher time-step resolution (e.g., sub-hourly) was implemented in the beta SAM code, and it allowed a better thermal energy yield prediction than previous, SAM liquid-HTF CSP Physical Trough models.

Moreover, during the pre-validation of the beta SAM liquid-HTF model, standard SI units have been widely introduced and the sensible liquid-HTF trough model has been supplemented by a transient energy balance for the headers and runners. Also, in the pre-validation, the default SAM liquid-HTF case used for the beta version was changed and was more representative of an SIPH application (e.g., 5-MW_{th} facility using pressurized water at 150°C), and some bugs have been removed, which make the beta SAM version more suitable for IPH application. For example, an overnight recirculation of hot fluid that occurred during simulations has been amended. An important real-world implication of SIPH solar fields was the alternating row distances between the rows of collectors (as in Saignelégier), which can lead to errors in the simulated shadowing losses when using fixed row distances. These findings have been incorporated and contributed to support the optimization of the SAM liquid-HTF process heat model. More details of ZAE Bayern's optimizing and pre-validation can be found in work by ZAE Bayern and SPF (Samoli 2016).

2.2 SAM process heat liquid-HTF and DSG model developments and changes

NREL engaged with ZAE Bayern in 2016 and 2017 to address questions and issues found in using the older SAM code for SIPH cases. Review of the ZAE report (Beikircher et al. 2016) helped NREL identify several issues that made the new SAM models more amenable to SIPH applications. NREL has worked to address ZAE Bayern's questions and concerns and to provide feedback and support to this experienced SAM user. The engagement with ZAE Bayern helped the NREL CSP team understand design and operational methodologies for SIPH sites. The work at ZAE Bayern has highlighted key issues such as SIPH sites having smaller piping diameters than the original piping library within SAM, and SIPH solar field layouts that differ from large power plant designs. This type of future engagement will be key to continuing to build and code robust SAM modules for SIPH applications. Working with ZAE Bayern/SPF and understanding how process heat modelling could be changed, the latest version of SAM released in 2017 (NREL 2017b) has the CSP process heat models developed for liquid-HTF and DSG systems. Compared to the previous SAM CSP models for power generation, the solar field model has undergone some significant changes to accommodate the nature of SIPH systems. For example, the solar field from the CSP electricity model had a minimum of two subsections with "H" or "I" configurations common for electrical systems (Wagner and Gilman 2011). This "H" solar field layout is shown in Fig. 2 .

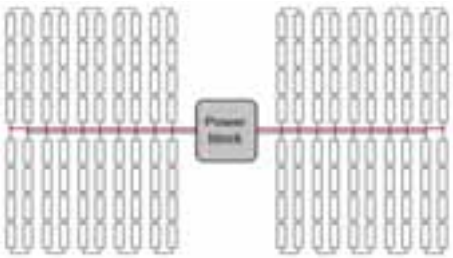

Fig. 2: Typical "H" power block and solar field layout for CSP solar fields for electricity generation (Wagner and Gilman 2011)

Since process heat systems can be much smaller and simpler, the solar fields in the liquid-HTF and DSG process heat models have been developed to utilize a single solar field section (effectively half or one section of the solar field in Fig. 2). In addition, the new models for both liquid-HTF and DSG systems allow for smaller pipe diameters. Also, since the heat sink or process heat exchanger between the solar field and the industrial site can be much closer to the solar field than for power generation sites, the fixed cold and hot header lengths of 50 m has been removed (Wagner and Gilman 2011). In addition, piping through the heat sink can be modeled to allow inclusion of additional thermal capacitance, thermal losses, and pressure drop across the solar-to-process heat exchanger. The DSG model has been developed to allow for modelling either a DSG PT or DSG LF system with a water/steam mixture, where the user can change the optical characteristics of the field. Both process heat models include a simple LCOH calculation and can include financial parameters such as the cost of debt.

3. SAM Model Validations

3.1. Liquid-HTF parabolic trough validation and results

For the final validation of the new liquid-HTF model, having finished the development and optimization, a detailed simulation of an existing parabolic trough solar field was undertaken. This site in Nevada, USA, uses pressurized water in the solar field, and the solar field has a thermal power of 17-MW_{th} (DiMarzio et al. 2015). The parabolic trough solar field was built to provide heat input for a hybrid process, and as such, it was considered a suitable SIPH application. Site operators supplied detailed operational data of the solar field.

The actual solar thermal energy output from the solar field was compared to the SAM simulations (which utilized the final SIPH-model) of the thermal yield generated. The operational data provided included site conditions such as DNI, wind speed, solar field thermal output, and ambient temperature for 58-days of continuous operation between March and April 2015. The validation used 58 days because this was the span of operational data provided, and it was long enough to understand the liquid-HTF model behavior in a variety of DNI conditions. To create the simulation model of the SIPH site, a site-specific weather file was developed, which included the site conditions for the approximate two-month period, and a Typical Meteorological Year (TMY) file was used for the remainder of the year to allow for an annual simulation. While an annual simulation was performed, the modelled simulation of the thermal energy yield was compared to the measured, real solar field thermal output for only the 58 days. This allowed a direct comparison between the simulated and the real thermal outputs and solar field behaviors.

Over the 58-day period, the measured solar field thermal output was recorded to be 4,832 MWh. The SAM model predicted energy output whenever adequate sunlight existed, as well as the cumulative generation that only includes time periods when the actual power plant was operating. Cumulative generation when the plant was operating was calculated by post-processing the SAM data to only sum energy values when the plant had a power output greater than 0 MW_{th}. In the former case, SAM overestimates generation by 1.8%, and in the latter case, SAM underestimates by 1.3%. It is not clear why the plant was idle during certain periods of acceptable sunlight, but the behavior highlights that SAM may need to provide additional user-defined constraints on plant operation. Fig. 3 shows three days of normalized operations data from the SIPH site compared to the simulation.

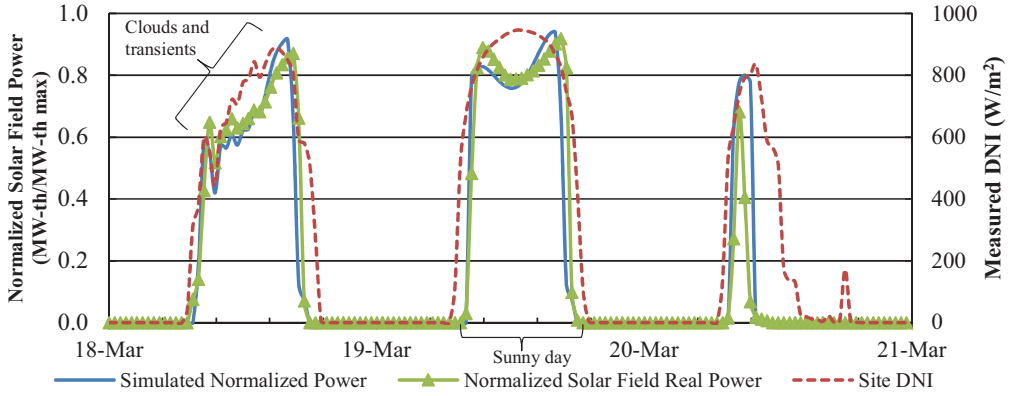

Fig. 3: Comparison of modelled normalized solar field output vs. the normalized solar field actual output for three days

The measured site DNI can also be seen (red dashes); for example, March 19, 2015 was a sunny day, after what was likely a cloudy day on March 18. As can be seen on March 18, the clouds and transients (e.g., the spikes in DNI) led to transient thermal output from both the simulated (green line) and actual operations (blue line). The modelled simulations using the final liquid-HTF model for that day are very similar to the actual site operations. As seen in Fig. 3, on March 20 the SIPH site suddenly stops operations near midday for an unknown reason. The simulated thermal output would normally follow the DNI shape more closely and calculate more thermal energy than the actual site produced on this date. In Fig. 3, an external constraint is applied to the simulation to limit production only to times when the actual plant is operating. Although appropriate for a validation study, such constraints need to be based on plant operation knowledge for a predictive simulation.

3.2. DSG linear-focus collector model validation and results

It has been possible to gain access to operational data for a DSG LF field in Calasparra, Spain. Through collaboration with Tubosol, the plant operators of the 30-MW_e Tubosol Puerto Errado 2 (Tubosol PE2) electricity generation plant, NREL has received and processed operational data for the entire 150-MW_{th} solar field (Novatec Solar 2011) for the month of June 2015. It was determined that the DSG process heat model (which does not include recirculation, but only once-through mode (OTM)), could be used to simulate the Tubosol PE2 solar field. This assumption seemed appropriate because there is no water/steam recirculation in the Tubosol PE2 solar field itself; also, the solar field can be considered to operate as if it were an OTM field, with the steam separation from the water/steam mix occurring after the solar field at the steam drum. The current DSG model would be unsuitable to simulate recirculating DSG fields.

These operational data allow for in-depth observation of the behavior of the solar field, both in normal and transient conditions. The data for the solar field (made up of 28 rows in total) are split into two equal segments (Tubosol PE2.1 and Tubosol PE2.2), where each segment is approximately 75-MW_{th} with 14 collector rows. The reason for the solar field segments is to allow in winter to direct steam from both solar fields to one 15-MW_e turbine. This arrangement ensures maximum electricity generation, rather than generating electricity from both 15-MW_e turbines at part load due to a lack of solar radiation. Each independent solar field segment has the following specification seen in Tab. 1 (Novatec Solar 2011). The data in Tab. 1 has been used for the SAM DSG model validation. It was decided since each segment can be operated independently, that the validation would be done only on one solar field segment. A weather file that uses site data, e.g., the DNI and ambient temperature, has also been created for the validation; again, a TMY file was used for the rest of the year.

Tab. 1: Data used for the SAM DSG validation of the Tubosol PE2 solar field segment

Parameter	Value	Unit
Product name	Nova-1	NA
Number of rows in solar field	14	NA
Solar field length	940	m
Aperture area	151,000	m^2
Operating temperature	270	°C
Operating pressure	55	bar
Peak thermal output	75	MW_{th}

The validation of the DSG process heat model has been done by comparing the predicted thermal energy by the SAM model with the plant data from the Tubosol PE2 segment, although an estimate of the solar thermal power has been made. It is important to note that since Tubosol PE2 has been designed for electricity generation (i.e., 30-MW_e), it was not possible to directly measure the solar thermal power output from the solar field, as the exit of the solar field is a two-phase fluid of steam and water. Unlike the validation of the SAM liquid-HTF process heat model, where the solar field thermal output was directly measured and compared to the SAM simulated solar field thermal output, this was not possible for the DSG validation. While SAM can undertake simulations sub-hourly, the minimum time step for the SAM DSG validation is 10 minutes. Therefore, the sub-minute data from the Tubosol PE2 solar field segment has been averaged to make 10-min time-step intervals, e.g., for the weather file for Calasparra and the estimation of the solar field power output.

Each solar field segment has measurements for pressure, temperature, and mass flow rate of the combined

water/steam fluid. Thus, the enthalpy and the steam quality are unknown at each measured interval at the exit of the solar field segment. Hence, to calculate the solar field thermal output power at each 10-min time step, the steam quality is estimated in two ways (identified as Case 1 and Case 2).

Case 1—where there was a constant steam quality of 0.7485 (i.e., approximately 75% steam in the steam drum). This was determined from the design conditions obtained from the balance of plant process diagram (Novatec Biosol 2011) and thus was used to calculate the enthalpy at each 10-min step.

Case 2—where variable steam quality is estimated from the steam-drum level given in the operations data, then averaged over every 10-min time step. The steam-drum level, as confirmed with Tubosol PE2, is a measure of the steam and water mix in the steam drum, where the steam drum separates the remaining water in the fluid from the steam produced by the solar field. Using the steam-drum level is an estimate of the steam quality produced by the solar field. The calculated enthalpy is multiplied by the mass flow rate to obtain an approximate value of thermal power delivered by the solar field. This estimated thermal power is then compared with the one predicted by the SAM simulation.

However, there are differences between the way the SAM DSG model predicts the solar field operation and the way the actual Tubosol PE2 solar field operates. Therefore, to make a better (and more realistic) comparison, there are a couple of constraints added for Case 2.

Constraint 1: The solar field has hot fluid in the field during the night periods (as well as the day), and the thermal energy can theoretically be calculated during this time. However, as no thermal power from the field is delivered during the night to generate steam, the solar field thermal power output from 9 pm to 6 am is ignored.

Constraint 2: When SAM thermal output is predicted, but the plant itself is for some reason not producing solar thermal power to generate steam for the turbine, this is excluded from the SAM output in a post-processing step.

Fig. 4 shows a plot of such a situation, where the thermal power predicted by the SAM model is shown against the real estimated solar field thermal power output. It can be seen the estimated solar field thermal output was barely present during the day (e.g., the green line), even though there was sufficient DNI for SAM to predict some thermal power generation. The thin blue line represents the SAM simulated power. As seen in Fig. 4, due to the DNI variations (e.g., perhaps due to several clouds that day), the model responded to the spikes in DNI with a considerable power production, whereas the estimated actual output was nearly zero through the day. Hence, the simulated thermal power for days like this was ignored in post-processing, as specific operational decisions such as this made at the site are not accounted for in the DSG model.

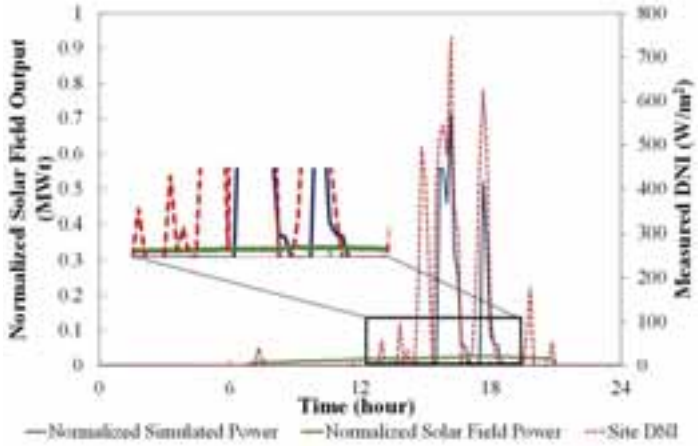

Fig. 4: Comparison of the simulated solar field power output and the estimated actual solar field power output on a day with transients, and showing the need for a constraint to exclude the SAM output when the estimated actual output was minimal

Tab. 2 shows the comparison between thermal energy generation predicted by the SAM DSG model and the calculated estimation using actual field data (for the constant and variable steam quality cases) for June 2015.

Tab. 2: Comparison of the thermal energy generated (MWh) between the actual estimated solar field and the simulated solar field, for the cases of constant and variable steam quality (Case 1 and Case 2, respectively)

Case	Condition	Real estimated thermal energy of solar field (MWh)	SAM thermal energy of solar field (MWh)	Difference in thermal energy (MWh)	Difference (%)
Case 1	Constant steam quality at design conditions	141,105	126,534	14,571	-10.32
Case 2	2.1: Estimated variable steam quality	130,864	126,534	4,330	-3.3
	2:2: Estimated variable steam quality with constraints	127,082	126,128	954	-0.75

As can be seen in Tab. 2, with constant steam quality (Case 1), the actual estimated thermal energy generated for June 2015, was approximately 141.1 GWh, compared to approximately 126.5 GWh from the SAM simulated solar field. In other words, the SAM thermal output was 10.32% less than the real estimated value. Case 1 (i.e., constant steam quality from the solar field) can be considered unrealistic, as there will be a varying steam quality produced by the actual Tubosol PE2 solar field segment. Discussions with the operators at Tubosol PE2 have confirmed that the steam quality can vary from 70% to 80% depending on the DNI conditions. As seen in Case 2 from Tab. 2, when variable steam quality is calculated for the Tubosol PE2 solar field segment, the estimated solar thermal energy generated in June 2015 from the field segment was 130.8 GWh, compared to the simulated output of 126.5 GWh. This is Case 2.1, without further constraints as mentioned being applied. As can be seen, the difference in the energy generated between the simulated solar field and the estimated actual is approximately -3.3%. When the constraints are added, the difference between the actual estimated thermal energy generated and the SAM output drops to 0.75%.

Fig. 5 and Fig. 6 shows the excellent comparison between the normalized simulation (blue) and the normalized estimated actual thermal power output for Case 2. Fig. 5 shows a day that had significant DNI variations (i.e., many clouds throughout the day); Fig. 6 shows a single transient in an otherwise very sunny day.

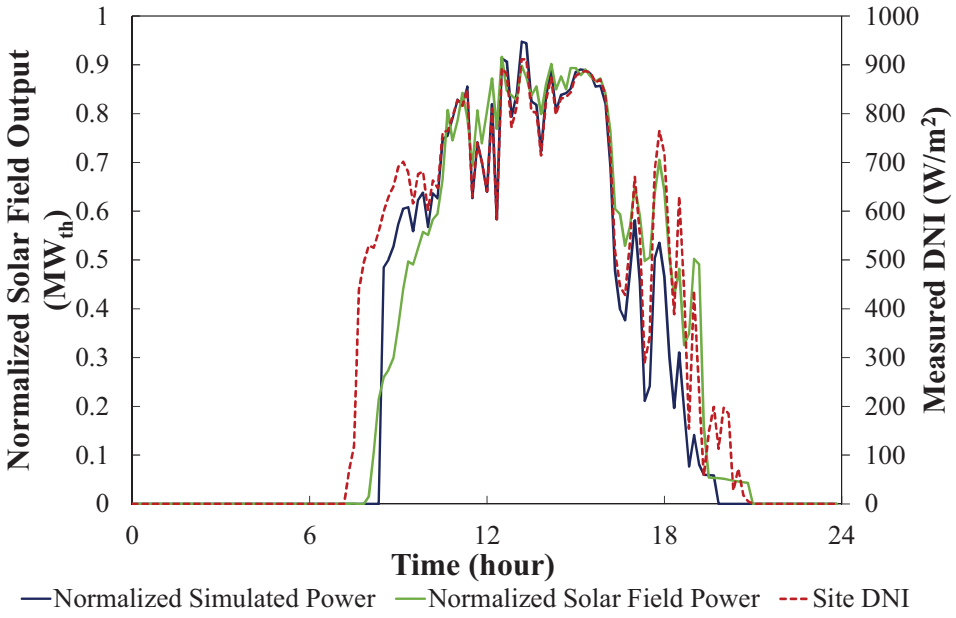

Fig. 5: Comparison of normalized simulated solar field power output and normalized actual estimated output on a day with significant DNI variations

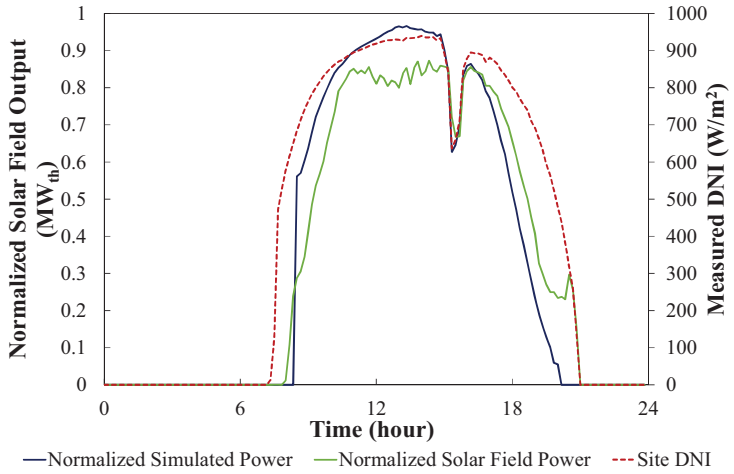

Fig. 6: Comparison of normalized simulated solar field power output and normalized estimated output with one DNI transient

As seen in Fig. 5 and Fig. 6, the simulated power output from the solar field tracks the DNI variations well throughout the day, although the simulated power output, in general, is smoother than the actual estimated solar field output. It is worth noting that near the start of the day, the simulated power compared to the real estimated power is generally slightly overestimating the power output, whereas the reverse is true in the evening. In Fig. 5 and Fig. 6, the simulated power is underestimated relative to the actual estimated amount in the evening. The -3.3% difference between the simulated DSG and the actual estimated energy output for the time period gives confidence that the DSG model is successfully modelling the conditions in the solar field and handling the energy flows. This shows that once the modeled solar field for DSG (at least in this DSG LF case) can be separated from the power generation aspect, the solar field can be well modelled.

4. Utilization of the SAM Liquid-HTF Process Heat Model

The use of both the liquid-HTF and DSG process heat models for potential actual commercial applications would have been ideal. But, it has only been possible to do an initial energy simulation and analysis with the liquid-HTF model. The DSG process heat model could be utilized in future analysis.

The concept of using SIPH for heat addition and integration into breweries is gaining strength, especially in Europe and South Africa, where several studies and operating demonstration SIPH plants for breweries exist (German Solar Association 2017; Mauthner et al. 2014). Either through concentrating or non-concentrating SIPH technologies, breweries that are located in regions having sufficient DNI for solar heat integration could significantly decrease the energy consumed from burning hydrocarbons (Lauterbach et al. 2009; Mauthner et al. 2014).

The newly developed SAM liquid-HTF process heat model has been used for an initial analysis of a brewery in California that is considering implementing a parabolic trough solar field to decrease natural gas usage. An important and potentially valuable financial incentive that currently exists in California is the maximum of up to $800,000 that a project can receive based on being able to show a metered decrease in natural gas due to the addition of a new solar thermal field (California Public Utilities Commission [CPUC] 2017).

The key parameters of the brewery's potential solar field include a design point yield of 1 MW_{th} and the use of unpressurized water as the HTF. The weather file for the site has been created using the National Solar Radiation Data Base, and the brewery site has a daily average DNI of greater than 6.5 kWh/m^2/day (NREL 2017a). The process heat thermal load requirement from the brewery has been highlighted as being approximately constant at 0.3 MW_{th}, 24 hours a day, 365 days a year. The Heat2Hydro solar field and system design also includes a mixed single-tank water storage unit of 50,000 gallons. The storage is expected to be charged fully and maintain an exit temperature to the brewery heat exchanger of 85°C. It is worth noting that SAM version 2017.9.5 has no storage built in. The potential new storage solution for the brewery cannot be directly modelled with the SAM 2017.9.5 version of the process heat model.

The SAM simulation file for the case has been created to model the annual heat input from the solar field to a brewery process heat exchanger. The parameters for the brewery's load (i.e., delivered thermal power to the heat exchanger) have been simulated using collector information provided by Heat2Hydro and Rackam Technologies. At present, since the publicly available SAM 2017.9.5 process heat module is without storage, the initial brewery case has been created whereby all the solar field output in excess of the process load can be absorbed by an ideal storage system. This is a reasonable assumption considering the large storage volume (50,000 gallons) for the Heat2Hydro storage that is charged with the excess thermal energy from the solar field. But this assumption will need to be tested in the future—particularly, how much of the excess energy from the solar field can be absorbed by the single mixed tank.

5. Conclusions

In on-going efforts to improve SAM, the models and use cases for SIPH will continue to be developed. Working with solar developers (e.g., SkyFuel), the SIPH process model developments, particularly for the liquid-HTF model, are likely to include thermal storage and dispatch strategies. With further investigation of the sizing of typical deployed SIPH systems, the default solar field size may be changed, e.g., to 1-MW_{th} for liquid-HTF SIPH fields. The DSG process heat model improvements include developing a recirculation mode to send the remaining water exiting the solar field back to the solar field for further evaporation. This would then allow SAM to better model actual DSG systems, as few DSG systems have been developed as OTM (Feldhoff 2012). Future use of the DSG model could provide a better understanding of the thermal yield generation and steam production for solar EOR.

The highlighted brewery initial case will be important to continue to develop into a case study, to develop both the energy yields and costs of the potential solution, and the financial models to understand economic viability e.g., the net present value (NPV) and the payback period. This will develop the understanding of SIPH applications in California, where the incentive scheme currently in place (e.g., for $800,000 granted to projects that can show a metered decrease in natural gas due to a solar thermal field). As of October 4, 2017, the legislative bill (Bill AB-797 Chapter 473) supporting the CPUC incentive scheme has been extended for two years (California Legislative Information 2017). Further investigation is needed of the financial implications of the extension of Bill AB-797 Chapter 473, particularly on potential projects in California.

The NREL SAM process heat models could help to show thermal energy generation and economic value for known and future applications of SIPH. As global use for SIPH applications continue, modelling tools such as SAM and Greenius can certainly provide an independent method to gauge the potential energy yield at the site. It is possible that the newly developed SAM process heat models could help some users looking to apply for the recently released U.S. Department of Energy (DOE) solar desalination Funding Opportunity Announcement (DOE 2017). The use of the process heat models could help prospects and awardees, better understand thermal energy yield generations and the potential LCOH of CSP process heat solutions, which could then provide heat for desalination activities.

6. Acknowledgements

The authors at NREL would like to thank Jana Möllenkamp, and Thomas Beikircher and Alexia Samoli at the SPF and ZAE Bayern research institutes, respectively, for their diligent and helpful work in the provision of an independent validation effort comparing SAM to operational data, and helping to use and improve the beta version of the SAM liquid-HTF process heat model. Without this type of user interaction, SAM would not be addressing the key issues faced in accurate modelling of end-user needs.

The NREL authors also thank and gratefully acknowledge the efforts and quality of the operational data provided by the operators of the solar fields and partners providing data for these studies. Without these data sets, validations of the SAM models comparing simulations to the real estimated or measured thermal outputs could not have been done. The validations have helped ensure that the SAM process heat models can provide results similar to real operating solar fields where the thermal energy can then be utilized for heat provision. The end-users and industries can put more trust in SAM and other tools such as Greenius, as these are a source of validated and readily available thermal energy generation and simulation tools.

This work was supported by the U.S. Department of Energy under Contract No. DE-AC36-08GO28308 to the National Renewable Energy Laboratory.

7. References

Artic Solar Inc. 2017. “About - Artic Solar.” Artic Solar. 2017. http://www.articsolar.com/.

Beikircher, Thomas, Jana Möllenkamp, Alexia Samoli, and W Schölkopf. 2016. “Validation of SAM Simulation Program Version 2015.6.30) for Process Heat Applications Using Data of a Small Parabolic Trough Solar Field in Switzerland.” Garching, Germany.

California Legislative Information. 2017. “Bill Text - AB-797 Solar Thermal Systems.” California Legislative Information. October 5, 2017. https://leginfo.legislature.ca.gov/faces/billTextClient.xhtml?bill_id=201720180AB797.

California Public Utilities Commission (CPUC). 2017. “California Solar Initiative-Thermal (CSI-T) Program Handbook - April 2017.” CPUC. http://www.gosolarcalifornia.ca.gov/documents/CSI-Thermal_Handbook.pdf.

Deutsches Zentrum für Luft und Raumfahrt (DLR). 2017. “Get FreeGreenius.” Free Greenius. 2017. http://freegreenius.dlr.de/index.php/get-freegreenius.

DiMarzio, Giuseppe, Lorenzo Angelini, William Price, Chun Chin, and Steve Harris. 2015. “The Stillwater Triple Hybrid Power Plant: Ntegrating Geothermal, Solar Photovoltaic and Solar Thermal Power Generation.” In *Proceedings World Geothermal Congress 2015*. Melbourne, Australia. https://pangea.stanford.edu/ERE/db/WGC/papers/WGC/2015/38001.pdf.

DOE. 2017. “Funding Opportunity Announcement: Solar Desalination | Department of Energy.” Energy.Gov. September 27, 2017. https://energy.gov/eere/sunshot/funding-opportunity-announcement-solar-desalination.

Feldhoff, Jan Fabian. 2012. “Direct Steam Generation (DSG) Technology Overview.” presented at the SFERA Summer School 2012, Almeriá, Spain, June 28.

Frank, Elimar, Heinz Marty, Lucien Hangartner, and Stefan Minder. 2014. “Evaluation of Measurements on Parabolic Trough Collector Fields for Process Heat Integration in Swiss Dairies.” *Energy Procedia*, 2013 ISES Solar World Congress, 57:2743–51.

German Solar Association. 2017. “Solar Heat for Industry.” http://www.solrico.com/fileadmin/solrico/media/doc/Solar_payback/Solar_Heat_for_Industry_Solar_Payback_April_2017.pdf.

IEA. 2017. “Solar Thermal Plants Database | Solar Heat for Industrial Processes (SHIP) Plants Database.” SHIP-Plants. 2017. http://ship-plants.info/solar-thermal-plants.

Kurup, Parthiv, and Craig S. Turchi. 2015. “Initial Investigation into the Potential of CSP Industrial Process Heat for the Southwest United States.” NREL/TP-6A20-64709. NREL. http://www.nrel.gov/docs/fy16osti/64709.pdf.

Lauterbach, C, B Schmitt, K Vajen, and U Jordan. 2009. “Solar Process Heat in Breweries Potential and Barriers of a New Application Area.” In *Proceedings ISES Solar World Congress 2009*. Johannesburg, South Africa: ISES. https://www.researchgate.net/publication/266877495_SOLAR_PROCESS_HEAT_IN_BREWERIES_-POTENTIAL_AND_BARRIERS_OF_A_NEW_APPLICATION_AREA.

Mauthner, Franz, Christoph Brunner, Matthaus Hubmann, and Christian Fink. 2014. “Solar Process Heat in Breweries.” AEE Intec.

MNRE. 2017. “SunFocus - Fourteenth Issue.” Minstry for New and Renewable Energy (MNRE). http://mnre.gov.in/file-manager/UserFiles/Sun-Focus_October-December-2016.pdf.

Möllenkamp, J., M. H. Rittmann-Frank, M. Caflisch, M. Rommel, A Häberle, T. Beikircher, W. Schölkopf, and S. Minder. 2016. “Evaluation of Thermal Losses in Parabolic Trough Collector Fields of Solar Process Heat Plants in Switzerland.” *ISES Solar Heating and Cooling (SHC) Palma de Mallorca* EuroSun 2016 Conference Proceedings (October). https://www.researchgate.net/profile/Thomas_Beikircher/publication/308967208_Evaluation_of_Thermal_Losses_in_Parabolic_Trough_Collector_Fields_of_Solar_Process_Heat_Plants_in_Switzerland/links/57fb4bce08ae886b89863c56.pdf.

Novatec Biosol. 2011. “Puerto Errado II BOP 30 MW Thermal Power Station - Process Diagram Water/Steam Balance Load Point 100%.” Tubosol PE2.

Novatec Solar. 2011. “NOVATEC SOLAR: Concentrating Solar Power - Puerto Errado 2 in Spain.” Novatec Solar. 2011. http://www.novatecsolar.com/56-1-PE-2.html.

NREL. 2017a. “NSRDB Data Viewer.” NREL NSRDB Data Viewer. 2017. https://maps.nrel.gov/nsrdb-viewer/?aL=8VWYIh%255Bv%255D%3Dt&bL=groad&cE=8VWYIh.0.0.1%255Ba%255D%3Df%268VWYIh.0.0.2%255Ba%255D%3Df%268VWYIh.0.0.3%255Ba%255D%3Df%268VWYIh.0.0.4%255Ba%255D%3Df%268VWYIh.0.0.5%255Ba%255D%3Df%268VWYIh.0.0.6%255Ba%255D%3Df%

268VWYIh.0.0.7%255Ba%255D%3Df%268VWYIh.0.0.8%255Ba%255D%3Df%268VWYIh.0.0.9%255Ba%255D%3Df%268VWYIh.0.0.10%255Ba%255D%3Df%268VWYIh.0.0.11%255Ba%255D%3Df%268VWYIh.0.0.12%255Ba%255D%3Df%268VWYIh.0.0.13%255Ba%255D%3Df%268VWYIh.0.0.14%255Ba%255D%3Df&lR=0&mC=49.54481568504451%2C-110.0006103515625&zL=8.

———. 2017b. “System Advisor Model (SAM).” NREL System Advisor Model. 2017. https://sam.nrel.gov/.

PWC India. 2013. " Using Parabolic Trough For Phosphating Process." PricewaterhouseCoopers (PWC) India. http://www.cshindia.in/images/pdf/SKF.pdf

Samoli, Alexia. 2016. “Dynamic Simulation of a Parabolic Trough Process Heat Plant: Comparison with Experimental Data and Simulated Results of a Linear Fresnel Collector.” ZAE Bayern Bavarian Center for Applied Science: TUM Department of Mechanical Engineering Technical University Munich.

Turchi, Craig S., Parthiv Kurup, and Guangdong Zhu. 2016. “Revisiting Parabolic Trough Concentrators for Industrial Process Heat in the United States.” In *ASME 2016 Power and Energy Conference PowerEnergy 2016*, V001T08A018. North Carolina, USA: ASME. https://doi.org/10.1115/POWER2016-59621.

Wagner, Michael J., and Paul Gilman. 2011. “Technical Manual for the SAM Physical Trough Model.” NREL/TP-5500-51825. NREL. http://www.nrel.gov/docs/fy11osti/51825.pdf.

INDIA'S QUEST FOR GLOBAL SOLAR THERMAL INDUSTRIAL PROCESS LEADER

- Jaideep N. Malaviya (Secretary General), Solar Thermal Federation of India
info@stfi.org.in, *Phone: +91-9890033399*

INTRODUCTION

Fifty-seven per cent (nearly 240 Metric tons of oil equivalent) of the final energy consumption in India is used for thermal applications. Industrial process heat, residential cooking, and water heating are the main thermal applications accounting for more than 90% of the thermal energy requirement. Presently India's thermal energy demand is primarily being met through coal, biomass, and petroleum fuels. Several areas in India receive good DNI and solar thermal energy has potential to convert this radiant energy to meet the heating needs up to 250 ^{O}C. 15 million tonnes of fuel oil in industries requiring heat up to 250 ^{O}C & 5,000 trillion kWh of electricity (excluding LPG consumption) in various sectors for heating water & air being consumed annually. Even if 1% of this energy requirement is met using concentrated solar thermal (CST) systems the potential estimated is over 2.5 million m^2. However, to achieve these targets there need to be market drivers and one of them suggested is to obligate solar thermal heating in high energy consuming industries and encourage Energy Service Companies (ESCo's).

INDIA'S ACHIEVEMENT IN CST SYSTEMS

More than 200 steam generating systems have been installed so far in the country with a cumulative figure of little over 75,000 m2 of dish area equivalent to about 50 MW. These are largely due to subsidy programmes of Ministry of New and Renewable Energy (MNRE), government of India and programmes under GEF-UNDP and GEF-UNIDO. Most of these have been installed mainly at places where steam generated through conventional boilers for process heating and community based steam cooking besides few demonstration projects for cooling. During the period April 2012 to March 2017 the country witnessed net installation of 44,949 m2 of dish area under the GEF-UNDP Concentrated Solar Thermal Heating programme. Solar Heat for Industrial Process had the lion's share of almost 70%. Table 1 below gives the break-up wise of installation occurred under this programme besides projects supported for revamping.

Sl.	Application	Area (m2)
1	Process Heating	28,188
2	Steam Cooking	9,208
3	Space Cooling	3,826
4	Repair and Maintenance	3,727
	TOTAL	44,949

Table 1: Application wise installations under GEF-UNDP programme

The true market potential of CST technologies in the industrial sectors has been assessed as 6.4 GW in India in a study recently commissioned by UNIDO. Fourteen industry sectors have been identified (Table 2) by UNIDO where CST technologies make economic and technical sense in terms of ready acceptability for their deployment for a variety of process heat applications in the temperature range up to 350°C.

Sl.	Sectors
1	Textiles (Weaving, Finishing)
2	Pharmaceuticals
3	Automobiles
4	Breweries
5	Pulp & paper

doi:10.18086/swc.2017.26.07 Available at http://proceedings.ises.org

6	Electroplating
7	Food processing (including Dairy & Sugar)
8	Rubber
9	Chemical & Fertiliser
10	Petroleum Refineries
11	Desalination
12	Ceramic tile & pottery
13	Plaster of Paris, Steel rerolling, Cement, Mining
14	Tobacco

Table 2: Highest potential sectors for solar thermal process heating

In India mainly 3 types of concentrating solar technologies are presently in promotion:

i) Manually tracked dish solar cookers to cook food for 10-40 people,

ii) Fixed focus E-W automatically tracked elliptical dishes (Scheffler) for direct indoor cooking for about 50-100 people & for steam generation for community cooking, laundry, space cooling etc. of any capacity and

iii) Dual axis fully tracked Fresnel dishes (Arun) for all such applications.

The CST systems can be broadly classified as below

- ★ Fixed Focus Elliptical Solar Dish (Scheffler)
- ★ Fresnel Reflector Based Dish
- ★ Linear Fresnel Reflector Concentrator
- ★ Compound Parabolic Collector
- ★ Parabolic Trough Concentrator
- ★ Paraboloid Dish

There are 22 Manufacturers offering 6 types of CSTs in promotion with varying designs & sizes. Figure 1 gives the technology-wise CST systems. There are couple of solar grade cut mirror glass manufacturers offering international standards quality developed technologies for edge sealing & back coating and state of the art parabolic trough mirrors.

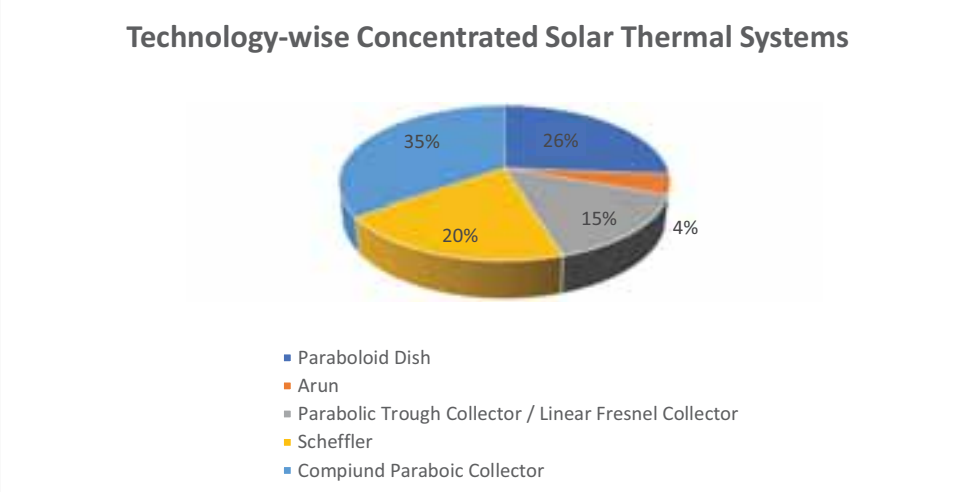

Figure 1: Technology-wise CST systems

DNI MAP OF INDIA

The Direct Normal Irradiation (DNI) in India varies from 4.0 to 6.0 kWh/m²/day as shown in the Figure 2 and is an indicator of the potential regions that can use solar thermal.

Figure 2: DNI Map of India (Geo Model Solargis, EU)

Based on the DNI the potential states with medium to high DNI that facilitate implementation of CST projects are listed in Table 3.

Sl.	Region	Indicative average DNI/ m² / day* (In kWh)	Sunshine days	Fixed focus elliptical dish^ / Non-evacuated heat receiver PTC		Evacuated heat receiver PTC/ LFTR		Fresnel reflector/ Paraboloid based dish	
				Efficiency at 150C**	Heat delivery*** / m²/ year (in million kcal)	Efficiency at 150C**	Heat delivery*** / m²/ year (in million kcal)	Efficiency at 150C**	Heat delivery*** / m²/ year (in million kcal)
1.	Leh Ladakh	6.5	320	35%	0.626	40%	0.715	60%	1.073

2.	Gujarat Rajasthan & western M.P.	6.0	300	40%	0.620	45%	0.697	65%	1.010
3.	Southern & Central	5.0	280	40%	0.482	45%	0.542	65%	0.783
4.	North, West & Himalayas	4.5	250	35%	0.339	40%	0.387	60%	0.581
6.	North – east & Eastern part of Orissa & A. P.	4.0	250	40%	0.344	45%	0.387	65%	0.559

Table 3: Potential states with medium to high DNI

^ Average effective aperture area of 16 m^2 fixed focus elliptical dish for receiving normal radiation during whole year is to be taken as 11 m^2. The heat delivery from a 16 m2 elliptical dish in a year in different regions will, therefore, be 11 multiplied by figures given in above table.
Also, dual axis automatic tracked elliptical dishes may have higher heat delivery by say 5% in comparison to single axis tracked dishes due to avoided errors in manual N-S adjustments.

* Can vary by +/- 10% at a location in the region

** Its average annualized efficiency and is linked with ambient temperature and wind conditions of particular region. It reduces in the regions having lower ambient temperature and high wind velocity. It also reduces marginally for CSTs working at higher temperatures due to higher heat losses, thereby reducing the heat delivery. Temperature range which can be achieved by various CSTs, their salient features, installed cost & payback period are given below.

*** Heat delivery will:

i) increase if the fluid temperature goes down due to less heat losses. Likewise, it will also decrease if working temperature is raised high say up to 350 ^{O}C or so especially in case of Fresnel reflector /Paraboloid dishes which are designed for such temperatures.

ii) decrease by 10% or more if the mirrors are not of solar grade quality.

INTRODUCING SOLAR THERMAL CERTIFICATE SCHEME

Perform Achieve and Trade (PAT) scheme of Bureau of Energy Efficiency, designed to accelerate energy savings in energy intensive and large industries by incentivizing energy savings. The identified industries classified as Designated Consumers (DC's) are aluminum, cement, chlor-alkali, fertilizers, iron and steel pulp and paper, railways, textiles, petroleum processing and refining, sugar, chemicals, commercial buildings and electricity distribution companies. The PAT – Part 1 scheme that ended in March 2015 achieved 8.67 million tonnes of oil equivalent (MTOE) and abated 31 million tons of CO_2. The PAT Part 2 scheme notified on 31st March 2016 has a target reduction of 8.869 MTOE assigned to 621 DC's.

These DC's who achieve reductions in their targets receive ESCerts (energy saving certificates) which can be traded with facilities that are having trouble meeting their targets, or banked for future use.

One tonne of oil equivalent (TOE) is One ESCert is issued.

1 TOE = 1 ESCert = INR 10,968

Each TOE at 890 kgs/m3 density is equivalent to 1,125 litres of fuel oil.

Concentrated Solar Thermal (CST) Technologies can provide a good alternative to reduce their specific energy consumption as shown in Table 4 below:

	Solar PV	Unit	Solar Concentrator (PTC/Dish) >120°C	Solar CPC (NIC) 80-90°C	Unit
Energy (TOE/Year)	1		1	1	
Equivalent Energy	**11,630**	**kWh**	10,000,000	10,000,000	kcal
Capacity	8	kWe	5	5	kWth
Area Required	84	m^2	14	11	m^2
Cost (INR)	6,00,000	INR	283,173	163,929	INR

Table 4: Cost Comparison of energy generation using solar PV, CPC and Parabolic/Dish

Hence for the same amount of TOE, CST technologies offer a viable alternative and hence including it in the reporting structure of PAT will ensure that designated consumers (DCs) will invest in CST technologies.

To encourage these DC to go for CST a scheme of s**olar thermal certificate (STCert)** to be launched by Bureau of Energy Efficiency (BEE). A defined target to be given to potential DC's to generate STCert. The minimum project size to qualify for STCert to be 250m^2 for single axis and 150m^2 for double axis. If the scheme is successful and finds more buyers of STCert, the incentive can be reduced gradually with time. Non-DC's can also apply for STCert and should be an entity consuming at least 5,000 litres/ year of fuel oil annually. Those DC's not able to meet their STCert can buy these STCert from non-DC's.

BARRIERS IN CST'S GROWTH

Major barriers listed in large-scale promotion of CSTs at the start of project were as follows:

- Lack of awareness about the technologies & their benefits.
- Information on successful projects not accessible to public.
- Lack of confidence on technologies. Lacking in trained manpower of technicians.
- No test standards & test set ups for measuring performance exists
- Space constraints for installations to beneficiaries
- Non-availability of solar grade mirrors in required sizes at reasonable prices.
- Non-availability of soft loans to beneficiaries & ESCOs
- Low returns on investments as compared to solar flat plate collectors. Requires higher support, especially for space cooling & standalone systems
- Very few manufacturers. Not much competition.
- Difficulties for cost control measures.

While most of the barriers have been addressed in the last five years however the demand creation has not occurred to a level of commercialisation.

PROJECT SOLAR PAYBACK

The Solar Thermal Federation of India (STFI) and the Indo-German Chamber of Commerce (IGCC) have teamed up for the international 'Solar Payback' project, which aims to increase the use of solar thermal energy in industrial processes. Supported by the German Federal Environment Ministry funded by the International Climate Initiative, the three-year project will be implemented in India, South Africa, Mexico and Brazil. It is coordinated by the German Solar Association BSW-Solar and eleven partner organisations: three German companies, plus each target country's national solar industry association and German Chamber of Commerce. The use of solar heat for cleaning, steam

production, bath heating and surface treatment in manufacturing is still a niche market in India and around the world

The initial study has so far focused on an in-depth analysis of market barriers and drivers by drafting a solar process heat roadmap and making policy recommendations. In addition, it intends to strengthen the industry by offering training for planners and raise awareness by organising an industry conference. The project partners will use a wide range of activities and communication tools to get in touch with the relevant stakeholders in politics, business and financing. Key activity targets include:

- Drafting a National Solar Process Heat Roadmap
- Developing a financing/business tool for planners and investors to offer preliminary analyses of solar process heat plants
- Developing policy recommendations for uptake of solar process heat at national level
- Organising train-the-trainer workshops on planning / designing solar process heat systems
- Implementing an online matchmaking network for investors and technology providers
- Organising a local industry / stakeholder conference

Conclusions:

Looking at the huge heating demand and reducing dependence on imports of fuel oil India has the quest to quest for becoming global leader for deploying solar thermal industrial process heat and meeting the identified target of 6.4 GW. The areas that need to be addressed can be summarised as below:

- MNRE to create demand worth INR 100,000 m^2 in 3 years in food processing industries, automobile and defence etc.
- MNRE to invite manufacturers to develop products and infrastructure to bring down the costs through R&D and have budget for
- Make the available DNI data of various locations to public at no cost.
- Introduce performance based incentive equivalent of MWth or MTOE avoided.
- Output be close to the manufacturer's claim & co-relate to the DNI of that area. Any reduction be suitably penalised. A Renewable Heat Incentive (RHI) policy need to be framed.
- Provide concessional loan to manufacturing industries to scale up operations and business.
- Perform Achieve Trade (PAT) operated by BEE must have a special mention about solar thermal heating in their curriculum.
- Large scale capacity building workshops for skilled personnel for better upkeep and maintenance
- Encourage ESCo model as it ensures proper operation of the installations and can give is the recovery. Easy funding be made available for ESCo projects.

REFERENCES:

Solar Thermal Federationof India (http://www.stfi.org.in)
Ministry of New and Renewable Energy, government of India (http://www.mnre.gov.in)
GEF-UNDP Concentrating Solar Thermal Programme (www.cshindia.in)

- X – X – X -

A Comparative Cost Assessment of Low Carbon Process Heat Between Solar Thermal and Heat Pumps

Steven Meyers, Bastian Schmitt and Klaus Vajen

University of Kassel, Kassel, Germany

Abstract

Lower temperature renewable process heat derived from the sun can be generated from solar thermal collectors and a photovoltaic powered heat pump. To determine which can produce lower cost heat under certain technical and financial parameters, a robust methodology was developed to determine the maximum solar thermal project investment for it to remain the lower cost technology. This result can also serve as a target for the solar thermal industry to ensure its role in the future of renewable heat.

The assessment methodology was used in a case study analysis, consisting of typical industrial process heat load and temperature profiles, meteorological conditions, technology costs and performance. Results indicated that for constant energy demand processes when a heat pump can operate the majority of the year, a photovoltaic heat pump system delivers lower cost heat. In a typical five day one shift work week where a heat pump has limited access to a heat source, solar thermal remains the lower cost heat provider. For the same five day one shift case but without a constrained heat source, allowing the heat pump to operate for 2000 hours a year, solar thermal plants must be built for less than 250 €/m^2_{ap} in low irradiation regions like Copenhagen and 525 €/m^2_{ap} in high irradiation regions like Chile or North Africa. For solar thermal to remain a primary renewable heat provider in the future, project investments should consistently be less than 200 €/m^2_{ap}.

The presented results are highly variable based on numerous technical and financial parameters. Therefore the use of the methodology described in this work is critical to quickly determine which technology produces lower cost solar derived renewable heat.

Keywords: process heat, solar thermal, PV, heat pump, techno-economic, renewable heat

1. Introduction

A major result of the climate change conference in Paris was the decision to attempt to limit the rise of Earth's global temperature at century's end to no greater than 1.5 °C. One major sector, Industry, accounted for 28% of global final energy use and 11% of emissions from heat and electricity production (IPCC, 2015). If the 1.5 °C goal is going to be achieved, swift action must be taken to replace all sources of carbon emissions. One such option is the use of the sun to generate renewable industrial process heat typically below 150 °C.

Two main technologies can convert solar irradiance to thermal energy; either directly through solar thermal (ST) collectors or indirectly via photovoltaics (PV) and an electrically driven vapor compression heat pump. Numerous studies have been conducted within the domestic sector which compares and/or utilizes both technologies for hot water production and space heating. In the industrial sector, where load profiles, temperature levels, and project specific costs are drastically different, few studies to date have been conducted to compare these two solar heating technologies. Meyers et al (2015; 2016) have developed a comparison methodology between solar thermal and direct resistance heating photovoltaics, crafting unique terms such as the levelized cost of heat (*LCOH*) ratio and project investment ratio (IR). These terms allow for a quick comparison of technology based on their project turn-key specific capital investments. Pérez-Aparicio et al. (2017) has subsequently undertaken similar methodological approaches, incorporating the use of PV powered heat pump, though is limited in its flexibility to adapt to different meteorological conditions, process temperatures (only 200 °C was tested), technology performance, and future costs. These results were also not supported by energetic simulation. The work presented here has expanded upon the prior Investment Ratio methodology of Meyers et al. (2016) and has incorporated the use of heat pumps to develop a universally applicable method to assess which technology can produce lower cost heat for nearly any possible combination of meteorological, technical, and financial parameters.

doi:10.18086/swc.2017.26.08 Available at http://proceedings.ises.org

2. Methodology

The analysis conducted within this work is an expansion of prior research (Meyers et al., 2015; 2016). Within this publication, detailed solar thermal and PV simulations were conducted and correlations made which determined the lower cost heat provider based on local solar irradiation, process temperature, and technology capital cost. The current work expands upon this methodology to include a PV electricity powered vapor compression heat pump.

2.1 Solar simulations and technical basis

2.1.1 Solar Thermal

The solar thermal (ST) plant design and simulation methodology has been described in Meyers et al. (2016) to calculate solar yields under various process loads, temperatures, and meteorological conditions with different collector types. The ST plant was designed to work in conjunction with an already existing heating facility, serving as a "fuel saver" when solar thermal energy is available, either directly or through a thermal store. In summary, two phases of simulations took place via TRNSYS, with a model that was validated through a currently operating industrial solar heating plant in Germany (Lauterbach, 2014; Schmitt et al., 2015). The first phase were "Infinite Load Case" (ILC) simulations which determined the maximum annual specific ST yield ($q_{sol}^{ST,ILC}$ in $kWh_{th}/(m^2_{ap}\cdot a)$) for 800+ global cities for four non-concentrating collectors (flat plate, flat plate double glazed, evacuated tube, compound parabolic (CPC)) at various mean process temperatures ($T_{P,m}$). The yields were considered as a "maximum" because the process load was constant and had a large heat demand which allowed for the exclusion of a thermal store and second heat exchanger (only the collector field, solar loop heat exchanger and pipes/pumps were modeled). This reduced the mean collector temperature and thus maximized yield.

The second phase consisted of the "Practical Load Case" (PLC) simulations which incorporated more realistic conditions found in industry. These conditions included various process load profiles (one or three shifts, operating five or seven days a week), load magnitude (quantity of daily energy required relative to installed solar field size), and storage volume. Only nine sites were simulated due to the computational intensity, but they represented a wide span of annual solar irradiation (H in kWh/m^2a), annual average daytime temperature ($T_{amb,day}$), with annual specific ST yield results reported ($q_{sol}^{ST,PLC}$) in $kWh_{th}/(m^2_{ap}\cdot a)$. To reduce dimensionality, a differential temperature term was coined, called T_{diff}, which was the difference between the mean process temperature ($T_{P,m}$) and annual average daytime temperature ($T_{amb,day}$). This term highly influenced the annual yield results.

Correction factors (F_{corr}^{PLC}) were calculated to adjust results from the ILC to the nine representative PLC cases, by simply dividing the PLC yield by the ILC yield for the same simulated cities ($F_{corr}^{PLC} = q_{sol}^{ST,PLC}/q_{sol}^{ST,ILC}$).

2.1.2 Photovoltaic Heat Pump

The photovoltaic driven heat pump (PVHP) plant was the combination of a PV plant installed on a factory's roof with a heat pump connected to a heat demanding industrial process. The PV plant was connected to the industry's internal electrical grid. When the PV plant generated electricity, it first went to power the HP and any deficit or excess was "bought" from or "sold" to the internal grid at no cost. This meant that the existing electrical infrastructure on site served as free exchange mechanism. In this light a HP, with a known Coefficient of Performance (COP in units of kW_{th}/kW_{el}), was operated only when needed using "banked" PV generated electricity. The annual thermal energy generated by the PVHP system (q_{sol}^{PVHP}) is shown in eq. 1, with the annual specific PV generated electricity denoted E_{sol}^{PV} in $kWh_e/(kW_p\cdot a)$.

$$q_{sol}^{PVHP}\left(kWh_{th}/\left(kW_p\cdot a\right)\right) = E_{sol}^{PV}\cdot COP \qquad \text{(eq. 1)}$$

This model, while not a true PVHP direct coupled system as seen in the household sector, does better represent typical industrial conditions. The onsite electrical demand of typical industries is often significantly larger than a PV plant could generate on its roof, meaning that all PV electricity would be internally consumed and not fed into the grid. Secondly, a PV plant would never be directly coupled with a HP because factories nearly always have an electrical grid connection and operating an electrically isolated HP directly off PV would require batteries to smooth transient and control HP performance. For both reasons, this design was not investigated.

The peak power or size of the HP relative to the PV plant was scaled to consume every kWh of the annual PV generated electricity. This symbolized that the heat is 100% renewable and zero carbon (ignoring the required carbon to produce the components and refrigerant leakages), thus similar to an ST plant. The HP peak power (P_{peak}^{HP}) was calculated by multiplying the annual solar PV yield (E_{sol}^{PV}) by a known onsite estimated *COP*, then divided by the number of full load operating hours (*FLH*) per year that the HP was expected to operate (eq. 2), in units of Watt thermal (HP) per Watt peak (PV). *FLH* and *COP* can be determined through knowledge of the industrial process and availability of a fitting heat source, often by conducting an energy audit. Through this equation, it is shown that smaller heat pumps are required when operating more hours and larger heat pump for fewer, in order to consume the same annual PV generated electricity.

$$P_{peak}^{HP}\left(kW_{th}/kW_p\right) = E_{sol}^{PV}\left(\frac{kWh_e}{kW_p}\right) \cdot COP\left(\frac{kW_{th}}{kW_e}\right)/FLH\ (h) \qquad \text{(eq. 2)}$$

The heat pumps (HP) used for this assessment were electrical powered vapor compression. An increasing number of industrial grade devices are currently on the market with heating performances well over 100 °C, capacities greater than 100 kW_{th} of heat, and with a *COPs* ranging between 2 and 5, depending on the source and sink temperature (Wolf et al., 2014). These types of HPs are very suitable to deliver similar levels and quantities of heat as ST. For this assessment, annual average HP *COPs* were assumed to be used, taking into account small changes due to part load operation during the year. Through the advent of multiple parallel compressors and variable speed drives currently available for industrial HPs, the variability in COP is quite small through the normal operating range. A small buffer tank was also recommended by HP suppliers to reduce temperature transient in both the source and sink side of the HP. Due to its relatively small size (15 l/kW_{th}), thermal losses were less than 0.5% of the overall HP generated heat and thus ignored.

Solar PV yields were determined through TRNSYS simulations for the same 800+ sites of the ILC using a well-known mono-silicon panel from a global producer, incorporating module temperature and irradiance dependent efficiency modifiers. A correlation between PV solar yield (E_{sol}^{PV}) in kWh_e/kW_p and the local irradiation (*H*) and latitude (φ) was created so an expected PV yield (necessary for heat pump sizing and economic considerations) can be quickly estimated when investigating a solar process heat plant at a specific site (eq. 3).

$$E_{sol}^{PV}(kWh/kWp) = \theta_0 + \theta_1 \cdot H + \theta_2 \cdot \varphi \qquad \text{(eq. 3)}$$

2.2 Solar Heating Project Investment

Specific solar thermal project investment (I_{ST} in €/m^2_{ap}) was the total turn-key cost for all components (collectors, store, pipes, pumps), installation, and process integration to realize a plant, inclusive of any locally available subsidies or financial support mechanisms. The project investment (I_{ST}) varied widely based on technology choice, integration difficulty, thermal store size, and installer expertise. Typical I_{ST} values can range from less than 250 €/m^2_{ap} for 10,000+ m^2_{ap} plants in Denmark to over 800 €/m^2_{ap} for smaller installations with high quality collectors, though typical values are between 300..600 €/m^2_{ap} for projects larger than 500 m^2_{ap} (BAFA, 2016), with subsidy.

Specific PVHP project investment (I_{PVHP} in €/W_p electric) was dependent on three factors, the specific PV field investment (I_{PV} in €/W_p), the specific HP investment (I_{HP} in €/kW_{th}) and the relative HP peak power

(P_{peak}^{HP}) as already discussed in eq. 2. The specific PV investment (I_{PV}) for megawatt scale projects is in the range of 1 €/W_p (Fraunhofer ISE, 2015). The specific HP investment (I_{HP}) is rather application and technology dependent, but values ranging between 200 and 800 €/kW_{th} can be expected (IEA Annex 35, 2014; Wolf et al., 2014). The HP contribution to the overall PVHP investment was determined by multiplying the relative HP peak power by the specific HP investment, shown in eq. 4.

$$I_{HP_{(PV)}}\left(€/W_p\right) = P_{peak}^{HP}\left(\frac{kW_{th}}{kW_p}\right) \cdot I_{HP}\left(\frac{€}{kW_{th}}\right) \quad \text{(eq. 4)}$$

Subsequently, the overall specific PVHP investment per Watt peak (electric) is shown in eq.5.

$$I_{PVHP}\left(€/W_p\right) = I_{HP_{PV}} + I_{PV} \quad \text{(eq. 5)}$$

Expected values of P_{peak}^{HP} and I_{PVHP} are shown in Tab. 1. For the few example cases, the HP investment was typically smaller than PV, which is why values were expressed in units per W_p electric (PV) instead of thermal (HP).

Tab. 1 – Example calculation to determine the overall PVHP investment in relation to the installed PV power

E_{sol}^{pv} ($kW_e h/kW_p$)	COP (kW_{th}/kW_e)	FLH (h)	P_{peak}^{HP} (kW_{th}/kW_p)	I_{HP} (€/kW_{th})	$I_{HP_{(PV)}}$ (€/W_p)	I_{PV} (€/W_p)	I_{PVHP} (€/W_p)
1000	2	4000	0.5	400	0.2	1.25	1.45
1250	3	2000	1.87	400	0.75	1.25	2
1500	4	1000	6	400	2.4	1.25	3.65

2.3 Financial Analysis

By expressing the turn-key PVHP plant investment per W_p electric, a similar methodology can be used from Meyers et al. (2016). In this work, the two technologies were compared by their dividing their installed specific capital investments, called the Investment Ratio (*IR*), a value which was calculated when the Levelized Cost of Heat (*LCOH*) of both were equal (Louvet et al., 2017). This methodology can be altered to fit this comparison by simply replacing the I_{PV} with I_{PVHP} and q_{sol}^{PV} with q_{sol}^{PVHP}.

For each infinite load simulation case (800 cities, 4 ST collectors, 3 process temperatures and 1 PV), ST and PVHP yields were calculated, assuming a known COP. Using the equivalent *LCOH* equation (eq. 6) and parameters in Tab. 2, I_{ST} and I_{PHVP} were iterated until convergence was found.

$$LCOH_{ST} = \frac{\boldsymbol{I_{ST}} + \sum_1^n \frac{OM_{ST}}{(1+DR)^n}}{\sum_1^n \frac{q_{sol}^{ST}\cdot(1-SD)^n}{(1+DR)^n}} = \frac{\boldsymbol{I_{PVHP}} + \sum_1^n \frac{OM_{PVHP}}{(1+DR)^n}}{\sum_1^n \frac{q_{sol}^{PVHP}\cdot(1-SD)^n}{(1+DR)^n}} = LCOH_{PVHP} \quad \text{(eq. 6)}$$

Tab. 2 – The required parameters to calculate the *LCOH*

Parameter	Definition	ST Value	PVHP Value
$\boldsymbol{I_{ST,PV}}$	Investment (/m^2_{ap} , /W_p)	Variable	
$\boldsymbol{OM_{ST,PV}}$	Operation and Maintenance (% of $I_{ST,PVHP}$)	2% (VDI, 2014)	1.75% (VDI, 2012; Shimura et al., 2016)
DR	Discount Rate	6.40% (Ondraczek et al., 2015)	
SD	Degradation Rate	0.4%/a (Fraunhofer ISE, 2016)	0.5%/a (Jordan and Kurtz, 2013)
n	Years of Operation	20 (Duffie and Beckman, 2013)	

Using the iterated I_{ST} and I_{PVHP} per simulation case when their heat costs were equal, the Investment Ratio ($IR^{CPC}_{ILC,local}$) was calculated in eq. 7. The superscript indicates which collector was being assessed and the subscript depicts the Infinite Load Case (ILC). Also in the subscript, the "*local*" denoted the calculated *IR* for that specific case of local meteorological conditions and is a precise value. The resulting "*local*" Investment Ratios were generalized as a function of T_{diff}, H, and COP, determined through linear regression in eq. 8, noted with "*gen*" in the subscript. $IR^{CPC}_{ILC,gen}$ is graphically depicted in section 3.1.1. The subscripts "*local*" and "*gen*" can be interchanged within the other equations in this work, as they approximately equal each other due to the regression analysis. A "*market*" subscript is the site specific known investment for heat pump, PV and solar heating plants to be realized, known by local installers.

$$IR^{CPC}_{ILC,local} = I_{ST}/I_{PVHP} \text{ in units of } (€/m^2_{ap})/(€/W_p) \quad \text{(eq. 7)}$$

$$IR^{CPC}_{ILC,gen} = \theta_0 + \theta_1 \cdot H + \theta_2 \cdot \sqrt{T_{diff}} + \theta_3 \cdot H \cdot T_{diff} \quad \text{(eq. 8)}$$

Using the calculated Investment Ratio for the Infinite Load Cases, one can determine the maximum ST investment required for it to remain the lower cost heating technology. Initially, the $IR^{CPC}_{ILC.local}$ is calculated from the simulation results and regression analysis (eq. 8). Next, a correction factor ($F^{CPC}_{corr,PLC}$) is determined using the simulation results which adjusted the ILC solar yields to a more typical value expect in real solar heating plants under industrial conditions, called "Practical Load Case". The $F^{CPC}_{corr,PLC}$ value typically ranges between 0.7 and 0.95 depending on the load profile, graphically shown in section 3.1.2. By multiplying these together (eq. 9), a more accurate Practical Load Case Investment Ratio ($IR^{CPC}_{PLC.local}$) is calculated which takes into account typical process load conditions and thermal losses.

$$IR^{CPC}_{PLC.local} = IR^{CPC}_{ILC,local} \cdot F^{CPC}_{corr,PLC} \quad \text{(eq. 9)}$$

Next, market insight is required for the known technology costs at a specific location. One must individually calculate the market price for a PVHP plant ($I_{PVHP,market}$) using eq. 2, 4, and 5, and then multiple this by the local PLC Investment Ratio ($IR^{CPC}_{PLC.local}$ in eq. 9) to determine the maximum ST investment ($I_{ST,local}$) a plant can be to remain the lower cost technology again PVHP (eq. 10).

$$I_{ST,local} = I_{PVHP,market} \cdot IR^{CPC}_{PLC.local} \quad \text{(eq. 10)}$$

Quite simply, if the known market investment for solar thermal ($I_{ST,market}$) is less than $I_{ST,local}$, then ST is the lower cost renewable heat producer. If not, PVHP produces heat at a lower price (eq. 11).

$$\begin{cases} ST\ chosen,\ I_{ST,market} < I_{ST,local} \\ PVHP\ chosen,\ I_{ST,market} > I_{ST,local} \end{cases} \quad \text{(eq. 11)}$$

3. Results

The thermal yield simulation results can be viewed in a prior publication (Meyers et al., 2016). The graphical depiction and required equation parameters of the Investment Ratio (*IR*), Correction Factor ($F^{CPC}_{corr,PLC}$), and PV Yield (E^{PV}_{sol}) are shown in section 3.1.1, 3.1.2, and 3.1.3 respectively, all required to for the economic comparison. Section 3.2 provides a short example of how to use the methodology. A focus is given to the CPC collector for this section, but graphs and equations for other cases will be made available in future publications.

3.1 Key Calculation Parameters

3.1.1 Investment Ratio

The generalized form of the ILC Investment Ratio for CPC collectors as a function of solar irradiation (*H*)

and differential between mean process and annual average daytime temperature (T_{diff}) was explained in eq. 8. The resulting parameter coefficients for a CPC collector are shown in Tab. 3. The regression had a root mean squared error (RMSE) of 2.7% and an R^2-adj of 0.982 with all parameters having a p-value less than 0.05, indicating significance.

Tab. 3 – The linear regression derived parameters to calculate the generalized Investment Ratio for Infinite Load Cases using a CPC collector

	$IR_{ILC,gen}^{CPC}$				
COP	1	2	3	4	5
θ_0	1064	532	355	266	213
θ_1	0.066	0.033	0.022	0.016	0.013
θ_2	-83.0	-41.5	-27.7	-20.8	-16.6
θ_3	5.92E-04	2.96E-04	1.97E-04	1.48E-04	1.18E-04

The resulting plot of this regression equation is shown in Fig. 1. The x-axis hosted the site and process dependent T_{diff}, ($T_{p,m}$ – $T_{amb,day}$). The global horizontal irradiation (H) is showed on the y-axis. The intersection of two selected points on the x- and y-axes, defined by its color and contour lines, was the Investment Ratio for various *COPs*, shown on the right hand side. The values on the contour lines of Fig. 1 were for a *COP* of one, essentially an electrical heater. This value helped, along with the color scheme, to orientate oneself to the right hand side table and subsequently determine the $IR_{ILC,gen}^{CPC}$ dependent on the *COP* of a HP.

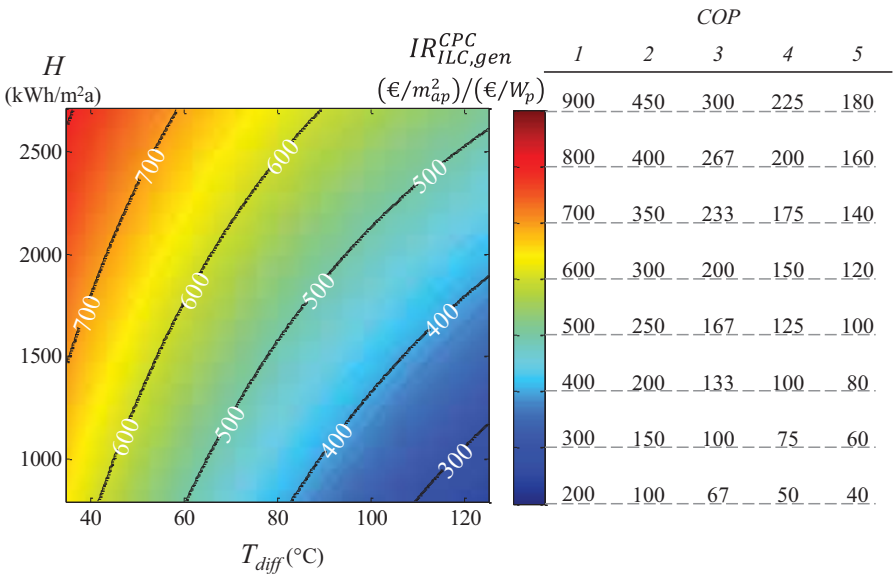

Fig. 1 – The results of a regression analysis from the energetic simulations which depict the Investment Ratio as a function of T_{diff} and H for a CPC collector under an Infinite Load Case

A brief observation of Fig.1 shows that the Investment Ratio increased as a function of global solar irradiation (H) and decreased due to a higher temperature difference between the process and ambient conditions (T_{diff}). This was expected, as this trend is in agreement with the solar collector efficiency equation (ISO, 2013). The performance of a PVHP system (or PV more specifically) was only slightly negatively influenced by higher ambient temperatures (i.e. increasing $IR_{ILC,gen}^{CPC}$).

3.1.2 Correction Factor

An example of a Correction Factor ($F_{corr,PLC}^{CPC}$) curve is shown in Fig. 2, for a seven day constant (three shift) load profile being heated with a CPC collector. The x-axis indicated the temperature difference (T_{diff}) between the mean process temperature ($T_{p,m}$) and the annual daytime average temperature ($T_{amb,day}$). The colored dots in the middle represented the average correction factor of the various locations and process

temperatures, colored by their respective annual solar irradiation (H). The dashed vertical lines per colored dot illustrated the range of correction factors based on various daily specific load requirements and the optimum storage. The upper range of the dashed vertical line represented relatively smaller ST plants relative to the process load achieving higher solar utilization but lower solar fractions. The lower range represented the opposite, relatively large ST plants with higher solar fractions but lower solar utilizations. The black dots within the dashed line indicated the specific simulated cases. A clear decreasing trend of $F_{corr,PLC}^{CPC}$ is shown as T_{diff} increases, nearly independent of annual solar irradiation.

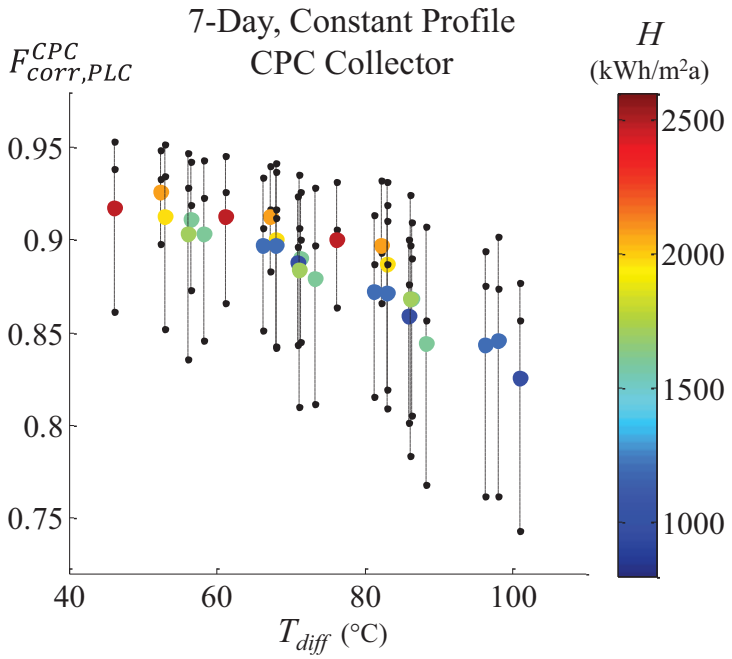

Fig. 2 – An assessment of the PLC correction factor for a 7 day constant load demand being met with a CPC collector

3.1.3 PV Yield

The specific yield of a PV plant in various climates can be calculated with numerous online tools and commercial software packages. While not specifically unique to this research, its presentation in a simple nomogram, calculated through numerous simulations and generalized with linear regression, is helpful for a quick assessment to later determine HP sizing and overall PVHP project investment. The resulting parameters from the linear regression (eq. 3) are show in Tab. 4, which had an RMSE of 2.81% and an R^2-adj of 0.972 with all parameters having a p-value less than 0.05, indicating significance.

Tab. 4 – Model coefficients used to estimate the specific PV yield with the global horizontal irradiation and latitude known for a location of interest

$E_{sol,gen}^{PV}$		
θ_0	θ_1	θ_2
-279.7	0.89	7.52

The results of this linear regression are plotted in Fig. 3. To use, a site's latitude (φ) in degrees was on the x-axis and its global horizontal irradiation (H) on the y-axis. Their intersection point was the estimated annual solar PV yield, in kWh_e/kW_p. The white dots indicate the sites used for the correlation at their specific φ and H. The model's parameter linked to H (θ_1) is 0.89, which is roughly a typical Performance Ratio for PV plants. Built into the latitude model parameter (θ_2) was also a crude ambient temperature correlation, so solar yield benefits not only from collector tilt at higher latitudes but also from lower ambient temperatures often observed there. Collectors were tilted to the site's latitude, minus 15 degrees with a minimum tilt angle of 15 degrees.

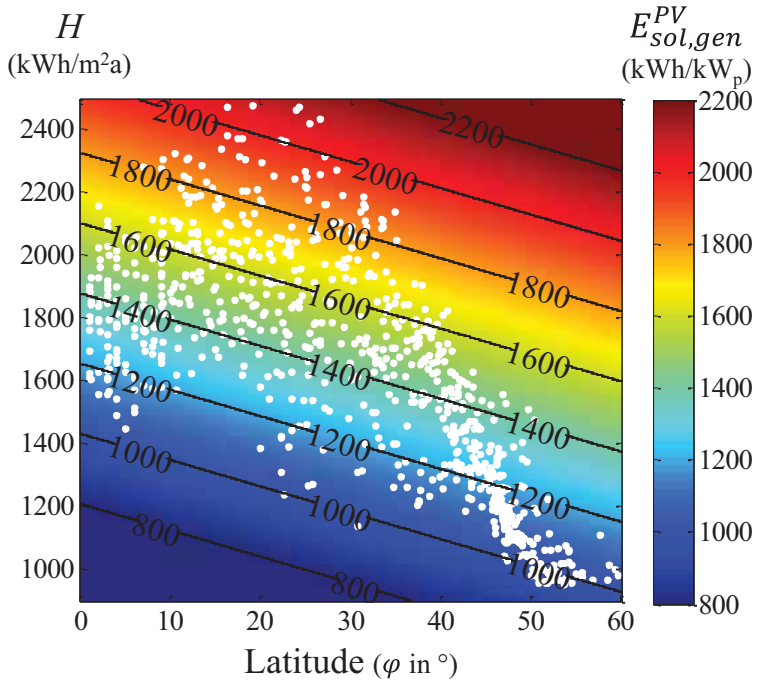

Fig. 3 – A graphical representation of the model used to estimate solar PV yield (E^{PV}_{sol})

3.2 Methodology Demonstration

To determine the use of the methodology, a step by step example is provided:

1 - Determine known process parameters through an energy audit, for example:

- Local meteorological conditions: H: 1250 kWh/m^{2}a, $T_{amb,day}$: 15 °C, φ: 40°
- Industrial process: 70..90 °C ($T_{P,m}$: 80 °C), operates 7 days a week for 3 shifts (Continuous profile)
- T_{diff}: $T_{P,m}$ - $T_{amb,day}$: 65 °C
- Waste Heat: Available 2000 hours per year (FLH: 2000)
- Estimated PV and HP figures – I_{PV} : 1.1 €/W$_p$, COP : 3 and I_{HP} : 500 €/kW

2- Use Fig. 1 or eq. 8 to calculate the Investment Ratio ($IR^{CPC}_{ILC,gen}$) with inputs of H, T_{diff}, and COP

- $IR^{CPC}_{ILC,gen}$= **175** in (€/m$^2_{ap}$)/(€/W$_p$)

3- Use Fig. 2 to estimate a Correction Factor ($F^{CPC}_{corr,PLC}$) with T_{diff} and the known process load profile

- $F^{CPC}_{corr,PLC} \approx$ **0.90**

4- Use Fig. 3 or eq. 3 to calculate E^{PV}_{sol} with inputs of H and φ

- $E^{PV}_{sol,gen}$ = 1133 kWh/kWp

5- Use eq. 2, 4, and 5 to calculate $I_{PVHP,market}$

- Size the Heat Pump: $P^{HP}_{peak}(kW_{th}/kW_p)$ = 1133·3/2000 = 1.7 kW$_{th}$/kW$_p$ (eq. 2)
- Heat Pump Investment: $I_{HP_{(PV)}}(€/W_p)$ = 1.7 · 500 = 0.86 €/W$_p$ (eq. 4)
- $I_{PVHP,market}(€/W_p) = I_{HP_{PV}} + I_{PV}$= 0.86 + 1.1 = **1.96** €/W$_p$ (eq. 5)

6- Use eq. 9 and 10 to determine the maximum ST Investment, $I_{ST,local}$

- $I_{ST,local} = I_{PVHP,market} \cdot IR^{CPC}_{ILC,gen} \cdot F^{CPC}_{corr,PLC}$ = **1.96·175·0.9** = **310** €/m$^2_{ap}$

When a ST plant can be built turn-key at this site ($I_{ST,market}$) for this industrial process for less than 310 €/m$^2_{ap}$, solar thermal is the lower cost renewable heat technology (eq. 11).

4. Case Study

Using the described methodology in this work and the stepwise procedure highlighted in section 3.2, case studies have been performed to estimate the maximum $I_{ST,local}$ under numerous conditions for an industrial process requiring heating from 60..90 °C with a CPC.

4.1 Boundary Conditions

Three site locations were chosen which had different levels of solar irradiation and ambient temperature. The "High" case had an H: 2400 kWh/m^{2}a and $T_{amb,day}$: 29 °C, the "Mid" case H: 1600 kWh/m^{2}a and $T_{amb,day}$:19.5 °C, and the "Low" case H: 1000 kWh/m^{2}a and $T_{amb,day}$: 10.5 °C. By using this range of meteorological parameters, a band of all feasible $I_{ST,local}$ was displayed.

Three process load profiles were selected to represent a range of potential $I_{ST,local}$. The first case, denoted in green, was a constant load profile, requiring heat 7 days a week for three shifts, during which a heat pump can operate continuous at 8000 full load hours (FLH) a year. The correction factor ($F_{corr,PLC}^{CPC}$) was estimated to be 0.90. The second, denoted in blue, was a typical weekly operating process (5 days) for only one daytime shift (8 hours), where a heat pump can operate full time at approximately 2000 hours per year. The third case, in red, was the same as the second, only that the heat source for the heat pump was constrained. This reduced its operating full load hours to 500 per year. The correction factor ($F_{corr,PLC}^{CPC}$) was estimated to be 0.80 for both the second and third case, though the graph is not depicted in this publication.

For the remaining required parameters I_{PV}, COP and I_{HP}, a range was given spanning the current highest and lowest thresholds. From pessimistic to optimistic, the ranges were for 2..0.5 €/W$_p$ (I_{PV}), 2..5 (COP), and 800..200 €/kW (I_{HP}).

4.2 Results

The case study results are displayed in Fig. 4. The x-axis is comprised of the range of pessimistic to optimistic values of I_{PV}, COP, and I_{HP}, from left to right. Each column of values noted on the x-axis were the input parameters to calculate $I_{ST,local}$ for the three process load profiles and three site locations. It was recognized that for real cases these values will not be as orderly but it serves to demonstrate how $I_{ST,local}$ on the y-axis is influenced by the parameters. Three process load cases are represented by their noted colors. The three site locations are identified by their location within each color band. The "High" case was always located on the upper edge, the "Low" case on the lower edge, and the "Mid" case was appropriately in the middle.

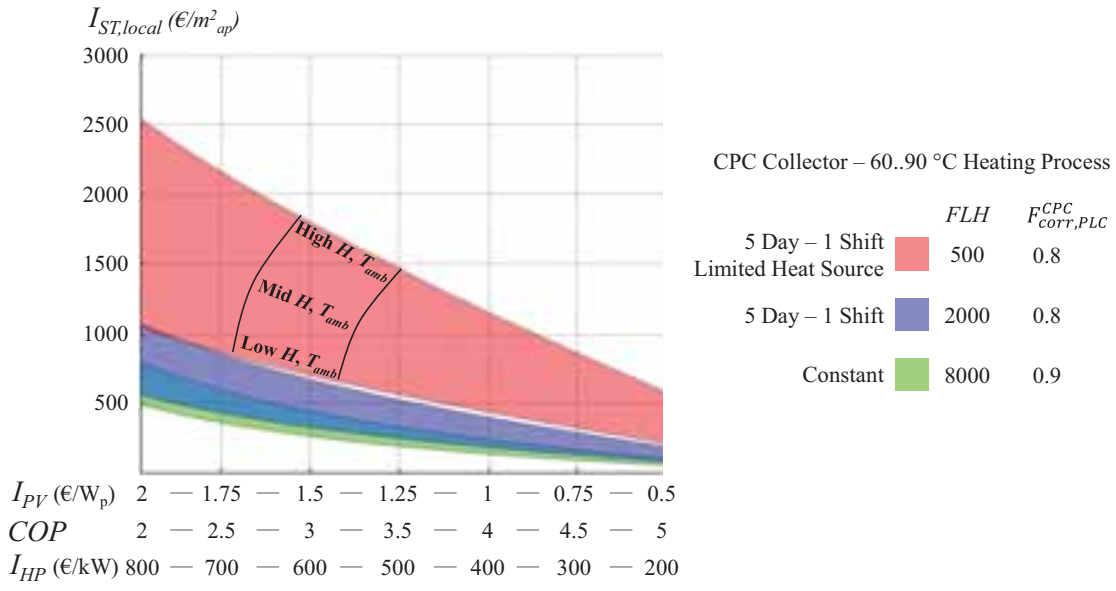

Fig. 4 – The case study results, illustrating the span of potential $I_{ST,local}$ values for numerous process inputs

Fig. 4 shows clear trends which immediately elucidate the sensitivity of certain parameters on $I_{ST,local}$. First and most obvious was that as the main PVHP financial and operating parameters (I_{PV}, *COP*, and I_{HP}) go from pessimistic to optimistic along the x-axis, $I_{ST,local}$ reduces significantly meaning PVHP became more competitive. Second, the process load has a marked influence. The PVHP plant is most competitive against ST (lowest $I_{ST,local}$) during a constant profile in which a heat pump can operate for nearly the whole year, shown in the green band at the bottom of Fig. 4. In turn the PVHP is least competitive (highest $I_{ST,local}$) during a 5 Day – 1 Shift process with limited heat pump operation (500 *FLH*), visible in red at the top of Fig.4. Site location or more specifically the greater available solar irradiation and ambient temperature positively influence $I_{ST,local}$, making ST more competitive when installed in more sunny and warmer regions. The area above an $I_{ST,local}$ of 1000 €/m$^2_{ap}$ should be of little interest because any well-built ST plant can be built for less, making any result above this value automatically in favor of ST over PVHP. To focus on $I_{ST,local}$ values less than 1000 €/m$^2_{ap}$, Fig. 4 was truncated into Fig. 5 by zooming in the region of interest on the y-axis.

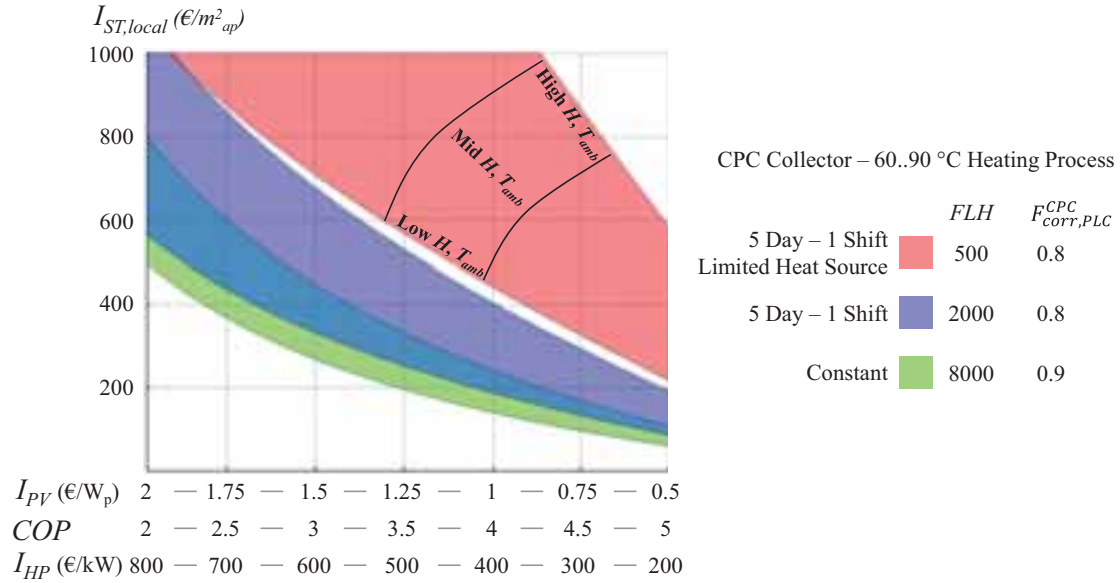

Fig. 5 – The case study results with a focus on $I_{ST,local}$ values less than 1000 €/m$^2_{ap}$

For the 5 Day – 1 Shift case with a limited heat source (red) in Fig. 5, the calculated $I_{ST,local}$ remains above 400 €/m$^2_{ap}$ for nearly every case, meaning that a well-built ST plant will remain the lower cost technology when FLHs are minimal. The opposite case, with a Constant load profile and a heat pump operating 8000 hours a year (green), indicated that for most situations, a PVHP will be the lower cost heat provider as $I_{ST,local}$ must be below 300 €/m$^2_{ap}$. ST can be competitive in cases when both PV and HP technologies are expensive and operate with a low *COP*. The final case, with a 5 Day – 1 Shift load (blue), both technologies could potentially be lower cost depending on the many boundary conditions. At current average PVHP technology costs (I_{PV}: 1.25 €/W$_p$, I_{HP}: 500 €/kW) with a reasonable *COP* of 3.5, $I_{ST,local}$ varied between 250 €/m$^2_{ap}$ to 525 €/m$^2_{ap}$ from the low to high solar irradiation and ambient temperatures locations. This range is the directly in-line with current $I_{ST,market}$ (BAFA, 2016), showing that the comparison between the two technologies is a stalemate, highly dependent on how cost effective can a ST plant be build. In the future, if PV and HP technology investments continue to reduce while HP performance increases, ST must similarly reduce investment below 200 €/m$^2_{ap}$ to remain the clear technology leader in the majority of industrial cases.

5. Conclusions

The quest for zero carbon process heat in industry often pits solar thermal and renewable electricity (by PV) powered heat pumps against each other. While any technology which reduces carbon emissions is welcome in the fight against climate change, industry often requires the lower cost path to reduce fossil fuel consumption and emissions. For the first time, a robust methodology based on numerous techno-economic

simulations is presented which clearly determines which technology is less expensive when primary industrial process and technology parameters are known.

A comprehensive case study analysis was conducted which used the described methodology to determine the maximum specific investment a solar thermal plant can have in order to remain economically competitive against a heat pump operated with PV generated electricity. In cases when thermal energy is constantly required by an industrial process and a heat pump can operate for the majority of the year, PV heat pump plants will likely be the preferred technology. Contrary to this, if a heat pump can only operate 500 hours or less per year, solar thermal will be the lower cost technology in nearly all cases. In between these two, when the process load and heat pump both require/generate heat for 2000 hours per year at current PV and heat pump investments, the maximum ST investment was between 250 €/m^2_{ap} for low irradiation climates to 525 €/m^2_{ap} for high irradiation climates. Depending on how well or cost effective a solar thermal plant can be built, it can be the lower cost technology. For solar thermal to remain a competitive renewable heat technology and "future proof" itself against others, installed projects must achieve investment levels no greater than 200 €/m^2_{ap} to be the lower cost renewable heat technology in most meteorological and process conditions.

6. Acknowledgements

Funding: This work was supported by the People Programme (Marie Curie Actions) of the Seventh Framework Programme FP7/2007e2013/under REA grant agreement n 317085 [PITN-GA-2012-317085], commonly known at the SHINE (Solar Heat INtegration Network) Program (https://www.uni-kassel.de/projekte/solnet-shine/home.html).

References

BAFA, 2016. Innovationsförderung – Bereitstellung von Prozesswärme. http://www.bafa.de/DE/Energie/Heizen_mit_Erneuerbaren_Energien/Solarthermie/Gebaeudebestand/Innovationsfoerderung_Prozesswaerme/prozesswaerme_node.html. Accessed 13 July 2017.

Duffie, J.A., Beckman, W.A., 2013. Solar engineering of thermal processes, 4th ed. John Wiley & Sons.

Fraunhofer ISE, 2015. Current and Future Cost of Photovoltaics. Long-term Scenarios for Market Development, System Prices and LCOE of Utility Scale PV Systems. A study on behalf of Agora Energiewende.

Fraunhofer ISE, 2016. Entwicklung beschleunigter Alterungstestverfahren für solarthermische Kollektoren und deren Komponenten. Fraunhofer-Institut für Solare Energiesysteme ISE.

IEA Annex 35, 2014. Applications of Industrial Heat Pumps. Final Report, Part 1 and 2. Report No. HPPAN35-1 and 2; ISBN 978-91-88001-92-4 and 978-91-88001-93-1.

IPCC, 2015. Climate Change 2014: Mitigation of Climate Change. Working Group III Contribution to the IPCC Fifth Assessment Report. Cambridge University Press, Cambridge, Online-Ressource.

ISO, 2013. 9806:2013 - Solar energy - Solar thermal collectors - Test methods. https://www.iso.org/obp/ui/#iso:std:iso:9806:ed-1:v1:en. Accessed 13 July 2017.

Jordan, D.C., Kurtz, S.R., 2013. Photovoltaic Degradation Rates. An analytical review. Progress in Photovoltaics: Research and Applications 21, 12–29.

Lauterbach, C., 2014. Potential, System Analysis and Preliminary Design of Low-Temperature Solar Process Heat Systems. Kassel University Press, Kassel.

Louvet, Y., Fischer, S., Furbo, S., Giovannetti, F., Mauthner, F., Mugnier, D., Philippen, D., Vajen, K., 2017. Entwicklung eines Verfahrens für die Wirtschaftlichkeitsbe-rechnung solarthermischer Anlagen: die LCOH Methode, in: 27. SYMPOSIUM "THERMISCHE SOLARENERGIE". Ostbayerisches Technologie-Transfer-Institut e.V. (OTTI), Regensburg.

Meyers, S., Schmitt, B., Vajen, K., 2015. Techno-Economic Comparison of Solar Thermal and PV for Heat Generation in Industrial Processes, in: Proceedings of the ISES Solar World Congress 2015. International Solar Energy Society, Freiburg, Germany, pp. 1–10.

Meyers, S., Schmitt, B., Vajen, K., 2016. Competitive Assessment Between Solar Thermal and Photovoltaics for Industrial Process Heat Generation, in: Proceedings of EuroSun2016. International Solar Energy Society, Freiburg, Germany, pp. 1–11.

Ondraczek, J., Komendantova, N., Patt, A., 2015. WACC the dog: The effect of financing costs on the levelized cost of solar PV power. Renewable Energy, 888–898.

Pérez-Aparicio, E., Lillo-Bravo, I., Moreno-Tejera, S., Silva-Pérez, M., 2017. Economical and environmental analysis of thermal and photovoltaic solar energy as source of heat for industrial processes, in: SolarPaces (Ed.), AIP Conference Proceedings, p. 180005.

Schmitt, B., Lauterbach, C., Ritter, D., Meyers, S., Vajen, K., 2015. Fast Feasibility Assessment for Solar Thermal Systems in Industry, in: Proceedings of the EuroSun 2014 Conference. International Solar Energy Society, Freiburg, Germany, pp. 1–10.

Shimura, S., Herrero, R., Zuffo, M.K., Baesso Grimoni, J.A., 2016. Production costs estimation in photovoltaic power plants using reliability. Solar Energy, 294–304.

VDI, 2012. 2067 - Economic efficiency of building installations. Verein Deutscher Ingenieure.

VDI, 2014. 6002 - Solar heating for potable water. Verein Deutscher Ingenieure. http://www.vdi.eu/nc/guidelines/vdi_6002_blatt_1-solare_trinkwassererwaermung_allgemeine_grundlagen_systemtechnik_und_anwendung_im_wohnun/. Accessed 13 July 2017.

Wolf, S., Fahl, U., Blesl, M., Voß, A., Jakobs, R., 2014. Analyse des Potenzials von Industrie-wärmepumpen in Deutschland.

Comparison of thermal losses due to heating-up of system components in two solar process heat plants with parabolic trough collectors

J. Möllenkamp[1], T. Beikircher[2], M. H. Rittmann-Frank[1], A. Häberle[1]

[1] SPF Institute for Solar Technology, 8640 Rapperswil (Switzerland)
[2]ZAE Bavarian Center for Applied Energy Research, 85478 Garching (Germany)

Abstract

Two solar process heat plants with liquid heat transfer parabolic trough collectors (PTC, 627 m² and 115 m² aperture) at Swiss dairies have been experimentally investigated in detail. They provide solar thermal heat for a hot water network of 102 °C and a steam network of 135 °C - 150 °C, respectively. Detailed yearly, monthly and daily evaluation with regard to usable solar gains Q_{use} and solar energy necessary for heating–up system components to required temperature T_{set} is presented. Thermal heat capacities of the primary circuit have been analyzed and the change in inner energy ΔU has been calculated and cumulated for periods with no usable heat output below $T_{set.}$ Over the year, the ratio of not usable solar energy required to heat-up the system to overall solar gains in the collectors ($\Delta U / (Q_{use} + \Delta U)$) varies between 14-18 % and 20-22 %, respectively. During winter months ΔU can even exceed Q_{use}. These capacitive losses can be reduced by lower heat capacities or an improved thermal insulation. With intermediate storages, inner energy contained in the hot system could be stored for re-heating after an idle period.

Keywords: solar process heat, parabolic trough collector, concentrating solar thermal, thermal heat capacity, thermal losses, heating-up.

1. Introduction

Nearly 70% of final energy consumption in European industry is required for process heat. Part of this energy could be provided by thermal collectors in order to reduce fossil fuel consumption and CO_2 emissions. Though, to date there is little experience with solar process heat plants (SPHP), especially at temperatures between 100 °C and 250 °C, where thermal losses of system components during stand-still periods play a major role compared to low temperature applications. After periods of non-operation, solar energy is required to heat up the components to operating temperature before solar heat can be delivered to the processes.

The work focuses on experimental analysis of two solar process heat plants with parabolic trough collectors quantifying daily and monthly inner energy ΔU required to heat-up heat transfer fluid and piping system and comparing it to useful solar energy gains Q_{use}. Both plants analyzed provide solar heat for dairies and are located in northwest (Saignelégier) and southeast (Bever) of Switzerland. They operate at different collector temperatures (120 °C/190 °C) and differ in size (627 m^2/115 m^2), integration concept (hot water/steam) and type of heat transfer medium (water-glycol/thermal-oil).

A methodology based on the system configuration in Saignelégier has been developed in order to experimentally quantify the required solar thermal energy during transient heat-up periods of the plant (Möllenkamp et al., 2016). In this work, the methodology has been adapted to the plant configuration of Bever and results of both plants are compared and discussed.

doi:10.18086/swc.2017.26.09 Available at http://proceedings.ises.org

Fig. 1: SPHP in Saignelégier, 1000 m above sea level, 627 m² (aperture) PTC collectors with axis orientation NS with 18° deviation counterclockwise

Fig. 2: SPHP in Bever, 1700 m above sea level, 115 m² (aperture) PTC-collectors, axis orientation NS with 19° deviation clockwise

2. Description of analyzed solar process heat plants

Saignelégier

The SPHP in Saignelégier produces thermal energy for a (cheese) dairy operated by Emmi. The collector field comprises of 17 parabolic trough collectors (PTC) PolyTrough 1800 by NEP Solar (SPF 2017) connected in parallel. It is mounted on the roof of a production hall and its orientation follows the roof geometry (north-south with 18 ° deviation counterclockwise). The total aperture area amounts to 627 m^2 and the row distance alternates between 2.98 und 3.84 m. As heat transfer fluid, a 25 vol.% water-glycol mixture with $c_{p(0\text{-}120\ °C)}$=3.9-4.2 kJ/kg/K is used. The primary circuit consists of solar field and return/supply pipes and delivers useful solar heat Q_{use} to the hot water network operated at 102 °C (secondary circuit) via a heat exchanger if a set point of T_{set} = 117 °C is exceeded (Fig. 3 and Fig. 4). Useful solar energy is either stored in a 15 m^3 water storage, used for pre-heating water in two oil-burners or directly delivered to the processes of the dairy (cleaning or thermal treatments of dairy products). Fluid temperatures are measured at inlet and outlet of the collector field and the heat exchanger. Minute mean values of highly resolved (up to 1 secs) measurements are used for the analysis.

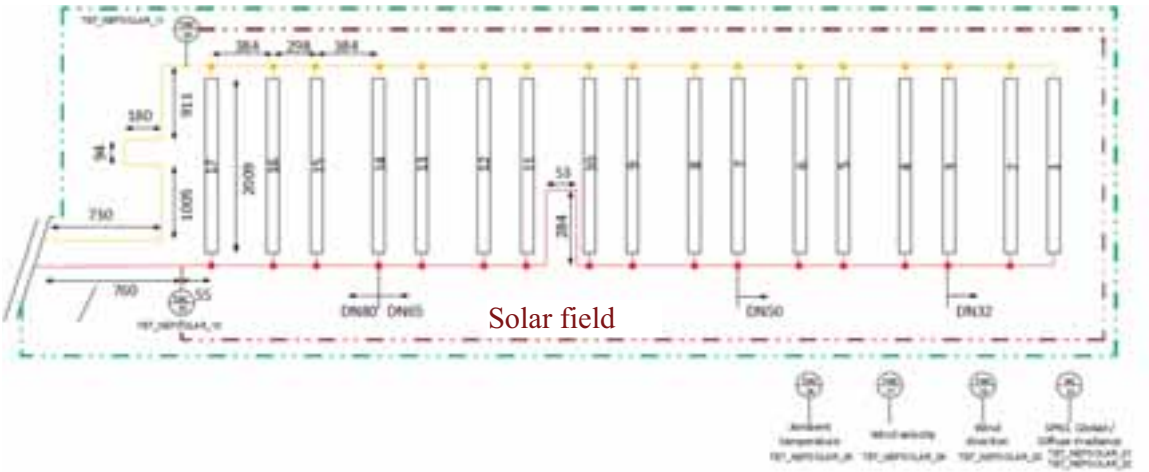

Fig. 3: Hydraulic Scheme of solar field in Saignelégier

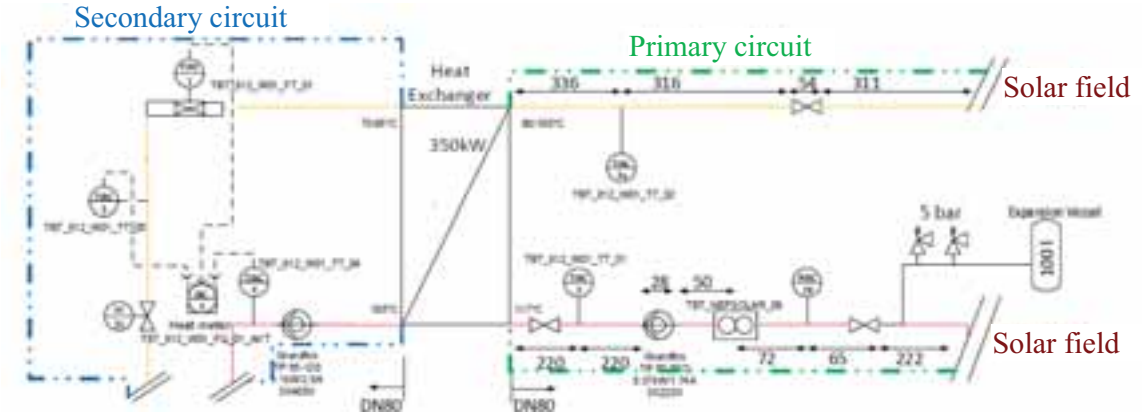

Fig. 4: Hydraulic scheme of SPHP in Saignelégier (solar field not included)

Bever

The second plant is located in Bever and produces thermal energy for a (cheese) dairy operated by Lesa. The collector field comprises of 4 collector rows with a length of 25 m each. Two rows are connected in series and the arising subfields connected in parallel. The solar field consists of parabolic trough collectors PolyTrough 1200 by NEP Solar and is mounted on the rooftop of a production hall. The axis orientation is north-south with 18.8 ° deviation clockwise. The total aperture area is 115 m^2 with and a row distance of 2.45 m (outer rows) and 3.42 m (in the middle). Here, thermal oil is used as heat transfer fluid with $c_{p(0\text{-}190\ °C)}$ = 2-2.7 kJ/kg/K. The solar heat is delivered to a steam network via steam generator. In Fig. 5, the SPHP again is divided into solar field, primary circuit (solar field plus return/supply pipes) and secondary circuit (steam network).Temperatures of the fluid are measured at inlet and outlet of the collector field and evaporator. Instantaneous measurement data with a frequency of one minute was available.

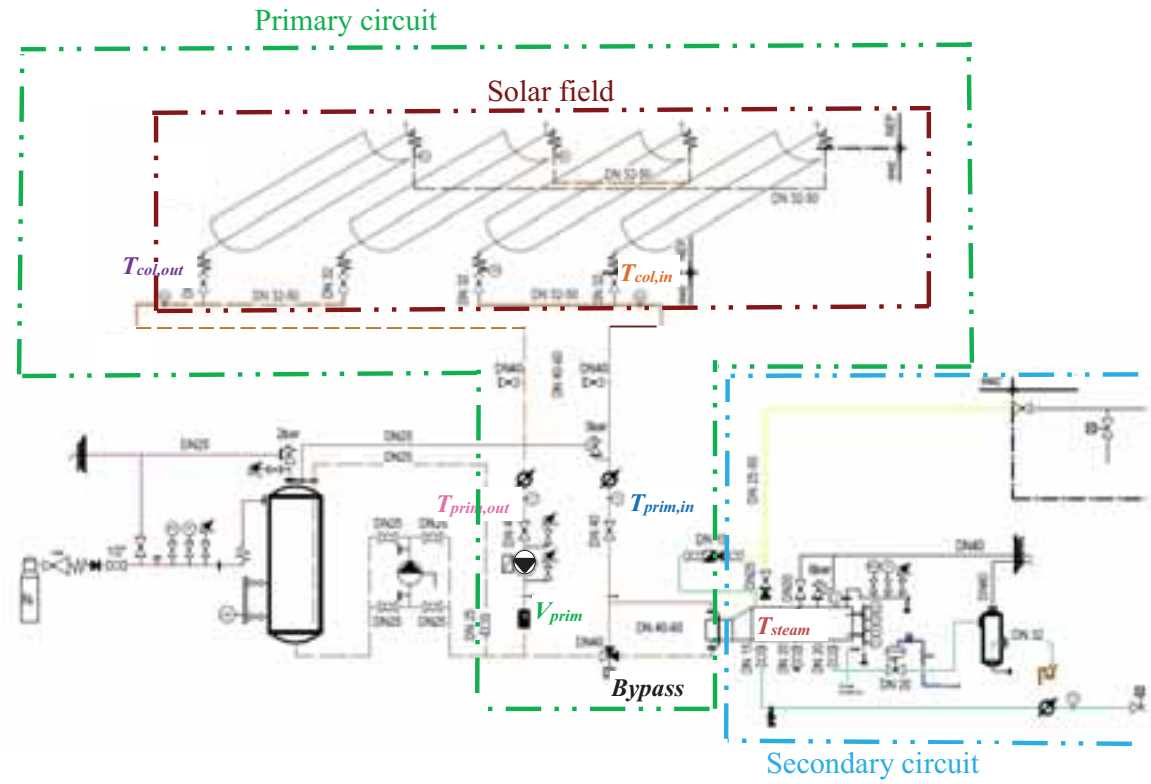

Fig. 5: Hydraulic scheme of SPHP in Bever

In Bever, the presence of a steam generator complicates the evaluation of Q_{use} due to no available information about incoming (feed water) and outgoing (steam) mass flowrates of the steam generator nor from pressure or temperature in the steam network. The steam generator contains 210 l water and is about half filled. Fig. 6 shows a typical operating day for the Bever plant and clarifies the operation modes. If the outlet temperature of the collector field T_{prim_out} exceeds the temperature in the steam generator T_{steam}, the bypass to the internal heat exchanger of the steam generator opens (i.e. at 9:50) and solar energy is used for heating up and evaporating the water in the steam generator. If the steam pressure in the steam generator exceeds the pressure in the steam network plus a certain unknown hysteresis-pressure (e.g. at 11:10 and 12:50), a valve opens their connection and useful solar heat is, driven by pressure forces, delivered to the processes until the pressure in the steam generator has decreased down to the pressure in the steam network (3.1 – 4.8 bar, varying during the day, see Fig. 6). Consequently, a steam temperature of 135 – 150 °C is required to feed useful energy into the steam network calculating T_{steam} from vapor pressure curve. Additionally, the primary circuit has to deliver the necessary temperature difference over the heat exchanger (25 K during operation, see Fig. 6). This leads to a minimal T_{prim_out} of 160 – 175°C (depending on varying steam net pressure) before usable solar heat can be transferred to the process. Though, set temperature for the pump control of the collector field is $T_{col,out}$=190 °C, which can also be seen in Fig. 6.

The dashed lines in Fig. 6 mark two heating up periods converting solar energy in enlargement of inner energy ΔU without providing Q_{use}.

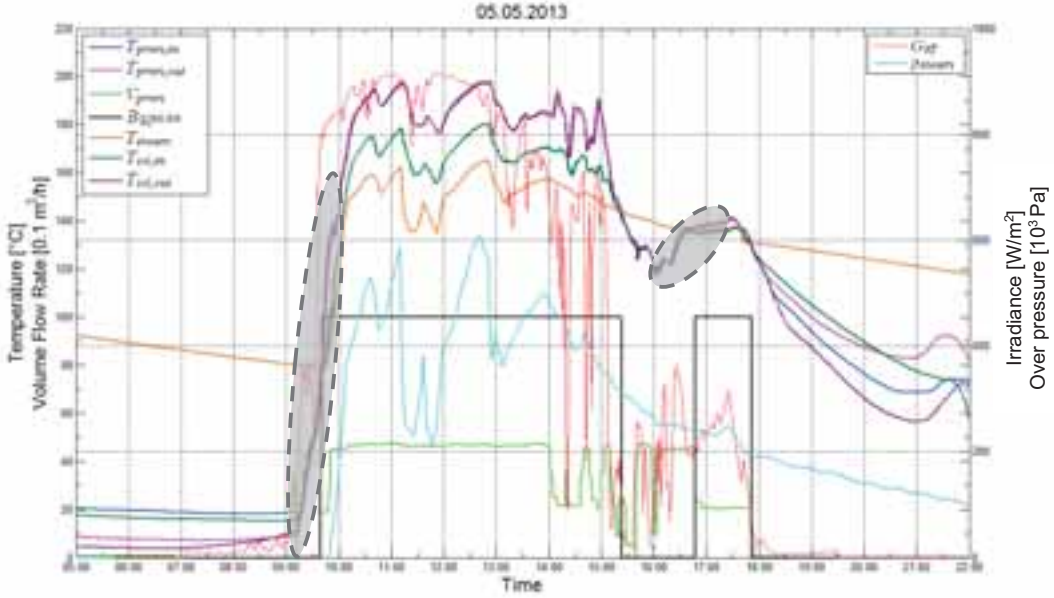

Fig. 6: Exemplary measurement data for the 5th of May 2013 at the SPHP in Bever showing inlet and outlet temperatures of the primary circuit ($T_{prim,in}$ and $T_{prim,out}$), volume flowrates in the primary circuit (V_{prim}), bypass signals (in %), steam temperatures (T_{steam}) and collector field inlet and outlet temperatures ($T_{col,in}$ *and* $T_{col,out}$) as well as direct normal irradiance on the aperture area (G_{bT}) and steam over pressure in the steam generator (p_{steam}).

Comparison of effective thermal capacity

The aperture area specific total thermal capacity C_{eff} [kWh/(Km^2)] of the primary circuit for Saignelegier comprises only of different fluid filled pipe sections (connecting tubes inside and outside the building and collector pipes), see Fig. 5. C_{eff} has been calculated from dimensions, density and specific heat capacities of heat transfer medium and pipe materials. The major part of C_{eff} (80 %) of the primary circuit in the Saignelégier plant is given by the pipes outside connecting the 17 collector rows, see left diagram in Fig. 7.

In contrast, only 50% of C_{eff} of the piping system in Bever (diagram a) Fig. 7, green segments) results from collector connecting pipes due to less collector rows (4), longer collector pipes (5 m longer) and serial connection. Besides the capacity of 198 l thermal oil with $c_{p(0\text{-}190\ °C)}$ = *2-2.7* kJ/kg/K, additionally the thermal capacity of 210 l

water with $c_p = 4.2$ kJ/kg/K in the steam generator (see diagram in Fig. 7, blue section) has to be considered being responsible for two third of the total C_{eff}. Note, that generally the metallic materials of system components like piping, heat exchangers and steam generator account for only about 10% of the total heat capacity, which is mainly determined by the contained fluid.

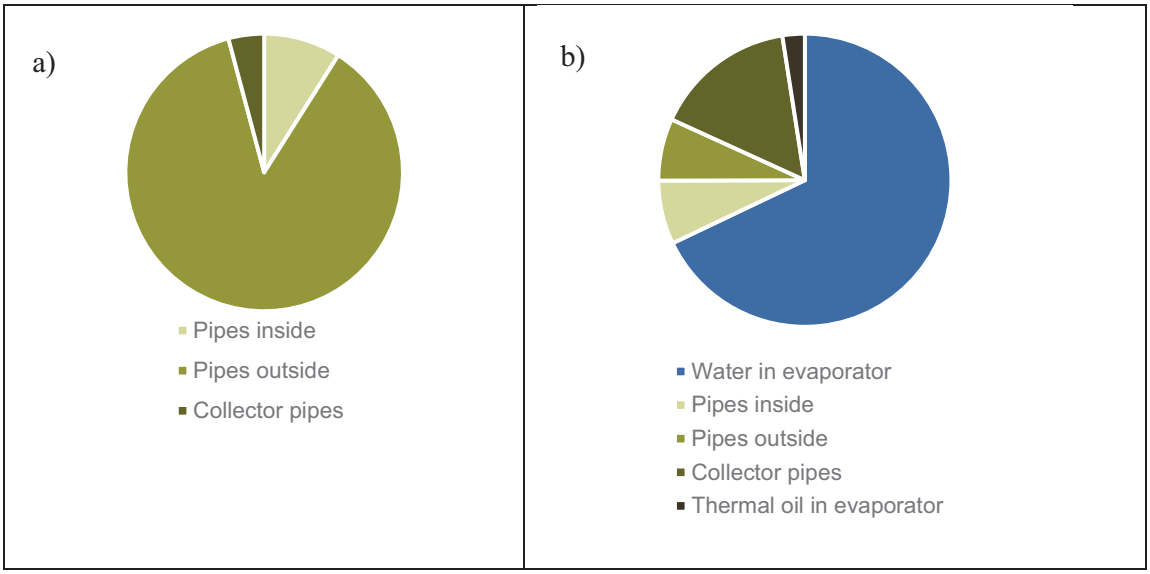

Fig. 7: Distribution of effective thermal capacity C_{eff} in primary circuit of SPHP in a) Saignelégier and b) Bever.

The total thermal capacities C_{eff} (related to the aperture area) for both plants are similar, see Table 1, though the collector fields are differently large by a factor of 6 in aperture area. Regarding only HTF and pipes, C_{eff} in Bever is three times smaller than in Saignelégier. However, in Bever results even a slightly higher total C_{eff}, additionally considering the water in the steam generator. Hence, compared to Saignelégier, the usable part of solar energy in Bever is expected lower, because principally more heat capacity has to be heated to usable temperature level T_{set}, which in Bever (at least 160 °C) is significantly higher than in Saignelégier (117 °C).

Tab. 1: Aperture-specific effective thermal capacity of pipes and HTF in Saignelégier and Bever as well as C_{eff} of water in the steam generator of Bever and the resulting total heat capacities

	C_{eff} [kWh/m²K]	
	Bever	**Saignelégier**
HTF and pipes	0.94	2.73
Water	2.15	
Total	3.09	2.73

3. Methodology for quantification of usable solar energy Q_{use} and solar energy required to heat-up ΔU

Thermal energy required to heat up system components after stand-still periods is calculated by (see Möllenkamp et al. 2016):

$$\Delta U = \sum_{i=1}^{m} \sum_{j=1}^{n} C_{eff,j} \cdot \left(T_{fl,j}\left(t_{2,j}^{i}\right) - T_{fl,j}\left(t_{1,j}^{i}\right) \right) \qquad \text{(eq. 1)}$$

with C_{eff} representing the effective thermal capacity of each capacitive section i and m and n the number of section and heating-up periods, respectively. $T_{fl}(t_1)$ represents the mean temperature of the fluid in each section at the beginning of each heating-up period and $T_{fl}(t_2)$ the temperature at the end, respectively.

Usable solar energy Q_{use} is determined by the energy transferred to the secondary circuit by integrating primary circuit power over periods with an operating pump in the secondary circuit:

$$Q_{use} = \int_{t_2}^{t_3} c_p \cdot \rho \cdot \dot{V}_{prim} \cdot \left(T_{prim,out} - T_{prim,in}\right) dt \qquad \text{(eq. 2)}$$

With t_2 and t_3 defining beginning and end of each period, respectively.

In Bever, the water filled steam generator represents an additional component which has to be considered for the analysis. As derived more above from typical measuring data (Fig. 6), it is simplifying assumed that solar heat is embedded into the steam network (and therefore represents useful energy) if collector outlet temperatures $T_{prim\_out} > T_{set}$. T_{set} corresponds to the minimum steam pressure in the steam network (3.1 bar) and leads to a threshold of $T_{prim\_out} > 160$ °C for useful solar energy. This means, all solar energy below 160° C is used for heating up collector pipes and steam generator. Due to measuring a maximum steam network pressure of 4.8 bar (corresponding to 150°C steam temperature) the evaluation has also been done for this threshold, whereas real conditions meet in between these two limiting cases.

For the evaluation in Bever it was distinguished between thermal energy required to heat up the collector field, the connection pipes inside and outside the building and the water in the steam generator considering different temperatures for each section. For example, the steam generator cools down to 80 °C during night, while the collector field components are at ambient in the morning and differ slightly inside and outside the building (see Fig. 6).

4. Q_{use} and ΔU: Results and discussion

Saignelégier

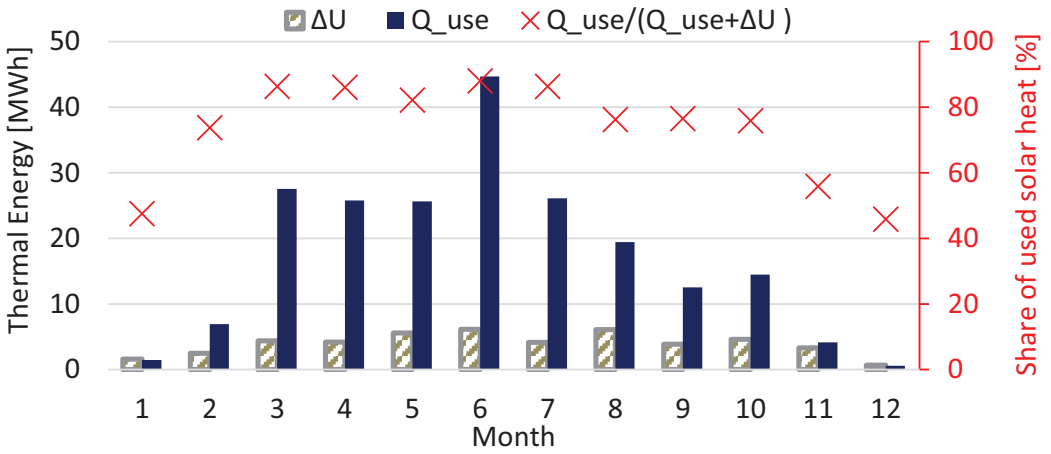

Fig. 8: Solar energy gains required to heat-up system components ΔU, useful solar gains for process heat Q_{use} and share of useful solar heat Q_{use} /(Q_{use} + ΔU) of the SPHP in Saignelégier 2014

According to Fig. 8 between 76 % and 88 % of the total solar gains Q_{tot} with

$$Q_{tot} = Q_{use} + \Delta U \qquad \text{(eq. 3)}$$

has been provided to the hot water network of the dairy between March and October of 2014 in Saignelégier. Here, pipe losses during the operation at $T_{prim\_out} > T_{set}$ have been neglected due to

- having been proven to be totally below 5 % of monthly Q_{tot}, if properly insulated (see Möllenkamp et al., 2016)
- time ratio with $T_{prim\_out} > T_{set}$ is below 20 % during the whole month, reducing part of pipe losses during operation with $T_{prim\_out} > T_{set}$ to less than 1 %

In contrast, the share of useful solar energy decreased down to 46 % in December 2014. This is mainly resulting from less daily direct irradiation on the collector plane and lower ambient temperatures. During the whole year, 18 % (ΔU=47 MWh) of the total thermal solar energy (Q_{tot}=256 MWh) is required for heating-up fluid and pipes of the SPHP in Saignelégier 2014.

In 2015 (see Fig. 9) the annual ratio of required heat for pre-heating is reduced to 14 % (ΔU=37 MWh, Q_{tot}=264 MWh), which is mainly resulting from higher direct irradiation on the aperture area ($H_{bT,2014}$=985 kWh/m² aperture area; $H_{bT,2015}$ =1138 kWh/m² aperture area) and hence higher useful energy gains (Q_{use}=257 MWh). The maximum share of used solar heat is recorded in April 2015 with 93 %. The SPHP was shut down in December 2015 due to snow blocking the tracker. The time of heating-up periods on sunny days in Saignelégier varied between at least 50 min in summer and up to 4.2 hours in winter during 2014 and 2015.

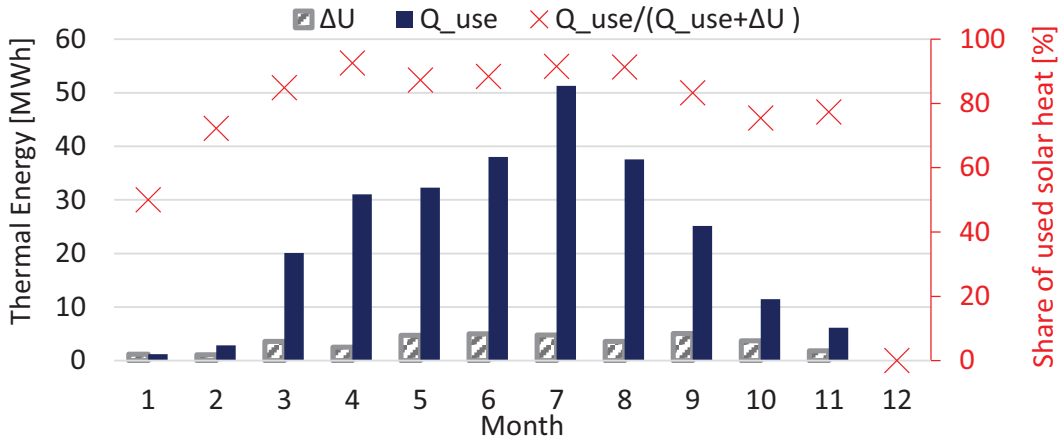

Fig. 9: Solar energy gains required to heat-up system components ΔU, useful solar gains for process Q_{use} and share of useful solar heat $Q_{use}/(Q_{use}+\Delta U)$ of the SPHP in Saignelégier 2015

Thermal losses due to heating-up periods could be reduced by implementation of an additional storage, which collects the heat of fluid and pipes at the beginning of each stand-still period and feeds the solar field with hot fluid before the next start of operation.

Bever

The SPHP in Bever was able to provide 55 % - 89 % of the total solar gains to the steam network from March until October of 2013, whereas in January only 18 % of the total solar thermal energy could be used for industrial processes (see Fig. 10). In 2013, 9 MWh of solar energy gains were used for heating-up system components, which represents 20 % of the total yearly solar gains ($Q_{tot,2013}$ = 44 MWh). Here, it can be distinguished between energy to heat-up water in the steam generator (10 % of Q_{tot}) and energy to heat-up thermal-oil and pipes (10 % of Q_{tot}).

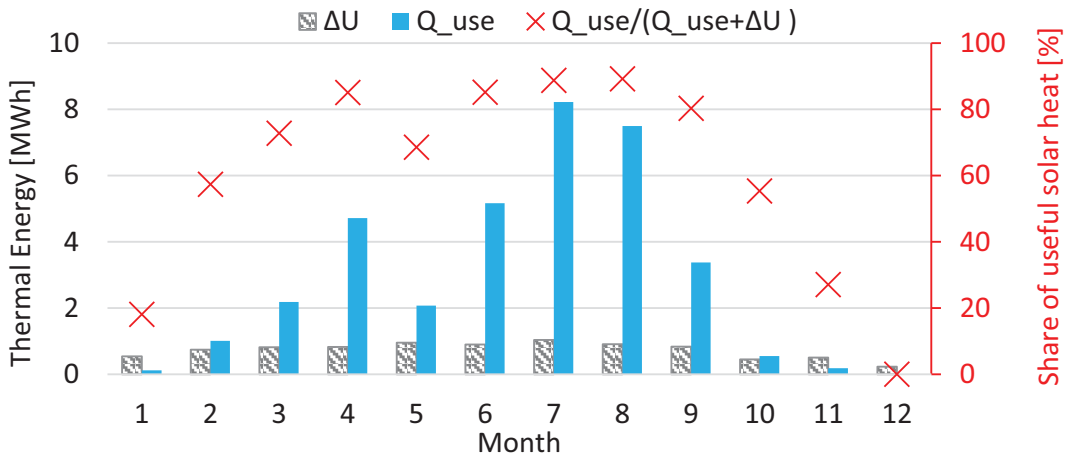

Fig. 10: Solar energy gains required to heat-up system components ΔU, useful solar gains for process heat Q_{use} and share of useful solar heat $Q_{use}/(Q_{use}+\Delta U)$ of the SPHP in Bever 2013

For the maximal pressure of 4.8 bar as measured in the steam network a collector field outlet temperature of 175 °C is required to evaporate the water. Under this assumption, a yearly $\Delta U/Q_{tot}$ =22 % and hence a higher ratio of solar energy used to heat up the system is experimentally obtained. The real value $\Delta U/Q_{tot}$ for Bever is between these two extremal cases (20 % for 160 °C and 22 % for 175 °C). Heating-up times in Bever varied between 1.5 and 2 hours.

For the Bever plant, it is recommended to further improve the insulation of the steam generator, before considering an additional storage for saving thermal energy during stand-still periods.

Comparison between the two plants

The evaluation of measurement data shows that the ratio of required solar energy to heat-up the system compared to overall solar gains do not differ much between both plants analyzed ($\Delta U/Q_{tot}$ 14-18 % in Saignelégier and 20-22 % in Bever) even though minimally acquired collector field temperatures in Bever (>160 °C) are much higher than in Saignelégier (117 °C) and thermal capacities per solar aperture area are comparable.

In spite of a similar total effective thermal capacity C_{eff}, it has to be considered that different temperature differences arise for heating up water and thermal-oil in the Bever plant. Due to its better insulation, the steam generator cools down to only 80°C during night, while the primary circuit cools down to ambient, see Fig. 6. Assuming an ambient temperature of 20 °C inside and outside the building, heating-up in the morning once a day consumes

$$\Delta U_{Bever} \approx C_{eff,water} \cdot (130-80)K + C_{eff,HTF+pipes} \cdot (190-20)K = 267\ kWh/m^2$$

$$\Delta U_{Saignelégier} \approx C_{eff,HTF+pipes} \cdot (120-20)K = 273\ kWh/m^2$$

of solar thermal energy in the morning.

Also the high yearly direct irradiation on the tilted aperture area H_{bT} in Bever (1285 kWh/m² yearly, monthly see Fig. 12) favors a lower $\Delta U/Q_{tot,}$ which can be seen from Fig. 11 showing monthly H_{bT} for the Saignelegier plant comparing the years 2014 and 2015: The yearly share of used solar heat in Saignelégier increases from 82 % to 86 % if yearly H_{bT} grows from 985 kWh/m² to 1138 kWh/m².

Nevertheless, distribution of direct normal irradiance (DNI) over the day also plays a role. For example, five sunny days and five cloudy days show a higher ratio of usable solar energy compared to ten days with fluctuating DNI but same cumulated DNI.

The exact influence of the parameters discussed on the share of usable solar energy Q_{use} and not usable solar energy required to heat-up ΔU can only be determined by dynamic simulations.

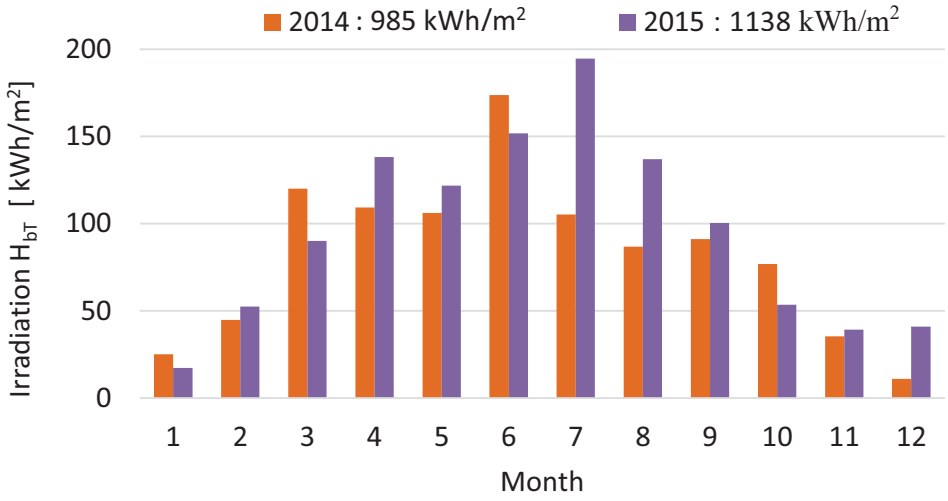

Fig. 11: Monthly direct irradiation on the tilted aperture area of the SPHP in Saignelégier 2014 and 2015

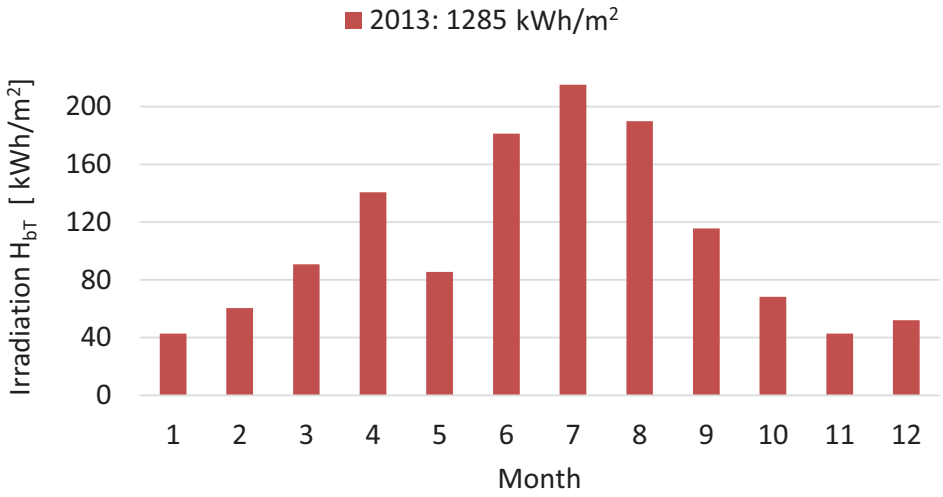

Fig. 12: Monthly direct irradiation on the tilted aperture area of the SPHP in Bever 2013

5. Summary and outlook

For two SPHP in Switzerland with PTC collectors at operating temperatures between 100 °C and 200 °C and collector aperture areas between 115 and 627 m² it could be shown experimentally that 14 to 22 % of potentially usable yearly solar energy, i.e. solar energy transferred to the collector fluid of a SPHP, are lost due to thermal losses in stand still periods which must be balanced by solar heating-up processes. In further studies both plants will be modelled with a dynamic simulation software in order to

- study the exact influence of the different parameters (thermal capacities of components, operating temperatures, integral solar radiation and its distribution, user behaviour) on solar energy required to heat-up ΔU and usable solar energy Q_{use}.
- quantify possible thermal energy savings with the developed optimization methods for each plant, which enlarge Q_{use} reducing ΔU by better thermal insulation and/or saving ΔU at the begin of a stand still period for the next heating up period by means of a thermal storage.

6. References

Möllenkamp, J., Rittmann-Frank, M.H., Caflisch, M., Rommel, M., Häberle, A., Beikircher, T., Schölkopf, W., 2016. Evaluation of thermal losses in parabolic trough collector fields of solar process heat plants in Switzerland. Conference Proceedings of EuroSun 2016, Palma de Mallorca.

SPF Insitute for Solar Technology, 2017. Solar Collector Factsheet NEP Polytrough 1800. URL http://www.spf.ch/fileadmin/daten/reportInterface/kollektoren/factsheets/scf1549en.pdf., accessed 13.10.2017.

An automated solar biomass hybrid dryer in rural communities in Ghana

George Obeng-Akrofi[1], Joseph Oppong Akowuah[1], Gifty Opoku-Agyeman[1], Isaac Nkrumah[1], Michael K. E. Donkor[1], Reuben Y. Tamakloe[1], Francis K. Ampong[1], Maike Waldhoff[2], Tobias Klaus[2], Alexander Olenberg[2], Eugeny Kenig[2], Stefan Krauter[2]

[1] Kwame Nkrumah University of Science and Technology, Kumasi (Ghana)

[2] University of Paderborn, Paderborn (Germany)

Abstract

Computational fluid dynamics (CFD) was used to simulate the drying process of a Solar-Biomass Hybrid Dryer (SBHD). CFD simulations were set up with the software StarCCM+ for investigating the temperature distribution inside a 5-tonne prototype in a rural community in Ghana. The predicted temperature distributions were compared to the experimental data of temperature distribution in the dryer. The simulated results of Levels 1 and 2 within the dryer were 5–15 K higher than the experimental data. This was due to the introduction of cold air at the bottom of the dryer and also, the absence of the effect of the fans in the dryer during the simulation process. The simulated results fit nearly perfect for Layers 3 and 4 in the dryer with a deviation of not more than 5 K. All in all, the predicted simulation agrees with the experimental data. In order to improve drying conditions in the SBHD, it is suggested that the integration of an automated system which will aid in the controlled introduction of hot air at high air flow at the lower levels of the shelves in the dryer would be required.

Keywords: CFD simulation, Solar-biomass hybrid dryer, performance

1. Introduction

Crop drying has been proven to be an essential process in the preservation of agricultural products (Mastekbayeva, et al., 1999). Being an old technique used for the preservation of food, drying can reduce postharvest loss associated with crops and also make produce lighter, smaller and easier to handle (Green and Schwarz, 2001).

Major drawbacks with open sun drying method as reported by Madholpa et al. (2002) have led to the introduction of enclosed solar structures for drying purposes. Drying of agricultural produce in enclosed solar structures is an attractive way of reducing both the qualitative and quantitative losses of the traditional open-sun drying (Forson et al., 2007). Studies have shown that solar drying techniques lead to a considerable reduction of the drying time and to a significant improvement of the product quality in terms of color, texture and taste as compared to the traditional open sun drying techniques (Fadhel et at., 2014; Srinivasan and Balusamy, 2015; Ajayi et al., 2017).

Solar dryers have a major downside of being weather dependent leading to longer drying times. This has been one of the factors which are impeding the commercialization of such systems in Ghana (Sekyere et. al., 2016). For reaching short drying times, high drying efficiency and product quality, a continuous drying process is targeted. This is the reason why solar biomass hybrid dryers (SBHD) are introduced for reaching constant drying temperatures and a continuous process. With the operation of an external heat source, like a furnace which runs on biomass, the drying process is independent of weather conditions.

The performance in terms of the temperature distribution in the SBHD systems have been studied based on experimental data with little attention geared towards simulated procedures. Carrying out CFD simulations of drying systems can contribute to better design, management and control of such systems. Such studies can help designers analyse spatial temperature and moisture distribution as well as drying time of drying systems prior to scale-up.

doi:10.18086/swc.2017.26.10 Available at http://proceedings.ises.org

The use of CFD modelling for carrying out simulation of drying systems has been proven to be effective and efficient. Such studies help engineers in analysing the performance of drying systems. This goes a long way in the optimization, control and improvement of drying systems in Ghana.

This paper, therefore, sought to study the performance of a 5-tonne capacity SBHD used for drying maize in Ejura, a farming community in Ghana. It was done by using CFD simulated models to validate experimental results.

2. Materials and methods

2.1. Experimental Setup

The 5-tonne capacity Solar Biomass Hybrid Dryer (Fig. 1) is located at Ejura (7° 23′ 0″ N, 1° 22′ 0″ W). It consists of three main parts; the drying chamber, the backup heat generation system and solar photovoltaic system. The dryer has a length of 13 m, the width is 7.85 m and height of 4.6 m. Inside the drying chamber, the shelves have 4 levels with 36 trays on each level.

Fig. 1. 5tonne capacity dryer located in Ejura

2.2. Data Collection of temperature and relative humidity data

Temperature and relative humidity conditions were determined by the use of Tinytag data loggers. The logging date was on 16th October 2016. The logging interval was set at 10 minutes to cater for weather changes at short intervals. During the determination the drying conditions, 5 loggers were placed at each level, 2 on the left and the right side, as well as in the middle, see Fig. 2. The positions of the sensors are implemented in the simulations, to get the temperature variations.

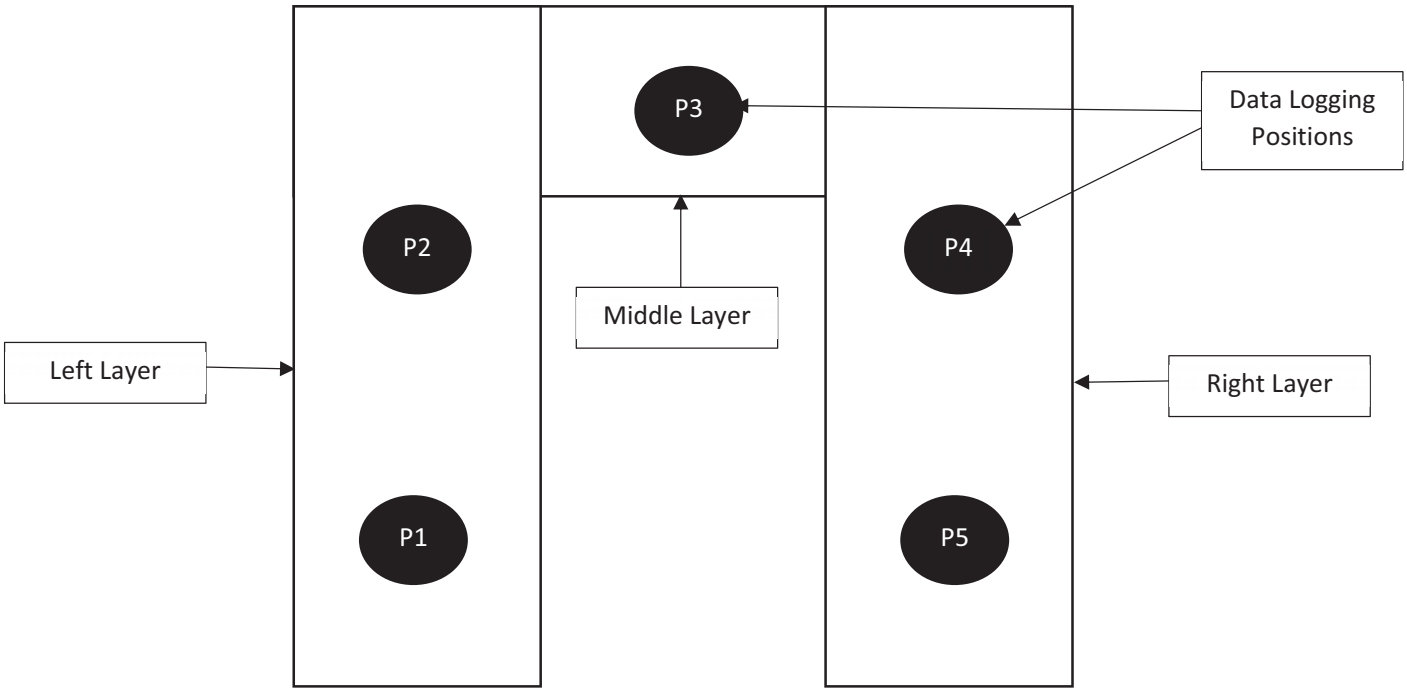

Fig. 2: Layout of shelves and logger positions at each level within the drying chamber

2.3. Physical properties of maize

2.3.1. Heat conductivity and specific heat of maize grain

Heat conductivity and specific heat of maize were determined by Eqn. 1 and Eqn. 2 (Scherer and Kutzbach, 1980; Schwerer and Mühlbauer, 1977)

$$\lambda = 0.108 + (1.80 \times 10^{3} x XM_{H2O}) + (1.79 \times 10^{-4}) \quad \text{(eq. 1)}$$

$$C_{Mp} = 1.294 + (3.44 \times 10^{-2} \times XM_{H2O}) \quad \text{(eq. 2)}$$

Where:

λ is the heat conductivity (W/mK)

XM_{H2O} is the mass water fraction in the maize grain

C_{Mp} is the specific heat capacity of maize (J/ (kg K))

2.3.2. Porosity of maize

The porosity of the maize grains was determined in the laboratory by the use of the water displacement method. Eqn. 3 was used to determine the porosity of the maize grains.

$$\epsilon = \frac{V_V}{V} = 1 - \frac{V_S}{V} \quad \text{(eq. 3)}$$

Where:

V_V is the volume of void

V_S is the volume of solid (maize grains)

V is the total volume of measuring cup

2.3.3. Diameter of maize grain

With the total volume of the maize grains, it was possible to determine the particle volume of a sphere, which is equivalent to the volume of one maize grain. The maize volume was divided by the number of maize grains to get the average volume of one maize grain. The diameter of the maize grain was calculated using Eq. 4.

$$d_p = \sqrt[3]{\frac{6V_g}{\pi}} \quad \text{(Eq. 4)}$$

Where:

d_p is the diameter of a maize grain

V_g is the volume of a maize grain

2.4. Geometry of the SBHD

3D model of the dryer was drawn in the software Autodesk Inventor and exported as a CAD file to StarCCM+ as shown in Fig. 3. In order to set up the simulation, not the original geometry was used, but the geometry in which the fluid flows. The shelves, the maize layers, the inlet, the outlet and the glass are separated in volumes to create single geometry parts for each volume during the import of the CAD file to StarCCM+. Afterwards, a region is created for each geometry part, in order to be able to set individual material properties for each region, e.g. heat conductivity for maize, air and PMMA. The fluid and the porous region are subtracted from the glass shape to get the fluid geometry. Four trays are combined to one maize region to reduce the computational effort, and as a result, each layer is divided into 9 sub-regions.

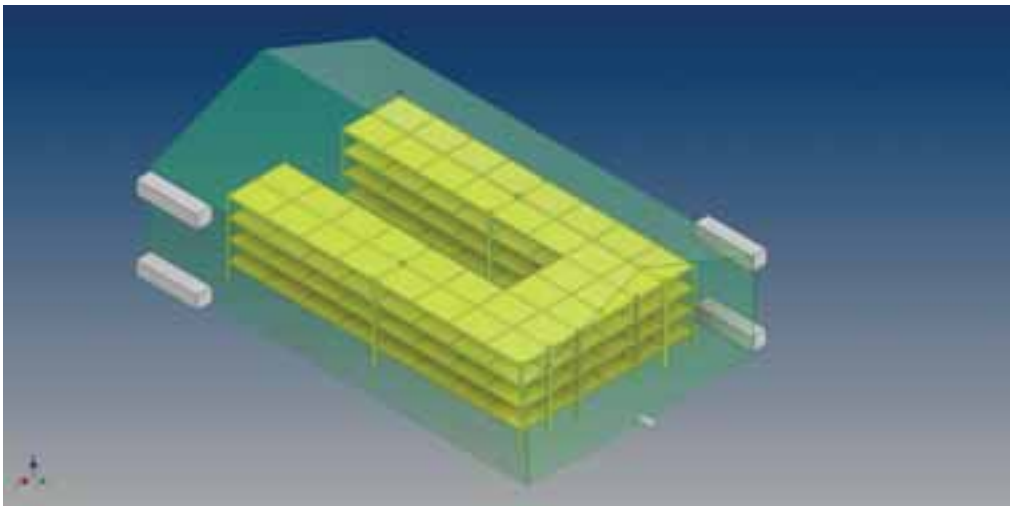

Fig. 3: 3D model of the SBHD

2.5. Boundary conditions

Boundary conditions are set to solve the differential equations. At the pipe, the boundary conditions velocity inlet with 0.25 m/s is defined. Furthermore, the state of the air is given by the data sheets with an average temperature of 305 K and an absolute water mass fraction of 0.025. The relative humidity was transformed into mass fraction xH_2O with Equation 5. The thermodynamic software REFPROP calculates the saturation pressure (REFPROP, 2017).

$$x_{H2O} = \varphi \frac{P_S(t)}{P_M} \quad \text{(Eq. 5)}$$

Where:

P_s is the saturation pressure

P_m is the pressure of the mixture

At the outlet of the drying chamber, a pressure boundary with a relative pressure of 0 Pa is set. The no-slip wall boundary condition is set for the PMMA sheets, the shelve of the maize layers and the floor. For modelling, the solar radiation, the transmissivity, the emissivity and the reflectivity are defined at the interfaces between the fluid and the PMMA region. Table 1 shows the boundary conditions set for the simulation.

Table 1: Boundary conditions for the simulation

Part	Region	Boundary Condition
input	**fluid**	**velocity inlet**
variable	**value**	**entity**
species mass fraction	0.972, 0.028	-
temperature	0.0006.t +296.88	K
emissivity	0.8	-
reflectivity	0.2	-
transmissivity	0.0	-
velocity	0.25	m/s^2
output	**fluid**	**pressure outlet**
pressure	0	P a
PMMA	**glass**	**wall**
emissivity	0.05	-
reflectivity	0.05	-
transmissivity	0.05	-
heat transfer co-efficient	3	$\frac{W}{m^2K}$

2.6. Simulation Procedure

CFD simulations were set up with the software StarCCM+ for investigating the temperature distribution inside the 5-tonne prototype. Before building up the final simulation, the physical phenomena (radiation, fluid flow, heat transfer and species transfer) which occur in the drying process were described by matching numerical models given by StarCCM+. Most important step in describing the drying process was to find an adequate approach for the heat and species transfer. With this approach, the temperature variations in the maize and drying air were calculated. The geometry, through which the fluid flows, was drawn in the software Autodesk Inventor and imported to StarCCM+. Then the given operating parameters (e.g. temperature, relative humidity and velocity at the inlet) and material properties (e.g. transmissivity for the PMMA, maize density) are implemented. Subsequently, the simulation is carried out and the resulting temperature distribution is compared to measurements to evaluate the used models and boundary conditions.

3. Results and discussion

3.1. Dynamics of fluid flow

The simulation of turbulent flow with velocities between $0\ \frac{m}{s}$ and $1.616\ \frac{m}{s}$ are shown in Fig. 4. As expected, the maximum and minimum velocities are close to the inlet and outlet of the dryer. Between the layers, the velocities decrease between $0.323\ \frac{m}{s}$ and $0.646\ \frac{m}{s}$. The velocities at the top of the dryer are approximately $0\ \frac{m}{s}$.

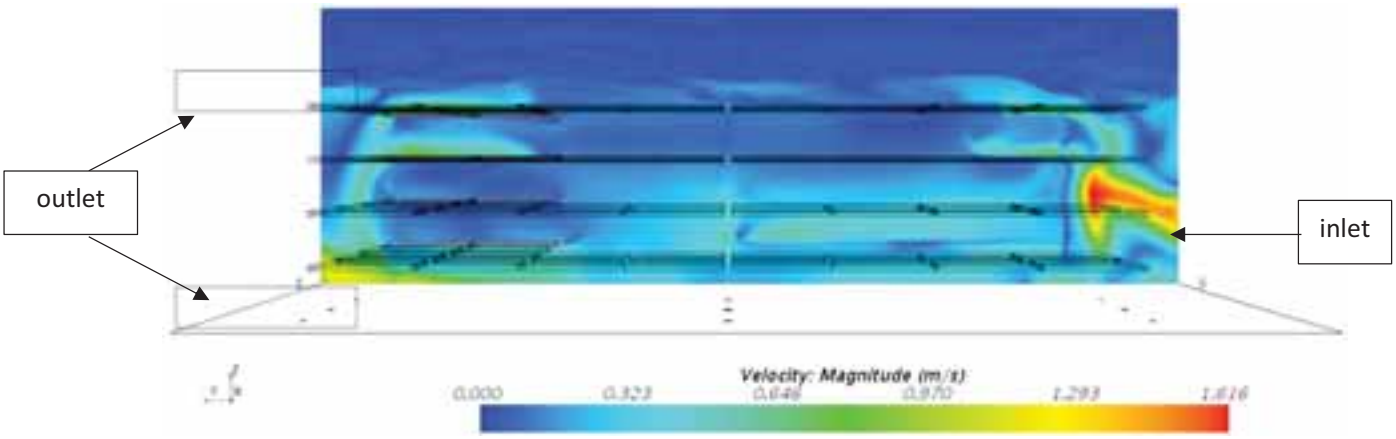

Fig. 4: Velocity field for the unsteady turbulent case

With a closer look at the turbulent viscosity ratio in Fig. 5, the laminar and turbulent flow can be evaluated. The turbulent viscosity ratio between the layers is 600. Hence, the laminar flow cannot be further evaluated, due to the turbulent areas between the layers. With this, the temperature distribution was observed for the turbulent flow.

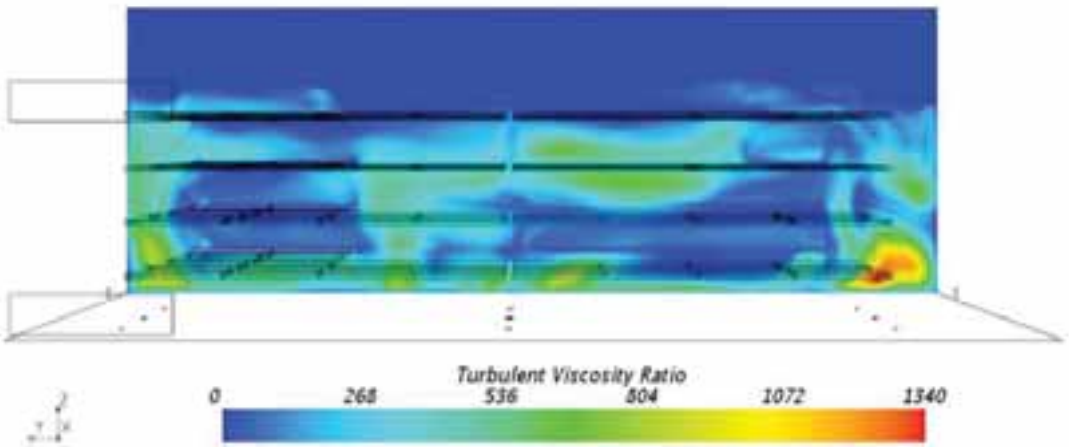

Fig. 5: Scalar Scene for the turbulent viscosity ratio

3.2. Temperature Distribution

Temperature changes are caused by the invading solar radiation and the incoming air; both variables depend on the daytime. The temperature distributions were carried out for a case where the heat transfer coefficient of the Perspex walls was $3\,\frac{W}{m^2K}$. The results for the temperature distribution inside the drying chamber are shown in Fig. 6. Two temperature fronds are developed in Fig. 6. The temperatures close to the roof reached between 340 K and 380 K, and the temperatures around the layers are between 305 K and 330 K. The intruding radiation heats up the drying chamber. This causes hot air to rise due to the density variations, whereas through the pipe at the input, cooler air gets in the drying chamber. The overheating at the top of the drying chamber can result in irregular product quality at the Layer 4 and Layers 1 to 3.

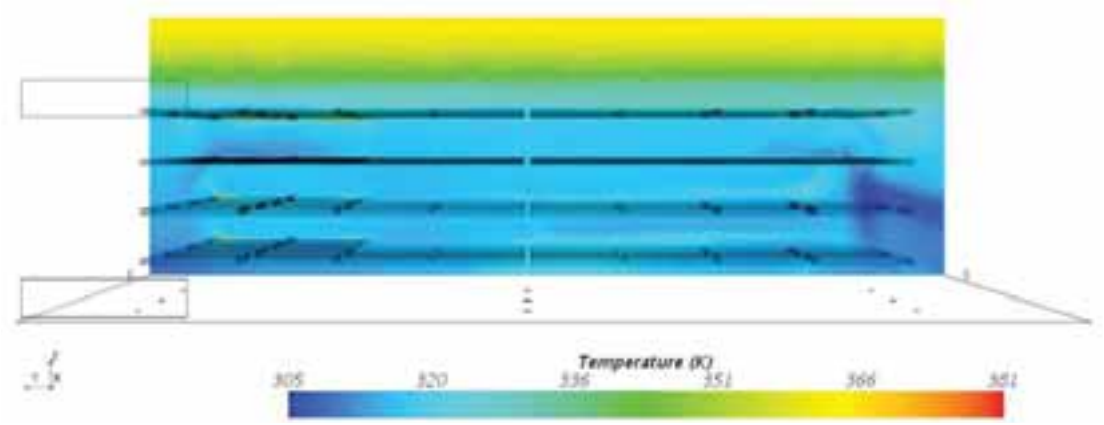

Fig. 6: Scalar Scene for the temperature distribution for the $3\frac{W}{m^2K}$ non-adiabatic wall

The simulation results are compared with experimental data to evaluate the simulations. Temperature distributions for Layers 1, 2, 3 and 4 for the non-adiabatic case are displayed in Fig. 7, 8, 9 and 10 respectively. The temperature function of the simulation results was calculated by Excel to get a smooth distribution and are displayed as dotted lines. The continuous lines display the experimental data. The data from sensor P1 and P2 are averaged to S1. Accordingly, P3 and P4 are averaged to S2. The simulation results for the temperature in Layer 1 (Fig. 7) are up to 15 K higher than the experimental data but the variation decreases in Layer 2 up to 5K (Fig. 8). The simulation results fit nearly perfectly in Layer 3 and Layer 4 (shown in Fig. 9 and 10) for the non-adiabatic case. The high temperatures from the simulation was due to the fact that the dryer was drawn as a continuous shape, but the constructed one in Ejura (Fig. 1) is leaking. Furthermore, temperature differences can be explained by changes in weather, whereas StarCCM+ calculates solar radiation without interruptions. Also, higher temperatures in Layer 1 and Layer 2 in the simulation, can be caused by the missing fans which are installed in the dryer but not considered in the simulations.

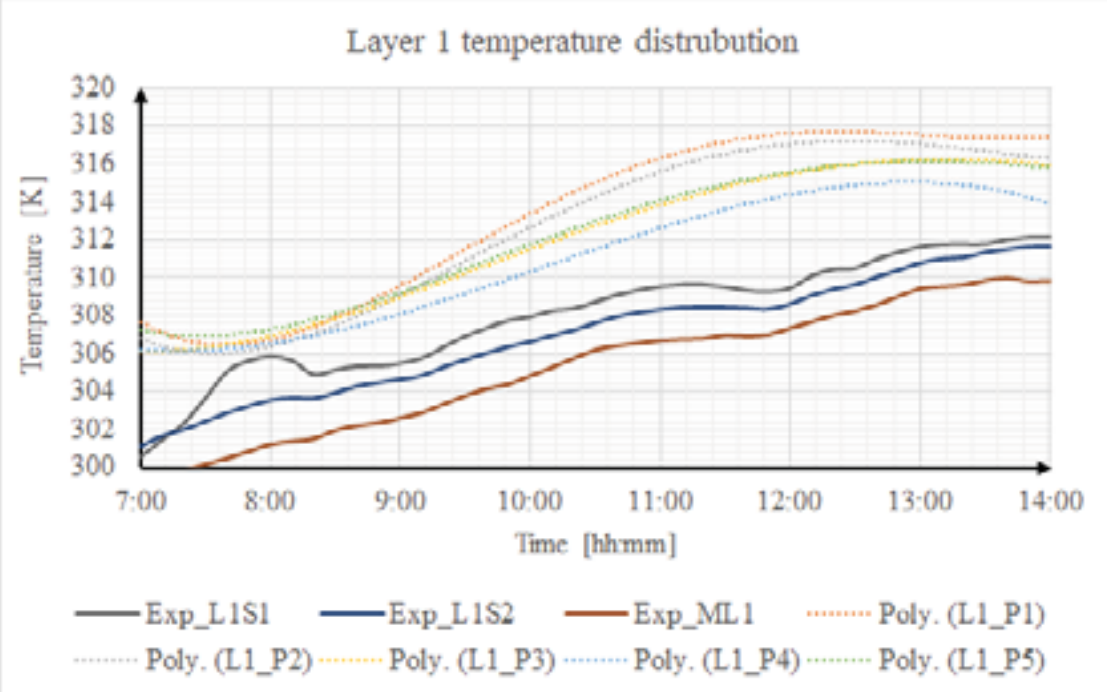

Fig. 7: Temperature distribution for Layer 1

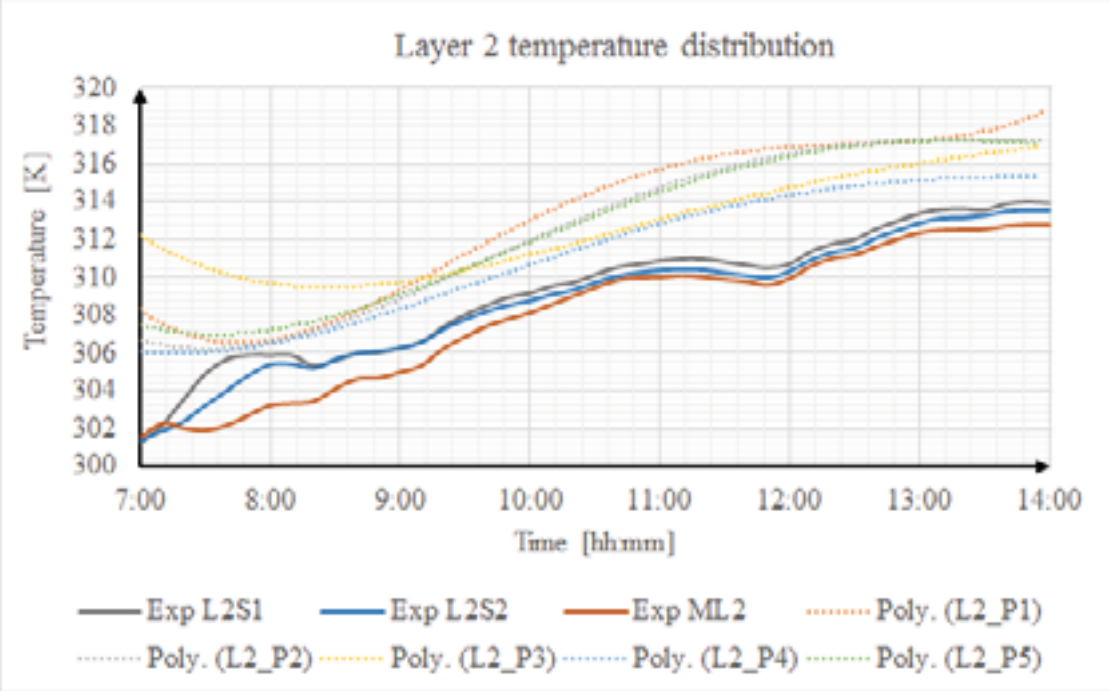

Fig. 8: Temperature distribution for Layer 2

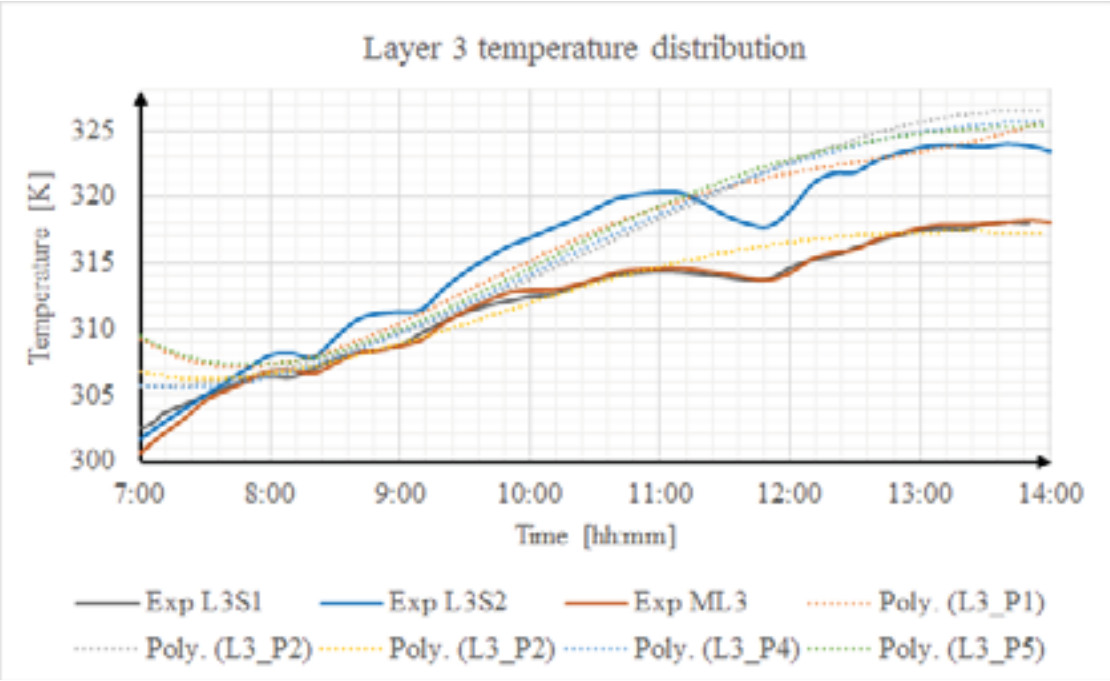

Fig. 9: Temperature distribution for Layer 3

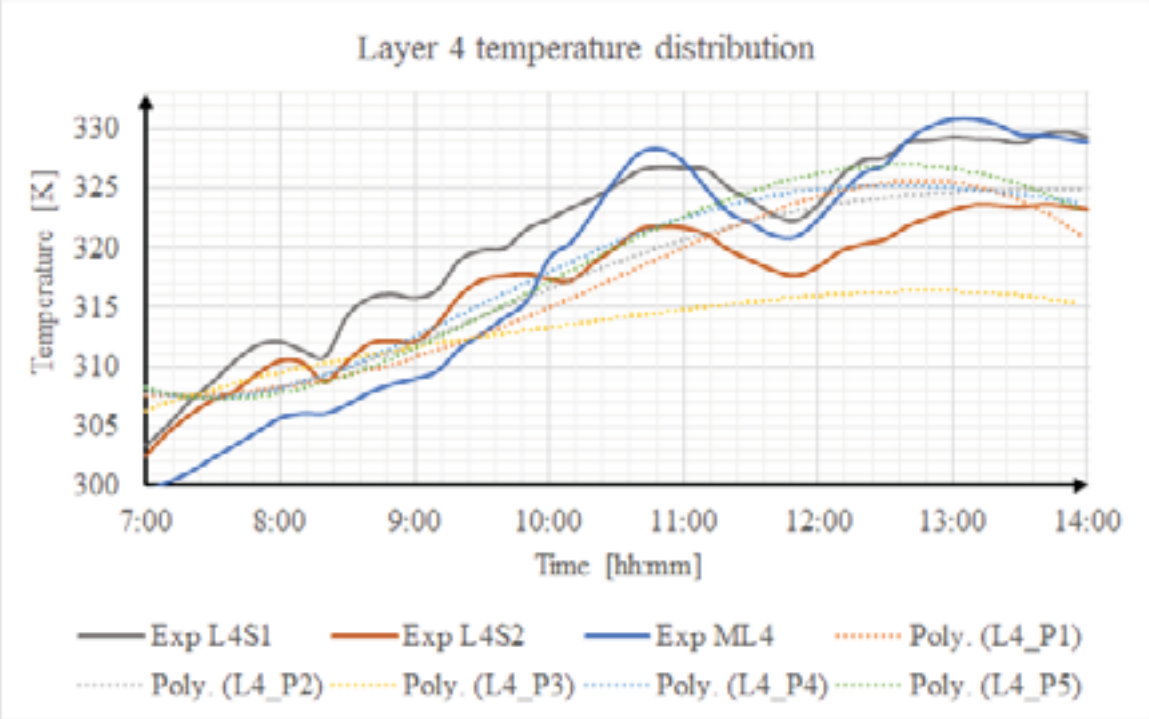

Fig. 10: Temperature distribution for Layer 4

3.3. The automated system

The uneven distribution of temperature in the SBHD could be resolved by the introduction of an automated system. This in addition could also help in the regulation of temperature in the dryer to provide drying conditions which will suit different types of crops.

An electronic circuit consisting of DHT22 temperature and humidity sensors would be designed by the use of Raspberry Pi microcontroller. The Raspberry Pi would be used because of its ability to run Graphic User Interface (GUI) application. The aim of the GUI interface is to enable the users of SBHD to easily interact with the automated system, control and be informed about drying conditions in the dryer. Instead of the conventional keyboard and mouse, an LCD touch screen would be attached to the device to provide a simple interface between the user and the drying system.

Fig. 11 shows the arrangement of the various systems in the automation with the input being the DHT22. The pump and servo motor serve as the outputs of the biomass furnace when the weather and/or drying conditions are not favourable. The DHT22 sensors get signals of temperature and humidity conditions inside the dryer and then relay these signals to the microprocessor. The microprocessor then sends information to the suction pump to either allow or disallow the driving of hot air from the biomass furnace into the dryer. The servo motor acts as the main mechanism to control the movement of shutters at the inlet from the suction pump in to the dryer as shown in Fig. 12. The operations of the suction pump and the servo motor depends on the drying conditions in the dryer. For instance, when temperature in the dryer is lower than the required drying temperature, DHT22 sensor will send signal to the microprocessor for the microprocessor to start the operation of the suction pump.

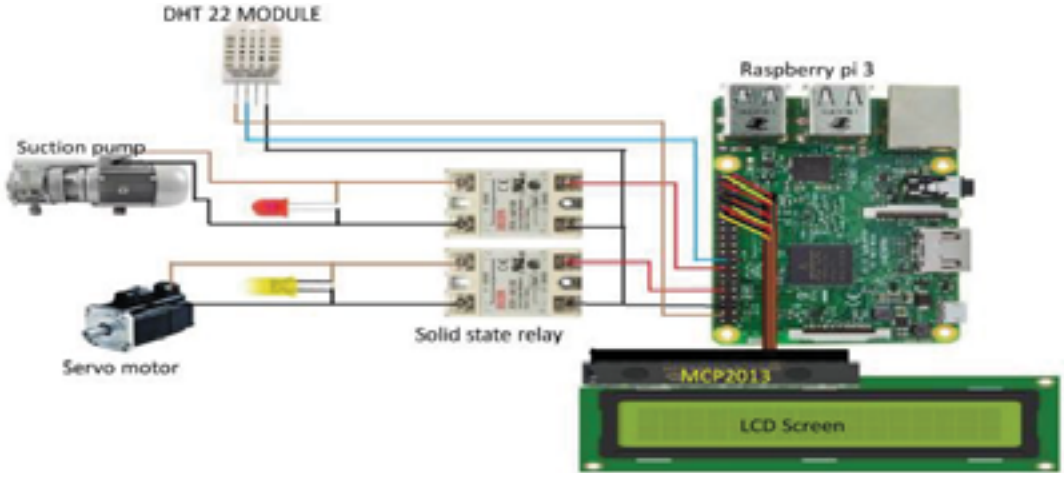

Fig. 11: Schematic circuit of the automated system

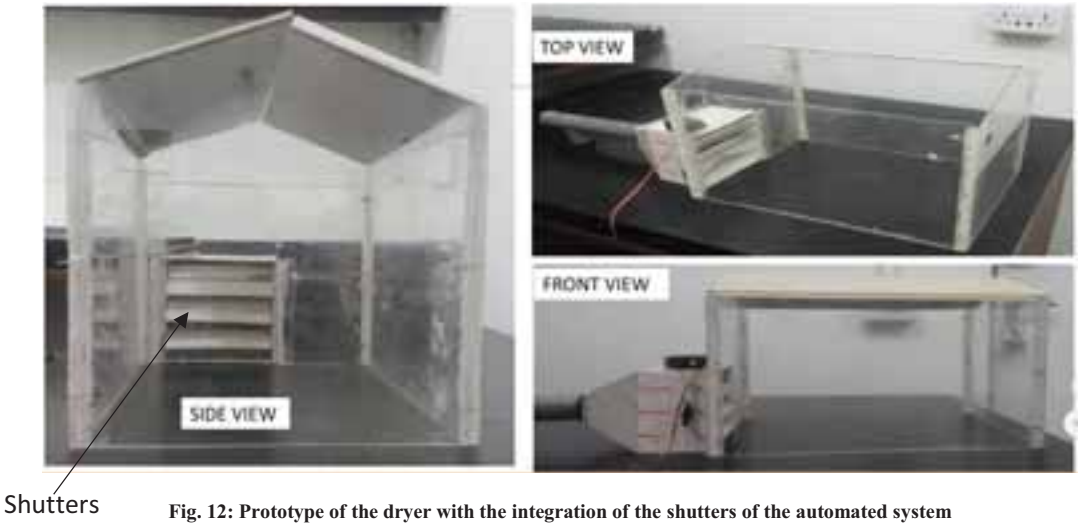

Fig. 12: Prototype of the dryer with the integration of the shutters of the automated system

4. Conclusion

The aim of this work was to develop a CFD model for the Solar Hybrid dryer. The resulting temperature distribution for the heat transfer was compared to experimental data. The comparison showed that the status quo of the dryer was abstracted in a suitable way by the CFD model. Although some deviations between the model and the data exist, they can be explained by the differences between the geometry of the model and the dryer at Ejura. In contrast to the ideal CAD geometry, the physical dryer has several leakages caused by the manufacturing process.

A satisfactory model for describing the status quo of the prototype is compulsory for performing further case studies. For example, case studies can be carried out to investigate the influence of different operation conditions (higher inlet temperature with the furnace, variation of inlet velocities) on the drying process. Furthermore, the dimensions of the shelves (height between the layers, depth of the maize on the layers) can be varied to display effects on the heat and moisture distribution. Again, the integration of an automated system which will aid in the controlled introduction of hot air at high air flow at the lower levels of the shelves in the dryer would help in controlling the temperature of the dryer and then introduce heat from the biomass furnace where weather conditions are not favourable.

5. References

1. Ajayi, O.A., Ola, O.O., Akinwunmi, O.O., 2017. Effect of drying method on nutritional composition, sensory and antimicrobial properties of Ginger (Zinginber officinale). International Food Research Journal, 24(2).
2. Ajayi, O.A., Ola, O.O., Akinwunmi, O.O., 2017. Effect of drying method on nutritional composition, sensory and antimicrobial properties of Ginger (Zinginber officinale). International Food Research Journal, 24(2).
3. Belessiotis V., Delyannis E., 2011. Solar Drying. Solar Energy 85, 1665–1691
4. Fadhel, A., Kooli, S., Farhat, A. and Belghith, A., 2014. Experimental study of the drying of hot red pepper in the open air, under greenhouse and in a solar drier. Int J Renew Energy Biofuels, 2014.
5. Fadhel, A., Kooli, S., Farhat, A., Belghith, A., 2014. Experimental study of the drying of hot red pepper in the open air, under greenhouse and in a solar drier. Int J Renew Energy Biofuels.
6. Forson, F.K., Nazha, M.A.A., Akuffo, F.O., 2007. Design of mixed-mode natural convection solar crop dryers: application of principles and rules of thumb, Renewable Energy 32 - 2306 - 2319.
7. Mastekbayeva, G.A., Bhatta, C.P., Leon, M.A. and Kumar, S., 1999, July. Experimental studies on a hybrid dryer. In ISES 99 Solar World Congress (pp. 4-9).
8. REFPROP accessed on 10th October 2017. <https://www.nist.gov/srd/refprop>
9. Scherer, R, Kutzbach, H.D., 1980. The heat and temperature conductivity of grains. Basic principles of Agricultural Engineering. Vol. 30 No.1:21–27.
10. Schwerer, R., Mühlbauer, W., 1977 The specific heat of grains. Basic principles of Agricultural Engineering. Vol 2 No. 2: 33-40.
11. Sekyere, C.K.K., Forson, F.K., Adam, F.W., 2016. Experimental investigation of the drying characteristics of a mixed mode natural convection solar crop dryer with back up heater. Renewable Energy 92, 532 – 542
12. Srinivasan, R. and Balusamy, T., 2015. Comparative studies on open sun drying and forced type (mixed mode) solar drying of bitter gourd. Journal of Chemical and Pharmaceutical Sciences www. jchps. com ISSN, 974, p.2115.

Eight Feasibility Studies Demonstrating the Potential of Solar Process Heat in the European Automotive Industry

Felix Pag, Bastian Schmitt and Klaus Vajen

University of Kassel, Institute of Thermal Engineering
Kassel, Germany

Abstract

Solar process heat is an important part of future decarbonised heat supply but has not been able to meet the expectations of the market penetration. The automotive industry is a globally leading industry sector cutting edge research and technical innovation. Together, a large-scale implementation within this sector could bring the much-needed breakthrough for the widespread use of industrial solar process heat. To enable such a reality, several case studies have been carried out within the research project "SolarAutomotive" to detail all relevant industrial heat sinks suitable for solar process heat integration. Within this paper, exemplar results are presented, demonstrating the potential of this application to reduce the CO_2-emissions in industrial heat supply. The collector potential identified in the presented case studies totals to more than 11,000 m^2_{gr} (gross area), which are currently being discussed internally within the companies.

Keywords: Solar process heat, SHIP, Feasibility study, Automotive, Industry, Depreciation, Solar economics

1. Introduction

The automotive industry and their suppliers comprise the most important global industry sectors based on turn-over and employees and have a leading role regarding technical innovations. More than three million people are employed in the European automotive and associated industries representing more than 10 % of the EU manufacturing employment. The sector accounts for about 4 % of the European gross domestic product (GDP). The overall energy consumption (heat and electricity) is 39 TWh and annual CO_2-emissions of 10 million (ACEA, 2017).

Solar heat for industrial processes (SHIP) is a reliable, carbon-free technology for industrial heat supply. Despite hundreds of implementations world-wide, a significant market penetration has not yet been still achieved. If the major automotive players begin to adopt the use of SHIP at their production sites, it can be a strong signal to begin a sustainable and self-reinforcing market uptake. The automotive industry and their suppliers are comprised of 12 sectors, from the OEMs (Original Equipment Manufacturer) themselves to comparably small companies producing textiles, plastics, or electronics. These sectors cover a wide spectrum of production processes required to generalise SHIP projects and eventually transfer the results to other industrial sectors. Therefore, within the research project "SolarAutomotive" several feasibility studies are conducted in the automotive industry. Based on a detailed analysis of various production sites, including heat supply and heat-consuming processes, integration concepts for solar process heat have been technically developed and economically evaluated. Twenty-five case studies in eight European countries have been conducted with eight presented with this paper.

2. Methodology

The case studies are targeted at the complete value chain in the automotive industry and their suppliers. They cover the most relevant heat sinks such as central heating networks, bath heating, drying, and supply of hot water. Very influencing boundary conditions are represented, such as different climatic conditions (irradiation and ambient temperature) and economic parameters (available subsidies, gas prices, internal CO_2-reduction goals and accepted mitigation costs). Within the feasibility assessment all relevant collector technologies such as flat plate collectors (FPC), evacuated tube collectors (ETC), compound parabolic concentrators (CPC) and air collectors (AirC) are considered depending on the respective heat sink and temperature level. The analysed production sites and the relating industry sectors are in Fig. 1.

doi:10.18086/swc.2017.26.11 Available at http://proceedings.ises.org

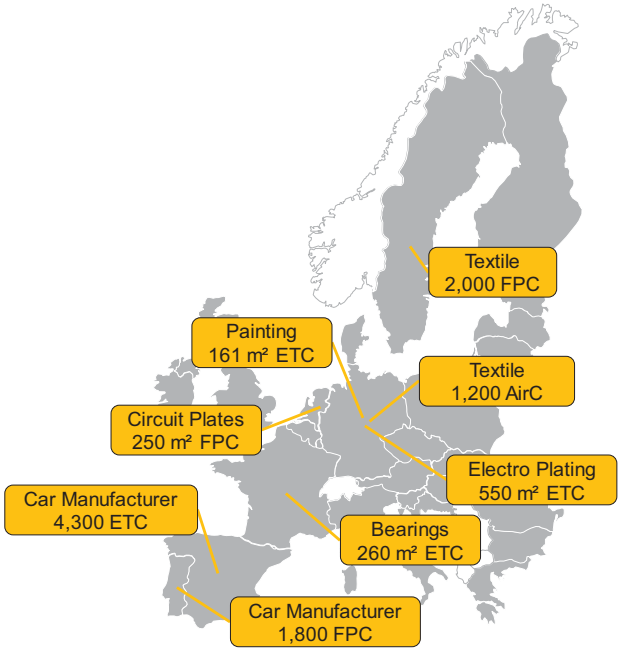

Fig. 1: Analysed production sites within Europe and related industry sectors

2.1 Technical Evaluation

Based on the daily summer heat demand and the heat sink (process) temperature, the maximum potential collector area is calculated. By this design, the solar heating plant produces no excess heat during regular operation and on sunny days the entire heat demand can be covered. This method allows both a relatively high solar specific yield and solar fraction in a highly economical way. Often, the largest solar process heat plant cannot be realised due to site limitations and zoning restrictions. Using Lauterbach (2014), the solar yield and the utilisation ratio of the solar heating plant can be determined for various daily heat demands and installed solar process heat plant size ratios. The energy analysis and solar heating plant performance is then discussed with the company's persons in charge. If there is further interest, a detailed on-site inspection is performed to refine the analysis, which includes suitable roof or ground areas identification and heat sinks as well as heat supply infrastructure. Based on the situation at the production site and the results from the inspection, the collector area of the solar heating plant is reassessed, which often leads to a reduced solar heating plant size and solar fraction. However, an undersized solar heating plant can operate at lower collector temperatures, thus increasing efficiency and utilisation factor. Finally, a detailed simulation with Polysun is performed to calculate the solar yield, utilisation ratio, and the solar fraction, inputs for the economic assessment.

This approach is distilled into a pre-design tool to calculate all relevant parameters within the feasibility assessment. It is based on hundreds of dynamic simulations with different load profiles, process temperatures, geographic locations, and collector technologies (Lauterbach, 2014). The tool uses the production site's latitude to estimate the annual irradiation and peak solar availability in summer for plant sizing purposes. Process flow and return temperatures and an estimated daily load and its profile can be selected by the user. With this information, the tool calculates the potential collector area and storage size, followed in an estimated solar yield and utilisation ratio. If the irradiation at the respective geographic location is known, the solar yield can be recalculated by the product of annual irradiation and utilisation factor for a more accurate result. The tool and its results for those feasibility assessments are validated with Polysun and prove very good compliance. The pre-design tool can be used free of charge (designtool.solar4industry.info).

2.2 Economic Evaluation

Two different economic evaluation approaches are considered. On the one hand, the levelised cost of solar heat are calculated over the life time of the system based on the recommendations of Task 54 (Louvet et al., 2017), comparing solar to conventional heat supply costs over a 25 year lifetime. The conventional heat supply costs are calculated using a gas price and an estimated utilisation factor of the boiler (typically between 75..85 %). On the other hand, the total cost of ownership method is used to determine payback time, internal rate of return and net present value. The solar heating plant investments are estimated by experience and detailed analysis of solar process heat systems in Germany based on size, collector technology, plant location, and integration effort. Other relevant parameters for the economic calculation are in Tab. 1.

Tab. 1: Technical and economic parameters for the calculation of the levelised cost of solar heat and for the total costs of ownership

Parameter	Value
Performance factor[1]	70..100
Price increase of fossil fuels	3 %/a
Inflation	0.8 %
Maintenance, repair, and insurance	0.7 %
Discount rate	4 %
Operation time	25 a

In addition to the natural gas savings, the depreciation of the solar heating plant is considered for a detailed economic assessment. Depreciation is an allocation method that enables a company to reduce the economic value of an asset over a certain time. The depreciated value of the asset reduces to company-wide profit and thus the tax load over the depreciation period. This can significantly decrease the payback time and increase the internal rate of return. Approaches not considering the depreciation of the solar heating plants cannot evaluate the investment correctly.

Assed depreciation is defined by the national tax law and varies between different countries in both number of years and its calculation method. The method of depreciation can either be straight-line or a declined-balanced method. Whereas the straight-line method continuously and equally depreciates the complete investment, the declined-balanced method has an accelerated depreciation in the first years and a decelerated in the final years. Therefore, it is not possible to depreciate the complete investment with the declined-balanced method. The actual additional benefit of a solar heating plant by reducing a company's tax burden is calculated on an annual basis by the product of the depreciation rate per year (DEP in €) and the respective business tax rate (TR in %) shown in eq. 1.

$$Tax\ Benefit = \sum_{i=1}^{Years\ of\ Depreciation} DEP_i \cdot TR \qquad \text{(eq. 1)}$$

In tab. 2**Fehler! Verweisquelle konnte nicht gefunden werden.** different depreciation parameters and tax rates are presented for the analysed countries showing the additional benefit of depreciating a solar heating plant. The depreciation duration plays a significant role regarding the tax benefit of the solar heating plant, most notable for the declined-balanced method within the first four years. Since nearly all companies solely base capital investment on payback time, the first years are most important in reaching a decision in industrial companies.

[1] Ratio of delivered solar heat to used electricity

Tab. 2: Overview of the depreciation methods and rates in the related countries of the EU

Country	Depreciation method	Depreciation factor[1]	Years of depreciation	Depreciated investment in the first 4 years	Corporate tax rates	Additional benefit[2] within the first 4 years
DE	Straight-line	-	10	40 %	29.88 %	12 %
ES	Straight-line	-	14	29 %	25 %	7 %
FR	Declined-balanced	2.25	10	64 %	34.43 %	22 %
NL	Straight-line	-	5	80 %	25 %	20 %
PT	Declined-balanced	2.5	4	98 %	25.5 %	25 %

As an example, the German depreciation method is fixed to the straight-line method with a 10 years depreciation period and the business tax of 29.83 %. In contrast, the Portuguese depreciation period is reduced to four years and applies the declined-balanced method (with an accelerating factor of 2.5). The business tax in Portugal is 25.5 %. Assuming 100,000 € investment, 40,000 € can be depreciated within the first four years in Germany, resulting in an additional economic benefit of 11,932 €. In contrast, the benefit in Portugal is more than double with 24,955 € within four years, nearly depreciating the entire solar heating plant. For a better understanding of the cash flows regarding both depreciation methods, Fig. 2 shows the annual depreciation rates (bars) and the additional benefit (dashed line) of solar heating plants. The Portuguese results for the declined-balanced method with four years depreciation period are in green and the German straight-line method over ten years is shown in red. Exemplarily, a corporate tax rate of 25 % has been assumed for both calculations for a better consistency. As quickly seen, the tax benefit of both methods is the same over ten years. In Portugal, a greater tax benefit is realised within the first years and as such the payback time is significantly reduced.

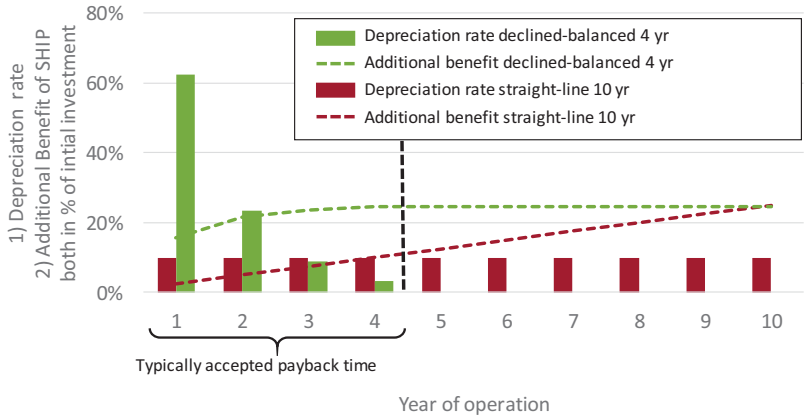

Fig. 2: Comparison between two depreciation methods and duration regarding the depreciation rate and additional tax benefit of a solar heating plant. The depreciation factor for declined-balanced method is 2.5 and the corporate tax rate is 25 %

To conclude, the payback time of solar heating plants in industry is reduced by depreciating capital investments. This boosts the market uptake, already seen in some countries, such as Portugal, France, and also in India. In addition, governmental tax revenue is not affected long term by the inclusion of depreciation and should not be a hinderance in future economic policy.

[1] Only existent for declined-balanced method
[2] In relation to the initial investment

3. Results

As already mentioned, numerous feasibility studies including solar heating plant pre-design are carried out within the project "SolarAutomotive". By several case studies in companies specialised in surface treatment, it is seen that this sector in general and electro plating in specific are very promising for the use of solar process heat. In this sector, many baths must be heated and kept at elevated temperatures, easily achievable for solar heating plants. In summer, there is a significant base heat load and any possible heat recovery barely reduces overall heat demand. Solar process heat integration for heated baths is also fairly easy through dimple plates or by external heat exchangers.

Only a few selected case studies are discussed in this work to provide a wide range of examples. For a more detailed assessment on a German electroplating company Pag et al. (2017) details a performed case study and proposes a concept to use of solar process heat in combination with a micro gas turbine.

Tab. 3 shows an overview of the selected feasibility studies, followed by a summarised explanation.

Tab. 3: Overview of the performed feasibility studies
Heating network, supply/return temperature; Heat recovery network, supply/return temperature; Hot water, start..set temperature; Bath heating, bath temperature; Drying, start..set temperature

Country	Sector	Heat sink	Pre-design[1]	Irradiation in kWh/m²a[2]	Specific solar yield in kWh/m²$_{gr}$a	Solar fraction[3]
ESP	Car manufacturing	Heating network, 130/110 °C	4,300 m² ETC	1,670	410	5 %
PT	Car manufacturing	Heating network, 70/40 °C	1,800 m² FPC, 75 m³	1,920	830	34 %
GER	Electro Plating of Plastics	Heating network, 80/70 °C	1,000 m² ETC + 317 kW$_{th}$ CHP,	1,010	350	18 %
NL	Circuit boards	Hot water 15..60 °C	250 m² FPC, 15 m³	1,130	430	5 %
FR	Bearings	Heat recovery network, 80/60 °C	260 m² ETC, 25 m³	1,210	485	5 %
GER	Textile processing	Drying, 10..60 °C	1,200 m² AirC	1,040	480	10 %
SWE	Textile processing	Hot water, 10..60 °C	2,000 m² FPC, 175 m³	1,040	550	23 %
GER	Painting	Bath heating, 43 °C	161 m² ETC, 8 m³	960	390	31 %

3.1 Car manufacturing in Spain

The production site analysis in northern Spain shows that the specific yield does not allow an economic integration of solar heat at the moment, even though there is a good irradiation and significant open land for plant construction. The return and flow temperatures of the central hot water network are unnecessarily high but cannot be lowered due to one single process (wax bath) with a high temperature level. In addition, there are six weeks in summer

[1] If not specified differently, the collector area given refers to the summarised gross area of the collector field
[2] On tilted surface
[3] Solar fraction is given with respect to overall heat consumption (central heating network) or to process heat demand (Hot Water, Bath heating, Drying) if not specified differently.

(two weeks in June and four weeks in August) when the production site is closed completely and the hot water network is shut down. To handle this long period during times of high irradiation without a heat sink, parabolic trough collectors that can be defocused and evacuated tube collectors with a built-in switch-off temperature are considered within the feasibility assessment. The latter concept with 4,300 m² collector area still reaches specific annual yields of more than 400 kWh/m²$_{gr}$. The potential plant site is located more than a kilometre away from the boiler site and complicates the integration. The closest reasonable integration point is 900 m away and still challenging. Due to no subsidy program for solar process heat plants in Spain, an implementation is not realistic and further investigations have been put on hold.

3.2 Car manufacturing in Portugal

Within the production site of a Portuguese car manufacturer, a hot water network is operated with a 70 °C flow and process dependent 40..50 °C return temperature. In addition to heat recovery from the thermal oxidiser in the paint-shop, three gas boilers with an overall capacity of 13 MW provide heat for an annual heat demand of 4.4 GWh. Process heat demand is distributed more or less evenly over the day with a light peak in the morning. Heat demand will be significantly increased due to a doubling of production capacity until the end of 2017. The future designed heat load is estimated to be 7 MWh/d to be served with a flat-plate collector field of 1,800 m². Due to the high local irradiance, a low temperature level and constant load profile, a specific solar yield of 830 kWh/m²a can be achieved. The levelised cost of heat were calculated with 25 €/MWh over 25 years. Despite the four-year declined-balanced deprecation period for solar heating plants in Portugal, the payback time is 15 years due to the low gas price and no other solar process heat plant subsidies.

3.3 Electro plating of plastics in Germany

The analysed electro plating line has a heat demand of 2 GWh/a. Due to a high electrical base load, a combined heat and power plant (CHP) is taken into consideration. In Germany, subsidies for a CHP are paid over a fixed period of full load hours. This opens up the possibility to change the typical dimensioning of a CHP and its operational mode because it is no longer necessary to continually operate the best economic return. To increase the share of heat supplied by CHP in winter, the plant is designed based on the winter load. In return, the CHP is switched off between May and September to avoid inefficient part load behaviour and increased burner cycling. This enables a larger solar heating plant to be integrated, covering a relevant share of the summer heat demand. The residual heat load is covered by a conventional gas boiler. The CHP has a thermal capacity of 318 kW. The collector field is designed with 1,000 m² ETC. This technology coupling covers more than two thirds of the heat demand with low carbon heating technologies (CHP: 50 %, solar: 18 %). The investment is estimated to be 570,000 €, with an internal rate of return of nearly 10 % over 15 years. Using the conventional design rules for CHP (summer load), a CHP with a thermal capacity of only 212 kW could be implemented with no further potential for solar heat due to the reduced heat load during summer that is already covered by CHP.

3.4 Production of circuit boards in the Netherlands

Circuit boards are produced in continuous loop and plunged consecutively into various baths. The company has several production lines with over 500 baths in total (several hundred litres each), with 56 requiring heat up to 60 °C. The baths are electrically heated with an overall nominal capacity of 455 kW. Due to the large number of baths and their small volume, solar process heat integration for direct bath heating would be very complex and expensive. However, the baths are fed with fresh water to compensate evaporation and carryover losses. This is currently done by cold water, which has to be electrically heated. A new concept is developed with a second feed line for fresh water at 60 °C. This enables a simple and cost-efficient possibility to integrate solar heat. The amount of hot water is estimated to be 7 m³/d with a FPC solar process heat potential of up to 250 m². Due to the constant load profile during the week (five days, two to three shifts), a specific yield of 430 kWh/m²a can be achieved (118 MWh/a) and corresponds to a solar fraction of about 5 % with respect to the overall heat demand at the production site. The levelised cost of heat is estimated between 24.5 €/MWh and 37.2 €/MWh depending on the development of the tariffs of the feed-in subsidy scheme.

3.5 Production of bearings in France

The heat for the French production site is currently supplied by a steam boiler. Within 2018, the steam network will be completely replaced by a hot water network with a 70 °C supply and 40 °C return temperature and a condensing gas boiler. Heat recovery from compressed air generation from compression chillers will be implemented and its recovered heat is fed into the network. There is a still a residual heat demand that can partially

be covered by solar heat. A solar heating plant is designed to have 260 m² ETC collectors and includes a storage of 25 m³ generating 126 MWh/a. The levelised cost of solar heat is approximately 20 €/MWh due to an existing national subsidy for solar process heat in France. Following detailed measurements after the implementation of the new heat network, the solar heating plant will be redesigned and built by the end of 2018 if the solar heating plant is still economically feasible.

3.6 Textile processing in Germany

This company with more than 140 employees covers the whole spectrum of product finishing with processes such as sizing, dyeing, and coating of textiles and relating materials. The three-shift operation over five days is very water and energy intensive, constantly needing massive amounts of hot water at different temperature levels up to 90 °C. Due to expansive use of heat recovery from a regenerative thermal oxidiser that purifies exhaust air, the hot water demand is nearly fully covered. The exhaust air originates from several stenters and a dryer that uses fresh air heated to 200 °C. By using all the heat recovery for water (pre-) heating, the fresh air for these applications must be heated internally by internal and external heat exchangers from the central steam network. Solar air collectors can be used to preheat the required air for these heat sinks. Based on the air volumetric flow rates and the set temperatures of the stenters (46,400 m³/h; 200 °C) and the dryer (8,000 m³/h; 140 °C), the heat demand has been estimated by 22.4 MWh/d in summer (ambient air temperature 20 °C), considering a simultaneity factor of 0.5 and 15 hours of operation per day. This results in a yearly heat demand of 5.2 GWh. To cover a relevant share by solar collectors, an air collector system with 1,200 m² is designed and simulated. These collectors preheat the incoming air from ambient temperature to a maximum of 60 °C. The solar heating plant obtains a collector yield of 707 kWh/m²a but only 481 kWh/m²a can be used in the processes due to the lack of storage. Still, a solar fraction of 10 % with respect to the process can be achieved. The estimated investment of 350,000 € including 50,000 € for installation, results in solar heating costs of 12 €/MWh.

3.7 Textile processing in Sweden

The production site is operated 24 hours per day and 6 days per week with a three weeks summer production break. More than 400 m³/d of 60 °C hot water is required for dyeing and washing leading to a daily heat demand of 21 MWh in the summer. The heat demand is met with a steam boiler at 190 °C. To cover the summer daily heat demand, nearly 5,000 m² FPC are theoretically required. A flat roof offers an area of about 10,000 m² but considering roof statics, skylights, and collector spacing the feasible collector area is approximately 2,000 m². Depending on the currently unknown actual hourly load profile the specific solar yield can range between 520 and 580 kWh/m²a and up to 1.2 GWh/a in total. This corresponds to an annual solar fraction of about 22.5 %. A hot water storage of 90 m³ is already installed to ensure the hot water supply during peak demand. This must be complemented with a solar heat storage with up to 175 m³, depending on the load profile and the actual peak loads. During the detailed planning, it will be investigated if the current storage can be used to store the solar heat. Given the size of the collector field, selected technology and integration type, a specific investment of 450 €/m² is estimated. This way, solar heat can be provided with levelised costs of heat of 49 €/MWh, currently below the actual cost of steam.

3.8 Painting process in Germany

This company is specialised in the painting of large scale parts, e.g. of commercial vehicles. In a pre-treatment step, these parts must be removed from rust and debris (pickling). This is done in a 15 m³ acid bath, kept at 43 °C with electrical heaters having a nominal capacity of 42 kW. Measurements show that 28 kW (67 % of the nominal capacity) are constantly required 24 hours per day. The electrical heaters are switched off midday on Saturday until early Monday morning to provide the set temperature for production. This corresponds to a daily heat demand of about 700 kWh in summer and 210 MWh per year.

Based on these data and available roof areas, four solar heating plants with different collector field sizes are designed and simulated with Polysun. Double sided evacuated tube collectors have been chosen due to their low static load when installed. The solar heating heat is integrated with an external heat exchanger into a circulation pipe, which constantly mixes the bath contents. The simulated result are in Fig. 3. The corresponding solar fractions range between 15 % (88 m², no storage) and 58 % (337 m², 32 m³). The company decided for a medium-sized collector field of 161 m² in combination with an 8 m³ storage having a solar fraction of 31 %. Due to expensive electrical energy used to currently heat the bath, a 35 % internal rate of return and a payback time of less than three years can be achieved.

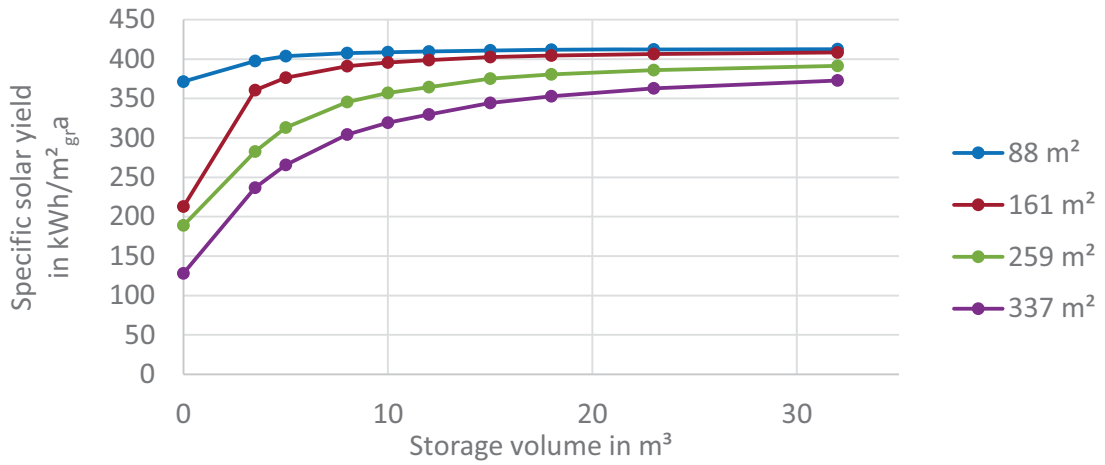

Fig. 3: Specific solar yields for the four different collector field sizes and storage volume variation

The painting hall, where the painting process itself is performed by hand, requires heat that can be covered by solar heat. During the painting process fresh air (74,000 m³/h) must be supplied at 20 °C to guarantee acceptable working conditions. Due to a high load of paint particles, the air cannot be circulated. Afterwards, the painted parts must be dried. Therefore, the hall is heated up to 60 °C with the same air volumetric flow rate as in the painting mode, whereas 67,000 m³/h (90 %) is recirculated and the rest is provided by fresh air. The air volumetric flow rates are provided by an air handling unit that can switch between the painting/drying operational modes and is heated by an air-to-water heat exchanger. A heat recovery system is installed for preheating the fresh air by the exhaust air. By conducting detailed air measurements, it is established that there are either one or two painting cycles per day followed by a drying period during night. Based on these measurements, the heat load profile for the air-handling unit can be calculated and in a further step extrapolated over the year taking into account the seasonal temperature profile of a near-by weather station. The yearly energy demand is estimated to be 270 MWh/a with a daily summer load of 800 kWh/d. By installing an additional heat exchanger, solar heat can be integrated. First simulations recommend a 250 m^2_{gr} ETC solar heating plant. The efficiency of the solar heating plant is increased by varying the supply temperature depending on the actual operation mode (painting vs. drying).

4. Conclusion

The automotive industry and their suppliers have many technical possibilities to integrate solar heat into various processes. In general, central heating networks are available that can be used for solar integration. Depending on the industry sector, there are also individual processes that allow an efficient decentralised use of solar process heat. Generally, companies who specialise in textile and surface treatment, operate multiple baths at a feasible temperature for solar process heat. If there are any restrictions on-site (e.g. space) and solar heat cannot be integrated easily into the baths, the pre-heating of feed-water for carry-over and evaporation loss compensation offers a possibility to cover a small fraction of the overall heat demand with solar heat. Drying for paint-shops, which is comparable to other industries plays a key role with respect to the energy demand. Since fresh air is often needed, the use of solar for air pre-heating can be a cost-effective solution.

Many economically feasible solutions were identified, which were highly dependent on national subsidy programs and on-site boundary conditions. Within the performed case studies, the levelised cost of solar heat ranged between 12 and 49 €/MWh. The most economical concept has an internal rate of return of 35 % and the least economical still has a return of 6 %. Unfortunately, the decision for or against a capital investment in efficiency and renewable energy is still primarily made based on the payback time, regardless of solar process heat's proven long term economic benefit. To help overcome this hurdle, regulations regarding depreciation and corporate tax have a major positive influence on payback time. As such the national tax legislation plays a significant role to obtain the required financial decision metrics by industry.

To date, only a few companies have committed themselves to significantly reduce CO_2-emissions in a way that may conflict with economic decision criteria. Additionally, low natural gas prices currently globally impede further market uptake of solar heating plants. The subsidy programs for solar process heat, if existent, are typically

not sufficient to satisfy the economic targets in industry due to the small difference between the conventional heating costs and the solar heating costs. If some stakeholders in the automotive industry and their suppliers can be encouraged to take the first step, it will be a tipping point for a wider adoption of this reliable, CO_2-free technology. Optimising the depreciation tax legislation for low carbon heat capital investments is a promising possibility to support the necessary market uptake.

5. Acknowledgement

The authors gratefully acknowledge the financial support provided by the German Federal Ministry for Economic Affairs and Energy (contract no. 0325863A) as well as the industry partners within “SolarAutomotive” for the cooperative and trustful cooperation.

6. References

ACEA (European Automobile Manufacturers Association), 2017. The Automobile Industry Pocket Guide 2017-2018

Lauterbach, C., 2014. Potential, system analysis and preliminary design of low-temperature solar process heat systems, kassel university press, Germany

Louvet, Y., Fischer, S., Furbo, S., Giovanetti, F., Mauthner, F., Mugnier, D., Philippen, D., 2017. LCOH for Solar Thermal Applications, Task 54, INFO Sheet A.2, available at (last access: 20 September 2017): http://task54.iea-shc.org/data/sites/1/publications/170306-IEA-SHC_Task%2054-Info_Sheet_LCOH-Final.pdf

Pag, F., Majewska, P., Schmitt, B., Vajen, K., 2017. Combination of solar process heat with a micro gas turbine in a medium-sized electro plating company, in: Proceedings OTTI Staffelstein, Germany (in German)

Solar Dryer and post-harvest management in Ethiopia: Design and CFD simulation

Asfafaw H. Tesfay[1,2], Brhane A. [2] , Ashenafi K. A[2] and Fana F. Nurhusien[2]

[1] Institute of Energy Mekelle University, Mekelle, Tigray, Ethiopia

[2] School of Mechanical and Industrial Engineering, Ethiopian-institute of Technology-Mekelle, Mekelle University, Mekelle, Tigray, Ethiopia

asfafaw.haileslassie@mu.edu.et

Abstract

A solar tunnel dryer system utilizes solar energy to heat up air and to dry any food substance loaded to it, this leads to reduce wastage of agricultural products and prolong their life by natural drying, and has limitations such as, exposure to sunlight, liability pests and rodents, and lack of proper monitoring. The aim of this paper is to design and simulation a solar tunnel dryer for drying of cereal's, fruits and vegetables. In this dryer, the grains have placed directly at absorber and exposed to direct solar radiation. The airflow and associated pressure development in the drying chamber is analyzed with CFD.

The initial and final moisture content considered were 35 and 15 percent for maize, and 94 and 10 percent for tomato. The dryer is designed to dry one-ton of maize in four days, and 250Kg of sliced tomato in two days. The dryer has an integrated fan to drive the moist air, which is powered by energy. The simulation considers Mekelle, weather data as its input.

Keywords: Tunnel dryer; solar dryer; postharvest loss; tomato dryer; simulation of tunnel dryer; Forced dryer

1. Introduction

Food security is a common problem in developing countries that happened not only because of less yields, but also because of poor harvesting and post harvesting management. Proper post-harvest management in developing countries can significantly contribute to the availability of food [2]. Common post-harvest losses are due to improper and/or untimely drying of foodstuffs such as cereal, grains, pulses, tubers, meat, fish, etc…[2]. Traditional drying, which frequently performed on the ground in an open air, is the most widespread method used in developing countries because of its simplicity and does not incur additional cost. Nevertheless, this drying technique has many drawbacks contamination, uneven drying, and uncontrolled moisture content of the products, which in return causes degradation in quality, insect infestation, and attack by animals etc. Traditional dried food items does not fulfil the international quality standards, and it has international market process [4].

To improve the traditional drying techniques, solar dryers have received considerable attentions to improve post-harvest management [1]. Though many developing countries are endowed with higher solar energy potential, unfortunately solar dryers have not well introduced, on these regions the reason for the less technology infiltration includes such as; economically unviable, unsatisfactory technology development and limited knowledge of the technology [3].

Like many developing countries; the, majority of the population of Ethiopia engaged in farming and about 80% the countries food products cultivated by small farmers, these farmers do not use proper postharvest management technologies, but the traditional open air dryer techniques. In this regard, the development and introduction of solar drying as post-harvest technologies are significantly important in improving livelihood development of developing countries [24].

Many solar dryers have been introduced, but accomplishing it is very important performed unsatisfactorily. There is a need to understand the overall operation of the dryer, the interaction between its component parts, the influence of various design and operating parameters on its performance, and the development of systematic design procedures and guidelines. These technical constraints have been limiting the use of natural convection solar dryers. In addition, during drying some materials absorb heat directly from the radiation of the sun and tends to

doi:10.18086/swc.2017.26.12 Available at http://proceedings.ises.org

decolorization of the product, which decrease the quality of the product.

Solar dryers of forced convection type can effectively be used. However, which needs power to drive the fan, and unfortunately many rural areas, do not have power. Because of this forced convection were not introduced widely in many developing countries. In direct driers have low drying rate compare to direct forced dryer, but they have better quality and have potential to access the market as a result it enhances the income of individual farmers [3].

According to FAO report in 2000, Ethiopia produces 115,000Mg from 7,800 hectare and increased to 10,000 ha and 150,000 Mg in 2008(FAO, 2010). Most of the fruits produced in Ethiopia are consumed locally.

Fresh fruits are regarded as highly perishable and bulky commodities as they contain more than 80% moisture. Consequently, their transportation to distant places is costly and their condition on arrival might be less than satisfactory. The best way to maintain the nutritional value of fruit is by keeping the products fresh. On the other hand, its cold chain is difficult to maintain throughout the developing countries. Fruits have an average shelf life of 7 to 36 days [6]. Those losses at fruits could be happen because of thing, poor postharvest handling, and market conditions. For example during the rain season harvesting period of these exist excess, but according many losses happened on the country shortage of supply happens during the other period of the year this cause fluctuation in market.

In this paper crop, fruit and vegetable have considered for drying, Modelling and Simulation of a forced convective solar tunnel dryer has studied. CFD has used to show the flow through the duct and to simulate air pressure and air velocity profiles in the drying chamber.

2. Materials and Methods'

2.1. Solar Tunnel Dryer Construction Material Selection

The construction materials of the solar tunnel dryer based on its quality and suitability. The materials include absorber, metal frame, drying tunnel, rolling bar, concrete block substructure, PV module and fan. Solar absorber is a device that receives solar radiation and converts it into thermal energy. The absorber material is mild steel of thickness 0.9mm or (24.2 × 2 × 0.0009 m). The absorber is black painted metallic in order to increase its absorbance thereby heating the air between it and the cover.

The absorber and the cover have created a triangular shaped tunnel. This tunnel volume of 0.044 m^3 air is heated and the hot air is transported by means of forced convection

The cover plate: of the dryer is transparent sheet used to cover the absorber, to prevent dust and rain entering to the absorber. It permits solar radiation into the system, but hinders reflected radiation from the system. This cover plate is made up of glass with thickness 4 mm or (24.2 × 2.3 ×0.002 m).

Drying Tunnel: is the drying chamber made of a highly polished plywood box (24.2×2 ×0.016 m) held in place by galvanized iron, the material has been chosen because of its poor thermal conductivity , its smooth surface finish, and minimized radiation loss. The cover of the drying chamber is corrugated plastic of thickness of 2-3 mm, or (24.2 ×2.3 × 0.002 m). In order to reduce with radiation and avoid moisture absorption by the wood aluminum foil is wrapped on the inside of the chamber, with Nail and glue fasteners.

Insect net at air inlet and outlet has used to prevent insects from entering into the dryer. The hinges and handle for the dryers door.

Brick block: have used to protect bending of the dryer and collectors structure with dimensions (0.4×0.4 ×0.5 m). The frame has covered by aluminum wire mesh to hold the product to be dried. Axial Fan has selected because of its low static pressure, is required to drive the moist air out of the dryer and the fan has 18 m^3/min with a power of 0.626 Hp (0.46 kW).

Insulators: the insulation material used in this system is fiberglass with 150 mm thickness under the absorber surface, which compromises 48.5 x2 x0.15 m^3 volume of material.

2.2. Methods

The design of the solar tunnel dryer taken into consideration different design criteria and parameters. Some of these were from literature while others were determined by a series of mathematical analysis. The design parameters included environmental conditions of the test location, drying temperature, amount of moisture to be removed, heat energy requirement and airflow required.

The test location is found at a latitude 13° 29′ N and longitude 39° 28′E with elevation of 2084 m. ambient temperature, Ta, of 24℃ and relative humidity 55 %.

Then the following models are applying through the tunnel dryer.

Mathematical

Geometric modelling

Simulation

The mathematical modelling developed for the tunnel dryer is standing form cooling law, and the geometrical modelling is verified using Catia or simply ANSYS software, finally the simulation of the solar tunnel dryer is going on ANSYS Fluent software with version 15.01 the helping of designed and environmental conditions.

3. Analysis

3.1. Input data

The weather condition of Mekelle is obtained from National Metrology Agency

- The average sunshine is 8 hours
- Average temperature is 240C
- Relative humidity 55%
- Drying temperature is 600C
- Solar radiation average 697.8W/m2

3.2. Design

The design analysis sets dimension components of solar tunnel dryer, and the thermal analysis of the tunnel dryer. The total load of the drying is one tone maize to be dried in 8 sunshine hours. The 5000 cobs of maize is required with an average mass 0.2Kg each Maize has fed at once. Referee in the tale shows the design parameter of the solar dryer.

Table 1:

No.	Description	Equation	Result
1.	The mass of water evaporated from the product	$m_w = m_t[(M_i - M_f)/(100 - M_f)]$	235.3Kg
2.	Equilibrium Moisture content	$M_e = \frac{w_m c k a_w}{(1 - k a_w)[1 + (c-1)k a_w]}$	10.33
3.	Water activity	$a_w = 1 - \exp[-\exp(0.914 + 0.5639\ln(M))]$	0.61
4.	Equilibrium relative humidity	$ERH = 100\, a_w$	61%
5.	Initial humidity ratio	$\varnothing_i$	0.012
6.	Final humidity ratio	$\varnothing_f$	0.021
7.	Initial Enthalpy	h_i	50KJ/Kg
8.	Final Enthalpy	$h_f = 1006.9T + \omega[2512131 + 1552.4T]$	115.13KJ/Kg
9.	Mass flow rate	$\dot{M}_a = \rho_a * V_a$	0.24Kg/s
10.	Total Energy	$E = M_a(h_f - h_i)$	1778MJ
11.	Area of collector	$A_c = \frac{E}{I\eta}$	56m^2
12.	Drying area	$A_{dr} = l * b$	48.5m^2
13	Volume flowrate of fan		420.3 CFM
14	Power of fan = $\frac{air\ flowrate(CFM) * static\ pressure}{6320 * fan\ efficiency}$		0.46 KW
15	Pv panel	Three panels	1020 W
16	Page Model $M(t) = (M_o - M_e)e^{-K t^n} + M_e$		K= 0.311 n = 0.873
17	Midilli et al model $M_R = a\, e^{(-K t^n)} + bt$		a = 0-99 K= 0.14 n = 0.711 b = 0.00108

Table 2: The loading rate per batch of the drying products

SN	Name of the drying products.	The loading rate per batch	Loading density in Kg/m2
1	Maize	1000 Kg	30.3
2	Tomato	250 Kg	7.6
3	Potato	330 Kg	10
4	Onions	300 Kg	9
5	Grape	315 Kg	9.5
6	Fish	335 Kg	10
7	Banana	310 Kg	9.4

3.3. fan

Drying depends on airflow rate and the ability of the air to carry moisture. The fan should move air through the grain by overcoming the resistance to flow. This resistance to airflow is the static pressure drop through the grain. Multiply this pressure drop for clean grain by a factor 1.3 to 1.5 to adjust for packing and foreign material in the grain. This value varies depending on the cleanliness and physical properties of the grain. A value of 1.3 is commonly used for wheat and 1.5 for other crops [21].

By considering the specific volume of air from the psychrometric chart, the volume flowrate required to be 731.6 m3/ hr.

3.4. Fan drive

The fan should run under forecasted weather conditions. The PV panel therefore needs to be chosen bigger. A factor of 2.5 is reasonable. If a fan requires 2W it should choose as 5 W panels [22]. It is best to select the PV panel with 340 watt per unit cell, and the solar tunnel dryer needs 3 panels to drive the fan.

3.5. Model preprocessing

Figure 1, shows the placement of Maize cobs inside the tunnel dryer. The cobs have ordered in parallel to the direction of airflow and have a gap of 5 mm each other in order to expose the surface of drying product to the heated air, and creates uniform drying products.

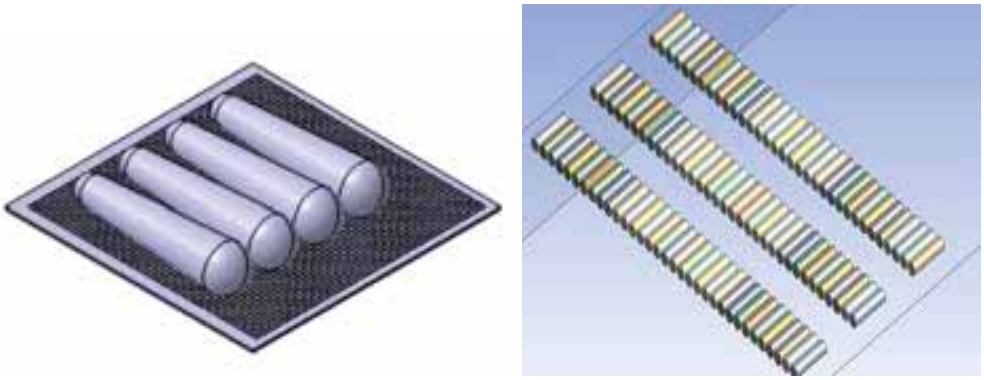

Figure1, Placement of Maize inside a solar tunnel dryer

The geometrical modeling of the dryer is shown in Figure 2 model consists of transparent glass, cob tray, absorber, insulation and the supporting walls.

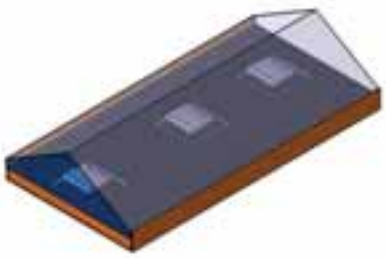

Figure2, Sample geometrical modeling of solar tunnel dryer.

Through this edge two types of meshing for three-dimensional models have applied, Cut cell and tetrahedrons. This study use Cut cell meshing type, because of its convenient for assembly better accuracies of analysing and come up with distributed loads. In additionally, the Cut cell algorithm is suitable for a large range of applications.

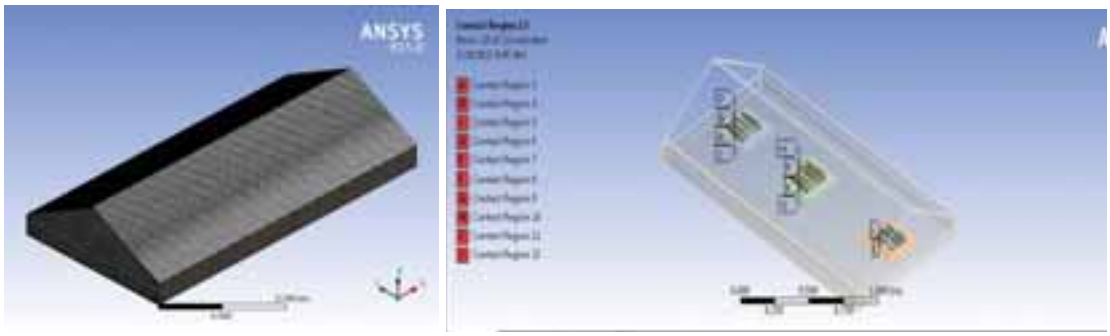

(a) (b)

Figure 3: cut cell meshing of the solar tunnel dryer. Figure 4, model contact regions of the product after meshing.

There are five types of zones considering the entire of solar tunnel dryers.

1. Inlet zones: this is the flowing of air in the inlet conditions.
2. Out let zones: this is the properties of air at the exit sides.
3. Absorber: Energy accumulated in the black painted sheets.
4. Insulation: this protects energy losses from absorber.
5. Wall zones: this is considered on both sides of the solar tunnel dryers.

The figure 5, shows the model contact regions of the product after meshing.

This show the continuity and energy equations converge to some constant value after some iterations.

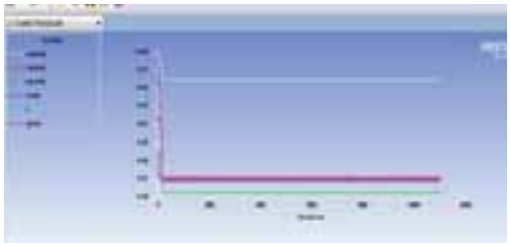

Figure 5, iteration of Maize for a solar tunnel dryer.

4. Results and discussion

4.1. Drying of Maize

Figure 6 and 7 moisture content on dry biases versus the drying time of maize. This model is based on the Midilli et al model since it is more convenient to describe on maize drying. Drying is faster in the first two days then it evaporates its moisture slowly until constant drying happen, there after the maize will reach its minimum moisture content or the equilibrium moisture content of the products.

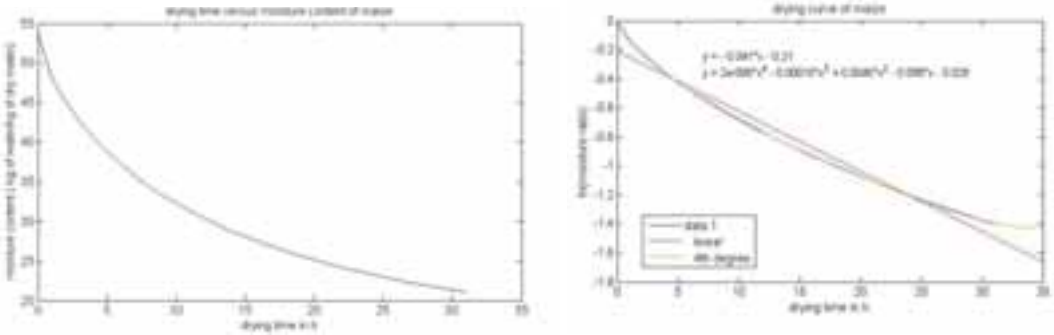

Figure 6, Drying time versus moisture content for Maize Figure 7, Drying curve of Maize

Figure 7, shows the log of moisture ratio versus drying time, which represents the typical characteristic-drying curve of maize during thin-layer drying operation when using solar tunnel dryer. The drying constants are = -0.041 and = 1.233 are the slops and constants of the linear drying curves respectively. The drying curve is above the linear trend for the first five hours and below the linear line up to twenty four hours.

The temperature contour of fluid flow is displayed here at the position of the solar tunnel dryer at different time intervals, then the maize absorbs heat and its moisture releases as the heated air passes over the maize. The flowing air rises up its temperature from the absorber to the upper glass, and reaches the maximum drying temperature.

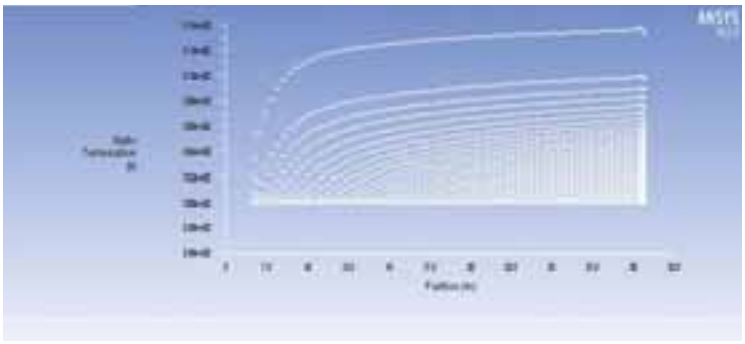

Figure 1, Temperature contour of interior fluid inside a solar tunnel dryer

Pressure contour is defined as the pressure distribution across the length of the tunnel dryer. It helps to define the pressure variation between flowing heated air. The streams of static pressure is maximum at the exit as seen from the figure 9.

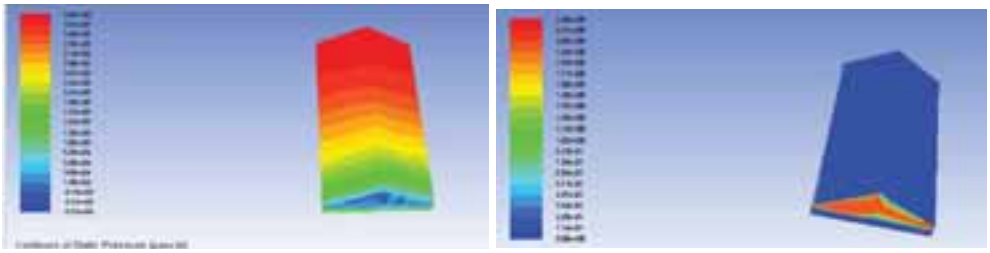

Figure 9, Pressure contour of interior fluid Figure10, Velocity contour of flow ai

Figure 9&10, shows velocity contour, which justifies the velocity distribution across the solar tunnel dryer.as the velocity is maximum at the center, and decreases from center towards the absorber and the cover plate sides. Therefore, grains remove its moisture content when exposure to warm air flow.

The velocity shown is the velocity of the interior fluid that passes through the drying products and the velocity is maximum near the center and drops down when the flow is near the walls. Line 15 which lies in the coordinate x (0, 24.2) and y (1, 1), and line 16 which lies in the coordinate x (0, 24.2) and y (2, 2) shown in the figure describes the velocity throughout the length of the solar tunnel dryer at the center and near the wall side respectively. Therefore, the two flows near the wall have frictional effects and have a zero velocities.

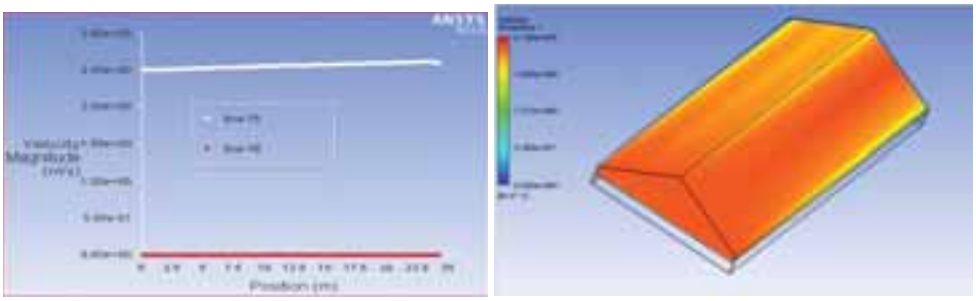

Figure11, Velocity flow interior fluid inside solar tunnel dryer Figure12, Velocity stream line flow

4.2. Modeling of Tomato in solar tunnel drying

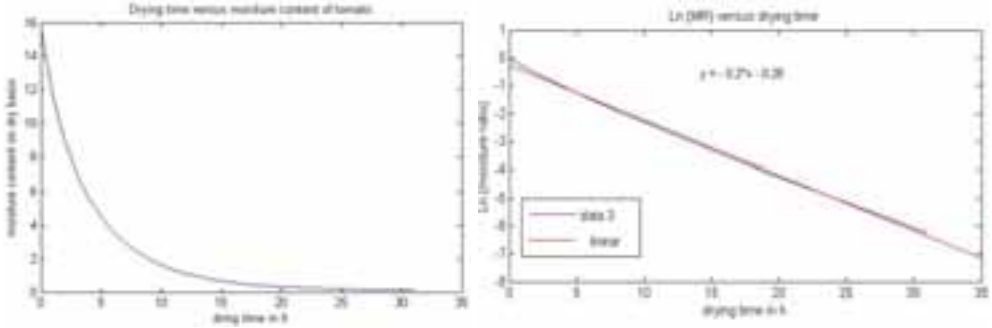

Figure13, Drying time versus moisture content of tomato Figure14, Drying curve of tomato

The figure above shows the moisture ratio versus drying time, which represents the typical characteristic-drying curve of Tomato during thin-layer drying operation. From the Henderson and Pabis model of equation (14) the slope and the constants are k = 0.2 and a = 0.755 respectively.

When we see the drying time characteristics of tomato and maize on same solar tunnel dryer tomato will have a faster drying rate than maize, this tells us products with higher moisture content have higher drying rate than lower moisture content on wet biases.

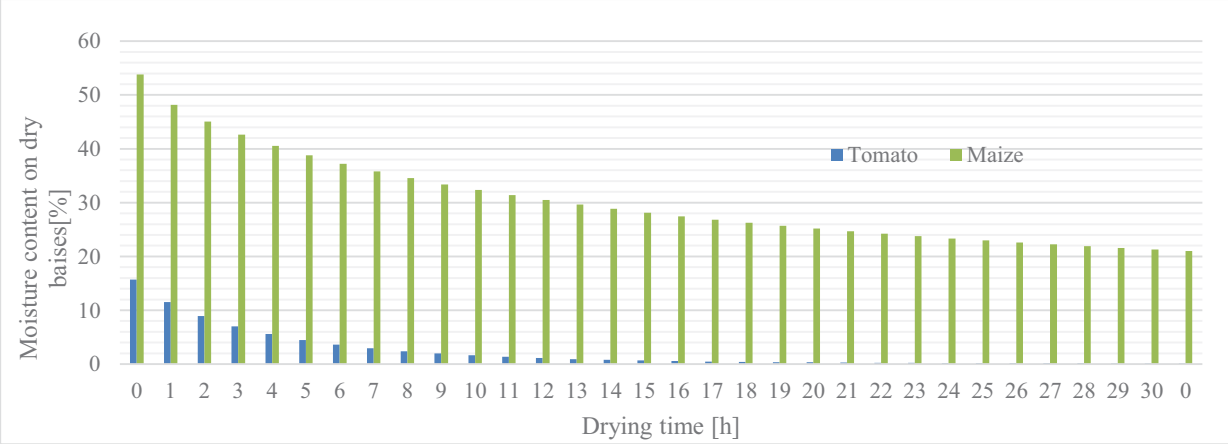

Figure15, Comparison of Tomato and Maize on moisture content versus drying time

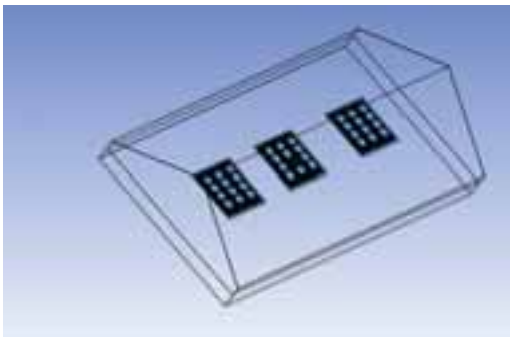

Figure16, This is the arrangement of the Tomato in the solar tunnel dryer

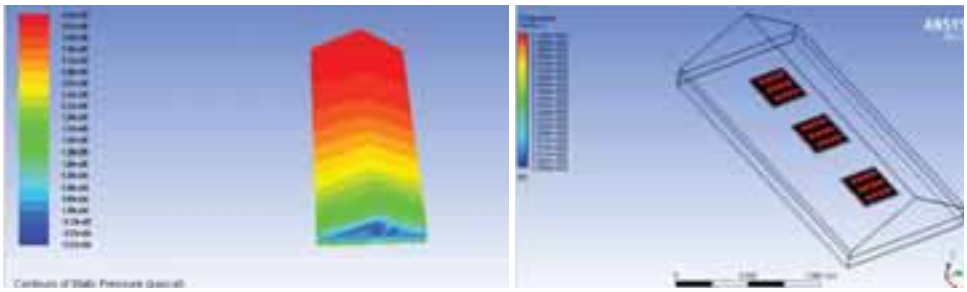

Figure17, Pressure contour of interior fluid. Figure 18, Temperature contour of tomato in side the solar tunnel dryer

The figure shown below is the velocity distribution of the solar tunnel dryer for Tomato, and has a velocity of around 2.4 m/s at the center and 1.12 m/s near the wall.

Figure 19, Velocity contour of tomato Figure20, Velocity of interior fluid flow inside a solar tunnel dryer throughout the length

The figure 20 shows the velocity flow inside a solar tunnel dryer and this velocity is turbulent effect near the walls and flow at the centers are as shown blow. Therefore, the given lines, line 14 or the coordinates of x (0, 24.2) and y (0, 0), line 15 or the coordinates of x (0, 24.2) and y (1,1), line 16 or the coordinates of x (0,24.2) and y (2,2), line17 or the coordinates of x (0, 24.2) and y (1.5) , and line 18 or the coordinates of x (0,24.2), y(0.5)

The figure 21, shown is the velocity stream line of Tomato, hence the flowing hot air is passing over the product which tells us the sliced tomato are in contact with flowing air and, evaporation takes place.

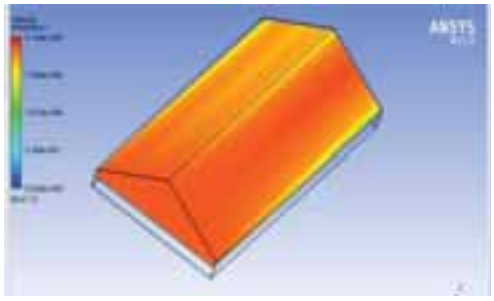

Figure21, Velocity streamline of tomato

5. Conclusion

A solar tunnel dryer was designed and simulated based on Preliminary investigations of maize. The designed solar tunnel dryer to be used to dry maize, tomato, potato and other under controlled conditions. The designed dryer with a collector area of 48 m2 is expecting to dry one-ton maize and 250 Kg of sliced tomato from 35 to15 percent and 94 to 10 percent wet basis in four and two days respectively during harvesting period. A proto type of the solar tunnel dryer was simulated and discussed the results.

6. References

[1.] Habtamu Tkubet "*Simulation of Solar Cereal Dryer using TRANSYS*",

[2.] Bala, B.K., Woods J.L.1994. "Simulation of the Indirect Natural Convection Sol Drying of Rough Rice,"

[3.] Abduieiah Ali, Abdias Mohamed, Mohamed, Ahmed, Fahd "Design and Construction of a Solar Drying System for Food Preservation".

[4.] B.K, Bala, J.L. WOODS, 1994. “Simulation of the Indirect Natural Convection Solar Drying of Rough Rice”, Vol.53.No.3

[5.] Ministry of New and Renewable Energy Block No: 14 C.G.O Complex Lodhi Road, New Delhi- 110003. “Hand Book of Solar Air Heating for Drying and Space Heating”

[6.] Lisa Kitinoja and AbelA. Kader “Small-Scale Postharvest Handling Practices: A Manual for Horticultural Crops (4th Edition)”.

[7.] C.L.Hii,S.V.Jangam,S.P.Ongand A.S.Mujumdar“SolarDryingFundamental Applications and Innovations”.

[8.] Ching Ling Hii, Schin vinayak Jangam, Sze Pheng Ong and Arun Sadashive Mujumdar “Solar Drying: Fundamentals, Applications and Innovations”

[9.] Hii, C.L., Jangam, S.V., Ong, S.P. and Mujumdar, A. S. (Ed.). Solar Drying: Fundamentals, Applications and Innovations. Transport Phenomena Group, Singapore, 2012, ISBN 978-981-07-3336-0. p 150.

[10.] Weiss, W. and Buchinger, J (2002). “Solar Drying. Austrian Development Cooperation,Austria”. Available from <http://t.aee-intec.at/0uploads/dateien553.pdf>. [17 June 2014].

[11.] El-Sebaii, A. A. and Shalaby, S. M. (2012). “Solar drying of agricultural products”: A Review. Journal of Renewable and Sustainable Energy Reviews, 16(1): 37–43

[12.] Seveda, M. S. (2013). “Design of a Photovoltaic Powered Forced Convection Solar Dryer in NEH Region of India” International Journal of Renewable Energy Research, 3(4): 1–7.

[13.] “Asian and Pacific Center for Transfer of Technology”

[14.] Josef, 2006

[15.] LIBERTY, JACOB TIZHE, 2014 “Design, Construction and Performance Evaluation of A postharvest Heat Storage Solar Energy Crop Dryer”.

[16.] F.W.Bakker-Arkema, M.D.Montross, Liu Qiang, and D.E.maier “Analysis of Continuous - flow Grain Dryers”.

[17.] Charies G. Moyers, PhD., P.E, Glenn W. Baldwin, M.S., P.E “Psychrometry, Evaporative Cooling, and Solids Drying”.

[18.] K.S Tonui, E.B.K. Mutai, D.A. Mutuli, D.O. Mbuge, and K.V. Too “Design and Evaluation of Solar Grain Dryer With a Back-up Heater”.

[19.] Osondu L.C, Chikelu C.C, Ukwuani S. T, Eze N. N “Projects Development Institute (PRODA), Emene Ind, Enugu, Nigeria”.

[20.] Anjum Munir, Umair Sultan and Muhammad Iqbal “Development and Performance Evaluation of a locally Fabricated Portable Solar Tunnel Dryer for Drying of Fruits, Vegetables and Medicinal Plants”.

[21.] Dr. Kenneth J. Hellevang, PE Extension Agricultural Engineer “Grain Drying”.

[22.] Google .com “Small Solar Tunnel Drer”.

[23.] K. Agbossou,*, K. Napo , S. Chakraverty “Mathematical Modelling and Solar Tunnel Drying Characteristics of Yellow Maize”.

[24.] Carmen, Rosselic, 1992. “Simple Mathematical Model to Predict the Drying Rates of Potatoes”,

Solar Ponds

Fatigue characterization of potable water certified PA and PPA grades for solar-thermal applications

Patrick R. Bradler[1], Joerg Fischer[1],
Gernot M. Wallner[1] and Reinhold W. Lang[1]

[1] Institute of Polymeric Materials and Testing / Johannes Kepler University, 4040 Linz (Austria)

Abstract

A material screening method for potable water certified plastics for solar-thermal applications based on superimposed cyclic mechanical loading was conducted. One aliphatic polyamide and three semi-aromatic polyphtalamide grades with various glass fiber contents were characterized on specimen level. Therefore, an electro-dynamic testing machine equipped with an in-situ testing device was used to obtain the crack growth kinetics at different temperatures (23°C and 80°C) in different media environments (air and H_2O) . At 80°C in H_2O, specimens revealed a significantly reduced fatigue crack growth resistance compared to tests at the reference conditions of 23°C in air. Comparing all investigated materials at 80°C in water, the polyamide grade and one polyphtalamide grade revealed the best performance. Due to different slopes in their FCG curves, PA-GF30 showed a superior crack growth resistance at low FCG rates.

Keywords: polyamide, polyphthalamide, fatigue crack growth, superimposed loading

1. Introduction

The performance of polymeric materials is strongly dependent on the mechanical and environmental loading conditions (Stern et al., 1998a; Stern et al., 1998b; Lang et al., 2005). Hence, tests are necessary under application relevant conditions. An objective in former research (Schoeffl et al., 2014; Fischer et al., 2016) was to develop and implement advanced testing methods for the evaluation of the long-term behavior of polymeric materials for solar-thermal collectors under service relevant loading conditions (e.g., for an integrated storage collector system). To fulfill the application requirements for pressurized integrated storage collectors maximum internal pressures of 4 bar and maximum application temperatures of 95°C should be considered (Solecrafte, 2017).

While in previous papers, fatigue crack growth kinetics of polyamide under superimposed mechanical loads were described properly (Fischer et al., 2016) and a lifetime prediction approach (Bradler et al., 2016) was presented, this paper deals with the investigation of potable water certified polyamide (PA) and polyphtalamide (PPA) grades with various glass fiber contents under different superimposed mechanical and environmental loads.

2. Background

Polyamides can be classified according to their composition in different polyamide types. Two of them are used in this study, namely (1) the aliphatic polyamides (PA) with an aliphatic main chain including the well known Nylon or PA 6.6 (Gilbert and Brydson, 2017), and (2) the polyphtalamides (PPA) with a semi-aromatic main chain (Wypych, 2016). In single-loop solar-thermal collector systems, potable water is acting as heat carrier fluid (Köhl et al., 2012). Hence, various system components are getting in contact with drinking water. Materials used for such applications should have an adequate drinking water certificate, which is limiting the use of stabilizers. Several studies are describing the negative impact of the lack of stabilizers on the fatigue crack growth (FCG) behavior and thus on the long-term failure (Lang et al., 1997; Pinter and Lang, 2003).

The long-term failure of polymers is usually characterized by the concept of linear elastic fracture mechanics (LEFM) (Hertzberg and Manson, 1980; Lang, 1980). For these tests, some requirements have to be fulfilled (i.e., small plastic zones and a linear-viscoelastic material behavior) (Lang, 1980; Lang et al., 1982). Based on results of fracture mechanics tests, a FCG kinetics curve can be plotted, which is a double logarithmic plot of the fatigue crack growth rate da/dN vs. the stress intensity factor range ΔK_I. The resulting plot can be subdivided into three characteristic regions, where region I describes the threshold, region II describes the stable crack growth which can be described by a power law equation (see eq. 1) (Paris and Erdogan, 1963), and finally region III describes the unstable crack

doi:10.18086/swc.2017.27.01 Available at http://proceedings.ises.org

growth at high plastic deformations. Details and the characteristic plot are described elsewhere (Fischer et al., 2016; Bradler et al., 2017).

$$\frac{da}{dN} = A \cdot \Delta K^m \qquad \text{(eq. 1)}$$

The stress intensity factor range ΔK_I for a cyclic loading (s. eq. 2) describes the difference between the maximum and minimum stress intensity factor ($K_{I,max}$ -$K_{I,min}$) in the loading mode I, which indicates crack opening. "$\Delta\sigma$" describes the difference between maximum and minimum global loading, "a" the crack length and "Y" a geometry and specimen dependent shape factor.

$$\Delta K_I = \Delta\sigma \cdot \sqrt{a} \cdot Y \qquad \text{(eq. 2)}$$

3. Methodology and experimental

Materials and specimens

One aliphatic polyamide (PA) and three different semi-aromatic polyphtalamide (PPA) grades were investigated regarding fatigue crack growth (FCG) resistance. An overview of selected information on these grades is given in Table 1. The grades are varying in chemical composition as well as in glass fiber content.

Tab. 1: Material designation, grade, and glass fiber content.

Material designation	Grade	Glass fiber content
PA-GF30	polyamide 6.6	30 w%
PPA-GF40	polyphthalamide	40 w%
PPA-GF50-1	polyphthalamide	50 w%
PPA-GF50-2	polyphthalamide	50 w%

Fig. 1 depicts a standardized compact type (CT) specimen (E08 Committee, 2000; ISO/TC 156 - Corrosion of metals and alloys, 2011). Specimens were manufactured via milling out of injection molded plaques. According to previous results (Schlaeger, 2015; Fischer et al., 2016), for FCG tests with glass fiber reinforced polyamides and a specimen thickness of 4 mm, specimens with the initial crack in flow direction are most critical.

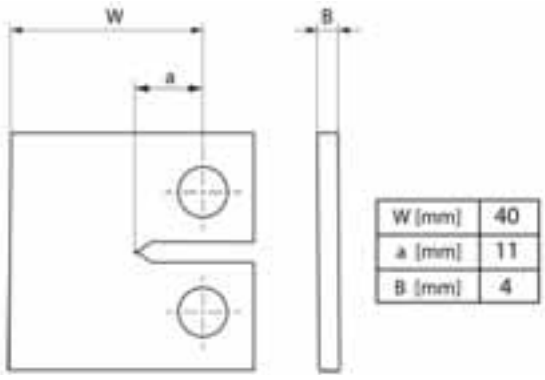

Fig. 1: Compact type (CT) specimen with relevant dimensions for data reduction.

Fatigue tests and data reduction

All FCG experiments were carried out on an electro-dynamic testing machine (Instron ElectroPls E3000; Nordwood, USA). For tests under different environmental conditions, an in-situ testing device was used, which was originally implemented for tests in liquid hydrocarbons by Schoeffl et al. (Schoeffl, 2014; Schoeffl et al., 2014). All tests were conducted with a frequency of 5 Hz and a sinusoidal loading with an R-ratio of 0.1. The R-ratio describes the ratio between the maximum to minimum applied stress intensity factor. The subsequent calculation of the stress intensity factor range "ΔK " was done according to eq. 3 (Gross and Seelig, 2011), where "ΔF" is the difference between maximum and minimum applied force, "B" the thickness of the specimen, "W" the width of the specimen and "f(a/W)" a geometry dependent shape factor.

$$\Delta K = \frac{\Delta F}{B \cdot \sqrt{W}} \cdot f(a/W) \qquad \text{(eq. 3)}$$

4. Results and discussion

The effect of different temperatures and different media on the fatigue crack growth resistance of the grade PPA-GF50-2 is shown in Fig. 2. In terms of temperature, in both media, the material performance was enhanced at the lower temperature of 23°C. At both temperatures, inferior FCG resistances were determined in water. These results are exhibiting hot water as the more critical environment compared to air and are in good agreement with conventional aging data obtained in another research (Geretschlaeger and Wallner, 2016). All further tests were carried out at the best and worst conditions, 23°C in air and 80°C in water, respectively.

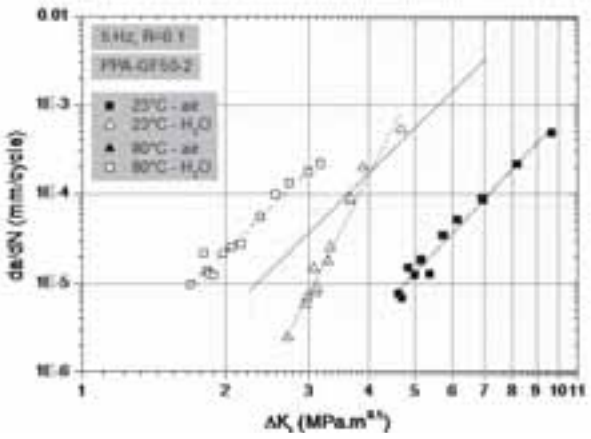

Fig. 2: Fatigue crack growth kinetics for the grade PPA-GF50-2 at various temperatures in various media.

A comparison of the FCG kinetics curves for the two polyphtalamide grades with the same glass fiber content of 50 w% (PPA-GF50-1 and PPA-GF50-2) tested at the best and worst environmental conditions is depicted in Fig. 3. Tests at 23°C in air exhibited a better FCG behavior for both materials compared with tests at 80°C in water, resulting in higher ΔK_I-values at specific fatigue crack growth rates. The material PPA-GF50-1 reveals a better FCG resistance at both conditions. At a comparable rather low crack growth rate of 2E-5 mm/cycle, the difference between the ΔK_I-values of the two materials at 23°C in air is given with a factor of about 1.2 and at 80°C in deionized water with a factor of about 1.6. The results obtained are exhibiting a higher sensitivity of the PA-GF50-2 grade against elevated temperatures and water environment.

Due to the same chemical composition of the matrix material, the grades PPA-GF40 and PPA-GF50-1 are only differing in their glass fiber content. Thus, for these two materials, the effect of glass fiber content on the FCG rates was investigated and is depicted in Fig.4. While the grade PPA-GF40 with the lower glass fiber content of 40 w% shows an inferior FCG resistance, the PPA-GF50-1 with 50 w% of glass fiber reinforcement reveal clearly a higher

FCG resistance.

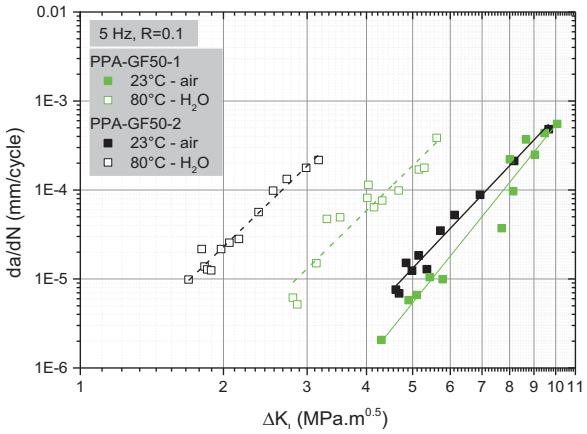

Fig. 3: Fatigue crack growth kinetics for PPA grades with 50 w% glass fiber reinforcement at 23°C in air and at 80°C in water.

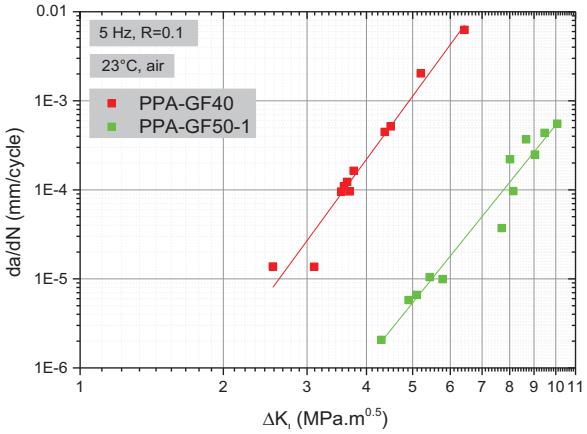

Fig. 4: Effect of glass fiber content on the fatigue crack growth kinetics for the PPA-grades at 23°C in air.

As, in this study, the most critical environmental condition for fatigue crack growth is 80°C in water, all materials were tested at this condition and resulting FCG curves are illustrated in Fig. 5. The grade PPA-GF40 shows a significantly lower FCG resistance, leading to a factor 2.6 lower ΔK_I-value at a crack growth rate of 2E-5 mm/cycle compared with PA-GF30, the best performing material at low crack growth rates. For PPA-GF50-2 and PPA-GF50-1 compared to PA-GF30, lower ΔK_I-values with a factor 1.9 and 1.2, respectively, were obtained. PA-GF30 exhibits a superior crack growth resistance at low crack growth rates. Due to a different slope in the FCG curve, at high FCG rates, PPA-GF50-1 is slightly better.

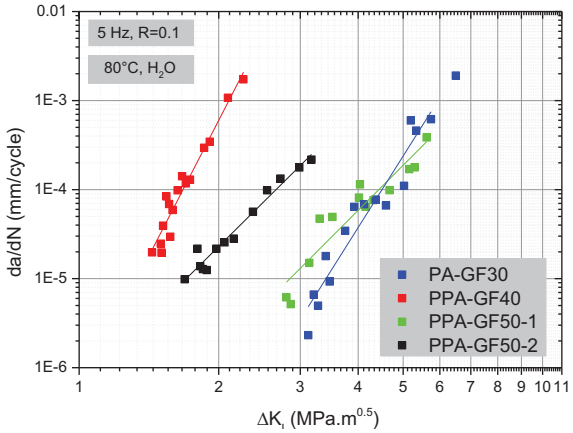

Fig. 5: Fatigue crack growth kinetics for all investigated material grades at 80°C in water.

5. Summary and outlook

The fatigue crack growth (FCG) resistance of one aliphatic polyamide and three semi-aromatic polyphthalamides varying in their glass fiber content was investigated. Due to their certification for the transport of potable water, these materials are of high relevance for solar-thermal applications. Fatigue crack growth measurements were performed at application relevant conditions in two environmental media (air and water) at two temperatures (23°C and 80°C). For the polyphtalamide PPA-GF50-2, tests at all four environmental combinations were conducted resulting in the best performance at 23°C in air and in inferior FCG resistance at 80°C in water. As to the glass fiber content of the polyphthalamides, PPA-GF50-1 showed superior FCG behavior and PPA-GF40 revealed inferior fatigue crack growth resistance. Comparing all investigated materials at 80°C in water, the aliphatic polyamide PA-GF30 and the polyphtalamide PPA-GF50-1 revealed the best performance. Due to different slopes in their FCG curves, PA-GF30 showed a superior crack growth resistance at low FCG rates. Conversely, at high FCG rates, PPA-GF50-1 is slightly better.

In this study, a very fast screening method for materials for solar-thermal applications, especially for reinforced plastics, was introduced. Based on an extension of the test program in terms of testing at different R-ratios, in a further study a lifetime prediction of these materials could be conducted.

Acknowledgements

This research work was performed in the cooperative research project *SolPol-4/5* entitled *"Solar-thermal systems based on polymeric materials"* (www.solpol.at). The project *SolPol-4/5* is funded by the Austrian Climate and Energy Fund (KLI.EN) within the program "e!MISSION.at" and the funding is administrated by the Austrian Research Promotion Agency (FFG).

6. References

Bradler, P.R., Fischer, J., Pohn, B., Wallner, G.M., Lang, R.W., 2017. Effect of stabilizers on the failure behavior of glass fiber reinforced polyamides for mounting and framing of solar energy applications. Energy Procedia 119, 828–834.

Bradler, P.R., Fischer, J., Schlaeger, M., Wallner, G.M., Lang, R.W., 2016. A Fracture Mechanical Based Lifetime Assessment Approach for Polyamide Used for Integrated Storage Collectors, in: Proceedings of EuroSun2016. International Solar Energy Society, Freiburg, Germany, pp. 1–7.

E08 Committee, 2000. Test Method for Measurement of Fatigue Crack Growth Rates. ASTM International, West Conshohocken, PA.

Fischer, J., Bradler, P.R., Schlaeger, M., Wallner, G.M., Lang, R.W., 2016. Novel Solar Thermal Collector Systems in Polymer Design – Part 5. Fatigue Characterization of Engineering PA Grades for Pressurized Integrated Storage

Collectors. Energy Procedia 91, 27–34.

Geretschlaeger, K.J., Wallner, G.M., 2016. Aging characteristics of glass fiber-reinforced polyamide in hot water and air. Polym. Compos.

Gilbert, M., Brydson, J.A. (Eds.), 2017. Brydson's plastics materials. Butterworth-Heinemann, Oxford, Singapore, xxxi, 859.

Gross, D., Seelig, T., 2011. Bruchmechanik. Mit einer Einführung in die Mikromechanik. Springer-Verlag Berlin Heidelberg, Berlin, Heidelberg.

Hertzberg, R.W., Manson, J.A., 1980. Fatigue of engineering plastics. Academic Press, New York, xv, 295.

ISO/TC 156 - Corrosion of metals and alloys, 2011. Corrosion of metals and alloys - Stress corrosion testing - Part 6: Preparation and use of precracked specimens for tests under constant load or constant displacement. ISO, Genf, CH.

Köhl, M., Meir, M.G., Papillon, P., Wallner, G.M., Saile, S. (Eds.), 2012. Polymeric materials for solar thermal applications. Wiley-VCH, Weinheim, XXIII, 393 S.

Lang, R.W., 1980. Applicability of linear elastic fracture mechanics to fatigue in poymers and short-fiber composites. Dissertation, Berhlehem (US).

Lang, R.W., Manson, J.A., Hertzberg, R.W., 1982. Effect of short glass fibers and particulate fillers on fatigue crack propagation in polyamides. Polym. Eng. Sci. 22 (15), 982–987.

Lang, R.W., Pinter, G., Balika, W., 2005. Konzept zur Nachweisführung für Nutzungsdauer und Sicherheit von PE-Druckrohren bei beliebiger Einbausituation. 3R International (1-2/2005), 32–41.

Lang, R.W., Stern, A., Doerner, G., 1997. Applicability and limitations of current lifetime prediction models for thermoplastics pipes under internal pressure. Angew. Makromol. Chemie 247 (1), 131–145.

Paris, P., Erdogan, F., 1963. A Critical Analysis of Crack Propagation Laws. J. Basic Engineering 85 (4), 528.

Pinter, G., Lang, R.W., 2003. Effect of stabilization on creep crack growth in high-density polyethylene. J. Appl. Polym. Sci. 90 (12), 3191–3207.

Schlaeger, M., 2015. Einfluss der Umgebungsbedingungen auf die mechanischen Eigenschaften von kurzglasfaserverstärktem PA 66 unter monotoner und zyklischer Belastung. Master Thesis, Linz, V, 64 Bl.

Schoeffl, P.F., 2014. Influence of Liquid Hydrocarbon Environments on High Density Polyethylene for Oil and Gas Applications. Doctoral Dissertation, Linz.

Schoeffl, P.F., Bradler, P.R., Lang, R.W., 2014. Yielding and crack growth testing of polymers under severe liquid media conditions. Polymer Testing 40, 225–233.

Solecrafte, 2017. The first compact hot water solar system. http://www.greenonetec.com/sites/default/files/downloads/broschure-solcrafte-blue-edition_-en-_2017-03-small.pdf. Accessed 14 October 2017.

Stern, A., Asanger, F., Lang, R.W., 1998a. Creep crack growth testing of plastics—II. data acquisition, data reduction and experimental results. Polymer Testing 17 (6), 423–441.

Stern, A., Novotny, M., Lang, R.W., 1998b. Creep crack growth testing of plastics—I. test configurations and test system design. Polymer Testing 17 (6), 403–422.

Wypych, G. (Ed.), 2016. Handbook of polymers. ChemTec Publishing, Toronto.

Field test results of an innovative PV/T collector for indoor swimming pools

Laetitia Brottier[1,2] and Rachid Bennacer[2]

[1] DualSun, Marseille (France)

[2] LMT /ENS-Cachan/CNRS/Université Paris Saclay, Cachan (France)

Abstract

Hybrid solar PV/T has the potential to become a major player in the renewable energy sector, but one of the most important barriers is the inexistence of a proven track record in terms of reliability and performance. In order to address this issue, a study was conducted to monitor in-field energy performances of two indoor swimming pool installations near Perpignan (France) equipped with an innovative unglazed PV/T collector (1.64m², 250Wp, 912Wth).

With 300m² of PV/T collectors for a 1100m³ indoor swimming pool and 6000L/day of hot water needs, an annual thermal production of 120MWh and an annual photovoltaic production of 64MWh were achieved. Performances were higher than simulated with the TRNSYS study.

Keywords: Photovoltaic thermal (PV/T) collector; Field test; Energy performance

1. PV/T characteristics

A review of PV/T technologies has been done by Zhang et al. (2012) and Good et al. (2015). The PV/T module in the study is based on the unglazed flat-plate liquid design described in these reviews. It has 60 monocrystalline cells for a nominal power of 250Wp. The photovoltaic characteristics are given in table 1.1. The thermal characteristics (table 1.2) were determined by tests conducted at the TÜV Rheinland laboratory following the Solar Keymark certification rules (ISO 9806 : 2013).

Tab. 1: Electrical and thermal characteristics

Electrical characteristics	
Dimensions	1677×990×40 mm³
Number of cells	60
Type of cells	Monocrystalline (6 inches)
Nominal power (P_{mpp})	250 Wp
PV module efficiency (η_{PV})	15.40% (Tolerance : ±3%)
Power loss /°C (βp)	-0.44% / °C

Thermal characteristics	
Heat transfer fluid (HTF)	Water/glycol mix
Absorber surface area	1.58 m²
Conversion factor (η_0)	57.8%
Heat loss coeffiient (b_1)	12.08 W/K/m²
Wind dependency of collector efficiency (b_U)	0.028 s/m
Wind dependency of heat loss coefficient (b_2)	1.842 W.s/K/m³

2. Presentation of the two field tests

Indoor swimming pool systems coupled with PV/T collectors have already been studied by simulation by Buonomano et al. (2015), but few experimental works have confirmed the expected performances with real installations, as has been done in this study.

For the two indoor swimming pools in the study, the PV/T modules are connected to heat exchangers and are used to preheat the water for the showers and to heat the pools. As an auxiliary heat source, a heat pump is connected in series to the solar heat exchanger to heat up the water instantly when needed. In the case that the system does not

doi:10.18086/swc.2017.27.02 Available at http://proceedings.ises.org

provide enough heat, the system is completed if necessary with a natural gas boiler. In order to monitor the system, a calorimeter is placed just before the solar heat exchangers.

Data were recorded every 5 minutes. A diagram of the system and the monitoring is given in Figure 1.

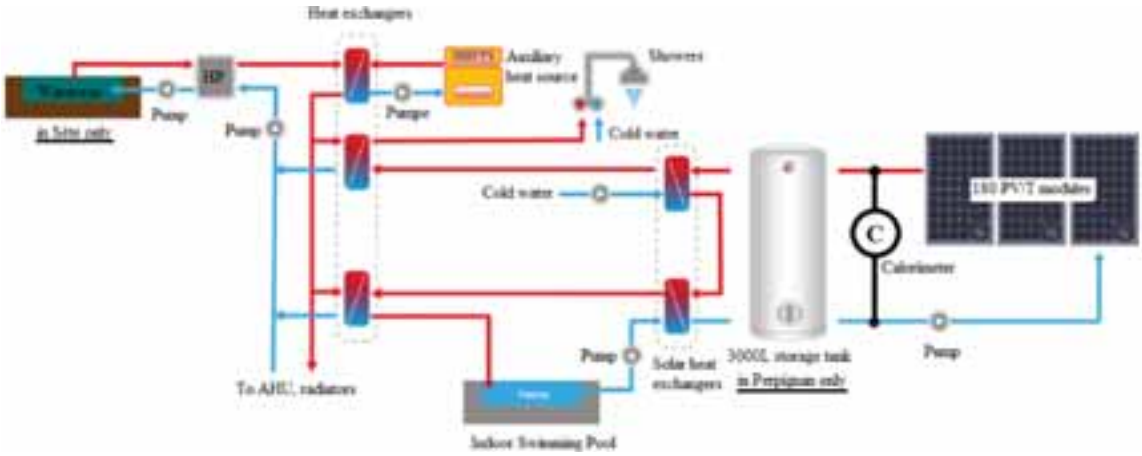

Fig. 1: Simplified hydraulic scheme and monitoring system put in place

In order to verify the in-situ reliability and performance for indoor swimming pools of the innovative hybrid solar PV/T module, two installations were monitored near Perpignan in the South of France (Lat/ Long. 42.6976 / 2.8954). In Perpignan according to Meteonorm, the maximum ambient daily temperature in the day is on average 19.6°C and the maximum daily irradiation in the day is on average 576W/m² over the year.

In Sete (Figure 2) as in Perpignan (Figure 3), 180 PV/T modules were installed as a solar canopy.

Fig. 2: picture of the PV/T canopy for the municipal swimming pool of Sète (France)

Fig. 3: picture of the PV/T canopy for the municipal swimming pool of Perpignan (France)

Key parameters of the two solar installations are provided in Table 2.

Tab. 2: parameter of the 2 installations

	Sète	Perpignan
Swimming pool dimensions	720 m² for 1100 m^3 = 1 056 MWh/an	730 m² for 1095 m^3 = 1 016 MWh/an
Pool temperature setup	28 °C	
Shower needs	~ 6000L/day = ~ 125 MWh/an	
Number of unglazed PV/T	180 (300 m²)	
Integration type	Solar canopy	
Orientation (0° = South)	South-East (-20°)	South (0°)
Slope	10 °	30 °

The solar energy goes to hot water preheating if the temperature of the panels is 6°C higher than the bottom of the sanitary tank or to the pool if it is higher than 30°C. The panels and the technical room, where the heat exchangers and the calorimeter are located, are separated by a distance of 70m. The pipes are buried over this distance.

3. TRNSYS study

A TRNSYS model has been performed, the diagram is given in Figure 4.

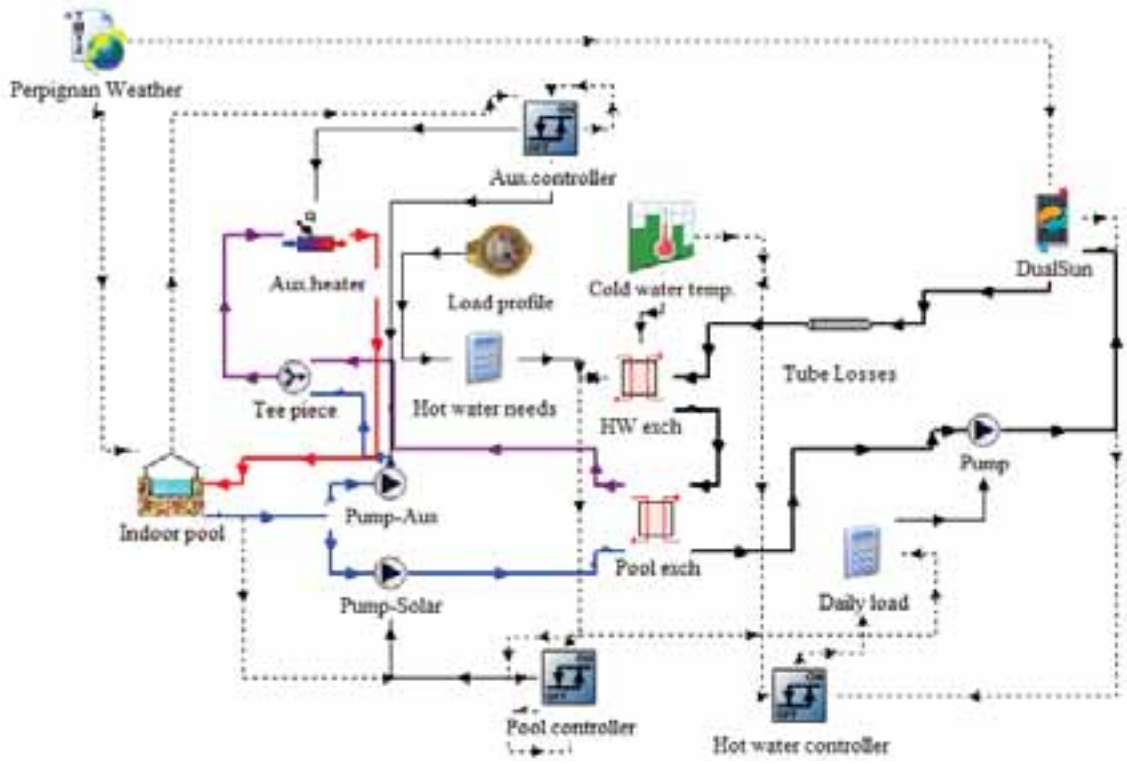

Fig. 4: TRNSYS diagram of the installation

The photovoltaic simulation does not take into account the cooling of the cells, and the storage of the heat for the showers in Perpignan is not included in the model.

The loss coefficient in the 70m buried pipe was taken at 24 W/(m².K).

The hot water profile was built from the scenario for sport facilities in the French thermal regulation method (RT 2012), and the typical day profile is given in Figure 5.

Fig. 5: Hot water need profile in the simulation

The hot water needs are estimated at 1.2GWh/yr, wich seemed very accurate with the 1,27GWh/yr (127 782 m^3 gas volume) consumed in Sète for a year before the solar installation. Recently a monthly detail of the previous gas consumption revealed some significative difference between the monthly distribution of the simulated consumption and the real one before the solar installation as seen in Table 3.

Tab. 3: Real and simulated global heat needs

Month	TRNSYS Heat needs (kWh)	Gas consumption (before solar) (m3)	Energy consumption (before solar) (kWh, η=90%)
January	139 937	16 911	167 727
February	120 905	16 770	166 321
March	117 706	15 725	155 961
April	101 207	13 218	131 099
May	88 562	9 463	93 853
June	65 746	7 491	74 294
July	60 373	5 460	54 150
August	58 353	4 001	39 684
September	72 506	5 091	50 493
October	101 365	7 121	70 628
November	118 812	12 617	125 137
December	135 364	13 914	137 996
Total /yr	**1 180 835**	**127 782**	**1 267 343**

At Sète, the production of the solar module to 81MWh/yr for the thermal part (6.9% of the heat needs) and 56MWh/yr for the electrical part (Table 4). At Perpignan were the slope and the orientation of the modules are more favorable, 97MWh/yr for the thermal part (8.5% of the heat needs) and 60MWh/yr for the electrical part (Table 5).

Tab. 4: TRNSYS model results for Sète

Month	Hot water needs (kWh)	Solar for hot water (kWh)	Pool needs (kWh)	Solar for pool (kWh)	PV electricity (kWh)
January	11 583	1 014	128 354	0	2 538
February	10 392	1 379	110 513	142	2 892
March	11 198	2 319	106 507	1 875	4 674
April	10 479	2 587	90 728	3 470	5 516
May	10 468	3 137	78 094	6 859	6 595
June	9 708	3 382	56 038	10 259	6 945
July	9 706	3 565	50 667	13 213	7 262
August	9 598	3 129	48 755	11 322	6 446
September	9 501	2 371	63 005	6 208	5 033
October	10 254	1 587	91 111	1 624	3 485
November	10 431	1 058	108 381	110	2 392
December	11 279	744	124 085	0	2 048
Total kWh/yr	**124 596**	**26 271**	**1 056 239**	**55 083**	**55 826**

Tab. 5: TRNSYS model results for Perpignan

Month	Hot water needs (kWh)	Solar for hot water (kWh)	Pool needs (kWh)	Solar for pool (kWh)	PV electricity (kWh)
January	11 583	1 772	123 747	432	3 441
February	10 392	2 019	104 845	1 014	3 798
March	11 198	2 748	106 154	3 206	5 454
April	10 479	2 775	90 286	4 587	5 644
May	10 468	3 103	76 208	6 342	5 831
June	9 708	3 336	54 972	9 641	6 203
July	9 706	3 696	44 745	13 078	6 663
August	9 598	3 345	44 316	12 616	6 408
September	9 501	2 719	60 786	9 015	5 645
October	10 254	2 188	85 017	4 250	4 592
November	10 431	1 648	104 041	1 569	3 608
December	11 279	1 584	120 807	394	3 247
Total kWh/yr	**124 596**	**30 932**	**1 015 924**	**66 144**	**60 535**

4. Field test results

The measured results of the PV/T panels are very close to the simulated results for the first year.

At Sète (Table 6), the thermal solar production is 2% higher than simulated, which confirms the accuracy of the model. At Perpignan (Table 7), the production is 23% higher, which proves the good impact of the storage for hot water to improve the solar share covering these needs.

The photovoltaic production measured are respectively 5,9% and 5,6% higher at Sète and at Perpignan, which is to attribute to the cooling of the cells that improves the performances.

Tab. 6: Comparison measurement and model for Sète

	Solar for heat (kWh)		Solar PV electricity (kWh)	
Month	**TRNSYS**	**MEASURED**	**TRNSYS**	**MEASURED**
Jan-17	1 014	1 000	2 538	3 280
Feb-17	1 521	1 000	2 892	1 828
Mar-17	4 194	4 000	4 674	4 904
Apr-17	6 057	8 000	5 516	6 452
May-17	9 996	8 000	6 595	6 575
Jun-17	13 641	12 000	6 945	4 361
Jul-17	16 778	16 000	7 262	6 669
Aug-16	14 451	15 000	6 446	8 604
Sep-16	8 580	8 000	5 033	6 386
Oct-16	3 211	7 000	3 485	4 514
Nov-16	1 168	2 000	2 392	3 239
Dec-16	744	100	2 048	2 301
Total kWh/yr	**81 354**	**82 100**	**55 826**	**59 113**

Tab. 7: Comparison measurement and model for Perpignan

	Solar for heat (kWh)		Solar PV electricity (kWh)	
Month	**TRNSYS**	**MEASURED**	**TRNSYS**	**MEASURED**
Jan-17	2 204	2 600	3 441	2 603
Feb-17	3 033	4 000	3 798	3 387
Mar-17	5 954	9 100	5 454	4 060
Apr-17	7 361	10 250	5 644	6 179
May-17	9 445	10 250	5 831	8 147
Jun-17	12 977	11 490	6 203	7 461
Jul-17	16 774	16 080	6 663	7 836
Aug-16	15 961	18 100	6 408	8 058
Sep-16	11 734	15 800	5 645	5 736
Oct-16	6 439	10 000	4 592	4 223
Nov-16	3 217	8 900	3 608	3 813
Dec-16	1 978	3 300	3 247	2 439
Total kWh/yr	**97 077**	**119 870**	**60 535**	**63 942**

The cost of these installations was around 250 k€ (no subsidies taken into account), around 100 k€ for the PV side and 150 k€ for the thermal solar side. If we assume a solar production of 20 years, which seems reasonable, the solar electrical price was around 9c€/kWh and the solar thermal price around 6c€/kWh for the swimming pool at Perpignan (in the South of France). It seems very promising for this innovation, and as the cost reduction potential exists still, the competitivity even with gas may be achieved in the few years.

5. Conclusion

The 300m² PV/T panels provide 30% of the energy for the 6000L/day shower needs and 20% of the heating needs for the 1100m^3 indoor swimming pool during 4 months of the year *(June – September)*.
The measured thermal results of the PV/T panels are very close in this first year, and to add a storage seem to better of 20% the share of solar energy in hot water needs. The positive effect of the cooling of the cells can be estimated around 5.5 and 6% in this type of installation.

With a global cost of energy over 20 years of 7c€/kWh, this promising innovation may be competitive even with natural gas in a few years.

6. References

Buonomano, A., et al., 2015. Dynamic simulation and thermo-economic analysis of a PhotoVoltaic/Thermal collector heating system for an indoor–outdoor swimming pool. Energy Conversion and Management. 99, 176–192.

ISO 9806:2013 Solar energy - Solar thermal collectors - Test methods

Good, C., et al., 2015. Hybrid photovoltaic-thermal systems in buildings – a review. Energy Procedia. 70, 683 – 690

Zhang X., et al., 2012,, Review of R&D progress and practical application of the solar photovoltaic/thermal (PV/T) technologies. Renewable and Sustainable Energy Reviews; Vol 16, Issue 1, p. 599–617

Solar thermal technologies for domestic hot water applications: An energy and economic investigation for the Australian climate

F. Ghani[1,2] and T. S. O'Donovan[1]

[1]Institute of Mechanical, Process, and Energy Engineering, Engineering and Physical Sciences, Heriot-Watt University, Edinburgh, EH14 4AS, United Kingdom

[2] Sunamp Ltd, Macmerry, United Kingdom

Abstract

By displacing the current heavy use of electricity and gas for domestic hot water applications, solar thermal technologies have significant potential to reduce Australia's fossil fuel emissions. Solar thermal systems prevalent in the current Australian market include a mixture of flat plate and evacuated tube collector types applied in either active or passive style circulation systems. The performance of these systems can vary significantly depending on a number of factors including; the characteristics of the solar collector, storage tank size, hot water load and usage, and climate. As all these factors can vary considerably, particularly the Australian climate, the optimal configuration (considering both performance and economics) of a solar hot water system can also be expected to vary substantially. The purpose of this study is to examine the performance of common solar thermal system designs operating in four climate zones of Australia (Rockhampton, Alice Springs, Sydney, and Melbourne) operating under the load of a four person detached dwelling. A total of six solar hot water systems were designed and simulated using the commercial software package POLYSUN operating in the four Australian climate zones mentioned.

The results showed that solar fractions and payback periods can vary considerably, ranging from 58 to 100 per cent and between 3.8 and 10.1 years respectively. It was found, in this work that, although the evacuated tube collector generally operates with a marginally higher annual thermal efficiency over the selective surface flat plate collector, the overall performance of a system comprising of two selective surface collectors, is greater than a 30 tube evacuated tube system due to its larger absorber area despite taking less roof area. Due to the ratio of absorber to gross collector area, the selective surface flat plate collector was shown, in this study, to yield a higher thermal output per unit area of roof over the evacuated collector making it an ideal choice for domestic hot water projects where roofing area is limited relative to the thermal load. Furthermore, for the regions of high solar irradiance in Australia (Rockhampton and Alice Springs) the cheaper, lower performance flat plate collector was found in this study to operate with very high solar fractions while lowering the stagnation temperature over the selective surface flat plate and evacuated tube collector alternatives and is therefore the preferred solution.

Keywords: solar, thermal, flat plate, evacuated tube, domestic hot water, simulation

1. Introduction

Net energy consumption is increasing steadily in Australia due to a combination of factors including population growth and an increase in living standards (Bush, Harris et al. 1997). A significant portion of the energy consumed within the Australian residential sector is the energy required in meeting domestic hot water needs. Here, Australia is heavily dependent on the use of electric and gas fuelled water heaters responsible for approximately 24% of residential sector greenhouse gas emissions (Ferrari, Guthrie et al. 2012). Solar water heaters have been shown in a number of previous studies to make significant reductions in conventional energy (i.e. electricity and gas) use (Czarnecki 1958, Czarnecki and Read 1978, Morrison, Tran et al. 1984, Crawford 2001, Lloyd 2001, Vieira, Beal et al. 2014) while also demonstrating energy pay back periods of less than two years in some studies (Crawford and Treloar 2004, Hernandez and Kenny 2012).

doi:10.18086/swc.2017.27.03 Available at http://proceedings.ises.org

In order to increase the penetration of solar hot water heaters into the hot water market and reduce greenhouse emissions, a number of incentives have been provided at both state and federal levels resulting in strong growth within the Australian solar hot water industry, particularly within the new housing market such as the Small-Scale Renewable Energy Scheme (CER 2015). In the southern state of Victoria, new homes now require the installation of either a solar hot water system or rainwater tank. This programme alone has resulted in an increase adoption of solar water heaters from approximately 5% in 2004 to over 70% in 2011 (Ferrari, Guthrie et al. 2012).

Although Australia has recently experienced an uptake in the penetration of solar hot water heaters, it is approximated that energy efficient hot water heaters (i.e. solar and heat pump water heaters) constitute only 13% of total current installed water heaters (Shrapnel 2010). With the total number of water heaters sold in Australia to be approximately 700,000 units annually, the future market for solar thermal installations is large, particularly considering the rapid increase in utility costs that is occurring in Australia.

Solar thermal collectors can efficiently convert incident solar energy directly into useful thermal energy. This energy can be utilised by a household and significantly reduce the usage of the traditional fossil fuel powered energy sources.

1.1 Solar hot water systems and components

The typical domestic hot water solar thermal system comprises of the following major components (Kalogirou 2009):

1. Solar thermal collectors
2. Storage tank
3. Energy transfer system
4. Method of providing auxiliary boosting

The principal component of the solar thermal hot water system is the collector. The solar thermal collector is a unique heat exchanger which consists of an absorber, the component which absorbs incident electromagnetic energy radiated from the sun and converts this energy to useful thermal energy via an absorption process. Thermal energy is then transferred to the transport medium (typically water or a water/glycol mixture) which is circulated within the absorber. Thermodynamically, the design of a solar thermal collector aims to maximise the absorption of solar radiation and the heat transfer from the absorber to the transport medium, while minimising heat losses to the environment. A number of collector designs currently exist to achieve these engineering goals, with the stationary non-concentrating type flat plate collector and evacuated tube collector predominant in the Australian solar hot water market.

The typical design of a flat plate collector is shown in Fig 1 with major components forming the assembly identified. Incident solar radiation is attenuated through the glazing, generally high transmission low iron glass, onto the absorber surface. The absorber is made from a material of high thermal conductivity such as steel, aluminium, or copper and coated to increase its absorptivity. As a result of the impinging solar radiation being absorbed the temperature of the absorber will increase. The majority of this energy is then transferred to the transport medium (e.g. water) that is flowing within a series of fluid risers that are placed in thermal contact with the absorber via convection heat transfer.

Analysing the performance of a solar collector can be simplified to highlight the influence of the most important materials. The optical efficiency (η_0) of a solar collector is dependent on the properties of the absorber and glazing. The absorber is a function of two dominant properties: the absorptance of the absorber coating and the collector efficiency factor (F') as shown by Eq. (1) (Frei and Brunold 2000).

$$\eta_o = F'(\alpha\tau)_e \tag{1}$$

Where α is the absorptance, τ is the transmission of the glazing, F' is the collector efficiency factor, and $(\alpha\tau)_e$ is the effective absorption-transmittance product. The efficiency of a collector while in operation is calculated using Eq. (2).

$$\eta = F'(\alpha\tau)_e - F'U_L\left(\frac{T_m - T_a}{G_t}\right) \tag{2}$$

Where U_L is the overall heat loss coefficient, T_m is the mean collector temperature, T_a is the ambient temperature and G_t is the solar insolation on the collector plane.

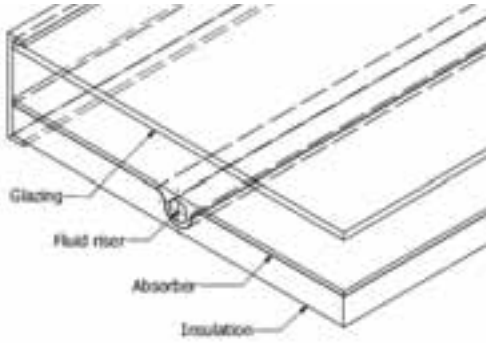

Fig 1: Typical components of a flat plate collector.

Examining Eq. (2), we can see that the thermal efficiency of a solar thermal collector is reduced by the heat loss term which is a factor of the temperature difference between the mean collector temperature (T_m) and the ambient temperature (T_a). As the mean absorber temperature rises above ambient, heat losses will inevitably occur via radiation, convection, and conduction modes reducing the thermal efficiency, and therefore yield of the collector. The characteristic performance of a solar thermal collector is typically expressed using Eq. (3) below.

$$\eta_{th} = a_1 - a_2\frac{(\bar{T} - T_a)}{G_t} - a_3\frac{(\bar{T} - T_a)^2}{G_t} \tag{3}$$

Where a_1, a_2, and a_3 are the collector performance characteristics determined by a laboratory to the local relevant test standard. It is of course ideal to maximise collector efficiency for the range of operating temperatures a solar collector will operate within which is dependent on the application (e.g. domestic hot water or industrial process heat application). For domestic hot water applications, this can range up to 70 degrees C, where a standard flat plate collector can experience significant heat losses reducing the useful energy gained by the transport medium. To minimise this loss, a number of strategies may be employed. One successful method which has been shown in previous studies (Jung 1988, Eisenhammer, Mahr et al. 1997, Schüler, Geng et al. 2000, Roberts 2013) to significantly improve the thermal performance of a collector is the use of spectrally selective absorber coatings onto the absorber substrate. By applying a spectrally selective coating onto the absorber, absorption (α) and emittance (ε) values can be altered and optimised such that thermal radiation losses can be reduced. Heat loss via convection may also be retarded by the evacuation of the air between the absorber and outer glazing reducing heat loss. This is the key feature of the evacuated tube collector (Gao, Fan et al. 2014). By creating a vacuum envelope, the thermal efficiency of the evacuated tube collector is less influenced by ambient conditions (temperature and wind) allowing higher collector operational temperatures.

The performance of a solar hot water system however, is not only dependent on the collector but the design of the whole system. Thermal energy collected from the collector must be stored in a thermally insulated container so that it can be later used by the household. The characteristics of the storage tank (size, heat loss, location of plumbing ports, etc.) will directly influence the collector and the quantity of hot water available to the household. A tank that is undersized for a given collector, application, and climate will lower the efficiency of the collector (due to an elevated mean collector temperature) and increase the likelihood of stagnation and the associated risks. An oversized tank on the other hand will increase the cost of the system and have a detrimental impact on the cost/performance ratio and excessive heat loss.

The manner in which energy is transferred between the collector and tank will have a significant influence on the performance of the system. This can be performed either by active or passive means. An active system is where an electrically driven circulator is used in conjunction with a controller to pump fluid around the collector loop. Alternatively, the passive or thermosiphon system works of the principle of natural convection and flow induced by a density differential and therefore does not need a pump or controller. Of these two methods, the active system will operate with the higher fluid velocity which will improve the heat transfer from the absorber to the transport medium, improving the thermal efficiency of the collector. The passive/thermosiphon system however will operate with reduced electricity consumption and potentially lower annual operational cost.

Finally, when designing a solar hot water system, a means to provide additional heating powered by conventional fuels (e.g. electricity/gas) is generally incorporated to ensure thermal loads are met during periods of insufficient radiation. A number of methods currently exist to achieve this with in-tank electric boosting and in-line continuous gas boosting methods the dominant methods in Australia. The in-tank electric boosting method is where an electric element is immersed in the tank and controlled via a thermostat. Although simple and cheap, a significant pitfall with this method is the addition of energy directly to the fluid being circulated through the collectors. As this will elevate the mean operating temperature of the collector, it will also reduce its operational efficiency. To avoid this issue, a gas booster can be placed between the outlet of the storage tank and the hot water supply line making an 'in-line' configuration. This way, energy is only added to the fluid when required and will not adversely affect the collector performance.

The combination of collector, tank, circulation method, and auxiliary boosting method will all contribute to the performance and cost of a solar hot water system. The optimal configuration will be dependent on a number of factors including the thermal load, installation parameters, and climate.

1.2 Aims of this study

It was discussed in the previous section that a number of collector types and system configurations are typically employed in Australia. When one considers the vast size of Australia, and consequently the vast differences in climate across the continent, the optimal configuration of solar thermal system components can also be expected to vary considerably when both thermodynamics and economics are taken into account.

The aim of this study is to conduct a computational study to determine the thermal performance of a number of solar hot water systems for a typical four-person household in Australia. This study will be limited to stationary, non-concentrating type collectors (i.e. flat plate and evacuated tube collectors only) that are boosted via an in-line continuous gas booster as discussed previously in Section 1.1. One area of focus for this study will be to compare performance and economic metrics between the flat plate and evacuated tube collectors. An emphasis will therefore be placed in this study to examine this specific issue further.

2.0 Method

A computational approach was applied in this work as it has now become common practice to incorporate simulations for the design of a solar thermal systems. Doing so allows the performance to be approximated for a specified system operating under transient environmental conditions. Computer simulations allow a number of system design parameters such as the characteristics of the collector, how it is orientated (azimuth and inclination), climate data, thermal loads, etc. to be varied so that their influence on output can be quantified and then examined and optimised. Although experimental work is the preferred method of acquiring data from an engineered system, it is often not practical and feasible considering time and costs. Such is the case for this study as we wish to investigate a number of system designs operating in different climate zones.

A number of sophisticated off-the-shelf computer simulation programmes for carrying out solar simulations are currently available such as TRNSYS (TRNSYS), T*SOL (T*SOL), and POLYSUN (POLYSUN). POLYSUN software package is used in this study and has also been applied successfully in previous studies (Kalogirou 2009, Bornatico, Pfeiffer et al. 2012, Carbonell, Haller et al. 2014). The accuracy of any computer simulation however, is not only dependent on the software package used but also by the quality of the simulation setup and the input of realistic parameters by the user and the consideration of system uncertainties (Dominguez-Munoz, Cejudo

Lopez et al. 2012). Details of the solar thermal systems and the parameters for the simulation are provided in the next section.

2.1 Simulation setup

In total, six solar thermal domestic hot water systems were investigated in this work operating under four climate zones of Australia. Details of each system configuration are provided in Tab 1. With regards to the types of solar thermal collectors investigated, high and low performance flat plate collectors as well as an evacuated tube type collector were examined in this work. All systems were coupled with a 300 litre storage tank with a daily draw-off of 200 litres per day at 50° Celsius, sufficient for a family dwelling of 4 people (50 litres/person). The energy draw-off pattern shown in Figure 3 was defined and assumed for all simulation studies conducted. All systems were auxiliary boosted via the in-line continuous gas boosted methodology discussed previously in Section 1.1.4. The gas booster chosen in this study was a generic 25kW natural gas fired type operating with a thermal efficiency (η_{th}) of 80 per cent.

The performance characteristics for each of the three solar thermal collectors are provided in Tab 2 below. In all simulations carried out, it was assumed that the collectors were orientated directly north and tilted at 25 degrees in accordance with the Australian standards relevant to the simulation of solar thermal systems (2008). All storage tanks (both active and thermosiphon) were 300 litres in storage capacity, fabricated from stainless steel and insulated with rigid polyurethane (PU). Additionally, piping length between the storage tank and collectors was fixed at 10m for all active systems with loose glass fibre\mineral wool type insulation (ρ = 250 kg/m^3 and k_{th} = 0.045 W/m.k) 20mm in thickness. For active systems, piping length between collectors and tank was fixed at 10m.

Tab 1: Details of the six solar thermal system configurations investigated in this work.

System	Type	Collector	Tank	Auxiliary booster
1	Active	2 x High performance flat plate	300L	25kW in-line gas booster
2	Active	2 x Low performance flat plate	300L	25kW in-line gas booster
3	Thermosiphon	2 x High performance flat plate	300L	25kW in-line gas booster
4	Thermosiphon	2 x Low performance flat plate	300L	25kW in-line gas booster
5	Active	1 x 30 Tube evacuated tube	300L	25kW in-line gas booster
6	Thermosiphon	1 x 30 Tube evacuated tube	300L	25kW in-line gas booster

Tab 2: Performance characteristics of each of the collectors investigated in this work.

Parameter	High performance flat plate (x1)	Low performance collector (x1)	Evacuated collector x 30 tube
$A_{absorber}$ (m^2)	1.62	1.87	2.84
A_{gross} (m^2)	1.8	2.01	4.4
η_0	0.785	0.687	0.71
a_1 (W/m^2/k)	3.35	5.761	1.65
a_2 (W/m^2/k^2)	0.012	0.014	0.008
T_{stag} (°C)	203	124	228

As previously stated, one of the key factors under investigation in this work is the influence of weather on system behaviour. Given the vast size of Australia, four climate zones have been identified in the Australian Standards (2008) to standardise the performance assessment of solar energy systems across the country. These four zones are shown in Fig 2 below. For each climate zone, the meteorological data is taken from a single city. These are Rockhampton, Alice Springs, Sydney, and Melbourne for Zones 1, 2, 3, and 4 highlighted in Fig 2 respectively.

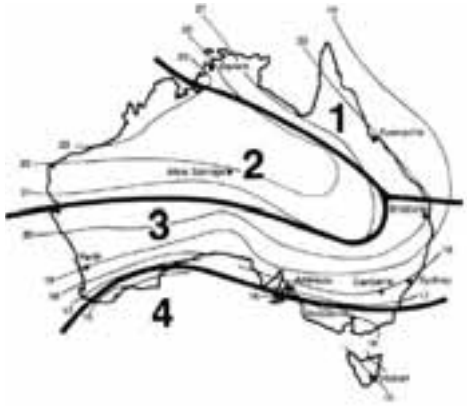

Fig 2: A map of Australia identifying the four climate zones used for simulation studies (2008).

With regard to thermal loading on the hot water system, user profiles will, of course, change considerably based on consumer preferences and seasonal variation. In this work, we will use the thermal load profile specified in the Australian standards (2008). This profile, shown in Fig 3, consists of morning and evening peaks with some usage shouldering the lunch time periods.

In summary, six solar thermal systems (see Tab 1) operating under four weather climates were investigated in this work. Results are presented in the next section.

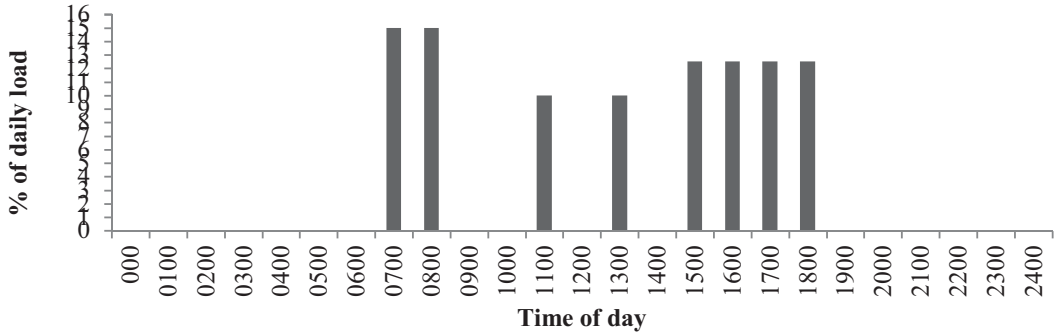

Fig 3: Thermal load profile for all solar hot water systems studied in this work (2008).

3.0 Results and Discussion

The results with respect to energy and economics are presented in this section.

3.1 Energy analysis

Quantitative annual energy results are provided in Tables A.1 to A.6 for Systems 1 through to 6 respectively. The following key performance metrics were taken from the POLYSUN generated results in order to evaluate the overall performance of the systems studied:

a) E_{tot} – the total annual energy that must be purchased by the consumer to operate the booster and if applicable, auxiliary equipment (kWh).
b) *Solar fraction (S_f)* – The POLYSUN total solar fraction is determined by equation Eq. (4).

$$S_f = \frac{Q_{sol}}{Q_{sol} + Q_{aux}} \tag{4}$$

Where Q_{sol} is the collector field yield (kWh) and Q_{aux} is the energy required by the auxiliary booster (kWh).

c) Collector field yield (Q_{sol}) – the total annual energy delivered by the collectors to the loop (kWh).

d) Specific collector field yield – The quotient of the annual collector field yield (Q_{sol}) and the gross collector area (kWh/m^2/year).
e) Collector efficiency ($\eta_{th,col}$) – the quotient of the annual collector field yield ($Qsol$) and the annual global irradiation incident on the collector aperture area.

From the data presented in Tables A.1 to A.6, a number of key findings can be extracted:

1. Comparing System 1 and System 5 we see that the evacuated tube collectors operate with a slightly higher thermal efficiency. However, solar fractions are higher for the flat plate system due to the larger absorber area of the two flat plate collectors resulting in greater collector field yield (Q_{sol}) and reduced auxiliary energy consumption.
2. The specific collector field yield for the high performance flat plate collector system is higher than the evacuated tube collector. This is explained by comparing the ratio of absorber to gross collector areas for both collectors. The flat plate collector has a ratio of A_{abs}/A_{gross} = 0.9 while the evacuated tube collector is 0.65.
3. For Zones 1 and 2, regions of Australia with high solar irradiance, the lower performing flat plate collector is a good choice as high solar fractions can be obtained in both active and thermosiphon systems while reducing the stagnation temperature.
4. Thermosiphon systems operate the minimum E_{tot} values due to the passive or natural circulation of fluid.
5. The difference in solar contribution from a solar hot water system is heavily influenced on its installed location in Australia.

Qualitatively examining the tabulated data presented in Appendix A specifically for Zone 3 (Sydney) we can visually compare the behaviour of each system for a single climate. Fig 4 compares the specific collector field yield and collector efficiencies between all six systems. From this figure we observe that an active system coupled with the high performance flat plate collectors (System 1) offers the maximum specific yield (Q_{sol}/A_{gross}) despite operating with a collector efficiency value slightly lower than the evacuated tube collector (System 5). This result which was similarly found in other work (Budihardjo and Morrison 2009), can be explained by comparing the collector characteristics, specifically the collector area values provided in
Tab 2. The ratios of absorber to gross collector areas are 0.9 and 0.65 for the high performance flat plate and evacuated tube collectors respectively. As the flat plate collector has a much higher ratio of absorber to gross collector area, it is able to compensate for its slightly lower thermal efficiency. This is again highlighted in Fig 5 which plots solar fraction and collector efficiency for each system for weather zone 3. The active system with high performance collectors offers the maximum solar fraction, greater than the 30 tube evacuated tube system. The system with the greatest solar fraction will require the least amount of purchased energy and potentially operate with the lowest annual running cost.

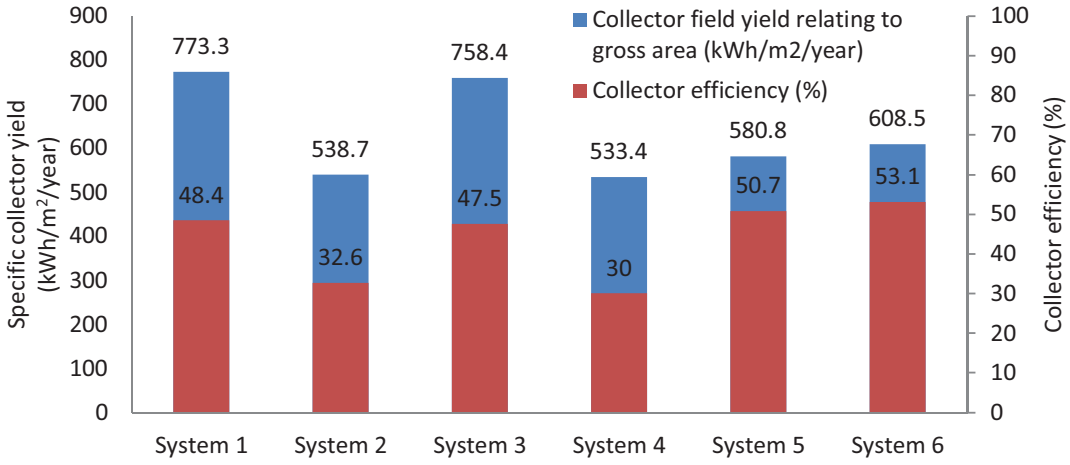

Fig 4: Comparing specific collector output and thermal efficiencies for all systems in climate Zone 3.

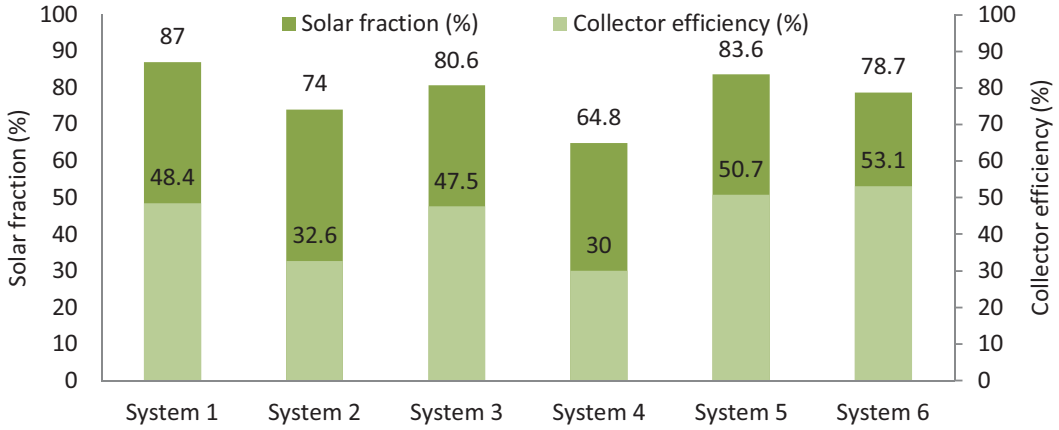

Fig 5: Comparing solar fractions and collector efficiencies for all systems in climate Zone 3.

3.2 *Economic analysis*

An economic analysis of the results was also conducted where the annual energy savings and return on investment (ROI) for each system and weather zone were calculated. System costs for each of the six solar hot water systems used for this step of the analysis are summarised in Tab 3. These figures were determined in consultation with Solimpeks Australia, one of Australia's distributors of solar thermal systems. Installation costs were also included to consider the differences in installing active and passive type solar thermal systems into the analysis. These figures were obtained from Australian Plumbing & Gas Australia Pty Ltd.

Tab 3: Approximate pricing for all six systems investigated in this work including installation. All prices are in Australian dollars.

	System					
	1	2	3	4	5	6
TOTAL (AUD)	$4,210.00	$4,190.00	$3,560.00	$3,540.00	$4,650.00	$4,000.00

Results for the average annual energy savings and ROI are presented in Fig 5 and Fig 6 respectively. Examining these two figures we can extract the following key results:

1. The thermosiphon system comprising of high performance flat plate system offers the maximum annual energy savings and fastest return on investment for all four weather climates investigated followed by a thermosiphon system coupled with an evacuated tube collector.
2. For all active type systems studied, the high performance flat plate collector system offered the greatest energy savings and fastest payback period.
3. A large variation in ROI values was calculated ranging from 3.8 to 10.1 years for the systems studied under the largely varying Australian climate.

The favourable payback period of the flat plate collector system over the evacuated tube system found in this study is supported by the experimental work carried out in a previous study (Chow, Dong et al. 2011). The results of this study highlight the importance of considering the system's holistic performance in its installed location and intended use as opposed to the thermal efficiency of the collector alone. However, under certain circumstances the evacuated tube collector may be the better choice particularly for applications which require higher fluid temperatures (> 70 degrees C) such as industrial process heat applications.

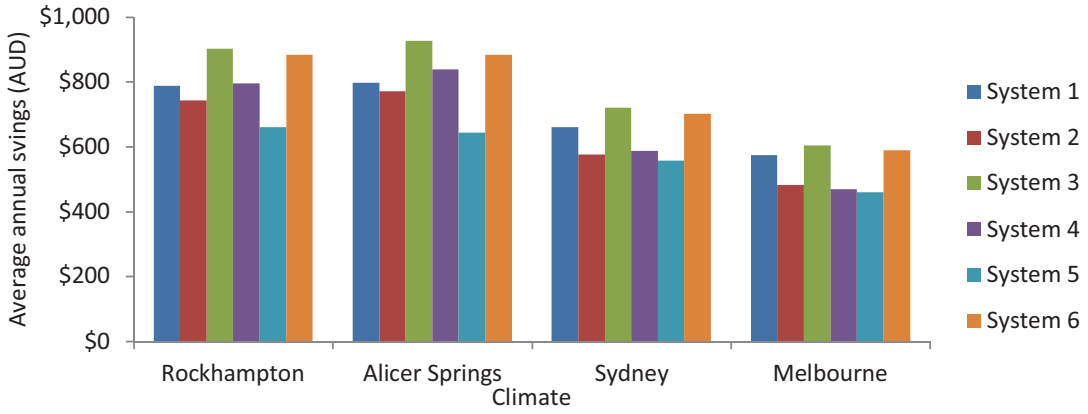

Fig 6: Average annual energy savings for each system in each of the four weather climates investigated.

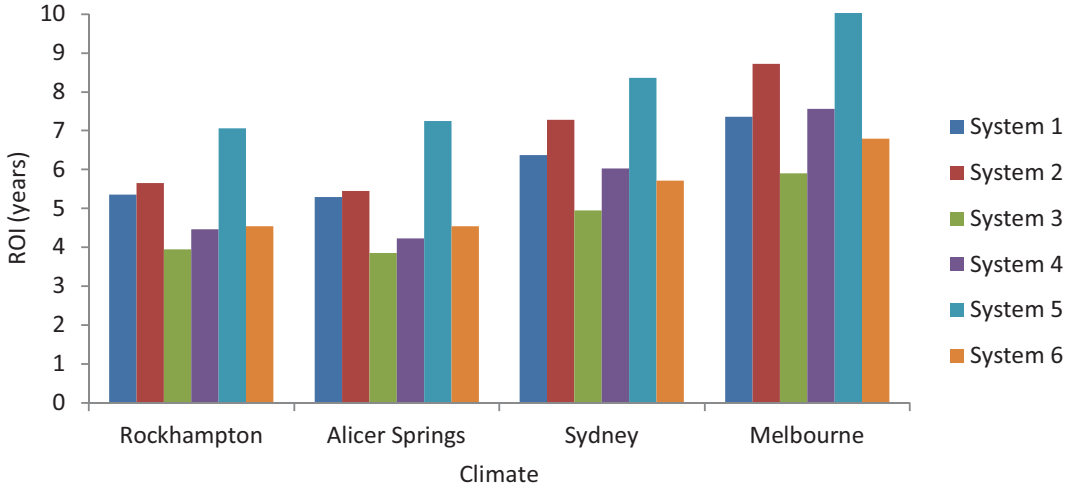

Fig 7: Payback periods for all systems investigated for all four climates in Australia.

4. Conclusions and recommendations

In this study, a number of computational simulations have been carried out on typical solar thermal systems typically deployed in Australia for domestic hot water purposes. Three collector types were investigated including high and low performing flat plate collectors and evacuated tube collectors which were integrated into both active and passive systems. From this work we can make the following conclusions:

1. The high performance flat plate collector operates with a slightly lower thermal efficiency in comparison to the evacuated tube collector, but contributes greater thermal yield per unit area of roof due to its comparatively higher absorber area.
2. The high performance flat plate collector offers the greatest thermal yield per unit area of roof of all collectors studied.
3. For Zones 1 and 2 of Australia, the low performance flat plate collector is a good choice based on its ability to operate with high solar fractions and its reduced cost and operational safety concern which arise from excessively stagnation temperatures.
4. A large variation in payback periods was found in this study highlighting the importance of system design for solar hot water applications in Australia.
5. Thermosiphon systems offer the fastest payback periods due to the lower capital and operational costs despite operating with reduced collector efficiency.

It is common in the solar thermal industry to emphasise the thermal performance of solar thermal collectors as a single component, but other considerations should be taken into account. The results from this study support the claim that the evacuated tube collector do indeed operate with a higher thermal efficiency over the flat plate

collector, however, it is important to assess the performance of the overall system, not just one component forming it. This study has shown for all four weather profiles studied (Rockhampton, Alice Springs, Sydney, and Melbourne) the cheaper high performance flat plate collector operates with a greater solar fraction over the evacuated tube collector and offers the household a faster payback period and lower cost of energy. Furthermore, the high stagnation temperature of evacuated tube collector should always be considered when proposing this technology. With stagnation temperatures over 220°C achievable with the evacuated tube collector, this can stress component materials and create safety concerns for the user.

Appendix A. Results tables

Tab A.1: Energy results for System 1 (active system with 2 x high performance flat plate collectors).

	Zone 1	**Zone 2**	**Zone 3**	**Zone 4**
	Rockhampton	**Alice Springs**	**Sydney**	**Melbourne**
E_{tot} **(kWh)**	672.4	629.4	1173	1522.6
S_f**, Solar fraction (%)**	100	100	87	79.9
Q_{sol}**, Collector field yield (kWh)**	3247	3617.3	2783.8	2776.6
Specific collector field yield (kWh/m^2/year)	901.9	1004.8	773.3	771.3
$\eta_{th,col}$**, Collector efficiency (%)**	47	46.3	48.4	49.7

Tab A.2: Energy results for System 2 (active system with 2 x low performance flat plate collectors).

	Zone 1	**Zone 2**	**Zone 3**	**Zone 4**
	Rockhampton	**Alice Springs**	**Sydney**	**Melbourne**
E_{tot} **(kWh)**	845.6	737.2	1509	1888.6
S_f**, Solar fraction (%)**	92.8	96.6	74	67.2
Q_{sol}**, Collector field yield (kWh)**	2589	2954.4	2165.7	2187.1
Specific collector field yield (kWh/m^2/year)	644	734.9	538.7	544
$\eta_{th,col}$**, Collector efficiency (%)**	32.4	32.7	32.6	33.9

Tab A.3: Energy results for System 3 (thermosiphon system with 2 x high performance flat plate collectors).

	Zone 1	**Zone 2**	**Zone 3**	**Zone 4**
	Rockhampton	**Alice Springs**	**Sydney**	**Melbourne**
E_{tot} **(kWh)**	214.7	114.9	937.8	1397.8
S_f**, Solar fraction (%)**	97.5	100	80.6	72.8
Q_{sol}**, Collector field yield (kWh)**	3267.7	3712	2730.4	2717
Specific collector field yield (kWh/m^2/year)	907.7	1031.1	758.4	754.7
$\eta_{th,col}$**, Collector efficiency (%)**	47.3	47.5	47.5	48.6

Tab A.4: Energy results for System 4 (thermosiphon system with 2 x low performance flat plate collectors).

	Zone 1	**Zone 2**	**Zone 3**	**Zone 4**
	Rockhampton	**Alice Springs**	**Sydney**	**Melbourne**
E_{tot} **(kWh)**	639.2	464.6	1465.7	1938.5

S_f, Solar fraction (%)	85.1	91	64.8	58.3
Q_{sol}, Collector field yield (kWh)	2463.7	2912	1994.9	2026
Specific collector field yield (kWh/m^2/year)	612.9	724.4	533.4	541.7
$\eta_{th,col}$, Collector efficiency (%)	30.9	32.3	30	31.4

Tab A.5: Energy results for System 5 (active system with 1 x 30 tube evacuated tube collector).

	Zone 1	**Zone 2**	**Zone 3**	**Zone 4**
	Rockhampton	**Alice Springs**	**Sydney**	**Melbourne**
E_{tot} (kWh)	1177.9	1245.3	1586	1973.5
S_f, Solar fraction (%)	97.8	99.3	83.6	75
Q_{sol}, Collector field yield (kWh)	2973.8	3249.5	2555.7	2503.8
Specific collector field yield (kWh/m^2/year)	675.9	738.5	580.8	569
$\eta_{th,col}$, Collector efficiency (%)	49.1	47.4	50.7	51.1

Tab A.6: Energy results for System 6 (active system with 1 x 30 tube evacuated tube collector).

	Zone 1	**Zone 2**	**Zone 3**	**Zone 4**
	Rockhampton	**Alice Springs**	**Sydney**	**Melbourne**
E_{tot} (kWh)	290.2	290.2	1015.5	1459.2
S_f, Solar fraction (%)	95.5	95.5	78.7	71
Q_{sol}, Collector field yield (kWh)	3159.8	3159.8	2677.5	2619
Specific collector field yield (kWh/m^2/year)	718.1	718.1	608.5	595.4
$\eta_{th,col}$, Collector efficiency (%)	52.1	52.1	53.1	53.5

References

(2008). AS/NZS 4234:2008, Standards Australia**:** 1-81.
Bornatico, R., M. Pfeiffer, A. Witzig and L. Guzzella (2012). "Optimal sizing of a solar thermal building installation using particle swarm optimization." Energy **41**: 31-37.
Budihardjo, I. and G. L. Morrison (2009). "Performance of water-in-glass evacuated tube solar water heaters." Solar Energy **83**(1): 49-56.
Bush, S., J. Harris and L. H. Trieu (1997). Australian energy consumption and production: historical trends and projections to 2009-10. ABARE Research Report. Canberra.
Carbonell, D., M. Y. Haller, D. Philippen and E. Frank (2014). "Simulations of combined solar thermal and heat pump systems for domestic hot water and space heating." Energy Procedia **48**: 524-534.
CER. (2015). "http://www.cleanenergyregulator.gov.au/RET/About-the-Renewable-Energy-Target/How-the-scheme-works/Small-scale-Renewable-Energy-Scheme." Retrieved 10th of November, 2015.
Chow, T.-T., Z. Dong, L.-S. Chan, K.-F. Fong and Y. Bai (2011). "Performance evaluation of evacuated tube solar domestic hot water systems in Hong Kong." Energy and Buildings **43**(12): 3467-3474.
Crawford, R. H. (2001). "Solar versus fossil fuels: A net energy analysis of domestic solar hot water systems in Australia." Refocus **2**(5): 38-39.
Crawford, R. H. and G. J. Treloar (2004). "Net energy analysis of solar and conventional domestic hot water systems in melbourne, Australia." Solar Energy **76**: 159-163.
Czarnecki, J. T. (1958). "Performance of experimental solar water heaters in Australia." Solar Energy **2**(3–4): 2-6.
Czarnecki, J. T. and W. R. W. Read (1978). "Advances in solar water heating for domestic use in Australia." Solar Energy **20**(1): 75-80.
Dominguez-Munoz, F., J. M. Cejudo Lopez, A. Carillo Andres and C. R. Ruivo (2012). "Design of solar thermal systems under uncertainty." Energy and Buildings **47**: 474-484.

Eisenhammer, T., A. Mahr, A. Haugeneder and W. Assmann (1997). "Selective absorbers based on AlCuFe thin films." Solar Energy Materials & Solar Cells **46**(1): 53.
Ferrari, D., K. Guthrie, S. Ott and R. Thomas (2012). "Learning from interventions aimed at mainstreaming solar hot water in the Australian market." Energy Procedia **30**: 1401-1410.
Frei, U. and S. Brunold (2000). Chapter 46 - Materials in High Performance Solar Collectors. World Renewable Energy Congress VI. A. A. M. Sayigh. Oxford, Pergamon**:** 241-252.
Gao, Y., R. Fan, X. Y. Zhang, Y. J. An, M. X. Wang, Y. K. Gao and Y. Yu (2014). "Thermal performance and parameter analysis of a U-pipe evacuated solar tube collector." Solar Energy **107**(0): 714-727.
Hernandez, P. and P. Kenny (2012). "Net energy analysis of domestic solar water heating installations in operation." Renewable and Sustainable Energy Reviews **16**(1): 170-177.
Jung, H. C. (1988). Selective Surface Coating for Solar Thermal Conversion. Advances In Solar Energy Technology. W. H. Bloss and F. Pfisterer. Oxford, Pergamon**:** 697-700.
Kalogirou, S. (2009). "Thermal performance, economic and environmental life cycle analysis of thermosiphon solar water heaters." Solar Energy **83**: 39-48.
Kalogirou, S. A. (2009). Solar Energy Engineering: Processes and Systems. Burlington, MA, Elsevier.
Lloyd, C. R. (2001). "Renewable energy options for hot water systems in remote areas." Renewable Energy **22**(1–3): 335-343.
Morrison, G. L., N. H. Tran, D. R. McKenzie, I. C. Onley, G. L. Harding and R. E. Collins (1984). "Long term performance of evacuated tubular solar water heaters in Sydney, Australia." Solar Energy **32**(6): 785-791.
POLYSUN. "http://www.velasolaris.com/english/home.html." Retrieved November, 2014.
Roberts, D. E. (2013). "A figure of merit for selective absorbers in flat plate solar water heaters." Solar Energy **98, Part C**(0): 503-510.
Schüler, A., J. Geng, P. Oelhafen, S. Brunold, P. Gantenbein and U. Frei (2000). "Application of titanium containing amorphous hydrogenated carbon films (a-C:H/Ti) as optical selective solar absorber coatings." Solar Energy Materials and Solar Cells **60**(3): 295-307.
Shrapnel, B. (2010). The Household Appliance Market in Australia. Vol. 4 Hot Water Systems. **4**.
T*SOL. "http://www.valentin-software.com/en/products/solar-thermal/14/tsol." Retrieved November, 2014.
TRNSYS. "http://sel.me.wisc.edu/trnsys/." Retrieved November, 2014.
Vieira, A. S., C. D. Beal and R. A. Stewart (2014). "Residential water heaters in Brisbane, Australia: Thinking beyond technology selection to enhance energy efficiency and level of service." Energy and Buildings **82**(0): 222-236.

Solar Refrigeration and Solar Air Conditioning

Monitoring and energy performance assessment of an advanced DEC HVAC system in Morocco

Marco Beccali[a], Pietro Finocchiaro[b], Vincenzo Gentile[c], Matteo Muscherà[d], Mario Motta[d]

[a] University of Palermo - Italy, [b] SolarInvent srl - Italy, [c] Polytechnic of Turin - Italy, [d] Polytechnic of Milan - Italy

Summary

This work addresses the energy performance of a solar Desiccant and Evaporative Cooling (DEC) system working with the freescoo technology. Freescoo is an innovative solar air conditioning concept for ventilation, cooling, dehumidification and heating of buildings in residential and tertiary sectors.
The monitoring of the system started in November 2016 and will continue until the end of 2017. Energy performances are evaluated according to the monitoring procedure for solar cooling systems developed by the Task 38 and 48 of the International Energy Agency experts.
The analysis based on monitoring data shows that, for typical operating conditions in cooling mode, the electricity saving in comparison to conventional HVAC systems can be over 70%.

1. Introduction

Within the agreement between Politecnico di Milano and AMEE (Agence Marocaine pour l'Efficacité Energétique), a solar cooling pilot plant had to be installed at a library in Marrakech. The aim was to develop, test and optimize a robust, low cost, low maintenance solar driven air-conditioning concept, suitable for Northern African climates. At the end of a call for tenders issued by Politecnico di Milano, freescoo by Solarinvent has been selected.

The building is a three-stage structure oriented NE-SW, and the last stage hosts the library. The library stage has a square shape. The roof is plane and presents a square-shaped skylight in the centre with a sloped roof. The skylight height is 1.30 m and his rooftop is 3.50 m above the plane level. The internal ambient is developed around the central space, corresponding to the square skylight. The ambient is composed of two different spaces. The first is assigned to the document shelves, while the other is designated to the hosts' seats. The net internal area is about 300 m^2. The internal ambient temperature is controlled by the pre-existing cooling system, made of four electrical split systems, with a global cooling power of about 18 kW. It has to be noted that only some split units operate properly causing frequent overheating during the summertime and insufficient heating during the wintertime.

Fig. 1: The libray at AMEE

Table 1: Main building data

Description	Data
Internal area	300 m^2
Existing air distribution system	Plaster air ducts
Installed cooling power of split system	18 kW
Existing HVAC system	Ventilation AHU + split system
Occupation pattern	Library 9:00 -16:00

doi:10.18086/swc.2017.28.01 Available at http://proceedings.ises.org

Global radiation on the horizontal on the site of Marrakech reaches 1100 W/m2, whereas global solar irradiation in one year is about 1.9 MWh/m2. Average temperatures vary from about 7°C to 35°C, peak temperature from 4°C to 43°C. Peak humidity ratio is about 16 g/kg in July.

2. Description of the system

The HVAC system is a freescoo AHU integrated with the solar collector; it has a maximum air flowrate of 1000 m^3/h and supplies fresh air to a room of 400 m^3. The max power needed is about 360 W. For driving the cooling process, about 2 litres of water per kWh of cooling energy are needed. In the wintertime, the system can provide also heating to the room when the sun shines and the required air change in the middle seasons.

Fig. 2: Picture of the freescoo system at AMEE

The freescoo concept is based on an innovative and patented DEC (Desiccant and Evaporative Cooling) open cycle technology: by using low enthalpy heat and water evaporation, Freescoo treats directly external hot and wet air to obtain a conditioned stream typically at 18-20°C and 50-60% of relative humidity, reducing drastically electrical demand in comparison to conventional HVAC systems based on vapor compression cycles.

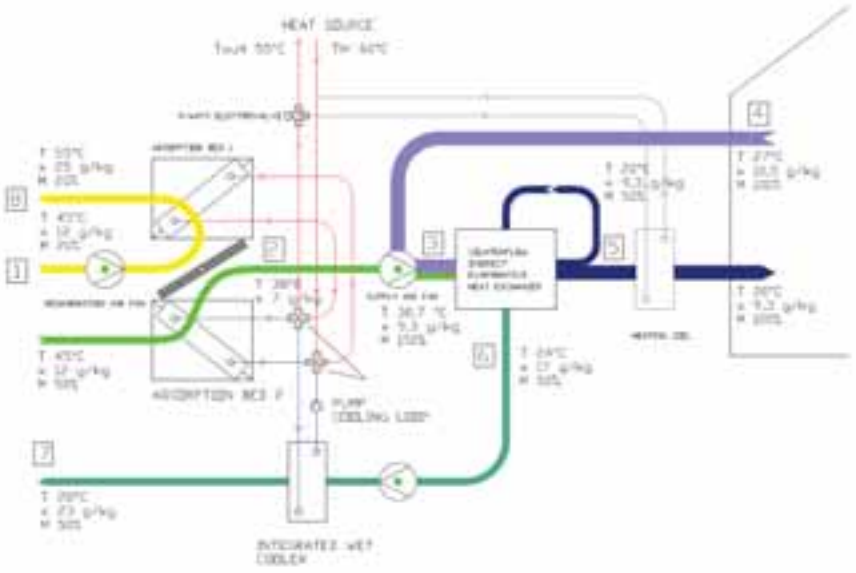

Fig. 3: Scheme of the operation in cooling mode

The innovative Freescoo DEC technology is based on two processes:

- Physical adsorption that reduces moisture content of external air up to the desired humidity rate by using two Cooled Package Beds of silica gel which are operated in a batch process. Each adsorption bed is realized with air to water heat exchanger filled with silica gel grains. The refrigerant used in the process is the water: so the adsorption material is cooled by water flowing through the tubes and a dry cooler is used to reject the adsorption heat generated by the desiccant bed operating in dehumidification mode. After hours of working the adsorption sorbent material reaches the maximum moisture content and it has to be regenerated by heating and drying the sorbent material with hot air.
- Evaporative cooling process takes advantage of advanced double stages indirect evaporative cooler which reduces air temperature up to the supply conditions without increasing the humidity content.

The cooling cycle is described here below. A flow rate of outside air (1) (moderate humidity and high temperature) is drawn through one of the adsorption beds. The moist air is simultaneously dehumidified (passing through the fins filled with silica gel grains) and cooled down (by the water flowing into the heat exchanger tubes). The coupling of dehumidification and cooling steps allows to increase the energy performance of the whole process in comparison to standard desiccant rotor based DEC cycles.

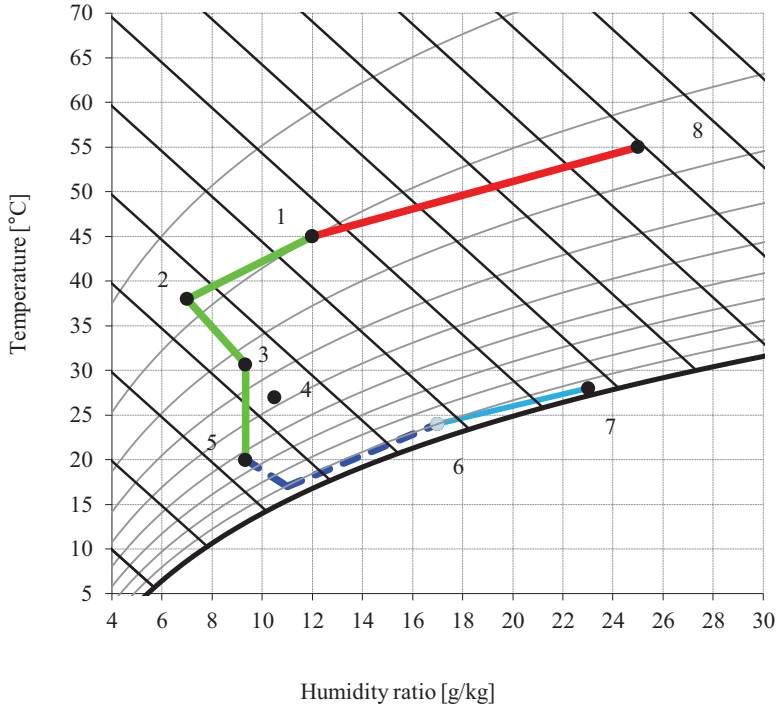

Fig. 4: Thermodynamics of the cooling cycle

Dehumidification process is carried out with a slight temperature decrease (2). Afterwards, dehumidified air is mixed with the return air extracted from the building (4), reaching the conditions of point (3). The mixed air enters the double-stages indirect evaporative cooler allowing to cool down the supply air without increasing its humidity reaching the supply conditions at point (5). In order to produce the cooling effect, a portion of the supply air is drawn to the secondary side (6). The air coming from the secondary side of the indirect evaporative heat exchanger, passes across the wet cooler and receives the adsorption heat caused by the dehumidification process in the adsorption bed (7). When the adsorbent material gets saturated with moisture, this must be reactivated by means of heat supply: outside air (1) is drown into the sorption bed which must be regenerated and receives the moisture released by the desiccant which is now heated up by the hot water (8).

Two adsorbent beds are included in the Freescoo unit to ensure a continuous operation of the system: while the first one is working in order to dehumidify the air, the other one is regenerated using heat from the heat distribution system at temperature > 55°C. A system of air dumpers provides the automatic commutation between the two adsorption beds to guarantee a continuous process.

Tab. 2: Air conditions at inlet and outlet of the internal components at design summer operation (Toutside = 45°C x outside = 10,5 g/kg, T bui = 27°C x bui = 10,5 g/kg)

Description	X	T	h	Position
-	g/kg	°C	kJ/kg	-
Outside air	12	45.0	76.2	1
Outlet ADS bed	7.0	38.0	56.2	2
Mixing	9.3	30.7	54.7	3
Outlet EVA heat exchanger	9.3	20	43.8	5
Building	10.5	27.0	53.9	4
Inlet EVA - secondary side	9.3	20.0	43.8	4
Outlet EVA - secondary side	17	24	67.4	6
Outlet wet cooler	23.0	28.0	86.8	7
Outside air	12.0	45.0	76.2	1
Regeneration	25.0	55.0	120.3	8

The main technical data at the design summer conditions typical for Marrakech are reported in Tab.3.

Tab. 3: Performance at design summer conditions (Toutside = 45°C x outside = 12 g/kg, T bui = 27°C x bui = 10,5 g/kg)

Description	Value	Unit
Supply air flow rate	0-1000	[m^3/h]
Rate of fresh air	50	[%]
Total max cooling power	5800	[W]
Heating power required for the regeneration	3000	[W]
Installed solar collector power	4800	[W]
Power absorbed	360	[W]
Thermal COP	1.9	[-]
EER	16,7	[-]

In addition to the mentioned cooling operation, in the wintertime, the system can provide free solar heat when the sun is shining and can be eventually integrated with different kinds of auxiliary heat sources (heat pump, boiler) in order to guarantee a continuous heating of the building.

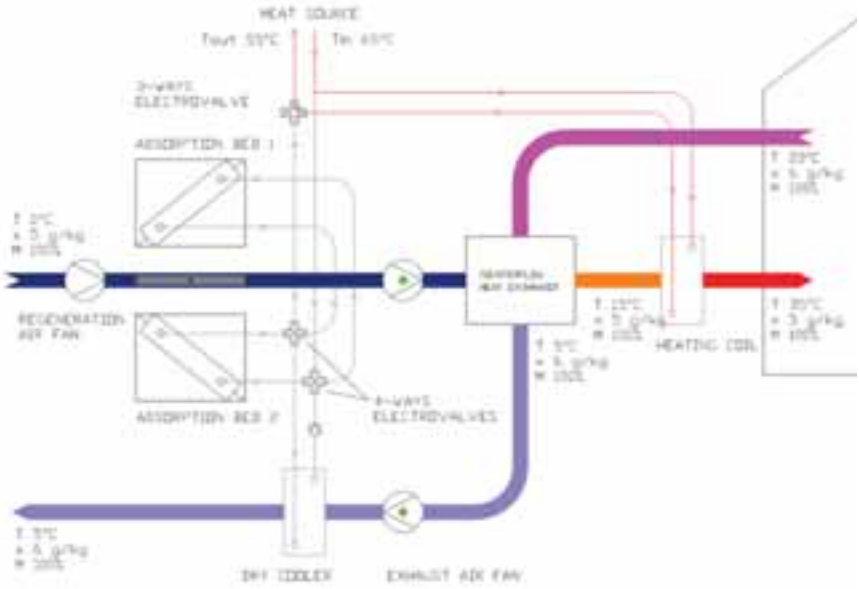

Fig. 5: Scheme of the operation in heating and ventilation mode

Outside air is drown into the counter-flow heat exchanger which is now used as heat recovery unit. Afterwards, the air is heated up in the heating coil which is connected with the heating source, reaching the supply conditions. Simultaneously, an equivalent portion of air is extracted from the building and used for pre-heating the outside air in the counter flow heat exchanger.

3. Results on the energy performance and discussion

In order to assess the energy consumption, an extended monitoring campaign has been performed during the 2017. For the heating mode data presented have been registered in January and February (59 days), whereas for cooling operation from May to September (159 days).

During the wintertime, daily operation hours varied according to the working hours of the solar collectors. In heating mode, being the system solar autonomous, it is operated only when temperature at the solar collectors exceeded 25°C. In summertime, the operation hours varied according to the decision of the users and varied from 10 to 24 hours a day. During the monitoring period, the building was occupied as normally.

Measurements of temperatures (accuracy ± 0.3°C) and humidity (accuracy ± 2.5% of measured value), air velocity (at supply, return, adsorption beds), accuracy of ± (0.5 m/s + 3% of measured value), electricity consumption (accuracy ± 0.5%), solar radiation (2° call accord to ISO9060), and water flowrates (accuracy ± 3%) have been measured at inlet and outlet of main components. Data acquisition has been performed using the GPRS 2 platform from SENECA at 16-bit together with 4 x 8 input analogue modules and 1 digital DI module.

Energy performances have been evaluated according to the monitoring procedure for solar cooling systems developed by the Task 38 and 48 of the International Energy Agency experts.

In the following pages the behaviour of the system will be analysed, and diagrams and instantaneous and long-term energy performances will be presented.

Typical winter operation is depicted in Fig. 5,6,7,8: first two graphs are related to a day of February in which there's a continuous and abundant solar radiation; in Fig. 7 and 8, a day of January with a lower total solar radiation and a discontinuous behaviour is reported. The external temperature has an excursion of 10-15°C between the day and the night time in both cases, instead the building temperature has a quasi-flat behaviour.

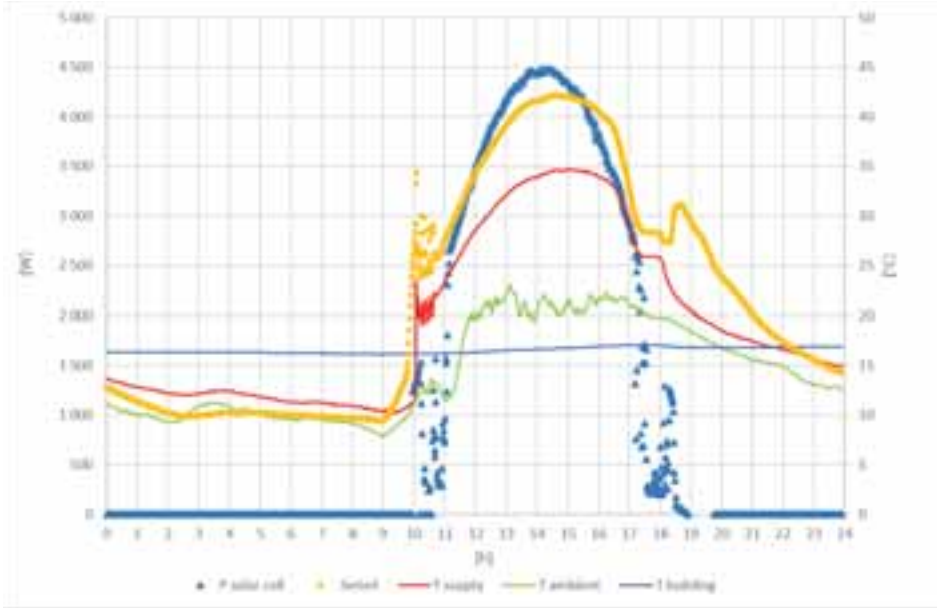

Fig. 5: Thermal performance of the AHU – Day 1, 03.02.2017

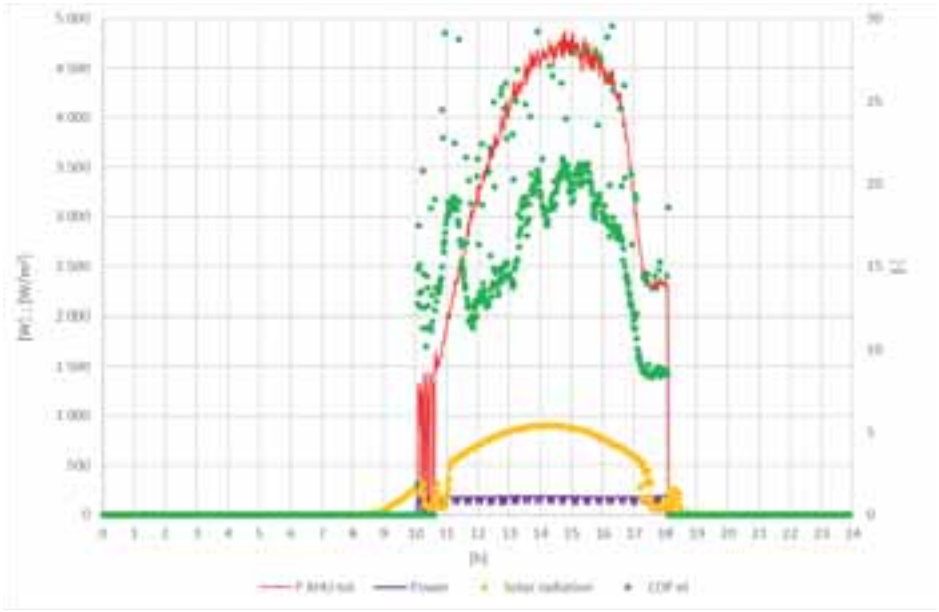

Fig. 6: Electrical performance of the AHU – Day 1, 03.02.2017

For the days considered, the supply temperature of the AHU ranges between 25 and 35°C, with the typical trend that follows the daily solar radiation. Evacuated solar collectors work quite efficiently, between 55-62 %, and the daily COP of the AHU during the winter operation ranged between 11-15. These values are strongly correlated to the total amount of solar radiation that influences directly the energy performances of the AHU. In fact, due to the malfunction of the internal split unit, the temperature of the building is always lower than the supply temperature, therefore the AHU works always at the maximum air flow rate with a constant electrical consumption. As a result, the working operation is quite similar during the winter season, between 6.5 and 8 hours per day. The higher incident solar radiation, the higher thermal power of the AHU, and consequently the higher values of the electrical COP.

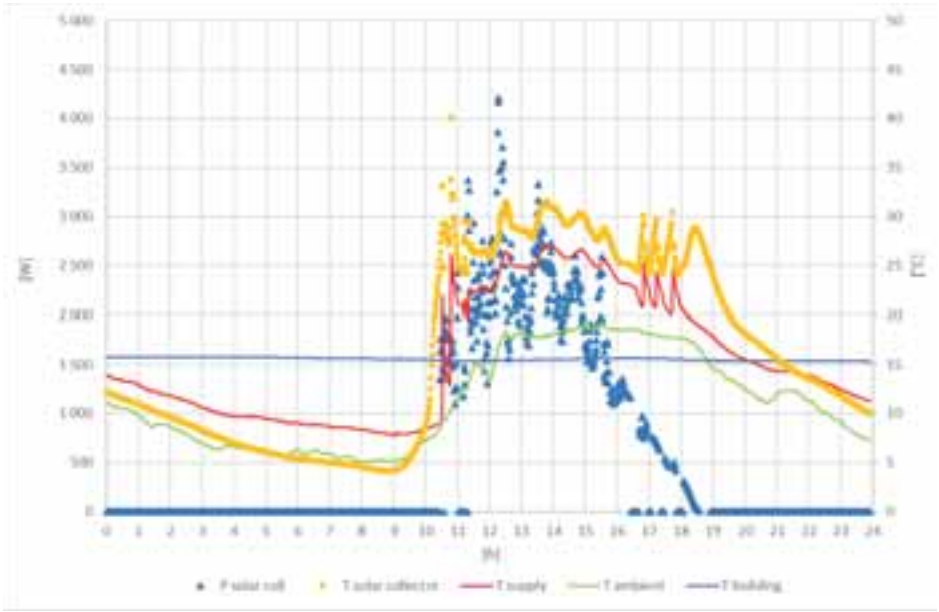

Fig. 7: Thermal performance of the AHU – Day 2, 08.01.2017

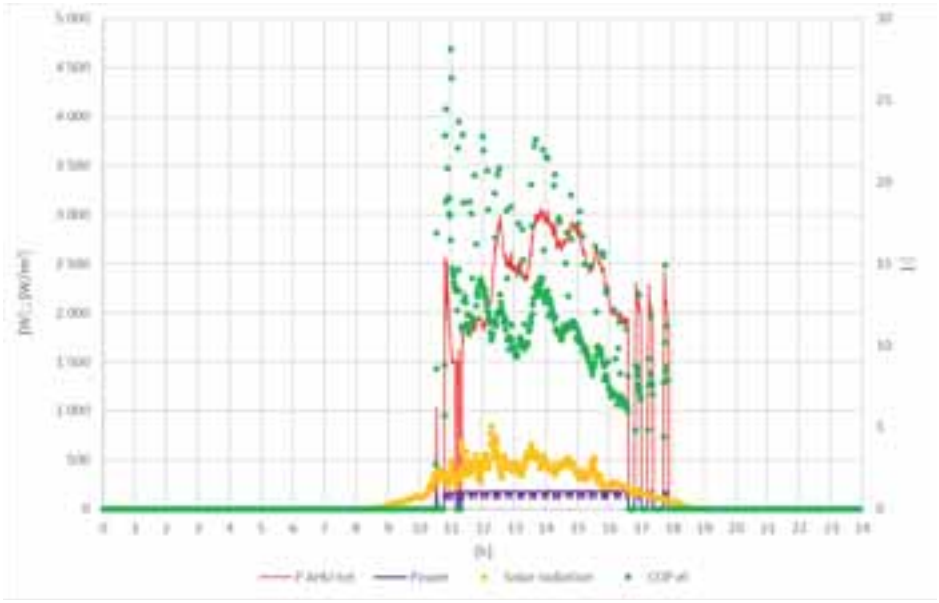

Fig. 8: Electrical performance of the AHU – Day 2, 08.01.2017

Tab. 4: Daily performance of the AHU for the two days considered

Description	Value Day 1	Value Day 2	Unit
Total electricity consumption	1.31	1.04	[kWh]
Incident solar radiation	40.6	21.9	[kWh]
Delivered thermal energy of AHU	22.0	11.9	[kWh]
Delivered thermal energy to the building	27.8	14.7	[kWh]
Solar heat produced	25.3	12.4	[kWh]
Operation hours	7.9	6.4	[h]
COP el	16.8	11.4	[-]
Solar collector efficiency	62%	57%	[-]

With regards of the cooling operation, two days of July are presented here below in Fig. 8 and 9 for the first day and in Fig. 10 and 11 for the second day.

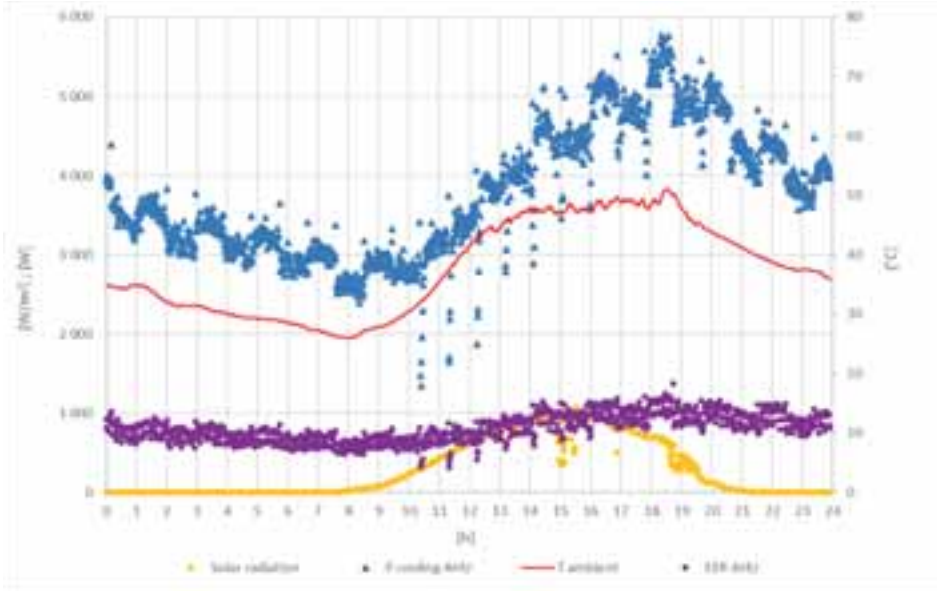

Fig. 8: Energy performance of the AHU – Day 1, 16.07.2017

Fig. 9: Temperature and humidity ratio in the AHU – Day 1, 16.07.2017

The total incident solar radiation ranges between 50-60 kWh/day, and the cooling power produced by the AHU is between 2.5-5.5 kW, with a supply temperature of 19-22°C. First day is characterized by high solar radiation, extreme ambient temperatures (maximum value about 50°C), whereas second day has lower solar radiation and ambient temperatures up to 40°C. System has been operated 24 hours during the first day, and 10 hours during the second day. In the first day, the cooling power of the AHU produced during the night is only due to the indirect evaporative cooling effect.

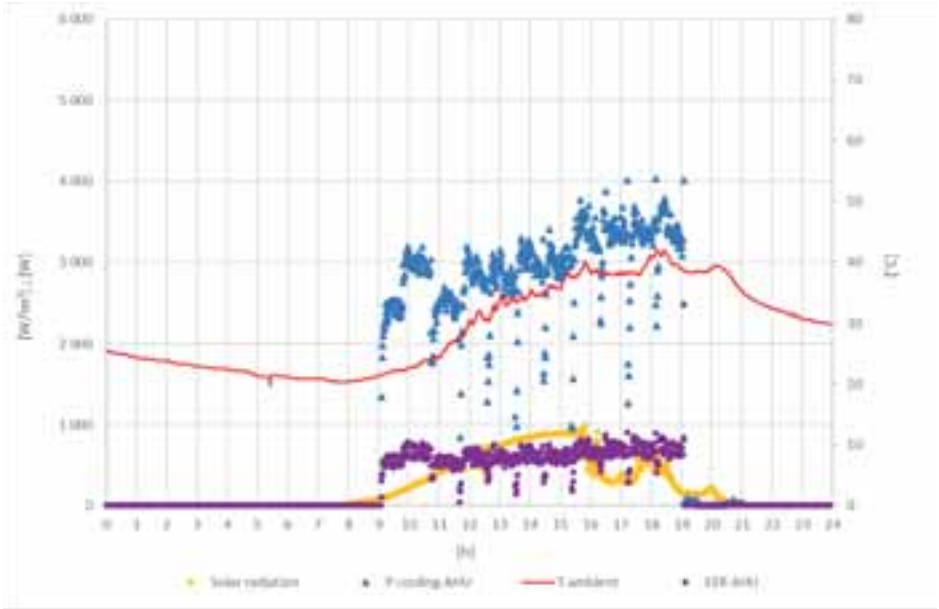

Fig. 10: Cooling performance of the AHU – Day 2, 23.07.2017

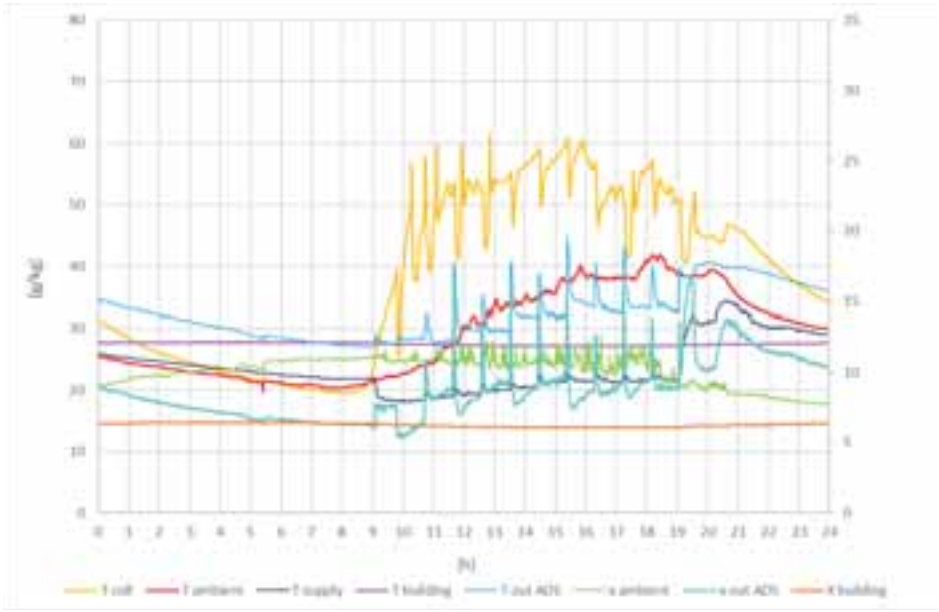

Fig. 11: Temperature and humidity ratio in the AHU – Day 2, 23.07.2017

Tab. 5: Daily performance of the AHU for the two days considered

Description	Value Day 1	Value Day 2	Unit
Cooling energy delivered by the AHU	91	29	[kWh]
Average flow rate	881	376	[m3/h]
Incident solar radiation	52.9	43.3	[kWh]
Solar collector heat	31.9	24.1	[kWh]
Electricity consumed	8.4	3.62	[kWh]
Specific power consumption for ventilation	0.40	0.96	[W/m^3/h]
Hours of operation	24	10	H
EER	10.8	7.92	[-]
COP th	2.88	1.12	[-]
Solar collector efficiency	60%	56%	[-]

In Fig. 12 the daily performances in July are reported. The EER is always higher then 5, with peak values higher then 10, and an average value of about 7. Thanks to the very good performance of the evaporative cooling module of the AHU, the thermal COP of AHU varies between 1 and 2, with a strong influence of the external environmental conditions both in terms of temperature and relative humidity.

In the summer period the air flow rate has a daily modulation, managed by the PID controller since the control strategy implemented uses the building temperature and humidity as input parameters. In Fig. 9, monthly performances of the machine are depicted. The average air flow rate has a minimum value in the month of May, 400 m^3/h and, whereas a maximum value of about 900 m^3/h is reached in the month of August. The electricity consumption varies correspondingly both for the increase of the air flow rate and the daily working hours.

Fig. 12: Daily energy performances of the AHU – July 2017

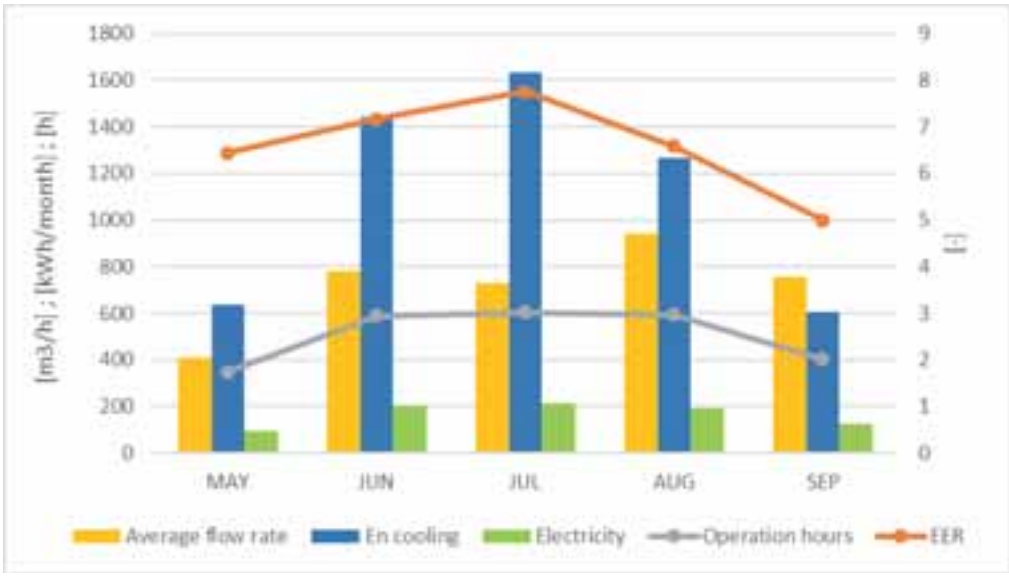

Fig. 13: Monthly energy performances of the AHU – July 2017

Tab. 6: Seasonal and yearly performance results

Description	Cooling	Heating	Year	Unit
Thermal energy – AHU	5527	960	6487	[kWh]
Thermal energy – BUI	2250	1109	3359	[kWh]
Average flow rate	714	623	668	[m^3/h]
Incident solar radiation	6859	2008	8867	[kWh]
Solar collector heat	3966	1235	5200	[kWh]
Electricity consumed	820	90	910	[kWh]
Water consumption	11.6	0	11.6	[m^3]
Mean daily water consumption	83	0	-	[liters/day]
Specific power consumption for ventilation	0.46	0.35	0.40	[W/m^3/h]
Hours of operation	2524	412	2937	[h]
Days of operation	139	59	198	[day]
EER	6.7	11	7.1	[-]
COP th	1.39	0.78	-	[-]
Solar collector efficiency	58%	61%	59%	[-]

According to the results obtained, a comparison with the energy performances of a conventional AHU coupled with a vapor compression reversible heat pump has been assessed. The main hypotheses regarding the conventional system concern the energy efficiency ratio of the chiller/heat pump and the electricity consumption for the ventilation. Results show an electricity saving of 70 % over the year.

Tab. 7: Calculated annual energy performances for a conventional AHU coupled with a vapor compression reversible heat pump

EER for the chiller/HP (assumed)	3	[-]
Electricity consumed by the chiller/HP	2162	[kWh]
Specific power consumption for ventilation (assumed)	0.30	[W/m^3/h]
Electricity consumed by the AHU for ventilation	589	[kWh]
Total electricity consumed	2751	[kWh]
Electricity saving	70	[%]

3. Conclusions

In this work the energy performance of a innovative DEC AHU working with the freescoo concept has been presented. The system has been monitored both in cooling and heating operation and results showed the high energy saving potential of technology.

Summer operation has been characterized by a lower electrical efficiency of the AHU in comparison to the winter operation (6.7 versus 11). The main reason is the dry climate that characterizes the summer season of Marrakech, and the low latent load of the building. As a result, the latent part of the cooling power produced by AHU was much lower than the maximum potentiality of the machine.

Global results can be considered anyway very good, both in terms of instantaneous and long-term behaviour.

The comparison with the energy performances of a conventional AHU coupled with a vapor compression reversible heat pump shows that the freescoo AHU can save 70% of electricity.

Water consumption amounted to about 12 m^3 for the summertime. This is a relevant aspect that can limit the application of the mentioned technology in climates with scarcity of water.

4. Acknowledgements

The mentioned project has been realized with the support of the Italian company Pleion srl which provided the solar collectors and their large experience in the solar thermal area.

4. References

Finocchiaro P, Beccali M, Innovative compact solar air conditioner based on fixed and cooled adsorption beds and wet heat exchangers. Energy Procedia 2014; 819:827–48.

Finocchiaro P, Beccali M, Gentile V. Experimental investigation of adsorption performances of an heat exchanger packed with silica gel for application in solar desiccant cooling systems. Proceedings of OTTI 5th Solar Air-Conditioning Conference, Black Forest: 25 – 27 Sept 2013, p. 210-215

Finocchiaro P, Beccali M, Lo Brano, Gentile V. Monitoring results and energy performances evaluation of freescoo solar DEC systems. SHC 2015 International Conference on Solar Heating and Cooling for Buildings and Industry Energy Procedia 2015;

PAPER ID 10796
Assessment of a Solar Powered Refrigerator Equipped with Thermal Storage for a Dairy Application

Adriana Coca-Ortegón[1], Victor Torres-Toledo[2], Joachim Müller[2], Alberto Coronas[1]

[1]Universitat Rovira i Virgili, Department of Mechanical Engineering, Tarragona (Spain)

[2] Universität Hohenheim, Agricultural Engineering Institute, Stuttgart (Germany)

Abstract

Typical agro-food value chains use electric refrigeration systems. However, in many non-industrialized countries, the cold chain is often not guaranteed due to lack of electricity access or unreliable electricity grids. In such cases, refrigeration systems must be equipped with electrical backups or other form of energy storage.

This study analyses the use of a commercial available vapour-compression horizontal refrigerator for small-scale cheese processing system. The studied refrigerator of 350 litres capacity is powered by photovoltaic panels, which provide electricity to a DC compressor. Encapsulated phase change materials were incorporated to the system as energy storage option, for a reliable operation at temperature at 11°C. This operating temperature is suitable for the analysed product, but it is also suitable for other agro-food applications, such as the preservation of fruits and vegetables. In particular, this study evaluates the incidence of the incorporation of Phase Change Materials on the stratification temperature inside the refrigerator, the raise temperature time of the refrigerated product, the number of on-off cycles of the compressor, the COP of the system, and the sizing of the conventional storage system with electrical batteries.

Keywords: Solar PV collectors, Compression refrigeration, Thermal energy storage, Phase change materials, Dairy sector

1. Introduction

Proper cold chain management in the agro-food sector is fundamental to preserve the quality of the products, reduce waste products, and also promote their effective commercialization (Gustavsson et al., 2012). Refrigeration systems in this sector typically use vapour-compression systems, powered by electricity, with direct expansion of refrigerant for small applications. In many developing countries, the cold chain cannot be guaranteed due to the lack of electricity supply or the frequent power outages. In such cases, refrigeration systems must be equipped with electrical backups or other form of energy storage.

In this context, several studies have analysed refrigeration systems powered by photovoltaic modules (Deshmukh and Kalbande, 2015; Katic et al., 2010) which use electrical storage and small size Direct Current (DC) compressors, eliminating the losses associated with DC / AC inverters. Energy storage plays a relevant role, especially when the cold production and energy demand are not matching (Dincer and Rosen, 2011; Lott and Kim, 2014). The use of Phase Change Materials (PCM) as a thermal energy storage option in this type of systems, can eliminate or reduce the size of the traditional electrical storage with lead-acid batteries (Pedersen and Katic, 2016). This type of electrical-storage has less useful life, generates a greater environmental impact, and in many cases has higher cost than some thermal storage options.

The integration of PCM into direct-expansion refrigeration systems can be done at the condenser as well as at the evaporator level. The integration at the evaporator level should consider factors such as the type of evaporator, its location within the cooled space, and the air diffusion system. In this regard, different studies have analysed the use of PCM in domestic and commercial refrigerators and freezers (Alzuwaid et al., 2015; Azzouz et al., 2008; Oró et al., 2012; Yusufoglu et al., 2015). In general, the results indicate that PCM provide more stable temperatures, a greater system autonomy and energy savings for refrigerators with non-regulated compressors. Most of these studies have been performed at typical operating temperatures of 4°C and -18°C, for refrigerators and freezers respectively, and in some cases without stored product; so we considered that it is convenient to carry out studies and develop models closer to the real conditions for each type of application.

doi:10.18086/swc.2017.28.02 Available at http://proceedings.ises.org

In this line, the present study analyses the performance of a horizontal refrigerator, of 350 litres of capacity, with a direct-current compressor powered by photovoltaic modules. The refrigerator will be used later in a small-scale cheese processing at an operating temperature of 11°C. This operating temperature is suitable for the analysed product, but also for other agro-food applications, such as preservation of fruits and vegetables. The refrigerator has been adapted for storing the product, as well as for the incorporation of encapsulated PCM, with a phase change temperature between 5 and 6°C. In particular, this study evaluates the incidence of the incorporation of PCM on the stratification and temperature stability inside the refrigerator, the raise temperature time of the refrigerated product, the number of on-off cycles of the compressor, the COP of the system, and the sizing of the conventional storage system with electrical batteries.

Nomenclature

H	Specific Enthalpy [kJ kg^{-1}]	η	Efficiency
Q	Heat [J]	D_t	Door open time factor [-]
q	Heat flow rate [W]	D_f	Door flow factor [-]
Q_T	Total thermal load [J]	E	Effectiveness of doorway protective device [-]
Q_{Losses}	Transmission heat gains [J]	a	Parameter "a" of photovoltaic model [-]
Q_{Pr}	Product thermal load [J]	F	Fractional state of charge of battery [-]
Q_{Int}	Heat gains due to internal equipment [J]		
Q_{Inf}	Infiltration heat gains [J]	**Subscripts**	
$Q_{Losses,d}$	Transmission heat gains for a day [J]	*ex*	Exterior
Q_{Useful}	Useful heat [J]	*in*	Interior
m	Mass [kg]	*p*	Time interval
T	Temperature [K]	*Ref*	Refrigerator
A	Area [m^2]	*air*	Air
x	Thickness [mm]	*PCM*	*Phase change material*
W	Electricity consumption [J]	*s*	Solid
w	Power [W]	*l*	Liquid
V	Voltage [V]	*S*	Series
I	Current [A]	*P*	Parallel
I_{SD}	Inverse saturation current of the diode	*F*	Photovoltaic
t	Time [s]	*i*	Initial
c_p	Specific heat [J kg^{-1} K^{-1}]	*f*	Final
k	Thermal conductivity [W m^{-1} K^{-1}]	*r*	Regulator
h	Convection heat transfer coefficient [W m^{-2} K^{-1}]	*b*	Battery
U	Global heat transfer coefficient [W m^{-2} K^{-1}]	*d*	Discharging
COP	coefficient of operation [-]	*c*	Charging

2. Methodology

2.1 Description of system and analysed application

The studied system is located in the district of Nyanza (Kenya), with a latitude of 0.08°N, longitude of 35.06°E, and 1914 m of altitude. The system consists of a horizontal refrigerator (Fig.1), which will be installed in a processing room, under controlled temperature between 21 and 25°C. The refrigerator is equipped with a direct current (DC) Compressor, with refrigerant R134a. The system will be powered by a multi-crystalline photovoltaic module, and has two types of energy storage: (1) Electrical storage with conventional lead-acid batteries, with a charge controller, and (2) Thermal energy storage with phase change materials, arranged next to the interior walls of the spaced refrigerated, since the evaporator is embedded in them.

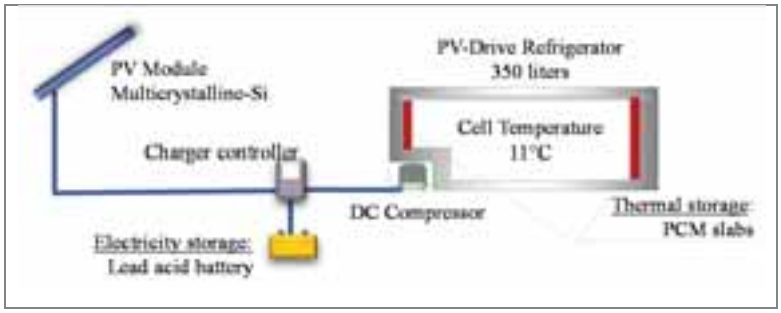

Fig. 1: Scheme of the system

The refrigerator was adapted to store the product (cheeses), incorporating four vertical structures that allow to process up to 16 kg of cheeses, and using forced convection with two small power fans installed in the upper area of the refrigerator.

2.2 Experimental setup for testing refrigeration cell

For performing this study, the refrigerator was tested in a climatic chamber taking measurements before and after installing the PCM. Taking into account that in real conditions the refrigerator will operate in an air-conditioned room, the tests were performed for an ambient temperature of 25°C and a relative humidity between 40 and 60%. During the tests, water was used as a refrigerated product, and in a later stage, a specific mixture will be used to simulate the system in conditions closer to the application.

The experimental setup is shown in Figure 2. The horizontal refrigerator, 350 litters capacity, is equipped with a direct current compressor, Secop BD 35F, with refrigerant R134a and a Danfoss 101N21C controller. The power supply in the test was performed at 12 volts, using a regulated source voltage. The phase change material (PCM) was incorporated in the internal side of the refrigerator, since the evaporator of the refrigerator is embedded in the wall.

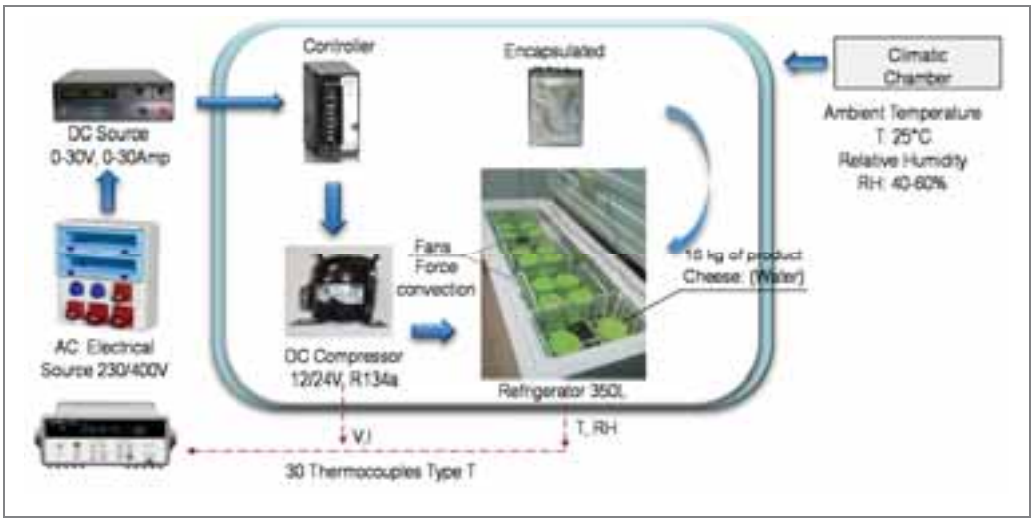

Fig 2: Experimental setup of refrigerator cell

The PCM-encapsulation consists of polyethylene bags with an aluminium layer, placed on a 1mm steel-sheet (Fig 3(a)) attached to the inner side of the refrigerated space (Fig 3(b)), since the evaporator is embedded in the refrigerated space walls. The melting temperature of the PCM, manufactured by Rubitherm, is between 5 and 6 ºC and the operating temperature inside the refrigerator is 11±2°C. The PCM slab has a thickness of 8mm, and the final mass installed was 8.9 kg.

(a) Detail of phase change material on one of the walls of the refrigerator.

(b) Refrigerator with PCM next to Evaporator-Wall

(c) Refrigerator, inside of the climatic chamber at the laboratory

Fig. 3: Details of the experimental setup of integration of PCM

In total, 30 T-type thermocouples were used to measure the temperatures in the product (cheese), PCM, and refrigerator walls, and ambient temperature. Current and voltage measurements were also taken in order to quantify the electrical consumption, with a measurement interval of 1 minute. Table 1 summarizes the number and types of sensors used in the experimentation.

Tab. 1: Resume of sensors used in the experimental setup of refrigeration cell

Type of sensor		Number of sensors	Location
Temperature sensors	T-type thermocouples	10	Interior walls of refrigerator
		10	Product
		9	Encapsulated PCM
		1	Climatic chamber
Electricity sensors	Voltage: Voltage Regulated Source Output	1	CC Circuits
	Current: Hall effect sensor, Arduino ACS712	2	CC Circuit 1: Compressor, CC Circuit 2: Fans
Humidity sensors	Relative humidity sensor	1	Climatic chamber

2.3 PCM selection and integration

The integration of PCMs in domestic and commercial refrigerators and freezers can be carried out through active and passive solutions. Active solutions are often more effective than passive ones in the heat transfer process; however, passive solutions are simpler for implementation.

Passive integration solutions can be done at the condenser as well as at the evaporator level. The integration at the evaporator level should consider factors such as the type of evaporator, its location within the cooled space, and the air diffusion system.

In relation to this, several previous studies have analysed different options such as: The installation of a PCM slab next to the external side of the evaporator and embedded in the wall of the refrigerator (Azzouz et al., 2008; Yusufoglu et al., 2015); the arrangement of PCM slabs inside freezers with internal evaporator (Oró et al., 2012), the arrangement of PCM next to the condenser, and also the arrangement of PCM in the refrigeration circuit (Cheng et al., 2011). In the case studied, the refrigerator has a wall evaporator, so the integration option adopted consists of placing a slab of the PCM on the inner wall of the refrigerator.

Tab. 2: Main Characteristics of Phase Change Material (PCM) Selected

Description	Value
Manufacturer	Rubitherm
Reference of the substance	RT5HC, Organic
Type of Substance	Paraffin, C5-C20
Phase change Temperature Range [°C]	5 to 6
Thermal storage capacity [kJ/kg]	250 (-2 to 13°C)
Specific heat capacity (solid) [J kg^{-1} K^{-1}]	2000
Specific heat capacity (liquid) [J kg^{-1} K^{-1}]	2000
Density (solid, -15°C) [kg m^{-3}]	880
Density (liquid, 20°C) [kg m^{-3}]	760
Thermal conductivity (solid) [W m^{-1} K^{-1}]	0.2
Thermal conductivity (liquid) [W m^{-1} K^{-1}]	0.2

Since the temperature required for the refrigerated product is 11 ° C, the evaporator temperature should be about 0 ° C, in order to provide a suitable temperature difference for an effective heat transfer process. In this case, the phase change temperature of the PCM should have a value between the evaporator temperature and the required product temperature. This ensures that the PCM material changes phase, without cooling the refrigerated product below the required temperature range.

In this way, the PCM finally selected is the RT5HC manufactured by Rubitherm, with a phase change temperature

between 5 ° C and 6 ° C. Table 2 presents the main characteristics of this material. The material is organic (Paraffin, C5-C20), and does not have a single-phase change temperature, as it happens, in pure substances. The main advantages of this type of PCM compared to the hydrated salts are the greater stability, and that the crystallization process requires less sub cooling of the material.

2.4 Data analysis and simulation

2.4.1 Scenarios considered

The experimental data provide information about the system for two scenarios: (1) Refrigerator without PCM and (2) Refrigerator with PCM. For both scenarios, two types of day were analysed: (1) "Initial day", in which the product is cooled from an initial temperature (25°C) to the required final temperature (11°C) , and (2) "Maintenance day" type, in which the product is only maintained within the required operating temperature range (11±2°C).

Base on the experimental data, two electrical power demand profiles were created for a full month of operation (With PCM and Without PCM). The month selected for analysis was November, since this month has the lowest photovoltaic production. The TRNSYS 16 software was used as a simulation tool for photovoltaic production, and other complementary analysis was carried out by using Matlab.

2.4.2 Total thermal load

Total thermal load (Q_T) was calculated according to ASHRAE (eq.1), which includes: Transmission heat gains or losses through the refrigerator enclosures (Q_{Losses}), the Product thermal load (Q_{Pr}), the heat gains due to internal equipment (Q_{Int}) and the infiltration heat gains (Q_{Inf}).

$$Q_T = Q_{Losses} + Q_{Pr} + Q_{Int} + Q_{Inf} \quad \text{(eq.1)}$$

Transmission heat gains or losses through the refrigerator enclosures (Q_{Losses}) were estimated according to equation 2 (ASHRAE, 2010; Azzouz et al., 2008), where U_{Ref} corresponds to the global heat transfer coefficient of the refrigerator, A_{Ref} corresponds to the refrigerator area, $\Delta T_{Ref,p}$ is the temperature difference between the inside face of the cooler and the outside air at each time interval (p), and the Δt corresponds to the time step of the measurement or simulation.

$$Q_{Losses} = \sum_{p=0}^{P} U_{Ref}.A_{Ref}.\Delta T_{Ref,p}.\Delta t \quad \text{(eq.2)}$$

The overall heat transfer coefficient of the refrigerator was estimated according to equation 3, where x_n and k_n correspond to the thickness and thermal conductivity of the wall layer "n", and h_{int} and h_{ext} correspond to the interior and exterior convection heat transfer coefficients.

$$U_{Ref} = \frac{1}{\frac{1}{h_{ex}} + \frac{x_1}{k_1} + \frac{x_1}{k_1} + .. + \frac{x_n}{k_n} + \frac{1}{h_{in}}} \quad \text{(eq.3)}$$

The layers considered on the refrigerator wall are presented in Table 3. The overall coefficient U_{Ref} is 0.4712 $Wm^{-1}K^{-1}$ without PCM and 0.4623 $Wm^{-1}K^{-1}$ with PCM.

Tab. 3: Properties of the materials of the enclosures of the refrigerator

Layer Number	Material	Thickness [mm]	Thermal Conductivity [$Wm^{-1}K^{-1}$]
1	Steel	1.5	50

2	Polyurethane	60	0.050
3	Aluminium	1	230
4	PE film	0.15	0.33
5	PCM	8	0.2
6	PE film	0.15	0.33
7	Steel	1	50

The heat extracted from the product (Q_{Pr}) includes only sensible heat for this application, since the refrigerated product does not change phase. Q_{Pr} is calculated by applying the basic expression of equation 4, where C_p and m correspond to specific heat and mass of the material, while T_i and T_f are the temperatures corresponding to the initial and final time of the evaluated period.

$$Q = C_p.m.(T_i - T_f) \quad \text{(eq.4)}$$

In relation to the heat gains due to internal equipment (Q_{Int}), the calculation considered two small power fans (1.8W) used for forced convection inside the refrigerated cell. Finally, the infiltration heat gains (Q_{Inf}) were estimated for a full day of operation of the refrigerator, applying equation 5 (ASHRAE, 2010), which includes the transmission heat gains in the enclosures for a stable day of operation ($Q_{Losses,d}$), the door open time factor (D_t), the door flow factor (D_f), and the effectiveness of doorway protective device (E).

$$Q_{Inf} = Q_{losses,d}.D_t.D_f(1 - E) \quad \text{(eq.5)}$$

2.4.3 Power demand profiles

The profiles of the electric power demand were defined based on experimental data for the two scenarios analysed (With PCM and without PCM). To do this, the power was calculated by multiplying the voltage (V) and current (I) measurements at each time step.

2.4.4 Heat transferred in the PCM

The total heat transferred in the PCM (Q_{PCM}) was estimated multiplying the mass of the installed PCM by the variation of enthalpy for each time step, from the initial to the final one, according to the equation 6.

$$Q_{PCM} = \sum_{p=1}^{P} m_{PCM}.\Delta H_{PCM,p} \quad \text{(eq.6)}$$

The specific enthalpy, , was calculated as a function of the temperature of the phase change material, according to equation 7 (Ozisik, 1993), where C_p is the specific heat capacity of the PCM, L is the specific heat of fusion, and the mushy region is between the temperatures T_s and T_l. When the temperature is lower than T_s, the material is in solid state, and when the temperature is higher than T_l, the material is in a liquid state.

$$H = \begin{cases} C_pT & for\ T < T_s\ Solid\ region \\ C_pT + \dfrac{T - T_s}{T_l - T_s}L & for\ T_s \le T \le T_l\ Mushy\ region \\ C_pT + L & for\ T > T_l\ Liquid\ region \end{cases} \quad \text{(eq.7)}$$

2.4.4 PV production

The photovoltaic production profile was calculated by using the component 194 available in the dynamic simulation software TRNSYS 16. This component uses the 5-parameter model (Duffie and Beckman, 2013), that consists of a voltage generator, a diode connected in parallel that represents the semiconductor material, a series resistance, and a parallel resistance.

$$I = I_F - I_{SD}.\left(e^{\frac{V+I.R_S}{a}} - 1\right) - \frac{V + I.R_S}{R_P} \quad \text{(eq.8)}$$

The output current of the photovoltaic module (I) is calculated by applying equation 8, where it is necessary to know the 5 parameters of the model: (1) The series resistance (R_S), (2) parallel Resistance (R_P), (3) the current produced by photovoltaic effect (I_F), (4) the inverse saturation current of the diode (I_{SD}), and finally the factor "a". These parameters can be calculated by using the manufacturer specifications at standard reference conditions according to Eckstein (1990) and De Soto et al (2006).

2.4.5 Electric battery and regulator

The electric battery as well as the load regulator/controller were simulated using the algorithm applied in the "Type 48b", available in the dynamic simulation software TRNSYS 16. In this model, the charging of battery is carried out by applying a global efficiency value (η_b); the regulator charges the battery while the fractional state of charge *(F)*, is between a minimum value (F_d) and a maximum value (F_c). In addition, the battery bank can be discharged when the fractional state of charge is below of a specific value (F_b). On the other hand, a direct current (DC / DC) conversion is performed on the regulator/controller with a global efficiency value (η_r). Table 4 presents the parameters used in the analysed case.

Tab. 4: Values of Fractional state of charge and efficiencies applied in the electric battery and the regulator model

Description	Value
Minimal value of Fractional state of charge (F_d)	0.3
Maximum value of fractional state of charge (F_c)	1.00
Fractional of Fractional state of charge for starting discharging the battery bank (F_b)	0.85
Charging battery efficiency (η_b)	0.85
Regulator efficiency (η_r)	0.95

2.4.6 Performance indicators

The system performance was analysed by reviewing the following variables and indicators: (1) the temperature stratification of the refrigerated product, (2) the number of on-off cycles of the compressor, (3) the rise temperature time and (4) the coefficient of operation of the system (COP). In addition, the process of charging and discharging of PCMs was also studied.

The temperature stratification of the product was revised from the experimental data, using the information of nine thermocouples in the refrigerated product arranged at three different heights and at different points in the refrigerator.

The rise temperature time was measured by turning off the power supply and quantifying the total time in which the temperature of the refrigerated product reaches the maximum permitted value. These measurements were made according the standard EN 62552 for household refrigerating appliances (IEC, 2013).

$$COP = \frac{Q_{Useful}}{W} \quad \text{(eq.9)}$$

The coefficient of operation (COP) of the system was calculated by applying equation 9, where Q_{Useful} corresponds to the effective heat extracted by evaporator, and W corresponds to the electricity consumption of the refrigerator during the period of time evaluated. The effective heat extracted by the evaporator was estimated by adding the heat extracted from the product, the heat gains by transmission through the enclosures, and the infiltration heat gains. In this case, the experimental temperature data measured minute by minute are used and equations 2 to 5 are applied.

In relation to the charging and discharging processes of the PCM, the transferred heat was also calculated from experimental temperature data and applying equations 6 and 7.

3. Results and discussion

3.1 Power demand

The electric power demand of the refrigerator was measured during 48 hours for the two analysed scenarios (with PCM and without PCM). According to these data, the power demand profile were elaborated for two types of days: (1) "Initial day" (Fig 4a), in which the product is cooled from an initial temperature of 25 ° C to the required final temperature of 11°C, and (2) "Maintenance day" (Fig 4b), in which the product is only maintained within the required operating temperature range (11±2°C).

The average power for the "Without PCM" scenario is 38.7W, with a minimum of 33.2W and a maximum of 45.8W, while the average power for the "With PCM" scenario is 41.6W with a minimum of 35.9W and a maximum of 48.4W. This implies that the incorporation of PCM in the refrigerator increases the average power demanded in 7%.

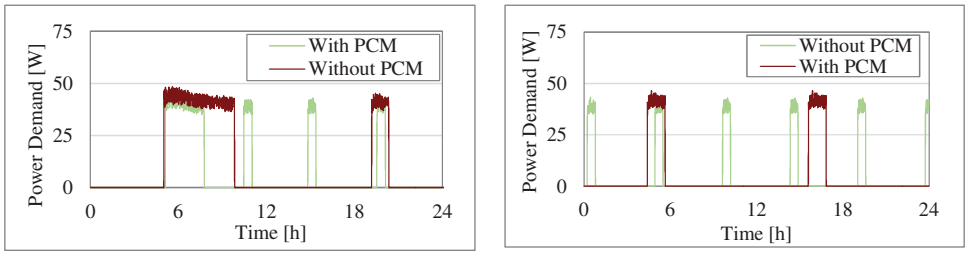

a) Initial day (b) Maintenance day

Fig. 4: Power demand profile for Initial and Maintenance day, with and without PCM

In relation to the electricity consumption, when the refrigerator does not have PCM, the values obtained are 709 kJ and 410 kJ for the "Initial day" and "Maintenance day" respectively. When the PCMs are incorporated in the refrigerator, these electricity consumption values are 929 and 396 kJ for the "Initial day" and "Maintenance day" respectively. Finally, for the analysed month of operation of the system, there is a slight reduction of 1.5% in the electricity consumption when the PCM are installed.

3.2 PV Production

Taking into account the daily demand for electrical energy, the proposed photovoltaic installation consists of a single multi-crystalline type module, 50Wp in STC (37WP in NOTC). The azimuth of the module is 0°, and the slope is 15°, this value is slightly higher than the latitude in order to improve the maintenance conditions. Fig 5 shows the production of the photovoltaic module, simulated in TRNSYS 16, for the month analysed (November). The average daily production of electricity is 870 kJ, with a minimum of 692 kJ on the 30th of the month, and a maximum of 1024 on the 3rd of the month.

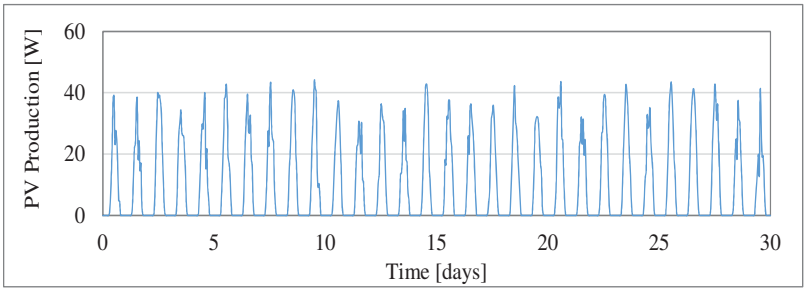

Fig. 5: Electricity production of the photovoltaic installation for analysed month

The electricity production does not match the demand, as shown in Figures 6a and 6b for the “Initial day” and the "Maintenance day" type respectively. Therefore, the installation must incorporate energy storage (thermal or electric) as is usually for the off-grid photovoltaic installations.

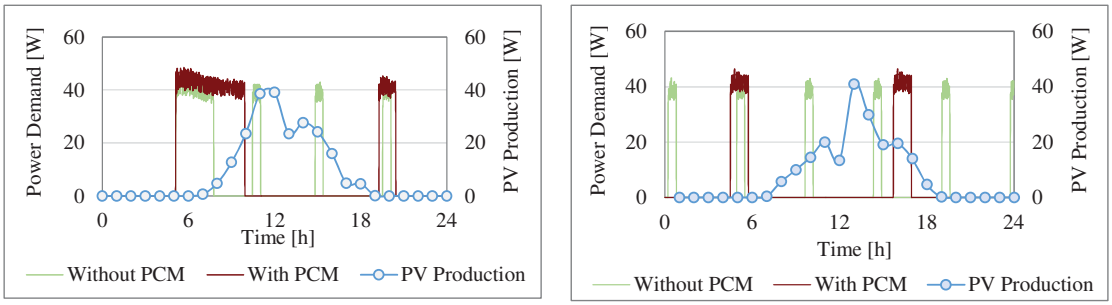

a) Initial day (b) Maintenance day

Fig. 6: Mismatch between electric production and power demand for initial and maintenance day

3.3 Evolution and stratification of product temperature

Figure 7 shows the evolution of the temperature in the top zone of the refrigerator as well as in the bottom zone, for the analysed scenarios (With PCM and without PCM). According to this information, the product temperatures in both refrigerator zones (top and bottom) are maintained within the required operating range (11 ± 2 ° C). The maxim temperature difference between the top and bottom zones is 5% for the "Without PCM" scenario and 6% for the "With PCM" scenario for the Maintenance cycles.

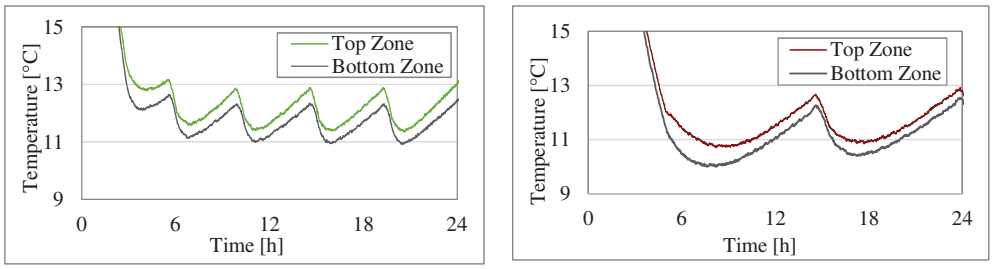

a) Without PCM (b) With PCM

Fig. 7: Product temperature evolution for Initial day

The data allow concluding that the influence of PCMs on stratification of product temperature is low. However, the temperature of the refrigerated product in the "With PCM" scenario is lower than the temperature in the "Without PCM" scenario. This difference of temperature between both scenarios reaches a value of 1.5°C.

The lower temperature of the "PCM" scenario is because the PCM is at a lower temperature than the product, so when the compressor stops, the heat transfer process continues until the equilibrium is reached. Therefore, it is advisable to take into account this behaviour in order to improve the control of the product temperature in the Scenario "With PCM".

3.4 Number of on-off cycles of the compressor

There are two types of operating cycles In the operation of the refrigerator: The "Initial Cycle" in which the product is cooled from the initial temperature (25 ° C) to set temperature (11 ° C); and the "Maintenance Cycle" in which the product is maintained in the required temperature range (11 ± 2 ° C). In both cycles, the compressor is "on" until the set-point temperature is reached, and then it continues "off" until the product temperature reaches the maximum allowed value.

According to the power demand profiles presented item 3.1, it is possible to verify that the number of off-on operations of the compressor are reduced from 4 to 2 for the "Initial Day" of operation, and from 5 to 2 for the "Maintenance Day" type. This implies that during the studied month, the number of off-on operations of the compressor decrease 59.7%, from 149 to 60 operations. This fact has a positive impact in the useful life of the compressor.

3.4 COP of the system

The COP was calculated according to 2.4.6, when the useful heat extracted by the evaporator was estimated by adding the heat extracted from the product, the heat gains by transmission through the enclosures, and the infiltration heat gains. The calculations were carried out for the "Initial" and "Maintenance" cycles, and for the two analysed scenarios (With PCM and Without PCM). Table 5 summarizes the results for the two analysed scenarios.

Tab. 5: COP of System

Cycle	COP Without PCM	COP With PCM
Initial cycle	2.19	1.90
Maintenance cycle	1.83	1.99

We can see that the scenario “With PCM” has a lower COP than the scenario “Without PCM” for the Initial cycle. However, the result is just the opposite when the maintenance cycle is analysed. This is because the smaller number of off-on operations of the compressor finally have a positive impact on the efficiency of the system, as some previous studies have verified.

3.5 Charging/discharging process in PCM

The charging and discharging process of PCMs can be analysed by monitoring the temperature in the encapsulation bags of PCM. Figure.8 shows the evolution of the average temperature of the PCMs located in the top, middle, and bottom zones of the refrigerator wall.

This information indicates that the PCMs located in the top and middle zones of the refrigerator wall reach the temperature required to change the phase (less than 5°C), and can storage sensible and latent thermal energy. However, the PCMs located in the bottom zone of the refrigerator wall do not reach the required temperature and only storage sensible thermal energy. This result makes necessary to adjust the integration solution of the PCMs in the bottom zone of refrigerator wall; one option can be to install insulation material in this part instead of the PCMs, and another option can be to use a PCM with a different phase change temperature.

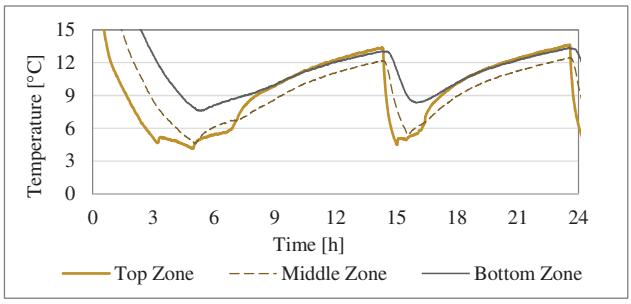

Fig. 8: Temperature evolution in the PCM

In relation to the energy rate transferred during the charging /discharging process of the PCM, the values obtained for the maintenance cycle were 177 W for charging process, and 44 W for the discharging process. These values can also be improved by other actions, such as the use of materials with better thermal conductivity to carry out the integration of PCMs.

3.6 Raise temperature time

The raise temperature time, correspond to the time from the compressor stops (off), until the refrigerated product reaches the maximum allowable temperature. The measurements were made according to “The Rise Temperature Test” included in the standards EN 62552 for household refrigerating appliances (IEC, 2013). Table 6 presents the duration of the different cycles (“Initial” and “Maintenance”), according to the state of the compressor ("on" and "off") and for each analysed scenario ("With PCM" and "Without PCM").

Tab. 6: Cycle duration time and raise temperature time

Description	Without PCM [h]			With PCM [h]		
	On	Off	Total	On	Off	Total
Duration of Initial Cycle	2.63	2.72	5.35	4.78	9.38	14.16
Duration of Maintenance Cycle	0.55	4.07	4.62	1.18	8.08	9.26
Raise Temperature Time		5.01	5.01		11.31	11.31

In general, the incorporation of the PCM in the internal side of the refrigerator increases the duration of the different cycles as well as the raise temperature time of the refrigerated product. According to these data, the raise temperature time changes from 5.01 h to 11.31 h; that means an increase of 126%. Thanks to this, the size of the energy storage with the electric batteries can be reduced as item 3.7 exposes.

3.7 Sizing of electrical battery

In order to sizing the electric storage with lead-acid batteries, we first consider the results of daily electrical consumption, presented in 3.1, and secondly we select a four-day autonomy for the system. According to this, for the “Without PCM” scenario, a battery bank should have a capacity 2345kJ, which correspond to 51Ah C20 for a voltage of 12V and a discharging time of 13.1h.

On the other hand, for the "With PCM" scenario, the initial capacity of the battery bank would be 2263kJ, which can be adjusted, taking into account the increase of the raise temperature time of the refrigerated product in this scenario. In this way, the capacity of battery bank can be reduced to 1996 kJ, which correspond to 46 Ah C20, for a voltage of 12V and a discharging time of 18.5h.

The result means a decrease of 10% in the size of the electric battery bank when the “With PCM” scenario is compared with the “Without PCM scenario”. This reduction is low, and the system should be optimized in order to improve the performance of the thermal storage with PCM.

Because of this, the experimental results will be used for validating a model and analysed different parameters in the system, such us the thickness of the PCM slab, the thickness of the insulation, and the velocity of the fans for the force convection.

4. Conclusions

This study analysed the performance of a commercial horizontal refrigerator, of 350 litres of capacity, with a direct-current compressor powered by a photovoltaic module. The refrigerator will be used later in a small-scale cheese processing at an operating temperature of 11°C. The system has an electrical storage with a lead-acid batteries and also the refrigerator incorporates a thermal storage with an inner slab of PCM, next to evaporator-wall, with a thickness of 8mm and phase change temperature between 5 and 6°C.

The analysis considers two scenarios, one is the refrigerator “Without PCM” and the other is the refrigerator “With PCM”. From the experimental data, two electrical power demand profiles have been created for a full month of operation (With PCM and Without PCM). The month selected for analysis was November, since this month has the lowest photovoltaic production throughout the year.

The incorporation of PCM, does not have a high impact in the stratification of product temperature, nevertheless the temperature of the refrigerated product is lower when the Refrigerator has the PCM slab. This is because the discharging process of the PCM continues once the compressor stops in each cycle. Taking into account, this behaviour the control system of product temperature can be improved.

Regarding to charging process of PCM, it was possible to verify that the PCM located in the top and middle zone of the refrigerator wall reach the temperature required for the freezing and took advantage of the latent energy storage; however, the PCM located in the lower do not reach the required temperature. This result makes necessary to adjust the integration solution of the PCMs in the bottom zone of refrigerator wall in order to improve the analysed thermal storage option.

The PCM gives more inertia to the system, since the number of daily on-off cycles of the compressor, has a reduction of 59.7% for an analysed month. This fact has an indirect positive impact in the useful life of the compressor and in the electricity consumption. With regard to this electricity consumption there is an increase of 31.0% in the "Initial cycle" and a decrease of 3.5% in the "Maintenance cycle". Finally, for the full-analysed month, there is a slight reduction of 1.5% in the electricity consumption.

As far the raise temperature time concern, this value increases 126%, going from 5.01h to 11.31h. This implies that conventional energy storage with electric batteries can be reduced about 10% for the analysed application. This reduction is low, and the system should be optimized.

5. Acknowledgement

The authors are grateful to URV-Solidaria, and AGAUR (FI-DGR 2017), program co-financed by the European Social Funds.

6. References

Alzuwaid, F., Ge, Y.T., Tassou, S. a., Raeisi, A., Gowreesunker, L., 2015. The novel use of phase change materials in a refrigerated display cabinet: An experimental investigation. Appl. Therm. Eng. 75, 770–778. doi:10.1016/j.applthermaleng.2014.10.028

ASHRAE, 2010. Handbook - Refrigeration. American Society of Heating, Refrigerating and Air-Conditioning Engineers (ASHRAE), Atlanta (US).

Azzouz, K., Leducq, D., Gobin, D., 2008. Performance enhancement of a household refrigerator by addition of latent heat storage. Int. J. Refrig. 31, 892–901. doi:10.1016/j.ijrefrig.2007.09.007

De Soto, W., Klein, S. a., Beckman, W. a., 2006. Improvement and validation of a model for photovoltaic array performance. Sol. Energy 80, 78–88. doi:10.1016/j.solener.2005.06.010

Deshmukh, S., Kalbande, S., 2015. Performance Evaluation of Photovoltaic System Designed for DC Refrigerator. Int. J. Sci. Res. 4, 18–23.

Dincer, I., Rosen, M.A., 2011. Thermal Energy Storage: Systems and Applications. Cap 1 Partial, Second Edi. ed. John Wiley & Sons, United Kingdom.

Duffie, J., Beckman, W., 2013. Solar engineering of thermal processes, 4th Editio. ed. John Wiley & Sons, Wisconsin-Madison.

Eckstein, J.H., 1990. Detailed modelling of photovoltaic system components. University of Wisconsin - Madison.

Gustavsson, J., Cederberg, C., Sonesson, U., Otterdijk, R., Meybeck, A., 2012. Losses and waste of food in the world, Nucleus. Roma, Italy. doi:10.3738/1982.2278.562

IEC, 2013. EN 62552 Household refrigerating appliances - Characteristics and test methods.

Katic, I., Pedersen, H., Jacobsen, E., 2010. Standalone cool/freeze cluster driven by solar PV energy.

Lott, M.C., Kim, S.-I., 2014. Technology Roadmap - Energy storage. doi:10.1007/SpringerReference_7300

Oró, E., Miró, L., Farid, M.M., Cabeza, L.F., 2012. Improving thermal performance of freezers using phase change materials. Int. J. Refrig. 35, 984–991. doi:10.1016/j.ijrefrig.2012.01.004

Ozisik, M.N., 1993. Heat Conduction, Second Edi. ed. John Wiley & Sons, Inc., New York. doi:10.1002/9781118411285

Pedersen, H., Katic, I., 2016. Direct drive solar coolers, in: 12th IIR Gustav Lorentzen Natural Working Fluids Conference. Papaer ID 1070. Edinburgh, p. 8. doi:10.18462/iir.gl.2016.1070

Yusufoglu, Y., Apaydin, T., Yilmaz, S., Paksoy, H.O., 2015. Improving performance of household refrigerators by incorporating phase change materials. Int. J. Refrig. 57, 173–185. doi:10.1016/j.ijrefrig.2015.04.020

Efficient Solar Cooling by Using Variable-Effect LiBr-H_2O Absorption Chiller and Linear Fresnel Solar Collector with Cavity Receiver

Yanjun Dai, Jishuai Ma

Institute of Refrigeration and Cryogenic Engineering, Shanghai Jiao Tong University, Shanghai (China)

Abstract

A solar cooling system, which mainly consists of a variable-effect LiBr-H_2O absorption chiller and arrays of linear Fresnel solar collector, has been investigated and analyzed by experiment. The 50 kW variable-effect absorption chiller, which can work from single to double effect mode continuously, depending on the temperature level of the linear Fresnel solar collector array, can obtain a COP span of 0.6–1.15. Compared to the conventional single- and double-effect solar absorption cooling, the solar variable-effect cooling is capable of operating for a longer time, leading to more cooling output. Such solar cooling plant has been tested and analyzed in depth. The experimental results show that thermal efficiency of the linear Fresnel solar collector is approximately 58.8%, and the operation temperature is as high as 147 °C. Thermal COP of the variable-effect LiBr-H_2O absorption chiller varies between 0.84–1.05 depending on the solar collector temperature. The solar cooling plant can convert solar radiation to cooling output accompanied by a solar COP span of 0.41–0.53 under given conditions.

Keywords: Solar cooling, variable effect, absorption chiller, Linear Fresnel solar collector, performance evaluation.

1. Introduction

Solar cooling is a promising approach to shift the peak of power grid due to its ability of converting effective solar radiation to cooling production which reducing the energy demand of city power grid. So far, it has been recognized as one of the best substitutes of conventional cooling, and is attracting more and more attention worldwide, especially in the regions with the hot and humid climate (Winston et al., 2014). Conventionally, a solar cooling plant is configured by single-effect LiBr-H_2O absorption chiller driven by stationary solar collectors (e.g. non-tracking flat plate or evacuated tubular solar collectors), or by double-effect LiBr-H_2O absorption chiller driven by concentrated solar collectors (e.g. trough or linear Fresnel solar collectors). For the first option, the conversion efficiency from solar radiation to cooling production (i.e. solar COP) is lower than 0.3. For the second option, the solar COP can be greatly upgraded due to the higher COP of double-effect chiller and high flux contributed by concentrated solar collector, however, the operation time of cooling output is limited because of a high driving temperature required by double-effect absorption chiller. To reach the target of high efficiency and longer time of solar cooling, it is urgent to develop a novel absorption chiller and the corresponding concentrated solar collector.

The predominant merit of linear Fresnel reflector (LFR) solar collector is the decrement manufacturing, operation and maintenance costs (Gharbi et al., 2011). LFR solar collector is becoming a potential method for solar thermal cooling and mid-temperature industrial utilization due to its simplicity in structural design and low investment cost. Chemisana et al. (2011, 2013) carried out a solar cooling system driven by LFR solar collector which provided thermal energy to a double effect LiBr-H_2O absorption chiller, where the rated COP of 1.35 and 150-170 °C driving temperature of chiller can be observed. The results showed that the LFR solar thermal cooling system has advantages and disadvantages. The advantageous is that a higher solar cooling COP can be realized with LFR solar collector under good conditions of solar irradiance. However, the disadvantageous in the system may be somewhat complex and expensive compared with the non-tracking solar cooling system. When comparing to evacuated tubular LFR collector, cavity receiver has its merits in cost benefit, and thermal stability, especially for pressure water cycle. Zhou et al., 2017 assessed

doi:10.18086/swc.2017.28.03 Available at http://proceedings.ises.org

the performance of a single/double hybrid effect absorption cooling system driven by linear Fresnel solar collectors with latent thermal storage, based on the parametric optimization. The variable-effect absorption refrigeration cycle previously proposed by Xu et al. (2013) indicates the COP of variable effect cycle increases with driving temperature. Based on the concept design, a 50 kW prototype of variable effect LiBr-H_2O absorption chiller was built and tested (Xu and Wang, 2016).

To date few reports of such similar detailed analysis of the performance in LFR solar thermal cooling system combined with the variable-effect absorption chiller has been produced. In this paper, an integrated LFR solar thermal cooling system with a variable-effect absorption chiller is introduced and studied experimentally. The individual test was carried out for major components including LFR solar collector arrays, and the variable-effect chiller. Finally, the solar COP of the entire cooling system was evaluated by dynamic test.

2. Description of the solar cooling system

The solar cooling system investigated in this paper is composed of a 50 kW variable-effect absorption chiller and LFR solar collector arrays with total aperture area of 144 m^2. In fact, the solar cooling system is originally a small part of a solar tri-generation system, for heating, cooling and power generation by using an ORC generator, shown in Fig. 1. Specifically, LFR solar collector arrays convert effective solar radiation to intermediate temperature heat, and then the heat is charged into a steam manifold that produces steam for the variable-effect absorption chiller (cooling), the ORC generator (power), and the domestic water (hot water). In this paper, the authors only focus on performance of the variable-effect absorption chiller driven by high-temperature steam heated by LFR solar collector arrays, outlined in Fig. 1.

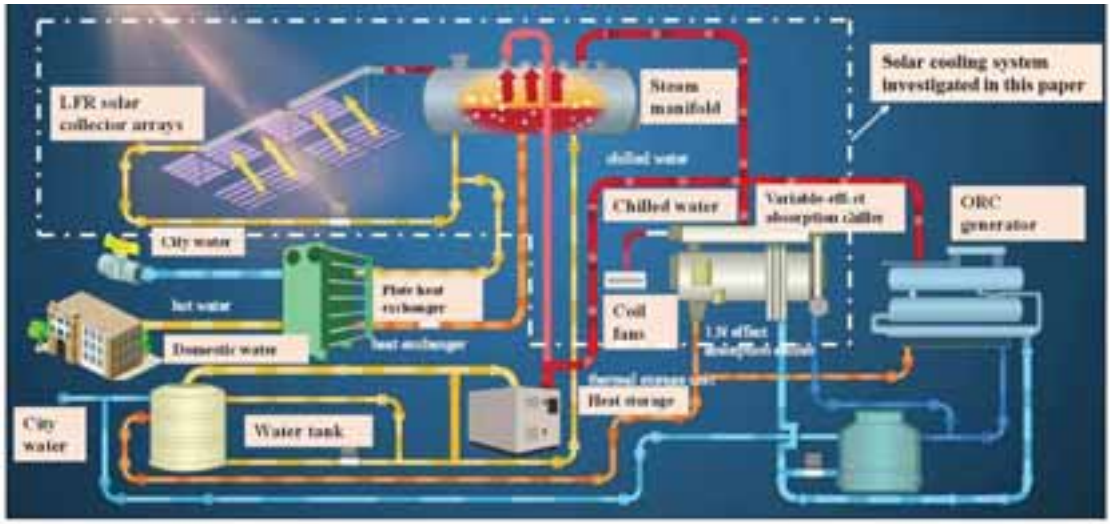

Fig. 1: Schematic diagram of the solar cooling plant with a variable-effect absorption chiller and LFR solar collectors

2.1. LFR solar collectors

A prototype of LFR solar collector employed steel tubular absorbers coated with selective absorption film was developed and serves as the thermal source. The schematic and prototype of LFR solar collectors are shown in Fig. 2.

The array of LFR collector consists of 8 individual LFR collector units, where each unit contains 12 rows of curved mirrors. The curved mirror was designed with an arch height of ΔH = 3 mm. To reduce the effect of shading and blocking caused by adjacent mirrors on the optical efficiency of LFR collector, the distance

between adjacent rows was set to be 7 cm based on the model proposed by Mathur et al. (1991). The semi-circle cavity receiver with reasonable optical efficiency, relatively low investment, operation, and maintenance costs (Xie et al., 2012) was located at the latitude of 4 m, where the semi-circle receiver is comprised of five copper pipes with the inner diameter of 38 mm. Selective black chromium coating was covered on the surface of absorber pipes with a ultra-white glass of 3 mm thickness. Besides, phenolic foam serves as the insulation material between absorber and steel frame to minimize the conductive heat loss. The structure and other main parameters of LFR collector are shown in Table.1.

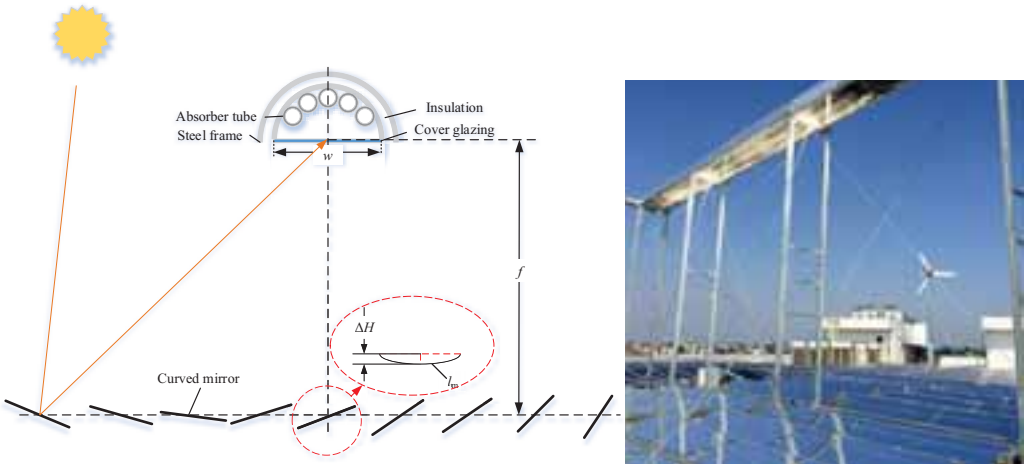

(a) (b)

Fig. 2: The schematic and photograph of LFR solar collectors: (a) schematic of the LFR solar collector, and (b) the prototype

Table 1: The geometric and thermos-physical properties of the LFR solar collector array

Component	Parameters	Value
Mirror array	Number of units	8
	Collector area of each unit	18 m^2
Curved mirror	Arch height	3 mm
	Mirror length	3 m
	Mirror width	50 cm
	Distance of the adjacent mirrors	7 cm
Cavity receiver	Altitude	4 m
	Inner diameter (D_i) of absorber tube	38 mm
	Aperture width (w)	53 cm
	Aperture area	1.59 m^2 (each LFR unit)
	Thickness of the cover glazing	3 mm
	Absorptivity	0.85
	Emissivity (at 353 K)	0.5

2.2. Variable-effect absorption chiller

The variable effect absorption chiller, which is configured by adding an additional low pressure generator for

harvesting the absorption heat, is the main section to improve the solar cooling efficiency. As is shown in Fig. 3, the main components of the chiller are presented. Fig. 3a (Xu et al., 2016) shows the thermodynamic cycle of the variable-effect absorption cooling. The variable absorption cooling works in three processes: (1) if the temperature of heat resource is enough high (> 140 °C), it works in double effect mode, and the chiller is a double effect absorption chiller; (2) if the temperature of heat resource is less than 100 °C, it works in single effect mode; (3) if the temperature level is in the range of 100-140 °C, the chiller works in the 1.N effect mode, namely, it can work almost linearly from single to double effect depending on the temperature level, thus the cooling output can be increased, in comparison with the normal single effect or double effect chiller, especially for solar cooling application. The key for realizing variable-effect absorption cooling is that the internal absorption heat recovery in the high pressure absorber, even when the temperature level can not effect complete operation of high pressure generator, it can still contribute some for cooling production by using the heat from the high pressure absorber to the additional low pressure generator. The detailed thermodynamic process of the solar energy conversion and the cooling production is investigated. The prototype of the variable-effect absorption chiller is shown in Fig. 3b. The detailed parameters of the 50 kW variable-effect absorption chiller were reported by Xu et al., 2015.

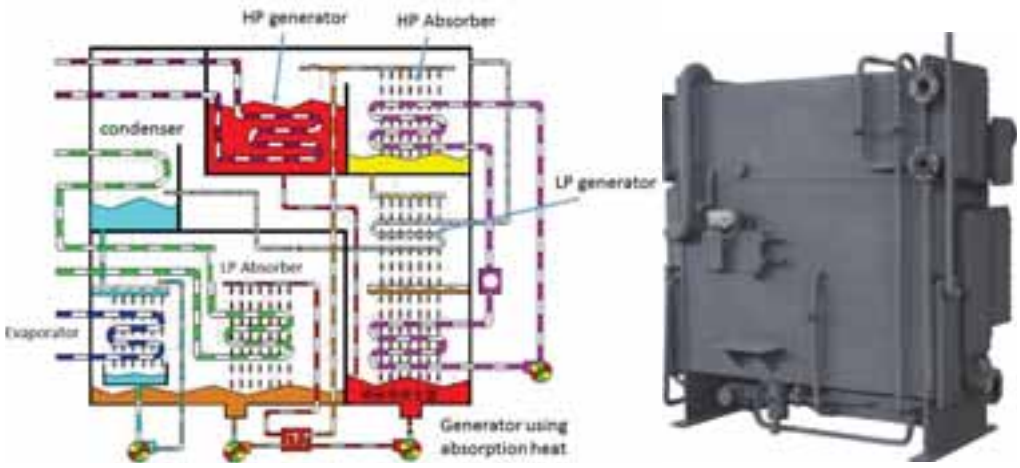

(a) (b)

Fig. 4: The variable-effect absorption chiller: (a) Flow streams and (b) a prototype

3. Performance indexes

3.1. LFR solar collector

Optical efficiency η_o of LFR solar collector can be introduced with respect to cosine efficiency, end loss, reflectivity of mirror, and absorptivity of the absorber. The similar theoretical models (Morin et al., 2012) are used to predict the solar-to-thermal performance of the proposed LFR solar collectors. According to energy balance, the heat absorbed by cavity receiver is equal to the difference of the heat reflected to cavity surface by mirrors and heat loss of cavity, which is shown as the following relationship:

$$\eta_{th} = F_R\left[\eta_0 - \frac{U_L(T_{i,LFR} - T_{amb})}{CI_b}\right] \quad \text{(eq. 1)}$$

where F_R is the heat removal factor of the solar collector. $T_{i,LFR}$ is inlet temperature of pressure hot water. I_b is direct normal irradiance (DNI). U_L is heat loss coefficient between HTF and ambience. T_{amb} is ambient temperature. Geometric concentration ratio C of the LFR collector is defined as the ratio of collecting area A_c and absorber area A_a of the receiver.

Thermal efficiency represents the ratio between absorbed energy by cavity receiver and total energy received by mirror fields in steady state or sufficiently good quasi steady state condition. Thermal efficiency can be calculated by

$$\eta_{\mathrm{th}} = \frac{\dot{m}c_p\left(T_{\mathrm{o,LFR}} - T_{\mathrm{i,LFR}}\right)}{I_{\mathrm{b}}A_{\mathrm{c}}} \quad \text{(eq. 2)}$$

where $\dot{m}$ is mass flow rate of pressure water. c_p is specific heat of HTF. $T_{\mathrm{o,LFR}}$ represents the outlet temperature of the LFR collector array.

The heat loss coefficient of LFR solar collector can be expressed as

$$F_R U_L = \frac{Q_{\mathrm{loss}}}{A_{\mathrm{a}}\left(T_{\mathrm{i,LFR}} - T_{\mathrm{amb}}\right)} = \frac{\dot{m}c_p\left(T_{\mathrm{i,LFR}} - T_{\mathrm{o,LFR}}\right)}{A_{\mathrm{a}}\left(T_{\mathrm{i,LFR}} - T_{\mathrm{amb}}\right)} \quad \text{(eq. 3)}$$

3.2. Variable-effect absorption chiller

Cooling capacity is calculated by

$$Q_{\mathrm{chw}} = \dot{m}_{\mathrm{chw}} c_{p\mathrm{chw}} (T_{\mathrm{chw,in}} - T_{\mathrm{chw,out}}) \quad \text{(eq. 4)}$$

where $\dot{m}_{\mathrm{chw}}$ is defined as the flow rate of chilled water. $c_{p\mathrm{chw}}$ denotes specific heat of chilled water. $T_{\mathrm{chw,in}}$ and $T_{\mathrm{chw,out}}$ are the inlet and outlet temperatures of chilled water.

Input power of the pressure hot water is calculated in terms of flow rate of hot water ($\dot{m}_{\mathrm{hw}}$), specific heat of hot water ($c_{p\mathrm{hw}}$), inlet and outlet temperatures ($T_{\mathrm{hw,in}}$ and $T_{\mathrm{hw,out}}$) of hot water. The equation can be expressed by

$$Q_{\mathrm{hw}} = \dot{m}_{\mathrm{hw}} c_{p\mathrm{hw}} (T_{\mathrm{hw,in}} - T_{\mathrm{hw,out}}) \quad \text{(eq. 5)}$$

Based on the cooling capacity and input power of pressure hot water, COP of the variable-effect absorption chiller can be expressed by

$$\mathrm{COP} = \frac{Q_{\mathrm{chw}}}{Q_{\mathrm{hw}}} \quad \text{(eq. 6)}$$

Considering the conversion performance from solar radiation to cooling production, the solar COP is defined as

$$\mathrm{COP}_{\mathrm{s}} = \frac{Q_{\mathrm{chw}}}{I_{\mathrm{b}}A_{\mathrm{c}}} \quad \text{(eq. 7)}$$

4. Results and discussion

Thermal performance of the solar cooling system was tested under outdoor field conditions on the roof of a building in Guangzhou. In order to conduct a practical assessment, the variable-effect absorption chiller and the LFR solar collector array were experimented under dynamic conditions. In the testing system, physical measurement parameters should include all temperatures at the inlet and the outlet of all units, circulating volume flow rates, ambient temperature, and DNI. Platinum resistance thermometers (PT100) were used to measure all temperatures. All temperature sensors were calibrated to an absolute measuring error of 0.1 K and a relative deviation between each other less than 0.05 K. To minimize temperature measurement error, two temperature sensors were located as close as possible to the inlet and outlet locations. A pyrheliometer with the measuring error less than 5% were employed to measure DNI. The ambient temperature sensor was housed in a well-ventilated instrumentation shelter above the ground and with its door facing north in order to shield from direct irradiation. A set of Keithley 2700 served as the data logger, which collects and records the data of sensors with a time interval of 10 s.

Fig. 5 shows the variations of DNI and ambient temperature as a function of local time in the test day. As seen, it was typical cloudy day. The DNI varied in a span of 100-650 W/m^2 due to the cloudy weather condition and the mean ambient temperature is about 32 °C.

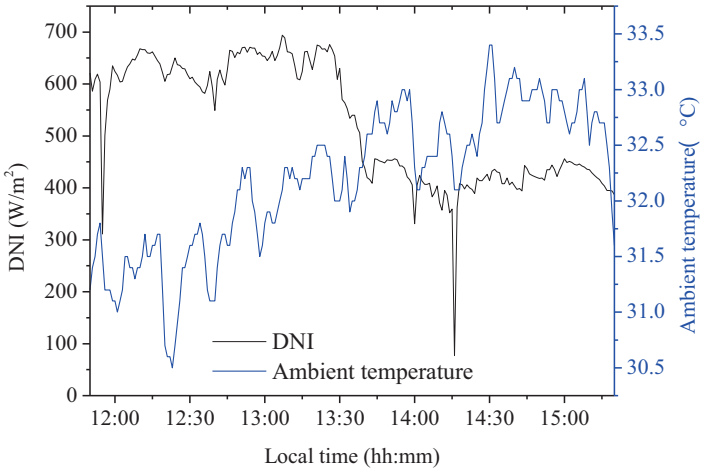

Fig. 5: DNI and ambient temperature as a function of local time

Fig. 6 shows the thermal performance of the LFR solar collector array including inlet and outlet temperatures, and thermal efficiency. The test results indicated that the peak temperature of the LFR solar collector array with cavity receiver can reach 150 °C under weather conditions shown in Fig. 5. It should be noted that the inlet and outlet temperatures of pressure hot water gradually increased, however, the DNI decreased hugely after 13:30. It is mainly contributed by the heat capacity of the steam manifold like storage tank. Thermal efficiency gradually decreased with the increasing temperature of hot water mainly due to the increasing heat loss of the cavity receiver.

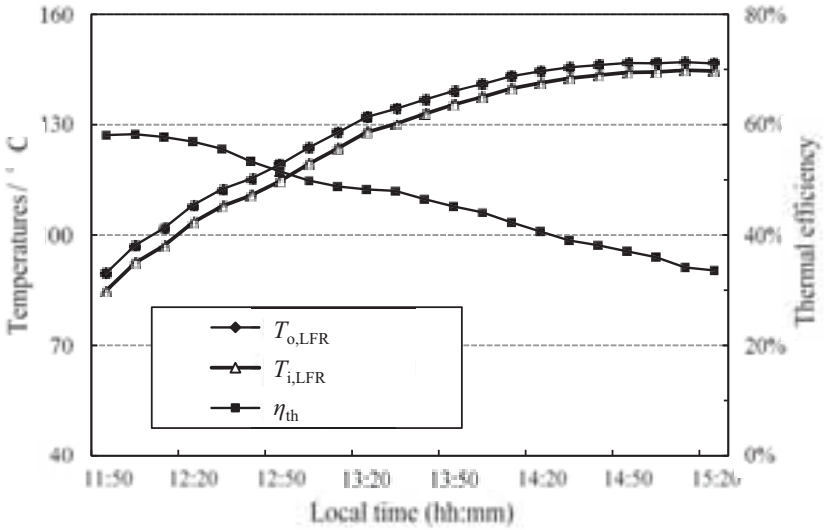

Fig. 6: Thermal performance of the LFR solar collector array

The details of performance of the variable-effect absorption chiller are depicted in Fig. 7. The cooling capacity of the variable-effect absorption chiller is around 50 kW, and the thermal COP of the chiller is about 1.05 during the operation period. During a typical cloudy day, the chiller COP varies from 0.84-1.05, much higher than the solar single effect absorption cooling system. It is found that the solar cooling system works well and the chiller COP is always above 0.8 during the given period. Fig. 8 further shows the variations of the system COP, indicating that 36-53% of solar radiation can be converted to cooling output. Also found is

that the solar thermal efficiency for the Fresnel solar collector varies from 36-58% during the operation period, and the operation temperature is within the range of 90-147°C. The cooling output changes (Q_{chw}) from 28-65.8 kW accordingly. It is important that the COP and the cooling output are almost linearly changing instead of step changing from single effect mode to double effect mode, and the operation time is also extended.

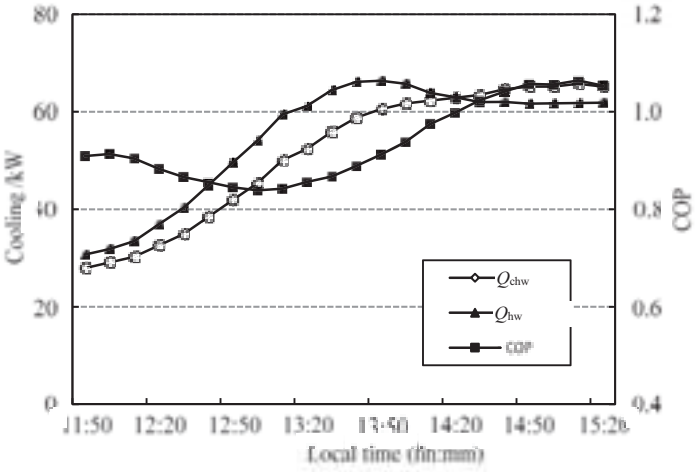

Fig. 7: Cooling output and chiller COP as a function of local time

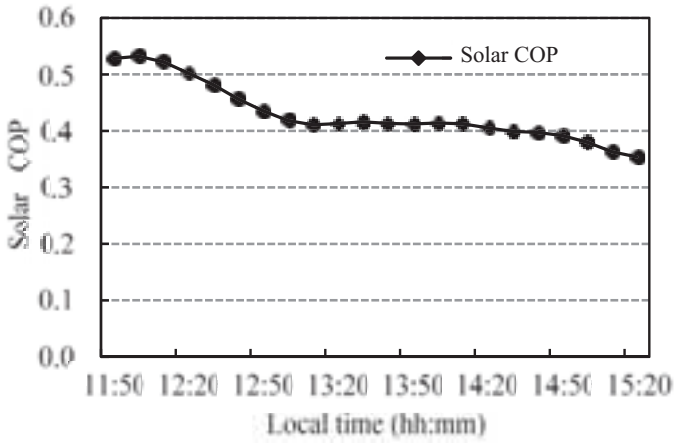

Fig. 8: Solar COP as a function of local time

5. Conclusions and Future work

A solar cooling system, composed of linear Fresnel reflector (LFR) solar collectors, a variable-effect absorption chiller and assistant components was established and investigated experimentally in this paper. A typical cloudy day test was conducted. The corresponding conclusions can be drawn:

(1) Thermal efficiency for the LFR solar collector varied from 36-58% during the operation period, and the operation temperature was in a temperature span of 90–147 °C.

(2) The solar cooling system COP is about 0.4–0.5, indicating that this design and configuration for solar cooling can convert 40-50% of solar radiation to cooling output. The results show that the variable-effect absorption chiller is one of the best choices for improving solar cooling output and efficiency.

Future work will be focused on detailed whole day and entire summer season test, parametric optimization of

such kind of solar cooling system, and cost benefit analysis.

6. Acknowledgment

This work is supported by Natural Science Foundation of China under Contract Number 51476099.

7. References

Chemisana, D., Rosell, J.I., 2011. Design and optical performance of nonimaging Fresnel transmissive concentrator for building integration applications. Energy Convers. Manage. 52 (10), 3241–3248.

Chemisana, D., López-Villada, J., Coronas, A., Rosell, J.I., Lodi, C., 2013. Building integration of concentrating systems for solar cooling applications. Appl. Therm. Eng. 50, 1472–1479.

Gharbi, N.E., Derbal, H., Bouaichaoui, S., Said, N., 2011. A comparative study between parabolic trough collector and linear Fresnel reflector technologies. Energy Procedia 6, 565–572.

Mathur, S.S., Kandpal, T., Negi, B., 1991. Optical design and concentration characteristics of linear Fresnel reflector solar concentrator II. Mirror elements of equal width. Energy Convers. Manage. 31, 221–232.

Winston, R., Jiang, L., Widyolar, B., 2014. Performance of a 23 kW solar thermal cooling system employing a double effect absorption chiller and thermodynamically efficient non-tracking concentrators. Energy Procedia 48, 1036–1046.

Xie, W.T., Dai, Y.J., Wang, R.Z., 2012. Theoretical and experimental analysis on efficiency factors and heat removal factors of Fresnel lens solar collector using different cavity receivers. Sol. Energy 86, 2458–2471.

Xu, Z.Y., Wang, R.Z., 2016. Absorption refrigeration cycles: Categorized based on the cycle construction, Int. J. of Refr. 62, 114–136.

Xu, Z. Y., Wang, R. Z., Xia, Z. Z., 2013. A novel variable effect LiBr-water absorption refrigeration cycle. Energy 60, 457-463.

Xu, Z.Y., Wang, R.Z., Wang, H.B., 2015. Experimental evaluation of a variable effect LiBrewater absorption chiller designed for high-efficient solar cooling system, Int. J. Refrig. 59, 135-143.

Zhou, L., Li, X., Zhao, Y., Dai, Y., 2017. Performance assessment of a single/double hybrid effect absorption cooling system driven by linear Fresnel solar collectors with latent thermal storage. Solar Energy 151, 82-94.

Development of a low carbon coupling device for solar cooling (photovoltaic + heat pump)

Philippe Esparcieux[1], Olivier Baup[1], Daniel Mugnier[2], Christophe Weber[3], Christophe Marvillet[3] and Laurent Pomathiod[4]

[1] Atisys Concept, Toulon (France)

[2] Tecsol, Perpignan (France)

[3] NeoTherm Consulting, Le Bourget du Lac (France)

[4] EED, Gigean (France)

Abstract

This paper presents a smart design named PV COOLING to produce solar cooling using low GWP heat pump system coupled with a standard photovoltaic plant. A maximum of self-consumption is promoted by means of a light bank of batteries and chilled water tank. For this, a test bench has been installed on the building roof in the south of France with the originality to be entirely controllable in terms of building load injected. Thereafter, this new system aims to be used for air-conditioning and/or dehumidification in the tertiary sector and positive cold storage in the industrial sector in countries where climatic, regulatory and technical conditions are suitable. PV COOLING potential is developed within a market study. The aim of this study is to assess the thermal / electrical performances of our test bench with the purpose to air-conditioning a building by means of several sensors and meters.

Keywords: solar air conditioning, photovoltaic, heat pump, self-consumption, batteries, inverter, thermal tank, glycol water, propane, R290, low GWP, air-conditioning, cold storage

1. Introduction

Until now, traditional PV economic model was based on feed-in tariff. However this trend is currently moving toward on-site self-consumption. PV self-consumption can be used in a straightforward manner for domestic purposes: lighting, heating, domestic hot water heating (DHW), cooking, domestic appliances, etc.

An example of application consists in using solar power to directly drive a thermodynamic device with a target to produce cooling or refrigeration. It can be noted that PV production perfectly matches cooling needs during the day. Besides, in many countries all over the world, the summer comfort in buildings becomes necessary in order to allow employees to work in good condition.

The use of renewable energy for powering heat pumps can solve environmental problems due to the ways of producing energy (e.g. CO2 emissions by coal thermal plants in China). Even if the energy problem is settled, it remains the issue of refrigerant fluid leakage which represents a non-negligible share of the greenhouse effect. Therefore, the use of low global warming potential (GWP) fluid in thermodynamic system allows to reduce the device carbon footprint.

2. The adopted strategy

At first glance, compressor power shall be adapted with PV output power. This may work within a certain range until a minimum threshold where chiller compressor has to be stopped. When PV output power is back, the main issue is to be sure that power remains sufficiently stable and reliable to start compressor again and avoid short-cycle. Indeed, the problem of driving a chiller compressor with PV lies in the fact that it may happen that irradiation may be temporary obstructed by some peculiar clouds.

doi:10.18086/swc.2017.28.04 Available at http://proceedings.ises.org

Using variable-frequency drive can solve the problem of high inrush current during compressor run-up. For the intermittent energy problem, storage using batteries or other electricity supply can easily sort this problem out. It's also possible to mix with thermal storage system which is a shorter-term storage mode. Both electricity and thermal storage allow to store a sufficient energy when the PV production exceeds and use it when the need becomes higher than the PV production.

To contribute to an environmentally friendly device, propane (R290) has been chosen as refrigerant for this project. This very low GWP refrigerant (GWP < 10) combined with an original configuration allows a significant reduction of refrigerant amount. To maximize the self-consumption, the inverter has to allow both electric powers issued from PV and batteries.

This research aims to study a test bench using PV cooling, installed on the building roof in the south of France. For a better understanding of the system behaviour, instead of cooling the building, cooling is distributed into a chilled water tank in which is fitted a power controlled heating resistor which simulated all sorts of building thermal load configurations.

3. Promoting solar photovoltaic on new market segments

3.1. Air-conditioning for the tertiary sector

To avoid an unfair competition with cheap traditional heat pump produced at ten millions samples yearly, PV cooling will be suitable for medium / high power in the tertiary sector and according to certain criteria. The criteria to lead the market study are classified into three main contextual families (climatic, economic and regulatory) and are summarized through a "bubble chart" (Fig. 1). These criteria are expressed inside the chart as:

- The cooling demand expressed in cooling degree days (CDD) on the x-axis.
- The annual global horizontal irradiation (GHI) per square meter on the y-axis.
- The market size of mid-sized / large heat pump in the tertiary sector is expressed by the percentage of the worldwide unit demand through the surface size of the bubble.
- The electricity price in the tertiary sector as a driver of renewable investment is expressed by the colour of the country, with cheap costs in light and high costs in black.
- Finally, self-consumption policy and fiscal incentives which are positive for renewables (e.g. feed-in-tariffs, subsidies, solar obligations) are marked with (+); others with (-) and unclear situation with (?).

Figure 1 shows only the final result of an ambitious market study. Indeed, several countries have been removed from previous "bubble charts" because of following weaknesses. First of all, many countries in Europe have an insufficient radiation like Germany and even if the radiation is enough like in South Europe, the cooling needs are only present during summer. Among countries which gather good natural conditions (both radiation and cooling needs), the low electricity price doesn't allow for photovoltaic to be profitable (e.g. Saudi Arabia).

Countries that appear qualitatively as the most mature to accommodate a short-term photovoltaic air-conditioning system according to Figure 1 are mainly countries with a tropical climate. Indeed, under this kind of climate, the cooling needs are constant during the full year. Electricity price appears as an important criterion which participates to have a return on investment the most quickly possible.

The market size is not an essential criterion because PV COOLING can find its place in a market niche where the tertiary sector is not developed like high-income countries. For instance, the air-conditioning for a cybercafe in Africa which doesn't have access to a reliable electrical grid. Indeed, more and more African cities have the means to propose services moving towards European standard for a category of population which are increasingly financially secure.

The self-consumption policy and fiscal incentives are the last criterion which may help PV solutions to be more attractive especially the right to self-consume. But it is difficult to be entirely exhaustive in each country because the PV policy changes quickly. PV outlooks show that each government will pass laws to tend towards a smarter way to consume photovoltaic which is self-consumption model. Besides, a lot of PV self-consumption projects take place in countries where no PV policy exists particularly in Western Africa. That means PV policy is not a necessary criterion to have the right to self-consume.

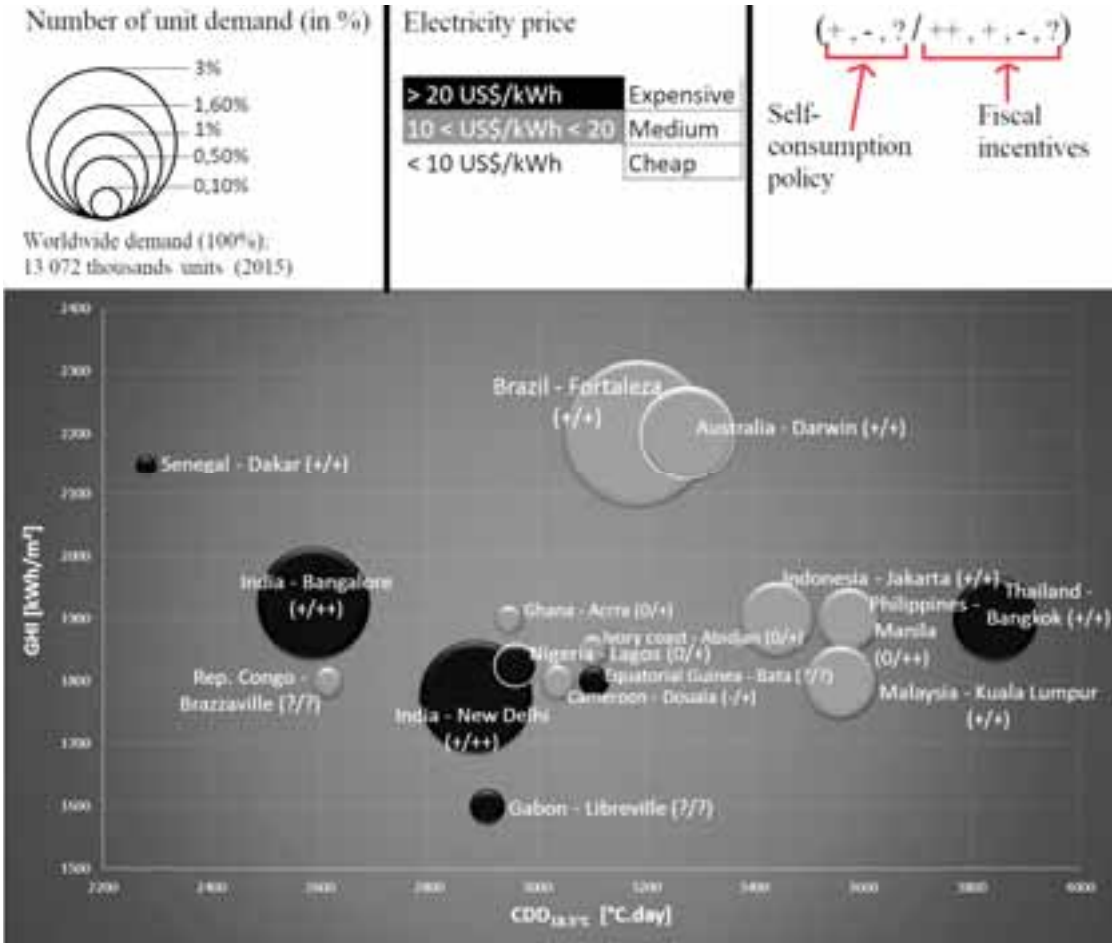

Fig. 1: Graph illustrating the attractiveness of cooling markets for PV COOLING

3.2. Cold room for perishables foods in industrial sector

The industrial sector which matches quite well with the natural condition is agri-food industry and more specifically storage for perishable food items with positive cold storage or refrigerated warehouse. The perishable foodstuffs which require positive cold storage to maintain a longer lifetime are mostly fruits & vegetables and roots & tubers. Countries with tropical climate appear to be regions where food harvest are significant and represent a considerable share of GDP. The majority of countries with tropical climate are low or middle-income, so the food cold chain is not developed as high-income countries. This is why due to

economic and climate problems (hot and damp), tropical climate regions have a significant food losses share caused by a lack of cold storage (Jenny Gustavsson et al., 2011).

As the air-conditioning study market, the “bubble chart” underlines the fact that tropical countries appear to be the most attractive for PV COOLING usage for positive cold storage food.

We can notice all the same a slight difference, with the apparition of very low-income countries in Africa in the “bubble chart” owing to the fact that agriculture is the only source of revenue.

4. R&D carried out for a properly sized system

Actual PV COOLING innovation mainly consists of setting together in a clever way, components which actually are highly improved, but never have been set together in a single goal system: PV plant dedicated to driving a thermodynamic fluid chiller as shown in Figure 2.

This is the fruit of two years co-operation with four French companies, with several decades’ expertise in solar energy (Tecsol), heat exchangers technology & design (NeoTherm Consulting), designing special thermodynamic equipment (EED) and designing & implementing innovative systems (Atisys).

Besides, the R&D project has also an academic dimension in France with an expert in cold industry from the Conservatoire National des Arts & Métiers (CNAM-Paris).

4.1. Overall PV COOLING architecture

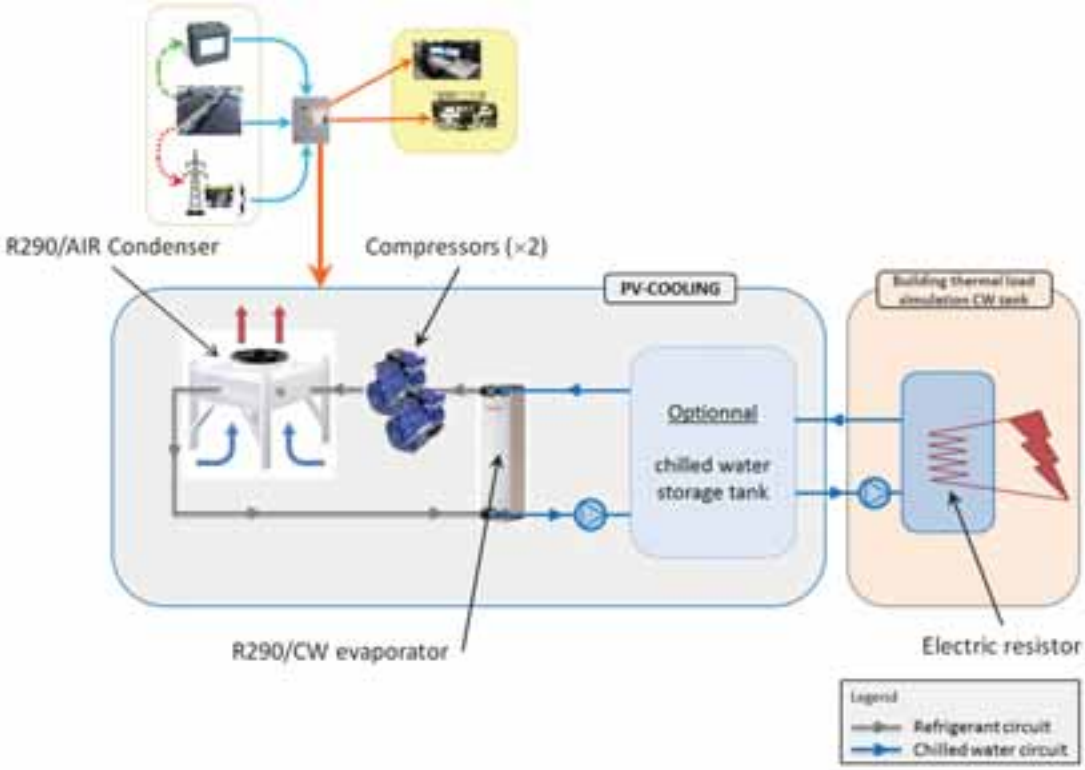

Fig. 2: Schematic architecture of PV-COOLING system

4.2. Layout description

The first test bench, installed on the Atisys head-office roof-top, is located in Toulon area (South East of France, lovely site in French Riviera).

Fig. 3: Picture of 19 mono-crystalline photovoltaic modules (280 Watts peak (Wp) for each module) on the Atisys roof top

Fig. 4: PV COOLING control and management system

In the pilot testing system, electrical production is delivered by 18 mono-crystalline photovoltaic modules (280 Watts peak (Wp) for each module) as illustrated on Figure 3, which represents a total power of 5.0 kWp. This power is quite enough for driving chiller compressors and all ancillary equipment dimensioned for 10 kW_{th} chilling power (condenser fan and chilled water circulation pump).

These photovoltaic panels are connected to a three-phase wired inverter along with batteries bank. The four selected 12-Volt batteries are connected in series to obtain a voltage of 48V. Their 150Ah capacity each with a 50% depth of discharge (DOD) allows to obtain a useful electrical storage energy about 3.6kWh. This is enough to drive the full load power installation at least for one hour.

For a real operational system, battery capacity may be chosen according to actual need.

In order to limit the inrush current during compressor run-up, a variable-frequency drive has been installed downstream from the inverter which makes possible to divide the inrush current by 6.

Figure 4 presents the complete electrical setting.

Two parallel-mounted semi-hermetic compressors were selected and adapted for propane. Each compressor can provide from 2.4 to 5.4 kW of cooling by varying its rotation frequency from 30 to 70 Hz. This allows a cooling capacity between 2.4 and 10.8 kW. For the future, commercial PV cooling systems will be able to reach high cooling power till 300 kW using bigger compressors. It is enough to size the other equipment accordingly.

Fig. 5: Picture of the Two parallel-mounted semi-hermetically compressors

The condenser is an air/R290 type heat exchanger, also called air-cooled condenser. In order to reduce refrigerant load, a microchannel type condenser has been chosen.

The evaporator selected for the project is brazed plate heat exchangers, also suitable for propane.

The major innovation regarding the heat pump system lies in the use of low Global Warming Potential (GWP) refrigerant.

The choice fell on propane (R290) with (<10) GWP, which is considerably low compared to a common refrigerant (e.g. 1300 GWP for R134a).

The only drawback with using propane is the necessity of additional security due to propane flammability. In our case and according with French safety regulation, setting the chiller outdoor (see Fig. 6) is considered as sufficient. Thus, no additional security is necessary.

The fluid that transports the refrigerating capacity from the cold unit to the chilled water tank is water/methyl propylene glycol (MPG) mixture, so as to avoid any freezing risk.

Fig. 6: Picture of the global chiller installation installed on the Atisys top roof

For this test bench, the chilled water tank is representative of a typical building whose thermal load is simulated with an electrical resistor heating the 180L chilled water tank (see heater on Fig. 6). That gives the advantage to fully control the building loads and consequently simulate several conditions which correspond to different building utilization/insulation and climate conditions.

A monitoring system has been set up with a view to monitoring performances of the system according to the needs throughout the year. Monitoring is powered by PV-COOLING itself.

4.3. PV COOLING management

Building thermal load is estimated as follows:

$$P_{Build-Load}(t) = G \times V \times \left[T_{ext}(t) - T_{set}(t)\right] + K \times S_{Build} P_{Sol.Ir}(t) * \delta(t-\tau) \qquad \text{(eq. 1)}$$

With:
- T_{ext} : outdoor temperature
- T_{set} : indoor setpoint temperature
- G : volume heat loss coefficient [W/m^3.°C] choosen as G=2.5 (poorly insulated building in our case)
- V: the cooled volume. V=325 m^3
- $P_{Sol.Ir}$: Power of solar irradiation [W/m^2]
- S_{Build} : time average wall surface of building exposed to solar irradiation (chosen to 40 m^2)
- K: solar power absorption sensitivity of building walls [non-dimensional, $0 \leq K \leq 1$], chosen to 0.20
- $\delta(t-\tau)$: delay function (Dirac), corresponds to thermal inertia of building to solar irradiation (τ = 1 hour)

For the automatic control of heat pump management, several approaches are tested between two main paradigms.

The first one is the **economy mode** (also designated as **"eco" mode**) in which compressor driving power is adapted to PV output power.

The second one is the **comfort mode** in which setpoint value consists in keeping constant chilled water feedback temperature (12°C) and if necessary take complementary power from the grid when both PV and batteries power are insufficient.

5. Results and discussion

PV COOLING test bench has been tested during several months with monitoring sequences of several days from June to September 2017. The electrical resistance of the heater has been controlled to model a 325 m^3 building (i.e. 125m^2 with a high ceiling of 2.60m). To correspond to reality, an outside temperature sensor has been installed.

PV COOLING major monitoring data and performance results are presented hereby, for both **"eco"** and **"comfort"** modes, and under both **sunny** and **intermittently disrupted sunny/cloudy** conditions.

On graphical displays of fig. 7 to 11, negative values of grid electric powers means that power in injected by PV system into the grid (red curve). For battery (black curve), it is the opposite (this was done for lisibility).

Data and performances results are obtained on a daily basis, from 8 a.m. up to 7 p.m. Those data may permit one to appreciating PV COOLING efficiency (fig. 12), especially EER (ratio of thermal energy produced to grid energy consumption, from 8 a.m. up to 7 p.m.).

5.1. "eco" mode

Figure 7 below shows PV COOLING monitoring data captured on Sept 5th. Although this was a very sunny day, weather was quite windy due to a northern dry and cold wind, designated as "Mistral" (quite typical of south of France) : Mistral blows clouds away and also pushes Mediterranean sea thermocline offshore, such that sometimes even in summer, swimming on the French Riviera is a matter of bravery !

That explains why despite of sunny conditions, thermal load is far below classical figure in this period of the year. Therefore, PV-COOLING power remains far below PV power until late afternoon (5:30 p.m.) and no any external source is required.

This case gives **EER = 106.3** ! (see fig. 12).

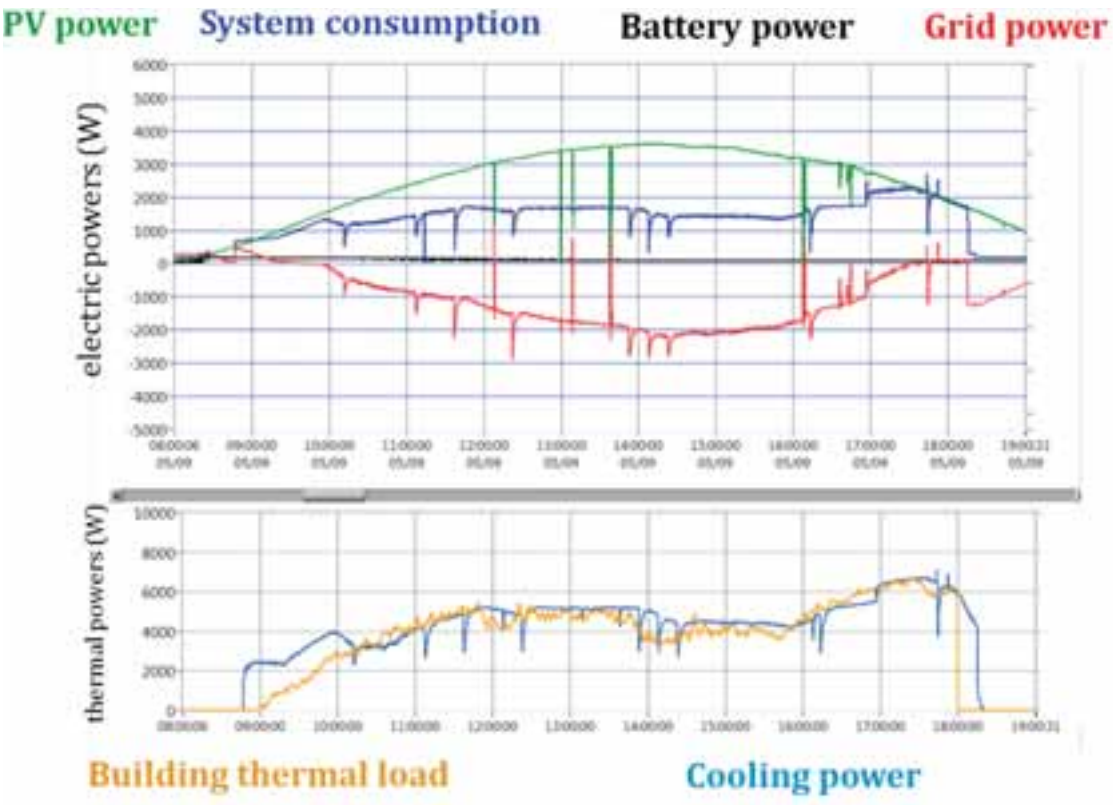

Fig. 7: Electric and thermal powers time history (Sept 5th 2017 – TOULON) – "eco" mode

It can be noticed that if PV-COOLING manager was configured as “comfort” mode, results would have been identical.

Figure 8 displays a much more significant case of ”eco” mode efficiency : Sept 6th was quite a disrupted sunny/cloudy day until 4:00 p.m. and in can be seen that system consumption (and thus cooling power) is limited by both PV power and thermal load.

One can notice that despite disrupted conditions, Sept 6th conditions show a much higher building thermal load than eve, and even in “eco” mode, cooling power matches quite well thermal load history.

This case gives **EER = 44** (see fig. 12).

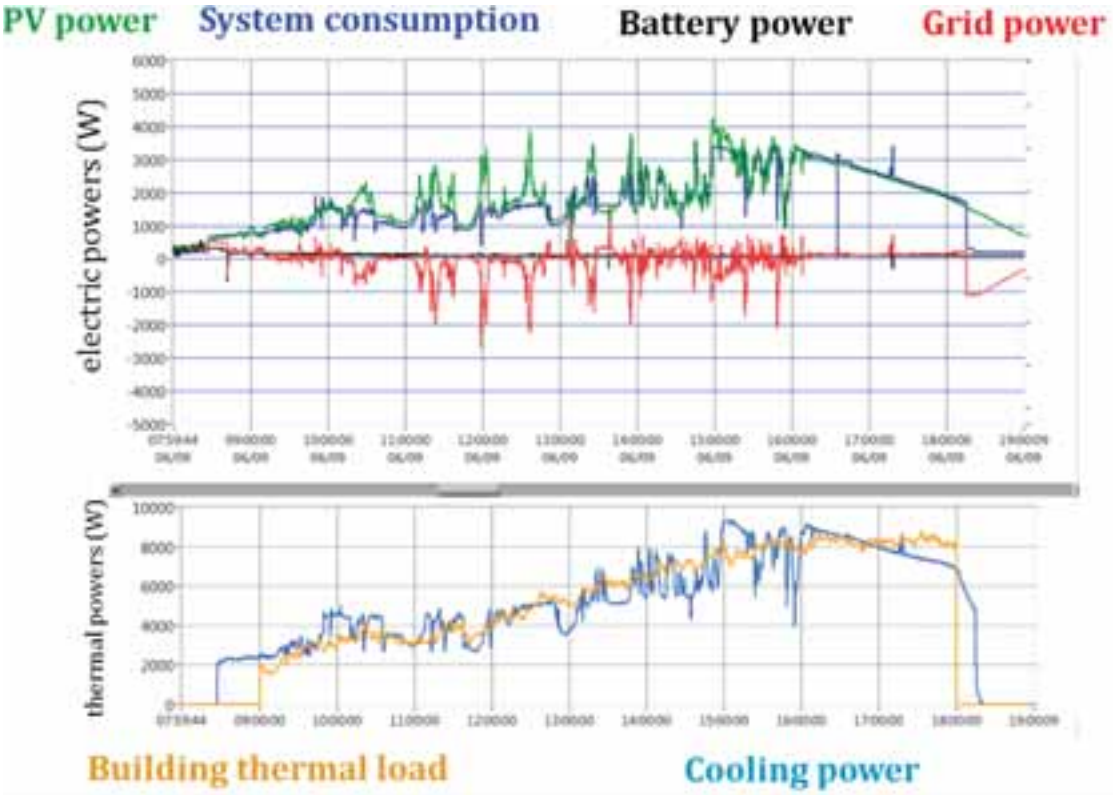

Fig. 8: Electric and thermal powers time history (Sept 6th 2017 – TOULON) – “eco” mode

5.1.”comfort" mode

Figure 9 displays PV-COOLING results obtained on Aug. 28th 2017, quite a sunny day and with high thermal load (71.15 kWh), a high cooling production (75.46 kWh) and a low grid consumption (0.47 kWh) which yields to **EER = 161.93** (see fig. 12).

Figure 10 displays following day (Aug 29th) which much more disrupted than previous example and still exhibits high thermal load (72.04 kWh) a high cooling production (75.14 kWh) and a low grid consumption (0.78 kWh). Here **EER = 95.82** (see fig. 12).

Similar comments can be done regarding Aug. 30st (fig. 11) where cooling power matches quite well building thermal load history. One may notice that battery power was limited to 1.5 kW as a security barrier set up to save battery lifetime, which yields to grid consumption (3.15 kWh) and consequently degrades performances to **EER = 24.71** (see fig. 12).

On all those examples, one can see that priority is given to battery as external supply (at the condition that battery charge level is sufficient).

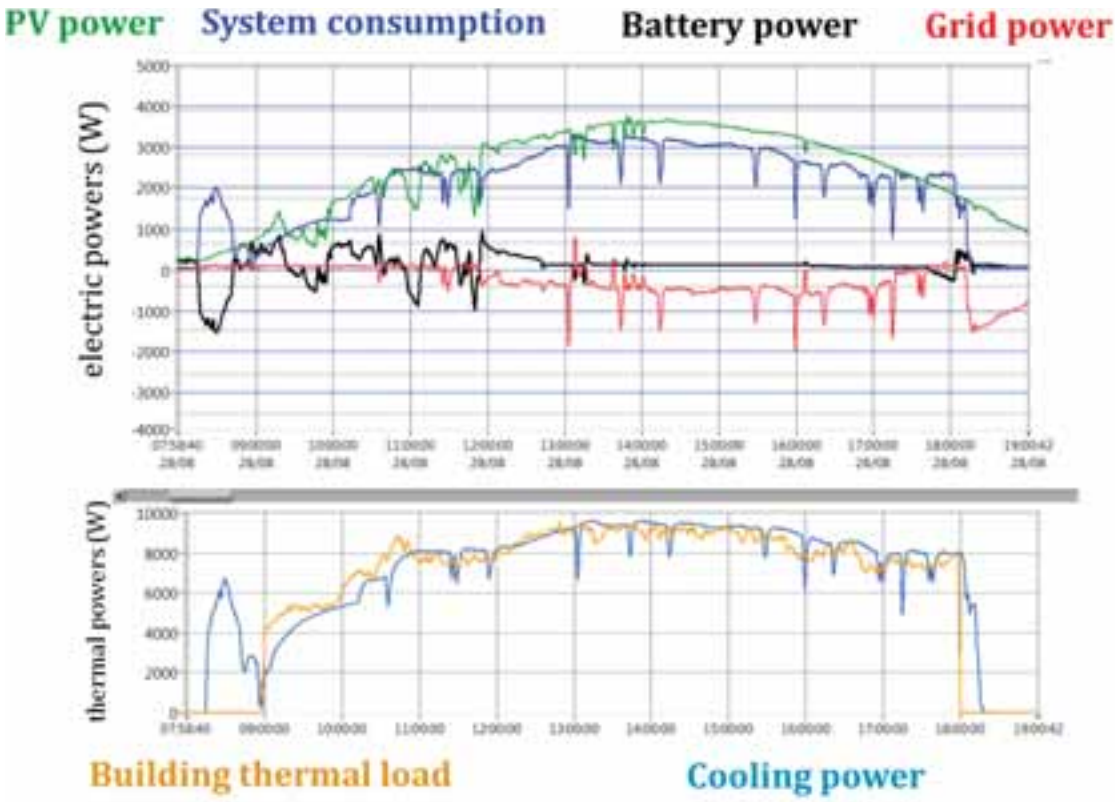

Fig. 9: Electric and thermal powers time history (Aug. 28th 2017 – TOULON) – "comfort" mode

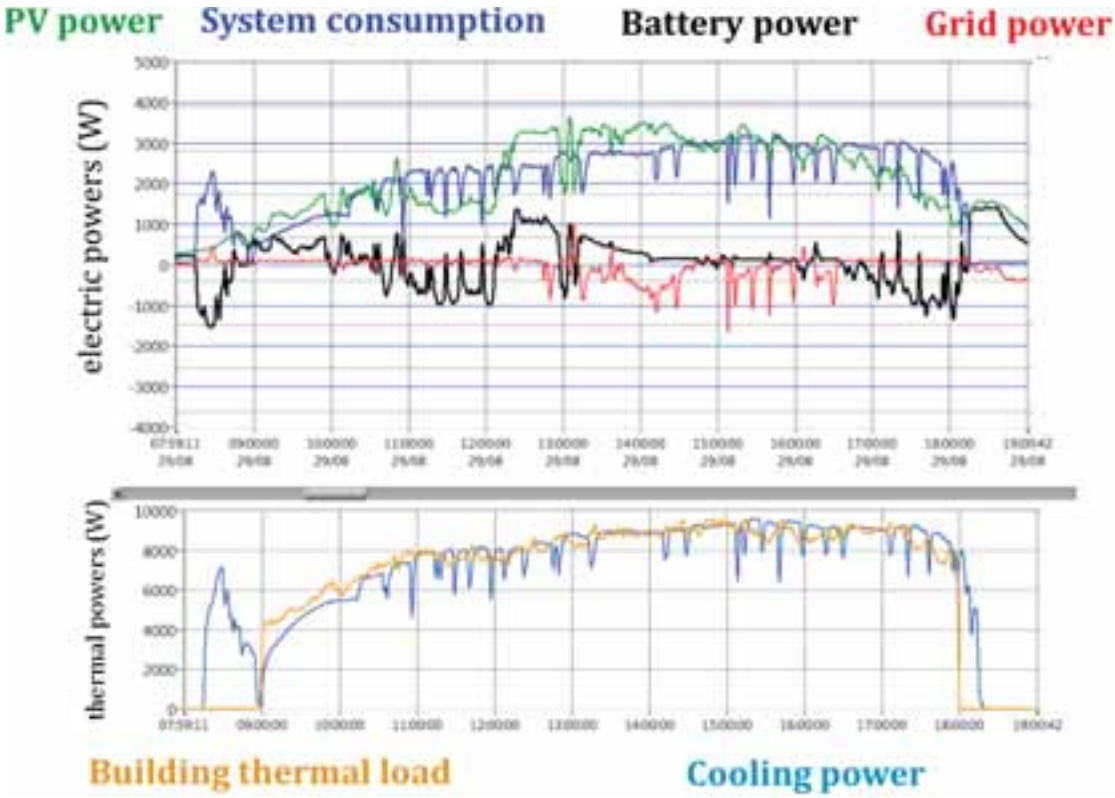

Fig. 10: Electric and thermal powers time history (Aug. 29th 2017 – TOULON) – "comfort" mode

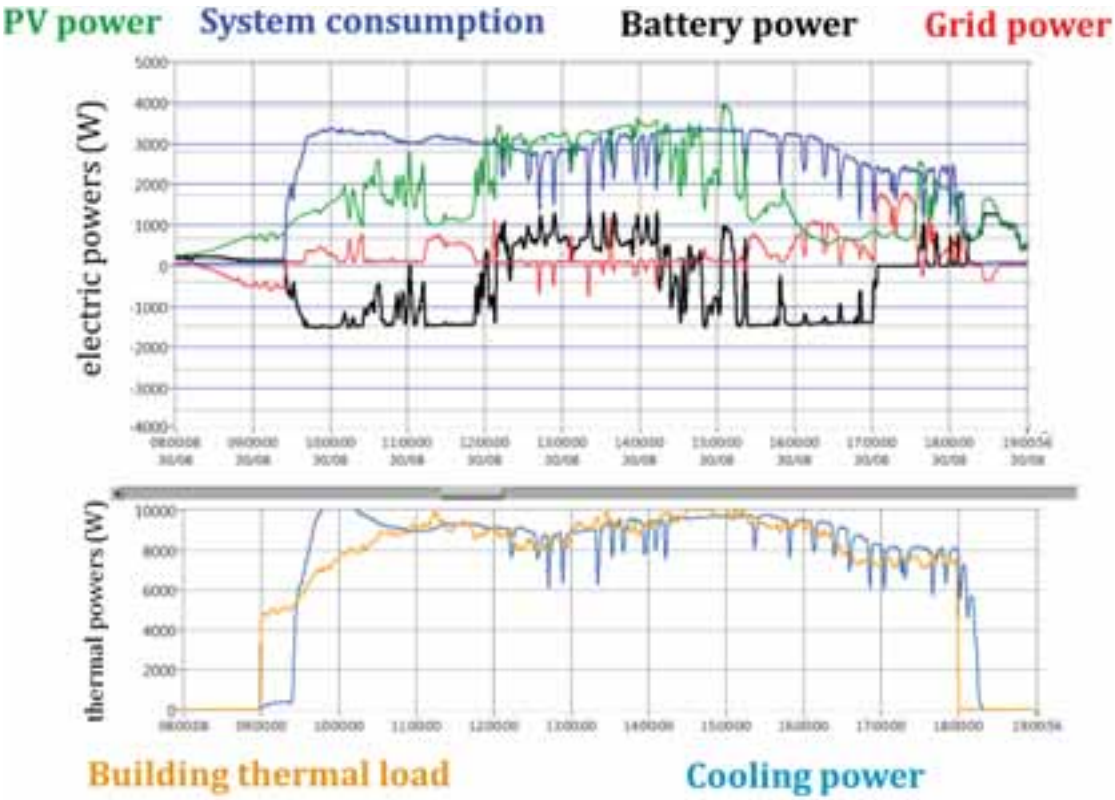

Fig. 11: Electric and thermal powers time history (Aug. 30th 2017 – TOULON) – "comfort" mode

Fig. 12 below is a synthetic table of significant values which permit one to appreciating PV-COOLING performances.
Surprisingly high values of EER are the result of very low grid consumption and have to be interpreted with humility: in fact, comparing EERs on Aug. 8th and 9th (respt. 162 and 96) is only du to 0.31 kWh difference in 11 hours !

	"ECO" mode		"COMFORT" mode		
data	**sept 5th**	**sept 6th**	**Aug. 8th**	**Aug. 29th**	**Aug. th**
overall electric PV-COOLING consumption (kWh)	14,52	17,87	22,62	22,22	25,24
PV-COOLING PV consumption (kWh)	14,11	16,64	21,29	19,26	15,95
PV energy production (kWh)	26,56	19,94	25,88	22,94	18,72
Battery consumption (kWh)	0,00	0,01	0,87	2,18	6,13
Grid consumption (kWh)	0,40	1,22	0,47	0,78	3,15
building thermal load (kWh)	38,64	51,74	71,15	72,04	75,99
Cooling production (kWh)	43,03	53,87	75,46	75,14	77,89
Compressor COP	**3,40**	**3,36**	**2,91**	**2,96**	**2,82**
PV-COOLING COP	2,96	3,02	2,72	2,76	2,64
PV-COOLING EER (Q_{th}/Q_{grid})	**106,34**	**44,11**	**161,93**	**95,82**	**24,71**

Fig. 12: Summary off significant values for different weather and management conditions

However, as a result of those examples, it may be concluded that PV-COOLING concept can be considered as efficient and quite acceptable values of EER were obtained which demonstrate possibility to run PV-COOLING independently from grid.

6. Conclusion

To conclude, the developed and tested PV-COOLING concept allows bringing following conclusions:

- PV-COOLING demonstrates that it is possible to combine improved technologies which are photovoltaic (PV) power plant to drive vapor compression thermodynamic system for the sake of producing cooling energy ;
- Securing PV plant with external power supply to drive thermodynamic system was successfully demonstrated ;
- Part of efficiency results in possibility to real-time adapting cooling power to solar irradiation ;
- EER obtained values shows that only a limited amount of grid supply is necessary and consequently, external generator may efficiently be substituted to grid ;
- Proper management permits one to consider fully autonomous systems disconnected from grid ;

Technically, existing system is planned to further investigate clever ways of using PV excessive power. This concerns mainly investigating cold storage (as shown on fig.2), but also electric storage and compare which is better to improve autonomy of PV-COOLING.

The marketing plans carried out target PV COOLING as a development tool in sunny and/or tropical regions for both air-conditioning system and positive food storage. Eventually, PV-COOLING concept open wide perspective for insulated areas and may constitute a tool for land-use planning, and especially in the developing world.

7. References

Jenny Gustavsson, Christel Cederberg, Ulf Sonesson, Robert van Otterdijk, Alexandre Meybeck 2011. Global food losses and food waste – Extent, causes and prevention. Report of Food and Agriculture Organization of the United Nations (FAO).

Control strategy approach based on the operational results of a small capacity direct air-cooled LiBr-Water absorption chiller

Joan Farnós[1], Jesus Castro[1], Giorgos Papakokkinos[1], and Assensi Oliva

[1] Heat and Mass Transfer Technological Center (CTTC)
Technical University of Catalonia-BarcelonaTech (UPC-BarcelonaTech)
ETSEIAT, C. Colom 11, 08222 Terrassa (Barcelona), Spain
Fax: +34 93 739 89 20 e-mail: cttc@cttc.upc.edu

Abstract

The scope of this paper is to give a short overview of the state of the art regarding control strategies, identify the role of different operating conditions, and provide useful suggestions for the design and operation of a solar assisted absorption cooling system, in line to the European regulation as well as its directly related directives.
The operation of a solar absorption cooling system under real conditions is subjected to various limitations regarding its ability to satisfy the required cooling demand, as well as to avoid certain internal conditions which would lead to problematic situations and jeopardize the smooth operation of the system - such as solution crystallization and water freezing. Thus, it is very important to define and refine new control operating strategies, from an internal and external perspective. Several control strategies are discussed, altogether with a new fuzzy logic approach, which shall be experimentally validated as future actions, due to its highly promising capability.

Keywords: *Air-cooled, numerical simulation, LiBr-Water, object-oriented, transient, single-effect, absorption, fuzzy logic, control.*

1. Introduction

In 2005, the Ecodesign Directive 2005/32/EC established a framework aimed at setting the ecodesign requirements for energy-using products. In 2009, the Ecodesign Directive was extended (Directive 2009/125/EC) to all energy-related products (ErPs). Thus, also products which do not necessarily use energy, but have an impact on energy consumption and can therefore contribute to save energy were included.
The most common available technologies that increase the energy efficiency of chillers, and thus help to comply with the normative, are: i) Electronic expansion valves (EEV), ii) Variable capacity compressors, iii) Variable frequency drives (VFD), iv) Evaporative cooling, v) Electronic fans and pumps, vi) Controllers and supervisory systems with energy-efficiency functionalities, and vii) High efficiency heat exchangers (e.g. micro-channels, flooded).
In this paper an extended discussion over the potential use of variable frequency drives is included, aiming to achieve a great performance of the chiller under different operating challenges. In fact, an intelligent operation of the absorption chiller may result in an adequate performance, together with a minimization of operating interruptions (freezing, crystallization, etc.).
Internal and external controls must be focused on the operation of air-cooled absorption chillers. In this work internal chiller processes are addressed by reviewing several control strategies present at the scientific literature and also from the industry. External control deals with external parameters of the chiller, such as the ones concerning low, medium and hot circuitry.
Controlling hot and cooling water is one of the most promising approaches but in a direct air-cooled machine is highly complicate, at least at the medium focus. Nevertheless, an optimal control of the chiller concerns on defining a good strategy for the whole system, including heating and cooling components (hot and cold storage, solar circuit, etc.).
The principal controlled parameters of a solar cooling system may be inner hot water temperature and mass flow, cooling air or inner water temperature and mass flow, and chilled water outer temperature and mass flow. Chilled water must be kept in certain limits to allow satisfactory operation (Kohlenbach and Ziegler, 2008). At

doi:10.18086/swc.2017.28.05 Available at http://proceedings.ises.org

the same time differential on/off operation of the external circuits should be avoided (Bong et al., 1987) (Yeung et al., 1992) (Labus et al., 2012).

Directly focusing on the direct air-cooled absorption chillers, these are attractive due to it is not necessary both cooling tower either the associated installation. However, the key technical barrier to operate an air-cooled absorption chiller using LiBr-Water as working fluid is crystallization because of high temperatures achieved inside the absorber which derives in a concentrated solution. It is the main difference towards water cooled absorption chillers. As air is used as coolant, low heat transfer characteristics must be taken into consideration because operational concentrations of the solution are very close to the crystallization limit. Therefore, not always the evaporator temperature can be maintained as low as it would be necessary to overcome the absorption pressure increase. LiBr begins to crystallize when the temperature solution is reduced under the crystallization limit or when concentration ratio is increased.
When high condensation temperature is required due to high ambient temperature (Florides et al., 2003) (Izquierdo et al., 2004), high temperature at the desorber is needed, with a possible overloading power to the desorber. Therefore, a high concentrated solution has to return to the absorber through the solution heat exchanger. On the other hand, for condensation temperatures over 40C, single-stage air-cooled absorption chillers cannot be operated by single glaze flat plate collectors (McNeely, 1979).
Other causes which allow the creation of slush are low ambient temperature and full load, electrical failure (shutdown dilution process) and when the chilled temperature is set too low (Liao and Radermacher, 2007). The presence of non-absorbable gases (air and hydrogen) which may vary according to the power input at the desorber and their effect on the performance of the absorption process phenomena have previously been studied at a basic research level (Garcia-Rivera et al, 2008, 2011, 2012, 2016). The effect on the performance of the chiller will be discussed in future works on the performance of the air-cooled absorption prototype.
Air leaks into the system raise the evaporating temperature and the chilled water leaving temperature. A higher temperature increases the heat input and the solution concentration to the point of crystallization. When the system is operated at full load, if the temperature of the cooling water is too low, the diluted solution temperature may fall low enough to reduce the temperature of the concentrated solution to the point of crystallization. If the electric power is interrupted, the system ceases to operate. The temperature of the concentrated solution in the heat exchanger starts to drop and may fall below the crystallization line.

Because of the particular operating principle of absorption chillers, novel and imaginative integration strategies have been proposed in the literature and shortly reviewed next. Several devices have been developed in order to minimize the possibility of crystallization. Moreover, several approaches can be found on the scientific literature as self-decrystallisation technique (DeVuono et al., 1991) by driving high temperature secondary fluid through the solution heat exchanger. It is only possible if high temperature drives the desorption process. Other techniques as controlling the absorbed mass by monitoring the fluid level at the evaporator or boosting the absorber pressure have also been studied by different authors (Zogg and Westphalen, 2006), (Xie et al., 2012). These approaches and an overview of control strategies can be found at Labus PhD dissertation, (J. Labus, 2011), where a new Artificial Neural Network (ANN) modeling and optimization approach is described. Another focus is to define a control strategy based on minimizing specific costs or the price for generation of cold (J. Albers, 2014).
A J-tube technology or by-passing the solution from the desorber to the absorber in order to avoid crystallization is widely applied on the industry [18], (Wang et al, 2011). When crystallization phenomena appear, a connection between the desorber and the absorber, which by-passes the solution heat exchanger, is opened. Therefore, immediately the concentrated solution is diluted and its temperature decreases, warming the low concentrated solution. At the same time, the mass flow over the solution heat exchanger will allow to avoid crystallization at the concentrated solution which is at low temperature.
Summarizing, regulation and control of the cycle is quiet challenging due to crystallization phenomena and environmental temperature dependence. In fact, mass flow driven from the generator to the absorber depends on the pressure gradient, which at the same time depends on the geometrical configuration. Therefore, it is important the mechanical design in order to define correctly all the input parameters at the numerical simulation. Transient numerical modeling helps to define an optimum control strategy.
Therefore, switch-on, standard operation and shut-down process must be aware not only of delivering cooling to overcome the cooling demand but on the protection of the components, i.e. the solution pump, to avoid

unexpected interruption of the machine and possible warnings (i.e. freezing). Several potential internal and external control strategies must be analyzed, and the authors have implemented different control strategies at the numerical platform tool called NEST (in-house developed object-oriented numerical tool) (López et al, 2012). The readiness of the chiller to deliver cooling demand is also considered, depending on the load demand and operating boundary conditions of the chiller. Operational data of a small capacity single-effect air-cooled LiBr-Water absorption chiller has been obtained and presented in this paper.

2. Numerical approach of the control strategy

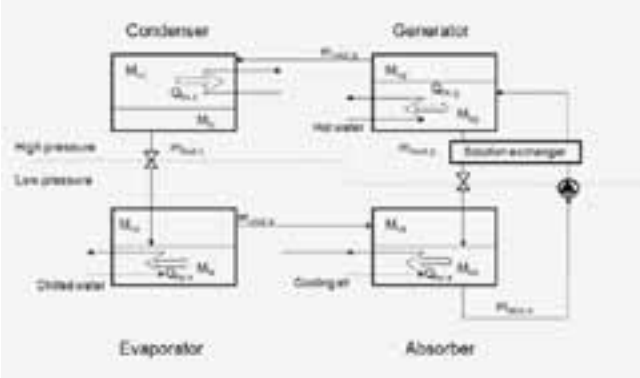

Fig. 1. Basic diagram of a single effect LiBr-H_2O absorption chiller based on parallel configuration

For performing the simulations a modular object-oriented simulation platform named NEST has been used, allowing the link among different components (solar field, pumps, tanks, heat exchangers, absorption chiller, etc.). In this numerical platform each component is an object, which can be an empirical-based model (e. g. heat exchangers, solar collector), lumped capacity models or a more detailed calculation if necessary. With this numerical platform, parallel computing is allowed. This model plant is capable to simulate the thermal and fluid dynamical behavior of the whole air-cooled absorption chiller (Farnós et al., 2017a, 2017b).

Numerical control strategy has been implemented considering a wide variety of causes which may interrupt the operation, basically in terms of crystallization and freezing. In fact, internal and external controls must be focused on the operation of air-cooled absorption chillers. External control deals with external parameters of the chiller, such as the ones concerning low, medium and hot secondary circuits.

Controlling hot and cooling water is one of the most promising approaches, but in air-cooled machines it is not possible, at least at the medium focus. However, an optimal control of the chiller is based on defining a good strategy for the whole system, including heating and cooling components (hot and cold storage, solar circuit, etc.). A multivariable approach presents a high performance control capability. The main controlled parameters of a solar cooling system may be water inlet temperature and mass flow at low, medium and high source.

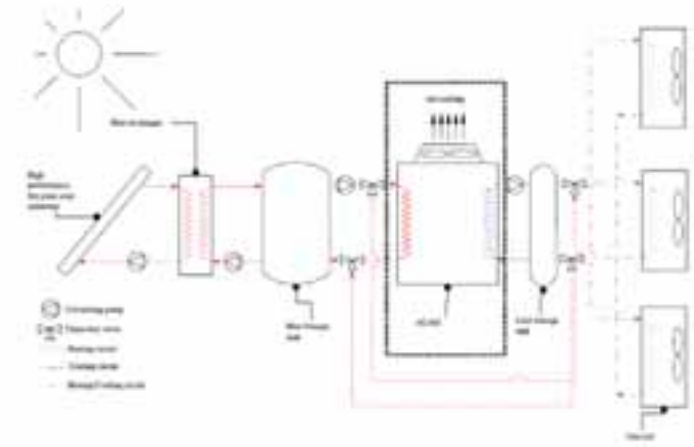

Fig.2. Solar cooling facility implemented in a virtual facility

Regarding the main technical characteristics of the secondary ciruitry, the total considered solar area is 30m^2 with flat plate collectors with an efficiency of: $\varepsilon = 0.803 - 2.4\frac{Tin-Tm}{G} - 0.0058\frac{(Tin-Tm)^2}{G}$. The cold water tank has a capacity of 1000 liters, and the hot water tank 5000 liters. Finally, the auxiliary source has a thermal power of 20 kW.

3. Technical Characteristics of a direct air-cooled absorption machine

A small, compact and cost-effective single-effect LiBr-Water absorption chiller has been designed, prototyped and commissioned not only from a scientific perspective but from an end-user perspective at the Heat and Mass Transfer Technological Center from the Technical University of Catalonia (UPC-BarcelonaTech). The use of standard components and procedures from the whole assembly has been mandatory during the whole development. The arrangement between the air-cooled heat exchangers is in parallel flow. The absorber takes more than the 50% the total air flow, the same proportion as the frontal area. All the heat exchangers have been divided in two parts in order to keep the design as compact as possible. On the other hand, and based on the EU regulation control approaches must also be focused and discussed.

Table 1. Equipment specifications and main results of the cycle simulation (* output value)

	Units		**Specification**	
Nominal capacity	kW		7.0	
COP	-		0.7	
Hot water stream	ºC	kg h^{-1}	88	1730
Cooling air stream	ºC	m^3 h^{-1}	35	16500
Chilled water stream	ºC	kg h^{-1}	9	1200

4. Analysis of the performance of the chiller under different control strategies

Data obtained from numerical simulation is used to manage the regulation based in a transient analysis, taking into account several heat and mass transfer phenomena like absorption, desorption, evaporation condensation etc., aiming to assure an acceptable performance of the chiller under different operating conditions, etc. Therefore, a great effort was done by obtaining mass transfer coefficients, which feed the transient numerical simulation, by solving the falling film phenomena in detail. Furthermore, thermal size of the components is not fixed but obtained in each time step (Farnós et al., 2017a, 2017b). Monitoring the performance focusing on heat rejection temperature dependency and crystallization phenomena is a very valuable data to reconsider state of-the-art strategies where air is not the most common used coolant.

In order to regulate the cooling capacity of the chiller according to the cooling demand, different strategies can be attended. The first one may be the regulation of the mass flow of the secondary stream at the desorber. Nevertheless, figure 2 demonstrates that the regulation of the cooling capacity becomes a challenge using this strategy because the delivered cooling mainly depends on the rate of the mass flow on the interval 0-25% of nominal mass flow. Between 25-75% of nominal flow the variation of cooling capacity is around 7-9% only. It agrees perfectly with scientific literature (Zamora et al, 2015).

On the other hand, and based on temperature regulation of the secondary source of the desorber, an other control strategy has been focused (Figure 3). Even though it shows a great potential, in a real solar cooling facility is not easy to implement due to the thermal inertia of the heat storage tank (a tank is used to storage heat when the solar circuit is not activated and to use as minimum as it would be possible the auxiliar heat source; a gas boiler). Therefore, temperature variation can not be reached in a short time in order to follow the cooling demand.
Finally, a third strategy is attended with the aim of following the cooling demand varying the air mass flow of the secondary sources at the absorbers and condensers. An accurate fuzzy logic control shows enough potential to analyze the chiller performance within different operational conditions of the chiller and improve the capabilities of the system, avoiding internal failures and reducing electricity consumption.

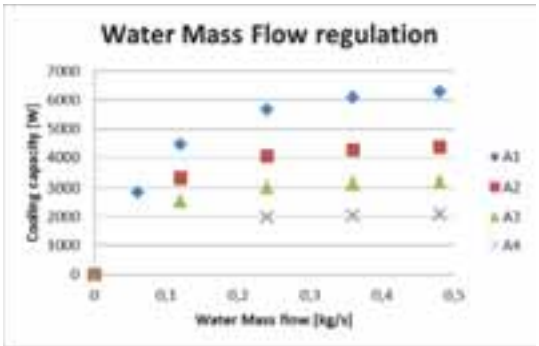

Fig. 3 Water mass flow regulation (*)

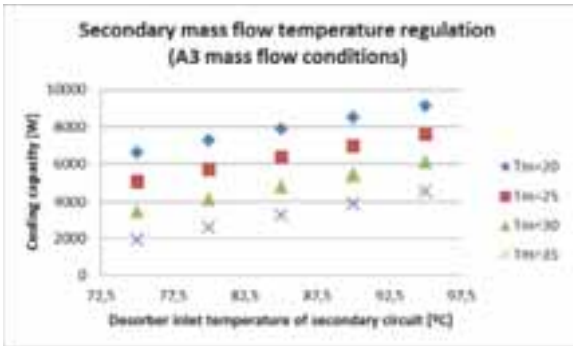

Fig. 4 Secondary mass flow temperature (Desorber) (*)

(*) Secondary nominal mass flows are:
A1: i) Desorber 0.48 kg s^{-1}, ii) Absorber 2.5 kg s^{-1}, iii) Condenser 1.5 kg s^{-1}, and iv) Evaporator 0.334 kg s^{-1}.
A2: i) Desorber 0.48 kg s^{-1}, ii) Absorber 1 kg s^{-1}, iii) Condenser 0.6 kg s^{-1}, and iv) Evaporator 0.334 kg s^{-1}.
A3: i) Desorber 0.48 kg s^{-1}, ii) Absorber 0.6 kg s^{-1}, iii) Condenser 0.36 kg s^{-1}, and iv) Evaporator 0.334 kg s^{-1}
A4: i) Desorber 0.48 kg s^{-1}, ii) Absorber 0.36 kg s^{-1} iii) Condenser 0.216 kg s^{-1}, and iv) Evaporator 0.334 kg s^{-1}

4.1 Air mass flow regulation

Here in this section are presented the results of a parametric analysis of the chiller (Figure 4). Secondary air mass flow streams have been varied from A1 to A4 conditions. Furthermore, a variation of the inner hot water temperature at the generator altogether with the environmental temperature is also presented. Different cooling capacities under different boundary conditions are obtained. Analyzing plotted results it is obvious the necessity of a well-performing control approach, which should be aligned with the EU regulations.

A first basic approach based on switching the operation of the secondary impellers has been considered and presented in Section 5. Nevertheless, it is important to match the cooling load with the cooling capacity, maintaining the internal and external conditions inside the working range and avoiding operating failures. It is the reason why a new fuzzy logic control strategy approach is described in Section 6 of this paper, as well as some examples for a transient operation of the chiller in Section 7.

Table 2: Parametric study: range of operation

Inlet T conditions secondary circuit [ºC]	Desorber	Absorber and condenser	Evaporator
Range	75-95	20-35	14

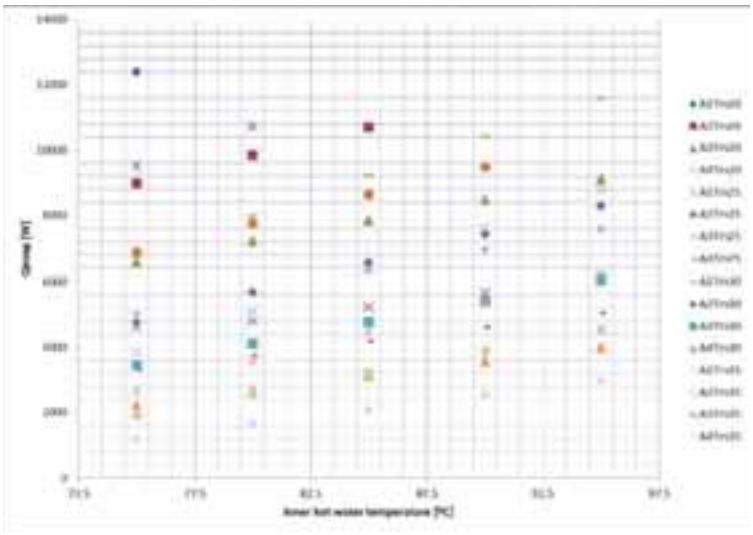

Fig. 5. Parametric study of the cooling capacity of the chiller under different mass flows and temperatures

An other interesting aspect is to analyze the performance of the chiller under different air flow regimes and temperatures, but for a fixed inner hot water temperature. In Figure 5 the cooling capacity over the frequency variation of the fan is presented, showing the wide range that the chiller can overcome under different cooling demands under different medium focus boundary conditions.

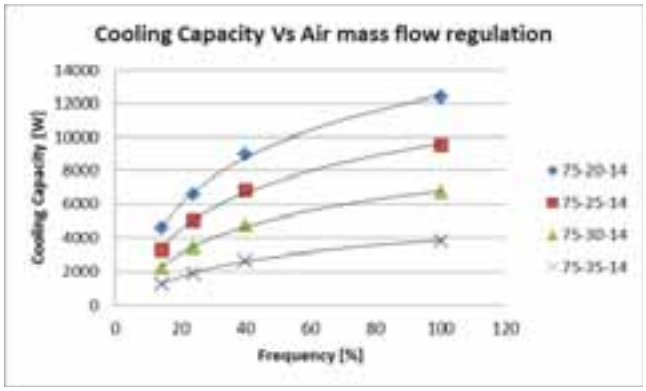

Fig. 6 Cooling capacity under frequency impeller variation

5. Basic control regulation: On/Off approach

Next it is shown the basic control diagram for an On/Off control approach. It is based on the WFC10 from Yazaki [25] and modified according to the direct air-cooled chiller necessities. Nevertheless, a basic On/Off control approach would lead into internal problems and cause failure operating conditions, and is not possible to achieve a high value of the electrical COP.

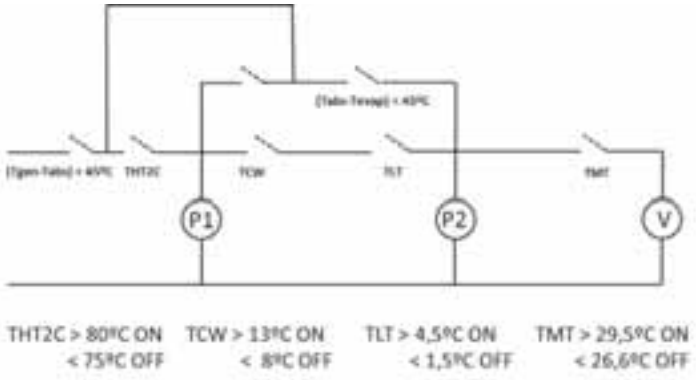

Fig. 7. Basic electric control diagram of the secondary circuitry

6. Basic fuzzy logic control strategy

A new fuzzy logic control of the cooling capacity of the chiller is based on the impossibility to modify the inlet secondary temperatures but having different cooling demands to satisfy. Therefore, in order to avoid processes of freezing or crystallization is important to know which is the maximum capacity of the chiller for each boundary conditions, aiming to change its capacity among the whole frequency range of the air impeller. This basic control strategy is compared to that widely used in other types of chillers based on switching the solution pump between ON and OFF operation (C.P. Underwood, 2015), and presented in Section 7.

A basic algorithm is presented next in order to achieve a high quality cost-competitive control strategy based on a basic sampling temperatures at the secondary circuits.

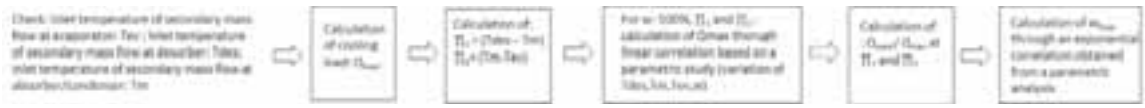

Equations related to obtain the output value of the fan frequency (w_{out}) are detailed next:

$$\pi_1 = T_h - T_m \quad (1)$$

$$\pi_2 = T_m - T_l \quad (2)$$

$$\dot{Q}_{max} = f(\pi_1, \pi_2, w_{max}) \text{ (Linear correlation)} \quad (3a)$$

Equation (3) is obtained by defining secondary mass flows and keep them constant. Then cooling capacity is obtained for different temperature conditions (a parametric numerical analysis has been carried varying inner hot water temperature from 75ºC to 95ºC and environmental temperature from 20ºC to 35ºC).

Once the cooling capacity has been calculated, eq. 1 and eq. 2 are used to calculate temperature differences. Finally, a relation between cooling capacity for arbitrary temperature conditions and the maximum cooling capacity obtained from the parametric study allows to obtain the value of the cooling ratio (Q/Qmax) for arbitrary conditions. Finally a correlation between π_1 and π_2 and Q/Qmax is obtained. The maximum error between the correlation and the Q/Qmax values obtained from the numerical simulation is lower than 2%, allowing to move forward on this control strategy approach.

$$Q_{wmax} = (0{,}059226879 + 0{,}019855119\pi_1 - 0{,}025693839\pi_2)\, Q_{ref} \quad (3b)$$

$$w_{out} = f(\dot{Q}_{demand}, \pi_1, \pi_2) \quad \text{(Exponential correlation)} \quad (4a)$$

Equation (4) has also been obtained by means of a parametric study of the prediction of the performance of the chiller under different boundary conditions (See Fig. 4).

$$w = 5.3145e^{2.9126(Q_{demand}/Q_{max})} \quad (4b)$$

The inner hot water temperature range varies between 75-95ºC and the environmental temperature oscillates among 20-35ºC. Then, for fixed mass flows over the secondary circuitry (Block A1,A2,A3 and A4) the cooling capacity is calculated for the whole temperature range defined. Then, defining Th,Tm and Tl the cooling capacity per block is obtained . Moreover, the maximum cooling capacity is referenced to the A1 block, but this Qref can also be either the nominal expected cooling capacity (7kW) or correspond to the maximum cooling capacity that the chiller is capable to deliver for a fixed Th,Tm,Tl. Then, the cooling ratio is calculated (Q/Q_{max}). Q/Qmax ratio is almost the same for all the same temperature case (fixing Th,Tm,Tl); varying the frequency of the air impeller.

Finally Figure 7 plots the cooling ratio versus the frequency of the impeller. Defined temperature conditions altogether with a variation of the air mass flow can oscillate the cooling capacity of the chiller, which will allow to follow the cooling demand, reducing the electricity consumption and avoiding internal challenges.

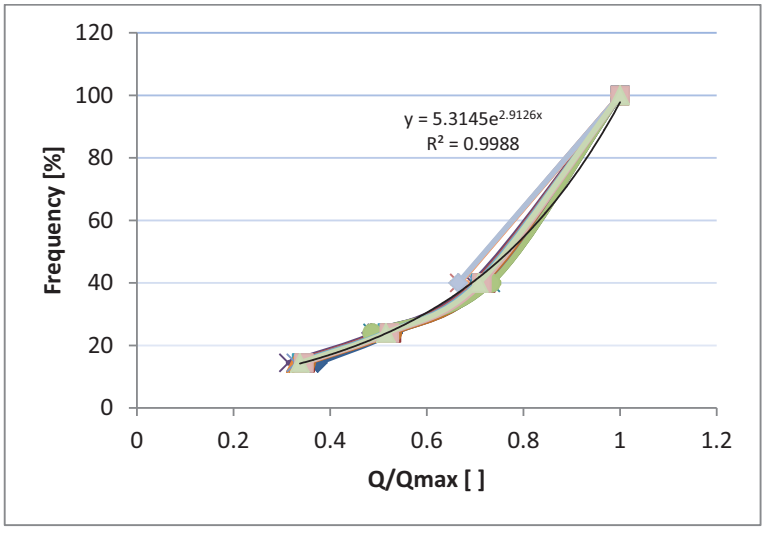

Fig. 8 Normalised exponential function (eq. 4)

7. Control demonstration: application, basic, fuzzy logic, and no control approach

A virtual laboratory has been created in order to analyze a solar cooling facility. Evaporator and generator secondary stream inlet temperatures are determined by two sinks, which are used as a buffer, in order to avoid oscillations on the driving temperature. Temperature inside the tanks is controlled so that the high temperature circuit (solar circuit) is activated only when is required. Hysteresis of the tanks is considered when the high temperature source is activated or deactivated. Moreover, there is an auxiliary circuit if solar circuit is not available to overcome heating demand. The low temperature circuit is controlled in order to avoid freezing at the chiller. In the figure 8 it is described:

7.1 Transient numerical simulation using a basic control strategy of the chiller

A characteristic day (8th July) in Barcelona (Spain) has been simulated in order to understand the performance of the chiller under different control approaches. In Fig. 8 the basic control described in Section 5 has been applied, and thermal power along 24h is plotted, according to a variable cooling demand of a house. It is observed that there are many switches which do not allow the system to operate in the best conditions, and achieve high energy savings. Nevertheless, it permits a very easy implementation on the electrical control device.

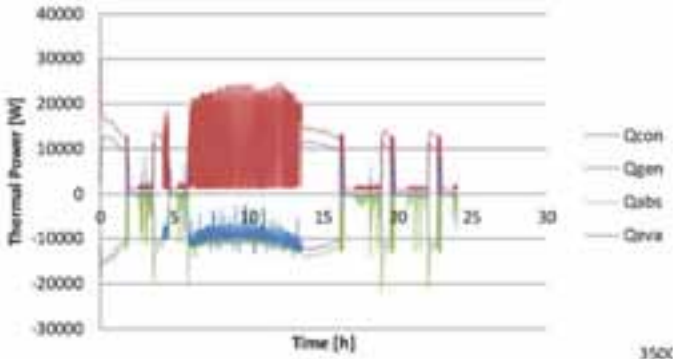

Fig. 9. 24h simulation based on a basic control strategy

7.2 Fuzzy logic control strategy of the chiller (application example):

In this section an example of how the fuzzy logic is applied is shown. Linear and exponential correlations described above are used.

Table 3: Example of a control strategy application

Qdemand [W]	Th [ºC]	Tm [ºC]	T [ºC]	(Th-Tm) [ºC]	(Tm-Tl) [ºC]	Qmax[W] (w=100%)	Qload/Qmax (w=100%)	Wout [%]	Qdelivered [W]
7000	90	30	14	60	16	10404	0,67	37,41	7000

7.3 Transient numerical simulation using a fuzzy logic control strategy

The fuzzy logic approach described above allows the system to reduce dramatically the energy consumption as well as to follow the cooling demand in an optimal way. Thus, internal challenges are reduced drastically and mean electrical COP is quite larger than the one obtained by using a basic control approach. In future works these values will be presented and compared.

For the same case presented in section 7.1, the performance of thermal power are smoother than using the implemented basic approach. It means that the operation of the chiller becomes easier as well as its potential to avoid internal and external failures. Nevertheless, all these control strategies must be improved and experimentally validated.

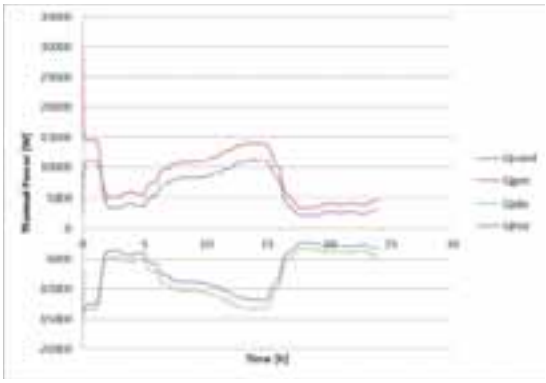

Fig. 10. 24h simulation based on a novel fuzzy logic control strategy

7.4 Comparison between a basic and a fuzzy logic control strategy

In figure 11 the evolution of the electrical COP is presented (same case than in Section7.1 and 7.3). It is clear that using a fuzzy logic approach the COPel is higher than the one achieved by means of a basic control strategy. Large electricity consumption would be expected to be saved by means of this novel approach.

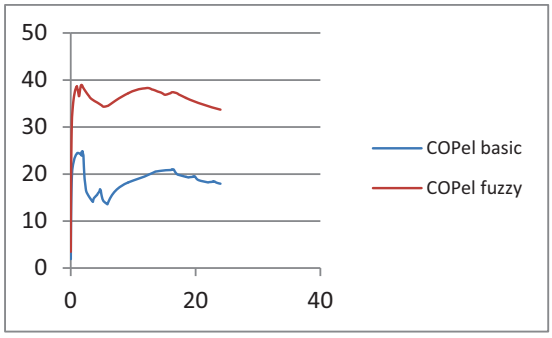

Fig.11 24h COPel evolution

7.5 No control approach

Based on a numerical simulation carried in May for half a day (12h), from 8 am to 8 pm, after 5 hours of a control-based operation (1pm), control is switched-off. Initial basic and fuzzly logic control both have been plotted before switching-off the control device. Then it is shown what would happen regarding freezing and crystallization after basic and fuzzy logic control during the first 5 hours of operation. In the first case we can observe in Fig. 12 the evolution of the primary evaporator temperature after the control is switched off. On the other hand, in Fig. 13 it is described the evolution of the concentration of the LiBr-Water solution inside the desorber vessel. Freezing and crystallization phenomena appear as internal failures. These may damage the absorption chiller operation, being impossible to avoid and leading to operating interruptions if no control strategies are considered, at least in a direct air-cooled absorption chiller.

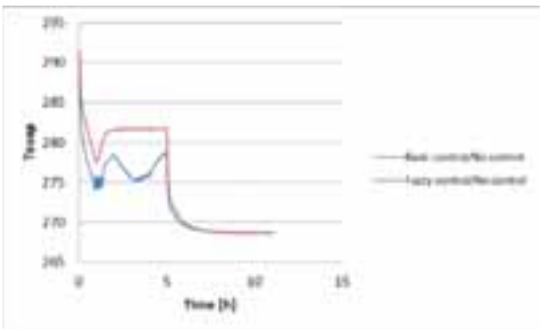

Fig.12 Internal failure if no control is considered (freezing)

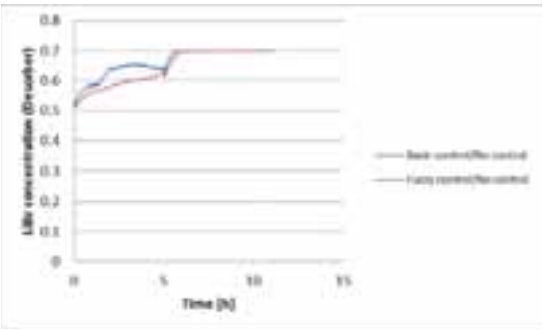

Fig. 13 Internal failure if no control is considered (crystallization)

8. Conclusions

In this work a dynamic model for an air-cooled H_2O-LiBr absorption machine has been used as the basis to implement different kind of control strategies. The model is based in the use of heat & mass transfer empirical correlations of the scientific literature, to avoid ad-hoc adjusts of the main parameters of the absorption refrigeration cycle.
Targeted end users of the absorption chiller must be enlarged in order to go further than domestic applications if an acceptable Return of Investment (ROI) wants to be achieved. In that sense several actions should be performed: increase of the temperature lifts to allow its operation as a heat pump, active/ passive improvements for heat & mass transfer, optimization of transient response, reduction of the total circulating mass flow, and new control strategies to optimize the performance of the chiller and the whole solar cooling facility. Based on this issue and taking into consideration EU regulation, different control approaches of the absorption chiller are herein presented and discussed: i) Inner hot water mass flow regulation, ii) Inner hot water temperature regulation, iii) Basic control regulation, and iv) A novel fuzzy logic control strategy applied to direct air-cooled absorption chillers.

A fuzzy logic approach seems to be the most valuable control strategy, keeping in mind that a multivariable approach, considering inner hot water mass flow regulation, should be focused in the near future. As it has been shown in Fig. 11 the obained COPel based on the fuzzy logic control strategy is clearly higer than the one obtained by means of a basic control strategy. Internal and external behavior are also smoother than a basic control, which help to avoid operation failures such as freezing or crystallization.Therefore, this tool is recommended to be numerically assumed and experimentally validated in further works, quantifying the total energy savings in terms of thermal load and electricity consumption.

9. References

[1] P. Kohlenbach and F. Ziegler. A dynamic simulation model for transient absorption chiller performance. Part ii: numerical results and experimental verification. International Journal of Refrigeration, 31:226{233, 2008.
[2] T.Y. Bong, K.C. Ng, and Tay A.O. Performance study of a solar-powered air-conditioning system. Solar Energy, 39(3):173-182, 1987.
[3] M. R. Yeung, P. K. Yuen, A. Dunn, and L. S. Cornish. Performance of a solar powered air conditioning system in Hong Kong. Solar Energy, 48(5):309-319, 1992.
[4] J. Labus, I. Korolija, L. Marjanovic-Halburd, Y. Zhang, and A. Coronas. ANN application to modelling and control of small absorption chillers. In Proceedings of the BSO12 - Building Simulation and Optimization Conference., pages 245-252, 2012.
[5] X.H. Liao and R. Radermacher. Absorption chiller crystallization control strategies for integrated cooling, heating and power systems. International Journal of Refrigeration, 30(5):904-911, 2007.
[6] GA. Florides, SA. Kalogirou, SA. Tassou, and LC. Wrobel. Design and construction of a LiBr-water absorption machine. Energy Conversion Management, 44:2483-2508, 2003.
[7] M. Izquierdo, M. Venegas, P. Rodríguez, and A. Lecuona. Crystallization as a Limit to Develop Solar Air-Cooled LiBr-H2O Absorption Systems Using Low-Grade Heat. Solar Energy Materials and Solar Cells, 81(2):205-216, 2004.
[8] L. McNeely. Thermodynamic Properties of Aqueous Solutions of Lithium Bromide. ASHRAE Transactions, 85(1):413-434, 1979.
[9] E. García-Rivera, J. Castro, J. Farnós, and A. Oliva. Two Mathematical Models of the Falling Film Absorption in Vertical Tubes. In Proceedings of the 8th IIR Gustav Lorentzen Natural Working Fluids Conference, pages 263-270, 2008.
[10] E. García-Rivera, J. Castro, J. Farnós, and A. Oliva. Simulation of Absorption of H2O in Falling Film of LiBr Aqueous in Vertical Tubes in Wavy Regime. In Proceedings of the International Absorption Heat Pump Conference 2011, pages 59-66, 2011.
[11] E. García-Rivera, J. Castro, J. Farnós, and A. Oliva. Modeling of absorption of h2o vapor in falling film of LiBr aqueous solution in vertical tubes with presence of non-condensables. In Proceedings of the 10th IIR Gustav Lorentzen Conference on Natural Refrigerants, 2012.

[12] E. García-Rivera, J. Castro, J. Farnós, and A. Oliva. Numerical and experimental investigation of a vertical LiBr falling film absorber considering wave regimes and in presence of mist flow. International Journal of Thermal Sciences, 109:342-361, 2016.
[13] A.C. De Vuono, W.T. Hanna, R.L. Osborne, and D.A. Ball. Development of a double-effect air-conditioner heater (DEACH). phase 3 and final report. Overall project report by Battelle and Gas Research Institute., Phase 3 and Final Report, January 1990-December 1991. Phase 3, September 1987-December 1991.
[14] R. A. Zogg and D.Westphalen. Developing Air-Cooled LiBr Absorption for Light Commercial Combined Heat and Power Applications. International Journal of Heat Ventilation Air Conditioning and Refrigeration Research, 12(3b):731-747, 2006.
[15] G. Xie, Q. Wu, X. Fa, L. Zhang, and P. Bansal. A novel lithium bromide absorption chiller with enhanced absorption pressure. Applied Thermal Engineering, 38:1-6, 2012.
[16] J. Labus. Modeling of small capacity absorption chillers driven by solar thermal energy or waste heat. PhD thesis, Universitat Rovira i Virgili, 2011.
[17] J. Albers. New absorption chiller and control strategy for the solar assisted cooling system at the German federal environment agency. International Journal of Refrigeration, 39:48-56, 2014.
[18] http://www.johnsoncontrols.com.
[19] K. Wang, O. Abdelaziz, P. Kisari, and E. Vineyard. State of the art review on crystallization control technologies for water/LiBr absorption heat pumps. International Journal of Refrigeration, 34(6):1325-1337, 2011.
[20] J. López, O. Lehmkuhl, R. Damle, and J. Rigola. A parallel and object-oriented general purpose code for simulation of multiphysics and multiscale systems. In Proceedings of the 24th International Conference on Parallel CFD, 2012.
[21] J. Farnós, G. Papakokkinos, J. Castro, and A. Oliva. Dynamic simulation of an air-cooled LiBr-water absorption chiller based on variable heat and mass transfer coefficients. In Proceedings of the International Sorption Heat Pump Conference, pages 1-3, 2017.
[22] Farnós, J., Papakokkinos, G., Castro, J., and Oliva, A. 2017. Dynamic modelling of an air-cooled LiBr-H_2O absorption chiller based on heat and mass transfer empirical correlations. 12th IEA-Heat Pump Conference.
[23] M. Zamora, M. Bourouis, A. Coronas, and M. Vallés. Pre-industrial development and experimental characterization of a new air-cooled and water-cooled NH_3 -$LiNO_3$ absorption chiller. International Journal of Refrigeration, 45:189-197,2014.
[24] C.P. Underwood. Fuzzy multivariable control of domestic heat pumps. Applied Thermal Engineering, 90:957-969, 2015.
[25] Manual de Instalación. Grupo refrigerantes por absorción de agua caliente WFC10 Yazaki. ESESA

Appendix: Units and Symbols

Table 4: Symbols

Quantity	Symbol	Unit
Mass flow rate	$\dot{m}$	kg s^{-1}
Heat flow rate	*Q*	*W*
Temperature	*T*	*ºC*
Frequency	*W*	*Hz*
Temperature difference	Π	*ºC*
ε	Efficiency	
G	Solar radiation	*W/m2*
THT2C	Thermostat of inner hot water temperature	*ºC*
TCW	Thermostat of temperature of chilled water	*ºC*
TLT	Thermostat of low water temperature of primary circuit	*ºC*
TMT	Thermostat of air mass flow temperature	*ºC*
P1	Pump 1. Chilled water pump	
P2	Pump 2. Hot water pump	
V	Fan	
COP	Coefficient of Performance	

Table 5: Subscripts

Quantity	Symbol
des	Desorber
h	High temperature focus
m	Medium focus (environment)
l	Low temperature focus
cond	Condenser
gen	Generator
abs	Absorber
evap	Evaporator
max	Maximum
in	Inlet value
out	Outlet value
demand	Demand
ref	Reference
el	Electrical
th	Thermal
1	Hot-medium focus temperature difference
2	Medium-low focus temperature difference

Performance Analysis Of a Solar-Powered Air-Conditioning System Using Absorption Refrigeration Cycle And High Efficiency Cooling Technologies Installed In Colombia

Caterina Fella[1], Paolo Silva [2] and Cesar I. A. Rolán [3]

[1] Politecnico di Milano, Milan (Italy)

[2] Politecnico di Milano, Milan (Italy)

[3] Universidad Pontificia Bolivariana, Medellín (Colombia)

Abstract

In this work an analysis of the performance of solar absorption air-cooling system installed to a building office of the Bolivarian Pontifical University (UPB) of Medellín in Colombia is presented. The solar powered, single-effect Li-Br absorption cooling system using evacuated heat pipe collectors, has a nominal capacity of 11,5 kW and it is implemented with a 17,6 kW indirect evaporative cooler (iec), responsible to improve the energy efficiency and to renovate the air in the building, for a total cooling capacity of more than 29 kW (more than 8 refrigeration tons). A system of chilled water capillary mats is implemented for air conditioning, where the heat transfer takes place through a radiant ceiling, reducing recirculation airflow and increasing the temperature of chilled water supplied, allowing a reduction in energy consumption by airflow and an improvement in energy efficiency of the solar-powered absorption cooling system. The performance is evaluated for three main subsystems composing the air conditioning system the absorption chiller, the heat pipe evacuated tube collectors and the indirect evaporative cooler. A series of test-measurements (TMs) are carried out varying the value of one or more particular parameters that affects the performance. Some indicators, which describe the performance, are calculated and compared, so an evaluation of the different TMs is provided. In more is presented an economic comparison with a conventional scheme in order to assess the potential energy savings of the system, the simple payback period of the investment is calculated for different size and cooling demand for Colombian and Italian case.

Keywords: Solar Cooling system, absorption chiller, heat pipe evacuated tube collectors, indirect evaporative cooler, performance analysis, experimental test-measurements, simple payback period

1. Introduction

Buildings produce high CO2 emissions as they consume almost 40% of worldwide energy, and a remarkable percentage of this energy is used for achieving thermal comfort conditions, both in heating and cooling. Thermal comfort is one of the first priorities, as it represents around 65% of building energy consumption [1]. Solar energy is the most widely renewable energy all over the World [2]. Solar power is sufficient to cover the thermal comfort demands in medium and low latitude regions [1] and it is not a fortuity that a solar-powered absorption cooling system was projected in Medellín, whose latitude is 6° 15' 6 N. Among the various solar air-conditioning alternatives, the absorption cooling system appears to be one of the most promising methods[3], because of the fact that the pick concentration of solar energy coincides with the hours when the cooling is required, in more as no chlorofluorocarbons (CFCs) are used, the system is presented as environmentally friendly. The project presented is the 7th out of 8 projects belonging to the National Strategic Plan of Energy Management that includes 4 years last projects in order to implement energy efficiency of Colombia's electric and thermal energy production systems, reduce the emissions and the environment resources depletion. This project was born as implementation of air-conditioning system for a building office, called Building 24, of UPB by Li-Br solar absorption cooling system with evacuated tube collectors. The office selected hosts about 50-80 persons and has an area of 239 m^2, for improving the energy efficiency of the air conditioning system, an indirect-evaporative air cooler (iec) responsible in

doi:10.18086/swc.2017.28.06 Available at http://proceedings.ises.org

renovation of the air, was installed, resulting that the air entering is provided at lower temperature than the temperature outside. Employing both system the thermal capacity needed for the office building is satisfied. The peculiarity of this air-conditioning system consists on the use of chilled water capillary mats instead of conventional fun coils. The heat transfer takes place through a radiant ceiling, reducing recirculation airflow and increasing the temperature of chilled water supplied, allowing a reduction in energy consumption by airflow and an improvement in energy efficiency of the solar-powered absorption cooling system.

2. System description

Medellín is also known as the city of eternal spring, presenting full year mostly sunny weather, with diurnal temperature which oscillate between 22°C and 35°C and a relative humidity between 40% and 75%. For this reason, it suits the solar powered air conditioning system very well. The figure below shows a schematic picture of the system with its principal component by the control screen of the engineering software used in order to test, measure and control its data. The picture with typical values from operation of 5th TM during chilled water production is shown below. For a good understanding, a brief description of the most important sub-system that characterize this configuration of Li-Br solar absorption air conditioning system, in order to justify the technologic choices that have been taken and focus on the specifications needed for proceed to a performance analysis is presented.

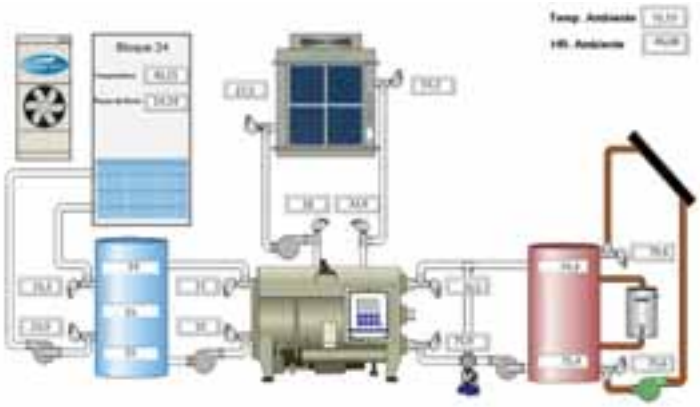

Fig. 1: LabView Control screen of the system

1. Evacuated heat pipe tube collectors (ETCs). The operating temperature of the hot water supplied to the generator of the LiBr-water absorption refrigeration system is about 70°C and 90°C. The lower temperature limit is imposed from the fact that hot water must be at a temperature sufficiently high to be effective for boiling the water off the solution in the generator[4]. For a number of 20 tubes for 10 collectors, the effective lighting area installed resulted of 20.4 m^2. The ETCs are connected directly to the hot water storage tank. Because no evaporation or condensation above the phase-change temperature is possible, the heat pipe offers inherent protection from freezing and overheating. The collectors were installed on the roof of the building chosen. Although it is recommended to incline the collector according to the latitude in order to catching the most direct radiation of the sun, it resulted that didn't permit the natural cleaning of the collectors by the rain and for this reason an inclination of 10° was chosen, and being installed in north hemisphere, they are directed to the south.

2. The absorption chiller constitute the core of the configuration: the refrigerant steam enter into condenser and is cooled down by cooling water flowing in the pipes, that passes from about 35°C to about 25°C, and the refrigerant water gathered in condenser enter into the evaporator by throttling. Because of low pressure (0,6 kPa) in the evaporator, obtained thanks to a vacuum pump, the refrigerant water will be evaporated by absorbing the heat of chilled water flowing in pipes, so that to lower the temperature of chilled water and realize the refrigeration; it is possible to obtain chilled water from 20°C until 7°C (in the picture the temperature in the evaporator are higher

because the screen shot is taken when chilled water production is still not started). In order to work, the temperature out of the tank could not be lower than 65°C and the cooling capacity increases with increase of this temperature.

3. Due to the intermittent nature of available solar energy, hot and chilled water storage tanks of a capacity of 1000 L are needed. They are carbon steel inertia buffer tanks, characterized of a high thermal inertia and insulation, allowing correct management of energy, ideals for the closed cooling circuit, because they act as the installation energy regulation[5]. Because of natural thermal stratification, the top zone of the tank is kept at the maximum temperature, and the bottom one at the lowest.

4. An auxiliary gas heater, of 40 kW of nominal power, directly connected to the tank, activated whenever the heat pipe collectors outlet temperature is less than the temperature required in the generator of the chiller, so that the temperature out of the chiller is not enough to assure the system functioning.

5. Since in an absorption-refrigeration cycle heat must be rejected from the absorber and the condenser, a cooling water system must be employed in the cycle. Because the absorber requires a lower temperature than the condenser, the cool water from the cooling tower is fist directed to the absorber and then to the condenser[4]. It has been chosen a particular closed circuit cooling tower because it is necessary that the water does not present problems of contamination and encrustation. The closed-circuit evaporative cooler is composed by wet panel type adiabatic cooler, in order to decrease the air temperature at the inlet of the coils, two coils of copper tubes and aluminum fins installed in V with an axial fan of variable volume installed on its top, so the air is cooled by ventilator and by adiabatic cooling, to assure high efficiency. The closed-circuit assure to minimize energy consumption and water consumption (the nominal power at maximum capacity is at 1,9 kW) and to avoid contamination problem.

6. Water capillary mats were chosen instead of conventional fun coils, because they result more efficient, exchanging heat by radiation. For this reason, they need a higher minimum temperature for being effective (about 7°C or even until 18°C water temperature, against the fun coil's temperature of 5°C), reducing recirculation airflow and increasing the temperature of chilled water supplied, allowing a reduction in energy consumption by airflow and an improvement in energy efficiency of the solar-powered absorption cooling system. This system is installed in a superimposed form on the "false ceiling", of the top of building 24, required in order to avoid to damage the ceiling in case of condensation of the water inside the tube.

7. Five pipe sections are identified in the system. The tabled below shows, at the sections considered, the diameter of the pipeline and the nominal parameters of the pumps selected (the head, the number of step-speed that could be selected and the power with respect to the working speed):

Tab. 1: Water Pipeline specifications

Section	Diameter internal	Head max	Speeds	Max power input
1 Hot water storage tank - Collectors	0.032 m	10 m	1	245 W
2 Hot water storage tank - Absorption chiller	0.032 m	10 m	1	245 W
3 Chilled water storage tank - Absorption chiller	0.032 m	9 m	3	150-179-196 W
4 Chilled water storage tank - capillary mats	0.063 m	8,5 m	Adapta ble	9..144 W
5 Cooling tower - Absorption Chiller	0.04 m	27 m	1	740 W

8. In order to improve the energy efficiency, to renovate the air in the building, a 17,6 kW indirect evaporative cooler (iec), called Coolerado, was installed, therefore the air entering is at lower temperature than outside; the system draws a maximum of 750 watts of power at full flow[6]. Coolerado system is based on Maisotsenko cycle, a particular case of indirect adiabatic (evaporative) cooling air conditioning system. Humid working air, that constitute about half of the air that enters the heat and mass exchanger is released back into the atmosphere, carrying energy removed from the conditioned air. Chilled fresh air with no added humidity is supplied.

9. Auxiliary and measurement components.

In order to evaluate the performance of the solar cooling system a performance analysis for the three main subsystem that characterised the air conditioning in the Building 24 is carried out: the absorption chiller, the solar collector and the Coolerado.

3. Absorption chiller performance analysis

In order to test the performance of the equipment a series of test measurements (TMs) in different conditions are carried out.

In order to describe and compare the performance of the absorption chiller in different TMs done the performance indicators are estimated by an overall steady-state energy balance on the absorption chiller, neglecting net losses that may occur to the surroundings. Being possible to experimentally calculate the flow rate into the cooling tower ($\dot{m}_{c\,tower}$) from the manifacture's pump flow rate delivered/ power supply curve [12], the power removed by the cooling tower, from the the absorber to the condenser, was calculate as

$$\dot{Q}_{c\,tower} = \dot{m}_{c\,tower} * (T_{cooling,out} - T_{cooling}) \quad \text{(eq.1)}$$

Where

$\dot{m}_{c\,tower} = 1{,}389$ kg/s

$T_{cooling}$ ($T_{c\,tower,out}$) is the temperature of condensation or "Cooling water inlet temperature" to the condenser, coming from the cooling tower.

$T_{cooling,out}$ ($T_{c\,tower,in}$) is the outlet temperature at the condenser, entering the cooling tower.Starting from the nominal performance curve of the equipment[11], furnished by the constructor, with respect to the chilled water outlet, cooling water inlet and hot water inlet temperature respectively, the equation curves of the cooling capacity were extrapolated. In particular, for each measure the cooling capacity ($\dot{Q}_{eva}$) with respect to the following parameter was calculated:

- Temperature of evaporation (T_{evap}) that is "Chilled water outlet temperature" at the evaporator, going to the chilled water tank, according to eq. 2

$$\dot{Q}_{eva} = 0{,}2698 * T_{evap} + 9{,}3811 \quad \text{(eq 2.) [11]}$$

- Temperature of condensation ($T_{cooling}$) according to equation 3

$$\dot{Q}_{eva} = -0{,}889 * T_{cooling} + 37{,}681 \quad \text{(eq.3) [11]}$$

- Temperature of generation (T_{hot}) that is "Hot water inlet temperature" to the generator, coming from the hot water tank), according to equation 4

$$\dot{Q}_{eva} = 0{,}3197 * T_{hot} - 17{,}482 \quad \text{(eq.4) [11]}$$

Indeed for each TM three cooling capacities were found and the correction factor calculated as

$$f_1(T_{evap}) = \frac{\dot{Q}_{eva}(T_{evap})}{\dot{Q}_{nom,evap}} \quad \text{(eq.5)}$$

$$f_2(T_{cooling}) = \frac{\dot{Q}_{eva}(T_{cooling})}{\dot{Q}_{nom,evap}} \quad \text{(eq.6)}$$

$$f_3(T_{hot}) = \frac{\dot{Q}_{eva}(T_{hot})}{\dot{Q}_{nom,eva}} \quad \text{(eq.7)}$$

Where

$\dot{Q}_{nom,eva}$ is the nominal capacity of the absorption chiller equal to 11,5 kW

Assuming valid the overlap of the effect the Coefficient of Performance was find for each TM ($COP_{i,TM}$) as

$$COP_{i,TM} = COP_{nom} * f_1(T_{evap}) * f_2(T_{cooling}) * f_3(T_{hot}) \quad \text{(eq. 8)}$$

Where:

COP_{nom} is the norminal Coefficient of Performance of the machine equal to 0,69.

f_1 is the correction factor of the cooling capacity due to the influence of the chilled water outlet temperature.

f_2 is the correction factor of the cooling capacity due to the influence of the cooling water inlet temperature.

f_3 is the correction factor of the cooling capacity due to the influence of the hot water inlet temperature.

The indicators of performance ($COP_{i,TM}$ and $\dot{Q}_{eva}$) were analyzed during a period in which the air-conditioning supplied by the transient operation of the chiller could be approximated to idealized steady-state operational conditions (the transient operation of the chiller leads to approximately 8% lower COP than would be expected if transients would neglected[7]). In order to compare the performance between each test measurement was chosen an equal period of 45 minutes.

Finally, knowing $COP_{i,TM}$ and $\dot{Q}_{i,c\,tower}$ for each TM, following parameters that characterize the system performance are calculated as:

$$COP_{i,TM} = \frac{\dot{Q}_{eva}}{\dot{Q}_{gen}} \quad \text{(eq. 9)}$$

$$\dot{Q}_{c\,tower} = \dot{Q}_{eva} + \dot{Q}_{gen} \quad \text{(eq. 10)}$$

$$COP_{i,TM} = \frac{\dot{Q}_{eva}}{\dot{Q}_{gen}} \quad \text{(eq. 11)}$$

$$\dot{Q}_{c\,tower} = \dot{Q}_{gen} * (COP_{i,TM} + 1) \quad \text{(eq. 12)}$$

$$\dot{Q}_{gen} = \frac{\dot{Q}_{c\,tower}}{(COP_{i,TM}+1)} \quad \text{(eq. 13)}$$

$$\dot{Q}_{eva} = \dot{Q}_{c\,tower} - \dot{Q}_{gen} \quad \text{(eq.14)}$$

Where

$\dot{Q}_{gen}$ is the heat consumption from the generator.

The results are shown in term of average in the table below:

Tab. 2: Performance results of the absorption cooling system during the five TMs.

	1st TM	2nd TM	3rd TM	4th TM	5thTM
Average during 45 minutes of air conditioning (stable period)					
$\overline{T_{hot}}$ [°C]	72,690	77,320	75,950	79,140	69,930
$\overline{\Delta T_{gen}}$ [°C]	3,484	3,28	3,166	3,380	4,560
$\overline{\dot{Q}_{gen}}$ [kW]	10,589	9,112	8,706	8,713	17,673
$\overline{T_{evap}}$ [°C]	15,330	13,670	16,150	14,140	13,560
$\overline{\Delta T_{evap}}$	2,648	2,308	2,697	2,652	4,030
$\overline{\dot{Q}_{eva}}$[kW]	**4,273**	**4,473**	**4,240**	**4,698**	**6,699**

$\overline{T_{cooling}}$ [°C]	29,530	29,520	29,460	29,430	27,600
$\overline{\Delta T_{cooling}}$ [°C]	2,56	2,340	2,230	2,310	4,198
$\overline{\dot{Q}_{c\ tower}}$[kW]	14,862	13,585	12,946	12,830	24,372
$\overline{COP}_{i,th}$	**0,404**	**0,491**	**0,487**	**0,539**	**0,379**
$\overline{P}_{\substack{air\ cond \\ entire\ period}}$ [kW]	2,8	2,65	2,5	2,4	3,4

Where

$\overline{\Delta T_{gen}}$, $\overline{\Delta T_{cooling}}$, $\overline{\Delta T_{evap}}$ are the average temperature difference inlet and outlet from the generator, the evaporator and the condenser respectively

$\overline{P}_{\substack{air\ cond \\ entire\ period}}$ is the average of total power required by the system.

During all the TMs was never reach the nominal cooling capacity of 11,5 kW, that because of an intrinsic limit of the system that never allows to work with a temperature in the generator (T_{hot}) equal to 90°C . During the start up period, indeed the period in which no vapor would have been involved, the generator consumes a lot of power, as initial and final temperature shown in Table 3. This behavior is more remarked during the 5th TM when working with a cooling temperature lower, and less remarked when working at partial load, during 3rd and 4th TMs.

Tab. 3: Start up period of TMs.

	1st TM	2nd TM	3rd TM	4th TM	5thTM
Start up period [min]	8	7	7	5	5
Lost in temperature [°C]	5,8	7,5	6,5	6,5	8,2

Passing from 1st TM to 2nd TM could be noticed that increasing the inlet temperature of the generator of an average of 5°C (it was necessary to heat the hot water storage tank of 13°C mores, from 79°C to 92°C) the COP increase of 17,7 %. Also the cooling capacity increase of 4% and the time employed in chilled water production decrease of about 48 minutes.

The 3rd TM and 4th TM are characterized by a reduction in evaporator's flow rate, working with the second speed of the pump. It brings to an improvement in the effectiveness of the heat exchange that could be reflected also in an improvement of the COP.

If compare the indicators of the 3rd TM with which were obtained in the 1st TM, that are characterized by more similar generator temperature, the COP passed from to be the 58,6 % of the nominal in the 1st TM to the 70,6 % in the 3rd TM. During 3rd TM, for almost the same cooling capacity, the machine exploit much less thermal power than in the 1st TM (8,7 kW versus 10,6 kW), indeed a better COP is reached allowing the machine to work longer. The air conditioning last 25 minutes more respect to the 1st TM: the machine worked longer, because the minimum conditions required in the generator are guaranteed longer.

The best COP is registered during the 4th TM that is characterized to high temperature in the generator (the thermal storage temperature arrived to 98,4 °C) and better heat exchange effectiveness (the highest difference in chilled temperature, due to reduction of the mass flow rate in the evaporator). In this measurement, it was capable in reaching the 78% of the nominal COP and the cooling capacity improve of 5% with respect to the 2nd TM and the lowest time in production of chilled water was registered.

The 5th TM presented the highest cooling capacity, about equal to the 60% of nominal, but presented the lowest COP registered (about the 55% of the nominal one). That is because in order to provide about 7kW of cooling power ($\dot{Q}_{evap}$) consume about 17 kW of thermal power stored. Such situation provoke that the minimum condition requested from the chiller are extinguished very quickly.

4. Collectors performance analysis

The performance of the collectors are described by the efficiency in term of useful energy delivered in joules: a solar collector receives solar radiation $\dot{Q}_s$ from the sun [product of the surface area, $A_c(m^2)$ and the solar radiation perpendicular to the surface I_p (kW/m^2)] and supplies $\dot{Q}_g$ to a heat engine at the temperature T_H. The ratio of supply heat $\dot{Q}_g$ to the radiation $\dot{Q}_s$ is defined as the thermal efficiency of a solar thermal collector[8]:

$$\eta_{coll} = \frac{\dot{Q}_g}{I_p * A_c} = \frac{\dot{m} c_p (T_O - T_i)}{A_c * I_p} = \frac{\dot{Q}_g}{\dot{Q}_s} \qquad \text{(eq.15)}$$

In order to calculate the flow rate $\dot{m}$ circulating into the collectors were assumed negligible energy loss into the hot water tank and the average flow rate came out from the energy balance was assumed as real constant flow rate delivered by the collectors' pump. The table below resume the collector's performance registered during 3rd TM, 4th TM and 5th TM (measurement for which was possible to measure the solar radiation I by means of the use of pyrometer). In the table below $\overline{\eta_{coll}}$ is the average efficiency of the solar collectors during the whole period of operation; $\bar{I}$ is the average solar radiation registered during the period of operation; P_{peak} is the maximum power output from the collectors registered; $\overline{P_{coll,inst}}$ is the average power output from the collectors; E_{tot} is the total amout of energy provided by the collectors.

Tab. 4: Results of performance analysis of solar collector installed in the Building 24.

	3rd TM (27/03/2017)	4th TM (28/03/2017)	5th TM (25/05/2017)	Weighted Average
$\overline{T_{amb}}$ [°C]	31,40	29,50	30,90	
$\bar{I}$ [W/m^2]	746,50 (725,08*)	723,20 (668,17*)	655,70 (775,6*)	
Collectors ON	11:29 (11:53*)	10:06 (11:23*)	11:12	
Collectors OFF	16:00	15:13	16:00 (13:30*)	
$\overline{\eta_{coll}}$	0,56 (0,57*)	0,50 (0,53*)	0,38 (0,50*)	0,53*
P_{peak}	14,91	15,60	11,08	13,86*
$\overline{P_{coll,inst}}$[kW]	9,82 (9,88*)	9,34(9,79*)	6,14 (8,30*)	9,50*
E_{tot}[kWh/day]	44,34 (40,65*)	47,82 (37,48*)	29,5 (21,9*)	40,97

*The value is referred to the average calculated during the period in which operate also the absorption chiller

The values remarked by the asterisk in the table, resulted higher because when the chiller works and exploit thermal power stored, the collectors' contribution is much more remarkable. Because the generator of the chiller is consuming the power collected into the tank, the temperature entering the collector is lower; indeed the collectors are much more effective, being the difference between temperatures in and out of the collectors higher. This is the condition C of the figure below that point out the performance of the collectors by the temperature difference in and out of the collector in orange related to the radiation incident on the collectors in blue, during the 4th TM. In particular collector efficiency, referring also to the system condition, is affected by the auxiliary heater contribution, that heating the water inside the tank increase its temperature inlet to the collector, so to make inefficient the collector contribution in case the radiation is not enough or the temperature inlet is too high (see Condition D in the figure). This phenomenon is even worse in case the chiller does not work and the auxiliary heater is switched on in order to heat the storage faster. When the Chiller is starting up, a not stable state persists (see Condition B) that addresses an appropriate control behavior; the same happens when the hot water pump is switched on in order to make the temperature into the tank homogenous (see Condition A).

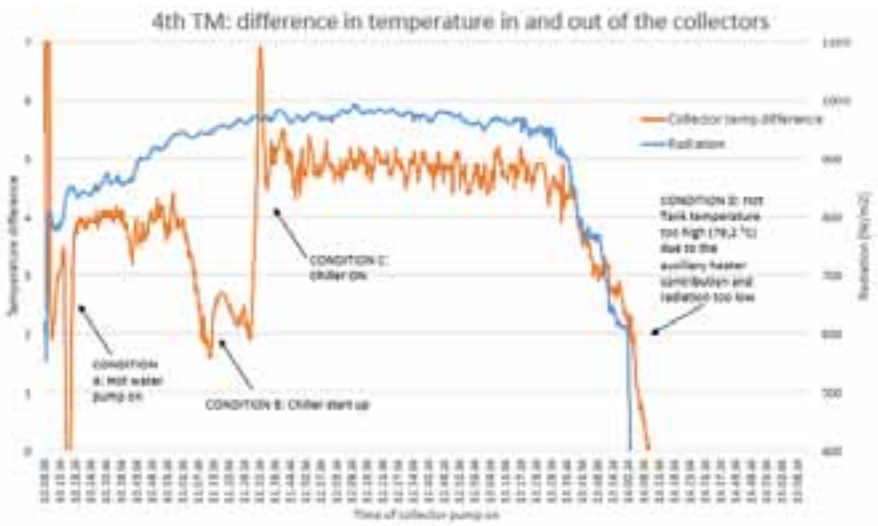

Fig. 2: Collector performance analysis during 4th TM

The 3rd TM registered the best value of global efficiency, instant power output and energy output because presented an higher average radiation and low generator temperature (see Table 4) indeed the condition D happen later. It is the longest measurement in which the collectors works simultaneously with the absorption chiller and the difference in temperature in and out from the collectors was higher (Condition C).

The 5th TM was the measurement in which the Condition C lasts less (only 2h 36min with respect to 3h 50min of the 4th TM and 4h 22 min of the 3rd TM) and indeed the global efficiency is lower. In more, the chiller during its operation required much more thermal power in order to produce a bigger cooling capacity: the collectors could only partially provide to it. This, in fact, suppose that the average temperature difference in and out of the collector, and so the global efficiency and the power output, during absorption chiller operation was lower than in the previous cases because the chiller faster consumes the power provided by them, together with the auxiliary heater.

5. Indirect Evaporative Cooler (iec) performance analysis

Being the IEC performance depending on temperature and relative humidity two different cases were simulated, assuming a constant volume air flow equal to $\dot{V}$= 0,76 m^3/s (maximum value registered in the measurement, assuming the ventilator of the iecworks always at the same speed). Were chosen two favorable weather condition typical of the city of Medellín: relative humidity (r.h.)equal to 30% and dry bulb temperature equal to 33°C. The product air temperature ($T_{product\ air\ flow}$) was calculated through equations furnished by the constructor: with respect to the external static pressure of Medellín the air product temperature should approach at 94% to the wet bulb temperature(T_{wb}). In equation is also considered an about of 2,5% of worsening in performance because of the height of Medellín of 1538 meters [13] :

$$(T_{amb} - T_{wb}) * 0{,}94 * (1 - 0{,}005 * 1538/305) = X \quad \text{(eq.16)}$$

$$(T_{amb} - X) = \text{Design } T_{wb} \quad \text{(eq.17)}$$

$$T_{product\ air\ flow} = \text{Design } T_{wb} + 1{,}1 \quad \text{(eq.18)}$$

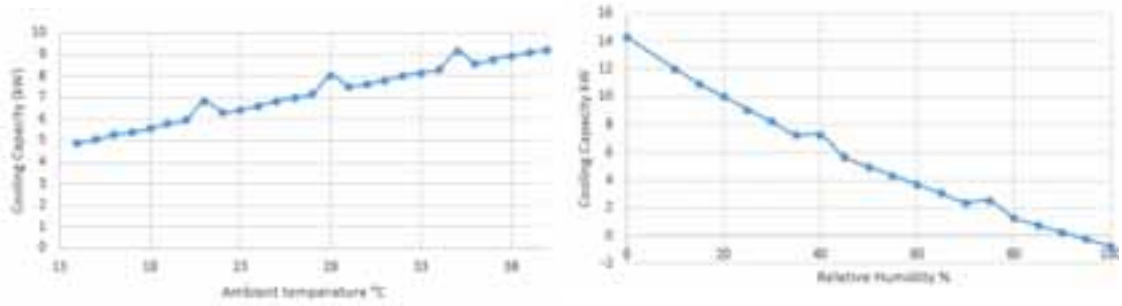

Fig. 3: Iec Performance at a defined relative humidity (r.h.=30%) and dry bulb temperature ($T_{amb} = 33\ °C$)

By these plots it could be seen that in these conditions it is never reach the maximum nominal capacity (17,6 kW): in the first simulation (at r.h.=30%) about 9,2 kW of cooling power is reach at the temperature equal to 40 °C and at temperature under 35°C the capacity is halved. At the ambient temperature of 21, 28 and 35 °C the capacity improve because the difference in wet and ambient temperature registered[9] is higher. Instead, in the second case (at T=33°C) the cooling capacity reaches a maximum of 14,3 kW but decrease really rapidly at relative humidity few lower (reaching negative values at high relative humidity, because the outlet temperature resulted even higher than inlet temperature).

Considering all the tests measurement done so far, it could be said that the air conditioning with the use of iec at Building 24 happens when the temperature oscillates between 33 °C to 23°C and relative humidity between 30% to 72% (without take in account the day in which rain, because in that case is not convenient to work with theiec). Indeed taking into account these ambient condition, and the maximum flow rate registered experimentally, the maximum cooling capacity of the iec is more than 8 kW (a cooling capacity of 8,2 kW was obtained at the best ambient conditions of the air cooling, T=33°C, r.h.= 30%) and an energy consumption of maximum 681,3 W (the maximum experimentally registered).

6. Economic analysis

In order to analyze the economic effort and justify the initial capital cost of the system a comparison with an air cooler Chiller, the most used conventional refrigeration system is done. An analysis of fixed and annual cost was done, taking in account only the purchased equipment costs (PEC) in the fixed capital investment (FCI). The simple payback period was calculated as [10]:

$$Simple\ Payback[years] = \frac{Cost}{Benefit} \qquad \text{(eq. 19)}$$

Where

the $Cost$ are represent by the fixed cost difference between solar and conventional [€]

the $Benefit$ are represented by the variable (annual) cost savings, in primary energy consumption and Operational and Maintenance (O&M) costs, represented by the variable cost difference between conventional and solar systems [€/year]. The analysis was carried on for different size of the system (indeed for different cooling capacity), from the actual case (about 30 kW_{fr}) up to 1300kW_{fr} , and assuming that the expenditure is justified over a long period of cooling demand, the analysis was also done for different operational hours ($t_{op\ hours,year}$) from 3000 h/year up to 1000 h/year. Two different cases were analyzed: Colombian and Italian case, differentiating only for the specific cost of Electrical Energy (EE). For both variable and fixed cost the following assumption were made:

- Specific costs decrease with the increase of the size of the equipment (exchange rate of June20th 2017)
- The sizing of the collectors installed was estimated accounting for cooling capacity and the thermal storage.
- For the equipment which was not possible to provide the specific costs the relationship between the size and the actual cost with a coefficient equal to 0,6 was used.

- The Balance of Plant (BOP) account for a 10% and a 30% of the PEC of the solar and conventional respectively.
- $\bar{P}_{\substack{air\ cond \\ period}} = 2{,}5\ kW$, whose 40% does not depend on the size of the cooling system.
- $COP_{\substack{air\ cooled \\ Chiller}} = 3 \div 4$ variable with respect to the size
- Renewable system works for the half time of its operational hours by thermal energy coming from the auxiliary heater
- $\eta_{auxiliary\ heater} = 0{,}92$
- The O&M costs equal to 4% of the equipment cost of the conventional cooling system and the middle for the solar one.
- $\dot{c}_{natural\ gas} = 0{,}3$ €/Smc (tax free)
- $\dot{c}_{EE,\,Colombia} = 0{,}16$ €/kWh for Colombian case, $\dot{c}_{EE,\,Italy} = 0{,}21$ €/kWh for Italian case (tax free).

The Figures below show the results of the analysis for the Colombian and Italian case.

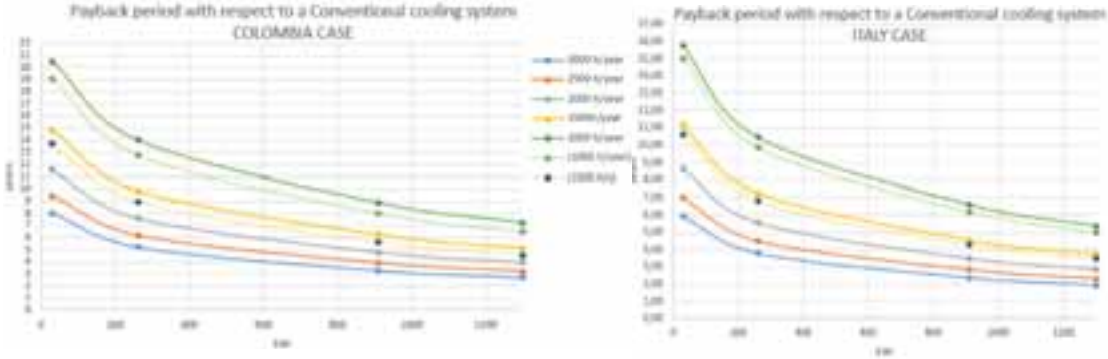

Fig. 4: Results of the payback period between Solar and Conventional cooling system

It is very clear the dependence in size of the equipment: the benefit, indeed the annual primary energy savings in term of money increase so that the ratio to the benefit over the cost decrease exponentially, increasing the size of the system. In Colombia, because of the very low cost of electric energy (0,16 €/kWh), this technology resulted economically convenient (payback period less than 6 years) from capacity few lower than 200 kW if the cooling demand is minimum of 3000 h/years. The situation seems much more convenient for Italy, where the price of electrical energy is 25% higher. The dotted lines represents the payback period for different size of the solar cooling system in case in which it operates 2/3 of the operational hours by sun radiation and 1/3 by thermal energy given by the auxiliary heater, indeed at different share in primary energy consumption. This assumption is done only when the operational hours are lower and indeed is enough to suppose that are present these conditions (1000 and 1500 h/year). For both cases a remarkable improvement could be seen passing from 1000 to 1500 h/year. That because the electric energy consumption has much more heavy contribution for high cooling demand, and the savings are more remarkable with respect to the cost of the investment: it might be not justifiable if the electric energy consumption is not so elevated. In more, should also be noticed that for the electrical energy consumption of the conventional system was assumed a COP that improves with the size; it is not always verified as true, even more if considered that over time the machine is affected by a drop in performance due to wear. Therefore, the payback period curve with respect to the size could present an even more inclined trend, that is traduced with the fact that even shorter period in return of the investment could be expected.

7. Conclusions

The absorption chiller evidenced a cooling capacity lowered of more than the 50 % of the nominal capacity, essentially due to impossibility of the system to maintain a high temperature in the generator. The machine, in fact cannot exploit the nominal thermal power required by the generator (that should be equal to 16,7 kW). Starting from the performance curve provided by the constructor and assuming a linear overlapping of the effects of the generator, evaporator and condenser temperature in the performance of the machine, a lower power furnished by the generator

was registered, (values between 10,5 to 8,7 kW). The problem could be solved doing some modification of the layout:

• The pump that goes from the hot water storage tank to the absorption chiller takes water from the bottom of the tank; indeed, it affects negatively the generator operation due to the thermal stratification inside the tank. It is appropriate to connect the pump to the top of the hot water storage tank, in order to bring into the generator always the hottest water stored.

• The auxiliary heater input is located directly to the hot water tank. A future simulation could be to connect the auxiliary heater in series with the thermal storage. It could lead to provide always the nominal temperature required by the machine, and to avoid the stoppage of the machine, assuring the minimum temperature required in the absorption chiller.

• The pump that goes from the chilled water storage tank to the absorption chiller takes water from the bottom of the tank; indeed, it always sent the coolest water to the evaporator, affecting negatively the heat exchange effectiveness in the evaporator. Move the downstream handle of the chilled water pump to the top part of the tank will increase the difference between inlet and outlet temperature of the heat exchange of the evaporator, increasing the cooling capacity.

With the actual layout, two different operational conditions of the system could be preferred: the one, which could lead to highest COP registered so far, and another that, provides the highest cooling capacity, at a cost of higher energy consumption. These two different configuration are obtained by the lasts two TMs, the 4th and the 5th, proving indeed that during the experimental tests, the right directions in varying operational conditions has being followed. The operational conditions, which lead to optimize the COP, have been reached at 4th TM. Working with the second speeds of the chilled water pump to the evaporator and at the highest temperature that actually could be possible to maintain in the generator, heating the thermal storage up to the limit that avoid the boiling (about 98°C), the effectiveness of the heat exchange in the evaporator improves and the machine produce chilled water exploiting less thermal power in the generator, indeed obtaining the highest values of COP so far registered, equal to 0,54 that is only 20% less of the nominal value. This configuration assure the longest period of work of the chiller because consumes less instantaneous power from the generator. In more, it is assure the lowest value of energy consumption, because both the cooling tower and the pump required less power input. This configuration could be more suitable in case is needed only to maintain the same temperature in the building, and indeed when the cooling demand is lower.

The operational conditions, which lead to optimize the Cooling capacity, have been reach at 5th TM. As the performance curves of the absorption unit shows, lowering the condensation temperature up to the limit that avoid crystallization of the refrigerant flow, increase the cooling capacity of the machine. In particular, it was working with a Tset in the cooling tower equal to 28°C and at maximum capacity in the evaporator, indeed with the third speed of the chilled water pump. It was possible to reach the 60% of the nominal cooling capacity, once have heated the thermal storage up to the boiling limit. This configuration is very useful in case the cooling demand is imminent and big.

The average maximum collectors capacity registered during the TMs done, resulted equal to 13,86 kW, indeed the actual capacity of the collectors does not resulted enough in order to furnished the nominal thermal power required by the absorption chiller. This justify the use of the auxiliary heater during the whole test measurements. Is evidenced an inappropriate control behavior is registered during start up period of the Chiller. In order to improve the capacity of the collectors some improvement have been proposed.

• The actual arrangement of solar collectors sees a series of 5 manifolds in parallel with the same series. In this way the flow rate provided by the pump is separated into two flux. Neglecting the heat loss from the hot tank, the flow rate resulted by the energy balance into the hot tank, is equal to 972 L/h per manifold. Reducing the flow rate, that referring to the datasheet of similar collectors could be even three times lower, the ΔT of the collectors and indeed the power output could improve. Positioning the collectors in series of two, indeed five in parallel could increase them performance.

• The actual arrangement of the auxiliary heater provoke that in case the radiation is low and the temperature inside the storage tank already high (due to the auxiliary heater contribution) the collectors contribution is not effective. The problem could be solved arranging the auxiliary heater in series with the hot water storage tank, so that the

thermal storage is completely depended by the solar energy contribution.

• The actual position of the collectors does not permit to exploit the solar radiation after 4 pm, because the collectors resulted covered by trees' shadows. Very recommended is to move the collector to a different point of the roof of the building.

In order to cover the nominal thermal power required by the absorption unit, dimensioning the capacity of the collectors assuming to receive always an instant power equal to 13, 86 kW, a total of 4,2 m^2 of absorption area of collectors should be added. This corresponds to 4 collectors more (each collectors has 10 tube and each tubes 0,102 m^2 of absorbed area).

From the iec performance analysis, responsible in renovate the air in the building, is evinced that the machine in Medellin condition, and at the actual state of cleaning of filters could furnish a cooling capacity about equal to 8 kW.

From the economic analysis, is evinced the very strong dependence of the simple payback period on the size of the solar cooling system. Increasing the size of the system the benefit, indeed the annual primary energy savings in term of money, increase, so that the ratio of the benefit over the cost decrease exponentially, also due to the lower specific cost of the machine. The payback period is strongly reduced passing from the solar cooling system of a capacity of 30kW to a system of 250 kW. For installed capacity higher than the system analyzed, the technology resulted very convenient not only for a typical Colombian cooling demand (3000 h /year) but also for demand halved, indeed also for an Italian case. Actually in Italy, where the electric energy cost is very high the payback period of the investment resulted in general, much reduced than in Colombia, where the electric energy costs 35% less, due to the wealth of rivers that allows low-cost hydroelectric power production. Considering a cooling demand that could be realistic for Italian weather, equal to 1500 h/year, the technologies proposed resulted convenient (payback period of 6 years) already for system with cooling capacity equal to 500 kW in Italy (the same capacity for Colombian cooling demand has a payback period about of 3years).

Should also be noticed that the economic analysis was carried out considering for the electrical energy consumption of the conventional system a COP that improves with the size; it is not always verified as true, even more considering that over time the machine is affected by a drop in performance due to wear. Therefore, even shorter period in return of the investment could be expected. Anyway, the very good news is that installing an air conditioning system that uses these technologies could make the user richer not only in term of money but also in term of sustainability, because the conditioned ambient in which he will live won't be responsible in remarkable CO2 emissions and won't use any type of refrigerant that impacts the ozone. The user will live not only on a cheap air-conditioned but also environmental-friendly room.

8. References

[1] O. Uribe, J. Martin, M. Garcia-Alegre, M. Santos, and D. Guinea, "Smart Building: Decision Making Architecture for Thermal Energy Management," *Sensors*, vol. 15, no. 11, pp. 27543–27568, Oct. 2015.

[2] M. Beerepoot, "Technology Roadmap Solar Heating and Cooling," *OECD/IEA ; Paris, Fr.*, 2012.

[3] P. J. Wilbur, C. E. Mitchel, "Solar absorption air conditioning alternative," *Sol. Energy*, vol. 17, 1975

[4] S. Kalogirou, *Solar Energy Engineering - Processes and Sistems*, 1st editio. Academic Press - Elsevier, 2009.

[5] "Domestic Hot Water Production and storaga Tanks," 2016.

[6] G. Viacheslav, "SYSTEMS BASED ON MAISOTSENKO CYCLE Coolerado Coolers," 2012.

[7] J. A. Duffie and W. A. Beckman, *Solar_Engineering_of_Thermal_Processes*, Second. John Wiley & Sons, 1980.

[8] S. Kalogirou, *Processes and System*, 1st ed. 2009.

[9]"http://www.meteorivierapicena.net," 2017. [Online]. Available: http://www.meteorivierapicena.net.

[10] J. R. Turner, The Handbook of Project Based Management. McGraw Hill, 2009

[11] S. Lucy, N. Energy, and T. Co, "Operation Manual of Hot Water Operated 目 录 Content."

[12] https://product-selection.grundfos.com/ - product nr 97568429

[13] J. O. B. Name and C. Fan, "M50 Submittal Data Sheet," pp. 1–3

Testing and simulation of a solar diffusion-absorption refrigeration system for low-cost solar cooling in India

James Freeman[1], Ahmad Najjaran[1], Robert Edwards[2], Michael Reid[2], Richard Hall[3], Alba Ramos[1], Christos N. Markides[1]

[1] Clean Energy Processes (CEP) Laboratory, Imperial College London, London (UK)

[2] Solar-Polar Ltd., Peterborough (UK)

[3] Energy Transitions Ltd., Pontypridd (UK)

Abstract

Solar cooling technologies have the potential to improve crop and vaccine supply chain management in areas with unreliable access to an electricity distribution network. The diffusion absorption refrigeration (DAR) cycle is a technology of interest for cooling in rural areas and developing countries due to its low capital cost, low maintenance requirements, and unique design in which the requirement for electrically-driven components are fully omitted. The main feature of DAR systems is a thermally driven bubble pump that is used to circulate the refrigerant and absorbent fluid components around the system. In this paper, we present results from a laboratory DAR system operating over a range of pressures and heat input rates with ammonia-water-hydrogen as the working fluid. By reducing the system pressure from 21 bar to 14 bar, a 17% increase in maximum coefficient of performance (COP) is reported, and the system start-up time is reduced by up to 58%. The results are used to calibrate a thermal model of a solar-DAR system, which is then used to determine the optimal system pressure and solar collector array configuration for summer operation in the location of Chennai, India.

Keywords: Solar cooling, diffusion absorption refrigeration, cold chain, solar thermal collectors

1. Introduction

The DAR cycle was patented by von Platen and Munters in 1928. Its principle of operation differs from that of absorption refrigeration systems based on dual-pressure cycles and binary fluid mixtures in that it is designed for "single-pressure" operation enabled by a third component, which imposes different partial pressures on the refrigerant. The basic design has changed little since the early systems, which use ammonia-water-hydrogen as the working fluid at system pressures of 20-25 bar to utilize thermal energy typically at temperatures of 180-250 °C.

A DAR system schematic is shown in Fig. 1. An ammonia-water solution is heated in the generator (1-2), and boils so that the depleted liquid solution (3) is lifted by the ammonia-rich vapour (4) to the top of the bubble pump. The vapour rises to the rectifier, where most of the remaining water is separated out (5), leaving a near-pure ammonia vapour (6). The ammonia returns to the liquid phase in the condenser (6-7a) and is precooled (7a-9) before entering the evaporator, where it evaporates and diffuses into a reduced partial pressure hydrogen environment, extracting heat from the evaporator's surroundings (9-10). Any uncondensed vapour leaving the condenser bypasses the evaporator entirely (7b-10). Saturated-vapour ammonia mixed with hydrogen exits the bottom of the evaporator and enters the reservoir, then rises through the absorber column where it is absorbed by the downwards flowing weak solution introduced at the top (8a). The hydrogen meanwhile is not absorbed and rises back to the evaporator (8b) via a gas heat exchanger where it is pre-cooled by the downward flowing refrigerant. The liquid solution, having absorbed the ammonia from the upward-flowing gas, settles in the bottom of the reservoir before proceeding to the generator via the liquid heat exchanger (11-1).

Recent research has considered how the DAR cycle can be adapted for use in a lower temperature range with solar thermal collectors. Approaches considered include the use of alternative working fluids (Zohar *et al*. 2009, Ben Ezzine *et* al. 2010, Acuña *et al*., 2013) and the configuration of the generator and bubble pump (Zohar *et al*. 2008, Damak *et al*., 2010). The UK company Solar-Polar has recently developed a solar-DAR system for use in rural cold chain applications. A field-test of the system is currently in preparation at Anna University in Chennai, India (see Fig. 2), where fifteen modular roof-top units will be used to provide cooling to a 34 m^3 insulated cold store. Each unit provides a nominal 60-70 W of cooling from a 0.72 m^2 array of solar heat pipe collectors. A one-year monitoring study will be undertaken in order to assess the seasonal performance of the system.

doi:10.18086/swc.2017.28.07 Available at http://proceedings.ises.org

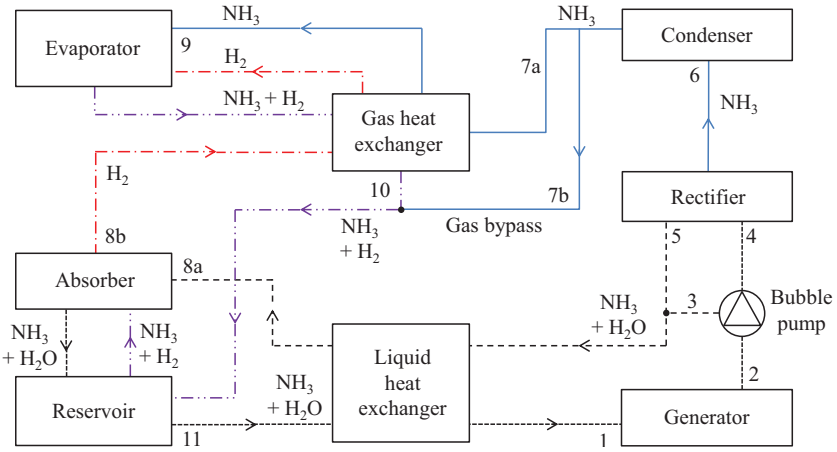

Fig. 1: Schematic diagram of the diffusion absorption refrigeration cycle showing the flows of the ammonia, water and hydrogen working fluid mixture components. For descriptions of the numbered cycle state points, refer to Fig. 3.

To ensure that the units in the pilot study are configured to provide maximum cooling output in Chennai conditions, a predictive model that can capture the performance of the system over diurnal and seasonal time-scales is an invaluable tool. The processes of the DAR cycle are well understood, however many of the models presented in the literature (Zohar *et al*. 2005, Starace and De Pascalis 2012, Taieb *et al*. 2016) use restrictive assumptions about the state of the system that are based on a limited range of operating conditions. In particular, there is a lack of experimentally-validated models for the ammonia-water-hydrogen DAR cycle operating over a wide range of system pressures and solution concentrations. The system pressure is an essential parameter for optimization in solar thermal applications, which represents a trade-off between the operating temperature and efficiency of the solar collector array, and the ability to reject heat from the cycle to the ambient air.

Fig. 2: Solar-Polar DAR demonstration system with heat pipe solar collector array, installed at Anna University campus, Chennai.

In this paper, the Solar-Polar DAR system will be used as the basis for a laboratory study in which the performance of the system will be characterized over a range of operating conditions. The experimental data will be used to calibrate a thermodynamic model of the system developed in earlier work (Freeman *et al*. 2016), and a whole-system solar-DAR model will then be used to simulate performance in the Chennai climate over a range of operating pressures and with various solar collector configurations.

2. Experimental methods

Steady-state tests were performed on the laboratory DAR units over a range of generator heat input powers ($\dot{Q}_{\mathrm{gen}}$) and system charge pressures (p_{ch}). In this paper, results will mostly be presented for a cooling delivery temperature (T_{cool}) of 5 ˚C. The main performance parameter of interest is the cooling power delivered by the DAR evaporator ($\dot{Q}_{\mathrm{evap}}$) and the coefficient of performance (COP), which is defined as the ratio of the cooling output delivered at the evaporator to the heat input provided to the generator. Therefore accurate measurements of both the heat input and cooling output from the system are required.

Heat was provided by five 9.5-mm diameter cartridge heaters, of similar dimensions to the condenser end of the heat pipe collectors used in the solar-DAR setup. The cartridge heaters were fitted into sockets welded to the outer surface of the generator tube. The full length of the bubble pump was insulated with 50 mm of rockwool insulation, while a larger thickness of 100 mm was used to insulate the generator and cartridge heaters. During each steady-state test, the electrical power to the cartridge heaters was maintained at a fixed value, set using an AC autotransformer (variac). The heater power was varied between 0-500 W at intervals of 50 W for each pressure level. Three system charge pressure settings were chosen for the experiments: (i) 14 bar; (ii) 17 bar; and (iii) 21 bar (absolute pressure, measured while the system was at rest under ambient temperature conditions).

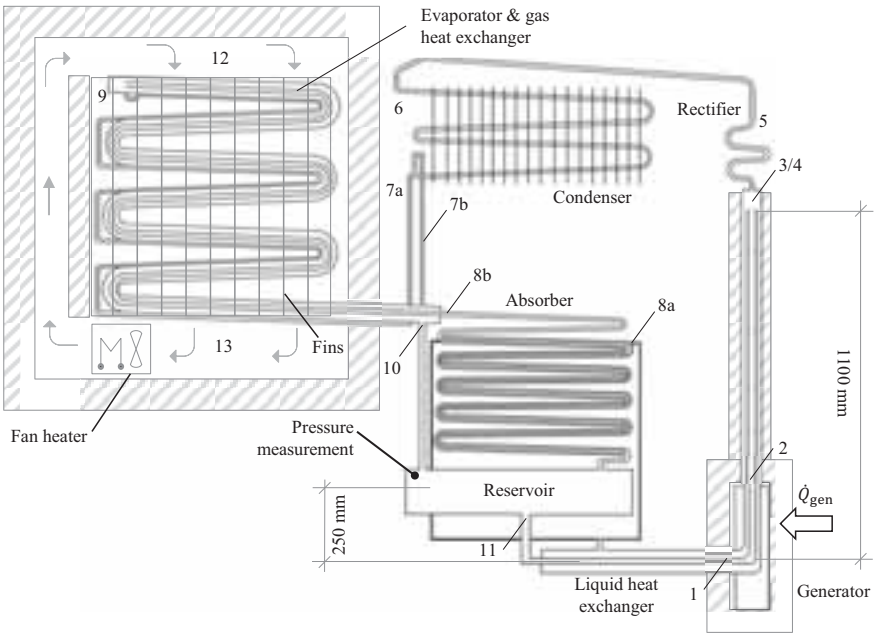

State points

1. Generator inlet	5. Rectifier	8a. Absorber, liquid inlet	11. Reservoir outlet
2. Generator outlet	6. Condenser inlet	8b. Absorber, gas outlet	12. Evaporator air on
3. Bubble pump outlet (liquid)	7a. Condenser outlet (liquid)	9. Evaporator inlet	13. Evaporator air off
4. Bubble pump outlet (vapour)	7b. Condenser outlet (gas bypass)	10. Evaporator outlet	

Fig. 3: Layout of the laboratory DAR system showing major components and numbered state points representing the locations of temperature measurements on the system.

In order to measure the cooling power $\dot{Q}_{\mathrm{evap}}$, a box was constructed around the evaporator using 100 mm thick layers of rigid polyurethane insulation. The internal dimensions of the cold box were 710 × 360 × 110 mm, giving an internal volume of 0.0281 m^3. Sealant was applied around all pipe penetrations in order to minimize air leakage to or from the surroundings. A small electric fan heater placed inside the box was used to control the temperature of the air delivered across the surface of the evaporator. Air was delivered in a downward direction via an insulated channel running along the edge of the box and was distributed between parallel aluminium fins attached to the outer surface of the steel evaporator tubing. The power delivered by the fan heater was controlled so that the "air off" temperature measured at the bottom of the evaporator was maintained at a constant value of 5 °C. Heat losses from the box were estimated in the final COP calculations by assuming a U-value of 0.24 W m^{-2} K^{-1} and an air leakage rate of 0.2 air changes per hour from the cold box.

Detailed temperature measurements were taken on each system sub-component in order to evaluate assumptions used in the thermodynamic model of the cycle (see Section 3.1). For some of the locations, measurement of fluid temperatures was challenging, for example in the concentric tube (pipe-in-pipe) heat exchangers in the evaporator and bubble pump. The apparatus was modified to include thermowells welded into the pipework so that fluid temperatures in the inner tube of the bubble pump could be measured more accurately at locations 2 and 3. Elsewhere in the system, most fluid temperatures were estimated from measurements in contact with the outer surfaces of the steel tubes. A direct measurement of system pressure during the tests was also provided by a pressure transducer located at the fluid reservoir. For each run, the system was operated under steady-state

conditions for a period of one hour while temperatures, pressure and electrical input power to the cartridge heaters and fan heater were measured at intervals of 1 second. Air temperature in the laboratory was maintained at approximately 25 ºC, although some variation of ± 2 ºC was found to occur between the tests.

Previous experimental studies by Mazouz *et al.* (2014) and Ben Jemaa *et al.* (2016), among others, have noted that the starting characteristic of DAR systems varies significantly with heat input rate. During the start-up process, the solution in the generator is heated until it transitions from nucleate boiling to a state where significant bubble coalescence takes place to provide lifting of the liquid solution through the entire length of the bubble pump. Shelton and White (2002) and Hanafizadeh *et al.* (2014) have discussed the conditions under which the bubble pump processes are dominated by slug flow or churn flow regimes. It is important to consider the dynamic behaviour of the system in any situation where the heat source is intermittent (such as solar applications), and therefore in the present work the temperature profiles of the generator during start-up will be used to determine the thermal capacity and minimum starting temperature under various operational settings.

3. Modelling methodology

A model of the solar-DAR system was developed to evaluate its performance under realistic climatic conditions and to select the most appropriate operational settings for the chosen location. In this paper, the model is used to investigate the optimal system pressure and solar collector array configuration for summer operation in Chennai. The sub-models of the DAR cycle and the solar collector sub-systems are described in the following sections.

3.1. DAR system sub-model

The thermodynamic model of the DAR cycle is based on the equations of Starace and De Pascalis (2012), and consists of 6 lumped sub-component models: (i) generator and bubble pump; (ii) rectifier; (iii) condenser; (iv) evaporator; (v) absorber; and (vi) liquid-solution heat exchanger. The energy balances for each component are shown in Eqs. 1-6, where $\dot{m}$ is mass flow rate in kg s^{-1}, $\dot{Q}$ is heat flow rate in W, h is specific enthalpy in J kg^{-1}, and "ig" denotes hydrogen (inert gas). The numbered state points correspond to those shown in Figs. 1 and 3.

$$\dot{Q}_{\mathrm{gen}} = \dot{m}_3 h_3 + \dot{m}_4 h_4 - \dot{m}_1 h_1 + \dot{Q}_{\mathrm{bp,loss}}, \quad \text{(eq. 1a)}$$

$$\dot{Q}_{\mathrm{bp,loss}} = \dot{m}_3[h_3 - h_{\mathrm{l}}(T_2)] + \dot{m}_4[h_4 - h_v(T_2)], \quad \text{(eq. 1b)}$$

$$\dot{Q}_{\mathrm{rect}} = \dot{m}_5 h_5 + \dot{m}_6 h_6 - \dot{m}_4 h_4, \quad \text{(eq. 2)}$$

$$\dot{Q}_{\mathrm{cond}} = \dot{m}_6(h_7 - h_6), \quad \text{(eq. 3)}$$

$$\dot{Q}_{\mathrm{evap}} = \dot{m}_9(h_{10} - h_{7\mathrm{a}}) + \dot{m}_{\mathrm{ig}}\left(h_{10,\mathrm{ig}} - h_{8\mathrm{b,ig}}\right), \quad \text{(eq. 4)}$$

$$\dot{Q}_{\mathrm{abs}} = \dot{m}_{11} h_{11} - \dot{m}_{10} h_{10} - \dot{m}_{8\mathrm{a}} h_{8\mathrm{a}} + \dot{m}_{\mathrm{ig}} h_{8\mathrm{b}} - \dot{m}_{\mathrm{ig}} h_{10,\mathrm{ig}} - \dot{m}_{7\mathrm{b}} h_{7\mathrm{b}}, \quad \text{(eq. 5)}$$

$$\dot{m}_3 h_3 + \dot{m}_5 h_5 - \dot{m}_{8\mathrm{a}} h_{8\mathrm{a}} = \dot{m}_1(h_1 - h_{11}). \quad \text{(eq. 6)}$$

The thermodynamic properties of the ammonia-water mixtures were calculated using the correlations of Patek and Klomfar (1995), and REFPROP was used to calculate the properties of hydrogen. The DAR system models presented in Zohar *et al*. (2005) and Starace and De Pacalis (2012) require temperatures to be specified as inputs at several points in the cycle, including the inlet and/or outlet of the generator, condenser, evaporator and reservoir. The aim in the present work is to predict DAR performance using only the local climatic conditions, and information on the system charge pressure and thermal input provided from the solar collector array. Thus the experiments in this study will be used to characterize the performance of the various system components, and the following additional relations will be formulated for the bubble pump, rectifier and condenser:

$$T_2 = f(p, \dot{Q}_{\mathrm{gen}}), \quad \text{(eq. 7)}$$

$$T_6 = T_4 - \varepsilon_{\mathrm{rect}}(T_4 - T_{\mathrm{a}}), \quad \text{(eq. 8)}$$

$$\dot{Q}_{\mathrm{cond}} = UA_{\mathrm{cond}}\Delta T_{\mathrm{LMTD}}. \quad \text{(eq. 8)}$$

The following assumptions were also used: (i) the mass fraction of the rich ammonia-water solution entering the generator from the reservoir is fixed at 30% NH_3, with no hydrogen present; (ii) the preheated solution enters the generator as a saturated liquid; (iii) the refrigerant enters the condenser as a saturated vapour.

3.2. Solar collector sub-model

Two types of solar heat-pipe collector will be investigated for use with the DAR system. Collector 1, shown on the left in Fig. 2a, is a classic low-cost design consisting of a heat pipe with an aluminium fin inside an all-glass tube formed of two concentric layers. The annulus is evacuated, and a solar absorbing coating is applied to the inner glazed layer. Collector 2, shown on the right in Fig. 2a consists of a single-glazed tube with a fully evacuated core that contains a copper tube with a textured fin. The heat pipe is inserted inside the copper tube, and the solar absorbing coating is applied directly onto the surface of the metal fin. The former type of collector is easily mass-produced and available at very low costs in bulk quantities, while the latter tends to be more expensive due to the high-quality glass-to-metal seal required at the copper tube penetration point.

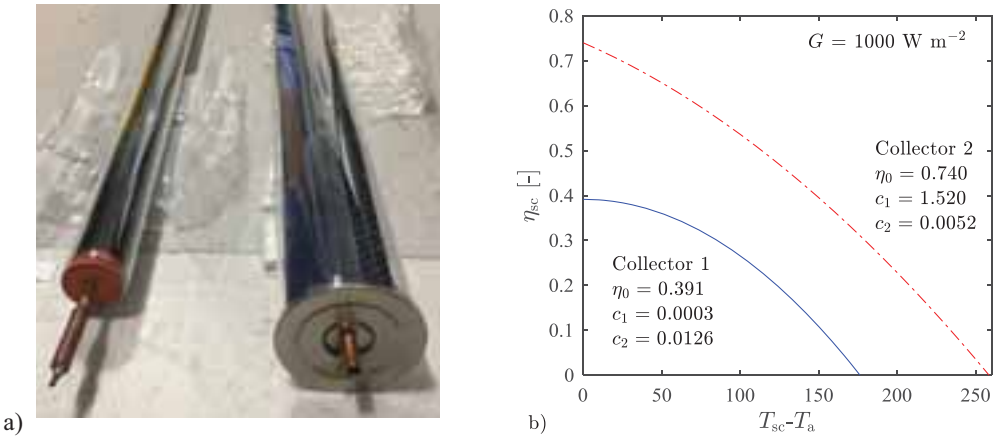

Fig. 4: (a) Photograph showing two heat pipe collector types investigated for use with the solar-DAR system: Collector 1 (left) and Collector 2 (right). (b) Efficiency curve plots for the two collectors (aperture area basis, G = 1000 W m^{-2}).

The efficiency curves for the two heat pipe collectors are compared in Fig. 2b, showing a higher zero-loss efficiency and stagnation temperature for Collector 2. The efficiency curve coefficients for Collector 2 were taken from a Solar Keymark performance test report (SPF, 2009). In the absence of existing performance data for Collector 1, the collector was tested in-house under irradiance conditions of 1000 W m^{-2} and a temperature range of 30-180 ˚C to obtain the efficiency curve coefficients η_0, c_1 and c_2 in Fig. 2b. The coefficients are used in the solar-DAR system model to calculate the collector's useful heat output $\dot{Q}_{\mathrm{sc}}$ as a function of the solar irradiance (direct and diffuse components G_{b} and G_{d}), collector temperature T_{sc} and ambient temperature T_{a}:

$$\dot{Q}_{sc} = \eta_0 A\left(K_{\theta,\mathrm{b}} G_{\mathrm{b}} + K_{\theta,\mathrm{d}} G_{\mathrm{d}}\right) - c_1 A(T_{\mathrm{sc}} - T_{\mathrm{a}}) - c_2 A(T_{\mathrm{sc}} - T_{\mathrm{a}})^2. \qquad \text{(eq. 9)}$$

The main dynamic component considered in the system model is associated with the thermal capacity C of DAR generator, which will be determined experimentally. The collector's effective thermal capacity is assumed to be small by comparison and is therefore not included in the model. The thermal conductance $(UA)_{\mathrm{gen}}$ between heat pipe collector and the DAR generator is also required to solve the following energy balance at 1-min intervals:

$$\dot{Q}_{\mathrm{sc}} = \dot{Q}_{\mathrm{gen}} + C\frac{dT_{\mathrm{gen}}}{dt} = (UA)_{\mathrm{sc-gen}}\left(T_{\mathrm{sc}} - T_{\mathrm{gen}}\right). \qquad \text{(eq. 10)}$$

3.3. Climate data for diurnal simulation

In the present study, the system operation will be simulated for a "peak solar" day in Chennai, India, using climate data published by ASHRAE (2001). The region of Chennai experiences high solar irradiance during the summer season, between the months of March to May. From June onwards, the weather is typically cloudier with periods of heavy rainfall. The day chosen for the simulation is the 3$^{\mathrm{rd}}$ of May.

4. Results and discussion

4.1. Experimental results – steady-state performance

Plots of cooling power and COP over the range of steady-state heat inputs are presented in Fig. 5 at the three system charge pressure settings 14 bar, 17 bar and 21 bar. It was found that for $p_{\mathrm{ch}} \geq 17$ bar, it was not possible to achieve the cooling delivery temperature of 5 ºC at $\dot{Q}_{\mathrm{gen}}$ values < 150 W.

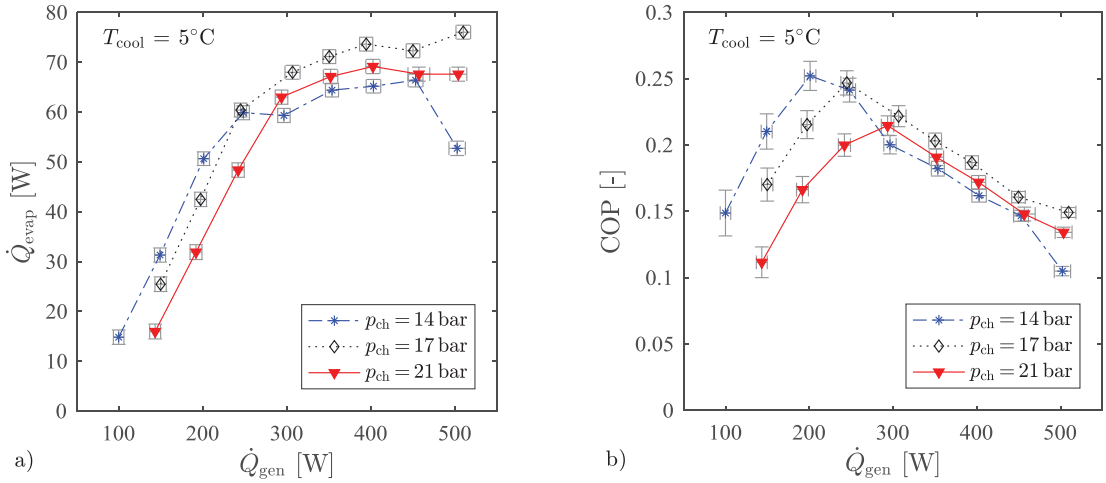

Fig. 5: Experimental results: (a) cooling power and (b) COP, at various charge pressures and for a cooling temperature of 5 °C.

The cooling output is shown to increase with generator heat input, however a change in the trend is observed at values of $\dot{Q}_{gen}$ around 200-300 W, that also corresponds to the peak COP of the system. The same behaviour was also observed in the study by Chen *et al.* (1996) who noted that for a further increase in heating input power beyond this point, liquid refrigerant begins to exit the evaporator.

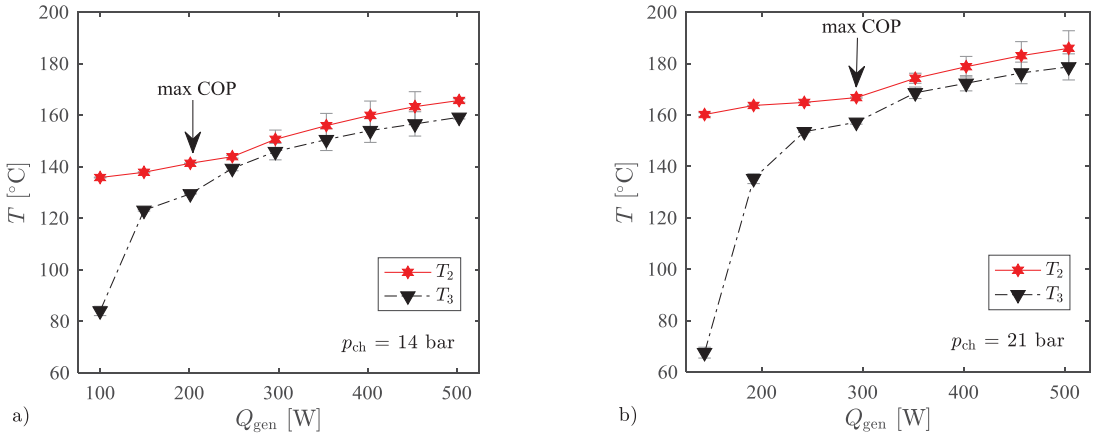

Fig. 6: Temperature at States 2 and 3 (generator outlet and top of the bubble pump, respectively), for system charge pressures of: (a) 14 bar and (b) 21 bar. Error bars denote standard deviation of measured values over the measurement period.

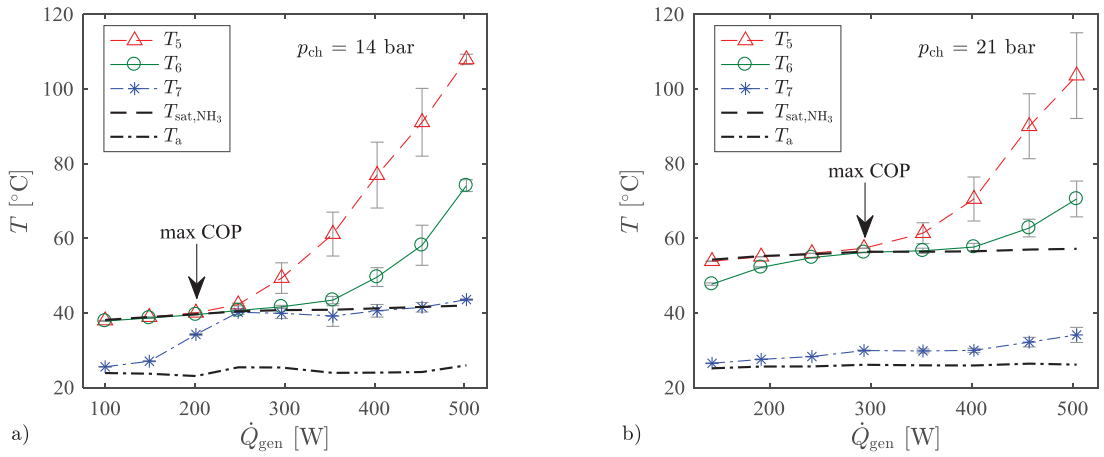

Fig. 7: Temperature at States 5, 6 and 7 (rectifier, condenser inlet and condenser outlet, respectively), for system charge pressures of: (a) 14 bar and (b) 21 bar. Also shown are the ambient air temperature T_a and the saturated liquid temperature of the refrigerant T_{sat,NH_3}. Error bars denote standard deviation of measured values over the measurement period.

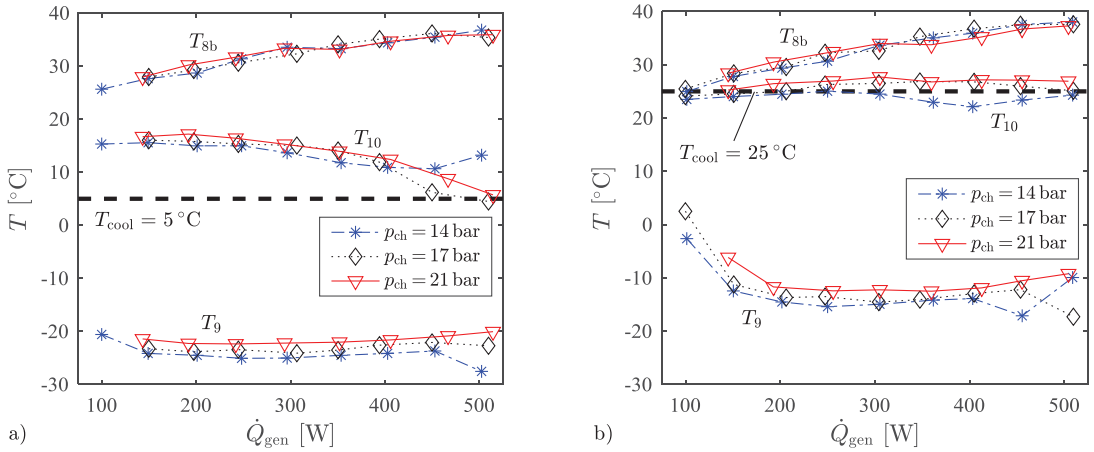

Fig. 8: Temperature at State 8b, 9 and 10 (absorber gas outlet, evaporator inlet and evaporator outlet, respectively), for cooling delivery temperatures (indicated by the dashed line) of: (a) 5 ºC and (b) 25 ºC, and for various values of p_{ch} and $\dot{Q}_{gen}$.

The mean temperatures measured along the bubble pump are plotted in Fig. 6. At low heat input rates, a large difference can be observed between the temperature at the top of the bubble pump T_3 and at the lower part of the bubble pump close to the generator T_2. At higher heat input rates this temperature difference is far smaller, indicating a change in flow regime that results in a lower level of heat dissipation according to Eq. 1b.

Full utilization of the rectifier and condenser is found to be a key factor in maximizing COP. Figure 7 shows the measured rectifier and condenser inlet and outlet temperatures; also indicated are the ambient air temperature and the saturation temperature of pure ammonia at the operating pressure of the DAR system. The highest COP is achieved at the point where the temperature at the condenser inlet (T_6) is very close to (slightly higher than) the saturation temperature of ammonia, such that the maximum flow-rate of ammonia with the minimum of water content was conveyed to the evaporator. At lower heat inputs, temperatures measured along the rectifier indicate that the condensation of ammonia occurs prior to the inlet of the condenser, thus resulting in some drain back of ammonia to the generator and a lower COP. At higher heat input rates, higher temperatures at the condenser inlet indicate that a larger fraction of water is present in the saturated vapour entering the condenser.

At the lowest heat inputs, significant subcooling is achieved at the condenser, where exit temperatures approach that of the ambient air. However, at the lowest system pressure p_{ch} = 14 bar and $\dot{Q}_{gen}$ > 250 W, Fig. 7a indicates that the fluid exiting the condenser is no longer subcooled, exiting the condenser in a two-phase state at the refrigerant saturation temperature. The uncondensed fraction of the refrigerant flow is diverted from the evaporator to the absorber via the gas bypass tube, and the result is a lower cooling output at higher values of $\dot{Q}_{gen}$ than achieved at p_{ch} = 17 bar (see Fig. 5a).

The evaporator inlet and outlet temperatures (T_9 and T_{10}, respectively) were found to vary with cooling delivery temperature more than system pressure or generator heat input. At a cooling delivery temperature of T_{cool} = 5 ºC (Fig. 8a), the evaporator inlet temperature is between -22 and -25 ºC across most of the heat input range, while for a cooling delivery temperature of T_{cool} = 25 ºC (Fig. 8b) it is between -12 and -15 ºC. In the former case, it should be noted from Fig. 8a that the evaporator outlet temperature is higher than the cooling delivery temperature due to the counterflow heat exchange with the warmer flow of hydrogen gas flowing upwards from the absorber, which enters the gas heat exchanger at the higher temperature of T_{8b}.

4.2. Experimental results – dynamic performance during system start-up

Figures 9a and 9b show generator temperature plotted against time during the start-up process, for a range of fixed heat input rates and for system charge pressures of 14 bar and 21 bar respectively. Temperature is shown to increase until the point at which the bubble pump begins to lift the solution from the generator, which is then replaced by a continuous flow of lower-temperature fluid from the reservoir. The start times and peak generator start-up temperatures for the range of test conditions are presented in Fig. 10.

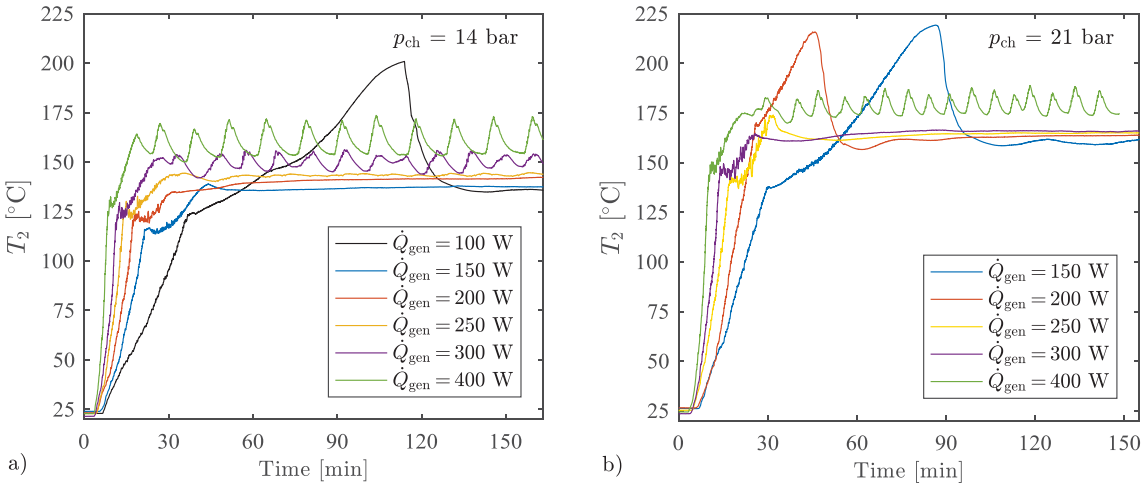

Fig. 9: Generator temperature at various steady heat input rates during start-up for: (a) 14 bar and (b) 21 bar charge pressure.

The lowest values of $\dot{Q}_{gen}$ are characterized by an "overshoot" of the generator temperature followed by a sudden drop in temperature as the system transitions to steady-state operation. Meanwhile, for the highest values of $\dot{Q}_{gen}$, an oscillating behaviour is observed for the generator temperature after the transition to steady-state. At intermediate values of $\dot{Q}_{gen}$ corresponding to peak COP, neither of these aforementioned behaviours are observed. In all cases there is a noticeable change in the rate of increase of the generator temperature during the initial heating of the solution that represents the onset of boiling, after which the temperature continues to increase at a slower rate (as is characteristic for non-isothermal phase-change processes in two-component mixtures) until the start of the bubble pump operation.

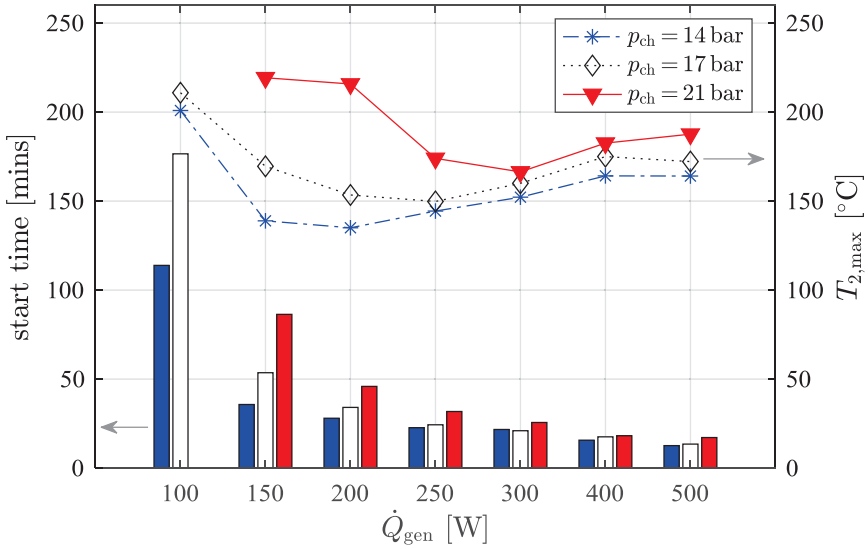

Fig. 10: Experimental results showing start-up time (bar plots) and peak generator start-up temperature (line plots) at various steady heat input rates. Shown for system charge pressures of 14 bar (blue), 17 bar (white) and 21 bar (red).

The peak in temperature observed at low values of $\dot{Q}_{gen}$ is significant. At p_{ch} = 14 bar and $\dot{Q}_{gen}$ = 100 W, the generator temperature reaches a maximum value of 201 ºC, which is 65 ºC above the temperature observed during steady-state operation. A likely reason for this is that slow nucleate boiling of stagnant fluid in the generator under low heat-flux conditions leads to a depletion of ammonia from the solution. This gradually raises the temperature at which the coalescence of bubbles is sufficient to lift liquid solution upwards in the bubble pump, before cooler solution can flow from the reservoir. At higher values of $\dot{Q}_{gen}$, there is a faster transition from nucleate boiling to flow boiling before significant depletion of the ammonia-rich solution occurs, with the result that no observable overshoot of the generator temperature occurs.

4.3. Model calibration

The results of the steady-state experiments were used to calibrate the system model. Table 1 contains a list of relations that were used to determine the state of the system according to certain environmental parameters or operational settings. The DAR system pressure p at each time instant in the model is determined as a function of the initial charge pressure p_{ch} and the generator temperature T_2. An additional equation is also included to describe the relationship between $\dot{Q}_{\mathrm{gen}}$, T_2 and p based on the experimental data. The conductance value $(UA)_{\mathrm{sc-gen}}$ describing the heat transfer between the solar heat pipe collectors and the generator was estimated from observations of the temperature difference between the cartridge heaters and generator during the tests. The parameters C and $(UA)_{\mathrm{gen-amb}}$ were estimated from the time constant of the temperature response of the generator during start-up and after shut-down. The conductance value $(UA)_{\mathrm{cond}}$ was estimated using temperature profiles measured along the two-phase (condensation) and single-phase (subcooling) zones of the condenser.

Figure 11 shows that the calibrated model gives a reasonably good prediction of cooling output, particularly at the lower end of the range of $\dot{Q}_{\mathrm{gen}}$ values, and correctly captures the trend of the COP curve. However, at higher values of $\dot{Q}_{\mathrm{gen}}$ (beyond those corresponding to the peak COP) the model is shown to over-predict $\dot{Q}_{\mathrm{evap}}$ by ~10% at $p_{\mathrm{ch}} = 14$ bar, and under-predict $\dot{Q}_{\mathrm{evap}}$ by ~15% at $p_{\mathrm{ch}} = 21$ bar.

Tab. 1: Supplementary equations and input parameters used in the solar-DAR system model.

Parameter	Value / Equation
p	$p = p_{\mathrm{ch}} + 0.123 \times 10^{-3} \cdot (T_2 - 25)^2$
$\dot{Q}_{\mathrm{gen}}$	$\dot{Q}_{\mathrm{gen}} = 14.2\,T_2 + 34.8\,p - 1293$
$\varepsilon_{\mathrm{rect}}$	$\varepsilon_{\mathrm{rect}} = 0.85$
$(UA)_{\mathrm{cond}}$	$(UA)_{\mathrm{cond}} = 5.5$
$(UA)_{\mathrm{sc-gen}}$	$(UA)_{\mathrm{sc-gen}} = 5$
$(UA)_{\mathrm{gen-amb}}$	$(UA)_{\mathrm{gen-amb}} = 0.3$
T_9	$T_9 = T_{\mathrm{cool}} - 28$
T_{10}	$T_{10} = T_9 + 37$
T_{11}	$T_{11} = T_{\mathrm{amb}} + \left(2.406 + 36.7\dot{Q}_{\mathrm{gen}}/1000\right)$
T_{8b}	$T_{8b} = T_{11} - 0.5(T_{11} - T_{\mathrm{a}})$
$\dot{Q}_{\mathrm{bp,loss}}$	$\dot{Q}_{\mathrm{bp,loss}} = \dot{Q}_{\mathrm{gen}}\left(0.65 + 0.025p - 0.0039\dot{Q}_{\mathrm{gen}}\right)$
$T_{\mathrm{gen,min}}$	$T_{\mathrm{gen,min}} = 85 + 3.6p_{ch}$
$T_{\mathrm{gen,start}}$	$T_{\mathrm{gen,start}} = 90 + 10.3p_{\mathrm{ch}} - 0.536\dot{Q}_{\mathrm{gen}}$

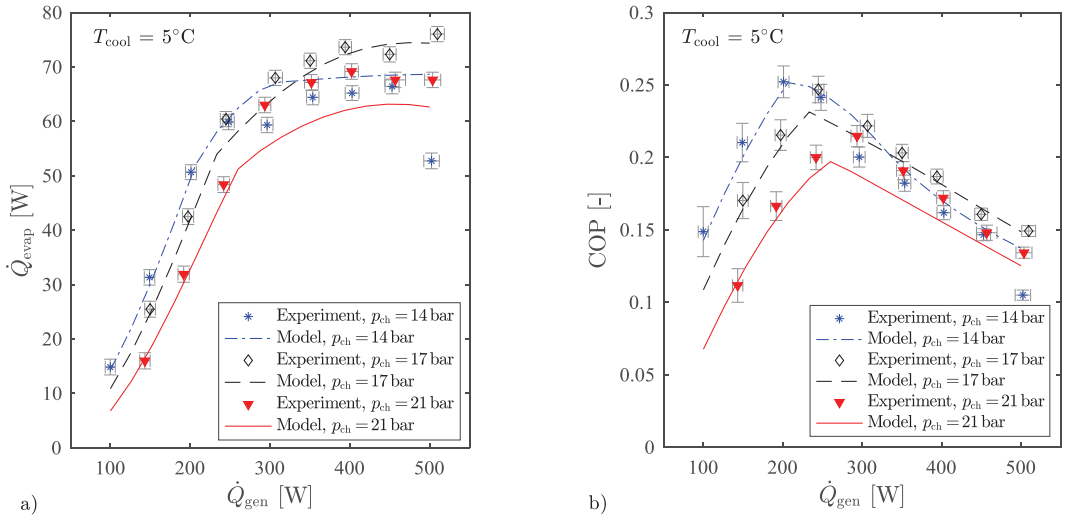

Fig. 11: Line plots showing predictions of (a) cooling power output and (b) COP from the calibrated DAR system model, overlaid with experimental data points for the corresponding charge pressures and heat input rates.

4.4. Solar-DAR system performance simulation

The solar-DAR system model, with the calibration parameters listed in Table 1 as inputs, was used to simulate the performance of the solar-DAR system on a "peak solar" day in Chennai, India. From the climate dataset, the maximum solar irradiation was found to occur on 3rd May. The peak ambient air temperature on this day is 39 ºC. Diurnal simulations were performed at system charge pressures between 12-21 bar and a delivered cooling temperature of 5 ºC. The solar collector array area was varied between 0.5-5 m^2, using Collector Types 1 and 2 presented in Section 3.2.

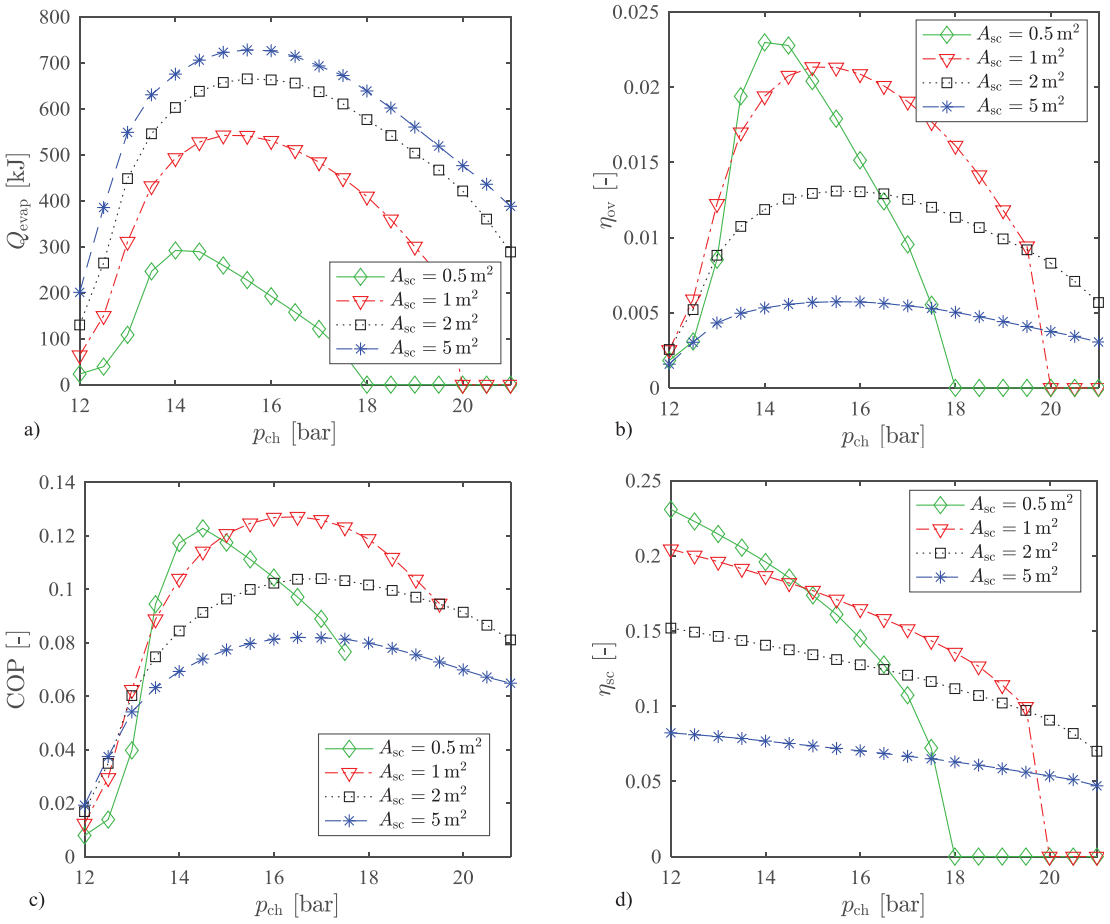

Fig. 12: Diurnal simulation results for the solar-DAR system with Collector Type 2, showing (a) total cooling output, (b) overall (solar to cooling) efficiency, (c) refrigeration cycle COP and (d) solar collector efficiency, plotted against DAR system charge pressure. Simulations are performed with various collector array areas, and a cooling delivery temperature of 5 °C.

The plots in Fig. 12a show the total daily cooling energy delivered with Collector 2 over the range of operating pressures and collector areas. As expected, cooling output increases with solar collector area, however for each doubling of the array size beyond 1 m^2, the improvement in maximum cooling output becomes smaller, indicating a higher cost per unit of cooling energy delivered; while maximum cooling output occurs at progressively higher system pressures as the array size is increased. Figure 12b shows that a maximum overall (solar to cooling) efficiency of 2.3% is achieved with 0.5 m^2 of collector array and a system pressure of 14 bar. For 1 m^2 of collector array area, a slightly lower maximum overall efficiency is achieved, however the system is able to operate over a wider range of system pressures and the DAR operates with a slightly higher COP, delivering an average power of 26 W over a 5.8 hour operating period. Figure 12c shows that with 1 m^2 of collector a DAR daily COP of up to 12.7% is achieved for a system pressure 16.5 bar. It can be seen in Fig. 12d that as system pressure is increased, the solar collector efficiency decreases due to higher collector temperatures and shorter operating periods of the DAR system; while larger collector array areas are needed to provide sufficient heat to the generator. Thus, from these results it can be predicted that an "optimal" summer-day configuration for the DAR system in Chennai is between 14-16.5 bar, with a collector array area of 0.5-1 m^2.

The simulated performance of the solar-DAR system was considerably poorer with Collector 1, delivering less than 25% of the daily cooling energy predicted with Collector 2 for an equivalent collector array area. Furthermore with Collector 1, a minimum array area of 2 m^2 was required in order to deliver sufficient thermal energy to start the system; while with an array area up to 10 m^2 the system could only operate at pressures < 14 bar.

Figures 13a and 13b show profiles of the system temperatures and energy flows over the diurnal operating period for the solar-DAR system charge pressure of 14 bar and 19 bar respectively, and with a 1 m^2 array area of the higher efficiency solar collectors (Collector Type 2) as the heat source. The figures illustrate the trade-off between the lower operating temperatures, higher collector efficiency, and longer operational period achieved at the lower system pressure; compared to the higher cooling power output during the middle of the day achieved at the higher system pressure. It can also be observed in Fig. 13a that at 14 bar the lower saturated liquid temperature of the working fluid in the condenser (shown by the green line) results in only partial condensation of the working fluid under the warm ambient conditions. As a result, 40% of the mass-flow of refrigerant bypasses the evaporator, resulting in a significant loss of cooling potential illustrated by the energy flow $\dot{Q}_{gb} = X_7 \dot{m}_r \Delta h_{fg}$. At the higher system pressure of 19 bar in Fig. 13b, the difference between the saturated liquid temperature of the working fluid in the condenser and the temperature of the ambient air is larger and therefore for most of the operating period, full condensation is achieved.

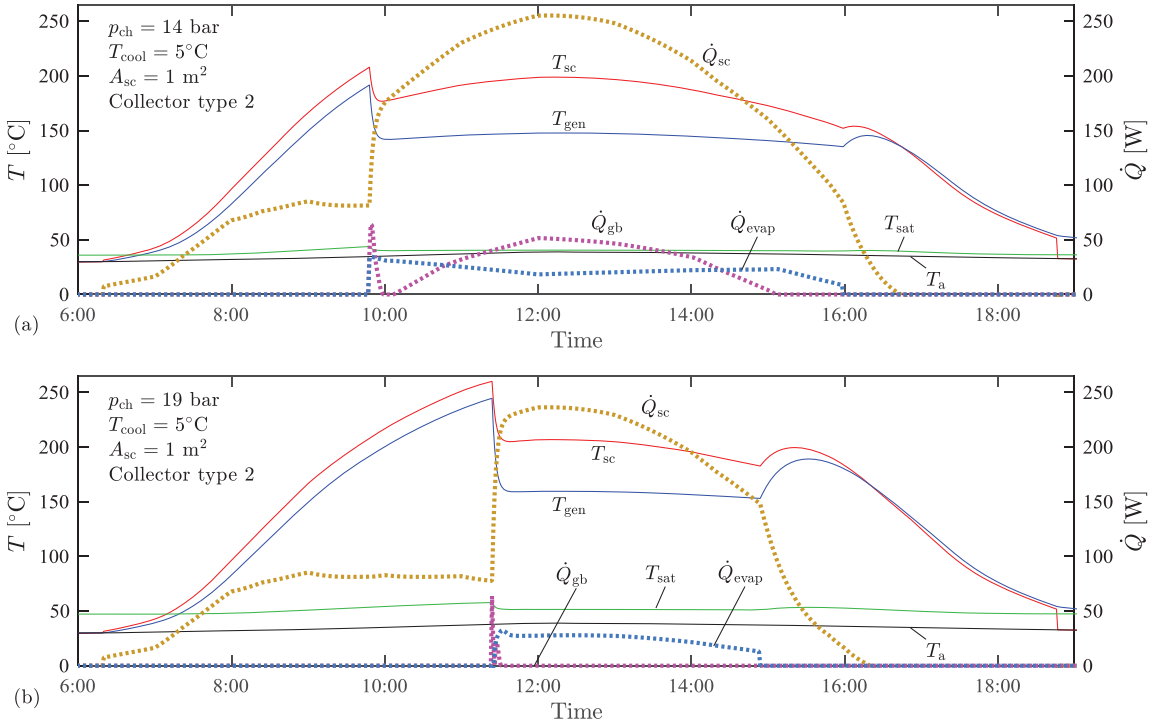

Fig. 13: Diurnal simulation profiles showing system temperatures and energy flow rates for two configuration cases.

5. Conclusions

A solar-cooling system based on a diffusion absorption refrigeration (DAR) cycle was presented, using heat-pipe solar collectors as the heat source. Based on experimental results from a DAR system operating over a range of charge pressures and heat input rates, a thermodynamic model was calibrated and used to simulate the system's performance in the climate of Chennai, India. The experimental analysis has shown that the DAR system can operate over a wide range of heat input rates, but that the maximum COP achieved is highly dependent on the system pressure. As the system pressure was lowered, a higher maximum COP was obtained for a lower corresponding generator heat input rate. For a cooling delivery temperature of 5 ºC and a charge pressure of 14 bar, a maximum COP of 0.25 was obtained with a heat input of 200 W. The observations relating to the condenser have shown that there is a limit to how far the lowering of the system pressure results in an increase in the COP of the system. This has further implications for the application of the system in the high-

ambient temperature environment of Chennai; the diurnal simulation of the solar-DAR system demonstrated that the optimal setting for the system pressure is a trade-off between reducing the generator temperature required to start the system and maximising the ability to reject heat in the condenser. Future work should investigate the effect of changing the ammonia-water solution concentration, while the diurnal simulation of the solar-DAR system should be extended to an annual analysis. The performance of this system in other geographical locations of interest with lower ambient temperatures should also be investigated.

6. Acknowledgement

This work was supported by Innovate UK and the UK Engineering and Physical Sciences Research Council (EPSRC) [grant number EP/P030920/1]. The authors would also like to thank Prof. R. Saravanan and S. Venkatakrishnan at Anna University, Chennai. Data supporting this publication can be obtained on request from cep-lab@imperial.ac.uk.

7. References

Acuña, A., Velázquez, N., Cerezo, J., 2013. Energy analysis of a diffusion absorption cooling system using lithium nitrate, sodium thiocyanate and water as absorbent substances and ammonia as the refrigerant. Appl. Therm. Eng. 51(1), 1273-1281.

ASHRAE, 2001. International Weather for Energy Calculations (IWEC) Weather Files. Available: https://energyplus.net/weather [Accessed 6 October 2017].

Ben Ezzine, N., Garma, R., Bellagi, A., 2010. A numerical investigation of a diffusion-absorption refrigeration cycle based on R124-DMAC mixture for solar cooling. Energy. 35(5), 1874-1883.

Ben Jemaa, R., Mansouri, R., Bellagi, A., 2016. Dynamic testing and modeling of a diffusion absorption refrigeration system. Int. J. Refrig. 67, 249-258.

Chen, J., Kim, K.J., Herold, K.E., 1996. Performance enhancement of a diffusion-absorption refrigerator. Int. J. Refrig. 19(3), 208-218.

Freeman, J., Ramos, A., MacDowell, N., Markides. An experimentally validated model of a solar-cooling system based on an ammonia-water diffusion-absorption cycle. The 8th International Conference on Applied Energy – ICAE2016, October 8-11, 2016, Beijing, China.

Mazouz, S., Mansouri, R., Bellagi, A., 2014. Experimental and thermodynamic investigation of an ammonia/water diffusion absorption machine. Int. J. Refrig. 45, 83-91.

Patek, J., Klomfar, J., 1995. Simple functions for fast calculations of selected thermodynamic properties of the ammonia-water system. Int. J. Refrig. 18(4), 228-234.

Shelton, S.V., White, S., 2002. Bubble pump design for single pressure absorption refrigeration cycles. ASHRAE Trans. 108, 1-10.

SPF Institute for Solar Energy, 2009. Thermostrom Strebel AS 100 HP16. Solar collector factsheet C1112. Available: www.solarenergy.ch [Accessed 6 October 2017].

Starace, G., De Pascalis, L., 2012. An advanced analytical model of the Diffusion Absorption Refrigerator cycle. Int. J. Refrig. 35(3), 605-612.

Taieb, A., Mejbri, K., Bellagi, A., 2016. Detailed thermodynamic analysis of a diffusion-absorption refrigeration cycle. Energy, 115, pp.418-434.

Von Platen, B.C., Munters, C.G., 1928. US Patent. US 1685764 A.

Zohar, A., Jelinek, M., Levy, A., Borde, I., 2005. Numerical investigation of a diffusion absorption refrigeration cycle. Int. J. Refrig. 28(4), 515-525.

Zohar, A., Jelinek, M., Levy, A., Borde, I., 2009. Performance of diffusion absorption refrigeration cycle with organic working fluids. Int. J. Refrig. 32(6), 1241-1246.

Experimental Study of a Solar Collector/Regenerator for Liquid Desiccant Systems

Fernando M. Gómez-Castro and Ursula Eicker

University of Applied Sciences Stuttgart/Centre of Applied Research Sustainable Energy Technologies zafh.net, Stuttgart (Germany)

Abstract

One of the key components of a solar liquid desiccant system is the regenerator, in which the diluted solution from the absorber is reconcentrated for its reuse in the air dehumidification task. Among the different types of regeneration units stands out the solar collector/regenerator (C/R), in which the liquid sorbent is exposed simultaneously to the solar radiation and the air stream, thus enhancing the regeneration process. In order to assess its thermal performance, an experimental study of a single-glazed forced convective C/R has been carried out using calcium chloride solution. The results of the conducted tests show that the water desorption rate increases strongly with the rise of the solar radiation and the inlet solution temperature as well as with the diminution of the gap height and the tilt angle. For the analysed measuring range, the water desorption rate firstly increases and then reaches a stable value by augmenting the air volumetric flow rate. Finally, the regeneration performance diminishes by increasing the solution volumetric flow rate.

Keywords: Liquid desiccant, solar collector/regenerator, experimental performance.

1. Introduction

The imperative need to mitigate the global environmental problems of greenhouse effect and ozone layer depletion, as well as the electrical energy consumption associated with the widespread use of vapour compression machines in air conditioning applications has recently contributed to renew the interest in direct solar thermally-driven liquid sorption systems, in which the diluted desiccant solution is reconcentrated by means of its simultaneous exposure to the solar radiation and the scavenging air stream into a single device named collector/regenerator (C/R). This equipment offers a great potential not only for simplifying and reducing the costs of liquid sorption systems via the elimination of the regeneration chamber, but also for improving the thermal regeneration efficiency through the further heating of the liquid sorbent.

When integrated to liquid desiccant systems, the solar collector/regenerator plays a key role since for every kilogram of water vapour absorbed by the concentrated solution in the dehumidifier, the same amount should be desorbed from the diluted one in the C/R (Collier, 1979), giving a direct measure of the system performance (Hawlader et al., 1992; Yang and Wang, 1995).

The solar collector/regenerators can be classified as open-type, closed-type and convective-type. Several theoretical works (Yang and Wang, 2001; Kaushik et al., 1992) and experimental studies (Gezahegn et al., 2013; Kabeel, 2005; Hawlader et al., 1997) carried out under different operating conditions have demonstrated that the convective C/R performs generally better than the other types in both humid and temperate climates, since its glazing limits the thermal losses to the ambient and also keeps the desiccant solution free from contamination due to dirt and rains. Furthermore, depending on the use of blowers, the convective collector/regenerators can operate in natural and forced ventilation modes.

Experimental studies on the performance of both counterflow forced and natural convective solar C/Rs operated under the hot humid climate of Kaohsiung, Taiwan, were realised by Yang and Wang (1994) by using aqueous LiCl solution as liquid desiccant Their findings indicated that, the water desorption rate of the forced convective C/R rose more significantly with increasing ambient temperature than for the natural convective one. Additionally, the forced convective C/R performed much better than the natural convective one for low inlet solution mass fractions from 40.90 to 42.50%. When the inlet mass fraction became higher than 42.50%, forced

doi:10.18086/swc.2017.28.08 Available at http://proceedings.ises.org

convection was unnecessary. It was also observed that the evaporation rate decreased with the glazing height for the forced convective C/R, while the natural convective C/R had an optimum glazing height.

Kabeel (2005) tested a cross flow forced convective collector/regenerator and a natural convective solar regenerator with aqueous $CaCl_2$ solution as liquid sorbent. It was observed that the desorption rate and the regeneration efficiency of both C/Rs rose strongly with enhancing the air mass flow rate. However, for higher air mass flow rates, said performance indices diminished again due to the fall of the solution temperature. Furthermore, the evaporation rate and the regeneration efficiency fell with rising the inlet solution mass fraction, operating the forced cross flow regenerator better than the natural one for medium solution mass fractions. Nevertheless, the performance difference between both C/Rs was small at higher mass fractions.

Despite the studies carried out by the aforementioned authors, the relevant experimental data of convective collector/regenerators are still very scarce. This work provides some light on this issue by experimentally investigating the effect of operating parameters such as the solar radiation, the inlet solution temperature and the volumetric flow rates of air and solution as well as geometric parameters such as the gap height and the tilt angle on the performance of a single-glazed forced convective C/R.

2. System description

In order to investigate the influence of both climatic and operating conditions on the performance of a forced convective collector/regenerator, a test bench comprising a collector/regenerator, fans, solution tanks, pumps, flow regulator/indicator, PID controller, and data acquisition devices was designed and constructed in the sorption laboratory at the University of Applied Sciences Stuttgart (see Fig. 1).

The collector/regenerator is made of polycarbonate and has a total area of 0.65 m² (0.5 m width × 1.3 m length), a gap height of 0.04 m or 0.1 m and a sprinkling area of 0.5 m² (0.5 m width × 1.0 m length). Its inclination angle can be variably set. The stainless steel absorber plate is painted with a special black nanocoating lacquer and is covered with a black cotton cloth for ensuring uniform wetting and absorption of the solar radiation. The C/R can be operated in both counterflow and parallel flow modes. The forced air is supplied by an axial fan with continuous flow control in the range of 2.5 to 25 m^3/h. A solution pump delivers the desiccant solution to the liquid distributor header at flow rates between 2.5 and 15 l/h. The temperature of the liquid sorbent is controlled before entering the C/R by the combination of an ARCTIC cold bath/circulation thermostat HAAKE AC 150-A10 and a plastic heat exchanger B3-12A-30-2.0. The volumetric flow rates, temperatures, relative humidities and the densities of the fluids involved in the regeneration process are measured both at the inlet and outlet of the collector/regenerator by means of the sensors summarised in Tab. 1. Data are taken at 5 seconds interval after the initial wetting and stabilising.

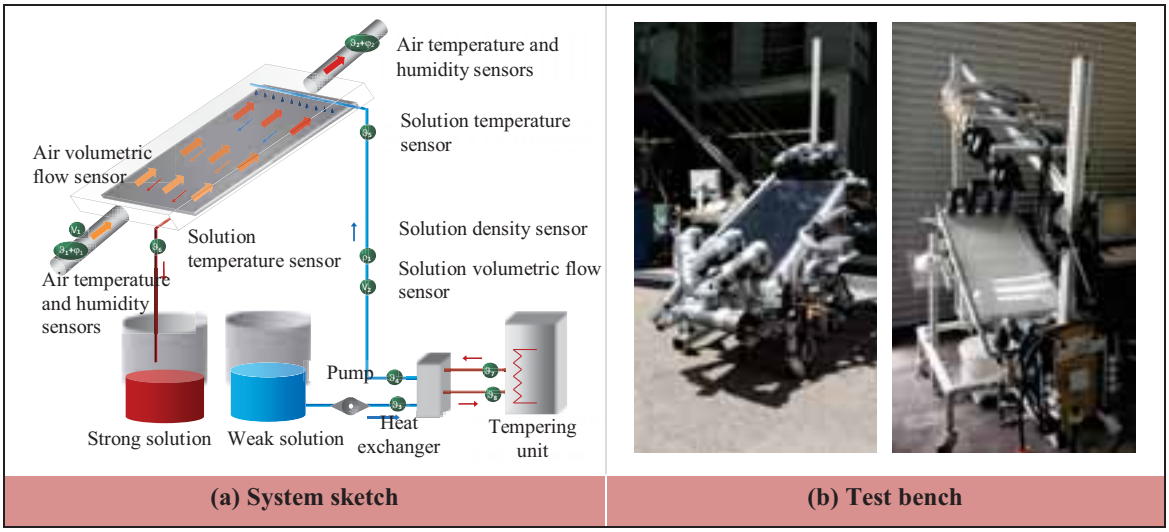

Fig. 1: System sketch and test bench of the collector/regenerator.

Tab. 1: Model parameters for the analysed air- and water-based solar collectors.

Manufacturer	Sensor	Measured parameter	Measuring range	Rated accuracy
Kobold	Flowmeter MIK-5NA	Volumetric flow rate solution/water	0,6 l/h-30 l/h	± 2 %
KEY Instruments	Flowmeter MR-3000		0,24 l/h -3,0 l/h 1,2 l/h -18,0 l/h	±4 %
Honeywell	Flowmeter AWM 720P	Volumetric flow air	0-12 m³/h	± 2 %
Rotronic	Sensor module HC2-S3	Air temperature	-10-90 °C	± 0,1 K
		Relative humidity	0-100 %	± 0,8 % R. H.
Fühlersysteme	Cable temperature sensor KT/E	Temperature solution/water	-50-250 °C	-
Anton Paar	Density transmitter L-Dens 313	Solution density	0,5-2 g/cm³	± 0,001 g/cm³
KippZonen	Pyranometer CMP 11	Global radiation	< 4000 W/m²	-

3. System performance measures

The performance of the collector/regenerator is evaluated on the basis of the water desorption capacity and the water desorption rate. The water desorption capacity ($\Delta\chi_{des}$) in [kg/kg] is defined as the amount of moisture added to an air stream during the regeneration process:

$$\Delta\chi_{des}=\chi_{a,out}-\chi_{a,in} \quad \text{(eq. 1)}$$

On the other hand, the water desorption rate ($\Delta\dot{m}_{des}$) indicates the change of the amount of water vapour transferred to the air stream $\dot{m}_a$, and therefore evaporated from the hygroscopic solution per unit time:

$$\Delta\dot{m}_{des}=\dot{m}_a\cdot(\chi_{a,out}-\chi_{a,in}) \quad \text{(eq. 2)}$$

Where $\chi_{a,in}$ and $\chi_{a,out}$ are the absolute humidities of the air at the inlet and outlet of a sorption unit, respectively.

The fluids involved in the regeneration process are characterised through the changes of their temperature ($\Delta T_{a/s}$) and mass fraction ($\Delta\xi_s$):

$$\Delta T_{a/s}=T_{a/s,out}-T_{a/s,in} \quad \text{(eq. 3)}$$

$$\Delta\xi_s=\xi_{s,out}-\xi_{s,in} \quad \text{(eq. 4)}$$

The mass and energy balance between air and desiccant solution are analysed through the dimensionless quantities κ_{mass} and κ_{energy}, which are given by (Jaradat et al., 2011):

$$\kappa_{mass}=\frac{\dot{m}_a\cdot\Delta\chi_{des}}{\dot{m}_s\cdot\Delta\zeta_s} \quad \text{(eq. 5)}$$

$$\kappa_{energy}=\frac{\dot{Q}_a+\dot{Q}_s}{\dot{Q}_{solar}} \quad \text{(eq. 6)}$$

Where ζ_s is the water content in the desiccant solution given as function of the solution mass fraction ξ_s by eq. 6.

$$\zeta_s=\frac{1-\xi_s}{\xi_s} \quad \text{(eq. 7)}$$

4. Experimental results and discussion

To analyse the performance potential of the collector/regenerator several measurement series were carried out

under different boundary conditions for the aqueous calcium chloride ($CaCl_2$) solution at natural sunlight. The volumetric flows of the regenerating air and the hygroscopic solution were varied between 2.5 m^3/h and 25.0 m^3/h and 2.5 l/h to 15.0 l/h, respectively.

4.1 Effect of the solar radiation on the C/R performance

Fig. 2 shows that the desorption rate, the desorption capacity, the temperature differences of air stream and $CaCl_2$ solution between inlet and outlet as well as the mass fraction difference of liquid sorbent between inlet and outlet increased strongly as the solar radiation rose at the boundary conditions summarised in Tab. 2, since the absorbed solar radiation is the energy source for water evaporation from the diluted solution. Furthermore, it can be observed from Fig. 2(d) that the values of κ_{mass} for test sequences at solution volumetric flow rates of 5.24 l/h and 9.77 l/h were very close to the unity, while the values of κ_{energy} exhibited an average relative deviation of 43.8%, which reflected the heat losses mechanisms such as the radiative heat transfer between the absorber plate and the collector glazing as well as the convective and radiative thermal losses to the environment.

Tab. 2: Boundary conditions for the experiments with fluctuating solar radiation (gap height = 4 cm, tilt angle = 30°).

Test seq.	Air volumetric flow [m^3/h]	Air temperature [°C]	Air absolute humidity [g/kg]	Solution volumetric flow rate [l/h]	Solution temperature [°C]	Solution mass fraction [%]
1	7.50	27.15	9.41	5.11	26.19	38.24
2	7.56	29.08	8.72	10.07	24.45	37.89

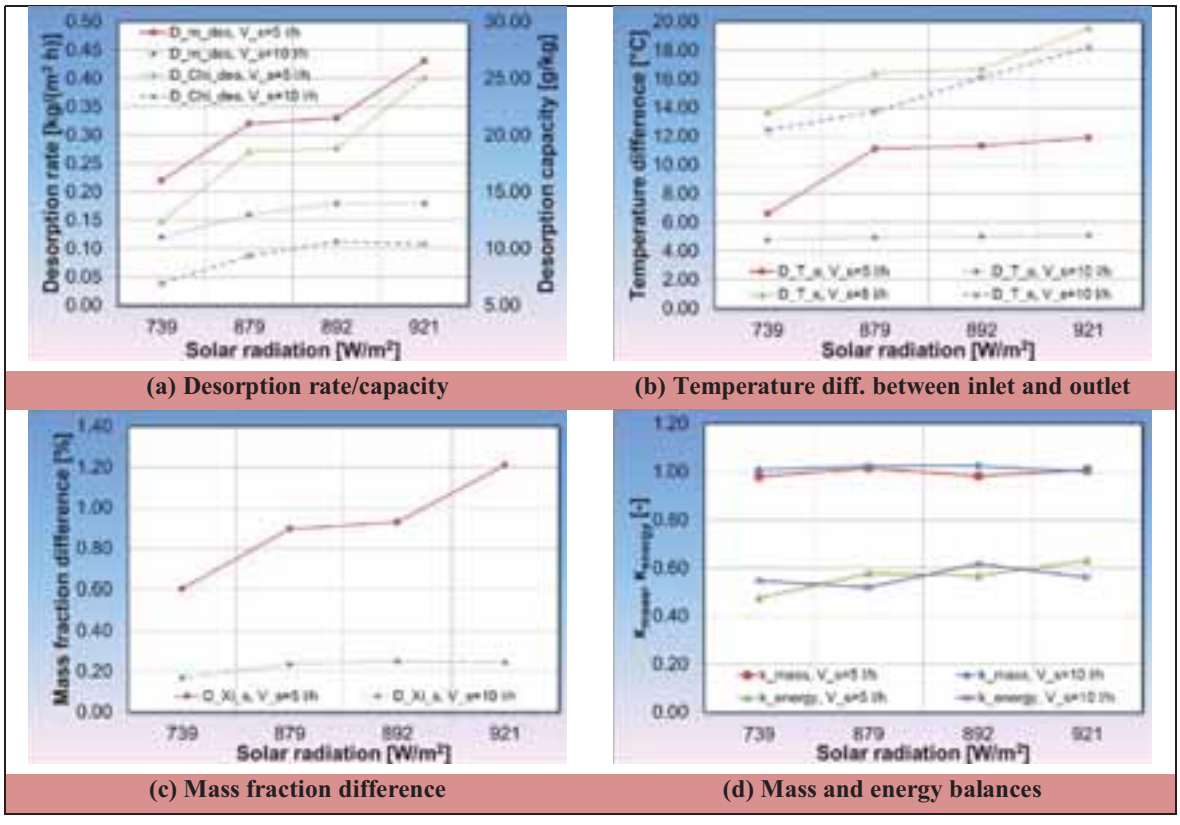

Fig. 2: Experimental results for the collector/regenerator with different solar radiation levels.

4.2 Effect of the inlet solution temperature on the C/R performance

From Fig. 3(a), it is clearly shown that both the desorption rate and the desorption capacity averagely increased by 56% as the inlet desiccant temperature rose from 25.1 °C to 37.3 °C at the boundary conditions summarised in Tab. 3. This was a consequence of the higher solution vapour pressure and the associated greater driving force for the mass transfer between the liquid sorbent and the regenerating air. According to Fig. 3(b), the

temperature difference of the regenerating air averagely augmented from 7.2 °C at an inlet solution temperature of 25.1 °C to 12.3 °C at an inlet solution temperature of 37.3 °C. Moreover, the temperature difference of the liquid sorbent fell from a high value of 12.5 °C to a low one of 5.8 °C at an inlet solution temperature of 37.3 °C due to the heat transfer from the desiccant film to the adjacent air stream. Conversely, the temperature difference of the hygroscopic liquid followed an upward trend at an inlet solution temperature of 25.1 °C because of the progressive solar heating of the liquid film. On the other hand, the mass fraction difference of desiccant solution between inlet and outlet averagely rose by 54% as the inlet solution temperature enhanced from 25.1 °C to 37.3 °C (see Fig. 3(c)). Finally, the values of κ_{mass} for test sequences 3 and 4 were very close to the unity, whereas the values of κ_{energy} for same tests exhibited average relative deviations of 39.1% and 55,6%, respectively (see Fig. 3(d)), which could be result not only of the heat losses from the collector/regenerator but also of sensors' accuracy and measurement errors.

Tab. 3: Boundary conditions for the experiments with fluctuating solution temperatures (gap height = 4 cm, tilt angle = 30°).

Test seq.	Solar radiation [W/m²]	Air volumetric flow [m³/h]	Air temperature [°C]	Air absolute humidity [g/kg]	Solution volumetric flow rate [l/h]	Solution temperature [°C]	Solution mass fraction [%]
3	909	7.43	30.53	9.80	5.21	37.33	36.78
4	848	7.46	25.67	9.41	5.05	25.07	38.56

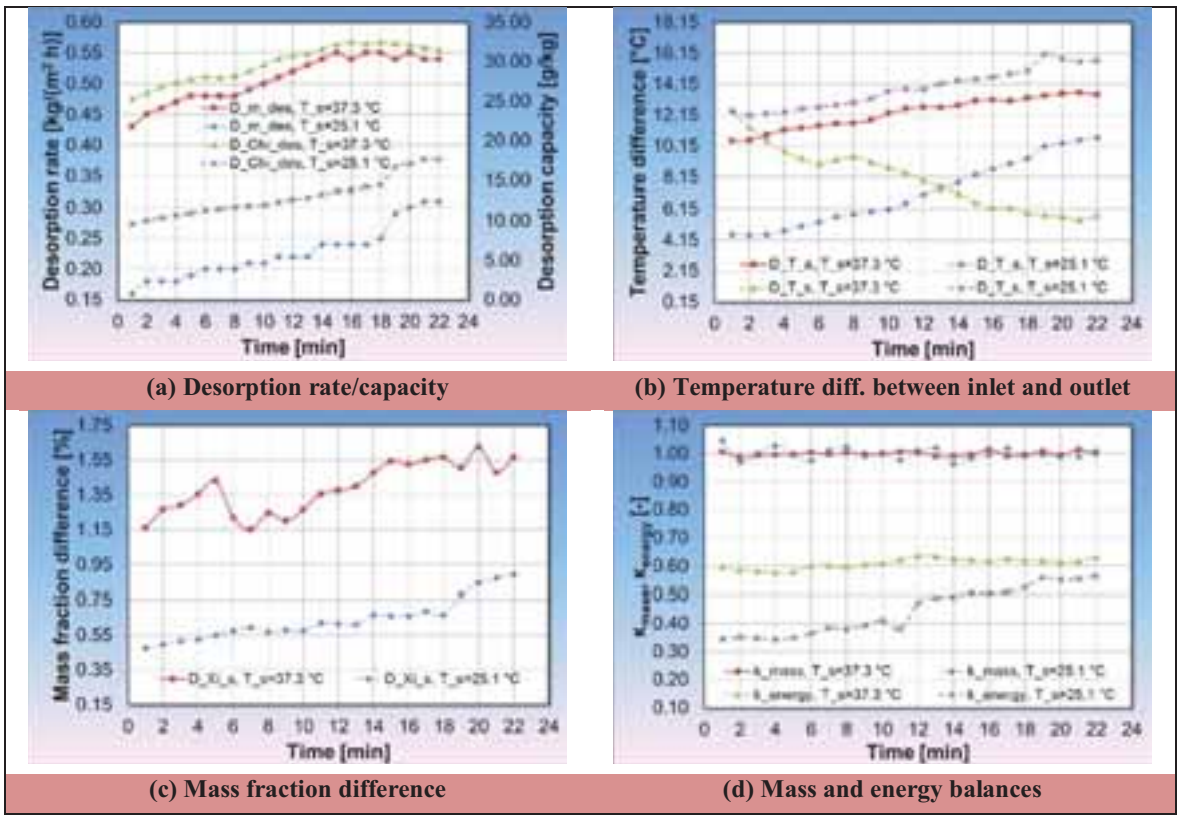

(a) Desorption rate/capacity **(b) Temperature diff. between inlet and outlet**

(c) Mass fraction difference **(d) Mass and energy balances**

Fig. 3: Experimental results for the collector/regenerator at different solution temperatures.

4.3 Effects of the fluid volumetric flow rates on the C/R performance

For the operating conditions analysed in experimental runs (see Tab. 4), the desorption rate obtained with the solar collector/regenerator firstly augmented with increasing the air volumetric flow rate, until it stabilised at a certain value as shown in Fig. 4(a). This net effect resulted from the combination of two facts:

- Increase of the mass transfer coefficient between the desiccant solution film and the regenerating air by enhancing the air volumetric flow rate.

- Further decrease of the solution temperature and consequently, of the solution vapour pressure and the driving force of mass transfer within the C/R by rising the air volumetric flow rate.

At a solution volumetric flow rate of 7.5 l/h, doubling the air volumetric flow rate from 5.0 m^3/h to 10 m^3/h increased the desorption rate by about 11% from 0.26 kg/(m^2 h) to 0.29 kg/(m^2 h). Said enhancement slightly rose by increasing the solution volumetric flow rate.

Conversely, as shown in Fig. 4(b), the desorption capacity decreased with augmenting the air volumetric flow rate due to the reduction in the temperature increase of the air stream in the collector/regenerator, which led to a lower vapour pressure difference between the desiccant solution and the air. At a solution volumetric flow rate of 7.5 l/h, doubling the air volumetric flow rate from 5.0 m^3/h to 10 m^3/h decreased the desorption capacity by about 43% from 21.65 g/kg to 12.26 g/kg.

Tab. 4: Boundary conditions for the experiments with fluctuating fluid volumetric flow rates (gap height = 4 cm, tilt angle = 30°).

Test seq.	Solar radiation [W/m^2]	Air volumetric flow [m^3/h]	Air temperature [°C]	Air absolute humidity [g/kg]	Solution volumetric flow rate [l/h]	Solution temperature [°C]	Solution mass fraction [%]
5	873-918	4.96- 25.08	28.57-30.03	9.52-10.40	2.47	24.93-25.87	37.70-38.18
6	870- 920	4.96-24.97	25.79-28.66	8.76- 9.80	4.98	24.61-25.80	37.49-38.16
7	886-928	2.52-25.03	26.03-32.40	9.43-9.93	7.44	24.53-25.47	37.42-38.25
8	875-922	2.61-24.95	25.45-31.37	8.64-9.44	10.03	24.59-25.22	37.42-38.12
9	872-904	2.41-24.99	24.70-28.88	8.93-9.85	15.01	24.78-25.23	37.30-38.00

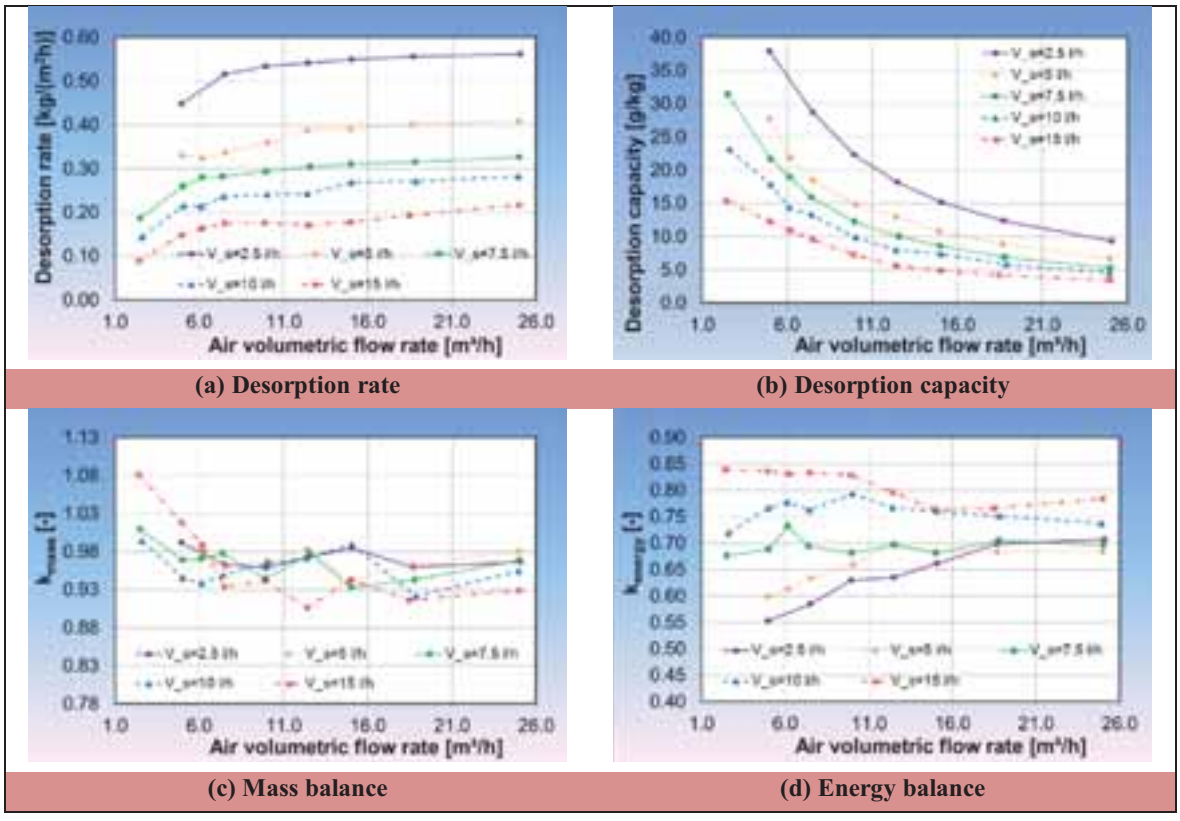

Fig. 4: Experimental results for the collector/regenerator at different fluid volumetric flow rates.

On the other hand, the desorption rate and the desorption capacity decreased with augmenting the solution volumetric flow rate as shown in Fig. 4(a) and Fig. 4(b). The higher the solution volumetric flow rate, the shorter the residence time of the liquid sorbent within the collector/regenerator. Consequently, the hygroscopic solution was heated little, thus reducing the vapour pressure difference between the solution film and the air. At

an air volumetric flow rate of 15.0 m^3/h, doubling the solution volumetric flow rate from 5.0 l/h to 10.0 l/h reduced both the desorption rate and the desorption capacity by about 31% from 0.39 kg/(m^2 h) to 0.27 kg/(m^2 h) and from 10.79 g/kg to 7.39 g/kg, respectively. These reductions slightly increased by enhancing the air volumetric flow rate. Finally, according to Fig. 4(c) and Fig. 4(d), the values of κ_{mass} were very close to the unity, whereas the values of κ_{energy} were deviated from the unity, especially at lower solution volumetric flow rates. These deviations reflected both the heat losses mechanisms from the collector/regenerator and problems related to sensors' accuracy and measurement errors.

4.4 Effects of the gap height on the C/R performance

At a constant air volumetric flow rate, the reduction of the gap height led to an average increase in the flow velocity of the regenerating air within the collector channel. The higher the air volumetric flow rate, the greater the enhancements in the air flow velocity and in the Reynolds number. As a result, the heat and mass transfer coefficients between the desiccant solution and the regenerating air also augmented. According to the operating conditions summarised in Tab. 4 and Tab. 5 for a solution volumetric flow rate of 7.5 l/h, the desorption rate and the desorption capacity averagely increased by about 5% by reducing the gap height from 10 cm to 4 cm (see Fig. 5). Greater increases in the regeneration performance were achieved at low air volumetric flow rates.

Tab. 5: Boundary conditions for the experiments with fluctuating fluid volumetric flow rates (gap height = 10 cm, tilt angle = 30°).

Test seq.	Solar radiation [W/m^2]	Air volumetric flow [m^3/h]	Air temperature [°C]	Air absolute humidity [g/kg]	Solution volumetric flow rate [l/h]	Solution temperature [°C]	Solution mass fraction [%]
10	863-909	5.09-25.20	30.06-35.03	9.09-11.08	2.41	24.58-26.48	37.54-38.13
11	885-923	4.87-25.03	31.64-33.98	9.38-11.39	4.96	24.65-25.78	37.39-38.07
12	883-934	2.48-25.10	29.57-33.66	9.57-11.79	7.52	24.84-25.59	37.36-37.90
13	891-918	2.55-24.90	28.36-32.80	10.16-12.16	10.00	24.82-25.43	37.47-37.90
14	877-913	2.63-25.06	25.98-31.46	9.85-12.25	15.01	24.97-25.26	37.54-37.82

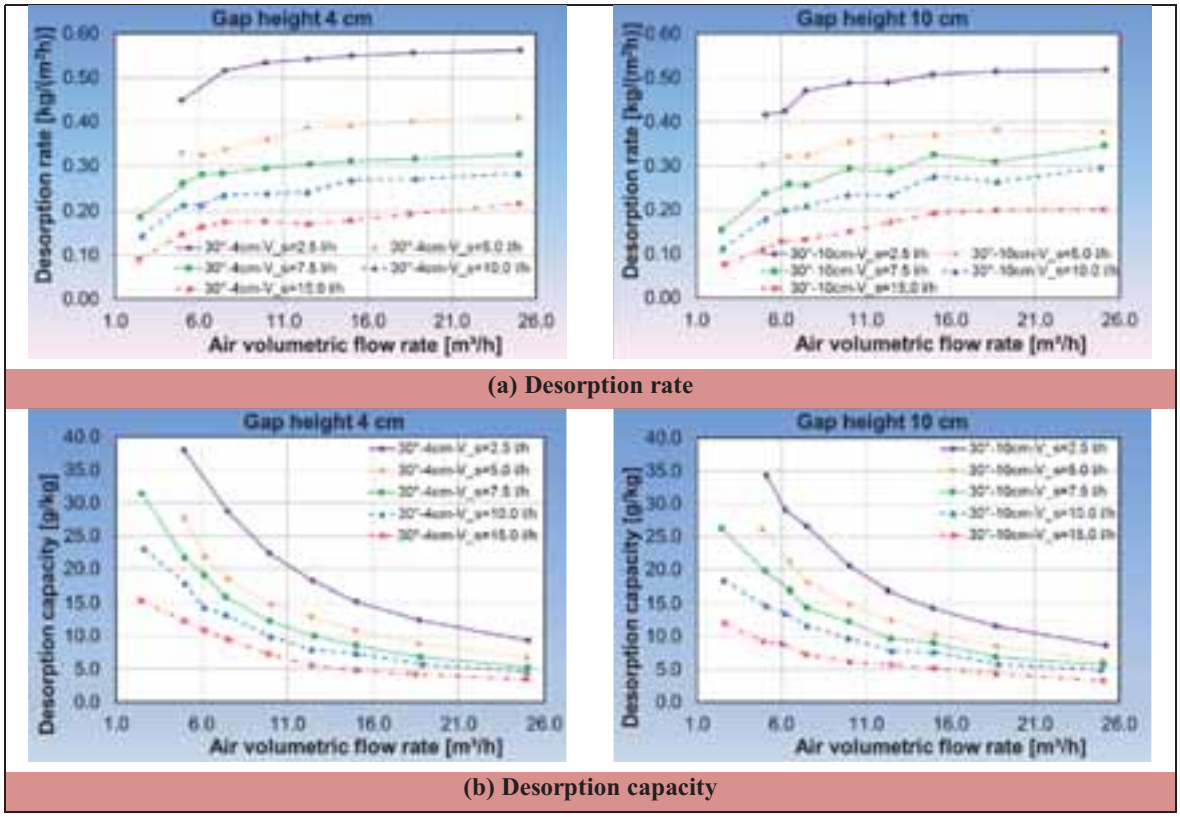

Fig. 5: Experimental results for the collector/regenerator at different fluid volumetric flow rates and gap heights.

4.5 Effects of the tilt angle on the C/R performance

From Fig. 6, the regeneration performance could be increased by reducing the inclination angle of the collector/regenerator from 30° to 15° due to the longer residence time of the desiccant solution on the absorber surface. Consequently, the liquid sorbent was quickly heated. According to the operating conditions summarised in Tab. 5 and Tab. 6 for a solution volumetric flow rate of 7.5 l/h, both the desorption rate and the desorption capacity averagely augmented by about 6% by decreasing the tilt angle from 30° to 15°.

Tab. 6: Boundary conditions for the experiments with fluctuating fluid volumetric flow rates (gap height = 4 cm, tilt angle = 15°).

Test seq.	Solar radiation [W/m²]	Air volumetric flow [m³/h]	Air temperature [°C]	Air absolute humidity [g/kg]	Solution volumetric flow rate [l/h]	Solution temperature [°C]	Solution mass fraction [%]
15	876-897	5.04-15.08	29.53-30.56	8.81-9.04	2.49	24.90-25.38	37.56-38.04
16	885-900	5.08-15.05	26.84-28.75	9.04-9.45	5.03	24.75-25.27	37.54-38.04
17	872-894	2.46-14.99	28.03-30.49	8.44-8.73	7.56	24.83-25.26	37.52-37.89
18	868-936	2.44-15.00	26.51-28.73	8.32-8.66	10.03	24.93-25.01	37.38-38.07
19	866-911	2.54-14.97	28.00-29.80	8.44-8.73	15.00	24.87-25.21	37.41-37.88

Tab. 7: Boundary conditions for the experiments with fluctuating fluid volumetric flow rates (gap height = 4 cm, tilt angle = 30°).

Test seq.	Solar radiation [W/m²]	Air volumetric flow [m³/h]	Air temperature [°C]	Air absolute humidity [g/kg]	Solution volumetric flow rate [l/h]	Solution temperature [°C]	Solution mass fraction [%]
20	873- 918	4.96-15.06	28.57-29.71	9.52- 9.89	2.48	24.93-25.87	37.77-38.18
21	883-911	4.96-14.96	25.79-27.96	8.76-9.17	4.95	24.82-25.80	37.49-38.11
22	905-928	2.52-15.01	29.60-32.40	9.66-9.93	7.41	24.53-25.47	37.42-38.25
23	875-922	2.61-15.05	29.22-31.37	8.64-8.95	9.94	24.59-25.22	37.44-38.12
24	872-904	2.41-24.99	24.70-28.88	8.93-9.85	15.01	24.78-25.23	37.30-38.00

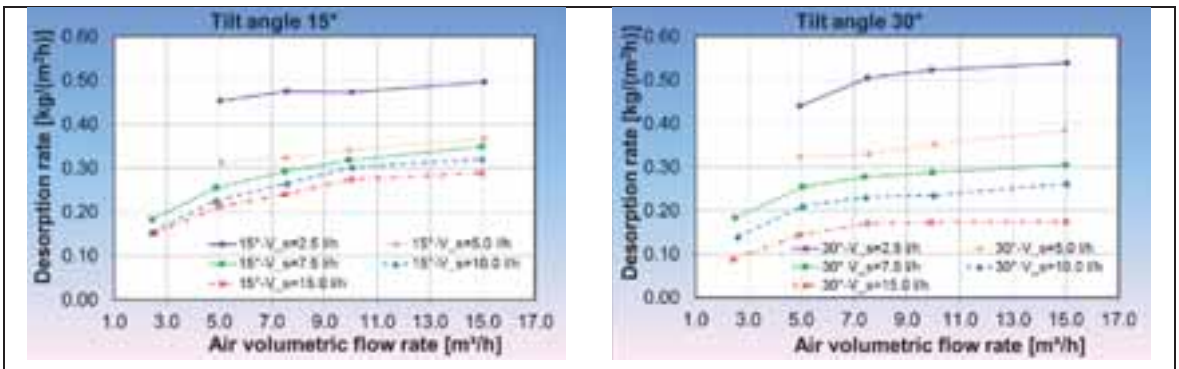

(a) Desorption rate

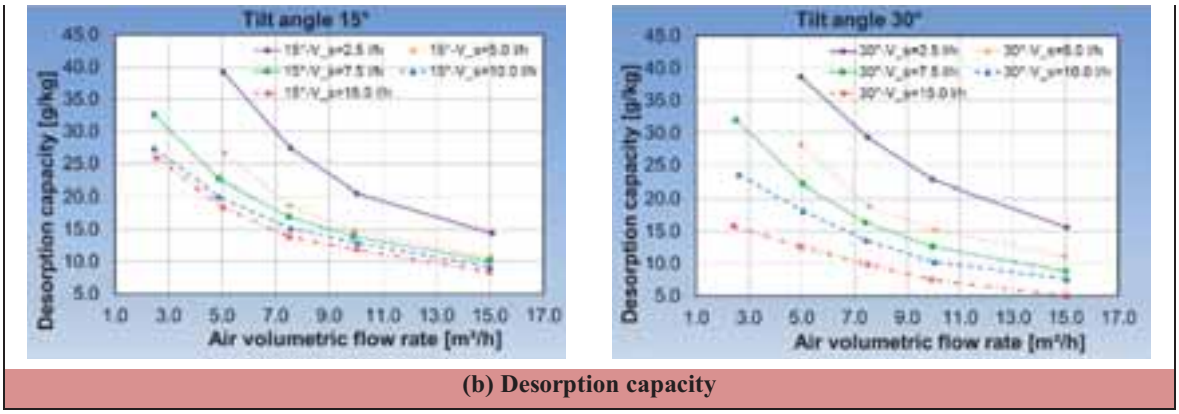

Fig. 6: Experimental results for the collector/regenerator at different fluid volumetric flow rates and tilt angles.

5. Conclusions

A single-glazed forced convective collector/regenerator was experimentally tested at the climatic conditions of Stuttgart. The experimental tests results indicated that the volumetric flow rates of the air and the desiccant solution as well as the gap height and the tilt angle of the collector played an important role in the assessment of the regeneration performance. Further studies will be carried out in order to optimise the construction of the C/R for specific requirements of air conditioning applications.

Acknowledgments

This work is sponsored by the Federal Ministry of Education and Research in framework of the program "Research at Universities of Applied Sciences – Funding stream Young Engineers" (contract number 03FH0041X4).

SPONSORED BY THE
Federal Ministry
of Education
and Research

References

Collier, R. K., 1979. The analysis and simulation of an open cycle absorption refrigeration system. Sol. Energy 23(4), 357-366.

Gezahegn, H., Mullick, S. C., Jain, S., 2013. Optical and thermal performance of a liquid desiccant solar regenerator. Proc. of International Congress on Renewable Energy, KIIT University, Bhubaneswar, Odisha, 15-27.

Hawlader, M. N. A., Wood, B. D., Folkman, C. C., Stack, A. P., 1997. Solar assisted open-cycle absorption cooling: Performance of collector/regenerators. Int. J. Energ. Res. 21(6), 549-574.

Hawlader, M. N. A., Stack, A. P., Wood, B. D., 1992. Performance evaluation of glazed and unglazed collectors/regenerators in a liquid absorbent open-cycle absorption cooling system. Int. J. Sol. Energy 11(3-4), 135-164.

Jaradat, M., Mützel, M., Schiemann, L., Heinzen, R., Vajen, K., Jordan, U., 2011. Experimental analysis of a liquid desiccant cross flow plate-type dehumidifier for air-conditioning applications, Proc. ISES Solar World Congress, Kassel (DE), 28.08. to 02.09.2011.

Kabeel, A. E., 2005. Augmentation of the performance of solar regenerator of open absorption cooling system.

Renew. Energ. 30(3), 327-338.

Kaushik, S. C., Kaudinya, J. V., Yadav, Y. K., 1992. Studies on some solar collector/regenerator systems for open cycle absorption air conditioning/liquid desiccant cooling systems. Heat Recov. Syst. CHP 12(4), 357-363.

Yang, R., Wang, P. L., 2001. A simulation study of performance evaluation of single-glazed and double-glazed collectors/regenerators for an open-cycle absorption solar cooling system. Sol. Energy 71(4), 263-268.

Yang, R., Wang, P. L., 1995. Experimental study of a glazed solar collector/regenerator operated under a humid climate. Int. J. Sol. Energy 16(3), 185-201.

Yang, R., Wang, P. L., 1994. Experimental study of a forced convection solar collector/regenerator for open-cycle absorption cooling. J. Sol. Energ.-T. ASME 116(4), 194-199.

Theoretical Analysis of Indirect and Direct Solar Regenerators for Liquid Desiccant Systems

Fernando M. Gómez-Castro and Ursula Eicker

University of Applied Sciences Stuttgart/Centre of Applied Research Sustainable Energy Technologies zafh.net, Stuttgart (Germany)

Abstract

Solar liquid desiccant air-conditioning systems have recently attracted attention due to their sustainability and good energy saving potential, since only heat is required in the solution regeneration process. The solar regenerators can be classified as indirect and direct regeneration units. In the first type, the solar heat can be transferred either to the air stream via solar air collectors or a combination of solar water collectors and water-to-air heat exchangers or to the liquid desiccant via a combination of solar water collectors and water-to-solution heat exchangers before entering the regeneration chamber. In the second type, the diluted solution is exposed simultaneously to the solar radiation and the air stream within a solar collector/regenerator. A performance comparison between both types of regeneration units is presented in this paper. The simulation results demonstrate that direct solar regenerators have a high potential for enhancing the water desorption rate from a diluted solution and, consequently, the air dehumidification capacity within the absorber.

Keywords: Liquid desiccant, indirect solar regenerator, solar collector/regenerator, performance comparison.

1. Introduction

Air conditioning in buildings is a large and growing market, almost exclusively covered with electrical compression systems. Therefore, in order to supply this market with sustainable technologies, cost-effective solar thermally-driven liquid sorption systems, which rely on the capacity of hygroscopic solutions in removing the air moisture content by the absorption process (Grossman and Johannsen, 1981) and on the solar heat for regenerating the solution in a temperature range of 40 to 70 °C (Katejanekarn and Kumar, 2008), need to be developed.

Indirect solar regenerated systems comprise the main components absorber, in which the moisture of the inlet process air is removed by bringing it into contact with sprinkled desiccant solution, and regenerator, in which the water content of the solution gradually diluted within the absorber is reduced by enhancing both its temperature and vapour pressure, and by subsequently removing the evaporated water through an air stream. Among the direct contact sorption chambers commonly used as heat and mass exchangers in both the air dehumidification and solution regeneration processes stand out the packed bed towers, which are filled with random or structured packing materials that increase the mass transfer area per unit volume as well as the contact time between the fluids involved in the sorption process, leading to more compact units (Martin and Goswami, 2000). Nevertheless, they require high enough solution mass flow rates for a proper wetting of the packing material as well as high fan energy consumption due to high air pressure drops. The heat required for the regeneration process can be supplied by either air-led (Kabeel et al., 2017) or water-based solar collectors (Jamar et al., 2016) and, more recently, by photovoltaic/thermal (PV/T) modules (Guo et al. 2017), which provide both heat for reconcentrating the liquid desiccant and electricity for powering the parasitic components (fans and pumps). The resulting strong solution is then stored without thermal losses for carrying out the air dehumidification process when solar radiation is not available. The dehumidified process air, heated by exothermic reactions during the moisture absorption in the desiccant solution, is generally precooled by the outdoor air or the return air from the room and moistened adiabatically in the next step to produce the desired cooling effect for air conditioning applications. However, some barriers like the high costs of manufacture and installation of the equipment, high system complexity due to the large number of individual components and the need of highly sophisticated control systems drastically limit the market entrance of indirect solar regenerated

doi:10.18086/swc.2017.28.09 Available at http://proceedings.ises.org

liquid desiccant systems (Gommed and Grossman, 2007).

The needed system simplification and its associated cost reduction can be accomplished by transferring the regeneration process into the solar collector. In this way, and contrary to the indirect solar regenerator, the hygroscopic solution is exposed simultaneously to the solar radiation and the air stream, which contributes to enhance the thermal regeneration efficiency. The direct solar regenerators can be classified as open-type, closed-type and convective-type. Several theoretical works (Yang and Wang, 2001; Kaushik et al., 1992) and experimental studies (Gezahegn et al., 2013; Kabeel, 2005; Hawlader et al., 1997) carried out under different operating conditions have demonstrated that the glazed forced convective collector/regenerator performs generally better than the other types in both humid and temperate climates, since its glazing limits the thermal losses to the ambient and also keeps the desiccant solution free from contamination due to dirt and rains.

However, there is a lack of works in the literature on the performance comparison between the indirect solar regeneration chambers and the solar collector/regenerators. This paper provides some light on this issue by comparing the performance curves obtained for both types of solar regenerators at specified operating conditions from calculation models developed in the equation-oriented simulation environment EES and by outlining under what conditions the direct solar regenerator outperforms the indirect ones.

2. System description

Three indirect solar regeneration units, which essentially comprise an adiabatic packed bed sorption reactor, an array of solar water/air heaters as well as heat exchangers, and a forced convective direct solar regenerator were theoretically analysed in this study. These configurations are depicted in Fig. 1 and described as follows:

- **Variant SWH+WA-HX+Reg (solar water heater + water-air heat exchanger for preheating of the regenerating air):** A 16 m² south-oriented collector field of solar water heaters (Topson TX) with 40% aqueous propylene glycol solution as working fluid and a tilt angle of 30° is connected with a finned coil water-air heat exchanger (WA-HX, Brazetek BT-HTL 12×12), in which the regenerating air stream is warmed-up before entering a counterflow adiabatic regeneration chamber (see Fig. 1(a)), whose packed bed (400 mm width × 400 mm length × 400 mm height) is filled with ceramic Novalox® saddles (volumetric mass transfer area = 255 m²/m³, void fraction = 0.74).
- **Variant SAH+Reg:** A similar field of compact solar air heaters (SAH TwinSolar) is directly coupled to the aforementioned packed bed regenerator as shown in Fig. 1(b).
- **Variant SWH+WS-HX+Reg:** The finned coil water-air heat exchanger of the variant SWH+WA-HX+Reg is replaced by a water-solution parallel plates heat exchanger (WS-HX, Kaori K095) for heating up the liquid sorbent before its entrance to the sorption reactor (see Fig. 1(c)).
- **Variant SWH+WS-HX+WA-HX+Reg:** A finned coil water-air heat exchanger and a water-solution parallel plates heat exchanger, identical to those of the variants SWH+WA-HX+Reg and SWH+WS-HX+Reg respectively, are connected in parallel with the solar water heaters field for simultaneously preheating the regenerating air and the desiccant solution (see Fig. 1(d)).
- **Variant SCR:** The diluted hygroscopic liquid and the regenerating air stream are simultaneously, directly heated through a field of counterflow, single-glazed solar collector/regenerators for reconcentrating the desiccant solution (see Fig. 1(e)).

Based on the energy conservation laws, thermodynamic equilibrium, as well as the heat and mass transfer laws for each system component, all these regenerator variants were modelled in the equation-oriented simulation environment EES to assess the water desorption rate ($\Delta \dot{m}_{des}$) for the specified operating conditions, which indicates the change of the amount of water vapour transferred to the air stream $\dot{m}_a$ and, therefore, evaporated from the hygroscopic solution per unit time:

$$\Delta \dot{m}_{des} = \dot{m}_a \cdot (\chi_{a,out} - \chi_{a,in}) \quad \text{(eq. 1)}$$

Where $\chi_{a,in}$ and $\chi_{a,out}$ are the absolute humidities of the air at the inlet and outlet of a sorption unit, respectively.

Indirect Use of the solar heat

Preheating of the regenerating air

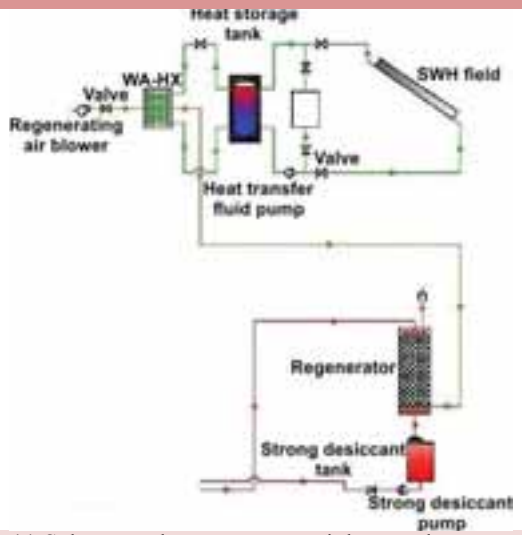

(a) Solar water heaters + water-air heat exchanger + regenerator (SWH+WA-HX+Reg)

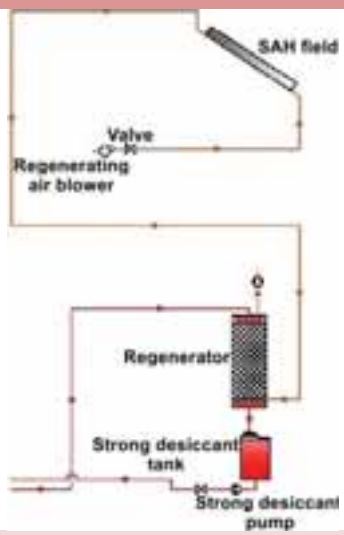

(b) Solar air heaters + regenerator (SAH+Reg)

Preheating of the desiccant solution

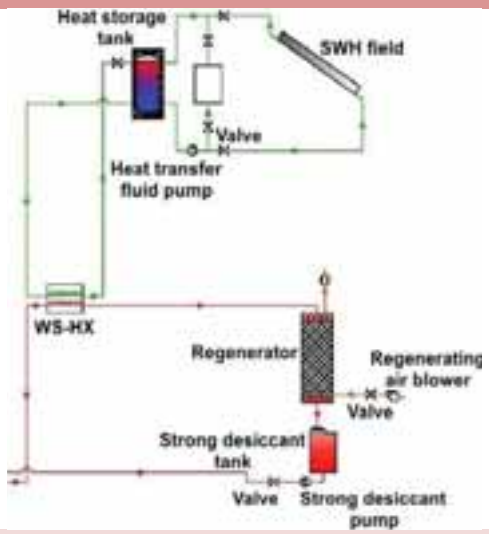

(c) Solar water heaters + water-solution heat exchanger + regenerator (SWH+WS-HX+Reg)

Simultaneous preheating of the regenerating air and the desiccant solution

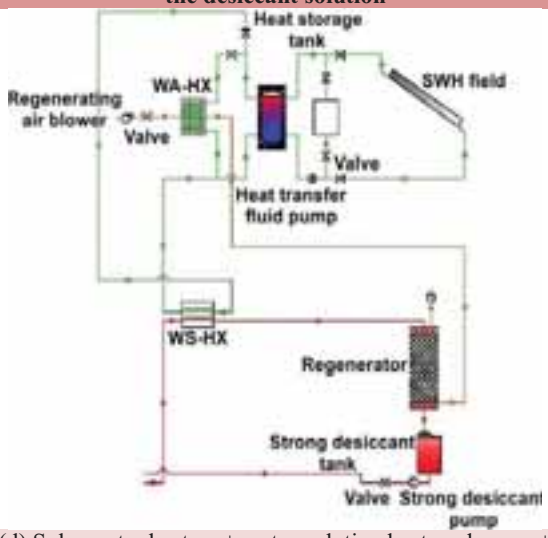

(d) Solar water heaters + water-solution heat exchanger + water-air heat exchanger + regenerator (SWH+WS-HX+WA-HX+Reg)

Direct use of the solar heat

Simultaneous heating of the regenerating air and the desiccant solution

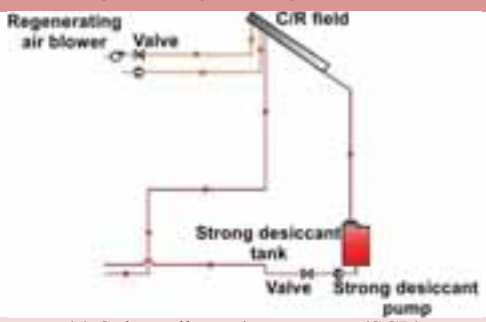

(e) Solar collector/regenerator (SCR)

Fig. 1: Analysed variants of the solar regenerators with indirect and direct (pre)heating of the regenerating air and the desiccant solution.

3. Mathematical modeling of the system components

3.1 Indirect solar regenerators

The efficiency of the sola collector η_c is given in terms of the average bulk temperature of the heat transfer medium $T_{f,m}$ and the ambient temperature T_{amb} by:

$$\eta_c=\eta_0-U_{L,1}\cdot\left[\left(T_{f,m}-T_{amb}\right)/G_{g,c}\right]-U_{L,2}\cdot G_{g,c}\cdot\left[\left(T_{f,m}-T_{amb}\right)/G_{g,c}\right]^2 \quad \text{(eq. 2)}$$

Where η_0, $U_{L,1}$, and $U_{L,2}$ are the collector optical efficiency, the linear heat loss coefficient and the quadratic heat loss coefficient for the solar collectors. For the collectors employed in this simulation, these coefficients are summarized in Tab. 1.

Tab. 1: Model parameters for the analysed air- and water-based solar collectors.

Parameter	TwinSolar compact	Topson TX
η_0 [-]	0.82	0.797
$U_{L,1}$ [W/(m² K)]	6.50	2.833
$U_{L,2}$ [W/(m² K²)]	0.032	0.0133

Fig. 2 shows a schematic diagram of the finite difference of a conventional counterflow regeneration unit with the heat and mass transfer interactions between the liquid desiccant and the regenerating air stream. By assuming negligible heat loss from or gain to the finite element, the 1D steady-state mass and energy balances can be written as follows:

Desiccant solution:

Mass balance

$$\dot{m}_{s,i}\cdot\xi_{s,i}=\dot{m}_{s,i-1}\cdot\xi_{s,i-1} \quad \text{(eq. 3)}$$

$$\dot{m}_{s,i}=\dot{m}_{s,i-1}-\Delta\dot{m}_{des,m,i} \quad \text{(eq. 4)}$$

Energy balance

$$\dot{m}_{s,i-1}\cdot h_{s,i-1}=\dot{m}_{s,i}\cdot h_{s,i}+h_{conv,s\text{-}a,m,i}\cdot A_{w,i}\cdot\left(T_{s,m,i}-T_{a,m,i}\right)+\Delta\dot{m}_{des,m,i}\cdot\left(h_{fg,i}+\Delta h_{d,i}\right) \quad \text{(eq. 5)}$$

Regenerating air:

Mass balance

$$\dot{m}_a\cdot\chi_{a,i-1}=\dot{m}_a\cdot\chi_{a,i}+\Delta\dot{m}_{des,m,i} \quad \text{(eq. 6)}$$

Energy balance

$$\dot{m}_a\cdot h_{a,i}+h_{conv,s\text{-}a,m,i}\cdot A_{w,i}\cdot\left(T_{s,m,i}-T_{a,m,i}\right)+\Delta\dot{m}_{des,m,i}\cdot\left(h_{fg,i}+\Delta h_{d,i}\right)=\dot{m}_a\cdot h_{a,i-1} \quad \text{(eq. 7)}$$

Where $\dot{m}$, h and T stand for the mass flow rate [kg/s], the specific enthalpy [J/kg] and the temperature [K] of the fluids involved in the regeneration process, while χ_a and ξ_s are the absolute humidity of the air [kg/kg] and the mass fraction of the hygroscopic liquid. The subscripts a and s stand for the air and the desiccant solution, whereas the subscripts i-1 and i denote the inlet/outlet and outlet/inlet characteristics of the solution/air. The symbols $h_{conv,s\text{-}a,m,i}$, $A_{w,i}$, $\Delta\dot{m}_{des,m,i}$, $h_{fg,i}$ and $\Delta h_{d,i}$ correspond to the local values of the convective heat transfer coefficient between the solution film and the air stream [W/(m² K)], the finite element area wetted by the

solution [m²], the water desorption rate [kg/s], the latent heat of water vaporisation [J/kg] and the differential enthalpy of dilution [J/kg], respectively.

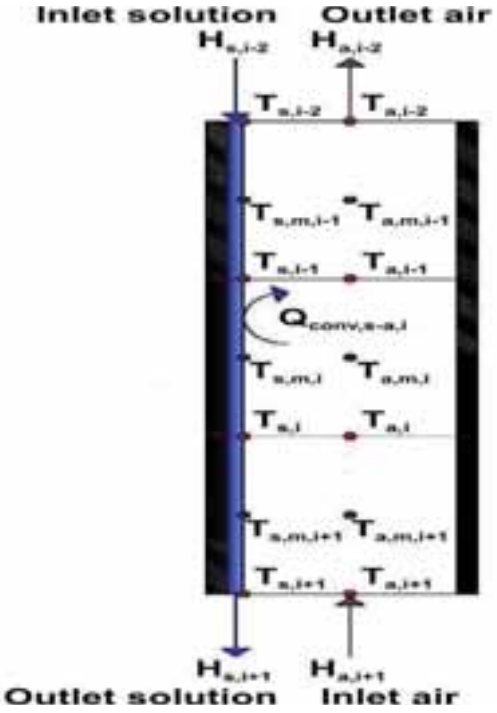

Fig. 2: Heat and mass transfer mechanisms in a finite element of the adiabatic counterflow packed bed regenerator.

On the other hand, the local water desorption rate $\Delta\dot{m}_{des,m,i}$ from the diluted liquid sorbent can be calculated as follows:

$$\Delta\dot{m}_{des,m,i}=\frac{\beta_{m,i}\cdot M_{H_2O}}{R_m\cdot T_{a,m,i}}\cdot A_{w,i}\cdot\left(p_{s,m,i}-p_{a,m,i}\right) \quad \text{(eq. 8)}$$

With M_{H_2O} and R_m as the molar mass of the water vapour (0.01802 kg/mol) and the molar gas constant (8.31451 J/(mol K)), and $p_{s,m,i}$ and $p_{a,m,i}$ as the vapour pressures [Pa] of the solution and the regenerating air at their average temperatures $T_{s,m,i}$ and $T_{a,m,i}$.

The local mass transfer coefficient based on the gas-phase concentration $\beta_{m,i}$ [m/s] is determined in terms of the heat transfer coefficient $h_{conv,s-a,m,i}$ by applying the Chilton-Colburn analogy:

$$\beta_{m,i}=\frac{h_{conv,s-a,m,i}}{\rho_{a,m,i}\cdot c_{p,a,m,i}\cdot Le_a^{2/3}} \quad \text{(eq. 9)}$$

Where $\rho_{a,m,i}$, $c_{p,a,m,i}$ and Le_a stand for the density [kg/m³], the isobaric specific heat capacity [J/(kg K)] of the regenerating air, and the Lewis number of the water vapour-air mixture. The local convective heat transfer coefficient between a fluid and the particles in the packed bed reactor is calculated according to the relationships given in the VDI Heat Atlas (Gnielinski, 2010).

3.2 Direct solar regenerators

The simultaneous heat and mass transfer mechanisms occurring within a single-glazed forced convective collector/regenerator are shown in Fig. 3. By neglecting the gradients of temperature and water content in both the air stream and the liquid film along the collector width, disregarding the heat conduction and mass diffusion

in both the air and the solution along their flow directions, and considering uniform wall temperature and concentration boundary conditions for the heat and mass transfer in the finite element, the following 1D steady-state mass and energy balances can be formulated for the counterflow case:

Collector housing;

Energy balance

$$U_{cond,p\text{-}h,m,i}\cdot\left(T_{p,m,i}-T_{h,m,i}\right)=h_{conv,h\text{-}amb,m,i}\cdot A_{c,i}\cdot\left(T_{h,m,i}-T_{amb}\right) \quad \text{(eq. 10)}$$
$$+h_{rad,h\text{-}sky,m,i}\cdot A_{c,i}\cdot\left(T_{h,m,i}-T_{sky}\right)$$
$$+h_{rad,h\text{-}gr,m,i}\cdot A_{c,i}\cdot\left(T_{h,m,i}-T_{gr}\right)$$

Absorber plate:

Energy balance

$$\left[\left(\tau_g\cdot\tau_s\cdot\alpha_p\right)_{eff}\cdot F_w+\left(\tau_g\cdot\alpha_p\right)_{eff}\cdot(1-F_w)\right]\cdot G_{g,c}\cdot A_{c,i}=U_{cond,p\text{-}h,m,i}\cdot A_{c,i}\cdot\left(T_{p,m,i}-T_{h,m,i}\right) \quad \text{(eq.11)}$$
$$+h_{conv,p\text{-}a,m,i}\cdot(1-F_w)\cdot A_{c,i}\cdot\left(T_{p,m,i}-T_{a,m,i}\right)$$
$$+h_{conv,p\text{-}s,m,i}\cdot F_w\cdot A_{c,i}\cdot\left(T_{p,m,i}-T_{s,m,i}\right)$$
$$+h_{rad,p\text{-}g,m,i}\cdot(1-F_w)\cdot A_{c,i}\cdot\left(T_{p,m,i}-T_{g,m,i}\right)$$

Desiccant solution:

Mass balance (see eq. 3 and eq. 4)

Energy balance

$$\dot{m}_{s,i-1}\cdot h_{s,i-1}+h_{conv,p\text{-}s,m.i}\cdot F_w\cdot A_{c,i}\cdot\left(T_{p,m,i}-T_{s,m,i}\right)=\dot{m}_{s,i}\cdot h_{s,i}+\Delta\dot{m}_{des,m,i}\cdot\left(h_{fg,i}+\Delta h_{d,i}\right) \quad \text{(eq.12)}$$
$$+h_{conv,s\text{-}a,m,i}\cdot F_w\cdot A_{c,i}\cdot\left(T_{s,m,i}-T_{a,m,i}\right)$$
$$+h_{rad,s\text{-}g,m,i}\cdot F_w\cdot A_{c,i}\cdot\left(T_{s,m.i}-T_{g,m,i}\right)$$

Regenerating air:

Mass balance (see eq. 6)

Energy balance

$$\dot{m}_a\cdot h_{a,i}+\Delta\dot{m}_{des,m,i}\cdot\left(h_{fg,i}+\Delta h_{d,i}\right)+h_{conv,s\text{-}a,m,i}\cdot F_w\cdot A_{c,i}\cdot\left(T_{s,m,i}-T_{a,m,i}\right) \quad \text{(eq.13)}$$
$$+h_{conv,p\text{-}a,m,i}\cdot(1-F_w)\cdot A_{c,i}\cdot\left(T_{p,m,i}-T_{a,m,i}\right)+h_{conv,g\text{-}a,m,i}\cdot A_{c,i}\cdot\left(T_{g,m,i}-T_{a,m,i}\right)=\dot{m}_a\cdot h_{a,i-1}$$

Glass cover:

Energy balance

$$\alpha_g\cdot G_{g,c}\cdot A_{c,i}+h_{rad,s\text{-}g,m,i}\cdot F_w\cdot A_{c,i}\cdot\left(T_{s,m,i}-T_{g,m,i}\right)+h_{rad,p\text{-}g,m,i}\cdot\left(1-F_w\right)\cdot A_{c,i}\cdot\left(T_{p,m,i}-T_{g,m,i}\right)= \quad \text{(eq.14)}$$
$$h_{conv,g\text{-}a,m,i}\cdot A_{c,i}\cdot\left(T_{g,m,i}-T_{a,m,i}\right)+U_{conv,g\text{-}amb,m.i}\cdot A_{c,i}\cdot\left(T_{g,m,i}-T_{amb}\right)$$
$$+U_{rad,g\text{-}sky,m,i}\cdot A_{c,i}\cdot\left(T_{g,m,i}-T_{sky}\right)+U_{rad,g\text{-}gr,m,i}\cdot A_{c,i}\cdot\left(T_{g,m,i}-T_{gr}\right)$$

With $\dot{m}$, h and T as the mass flow rate [kg/s], the specific enthalpy [J/kg] and the temperature [K] of the fluids involved in the regeneration process. The subscripts *h*, *p*, *s*, *a*, *g*, *amb*, *sky* and *gr* refer to the collector housing, the absorber plate, the hygroscopic solution, the regenerating air, the glass cover, the ambient, the sky and the ground, while the subscripts *i-1* and *i* indicate the inlet/outlet and outlet/inlet conditions of the solution/air. The symbols F_w, $A_{c,i}$, $\Delta\dot{m}_{des,m,i}$, $h_{fg,i}$ and $\Delta h_{d,i}$ correspondingly stand for the wetting factor, the total finite element

area [m²] as well as the local values of the water desorption rate [kg/s], the latent heat of water vaporisation [J/kg] and the differential enthalpy of dilution [J/kg]. The approaches to estimate the effective transmittance-absorptance products for the glass cover-absorber plate $\left(\tau_g \cdot \alpha_p\right)_{eff}$ and the glass cover-desiccant solution-absorber plate $\left(\tau_g \cdot \tau_s \cdot \alpha_p\right)_{eff}$ optical systems are given by Duffie and Beckman (2013). Finally, h_{conv}- U_{conv}, h_{rad} - U_{rad}, and U_{cond} denote the convective heat transfer coefficients, the radiative heat transfer coefficients, and the heat conductance value, respectively.

The air channel of a forced convective collector/regenerator is asymmetrically heated since its absorber plate is considerably warmer than its glass cover. For analysis purposes, the convective heat transfer coefficients between the absorber plate and the air stream ($h_{conv,p\text{-}a,m,i}$), the desiccant solution and the air stream ($h_{conv,s\text{-}a,m,i}$), and the glazing and the air stream ($h_{conv,g\text{-}a,m,i}$) are considered to be equal. In this way, the convective heat transfer coefficient $h_{conv,s\text{-}a,m,i}$ [W/(m² K)] is evaluated as follows:

$$h_{conv,s\text{-}a,m,i} = Nu_{s\text{-}a} \cdot k_{a,m,i} / D_h \qquad \text{(eq. 15)}$$

For laminar flow ($Re_{a,D_h} \leq 2300$), the Nusselt number $Nu_{s\text{-}a,lam}$ can be determined by means of the correlation of Mercer et al. (1967) for one-sided heated air channels at constant wall temperature:

$$Nu_{s\text{-}a,lam} = 4.86 + \frac{0.0606 \cdot \left(Re_{a,D_h} \cdot Pr_a \cdot D_h / L_c\right)^{1.2}}{1 + 0.0909 \cdot \left(Re_{a,D_h} \cdot Pr_a \cdot D_h / L_c\right)^{0.7} \cdot Pr_a^{0.17}} \qquad \text{(eq. 16)}$$

For turbulent flow ($Re_{a,D_h} \geq 3000$), in which the influences of the boundary conditions and the channel geometry are minor, the modified equation of Petukhov (Gnielinski, 1976) is used for assessing the Nusselt number $Nu_{s\text{-}a,turb}$:

$$Nu_{s\text{-}a,turb} = \left[\frac{(f/8) \cdot Re_{a,D_h} \cdot Pr_a}{1 + 12.7 \cdot \sqrt{f/8} \cdot \left(Pr_a^{2/3} - 1\right)}\right] \cdot \left[1 + \left(\frac{D_h}{L_c}\right)^{2/3}\right] \qquad \text{(eq. 17)}$$

$$f = \left\{0.78 \cdot Ln\left(Re_{a,D_h}\right) - 1.5\right\}^{-2}$$

With L_c and D_h as the channel length [m] and the hydraulic diameter [m].

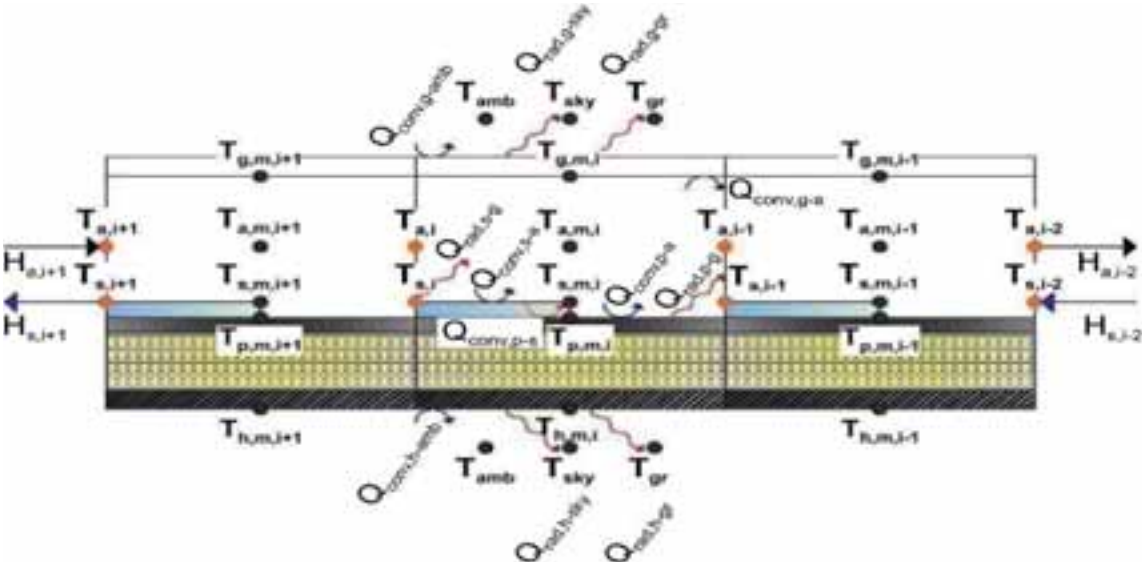

Fig. 3: Heat and mass transfer mechanisms in a finite element of the counterflow collector/regenerator.

4. Simulation results and discussion

This section presents the performance comparisons between the indirect and direct solar thermal regeneration units. Aqueous lithium chloride solution (LiCl-H_2O) was used as liquid desiccant. The parameters for this simulation study are summarised in Tab. 2.

Tab. 2: Parameters for the simulation of the analysed solar regeneration systems.

Component	Operating parameter	Unit	Range (reference value)	Variant
Solar water heater	Solar radiation	W/m²	800	SWH+WA-HX+Reg, SWH+WS-HX+Reg, SWH+WS-HX+WA-HX+Reg
	Collector area	m²	16	
	Tilt angle	°	30	
	Fluid volumetric flow rate	l/h	240	
	Fluid mass fraction	%	40	
	Inlet fluid temperature	°C	40	
WA-HX	Fluid volumetric flow rate	l/h	240	SWH+WA-HX+Reg
			120	SWH+WS-HX+WA-HX+Reg
	Air volumetric flow rate	m³/h	100-400 (300)	SWH+WA-HX+Reg, SWH+WS-HX+WA-HX+Reg
	Inlet air temperature	°C	24-40 (30)	
	Inlet air absolute humidity	g/kg	10.6-18.8 (10.6)	
WS-HX	Fluid volumetric flow rate	l/h	240	SWH+WS-HX+Reg
			120	SWH+WS-HX+WA-HX+Reg
	Solution volumetric flow rate	l/h	100-400 (200)	SWH+WS-HX+Reg, SWH+WS-HX+WA-HX+Reg
	Inlet solution temperature	°C	40-70 (50)	
	Inlet solution mass fraction	%	34-42 (37)	
Solar air heater	Air volumetric flow rate	m³/h	100-400 (300)	SAH+Reg
	Inlet air temperature	°C	24-40 (30)	
	Inlet air absolute humidity	g/kg	10.6-18.8 (10.6)	
Regenerator	Air volumetric flow rate	m³/h	100-400 (300)	SWH+WA-HX+Reg, SAH+Reg, SWH+WS-HX+Reg, SWH+WS-HX+WA-HX+Reg
	Inlet air temperature	°C	24-40 (30)	SWH+WS-HX+Reg
	Inlet air absolute humidity	g/kg	10.6-18.8 (10.6)	SWH+WA-HX+Reg, SAH+Reg, SWH+WS-HX+Reg, SWH+WS-HX+WA-HX+Reg
	Solution volumetric flow rate	l/h	100-400 (200)	
	Inlet solution temperature	°C	40-70 (50)	SWH+WA-HX+Reg, SAH+Reg
	Inlet solution mass fraction	%	34-42 (37)	SWH+WA-HX+Reg, SAH+Reg, SWH+WS-HX+Reg, SWH+WS-HX+WA-HX+Reg
Collector/regenerator	Air volumetric flow rate	m³/h	100-400 (300)	SCR
	Inlet air temperature	°C	24-40 (30)	
	Inlet air absolute humidity	g/kg	10.6-18.8 (10.6)	
	Solution volumetric flow rate	l/h	100-400 (200)	
	Inlet solution temperature	°C	40-70 (50)	
	Inlet solution mass fraction	%	34-42 (37)	

4.1 Effects of inlet air parameters on the regeneration performance

Fig. 4 shows that, for all configurations, the desorption rate increased with the rise of the inlet air temperature due to the enhancement in the driving force for the heat transfer between the regenerating air and the hygroscopic solution, which consequently augmented the temperature and the vapour pressure of the liquid sorbent. The desorption rate obtained from the direct solar regenerator (SCR) was in average 11% and 9% greater than those respectively achieved from the variants with indirect solar preheating of both air and liquid sorbent (SWH+WS-HX+WA-HX+Reg) and of only desiccant solution (SWH+WS-HX+Reg), which were the best indirect solar regeneration units at the analysed operating conditions. By contrast, the regenerators with air preheating via solar air heaters (SAH+Reg) and solar water heaters (SWH+WA-HX+Reg) exhibited the worst performances among the conventional regeneration units with average desorption rates 37 % and 49% lower than that from the direct solar regenerator.

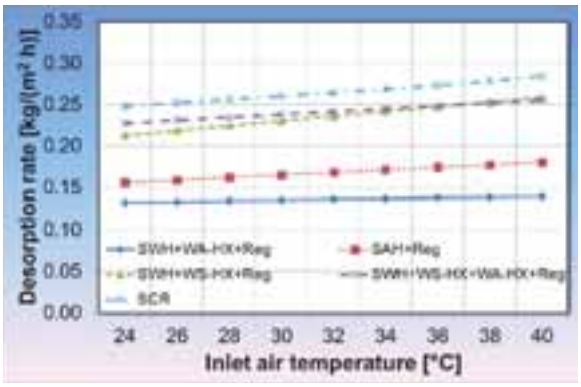

Fig. 4: Effect of the inlet air temperature on the desorption rate of the solar regenerators with indirect and direct (pre)heating of the regenerating air and the desiccant solution.

The desorption rate linearly decreased in all analysed solar regenerators with increasing absolute humidity of the air stream (see Fig. 5) due to the inherent rise in the air vapour pressure, which indeed diminished the vapour pressure difference between the desiccant solution and the air. This decrease was less severe in the direct solar regenerator than in the conventional regeneration units at the analysed operating conditions. The desorption rates achieved with the variants with simultaneous indirect solar preheating of the liquid sorbent and the air (SWH+WS-HX+WA-HX+Reg) and indirect solar preheating of the desiccant solution came next and were on average about 17% and 21% lower than those for direct solar regenerators, respectively. On the other hand, the regeneration systems with air preheating through solar air heaters (SAH+Reg) and solar water heaters (SWH+WA-HX+Reg) had the worst desorption rates, which were approximately 47% and 60% less than the respective value for collector/regenerators.

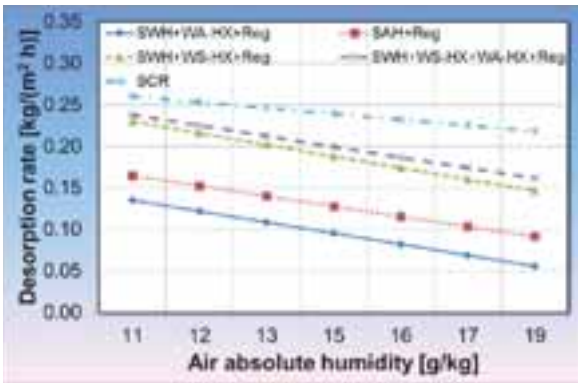

Fig. 5: Effect of the air absolute humidity on the desorption rate of the solar regenerators with indirect and direct (pre)heating of the regenerating air and the desiccant solution.

According to Fig. 6, the desorption rate for all configurations augmented at the analysed operating conditions by increasing the air volumetric flow rate due to the enhancement in the mass transfer coefficient, which counteracted the decrease in the solution temperature and its vapour pressure. From an air volumetric flow rate

of 300 m^3/h ($\dot{m}_a/\dot{m}_{s,in}=1.187$ with $\dot{V}_{s,in}=200\,l/h$), the direct solar regenerator exhibited considerably high values of said performance index compared with those of indirect solar regenerators because of the proximity to the turbulent regime of air flow within the collector/regenerator channel ($Re_{a,ch}=2374$). In average, the desorption rate achieved with the direct solar regenerator was 14% greater than those for the variants with indirect solar preheating of air and liquid desiccant (SWH+WS-HX+WA-HX+Reg and SWH+WS-HX+Reg). Moreover, the variants with indirect solar preheating of air by means of solar air heaters (SAH+Reg) and solar water heaters (SWH+WA-HX+Reg) were clearly outperformed with average desorption rates 44% and 53% lower than that of the direct solar regenerator.

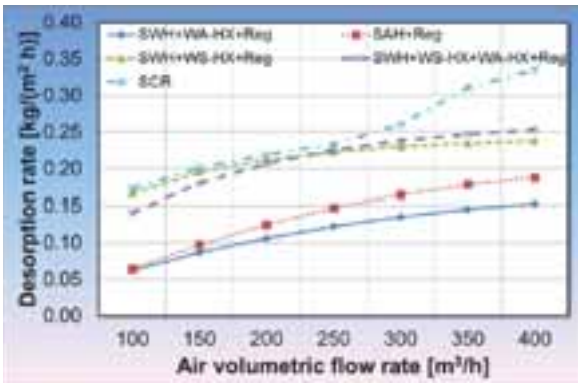

Fig. 6: Effect of the air volumetric flow rate on the desorption rate of the solar regenerators with indirect and direct (pre)heating of the regenerating air and the desiccant solution.

4.2 Effects of inlet solution parameters on the regeneration performance

When the desiccant solution entered the analysed regeneration units at high temperatures, the consequent increasing in the heat and mass transfer driven potentials led to higher desorption rates (see Fig. 7). Comparing with the effect of the inlet air temperature, it can be concluded that preheating the desiccant solution was more efficient than preheating the air stream. Although the average desorption rate attained with the direct solar regenerator was approximately 11%, 17%, 26% and 37% higher than those corresponding to the conventional regeneration units SWH+WS-HX+WA-HX+Reg, SWH+WS-HX+Reg, SAH+Reg and SWH+WA-HX+Reg, the performance differences among them were considerably reduced from an inlet solution temperature of 60°C.

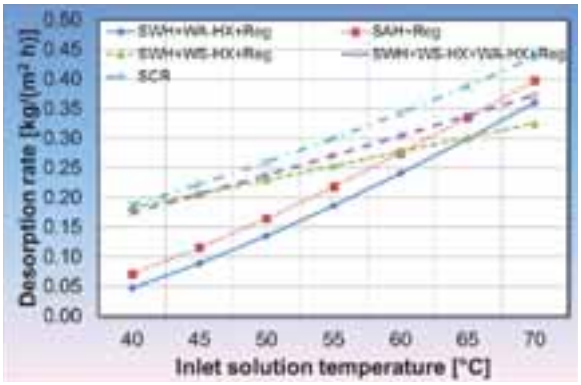

Fig. 7: Effect of the inlet solution temperature on the desorption rate of the solar regenerators with indirect and direct (pre)heating of the regenerating air and the desiccant solution.

Under the given operating conditions, the higher the solution mass fraction, the lower the desorption rate for all the analysed regeneration units due to the lower vapour pressure of the solution, which indeed reduced the mass transfer driven potential as shown in Fig. 8. The desorption rate achieved with the direct solar regenerator was 10% and 13% higher than the corresponding values for the variants with indirect solar preheating of both the air and desiccant solution (SWH+WS-HX+WA-HX+Reg) and of only liquid sorbent (SWH+WS-HX+Reg). Besides, the performance of the configurations with indirect solar preheating of air by using solar air heaters (SAH+Reg) and solar water heaters (SWH+WA-HX+Reg) were widely surpassed with average desorption rates 39% and 51% lower than that of the solar collector/regenerator.

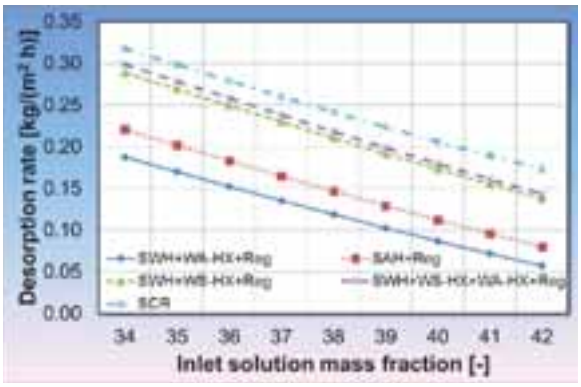

Fig. 8: Effect of the inlet solution mass fraction on the desorption rate of the solar regenerators with indirect and direct (pre)heating of the regenerating air and the desiccant solution.

For the analysed range of operating conditions, the increase of the solution volumetric flow rate affected in different ways the desorption rate for direct and indirect solar regenerators (see Fig. 9). In the case of the collector/regenerator, the desorption rate strongly decreased with the rise of the solution volumetric flow rate due to the reduced residence time of the liquid sorbent within said device, which contributed to diminish both the solar warming of the solution and the resulting mass transfer potential. On the other hand, the desorption rate obtained from the indirect solar regeneration units exhibited the inverse behaviour since the shortening of the residence time of solution within the sorption reactor led to the decrease of the temperature falls for both the air and the liquid sorbent, thus keeping the heat and mass transfer driven potentials relatively high. It was observed that the direct solar regenerator clearly outperformed the investigated indirect solar regeneration units until reaching a critical solution volumetric flow rate of approximately 225 l/h ($\dot{m}_a/\dot{m}_{s,in}=1.282$ with $\dot{V}_a=300\ m^3/h$). At higher flow rates, the performance of the collector/regenerator was clearly surpassed by that of the indirect solar regenerator with preheating of liquid desiccant (SWH+WS-HX+Reg).

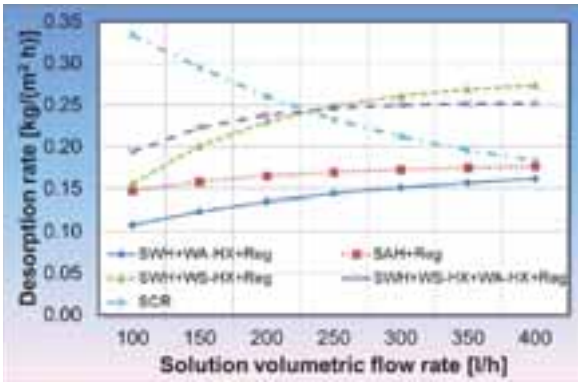

Fig. 9: Effect of the solution volumetric flow rate on the desorption rate of the solar regenerators with indirect and direct (pre)heating of the regenerating air and the desiccant solution.

5. Conclusions

The use of collector/regenerators contributes to reduce the installation costs and complexity of liquid desiccant systems by diminishing their number of components and by simplifying their control strategies. Moreover, the direct solar regenerator clearly outperforms the indirect ones at high absolute humidities, air volumetric flow rates higher than 300 m^3/h ($\dot{m}_a/\dot{m}_{s,in}$ = 1.187 with $\dot{V}_{s,in}=200\ l/h$), high inlet temperatures of air and solution as well as solution volumetric flow rates lower than 225 l/h ($\dot{m}_a/\dot{m}_{s,in}=1.282$ with $\dot{V}_a=300\ m^3/h$) while keeping constant the other operating parameters.

Acknowledgments

This work is sponsored by the Federal Ministry of Education and Research in framework of the program "Research at Universities of Applied Sciences – Funding stream Young Engineers" (contract number 03FH0041X4).

References

Duffie, J. A., Beckman, W. A., 2013. Radiation transmission through glazing: absorbed radiation, in: Solar engineering of thermal processes. John Wiley & Sons, Inc. pp. 202-214.

Gezahegn, H., Mullick, S. C., Jain, S., 2013. Optical and thermal performance of a liquid desiccant solar regenerator. Proc. of International Congress on Renewable Energy, KIIT University, Bhubaneswar, Odisha, 15-27.

Gnielinski, V., 2010. Fluid-particle heat transfer in flow through packed beds of solids, in: VDI Heat Atlas, V.-G.V.u. Chemieingenieurwesen, Springer, pp. 743-744.

Gnielinski, V., 1976. New equations for heat and mass transfer in turbulent pipe and channel flow. Int. Chem. Eng. 16(2), 359-367.

Gommed, K., Grossman, G., 2007. Experimental investigation of a liquid desiccant system for solar cooling and dehumidification. Sol. Energy 81(1), 131-138.

Grossman, G., Johannsen, A., 1981. Solar cooling and air conditioning. Prog. Energy Combust. Sci. 7(3), 185-228.

Guo, J., Lin, S., Bilbao, J. I., White, S. D., Sproul, A. B., 2017. A review of photovoltaic thermal (PV/T) heat utilisation with low temperature desiccant cooling and dehumidification. Renew. Sustain. Energy Rev. 67, 1-14.

Hawlader, M. N. A., Wood, B. D., Folkman, C. C., Stack, A. P., 1997. Solar assisted open-cycle absorption cooling: Performance of collector/regenerators. Int. J. Energ. Res. 21(6), 549-574.

Jamar, A., Majid, Z. A. A., Azmi, W. H., Norhafana, M., Razak, A. A., 2016. A review of water heating system for solar energy applications. Int. Commun. Heat Mass Transf. 76, 178-187.

Kabeel, A. E., 2005. Augmentation of the performance of solar regenerator of open absorption cooling system. Renew. Energ. 30(3), 327-338.

Kabeel, A. E., Hamed, M. H., Omara, Z. M., Kandeal, A. W., 2017. Solar air heaters: design configurations, improvement methods and applications - a detailed review. Renew. Sustain. Energy Rev. 70, 1189-1206.

Katejanekarn, T., Kumar, S., 2008. Performance of a solar-regenerated liquid desiccant ventilation pre-conditioning system. Energy Build. 40(7), 1252-1267.

Kaushik, S. C., Kaudinya, J. V., Yadav, Y. K., 1992. Studies on some solar collector/regenerator systems for open cycle absorption air conditioning/liquid desiccant cooling systems. Heat Recov. Syst. CHP 12(4), 357-363.

Martin, V., Goswami, Y., 2000. Effectiveness of heat and mass transfer processes in a packed bed liquid desiccant dehumidifier/regenerator. HVAC&R. Res. 6(1), 21-39.

Mercer, W. E., Pearce, W. M., Hitchcock, J. E., 1967. Laminar forced convection in the entrance region between parallel flat plates. J. Heat Transfer 89(3), 251-256.

Yang, R., Wang, P. L., 2001. A simulation study of performance evaluation of single-glazed and double-glazed collectors/regenerators for an open-cycle absorption solar cooling system. Sol. Energy 71(4), 263-268.

Establishment and Theoretical Analysis of a Solar Driven NH_3-H_2O Resorption Heat Pump Cycle

Teng Jia, Yanjun Dai*

Institute of Refrigeration and Cryogenics, Shanghai Jiao Tong University, Shanghai (China)

Abstract

To make full utilization of low-temperature solar thermal, a novel balanced-type absorption-resorption heat pump (ARHP) cycle with a simple construction is proposed in this paper. The novel cycle is based on concentration difference of strong solution, weak solution and ammonia vapor (in fact a very small amount of water vapor inside). In order to achieve the optimal operating conditions, a mathematical model is developed and the feasibility and performance are investigated when factors like high and low generation pressure and ambient air temperature vary. Performance of the novel cycle is compared with that of the conventional single-stage absorption heat pump (AHP) cycle. The novel cycle is proved to have a smaller operation pressure differential compared to the conventional AHP cycle and is more suitable for the temperature characteristics of commonly used solar collectors. Coefficient of performance (COP) value of 1.42 can be obtained when high pressure (P_H) and low pressure (P_L) are respectively 1.40 MPa and 0.41 MPa under given working conditions. COP increases with the increasing of solar thermal temperature and ambient air temperature.

Key words: Solar thermal, absorption-resorption heat pump, simulation, COP

Nomenclature	
COP	coefficient of performance
PV	photovoltaics
AHP	absorption heat pump
GAX	generator–absorber exchanger (GAX)
FPC	flat plate collectors
ETC	evacuated tube collectors
HPG	high pressure generator
LPG	low pressure generator
HPA	high pressure absorber
LPA	low pressure absorber
SHX	solution heat exchanger
FRV	flow regulating valve
TV	throttling valve
Subscripts	
hpg	high pressure generator
lpa	low pressure generator
a	absorption
e	evaporation
c	condensation
H	high
L	low
h	heat source
lpg	low pressure absorber
hpa	high pressure absorber
*P*1	solution pump 1
m	mass flow rate [kg/s]
h	specific enthalpy [kJ/kg]
Q	heat exchanged [kW]
W	work, power [kW]
x	concentration [kg/kg]
T	temperature [°C]

doi:10.18086/swc.2017.28.10 Available at http://proceedings.ises.org

1, 2, …	state points
Greek symbols	
ξ	concentration [kg/kg]

1. Introduction

Heat pumps gain popularity by helping improve the quality of life by means of supplying heating in heating seasons and producing domestic hot water throughout the year. Improving their performance, reliability, and environmental impacts has been an ongoing concern (Chua et al. 2010). Conventional compression heat pumps are driven by electric power, and high-power compressors are often required to improve the performance (Fatouh and Elgendy 2011), which leads to many environmental problems. Solar energy is potential in driving heat pumps for different applications due to its cleanliness and accessibility (Fraga et al. 2015; Jradi et al. 2017; Zhou et al. 2016; Dai et al. 2015; Ozcan and Dincer 2013). Solar driven heat pumps can be divided into 3 kinds, i.e. heat pumps driven by thermal arrested by solar collectors, vapor compression heat pumps driven by solar photovoltaics (PV) and those combining solar thermal and vapor compression heat pumps. Among all the technical routes of solar driven heat pumps, the first kind has the highest solar thermal efficiency, which can theoretically convert 80% of the incident solar radiation energy into heating capacity. The combined heat pump systems use solar energy as the low-temperature heat source and are often combined with periodic heat storage devices to improve the cycle's COP by lifting the evaporation temperature (Omojaro and Breitkopf 2013). Electricity is still the basic power source for winter heating. Wu et al. (2014a, 2014b) reviewed recent absorption heating technologies and ammonia-based absorption heat pumps and pointed out that vapor compression and resorption heat pumps were suitable for wider temperature range than absorption ones. Van de Bor D. M. et al. (2014) numerically investigated many compression-resorption heat pumps with ammonia-water as working fluid for 50 specific industrial cases. The simulation results showed that the optimal performance, along with the lowest compression power and reduced investment and operating costs, is obtained under conditions which make the quality of vapor into the resorber be exact 100%. In practice, the vapor quality cannot reach 100% and compressors often work in the wet compression regime with a lower isentropic efficiency. Limited by cycle modes and high driven temperature, these products didn't utilize solar energy. Velázquez N. et al. (2002) presented a methodological analysis and energy evaluation of an air-cooled ammonia–water absorption heat pump with a generator–absorber heat exchanger (GAX) and operated by a hybrid natural gas–solar energy source. The heat pump allowed 19% of solar contribution at full load. A COP value of up to 1.86 was calculated by using ambient air up to 40°C with a relative humidity of 24% as cooling source. The system had a working pressure difference of up to 1.50 MPa and must be equipped with a rectifier. The required temperature of heat source is up to 150 °C, making function time of solar thermal relatively short, which together with the complex structure and high investment cost limited its application.

An absorption-resorption heat pump is formed when the evaporator and condenser in a conventional absorption heat pump are displaced by a low-pressure generator and a high-pressure absorber, respectively, and it completes the inner cycle relying on the concentration difference change of the binary mixtures. Although solar energy utilization is plagued by its intermittence and volatility, absorption-resorption heat pumps are still viable alternatives to supply winter heating in low-temperature environment when utilizing proper working fluid and high-temperature heat sources. Moreover, efficient and stable heating can be achieved by capacity regulating, energy complementary and working fluid storage, making solar driven absorption-resorption heat pump a research hotpot in the field of solar heating worldwide. Du et al. (1991, 1993) analyzed an unbalanced type of absorption -resorption heat pump with ammonia-water as working fluid. The simulation results showed that the system's highest working pressure is determined by the ammonia concentration in the cycle. The cycle appeared stronger adaptability to the environment by regulating ammonia concentration under varying operating conditions. The system was equipped with two solution pumps and the required temperature of generating is too high for efficient application of solar thermal.

This paper presents a novel balanced-type ammonia-water absorption-resorption heat pump which can be driven by solar thermal of lower temperature and of wider temperature range than the abovementioned GAX ones and the unbalanced types, which makes it possible to use flat plate collectors (FPC) and evacuated tube collectors (ETC).

As depicted in Fig. 1, in a conventional AHP cycle, concentration of solution out from condenser is 100%, while in a balanced ARHP cycle, outlet solution concentration of HPA is lower than 100%. Therefore, given the same temperature of solutions out from HPA and condenser, P_H of the novel cycle is lower than that of a conventional AHP cycle (ΔP_H), consequently resulting in a temperature decline of ΔT_h at the generator side, which makes it possible to utilize low-temperature heat source to drive ARHPs for space heating. Besides, given the same inner pressure difference in the two types of heat pumps, a pressure difference (ΔP_L) can also be achieved between evaporator and LPG. "Balanced" here means that there is overlap between the solution concentration range of the left and right sub-cycle Solution streams out from LPG and LPA are mixed together and then pumped to HPA and HPG to complete high-pressure absorption and generation process, respectively.

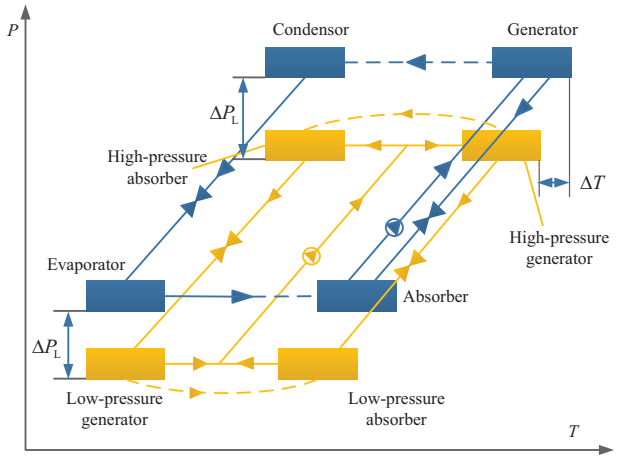

Fig. 1: Comparison of the conventional AHP cycle and the ARHP cycle proposed in this paper

2. Cycle description

The schematic diagram of the proposed balanced ARHP cycle is shown in Fig. 2. The pressure-temperature ($P-T$) diagram of the aqueous ammonia is shown in Fig. 3. The novel cycle comprises the following main components: HPG (high pressure generator), SHX1, 2 (solution heat exchanger 1, 2), TV1, 2 (throttling valve 2), LPA (low pressure absorber), solution mixing tank (SMT), P1 (solution pump1), solution separation tank (SST), HPA (high pressure absorber), LPG (low pressure generator). In order to clarify different heat absorption processes in low pressure generator, LPG is functionally divided into two parts, LPG1 which takes heat from the ambient and LPG2 which recovers heat from warm solution out from HPA. Ammonia/water is utilized as working pair in this work. The working principle is detailed as follows.

1-2-3-4-5-6-7-8-9-1 is a closed solution circuit. The weak solution out from HPG (1) is precooled by the solution out from SHX1 to state point (2) and then throttled in TV2 to low-pressure (P_L) (3). The solution (3) then absorbs the vapor (16) from LPG, releasing the absorption heat and becoming strong solution (4). The strong solution discharged from LPA (4) is then blended in the SMT with the solution (5) from LPG to make solution (6). The solution (6) is preheated in SHX2 by the hot solution from HPG to solution (7). The solution (7) is pressurized through P1 to high-pressure solution (8). Solution (9) (a portion of solution (8)) then enters HPG and heated by solar thermal to generate, making high-temperature and high-pressure vapor (17/18) and weak solution (1). The solution circuit of the right sub-cycle is finished.

15-6-7-8-9-10-11-12-13-14-5 is another solution circuit. The weak solution out from LPA (5) (which is stronger than the solution (1)) is blended in the solution mixing tank with the solution out from LPA (4) into the solution (6). The solution (6) is then preheated in SHX2 by the solution (1) out from HPA to (7). The solution (7) is pressurized through P1 to high-pressure solution (8). Solution (10) (the remaining portion of solution (8)) then enters LPA and absorb the vapor (18/17), giving off the resorption heat and forming strong solution (which is stronger than solution (4)). The strong solution out from HPA (11) is precooled by solution (14) in LPG2 to solution (12). The high-pressure solution (12) is then depressurized by TV1 to low-pressure solution (13). The low-temperature solution (13) then enters LPG and takes heat from the ambient to

generate, discharging low-temperature and low-pressure vapor in turn in LPG1 and LPG2 and making weak solution (5) (which is stronger than solution (1)). The solution circuit of the left sub-cycle is finished.

t should be pointed out that the amount of solution (4) and solution (9) are not the same due to the different amount of vapor (17/18) and (16). In the same way, the amount of solution (14) and solution (10) are different.

17-18 and 15(15a)-16 are the high- and low-pressure ammonia vapor flow, respectively. 23-24 is the ambient air flow acting as the low-temperature heat source. 19-20-21-22 is the series supply/return water flow. 25-26 is the working medium out from/ into solar collectors, which serves as the high-temperature heat source (80~100 °C in this paper).

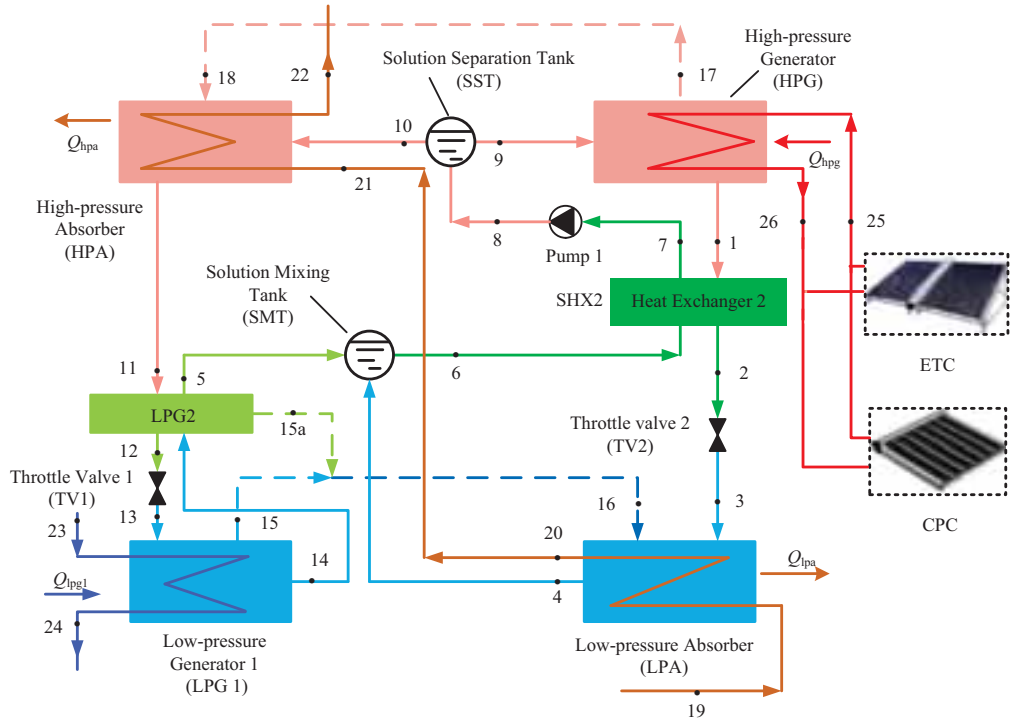

Fig. 2: Schematic diagram of the novel ARHP cycle

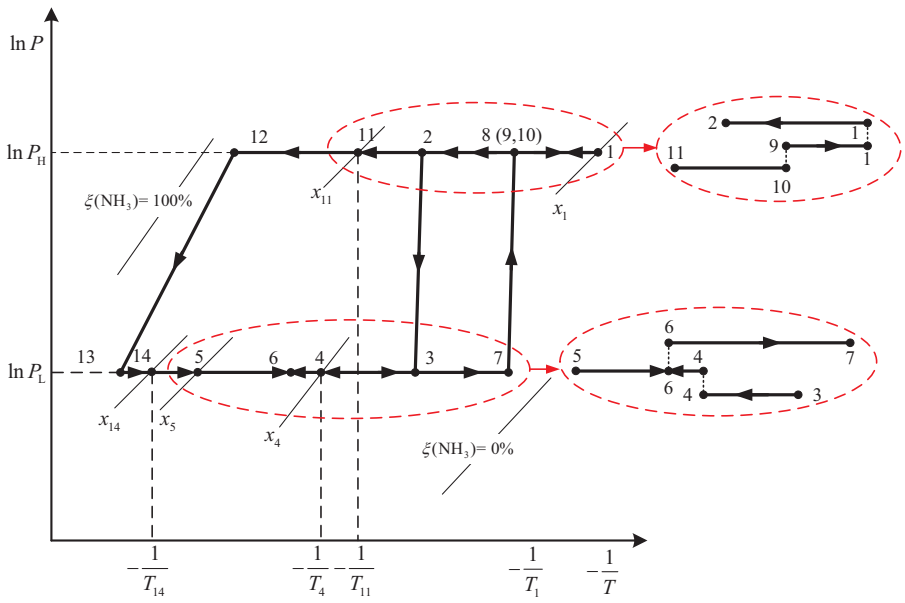

Fig. 3: *P-T* diagram of the novel ARHP cycle

3. Mathematical model

In this paper, low-temperature solar thermal of about 80℃-100℃ works as the high-temperature heat source. A mathematical model is developed to analyze the performance of the proposed cycle. Performance of the proposed cycle is simulated and compared to conventional single-stage cycle. The model can be simplified by the following assumptions:

(1) The system runs in a steady state;

(2) Heat losses to the surroundings and pressure drops along the pipelines are neglected;

(3) The solutions out from the LPG, HPG, LPA and HPA are all saturated;

(4) The vapor out from the LPG and HPG are saturated;

(5) The process in the solution pump is adiabatic.

(6) The expansion processes in throttling valves are isenthalpic.

(7) The mixing process in the solution mixing tank is adiabatic.

The proposed cycle comprises several relatively simple components such as the solution pump, heat exchangers, solution mixing tank, valves, and solution separation tank, HPG, LPG (1 and 2), HPA and LPA. Each component can be taken as a control volume with inlet and outlet fluid, heat transfer and work interactions (Hong 2011). The basic models for all of the components include energy balance equation, solution mass balance equation and ammonia mass balance equation, which are shown respectively as follows in Table 1.

ab. 1: Basic equations of the main components in the heat pump cycle

Components	Balance equations	
HPG	$m_9 h_9 + Q_{hpg} = m_1 h_1 + m_{17} h_{17}$	(eq. 1)
	$m_9 = m_1 + m_{17}$	(eq. 2)
	$m_9 x_9 = m_1 x_1 + m_{17} x_{17}$	(eq. 3)
SHX2	$m_1 h_1 + m_6 h_6 = m_2 h_2 + m_7 h_7$	(eq. 4)
	$m_1 = m_2$	(eq. 5)
	$m_1 x_1 = m_2 x_2$	(eq. 6)
	$m_6 = m_7$	(eq. 7)
TV2	$m_2 h_2 = m_3 h_3$	(eq. 8)
	$m_2 = m_3$	(eq. 9)
	$m_2 x_2 = m_3 x_3$	(eq. 10)
LPA	$m_3 h_3 + m_{16} h_{16} = m_4 h_4 + Q_{lpa}$	(eq. 11)
	$m_4 = m_3 + m_{16}$	(eq. 12)
	$m_4 x_4 = m_3 x_3 + m_{16} x_{16}$	(eq. 13)
SMT	$m_5 h_5 = m_4 h_4 + m_{14} h_{14}$	(eq. 14)
	$m_5 = m_4 + m_{14}$	(eq. 15)
	$m_5 x_5 = m_4 x_4 + m_{14} x_{14}$	(eq. 16)
LPG1	$m_{13} h_{13} + Q_{lpg1} = m_{14} h_{14} + m_{15} h_{15}$	(eq. 17)
	$m_{13} = m_{14} + m_{15}$	(eq. 18)
	$m_{13} x_{13} = m_{14} x_{14} + m_{15} x_{15}$	(eq. 19)
TV1	$m_{12} h_{12} = m_{13} h_{13}$	(eq. 20)
	$m_{12} = m_{13}$	(eq. 21)
	$m_{11} h_{11} + m_5 h_5 = m_{12} h_{12} + m_6 h_6$	(eq. 22)
SHX1	$m_{11} = m_{12}$	(eq. 23)
	$m_{11} x_{11} = m_{12} x_{12}$	(eq. 24)
	$m_6 = m_5$	(eq. 25)
	$m_6 x_6 = m_5 x_5$	(eq. 26)
	$m_{10} h_{10} + m_{17} h_{17} = m_{11} h_{11} + Q_{hpa}$	(eq. 27)

HPA	$m_{11}x_{11} = m_{10}x_{10} + m_{17}x_{17}$	(eq. 28)
	$m_{11} = m_{10} + m_{17}$	(eq. 29)
P1	$m_7h_7 + W_{p1} = m_8h_8$	(eq. 30)
	$m_7 = m_8$	(eq. 31)
	$m_7x_7 = m_8x_8$	(eq. 32)
SST	$m_8h_8 = m_9h_9 + m_{10}h_{10}$	(eq. 33)
	$m_8 = m_9 + m_{10}$	(eq. 34)
	$m_8x_8 = m_9x_9 + m_{10}x_{10}$	(eq. 35)
LPG2	$m_{14}h_{14} + m_{11}h_{11} = m_{12}h_{12} + m_5h_5 + m_{15a}h_{15a}$	(eq. 36)
	$m_{14} = m_5 + m_{15a}$	(eq. 37)
	$m_{14}x_{14} = m_5x_5 + m_{15a}x_{15a}$	(eq. 38)

In this paper, COP is adopted to evaluate performance of the proposed NH_3-H_2O absorption-resorption cycle. It can be defined as heating capacity output divided by the total energy input, given by

$$\mathrm{COP} = \frac{Q_{\mathrm{hpa}} + Q_{\mathrm{lpa}}}{Q_{\mathrm{hpg}}} = 1 + \frac{Q_{\mathrm{lpg1}}}{Q_{\mathrm{hpg}}} \quad \text{(eq. 39)}$$

Where Q_{lpg1} and Q_{hpg} are the total heat input of LPG1 and HPG, respectively.

All the properties of ammonia-water and pure ammonia are calculated by the REFPROP 8.0.

4. Results and discussion

In this paper, all the simulation results are based on the assumption that mass flow rate of low-pressure refrigerant vapor is 0.034 kg/s, i.e. m_{16} = 0.034 kg/s. The initial working conditions are listed in Table 2.

Tab. 2 Initial working condition

Working conditions	Given values (°C)
Temperature of solution out from HPG (1)	90
Temperature of solution out from HPA (11)	40
Temperature of solution out from LPA (4)	35
Temperature of the return water (19)	30
Ambient air temperature	10
Temperature difference between ambient air and solution (14)	3
Cold end temperature difference of SHX2, i.e. $T_2 - T_6$	10
Temperature difference between HTF outlet and solution (1), $T_{25} - T_1$	5
Temperature difference in LPG2, i.e. $T_5 - T_{14}$	5

Performance of the proposed cycle has been simulated under working conditions listed in Table 2. Simulation results are illustrated in Figs. 4-8.

Fig. 4 shows the effect of P_H (high generation pressure) values and P_L (low generation pressure) values on COP of the novel cycle. It can be seen that for a given P_H value, the COP increases rapidly with the increasing of P_L at first and then decreases with the increasing of P_L value. Under given working conditions, each P_H value corresponds to an optimum P_L to make the cycle's COP to its maximum value. The optimum P_L value increase with the increasing of P_H value, and so does the maximum value of COP. For instance, the maximum COP values for P_H values of 0.80 MPa, 0.90 MPa, 1.00 MPa, 1.10 MPa, 1.20 MPa, 1.30 MPa and 1.40 MPa are 1.17, 1.20, 1.23, 1.26, 1.31, 1.36, 1.42, respectively, and the corresponding optimum P_L values are 0.18 MPa, 0.21 MPa, 0.24 MPa, 0.28 MPa, 0.31 MPa, 0.36 MPa and 0.41 MPa, respectively. For a given P_H value, the corresponding P_L value is limited in a certain range and the proposed heat pump cycle will not work beyond that range.

Fig. 5 depicts effect of P_H and P_L values on ΔT_1 of LPG1, ΔT_2 of LPA, ΔT_3 of HPG and ΔT_4 of HPA. It can be seen that ΔT_1, ΔT_2 and ΔT_4 decreases while ΔT_3 increases with the increasing of P_L value within its range. It indicates that when P_L increases, the amount of heat needed to drive the high-pressure generation process

increases.

Fig. 6 describes heat source temperature (T_{hs}) corresponding to different P_H and P_L values. It can be seen that for given P_H value, T_{hs} increases with the increasing of P_L value. It is also obvious that the maximum T_{hs} of the cycle under given working conditions reaches 51.0 °C when P_H and P_L are with the value of 0.80 MPa and 0.22 MPa, respectively, where the cycle's COP is 1.114. It can basically meet the temperature demand of winter hot water supply. It is worth mentioning that, when the cycle is operated at its maximum COP (1.42) when P_H and P_L are 1.40 MPa and 0.41 MPa, respectively, T_{hs} can still reach 43.7 °C, which can meet the temperature demand of building floor heating. Furthermore, for other selected P_H/P_L values such as 1.30/0.36 MPa, 1.20/0.31 MPa, 1.10/0.28 MPa, 1.00/0.24 MPa, 0.90/0.21 MPa and 0.80/0.18 MPa the T_{hs} values are 44.1 °C, 44.3 °C, 45.2 °C, 45.4 °C, 46.1 °C and 46.7 °C, which are all suitable for fan coil heating.

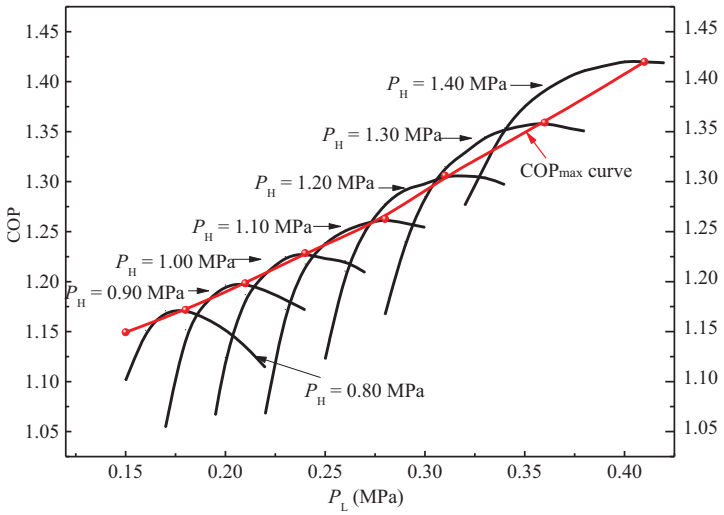

Fig. 4: The effect of P_H and P_L values on COP

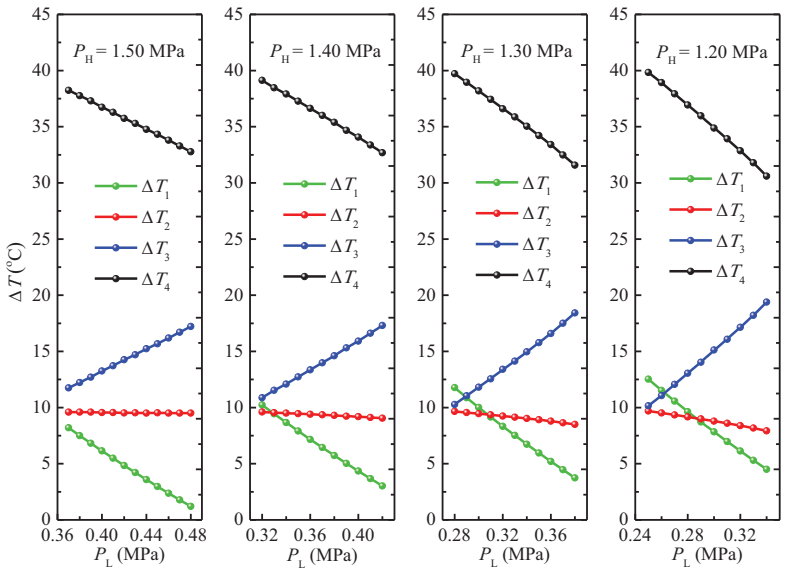

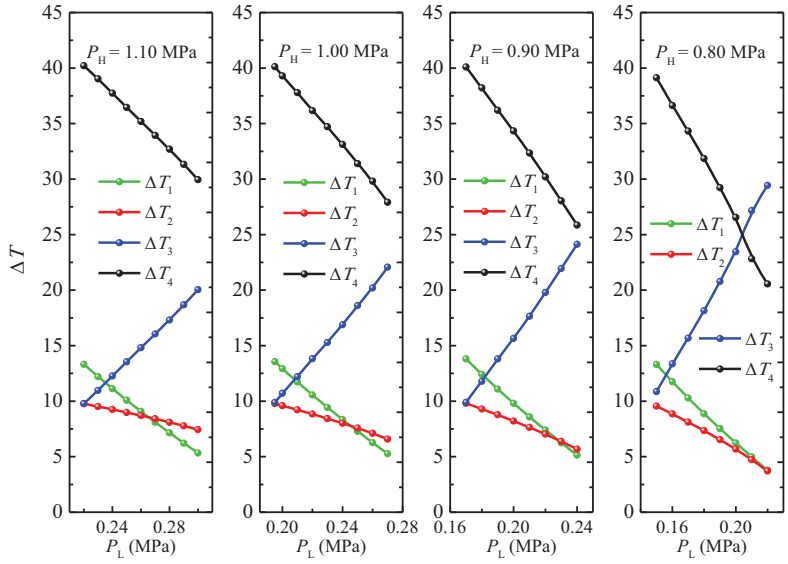

Fig. 5: Effect of P_H and P_L values on ΔT_1 of LPG1, ΔT_2 of LPA, ΔT_3 of HPG and ΔT_4 of HPA

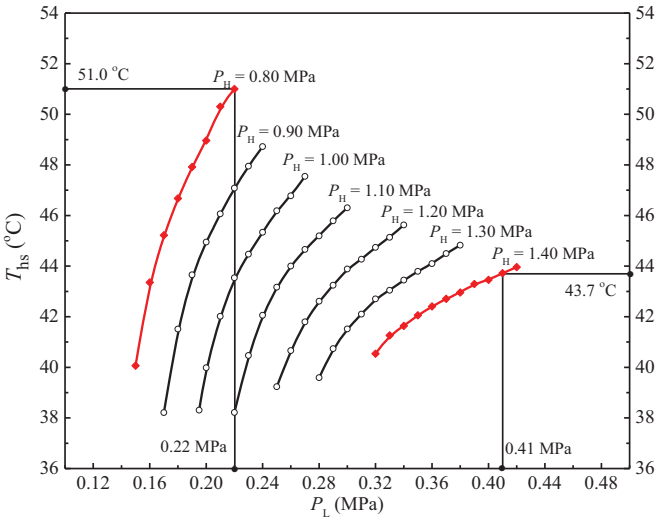

Fig. 6 Heat supply temperature (T_{hs}) corresponding to different P_H and P_L values

Fig. 7 depicts the effect of heat source temperature (T_h) on COP under the P_H/P_L pair values corresponding to the maximum COPs obtained in Fig. 4. It can be found that for the novel balanced ARHP cycle, T_h must be above 85 °C which happens when P_H/P_L pair value is 1.40/0.41 MPa and the corresponding COP value is 1.17. Meanwhile, For given P_H/P_L pair, COP firstly ascends rapidly with the increasing of T_h, and then increases slowly when T_h is higher than 95 °C. The maximum COP under given working conditions can reach 1.425.

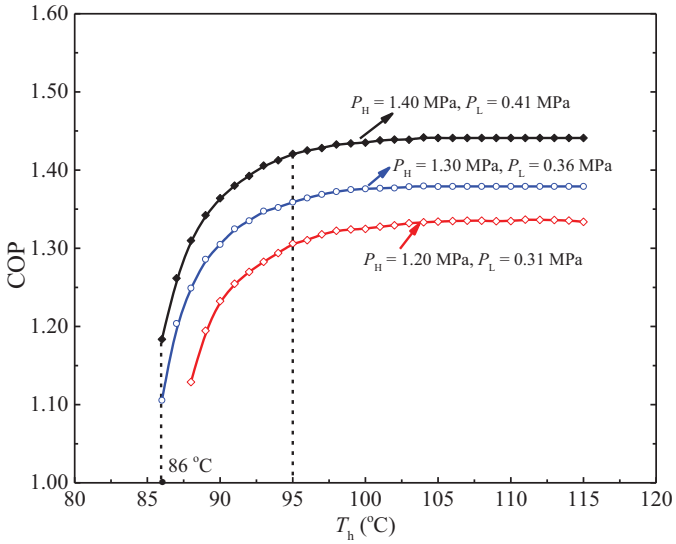

Fig. 7: Effect of heat source temperature (T_h) on COP

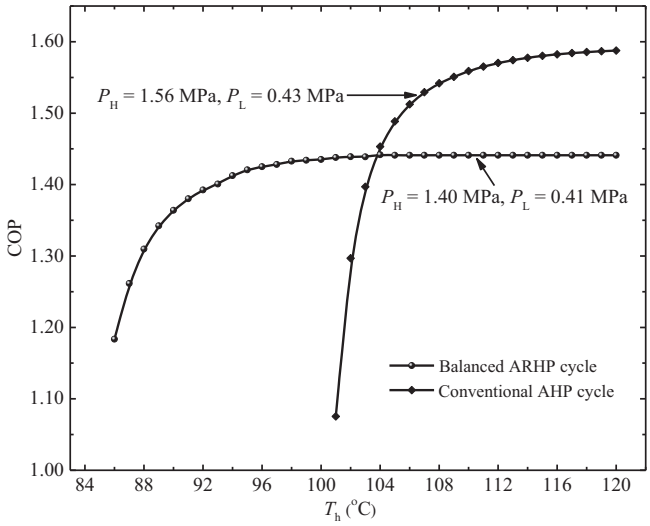

Fig. 8 Comparison of the novel ARHP cycle and the conventional AHP cycle

For comparison, effect of T_h value on COP of the conventional AHP cycle when T_e, T_c, T_a are 0 °C, 40 °C, 48 °C, respectively, and effect of T_h value on COP are also illustrated in Fig. 8. For the conventional AHP cycle, T_h must be higher than 101 °C, and when T_h is higher than 104 °C, COP of the balanced ARHP cycle is lower than that of the conventional AHP cycle. However, COP of the conventional AHP cycle declines quickly when T_{hd} is lower than 108 °C. Furthermore, the AHP cycle will stop working whereas the balanced ARHP cycle could still operate when T_h is lower than 100 °C. Apparently, the balanced ARHP cycle we proposed could function under a larger heat source temperature range than the conventional AHP cycle.

5. Summary and conclusions

To make efficient use of low-temperature solar thermal, this paper proposes a novel absorption-resorption heat pump cycle. The new resorption heat pump cycle without distillation device is more suitable for temperature characteristics of the solar heat source. Parameters like the pressure of the cycle, heat source temperature and heat supply temperature are investigated. COP of the novel cycle in this paper can reach up to 1.42 with low temperature of solar thermal acting as the high-temperature heat source. P_H and P_L value are important on the performance of the heat pump cycle. Pressure of the high-pressure generator and pressure of the low-pressure generator could be optimized to get a maximum COP at any given working conditions. The novel cycle can supply water that can meet space heating temperature demand.

Multiple heat sources with different temperatures can also be efficiently used at the same time by slightly modifying the configuration of the cycle. And when the ambient temperature is too low to drive the cycle, solar thermal collectors can be used to lift the temperature in the low-pressure generator.

References

Chua, K.J., Chou, S.K., Yang W.M., 2010. Advances in heat pump systems: A review. Appl. Energy. 87(12), 3611-3624.

Fatouh, M., Elgendy, E., 2011. Experimental investigation of a vapor compression heat pump used for cooling and heating applications. Energy. 36(5), 2788-2795.

Fraga, C., Mermoud F., Hollmuller P., et al., 2015. Large solar driven heat pump system for a multifamily building: Long term in-situ monitoring. Solar Energy. 114, 427-439.

Jradi, M., Veje, C., Jørgensen, B.N., 2017. Performance analysis of a soil-based thermal energy storage system using solar-driven air-source heat pump for Danish buildings sector. Appl. Therm. Eng. 114, 360-373.

Zhou, J., Zhao, X., Ma, X., et al., 2016. Experimental investigation of a solar driven direct-expansion heat pump system employing the novel PV/micro-channels-evaporator modules. Appl. Energy. 178, 484-495.

Dai, Y.J., Li, X., Wang, R.Z., 2015. Theoretical analysis and case study on solar driven two-stage rotary desiccant cooling system combined with geothermal heat pump. Energy Procedia. 70, 418-426.

Ozcan, H., Dincer, I., 2013. Exergy Analysis and Environmental Impact Assessment of Solar-Driven Heat Pump Drying Systems, Causes. Impacts and Solutions to Global Warming. New York, 839-858.

Omojaro, P., Breitkopf, C., 2013. Direct expansion solar assisted heat pumps: A review of applications and recent research. Renew. Sust. Energy Rev. 22, 33-45.

Wu, W., Wang, B., Shi, W., et al., 2014a. Absorption heating technologies: a review and perspective. Appl. Energy. 130, 51-71.

Wu, W., Wang, B., Shi, W., et al., 2014b. An overview of ammonia-based absorption chillers and heat pumps. Renew. Sust. Energy Rev. 31, 681-707.

Van de Bor, D.M., Ferreira, C.A.I., Kiss, A.A., 2014. Optimal performance of compression–resorption heat pump systems. Appl. Therm. Eng. 65(1),219-225.

Velázquez, N., Best, R., 2002. Methodology for the energy analysis of an air cooled GAX absorption heat pump operated by natural gas and solar energy. Appl. Therm. Eng. 22(10),1089-1103.

Du, K., Yang, S.W., Zhang, S.Q., 1991. Experimental analysis and research of an aqua ammonia absorption-resorption heat pump, J. Eng. Thermophys. 3(12), 229-233 (in Chinese).

Du, K., Yang, S.W., Zhang, S.Q., 1993. Performance simulation and analysis of aqua ammonia absorption-resorption heat pump, J. Southeast Univ. 2(23), 26-32 (in Chinese).

Hong, D.L., Chen, G.M., Tang, L.M., et al, 2011. Simulation research on an EAX (Evaporator-Absorber-Exchange) absorption refrigeration cycle. Energy. 36(1), 94-98.

NIST Reference Fluid Thermodynamic and Transport Properties Database (REFPROP): Version 8.0.

Preliminary Assessment of a Solar Absorption System for Air Conditioning Applications

J.C. Jiménez-García, W. Rivera

Instituto de Energías Renovables, Universidad Nacional Autónoma de México, Temixco, Morelos, México.

Abstract

A low-capacity solar absorption system for air conditioning applications has been developed. The system uses the mixture ammonia-lithium nitrate and plate heat exchangers as the main components. Several experimental test runs were carried out at different operating conditions for the generator, condenser and absorber. The system achieved an internal cooling power close to 3.1 kW, with cooling temperatures around 6 °C and an internal coefficient of performance around 0.62.

Key-words: absorption cooling system, solar air conditioning, ammonia-lithium nitrate

1. Introduction

In the last years absorption systems have gained increasing interest by the fact that they can be operated with either solar thermal energy or residual heat from industries. Around 15% of the electricity produced worldwide is used for air-conditioning and cooling (Statistics, I. E. A., 2011), so absorption systems may help to reduce this percentage. Currently, the research on absorption systems has focused in three main aspects:

(i) the study of alternative mixtures,
(ii) the development of more efficient and low cost components, and
(iii) the development of advanced systems

Up to now, several studies have been carried out on the development of absorption cooling prototypes operating with ammonia-water (Jakob et al., 2008) and water/lithium bromide (Achuthan et al., 2011; Agyenim et al., 2010; González-Gil et al., 2011; Lizarte et al., 2012, 2013; Qu et al., 2010; Venegas et al., 2011; Yin et al., 2013;). These two mixtures have been the most used since they possess great advantages. However due to their well-known drawbacks, Best and Rivera (2015) presented a review of thermal cooling systems. According to their study, the ammonia-lithium nitrate mixture possesses some advantages over the conventional ones. Regarding ammonia-lithium nitrate mixtures, some of the most relevant studies are cited below. Rivera et al. (2012) and Moreno-Quintanar et al. (2012) reported the assessment of an intermittent solar absorption refrigeration system operating with NH_3-$LiNO_3$ using a cylindrical parabolic collector as a generator–absorber. The results showed that it was possible to produce up to 8 kg of ice per day. Generation temperatures varied from 75 °C to 110 °C achieving evaporation temperatures as low as -11 °C and solar coefficients of performance of 0.08. Llamas et al. (2007, 2014) reported the results of a 10 kW solar absorption air conditioning system for a cooling capacity between 5 and 10 kW operating with the ammonia-lithium nitrate mixture. The system was air cooled and the heat was supplied by evacuated solar collectors. Coefficients of performance up to 0.53 were achieved with chilled water temperatures as low as 0 °C. Hernández-Magallanes et al. (2014) reported the experimental assessment of an absorption cooling system operating with the ammonia-lithium nitrate mixture. The generator and absorber were helical coil falling film heat exchangers while condenser, evaporator and economizer were plate heat exchangers (PHE). The COP values varied between 0.45 and 0.7 while the cooling capacity was between 0.52 to 2.52 kW, for generator temperatures between 85 °C and 105 °C and condenser temperatures from 18 °C to 36 °C. Zamora et al. (2014, 2015) reported two studies on the assessment of an absorption chiller operating with the ammonia-lithium nitrate mixture using compact heat exchangers as the main components. The authors reported that the water-cooled

doi:10.18086/swc.2017.28.11 Available at http://proceedings.ises.org

prototype yields 12.9 kW of cooling capacity and an electrical COP of 19.3, when operating at 15 ºC for chilled water, 90 ºC for heating water and 35 ºC for cooling water. Dominguez-Inzunza et al. (2016) carried out the evaluation of an ammonia/lithium nitrate absorption cooling system. The generator temperatures varied between 80 °C and 100 °C, while the cooling water temperatures varied from 20 °C to 34 °C. Cooling capacities up to 4.5 kW and evaporator temperatures as low as 4 °C were achieved with coefficients of performance ranging from 0.3 to 0.62.

On the other hand, regarding to the use of PHE as components in absorption cooling systems, some of the most relevant works are the following: Goyal et al. (2017) reported the evaluation of a small-capacity, waste-heat driven ammonia-water absorption chiller. The system developed used waste heat from diesel generator exhaust to desorb the refrigerant solution. The system was designed to deliver 2.71 kW of cooling at extreme ambient temperature of 51.7 °C obtaining a coefficient of performance of 0.55. The system utilizes air-cooled finned-tube in the absorber and condenser and microchannel array in the evaporator. Experiments were carried out at ambient temperatures of 29.7–44.2 °C, delivered cooling duties of 2.54–1.91 kW. Zacarías et al. (2013) reported the results on the experimental assessment of the adiabatic absorption of ammonia vapor in an ammonia-lithium nitrate solution using a fog jet nozzle. The system utilizes compact heat exchangers in all the components with exception of the absorber. The authors reported that the approach to adiabatic equilibrium factor for the conditions essayed was always between 0.82 and 0.93. Khan et al. (2012a, 2012b) carried out an experimental investigation on evaporation heat transfer and pressure drop for ammonia in 30º and 60º chevron PHE. The experiments were performed for saturation temperatures ranging from 25 ºC to 2 ºC and the heat flux varied between 21 kW m^{-2} and 44 kW m^{-2}. The experimental results showed a significant effect of saturation temperature, heat and exit vapor quality on heat transfer coefficient and pressure drop. The authors proposed correlations for the Nusselt number and friction factor. Stasiek (1998) carried out experimental studies of heat transfer and fluid flow across corrugated-undulated heat exchanger surfaces. The authors used a true color image processing of liquid crystal images for temperature and heat transfer distribution measurements in six element-shapes of heat exchangers. The authors reported that the technique could be of considerable use in improving the design of all types of plate heat exchangers. Ibarra-Bahena et al. (2015) reported the experimental results of a single stage heat transformer using PHE in all its main components. The system operated with the water-carrol mixture. The experimental gross temperature lift achieved values from 18.5 to 22.2 ºC and the coefficients of performance varied from 0.30 to 0.35.

From the literature review it can be seen that just a few prototypes have been developed using the ammonia-lithium nitrate mixture and only the research carried out by Zamora et al. (2014, 2015) involves plate heat exchangers as main components. However, their studies only present some global results for the coefficients of performance for very specific conditions and they did not do a parametric study in order to evaluate the system's performance under several operating conditions. Therefore, this paper presents the evaluation of a single-stage absorption cooling system operating with the ammonia-lithium nitrate mixture at different temperatures heating and cooling water.

2. System description

2.1 Experimental setup

The absorption system proposed consists of the following components: generator, absorber, condenser, evaporator, economizer, pump, throttle device, and a couple of tanks. The system was operated with the ammonia-lithium nitrate mixture, and it was built using five plate heat exchangers (PHE) as the main components which were oriented in vertical configuration. The PHE utilized in the system were manufactured by *Alfa Laval*, and it was considered the model *Alfanova 52* for generator, economizer and absorber, the number of plates for each heat exchanger is 40, for condenser and evaporator the model *Alfanova 27* was chosen with 20 plates in each heat exchanger. A *Milton Roy* diaphragm pump with a nominal power of 745 W was used in order to pumping the working fluid from the absorber to the generator. The throttle device used was a stainless steel low-pressure metering valve coupled with vernier handle, which has a maximum flow

coefficient equal to 0.004. Besides, a couple of tanks with a volume capacity near to 2 liters were included in the system: one of them is located at the exit of the generator, whose function is to enable the phases' separation, thus it allows the ammonia vapor flow to the condenser and the liquid solution flow to the absorber. On the contrary, the second tank acts as a mixing chamber, because the solution with a low refrigerant's concentration (weak solution) that comes from the generator and the solution that is being recirculated get mixed there. The system's measures are: 1.06 x 1 x 0.65 meters (front-height-depth). All the components utilized in the system are 100% stainless steel, in order to avoid their degradation caused by ammonia and lithium nitrate. The described components can be seen in the system's schematic diagram shown in figure 1.

Although the aim of the system is to be driven by solar energy, in order to perform the experimental assessment under controlled conditions, up to now, the experimental tests were carried out using three auxiliary systems. The thermal energy required to separate the refrigerant from the working mixture is supplied to the generator by means of an auxiliary heating system. This auxiliary system uses an electric resistance to heating up a mass flow rate of water, the hot water is supplied to the generator at a gauge pressure near to 200 kPa (2 bar), thus, avoiding the boiling of the water at generation temperatures.

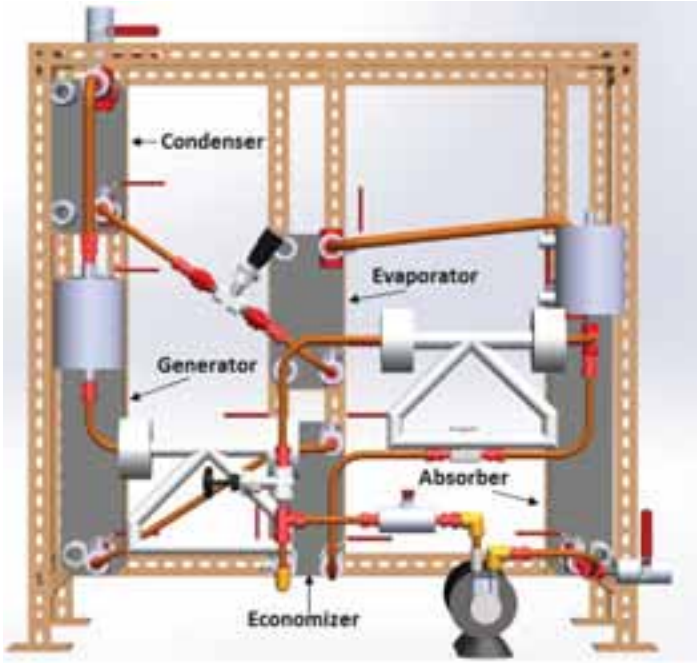

Fig. 1: Schematic diagram of the absorption cooling machine

On the other hand, the thermal power removed from the condenser and absorber is dissipated by means of an auxiliary cooling system, this cooling system consists of a storage tank, a recirculating water pump and a commercial chiller. Once the flow of water has removed heat from the condenser and absorber, its temperature is reduced in the chiller, transferring the heat to the ambient air, when the water leaves the chiller it is stored in the tank, the recirculating pump takes the low-temperature water from the storage tank and pumps it to the condenser and absorber, hence, the water is able to take thermal energy from the condenser and absorber again. The third auxiliary system is intended to supply a mass flow rate of water to the evaporator, in order to be cooled by the absorption system. This system also has a storage tank, a pump and an electric resistance, and it was designed to provide the heat necessary to keep the water's temperature constant.

2.2 Operation of the system

A mass flow rate of hot water is supplied to the generator in order to get the ammonia and the solution separated. The two phase mixture (ammonia vapor and weak solution) leaves the generator and enters to a separation tank, there, the ammonia vapor flows to the condenser where it is liquefied by means of the cooling water supplied by the chiller. The ammonia in liquid phase, leaves the condenser and goes through the

expansion valve, reducing its pressure and temperature. Once the ammonia has passed through the valve, its thermodynamic state is a saturated liquid-vapor mixture and its temperature is the lowest temperature of the entire cycle. Under these conditions, the ammonia mixture enters into the evaporator extracting a thermal load from the water circulating in the adjacent channels of the PHE as a countercurrent flow, producing the system's cooling effect. The ammonia leaves the evaporator as superheated vapor and goes to the absorber where it is mixed with the weak solution coming from the generator. This mixture process releases thermal energy, which is transferred to the cooling water that flows in the absorber. Finally, the solution with high concentration of refrigerant (strong solution) leaving the absorber is pumped to the generator starting the cycle again.
Furthermore, an economizer is included in the system, whose purpose is to exchange heat between the solution flows going to and leaving the generator, in order to enhance the coefficient of performance (COP) by reducing the heat rejection in the absorber as well as the heat supplied to the generator.

2.3 Instrumentation

In order to evaluate the system's performance while the operative conditions are modified, a set of temperature, pressure and mass flow rate sensors were included in the absorption system. The pressure in the system was measured in the generator, condenser, evaporator and absorber. *Ashcroft* piezoelectric transducers were utilized. Regarding the mass flow rates in the absorption system: two types of sensors were considered: in order to obtain the refrigerant produced and the weak solution mass flow rates, a couple of *Micro Motion Elite Coriolis Flow Meters* was used. The strong solution as well as the external mass flow rates of water were registered by several turbine flow meters. The temperature for each current was measured at the inlet and outlet ports in every PHE. Every measuring device used for the system's experimental assessment was calibrated and a set of calibration equations was obtained. Each outlet signal was received, processed and stored by a *HP* data acquisition system using the software *Agilent VEE Pro 9.3*, were the equations obtained were utilized in order to find the expected values. The sensors' position in the system is shown in the schematic diagram presented in figure 2.

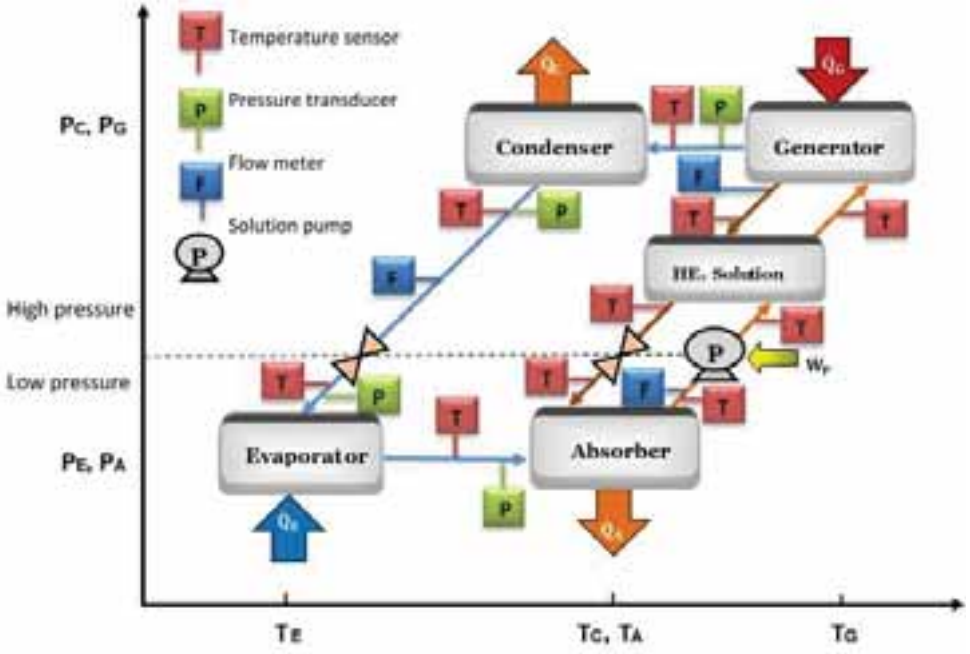

Fig. 2: Schematic diagram showing the sensors location in the absorption cooling machine

Fig. 3: Developed absorption cooling machine

The uncertainties associated to the cited instrumentation are presented in Table 1.

Tab. 1: Instruments uncertainties

Measuring instrument	Uncertainty
Elite Coriolis flowmeter	± 0.10%
Omega rotameter	± 1%
Turbine flowmeter	± 1%
Pressure transducer	± 1%
RTD sensor	± 0.3°C

3. Main equations

The coefficient of performance is a measure of the system's efficiency and it can be determined based on internal or external parameters. Internal parameters are related to the conditions for the weak and strong solutions and the refrigerant produced. External parameters are influenced by the conditions of the mass flow rates of heating and chilled water, at inlet and outlet of the generator and evaporator, respectively, as well as the work supplied by the related pumps.

The internal coefficient of performance (COP_{int}) can be determined by equation 1:

$$COP_{int} = \frac{\dot{Q}_{e,int}}{\dot{Q}_{g,int} + \dot{W}_{b,int}} \qquad \text{(eq. 1)}$$

In equation 1 $\dot{Q}_{e,int}$ represents the system's cooling power, this term is the thermal power transferred to the ammonia in the evaporator and it is calculated as shown in equation 2.

$$\dot{Q}_{e,int} = \dot{m}_{ref}(h_{e,o} - h_{e,i}) \quad \text{(eq. 2)}$$

On the other hand, the term $\dot{Q}_{g,int}$ represents the actual heat power supplied to the strong solution in the generator, it is calculated as an energy balance considering the mass flow rates across the PHE. The energy balance calculation can be advertised in equation 3.

$$\dot{Q}_{g,int} = \dot{m}_{weak}\left(h_{g,o-weak}\right) + \dot{m}_{ref}\left(h_{g,o-NH3}\right) - \dot{m}_{strong}\left(h_{g,i}\right) \quad \text{(eq. 3)}$$

The term $\dot{W}_{b,int}$ in equation 1 expresses the mechanical power supplied to the system in order to pump the strong solution from the absorber to the generator. It is determined calculating the enthalpies difference (before and after the pump) for the strong solution mass flow rate. Equation 3 exposes the manner in which the mechanical power for the internal pump is determined.

$$\dot{W}_{b,int} = \dot{m}_{strong}\left(h_{ec,i-strong} - h_{a,o}\right) \quad \text{(eq. 4)}$$

The properties for the ammonia-lithium nitrate mixture were calculated using the equations reported by Farshi et al. (2014). The ammonia properties were determined from the *REFPROP* software using the international institute of refrigeration (IIR) reference state.

4. Results

In order to assess the absorption cooling system, approximately 40 test runs have been carried out. A parametric analysis was performed with the aim of demonstrating the effects of the change in a parameter on the others. Thus, the condensation temperature was varied while parameters as the strong solution mass flow rate and temperatures of heating water and water to be chilled, were kept constant. The working mixture employed in the experimental assessment had an ammonia's mass concentration equal to 54 % and it was kept constant for the test runs presented.

The preliminary assessment was performed for generation temperatures between 80 and 95 °C, and condensation temperatures from 22 °C to 32 °C. Generation temperature was varied in 5 °C increments. The condensation temperature steps were equivalent to 2 °C.

For each test run steady state conditions were achieved and kept by a minimum period of 30 minutes. The figures 4 to 7 present the temperature profiles obtained in the main components for a chosen test run, where the generation temperature was 80 °C while the condensation temperature was 28 °C. The mass flow rate values utilized for the system's assessment are presented in table 2.

Tab. 2: Mass flow rate values for parameters enternal and internal

Parameter	Mass flow rate (kg/s)
Heating water	0.25
Cooling water	0.2
Chilled water	0.183
Solution to generator	0.016

In figure 4 is advertised that generator temperatures are constant for the test's period of time. The highest temperature corresponds to heating water entering to generator (Tg,wi). On the contrary, the lowest temperature is the solution going into the generator (Tg,i), which almost reaches the highest temperature when it leaves the PHE. That means the selected parameters such as solution mass flow rate and flow arrangement (countercurrent arrangement) are adequated for the conditions presented. The average temperatures for the solution entering and leaving the generator are 64.1 °C and 78.2 °C, respectively.

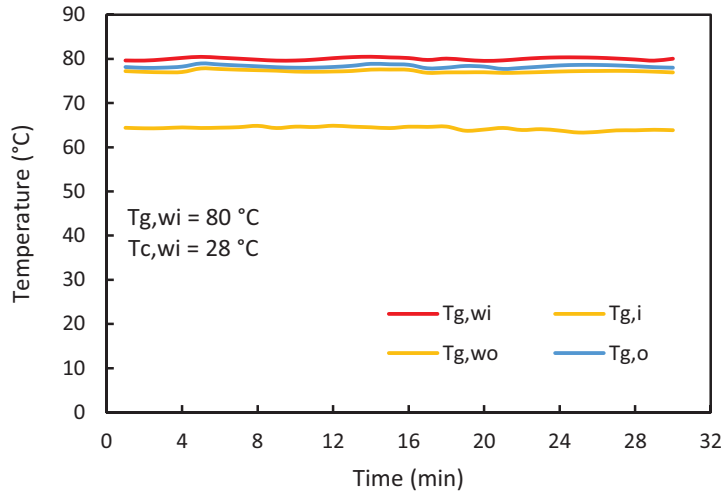

Fig. 4: Temperature profiles in generator during the test run

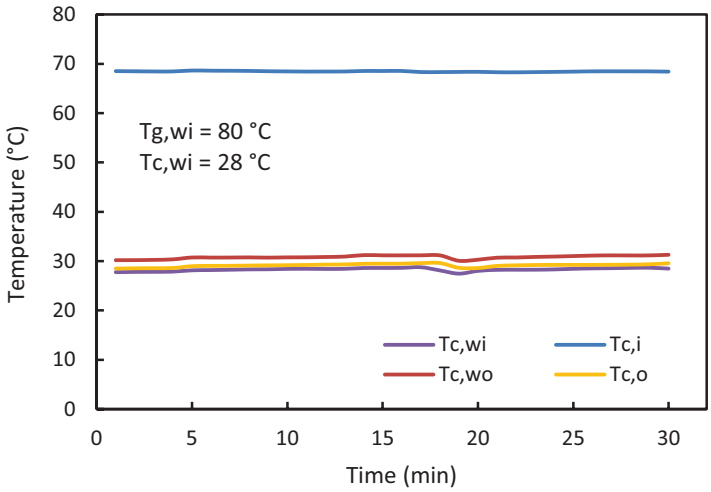

Fig. 5: Temperature profiles in condenser during the test run

In the case of the temperature profiles in condenser, from figure 5 it can be seen the steady state is also kept. The refrigerant enters to the condenser at an average temperature of 68.5 °C ($\mathbf{T_{c,i}}$), and leaves the heat exchanger at an average temperature near to 29.12 °C ($\mathbf{T_{c,o}}$). The pressure measured in this test run is approximated to 1.25 MPa (12.5 bar) which means that for the $\mathbf{T_{c,o}}$ measured it is assured that refrigerant condensation is achieved. In the case of cooling water an average temperatures difference between the inlet and outlet near to 2.6 °C is accomplished.

The profiles for attained temperatures in evaporator are shown in figure 6, where it is possible to observe that for the test conditions, the refrigerant at the inlet's port in evaporator ($\mathbf{T_{e,i}}$) had a temperature near to 10 °C. The water to be chilled ($\mathbf{T_{e,wi}}$) entered the evaporator at an average temperature of 20 °C and experimented a reduction of 2.5 °C in average. It is important to mention the refrigerant temperature leaving the evaporator ($\mathbf{T_{e,o}}$) is very close to $\mathbf{T_{e,wi}}$, this probably means that refrigerant is overheated, which would imply that the mass flow rate of refrigerant produced is low, regarding the evaporator's capacity.

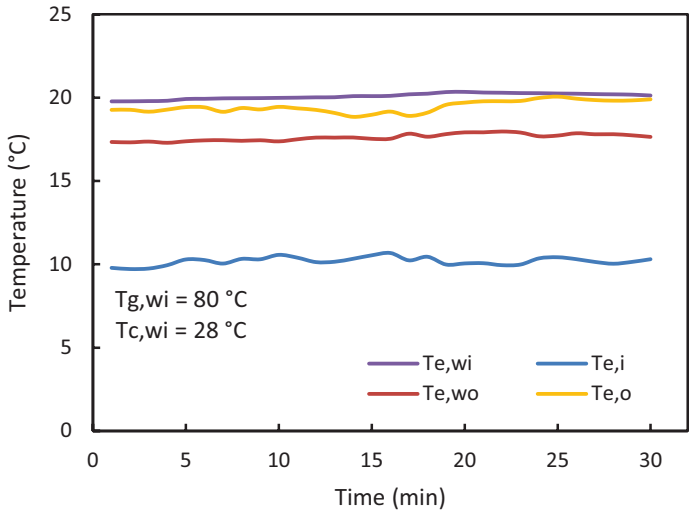

Fig. 6: Temperature profiles in evaporator during the test run

In figure 7 is possible to see the temperature profiles through the absorber. The cooling water entering the PHE has an average temperature of 28 °C ($\mathbf{T}_{a,\mathbf{wi}}$) and leaves it at an average temperature of 30.65 °C ($\mathbf{T}_{a,\mathbf{wo}}$). On the other hand, a two phase mixture of ammonia vapor and weak solution arrives at an average temperature ($\mathbf{T}_{a,\mathbf{i}}$) near to 47 °C. After the absorption process has taken place, the solution with a higher ammonia concentration leaves the absorber at an average temperature approximated to 32.4 °C.

In figures 5 and 7 a temperature perturbation is seen on the water profiles, this disturbance is induced by the auxiliary cooling system which has an intermittent behavior which is determined by the temperature variations in the storage tank. The described disruption causes, at the same time, a disturbance on the exit temperature of the opposite flow, which is reflected on its temperature profile of both PHE: condenser and absorber.

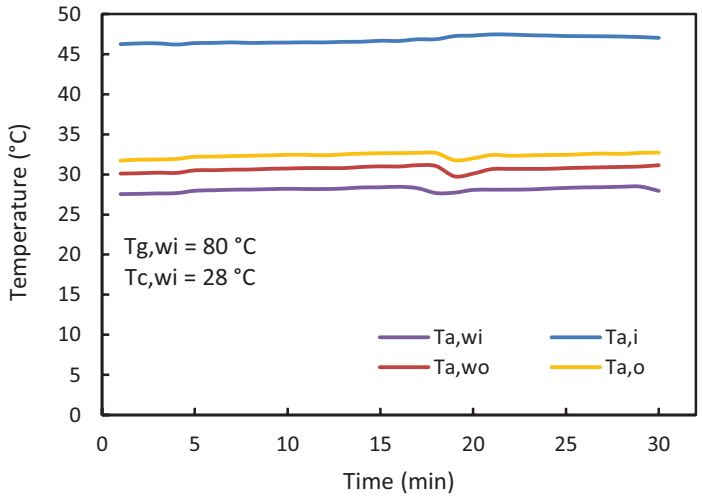

Fig. 7: Temperature profiles in absorber during the test run

The thermal power transferred to ammonia in evaporator (calculated as $\dot{\boldsymbol{Q}}_{\boldsymbol{e,int}}$ from eq. 2) is presented in figure 8. Figure 8 shows the downward trend for this parameter as the condensation temperature grows up. In other words, the system's cooling capacity is reduced at higher condensation temperatures. This fact was expected

because the higher condensation temperatures the higher pressures in the components are gotten, and higher evaporation temperatures for ammonia are obtained, which means the cooling capacity is reduced. The figure 8 also shows a direct relationship between generation temperatures and cooling power, having that the lowest generation temperatures the lowest cooling capacities are attained. When the system was operated at $\mathbf{T_{g,wi}} = \mathbf{95\ °C}$, the pressures attained were very similar to those for $\mathbf{T_{g,wi}} = \mathbf{90\ °C}$, for that reason some key temperatures and thermal powers are very close, as it can be seen in figure 8.

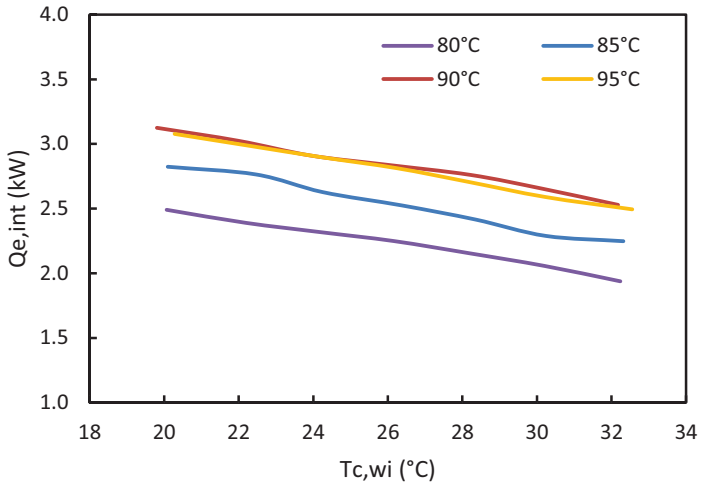

Fig. 8: Internal thermal power transferred in evaporator for several generation temperatures

Figure 9 exhibites the ammonia mass flow rate produced for every generation temperature tested. As condensation temperature increased, the ammonia mass flow rate produced was diminished, presenting a downward linear changement for every trend. On the other side, it could be seen from figure 9 that there is a direct relationship between the generation temperatures and the amount of ammonia circulating throught the condenser and evaporator. Thus, at higher generation temperatures a higher amount of ammonia is produced and a higher cooling effect is obtained as it is demonstrated in figure 8.

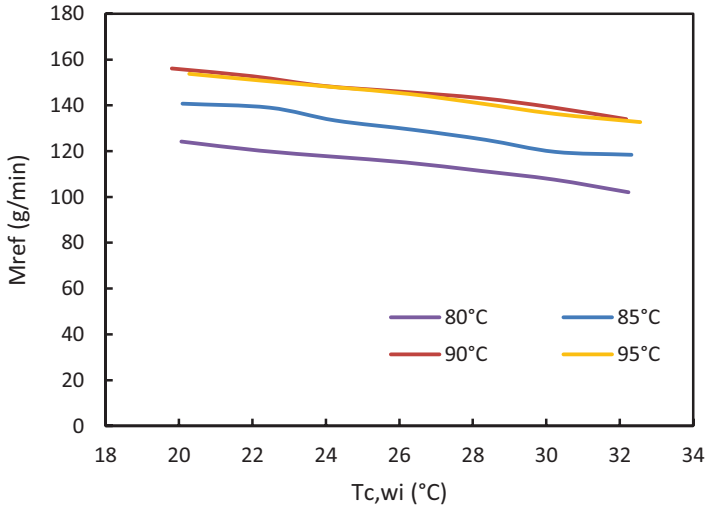

Fig. 9: Refrigerant mass flow rate produced during the assessment

The lowest system's temperature is reached after the ammonia has passed through the throttle valve ($\boldsymbol{T_{e,i}}$), just before the inlet to evaporator. The ammonia temperature was measured at this point and it was plotted in figure 10 against condensation temperature, for each generation temperature considered. As it is presented in figure 10, this temperature augmented as condensation temperature grew up. This was due to the fact that at higher condensation temperatures higher pressures in absorber and evaporator are gotten, which causes the saturation temperature for ammonia to increase.

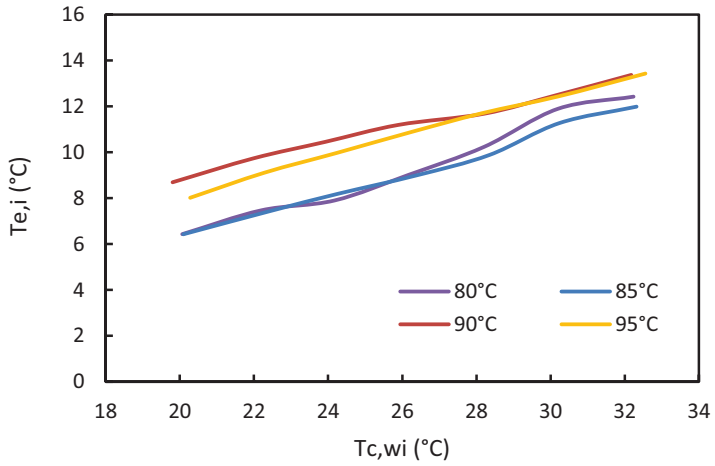

Fig. 10: Ammonia evaporation temperatures registered

The variation of internal COP with respect to condensation temperatures for each generation temperature tested is shown in figure 11. From this figure, it is possible to see that, as a general trend, the internal COP decreases as the condensation temperature increases, besides this, the figure 11 makes evident that for higher generation temperatures, higher coefficients of performance are reached, according to what was expected.

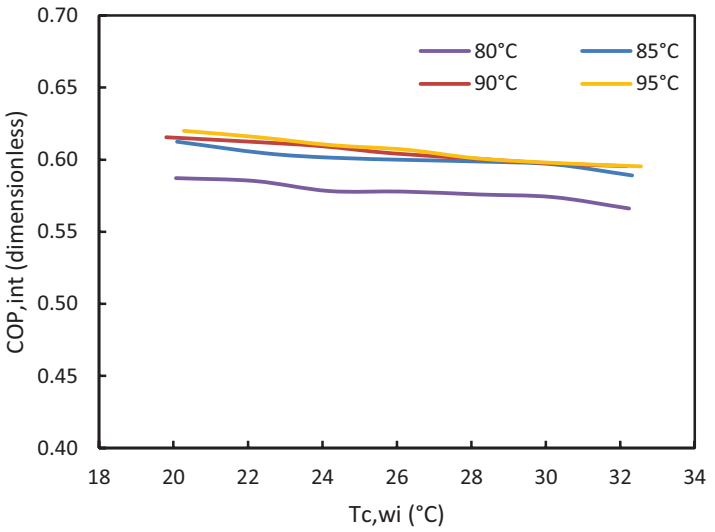

Fig. 11: Internal coefficient of performance for the absorption system

For the lowest $\boldsymbol{T_{g,wi}}$ (80 °C) the highest $\boldsymbol{COP_{int}}$ value was 0.587 when $\boldsymbol{T_{c,wi}}$ was 20 °C, while the minimum COP was 0.566 when 32 °C were kept in condenser. The $\boldsymbol{COP_{int}}$ for $\boldsymbol{T_{g,wi} = 85\ °C}$ varied from 0.612 to 0.589 for the condensation range specified. Regarding 90 and 95 °C generation temperatures, the highest $\boldsymbol{COP_{int}}$ obtained were 0.612 and 0.619 at $\boldsymbol{T_{c,wi} = 20\ °C}$ respectively, while the lowest value was close to 0.595 for both cases.

5. Conclusions

The preliminary assessment of an experimental absorption cooling system operating with the ammonia-lithium nitrate working mixture was presented. The assessment was performed for generation temperatures from 80 to 95 °C, while condensation temperatures were varied from 20 to 32 °C. A mass flow rate of solution going to generator was kept constant at 0.016 kg/s (1 kg/min). Key parameters such as main temperatures, cooling powers, mass flow rates of refrigerant produced and internal coefficients of performance were presented and discussed. It was found the system achieved a cooling power close to 3.1 kW for a generation temperature equal to 90°C. On the other hand, for the lowest generation temperatures, cooling temperatures around 6 °C were attained. A maximum internal coefficient of performance near to 0.62 was obtained when $T_{g,wi} = 95\ °C$ and $T_{c,wi} = 20\ °C$.

6. References

Achuthan, M., Venkataraman, A., & Rathnasamy, R. (2011). Experimental analysis on the performance and characteristics of compact solar refrigeration system. Distributed Generation & Alternative Energy Journal, 26(3), 66-80.

Agyenim, F., Knight, I., & Rhodes, M. (2010). Design and experimental testing of the performance of an outdoor LiBr/H_2O solar thermal absorption cooling system with a cold store. Solar energy, 84(5), 735-744.

Best, R., & Rivera, W. (2015). A review of thermal cooling systems. Applied Thermal Engineering, 75, 1162-1175.

Domínguez-Inzunza, L. A., Hernández-Magallanes, J. A., Soto, P., Jiménez, C., Gutiérrez-Urueta, G., & Rivera, W. (2016). Experimental assessment of an absorption cooling system utilizing a falling film absorber and generator. Applied Thermal Engineering, 103, 1105-1111.

Farshi, L. G., Ferreira, C. I., Mahmoudi, S. S., & Rosen, M. A. (2014). First and second law analysis of ammonia/salt absorption refrigeration systems. *International journal of refrigeration*, *40*, 111-121.

González-Gil, A., Izquierdo, M., Marcos, J. D., & Palacios, E. (2011). Experimental evaluation of a direct air-cooled lithium bromide–water absorption prototype for solar air conditioning. Applied Thermal Engineering, 31(16), 3358-3368.

Goyal, A., Staedter, M. A., Hoysall, D. C., Ponkala, M. J., & Garimella, S. (2017). Experimental evaluation of a small-capacity, waste-heat driven ammonia-water absorption chiller. International Journal of Refrigeration, 79, 89-100.

Hernández-Magallanes, J. A., Domínguez-Inzunza, L. A., Gutiérrez-Urueta, G., Soto, P., Jiménez, C., & Rivera, W. (2014). Experimental assessment of an absorption cooling system operating with the ammonia/lithium nitrate mixture. Energy, 78, 685-692.

Ibarra-Bahena, J., Romero, R. J., Velazquez-Avelar, L., Valdez-Morales, C. V., & Galindo-Luna, Y. R. (2015). Experimental thermodynamic evaluation for a single stage heat transformer prototype build with commercial PHEs. Applied Thermal Engineering, 75, 1262-1270.

Jakob, U., Eicker, U., Schneider, D., Taki, A. H., & Cook, M. J. (2008). Simulation and experimental investigation into diffusion absorption cooling machines for air-conditioning applications. Applied thermal engineering, 28(10), 1138-1150.

Khan, T. S., Khan, M. S., Chyu, M. C., & Ayub, Z. H. (2012a). Experimental investigation of evaporation heat transfer and pressure drop of ammonia in a 60 chevron plate heat exchanger. International journal of refrigeration, 35(2), 336-348.

Khan, M. S., Khan, T. S., Chyu, M. C., & Ayub, Z. H. (2012b). Experimental investigation of evaporation heat transfer and pressure drop of ammonia in a 30 chevron plate heat exchanger. International journal of refrigeration, 35(6), 1757-1765.

Lizarte, R., Izquierdo, M., Marcos, J. D., & Palacios, E. (2012). An innovative solar-driven directly air-cooled LiBr–H 2 O absorption chiller prototype for residential use. Energy and Buildings, 47, 1-11.

Lizarte, R., Izquierdo, M., Marcos, J. D., & Palacios, E. (2013). Experimental comparison of two solar-driven air-cooled LiBr/H 2 O absorption chillers: indirect versus direct air-cooled system. Energy and Buildings, 62, 323-334.

Llamas, S. U., Herrera, J. V., Cuevas, R., Gómez, V. H., García-Valladares, O., Cerezo, J., & Best, R. (2007, October). Development of a small capacity ammonia-lithium nitrate absorption refrigeration system. In 2nd Int Conference on Solar Air-Conditioning, Tarragona (pp. 470-475).

Llamas-Guillén, S. U., Cuevas, R., Best, R., & Gómez, V. H. (2014). Experimental results of a direct air-cooled ammonia–lithium nitrate absorption refrigeration system. Applied Thermal Engineering, 67(1), 362-369.

Moreno-Quintanar, G., Rivera, W., & Best, R. (2012). Comparison of the experimental evaluation of a solar intermittent refrigeration system for ice production operating with the mixtures $NH_3/LiNO_3$ and $NH_3/LiNO_3/H_2O$. Renewable energy, 38(1), 62-68.

Qu, M., Yin, H., & Archer, D. H. (2010). A solar thermal cooling and heating system for a building: experimental and model based performance analysis and design. *Solar Energy*, *84*(2), 166-182.

Rivera, W., Moreno-Quintanar, G., Rivera, C. O., Best, R., & Martínez, F. (2011). Evaluation of a solar intermittent refrigeration system for ice production operating with ammonia/lithium nitrate. Solar Energy, 85(1), 38-45.

Stasiek, J. A. (1998). Experimental studies of heat transfer and fluid flow across corrugated-undulated heat exchanger surfaces. International Journal of Heat and Mass Transfer, 41(6-7), 899-914.

Statistics, I. E. A. (2011). CO2 emissions from fuel combustion-highlights. *IEA, Paris http://www. iea. org/co2highlights/co2highlights. pdf. Cited July*.

Venegas, M., Rodríguez-Hidalgo, M. C., Salgado, R., Lecuona, A., Rodríguez, P., & Gutiérrez, G. (2011). Experimental diagnosis of the influence of operational variables on the performance of a solar absorption cooling system. Applied Energy, 88(4), 1447-1454.

Yin, Y. L., Zhai, X. Q., & Wang, R. Z. (2013). Experimental investigation and performance analysis of a mini-type solar absorption cooling system. *Applied Thermal Engineering*, *59*(1), 267-277.

Zacarías, A., Venegas, M., Lecuona, A., & Ventas, R. (2013). Experimental evaluation of ammonia adiabatic absorption into ammonia–lithium nitrate solution using a fog jet nozzle. Applied Thermal Engineering, 50(1), 781-790.

Zamora, M., Bourouis, M., Coronas, A., & Valles, M. (2014). Pre-industrial development and experimental characterization of new air-cooled and water-cooled ammonia/lithium nitrate absorption chillers. International journal of refrigeration, 45, 189-197.

Zamora, M., Bourouis, M., Coronas, A., & Vallès, M. (2015). Part-load characteristics of a new ammonia/lithium nitrate absorption chiller. International Journal of Refrigeration, 56, 43-51.

7. Appendix

Nomenclature

Parameter	Symbol	Units
Coefficient of performance	COP	dimensionless
Thermal power	$\dot{Q}$	kW
Mechanical power	$\dot{W}$	kW
Mass flow rate	$\dot{m}$	Kg/s
Specific enthalpy	h	kJ/kg
Temperature	T	°C

Subscripts

Reference	Symbol
Internal	int
Evaporator	e
Condenser	c
Generator	g
Absorber	a
Economizer	ec
Input	i
Output	o
Refrigerant	ref
Diluted/weak solution	weak
Concentrated/strong solution	strong
Water	w

Potential Application of Commercial Refrigerants as Adsorbate in Adsorption Refrigeration System

Michael John[1], Cuthbert Z.M. Kimambo[1], Trygve M. Eikevik[2], Ole J. Nydal[2]and Joseph Kihedu[1]

[1] University of Dar es Salaam, Dar es Salaam (Tanzania)

[2] Norwegian University of Science and Technology, Trondheim (Norway)

Abstract

Commercial refrigerants used for vapour compression cycle show positive adsorption capacity with various activated carbon adsorbents however most of them appeared to have high global warming potential (GWP) values. Nevertheless, refrigerants such as R1234yf, R1234ze (E), R450A, R290, R600a, R744 and R717 have been proposed as low GWP alternatives in vapour compression cycles.

Properties of some vapour compression cycle refrigerants qualify them as the good alternative adsorbate for solar adsorption refrigeration systems. Maximum adsorption capacity of 2kg/kg-adsorbent reported for commercial refrigerant R134a on activated carbon, while the maximum for classical adsorption pairs is 0.259 kg/kg-adsorbent which appears for activated carbon-methanol pair.These refrigerants will add the availability of the adsorbates, reduced scale of problems associated with material compatibility and leakages. These systems have good potential applications in off grid areas in developing countries with abundant availability of solar energy including food preservation, vaccine and medicine storage.

Keywords: Refrigerant, GWP, Adsorption refrigeration, off grid application,

1. Introduction

Refrigeration is the cooling effect of the process of extracting heat from a lower temperature heat source, a substance or cooling medium, and transferring it to a higher temperature heat sink, probably atmospheric air and surface water, to maintain the temperature of the heat source below that of the surroundings for purposes of comfort or preservation (Kreith et al., 1999). Refrigeration technology includes the classical cycle with a compressor and an expansion valve, absorption processes, adsorption processes and desiccant systems. Vapour compression cycle is the common refrigeration technology however, significant implications of refrigerants to the environment such as ozone layer depletion, greenhouse effect, global warming and huge electrical energy consumption have forced scientists to develop environmentally friendly refrigerants and refrigeration technologies (Anupam et al., 2016).

Refrigerants are used in a wide variety of heating, ventilation, air conditioning and refrigeration (HVAC&R) equipment in both industrial and domestic equipment from household refrigerator, cooling chambers and air conditioners (Benhadid-Dib and Benzaoui, 2011; Goetzler et al., 2014). The first generation of refrigerants involved whatever worked and was available, including familiar solvents and other volatile fluids of which majority were flammable, toxic, or both and some were also highly reactive included substances such as hydrocarbons, ammonia and carbon dioxide. The second generation refrigerants shifted to fluorochemicals for safety and durability which included CFCs and HCFCs which became widely used because were efficient, non-flammable and non-toxic. However, in the 1980s CFCs and HCFCs were determined to play a major role in depleting the stratospheric ozone layer, therefore phased out in the 1990s in favor of a third generation of refrigerants HFCs which presented zero ODP but along with CFCs and HCFCs were greenhouse gases that contribute to the radiative forcing of climate with significantly GWP when released to the atmosphere (Calm, 2008; Goetzler et al., 2014; Velders et al., 2009). This shifts ignited renewed interest in natural refrigerants particularly ammonia, carbon dioxide, hydrocarbons and water (Calm, 2008).

The growing international emphasis on global warming mitigation stimulated interest for the fourth generation of

doi:10.18086/swc.2017.28.12 Available at http://proceedings.ises.org

low GWP refrigerants with countries like the United States, Canada and Mexico proposed an amendment to the Montreal Protocol in 2014 to reduce production and consumption of HFCs by 85% during the period 2016-2035 for Non A5 (developed) countries and the European F-gas legislation issued in 2014 which will reduce HFC consumption by 79% over the period 2016-2030 (Goetzler et al., 2014).

On other hand, adsorption refrigeration systems can utilize environment friendly refrigerants and low temperature waste heat and renewable energy sources like solar radiation and biomass derived thermal energy to generate the cooling effect (Anyanwu, 2004; El-Sharkawy et al., 2008).

2. Low GWP refrigerants for vapour compression cycle refrigeration

Various researchers are on board searching for new refrigerants which will be both efficient and environmental friendly. Velders et al. (2009) reported the hydrocarbons, ammonia and CO_2 as the suitable low GWPs refrigerants if compared to HFCs for small refrigerant charges systems where a refrigerant leak would not pose unacceptable flammability or toxicity risk, however for industrial systems with large refrigerant charges expert to managed fire and toxicity risk were required. Koyama et al. (2010) carried out drop-in experiments in order to investigate the possibility to introduce R1234ze (E) and its mixture with R32 as low GWP alternatives for vapour compression heat pump/refrigeration systems. The results obtained proved that the heating effect and COP of R1234ze (E) could be improved by adding R32 as the second component into R1234ze (E) and the mixtures found to be strong candidates for replacing R410A in domestic heat pump system. The mixture of 50% R1234ze (E) and R32 produced the COP of about 7.5% lower than that of R410A at the same heating load of 2.8 kW. Pure R1234ze (E) at 1.6 kW produced the COP value of 20% lower than that of R410A at 2.8 kW. Evaporator and condenser sides pressure drops in both HFO-1234ze(E) and its mixture with R32 were almost at the same level as R410A though the refrigerant flow rates were lower, enlargement of diameter of heat transfer tubes and connecting tubes required as compared with the case of R410A. Drop-in replacements of R1234yf and R1234ze to R134a refrigerants were also tested with no performance enhancing modifications to the refrigerators to evaluate energy consumption, results indicates that R1234yf was a suitable drop-in replacement for R134a in domestic refrigeration applications however the lower capacity of R1234ze in domestic refrigerators would need to be addressed therefore R1234ze might not be suitable for drop-in replacement (Karber et al., 2012). Table 1 show low GWP refrigerants for vapour compression cycle.

Tab. 1: Alternative Vapour Compression Refrigerant (Low GWP refrigerants)

S/N	Refrigerant	Chemical formula	ODP	GWP 100 yrs.
1	R1234yf	CH2=CFCF3	0	<4.4
2	R1234ze (E)	CHF=CHCF3	0	6
3	R450A	(R134a/R1234ze commercial mixture)	NA	NA
4	R290	CH3CH2CH3-propane	0	20
5	R600a	CH(CH3)2CH3-isobutane	0	20
6	R744	CO2-carbon dioxide	0	1
7	R717	NH3-ammonia	0	<1

Navarro-Esbrí et al. (2013) did an experimental analysis of a vapour compression system using R1234yf as a drop-in replacement for R134a in vapor compression system. The tests were performed by varying the condensing and evaporating pressure, superheating degree, the compressor speed and the use of IHX. The energetic comparison was performed on the basis of the cooling capacity, volumetric efficiency, compressor power consumption and the COP. The energy performance parameters of R1234yf in a drop-in replacement were close to those obtained with R134a at high condensing temperatures and making use of an IHX. The cooling capacity of R1234yf was 9% lower in an R134a refrigerant facility in the tested range of which difference decreased when the condensing temperature increases and when an IHX was used. The volumetric efficiency was about 5% lower for R1234yf compared with R134a. Also, the compressor volumetric efficiency using R1234yf showed a greater dependence on the compressor speed. The values of the COP obtained using R1234yf were between 5% and 30%

lower than those obtained with R134a. However, when the condensing temperature raises from 313.15 K to 333.15 K the difference decreases from 25% until 8%, even more when using an IHX.

Mota-Babiloni et al. (2014) did energy performance evaluation of two low GWP refrigerants, R1234yf and R1234ze (E) as drop-in replacements for R134a. Tests were carried out in a monitored vapour compression system combining different values of evaporation and condensation temperature without/with the adoption of an internal heat exchanger. The volumetric efficiency, cooling capacity and COP taking R134a as baseline were analyzed with results showed that without IHX the average volumetric efficiency for R1234yf and R1234ze was 4% and 5% lower compared with R134a. The cooling capacity obtained with R1234yf and R1234ze was reduced, with an average difference of 9% and 30% without IHX. Also, COP values were about 7% lower for R1234yf and 6% lower for R1234ze than those obtained using R134a. The use of an internal heat exchanger reduced the COP differences for both replacements as shown in Table 2.

Tab. 2: R1234yf and R1234ze (E) as drop-in replacements for R134a without IHX (Mota-Babiloni et al., 2014)

Refrigerant	Volumetric efficiency	Cooling Capacity	COP
R134a (baseline)	100%	100%	100%
R1234yf	4% lower (96%)	Reduced 9%	7% lower (93%)
R1234ze(E)	5% lower (95%)	Reduced 30%	6% lower (94%)

Mota-Babiloni et al. (2015a) presented a drop-in analysis of an internal heat exchanger (IHX) used in a monitored vapour compression system. They compared R134a and two of its alternatives, R1234ze and R450A (R134a/R1234ze commercial mixture). Study, concluded that IHX produced benefits for all refrigerants tested and could be considered its use for R450A as drop-in or retrofit R134a replacement and new design installations using R1234ze. However, without IHX in an R134a system, alternative R450A would overcome the R134a COP results but for R1234ze more system modifications would be needed. Experimental performance of non-flammable refrigerant R450A (contrary to R1234ze and R1234yf) as R134a replacement in a vapour compression system under a wide range of operating conditions were studied by Mota-Babiloni et al. (2015b) . The cooling capacity of R450A found to be slightly lower than those obtained with R134a (6% lower as average). The COP of R450A found to be 1% average higher than R134a due to compressor power consumption for R450A being much lower than R134a. The IHX affected positively the R450A energy efficiency in a similar proportion to R134a. The discharge temperature of the alternative was found to be lower, 2K as average than of R134a. R450A could be used directly in R134a systems with slightly lower cooling capacity and similar COP, however redesign and optimisation would lead to better energy performance and hence, lower power consumption.

Janković et al. (2015) reported the analysis of R1234yf and R1234ze (E) as drop-in replacements for R134a in a small power refrigeration system. The first analysis was based on equal evaporation and condensation temperatures before and after the refrigerant replacement. The second analysis was carried out for equal cooling medium conditions in the condenser, so that the transport properties and the heat transfer features in the condenser were considered for the three refrigerants. Results showed that different conclusions may be drawn if the drop-in analysis was carried out for equal condensation temperatures or for equal temperatures of the cooling medium in the condenser, as well as that these results were affected by the condenser design. R1234yf was found as an adequate drop-in refrigerant for R134a, but R1234ze (E) may perform better when used an overridden compressor to match the refrigerating system cooling power. Sethi et al. (2016) evaluated the performance of R1234yf and R1234ze (E) in a representative vending machine system and compared against the baseline refrigerant R134a as promising replacements for new small refrigeration systems. In the theoretical analysis, it was estimated that R1234yf has pressures similar to R134a whereas R1234ze (E) has pressures lower than R134a. Based on actual drop-in system testing, it was found that R1234yf shows capacity and efficiency similar to R134a as estimated based on thermodynamic properties. R1234ze (E) was estimated to have about 25% lower capacity. To match the capacity of R134a larger compressor was needed as result lower efficiency observed due to higher pressure drop in the system. R1234yf may show even better performance by using a slightly larger diameter suction line and employing a suction line liquid line heat exchanger in new systems. R1234ze (E) may show performance similar to R134a by use of a compressor with larger displacement, a slightly larger diameter suction line and by increasing the number of refrigerant circuits in the heat exchangers.

Brown et al. (2010) reported thermodynamic properties of eight fluorinated olefins, namely: R-1225ye(E), R-1225ye(Z), R-1225zc, R-1234ye(E), R-1234yf, R-1234ze(E), R-1234ze(Z), and R-1243zf. The group contribution method were used to predict the critical temperatures, critical pressures, critical densities, acentric factors, and ideal gas specific heats at constant pressure. The Peng-Robinson equation of state was used to predict thermodynamic properties and the results were presented in pressure-enthalpy and temperature-entropy state diagrams. Higashi (2010) presented the thermo physical properties of R1234yf and R1234ze (E). He predicted the difficulties of finding the next generation refrigerant from pure substances hinted that, the combination among HFCs, HFOs, and HCs should be expected in the next generation refrigerant. Lai (2014) described the thermodynamic properties of the R1234ze (E) with the molecular based BACKONE and PC-SAFT equations of state (EOS). The investigation indicated that the relative deviations among corresponding cycles' characteristics were mostly within 1% compared with multi-parameter EOSs. Thus, molecular based EOSs could be used in the investigation of a refrigeration cycle in case of no multi-parameter EOS due to the insufficient numbers of accurate experimental data in full fluid region. For the refrigeration cycle using R1234ze (E), R1234yf, R22, R134a, and R32 as refrigerants, R1234ze (E) and R1234yf were reported to be potential alternative refrigerants for the replacement of R134a.

Mota-Babiloni et al. (2015c) reviewed the current status of commercial refrigeration for food freezing and conservation in retail stores and supermarkets as one of the relevant energy consumption sectors. They reported that new GHG regulations impose strong GWP limitations that were going to phase out currently used HFC refrigerants in commercial refrigeration (R404A and R507A). In low charge applications propane, showed a good performance, while low GWP HFC or HFC/HFO mixtures as drop-in or retrofit replacements (with little system modifications), and CO_2 systems in trans-critical systems or at the low-stage of cascade systems were proposed as the different alternatives. Mota-Babiloni et al. (2016) reviewed thermo physical and compatibility properties, heat transfer, pressure drop characteristics and vapour compression system performance of R1234ze (E) HFO refrigerant. Pure R1234ze (E) was found to be a good option only in new HVACR systems. Nevertheless, if it was combined with other refrigerants, the final GWP value was also considerably reduced and maintaining the efficiency parameters at levels that allow them to replace R134a, R404A or R410A in existing systems with minor modifications.

There are importance of proper selection of refrigerant (Calm, 2012). Most refrigerant were selected as per the application, the environmental and physical properties together with performance parameters. Global warming issues suggested to phase out presently most used refrigerant R134a and use natural refrigerants such as ammonia, carbon dioxide and hydro carbons (isobutene R600a and propene R290) in vapour compression refrigeration system for sustainable environment. R1234yf also reported to be a suitable candidate for refrigeration and air conditioning systems. However eco-friendly technologies like thermo-electric, magnetic and adsorption refrigeration will receiving more attention as energy environmental problems keep increasing (Bhatkar et al., 2013)

3. Performance of commercial refrigerants as adsorbate in adsorption refrigeration system

Several researchers have reported the performances of commercial vapour compression refrigerant in adsorption studies. Akkimaradi et al. (2001) presented adsorption isotherms for R134a on activated charcoal, in the temperature range of 273-353 K and pressures up to 0.65 MPa using volumetric method. Experimental isotherm data were obtained for three specimens of activated charcoal (Chemviron, Fluka and Maxsorb Charcoal) adsorbing R134a. A mathematical description of the isotherms was provided by using the D-A equation and the isosteric enthalpy of adsorption evaluated from the transformed isotherm data. Habib et al. (2010) measured adsorption rates of R134a and R507A onto pitch based activated carbon of type Maxsorb III with temperatures varying from 20-60 ^{0}C. The experimental data were found to match fairly with the Fickian diffusion model while the surface diffusions followed the classical Arrhenius trend for both pairs. It was noted that Maxsorb III can adsorb R134a as high as 1.6 kg/kg within an adsorption time interval of 1200 s at an adsorption temperature of 25 ^{0}C, while R507A can adsorb as high as 1.3 kg/kg within an adsorption time interval of 1100 s at adsorption temperature of 20 ^{0}C.

Askalany et al. (2013a) designed and built an adsorption cooling system using granular activated carbon GAC-R134a pair. The theoretical mathematical model results presented good agreements with experimental results. COP was theoretical 0.35 at 373 K driving temperature and 293 K evaporator temperature. The system operated between the pressures of 3.3 bar and 7 bar where the difference in the adsorption uptake reached up to 0.3 kg/kg and time of the intermittent cycle of about 900 s. The experimental SCE was up to 70 kJ/kg, while the theoretical SCE was 83 kJ/kg at 373 K driving temperature and 295 K evaporator temperature. SCE and COP was increased by raising the driving or evaporator temperatures. Increase of cycle time increased COP and SCE at constant evaporator temperature and decreased COP and SCE at constant driving temperature. Attalla et al. (2014) investigated experimentally the adsorption capacity of R134a on a GAC for adsorption/desorption process. The bed was designed and built with finned tubes heat exchanger to increase the heat transfer area. The experiments were conducted over a temperature range from 20 ºC to 60 ºC and pressure up to 10 bars. The data were correlated with D–A equation corresponding to adsorption/desorption process. The maximum adsorption capacity uptake found to be 1.92 kg/kg at 20 ºC after 1200 s, later Attalla and Sadek (2014) found the isosteric heat of adsorption which varied from 120 to 340 kJ/kg for adsorption capacities ranging from 0.2 to 1.8 kg/kg-adsorbent. AquaSorb 2000-R407C pair was tested over a temperature range of 25-75 ^{0}C, maximum adsorption capacity of 0.43 kg·kg-1 of adsorbent was obtained (El-Sharkawy et al., 2016).

Askalany et al. (2013b) reported adsorption isotherms for refrigerant R32 on activated carbon powder (ACP) and fiber (ACF) forms over the range of 25-75^{0}C and pressures up to 1400 kPa, measured using constant volume apparatus. The data were correlated by Toth and Dubinin-Astakhov with the adsorbed phase volume correction isotherm models. Adsorption parameters were evaluated from the least-squares fit of experimental data, whereas the D-A equation with volume correction fitted the data better. The uptake and pressure dependence of the isosteric heat of adsorption was extracted from the D-A equation using the Clapeyron equation. ACP observed to have better adsorption than ACF. Adsorption isotherms and kinetics of R410A onto ACP (Maxsorb III) and ACF (A-20) studied by Askalany et al. (2014), the maximum adsorption capacity of the ACP was found to be 1.6 times higher than that of ACF at same adsorption temperature. Both investigated adsorption isotherms (Tóth and D-A) models and kinetics (LDF) models have been found to fit the experimental data within ±5% deviations. D-A equation was used to determine the isosteric heat of adsorption pairs. Adsorption isotherms and kinetics were also investigated experimentally and theoretically over a temperature range of 25-75 0C for Maxsorb III-R152a and AquaSorb 2000-R404A pairs (Ghazy et al., 2016a; Ghazy et al., 2016c). Table 3 shows the commercial vapour compression refrigerant reported on adsorption studies.

Tab. 3: Commercial Vapour Compression Refrigerants used in Adsorption Research

S/N	Refrigerant	Chemical formula	Adsorption capacity kg/kg	ODP	GWP 100 yrs. (CO_2 =1)
1	R134a	CH2FCF3	1.6-2.0 with ACP	0	1,370
2	R32	CH2F2-methylene fluoride	1.29 ACP/0.94 with ACF	0	716
3	R404A	R-125/143a/134a (44.0/52.0/4.0)	0.52 with AquaSorb 2000	0	3,700
4	R507A	R-125/143a (50.0/50.0)	1.3 with ACP	0	3,800
5	R410A	R-32/125 (50.0/50.0)	NA	0	2,100
6	R152a	CH3CHF2	1.3 with ACP	0	133
7	R407C	R-32/125/134a (23.0/25.0/52.0)	0.43 with AquaSorb 2000	0	1,700

Askalany and Saha (2015) investigated experimentally and theoretically the adsorption kinetics of Difluoromethane (R32) onto activated carbon powder (Maxsorb III) and activated carbon fiber (A-20) at various adsorption temperatures ranging from 25-65 ^{0}C. Two commonly used theoretical models (LDF and FD) fitted experimental data well within ±5% error. Jribi et al. (2013) reported a transient mathematical model of a 4-bed adsorption chiller using Maxsorb III as the adsorbent and low GWP refrigerant R1234ze (E). The performance of

the cyclic-steady state of the system for different heating and cooling water inlet temperatures presented. With 80 kg of Maxsorb III the chiller produced 2 kW of cooling power at driving heat source temperature of 85 ^{0}C along with a cooling temperature of 30 ^{0}C, the performance which compared slightly higher than that of the Maxsorb III-R134a based adsorption cooling cycle. Consequently propose R1234ze (E) as potential replacement of R134a based adsorption cooling system. Ghazy et al. (2016d) reported adsorption isotherms and kinetics of HFC-152a onto activated carbon of type Maxsorb III over a temperature range of (25 to 75) ^{0}C. The D-A and Toth equations were used to correlate the adsorption isotherms with D-A found to be more suitable. Maxsorb III adsorbed up to 1.3 kg of HFC-152a per kg of adsorbent. Adsorption kinetics data were correlated using LDF and FD models and isosteric heat of adsorption was estimated. Activated carbon/CO_2 pair reported to show the maximum COP of 0.16 for evaporation and desorption temperatures of 15ºC and 80ºC (Jribi et al., 2010).

Ghazy et al. (2016b) investigated experimentally and theoretically over a temperature range of 25-75 ^{0}C adsorption isotherms and kinetics of AquaSorb 2000-R404A pair. D-A and Tóth equations were used to fit equilibrium uptake while adsorption kinetics was correlated using LDF and FD models. The experimental maximum adsorption capacity of AquaSorb 2000-R404A pair was about 0.52 kg/kg. The activation energy and the pre-exponential coefficient were estimated to be 10488.49 J/mol and 1.11 respectively. Using the Clausius-Clapeyron equation, Isosteric heat of adsorption found to vary from 145 to 330 kJ/kg depending on the adsorbate loading. Both LDF and FD models found suitable to simulate the adsorption kinetics of AquaSorb 2000-R404A with an acceptable error of ±5%. The D-A equation was used to fit the P-T-C diagram of AquaSorb 2000-R404A.

Classical pairs which includes activated carbon-methanol, activated carbon-ethanol, activated carbon-ammonia, silica gel-water and zeolite-water reported to have the maximum adsorption capacity of 0.259 kg/kg-adsorbent which occurs on activated carbon-methanol pair, while the commercial refrigerant R134a presented maximum adsorption capacity of 2 kg/kg-adsorbent with activated carbon adsorbent (Shmroukh et al., 2015). The application of commercial refrigerants as adsorbates will positively contribute to adsorption refrigeration systems as it will add the availability of the adsorbate, reduce the problems associated with material compatibility like on ammonia with copper and reduced leakage problems associated with the negative pressure systems (Zhong et al., 2006). These adsorption refrigeration systems have good potential for off grid applications in developing countries with abundant availability of solar energy including food preservation, vaccine and medicine storages.

4. Conclusions

The potential for adsorption refrigeration system using the commercial refrigerants is evident. The maximum adsorption capacity for the classical working pairs (activated carbon-methanol, activated carbon-ethanol, activated carbon-ammonia, silica gel-water and zeolite-water) of 0.259 kg/kg which appeared for activated carbon-methanol is small compared to adsorption capacity of 2 kg/kg-adsorbent which appeared for modern adsorption working pair of activated carbon-R134a (Shmroukh et al., 2015).

Commercial refrigerants such as R134a, R32, R404A, R507A, R410A, R152a and R407C have been studied as the potential adsorbates for adsorption cooling systems or for mixture separation in the blended refrigerant (Akkimaradi et al., 2001; Askalany and Saha, 2015; Askalany et al., 2013a; Askalany et al., 2014; Askalany et al., 2013b; Attalla and Sadek, 2014; Ghazy et al., 2016b; Ghazy et al., 2016d; Habib et al., 2010). Though they have shown the positive adsorption capacity with various type of activated carbon adsorbents, they also possess high GWP values (Calm and Hourahan, 2007).

Several refrigerants including R1234yf, R1234ze (E), R450A, R290, R600a, R744 and R717, have been proposed to be possible alternatives or drop in replacement of commercial high GWP refrigerants in vapour compression cycles (Bhatkar et al., 2013; Brown et al., 2010; Higashi, 2010; Koyama et al., 2010; Lai, 2014; Mota-Babiloni et al., 2015a, 2015b; Mota-Babiloni et al., 2015c; Navarro-Esbrí et al., 2013; Sethi et al., 2016). These refrigerant could be the good alternative for adsorption pairs for solar adsorption refrigeration system. And therefore increase the availability and options for the adsorption refrigerants, reduced scale of problem associated with material compatibility as is there ammonia system and copper, positive pressure system therefore avoiding the leakage problem associated with the vacuum systems.

Besides the adsorption properties, it is also important to understand the kinetics of these adsorption pairs before

the conclusions of best adsorption pairs as the kinetics data are essential and useful in designing adsorption refrigeration systems.

5. References

Akkimaradi, B.S., Prasad, M., Dutta, P., Srinivasan, K., 2001. Adsorption of 1, 1, 1, 2-tetrafluoroethane on activated charcoal. J. Chem. Eng. Data 46(2), 417-422.

Anupam, K., Palodkar, A.V., Halder, G., 2016. Experimental study on activated carbon–nitrogen pair in a prototype pressure swing adsorption refrigeration system. Heat Mass Transf. 52(4), 753-761.

Anyanwu, E.E., 2004. Review of solid adsorption solar refrigeration II:: An overview of the principles and theory. Energy Convers. Manage. 45(7-8), 1279-1295.

Askalany, A.A., Saha, B.B., 2015. Experimental and theoretical study of adsorption kinetics of Difluoromethane onto activated carbons. Int. J. Refrigeration 49, 160-168.

Askalany, A.A., Saha, B.B., Ahmed, M.S., Ismail, I.M., 2013a. Adsorption cooling system employing granular activated carbon–R134a pair for renewable energy applications. Int. J. Refrigeration 36(3), 1037-1044.

Askalany, A.A., Saha, B.B., Ismail, I.M., 2014. Adsorption isotherms and kinetics of HFC410A onto activated carbons. Appl. Therm. Eng. 72(2), 237-243.

Askalany, A.A., Saha, B.B., Uddin, K., Miyzaki, T., Koyama, S., Srinivasan, K., Ismail, I.M., 2013b. Adsorption isotherms and heat of adsorption of difluoromethane on activated carbons. J. Chem. Eng. Data 58(10), 2828-2834.

Attalla, M., Sadek, S., 2014. Experimental investigation of granular activated carbon/R-134a pair for adsorption cooling system applications. Journal of Power and Energy Engineering 2(02), 11-20.

Attalla, M., Sadek, S., Abd El-Fadeel, W., 2014. Adsorption characteristics and heat of adsorption measurements of R-134a on granular activated carbon. IJACR 22(03), 1450014.

Benhadid-Dib, S., Benzaoui, A., 2011. Refrigerants and their impact in the environment. Use of the solar energy as the source of energy. Energy Procedia 6, 347-352.

Bhatkar, V., Kriplani, V., Awari, G., 2013. Alternative refrigerants in vapour compression refrigeration cycle for sustainable environment: a review of recent research. International Journal of Environmental Science and Technology 10(4), 871-880.

Brown, J.S., Zilio, C., Cavallini, A., 2010. Thermodynamic properties of eight fluorinated olefins. Int. J. Refrigeration 33(2), 235-241.

Calm, J.M., 2008. The next generation of refrigerants–Historical review, considerations, and outlook. Int. J. Refrigeration 31(7), 1123-1133.

Calm, J.M., 2012. Refrigerant Transitions... Again. Moving Towards Sustainability, proceedings of the ASHRAE/NIST Conference, Gaithersburg, MD, USA. pp. 29-30.

Calm, J.M., Hourahan, G., 2007. Refrigerant data update. HPAC Engineering 79(1), 50-64.

El-Sharkawy, I.I., Saha, B.B., Koyama, S., He, J., Ng, K.C., Yap, C., 2008. Experimental investigation on activated carbon-ethanol pair for solar powered adsorption cooling applications. Int. J. Refrigeration 31(8), 1407-1413.

El-Sharkawy, M.M., Askalany, A.A., Harby, K., Ahmed, M.S., 2016. Adsorption isotherms and kinetics of a mixture of Pentafluoroethane, 1,1,1,2-Tetrafluoroethane and Difluoromethane (HFC-407C) onto granular activated carbon. Appl. Therm. Eng. 93, 988-994.

Ghazy, M., Askalany, A.A., Harby, K., Ahmed, M.S., 2016a. Adsorption isotherms and kinetics of HFC-404A onto bituminous based granular activated carbon for storage and cooling applications. Appl. Therm. Eng. 105, 639-645.

Ghazy, M., Askalany, A.A., Harby, K., Ahmed, M.S., 2016b. Adsorption isotherms and kinetics of HFC-404A onto bituminous based granular activated carbon for storage and cooling applications. Applied Thermal Engineering.

Ghazy, M., Harby, K., Askalany, A.A., Saha, B.B., 2016c. Adsorption isotherms and kinetics of activated carbon/Difluoroethane adsorption pair: Theory and experiments. Int. J. Refrigeration 70, 196-205.

Ghazy, M., Harby, K., Askalany, A.A., Saha, B.B., 2016d. Adsorption isotherms and kinetics of activated carbon/difluoroethane adsorption pair: theory and experiments. International Journal of Refrigeration.

Goetzler, W., Sutherland, T., Rassi, M., Burgos, J., 2014. Research & development roadmap for next-generation low global warming potential refrigerants. www.osti.gov/home/ (Accessed 18/10 2016).

Habib, K., Saha, B.B., Rahman, K.A., Chakraborty, A., Koyama, S., Ng, K.C., 2010. Experimental study on adsorption kinetics of activated carbon/R134a and activated carbon/R507A pairs. Int. J. Refrigeration 33(4), 706-713.

Higashi, Y., 2010. Thermophysical properties of HFO-1234yf and HFO-1234ze (E), International Symposium on Next-Generation Air Conditioning and Refrigeration Technology. Tokyo, Japan.

Janković, Z., Sieres Atienza, J., Martínez Suárez, J.A., 2015. Thermodynamic and heat transfer analyses for R1234yf and R1234ze(E) as drop-in replacements for R134a in a small power refrigerating system. Appl. Therm. Eng. 80, 42-54.

Jribi, S., El-Sharkawy, I.I., Koyama, S., Saha, B.B., 2010. Study on activated carbon-CO_2 pair: adsorption characteristics and cycle performance, Proc. Int. Symp. On Next-Generation Air Conditioning and Refrigeration Technology, Tokyo Japan.

Jribi, S., Saha, B.B., Koyama, S., Chakraborty, A., Ng, K.C., 2013. Study on activated carbon/HFO-1234ze(E) based adsorption cooling cycle. Appl. Therm. Eng. 50(2), 1570-1575.

Karber, K.M., Abdelaziz, O., Vineyard, E.A., 2012. Experimental Performance of R-1234yf and R-1234ze as Drop-in Replacements for R-134a in Domestic Refrigerators, IRACC. p. Paper 1228.

Koyama, S., Takata, N., Fukuda, S., 2010. Drop-in experiments on heat pump cycle using HFO-1234ze (E) and its mixtures with HFC-32, IRACC. , p. Paper 1155.

Kreith, F., Wang, S.K., Norton, P., 1999. Air conditioning and refrigeration engineering. CRC Press.

Lai, N.A., 2014. Equations of state for HFO-1234ze (E) and their application in the study on refrigeration cycle. Int. J. Refrigeration 43, 194-202.

Mota-Babiloni, A., Navarro-Esbrí, J., Barragán-Cervera, Á., Molés, F., Peris, B., 2014. Drop-in energy performance evaluation of R1234yf and R1234ze(E) in a vapor compression system as R134a replacements. Appl. Therm. Eng. 71(1), 259-265.

Mota-Babiloni, A., Navarro-Esbrí, J., Barragán-Cervera, Á., Molés, F., Peris, B., 2015a. Drop-in analysis of an internal heat exchanger in a vapour compression system using R1234ze (E) and R450A as alternatives for R134a. Energy 90, 1636-1644.

Mota-Babiloni, A., Navarro-Esbrí, J., Barragán-Cervera, Á., Molés, F., Peris, B., 2015b. Experimental study of an R1234ze (E)/R134a mixture (R450A) as R134a replacement. Int. J. Refrigeration 51, 52-58.

Mota-Babiloni, A., Navarro-Esbrí, J., Barragán-Cervera, Á., Molés, F., Peris, B., Verdú, G., 2015c. Commercial refrigeration-an overview of current status. Int. J. Refrigeration 57, 186-196.

Mota-Babiloni, A., Navarro-Esbrí, J., Molés, F., Cervera, Á.B., Peris, B., Verdú, G., 2016. A review of refrigerant R1234ze (E) recent investigations. Appl. Therm. Eng. 95, 211-222.

Navarro-Esbrí, J., Mendoza-Miranda, J.M., Mota-Babiloni, A., Barragán-Cervera, A., Belman-Flores, J.M., 2013. Experimental analysis of R1234yf as a drop-in replacement for R134a in a vapor compression system. Int. J. Refrigeration 36(3), 870-880.

Sethi, A., Becerra, E.V., Motta, S.Y., 2016. Low GWP R134a replacements for small refrigeration (plug-in) applications. Int. J. Refrigeration 66, 64-72.

Shmroukh, A.N., Ali, A.H.H., Ookawara, S., 2015. Adsorption working pairs for adsorption cooling chillers: A review based on adsorption capacity and environmental impact. Renew. Sustain. Energy Rev. 50, 445-456.

Velders, G.J., Fahey, D.W., Daniel, J.S., McFarland, M., Andersen, S.O., 2009. The large contribution of projected HFC emissions to future climate forcing. PNAS 106(27), 10949-10954.

Zhong, Y., Critoph, R.E., Thorpe, R., 2006. Evaluation of the performance of solid sorption refrigeration systems using carbon dioxide as refrigerant. Appl. Therm. Eng. 26(16), 1807-1811.

Modeling and Optimization for Contribution Rates of Solar Heating and Cooling Systems in Building Energy-Saving

Bojia Li[1], Tao He[1], Xinyu Zhang[1], Boyuan Wang[1], Motomi Inagaki[2], Yohsuke Yamada[2] and Xin Shi[3]

[1] China Academy of Building Research, Beijing (China)

[2] Yazaki Energy System Corporation, Hamamatsu (Japan)

[3] Yazaki Energy System Corporation Beijing Rep. Office, Beijing (China)

Abstract

With the increased emphasis on building energy-saving in China, solar heating and cooling (SHC) has become one of the best promised technologies to achieve ultra-low energy consumption. To achieve improved economy performance, enhancing energy system efficiency, SHC system requires scientific calculation and analysis according the architectural features. In this paper, building and system models have been established for hourly simulation of energy consumption. The deviation of tested and simulated solar fraction and system COP is about 5%. It indicates the system model established in this paper is accurate enough for design and optimization of SHC systems. With verified models, SHC system has been optimized considering the solar contribution and economy index. Results show that, after the system scheme and configuration optimization, SHC system applied in office building in Turpan can be achieved in the solar contribution of more than 30%. Meanwhile, the payback period could be reduced to less than 20 years.

Keywords: solar heating and cooling, solar contribution, system design and optimization, payback period

1. Introduction

With the increased emphasis on building energy-saving in China, the limit of building energy consumption is stricter than ever. Nearly zero energy building, passive building has become a new trend (Xu et al. 2016). As the energy consumption for space heating and cooling accounts for a large part of the building energy consumption, solar heating and cooling (SHC) has become one of the best promised technologies to achieve ultra-low energy consumption.

After years of development, SHC technology has made great progress in the technical maturity and practical application. However, SHC system has not been promoted widely because its high initial cost and low efficiency. Sarabia et al. (2011) proposed a design method for solar cooling systems with single effect absorption cooling machine directly coupled to a solar collector field, then analyzed the feasibility of the system in 12 Spanish Cities. Syed et al. (2005) designed a solar cooling system for residential buildings in Madrid. And the test results showed that the average coefficient of performance is around 0.6. Mateus et al. (2009) investigated solar absorption cooling and heating system in different building types and climates. With TRNSYS software, contributions of SHC system in building energy-saving had been analyzed. Li Z. et al. (2000, 2001) proposed a solar absorption cooling system with a layered heat storage tank, and the system was optimized and applied in Hong Kong.

To achieve improved economy, enhancing energy system efficiency, SHC system requires scientific calculation and analysis according the architectural features. In this paper, building and system models have been established for hourly simulation of energy consumption. With verified models, SHC system has been optimized considering the solar contribution and economy index.

doi:10.18086/swc.2017.28.13 Available at http://proceedings.ises.org

2. Method

2.1. Contribution rates

Similar to solar fraction, contribution rates of solar heating and cooling systems in building energy-saving means the proportion of building heating and cooling demands meet by solar energy. The calculation method is as follows:

$$f_s = \frac{E}{Q} \qquad \text{(eq. 1)}$$

Where, f_s is the contribution rates in building energy-saving; E is building heating and cooling demands meet by solar energy; Q is total heating and cooling demands.

2.2. Optimization method

Contribution rate of SHC systems is affected by many factors. To achieve an optimal contribution rate, building and system models have been established first. Then hourly energy consumption and system performance have been simulated. During the simulation, Effects of climate, building type, and SHC system type have been considered, as shown in Fig. 1. With simulation results, the system contribution rates in building energy-saving could be determine considering following key indicators:

- *Indoor temperature*, *heating and cooling capacity*: the indoor temperature, system heating and cooling capacity have to meet the design requirements;
- *Energy saving*: reduction rate of primary energy consumption as the main index;
- *Economy*: payback period as the main index.

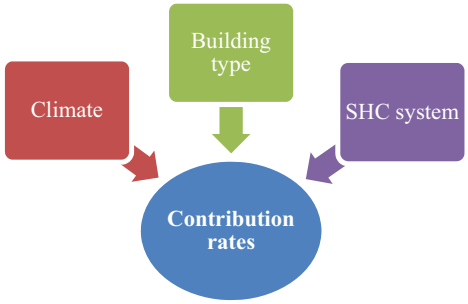

Fig. 1: Affect factors on contribution rate

3. Modeling

3.1. Building model

An office building model and an inpatient building model have been established to analyze the heat and cooling demands in different building types. Construction dimensions of both models are determined according to the design drawings of actual buildings. Building envelope conditions meet requirements of the *Design standard for energy efficiency of public buildings* (GB 50189-2015) in China. Operation time of the office building and inpatient building is different: the office building is used from 08:00 to 18:00 during workdays while the inpatient building is used 24 hours all year round.

As the actual buildings is still under construction, another office building is selected and modeled to verify the building and system models. Brief information of three buildings are shown in Tab. 1.

To analyze the effect of climates on contribution rates, heating and cooling loads of both office building and inpatient building have been calculated according the climates of different locations, results shown in Tab. 2.

Tab. 1: Building Information

Building	Height	Floors	Gross floor area (m^2)
office building	18.6 m	4 floors above ground 1 floor under ground	6144
inpatient building	24.9 m	6 floors above ground	5904
office building for validation	11.8 m	2 floors above ground	1850

Tab. 2: Heating and cooling loads of the office building and inpatient building in different locations

Location	Building	Cooling		Heating	
		Load (kW)	Annual demand (MJ)	Load (kW)	Annual demand (MJ)
Beijing (Northeast China)	office building	512	254,715	580	93,340
	inpatient building	504	348,776	456	146,808
Turpan (Northwest China)	office building	644	274,512	494	110,243
	inpatient building	625	374,172	381	141,172

3.2. System description

Based on investigation and analysis of practical projects, three types of SHC systems are summarized and compared with the conventional system. The SHC systems and conventional system are listed in Tab. 3.

Tab. 3: The SHC systems and conventional system

System			Heating and Cooling Souce
SHC systems	System I：Solar absorption cooling + Water cooled chiller + Gas boiler	Cooling	Solar collectors＋WFC + Water cooled chiller
		Heating	Solar collectors＋Gas boiler
	System II：Solar absorption cooling+ WSHP + Gas boiler	Cooling	Solar collectors＋WFC＋WSHP
		Heating	Solar collectors＋WSHP＋Gas boiler
	System III: Optimized SHC system	Cooling	Solar collectors＋WFC＋WSHP
		Heating	Solar collectors＋WSHP＋Gas boiler
Conventional system	Water cooled chiller + Gas boiler	Cooling	Water cooled chiller
		Heating	Gas boiler

WFC: Hot water fired absorption chiller WSHP: Water source heat pump

System I: Solar absorption cooling + Water cooled chiller + Gas boiler

The main components of this system include the Solar collectors, an Hot water fired absorption chiller (WFC), a Heat storage tank, Cooling towers, a Gas boiler and a Water cooled chiller for summer cooling. The system schematic is showed in Fig. 2.

Cooling mode:

1. When the heat storage tank temperature is higher than the set point, WFC is used in priority to meet the cooling demand. When WFC cooling capacity can not meet the cooling demand, Water cooled chiller starts.

2. If the heat storage tank temperature is below the set point, Water cooled chiller is used to meet the cooling demand.

Heating mode:

1. If the heat storage tank temperature is higher than the heating requirement in winter, heating demand is satisfied directly by solar.

2. If the heat storage tank temperature is lower than the requirement, Gas boiler starts to satisfy the heating demand.

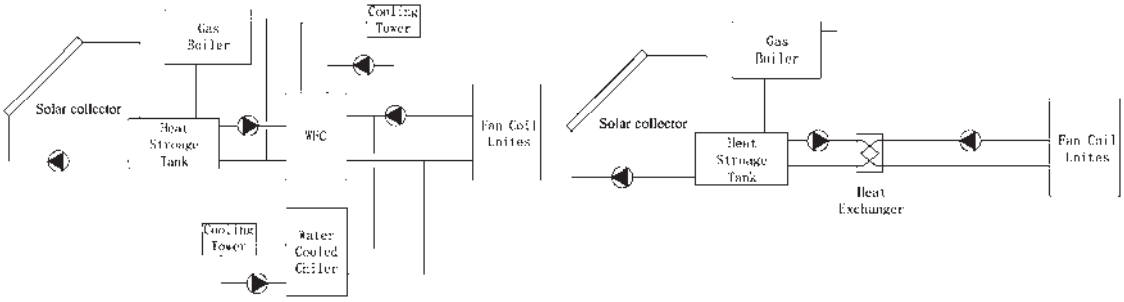

(a) cooling mode (b) heating mode

Fig. 2: Schematic of System I

System II: Solar absorption cooling+ WSHP + Gas boiler

The main components of this system include the Solar collectors, an Hot water fired absorption chiller (WFC), a Heat storage tank, Cooling towers, a Gas boiler and a Water source heat pump (WSHP) for both heating and cooling. The system schematic is showed in Fig. 3.

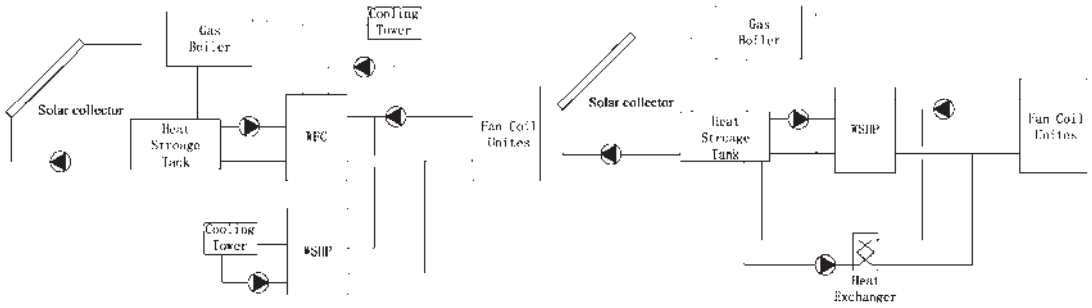

(a) cooling mode (b) heating mode

Fig. 3: Schematic of System II

Cooling mode:

1. When the heat storage tank temperature is higher than the set point, WFC is used in priority to meet the cooling demand. When WFC cooling capacity can not meet the cooling demand, WSHP starts.

2. If the heat storage tank temperature is below the set point, WSHP is used to meet the cooling demand.

Heating mode:

1. If the heat storage tank temperature is higher than the heating requirement in winter, heating demand is

satisfied directly by solar.

2. If the heat storage tank temperature is lower than the requirement, but higher than WSHP's requirement, WSHP starts to satisfy the heating demand.

3. System could also provide heating by Gas boiled directly.

Main difference between System I and System II is that the WSHP could provide heating by lower temperature water. Solar contribution rate could be increased in winter.

System III: Optimized SHC system

The main components of this system is same as System II. Main difference between System III and System II is that the heating capacity of WSHP can fully satisfy the heating load, but the cooling capacity is not required to meet the cooling load. So, the system could use a WSHP with lower volume to improve the economy indexes.

When cooling in summer, if the heat storage tank temperature is below the set point, WSHP co-works with WFC to meet the cooling demand.

3.3. System model

With TRNSYS software, all systems have been modeled and simulated based on typical meteorological year (TMY) weather data and building data of both Beijing and Turpan. The TRNSYS model of System I is shown in Fig. 4. The TRNSYS model of System II & System III is shown in Fig. 5.

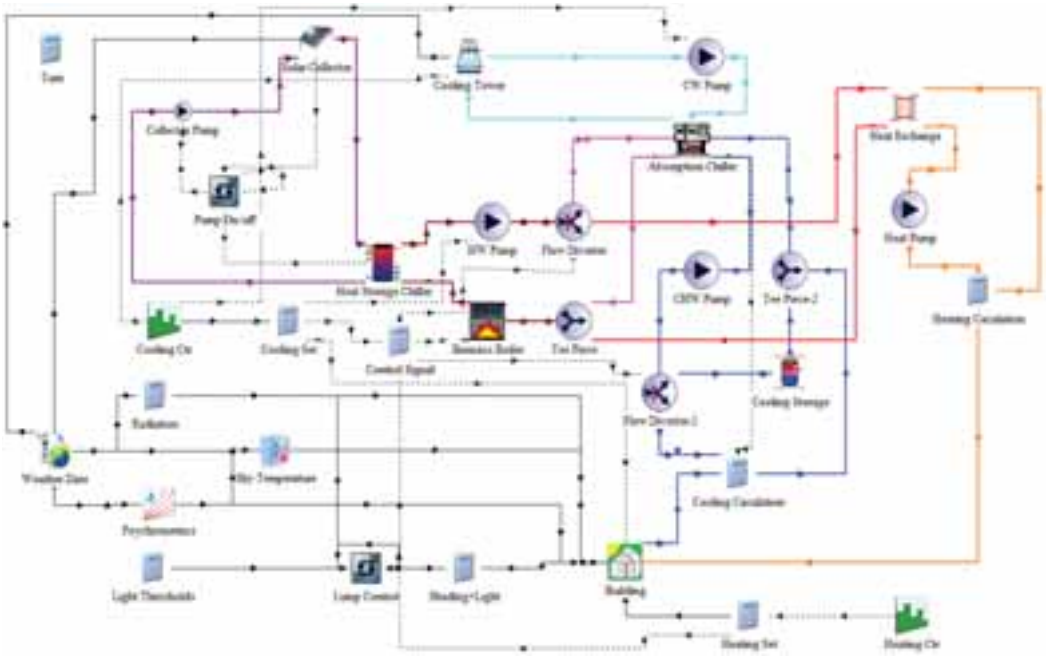

Fig. 4: The TRNSYS model of System I

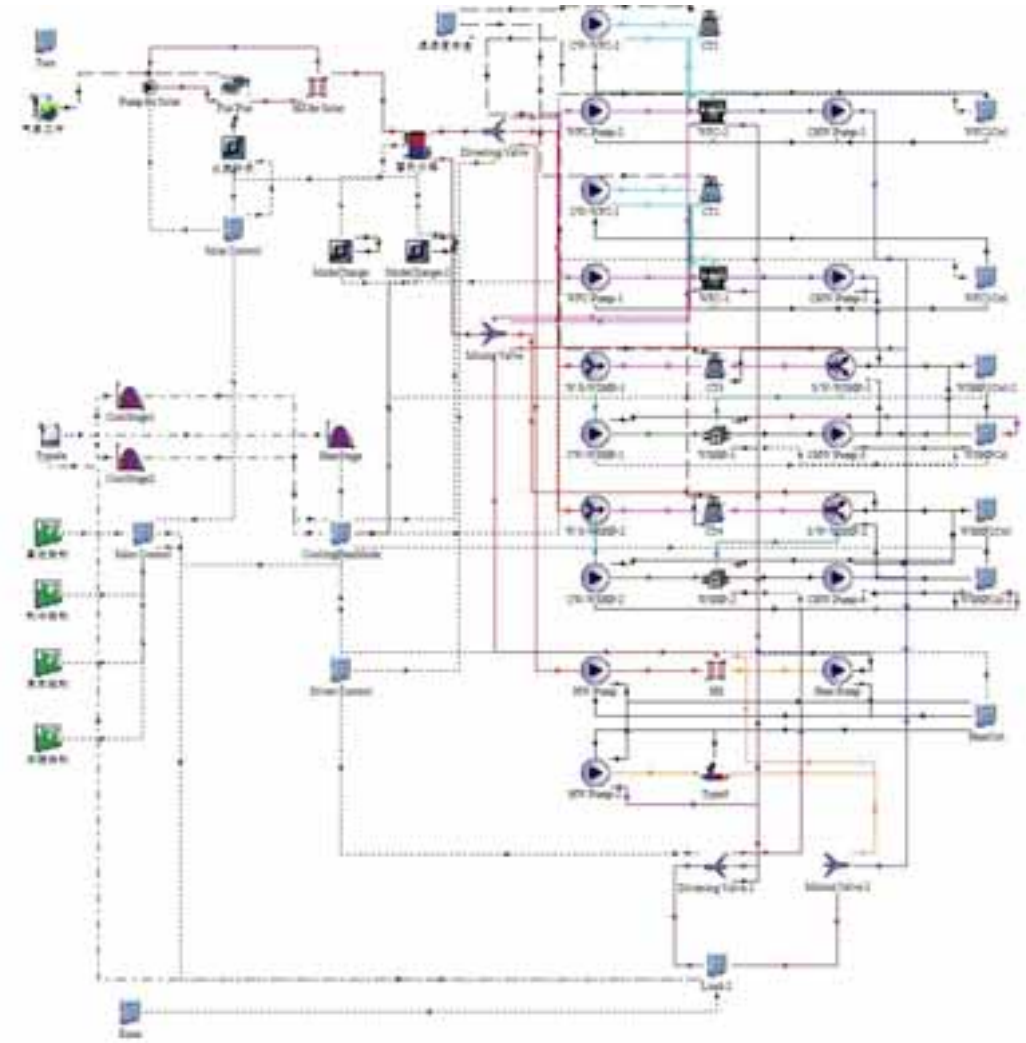

Fig. 5: The TRNSYS model of System II & System III

4. Model Validation

In this study, an office building with SHC system in Beijing is selected and modelled. Simulated and measured results are compared to verify the system model.

This two floors office building is located in Beijing, China. The SHC system applied for space cooling and heating is same as System I. Building and system information is published in previous study (He et al. 2014). The system had been tested during the summer of 2013 by China Academy of Building Research. There were 4 days selected to test the system performance under typical weathers. The solar irradiation levels of the 4 days were respectively very good, good, medium and poor.

To verify the system model, measured data of environmental parameters was integrated into the weather data of TRNSYS model of System I. Then Several operating data, such as tank temperature, flow rate, had been used to set the initial simulate conditions. Tested COP and solar fraction were compared with simulated results, as shown in Fig. 6.

Comparison of tested and simulated results show that the deviation of tested and simulated solar fraction and system COP is about 5%. It shows that the system model is accurate enough to caculate system performance.

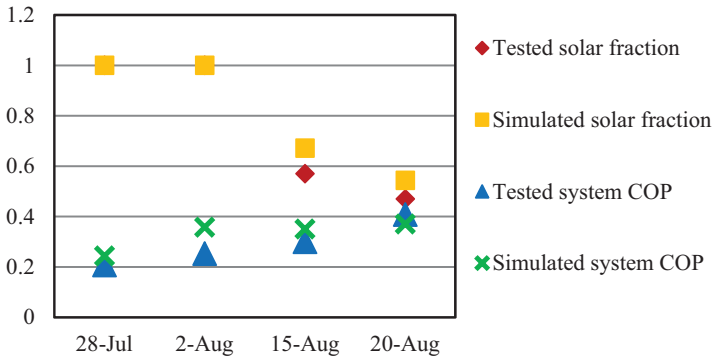

Fig. 6: Comparison of tested and simulated results

5. Optimization

5.1. Simulation results

In this study, Solar contribution rates of System I and System II applied in different building types and climates have been simulated separately. Results is shown in Fig. 7 to Fig. 8.

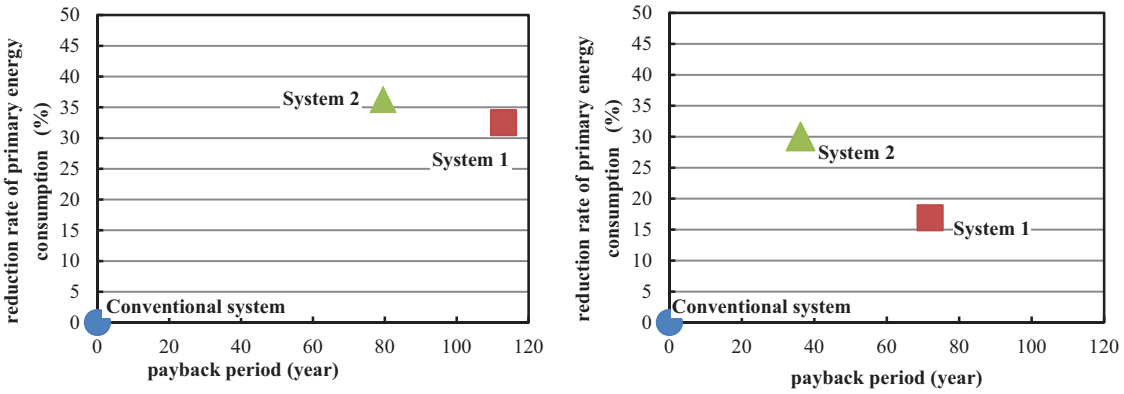

(a) Turpan (Northwest China) (b) Beijing(Northeast China)

Fig. 7: Simulated results of System I and System II in office building

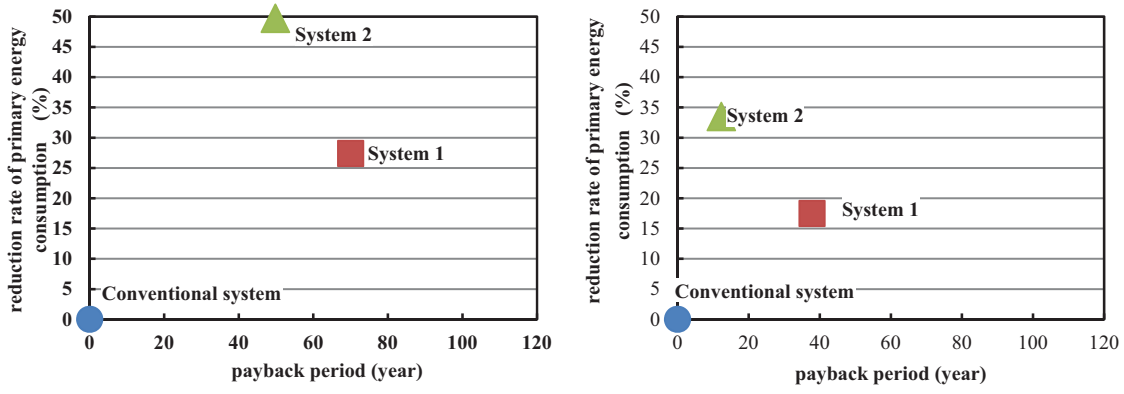

(a) Turpan (Northwest China) (b) Beijing(Northeast China)

Fig. 8: Simulated results of System I and System II in inpatient building

Results shows that the reduction rate of primary energy consumption of System II is larger than 30% in all buildings. In the inpatient building, the primary energy consumption could be reduced by 50%. It indicates the

SHC system has significant effect in energy-saving. But nearly all payback periods are more than 30 years, except the System II applied in inpatient building in Beijing. These unacceptable payback periods show the optimization of SHC system needs to focus on enhancing the economic performances.

5.2. System optimization

Based on System II, System III is proposed to improve the economic performances of SHC systems. Compared with System II the optimization includes:

- The heating capacity of WSHP can fully satisfy the heating load, but the cooling capacity is not required to meet the cooling load. The system could use a WSHP with lower volume to reduce initial cost.
- When cooling in summer, if the heat storage tank temperature is below the set point, WSHP co-works with WFC to meet the cooling demand.
- Increasing system scale, solar contribution rate of solar district heating and cooling system in regional heating and cooling has been simulated.

Tab. 4 shows the simulated results of System III applied in a district heating and cooling project in Turpan. The simulated results indicates that the economic performance of System III has been improved while the energy-saving effect is still significant (Reduction of primary energy consumption is more than 30%). After system optimization, the contribution rate of System III in energy-saving is about 36.8%.

Tab. 4: Simulated results of System III applied in a district heating and cooling project in Turpan

		System III	Conventional system
Summer	Cooling capacity (kW)	4269.4	4357
	Heat gain by collectors (MJ)	6.75E+06	0
	Cooling load (MJ)	1.21E+07	1.21E+07
	Solar contribution	40%	0%
Winter	Heat gain by collectors (MJ)	3.38E+06	0.00
	Heating load (MJ)	1.02E+07	1.02E+07
	Solar contribution	33%	0%
Electricity (kW/h)		**841431**	**1173764**
Gas consumption (m^3)		**206015**	**308216**
Reduction rate of primary energy consumption		**30.8%**	**-**
Increased investment (thousand Yuan)		**6311.9**	**-**
Reduction of operation cost (thousand Yuan)		**343.2**	**-**
Payback period (Year)		**18.4**	**-**

6. Conclusion

With the increased emphasis on building energy-saving in China, solar heating and cooling (SHC) has become one of the best promised technologies to achieve ultra-low energy consumption. To achieve improved economy, enhancing energy system efficiency, SHC system requires scientific calculation and analysis according the architectural features.

In this paper, building and system models have been established to simulate the contribution rate of different SHC systems in energy-saving. Effects of climate, building type, and SHC system type have been considered during simulation. Results show that:

- The deviation of tested and simulated solar fraction and system COP is about 5%. The system model

established in this paper is accurate enough for design and optimization of SHC systems.

- Traditional SHC system has significant effect in energy-saving, but the economic performance needs to be enhanced.
- After the system scheme and configuration optimization, SHC system applied in office building in Turpan can be achieved in the solar contribution of more than 30%. Meanwhile, the payback period could be reduced to less than 20 years.

7. Acknowledgement

The research is part of the CABR-YAZAKI joint research project “Technical and Economic Analysis of Different Types of Solar Heating and Cooling Systems in Different Region”. All authors are also grateful for the financial support provided by the *National Key R&D Program of China* (Grant No. 2016YFC0700405) and the *Youth Technology Research Fund of CABR* (Project No. 20160109331030062).

8. References

He T., Zhang X., Wang C., Wang M., Li B., Xue N., Shimizu K., Takahashi K., Wu Y., 2014. Application of solar thermal cooling system driven by low temperature heat source in China. Energy Procedia. 70, 454-461.

Li Z., Sumathy K., 2000. Technology development in the solar absorption air-conditioning systems. Renewable and Sustainable Energy Reviews. 4(3), 267–293.

Li Z., Sumathy K., 2001. Simulation of a solar absorption air conditioning system. Energy Conversion and Management. 42(3), 313–327.

Mateus T., Oliveira A. C., 2009. Energy and economic analysis of an integrated solar absorption cooling and heating system in different building types and climates. Applied Energy. 86(6), 949–957.

Sarabia Escriva E. J., Lamas Sivila E. V., Soto Frances V. M., 2011. Air conditioning production by a single effect absorption cooling machine directly coupled to a solar collector field. Solar Energy. 85(9), 2108–2121.

Syed A., Izquierdo M., Rodríguez P., 2005. A novel experimental investigation of a solar cooling system in Madrid. International Journal of Refrigeration. 28(6), 859–871.

Xu W., Liu Z., Chen X., Zhang S., 2016.Thoughts of Development of Chinese Nearly Zero Energy Buildings. Building Science. 32(4), 1–5.

Energy Storage for PV-Driven Air-Conditioning for an Off-Grid Resort – A Case Study

Christoph Luerssen[1,2], Arifeen Wahed[1], Thomas Reindl[1], Clayton Miller[2], David Cheong[2] and Chandra Sekhar[2]

[1] Solar Energy Research Institute of Singapore (SERIS), National University of Singapore (NUS), Singapore (Singapore)

[2] Department of Building, National University of Singapore (NUS), Singapore (Singapore)

Abstract

The current paper presents a case study of a PV-driven air-conditioning system with battery and latent heat storage applied for an off-grid resort in Bintan (Indonesia). The lead-acid battery bank has a nominal energy storage capacity of 47 kWh and the ice storage can store up to 92 kWh latent heat. The entire energy system of the resort was equipped with a comprehensive real-time data acquisition system to measure different parameters such as solar irradiation, temperatures, flow rates and power consumptions. More than 100 parameters are transferred minutely and monitored remotely across country borders. A TRNSYS model has also been developed to simulate the case study system dynamically. To assure accurate simulation results, the chiller and the Thermal Energy Storage (TES) models were calibrated using measured data from the monitoring system. Initial simulation results show the usage of the energy storages. The battery is utilised as a buffer to run the chillers with least disruptions and the TES is used to shift the cold generated during daytime to cool bedrooms at nighttime. The later one can also serve as a short-term energy storage over a few rainy days. For future works, we propose a comparative study of chilled water, ice and battery storage to design an optimal energy storage system for the resort based on the insights provided by this case study.

Keywords: Solar air-conditioning, PV-driven cooling, energy storage solutions, off-grid

1. Introduction

At present, a significant reduction in PV module costs pares the broader integration of PV systems. Hence, PV-driven cooling systems have gained attention. Compared to solar thermally driven cooling systems, at present PV-driven cooling systems' footprint is lower (Otanicar et al., 2012; Noro et al., 2014; Eicker et al., 2014) and they are economically more favorable (Otanicar et al., 2012; Noro et al., 2014; Eicker et al., 2014). The primary driver for the superior results of PV-driven cooling is the substantial decrease in PV costs and the higher Coefficient of Performance (COP) (Otanicar et al., 2012; Noro et al., 2014). Furthermore, the individual components are well-known, and the solution is flexible, which has the potential to improve situations in off-grid areas where grid-connections are not viable so far (Wang and Ge, 2016). However, there are challenges, since the PV power output does not match cooling demand, as the first depends on the solar irradiation whereas the second is also influenced by the ambient temperature and the occupancy. Thus, energy storage is required to buffer the imbalance between power demand and supply.

In the tropics, load-shifting is required to buffer energy and shift it from daytime to nighttime; occasionally also over a few rainy or cloudy days. Typically, battery storage technologies are considered for this energy storage duration of solar energy in an off-grid system (Merei et al., 2013; Eltawil, 2007). Looking at the Southeast Asian region in particular, a significant part of the energy consumption in buildings accounts for air-conditioning. This is a thermal load that allows for Thermal Energy Storage (TES). There are different TES solutions for cooling applications. Sensible energy storage is the most commonly realised in the form of chilled water (Arteconi et al., 2017). On district cooling scale or in large-scale office buildings also latent heat storage in the form of ice is common practice (Sehar et at., 2012; Chan et al. 20016). Other Phase Change Materials (PCM) have been commercialised and are investigated for application in TES systems (Souayfane et al., 2016; Ewert, 2000; Foster, 2017).

In grid-connected systems, the effective utilization of an energy storage such as a chilled water tank depends on the economic viability, i.e., increase the self-consumption of solar energy instead of selling it to the grid for a lower price

doi:10.18086/swc.2017.28.14 Available at http://proceedings.ises.org

(Arteconi et al., 2017). However, in an off-grid environment, energy storage is a necessity. An off-grid PV-driven cooling system can be configured as shown in Figure 1. Energy generated by a PV system is often stored directly via a battery. However, it is also possible to store the cold produced by the chiller via TES.

A prototype of such a system using latent heat and battery storage is installed at the LooLa resort in the rural and remote south-east of Bintan Island (Pulau Bintan) in the Riau Archipelago of Indonesia. The resort focusses on environmental and sustainable aspects as well as empowering their local staff and it is not connected to the public grid. The Solar Energy Research Institute of Singapore (SERIS) was selected as an R&D partner to monitor the existent prototype to optimise its performance and use it as a starting point for further investigation and research.

The objective of the present case study is to gain insights regarding operational and energy performance. It prepares a comparative study of different energy storage for the PV-driven cooling system at the resort. Therefore, the existing system is described, equipped with a monitoring system and dynamically modelled. Preliminary results are shown and research opportunities are discussed to round the study off.

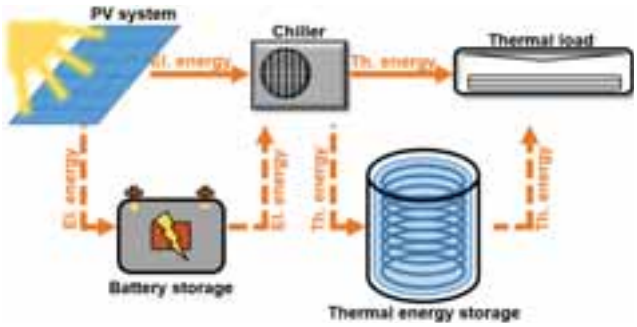

Fig. 1: Schematic of the system concept of an off-grid solar PV-driven air-conditioning system showing the variety of energy storage opportunities.

2. Case study description

The LooLa eco-resort has two villas offering higher-class hotel rooms with air-conditioning at night. To demonstrate sustainable technologies, a prototype of a PV-driven air-conditioning system was implemented in each of the villas. Additionally, a diesel generator is operated during nighttime to augment the power requirement in the resort. There is no public electricity grid access available in this part of Bintan. The main components of the PV powered air-conditioning system are electrical in nature including the PV system, the diesel generator and the chillers. It is only after the chillers that there is the switch to a thermal energy system as shown in Fig. 2.

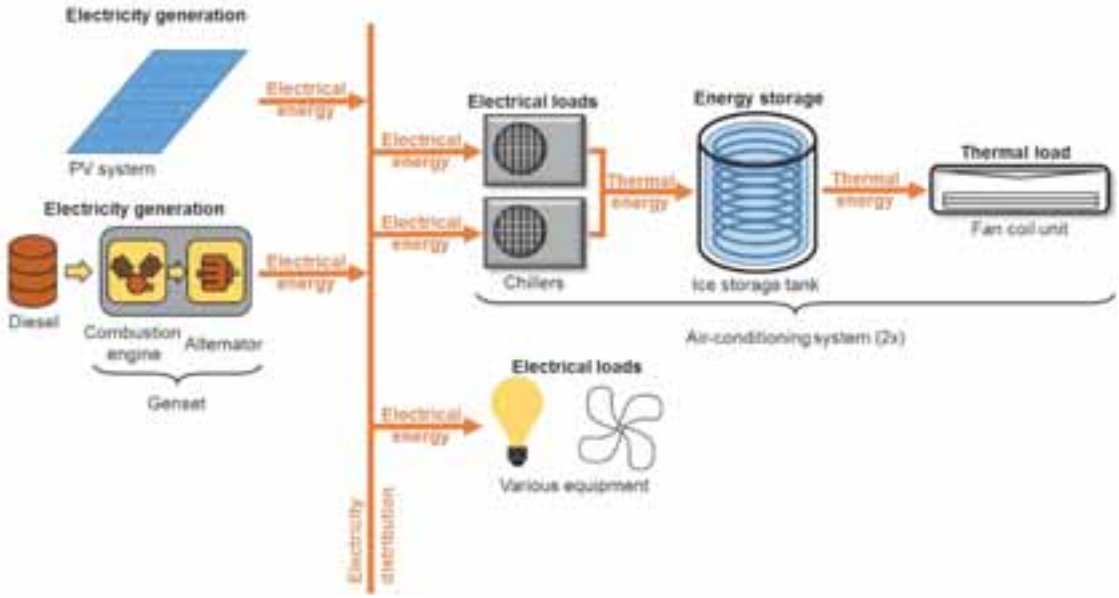

Fig. 2: Schematic of the energy system of the resort. On the left side PV system and diesel generator supply electricity to the distribution network. On the right side, both electrical and thermal loads are shown.

The PV system consists of different components – PV modules, PV inverters, batteries and battery inverters. During

daytime, it powers the air-conditioning systems for storing solar energy in the form of ice and supplies power for the shop, kitchen and office. The space cooling is scheduled to operate only during nighttime by discharging the thermal energy from the ice storage tank. To maintain the set point (room) temperature, FCUs supply cold air utilizing the latent energy from the ice storage tank without the need of operating the energy-intensive chillers. From 5.00PM to 8.00AM, the diesel generator supplies electricity for the entire resort. The switching of power sources is not automated, but manually conducted. An overview of the systems' and components' specifications is provided in Table 1.

Tab. 1: System and components specifications of the energy system at the LooLa resort

System	Component	Quantity	Specifications
PV system	PV module	72	Chinaland Solar Energy CHN240-60P; module power 240 W_p; multicrystalline silicon cells; 6 strings each having 12 modules; system power 17.3 kW_p
	Battery	48	RITAR OPzV2-490; tubular plate VRLA gel battery; capacity 490Ah
	PV inverter	3	SMA Sunny Boy 5000TL; rated AC power 4600 W
	Battery inverter	2	SMA Sunny Island 6.0H; rated AC power 4600 W; battery depth of discharge 50%
Diesel generator	Diesel Generator	1	Power 30 kVA
Two air-conditioning systems	Condensing unit	4 (2 per system)	Tecumseh FHT4525YHR; cooling capacity 2.4 kW and Power consumption 1.5 kW at 32 °C ambient temperature and -15 °C evaporation temperature; refrigerant R134a
	Evaporator (Heat exchanger)	4 (2 per system)	Gimleo GBH05-CMF; tube in shell heat exchanger; cooling capacity 9.5 kW
	Ice storage tank	2 (1 per system)	Customized design (cuboid shape); volume 1045 l; fiberglass; copper pipe; 15 cm Polyurethane foam insulation
	Water tank	2 (1 per system)	Guangdong LuckingStar New Energy LWT300-T&H-02; volume 300 l; stainless steel
	Fan coil unit small	6 (3 per system)	Eurostars 300WM2; cooling capacity 2.9 kW (max); power consumption 52 W
	Fan coil unit big	2 (1 per system)	Eurostars 400WM2; cooling capacity 3.7 kW (max); power consumption 62 W

2.1. Air-conditioning system design and operation

In order to understand the air-conditioning system design and operation, we look at a single air-conditioning system. The top part of Fig. 3 shows a simplified schematic focusing on the heat exchangers and fluid circuits. This schematic includes only one chiller, whereas the real system has two chillers. Therefore, the bottom part of Fig.3 provides a complementary Piping & Instrumentation (P&I) diagram for deeper understanding of the actual design. The top and the bottom part of Fig. 3 are linked in terms of color coding of key components.

At daytime, the chillers (conventional vapor-compression systems consisting of compressor, condenser, evaporator, expansion valve and refrigerant) operate at an evaporation temperature of below 0 °C. The chiller refrigerant exchanges heat to the ethylene glycol based water solution (glycol) in the evaporator. The glycol flows through the left side of the circuit in order to exchange heat with the water in the ice storage tank. The process is carried out through a tube and shell heat exchanger. Since the temperature of the glycol is below 0 °C, ice is generated in the storage tank. The ice storage is charged and the thermal energy is stored as latent heat.

During nighttime, the glycol exchanges heat with the ice in order to cool the water in the water tank to ~17 °C temperature. The chilled water from the water tank is pumped through the fan coil units that blow the cool air out, providing thermal comfort in the sleeping areas. The air-conditioning operation causes melting of the ice, i.e., discharging of the thermal energy storage.

On a sunny day, the condenser units and the auxiliary equipment run on the PV system for 8 hours, from 8AM to 4PM. In case of heavy rains and prolonged presence of clouds, the PV system is disconnected manually at the discretion of the operators, which means that there is no electricity available in the resort at that time. The loads are then manually reconnected to the PV system when the weather changes to more favorable conditions. This procedure is conducted to keep some buffer storage in the batteries. If there is not enough cooling energy stored in the thermal energy storage on a cloudy or rainy day, the chillers are powered by the batteries of the PV system until they are completely discharged. At night, the auxiliary power for devices such as pumps, valves and FCUs are sourced from the diesel generator.

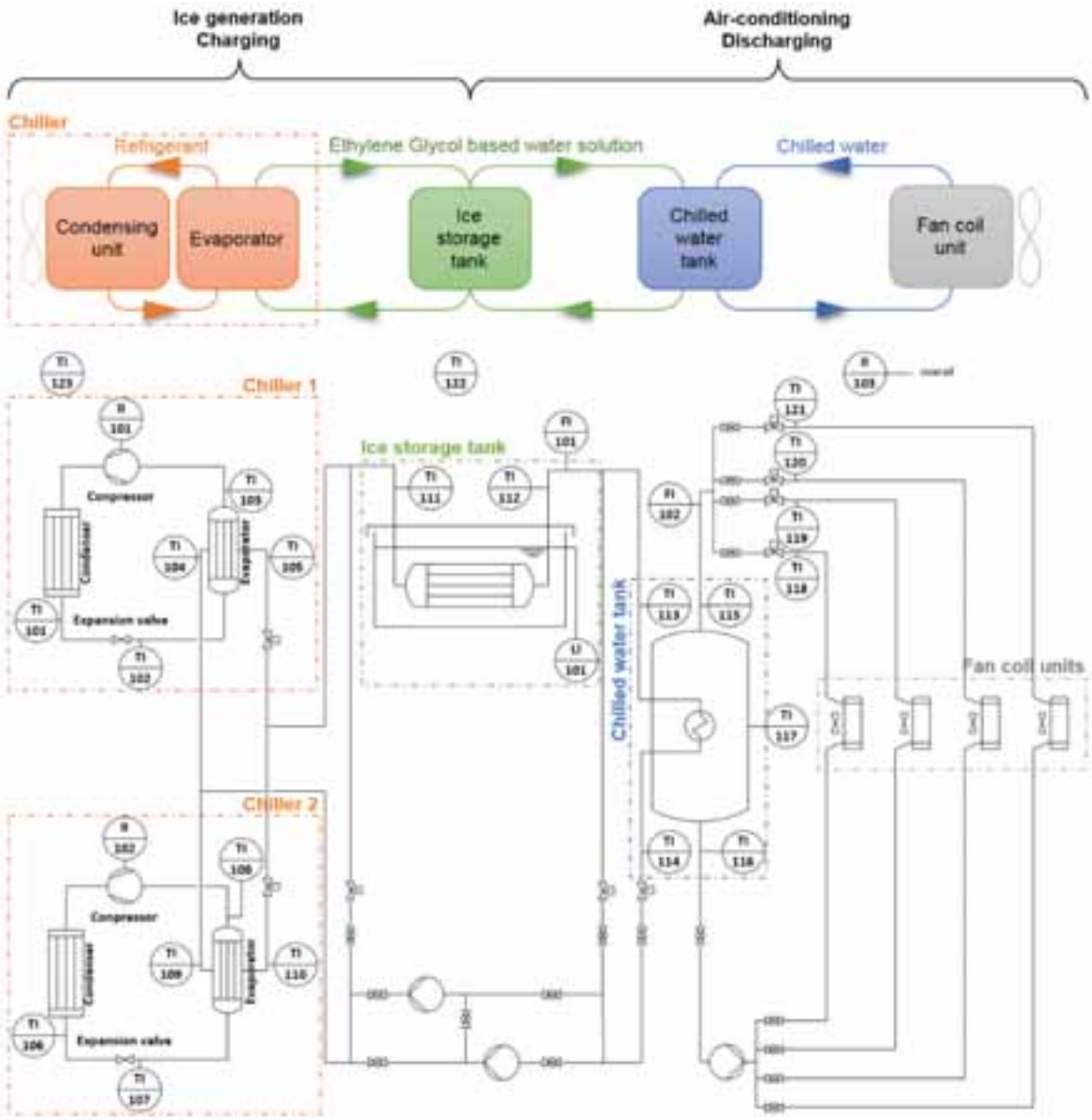

Fig. 3: Simplified schematic diagram describes the operation process of an air-conditioning system with thermal energy storage (top); Piping and Instrumentation diagram of a single air-conditioning system to show the sensor positions: temperature indicator (TI), flow indicator (FI), level indicator (LI), power indicator (II) (bottom)

3. Monitoring system

The prototypes of the PV-driven cooling systems enable the LooLa resort to provide air-conditioning to the clients

staying in the villas in an ecological way. However, the assessment of the performance was not possible due to insufficient data acquisition. Therefore, deployment of a monitoring system was the consequence. The developed monitoring architecture acquires sensor data throughout the entire resort. Three remote stations were deployed, one for each air-conditioning system and one that acquires PV system and diesel generator data. The top part of Fig. 4 shows the monitoring system architecture. On the field level, the relevant heat flows, components' performances/statuses and power consumptions need to be identified. Therefore, the ultrasonic flowmeters, ultrasonic level sensors for the ice storage tanks, temperature sensors and a silicon irradiance sensor are required for the PV and the cooling system. The sensors are hardwired to National Instruments (NI) CompactRIO controllers (cRIO), which are part of the control level. The remote stations consist of a cRIO, an Ethernet switch and a router. The bottom part of Fig. 4 provides a photo of one remote station and its components. They are lightning protected and backed-up through an uninterruptible power supply. The three cRIOs are capable of processing the acquired parameters remotely and fully automated. The LabVIEW software is capable to acquire the data from all the sensors as well as power meters and inverters. The later ones are directly accessed by MODBUS TCP. The cRIOs log the acquired data and transfer it from the remote stations in Bintan to the Central Monitoring Station (CMS) in Singapore by use of cellular network routers. The cellular network was observed to be rather weak at the resort and its vicinity. In order to find the most suitable locations for the routers, location-based tests were conducted a priori. Three spots, all close to one of the cRIOs, were found to have sufficient coverage for the data transmission. The routers are configured for a local SIM card and Virtual Private Network (VPN) to access the internet. At the process control level, the CMS receives one-minute live-data and initiates nightly download routines. The data is sorted into files and databases by the CMS to make it available for analysis.

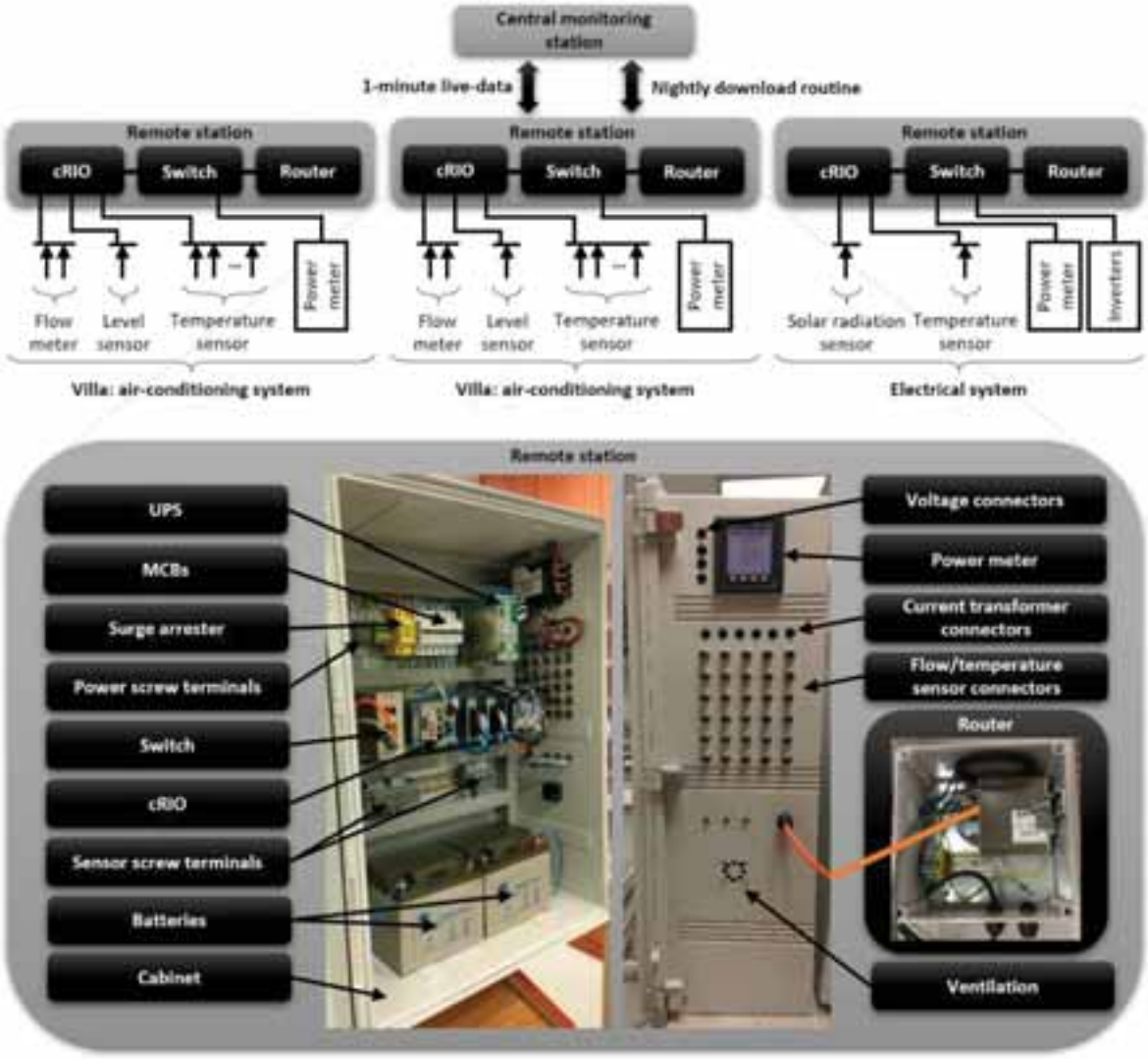

Fig. 4: System architecture of the monitoring system for the energy system at the LooLa resort (top); exemplary remote monitoring station (bottom)

This case study uses data measured by temperature sensors, flow meter and power meter to calibrate parts of a simulation model in Chapter 5. Detailed specifications of the utilised sensors is given in Table 2. To ensure the accuracy of the sensor/meter readings, additional calibration of certain sensors is required. The manufacturer of the temperature sensors provides accuracy class A. However, an additional multi-point calibration with a reference sensor (Isotech Hyperion Site & 935-14-61, overall accuracy: 0.04 °C) was conducted in a cooling bath from -20 °C to 40 °C for each sensor under laboratory conditions. The ultrasonic flow meters are also calibrated for the respective pipe dimensions and fluids, following similar laboratory conditions on-site. The calibration was conducted for the range of 0 to 15 l/min with an in-line reference flow meter (Rosemount 8732E, overall accuracy: ±0.02349 l/min). For both temperature sensors and flow meters, regression analysis was implemented in order to determine the correlation factors. The power meter meets IEC 61557-12 requirements and needs no further calibration.

The sensors were installed according to the P&I diagram in the bottom part of Fig. 3. Condensation and evaporation temperatures of the vapor-compression cycles are measured as well as stream temperatures before and after the ice storage tank, water tank and FCUs. Additionally, the water tank is equipped with a sensor measuring the temperature inside. The flow rates of the glycol and water are measured to be able to calculate the transferred thermal energy. The power meter measures the power consumption of the two chillers and the overall air-conditioning system.

Tab. 2: Specifications of the utilized sensors of the monitoring system

Parameter	Sensor	Range	Accuracy
Temperature	RTD, PT100, 4-wire, Thermotron	-30 to 100 °C	Class A
Flow rate	Ultrasonic flow meter Transmitter: Flexim F704 Transducer: Flexim FSQ	Plow velocity 0.01 to 25 m/s	Repeatability 0.15 % of reading ±0.01 m/s With standard calibration ±1.6% of reading ±0.01 m/s
Power	Current and voltage Schneider Electric PM5320	Depends on current transformers	Class 0.5S

4. Simulation model

A simulation model for the PV-driven cooling system at LooLa was set up using TRRNSYS 17.1, a dynamic simulation software. The model is divided into three main parts, cooling system 1, cooling system 2 and PV system, as displayed in Fig. 5. Additionally, weather data is utilised by all three parts. In the bottom part of Fig. 5, the outputs are processed, plotted and compiled in a text file for further analysis.

Cooling system 1 represents the actual system described in Chapter 2.1. Two chillers charge the ice storage tank (provided by Lerch and Heinz (2012)) during scheduled hours at daytime. Similar to the real system, the air-conditioning is scheduled during certain hours at night. Additionally, an occupancy calendar using the booking data of the resort in 2016 was implemented. The given data provides information about whether a villa is booked, but not how many rooms in which villa are booked, hence the occupancy is a binary input. In the discharging circuit, the chilled water tank was replaced by a controlled tempering valve keeping the glycol solution temperature at 12 °C and the four FCUs are simulated using a single FCU model. The input parameters for the FCU were determined using the psychrometric chart in Fig. 6. The return air is mixed with 15% outdoor air. One air change per hour is achieved by an air flow rate of 790 kg/h for four bed areas, each 12.5 m² and 2 m celling height. This results into a cooling load of 2.76 kW according to the mixed air and supply air conditions from the psychometric chart.

Cooling system 2 is only represented by the electrical load of the two chillers, because the system is similar to cooling system 1. The PV system powers the four chillers of the cooling systems. The power consumption of the auxiliary equipment, such as pumps, valves, control and FCUs, as well as the other loads at the resort that are connected to the PV system are neglected. The parameters for PV modules, batteries and control strategy are chosen according to the on-site system.

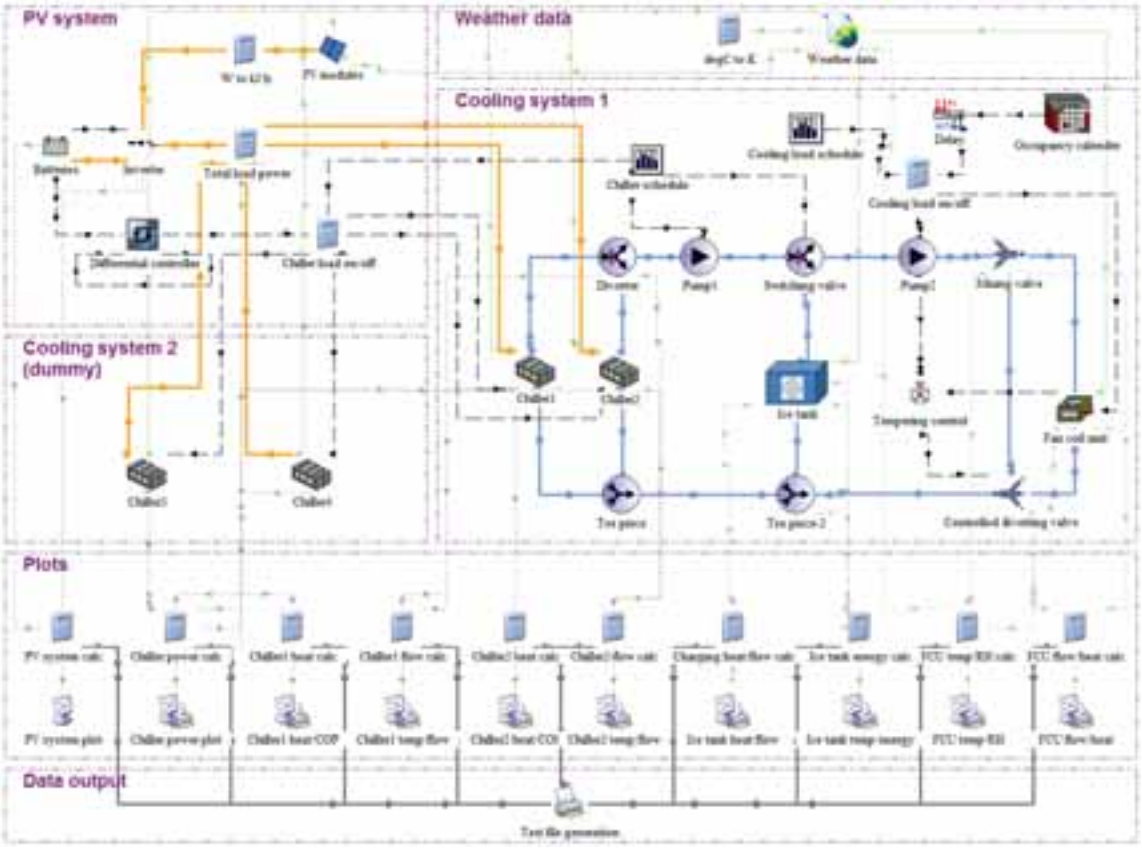

Fig. 5: TRNSYS simulation model of the PV-driven cooling system at the LooLa resort; Lines: power line – orange bold, weather data – green, output data – grey dotted, control lines – black dashed, pipes – blue bold.

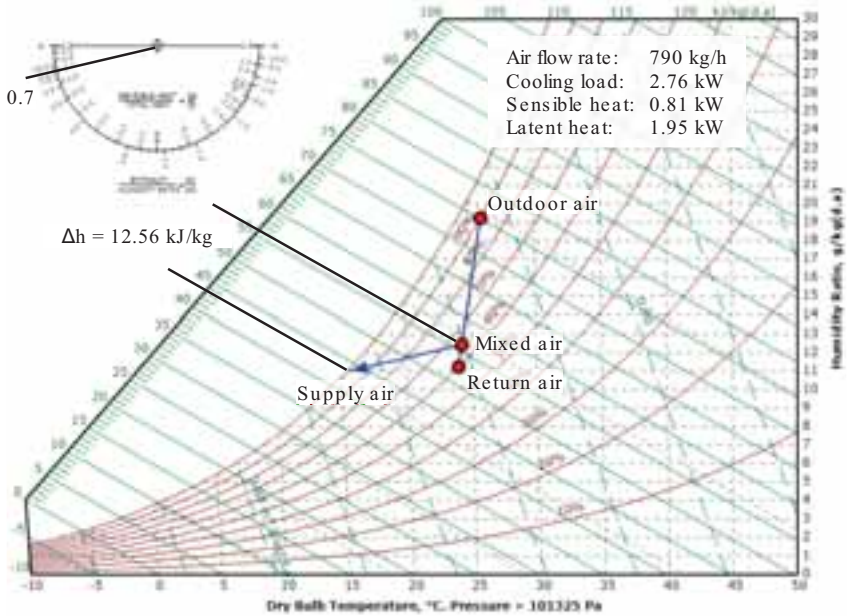

Fig. 6: Cooling load estimation via psychrometric chart; created with http://www.flycarpet.net/en/PsyOnline

5. Calibration results

The critical components, chiller and TES, were tested utilising data acquired by the monitoring system. Therefore, a simplified version of the simulation model was used, see Fig. 7. The chiller model is from the TESS library, Type655 and cuboid storage tank model Type843 was developed by Lerch and Heinz (2012). The TES model can operate as chilled water and ice tank.

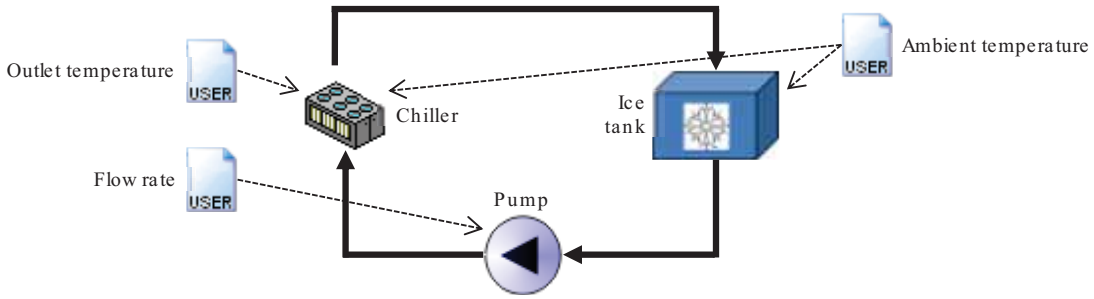

Fig. 7: Simplified TRNSYS simulation model for calibration of chiller and storage tank with measured data inputs

First, the operation as chilled water tank during charging is tested. Therefore, eight hours of measured data with the sample rate 1/min for chiller outlet temperature, ambient temperature and flow rate are used as inputs for the model. The model outputs to be compared with actual measured data are chiller power and tank outlet temperature. The result is plotted in graph 1a and 2a in Fig. 8. The non-fitting chiller power graph is caused by the performance data files of Type 655 that assume the chiller to be capable of operating in part load, which is not the case in the actual system. After adjustment of the performance data files, the Root Mean Square Error (RMSE) is merely 30 W as shown in graph 1b (Fig. 8). The tank outlet temperature decreases faster in the simulation than in the real setup, when the tank inlet temperature is prescript by measured data. This means that the actual heat transfer is lower than the simulated heat transfer. As the heat depends on flow rate, temperature difference and specific heat, where the temperature difference and the flow rate are measured, the specific heat serves as a parameter to match the model performance with the actual performance; the value is adjusted from 3.54 kJ/kgK to 1.7 kJ/kgK. The result is plotted in graph 2b of Fig. 8 and the RMSE has decreased to 0.18 °C.

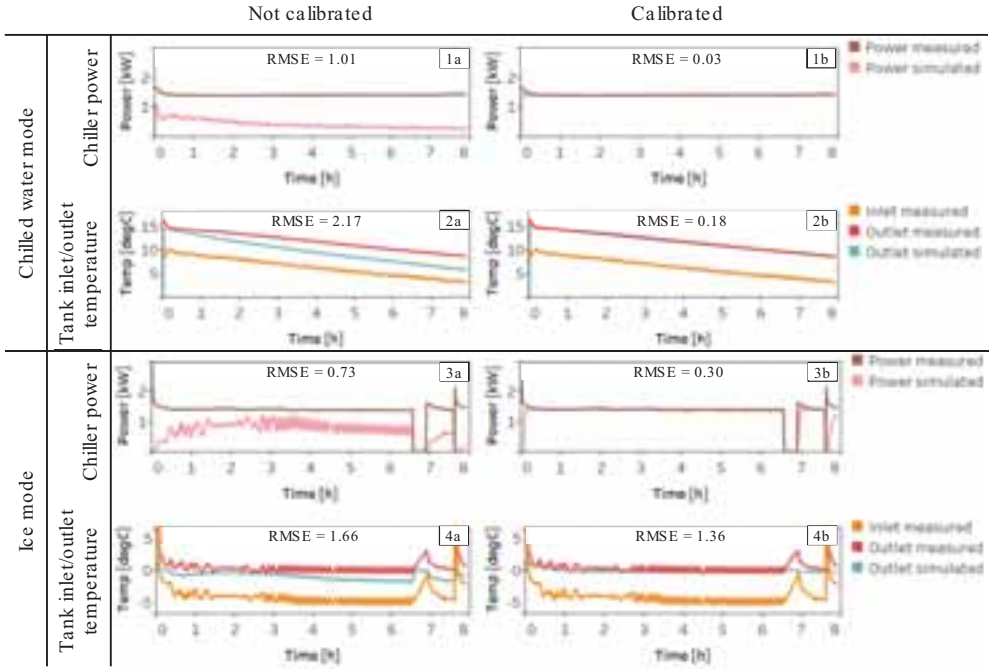

Fig. 8: Calibration of the chiller and storage tank models in chilled water mode (top) and ice mode (bottom) with measured data

The calibrated model represents the actual system accurately as shown by the RMSE values. However, the TES from Lerch and Heinz (2012) can also simulate the phase change from water to ice and, hence, operate as latent heat storage. Therefore, the input data from a day where the TES operates as ice tank during charging is chosen to test the simulation model for this condition. The simulation was run without calibration (graphs 3a and 4a in Fig. 8) and with the calibration measures described above (3b and 4b in Fig. 8). The chiller power RMSE is ten times higher compared to the chilled water operation, however a precise fit can be observed between 0.5 h and 6.5 h. in graph 3b (Fig. 8). The increased error is caused by two operation interruptions after 6.5 h and the starting current that is not modeled. The increase of the RMSE for the outlet temperature can be explained by the chiller operation interruptions as well. An additional factor is the oscillating temperature sensor reading that might have been caused by parasitic frequencies along the sensor wires. Overall, the TRNSYS simulation models the real system sufficiently accurate to produce

initial annual simulation results.

6. Initial simulation results

The TRNSYS simulation was performed for an entire year (8760 h) with a time step of 0.5 h. The initial results discussed in this chapter focus on the utilisation of the energy battery storage (Fig. 9) and the TES (Fig. 10).

The battery is charged to store surplus solar energy and discharged to supply energy for the chillers in case of insufficient solar energy availability. The usable storage capacity is 23.5 kWh considering 50% DoD. The four chillers consume 5.67 kW, which means the battery will ensure continuation of chiller operation for 4.15 h when it is fully charged. On a rainy or overcast day, chiller operation disruptions can occur due to the battery being fully discharged. This situation can be seen in the bottom chart of Fig. 9 when the graph approaches 0 kWh stored energy. Furthermore, the chart shows a high cycling frequency, which means that the battery serves as buffer storage. The bar chart in the top of Fig. 9 supports the finding, as the daily charged and discharged energy even exceeds the usable storage capacity of the battery (23.5 kWh) on many days. On those days, more than one cycle is performed.

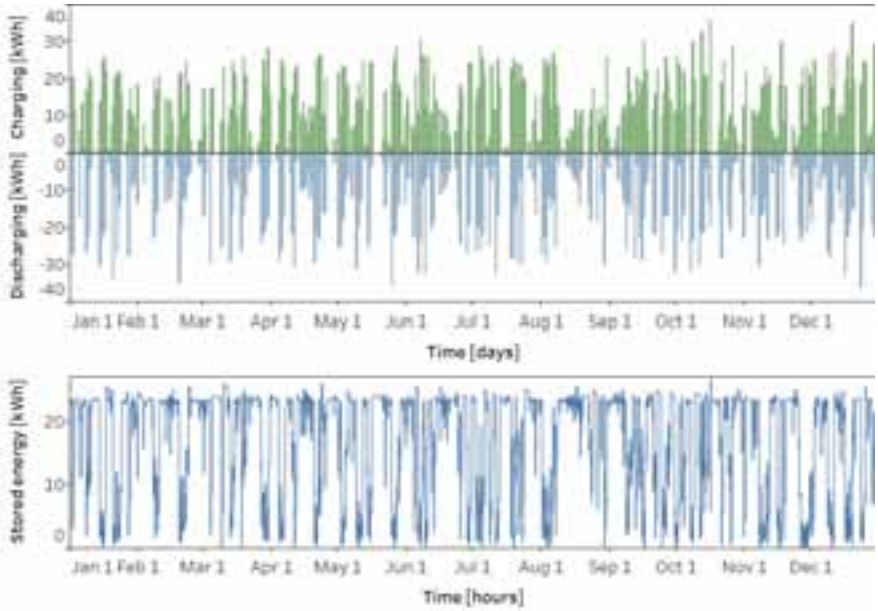

Fig. 9: Battery storage utilization; daily charged and discharged energy (top); stored energy again hours (bottom)

While the utilization of the battery storage occurs during chiller operation hours at daytime, the TES is only charged during that time. The discharging happens at nighttime. Unlike the battery, charging and discharging of the TES cannot occur simultaneously. Thus, the bottom graph of Fig. 10 (stored energy in the TES against time) shows a different pattern than the bottom graph of Fig. 9 (stored energy in the battery against time). The TES is charged nearly every day, but the discharging depends on the occupancy calendar; no occupancy means no discharging (see top chart in Fig. 10). The amount of charged energy (top chart in Fig. 10) decreases with increasing amount of energy stored, because the ice generated in the tank has lower heat conductivity than water, hence, insulating properties. Furthermore, the daily amount of charged energy also depends on the chiller operation hours during that day. In Fig. 10, 0 kWh stored energy is defined as 0% ice in the tank. Below that, it operates as chilled water tank. During high occupancy in December, the tank operates frequently as chilled water tank and might not meet the space cooling requirements.

The TES is cycled less frequently compared to the battery storage. It can store up to 93 kWh of latent heat, approximately four times the storage capacity of the battery. Thus, the TES serves as short-term energy storage that can shift the energy generated during daytime to serve the cooling needs during nighttime. Moreover, it can supply sufficient cooling over a few rainy or cloudy days.

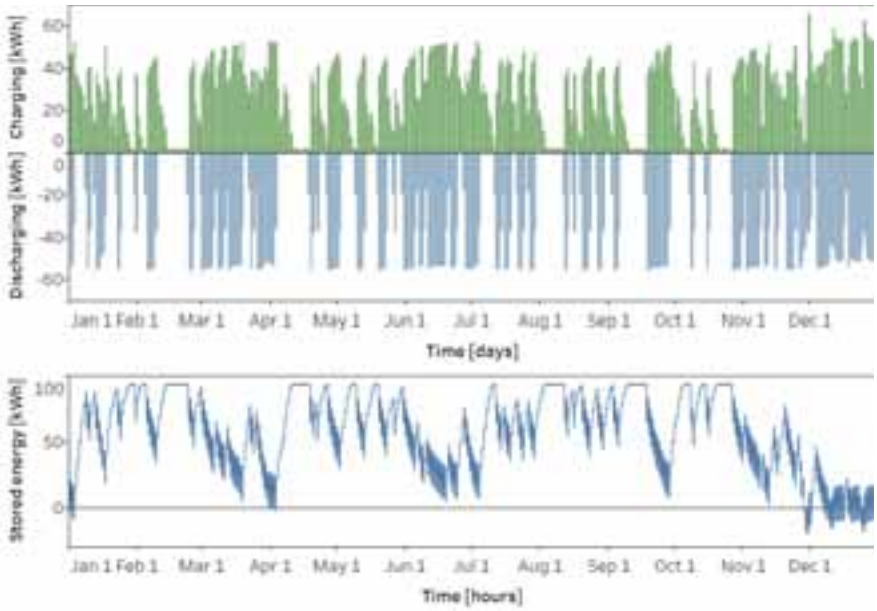

Fig. 10: TES utilization; daily charged and discharged energy (top); stored energy again hours (bottom)

7. Conclusion and outlook

The case study system is monitored in real-time and the data is used to calibrated components of a simulation model. Initial results emphasise the role of the battery and TES in the operation of this PV-driven cooling system. However, the simulation reflects not exactly the on-site situation, because of the following simplifications:

- The load of the PV system consists only of the chiller power consumption. In reality other parts of the resort (e.g. kitchen, shop and office) are also powered by the PV system during daytime, hence frequency of the power outages is likely to be higher.
- The power consumption of the auxiliary equipment of the cooling system, e.g. pumps, valves and control, were neglected. They are powered by the PV system during daytime and by the diesel generator during nighttime.
- The TRNSYS chiller model Type 655 requires a set temperature input, but the real chillers do not have a set temperature; only the evaporation temperature can be adjusted through the expansion valve.
- The cooling load was estimated via space volume and psychrometric chart and not derived from measured data. Furthermore, a binary value was used for the occupancy due to limited booking data.
- On the thermal load side, the water tank and 4 FCUs were replaced by a single FCU and a tempering valve.
- The charging process of the TES was only calibrated by a data set of 8 h and the discharging process was not calibrated.
- Pipe losses were not considered in this simulation.

Further work on enhance the simulation model will be done. Subsequently, three main topics will be addressed to complete the case study:

- A parametric study to size a battery storage, a chilled water tank and an ice storage tank for the prototype system.
- An economic analysis of the PV-driven cooling system at the LooLa resort.
- A comprehensive comparative study of the PV-driven cooling system with the three different energy storage solutions compared to a baseline system powered by a diesel generator in terms of energy and economic performance.

Eventually, the modelling and analysis shall be generalised towards a workflow that can be applied to various cooling applications.

8. Acknowledgements

The study is part of a research project funded by the LooLa Adventure Resort. The authors gratefully acknowledge the cooperation with the local LooLa staff in Bintan and the CEO, Dr. Marc van Loo. Moreover, we want to thank Shantanu Vachhani, a SERIS intern, for investigating various TES models and selecting the ice tank model for this paper. We are glad to be able to fall back on his work, when selecting the ice tank model for this paper. Last but not least, we are more than grateful for the selflessness of Dr. Andreas Heinz who provided the utilised ice tank model (Type 843) for this study.

9. References

Arteconi, A., Ciarrocchi, E., Pan, Q., Carducci, F., Comodi, G., Polonara, F., Wang, R., 2017. Thermal energy storage coupled with PV panels for demand side management of industrial building cooling loads. Applied Energy 185, 1984–1993.

Chan, A.L.S., Chow, T.-T., Fong, S.K.F., Lin, J.Z., 2006. Performance evaluation of district cooling plant with ice storage, Energy 31, 2750–2762.

Eicker, U., Colmenar-Santos, A., Teran, L., Cotrado, M., 2014. Economic evaluation of solar thermal and photovoltaic cooling systems through simulation in different climate conditions: An analysis in three different cities in Europe. Energy and Buildings 70, 207-223.

Eltawil, M.A., Samuel, D.V.K., 2007. Vapour Compression Cooling System Powered By Solar PV Array for Potato Storage. Agricultural Engineering International: the CIGR Ejournal. Manuscript EE 06003. Vol. IX.

Foster, R., Jensen, B., Dugdill, B., Hadley, W., Knight, B., Faraj, A., Mwove, J.K., 2017. Direct Drive Photovoltaic Milk Chilling Experience in Kenya. IEEE Photovoltaic Specialists Conference 44.

Ewert, M.K., Bergeron, D.J., Foster, R.E., LaFleur, 2002. Photovoltiac direct-drive, battery-free solar refrigerator field test results. Solar 2002 - American Solar Energy Society.

Lerch, W., Heinz, A., 2012. Solare Wärmepumpen – Kombianlagen inkl. Abwasser Wärmerückgewinnung: Energetische Bewertung durch dynamische Anlagensimulationen in TRNSYS, Solar 2012, Gleisdorf (Austria).

Merei, G., Berger, C., Sauer, D.U., 2013. Optimization of an off-grid hybrid PV–Wind–Diesel system with different battery technologies using genetic algorithm. Solar Energy 97, 460–473.

Noro, M., Lazzarin, R.M., 2014. Solar cooling between thermal and photovoltaic: An energy and comparative study in the Mediterranean conditions. Energy 73, 453-464.

Otanicar, T., Taylor, R.A., Phelan, P.E., 2012. Prospects for solar cooling – An economic and environmental assessment. Solar Energy 86, 1287-1299.

Sehar, F., Rahman, S., Pipattanasomporn, M., 2012. Impacts of ice storage on electrical energy consumptions in office buildings, Energy and Buildings 51, 255–262.

Souayfane F., Fardoun, F., Biwole, P., 2016. Phase change materials (PCM) for cooling applications in buildings: A review. Energy and Buildings 129, 396–431.

Wang, R.Z., Ge, T.S., 2016. Advances in Solar Heating and Cooling, Elsevier, United Kingdom.

Sensitivity analysis on the technical and economic performance of thermal and PV driven solar heating and cooling systems

Daniel Neyer[1,2] and Rebekka Köll[3]

[1] daniel neyer brainworks, 6700 Bludenz (Austria)

[2] University of Innsbruck, 6020 Innsbruck (Austria)

[3] AEE INTEC, Feldgasse 19, 8200 Gleisdorf (Austria)

Abstract

Solar heating and cooling is proposed to be an environmental sound alternative to conventional systems. Both, solar electrical and thermal driven systems can be a suitable solution and are currently under a controversial discussion. Therefore, the comparison of technical and economic performance of Solar Heating and Cooling (SHC) systems becomes a major issue. The assessment in a common comparable format is complicated by the numerous, alternative energy sources and design possibilities. A generalized technical and economic assessment methodology was developed and tested in the course of IEA SHC Task 53.

Ten case studies and best practice plants were analyzed and compared. All systems can achieve non-renewable primary energy savings greater than 40%, and some can show up a cost ratio lower than 1. Trend wise the PV and ST system are compared for southern and northern locations. Although the differences are rather small solar thermal seems to have advantages against PV driven systems. But in certain cases the situation is reversed and PV is advantageous.

A comprehensive sensitivity analysis on boundary conditions is showing the technical and economic performance in the same range for solar thermal and PV. Finally the analysis points out that both technologies - solar thermal and PV driven systems - can become an economic solution.

Keywords: Solar heating and cooling, assessment, benchmarking, solar thermal, photovoltaic

1. Introduction

The growing comfort demand and the increasing number of highly glassed buildings will provoke a further increase of the energy demand for cooling in future. Therefore the usage of an environmentally friendly cooling technology is inevitable. Solar cooling is an interesting alternative to conventional cooling systems when considering a significant reduction of non-renewable energy consumption. An increase on realized solar cooling systems could be observed in the past.

Solar cooling systems have a high diversity of different system designs including different cooling technologies as well as different combinations with renewable or non- renewable backups and storage tanks. In addition the systems are often designed to cover space heating or domestic hot water demand as well.

The IEA SHC Task 53 “New generation solar cooling and heating systems” is dealing with the cost effectiveness and performance of the latest solar cooling and heating systems to make them competitive on the market. (Mugnier, 2016).

One focus is on the analysis and benchmark of solar heating and cooling systems (SHC) against a reference system but also against other renewable technologies. Therefore an overview of realized as well as simulated systems in field tests or laboratory tests has been collected. The most important design issues are described and summarized. Some representative systems are selected for the detailed technical and economic analysis with a tool developed in the Task.

The T53E[4]-Tool is an enhanced Version of earlier developments in IEA SHC Task 48 and enables the

doi:10.18086/swc.2017.28.15 Available at http://proceedings.ises.org

comparison of different system designs. It considers several renewable and non-renewable energy sources as primary heat source or backups, as well as different types of heating and cooling technologies in combination with hot or cold storages. A more detailed analysis is separating the results by their applications (e.g. space heating, domestic hot water or cooling). This ensures that the analysis distinguishes further optimization potentials but the analysis also highlights good performing subsystems. An overview of considered energy flows and division of the subsystems is shown in Fig. 1.

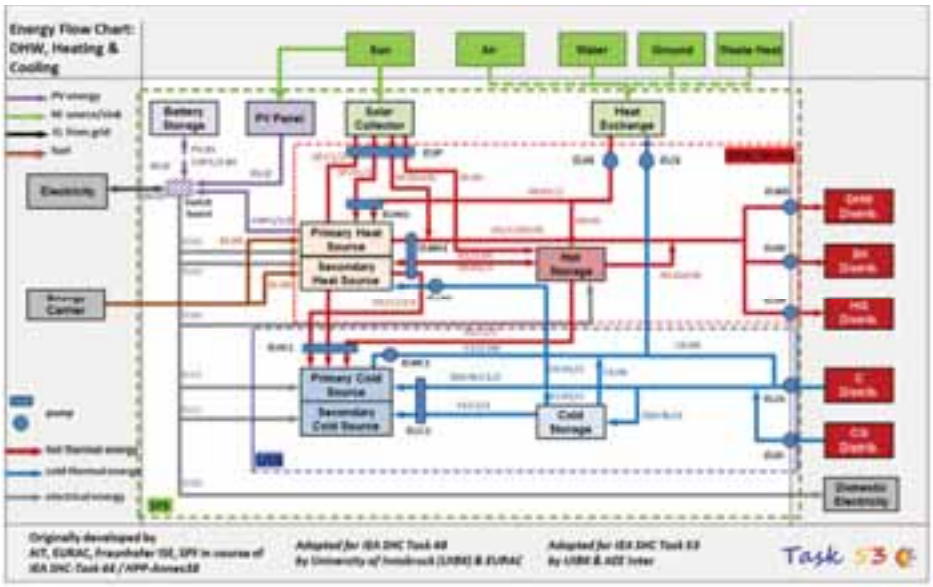

Fig. 1. Energy-flow-chart of all system components that can be taken into account for the assessment by consideration of the different subsystems in T53E[4]-Tool (Neyer et al. 2016)

The main focus of the analysis is on the comparison of solar-thermal and PV driven SHC systems. In the last years more and more conventional compression chiller/heat pumps are combined with a PV system, which is less complex and difficult to control than a solar-driven system. The assessment of the plants should lead to the conclusion which system is more cost effective and can lead to higher reduction of non-renewable energy sources. A number of simulated and demonstrated systems were selected and analyzed with the T53E[4]-Tool. In total 18 SHC systems are considered; their apportionment between technologies and data source is shown in Fig. 2.

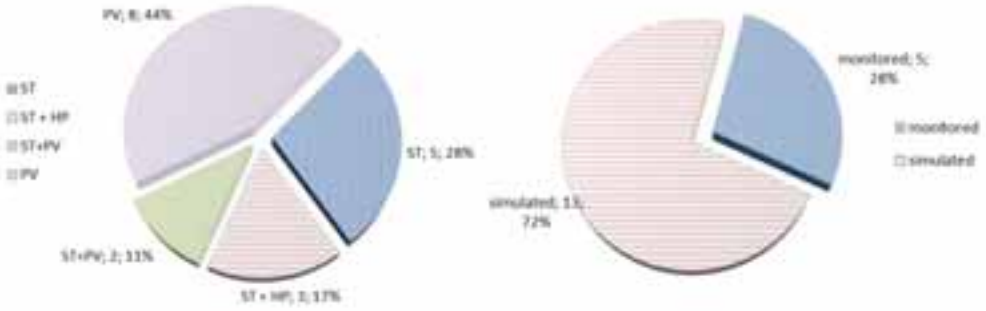

Fig.2: Overview of chosen SHC systems for the assessment summarized by the used technology (left) and the source of annual data for the assessment (right).

Eight of the selected systems are solar thermal driven systems, whereas 5 have thermal backups and 3 an electrical (HP). Eight systems are PV-driven and the remaining 2 include both, PV and solar thermal collectors. Most of the data analyzed is a result of simulation which offers the advantage to compare the same load-profile with different technologies. Five plants are in operation and the monitored data were analyzed.

Tab. 1: Nomenclature and Subscripts

ACM	Absorption chiller	in	input	Qout,cold	Useful cold
AHP	Absorption heat pump	MON	Monitored	Qout,heat	Useful heat output
AWHP	Air water heat pump	NRE	Non-renewable energy	QPV,in	Electricity from PV system
C	Cooling	out	Output	QSolar,in	Heat from solar collector
Can.i	Annualized costs of i categories	PER	Primary Energy Ratio (-)	QWD.sys	Domestic hot water demand
Can.tot	Total annualized costs	$PER_{NRE,ref}$	Non-renewable primary energy ratio of reference system	ref	reference system
CR	Cost ratio (-)	PER_{NRE}.sys	Primary energy ratio of solar system	SEER	Seasonal Energy Efficiency Ratio (-)
Ctot,ref	Total levelized costs of reference system	Q	Energy	SF	Solar Fraction
Ctot.SHC	Total levelized costs of solar heating and cooling system	QBackup	Energy from backup source	SH	Space heating
DE	Domestic electricity	QCD.sys	Cold water demand	SHC	Solar Heating and Cooling
DHW	Domestic hot water	QDC.sys	District cooling demand	SIM	Simulated
ε	Primary Energy Factor (kWh/kWh_{PE})	QDH.sys	District heating demand	SPF	Seasonal Performance Factor (-)
EC	Energy Carrier (=fuel)	Qel,ref	Electrical demand of reference system	SPFc,ref	Seasonal performance factor of cooling for reference system
el	Electrical	Qel.sys	Electricity demand	sys	Overall system (C & DHW & SH)
equ	equivalent	Qgrid	Electricity from grid	VCC	Vapour compression chiller
fsav.NRE	Non-renewable primary energy savings	QHD.sys	Heat demand	ηHB,ref	Efficiency of reference boiler
HP	Heat Pump	Qloss,ref	Heat losses of reference system		

2. Methodology

2.1 Assessment – T53E^4-Tool

The T53E^4-Tool enables a technical and an economical comparison of renewable and non- renewable systems for heating and cooling. The analysis is based on monthly energy balances of heat and electricity. For an entire assessment the values have to include annual measured or simulated energy quantities. The defined KPI's are compared to a reference system defined in Neyer et al (2016). The reference system uses a natural gas boiler for heating and an air cooled vapor compression chiller (VCC) for cooling. The efficiency of the reference system is depending on the size (technology), energy delivered (full load) and other parameters. The reference system is used to compare the technical and economic performance of the entire SHC system and to calculate the primary energy savings and cost competitiveness.

Technical Assessment

The key performance indicators (KPI) that are calculated are the non-renewable Primary Energy Ratio (PER_{NRE}), the non-renewable primary energy savings ($f_{sav,NRE}$) and the electrical equivalent Seasonal Performance Factor (SPF_{equ}). They are considered as appropriate indicators for the comparison of the high diversity of SHC systems analyzed with the T53E^4-Tool. The KPI's are calculated by the tool for the overall system, as well as the subsystems.

- Non-Renewable Primary Energy Ratio

The non-renewable primary energy ratio (PER_{NRE}) is calculated over a longer period of time (annual or monthly). It is defined as the ratio of useful energy, supplied to satisfy the needs of the application (DHW, SH, Cooling), to non-renewable primary energy input from any energy source (electric or thermal) used within the defined system boundaries.

$$PER_{NRE} = \frac{\sum Q_{out}}{\sum\left(\frac{Q_{el,in}}{\varepsilon_{el}} + \frac{Q_{in}}{\varepsilon_{in}}\right)} \quad \text{(eq. 1)}$$

The higher the PER_{NRE} (in a magnitude of 1 to 2.5) the less non-renewable energy is used by the SHC system to cover the heat and cold demand.

The reference System $PER_{NRE,\ ref}$ is also calculated for the equal heat and cooling demand. The reference system

calculation follows Napolitano (2011) and has a natural gas boiler for covering the heat demand and an air-cooled VCC system for cooling. It includes a small hot water storage for domestic hot water (DHW) purposes and a cold storage volume for a smooth operation of the air cooled VCC. The T53E^4-Tool also provides the possibility to define a specific reference case for individual assessment, but here the defined standard reference system is used.

$$PER_{NRE.ref} = \frac{\sum Q_{out}}{\sum\left(\frac{Q_{out.heat}+Q_{loss.ref}}{\varepsilon_{in}*\eta_{HB.ref}}+\frac{Q_{out.cold}}{SPF_{C.ref}*\varepsilon_{el}}+\frac{Q_{el.ref}}{\varepsilon_{el}}\right)} \quad \text{(eq. 2)}$$

- Non-renewable primary energy savings ($f_{sav.NRE}$)

The $f_{sav.NRE}$ compares the $PER_{NRE.sys}$ of the entire SHC system to the $PER_{NRE.ref}$.

$$f_{sav.NRE} = \frac{PER_{NRE.sys} - PER_{NRE.ref}}{PER_{NRE.sys}} = 1 - \frac{PER_{NRE.ref}}{PER_{NRE.sys}} \quad \text{(eq.3)}$$

The result for $f_{sav.NRE}$ is always below 1 and shows the non-renewable primary energy savings of the SHC system compared to the reference system. A high value indicates also a high solar fraction and low energy input from fossil derived fuels. A negative value points out that the SHC system has a higher non-renewable primary energy consumption than the reference system and no savings could be achieved with the SHC system.

- Electrical equivalent Seasonal Performance Factor (SPFequ)

However, values for PER_{NRE} are not directly comparable with any widely available industry figures of merit such as the EER or SEER of a vapor compression chiller. Therefore the electrical equivalent Seasonal Performance Factor was introduced and enables a comparison with the SEER of VCC systems or the SPF of electric driven heat pump systems. All energy flows are converted into electrical equivalent units by dividing the PER_{NRE} with the primary energy factor of electricity (ε_{el})

$$SPF_{equ} = \frac{PER_{NRE}}{\varepsilon_{el}} = \frac{\sum Q_{out}}{\sum\left(Q_{el,in}+\frac{Q_{in}}{\varepsilon_{in}}*\varepsilon_{el}\right)} \quad \text{(eq.4)}$$

Economic assessment

The bases for the economic assessment are the total annual costs of the system. This is the sum of the annual costs for investment, replacement, residual value, maintenance, energy and water costs and is calculated by the T53E^4-Tool by inserting information of the type and size of system components. If the real costs are known the tool enables the possibility to enter the specific values. The annualized costs for the entire system are calculated by using the annuity method. The calculation for investment costs are considering economy of scale prices, which means that the capacity of the components is taken into account when calculating the specific costs. The maintenance, energy and water costs are based on the consumption and are defined under the consideration of VDI 2067. All the costs (investment, replacement, residual value, maintenance, energy and water costs) are expressed in annualized costs C_{an} and summed up to the total annualized costs $C_{an.tot}$ of the SHC system. The Levelized Costs of Energy is the ratio of annualized costs and the overall annual useful energy provided to the application.

$$LCOE = \frac{C_{an.tot}}{Q_{CD.sys}+Q_{DC.sys}+Q_{HD.sys}+Q_{WD.sys}+Q_{DH.sys}+Q_{el.DE}} \quad \text{(eq.6)}$$

Since the uncertainties in cost calculation are varying, the comparison of absolute costs of different SHC systems is resigned and the economic assessment concentrates on the cost ratio by comparing the total levelized energy costs of the SHC system $C_{an.tot-SHC}$ to the total levelized energy costs of the reference system $C_{an.tot-REF}$.

$$CR = \frac{LCOE_{SHC}}{LCOE_{REF}} = \frac{C_{an.tot-SHC}}{C_{an.tot-REF}} \quad \text{(eq.7)}$$

2.2 Examples

The 10 examples (with extra 8 variations) included in this work are described briefly and summarized in table 2.

- Example 1, SERM (Mugnier, 2015)

The SHC system of the SERM project is realized for a building with different purposes: offices, dwelling and shops in the urban zone "Jacques Coeur" in Montpellier, France. The system provides cooling mainly for the office and shops and domestic hot water for the dwellings. The centralized system consists of 240 m² flat plate collectors, 1.5 m³ buffer storage, a single stage adsorption chiller with a capacity of 35 kW and a hybrid cooling tower (adiabatic aero-cooling device) with a capacity of 85 kW. As backup for DHW purpose a natural gas boiler with a capacity of 70 kW is installed.

- Example 2, iNSPiRe (Fedrizzi et al., 2015)

The iNSPiRe project has created a simulation data-base of performance and costs of different HVAC systems at an extensive variation of boundary conditions in the field of refurbishment. Some crucial examples are selected for the analysis. A single-family house, as well as a multi-family house, with different solar thermal collector field areas or amount of PV modules or a combination of solar thermal collectors and PV at the locations Madrid and Stuttgart are analyzed. In all cases space heating (SH), cooling and domestic hot water production is provided with a centralized air to water heat pump which is connected to a 430 l tank for DHW and SH.

- Example 3, ZAE (Sipilä et al, 2017)

Within the finish-german joint research project "Solar Heating and Cooling for Central and Northern Europe" a small scale solar thermal cooling (10 kW) and heating (24 kW) plant was installed at the Savo-Solar headquarter in Mikkeli, Finland in 2016. It is designed to supply the office building of Savo-Solar. The system consists of the main components solar-thermal collectors, vacuum insulated storage tank, dry air cooler and reversible absorption chiller/heat-pump. The main heat source for driving the chiller is a solar thermal collector field with 36 m² aperture area. A wood chip fired district heating access serves as backup heat. In summertime, cooling is done by an advanced single-effect absorption process. At insufficient solar radiation, the driving heat is provided by the heat storage or the district heating network. In wintertime the system works as thermal driven heat pump, using the biofuel fired district heat to upgrade ambient heat to a useful temperature level.

- Example 4, UMH DHW (Aguilar et al., 2016)

In this example an air to water heat pump is used for the preparation of domestic hot water with a nominal heating capacity of 1.5 kW. The electricity consumption of the heat pump is covered by two PV modules with 470 Wp or electricity from the grid. The system also includes a buffer tank of 190 l and is located at the university in Elche, Spain. The DHW demand is 6.26 kWh/d distributed in 6 extractions.

- Example 5, UMH HVAC (Aguilar et al, 2017)

A PV-driven HVAC system is realized in an office with a heated/cooled area of 35 m² in Alicante, Spain. The inverter air-conditioner is used to cover the cooling and space heating demand of the office. The cooling capacity is 3.52 kW, whereas the heating capacity is 3.81 kW. It is connected to three PV panels with 705 Wp as well as to the grid to provide the necessary electricity consumed by the HVAC system. The indoor temperature was set to 23ºC in cooling mode and the relative humidity was not controlled.

- Example 6, Högskolan Dalarna (Psimopoulos et al. 2016)

The simulated house is a typical Swedish single floor, single family house with a heated area of 143 m² placed in Norrköping. A variable speed, exhaust air heat pump (HP) with a capacity of 5 kW delivers heat both for SH and DHW. A hot water storage tank of 180 litres is used for DHW. If the heat from the HP is not sufficient an electrical auxiliary heater with a power of 6.5 kW is turned on. The system also includes a 5.7 kWp PV System

and lithium-ion battery storage with a capacity of 7.2 kWh.

- Example 7, AEE INTEC (Fink, 2011)

The SHC system is applied for heating, domestic hot water and cooling of a small juice producer. The heat is produced by 100 m² of double-glazed flat plate collectors and as a backup-heater a wood chip boiler with a capacity of 100 kW is used. The heat is stored in a 20 m³ buffer storage and connected to a single-stage absorption chiller with a capacity of 19 kW and a dry cooling tower with a capacity of 50 kW. The chilled water is used for the juice refrigeration only. If no cooling is needed the heat is used for the juice production process, for DHW preparation or to cover the space heating demand of the residential house next to the juice production.

- Example 8, TheBat (Thür et al., 2016)

In the project "TheBat" a single family house located in Innsbruck is simulated with different control concepts with the goal to maximize the PV-self consumption by using a heat pump and the available heat capacities in the building as "thermal battery". The chosen example is covering the space heating and domestic hot water demand with a brine heat pump with a thermal capacity of 10 kW. The HP can charge a water storage (TES) or directly heat the building via thermal activated building structure (TABS). The heat pump is controlled by matching the compressor speed to the available power of the PV and store the produced heat preferably in the TABS or the TES. First, the electricity from the PV is used for running the HP, the remaining electricity is fed into the grid (no household electricity consumption is considered in the simulation studies).

- Example 9, SolarHybrid (Neyer et al 2016a)

In the project SolarHybrid a solar thermal and PV driven HVAC system for a hotel located in Innsbruck and Sevilla is simulated. The cooling of the hotel is provided by a vapour compression chiller (VCC) in combination with an ammonia/water-absorption chiller (ACM). A solar thermal (ST) driven system is compared with a PV supported system. The ST feeds a hot water storage tank, which is used to ensure the heat supply and operation of the ACM. A natural gas backup boiler is used for DHW and SH only. The ACM is used to cover the base load (19 kW) and the conventional VCC (70 kW) covers the remaining demand using grid electricity. Both refrigerators operate with dry back-cooling. The PV supports the heat pump, which operates reversible and feeds the hot water storage tank for domestic hot water and a cold water storage. A PV area, which is designed exclusively for the operation of the reversible HP complements the system.

- Example 10, Yazaki (Inagaki et al. 2017)

The passive house office is located in JINAN in P.R.China, a humid continental climate. The thermal energy for the solar collector fields of 110 m² is stored in a 5 m³ hot water tank. In summer case the heat is used to run the absorption chiller (WFC10) with 35 kW nominal capacity and the heat is rejected via a wet cooling tower. The chilled water is stored in a 1.5 m³ tank and complemented by a reversible air-water electrical heat pump. The energy is delivered into the rooms over a radiant ceiling and the ventilation unit. The ventilation unit includes a heat recovery system, a pre heating/cooling coil, a 20 kW air-air heat pump as backup and the re-heating coil.

A summary of the most important information of the plants is shown in Tab. 2. The solar fraction should give a hint weather the plants are designed for full load (100%) or base load (<30%) only. The solar fraction for thermal (SF_{th}) or PV-driven systems (SF_{el}) is calculated according to Eq. 8 and Eq. 9 respectively.

$$SF_{th} = \frac{Q_{solar,in}}{(Q_{solar,in} + Q_{backup})} \quad \text{(eq. 8)}$$

$$SF_{el} = \frac{Q_{PV,in}}{(Q_{PV,in} + Q_{grid})} \quad \text{(eq. 9)}$$

Tab. 2: examples analyzed with T53E4 Tool

Plant #	Status	Demand		Solar			Boiler		Chiller	
	Monitored (MON) Simulated (SIM)	Type: DHW / SH / C	Energy demand (MWh)	Technology: ST / PV	Size: ST (m²), PV (kW_p)	Solar fraction (%)	Type	Capacity (kW)	Type	Capacity (kW)
1	MON	DHW C	133 / 9	ST	240	74	natural gas	70	ACM	35
2	SIM	DHW SH C	11 / 28 / 21	PV	4.8	5	Reversible AWHP	34	Reversible AWHP	34
2a				ST	27.6	39				
2b			11 / 25 / 8	PV	4.8	25				
2c				ST	27.6	46				
2d			2 / 5 / 3	PV & ST	9.2 & 2.4	th:58 el: 54		8		8
2e			2 / 5 / 1			th:56 el: 40				
3	MON	SH / C	17.2 / 1.8	ST	36	32	reversible AHP	24	reversible AHP	15
4	MON	DHW	3 / 3.5	PV	0.47	35	AWHP	1.5	-	-
5	MON	SH/C	2.2	PV	0.705	42	split	3.81	split	3.52
6	SIM	SH/DHW	14.3 / 3	PV	5.7	27	air HP	5	-	-
7	MON	SH&DHW/ process heat/C	62 / 30 / 4.5	ST	100	25	wood chip boiler	100	ACM	19
8	SIM	DHW / SH	2 / 7	PV	2.5	49	HP	10	-	-
9	SIM	DHW / SH / C	562 / 545 / 82	ST	720	35	Natural gas	500	ACM VCC	19 70
9a				PV	84.5	27			VCC	80
9b			541 / 534 / 299	ST	720	66			ACM VCC	19 100
9c				PV	84.5	52			VCC	110
10	SIM	SH / C	9 / 32	ST	111	45	Reversible air HP	61	Reversible air HP	51

3. Results

A wide variety of SHC systems is included in the assessment. Systems with different heating and cooling technologies, with different capacities, with simulated and monitored data base as well as a mixture of cooling, space heating and domestic hot water application were selected. An overview of the selected systems on basis of the total capacity and the type of heat source technology is shown in Fig. 3:

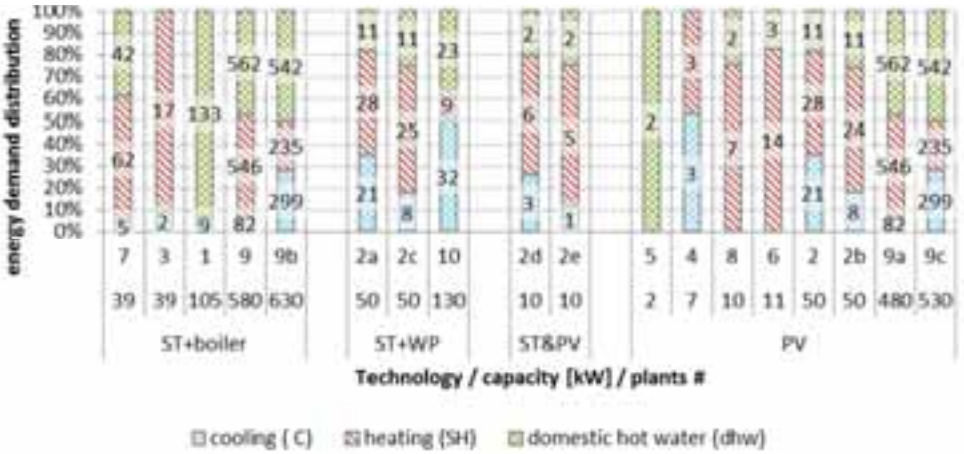

Fig.3: distribution of annual energy demand between cooling (C), heating (SH) and domestic hot water (dhw); numbers in the bars are in MWh; arranged according to the Technology used and total installed heating and cooling capacity (kW)

Seventeen systems include DHW demand, fifteen systems include cooling and sixteen systems include SH. In total eleven systems cover all three demands: SH, DHW and cooling. There is also a wide spread in the size of the systems. The total installed heating and cooling capacity of the systems is between 2 kW and 630 kW, but more than half of the systems are in the range between 10 kW and 130 kW. The graph also illustrates the total yearly energy demand in MWh. Whereas the smallest system covers a heat demand of 2 MWh/y the highest total energy demand which is covered by a system is 1190 MWh.

The base of the economics is presented in Figure 4 by showing the specific investment cost of the entire system and the related reference system. The ratio of investment ($Invest_{SHC}/Invest_{REF}$) is calculated and shown in connection with the achieved non-renewable primary energy savings ($f_{sav.NRE}$).

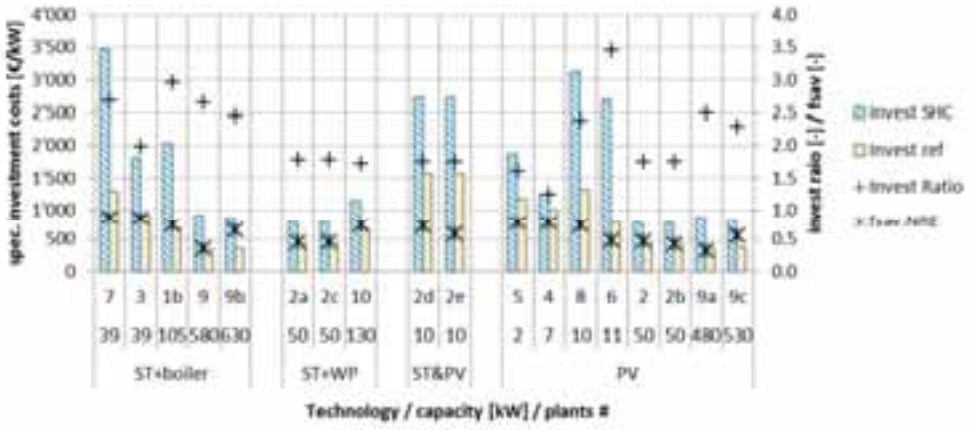

Fig.4: specific Investment costs for each SHC plant and corresponding reference system according to T53E4 Standard (left axis); Investment ratio (SHC/REF) and non-renewable primary energy savings (right axis); arranged according to the Technology used and total installed capacity (kW);

All costs are compiled with the Task 53 Standard values. Trend wise the smaller systems and those with higher savings show higher absolute investment costs and higher investment ratio. But both values are further influenced by the design (size of components, storages…) and the choice of components (HP vs. boiler, etc.). Comparing ST and PV systems produces an equal picture. Roughly half of the plants present investment costs higher 1'500 €/kW, the other half costs below 1'000 €/kW.

The investment is usually the main cost factor, but the total cost also include cost for replacement, electricity, energy carrier, water, maintenance and for grid connected PV systems the feed-in remuneration. The total annualized cost distribution of all systems is shown in Figure 5. The more energy a system is providing the higher the ratio of energy costs; the smaller the system the huger is the ratio of investments. The ratio of investment costs varies from roughly 30% up to almost 60%; if replacement costs are considered the ratio related to investment adds another 5-10%. Maintenance cost ratios are slightly higher for the solar thermal driven system compared to PV supported system. A high PV self-consumption can be observed in almost all system thus the feed-in remuneration does play a minor role.

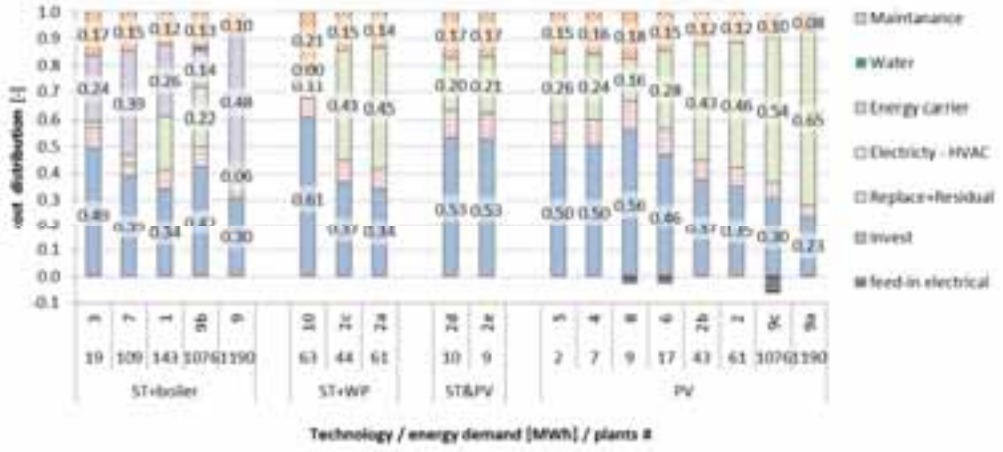

Fig.5: annualized cost distribution for each SHC plant; the fraction for investment, electricity, energy carrier and maintenance are stated in the bars; arranged according to the Technology used and total energy demand (MWh)

Figure 6 presents the summary of non-renewable savings in relation to the entire costs, expressed as CostRatio (CR). Each plant is represented as individual dot. The CR is displayed in reversed order thus the more cost effective and the higher the savings the more the results appear in the upper right side. Further 4 trend lines are drawn summarizing the results technology and location wise.

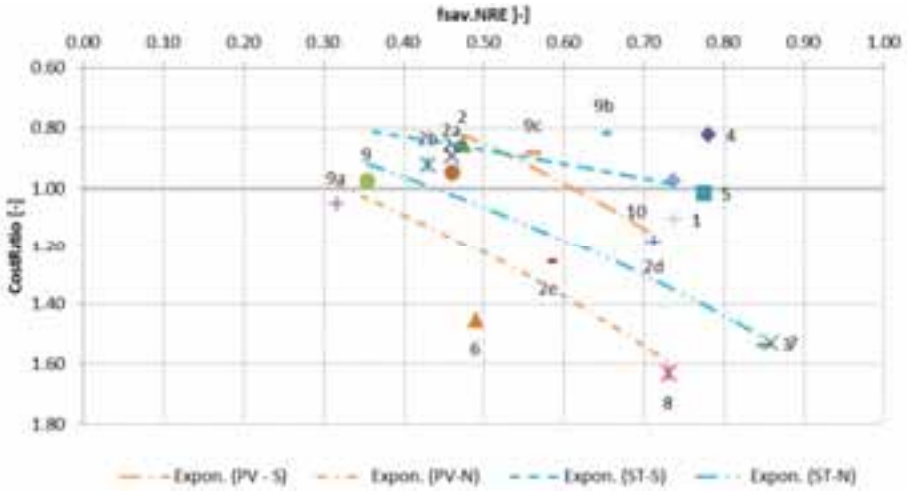

Fig.6: CostRatio (CR) in reverse order vs. non-renewable primary energy savings ($f_{sav.NRE}$); cluster in four groups (i) PV supported system in southern climate (PV-S), (ii) PV system in northern climates (PV-N), (iii) solar thermal supported system in south (ST-S), (iv) solar thermal system in north (ST-N)

The clustering for the trend lines of the results is arranged in the following order (i) PV-S: #2, #2d, 9c; (ii) PV-N: # 2b, #2e, #6, #8, #9a; (iii) ST-S: #1, #2a, #9b, #10; (iv) ST-N: #2c, #3, #7, #9. Only plant #4 and #5 cannot be clustered as they are a not comparable in size and technology used. The quantity of examples is not high enough to dare on the trend lines; nevertheless they can be used for general statements and to show the results of the sensitivity analysis.

Considering the cost ratio, it can be seen that the majority of systems can compete with a conventional system or are even more cost efficient. The most effective plants are PV driven #4, #5 and ST driven #9b, #10 and #1. They represent a good relationship of cost and savings. All these plants have a year around solar usage and either a low investment ratio (small plants) or a low share of investment costs of total annualized costs. ST systems in north and south represent more even gradient than the PV driven systems. The southern locations represent more efficient (higher savings) and more economic (higher solar yield) systems. In southern location the trend lines cross each other, in the northern location the trend line of ST reclines higher. This indicates that solar thermal at the same saving is cheaper than PV or at the same CostRatio the solar thermal can reach higher saving. This might be true as a general finding but individual example (especially #2) show reversed conclusions. Thus the trend line and their interpretation should be used with care!

The question arises whether the chosen boundary conditions are affecting the results or if the design and location is more important. Thus a sensitivity analysis was performed and the effect is shown by means of the shift of the trend lines. The parameters that are varied are the total investment costs (40%~130%), the electricity price (50%~350%), the natural gas price (50%~200%), the conversion factor for electricity (80%~140%) and the electrical efficiency of the systems (90%~200%). As not all results can be presented in this paper two (investment costs in Fig. 7 and electrical efficiency in Fig.8) are selected and discussed here, all other will be published in the course of IEA SHC Task 53.

The result of the sensitivity analysis on investment costs is shown in figure 7 in two diagrams separated according to the location. The results for ±15% of the initial costs are presented in figure 7 in red (+15%) and in blue (-15%). It is obvious that if the costs are dominated by investments the CostRatio will response more intense than if the investment costs ratio is smaller. The analysis will only affect the CostRatio, the non-renewable primary energy savings keep unaffected.

In the northern locations (Fig 7. left) the +15% in solar thermal and -15% in PV systems are overlapping strongly and the results get equal. The same behavior occurs in the southern locations. If the investment costs are changed in the same direction (e.g. -15%) in norther location the difference gets smaller (PV is more investment driven), in the southern locations the difference gets larger (ST is more investment dominant). The effect of minus 15% can take shape in a magnitude of -5 to 20 %points in the CostRatio

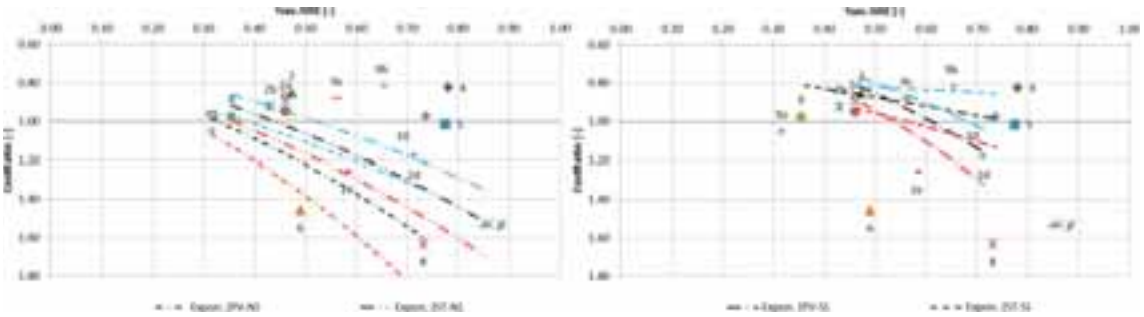

Fig.7: sensitivity analysis on investment costs; +15% investment in red; -15% investment in blue; for northern located system (left) and south located system (right)

The sensitivity analysis on the electrical efficiency of the systems is shown in figure 8. The electrical efficiency is changed by changing the total grid electricity drawn by the entire system. The effect is shown for +25% (red) and for +40% (blue). It is obvious that if the system is electricity driven and the larger the electricity costs ratio is, the more sensitive a system will be. The sensitivity analysis will affect the cost ratio (lower electricity cost) as well as the non-renewable primary energy savings.

For both locations the gap between PV driven and solar driven system gets smaller. Even with (probably unrealistic) 40% efficiency increase the solar thermal systems keep upfront the PV systems. In general the lower efficient systems (lower $f_{sav.NRE}$) benefit more than the already high efficient systems. Thus curves shift to the right and the gradients get steeper. If the efficiency could be increased by 25% the savings increase by a factor of 10 to 15%points, the CostRatio keeps almost unaffected (up -5%points).

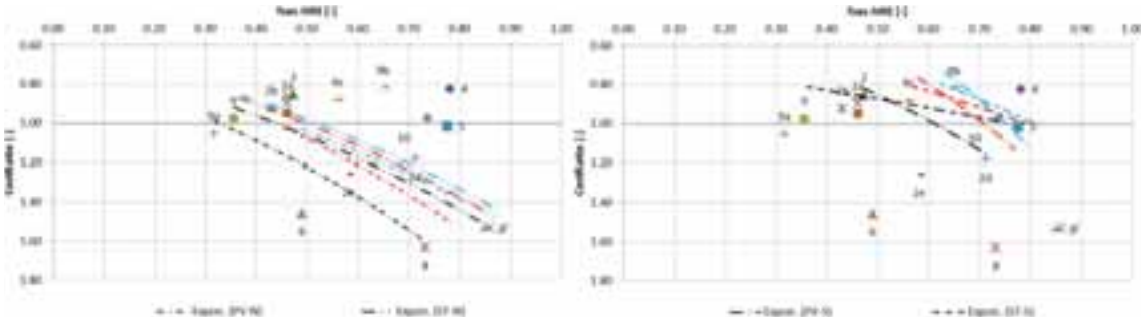

Fig.8: sensitivity analysis on electrical efficiency changes (+25 % red lines; +40% blue lines) for northern located system (left) and south located system (right)

The other sensitivity analyses are showing a similar picture. Decreasing costs lead to lower CostRatio's increasing the efficiency increases the non-renewable primary energy savings and reduces the CostRatio. The natural gas costs effects all system as the reference system is a natural gas boiler. Within a reasonable change of boundary conditions (±20~30%) the magnitude of change in key figures can be expected in the range presented within the two analyses.

Overall it falls into place that with a clever design and a decrease of investment costs the solar technologies are already less expensive than a conventional system for heating and cooling applications or can reach cost equity with minor effort.

4. Summary & outlook

A comprehensive tool was developed in the course of IEA SHC Task 53 and is available for the analysis and assessment of new generation of solar heating and cooling systems. The key figures that are calculated allow a benchmarking and simplify the comparison of different system configurations. The T53E^4-Tool can be used to benchmark against a standardized reference systems or against other renewable heating and cooling technologies. Still, the comparability is challenging if applications and configurations are mixed. Nevertheless, a trend wise comparison of magnitudes can definitely be achieved. The T53E^4-Tool is expected to be published in 2018.

The methodology presented is based on monthly energy balances and focusing on non-renewable primary energy. Thus the results are depending on the non-renewable primary energy conversion factors which depend on the season (summer / winter), daytime (peaks), on political decision (balancing methods) and the repercussion of the entire system on factors itself. Future developments of costs but also primary energy conversion factors are difficult to forecast. Thus a sensitivity analysis on the influencing boundary conditions should be performed anyway.

A majority of the systems can be classified as small or medium scale systems. The economics are investment dominated and the electrical or thermal efficiency is of minor order. Nevertheless a high efficiency is essential for acceptable non-renewable primary energy savings, being aware that the efficiency or technology of the reference system will change in future.

The southern locations represent more effective (higher non-renewable primary energy savings) and more economic systems mainly due to higher solar yields. Southern examples can already reach CostRatio's below one. Accordingly the systems are cost competitive compared to the standard reference system calculated within the T53E^4-Tool.

Summarizing the comparison of ST and PV driven system expresses a clear conclusion that ST is more effective at lower costs. Nevertheless the difference is probably within the uncertainties and when changing the boundary conditions accordingly the results are overlapping. In the end the advantage of the one or other technology is depending on local conditions, the design of the plant and its control strategies. Both Technologies can be optimized intensively to become cost competitive and an attractive alternative compared to conventional heating and cooling systems.

5. Acknowledgment

The Austrian part of the IEA SHC Task 53 is carried out within the framework of the IEA research co-operation on behalf of the Austrian Ministry of Transport, Innovation and Technology.

A special thanks to all Task 53 participants that provided examples with monthly and annual energy data and their agreement for the usage of the data for assessment, benchmarking and publication. In particular to:

- TECSOL – Daniel Mugnier
- EURAC – Chiara Dipasquale and Roberto Fedrizzi
- ZAE Bayern – Richard Schex and Martin Helm
- Universidad Miguel Hernandez – Pedro G. Vicente Quiles
- University Högskolan Dalarna – Emmanouil Psimopoulos and Chris Bales
- University of Innsbruck – Alexander Thür
- YAZAKI Energy Systems – Wei Zheng

6. References

Aguilar et al., 2016: Aguilar F.J., Aledo S., Quiles P.V.; Experimental study of the solar photovoltaic contribution for the domestic hot water production with heat pumps in dwellings, Applied Thermal Engineering Vol.101, pp. 379-389, 2016

Aguilar et al., 2017: Aguilar F.J., Aledo S., Quiles P.V.; Experimental analysis of an air conditioner powered by photovoltaic energy and supported by the grid, Applied Thermal Engineering Vol.123, pp. 486-497, 2017

Fedrizzi R. et al. 2015, D6.3a - Performance of the Studied Systemic Renovation Packages – Methods, iNSPiRe, 2015

Fink et al, 2011: Fink C., Knabel S., Wagner W., Stelzer R., Windholz B., Helminger F.: Endbericht zum Projekt Wissenschaftliche Begleitforschung zum Förderprogramm „Solarthermie – Solare Großanlagen 2011“, 2011

Inagaki Motomi, Kazuhide Ishida, Yohsuke Yamada, Xin Shi, Wei Zheng, Neyer, Daniel (2017). Yazaki Future Energy System, Joined research project of Yazaki Corporation (Japan) and University of Innsbruck (Austria)

Psimopoulos, E., Bales, C., Leppin, L., Luthander, R. (2016) Control Algorithms for PV and Heat Pump System Utilizing Thermal and Electrical Storage, 11th ISES EuroSun 2016.

Mugnier, D., 2015. DHW/cooling hybrid strategy for solar cooling: two successful year monitoring results, 6th International Conference Solar Air Conditioning. Roma, Italy, September 25th-27th, 2015.

Mugnier D., 2016: SHC Task 53 New generation solar cooling & heating systems – Task description and work plan, France, 2016

Neyer D., Neyer J., Stadler K., Thür A., 2016. Deliverable C3-1: TASK 53 - Energy-Economy-Ecology-Evaluation Tool T53E4-Tool, Tool Description and introductory Manual, Solar Heating and Cooling Programme, Task 53, 2016

Neyer, Daniel; Gritzer, Florian; Thür, Alexander; Luger, Stefan; Furtner, Jürgen; Kefer, Patrik; Focke, Hilbert (2016a): Towards a Solar Hybrid Solution for Heating and Cooling. 11th ISES EuroSun 2016.

Sipilä et al, 2017: Sipilä K., Reda F., Pasonen R., Löf A., Viot M., Pischow K., Helm M., Möckl M., Menhart F., Kausche M., Osgyan P., Streib G.: Solar heating and cooling in northern and central Europe, Finland, 2017

Thür, Alexander; Calabrese, Toni; Streicher, Wolfgang (2016): Smart Grid and PV driven Heat Pump as Thermal Battery in Small Buildings for optimized Electricity Consumption. 11th ISES EuroSun 2016.

Solar-electric driven Heating and Cooling System with PCM-Storage for improved Grid Connection

Richard Schex[1], Andreas Krönauer[1], Michael Remy[1], Johannes Linn[1], Timo Korth[2], Felix Loistl[2], Christian Schweigler[2]

[1] Bavarian Center for Applied Energy Research (ZAE Bayern), Garching (Germany)

[2] Munich University of Applied Sciences, Munich (Germany)

Abstract

This study presents the coupling of a solar-electric driven air conditioning system (VRF, 3-pipe) with thermal storages based on Phase Change Material (PCM). The main objectives are the reduction of PV-related peak feed-in, to give a possibility for applying Demand Side Management and increasing self-consumption of such grid-connected PV-HVAC systems. To accomplish these goals the PCM-storage will be implemented directly in the refrigeration cycle of the system. Using PCM whose melting temperatures are adapted to the cooling process, cold/heat could be used directly without additional brine loops, accompanied by a negative effect on the EER. Furthermore the storage can be used to improve the system efficiency in case of discharge, which lowers the electrical demand when it is appropriate to reduce grid stress. Key issues are the development of the heat exchanger for the storage, the storage integration in the refrigeration cycle and the control strategies how to use the PCM-storage.

Keywords: Air Conditioning, Variable Refrigerant Flow (VRF), PCM, Heat Exchanger, Two-Phase-Flow, PV self-consumption, Demand Side Management

1. Introduction

Air Conditioning and heating based on electrically driven heat pumps is worldwide increasing in residential as well as in business buildings. Due to easy installation and easy access of the energy source/heat sink, air/air based systems are getting more and more relevant. The capability to store energy is limited in these systems. Systems with electric battery are expensive and sensible thermal storages do not fit well to the refrigeration cycle due to exergetic losses. The ability to store energy is mandatory to achieve better integration of PV-production for such combined systems. Especially in future when the numbers of installations will increase and capability to store energy is not given, a significant, negative impact on the electrical grid is expected, because the peak of cooling demand does not correspond to the peak of PV-production during the day.

The project approach is to integrate a thermal PCM-based storage into the refrigeration cycle of an air/air based 3-pipe VRF system. The efficiency of a heat pump corresponds directly to the temperature lift the compressor has to overcome. The approximately constant temperature of PCM at phase change can cause significant advantages in the system efficiency compared to sensible storage materials (Loistl et al., 2016). Therefore it is mandatory to choose materials whose melting temperature is appropriate for the desired effect of the heat storage, acting as heat sink, heat source or subcooler for the refrigeration cycle or as direct heat/cold storage.

doi:10.18086/swc.2017.28.16 Available at http://proceedings.ises.org

2. Modelling Phase

Several melting temperature ranges can be taken into account for implementing the PCM into the system. To get an idea which ranges will be most promising for the integration of PV-production and for the design of the entire system, load and PV-yield simulations have been made in TrnSys. The model consists of transient load simulations of a specific office building in which a pilot installation, based on a 3-pipe VRF system will be built up. Furthermore it contains transient PV-yield simulations, varying the installed peak-power. To simulate the theoretically possible thermal supply of the PV-driven heat pump the model is also fed with ambient temperature- and part load- dependent data of the EER/COP.

To gain reliable load data of the specific building, the known building characteristics and its geometry had been set up in the TRNBuild Editor. The building which is considered is located in Garching, in the south of Germany. It can be classified as a light construction building. The heating and cooling system supplies offices, laboratories and a small server room. The major part of the equipped building is shown in Figure 1.

Figure 1 Main part of the institute building which will be equipped with Indoor Units (IU).

The main thermal features and data of the building are shown in table 1.

Tab. 1: General data and main thermal features of the modeled institute building in Garching.

Main thermal features of the building	
	U Value
Wooden structured external wall	0.24 W/m²K
External Roof	0.18 W/m²K
On-ground concrete floor slab	0.25 W/m²K
Insulated glazing	1.1 W/m²K
General data of building	
Location	Garching, N 48°15´, E 11° 40´
Floor surface Offices	160 m²
Floor surface Laboratories	150 m²
Air change rate	40 m³/h·person
Cooling/Heating set point temperatures	24 °C – 21 °C

For the PV-yield simulation the Standard TrnSys Type 194b for Photovoltaic-Arrays including inverter losses is used. For the investigation the reachable PV-yield was maximized using PV-panels facing south with an inclination of 30°. Under typical operating conditions, there is only limited congruence of PV-generator yield and electric building load. Thus, the storage is applied in order to accomplish a better match, avoiding losses of the possible PV-yield.

The pilot installation will be equipped with a Fujitsu V-II R VRF-System. To implement this system to the model the part-load and ambient temperature dependent data was fed in. This data is published by Fujitsu down to a part-load-ratio of 50%. (Fujitsu, 2014)

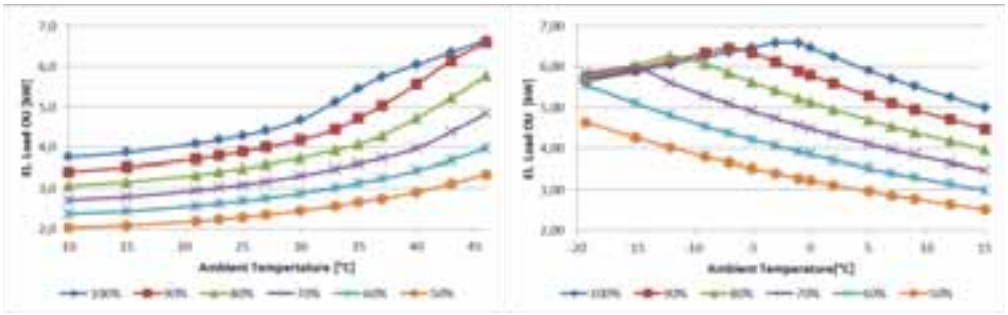

Figure 2 Electrical Load depending on ambient temperature and part-load ratio for cooling (left) and heating mode (right). Database for Fujitsu V-II R Type 72GALH with a rated cooling capacity of 22.4 kW and a rated heating capacity of 25 kW. The nominal electrical load is specified with 5.5 kW.

Figure 2 shows the electrical load of the Outdoor Unit 72GALH of the Fujitsu-System. Every curve represents a different part-load of the system in a range from 50% to 100%. Down to a part load ratio of 50% the EER as well as the COP depends mainly on the ambient temperature and only slightly on the part load of the system. A curve fitting method was used to get continuous data for the electrical load within the known ranges. Using the entire model it is possible to determine sizing and design parameters. Also an assessment of storage temperature levels can be made with the target of maximum reduction of grid stress caused by PV feed in.

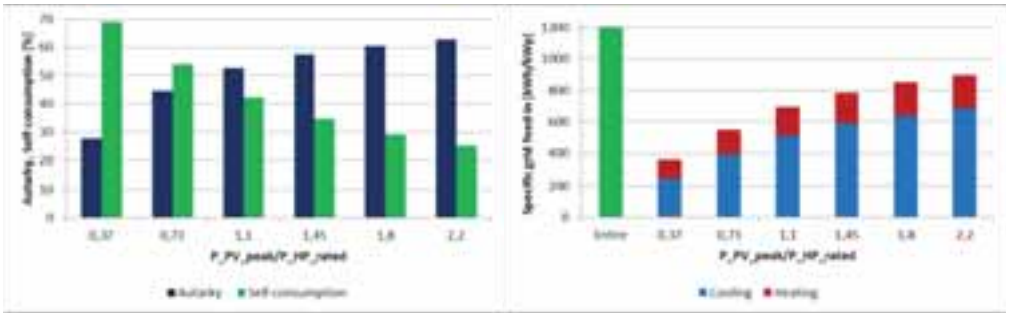

Figure 3 Autarky and self-consumption of system for different PV-installation (left). Specific remaining grid feed-in (right).

Figure 3 on the left hand side shows the possible autarky and self-consumption rate of the PV-HVAC system according to the electric power ratio of installed PV power related to the electric power rating of the heat pump. The right hand side shows the remaining grid feed-in during cooling and heating according to the above mentioned power ratio. Weniger et al. (2015) already shows that oversizing of the PV-generator in PV-storage systems leads to a saturation of autarky, while self-consumption is decreasing. Consequently, PV-peak feed in to the grid is increased. This effect can only be reduced by non-economic, oversized storages. The residual feed in to the electrical grid on the right figure is divided into the main cooling (blue) and main heating (red) period. It can be seen clearly, that the major part of remaining grid feed-in appears in cooling mode.

The model is capable for analyzing the system design aiming at optimal matching of PV, heating and cooling load and PCM-storage capacity. Figure 4 on the left hand side shows the amount of thermal energy which can be charged (blue) and discharged (red) daily in July for different electrical power ratios of PV and VRF (HP) system.

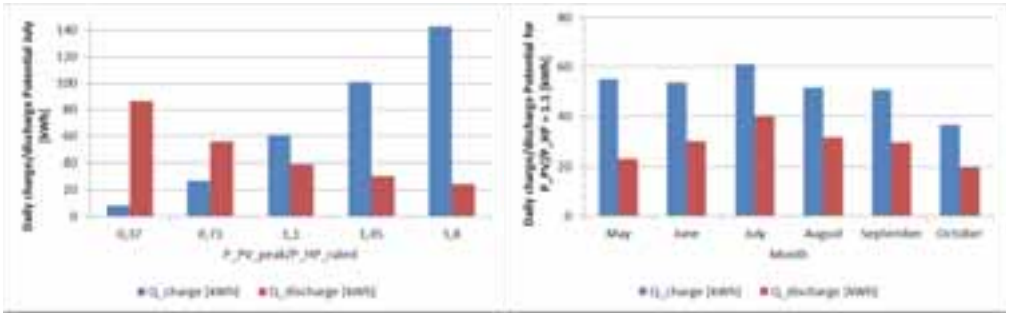

Figure 4 Daily charge/discharge potential of the storage. In July for variable PV-power (left). Daily charge/discharge potential for the entire cooling period with a relation of PV-power/rated power (HP) = 1.1 (right).

While for small scale PV the storage cannot be charged during the day, large scaled PV installations cannot use the stored energy the same day. The diagram on the right hand side shows the results for a slightly oversized PV-plant with a fix power ratio of 1.1. Regarding the average thermal energy which can be charged and discharged in one day during the whole cooling period, a storage capacity between 20 kWh and 30 kWh is found to be suitable for the considered system. It is important to say that this shows the maximum capacity which can be used. Furthermore there can be limits for the useable capacity due to the refrigerant cycle and the implementation/characteristic of the storage. Therefore another model for the cooling circuit and for the PCM-storage had been set up in EES (Engineering Equation Solver). These models are described in the upcoming Chapter.

3. Storage Implementation and Development

3.1. Possible Storage Implementations

As already mentioned there are different options for integration of a PCM-storage into the heat pump cycle. With regard to the desired function different melting temperature ranges can be taken into account. Figure 5 gives a general overview of the different possible storage functions and their operation. The left side shows the functions with the temperature range of each application, while on the right side a description of the cyclic operation of the system is given with charging and discharging phases.

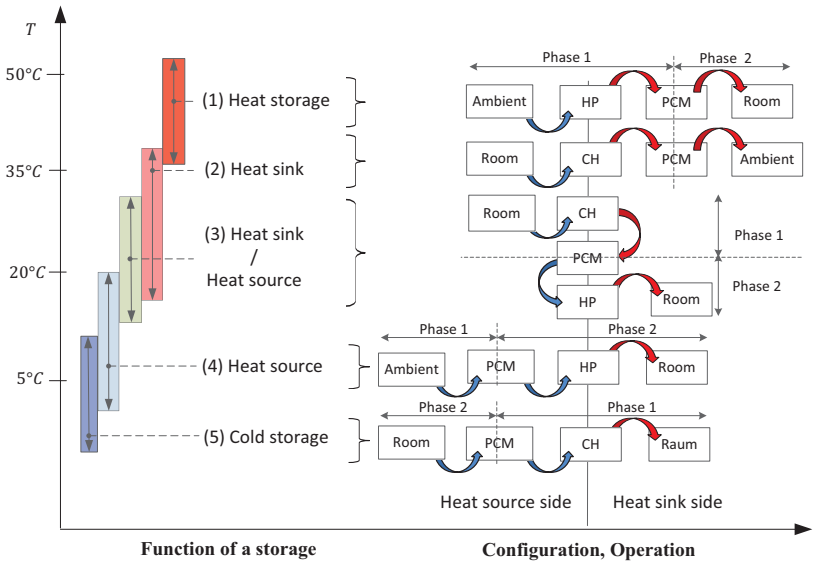

Figure 5 Different implementations of the Storage. Function of the storage with corresponding application temperature (left). Phases of operation on the right for chiller (CH) and heat pump (HP) applications (right). (Loistl et al., 2017)

For example configuration (1) represents a heat storage. In phase one the storage is charged with energy by heat pump (HP) operation, using the ambient as heat source. Subsequently in phase 2 the energy can be used for a heating purpose. Due to results of the TrnSys modelling phase, the possibilities to implement the storage as central cold storage (5), or as subcooler, which can also be categorized as heat sink were considered in more detail. For that purpose an EES model for the cooling circuit had been set up.

The model comprises enthalpy balances for the different steps of the refrigerant cycle characterized by the state points listed in table 2. For the refrigerant the dataset of R410A is used, which is the common refrigerant in state of the art VRF-systems.

Tab. 2: State points of the modelled refrigerant circuit.

Number	Definition
[1]	Beginning of Vaporising
[2]	End of Vaporising
[3]	Superheat of refrigerant
[4]	Hotgas after Compressor
[5]	Hotgas, beginning of Condensation
[6]	Liquid refrigerant, end of condensation
[7]	Liquid, subcooled refrigerant

The considered VRF-system operates with nearly fixed levels of evaporating and condensing temperatures. The following log(p)/h diagrams respect that with the shown isotherms for $T_{Condens}$ and T_{Evap}.

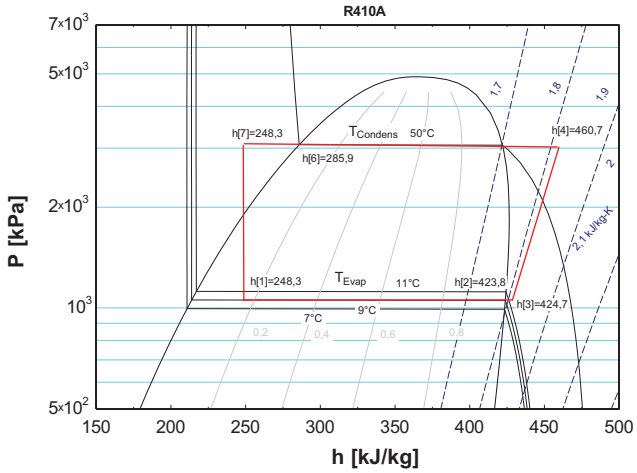

Figure 6 log(p)/h diagram. Example for the calculation of the refrigerant cycle.

Figure 6 shows the cycle state points in a log(p)/h diagram as given in Table 2 for the common system without any modifications of the refrigerant cycle. In this example the system works at its nominal cooling capacity of 22.4 kW with an evaporating temperature of 9 °C and a condensation temperature of 50 °C. The superheating is set to 4 K and the isentropic efficiency of the compressor is assumed to 0.7.

For a better understanding of the system, the storage configuration as subcooler is shown more detailed.

PCM-Storage working as subcooler

One possible implementation of the storage is to use it as additional subcooler in the refrigerant cycle. The idea using a thermal storage for subcooling the refrigerant is not completely new. The Electric Power Research Institute in California already worked on a combination of a VRF-system using an ice-storage for subcooling (Amarnath, 2009). The ice-storage there was charged in nighttime and discharged during the day to prevent peak loads. The main difference to this approach in the present investigation is the possibility to charge the storage in parallel to the regular cooling operation. Therefore it will be possible to charge the storage when PV-peaks occur.

First a simplified P&ID scheme of each storage implementation in case of charge (left hand side) and in case of discharge (right hand side) is shown. The scheme is reduced to a 2-pipe system working in cooling mode. The P&ID is followed up by the corresponding log(p)/h diagram both in case of charge (left) and discharge (right).

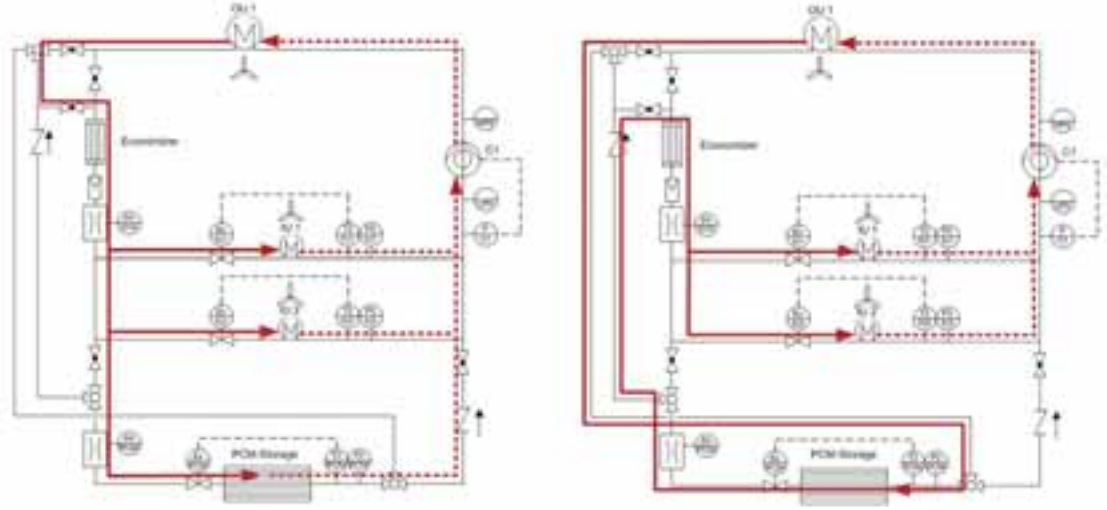

Figure 7 P&ID VRF system with a storage working as subcooler. 1 Outdoor Unit (OU), 2 Indoor Units (IU), Economizer and the PCM-Storage. Charging PCM-Storage on the left. Discharging PCM Storage on the right hand side.

Figure 7 shows on the left hand side the charging of the storage at the common evaporating level of the system, using PV surplus energy. Therefore, the phase change temperature has to be above this level. While charging, the storage is connected to the system like an additional Indoor Unit. Using the common evaporating level, there are no EER losses expected while charging. The storage works as additional load. Due to a higher part load ratio, positive effects on the EER while charging are expected. The right hand side of the P&ID shows the discharge case. When thermal load exceeds solar supply, the liquid refrigerant is led through the storage and is subcooled near the melting temperature of the chosen material. The already subcooled refrigerant is now led through the conventional economizer to ensure safely a sufficient subcooling before the refrigerant is led to the Indoor Units.

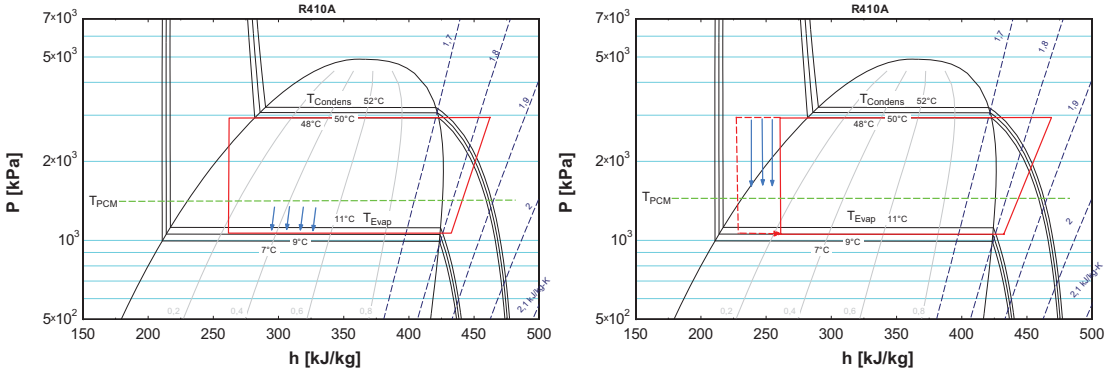

Figure 8 PCM storage used as additional subcooler in case of discharge (right). Charging on the common evaporating level of the system (left).

Figure 8 illustrates the refrigerant cycle of the process while charging (left) and discharging (right). The green line represents the melting temperature of the PCM, which has to be above the common evaporating temperature. With the storage used as subcooler there are two benefits to achieve:

- A higher usable enthalpy difference for cooling compared to conventional subcooling.
- Reaching sufficient subcooling by the storage can relieve the conventional economizer. Those systems usually subcool the refrigerant by evaporating a part of the condensed refrigerant to low pressure level. This part of the refrigerant is lost for the energy conversion but has to be transported by the compressor.

Both benefits lead to an increase of the EER during the discharge phase of the storage compared to conventional systems. This gives the possibility for a lower electrical demand when it is appropriate.

Figure 9 shows the EER improvement of the system at discharging the storage over varying melting temperature for the PCM-storage. It is assumed that the system works on its nominal conditions at an evaporating level of 9 °C. Lower melting temperatures improve the subcooling and also the EER up to 24% during the discharging cycle. On the other hand, a sufficient temperature difference between melting temperature and evaporating temperature needs to be ensured in case of charging. Taking both into account, the ideal melting temperature range for this implementation is between 16 °C and 21 °C. It has to be stated that the increased evaporator efficiency and the related improvement of the EER is a result of an additional input of driving energy during loading of the storage. Integrally, only minor changes of the average EER of the system should occur, related to the change of the load profile along the day.

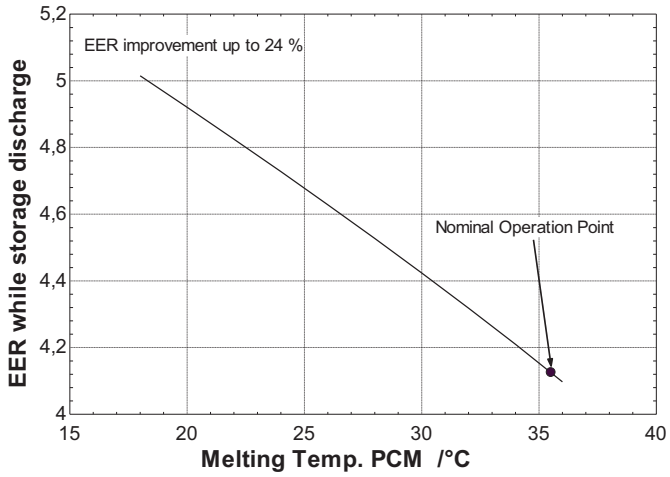

Figure 9 EER improvement in case of discharge for different melting temperatures of the PCM. Comparison to the nominal operation point of the system (storage working as subcooler).

3.2. Sizing/Development of Subcool Storage

Selection of storage material

Since it has been determined that the storage for the pilot installation should be working as a subcooler, a PCM material with a melting range around 16 °C and 21 °C had to be found. Besides a fitting melting point other important factors were a high latent heat and an economically viable price. To improve heat transfer rates it was decided to work with a metal heat exchanger. Hence a non-corrosive storage material was needed which excluded most salt-hydrates.

Regarding the temperature range, paraffin waxes are a good alternative. Their advantages include non-corrosivity, freezing without much supercooling, the ability to melt congruently, no segregation and they are non-hazardous. Parafol 16-97 from Sasol with an onset temperature around 16.5 °C, a latent heat of at least 220 J/g was found to be suitable(Sasol Performance Chemicals, 2017). The relatively low melting temperature range around 18 °C ensures a high temperature difference to the condensation point and therefore leads to a higher EER gain.

Since Parafol 16-97 like most paraffin waxes has a low thermal conductivity, graphite powder will be added to the storage medium to improve the thermal conductivity and allow higher power rates. The used graphite is SIGRATHERM® GFG 600. Tests with the mixture showed that with a mass ratio of 1:5 the thermal conductivity is sufficient and the mixture is still pumpable and therefore easy to fill into the storage container.

Construction of the storage unit

The test building is the institute of the ZAE Bayern located in Garching, Bavaria. Figure 10 shows the modeling result for the available cooling output of the PV driven VRF system and the cooling demand for a typical cooling day in August (left) and a day in transition time at the beginning of May (right, day with solar radiation). The data was generated by available weather data and the TrnSys model explained in chapter 2. Electricity is generated by photovoltaic panels. This electrical power is used to run the cooling cycle of the VRF system. The calculated possible total thermal power output is shown in red. The cooling demand of the building is shown in blue. The difference between available cooling power and cooling demand is shown in green (excess thermal energy) and black (cooling demand exceeding the thermal power output). Due to the lightweight construction of the investigated building, the cooling demand and the solar peak correlate very well as shown in Figure 10. Hence the potential for a load shift is comparably small. The analysis of the data from April to October, which are the months with a sizeable cooling demand in Germany, suggested a storage capacity of about 20 kWh to be sufficient. Would a building with a heavier construction with building materials such as concrete or stone be used, it would take a longer time to heat up the interior. The cooling demand would shift to a later time and therefore the peaks of demand and production would not correlate so well. This would lead to a bigger storage demand.

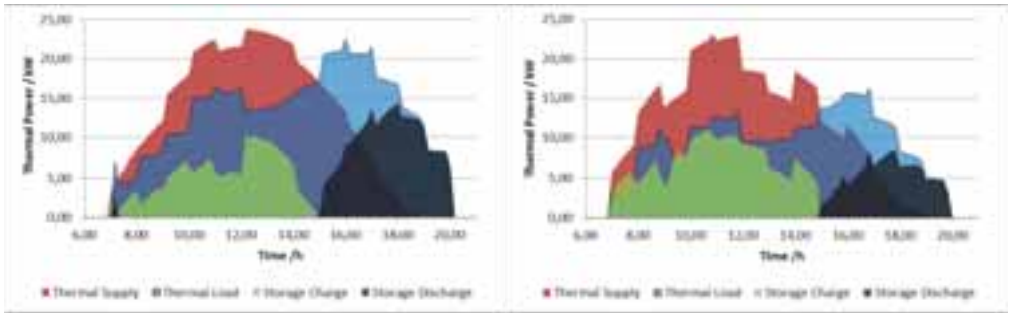

Figure 10 Exemplary thermal course of a typical cooling day for August (left). Thermal course of a day in transition time with solar radiation in May (right). The storage charge (green) and discharge (black) areas are representing potentials.

However, the possible maximum charging and discharging power is not arbitrary, but is limited by the construction of the storage and the heat exchanger. Furthermore it is influenced by the charging history. Hence, an iterative process was necessary to determine an appropriate storage size and heat exchanger construction.

First the volume of the storage container was calculated with the estimated 20 kWh storage capacity. A suitable heat exchanger was modelled using the Engineering Equation Solver (EES) software. Afterwards, the charging and the discharging process were simulated.

Charge

The cooling fluid R410A is injected into the heat exchanger of the storage unit and evaporates, cooling the PCM material. As a result, the selected PCM Parafol 16-97 crystallizes along the heat exchanger. The model took into account the evaporation of cooling fluid on the inside of the heat exchanger as well as the heat transfer through and the phase change in the PCM material. It includes different pressure loss phenomena (static, acceleration, frictional, pipe bends) and the flow boiling effects after Shah (VDI-Gesellschaft Verfahrenstechnik und Chemieingenieurwesen, 2002, Nellis and Klein , 2009). Depending on the distance between phase front within the Parafol 16-97 and the heat exchanger the transferable power varies.

Therefore, the maximum transferable power depends on the way the storage was charged and discharged before. To simplify the model it was assumed that each day was independent of the one before. That means the storage was discharged every morning. The system is not highly reactive, meaning switches between charging and discharging in a short time scale are not favorable. Therefore one can assume that there is only one charging and one discharging cycle per day. Under these assumptions, the possible power transfer is a function of the state of charge (SoC) of the storage, because the distance between the heat exchanger surface and the phase front in the PCM is growing with a larger SoC. The higher the SoC, the larger is the fraction of PCM in the solid state.

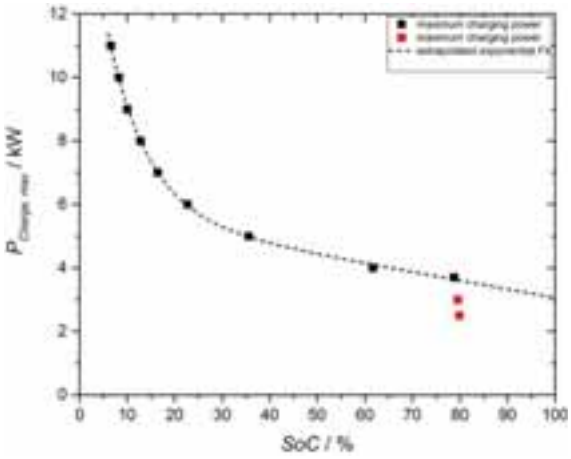

Figure 11 Maximum charging power depending on the SoC

Figure 11 shows the maximum transferable charging power depending on the SoC. Until about 80% of SoC it can be fitted by an exponential function. At higher SoC values (red squares) the maximum charging power decreases rapidly. This is because in the simulation the phase fronts reach symmetric borders at that point. Consequently, the calculated heat exchange surface decreases rapidly, which reduces the transferable power. However, in this simplified model heat transfer parallel to the heat exchanger was not considered. Therefore it is expected, that the decline in the maximum transferable power is not that sharp in a real storage device. This was already confirmed in preliminary tests. For further calculations, the exponential fit was extrapolated to a SoC of 100%.

To calculate the maximum charging energy, the minima of the available thermal power and the maximum possible charging power resulting from the actual SoC were determined.

Discharge

During discharging liquid R410A is injected at high pressure and temperature into the heat exchanger of the storage unit. Within the storage, the cooling fluid is cooled from about 48 °C to nearly the phase change temperature of the PCM (18 °C), melting Parafol 16-97. The maximal possible discharge power can be calculated via equation 1.

$$P_{Discharge} = \dot{m}_{R410A} \cdot \int_{T_c}^{T_h} c_{p,l}(T) \cdot dT \qquad \text{(eq. 1)}$$

Hereby $P_{Discharge}$ is the maximum discharge power. $\dot{m}_{R410A}$ is the mass flow rate of the cooling liquid, $c_{p,l}(T)$ the temperature dependent heat capacity, and T_h and T_c are the temperatures at the in- and outlet of the PCM storage unit. The mass flow rate is given by the actual cooling demand. The cooling power is provided by the evaporation of R410A. Hence, the mass flow rate is given by:

$$\dot{m}_{R410A} \approx \frac{P_{Cooling}}{\Delta h_{R410A}} \qquad \text{(eq. 2)}$$

For a fixed inlet temperature T_h of 48 °C the discharge power is found to be limited to about 28% of the cooling power. The excess energy is necessarily provided by the cooling cycle (liquefaction).

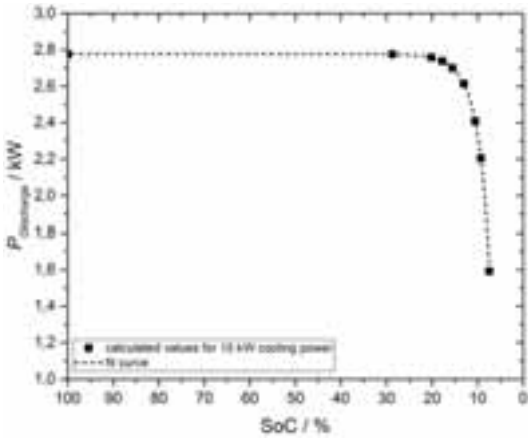

Figure 12 Discharge power depending on the SoC for a cooling power of 10 kW

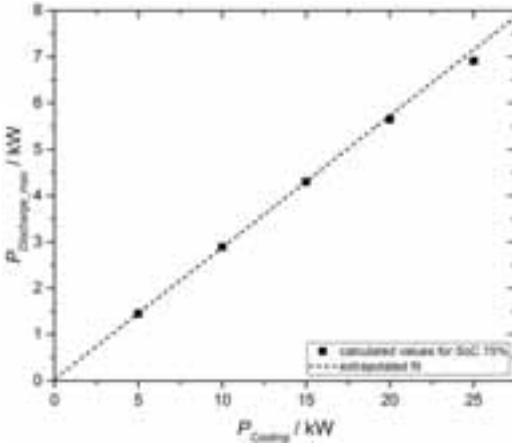

Figure 13 Maximum discharge power depending on the cooling power for a SoC of 75 %

The discharge power is in most cases rather limited by this fact then by the discharge characteristics of the storage unit. Figure 12 shows the SoC dependent discharge power for a cooling power of 10 kW. Down to around 20% SoC the discharge power is virtually constant (100% means the PCM is solid, while 0% means it is liquid). After that there is a fast decay. It results from the heat transfer which in this region limits the discharge power. However, this is a worst case estimation. For example heat conduction parallel to the heat exchanger was not taken into account in these calculations. Hence, it can be expected that the decay is not as steep in reality. In most operating conditions the discharge power will be limited by the cooling power.

In Figure 13 the maximum discharge power is shown as a function of the cooling power for a SoC of 75%. The data yields a nearly linear relation. Only at very high power rates the slope flattens. It confirms that the discharge power is generally limited by about 28% of the cooling power.

Hence, the calculation of the maximum theoretical available discharge energy per day was simplified and calculated by multiplying the cooling demand with a factor of 0.28 when cooling demand exceeds the generated cooling output of the VRF system.

Results of the iteration

The found limits of charging and discharging power have been implemented in the system model. For each day of the cooling period a possible maximum thermal energy which can be shifted was calculated again. These restrictions on the transferable power led to a lower reasonable storage size. The iterative process was continued and a latent heat storage capacity of 16 kWh was determined.

The final heat exchanger unit contains six heat exchangers with each 23 m length which will enable the storage to a peak power of more than 10 kW while charging.

The storage dimensions will be 1400 x 600 x 600 mm. 390 l of the PCM-Graphite compound will be used. This corresponds with a latent heat capacity of 16 kWh. A schematic drawing of the storage and the heat exchanger unit is shown in Figure 14.

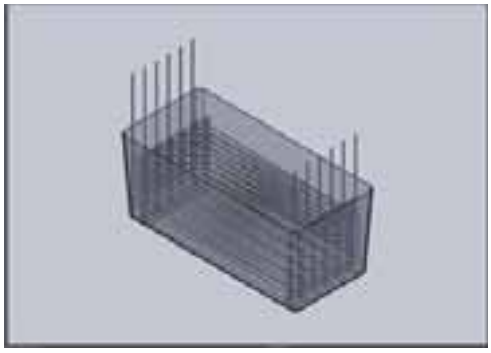

Figure 14 Schematic drawing of the storage container and the heat exchanger

3.3. Implementation of Storage Characteristic to Refrigerant Cycle Model

After the design phase for the storage and the iteration to work out a suitable storage capacity, the characteristic curves for the storage were implemented to the refrigerant cycle model. Figure 15 shows the course of a typical cooling day in August. The data is related to the thermal course shown in Figure 10 on the left representing the theoretical charge and discharge potential independent from the kind of storage implementation.

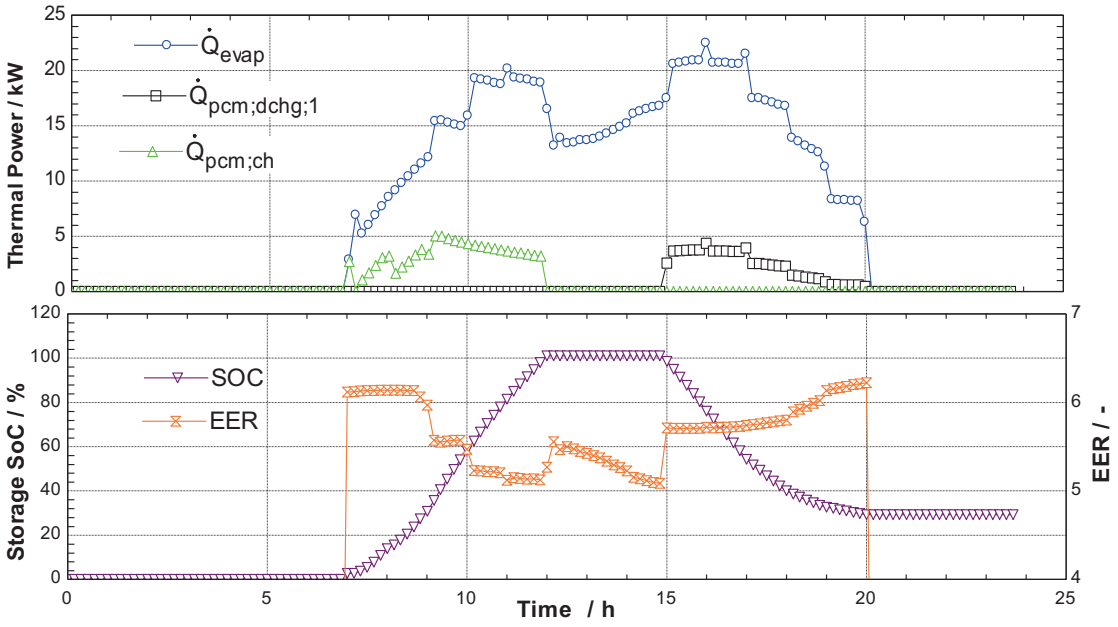

Figure 15 EES model of the refrigerant cycle fed with thermal load data and storage characteristics. Thermal course for a typical cooling day in August (Data out of Figure 10 on the left showing the potential). Thermal load, storage charging and discharging power in the upper part. SOC and EER in the lower part.

The upper part of Figure 15 shows the cooling load (blue, circled) of the system including storage charging. The green line (triangular) represents the storage charging power taking into account the characteristics described by Figure 11. The black line (squares) shows the possible discharge of the storage with respect to the limitation through the current thermal load. The bottom part of Figure 15 shows the variation of the systems EER (orange curve) and the storage SOC (violet, triangular) during the day. As already mentioned due to a higher part load ratio while charging, a slight EER-gain through charging can be expected. The real benefit is shown when discharge begins at 15:00 pm and the EER increases from 5 to nearly 6.

This EER gain while discharging the PCM-storage will significantly reduce electrical load when it is appropriate. In this example, the storage will be completely charged before the PV peak occurs. Thus, the course of the SoC trend line directly indicates that measures have to be taken for controlling the operation of the storage. A predictive control strategy is required in order to charge the storage completely while covering the PV-peak.

4. Summary and Outlook

The study describes the modelling and sizing phase for a PV driven VRF system coupled with a thermal PCM-storage. The integration of the storage as subcooler is described in detail. Considering the thermal load, PV-supply and the systems boundary conditions an adequate PCM was chosen and a storage with sufficient thermal characteristic was designed.

Next steps are the installation and start-up of the VRF pilot installation in Garching. In parallel the designed PCM-storage will be built up for laboratory tests. In a second step a tested and optimized pilot-storage will be implemented to the VRF installation. For the integration of the PV peak without losses of solar fraction, predictive control strategies will be worked out and tested during operation of the system.

5. References

Amarnath K., 2009. Performance Assessment of a Variable Refrigerant Flow Air Conditioner with Ice Storage System. Electrical Power Research Institute, Palo Alto, California

Fujitsu General Limited, 2014, Design and Technical Manual Airstage VR-II Variable Refrigerant Flow System, Japan

Loistl, F., Korth, T., Schweigler, C., 2016. Einsatz von Latentwärmespeichern in Klimageräten, Deutsche Kälte- und Klimatagung, Kassel

Loistl, F., Korth, T., Schweigler, C., 2017. Latentwärmespeicher für Luft/Luft-Wärmepumpen, KI – Kälte-, Luft- und Klimatechnik, p. 50-55, 10/2017

Nellis, G., Klein, S., 2009. Heat Transfer, Cambridge University Press, New York

Sasol Performance Chemicals, PARAFOL C12–C22, High purity normal paraffins, http://www.pcm-ral.org/pcm/wp-content/uploads/2016/08/Brochure_PARAFOL_2016.pdf, [Stand 05.10.2017]

VDI-Gesellschaft Verfahrenstechnik und Chemieingenieurwesen, 2002. VDI-Wärmeatlas: Berechnungsblätter für den Wärmeübergang, Heidelberg

Weniger, J., Bergner, J. Tjaden, T., Quaschning, V., 2015. Dezentrale Solarstromspeicher für die Energiewende. Hochschule für Technik und Wirtschaft Berlin

Acknowledgment

The project SolarSplit is funded by the BMWi (German Federal Ministry for Economic Affairs and Energy) under grant No. 0325900A, B and C.

Increase of the Ventilation Effectiveness of Solar Chimneys with Consideration of Wind-Effects applying CFD Simulations and Measurements

Lukas Schwan[1], Hannes Rütschlin[1], Madjid Madjidi[1] and Thomas Auer[2]

[1] University of Applied Science Munich, Department of Building Services Engineering, Munich (Germany)

[2] Technical University of Munich, Chair of Building Technology and Climate Responsive Design, Munich (Germany)

Abstract

Solar chimneys have been used for natural ventilation and cooling in the Middle East already hundreds of years ago. In modern buildings, the concept could contribute to energy savings and reduction of greenhouse gas emissions. An optimized system would enable a sustainable and permanent operation of this natural ventilation concept. This study analyzes the effect of wind and the possibilities to increase the ventilation effectiveness of solar chimneys by optimizing the design of the chimney outlet. Computational fluid dynamic (CFD) simulations have been used to investigate the general influence of the wind effects on a building which is naturally ventilated with solar chimneys. The results show that the air change rate increases or decreases depending on the predominating wind direction. To be able to accomplish a system which supports the natural ventilation irrespective of the wind direction, different wind cowls were tested at a test rig located at the University of Applied Sciences Munich. As a result of this study, the flow velocity can be shown as a square root function of the wind speed. An average flow velocity between 0.6 – 1.1 m/s can be reached by using turbine ventilation systems.

Keywords: Solar chimney, wind cowl, energy savings, natural ventilation, CFD simulation, ANSYS FLUENT

1. Introduction

Approximately 15 % of the total electrical energy demand of today's office and factory buildings is used by mechanical ventilation (EnOB 2016). The use of natural ventilation and natural cooling systems could be a possible solution to reduce the energy consumption in the building sector. This paper explores the concept and the potential of an enhanced solar chimney which uses just the sun and the wind as its driving forces. Therefore, no conventional sources of energy are used.

During sunshine, solar radiation enters the chimney through a transparent cover and heats up an absorber surface. The difference between the chimney temperature and the ambient air temperature generates a buoyancy effect. As a result, the air is drawn out of the building. To generate this buoyancy effect also during the night-time, for night cooling or periods with cloudy sky, the effectiveness of such a system needs to be increased. Permanent and sufficient ventilation could be provided by using wind effects with an optimized design of the chimney outlet and wind cowls in addition to the buoyancy effect.

Khan, Su and Riffat (Khan et al. 2008) give a good overview about historical wind towers and modern techniques for wind driven ventilation systems. Kisteledgi and Haber (Kistelegdi, Háber 2012) discuss the direction of wind towers and the design of their outlets for the natural ventilation of a plus-energy manufactory in the South of Hungary. Ismail and Rahman (Ismail, Rahman 2012) show possibilities for future configurations of wind turbines, fans and solar panels and combinations of static and dynamic systems.

doi:10.18086/swc.2017.28.17 Available at http://proceedings.ises.org

To study the effect of wind and its benefit for a natural ventilation concept with a solar chimney, the investigation of this study contains two major parts. The first part describes the general impact of wind on a reference building which is naturally ventilated with solar chimneys. This analysis was done using CFD simulations to see the influence of wind direction and the positioning of the solar chimneys. Afterwards an experimental investigation was conducted to investigate different wind cowl systems which could be integrated in a solar chimney concept using measurement data from a test rig.

2. Impact of wind on natural ventilation of a reference building

2.1. Methodology and simulation set-up

The impact of wind on a building regarding the ventilation effectiveness is analyzed using a standard building model as a reference for the location of Munich, Germany. The reference model is a three story office building and it was taken from the VDI Norm 6009 (VDI 2001). The same model has been used in previews studies to investigate the viability of using solar chimneys for natural ventilation in Germany (Schwan et al. 2017a). A solar chimney was attached to the south façade of each floor, respectively. The inlet window sizes and building geometry for the three floors was identical to the reference model.
The building model was simulated with the software ANSYS workbench 16.2, which consists of different applications. The geometry of the building model was set up using the DesignModeler. In addition to the building, a surrounding area was simulated as well. Both, reference building and its surrounding area can be seen in Fig. 1.

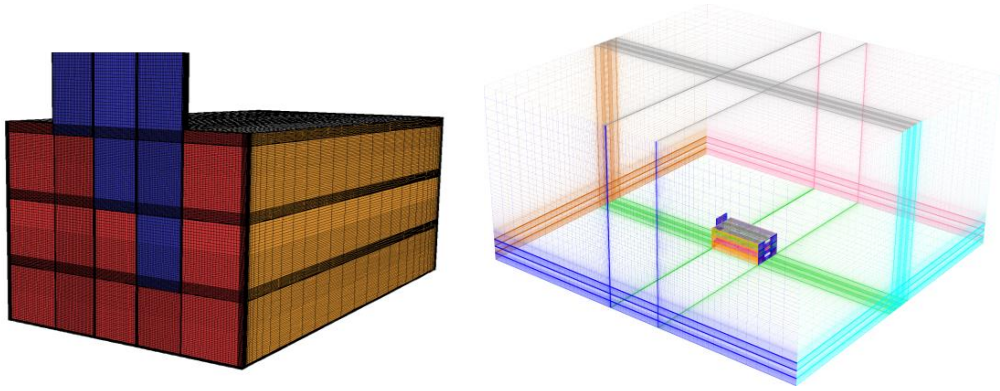

Fig. 1: Model of the reference building (left) and surrounding (right) developed in ANSYS FLUENT

The reference building is 30.6 m long and 16.6 m wide. The solar chimneys are 4 m, 8 m and 12 m high; depending to which floor they are attached to. Every solar chimney is 3 m wide and has an inside air gap of 0.3 m. In previous investigations an air gap of 0.3 m was found to be the ideal size for a maximum air flow without the appearance of backflows (Schwan et al. 2017b). The building, including the solar chimneys, has a height of H = 16 m. In every direction the building is 5H away from the boundaries of the surrounding, respectively. The simulation of the surrounding is necessary to be able to simulate the wind effect properly. It is limited to 5H to retain a manageable simulation time. The distance is chosen to be the same in all directions, because different wind directions are investigated. The parameters for the building and the solar chimneys (SC) can be seen in Table 1 and Table 2.

Table 1: Building parameters

Parameter	Symbol	Value	Unit
Height of building	H_B	16.00	m
Length of building	L_B	30.60	m
Width of building	W_B	16.60	m
Window size (north)	A_W	9.50	m²
Area of each floor	A_F	507.96	m²
Total floor area	$A_{F,ges}$	1523.88	m²

Table 2: Solar chimney parameters

Parameter	Symbol	Value	Unit
Cross section area	A_{SC}	0.841	m²
Height of SC ground floor	H_{SC1}	12	m
Height of SC first floor	H_{SC2}	8	m
Height of SC second floor	H_{SC3}	4	m

The major influence factor for the both, simulation time and the accuracy of the simulated results, is the applied mesh. For this investigation the software package ANSYS ICEM CFD was used for the mesh generation. High numbers of cells are used in the solar chimney and the building floors to provide reliable results in these areas. Lower numbers of cells are used in the surrounding area to reduce the calculation time. A hexahedral mesh was used due to lower numbers of cell element and a higher quality of the mesh compared to a tetrahedral mesh. The used mesh consists of more than 2,000,000 hexahedron cell elements. ANSYS FLUENT was used for the calculation of the fluid dynamics. The post processing and evaluation of the results have been done with ANSYS CFD Post. The investigations were performed with steady simulations for specific reference days to be able to reduce the simulation time. The turbulence of the air flow is calculated with the k-ε model, considering gravity and buoyancy effects. An enhanced wall treatment was used to compensate inaccuracies of the turbulence model for areas next to the walls. The air density was calculated using the Boussinesq model.

2.1. Investigated aspects

The ventilation effectiveness was studied according to the position of the solar chimney, the wind direction and the wind speed for different seasons. Steady simulations were conducted for three reference days (two in summer and one in winter) to be able to validate the impact of the wind on the natural ventilation system. The weather data for the city of Munich was taken from the German Test Reference Year (TRY) of 2010 for the chosen reference days (Deutscher Wetterdienst 2014). The used data can be seen in Table 3.

Table 3: Weather of used reference days

Month, day, time	July, 23rd, 12 pm	August, 12th, 5 pm	December, 5th, 12 pm	Unit
Wind direction	260 (SW)	190 (S)	100 (SE)	°
Wind velocity (H = 10 m)	3	1	5	m/s
Wind velocity (H = 16 m)	3.70	1.23	6.16	m/s
Air temperature (H = 2 m)	24,8 297,95	32,8 305,95	-2,4 270,75	°C K
Air pressure	96,09	95,45	95,54	kPa
Direct solar irradiation	550	59	24	W/m²
Diffuse solar irradiation	291	201	128	W/m²

2.2. Comparison between reference days

The weather data of the three reference days are completely different, as it can be seen in Table 3. The largest influences on the buoyancy effect of the solar chimney are the height of the chimney and the temperature difference between the inner part of the solar chimney and the ambient air temperature.

On the December reference day, the temperature difference is high, because of the low ambient air temperature. As a result the air changes per hour (ACH) are high as well. All simulated results of the ACH for the three reference days can be seen in Fig. 2. The ACH will be even higher with an increased height of the solar chimney. Therefore, the ACH of the ground floor is higher than the ACH of the first and second floor. The wind has a positive effect on the results of the ACH for the December reference day. The ambient air temperature on the reference day in August is significantly higher than the temperature in the building. In addition, the solar irradiation is not strong enough to rise the temperature in the solar chimney. As a result, backflows occur in the solar chimney. Just the wind can balance that effect, although sufficient ventilation cannot be provided. On the July reference day, the ACH is higher and the effect of the height of the solar chimneys can be seen as well. The wind from south west has no significant positive effect of the ACH on that day. These results show the effect of the ambient air temperature as well as the effect of the wind.

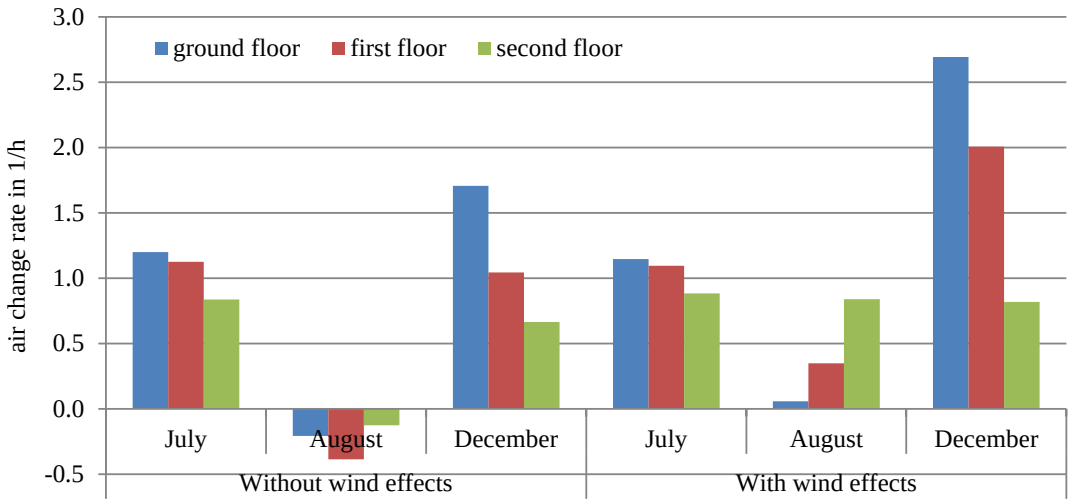

Fig. 2: Air changes per hour without and with wind effects for three reference days

2.3 Investigation of wind direction

Different wind directions have been investigated for the same reference day in July, to ensure a better comparability of the results to neglect the other effects. The considered wind directions can be seen in Fig. 3.

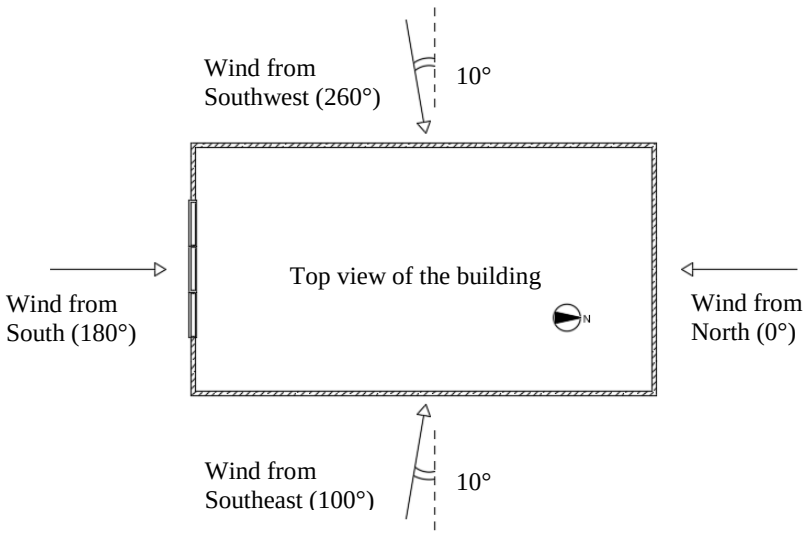

Fig. 3: Considered wind directions

The simulations have been conducted for the four wind directions. The results show that the effect of wind depends considerably on the wind direction. The results of the ACH can be seen in Fig. 4.

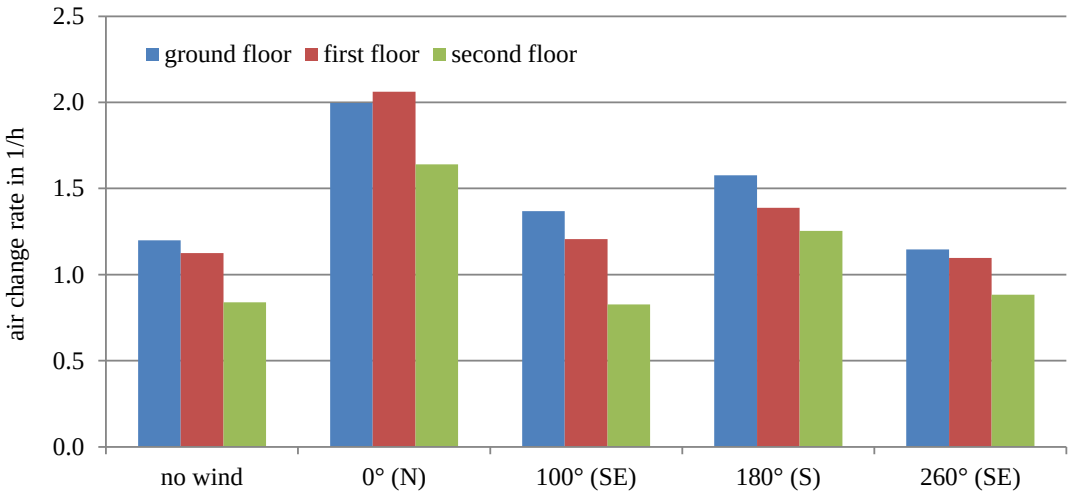

Fig. 4: Air changes per hour for different wind directions for a reference day in July

If the wind direction was North (0°) or South (180°), then a distinct wind profile occurs. The wind increased the provided volume flow in the solar chimney and therefore the ventilation effectiveness (compared to simulations without wind) for all three floors. A velocity profile for the air around the reference building and inside the chimney can be seen in Fig. 5. The air change rate is approximately 30 % higher compared to simulations without wind.

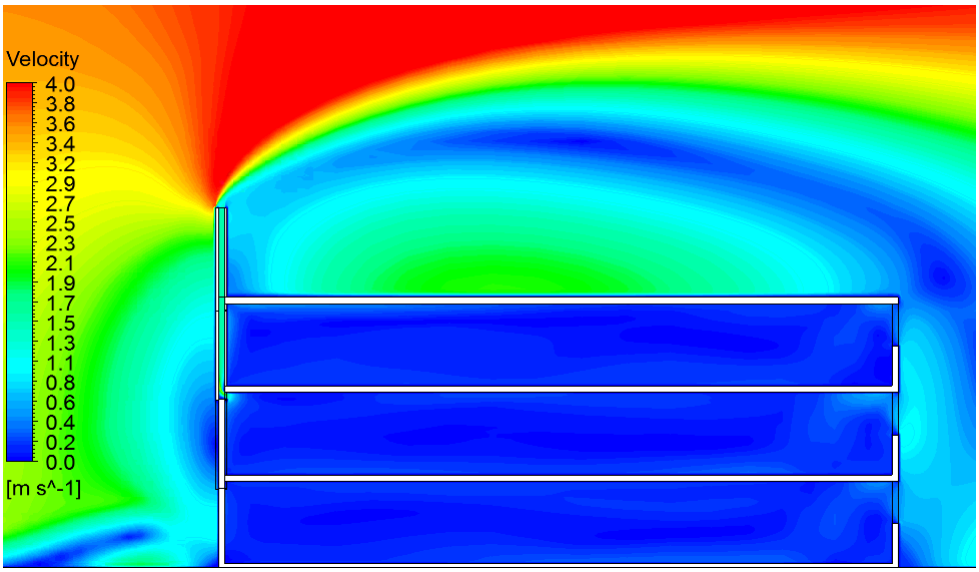

Fig. 5: Velocity profile for air around the reference building (wind direction: South)

If the wind direction is inclined and non-parallel to the small side of the solar chimney, for example for wind from South-West (260°) or South-East (100°), there is a significant change in the resulting air volume flows. At least in one of the three solar chimneys, a reduced volume flow occurred for these wind directions compared to simulations without wind. The air change rate was reduced by up to 10 % in these cases. These results highlight the importance to optimize the design of the solar chimney outlet in order to avoid negative influence of wind effects and rather use wind effects to enhance the ventilation effectiveness.

3. Optimization of the solar chimney outlet through integration of wind driven systems

3.1. Methodology and test-rig

Using wind-driven ventilation systems at the top of a solar chimney should offer permanent and sufficient ventilation and avoid negative influences on the performance of the thermally driven solar chimney. Therefore, different types of cowls and roof ventilation systems were analyzed for their contribution to natural ventilation. Only systems without additional gears (e.g. photovoltaic-wind driven systems) were considered. The systems work independent of the wind direction, which should avoid the problems discussed in the previous chapter. The experimental investigation was mainly focused on findings about the ventilation rate in general and as a function of the wind speed. Also, the influence by the thermal buoyancy effect and the solar radiation was part of the study.

With a height of 4.5 m, the chimney overlapped the adjacent building and enabled an incident flow from all directions. The length of the chimney was 1 m and the width 0.5 m. The diameter of the air inlet and outlet was 0.3 m. The test rig was located at the University of Applied Science in Munich and faced in southwestern direction. The test rig can be seen in Fig. 6.

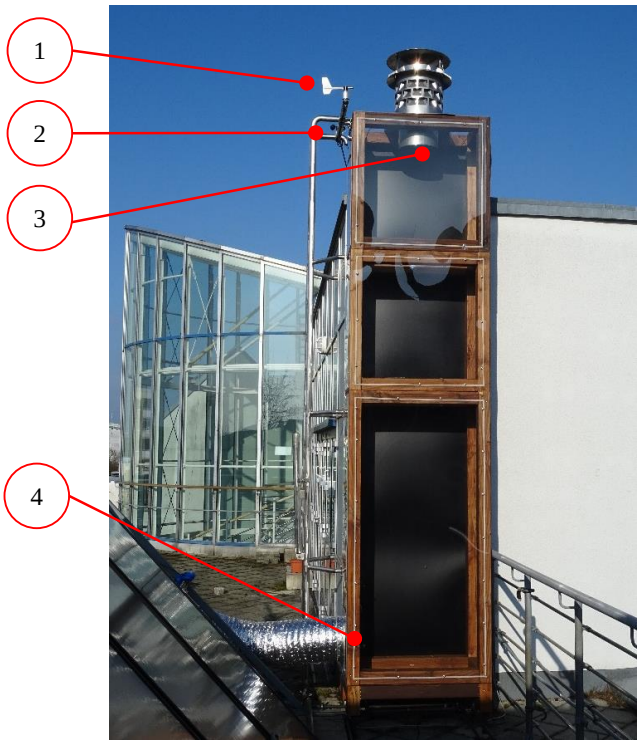

Fig. 6: Test rig at University of Applied Science Munich

A wind direction transmitter (1) and a vane anemometer (2) recorded the wind regimes. Inside the chimney, the flow velocity, pressure and temperature of the air were measured. Therefore, two thermoanemometers were installed at the air outlet (3) and inlet (4). Table 4 shows the installed measurement instrumentation and corresponding measuring range.

Table 4: Installed measurment instrumentation at the test rig

Measured variable	Measuring instrument	Measuring range
Wind speed	Vane anemometer	0 – 50 m/s
Wind direction	Wind direction transmitter	0 – 360 °
Air velocity, pressure and temperature	Thermoanemometer	0.08 – 2 m/s

On a test rig, three different types of dynamic turbine ventilation systems by Rotovent Systems (RS) and an inject nozzle by Euro Windkat were tested (see Fig. 7). The turbine ventilation systems differ from the shapes of their blades.

RS cyclone | RS | RS premium | Injection nozzle

Fig. 7: Three different types of turbine ventilation systems (left) and an inject nozzle (right)

3.2. Correlation between wind speed, buoyancy effect and chimney airflow velocity

During the experimental investigation, global solar radiation, wind speed, the flow velocity inside the chimney, the temperatures inside the chimney and the ambient air temperature have been measured. For each wind cowl systems the data was recorded for at least two weeks to ensure to have different weather situations with varying intensities of wind and solar radiation.

Fig. 8 shows the global solar radiation, the wind speed and the resulting flow velocity in the solar chimney for an exemplary hour of the wind cowl system with straight blades (RS cyclone).

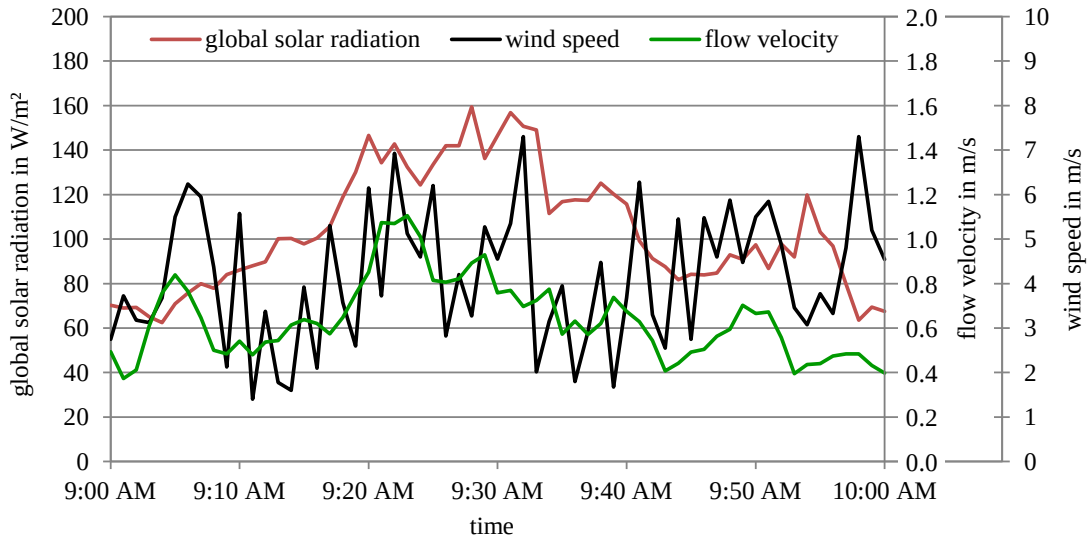

Fig. 8: Solar radiation, wind speed and flow velocity inside the solar chimney (18th March 2017, 9:00 – 10:00 am)

The buoyancy effect and the wind effect are the two major impact factors for the resulting flow velocity inside the solar chimney. The buoyancy effect is mainly influenced by the temperature difference between the ambient air temperature and the temperature inside the chimney and therefore indirectly influenced by the solar radiation as well. To quantify the share of both of these factors – wind and buoyancy – further investigations have been conducted, in which the thermal influence was neglected.

Fig. 9 shows the flow velocity inside the solar chimney as a function of the wind speed for the dynamic turbine ventilation system with straight blades. An average flow velocity more than 1 m/s can be reached. The development of the flow rate equates a root function. In comparison to the thermal buoyancy due to an increased absorber temperature, dynamic wind cowls show the same speed level. Therefore, the integration of wind-driven cowl systems in the concept of a solar chimney shows great promise.

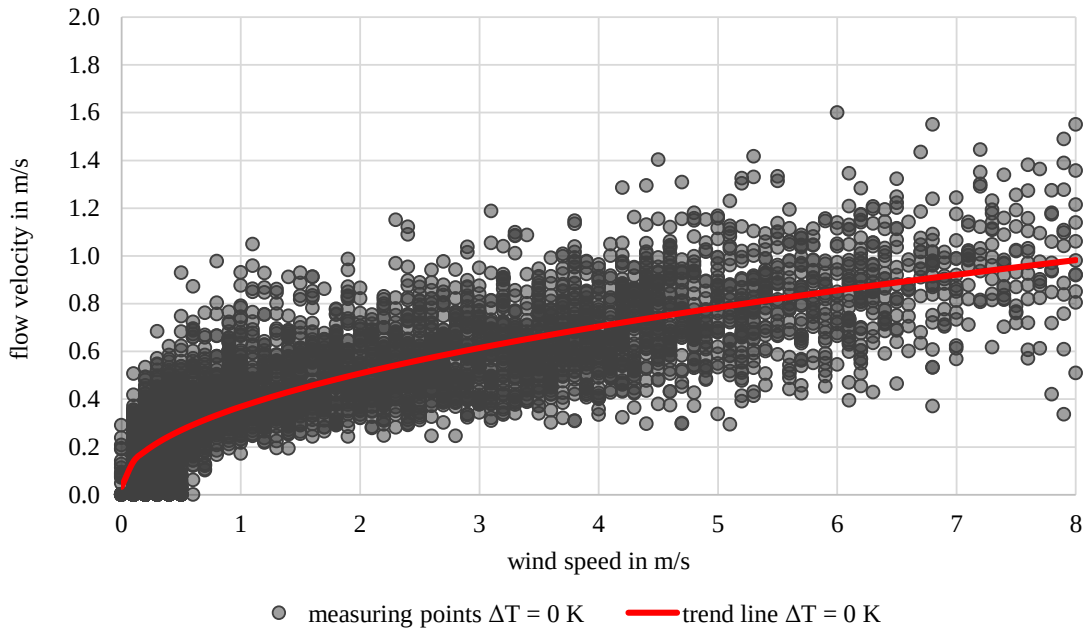

Fig. 9: Flow rate without thermal buoyancy for a turbine vent with straight blades (RS cyclone)

To consider the influence of the two driving forces wind and sun, the flow velocity can also be shown including the thermal buoyancy. Therefore, the air temperature difference between inlet and outlet was divided into six temperature ranges. Fig. 10 shows the flow velocity as a function of the wind speed and thermal buoyancy for a turbine ventilation system with straight blades. In comparison to Fig. 9 the flow velocity increased up to 1.8 m/s.

The measurements also illustrate, that the two driving forces interferer each other. For low wind speed, the impact of the thermal buoyancy is high. Otherwise the temperature differences between inlet and outlet decreased for increasing wind speed. This trend was noticed for all four ventilation systems.

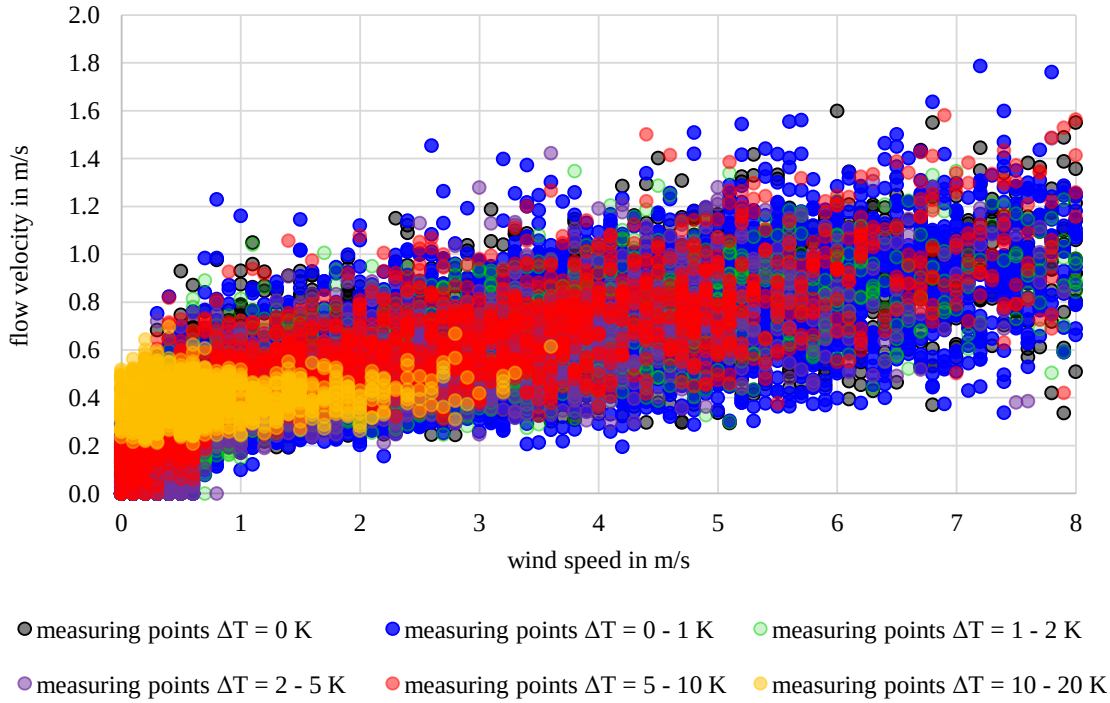

Fig. 10: Flow rate with thermal buoyancy for a turbine vent with straight blades (RS cyclone)

3.3. Comparison between different wind cowl systems

The flow velocity inside the chimney increases with higher wind speeds according to a square root function.

$$f(x) = a\sqrt{x} + b \qquad \text{(eq. 1)}$$

For time steps with a temperature difference between the inner part of the solar chimney and the ambient air, a buoyancy effect occurs. This results in positive flow velocity even in situations without wind with wind speed = 0 m/s. In eq. 1 this offset to the origin of coordinates is represented by the constant b. For time steps without buoyancy effect, the graph starts in the origin of coordinates. The gradient of the graph a is different for all four investigated systems. The different gradients and the trend lines of the measurement points of all four systems can be seen in Table 5 and Fig. 11.

Table 5: Gradient of graph and average flow velocity for a wind speed of 10 m/s for all wind cowl systems

Wind cowl system	Gradient of graph a	Average flow velocity for a wind speed of 10 m/s
RS	0.21	0.66 m/s
RS cyclone	0.34	1.08 m/s
RS premium	0.31	0.98 m/s
Injection nozzle	0.33	1.04 m/s

Based on the measurement results, it can be seen that the best values can be achieved with the RS cyclone system. The measured points of the injection nozzle have the highest deviation compared to the dynamic RS systems.

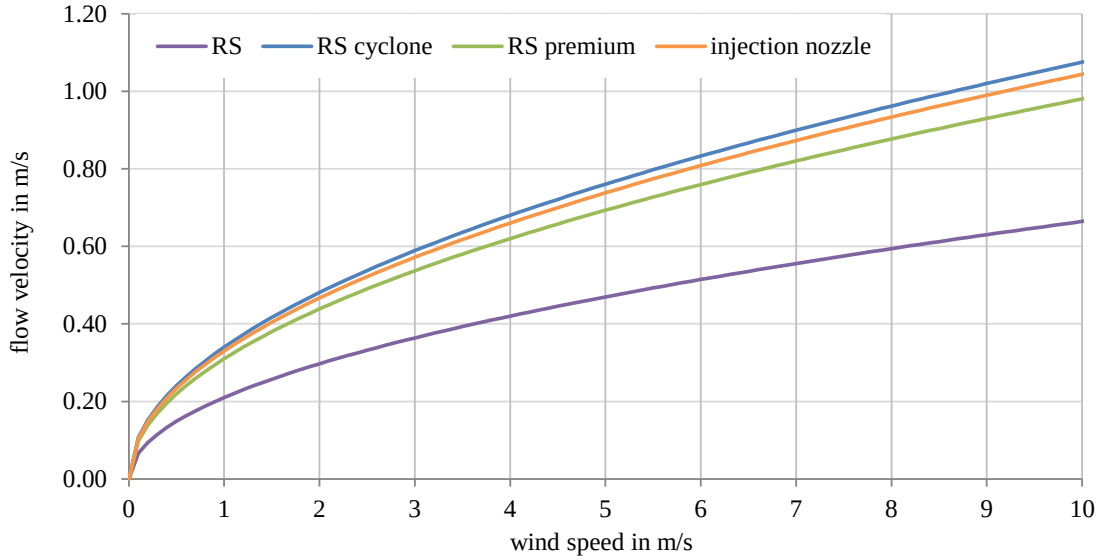

Fig. 11: Trend lines of the flow velocity without buoyancy effect for all four systems

4. Conclusion and Outlook

In this study the influence of wind effects on natural ventilation systems with solar chimneys has been investigated applying CFD simulations and measurements. The results showed the importance of considering wind effects for solar chimney projects and the huge impact of wind on the resulting air change rates. Especially the wind direction is important and can either lower or enhance the effectiveness of the solar chimney. A suitable solution to achieve a system which utilizes the wind effects irrespective of the wind direction, are wind cowl systems. Turbine vents showed the best performance and generated average flow velocities above 1 m/s. A higher effectiveness of solar chimneys can be reached through the integration of wind cowl systems. This offers a longer time of operation of the natural ventilation system, saves more energy and reduces greenhouse gas emissions.

In the future, the presented findings will be used in further research work to develop a planning tool for solar chimney projects. This planning tool should provide information about the expected ventilation rates and increase of the effectiveness of solar chimneys by using wind effects for the specific place of installation. Further research needs to be done to integrate the findings to a simplified calculation method to predict the effectiveness and efficiency of different solar chimney concepts.

5. References

Deutscher Wetterdienst (2014): Testreferenzjahre von Deutschland für mittlere, extreme und zukünftige Witterungsverhältnisse. Available online at https://www.dwd.de/DE/leistungen/testreferenzjahre/testreferenzjahre.html.

EnOB (2016): EnBau: "Energy-optimised new buildings" model projects. Available online at http://www.enob.info/en/research-areas/enbau/, checked on 9/6/2016.

Ismail, Mazran; Rahman, Abdul M. A. (2012): Stack ventilation strategies in architectural context: A brief review of historical development, current trends and future possibilities. In IJRRAS (11 (2)). Available online at www.arpapress.com/Volumes/Vol11Issue2/IJRRAS_11_2_14.pdf, checked on 3/23/2017.

Khan, Naghman; Su, Yuehong; Riffat, Saffa B. (2008): A review on wind driven ventilation techniques. In Energy and Buildings 40 (8), pp. 1586–1604. DOI: 10.1016/j.enbuild.2008.02.015.

Kistelegdi, István; Háber, István (2012): Gebäudeaerodynamische Untersuchungen einer Plusenergie-Produktionsstätte mit passiven Lüftungstürmen in Sikonda (Südungarn). In Bauphysik 34 (3), pp. 107–120. DOI: 10.1002/bapi.201200016.

Schwan, Lukas; Kiluthattil, Eabi; Madjidi, Madjid; Auer, Thomas (2017a): Viability study of Solar Chimneys in Germany – Analysis and Building Simulation. In TU Delft Open (Ed.): Powerskin Conference. Proceedings. With assistance of Thomas Auer, Ulrich Knaak, Jens Schneider. Powerskin Conference. München, 19.01.2017. TU Delft Open. Delft: TU Delft Open.

Schwan, Lukas; Madjidi, Madjid; Auer, Thomas (2017b): Geometric optimization of thermally activated small scale solar chimneys for natural ventilation applying CFD simulations and measurements. In ECOS (Ed.): 30th International Conference on Efficiency, Cost, Optimization, Simulation and Environmental Impact of Energy Systems. Proceedings. ECOS 2017. San Diego, July 2-6. San Diego State University.

VDI (2001): Facility Management - Anwendungsbeispiel aus dem Gebäudemanagement. VDI 6009 - Blatt 1. VDI.

MULTI-FUNCTIONAL FAÇADE WITH PV FOR SOLAR AUTONOMOUS COOLING APPLICATIONS

T. Selke[1], T. Schlager[1], M. Rennhofer[1], A. Heinz[2], D. Brandl[2], T. Mach[2]

[1] AIT Austrian Institute of Technology GmbH, Vienna (Austria)

[2] Graz University of Technology, Institute of Thermal Engineering (Austria)

Abstract

The objective of the Austrian research project COOLSKIN is the development, assessment and functionality approval of a façade-integrated energy system for cooling. Façade integrated photovoltaic modules directly convert the solar irradiation onto the vertical surface into electricity, which operates the compressor unit of a heat pump cycle for controlling the indoor temperature of the adjacent room. The COOLSKIN system concept addresses a) decentralization of the energy supply and b) energy autarky by the usage of solar electricity, i.e. no external energy sources are required. Methods to fulfil the project requirements are i) elaborated system simulations, ii) experimental tests with a functional model of the system and iii) field tests under real operating conditions. With this paper, the authors present the a) specification of the COOLSKIN system design and b) first results and findings of both conducted system simulation and laboratory test measurements of electric components.

Keywords: Multi-functional façade, solar autonomous cooling, façade integrated Photovoltaics

1. Introduction

In 2015 the Austrian research project COOLSKIN was launched, in which a multidisciplinary team aims to develop, assess and test different façade concepts with the technical integration of both photovoltaics (PV) and air-conditioning or cooling system into the façade construction. There is a good coincidence between the daily and/or seasonal profiles of the cooling demand in buildings and the solar irradiation hitting the surface area of the façade. Furthermore, there has been a significant cost reduction of photovoltaic modules in the last decade (Fraunhofer ISE). The COOLSKIN energy design concept focusses on technical solutions for achieving high level of energy autarky in the operational phase, i.e. there is no connection to the public grid. The COOLSKIN concept addresses as well a high level of pre-fabrication of the technical façade solution.

The COOLSKIN team formulated additional framework conditions for the development:

- Office buildings offers a greater potential for decentralized cooling system solutions compared to residential buildings. Therefore, primarily office buildings are investigated. The technical configurations of the façade do respect the boundary conditions and specifications of an office façade.
- Europe is the primary target market – Increasing demand for cooling and air-conditioning in the building sector and the climate change will lead to additional markets. All European cities are considered for being a potential application field.
- COOLSKIN concept addresses primarily technical solution for covering the cooling demand in buildings. Nevertheless, there is an emphasis on technical solutions for all-year operation, and other energy demands like heating and electricity for other appliances are going to be investigated as well.

For achieving the COOLSKIN target the research project is sub-divided into three development steps: i) evaluation of promising system configurations, ii) construction and dimensioning of a functional model and iii) implementation and energy monitoring with the help of a field test façade. This paper reports on first results and findings of the two first development steps i) and ii).

doi:10.18086/swc.2017.28.18 Available at http://proceedings.ises.org

2. System design by simulation

Definition of boundary condition

As a first working step, boundary conditions were defined with regard to climatic, geometrical and utilization-related aspects. The definitions serve as the basis for the calculation of cooling and heating loads to be covered, the system considerations and simulations. An office was defined as a reference room, which was analyzed under different conditions with regard to climate and orientation. Three climatic data sets were selected as climatic boundary conditions, in order to represent a cold, medium and warm European climate. A comparison of all European capitals has shown that the cities of Helsinki (cold), Ljubljana (moderate) and Madrid (warm) are well suited to show the range of climatic conditions to be expected in Europe. For these cities a 10-year average climate was therefore created with the software Meteonorm (Meteotest, 2009).

Definition of the reference room

An office with an occupancy of three persons was defined and implemented as a thermal building model in the simulation environment (TRNSYS, 2011). The room has a net floor space of 25 m² and was simulated as four separate thermal zones facing into the main compass directions. An additional space or a thermal zone was positioned in the center as shown in Figure 1 (left). The used wall constructions and U-values are summarized in Figure 1 (right). It is assumed that the rooms are positioned in an intermediate store, thus there is no heat exchange through the floor and ceiling. The same applies to the partition walls, as it is assumed that a similarly conditioned room is adjacent. A façade configuration has been defined concerning the layout and the dimensions of the glazing surfaces, as depicted in Figure 2.

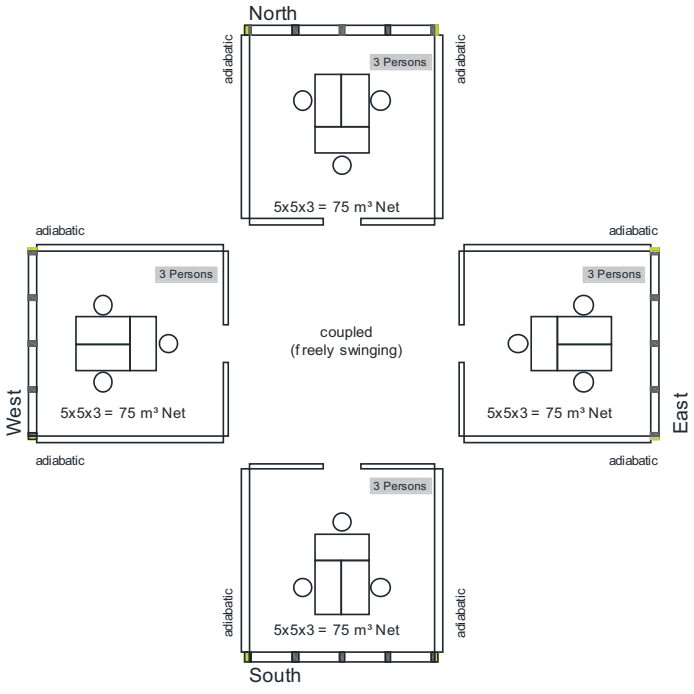

Fassade, opaque	d	λ	R	
steel	0.008	15.00	0.001	
insulation	0.033	0.04	0.825	
steel	0.008	15.00	0.001	
		Σ	0.826	[m²K/W]
		h i	0.130	[m²K/W]
		h e	0.040	[m²K/W]
		Rges	0.996	[m²K/W]
		Uges	**1.004**	[W/m²K]

Partition wall, adiabatic	d	λ	R	
plasterboard	0.030	0.21	0.142	
insulation	0.140	0.04	3.500	
plasterboard	0.030	0.21	0.142	
		Σ	3.784	[m²K/W]
		h i	0.130	[m²K/W]
		h e	0.040	[m²K/W]
		Rges	3.954	[m²K/W]
		Uges	**0.253**	[W/m²K]

Partition wall	d	λ	R	
plasterboard	0.020	0.21	0.095	
insulation	0.109	0.04	2.725	
plasterboard	0.020	0.21	0.095	
		Σ	2.914	[m²K/W]
		h i	0.130	[m²K/W]
		h i	0.130	[m²K/W]
		Rges	3.174	[m²K/W]
		Uges	**0.315**	[W/m²K]

Ceiling, adiabatic	d	λ	R	
wallboard	0.050	0.17	0.295	
air (massless layer)	0.250		0.169	
concrete	0.300	2.10	0.143	
		Σ	0.607	[m²K/W]
		h i	0.130	[m²K/W]
		h i	0.130	[m²K/W]
		Rges	0.867	[m²K/W]
		Uges	**1.154**	[W/m²K]

Window			
g-value	0.59		[-]
U glazing	0.59		[W/m²K]
U frame	2.08		[W/m²K]

Figure 1: Reference office room geometries (left), wall construction details (right)

Determination of energy demand and generation profiles

In the simulation the thermal conditioning (heating and cooling) of the reference office room is ideally regulated. This means that the room is supplied with precisely the thermal power, which is necessary in order to maintain a room temperature above 21 °C (heating) and below 26 °C (cooling). An additional thermal zone was positioned in the center of the four virtual rooms, which is in heat exchange with the four rooms and assumed to be "free swinging", i.e. which is not thermally conditioned (Figure 1). External shading was assumed for the transparent surfaces, which is activated with a shading factor of 0.75, when the room temperature rises above 24 °C and deactivated, when it drops below 22 °C. A fresh air supply of 108 m³/h is assumed during the presence time

(working time varying between 8:00 and 18:00), with a controlled ventilation and exhaust air heat recovery (recovery rate 60 %). In the cooling case the heat recovery is deactivated, when the outside temperature is lower than the room temperature.

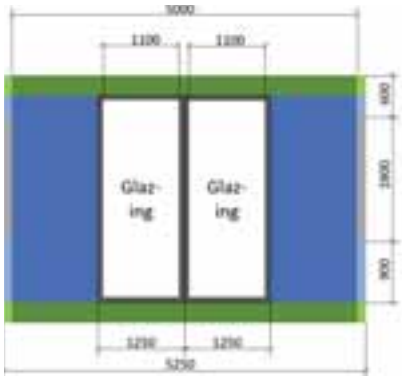

	Area m²	Fraction %
PV	11.22	59.9
Frame	1.31	7.0
Glazing	6.19	33.1
Sum	18.72	100

Figure 2: Façade configuration

Photovoltaics

For the simulation of the photovoltaics, the model Type 94a included in the TRNSYS library, which is based on a 4-parameter approach (TRNSYS, 2012), is used. The parameterization was carried out according to the manufacturer data of a polycrystalline PV module available on the market. It is assumed that the PV is integrated vertically into the façade with the maximum possible area for the particular façade configuration, as specified in Figure 2.

Heat demand and PV-yield

Simulations with a time step of one hour were carried out for the described configurations concerning the orientation of the room and different climates. As an example, the results on a monthly base are shown in Figure 3 for the location Ljubljana. According to these results the cooling demand coincides well with the PV yield and it can be assumed that sufficient PV electricity is available to cover the cooling demand for all four orientations, assuming a *Coefficient of Performance* (COP) of a hypothetical cooling unit of 2 to 3. With the assumed dimensioning of the PV it should also be possible to cover the heating demand of the room.

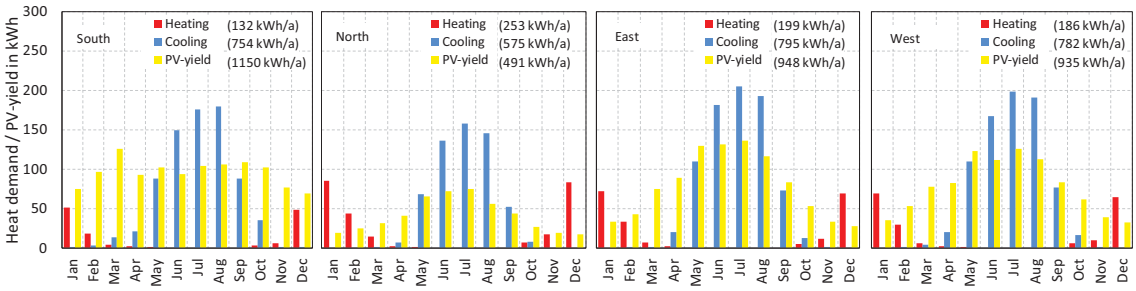

Figure 3: Simulation results: Monthly sums of heating demand, cooling demand and PV-yield for Ljubljana, yearly sums in brackets

However, for a real system it is essential, how well the demand and the PV electricity generation coincide on a smaller time scale and how much energy has to be stored, in order to be able to compensate times with an excess supply or an undersupply of electricity. For an exemplary week in July, hourly values of the cooling demand and the PV-yield are shown in Figure 4. Depending on the orientation, the peaks for both values occur at different times and with different size.

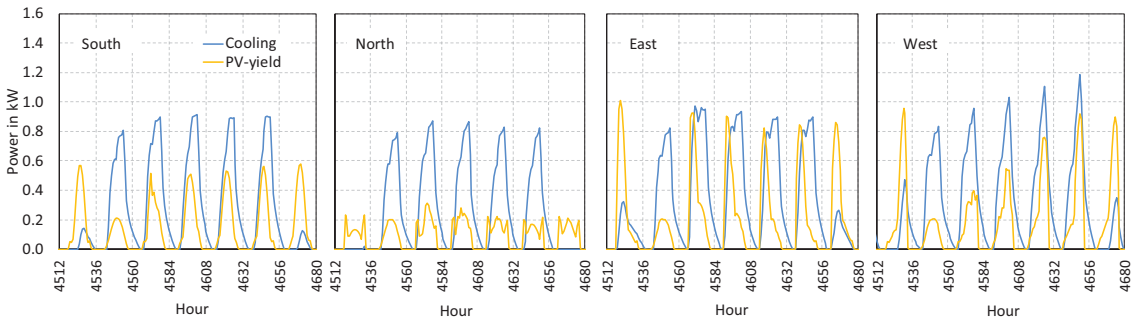

Figure 4: Simulation results: Hourly values of the cooling demand and the PV-yield for an exemplary week in July in Ljubljana

Analysis of the time shift between supply and demand and the need for energy storage

Based on the simulation results described above, an analysis of the temporal shift between supply and demand as well as a rough estimation of the necessary capacity of an energy storage was carried out. A very simple model of a compression chiller is used for the supply of the cooling demand, the cooling capacity and the electrical power consumption being assumed as a function of the room temperature and the outside temperature. In order to compare the occurrence of the power consumption and supply of cooling capacity of the chiller with the cooling load of the building and the PV-power the approach described in the following is used.

It is assumed that the chiller is capacity-controlled and that it is only running, when a cooling load occurs. Due to the temporal offset of the PV yield and the power consumption of the compressor, electrical energy has to be stored. This is shown qualitatively in Figure 5. As cooling capacity is provided at times of an occurring cooling load, the previously generated PV electricity has to be stored in an electrical storage in order to use it at later times. This is indicated by the gray surfaces in the diagram. The green surface represents the share of energy, which can be covered simultaneously and without storage.

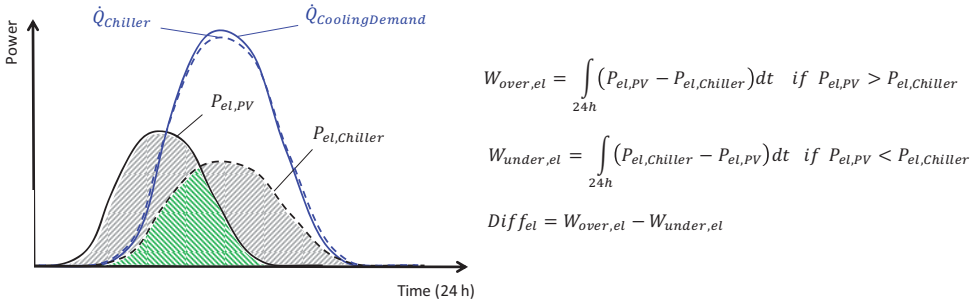

Figure 5: Qualitative daily sequences for the comparison of the electricity consumption of the chiller (Pel,Chiller) and the electricity generation of the PV (Pel,PV)

For each day of the year the electrical over- and under-supply as well as the difference between the over- and under-supply is calculated (equations in Figure 5). Figure 6 shows the results for the Ljubljana climate and the south-orientation in the form of ordered duration curves for two different sizes of the PV (5.6 m² on the left and 8.4 m² on the right). In this example, a chiller with a cooling capacity of 0.85 kW is used. For each case the right diagram shows, on how many cooling days a certain amount of over- and under-supply is exceeded.

According to these results, an under-supply of maximum 2 kWh has to be covered out of an electrical storage. Of course for this a corresponding over-supply is needed beforehand, in order to charge the storage. From the diagram on the left it can be seen that this is not the case on every day for both dimensioning's (negative $Diff_{el}$), of course with better results for the larger PV area. But it has to be mentioned, that these results are of course quite theoretical, as every single day is treated individually, i.e. it is assumed that the storage is empty at the beginning of each day. However, for the desired purpose (rough dimensioning of the storage capacity), the method is considered to be appropriate and a storage of 2 kWh should be appropriate for the considered application. For the other orientations, the results are slightly different, but the required storage capacity of 2 kWh stays the same.

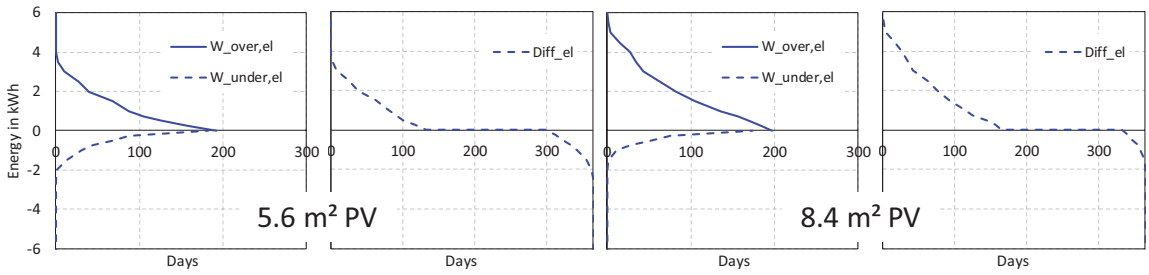

Figure 6: Duration curve of electrical over- and under-supply and daily difference between over- and undersupply for Ljubljana, south orientation for two different PV sizes (cooling capacity chiller 0.85 kW)

3. Experimental components and system tests

This chapter reports on the laboratory tests of the operational behavior of each single electric component and the compatibility test of the overall system. Main components of the setup are shown in Figure 7. Photovoltaic modules (1) generate electricity used as energy source for the cooling process. The maximum power point (MPP) tracker (2) ensures that the photovoltaic system operates in its most efficient operating point and it controls the battery charging process. A Lithium iron phosphate ($LiFePO^4$) battery (3) functions as an energy storage, when the current PV electricity generation for the compressor motor of the cooling system is not sufficient. The battery voltage of 25.6 V is transformed to 230 V, 50 Hz AC-Voltage by the inverter (4) in order to run the AC-Compressor motor. Due to the energetic conversation losses of MPP-Tracker (η_{MPP}), Battery (η_{Bat}) and Inverter (η_{Inv}), not more than 85 % of energy harvested by the photovoltaic modules can be used to operate the compressor motor of the cooling machine. In part load operation or extreme environmental conditions, the efficiency might be even worse. These energy losses are transformed into 100% heat, which requires an internal active cooling of these electric components. MPP-Tracker and Inverter stop working in case of temperatures higher than 60 °C.

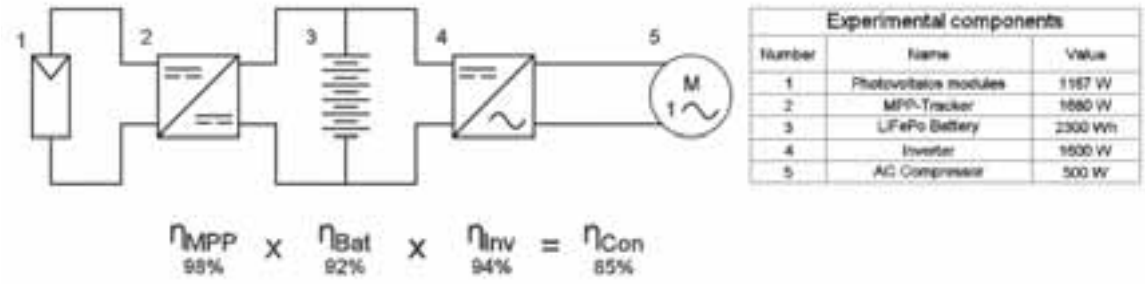

Experimental components

Number	Name	Value
1	Photovoltaic modules	1167 W
2	MPP-Tracker	1680 W
3	LiFePo Battery	2300 Wh
4	Inverter	1500 W
5	AC Compressor	500 W

Figure 7: Block diagram of the electric circuitry with conversation efficiency.

After the successful completion of the laboratory tests, all components were assembled to enable a simple installation at the mounting site. Figure 8 shows the two test boxes at the campus of Graz University of Technology with the installed PV modules. The box on the right with the installed “black line” photovoltaic modules is used as test box where the cooling system will be installed for a long run test under real climate conditions. The box on the left side where the “digital print” photovoltaic modules are installed is the reference box.

Figure 8: Test boxes with installed aluminum frame and the photovoltaic modules, the right box is the test facility with the installed cooling system while the left box is used as reference box (Source: TU Graz)

4.1 Test photovoltaic modules

Two different glass-glass photovoltaic module types, both with mono crystalline cells, were tested: i) “black line”, with blackened bus bars and ii) “digital print”, with screen printed front glass. Four modules of each type were produced. The size of the “digital print” modules are the same as the “black line” modules. Pictures of the used modules are shown in Figure 9. Mounted at the test boxes either the “black line”- or the “digital print”- modules will be used to run the cooling machine. The COOLSKIN project aims to demonstrate that the designed façade integrated energy system operates even when architecturally appealing photovoltaic modules with relatively low efficiency are applied.

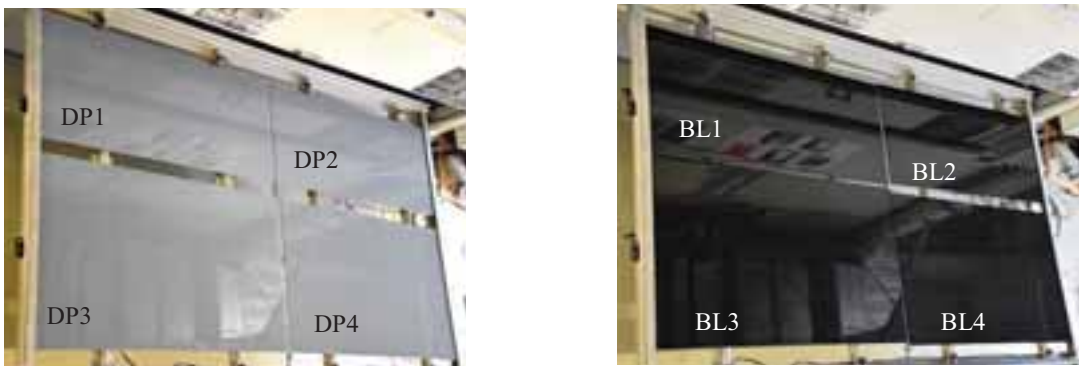

Figure 9: Photovoltaic module type “digital print” DP (left) and type “black line” BL (right) (Source: AIT)

Measurement results show that the module type “digital print” has approximately 2.6 percentage points lower efficiency than the “black line” modules. The cumulated power of the four “digital print” modules is 952 W, which is roughly 18 % lower than the cumulated power of the four “black line” modules with 1167 W. Additionally all glass-glass photovoltaic modules were checked in advance before its test box installation regarding cell cracks. Figure 10 displays an electroluminescence picture of one of the eight tested glass-glass photovoltaic modules.

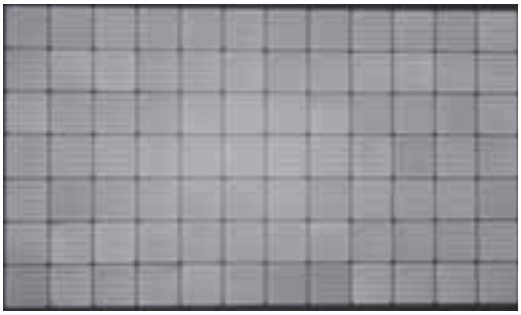

Figure 10: Electroluminescence picture of glass-glass photovoltaic modules without any cell cracks.

4.2 Test batteries

Two Lithium iron phosphate ($LiFePO^4$) batteries are used as buffer storage between the photovoltaic system and the cooling machine. $LiFePO^4$ batteries are a type of lithium-ion battery, with the advantage of a higher energy density, higher power density, longer lifetime and, because of its thermal and chemical stability, improved battery safety. Cell voltage of a $LiFePO^4$ stays close to 3.2 V during discharge until the cell is exhausted. Due to that, the cell can deliver nearly full power until it is discharged. In one battery, four cells are connected in series for a nominal battery voltage of 12.8 V. At cell voltages beyond 3.6 V or under 2.5 V, severe damage will occur in most instances. Therefor a so-called battery management is needed, which balances the cell voltages, stops charging in case of over voltage and stops discharging in case of under voltage.

The two $LiFePO^4$ batteries are connected in series to a nominal Voltage of 25.6 V and a capacity of 2304 Wh when discharged with less than 90 A.

As the used charging system has no temperature compensation, the temperature behavior of a battery cell was tested in a climate chamber. A fully charged $LiFePO^4$ cell was cooled down to -25 °C and heated up to 55 °C while the cell voltage was measured.

Measurement results are shown in Figure 11. The cell voltage is nearly stable from -25 °C to 45 °C. In this temperature range, no temperature compensation is needed for the charging process. At temperatures beyond 45 °C, cell voltage decreases and a battery management with temperature compensation would be recommended. The COOLSKIN system design contains an active cooling system in the façade mock-up to keep temperatures below 45 °C.

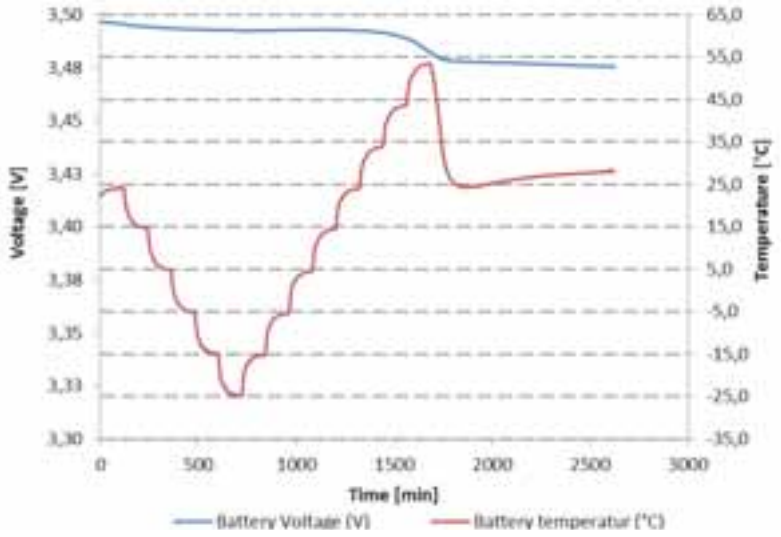

Figure 11: Voltage curve of a LiFePO4 cell in a temperature range from -25 °C to 55 °C.

4.3 System test

Charge process is started in case that the battery voltage is lower than the charge cut-off voltage of 28.4 V and the available photovoltaic power is higher than the load plus conversion losses. The MPP-Tracker (i.e. charge controller) controls the charging progress according to the charge level, which is indicated by the voltage level of the battery. The controller is configured for a three-phase charging process:

1. Bulk: The controller delivers as much charge current as possible to rapidly recharge the batteries.
2. Absorption: When the battery voltage reaches the absorption voltage setting, the controller switches to constant voltage mode. When only shallow discharges occur, the absorption time is kept short in order to prevent overcharging of the battery. After a deep discharge the absorption time is automatically increased to make sure that the battery is completely recharged. Additionally, the absorption period is also ended when the charge current decreases to less than 2A.
3. Float: During this stage, float voltage is applied to the battery to maintain it in a fully charged state. When

the battery voltage drops below float voltage during at least 1 minute a new charge cycle will be triggered.

An example for the three-phase charging process is shown in Figure 12.

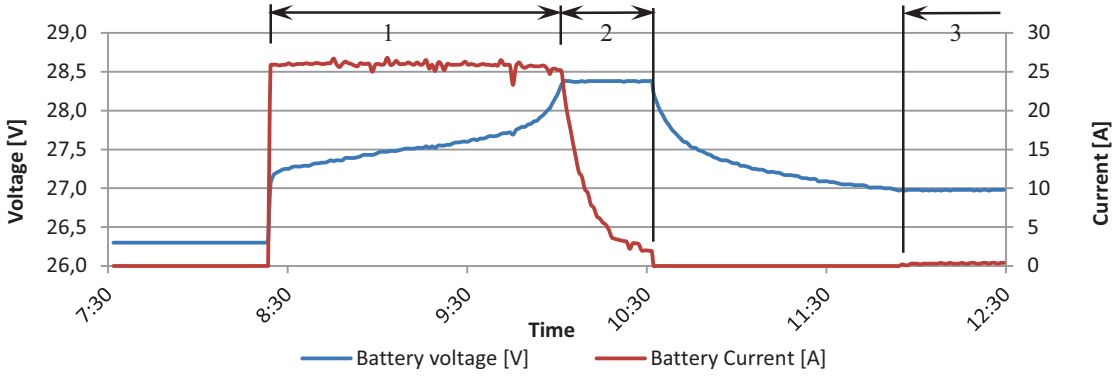

Figure 12: Example of three-phase charging process.

Discharging process starts when the load is higher than the photovoltaic yield. In this application, the main load would be the compressor of the cooling machine with 500 W. Nevertheless also, the monitoring system, the inverter and the MPP-Tracker have standby energy consumptions. In total this standby losses are in a range of 10 W to 20 W. However, a discharge protection is needed to disconnect any load before deep discharging the battery. In this application, the inverter stops before the battery voltage decreases below 23 V. In addition to that a battery protect relay cut off the battery from all loads, including standby consumers, if its voltage decrease below 22 V.

Figure 13 shows a measured battery discharge processes. The average battery voltage of 25.8 V and the average battery current of about -25 A result in an average battery power output of 640 W. The compressor motor consumes 500 W electric power, 140 W can be assigned to conversion losses and standby energy consumptions. This results in an overall efficiency of 78 %. According to the datasheet the total capacity of the battery pack is 2,304 Wh. Concerning a power output of 640 W, this would result in an operation time of 3.6 hours, which correlates to our measurement results.

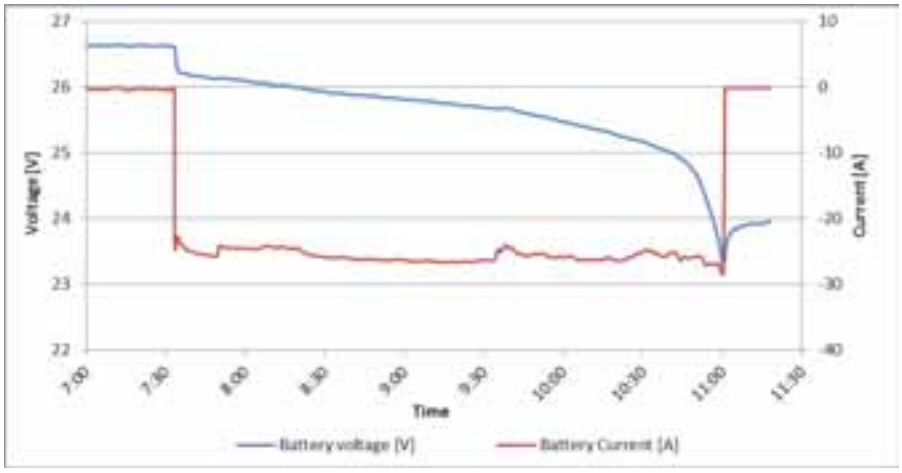

Figure 13: Battery discharge process with a 500 W compressor as load.

Once the inverter stopped because of deep battery voltage, it will not restart until the battery it is recharged to 25 V. In case that battery voltage is low and the energy consumption of the load is higher than the photovoltaic yield, the inverter will start and stop periodically. An example of this undesirable behaviour is shown in Figure 14. The energy need of the load is higher than the photovoltaic yield, which leads to a discharge of the battery and hand in hand with that to a negative battery current. Due to the discharge process, the battery voltage decreases until the inverter stops. As the major part of the load is disconnected when the inverter stops and photovoltaic yield is still available, the battery is charged. The inverter restarts if the battery voltage is higher than 25 V.

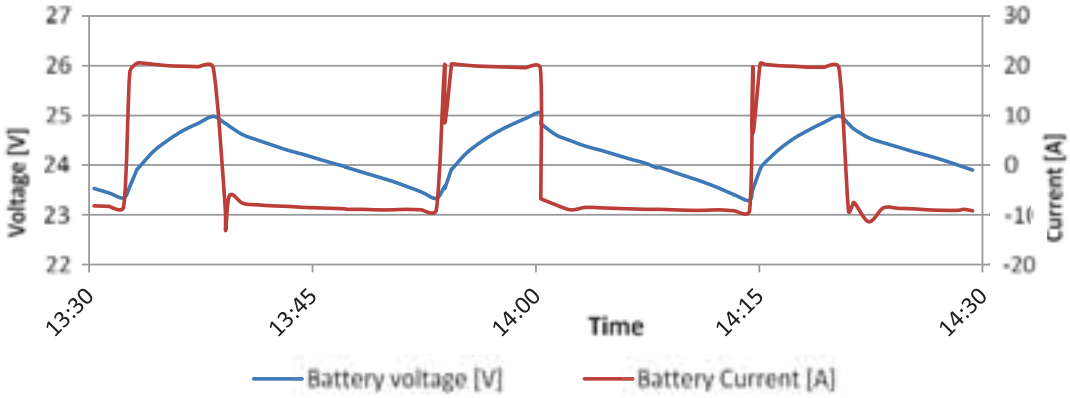

Figure 14: Start-stop behaviour of the inverter at low battery charging state and higher energy consumption than production.

A disadvantage of the used compressor type is shown in Figure 15. The relatively high starting power that may be four to eight times the nominal power could rapidly decrease the battery voltage which would strengthen the above mentioned start-stop behaviour. To avoid this effect a speed controlled compressor will be used in the field tests.

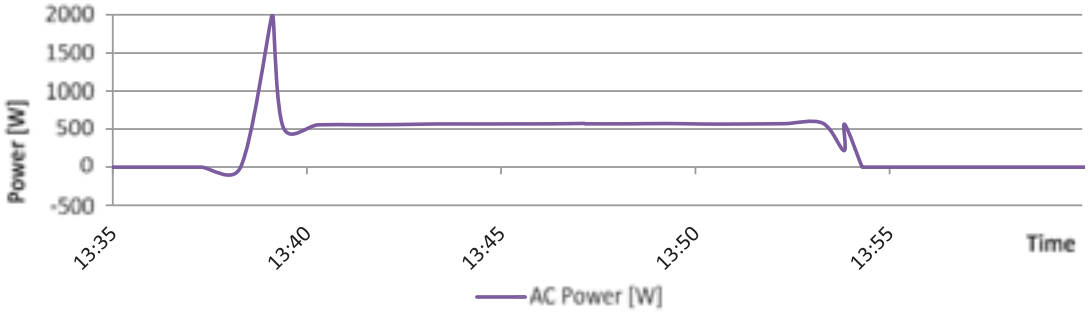

Figure 15: Start-stop behavior of the compressor.

4. Findings

Following key findings were made on the results from the simulations and laboratory tests

(a) Simulation

Based on results of the energy demand simulation some facts could be revealed which are important for the operation of a decentralized cooling system like the one of COOLKSIN. First, it was shown that under the configuration of the free-swinging coupling of the rooms the monthly cooling demand (see Figure 3) of north and south oriented rooms is only slightly different while the energy production from the PV-system is differing significantly. The corresponding analysis of the east orientation towards the west orientation shows that for them the monthly demand and production are more equal. From this, it can be concluded that a completely decentralized supply is mainly possible for south, east and west, where south might produce more than needed. If a north façade should be used for cooling excess energy from the other facades has to be provided via battery storage.

Analyzing the highly resolved data from Figure 4 one finds that for daily cycles the main result stays the same as for Figure 3. The south and north façade consume about the same amount of cooling demand, but the production at north is poor. For the east and west façade one finds that during the week under analysis the cooling demand of east and west façade differs significantly first for its daily evolution and then also for its evolution during the week. This behavior is strongly dependent on the daily and weekly distribution of sun hours. Even for a series of clear sky days the east and west would differ, as during the day the environmental temperature also raises.

An analysis with a simple worksheet approach showed that an electrical storage with a capacity of about 2 kWh should be sufficient to compensate the offset in time between the PV-yield and electricity consumption of the chiller.

(b) Experimental test in laboratory

From the experiments as shown in Figures 11-15 the main advantages and disadvantages of the system set-up can be extracted. First, the direct coupling of the battery and the load in series does not allow to bypass the battery. This might be useful in a real setting, when the battery is empty and should be loaded, there is enough solar energy to run the load, but it will take some time to recover the battery voltage above the security threshold (here this was between: switch off: 23 V, switch back on: 25 V. If load priority is a set target; the bypass is essential, in a setting similar to Figure 14.

Further is was important to test all critical settings of the systems: the lower voltage of the battery and switch of, meaning that there is not enough solar electricity but the load was powered (see again Figure 13, as it is). Very important for the real running of the system out-doors was also the operation point where the load is powered, the battery is full, but the solar production is slightly decreasing, leading to a discharging of the battery. This behavior can show if the PV-system size it at all big enough (including the losses due to the inclination for the modules in the façade).

In a worst case scenario there will be day with cooling demand but not sun irradiation to run the system. From this scenario the needed storage size could be extracted for running the cooling system only via the battery: then the storage system capacity SC is given by the time interval t where the demand is provided, the electric load demand ELD and the DoD of the battery system by: SC = t*ELD / DoD (Compare, 2016). For running for n days this can be expanded by n*t.

The last important test is the test showing the “flickering” of the whole system in Figure 14. It shows that for a certain irradiation budget the system layout from battery capacity and PV-array size is too weak. From such a behavior it would follow that the PV-size or the battery size and the PV-size should be increased. In a setting where the system components can be programmed one should try to avoid this behavior, e.g. by increasing the level, where the battery is reconnected to the load (e.g. from 25 V to 26 V or even above).

(c) Experimental test set up in the façade

Technical description

The setup was built in a way that the most flexible alterations can be done between battery, PV-system and cooling equipment. The system contains of 4 subsystems of PV-arrays. The black-line is high efficient while the colored edition is reduced in its efficiency. It was taken care in the irradiation simulation of the laboratory experiments to include this behavior also. Then the lower panels and the upper panels differ in electric output power also, see table 1. The corresponding sub-arrays of upper digi-print, lower digi-print, upper black-line, lower black-line then give then a maximum electric power of 220 W, 551 W, 481 W and 685W, respectively. This power output has then to be considered also with approx. 0.65 for the daily energy yield compared to an optimal oriented PV-facility due to the façade integration. By standard setting all digital-print or all black-line modules are connected in series to MPP tracker and the battery system. The setting can be switched. Also, only the small systems or only the lower systems can be connected separately in order to simulated bad system layouts with too small PV-capacity.

Field tests planned

For the field tests several runs are planned. The most important experiments are those of continuous running with parallel data evaluation in order to identify times of system behavior reflecting cases from Figure 11 to Figure 15. These are:

- Continuous loading while load is connected
- Continuous de-charging while load is connected
- Voltage all day between 23 V and 28 V
- Flickering

After doing that, single cases can be investigated to higher extent, like altering the system configuration by the PV-panels connected to the battery. Also, the comparison of the influence of the power loss from digi-print will be done systematically

5. Outlook

Next activities in the COOLSKIN project are dedicated to a) the assembling of the outdoor test facility including cooling system and b) the examination of the long-term observation of the energy performance by a scientific monitoring till august 2018. Figure 16 shows a three-dimensional CAD model of the aluminum frame with the integrated cooling system. According to this CAD model, this system will be attached to the test box for long-term tests. The cooling system consists of five main assembly units. The first unit is the electric cycle that receives electricity from the photovoltaic modules, charges the batteries and serves as electrical source for the other units inside the cooling system. The next unit is the heat pump cycle, where energy for cooling as well as for heating is generated. The heat pump cycle is connected with an air channel by an integrated heat exchanger, which serves as condenser in cooling mode and as evaporator in heating mode. The heat pump cycle can either charge into a water cycle via a plate heat exchanger or into the room air. The water cycle is connected to the cooling and heating system of the test box (activated ceiling and/or floor). On the other hand the room air of the test box can be directly conditioned through a conventional air conditioning system (fan coil), which is also integrated in the aluminum frame.

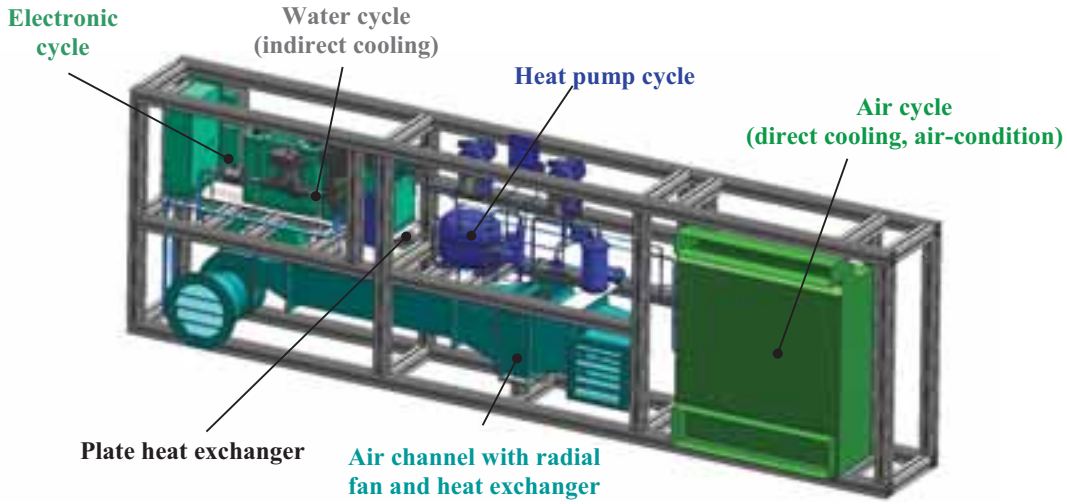

Figure 16: 3D CAD model of the aluminum frame with the integrated cooling system (Source TU Graz)

The whole system is going to be assembled and put into operation in the laboratory of the Institute of Thermal Engineering. After the system is working, it will be attached to the test box (see in Figure 8) for long-term tests under real climate conditions (covering all seasons). In this test, it will be figured out if the system is able to cover the cooling and heating demand for a comfortable indoor climate. Furthermore, the thermal behavior of the interior room can be compared with the indoor climate of the reference box (see in Figure 8). The reference box has only a floor heating system and allows no cooling. For the long run tests, the boxes´ interior rooms will be simulated as an office. Among others in the test boxes are considering interior heat loads and hygienic air exchange from 8 am to 4 pm at working days.

6. Acknowledgement

This project ‘COOLSKIN’ is funded by the national ‘Klima- und Energiefonds’ within the programme ‚e!MISSION’ 1st Call 2014.

7. References

(Fraunhofer ISE); Current and Future Cost of Photovoltaics; Long-term Scenarios for Market Development Prices and LCOE of Utility-Scale PV Systems, Study on behalf of Agora Energiewende; February 2015, page 6

(Meteotest, 2009): Meteonorm 6.1.0.9, Global Meteorological Database for Engineers, Planners and Education, Software and Data on CD-ROM. Meteotest, Bern, Switzerland.

(TRNSYS, 2011): TRNSYS 17, A Transient System Simulation Program, V 17.00.0019, Solar Energy Lab, University of Wisconsin – Madison, USA

(TRNSYS, 2012): TRNSYS 17, A Transient System Simulation Program, Mathematical Reference, Volume 4. Solar Energy Laboratory, University of Wisconsin-Madison

(Compare, 2016): Y. Abawi, M. Rennhofer, K. Berger, H. Wascher and M. Aichinger; COMPARISON OF THEORETICAL AND REAL ENERGY YIELD OF DIRECT DC-POWER USAGE OF A PHOTOVOLTAIC FAÇADE SYSTEM; In Renewable Energy; 89; p 616-626 (2016)

Highest Efficiency Ice Storage for Solar Cooling Systems – Experiences with a Vacuum Ice Slurry Cold Thermal Energy Storage

Christoph Steffan[1], Carsten Heinrich[1], Mathias Safarik[1] and Marcus Honke[1]

[1] Institute for Air Handling and Refrigeration, Dresden (Germany)

Abstract

With an increasing share of renewable energies efficient storage technologies are in high demand. Due to the high specific enthalpy of fusion pumpable water-based ice slurry represents a thermal storage medium which is ecological as well as economical advantageous. A further need for research can be seen in the increase of efficiency for ice slurry generation processes. The high efficient process of ice slurry generation by direct evaporation under rough vacuum conditions including its potential for solar cooling systems is presented in this paper. After installing a first pilot of an integrated ice slurry generation and storage system based on the R718 turbo vapour compression technology a new facility concept for higher capacities has been developed and commissioned. Findings from recent research projects flowed into the conceptional work and have been implemented. The facility has a nominal ice generation capacity of 180kW, a storage capacity of 1MWh and a discharging capacity of max. 300kW.

Keywords: Thermal Energy Storage, Vacuum Ice Slurry, Solar Cooling, water as refrigerant (R718), Natural Refrigerants, Secondary Refrigerants, Load Management, District Cooling

Introduction

In fields of refrigeration and air conditioning technologies the current research focus lies on the transition towards natural refrigerants combined with an increase of efficiency for the whole compression cycle, e.g. development of new compressors with higher efficiencies especially for part load conditions (Heinrich, 2012). In the near future an increasing expansion of the renewable energy sector will gradually challenge us worldwide to use generated power when it is made available. A main question will be how to store energy that is not immediately needed at time of generation. The reduction of peak loads and the compensation of fluctuating availabilities of renewable energy sources requires a comprehensive planning approach. With the integration of a thermal storage system energy demand and availability can be adapted. For refrigeration and air conditioning systems several approaches to store cold thermal energy are applicable. Fig. 1 gives an overview of available storage technologies according to the type of storage media (Urbaneck, 2012).

Fig. 1: Technologies for water-based cold thermal storage systems

From an economical as well as ecological perspective systems with water as storage medium represent a safe, environmentally friendly and efficient approach to store thermal energy (Kauffeld et. al, 2005). The synergy effect of a pumpable secondary refrigerant with the characteristics of a phase change material are the key argument for the usage of water-based ice slurries (see Fig. 2). Besides the high enthalpy of fusion (transport capacity) higher heat transfer coefficients can be achieved. Hence, the dimensions of cooling distribution networks and related pump capacities can be reduced significantly (Kauffeld et. al, 2010).

doi:10.18086/swc.2017.28.19 Available at http://proceedings.ises.org

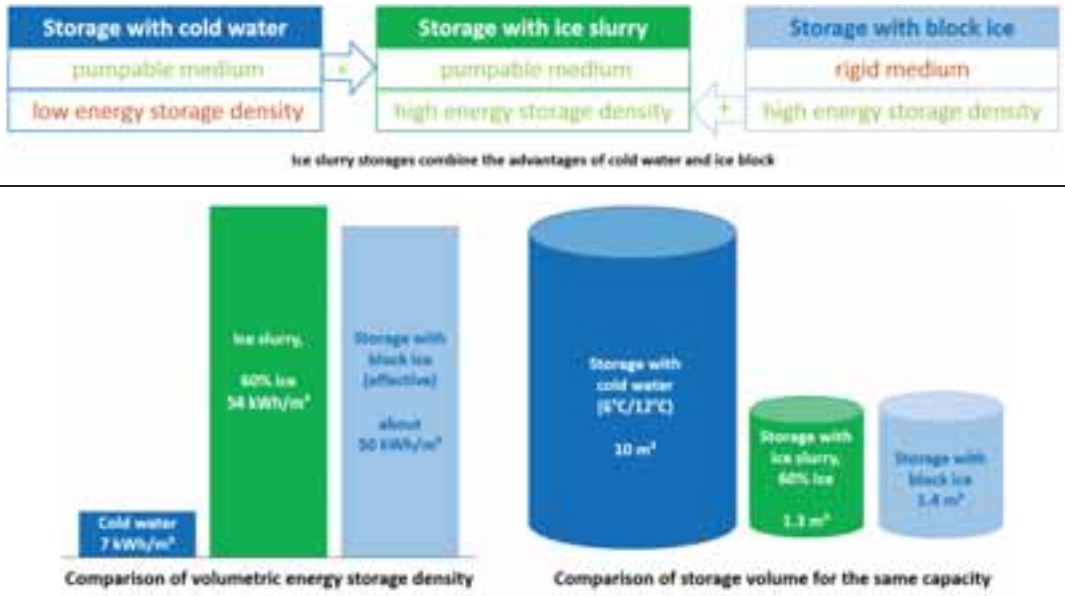

Fig. 2: Synergy effects of ice slurry as thermal storage medium

To date ice slurry based cooling systems are mainly applied in cooling processes for food products, e.g. breweries, fishing and refrigerating counters. In Japan first air conditioning applications were installed by using ice slurry only as storage medium (Snoek, 1993).

For the production of ice slurry various processes have been developed and are available on the market (Kauffeld et. al, 2010). From an energetic perspective vacuum ice slurry technology is a promising approach in terms of efficiency of cold generation for all traditional applications of industrial refrigeration processes and air conditioning of buildings (Albring, 2009). The system can be integrated for cold thermal energy storage in larger PV driven cooling systems to increase efficiency, availability and comfort or to minimize back-up needs. The current research work focuses on the optimization of the vacuum ice generation process as well as investigating new fields for ice slurry applications, e.g.:

Fig. 3: General fields of application for ice slurry as secondary refrigerant and storage medium

Vacuum Ice Slurry Technology

2.1. Process description

The process of ice generation by direct evaporation in a rough vacuum runs at low pressure conditions below the triple point of water (p_{Tr}=611 Pa, ϑ_{Tr}=0.01 °C). Within a vessel which is initially pre-evacuated down to saturation conditions water is cooled sensibly by heat loss through evaporation (Figure 1). Below triple point conditions water cannot cooled down anymore. Thus, the energy for evaporation must be provided by a further phase change – the generation of ice particles within the sump of the evaporator. The quotient between enthalpy of fusion ($h_{lg}\approx 2500\,kJ\cdot kg^{-1}$) and the freezing enthalpy ($h_{ls}\approx 333.4\,kJ\cdot kg^{-1}$) provides the mass relation between evaporated vapor and the amount of produced ice particles. Hence, evaporating one kilogram of water would lead to a generated ice mass of 7.5 kg. Under vacuum conditions the corresponding volume flow is high due to the low density of water vapor ($\rho_g\approx 0.005\,kg\cdot m^{-3}$). The driving thermodynamic potential in the evaporator is given by the pressure difference between saturation pressure (p_{lg}) and the pressure (p_g) in the gas phase above. High energy efficiency can be achieved because of a minimal thermal resistance through direct evaporation. Direct contact between storage medium and refrigerant requires low subcooling temperatures in comparison to other ice slurry generation processes. By increasing the evaporating surface A_O and the heat transfer coefficient α the evaporating performance can be further increased. In order to achieve stable ice generating conditions in the sump of the evaporator the pressure difference must be kept stable, e.g. by using a vacuum pump. Higher water vapor volume flows can be conveyed by applying a centrifugal compressor technology.

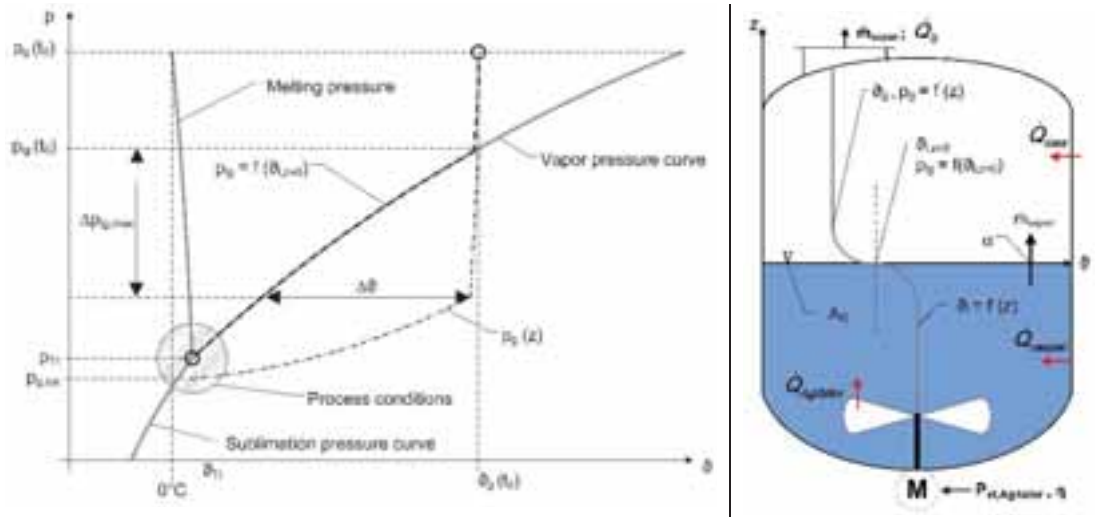

Figure 1: Ice slurry generation by direct evaporation in a rough vacuum

2.2. Efficiency comparison

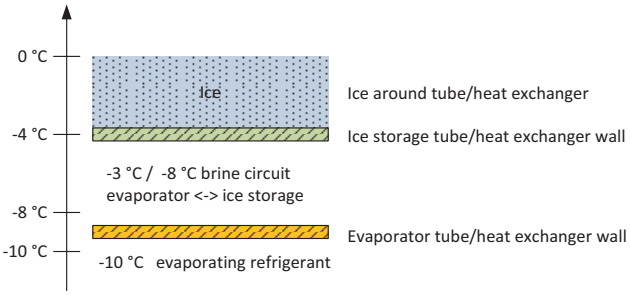

Fig. 4: Exemplary temperatures during charging of a block ice storage using a cold brine circuit

One major disadvantage of conventional ice generators (e.g. in block ice storages) is the low effective evaporation temperature of the cooling cycle which is often operated in the range of -10 °C to -13°C. The low evaporation temperature is caused by the temperature differences necessary for heat transfer between the evaporator of the chiller and the heat exchanger inside the ice storage/ice generator, see Fig. 4. Hence, the low evaporation temperature results in a lower efficiency of the ice generation process. Generating ice slurry by direct evaporation

of water the heat exchanger between the refrigerant and the phase change material water/ice can be eliminated. Here, the water itself is used as refrigerant. The effective evaporation temperature is as high as -0°C which leads to highest efficiencies for ice generation using the direct evaporation process.

Tab. 1: Calculation scenarios and results

Process	t_e [°C]	t_c [°C]	EER	Specific energy demand [kW_e/kW_{th}]
1) On-time chilled water generation 6/12 °C (chiller with R717, η_{is} = 0.7)	4	34	5.71	0.175
2) Ice slurry generation by direct evapocation (refrigerant R718, η_{is} = 0.65)	-0.5	6	26.2	0.038
3) Combined (cascaded) ice slurry generation using the conventional chiller for condensing the compressed water vapour of the vacuum ice process -> combination of 1) and 2)	-0.5	34	4.69	0.213
4) Combined (cascaded) ice slurry generation at nighttime conditions with reduced condensation temperature	-0.5	24	6.67	0.150
5) Conventional ice slurry generation (scraped surface) or block ice storage (chiller with refrigerant R717, compressor η_{is} = 0.7)	-10	34	3.49	0.287
6) Conventional ice slurry generation (scraped surface) or block ice storage at nighttime conditions with reduced condensation temperature	-10	24	4.71	0.212

Tab. 1 shows a comparison of thermodynamic efficiencies of two different approaches for ice slurry generation. Here only the required electrical capacity for the compressor is taken into account. Necessary capacities for mixing or scraping devices and auxiliary systems, e.g. initially or sequentially operating vacuum pumps should not be part of a general comparison and have to be evaluated case by case. Using the method of direct evaporation additional energy demand for ice production compared to chilled water generation can be reduced significantly. If ice generation (charging of storage) can be done during nighttime the efficiency can be further increased by taking advantage of lower ambient temperatures, see #4 and #6 in Tab. 1. The comparison between case 1 in (on-time chilled water generation) and case 4 (vacuum ice slurry generation during nighttime) shows that additional energy demand for ice generation can be overcompensated by saving that results from the decrease of the condensation temperature.

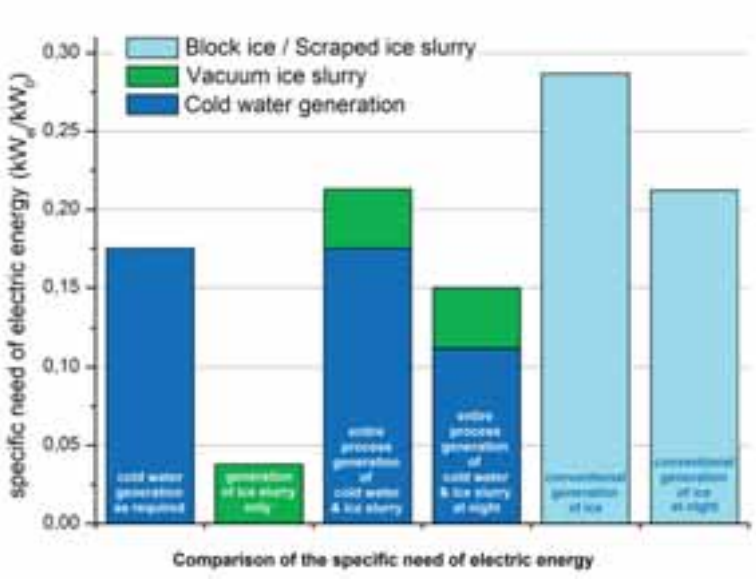

Fig. 5: Efficiency comparison

2.3. Facility Scheme

At Göttingen University a second pilot facility of a vacuum ice slurry thermal storage system has been installed. The system is integrated in the chilled water network of a chemistry building in order to reduce peak loads. An overall scheme of the facility is shown in Fig. 6. The chilled water network is run at 6°C/12°C. The conveyed and compressed water vapor is condensed by a direct condenser which is supplied by an intermediate cold water circuit. The produced condensation heat is transfered to the subordinate chilled water network. This is done by HX2.

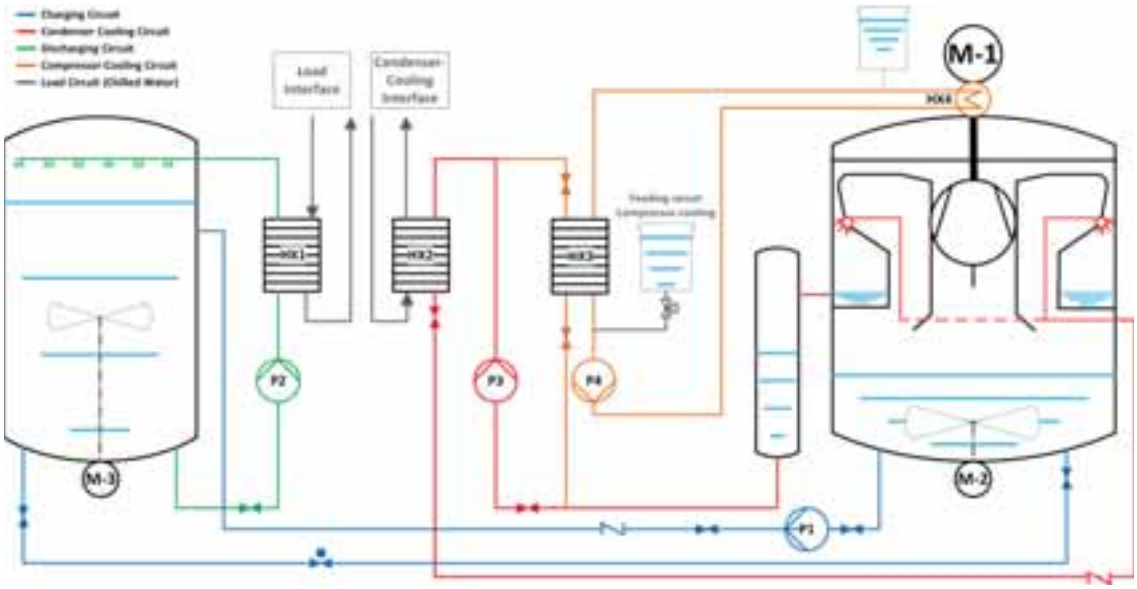

Fig. 6: General scheme of the pilot facility at University of Göttingen

A small fraction of the volume flow (condensed vapor, destillate) is used as return flow to the sump of the evaporator. For cooling parts of the compressor (contour plates, rotary shafts and seals) chilled water from the condenser cooling circuit is used. An agitator in the sump of the evaporator was installed in order to increase evaporation surface and thermal heat transfer coefficients for maximizing the evaporation performance. For discharging the storage a 300kW plate heat exchanger (HX 1) tranfers heat from the chilled water network to the ice slurry. The storage vessel has a diameter of 3 m and takes 28m³ of water. The fully charged storage reaches a capacity of 1.000 kWh which correlates with a mass fraction of 50 % ice produced. As well as for other ice slurry generating processes a freezing point depressant additive has to be used in order to reach smaller crystal sizes and minimizing the risk of frozen evaporation surfaces. At ILK's vacuum ice slurry generators sodium-chloride-solution (1%) is applied which lowers the initial saturation temperature by 0.61 K. The demonstration facility is fully-integrated within the subordinate control system. With an installed data logging and the access via remote control error messages and failure reports can be analyzed. An additional LabVIEW-programme is used for monitoring and data analysis.

2.4. Solar Cooling with Vacuum Ice Slurry

Using solar energy fluctuating availabilities lead to high requirements in order to level supply voltages in power grids. Besides electrical storage technologies peak availabilities can be used to converse and store effective energy for a delayed use, e.g. for cooling purposes. Even conversion losses can be shifted. Consequently energy consumption for the provision of cold thermal energy during trough periods can be minimized significantly. Nevertheless cooling load and energy availability curves has to be analyzed. In Fig. 7 two generic charts for load shifting describe the main approaches for the use of cold thermal energy storages. The upper chart shows an efficiency orientated approach with focus on ideal condensing conditions at times with low ambient temperatures. For instance in continental climate areas (e.g. deserts) high day / night temperature differences resulting in high efficiency values. For the application of solar cooling an availability orientated approach has to be applied. Mainly, this approach can be reasoned by a higher reliability of supply (autonomous energy provision) or overcapacities of solar energy. As a result, financial aspects play more and more an important role. When it comes to troughs in energy availability market prices for energy provision tend to increase. In times of higher availabilities or even overcapacities low market prices or negative market prices can be achieved.

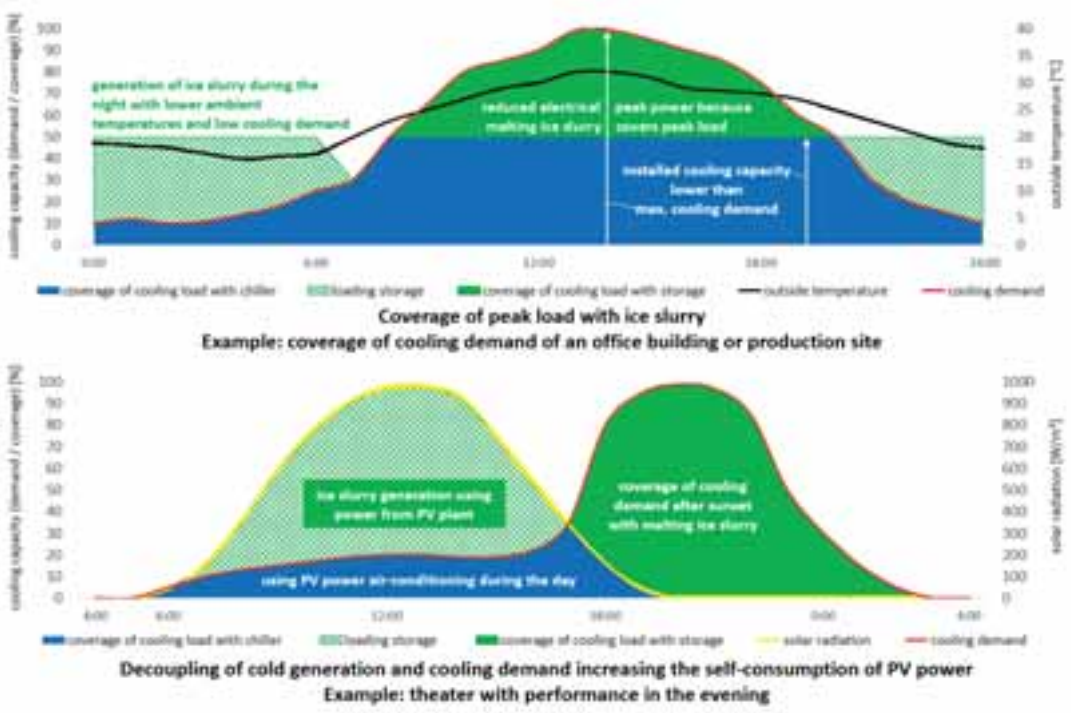

Fig. 7: Schematic charts for load shifting of cold thermal energy

Outlook

The paper presents a comprehensive approach for using water as refrigerant. Taking into account further requirements to integrate renewable energy sources into innovative refrigeration concepts cold thermal energy storages based on ice slurry are a preferable solution. Thermodynamically the process of direct evaporation under triple point conditions reflects a high efficient approach to generate a pumpable ice slurry solution which can be isochronously used as secondary refrigerant and storage medium. At ILK Dresden a further pilot facility was developed and has been tested under laboratory conditions. Due to a delay at customers chilled water system practical experiences cannot be discussed so far. Final commissioning is terminated for the first quarter 2018 and operational data will be presented.

References

M. Kauffeld, M. Kawaji, and P. W. Egolf, Handbook on Ice Slurries - Fundamentals and Engineering. International Institute of Refrigeration, 2005, p. 360.

Urbaneck, T., 2012. Kältespeicherung: Grundlagen, Technik, Anwendung. Oldenbourg Wissenschaftsverlag, Chemnitz.

M. Kauffeld, M. Wang, V. Goldstein, and K. Kasza, “Ice slurry applications,” International Journal of Refrigeration, vol. 33, no. 8, pp. 1491–1505, 2010.

C. W. Snoek, The design and operation of ice slurry based district cooling systems. IEA Report, 1993.

P. Albring, “Eiserzeugung und Eisspeicherung mit Wasser als Kältemittel,” 2009.

C. Steffan, M. Honke, and Safarik, “Operational experiences with an ice slurry cold thermal storage system using the R718 direct evaporation ice generation process,” in 12th IIR Gustav Lorentzen Natural Working Fluids Conference, Edinburgh, 2016.

EXPERIMENTAL STUDY ON SOLAR DRIVEN DEHUMIDIFICATION SYSTEM WITH SILICA GEL COATED HEAT EXCHANGER IN WINTER

Yao Zhao, Yanjun Dai, Jingyu Zhang

Institute of Refrigeration and Cryogenic Engineering, Shanghai Jiao Tong University, Shanghai (China)

Abstract

In this paper, a desiccant coated heat exchanger (DCHE) system driven by solar energy is built and tested under winter condition. The purpose of this experimental research is to explore the heating and humidification performance of DCHE system. Effects of hot water temperature, hot water mass flow rate and regeneration air flow flux are discussed as vital factors impacting system performance. Results show that increasing of heat water temperature as well as of hot water mass flow rate both have positive effects on humidification capacity and thermal coefficient of performance (COP) of the DCHE system. Moreover, the latter has a more remarkable influence. When a tradeoff is made between the performance of DCHE system and the thermal comfort of supply air, 40oC and 0.4 kg/s are selected as optimum hot water condition. Under this operation condition, average humidity ratio of supply air is 5.15 g/kg, almost twice of ambient air. Maximum thermal COP can reach 1.78 with a comfortable average temperature of supply air (28.3 ^{o}C). To provide a better supply air state under low humidify ratio of ambient air, small regeneration air flow flux is implemented, which effectively increases the humidity ratio of supply air with the decrease of COP.

Keywords: Silica gel coated heat exchanger, solar energy, experimental study, COP.

1. Introduction

Desiccant coated heat exchanger air conditioning system is a recently developed solid desiccant technology which obtains more and more attention in the HVAC field. Compared with vapor compression (VC) system which is widely used at present, solid desiccant system has several obvious advantages. For example, it can control both sensible and latent loads under summer and winter condition, while VC system has limited capacity in moisture control through heat pump cycle, especially cannot meet the demand of humidification in winter [1,2]. Without the use of refrigerants containing more or less CFCs which generally applied to the VC system, solid desiccant technology has an environmentally friendly property. Moreover, after the Copenhagen Conference, how to reduce building energy consumption and greenhouse gas emission has aroused unprecedented attention[3,4]. The solid desiccant air conditioning system which usually selects silica gel as desiccant provides a promising alternative solution. Since silica gel with a relative low desorption temperature can take advantage of renewable

doi:10.18086/swc.2017.28.20 Available at http://proceedings.ises.org

energy and low-grade thermal energy[5], such as solar energy and waste heat, which can be used as the regeneration heating source instead of electricity. Solid desiccant technologies possess extensive application perspective in new energy utilization and industrial commercialization.

In recent years, a novel concept of desiccant coated heat exchanger (DCHE) air condition system has been proposed and developed in solid dehumidifying. DCHE is based on the traditional fin-tube heat exchanger with the reprocessing on the out surface coated by the desiccant materials. Comparing with rotary desiccant wheel that a common equipment in solid desiccant system, DCHE is chilled by inner cooling water flowing in the copper pipes of heat exchanger, and the adsorption heat can be timely taken away in the dehumidification process. This improvement can realize the approximately isothermal dehumidification and overcome the side effect of adsorption heat accumulation due to the structure limit of rotary desiccant wheel. Therefore, DCHE system effectively enhances the moisture removal obviously which leads to a better control of the latent load. Meanwhile, there is no rotatable part in DCHE system with longer service life and less noisy in operation. Aynur et al. [6] introduced DCHE into VRV (variable refrigerant volume) air conditioning system instead of the traditional heat exchanger, and better dehumidification capacity could be achieved with less energy consumption were confirmed in the field performance test under both cooling season and heating season. Using more environmentally friendly water as working medium, Ge et al. [7] experimentally verified that DCHE could effectively handle both the sensible heat and the latent heat of process air in the dehumidification process. Further works by Zhao et al. [8] successfully introduced solar energy to drive DCHE system and used two paratactic DCHE units to provide continuous dehumidification capacity. Later, Zhao et al. [9] added internal heat recovery to build a new type of DCHE cycle and both the thermal and electrical coefficient of performance significantly increased (1.2 and 13.8, respectively), while providing better indoor thermal comfort in summer condition.

The dehumidification abilities of DCHE which is applied in summer condition have caught the main attention of scholars on no matter in experimentally or theoretically investigations. However, few researches on regeneration process of DCHE system have been done to meet the demand in winter. The main objectives of this paper are to utilize a solar powered desiccant coated heat exchanger humidification air conditioning system and to validate the heating and humidification performance under winter condition. What's more, how the different regeneration conditions (including hot water temperature, hot water mass flow rate and regeneration air flow flux) affect the humidification process are experimented and analyzed.

2. Description of experimental system

Fig.1 shows photographic view of the experimental setup and main components. The DCHE air conditioning system consists of three main components: desiccant humidification unit, solar collecting unit and cooling unit. And its function covers humidification in winter and dehumidification in summer simultaneously.

As the core device of the system, DCHE is based on the traditional fin-tube heat exchanger, the size

of which is 400 mm (length)×150 mm (width)× 400 mm (height). After being soaked by desiccant and dried for 3-5 times, the surfaces of all pipes and fins of the heat exchanger are coated. Solid silica gel with 0.15 mm particle diameters and liquid silica gel are used as the desiccant materials in the experiment. And the final glue quantity of DCHE is 2.53 kg with 0.316 kg on per square meter. The detailed structural parameters of the heat exchanger and specifications of silica gel are shown in Table 1.

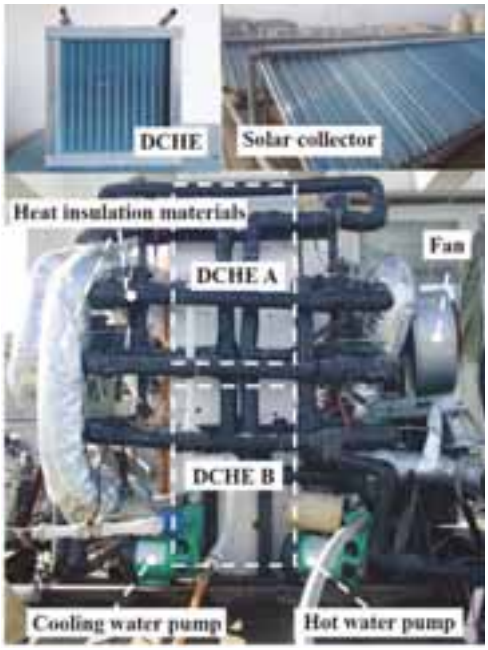

Fig.1 Photographic view of experimental setup and main components

Table 1 The structural parameters of the heat exchanger and specification of silica gel

Name	Parameter
Structural size (mm)	400 (length)×150 (width)×400 (height)
Thickness of the fin (mm)	0.15
Spacing of the fin (mm)	3
Outer diameter of the tube (mm)	9.87
Inner diameter of the tube (mm)	8.67
Silica gel column chromatography	Macro pore, ZCX- II . JN30,30%
Particle diameters of silica gel (mm)	0.15
Glue quantity (kg)	2.53

Solar energy is used as regeneration source in the experiment. The vacuum tube solar collector can supply 8.5 kW heating power with 22 m2 area. The capacity of the matched tank is 500 L. Through adjusting heating time and mass flow rate of circulating water in solar collecting unit, the temperature of hot water can meet the experiment requirements in different sunlight intensity. The cooling water after the dehumidification process flows back to cooling tower. In the cooling tower, the temperature of water decreases by air cooling.

The cooling water and hot water are dominated by two pumps in the water loops. In the experiments, the mass flow rate of cooling water is constant at 0.32k g/s. By adjusting the valve opening of the water loop, the water mass flow rate of hot water can be regulated. The maximum water mass flow rates of the cooling water and hot water provided by two pumps are 0.32 kg/s and 0.4 kg/s, respectively.

Moreover, it is extremely important to complete the airtightness and heat insulation of both air and water pipes to ensure good performance of the system. The leakage of water and air have been checked and precluded before the experiment. To minimize the heat loss, all the pipes are wrapped with heat insulation materials, including fiber-glass on air pipelines and heat insulation felt on water loop.

The basic operation principles of DCHE system consist of dehumidification process and regeneration process. In dehumidification process, ambient air (AA) is dehumidified and cooled in the air side of DCHE, by the desiccant and cooling water, respectively, then the cold dry air discharged to the environment as the exhaust air (EA). Meanwhile, the desiccant absorb moisture from the ambient air with adsorption heat taken away by cooling water and moisture content rise which is well prepared for the regeneration process. Then heat and mass transfer process between air and desiccant has basically completed in the end of dehumidification process. And cooling tower provides cooling water for dehumidification process in the system. In the following regeneration humidification process, when regeneration hot water flows into the copper pipes of DCHE, the humid desiccant coated on the heat exchanger is heated , and it enters the desorption process. As a result, the heat and moisture are taken away by ambient air (AA) which is supplied to the conditioned space with an increase of temperature and humidity ratio as supply air (SA). The sensible and latent loads of the supply air are promoted at the same time in the regeneration process. Then the desiccant become relatively dry which recovers the dehumidification capacity. And hot water in the system for the regeneration process is from solar collecting unit.

Based on above principles, the experimental setup is established, and two alternate operation modes are proposed to realize the continuous operation of the system as shown in Fig.2 (a),(b). Two DCHEs, including DCHE A and DCHE B which are installed in two paratactic air ducts, compose the desiccant humidification unit. In the MODE 1, the two water values (WV1,WV2) in hot water loop open 2’ and 1’ direction, respectively, which provide the regeneration water to DCHE A. The other two water values (WV3,WV4) in cooling water loop open 1’ direction and pump the cooling water into the DCHE B. As a result, DCHE A operates in regeneration process, and DCHE B operates in dehumidification process. Meanwhile, the four 3-way air values open 1’ direction that the cold dry AA through DCHE A is handled

into hot humid SA supplied into conditioned space. In the MODE 2, the two water values (WV1,WV2) in hot water loop open 1' and 2' direction, respectively, which provide the regeneration water to DCHE B. The other two water values (WV3,WV4) in cooling water loop open 2' direction and pump the cooling water into the DCHE A. DCHE B operates in regeneration process, and DCHE A operates in dehumidification process. Meanwhile, the four 3-way air values open 2' direction. The air flowing through the surfaces of DCHE B is heated and humidified which is supplied to the conditioned space. By switching multiple 3-way water valves and air valves completing the conversion of the two modes, DCHE A and DCHE B alternately complete dehumidification and regeneration humidification process which realize the continuous hot and moist air supply.

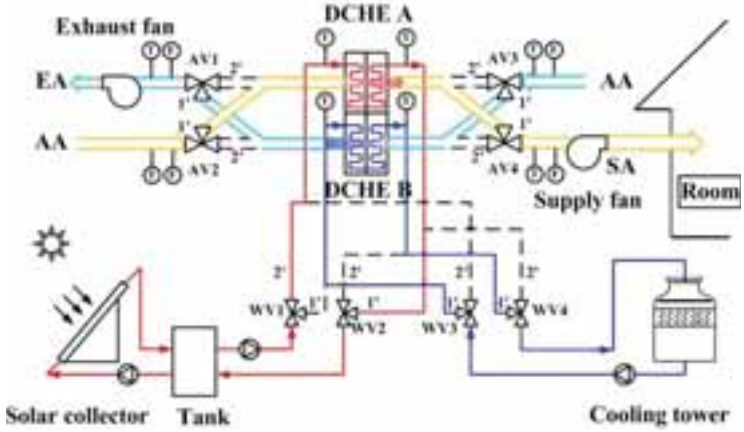

(a)

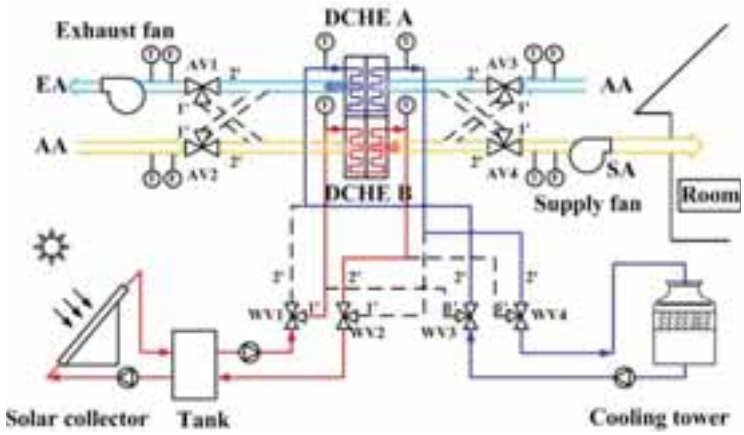

(b)

Fig.2 Schematic diagram of the experimental setup:(a) MODE1: DCHE A in regeneration process and DCHE B in dehumidification process (b) MODE2: DCHE A in dehumidification process and DCHE B in regeneration process

3. Performance indices

Performance of DCHE humidification air conditioning system in winter is evaluated by the

following indices:

(1) Supply air state(T_t, d_t, T_{ave}, d_{ave})

The temperature and humidity ratio of supply air are the primary criterion to judge whether the system can achieve the required heating and humidification capacity in winter condition.

Among them, transient temperature T_t and transient humidity ratio d_t indicate the change regularity of supply air state in each cycle. And during the humidification process t_e, the average temperature T_ave and humidity ratio d_ave are another two important indices to assess the performance of the whole system. And they are expressed as following Eq. (1) and Eq. (2), respectively:

$$T_{ave} = \overline{\sum_{0 \to t_e} T_t} \tag{1}$$

$$d_{ave} = \overline{\sum_{0 \to t_e} d_t} \tag{2}$$

(2) Average moisture addition (Δd_{ave})

Δd_{ave} is the most intuitive parameter adopted to evaluate the capacity of humidification of the system, which is expressed by average moisture adding of supply air in per cycle as the following Eq. (3):

$$\Delta d_{ave} = \overline{\sum_{0 \to t_e} \Delta d_t} = \overline{\sum_{0 \to t_e} (d_t - d_{in})} \tag{3}$$

where Δd_t is transient moisture addition, d_{in} and d_t are humidity ratio of inlet air and outlet air in regeneration process, respectively in g/kg.

(3) Thermal coefficient of performance(COP)

The energy utilization of the system is measured by COP, which is the ratio of Q_t and Q_w. Q_t is the average enthalpy exchanged of process air in effective dehumidification process, and Q_w is the average enthalpy exchanged of water in effective regeneration process, respectively in kW.

$$COP = \frac{Q_t}{Q_w} = \frac{M_a(h_{a,out} - h_{a,in})}{c_w M_w(T_{w,in} - T_{w,out})} \tag{4}$$

where M_a and M_w are mass flow rate of air and hot water, respectively in kg/s. h is the enthalpy in kJ/kg. $T_{w,in}$ and $T_{w,out}$ are inlet and outlet temperature of hot water, respectively in K. c_w is the specific heat of water in kJ/(kg·K).

4. Results and discussions

The solar powered DCHE humidification air conditioning system is tested to evaluate the feasibility of heating and humidification in the typical winter condition from 15 December 2015 to 31 January 2016 in Shanghai. And the system performances are compared and discussed based on three crucial regeneration factors, including hot water temperature $T_{w,in}$, hot water mass flow rate m_w and regeneration air flow flux V_a. Because the thermo-hygrometric condition of the environment air changed every day, even unstable from day to night. Based on a great deal of experiments, the data is selected and compared with the principle of a single variable. Besides, 600 s is recommended as the experiment cycle

in order to guarantee the experiment performance.

4.1 Effect of hot water temperature

The temperature of hot water has an important influence on the regeneration process of DCHE and makes a further effect on the humidity and temperature of supply air. To explore how the hot water temperature affect the performance of the system, the test water temperatures are specified at 30, 35, 40 and 45 ºC. In addition, the humidity ratio of ambient air is around 2.91 g/kg-3.10 g/kg, the hot water mass flow rate and regeneration air flow flux are 0.4 kg/s and 400 m^3/h, respectively. These three parameters remain constant under this test condition.

The transient humidity ratio of supply air under different hot water temperature is shown in Fig.4. There is an obvious increase of moisture content under every condition compared with ambient condition, which demonstrates that the solar powered DCHE humidification air conditioning system can effectively improve the air humidity ratio in winter condition.

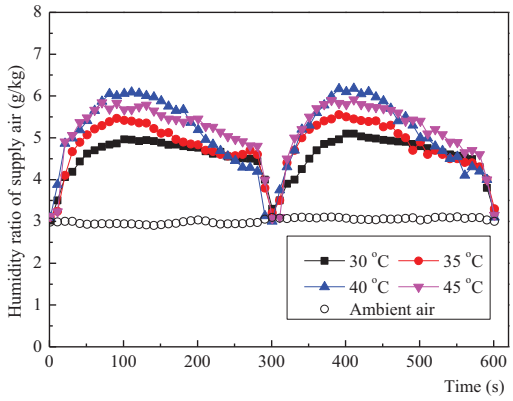

Fig.3 The transient humidity ratio of supply air with different hot water temperatures

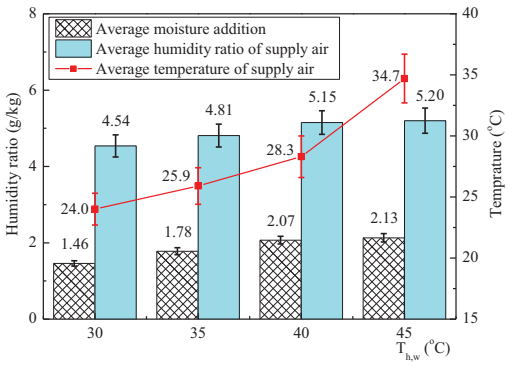

Fig.4 The average moisture addition, humidity ratio and temperature of supply air with different hot water temperatures

With the rising of $T_{w,in}$, the transient and average humidity ratio of supply air both increase as shown in Fig.3 and Fig.4. And the average value increases from 4.54 g/kg to 5.20 g/kg, up 15 %. The average moisture addition rises from 1.46 to 2.13, up 46%. Due to higher hot water temperature for desiccant material more heating power and humidification capacity can be obtained, then the regeneration process is completed thoroughly, which directly leads to the increase of moisture addition and humidity ratio of supply air. On the other hand, the surface of solid desiccant becomes drier at the end of the regeneration process with the rising of $T_{w,in}$, which increases the moisture removal and indirectly accelerates the next regeneration process. As it shows in Fig.4, the temperature of supply air rises from 24.0 ºC to 34.7 ºC due to the increment of the temperature difference between hot water and air/desiccant. And the slope of the curve is elevated. Through analyzing the above variation trends, the increase of $T_{w,in}$ has more effect on the rise of sensible load than latent load in the test condition which reflects on the tendencies of temperature and humidity ratio of supply air, respectively. At the same time, COP increases from 1.05 to 1.85, up 76 %, which increases obviously from 30 ºC to 35 ºC, then gradually

become flat when from 35 ºC to 45 ºC.

Transient supply air states in one cycle are plotted in the psychrometric figure(Fig.5) to measure whether the system can provide satisfied supply air under test condition. The black solid dot represents ambient air state, area circled by blue dashed lines show the designed standard of indoor air in winter China (temperature: 18 ºC-24 ºC, relative humidity ratio: 30 %RH-60 %RH)[24] []and the hollow points are the supply air state under different hot water temperatures. It is found that the supply air states gradually enter the designed standard area with the temperature increase from 30 ºC to 40 ºC. However, the supply air states is far from the area when $T_{w,in}$, is 45 ºC, mainly because the temperature of supply air is too high(the average temperature of supply air is 34.7 ºC). To balance the performance of the system and the thermal comfort of supply air, in spite of the performances of system (including d_{ave}, Δd_{ave}, COP) best in 45 ºC, 40 ºC is selected as the appropriate hot water temperature whose average humidity ratio is 5.15 g/kg, average temperature is 28.3 ºC , average moisture addition is 2.07 and COP is 1.78.

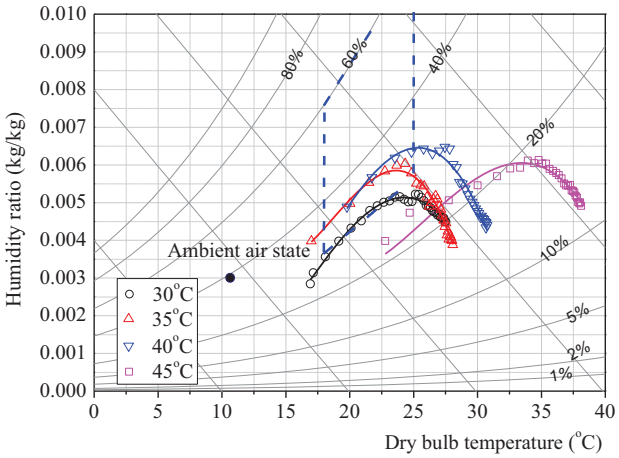

Fig.5 Transient supply air states in psychrometric figure with different hot water temperatures

4.2 Effect of hot water mass flow rate

In the solar powered DCHE system, the hot water flowing in the DCHE provides the desorption heat in regeneration process. The mass flow rate of hot water directly affects the heat exchanger efficiency between air and water, and crucially impacts the humidification and heating performance of the system. In order to explore the effect of m_w, the system is tested under constant condition that the humidity ratio of ambient air is around 2.42 g/kg-2.59 g/kg, the hot water temperature is 40 ºC and regeneration air flow flux is 400 m^3/h. Through adjusting the valve opening of the hot water loops, the different mass flow rates of hot water are controlled to 0.1, 0.2, 0.3, 0.4 kg/s, respectively. And the transient and average experimental results are summarized in Fig.6-9. In Fig.6, when the mass flow rate of hot water is greater than or equal to 0.2 kg/s, transient humidity ratio of supply air first rapidly increases to a maximum value and then gradually falls down. In the beginning period, there is a bigger relative humidity ratio difference between ambient air and pores within desiccant material, which acts as the main driving force for mass transfer and brings in the increase of moisture addition. However, water

in desiccant material is limited, which is the main reason why the humidity ratio of supply air decreases in the following process. But when mass flow rate of hot water is 0.1 kg/s, the variation trend is different. Transient humidity ratio of supply air increases in the beginning and then becomes flat without a drop process. This phenomenon occurs because the mass flow rate (0.1 kg/s) is too small to provide enough desorption heat in regeneration process and the regeneration process proceeds slowly which has not yet emerged the obvious influence due to the water decrease in desiccant material.

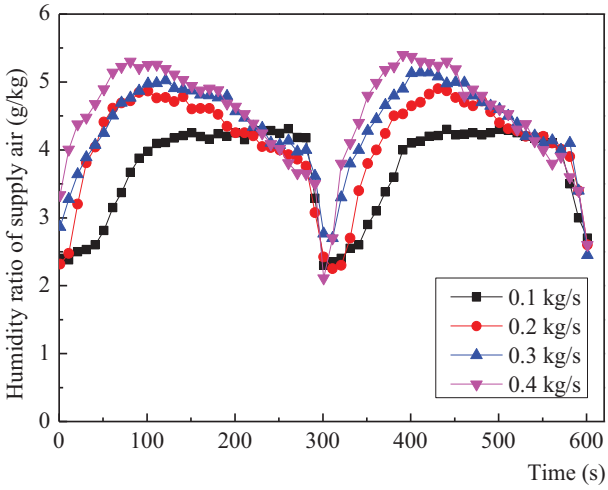

Fig.6 The transient humidity ratio of supply air with different hot water mass flow rate

With the increase of mass flow rate of hot water from 0.1 kg/s to 0.4 kg/s, all the performance indices are enhanced. Average humidity ratio of supply air, moisture addition and COP have approximately linear rises, up 24 %, 71 % and 102 %, respectively. And the increase trend of average temperature differs from others, which is from sharp to flat. This phenomenon indicates that the effect of hot water flow mass on the supply air temperature weaken when it is above 0.2 kg/s. Comparing with hot water temperature(up 15 %, 46 %, 76 %, respectively), mass flow rate of hot water has a greater influence on system performance indices when other parameters remain the same.

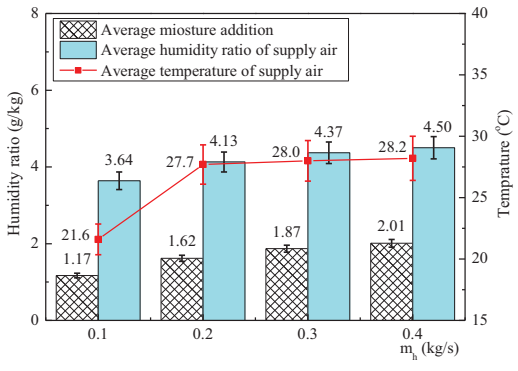

Fig.6 The average moisture addition, humidity ratio and temperature of supply air with different hot water mass flow rate

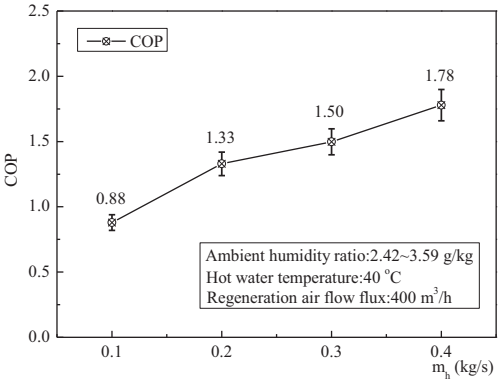

Fig.7 The average COP of the system with different hot water mass flow rate

Except for the performance of system, the thermal comfort of supply air also needs to be taken into account. Fig.8 shows the transient supply air states in psychrometric figure with different mass flow rate of hot water. When mass flow rate of hot water increases, the curves moves towards the upper right of the figure due to the promotion of heating and humidification performance. Compared with the experimental results of 0.1, 0.2, 0.3 kg/s, more points of supply air curve in 0.4 kg/s are included in the designed standard of indoor air, which can provide more comfortable temperature and humidity ratio to the conditioned space.

To sum it up, the maximum hot water mass flow rate (0.4 kg/s) is recommended in this system in order to improve regeneration process and provide better supply air condition.

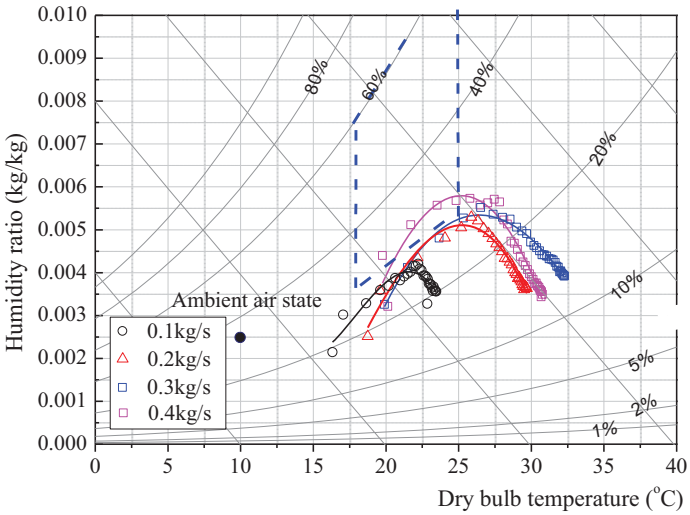

Fig.8 Transient supply air states in psychrometric figure with different hot water mass flow rate

5. Conclusion

In this paper, the solar powered DCHE air conditioning system is established and tested to research the humidification performance of DCHE in winter condition. Three important factors impacting regeneration process are discussed. The main conclusions are as follows:

(1)Experimental results of supply air humidity ratio validate that DCHE system possessed a good humidification and heating performance in winter condition.

(2)Under a single variable, humidification capacity and COP of DCHE system have a prominent increase with the rising of heat water temperature, as well as hot water mass flow rate. And through analysis of results, mass flow rate has a greater influence on all performance indices of the system than water temperature.

(3)To balance the performance of the system and the thermal comfort of supply air, 40 ºC and 0.4 kg/s are optimum temperature and mass flow rate of hot water, respectively. And the best operation state of the system in this hot water condition is concluded that average humidity ratio of supply air is 5.15 g/kg, average temperature of supply air is 28.3 ºC and COP is 1.78.

6. ACKNOWLEGEMENT

The authors acknowledge the financial support of the National Natural Science Foundation of China (Grant No.51576121 and No. 51336004).

7. References

[1] Daou K,Wang R, Xia Z. Desiccant cooling air conditioning: a review. Renew Sust Energ Rev. 2006, 10(2): 55-77.

[2] Mazzei P, Minichiello F, Palma D. HVAC dehumidification systems for thermal comfort: a critical review. Appl Ther Eng. 2005, 25(5-6): 677-707.

[3] Zouaoui A, Zili-Ghedira L, Nasrallah SB. Open solid desiccant cooling air systems: A review and comparative study. Renew Sust Energ Rev. 2016, 54:889-917.

[4] Qu M, Yin H, Archer DH. A solar thermal cooling and heating system for a building: Experimental and model based performance analysis and design. Solar Energy. 2010, 84(2): 166-182.

[5] Misha S, Mat S, Ruslan MH, Sopian K. Review of solid/liquid desiccant in the drying applications and its regeneration methods. Renew Sust Energ Rev. 2012, 16(7): 4686-4707.

[6] Aynur TN, Hwang YH, Radermacher R. Field performance measurements of a heat pump desiccant unit in dehumidification mode. Energy Buildings. 2008, 40(12): 2141-2147.

[7] Ge TS, Dai YJ, Wang RZ, Peng ZZ. Experimental comparison and analysis on silica gel and polymer coated fin-tube heat exchangers. Energy. 2010, 35(7): 2893-2900.

[8] Zhao Y, Ge TS, Dai YJ, Wang RZ. Experimental investigation on a desiccant dehumidification unit using fin-tube heat exchanger with silica gel coating. Appl Therm Eng. 2014, 63(1): 52-58.

[9] Zhao Y, Dai YJ, Ge TS, Wang HH,Wang,RZ. A high performance desiccant dehumidification unit using solid desiccant coated heat exchanger with heat recovery. Energy Build. 2016, 116:583-592.

Solar Space Heating and Hybrid Applications

Performances analysis of combined rankine and absorption refrigeration cycles for a small size solar power plant

Alain C. Biboum[1], Mabvuto Mwanza[1] and Ahmet Yilancı[2]

[1]Ege University, Graduate School of Natural and Applied Sciences, Solar Energy Science Branch, 35100,Bornova, Izmir, Turkey

[2]Ege University, Solar Energy Institute, 35100, Bornova, Izmir, Turkey

Abstract

The use of Concentrating Solar Power (CSP) systems for combined cooling and power (CCP) is increasing daily across the global. However, due to some land and other limitations various types of solar fields, CSP technology and specially solar trough Collector (STC) configuration which may have effect on overall performance of Solar thermal power plant (STPP) are used. Thus, performance analysis of these configurations is vital in order to identify their performance uncertainties and weakness. This paper studies and analysis the performance of three types of STC configuration used in most experimental and non conmmercial plants, using Matlab software and analytical approach. The results shows that for the same modules number, 5Loops configuration has higher performance with energy efficiency of 32.75%, exergy efficiency of 32.07% and lowest coefficient of performance for cooling of 0.5751, followed by 10-SCAs configuration, and 15-SCAs configuration has the lowest performance with energy efficiency of 26.45%, exergy efficiency of 25.91%, and highest coefficient of performance of cooling (COPc) of 0.7706. This study is important for identifying the performance uncertainties of various STC configurations using indirect stem generation (ISG) and selecting the most optimal configuration for small size plant in order to maximize the utilization of solar energy in CSP systems.

.

Keywords: CSP, Solar Collector Assemblies (SCAs), Configuration, CCP, STC, STPP, COPc, ISG, Loop

1. Introduction

Concentrating Solar Power (CSP) systems require direct normal irradiation to effectively function. In order to concentrate the sunlight, the lenses or mirror are used. At the same time, the tracking systems are used to optimize solar thermal power output. The solar trough Collector (STC) can be considered as the most efficiency CSP technology, according with plant number in the world and total energy thermal and electricity production [1]. In California's Mojave Desert Since the 1980s, more than 350 MW of capacity has been developed by the Solar Electric Generating Station (SEGS) using STC technology [2]. A viable alternative that helps to alleviate the challenges associated with renewable energy is a combined cycle (CC) or Rankine cycle power blocks. Solar combined cycle (SCC), uses concentrating solar thermal (CST) energy as the renewable source. V. Zare and M. Hasanzadeh studied closed Brayton cycle combined with Organic Rakine cycle for solar power tower plants in order to optimize electricity generation, in their study they found the efficiencies of the system to be 23.2% [3]. Spelling et al. studied thermodynamic and economic performance of a combined-cycle, based on open air Brayton and steam Rankine cycle was analyzed , in this study it was concluded that the efficiencies of the system was between 18–24% [4]. Organic Rankine cycle (ORC) is a special kind of Rankine cycle that uses an organic fluid as a working fluid instead of water, which is currently used for combined cycle study. ORC could be used with diffferent kinds of low temperatures coming from various heat sources such as geothermal energy, solar energy, biomass energy and waste heat. Suna et Li [5] provided the organic Rankine cycle heat recovery power plant using R134a as working fluid to evaluate and optimize the plant performance. Sun L. et al. [6] proposed an combined power and cooling system power able to use mid/low temperature from heat source, this system consisted of a combination of Rankine cycle (RC) and absorption refrigeration cycle (ARC). During this study Sun L. et al. used the more import portion of waste heat for power generation uusing ORC as was done by V. Zare and M. Hasanzadeh, whereas another portion of this waste heat was used for cooling generation. Today, in order to increase opportunities offered by

doi:10.18086/swc.2017.29.01 Available at http://proceedings.ises.org

renewable energy sources, significant market for the ORC is ready to make more attracted combination of cooling heat and power (CCHP) using waste heat from soloar thermal power plant (STPP) specially. Organic Rankine cycle technology is a challenge to develop an appropriate CCHP scale to meet both energetic, economic and environmental needs increase [7–8]. This paper focus on SCC power plant configuration and performance analysis, in order to show both energetic and exergetic efficiency values of different configurations. In either case this study integrated ARC analysis using waste water from Power combined cycle (PCC) with objective to decrease heat loses.

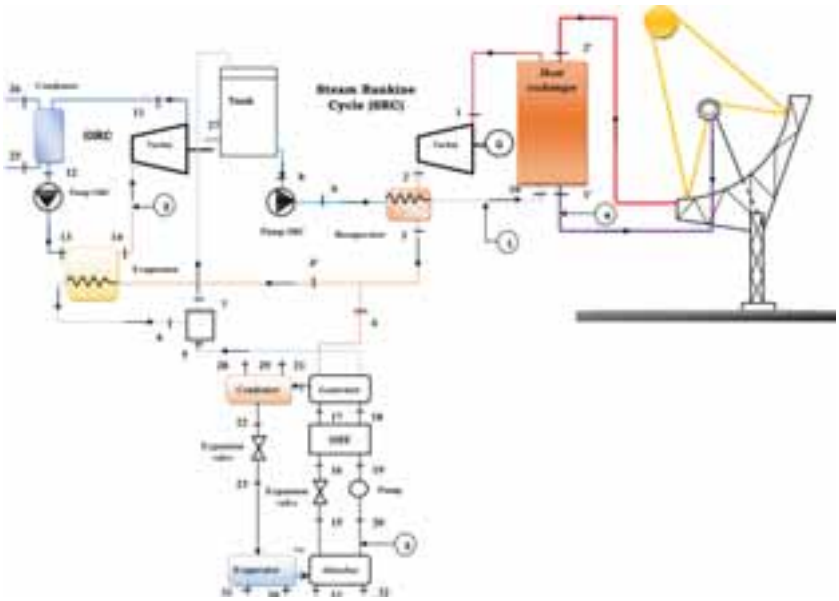

Figure 1: System description

2. System descriptions and assumptions

The following assumptions have been considered in the study

- The system is operating in steady state conditions.
- The kinetic and potential energies and exergies are negleable, due to absence of chemical reactions in the considered system and also in heat transfer fluid.

2.1 System descripton

Fig.1 shows layout of CCP system containing parabolic trough collectors (PTC), heat exchanger , thermal heat transfer fluid and combined power systems able to provide waste heat necessary for cooling system, by using ARC. PTC is a known and commercialized technology. In this study, Luz-S2 and PTR schott technologies are used as receiver type and absorber type respectively. This technology is generally used to provide heat around 500°C using heat tranfer fluids (HTFs) depending o configurtion type, Direct steam generating (DSG) or ISG system. In this case study we are using ISG system on by using Therminol VP-1 as thermal HTF. There after, thermal energy is transfered to water in Intermediate Heat Exchanger (IHE). Before going through IHE, cool water have to be heated by recuperator, to increase its temperature.Steam generated has the temperature close to HTF's temperature according to mass flow rate of water. As indicated in Fig.1 exiting steam from turbine is used for preheating water from tank by using recuperator. Exiting steam from recuperator is used to provide heat for auxilaries cycles both Organic Rankine and Absorption refrigeration. For ORC exiting hot water go through evaporator directly to increase organic heat tranfser fluids temperature (satured vapor state) and for absorption system the hot water is used to seperate Lithium Bromide and Water inside of generator.

2.2 Solar field

Solar energy is one of main key alternative energy sources in Turkey. Therefore, it improtant to consider its utilization in future energy generation mix in the country and especially in Izmir.
Izmir has a mediterranean climate which is characterized by long hot and dry summer with mild to cool and rainy winters[9]. The total average of precipitation for Izmir is around 686 mm per year. However, 77% of the rain falls during December through to March. The maximum temperature during winter months are usually between 10 to 16°C. During summer the ambient air temperature can rise high to as much as 40°C from June to

September. Average relative humidity is between 42 and 70%. Mean monthly sunshine hours are between 124.0 hours in december and 375.1hours in July [9]. Solar energy potential of Izmir is considerable and advantageous due to its geographical position in northern hemisphere as shown in Table 1 [10-11].
During this study direct normal irradiation value used for calculation is 523.7 W/m^2, which correspond to Average value of solar radiation during 1 year in Izmir.The solar field can be defined as a system containing a number of loops, with each Loop consisting of two solar collector assembly which is made of connected modules. The specifications of module and Solar Collectors Assemblies is shown in Table 2.

3. Method and Formula

3.1 Configuration Description

Usually there are two arrangement types in Solar thermal collector plant using parabolic trough collectors, I and H. In this study, three differents configurations of STC fied have been analyzed using a same modules number and characteristics. The main aim of this work is to show which configurations can provide better energetic and exergetic efficiencies using CCP system. The configuration type-A contains 15 SCA's and each one has 8 modules without any loop. Configuration type-B contains10 SCA's each with 12 modules without any loop. Configuration type-C contains 5 loops with each one having 24 modules.

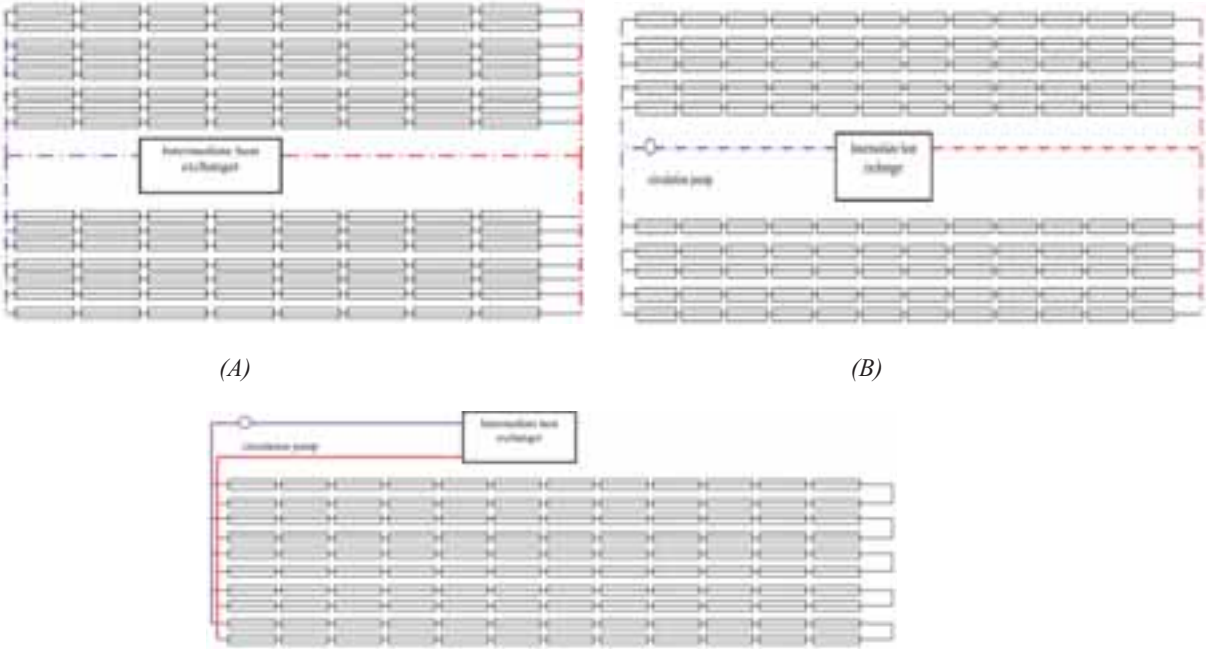

(A) *(B)*

(C)

Figure 2: solar field configurations A, B and C

3.2 Solare collector efficiency

The thermal efficiency of solar collector is the ratio of collector thermal power output to the solar power input [13-15] and can be expressed by eq.1:

$$\eta_c = \frac{\dot{Q}_{abs}}{\dot{Q}_{solar}} \qquad \text{(eq. 1)}$$

Where $\dot{Q}_{solar}$ is the solar power input (kW) and $\dot{Q}_{abs}$ is useful energy output of collector(kW). The solar power input can be calculated from the average direct normal irration G_b and total collector aperture area A_{ap} . Thus, the total available solar on the PTC's cover glass has been estimated using the given eq. 2[15]:

$$\dot{Q}_{Solar} = A_{ap}.G_b \qquad \text{(eq. 2)}$$

The amount of total solar radiation that is striking the collector and used as input heat, which is necessary to heat transfer fluid inside of absorber has been calculated using eq. 3[15].

$$\dot{Q}_{use,in} = A_{ap}.F_R.S \qquad \text{(eq. 3)}$$

Where $\dot{Q}_{use,in}$ is the absorber input solar energy, F_R. is heat removal factor, and S is the heat absorbed by receiver. These parameters can be expressed respectively as[15]:

$$A_{ap} = \left(W - D_{r,o}\right).L \qquad \text{(eq. 4)}$$

$$F_R = \frac{\dot{m}.C_P}{A_r.U_L}\left[1 - exp\left(-\frac{A_r.U_o}{\dot{m}.C_P}\right)\right] \qquad \text{(eq. 5)}$$

$$S = G_b.\eta_o \qquad \text{(eq. 6)}$$

Where η_o is optical efficiency, $U_o$is overall heat transfer coefficient, and $\dot{m}$ is mass flow rate of HTF. The values of a receiver and cover surface area, optical parameters and other can be found in Table 2.
The useful energy output of collector has been estimated using eq. 7 written as[15]:

$$\dot{Q}_{abs} = A_{ap}.F_r.\left(S - \frac{A_r}{A_{ap}}U_L.(T_{ri} - T_o)\right) \qquad \text{(eq. 7)}$$

Where receiver area aperture is A_r (Table), U_L is heat losses coefficience, T_{ri} is input temperature of HTF inside receiver, T_o ambient air temperature. Table 3 summarizes the defination of the optimal parameters of the parabolic trough collector.

3.3 Optical and Thermal analysis of parabolic collector

Therminol VP-1 oil has been used as HTF in this study due to its good temperature control and heat transfer properties (Table 5) [16]. Generally mass flow rate of the heat transfer fluid per row is between 0.35 and 0.8 kg/s according with solar collector assembly length [17]. In order to determine thermodynamic properties of heat transfer fluid entering the IHE and also working fluid properties entering in the steam turbine of Rankine cycle. All the equations below have to be used to calculate the temperature of receiver's cover and the value of solar heat absorbed by the receiver of parabolic trough collector.

A. Optical analysis

The concentration ratio (C) of parabolic trough collector is calculated by the given eq.8 [18]:

$$C = \frac{A_{ap}}{A_{c,o}} \qquad \text{(eq. 8)}$$

The geometric factor is a ratio of lost area to aperture area which is estimated using the following eq. 9[18]:

$$A_f = \frac{A_L}{A_{ap}} \qquad \text{(eq. 9)}$$

Whereas the lost area has been estimated using the expression eq. 10 [18]:

$A_L = \frac{2}{3}W_a.H_p + fW_a\left[1 + \frac{{W_a}^2}{48f^2}\right]$ Where H_P is height of parabola and f is parabola focal distance

Optical efficiency is defined as ratio of the energy incident on the collector's aperture [18]. It depends on optical properties of materials involved, geometric of collector and other parameters as errors related to the construction collector. The optical efficeiency has been estimated using the expression as given in eq11[18].

$$\eta_o = \rho_c.\tau_g.\alpha_r.\gamma\left[\left(1 - A_f.\tan(\theta)\right)cos(\theta)\right] \qquad \text{(eq. 11)}$$

Parabolic Trough collector (PTC) structure uses a two axis tracking, the main advantage of using the tracking system is that solar collector assembly can collect all available direct solar energy during the day, because incidence angle of solar radiation is always equal to zero.

B. Thermal analysis

Generally, in order to decrease the heat losses, a cover glass tube is employed around receiver . The space between the receicer and the cover glass is evacuated in order to minimize the conventional losses. The heat losses coefficient has been calculated usıng eq. 12 given by [18].

$$U_L = \left(\frac{A_r}{(h_{c,c-a}+h_{r,c-a})*A_{c,o}} + \frac{1}{h_{r,r-c}}\right) \qquad \text{(eq. 12)}$$

The heat transfer coeefficients between receiver and cover glass and between cover glass and ambient temparature of have been estimated using eq.13a and 13b written as[18].

$$h_{r,\ r-c} = \sigma\left(T_g + T_a\right)\left(T_g^2 + T_a^2\right).\left(\frac{1}{\varepsilon_r} + \frac{A_r}{A_g}\left(\frac{1}{\varepsilon_g} - 1\right)\right)^{-1} \qquad \text{(eq. 13a)}$$

$$h_{r,\ c-a} = \varepsilon_g\sigma\left(T_g + T_a\right)\left(T_g^2 + T_a^2\right) \qquad \text{(eq. 13b)}$$

The overall heat transfert coefficient, including external walls of the cover glass has been calculated using the following expression eq.14 [18].

$$U_o = \left(\frac{1}{U_L} + \frac{D_{r,o}}{h_{c,r-c}.D_{r,i}} + \frac{D_{r,o}.ln\left({}^{D_{r,o}}/_{D_{r,i}}\right)}{2k_r}\right) \qquad \text{(eq. 14)}$$

Between receiver and cover glass , cover glass and ambient terms of heat trnasfer coefficient are written as eq. 15a and 15b [18]:

$$h_{c,\ c-a} = \frac{(Nu_{air}.k_{air})}{D_g} \qquad \text{(eq. 15a)}$$

$$h_{c,\ r-c} = \frac{(Nu_r.k_r)}{D_g} \qquad \text{(eq. 15b)}$$

Where Nu is Nusselt number, k is the thermal conductivity and D is the diameter of cross section . The Reynold and Prandt number has been estimated using eq.16 and 17 [18]:

$$Re = \frac{V_f.D_{cross}}{\vartheta_f} \quad \text{(eq. 16)}$$

$$Pr = \frac{\rho.Cp.\vartheta}{k} \quad \text{(eq. 17)}$$

By ignoring the radiation absorbed by the cover glass, T_c has been estimated from this energy balance eq.18 :

$$A_c.\left(h_{c,c-a} + h_{r,c-a}\right).(T_c - T_a) = A_r.h_{r,r-c}(T_r - T_c) \quad \text{(eq. 18)}$$

Temperature of receiver cover has been calculated as follows eq. 19 [18].

$$T_c = \frac{h_{r,rc}.T_{r,a} + \frac{A_c}{A_r}(h_{c,ca} + h_{r,ca})T_o}{h_{r,rc} + \frac{A_c}{A_r}(h_{c,ca} + h_{r,ca})} \quad \text{(eq. 19)}$$

C. Thermal efficeincies

The collector efficiency factor for this study has been calculated using eq.20 given by[15-18].

$$F' = \frac{U_o}{U_L} \quad \text{(eq. 20)}$$

The collector efficiency has been found by dividing energy useful by solar energy input. Therefore, the collector efficiency is estimated using the following eq. 21[18].

$$\eta = F_R\left[\eta_o - U_L\left(\frac{(T_{ri} - T_o)}{G_b C}\right)\right] \quad \text{(eq. 21)}$$

The thermodynamic properties of the heat transfer fluid used in the study is given in the Table 5 (Appendix1). Using the heat transfer fluid the usefull energy output of collector has been determined using eq. 22 [15-18].

$$\dot{Q}_{abs} = \dot{m}_{Th}\left(Cp_{Th,o}.T_{Th,o} - Cp_{Th,i}.T_{Th,i}\right) \quad \text{(eq. 22)}$$

Where $\dot{m}_{Th}$, Cp_{Th} and T_{Th} are the mass flow rate , the specific heat and temperature of Therminol VP-1 going trough PTC's receiver respectively. The subscripts o and i refer to outlet and inlet position of Therminol VP-1 inside of that receiver.

3.4 Thermodynamic analysis

Overall system is divided into three subsystems namely, Solar Collector system, Power cycle (Steam and Organic Rankine Cycle), and Absorption system. For each subsystem, thermodynamic models are developed and the components of each subsystem are studied using MATLAB program to simulate the subsystem models. For a control volume accompanying a steady state process the energy and exergy balance equations [19]. Where $\dot{\psi}_{out}$ and $\dot{\psi}_{int}$ are the total exergy rates entering and exiting to the control volume respectively, while $\dot{\psi}_D$ is the exergy destruction rate within the component as defined in Appendix 1.

A. Solar sub -system

Solar subsystem contain essentially PTC and intermediate heat exchanger using Therminol VP-1 oil as working fluid. On the other hand, it's one of the most important part of this system. Its major purpose is provide heat collected from concentrated sun rays to power cycle by intermediate heat exchanger. The energetic efficiency of solar subsystem is the ratio of heat provided by working fluid inside of intermediate heat exchanger to heat obtained through absorber . It has been calculated using eq.28 written as[3,20]:

$$\eta_{th,S} = \frac{\dot{Q}_{IHE}}{\dot{Q}_{use}} \quad \text{(eq. 28)}$$

The exergetic efficiency of solar sub-system is the ratio of the usefull exergy input to power cycle and exergy of heat obtained through absorber. It has been determined using eq. 29 given below[3-20].

$$\eta_{ex,S} = \frac{\dot{\psi}_{2'} - \dot{\psi}_{1'}}{\dot{Q}_{use}\left(1 - \frac{T_o}{T_{ref,sun}}\right)} \quad \text{(eq. 29)}$$

Where $T_{ref,sun}$ is apparent sun temperature as the equivalent heat source temperature (Tref, sun = 5739 K).

The exergy destruction of solar subsystem is the sum of destroyed exergy in intermediate heat exchanger and solar field. It has been estimated using the eq. 30 presented by[3]:

$$\dot{\psi}_{D,solar\ ss} = \dot{\psi}_{D,abs} + \dot{\psi}_{D,IHE} \quad \text{(eq. 30)}$$

B. Power cycle (Steam and Organic Rankine Cycle)

The following assumptions have been considered in the study of the power cycle**:**

- For turbines and pump in Rankine cycles , isentropic efficiencies are assumed as given in Table.
- The appropriate value of the efficiency for recuperator has been assumed as given in table.
- Pressure drop and losses inside of Rankine cycles are neglegible.

$\dot{\psi}_{2'} - \dot{\psi}_{1'}$ represents the usefull exergy input to the combined rakine cycle. Heat provided to power cycle is generated inside of IHE, it has been estimated using the expression given by eq.31[18].

$$\dot{Q}_{IHE} = \dot{m}_w(h_1 - h_{10}) = \dot{m}_f(h_{1'} - h_{2'}) \quad \text{(eq. 31)}$$

While the net output power work $\dot{W}_{net}$ of the combined Rankine cycle has been calculated using eq. 32[15].

$$\dot{W}_{net} = \left(\dot{W}_T - \dot{W}_{Pump}\right)_{SRC} + \left(\dot{W}_T - \dot{W}_{Pump}\right)_{ORC} \quad \text{(eq.32)}$$

Power generation unit converts thermal solar energy absorbed in imtermediate heat exchanger to the net power generated.Thus, the efficiency for both energetic and exergetic of power cycle have been estimated using the following eqs. 33 and 34 respectively[3, 20]:

$$\eta_{th,cc} = \frac{\dot{W}_{net}}{\dot{Q}_{IHE}} \quad \text{(eq. 33)}$$

$$\eta_{ex,cc} = \frac{\dot{W}_{net}}{\dot{\psi}_{2\prime} - \dot{\psi}_{1\prime}} \quad \text{(eq. 34)}$$

For the considered solar power plant the overall energy and exergy efficiency can be defined as ratio of the net output power to the energy or exergy input due to solar irradiation on parabolic collector field. More clearly, power plants overall can be expressed as product of solar field efficiency and power cycle efficiency.
The overall energetic efficiency of power plant has been calculated using eqs. 28 and 33[3]:

$$\eta_{th,PP} = \frac{\dot{W}_{net}}{\dot{Q}_{IHE}} * \frac{\dot{Q}_{IHE}}{\dot{Q}_{use}} \quad \text{(eq. 35)}$$

While the overall exergetic efficiency of power plant has been estimated using eqs. 29 and 34.

$$\eta_{ex,PP} = \frac{\dot{W}_{net}}{\dot{\psi}_{2\prime} - \dot{\psi}_{1\prime}} * \frac{\dot{\psi}_{2\prime} - \dot{\psi}_{1\prime}}{\dot{Q}_{use}\left(1 - \frac{T_o}{T_{ref,sun}}\right)} \quad \text{(eq. 35)}$$

Where $T_{ref,sun}$ is apparent sun temperature.

C. Absorption system analysis

In order to estimate the size of equipment and optimize single effect Water -Lithium bromide absorber cooler. The following assumptions and input values have been considered.

- Absorption system is operating in steady state and refrigerant is pure water.
- There are no pression variation, except through the flow restrictors and the pump (i.e pump and flow restrictors are considered as isentropic and adiabatic respectively).
- Environmental heat losses are neglegible.
- There are no jacket heat losses, and at points 20,17,22 and 24 there is only saturated state.

The cooling COP of absorption system is defined as the ratio of the heat load inside of evaporator and the heat load inside of generator and has beeen determined using expression 38 [22,23] :

$$COP_C = \frac{\dot{Q}_E}{\dot{Q}_G + \dot{W}_P} \quad \text{(eq. 38)}$$

$$= \frac{\dot{m}_{21}(h_{23} - h_{24})}{\dot{m}_{20}(h_{19} - h_{20}) + m_{21}h_{21} + \dot{m}_{17}h_{17} - \dot{m}_{18}h_{18}}$$

Where m is mass flow rate and h is the enthalpy of working fluid at each corresponding state point. The heating COP of absorption system is the ratio of combined heating capacity , obtained through absorber and condenser and heat load provided by an external source, specifically inside of generator calculated using eq.39 [22,23]:

$$COP_H = \frac{\dot{Q}_A + \dot{Q}_C}{\dot{Q}_G + \dot{W}_P} = 1 + COP_C \quad \text{(eq. 39)}$$

The exergetic efficiency of absorption system for cooling is exergetic ratio between chilled water at evaporator and heat source at the generator. Which has been calculated using eq.40 [24,25].

$$\psi_C = \frac{\dot{\psi}_{30} - \dot{\psi}_{31}}{(\dot{\psi}_4 - \dot{\psi}_5) + \dot{W}_P} \quad \text{(eq. 40)}$$

The exergetic efficiency of absorption system for heating is exergetic ratio of combined supply of hot water at absorber and condenser to heat source at the generator. Which can be expressed as given in eq.41 [26,27].

$$\psi_H = \frac{(\dot{\psi}_{29} - \dot{\psi}_{28}) + (\dot{\psi}_{33} - \dot{\psi}_{32})}{(\dot{\psi}_4 - \dot{\psi}_5) + \dot{W}_P} \quad \text{(eq. 41)}$$

The exergy destruction of absorption system is defined as the sum of destroyed exergy in each component and can be calculated using the following eq. 42 [28].

$$\dot{\psi}_{D,abs} = \dot{\psi}_{D,Gen} + \dot{\psi}_{D,Con} + \dot{\psi}_{D,\ Eva} + \dot{\psi}_{D,abs}\ \dot{\psi}_{D,she} + \dot{\psi}_{D,Val} \quad \text{(eq. 42)}$$

Table 1 : Energy and exergy balance

Components	Energy Q (kW)			Exergy destroyed I (kW)		
	#1	#2	#3	#1	#2	#3
Absorber	124.1	84.1	55	5.04	6.87	6.82
Generator	124.7	85	57.7	13.81	12.57	11.02
Condens.	101	64.5	35.4	5.77	2.21	1.51
S. he	33	27.4	12.2	2.8	2.58	1.1
Evaporat.	96.1	61.3	33.2	3.15	3.68	1.87
Total				**30.57**	**27.91**	**22.3**

4. Results and Discussion

4.1 Validation of PTSC assemblies

The SCA study is based on the pysical and optical characteristics of the parabolic collector used for its assembly. But for this study the parabolic collector used is the same for all the configurations, moreover we must know that the arrangement of the collectors is in series even if the size and the shape of the SCA show some differences. This validation of the SCA technology was based essentially on the Removal factor, thermal efficiency and thermal efficiency factor (0.85).

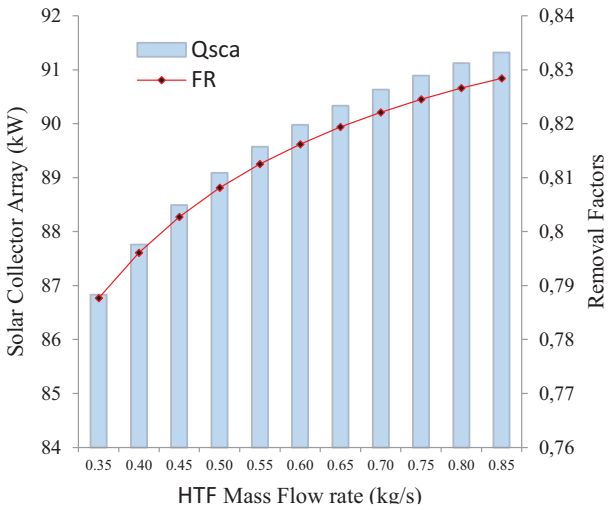

Fig.2: Absorbed energy and Removal factor of SCA. in configuration Type - A

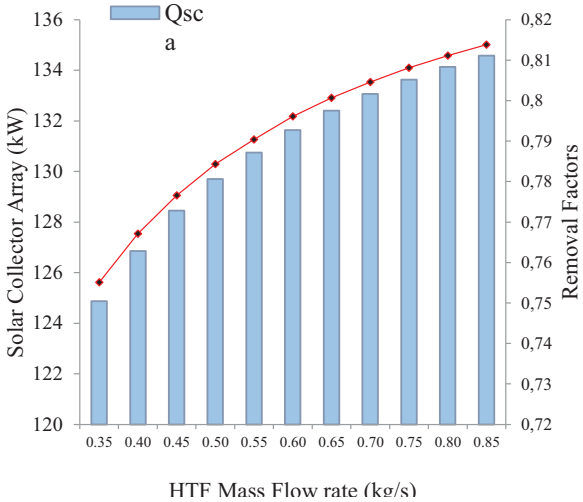

Fig.3: Absorbed energy and Removal factor of SCA. in configuration Type - C

The fig. 2 shows that the SCA used in the configuration type -A has a Removal factor of 0.812 and its energy absorbed of 89.9 kW, while Fig.3 presents a configuration type -B with a Removal factor of 0.791 and an energy absorbed of 131 kW when working with a mass flow rate of 0.55 kg/s. The configuration type-C not shown in this section has a Removal factor of 0.7543 and an energy absorbed of 249.46 kW working at a mass flow rate of 0.65 kg/s.

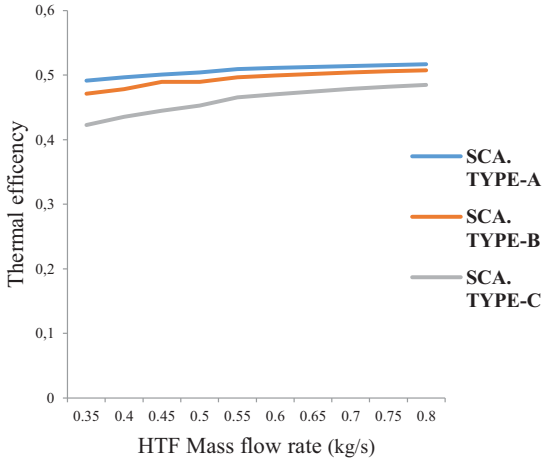

Fig. 4 : Effect of HTF mass flow rate on thermal efficiency.

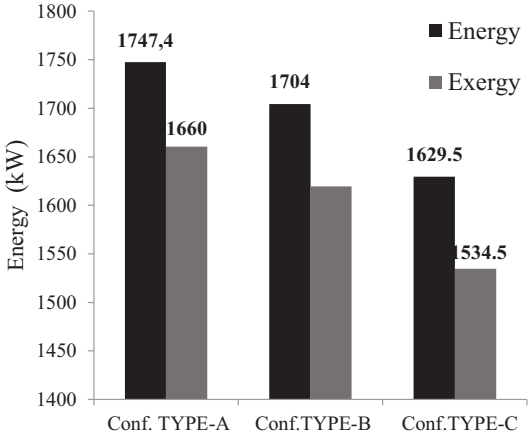

Fig.5: Effects of configuration type on Energy -exergy output

The fig.4 shows a negligible variation of the Thermal efficiency when the mass flow rate increases for the configuration type-A. On the other hand for the configuration type -C there is a considerable variation in the Thermal efficiency when there is a variation of the mass flow rate between 0.35 and 0.7 kg /s. For this study, a mass flow rate of 0.55kg/s will be used for Type-A and Type B configurations and 0.65kg/s for Type-C configuration

4.2 Validation of solar field configuration Type

Fig. 5 shows that the energy absorbed in the configuration type-A is greater than other configurations. It should be noted that the energy absorbed by the configuration of the solar field is closely related to the volume

of transfer fluid used to absorbe that energy. Futhermore outlet temperatures of the transfer fluid in the other types are significantly higher than configuration type-A.
In summary, we will say that the energy absorbed by the solar field changes inversely with the outlet temperature of the transfer fluid. The use of the ORC in the production of electricity does not influence the choice of the appropriate configuration. On the other hand, it contributes to the growth of electricity production in a significant way (Figures 6 and 7).

4.3 effects of configuration on power system performance

A comparative study of the results obtained in Tables 9, 10 and 11 between the CRC and SRC for different configurations shows a relative increase in electricity production according to the type of configuration. The configuration Type -A presents an increase of 5.05%, while configurations type -B and C show 3.1% and 1.95% increase in power generation respectively.

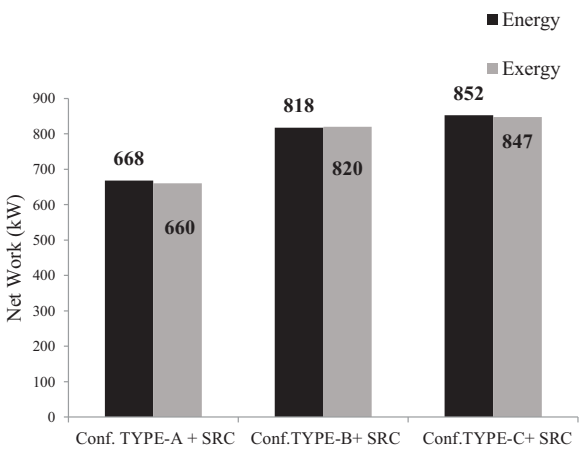

Fig.6: Net work of overall plant without ORC system

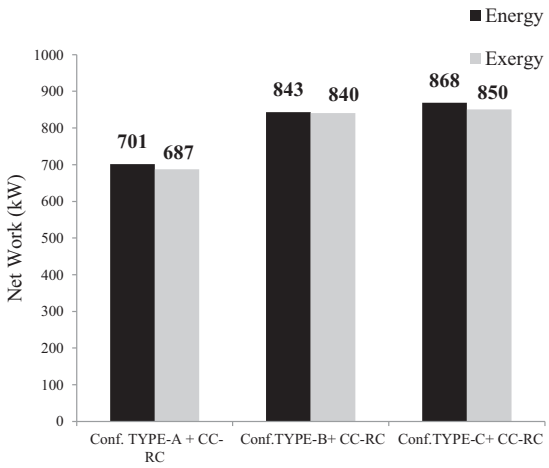

Fig.7: Effect of ORC on power system performance

4.4 effects of additive subsystem on system performance

The figures 8 et 9 show overall performance of studied configurations, configuration Type-C presente an higher performance with energy efficiency of 32.75%, exergy efficiency of 32.07% and lowest coefficient of performance for cooling and heating of 0.5751 and 1.5751 respectively.The configuration Type-C is followed by configuration Type -B, and configuration Type- A. The configuration Type- A has the lowest performance with energy efficiency of 26.45%, exergy efficiency of 25.91%, and highest coefficient of performance of cooling of 0.7706. The fig. 8 presents impact of both ORC and ARC in combined cooling power system analyzed.

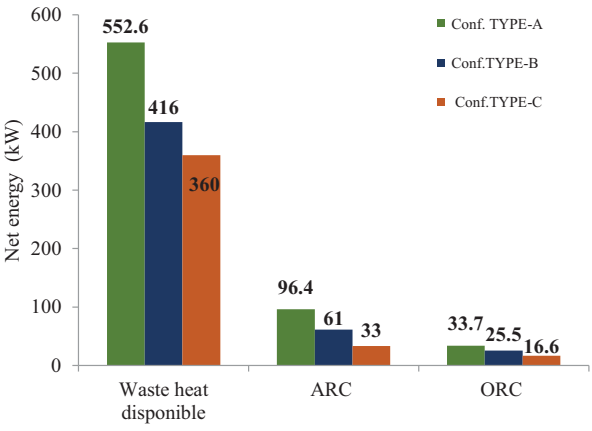

Fig.8: Effect of ARC and ORC on power system performance

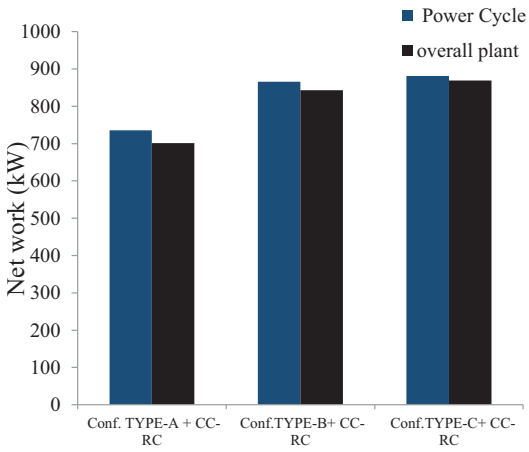

Fig.9: Effect of htf Pumping system on power system performance

Fig. 9 shows direct impact of htf pumping system of solar field configuration type on overall power plant. This study present configuration Type -A as a configuration which transfer 8.25 kg of Therminol oil per second too feed its piping network.

4.5 presentation of other results

Figure 10 presents a complete resume of this study through energy analysis of described system (fig.1). During this study optical, thermal conversion, transport and CCP losses has been analyzed for each solar plant configuration in order to show which of them is more efficiently and can be use to use provide power and cooling more suitably. fig.10.a shows repartition of these losses and overall plant production in configuration Type-A. The total losses evaluated for configuration is 68.62%, where optical losses contribute the highest value of 34.11%, followed by CCP production contributing 26.45% while cooling production contribute the second lowest value of 3.64% and external energy contribute the least lowest value of 1.29%.

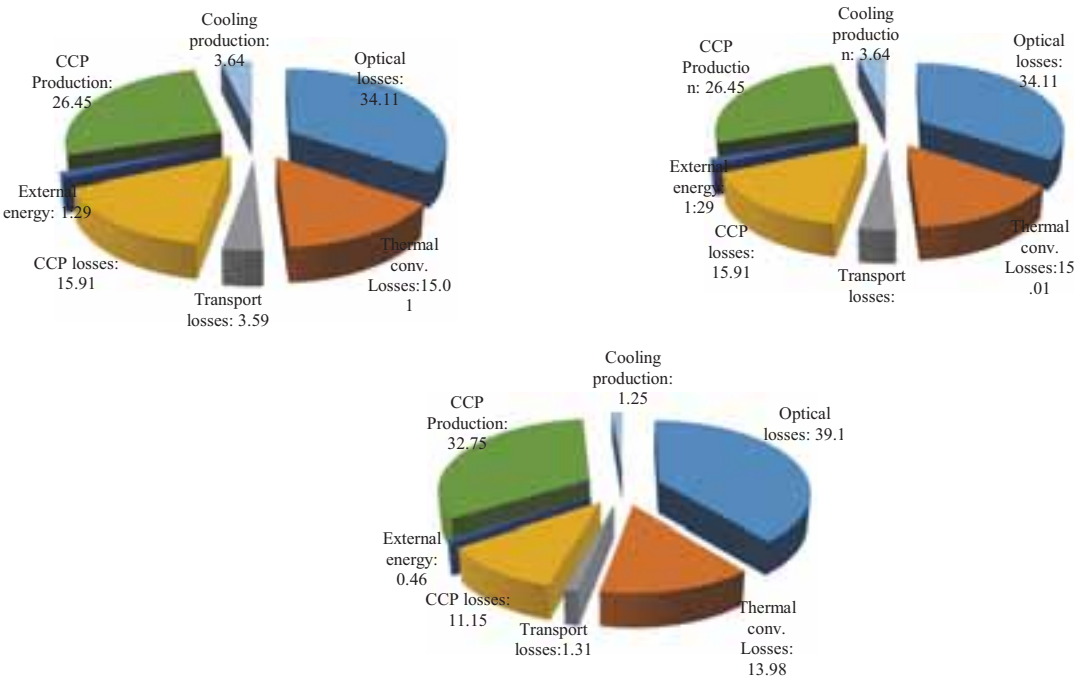

Figure 10: Repartition of energy losses of CCP in plant (a) configuration Type -A (b) configuration Type -B, (c) configuration Type -C

Fig.10.b shows the distribution of the total losses of configuration Type -B with the value of 65.54% , here CCP production contribute 32.75% of the total losses, while cooling production contribute 1.25% and external energy contribute the least value of 0.46%. It is worth to note that in all the configuration, optical losses contribute the highest to losses while external energy contribute the least. Furthermore, among the three configuration studied, configuration type-A had the highest losees followed by configuration type-B, while configuration type-C had the least.

In all the configurations presented, configuration type-C had a higher optical loss and lowest transport, thermal conversion and combined cycles power losses due to higher operating temperature, low mass flow rate of heat transfer fluid and short pipeline network.

5. Conclusion

The complete energy and exergy analysis on combined cooling power using combined Rankine cycles has been analyzed in this paper. This study has considered three differents configuration of same CSP system containing 120 modules. During this study effect of operating parameters such as temperatures, mass flow rates of working, transfer fluids are included, by a situable rate values of each one. Besides this, analysis of individual components of ecah subsystem is also done in order to improve global efficiency of system. This study shown that configuration type-C is more siutable for electricity produce in CSP commercial plant. This configuration despite working with higher temperature and lower mass flow rate, it has higher efficiency for power production. However, the system has lowest absorption refrigeration (AR) system efficiency due to lower exergy transfer by Steam Rankine cycle on the AR system. This study is important for identifying the performance uncertainties of various STC configurations using indirect stem generation (ISG) and selecting the most optimal configuration for small size plant in order to maximize the utilization of solar energy in CSP systems. Thus, its hoped that the results found in this study will be usefull for decision making regarding the selection of CSP systems configurations for optimal solar energy utilization.

References

[1]http://www.nrel.gov/csp/solarpaces/by_country_detail.cfm/country=US%20("_self") [access on23.12.16]
[2] David Ugolini, Justin Z. and John P. 2009. Options for hybrıd solar and Conventional fossil plants, Bechtel Technology Journal.
[3] V. Zare, M. Hasanzadeh 2016. Energy and exergy analysis of a closed Brayton cycle-based combinedcycle for solar power Tower plants, Energy Conversion and Management. 128, 227–237.
[4] Spelling J, Favrat D, Martin A, Augsburger G. 2012. Thermoeconomic optimization ofa combined-cycle solar tower power plant. Energy. 41, 113–20.
[5] J. Suna, W. Li, 2011. Operation optimization of an organic Rankine cycle (ORC) heat recovery power plant, Appl. Therm. Eng. 31, 2032–2041.
[6] Sun L, Han W, Jing X, Zheng D, Jin H. 2013. A power and cooling cogeneration system using mid/low-temperature heat source. Appl Energy.112, 886–897.
[7] M. Imran, B.S. Park, H.J. Kim, D.H. Lee and Al. 2014. Thermo-economic optimization of regenerative organic Rankine cycle for waste heat recovery applications, Energy Convers Manage.87, 107–118.
[8] H. Esen, M. Inalli, M. Esen, 2007. A techno-economic comparison of ground-coupled and air-coupled heat pump system for space cooling, Build. Environ. 42,1955–1965.
[9] https://en.wikipedia.org/wiki/İzmir#Climate [accessed on 15.11.16].
[10] Senol R. An analysis of solar energy and irrigation systems in Turkey. EnergyPolicy 2012;47:478-486.
[11] Topkaya SO, 2012. A discussion on recent developments in Turkey's emerging solar power market. Renew Sustain Energy Rev.16,3754-3765.
[12] https://eosweb.larc.nasa.gov
[13] Janotte, N., Lu¨pfert, E., Pitz-Paal, R., Pottler, K., Eck, M., Zarza, E., Riffelmann, K.-J., 2008. Influence of measurement equipment on the uncertainty of performance data from test loops for concentrating solar collectors. Proceedings of the 14th SolarPACES Conference, Las Vegas, NV (USA).
[14] Kutscher, C., Burkholder, F., Stynes, J.K., 2012. Generation of a parabolic trough collector efficiency curve from separate measurements of outdoor optical efficiency and indoor receiver heat loss. J. Sol. Energy Eng. 134, 11012–11016.
[15] Mohamed S. , Mehmet F. , F. Uygul, 2016.Thermodynamic analysis of parabolic trough and heliostat field solar collectors integrated with a Rankine cycle for cogeneration of electricity and heat, Solar Energy. 136,183–196.
[16] Therminol VP-1, heat transfer fluids by solutia, Applied chemistry, creative solutions, Group Provoc T.B.S 10-04 (12/98) E.
[17] Valenzuela, L., Zarza, E., Berenguel, M., Camacho, E.F., 2005. Control concepts for direct steam generation in parabolic troughs. Sol. Energy. 78, 301–311.
[18] Soteris A. Kalogirou, 2014. Solar Energy Engineering Processes and Systems 2nd edition, ISBN–13: 978-0-12-397270-5
[19] C¸engel YA, Boles MA.. 1994. Thermodynamics: an engineering approach. New York: McGraw-Hill.
[20] Xu C, Wang Z, Li X, Sun F., 2011. Energy and exergy analysis of solar power tower plants. Appl Therm Eng.31,3904–3913
[21] Talbi MM, Agnew B., 2000. Exergy analysis: an absorption refrigerator using lithium bromide and water as working fluids. Appl Therm Eng.20, 619–630.
[22] Herold KE, Radermacher R, Klein SA., 1996. Absorption chillers and heat pumps. Boca Raton, FL: CRC Press.
[23] Tozer RM, James RW., 1997. Fundamental thermodynamics of ideal absorption cycles. Int J Refrigeration. 20(2), 120–135.
[24] Lee SF, Sherif SA., 2001. Thermodynamic analysis of a lithium bromide/water absorption system for cooling and heating applications. Int J Energy Res. 25,1019–1031.
[26] Talbi MM, Agnew B., 2000. Exergy analysis: an absorption refrigerator using lithium bromide and water as working fluids. Appl Therm Eng.20, 619–30.
[27] Sun DW. Thermodynamic design data and optimum design maps for absorption refrigeration systems.
[28] Kotas TJ., 1985. The exergy method of thermal plant analysis. Great Britain: Anchor Brendon Ltd;
[29] http://re.jrc.ec.europa.eu/pvgis/apps4/pvest.php [accessed on 30.12.16]

Appendix A: Main data and equations

1. Solar Fields and Collector Specification

Table 1: Global solar radiation in izmir [12]

Months	Daily global solar radiation (kW.h/m^2.d.a) [12]	Daily sunshine duration (h/Day) [29]	Av. solar Radiation during Sunshine h. (W/m^2)
January	3.56	9	395.5
February	3.83	9.5	403.2
March	4.99	11	453.6
April	5.33	11.25	473.7
May	6.94	12.75	544.3
June	8.54	11.75	726.8
July	8.83	11.75	751.5
August	8.05	11.75	685.1
September	7.10	11.75	605
October	5.39	11.75	513.3
November	3.75	9.5	394.7
December	2.92	8.75	333.7
Av. values	**5.78**	**11.03**	**523.7**

(source: NASA and JRC)

Table 2: specifications of SCA (SAM Software)

Receiver type	**Luz LS-2**	**Absorber type**	**Schott** PTR80
Reflective area Apperture A_{ap} (m^2)	160.7	Height of receiver in ⊥	4.92
Av. surface to focus path length	1.80	***Absorber tube diameter***	***mm***
Apperture width, W total structure (m)	5	İnner ($D_{r,i}$)	76
Ext. surface areaof Cover glass A_c (m^2)	12.32	Outler ($D_{r,o}$)	80
Ext. surface areaof receiver A_r (m^2)	8.12	***Cover glass . diameter***	***mm***
Length of Module L (m)	8.166	İnner ($D_{g,i}$)	115
Nb modules per collector	-	Outler ($D_{g,o}$)	120
Reflectance mirror (ρ_c)	0.935	İncidence angle modifier (k_r)	1.0
Optical parameters	0.96	***Absorber flow plug***	
Optical efficiency at design	0.87	Internal surface roughness	4.5 e-02
Cover glass Absorbance (α_g)	0.02	Absorber material type	B42 copper
Cover glass Emittance (ε_g)	0.86	receiver absorbance (α)	0.963
Cover glass Transmittance (τ_g)	0.964	Receiver emittance (ε_r)	0.65
Everage heat losses (W/m)	210	İntercept factor (γ)	0.93

Table 3 : Optimal parameters of the parabolic trough collector

Parameter	**Value**	**Symbol**
Useful energy input	-	$\dot{Q}_{use}$
Amount of solar radiation (kWth)	2652	$\dot{Q}_{solar}$
Temperature glass cover (K)	343.5 - 377	T_c
Collector efficiency factor	0.858	F'

2. Heat transfer fluids parameter

$0.1 < Re < 1000$: $Nu_{air} = 0.4 + 0.54.Re^{0.52}$

$1000 < Re < 5.10^4$: $Nu_{air} = 0.3.Re^{0.6}$

$Re < 2300$: $Nu_r = 0.023.(Re)^{0.8}(Pr)^{0.4}$

$Re > 2300$: $Nu_r = 4.364$

Table 5:Properties of thermal Htf and PTC's receiver [16]

Parameter	**Value**	**Symbol**
Therminol / HTF		
Density of HTF @ 15°C	1068 kg/m^3	ρ_{htf}
Thermal conductivity	0.096W/m.K	k_r
Kinematic viscotivity	9.9 10^{-7}m^2/s	υ_{htf}
Thermal conductivity of water	W/m.K	k_{water}
Receiver		
Receiver mass flow rate	> 0.65 kg/s	$\dot{m}_{htf}$
output temprature of receiver	> 665.5K	T_{ro}
input temperature of receiver	503K	T_{ri}
Average solar irradiation	523.7 W/m^2	G_b
Ambient temperature	298.15 K	T_o

3. Thermodynamic of working fluids

Exergy balance equations are expressed in eq.23a, b, and c given below have been used in this study[19]:

$$\dot{E}_{int} - \dot{E}_{out} = \Delta\dot{E}_{syst} \quad \text{(eq. 23a)}$$

$$\dot{\psi}_{int} - \dot{\psi}_{out} - \dot{\psi}_D = \Delta\dot{\psi}_{syst} \quad \text{(eq. 23bc)}$$

$$\dot{S}_{int} - \dot{S}_{out} + \dot{S}_{gen} = \Delta\dot{S}_{syst} \quad \text{(eq. 23c)}$$

For the first law of thermodynamics yields, energy balance of each component is given by eq.23 [19] :

$$\sum(\dot{m}h)_i - \sum(\dot{m}h)_o - \left[\sum Q_i - \sum Q_o\right] + W = 0$$

$$\dot{E} = \dot{m}h \quad \text{(eq. 24)}$$

The exergy of fluid has been estimated using the following expression

$$\psi = (h - h_o) - T_o(s - s_o) \quad \text{(eq. 24)}$$

The exergy destruction in each component has been calculated using :

$$\dot{\psi}_D = \dot{\psi}_{int} - \dot{\psi}_{out} - \left[\sum Q\,(1 - \tfrac{T_o}{T})_i - \sum Q\,(1 - \tfrac{T_o}{T})_o\right] + \sum W$$

$$\dot{\psi} = \dot{m}.\psi \quad \text{(eq. 25)}$$

The exergy destruction of system is the sum of destroyed exergy, can be presented by:

$$\dot{\psi}_{D,Total} = \sum_i \dot{\psi}_{D,i} \quad \text{(eq. 26)}$$

The system performance and optimatization has been done using the presented Thermodynamic law.

The equivalent heat source temperature is given by:

$$\dot{\psi}_{D,CC} = \sum_i \dot{\psi}_{D,T} + \sum_i \dot{\psi}_{D,P} + \dot{\psi}_{D,cond} + \dot{\psi}_{D,Eva} + \dot{\psi}_{D,rec}$$

The governing equations of mass and type of material conservation for a steady state and steady flow system are expressed by eqs. 36a and b[21]:

$$\sum \dot{m}_i - \sum \dot{m}_o = 0 \qquad \text{(eq. 36)}$$
$$\sum(\dot{m}x)_i - \sum(\dot{m}x)_o = 0$$

The heat exchanger efficiency has been estimated using eq. 37 as presented below[18].

$$\pi_{she} = \frac{T_{17}-T_{16}}{T_{17}-T_{19}} \qquad \text{(eq.37)}$$

4. Nomenclature

Table 1: Symbols for Solar Collector and HTF

Quantity	Symbol	Unit
Area Aperture area	A_{ap}	m^2
Area of receiver	$A_{c,o}$	m^2
Lost area	A_L	m^2
Aperture width	W	m
Geometric factor	A_f	
Heat transfer coefficient	h	$W.m^{-2}.K^{-1}$
System mass	m	kg
Concentration ratio	C	
Mass flow rate	$\dot{m}$	$Kg.s^{-1}$
Heat	Q	J
Heat flow rate	$\dot{Q}$	W
Heat flux	q	$W.m^{-2}$
Heat abs. receiver	S	$W.m^{-2}$
Temperature	T	K
Overall heat transfer coefficient	U	$W.m^{-2}.K^{-1}$
Stefan-Boltzmann constant	σ	$W.m^{-2}.K^{-4}$
Removal factor		

Table 2: symbols for materials properties

Quantity	Symbol	Unit
Specific heat	c	$J\ kg^{-1}\ K^{-1}$
Thermal conductivity	k	$W\ m^{-1}\ K^{-1}$
Absorptance	α	
Emittance	ε	
Reflectance	ρ	
Transmittance	τ	
Prandt number	Pr	
Nusselt number	Nu	
Reynold number	Re	

Table 3: symbols for radiation quantities and efficiencies

	Preferred name	Symbol	Unit
a)	Usefull energy output	$\dot{Q}_{abs}$	kWth
	Solar power input	$\dot{Q}_{solar}$	kWth
	Absorbed energy input	$\dot{Q}_{use,in}$	kJ
	Energy	E	kW
	Exergy	ψ	kW
b)	Collector efficiency	η	
	Overall heat transfer	U_o	$W.m^{-2}.K^{-1}$
	Heat losses coefficient	U_L	$W.m^{-2}.K^{-1}$
	Efficiency factor of collector	F'	
	Optical efficiency	η_o	
	Energetic efficiency	η_{th}	
	Exergetic efficiency	η_{ex}	
	Efficiency of exchanger	π	

Table 4 : subscripts

Quantity	Symbol
Glass, Cover glass	*g, c*
destruction	*D*
solar subsystem	*ss*
Absorber, Receiver	*Abs, r*
power plant	*pp*
condenser	*Cond*
evaporator	*Eva*
absorber	*abs*
Thermal	*th*

Residential buildings retrofit: the role of solar technologies

Alessandro Bellini[1,2], Chiara Dipasquale[1] and Roberto Fedrizzi[1]

[1] Institute for Renewable Energy, Eurac Research, Bolzano (Italy)

[2] Free University of Bolzano, Bolzano (Italy)

Abstract

In line with the last European directives that boost actions for reducing the energy consumption in the residential sector, buildings refurbishment becomes key. On one hand, a deep building retrofit concerns actions aimed at reducing the building demands and the final energy consumption. In particular, the replacement of existing windows, the addition of an insulation layer on the external surfaces and the installation of a mechanical ventilation system with heat recovery (MVHR) help to drastically reduce the building demands. On the other hand, the installation of a system with improved performance can additionally decrease the final energy used for space heating and cooling (H&C) and Domestic Hot Water (DHW) preparation with respect to a traditional system. Once the retrofit measures have acted on improving the energy efficiency of both building envelope and HVAC system, an additional contribution can be given by solar technologies integrated in the building.

In this context, this paper wants to show the amount of final and primary energy consumption reduction through a deep renovation on existing buildings and the contribution that solar technologies gives in this perspective.

Keywords: Building retrofit, solar technologies, simulation-based analysis, residential buildings

1. Introduction

In line with the last European directives that boost actions for reducing the energy consumption in the residential sector, buildings refurbishment becomes key. The construction period of half of the existing European residential building stock dates back to before 1970. The average heating demand of these buildings over Europe is higher than 200 kWh/(m²y) (Birchall et al., 2014). This means a big potential for buildings refurbishment although up to now the yearly retrofit ratio is around 1-2%. For achieving high energy savings, what is needed is a deep building retrofit that involves both the envelope and the HVAC system of a building. The integration of solar technologies can even increase the reduction of energy consumption due to space Heating & Cooling (H&C) and Domestic Hot Water (DHW) preparation.

Deep building retrofit concerns actions aimed at reducing building demands and final energy consumption. On one hand, the replacement of existing windows, the addition of an insulation layer on the external surfaces and the installation of a mechanical ventilation system with heat recovery (MVHR) help drastically to reduce the building demands. On the other hand, the installation of a system with improved performance can contribute additionally to decrease the final energy needed for covering the building uses. Intervention on the envelope, in fact, are effective only if also the HVAC system is performing. The effect that one solution could have on another one and the contribution that solar thermal panels (ST) and photovoltaics (PV) without battery can have on the final energy consumption are not easy to be estimated during the design phase. For this purpose, dynamic simulations could help for accounting for the loads to be covered and production contemporaneity.

For the abovementioned reasons, this paper aims to present simulation-based results of renovation packages solutions applied to residential existing buildings. In particular, the paper reports building demands reduction due to envelope solutions, final energy consumption and HVAC system performance, solar fraction obtained with the integration of STC and PV production, self-consumption and energy fed into the grid. Simulations are carried out in the TRNSYS environment (Klein et al., 2011).

doi:10.18086/swc.2017.29.02 Available at http://proceedings.ises.org

The paper presents results collected in an online database (iNSPiRe, 2016) useful in a pre-design phase for giving an idea about energy and economic performance of market-available renovation packages solutions. The validity of this database concerns the possibility to consult easily renovation measures performance obtained through detailed models. The numerical models of the analysed cases take also into account the contemporaneity of available solar energy and building loads (thermal or electrical), the presence of thermal storages and the implementation of the system control. The analysis has been performed through seven European climates, seven building construction periods, four heating demand levels and five building typologies. Moreover, the database reports results on the investment, maintenance and running costs of each solution. For the scope of the paper, only a selection of these results is commented.

In this paper, in particular, the authors want to underline the impact that solar technologies have in a retrofit process for the reduction of the final and primary energy consumption. Additionally, the paper provides suggestions on the optimal solar field size to match the building needs and reduce stagnation hours in solar thermal field and fed-into-the-grid energy in PV installations.

2. Retrofit packages for residential buildings

The study refers to reference buildings individuated in a previous study developed within the iNSPiRe FP7 project (Birchall et al., 2014). Based on an extensive literature review through national statistics, public papers, other sources and previous European projects, two main building typologies, Single Family Houses (SFHs) and Multi Family Houses (MFHs) are identified. In addition, some variations of surface over volume (S/V) ratio through detached/row houses for SFHs and number of floors for MFHs, it was possible to have models that covered around 70% of the existing residential building stock in Europe.
Building typologies are classified based on information collected through the study: geometric and physic characteristics are defined by building typology, construction period and climate (Birchall et al., 2014). In particular, the SFH reference building is a two-storeys building with a total heated area of 96 m². Glazing ratio in the north façade is 10%, 12% in the east and west facades and 20% in the south façade. The building covering is a pitched roof; the ground floor bounds with a cellar. In order to enlarge the cases availability, together with the detached SFH, also row-houses are considered: east and west facades of the detached ones are taken as adiabatic surfaces instead of external. From detached to row-houses, the S/V ratio reduces from 0.87 to 0.58.
The MFH reference building here considered is a small MFH (s-MFH) composed by ten apartments distributed through five floors. Each dwelling is 50 m²; the staircase is embedded in the building between the two apartments. In this case, the roof is flat and the cellar is not present. In MFHs, the number of floors varied from three to seven in order to cover cases with S/V ratio from 0.48 to 0.61.
In the study, numerical models of the reference buildings were therefore developed and in particular, one model per building typology, construction period and climate were created. For each of these, the assessed heating and cooling demands were benchmarked with statistics data in order to prove the models validity (Dipasquale et al., 2014).
For the reference cases, energy consumption was calculated assuming that heating and DHW were provided by a gas boiler with efficiency of 0.8, while cooling demand was covered by a split unit with EER equal to 2.5. For the Primary Energy (PE) consumption calculation, conversion factors of 2.878 kWh_{PE}/kWh_{FE} for electricity and 1.194 kWh_{PE}/kWh_{FE} for gas are used (Malenkovic et al., 2012).

The abovementioned buildings models represent the reference cases for the retrofit solutions to be investigated.
The studied retrofit packages are defined with market-available products. In this way, the final user of the database, that could be the decision maker or a technician of the residential sector, can find in it a generic building similar to the specific case.
In this paper, the interventions of a deep renovation are studied in three steps: measures on the envelope, improvement of the HVAC system performance and integration of solar technologies.
The retrofit measures for the envelope concern the replacement of the existing windows with double or glazed windows, the installation of a mechanical ventilation machine with heat recovery (MVHR) with efficiency of 0.85 and the insulation of the external surfaces. The specific measure or insulation thickness are decided based on the climate (one of the seven, Nordic, Northern Continental, Continental, Oceanic, Southern Continental, Southern

Dry and Mediterranean) and the heating demand energy level (EL) to be achieved, 15, 25, 45 and 70 kWh/(m²y). Once defined the window quality, the presence of the MVHR system and, consequently, the new infiltration rate, the insulation thickness is calculated for achieving the targeted EL. For this study the insulation layer is an EPS (expanse polystyrene) with conductivity 0.039 W/(mK).
Details on the envelope renovation measures are reported in (Fedrizzi et al., 2016a) for SFHs and in (Fedrizzi et al., 2016b) for s-MFHs.

In the study, the existing generation and distribution system is supposed to be replaced with a more efficient HVAC system. Different configurations are studied with a modular approach that allows to investigate the performance of different devices for the energy generation and terminals using the same energy plant layout and working modes. Also for the HVAC system, the choice of the renovation solutions moves on the most common and promising market-available solutions. In particular, the investigated generation systems are: air-to-water heat pump, ground-source heat pump, condensing boiler and pellet boiler.
With regard to the distribution system, the different behavior and energy consumption of radiant panels, fan coils and radiators is taken into account.

Finally, the contribution of solar technologies is considered for even reducing the energy consumption. In the study, solar thermal collectors (STC) and photovoltaics (PV) fields were analysed accounting for the effect of either one of them or both together. Three different areas and two slopes, 30° on the roof and 90° on the façade, were studied. The below tables report the solar fields size for STC and PV.

Table 1: Solar thermal collectors field size

	Unit	SFH	s-MFH
STC_1	*m²*	4.6	18.4
STC_2	*m²*	9.2	27.6
STC_3	*m²*	13.8	36.8

Table 2: PV field size

	Unit	SFH	s-MFH
PV_1	*kWp*	1	3
PV_2	*kWp*	2	4
PV_3	*kWp*	3	5

3. Results and discussion

The abovementioned renovation measures aim at reducing the total energy consumption of the existing residential building stock keeping thermal comfort inside the dwellings. Each measure contributes differently: envelope solutions decrease the building demands, an efficient HVAC system reduce the final energy consumption and solar technologies contribute to the energy savings with the use of renewable energy.

Within all the cases presented in the database (iNSPiRe, 2016), in the following paragraphs only a selection of these will be reported. For the sake of clarity, extreme climates will be shown, that is Nordic, with reference weather conditions of Stockholm (STO), and Mediterranean – Rome (ROM). These two cases in fact represent a heating and a cooling dominated climates. For the generation systems, air-to-water heat pump (AWHP) only is chosen as one of the most common and innovative solution. Performance of this generation system is compared with the reference one. In terms of final energy consumption, ground-source heat pump differs from AWHP for a higher electricity consumption due to the hydraulic pump used in the source/sink side of the heat pump. However, exchanging with the ground instead of external air, the heat pump performance improves and consequently final energy consumption decreases keeping the same delivered thermal energy. A condensing boiler has higher efficiency than a normal boiler. The pellet boiler, since it has a smaller primary energy factor, outperforms the condensing boiler in terms of primary energy despite its performance is lower.

With regard to the distribution system, results refer to a system with radiant ceilings working with a supply temperature of 35°C. These units better suit the possibility to deliver heating and cooling with the same generation device working at low temperatures. Differently from the radiant panels, radiators and fan coils distribute heating/cooling with a lower radiative fraction. This means that with radiant panels the operative temperature in the zone is closer to the sensible temperature that is used by the thermostat. Consequently, more thermal energy, in a range of 3-5%, is required for keeping the internal set temperature and therefore balance the extra transmission losses due to surfaces higher temperature. However, fan coils consume additional electricity required by the fan

embedded in the device, while radiators, instead, cannot deliver cooling needing, therefore, another device for that purpose. In the case of boilers and radiators, space cooling is covered by split units.

3.1. Envelope renovation measures

The improvement of the envelope energy performance can allow important heating demand reductions.
In SFHs despite the different weather conditions of the Nordic and Mediterranean climates, the average heating demand for buildings built between 1945-1970 in both climates is around 170 kWh/(m²y). This behaviour is due to a better wall constructions adopted in the northern climates for the existing buildings. In the here reported case, the envelope measure aims at achieving a fixed heating demand of around 50 kWh/(m²y). For this energy level (EL) target, in the Nordic it is necessary to install a triple glazed window, a MVHR system, 8 cm of insulation on the external façade, 5 cm on the ground floor and 15 cm on the roof. In the Mediterranean, instead, the EL is reached by installing double glazed windows, 12 cm of insulation on the façade and 18 cm on the roof. These interventions on the envelope allow reducing the building heating demand of around 70% in both cases. A better quality window and the use of external shadings for both climates bring also a reduction of the cooling demand of 55% in Rome and 44% in Stockholm.
s-MFHs with same construction period as SFHs have heating demand around 86 and 95 kWh/(m²y) respectively in the warmer and colder climate. The lower demand is due to the lower S/V ratio. For this building typology for both climates, the EL target is achieved without the need of a MVHR system neither triple glazed windows. Regarding insulation, while in Rome only 5 cm are needed on the façade, in Stockholm it is required 10 cm on the façade and 10 cm on the roof. As shown, a small intervention on the envelope allows to reduce the heating demand of 40-45%. Differently with SFHs, the cooling demand in s-MFH slightly reduces (see Table 3).

Table 3: Heating and cooling demand before and after envelope renovation

Building	Space Heating [kWh/(m²y)]		Demand	Space cooling [kWh/(m²y)]		Demand
	Existing case	Post renovation	reduction [%]	Existing case	Post renovation	Reduction [%]
SFH_ Rome	171.2	53.7	68.6%	44.7	25.7	42.6%
SFH_Stockholm	173.9	51.3	70.5%	16.8	7.4	55.8%
sMFH_ Rome	86.3	55.1	36.2%	42.1	40.4	4.0%
sMFH_Stockholm	95.4	49.7	47.9%	14.7	14.5	1.4%

3.2. HVAC system renovation measures

A building with a good performance envelope is not enough for achieving important energy savings if also the HVAC system is not efficient. The replacement of the existing system with a more efficient one is able to bring relevant savings on the final energy consumption. Starting from the demands obtained after renovation (Table 3), Primary Energy consumption for space heating (SH) and space cooling (SC) is calculated considering the reference system (Reference) and the AWHP system (AWHP). The reference system is the one used for calculating the final energy for the existing buildings (see Par.2). Final energy consumption obtained after retrofit are instead calculated through simulations and are available on the database. The results reported in Table 4 show as an improvement of the HVAC system performance allows a PE reduction for SH of 44%-46% in Rome and 36-37% in Stockholm respectively for the SFH and s-MFH buildings. For SC the savings depend on a better EER of the cooling device bringing for Rome and Stockholm 23-27% of PE consumption in the SFHs and 33-36% in s-MFHs.

Table 4: Primary Energy consumption before and after HVAC system renovation

Building	PE heating [kWh/(m²y)]		PE for SH	PE cooling [kWh/(m²y)]		PE for SC
	Reference	AWHP	reduction [%]	Reference	AWHP	reduction [%]
SFH_ Rome	80.0	44.9	43.9%	29.6	21.6	27.0%
SFH_Stockholm	76.4	49.3	35.5%	8.5	6.5	23.4%
sMFH_ Rome	82.1	44.2	46.2%	46.5	31.2	32.9%
sMFH_Stockholm	74.0	46.3	37.4%	16.7	10.7	35.7%

Comparing the PE consumption for the cases before retrofit and the ones with the envelope renovation measures and the more efficient HVAC system, the energy savings that can be achieved amount to around 80% for the SH of the SFH and 66% for the SH of s-MFHs (regardless the climate). For the SC the percentage is lower due to also to the lower demand, but even not negligible: in the SFH, PE for SC is reduced of 58% in Rome and 66% in

Stockholm, while in the s-MFH the reduction is of around 36% in both climates (see Fig 1).

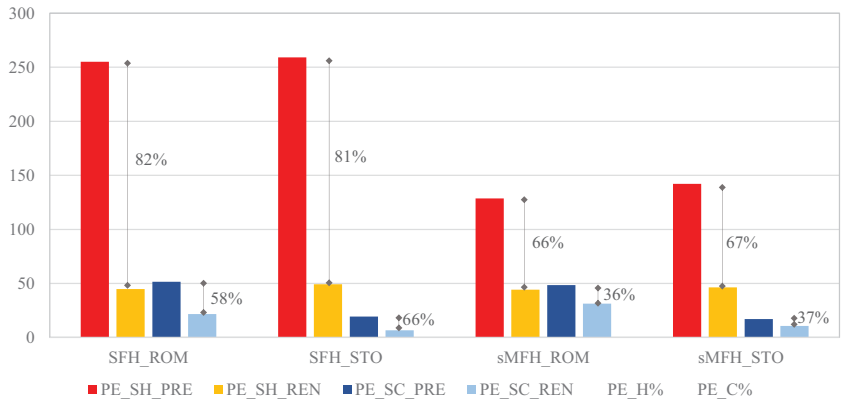

Fig 1 Primary Energy consumption of the two buildings typologies in the two climates before renovation (PRE) and after the envelope and HVAC system renovation (REN)

3.3 Solar technologies contribution

In a deep renovation process, a strongly reduction of the energy consumption is favoured by the installation of solar technologies as solar thermal panels (STC) and photovoltaics (PV). Depending on the building loads and climate, one or the other technology can have a higher impact on the total final consumption. However, even a small solar field can bring important savings against a small investment cost, with respect to the cost of the whole renovation.

Solar thermal collectors

In the following, results for cases STC_1 and STC_3 (see table 1) referred to SFHs and s-MFHs are reported.

In SFHs, a solar field of 4.6 m² installed on the roof is able to cover around 74% of the DHW load in the Mediterranean climate and 40% in the Nordic one. If the panels are installed on the façade (90°), the production is reduced respectively in the two climates of 18%-10%. This difference amounts to only 3 % if calculated over the whole heating production.

In the Mediterranean, a three times bigger solar field can double the solar fraction for the heating production (DHW demand and space heating) but the number of hours where the stagnation phenomena can occur drastically increases. To reduce this effect or even eliminate it, solar collectors can be installed on the façade with only 4% of solar fraction reduction with respect to the installation on the roof.

In a Nordic climate, the behavior is similar, moving from STC_1 to STC_3 the solar fraction for heating production almost double, but also stagnation hours occur. The installation of solar panels on the façade strongly limits the stagnation hours with only 1% less of solar fraction.

Accordingly, similar trend is observed also in the s-MFHs (see Table 5). The percentage of solar collectors over living are is smaller in s-MFH with respect to SFH because of the lower available surface. Despite this, a solar field of almost 37 m² on the roof causes the stagnation phenomena both in the Mediterranean and in the Nordic climate. Again in this case, stagnation disappears if the panels are installed on the façade with a solar fraction reduction of 3% (see Table 5).

Table 5: Solar fraction for heat production

AREA	Slope	ROM_SFH	STO_SFH	ROM_s-MFH	STO_s-MFH

		SF [%]	[hr]	SF [%]	[hr]	SF [%]	[hr]	SF [%]	[hr]
no ST	0	0%	0	0%	0	0%	0	0%	0
STC_1	*30°*	21%	101	12%	0	22%	37	13%	0
STC_3	*30°*	44%	1985	21%	374	34%	624	20%	68
STC_1	*90°*	17%	0	9%	0	17%	0	11%	0
STC_3	*90°*	40%	30	20%	0	31%	0	18%	0

In terms of final energy consumed for covering heating and DHW demands, the savings of using STC_1 amount to 26% in Rome – SFH and 12% in Stockholm - SFH. Despite the lower ratio of solar panels area over living area, same behavior is observed in the s-MFH. The STC_3 instead, that corresponds to around one fourth of the SFH roof surface, in the warmer climate can cover 43% of the heating production while in the colder one 20%. For the s-MFHs the final energy for heating production reduction with STC_3 amounts to 34% and 18% respectively in Rome and Stockholm (Fig. 2).

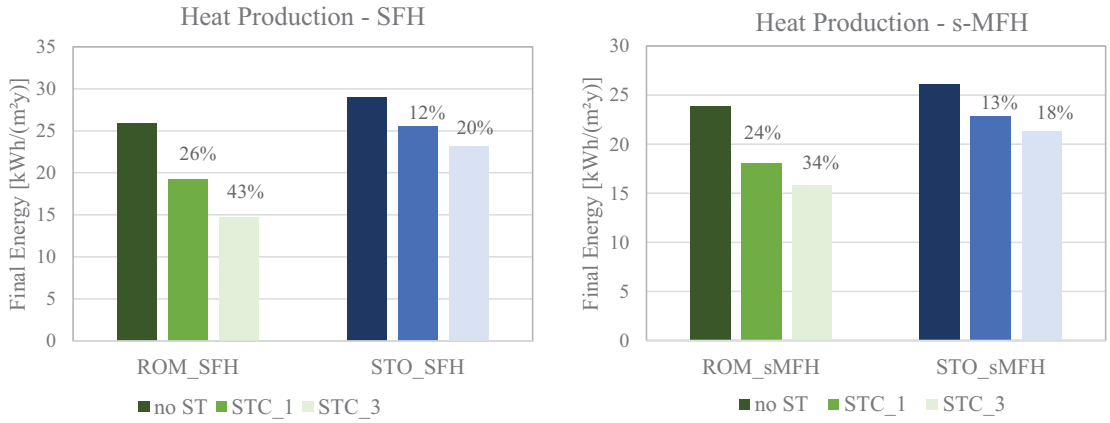

Fig 2 Final Energy consumption for heating production for two solar thermal fields in comparison with the case without thermal panels in SFH (left) and s-MFH (right)

In addition to two panels slope, the database contains also results for two different solar tank sizes, 50 l/m² and 100 l/m² of solar area. With respect to the final energy consumption for heating purposes, a slightly better performance is observed with the bigger storage, in the order of 2-3%.

Solar thermal panels influence only the consumption due to space heating and DHW consumption, so their contribution on the total building consumption depends on the share between the different uses. In particular for the cases here analysed, these quantities on the total energy consumption of a SFH for STC_1 and STC_3 fields amount to 20% and 33% in the Mediterranean, and 10% and 16% in the Nordic. In a s-MFH instead, the energy reduction due to the installation of a solar thermal field can achieve 23% in Rome and 16% in Stockholm if the biggest studied area is installed.

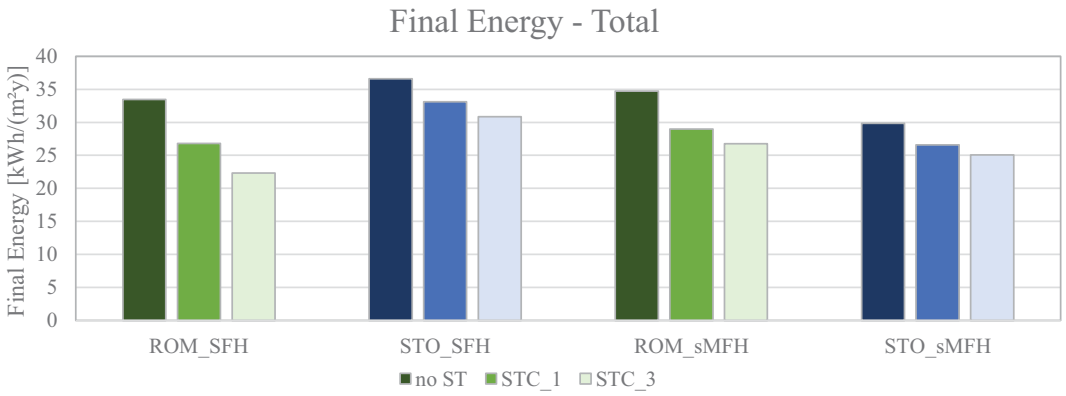

Fig. 3 Total Final Energy consumption for two solar thermal fields in comparison with the case without thermal panels

Photovoltaics

The analysis on the contribution that a photovoltaic field could give on the total energy consumption of a building focuses first on the share between self-consumption versus fed-into-the grid and then on the savings that this technology can bring to the building total final consumption.

Fig. 4 shows the share options of PV production between the energy used by the HVAC system (red bar), by other building uses like appliances (orange bar) and fed into the grid (yellow bar). The following comments do not consider any feed-in-tariff for the latter share option as every country has its own regulation that often changes.

In this contest, a solution that maximizes the auto-consumption is considered more favorable. Looking at the left graph of Fig. 4, the solution with only 1 kWp installed represents the best compromise between production and consumption. Most of renewable energy production is in fact used by the HVAC system itself or by other uses. Installing 3 kWp, instead, around 60% of the produced energy is not consumed by the building. This scenario becomes favorable only if convenient fees are foreseen. On the total PV production, the installation of the PV panels on the façade in place of on the roof brings less energy production of 24% in Rome and 13% in Stockholm. In the following it will be shown as the lower energy production has a minor effect on the single uses.

Different behavior is observed for the s-MFHs where, as for the STC, the percentage of PV area on the living area is lower than in the SFH. Electricity production of a 3 kWp PV field is used for 95% from the building uses. If instead 5 kWp of PV is installed, that means covering 6.5% of the roof area, the self-consumption amounts to around 85-90% both in the northern and in the southern climate.

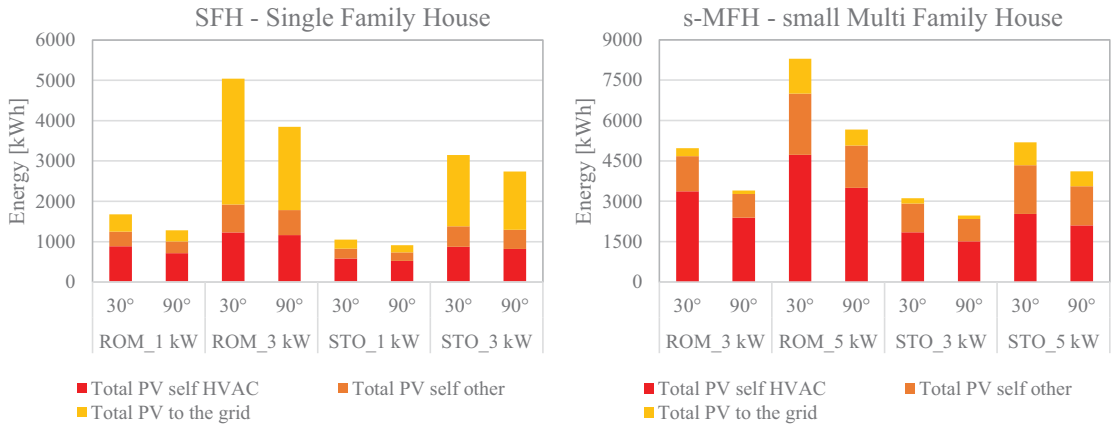

Fig.4 PV production and self-consumption for SFHs (left) and s-MFH (right) for two climates and two field sizes

Looking at the savings that the analysed solar fields bring on the different energy uses consumption, 1 kWp of PV in a SFH is able to reduce space heating consumption of 7% in Rome and 3% in Stockholm. If instead 3 kWp are installed, the reduction is respectively of 12% and 7%. The advantage in this case seems to be not relevant, but doing the same consideration for the cooling load, the reduction is higher than 80% in both climates. Together with the space heating and cooling, PV contributes also in the decrease of DHW preparation energy need. Looking at the total building consumption, we can observe that 1 kWp of PV field in a SFH reduces 27% of the total electricity in the southern climate and 16% in the northern one. A three times bigger field helps in achieving 38% and 24% lower electricity consumption respectively in the two climates (Fig. 5).

The above considerations refer to a PV field installed on the roof. If it is positioned on the south façade, the winter harvesting slightly decreases, in the order of 1-2%, but the summer harvesting increases. The yearly electricity reduction therefore amounts to 36% in the Mediterranean and 23% in the Nordic climate.

Although in s-MFHs the share of PV field over living area is lower than in SFHs, the higher percentage of self-consumed electricity makes the electricity savings similar in both building typologies. In particular, the bigger PV field – 5 kWp – brings 16% and 7% of energy reduction in winter for the two climates, Mediterranean and Nordic, while for the cooling the reduction amounts to 34% and 46%. Accounting for also the DHW production and the yearly behavior, the PV_3 field (Table 2) is able to reduce the total final consumption for the HVAC system of 30% in the Southern climate and almost 20% in the Northern one. If the PV field is installed on the façade, the total energy savings for the two climates reach respectively 23% and 16%.

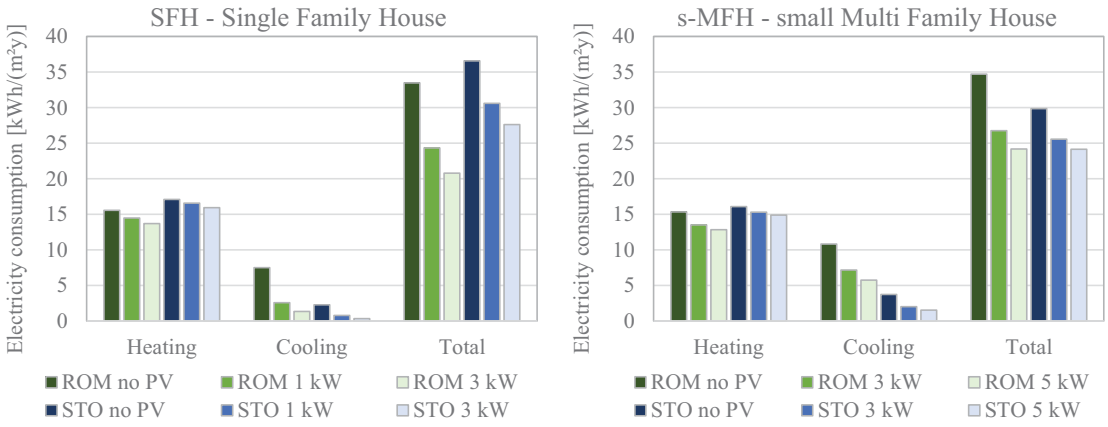

Fig.5 Final energy consumption for space heating, space cooling and total for SFH (left) and s-MFH (right) in two climates by different PV field sizes.

3.4 Retrofit solutions total savings

In the previous paragraphs, each retrofit measure has been analysed separately. In Fig.6 the initial PE consumption for space heating, space cooling and DHW preparation is compared with the PE savings that each measure gives to the total energy consumption. For the solar technologies, it has been considered the contribution of STC and PV together, considering the PV_3 size on the roof and STC_3 on the façade.

Table 6 summarizes the savings in percentage on the initial total primary energy consumption by each retrofit solution. The last line instead indicates the percentage of PE consumption after retrofit on the one before retrofit.

In the study, the retrofit measures for the envelope were decided once fixed the heating demand energy level. Consequently, depending on the initial building demand, the savings obtained by the envelope are larger where the initial building demand is higher. Buildings with same external surfaces thermal characteristics but different S/V ratio, i.e. SFH and s-MFH, can have heating demand one the double of the other. As a consequence for the studied cases, especially in SFH, the retrofit measures applied to the envelope are the ones that mostly contribute on the primary energy consumption reduction. An efficient HVAC system has a major impact on the heating production consumption than on the consumption for cooling because of the performance of the reference case. With this regard, the savings due to the HVAC system only amount to 32% and 23% in SFH respectively southern and northern climate and 38% and 31% in s-MFHs. This means that with respect to a boiler with 0.8 efficiency and split units with 2.5 EER, the final primary energy consumption can be reduced by around one third thanks to the use of a more efficient system composed by an air-to-water heat pump.

Additionally, even small surfaces of solar technologies as PV and thermal collectors, have an important impact on the total energy consumption. In fact in Southern climates as Rome, the combination of 3 kWp of PV and 6 panels in STC can almost halve the final consumption in SFHs. 5 kWp of PV and 16 panels of STC in s-MFH instead allow 43% of the total primary energy reduction. Due to climate conditions in the Northern climate the contribution of solar technologies on the total energy consumption is slightly lower, but still 34% in SFH and 29% in s-MFHs.

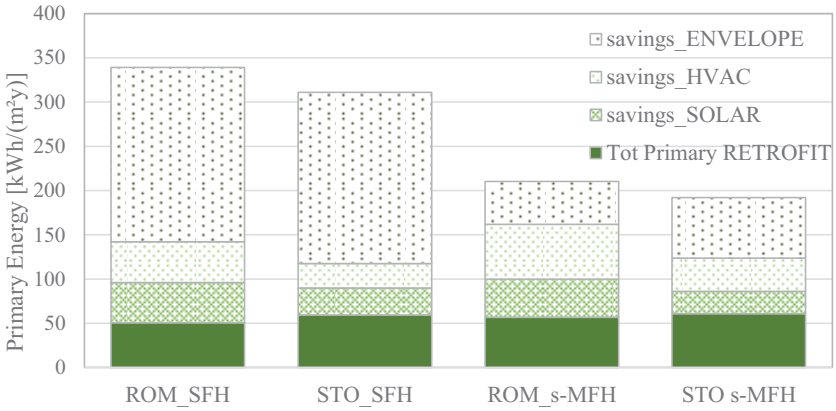

Fig. 6 Primary energy savings due to the retrofit solutions

Table 6: Energy savings of each retrofit solution on the total PE consumption pre-retrofit

Primary Energy	*Units*	SFH Mediterranean	SFH Nordic	s-MFH Mediterranean	s-MFH Nordic
savings_envelope	*kWh/(m²y)*	58%	62%	23%	36%
savings_HVAC syst	*kWh/(m²y)*	14%	9%	29%	20%
savings_PV+STC	*kWh/(m²y)*	13%	10%	21%	13%
Total PE retrofit	***kWh/(m²y)***	**15%**	**19%**	**27%**	**32%**

Finally, thanks to the interventions on the building envelope, HVAC system and use of renewable energies, primary energy consumption for space heating, cooling and DHW preparation of a SFH located in the Mediterranean climate is reduced up to 15% of the consumption before retrofit. Similarly, if the building is located in the Nordic climate, the PE consumption after retrofit amounts to 19%.

Due to the lower PE consumption already pre-retrofit of s-MFHs with respect to SFHs, the application of the renovation measures in this case reduces the primary energy consumption up to 27% in the southern climate and 32% in the northern one.

4. Conclusion

The large share of European residential buildings built before 1970 with high energy consumption requires measures that can contribute to the reduction of the final energy consumption. In this contest, this work wants to show how market-available solutions can drastically reduce the energy consumption for space heating, cooling and DHW of a building. In particular, the paper focuses on the contribution that solar technologies, e.g. photovoltaic and solar thermal collectors, gives on the final energy consumption reduction. In this contest, considerations are given with respect to the influence of each technology on the final uses, the installation position on the building and solar field size.

Regarding the panel position, both for PV and STC the installation on the façade obviously reduces the solar energy harvesting, but this does not mean a relevant difference on the final energy consumption. In fact, thanks to the solar radiation direction through the year, thermal panels vertically positioned become advantageous in reducing the stagnation hours in summer and in maximizing the winter harvesting. On the contrary, the PV contribution is mostly exploited during summer period due to the cooling demand that is covered by electricity. In this case, the difference on the solar radiation harvesting between the two positions is higher for the summer period. Despite that, even in the southern climate, the impact of the vertical position instead of on the roof on the total energy consumption is less than 10%.

Another important achievement of the study is that even small ratios of solar fields on living area can help on achieving relevant energy savings. In fact, looking at SFHs, solar thermal collectors of 2 to 6 panels can reduce the heating production (space heating and DHW preparation) of 26-43% in the southern climate and 12-20% in the northern. In s-MFHs due to the lower ratio between solar field versus living area, 8 to 16 panels contribute with 24-34% in the southern climate and 13-18% in the northern climate for the heating production reduction.

Regarding the PV, especially if it is not foreseen a feed-in-tariff policy, the solar field should be sized with the self-consumption capacity. From the study, 1 kWp for SFH and 3 kWp for s-MFH use respectively 80% and 95% of the PV production for self-consumption.

Concluding, in a deep renovation process of a residential building, in addition to retrofit measures on the envelope and HVAC system, even limited solar fields areas of PV and/or STC can contribute on an additional final energy consumption reduction. In fact, with respect to the case without solar technologies, these can allow additional energy savings of around 45% in the Mediterranean climate and 30% in the Nordic climate.

5. References

Birchall, S, Wallis, I., Churcher, D., Pezzutto, S., Fedrizzi, R., Causse, E. 2014. D2.1a Survey on the energy needs and architectural features of the EU building stock. Final report. EU FP7 iNSPiRe grant agreement n°314461

Klein, A., Beckman, A, Mitchell, W, Duffie, A. 2011. TRNSYS17 – A Transient SYstems Simulation program, Solar Energy Laboratory, University of Wisconsin, Madison

iNSPiRe, 2016. Retrofit Solutions Database - Target Building Simulations. Available from: http://inspirefp7.eu/retrofit-solutions-database/target-building-simulations/.

Dipasquale C., Fedrizzi R., Bellini A., D'Antoni M., Bales C., Gustafsson M., Ochs F., Dermentzis G. 2014. D2.1c Simulation Results of Reference Buildings, EC FP7 project iNSPiRe, Grant agreement no. 314461

Malenkovic, I, Eicher, S., Bony, J., 2012. Definition of main system boundaries and performance figures for reporting on SHP systems-A technical report of Subtask B - Deliverable B1.1. IEA SHC Task 44, HPP Annex 38

Fedrizzi R., Dipasquale C., Bellini A., Gustafsson M., Bales C., Ochs F., Dermentzis G., Nouvel R., Cotrado M. 2016. D6.3b - Performance of Studied Systemic Renovation Packages –Single Family Houses, EC FP7 project iNSPiRe, Grant agreement no. 314461

Fedrizzi R., Dipasquale C., Bellini A., Gustafsson M., Bales C., Ochs F., Dermentzis G., Nouvel R., Cotrado M. 2016. D6.3c - Performance of Studied Systemic Renovation Packages –Multifamily Houses, EC FP7 project iNSPiRe, Grant agreement no. 314461

Techno-Economical Optimization of Solar Energy Supply Concepts for Residential Buildings

Thomas Duschner[1,2], Michael Klärner[1], Christoph Trinkl[1], Wilfried Zörner[1] and Thomas Hamacher[2]

[1] Institute of new Energy Systems, Technische Hochschule Ingolstadt (Germany)

[2] Institute of Renewable and Sustainable Energy Systems, Technical University of Munich (Germany)

Abstract

The German energy transition must take place in the heat as well as in the power sector. In the field of solar energy, however, competition between solar-thermal systems and photovoltaic systems arises. A decreasing feed-in tariff leads to an increasing demand for solutions enabling self-consumption of energy. As a result, traditional heat generation systems, both fossil (e.g. gas heating boiler) and renewable (e.g. solar-thermal), enter a competition with systems being able to couple the electricity with the heat sector (e.g. photovoltaic + heat pump). The objective of this contribution is to analyze this competition and to evaluate the combination of solar-electric and solar-thermal systems in residential buildings. For this purpose, a linear optimization model is used. It also turns out that above all the investment costs for solar-thermal systems must fall, but also costs for battery storages are still too high. Only if several factors change, a combination of solar-thermal energy and photovoltaics becomes interesting from an economic point of view. For a reduction in emissions, the solar-thermal system competes with battery storage.

Keywords: solar systems, residential application, mathematical optimization, cost optimal

1. Introduction

The Paris climate agreement limits global warming to less than 2 °C, ideally less than 1.5 °C. To achieve this, a complete decarbonization is necessary by 2040 (Quaschning, 2016). Therefore, the share of renewable energy sources (RES) must be increased by a factor of 4 to 5 with respect to present values. In Germany, the implementation of RES primarily takes place in the electricity sector. This can mainly be determined by the coverage ratio. In 2016, the percentage of RES in electricity consumption was 32 % (Umweltbundesamt, 2017), while in final energy consumption it was only 12.6 % (BMWi, 2017). The integration of RES in the electricity system gets more and more difficult. Thus, the cost of redispatch in 2015 was 402.5 million euros (BDEW, 2017), because RES (predominantly wind power) had to be shut down in the north while conventional power plants had to be restarted in the south. This is due to grid bottlenecks, which do not permit enough power transfer from north to south or vice versa. This example shows that also the market is not always able to use the electricity sensibly.

One possible solution for dealing which such bottlenecks in the electricity grid is to couple different energy sectors, allowing more local self-consumption of the locally energy produced. Nevertheless, the question remains which sectors are best suitable to be coupled. In addition to mechanical energy (39 %), a large proportion of energy consumption in the domestic sector is attributable to space heating (27 %) and hot water preparation (5 %) (BMWi, 2017). Hence, there is great potential for coupling the electricity system with these sectors. A total of 56 % of the final energy consumption is due to heating demand (Quaschning, 2016). Thereby, the energy supply is still strongly based on fossil fuels. The share of fossil fuels in space heating is 75.1 % and in domestic hot water, it is 66.4 %. Only 13.7 % (space heating) respectively 9.3 % (domestic hot water) are covered by RES. The remaining demands are covered by district heating (9 % space heating, 4.4 % domestic hot water) and electricity (2.2 % space heating, 19.9 % domestic hot water) (Quaschning, 2016). Dominating RES for space heating and domestic hot water is still biomass (11 %). Solar-thermal systems as well as heat pumps are still less important, as the cover ratio of both technologies is only 1 % in 2014. Economic aspects prevent a stronger expansion of solar-thermal as well as geothermal systems (Quaschning, 2016). On the long term, efficient heat pumps must largely take over the supply of space heating and domestic hot water preparation, also due to the possibility of coupling with the electricity sector. However, the use of electric heaters can lead to more than double the current electricity requirement in Germany of 648 TWh in 2016 by an additional requirement of 770 TWh. This would be the case, if only gas heat pumps were used and the gas produced through power-to-gas (Quaschning, 2016). This in turn shows that the energy transition must take place both in the heat and power sector.

doi:10.18086/swc.2017.29.03 Available at http://proceedings.ises.org

In the field of solar energy supply, however, solar-thermal energy competes with photovoltaic systems, which is also due to the coupling of photovoltaics and heat pumps. Another aspect is the grid parity. This is the turning point where the use of self-produced PV power is more cost-effective then the consumption of grid electricity. Therefore, covering the heat demand with electric energy will become an interesting opportunity to increase self-consumption. The aim of this investigation is to analyze, under which conditions it may be useful to use a combination of solar-thermal and photovoltaic system and how the framework conditions would have to be changed, so that these systems can prove to be more cost-effective alternatives.

2. Simulation Model and Mathematical Description

To assess the research question stated above, the linear programming model urbs (lat.: city) (Dorfner and Hamacher, 2017) is used. The focus of the urbs model is to analyze urban energy systems. Amongst others, a low-carbon power system for Indonesia, Malaysia and Singapore was modelled (Stich et al., 2014). Currently, the model is used, in combination with the single-node variation of the model urbs, to optimize the energy supply of mixed use areas taking as example the Garching campus of TU Munich (Schweiger and Wedel, 2017). To answer the question concerning the competition of photovoltaic and solar-thermal systems, the original model, designed for the urban structures, was adapted to residential application.

2.1. Simulation Model

The urbs model (a mixed integer linear programming model (MILP)) is a simulation model for identifying cost-optimal system sizes and operation times for a portfolio of technologies and a given demand. The model consists of three main tuples[1], the commodities (*com*), the processes (*pro*) and the storages (*sto*). The commodities describe the different energy demands and external energy sources. Tab. 1 lists the implemented commodities.

Tab. 1: Different commodities implemented in urbs

commodity	***com***	**description**
Solar energy	solar	solar irradiation
Electricity	elec	electricity demand of the building
Heat	heat	heat demand of the building
Gas	gas	natural gas from the gas supply
CO_2	CO2	CO_2-emissions of the processes
Elec-buy	buy	electricity bought from the grid
Elec-sell	sell	electricity fed into the grid

With processes, it is possible to convert one commodity into another (e.g. electricity to heat by utilizing the process “heat pump”, cf. Tab. 2). These processes are defined by various parameters, e.g. input and output ratios, investment costs or the required roof area for solar energy systems. Tab. 2 shows the different investigated processes.

Tab. 2: Portfolio of processes in urbs

Process	***pro***	***com_in***		***com_out***
photovoltaic system	photovoltaic	solar	→	elec
solar-thermal system	solar-thermal	solar	→	heat
gas boiler	gas boiler	gas	→	heat
heat pump	heatpump	elec	→	heat
heating rod	rod	elec	→	heat
mini CHP	CHP	gas	→	elec
			→	heat
electrical grid	purchase	buy	→	elec
	feed-in	elec	→	sell

The last tuple, the storages, allows the time shift of different forms of energies and commodities. For residential buildings, there is a battery storage and a thermal energy storage (cf. Tab. 3).

[1] Ordered list of elements

Tab. 3: Considered storage types

storage	*sto*	description
Battery	elec	battery storage
Tank	heat	thermal energy storage

Fig. 1 shows the basic structure and layers of the urbs model. A detailed description of the individual parameters is given in the following sections.

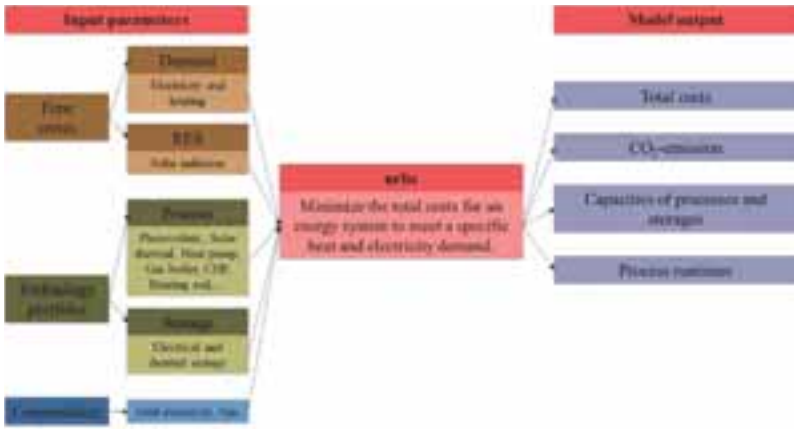

Fig. 1: Overview of the model urbs and the different components

2.2. Mathematical Formulation

The main aim of the model urbs is to minimize the total costs (c) for an energy system to meet a specific heat and electricity demand. These costs are composed of the investment costs $c_{pro,sto}^{invest}$, the variable costs $c_{pro,sto}^{var}$ (related to the operation of the system), the fixed costs $c_{pro,sto}^{fix}$ (independent from the operation of the system), the fuel costs $c_{pro,sto}^{fuel}$, the purchase costs $c_{pro,sto}^{purchase}$ (electricity costs), the startup costs $c_{pro,sto}^{startup}$ and the income from the feed-in $c_{pro,sto}^{revenue}$ for each process (*pro*) and storage (*sto*):

$$\min c = \min \sum_{pro,sto} [c_{pro,sto}^{invest} + c_{pro,sto}^{var} + c_{pro,sto}^{fix} + c_{pro,sto}^{fuel} + c_{pro,sto}^{purchase} + c_{pro,sto}^{startup} - c_{pro,sto}^{revenue}] \quad \text{(eq.1)}$$

(Dorfner and Hamacher, 2017) provide a detailed description of the objective function and the constraints. The essential constraint is that the power from processes (*pro*), storages (*sto*) and the electrical grid (*grid*) has to meet the thermal (d_{therm}) and electrical (d_{elec}) demand for every time step (t):

$$\sum_{pro} p_{pro,elec}(t) + \sum_{sto} p_{sto,elec}(t) + grid(t) \geq d_{elec}(t) \quad \text{(eq.2)}$$

$$\sum_{pro} p_{pro,therm}(t) + \sum_{sto} p_{sto,therm}(t) \geq d_{therm}(t) \quad \text{(eq.3)}$$

To use urbs for residential buildings means some changes. For urban structures, it is often possible to use several technologies, whereas in a residential building, besides solar-thermal systems, only one backup technology (e.g. heat pump or gas boiler) is used. Therefore, the number of back-up processes ($num_{pro,backup}$) is limited to one:

$$\sum_{pro} num_{pro,backup} \leq 1 \quad \text{(eq.4)}$$

The power demand and the power distribution in urban areas are much higher than in the domestic field. Hence, it is no problem to find the appropriate component sizes (cap_{pro}) on the market. For residential buildings, the necessary power would be partially below the power of available components, for example a heat pump with a thermal power less than 1 kW. Therefore, a minimum capacity ($cap_{pro,min}$) is defined, which the components must have at least:

$$cap_{pro} \geq cap_{pro,min} \quad \text{(eq.5)}$$

The thermal load for room heating and for domestic hot water specifies the minimum power required for the backup system:

$$cap_{pro,backup} = d_{therm,max} \quad \text{(eq.6)}$$

In addition, the step size of the possible extension of a process ($cap_{pro\text{-}new}$) is restricted, in other words, if the power is not sufficient, the next-largest component must be used. This is essential especially for the solar collectors, since here only the expansion by one collector is technically possible:

$$cap_{pro,new} \geq cap_{pro,new,min} \quad \text{(eq.7)}$$

Since the solar energy is free of charge for an installed capacity, it can be economic to 'destroy' surplus energy using the storage efficiency. This is not possible in a residential building, especially for thermal energy. For this reason, the storage must not be charged and discharged at the same time. This can be prevented by considering additional variable costs for the storage systems. The costs also show that turn-off is associated with higher maintenance costs.

Nevertheless, it can be useful to control the power distribution of the solar energy systems, especially in case of a solar-thermal system. For this reason, a process shunt is implemented which enables the solar process to be deactivated and to analyze how much energy is not used. Fig. 2 shows a comparison of a simulation with (c.f. Fig. 1, upper diagram) and without (c.f. Fig. 1, lower diagram) the shunt process for the month of May. It is seen that part of the solar-thermal generation is not used for economic reasons (green area), leading to a reduction of the thermal storage from approx. 100 kWh to approx. 10 kWh. It can also be seen that only the energy of the solar-thermal system is 'destroyed'.

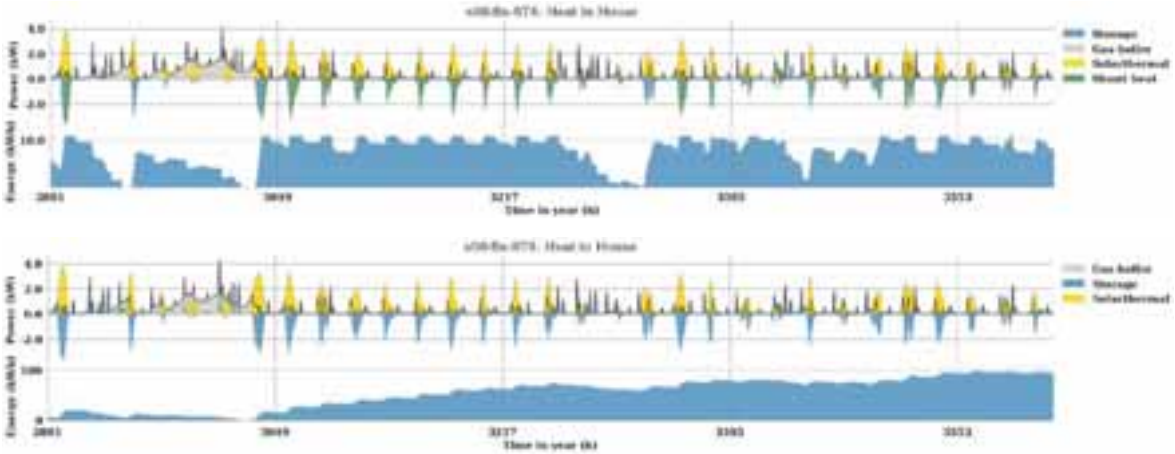

Fig. 2: Thermal energy flow with and without a shunt process for the month of May

3. Input Data

3.1. Technical and Economic Parameter

The different processes are defined with respect to their technical and economic parameters. The economic parameters are essentially the investment costs, the variable costs and the fixed costs. Added to this are the prices for the commodities/fuels.

The investment costs as well as the variable and fixed costs are stated in €/kW respectively €/kWh. Market surveys and data from scientific literature are used to determine the necessary investment costs. The costs of the solar-thermal system are composed of the costs for the flat-plate collector (320 €/m^2 (Sonne Wind & Wärme, 2017)), other component costs (90-160 €/m^2 (Kaltschmitt et al., 2014)) and installation costs (190 €/m^2 (Kaltschmitt et al., 2014)). This results in total system costs for the solar-thermal system of 620 €/m^2 (without storage). The specific solar yield for Germany is 425 kWh per square meter collector surface area (Eicker, 2012). By means of solar full-load hours, which amount to 1.140 h/a for the used weather data set (TRY Zone 13 (DWD, 2011)), the specific costs of the solar-thermal collector can be calculated (1,665 €/kW). The costs of photovoltaic systems are about 180 €/m^2 for the investigated sizes (5 m^2 -50 m^2), whereas a roof area of 8 m^2 is required for a capacity of 1 kW$_p$ (Solaranlagenportal, 2017). This results in costs of 1,440 €/kW$_p$ of the photovoltaic system. The cost of a thermal storage tank can vary between 1.50 €/l and 7.00 €/l (Kaltschmitt et al., 2014). This figures are in accordance with data available from an energy database, specifying an average cost of solar-thermal storages of 2.50€/l (Sonne Wind & Wärme, 2017). In

addition, installation costs of 0.50 €/l are taken into account. The usable temperature spread is 65°C for the thermal storage. The prices of the batteries are currently changing very fast. In the second half of 2015, the system prices were already down to around 1,300 €/kWh with an annual average price reduction of 18 % (Hegner, 2017). For this reason, a price of 1,066 €/kWh_{el} (a decrease of 18 % compared to the previous year) is assumed. The cost of the gas system is 600 €/kW_{therm} (Kilburg, 2015), of the air/water heat pump 900 €/kW_{therm} (Henning, 2012; Kilburg, 2015) and of the heating rod 75 €/kW_{therm} (Fuhs, 2015). For the heating rod costs for the installation of 25 €/kW_{therm} are added. The mini-CHP (combined heat and power) is the most expensive component with 6,430 €/kW_{el} (ASUE e.V., 2014). Every process converts the related commodities with a certain degree of efficiency. The interest rate of all technologies is 3 %.

The variable costs of a photovoltaic system are near-zero (Dorfner, 2016). The solar energy system has variable costs due to the power of the solar pump, these electricity costs amount to 3-5 % of solar-thermal gains (Weyres-Borchert et al., 2015). The considered variable costs of the other systems are taken from (EIA, 2014) and range between 1.5 % and 8 %. The fixed costs are mainly maintenance costs, typically specified as a percentage of the investment costs (Verein Deutscher Ingenieure, 2012). The prices of the commodities/fuel are average prices for the year 2016 (BMWi, 2016). Tab. 4 summarizes the assumed cost parameters. The current feed-in tariff of photovoltaic electricity is 12.3 ct/kWh (Bundesnetzagentur, 2017). The remuneration of the CHP will change as a function of the electricity prices on the European Power Exchange. On average, it is about 11.8 ct/kWh (Verbraucherzentrale, 2015). This value differs only slightly from the feed-in tariff of the photovoltaic system, which is why only one tariff is used for this calculation.

Tab. 4: Cost parameters for the considered different technologies (depreciation period: 20 years)

Process	*com*	Investment costs [€/kW]	Variable Costs [€/kWh]	Fixed Costs [$\%_{inv}$]	Fuel Costs [€/kWh]	Efficiency
photovoltaic system	solar	1,440	0	1,5	0	
solar-thermal system	solar	1,665	0.003	1,5	0	
gas boiler	gas	600	0.006	2	0.07	0.95
heat pump	elec	900	0.02	2	0.29	2.7 (COP)
heating rod	elec	100 €	0.005	3	0.29	0.99
mini CHP	gas	6,430 (elec)	0.5	8	0.07	0.23 elec 0.62 therm
Battery	elec	1,066	0.001	2		0.90
Tank	heat	30	0.001	2		0.92
Purchase	buy	0	0	0	0.29	
Feed-in	sell	0	0	0	-0.123	

3.2 Time Series

The time series are an essential part of the model. There are two possible types. On the one hand, the model requires time series for the demand. For the residential building, these are the electricity (d_{elec}) and thermal energy demand (d_{therm}). This energy demand must be covered by every simulation time step (t). On the other hand, since solar processes cannot provide a constant power due to irradiation, an intermittent supply for this commodity (*solar*) must be defined. In contrast to the demand curves, which indicate the actual demand in kWh/h, the intermittent supply curve is normalized to a value of 1.This is because the output of these processes depends on the installed capacity, which is variable in the simulation model.

The VDI guideline (Verein Deutscher Ingenieure, 2008) defines an electrical load profile as a function of the building location, the day of the weak, the ambient temperature and the cloudiness, which serves as the basis for the annual simulations. For a 4-person household, an annual electricity requirement of 4,000 kWh is assumed. The VDI guideline also defines the hot water tapping profile with an overall annual demand of 2,000 kWh. The heating energy demand as well as the yields of the solar-thermal system are generated by means of parametric models, requiring only a limited amount of parameters (Dittmar, 2004). Characteristic parameters such as areas, window sizes and opaque elements for the building model are taken from IEA-SHC Task 44. This publication defines reference buildings for use in simulations, ensuring a fair comparison of different technological concepts (Dott et al., 2013). The SFH45 building standard represents current legal requirements of a renovated building with a building envelope

of good thermal quality, whereby SFH stands for **S**ingle **F**amily **H**ouse and 45 indicates the specific heating demand in kWh/m²a. With the used weather data set, the heat demand amounts to 8,000 kWh/a. The parameter model of the building is implemented in the simulation environment Matlab/Simulink and the additional CARNOT blockset (Hafner et al., 1999) to get the annual load curves as an input for the urbs model. In Simulink/CARNOT, a standard building, equipped with a boiler, a thermal storage and a solar-thermal system is implemented. The created load curves (Electricity and DHW) as well as the parameter model for the building are integrated in this model in order to get the necessary load curves for the subsequent linear optimization.

The annual simulation is used to get the necessary demand profiles for domestic hot water and space heating. Besides this, the simulation also enables to get the necessary input curves for the solar energy processes. The model urbs is a linear system. A large part of the examined components such as the photovoltaic system or the gas boiler can easily be linearly simulated and scaled. However, the solar-thermal system strongly depends on the ambient temperatures and supply temperature. In order to obtain a medium solar energy generation profile, simulations with 1-8 collectors were carried out in a Matlab/Simulink model. The area of a collector is 2.38 m^2. The storage size is adjusted according to the collector area and increased by 50 liters per square meter (Eicker, 2012). The volume flow is also increased linearly. Fig. 3. shows the annual yield of the various systems. The solar-thermal energy yields based on the number of collectors generally show logarithmic behavior. However, this behavior can be linearized for the collector areas as used in residential buildings (ca. 2–20 m^2). This is only possible for a small collector area, hence an extrapolation of the line leads to incorrect results.

In order to make a statement about the linear correlation, the Pearson correlation coefficient r and the coefficient of determination r^2 are calculated. With a correlation coefficient of 1, there is a completely linear coherence between the observed features. The correlation coefficient of the investigated systems is 0.988. The coefficient of determination is a quality measure for the linear adaption. The closer the coefficient of determination r^2 is to 1, the higher the probability of the linear coherence. Here the value is 0.976. These deviations are within the tolerance and a linearization and scaling of the solar-thermal system is possible without loss of accuracy. The normalized power curves of the 8 systems are averaged and act as input variables for the solar-thermal process.

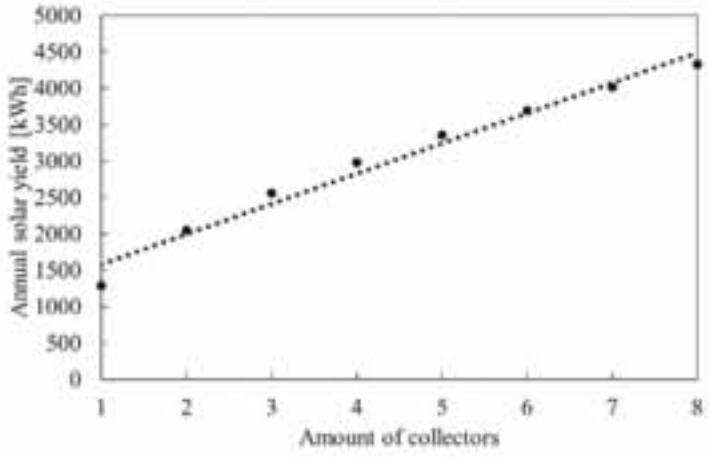

Fig. 3: Annual solar yields for 1-8 solar-thermal collector(s)

Fig. 4 shows a comparison of the solar-thermal performance for the parameter model in Matlab/Simulink and the linear model in urbs over a period of one week for two solar collectors. The results indicate that the generated solar-thermal power is nearly identical. The linear model produces a slightly higher peak load. However, the energy amounts are very low. The relative deviation between the CARNOT and the urbs model, as determined by eq. 8,

$$f = \frac{p_{CARNOT} - p_{urbs}}{p_{urbs}} * 100\ \% = \left(\frac{p_{CARNOT}}{p_{urbs}} - 1\right) * 100\ \% \qquad \text{(eq.8)}$$

is only 1.53 % for the solar-thermal power of an annual simulation. For the energy, the deviation is 0.17 % and thus even below one percent.

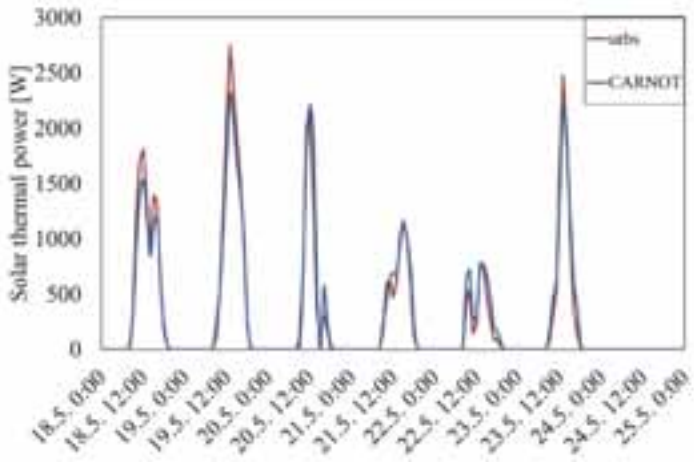

Fig. 4: Comparison of the generated solar power for the simulation models CARNOT and urbs

4. Scenario Results

This study is intended to show how solar-thermal and photovoltaic systems compete and under which conditions a joint use is economically reasonable. For that reason, various framework conditions are examined. On the one hand, the investment costs of individual technologies are modified and on the other hand, fuel prices and the remuneration are changed.

4.1. Variation of the Investment Costs

First, the study investigates the changes in system configurations for varying investment costs for the different processes. The investment costs for photovoltaic systems have declined in recent years (Wirth and Schneider, 2017). For this reason, one investigated scenario assumes drastically decreased investment costs of 50 % compared to today´s costs (s02). Solar-thermal systems have not experienced such a steep learning curve. Scenario s03 describes a potential cost reduction of solar-thermal systems by 50 %. A further scenario (s04) assumes even lower investment cost (75 % cost reduction compared to today`s cost level). The prices for batteries have also decreased in recent years. Similarly to the scenarios described above, a further cost reduction of 50 % compared to nowadays investment costs is assumed (s05). A technology that is currently too expensive for domestic applications is CHP. To make this technology competitive with the aforementioned, a cost reduction of 75 % is assumed (s06). Lastly, it is assumed that a solar-thermal system is already installed, on the one hand only for domestic hot water heating (2 solar collectors) (s07) and on the other hand for domestic hot water and space heating (4 solar collectors) (s08). All systems are compared with the base system as described before (s01).

Fig. 5 shows the results and the energy flows for the different investigated investment costs. The individual scenarios are listed vertically. This list shows the most cost-effective system for each scenario. Therefore, no comparison of the systems with one another is not possible. The annual costs for the different cost types are shown on the left. Revenue through feed-in is shown negative. The energy generation of the technologies used can be seen in the centre. Energy, which is not used by the building (feed-in, shunt process), is negative, too. This presentation allows a quick conclusion on how the system changes in the individual scenarios. On the right are the retrieved energies of the storages. It can be recognized, that the systems do not change with the investment costs. This is due to the low system costs for the gas boiler as well as the currently very low gas prices. The existing roof surface is completely covered with photovoltaic modules. If a solar-thermal system is already installed, a gas boiler is also used as the backup system. In this case, the thermal storage needs to be increased. However, because of the feed-in remuneration, this is economically more reasonable than buying a battery storage.

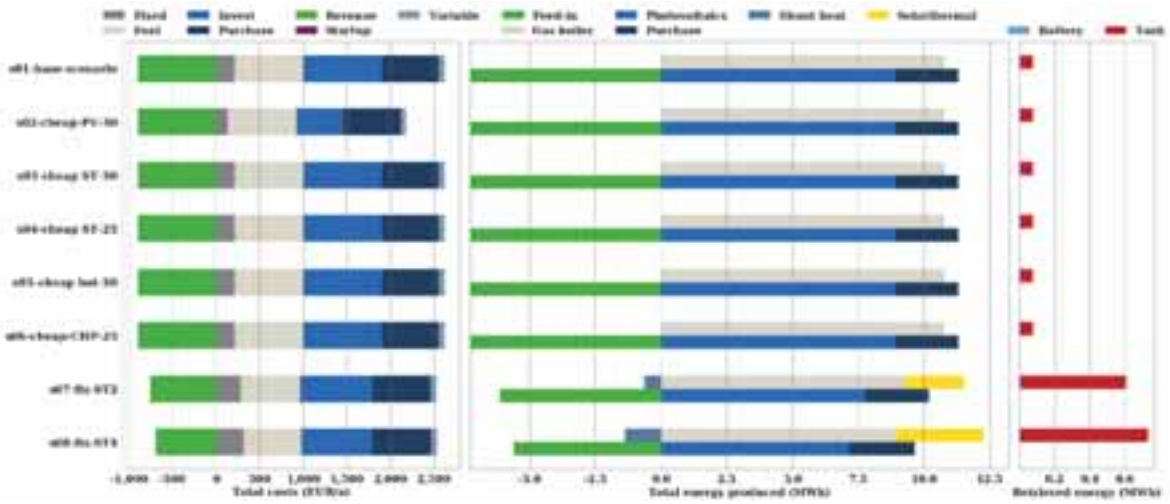

Fig. 5: Costs and energy flows for varying investment costs for the investigated systems

To account for a potential CO_2 tax, a CO_2-neutral energy demand of 15 % is assumed. This is in accordance with the requirements of the German Renewable Energies Heat Act (EEWärmeG). The different processes have a specific CO_2 emission per kWh. The basic system with gas boiler generates emissions of approx. 4,400 kg/a. The maximum annual CO_2 production is, therefore, limited to 3,750 kg.

Fig. 6 shows two essential findings. If there is no solar-thermal system, a battery storage must be installed to meet the emission limit. This reduces the emissions due to the purchase. At current prices, it is economically better to invest in a battery storage than in a solar-thermal system. Only in case of halved system costs, solar-thermal becomes competitive. A further cost reduction leads to the same result. In addition, the price of the battery storage does not affect the installed capacity.

The investigation with regard to the investment costs shows that these costs hardly affect the cost-optimal system configuration. Gas systems are the most economic at present prices. Only if CO_2 emissions are limited, some of the heat demand needs to be covered by the solar-thermal system. For this reason, the effect of the supply costs on the system is investigated, too.

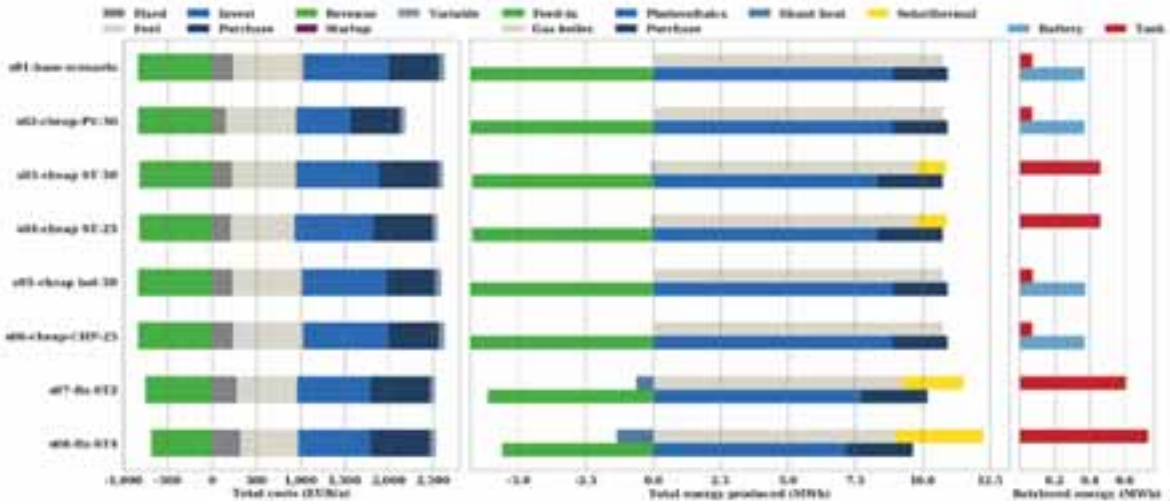

Fig. 6: Costs and energy flows for varying investment costs for the investigated systems and a CO_2 limit of 3,750 kg/a

4.2. Variation of Fuel Prices and Remuneration

In a further step, the energy supply costs and the remuneration are varied. In addition to an adjustment of the electricity costs with an increase (s09) as well as a decrease (s10) of 50 %, another gas price is also examined. The assumed gas prices represent a doubling (s11) and a tripling (s12) of current gas prices. This study also examines, what happens, when the remuneration is halved (s13) or when there is no longer any remuneration (s14).

Compared to the investment costs, it can be seen that the fuel prices have a much higher influence on the most economic system (cf. Fig. 7). A doubling of the electricity rate results in a battery storage being economically reasonable. If the electricity price is halved, the heat pump is more cost-effective than the gas boiler. This is also the case, if the gas price increases. For better economy of the heat pump, a doubling is already sufficient. Photovoltaic plants are economically unattractive with a reduction of the feed-in tariffs. The size is dimensioned in such a way that a high self-consumption can be reached. Thus, battery storages are again advantageous. The remaining roof area due to the small number of photovoltaic modules is, however, not used for a solar-thermal system.

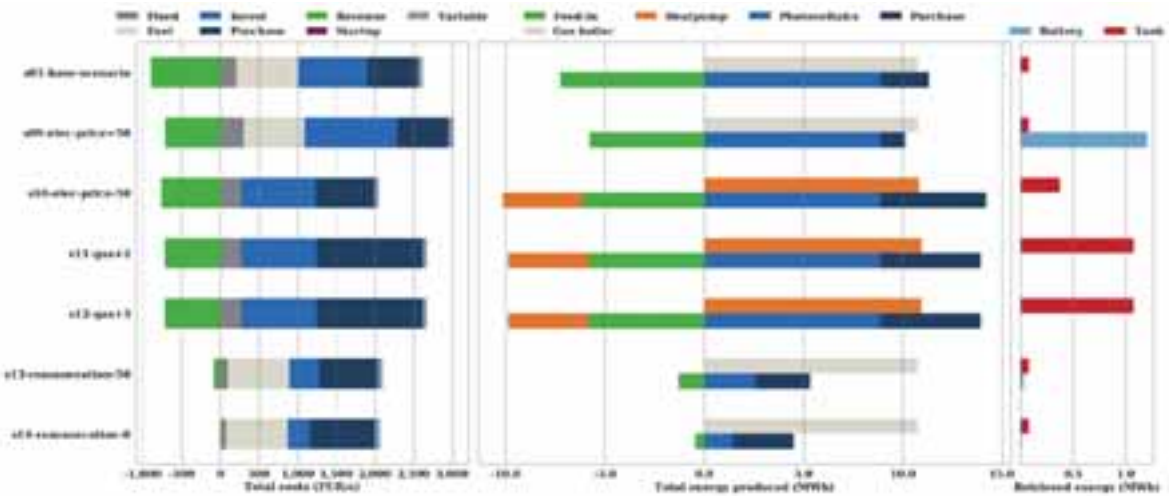

Fig. 7: Costs and energy flows for varying fuel prices and remuneration for the investigated systems

This shows that the decisive factor for a change in the energy systems is the price for the commodities. Investment costs have only a minor impact. A competition between photovoltaic system in combination with a heat pump and solar-thermal system cannot be observed. A reasonable combination of these three systems would require several boundary conditions to change at the same time.

5. Conclusions and Outlook

This study analyses the competition between photovoltaic and solar-thermal systems for residential applications. For this, the urbs model was adapted and extended for an application for single family houses. Due to the linearity of the model, it was shown that the yields of the solar-thermal system, which are strongly dependent on temperature, can be linearized with very high accuracy for the system sizes under investigation.

A major finding is that the cost-optimal system configuration is almost independent of the investment costs of the components. Gas-driven systems are currently the most economic ones. Only if the prices for electrical energy and gas vary, the system configuration changes. With a reduction in electricity prices as well as an increase in gas prices, the heat pump is more cost-effective than the gas system. An increase in the electricity price provokes an investment in a battery storage. A battery storage is also necessary if the CO_2 emissions are limited, whereby the size is independent of the investment costs. However, in the case of a reduction in the costs for solar-thermal systems, these are advantageous in comparison to the electrical storage. This shows that solar-thermal energy is an essential technology for decarbonisation.

However, there is no competition between photovoltaic and solar-thermal systems under current conditions. The combination of photovoltaic and heat pump is currently no more economic than a gas-driven system. This is due, on the one hand, to the feed-in tariff and, on the other, due to the currently low gas prices.

The aim of the study was to find the most economic system configuration for different boundary conditions. In this case, the solar-thermal system is disadvantageous compared to the photovoltaic system. However, not only economic optimization should be investigated. Further research must be conducted to answer how the different systems behave with different optimization objectives: (1) maximizing self-sufficiency, (2) maximizing self-consumption and (3) maximizing the use of solar energy. These questions will be addressed in further investigations.

References

ASUE e.V., 2014. BHKW-Kenndaten 2014/2015. Module, Anbieter, Kosten, Berlin.

BDEW, 2017. Redispatch in Deutschland. Auswertung der Transparenzdaten. April 2013 bis einschließlich März 2017, Berlin.

BMWi, 2016. Energiedaten: Gesamtausgabe. Stand: November 2016. Bundesministerium für Wirtschaft und Energie, Berlin. http://www.bmwi.de/DE/Themen/Energie/Energiedaten-und-analysen/Energiedaten/gesamtausgabe,did=476134.

BMWi, 2017. Energiedaten: Gesamtausgabe. Stand: Mai 2017, Berlin. http://www.bmwi.de/Redaktion/DE/Downloads/Energiedaten/energiedaten-gesamt-pdf-grafiken.html.

Bundesnetzagentur, 2017. Bundesnetzagentur - Archiv Datenmeldungen. https://www.bundesnetzagentur.de/DE/Sachgebiete/ElektrizitaetundGas/Unternehmen_Institutionen/ErneuerbareEnergien/ZahlenDatenInformationen/EEG_Registerdaten/ArchivDatenMeldgn/ArchivDatenMeldgn_node.html. Accessed 13 September 2017.

Dorfner, J., 2016. Open Source Modelling and Optimisation of Energy Infrastructure at Urban Scale. Dissertation, München, 205 pp.

Dorfner, J., Hamacher, T., 2017. urbs: A linear optimisation model for distributed energy systems — urbs 0.7.1 documentation. Chair of Renewable and Sustainable Energy Systems, Technical University of Munich. https://urbs.readthedocs.io/en/latest/. Accessed 15 September 2017.

Dott, R., Haller, M.Y., Ruschenburg, J., Ochs, F., Bony, J., 2013. The Reference Framework for System Simulations of the IEA SHC Task 44 / HPP Annex 38 Part B: Buildings and Space Heat Load. A technical report of subtask C Report C1 Part B.

DWD, D.W., 2011. Wetter und Klima - Deutscher Wetterdienst - Leistungen - Testreferenzjahre (TRY). DWD. http://www.dwd.de/DE/leistungen/testreferenzjahre/testreferenzjahre.html. Accessed 15 September 2017.

EIA, 2014. Assumptions to the Annual Energy Outlook 2014, Washington. https://www.eia.gov/outlooks/aeo/assumptions/pdf/0554(2014).pdf. Accessed 15 September 2017.

Eicker, U., 2012. Solare Technologien für Gebäude. Grundlagen und Praxisbeispiele, 2nd ed. Vieweg+Teubner Verlag / Springer Fachmedien Wiesbaden GmbH Wiesbaden, Wiesbaden.

Fuhs, M., 2015. Übersicht regelbare Heizstäbe. pv magazine 2015 (01), 25–27.

Hafner, B., Plettner, J., Wenhöner, C., Wenzel, T., 1999. CARNOT Blockset Version 1.0. Conventional And Renewable eNergy systems OpTimization Blockset User´s Guide, Juelich.

Hegner, M., 2017. Energiespeicher - Eine entscheidende Säule der Energiewende. Stationäre Energiespeicher und deren Netzintegration, 2017, Regensburg.

Henning, H.-M., 2012. Energetisch-ökonomische Bewertungsgrößen für solarthermische Anlagen., in: 22. Symposium Thermische Solarenergie.

Kaltschmitt, M., Streicher, W., Wiese, A. (Eds.), 2014. Erneuerbare Energien. Systemtechnik, Wirtschaftlichkeit, Umweltaspekte, 5th ed. Springer Vieweg, Berlin, 931 pp.

Kilburg, S., 2015. Kostenvergleich verschiedener Heizsysteme im Gebäudebestand, Straubing. http://www.carmen-ev.de/files/festbrennstoffe/Kostvgl_05_2015.pdf.

Quaschning, V., 2016. Sektorkopplung durch die Energiewende. Anforderungen an den Ausbau erneuerbarer Energien zum Erreichen der Pariser Klimaschutzziele unter Berücksichtigung der Sektorkopplung. Hochschule für Technik und Wirtschaft Berlin, Berlin.

Schweiger, B., Wedel, W.G., 2017. CleanTechCampus Garching. Development of holistically optimised, sustainable and transferable energy concepts taking as example the Campus Garching of the TUM. http://www.es.mw.tum.de/en/research/projects/cleantechcampus/. Accessed 15 September 2017.

Solaranlagenportal, 2017. Photovoltaik Kosten - Was kostet eine Photovoltaikanlage? https://www.solaranlagen-portal.com/photovoltaik/kosten. Accessed 7 September 2017.

Sonne Wind & Wärme, 2017. Energie-Datenbank. http://www.energie-datenbank.eu/. Accessed 13 September 2017.

Stich, J., Mannhart, M., Zipperle, T., Massier, T., Huber, M., Hamacher, T., 2014. Modelling a Low-Carbon Power System for Indonesia, Malaysia and Singapore, in: 33rd IEW International Energy Workshop.

Umweltbundesamt, 2017. Erneuerbare Energien in Deutschland. Daten zur Entwicklung im Jahr 2016, Dessau-Roßlau. https://www.umweltbundesamt.de/publikationen.

Verbraucherzentrale, 2015. Kleine Blockheizkraftwerke: Die Heizung, die auch Strom liefert. https://www.verbraucherzentrale.de/BHKW-Verguetung. Accessed 18 September 2017.

Verein Deutscher Ingenieure, 2008. Reference load profiles of single-family and multi-family houses for the use of CHP systems.

Verein Deutscher Ingenieure, 2012. Economic efficiency of building installations Fundamentals and economic calculation, 44 pp.

Weyres-Borchert, B., Kasper, B.-R., Drück, H., 2015. Solare Wärme. Technik - Planung - Hausanlage. Fraunhofer IRB-Verl., Stuttgart, 168 pp.

Wirth, H., Schneider, K., 2017. Aktuelle Fakten zur Photovoltaik in Deutschland, Freiburg.

Energetic and Economic Efficiency Evaluation of Solar Assisted Heating Systems for Multi-Family Houses

Sonja Helbig[1], Daniel Eggert[1], Mario Adam[2]

[1] Institut für Solarenergieforschung Hameln (ISFH), Am Ohrberg 1, 31860 Emmerthal (Germany)

Phone: +49 5151 999 642, E-Mail: s.helbig@isfh.de

[2] Hochschule Düsseldorf (HSD), ZIES, Münsterstraße 156, 40476 Düsseldorf (Germany)

Abstract

For holistic efficiency evaluation of solar-assisted heating systems in multi-family houses common system designs are tested with hardware-in-the-loop measurements. The experimental results provide the basis for the subsequent energetic and economic efficiency analysis. A previously introduced efficiency measure called "central performance factor of the heating facility" (CPF) is used to evaluate energetic efficiency of the overall heating system. Using this measure it can be explained, how system designs comprising low heat distribution losses (e.g. 2-pipe heat distribution networks or an ultrafiltration module in the DHW circulation return flow) feature the highest CPF. Cost analysis show, however, that such designs incorporate elevated levelized cost of heat compared to the other systems under investigation. Carbon abatement cost are combining the energetic and economic evaluation into one parameter. The results show that concepts with a bivalent heat storage tank and a fresh water unit connected to a 4-pipe heat distribution network, are leading to the lowest carbon abatement cost, at a minimum value of 46 €/tCO_2.

Keywords: solar combisystems, whole system testing, levelized cost of heat, carbon abatement cost

1. Introduction

There are various hydraulic design concepts for the integration of solar thermal energy into the heat supply of multi-family houses. Additionally, the control algorithms and the type of heat distribution network may vary. The variety of technical solutions therefor are hardly comparable for planners and installers due a lack of comprehensive system evaluation. This establishes a general obstacle for the application of solar thermal systems, especially in Germany, where solar thermal systems are used almost exclusively (97 %) for the heat supply of houses with one to three residential units (BSW, 2007), although more than 50 % of the apartments are situated in multi-family houses (IWU, 2010). In this paper selected solar-assisted heat supply concepts are evaluated in an energetic and cost-effective manner, in order to identify or derive optimal system concepts.

1.1 Evaluation method

Functional system evaluations (Helbig et.al, 2016) are carried out using a hardware-in-the-loop (HIL) test procedure (see Figure 1). For this purpose, the central components of the heat supply system (referred to "central heating facility" in the sequel) are implemented according to manufacturer´s instructions and tested under emulated, real operation conditions. Weather data and solar thermal collectors as well as the building with the heat distribution system are part of a dynamic simulation model in TRNSYS to ensure standardized and reproducible boundary conditions for system tests. The central heating facility is connected to thermostatic emulators during the tests, which supply the simulated heat gain or remove the required heat. The behavior of the emulators is calculated by means of real-time simulations in TRNSYS. With a time interval of one minute measured values are passed as input data to the simulation environment. Thus the HIL system can react dynamically to the behavior of the central heating facility. The test device allows the emulation of heating capacities sufficient for 20 residential units under central-European climate conditions and a solar thermal collector power of up to 60 kW.

doi:10.18086/swc.2017.29.04 Available at http://proceedings.ises.org

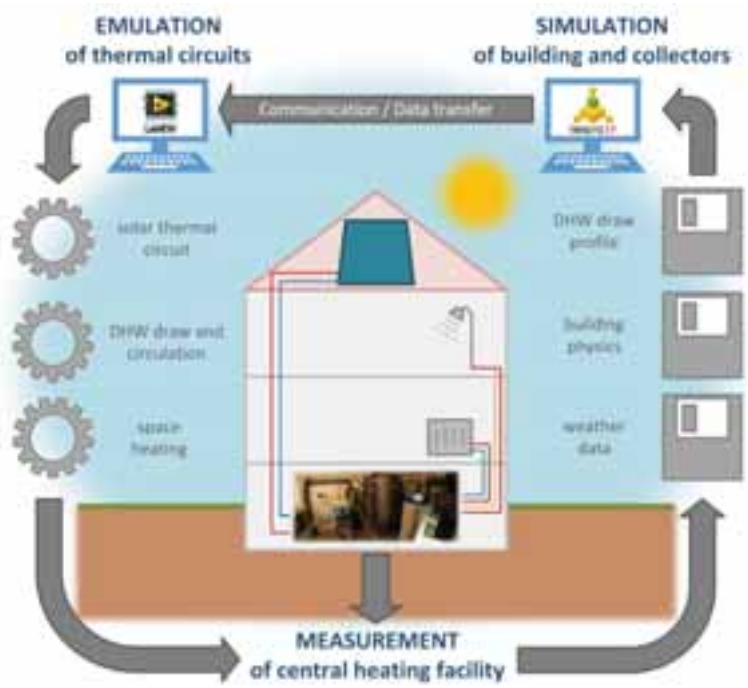

Fig. 1: Hardware-in-the-loop (HIL) test procedure for central heating facilities

The subsequent energetic evaluation is based on the results of high-resolution annual simulations of the solar-assisted heat supply systems under investigation. The simulation models are derived from the TRNSYS models of the HIL tests. Thereby, the performed measurements provide the data basis for model validations which allows a very precisely parametrization of the components of the central heating. While the HIL measurements are carried out for up to eight selected days, which generate all typical operation conditions within a year, the system simulations cover a complete year.

Finally, an economic analysis of the systems under investigation has been done. The economic evaluation is based on the results of the energetic system evaluation and a cost analysis of the single components of the central heating facility. Thereby two different evaluation parameter are used: levelized cost of heat (LCOH) and carbon abatement cost (AC_{CO2}).

1.2 Tested systems and applied boundary conditions

The tested solar-assisted heating systems for multi-family houses can be distinguished according to the type of heat distribution system, their solar heat storage and the hot water and boiler connection. In figure 2 the distinguishing features of the tested systems for the DHW preparation is shown. Additionally, all systems have solar support for space heating. The reference case has no solar support and is characterized by a domestic hot water storage and a 4-pipe distribution network.

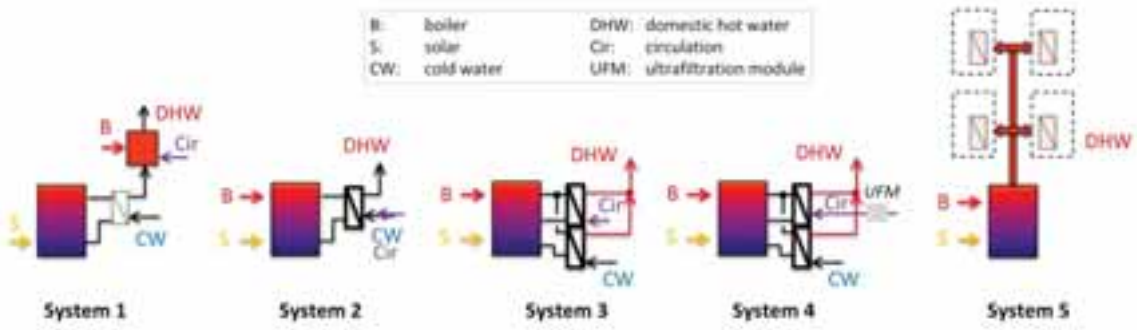

Fig. 2: Simplified hydraulic schemata for the DHW preparation of the tested systems (Adam et.al, 2016)

System 1 to System 4 are characterized by a 4-pipe distribution network, while System 5 has a 2-pipe distribution network. In system 1, solar heat is transferred exclusively to the monovalent solar heat storage tank.

The solar storage is used to preheat domestic hot water via a fresh water unit. Systems 2 to 4 differ in the number of heat exchangers in the fresh water unit. While system 2 has a common heat exchanger for heating both the domestic hot water (DHW) and the circulation return, the systems 3 and 4 have two separate heat exchangers for these tasks. System 4 is furthermore characterized by an ultrafiltration module in the circulation return. This provides a mechanical legionella treatment whereby the DHW flow line temperature can be lowered to little above the desired tap temperature (e.g., 47°C). System 5 has a bivalent heat storage tank from where the heat is distributed to the decentralized apartment transfer stations. The flow line temperature in the 2-pipe heat distribution network is constant at 50°C.

Tab.1: Boundary conditions for hardware-in-the-loop measurements and dynamic system simulation

	Description	Values
weather data	Meteonorm (version 5), location: Zurich, Switzerland	• days for HIL measurements: 38, 71, 99, 112, 175, (230), 250, (356)
solar thermal circuit	flat plate collectors as well as pipes between roof and central heating facility	• aperture area: between 14 m² and 33 m² • inclination: 45°, orientation: south • total pipe length: 53.5 m
space heating and distribution	multi-family house in Germany with a construction year between 1958 and 1968 and an energy-focused refurbishment according to the standards of EnEV 2009	• multi-zone simulation model (52 thermal zones) • number of apartments: 8 • detailed heat distribution network with more than 100 pipe sections • size of an apartment: 65 m² • heating system: radiators
domestic hot water draw	draw profile generated with DHWcalc (Jordan, Vajen, 2014)	• 55 litre per apartment and day (assumption of 1.8 inhabitants per flat)
domestic hot water circulation	constant circulation 24 hours a day	• 19 litre per hour and apartment (according to a maximum temperature difference in the flow line of 5 K)

2. Energetic efficiency evaluation

2.1. System boundaries and evaluation parameter

Figure 3 shows the system boundaries employed for balancing the energy fluxes of a solar assisted heat supply system for a multi-family house. Of particular interest is the boundary around the central heating facility with its energetic inputs and outputs. The central heat demand of the building ($Q_{central}$) combines the space heat demand and distribution losses as well as the heat demand for DHW and circulation. An efficiency measure previously introduced (Helbig et.al, 2016) is employed for the energetic evaluation of the investigated central heating facilities: the central performance factor of the heating facility (CPF). It represents the ratio of the central heat demand of the building as energetic benefit to final energy demand (E_{final}) as energetic expenditure:

$$CPF = \frac{Q_{central}}{E_{final}} [-] \quad \text{(eq. 1)}$$

For an overall evaluation of the energy conversion chain, the central performance factor of the heat supply chain (CPF_{plus}) is additionally introduced as an assessment parameter. In this case, the useful energy (Q_{use}) is set in relation to the primary energy (E_{prim}). The CPF_{plus} thus represents the reciprocal value of the plant effort (e_P) according to DIN V 4701:

$$CPF_{plus} = \frac{1}{e_P} = \frac{Q_{use}}{E_{prim}} [-] \quad \text{(eq. 2)}$$

In contrast to the CPF, the CPF_{plus} also allows the comparison of systems with different fossil energy sources and thus different primary energy factors. In addition, effects for reducing distribution heat losses can be assessed. However, a disadvantage of the CPF_{plus} is that both the useful energy and the primary energy are not measurable variables.

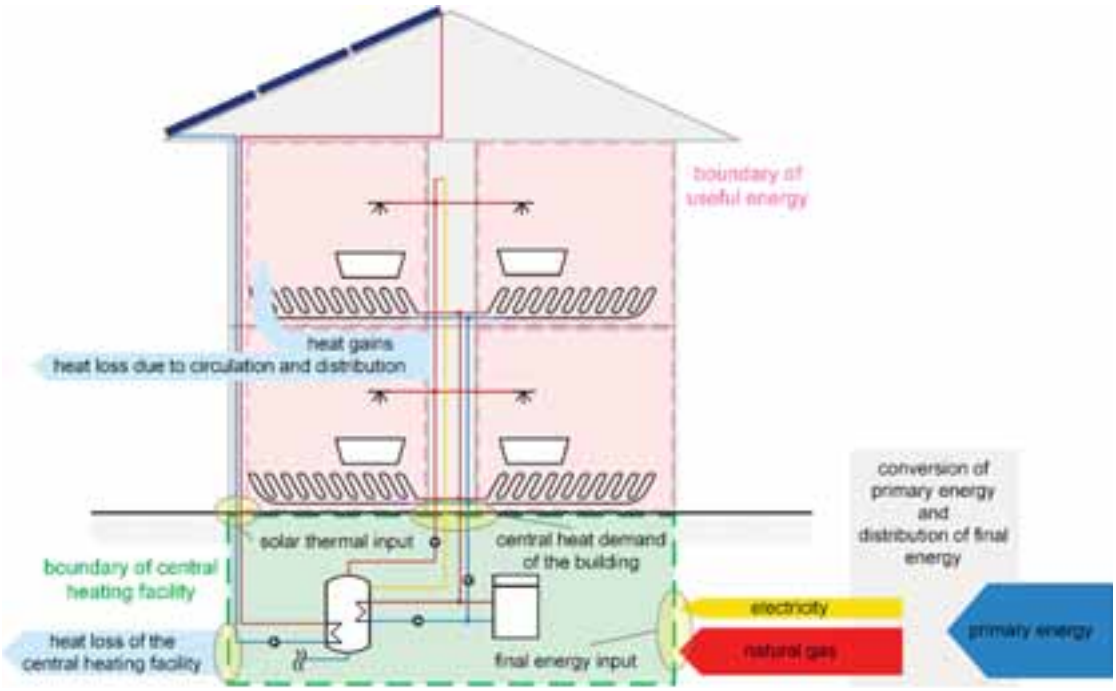

Fig. 3. Definition of system boundaries for the energetic efficiency evaluation (Helbig et.al, 2016)

Both the CPF and the CPF_{plus} are strongly dependent on the chosen boundary conditions (solar thermal collectors, weather and building characteristics, see Table 1). Accordingly, the demand-specific collector area (a_{dsc}) is selected as the reference parameter. It forms the quotient from the collector area (aperture) to the central heat demand of the building:

$$a_{dsc} = \frac{A_{col}}{Q_{central}} \left[\frac{m^2}{MWh}\right] \quad \text{(eq. 3)}$$

The benchmark procedure according to (Steinweg et.al, 2016) is used to calculate the maximum possible CPF or CPF_{plus} of an idealized central heating facility. For this purpose, the maximum collector circuit yield is determined by taking into account the temperature levels of the heat sinks in the monthly balance method. The central heating facility has no conversion losses from final energy to building energy. A comparison between the investigated systems and the benchmark makes it possible to determine the theoretical optimization potential of the individual systems (Helbig et.al, 2016).

2.2 Results

Figure 4 shows the CPF over the demand specific collector area for the systems 1 to 5, as well as for the reference system without solar support and the benchmark. It can clearly be seen that the central heating facilities 1 and 2 without solar support ($a_{dsc} = 0.0$) have identical energy efficiency (CPF) as the reference system. Systems 3 to 5, on the other hand, show an efficiency increase compared to the reference system without any solar support. The second heat exchanger in the fresh water unit (system 3 and 4) is leading to a better stratification of the heat storage tank whereas the ultrafiltration module in the circulation return (system 4) as well as the 2-pipe heat distribution network (system 5) are lowering the heat distribution losses. An increasing demand-specific collector area always leads to an increase in efficiency of the central heating facilities. For example, a solar support due to a demand specific collector area of 1.0 m² / MWh is leading to an efficiency increase of the central heating facilities of 15 to 37 %-points compared to the reference system. It can be seen that this increase in efficiency between the tested systems with solar support can differ by up to 22 %-points. However, system 5 as the most efficient of the systems under investigation still has a theoretical optimization potential of the CPF of a further 45 %-points (difference to the benchmark) with a demand-specific collector area of 1.0 m²/MWh. The theoretical optimization potential is made up of technical optimization measures and system idealization (Helbig et.al, 2016).

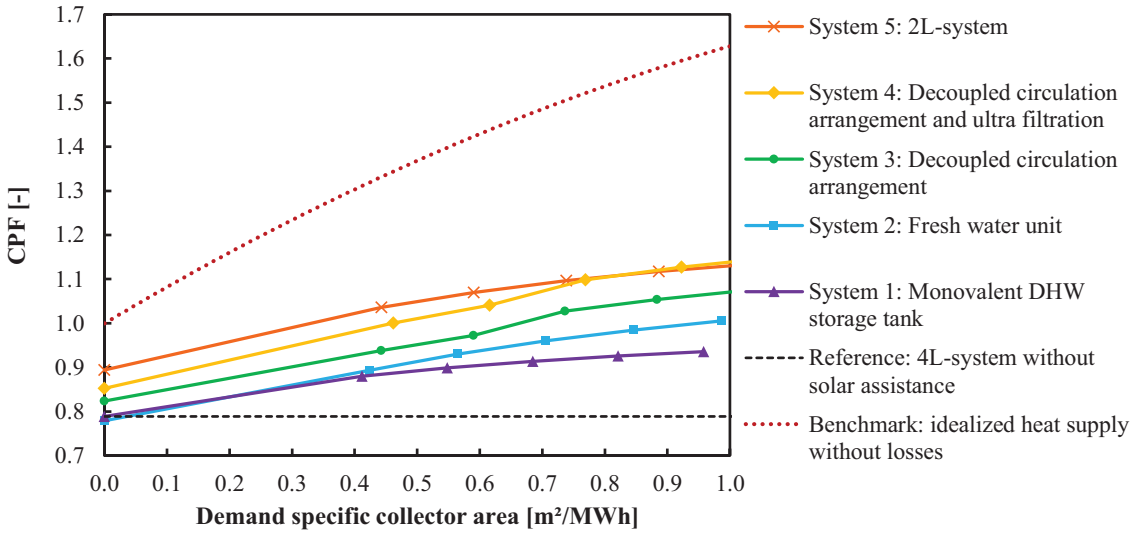

Fig. 4: Central performance factor of the heating facility over the demand specific collector area

Figure 5 shows the CPF_{plus} as a function of the demand-specific collector area. Since the CPF_{plus} evaluates a larger section of the energy conversion chain, its values always lie below those of the CPF.

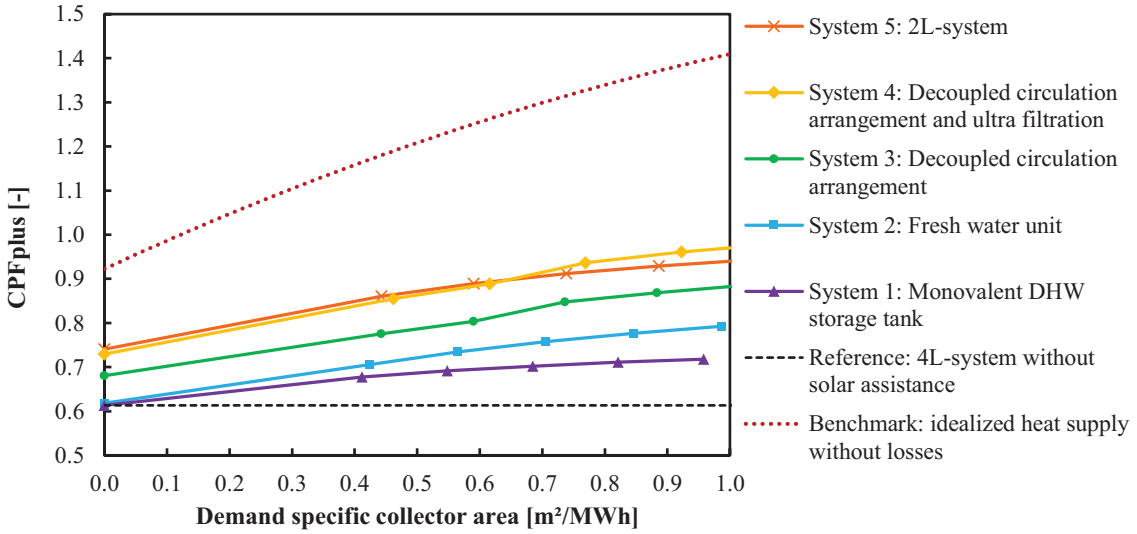

Fig. 5: Central performance factor of the heat supply chain over the demand specific collector area

A comparison between the CPF_{plus} in figure 5 and the CPF in figure 4 shows that both evaluation variables lead to a similar result in the efficiency assessment of the investigated systems. However, it can be seen in detail that the systems 4 and 5, compared to systems 1 to 3, have a relative efficiency increase in the heat supply which is attributable to lower heat distribution losses. In system 4 the reduction of those losses are a result of reduced DHW flow line temperatures because of the ultrafiltration module. The reduced heat distribution losses in system 5 are due to the application of a 2-pipe heat distribution network instead of a 4-pipe system. But it appears that the relative efficiency increase due to the ultrafiltration module is higher than the one due to the 2-pipe heat distribution network.

3. Economic efficiency evaluation

3.1 Evaluation parameter

In order to assess the economic efficiency of solar-assisted heating systems, levelized cost of heat (LCOH, see equation 5) as well as carbon abatement cost (AC_{CO2} see equation 6) are calculated and compared for the

systems under investigation. Both evaluation parameter rely on the calculation of the equivalent annual cost (EAC) which is determined by multiplying the annuity factor (a) with the net present value (NPV) (see VDI 2067):

$$\mathrm{EAC} = \mathrm{a} \cdot \mathrm{NPV} = \frac{i}{1-(1+i)^{-T}} \cdot \sum_{t=0}^{T} \frac{R_t}{(1+i)^t} \left[\frac{€}{a}\right] \quad \text{(eq. 4)}$$

where: i: annual interest rate [-]
T: observation period [a]
t: year [a]
R: net cash flow [€]

In the net cash flow (R) different types of costs (capital-related costs, demand-related costs, operation-related costs) as well as price change factors are considered. The investment costs as part of the capital-related costs come from real offers of an installation company for heating technology. The offers distinguish between component, delivery and assembly costs. Disbursements for replacements, which correspond to the depreciation period of the single components (VDI 2067), are also part of the capital-related costs as well as the possible payments by a residual value and incentives for thermal solar collectors of the German Federal Office of Economics and Export Control (BAFA, 2017a). The demand-related costs include the costs for electricity and natural gas. The operation-related costs are composed of the costs for maintenance, which were also selected according to the VDI 2067, as well as the costs for maintenance and inspection. The latter are from the offerings of the installation company, which contains a maintenance contract.

In addition to the offers for the systems under investigation, alternative offers were also made which have a quite similar hydraulic specification compared to the systems under investigation, but originate from another manufacturer. The alternative offers serve to assess the cost differences between the systems as well as between the manufacturers. The evaluation is done anonymously. It should be considered that to calculate the levelized cost of heat for the alternative manufacturers' systems, the respective energy efficiency of the systems under investigation is assumed. Accordingly, the levelized cost of heat of the alternative manufacturers are associated with additional uncertainty, which must be taken into account when interpreting and evaluating the results. Further boundary conditions for the economic efficiency calculation are summarized in table 2.

The levelized cost of heat describe the monetary expenditure for one heat unit. Therefor the equivalent annual cost are divided by the annual useful energy of the system:

$$LCOH = \frac{\mathrm{EAC}}{Q_{use}} \left[\frac{€}{kWh}\right] \quad \text{(eq. 5)}$$

Carbon abatement cost describe the additional cost for the carbon saving measure per unit CO_2 avoided. Consequently, for the calculation of abatement costs a reference system (ref) needs to be defined (see section 1.2). The annual CO_2 emissions caused by each system are determined by adding up the product of the carbon intensity per kilowatt-hour (CIPK) and the final energy demand for all energy sources used (n):

$$AC_{CO2} = \frac{\mathrm{EAC}_{Sys} - EAC_{ref}}{\left(\sum_{j=1}^{n} CIPK_j \cdot E_{final,j}\right)_{Sys} - \left(\sum_{j=1}^{n} CIPK_j \cdot E_{final,j}\right)_{ref}} \left[\frac{€}{tCO_2}\right] \quad \text{(eq. 6)}$$

Tab. 2: Applied boundary conditions for the economic efficiency analysis

annual interest rate	0,4 %
prices for energy	electricity: 29,7 €-cent/kWh and natural gas: 6,1 €-cent/kWh
price change factors	capital-related: 1,4 %/a and salary: 2,2 %/a electricity: 3,6 %/a and natural gas: 3,7%/a
observation period	20 years
CIPK	electricity: 526 gCO_2/kWh and natural gas: 202 gCO_2/kWh

3.1 Results

Figure 6 shows the LCOH and figure 7 the AC_{CO2} for the systems 1 to 5 and the reference system. The LCOH and AC_{CO2} for the benchmark are not shown, since this is not a real system. While the solid lines in figure 6 and 7 indicate the results for the systems tested in the HIL test, the dotted lines represent the results for systems with similar hydraulic specification, but from alternative manufacturers. In both figures the unsteady steps in the graphs of system 5 and system 1 (alternative offer) result from a nonfulfillment of a requirement for the incentives of solar thermal collectors from the German Federal Office of Economics and Export Control. The critical requirement states that the collector specific volume of the heat storage tank has to be larger than 40 l/m² (BAFA, 2017a). If it is clearly shown that a system has a solar support also for space heating and not just for the DHW preparation the limit of 40 l/m² can be undercut by 10 % (BAFA, 2017b). Nevertheless the systems 5 and 1 (alternative offer) do not fulfill the incentive requirement for all demand specific collector areas under investigation although the storage tanks have been replaced by similar models of the manufacturer with a larger volume as the collector surface area increases. However, a storage volume of 1500 liters was assumed as the upper limit, since the installation of even larger individual storage units in multi-family buildings is regarded as unrealistic and a possible storage cascading has so far not been used in the investigated systems.

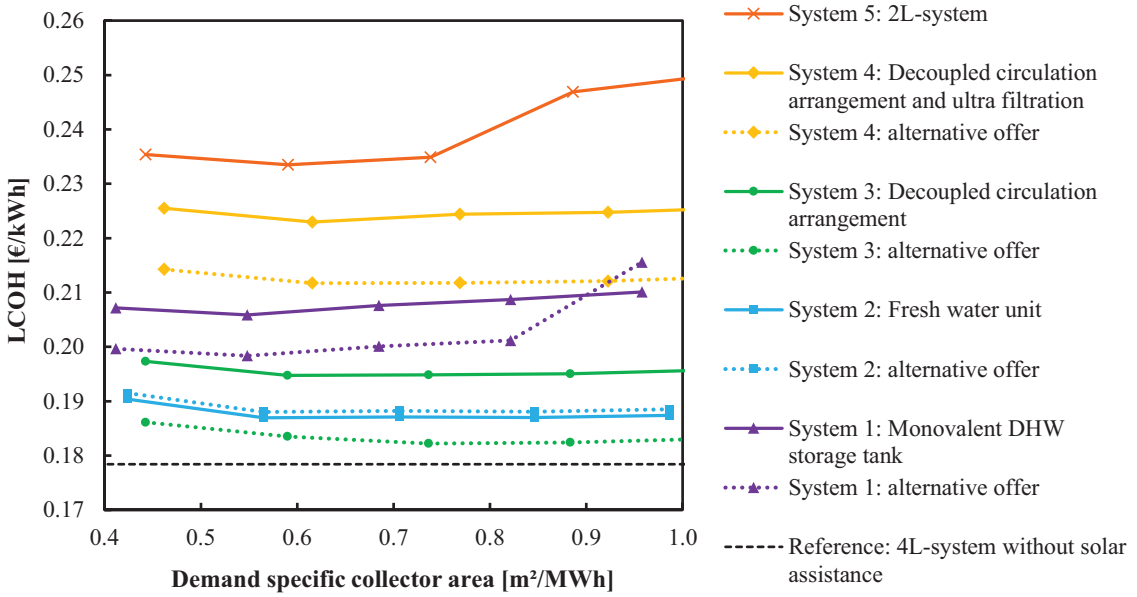

Fig. 6: Levelized cost of heat over the demand specific collector area for the investigated systems and alternative offers with a similar hydraulic specifications

It can be seen in figure 6 that all solar-assisted systems have higher levelized cost of heat than the reference system. When comparing the solar-assisted systems with each other, it appears that systems 2 and 3 have the lowest LCOH, with system 3 showing a greater difference between the considered manufacturers. In system 1, the large number of components and the low energy efficiency lead to high LCOH. The two most energy efficient systems under investigation are at the same time the ones with the highest LCOH. While for system 4 that is a result of the high costs for the ultrafiltration module, for system 5 the high costs for eight decentralized apartment transfer stations and their installation are leading to LCOH of more than 0.23 €/kWh.

Looking at figure 7 it appears that the systems with the lowest LCOH (systems 2 and 3) also feature the lowest AC_{CO2}. The alternative offer of system 3 is reaching 46 €/tCO_2 at its lowest point (at 0.74 m²/MWh). In contrast to that, system 1 shows to have the highest AC_{CO2} with over 1000 €/tCO_2 (at 0.4 m²/MWh). Although the AC_{CO2} is an economical parameter it is combining the energy efficiency analysis (CPF) and the economic efficiency assessment (LCOH). As a result, system 5 with the highest LCOH but also the highest CPF features lower AC_{CO2} than system 1 which is representing the most inefficient solar-assisted system under investigation.

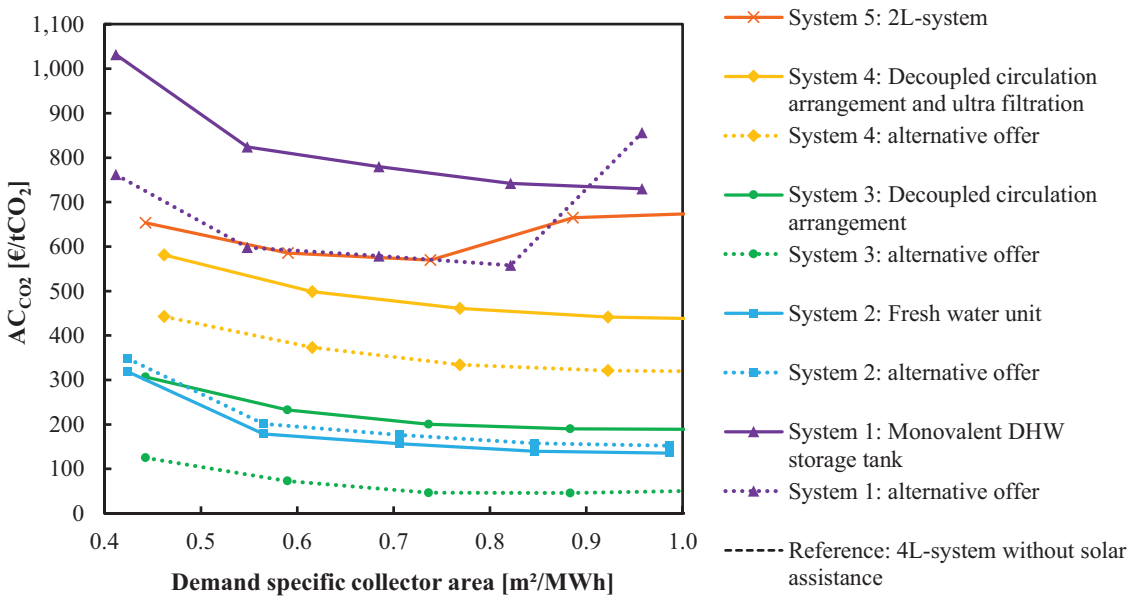

Fig. 7: Carbon abatement cost over the demand specific collector area for the investigated systems and alternative offers with similar hydraulic specifications

4. Conclusion

The overall assessment of solar-assisted heat supply concepts requires not only single component tests, but also tests of the entire system. The investigation shows that a significant increase in efficiency and utilization of the available solar heat can be achieved through compact installation (small number of components or short piping between components), the maintenance of the temperature layering in the heat storage tanks (e.g. stratified charging devices or circulation decoupling) and reduction heat distribution losses (e.g. 2-pipe heat distribution network or ultrafiltration module). The latter is not just reducing distribution heat losses within the building but also conversion losses within the central heating facility. Accordingly, systems that aim for reduced system temperatures show also a higher efficiency in the CPF and not just in the CPF_{plus}, which is explicitly considering distribution heat losses due to the chosen evaluation boundaries. In contrast to the CPF_{plus} the CPF can be easily determined in almost every building, since the input variables end energy and central heat demand of the building can be recorded without much effort with standard measuring technology.

The economic efficiency analysis shows that solar-assisted heat supply systems under investigation have higher levelized cost of heat than the reference system without solar support. A clear economic assessment of the systems is only possible to a limited extent, since the differences in the levelized cost of heat between the systems are roughly the same as the differences between the manufacturers. However, the increase in the number of components and therefore the complexity of the system also means that the levelized cost of heat are increasing.

The carbon abatement cost allows a combined energetic and economic evaluation of the systems and should therefore be the parameter used for the overall assessment of solar-assisted heat supply concepts. Moreover the carbon abatement cost offer the possibility to compare solar-assisted heat supply concepts with other activities where CO_2 emissions are avoided, like electricity production from photovoltaics or wind. The investigation presented in this paper disclosed large differences between the carbon abatement costs of the different solar-assisted heat supply concepts in multi-family houses. The carbon abatement cost moved in a span between 46 and over 1000 €/tCO_2. The most efficient systems in the meaning of a combined energetic and economic efficiency showed to be the systems 2 and 3 where the carbon abatement cost varied between 46 and 300 €/tCO_2 depending on the manufacturer and the demand specific collector area.

5. Acknowledgement

The project SUW-MFH presented in this paper is funded by the German Federal Ministry for Economic Affairs and Energy based on a decision of the German Federal Parliament (reference number: 03ET1212B). The project is carried out in cooperation with the University of Applied Sciences Düsseldorf. The authors are grateful for the financial support and responsible for the content.

6. References

Adam, M., Backes, K., Ille, F., Eggert, D., Steinweg, J., 2016. Klassifizierung und Laborfeldtest von solar unterstützten Wärmezentralen in Mehrfamilienhäusern, 26. Symposium Thermische Solarenergie, Bad Staffelstein

BAFA (Bundesamt für Wirtschaft und Ausfuhrkontrolle), 2017a. Förderübersicht Solar (Basis-, Innovations- und Zusatzförderung), https://www.bafa.de/SharedDocs/Downloads/DE/Energie/ee_solarthermie_foerderuebersicht.pdf?__blob=publicationFile&v=4

BAFA (Bundesamt für Wirtschaft und Ausfuhrkontrolle), 2017b. Oral assurance of the person in charge for incentives of Renewable Energy (Reiner Warsinski). Conversation from 11th of May 2017, Bad Staffelstein

BSW (Bundesverband Solarwirtschaft e.V.), 2007. GroSol - Studie zu großen Solarwärmeanlagen, Berlin, http://www.solarthermietechnologie.de/fileadmin/img/Intranet/AG2/PDF/GROSOL_Studie_BSW_final.pdf

DIN (Deutsches Institut für Normung e.V.): DIN V 4701-10, 2003. Energy efficiency of heating and ventilation systems in buildings - Part 10: Heating, domestic hot water, ventilation, Berlin

Helbig, S., Steinweg, J., Eggert, D., Adam, M., 2016. Performance Testing and Optimization of Solar Assisted Heating Systems for Multi-Family Houses. Conference proceedings – EuroSun, Palma de Mallorca

IWU (Institut Wohnen und Umwelt), 2010. Datenbasis Gebäudebestand - Datenerhebung zur Energetischen Qualität und zu den Modernisierungstrends im deutschen Wohngebäudebestand, Darmstadt, http://www.datenbasis.iwu.de/dl/Endbericht_Datenbasis.pdf

Jordan, U., Vajen, K., 2014. Manual DHWcalc – Tool for the Generation of Domestic Hot Water (DHW) Profiles on a Statistical Basis, Version 1.20, Universität Kassel, Institut für Thermische Energietechnik

Steinweg, J., Eggert, D., Rockendorf, G, Backes, K., Adam, M., 2016. Leistungsbewertung und Optimierung von solar unterstützten Wärmezentralen in Mehrfamilienhäusern; 26. Symposium Thermische Solarenergie, Bad Staffelstein

VDI (Verein Deutscher Ingenieure e.V.): VDI 2067 Part 1, 2012. Economic efficiency of building installations – Fundamentals and economic calculation, Beuth Verlag, Berlin

7. Appendix

Nomenclature		
A_{col}	collector area	[m²]
AC_{CO2}	carbon abatement cost	[€/tCO_2]
a	annuity factor	[a^{-1}]
a_{dsc}	demand-specific collector area	[m²/MWh]
CIPK	carbon intensity per kilowatt-hour	[gCO_2/kWh]
CPF	central performance factor of the heating facility	[-]
CPF_{plus}	central performance factor of the heat supply chain	[-]
EAC	equivalent annual cost	[€/a]
E_{final}	final energy demand	[kWh]
E_{prim}	primary energy demand	[kWh]
e_P	plant effort	[-]
i	annual interest rate	[%]
LCOH	levelized cost of heat	[€/kWh]
NPV	net present value	[€]
$Q_{central}$	central heat demand of the building	[kWh]
Q_{use}	useful energy	[kWh]
R	net cash flow	[€]
T	observation period	[a]

SOLAR THERMAL BASED NEW AND RENEWABLE ENERGY HYBRID SYSTEM FOR THE DISTRICT HEATING AND COOLING IN SOUTH KOREA

Jaehyeok Heo[1], Minhwi Kim[1] and Dong Won Lee[1,*]

[1] New and Renewable Energy Research Division, Korea Institute of Energy Research, Daejeon (Korea)

* corresponding author (dwlee@kier.re.kr)

Abstract

Considering the renewable energy ratio of only 4% in South Korea, the centralized renewable hybrid district heating and cooling demonstration complex would be new alternatives to expand new and renewable energy. In this paper, the current status of recently completed the first centralized renewable hybrid district heating and cooling demonstration complex is introduced. In addition, the methods for load estimation, installed capacities of installed new and renewable energy equipment, and control strategies with operation modes are simply explained.

Key-words: renewable hybrid, district heating, solar thermal system, seasonal thermal energy storage

1. Introduction

South Korea is one of the countries where the amount of energy usage is continuously increasing, but it imports about 95% of its energy sources from abroad because there are few natural energy resources available. Since more than 83% of the consumed primary energy is fossil energy, and with the dependency on nuclear power generation so high in the area of power generation, the ratio of renewable energy is only about 4% whereas the ratio of nuclear energy is about 12% as shown in Fig. 1.

Most of the new and renewable energy accounts for waste incineration and bio energy, and solar thermal energy and geothermal power are only about 1.2%. The reason why the spread of solar thermal energy is

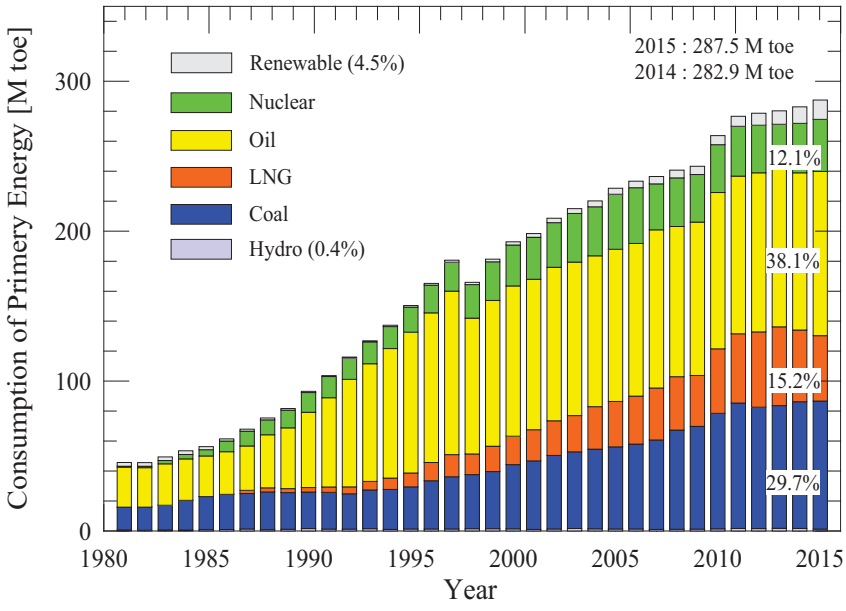

Fig. 1: Consumption of primary energy and the ratio with energy resource types in South Korea

doi:10.18086/swc.2017.29.05 Available at http://proceedings.ises.org

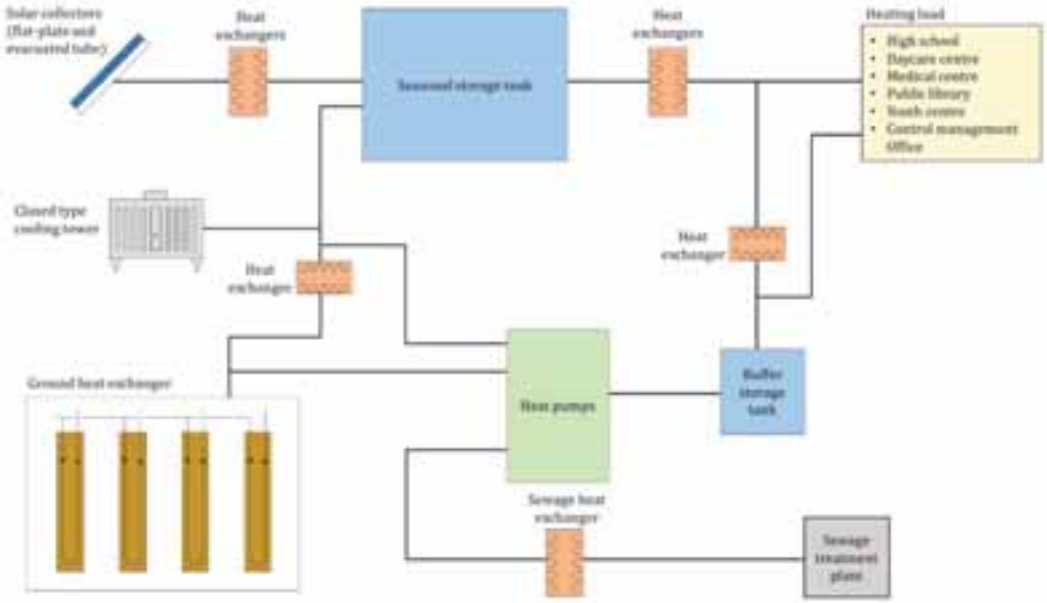

(a)

(b)

Fig. 2: New and renewable energy hybrid system configuration (a) and current on-site pictures (b) of demonstration complex

slow is that the consumer confidence on the solar thermal system applied in the household is not high enough. Most companies related with solar thermal energy are small and follow-up service is not managed satisfactorily. In addition, relatively inexpensive cost of other heat energy sources is the one of the reason why consumers are reluctant to use solar thermal system. Therefore, in order to expand the use of solar energy, it is necessary to supply a large-scale solar thermal system that can be equipped with maintenance system in addition to a small domestic solar heater. The primary goal of this project is to construct a centralized renewable hybrid district heating and cooling demonstration complex based on a large-scale solar thermal system, targeting sewage treatment plants area and six public buildings (schools, libraries, etc.) located in Jincheon, Chungbuk Innovation City. The ultimate goal is to secure the necessary control technologies for the optimal hybrid operation while demonstrating the facilities, and establish a basis for expanding and distributing similar systems in the future.

2. Estimation of heating and cooling loads

In this project, it is aimed to build an energy independence demonstration complex that can provide annually stable heat and electric energy through the various new and renewable energy hybrid facilities. Seasonal thermal energy storage (STES) was applied for the stable thermal energy supply. The electric energy is produced by photovoltaic and fuel cell systems as much as the electricity demand in the demonstration complex for net energy independence, but it is connected to grid line to sell the produced electricity energy instead of self-consumption due to the economical factor. Initially, it was planned to supply only the heat energy necessary for heating and hot water supply. However, since the heat pump is used as an auxiliary system, it was decided to supply cold heat required for cooling to public buildings (except for a high school). In case of a high school, additional cooling system is installed, because the cooling load of high school is too much to be covered by the originally planned heat pump facilities.

In order to determine the capacity of the required renewable energy facility, the heating and cooling load of each public building was estimated first. The energy load is estimated based on the detailed building design and operating statistics on similar buildings (Lee et al., 2014). EnergyPlus was used for the heating load analysis. The thermal load of high school was estimated based on operating statistics of sites near high school, although exact load estimation was very difficult because operating circumstances are different in each school. Table 1 shows total annual heating and cooling load calculated based on the ambient temperature conditions of 24^{o}C and 26^{o}C in winter and summer, respectively. Total thermal energy load for heating and hot water supply were estimated as 761.5 MWh.

3. Capacity of installed new and renewable energy equipment and status

The capacities of new and renewable energy systems were determined based on the estimated thermal energy load and the TRNSYS-based simulation program. Due to field spatial limits, maximum installation area of solar thermal collector and size of STES were about 1,600 m^2 and 4,000 m^3, respectively. To cover the deficient thermal energy, water source heat pump (WSHP) of 350 kW and ground source heat pump (GSHP) of 175 kW were designed. In case of heating operation, totally 350 kW WSHP is operated to raise the residual heat in STES, and GSHP of 175 kW will be used as the auxiliary system. When the residual heat in STES is insufficient, sewage heat in the water purification center is used as the heat source. In case of cooling operation, alternating operation of WSHP would be possible with additional WSHP of 175 kW among 350 kW, because the cooling load of 4 public buildings can be covered by a GSHP of 175 kW and a WSHP of 175 kW. In addition, it is estimated that about 750 kW of photovoltaic power generation equipment is needed to produce about 850 MWh/year of electricity, which is expected to be consumed in public buildings in the demonstration complex.

Fig. 2 shows the new and renewable energy system configuration and current on-site pictures, respectively. All public buildings except for a youth center have been completed, and renewable energy facilities and seasonal thermal energy storage have been installed. The solar thermal systems were installed on the parking lot and the grounds where the geothermal heat exchanger was installed, and the photovoltaic systems were distributed on the installable space. The heat pump, the fuel cell, and the buffer storage tank were installed in the machine room including the monitoring center.

Tab. 1: Heating and cooling load for public buildings

Building	Heating load [MWh]	Cooling load [MWh]
High school	219.7	(250.7)
Library	76.1	81.0
Youth center	32.8	19.1
Child care center	31.7	21.6
Public health center	17.9	6.2
SUM	378.2	127.9

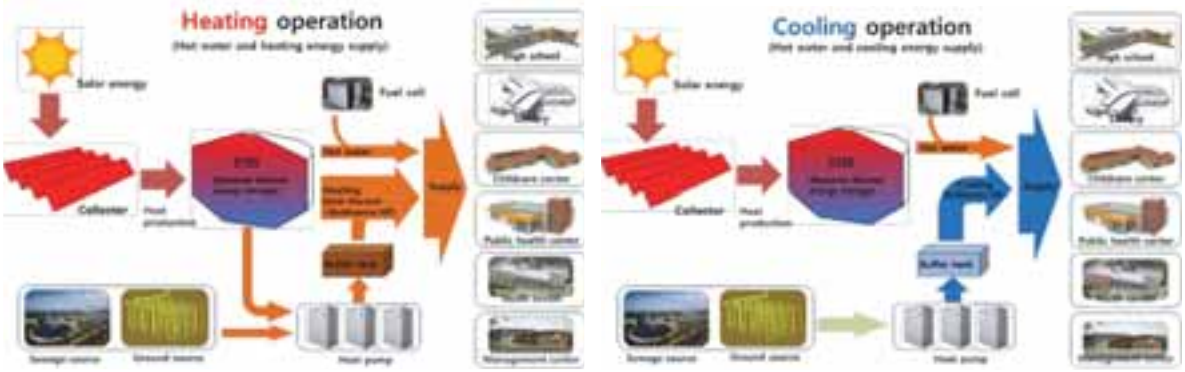

(a) (b)

Fig. 3: Operating options with heating (a) and cooling operations (b)

4. Operating methods

Operating options for new and renewable energy hybrid district heating system are divided into four operational methods as explained in section 4.1-4.4, and Fig. 3 shows the operation options with heating and cooling mode.

4.1. Operation based on solar thermal system

The heat energy produced in the flat plate and evacuated tube collectors is stored as hot water in the seasonal thermal energy storage through the heat exchanger. The stored hot water is supplied to public buildings for heating and hot water supply, and two separate heat exchangers were installed with purposes for separating the heat storage fluid in the STES and circulating fluid in the supply/return circulation pipe. At this time, the return temperature is controlled lower than 40^{o}C for the thermal stratification in STES by using both a variable speed pump and a 3-way valve. The return temperature will be preferentially controlled by the inverter pump, but 3-way valve might be additionally used according to the operation status by the inverter control. In the heating and hot water supply operation, the supply water is continuously circulated during business hours. When the heating and hot water load occur in public buildings, the temperature difference between supply and return water was observed. By this temperature difference detection, the heat energy in STES is supplied to the load. When the heat supply water temperature is less than 50^{o}C, operation mode is changed from the mode based on solar thermal system to the mode based on heat pump system because it can be considered that the thermal energy in STES is not available to supply to the load.

4.2. Operation for solar thermal overheating protection

In case that the STES is overheated by the over produced heat energy from solar collectors, overheating protection operation mode is provided to reduce the high temperature in STES. Except for summer season for cooling operation, the over produced heat is first released to underground through borehole heat exchangers, and the leftover heat is released to atmosphere by an additional cooling tower.

4.3. Heating operation based on heat pump system

Ground and sewage source heat pumps were installed as the auxiliary heating system. Besides, water source heat pump that uses residual heat less than 40^{o}C in STES as the heat source is also utilized. The hot water produced from heat pump is stored in the buffer storage tank and then supplied to the load. The reason why the buffer tank is used is to utilize the off-peak load time power. The operational cost can be reduced when hot water produced by heat pump operation during the night time is supplied to the load in day time. Of course, in case of heavy heating and hot water load, the heat pump should be operated during the day time.
It was checked that the capacities of heat pump and buffer storage tank can afford to respond to the maximum load of public buildings. The exchanger is installed for the separation between the heat storage fluid in the buffer storage tank and the circulating fluid in the supply / return circulation pipe. The heat pump operation in day time was set based on the temperature of hot water supplied to the load side.

4.4. Cooling operation based on heat pump system

In summer, cold heat is supplied to public buildings (except for a high school). Ground source and sewage source heat pumps are used as the cooling equipment, and the cold heat is supplied to the load side through

buffer storage tank. Buffer storage tank is applied for the utilization of the night time power as in the case in heating operation. In high school, additional direct-fired absorption chiller is used for the cooling. During the cooling operation, it is possible to supply hot water to the load side by using the stored heat in STES.

5. Conclusion

In November 2016, the first centralized renewable hybrid district heating and cooling demonstration complex based on a large-scale solar thermal system has been constructed in South Korea. The method for load estimation and capacities of installed new and renewable energy equipment were introduced, and the concept of major operation modes and control strategies were simply explained. While demonstrating the facilities, control technologies for the optimal hybrid operation will be improved and this experience will be a valuable basis for expanding and distributing similar systems in the South Korea.

6. Acknowledgement

This research was sponsored by MSIP (Ministry of Science, ICT and Future Planning) Eco-Friendly Energy Town Program (Grant No. NRF- 2015M3D2A1032742).

7. References

Lee, D. W. et al., 2014, Development of the environment-friendly new and renewable energy convergence town, Korea Institute of Energy Research Report, KIER-B42426.

High latitude solar heating using photovoltaic panels, air-source heat pumps and borehole thermal energy storage

Janne Hirvonen[1], Kai Sirén[1]

[1] Aalto University School of Engineering, Espoo (Finland)

Abstract

A solar community of 100 passive houses was designed for high latitude Finnish conditions. Typical solar thermal energy generation was replaced by solar electric system which was used to operate heat pumps. Short-term water-based thermal storage tanks were charged with an air-to-water heat pump and then discharged to a seasonal thermal storage system in the form of borehole thermal energy storage (BTES).

With total PV capacities of 240 to 600 kW, 78 to 97% of space heating and domestic hot water was provided by renewable energy from the local heating grid. Utilizing a water-to-water heat pump between low and high temperature water tanks increased the efficiency of the air-source heat pump. Varying the flow rate of borehole storage provided very minimal benefit.

Keywords: Solar community, seasonal thermal storage, solar electricity, heat pump,

1. Introduction

Solar energy availability varies between day and night and with seasons. The seasonal variability is different from country to country, with locations far from the equator experiencing larger changes in insolation. Finland is located above 60 °N latitude, which means that in summer the day can be 18 hours long, while in winter it might last only 6 hours. Correspondingly, energy demand for heating is greatest during winter, when there is little, if any, solar energy available. For this reason, conventional solar heating system with a short-term water storage is of limited utility in Finnish conditions. However, seasonal thermal storage may offer a solution.

Seasonal thermal storage allows the storage of heat for several months. The most popular seasonal storage methods are tank storage, aquifer storage, pit storage and borehole storage (Hesaraki, et al., 2015). Borehole thermal energy storage (BTES) consists of a grid of boreholes that have been drilled into the ground and fitted with heat transfer pipes (Lanahan & Tabares-Velasco, 2017). Hot fluid is circulated in the boreholes to heat the ground. If the size of the storage is large enough, thermal losses to the environment remain manageable and make it possible to provide a large fraction of heating by solar energy. Typically, the seasonal storage is heated by solar thermal collectors, which produce heat directly, as was the case in the Drake Landing Solar Community (Sibbitt, et al., 2012). Similar designs for Finnish conditions have been tested in an optimization study (Hirvonen, et al., 2017).

In Finland, the current market for solar thermal collectors is small, but installations of solar photovoltaic (PV) panels are accelerating and a new record for the country's largest PV system installation is set several times per year. Heat pumps are also replacing conventional district heating in many locations. Thus, combining these two technologies was considered in this paper. Solar electricity was used not only to meet the electric load of house appliances, but also to run an air-to-water heat pump to charge the seasonal thermal storage through a large water storage tank. The goal was to make an initial test of concept and find out the effect of different controls and solar generation capacity on the reduction of imported external energy.

2. Methodology and system description

This study looked at the energy matching in a virtual solar community of 100 single-family houses, located in Helsinki, Finland. The study was based on dynamic simulations performed with TRNSYS 17, using the weather data from Helsinki Test Reference Year 2010. The space heating (SH) demand in the houses was based on the

doi:10.18086/swc.2017.29.06 Available at http://proceedings.ises.org

simulated performance of a 100 m^2 passive level house with 25 kWh/m^2 annual energy demand according to heated floor area. The domestic hot water (DHW) demand was based on profiles gained from an IEA study (Jordan, 2001), normalized to 35 kWh/m^2. Electricity consumption of appliances was based on measured demand from 50 real district heated houses in the Helsinki region, normalized to 40 kWh/m^2.

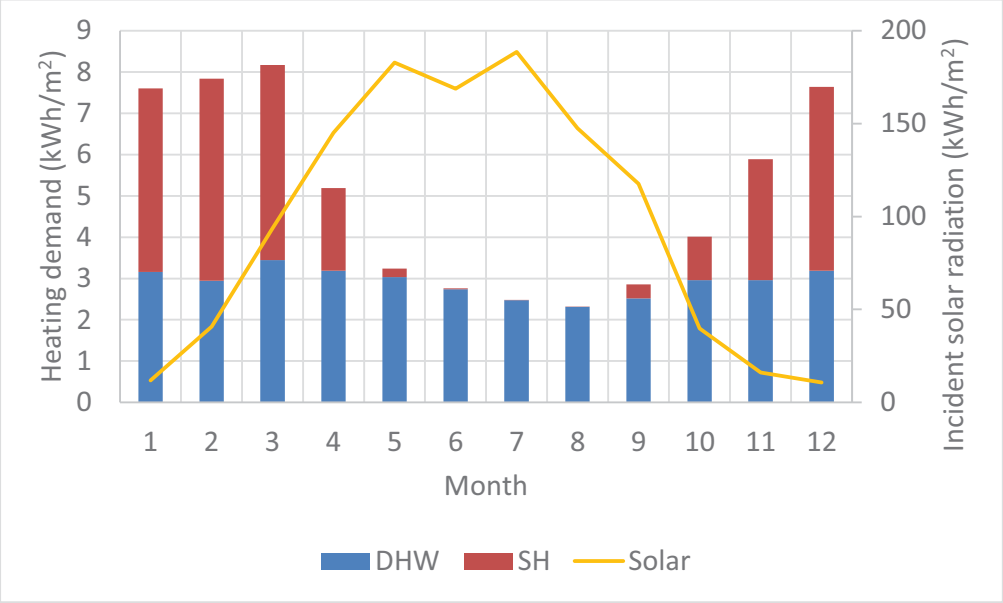

Figure 1: Monthly solar energy potential (vs. collector area) and heating demand in the houses of the community (vs. floor area).

The modeled energy system is shown in Figure 2. All the houses in the community were connected to a local heating grid that was fed from two large water storage tanks. The warm tank (300 m3) was used to supply space heating (SH) at 30 to 35 °C (floor heating) and to preheat the domestic hot water (DHW). The hot tank (150 m3) was used to superheat the DHW to the required temperature of 55 °C. The warm water tank was heated by an air-to-water heat pump (AW-HP, Figure 3) powered by solar photovoltaic (PV) panels, using ambient air as the heat source. The hot tank was heated by a water-to-water heat pump (WW-HP, Figure 4), using the warm tank as the heat source. Thus, the two heat pumps formed a type of cascade heat pump. Solar electricity was also used to run the house appliances. In case there was not enough solar power for all needs, the first priority of solar energy use was with the appliances, second priority with the WW-HP and third priority with the AW-HP. It was assumed that the heat pumps could be operated at any part-load between 10 and 100%. If solar electric power was not enough to run the AW-HP at the minimum part-load, the HP would not start. The ratios of the source-side (ambient air or warm water) and load-side flows (warm or hot water) in the heat pumps were kept constant. The flows adjusted according to heat pump power, to keep the load-side temperature change roughly constant at 12 °C.

If the warm tank cooled down and there was not enough solar energy available, it was be heated by discharging the seasonal storage. If the warm tank temperature rose above 50 °C by the use of the AW-HP, the extra heat was transferred to the seasonal storage. When the BTES temperature was above the tank temperature and the required SH temperature, energy from the ground was transferred back to the tank.

The seasonal storage was a borehole thermal energy storage system, contained in rock with thermal conductivity of 3.5 W/mK and total volume of 30 000 m3. There were 216 boreholes, each 37 m deep, evenly distributed along the BTES cross-section. The boreholes were connected in groups of 4, to generate a radial temperature distribution in the BTES. During charging, hot fluid entered from the center, flowed through 4 boreholes and exited at the edge of the BTES. During discharging, cold fluid entered from the edge and exited through the center. As it takes several years for a BTES system to reach stable conditions, a three-year simulation period was used. The results reported in this study were for the final year, on the assumption that long-term steady-state conditions had been achieved.

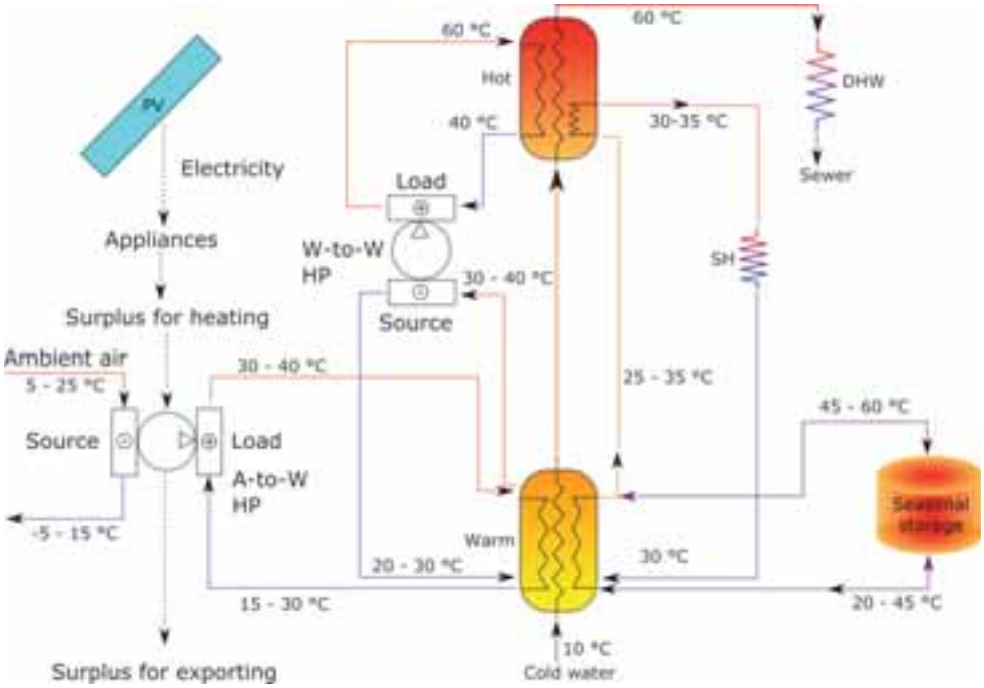

Figure 2: Energy system diagram.

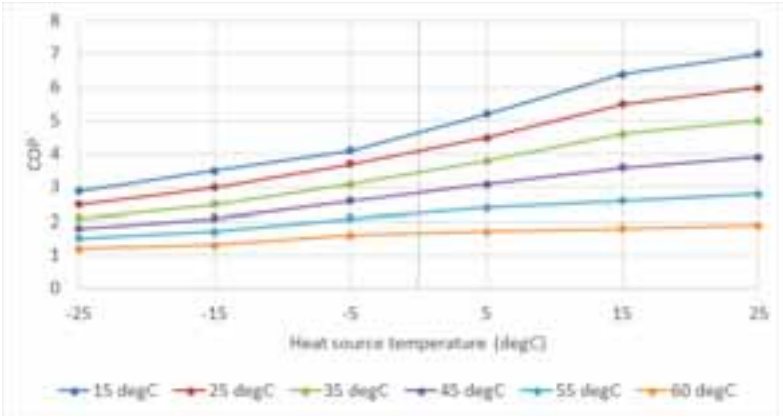

Figure 3: COP of the air-to-water heat pump with different load-side inlet temperatures. Based on model NIBE-2120.

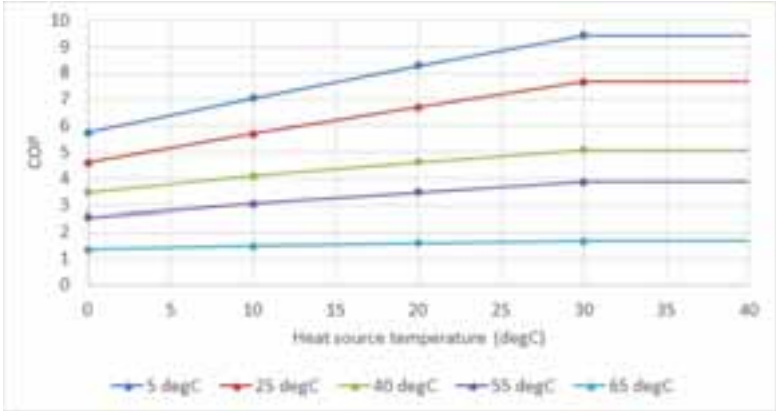

Figure 4: COP of the water-to-water heat pump with different load-side inlet temperatures. Based on model NIBE-F1345.

The total AW-HP thermal capacity was set to 960 kW, which corresponds to 240 kW electricity consumption in standard conditions. In addition, the WW-HP thermal capacity was set to 180 kW, which corresponds to 60 kW electricity consumption. Both heat pumps could be operated in part-load mode, with a minimum power of 10%. Actual ratio of thermal and electric ratio depended on the heat source temperature and load temperature, as shown in Figures 2 and 3.

2.1. Equations

Renewable energy fraction (REF) is the portion of end-use heat energy that is provided by the renewable energy of the local heating grid. Since electricity was the only external energy source, we can determine the REF indirectly

$$\mathrm{REF} = 1 - \frac{E_{imported\ heating\ elec}}{E_{SH}+E_{DHW}}, \qquad \text{(eq. 1)}$$

where $E_{\text{imported heating elec}}$ is the additional imported grid electricity needed for heating (heat pumps, backup system, pumps) after solar electricity has been accounted for, E_{SH} is the building-side space heating thermal energy demand and E_{DHW} is the building-side domestic hot water thermal energy demand. There was no electric energy storage, which limited the maximum amount of appliance related solar energy use. Thus, the REF only accounts for heating related energy, not electric appliances.

Efficiency of the seasonal storage is defined as the ratio of energy taken from the storage vs. the energy stored into the system

$$\eta_{\mathrm{BTES}} = \frac{E_{BTES\ discharge}}{E_{BTES\ charge}}. \qquad \text{(eq. 2)}$$

The PV system produces only electricity, but when connected to the heat pump the combined efficiency has the same meaning as the efficiency of a solar thermal collector. The combined thermal efficiency is defined as

$$\eta_{\mathrm{PV,thermal}} = COP_{HP}\frac{E_{PV,HP}}{G}, \qquad \text{(eq. 3)}$$

where COP_{HP} is the coefficient of performance for the heat pump, $E_{PV,HP}$ is the electricity consumed by the heat pump that was supplied by the PV system and G is the incident solar insolation on the solar panels.

2.2. Study parameters

To gain understanding of how the heating system and solar electricity interact, three parameters were chosen for analysis: PV capacity, BTES flow setting and WW-HP control mode.

PV capacity was selected as multiples of the nominal electricity consumption of the AW-HP (multiples 1, 1.5, 2, 2.5) to see how much excess capacity relative to the heating capacity is needed before there is enough power to both run the appliances and heat the BTES.

The BTES was operated in two different modes. In the Constant mode, all charging and discharging was done at a constant flowrate. In the Variable mode, the flowrate was changed according to the difference between the average BTES temperature and the temperature at the top of the warm tank. A high temperature difference corresponded to high flow and a low temperature difference to a low flow. The base flow rate for the BTES was 1600 kg/h per pipe loop. With a ΔT below 1, below 5, below 10 and above 10, the flow rate fraction was 25%, 50%, 75% and 100%, respectively.

The HP control setting decided whether the WW-HP was only run when the hot tank required recharging (setting 0) or if the hot tank was charged whenever there was available solar energy and the temperature at the top of the tank was less than 70 °C (setting 1). Additional use of the WW-HP lowers the temperature in the warm tank, thus increasing the COP of the air-to-water heat pump.

Table 1: Simulation parameters.

Case	PV capacity (kW)	BTES flow	HP control
0	0	-	0
1	240	Constant	0
2	240	Constant	1
3	240	Variable	0
4	240	Variable	1
5	360	Constant	0
6	360	Constant	1
7	360	Variable	0
8	360	Variable	1
9	480	Constant	0
10	480	Constant	1
11	480	Variable	0
12	480	Variable	1
13	600	Constant	0
14	600	Constant	1
15	600	Variable	0
16	600	Variable	1

3. Results

3.1. Renewable energy fraction

An important measure for energy system performance is the renewable energy fraction. Figure 5 shows the fraction of end-use heat energy that was met by the solar heating system. Even without any solar energy, 66% of heating was provided by the heat pump system alone. When solar capacity was set to 2.4 kW/house, which was equivalent to the maximum electricity use of the AW-HP, REF of heating was increased to 78%. Increasing the PV capacity to 3.6 kW/house, up to 88% REF was achieved. Increasing PV capacity further showed diminishing returns, as at 4.8 kW/house the maximum REF was 95% and at 6 kW/house it was 97%.

While PV capacity was the main determinant of REF, heat pump and BTES configurations also affected the results. With the smallest PV capacity (240 kW), increasing the WW-HP utilization during peak solar generation lowered REF compared to only running the WW-HP as needed by the hot tank. With all the larger solar generation capacities it had the opposite effect; increased use of WW-HP increased total REF. With a small PV capacity, the higher priority of the WW-HP prevented the operation of the AW-HP, since little extra solar energy was available for heating the warm tank and subsequently the BTES. With larger PV capacities there was enough energy to operate both the AW and WW heat pumps. In these cases, the WW heat pump cooled down the warm tank (which it used as an energy source), improving the COP of the AW-HP due to lower load-side temperatures. Increased use of WW-HP changed REF by -2.2%, +0.9%, +2,3% and +3.6% for the 240, 360, 480 and 600 kW cases, respectively. The effect of the variable BTES flow was less significant, though it was positive in all cases. The increase in heating REF was 0.2 to 0.6%, the largest gains found in the 360 kW case.

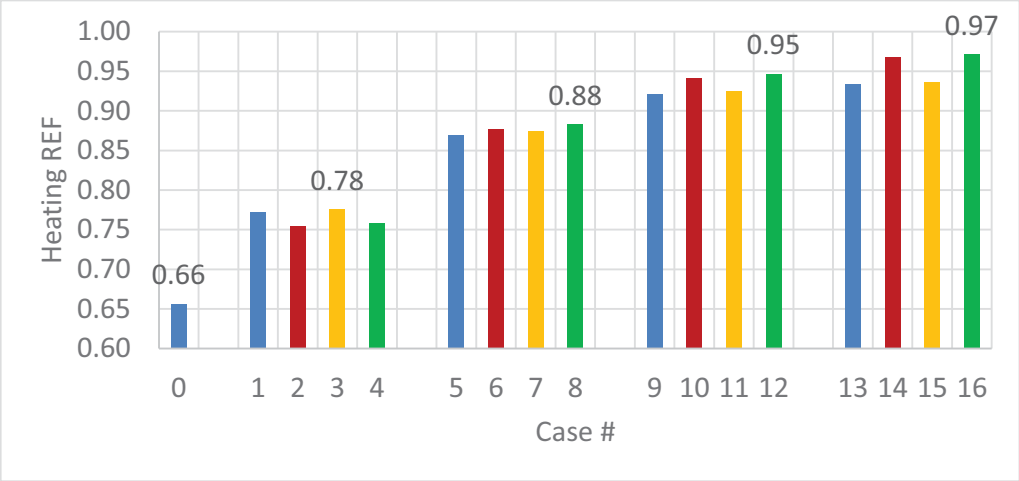

Figure 5: Annual renewable energy fraction of heating for the simulated cases. Bars with the same color have the same BTES and HP flow settings, but different PV capacity, as shown in Table 1. The numbers show the highest REF for each PV capacity.

3.2. Solar energy use

The solar energy generated by the PV panels was used for appliances, heat pumps and exporting. Increasing the PV capacity by 150% from 240 kW to 600 kW increased the PV use for appliances only by 25%, due to the mismatch in energy use and generation patterns. Most of the added solar energy generation was used by the AW-HP, as shown in Figure 6. Increasing the use of the WW-HP increased its electricity consumption by 230 to 420%, according to PV capacity. However, the total sum of the AW and WW heat pump electricity consumption remained practically constant in all the cases with the same PV capacity. In the cases with 240 and 360 kW PV capacity, 1% of PV generation was exported to the grid. With 480 and 600 kW, exports were 4 and 7% of PV generation.

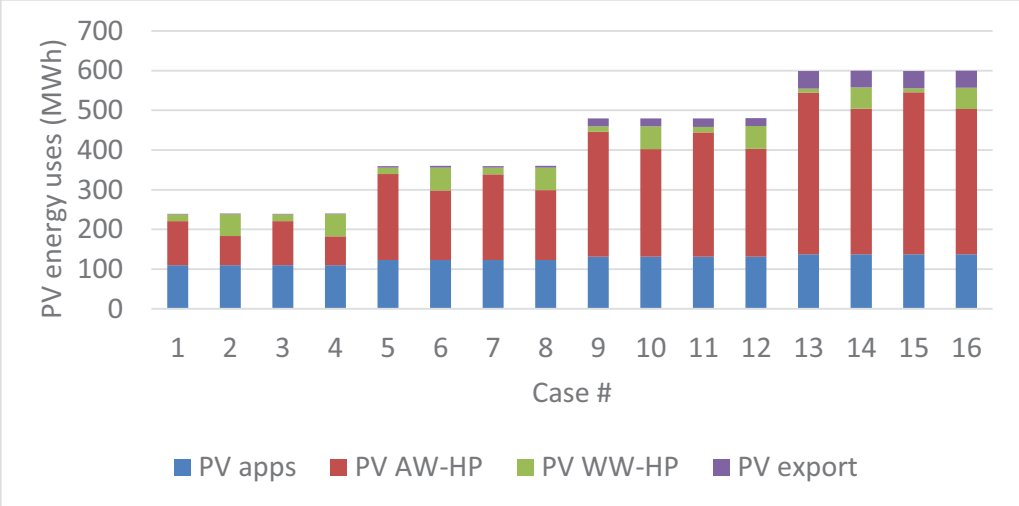

Figure 6: Annual distribution of PV generated energy for different uses.

3.3. Thermal efficiency of solar electric heat generation

Effective efficiency of solar panels when producing heat with heat pumps, hourly duration curve. Choose the best case of all PV sizes and put them in the same figure.

Since solar electricity was used to run the heat pumps, we can calculate the thermal efficiency of solar heat generation. Figure 7 shows the duration curves for the thermal efficiency of both heat pumps in the best cases of each PV capacity. The total running time of the AW heat pump was increased by adding more PV capacity, because after meeting appliance needs extra power was available more often. There was also a clear decrease in average efficiency as the PV capacity was increased. This is due to the AW HP operating at higher temperatures due to charging of the thermal storage tank. With WW HP, the longest running time and highest efficiency was

obtained in the 360 kW case. Conversely, the lowest efficiency was obtained with the 600 kW system.

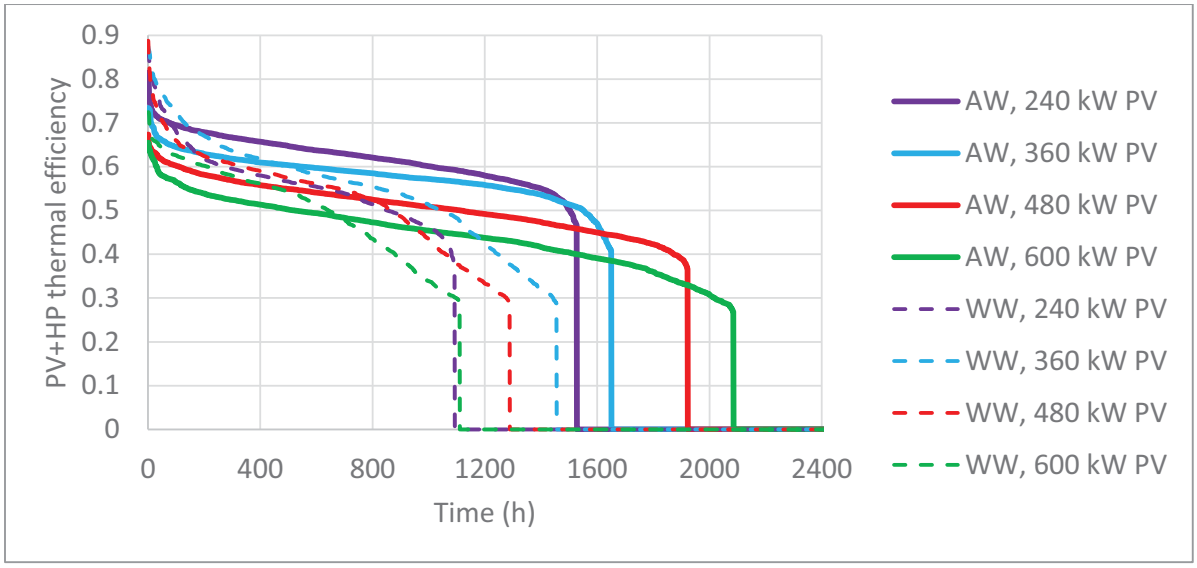

Figure 7: Duration curves of the thermal efficiency of heat pump energy generation using solar electricity.

3.4. BTES performance

Figure 8 shows the average temperature in the BTES during the seasonal cycle of the last simulated year. The bottom and top end of the bars represent the annual minimum and maximum temperatures, respectively. Also shown is the storage cycle efficiency. In the 240 kW PV cases, there was not enough energy to heat the BTES to the temperature levels required to meet space heating demand. The low temperature resulted in a very high cycle efficiency. Higher PV capacity raised the storage temperature.

The borehole flow setting had no practical effect on the temperature. The more active operation mode of the WW HP, however, decreased temperature and increased BTES efficiency for most cases. In the 360 kW cases, the lower temperature was also joined by lower efficiency.

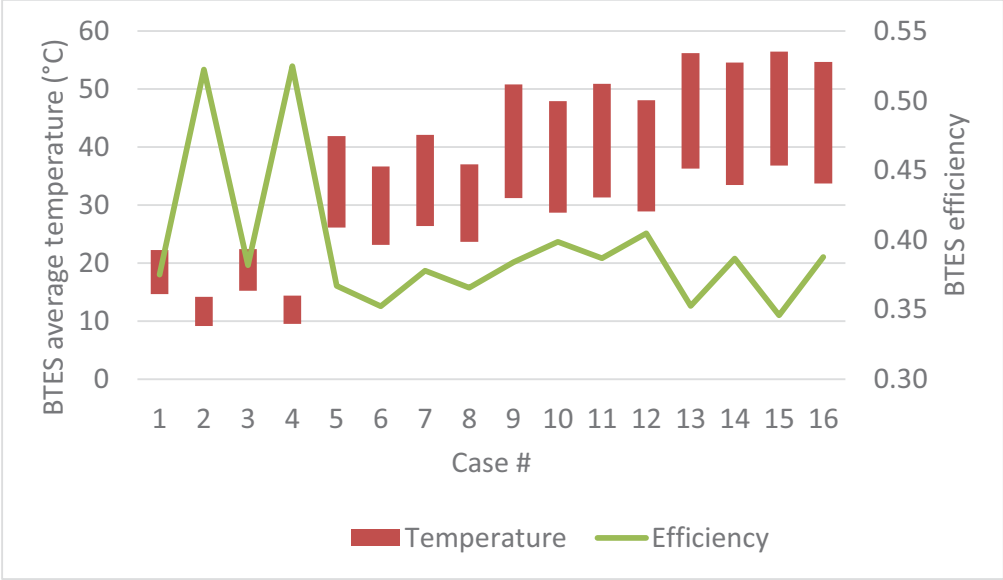

Figure 8: Range of average seasonal storage temperature and the annual seasonal storage efficiency.

3.5 Monthly comparison

Figure 9 shows the third year monthly electricity flows and seasonal storage temperatures in Case 1. Generation from the PV system was distributed between appliances, AW-HP and WW-HP. The minimum need for external energy happened in July, with 15 MWh of electricity imported. The maximum happened in December, with

66 MWh of electricity imported. The low amount of 2.4 kW solar panels per building didn't have enough excess energy to allow the charging of the seasonal storage. Thus, the maximum temperature achieved by the BTES was 22 °C, which was not enough to provide heating in winter.

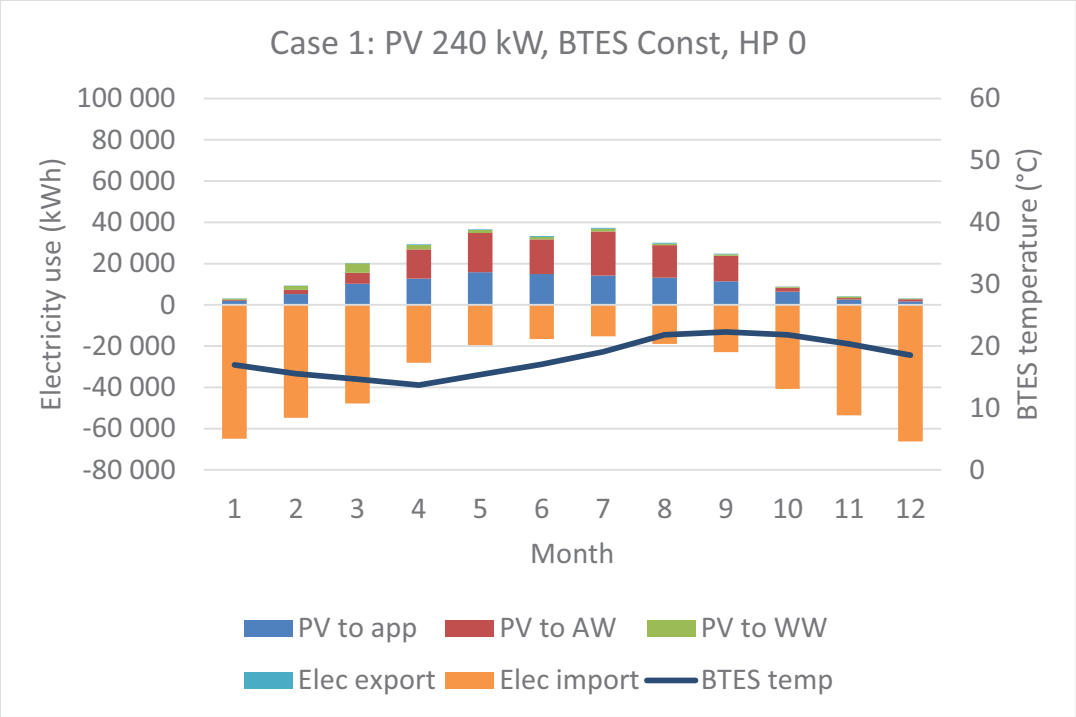

Figure 9: Electricity flows and seasonal storage temperatures in Case 1.

Figure 10 shows the third year monthly electricity flows and seasonal storage temperatures in Case 16. Now the higher solar capacity allowed diverting a large amount of solar electricity to the operation of the AW-HP. The extra heat was then used to charge the BTES up to 55 °C, while the annual cycle only dropped the temperature down to 34 °C. The need for imported energy was reduced compared to Case 1, as the minimum imports were 10 MWh in July and maximum 45 MWh in December. This highlights the difficulty of utilizing significant amounts of solar energy in high latitude conditions, which have a high seasonal mismatch in demand and generation. Increasing nominal solar energy capacity by 150%, compared to Case 1, reduced the need for external energy by only 32% during the peak month.

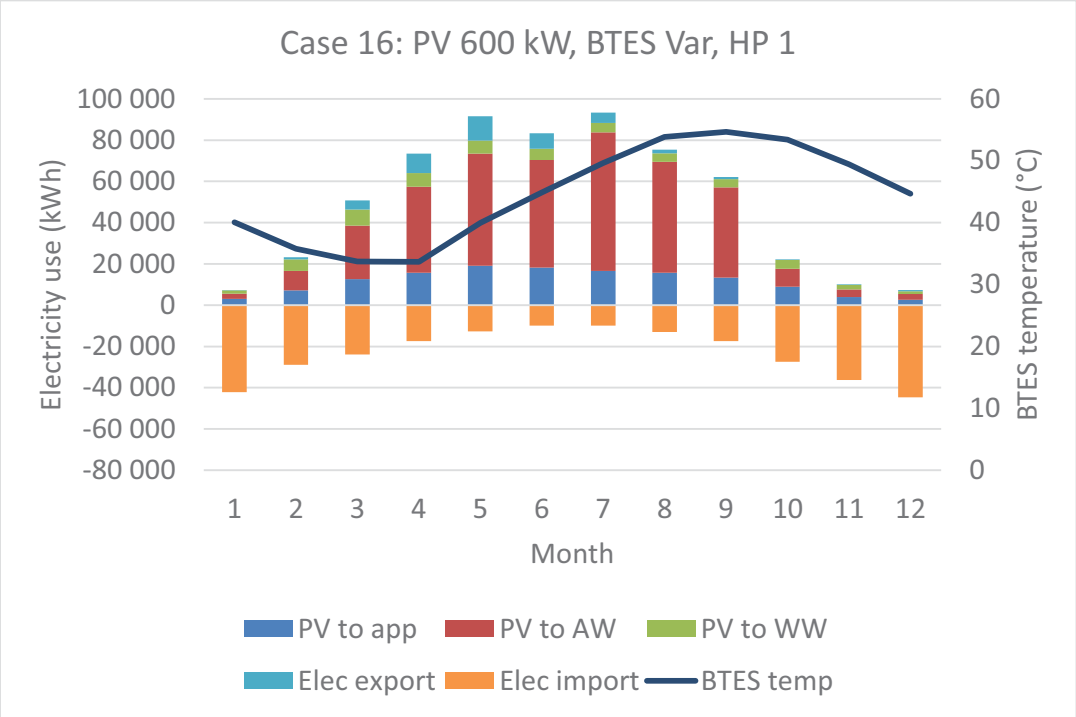

Figure 10: Electricity flows and seasonal storage temperatures in Case 16.

4. Discussion and conclusions

The heat pump based solar heating concept introduced in the paper worked well. A renewable energy fraction of up to 97% was achieved by having a nominal solar electric capacity of 600 kW. This was equal to 2.5 times the maximum electricity consumption of the air-to-water heat pump. However, even with a PV capacity of 360 kW, 1.5 times the maximum electric power of the AW-HP, the REF could be as high as 88%. Thus, with passive houses, a relatively low amount of PV generation per house was needed to achieve a high REF. Using the solar photovoltaic system simplifies the solar community design compared to a solar thermal collector design, because the same solar panels can supply both the heat and the electricity. In addition, no piping is required between the solar collectors and storage tanks.

Varying the BTES flowrate did not significantly influence the system performance. This implies that using a constant flow rate is effective enough, though the optimal flow rate could still be different than what was selected in this study.

Combined with the air-to-water heat pump, the average thermal efficiency of solar heat generation could be above 50%, even when heating REF was above 90%. The thermal efficiency of this electric heating system compared favorably to the 33% solar thermal efficiency obtained in the Drake Landing Solar Community (DLSC, 2012). Utilizing the water-to-water heat pump between the two buffer storage tanks increased total system efficiency by lowering the input temperature of the air-to-water heat pump, but only if PV capacity was large enough to also allow additional use of the AW heat pump. It should be noted that the ideal heat pump modeled here suffered no ill effects from part-load use or fast on-off behavior and could always adjust perfectly to the current solar conditions. A real-life system may face more difficulties in these aspects, which might lower total system efficiency.

A high REF solar community based on solar electricity and heat pumps was found to be technically feasible in a high latitude country like Finland. However, the seasonal energy mismatch and large losses in the seasonal thermal energy storage cause diminishing returns for increased solar capacities. Further optimization is needed to find out economical implementations of the basic design.

5. References

DLSC, 2012. *Drake Landing Solar Community, monthly reports.* [Online]
Available at: https://www.dlsc.ca/reports.htm
[Accessed 16 August 2017].

Hesaraki, A., Holmberg, S. & Haghighat, F., 2015. Seasonal thermal energy storage with heat pumps and low temperatures in building projects - A comparative review. *Renewable and Sustainable Energy Reviews,* pp. 1199-1213.

Hirvonen, J., Rehman, H. u., Deb, K. & Sirén, K., 2017. Neural network metamodelling in multi-objective optimization of a high latitude solar community. *Solar Energy,* Volume 155, pp. 323 - 335.

Jordan, U., 2001. *Realistic domestic hot-water profiles in different time scales,* Marburg: International Energy Agency.

Lanahan, M. & Tabares-Velasco, P. C., 2017. Seasonal thermal-energy storage: A critical review on BTES systems, modeling, and system design for higher system efficiency. *Energies.*

Sibbitt, B. et al., 2012. The performance of a high solar fraction seasonal storage district heating system - Five years of operation. *Energy Procedia,* Volume 30, pp. 856 - 865.

THE CHARACTERISTICS OF SOLAR THERMAL COLLECTOR AND STORAGE SYSTEM INCLUDING SEASONAL THERMAL ENERGY STORAGE IN SOUTH KOREA

Minhwi Kim[1], Jaehyeok HEO[1] ,Schilt Ueli[1] and Dong Won LEE[1,*]

[1] New and Renewable Energy Research Division, Korea Institute of Energy Research, Daejeon (Korea)

[*] corresponding author (dwlee@kier.re.kr)

Abstract

A renewable hybrid energy system using seasonal thermal energy storage (STES) has been recently constructed in Jincheon, South Korea. The eco-friendly energy town was proposed and constructed in Jincheon to supply the heat from the solar thermal system and new and renewable hybrid energy systems with seasonal thermal energy storage (STES) to six buildings contained in town. In this research, the thermal behavior of the series connected solar thermal systems, which are flat-plate solar collectors and evacuated tube solar collectors, and the STES have been investigated. During the 21 days of trial operation period in January 2017, the ambient air conditions, irradiation, useful thermal energy gain, and internal thermal energy variation in STES were estimated by using measuring data. It was found that the efficiencies of solar thermal systems were 2.4 to 25.4%, and that of the STES were 90%, during the whole test period.

Keywords: solar thermal systems, seasonal thermal energy storage, control logic, experimental results, efficiency

1. Introduction

In South Korea, where the usage ratio of renewable energy among the national energy consumption is still low, the policies have been established to expanding the heat supply from renewable energy facilities including solar thermal systems. As part of these policies, the eco-friendly energy town constructed in Jincheon, South Korea has adopted a centralized heat supply system combined with various new and renewable hybrid energy systems, focusing on the solar thermal systems and seasonal thermal energy storage (STES).

This proposed eco-friendly energy town is the first case in South Korea that uses STES for stable heat supply to the buildings. The eco-friendly energy town contains six buildings with the new and renewable hybrid energy systems which includes a solar thermal system, STES, 3 heat pump systems which have different heat sources, buffer tank, and a district heating loop system. The six buildings are consisted of high school, library, youth center, child care center, public health center. Figure 1. shows the new and renewable energy hybrid system configuration installed in Jincheon. The two types of solar collectors are connected in series, and then the collected heat is stored in the STES through the whole year. The stored heat in the STES is supplied to the building for heating the space and supplying the hot water through the winter season. In the end of heating season, when the stored water temperature in STES is lower than the target supply heating water temperature, the heat pump system increases the supply water temperature with supplying the hot water in the STES to the source side of the heat pump. During the cooling season, two heat pumps which uses the ground heat source and sewage heat source, respectively, are operated to produce cooling water. The produced cooling water is stored during the nighttime in the buffer storage tank, and then the cooling water is sent to the district loop system to cool the buildings during the daytime.

Over the last decades, many researches have been conducted on seasonal heat storage and solar thermal systems focused on European countries. Schmidt et al. (2004) demonstrated the central solar heating plants using seasonal thermal storage. The demonstration plants that had been built up to this point through the government-funded research program, “Solarthermie2000” in Germany were presented in detail. Bauer et al. (2010) showed several central solar heating plants with seasonal storage in Germany while comparing and summarizing the results of

doi:10.18086/swc.2017.29.07 Available at http://proceedings.ises.org

extensive monitoring programs which were carried out within the framework of “Solarthermie2000”. Four different types of thermal energy storage were investigated, such as hot water, gravel-water, borehole, and aquifer. Novo et al. (2010) presented a review of technologies and conducted projects for central solar heating systems which employ seasonal sensible water storage. Different technologies for the storage of heat were available and researched. Xu et al. (2014) reviewed three forms of heat storage, namely sensible, latent and chemical heat storage. It was concluded that in comparison, sensible heat storage is most applicable for practical use whereas latent and chemical heat storage still need to be investigated and developed further.

In this study, we investigated the efficiency of solar thermal system and the thermal storage performance of the STES based on the measured data during the trial operation period.

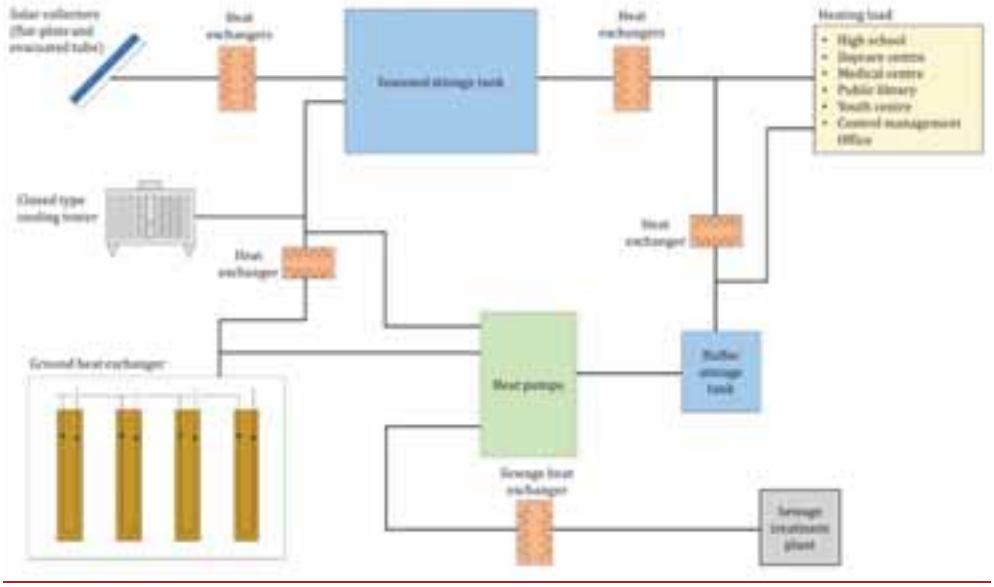

Fig. 1: New and renewable energy hybrid system configuration

2. System overview

The solar thermal systems in the proposed system consisted of 800 m2 of flat-plate type solar collectors, 800 m2 of evacuated type solar collectors, and 4000 m3 of a STES. As shown in Figure 2, the flat-plate type solar collectors and evacuated type solar collectors are connected in series. The solution that passes through the flat-plate type solar collectors is also heated by passing through the evacuated type solar collectors. The aqueous brine solution is used as a heat transfer medium for antifreeze. The collected thermal energy is transferred to the water, and then the water is used as a heat storage medium in STES. Figure 3 shows the installed solar collectors and STES in Jincheon.

The STES is a rectangular-shaped water tank. The STES consisted of concrete walls and a ceiling which are covered with a 700 mm thick insulation on the outside. The inside of the tank has a height of 10.3 m, a width of 16.7 m, and a length of 24.7 m. There is another concrete wall some distance away from the insulation surrounding the STES which creates a space that is filled with ambient air. For observing the stratification performance of the STES, nine temperature sensors are placed at the center of STES with 1 m different heights above the floor of the STES.

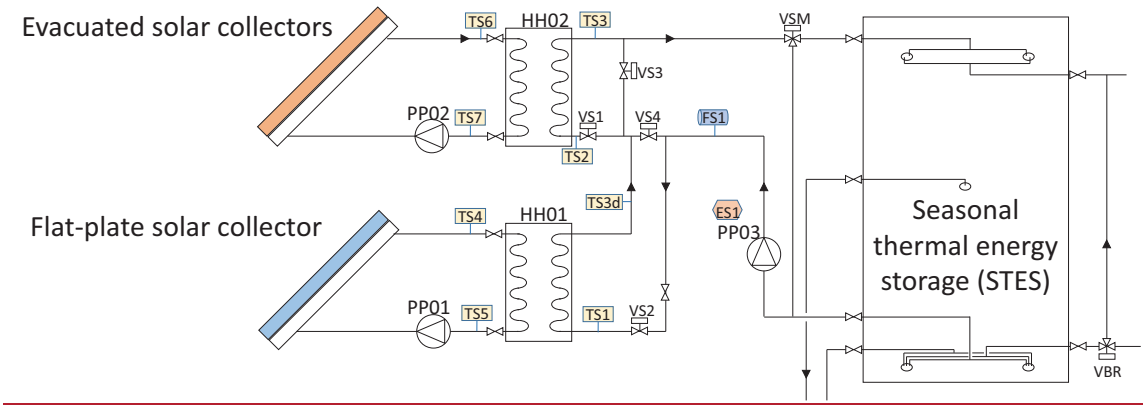

Fig. 2: Configuration of solar thermal collectors and seasonal thermal energy storage (STES)

(a) Solar thermal collectors

(b) STES

Fig. 3: Solar thermal collectors and STES in Jincheon, South Korea

3. Estimation of system performance

3.1 Control logic of solar thermal systems

The hydraulic loop of the proposed system is divided into two parts: the solar thermal system loop and STES loop. The each loop of solar thermal system is closed-circuit with solution, and the water that used to storage heat in STES is firstly passing through the heat exchanger in the circuit of flat-plat type solar collectors, and then the heat exchanger in the circuit of evacuated type solar collectors heats the water. The heated water is distributed into the top of the STES, the water that located in the bottom of STES goes to the solar thermal systems. The each pump of solar thermal system loop is operated when the tilted solar radiation is reached at 400 W/m^2. And then, by comparing the middle or bottom of the water temperature of the STES, the pump of STES is operated. This control logic is primarily for maintaining the temperature stratification of STES. After that, the 3-way valve (VSM) is modulated to maintain the water temperature that higher than the water located in the top of the STES.

3.2 Efficiency of seasonal thermal energy storage (STES)

In order to observe the temperature stratification of STES, the nine temperature sensors were installed in the middle of STES. Each temperature sensor were located from the bottom to top of the tank, and the water inside the tank can be divided into nine sections. For simplifying estimation the efficiency of STES, the volume of the water inside the tank was divided into nine sections according to the nine temperature sensors, and it was assumed that the water temperature within a volume-section is constant and that it only changes with time. Each temperature sensor therefore displays the temperature of one volume-section.

The temperature variation were measured every 30 seconds. Based on the STES, the system can be divided by three circuits, that are the collector circuit, the load circuit, and the auxiliary circuit. For the collector circuit, the added energy is typically positive because heat is delivered from the solar collectors to the tank. When the temperature of STES was increased, the energy is added (i.e., positive) and it also can be mentioned that the more heat was collected from the solar thermal system than the used energy in the load side. On the other hands, when the energy delivered to the load circuit is larger than the energy collected from the solar thermal system, the temperature of STES should be decreased (i.e., negative). The energy added to the tank by the auxiliary circuit can either be positive or negative depending on the application. For the calculations presented in this article however, the auxiliary circuit does not contribute significantly to the results as it has not been activated during the time period from which the measured data was chosen. The energy added to the system through the collector circuit during time step n is calculated as follows.

$$\Delta Q_{\mathrm{C},n} = \dot{V}_{\mathrm{C},n}\left(\rho c_{\mathrm{p}} T_{\mathrm{C,in},n} - \rho c_{\mathrm{p}} T_{\mathrm{C,out},n}\right)\Delta t_n \qquad \text{(eq. 1)}$$

where $\dot{V}_{C,n}$ is the flow rate of the collector circuit in and out of the tank during time step n. $T_{C,\mathrm{in},n}$ and $T_{C,\mathrm{out},n}$ denote inlet and outlet temperature of the water stream, respectively. The length of the time step is denoted with Δt_n. Temperature-dependent values of water density ρ and heat capacity c_{P} have been used for the calculation. The energy added through the load and auxiliary circuits can be calculated in the same way as in Eq. (1):

$$\Delta Q_{\mathrm{L},n} = \dot{V}_{\mathrm{L},n}\left(\rho c_{\mathrm{p}} T_{\mathrm{L,in},n} - \rho c_{\mathrm{p}} T_{\mathrm{L,out},n}\right)\Delta t_n \qquad \text{(eq. 2)}$$

$$\Delta Q_{\mathrm{aux},n} = \dot{V}_{\mathrm{aux},n}\left(\rho c_{\mathrm{p}} T_{\mathrm{aux,in},n} - \rho c_{\mathrm{p}} T_{\mathrm{aux,out},n}\right)\Delta t_n \qquad \text{(eq. 3)}$$

The total energy added by the three circuits is the energy increase of the storage tank under ideal conditions, meaning when there is no heat loss to the environment. This energy increase is calculated as follows for one time step.

$$\Delta Q_{\mathrm{ideal},n} = \Delta Q_{\mathrm{C},n} + \Delta Q_{\mathrm{L},n} + \Delta Q_{\mathrm{aux},n} \qquad \text{(eq. 4)}$$

The change of internal energy in the tank is calculated based on the change in water temperature. For each of the nine sections the change in internal energy is calculated separately before it is added up to yield the change in internal energy for the whole storage tank. The change in internal energy is calculated directly from measurements from the first and last timestamp of the examined time period, which is typically one day. The change in internal energy for volume-section i over this time period is calculated with Eq. (5).

$$\Delta Q_{\mathrm{int},i} = V_i \rho c_{\mathrm{p}} (T_{\mathrm{S},N,i} - T_{\mathrm{S},n1,i}) \qquad \text{(eq. 5)}$$

The storage efficiency during charging is calculated by comparing the change of internal energy with the total added energy over the whole charging period:

$$\eta_{\mathrm{s,chg}} = \frac{\Delta Q_{\mathrm{int},i}}{\Delta Q_{\mathrm{ideal},n}} \qquad \text{(eq. 6)}$$

4. Results

4.1 Efficiency of solar thermal collectors

The produced thermal energy difference from the solar collectors and stored thermal energy into the STES was caused by the operation time difference of the pumps in solar thermal system loop and that in STES loop. Therefore, the useful output thermal energy from the solar collectors was calculated using the water temperature difference between inlet of HH01 (TS1) and outlet of HH02 (TS3).

The trial operation test was conducted during the commissioning period. The tests were done in January 1st to 21th in 2017. As shown in Figure 4(a), during the test period, the average ambient air temperature, relative humidity, and tilted surface irradiation were ranged from -5.4 to 8.6°C, 42.1 to 75.8%, and 1.9 to 6.2 kWh/m^2, respectively. Figure 4(b) shows the produced useful thermal energy from the solar collectors in each day. One can see that the 72.5 to 2365.5 kWh of useful thermal energy could be obtained in each day. It also found that the efficiency of solar thermal collectors based on the useful thermal energy was from 2.4 to 25.4% in each day.

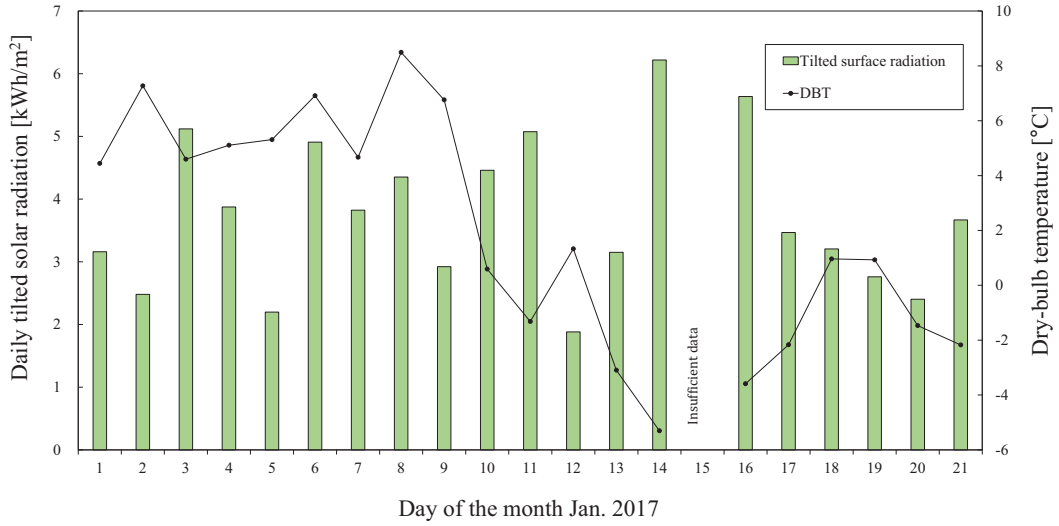

(a) Ambient conditions of test site

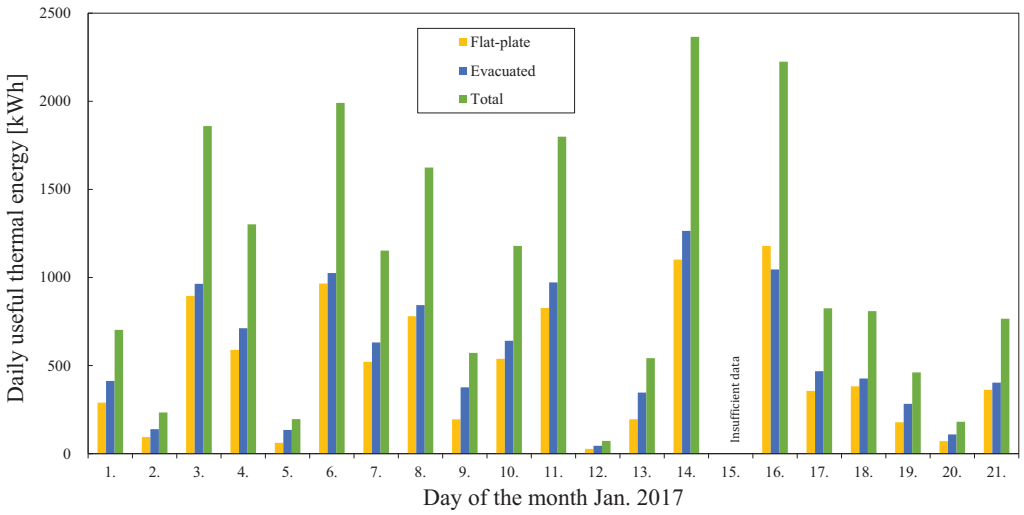

(b) Daily obtained heat energy

Fig. 4: Test results of solar collectors

4.2 Efficiency of seasonal thermal energy storage (STES)

Based on the produced thermal energy from the solar collectors and the internal energy variations of the STES, the efficiency of the STES was estimated. For estimating the internal energy variation, the installed nine temperature sensors were used, and the STES was divided into nine sections attributed to the nine temperature sensors. It was assumed that the water temperature within a volume-section is constant. The efficiency of STES was calculated by the change of internal energy variation in the STES over the useful thermal energy produced by the solar thermal systems. Figure 5(a) shows the comparison of the useful thermal energy and internal energy change in each day. One can see that the 90% of thermal energy storage efficiency was shown during the whole test period. As shown in Figure 5(b), the stratification of STES was well maintained during the test period.

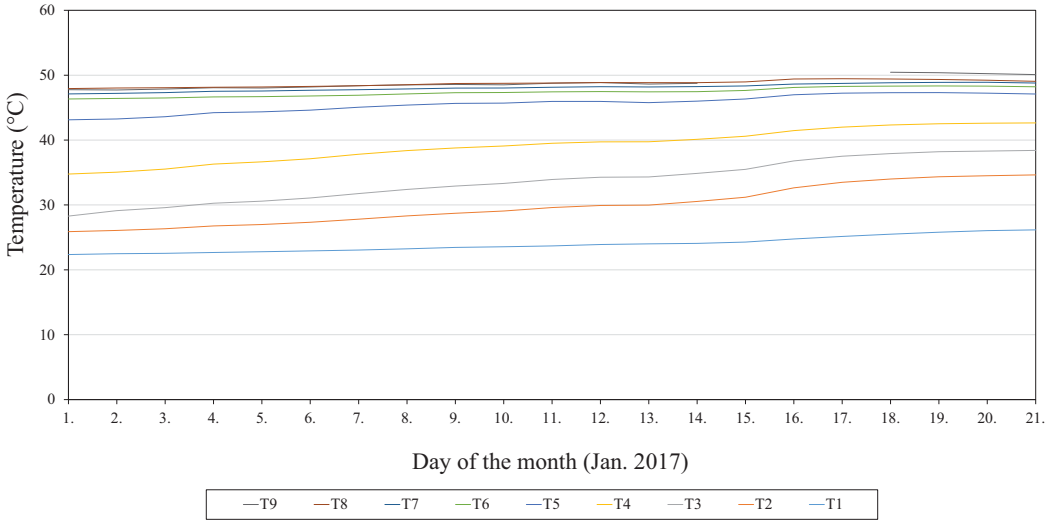

(a) Daily heat gain compared to daily change in internal energy of the STES

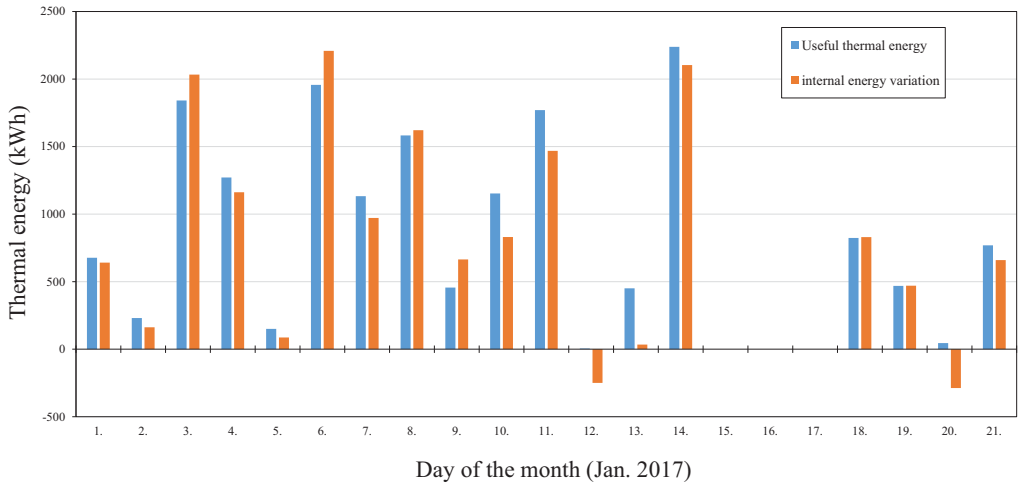

(b) STES water temperatures and load circuit volume flow rate
Fig. 5: Test results of the STES

5. Conclusion

This research investigated the thermal performance of the proposed system, which was tried for the first time to use the STES in South Korea. For observing the thermal performance of the proposed system, the efficiency of solar thermal collectors and STES was estimated based on the experimental data during the commissioning period. It was found that the efficiency of solar thermal collectors based on the useful thermal energy was from 2.4 to 25.4% in each day. One can also see that 90% of thermal energy storage efficiency was shown during the whole test period.

6. Acknowledgement

This research was sponsored by MSIP (Ministry of Science, ICT and Future Planning) Eco-Friendly Energy Town Program (Grant No. NRF- 2015M3D2A1032742).

7. References

Bauer, D., Marx, R., Nußbicker-Lux, J., Ochs, F., Heidemann, W., Müller-Steinhagen, H., 2010. German central solar heating plants with seasonal heat storage. Solar Energy. 84, 612-623.

Schmidt, T., Mangold, D. and Müller-Steinhagen, H., 2004. Central solar heating plants with seasonal storage in Germany. Solar energy, 76(1), 165-174.

Novo, A.V., Bayon, J.R., Castro-Fresno, D., Rodriguez-Hernandez, J., 2010. Review of seasonal heat storage in large basins: Water tanks and gravel–water pits. Applied Energy, 87(2), 390-397.

Xu, J., Wang, R.Z. and Li Y., 2014. A review of available technologies for seasonal thermal energy storage. Solar Energy, 103, 610-638.

Experimental Characterization of a Solar Combisystem with Seasonal Storage for a Single Detached House

Curtis Meister[1] and Ian Beausoleil Morrison[1]

[1] Carleton University, Ottawa (Canada)

Abstract

A solar combisystem with seasonal thermal energy storage has been designed and installed at the Urbandale Centre for Home Energy Research in Ottawa, Ontario, Canada. The system features a 28 m^2 evacuated tube solar array, 1350 litres of diurnal heat storage tanks, and a 37 m^3 buried water tank for seasonal heat storage. The single-detached research house is warmed through radiant floors supplied by either the diurnal or seasonal storage tanks, and domestic hot water is supplied with the diurnal tanks. This research aims to determine the performance of such a system over a full-scale one-year experiment, with the goal of demonstrating a high solar fraction. Preliminary results show that heat losses from the seasonal store exceed those expected from design values. Future experiments are identified.

Keywords: Solar thermal, solar combisystems, seasonal storage, solar domestic hot water

1. Introduction

The majority of energy consumed in cold-climate homes is used for space heating and domestic hot water (DHW). Our reliance on fossil fuels in the residential sector could be drastically reduced by replacing conventional space and hot water heating systems with solar combisystems. Solar combisystems provide space heating and hot water through solar-thermally-charged hot water storage tanks. Combisystems equipped with diurnal thermal energy storage (DTES) can be expected to achieve solar fractions (the fraction of energy demands met with solar energy alone) of 50-60% (Dincer and Rosen (2011), Edwards (2014)). For combisystems to achieve solar fractions approaching 100%, they will almost certainly require long term energy storage.

The focus of this research is an experimental facility equipped with a solar combisystem and seasonal storage in the form of a 37 m^3 buried water tank. In this paper, we describe the full-scale experiment that has been developed for this system and report on findings from preliminary heat loss tests. A high-level overview of the facility is given, followed by a detailed description of the system's instrumentation and control system. Finally, preliminary results of heat losses from the STES tank are presented and discussed.

a) b)

Fig. 1: a) The Urbandale Centre for Home Energy Research and b) installation of the seasonal storage tank

doi:10.18086/swc.2017.29.08 Available at http://proceedings.ises.org

2. Past Studies on Seasonal Storage

Thermal energy storage (TES) was studied extensively under Tasks 7 and 32 of the IEA (International Energy Agency) SHC (Solar Heating and Cooling) program. The programs explored many methods of thermal energy storage, including sensible, chemical and latent heat storage. Pinel et al. (2011) presented a comprehensive review of these methods for seasonal thermal energy storage, and concluded that for residential applications, sensible heat storage was currently the simplest, most cost effective and best-understood method. Indeed, most installed STES systems are simple sensible heat stores, using water or earth as a storage medium. This section briefly summarizes the relevant work in this area, particularly studies relating to STES for single homes.

2.1 Simulation Studies on Seasonal Storage

Simulation studies on STES have typically aimed to determine the optimum size of components in a solar combisystem with STES (array size, STES size). Sillman (1981) conducted simulation studies on buildings with long term heat storage, and determined that solar fractions increased with storage volume up until the "point of unconstrained operation", when all excess solar gained could be stored. Braun et. al (1981)'s simulations agreed that increasing STES volume for a constant array size led to higher solar fractions until all collected heat could be stored. Wills (2013) looked at larger STES tank volumes (80-130 m^3 for single detached homes) than the latter two studies, and found that larger tank volumes decreased solar fractions due to the lower quality of energy (exergy) that could be stored. Kemery (2017) simulated the as-built combisystem and STES tank presented in this study, and found that a high solar fraction (over 90%) could be achieved.

Losses from seasonal stores have been consistently identified as a source of uncertainty in STES models. This is largely due to the complexity involved in simulating the ground domain. Some tank models (TRNSYS Type 534, Thermal Energy System Specialists (2017)) take a simplified approach, imposing a constant boundary temperature on the tank's exterior wall. Other models, like those employed by Ochs (2009), Marazella(), and Wills (2013) employ 2D or 3D finite differencing to represent the ground temperature distribution. Pinel et al. (2011) point to a lack of consideration of a number of factors in ground heat transfer: humidity diffusion in soil, thermal coupling between the storage and house, and uncertainty in ground surface conditions. There are also uncertainties in the selection of material properties for models, particularly the thermal conductivity of insulating materials. This is treated in the next section.

2.2 Experimental Studies

Experimental facilities equipped with seasonal storage have mostly been limited to district scale systems, such as the heating system in Hannover, Germany (Ochs(2009), Raab(2005)) and Drake Landing (Sibitt et al. (2012)). However, there have been a few attempts to demonstrate STES on the single detached house scale. Most of these systems were designed for very low energy houses, and feature solar thermal arrays ranging from 10-42 m^2 and seasonal storage tanks ranging from 12-40 m^3. The interested reader is directed to the designs of Besant et al. (1979) and Esbensen and Korsgaard (1977), though neither present experimental results.

Colclough et al. (2011) present a STES system installed on a low energy home in Ireland. The system featured a 10.8 m^2 evacuated tube solar array, 300 litre DTES tank and a 23 m^3 STES tank. The system achieved solar fractions of 56% and 93% for space heating and domestic hot water, respectively. Heat losses from the STES tank were found to be more significant than predicted. The experimental heat loss coefficient found was approximately 10 W/K, despite calculations from nominal insulation properties giving 4.2 W/K (Clarke (2014)).

Other STES installations have shown higher heat losses than expected as well. Marazella's XST model was validated by Raab (2005) for the STES tank in Hannover. A parameter investigation based on measured data suggested that the thermal conductivity of the granular glass STES insulation must be approximately 0.10 W/mK. This was approximately 40% higher than the value found for dry granular glass (0.072 W/mK) when measured in a lab setting. The authors attribute this to moisture migration in the insulation and thermal bridging in the tank support materials. It is clear from the literature that care should be taken when using nominal insulation properties in designing and simulating STES tanks.

3. Experimental Setup

This section provides an overview of the design of the research home and solar thermal system, as well as its instrumentation and control system. The section concludes with a brief discussion of cooldown tests commenced to determine heat loss rates in the STES tank.

3.1 The Urbandale Centre for Home Energy Research

The Urbandale Centre for Home Energy Research (CHEeR) is an experimental research house built to study various innovative home energy systems. The house, pictured in Figure 1, contains a basement and two above-ground storeys with 149 square-meters of heated floor area. The house was intended to exceed current Canadian energy standards (i.e. R-2000) but to remain realistic under current building practices. The east, west and south walls have a nominal U-value of 0.21 W/m^{2}K, while the north walls are more heavily insulated at 0.12 W/m^{2}K. The attic is freely ventilated, and contains blown-in insulation with a U-value of 0.11 W/m^{2}K. The basement slab is insulated with rigid foam board with a U-value of 0.36 W/m^{2}K, and the basement walls have a U-value of 0.21 W/m^{2}K. The building's airtightness at 50 Pa depressurization was measured to be 1.3 ac/h. Almost all of the windows are placed on the south side of house to maximize solar gains. The total south-facing window area of the house is 20 m^2. All windows are triple-glazed with an argon fill and two low-emissivity coatings.

CHEeR has several redundant heating and cooling systems. An air-source heat pump connected to rock bed heat storage can heat or cool the house. An extensive hydronic network connects an evacuated tube solar array with one of two buried seasonal stores; a large insulated sandbox and a large buried water tank. The collectors can also charge a number of smaller hot water tanks for diurnal storage and to provide DHW. The hydronic network can supply either a radiant floor or a hydronic air handler.

The house is equipped with a large suite of instrumentation. Indoor air temperatures are measured at several locations on each storey using shielded, aspirated thermocouples. On the roof sits a weather station that can measure outdoor air temperature, humidity, and wind speed. A number of pyranometers measure direct and diffuse radiation on the horizontal, vertical and collector tilt (60°) planes.

3.2 Solar Combisystem with Seasonal Storage

The solar thermal system used in this research is shown schematically in Figure 2. The solar array consists of ten Apricus AP-30 evacuated tube collectors in two parallel lines of five. The collectors face south, and are tilted at 60° to bias solar collection towards winter. An antifreeze solution consisting of 60% Intercool Biogreen and 40% water is run through the collectors to prevent freezing in winter. Actuated valves allow the solar array to charge either the diurnal storage tanks or the seasonal storage tank. The antifreeze solution indirectly charges these loads through heat exchangers.

The diurnal store consists of three insulated 450-litre tanks. The primary diurnal tank, Tank A in Figure 2, is charged through an immersed-coil heat exchanger. A circulator pump can move hot water from the primary tank (A) to the secondary and tertiary tanks (B and C). Tank A is used to supply DHW to a load mimicry system, while Tanks B and C can provide hot water to the radiant floor. The seasonal storage tank is used only for space heating, and can heat the radiant floor through a heat exchanger.

Because the research home does not have mains water connection, domestic hot water draws must be mimicked experimentally. To do this, the solar collector loop is used to cool two 450 litre "DHW mimicry" tanks overnight. Flow in the collector loop is directed through heat dissipators mounted on the northern roof of the research house, which cools the DHW tanks through a heat exchanger. To mimic draws, water is exchanged between DTES Tank A and the DHW mimicry cool tanks. Hot water draws follow a typical Canadian hot water draw schedule developed by Edwards (2015)

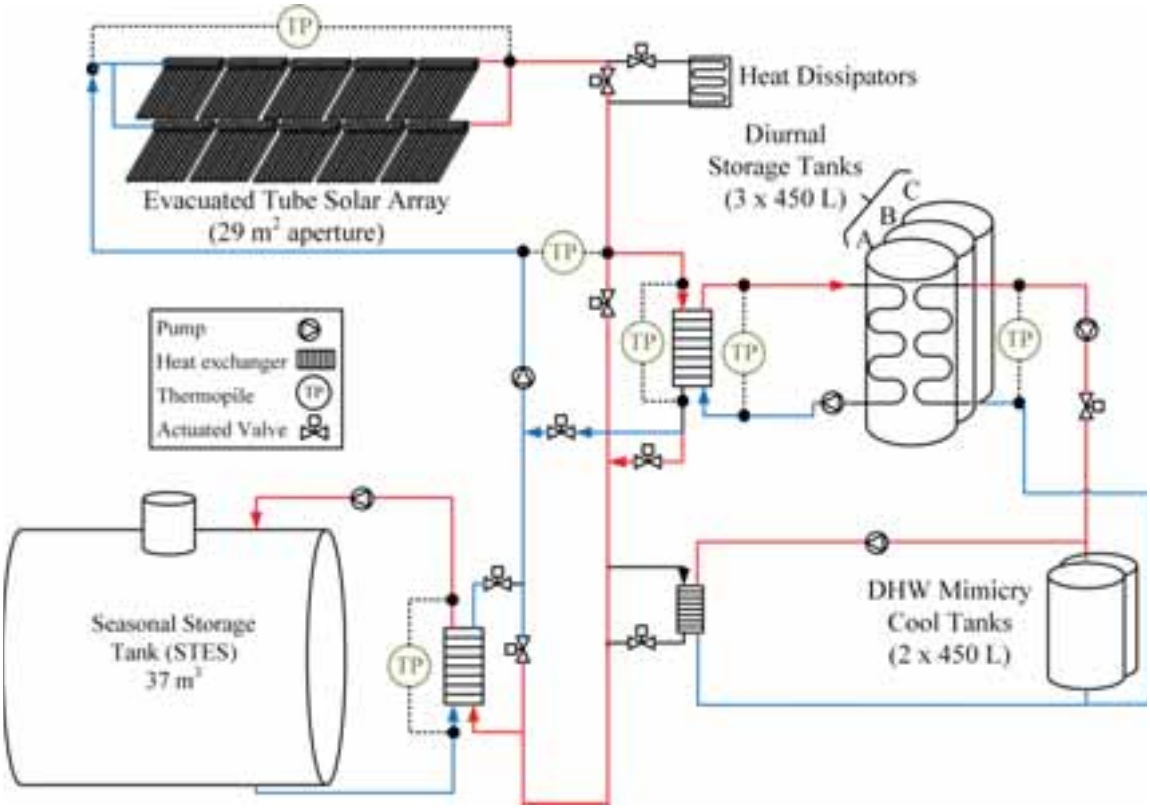

Fig. 2: Simplified schematic of CHEeR's solar thermal system with seasonal storage

The seasonal storage tank (Figure 1.b) couples to the collector loop (Fig. 2) and radiant flooring loop (not pictured) through heat exchangers. The tank is approximately 37 m^3 in volume, and features two sets of inlets and outlets for charging and discharging (Figure 3). The tank inlets and outlets were designed to promote stratification in the tank; the pipes are 10 cm in diameter to produce low flow velocities, and the inlet tubes are perforated to encourage water to reach its appropriate temperature level. The perforations are 9.5 mm in diameter and spaced 5 cm apart vertically. The tank was insulated with 30.5 cm of spray-on polyurethane insulation, which gives it a nominal U-value of 0.075 W/m^2K.

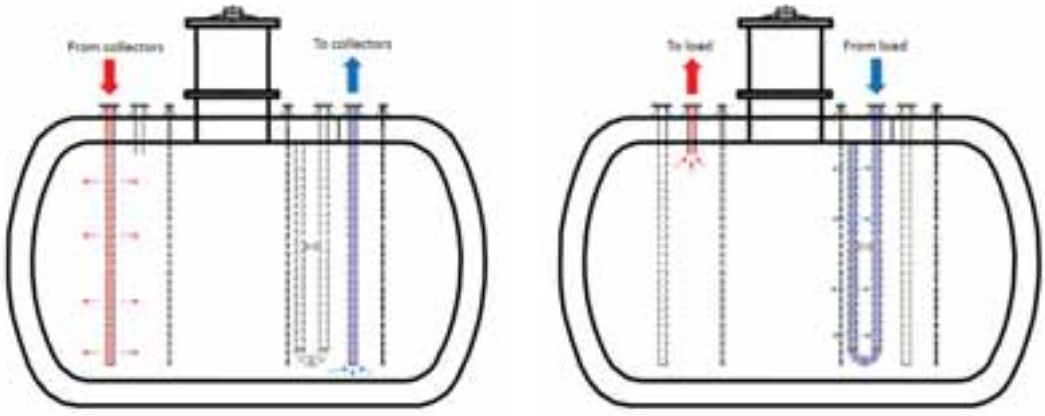

a) b)

Fig. 3: Seasonal storage tank, with a) solar charging inlet and outlet, and b) space heating inlet and outlet

The tank's access hatch is above ground. To insulate the hatch, a small structure was created. Figure 4 shows a cross-sectional view of the hatch insulating structure. Five sheets of 7.6 cm rigid foamboard (nominally RSI 2.6 each) surround the hatch on each side. The cavity formed between the foamboard and hatch is stuffed with batt insulation (not shown). The foamboard pieces are affixed to one another with adhesive spray foam. The foamboard structure is surrounded by an air barrier, which is buried under a layer of soil. The design U-value of this structure is intended to match that of the tank's insulation (0.075 W/m^{2}K).

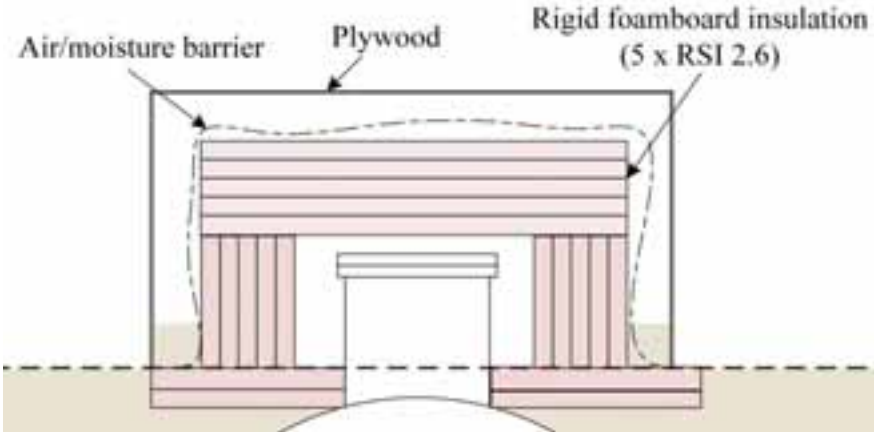

Fig. 4: Insulation of the STES access hatch

2.3 Instrumentation

We are primarily interested in measuring heat transfer rates within the solar thermal system. Heat transfer rates can be determined using the 1st law of thermodynamics and by treating the fluid (water or antifreeze) as an incompressible with constant density and specific heat:

$$\dot{Q} = (\rho c_p)\big|_T \dot{V} \Delta T \qquad \text{(eq.1)}$$

Where $\dot{V}$ is volumetric flow rate and ΔT the temperature rise in the fluid. Volumetric flow rates are measured by positive displacement oval gear flowmeters, which are manufacturer-calibrated to a bias error of ±1% of reading.

Temperature differences are measured with six-junction thermopiles. An example of a typical heat transfer station is shown in Figure 5.

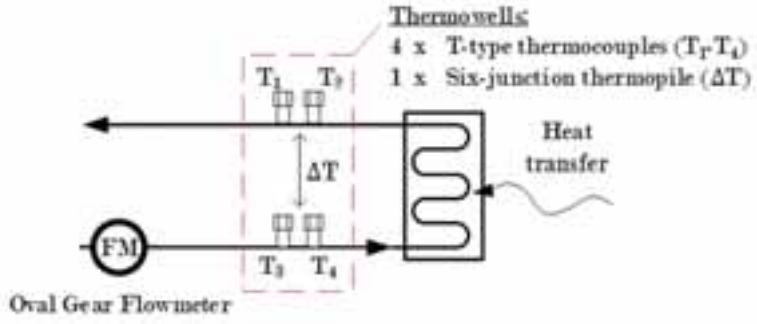

Fig. 5: Example of instrumentation on a heat transfer station

The thermopiles were calibrated using highly accurate platinum RTDs, and the bias error was calculated according to the methods detailed by Moffatt (1988) considering all sources of error. This included the voltage reading error of the data acquisition system, curve-fitting errors, and the bias error of the platinum RTDs themselves. Assuming negligible uncertainty is associated with material properties (density, specific heat), the total bias error for heat flows is less than 2% for temperature differences of 3°C and above. Some (but not all) thermopiles are shown on Figure 2. Eleven heat flows are monitored in total.

Stratification and heat loss performance of the seasonal storage tank can be inferred from three vertical racks of

25 T-Type thermocouples (Figure 3) that are immersed along the tank's vertical mid-plane. As with the thermopiles, a calibration was performed on the thermocouples. The bias error associated with a single thermocouple measurement was found to be 0.45°C when all sources of bias were considered.

2.4 Controls

The control scheme for the solar thermal system was designed to be similar to Wills (2013) and Kemery (2017). While it is almost certainly non-ideal, it was selected for its simplicity and ease of implementation in preliminary experimentation. Future work will examine optimum control configurations, for instance, the use of variable speed pumps to increase collector temperatures during low irradiance. The control algorithm is written in NI LabVIEW (National Instruments, (2017)) which runs in real-time on three NI data acquisition (DAQ) systems, which in turn actuate the pumps and valves in the system.

The control scheme for solar charging is given in Figure 6. When a given level of solar irradiation on the collector plane or sufficient collector temperature is sensed, the solar collector pump is triggered. If hot enough to charge the loads in the system (i.e. the collector outlet temperature T_{coll} exceeds the load temperature plus the "on" setting ΔT_{ON}), the algorithm selects a load to charge based on a pre-set priority list. The highest priority load is DTES Tank A. The tank is maintained at a set point T_{DHW} so that it can always supply domestic hot water. When charged in heating season, DTES B and C are prioritized over the seasonal store. If the system is charging the DTES, the temperature of the antifreeze after the DTES heat exchanger is sensed to see if it exceeds the mean seasonal store temperature. If so, the seasonal store is charged in series with the DTES. If the collector temperature falls below a certain level (determined by the load temperature plus setting ΔT_{OFF}), the solar pump is shut off.

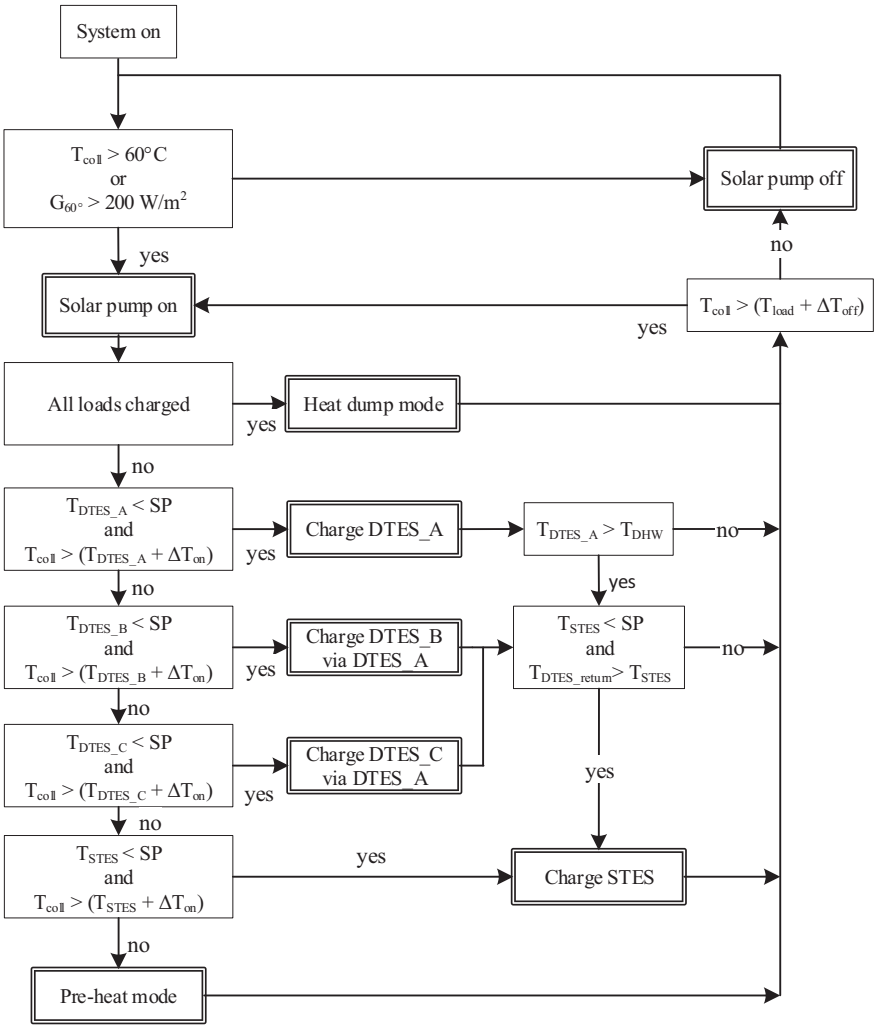

Fig. 6: Control strategy for charging the solar thermal system

A description of the control variables mentioned in Figure 6 are given in Table 1.

Tab. 1: Description of solar control parameters

Variable	Setting
T_{coll}	Temperature determined by an RTD placed on the solar collector
$G_{60°}$	Solar irradiance measured by a pyranometer on the collector plane
SP	Set point
T_{DTES_i}, T_{STES}	Temperature of a diurnal tank *i*, temperature of the seasonal storage tank
T_{load}	Temperature corresponding to the current load being charged

3.4 Cooldown Tests

The ability of the seasonal storage to preserve thermal energy has obvious implications on its yearly performance. Two cooldown tests of the seasonal store, performed in July of 2016 and 2017 respectively, show early indications of the tank's heat loss performance. During the cooldowns, solar charging of the tank was ceased so that all energy transfer could be attributed to heat losses. The temperature distribution in the tank was then monitored over 2-3 weeks. During the July 2016 test, the tank began the test well-mixed at an average temperature of 72.2°C, while in 2017 the tank began approximately 5°C hotter at the top than bottom with an average temperature of 63.6°C. The results of these tests are given in the next section.

4. Results

Cooldown results for both tests are given in Figure 7. Results are given for the average temperature of 5 stratums within the tank, each containing 5 thermocouples (S1 through S5) from each of the three thermocouple racks. No significant temperature differences were found between the three thermocouple racks in the tank.

For the well-mixed test, the average heat loss rate was 530 W. No development of natural stratification due to heat loss is apparent during this time, and similar heat loss rates are seen in all layers of the tank. The stratified cooldown shows accelerated temperature loss at the top and bottom of the tank (S1, S5) relative to the middle layers. Destruction of stratification can be seen as layers S2 through S5 converge to a similar temperature around 300 hours. However, the bottom layer of the tank remained 5°C below the top layer throughout the test. The average late of heat loss for this test was approximately 350 W.

In both test cases, measured heat loss rates exceed expected values. According to Kemery (2016), even if a conservative ground temperature of 10°C is assumed, heat loss rates for a 72°C tank with 0.075 W/m^{2}K insulation should not exceed about 285 W. It is possible that these higher than expected losses are the result of heat loss from the tank's above-ground access hatch. It should be noted that during the 2016 tests, the foamboard sheets used to insulate the hatch did not extend underground as shown in Figure 4. Instead, they simply sat on the ground surface. The air barrier was also not installed until 2017. Hatch losses would not explain higher than expected losses from the bottom layer of the tank. Moisture migration in insulation is a typical cause for greater than expected losses, but this is deemed unlikely, as product specifications show the spray-foam insulation to be unaffected by moisture content. Further, the tank has a double-wall construction that should prevent moisture migration. Thermal bridges within the insulation are another possible explanation. Thermal bridges could be caused by either structural members within the tank or non-uniformities in the insulation coverage.

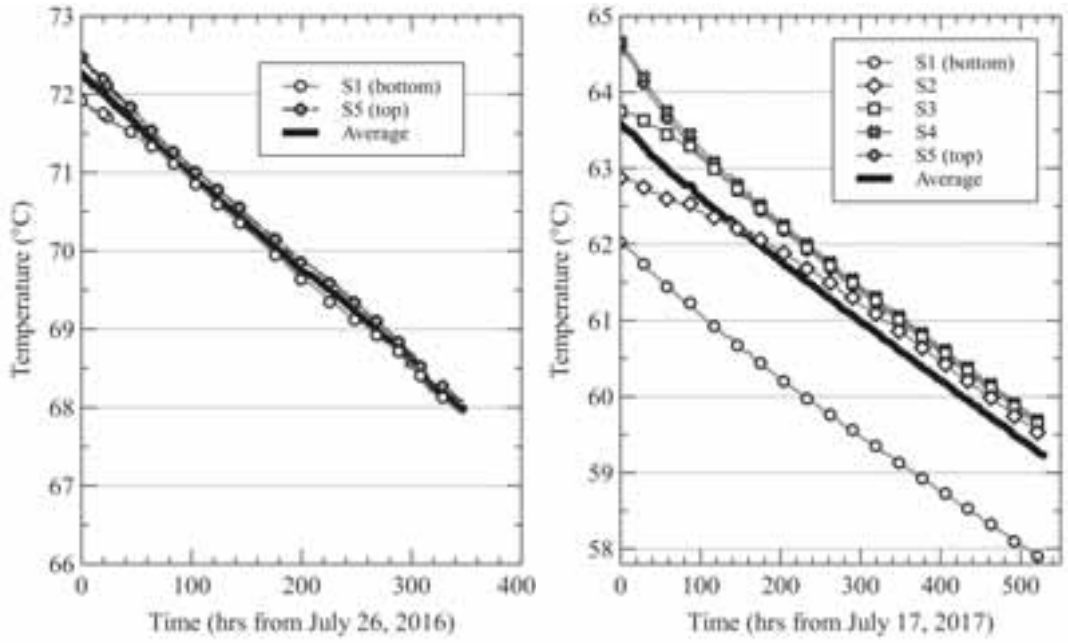

a) b)

Fig. 7: Temperature loss during seasonal storage cooldowns with a) well-mixed and b) 5°C stratified starting conditions

Regardless, as evidenced by the work of Colclough (2011) and Raab (2005) referenced earlier in this paper, excess losses appear to be a common trend with buried STES tanks, and may not indicate poor performance for the combisystem. Kemery (2016) performed a sensitivity study wherein the ground temperature was varied from 5 to 25°C. The ground temperature was used as a constant boundary temperature for the seasonal store. Simulation results showed that the solar thermal system's performance was not particularly sensitive to heat losses. This might be explained by the relatively high ratio of collector area to storage volume at CHEeR; lost heat can be quickly recovered by the large array. However, even with an imposed 5°C boundary temperature, predicted heat losses were less than those found through experiment. Predicted losses ranged from 6.9 to 9.5 GJ yearly. If we consider the experimental heat loss tests to represent typical average losses for the year, approximately 11 to 17 GJ of heat would be lost from the as-built tank yearly. That would represent 16 to 28% of the total solar energy collected by the solar array, based on Kemery's estimation of 60-70 GJ collected yearly. It should be noted that at the time of writing, the seasonal storage tank has only undergone one full annual charge and discharge cycle. It is possible that the surrounding ground is still in a transient state; that is, heat losses from the tank could be reduced as the ground warms up. Kemery (2016) notes that 4 years of simulation were required before the STES system reached a consistent cyclical behavior.

5. Conclusions and Future Work

This paper has presented an overview of the design of a solar combisystem with seasonal thermal energy storage. The system's components, instrumentation and control system were described. Preliminary results from heat loss tests show that the seasonal storage tank loses heat at faster rate than would be expected based on nominal properties of the insulation. Explanations for larger than expected losses are postulated, including losses through the access hatch and thermal bridging.

Future work will quantify the energy performance of the solar combisystem over a full heating and cooling season. A model of the as-built seasonal storage tank will be developed and validated in TRNSYS software (Thermal Energy Storage Specialists (2017)), and coupled to a full building model of the CHEeR house in ESP-r (Energy Systems Research Unit, University of Strathclyde (2017)), following the work of Wills (2013) and Kemery (2016). Parametric studies will re-examine the sizing and control of the solar combisystem, and multi-objective optimization will be performed for system performance and economic consideration.

6. References

Besant, R., Dumont, R., and Schoenau, G., 1979. The Saskatchewan conservation house: Some preliminary performance results. Energy and Buildings, 2(2):163-174

Braun, J., Klein, S. and Mitchell, J., 1981. Seasonal storage of energy in solar heating. Solar Energy, 26(5):403-411.

Clarke, J., Colclough, S., Griffiths, P., and McLeskey Jr., J.T., 2014. A Passive House with Seasonal Solar Energy Store: In Situ Data and Numerical Modeling, International Journal of Ambient Energy, 35(1): 37-50.

Colclough, S., Grihs, P., and Hewitt, N.,2011. A year in the life of a passive house with solar energy store. In Energy Storage Conference, (Belfast, Ireland), IC-SES.

Dincer, I. and Rosen,M., 2011 Thermal Energy Storage: Systems and Applications, second ed. John Wiley & Sons, Hoboken, NJ, USA.

Edwards, S., 2014. Sensitivity Analysis of Two Solar Combisystems Using Newly Developed Hot Water Draw Profiles. M.A.Sc Thesis, Carleton University.

Edwards, S., Beausoleil-Morrison, I., and Laperriere, A., 2015. Representative hot water draw profiles at high temporal resolution for simulating the performance of solar thermal systems. Solar Energy, vol 111, pp.43-52.

Esbensen, T. and Korsgaard, V., 1977. Dimensioning of the solar heating system in the zero energy house in Denmark. Solar Energy, 19(2):195-199.

ESP-r, 2017. Energy Systems Research Unit, University of Strathclyde, Accessible online at http://www.esru.strath.ac.uk/Programs/ESP-r.htm.

Kemery, B., 2017. Analysis and design of a solar-combisystem for high solar fraction Canadian housing with diurnal and seasonal water-based thermal stores, M.A.Sc. thesis, Carleton University.

LabVIEW, 2015. Version 15.0. National Instruments.

Marazella, L., 1992. Multi–flow stratified thermal storage model with full–mixed layers PdM-XST. Technical report., University of Stuttgart and Dipartimento di Energetica Politecnico di Milano.

Moffat, R., 1988. Describing the uncertainties in experimental results. Experimental Thermal and Fluid Science, 1(1):3-17.

Ochs, F., 2009. Modeling large-scale thermal energy stores. Ph.D. thesis, University of Stuttgart.

Pinel, P., Cruickshank, C., Beausoleil-Morrison, I. and Wills,A., 2011. A review of available methods for seasonal storage of thermal energy in residential applications. Renewable and Sustainable Energy Reviews, 15(7): pp. 3341-3359.

Raab, S., Mangold, D. and M¨uller-Steinhagen, H., 2005. Validation of a computer model for solar assisted district heating systems with seasonal hot water heat store. Solar Energy 79(5): 531–543.

Sibbitt, B., McClenahan, D., Djebbar, R,. Thornton, J., Wong, B., Carriere, J. And Kokko, J., 2012. The performance of a high solar fraction seasonal storage district heating system - five years of operation. Energy Procedia, 30:856-865.

Sillman, S., 1981. Performance and economics of annual storage solar heating systems. Solar Energy, 27(6):513-528.

TRNSYS, 2017. A Transient System Simulation Program, Version 17, Thermal Energy System Specialists.

Wills, A., 2013. Design and co-simulation of a seasonal solar thermal system for a Canadian single-family detached house. M.A.Sc. thesis, Carleton University.

Design and optimization of a De-centralized community sized solar heating system for Nordic Region

Hassam ur Rehman[1,*], Janne Hirvonen[1] and Kai Siren[1]

[1] Aalto University, School of Engineering, Department of Mechanical Engineering, HVAC group, PO Box PL 14400/Vi 351, 00760 Aalto, Finland

Abstract

There is a need to accelerate the application of advanced clean energy technologies to resolve the challenges of climate change. Solar heating is a feasible solution among clean energy technologies. These technologies are not yet highly used in high latitudes due to various challenges. This paper focuses on the community sized solar district heating system configuration for cold climates. The proposed configuration consists of a partially de-centralized heating system. Each individual house heat pump was connected between large centralized solar-charged low temperature tank and smaller de-centralized individual high temperature tank in each house. Additionally, the large centralized tank was directly charged by solar-charged borehole storage during winters. Dynamic simulation approach was used through TRNSYS software coupled with MOBO (multi-objective building optimizer) for NSGA-II optimization algorithm. The purchased electricity and investments were two objectives minimized. The impact of the energy system on the renewable energy fraction, purchased electricity and investments as a function of the building heating demand, collectors and photovoltaic areas, short-term tanks storages and boreholes volumes were evaluated. Results showed that purchased electricity varied 47 kWh/m^2/yr—25 kWh/m^2/yr and renewable energy fraction 75%—91%.

Keywords: De-centralized solar district heating, multi-objective optimization, cold climate, seasonal storage.

1. Introduction

Buildings are one of the largest consumers of the energy in European Union (EU). They consume around 40% of the total energy (Nielsen, 2012). Buildings in the urban and community setup play a significant role in the energy demand of the community. Furthermore, in Finland huge amount of energy is being used by space heating and domestic hot water for the residential buildings. This causes large emissions of CO_2 (Official Statistics of Finland (OSF), 2016). Therefore, with increase in the emissions, and interest on the environmental impact of residential areas, there is an increased interest in using of renewable energy for the buildings. Solar communities can provide a good alternative to the conventional communities that are being provided with fossil based heat energy. These community concepts have not been built at high latitudes in cold regions such as Finland. The cold temperature, demand and supply mismatch and expensive storage system does limit the operations of such systems in building heating requirements. On the contrary, solar thermal can be used effectively if designed properly. It is important to mention that designs and parameters cannot be used directly from other locations as each location has different conditions and climate (Flynn & K.Siren, 2015).

Solar district heating is a very promising alternative to fossil fuel district heating. Solar thermal (ST) systems are key technologies for achieving emission reduction goals. Their use is spreading in European countries. In Europe, there are around 141 heating plants which have more than 500 m^2 solar collector area (Dalenbäck & Werner, 2012). Since 1979 onwards several countries have participated in operating central solar heating plants with seasonal storage under IEA Task 7 to boost the progress of large scale heating technologies (International Energy Agency Solar Heating and Cooling Programme, IEA-SHC, Task 7, 2016). Since 1980s onwards, in Germany many plants have been built that provide district heating via solar thermal energy (Schmidt, et al., 2004). In Denmark, due to its competitive price in comparison to biomass and gas there is a boom in the solar district heating market (Nielsen, 2012). Similarly, many solar district networks are built in different parts of the Europe and North America. For instance, there are large scale pilot plants located in Norway, Denmark, Sweden, the Netherlands, Canada and the USA that uses solar energy with seasonal storage (Nielsen, 2012),

doi:10.18086/swc.2017.29.09 Available at http://proceedings.ises.org

(Solar District Heating, 2016), (Mangold, 2007), (M. Lundh, 2008), (Bauer, et al., 2010). It is found that community-scale solar energy systems are economical even without support payments. Community-scale allowed the use of seasonal thermal storage, which is a key technology for achieving a high degree of utilization of solar energy in Finland. However, no such community has been built in Finland yet. Instead of zero energy buildings, the focus should shift to developing zero energy communities, which can benefit from the best features of both distributed and centralized energy systems (Hirvonen, 2017). The reason and the challenges to build such community in Nordic region are: (a) the energy cost is still not yet competitive enough and (b) solar energy is not typically available when needed.

In community sized system, the energy storage plays an important role to improve the performance of the system. Moreover in Nordic conditions where the mismatch between the irradiation and demand is significant, seasonal storage is vital. Using thermal storage for viable solar energy utilization through solar thermal panels to meet building heat loads becomes an important discussion. Excess energy generated during long summer hours can be stored for seasonal periods (Kalaiselvam & Parameshwaran, 2014). Seasonal thermal storage stores thermal energy when solar radiation is abundant. The cost and size of the seasonal storage are important factors that influence the decision while choosing the type of seasonal storage to be used in such solar community concepts. Ground thermal energy storage has cost advantage due to its size and capacities compared to short term tanks storage (Fisch, et al., 1998), (Rad & Fung, 2016). However, ground storages have higher losses issues due to ground conductivity. Therefore, the properties of the ground, time of storage, temperature, location and geometry are critical (Nordell, 2000). Sensible thermal storage collects energy by increasing the temperature of a medium with finite heat capacitance (typically water) (V.Novo, et al., 2010). It is stored in a variety of medium for the use during winters. The most prominent modes of storage found in the literature are: (1) Hot Water Energy Storage (HWTES), (2) Gravel-Water Thermal Energy Storage (GWTES), (3) Aquifer Thermal Energy Storage (ATES), and (4) Borehole Thermal Energy Storage (BTES) (Schmidt, et al., 2004). Each method provides certain advantages such as location, capacity and cost. Among these four methods, BTES is the most flexible storage technique (Rehman, et al., 2017) and therefore is the primary focus of this analysis.

It is found that in most of the existing solar communities the focus is on space heating demand (SPH). This approach minimizes the heat losses in the seasonal storage (Chapuis & Bernier, 2009). This low grade temperature present in the seasonal storage can be increased using a heat pump. Heat pump (HP) can be used with the ground with any combination, i.e. regardless the ground is charged or not via solar energy. It is found that charging of the ground can improve the heat pump performance as the evaporator temperature increases. Hence, it improves the coefficient of performance (COP) of the heat pump (Rehman, et al., 2017). The heat pump can be integrated with the solar thermal system in multiple ways and with varying control strategies. The way and the strategy used to integrate the heat pump can also vary the overall solar thermal system performance and behaviour. In this study, a particular methodology is described to integrate HP with the solar thermal district network.

The novelty in the present study is the proposed partially de-centralized solar district heating system and the multi-objective optimization of such system. The proposed system has a centralized large tank that is at lower temperature and provides most of the space heating. While the de-centralized part consists of a small tank in each individual house that operates at higher temperature, it is being charged by the centralized tank and heat pump, and part of the space heating along with domestic hot water is provided through this tank. In this configuration the placement of the heat pump, hot short term storage tank and the overall control strategy is altered compared to the previous studies (Rehman, et al., 2017), (Sibbitt, et al., 2012). In the previous study carried out, the heat pump is centralized with the two large centralized short term storage tanks charged via solar energy and seasonal storage in parallel (Rehman, et al., 2017). These large tanks are divided into warm and hot tanks in order to meet the space heating (SPH) and domestic hot water demand (DHW) of the community respectively (Rehman, et al., 2017). Whereas in the present study, instead of a large centralized hot tank, a small tank is places in each of the 100 houses. Similarly, instead of a centralized large heat pump, 100 small sized heat pumps are distributed among the 100 houses to charge the small hot tank. Furthermore, only the large centralized warm tank is charged by the solar energy, and the small hot tank is charged via the heat pump directly instead of the solar energy. Likewise, the difference between the present study and the Drake Landing Solar Community, Canada is that for domestic hot water a dedicated individual collectors and natural gas heaters is installed to provide hot water (Sibbitt, et al., 2012). On the contrary in the present study, the individual

house hot tank is charged via heat pump using energy from the centralized solar heating network. The aim of this research is to design, optimize and assess the performance of such de-centralized solar thermal district heating system in Nordic location. The challenges mentioned above are addressed. The impact of the mentioned configuration of solar and ground loop on the annual energy consumption is evaluated. In particular the influence of varying solar thermal (ST) size, short-term storage tank volume, borehole (BTES) size, photovoltaic (PV) size, and building heating demand on the purchased electricity, investments and renewable energy fraction are evaluated. The energy system is designed by using dynamic simulation software i.e. TRNSYS (Thermal Energy System Specialists, LLC, 2012) and then optimized using multi-objective optimization algorithm (NSGA-II) where the purchased electricity and investments are minimized.

2. Methodology

The paper focuses on the modelling and the multi-objective optimization of the de-centralized community sized solar district heating system. Therefore the energy system is first design on dynamic simulation software i.e. TRNSYS (Thermal Energy System Specialists, LLC, 2012) and then the model is optimized using multi-objective optimization algorithm (NSGA-II) (Hirvonen, 2017) where purchased electricity and investments are minimized together. Renewable energy fraction (Hirvonen, 2017), (Rehman, et al., 2017), final purchased electricity, and investment costs (IC) are calculated to evaluate the system.

2.1. Energy system

The energy system consists of ST collectors, short-term tanks, boreholes, PV modules, heat pumps and buildings. The energy system is designed based on Drake Landing Solar Community (DLSC), Canada (Sibbitt, et al., 2012) as it has shown good performance in cold climatic conditions.

The solar energy system is used to provide DHW and SPH through the network and secondarily for charging the ground. The control is designed in a hierarchical pattern. Solar thermal pump draws the cold water from the large centralized low temperature tank bottom and into the heat exchanger to collect heat from solar collector loop. Meanwhile, heated water from collector transferred heat to the centralized tank directly via heat exchanger after attaining the desired temperature based on the set point. For this study, temperature tracking control mode is selected where the collectors typically aims for an outlet temperature that is one degree higher than the warm tank top temperature connection for charging (ur Rehman, et al., 2016).

If the large centralize tank temperature is lower than 40 ^{o}C, it is heated to 45 ^{o}C. Excess heat from solar collectors is transferred to BTES to avoid overheating of this large tank. Heat from storage tank is transferred when tank temperature reached 50 ^{o}C and stopped once the temperature dropped to 45 ^{o}C. If energy from solar collectors is not available, heat can be transferred back from BTES into the centralized tank directly. If the centralized tank temperature is less than 35 ^{o}C and the BTES average temperature is higher than the tank top temperature, the energy is transferred via BTES and tank is charged till 40 ^{o}C. The cold fluid entered from the cool outer edge of the BTES and exits from the hot centre. Low temperature is maintained in the collectors and centralized tank circuit to improve the collectors' efficiency. The energy from this centralized large tank is distributed in the low temperature space heating district heating network of the community. Moreover, the space heating return network is used by individual heat pump (NIBE, 2017) present in each of the 100 houses in the community to heat each of the small sized hot tanks present in each of the houses. If the hot tank temperature is lower than 60 ^{o}C, it is heated to 65 ^{o}C by the heat pump.

The space heating is provided by passing the space heating (SPH) water through the warm tank and then through the bottom node of the small hot tank. This heated water is then provided to the houses at temperature between 30 ^{o}C to 40 ^{o}C depending upon the outdoor temperature. Domestic hot water (DHW) is provided to houses by passing the cold water from the bottom of the hot tank and till the top of the tank until it reached the desired temperature of 60 ^{o}C. If the heat pump and solar energy are not enough to meet the temperature needs, backup heating is handled by direct electric heaters. A schematic representation of the system is shown in Fig. 1. The centralized section of the energy system i.e. solar thermal collectors, seasonal storage and warm tank along with de-centralized section of energy system i.e. the heat pump and the hot tank in each house is shown in Fig.1.

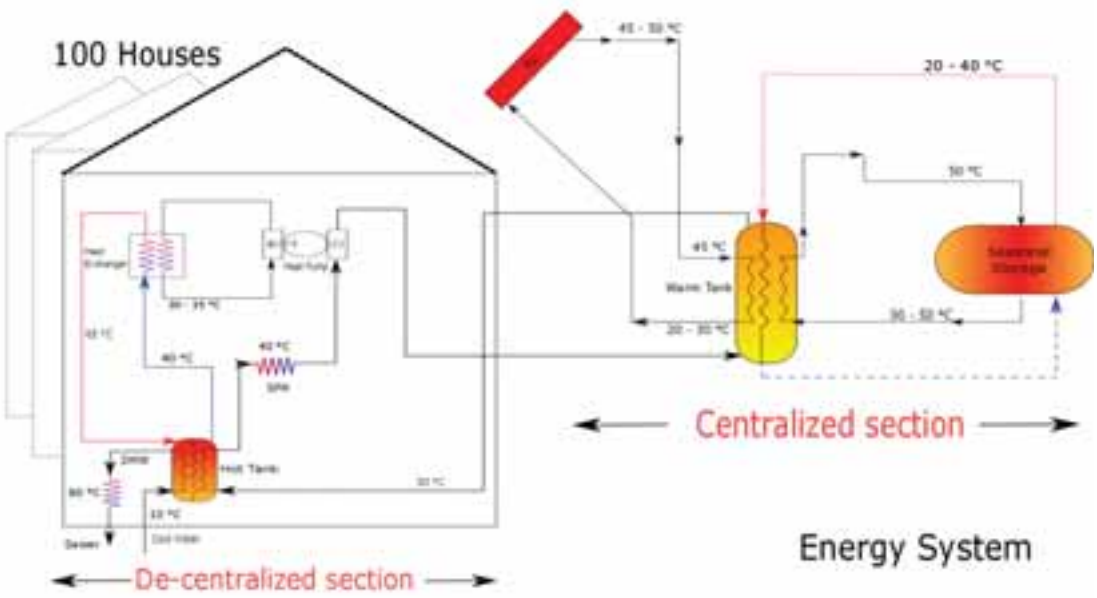

Fig. 1: Simple schematic representation of the partial centralized and de-centralized energy system.

2.2. Simulation environment

A 100-house community is studied, located in Helsinki, Finland. The system is simulated using TRNSYS simulation studio (Thermal Energy System Specialists, LLC, 2012). TRNSYS type 1b, type 543, type 557a, type 668, type 194 and type 15 are used for solar thermal collectors, buffer tanks, boreholes, heat pump, photovoltaic panels and weather data respectively (Rehman, et al., 2017). The buildings are built and simulated in TRNBuild (Thermal Energy System Specialists, LLC, 2012), a subroutine of TRNSYS that generated the thermal loads profile of the building. Each house is a single story house and has pitched roof with a tilted angle of 20°. Three different types of buildings with varying heating demands are selected for the study. Buildings with space heating demand (SPH) of 25, 37 and 50 kWh/m^2/yr are selected. The domestic hot water (DHW) demand is 45 kWh/m^2/yr and electricity appliances demand is 40 kWh/m^2/yr for all three building type cases (Hamdy, et al., 2013). For optimization, TRNSYS simulation model was integrated with the NSGA-II algorithm by optimization integrator software i.e. MOBO also known as multi-objective building optimizer (Hamdy, et al., 2011).

2.3. Optimization problem

In district heating system the optimization problem deals with multiple objectives of conflicting nature. Therefore, in this study the optimization problem consists of minimization of purchased electricity and the investments as both are of conflicting nature.

2.4. Objective functions

In this study, purchased electricity and investment costs (IC) are set as objective functions to be minimized. The purchased electricity and investments costs (IC) are of interest because purchased electricity is in the interest of the user and the investment is in the interest of the contractors and construction companies.

The solar energy system is simulated together with the houses energy demand. Two functions that are analysed are the purchased electricity and the investment costs (IC) together. It is given as:

Min, {F1 (x) = Purchased electricity, F2(x) = Investment cost(IC)} for all x= $[x_1, x_2, \dots, x_6]$,

where 'x' is the vector of the design variables (x_1, x_2, …, x_6) as defined above, F1 is the purchased electricity for the system and F2 is the investment cost of the system. In this problem, the number of considered design variables are six (i.e., x= $[x_1, x_2, \dots, x_6]$). MOBO is integrated with TRNSYS simulation to perform multi-objective optimization. NSGA-II algorithm is used to perform optimization.

The mathematical expression for purchased electricity is,

$$E_{PUR} = E_{PUMP} + E_{HP} + E_{BH} + E_{BUL} - E_{EXP,} \quad \text{(eq. 1)}$$

where E_{PUR} is the purchased electricity, E_{PUMP} is the energy consumed by all pumps, E_{HP} is the heat pump energy consumed to heat the hot tank, E_{BH} is the energy use of the direct electric backup heating, used to maintain the temperature in the space heating and domestic hot water network in case heat pump and solar energy is not sufficient, E_{BUL} is appliance electricity demand of buildings and E_{EXP} is the excess electricity that is produced by PV panels and exported.

The second function, investment cost is the sum of the present value of the investments cost of the system. It is expressed as,

$$IC = C_{ST}+C_{PV}+C_{BTES}+C_{WT}+C_{HT}+C_{B}, \quad \text{(eq. 2)}$$

where IC is the overall investment cost, C_{ST} is the solar collectors, C_{PV} is the photovoltaic, C_{BTES} is the borehole, C_{WT} is the warm tank, C_{HT} is the hot tank and C_B is the building costs. No maintenance costs are considered. The system is simulated and optimized in parallel for the three years to allow the slow temperature rise in the BTES to take effect.

2.5. Design variables

The energy performance of the energy systems may depend mostly upon the six parameters or design variables which are defined and considered in this paper (Idman, 2013). These are the parameters that can be altered by the designer. The importance of these parameters can vary depending upon the system configuration. The six parameters considered in the system are: (1) ST collectors area, (2) hot tank volume, (3) warm tank volume, (4) BTES volume, (5) photovoltaic area, and (6) building heating demand.

The values of all the design variables and investment costs of design variables are shown in Table 1 including the selected buildings. A constant unit price is used for some energy system components. On the other hand the costs of some design variables are assumed to vary depending upon its size. The cost of the collectors varied as found in the study, large collector field tends to be much cheaper compared to smaller field, caused by economies of scale (Mauthner & Herkel, 2016), (Ahola, 2015), (Dalenbäck & Werner, 2012), (Hirvonen, 2017). The collectors used in the study are roof mounted solar collectors which are expensive compared to ground mounted collectors (Mauthner & Herkel, 2016). Finnish market is still under development therefore higher prices can be assumed for the collectors, tanks and PV panels (including taxes). In Crailsheim, Germany borehole thermal energy storage (BTES) is used as seasonal storage therefore, same cost is used here for BTES cost (Schmidt & Miedaner, 2012). The cost of the BTES is assumed to be constant per unit volume (includes drilling, insulation, construction and taxes) as shown in Table 1. It is computationally expensive to explore all designs. Hence, a multi-objective non-dominated sorting genetic algorithm (NSGA-II) is used to perform the simulation (Hamdy, et al., 2013). MOBO uses NSGA-II algorithm with an initial population of 16 individual for 100 generations i.e. 16 x100 = 1600 simulation run.

Tab. 1: System configuration variations for the simulations and investment cost of the components used in energy systems.

Design variables	Type of variables	Ranges/ Values	Prices (€)	Options
Roof mounted solar thermal area (m^2)	Continuous	50—6000	1000—550 €/m^2	
Warm tank volume (m^3)	Continuous	300—500	825—810 €/m^3	
Hot tank volume /house (m^3)	Continuous	0.5—5	900—810 €/m^3	
BTES volume (m^3)	Continuous	10000—60000	17.19 €/m^3	
Photo voltaic area (m^2)	Continuous	50—6000	450—200 €//m^2	
Building configurations	Discrete	Type 1: space heating demand= 25kWh/m^2/yr	15 628€/building	3
		Type 2: space heating demand= 37kWh/m^2/yr	13 260 €/building	
		Type 3: space heating demand= 50kWh/m^2/yr	12 655 €/building	

2.6. Renewable energy fraction

The renewable energy fraction (REF_{heat}) for heating is defined as (Rehman, et al., 2017),

$$REF_{heat} = 1 - \frac{(HP+backup\ direct\ heating+pumping)electricity\ consumption\ per\ year}{SH\ demand\ per\ year+DHW\ demand\ per\ year}, \quad \text{(eq. 3)}$$

the above equation (eq.3) accounts the heat losses through the grid. The household appliances electricity demand is not included in the calculations.

2.7. On-site energy matching (OEM) and on-site energy fraction (OEF)

The onsite-energy matching (OEM) for electricity is defined as the ratio between exported electricity and total on-site electricity generated through photovoltaic panels (Cao, et al., 2013). The OEM provided the values that indicated the portion of the on-site generated electricity that is used in the local demand rather than being dumped or exported. The onsite-energy fraction (OEF) for electricity is defined as the ratio between annual purchased electricity and total electricity demand of the community (Cao, et al., 2013). The OEF provided the values that indicated the portion of the demand covered by the on-site generated electricity through photovoltaic panels. Higher the value of OEF and OEM better is the matching.

3. Results and discussion

The relationship between the purchased electricity and the investments costs of the non-dominated solutions are shown in Fig. 2. In total there are 132 non-dominated solutions for the energy system (red points). All the simulations results cloud is also shown in Fig. 2 (blue points).

The solutions on the Pareto front in Fig.2 (red points) are called non-dominated solutions. All simulations run (blue points) converged on the Pareto front (red points) as shown in Fig. 2. It shows that due to the increase in the investments there is a reduction in the purchased electricity. The solutions on the left side of the Fig.2 are less energy intensive compared to the solutions on the right (red points). The purchased electricity varied from 47.4 kWh/m^2/yr to 25.7 kWh/m^2/yr, this correspond to the investments cost (IC) from 180.7 €/m^2, floor area to 526 €/m^2, floor area. The solution shows that there are wide ranges of the optimal solution available which can be selected by the contactors and the end users based on their expectation and demand. It is found that the left most solutions contained a large photo voltaic and medium sized solar thermal areas. On the other hand the majority of the solutions on the right hand side in Fig.2 contained solutions with smaller photovoltaic panels and solar thermal area. Furthermore, other important design parameters that followed a certain trend on the Pareto front are building heating demand.

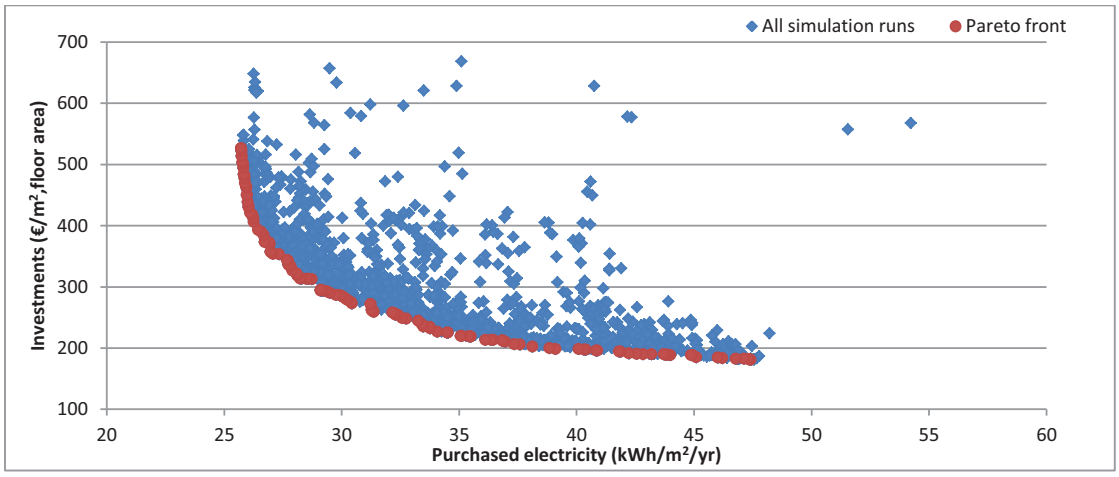

Fig. 2: Purchased electricity versus investments of the non-dominated optimal combinations of the design variables.

The cost breakdowns of the non-dominated solutions are shown in Fig.3.

The solutions on the left hand side of Fig.3 are the least expensive solutions. These solutions have higher purchased electricity. On the contrary the solutions on the right side of Fig.3 are expensive solutions and the corresponding purchased electricity is less.

It is observed that in Fig.3 photo voltaic area, solar thermal area, building heating demand and storage tanks volume played a significant role in the overall investments and also in the change in the purchased electricity. Due to the cheaper cost of the photovoltaics panels compared to the solar collectors, PV area is increased

initially by the algorithm to reduce the purchased electricity, and later solar collectors area is increased. Since hot tank is not charged by the solar thermal energy and it is only charged via the heat pump therefore, there is a large requirement of the electricity compared to the thermal energy. As a consequence, large photovoltaic area played significant role in reducing the purchased electricity compared to solar thermal area. Small-medium ST area is used to charge the warm tank at adequate level in all non-dominated solutions. Large PV panels area is used to provide electricity to the heat pump to charge the hot tank. Nevertheless if hot tank is charged by the solar thermal area then larger ST area would have been beneficial.

Furthermore, the solar thermal area also played important role in the reduction of the purchased electricity. The Fig.3 showed that on the left side, most of the cases has small solar thermal area of around 100—700 m^2. On the other hand, in the most expensive cases where the purchased electricity is less, the optimization algorithm selected medium sized solar thermal collectors of around 1000—2800 m^2. A very larger solar thermal area of around 3000 m^2 and above had minimal advantage in reducing the purchased electricity and also it is expensive, therefore the algorithm did not select a very large solar thermal collectors area. Hot tank is not charged by the solar energy therefore, large collector area had minimal advantage.

Building demand also contributed in improving the performance of the system. Initially, in most of the optimal cases building with heating demand of 50 kWh/m^2/yr are chosen because it is the cheapest option among others as shown in Fig.3 (left side). In the cases where the purchased electricity is less, on the right side of the Fig.3, the building with heating demand of 37 kWh/m^2/yr and 25 kWh/m^2/yr are chosen in majority. With higher investments, building demand could be reduced from 50 kWh/m^2/yr to 37 kWh/m^2/yr and up to 25 kWh/m^2/yr.

The size of the short term tanks also increased gradually from the least expensive to the expensive solution. This indicated that a large tank volume would improve the performance of the system. As this would provide the instantaneous energy needed for the system to meet the heating demand of the buildings. Larger the volume, large is the energy available. Larger tank volumes are also selected in high performing cases due to cheaper cost of the tank.

The solution on the right side of the Fig.3 shows that a combination of medium to large photovoltaic area, medium sized solar thermal area, and large volume of the tanks, energy efficient building and medium size of BTES volume could improve the performance of the energy system. On the other hand, this would have higher cost. A combination of small photovoltaic and solar thermal area, small BTES volume and building with highest heating demand would be the cheapest solution. This resulted in high purchased electricity by the system.

The solution with lowest solar thermal collectors area has minimal renewable energy fraction on left side in Fig.3. The renewable energy fraction increased with increase in the collectors area.

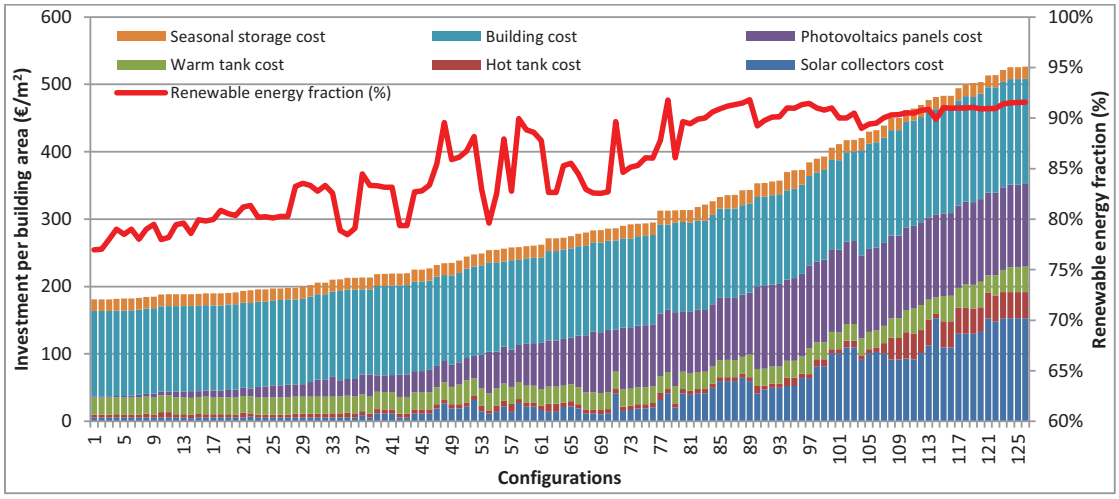

Fig. 3: The cost breakdown of the non-dominated optimal solutions.

The on-site energy fraction (OEF) varied between 2% and 38% as shown in Fig.4. This indicated that PV panels are able to meet 2%—38% of the local demand of the system, depending upon the PV panels size and annual electricity demand. The OEF is less when the PV panels area is less on the left side of the Fig.4, hence the on-

site generation of electricity is not enough to meet the high load. It improved until 38% when the PV and ST areas are large on the right side of Fig.4, resulting in large on-site electricity generation and lesser demand. The maximum OEF is 38% because of the mismatch between the generation and consumption and no electrical storage is considered. Since there is no electricity storage, therefore in the cases where the PV area is large the maximum OEM achieved is 20% as shown in Fig.4. This indicated that in highest performing cases 20% of the on-site generation by PV panels is used locally while the rest of the 80% is exported due to mismatch and lack of electricity storage in the system. On the other hand, the OEM is 100% when the PV area is small (no exported electricity), however this resulted in 2% OEF only.

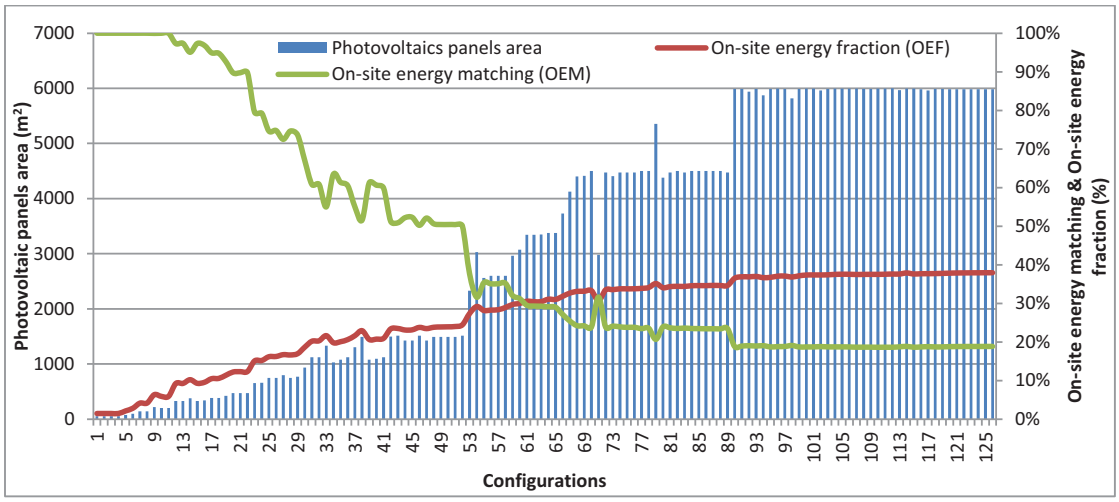

Fig. 4: The On-site energy fraction and On-site energy matching for electricity, correspond to the photovoltaic panels area.

3.1. The benefits of centralized space heating and de-centralized hot water

The simulation results provided some worthwhile findings. Firstly, size of the solar thermal area can be reduced in such system compared to the complete centralized system. It is found that in most of the optimized cases the size of the collectors ranged from 100— 2800 m^2. Large solar thermal area from 3000 m^2 onwards is not needed in such partial decentralized system. Because low temperature centralized tank can be charged with small-medium sized collectors and warm tank is used to preheat the space heating water therefore larger areas of collectors are not required. Furthermore, the decentralized hot tank is charged by the heat pump only and not via collectors. This also reduced the need of a larger collectors area in the optimized cases. Due to such partial centralized and decentralized configuration the size of the BTES is around 10700 m^3 in majority of the optimized cases. The discharge from the BTES is not significant in the cases where solar thermal capacity is less (cheapest cases), therefore in such cases BTES can be excluded from the system. Only in most expensive cases large volume of BTES (12000 m^3) is proposed that slightly improved the performance of the system. However large photovoltaic panels reduced the purchased electricity because hot tank is charged through electricity (heat pump) and not through solar thermal energy (collector) therefore large photovoltaic panels area are proposed.

Secondly, the partial decentralized system can be implemented at lower investment cost because the size of the solar thermal collectors and the BTES are less in most of the optimized cases. Since larger modules of both the solar collectors and BTES are not needed to improve the performance, hence the investment costs are less. Moreover, solar thermal collectors are the most expensive component in the solar community compared to photovoltaic panels. Hence lesser size of collectors is beneficial in terms of cost reduction.

Lastly, the results showed that by having de-centralized high temperature (domestic hot water) system inside houses, the losses through the piping reduced as the length of the high temperature pipe reduced from 4000 m (centralized) to 200 m (decentralized). The reduction in the losses through the domestic hot water piping is around 90%.

4. Conclusion

The goal of the research is to investigate the performance and optimize the solar district heating system for community in Nordic conditions. For this study de-centralized system is proposed. The proposed system

consists of individual house heat pump connected between large centralized solar-charged low temperature tank and smaller de-centralized individual high temperature tank in each house. Additionally, the large centralized tank is directly charged by solar-charged borehole storage during winters. The boreholes are charged by the centralized warm tank during summers. Multi-objective optimization is carried out in order to improve the performance of the system. The two objectives that are minimized are purchased electricity and investments cost.

Generally, it is found that solar energy can be used to provide both DHW and SPH, or also to charge the ground. Balancing the use of the solar energy throughout the year integrated with a HP is effective in energy system. In particular, storing energy in the seasonal storage increases the performance of the system by reducing the purchased electricity. The advantage of using the de-centralized system is that losses through the system and BTES are less. Since the size of the ST area is smaller therefore the temperatures in the seasonal storage is limited and it operates on lower temperature. Furthermore, the losses through the high temperature district heating grid are less compared to the centralized system because the high temperature tank is smaller in size and present inside the houses. This reduced the length of the piping from 4000 m to 200 m for 100 houses, as a consequence the losses through the high temperature DHW piping are reduced.

In terms of energy system, it is found that each component has varied effect on the performance of the system. In order to increase the performance of the system it is essential to have correct combinations of the system. The correct sizing of the design variables like: ST area, photovoltaic area, short-term storages tanks volume, BTES volume and the building heating demand is important. The analysis showed that the highest purchased electricity is 47.4 kWh/m^2/yr, on the contrary, the lowest purchased electricity is 25.7 kWh/m^2/yr. This is mainly caused by the variation in the heat pump consumption. The heat pump is used only to charge the small sized hot tank while taking energy from the space heating return line instead of the BTES. Hence, the source is relatively warmer on the evaporator side. The system can be implemented with the investments ranging from 180.7 €/m^2, floor area to 526 €/m^2, floor area. In most of the best cases, where purchased electricity is minimal, it is found that a combination of small-medium sized solar thermal collectors area, small-medium sized BTES and high energy intensive buildings are proposed in most of the optimal cases. However, purchased electricity can further be reduced by having a combination of medium solar thermal area, large volume of BTES and buildings with lowest heating demand. The results also showed that, photovoltaic area is vital for the overall system performance. Large photovoltaic area reduced the purchase electricity, however due to mismatch excess energy is exported to the grid. No electricity storage is considered in this study. As for the tank sizes, firstly it is beneficial to have small to medium sized decentralized hot tank in most of the optimal cases in each house. Secondly, it is beneficial to have large volume of centralized low temperature tank of around 300—460 m^3.

For the solar thermal collectors, a small to medium sized ST area is beneficial in most of the optimal cases. A large area of 3000—6000 m^2 is not selected in optimal cases. Large ST area had minimal benefit because high temperature is not needed in de-centralized system. In addition to that, the cost of the ST area played important role in selecting the solar thermal area, due to high cost of the collectors the algorithm selected small to medium sized collectors.

The on-site energy fraction (OEF) for electricity varied around 2%—38%. This correspond to the on-site energy matching (OEM) from 100%—20%. Both the OEF and OEM varied based on the PV panels area and the demand of the system. Large PV area and low purchased electricity resulted in higher OEF and low OEM. On the other hand, small PV area and high purchased electricity resulted in lower OEF and high OEM. PV panels installation is beneficial along with the ST collectors because without the PV panels the OEF for electricity would be zero and all the electricity has to be purchased via the grid. This would increase the purchased electricity and the operational cost of the community.

The renewable energy fraction varied from 75%—91%. This again illustrates the significance of the design variables and configuration on the system performance. This study clarified some important aspects of the energy system behaviour. It provides better in-depth understanding of the effect of each individual design variable on the system behaviour. This study gave the methodology and interactions between design variables for a proposed system configuration. In particular, their effect on the system performance in presented. An extended study could be made by changing the controls and other design variables, like the set points of the system in order to optimize the control algorithm. Additionally it is planned to include electricity price (operational cost) and emission price in the energy system optimization to show complete picture in the future

study. With increase in the popularity of the solar community concept in Nordic region, finding the best strategies and combinations would be important. This information is useful for the designers and contractors in making early stage decisions.

5. Acknowledgement

The project has been funded by the Academy of Finland, through the New Energy research program.

6. References

Ahola, J., 2015. *National Survey Report of PV Power Applications in FINLAND,* Lappeenranta: International Energy Agency (IEA).

Bauer, D. et al., 2010. German central solar heating plants with seasonal heat storage. *Solar Energy,* 84(4), pp. 612-623.

Cao, S., Hasan, A. & Siren, K., 2013. On-site energy matching indices for buildings with energy conversion, storage and hybrid grid connections. *Energy and Buildings,* Volume 64, pp. 423-438.

Chapuis, S. & Bernier, M., 2009. *SEASONAL STORAGE OF SOLAR ENERGY IN BOREHOLE HEAT EXCHANGERS.* Glasgow, Scotland, Eleven International IBPSA Conference.

Dalenbäck, J.-O. & Werner, S., 2012. *Market for Solar District Heating, WP2 – European Market Study.* [Online]
Available at: http://solar-district-heating.eu/portals/0/sdh-wp2-d2-3-market-aug2012.pdf
[Accessed 15 9 2016].

Fisch, M., Guigas, M. & Dalenbäck, J., 1998. A review of large-scale solar heating systems in Europe. *Solar Energy,* 63(6), pp. 355-366.

Flynn, C. & K.Siren, 2015. Influence of location and design on the performance of a solar district heating system equipped with a borehole. *Renewable Energy,* Volume 81, pp. 377-388.

Hamdy, M., Hasan, A. & Siren, K., 2011. Applying a multi-objective optimization approach for design of low-emission cost-effective dwellings. *Building and Environment,* 46(1), p. 109–123.

Hamdy, M., Hasan, A. & Siren, K., 2013. A multi-stage optimization method for cost-optimal and nearly-zero-energy building solutions in line with the EPBD-recast 2010. *Energy and Buildings,* Volume 56, p. 189–203.

Hirvonen, J., 2017. *Towards zero energy communities: Increasing local and renewable energy utilization in buildings through shared energy generation and storage.* [Online]
Available at: https://aaltodoc.aalto.fi/handle/123456789/26235
[Accessed 2017].

Idman, T., 2013. *Parametrization of energy simulation and development of energy efficient building design analysis and decision making process,* Espoo, Finland: Aalto University, School of Engineering, Department of Energy Technology.

International Energy Agency Solar Heating and Cooling Programme, IEA-SHC, Task 7, 2016. *Task 7-Central Solar Heating Plants With Seasonal Storage.* [Online]
Available at: http://task07.iea-shc.org/

Kalaiselvam, S. & Parameshwaran, R., 2014. *Thermal Energy Storage Technologies for Sustainability: Systems Design, Assessment and Applications.* 1st Edition ed. Amsterdam, The Netherlands: Elsevier.

M. Lundh, J.-O. D., 2008. Swedish solar heated residential area with seasonal storage in rock: initial evaluation. *Renewable energy,* 33(4), pp. 703-711.

Mangold, D., 2007. Seasonal storage-a German success story. *Sun Wind Energy,* Volume 1, pp. 48-58.

Mauthner, F. & Herkel, S., 2016. *Task 52: Solar heat and energy economics in urban environments, TECHNOLOGY AND DEMONSTRATORS, C1: Classification and benchmarking of solar thermal systems in*

urban environments, Gleisdorf: International energy agency: Solar heating and cooling programme.

NIBE, 2017. *NIBE-F1345.* [Online] Available at: http://www.nibe.fi/tuotteet/maalampopumput/nibe-f1345/ [Accessed 2017].

Nielsen, J., 2012. IEA-SHC Task 45: large solar heating/cooling systems, seasonal storage, heat pumps. *Energy Procedia,1st International Conference on Solar Heating and Coolingfor Buildings and Industry (SHC 2012),* Volume 30, p. 849–855.

Nielsen, J. E., 2012. IEA-SHC Task 45: Large Solar Heating/Cooling Systems, Seasonal Storage, Heat Pumps. *Energy Procedia, 1st International Conference on Solar Heating and Coolingfor Buildings and Industry (SHC 2012),* Volume 30, pp. 849-855.

Nordell, B., 2000. *Large-scale thermal energy storage, Lulea, Sweden.* [Online] Available at: http://large.stanford.edu/courses/2013/ph240/lim1/docs/nordell.pdf [Accessed 2017].

Official Statistics of Finland (OSF), 2016. *Dwellings and housing conditions [e-publication].* [Online] Available at: http://www.stat.fi/til/asas/index_en.html [Accessed 2016].

Rad, F. & Fung, A., 2016. Solar community heating and cooling system with borehole thermal energy storage-review of systems. *Renewable and Sustainable Energy Reviews,* Volume 60, pp. 1550-1561.

Rehman, H. u., Hirvonen, J. & Sirén, K., 2017. A long-term performance analysis of three different configurations for community-sized solar heating systems in high latitudes. *Renewable Energy,* Volume 113, p. 479–493.

Schmidt, T., Mangold, D. & Müller-Steinhagen, H., 2004. Central solar heating plants with seasonal storage in Germany. *Solar Energy,* 76(1-3), pp. 165-174.

Schmidt, T. & Miedaner, O., 2012. *Solar district heating (SDH), Solar district heating guidelines-Storage.* [Online]
Available at: http://solar-district-heating.eu/Portals/0/Factsheets/SDH-WP3_FS-7-2_Storage_version3.pdf

Sibbitt, B. et al., 2012. The performance of a high solar fraction seasonal storage district heating system – five years of operation. *Energy Procedia,* Volume 30, p. 856 – 865 .

Solar District Heating, 2016. *Ranking List of European Large Scale Solar Heating.* [Online] Available at: http://solar-district-heating.eu/ServicesTools/Plantdatabase.aspx [Accessed 2017].

Thermal Energy System Specialists, LLC, 2012. *TRNSYS 17.* Madison, WI 53703– U.S.A.: Solar Energy Laboratory, University of Wisconsin-Madison.

ur Rehman, H., Hirvonen, J. & Sirén, K., 2016. Design of a Simple Control Strategy for a Community-size Solar Heating System with a Seasonal Storage. *Energy Procedia,* Volume 91, pp. 486-495.

V.Novo, A., R.Bayon, J., Castro-Fresno, D. & Rodriguez-Hernandez, J., 2010. Review of seasonal heat storage in large basins: Water tanks and gravel–water pits. *Applied Energy,* 87(2), pp. 390-397.

Solar Supported Agriculture in Desert Regions

Modeling of a solar dryer for fruit preservation in developing countries

Juliette Chaignon[1], Henrik Davidsson[1]
[1] Lunds Tekniska Högskola, Lund (Sweden)

Abstract

About 25,3 % of the Mozambican population is suffering from undernourishment even though a sufficient amount of food and specifically fruits are produced. Post-harvest losses are estimated to 25 % to 40 % and part of the production is not even harvested due to a short season. A solution has to be found to improve fruit preservation and allow the population to consume what is harvested later. Drying fruits is a solution to preserve them. However, juicy fruits are harder to dry than other fruits since they contain more water. One small-scale solution is drying juicy fruits in a specific membrane which allows water vapor to escape from the fruit and the fruit juice to dry. It is possible to couple these membranes with solar dryer technology to control parameters such as temperature, relative humidityand air velocit) in order to improve the drying process

Two types of solar dryers are tested and preseted in this paper: an indirect and a direct dryer. Both solar dryers are modeled using a CFD tool (COMSOL Multiphysics) and the modeling work is based on former research to elaborate a mathematical model of the dryer physics. The simulations results produced by COMSOL allow to study the influence of several parameters such as geometry of the solar dryers, ambient conditions and solar dryer materials in order to improve the design of the dryers. The results from the modeling are compared to on-site measurements, in Mozambique, in order to calibrate and validate the models. The models estimated temperatures and relative humidity with an average relative error inferior to 20 %.

Keywords: solar dryers, modeling, CFD, indirect solar dryer, direct solar dryer, fruit preservation

1. Introduction

1.1 Food insecurity and fruit preservation

Mozambique is a developing country which presents a high rate of undernourished people. Around 6,9 million inhabitants are undernourished which represents 25,3 % of the total population in Mozambique (Food Agricultural Organization of the United Nations, 2016). The situation is even more concerning for children since 43 % of the children under 5 years old suffer from chronic malnutrition and 6 % are considered as sharply malnourished (Instituto Nacional de Estatística, 2012).

Although an acceptable amount of food is grown, a significant part is not consumed due to harvest losses or spoilage before it can be consumed. Post-harvest losses are estimated between 25 % and 40 % in Mozambique and a large part of the fruit production is not even harvested due to a short season (Phinney, R. et al. , 2015).

A solution to cope with this issue is to provide a fruit processing technology to safely and cost-efficiently preserve fruits when they can be harvested in order to consume them later. Large-scale solutions such as canning or aseptic processing are economic but they also require a considerable amount of resources (clean water, energy, transport facilities) which are not necessarily available in developing countries like Mozambique.

1.2 Solar-assisted pervaporation

A small-scaled solution, solar-assisted pervaporation, is used to dry fruits in this work. It consists in putting fruit juice or fruit purée in a semipermeable membrane bags which allow water vapor to escape the bags but prevent it to enter back in it. A minimum temperature of 50 °C is required in order to avoid bacterial growth. The temperature also has to stay below 70 °C to avoid the degradation of acid ascorbic (Vitamin C) (Paul and Ghosh, 2011).

The criteria used to determine if a product has been dried enough and is suitable for conservation at room temperature is the water activity level a_w . The water activity corresponds to the ratio between the vapor pressure

doi:10.18086/swc.2017.30.01 Available at http://proceedings.ises.org

of the food, P_w, to the vapor pressure of water at the same temperature and pressure, P_{ws} (Phinney et al., 2015) and can also be expressed as the equilibrium relative humidity of the product divided by 100 (Singh, P. and Heldman, D.R. 2013). This relation is found in equation 1.

$$a_w = \frac{P_w}{P_{ws}} = \frac{RH}{100} \text{ (eq. 1)}$$

According to Phinney et al. (2015), several conclusions can be made concerning solar-assisted pervaporation pouches :

- The drying process using SAP-pouches allows to reach water activities below 0,7. For instance, the water activity in mango purée went from 1,0 to 0,48 after 45 hours of drying.
- Ambient relative humidity is a key parameter in the drying process and is related to the temperature. A lower relative humidity will provide a higher evaporation rate of the product inside the pouch.
- Ambient wind velocity that is the velocity of the air flow around the pouch decreases the drying time.

Given these conclusions, it is interesting to combine these SAP pouches with solar dryers.

1.3 Solar drying

Several types of solar dryers exist and this work aims to model two different types of them :

- A direct active solar dryer (Fig. 1)
- A tilted passive solar dryer (Fig. 2)

In a direct solar dryer, the drying product receives directly the solar radiations. In an active solar dryer, the heated fluid (air in this case) is forced to circulate by a fan, a blower or any equivalent. On the opposite, the drying product is not directly exposed to solar radiations in an indirect solar dryer and a passive solar dryer only relies on natural convection due to the temperature difference between the absorber and the air circulating in the solar dryer.

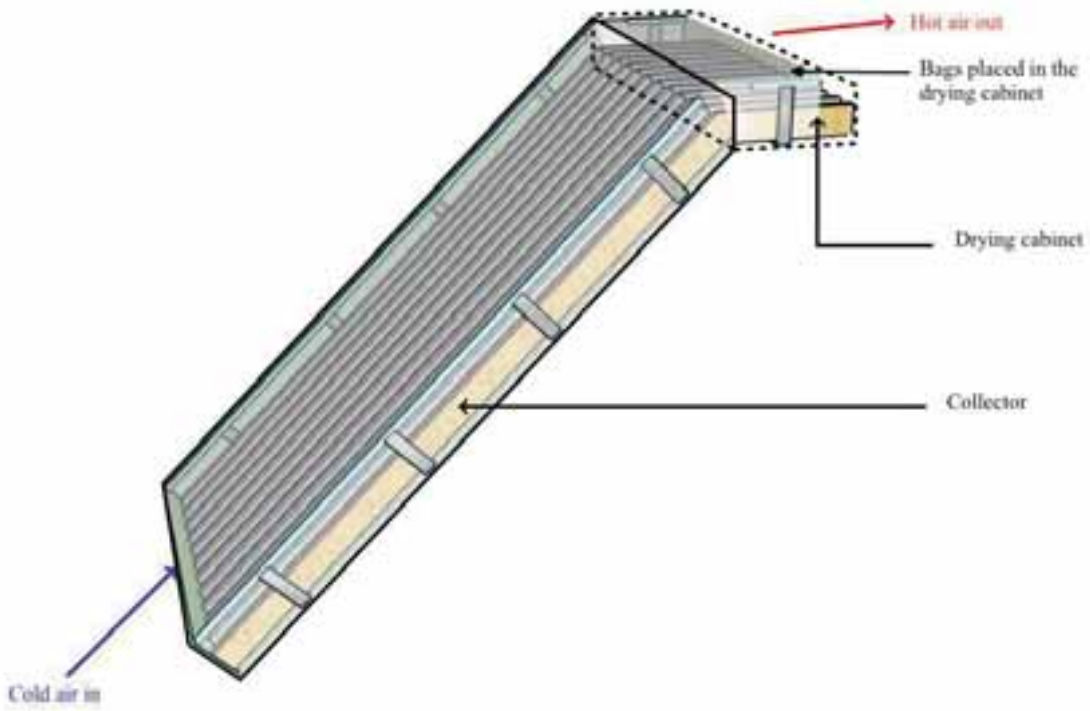

Figure 1 : Tilted passive solar dryer

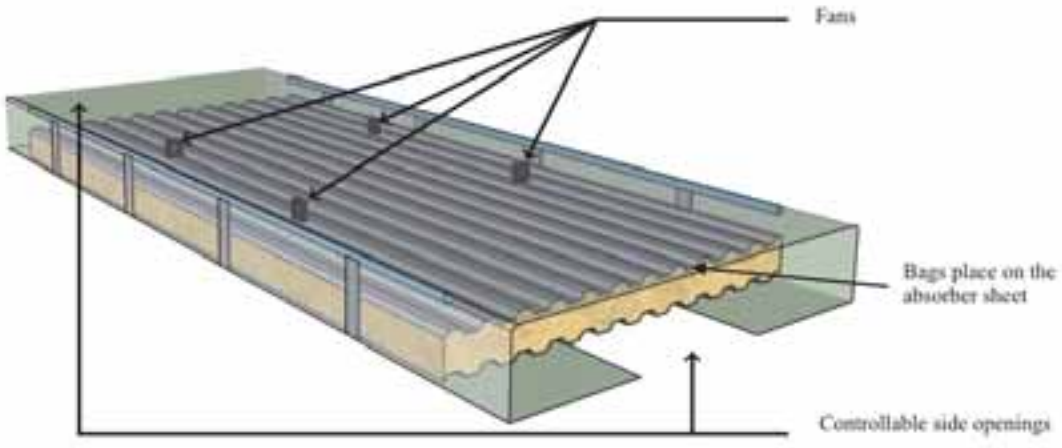

Figure 2 : Active direct solar dryer

2. Theory

The heat transfer exchanges in a solar dryer are presented on Figure 3. The solar radiation (1) is transmitted through a plastic sheet and absorbed by the absorber plate or on the fruit itself. Once the radiation is absorbed, part of it is emitted back to the plastic sheet. The rest is used to heat the air by convection on the absorber plate and the inner sides (4). The role of the absorber is thus to convert radiation in heat, by absorption and emission. Convection also happens on the plastic sheet (3) and the outer sides with the ambient air. Losses occur by radiation (2) from the plastic sheet from the sides of the solar dryer to the sky and from the bottom sheet of the collector to the ground. Finally, heat is transferred by conduction in the different materials.

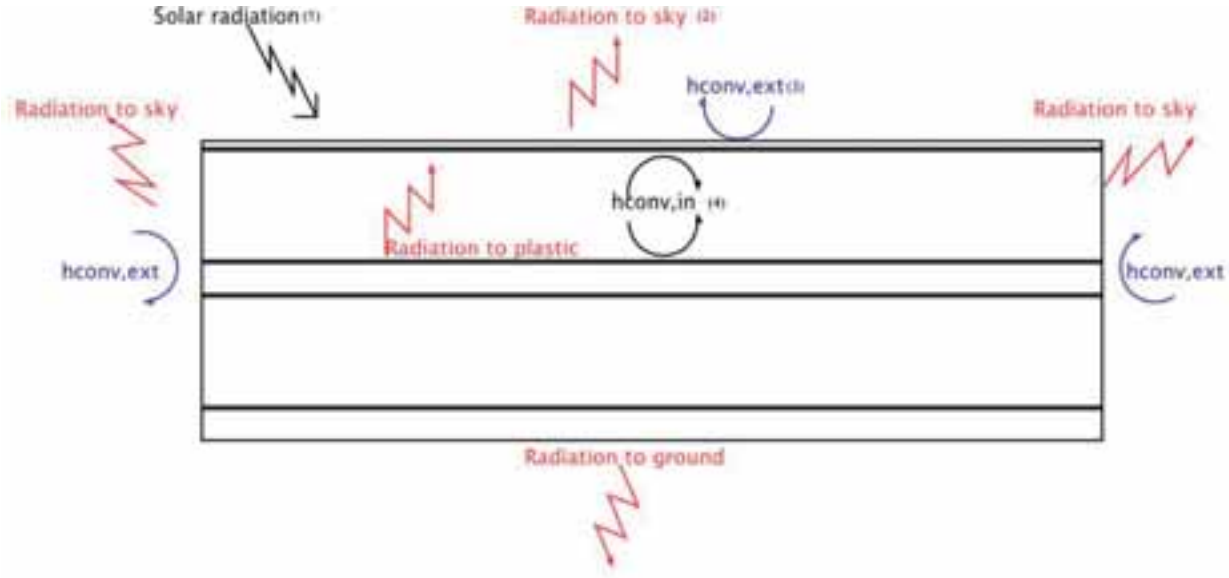

Figure 3 : Heat transfer in a solar dryer

3. Method

3.1 Models' description

The aim of this work is to model two types of solar dryers using the software COMSOL. The two main parameters taken into account in the studies are temperatues of the different elements of the solar dryers and relative humidity

of the air circulating in the solar dryers.

A first model, referred as Model 1, aims to represent the tilted collector, Figure 3, with a tilt angle of $\theta = 45°$. The computer model of this solar dryer enables to quantify heat transfer. In this model, the air inlet velocity is set to a constant value. This value is kept in the whole collector. In this model, the study focuses on the air characteristics circulating in the collector (temperature distribution, relative humidity). The velocity profile is not modeled using fluid dynamics equation. The airflow velocity value is used to calculate the Nusselt number and deduce the convective heat transfer occurring on the absorber plate.

A second model, referred as Model 2, represents an active flat dryer (Fig. 2) containing bags full of water. To create this model, the Heat Transfer Module is used in COMSOL. In this model, the solar dryer is the same as the indirect solar dryer, except that the direct solar dryer is flat and the bags are put directly in the solar dryer. The temperature distribution in the dryer and the relative humidity are the two main parameters studied.

3.2 Assumptions

The following assumptions are made to model the active direct solar dryer and the passive indirect solar dryer :

- The solar dryers' studies are steady state for a constant solar irradiation. This is an approximation since the solar irradiation varies with time and weather conditions (clouds).
- The calculations can be run on half of the solar dryer without affecting the accuracy of the results given the symmetry of the considered geometry.
- The solar dryers which are modeled are built with a black net put on top of the absorber. This net is neglected.
- The plastic sheet does not absorb visible radiation, $a_p = 0$.
- The outward radiation from the sides is assumed to be radiated toward the sky while the radiation from the bottom goes to the ground.
- The heat radiation between the absorber and the plastic sheet is taken into account and a view factor is calculated for this.
- The inner sides are assumed not to reflect radiation
- There are no air leakages

3.3 Model validation method

In order to validate the models created for the two solar dryers, the results obtained through the model calculations are compared to field measurements. The values compared are five temperatures, plastic sheet, inlet air, outlet air, absorber plate, rock-wool insulation, bottom sheet and the relative humidity of the outlet air. The experimental set-up is presented in Section 3.3.

The mathematical tool used to compare the values from the model and from measurements is the relative error, defined by equation 2.

$$\varepsilon = \frac{x_{model} - x_{measured}}{x_{measured}} \text{ (eq. 2).}$$

3.4 Experimental set-up

The measurements collected are temperatures and relative humidity at chosen points on the solar dryer (Figure below).

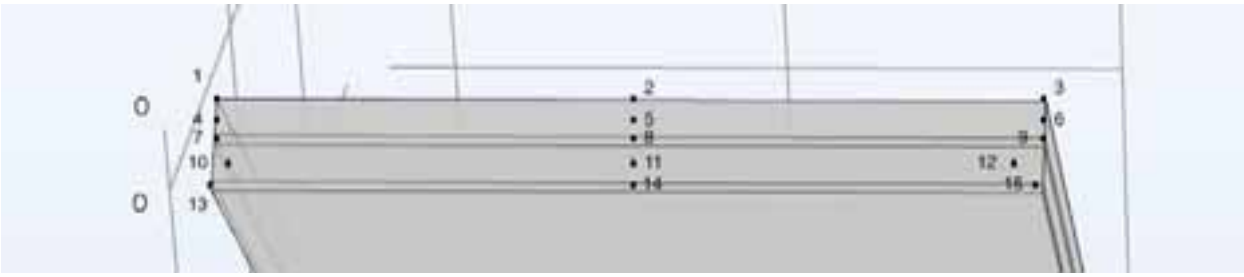

Figure 4 : Measurement points on the air outlet of the collector

The measurements collected are temperatures and relative humidity at chosen points on the solar dryer. To do so, two measurements tools have been used :

- four Vernier© sensors patched on strategic points on the solar dryer
- a Testo probe connected to a Testo435-2 logger, able to measure temperature and relative humidity

The measurements were taken during 30 minutes to reach stable values. The logs were stored on the Vernier© device and then transferred to a computer to be exploited on Excel. Each measurement has been done twice to deal with the repeatibility aspects of the experiments.

The ambient conditions were measured during 3 hours. Then, an average of the ambient temperature, ambient relative humidity and ambient solar irradiation has been done and used as intial values in the COMSOL models.

4. Results

4.1 Input data

The input data used for both the tilted passive and the flat active solar dryers is presented in the following table (Tab.1).

Tab. 1 : Input data

Parameter	Value	Unit
Collector width	1,1	m
Collector length	1,8	m
Insulation thickness	0,05	m
Global solar irradiation	916	W/m^2
Ambient temperature	31,6	°C
Ambient relative humidity	34,4	%

4.2 Model 1 : Tilted passive collector

The results from the computer model give the temperatures of the different elements of the solar dryer are given in Table 1 below. Here are presented the average temperature for each component of the tilted passive solar dryer.

Tab. 2 : Temperatures of the different elements of the titled passive solar dryer

Element	Temperature / (°C)
Plastic sheet	55,2
Outlet air	59,7
Absorber sheet	76,0
Insulation	43,0
Bottom sheet	33,2

The air temperature is above 50 °C and below 65 °C which means that the drying is performed in the correct range of temperatures to ensure the quality of the drying product, as shown on Figure 4. Less than 15 % of the collector length is necessary for the different elements to reach 80 % of the outlet temperature.

The value measured on-site for the ambient relative humidity is 34,4 % and is the one used in simulations. The calculations done by COMSOL show that at the outlet of the collector, the relative humidity drops to 10,1 % at

the center of the air outlet surface.

4.3 Model validation

In order to validate Model 1 (resp. Model 2) for the tilted passive (resp. flat active) solar dryer, the temperatues values and the relative humidity value of the air obtained through COMSOL calculations are compared to the measurements of the same values, done on-site.

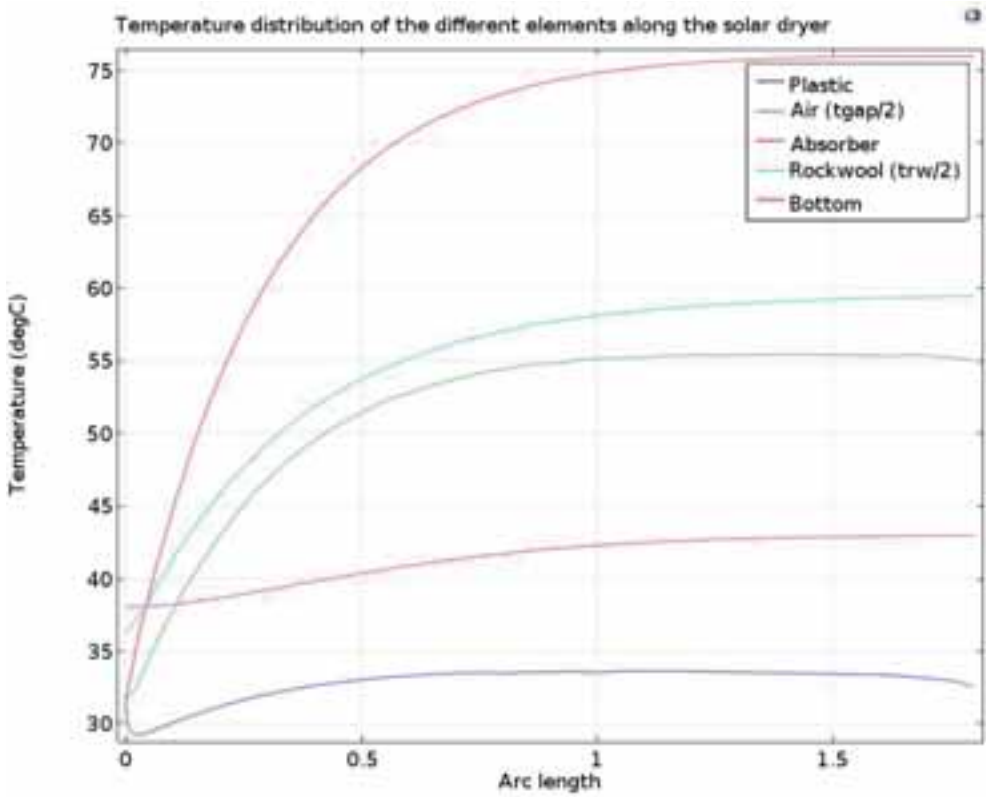

Figure 5 : Temperature of the different elements along the tilted passive solar dryer

For Model 1, the relative error for the temperatures given in Celsisus degrees varies from 2,6 % to 29,2 %. The average relative error for each element of the collector is given in Table 3 below, showing that the temperatures calculated by the model can be considered as accurate, except for the plastic sheet. For the relative humidity, a relative error of 8 % is obtained when the outlet air relative humidity measured is compared to the estimation from the computer model.

Tab. 3 : Relative errors for the temperature and relative humidity values – Model 1

Element	Average temperature measured on-site (°C)	Average temperature calculated by the model (°C)	Relative error on temperature
Plastic sheet	46	34	24 %
Outlet air	58	52	10 %
Absorber sheet	61	67	10 %
Insulation	61	55	11 %
Bottom sheet	40	41	3 %

The same is done with Model 2 and the relative error for the temperature values varies from 2,7 % to 33,2 %. The average relative error for each element of the collector is given in Table 4 below, showing again that the temperatures calculated by the model can be considered as accurate, except for the plastic sheet. For the relative humidity, a relative error of 8 % is obtained too when the outlet air relative humidity measured is compared to the estimation from the computer model.

Tab. 4: Relative errors for the temperature and relative humidity values – Model 2

Element	Temperature measured on-site (°C)	Temperature measured on-site (°C)	Relative error on temperature (°C)
Plastic sheet	41	28	32 %
Outlet air	49	43	12 %
Absorber sheet	44	51	17 %
Insulation	45	43	4 %
Bottom sheet	38	35	8 %

4.4 Parametric studies

The influence of the following parameters is studies through parametric studies in which all the parameters are fixed except the one studied.

The first parameter studied is the airflow velocity, which is constant in the solar dryer. The influence of the airflow velocity on the outlet temperatures, the internal convective heat transfer coefficient and the energy losses is studied. Six values of airflow velocity are studied : 0,1 ; 0,5 ; 1,0 ; 1,5 ; 2,0 ; 2,5 m/s. The higher the velocity, the lower the air temperature will be at the outlet. The same is observed for the absorber temperature at the outlet. This is due to the increased convection effects when increasing the airflow velocity. The air circulates faster in the absorber sheet and the heat will leave it faster. The relative humidity does not vary much as well and remains at about 10 % varying from 5 % for the lowest velocity to 12 % for the highest. Since the relative humidity depends on the temperature value, it is normal that a higher speed induces a higher relative humidity rate, because a higher airflow velocity is responsible for a lower temperature in the air. The internal convective heat transfer coefficient is affected by a change in the inlet airflow velocity. It is higher when the velocity is higher as shown on Figure 5. The range of values for this coefficient remains around [0,5; 2,0] $W/m^2/K$.

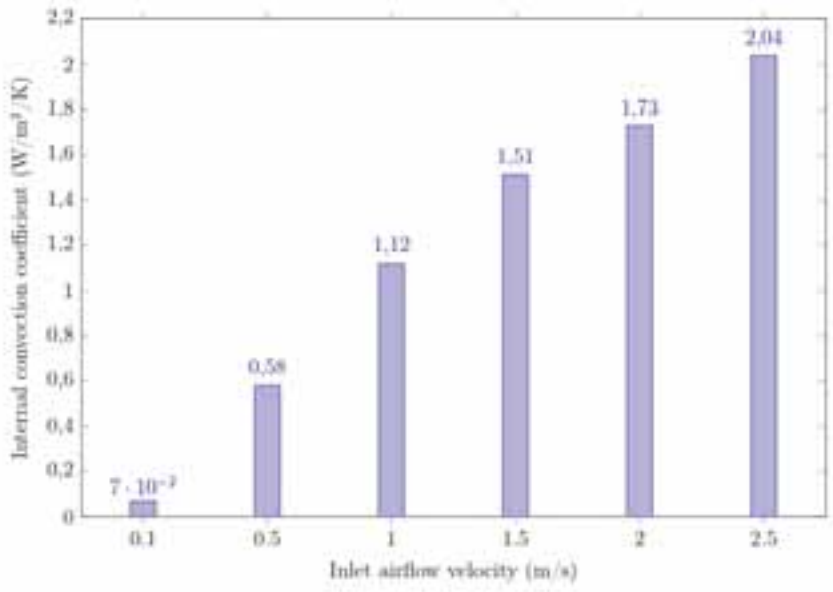

Figure 6 : Internal convection coefficient depending on the airflow velocity - Tilted passive collector

Then, the influence of the internal convection coefficient on the absorber plate is studied. The internal convective heat transfer coefficient on the absorber has a major influence on the outlet air temperature, the relative humidity and the outlet absorber temperature. When increasing the internal convective heat transfer coefficient on the absorber, the air at the outlet is at a higher temperature. For a constant velocity, increasing the internal convection coefficient on the absorber results in a lower relative humidity for the outlet air. The graph of the evolution of the outlet air temperature depending on the internal convective heat transfer coefficient is shown on Figure 6.

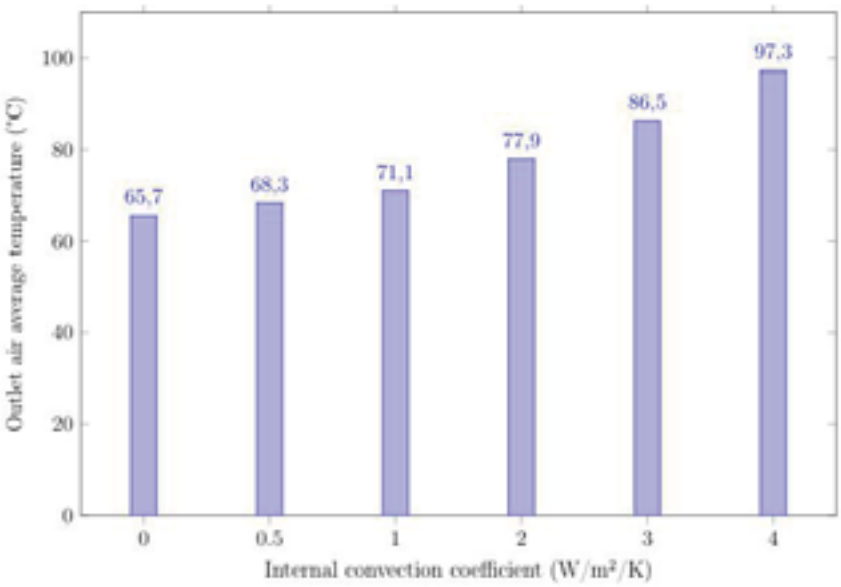

Figure 7 : Evolution of the outlet average air temperature depending on the internal convection coefficient for the tilted passive solar dryer

The radiative properties such as the transparency of the plastic sheet and of the absorptance and the emissivity of the absorber are some other important parameters which influence is studied. Simulations were run with the following values for the absorber emissivity : 0,1 ; 0,3 ; 0,5 ; 0,7 ; 1. The value of 1 corresponds to an ideal black body. The lower the emissivity, the higher the absorber temperature will be and thus the higher the air will be. A low emissivity means that the absorber is loosing less heat by radiation since it emits less thermal radiation (visible and infrared). This parameter is material-dependent.

Finally, the last parameters which influence is studied is the insulation thickness. The insulation thickness values tested are: 0.1 cm, 1 cm, 3 cm, 5 cm, 10 cm, 15 cm, 20 cm. Increasing the insulation thickness allows to get higher outlet air temperature to a certain point as shown on Figure 7. After 15 cm, the gain in the outlet air temperature is less perceptible. The temperature of the bottom part of the solar dryer is highly impacted by the insulation thickness.

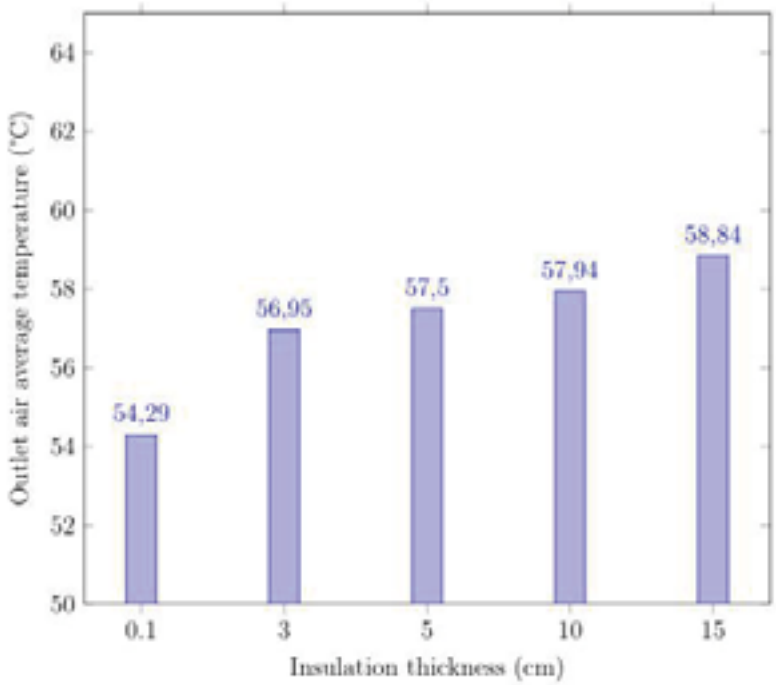

Figure 8 : Evolution of the outlet average air temperature depending on the insulation thickness for the tilted passive solar dryer

4.5 Design optimization

Some design optimization can be deduced from the previous parametrics. First of all, the insulation thickness needs to be chosen carefully. A too thick insulation layer is not useful but 5 cm seems to be a minimum value to limit the heat losses and keep the bottom part of the solar dryers at a reasonable temperature. Increasing the thickness of the insulation layer also increases the absorber temperature and in this case, even if more heat is transferred by convection to the air, the temperature difference between the absorber and the plastic sheet is higher and so are the radiative losses from the absorber to the plastic sheet. Finding the minimum thickness needed for the insulation layer allows also to reduce the price of the material needed.

The absorber material should be chosen carefully with the highest absorptance possible and the lowest emissivity. For this, low emitting coating absorbers would of course provide better drying performances. However, the quite high emittance of the absorber (0,8) used to build the solar dryers is sufficient to ensure an air temperature between 50°C and 65°C and thus food safety regarding the drying product. Since the solar dryers will be built and used in Mozambique, the emittance of the absorber is not a prior concern given the price difference between a classic corrugated metal sheet and a low-emitting coating. The plastic sheet material choice could be improved by choosing a more transparent material to increase the fraction of solar radiation transmitted to the absorber.

Then, increasing the convection on the absorber plate is a way of transferring more heat to the air. It can be done by increasing the surface of contact between the air and the absorber. Then, a better way of increasing the convective heat transfer is to increase the convective heat transfer coefficient, which means increasing the Nusselt number or the hydraulic diameter (the effective surface of the absorber). It could be possible to increase the natural convection thanks to a double-pass system with the air entering on the backside of the passive solar dryer and then going around the absorber plate and exiting the solar dryer on the opposite side to the one the air entered. The

convection around the bags is also very important. As explained by Phinney and Tivana (2016), the higher the airflow velocity around the bags, the higher the drying rate. One idea to increase the amount of air passing around the bags could be to have air passing above and under the bags. In the passive solar dryer, the bags should be put higher in the drying chamber joined to the collector. However, a balance has to be found because the driest air is located close to the absorber plate. In the active solar dryer, the fans already provide a good circulation of air around the bags. The point in this is also to avoid the moisture to stay on the bag so the relative humidity does not increase too consequently around the bags.

5. Discussion and conclusion

The model validation has been done by comparing measurements to values calculated by COMSOL. However, the tools used to take measurements are a source of error. In both models (passive tilted and flat active), the plastic sheet temperature is underestimated. This is an example of the difficulty to measure temperatures on certain elements of the solar dryer. Also, the model used to represent the solar dryers used an internal convective heat transfer coefficient based on a Nusselt number calculated using correlations. This is another source of error. One approximation has been done regarding the absorber plate shape. The material used in the solar dyers is a corrugated metal sheet. To simplify the problem, it is modeled as a flat sheet which thickness is equal to half of the height of the bumps of the corrugated metal sheet. When measuring the absorber temperature, it is always the temperature at the top of the bumps which is collected. A difference of 2,5 to 4°C is observed between the temperatures on the bumps or the hollows.

The internal convection in the solar dryer is one of the most delicate point in this modeling task. There are several solutions to do so. One solution is to determine an equivalent conductivity to the convection phenomenon. For the solar dryer, convection in the fluid would occurs in the case of an "horizontal cavity heated from below". COMSOL requires to give the dimension of the cavity (distance plastic sheet - absorber) and the temperature difference between the air and the horizontal plate heating the air. This solution might not be the best, first because knowing the temperatures of the air and absorber are one of the goal of the study and are not meant to be set. Also, the software uses some correlations that are not easily accessible. Another solution is to use another module in the software to model the flow behaviour. Thanks to the Boussinesq approximation for instance, it would be possible to model the natural convection inside a passive solar dryer (Motte et al., 2011). However, in this case, it is time consuming and it could not have been possible to carry out parametric studies with such a model. Finally, the chosen solution was to calculate the Nusselt number and give it as a parameter in the software. COMSOL allows to determine the different elements of the Nusselt number formula (specific heat at constant pressure, density, etc) depending on the temperature in each cell of the mesh of the air domain.

Finally, it could have been possible to model the airflow using the Navier-Stokes equations in the Non-Isothermal Flow Module available in COMSOL. However, this method is time-consuming, even using simplifications such as symmetry in the geometry. Some models have been built taking into account the fluid behavior. The results for the temperature and the relative humidity were close to the results given by the model not including the fluid behavior modeling.

To conclude, the models created in COMSOL Multiphysics give sufficient information regarding the temperatures and air relative humidity in several parts of both a direct and indirect solar dryer. Even if the exact temperatures might not be found, the models give correct approximation of it. The main purpose of these models is to study the effect of different parameters variation. The main conclusions of this work are that:

- COMSOL is a sufficient tool to build models. It will also allow to improve the modeling by including more phenomena (water vapor transport for instance).
- The models give a sufficient estimation of the temperature and relative humidity in a direct and in an indirect solar dryer with a maximum relative error of 10% for the outlet air temperature.
- The calculations of the external convective coefficient can be done with different formulas without changing the results in a significant way. However, the calculation of the internal convective coefficient is more important and the formula used to calculate requires to be chosen carefully depending on the flow characteristics (Reynolds and Prandtl numbers).
- It is possible to increase the performance of the two solar dryers tested by reducing the space between the absorber and the plastic sheet and by using an insulation layer of at least 5 cm.

- The choice of a low-emissivity material for the absorber is not of prime importance. However, the plastic sheet could be of higher quality with a higher transparency.

6. References

Food Agricultural Organization of the United Nations. 2016. Evolution of the number of people undernourished (1990-2015). URL : http://www.fao.org/faostat/en/#compare [Accessed : 03/05/2017]

Instituto Nacional de Estatística. 2012. Moçambique Inquérito Demográfico e de Saúde 2011.

Paul R. and Ghosh,U., 2012. Effect of thermal treatment on ascorbic acid content of pomegranate juice. Indian Journal of Biotechnology. Vol 11, pp 309-313.

Phinney R., Rayner M. and L. Tivana., 2016. “Solar Assisted Pervaporation (SAP) for Preserving and Utilizing Fruits in Developing Countries”.

Phinney, R., Rayner, M., Sjöholm, I., Tivana, L. and Dejmek, P., 2015. “Solar Assisted pervaporation (SAP) for preserving and utilizing fruits in developing countries”. In: Third Southern African Solar Energy Conference. South Africa.

Motte, F., Cristofari, C. and Notton, G., 2011. “Thermal Modeling of a Solar Water Collector Highly Building Integrated”. In: [Accessed 23/05/2017]. Proceedings of the 2011
COMSOL conference. Stuttgart. URL : https://www.researchgate.net/profile/G _ Notton /publication / 266412238 _ Thermal _ Modeling _ of _ a _ Solar_ Water _Collector _ Highly _ Building _ Integrated /links / 55293d530cf2779ab79077be /Thermal-Modeling-of-a-Solar-Water-Collector-Highly-Building-Integrated.pdf [Accessed : 15/06/2017]

Singh, P. and Heldman, D.R., 2013. Introduction to Food Engineering. Edition S.L. Taylor. 4th edition. Food Science and Technology, International Series. Elsevier. Chap. 1

Solar Water Pumping for Productive Uses in Nepal

Robert Foster[1], Bikash Pandey[1], Bikash Uprety[1b] Binod Shresta[1b], Resha Piya[1b]
1 Winrock International, Arlington, Viriginia (USA)
1b Winrock International, Khatmandu (Nepal)

Abstract

The market for solar pumps is rapidly increasing due to rapidly declining costs and technology improvements that are replacing traditional manual (hand) pumps, mechanical windmills, and diesel engines around the globe. They are also reducing the demands on local and national power grids. Solar pumping has become a significant and growing niche for the solar energy industry. Solar pumps are an important way for smallholder farmers to increase crop yields through irrigation; fish farmers can increase fish yields through reliable water and improved aeration; and livestock herders can increase income through a reliable water supply for their animal's welfare. This paper details solar water pumping advances and example economic impacts that are making a real difference in the daily lives of rural Nepali farmers and communities.

1. Modern Solar Water Pumping

Solar photovoltaic water pumping (PVWP) systems are simple, reliable, cost competitive, and low maintenance. There is typically an excellent match between seasonal solar resource and seasonal water needs, when it is sunnier and hotter, is precisely when there is more solar energy to pump water (Foster, 2009). Small and medium scale solar water pumping systems are more econmical to operate than diesel or even many electric grid powered pumps, and provides a good return on investment. Their positive impact is most significant in rural communities like those in Nepal where conventional grid electrical power does not exist. Modern PVWP systems are characterized by their reliability, durability, and low maintenance. These qualities translate into a long-term lower cost when compared with other alternatives like diesel, not to mention the environmental benefits (they do not pollute the air or water, and operate queitly). In addition, PVWPs are easily automated and do not require an operator. PVWPs also provide system modularity, which provides the owner with the ability to flexibly meet specific need at any given moment.

There have been significant advances with solar water pumping systems over the past decade. PVWP systems costs have dropped by ~2/3 since 2000. Photovoltaic module prices have decreased by over 90 percent since 2010. As a result, solar water pumping system costs have declined significantly, from a high of over US$25 per peak Watt 20 years ago, to under US$5 a Watt today. Market estimates are that PV module prices may decrease by another 50 percent in only the next 5 or so years. There have also been improvements with pump system controllers using maximum power point tracking. Solar water pumping is now competitive with retail electric grid pumping costs (Kunen, 2015).

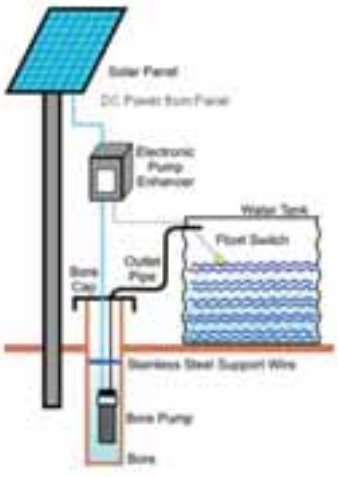

Fig. 1: Typcal solar water pumping system layout for a borehole (well) in Nepal.

doi:10.18086/swc.2017.30.02 Available at http://proceedings.ises.org

1.1. Centrifugal Solar Water Pumps

In Nepal, WI has been mostly deploying both DC and AC submersible and surface centrifugal water pumps. These pumps are readily available and affordable in the Nepalese Market. For a centrifugal pump, water enters at the center of the pump through a rotating impeller. The impeller spins the water, creating centrifugal force. The water gains both pressure and velocity as it flows through the impeller and is directed outward. A centrifugal pump can have multiple stages to increase its lift capacity. Each stage consists of one impeller with the output of the first stage feeding the input of the next. This is called a multi-stage centrifugal and may use up to about 20 stages to attain higher lifts. Each stage adds pressure, thus greater lift capacity. However, each stage also imposes friction, resulting in an efficiency loss of about 5 percent per stage.

Centrifugal pumps are especially efficient for higher flows > 40 lpm and for lifts of < 30 m. At lower flow rates and/or higher lifts, the efficiency is poor even under optimal conditions. To work efficiently, they need to run close to their full speed. Conventional power sources (grid or generator) provide stable power to maintain optimum rotational speed. Most solar pumps use variable power direct from a solar array; when power varies with the weather and the time of day, the speed of a pump will also vary (Foster, 2009). Centrifugal pumps are easily repairable locally in Nepal.

Any pump will have an optimum peak in its operating range, at which its energy efficiency is highest. Centrifugal pumps tend to have a narrow efficiency peak. A reduction in solar intensity reduces a centrifugal pump's performance disproportionately. This is because pressure is produced by centrifugal force, which is proportional to the square of the rotational speed. Thus, at half-speed, a centrifugal pump will produce only one-quarter pressure. Variation in water lift will also cause disproportionate drops in performance, if it falls outside the pump's range of efficiency. During late afternoon or early morning, or as cloud shadow appears, the pump may be spinning but the flow can stop completely.

A submersible pump is often simpler to install than a surface pump. It will not require intake piping or an intake valve. Nor will it require priming (being filled initially with water). It is less likely to be damaged from running dry due to pipe or valve leakage. Under ground and under water, it is protected from temperature extremes (e.g., freezing) and from human tampering.

Fig. 2: Pedrollo (Italian) surface centrifugal AC solar pump used in Odaltal village of Surkhet District for rice irrigation.

Horizontal submersible centrifugal pump installation (Fig. 3) is fine, but the lack of screen on the pump intake will cause the pump impellers to eventually clog from gravel and silt buildup that will require frequent cleaning of the pump stages. Pump intakes should be installed at least 1 meter from the bottom of well or river and with an intake screen to prevent large debris from entering. The community agreed to improve the pump setup.

Centrifugal pumps are useful for pumping large volumes of water and in situations of low head and are often the most efficient and economical. For example, in seeking a system to irrigate a large field requiring over 100 m3 per day, centrifugal pumps aer superior to positive displacement pumps.

Fig. 3: Grundfos submersible centrifugal pump used in a river for Taule village.

Fig. 4: Flood irrigation via a surface centrifugal solar water pump managed by Phattu Tharu of Bansgadhi, Bardiya.

The system above (Fig 4.) includes 8 TrinaSoar PV modules that are 315 Wp each (8 S X 1P configuration), directly powering a 1,800 W Italian Pedrollo AC surface centrifugal pump. The project irrigates rice and vegetables was implemented by the Hariyali Krishak Samuha farmer association in Bardiya in cooperation with the USAID Kisan project.

2. Accelerated Commercialization of Photovoltaic Water Pumping for Nepal

The USAID Accelerated Commercialization Solar Photovoltaic Water Pumping (AC-PVWP) project managed by Winrock Interational (WI) from 2015-17 is designed to expand the commercialization and adoption of PVWP systems for irrigation, livestock watering and community water supply in Nepal. The AC-PVWP project has worked closely with the USAID Knowledge-based Integrated Sustainable Agriculture and Nutrition (KISAN) Project in Nepal also managed by WI in supporting small scale farmers to transition from subsistence to commercial vegetable farming by helping implement new techniques and technologies such as solar water pumps, as well as the use of plastic houses and raised beds that replaced less effective traditional cultivation practices. Capacity building and market development activities have helped expanded commercialization and adoption of solar water pumping systems for irrigation, livestock watering, and community water supply. " Irrigation is a game changer for agricultural households in Nepal because they can grow during more seasons outside of the monsoon season and yields can be tremendously higher," states Phil Broughton, Chief of Party for the USAID

KISAN project (Warren, 2017).
The AC-PVWP project has been successful in establishing scalable and profitable business models. While higher upfront initial capital costs are always a barrier for the adoption of PVWP technology for rural communities and smallholder farmers in Nepal, the AC-PVWP project has worked closely with private suppliers, banks and financial institutions to develop business models such as credit financing, rent-to-own, water entrepreneurship, vendor financing to overcome this barrier and scale up installation of the technology. Furthermore, the project introduced new and affordable product with wide range of technology considering the need and affordability of the farmers for scaling up PVWP .market.

The first phase of the AC-PVWP project in 2016 installed over 69 pilot PVWP systems with installed capacity of 53.15 kWP benefiting 392 farmer groups in 16 districts as follows: Jhapa, Morang, Siraha, Rautahat, Makwanpur, Chitwan, Kathmandu, Kapilvastu, Syangja, Dang, Banke, Surkhet, Dailekh, Bardiya, Kailali and Kanachapurt. An additional ~120 replicated systems will be deployed in the second phase by the end of 2017. The business models employed and the district wise installations as shown below:

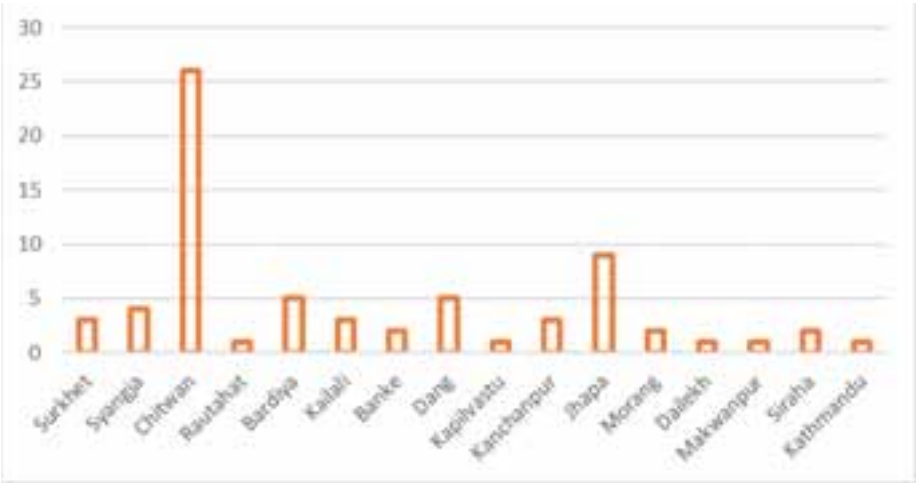

Fig. 5: Number of first phase AC-PVWP system installations by District in Nepal

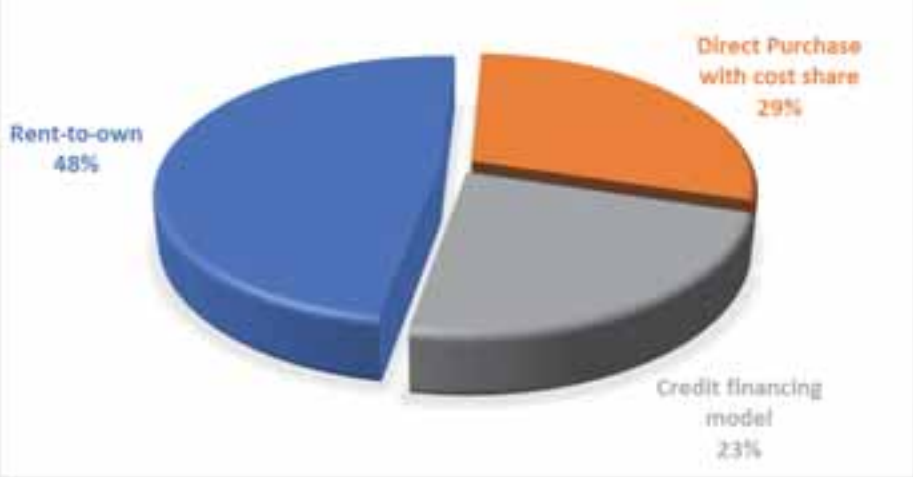

Fig. 6: Finance models for AC-PVWP projects installed in Nepal

3. Empowering Rural Women and Improving Livelihoods

"I can now earn enough to invest on the education of my children and I feel empowered" - Ms. Dila Gurung

Ms. Dila Gurung, 35 years old from the off-grid Taule village in Surkhet District, was in a difficult economic situation before acquiring a solar water pump which helped improve her livelihood. Even though she owned 5 Ropani (0.62 acres) of land, she was dependent on intermittent rainfed agriculture with no prospects for irrigation to increase productivity. WI approached the farmers about the potential to extend their ability to grow crops during the dry season through solar powered irrigation and that a solar-powered irrigation system would help transport 10,000 liters of water per day uphill from the nearby river to the fields where it was needed.

Her land is now green with high value commercial vegetables made possible with a PVWP system in collaboration with the Sitaram Agricultural Group. The financing for the PVWP was made accessible through the Small Farmer Saving and Credit Cooperative for commercial vegetable farming. Technical support was from WI from the USAID AC-PVWP project in collaboration with the Veri-Ganga municipality and USAID KISAN project.

The 1,260 Wp PVWP system installed at Taule-10 is primarily used for vegetable farming. The system includes 9 PV modules (140 Wp each) installed 9S X 1P. The mono-crystalline solar modules are manufactured by Ningbo Komaes Solar Technology Co. The system is community-based and owned by Sitaram Krishi Samuha benefiting 11 active farmers out of 16 members. The system pumps 10,000 liters per day of water at a total dynamic head (TDH) of 60 meters. The PVWP system was installed at a total cost of US$4,766 using a 1.26 kW SQF-3A10 manufactured by Grundfos. KISAN helped surmount that financial hurdle by arranging a cost-sharing agreement in which eight farmers took out a loan of $3,000 from a local farmers' cooperative, which would be paid back thanks to additional income from vegetable sales. In addition, Winrock, KISAN and the local Veri Ganga Municipal government contributed grants totaling $2,200. With labor supplied by the farmers and technical expertise from Winrock, the solar irrigation system was installed in May, 2015 (Warren, 2017).

Fig. 7: Solar water pumping array (9s x 1p) rated at 1.26 kWp used for irrigation by the Taule village farmers.

The difference consistent access to water has made in the amount of vegetables Gurung and his fellow farmers can grow has been dramatic. "After the solar pump the production has increased 70 or 80 percent," says Gurung. Household incomes have also risen between $300 and $2,750 annually, allowing the farmers to pay off the loan for the solar irrigation system (Warren, 2017).

The PVWP in Taule has completely changed Mrs. Gurung's lifestyle. She appreciates that the PVWP system has very low maintenance and running costs, quietly and reliably providing daily irrigation throughout the year. Her traditional subsistence farm was completely changed into a highly profitable enterprise based on using a PVWP systems for irrigation. She now harvests high value commercial vegetables and has seen a fivefold increase in her annual income from her former subsistence farming lifestyle. She grows cauliflower, cabbage, and red chilies and sells to the local markets. She is financially empowered and earned US$1,9145[1] last year from selling vegetables. She has better finances, improved self-esteem, and new technical skills attained from KISAN farmer trainings. "I feel socially, financially and technically empowered after commercial vegetable farming. I shared my journey of transition and boundless opportunities brought by the solar pump to Haree village to inspire women to switch to commercial vegetable farming." She looks forward to the returning of her husband from Qatar and she believes in their new potential to commercially grow vegetables together with no need for him to return to Qatar.

4. Case Study: Replacing Diesel Pumps for Solar Pumps for Fish Farming

"We are easily paying off the installation of our solar pump from the savings of diesel fuel costs" - Ms. Bhundi

[1] Exchange rate for 24 March, 2017: 1 US$=NPR 104.45

Chaudhary

Mrs. Bhundi Chaudhary, a 47 year old fish farmer from Maijui village of Chitwan district, whch is populated with indigenous Tharu residents whose main livelihood is fish farming. Mrs. Chaudhary decided to switch to solar water pumping system to fill her fish pond and aerate in order to eliminate the expense of her previous diesel powered water pump. Before installing solar water pumping system in her field, she used to fill the fish pond and irrigate her 13 Kattha (1.08 Acres) of land using an oversized 5 HP diesel water pump set. They used to operate diesel pump for 3 to 4 hours in every other day to meet their water requirements. They used to spend about US$ 81 per month for fuel to operate diesel pump.

Ms. Chaudhary learned about solar water pumping technology through a farmer's interaction program at Khareni, Chitwan organized by WI where she learned about a rent -to-own business financing program provided by Sun-Farmer Nepal. Leveraging the program, Ms. Chaudhary installed a 750 Wp solar pumping system that operates 0.8 HP submersible DC pump which pumps about 20,000 liters of water daily under this affordable financial model.

The PVWP was installed in December of 2015 at a total system installed cost of US$3,350, which included three years of vendor post-sales service. Since this was the first pilot in this region, and as incentive to buy down the technology risk for her as an early adopter, a subsidy of US$1,379 was provided jointly by WI and the Nepal Government Renewable Energy for Rural Livelihood project. As part of the subsidy agreement, she had to make her installation available as a demonstration for other area farmers. After providing equity of US$575 as up-front payment, NPR US$1,398 of the system and service cost was arranged under a rent-to -own business model through SunFarmer Nepal with a 3 years term. Under this scheme Ms. Chaudhary must pay monthly installment of US$39. Through productivity gains, she is paying back the installment from the savings of diesel fuel costs displaced. "Other farmers in the village were struggling to find diesel to run their diesel pump set during the Indian border blockade and were forced to buy diesel at higher price ranging up to NPR 350 (US$3.35) per liter. But, we were worry free as our solar water pump operated from the sun which was free from a blockade without incurring any cost and troubles" is Ms. Chaudhary's observation.

The 750 Wp Solar Water Pumping is used to draw water from an open-well to a canal to the pond. 3 panels each of 250 Wp are installed in configuration of 3 Sun-Worth PV models in series and 1 in parallel (3S X 1P). The pump is 600 W (48VDC submersible pump) from Solar Tech model SPM600C with a water output of 25,000 liters/day at 4.2-meter head for 6 kWh/m^2/day solar radiation. The system cost of the PVWP is NPR 350,000 (US$3,350.88). The system was installed under rent-to-model. In this model, the farmers provide a down payment upfront, and the remaining amount is financed by the company for a 3 years period. During the financed period, the PVWP vendor will be responsible for system operation and maintenance.

Fig. 8: Mrs. Chaudhary with her 750 Wp PV water pumping system in the background in between her aquaculture ponds

Besides the fish farm, Ms. Chaudhary also used water from solar pump to irrigate her land. She appreciates solar pump for several benefits such as minimal maintenance, effortless operation, minimal attention and continuous water supply compared to a diesel pump. The operation of diesel pump was not easy as it required physical strength to start and she had to look for help every time. She also had to remain standby to check the proper operation of diesel pump. Now, she is free as her solar pump is automated. The solar pump starts pumping water with the rising sun and stops as the sunset. She invests her saved time into productive works like vegetable farming, livestock rearing, and fencing her land. Her field is green with several types of vegetables. She is

growing green peas, cauliflower and other seasonal vegetables. She made profit of US$718 by selling of fish and US$287 by selling green peas and vegetables last year.

According to Ms. Chaudhary, "Installation of the solar pump was my sole decision and it feels good to be appreciated by my husband and family." She is now a model fish farmer in her village her self-confidence has been boosted from the interest and visits of other farmers to see her aquaculture operation and how they can also boost their productivity using a solar pump.

5. Case Study: Replacing Diesel Pumps for Solar Pumps for Fish Farming

"We no longer have to rely on rain to cultivate land. The barren land is now green with commercial vegetable farming" - Ms. Ganga Garanja

Ms. Ganga Garanja, 44 is a single mother of Pingale village of Pokharikada in Surkhet District who was a subsistence farmer who grew limited cereal crops to feed her family throughout the year. She owns 6 Ropani (0.75 acres) of mountain side land that was barren as irrigation was not feasible and she had to depend on inadequate rainfed agriculture compelling her to take out a loan just to feed her family. She along with her 2 daughters and a son were stuck in grinding poverty. Likewise, 29 other village households in Pingale were faced with a similar situation.

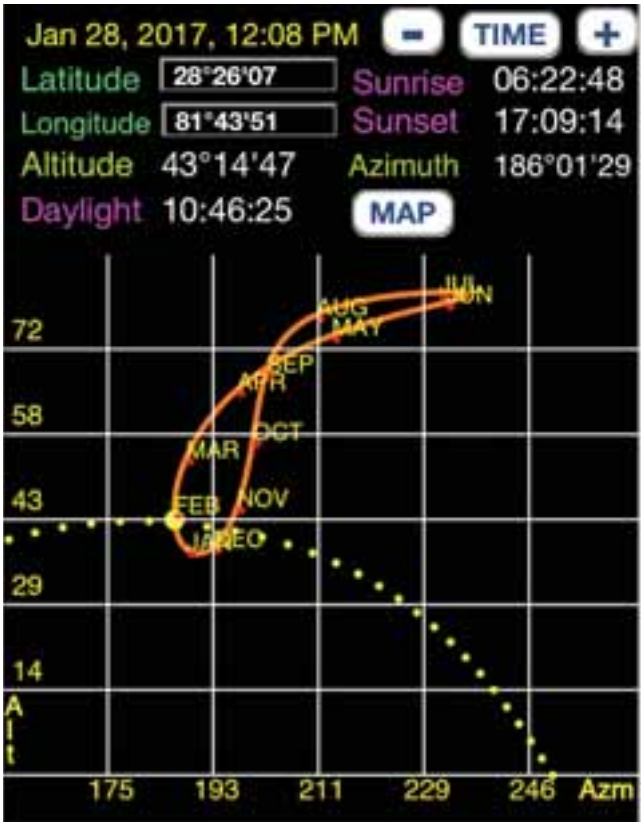

Fig. 9: Solar analemma near solar noon for Pokharikada (Solar Track App)

Despite owning land, the people of the village had to work as day laborers to survive. However, the money earned as day laborers was never sufficient to provide a good education and sufficient food for their children. Villagers intially tried to organize into a group named Milijuli Tarkari Utpadan Samuha to initiate commercial vegetable farming in 2009, but it was of no help as the group had no means for irrigation and depended on rain-fed agriculture.

Figure 10: Solar power array using German made Komaes140 Wp PV modules (9s x 1p) for t Pokharikada using a Grundfos submersible centrifugal solar water pump.

After 6 years in 2015, in collaboration with the AC-PVWP and KISAN projects, the Pingale village group installed a PVWP system for crop irrigation. The PVWP system helps farmers to irrigate throughout the year from a natural spring utilzing a spring catchment reservoir pumping to a higher altitude storage tank from where the water is distributed for irrigation. The villagers paid NPR. US$ 3,407 for the installation of the system. WI provided a pilot subsidy of US$1,436 through the AC-PVWP project and KISAN project provided US$192 to create a regional demonstration for other farmers in the district. Similarly, RISMFP and Pokharikanda VDC also provided grants of US$ 2,528 and US$ 1,292 for the installation of the system. .The system is managed and owned Milijuli Tarkari Utpadan Krishak Samuha farmer group.

Fig. 11: Pokharikada main water storage tank for solar water pumping from a spring for irrigation.

The PVWP helped the villagers make the transition from subsistence to commercial vegetable farming. The results for villagers has been life-changing from subsistence to commercial farming which has increased Ms. Granaja's income by 3-fold and enabled her to cultivate tomatoes and boost the quantity and quality of her crops. Now Ms. Granaja makes an annual profit of more than US$ 478.69 from tomatoes and US$ 287 from selling other seasonal vegetable and US$ 191 from livestock.

The technical skills provided by the KISAN project on commercial vegetable farming regarding the better seeds, vitamins, tillage, plant spacing, varieties and scheduling irrigation has been very effective. Mrs. Granaia

concludes that “The technical assistance from Winrock International has helped us to have received the solar water pump that requires less attention, effortless operation, and minimal maintenance.” The villagers now have a better financial status because of solar powered irrigation for commercial vegetable farming.

6. Commercial Rice Irrigation

A solar water pumping system was installed with WI assistance in the village of Odaltal of Surkhet District by Ghampower Pvt. Ltd. in November, 2016. The farmer group installed the distribution pipes and water storage tank in mid-2017. The system is managed by Jagaran Krishak Samuha, who is part of a 30 farmer cooperative group, whose chairperson is Ms. Tej Kumari Sunar.

The system consists of a 2,340 Wp array TrinaSolar modules from China (9S X 1 P configuration), each solar panel is 260 Wp. A 2,300 W Italian Pedrollo 2 HP AC surface pump is used to deliver water to the water storage tank from the spring reservoir. The total PVWP system cost was US$5,170, which excludes civil works such as the spring reservoir, storage tank, and distribution pipes. The irrigation system only became operational in mi-2017 and economic impacts for rice irrigation season have not yet been determined.

Figure 12: WI technicians measuring solar irradiance for the PVWP installed in Odaltal village of Surkhet District.

6.1. Rice and Vegetable Irrigation

A large solar water pump system was installed in November 2016 in Piparkoti, Valkachuha in Kailali District using a Trina Solar 3,120 kWp solar power array used for irrigation of rice and vegetables. The farmer group that uses this system was formed by USAID-KISAN project and has 20 members. The solar power system is owned and managed by Sirjana Krishak Samuha from the farmer group. The PV system is somewhat unique for solar water pumpoing in that it charges a battery bank to operate the solar pump and a crop grinder processing unit.

The battery bank is comprised of eight 150 Ah 12 V Asian batteries (made in Nepal) that are wired in a 4S X 2P configuration for a total capacity of 300 Ah at 48 V. (14,400 kWh). The battery bank is used to power a Chinese made 4 kW VOP Solar Hybrid Inverter model InfiSolar V 4000-48 operating at 220 V and 50 Hz. The PV power system operates an AC powered 1.5 HP Pedrollo AC surface centrifugal pump for irrigation. The total system cost of the PVWP was US$7,430 which includes the balance of system (batteries, inverter, etc.), as well as the crop grinder; it excludes civil works and power house costs.

Fig. 13: Piparkoti village inverter and controls for large scale rice irrigation

7. Lessons Learned

Solar water pumping technology ensures sustainable and effective access to water for irrigation, livestock watering and drinking water supply for smallholder farmers in Nepal. Easy access to water encourages smallholding farmers to carry out or increase their economic activity graduating them from subsistence farming to commercial farming. However, the key barriers for generating large scale commercial sales of solar water pumping systems are related to financial and market access issues, rather than technology which is reliable and mature. PVWP water pumping systems have dropped dramatically in price over the past decade, but still require a somewhat higher initial capital investment than diesel pumps. Experience in Nepal has shown that with access to financing, the challenges can be overcome by taking advantage of relative cost savings, increased reliability for both electricity and irrigation systems, increasing access to technology and technological assistance, and reduced greenhouse gas emissions, when compared with diesel pumps. Efforts to commercialize PVWP technology for irrigation are ongoing, by embedding the technologies in value chain projects which support farmers to increase income by growing off-season vegetables and fruits, fish, and livestock. Barriers include lack of awareness about the technology, high upfront costs, and absence of technical repair services can be overcome through demonstration projects, linkage with finance institutions, and partnerships with technology providers.

8. References

Kunen, E., and Pandey B., Foster, R. et al, 2015. “Solar Water Pumping: Kenya and Nepal Market Acceleration, Solar World Congress”, International Solar Energy Society (ISES), Daegu, Korea.

Foster, R., Ghassemi M., Cota A., 2009. Solar Energy, Renewable Energy and the Environment Series, Volume 2, Taylor and Francis Publishing, CRC Press, ISBN: 13:9781420075663, Boca Raton, Florida.

Warren, Chris, 2017. Winrock International, blog, www.winrock.org/water-from-the-sun

Accelerating Solar Water Pump Sales in Kenya: Return on Investment Case Studies

Jennifer Holthaus[1], Bikash Pandey[1], Robert Foster[1], Bernard Ngetich[2], James Mbwika[3], Evgenia Sokolova,[4] and Philip Siminyu[5]

[1] Winrock International, Arlington, Virginia (United States)

[2] Winrock International, Nairobi (Kenya)

[3]Value Chain Consultant, Nairobi (Kenya)

[4]Enterprise Finance Consultant, Madrid (Spain)

[5]Agricultural Economics Consultant, Nairobi (Kenya)

Abstract

Irrigation allows smallholder farmers to increase their yields and to grow two or even three crops of high-value vegetables and fruits a year, receiving higher commodity prices during the off-season. In Kenya in 2010, 2.5 million smallholders generated 80% of national horticulture production. Inexpensive diesel water pumps (US $200) are available, but fuel purchase and transport costs are significant (typically US $100–$300 per 3-month season for one acre); as a result farmers are conservative with, or cannot afford, diesel irrigation. Return on Investment case studies by Winrock International show an increase in gross profits of up to 186% within one to two crop seasons after purchase of a solar water pump (SWP). Between August 2015 and December 2016 Winrock demonstrated SWPs to more than 16,000 smallholder farmers in Kenya and found that despite strong demand, the lack of smallholder credit options for solar irrigation is a key obstacle preventing SWP sales from increasing rapidly; financial institutions and SWP retailers need technical assistance to facilitate smallholder access to credit.

Keywords: smallholder, solar irrigation, solar water pump, finance, return on investment, Kenya

1. Introduction

In Kenya in 2010, 2.5 million smallholders generated 80% of horticulture production. 80% of the country's land surface is classified as arid and semi-arid; the majority of people living in rural areas depend on rain-fed agriculture for their livelihoods. Historically, rains occurred in January, February, November and December, with dry conditions the rest of the year. Climate change is affecting rainfall patterns, which in turn is causing increased crop failures and lower yields. Expanding irrigation is a key mitigation strategy for smallholders (Karina 2011). Irrigation can assist in agricultural diversification, enhance food self-sufficiency, increase rural incomes, generate foreign exchange and provide employment opportunities when water is a constraint (Ngigi 2002). Irrigation can allow smallholder farmers to increase their yields and grow two or even three crops of high-value vegetables and fruits a year, receiving higher commodity prices in the dry seasons.

Winrock International is a non-profit organization that works to empower the disadvantaged, increase economic opportunity and sustain natural resources around the world. Winrock has been working to increase smallholder productivity and income through affordable on-farm solar technologies, including solar chillers and solar water pumps.

Solar water pumping is a mature, reliable, and economically attractive solution for off-grid irrigation, livestock water, and community water supply. A 2008 Rutgers University study showed that vegetable growing using solar irrigation is cost effective compared to grid-connected drip irrigation. Given that rural smallholders in Kenya have an increasing need for irrigation but limited access to conventional energy sources, solar water pumps (SWPs) are a critical tool for ensuring food security and decreasing poverty. However, smallholder adoption of solar irrigation is hampered by lack of awareness of affordable, high-quality solar pump products, and lack of access to finance for solar pump purchases.

2. Solar Water Pumps in Kenya: Supply and Demand

doi:10.18086/swc.2017.30.03 Available at http://proceedings.ises.org

In mid-2015, when Winrock International began demonstrating solar water pumps (SWPs) in Kenya under the USAID-funded Kenya Smallholder Solar Irrigation (KSSI) project, there were two high-quality, affordable small scale SWPs locally available. The US $450 SunFlower pump by Futurepump was designed to operate up to 10 meters Total Dynamic Head (TDH), and the US $2,200 SunCulture SP-300 pump was designed to operate up to 50 meters TDH (Kunen, 2015). SWP retailers were receiving individual pump orders but having difficulty aggregating purchases from smallholder farmers (<2 acres). During farmer field days attended by more than 16,000 farmers between August 2015 and December 2016, Winrock found very high interest in SWPs among farmers, but few had the cash needed to purchase a SWP. The most frequent comments from farmers were that the SWPs should be cheaper, and that financing would greatly facilitate purchases.

By early 2017 there were four high-quality affordable small scale SWPs locally available, including the new $350 Majipump MP 400 offered by Chloride Exide, and the $1,500 D3Solar offered by Davis & Shirtliff. The SunFlower had increased in price to US $650 and the SunCulture SP-300 pump had decreased to US $1,740. In October 2017 SunCulture launched the US $500 RainMaker pump, which claims to pump 7,000 liters per day at 100 meters total dynamic head, but has not yet been tested by Winrock. Given that the majority of the 5 million smallholder farmers in Kenya live in areas where TDH is between 10 and 50 meters (**Fig. 1**), Winrock estimates conservatively that 2 million smallholders in Kenya could achieve significant income benefits from the SWPs currently on the market. An efficient way to accelerate commercial sales of SWPs is through existing aggregation mechanisms targeting smallholder horticulture producers, including cooperatives, wholesale buyers, exporters, and processors.

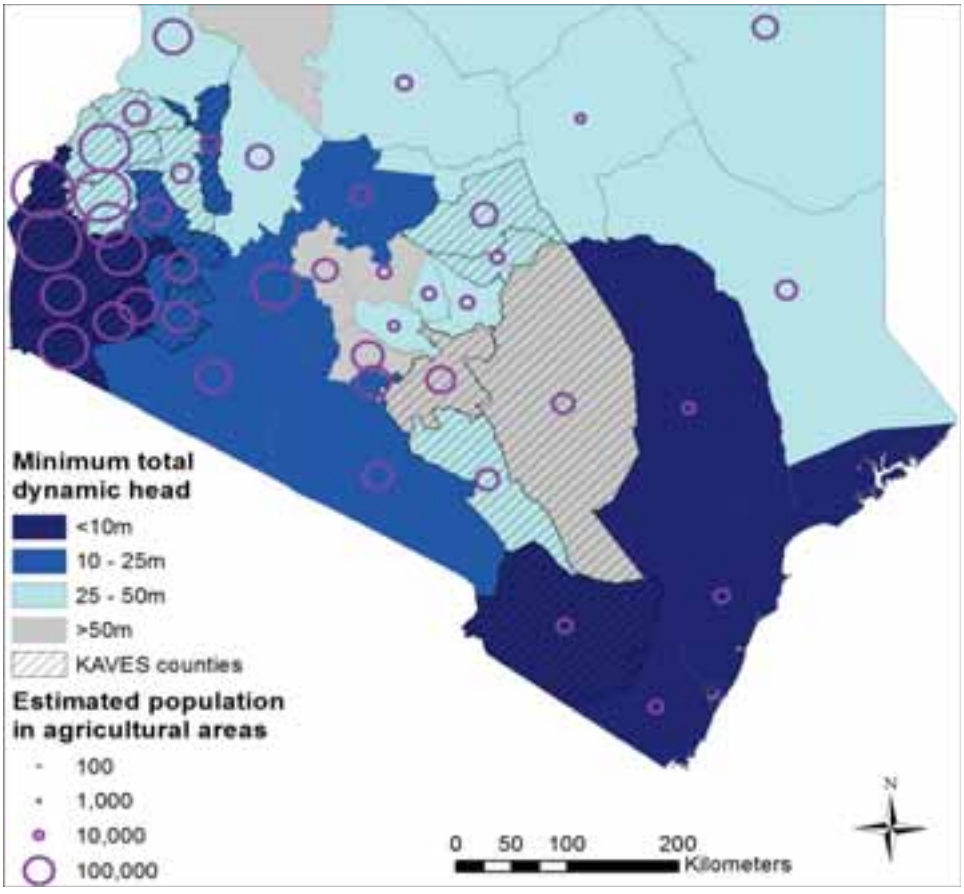

Fig. 1: Minimum total dynamic head vs estimated farmer population in Kenyan counties.

3. Smallholder Finance Options

Between August 2015 and May 2016, KSSI facilitated demonstrations of the Futurepump SWP at farmer

field days hosted by the Kenya Agricultural Value Chain Enterprises project. More than 8,000 farmers visited the Futurepump booth, yet only 9 SWPs were sold for cash during the events. In late 2015 Winrock began an effort to facilitate solar pump finance from Kenyan financial institutions (FIs). At the time Winrock could only identify one FI, Equity Bank Kenya, with an existing solar pump loan product for smallholders. Equity reported that, because of perceived high credit risk, they had rejected most of the 200 solar pump loan applications they had received since they created the loan product. Reasons included lack of farming experience or an alternative salaried income; lack of land ownership; and lack of required collateral.

Interviews with more than 20 Kenyan FIs showed that prevailing loan terms – if solar pumps were classified as agricultural loans – would be difficult for most smallholders to meet. Annual interest rates were 22% and up; a 20-30% down payment was required; and some FIs also required credit and crop insurance, which each added up to 10% in one-off interest fees. However, every FI interviewed by Winrock expressed interest in solar pumps as a way to mitigate risks of rainfall variability and drought, therefore lowering overall default rates in their existing agricultural portfolios. FIs acknowledged the high demand for solar pumps from their clients, but were hesitant to enter the market because of uncertainties about supply, performance, and cost of solar pump products.

Winrock selected five FIs as potential partners to create solar pump loan products. All five FIs had offices in areas with high solar pump demand and strong distribution and after-sales support from retailers. Three FIs – Juhudi Kilimo, ECLOF Kenya (through its affiliate Ecosmart Energy Limited, a renewable energy distributer), and the Kenya Union of Savings and Credit Co-operatives (KUSCCO) – moved forward with Winrock-supported loan pilots under the following terms:

- Commitment to lend to at least 50 SWPs over a period of 3 months;
- Affordability of credit to smallholder farmers, defined as owning less than 5 acres and having limited financial history and physical collateral;
- Availability of capital to put toward SWP loans;
- Willingness to share training costs;
- Strong senior management buy-in; and
- Readiness of systems and internal processes to lend into a new product.

Winrock served as a bridge between two FIs and a solar pump retailer, assisting them to negotiate terms for pricing, target sales volumes, demonstration pump units, distribution and after-sales support. FIs were reluctant to handle stock (which also results in a Value-Added Tax that they are not able to charge to loan clients), so an intermediary distributor or stockist was engaged near FI branch offices.

To decrease the risk perception of the FIs, Winrock provided data on farm-level return on investment case studies (**Section 5**), which showed payback times of 1.5 years or less; and on typical solar pump warranties (20 years for solar panels, 2 years for pumps). The warranty and payback periods match well with a 2-year loan tenor. Winrock advised the FIs to classify solar pump loans as asset financing, typically viewed as less risky, requiring less collateral and enabling better loan pricing. Winrock also provided solar pump technical training to FI senior management teams and branch loan officers.

During an initial loan marketing phase, issues that required troubleshooting from Winrock included miscommunication over pump delivery logistics, and adjustments to the marketing strategy to ensure that loan officers were targeting savings groups that had the capacity to take on new loans.

After 6 months, results included 5 solar pump loans made by Juhudi Kilimo, and 40 smallholders who had initiated savings with Ecosmart to qualify for a solar pump loan. One year later, the emergence of two lower-cost SWPs on the market has caused Juhudi Kilimo to adjust its SWP product offering, since many of its clients need a higher-powered pump than the one they had been offering. They plan to incresae the SWP loan size to include a water tank, piping and drip irrigation kit. Given the 2017 drought in Kenya they are also assessing other solutions including water conveyance and storage. Ecosmart is also seeking to offer one of the new lower-cost SWPs, as many of their clients felt the price of the original SWP product was too high. ECLOF's members have saved US $3,000 toward SWP loans.

Key lessons learned were:

- Co-guarantees in a group lending arrangement did alleviate prohibitive collateral requirements, but required a lead time of at least 3 months or more for existing loan groups to build up the required savings for credit disbursal. For new farmer groups the lead time was nearly double that of existing loan groups.

- Solar pump products must match smallholder needs in several key ways: the pump must perform at the required TDH; accessories must also be offered on credit if needed by farmers (e.g. pipes, water tank and/or irrigation drip kit); and smallholders must perceive that the SWP price is affordable.
- Aggregation mechanisms are an effective next step to gain scale and reduce costs when commercializing a new technology. Aggregation brings about volumes and bulk pricing discounts that eventually lead to lower prices for smallholders. For technical assistance providers, aggregation also offers economies of scale to reach thousands of farmers while minimizing program costs.

4. Pump Technologies Deployed

The KSSI project installed several types of solar water pumps for crop irrigation and aquaculture. There are two families of pump mechanisms with a range of options depending on water volume needs, pumping depth, and lift; thus there are two mechanical principles by which a pump can create pressure. Displacement pumps (also called positive displacement or volumetric pumps) move water by isolating it in sealed chambers, and applying mechanical action to force it upward. Displacement pumps work efficiently through wide ranges of speed and head. The KSSI project used mostly positive displacement pumps for small pumpig systems <2kW in both surface and submersible configurations as described in the following sections.

3.1 Reciprocating Displacement Pump

The SunFlower pump (**Fig. 2**), sold by Futurepump, is a portable solar irrigation pump manufactured in India. It raises a close-fitting piston in a submerged pipe to draw water up behind it to fill the vacuum which would otherwise occur; this works only up to a certain limit of the height water can be pulled by suction (~10 m maximum limit), see **Fig. 3**. The piston serves to create a vacuum and the water is actually displaced by atmospheric pressure pressing on its external surface. So water is displaced by "pulling." The KSSI project facilitated deployment of 172 SunFlower pumps, mostly in the Lake Victoria region of Kenya (**Section 5.2**).

Fig. 2: Futurepump SunFlower (SF1) is a micro-size piston pump for small-farm irrigation. To reduce cost and complexity, it uses a two-speed manual transmission instead of an electronic controller, and manual solar tracking. Photo: Winrock International Kenya.

4.2 D

iaphragm Pumps

Diaphragm pumps displace water by means of a diaphragm made from a flexible synthetic material (elastomer). Normally there are three or four pumping chambers, each with a check valve for the intake, and another for the outlet. Diaphragm pumps supply low volume water needs at high efficiency and low cost. A diaphragm pump may be used for solar pumping where the initial cost must be minimal, the water volume requirement is very low, and the future cost of maintenance frequent replacement is acceptable. Diaphragms normally need to be replaced after a two or three years of continuous use, due to normal material fatigue and wear. Manufacturers of these pumps provide replacement kits, or the entire pump may be replaced at low cost. Pumps that provide low lifts (the lower half of their capacity) can last longer than those operating at higher lifts. Diaphragm pumps are generally not a good choice for communal water pumping systems due to their higher maintenance requirements.

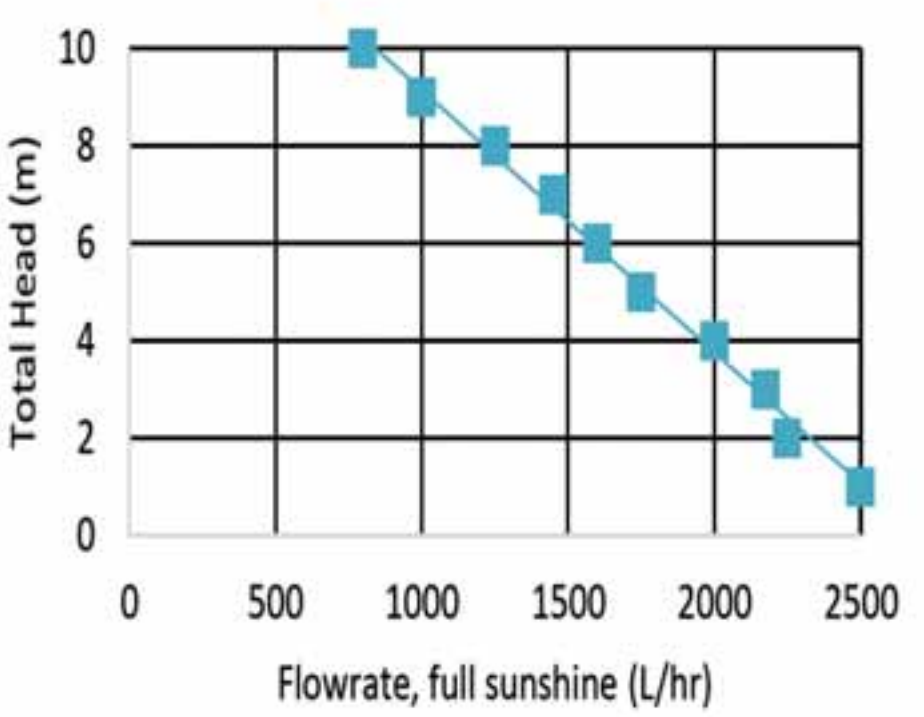

Fig. 3: As shown by the SunFlower pump manufacturer's performance curve, it can lift 2,000 lph at 4 m head at 1,000 W/m² irradiance using only an 80 Watt PV module. Courtesy: Futurepump

Diaphragm pumps are most appropriate for small volume requirements such as single-family drinking water or livestock pumping. If the pump is to be run every day, year-round, a HR pump should prove more economical in the long run.

Fig. 4: Winrock technicians inspecting two Ubink PV modules made in Kenya for the Machakos solar diaphragm pump system. The farmer brings her PV modules in at night for security reasons.

4.3 Helical Rotor Pumps

A helical rotor pump (HR) is a positive displacement pump that offers a wide range of volume and lift capacities at high efficiency. The pump end has only one moving part lubricated by water that produces continuous flow, free of pulsation (unlike a diaphragm pump) and requires no preventive maintenance. The HR pump has the best characteristics of any type of displacement pump due to its simplicity and reliability. It is optimum for flow ratesup to ~60 lpm for vertical lifts that exceed 20 m.

The HR pump's rotor is a helix made of stainless steel which fits precisely into a rubber stator (stationary outside tube), see **Fig. 5**. The inside surface of the stator is formed of two intertwined helixes, with an ovoid cross-section. The surfaces of the rotor and stator intersect to form a series of sealed cavities (hollow spaces). As a cavity forms at the intake end, it draws water in. As the rotor turns, the cavity seals and progresses upward (also called a progressive cavity pump). The pumped water lubricates the rotor. As with any pump, a high concentration of abrasive particles will cause premature wear of the rotor and stator.

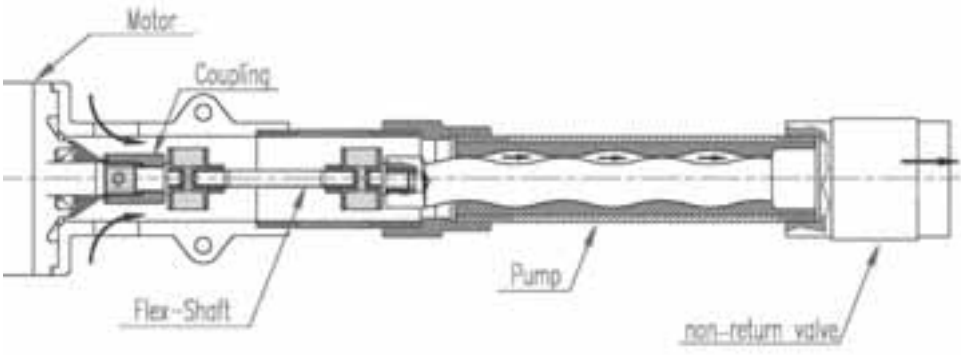

Fig. 5: Cross-section of typical helical rotor pump end (Foster et al, 2009).

A check valve at the pump's outlet prevents possible leakage downward when the pump is stopped. By relieving pressure, it tends to make the pump easier to start. The check valve closes only when the pump stops. Electronic controllers for HR pumps supply a boost of current, and precise control during startup. The KSSI project facilitated the installation of a relatively large solar pumping system in Nyandarua county, which uses an HR pump (**Fig. 6**).

Fig. 6: Lorentz helical rotor 8.1 kW_p solar water pumping system providing community and irrigation water supply to 500 farmers in Nyandarua County. The borehole is 230 meters.

5. Solar Pump Return on Investment Case Studies

Winrock conducted detailed farm-level return on investment case studies from 2015 to 2017. The case studies, which represent different pump price points, show strong returns within one to two crop seasons.

5.1 Solar drip irrigation in Machakos County

Mr. Shadrack Nzioka has farmed since 2006 in Muuani Village, Machakos County. He was using a diesel pump to transfer water to a pond, from which he irrigated 0.25 acre of onions with a treadle pump. In August 2015 Mr. Nzioka invested US $2,670 in a 27 meter borehole, a water tank, and land clearing. He purchased a US $2,500 SunCulture SWP and drip kit through a US $2,000 loan from Equity Bank at 18% interest; he will make a monthly loan payment of US $100 for two years. The helical rotor solar pump, which is powered by a 300 Wp solar module, automatically fills a water tank connected to drip irrigation (**Fig. 7**). During the first season after purchasing the SWP Mr. Nzioka irrigated 0.25 acres of onions. During the second season after purchasing the SWP Mr. Nzioka increased to a total of 0.875 acre: 0.25 acre of onions, 0.5 acre of passion fruit and 0.125 acre of tomatoes.

Fig. 7: Installation of water tank and drip lines at Shadrack Nzioka's farm.

The solar pump allowed Mr. Nzioka to increase his irrigated acreage from 0.25 to 0.875 acre, eliminate diesel fuel costs, and grow two crops per year instead of one. Using conservative estimates, he maintains his gross profit while paying off the two-year solar pump loan. Using conservative estimates, his gross profit is projected to increase by 100% after he pays off the loan. A profit and loss analysis for Mr. Nzioka is shown in **Table 1**.

Table 1: Shadrack Nzioka Profit and Loss Analysis

	Year 1 Actual		Year 2 Actual	Year 3 Projected
	Season 1 (Pre-SWP)	**Season 2 (Post-SWP)**	**Season 2**	**Season 2 (Post Loan)**
Farmer Profit and Loss Statement				
Acreage Planted	Onions 0.25	Onions 0.25	Onions 0.25; PF 0.50; Tomatoes 0.125	Onions 0.25; PF 0.50; Tomatoes 0.25
Total Yield (kg)	3,125	3,500	5,500	8,500
Yield change, %		*12%*	*57%*	*55%*
Total Revenues	**312,500**	**350,000**	**475,000**	**720,000**
Revenue growth, %		*12%*	*36%*	*52%*
Operating Costs	77,100	83,600	158,450	195,150
Diesel Pump Fuel and Transport	11,000	-	-	-
Pump maintenance	2,000	500	600	1,040
Total Operating Costs	**90,100**	**84,100**	**159,050**	**196,190**
Gross Profit	**222,400**	**265,900**	**315,950**	**523,810**
Gross Profit Margin, %	*71%*	*76%*	*67%*	*73%*
Loan + interest payment (6 months)	-	60,000	60,000	-
Earnings Before Taxes (EBIT)	**222,400**	**205,900**	**255,950**	**523,810**
Debt Coverage and Investment Returns				
SWP Total Upfront Investment	480,500		5 Yr Return on Investment (ROI)	3.61
financed by own savings	280,500		5 Yr Internal Rate of Return (IRR)	36%
financed by Bank Loan (18%, 2 yrs)	200,000		Incremental Gross Profit/Initial Investment	3.91x
Loan Principal and Interest due in 2yrs	240,000		Cash Flow/Total Debt Coverage	3.72x
vs Cash flows generated in 2 years	892,560			

5.2 Solar irrigation in Homa Bay county

Ms. Lilian Akinyi rents a farm in Homa Bay County near Luala Kambuya village. She was using a diesel pump to transfer water from a canal which is fed by the Sondu Miriu River. She hired the diesel pump one day a week for US $5.50, which included pump rental, petrol and transport. She irrigated 0.75 acre of tomatoes with the diesel pump and 0.25 acre of kale with a watering can. In September 2016 Ms. Akinyi purchased a Futurepump solar pump powered by a 80 Wp solar module and a 12-meter pipe (US $36) through Futurepump's Pay-As-You-Go program. She paid US $236 down, and will make a monthly loan payment of US $20 for 22 months. She stopped using the diesel pump as soon as she purchased the solar pump.

Fig. 8: Lilian Akinyi with her 0.75 acre maize crop, December 2016.

Ms. Akinyi no longer has diesel pump rental, fuel and transport costs, has increased her irrigated area from 1 to 1.25 acres, has added a maize crop (**Fig. 8**), and is irrigating more frequently than before. We assume she will increase to 1.5 acres by the second season after purchasing the solar pump. Using conservative estimates, her gross profit is projected to increase by 186% by her second season after purchasing the solar pump. A profit and loss analysis for Ms. Akinyi is shown in **Table 2**.

Table 2: Lilian Akinyi Profit and Loss Analysis

	Year 1 Actual		Year 2 Actual	Year 3 Projected
Lilian Akinyi Farm	**Season 1 (Pre-SWP)**	**Season 2 (Post-SWP)**	**Season 1**	**Season 2 (Post Loan)**
Farmer Profit and Loss Statement				
Acreage Planted	Tomatoes: 0.75; Kale 0.5	Tomatoes: 0.25; Kale 0.25; Maize 0.25	Tomatoes: 0.5; Kale 0.5; Maize: 0.5	Tomatoes: 0.5; Kale 0.5; Maize: 0.5
Total Yield (kg)	2,517	3,683	6,300	6,900
Yield change, %		*46%*	*71%*	*10%*
Total Revenues	**99,200**	**144,890**	**250,600**	**282,800**
Revenue growth %		*46%*	*73%*	*13%*
Operating Costs	29,530	38,063	50,246	52,700
Pump Fuel and its Transport	2,500	1,000	-	-
Pump Hire and Maintenance	3,000	3,700	1,500	1,800
Total Operating Costs	**35,030**	**42,763**	**51,746**	**54,500**
Gross Profit	**64,170**	**102,127**	**198,854**	**228,300**
Gross Profit Margin, %	*65%*	*70%*	*79%*	*81%*
Loan + interest payment (6 months)	-	15,000	15,000	-
Earnings Before Taxes (EBIT)	**64,170**	**87,127**	**183,854**	**228,300**
Debt Coverage and Investment Returns				
SWP Total Upfront Investment	78,600	5 Yr Return on Investment (ROI)		18.14
financed by own savings	23,600	5 Yr Internal Rate of Return (IRR)		197%
financed by Vendor Loan (10%, 2 yrs)	55,000	Incremental Gross Profit/Initial Investment		2.56x
Loan Principal and Interest due in 2yrs	65,000	Cash Flow/Total Debt Coverage		10.63x
vs Cash flows generated in 2 years	691,011			

6. References

Kunen, E., Pandey B., Foster R., Holthaus J., Shrestha B., Ngetich B., 2015. "Solar water pumping: Kenya and Nepal market acceleration," Solar World Congress, International Solar Energy Society (ISES), Daegu, Korea.

Foster, R., Cota, A., 2009. Solar Energy, Renewable Energy and the Environment Series, Volume 2. Taylor and Francis Publishing, CRC Press, Florida.

Karina, Francis Z., Wambua Mwaniki, Alex, 2011. Irrigation Agriculture in Kenya: Impact of the Economic Stimulus Programme and Long-term Prospects for food Security in an Era of Climate Change. Heinrich Boll Stiftung, East and Horn of Africa.

Ngigi, S.N, 2002. Review of irrigation development in Kenya. In: Blank, H.G., C.M. Mutero and H. Murray-Rust (eds.), 2002. The changing face of irrigation in Kenya: Opportunities for anticipating change in Eastern and Southern Africa. International Water Management Institute, Colombo, Sri Lanka.

Tietjen, W. H., Grande, J., Nitzsche, P. J., Manning, T., Dager, E., 2008. Solar pump drip irrigation for vegetable production, ASP proceedings. Rutgers CES of Warren County.

Solar Thermal Collectors

Experimental Investigation of the Performance of a Transpired Solar Collector Acting as a Solar Wall

Andrei-Stelian Bejan[1], Abdelouhab Labihi[1, 4], Cristiana-Verona Croitoru[1, 2], Florin Bode[2, 3], Mihnea Sandu[1],

[1] Technical University of Civil Engineering Bucharest, Faculty of Engineering for Building Services, Bucharest (Romania)

[2] CAMBI Research Center, Bucharest (Romania)

[3] Technical University of Cluj-Napoca, Cluj-Napoca (Romania)

[4] LP2M2E Laboratory, Cadi Ayyad University, Marrakech (Morocco)

Abstract

It the current energy context it is necessary to implement highly efficient and cost-effective systems in order to reach indoor comfort conditions with minimum energy consumption. This paper aims to analyze the performance of an unglazed transpired solar collector (UTSC), which represents a building envelope element, and to assess the efficiency of two types of external metal cladding: with circular orifices and with lobed orifices. Several experimental campaigns were conducted using different approaches and the results are very interesting: the metal plate with lobed orifices increases the efficiency of the solar collector, providing an enhanced thermal transfer and higher exhaust temperatures. The use of lobed orifices rises the outlet air temperature with 10% more than in the case with circular orifices by enhancing the heat transfer between the metal plate and the air flow due to the more complex dynamic of the lobed flows near the metal absorber. The rise in temperature in case of using lobed orifices is 22.9°C and the metal plate temperature is 64.5°C. An experimental study regarding the implementation on phase changing materials (PCM) in transpired solar collectors was also conducted.

Keywords: Transpired solar collector, TSC, solar wall, energy efficiency, lobed orifices, circular orifices, PIV, phase changing materials, PCM

1. Introduction

Nowadays, the buildings sector is responsible for over one-third of the total energy consumption and CO_2 emissions, being the largest energy consuming sector in the world (IEA, 2013), while the requirements regarding energy use reduction and the CO_2 emissions are more and more strict (EU, 2015).

After the COP21 conference all the members of the UN agreed to limit the global warming even to 1.5°C above preindustrial level in next eighty years (Gütschow et al., 2015) and furthermore all the European Union states must reduce the CO_2 emissions with 20% until 2020 and 40% until 2030, and must reduce the primary energy consumption with 27% until 2030 (EU, 2014). Therefore, in order to reach these goals it is necessary to implement highly efficient systems and solutions by using renewable energy sources to obtain the indoor comfort parameters with minimum energy consumption.

One of the most promising strategies that could be used in this purpose is the use of the solar air collectors which can represent a cost-effective solution (Dymond and Kutscher, 1997, Gill et al., 2012). There are many types of solar collectors used in order to pre-heat the air (Shukla et al., 2012). Thermal solar walls can be classified in several types and categories (Hami et al., 2012) but the two main categories are: glazed solar collectors (GSC, e.g. Trombe walls) and unglazed transpired solar collectors (UTSC – usually used as façade elements). Transpired solar collector are more efficient than plane solar collectors (Belusko et al., 2008) and the efficiency can be even higher with 50% (Chan et al., 2014). According to the literature transpired solar

Selection and/or peer review under responsibility of Scientific Committee
doi:10.18086/swc.2017.31.01 Available at http://proceedings.ises.org

collectors have lower investment costs and also lower operation costs, being an excellent cost-benefit, energy-efficient system (Nkwetta and Haghighat, 2014, Wang et al., 2017).

The UTSC usually presents a perforated metal plate which, together with the building wall, creates a cavity for the air flow. The metal plate is heated by the solar radiation and the energy is yielded to the air which is extracted from the top of the wall and afterwards, it is introduced in the building. The operating principle of the unglazed transpired solar collector which acts as a solar wall for the building envelope is highlighted in figure 1.

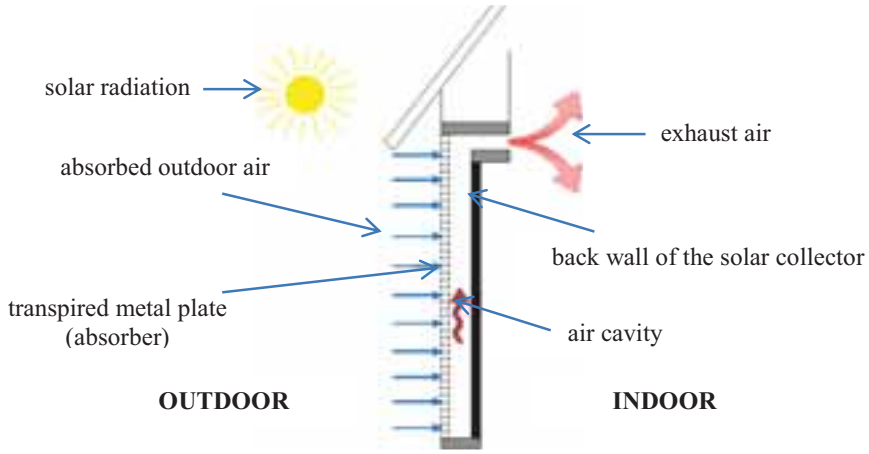

Fig. 1: The operating principle of an unglazed transpired solar collector acting as a solar wall

The solar radiation, ambient (outdoor) temperature, air flow, orifices geometry, pitch, collector geometry, solar absorber material are very important parameters which defines the efficiency of a solar collector (Zhang et al., 2016). Also in order to assess the impact of a transpired solar collector it is important to determine the rise in temperature (ΔT, difference between the outlet air temperature and ambient air temperature), the efficiency of the solar collector (η) and the efficiency of heat transfer or heat exchange effectiveness (η_t) (Van Decker et al., 2001, Leon and Kumar, 2007).

According to Wang et al. (2017) these parameters can be calculated with the following formula, where: c_{air} is specific heat capacity of air (J kg^{-1} K^{-1}), $\dot{m}_{air}$ is air mass flow rate (kg s^{-1}), $T_{air,out}$ is outlet air temperature (°C), T_a is the ambient air temperature (°C), G_s is the incident solar radiation on the collector (W m^{-2}), A_s is collector area (m^2) and T_p is the average absorber plate temperature (°C):

$$\eta = \frac{c_{air}\dot{m}_{air}(T_{air,out}-T_a)}{G_s A_s} \quad \text{(eq. 1)}$$

$$\Delta T = T_{air,out} - T_a \quad \text{(eq. 2)}$$

$$\eta_t = \frac{T_{air,out}-T_a}{T_p-T_a} \quad \text{(eq. 3)}$$

A very interesting study found in the literature emphasize that if the orifices diameter and the pitch have lower values, the heat transfer efficiency is enhanced (Leon and Kumar, 2007). An experimental study (Wang et al., 2017) shows that a transpired solar collector could reach a rise in temperature up to 31.16°C and an efficiency up to 74.93% depending on the input conditions (tests were made for solar radiation from 400 W m^{-2} to 1000 W m^{-2} and air flow between 80 (m^3 h^{-1}) and 200 (m^3 h^{-1})).

According the literature a UTSC could reach a rise in temperature between 6°C and 35°C, and an efficiency between 19% and 75% (Konttinen et al., 2005, Leon and Kumar, 2007, Cordeau and Barrington, 2011, Li, 2013, Perisoglou and Dixon, 2015, Wang et al., 2017). Even if there are many studies regarding the performance of the transpired solar collectors, very few authors focused their attention on the geometry of the orifices even if, according to the studies, 28% of the heat is transferred to the air in the orifice (Van Decker et al., 2001). Usually the metal plate orifices have circular shape. However, the lobed geometries studied before by researchers could improve the heat transfer because of the complex dynamics of the flows and streamwise vortices induced (Nastase et al., 2008, Nastase and Meslem, 2010).

The main objective of the present paper is to assess the impact of the geometry of orifices on the thermal efficiency of an UTSC in to cases (circular orifices plate and lobed orifices plate) and to determine new ways to improve the efficiency of the transpired solar collector.

2. Experimental setup and methodology

In order to achieve the objective presented above a physical model was built and tested. The graphical representation is emphasized in figure 2 and the physical experimental stand is pointed in figure 3 and figure 4.

The unglazed transpired solar collector proposed consists of a rectangular box with the following dimensions: 116x70x23 cm (figure 2). In addition to the UTSC built, the following materials and equipment were used for the experimental study (see figure 2, 3 and 4):

- Fan with variable flow (1)
- Interchangeable metal plates (2a – with circular orifices and 2b – with lobed orifices)
- Six halogen lamps (3) in order to simulate solar radiation (800 Wm^{-2}).

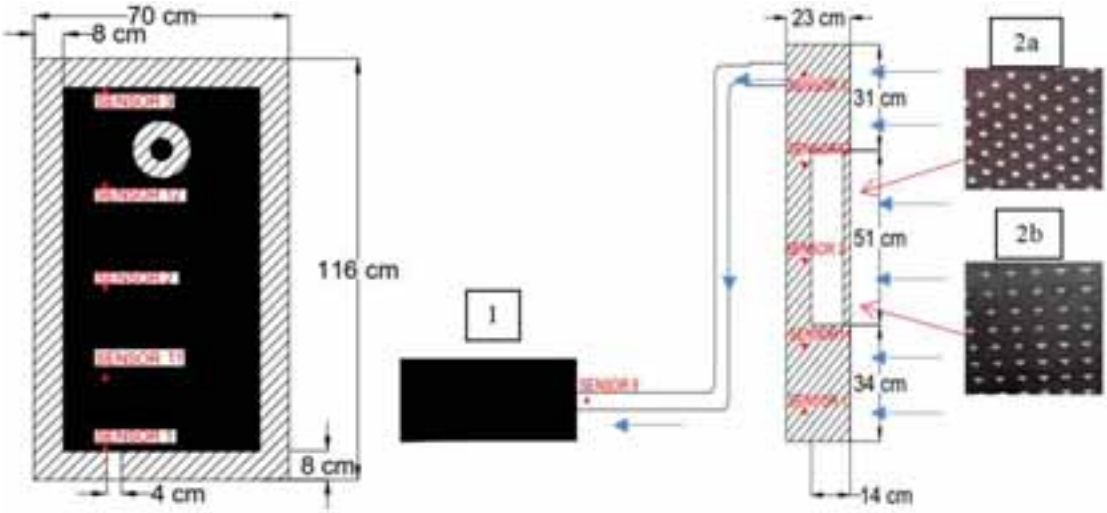

Fig. 2: Graphical representation of the UTSC (front and side view, dimensions, location of the temperature sensors)

The cavity formed between the metal plate and the back wall has 20 cm width and the wall is insulated with 5 cm of extruded polystyrene. The solar radiation is simulated by six halogen lamps placed on a stand 50 cm from the solar wall which generates 800 W m^{-2} (figure 4). Furthermore, the heat is embodied in the metal plate which acts as a solar absorber and then it is ceded to the air that passes through the orifices (circular or lobed). The heated air is extracted from the upper part of the UTSC through a 15cm hole using a fan with variable flow which forces the ambient air to pass through the transpired metal plate.

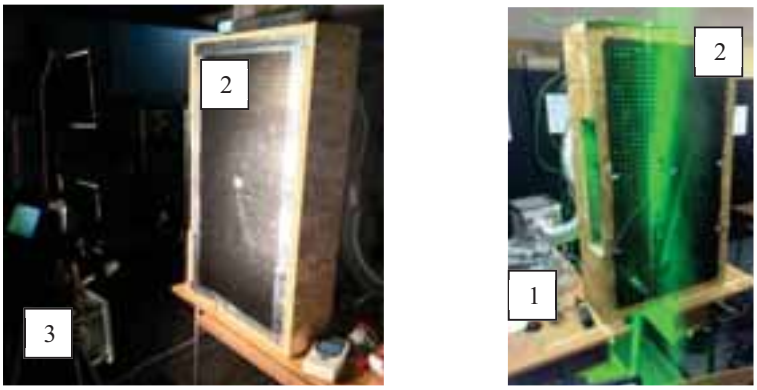

Fig. 3: Experimental setup of the UTSC during the measurements (temperature and velocity)

In order to measure the gradient of temperature within the UTSC, five sensors were placed inside the box in different places at 25 cm distance from each other (1, 11, 2, 12 and 3).

Other three sensors were used in order to assess the impact of the UTSC on the rise in temperature between ambient air extracted and the air exhausted:

- Thermocouple placed on the metal plate (sensor 4, T_p)
- Thermocouple located in ambient (sensor 14, T_a)
- Thermocouple placed on the exhaust/outlet duct (sensor 9, $T_{air,out}$).

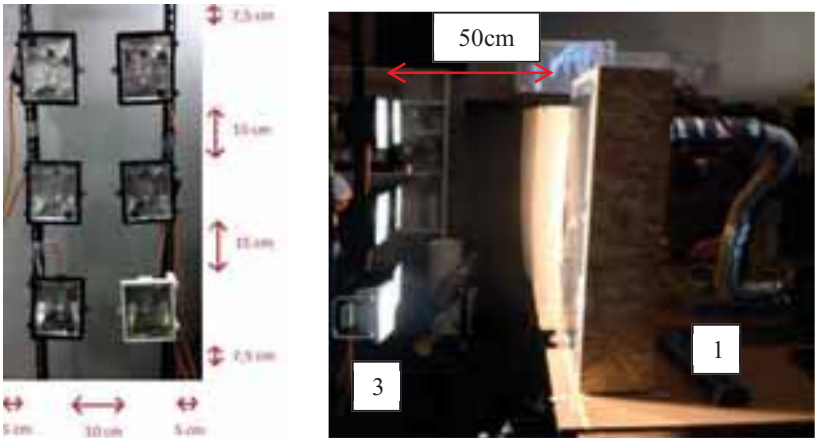

Fig. 4: Positioning of the halogen lamps in the experimental setup

All the data was collected using a very precise data logger. We also used the PIV measuring technique (Particle Image Velocimetry) in order to evaluate the velocity induced by the circular and lobed orifices (figure 3) and to determine the impact of the lobed geometry on the air flow, air mixing and efficiency of the solar collector.

3. Results and interpretations

Following the experimental campaigns conducted we have obtained interesting results. The measurements were made at different air flows and the most representative results are highlighted bellow for 29 (m^3 h^{-1}). Because the ambient temperature has a constant value, we waited for the other values to stabilize (metal plate temperature and exhaust temperature) and we collected the data which is presented below.

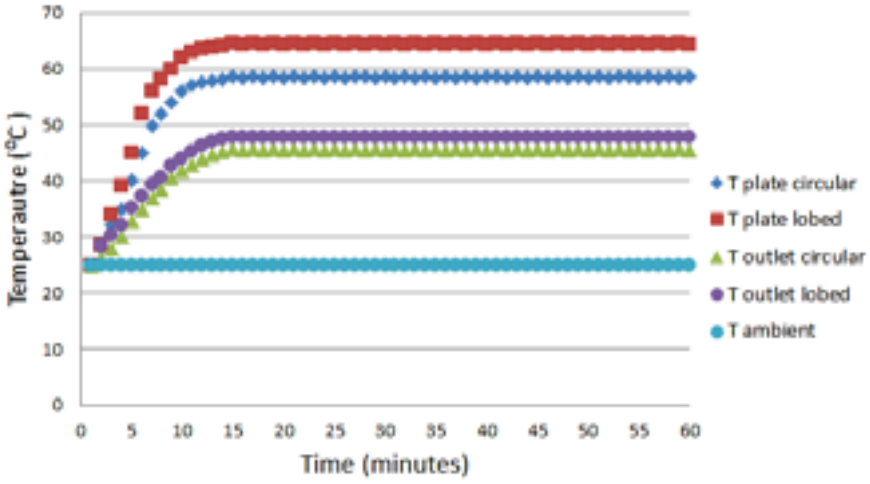

Fig. 6: Temperature variation inside the experimental setup for 29 (m^3 h^{-1})

As it can be observed in figure 6, the metal plate temperature stabilizes after almost 9 minutes of functioning

at approximately 58.5°C in case of the metal absorber with circular orifices and at almost 64.5°C in case of the metal plate with lobed orifices. Furthermore, the outlet air temperature stabilizes after 14 minutes of functioning at approximately 45.7°C in case of the metal absorber with circular orifices and at almost 47.9°C in case of the metal plate with lobed orifices.

The measurements conducted analyze the behavior of the unglazed transpired solar collector studied from two points of view: thermal and dynamic.

3.1. Thermal analysis

In figure 6 it is emphasized the variation of exhaust air temperature and also, the temperature on the metal plate, in both cases (metal plate with circular orifices and metal plate with lobed orifices). It can be observed that at the same ambient temperature (25°C), the temperature on the metal plate is 58.5°C in the case of using circular orifices and 64.5°C in case of using lobed shaped orifices. In this case, the temperature on the metal plate is higher with 6°C (which means almost 9.2% more) when using the plate with lobed orifices which clearly means that the geometry improves the heat exchange and the efficiency of the solar collector.

Moreover, it can be noticed from figure 6, that at the same ambient temperature (25°C), the exhaust temperature is with 2.2°C higher when using the plate with lobed orifices (47.9°C unlike 45.7°C), which means 5% more compared to the use of the metal plate with circular orifices. The rise in temperature in the case of the experimental study conducted with the plate with circular orifices is approximately 20.7°C and, in the second case, with the metal absorber with lobed orifices, the rise in temperature is approximately 22.9°C which means an increase of 10%.

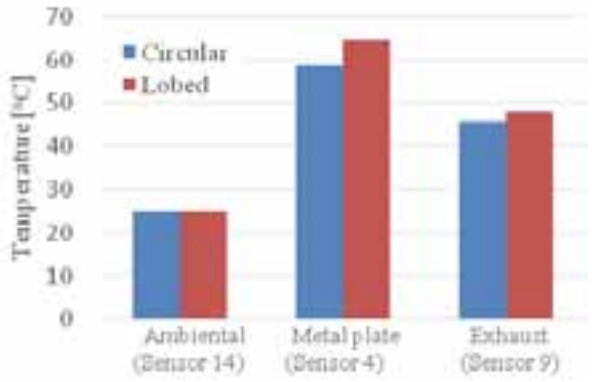

Fig. 6: Metal plate temperature variation and exhaust air variation for 29 (m^3 h^{-1})

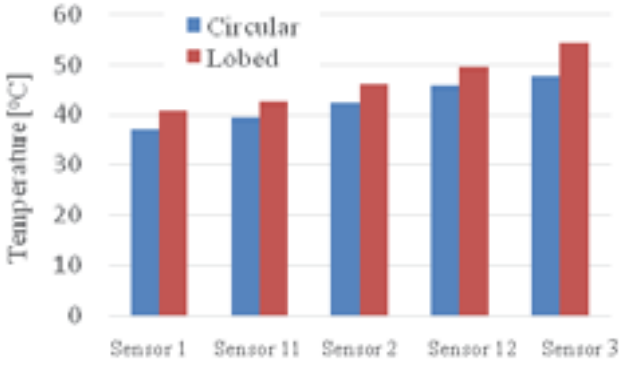

Fig. 7: Temperature measured in several points in the UTSC for 29 (m^3 h^{-1})

In figure 7 it is represented the vertical temperature variation inside the UTSC, also in both cases with circular and lobed orifices. It can be observed that the metal plate with lobed orifices enhances the heat transfer and air reaches a temperature of 54.3ºC at the top of the experimental setup (sensor 3), while in case of the metal plate with circular orifices, the air temperature reaches 47.6ºC, which means an increase in efficiency of 14%. Also, in every point where the sensors are placed, the temperature values are bigger in case of using the lobed orifices. Sensor 1 measures 40.5ºC in case of using lobed orifices unlike 37.5ºC in

case of using circular shaped orifices, sensor 11 measures 42.5ºC unlike 39.7ºC, sensor 2 measures 46.2ºC unlike 42.1ºC and sensor 12 measures 49.8ºC unlike 45.6ºC.

3.2. Dynamic analysis

Regarding the dynamical analysis, the plate with lobed orifices presents several advantages. From the results obtained using the PIV methodology, it can be noticed (figure 8) that the metal plate with lobed orifices provides higher velocities (in longitudinal section) and a uniform velocity variation. In case of using the plate with lobed orifices the maximum air flow velocity is 0.6 m s^{-1} and in case of using the plate with circular orifices the maximum air flow speed is 0.3 m s^{-1}. Moreover, the jet length is bigger for plate with lobed orifices (with 3.1 mm), resulting a better air mixing.

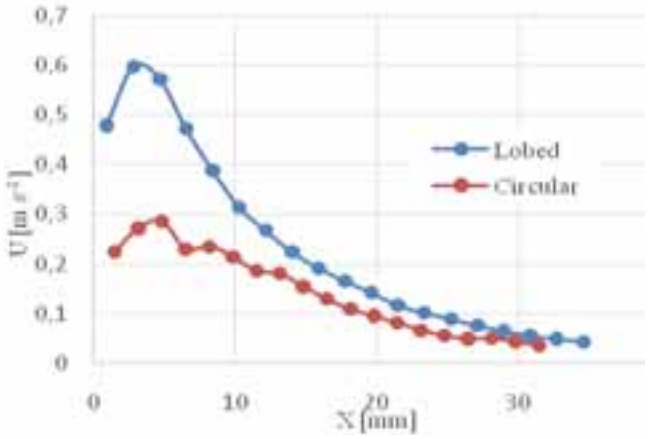

Fig. 8: Air flow velocity profile along the jets axis for airflow of 29 (m^3 h^{-1})

The difference between the jets and the flows in both cases can be seen in figure 9, which represents the velocity fields for the airflow of 29 (m^3 h^{-1}). As it can be observed, in case of using the lobed orifices it results a better air mixing and a stabilization of the jet flows inside the cavity determined by streamwise vortices created by this geometry. Moreover, because of the more complex dynamic of the lobed flows near the metal plate (absorber) the heat transfer is enhanced which determines a higher air temperature inside the cavity and a higher outlet air temperature, as it has been presented in the previous chapter.

With all these important results taken into account we can conclude that the lobed geometry provides a better flow profile and enhances the thermal transfer while increasing the efficiency of the unglazed transpired solar collector.

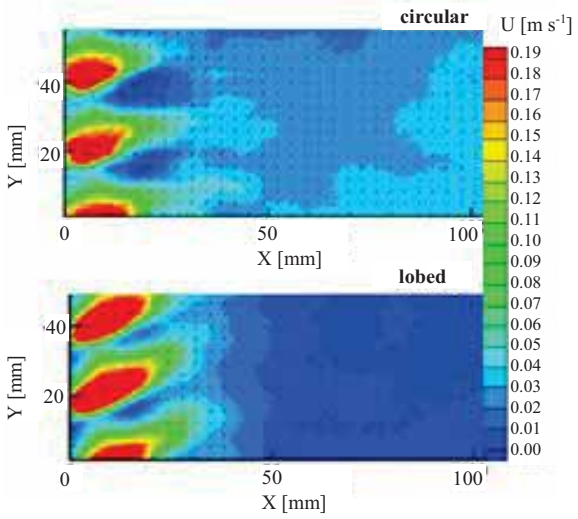

Fig. 9: Velocity fields of the circular and lobed jets extracted from PIV measurements (m^3 h^{-1})

3.3. Further studies and perspectives

According to the literature, the solar air collectors which are using renewable solar energy could be improved by adding thermal storage (Goyal et al., 1998, Khadiran et al., 2016). Thermal inertia can increase the operation time of the unglazed transpired solar collector, could stabilize the outlet air temperature (also increasing the comfort) and could increase its overall efficiency by overcoming the periods when the solar radiation is unstable/variable (during the day or during the night-time).

One of the most effective way to store energy is the use of latent heat storage materials or Phase Changing Materials (PCM) which can store 5 to 14 times more energy than classical materials (Kuznik et al., 2011).

In order to assess the impact of thermal inertia implemented in the solar collector we used the RT-25 phase change material from Rubitherm, an organic material (paraffin) with the following characteristics:

- Melting temperature: 22-26ºC
- Congealing area: 26-22ºC
- Heat storage capacity: 170 kJ kg^{-1}
- Specific heat capacity: 2 kJ kg^{-1} K^{-1}
- Heat conductivity: 0.2 W m^{-1} K^{-1}
- Density: 0.88 kg l^{-1} (solid), 0.76 kg l^{-1} (liquid).

The PCM was macro-encapsulated in four aluminum recipients with the following dimensions: 200x100x10 mm which were placed on the back wall of the UTSC presented in the previous chapters, with the same geometry and with the same conditions. For this experimental study we used the metal plate absorber with lobed orifices and the ambient temperature was 21ºC.

The study was conducted for two hours, respectively 7200 seconds. The test was divided in two equal steps: heating (the lamps are on, simulating solar radiation) and cooling (lamps are off, simulating cloudiness or night-time). As it can be observed in figure 10, the outlet air temperatures are stabilizing very quickly, after approximately 9 minutes. During the heating phase the outlet air temperature is lower in case of using PCM (with approximately 7ºC) which means that the materials store the heat. After the heating phase is over, the outlet air temperature drops also quickly (almost 15 minutes) but for the remaining time, the outlet air temperature is higher with 1.3ºC in case of using phase changing materials in the cavity of UTSC, which means that PCM are slowly releasing the heat stored.

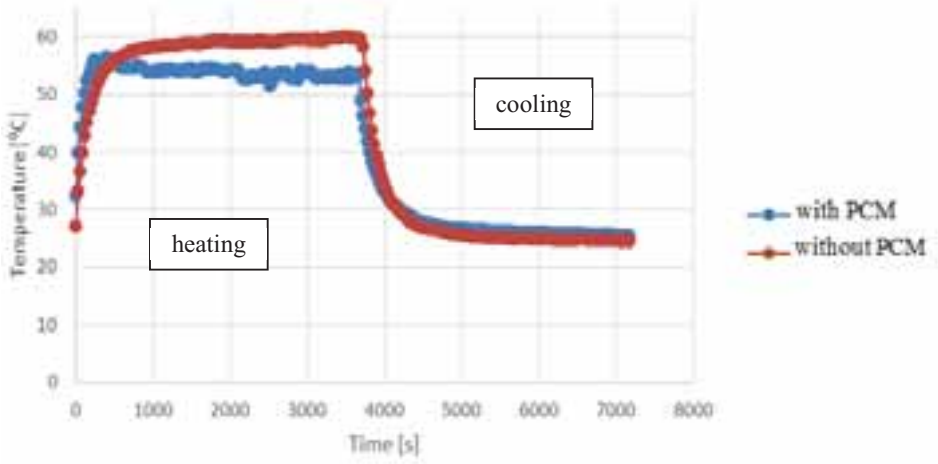

Fig. 10: Outlet air temperature variation in both cases: with and without PCM mounted on the back wall

This phenomenon still needs to be investigated and it opens new perspectives regarding the improvement of transpired solar collector efficiency by storing solar energy. More thermal storage could be added which can enhance the total capacity and a higher phase changing temperature is needed, near to the average temperature inside the cavity.

4. Conclusions

Transpired solar collectors are cost-benefit solutions which can significantly reduce the heating systems consumptions by heating or preheating the fresh air and could contribute to the reduction of CO_2 emissions around the world.

This paper is assessing a transpired solar collector performance by comparing and highlighting the importance of metal plate absorber by means of orifices geometry. Two types of orifices were studied: circular and lobed, and many interesting results were obtained.

After several experimental campaigns conducted we can conclude that:

- In case of using circular orifices the metal plate temperature is stabilized at 58.5ºC, while using lobed orifices the metal plate temperature is approximately 64.5ºC
- In case of using circular orifices the outlet air temperature is stabilized at 45.7°C, while using lobed orifices the outlet air temperature is approximately 47.9°C (5% more)
- The UTSC using metal plate with lobed orifices is more efficient, the temperature at the upper side of the UTSC being higher with 14% (6.7°C)
- The rise in temperature in case of the metal plate with lobed orifices is being higher with 10% (2.2°C)
- The rise in temperature in case of using lobed orifices is 22.9°C (unlike 20.7°C in the case of circular orifices)
- After the dynamic analysis we can observe that in case of using the lobed orifices it results a better air mixing and a stabilization of the jet flows inside the cavity determined by streamwise vortices created by this geometry
- In case of using the metal plate with lobed orifices the maximum air flow velocity is 0.6 m s^{-1} and in case of circular orifices the maximum is 0.3 m s^{-1} resulting a better air mixing (the jet length is also bigger with 3.1 mm)
- Because of the more complex dynamic of the lobed flows near the metal plate (absorber) the heat transfer is enhanced which determines a higher air temperature inside the cavity and a higher outlet air temperature.

We've also conducted studies with thermal inertia materials, such as phase changing materials and the preliminary results are promising. The thermal storage implemented in the transpired solar collector can increase the operation time of the unglazed transpired solar collector and could increase its overall efficiency by lagging the solar energy absorbed during the day-time and using it during the periods when the Sun is not available. During the heating period the PCM are storing the heat and the outlet air temperature is lower than in the case without PCM (with almost 7ºC) and furthermore, in the cooling stage, the heat stored is released slowly, the outlet temperature being higher with almost 1.3ºC.

The implementation of the PMC in UTSC needs to be further investigated. Further studies will be conducted with different types of thermal inertial elements which could improve the effect of the plate with lobed orifices implemented in a UTSC, with different phase change temperatures, different quantities and different orifices geometries.

5. Acknowledgement:

This work was supported by the grants of the Romanian National Authority for Scientific Research, CNCS – UEFISCDI, project number PN-III-P2-2.1-PED-2016-1154. Student Daniel Bordianu is also gratefully acknowledged for his contributions to this project.

6. References:

Belusko, M., W. Saman and F. Bruno, 2008. Performance of jet impingement in unglazed air collectors. Solar Energy 82(5): 389-398.

Chan, H.-Y., J. Zhu, M. H. Ruslan, K. Sopian and S. Riffat, 2014. Thermal Analysis of Flat and Transpired Solar Facades. Energy Procedia 48: 1345-1354.

Cordeau, S. and S. Barrington, 2011. Performance of unglazed solar ventilation air pre-heaters for broiler barns. Solar Energy 85(7): 1418-1429.

Dymond, C. and C. Kutscher, 1997. Development of a flow distribution and design model for transpired solar collectors. Solar Energy 60(5): 291-300.

EU, 2014. Communication from the Commission to the European Parliament, the Council, the European Economic and Social Committee and the Committee of the Regions - A policy framework for climate and energy in the period from 2020 to 2030, European Commission. from http://eur-lex.europa.eu/legal-content/EN/TXT/?uri=CELEX:52014DC0015.

EU, 2015. Communication from the commission to the European Parliament and the council – The Paris Protocol – A blueprint for tackling global climate change beyond 2020. European Commission, from https://ec.europa.eu/clima/sites/clima/files/international/paris_protocol/docs/com_2015_81_en.pdf.

Gill, R. S., S. Singh and P. P. Singh, 2012. Low cost solar air heater. Energy Conversion and Management 57(Supplement C): 131-142.

Goyal, R. K., G. N. Tiwari and H. P. Garg, 1998. Effect of thermal storage on the performance of an air collector: A periodic analysis. Energy Conversion and Management 39(3–4): 193-202.

Gütschow, J., R. Alexander, L. Jeffery, B. Hare, M. Schaeffer, M. Rocha, N. Höhne, H. Fekete, P. v. Breevoort and K. Blok, 2015. INDCs lower projected warming to 2.7˚C: significant progress but still above 2 degrees celsius. from http://climateactiontracker.org/assets/publications/CAT_global_temperature_update_October_2015.pdf.

Hami, K., B. Draoui and O. Hami, 2012. The thermal performances of a solar wall. Energy 39(1): 11-16.

IEA, 2013. Transition to Sustainable Buildings - Strategies and Opportunities to 2050. from https://www.iea.org/publications/freepublications/publication/Building2013_free.pdf.

Khadiran, T., M. Z. Hussein, Z. Zainal and R. Rusli, 2016. Advanced energy storage materials for building applications and their thermal performance characterization: A review. Renewable and Sustainable Energy Reviews 57: 916-928.

Konttinen, P., T. Salo and P. D. Lund, 2005. Degradation of unglazed rough graphite-aluminium solar absorber surfaces in simulated acid and neutral rain. Solar Energy 78(1): 41-48.

Kuznik, F., J. Virgone and K. Johannes, 2011. In-situ study of thermal comfort enhancement in a renovated building equipped with phase change material wallboard. Renewable Energy 36(5): 1458-1462.

Leon, M. A. and S. Kumar, 2007. Mathematical modeling and thermal performance analysis of unglazed transpired solar collectors. Solar Energy 81(1): 62-75.

Li, Y. (2013). Thermal Performance Analysis of a PCM Combined Solar Chimney System for Natural Ventilation and Heating/Cooling (Thesis), Coventry University.

Nastase, I. and A. Meslem, 2010. Vortex Dynamics and mass entrainement in turbulent lobed jets with and without lobe deflection angles. Experiments in Fluids 48(4): 693-714.

Nastase, I., A. Meslem and P. Gervais, 2008. Primary and secondary vortical structures contribution in the entrainement of low Reynolds number jet flows. Experiments in Fluids 44(6): 1027-1033.

Nkwetta, D. N. and F. Haghighat, 2014. Thermal energy storage with phase change material—A state-of-the art review. Sustainable Cities and Society 10: 87-100.

Perisoglou, E. and D. Dixon, 2015. Experimental Monitoring of Different Dimensions of Transpired Solar Collectors. Energy Procedia 70: 111-120.

Shukla, A., D. N. Nkwetta, Y. J. Cho, V. Stevenson and P. Jones, 2012. A state of art review on the performance of transpired solar collector. Renewable and Sustainable Energy Reviews 16(6): 3975-3985.

Van Decker, G. W. E., K. G. T. Hollands and A. P. Brunger, 2001. Heat-exchange relations for unglazed transpired solar collectors with circular holes on a square or triangular pitch. Solar Energy 71(1): 33-45.

Wang, X., B. Lei, H. Bi and T. Yu, 2017. A simplified method for evaluating thermal performance of unglazed transpired solar collectors under steady state. Applied Thermal Engineering 117: 185-192.

Zhang, T., Y. Tan, H. Yang and X. Zhang, 2016. The application of air layers in building envelopes: A review. Applied Energy 165: 707-734.

EFFECT OF AGING IN HOT CHLORINATED WATER ON THE MECHANICAL BEHAVIOR OF POLYPROPYLENE FOR SOLAR-THERMAL APPLICATIONS

Joerg Fischer[1], Susan C. Mantell[2], Patrick R. Bradler[1],
Gernot M. Wallner[1] and Reinhold W. Lang[1]

[1] Institute of Polymeric Materials and Testing - Johannes Kepler University Linz, 4040 Linz (Austria)

[2] Department of Mechanical Engineering - University of Minnesota, Minneapolis, MN 55455 (USA)

Abstract

Polypropylene (PP) is increasingly considered as a material choice for pressurized components in solar-thermal systems. In these systems, the materials are exposed to superimposed mechanical and environmental loads. The objective of this research is the characterization of the mechanical behavior of three different black-pigmented polypropylene (PP) grades immersed for up to 750 h in chlorinated water (5 ppm chlorine content) at an elevated temperature of 60°C. Hence, values for strain-at-break and essential work of fracture were determined by tensile tests. For the strain-at-break values and for the essential work of fracture values a similar exposure dependence was obtained. Depending on the PP grade, time-to-embrittlement values of 250 h and 750 h were achieved. For one PP grade, both testing methods led to an identical time-to-embrittlement value of 750 h.

Keywords: polypropylene, solar-thermal collector, chlorinated water, aging, mechanical properties

1. Introduction

In novel pumped and non-pumped solar-thermal systems, a growing share of polyolefins, especially polypropylene (PP), is considered for pressurized component applications (Koehl et al., 2012). In conventional solar-thermal systems, polypropylene is mainly utilized for hot water piping applications, whereas in systems with overheat control, polypropylene can also be used as an absorber material (Koehl et al., 2012; Lang and Wallner, 2012; Meir et al., 2008; Wallner et al., 2012). In either configuration, all components are simultaneously loaded with elevated temperatures, mechanical stresses and different environmental media. While the outside of such components may be surrounded by air, the inside is part of the hot water supply system and is exposed to a liquid medium. Usually, water is used as the heat carrier fluid in single-loop solar-thermal collector system. In many regions of the world, water is polluted with bacteria, viruses and parasites. Disinfection of contaminated water is required as a prevention of waterborne diseases (WHO, 2011). Chlorine is the most widely utilized and the most affordable water disinfectant. Chlorine is easy to use and highly efficient against different kinds of waterborne pathogens (Deborde and von Gunten, 2008; WHO, 2011; WCC, 2008). The maximum allowed chlorine content in drinking water is 5 ppm (mg/l) to ensure no further risk for human health (WHO, 2011). Polyolefins exhibit a significant degree of aging when exposed to water disinfectants (Cosgriff et al., 2017; Fischer et al., 2016; Ge et al., 2012; Hassinen et al., 2004; Mitroka et al., 2013; Mittelman et al., 2008; Vibien et al., 2001). Hence, product lifetimes are substantially reduced and, in many cases, premature failure occurs. The structural performance of polymeric materials is dependent on the mechanical and environmental loading conditions (DeCoste et al., 1951; Krishnaswamy, 2005; Lang et al., 1997; Lang et al., 2005; Stern et al., 1998a; Stern et al., 1998b). Therefore, tests of plastics for solar-thermal applications should consider service relevant loading conditions. In previous research, polymer properties were investigated by tests of specimens which were affected by various environmental conditions (Altstaedt and Kausch, 2005; Brown, 1999; Cosgriff et al., 2017; DeCoste et al., 1951; Fischer et al., 2016; Freeman et al., 2005; Ge et al., 2012; Grabmayer, 2014; Lang et al., 1997; Povacz et al., 2016; Schoeffl, 2014; Stern et al., 1998a; Stern et al., 1998b).

This paper describes the characterization of the effect of aging in hot chlorinated water on the mechanical behavior of three different black-pigmented PP grades for solar-thermal applications. Micro-sized specimens of two commercial PP grades and one development PP grade were immersed in a water bath and were removed after

doi:10.18086/swc.2017.31.02 Available at http://proceedings.ises.org

different intervals. To ensure a constant environment, the temperature, the pH and the chlorine content of the water bath were controlled. The exposure time dependent values for strain-at-break and essential work of fracture were determined by tensile tests.

2. Experimental

Three polypropylene (PP) grades were characterized in terms of their aging behavior. While two materials are commercially available, black-pigmented PP pipe grades from two different manufacturers (PP-B1 and PP-B2), the third material represents a modified PP-B2 grade (PP-B2 mod) containing additional phenolic-based antioxidants (see Table 1). To investigate the aging effect of chlorinated water with a chlorine content of 5 ppm at an elevated temperature of 60°C, micro-sized specimens with a thickness of 0.1 mm (Grabmayer, 2014; Wallner et al., 2013) were immersed in a water bath with controlled temperature, pH and chlorine content (Cosgriff et al., 2017; Freeman et al., 2005; Ge et al., 2012). In order to achieve a range of degradation levels, the exposed micro-sized specimens were removed from the aging device at different intervals (0 h, 125 h, 250 h, 375 h, 500 h, 750 h).

Tab. 1: Material designation and material composition

Material designation	Matrix polymer	Stabilizer system
PP-B1	Polypropylene blockcopolymer	Basic stabilization
PP-B2	Polypropylene blockcopolymer	Basic stabilization
PP-B2 mod	Polypropylene blockcopolymer	Basic stabilization with additional phenolic-based antioxidants

Based on tensile tests, the strain-at-break values of the removed PP specimens were determined. The tensile tests were conducted with specimens with the dimensions 150 mm x 2 mm x 0.1 mm (length x width x thickness) to achieve the relevant stress-strain curves. The time-to-embrittlement was defined as that exposure time when the strain-at-break value of the exposed specimen dropped below the strain-at-yield value of the unexposed specimen.

Furthermore, to characterize the aging effect on the fracture behavior, the essential work of fracture (EWF) method was utilized. Therefore, tensile tests were carried out with specimens with the dimensions 80 mm x 30 mm x 0.1 mm (length x width x thickness). To obtain the EWF values, different ligament lengths (6 mm, 8 mm, 10 mm, 12 mm and 14 mm) are necessary (Bárány et al., 2010) and were realized with a unique cutting device. Based on the load-displacement curves the total work of fracture values were evaluated. EWF values were obtained by plotting the specific total work of fracture as a function of ligament length.

All tensile tests were conducted at 23°C using a screw-driven universal testing machine. The gauge length was 20 mm and the test speed was 50 mm/min.

3. Results and Discussion

Exposure of the three PP grades PP-B1, PP-B2 and PP-B2 mod to hot chlorinated water led to an oxidation induced material degradation indicated by significant changes in the stress-stain curves, which are illustrated in Fig. 1. The exposure time dependent values for strain-at-break and strength are depicted in Fig. 2.

Due to aging, a significant decrease of the strain-at-break and strength was obtained for all PP grades. The lowest initial strain-at-break (for the unexposed specimen) of 364 % was determined for PP-B1. After 250 h of exposure, this material reached the time-to-embrittlement, defined as the exposure time for which the strain-at-break value of the exposed specimen dropped below the strain-at-yield value of the unexposed specimen. PP-B2 and PP-B2 mod exhibit significantly higher initial strain-at-break values of 732% and 1177%, respectively. For both materials, a time-to-embrittlement of 750 h was measured. Up to an exposure time of 500 h for PP-B2 mod the highest strain-at-break values were determined, which indicates a positive effect of the additional stabilization

with the phenolic-based antioxidants. In terms of strength for PP-B1, PP-B2 and PP-B2 mod initial values of 31 MPa, 25 MPa and 30 MPa, respectively, were established. After 750 h of exposure, the strength dropped to 3.8 MPa, 6.1 MPa and 7.4 MPa, respectively. Comparing the strength of the three PP grades, the highest exposure time dependent values were obtained for PP-B2 mod.

For all three polypropylene grades, the exposure time dependent values of specific total work of fracture are depicted as a function of ligament lengths in Fig. 3. As alluded to above, exposure to hot chlorinated water led to oxidation induced degradation of the polymers and thus to a more brittle behavior at higher aging times. Hence, with increasing exposure times ligament yielding and crack initiation/growth were superposed. Thus, the EWF preconditions were not fully met. Nevertheless, up to certain exposure times, the EWF concept requirement of self-similar load-displacement curves was fulfilled (Bárány et al., 2010; Mai et al., 2000). For the EWF tests, the time-to-embrittlement was defined as that exposure time when no self-similarity of the load-displacement curves was obtainable. Above this aging time, the EWF preconditions were not met and thus the test conditions and furthermore the results were not valid.

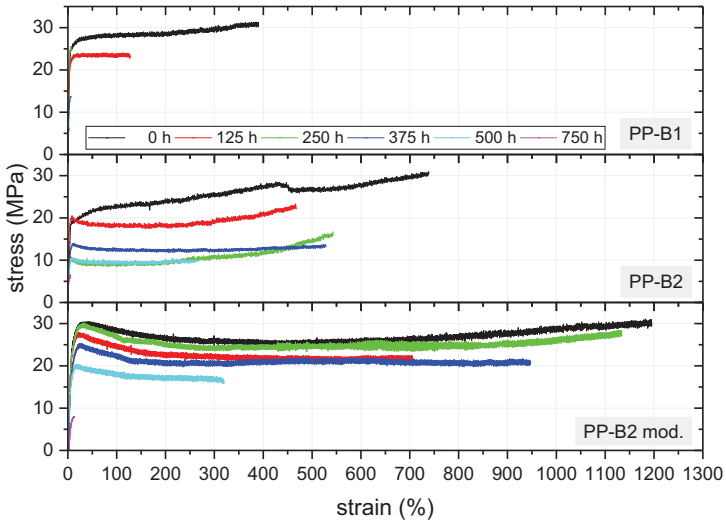

Fig. 1: Exposure time dependent stress-strain curves for the three PP grades.

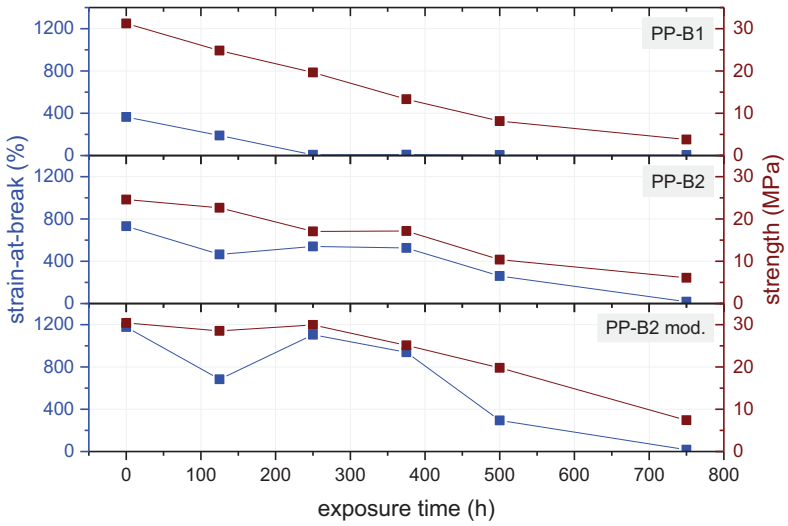

Fig. 2: Strain-at-break and strength as a function of exposure time for the three PP grades.

Based on the curves depicted in Fig. 3, the values for the specific non-essential work of fracture and for the specific essential work of fracture were evaluated. In Fig. 4, these values are plotted against the exposure times. Again, for all PP grades, the essential work of fracture decreased with increasing aging times. For the two commercial

PP pipe grades PP-B1 and PP-B2, the time-to-embrittlement was 375 h, for the additionally stabilized PP grade PP-B1 mod the time-to-embrittlement was 750 h. For PP-B2 and PP-B2 mod exposed up to 250 h, the aging dependent values of specific non-essential work of fracture and specific essential work of fracture are similar. However, due to the additional stabilization with phenolic-based antioxidants, the time-to-embrittlement was greatest for PP-B2 mod (500 h vs. 250 h for PP-B1 and PP-B2)

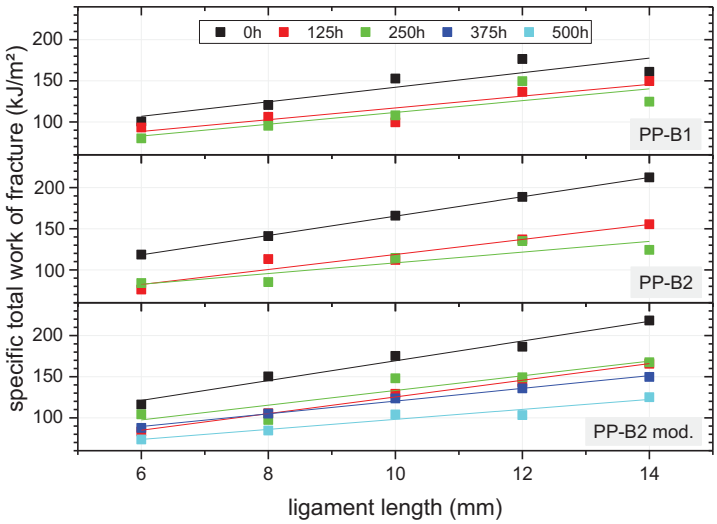

Fig. 3: Exposure time dependent curves of specific total work of fracture vs. ligament length for the three PP grades.

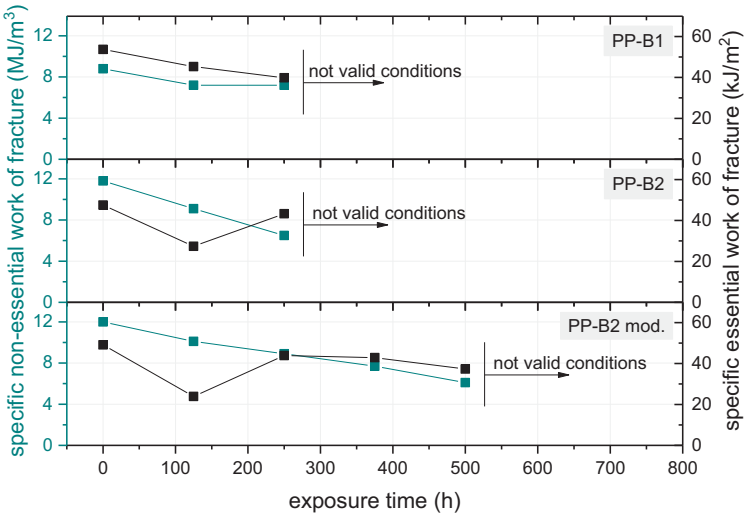

Fig. 4: Specific non-essential work of fracture and specific essential work of fracture as a function of exposure time for the three PP grades.

Exposure time dependent values for strain-at-break and specific essential work of fracture are illustrated in Fig. 5. For all PP grades, the strain-at-break curves exhibit similar aging effects as the EWF curves. Nevertheless, in terms of time-to-embrittlement, only for PP-B2 mod did both methods yield identical values. A comparison of the time-to-embrittlement data (all below 1000 h) with published data for similar materials tested in hot air and in hot heat carrier fluid (Povacz et al., 2016) reveals hot chlorinated water as the most aggressive environment.

Due to the simple specimen preparation and test procedure, the strain-at-break method is recommended for embrittlement tests. To receive further information on the fracture mechanism and the fracture toughness, the EWF method should be utilized.

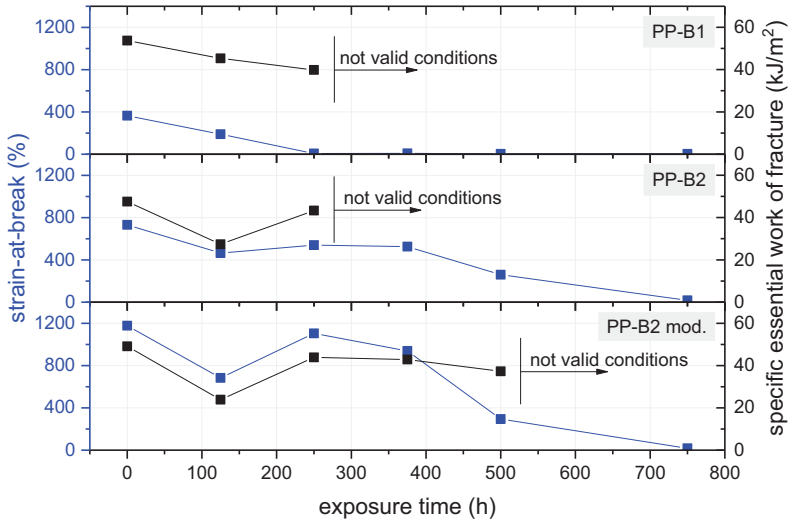

Fig. 5: Strain-at-break and specific essential work of fracture as a function of exposure time for the three PP grades.

4. Summary and Conclusions

Three different polypropylene grades were immersed for up to 750 h in a controlled water bath filled with chlorinated water (5 ppm chlorine content) at an elevated temperature of 60°C. To detect the extent of degradation over time, exposed specimens were removed at time intervals. Based on tensile tests on micro-sized specimens with method specific dimensions, values for strain-at-break and essential work of fracture were determined as a function of exposure time. The strain-at-break data exhibited a similar exposure time dependence as the essential work of fracture data. Depending on the PP grade, time-to-embrittlement ranged from 250 h to 750 h. For the PP grade that included additional phenolic-based antioxidants, the time-to-embrittlement was greatest at 750 h for both test methods.

Acknowledgements

This research work was performed in the cooperative research project *SolPol-4/5* entitled *"Solar-thermal systems based on polymeric materials"* (www.solpol.at). The project *SolPol-4/5* is funded by the Austrian Climate and Energy Fund (KLI.EN) within the program "e!MISSION.at" and the funding is administrated by the Austrian Research Promotion Agency (FFG).

References

Altstaedt, V., Kausch, H., 2005. Ed. Intrinsic molecular mobility and toughness of polymers II, Berlin, New York: Springer.

Bárány, T., Czigány, T., Karger-Kocsis, J., 2010. Application of the essential work of fracture (EWF) concept for polymers, related blends and composites, A review, Progress in Polymer Science 35 (10), 1257-1287.

Brown, R., 1999. Handbook of polymer testing: Physical methods, Marcel Dekker, New York.

Cosgriff, E., Mantell, S.C., Bhattacharya, M., 2017. Method for degrading polyethylene sheet samples in an oxidative environment, ANTEC, Conference Proceedings, 1228-1233.

Deborde, M., von Gunten, U., 2008. Reactions of chlorine with inorganic and organic compounds during water treatment – Kinetics and mechanisms: A critical review, Water Research 42, 13-51.

DeCoste, J.B., Malm, F.S., Wallder, V.T., 1951. Ind. Eng. Chem. 43 (1), 117-121.

Fischer, J., Bradler, P.R., Lang, R.W., Wallner, G.M., 2016. Fatigue crack growth resistance of polypropylene in chlorinated water at different temperatures, Conference Proceedings of the 18th Plastic Pipes Conference.

Freeman, A., Mantell, S.C., Davidson, J.H., 2005. Mechanical performance of polysulfone, polybutylene, and polyamide 6/6 in hot chlorinated water, Solar Energy 79 (6), 624-637.

Ge, H., Singh, G., Mantell, S.C., 2012. Fracture behavior of degraded polyethylene thin films for solar thermal applications, Energy Procedia 30, 783-792.

Grabmayer, K., 2014. Polyolefin-based Lining Materials for Hot Water Heat Storages Development of Accelerated Aging Characterization Methods and Screening of Novel Compounds, Dissertation, Johannes Kepler University, Linz, Austria.

Hassinen, J., Lundbaeck, M., Ifwarson, M., Gedde, U., 2004. Deterioration of polyethylene pipes exposed to chlorinated water, Polymer Degradation and Stability 84 (2), 261-267.

Koehl, M., Meir, M.G., Papillon, P., Wallner, G.M., Saile, S. (Eds.), 2012. Polymeric Materials for Solar Thermal Applications, first ed., Wiley-VCH.

Krishnaswamy, R.K., 2005. Polymer 46 (25), 11664-11672.

Lang, R.W., Stern, A., Doerner, G., 1997. Angew. Makromol. Chemie 247 (1), 131-145.

Lang, R.W., Pinter, G., Balika, W., 2005. 3R international 44, 33-41.

Lang, R.W., Wallner, G.M., 2012. Herausforderungen und Möglichkeiten für den Einsatz von Polymermaterialien in solarthermischen Anwendungen, in: Tagungshandbuch Gleisdorf Solar, pp. 285-288.

Mai, Y.W., Wong, S.C., Chen, X.H., 2000. Application of fracture mechanics for characterization of toughness of polymer blends, Polymer blends: formulations and performance, in: Paul, D.R., Bucknall, C.B., editors, Vol 2, Wiley-VCH, New York, pp. 17-58.

Meir, M.G., Buchinger, J., Kahlen, S., Koehl, M., Papillon, P., Rekstad, J., Wallner, G.M., 2008. Conference Proceedings, Lissbon.

Mitroka, S., Smiley, T., Tanko, J., Dietrich, A., 2013. Reaction mechanism for oxidation and degradation of high density polyethylene in chlorinated water, Polymer Degradation and Stability 98 (7), 1369-1377.

Mittelman, G., Davidson, J.H., Mantell, S.C., Su, Y., 2008. Prediction of polymer tube life for solar hot water systems, Solar Energy 82 (5), 452-461.

Povacz, M., Wallner, G.M., Grabmann, M.K., Beißmann, S., Grabmayer, K., Buchberger, W., Lang, R.W., 2016. Novel Solar Thermal Collector Systems in Polymer Design – Part 3, Aging Behavior of PP Absorber Materials, Energy Procedia 91, 392-402.

Schoeffl, P., 2014. Influence of Liquid Hydrocarbon Environments on High Density Polyethylene for Oil and Gas Applications. Dissertation, Johannes Kepler University, Linz, Austria.

Stern, A., Novotny, M., Lang, R.W., 1998a. Polymer Testing 17 (6), 403-422.

Stern, A., Asanger, F., Lang, R.W., 1998b. Polymer Testing 17 (6), 423-441.

Vibien, P., Couch, J., Oliphant, K., Zhou, W., Zhang, B., Chudnovsky, A., 2001. Assessing Material Performance in Chlorinated Potable Water Applications, Proc. of the 11th Plastic Pipes, Munich.

Wallner, G.M., Lang, R.W., Povacz, M., Grabmayer, K., Koller, W., Brandstaetter, A., et al., 2012. Solarthermische Kollektorsysteme mit Kunststoffabsorber - Materialien und Eigenschaftsprofile, in: Konferenzband Gleisdorf Solar.

Wallner, G.M., Grabmayer, K., Beißmann, S., Schobermayr, H., Buchberger, W., Lang, R.W., 2013. Methoden zur beschleunigten Alterungsprüfung von Kunststoffen, Erneuerbare Energie 1, 18-20.

WCC - World Chlorine Council, 2008. Drinking Water Chlorination, Report: position paper.

WHO - World Health Organization, 2011. Guidelines for drinking-water quality, fourth ed., Geneva.

Characterization of polymeric materials for solar-thermal collector mounting systems

Joerg Fischer[1], Patrick R. Bradler[1], Sandra Leitner[1], Gernot M. Wallner[1] and Reinhold W. Lang[1]

[1] Institute of Polymeric Materials and Testing / Johannes Kepler University, Linz (Austria)

Abstract

In this research, three unreinforced and two glass fiber reinforced plastics for the application in mounting systems of solar-thermal collectors were investigated comprehensively. Therefore, morphological, thermomechanical, mechanical and cyclic fracture mechanical tests were performed. Focus was given on the mechanical properties and the fatigue crack growth (FCG) resistance at service relevant temperatures. In the morphological characterization, for the five materials primarily homogenous material distributions were detected. However, the polymer blend ASA/PC showed a limited miscibility. This was confirmed by the separated glass transition temperatures, which were determined by dynamic mechanical analysis. In terms of mechanical properties, significantly higher values for Young's modulus and strength as well as lower strain-at-break values were obtained for the glass fiber reinforced polymer grades. Increasing temperatures led to decreasing Young's moduli and strengths as well as to higher strain-at-break values. The unreinforced plastics revealed an inferior FCG resistance. For all materials, temperature increase evoked a declining FCG behavior. The FCG resistance of the reinforced plastics was influenced by the fiber orientation.

Keywords: plastics, solar-thermal collectors, mounting systems, mechanical properties, fatigue crack growth

1. Introduction and scope

Currently, mounting systems of solar-thermal collectors are constructed from aluminum or stainless steel (Erfurth et al., 2001; Koehl et al., 2012). For the reduction of costs and weight, it is a common practice to replace conventional materials with advanced polymeric material solutions. For an appropriate material replacement, various aspects must be carefully considered. Materials for mounting and framing must withstand environmental loads (e.g., temperatures, environmental media) and mechanical loads (e.g., weight of the mounted solar-thermal collector, snow weight, wind load, hail) (Erfurth et al., 2001; Koehl et al., 2012). The loading conditions can adversely affect the structural performance of polymeric materials (Altstaedt, 2005; DeCoste et al., 1951; Fischer et al., 2016a; Lang et al., 1997; Lang et al., 2005; Stern et al. 1998a; Stern et. al. 1998b). A comprehensive understanding of the material behavior under service relevant loading conditions is of utmost importance. Thus, previous research focused on the effect of superimposed mechanical and environmental loads on the properties of polymeric materials (Bradler et al., 2016; Bradler et al., 2017; Fischer et al., 2016a; Fischer J. et al., 2016a; Schoeffl and Lang, 2015).

The main objective of this research was the characterization of the morphological, thermomechanical, mechanical and fatigue crack growth (FCG) behavior of polymeric materials for mounting systems of solar-thermal collectors under application relevant temperatures. Therefore, infrared spectroscopic microscopy, dynamic mechanical analysis, monotonic tensile tests and cyclic fracture mechanics tests were performed at three different temperatures (0°C, 23°C, 60°C) in air environment.

2. Background

The linear elastic fracture mechanics concept was used for the investigation of the fatigue crack growth (FCG) behavior of plastics (Anderson, 2017; Bradler et al., 2016; Bradler et al., 2017; Fischer et al., 2016a; Fischer J. et al., 2016b; Lang, 1980; Schoeffl and Lang, 2015). In this concept, the fatigue crack growth rate (da/dN) is plotted against the stress intensity factor range ΔK. While the crack growth rate indicates the crack growth per cycle, the

doi:10.18086/swc.2017.31.03 Available at http://proceedings.ises.org

ΔK_I-value, described in eq. 1, is the difference between maximum and minimum stress intensity factor ($K_{I,max}$-$K_{I,min}$) of a cycling loading profile in loading mode I (pure tensile loads). In this equation, "$\Delta\sigma$" describes the global loading, "a" the crack length and "Y" a factor which is dependent on the geometry of the specimen used.

$$\Delta K_I = \Delta\sigma \cdot \sqrt{a} \cdot Y \tag{1}$$

In the double-logarithmic fatigue crack growth kinetics curve, region II represents the stable crack growth of the material. In a comparison of different polymeric materials or of different test conditions, improved fatigue crack growth resistance is revealed by a shift of the FCG curve to higher ΔK-values. Additionally, also slope decrease of the FCG curve exhibits improved FCG behavior (Haager, 2004; Lang, 2005).

3. Experimental

Materials

An overview of all investigated materials is given in Table 1, comprising three unreinforced and two glass fiber reinforced plastics. These materials were characterized with different methods at service relevant temperatures (0°C, 23°C, 60°C). The unreinforced polymer grades contain an acrylic ester-styrene-acrylonitrile copolymer (ASA), a polymer blend of ASA and polycarbonate (ASA-PC) as well as a polymer blend of polybutylene terephthalate and polycarbonate (PBT-PC). The reinforced plastics include a short glass fiber reinforced polyamide grade with a fiber content of 30 w% (PA-GF30) and a long glass fiber reinforced polyamide grade with a fiber content of 40 w% (PA-LGF40).

Tab. 1: Material designation and material composition.

Material designation	Material	Reinforcement type	Reinforcement content
ASA	Acrylic ester-styrene-acrylonitrile copolymer	-	-
ASA-PC	Polymer blend of acrylic ester-styrene-acrylonitrile copolymer and polycarbonate	-	-
PBT-PC	Polymer blend of polybutylene terephthalate and polycarbonate	-	-
PA6-GF30	Polyamide 6	Short glass fibers	30 w%
PA6-LGF40	Polyamide 6	Long glass fibers	40 w%

Infrared spectroscopic microscopy

To analyze the morphology and the fiber orientation within the compounds, the specimens were characterized with an infrared spectroscopic microscope PerkinElmer Spotlight 400 FT-IR Imaging System (Perkin Elmer Inc., USA. Tests were carried out with an attenuated total reflection mode (ATR). The spectral range was 650 cm^{-1} to 4000 cm^{-1}.

Dynamic mechanical analysis

Dynamic mechanical analysis (DMA) measurements were performed on an Anton Paar Physica MCR 502 (Anton Paar GmbH, Austria) for determining the temperature dependency of the storage modulus and the loss factor. The loss factor can be calculated out of the ratio between the storage modulus and the loss modulus. All DMA tests were conducted in a temperature range of -70°C and 220°C with a heating rate of 3 K/min. The applied frequency was set to 1 Hz and a torsional loading mode was applied. The samples were cut from the parallel part of the 1B multi-purpose specimen (ISO 527) with the dimension 40 mm x 10 mm x 4 mm.

Tensile tests

The mechanical properties (Young's modulus, strength and strain-at-break) were examined with a universal testing machine Z020 (Zwick Roell, Germany) equipped with a multi-extensometer and a temperature chamber for test at 0°C, 23°C and 60°C. Test parameters and multi-purpose specimens were used according to ISO 527 with a traverse speed of 1 mm/min for Young's modulus determination until a strain of 0.25 % and 50 mm/min until failure.

Fatigue crack growth

In order to investigate the fatigue crack growth (FCG) behavior, all five materials were tested with an in-situ testing device (Schoeffl et al., 2014) allowing fatigue tests at different temperatures within service-relevant environmental environments. Therefore, an electro-dynamic testing machine of the type ElectroPuls E3000 (Instron Inc., USA) was used. Compact type (CT) specimens with an initial crack in mold direction and in cross direction were utilized for investigations of the crack growth (Fischer et al., 2016b). A sinusoidal loading profile with a frequency of 5 Hz and an R-ratio of 0.1 was applied. Characteristic double-logarithmic FCG kinetic curves were plotted providing the relation between the FCG rate, da/dN, and the stress intensity factor range, ΔK_I, describing the local crack tip stress field.

4. Results and discussion

In the morphological characterization via infrared spectroscopic microscopy, for the two blends (ASA/PC and PBT/PC), a predominantly homogenous color distribution was found (see Fig. 1), with a limited miscibility of the ASA/PC blend. The reinforced grades revealed in the middle of the specimen a clear fiber orientation in cross mold direction. Conversely, due to higher shear loads, a fiber orientation in mold direction was found on the surfaces of the specimens. Fischer et al. reported this effect before (Fischer et al., 2016).

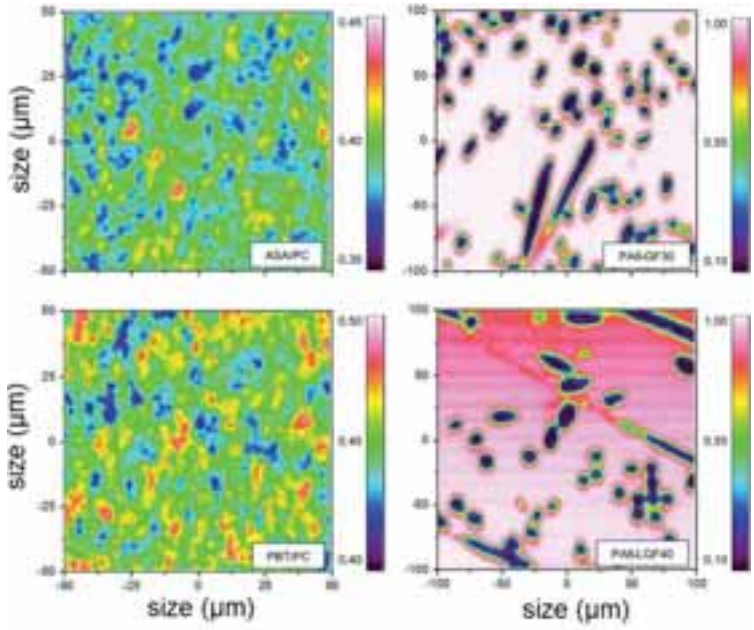

Fig. 1: Infrared spectroscopic map of the morphology of two polymer blends (left) and fiber orientation of two glass fiber reinforced polymers (right).

Curves of the storage modulus and the loss factor as a function of temperature (see Fig. 2) were attained via dynamic mechanical analysis (DMA). For the unreinforced materials, the highest storage moduli were exhibited for ASA and the lowest storage moduli for the PBT-PC blend. The glass transition temperature is depicted as a maximum of the loss factor curve. The ASA grade shows a peak at 124°C, for the ASA-PC compound two peaks are detectable, one for the ASA component at about 115°C, and a second at 149°C for the PC component. Hence, the limited miscibility obtained by infrared spectroscopic microscopy was assured. For the PBT-PC blend, a glass transition temperature of 140°C was found. The DMA data of the reinforced grades exhibit higher modulus values for the PA-grade PA6-LGF40 with 40 w% glass fiber reinforcement compared to the PA-grade PA6-GF30 with

30 w% glass fiber reinforcement. The glass transition temperatures of both PA-grades are similar (60°C for PA6-GF30 and 63°C for PA6-LGF40).

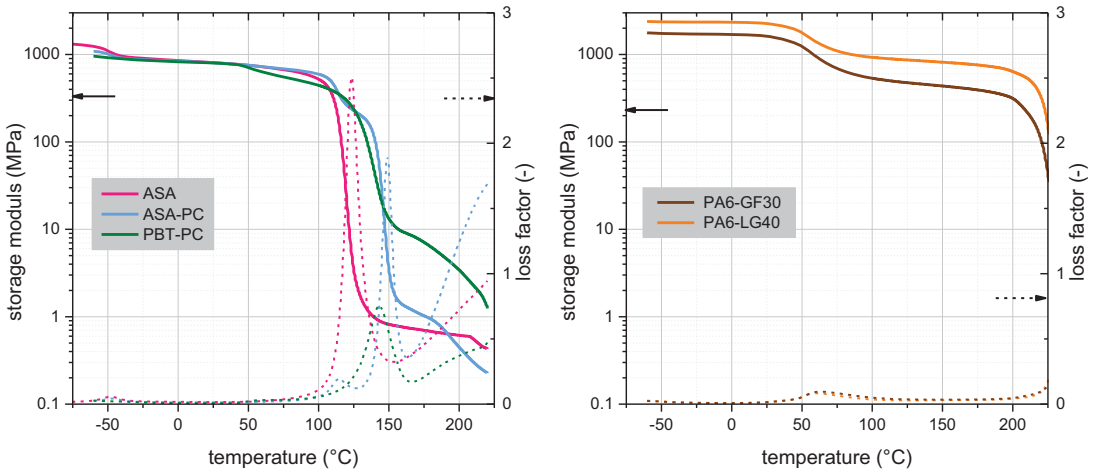

Fig. 2: Curves of the storage modulus and loss factor against temperature for unreinforced (left) and reinforced (right) plastics.

Storage moduli at the three application relevant temperatures 0°C, 23°C and 60°C are depicted in Fig. 3. Within each grade, highest moduli were obtained at 0°C. In the material comparison, at each temperature, the highest storage moduli were detected for the grade PA6-LGF40. At 60°C, the moduli of the grades ASA and ASA-PC are only moderate decreasing compared to 23°C. The PBT-PC compound shows a higher decrease, which is also visible in the DMA-curve (storage modulus against temperature) starting with diminishing storage moduli at 50°C. The reinforced grades PA6-GF30 and PA6-LGF40 exhibit a significant reduction of storage moduli between 23°C and 60°C. This is related to the immediate vicinity to the glass transition region of PA6.

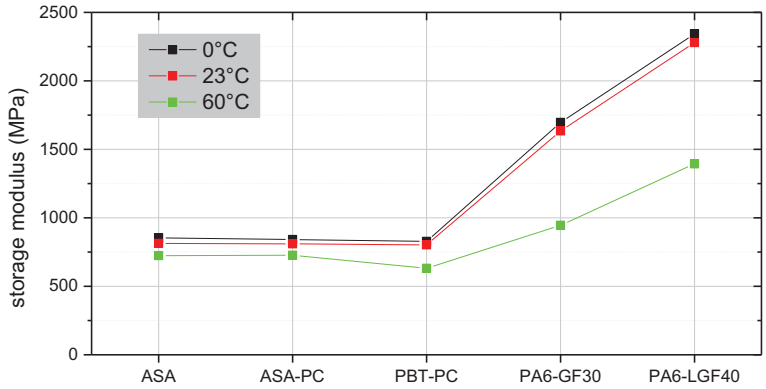

Fig. 3: Storage moduli at three different temperatures for three unreinforced and two reinforced plastics.

Temperature dependent stress-strain curves for the five plastics are plotted in Fig. 4. Based on the stress-strain curves, the values for Young's modulus, strength and strain-at-break were evaluated (see. Fig. 5). For all temperatures, the reinforced polymeric materials revealed significantly higher Young's moduli (factor 3 to 6) and strengths (factor 3 to 4). In contrast, the obtained strain-at-break values were much lower (factor 2 to 27). An increase in testing temperature led to declining Young's moduli and strengths. While the lowest values were determined for the polymer blend PBT-PC, for PA6-LGF40, the highest values were achieved. With a higher glass fiber content, an increase in Young's modulus was determined. Increasing temperatures led to higher strain-at-break values. The highest strain-at-break values were obtained for PBT-PC. For the glass fiber reinforced grades, a brittle failure and small strain-at-break values were received due to the dominating fiber influence.

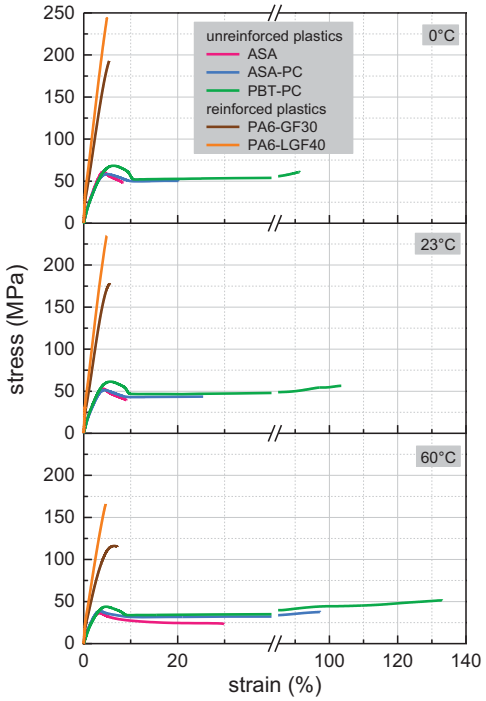

Fig. 4: Temperature dependent stress-strain curves for the three unreinforced and the two glass fiber reinforced plastics.

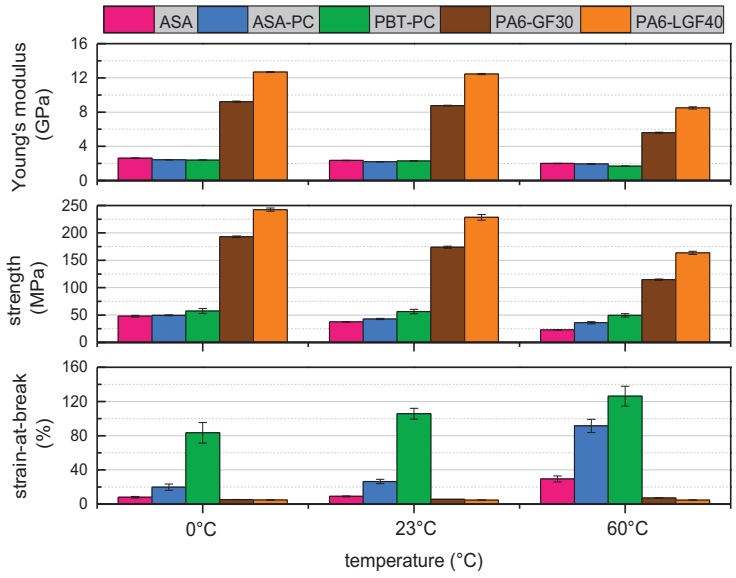

Fig. 5: Temperature dependent values of Young's modulus (top), strength (middle) and strain-at-break (bottom) for the five plastics.

In Fig. 6, the fatigue crack growth behavior of the five plastics for each testing temperature is depicted. Furthermore, the influence of different fiber orientation on the FCG resistance is revealed. For all materials, temperature increase led to a declining FCG resistance. In terms of the material comparison, for all temperatures, the glass fiber reinforced plastics revealed a significantly improved fatigue crack growth behavior. Conversely, the FCG resistance of ASA was inferior. In terms of fiber orientation, PA6-LGF40 and thus the PA grade with the long glass fiber reinforcement and the higher fiber content revealed an enhanced FCG behavior in the tests with the initial crack in mold direction. Nevertheless, tests with the initial crack in cross direction showed comparable FCG resistances for both glass fiber reinforced plastics.

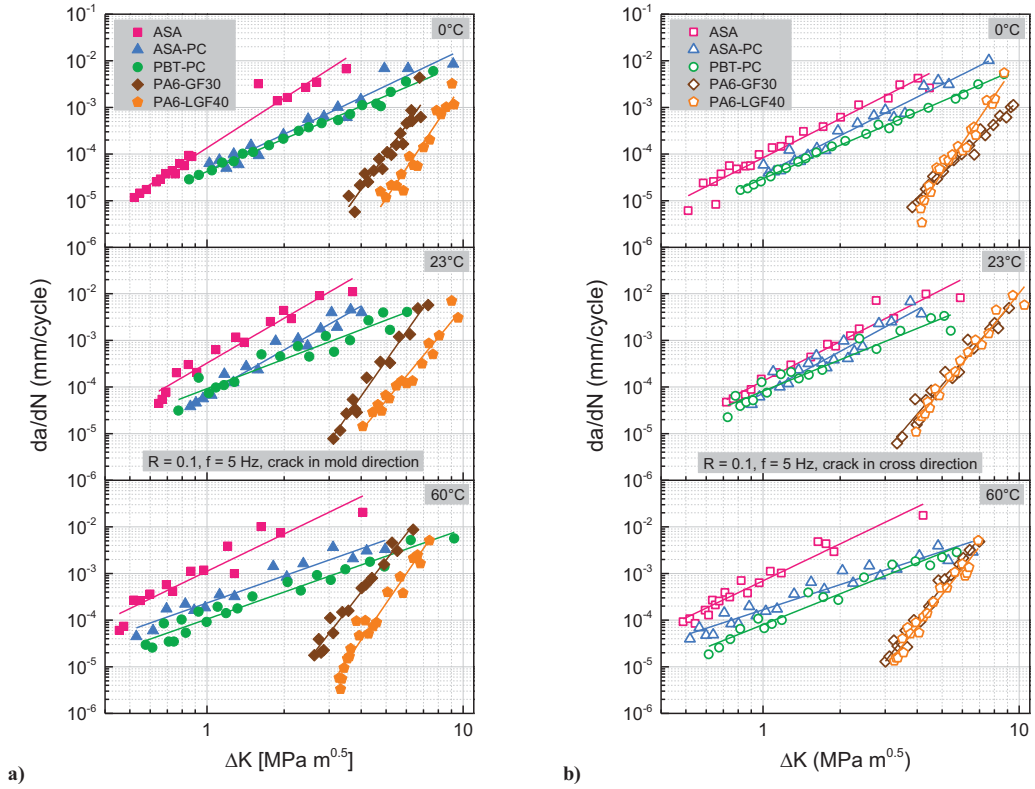

Fig. 6: Temperature dependent fatigue crack growth kinetics for the three unreinforced and the two glass fiber reinforced plastics tested with the crack in (a) mold direction and (b) cross direction.

5. Summary and conclusions

Three unreinforced and two glass fiber reinforced plastics for the application in mounting systems of solar-thermal collectors were characterized with regard to their morphological, thermomechanical, mechanical and fatigue crack growth (FCG) behavior. The three unreinforced polymeric materials included an elastomer-modified copolymer (acrylic ester-styrene-acrylonitrile, ASA) and two polymer blends (acrylic ester-styrene-acrylonitrile/polycarbonate, ASA/PC and polybutylene terephthalate/polycarbonate, PBT/PC). In the category of the reinforced materials one short glass fiber reinforced polyamide grade with a glass fiber content of 30 w% (PA6-GF30) and one long glass fiber reinforced polyamide grade with a glass fiber content of 40 w% (PA6-LGF40) were investigated. The morphological characterization revealed homogenous material distributions for all material grades. However, the polymer blend ASA/PC showed a limited miscibility leading to separated glass transition temperatures. For the three unreinforced plastics, significantly lower values for Young's modulus and strength were determined. A comparison between the strain-at-break values of the unreinforced and the reinforced plastics revealed higher values for the former materials. Decreasing Young's moduli and strengths as well as to higher strain-at-break values were detected with higher testing temperatures. At all temperatures, the reinforced plastics showed a superior FCG behavior. Increasing temperatures led to a diminishing FCG resistance. In order to investigate the effect of fiber orientation on the fatigue crack growth of the reinforced plastics, tests were carried out with specimens containing the initial crack in mold direction and in cross direction. While tests with the initial crack in cross direction revealed a similar FCG resistance, tests with the initial crack in mold direction showed a significantly better performance for the polymer with the higher fiber content.

Acknowledgement

This research work was performed in the cooperative research project *MidTempColl*. The project was funded by the Austrian Climate and Energy Fund (KLI.EN) within the program "Neue Energien 2020" and the funding was administrated by the Austrian Research Promotion Agency (FFG).

References

Altstaedt, V., 2005. The Influence of Molecular Variables on Fatigue Resistance in Stress Cracking Environments. In: Kausch HH, editor. Intrinsic molecular mobility and toughness of polymers, vol. 188. Berlin, London: Springer, pp. 105–152.

Anderson T.L.; 2017. Fracture mechanics: Fundamentals and applications. Boca Raton, FL: CRC Press.

Bradler, P.R., Fischer, J., Pohn, B., Wallner, G.M., Lang, R.W., 2017. Effect of stabilizers on the failure behavior of glass fiber reinforced polyamides for mounting and framing of solar energy applications, Energy Procedia 119, 828-834.

Bradler P.R., Fischer J., Schlaeger M, Wallner GM, Lang RW; 2016. Conference Proceedings of EuroSun 2016.

DeCoste, J.B., Malm, F.S., Wallder, V.T., 1951. Cracking of Stressed Polyethylene; Ind. Eng. Chem. 43 (1), 117-121.

Erfurth, R., Goering, J., Delzer, T., 2001. Tragkonstruktionen für Solaranlagen – Planungshandbuch zur Aufständerung von Solarkollektoren, first ed., Solarpraxis AG, Berlin, D.

Fischer, J., Bradler, P.R., Lang R.W., Wallner G.M.; 2016a. Fatigue crack growth resistance of polypropylene in chlorinated water at different temperatures, Conference Proceedings of the 18th Plastic Pipes Conference, 2016.

Fischer, J., Bradler, P.R., Schläger M.; Wallner, G.M., Lang, R.W., 2016b. Novel Solar Thermal Collector Systems in Polymer Design – Part 5; Energy Procedia; 91:27–34.

Haager M, Pinter G, Lang R.W.; 2004. Estimation of Slow Crack Growth Behavior in Polyethylene after Stepwise Isothermal Crystallization; Macromol. Symp.; 217(1):383–90.

Koehl, M., Meir, M.G., Papillon, P., Wallner, G.M., Saile, S. (Eds.), 2012. Polymeric Materials for Solar Thermal Applications, first ed., Wiley-VCH.

Lang R.W., Manson J.A., Hertzberg R.W.; 1982. Effect of short glass fibers and particulate fillers on fatigue crack propagation in polyamides; Polym. Eng. Sci.; 22(15):982–7.

Lang, R.W., Stern, A., Doerner, G., 1997. Applicability and limitations of current lifetime prediction models for thermoplastics pipes under internal pressure; Angew. Makromol. Chemie; 247(1):131–45.

Lang R.W.; 1980. Applicability of linear elastic fracture mechanics to fatigue in poymers and short-fiber composites. Dissertation. Berhlehem (US).

Lang, R.W., Pinter, G., Balika, W., 2005. Konzept zur Nachweisführung für Nutzungsdauer und Sicherheit von PE-Druckrohren bei beliebiger Einbausituation; 3R International (1-2/2005):32–41.

Schoeffl P.F., Bradler P.R., Lang R.W.; 2014. Yielding and crack growth testing of polymers under severe liquid media conditions; Polymer Testing; 40:225–33.

Schoeffl P.F., Bradler P.R., Lang R.W.; 2015. Effect of liquid oilfield-related media on slow crack growth behavior in polyethylene pipe grade materials; International Journal of Fatigue 72, 2015, 90-101.

Stern, A., Asanger, F., Lang, R.W.; 1998a. Creep crack growth testing of plastics—II. data acquisition, data reduction and experimental results. Polymer Testing 17 (6), 423–441.

Stern, A., Novotny, M., Lang, R.W.; 1998b. Creep crack growth testing of plastics—I. test configurations and test system design. Polymer Testing 17 (6), 403–422.

Development of a high accurate numerical platform for the thermal and optical optimization of linear Fresnel receivers

Erick Guadamud[1], Jorge Chiva[1], Guillem Colomer[1], Joan Farnós[1], Ahmed Al Mers[2], Joaquim Rigola[1] and Carlos David Perez-Segarra[1]

[1] Heat and Mass Transfer Technological Center (CTTC), Terrassa (Spain)
Universitat Politècnica de Catalunya-BarcelonaTech (UPC), Terrassa (Spain)
ESEIAAT, Colom 11, E-08222 Terrassa, Barcelona, Spain
[2] Department of Energy, Ecole Nationale Superieure d'Arts et Metiers, Meknés, Morocco.

Abstract

This paper represents an advanced methodology for the detailed modeling of the heat transfer and fluids dynamics phenomena in Linear Fresnel receivers. The present work aims at modeling Linear Fresnel elements (e.g. insulation material, glass cover, tube, pipe, etc.) by proposing a parallel modular object-oriented methodology. The heat conduction, natural convection, single & two-phase flow, and solar & thermal radiation are solved and coupled in an adequate manner. The Navier-Stokes 3D equations with incompressible and turbulent fluid hypotheses are used to solve the fluid inside the cavity by means of a CFD&HT coupling with thermal and solar radiation. The heat flux incident on the tube is analyzed by a 3D conduction model to determine the temperature distribution, single or multiphase models can be used for the HTF. A Monte Carlo Ray-tracing method is applied to obtain the estimated solar radiation source as a function of the altitude and azimuth solar angles. This work presents a comparison of three configurations, their optical behavior, the effects of the receiver height, the orientation of the mirrors and the shadows, temperature, velocity and thermal flow profiles are analyzed and presented hereafter.

Keywords: Linear Fresnel Receivers, CFD&HT, Numerical Model, TermoFluids.

1. Introduction

Many authors have carried out experiments on several prototypes with innovative design concepts and studied the performance characteristics of LFR for different optical and geometric parameters (Barale et al., 2010 [1]; Beltagy et al., 2017 [2]; Bernhard et al., 2008 [3]; Häberle et al., 2001[4]; Negi et al., 1989 [5]; Singh et al., 1999 [6]). Linear Fresnel reflectors usually employ a secondary concentrator that enlarges the target área for primary mirrors, and also acts as protective cover to reduce convective losses. A number of authors have been studied different types of receivers such as trapezoidal cavity with multiple absorber tubes (Facão and Oliveira, 2011 [7]) triangular, rectangular, arc-shaped and semi-circular cavity receivers (Lin et al., 2014 [8]), modified V-shaped cavity. Qiu et al. (2015) [9] investigated the thermal performance of LFR that employs a compound parabolic concentrator (CPC) with an evacuated absorber. They concluded that uniformity of flux distribution can be improved by choosing a proper slope error, but with a small sacrifice in the optical efficiency.

The present work develops an advanced model of LFR, through a modular platform that works each part of the system as a unique element with the capacity to transfer information between one element and another, this union is realized by coupling heat flow and temperature, which provides numerical stability. This modular system allows to apply different models for the various heat transport mechanics (solids are treated with a 3D conducting solver, the fluid inside the cavity is treated with a CFD & HT coupled with a solver of thermal and solar radiation, the HTF you can apply a single/two phase model depending on an industrial oil, molten salt or water vapor).

A scheme of the Linear Fresnel Collector (LFC) is given in Fig 1. The cavity receiver of LFC consists of an absorber tube and a secondary concentrator. The Fresnel cavity profile is defined by an equation from the literature [13]. The absorber is usually protected with glass cover at the bottom of the cavity to reduce heat losses. The primary mirror field reflects the direct normal radiation into the cavity and due to astigmatism and optical inaccuracies only part of the reflected radiation hits the absorber directly. A fraction of the radiation interacts with the secondary reflector and is redirected onto the absorber. While the absorber is being heated, it

doi:10.18086/swc.2017.31.04 Available at http://proceedings.ises.org

loses heat by long wavelength radiation and convection to the surroundings.

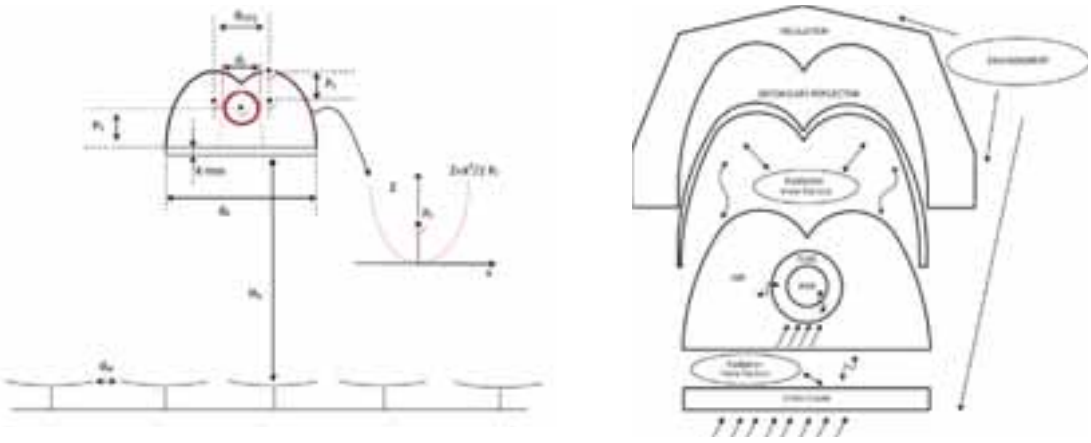

Fig. 1: NEST scheme of the modular system and Fresnel receiver

Nomenclature

c_p	Specific heat capacity, J kg^{-1} K^{-1}	Greek letters	
D_{in}	Internal diameter of the tube, m		
L_M	Width of mirror	ε	Thermal emissivity
f_M	Maximum deflection of the mirror	α	Sup. heat transfer coefficient, W m^{-2} K^{-1}
H_R	Receiver height	β	Thermal expansion coefficient, K^{-1}
d_R	Aperture of the receiver	η	Smallest turbulent scales of the flow, m
d_M	Distance between rows of mirrors	κ	Thermal diffusivity, m^2 s^{-1}
d_{F1F2}	distance between focal points	λ	Thermal conductivity, W m^{-1} K^{-1}
P_F	The focal parameter of the parabolic portions		
d_T	External tube diameter	μ	Dynamic viscosity, kg m^{-1} s^{-1}
P_T	Position of the tube in the cavity	ν	kinematic viscosity, m^2 s^{-1}
e_g	Thickness of the transparent glass	ξ	Turbulent kinetic energy dissipation rate, m^2 s^{-3}
η_{opt}	Optical efficincy	ρ	Density, kg m^{-3}
H	Height, m	σ	Stefan-Boltzmann constant, 5.67x10^{-8} W $m^{-2}K^{-4}$
g	Gravity vector, m s^{-2}	Γ_v	Stress tensor, m^{-2} s^{-2}
I	Identity matrix	Ω	volume, m^3
$\dot{m}$	Mass flow rate, kg s^{-1}	$\partial\Omega$	Surface which enclosed the volume **Ω**, m^2
Nu	Nusselt number	Δ	Magnitude increment
n	normal direction vector		
Pr	Prandlt number, $Pr = \mu c_p/\lambda$	Subscripts	
Pr_t	Turbulent Prandlt number, $Pr_t=\nu_{sgs}/\kappa_{sgs}$		
$\dot{Q}$	Heat losses, W	conv	Convection
$\dot{q}$	Specific heat flux, W m^{-2}	rad	Radiation
Ra	Rayleigh number, $Ra = g\beta\Delta TH^3/\nu\kappa$	cond	Conduction
S	Surface area, m^2	ins	Insulation
S_{ij}	Rate-of-strain, m^2	gc	Glass cover
$\bar{S}_{ij}$	Mean rate-of-strain fluctuations, s^{-1}	amb	Ambient conditions
T	Temperature, K	ref	Reflectors
t	time, s	tube	Tube
z	extruded direction, m	in	Inlet conditions
f(t)	Function of the time	out	Outlet conditions
u	velocity vector, m s^{-1}	sgs	Subgrid scales
g_k	Irradiosity on surface *k*, W m^{-2}	dir	Direct Radiation
j_k	Radiosity on surface *k*, W m^{-2}	max	Maximum
<u>	Average velocity u, m s^{-1}		
DNI	Direct Normal Irradiance		

A modular object-oriented methodology for the design and optimization of Linear Fresnel receivers is proposed (NEST platform [10]). This methodology considers the different parts of the Linear Fresnel receiver as independent models and the coupling between global models and advanced computational fluid dynamic and

heat transfer (CFD&HT) mainly based on large-eddy simulation (LES) techniques (TermoFluids[11]).

TermoFluids [11], a general purpose unstructured and parallel object-oriented CFD code developed to solve industrial flows, is used to optimize the optical and thermal performance of a defined system (geometry, optical and thermal properties of the materials).

The presented methodology was explained by Guadamud et al (2014), [12]. For each element of the receiver more than one model approach is considered depending on the desired accuracy. The use of a modular simulation allows that for the same element one-, two- or three-dimensional models can be used. At the same time, each element can receive a special treatment from the physical point of view.

The implementation of the Fresnel receiver methodology has been made within the existing NEST platform which allows the linking between different elements to perform a specific system or configuration. In the present implementation, Fresnel receiver is considered as the sum of different parts, e.g. insulation, glass cover, air inside the cavity, tube, pipe, etc., such as shown in Fig 1.

2. Geometry configurations and optimization

Three different configurations were selected; table 1 shows all the parameters.

Table 1. Different configurations for the Linear Fresnel receivers

Parameters	Configuration 1	Configuration 2	Configuration 3
L_M	12.5% H_R	5% H_R	10.5% H_R
d_{F1F2}	8.5% d_R	0% d_R	0% d_R
p_F	10.2% d_R	15% d_R	12% d_R

The H_R represents the height of the receiver, for optical analysis, this value will vary to determine its effect on optical performance, in the thermal analysis will set this value constant for all three configurations to a value in which its optical behavior is the most optimum. The d_R (aperture of the receiver) will be fixed constant in both analysis, based on this, various aspect ratios are obtained as shown in Table 1.

The procedure of the optimization consists in fixing certain parameters (taking into account some technical criteria) and calculating the others parameters by maximizing the optical efficiency (considered as the objective function).

The variation of the DNI during the day is simulated by a cosine expression:

$$DNI(t) = DNI_{max} * \cos\left(\left(-\frac{\pi}{12}\right) * t + \pi\right) \quad \text{(eq. 1)}$$

For the optical efficiency (η_{opt}) is evaluated by the total energy received by the tube during the day between the direct normal irradiance with the reflectors surface, the second optical efficiency (η'_{opt}) is the total energy received by the tube during the day between the direct normal irradiance with the total surface of the land requirements.

3. Mathematical Model

3.1 Heat conduction in the solid elements of the Fresnel receiver (tube, glass cover and insulation).

Transient conduction heat transfer can be solved directly from the governing equation. For the case of the transient heat conduction without volumetric sources, the energy transport equation can be written in integral from as:

$$\rho c_p \frac{\partial T}{\partial t} = \nabla \cdot (\lambda \nabla T) \quad \text{(eq. 2)}$$

where T represents temperature, t is the time, ρ is density, c_p is the specific heat and λ the thermal conductivity. In this work, a non-structured mesh and a uniform distribution has been used in some elements like the tube and

the glass cover, but due to the geometric singularity in the element insulation the mesh has been adapted to this form.

In TermoFluids, for the integration of the governing equations the finite volume method has been used. A modified least-square method has been chosen for the calculation of the gradients. The resulting system of equations is solved by means of the Conjugate Gradient method [15].

3.2 CFD&HT of the air inside the cavity receiver

The objectives for using a CFD&HT object for modeling the air inside the cavity are twofold: (i) due to the complex geometry of the cavity, there are not specific correlations for the heat transfer inside irregular cavities, thus results of such modeling would be used for proposing new correlations to be used in the global model for the convective process and (ii) it would shed some light into the complex physics presents in this kind of receivers. The CFD&HT air cavity object calls TermoFluids CFD&HT code [11] which is an object-oriented parallel and unstructured CFD&HT code for the resolution of industrial flows. In this object, the three-dimensional Navier-Stokes equations are spatially filtered. Therefore, some level of modelisation for the filtered non-linear convective terms is required. This approach is known as large-eddy simulation (LES) of the turbulent flow. In LES, all temporal scales of the flow together with the largest spatial scales are solved, and only the small scales of the flow are modeled by means of a sub-grid scale model (SGS).

The discretised continuity, momentum and energy filtered equations, assuming constant thermophysical properties and negligible viscous dissipation effects in the energy equation read,

$$M\vec{u} = 0 \qquad \text{(eq. 3)}$$

$$\Omega\frac{\partial\vec{u}}{\partial t} + C(\bar{u})\bar{u} + \nu D\bar{u} + \rho^{-1}\Omega\bar{\mathrm{p}} - f = C(\bar{u})\bar{u} - \overline{C(u)u} \approx -M\Gamma \qquad \text{(eq. 4)}$$

$$\Omega\frac{\partial\overline{\mathrm{T}}}{\partial \mathrm{t}} + C(\bar{u})\bar{T} + \frac{\nu}{Pr}D\bar{T} - \overline{\nabla\cdot q_{rad}} = C(\bar{u})\bar{T} - \bar{C}(u)T \approx -M\Gamma_T \qquad \text{(eq. 5)}$$

where $\vec{u} \in R^{3m}$, $\bar{p} \in R^m$ and $\bar{T} \in R^m$are the filtered velocity vector, pressure and temperature, respectively (here m applies for the total number of control volumes (CVs) of the discretised domain). $\Omega \in R^{3m}$ is a matrix with the cell control volumes. f are the body forces, $f = \beta(T - T_{ref})\boldsymbol{g}$. Convective and diffusive operators are given by $C(\vec{\boldsymbol{u}}) = (\vec{\boldsymbol{u}}\cdot\nabla) \in R^{3m\times m}$, $D = -\nabla^2 \in R^{3m\times 3m}$ respectively. Gradient and divergence (of a vector) operators are given by $G = \nabla \in R^{3m\times m}$ and $M = \nabla\cdot R^{m\times 3m}$ respectively.

The last term in Eqs. (6) and (7) indicate some modelisation of the filtered non-linear convective term. M represents the divergence operator of a tensor, and Γ is the sub-gird scale (SGS) stress tensor, which is defined as[4],

$$\Gamma = -2\upsilon_{sgs}\overline{S_{ij}} + (\Gamma{:}\,\mathrm{I})I/3 \qquad \text{(eq. 6)}$$

where $\overline{S_{ij}} = 1/2[G(\vec{\boldsymbol{u}}) + G^*(\vec{\boldsymbol{u}})]$, and G^* is the transpose of the gradient operator. Γ_T term is evaluated as in Γ term, but ν_{sgs} is substituted by ν_{sgs}/Pr_t, where $Pr_t$is the turbulent Prandlt. To close the formulation, a suitable expression for the subgrid-scale (SGS) viscosity, ν_{sgs}, must be introduced. The QR-model based on the invariants of the rate-of-strain tensor [15] has been used.

The governing equations used in TermoFluids CFD&HT code are discretised on a collocated unstructured grip arrangement by means of second-order conservative schemes [15], i.e. they preserve the kinetic energy equation which ensures stability and conservation of the kinetic-energy balance even at high Reynolds numbers and with coarse grids.

In the context of the large-eddy simulation of turbulent flows, the time advancement algorithm should be capable of solving all the relevant temporal scales while, at the same time, it should be kept within the stability domain. Different temporal schemes have been proposed in the literature to deal with time marching algorithm for turbulent flows (see for instance [16-18]). In this work, a two-step linear explicit scheme on a fractional-step method proposed by Trias and Lehmkuhl [19] is used. Its main advantage relies on its capacity of dynamically adapt the time step to the maximum possible value while at the same time it is kept within the stability limits. This strategy reduces the computational time required without lost accuracy. The method has been successfully

tested in different flows in [20-22].

3.3 Single phase flow

In this work, a one dimensional model has been chosen to represent the forced convection in the tube, solved by step by step method. The fact that this code is one dimensional makes difficult the communication between the fluid flow and the code for the tube heat conduction element. This problem has been solved by heat coupling between the tube and the pipe elements, evaluating the average heat flux of each n volume controls of the 3D tube element per plane of extrusion and passed to the pipe element, this average heat flux has been used to solve the fluid flow and a new temperature profile has been obtained, then this new temperature field has been used to evaluate the heat flow that has been send to the tube. A heat transfer coefficient has been calculated each time iteration considering the convective heat flux between the tube and the pipe in the extruded direction as:

$$\vec{q}_{tube-pipe,conv} = \sum_j \alpha_f \left(\bar{T}_{tube} - T_f^i\right) \frac{\pi D_{in}}{\Delta z} \qquad \text{(eq. 7)}$$

where α_f is the HTF convection heat coefficient at T_{tube} and is evaluated as a function of the Nusselt number Nu_{Din}, the Nusset number and the properties are evaluated at medium temperature between the temperature of the tube and the temperature of the fluid inside the tube. Due to the lack of specific correlations in literature for evacuation the Nusselt number taking into accont the temperature distribution of the tube, correlations for isothermal cylinders are considered. Specifically, the Gnielinski correlation [23] is used for turbulent and transitional flow (Re>3200) in circular ducts, which reads,

$$Nu_{D_{in}} = \frac{(C/2)\left(Re_{D_{in}} - 1000\right)Pr}{1+12\sqrt{C/8}\left(Pr^{2/3}-1\right)} \left(\frac{Pr}{Pr_w}\right)^{0.11} \qquad \text{(eq. 8)}$$

with $C = (1{,}82\log(Re_D)-1{,}64)^{-2}$.

A silicone HTF(Syltherm800)has been used, this fluid is normally used in CSP due to a highly stable at high temperature liquid phase operation. The thermo-physical properties of the syltherm 800 have been obtained from the datasheet [24], and the approaches have been made by a polynomial correlation, these properties correlation are presented in Table 2.

Table 2. Thermo-physical properties correlation of the Syltherm 800.

Property	Polynomial correlation
ρ	$1.269 \cdot 10^3 - 1.52\bar{T} + 1.8 \cdot 10^{-3}\bar{T}^2 - 2 \cdot 10^{-6}\bar{T}^3$
cp	$1.109 \cdot 10^3 + 1.7014\bar{T} + 1 \cdot 10^{-5}\bar{T}^2 - 9 \cdot 10^{-9}\bar{T}^3$
μ	$0.6527 - 6.451 \cdot 10^{-3}\bar{T}^3 + 2.552 \cdot 10^{-5}\bar{T}^2 - 5.023 \cdot 10^{-8}\bar{T}^3 + 4.905 \cdot 10^{-11}\bar{T}^4 - 1.9 \cdot 10^{-14}\bar{T}^5$
λ	$1.907 \cdot 10^{-1} - 2 \cdot 10^{-4}\bar{T} + 1 \cdot 10^{-8}\bar{T}^2 - 8 \cdot 10^{-12}\bar{T}^3$

3.4 Radiation

3.4.1 Solar Radiation from mirrors to receiver

The estimation of the incident solar energy was done by means of the Monte-Carlo Ray-tracing method, where a lightning sweep is performed on the various mirrors, the amount of energy incident on the tube is analyzed, and this amount of energy is saved for the different positions and is treated as a source term for the simulation of the system. The different matrixes obtained in the method will be loaded one by one each time it is considered suitable for which there has been a change of solar position and it is verified how it affects the Fresnel System.

a b

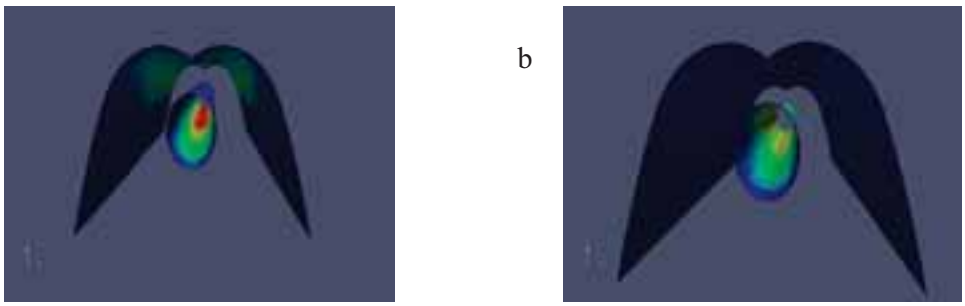

Fig. 2. Ray-tracing model obtained. (a) without a secondary reflector; (b) with a secondary reflector

Figure 2 shows the flux distribution of the incident solar radiation, comparing it qualitatively between a receiver without reflector (Fig. 2a) and with secondary reflector (Fig. 2b). In the first receiver the energy concentrates at lower part of the tube, losing many rays that go towards the upper part of the interior of the cavity, while having a secondary reflector distributes better the rays that do not directly affect the tube, and suffer second reflections increasing the optical performance of the system.

3.4.2 Thermal radiation inside the cavity

A Radiosity-Irradiosity method [25] has been applied to solve the non-participating media inside the cavity. The radiosity and the irradiosity can be expressed as:

$$j_k = \varepsilon_k E_{b,k} + \rho_k g_k \quad \text{(eq. 9)}$$

$$g_k = \sum_{l=1}^{N} F_{k\to l} j_l \quad \text{(eq. 10)}$$

For N surfaces, equations (11) and (12), define a linear system with N unknowns, the radiosities j_K. Once this system is solved, the toal heat flux, per unit area, is simply $q_K=j_K-g_K$. Considering the total heat flux $Q_K=A_K q_K$.

A Monte-Carlo Ray-tracing tool is applied to obtain the specular view factors needed, this factors are implemented on a Radiation model to solve a combined case with natural convection phenomena inside the cavity and their effects between the surfaces of the cavity and their surroundings.

4. Results

The need to analyze the behavior of a Fresnel Linear Receiver allows us to identify two important criteria, from the optical and thermal points of view.

The following is an intensive analysis of the various configurations, the parameters that determine its sensitivity, and has been compared with a commercial code such as OPSOL, obtaining very close results between those proposed by the RT-method of the CTTC and OPSOL [26]

Table 3. Optical efficiency comparison between this work and OPSOL code.

Parameters	Configuration 1	Configuration 2	Configuration 3
η_{opt}	*55%*	*57.5%*	*62.4%*
η'_{opt}	*39.5%*	*45.9%*	*48.4%*
η_{opt} **(OPSOL)**	*55%*	*60%*	*63%*
η'_{opt} **(OPSOL)**	*38.32%*	*46.8%*	*47.6%*

4.1 Optical performance of Linear Fresnel configuration

The instantaneous optical efficiency for the three configurations proposed was calculated for some day in April 2016 and based in Taroudant, Morocco. The analysis of the solar field behavior consisted on calculating the instantaneous power received by the tube during a whole day, from sunrise to sunset. The criteria to be optimized will be the effect of the receiver height, orientation of the mirrors, distribution of power in the symmetry plane, shadows basically.

4.1.1 Effect of receiver height.

It has been observed that increasing the height of the receiver results on a slightly higher performance. The reasons identified were: the orientation of the heliostats becomes more favorable, and the receiver being at a larger height casts less shadow on the mirrors.

4.1.2 Shadows

The shadows play a role in the efficiency of the system in two different ways. For the first and last hours of the day, when the sun altitude is low, some mirrors cast shadows onto other mirrors, thus decreasing the mirror surface area that reflects solar radiation to the receiver. On the other hand, when the sun is high in the sky, the receiver successively cast shadows one mirror by one mirror, thus also decreasing the effective area of the mirror. These two effects are illustrated in Figure 6.

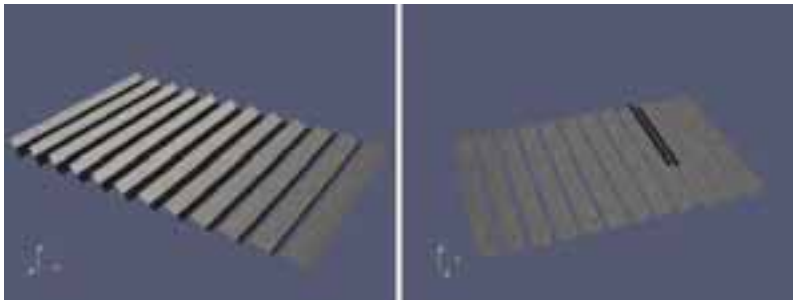

Fig. 6 Shadows cast on the mirrors are shown in black. Left: mirrors casting shadows on other mirrors when the sun is low in the sky. Right: receiver casting shadows on two mirrors when the sun is high in the sky.

It can be observed that the shadow casted by the receiver has less impact the higher the receiver is placed, because the shadow lasts for less time and covers less area of the mirrors. The fraction of the mirror that is illuminated during the course of the day, for several heights of the receiver, can be seen in Figure 7. The dents in the graphs correspond to the shadow of the receiver crossing the mirror, while the linear decrease at the end of the day (for outer mirror) and at both the beginning and end of the day (for the inner mirror) are due to the shadows cast by other mirrors. It is apparent from the figure that the effect of the shadows cast by the receiver is more detrimental for the configurations where the receiver is placed at lower a height. The effect of the shadows cast by other mirrors is (nearly) independent of the receiver height.

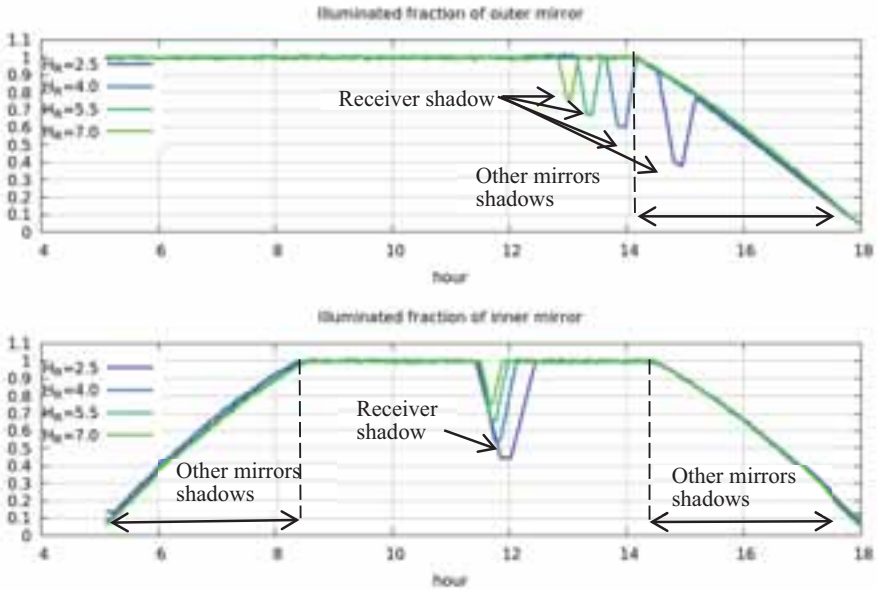

Fig. 7 Illuminated fraction of outer (top) and inner (bottom) mirrors, for several receiver heights.As the receiver height increases, both the size and duration of the shadow cast by the receiver decrease, making the mirror more effective.

4.1.3 Orientation of the mirrors

The orientation of the mirrors has an effect on the total power that can be reflected by the mirrors to the receiver and to the tube. Ideally, the mirrors should be facing a direction perpendicular to the direct solar radiation, but

there is a constraint that the orientation of the mirror is in fact determined by the point where it is supposed to focus the incoming solar radiation. Therefore, for a given receiver height and sun position, the orientation of the mirror is fixed. Looking at Fig. 3 one can expect that the orientation is more favorable the higher the receiver is placed, because the mirror will present a larger cross section to the solar radiation.

Fig. 3 Orientation of mirrors at noon. Blue mirrors: receiver height of 2m. White mirrors: receiver height of 8m. Taking into account that solar radiation at noon comes in Y direction (with some amount of Z component), clearly the higher the receiver height, the more effective area the mirrors present to the solar radiation. This effect is more important for the outer mirrors.

The influence of the orientation of the mirrors throughout the day is plotted in Figure 4. The inner mirror is the closest to the receiver, and the outer mirror is the furthest. The power reflected by the inner mirror due to its orientation is nearly independent of the receiver height. On the other hand, for the outer mirror the power reflected varies significantly with the receiver height.

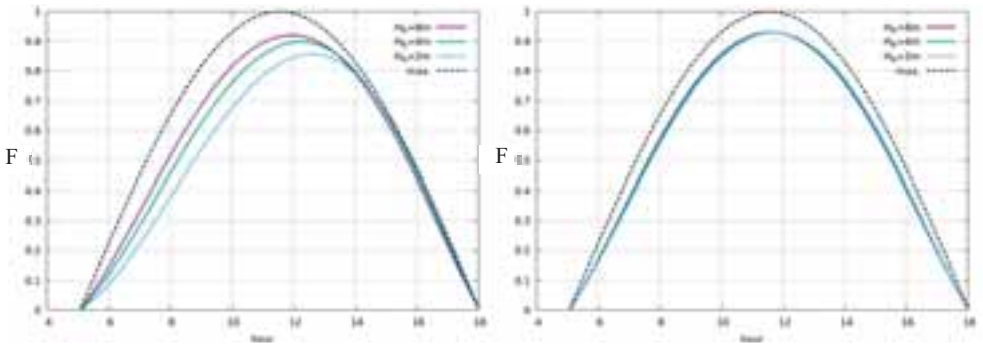

Fig. 4 Fraction of available solar power reflected by mirrors during the day. Geometric considerations only, i.e., the surface reflectivity of the mirror is not considered in these plots. Left: outer mirror (the higher the receiver, the more solar radiation is reflected). Right: inner mirror.

The daily integrated energy is shown in Figure 5. The closer the mirror is to the receiver (higher mirror index), the less influence the receiver height has on the power it can deliver. Note that the power reported is all of the power that is going to be reflected by the mirrors, without taking into account the distribution of this power in the zone near the receiver and the tube. In fact, not all of this power is going to be absorbed by the tube.

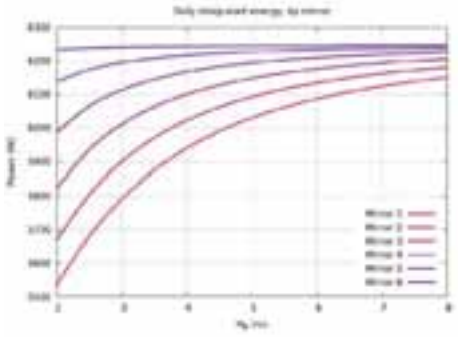

Fig. 5 Daily integrated energy for every mirror as a function of the receiver height. Inner mirror (6) is almost independent of H_R, while for outer mirrors (lower mirror index) the influence of H_R becomes noticeable.

4.1.4 Combination of all effects

To summarize, the receiver was collocated as high as possible so as to get less shadowing and higher cross section of the mirrors with respect to the incident solar radiation, but less power to the tube could available.

In Figure 8 the instantaneous power transferred to the tube is plotted for several heights of the receiver. It can be seen that the most optimal height roughly corresponds to that of the focal length of the parabolic mirrors. Also, the passage of the shadow of the receiver over the mirrors lasts less for higher heights (the wiggles start later and end before, and the time between two successive maxima is also shorter), and blocked area is smaller (the peak of variation is less pronounced).

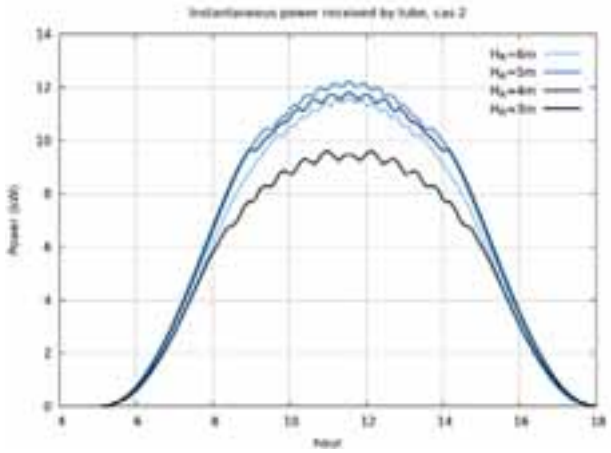

Fig. 8. Instantaneous power received by the tube in configuration "Cas 2" for several receiver heights.

4.2 CFD&HT modelling of the Fresnel receiver

4.2.1 CFD&HT modelling of the Fresnel receiver with radiation

The simulations were carried out with a direct intensity of variable radiation throughout the day. Similarities in the behavior and certain differences are presented in the different configurations. Due to the aspect ratio, visually there are differences, as shown in Figure 9. The first configuration has a double curve since there is a distance d_{F1F2} different from zero, whereas in the other two configurations only a single curve is presented. In the first configuration, the tube is situated at the vertical center of the cavity, in the second one is closer to the glass cover and in the third configuration; the tube is slightly higher than the vertical center of the cavity. At the energy level, the differences in position of the absorber tube, as well as the fact that there is a double parabola or only one, affect the temperature distribution. Higher values are observed in C1, than in the other two. Configurations 2 and 3 show similar temperatures.

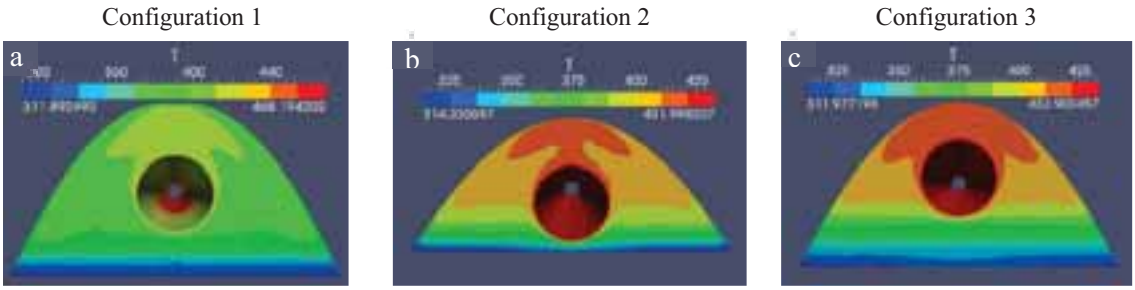

Fig. 9. Average air temperature (a) configuration 1; (b) configuration 2; (c) configuration 3

In the three configurations the tube with a higher temperature than its surroundings is observed, in configuration 3 there is a more closed concentration in the upper part of the cavity due to its closed curve, while in the two it is the more open, it is better distributed the temperature profile in this zone. In configuration 2, as the tube is closest to the glass cover, the Nusselt number is slightly higher, but the profile that reaches a higher peak is that of the first configuration. Figure 10 shows the distribution of the Nusselt number averaged in the air-tube absorber contact zone (Figure 10a) and in the air-insulation contact zone (Figure 10b). There is a change of trend in the Nusselt between the air and the insulation, because at the ends it is glued to the glass, where the air is at a lower temperature than that reached by the insulation, thus reversing the heat flow.

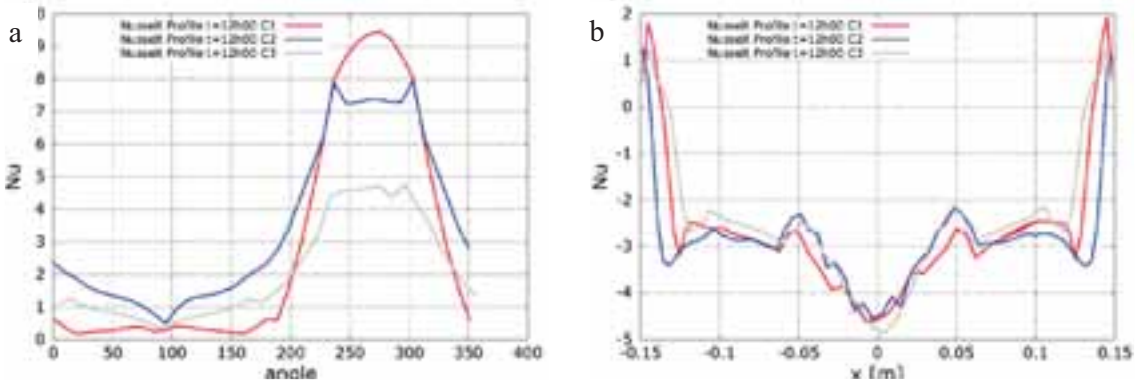

Fig. 10. Profiles of the average Nusselt number (a) boundary with tube; (b) boundary with insulation

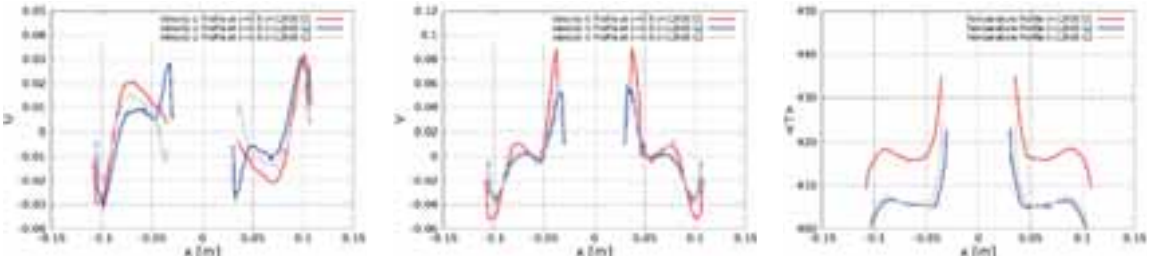

Fig. 11. Average profiles at middle of the cavity, plane z=1.0 (a) Velocity u profile from horizontal axis; (b) Velocity v profile from horizontal axis; (c) Temperature profile from horizontal axis.

Figure 11 shows the velocity profile for the various configurations at 12:00 solar time and ate the middle plane of the geometry (located at z = 1.0) in a horizontal line (parallel to the x-axis). In Figure 11a., it can be observed that the horizontal velocity u has a symmetrical but inverted behavior due to the geometry. In configuration 2, a more pronounced peak of horizontal velocity (u) is shown in the zone of contact with the tube. The accelerated decay of the value of u is due to the boundary layer conditions. The other two configurations show a lighter decay but with the same tendency. Figure 11b- shows the vertical velocity profile (v), where the symmetry of the case is visualized with respect to the center of the cavity. It is observed that, for this component of the velocity, the configuration with the highest peak is in the first. Moving away from the center, the downward tendency of the air is observed, reaching 0 at the contact end with the insulation. Figure 11c shows the temperature profile across the cavity from the zone of contact with the tube towards the insulation. It can be seen that the temperature is higher in the area close to the tube and decrease as it moves away towards the insulation. These values of temperatures could enhance the thermal wear of the system configurations 2 and 3 are more interesting.

4.2.2 Heat Conduction (Tube, Insulation and Glass Cover) and HTF inside the tube.

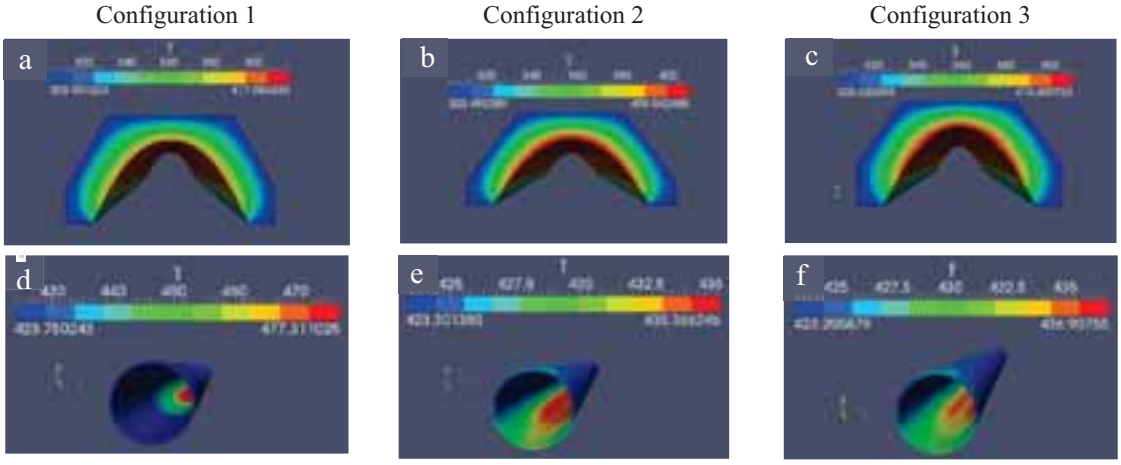

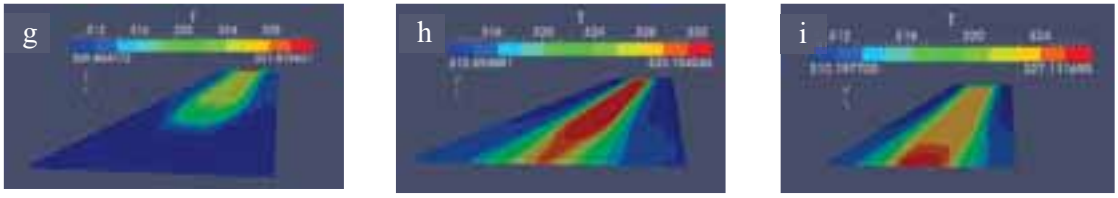

Fig. 12. Instantaneous distribution of the temperature, from top to bottom: insulation element, tube and glass cover. (a), (d), (g) configuration 1; (b), (e), (h) configuration 2; (c), (f), (i) configuration 3.

Figure 12 shows the instantaneous temperature profiles for each configuration and for each element of the system (insulation, absorber tube and glass cover). It is observed that the insulation has similar temperatures in the three configurations, even in the first case where a higher temperature is reached; it remains very similar, thermal expansion wear in this configuration must be taken into account. The absorber tube also has a high gradient between the inlet and the outlet, so it should be properly sized to withstand these temperatures and avoid thermal expansions that punish the element, configurations 2 and 3 exhibit similar behaviors with a variation of less than 2% of temperature in the tube and somewhat higher in the profile of the glass cover.

5. Conclusions

An advanced global model of a Fresnel linear system with couplings between natural convection, solar and thermal radiation, and its simultaneous multi-physics resolution allows us to estimate, study and analyze, the behavior of these systems in order to determine how is affected by the variation of the various parameters such as the height of the receiver, the shadows between mirrors, the orientation from the optical point of view. From the thermal point of view allows simulating diverse scenarios, to know maximum permissible temperatures. The coupled resolution also helps to determine the outlet temperature of the carrier heat fluid with a correct estimate, to test new materials, lighter or with lower optical properties, but to meet the energy requirements of these systems with the aim of reducing costs and making them more competitive with respect to other technologies of solar concentration.

The implementation of the system through a block where it can be varied of physical properties, the fluid carrier heat and the different models that are applied for its resolution, hypothesis, numerical approximations, etc., make this multidimensional model a versatile tool with many applications at industrial and energy sector level.

6. Acknowledgments

This research has been financed and supported by the European Institute of Technology and IRESEN through the Maghrenov project: “Solar Boiler based on Fresnel concentration system” (Ref. SIROCCO.EIT/KIC InnoEnergy/FPA/1).

7. References

[1] Barale, G., Heimsath, A., Nitz, P., Toro, A., 2010. Optical design of a Linear Fresnel collector for Sicily. In: SolarPaces Conf., pp. 1-7.

[2] Beltagy, H., Semmar, D., Lehaut, C., Said, N., 2017. Theoretical and experimental performance analysis of a Fresnel type solar concentrator. Renew. Energy 101, 782–793. http://dx.doi.org/10.1016/j.renene.2016.09.038.

[3] Bernhard, R., Laabs, H., De Lalaing, J., 2008. Linear Fresnel collector demonstration on the PSA, Part I–Design, construction and quality control. In: SolarPaces Conf., pp. 1–10. Breault Research Organization [WWW Document], n.d. (Accessed 04.10.17).

[4] Häberle, A., Zahler, C., De Lalaing, J., Ven, J., Sureda, M., Graf, W., Lerchenmüller, H., Wittwer, V., 2001. The solarmundo project - advanced technology for solar thermal power generation. In: ISES Sol. World Congr., pp. 961–970.

[5] Negi, B.S., Mathur, S.S., Kandpal, T.C., 1989. Optical and thermal performance evaluation of a linear Fresnel reflector solar concentrator. Sol. Wind Technol. 6, 589–593.

[6] Singh, P.L., Ganesan, S., Yàdav, G.C., 1999. Performance study of a linear Fresnel concentrating solar

device. Renew. Energy 18, 409–416. http://dx.doi.org/ 10.1016/S0960-1481(98)00805-2

[7] Facão, J., Oliveira, A.C., 2011. Numerical simulation of a trapezoidal cavity receiver for a linear Fresnel solar collector concentrator. Renew. Energy 36, 90–96. http://dx.doi.org/10.1016/j.renene.2010.06.003.

[8] Lin, M., Sumathy, K., Dai, Y.J., Zhao, X.K., 2014. Performance investigation on a linear Fresnel lens solar collector using cavity receiver. Sol. Energy 107, 50–62. http:// dx.doi.org/10.1016/j.solener.2014.05.026

[9] Qiu, Y., He, Y.-L., Cheng, Z.-D., Wang, K., 2015. Study on optical and thermal performance of a linear Fresnel solar reflector using molten salt as HTF with MCRT and FVM methods. Appl. Energy 146, 162–173. http://dx.doi.org/ 10.1016/j.apenergy.2015.01.135

[10] Damle, R., Lehmkuhl, O., Colomer, G., Rodríguez, I., 2011. Energy simulation of buildings with modular object oriented tool. In: ISES World conference; P. 1-8.

[11] Lehmkuhl, O., Pérez Segarra, C. D., Borrel, R., Soria, M. And Oliva, O., 2007, TermoFluids: A new Parallel unstructured CFD code for the simulation for turbulent industrial on low cost PC CLUSTER. Proceddings of Parallel CFD 2007 Conference, pq. 1-8.

[12] Guadamud, E. Oliva, A., Lehmkuhl, O., Rodríguez, I. And González, I. 2014. Thermal analysis of a receiver for Linear Fresnel reflectors. SolarPaces2014: International Conference on Concentrating Solar Power and Chemical Energy Systems: proceedings, at "Energy Procedia", vol. 69, Pags: 405-414. ISBN/ISSN: 1876-6102, May 2015.

[13] Dixon, J. D., Davies, P. A., 2012 Cost-exergy optimisation of linear Fresnel reflectors. Solar Energy, Vol. 86, pp 147-156.

[14] Sagaut P, Germnao M: Large eddy simulation for incompressible flows. Sporinger-Verlag; 2001.

[15] Verstappen RWCP, Veldman AEP. Symmetry-preserving discretization of turbulent flow. Jornal Of Computational Physics, 187:343-368, May 2003.

[16] Le H, Moin P. An improbvement of fractional step methods for incompressible Navier-Stokes equations. Journal of Computational Physics 1991;92(2):369-79.

[17] Kim D, Choi H. A second order time-accurate finite volume method for unsteady incompressible flow on hybryd unstructured grids. Journal of Computational Physics 2000;162(2):411-28.

[18] Fishpool G, Leschziner M. Stability bounds for explicit fractinal-step schemes for Navier-Stokes equations at high Reynolds number. Computers & Fluids 2009;38:1289-98.

[19] Trias F, Lehmkuhl O, A self-adaptive strategy for time integration of Navier-Stokes equations. Numerical Heat transfer Part B 2011;60(2):116-34.

[20] Trias F, Gorobets A, Soria M, Oliva A. Direct numerical simulation of a differentially heated cavity of aspect ratio 4 with rayleigh numbers up to 1011. Part i: numerical methods and time-averaged flow. International Journal of Heat and Mass Transfer 2010;53(4):665-73.

[21] Rodríguez I, Lehmkuhl O, Borrell R, Oliva A. Flow dynamics in the wake of a sphere at sub-critical Reynolds numbers. Computers & Fluids 2012.

[22] Jaramillo J, Trias F, Gorobets A, Pérez-Segarra C, Oliva A. DNS and RANS modelling of a turbulent plane impinging jet. International Journal of Heat and Mass Transfer 2012;55(4):789-801.

[23] Gnielinski V. New equations for heat and mass transfer for turbulent pipe and channels flow. Int Chem Eng 1976:16(2):359-63.

[24] Syltherm 800, Heat Transfer Fluid. Availabled in: www.loikitsdistribution.com/files/syltherm-800-product-brochuere.pdf

[25] Michael F. Modest. Radiative Heat Transfer. McGraw Hill, 1993.

[26] Soukaina El Alj, Ahmed Almers, et al. "Optical Modelling and Analysis of the First Moroccan Linear Fresnel Solar Collecto Prototype", Journal of Solar Energy Engineering, Transactions of ASME; 139[5], 0410091-12, 2017.

Enhanced Performance Analysis of Solar Chimney Power Plant Aided with Reflectors

Faisal M. Hussain[1,2], Fahad A. Al-Sulaiman[1,2 *] and Ahmed S. Abd-Elrazik[1,2]

[1] Department of Mechanical Engineering, King Fahd University of Petroleum and Minerals, Dhahran (Saudi Arabia)

[2] Center of Research Excellence in Renewable Energy (CoRERE), King Fahd University of Petroleum and Minerals, Dhahran (Saudi Arabia)

*Corresponding Author: fahadas@kfupm.edu.sa, Tel: +966 (13) 860-4628.

Abstract

Solar Chimney Power Plant (SCPP) is guided through natural draft utilizing solar radiant energy to impart ascending thrust to the flow of air and therefore, transforming the radiant energy to run the turbine. A simplified model for a solar chimney power plant aided with reflectors is developed and a comparative study is conducted with an SCPP model without reflectors. This paper presents the enhanced performance analysis of the SCPP model with the aid of reflectors by increasing the radiant energy incident onto the floor and presents its performance for Dhahran, Saudi Arabia. For solar radiation data of 2016, the reflector aided SCPP model can produce on average, around 331kW during daytime and has an average air mass flow rate of around 432 kg/s, when compared with traditional SCPP of same geometry which produces 123kW. The energetic efficiency and power output are found to increase by 40% and 167%, respectively. Moreover, power produced, energy efficiency, the variation of temperature for the floor, the variation of mass flow rate and inlet velocity of the turbine for each month of the year are reported.

Keywords: Solar Chimney Power Plant (SCPP), Reflectors, Energy, Efficiency.

1. Introduction

SCPP is an agglomeration of three traditional mechanisms: the green house, the lengthened chimney at the center, and the wind turbine seated within the chimney. This setup fulfills the effort of transformation into electrical energy from the radiant energy of sun. This transformation involves two steps. During the first step, air flowing radially inwards under the collector transforms the radiant energy into thermal energy and this stride is fulfilled by the greenhouse effect. During the next step, the chimney transforms the developed thermal potential into kinetic energy and finally into electricity through the generator connected to the wind turbine.

In the simple model, the collector is built with the film of glass or plastic cover drawn out evenly and advanced on the top of the ground, thus the cover fulfills the objective of trapping the heated air, and in turn allows the radiation of the smaller wavelength from sun and on the other side below arresting the radiation of smaller wavelength emanated from the ground. Consequently, temperature above the ground rises up, which in turn heats the air flowing beneath the film. The elevation of the collector cover, just above the ground increases evenly towards the middle of the SCPP. This accommodates continuous smooth passage of the hot air flowing through the long tubular chimney and therefore, downsizing the disturbance within the flow and thereby diminishing the eddy loss. A flat collector of these characteristics can transform a considerable fraction of the radiant energy into thermal energy.

The idea of SCPP was conceived by (Schlaich Jorg 1995) and (Haaf et al. 1983) in the 1970s. The very first operational 36 kW pilot plant was constructed in Manzanares which is near Madrid in Spain. The concept of SCPP was developed gradually over the years, several research issues argued distinct facets of the SCPP, in which intricate mechanism of heat transfer and fluid mechanics appear. But a very few attempts have been reported to enhance the performance of the system.

One of the technique was to introduce water filled tubes for thermal storage as reported by (Kreetz, H. 1997), water filled tubes are placed on the ground upon which radiation is incident, thermal energy is stored during day time and during night time when there is no solar radiation, temperature of air in the collector drops. Then water inside the tubes releases the heat that is stored during the day. But in the extended study of (Bernardes 2004) it is reported that the power produced during the peak hours of sunshine is decreased as the heat is absorbed by the water filled tubes.

doi:10.18086/swc.2017.31.05 Available at http://proceedings.ises.org

Anyhow, uniform power output is produced throughout day and night i.e., approximately 40% of the peak power of a traditional SCPP without water tubes is produced depending upon the depth of water stored.

Later (Pasumarthi and Sherif 1997, 1998a, 1998b) developed mathematical model, performed theoretical and experimental analysis. They suggested two designs, one is to elongate the sloped collector and the other was to introduce absorber plate in between ground and glass cover, both the designs were found to enhance the energy output by 10-15% compared with previous designs. Considering the first design suggested by (Pasumarthi and Sherif 1997, 1998a, 1998b) with the increase in the elongated sloped collector would surely increase the area subjected to solar radiation, but due to geometric constraints owing to negative draft it will also increase the height of chimney which is not desirable from construction and functioning aspect of SCPP.

(Bilgen and Rheault 2005) designed sloped SCPP for hills at high latitudes and evaluated its performance. As natural hills are used as collector field, the chimney height is reduced by 90%, which reduces the construction and maintenance cost. But construction of sloped collector increases the cost as it involves much civil work. Anyhow the authors claimed the efficiency of 0.48%, which is slightly better than the traditional SCPP. (Zhou et al. 2009) proposed a novel concept for producing energy by integrating a solar collector with a man-made mountain hollow. The mountain hollow, formed by excavation in a large elevation mountain, can avoid the issues of concrete chimneys which could reduce the usage of material and construction cost.

(Islamuddin et al. 2013a, 2013b) proposed a new idea of providing an external heat source to the SCPP by placing the hollow rectangular channels beneath the collector cover and passing the exhaust gases (flue gases) through it. They developed the mathematical model and investigated the numerical simulation, they validated their result with the analytical model of (Petela 2009c). But increase in overall efficiency of the system is found to be 1.14%. Anyhow, short coming of this hybrid technique is that flue gas is to be transported to the location of SCPP or thermal power plant should be in the vicinity of SCPP.

It can be observed from the literature review that no technique is able to enhance the efficiency of SCPP by more than 1.5%. In this article, study on new technique is emphasized, keeping the geometric parameters of SCPP same as that mentioned in the literature, an effort has been made to increase the radiation incident on solar collector with the aid of reflectors. Enhancement in the performance of SCPP was observed which is described in detail by performing energy analysis for Dhahran, Saudi Arabia. The results of the current research will be a valuable reference for researchers extending their studies for enhancing the efficiency of SCPP.

2. System Description

Air enters the collector through (point 0) via a gap of H_e. The floor of the collector is of diameter D_f, which is under the transparent cover which rises proportionally to ensure a constant radial cross-section area of flow for the radially directed air. The assumption of a constant radial cross-section implies

$$\pi \, x \, D_f \, x \, H_e \; = \; \pi \, x \, D_1 \, x \, H_1 \; = \; \pi \, x \, D_1^2/4 \qquad \text{(eq. 1)}$$

The values of H_e and D_f allows to determine inlet turbine diameter and height.

$$D_1 \; = \; \left(4 \, x H_e \, x D_f \right)^{\frac{1}{2}} \qquad \text{(eq. 2)}$$

$$H_1 = \frac{D_1}{4} \qquad \text{(eq. 3)}$$

The Collector floor heats the air from state 0 to a state 1. Heated air expands in the turbine to state 2. The inlet and outlet diameters of the turbine are D_1 and D_2, respectively. Height of the turbine is H_T; ($H_1 + H_T = H_2$). Air after expansion leaves the SCPP through the top of chimney of height H_3. Fig. 1 depicts the schematic representation of the SCPP taken into consideration for the present study.

Tab. 1: Dimensions of SCPP considered for present study

Geometric Parameter	Dimensions in Meter
D_f (Diameter of floor surface)	240
H_3 (Height of Chimney)	195
H_e (Height of Deck at Point 0)	0.3

The above dimensions from Tab.1 are substituted in afore mentioned geometric correlations to obtain overall dimensions of SCPP, owing to the fact to keep constant radial cross sectional area throughout the flow.

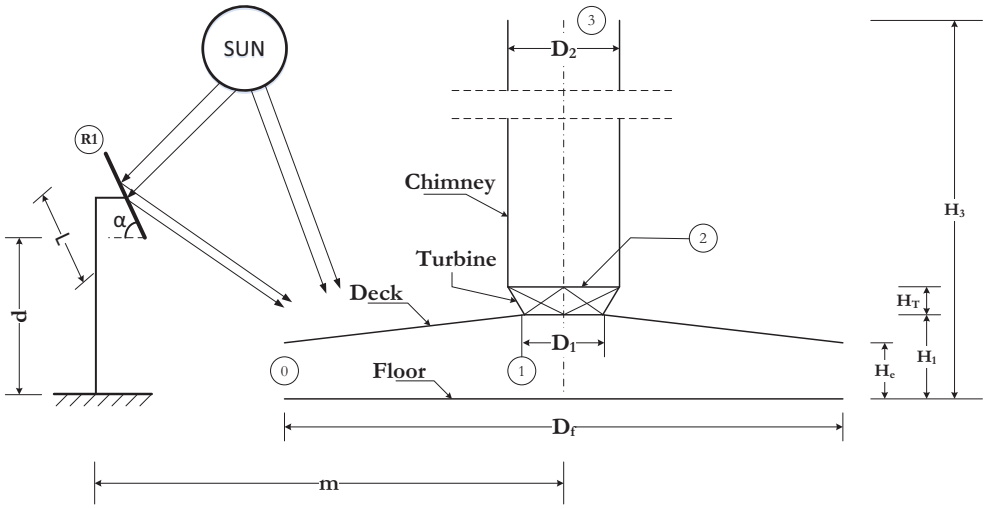

Fig. 1: Schematic Diagram of Solar Chimney aided with reflector

Once the geometric parameters of SCPP are determined then the location of reflectors is set such that the radiation incident on the mirror is reflected on to the collector field. Here, m denotes the distance of mirror from the center of SCPP, d, denotes the height between lower edges of mirror to the ground, L, denotes the length of mirror placed at an angle α. Since the mirrors are placed around the deck in concentric pattern, in our analysis, we consider the location of mirror along the mean position of the mirror field.

The ratio of reflection of mirror on deck to each mirror area is assumed to be one, which implies total area of mirrors required is equal to area of deck.

$$Number\ of\ mirrors = \frac{Total\ area\ of\ deck}{Area\ of\ each\ mirror} \qquad \text{(eq. 4)}$$

The dimensions of SCPP and positioning of mirror with respect to SCPP evaluated in this study are provided in Tab.2.

Tab. 2: The dimensions of the SCPP aided with reflectors under evaluation

Geometric Parameter	Dimensions
Area of each mirror	4 m2
Number of mirrors	11260
m	150 m
L	2 m
d	10 m
Alpha	70^0

3. Mathematical Modeling

First geometric modelling of SCPP is performed which is followed by energy analysis of the SCPP. The thermodynamic equations are derived by obtaining the correlation between the solar input energy, energy losses at various locations, and final output power. Then, it is followed by analyzing SCPP model for Dhahran conditions depending up on the solar irradiation data. Once all the correlations between energy input and final output are obtained, all the equations are solved simultaneously using EES.

3.1. Energy Analysis

Energy conservation principle using control volume approach is applied to each part of the SCPP. The energies are represented by E and the six energy balance equations are used considering the floor surface, collector (includes floor, air and deck), turbine, air in collector, chimney as presented by (Hussain and Al-Sulaiman 2016).

$$E_{s-f} + S_R = E_{f-a} + E_{f-d} \quad \text{(eq. 5)}$$

$$E_{f-a} + E_{d-a} = E_{a1} + E_{w1} + E_{p1} \quad \text{(eq. 6)}$$

$$E_{S-f} = E_{a1} + E_{w1} + E_{p1} + E_{d-sky} + E_{d-amb} + E_{d-ch} \quad \text{(eq. 7)}$$

$$E_{a1} + E_{w1} + E_{p1} = E_{a2} + E_{w2} + E_{p2} + E_{Power} \quad \text{(eq. 8)}$$

$$E_{a2} + E_{w2} + E_{p2} + E_{d-ch} = E_{a3} + E_{w3} + E_{p3} + E_{ch-amb} + E_{ch-sky} + E_{ch-gr} \quad \text{(eq. 9)}$$

$$E_{a-ch} + E_{d-ch} = E_{ch-amb} + E_{ch-sky} + E_{ch-gr} \quad \text{(eq. 10)}$$

Subscripts used in the above equations have the following definitions:

Tab. 3: Definition of subscripts in the above equations (5)-(10).

Subscript	Definition	Subscript	Definition
S-f	The solar radiation reaching the floor.	S_R	Radiant energy obtained by reflectors.
f-a	Heat transfer by convection from floor to air. .	ch-sky	Heat transfer by radiation from chimney to sky.
f-d	Heat transfer by radiation from floor to deck.	ch-gr	Heat transfer by radiation from chimney to ground.
d-a	Heat transfer by convection from deck to air.	a-ch	Heat transferred from the air in chimney to the surface of chimney.
d-ch	Heat transfer by radiation from deck to chimney.	a1, a2, a3	Enthalpy of air at different points.
d-sky	Heat transfer by radiation from deck to sky.	w1,w2, w3	Kinetic energy of air at different points.
d-amb	Heat transfer by convection from deck to atmosphere.	p1, p2, p3	Potential energy of air at different points.
ch-amb	Heat transfer by convection from chimney to atmosphere.	P	Power generated by turbine.

The Kinetic energies are calculated using the well-known formula:

$$E_w = m \times w^2/2 \quad \text{(eq. 11)}$$

The mass flow rate m is calculated as:

$$m = 0.25 \times \pi \times D_1^2 \times w_1 \times \rho_{a1} \quad \text{(eq. 12)}$$

Where, w represents velocity and ρ represents density.

Enthalpy of air is calculated using the formula:

$$E_a = m \times c_p \times (T_a - T_0) \quad \text{(eq. 13)}$$

The potential energies of air are calculated using the formula derived by (Petela 2009b):

$$E_p = m\left\{-\frac{1}{\rho}\left[\frac{b}{6d}(\rho - e)^3 + \frac{a}{2}(\rho - e)^2\right]\right\} \quad \text{(eq. 14)}$$

Where, a, b, d and e are constants having a particular value, given by (Petela 1964, 2003, 2008a, 2008b, 2009a).

The solar energy received by the floor of the collector is given as:

$$E_{S-f} = \tau_d \varepsilon_f I A_d \quad \text{(eq. 15)}$$

Where, I is the incident solar radiation on the earth surface, τ_d is the transmissivity of deck, and ε_f is the emissivity of the collector floor, A_d is the floor surface area, which receives the solar radiation and defined as:

$$A_d = \pi(D_f^2 - D_1^2)/4 \quad \text{(eq. 16)}$$

The additional solar energy S_R received by the floor with the aid of reflectors is defined as:

$$S_R = r_1 \tau_d \varepsilon_d I A_d \quad \text{(eq. 17)}$$

Where r_1 represents the reflectance of reflector R1, and was assumed to be 0.9, τ_d is the transmissivity of deck, and ε_f is the emissivity of the collector floor reflectors are assumed to be of same area as of floor surface area.

The energy radiated by the deck to chimney is calculated as:

$$E_{d-ch} = \varepsilon_d \frac{\pi}{4}\left[D_f^2 - (c_D D_2)^2\right]\sigma(T_{dE}^4 - T_{ch}^4) \quad \text{(eq. 18)}$$

T_{dE} is the effective temperature of the deck, c_D is factor which is used to account for the thickness of the chimney wall. The shape factor for radiation from the deck to the chimney ϕ_{d-ch} can be calculated as:

$$\phi_{d-ch}\frac{\pi}{4}\left[D_f^2 - (c_D D_2)^2\right] = \phi_{ch-d}\pi c_D D_2(H_3 - H_2) \quad \text{(eq. 19)}$$

Where, ϕ_{ch-d} can be determined from

$\phi_{ch-d} = 0.5 \times (90 - \beta)/90$, the value for β is found from $\tan\beta = 2 \times H_3/D_f$

Energy radiated from the floor to the deck is given by:

$$E_{f-d} = A_d \sigma(T_{fE}^4 - T_{dE}^4) \quad \text{(eq. 20)}$$

Where, T_{fE} is the effective temperature of the floor.

Energy transfer from the floor to air by convection is given as:

$$E_{f-a} = A_d h_{f-a}(T_{fE} - T_{aE}) \quad \text{(eq. 21)}$$

Energy transfer from the deck to air by convection is given as:

$$E_{d-a} = A_d h_{d-a}(T_{dE} - T_{aE}) \quad \text{(eq. 22)}$$

Energy transfer from the deck to ambient by convection is given as:

$$E_{d-amb} = A_d h_{d-amb}(T_{dE} - T_{amb}) \quad \text{(eq. 23)}$$

Energy transfer from the chimney to environment by convection is given as:

$$E_{ch-amb} = A_{ch} h_{ch-amb}(T_{ch} - T_{amb}) \quad \text{(eq. 24)}$$

Energy transfer from air inside the chimney to the chimney wall by convection is given as:

$$E_{a-ch} = \pi D_2(H_3 - H_2) h_{a-ch}\left(\frac{T_{a2}+T_{a3}}{2} - T_{ch}\right) \quad \text{(eq. 25)}$$

In the above equations h is the convective heat transfer coefficient for the respective pair of the surfaces, and the chimney surface area is defined as:

$$A_{ch} = \pi \times c_D \times D_2 \times (H_3 - H_2) \quad \text{(eq. 26)}$$

The convective heat transfer coefficient h_{a-ch} can be determined as, $h_{a-ch} = Nu \times k/D_2$. The Nusselt number is calculated from $Nu = 0.023 \times Re^{0.8} \times Pr^{0.4}$. Here Reynolds number is calculated as $Re = w_2 D_2/\nu$, and the Prandtl number (Pr) is taken as constant for air, Pr=0.7.The convective heat transfer coefficient h_{f-a} is determined considering forced convection. The calculations for h_{f-a} is made using Reynold's Number, instead of Grashoff Number. For this the average flow velocity of the air is assumed. Energy radiated from the deck to the chimney is given as:

$$E_{d-ch} = \phi_{d-ch} A_d \sigma (T_{dE}^4 - T_{ch}^4) \quad \text{(eq. 27)}$$

Energy radiated from the deck to sky is given as:

$$E_{d-sky} = \phi_{d-sky} A_d \sigma (T_{dE}^4 - T_{sky}^4) \quad \text{(eq. 28)}$$

Energy radiated from the chimney to sky is given as:

$$E_{ch-sky} = \phi_{ch-sky} A_{ch} \sigma (T_{ch}^4 - T_{sky}^4) \quad \text{(eq. 29)}$$

Energy radiated from the chimney to the ground which is not a part of the collector is given as:

$$E_{ch-gr} = \phi_{ch-gr} A_{ch} \sigma (T_{ch}^4 - T_{gr}^4) \quad \text{(eq. 30)}$$

The shape factor relations are as follows:

$$\phi_{d-sky} + \phi_{d-ch} = 1 \quad \text{(eq. 31)}$$

$$\phi_{ch-sky} + \phi_{ch-d} + \phi_{ch-gr} = 1 \quad \text{(eq. 32)}$$

Where, $\phi_{ch-sky} = 0.5$.

Temperature T_{a2} is calculated using the equation for isentropic expansion in turbine, which is defined as

$$\frac{T_{a2}}{T_{a1}} = \left(\frac{p_2}{p_1}\right)^{\frac{\kappa}{\kappa-1}} \quad \text{(eq. 33)}$$

Where κ for air is 1.4. Internal efficiency of turbine is η_T. Energy is converted into electric power at an overall efficiency η_0, which also includes mechanical and electrical efficiencies of the turbine generator. Further as mentioned in (Petela 2009b, 2009c), the temperature drop in the chimney can be estimated using eq. 34.

$$T_{a2} - T_{a3} = 0.154 \times D_2 \times H_3/m \quad \text{(eq. 34)}$$

Air distribution inside the collector was assumed to be linear. Therefore, the average temperature of air inside the collector was calculated as:

$$T_{aE} = (T_{amb} + T_{a1})/2 \quad \text{(eq. 35)}$$

Relative pressure drop across the chimney for maximum fluid power was given by (Backstrom and Fluri 2006) as:

$$\frac{P_1 - P_2}{P_1 - P_3} = \frac{2}{3} \quad \text{(eq. 36)}$$

The energetic efficiency of an SCPP aided with reflectors is described as below.

$$\eta_{energy} = \frac{E_{power}}{E_{sf} + S_R} * 100 \quad \text{(eq. 37)}$$

The following assumptions are used:

$T_{gr} = T_{amb}$, $c_D = 1.015$, $c_p = 1000 \frac{J}{kg} K$, $\kappa = 1.4$, $\eta_T = 0.7$, $H_T = 1\ m$, $h_{ch-amb} = 7 \frac{W}{m^2} K$, $h_{d-amb} = 5 \frac{W}{m^2} K$, $H_0 = 0.3\ m$

4. Results and Discussion

All the above formulated energy equations have been solved using sufficient and necessary assumptions with the help of EES software simultaneously, considering all the losses into account which eased in determining the theoretical final power output and hence forth the theoretical efficiency as well. Taking monthly average data into consideration, energy output and efficiency were determined for the SCPP model with and without reflectors for Dhahran, Saudi Arabia. The direct relationship between the energy output and the efficiency could not be drawn as they are dependent on many inter-dependent parameters, such as solar insolation, wind speed, atmospheric temperature. Furthermore, the geometry of the solar chimney model plays a vital role, which was clearly depicted in the results below. All the required data such as average insolation, wind speed, and atmospheric temperature for Dhahran, Saudi Arabia, was taken from NASA metrological website for the year 2016 which has a record of data for past 22 years.

From Fig. 2(a). With the aid of reflectors it is evident that there was increase in amount of irradiation incident on collector surface area by 90.25%, maximum intensity is found during the summer months vice versa along the winter months it is found to be minimum. It followed the same pattern as that of the available solar radiation over a period of one year. Fig. 2(b). Depicts the temperature of the floor upon which solar radiation is incident. The average ambient temperature for Dhahran is 297K, average floor temperature for SCPP model with and without reflectors are found to be 423K and 387K. Increase in floor surface temperature when aided with reflectors is found to be 9.3%, the higher floor temperature causes the density variation in air which in turn moves air towards the center i.e., low density area which helps in driving the turbine. The maximum temperatures were found to be for the summer months, which also correspond to maximum power generated. Across the winter months the temperatures were observed to be lower which corresponds to a lower power output as well.

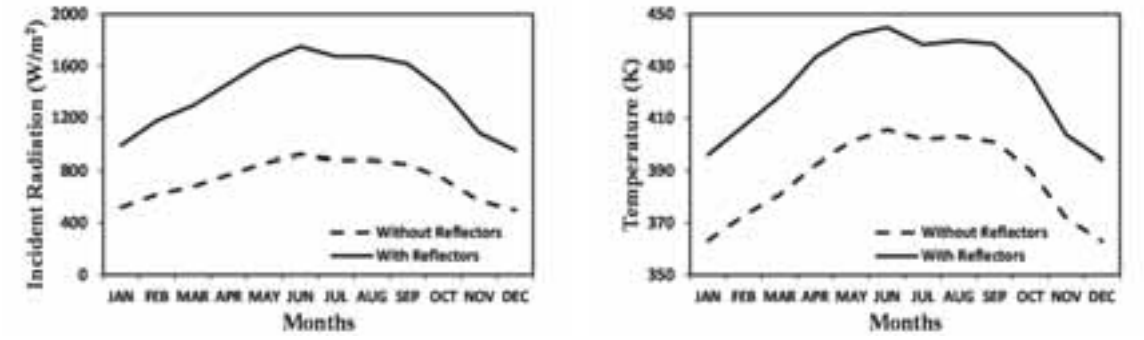

2 (a) **2 (b)**

Fig. 2: (a) Variation of incident radiation on SCPP model at Dhahran, Saudi Arabia. (b) Variation of floor temperature.

Variation of Mass flow rate and velocity at the inlet of the turbine are summarized in Fig. 3. The highest velocity and greater mass flow rate are observed for the month of July and August which has the highest incident solar radiation, as well as, higher energy output. With the aid of reflectors, average increase in velocity and mass flow rate are found to be 180% and 172% respectively.

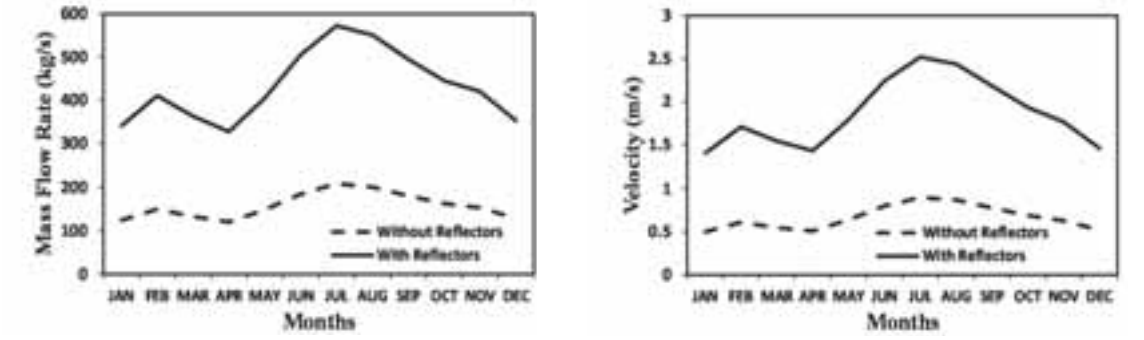

3 (a) **3 (b)**

Fig. 3: (a) Variation of mass flow rate. (b) Variation of velocity at the inlet of turbine.

Theoretical power output and efficiency of SCPP model for both the cases are determined and summarized in Fig. 4. Increase in power output due to reflectors is found to be 167% whereas efficiency was increased by 40%, which is much higher than the design suggested by Pasumarthi and sherif (Pasumarthi and Sherif 1997, 1998a, 1998b).

From Fig. 2(a). Fig. 4(a). Fig. 4(b). an important conclusion can be drawn though the energy output was found to be less for the months of January and December, but SCPP model is found to have a maximum efficiency during this period, it is because of the fact that the velocities obtained are less which increases the duration of contact between air and floor in which air absorbs more heat from floor, when compared with summer months; thereby making the system more efficient for the winter months but less energy output because of lower solar irradiation.

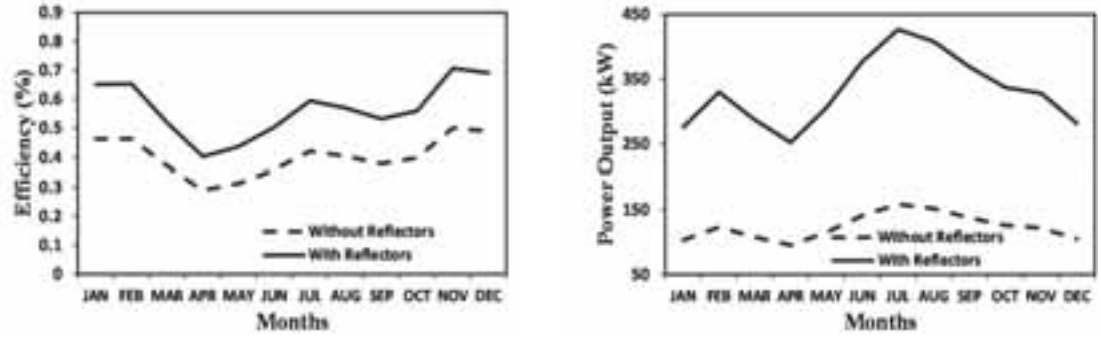

4 (a) **4 (b)**

Fig. 4: (a) Variation of efficiency. (b) Variation of energy output of the SCPP model.

5. Conclusions

This paper presents the enhanced performance analysis of the SCPP model with the aid of reflectors by increasing the radiant energy incident on to the floor and presents its performance for Dhahran, Saudi Arabia.

- It can be concluded that, the energy output is nearly directly dependent on the mass flow rate, which in turn is dependent on the geometry of the model, wind speed, and density.
- The reflector aided SCPP has an average air mass flow rate of around 432 kg/s, when compared with traditional SCPP which has an air mass flow rate of 158 kg/s.
- The SCPP aided with reflector is found to increase floor temperature by 9.3%.
- The reflector aided SCPP can produce on average, around 331kW during daytime when compared with traditional SCPP of same geometry which produces 123kW.
- The energetic efficiency found to increase by 40% and energy output is increased by 167%.

6. Acknowledgements

The authors would like to acknowledge the Deanship of Research, King Fahd University of Petroleum & Minerals for the financial support of this work under the project number IN141031.

7. References

Backstrom, Theodor W. and Thomas P. Fluri. 2006. “Maximum Fluid Power Condition in Solar Chimney Power Plants - An Analytical Approach.” *Solar Energy* 80(11):1417–23.

Bernardes, M. A. 2004. “Technical, Economical and Ecological Analysis of Solar Chimney Power Plants. Diss. Ph. D. Thesis.” Stuttgart University.

Bilgen, E. and J. Rheault. 2005. “Solar Chimney Power Plants for High Latitudes.” *Solar Energy* 79(5):449–58.

Haaf, W., K. Friedrich, G. Mayr, and J. Schlaich. 1983. “Solar Chimneys Part I: Principle and Construction of the Pilot Plant in Manzanares.” *International Journal of Solar Energy* 2(August 2013):3–20.

Hussain, FM and FA. Al-Sulaiman. 2016. “Exergy Analysis of Solar Chimney for Saudi Arabian Weather Conditions.” in *ASME. Energy Sustainability*.

Islamuddin, A., Hussain H. Al-Kayiem, and Syed I. Gilani. 2013a. “Simulation of a Collector Using Waste Heat Energy in a Solar Chimney Power Plant System.” Pp. 933–44 in *WIT transactions on Ecology and The Environment*, vol. 179.

Islamuddin, A., Hussain H. Al-Kayiem, and Syed I. Gilani. 2013b. “Simulation of Solar Chimney Power Plant with an External Heat Source.” *IOP Conference Series: Earth and Environmental Science* 16:12080.

Kreetz, H. 1997. “Theoretische Untersuchungen Und Auslegung Eines Tempora ¨ren Wasserspeichers Fu¨r Das Aufwindkraftwerk.” Technical University Berlin.

Pasumarthi, N. and S. A. Sherif. 1997. *Performance of a Demonstration Solar Chimney Model for Power Generation.* Sacremento, CA, USA.

Pasumarthi, N. and S. A. Sherif. 1998a. “Experimental and Theoretical Performance of a Demonstration Solar Chimney Model — Part I : Mathematical Model Development.” *International Journal of Energy Research* 22(3):277–88.

Pasumarthi, N. and S. A. Sherif. 1998b. “Experimental and Theoretical Performance of a Demonstration Solar Chimney Model — Part II : Experimental and Theoretical Results.” *International Journal of Energy Research* 22(5):443–61.

Petela, Richard. 1964. “Exergy of Heat Radiation.” *Journal of Heat Transfer* 86(2):187–92.

Petela, Richard. 2003. “Exergy of Undiluted Thermal Radiation.” *Solar Energy* 74(6):469–88.

Petela, Richard. 2008a. “An Approach to the Exergy Analysis of Photosynthesis.” *Solar Energy* 82(4):311–28.

Petela, Richard. 2008b. “Influence of Gravity on the Exergy of Substance.” *International Journal of Exergy* 5(1):1–17.

Petela, Richard. 2009a. “Gravity Influence on the Exergy Balance.” *International Journal of Exergy* 6(3):343–56.

Petela, Richard. 2009b. “Thermodynamic Analysis of Chimney.” *International Journal of Exergy* 6(6):868–80.

Petela, Richard. 2009c. “Thermodynamic Study of a Simplified Model of the Solar Chimney Power Plant.” *Solar Energy* 83(1):94–107.

Schlaich Jorg. 1995. *The Solar Chimney-Electricity from the Sun*. Axel Menges.

Zhou, Xinping, Jiakuan Yang, Jinbo Wang, and Bo Xiao. 2009. “Novel Concept for Producing Energy Integrating a Solar Collector with a Man Made Mountain Hollow.” *Energy Conversion and Management* 50(3):847–54.

Experimental and Modeling Study on Nighttime Heat Loss and Anti-Freezing Analysis of FPC Group

Zhenghao Jin[1], Yin Zhang[2], Yanru Li[2], Fei Liang[2], Xinhui Zhao[2], Qinjian Liu[2], Enshen Long[1,2,*]

[1]Institute for Disaster Management and Reconstruction, Sichuan University, Chengdu, Sichuan, 610065, China

[2]College of Architecture and Environment, Sichuan University, Chengdu, Sichuan, 610065, China

Abstract

The low-temperature-caused freezing of outdoor pipes and solar collectors in winter night is one of the most serious problems in solar thermal system. Studying the heat loss characteristic of the solar connector groups in nighttime is greatly significant for solar collector groups anti-freezing and maintaining system safety. In this paper, a heat loss mathematical model was established and validated through on-site measurement, to investigate the heat loss characteristic of the flat plate solar collectors (FPC) groups. Furthermore, the anti-freezing critical flow rate was analyzed when outdoor temperature and inlet water temperature vary. As an illustrative example, the anti-freezing analysis for Harbin, a northern city in China, was conducted. The results show that, the front heat loss and connecting pipes constituted the main heat loss of the solar collector group in nighttime, which accounted for 63.32% and 15.53% respectively. Besides, making anti-freezing flow rate equal to daytime working design flow rate is not suitable. Hence, the flow rate should be reduced through the water pump frequency conversion methods. Moreover, winter minimum temperature in China severe cold area can be 28.7℃. On that occasion, a single set of solar connector group should keep the inlet temperature higher than 15℃, while the flow rate larger than 0.5L/min.

Keywords: flat plate solar collectors, nighttime heat loss, heat loss mathematical model, anti-freezing

1. Introduction

With the extensive use of fossil fuels, global pollution problem is getting increasingly serious. The use of renewable energy has been paid more and more attention to by many countries around the world, in which the solar energy is promoted for the similarity to that of traditional energy maneuverability and adaptability (F. Dinter and Mayorga Gonzalez, 2014; Xiaolei Li et al., 2017) . Solar energy utilization can be either photovoltaic or photothermal. While the hot water system, which is a kind of photothermal, is of high working stability and easy for thermal energy storage, making it suitable for heating in winter (BillyAnak Sup et al., 2014; CJ Porras-Prieto et al., 2014; L.M. Ayompe et al., 2011). However, in severely cold areas, the freezing of outdoor pipes and collectors is one of the most serious problems, which, to a certain degree, limits the utilization of solar energy and decreases the system economic performance (Huifang Liu et al., 2015). As a result, studying the heat loss characteristic of the solar connector groups at night to avoid frost crack and maintain the system working safe and stable really makes a great difference.

According to available literatures, many scholars studied the solar connector anti-freezing. The conventional measures include the use of antifreeze fluid, electric tracing tapes, draining water from the collectors and using the hot water in a thermal storage tank to heat the outdoor pipes by circulation (BV Bourke, 1995; HMS Hussein et al., 1999; M Smyth et al, 2001; PW Cronin et al., 1997; R.H. Lewis and JB Carr, 1981). For FPC, KLEINS (S.A. Klein, 1975) proposed a method to calculate the heat loss coefficient, and respectively, put forward the top, bottom and side heat loss coefficient calculation method. Gao Liuhua (Gao Liuhua et al., 2014) proposed a one-dimensional steady state mathematic model of single FPC. He took overall heat loss coefficient of collector as a variable quantity. And absorber plate thickness and tube spacing of copper-aluminum FPC were optimized based on efficiency factor and metal consumption of collector. Th Beikircher (Th. Beikircher et al., 2014) studied heat loss measurements without insolation and a novel conversion towards daytime conditions. This research thought a broader application and test of the new method for further types of solar collectors by independent researchers is desirable. Fan Zhou (Fan Zhou et al., 2017) did experimental and numerical study of the freezing process of

doi:10.18086/swc.2017.31.06 Available at http://proceedings.ises.org

FPC, finding that narrowing the pipe space, increasing the pipe diameter or header diameter and reducing the emissivity of absorber and glass-cover are the effective ways of enhancing the antifreeze performance of flat-plate collector. But the reported studies rarely analyze the influence of the environment temperature, the inlet temperature, and the flow rate to a FPC group anti-freezing.

In this paper, a heat loss mathematical model was established and validated through on-site measurement, to study the heat loss characteristic of the FPC groups. Furthermore, the anti-freezing critical flow rate was analyzed when outdoor temperature and inlet water temperature vary. And we had an anti-freezing analyze of Harbin as a typical case. This study can provide meaningful references for practical engineering.

2. Experimental System

In order to study the heat loss characteristic of FPC groups in nighttime, we built a test bench at Sichuan University, which is at east longitude 30.67° and north latitude 104.06°. Fig.1 is the schematic diagram of the experiment system. From the figure, the test bench includes two FPC groups, which can control the flow rate independently. Besides, each FPC group is set up by two pieces of 2000mm×1000mm×700mm FPCs in parallel. The FPCs is facing south while the installation angle is 40°. Within each FPC group, the connecting pipes between two FPC is 74mm long and is made of copper.

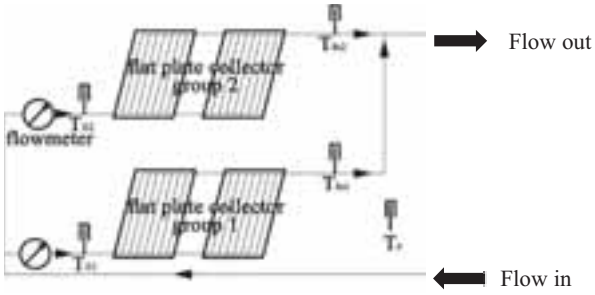

Fig.1 experiment system diagram

Fig.2 is the FPC configuration diagram, which shows the PFC comprises glass cover-plate, sheet absorber, pipe, insulating layer and housing. The sheet absorber is made of pure aluminum anodic oxide film plating. The insulating layer is made of polyurethane foam. And the pipe is made of copper. The heat loss of FPC can be divided into front heat loss, bottom heat loss, and side heat loss. Tab.1 shows detailed parameters for the FPC and connecting pipes.

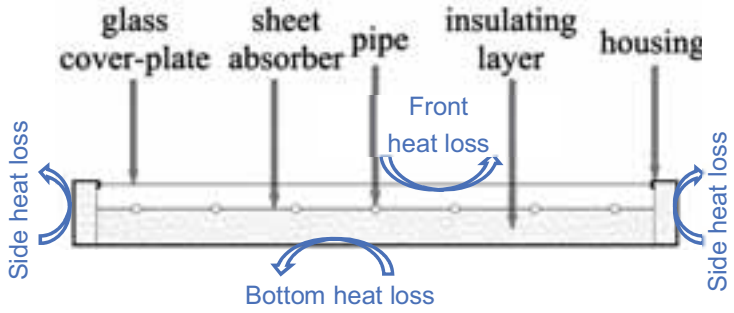

Fig.2: FPC configuration diagram

Tab. 1: Detailed parameters for the FPC and connecting pipe

Item	Value	Item	Value
FPC length /mm	2000	Connecting pipe number	2
FPC width/mm	1000	Connecting pipe length/m	0.074
FPC thickness/mm	70	Connecting pipe thermal	386.4

		conductivity/W·(m·K)$^{-1}$	
FPC lighting area /m2	1.85	FPC pipe outer diameter / mm	8
Sheet absorber length/mm	1940	FPC pipe wall thickness /mm	0.5
Sheet absorber width/mm	950	FPC pipe thermal conductivity / W·(m·K)$^{-1}$	386.4
Sheet absorber thickness/mm	0.4	Glass cover-plate emissivity	0.9
Sheet absorber emissivity	0.09	Glass cover-plate number	1
Sheet absorber absorptivity	0.95	Insulating layer thermal conductivity / W·(m·K)$^{-1}$	0.023
Sheet absorber thermal conductivity /W·(m·K)$^{-1}$	202.8	Bottom insulating layer thickness /mm	20
Connecting pipe outer diameter / mm	22	Side insulating layer thickness /mm	20
Connecting pipe wall thickness /mm	0.6		

The pipe between temperature measuring point and inlet or outlet water gates for FPC group is short and has a good thermal insulation, so it is assumed that the tested temperature is the temperature of water inlet or outlet gates for FPC group. T-type thermocouples (with accuracy of 2%) were used to measure the inlet temperature and outlet temperature of each groups, as well as the ambient temperature. All measurement data is collected by a JTRG-II building thermal temperature automatic tester. And flow meters (with accuracy of 5%) were used to measure the flow of every FPC group. Testing started from 20:15 Mar. 11 to 7:00 Mar. 12, with 1 min recording interval.

3. Heat Loss Mathematical Model

In this paper, one group of FPCs in Fig.1 is the studying object for the heat loss mathematical model, which includes two pieces of FPCs and two pieces of connecting pipes.

3.1 Heat Loss Mathematical Model for the FPC

In nighttime, the total heat loss of FPC group equals the FPC heat loss plus the connecting pipes heat loss plus the FPC group heat storage change. The heat loss equation can be written as Eq. (1):

$$Q_u = Q_{lh} + Q_p + \triangle Q_s \quad \text{(eq. 1)}$$

Where Q_u is the total heat loss of FPC group, W; Q_{lh}, Q_p and $\triangle Q_s$ denote the FPC heat loss, the connecting pipes heat loss, and the FPC group heat storage change, W. The FPC group heat storage is negligible, so we make an assumption that $\triangle Q_s = 0$.

The FPC heat loss can be calculated by the FPC lighting area, the total heat loss coefficient, the sheet absorber temperature and environment temperature (Eq. (2)).

$$Q_{lh} = A_a U_L (T_a - T_e) \quad \text{(eq. 2)}$$

Where the A_a is the FPC lighting area, m^2. The U_L is the total heat loss coefficient, W/m^2·K. The T_a and T_e are the sheet absorber temperature and environment temperature，K。

The total heat loss coefficient is a comprehensive and equivalent value that integrate the front heat loss coefficient, the bottom heat loss coefficient, and the side heat loss coefficient (Eq. (3)).

$$U_L = U_t + U_b + \frac{A_e}{A_a} U_e \quad \text{(eq. 3)}$$

Where the U_t、U_b、U_e denote the front, bottom and side heat loss coefficient, W/m^2·K. The A_e denote the FPC side area, m^2.

The U_t is calculated by the formula (Eq. (4)-Eq. (7)) put forward by Klein (S.A. Klein, 1975), which has

considered the heat loss caused by cold radiation of the sky. And the error of the formula can be controlled in ± 0.3W/(m2 • K)。

$$U_t=\left[\frac{N}{\left(\frac{c}{T_p}\right)\left(\frac{T_a-T_e}{N+f}\right)^e}+\frac{1}{h_w}\right]^{-1}+\frac{\sigma\left(T_a^2+T_e^2\right)\left(T_a+T_e\right)}{\left(\varepsilon_p+0.00591Nh_w\right)^{-1}+\frac{2N+f-1+0.133\varepsilon_p}{\varepsilon_g}-N} \quad \text{(eq. 4)}$$

$$f=\left(1+0.089h_w-0.1166h_w\varepsilon_p\right)\left(1+0.07866N\right) \quad \text{(eq. 5)}$$

$$C=520\left(1-0.000051s^2\right) \quad \text{(eq. 6)}$$

$$e=0.43\left(1-100/T_a\right) \quad \text{(eq. 7)}$$

Where the N is the glass cover-plate number. The h_w is the convective heat transfer coefficient between the air and the surface. The ε_p and ε_g are the sheet and glass cover-plate absorber emissivity. The s is the installation angle of FPC.

The U_b and U_e can be calculated by Eq. (8) and Eq. (9).

$$U_b=1\Big/\left(\frac{1}{h_b}+\frac{1}{h_w+h_r}\right) \quad \text{(eq. 8)}$$

$$U_e=1\Big/\left(\frac{1}{h_e}+\frac{1}{h_w+h_r}\right) \quad \text{(eq. 9)}$$

Where the h_b, h_e and h_r are bottom, side, and radiation heat loss heat transfer coefficient, W/ m^2·K. We made the assumption that $h_r \approx 0$ (Y. Lu et al., 2013). The h_w can be achieved by outdoor wind speed (Li Ming, 2004), which is 1m/s according to Chengdu Tianqi net (Chengdu weather net, 2017).

$$h_w=5.7+3.8v \quad \text{(eq. 10)}$$

Because the sheet absorber is too big and has a non-uniform distribution of temperature, we introduce efficiency factor *F'* for modification (JA Duffie et al., 1980), in order to use the inlet and outlet average temperature instead of the sheet absorber temperature (Eq. (11)).

$$Q_{lh}^{'}=A_aU_LF'(T_f-T_e) \quad \text{(eq. 11)}$$

Where the T_f is the inlet and outlet average temperature (Eq. (12)).

$$T_f=\frac{T_{fi}+T_{fo}}{2} \quad \text{(eq. 12)}$$

Where the T_{fi} and the T_{fo} denote the inlet and outlet temperature.

FPC pipe and sheet absorber has three kinds of welding method, welding way adopted in the experiment are shown in figure 2. The *F'* for this kind of welding can be got through Eq. (13).

$$F'=1\Big/\left(\frac{WU_L}{h_i\pi D_i}+\frac{W}{D_o+(W-D_o)F}\right) \quad \text{(eq. 13)}$$

Where the W, D_i and D_o denote the sheet absorber width, the FPC pipe inner diameter and outer diameter, m.

The h_i is the convective heat transfer coefficient between the water and the FPC pipe wall, W/ m^2·K. The F is the sheet absorber efficiency. And the h_i has a connection with the inlet and outlet average temperature, the flow velocity, and the FPC pipe inner diameter (Eq. (14)) (Badescu V, 2006).

$$h_i = \left(1430 + 23.3T_f - 0.048T_f^2\right) v_w^{0.8} D_i^{-0.2} \quad \text{(eq. 14)}$$

Where the v_w is the flow velocity for FPC pipes, m/s. The F can be got through Eq. (15).

$$F = th\left[\frac{\sqrt{U_L/\lambda_a\delta}(W-D_o)}{2}\right] \Big/ \frac{\sqrt{U_L/\lambda_a\delta}(W-D_o)}{2} \quad \text{(eq. 15)}$$

Where the λ_a is the sheet absorber thermal conductivity, W/m·K . The δ is the Sheet absorber thickness.

3.2 Heat Loss Mathematical Model for the connecting pipes

The two connecting pipes are symmetrical in the PFC group, so it is assumed that the inlet and outlet average temperature is equal to the average temperature for connecting pipes. The connecting pipes heat loss can be calculated by Eq. (16)

$$Q_p = q_l l \quad \text{(eq. 16)}$$

Where the q_l is the heat loss of unit length, W/m. The l is the length of connecting pipes. The q_l can be got by the formula of thermal conductivity for a cylindrical wall (Eq. (17)).

$$q_l = (T_f - T_e) / \left(\frac{1}{h_i' D_i' \pi} + \frac{1}{2\pi\lambda} + \frac{1}{h_w D_o' \pi}\right) \quad \text{(eq. 17)}$$

Where the D_i' and D_o' denote the connecting pipe inner diameter and outer diameter, m. The v_w' denote the flow velocity for connecting pipes, m/s. The λ is the connecting pipe wall thermal conductivity, W/m·K. The h_i' is the convective heat transfer coefficient between the water and the connecting pipe wall, and can be obtained by Eq. (18).

$$h_i' = \left(1430 + 23.3T_f - 0.048T_f^2\right) v_w'^{0.8} D_i^{-0.2} \quad \text{(eq. 18)}$$

3.3 Heat Loss Mathematical Model for the working fluid

The heat loss for working fluid circulating within the FPC group can be calculated by the flow rate and the inlet and outlet temperatures (Eq. (19)), which are obtained directly by the experiment.

$$Q_u' = \rho c V (T_{fi} - T_{fo}) \quad \text{(eq. 19)}$$

Where the ρ and c are the density(kg/m^3) and specific heat capacity of water(J/(kg·K)). The V is the flow rate of the connect pipe.

3.4 Anti- freezing Analysis Method

According to the energy conservation law, the heat loss for heat carrying fluid flowing through the FPC group is equals to the total heat change of FPC group (20).

$$Q_u' = Q_u \quad \text{(eq. 20)}$$

From the Eq. (1)-Eq. (20), We can get the relationship among all the major parameters, which include the T_e, the T_{fi}, the T_{fo}, and the flow rate of FPCs. If we set outlet temperature equal to 0 as the critical condition of pipe freezing, we can obtain the critical flow rate in different environment temperature and inlet temperature.

4. Results and Discussion

4.1 Experimental Results

During the experiment, the flow rate for FPC group 1 and 2 were 3.09L/min and 1.67 L/min. The T_{fi} and T_{fo} for each group and the T_e are showed in Fig. 3. The Fig. 3 indicates that the inlet temperatures for the two group were similar, while the outlet temperature for FPC group 1 was higher than that for FPC group 2. It was because the flow rate for FPC group 1 was higher than that for FPC group 2, making heat transfer time shorter for every unit of fluid.

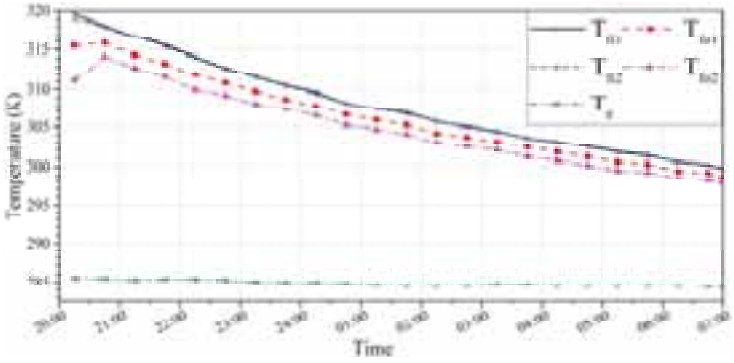

Fig. 3: Environment temperature, inlet temperature, and outlet temperature for every minute

In general, heat storage water tank has a limited capacity. With the operation of the anti-freezing working at nighttime, the inlet temperature become lower and lower, calling for a higher flow rate. So, it makes a difference to investigate the critical flow rate, which leads to the system antifreeze, in different environment temperature and inlet temperature.

Fig.4 shows the proportions of the PFC group front, bottom, side heat loss, and the connecting pipe heat loss. The front part of the PFC group occupied 62.32% of the heat loss, which constitutes the dominant part, because the cold radiation was large at night, and the top surface was large and has no heat insulation layer. The side part of the PFC group accounted for 3.57% of the heat loss, which serves as the smallest part, because the side surface was small and had a good heat insulation layer. The bottom part of the PFC group accounted for 18.57% of the heat loss, which was much smaller than the front part but had the same surface area as the front part. It was because of the bottom surface had a good heat insulating, substantiating the importance of heat insulating measures. The connecting pipes of the PFC group accounted for 15.53% of the heat loss, which was higher than the side part but lower than underside part. It was because of the connect pipe has no heat insulating layer, and was made by copper which had a high absorber thermal conductivity. In summary, reducing the heat loss in front part and making insulation layer for connecting pipes in practical engineering are very important, otherwise, the high heat loss of PFC groups will cause the outlet temperature too small, inevitably increasing the risk of system freezing.

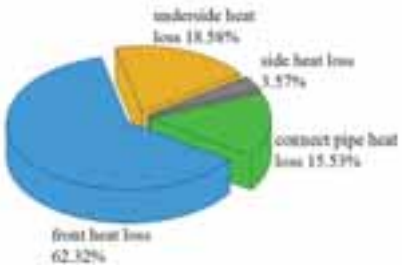

Fig. 4: The proportions of the PFC group front, bottom, side heat loss, and the connecting pipe heat loss

4.2 model verification

To verify the aforementioned heat loss mathematical model, we use Eq. (20) to compare the total heat loss of FPC (Q_u) with the heat loss for heat carrying fluid flowing through the FPC group (Q'_u).

Fig. 5 is the minutely variation of the Q_u and the Q'_u for the two groups. The Q_u and the Q'_u decrease gradually along the process of FPC groups dissipating heat at night. While the Q_{u1} is higher than Q_{u2} in most time, implying that the flow rate will be higher with the increase of the heat loss of the FPC group. Besides, since the Q_{u1} is always close and fit well to Q'_{u1}, so does the Q_{u2} to Q'_{u2}, the heat loss mathematical model can well describe the FPC group cooling process.

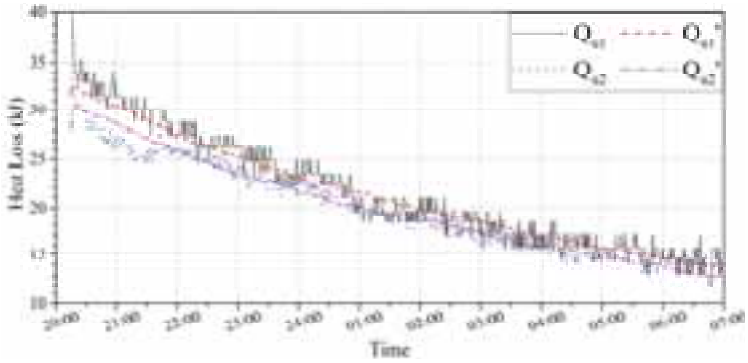

Fig. 5: The minutely variation of the Q_u and the Q'_u for the two groups

Fig. 6 is the cumulative variation of the Q_u and the Q'_u for the two groups. The $\sum Q_{u1}$ for one time is the cumulative Q_u before the time, so does the $\sum Q_{u2}, \sum Q'_{u1}, \sum Q'_{u2}$ to Q_{u2}, Q'_{u1}, Q'_{u2}. The $\sum Q_{u1}$ and the $\sum Q_{u2}$ increase gradually along the process of FPC groups dissipating heat at night. While the $\sum Q_{u1}$ is higher than $\sum Q_{u2}$ in most time, implying that the flow rate will be higher with the increase of the heat loss of the FPC group. Besides, the $\sum Q_{u1}$ is always close and fit well to $\sum Q'_{u1}$ with an error of only 1%, so does the $\sum Q_{u2}$ to $\sum Q'_{u2}$, so the heat loss mathematical model can well describe the FPC group cooling process, and the model can be used to study the heat loss of FPC group anti-freezing process.

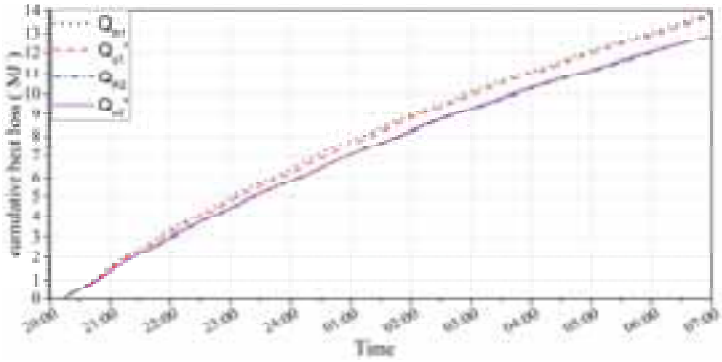

Fig. 6: The cumulative variation of the Q_u and the Q'_u for the two groups

4.3 Anti-freezing analysis for FPC group

In practical engineering, when the PFC group outlet temperature is lower than 0℃, the water in the system will be frozen. We define the flow rate of the system leading to 0℃ outlet temperature as the anti-freezing critical flow rate. When the inlet and ambient temperatures are constant, the heat loss increases with increasing flow rate, so the outlet temperature will be higher than 0℃ when the flow rate is higher than the anti-freezing critical flow rate.

Fig. 7 shows the anti-freezing critical flow rate varies with the ambient temperature and the inlet temperature. When the ambient temperature is constant, with the increase of inlet temperature, the anti-freezing critical flow rate is decreased fast when the inlet temperature is lower than 15℃ and is decreased slowly when the inlet temperature is higher than 15℃. When the inlet temperature is constant, with the increase of environment temperature, the anti-freezing critical flow rate is decreased fast when the inlet temperature is small and is decreased slowly when the inlet temperature is large. When the inlet temperature is 5℃, the anti-freezing critical

flow rate is decreased by 0.2L/min when the environment temperature is increased by 5℃. While when the inlet temperature is 30℃, the anti-freezing critical flow rate is decreased very slow when the environment temperature is increased.

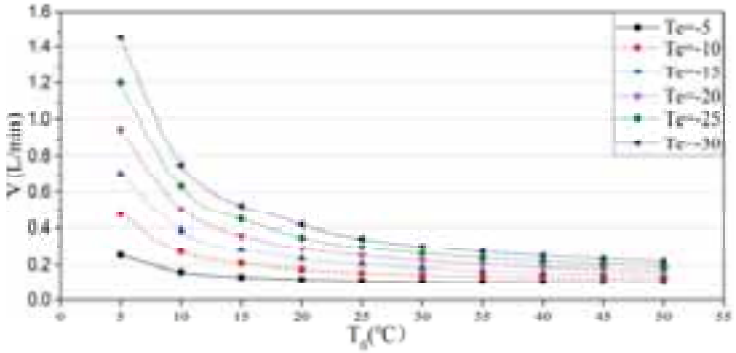

Fig. 7: The anti-freezing critical flow rate varies with the environment temperature and the inlet temperature

According to the standard (Hu Hanxin, 2016), the flow rate of the FPC group in daytime working is 4.8L/min, which is three times higher than the maximum anti-freezing critical flow rate in Fig. 7. In other words, the anti-freezing critical flow rate at night is much lower than the flow rate in daytime, so making anti-freezing flow rate equal to daytime working design flow rate is not a reasonable and desirable choice. By contrast, the flow rate should be reduced through the water pump frequency conversion methods.

4.4 Illustrative Example

We choose Harbin as a case of typical anti-freezing analyzing city, which is located in severe cold area of China and has the minimum temperature of -28.7℃ (U.S. Department of Energy and Lawrence Berkeley National Laboratory, 2017) in winter. Studying the anti-freezing critical flow rate in the winter extreme temperature of Harbin can provide meaningful references for practical engineering.

Fig.8 is the outlet temperature varies with the inlet temperature and flow rate in the winter extreme temperature. When the outlet temperature equals 0℃, the flow rate is the anti-freezing critical flow rate. Firstly, when the inlet temperature is constant, as the flow rate is increased, the outlet temperature is increased faster. Besides, when the flow rate is constant, as the inlet temperature is increased, the outlet temperature is increased. And when the flow rate is 1.5L/min, the outlet temperature is increased by 8℃ when the inlet temperature is increased by 5℃. Furthermore, when the inlet temperature ranges from 5℃ to 15℃, the anti-freezing critical flow rate is increased very fast when then inlet temperature is decreased, which is unfavorable for the anti-freezing flow rate control. So, in that situation, the inlet temperature should be higher than 15℃, and the anti-freezing flow rate should be higher than 0.5L/min.

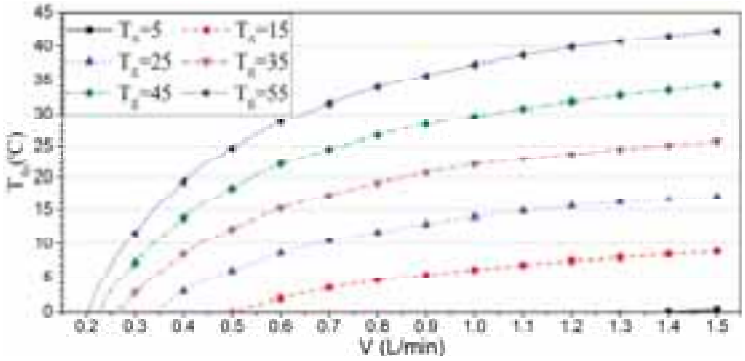

Fig. 8: The outlet temperature varies with the inlet temperature and flow rate in the winter extreme temperature

4. Conclusion

This paper studied the heat loss characteristic of the solar connector groups in nighttime through a heat loss mathematical model. A test bench which included two FPC groups has been built and solved analytically. The measured data well validated the analytical model. And main conclusions of this paper are as follows:

Firstly, when the FPC groups is anti-freezing working at night and the inlet temperature is constant, the outlet temperature increased when the flow rate increased, which keeps the system from freeze. But heat loss of FPC groups also increased when the flow rate increased. Secondly, the front part of the PFC group and connect pipes respectively accounted for 62.32% and 15.53% of the total heat loss, so reducing the heat loss in front part and making insulation layer for connecting pipes in practical engineering can make sense. But there is a pity that the front heat loss coefficient (Eq. (4)) did not independently show the radiant heat loss and the heat conduction, which is worth a further study. Besides, making anti-freezing flow rate equal to daytime working design flow rate is not suitable. By contrast, the flow rate should be reduced through the water pump frequency conversion methods. Furthermore, in the winter extreme temperature of Harbin, where the minimum temperature is -28.7℃, the input temperature should be higher than 15℃, and the anti-freezing flow rate should be higher than 0.5L/min.

This study can provide meaningful references for practical PFC groups anti-freezing engineering.

5. Acknowledgements

This project is funded by the National Key Research and Development Program (2016YFC00406), and the National Natural Science Foundation of China (No.51478280).

6. References

B.V. Bourke, 1995. Solar collector with freeze damage protection (P), in: United States Patent 5413091

Badescu V, 2006. Optimum fin geometry in flat plate solar collector systems (J). Energy Conversion and Management, v 47, n 15-16, p 2397-2413

BillyAnak Sup, TantiZanariahShamshir Ali, MohdFarid Zainudin, RosliAbu Bakar, 2014. Experimental study of water heating efficiency between aluminium and copper absorber plate in solar flat plate collector (J). Applied Mechanics and Materials, v 660, p 709-713

CJ Porras-Prieto, FR Mazarrón, VDL Mozos, JL García, 2014. Influence of required tank water temperature on the energy performance and water withdrawal potential of a solar water heating system equipped with a heat pipe evacuated tube collector (J). Solar Energy, v 110, p 365-377

Chengdu Tianqi Net, 2017. Chengdu Weather Net (EB/OL), in: http://chengdu.tianqi.com/20170311.html, 2017-3-12

F. Dinter, D. Mayorga Gonzalez, 2014. Operability, reliability and economic benefits of CSP with thermal energy storage: first year of operation of ANDASOL 3 (J). Energy Procedia, v 49, p 2472-2481

Fan Zhou, Jie Ji, Jingyong Cai, Bendong Yu, 2017. Experimental and numerical study of the freezing process of flat-plate solar collector (J). Applied Thermal Engineering, v 118, p 773-784

Gao Liuhua, Zhao Jun, Gao, Teng, 2014. Effect of absorber plate parameter on thermal performance of flat plat solar collector (J). Taiyangneng Xuebao/Acta Energiae Solaris Sinica, v 35, n 10, p 2054-2059

HMS Hussein, MA Mohamad, AS El-Asfouri, 1999. Optimization of a wickless heat pipe flat plate solar collector (J). Energy Conversion and Management, v 40, n 18, p 1949-1961

Huifang Liu, Shicong Zhang, Yiqiang Jiang, Yang Yao, 2014. Feasibility study on a novel freeze protection strategy for solar heating systems in severely cold areas (J). Solar Energy, v 112, p 144-153

Hu Hanxin, 2016. Design Standard for Heating and Ventilation of Civil Buildings in Sichuan Plateau-cold Zone (S). Northwestern Polytechnical University Press, Sichuan.

JA Duffie, WA Beckman, J Mcgowan, 1980. Solar Engineering of Thermal Processes (J). Journal of Solar Energy

Engineering, v 116, n 1, p 549

Li Ming, 2004. Theoretical and experimental analysis of the property of solar solid adsorption ice maker (J). Taiyangneng Xuebao/Acta Energiae Solaris Sinica, v 25, n 4, p 503-508

L.M. Ayompe, A. Duffy, S.J. McCormack, M. Conlon, 2011. Validated TRNSYS model for forced circulation solar water heating systems with flat plate and heat pipe evacuated tube collectors (J). Applied Thermal Engineering, v 31, n 8-9, p 1536-1542

M. Smyth, P. Eames, B. Norton, 2001. Evaluation of a freeze resistant integrated collector/storage solar water-heater for northern Europe (J). Applied energy, v 68, n 3, p 265-274

PW Cronin, PH Ottmar, EF Root, HM Simmons, 1997. Solar collector automatic freeze protection system (P), in: United States Patent 4044754

R.H. Lewis, Jr., J.B. Carr, 1981. Drain down freeze prevention control system for a solar collector (P), in: United States Patent 4256089

S.A. Klein, 1975. Calculation of flat-plate loss coefficients (J). Solar Energy, v 17, n 1, p 79

Th. Beikircher, P. Osgyan, S. Fischer, H. Druck, 2014. Short-term efficiency test procedure for solar thermal collectors based on heat loss measurements without insolation and a novel conversion towards daytime conditions (J). Solar Energy, v 107, p 653-659

U.S. Department of Energy and Lawrence Berkeley National Laboratory, 2017. EnergyPlus Energy Simulation Software (EB/OL), in: https://energyplus.net/weather-region/asia_wmo_region_2/CHN, 2017-10-10

Xiaolei Li, Ershu Xu, Shuang Song, Xiangyan Wang, Guofeng Yuan, 2017. Dynamic simulation of two-tank indirect thermal energy storage system with molten salt (J). Renewable Energy, v 113, p 1311-1319

Yu Lu, Hongwen Yu, Haicheng Ding, Yanli Zhang, Zongming Liu, 2013. Mathematical modeling and simulation of thermal properties of flat-plate solar collector (J). JOURNAL OF UNIVERSITY OF JINAN, v27, n3, p 293-297

Development, Optimization and Test Performance of Highly Efficient Flat Plate Solar Collector with Transparent Insulation and Low-Cost Overheating Protection

Deniz Kizildag[1], Jesús Castro[1], Hamdi Kessentini[2], Joaquim Rigola[1] and Assensi Oliva[1]

[1]Heat and Mass Transfer Technological Center (CTTC)

Universitat Politècnica de Catalunya-BarcelonaTech (UPC)

ETSEIAT Colom 11 08222 Terrassa, Barcelona, Spain

cttc@cttc.upc.edu, http://www.cttc.upc.edu

[2]Université de Tunis El Manar, Ecole Nationale d'Ingénieurs de Tunis (ENIT)

Laboratoire de Matériaux, Optimisation et Énergie pour la Durabilité (MOED), 1002 Tunis, Tunisia

Abstract

The present work addresses a flat plate solar collector with transparent insulation material (TIM) and high temperature protection system. The design and optimization of the collector have been numerically carried out by means of a parallel object-oriented simulation tool which is capable of simulating all the entities constituting the system as a whole, using efficient coupling between the elements. Three variants of the design are chosen to first test them under laboratory conditions. These collectors then are mounted in the roof of a hospital building, where their performance are comparatively tested along with a conventional flat plate solar collector, under real meteorological conditions and during long periods of time. Thus, due to long term exposure of the collectors, aspects such as reliability, durability, energy performance, correct functioning of the protection system will be analyzed, with the objective of improving the detected shortcomings for the future generations of the present design.

Keywords: Flat plate solar collector, thermal insulation material, thermal protection system, collector testing

1. Introduction

Flat plate solar collectors are generally designed for working temperatures between 40 and 60 ºC, which makes them ideal for their application in domestic hot water systems. Despite the variety of the products which have appeared in the market dedicated to the solar energy capturing, flat plate solar collectors have a privileged share in the market due to their simplicity, relatively lower cost, ease to manufacture, and the capability to collect radiation being stationary in any roof. By using highly selective absorbers, these collectors can work at temperatures up to 80 ºC with good efficiency (Kalogirou, 2003). To extend the application of these devices to higher working temperature, thus making them more available for applications such as food, drying of wood, crops, fruits, distillation, desalination, solar cooling (Nkwetta and Smith, 2012; Sharma et al., 2017), the transparent insulation materials (TIM) between two transparent covers or between absorber and outer glazing were used (Rommel and Wagner, 1992; Platzer, 1992). In some of these works, glass capillary tubes were considered, which despite their good resistance to temperature, increased the cost and weight of the collectors considerably. For commercial solar collectors, plastic TIM is potentially a good solution due to its advantage over glass capillary tube solution in terms of cost and weight. The main drawback is its vulnerability under the stagnation conditions. To overcome this problem, different solutions were proposed. Martínez et al. (2013) proposed a thermoelectric self-cooling system designed to dissipate the excess heat. A flat plate collector with plastic TIM and passive overheating system based on closed loop heat-pipe was recently introduced to the market showing good thermal performances (Adel, 2013).

In the present work, a flat plate solar collector with transparent insulation material is addressed. The scheme of the collector is shown in Fig. 1. The collector aims at delivering heat at the range from 80 to 110 ºC. The losses due to natural convection between the absorber plate and the cover glass is expected to be reduced due to employment of a layer of cellulose triacetate honeycomb TIM. According to the TIM manufacturer, this material can typically withstand a temperature of 140ºC, which can easily be reached under stagnation conditions. Indeed, yellowing and embrittlement can already be observed at temperatures above 100°C, well below the expected temperatures according to manufacturer's data. Moreover, outgassing, which affects both the optical efficiency and the appearance of the

Selection and/or peer review under responsibility of Scientific Committee
doi:10.18086/swc.2017.31.07 Available at http://proceedings.ises.org

collector, may occur at temperatures below 100 °C (Giovannetti et al., 2011). Thus, to protect TIM, the collector involves a ventilation channel between the absorber and back insulation, which operates thanks to a thermally actuating door which uses a shape memory alloy. When the system reaches high temperatures, the door opens, thus ventilating the collector to safer temperature levels. The collector is designed by means of a numerical model based on the numerical resolution of different components of the collector in the framework of a modular, object-oriented platform. The design is first tested in laboratory conditions, where the correct functioning of the system is tested and the characteristic curve of the collector is obtained. During the laboratory tests, different issues related with TIM and overheating protection system are identified and improved. The tested prototypes are then installed in the roof of a hospital building, where they are used along with the conventional flat plate solar collectors to cover the domestic hot water and space heating demand of the building. The site is properly instrumentalized so as to compare both developed and commercial collectors in terms of energy performance. Moreover, the prolonged exposure of the prototype under real climatic and working conditions constitutes a useful test for the reliability and durability of the design.

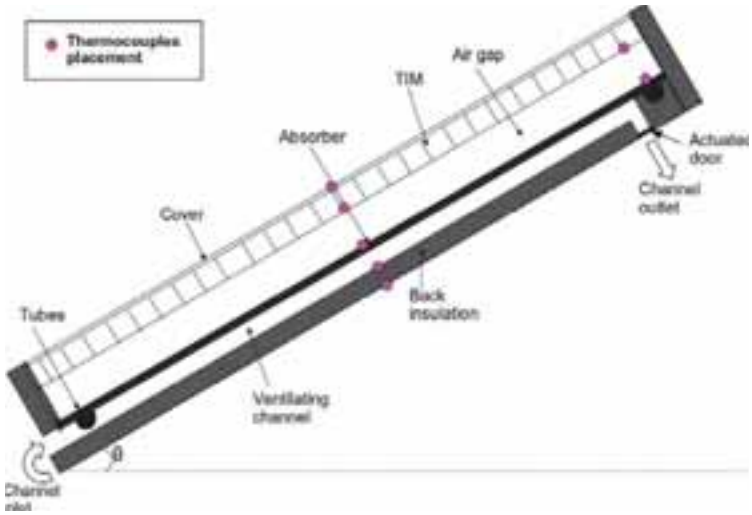

Fig. 1 Schematic view of the flat plate solar collector with TIM and ventilation channel.

2. Mathematical and numerical method

A mathematical model was developed (Kessentini et al., 2014b) where the flat plate solar collector with TIM and thermal protection can be numerically studied. In this model, the thermal and fluid dynamic phenomena taking place in each of the components that make up the prototype, i.e., glass cover, TIM, air gap, absorber plate, working fluid, ventilation channel, opaque insulation material, are numerically resolved considering different levels of complexity. In Figure 2, the detail of the mathematical model and the heat flux terms considered in the cross-section of the prototype and the absorber are schematically depicted.

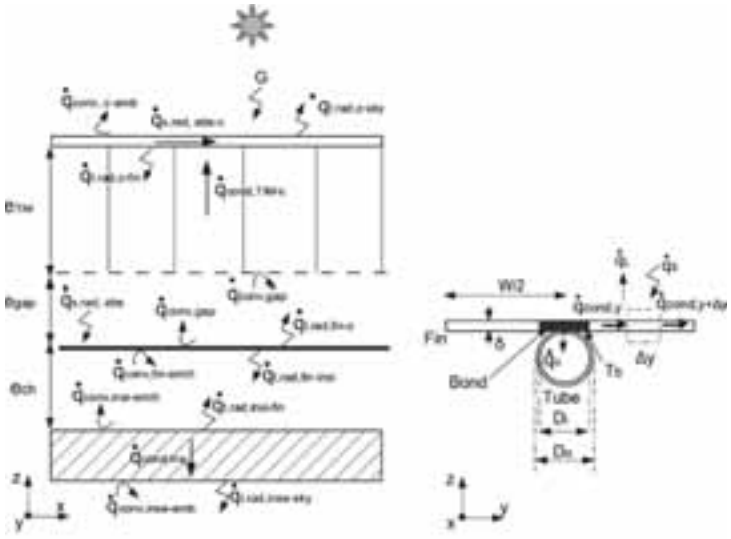

Fig 2. Detail of the heat flux terms. A cross section of the collector with TIM (left) and heat transfer at the absorber (right).

The object-oriented platform, called NEST (López et al., 2012), enables proper interaction between related components. The components, which can be treated as independent objects, can be linked with other related components through a global resolution algorithm. The numerical platform allows for efficient communications between the components (see Figure 3). Depending on the desired level of detail in the resolution of a particular element, even a high-level CFD object can be employed in the resolution of parts of the system. Given the computationally demanding nature of such a system composed of one or more CFD objects, the NEST framework provides parallelization to distribute the available computational power depending on the demands of each component, thus reducing computational time. Besides the active solar energy systems, like flat plate solar collectors (Kessentini et al., 2014a), this framework was also employed in the study of passive systems (Kizildag et al., 2014). Further details of the mathematical and numerical model used in this study are presented in Kessentini et al., 2014b.

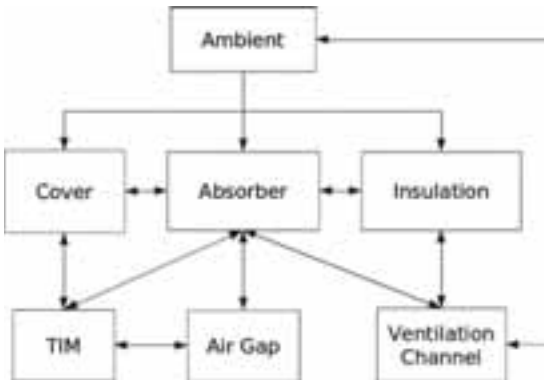

Fig. 3 Representation of the system composed of different components and their communications between each other.

3. Lab-scale testing and improvements

In line with the outcomes of the predesign performed using the numerical tool, prototypes with different TIM layer thicknesses were initially considered to observe their influence on the overall performance. In order to perform the characterization of the optical properties of the selected options, a set of preliminary glass-TIM configurations were initially tested under real outdoor conditions, as shown in Figure 4.

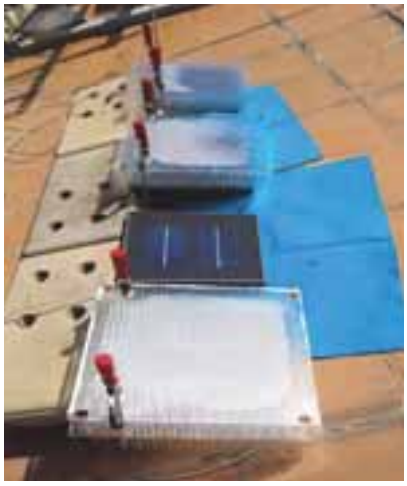

Fig. 4 Transmittance test set-up for different glass-TIM configurations under real climate conditions

As a result of previous analysis, and considering the numerical results, prototypes with four different TIM layer thicknesses (40mm, 50mm, 60mm, and 75mm) were manufactured to observe their influence on the overall performance. These prototypes were tested in the CTTC Solar Cell (see Figures 5 and 6), where tests up to 150 ºC and 8 bars can be performed using pressurized water. This experimental infrastructure allows for a comparative test employing two collectors in a parallel configuration.

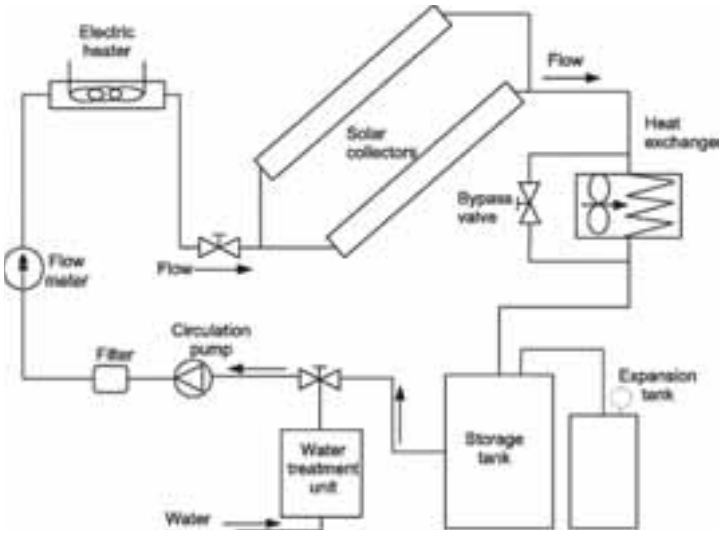

Fig. 5 Schematic view of the CTTC Solar Cell.

The main elements of the CTTC Solar Cell are the heater, water pump, filter, visor, expansion vessel, regulation and mixing valves, Coriolis flowmeter, storage tank, water treatment unit, heat exchanger, pyranometers for total and diffuse radiation in the plane of the tested collector, cup anemometer, 2D ultrasonic anemometer, temperature sensors, air vents. Some of these elements can be visualized in Figure 6. The experimental data is gathered using a data acquisition system, composed of a PC, an HP 3852A and two Agilent 34970A data acquisition units.

Fig. 6 Pictures of the key elements constituting the CTTC Solar Cell.

The manufactured prototypes are first subjected to the stagnation test, which is carried out to determine the maximum

temperature the collector can reach in the absence of mass flow. As no heat is transferred to fluid, the internal energy of the solar collector gradually increases, finally rising the temperature of the system up to an elevated temperature. It has been observed that the collector reached at the temperature of approximately 108 ºC when the thermally actuated door opened and started to cool down the collector. At that moment, TIM temperature was observed to be approximately 95ºC, which is well below the maximum temperature this element can resist. Visually inspecting the collector, TIM apparently was not damaged during the stagnation test, confirming that the effectiveness of the overheating protection system. In Figure 7, different temperatures registered during the stagnation test of a first generation prototype is depicted.

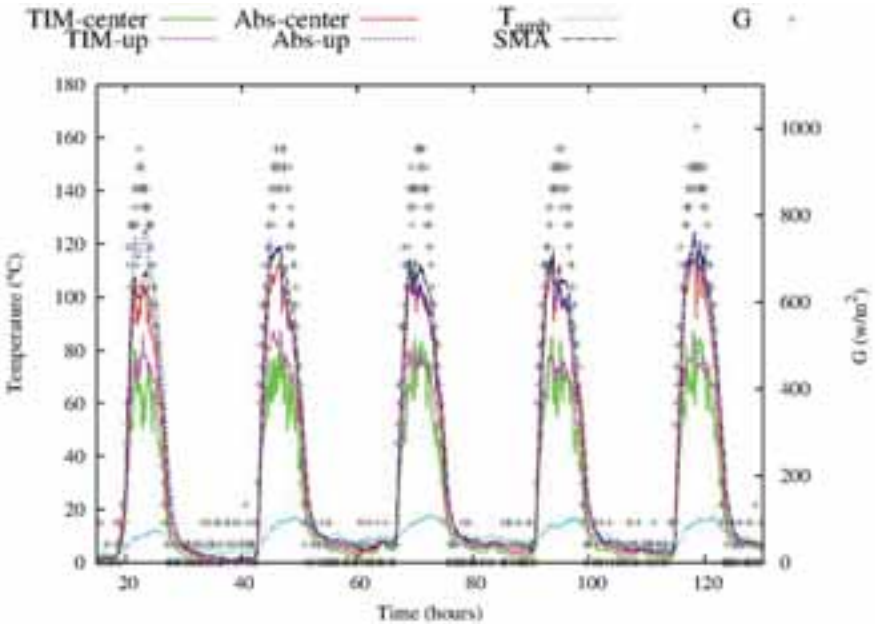

Fig. 7 Temperatures corresponding to different locations of TIM, absorber plate, sma spring, outdoor and total radiation on the tilted plane of collector registered during the stagnation test for an initial prototype.

After confirming that the prototypes are stagnation-proof, the outdoor steady-state efficiency test was performed following the recommendations of the international standard procedure described in ISO 9806-1. Accordingly, the prototypes were exposed to outdoor conditions for prolonged periods of time, assuring a constant temperature of the collector at the inlet. A mass flow rate of 0.042 kg/s was employed considering the collector absorber area. The collector is tested at 35, 50, 70, 90, and 110 ºC. The measurements obtained in periods close to solar midday are selected in order to fulfill criteria related with the angle of incidence. Other criteria regarding the amount of total solar radiation, the percentage of diffuse radiation, permitted variations in outdoor temperature and collector inlet temperatures throughout the test period are carefully attended. As the test were carried out under real climatic conditions in outdoors, it was not always possible to obtain favorable conditions for the collector testing. This caused requiring an important period of time to conduct the experiments and having to repeat the tests at different inlet temperatures.

The manufactured prototypes are tested in lab-scale where some of the shortcoming of the design were detected and improved, such as the condensation phenomenon observed due to the humidity absorbed by the plastic TIM material (see Figure 8). This problem was solved by means of introducing small ventilation holes, thus improving the ventilation and reducing the differences between the micro-climate of the collector and the outdoor ambient conditions. During the lab-scale tests, the emphasis is given to the influence of TIM material

Functioning of the thermally actuating door system is adjusted, with the objective of improving the phenomenon of premature opening of the channel. An experimental trial-error procedure was followed in order to determine the location and configuration of different elements constituting the overheating protection system, to make sure that thermally actuated spring is able to activate the ventilation channel under stagnation conditions while the channel can effectively be deactivated as the system is cooled down as a result of the heat evacuation by means of the ventilation channel.

Attachment of the TIM layer to the glass has been secured by more effective mechanisms, avoiding detachment of the cheap transparent insulation material under extreme conditions.

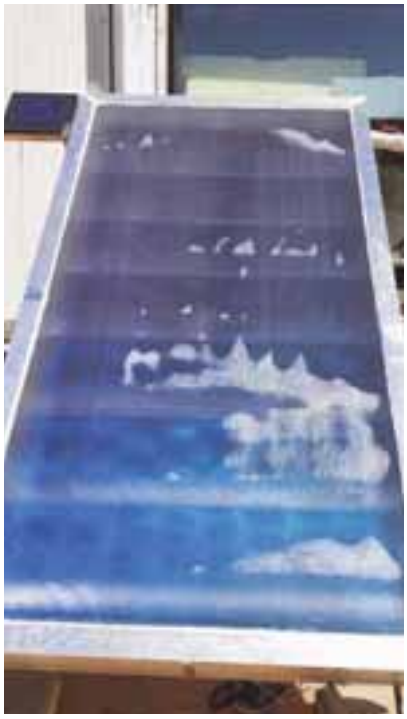

Fig. 8 Condensation phenomenon observed in a preliminary prototype

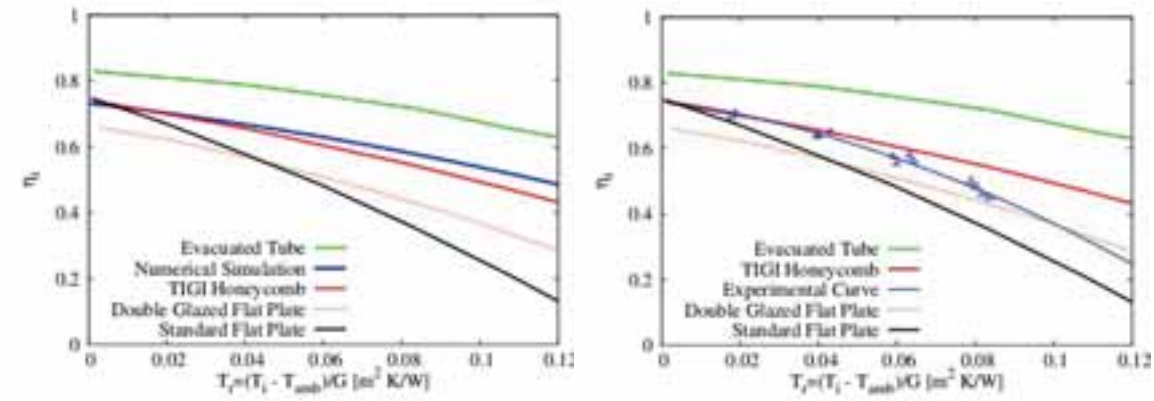

Fig. 9 Numerical (left) and experimental (right) steady-state efficiency curves of the prototype with 60mm TIM compared with solutions in the market.

In Figure 9, both numerical and experimental results during lab-scale tests are presented. The experimental curve corresponding to a first generation of prototypes is depicted in this graph. Note that these results anticipate an improvement with respect to the standard flat plate solar collector, at only slightly higher cost, since both TIM and overheating protection system use low-cost materials. The prototype achieves a somewhat lower performance with respect to the evacuated tube collector, though this type is expected to be approximately twice as costly as the manufactured prototype. In order to achieve the theoretical expected performance, improvements were implemented, especially affecting the insulation of the whole collector.

After the improvements with respect to the first generation of prototypes, a second generation was manufactured. In this second generation, a TIM layer of 75mm was used. This collector was also tested in laboratory conditions, obtaining finally the following steady-state efficiency curve given in eq.1:

$$\eta_i = 0.698 - 0.985\frac{(T_i - T_{amb})}{G} - 0.025\frac{(T_i - T_{amb})^2}{G} \qquad \text{(eq. 1)}$$

This curve is depicted comparatively in Figure 10, together with the curves of the previous generation of prototypes and commercial flat plate solar collector with TIM (TIGI LTD., 2011).

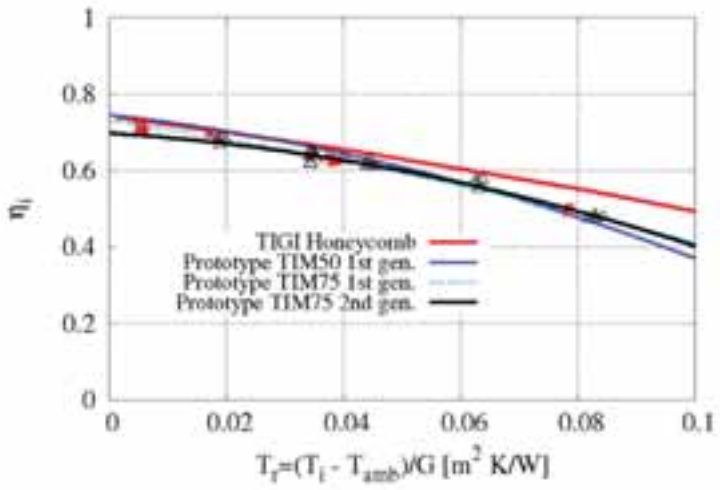

Fig. 10 Steady-state efficiency curves of different prototypes, compared with commercial flat plate solar collector with TIM.

Considering that the prototype involves a layer of TIM, it is of interest to the analyze the influence of the angle of incidence on the performance. Note that the steady-state efficiency curve is obtained for irradiation at or near normal incidence conditions. To that end, the prototype with TIM75mm is tested in outdoor conditions for a set of days in summer and autumn, always in clear sky conditions. In Figure 11, the results of the incidence angle modifier test are depicted. The experimental results reveal that the optical effects penalize the collector of the order of approximately 7 %, 10 %, and 32 % for the angles of incidence of 30º, 45º, and 60º, respectively. The methodology followed was to obtain the efficiencies for steady-state periods of 15 minutes, for symmetric intervals of time before and after solar midday, assuming an average angle of incidence of the given interval, and comparing it with the normal incidence efficiency for that particular conditions.

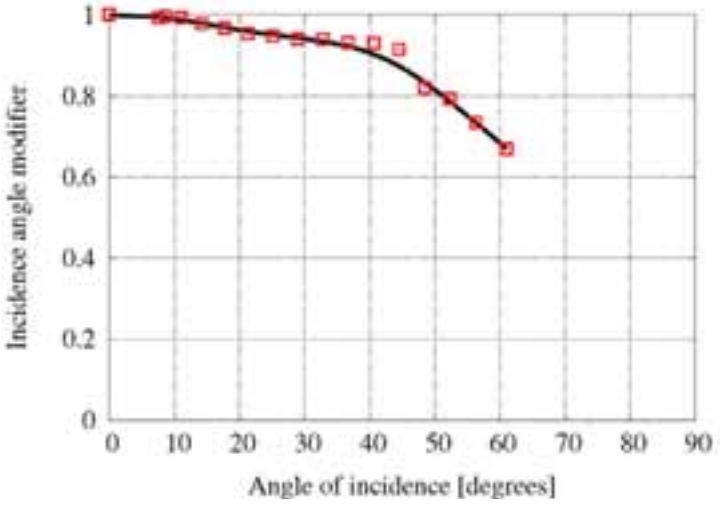

Fig. 11 Incidence angle modifier of the Prototype with TIM75mm, obtained by outdoor testing using a stationary test rack.

4. Long-term performance in demo site

Three prototypes, only differing in the TIM layer thickness (40mm, 50mm, and 60mm) are installed in the roof of a hospital building close to Barcelona (see Figure 12), where they are being tested comparatively with a commercial flat plate solar collector under real working and meteorological conditions during prolonged periods of time. The commercial collectors installed in the roof of the demo building do not have a layer of TIM. The steady-state efficiency curve provided by the manufacturer is given in eq. 2:

$$\eta_i = 0.739 - 3.706\frac{(T_i - T_{amb})}{G} - 0.017\frac{(T_i - T_{amb})^2}{G} \qquad \text{(eq. 2)}$$

The site is instrumentalized by means of mass flow, temperature, and radiation sensors. The long-term performance test in demo site provides realistic data for the functioning of the solar collectors, especially considering the solar heat delivered to the system and the reliability of the prototypes during prolonged periods of time. In the present work, demo site performance of the collectors are analyzed for winter and spring conditions.

Fig. 12 Solar energy capturing field of the Albada Building in Parc Tauli Hospital. The three prototypes are tested alongside the conventional flat plate solar collectors without TIM.

4.1 Winter Performance:

The prototypes, due to the employment of TIM are expected to have improved performance with respect to the standard flat-plate solar collectors, especially under the winter conditions where the losses to the ambient are pronounced as a result of important temperature gradient between intermediate collector working temperatures and outdoor conditions. In Figure 13, the ambient temperature and the total solar radiation on the plane of the collectors are depicted for a typical sunny day in the demo site location. Considering that the temperature in the inlet of the collectors was between 65-70ºC for this period, which is optimized considering the domestic hot water and space heating system installed in the hospital services building, important losses to the ambient can be anticipated.

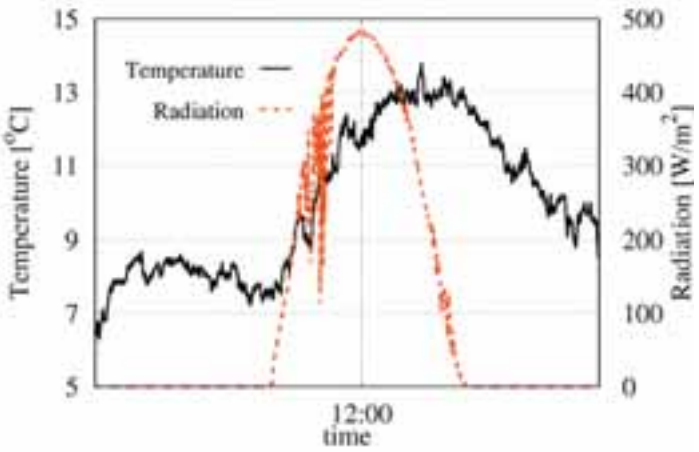

Fig. 13 Ambient temperature and solar radiation in the plane of the collectors for a sunny day in January 2017, mesured in Parc Tauli.

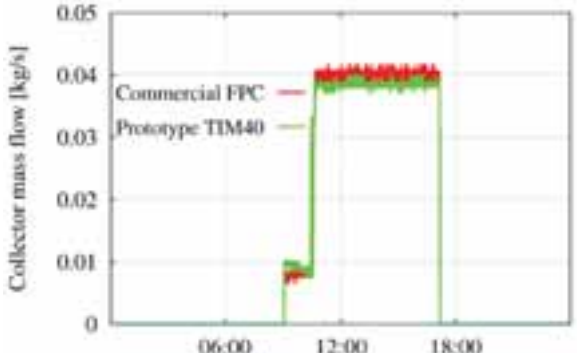

Fig. 14 Mass flow through the prototype and commercial flat plate collector without TIM for a representative sunny day in January 2017.

Note that the solar energy capturing circuit is activated only when a critical solar energy availability is reached. See Figure 14 for the registered mass flow through a prototype and a conventional flat plate solar collector without TIM.

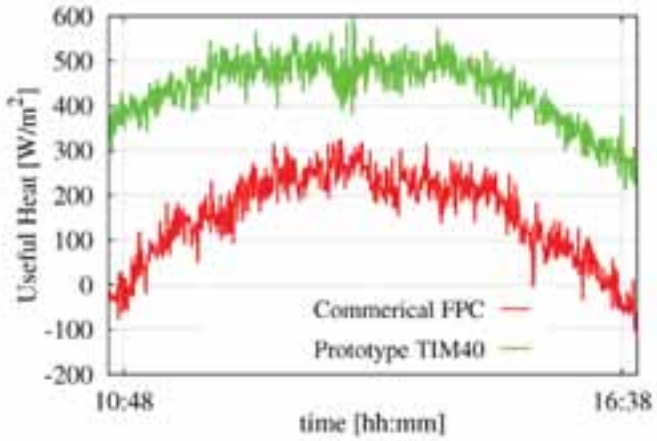

Fig. 15 Delivered useful heat for a representative day in January 2017 for the compared collectors.

In Figure 15, instantaneous useful heat delivered to the system is depicted both for the prototype and conventional flat plate collector without Tim for the day represented in Figure 14. This figure indicates a substantially better performance of the prototypes with TIM with respect to the conventional flat plate collectors, especially in winter conditions, when the losses from the collectors to the ambient are naturally enhanced, and the demand for space heating and domestic hot water is relatively higher.

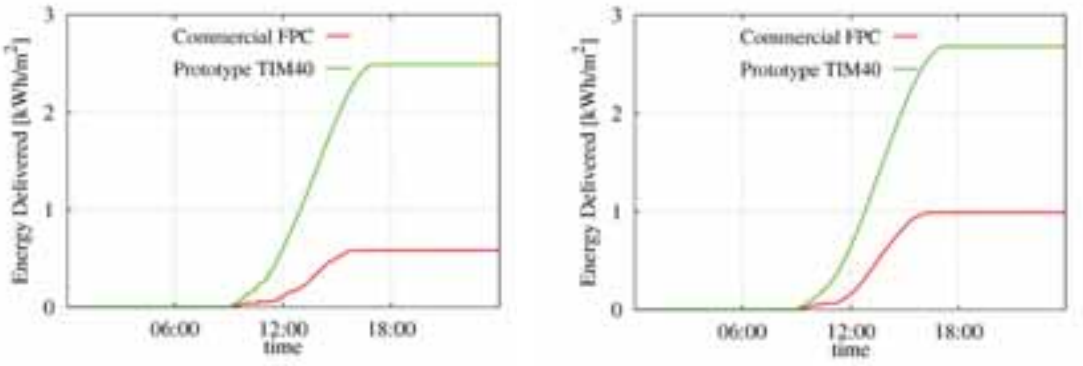

Fig. 16 Accumulative energy delivered to the system by the prototype and conventional flat plate collector without TIM for consecutive days in winter.

The trend captured in Figure 15 can be observed for other days during winter period of dissimilar solar availabilities, as shown in Figure 16, where the accumulative energy delivered to the system by the two compared collectors are depicted.

The steady-state efficiency curves of the collectors give valuable information on the thermal behavior of the collector under steady-state conditions with near-to-normal solar angle of incidence, together with some other additional conditions. However, a daily average collector efficiency can be defined, based on the energy delivered during the whole day by a collector and the solar energy available on the collector surface. Note that, this daily average efficiency will naturally have lower values with respect to the corresponding efficiencies indicated by the characteristic curve of the collector, as the curve is obtained by considering only the optimum conditions. Using the average data obtained in the vicinity of these days, which indeed are close approximation of the average day of the month considering the declination angles of the sun for this month, the daily average efficiencies for the prototype and conventional flat-plate collector are found as 41% and 16%, respectively.

In the absence of continuous readings due to technical problems in the demo site, these observed daily average efficiency values can be employed to obtain an approximation of the energy savings by both collectors for the winter meteorological conditions of the demo site. In Table 1, the total solar radiation in the vicinity of the demo site is provided, using the database of Meteonorm © software. The present estimation anticipates important savings as the high efficiency solar thermal collectors are employed for the given working conditions of the demo site.

Tab. 1: Total radiation on the inclined surface of the collectors and the estimated delivered heats during winter months.

Month	Total Radiation on Titled Plane (kWh/m^2)	Energy Delivered by Commercial Collector (kWh/m^2)	Energy Delivered by Prototype (kWh/m^2)
December	111	17.76	45.51
January	123	19.68	50.43
February	131	20.96	53.71
Winter Total	365	58.40	149.65

4.1 Spring Performance:

During the months of Spring, some experimental data could also be gathered in the demo site. Note that, due to relatively increased ambient temperatures, general losses of the collectors are reduced with respect to those in the winter season. Collectors are expected to work at higher efficiencies, which, especially in the case of the conventional collector, is expected to close the gap with the prototypes employing TIM.

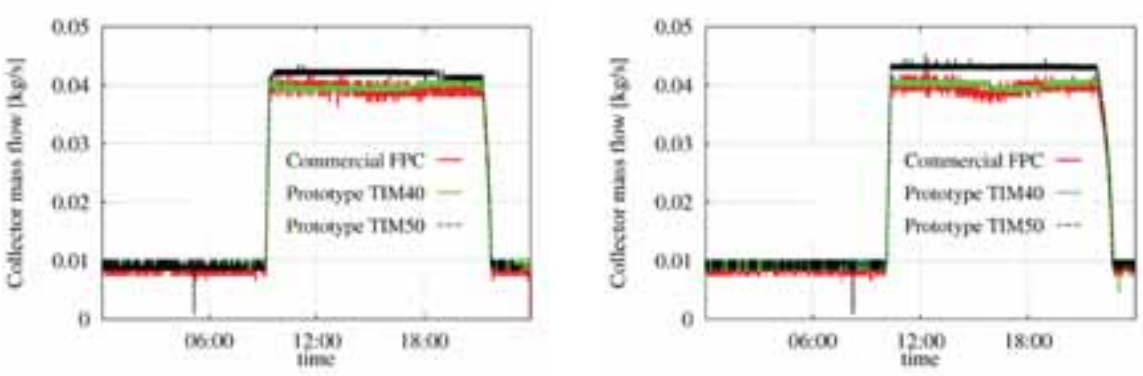

Fig. 17 Mass flow through two prototypes (TIM40 and TIM50) and commercial collector without TIM for two days with solar avaliability in March 2017.

In Figure 17, mass flows passing through the analyzed collectors are depicted for March 2017. Note that, due to requirements of the installer of the hydraulic circuit, the mass flow was not set to zero during periods of insufficient solar radiation. In the calculation and comparison of the accumulated energy delivered to the system by the analyzed collectors (see Figure 18), the effect of the nighttime flow was not taken into account, as it is considered as a temporary practice.

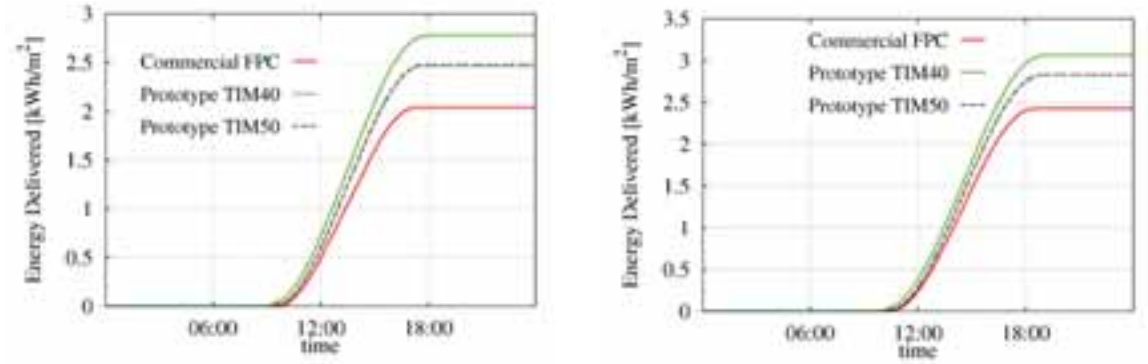

Fig. 18 Accumulative energy delivered to the system by the prototypes (TIM40 and TIM 50) and commercial flat plate collector without TIM for two representative days with solar availability in March..

Note that the commercial flat-plate collector improves its performance with respect to the winter period, even though it still delivers less amount of energy per area when compared with the prototypes. 40mm TIM layer prototype was observed to show better performance. Following the previous approach for defining an average efficiency for the

collectors based on these two test days, daily average efficiencies of 43% and 31% are obtained for 40mm layer TIM collector and commercial flat-plate collector, respectively. This information is used to estimate the delivered energies per area for both collectors during the tested spring period, as shown in Table 2.

Tab. 2: Total radiation on the inclined surface of the collectors and the estimated delivered heats during spring months.

Month	Total Radiation on Titled Plane (kWh/m^2)	Energy Delivered by Commercial Collector (kWh/m^2)	Energy Delivered by Prototype (kWh/m^2)
March	165	51.15	70.95
April	168	52.08	72.24
May	173	54.68	73.40
Spring Total	506	157.91	216.59

5. Conclusions

It has been demonstrated that different variants of the designed prototypes are capable of delivering higher amounts of heat to the domestic hot water and space heating system of a specific hospital building when compared with the conventional flat plate solar collector. The employment of the designed novel collector is especially interesting for the present application, as the practical working temperatures give rise to important losses during winter periods. The visual inspection of the prototypes does not present any issues related with ageing of TIM, problems with TIM adhesion, any damage of TIM due to stagnation conditions, which indicate a proper functioning of the overheating protection system. It is worth noting that due to the faults registered in different elements of the circuit, not necessarily related with the solar energy capturing field, the hydraulic circuit of the system did not function during prolonged periods of time in spring and summer. Thus, it can be stated that, this circumstance provided the necessary exposure of the designed prototypes to the stagnation conditions, building confidence in the reliability of the prototype collectors.

Thus, although the tested period does not yet cover a representatively long time span, the initial outcomes indicate promising results in terms of both energy efficiency and reliability of the present design.

6. Acknowledgments

This work has been financially supported by the European Community FP7 Programme, EeB.NMP.2013-3 No 609377 “RESSEEPE Project”. The authors thankfully acknowledge this support.

The authors would also like to acknowledge Manuel Ordoño, Cristóbal Galleguillos for their technical support during the lab-scale tests; and *Consorci Corporació Sanitària Parc Taulí de Sabadell* for their support and contributions in the building of the experimental facility in the demo site.

7. References

Adel M., 2013. Honeycomb collectors for high temperature differential solar thermal applications. In: International conference on solar heating and cooling for buildings and industry [ref:47634].

Giovannetti F., Kirchner M., Rockendorf G., Kehl O., 2011. Cellulose Triacetate Honeycomb Compounds for Improved Flat-Plate Collectors: Performance and Reliability. 30th ISES Biennial Solar World Congress 2011, SWC 2011.

Kalogirou S., 2003. The potential of solar industrial process heat applications. Applied Energy 76, 337-361.

Kessentini H., Capdevila R., Castro J., Oliva A., Bouden C., 2014. Three dimensional heat transfer analysis of combined conduction and radiation in honeycomb transparent insulation. Solar Energy 105, 58-70.

Kessentini H., Castro J., Capdevila R., Oliva A., 2014. Development of flat plate solar collector with plastic transparent insulation and low-cost overheating protection system. Applied Energy 133, 206-223.

Kizildag, D., Lehmkuhl, O., Rigola, J., Capdevila, R., Oliva, A., 2015. Thermal optimization of multi-functional façades as energy efficient solution in retroffiting public buildings, IPBSA, Hyderabad, India.

Lopez J., Lehmkuhl O., Damle R., Rigola J., 2012. A parallel and object-oriented general purpose code for simulation of multiphysics and multiscale systems. 24th Int. Conference on Parallel CFD, Atlanta.

Martínez A, Astrain D, Rodríguez A, Aranguren P., 2013. Thermoelectric self-cooling system to protect solar collectors from overheating. Journal of Electronic Materials 43(6), 1480-1486.Nkwetta D.N., Smyth M.,2012. The potential applications and advantages of powering solar air-conditioning systems using concentrator augmented solar collectors. Applied Energy 89(1), 380-286.

Platzer W.J., 1992. Total heat transport data for plastic honeycomb-type structures. Solar Energy 49(5), 351-358.

Rommel M., Wagner A.,1992. Application of transparent insulation materials in improved flat-plate collectors and integrated collector storages. Solar Energy 49(5), 371-380.

Sharma A.K., Sharma C., Mullick S.C., Kandpal T.C., 2017. Solar industrial process heating: A review. Renewable and Sustainable Energy Reviews 78, 124-137.

TIGI LTD., 2011. System and method for temperature limiting in a sealed solar energy collector. WO/2011/086534, A1: 1-40.

EXPERIMENTAL AND CFD OPTIMIZATION ON FLOW AND HEAT TRANSFER TO A SOLAR FLAT-PLATE GLASS COLLECTOR

Pascal Leibbrandt, Thomas Schabbach, Michael Dölz, Martin Rhein
Institut für Regenerative Energietechnik, University of Applied Sciences Nordhausen (Germany)

Abstract

In the project solar flat-plate glass collector, a new type of solar collector will be developed which, simplified, consists of four glass plates. As part of the project, the full volumetric flow in the fluid layer and the convective heat transfer in the insulating gas layer were investigated by using experimentally and numerically methods. Regarding to the fluid layer, an optimal fluid layer structure has been found which distributes the fluid well and ensures an optimal collector efficiency factor of nearly 99%. With the numerical simulation of the convective flow in the isolation gas layer it was shown, that the most used equation by Hollands (1976) presumably needs to be extended by the aspect ratio of the gas volume and other boundary conditions. These results are currently being validated experimentally. In addition, the filling/drainback process was examined for a potential drainback application.

Keywords: glass collector, fluid distribution, convective losses, CFD, validation

1. Collector construction and operation

In context of the research project “Nurglas-Solarflachkollektor” a collector with lower production costs is developed which consists primarily of glass. Due to the simplified construction, cost intensive production steps such as the absorber welding are unnecessary and enable an automated production process with fewer production steps. Manufacturing costs can thus be reduced by approximately 20% compared to conventional standard flat-plate collectors. Another advantage is the reduced collector thickness of < 40 mm which allows an simplified installation and collector field connection, so that other application areas (especially in facade) can be opened up.

The glass collector consists of four planar glass plates, which are glued and sealed by a frame and a fluid layer structure. As shown in Fig. 1, the heat transfer medium (yellow) passes directly through the middle rectangular space. The coatings on the glasses ensure optimal radiation absorption in the fluid layer and minimize the radiation losses due to reflection and emission, see also Leibbrandt et al. (2014). The heat transfer fluid has to be distributed full volumetric through the flow channel to ensure an optimal heat transfer coefficient $\mathbf{h_{fl}}$ in the fluid to optimize the collector efficiency factor. The fluid layer structure should also be able to absorb inner/outer forces from/to the fluid layer. Insulating gas layers (green) minimize convective heat losses to the front ($\mathbf{h_{igf}}$) and back ($\mathbf{h_{igb}}$).

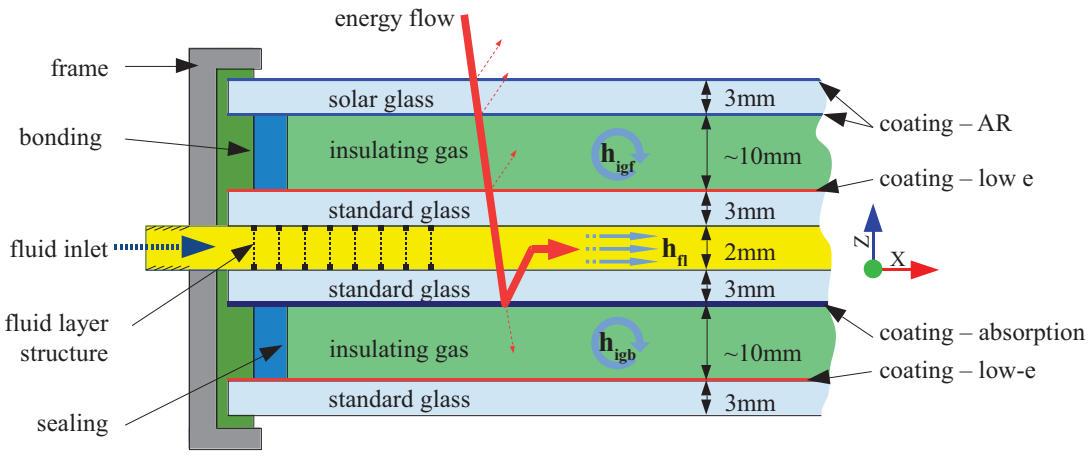

Fig. 1: Construction of the glass collector

doi:10.18086/swc.2017.31.08 Available at http://proceedings.ises.org

2. Fluid layer: full volumetric flow and heat transfer

With an optimal collector efficiency factor F′, the overall collector efficiency is ensured. F′ is the theoretical ratio of the useful energy gain to the useful gain that would result if the absorbing surface would be at the fluid temperature, Duffie Beckman (2013). The collector efficiency factor is at its maximum if the flow would be full volumetric. For flat-plate collectors with a fin width of 90-120 mm, the collector efficiency factor is about 88-94%, Wesselak et al. (2017). The internal heat transfer U_{int} is at its maximum when the flow is fully homogeneous (without flow areas with no/low flow velocity) and turbulent. It is

$$F' = \frac{U_{int}}{U_{int} + U_{loss}} \qquad \text{(eq. 1)}$$

Fluid layer full volumetric flow

The flow channel with size L x B s_f = 2000 x 1000 2 mm should be flowed through full volumetric in the ideal case. In flow channels without internals, a flow like in Fig. 2 - A results. The flow field $\overrightarrow{u_i}$ consist of local velocity components in each direction. The ideal homogeneous velocity field (Fig. 2 - B) consists only of velocity components in x-direction and is equal in any position of the flow channel. It is

$$\boldsymbol{A}\text{: } \overrightarrow{u_i} = \begin{pmatrix} u_i(x,y,z) \\ v_i(x,y,z) \\ w_i(x,y,z) \end{pmatrix} \qquad \boldsymbol{B}\text{: } \overrightarrow{u_i} = \begin{pmatrix} u_i(x) \\ 0 \\ 0 \end{pmatrix} \qquad \text{(eq. 2)}$$

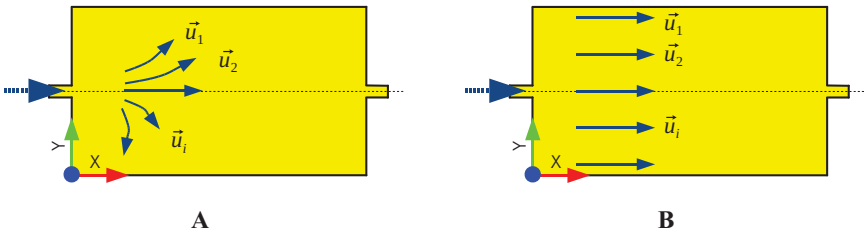

Fig. 2: Fluid Layer velocity fields

First 2D CFD simulations are able to model the flow in the fluid layer sufficiently precisely so that a further optimization of the fluid layer structure is carried out with CFD simulations. Results of the optimized version from a detailed 3D CFD model (flow channel 2000 x 1000 x 2 mm) with different fluid layer structure are illustrated in Tab. 1. The fluid layer structures with rectangular flow channels in meandering shape led to the best results in terms of flow distribution.

In addition to the local scalar velocities (row **1**) in the fluid layer (at z = 1 mm), the volume uniformity of the local velocities uni_u over the flow volume V was used to determine the homogeneity of the flow (row **2**). It is

$$uni_u = 1 - \frac{\sum_i |u_i - \bar{u}| \cdot V_i}{2|\bar{u}| \sum_i V_i} \qquad \text{(eq. 3)}$$

Tab. 1: Flow results for different fluid layer structures

	Structure 0 no inner web	**Structure 1** web with narrow bars (1 mm)	**Structure 2** web with wide bars (10 mm)	**Structure 3** web with wide bars (10 mm) and end gaps	**Structure 4** web with wide bars (10 mm) and end roundings
1	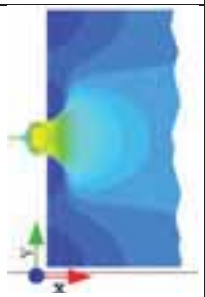		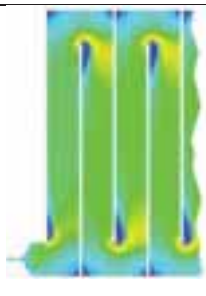		
2	uni_u = 0.723 m/s (reference)	uni_u = 0.812 m/s (+12,4%)	uni_u = 0.817 m/s (+13,0%)	uni_u = 0.799 m/s (+10,5%)	uni_u = 0.823 m/s (+13,9%)

An appropriate fluid layer structure, which distributes the heat transfer fluid almost full volumetric in the 2 mm fluid layer results of the detailed 3D CFD model. Experimental investigations of fluid layer prototypes confirm the simulation results and the flow behavior. In Fig. 3, an optical measurement of the flow field (left) is compared with 3D CFD results (right), see also Leibbrandt et al. (2017).

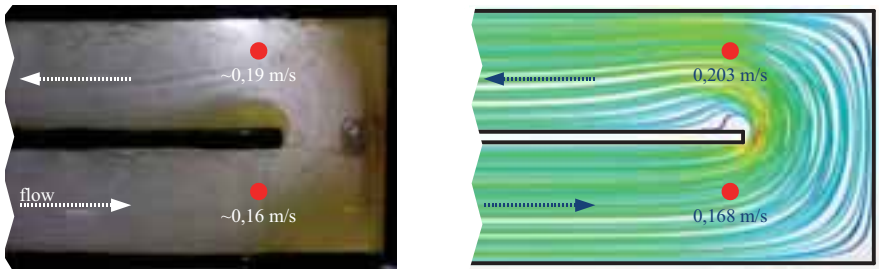

Fig. 3: Experimental and 3D CFD velocity field

At the same time the pressure drop and the filling/drainback performance is determined by experiments for a potentially drainback system application.

Fluid layer heat transfer

After the optimization of the fluid layer structure, the influence on heat transfer is investigated. The fluid layers' dimension is set to L x B x s_{fl} = 2000 x 1000 x 2 mm, the inclination of the layer is 45°.

For the simulations two fluid layer structures, similar to structure 0 and 2 are analyzed. The backside of the fluid channel is set up with a constant heat flow density $\dot{q}_{abs} = 700\ W/m^2$, which corresponds to the absorbed solar radiation power. At the front convective heat transfer with a constant heat transfer coefficient and fixed ambient temperature is assumed. In reality, the convective heat transfer coefficient depends on the front side temperature, too. The sides of the fluid channel have been supposed to be adiabatic. The fluid inlet temperature is 20 °C; the inlet velocity is varied between 0.25 – 1.00 m/s (35 – 140 l/(m² h)).

To rate the quality of the heat transfer coefficient h_{fl} through the fluid layer the useable enthalpy-flow $\dot{q}_{use}$ at the layer outlet is set into relation to mean fluid and absorber temperature difference. It is:

$$h_{fl} = \frac{\dot{q}_{use}}{\overline{T_{abs}} - \overline{T_{fl}}} \qquad \text{(eq. 4)}$$

To compare the collector efficiency factor of the fluid layer F_f' with standard flat-plate collectors it is assumed, that the overall loss heat transfer coefficient is $U_{loss} = 4\,W/(m^2K)$. U_{loss} describes the collector heat losses over the sides and the back of the collector which are not part of the presented CFD simulations. The efficiency factor of the fluid layer F_{fl}' is:

$$F_{fl}' = \frac{h_{fl}}{h_{fl} + U_{loss}} \qquad \text{(eq. 5)}$$

Tab. 1: Influence of fluid layer structures on heat transfer (3D CFD results)

		u_{in} in m/s		
		0.25	0.50	1.00
Structure 0	$\dot{q}_{use}$ in W/m²	565.95	630.53	657.35
	h_{fl} in W/m²/K	372.86	365.07	360.68
	$\boldsymbol{F_{fl}'}$	**98.9%**	**98.9%**	**98.9%**
Structure 2	$\dot{q}_{use}$ in W/m²	556.11	617.33	651.18
	h_{fl} in W/m²/K	343.25	421.14	625.53
	$\boldsymbol{F_{fl}'}$	**98.8%**	**99.1%**	**99.4%**

The useable enthalpy-flow $\dot{q}_{use}$ of structure 2 is less than in structure 0 because the heat loss to the front side is greater due to higher internal heat transfer and higher fluid temperatures.

Fig. 4 shows the temperature field inside the flow channels. A temperature inhomogeneity can be seen especially at the end of the individual fluid channels. They are formed due to the lower flow velocity and lead to local temperature maxima (hot spots). They should be minimized by a suitable flow guidance. At these hotspots the heat transfer reduces and high temperature gradients occur which also lead to stresses in the glasses.

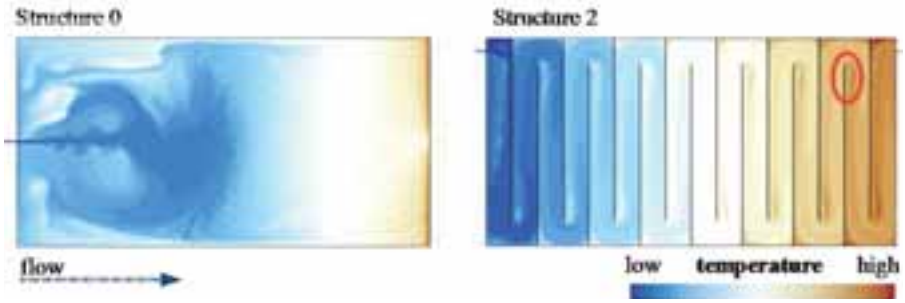

Fig. 4: Fluid Layer temperature fields (3D CFD results)

3. Insulating gas layer heat transfer

To ensure an optimal collector efficiency the convective front losses through the insulating gas layer is investigated. The gas volume, filled with insulating gas has a length L, a width B and a glass distance s, see Fig. 5. The resulting aspect ratio AR = L/s is about 80 at standard flat-plate collectors (distance between absorber and front glass) and about 200 at the presented glass collector. The most used approach to calculate the convective heat transfer was investigated by Hollands et al. (1976).

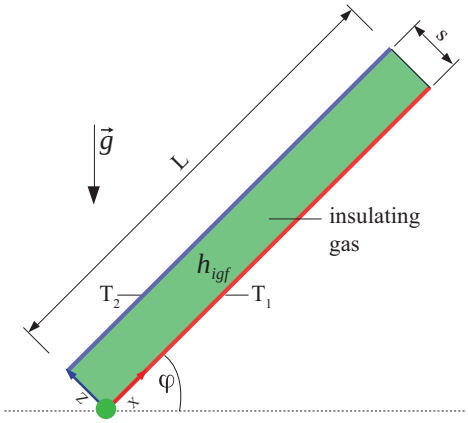

Fig. 5: Problem definition insulating gas layer

The internal heat transfer coefficient h_{igf} is at its minimum at the point where the gas flow velocity is low and the conductive isolating behavior of the gas is at its maximum.

The boundary conditions (e.g. temperature difference, homogeneity and level) and the geometric relationships (aspect ratio and vault of glasses) of the glass collector do not match those by Hollands et al. (1976). The deviations, when using the Hollands equation, for varying boundary condition were demonstrated, for example, by Föste (2013) by investigating an insulating glass flat-plate collector experimentally. Eismann (2014) showed the influence of the temperature inhomogeneity on the basis of collector simulations. The data in Tab. 2 show the wide range of geometry and boundary conditions. The error in calculating the heat transfer, as mentioned above, presumably results in these deviations.

Tab. 2: Geometry and boundary conditions

	Glass collector	Standard collector	Hollands et al. (1976)
Length L in mm	2,000	2,000	610
Glass distance s in mm	10	25	12.7
Aspect ratio AR	200	80	48
Insulating gas	argon	air	air
T_1 in C	70	120	26.67 (80 F)
T_2 in C	35	20	15.56 (60 F)
ΔT in K	35	100	11.1

The internal heat transfer is calculated with

$$\dot{Q} = A \cdot h_{igf} \cdot (T_1 - T_2). \qquad \text{(eq. 6)}$$

The heat transfer coefficient h_{igf} is calculated from the Nusselt number Nu, which depends on the Rayleigh number Ra. The Rayleigh number describes the internal free convection.

$$Nu = Nu(Ra) \qquad \text{(eq. 7)}$$

The Rayleigh number depends on the Grashof number Gr (ratio of lift forces and internal viscous friction forces) and the Prandtl number (material data).

$$Nu = \frac{h_{igf} \cdot s}{\lambda} \qquad \text{(eq. 8)}$$

$$Ra = Gr \cdot \mathrm{Pr} = \frac{g \cdot \beta \cdot \Delta T \cdot s^3}{\nu \cdot a} \qquad \text{(eq. 9)}$$

Hollands et al. (1976) developed the following Eq. from experimental measurement. The Eq. is split in three parts, depending on the Rayleigh number of the problem. The part $[\dots]^+$ activates the terms in brackets for different Rayleigh numbers.

$$Nu = 1 + 1.44\left[1 - \frac{1708\,(\sin(1.8 \cdot \varphi))^{\frac{1}{6}}}{Ra \cdot \cos(\varphi)}\right]\left[1 - \frac{1708}{Ra \cdot \cos(\varphi)}\right]^{+} + \left[\left(\frac{Ra \cdot \cos(\varphi)}{5830}\right)^{\frac{1}{3}} - 1\right]^{+}$$

Three different flow types, regarding to $Ra^* = Ra \cdot \cos(\varphi)$ are illustrated in Fig. 6. For $Ra^* < 1708$, the flow is quasi-conductive because the heat transfer media does move with very slow velocity. In the transition area $Ra^* = 1708 \dots \sim 5830$, the flow topology is characterized by a mono-cellular base flow. A multi-cellular flow regime arise for $Ra^* > 5830$. The optimal point of minimum heat transfer is at about $Ra^* \approx 1708$, where the isolating behavior of the gas is at its maximum.

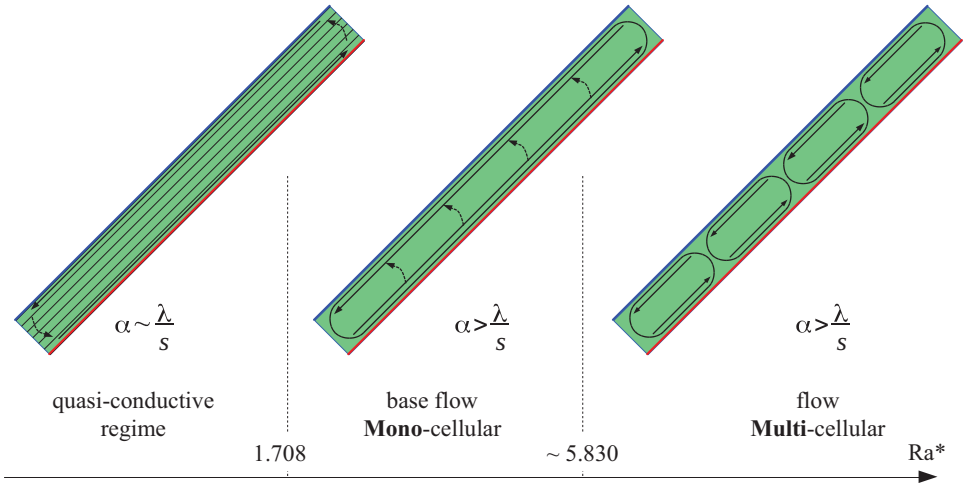

Fig. 6: Flow regimes

Based on intensive literature research, see Leibbrandt et al. (2016), the following conclusions for internal free convective flows in inclined cavities are known until now:

- Hollands et al. (1976) developed the correlation (see above) from experimental measurement and based on earlier theoretical research. The gas volume was captured between two nearly isothermal copper plates in a vacuum vessel. The change in Rayleigh number was set with varying pressure inside the vessel. So the aspect ratio AR was constant because of constant distance s. Also the humidity of the captured air was not documented, which led to an uncertainty in the heat transfer coefficient up to 6%. The correlation from Hollands et al. (1976) is based on an evaluation of the heat transfer in a central area (130 x 130 mm)of the copper plates. Later investigations show that the total heat transfer is significantly influenced by higher local heat transfer coefficients at the ends (top and bottom) of the gas volume, too.
- Bartelsen et al. (1993) and Föste (2013) showed that measured data from flat-plate collectors led to higher heat transfer coefficients about 10% regarding to Hollands et al. (1976). Measurements by Föste (2013) on isolating glass collector showed a deviation up to 32%. Yiqin et al. (1991) also investigated mean differences up to 10% in the heat transfer.

Insolating gas layer CFD simulation and validation

In this project, a CFD model is used to check the influence of varying boundary conditions and geometry. Numeric discretization and physics models are checked first in a simplified 2D CFD model and are validated with a 3D CFD model. Based on the experimental setup from Hollands et al. (1976) a detailed 3D CFD model calculates the internal flow and the heat transfer. The geometry, boundary conditions and report area (central) are the same as in Tab. 2 (Hollands). The Rayleih number is set with varying pressure from 70 Pa up to 700,000 Pa to capture the range of the setup from Hollands et al. (1976).

In Fig. 7 (left) the influence of varying discretization of the 3D CFD model is shown. For normal (cell size 1.0 mm) and coarse discretization (cell size 2.0 mm), the flow topologies and the heat transfer phenomena are captured unsatisfactory. Just the fine discretization (cell size 0.5 mm) is able to capture the behavior of the flow well. The discretization accuracy confirm the former 2D CFD results. An even finer discretization would lead to a disproportionate simulation time with no appreciable increase of the accuracy. Fig. 7 (right) shows the simulation results with two different flow models. The chosen one (LowRe: Reynolds-averaged Navier-Stokes model, coupled energy and flow with standard K-Epsilon Low-Re formulation) is able to model the flow well. The maximum deviation in h_{igf} is about 6.5% at 400,000 Pa.

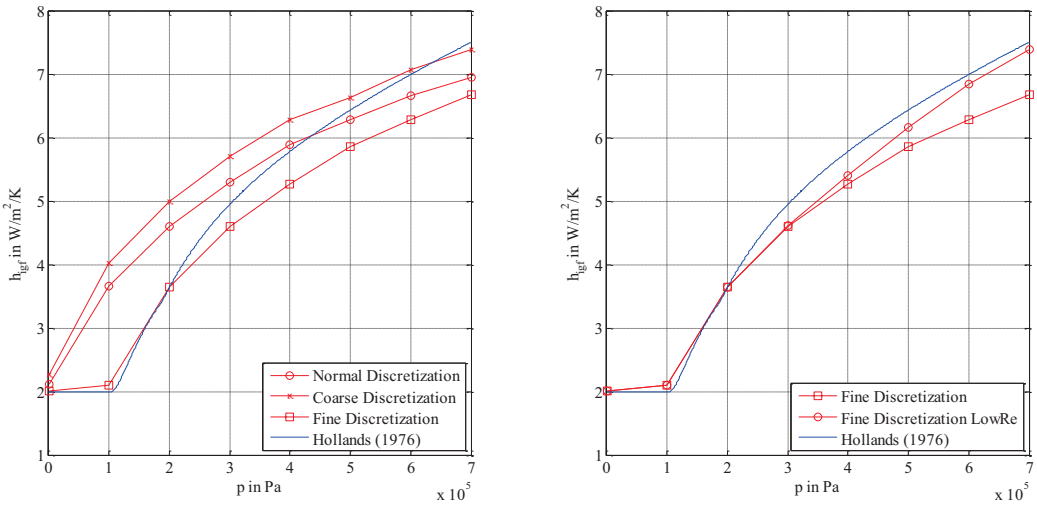

Fig. 7: Discretization influence (left) and flow model influence (right) of the 3D CFD model

Tab. 3 gives an overview of the different flow regimes. These results are scalar velocity- and temperature fields from a central section (bottom end) of the mentioned setup by Hollands et al. (1976) for fine discretization and LowRe flow model. The above-described flow regimes can clearly be seen in Tab. 3: for $p = 70\,Pa$ semiconductive behavior dominates, for $\mathrm{p} = 100{,}000$ Pa a mono-cellular flow topology is visible, for $\mathrm{Ra} > 200{,}000$ Pa turbulent multi-cellular flow cells are visible.

Tab. 3: Velocity- and temperature fields

p in Pa	Ra	Velocity field	Temperature field
70	0.001134		
100,000	2,313		
200,000	9,253		
300,000	20,820		
400,000	37,013		
500,000	57,832		
600,000	83,278		
700,000	113,351		

CFD simulation with varying boundary conditions

In the next step, the validated 3D CFD model is used to check the influence of heat transfer for varying geometry and boundary conditions. For this purpose all models and CFD setups are used, but for the first appraisal a 2D geometry is applied.

As mentioned above, the aspect ratio AR seems to have an influence on the flow regimes and so on the heat transfer phenomena. For this, simulations with varying $AR = 40 \dots 200$ are presented in Fig. 8. It is obvious that the variation of AR results in an a difference of h_{igf} and Nu. Nu differs up to 11.6% for high Rayleigh numbers.

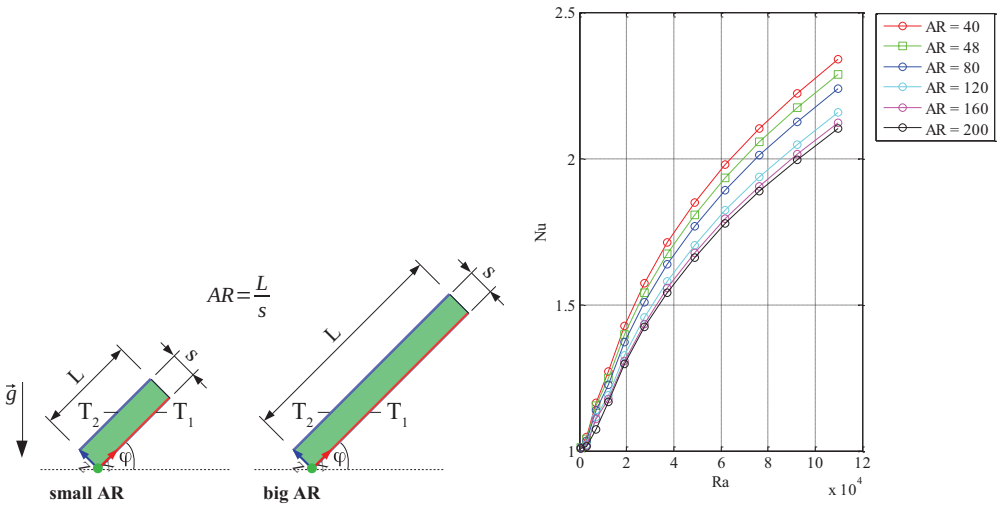

Fig. 8: Influence of varying AR (total area)

Another influence factor is the curvature of the glass plates. By default, the glass plates are considered as planar without any curvature. Due to varying temperatures while the collector operation, the resulting change in the density of the filling gas leads to a volume change of the gas and so to a curvature of the glasses. In the first step the glass planes are set to be parallel, so $s = const.$ and $ds = f(x)$, $ds(L/2)$ is varied with $ds_0 \dots ds_2 = 0 \dots 2 \dots 4\ mm$. Results are presented for $AR = 20 \dots 80$. For $AR = 20$, Nu differs up to 1.0% for $ds = 4\ mm$ and for $AR = 80$, Nu differs up to 0.7% for $ds = 4\ mm$, see Fig. 9.

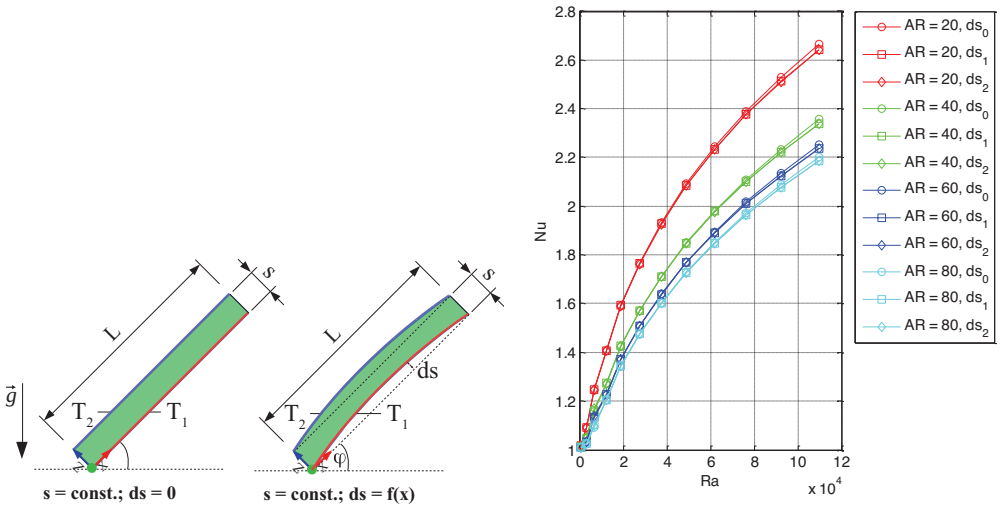

Fig. 9: Influence of varying ds (total area)

Last, the influence of a linear temperature profile $T_1 = f(x)$ is shown. In real collectors the fluid temperature increases over the collector length L due to the radiation absorption by a given flow direction. This effect is modeled by an linear temperature profile $T_1 = f(x)$, while the mean temperature $\overline{T_1}$ is constant. The influence of the linear temperature profile $dT/dL = 0 \dots 2 \dots 4\ K$ in Nu is maximum about 1.1% for $AR = 20$ and 0.5% for $AR = 80$.

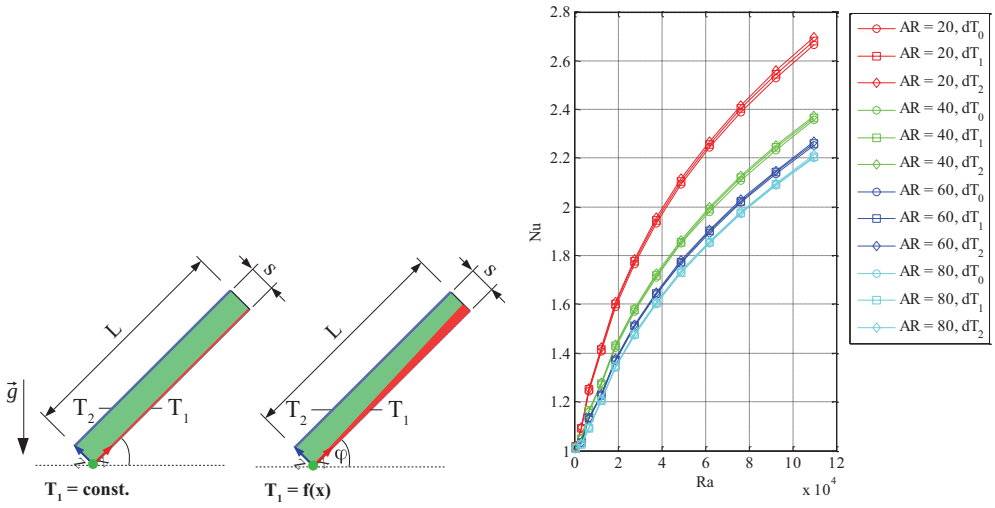

Fig. 10: Influence of varying T_1 (total area)

With CFD simulations, it is shown that the heat transfer coefficient h_{igf} depends on the boundary conditions mentioned above. This results for different AR in variation of h_{igf} up to 11.6%. The influence of AR is not component of the equation by Hollands et al. (1976), so that an extension of that equation should be carried out. For inhomogeneous temperatures and vaulted gas volumes, the influence is lower but not negligible.

Experimental investigations

To validate the simulation results, an experimental setup is under construction at the moment. A heating mat generates a one dimensional heat flux $\dot{q}(x,y)$ field, which is determined by a measurement layer and allows to measure the heat transfer trough the insulating gas layer. With temperature sensors, a spatially resolved heat flux field is used to calculate a spatially resolved heat transfer coefficient field $h_{igf}(x,y)$. The measurements are used to validate the simulation results and should allow to extend the present calculation approaches.

4. Outlook

In continuation to the project collector prototypes will be investigated experimentally. Target will be to increase the flow homogeneity, heat transfer and stability of the fluid layer. The pressure loss, manufacturability and long term stability must also be considered. The performance of the entire collector will be checked during QDT-testing. Mechanical load tests with internal and external forces will also take place.

5. Acknowledgement

The project “NUGLACOL – Development of a low cost solar flat-plate collector system based on glass”, FKZ 0325557, is carried out in cooperation with the companies Wagner Solar, Energyglas and Kömmerling and funded by the German Federal Ministry for Economic Affairs and Energy (BMWi) based on a decision of the German Federal Parliament. The authors are grateful for the financial support.

CFD analysis are carried out with the flow simulation software STAR-CCM+ by CD-adapco. Thanks for the support.

6. References

Bartelsen et al. 1993. Heat Transfer by Natural Convection in the Air Gap of Flat Plate Collectors. Proceedings ISES Solar World Congress, pp. 267-273, Budapest

Dölz; Schabbach; Leibbrandt; Rhein, 2016. Low-Cost-Kollektorprüfstand für quasidynamische Messungen im Hochtemperaturbereich. 26. OTTI Symposium Thermische Solarenergie, Bad Staffelstein

Duffie, Beckman, 2013. Solar Engineering of Thermal Processes, fourth ed. John Wiley & Sons Inc., Hoboken, New Jersey

Eismann, R. 2014. Thermohydraulik von Solaranlagen. ETH Zürich, Dissertation

Föste, S. 2013. Flachkollektor mit selektiv beschichteter Zweischeibenverglasung. Gottfried Wilhelm Leibniz Universität Hannover, Dissertation

Hollands et al. 1976. Free Convective Heat Transfer Across Inclined Air Layers. J. Heat Transfer 98(2), 189-193

Leibbrandt; Schabbach; Weber, 2014. Flachkollektoren aus Glas – erste Untersuchungsergebnisse. 24. OTTI Symposium Thermische Solarenergie, Bad Staffelstein

Leibbrandt; Schabbach; Dölz; Rhein, 2016. CFD-Untersuchungen zu konvektiven Wärmeverlusten in Scheibenzwischenräumen mit großem Seitenverhältnis. 26. OTTI Symposium Thermische Solarenergie, Bad Staffelstein

Leibbrandt; Schabbach; Dölz; Rhein, 2017. Experimentelle und numerische Untersuchungen zur vollvolumetrischen Durchströmung von Isolierglaskollektoren. 27. OTTI Symposium Thermische Solarenergie, Bad Staffelstein

Rhein; Schabbach; Dölz; Leibbrandt, 2016. Strukturanalyse eines Nurglaskollektors unter Berücksichtigung statischer und dynamischer Lasten. 26. OTTI Symposium Thermische Solarenergie, Bad Staffelstein

Wesselak et al. 2017. Regenerative Energietechnik, 3. ed. Springer Vieweg, Berin, Heidelberg

Yiqin et al. 1991. Measured Top Heat Loss Coefficients for Flat Plate Collectors with Inner Teflon Covers. Proceedings of the Biennial Congress of the International Solar Energy Society, Denver, Colorado

Solar Cooker Green Cooking

Md. Abdul Mozid

Orbit Solar Energy, Dhaka, Bangladesh

Abstract:

Food is one of the fundamental needs of mankind. Food preparation requires fuel which may be wood, coal, cow dung, liquid petroleum gas, and electricity consuming induction heaters or microwave oven. Availability of these non-renewable sources is a burning task. Moreover, it produces pollution which leads to the imbalance in nature. Solar cooker shall be a solution for cooking food. Solar Cooker is used for cooking food by sunlight only. No need fuel. Only sunlight is enough to cook a day's required food for an average family of Bangladesh. Bangladesh is situated underline of cancer as a result whole year has enough sun to cook the meal for a family by using Solar Cooker. There is a huge opportunity to use solar cooker in a village, suburban even some time in urban also.

Introduction:

Bangladesh is a highly populated country. We have around 170 million people in Bangladesh out of the 60 percent live in a village. The main food of our people is rice and curry. Village people are used to using wood, leaf, residual of crops and some time Bottled LPG for their cooking. There are very few Bio Gas plants are in village areas. Most people do not know about Co2 emission and environmental effect but they understand the cost. Now the above-discussed fuels are costly and emit CO2 gas which is hampering environment. They also lose their working hour and money to collect the fuel and the mothers lose their health to cook with the above fuels because that creates a lot of smoke which contaminate with air and hit their lungs directly.

We Orbit Solar Energy introduce a solar cooker considering food quantity of a family by using Solar Evacuated tube thermal cooking. We have two types of tube cooker with different quantity of food cooking at once.

Type OT-170:

The diameter of the tube is 170mm and the length is 900mm, there are three equal pots which capacity are 1.8 liters each. It can cook 5.4 liters foods at one time. This is portable and enough for a family contain 6-10 people

Type OT-125

The diameter of the tube is 125mm and length 800mm. there are three pots which capacity is 1x1.6 liter one and 2x0.8 liter. It can cook 3.2-liter foods at one time. This is portable and enough for a family of 4-5 people.

Technology& Design:

Solar cookers utilize the simple principles of reflection, concentration, absorption, glazing, insulation and the greenhouse effect to produce heat. **Solar Oven Evacuated Tube works as the same principle of solar cooking.** The evacuated tube style solar cookers are somewhat new on the market and in the solar cooking world, though they have been used for solar cooking by tinkerers and inventors for a few short

doi:10.18086/swc.2017.31.09 Available at http://proceedings.ises.org

years they have not been largely available to the commercial market until now. The older style box (ovens) cookers panel cookers and parabolic cookers have been around for much longer, some as long as fifty years, but now there is a new and very effective method of solar cooking in the form of the compact and very fast evacuated tube solar cookers.

We know that in a sunny day the sunlight energy per square meter is around 1KW, here we use the technology that direct light and reflected light is trapped (Greenhouse technology) in an evacuated tube which has very high thermal insulation, the trapped light turned into heat and this heat can cook food. The temperature rises up to 300 Degree centigrade.

Tube Glass

The tubes are made from a type of glass called Borosilicate. Borosilicate glass has the characteristic of being very strong and also has excellent light transparency (>92% @ 2mm thick).

Efficiency

The combination of the highly efficient absorber coating and the vacuum insulation means that the coating can be well over 200oC / 392oF and the outer glass is cool to touch. In strong sunlight, each evacuated tube can provide over 60 Watts / 204 Btu of water heating output.

Vacuum Insulation

The name "evacuated" is used to describe the process that expels the air from within the space between the glass tubes, forming a vacuum. A vacuum is an excellent insulator against heat loss, and so evacuated tubes are able to operate very efficiently

Evacuated Tube Oven Design:

The **Stove showed here**

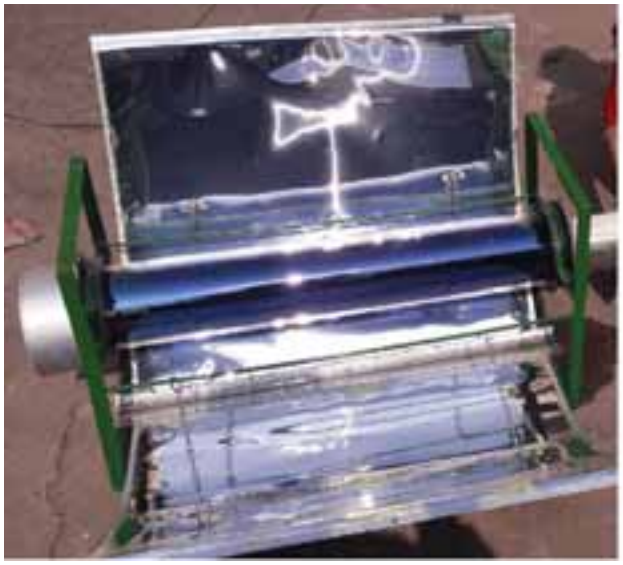

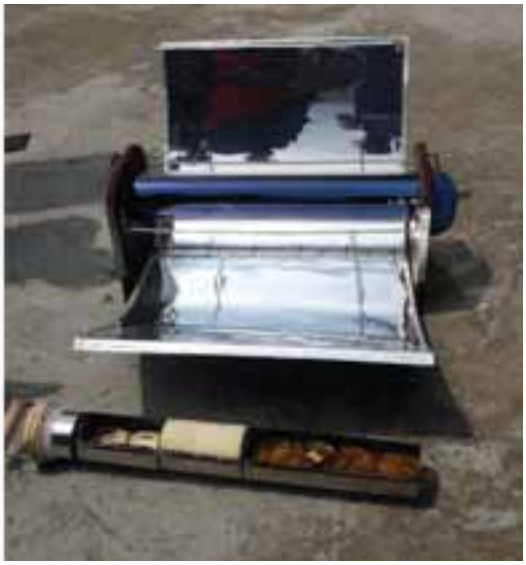

Tube:

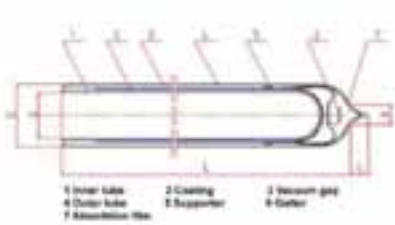

The evacuated tube design has an advantage in that it holds and retains its heat better than any other style of solar cooker, and it will heat up quite well even in less than optimum conditions.

Tube Dia: 125mm & 170mm

Length: 785mm & 900mm

SS Drum:

Inside the vacuum tube, there is a protection barrel inserted as the cooking chamber, which is made of stainless steel. Cooking Chamber, protect the tube from thermal shock.

Food Tray & Food Pots:

Made from SS and use for food holding and cooking, it's easy to load and unload these solar cookers using a sliding tray to place food inside.

Frame and Reflector:

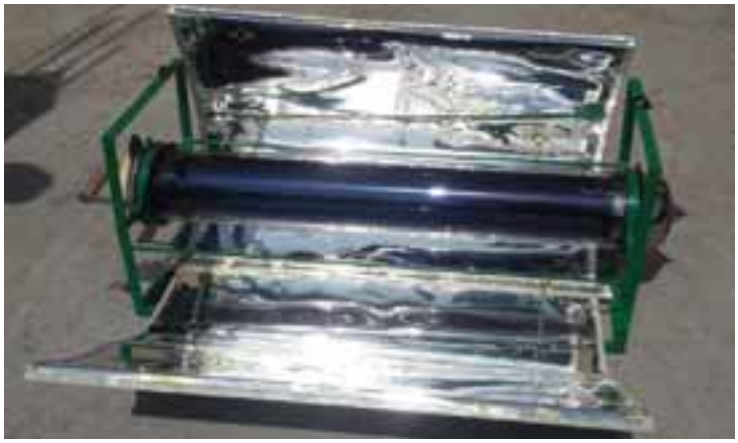

One metal frame holds the tube over ground and support to parabolic anodized aluminum mirror reflector.

The material of the reflector panel is the aluminum reflector, hard-anodized.

The material of the backboard for the aluminum reflector is hot dip galvanized sheet.

The material of the support structures is colored MS Bar.

This solar oven tube allows you to cook anything that you can cook in a conventional oven. The inside and outside tube are nice clean Pyrex type glass with no coatings on it. This makes cleanup a breeze. It can be washed normally. If you are cooking a roast, you can use either an elongated tray or aluminum foil to hold the meat and allow you to slide it in and out. If you are boiling water, just fill pots with water and insert into the tube and put it in the Sun. The same goes for soups, stews, etc. Cooking temperatures regularly reach up to 120 degrees without reflectors, or if you add a reflector, temperatures can reach 200-300 degrees centigrade.

The Orbit Solar Oven Evacuated Tube:

Highly transportable

Compact

Mid-weight

Easy to set up

Easy to load

Cooks at high and fast temperatures

Retains heat well due to evacuated glass tubes

Cooking Option:

With the Orbit Solar Oven Evacuated Tube style cooker you can cook almost any kind of food that you desire, including:

Chicken, Fish, Meat, Breads-rolls and cakes, Soups, Vegetables, Pasta, rice and more.

Cooking Process:

Rice:

Clean rice, put rice in the pot with required water.

Fish and Meat or Chicken:

Clean, Mix with spices and vegetable.

No water or minimum water as per requirement and taste.

Vegetable:

Clean and mix with spices, no water required.

Boiling of Egg/Vegetable:

Clean and put into the pot and insert to a cooker, no water required.

Baking:

You can bake cake, biscuit and etc.

Cooking Time

Cooking Span: Whole day, best time from 8 am to 4 pm

Cooking Time: 1-2 hours depending on load (quantity of food)

Spending Time: 5-10 minutes for one cooking

Cooking days in a year considering Bangladesh weather is 280 days

Benefits:

No Fuel required, Energy from Sun is free

Direct saving Tk 1000-2000/month

Time-saving 2hours /day

No monitoring

Long Life 10-15 years

Maintenance free

No chance to burn food if there is a delay to take out the food.

Energy Savings:

As we discussed that the energy of sunlight per square meter is 1kw, our covered area is 0.8m square (appx,), considering 50% efficiency, total trapped power is 400w.

Total trapped Power in a day - 2.4 KWh

Total Trapped power in a year- 672 KWh

Environmental Benefit:

No fuel burn so no Smoke and no Co2 produce at cooking

Co2 emission saving = 0.82kg/KWh (Avg for KWh Electricity Generation)

Considering above calculation total Co2 emission saving is 672*0.82=551kg/ year

Social Effect

No monitoring required for cooking, Women can save their time to other works, it will be honored and empowered our mothers. Around 2 hours can be saved for cooking per day and 2*280=560 hours per year.

Around the globe, hundreds of millions of people have limited access to cooking fuels [source: SCI]. In most cases, electricity and gas are out of the question; only charcoal and firewood are within reach, and even charcoal can be too expensive. So we're left with wood. The problem is that in many poor, rural areas in places, trees are scarce. It takes a lot of wood to cook meals for an entire family every day, and what few wood sources there are continue to dwindle. Families have to walk for hours to collect cooking wood, and they end up spending what little money they have on their fuel, leaving less money to buy food.

Solar cookers are useful during times of disaster or power outages. A solar cooker can be used at any time of the year, any place in the world. They're great for family camping trips since they're lightweight and easy to transport. But solar cookers are also smart to have on hand during disasters.

Nutrition Benefit:

It can result in healthier cooking. Solar cooking doesn't use smoke that can contain carcinogens or microwaves that expose your food to potentially dangerous radio waves. When you cook over a campfire, the smoke can irritate your eyes and respiratory system, and open fires present dangers to children.

Plus, when you cook in a solar appliance, the nutrients stay in the food and don't leach out. That's because you don't use water in solar cooking. And, the temperatures in a solar oven are moderate – around 325 F – so nutrients aren't destroyed during cooking at a high temperature like on a grill or over an open flame.

Health Benefit:

Another problem that can be solved by solar cooking has to do with the simple act of burning wood. Fires release pollution into the air. This smoke, filled with particulates, is bad for the environment, but it's even worse for the people who are breathing that air. When people use open fires to cook indoors, they end up inhaling microparticles that can cause all sorts of health problems, including both lung and heart disease. One estimate puts the number of people who die from this type of air pollution at 1.5 million per year [source: Madrigal]. A solar cooker eliminates the need for an open flame, meaning cleaner air.

Geographic Benefit:

Bangladesh is situated under Line of Cancer (23.5 deg north) as a result whole year has enough sun to cook a meal for a family except disturbance of weather. There is a huge opportunity to use solar cooker in the village, suburban even some time in urban also.

Prospect:

Bangladesh is a small country by area but in population, it is very big, geographically and weather wise very much suitable for a solar cooker. There are few units we provide to people and they are happy with the performance of cooker.

The challenges are as follows:

This is a very new concept for people. It is required huge campaigning. People are used to traditional cooking habit. The initial price of Solar Cooker is high compared to traditional cookers. People cannot cook at night and windy day, we made a solution by using an Electric heater inside the tube for the night and windy days (Evacuated Tube Hybrid Solar Cooker).

Life of Cooker:

Since it is made of glass, it will last virtually forever if it isn’t chipped or otherwise broken.

Safety:

Use gloves or cloth at put on and off the tray from the tube.

Do not put a hand inside the tube because the temperature may rise 300 degree centigrade.

Our Mission:

Our mission is to aware people to use solar cooker all over the country.

Pilot Cooking:

In a village rice Cooking:

Roof Top at Dhaka City:

In a Fair at Dhaka:

Reference:

1. https://www.google.com/url?sa=t&rct=j&q=&esrc=s&source=web&cd=2&cad=rja&uact=8&ved=0ahUKEwiFldyOmLPVAhVCq48KHdP8DcAQFghEMAE&url=https%3A%2F%2Fwww.researchgate.net%2Ffile.PostFileLoader.html%3Fid%3D589af6df3d7f4b9b6c1fa205%26assetKey%3DAS%253A459441301659648%25401486550750760&usg=AFQjCNEzyO2nRDqDFFvQW-PORMWvjDnwDg
2. http://www.elgas.com.au/blog/389-lpg-conversions-kg-litres-mj-kwh-and-m3

3. https://www.eia.gov/tools/faqs/faq.cfm?id=74&t=11
4. https://www.epa.gov/energy/ghg-equivalencies-calculator-calculations-and-references
5. Federal Register (2010). Light-Duty Vehicle Greenhouse Gas Emission Standards and Corporate Average Fuel Economy Standards; Final Rule, page 25,330 (PDF) (407 pp, 5.7MB, About PDF).

Flat Plate Collectors with Thermochromic Absorber Coating under Dynamic System Tests

Sebastian Müller[1], Rolf Reineke-Koch[1], Federico Giovannetti[1], Bernd Hafner[2]

[1] Institut für Solarenergieforschung Hameln (ISFH), Am Ohrberg 1, D-31860 Emmerthal (Germany), Phone: +49 5151 999-646, E-Mail: mueller@isfh.de

[2] Viessmann Werke GmbH & Co. KG, Viessmannstraße 1, D-35108 Allendorf (Germany)

Abstract

Thermochromic absorber coatings switch their emissivity for long wave radiation depending on the absorber temperature. Below the specific switching temperature of 68 °C the coating's emittance is quite similar to a commercial, highly selective absorber coating ($\varepsilon \approx 5$ %). At higher absorber temperatures the emittance reaches $\varepsilon \approx 35$ %, whereby the collector heat losses increase. As a result, the stagnation temperature is reduced by 30 K and an overheating or vaporization of the heat transfer fluid can be entirely prevented. We have carried out collector performance measurements according to ISO 9806. By means of dynamic system tests (ISO 9459-5) we predict the performance of a domestic hot water system with standard and thermochromic collectors. At typical daily tapping rates the marginally lower absorptance of the thermochromic coating raises the auxiliary energy demand up to 2.5 % and reduces the solar fraction by about 1 %-absolute. In additional system stagnation tests, we analyzed the stagnation behavior of thermochromic collectors, especially the vaporization of the heat transfer fluid, the steam expansion into the solar pipes and the thermal stagnation load on sensitive solar loop components. A reduction of the stagnation period by 60 % and a limitation of the stagnation temperature to 145 °C were investigated.

Keywords: thermochromic absorber coating, flat plate collector, dynamic system testing, stagnation load

1. Introduction

The steady performance enhancement of solar flat plate collectors leads to higher thermal solar system gains but increases the temperatures in the whole solar loop as well. The stagnation temperature of standard flat plate collectors can easily reach up to 200 °C. Thus, temperature resistant and also cost intensive system components have to be used, to withstand the thermal stagnation loads and temperature distribution in the solar loop. Additional measures need to be taken, especially for larger thermal collector arrays or systems with short solar piping, to protect the whole system against thermal damages (e.g. degradation of heat transfer fluid), as Scheuren (2006) investigated.

Hausner et al. (2003) investigated the stagnation behavior in detail and characterized different collector types on the basis of their steam production performance. To prevent overheating and handle the stagnation loads, Harrison et al. (2012) and Frank et al. (2015) summarized different protective arrangements and stagnation control strategies. Föste et al. (2016a) developed different heat pipe collectors with reduced stagnation temperature and protection against vaporization of the heat transfer fluid. To reduce the stagnation loads in flat plate collectors, Brunold et al. (2007) suggested thermochromic layers as a potential method and Föste et al. (2016b) investigated industrially manufactured thermochromic flat plate collector models first. Drainback solar thermal systems can prevent any vaporization in the solar loop, as Botpaev 2016 summarized.

2. Thermochromic absorber coating

Thermochromic absorber coatings have a highly temperature dependent emissivity for thermal radiation. This innovative smart selective coating increases its emittance ε above a predetermined "switching point" ($T_S \approx 68$ °C

doi:10.18086/swc.2017.31.10 Available at http://proceedings.ises.org

absorber temperature) from 5 % up to 35 %. The increase of the emittance above T_S can be explained as a first-order phase transition, which changes the internal crystalline structure in the thermochromic layer. The electronic band structure is altering from a semi-conductive to metallic character, whereby the electrical conductivity increases and influences the emittance. Pazidis et al. (2015) and Mercs et al. (2016) investigated, that this "switching" is a fully reversible process, as can be seen in Figure 1.a, as well as the long-term stability with accelerated aging tests. The layer stack on aluminum substrate consists of the active vanadium dioxide (VO_2) layer with an antireflective coating (SiO_2) on top (Figure 1.b).

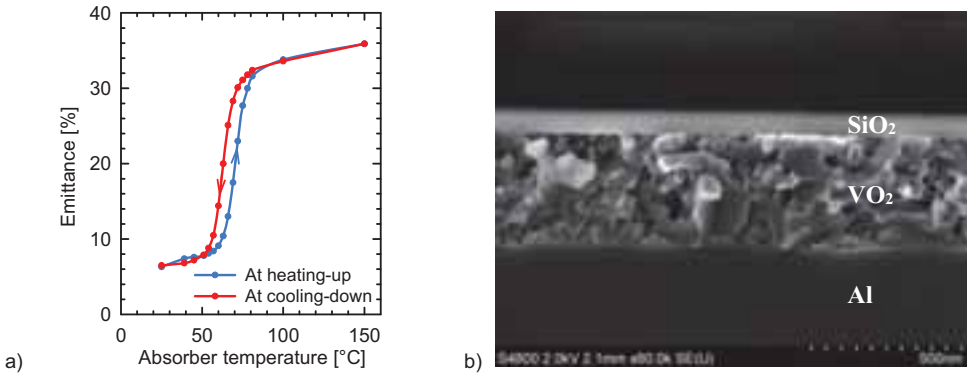

Fig. 1: Temperature dependent, fully reversible switching of emittance (a) and SEM cross section of absorber coating (b)

The thermochromic collector's behavior in the typical operating range is quite similar to a standard flat plate collector with a commercially available highly selective absorber coating ($\alpha > 94$ %, $\varepsilon \approx 5$ %). But in the switched state, the heat losses from the absorber to the glass cover increase significantly. Hence, the stagnation temperature is reduced by 30 K, the vaporization of the heat transfer fluid could be prevented more easily and the thermal stress for sensitive solar loop components (e.g. solar pump or membrane expansion vessel) could be lowered. Because of the reduction of thermal loads during stagnation, the components in typical solar thermal applications can be re-dimensioned or substituted to reduce the specific system costs and maintenance efforts.

3. Collector efficiency measurement

We have carried out collector performance measurements on an industrially manufactured thermochromic flat plate collector according to ISO 9806 (2013). Due to the fact, that our innovative coating changes its characteristic after the switching point with temperature T_S, the collector efficiency curve is splitted in two sections: the first describes the efficiency below the switching temperature and the second is valid for temperatures above T_S, both with their explicit collector efficiency parameters η_0, a_1 and a_2. For the evaluation we measured stationary collector efficiencies at three different absorber temperatures in each section as shown in Figure 2.

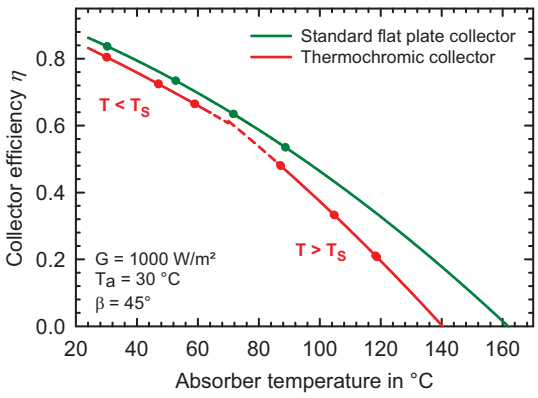

	$\eta_{0,Ap}$ -	a_1 W m^{-2} K^{-1}	a_2 W m^{-2} K^{-2}
Standard collector	0.786	4.19	0.0135
$T < T_S$	0.757	4.27	0.0065
$T > T_S$	0.830	6.17	0.0103

Fig. 2: Collector efficiency curves of a thermochromic and a standard flat plate collector related to their absorber temperature

Due to a marginally lower absorptance of the thermochromic absorber coating, the conversion factor η_0 is 3 %-absolute lower compared to an identically designed standard flat plate collector (η_0 = 0,786, related to

aperture area). The characteristic in the un-switched state is otherwise comparable to that of a standard collector. The higher emittance and heat losses at temperatures above T_S reduce the collector efficiency, which can be expressed in the gain of the linear heat loss coefficient a_1 from 4.27 to 6.17 W m^{-2} K^{-1}. Thus, the stagnation temperature was measured to 167 °C, 25 K lower compared to a standard flat plate collector (192 °C).

The splitted collector efficiency curve represents its characteristic sufficiently accurate. In system simulations with TRNSYS, the collector efficiency parameters switch instantaneously (without any hysteresis (cf. Fig. 1.a)), if the absorber temperature exceeds the temperature T_S. In the Solar Keymark certificate both curve sections are displayed as well as the "mixed" curve, which includes all measured stationary points. The annual collector outputs at mean fluid temperatures of 25 °C and 50 °C are calculated with the lower ($T < T_S$) efficiency parameters.

4. Experimental system yield prediction

4.1 Dynamic system testing

For an experimental performance assessment of the innovative selective absorber coating, we carried out dynamic system testing (DST) according to ISO 9459-5 (2007) on a solar domestic hot water (SDHW) system equipped with thermochromic collectors. The DST describes a dynamic short term measurement method for the evaluation of a SDHW system within 3…4 weeks, without testing each component by its own and no requirements of steady-state conditions. To acquire sufficient measurement data, the system operates in three different test sequences predefined by the standardization, to identify the thermal behavior of a SDHW system by pursuing it in all its relevant states. There is no need of measuring internal quantities, why this method is also compared with a "black box" approach. So only eight external quantities (e.g. irradiance, auxiliary energy demand, temperature of domestic hot water, wind velocity) have to be measured meanwhile as a function of time.

Mathematically, the whole system is described by seven system specific parameters, which have to be identified on the basis of measured data by dynamic fitting (DF) algorithm. The software minimizes the difference between measured and simulated system performance of the implemented physical SDHW system model. This physical model and the software DF are described by Visser and Pauschinger (1997) and Spirkl (1997), respectively. A long term performance (LTP) prediction of the annual solar system gain, auxiliary energy demand and solar fraction can be calculated with the mentioned short term test procedure from the identified parameters under arbitrary weather conditions.

The two SDHW systems were installed on an outdoor testing roof. The thermochromic system is compared to an identical solar thermal system equipped with standard collectors. Both systems have a gross area of 5 m² (2 collectors per array) each and a domestic hot water tank with a volume of 300 liters. An electrical immersed heater with a power of 6 kW is used for providing the auxiliary energy demand. The collector arrays are sloped by 38° and faced to south. The measurement and the investigations are carried out synchronously under the same environmental conditions, so that the systems can be compared directly with each other.

4.2 Evaluation and long term prediction

The identified system parameters (by DF) represent basically a combination of several physical phenomena, interactions between system components and even neglected effects. However, according to Spirkl (1992) it is possible to interpret some of them as real physical parameters, referring directly to a system component. Therefore U_S, C_S and f_{Aux} describe the total hot water tank heat loss rate, the thermal capacity and the share of store volume heated up with the immersed heater. The auxiliary parameters D_L and S_C characterize the mixing effects during hot water tapping and the SDHW tank stratification while storage charging, respectively. A_C* and u_C* are related to the collector area and its overall heat loss coefficient and describe mathematically the whole solar loop.

The parameters identified by the synchronous DST measurement are shown in Table 1. Due to the marginally worse optical properties of the thermochromic layer, as mentioned in chapter 3, the identified effective collector area A_C* of the thermochromic system is 3.4 % smaller than the standard collector one. The rising collector heat losses in the switched state are responsible for the higher u_C* of the thermochromic collector. Some other identified system parameters can be compared with measured data as well. For example the total heat loss rate

of the SDHW tank U_S amounts to 2.2 W K^{-1} and the thermal capacity C_S to 1.25 MJ K^{-1}. According to manufacturer's data sheet of the installed SDHW tank, the share of auxiliary heated volume f_{Aux} should be 0.44. The identified D_L value of almost 0 is equal to no mixing during draw-off, which can be expected for this kind of bivalent SDHW tank.

Tab. 1: System specific parameters identified by the DF alogrithm

Parameter	A_C* m²	u_C* W m^{-2} K^{-1}	U_S W K^{-1}	C_S MJ K^{-1}	f_{Aux} -	D_L [1] -	S_C [2] -
Standard collector system	2.96	10.16	2.44	1.27	0.54	0.018	0.042
Thermochromic collector system	2.86	10.55	2.33	1.28	0.55	0.017	0.034

[1] $D_L = 0$ is equal to no mixing during draw off
[2] $S_C = 0$ is equal to a solar heat exchanger, immersed at the bottom

For the LTP prediction of the system performance the predefined boundary conditions in ISO 9459-5 (2007) were used, with a draw-off temperature of 45 °C, an auxiliary set-point temperature of 60 °C and an ambient store temperature of 15 °C. The weather data for the four reference locations (Athens, Davos, Stockholm, Würzburg) given in the Standard were substituted by data from Meteonorm 7 (2012), due to comparability with system simulations done in TRNSYS.

The system performance is assessed by the auxiliary energy demand Q_{Aux}, which is provided by the immersed electrical heater into the SDHW tank in addition to the solar thermal gain to cover the domestic hot water energy demand Q_{DHW}. For this kind of investigation and system comparison it is the most meaningful parameter, because an increase of Q_{Aux} due to the installation of thermochromic instead of standard flat plate collectors leads to higher annual costs for the operator. At the reference location of Würzburg, the increase of auxiliary energy demand is less than 2.5 % over a wide range of daily tapping rates as shown in Figure 3. This is equal to 33 kWh a^{-1} at a daily tapping rate of 140 liters. At the other locations we predicted qualitatively the same increase of Q_{Aux} with maximum values of 5.6 % (Davos), 5.1 % (Athens) and 1.7 % (Stockholm).

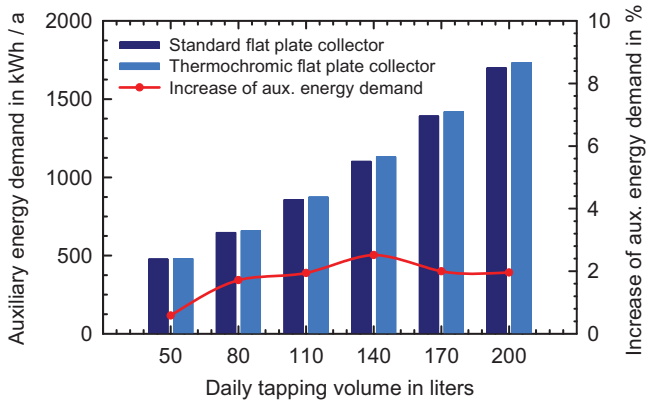

Fig. 3: Auxiliary energy demand for the thermochromic and standard SDHW system at the reference location of Würzburg

The solar fraction of a SDHW system characterizes the share of solar thermal gain into the SDHW tank, related to the domestic hot water energy demand Q_{DHW}. Furthermore and in reference to the Standard, the thermal gain can be expressed as the difference between the load energy Q_L and auxiliary energy demand Q_{Aux}.

$$f_{Sol} = \frac{Q_L - Q_{Aux}}{Q_{DHW}} \qquad (eq.1)$$

Figure 4 shows the solar fraction for all four reference locations over a wide range of daily tapping volumes (50…600 liters per day). At Würzburg, the f_{Sol} of the standard SDHW system reaches its maximum of 47.5 % at daily tapping rates of 110 liters and decreases for lower and higher tapping rates. These are typical values for this combination of collector gross area and SDHW tank volume. The SDHW system with thermochromic collectors exhibits qualitatively the same characteristic, but the solar fraction is 1 %-absolute lower than the standard system. The difference in solar fraction is nearly independent from the daily tapping rate. So it can be

assumed, that the difference in system performance depends primarily on the slightly worse optical properties of the thermochromic coating as on the increased thermal losses in the switched state.

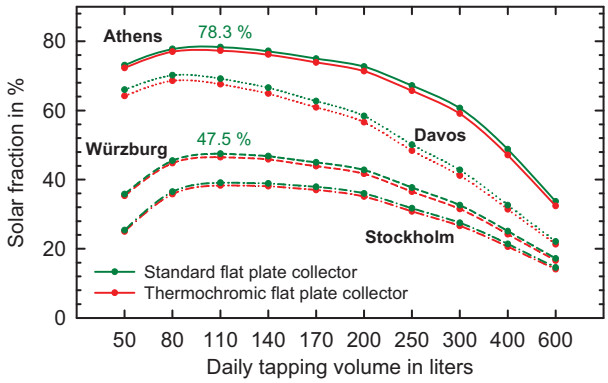

Fig. 4: Solar fraction for all four reference locations, variation of daily tapping volume and measured SDHW systems

Similar results are achieved considering the other reference locations. The mean difference in f_{Sol} over the whole range of tapping rates can be assessed to 1.2 (Athens), 1.6 (Davos) and 0.9 (Stockholm) %-absolute.

4.3 Cross-check with TRNSYS replica

To check the plausibility of the DST procedure and especially the LTP of the annual thermal system gain, we carried out system simulations with the software TRNSYS. Furthermore, a cross-check for the use of the implemented collector model with thermochromic collectors was investigated, as well. Thus, the installed SDHW system was modelled in TRNSYS in detail, considering all system parameters, e.g. length of solar piping, collector gross area, heat loss rate of SDHW tank, auxiliary power, etc. (cf. chapter 4.2). Even the matched flow operation mode was implemented into the system controller. The SDHW tapping was adjusted to the requirements of the Standard (one tapping per day; tapping rate 10 liters per minute; six hours after solar noon).

The comparison between the system simulations with the TRNSYS SDHW-replica and the DST long-term performance prediction was assessed by considering the solar fraction and the auxiliary energy demand again. The solar fraction of the thermochromic collector at the reference location of Würzburg can be modelled with an accuracy of less than 2 %-absolute within a wide range of daily tapping volumes (50…600 liters per day). As can be seen in Figure 5.a, within the range of 140…600 liters per day the difference decreases to less than 1 %-absolute. The auxiliary energy demand (see Figure 5.b) reports maximum differences of 3.1 %. For typical daily tapping rates (80…170 liters per day) the deviation does not exceed 1.5 %.

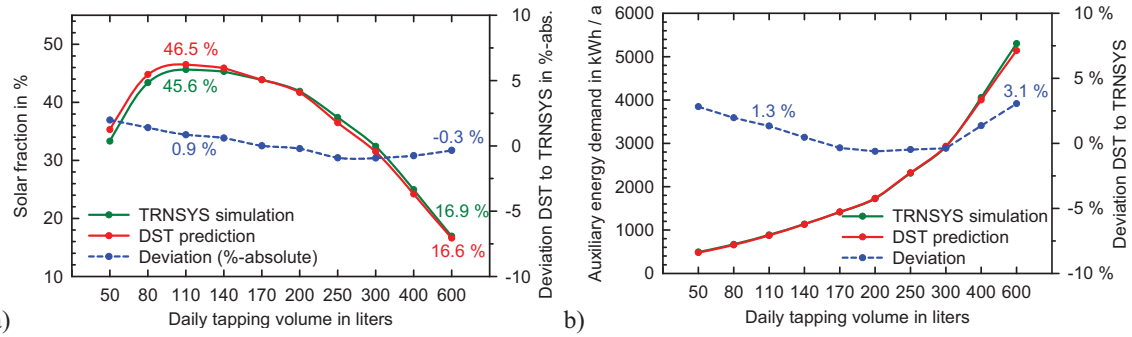

Fig. 5: Comparison of solar fraction (a) and auxiliary energy demand (b) for a system with thermochromic collectors between TRNSYS simulation and DST long-term performance prediction

For the standard collector array, we achieve similar results. Over the whole range of daily tapping rates, the auxiliary energy demand and the solar fraction are simulated with deviations of less than 5 % and 3.5 %-absolute, respectively compared to the DST long-term prediction.

The evaluation was carried out for the other three reference locations as well. The results for Athens are similar to those for Würzburg. At Stockholm, the deviations between simulation and DST prediction are marginally

lower, with maximum differences in auxiliary energy demand and solar fraction of 1.8 % and 1.4 %-absolute, respectively. The solar fraction at Davos can be modelled within 2.8 %-absolute and the auxiliary energy demand with deviations less than 6 %.

The results of our TRNSYS simulations with both SDHW systems confirm the DST long-term performance prediction as well as the applicability of the DST method to thermochromic flat plate collectors.

5. Stagnation tests

Pazidis et al. (2015) reported in a previous simulative study, that a thermochromic SDHW system could lower the stagnation time (here: timespan, in which the absorber temperature is above 120 °C) by more than 70 %. According to the simulation results, the maximum absorber temperature under normal operating and environmental conditions can be limited to 145 °C (Würzburg). To verify these investigations and experimentally evaluate the stagnation behavior of thermochromic collectors, we have carried out additional stagnation tests to analyze the steam expansion in the solar pipes due to the vaporization of the heat transfer fluid, the stagnation load on the collector itself and the temperature distribution in the whole solar loop. We focused especially on the thermal load on sensitive components, like the membrane expansion vessel or solar pump. An increase of the system pressure will be investigated in detail to raise the saturated steam temperature of the heat transfer fluid and prevent vaporization in the solar collector.

5.1 Experimental setting

We used both SDHW systems for our investigations, with the specifications mentioned in chapter 4.2 (see Figure 6.a). The overall solar loop length is 30 m per system to measure the steam expansion in detail, which is the most representative indicator for stagnation loads. Therefore, we installed temperature sensors (Pt1000) directly onto the solar piping, starting from the collector in- and outlet at intervals of 1.5 meters. The temperature distribution in the collector array is measured with four sensors at each absorber. Some more sensors were installed to quantify the thermal load on the solar pump and the membrane expansion vessel. One pressure sensor was added at the collector array outlet to investigate the stagnation dynamics and possible hydraulic shocks during stagnation. All sensors and their positions are displayed in the hydraulic schema in Figure 6.b.

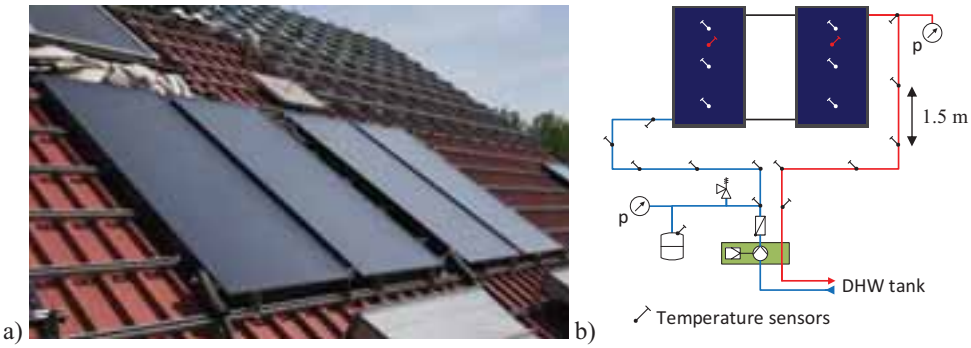

Fig. 6: Investigated SDHW collector arrays on the outdoor testing roof (a) and hydraulic schema with temperature and pressure sensor positions

The survey started in late 2016. During the tests the two systems were operated synchronously under well-defined stagnation conditions. We detected eight stagnation events, whereof four days under clear sky conditions. On these four representative days, the system operated at three different relative system pressures (2.0 bar, 2.2 bar, 3.2 bar). On one of these days, a so called “noon stagnation” was manually performed, by switching off the solar pump only at solar noon.

5.2 Evaluation of representative days

Maximum absorber temperatures occur usually at two-third of collector’s height. Figure 7.a compares these temperatures for the thermochromic and the standard flat plate collector at three different relative system pressures. The stagnation temperature of a collector is independent from its system pressure. Due to higher heat losses, the stagnation temperature of the thermochromic collector is limited to 145 °C under natural conditions

(including wind). Hence, we report a reduction of 30 K.

If the absorber temperature exceeds at any position in the collector array the saturated steam temperature of the used heat transfer fluid (TYFOCOR LS) at the specific relative system pressure, the fluid starts to vaporize. The saturated steam temperatures for the three investigated system pressures 2.0 bar, 2.2 bar and 3.2 bar are 139 °C, 141 °C and 150 °C, respectively. The steam expands into the solar pipe with increasing steam volume. We could detect the steam front, by comparing the pipe temperature recorded by the sensors to the current saturated steam temperature. The start of the fluid vaporization is attended by a soaring temperature at the collector outlet, as displayed in Figure 7.b. If the temperature at the collector outlet falls below the saturated steam temperature, the vapor condensates completely and no steam fills the solar piping anymore.

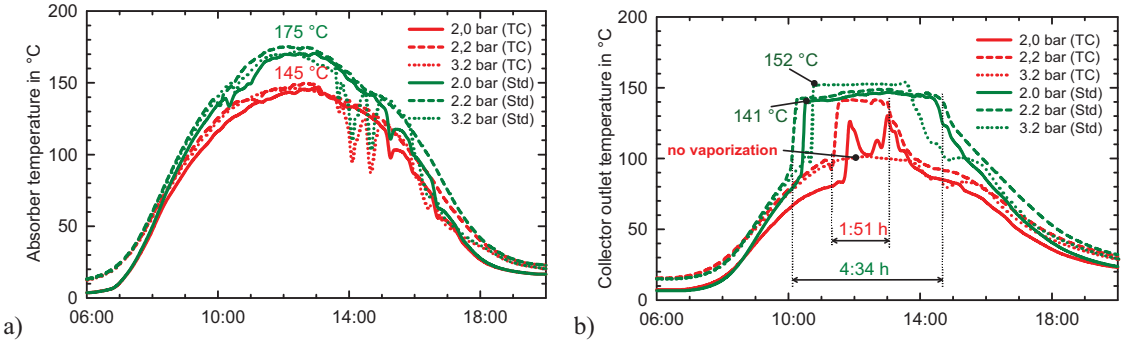

Fig. 7: Absorber temperature of thermochromic (TC) and Standard (Std) collector at two-third of the collector's height (a) and collector array outlet temperatures (b) for various relative system pressures

We define "stagnation period" as the timespan between the start of vaporization and the time, at which the entire system is free from steam again. For the evaluation with a system pressure of 2.2 bar, the stagnation period is reduced by 60 %, from 4:34 hours (standard collector array) to 1:51 hours. At 2.0 bar the stagnation period could be halved. The entire vaporization could be prevented at system pressures higher than 3.2 bar (see Figure 7.b). In this case, no steam expands into the pipes and the thermal load and the temperature distribution in the solar loop could be significantly lowered. The maximum outlet temperature is reduced from 154 °C in the standard collector array to 102 °C in the thermochromic collectors.

Insufficient data acquisition for the evaluated period in 2016, with a few stagnation events only, could not represent the stagnation behavior of both SDHW systems in detail. We will carry out the measurement and double the collector area in addition. To investigate the stagnation dynamic and the draining behavior more in detail, a high frequency pressure measurement at collector array outlet is planned. For further investigations, we calibrated both membrane expansion vessels to determine the whole steam volume in the collector loop only by measuring its fluid inlet temperature and the system pressure at the expansion vessel. This method was developed and introduced by Scheuren (2008). With the system steam volume and qualitative measured steam expansion, an evaluation of residual fluid and draining behavior is feasible.

6. Conclusions and outlook

By means of synchronous dynamic system tests according to ISO 9459-5 we predicted and compared the long-term performance of SDHW systems equipped with thermochromic and standard flat plate collectors. Our results confirm the high performance of a SDHW thermochromic system. The increase of auxiliary energy demand, by installing thermochromic instead of standard collectors, is less than 2.5 % for daily tapping rates between 50 and 600 liters at the reference location of Würzburg. Even for the warmer reference location Athens, the gain in auxiliary energy demand does not exceed 5.1 %. The low increase in auxiliary energy demand and the marginally low difference in solar fraction over a wide range of daily tapping volumes and locations reveal, that the slightly worse optical properties of the thermochromic collector influence the system performance more than the higher heat losses in the switched state.

On the basis of system simulations with TRNSYS, we could cross-check the DST long-term performance prediction and confirm the applicability of the implemented DST collector model on thermochromic flat plate collectors. We assume that the dynamic short-term measurement method can be extended to all kind of

collectors with unsteady efficiency behavior, e.g. collectors with thermally actuated ventilation door (cf. Frank 2015) or heat pipe collectors (cf. Föste 2016a). The results confirm the high performance of the thermochromic collectors in a SDHW system, which is comparable to that of a standard collector.

The stagnation behavior was analyzed by additional experimental stagnation tests. We report a limitation of the stagnation temperature at 145 °C and, thus, a reduction of 30 K compared to a standard flat plate collector. The stagnation period – the timespan, in which any steam is detected in solar thermal system – could be reduced during the measurement up to 60 % at normal system pressures. The vaporization can be entirely prevented by a slight pressure rise, which offers great potential for further reduction of system costs. We assume a significant reduction in installation and maintenance costs or the use of cost-effective (not high temperature-resistant) materials by avoiding vaporization and therefore less thermal loads for the whole system.

The thermochromic coating is currently under further development, with the aim to improve its optical properties and extend its temperature operating range. The main goals are the increase of the solar absorptance (α > 95 %), as well as the thermal emittance in switched state (up to 60 %) and a shift of the switching temperature T_S to 80 °C. We expect a gain in collector performance and a further reduction of the stagnation temperature at once.

Acknowledgement

The project “Process technology, quality assessment and system solutions for thermochromic absorbers in solar thermal collectors” presented in this paper is funded by the German Federal Ministry of Economic Affairs and Energy based on a decision of the German Federal Parliament (reference numbers 0325858 A and B). The project ProTASK is carried out in cooperation with Viessmann Werke GmbH & Co. KG.

The authors are grateful for the financial support and responsible for the paper’s content.

References

Botpaev, R., Louvet, Y., Perers, B., Furbo, S., Vajen, K., 2016. Drainback solar thermal systems: A review. Solar Energy 128 (2016), pp. 41 – 60.

Brunold, S., Vogelsanger, P., Marty, H., 2007. Beurteilung der Möglichkeiten von thermochromen Schichten als potenzielle Überhitzungsschutzmaßnahmen für solarthermische Kollektoren. Institut für Solartechnik SPF, Rapperswil.

Föste, S., Schiebler, B., Giovannetti, F., Rockendorf, G., Jack, S., 2016. Butane heat pipes for stagnations temperature reduction of solar thermal collectors. Energy Procedia 91 (2016), pp. 35 – 41.

Föste, S., Pazidis, A., Reineke-Koch, R., Hafner, B., Mercs, D., Delord, C., 2016. Flat plate collectors with thermochromic absorber coatings to reduce loads during stagnation. Energy Procedia 91 (2016), pp. 42 – 48.

Frank, E., Mauthner, F., Fischer, S., 2015. Overheating prevention and stagnation handling in solar process heat applications. IEA SHC Task 49, Technical Report A.1.2.

Harrison, S., Cruickshank, C. A., 2012. A review of strategies for the control of high temperature stagnation in solar collectors and systems. Energy Procedia 30 (2012), pp. 793 – 804.

Hausner, R., Fink, C., Wagner, W., Riva, R., Hillerns, F., 2003. Entwicklung von thermischen Solarsystemen mit unproblematischem Stagnationsverhalten. Berichte aus Energie- und Umweltforschung, 9/2003, Wien.

ISO 9806, 2013. Solar energy – Solar thermal collectors – Test methods. Beuth Verlag, Berlin.

ISO 9459-5, 2007. System performance characterization by means of whole-system tests and computer simulation. Beuth Verlag, Berlin.

Mercs, D., Didelot, A., Capon, F., Pierson, J.-F., Hafner, B., Pazidis, A., Föste, S., Reineke-Koch, R., 2016. Innovative smart selective coating to avoid overheating in highly efficient thermal solar collectors. Energy Procedia 91 (2016), pp. 84 – 93.

Meteonorm 7, 2012. Handbook, Parts I and II. Bern, www.meteotest.com.

Pazidis, A., Föste, S., Reineke-Koch, R., Hafner, B., Mercs, D., 2015. Development of an absorber for solar thermal collectors with stagnation temperature below 140°C and high efficiency. Final report of project „TASK“, Reference numbers 0325988 A and B, Hameln / Allendorf (Eder). (in German)

Scheuren, J., 2006. Reduction of Stagnation Load of Large-Scale Collector Arrays. Proceedings Eurosun 2006, International Solar Energy Society (ISES), Freiburg.

Scheuren, J., 2008. Untersuchung zum Stagnationsverhalten solarthermischer Kollektorfelder. Kassel University Press.

Spirkl, W., Muschaweck, J., 1992. General model for testing solar demostic hot water systems. Solar Energy Materials and Solar Cells 28 (1992), pp. 93 – 102, North-Holland.

Spirkl, W., 1997. Dynamic System Testing Program Manual Version 2.7. InSitu Scientific Software, Germering.

TRNSYS, 2008. Transsolar Energietechnik GmbH: TRNSYS Version 16.1.

Visser, H., Pauschinger, T., 1997. Dynamic Testing of Active Solar Heating Systems. IEA SHC Task 14, Final report.

Prototype of Integrated Collector Storage (ICS) Using Phase Changes Material and Thermosyphon Heat Pipes

Mickaël Pailha[1], Gilles Fraisse[1], David Cloet[1]

[1] CNRS, LOCIE, Université de Savoie, Le Bourget du Lac (France)

Abstract

Conventional thermal solar systems consist of roof-mounted collectors, a storage tank inside the building and various elements that ensure the operation of the system (controller, pump, etc.). This ultimately leads to relatively complex systems, leading to major disadvantages such as a relatively high cost, storage volume footprint and maintenance. The development of "passive" solar systems is therefore a strategy to be favored. It is in this context that we have studied numerically and experimentally a new concept of integral collector storage with phase change materials and heat pipes.

A prototype was tested in outside conditions at INES. Thermosiphon heat pipes work very well by transferring the absorbed solar energy to the storage located at the back of the absorber, and by acting as a thermal diode. Concerning storage, a small difference in temperature is observed between the 2 faces of the cavity containing the phase change material, which shows the efficiency of the honeycomb to transfer the heat. In terms of performance, the prototype is very well placed for its productivity. However, storage is largely discharged at night. This implies a low annual solar fraction. The metallic fixation which maintains the cavity is largely responsible for these losses. It is therefore sufficient to limit the thermal bridges to greatly improve the solar fraction.

Keywords: Type your keywords here, separated by commas,

1. Introduction

1.1. Context and Issues

Market development of solar thermal systems in France is penalized by the cost of investment compared to other solutions that use fossil fuels or electricity. Moreover, today's solar solutions are more adapted to the new than the renovation (additional space required for storage) that is the major energy issues in the building sector. The research activities should encourage the development of innovative solutions integrating these two issues. The integrated collector storage (ICS) are very interesting because they allow financial savings compared to a conventional solar thermal system: fewer components, simplicity, passive operation, possibility of industrialization "all in one" and setting work faster (Sadhishkumar and Balusamy, 2014). The first ICS exist since the end of 19th century (Smyth and Al, 2006). Currently, about ten companies propose ICS of various geometries and using water as a storage medium (http://www.sunwindenergy.com/ 1+2/2013). The ICS are suitable both for new buildings and at an energy renovation (Timilsina and Al, 2012). They avoid putting storage in a room, which is generally disadvantageous for reasons of space available in existing system and of cost of square meters in the new. The ICS are thus promising systems for the development of the solar thermal market. However, the main drawback of such systems is related to high thermal losses knowing that the storage is generally poorly isolated to the outside. Consequently, the ICS are rather used in soft climates of Mediterranean type.

The work suggested in this article presents a new prototype of integrated collector storage using phase-change materials (PCM), and thermosyphon heat pipes to transfer solar energy from a plane collector to storage. The use of PCM allows to reduce the thickness of the storage cavity as compared to water. Architectural integration is thus greatly improved knowing that it is about major problems for most currently available ICS. Through the use of PCM, storage presents no problem with the gel. A coil type heat exchanger finally allows to draw the energy contained in the ICS. The prototype is fully instrumented with flow rate, temperature and weather condition measurements. Tests are realized under real outdoor conditions.

doi:10.18086/swc.2017.31.11 Available at http://proceedings.ises.org

2. Experimental setup

2.1. Proposal for a new ICS concept

We have designed a new generation of ICS from very difficult specifications to satisfy: high energy performance in a cold climate, considering the risks of frost, simplicity of operation, quality architectural integration (low thickness), great reliability and cost comparable to conventional systems. This is the challenge of this project, which aims to demonstrate the feasibility of the new concept of ICS thanks to the experimental study carried out on a prototype. The originality of the concept is based on the use of heat pipes for the solar circuit and phase change materials (PCM) contained within an aluminum honeycomb structure for storage (figure 1).

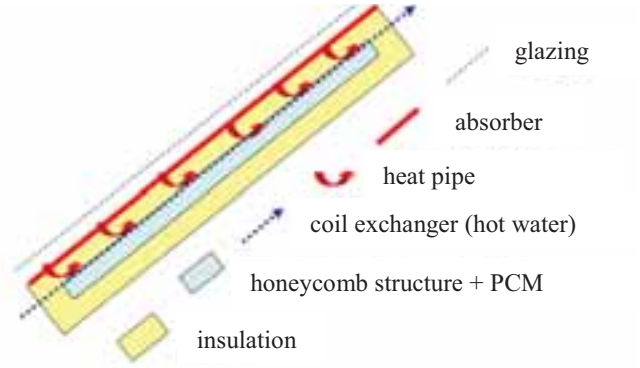

Fig. 1: Schematic of a new concept of ICS with PCM and heat pipes

We have thus developed the new concept of ICS around three points:

- Use of thermosiphon heat pipes: thermal diode operation possible, high thermal transfers and no risk of frost in the heat transfer between the sensor and the storage.

- Complete insulation of the storage volume to achieve energy performance comparable to conventional systems with hot water tank. This is very rarely the case for self-storage sensors.

- The PCM combined with an aluminum honeycomb structure seems well suited for storage in a self-storage sensor: low thickness (architectural integration), no problem with frost for the PCM (phase change), excellent characteristics of the honeycomb structure both in terms of heat transfer (compensation of the low thermal conductivity of the PCM by a large exchange surface) and mechanical strength (specific to the geometry of the honeycomb).

Concerning freezing, roof integration must be designed so that the cold-water supply to the rear is in an isolated volume. If this is not the case, an anti-freeze fluid and an exchanger must be used. This may be relevant in the case of a collective installation (limited cost). Finally, heat recovery is not provided within the self-storage sensor in the ADEME project. We considered it simply downstream of the auto-storing sensor.

We did not identify in the bibliography a ICS combining the use of heat pipes, the presence of a completely isolated storage and the use of a nida / PCM storage cavity. This is the originality of this ADEME project.

2.1. Principle of operation

The operating principle of the new ICS concept using heat pipes and PCM in a honeycomb structure (figure 2) is described in this section. Our solution is based on a conventional flat-plate collector. It has on the upper face a glazing beneath which is placed an absorber which converts the incident solar rays into heat. In our case, the solar loop is replaced by thermosiphon heat pipes which transfer the heat directly from the absorber to the storage (exchange n° 1 in figure 3). The heat pipes are in direct contact with the absorber on its rear face. This is called the "evaporator" part of the heat pipes. The heat pipes (six on the height of the prototype) are elements that conduct

heat by using the phenomenon of phase change as soon as a temperature difference is observed between the evaporator and the other end designated "condenser" which is in contact with the cavity. The heat pipes are in fact hermetic copper tubes containing a fluid (methanol in our case) filled to about 30%. Methanol vaporizes due to an energy input from the absorber. The steam goes up along the heat pipes to reach the level of the storage cavity. This is the condensation zone: the vapor of the fluid contained in the heat pipes condenses because the temperature in the storage is lower than that of the steam. The fluid releases the latent heat by condensing and then transmits it to the storage (exchange n ° 2). The designation "heat pipes" in this study corresponds in fact to thermosiphons since the flow of the liquid phase is by gravity. The heat pipes used have a very particular geometrical configuration since the slope is rather small: the inclination is not directly in the direction of the height of the sensor but over its length since the cavity is at the rear of the absorber, as in Fig. 4.

About phase change material, we used polyethylene glycol (PEG). The PEG6000 is placed in the cells of the honeycomb (figure 2). Each of the cells are filled with 75% in our case. A filling level of less than 100% is necessary because of the mechanical stresses associated with the volume change accompanying the phase change (during the fusion, the volume of PCM increases). The honeycomb is closed on both sides by aluminum plates. The assembly system by bonding makes it possible to hope for the sealing of each cell containing the PCM.

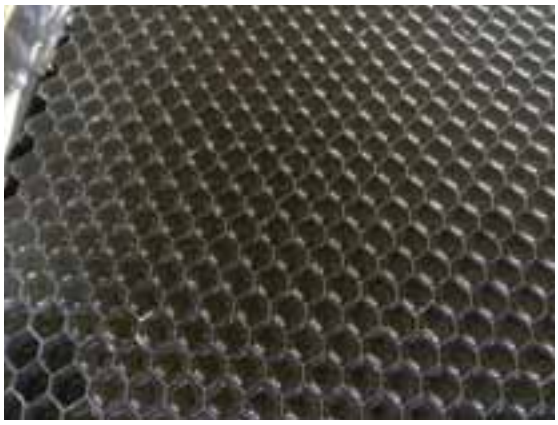

Fig. 2: Honeycomb filled with PCM

A water circuit (copper coil) is also present on the upper surface of the cavity where the condenser part of the heat pipe is located. Cold water from the water supply is injected during the withdrawals linked to the needs of the users. This water circulates in the coil exchanger which is pinned around the heat pipes on the upper aluminum plate of the cavity. PCM in a liquid state releases the latent heat and solidifies when there is a transfer between the PCM and the pulsed water (exchange No. 3). The melting / crystallization temperature of the PCM is chosen close to the set point (about 55 °C.). The water circuit placed on the front of the storage with the heat pipes is an advantage which allow a direct transfer of thermal energy from the heat pipe. This is exchange 4.

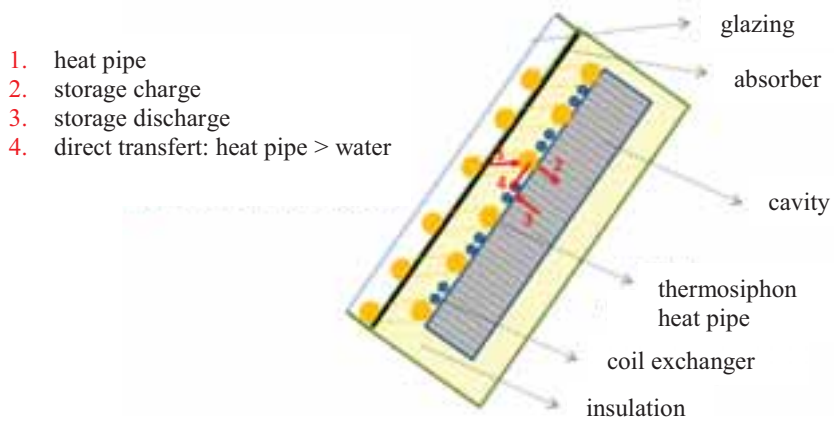

Fig. 3: Operating principle of the new concept of ICS

The table 1 shows all the characteristics of one module. For a complete installation, several modules will be required. The amount of module required will be sized according to the needs.

Tab. 1: Characteristics for each prototype module

Data for each prototype module
Surface d'ouverture : 1m x 0,5m
Storage cavity : aluminium, filled with 75% of PCM
Storage cavity size : 1m x 0,5m x 0,04m
Insulation of the cavity : 10 cm roch wool, λ: 0,04 W/(m.K)
Area of a honeycomb cell: 0,74 cm² (aluminium)
PCM : Polyethylen glycol (PEG 6000), latent heat of fusion: 192 kJ/kg ; Tfusion : 58,5°C ; 1 210 kg/m3 ; λ: 0,2 W/m.K ; volum in the cavity : 0,015 m3
Heat pipes : 6 made of copper, filled with 30% of methanol
Glazing : 4mm thick, Dim. 1006*605 mm, absorption coefficient 0,07, solar factor : 87%
Absorber : copper, λ : 380W/(m.K), 0,2mm thick
Water coil exchanger : cuivre, 12m long (diam int : 6mm, diam ext: 8mm)
ICS inclination : 30°

Photos of the prototype installed on the test platform are presented on figure 4.

Fig. 4: Front and back view of the prototype

2.3. Instrumentation of the prototype

The prototype is fully instrumented with flow rate measurements at the inlet and outlet of the coil exchanger. Weather conditions are recorded, included global solar irradiance within the ICS plane, and the temperature at back of the system. Temperatures are measured with 35 thermocouples on the absorber, on the cavity and on either side of the insulation. These thermocouples have previously been calibrated by performing cold junction compensation. The measurement accuracy of the thermocouples thus obtained is 0.1°C. All data is recorded with an Agilent 34972A acquisition unit. These measurements allow to characterize the system.

2.2. Withdrals

Water withdrawals are made to discharge the storage of the sensor. The withdrawal flow is regulated by a valve

placed upstream of the ICS and is measured by a flow meter. The programming of the withdrawal scenarios is made possible by a solenoid valve which opens at specific times and for fixed periods of time. The energy withdrawn by the water is determined by measuring the flow rate and the temperature at the inlet and the outlet of the water exchanger.

3. Experimental results

Experiments were carried out at the INES (National Institute for Solar Energy). Different withdrawals scenarios are carried out to allow the study of the charge of the discharge as well as stagnation temperature tests at the hottest of summer.

3.1. Study of the charge

The programmed withdrawal to study the charge is the following: a flow rate of 9.3L / min for 19min every morning at 6h, which represents approximately 177 liters of water per day evacuated in a single withdrawal. This choice was made to unload as much storage as possible at the beginning of each day to concentrate initially on the storage phase. This also made it possible to start each day with a maximum unloaded cavity. The first study week (May 24 to 19, 2017) revealed the following results (figure 5).

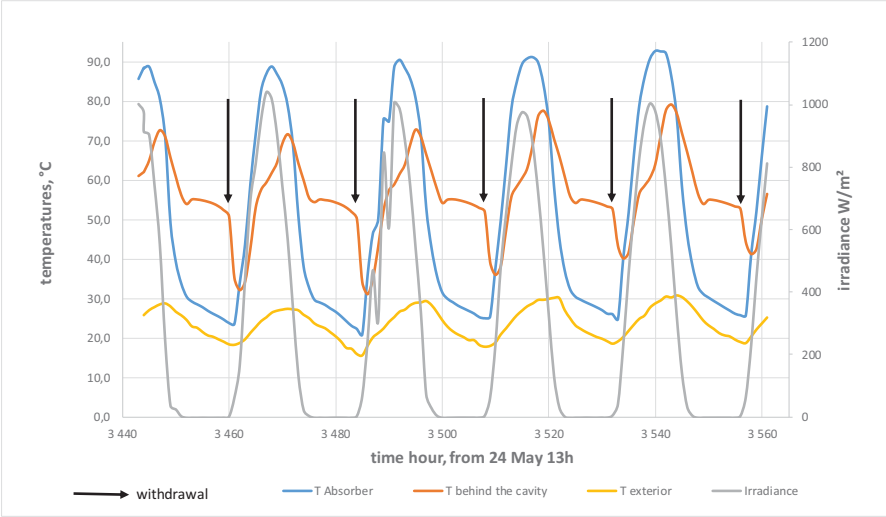

Fig. 5: Experimental results from 24 to 29 may 2017 (arrows indicate a withdrawal)

During these summer days, the irradiance reaches maximum values close to 1000 W/m² in the plane of the absorber (inclination 30°). The absorber temperatures reach 90 to 95°C in the middle of the day and follow the irradiance curve quite well. About storage (measured at the rear of the cavity), its temperature increases over the day, reaching a maximum of 70°C to 90°C in the middle of the afternoon. It is observed that the rise in temperature of the storage is rather fast in the solid phase (sensible heat). The phase change then limits this rise. The temperature change is again faster in the liquid phase (sensible heat) when the whole MCP is melted. The maximum temperature observed is approximately 90°C. Limiting the maximum temperature reduces the risk of degradation of the cavity. A plateau appears on the storage temperature every day around 9 pm for several hours because of the phase change (around 55°C) because of the crystallization of the PCM. The thermal losses of the cavity cause this phase change to be rather slow and create a long "plateau" on the temperature curve. The melting stage is much faster due to the higher solar contributions. We will again discuss the heat loss afterwards, knowing that they seem already quite important because the PCM goes down in temperature up to the level of crystallization during each night. It should be noted that this temperature profile is linked to our withdrawal profile: it would be radically different with a withdrawal in the day for example. A slight phenomenon of supercooling also appears at the end of each day. This phenomenon is related to the fact that the temperature of the PCM drops below its solidification temperature while remaining liquid. This is not inconvenient in our case given the large amplitudes of variation of the temperatures. We can also note that the daily withdrawal (indicated by the arrows) causes the temperature of the storage to drop to about 35°C before rising due to the solar contributions the following day.

This first week of study makes it possible to say that the rise in temperature of the PCM on its sensitive part is rather fast. In order to show this, the following comparison was made (from the experimental data collected):

Tab. 2: Temperature rise of PCM and water

	PCM (PEG 6000)	Water: traditional Solar water heater (TRNSYS simulation)
Initial temperature	30°C	30°C
Setpoint temperature	55°C	55°C
Temperature rise	8.3°C/h	6.2°C/h

This comparison shows the rapid rise in temperature with PCM compared to water. This phenomenon therefore implies, for an installation in operation, a reduced use of the make-up because the PCM reaches the desired setpoint more quickly. This is a particularly interesting point in terms of energy efficiency.

If the temperature of the absorber is analyzed with the outside temperatures, it is realized that for the night the absorber temperature drops very rapidly and reaches a difference of lower than 10 ° C between the absorber and the exterior (the absorber is protected from the outside by the glazing). The heat pipes thus appear to play their role as thermal diodes. Otherwise, the absorber would have a higher temperature.

A second withdrawal was scheduled for a few weeks. The flow rate was decreased from 9 to 3.3L / min for 1 hour at 3am. The total quantity of water discharged remains approximately the same, i.e. approximately 180 liters of water drawn off daily. A lower flow rate was chosen to analyze more finely the evolution of the water temperatures at the inlet and outlet of the sensor. The acquisition step has also been refined (from 1 minute to 3 seconds). The withdrawal was shifted from 6 to 3am in the morning because it coincids with the beginning of the next day's sunlight.

This second scenario allowed us to follow more precisely the evolution of the water temperatures at the inlet and the outlet of the sensor (figure 6).

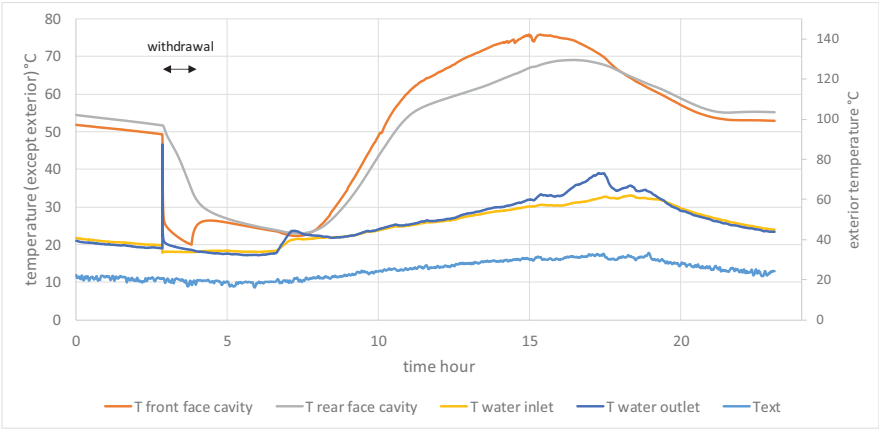

Fig. 6: Evolution of the temperature at the front and rear faces of the cavity, the exterior temperature and the water temperatures at the inlet and outlet, 5 July 2017

By considering a lower flow rate and a finer acquisition step, it is possible to observe more precisely the temperature changes during the withdrawal. Regarding the temperatures on either side of the cavity, their evolutions are similar to what was previously studied.

For water temperatures, it should first be stressed that only the withdrawal periods are meaningful because, without drawing off, the thermocouples measure stagnant water temperatures in the pipes. At the time of the withdrawal, the water in the pipes having been previously renewed, the inlet has a temperature close to 18°C. The outlet temperature rises rapidly to the temperature Tpe (front face of the cavity) which is close to 50°C (figure 6). This temperature decreases to about 25°C. very rapidly after the withdrawal. This hot water is actually stagnant water in the sensor that has been evacuated. The fact of not having water at 50°C for a sufficient time is mainly linked to the high value of the withdrawal flow rate compared to a conventional withdrawal. Moreover, the analysis of the losses during the night rises that the destocking is quite important. This is also due to the temperature of the front face of the cavity: before the withdrawal, it is at 48°C. The PCM has therefore resolidified (at least partly) because of the losses.

3.2. Case without withdrawal

The summer temperature made it possible to carry out a stagnation test on the prototype by not performing any withdrawal. The period concerned was from 13 July to 24 August. The interest is to subject the prototype to high heat and then check that it has not been damaged. During this summer period, outdoor temperatures reach up to 37°C for the hottest days and irradiance exceeds 1000W / m² in the middle of the day for almost all the study days (figure 7).

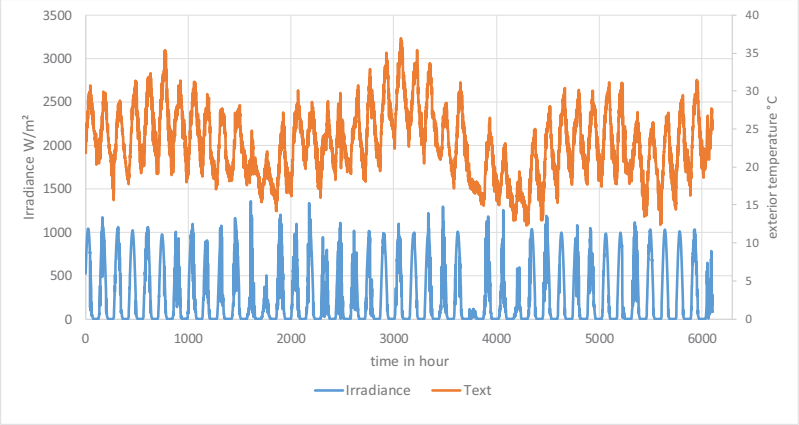

Fig. 7: Irradiance and exterior temperature from 13 July to 24 August

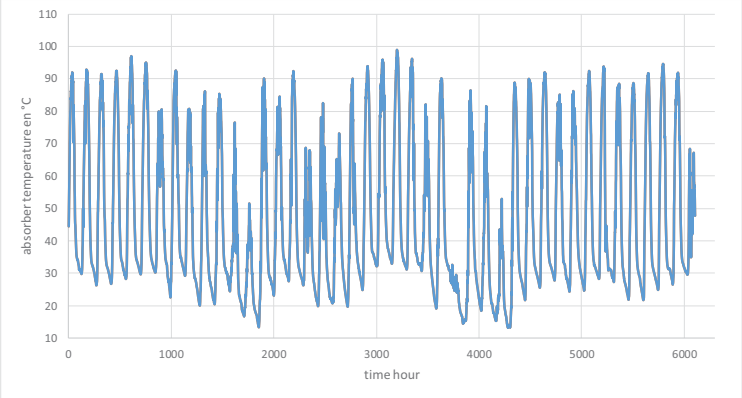

Fig. 8: Absorber temperature without withdrawal, from 13 July to 24 August

When the absorber temperatures are analyzed (figure 8), it can be seen that the absorber does not exceed 100°C. on any day and remains within the range of values observed with a withdrawal.

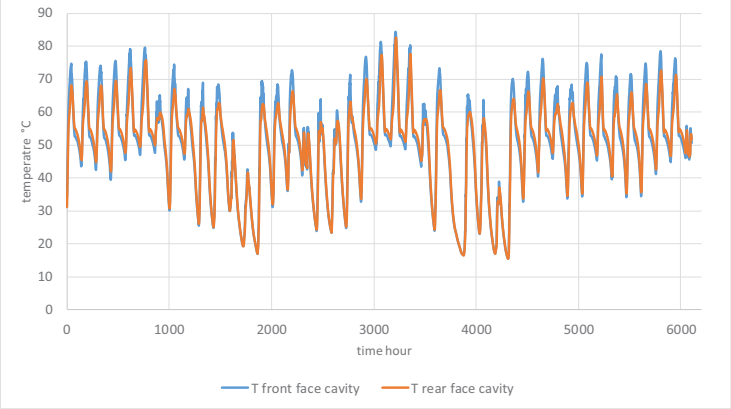

Fig. 9: Temperatures of the front and rear faces of the cavity, from 13 July to 24 August, period without withdrawal

The cavity temperature reaches a maximum of 80°C (figure 9), i.e. slightly higher levels than with a daily withdrawal. Moreover, temperatures generally do not fall as low as with a withdrawal: they are maintained between 30 and 40 ° C (or even more for warm nights) against an average of 20°C with a water withdrawal.

The results obtained in that stagnation test show that, on the one hand, the maximum temperatures reached by the absorber and the cavity remain within acceptable values: there is no rise in temperature which can damage the system. So from a reliability point of view, this is rather reassuring. On the other hand, the fact of not having higher temperature rises in this configuration shows that the sensor exhibits too high thermal losses. With an optimized prototype reducing the thermal losses of the storage, we evaluated, using a numerical model, a maximum temperature between 130°C and 140°C.

3.3. Study of the discharge

This last phase of the test was aimed at studying the phenomenon of discharge of the storage with a realistic flow. A lower withdrawal rate was selected: 0.87 L / min for 30 minutes at 17h. The withdrawal scenario was shifted at the end of the day to estimate the energy recovered by the withdrawal before the night losses partially discharge the cavity. The figure 11a represents the withdrawal at 17:00 for the day of 22 September. The same day, at 12h, flow adjustments were carried out on the experiment, resulting a short withdrawal, hence the first peak on the outlet temperature. The small temperature difference between the 2 faces of the cavity can be observed throughout the day (less than 10°C.). The thermal transfer by the honeycomb is therefore done correctly. The upper surface is logically warmer during the day (sunspot) and colder at night due to the larger losses on the front which is more exposed to the outside environment.

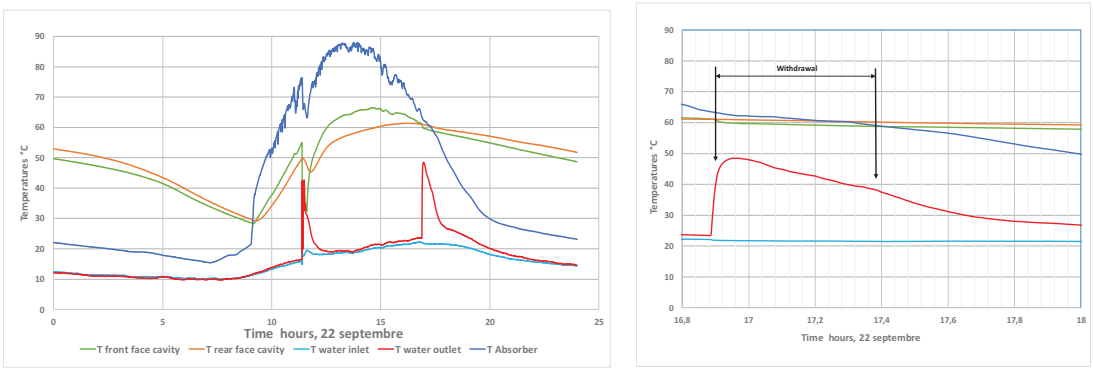

Fig. 10 : Evolution of the temperature on the front and rear faces of the cavity, on the absorber and the water temperatures at the inlet and outlet, 22 September 2017

The temperature of the absorber does not seem to be influence by the withdrawal at 17h, whereas the first at noon is accompanied by a decrease of its temperature and the cavity temperature. An explanation is that in the morning, the storage was not sufficiently charged (mainly sensitive part). Thus, when water has been drawn off, mainly the sensible heat has been removed, causing a drop in temperature. At 17h, the stored energy being mainly in latent form, the withdrawal allowed to partially discharge the cavity without causing a drop in temperature on the elements of the front face of the cavity.

If we look more specifically at the second withdrawal (figure 10b), the evolution of the temperatures allow to calculate the power extracted during the drawing (figure 11). It is about 1.6 kW for 0.5m² of sensor (ie 3.2 kW / m²), which is almost half of what was envisaged in the best case (6 kW / m²). Although the flow rate is slightly lower than expected (0.87 l / min instead of 1 l / min), it is likely that the contact between the coil and the top plate of the cavity should be improved. This explains why the outlet temperature does not reach the temperature of the cavity. Nevertheless, the outlet temperature is maintained at a level above 40°C during the withdrawal period (30 minutes), which is quite suitable.

The maximum outlet temperature is 48.7°C (61°C in the cavity at the same time), 43.5°C after 15 minutes and 40.0°C after 30 minutes. The discharge of the storage is therefore done correctly. The temperature in the cavity decrease only by 1°C.

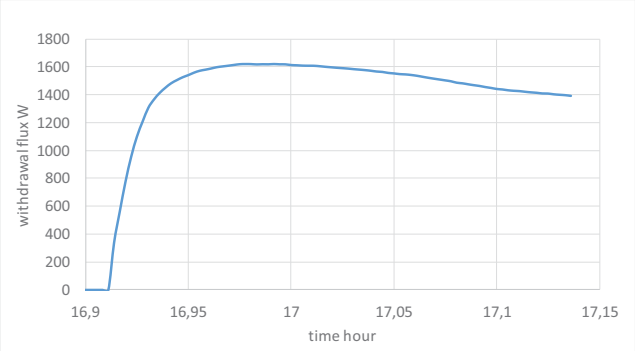

Fig. 11: Puissance récupérée grâce au soutirage d'eau le 22 septembre

4. Conclusion

This study focused on an innovative integrated collector storage concept which couples heat pipes to an MCP storage in a honeycomb. It appears that the rise in temperature of such a storage is much faster than with conventional water storage: 8.3°C/h (experimental) versus 6.2°C/h for a conventional CESI of 300L. In addition, the volume gain from this technology is important (counting at least a factor of 1.65). However, the implementation of the heat pipes proves to be quite complex. The phenomenon of thermosiphon requires to place the condenser above the evaporator.

A prototype was tested in real conditions at the INES. The concept has thus been validated experimentally. It appears that the prototype showed no signs of malfunction (leakage of MCP ...). It is charged correctly every day, the temperature levels reached by the cavity are satisfactory for the durability of the system (including without withdrawal). The solar energy is well transmitted to the storage: the heat pipes play their role well as expected. The thermal diode effect (of the thermosiphons) is also validated. A small temperature difference is observed between the 2 faces of the cavity, which shows the efficiency of the honeycomb structure to transfer the heat.

In terms of performance, it appears that the prototype is relatively well placed in terms of its productivity compared to a traditional individual solar water heater. However, storage is largely discharged at night, which explains why there is no rise in temperature during non-withdrawal periods (experimentally tested). The complete crystallization of the MCP shows that losses are almost equivalent to storage. The losses represent an average power of the order of 100W/m² permanently. This implies a fairly low solar coverage over the year. It is clear that the U-shaped profiles and the metallic fasteners which hold the cavity strongly accentuate the losses of the cavity. All this is not really worrying knowing that these problems of thermal bridges can easily be solved.

If one considers a more efficient version of the ICS, the maximum temperatures reached by the cavity could be between 130°C and 140°C. If it is desired to limit this maximum to a hundred degrees, the ICS must not have an excessive transmission coefficient of glazing and / or an absorber with low emissivity coating.

References

Sadhishkumar, S., Balusamy, T., 2014. Performance improvement in solar water heating systems—A review. Renewable and Sustainable Energy Reviews, 37 :191–198.

Smyth, M., Eames, P. C., Norton, B., 2006. Integrated collector storage solar water heaters. Renewable and Sustainable Energy Reviews, 10(6) :503–538.

Timilsina, G. R., Kurdgelashvili, L., Narbel, P. A., 2012. Solar energy : Markets, economics and policies. Renewable and Sustainable Energy Reviews, 16(1) :449–465.

Numerical Model for Solar Thermal Collectors and Thermal Energy Storages Based on Phase Change Slurry

Gaia Prearo, Gianluca Serale and Marco Perino

Politecnico di Torino, DENERG Energy Department, Turin (Italy)

Abstract

The efficiency of conventional solar thermal collectors and related thermal energy storages is often reduced by the requirement for high irradiation levels and the heat losses due to the relatively high temperature of the heat transfer fluid. In order to overcome those limitations, a solar thermal system capable of working at low temperatures through the exploitation of latent heat storage is presented in this paper. The proposed system was based on a novel heat transfer fluid and storage media, composed by a mixture of water and micro-encapsulated phase change material (PCM), named Phase Change Slurry (PCS). This paper introduces a numerical model capable of accurately describe the physical process and the dynamics of the proposed technology (collector, thermal energy storage and control logics). Results were validated by means of experimental tests and a long-term monitoring on a real full-scale prototype. Furthermore, experimental tests were performed to carry out the actual PCS thermo-dynamical properties that are strongly dependent on the concentration of micro-capsules in the heat transfer fluid.

Keywords: Phase Change Material (PCM), HVAC system, solar thermal system, Phase Change Slurry (PCS), Latent Heat Thermal Energy Storage (LHTES),

1. Introduction

The pursuit to obtain higher levels of comfort has led to a dramatic increase of the energy demand in buildings. In Europe the overall energy demand of the building sector accounts for about 40 % of the total energy consumption (Pérez-Lombard et al., 2008). Solar technologies are a leading solution to face the challenge of reducing the impact of the building sector (http://www.iea-shc.org/programme-description). However, the full profitability of RES is often limited to a great extent by their stochastic variation and the time mismatch between availability and demand (Heier et al., 2015). Thus, energy storage strategies are becoming a crucial requirement to partially mitigate this gap.

A field that is particularly promising is represented by active Thermal Energy Storage (TES) technologies, (SHC Annual Report, 2012). Indeed, in buildings the active TESs allow the surplus of energy production to be stored and then released whenever demanded by the occupant. In particular, the peak power consumption can be mitigated by means the adoption of the TES. In this way the RES are better exploited and the size of the auxiliary systems can be effectively reduced. For the implementation of storage technologies directly into the buildings, compact tank solutions are required.

A further improvement in TES performance has been represented by the introduction of solutions exploiting latent heat exchanges. These solutions are commonly referred as Latent Heat Thermal Energy Storages (LHTES) and can be based on different technologies and storage media (e.g.: ice cold storages, salt hydrates, Phase Change Materials). Advances in industrial technologies have led to the development of Phase Change Materials (PCM), whose phase transition process occurs in many temperature ranges. Thus it is possible to select the material whose features are the most suitable for each specific application. The exploitation of latent heat represents a possible benefit in terms of reducing the size of the component and improving the overall system performance (Rodriguez-Ubinas et al., 2012). Indeed, on one hand the great amount of energy due to the phase change increases the energy stored density. On the other hand, the phase change can be exploited to reduce the temperature differences affecting the system, thus improving the overall system performance by

doi:10.18086/swc.2017.31.12 Available at http://proceedings.ises.org

means of a reduction of both the dispersion and the internal entropy dissipations.

Nowadays, the scientific literature offers numerous works dealing with technologies and solutions concerning LHTES. Particularly encouraging are those in which LHTES is coupled with solar thermal systems. In general, the presence of a PCM leads to an overall annual increase in the solar fraction, a higher efficiency of the system and major storage heat capacity. In the last few years, the use of PCMs has been tested in several different types of solar thermal systems. Three different methods in particular have been proposed to incorporate PCMs into solar thermal systems: the integration of a PCM directly in a layer of the solar collector (Sharma and Chen, 2009 and Eames and Griffiths, 2006), the addition of PCM nodes to the primary HTF solar loop pipes (Haillot et al., 2013) and the addition of PCM elements to the inside of a storage tank (Cabeza et al., 2006).

In 2015, some of the authors of the present paper (Serale et al., 2015) proposed an innovative solar thermal system based on Phase Change Slurry (PCS). The PCS is a mixture of water with glycol and a dispersed micro-encapsulated Phase Change Material (PCM). Micro-capsules allow the PCS to be pumpable regardless the state of aggregation of the material contained in their core. For this reason, it was possible to use the PCS both as the storage media and the Heat Transfer Fluid (HTF) in the primary loop of the solar thermal system. In this way, the phase change transition occurred also in the collector reducing the operating temperatures of the system due to the exploitation of latent heat exchange instead of a traditional sensible HTF temperature increasing. On the one hand the system dispersions to the ambient were reduced and on the other hand the fraction of hours of exploitable solar radiation were also increased, due to a reduction of the threshold limit of the solar radiation necessary to produce energy.

In order to investigate the potentialities of this PCS-based technology, a numerical model for solar thermal collector based on latent heat exchanged was formulated extending the Hottler-Willier for traditional solar thermal collectors (Serale et al., 2016). The present paper is an extension of the numerical model formulated in (Serale et al., 2016). In particular, the extended model herewith presented considers not only the collector, but the entire solar thermal system, including also the system PID controller and the LHTES tank. The integration of these models with the one previously built of the solar thermal collector, allowed a simulation of the prototype as a whole. Eventually, the paper shows the validation process of the numerical model using data gathered during an experimental campaign and a field test on a real-scale prototype.

The work is organised as follow. Section 2 summarises the main features of the numerical model of the collector, the TES and the closed-loop controller for solar thermal system capable of exploiting both latent and sensible heat. Section 3 briefly introduces and describes the solar thermal system analysed as case study. Section 4 reports the results of the experimental tests necessary to characterise the PCS used as HTF. Section 5 outlines the results of an experimental campaign undertaken to validate the numerical model with real data gathered on field. Section 6 is the conclusion of the work.

2. Methods: a numerical model for solar thermal systems exchanging latent heat and sensible heat

In order to better investigate the opportunities offered by the adoption of PCS in solar thermal system, a numerical model was necessary to perform simulation and parametrical analysis. These allow the system performance to be tested under different boundary conditions and climatic parameters. The numerical model had to be capable to describe both the sensible and the latent heat exchanges occurring in the system. In this way both traditional water-based and innovative PCS-based HTF can be tested and the system performance compared. The following Figure 1 provides a comprehensive framework of the numerical model carried out in the present work.

The solar thermal system model was characterised by 3 key elements: the collector model, the TES model and the closed loop controller that regulates the pump speed, thus the flow rate flowing in the system. Both the collector model and the TES model were finite elements thermodynamic models capable to describe the system evolution in terms of internal energy and temperature of the nodes. The model was entirely developed by means of Matlab scripts and Simulink flows. The model can be used to simulate both traditional water-based and PCS-based solar thermal systems. The switch between the two options can be uptaken by different setting of the features of the heat transfer fluid and storage media. Since the numerical model has to work both with water and with a phase change material, an enthalpy approach, instead of a temperature one, was used to

evaluate the internal energy of the system. In this way it was exploited the property of the enthalpy itself of being a continuous and invertible function of the temperature ($h=h(T)$).

The external disturbances influencing the system were the external weather conditions and the energy demand by the occupants. The external weather conditions that mainly affect the system heat exchanges were the ambient temperature T_a, the beam solar radiation G_b, the diffuse solar radiation G_d, the angle of incidence of the solar radiation θ on the collector, the wind velocity w_a, and the radiative temperature of the sky T_{sky}. The TES model considered the ambient temperature as unique weather disturbance, while the solar thermal collector model was affected by all the previous parameters. The occupancy energy demand affected the model of the TES and in particular the inlet temperature of the heat exchanger $T_{hx,in}$ and the thermal energy required in the heat exchanger Q_{hx}. Some general assumptions and simplifications were made in the model to make the physical–mathematical description of the components easier:

- quasi steady-state of the collector components (cover, plate, back insulation casing);
- uniform weather boundary conditions over all the system components;
- heat loss toward the same heat sink, considered at the outdoor air temperature;
- the HTF has constant density and thermal conductivity;
- the temperature of the HTF in the outlet of the collector is, unless a negligible error, the temperature in the inlet of the TES.
- the temperature in the outlet of the TES is approximately equal to the inlet temperature of the solar collector.

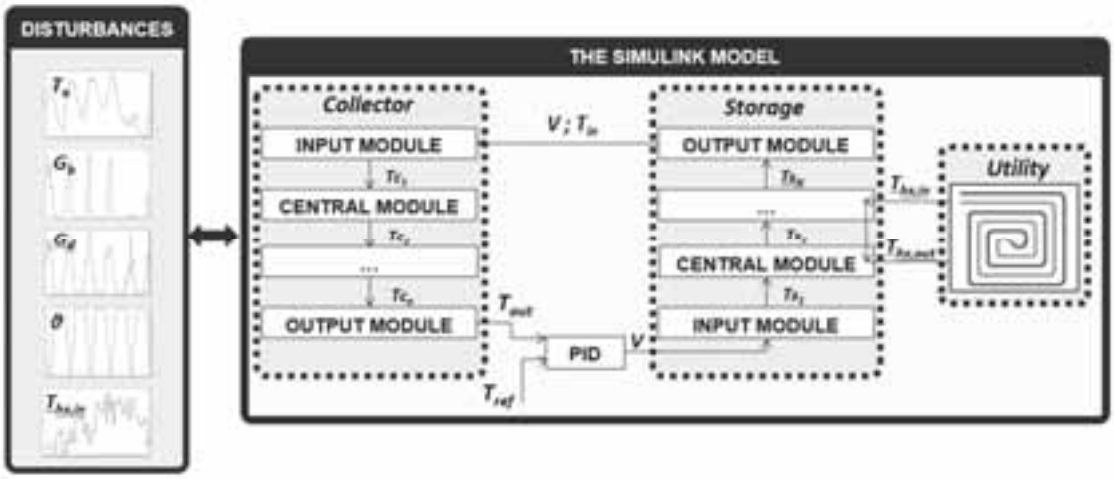

Fig. 1: General framework of the numerical model for solar thermal systems exchanging latent and sensible heat.

2.1 Numerical model for solar thermal collectors based on sensible or latent Heat Transfer Fluids

The solar thermal collector numerical model is the evolution of the previous version presented in (Serale et al., 2016). The numerical model was suitable to simulate different type of HTFs, thus with different thermo-physical properties. In this new version of the numerical model, the collector was a-priori discretised in 10 segments of the same length. Each segment was a lumped node having constant thermodynamic properties (e.g., temperature, specific enthalpy, conductivity, etc.). For each segment an energy balance based on the Hottel-Willier model for solar thermal collector was formulated and computed in order to carry out the temperatures of the components and the heat fluxes involved in the process (Duffie & Beckman, 2013). The solution of this energy balance depended on the HTF used, thus the thermal and rheological proprieties of the HTF had to be set in the model as a function of its temperature. In particular, the adoption of specific enthalpy vs. temperature curves defined by means of look-up tables allowed the model to be easily switchable from sensible to latent heat exchanges.

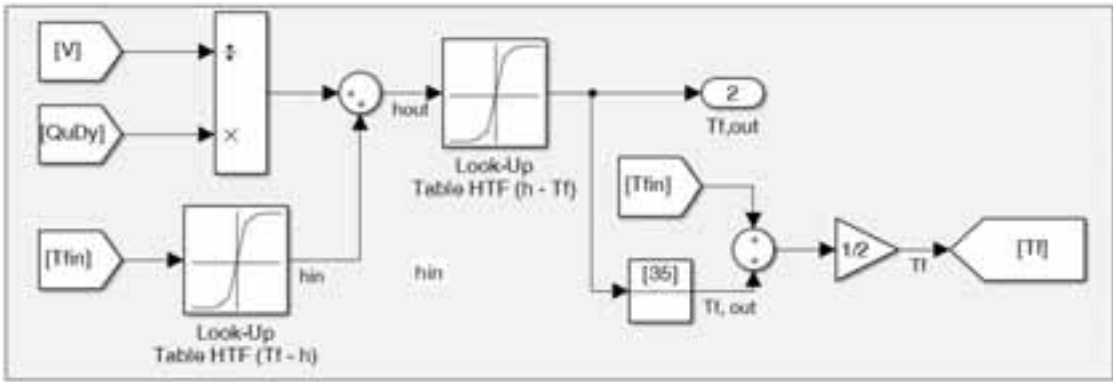

Fig. 2: The sub-section of the Simulink model exploiting the look-up tables used to define the HTF temperature as a function of the enthalpy.

2.2 The multi-node Thermal Energy Storage numerical model

A dynamic lumped energetic model was used to reproduce the thermal behaviour of the TES. In particular, a multi-node model (Streicher, 2008) was selected as the most suitable one to simulate with good accuracy the TES filled either with water or with PCS. Consequently, the TES tank has been virtually segmented into 7 lumped nodes representing finite horizontal volumes. Each node was considered filled with the internal storage media perfectly mixed, thus at one uniform temperature. Likewise the collector model, every node is influenced only by the flow rate entering from the previous one and it influences only the subsequent. The initial node receives the outlet flow rate of the collector, while the terminal node determines the inlet flow rate of the collector.

For each TES node the energy balance was defined by means of Eq.1.

$$\dot{Q}_{dp,j} + \dot{Q}_{hx,j} + \dot{Q}_{aux,j} + \dot{Q}_{cond,j} + \dot{Q}_{loss,j} = m_j \cdot \frac{h_j^{n+1} - h_j^n}{dt} \qquad \text{(eq.1)}$$

This balance considered negligible the pressure drop inside the tank and the heat losses to the ambient were taken into account using a global heat transfer coefficient. Referring to each *j*-th node of mass m, $\dot{Q}_{dp}$ is the heat flux due to the mass flow rate coming from the solar collector, $\dot{Q}_{hx}$ is the heat flux exchanged with the heat exchanger that delivers the space heating energy, $\dot{Q}_{aux}$ is the heat provided by an auxiliary heating source (e.g., a backup boiler or a backup electric heater), $\dot{Q}_{cond}$ is the heat flux exchanged by conduction between two adjacent nodes and $\dot{Q}_{loss}$ is the energy losses to the outdoor environment. The adoption of specific enthalpies h discretised over time on the right term of eq. 1 allowed the TES model to be easily adapted to the HTF used as storage media by means of the same temperature dependent look-up tables adopted for the model of the collector.

During an experimental campaign, every term of eq. 1 for each *j*-th node could be easily derived from the data gathered by thermocouples suitably placed into the TES. If the thermocouples in the TES were not enough to enable the direct solution of the balance in each node (e.g., temperatures monitored in the TES inlet and outlet only), the intermediate node temperatures would be linearly interpolated from these terminal data. Indeed, a quasi-linear trend could be justified by the very small temperature difference between the inlet and the outlet (e.g., at most 10 °C).

2.3 The control loop in the numerical model

Coping with a phase change fluid, the control logic was more complicated compared to traditional water based solar thermal systems. On one side, the controller had to avoid the overcoming of some technology limits of the system components (e.g., not exceed the 60°C maximum temperature thresholds that can damage the system). These control logics for the PCS-based solar thermal system could be based on Rule Based Controllers (RBC) extensively discussed in (Serale et al., 2015).

On the other side, an effective control logic was essential to fully exploit the available solar radiation and to optimise the coupling of the production with the users' demand. In order to maximise the overall energy

efficiency of the system the HTF latent heat should be exploited as much as possible. For this reason, the optimal working condition of the solar collector could be approximated to the one in which the PCS concludes its transition phase (around 40 °C) exactly at the collector outlet. In this way the heat for the isothermal phase change could be fully exploited and the thermal losses can be minimised by maintaining the lowest possible average working temperature of the solar panel. This control logic was addressed by means of a PID controller that managed the primary collector loop pump speed, thus the HTF flow rate flowing in the solar thermal collector. The target of the PID was to maintain the collector outlet temperature as much closer as possible to the set-point equal to the end of PCM transition phase.

The PID controller was implemented in the numerical model to control the flow rate flowing between the solar thermal collector and the TES tank. In the case of PCS the collector outlet temperature, which is the PID set-point, was set equal to 40 °C, a temperature slightly above the upper limit of the material phase change transition and always sufficient to guarantee the supply temperature for space heating. This allows the latent heat of the PCM to be fully exploited. The parameters of the PID controller were changed in the simulation model to evaluate the dynamic response of the system, and to tune the real controller of the prototype. Whereas the P value allows to reach the set-point faster, the I value deletes the error in regime permanent when the disturbances are constants and the D value allows to anticipate the future trend of the error. After preliminary tests, the controller was simplified to a Proportional-Integral controller and the Derivative term was neglected. Indeed, in this specific application, the disturbances - such as the solar radiation and the ambient temperature - are extremely variable, thus predicting the future error would also increase the instability of the system.

2.4 Auxiliary equations for considering the Phase Change Slurry features

A numerical model for a PCS-based solar thermal system required the proper setting of the PCS thermo-physical and rheological properties. These properties strongly depended on the concentration of the micro-encapsulated PCM in the PCS mixture. However, whereas the thermal properties could be easily calculated as the mass weighted average of the properties of the two components of the slurry, the rheological features showed a highly non-linear behaviour. Thus, the choice of the concentration of micro-encapsulated PCM dispersed in the mixture was not trivial. Indeed, it affected both the energy required in pumping and heat transfer, thus in the efficiency and in the energy savings of the system in real building applications. The selection of the most suitable concentration was a quite tricky trade-off, since enhancing a characteristic may cause the worsening of the other one. Indeed, boosting the concentration of micro-encapsulated PCM increased the available latent energy stored in the PCS mixture, but at the same time it determined higher pressure drops due to the increased fluid viscosity, which in turn means higher energy demand for pumping. However, higher thermal storage capacity also implied lower flow rate, and thus a reduction in electric energy demand from the pump (Serale et al., 2014). For these reasons, the authors decided to develop the model with PCS thermal and rheological characteristics that varies accordingly to the micro-encapsulated PCM concentration in the mixture, defined as φ. PCS viscosity and thermal conductivity were defined by means the following eq.2, eq.3 and eq.4, while the enthalpy or specific heat vs. temperature curves were determined with experimental tests for different concentrations.

On the one hand, the PCS dynamic viscosity has been calculated taking advantage from the Vand's model (eq 2):

$$\frac{\eta_b}{\eta_f} = (1 - \varphi - A\varphi^2)^{-2,5} \qquad \text{(eq.2)}$$

where η_b is the dynamic viscosity of the micro-encapsulated PCM, η_f is the dynamic viscosity of the dispersing phase, thus the water with concentration, φ is the volumetric concentration of the micro-encapsulated PCM in the mixture and A is a constant value that depends on the diameter and the geometry of the micro-capsule.

On the other hand, the PCS thermal conductivity was estimated by means of the (eq.3 and eq.4):

$$\frac{\lambda_{eff}}{\lambda_b} = 1 + B\ \varphi\ Pe_p^m \qquad \text{(eq.3)}$$

$$\frac{\lambda_b}{\lambda_f} = \frac{\left(2+\frac{\lambda_p}{\lambda_f}+2\varphi\left(\frac{\lambda_p}{\lambda_f}-1\right)\right)}{\left(2+\frac{\lambda_p}{\lambda_f}-\varphi\left(\frac{\lambda_p}{\lambda_f}-1\right)\right)} \qquad \text{(eq.4)}$$

where λ_{eff} is the thermal conductivity for the flowing PCS fluid, λ_b is the conductivity of the PCS in static conditions, λ_f is the conductivity of the fluid in which the micro-encapsulated PCM is dispersed, whereas Pe_p is the Péclet number of the particle. This last parameter depends on the dimension of the particle and of the pipe in which the fluid flows, on the radial position of the particle in the pipe and, moreover, on the mean velocity of the fluid. Finally, B and m can be considered as constants for defined ranges of the Péclet number.

3. Materials: a PCS-based solar thermal system

In order to validate the model, a real-scale prototype was necessary to undertake an experimental campaign and gather monitored data. In particular, the solar thermal collector and TES prototype described in (Serale et al., 2015) was used to this purpose. This prototype was designed to couple well with low temperature space heating terminals (e.g. radiant panels or Thermal Activated Building Elements). The prototype can use as HTF and storage media either water, eventually with glycol, or a PCS, which exploits the latent heat. The TES was powered by a flat plate solar thermal collector and heat was delivered to the building through a secondary heat exchanger placed inside the component. Furthermore, a complete monitoring system was installed in the prototype to gather data every second about the temperatures and the flow rates of the various components. In particular, energy meters monitored the electrical consumption of the auxiliaries, 20 thermocouples were placed in the collector, in the TES and in some crucial points of the pipes, 2 manometers (one for each loop) and a Corioli's flow meter were used in the secondary loop to measure the fluid flow rate inside the heat exchanger of the TES. On one side of the collector, a pyranometer measures the global solar radiation on the collector tilted plane.

Fig. 3: Left: schematic of the analysed PCS-based solar thermal system. Right: the full scale prototype at Politecnico di Torino.

Figure 3(left) reports a schematic of the prototype and its monitoring system, while Figure 3(right) is a picture of the real scale system installed on the roof of the energy laboratories of Politecnico di Torino. The main component was the solar thermal collector with a net area of 2.1 m^2. The panel was equipped with a motorised cover that worked both as a protection for adverse weather conditions and as a strategy to avoid an undesired overheating of the HTF. The TES tank volume was equal to 200 l. The TES connected the primary collector loop with the demand side heat exchanger that was an internal copper coil of 2.5 kW. A fiberglass insulation layer of 10 cm limited the TES thermal losses to the external ambient. Moreover 8 visors were installed in the TES to visually evaluate the fluid inside the tank. To move the PCS without damaging the PCM micro-capsules dispersed in the mixture, two peristaltic pumps were used, one for the primary collector loop and one in the TES to continuously recirculate the fluid and thus limit the creaming phenomenon (Fan et al., 2015). The peristaltic pump in the primary collector loop was the one controlled by means of the PID controller. Four

solenoid valves were used to control the RBC logics and the operating modes of the solar thermal system (Serale et al., 2015).

4. Experimental tests undertaken to derive the PCS features

The PCS used as HTF was a mixture of water with glycol and a dispersed micro-encapsulated PCM. The PCM contained in the micro-capsules core selected for this application was n-eicosane with a nominal melting temperature of about 36 °C and a specific enthalpy of fusion equal to 195 kJ/kg. Since the thermal properties of the whole PCS mixture strongly depended on the capsule concentrations experimental tests were necessary to define the enthalpy or specific heat vs. temperature curves. The T-History method was selected as the most suitable experimental test for this approach. T-History method defines the correlation between the fluid temperature and its enthalpy at the various micro-encapsulated PCM concentrations. In this case the concentration suitable for the adoption in the solar thermal system were investigated. An extensive description of the T-History tests for the analysed PCS can be find in (Buttitta et al., 2015).
Elaborating the monitored data of the T-history method experiments it was possible to find the enthalpy vs temperature curves at different concentrations using the correlations of Marvin et al. (Marin et al., 2003) (eq. 5-7).

$$H_m = \frac{m_w c_{p,w} + m_t c_{p,t}}{m_t} \frac{A_2}{A_1'} (T_0 - T_s) \qquad \text{(eq.5)}$$

$$\Delta H_p(T_i) = \left(\frac{m_w c_{p,w} + m_t c_{p,t}}{m_p}\right) \frac{A_i}{A_i'} \Delta T_i - \frac{m_t}{m_p} c_{p,t}(T_i) \Delta T_i \qquad \text{(eq.6)}$$

$$H_p(T) = \sum_{i=1}^{n} \Delta H_{p,i} + H_{p,r} \qquad \text{(eq.7)}$$

where H_m is the latent heat, H_p is the enthalpy of the micro-capsule of PCM, $H_{p,r}$ is the enthalpy of a reference fluid whose value is assumed known (in this case distilled water was used as reference fluid), T_0 is the fluid temperature at the experiment initial condition, T_s is the initial temperature of the phase change transition, A_1' is the integral of the temperature difference between the reference fluid and the ambient temperature, A_2 is the integral of the temperature difference between the PCS fluid and the ambient temperature. Both the integrals refer to a period of time ranging from the beginning till the end of the phase change transition. The subscript w indicates the water, whereas t is the tube of the sampler and i is the i-th time instant.
Afterwards, the calculation of the specific heat was possible. The specific heat is defined as the derivative of the enthalpy - temperature curve. The trend of the specific heat can be described as the combination of two Gaussian curves, one for the liquid part and the other one for the solid part (eq. 8).

$$c = \begin{cases} c_s + (c_m - c_s) e^{-\left(\frac{T_m - T}{\omega_s}\right)^2} & T \leq T_m \\ c_l + (c_m - c_l) e^{-\left(\frac{T_m - T}{\omega_l}\right)^2} & T > T_m \end{cases} \qquad \text{(eq.8)}$$

in which the subscribe s refers to the solid state, l to the liquid state and m is the peak value.
Thus, the final equation for the enthalpy curve results in eq. 9.

$$h = \begin{cases} c_s(T - T_{min}) - (c_m - c_s) \frac{\sqrt{\pi}}{2} \omega_s \left[\operatorname{erf}\left(\frac{T_p - T}{\omega_s}\right) - \operatorname{erf}\left(\frac{T_p - T_{min}}{\omega_s}\right)\right] & T \leq T_p \\ c_l T - (c_m - c_l) \frac{\sqrt{\pi}}{2} \omega_l \operatorname{erf}\left(\frac{T_p - T}{\omega_l}\right) + (c_m - c_s) \frac{\sqrt{\pi}}{2} \omega_s \operatorname{erf}\left(\frac{T_p - T_{min}}{\omega_s}\right) - c_s T_{min} + T_p(c_s - c_l) & T > T_p \end{cases}$$

(eq.9)

A possible drawback occurring in test regarding PCS was the so called creaming effect. Indeed, the PCM micro-capsules showed a density that was lower than the one of the water in which they were dispersed. Thus, there was a migration process of the PCM micro-capsules in the upper part of the tubes. To limit the phenomenon during the T-History method, the tubes were placed horizontally and this allowed the results accuracy to be improved up to 18 % compared to the vertical position.
The results of the T-History method are shown in Figure 4. These results were implemented in the Simulink numerical model using Look-up tables. Moreover, Table 1 highlights the available latent heat for each analysed concentration. The creaming effect somehow influenced the reliability of the results and the lower the micro-encapsulated PCM concentration the higher this effect. Indeed, for 5 % w.t. concentration of micro-encapsulated PCM the MAPE was 18 %, while for 15 % w.t. of micro-encapsulated PCM concentration the MAPE decreased to 5 %.

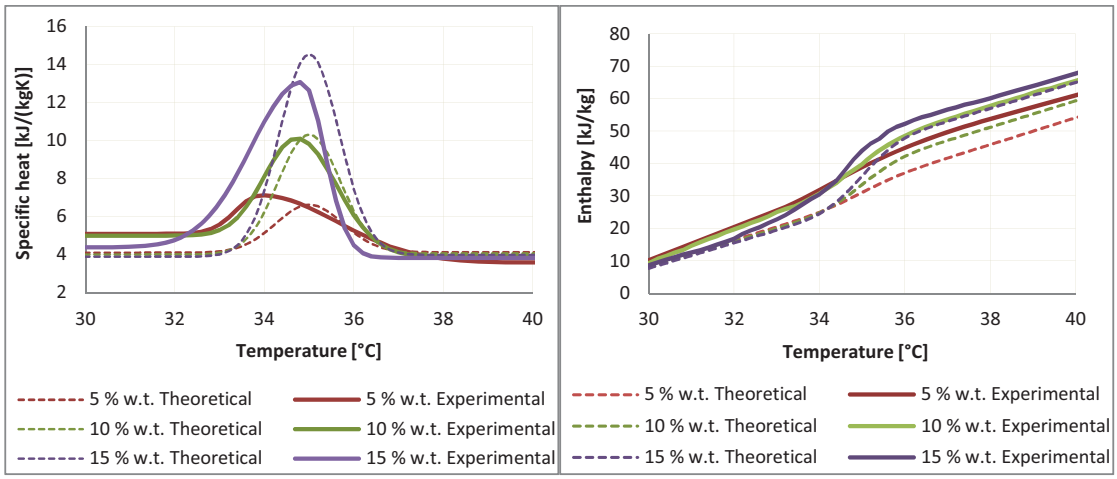

Fig. 4: Left: Enthalpy vs Temperature curves at different weight total concentrations of PCM. Right: Specific heat vs Temperature curve at different weight total concentrations of PCM.

Tab. 1: Comparison between theoretical end experimental PCS latent heat for different concentration of micro-encapsulated PCM in the mixture.

Concentration w.t. [-]	Theoretical latent heat [kJ/kg]	Experimental latent heat [kJ/kg]	MAPE [-]
5 %	4.73	5.74	18 %
10 %	10.97	11.14	2 %
15 %	17.81	18.77	5 %

5. Experimental tests to validate the model

The solar thermal collector and TES prototype were monitored in order to properly identify the parameters of the numerical model that best-fit the actual performance of the prototype. Firstly, the solar thermal collector and the TES were tested as stand-alone elements for 5 days each, afterwards the overall system was monitored for other 5 days. Thus, an uncertainly analysis between the data gathered from the plant and the results obtained from the numerical model has been done.

The implementation of the PID controller in the numerical model allowed not only to perform realistic simulations replicating the real control logics of the prototype, but also to investigate and improve the best Proportional, Integral and Derivative setting. Figure 5(left) shows the comparison of the temperature trend at the outlet of the real collector with the simulated data obtained introducing a P controller and a PI controller. The set-point tracked by the controller was a temperature of 40 °C at the outlet of the solar collector. The P value allowed the set-point temperature to be reached faster, while the I value deleted the error in permanent

regime where the disturbances were constants. The changes in the collector outlet temperature were due to the variation of the flow rate, influenced by controlling the peristaltic pump speed.

On the one hand adopting the P controller, when high level of solar radiation became available, the rotation speed of the pump decreased until the set-point temperature was reached (Figure 5(right)). However, if the solar radiation remained constant, it would not be possible to maintain the 40 °C set point with the P controller and the collector outlet temperature raised up to 44 °C. On the other hand, the combination of a P value with a I value solved this issue. Indeed, it is possible to infer from Figure 5(left) as the set-point was maintained also during all the central hours of sunny days when the solar radiation reached the highest levels. On the contrary, with either P or PI controller during cloudy days (e.g. the fourth and the fifth days of the monitored week), also maintaining the pump speed at the minimum value, the system was not able to reach the set-point could.

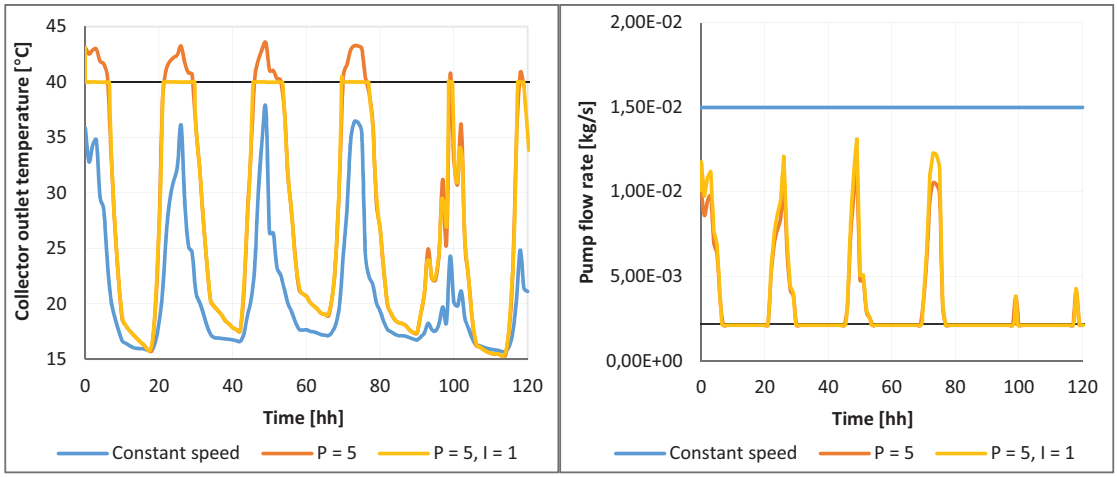

Fig. 5: Experimental results with different combinations of P and PI values. Left: Temperature at the outlet of the collector. Right: HTF pump flow-rates.

At the end of the calibration process for the solar thermal collector, the MAPE between measured and simulated outlet fluid temperatures with water was 1.8 % (i.e., a MAE of 0.5 °C). While the tests of the TES tank temperatures provided a MAPE equal to 1.6 % (i.e., a MAE of 0.3 °C). After those satisfactory results, the analyses of the entire closed loop system were performed. In this case, the difference between the simulated and the monitored data slightly increased. Nevertheless, the error indicators remained smaller than a MAPE of 8 % for the outlet temperature of the solar thermal collector and of 1.8 % for the TES nodes temperatures. The following Figure 6(left) shows the comparison between the simulation and monitored results obtained for the closed loop solar thermal system for 7 monitored temperature in the TES, whereas Figure 6(right) shows the collector outlet temperature.

The simulated trend of the collector outlet temperature followed the experimental results proving a good accuracy. Some small discrepancies were outlined only during peak loads of solar radiation and morning time. This was mainly due a difficult calibration of the solar radiation transmission coefficient of the solar collector glass cover as a function of the incidence angle. Indeed, this transmission coefficient strongly affected the panel performance, influencing the amount of the radiation effectively incident to the absorption plate of the collector. A delay affected the simulated results of the first hours of the day also concerning the TES temperature trends. This was influenced again by the uncertainties affecting the solar collector. Indeed, the outlet of the solar collector was the inlet of the TES.

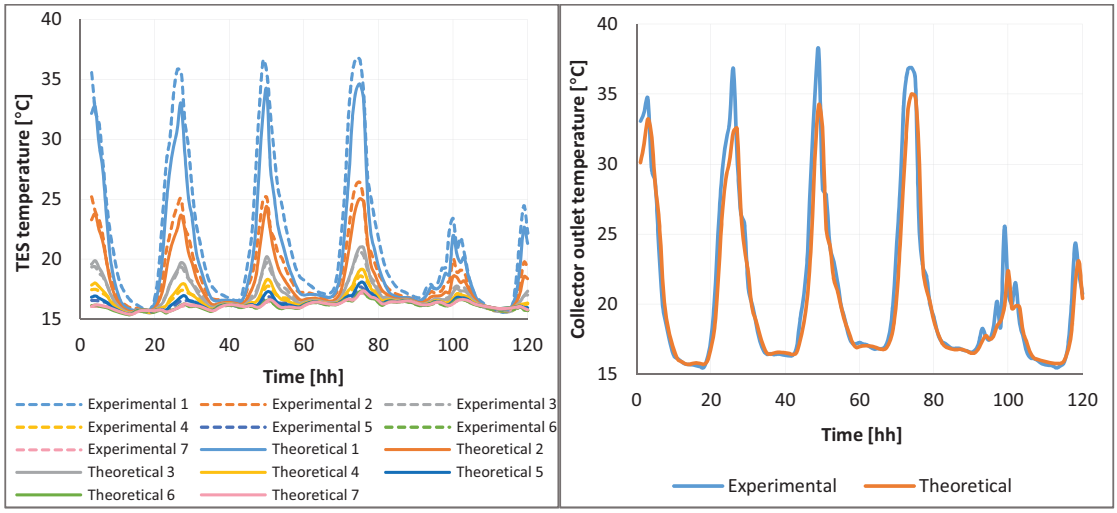

Fig. 6: Experimental vs simulation results. Left: Temperature at the outlet of the collector. Right: Temperatures of the 7 nodes of the TES tank.

The simulated trend of the collector outlet temperature followed the experimental results proving a good accuracy. Some small discrepancies were outlined only during peak loads of solar radiation and morning time. This was mainly due a difficult calibration of the solar radiation transmission coefficient of the solar collector glass cover as a function of the incidence angle. Indeed, this transmission coefficient strongly affected the panel performance, influencing the amount of the radiation effectively incident to the absorption plate of the collector. A delay affected the simulated results of the first hours of the day also concerning the TES temperature trends. This was influenced again by the uncertainties affecting the solar collector. Indeed, the outlet of the solar collector was the inlet of the TES. Eventually, a further discrepancy between real monitored data and simulation results was related to a temperature peak shift in the TES nodes farer from the TES inlet. Simulation results generally anticipated the real monitored data. This was due to some TES internal partitions that slowed down the HTF motion in the real tank and were not modelled in the lumped numerical model.

6. Conclusions

In the present paper a numerical model to describe the physical behaviour and the system dynamics of a complete PCS-based solar thermal system (collector, thermal energy storage and control logics) was presented. The HTF thermal properties were defined by means experimental laboratory tests whose results were herewith reported. Simulation performed by means of the numerical model resulted accurate enough to reproduce the real data gathered in-field during a monitoring campaign on a real scale prototype. Thus, the numerical model can be used in future works to perform comparative analyses to outline the possible benefits achievable by means of the proposed technology. Future works will also deal with additional experimental campaign aiming at adopting as HTF a PCS at different concentrations.

7. References

Buttitta, G., Serale, G., Cascone, Y. 2015. Enthalpy-temperature evaluation of slurry phase change materials with T-history method. Energy Procedia 78, 1877-1882

Cabeza, LF., Ibanez, M., Sole, C., Roca, J., Nogues, M. 2006. Experimentation with a water tank including a PCM module. Solar Energy Materials & Solar Cells 90, 1273–1282

Duffie, J. A., Beckman, W. A. 2013. Solar engineering of thermal processes. John Wiley & Sons.

Eames, PC., Griffiths, PW. 2006. Thermal behaviour of integrated solar collector/storage unit with 65°C phase change material. Energy Conversion and Management 47, 3611–3618

Fan, X., Serale, G., Capozzoli, A., Perino, M. 2015. Experimental measurement and numerical modeling of the creaming of mPCM slurry. Energy Procedia 78, 2010-2015

Haillot, D., Franquet, E., Gibout, S., Bédécarrats, JP. 2013. Optimization of solar DHW system including PCM media. Applied Energy 109, 470–475.

Heier, J., Bales, C., Martin, V. 2015. Combining thermal energy storage with buildings - A review. Renewable and Sustainable Energy Reviews 42, 1305–1325.

Marìn, J., Zalba, B., Cabeza, L. F., Mehling, H. 2003. Determination of enthalpy – temperature curves of phase change materials with the temperature-history method : improvement to temperature dependent. IOP Science, 184.

Pérez-Lombard, L., Ortiz, J., Pout, C. 2008. A review on buildings energy consumption information. Energy and Buildings 40(3), 394–398.

Rodriguez-Ubinas, E., Ruiz-Valero, L., Vega, S., Neila, J. 2012. Applications of Phase Change Material in highly energy-efficient houses. Energy and Buildings 50, 49–62.

Serale, G., Baronetto, S., Goia, F., Perino, M. 2014. Characterization and energy performance of a slurry PCM-based solar thermal collector: A numerical analysis. Energy Procedia 48, 223–232.

Serale, G., Fabrizio, E., Perino, M. 2015. Design of a low-temperature solar heating system based on a slurry Phase Change Material (PCS). Energy and Buildings 106, 44–58.

Serale, G., Goia, F., Perino, M. 2016. Numerical model and simulation of a solar thermal collector with slurry Phase Change Material (PCM) as the heat transfer fluid. Solar Energy 134, 429–444.

Sharma, A., Chen, CR. 2009. Solar Water Heating System with Phase Change Materials. International Review of Chemical Engineering 1, 297–307.

Streicher, W., Bony, J., Citherlet, S., Heinz, A., Pusching, P., Schramzhofer, H., Schultz, J. M. 2008. Simulation models of PCM storage units. A report of IEA solar heating and cooling programme. Task 32, Report C5 of Subtask C. “Advanced storage concepts for solar and low energy buildings”. IEA SHc- Task 32, 1–83.

Various authors, 2012. SHC Annual Report.

IEA-SHC, 2017. URL http://www.iea-shc.org/programme-description (accessed 9.20.17).

SolCoSi: A new online software for evaluate the thermal performance of flat plate solar collectors

Rodolfo Pérez-Espinosa[1], Octavio García-Valladares[2]

[1] Posgrado en Ingeniería (Energía), Unviersidad Nacional Autónoma de México, Privada Xochicalco S/N, Centro, C.P. 62580 Temixco, Morelos, México.
jrpee@ier.unam.mx

[2] Instituto de Energías Renovables, Universidad Nacional Autónoma de México, Privada Xochicalco S/N, Centro, C.P. 62580 Temixco, Morelos, México.
ogv@ier.unam.mx

Abstract

SolCoSi (SOLar COllector Simulator) is a software program developed in order to determine the thermal performance of flat plate solar collectors used in solar water heating systems. SolCoSi can be used as a tool for design and optimize flat plate solar collectors, it enables an analysis of different materials and dimensions of the absorber, transparent covers, number of tubes, types and dimensions of insulation, selective surface, and different working conditions (mass flow rate, wind speed, solar radiation, etc.). The mathematic model consist in a two-dimensional arrange of nodes disposed in longitudinal and axial direction; in order to determine the temperature in each node, an energy balance was solved. As a result, SolCoSi predicts the thermal efficiency curves (lineal or quadratic), the incident angle modifier factor, the stagnation temperature (calculated for the particular case when the mass flow rate is near zero) and the temperature distribution in fluids and solids. The model developed is available as free online software in English and Spanish on the following website: http://solcosi.ier.unam.mx/

Keywords: Numerical model, flat plate solar collector, water heating, free software

1. Introduction

SolCoSi (SOLar COllector Simulator) is a software program developed by the Instituto de Energías Renovables – UNAM. This software can be used to predict the thermal efficiency curves (lineal or quadratic), the incident angle modifier factor, the stagnation temperature (considering as the outlet water temperature in the solar collector when the water mass flow rate is near zero) and the temperature distribution in fluids and solids of flat plate solar collectors used in water heating systems. In order to design new prototypes of solar collectors, it is necessary to modify the principal parameters of these equipment such as: materials and dimensions of the absorber, transparent cover, number of tubes, types and

doi:10.18086/swc.2017.31.13 Available at http://proceedings.ises.org

dimensions of insulation, selective surface, and its working conditions (mass flow rate, wind speed, solar radiation, etc.).

2. Mathematical model

2.1 Equation of energy balance

The model combines the multilayer method proposed by Cadafalch (2009) with a discretization also in the longitudinal axis proposed by García-Valladares and Velázquez (2009) in order to take into account the temperature profile along the risers. The discretization used for SolCoSi is shown in Fig. 1.

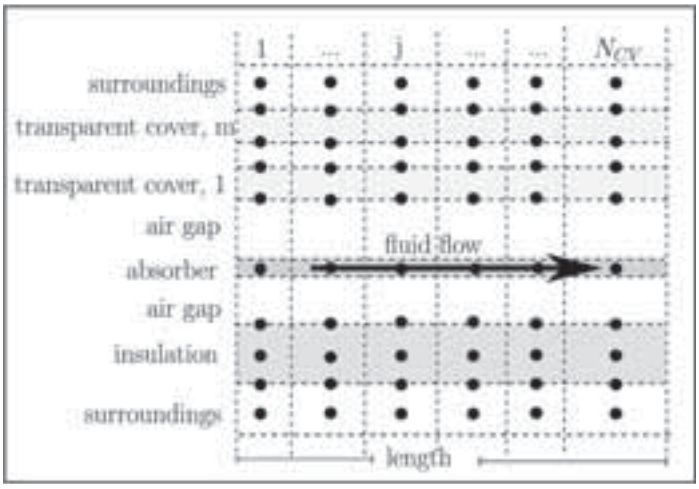

Fig. 1 Internal discretization of flat plate sola collector used for SolCoSi.

The eq. (1) shows the general form of the energy equation applied to each control volume. The model takes into account the following assumptions: steady state conditions, heat transfer in axial and longitudinal directions, the total water mass flow rate is divided into equals parts in each riser.

$$\left(Z_K + Z_{k-1} + Zs_j + Zs_{j-1}\right)T_{j,k} = Z_k T_{j,k+1} + Z_{k-1} T_{j,k-1} + \\ + Zs_j T_{j+1,k} + Zs_{j-1} T_{j-1,k} + q_{g,k} \qquad \text{(eq. 1)}$$

Where Z and Zs values correspond to heat transfer coefficients (conductive, radiative and convective) in each node in W/m^{2}K. The conductive and radiative coefficients are calculated with the Fourier and Boltzman's laws respectively using the thermophysical properties of the different materials. The convective coefficient are calculated using empirical correlations for each specific layer: (a) for the environmental heat transfer coefficient, the equations proposed by Duffie and Beckman (Duffie and Beckman, 2013); (b) for the fluid inside the tubes, the equation developed by Gnielinski (Gnielinski, 1979); and (c) for the air gaps between the back insulation and transparent cover the method suggested by Bejan (Bejan, 1993) are used respectively.

The $q_{g,k}$ term is the heat generation in W/m^2, $T_{j,k}$ is the temperature of the node analyzed and $T_{j,k-1}$, $T_{j,k+1}$, $T_{j+1,k}$ and $T_{j-1,k}$ are the temperatures of its neighbor nodes. The set of energy balance equation in each control volume is solved using the Tri-Diagonal Matrix Algorithm (TDMA) according to Patankar (Patankar, 1980). For more details see the following article (Pérez-Espinosa and García-Valladares, 2018).

3. Validation

In order to validate SolCoSi, a comparison with the experimental data of different commercial flat plate solar collectors (evaluated according to the international standard ISO-9806:2013 (2013) in different accredited solar laboratories around the world) has been carried out. A statistical analysis between the thermal efficiency curve predicted by SolCoSi (referred as the y−dependent variable) and the experimental thermal efficiency curve (defined as the x−independent variable) was used according to Verma and Santoyo (1997). In this statistical method, an ideal correlation is obtained when y=x; for this reason a ±3% error band was plotted in Fig. 2, this figure shows that 78.3% of the 23 numerical data points obtained were within and error band of ±3% and 95.7% were within and error band of ±5%. The mean deviation between experimental and numerical results was ±2.55%. With this analysis, a good agreement between numerical and experimental results has been observed. Appendix B shows the thermal efficiency data points of experimental and numerical results used in Fig. 2.

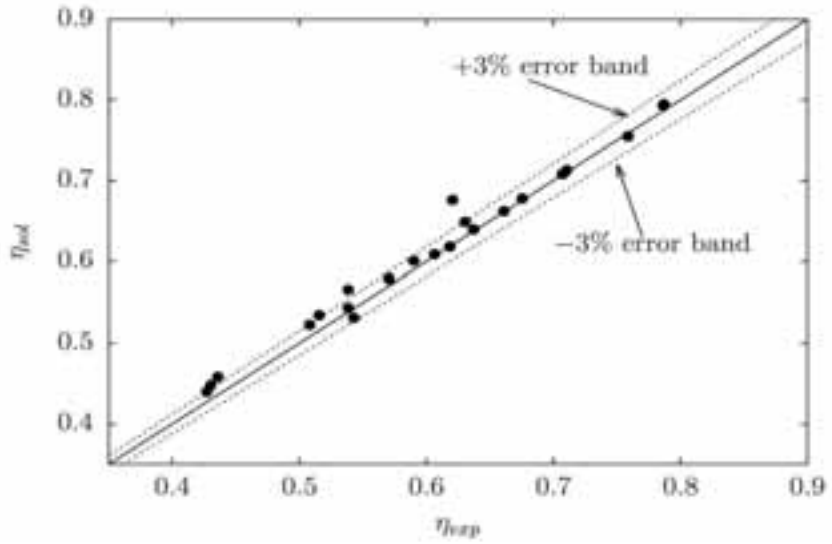

Fig. 2 Comparison of thermal efficiency between numerical and experimental data points.

4. Results

Once the SolCoSi was validated, the software was written in Java code and the program is now available in the website http://solcosi.ier.unam.mx with a visual interface and an English and Spanish versions. The result is a new software program named SolCoSi than can be used to evaluate the thermal performance of a flat plate solar collector: the thermal efficiency curve, the incident angle modifier and the stagnation temperature. These results can be download in a .pdf file as a report, the report includes: in the first section the principal values used in the simulation (values given by the user), after that it shows the linear and quadratic equations of the thermal efficiency (see Fig. 3); in the third section, it is shown the equation to determine the incidence angle modifier factor and the curve obtained with this equation (see Fig. 4); in the fourth section the stagnation temperature obtained by the simulation when the water mass flow rate is close to zero is shown. The main menu of the SolCoSi website is observed in Fig. 5.

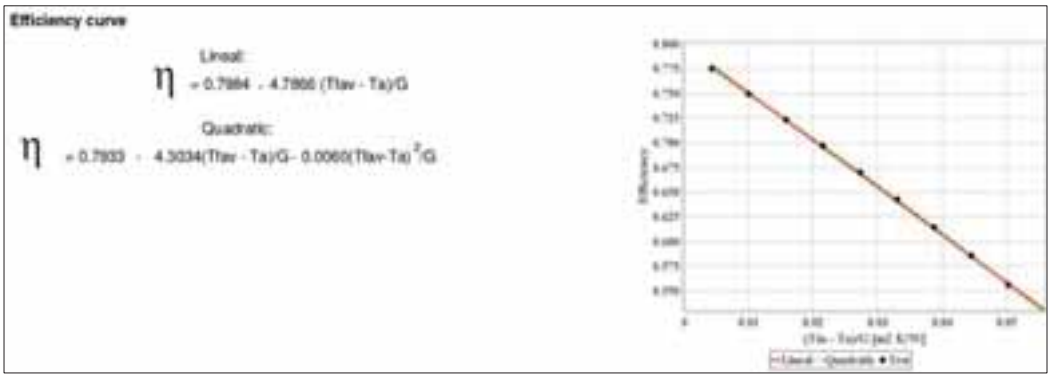

Fig. 3. Thermal efficiency equations and curves obtained by SolCoSi.

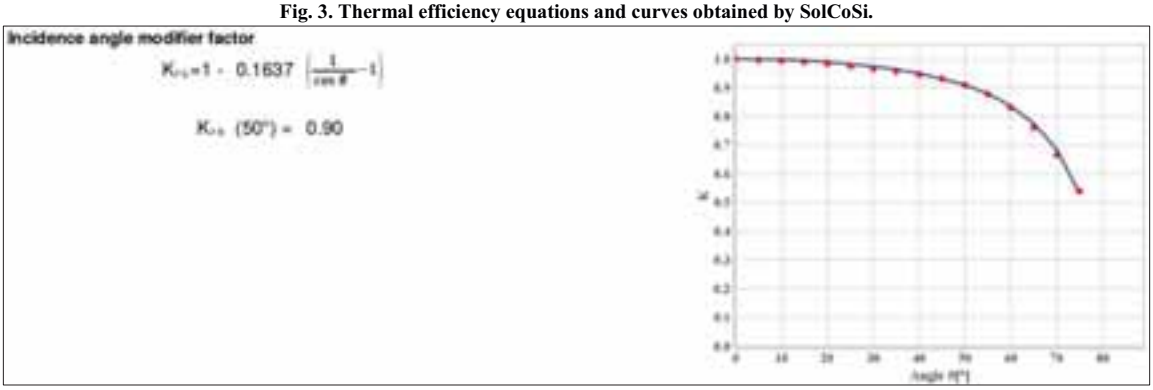

Fig. 4. Incidence angle modifier factor and its respective curve.

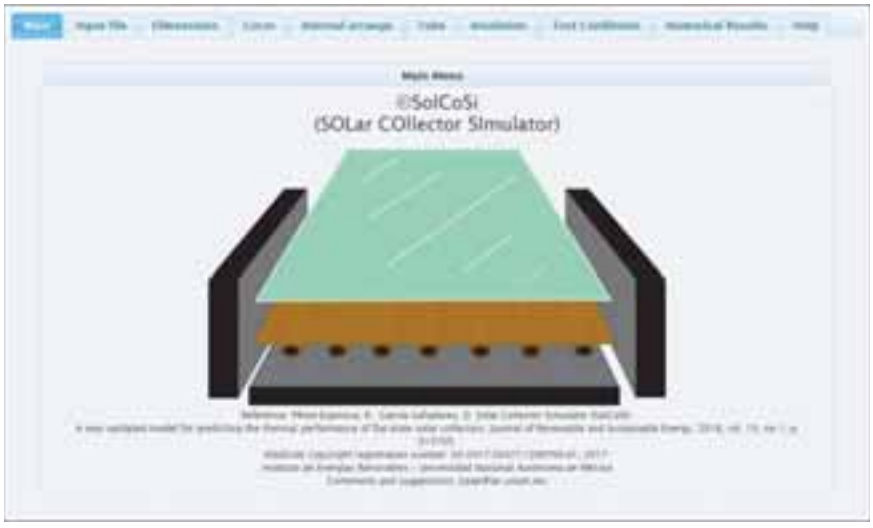

Fig. 5. Main menu of SolCoSi website.

5. Concluding remarks

A Solar Collector Simulator (SolCoSi) has been successfully developed. The model discretize the flat plate solar collector in the axial and longitudinal directions and it can be used to evaluate the thermal efficiency curve, the incident angle modifier factor, the stagnation temperature and the temperature distribution in fluid flow and solids.

SolCoSi was validated against a wide range of experimental data (70 experimental data points grouped in 23 groups) of different commercial flat plate solar collectors fabricated with different geometries, materials and working under different operating conditions; this

validation includes a comprehensive statistical analysis based on error bands. A good agreement between numerical and experimental results has been observed with a mean deviation of ±2.55%.

6. Acknowledgements

This work was partially supported by CEMIE-Sol project 12.

7. References

Bejan, A., 1993. Heat transfer, John Wiley & Sons, Inc.

Cadafalch, J., 2009. A detailed numerical model for flat-plate solar thermal devices. Solar Energy 83 (12), 2157-2164.

Duffie, J. A. and Beckman, W. A., 2013. Solar engineering of thermal processes, John Wiley & Sons.

García-Valldares, O. and Velázquez, N., 2009. Numerical simulation of parabolic trough solar collector: improvement using counter flow concentric circular heat exchangers. International Journal of Heat and Mass Transfer 52 (3), 597-609.

Gnielinski, V., 1976. New equations for heat and mass-transfer in turbulent pipe and channel flow, International chemical engineering 16 (2), 359-368.

Patankar, S., 1980. Numerical heat transfer and fluid flow. CRC press.

ISO9806: 2013. Solar energy, solar thermal collectors and test methods, in: International standard, 2013.

Pérez-Espinosa, R. and García-Valladares, O., 2018. Solar Collector Simulator (SolCoSi): A new validated model for predicting the thermal performance of flat plate solar collectors. Journal of Renewable and Sustainable Energy 10. View online: https://doi.org/10.1063/1.5004428

Verma, S. P. and Santoyo, E., 1997. Improved Equations for Na/K, Na/Li, and SiO2 geothermometers by outlier detection and rejection. Journal of volcanology and geothermal research 79, 9-23.

8. Appendixes

Appendix A: units and symbols

Table 1 shows all the symbols used in to the paper.

Table 1: Symbols used in this paper.

Quantity	Symbol	Unit
Global irradiance	G	W m^{-2}
Incidence angle modifier	Kτα	
Number of the control volumes	Ncv	
Heat generation	q	W m^{-2}
Temperature	T	K
Longitudinal thermal resistance	Zs	W $m^{-2}K^{-1}$
Subscripts		
Ambient	a	
Fluid at average temperature	fav	
j-th longitudinal control volume	j	
k-th axial control volume	k	
Greek letters		
Thermal efficiency (SolCoSi)	η_{sol}	
Thermal efficiency (experimental)	η_{exp}	
Collector incidence angle	θ	°

Appendix B: data of the tests

Table 2 shows the experimental and numerical results used in Fig. 2.

Table 2. Experimental and theoretical thermal efficiency data points

Test group	η_{sol}	η_{exp}
1	0.7105	0.7129
2	0.6305	0.6489
3	0.5385	0.5662
4	0.7080	0.7090
5	0.6065	0.6089
6	0.5080	0.5228
7	0.4270	0.4397
8	0.6205	0.6760
9	0.4358	0.4583
10	0.7865	0.7928
11	0.6610	0.6621
12	0.5706	0.5793
13	0.4303	0.4481
14	0.7870	0.7947
15	0.7070	0.7080
16	0.6185	0.6183
17	0.5385	0.5438
18	0.6372	0.6394
19	0.5428	0.5315
20	0.7587	0.7550
21	0.6755	0.6779
22	0.5901	0.6007
23	0.5156	0.5347

Design of non-imaging solar collectors for process heat

K. S. Reddy* and T. Srihari Vikram

Heat Transfer and Thermal Power Laboratory, Department of Mechanical Engineering,
Indian Institute of Technology Madras, Chennai, INDIA

*Corresponding Author, Email: ksreddy@iitm.ac.in

Abstract

In this article, a comprehensive optical analysis of a non-imaging elliptical hyperbolic concentrating collector has been carried out. This collector system has a wide acceptance angle so that it can be operated with no/minimum tracking based on the location of operation. Two types of receivers say flat and trapezoidal surface are considered and the flux distribution over these receivers are estimated and compared. It is found that maximum peak flux is intercepted by the trapezoidal surface receiver. The effect of concentrator geometrical parameters such as concentrator height (H_c) and concentration ratio (CR); receiver geometrical parameters such as aperture width (W_r) and receiver height (H_r) on optical performance of the collector has been studied. The optical efficiency varies between 5 – 15 % for the concentrators with height less than 1 m whose acceptance angle is about 60°, whereas for the concentrator height greater than 1m, the acceptance angle is ±45° and the optical efficiency varies between 20 – 30 % for incidence angles ±30°. The maximum flux incident on the trapezoidal surface is about 60585 W/m^2, however for flat surface, it is 40468 W/m^2. Based on the optical analysis, it can be seen that this system can be widely used for applications such as low and medium temperature applications and it requires less/no tracking with wider acceptance angle.

Keywords: Solar energy, non-imaging collector, hyperbolic concentrator, optical performance

1. Introduction

Non-imaging concentrators are widely used in low temperature solar process heating applications like water heating, air conditioning etc., For given concentration ratio, non-imaging systems provide wide acceptance angles for solar applications. Hence, these collectors require minimum or no tracking. A new type of non-imaging concentrator called elliptical hyperbolic concentrator has been developed which has wider acceptance angle and require less or no daily tracking and minor adjustment for seasonal tracking depending on the location of installation of collector. The use of hyperbolic concentrators were studied by Garcia-Botella et al. (2009). It has been concluded that the concentrators with hyperbolic profile have higher acceptance angle. Ali et al. (2009) compared the optical performance of 2-D and 3-D elliptical hyperbolic concentrator (EHC) and found that the optical efficiency of 2D and 3D system are 63% and 78% respectively. Ali et al.(2010) presented optical performance of 3D static circular and elliptical hyperboloids. Four different configurations of hyperboloids are studied based on the ray tracing techniques and flux distribution at the receiver aperture has been presented. A detailed parametric study on the elliptical hyperbolic concentrator has been performed by Ali et al.,(2013). Thermal analysis of concave cavity surface receiver of EHC was carried out by Reddy and Vikram (2015). In the present work, optical analysis of elliptical hyperbolic concentrator with two types of receivers are carried out and effect of various parameters such as concentrator height, concentration ratio, receiver height, receiver aperture on optical performance of the elliptical hyperbolic concentrator with trapezoidal/concave cavity surface receiver are studied.

2. Design of Elliptical Hyperbolic Concentrator

The elliptical hyperbolic concentrator is a non-imaging concentrator, which consists of a hyperbolic profile along the concentrator height with an elliptical aperture. This concentrator is the development of 3-D surface of revolution and falls under the category of family of surfaces called hyperboloid. The hyperboloidal surface considered in the present work is one-sheeted hyperboloid.

The equation of one-sheeted hyperboloid is given by (Gottwald, 2012):

$$\frac{x^2}{a^2}+\frac{y^2}{b^2}-\frac{z^2}{c^2}=1 \qquad \text{(eq. 1)}$$

doi:10.18086/swc.2017.31.14 Available at http://proceedings.ises.org

The length of the major axis and minor axis at the top aperture of the concentrator is termed as 2A and 2B whereas at bottom aperture, it is termed as 2a and 2b respectively, and Hc being the height of the concentrator. The geometrical parameters of elliptical hyperbolic concentrator are shown in Fig. 1.

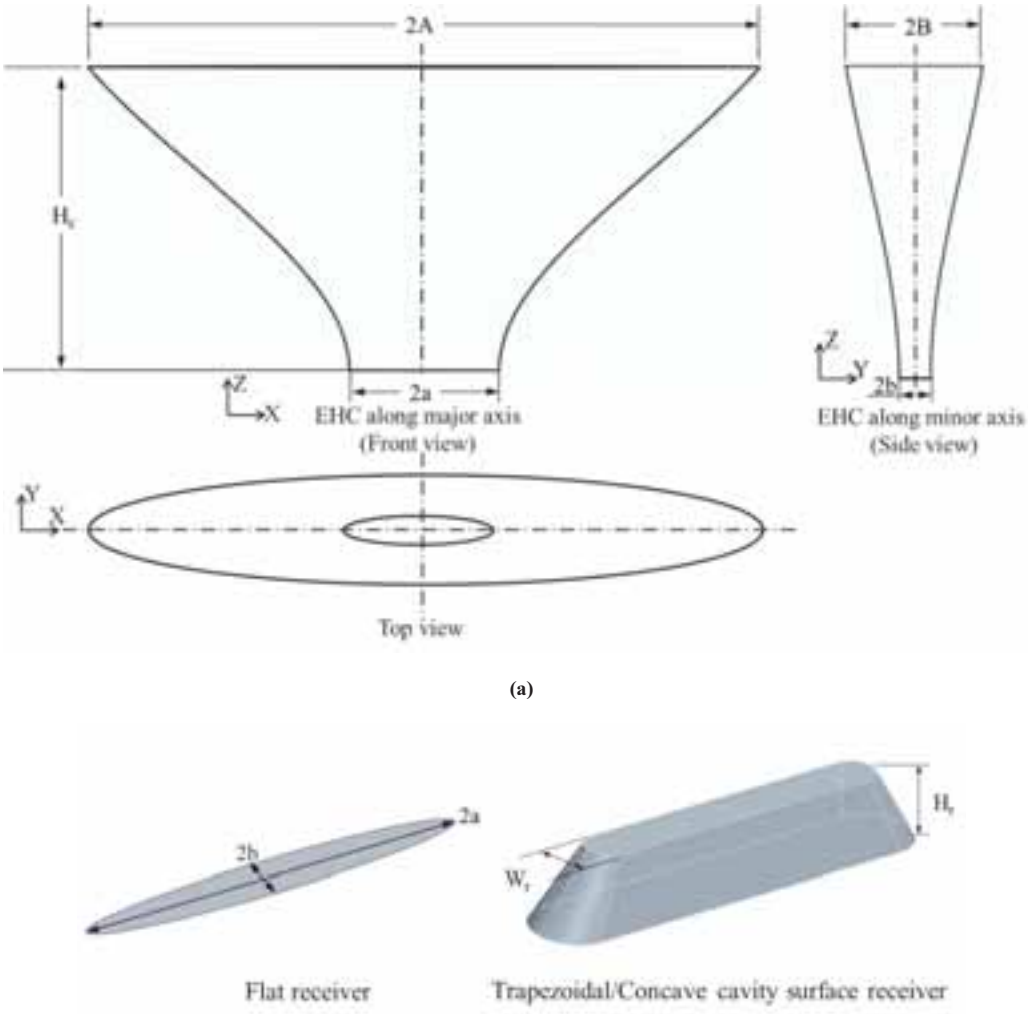

Fig. 1 (a) Elliptical hyperbolic concentrator and (b) receiver showing geometrical parameters

3. Modeling of Elliptical Hyperbolic Concentrator with receiver

The equation for hyperbolic profile is obtained by rewriting the Eq. (1) for two planes X-Z and Y-Z by substituting Y = 0 and X = 0.

For hyperbolic profile along X-Z plane (major axis side), substitute y = 0 and rewriting eq. (1) in terms of z, we get,

$$z_1 = c \times \sqrt{(x/a)^2 - 1} \qquad \text{(eq. 2)}$$

Similarly, for hyperbolic profile along Y-Z plane (minor axis side) is obtained by substituting x = 0 in Eq. (1), we get,

$$z_2 = c \times \sqrt{(y/b)^2 - 1} \qquad \text{(eq. 3)}$$

The equation for elliptical profile (at top and bottom aperture) is obtained by considering different values of z, ranging from 0 to H (height of the concentrator).

$$\frac{x^2}{a^2} + \frac{y^2}{b^2} = 1 + \frac{z^2}{c^2} \qquad \text{(eq. 4)}$$

The ratio of semi major and semi minor axis (a/b) remains one of the important parameter in designing the elliptical hyperbolic concentrator. This ratio plays a role in deciding the shape of elliptic aperture. The value 1 corresponds to circular cross section of aperture, whereas 10 correspond to narrow elliptical cross section (i.e.,) lower major axis compared to minor axis. Hence a medium or average value of 5 is considered for the ratio of semi major and minor axis (a/b) in the present study. The ratio of height to aperture (H_c/a) plays a role in the amount of solar radiation entering the concentrator and reaching the receiver. An optimum ratio of H_c/a ratio is considered as 4 based on the previous studies by Ali et al., (2013). It can be seen that when the ratio of height to aperture is varied from 1 to 10, the effective concentration ratio increases or decreases depending on the incidence angle of the solar radiation. For incidence angles of 0 and 15°, the effective concentration ratio increases whereas, for 30° and 45°, the effective concentration ratio decreases beyond 4. It can be concluded that the optimum Hc/a ratio seems to be 4 and corresponding H_c/b ratio seems to be 20. The geometrical values of parameters considered for the design of elliptical hyperbolic concentrator are shown in Table 1. Based on the values provided in Table 1, the design of EHC is carried out by obtaining the equations for hyperbolic profiles along major and minor axis and elliptical apertures at bottom and top of the concentrator using Eq. (2) – (4).

Tab. 1: Geometrical specifications considered for design of EHC

Parameters	Values
Semi major axis at receiver aperture (a)	0.4 m
Ratio of semi-major to minor axis (a/b)	5
Height to aperture ratio (H_c/a)	4

The geometry of EHC is modelled using modeling software, AutoCAD 2012. The points for the profiles along the major and minor axis is calculated for different values of x and y. These coordinate points are generated and is used to model the geometry of the concentrator. The receiver converts the incident concentrated solar radiation into thermal energy with the help of fluid circulated through it. Hence the design of the receiver becomes necessary for its efficient conversion of solar radiation. The amount of solar radiation incident on the receiver depends on the concentrator and the receiver shape. In the present study, two different configurations of the receivers such as flat surface and trapezoidal surface are analyzed. The flat surface receiver has the dimensions same as the bottom aperture i.e., the shape of ellipse with major and minor axis dimensions equal to that of the bottom aperture of the concentrator. Fig. 2 shows the EHC system with receivers placed at bottom aperture of the concentrator.

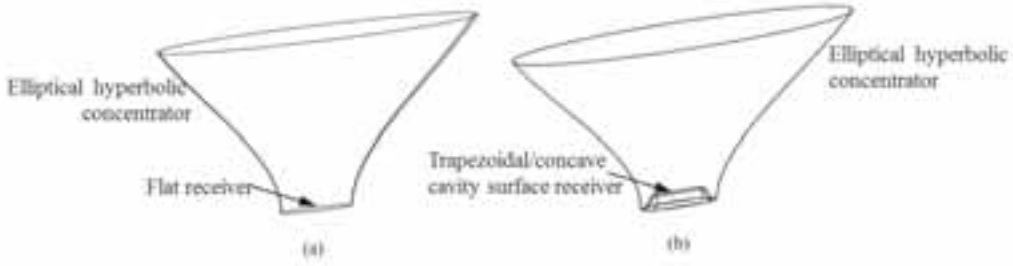

Fig. 2 EHC systems with receivers at bottom aperture (a) flat surface (b) trapezoidal surface

4. Optical ray tracing analysis

The optical ray tracing analysis is carried out to estimate the flux that is incident on the receiver and to calculate the optical efficiency of the system. ASAP (Advanced Systems Analysis Program) is an optical system-modelling software/tool based on Monte-Carlo ray tracing technique, which simulates the interaction of light with optical and mechanical structures (BRO, 2013). The geometrical model developed is imported to the ASAP software using suitable (iges or stp) format. After importing the model in ASAP, the system settings such as units, wavelengths are set. Then, the optical properties such as optical materials/coatings, refractive indices, reflectivity, and absorptivity are specified. Once the model is imported and the properties are defined, source is defined and appropriate number of rays for simulation is specified in the program. The source emitting the rays considered should have the properties of sun hence, subtended angle by the sun is specified while defining the source. After specifying the source, the ray tracing is carried out to concentrate the solar rays over the receiver through the concentrator. In the

present study, the reflectivity of the concentrator is considered as 0.94. This reflectivity corresponds to the reflectivity of Reflectech sheet (DiGarcia and Jorgenson, 2010) that is used over the concentrator. The ray tracing diagram for different incidence angles are shown in Fig. 3.

The optical efficiency is given by (Kalogirou, 2009):

$$\text{Optical efficiency},\eta_o = \frac{\text{Flux absorbed by the receiver}}{\text{Flux incident on the concentrator}} \quad \text{(eq. 5)}$$

$$= \frac{\sum_{i=1}^{N} I_i \rho_r^{\ m}}{I_o} \quad \text{(eq. 6)}$$

where, N and m corresponds to number of rays and number of reflections respectively.

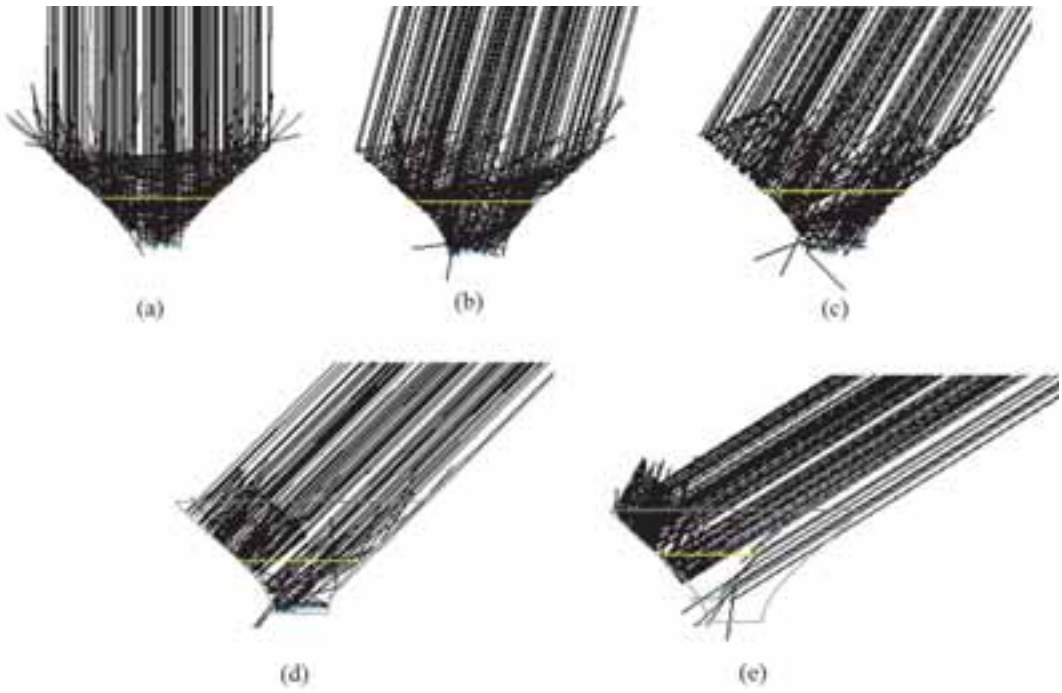

Fig.3 Ray tracing diagram for different incidence angles (a) 0º (b) 15º (c) 30º (d) 45º

The optical model/procedure needs to be validated to assure the correctness of the procedure that is followed. To validate the present optical model, the procedure is validated with optical analysis of two different geometries by Ali et al. (2010) and Abdullahi et al. (2013). Ali et al., (2013) carried out optical analysis of EHC system with flat receiver. The validation of present model with Ali et al. (2010) for Hc = 0.4 m, CR = 20, a/b = 5, a = 0.04 m was carried out. It can be seen that the variation of present model with the other model is minimum and found to have maximum deviation of 4.75%. Abdullahi et al. (2013) carried out optical ray tracing analysis of compound parabolic collector (CPC) with single and double receiver configurations. The geometry of CPC with single absorber of 11 mm radius is considered. It can be seen that the variation of optical efficiency with Abdullahi et al. (2013) is minimum.

5. Comparison of flat surface and trapezoidal surface receivers

The flux available at the bottom aperture of the elliptical hyperbolic concentrator is estimated and the receiver for EHC system has been designed based on the ray tracing analysis. The flux distribution on the receiver is important for conversion of incident solar radiation into useful heat. Hence, the receiver is designed as trapezoidal surface to intercept maximum amount of radiation that is entering the EHC system. The variation of optical efficiency for both flat and trapezoidal receiver surface is shown in Fig.4. The flux on a flat surface and trapezoidal surface for the solar incidence angle of 0° is shown in Fig.5. The optical efficiency of the flat and trapezoidal surface receiver is 27.3 % and 27.1% at normal incidence. The optical efficiency for the flat surface is slightly higher than the

trapezoidal surface at the maximum of 5 % at 30° incidence angle, however at other incidence angles, the variation of optical efficiency seems to be less than 5 %. This reduction of optical efficiency might be due to the geometry of the surface as the rays might miss the surface. Although the optical efficiency of the two receivers is close enough, the variation of flux incident on the receiver seems to be large.

The maximum flux incident on the trapezoidal surface is about 60585 W/m^2, however for flat surface, it is 40468 W/m^2. From Fig. 5, it can be seen that the maximum flux over the trapezoidal surface is 1.5 times higher than that of flat surface. An average flux of about 4236 W/m^2 and 4197 W/m^2 has been observed for trapezoidal surface and flat surface. The profile represented below and right side of the flux distribution corresponds to the flux along the centre line as indicated in the flux distribution diagram. Hence, using trapezoidal surface as receiver intercepts more flux than the flat surface. Hence, the trapezoidal surface receiver is considered for further analysis.

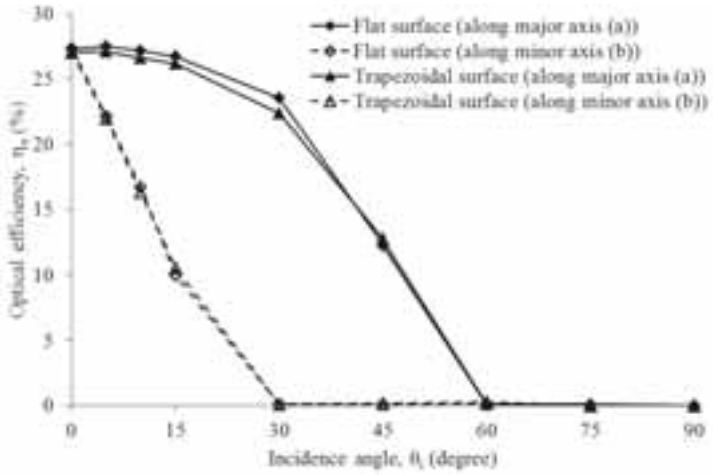

Fig. 4 Variation of optical efficiency for flat and trapezoidal surface receiver at normal incidence

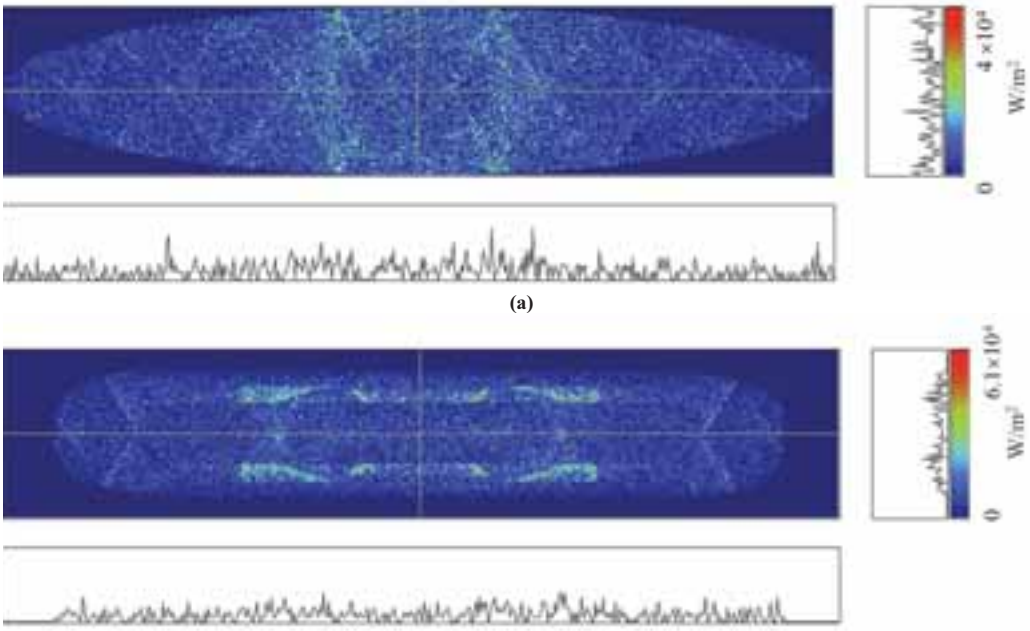

(a)

(b)

Fig. 5 Flux distribution over (a) flat surface and (b) trapezoidal surface receivers

6. Optical analysis of EHC

6.1 Effect of concentrator height

The variation of optical performance for different height of concentrator (H_c) ranging from 0.4 m to 2 m is studied. The effect of concentrator height for different incidence angles on optical efficiency is shown in Fig 6. The optical efficiency increases with increase in the height of the concentrator. The height of the concentrator decides the

acceptance angle of the concentrator. Higher the concentrator, lower will be acceptance angle depending on the aperture of EHC. When the concentrator height is less, for any ray to undergo multiple reflection is minimum. The optical efficiency is found to be maximum at normal incidence angle and varies for different incidence angles. The optical efficiency varies between 5 – 15 % for the concentrators with height less than 1 m whose acceptance angle is about 60°, whereas for the concentrator height greater than 1m, the acceptance angle is 45° and the optical efficiency varies between 20 – 30 % for incidence angles ± 30° and 5 – 20 % for another 15° variation in incidence angle.

The intensity of the flux incident on the receiver also depends on the concentrator height. As the concentrator height increases, the flux intensity increases. It can be observed that for the concentrator height of 0.4 m, the peak intensity of the flux incident on the receiver is 2.5×10^4 W/m^2, whereas for concentrator height of 2 m, peak intensity is 6.9×10^4 W/m^2 Fig. 7 shows the flux distribution over trapezoidal surface receiver at different incidence angles along major axis.

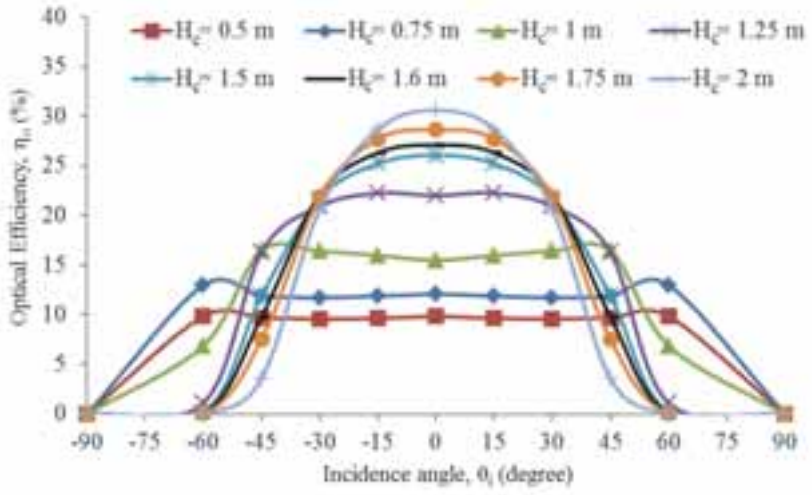

Fig. 6 Variation of optical efficiency for different concentrator heights

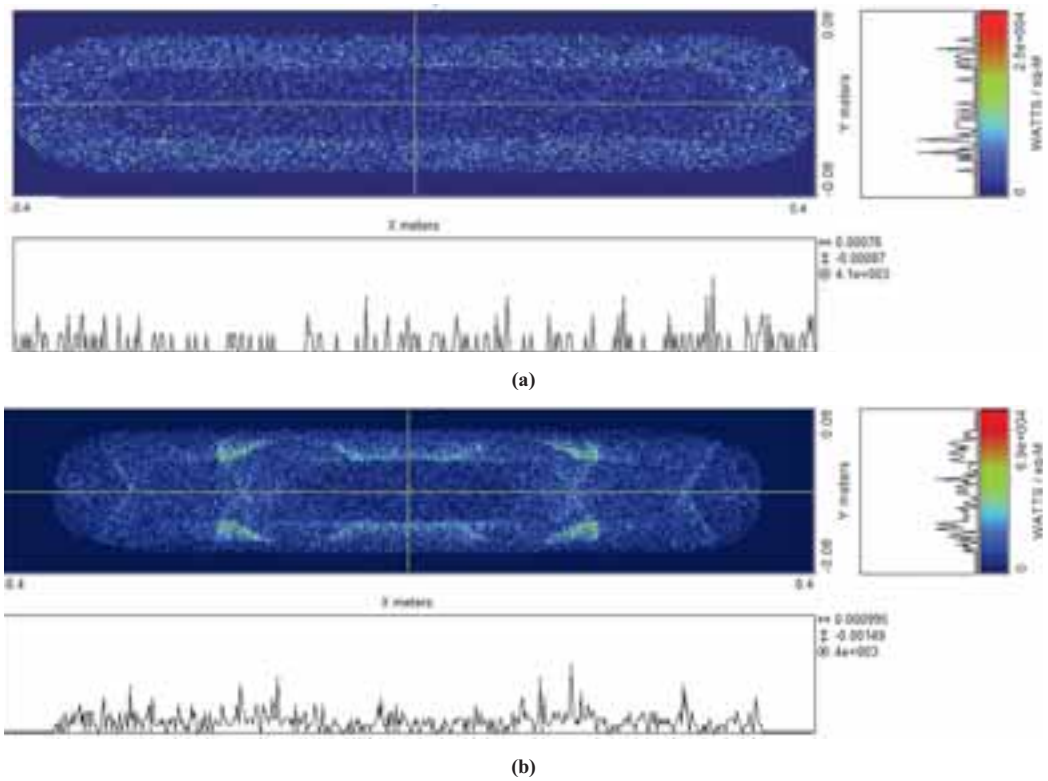

(a)

(b)

Fig. 7 Flux (2D) on receiver for two different heights of the concentrator (a) H_c = 0.4 m (b) H_c = 2 m

6.2 Effect of concentration ratio

The effect of concentration ratio (CR) of the EHC system is studied by varying from 5 to 30 in the steps of 5 by keeping H_c = 1.6 m. The aperture area at the bottom (receiver side) is kept constant and the aperture area at the top (entry of the concentrator) is varied to get different concentration ratio. The concentration ratio is defined as the ratio of aperture area of concentrator (A_{ap}) to that of aperture area of receiver (A_r). It is given by:

$$\mathrm{CR} = \frac{A_{ap}}{A_r} \qquad \text{(eq. 7)}$$

The effect of concentration ratio on optical efficiency is shown in Fig. 8. Lower the concentration ratio, higher the optical efficiency and it is peaked at normal incidence and drops drastically for other incidence angles. It can be seen that for CR of 5, the optical efficiency is 80% at normal incidence, however, at incidence angle of 15°, it reduces to 60%. Similarly for incidence angle of at 30° and 45° incidence angle, optical efficiency further reduces to 33% and 10% respectively. As the CR increases, optical efficiency reduces. It can be seen that for higher concentration ratios (CR = 20, 25 and 30), the variation of optical efficiency for incidence angles ranging between ± 45º do not vary much. This is due to fact that aperture area at top is wider and hence it accepts more amount of solar radiation for wide range of incidence angles. Variation in CR is the variation of the aperture area of the concentrator with respect to the aperture area at the bottom (receiver), which is kept constant. Higher concentration ratio ensures higher concentration of the solar radiation on the receiver but, the optical efficiency of the system decreases to very low say, about 10%, which is not a desirable factor for the design of the concentrator.

The variation of flux on the receiver for CR 5 and CR 30 is shown in Fig. 9. The maximum flux on the receiver for CR 5 is about 4.8×10^4 W/m^2, whereas, for CR 30, it is about 3.6×10^4 W/m^2. The maximum flux of CR 5 is higher than that of CR 30, because more number of rays are reflected towards the same location of the receiver from small surface area of concentrator in case of CR 5. But, in case of CR 30, the rays are reflected from wider surface area of concentrator. It can be seen that for CR of 5, more rays are incident on the left and right side surface of the receiver than on the top on the receiver.

But for CR 30, the flux is seen distributed over the entire surface of the receiver. Figure 10 shows the flux distribution over the concentrator surface for two different concentration ratios 5 and 30. The distribution of flux on the concentrator is more uniform for lower concentration ratio system than the higher concentration ratio system. It can be seen that the flux distribution over the concentrator for CR 30 is uneven and non-uniform showing peak flux at certain points on the concentrator. Hence, the aperture area of the concentrator plays a major role in deciding the flux incident on the receiver. The effect of the geometry of the concentrator on the optical performance of EHC have been discussed. It can be seen that the height of the concentrator plays a major role on the flux incident on the receiver and the acceptance angle of the solar rays. The aperture area of the concentrator (other words concentration ratio) is also important to which level the concentration of the solar rays on the receiver are desired.

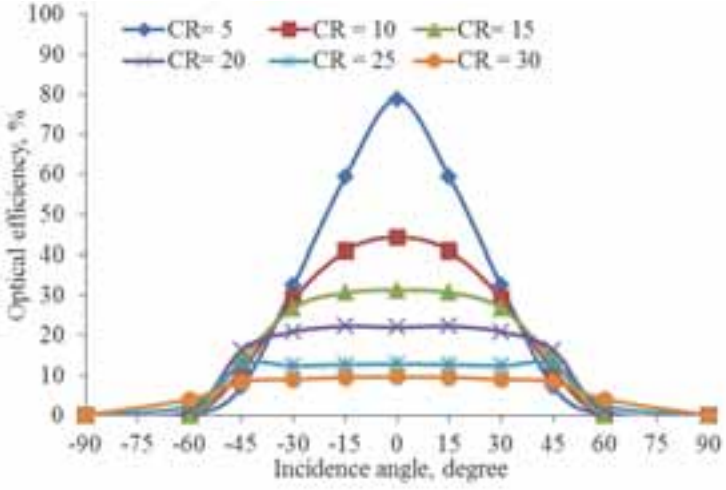

Fig. 8 Variation of optical efficiency with concentration ratio for different incidence angles

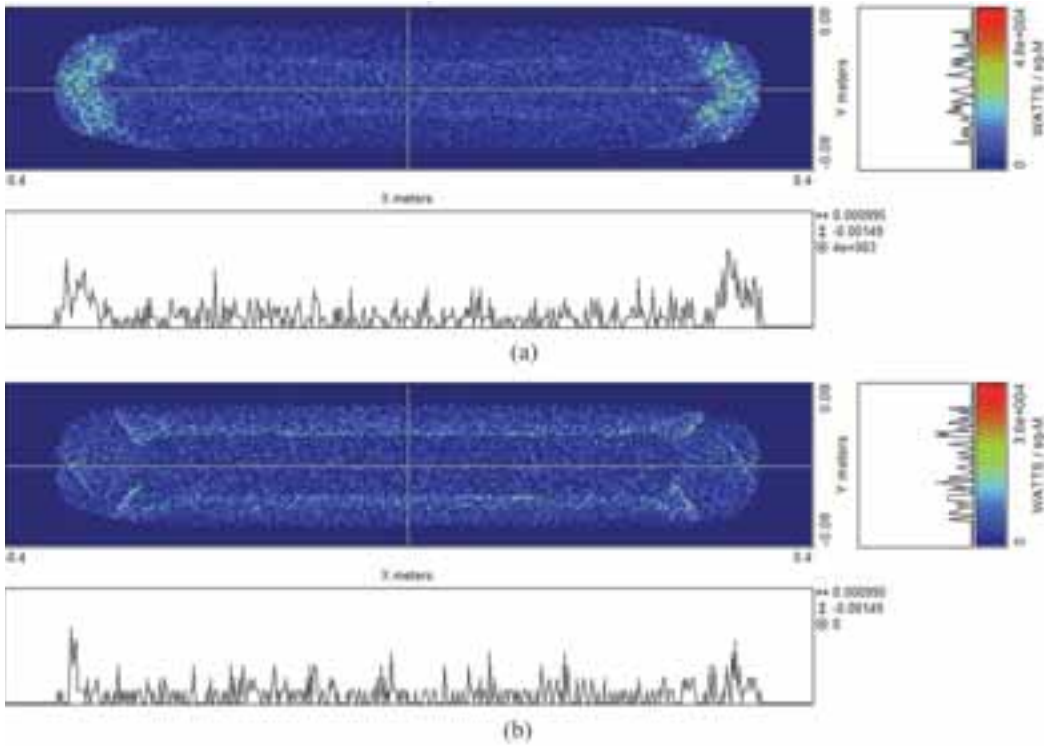

Fig. 9 Flux distribution (2-D) on the receiver for different concentration ratios (a) CR = 5 and (b) CR = 30

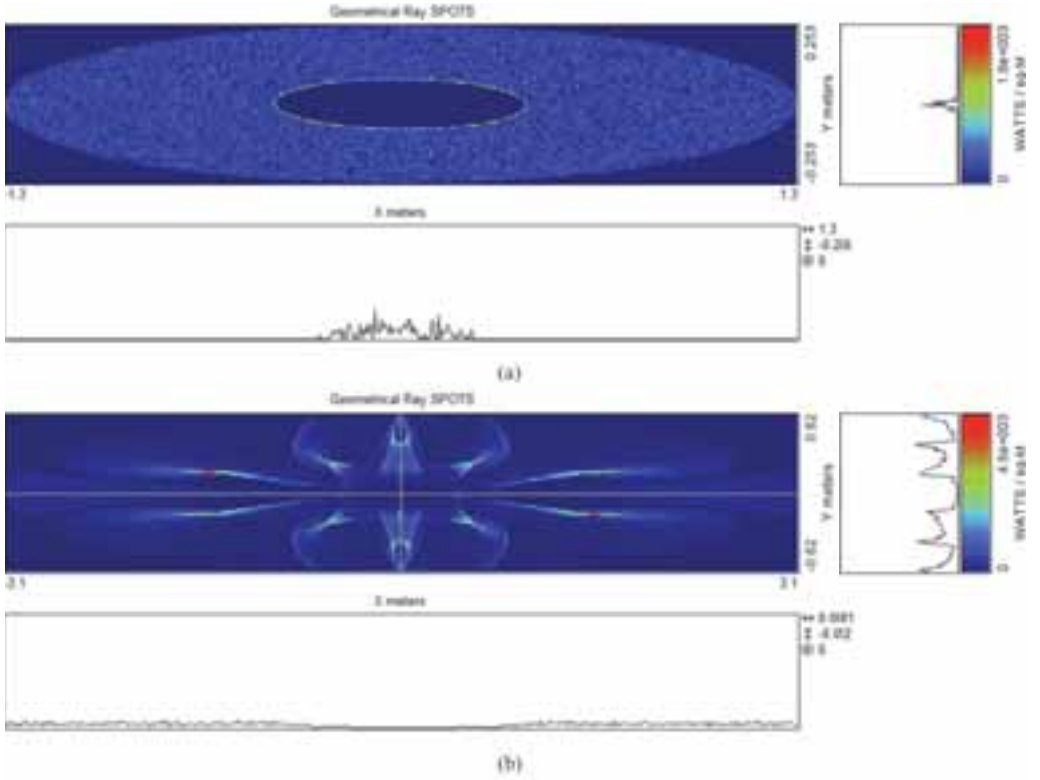

Fig. 10 Flux distribution (2-D) on the concentrator at different concentration ratios (a) CR = 5 and (b) CR = 30

6.3 Effect of receiver aperture

The effect of aperture width (W_r) of the top surface of the trapezoidal surface receiver of EHC on the optical performance is studied by keeping CR = 20 and H_r = 1.6 m. The different aperture width say, 30 mm, 45mm, 60mm, 90mm and 120 mm are studied. The variation of the optical efficiency of EHC for different aperture width is shown in Fig. 11. It can be seen that the variation of the optical efficiency for different aperture width is

negligible and it is found to vary around 22% for all aperture width considered. The flux distribution (2-D) on the receiver for different aperture width of 30 mm and 120 mm is shown in Fig. 12. When the receiver aperture width increases, the flux that is intercepted on the inclined surface is reduced, hence reducing the flux on the side surfaces of the receiver. Hence, it can be concluded that the effect of aperture width on the optical performance is negligible.

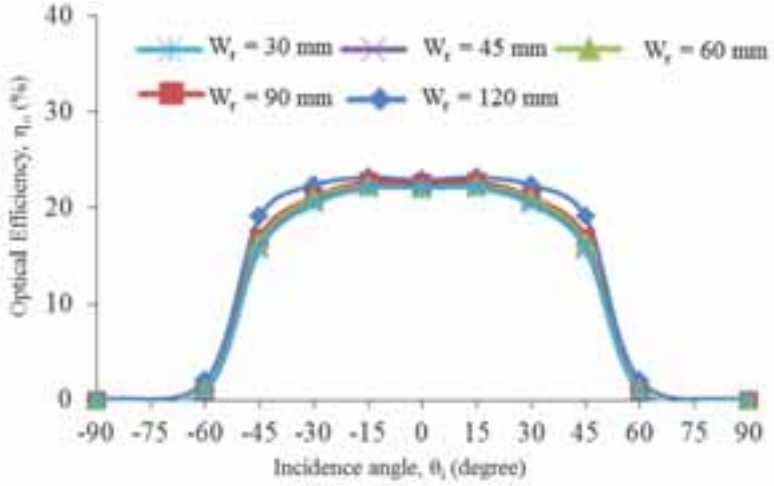

Fig. 11 Variation of optical efficiency for different aperture width

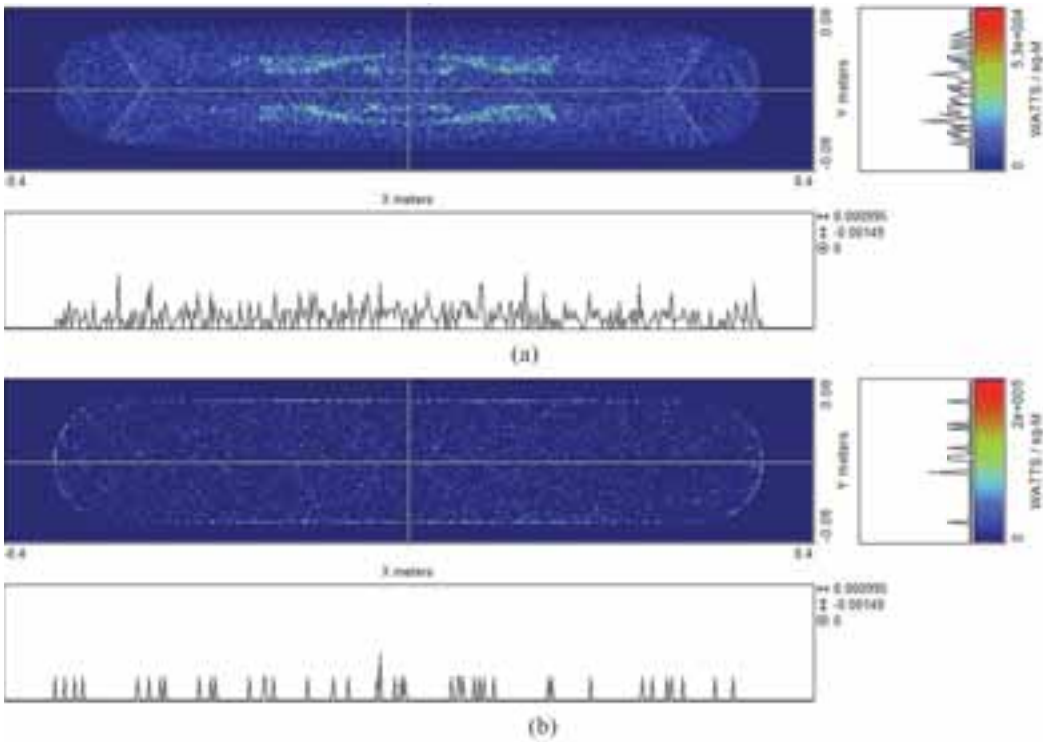

Fig. 12 Flux distribution on the receiver for different aperture width (a) 30 mm (b) 120 mm

6.4 *Effect of receiver height*

The effect of receiver height on the optical performance of EHC has been studied by varying the receiver height in four different values say 60, 90, 120 and 150 mm. Fig. 13 shows the variation of optical efficiency for different receiver height and it can be observed that the optical efficiency increases with receiver height. The flux variation on the receiver for different receiver height is shown in Fig. 14. It can be seen that, when the receiver height is varied, the amount of flux intercepted by the receiver is affected, consequently the optical efficiency of the system. It can be seen that the location of peak flux shifts from centre and moves outward when the height is increased. The variation of maximum flux on the receiver for different receiver height is found to be varying between 12kW/m^2 to 13 kW/m^2.

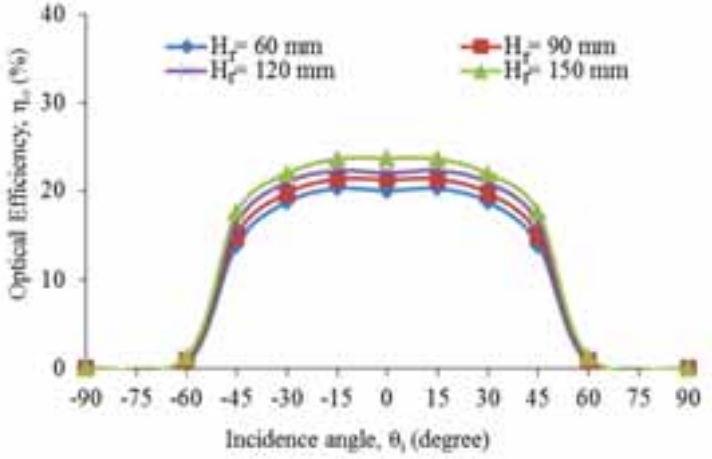

Fig. 13 Variation of optical efficiency for different receiver height

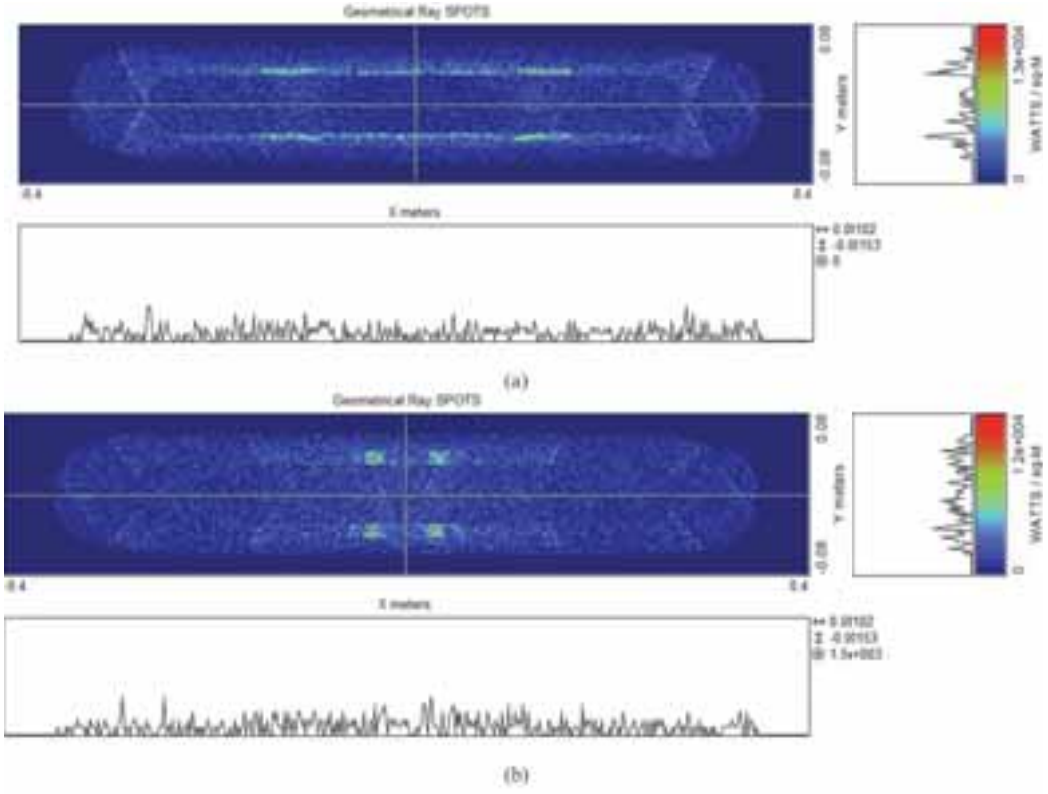

Fig. 14 Flux distribution on the receiver for different aperture width (a) 150 mm (b) 60 mm

7. Conclusion

The optical ray tracing analysis of a non-imaging concentrating collector with two types of receiver is studied. The effect of various parameters such as concentrator height, concentration ratio, receiver width and receiver height on optical performance of the system is studied. The flux distribution and optical performance of two types of receiver say flat receiver and trapezoidal surface receiver are compared and further based on the performance, trapezoidal receiver is considered for further analysis. The optical efficiency of the EHC system was found to be maximum at normal incidence and varies for different incidence angles. The optical efficiency varies between 5 – 15 % for the concentrators with height less than 1m whose acceptance angle is about ± 60º, whereas for concentrator height greater than 1m, acceptance angle is ± 45º and optical efficiency varies between 20 – 30 %. It can be observed that, for concentrator height of 0.4 m, peak flux intensity is 2.5×10^4 W/m^2 whereas for concentrator height of 2 m, it is 6.9×10^4 W/m^2. The effect of variation of CR is also studied. The effect of receiver aperture and height also play role in deciding the flux incident on the receiver. The effect of variation of receiver aperture width is negligible and it is found to vary around 22%. Similarly or variation of receiver height, flux incident varies between 12 –

13kW/m^2. This system can be effectively used for low and medium temperature applications based on the location with less/no tracking.

Nomenclature

a	Semi-major axis of concentrator at bottom aperture (m)
A	Semi-major axis of concentrator at top aperture (m)
A_{ap}	Aperture area (m^2)
A_r	Area of receiver (m^2)
b	Semi-minor axis of concentrator at bottom aperture (m)
B	Semi-minor axis of concentrator at top aperture (m)
c	Distance between focal point and centre of ellipse (m)
H_c	Height of concentrator (m)
H_r	Height of EHC receiver (m)
I	Flux (W/m^2)
m	Number of reflections
N	Number of rays
Wr	Aperture width of EHC receiver (m)
X,Y,Z	Cartesian coordinates (m)

Greek symbols

θ_a	Half acceptance angle (degrees)
θ_i	Solar incidence angle (degrees)
η_o	Optical efficiency (%)

Abbreviations

ASAP	Advanced Systems Analysis Program
CR	Concentration Ratio
EHC	Elliptical Hyperbolic Concentrator

References

Abdullahi, R.K. Al-Dadah, S. Mahmoud, R. Hood, 2015. Optical and thermal performance of double receiver compound parabolic concentrator, Appl. Energy. 159, 1–10.

Ali, I.M.S., Kew, P. A., O'Donovan, T. S., Reddy, K.S., Mallick, T.K., Optical performance evaluation of a 2-D and 3-D novel hyperboloid solar concentrator, In: World Renewable Energy Congress XI, Abu Dhabi, 1738–1743, 2009

Ali, I.M.S., O'Donovan, T. S., Reddy, K.S., Mallick, T. K., Optical performance of circular and elliptical 3-D static solar concentrators. In: ASES National Solar Conference, Phoenix AZ, USA, May 17 – 22, 2010

Ali, I.M.S., O'Donovan, T. S., Reddy, K.S., Mallick, T.K., 2013. An optical analysis of a static 3D concentrator, Sol. Energy. 88, 57–70.

BRO (Breault Research Organization, Inc.) 2013. ASAP Technical Publication, Tucson, Arizona. (www.brenault.com)

DiGarcia, M., and Jorgenson, G., Reflectech mirror film design flexibility and durability in reflecting solar applications, In: ASES National Solar Conference, Phoenix AZ, USA, May 17 – 22, 2010

Garcia-Botella, A.A. Fernandez-Balbuena, D. Vázquez, E. Bernabeu, Ideal 3D asymmetric concentrator, Sol. Energy. 83 (2009) 113–117.

Gottwald, S., 2012. The VNR Concise Encyclopedia of Mathematics, 2nd Edition, Springer, Netherlands.

Kalogirou, S. A., 2009. Solar Energy Engineering: Processes and Systems,1st Edition, Academic Press, USA

Reddy K.S. and Vikram T.S., Performance analysis of concave cavity surface receiver for a non – imaging solar collector, Proceedings of ISES Solar World Congress (SWC 2015), Daegu, Korea, 8-12 November 2015. http://doi:10.18086/swc.2015.10.11

Heat Loss Prediction from Solar LFR Linear Evacuated Surface Receiver with Variable 2-Stage Concentrated Flux

K. S. Reddy[1*], Shanmugapriya Balaji[1], T. Sundararajan[2]

[1]Heat Transfer and Thermal Power Laboratory,

[2]Thermodynamics and Combustion Engineering Laboratory

Department of Mechanical Engineering

Indian Institute of Technology Madras, Chennai – 600036, India

*Corresponding Author, Email:ksreddy@iitm.ac.in

Abstract

A numerical study has been carried out to analyse the thermal performance of the receiver system of solar Linear Fresnel Reflector (LFR) module. Realistic flux conditions obtained by the optical analyses are applied as the boundary condition to the circumference of the absorber. Heat losses caused by convection as well as radiation from the parabolic secondary receiver are investigated under evacuated and non-evacuated annular region between the absorber and the glass tube. The investigation has been carried out to determine the heat loss by varying the annular gap between the absorber tube and the protective glass.

Keywords: Solar flux, variable flux distribution, evacuated, non-evacuated condition

1. Introduction

A progressive method observed is the Linear Fresnel reflector (LFR) technology to harness the solar energy for power and thermal needs of the society. An LFR system consists of the primary mirror strips in conjunction with the uniaxial tracking system, receiver system comprising a glass tube enclosing the absorber with a secondary reflector.The receiver system of solar Linear Fresnel Reflector (LFR) module plays a vital part in the conversion of the solar rays to thermal energy (Reddy and Kumar, 2014), (Singh et al., 2010)) and the schematic of the LFR is shown in Fig. 1(a).The present work has been carried out based on the study carried by peers on a wide range of collectors. Zou et al., 2017 comprehensively studied the optical performance of parabolic trough collector based on Monte Carlo Ray Tracing method (MCRT) and theoretical method. The angle span of each flux distribution region was derived theoretically, and the variations of those parameters with different geometrical configurations were displayed. Geometrical parameters such as aperture width, focal length and absorber diameter had a greater influence on the performance of the system. It was concluded that the absorber diameter had to be larger than the spot size of the reflected light cone on the absorber to avoid rays escaping which can cause great optical loss. Guadamud et al., 2015 modelled an LFR with a parallel modular object-oriented methodology which considered the elements of the receiver system namely the insulation material, glass cover, tube, pipe, etc. The global model is composed of 4 submodels -heat conduction, two/single-phase flow, thermal radiation and natural convection. It was found that the CFD&HT simulations using LES modelling allowed more realistic results. Chaitanya Prasad et al., 2017 used the variable aim lines for primary mirrors to defocus and spread the radiation flux in a more uniform manner over the absorber. Both the tilt angles and the radii of curvature of the individual Fresnel mirrors are modified to obtain a better flux uniformity. With the variable aim line concept high optical efficiency of 76.4% and a coefficient of flux variation value of 0.13 were obtained. On the other hand, 74.9% and 70.9% of optical efficiencies along with 0.17 and 0.33 values of coefficient of variation were obtained with compound parabolic concentrator and trapezoidal concentrator profiles respectively. Okafor et al., 2017, 2014 carried out a numerical study on the influence of circumferential uniform and non-uniform solar heat flux distributions on the internal and overall heat transfer coefficients of the absorber tubes of a linear Fresnel solar collector was investigated. A 3D steady-state numerical simulation was implemented based on ANSYS Fluent code version 14. The non-uniform solar heat flux distribution was modelled as a sinusoidal function of the concentrated solar heat flux incident on the circumference of the absorber tube. The k–e model was used to study the turbulent flow of the heat transfer fluid through the absorber tube. Hence it is clear that study of modelling and the heat loss analysis from the receiver system becomes crucial to determine the efficiency of the system. In the present heat loss analysis, circumferential non-uniform heat flux distribution on the outer wall of the absorber tube is considered. Investigation of non-

doi:10.18086/swc.2017.31.15 Available at http://proceedings.ises.org

uniform flux distribution around the absorber is the more practical way of analysis compared to the constant flux conditions carried out by the peers. In the present work the investigation is carried for two cases: First, the annular area between the absorber tube and the protective glass tube is considered to be in the non-evacuated state and secondly, in the evacuated state. Heat losses in the convection and radiation mode are analysed for different flux conditions.Investigation on the heat loss dependent on the annular gap between the absorber and the protective glass tube are studied. Initial work deals with the optical distribution of the flux and the distribution have been homogenised with the parabolic profiled secondary reflector (Balaji et al., 2016). The variable distribution around the absorber is shown in Fig. 1(b).

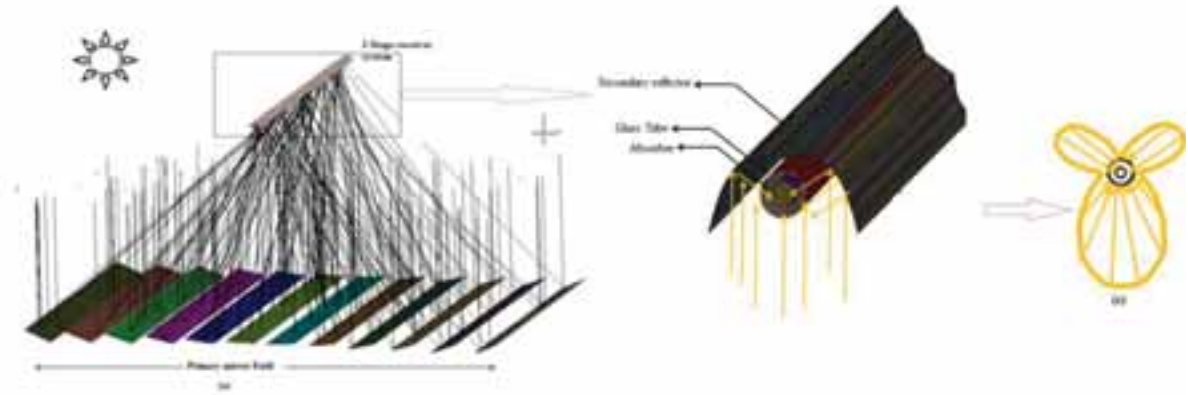

Fig. 1: (a) Schematic representation of Linear Fresnel Concentrator with secondary reflector (b) 2-Stage reflector system with solar ray (c) variable flux distribution around absorber

2. Description of LFR system

The Linear Fresnel Reflector/Concentrator(LFR) consists of an array of twelve long, parallel mirrors. The primary mirrors are tilted suitably and are equipped with one-dimensional tracking such that the solar rays from each mirror can be focused on one or more number of absorbers.An evacuated glass cover surrounds the absorber to prevent convective heat losses to the atmosphere. In the absence of the evacuated glass cover, the aperture opening of the secondary reflector covered by a glass pane. The absorber with the glass cover is mounted inside the secondary reflector module. Parameters of the pilot plant developed in Vallipuram (12.65N, 79.74E), Tamil Nadu, India is considered for the comprehensive study. The LFR system consists of a storage-integrated solar collector field of approximately 125 kWth capacity with the variable steam output (50 bar pressure and 350–400 °C temperature). Twelve primary reflectors with mild parabolic curvature are managed by a single axis tracking system. An absorber tube placed inside an evacuated glass cover for the reduction of convective heat losses is placed at the focal point of the primary reflectors. A selectively coated absorber tube for higher optical emissivity is used. A secondary reflector parabolic in profile surrounds both the absorber with the glass tube. In order to improvise the flux distribution along the circumference of the absorber thereby increase the concentration ratio, secondary reflectors are used. The second stage reflector maximizes the flux coverage area by re-reflecting the rays to the surface of the absorber. The 2 –stage reflector also ensures to enlarge the focused rays on the absorber thereby preventing the hot spots. Progressive analysis has been carried out to estimate the heat losses from the receiver system. Initially, the optical analysis is done to obtain an optimized flux along the circumference of the absorber and then the thermal study is performed.

3. Thermal Analysis

The thermal investigation is carried out for the receiver system comprising of the parabolic secondary reflector with an absorber tube placed in a glass tube. Optically optimised parameters from the earlier study namely the acceptance angle of the 2-stage reflector, truncation point on the reflector, the focal position of the absorber tube, the ratio of the gap between the reflector and the absorber to the height of the reflector are considered for the numerical study. The flux thus obtained from the optical analysis is applied as a user-defined function (UDF) in the form of a polynomial curve. The curve is a function of the angular position of the flux along the circumference of the absorber. The investigation is carried out with the different flux conditions and a parametric analysis is carried out to determine the heat loss for the different annular gap between the absorber and the glass tube. Laminar, steady state, 2D governing equations are solved in Fluent 14.5.The flow and thermal behaviours of the receiver system are considered under non-Boussinesq conditions.

3.1 Governing Equations

Flow and the heat transfer in the 2-stage reflectors are solved simultaneously by the mass, momentum and energy equations with Cartesian coordinates by Fluent Inc (2005). By the law of conservation of mass, the continuity equation is given by:

$$\frac{\partial(\rho_f u)}{\partial x} + \frac{\partial(\rho_f v)}{\partial y} = 0 \quad \text{(eq. 1)}$$

x- y Momentum equations:

$$\rho_f\left(u\frac{\partial u}{\partial x} + v\frac{\partial u}{\partial y}\right) = -\frac{\partial P}{\partial x} + \frac{\partial}{\partial y}\left(\mu\frac{\partial u}{\partial y}\right) + \frac{\partial}{\partial x}\left(\mu\frac{\partial u}{\partial x}\right) \quad \text{(eq.2)}$$

$$\rho_f\left(u\frac{\partial u}{\partial x} + v\frac{\partial u}{\partial y}\right) = -\frac{\partial P}{\partial x} + \frac{\partial}{\partial x}\left(\mu\frac{\partial v}{\partial y}\right) + \frac{\partial}{\partial y}\left(\mu\frac{\partial v}{\partial y}\right) + \rho g\beta(T-T_{ref}) \quad \text{(eq.3)}$$

Energy equation is solved by:

$$\rho_f C_p\left(u\frac{\partial T}{\partial x} + v\frac{\partial T}{\partial y}\right) = \frac{\partial}{\partial y}\left(k_f\frac{\partial T}{\partial y}\right) + \frac{\partial}{\partial x}\left(k_f\frac{\partial T}{\partial x}\right) \quad \text{(eq.4)}$$

where u,v represents the velocity components in x and y-direction respectively,ρ is the density of the air inside the cavity in kg/m^3, P is the pressure in N/m^2,k_f represents the thermal conductivity of the fluid in W/mK.

Surface-to-Surface (S2S) radiation model is used to model the radiation heat transfer of the secondary reflector system. This model helps to assume the receiver system in an air enclosed domain to be a non-participating medium by ignoring the emission and the scattering effects. The incident flux from the surface comprises of two components, the emitted flux and the reflected flux. Both the components of flux together constitute the radiosity (J_i) of the surface. The radiated flux depends on the flux falling on the surface from the surrounding and it is given by (Siegel, R., Howell, 2002) as

$$q_{out,i} = \varepsilon_i \sigma T_i^4 + (1-\varepsilon_i) q_{in,i} \quad \text{(eq.5)}$$

Interception by the two surfaces by radiation is defined as view factor F_{ij} that is independent on the surface properties and temperature. Hence the incident flux is given by.

$$A_i q_{in,i} = \sum_{j=1}^{N} A_j q_{out,j} F_{ji} \quad \text{(eq.6)}$$

Based on the reciprocity theorem

$$A_j F_{ji} = A_i F_{ij} \quad \text{(eq.7)}$$

Replacing (7) in (6),

$$q_{in,i} = \sum_{j=1}^{N} q_{out,j} F_{ji} \quad \text{(eq.8)}$$

$$q_{out,i} = \varepsilon_i \sigma T_i^4 + (1-\varepsilon_i) \sum_{j=1}^{N} F_{ij} q_{out,j} \quad \text{(eq.9)}$$

The sum of the reflected and the emitted fluxes, radiosity J_i is defined as the total radiation energy leaving a surface per unit time and per unit area. Hence

$$E_i = J_i - (1-\varepsilon_i) \sum_{j=1}^{N} F_{ij} J_j \quad \text{where } E_i = \varepsilon_i \sigma T_i^4 \quad \text{(eq.10)}$$

$E_i = \sum_{j=1}^{N} (\delta_{ij} - (1-\varepsilon_i) F_{ij}) J_i$ where δ_{ij} is the kronector delta given by $\delta_{ij} = \begin{cases} 1 \; when \; i = j \\ 0 \; when \; i \neq j \end{cases}$

Hence the radiosity expression is given by $E = KJ$ where K is a $N \times N$ matrix of the form

$$K = (\delta_{ij} - (1-\varepsilon_i) F_{ij)} \quad \text{(eq.11)}$$

In the above equations, J is the radiosity vector and E is the emissive power vector.

3.2. Boundary conditions

The 2-stage receiver system under study is an open aperture system and all the modes of heat transfer conduction, convection and radiation re influenced by the atmospheric condition. Hence the simulation is carried out by enclosing the receiver system in a domain property is simulated with the ambient conditions of temperature and pressure. The inlet of the domain is provided with pressure inlet boundary condition and the outlet of the domain is pressure outlet conditions, while the sides of the domain are pressure inlet conditions. The absorber tube is exposed to the flux reflected by the primary mirrors and the flux re-reflected by the secondary reflectors. Hence the non-uniform flux obtained from the optical study is imbibed as the boundary condition. The non-uniform flux is applied as the user-defined function. The absorber is coated with sputtered cermet of emissivity 0.075.The coupled condition is provided as a boundary value for the glass tube with the transmissivity of 0.95.Figure 2 shows the boundary condition of the 2-stage secondary reflector.

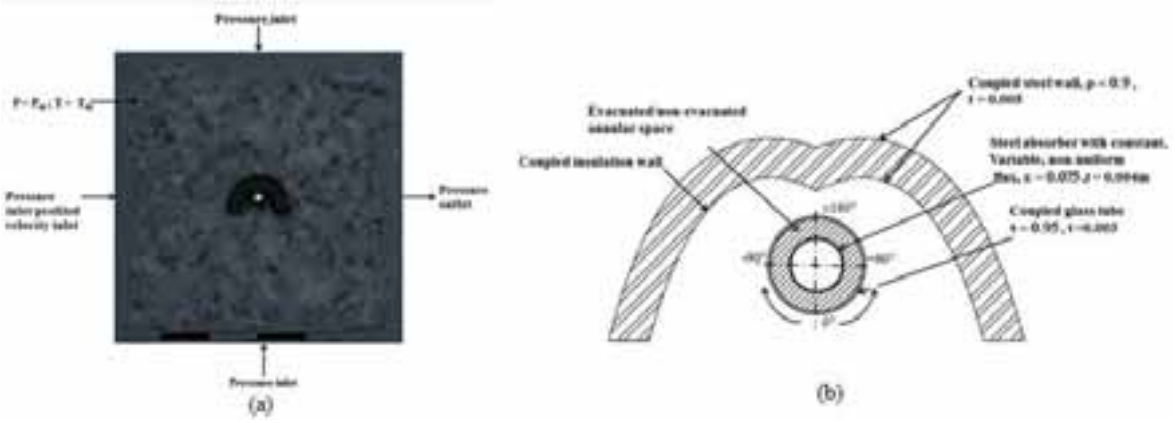

Fig. 2: Boundary condition of domain with 2-stage reflector of Linear Fresnel Concentrator (b) Boundary condition of 2-Stage reflector system

3.3. Boundary conditions

The size of the simulated domain is crucial since the heat loss output is dependent on it. Hence simulation is optimised by varying the inlet, side wall and the output length of the domain. Optimised domain size is assessed to be about 20D from the absorber on all the four sides. Skewness–Neighbor coupling of PSO algorithm is adopted with the convergence criterion of 10^{-6} on the residuals of the continuity equation and momentum equation. Deviation observed for the grid size with elements 8, 56,178 is appreciable to proceed the simulation. Validation of the present work was done with the work carried on by Reddy and Kumar, 2014; Sahoo et al., 2012 and the deviation in the results were found to be less than 10% which is acceptable.

4. Results and Discussion

A parametric study has been carried out based on the direct normal irradiance (DNI) and the annular gap between the absorber and the protective glass. The annular gap is non-dimensionalized by considering the ratio of the diameter of the absorber and the diameter of the protective glass. The study has been carried out for two different conditions of the annular gap: one, when the annular gap is filled with air as the residual gas and second, considering vacuum in the annular region.

4.1 Effect of DNI on the heat loss from the 2-stage receiver system

Temperature contours of the parabolic secondary reflector for DNI for 750W/m^2 and 1000W/m^2 for non-evacuated and evacuated annular region are shown in Fig.3.It is observed that because of the presence of air in the annular space between the absorber tube and the protective glass tube, buoyancy effect exist in the annular space. The hot wave in the annular space move upwards and the heat transfer occurs to the entire cavity region. Plume formation apparently illustrates the heat loss to the atmosphere. Whereas when the annular region is evacuated, the heat transfer from the upper portion of the absorber spread out symmetrically on both sides of the absorber within the cavity region. As the DNI increases the temperature increases and the hot wave distributes throughout the cavity and heat losses from the aperture opening.

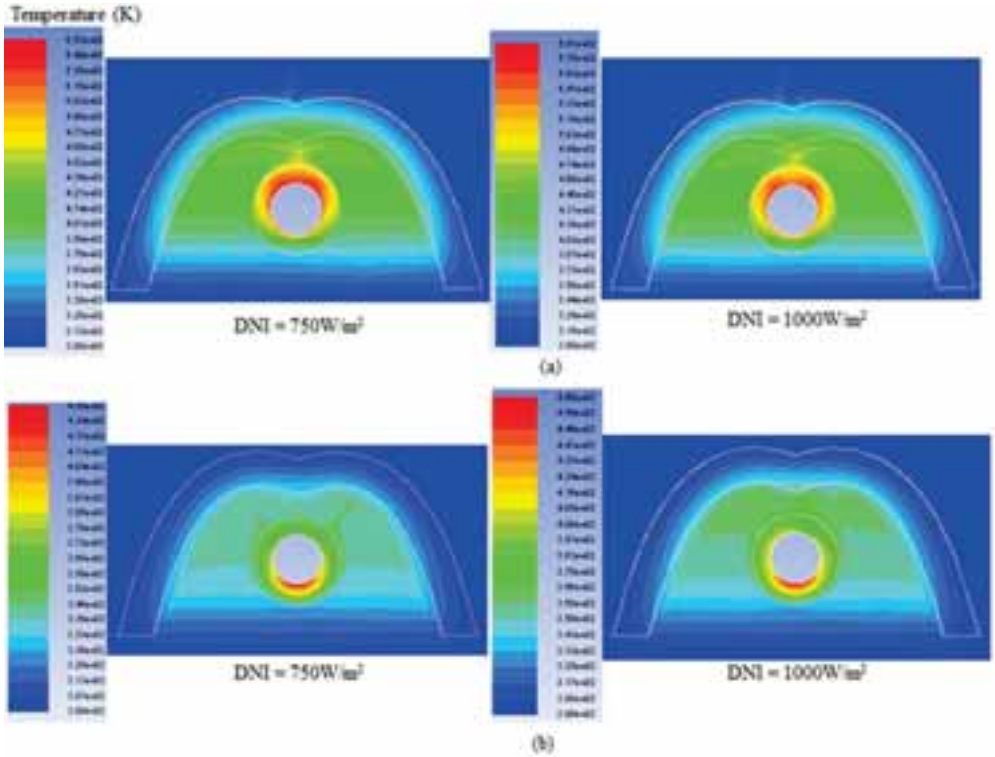

Fig. 3: Temperature contours of PB secondary reflector for different non-uniform flux distribution around the absorber tube with (a) non-evacuated annular (b) evacuated annular region

Figure 4 shows the total heat loss from the receiver system for the DNI ranging from 250W/m^2 to 1000W/m^2.under the non- evacuated condition i.e., when the annular gap is filled with air, the heat loss varies from 47.14W/m to 172 W/m for 250W/m^2 to 1000W/m^2 respectively .When the annular region is evacuated, the percentage of heat loss is reduced from 16% to 70%.It is observed that at lower DNI, the percentage of deviation is less compared to that at higher DNI.As expected, as the DNI increases, the percentage of heat loss also increases.

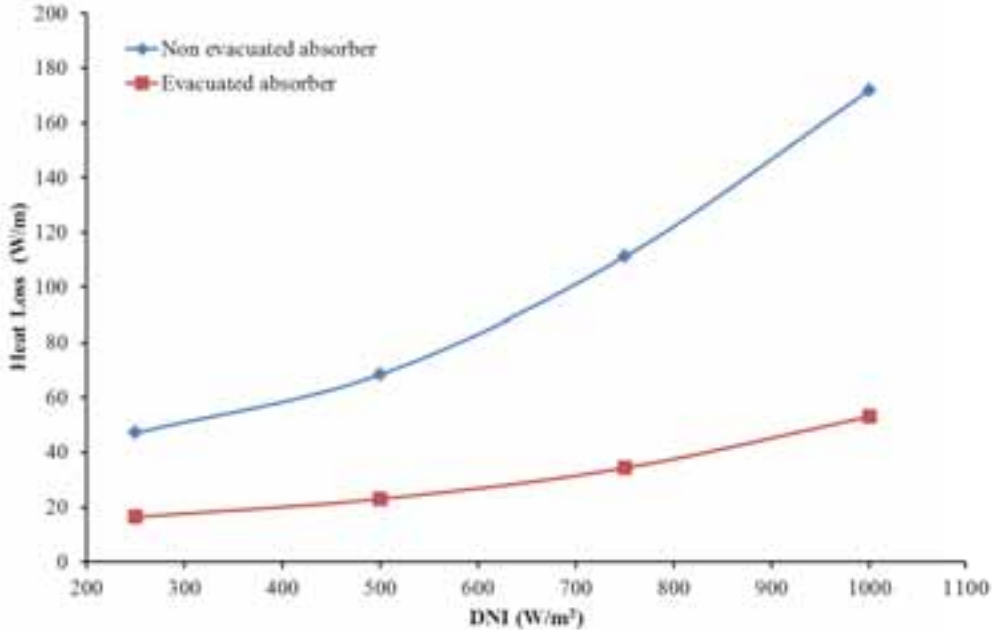

Fig. 4: Total heat loss for different DNI from the 2-stage receiver system

Figure 5 shows the convective and radiative heat losses for DNI ranging from 250W/m^2 to 1000W/m^2 for evacuated and non-evacuated annular region between the absorber and the glass tube. It is observed that the convection heat loss gets reduced by 40% under evacuated condition. Percentage of radiation heat loss varies between 28% and 57.5% from lower to higher flux conditions

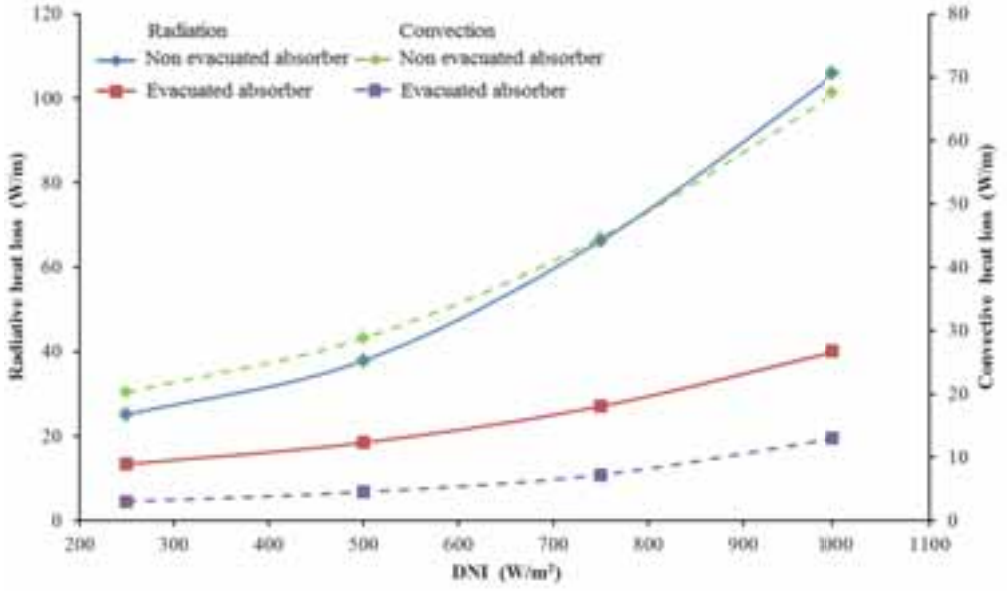

Fig. 5: Radiative and convective heat losses for different DNI

The individual components of heat loss, the radiative and the convective heat losses are studied. It is perceived that as the annular region is evacuated, the convective mode of heat transfer is minimized to a negligible amount and is shown in Fig. 5.When the residual gas in the gap is filled with air, the convective heat loss lies in the range of 30W/m to 100W/m for 250W/m^2 to 1000W/m^2. When the tube is evacuated, the convective heat loss reduces from 3W/m to 15W/m while the radiative loss is about 13W/m to 40W/m. It is obvious that as the tube is evacuated, the convective component of the heat loss is completely negligible.

4.2. Effect of gap between the absorber and the glass tube on the heat loss

Non-dimensionalization of the annular distance between the absorber and the glass tube is carried out by considering the ratio of the diameter of the absorber to the diameter of the protective glass.Total and the individual

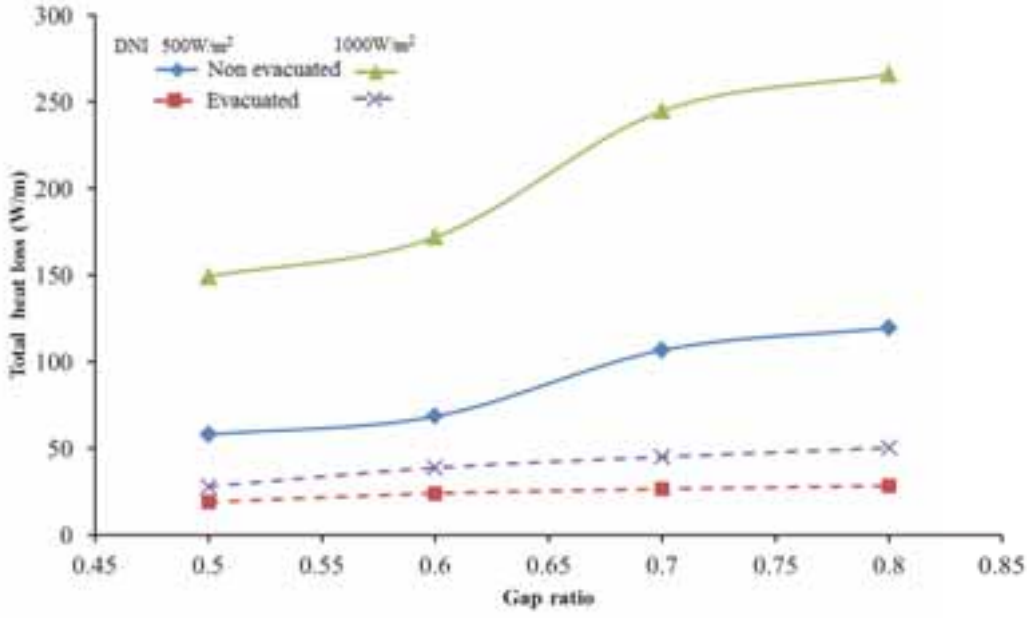

Fig. 6: Total heat losses for gap ratio between the absorber and the glass tube

components of heat transfer are studied.Variation in the heat loss for DNI of 500W/m^2 and 1000W/m^2 are investigated for both the evacuated and the non-evacuated conditions.Based on the commercial availability of SS absorber tube, the diameter of the absorber tube and the protective glass tube for the present study is chosen.Without compromising the diameter with the performance of the receiver system, it is observed from Fig. 6 that, the ratio of 0.6 has better performance and optimized annular region for less heat loss. When the tube is evacuated, the heat loss is observed to be constant for the range of gap ratio.The convective and the radiative heat loss components for the gap ratio between 0.5 and 0.8 for DNI of 500W/m^2 and 1000W/m^2 are shown in fig.7 and fig. 8 respectively. When the tube is non-evacuated both the

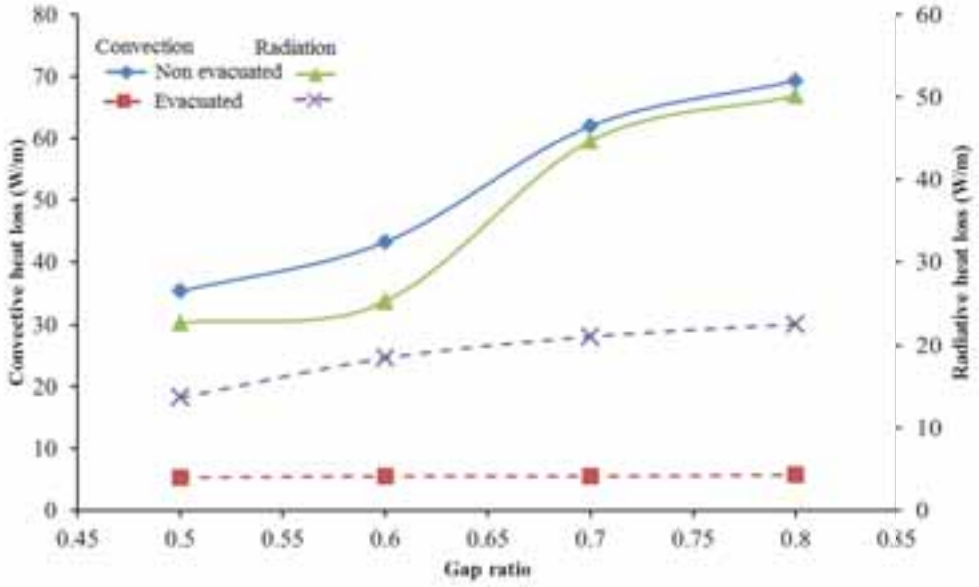

Fig. 7: Convective and radiative heat losses for different ratio of gap between the absorber and the glass tube for DNI of 500W/m^2

convective and the radiative components equally play a role in the heat loss. From Fig. 7, gap ratio of 0.5 to 0.6, heat loss of 35W/m and 22W/m on convective and radiative mode were observed. While at a higher ratio, convection and radiation heat loss exceed till 69W/m and 50W/m respectively. When the tube has vacuum, radiation component increases from 13.67W/m to 22.6W/m for the gap ratio from 0.5 to 0.8.

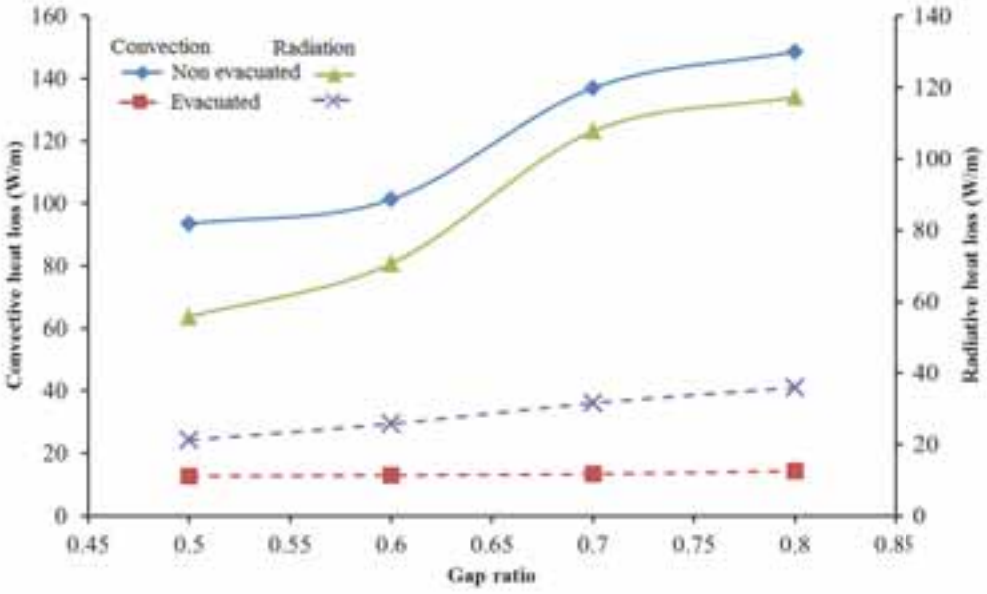

Fig. 8: Convective and radiative heat losses for different ratio of gap between the absorber and the glass tube for DNI of 1000W/m^2

The convective heat loss is at a constant level for different gap ratio.In Fig. 8, similar trend as of Fig. 7 is perceived.The convection and the radiation heat losses from the non-evacuated receiver increases by 57.5% and 58.5% and for evacuated conditions 36% and 59% respectively as the DNI increases from 500W/m^2 to 1000W/m^2 for the range of gap ratio.

5. Conclusion

A numerical study has been carried out to determine the heat loss from the 2-stage receiver system of the pilot plant in Vallipuram (12.65N, 79.74E), Tamil Nadu, India. Comprehensive analyses have been carried out to optimize the profile of the receiver system and then the thermal performance has been carried out. In the present work, the 2-stage receiver system is investigated when the absorber is under evacuated and non-evacuated conditions. A parametric study has been carried out by varying the DNI and the annular gap between the absorber and the protective glass. When the gap is filled with air, the heat loss varies from 47.14W/m to 172 W/m for 250W/m^2 to 1000W/m^2 respectively and when the region is evacuated, the percentage of heat loss is reduced from 16% to 70%. The convection and the radiation heat losses from the non-evacuated receiver increases by 57.5% and 58.5% and for evacuated conditions 36% and 59% respectively as the DNI increases from 500W/m^2 to 1000W/m^2 for the range of gap ratio.

6. References

Balaji, S., Reddy, K.S., Sundararajan, T., 2016. Optical modelling and performance analysis of a solar LFR receiver system with parabolic and involute secondary reflectors. Applied Energy 179. doi:10.1016/j.apenergy.2016.07.082

Chaitanya Prasad, G.S., Reddy, K.S., Sundararajan, T., 2017. Optimization of solar linear Fresnel reflector system with secondary concentrator for uniform flux distribution over absorber tube. Solar Energy 150, 1–12. doi:10.1016/j.solener.2017.04.026

Guadamud, E., Oliva, A., Lehmkuhl, O., Rodriguez, I., González, I., 2015. Thermal Analysis of a Receiver for Linear Fresnel Reflectors. Energy Procedia 69, 405–414. doi:10.1016/j.egypro.2015.03.047

Okafor, I.F., Dirker, J., Meyer, J.P., 2017. Influence of non-uniform heat flux distributions on the secondary flow, convective heat transfer and friction factors for a parabolic trough solar collector type absorber tube. Renewable Energy 108, 287–302. doi:10.1016/j.renene.2017.02.053

Okafor, I.F., Dirker, J., Meyer, J.P., 2014. Influence of circumferential solar heat flux distribution on the heat transfer coefficients of linear Fresnel collector absorber tubes. Solar Energy 107, 381–397. doi:10.1016/j.solener.2014.05.011

Reddy, K.S., Kumar, K.R., 2014. Estimation of convective and radiative heat losses from an inverted trapezoidal cavity receiver of solar linear Fresnel reflector system. International Journal of Thermal Sciences 80, 48–57. doi:10.1016/j.ijthermalsci.2014.01.022

Sahoo, S.S., Singh, S., Banerjee, R., 2012. Analysis of heat losses from a trapezoidal cavity used for Linear Fresnel Reflector system. Solar Energy 86, 1313–1322. doi:10.1016/j.solener.2012.01.023

Siegel, R., Howell, J., 2002. Thermal Radiation Heat Transfer, 4th Editio. ed. Taylor & Francis, New York.

Singh, P.L., Sarviya, R.M., Bhagoria, J.L., 2010. Heat loss study of trapezoidal cavity absorbers for linear solar concentrating collector. Energy Conversion and Management 51, 329–337. doi:10.1016/j.enconman.2009.09.029

Zou, B., Dong, J., Yao, Y., Jiang, Y., 2017. A detailed study on the optical performance of parabolic trough solar collectors with Monte Carlo Ray Tracing method based on theoretical analysis. Solar Energy 147, 189–201. doi:10.1016/j.solener.2017.01.055

7. Nomenclature

Quantity	Symbol	Unit
Area	A	m^2
Heat loss	$\dot{Q}$	W/m
Temperature	T	K
Emissivity	ε	
Stefan-Boltzmann constant	σ	W m^{-2} K^{-4}
Density	ρ	Kgm^{-3}

Experimental evaluation of evacuated tube collectors with heat pipes to avoid stagnation loads in a domestic hot water system

Bert Schiebler, Finn Weiland, Federico Giovannetti

Institut für Solarenergieforschung Hameln (ISFH), Am Ohrberg 1, 31860 Emmerthal (Germany)

Abstract

Heat pipes in solar thermal collectors can reduce thermal loads in the solar circuit by using the physical effect of dry out limitation. By avoiding high temperatures and vapor formation, simplified, more reliable and cost effective solar thermal systems can be designed. The paper investigates a newly developed evacuated tube collector based on optimized heat pipes able to limit the temperature loads at the manifold up to a desired value. On the basis of efficiency measurements on a prototype heat pipe collector, we determine the annual yield of a collector field in a domestic hot water system compared to an identical system with direct flow collector according to ISO 9459-5. The results are validated by simulations with TRNSYS and show no significant difference between the performances of the two systems. By means of extensive outdoor stagnation tests on the same fields, we report a maximum temperature of 125 °C in the solar circuit of the heat pipe system, which is 95 K lower compared to temperature measured in the reference system.

Keywords: heat pipe, stagnation temperature, overheating protection, evacuated tube collector, dynamic system testing

1. Introduction

Heat pipes in solar thermal collectors are state-of-the-art devices for the heat transfer from the absorber plate to the solar circuit. In comparison to direct flow collectors the heat pipe represents an additional thermal resistance in the heat flow path. Therefore, a high thermal performance of the heat pipes is essential to achieve a high collector efficiency. Beside the simplified collector hydraulic the use of heat pipes provides the advantage of decoupling the absorber plate from the fluid circuit. If the two-phase flow inside the heat pipe is suppressed beginning from a certain temperature, no more heat is transferred from the absorber plate to the manifold. By taking advantage of this physical effect, which is called the dry-out limit of heat pipes, the maximum temperature in the solar fluid can be limited to reduce thermal loads. The shut-off behavior and the maximum temperature are mainly determined by the type and the mass of working fluid in the heat pipe. Above this temperature, the fluid exists only in the vapor phase, so that the heat pipe heat transport ability is disabled. The maximum temperature in the connected solar circuit can be limited to such an extent that the evaporation of the solar circuit fluid can be completely avoided. In contrast to other technologies, the temperature limitation by heat pipes is inherently safe and independent from thermomechanical devices. The suppression of vapor formation in the solar circuit leads to simplified and more reliable system configurations and to a reduction of the overall system costs.

2. Evacuated tube collector prototype with novel heat pipes

We developed and investigated an evacuated tube collector prototype with novel heat pipes by means of indoor performance measurements with a sun simulator according to EN ISO 9806. The evacuated tubes with pentane-filled heat pipes were manufactured in cooperation with the German company NARVA Lichtquellen GmbH & Co. KG. The prototype collector consists of ten single tubes, which are connected with the solar circuit by a typical manifold. The collector power curve was measured at an average wind speed of 3 m/s and an ambient temperature of about 26°C. Figure 1 shows the measurement results and compares the efficiency curve of the heat pipe collector to that of a similar direct flow collector (standard collector). The conversion factor of the new prototype amounts to 75.4 % and is about 2 %-absolute lower than the standard collector, which is a typical difference caused by the additional thermal resistance of the heat pipe in the heat transfer path. Up to an operating temperature of about 75 °C both collectors have nearly the same heat loss coefficients. Above this

doi:10.18086/swc.2017.31.16 Available at http://proceedings.ises.org

temperature the heat loss coefficient of the heat pipe collector changes significantly as a result of the starting dry-out process, as represented by the characteristic kink point of the efficiency curve. As consequence of this, the stagnation temperature in the solar circuit takes place at 125 °C (measured without wind), which is significantly lower compared to the standard collector.

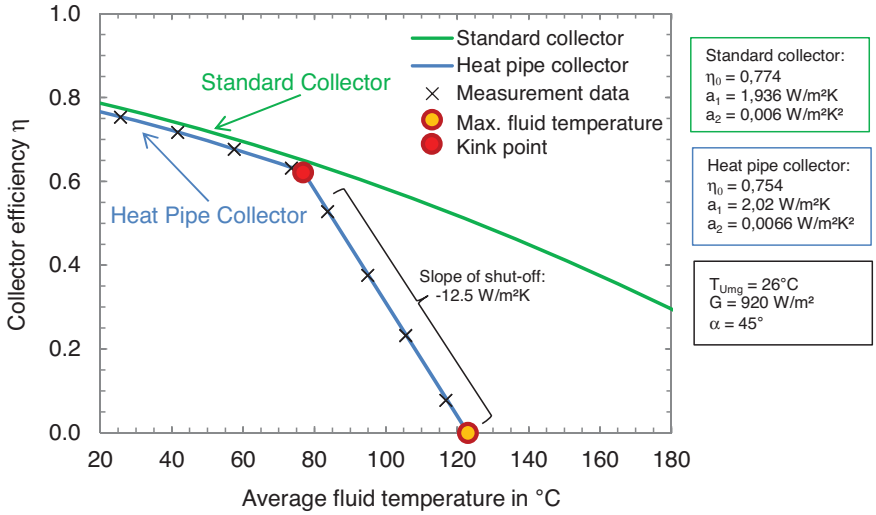

Fig. 1: Efficiency curve and coefficients of the prototype (measurement) and of a similar standard collector (TÜV-Rheinland 2014)

3. Experimental investigation of the system behavior

3.1. Experimental setup

For a comprehensive evaluation of the system behavior of heat pipe collectors with temperature limitation two identical experimental setups were installed on our test roof, which differ only in the collector hydraulic. We compared a prototype collector with deactivating heat pipes with an evacuated tube collector with direct flow as reference (Figure 2). Both systems consist of a field with an aperture area of 6 m² and a hot water tank with a volume of 400 l, which represent a common design for domestic hot water systems. The expansion vessel and all other solar circuit components are dimensioned in conformity with common guide lines. The specific system parameters of both systems are listed in Table 2 in the Appendix. Both solar plants are equipped with the necessary measurement and system technology according to ISO 9459-5 (see Figure 3, left). Additional temperature sensors and pressure measurement devices are installed in both solar circuits for investigating the stagnation loads (see Figure 3, right).

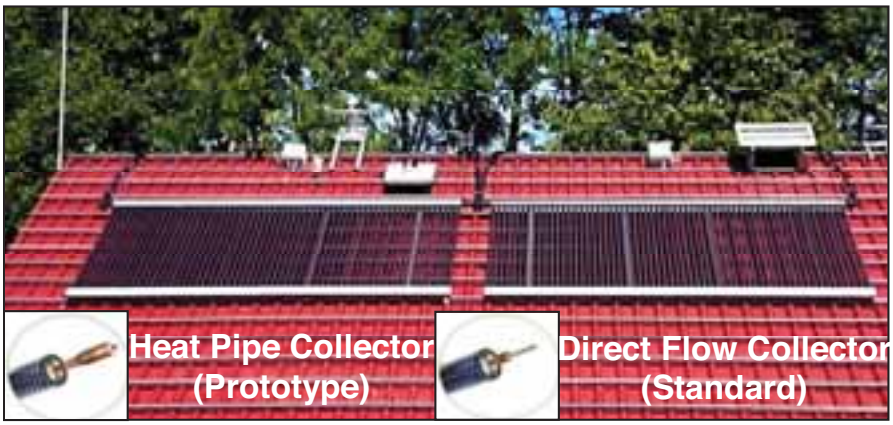

Fig. 2: Test roof with both prototype and reference evacuated tube collector fields

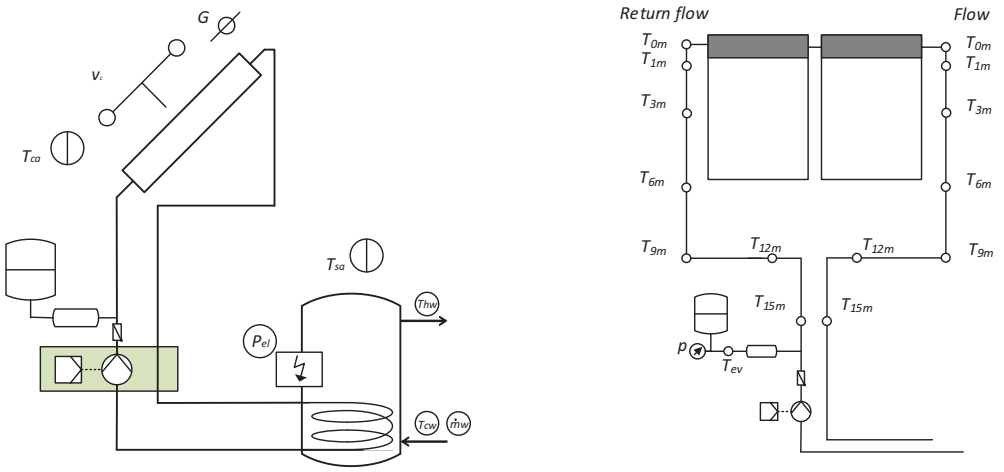

G	Global radiation	T_{ca}	Collector ambient temp.
P_{el}	Power of auxiliary heater	T_{st}	Storage ambient temp.
$\dot{m}_W$	Mass flow rate	T_{cw}	Inlet temp. storage
v_c	Wind speed	T_{hw}	Outlet temp. storage

T_{im}	Temperature of solar piping (i = distance from collector)
T_{ev}	Temperature of expansion vessel
p	System overpressure

Fig. 3: System scheme according to ISO EN 9459-5 (left) and additional sensors in the solar circuit (right)

The aim of the DST procedure is to determine the performance of complete solar systems under real conditions. The system is investigated under characteristic operating conditions by setting defined test sequences. Each sequence represents a separate period of measurement and needs several days. A complete data set consists of four measurement files, each with one sequence. These data can be used in a system simulation to determine the annual yield. The identified model parameters of both systems are shown in Table 1. The effective collector area *Ac** describe not only the collector geometry but also its optical properties. The slight difference can be explained by the lower conversion factor of the heat pipe collector (see Figure 1). The other parameters are almost in the same range.

Tab. 1: Identified model parameters of the dynamic system testing procedure for both the heat pipe and the standard system

Parameters	Symbol	Unit	Heat pipe system	Standard system
Effective collector loop area	A_C*	m^2	4.44	4.61
Heat-loss coefficient of the collector loop	u_C	$Wm^{-2}K^{-1}$	4.47	4.39
Heat-loss rate of the store	U_S	WK^{-1}	2.60	2.62
Heat capacity of the store	C_S	MJK^{-1}	1.54	1.48
Fraction of the store heated by the auxiliary heater	f_{aux}	-	0.573	0.595[1]
Draw-off mixing parameter	D_L	-	0.017	0.019
Collector loop stratification parameter	S_C	-	0.009	0.005

3.2. System performance in operation mode

The system performance is expressed by the annual yield and was determined by operating the two systems in parallel operation under identical conditions according to the DST procedure described in ISO 9459-5 (2007). The results depend on the tapping rates and on the climatic conditions of the considered locations. In general, the differences between the prototype and the reference system are almost negligible, as shown in Figure 4 (left) at a tapping rate of 200 l/d. For Würzburg, representing middle European climate, the deviation in annual yield amounts to 20 kWh/a (0.8 %). Thus, the auxiliary energy demand is increased by 20 kWh/a (2 %). For locations

[1] The annual yield is simulated with the same fraction values f_{aux} = 0.57 for both systems, because identical storages and auxiliary heaters are used.

with higher solar irradiation such as Athens or Davos the annual yield reduction of the heat pipe system further decreases down to 0.4 %. For locations with lower solar irradiation such as Stockholm, on the contrary, it increases up to 1.2 %.

The quotient of the annual yield Q_{sol} and the whole energy demand for domestic hot water Q_{DHW} is defined as the fractional system gain f_{sol} and is expressed by Equation 1. In general, the fractional system gain for both systems decreases with higher daily tapping rates (see Figure 4, right for Würzburg). For small tapping rates (< 100 l/d), the required temperature level, which has to be reached by the solar collector for contributing to the energy supply, has a negative impact on the performance, due to the prolonged standstill time and the increased heat losses. For common tapping rates of 100 to 300 l/d, the fractional system gain of both solar systems ranges between 77 and 60 %.

$$f_{sol} = \frac{Q_{Sol}}{Q_{DHW}} \qquad \text{(eq. 1)}$$

The deviations of the fractional system gain of the heat pipe system compared to the standard system are almost constant, between -0.5 and -0.8 %-absolute over the whole range of the considered tapping rates. That can be explained by the slightly lower annual yield of the heat pipe system. The losses in annual yield amount to about 1 % compared to the standard system (see Figure 4 right). That leads to higher auxiliary energy demands, which range between 1.5 and 3.5 % (about 2 % for typical tapping rates).

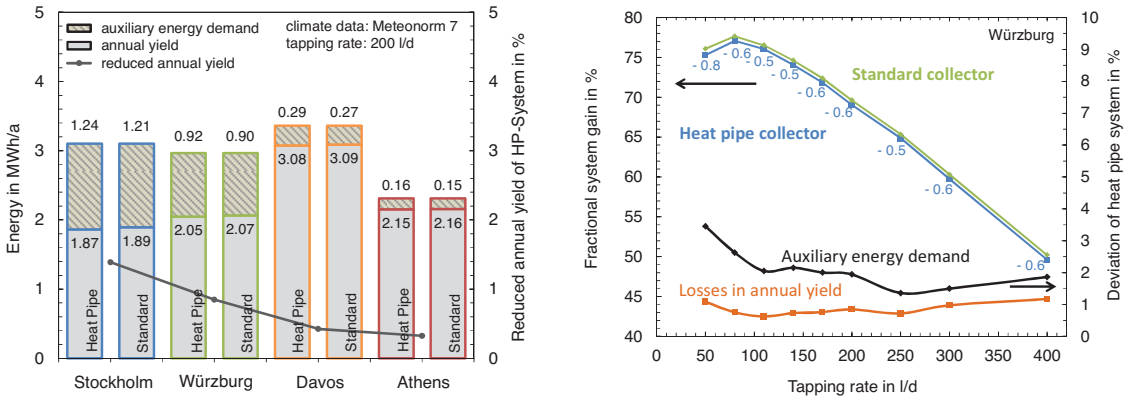

Fig. 4: Annual energy balances for all considered locations at a tapping rate of 200 l/d (left) and fractional system gain, deviations in annual yield and auxiliary energy demand for Würzburg against the tapping rate (right)

3.3. Validation with TRNSYS simulations

To validate the results of the DST procedure, the performances of both systems were simulated in TRNSYS. The characteristics of heat pipe collectors with inherently temperature limitation were implemented in a newly developed collector type model. Conditions such as the tapping and meteorological data were set equal to the DST procedure. The fractional system gain is determined as f_{save} according to IEA TASK 26, as the quotient of the auxiliary energy demand for domestic hot water with solar thermal system and the auxiliary energy demand of the same system without a solar thermal system (Streicher et al. 2003). Thus, storage losses generated by the solar system can be estimated and separated from conventionally generated losses. In the DST model the detailed procedure for calculating the heat storage losses is unfortunately unknown. For validation purpose, the electrical energy demand for the controller and pumping is not considered in both models, since their influence is negligibly small.

In the case of the heat pipe system the fractional system gain calculated according to both approaches have a maximum deviation of 5 %-absolute for all four locations and over a wide range of tapping rates (see Figure 5, left). Small tapping rates show the greatest differences. The reason could depend on the different consideration of the heat losses of the storage tank. In Würzburg and at a typical tapping rate of 200 l/d the fractional system gain differs by 1.0 %-absolute and the auxiliary energy demand by about 6.0 % (55 kWh), as shown in Figure 5, right.

According to the TRNSYS simulations the annual performance of the heat pipe system is, unlike the results of the DST model, slightly better ($\Delta f_{sol} \approx 0.5$ %-absolute) than that of the standard system. This difference can be

explained by the extremely simplified system modelling of the DST procedure. For example, the heat capacity of the collector, which is significantly lower for the heat pipe prototype, is not considered in the DST performance prediction. Only the simulation in TRNSYS can realistically represent the comparison in that point. Apart from these explainable small differences, both approaches confirm with sufficient accuracy, that the considered heat pipe collector prototype exhibits the same annual system performance as the standard collector.

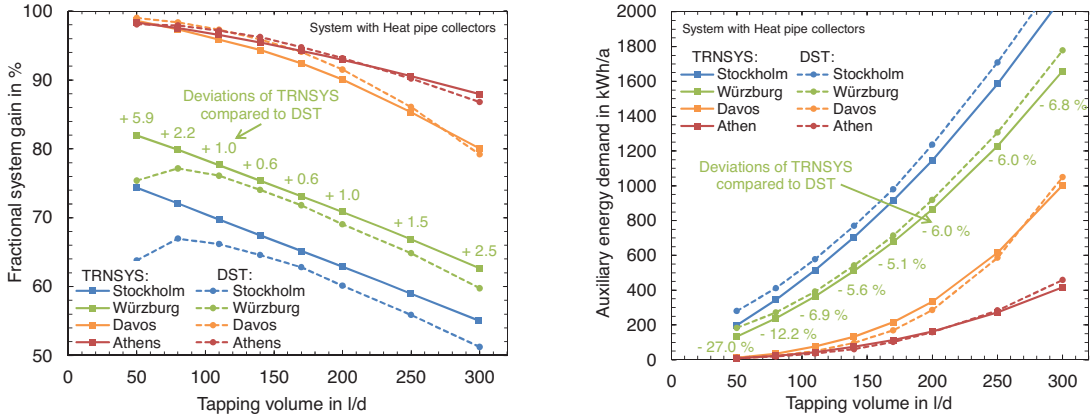

Fig. 5: Fractional system gain (left) and auxiliary energy demand (right) calculated with TRNSYS compared to the DST results against the daily tapping rate

3.4. Stagnation mode

In addition to the annual performance prediction, we investigated the stagnation behavior of both systems over several experimental test periods. During the tests the standstill of the solar circuit was realized by simultaneous switching-off the solar pump at solar noon and at an irradiance of about 1000 W/m². To evaluate the stagnation behavior we considered 30 stagnation days. The vapor formation has been investigated at different system pressure levels in the range between 1.0 / 1.8 and 2.0 / 2.8 bar system overpressure / absolute pressure at the collector.

In the case of the heat pipe collector we measured a maximum collector outlet temperature of 125 °C, which is up to 95 K lower than the maximum temperature recorded with the standard system. Figure 6 shows a typical stagnation sequence for both systems and the respective response of representative temperatures after deactivating the solar pumps at an overpressure level of 2 bars. For the standard system (red), a rapid increase takes place, so that the collector temperature significantly steps over the boiling temperature. The temperature at the inlet of the expansion vessel rises quickly to 115 °C. As a result of the vaporization, the system pressure increases in this case until the safety valve is triggered (> 6 bar). On the contrary, the temperature of the system with heat pipe collector (blue) achieves a maximum value of approx. 116 °C and the boiling temperature is not reached. The temperature at the expansion vessel is not affected by the stagnation sequence at all.

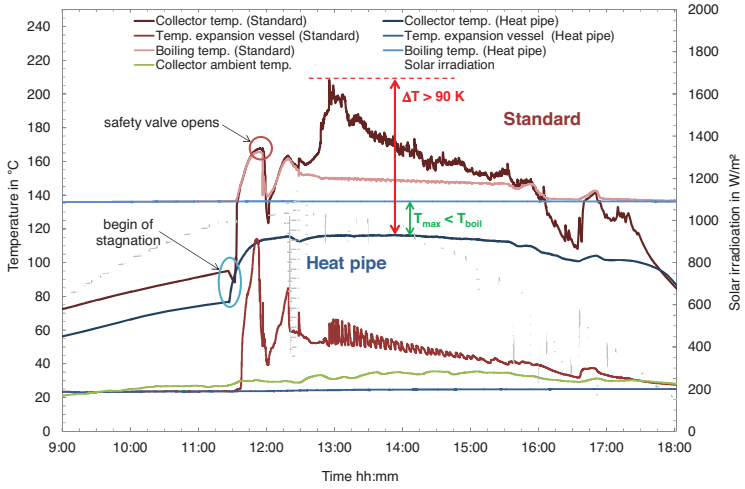

Fig. 6: Representative system temperatures over a stagnation sequence at an overpressure level of 2 bars

The boiling temperature of the solar fluid depends on the occurring system overpressure. For low system overpressures of only 1 bar, vapor formation takes place in the heat pipe collector, too. Figure 7 shows the maximum temperatures and pressures in both systems, as well as the resulting vapor formation in the solar circuit on the selected stagnation day. In the case of the standard system, the vapor at a temperature of about 155 °C is transported up to the solar station and the expansion vessel. In contrast to that, the maximum temperature at the heat pipe collector reaches 123 °C instead of 210 °C. The vapor transport is limited to few meters. The major part of the solar circuit shows a maximum temperature below 100 °C, which is significantly lower compared to the reference system.

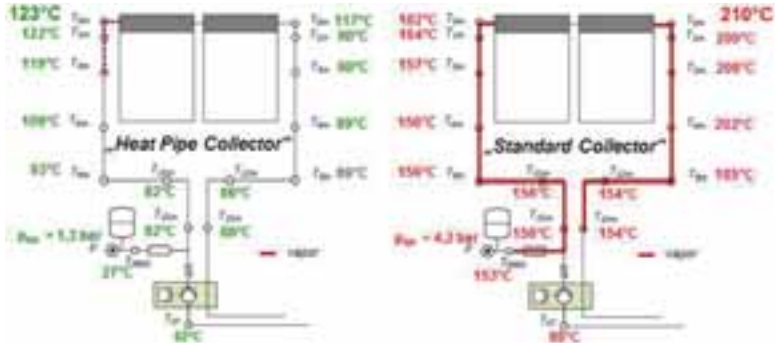

Fig. 7: Maximum temperature and pressure load in the solar circuit of heat pipe and reference system at a low system overpressure level of 1 bar

4. Parameter study with TRNSYS

4.1 System dimensioning

In addition to the annual performance both systems, as described in chapter 3, we investigate by means of TRNSYS simulations the influences of other boundary conditions, such as smaller designed collector fields. It was expected, that the differences of the annual performance between the systems could increase significantly with smaller collectors. Therefore the aperture area in the simulation was reduced whereby the storage tank volume was kept constant at 400 l. In general, the annual yield as well as the fractional system gain decreases and the auxiliary energy demand increases for both systems (see Figure 8 for Würzburg and for a tapping rate of 200 l/d). By reducing the aperture area to 4 m² (-33 %) the annual yields are correspondently reduced by about 20 % and the auxiliary energy demands rise by 40 %. If we focus on the differences between the collector types, the influence of the system performance is almost negligible. With refer to the annual yield, the relative deviation of the heat pipe system ranges from +0.6 % to -0.9 % by reducing the aperture area from 6 m² to 4 m². In consequence of this, the deviation in auxiliary energy demand varies from -1.2 % to +1.1 %. Contrary to our expectations the simulation results show that the annual performance of the heat pipe system is not significantly affected by smaller designed collectors compared to the standard system.

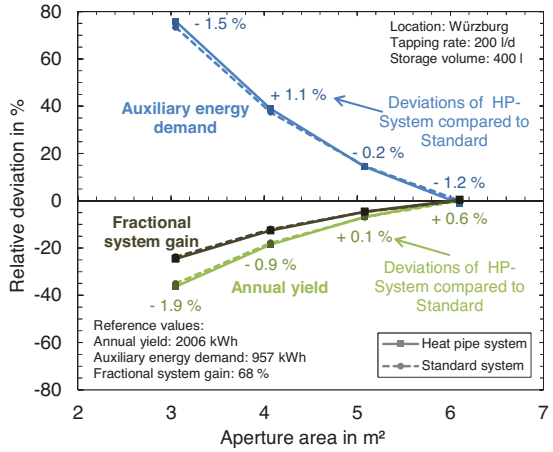

Fig. 8: Deviation of annual yield, fractional system gain and auxiliary energy demand for the heat pipe and standard system in dependency of the aperture area of the collector field

4.2 Shut-off behaviour and maximum temperature

The maximum fluid temperature of the heat pipe collector depends on several conditions. In particular, the type and amount of working fluid, which is inside the heat pipe, are the most important parameters. As a general rule, less fluid leads to lower maximum temperatures. A temperature shift by about ± 20 K can be simply managed by properly dosing the mass of a selected fluid in the heat pipe. Another important parameter is the slope of the collector power shut-off, which affects the kink point[1] (see Figure 9, left) and therefore the collector efficiency in the operating range. The slope of shut-off can be influenced i.e. by the type of working fluid, the heat losses and the internal thermal conductivity of the collector. Low heat transfer coefficients lead to flatter curves. By designing solar heat pipes for temperature limitation, both aspects have to be taken into consideration in order to achieve a significant reduction of the maximum temperature without compromising the annual system performance.

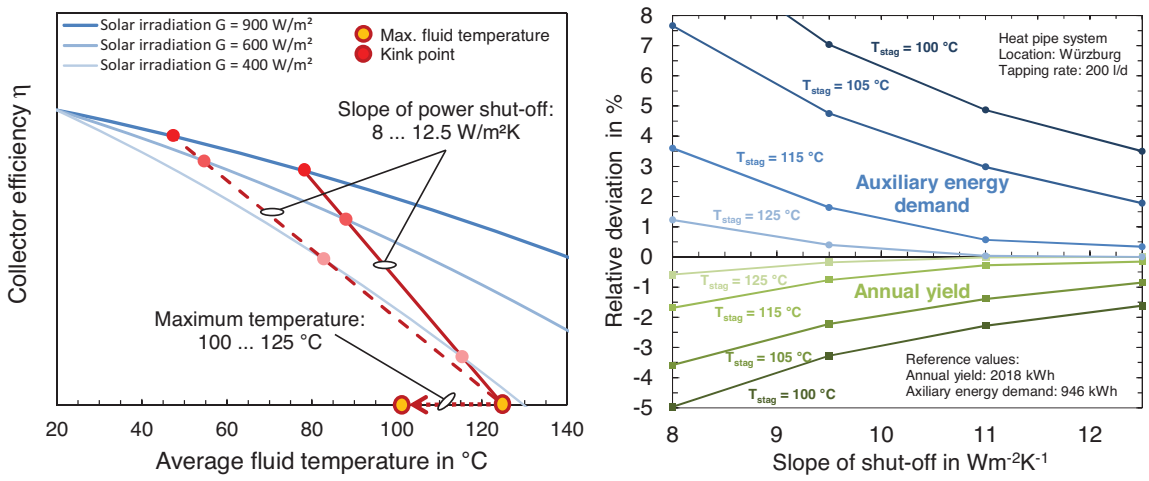

Fig. 9: Illustration of the varied parameters maximum temperature and slope of heat pipe power shut-off (left) and the annual yield and auxiliary energy demand as result of the parameter study (right)

The presented heat pipe prototype collector featured a maximum stagnation temperature of 125 °C and power limitation slope of 12.5 W/m²K. For a comprehensive evaluation, we further investigated the system performance for lower maximum temperatures and different slopes of power shut-off (see Figure 9, right). On the basis of our previous experience with different heat pipe prototypes, the maximum temperature was varied between 100 and 125 °C and the slope between 8 and 12.5 W/m²K. The parameter study was carried out with the system dimensions described in chapter 3 (collector area: 6 m², storage tank: 400 l). At a maximum temperature of 100 °C and a slope of 12.5 W/m²K the solar yield is reduced by 1.6 %, which leads to an increase in auxiliary energy demand by 3.5 %. If the stagnation temperature is limited to 105 °C, the solar yield is reduced by only 0.8 % and the auxiliary energy demand is increased by 1.8%. If lower values of the power limitation slope are considered, the effect is approximately negligible at T_{max} = 125 °C. In the case of T_{max} = 100 °C, significant losses are expected. A slope of 9.5 W/m²K, for example, leads to a lower annual yield by 3.5 % and a higher auxiliary energy demand by 7 %.

The parameter study shows, that a further reduction of the maximum temperature has a negative impact on the system performance. If a higher auxiliary energy demand by about 2 % is tolerated, the maximum temperature can be reduced to 115 °C with a minimum slope of 9.5 W/m²K or to 105 °C with a minimum slope of 12.5 W/m²K. If a temperature limitation to 115 °C is reached with a slope of 12.5 W/m²K, the demand of auxiliary energy increases by only 0.3 %. In consequence of this, vapor formation and the transportation of high temperatures in the solar circuit can be further reduced, in particular at a low system overpressure level, as shown in Figure 7.

[1] The kink point is not fixed at a certain temperature, but is affected by the slope of the shut-off and the occurring solar irradiation

5. Conclusion

We investigated a newly developed evacuated tube collector based on optimized heat pipes able to limit the temperature loads at the manifold to a maximum temperature of 125 °C. Additionally to collector efficiency measurements, we compared the annual yield of a heat pipe collector field in a domestic hot water system with an identical system with direct flow collector according to ISO 9459-5. The results show, that the heat pipe collector reaches almost the annual system performance of the reference collector. The system simulations in TRNSYS have confirmed the results of the DST procedure with a sufficient accuracy.

By means of extensive stagnation tests, we report a maximum temperature at the solar circuit of 125°C, which is 95 K lower compared to the reference system. As a main result, the vaporization can be completely avoided for a typical pressurized system and significantly reduced for low system overpressures. The use of these heat pipes can thus prevent the propagation of high temperatures in the system. The major part of the solar circuit shows a maximum temperature level below100 °C. Due to the significant reduction of thermal and pressure loads in the whole solar system the system design can be adapted and simplified. According to our parameter study with TRNSYS, a further reduction of the maximum temperature to 115 °C is possible without significantly affecting the annual performance.

As a result of the already achieved limitation of the maximum temperature to 125 °C and of the successful suppression of vapor formation, solar circuit components, such as the expansion vessel, the ballast vessel and the solar piping, can be resized or made by less expensive materials, i.e. by polymerics. According to our current estimation, the investment costs for the considered domestic hot water system can be reduced by about 8 – 10 %. Further simplifications in the installation procedure, i.e. by simpler filling and degasification of the solar circuit are possible. Finally, the lower system load can significant reduce the maintenance effort, in particular thanks to the prolonged life-time of the solar fluid. Taking into account the overall costs during the life-time of the system, the use of heat pipe collectors with temperature limitation can achieve a cost saving of 20 – 30 % compared to a state-of-the-art solution.

6. Acknowledgement

The project "Cost effective and reliable solar systems with novel heat pipe collectors" underlying this publication is funded by the German Federal Ministry of Economy and Energy (reference number 0325550A-C), following a decision of the German Parliament. The investigations are carried out in cooperation with the companies KBB Kollektorbau GmbH, NARVA Lichtquellen GmbH & Co. KG and AkoTec Produktions-gesellschaft mbH.

The authors are grateful for the support. The responsibility for the content of this publication lies with the authors.

7. References

Eisenmann W., Pujiula F., Köln H., Baumann A., 2004. On the Determination of the Effective Thermal Capacity of Solar Collectors, Proceedings 14. EuroSun Conference, Freiburg im Breisgau

Föste S., Schiebler B., Giovannetti F., Rockendorf G., Jack S., 2015. Butane heat pipes for stagnation temperature reduction of solar thermal collectors, Energy Procedia 91 p. 35-41

ISO 9459-5, 2007: System performance characterization by means of whole-system tests and computer simulation. Beuth Verlag, Berlin

Jack S., Rockendorf G., 2013. Wärmerohre in Sonnenkollektoren – Wärmetechnische Grundlagen und Bewertung sowie neue Ansätze für die Integration, final project report (published in german), FKZ 0325962A

Jack S., Parzefall J., Luttmann T., Giovannetti F., 2014. Flat plate aluminium heat pipe collector with inherently limited stagnation temperature. Energy Procedia 48 p. 105-113

Mientkewitz, G.; Zabel, J., 2010. Möglichkeiten eines Heatpipe-Kollektors ohne Stagnationsprobleme. Conference proceedings 20. OTTI Symposium Thermische Solarenergie, Bad Staffelstein

Reay D.A., Kew P.A., 2006. Heat Pipes: Theory, Design and Applications. 5th edition, Butterworth Heinemann, Oxford

Spirkl W., 1990. Dynamische Vermessung von Solaranlagen zur Warmwasserbereitung, VDI-Fortschrittberichte, Reihe 6: Energieerzeugung Nr. 241

Spirkl W., 1997. Dynamic System Testing Program Manual, InSitu Scientific Software

Streicher, W. et al., 2003. Report on Solar Combisystems Modelled in Task 26 (System Description, Modelling, Sensitivity, Optimisation), Report of IEA SHC – Task 26 Solar Combisystems

TÜV-Rheinland, 2014. Solar KEYMARK Certificate Licence Number 011-7S471 R. DIN CERTCO, Berlin

Visser H., 1997. Dynamic Testing of Active Solar Heating Systems, Final Report of the IEA SHC – Task 14 Dynamic Component and System Testing Subtask Software

8. Appendix

8.1 Specific system parameters

The specific system parameters of both systems are listed in Table 2. The collector coefficients as well as the stagnation temperature of the heat pipe collector were determined at the ISFH (see Figure 1). For the direct-flow collector, the parameters were taken from a referenced Solar Keymark certificate (TÜV-Rheinland 2014). The effective heat capacities of both collectors have been determined according to DIN EN 12975-2 by weighting the physical capacities of the single components. The significant difference is due to the substantially lower mass of solar fluid in the heat pipe collector.

Tab. 2: Specific system parameters used for performance simulation with both the heat pipe and the standard system

Parameters	Symbol	Unit	ETC with heat pipe	ETC Standard
Collector:				
Aperture area	A^*	m²	6.1	6.1
Conversion factor	η_0	-	0.754	0.774
Linear heat loss coefficient	a_1	$Wm^{-2}K^{-1}$	2.02/12.50[1]	1.94
Quadratic heat loss coefficient	a_2	$Wm^{-2}K^{-2}$	0.007	0.006
Maximum fluid temperature in stagnation	T_{stag}	°C	125	300
Effective collector capacity	C_{eff}	$kJm^{-2}K^{-1}$	4.75	10.19
Solar controller:				
On/off – criteria	$\Delta T_{on/off}$	K	7/3	7/3
Max. storage temperature	$T_{max,st.}$	°C	90	90
Max. collector temperature	$T_{max,coll.}$	°C	130	130
System:				
Storage volume	$V_{st.}$	l	400	400
Electrical auxiliary power	P_{aux}	kW	6	6
Heat loss rate storage	$U_{st.}$	WK^{-1}	2.69	2.69
Length of solar circuit piping (flow + return)	L_{sc}	m	30	30
Heat loss rate solar circuit	$U_{sc.}$	$Wm^{-2}K^{-2}$	3.19	3.19
Expansion vessel	V_{ev}	l	50	50
Ballast vessel	V_{bv}	l	12	12

[1] Slope of the power shut-off

Investigation on Dustfall and Rainfall to Cover Transmittance of Flat-plate Solar Collectors in Beijing

Min Wang, Bojia Li, Tao He, Xinyu Zhang, and Boyuan Wang

China Academy of Building Research, Beijing (China)

Abstract

Nature dustfall influences on transmittance of flat-plate solar collectors cover and will furtherly influences on its working efficiency. A 12-month experiment of dustfall and cover transmittance has been conducted in Beijing. A dust deposition model describing the effect of rain on dust deposition has been studied. And the correlation of environmental factors, such as dustfall and rainfall, on cover transmittance has also been established. The maximum relative deviation between calculated and experiment transmittance is 6.42%. Therefore, the correlation is accurate enough and can be used for further analysis such as maintenance strategy of solar thermal system operating in Beijing or other areas with similar climate.

Keywords: dustfall, rainfall, flat-plate solar collector, cover transmittance, rainfall facto, extinction coefficient

1. Introduction

Flat-plate solar collector (FPC) is getting higher installed capacity in China due to its better safety performance and advantage of integrating with buildings. Normally, effect of environmental factors, such as dust deposition, rainfall and wind, would not be considered when calculating the thermal performance of FPC. That results in a significant difference between designing output and actual operation, especially in the special area with severe dust or wind. El-Nashar (2009) pointed out that in arid regions such as the United Arab Emirates, collector's thermal performance will drop by 40% in a year without cleaning. Elminir et al. (2006) proposed that the transmittance of glass fell 52.5%~12.4% according different slope and azimuth in Egypt. Research in China showed that thermal performance of flat-plate collector would drop 9.69% after 3 months in Lanzhou, the transmittance would fall 12.3% after 12 days in Xi'an (Liu, 2014; Hou, 2015).

Based on the analysis of effect mechanism of dustfall and rainfall on cover transmittance, A 12-month experiment of dustfall and cover transmittance has been conducted in Beijing. A dust deposition model describing the effect of rain on dust deposition has been studied. And the correlation of environmental factors, such as dustfall and rainfall, on cover transmittance has also been established. With the correlation, further analysis, such as maintenance strategy of solar thermal system operating in Beijing or other areas with similar climate, could be analyzed.

2. Effect mechanism

2.1. Working principle

The working principle of flat-plate solar collectors can be described as following:

- Solar radiation through the glass cover is absorbed by the absorber panel with selective coating;
- The temperature of the absorber panel increases, and the heat transfer to fluid in tubes;
- Fluid is heated and deliver heat to outside.

Heat transfer process between components is showed in Fig. 1.

doi:10.18086/swc.2017.31.17 Available at http://proceedings.ises.org

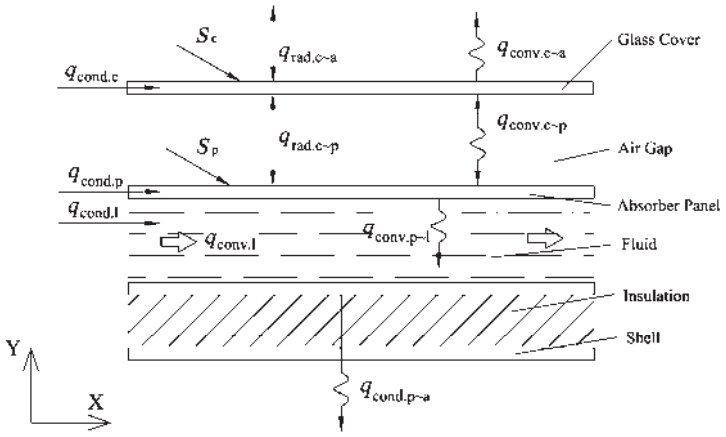

cond	Conductive heat transfer	c	Glass cover	a	Ambient
conv	Convective heat transfer	p	Absorb panel	*S*	Solar radiation
rad	Radiation heat transfer	l	Fluid	*q*	Heat transfer

Fig. 1: Schema of heat transfer in flat-plate solar collector

According to the working principle, transmittance of the glass cover has significant effect on collector's thermal performance. Decrease of the transmittance would reduce heat received by the absorber panel, which eventually leading to decline of heat gain and thermal efficiency.

For a flat-plate solar collector in operation, the cover transmittance is affected by the dustfall and rainfall. The effect mechanism could be described as following:

- Dust falls and deposited on the collector cover.
- Then it is washed by the rainfall.
- If the transmittance of clean glass cover is τ_c , transmittance of dust layer is τ_d, Then the transmittance of glass cover with dust is down to $\tau_m=\tau_c \cdot \tau_d$.

To describe the effect of dustfall and rainfall on cover transmittance, a dust deposition model has been studied as following.

2.2. Dust deposition

By deposition mechanism, the dustfall on the tilted collector cover could be divided into 2 parts: the gravity settling dust and particulate matter. The dust deposition on the tilted collector cover can be calculated from the following equation:

$$D_{d,\theta} = d_{1,\theta} + d_{2,\theta} = d_d \cos\theta + v_{d,\theta} C_{dp} T \times 10^{-3} \quad \text{(eq. 1)}$$

Where，θ is the titled angle of inclination surface; $D_{d,\theta}$ is the total dust mass on titled surface, g/m^2; $d_{1,\theta}$ is gravity settling dust mass on titled surface, g/m^2; $d_{2,\theta}$ is particulate matter mass on titled surface, g/m^2; d_d is daily gravity settling dust mass, g/m^2; v_d is particulate matter settling velocity，m/s; C_{dp} is particulate matter concentration, mg/m^3; T is calculation period of particulate matter，86400s.

2.3. Effect of rainfall on dust deposition

The rain will wash away part of the dust on the collector cover, but part of the sticky dust will still remain on the collector cover. Therefore, when describing the effect of rainfall on dust deposition, four different scenarios are proposed:

1) No rain, dust on the cover is not affected;

2) Little rain, but the rain is not strong enough to wash away the dust on the cover;

3) Small rain, the rain can only wash away part of the dust on the cover;

4) Heavy rain, the rainfall exceeds a certain threshold. Almost all the dust is washed away, but there will be a small part of sticky dust still stay on the cover.

Rainfall factor R is introduced as eq. 2 to describe the effect of rainfall on dust deposition. And the dust deposition model including rainfall effect has been established as eq. 3 ~ eq. 5.

$$R=\begin{cases}1 & r_{24}\le b_1\\ r' & r_{24}=b_2\\ r'' & r_{24}\ge b_3\\ 1+(r'-1)\dfrac{r_{24}-b_1}{b_2-b_1} & b_1<r_{24}<b_2\\ r'+(r''-r')\dfrac{r_{24}-b_2}{b_3-b_2} & b_2<r_{24}<b_3\end{cases} \quad \text{(eq. 2)}$$

Where, b_1, b_2, b_3 are different rainfall threshold, mm; r', r'' are the left dustfall proportion after rainfall flush, %.

$$D_r(i)=D_{r,1}(i)+D_{r,2}(i) \quad \text{(eq. 3)}$$

$$D_{r,1}(i)=R(i)\left[D_{r,1}(i-1)+d_d(i)\cos\theta\right] \quad \text{(eq. 4)}$$

$$D_{r,2}(i)=R(i)\left[D_{r,2}(i-1)+v_d C_{dp}(i)T\times10^{-3}\right] \quad \text{(eq. 5)}$$

Where $D_r(i)$ is the total dust mass after rainfall flush on i day, g/m^2; $D_{r,1}(i)$ is the total gravity settling dust mass after rainfall flush on i day, g/m^2; $D_{r,2}(i)$ is the total particulate matter after rainfall flush on i day, g/m^2.

2.4. Transmittance of collector cover with dust

According to Zhao (2006) and Katzan's (1991) research, the correlation between cover transmittance and dust deposition could be described as eq. 6 by defining the extinction coefficient of dust deposition K_d :

$$\tau=\tau_c\cdot\exp\left[K_d\left(\frac{D_{r,1}}{\phi_1}+\sum_{j=1}^{n}\frac{D_{r,2,j}}{\phi_{2,j}}\right)\right] \quad \text{(eq. 6)}$$

Where τ is the transmittance of dirty cover; τ_c is the transmittance of clean cover; φ_1 is equivalent diameter of gravity settling dust mass, m; $\varphi_{2,j}$ is equivalent diameter of particulate matter j, m.

To determine the rainfall factor R and extinction coefficient K_d in the correlation of dustfall and rainfall on cover transmittance of flat-plate solar collector, a 12-month experiment of dustfall and cover transmittance has been conducted in Beijing.

3. Experiment methods

3.1. Location

The dustfall and cover transmittance experiment has been carried out on the roof of a 3-floor building in Shunyi District, Beijing. There is no high-rise building around, and there is no obvious source of pollutants. The latitude of experimental site is 40°, longitude is 116°, average elevation of 35 m. Experimental site is 50 km away from city center.

The climatic character in Beijing is rainy and hot in summer, cold and dry in winter. 75% of the annual rainfall is in summer. Average annual rainfall is 571.3 mm. In January the average temperature is -4°C, and monthly rainfall is 2.8 mm. In July the average temperature is 26.3°C, and monthly rainfall is 177 mm.

3.2. Method

Experiment included 2 parts: dustfall measurement and cover transmittance measurement. Experiments period was 12 months, from April 2015 to March 2016. The dustfall measurement and cover transmittance measurement were carried out at the same time in each month. The rainfall data and daily PM_{10} concentration

from China Meteorology Data Center is recorded at the same time.

3.2.1. Dustfall measurement

The experiment was carried out according to the national standard GB/T 15265-94 "Ambient air -Determination of dustfall - Gravimetric method". The glycol water (Mixture of 100 mL $C_2H_6O_2$ and 100 mL water) was placed in a glass collection tank to collect the dustfall. The inner diameter of glass collection tank was 15 cm, and the height was 30 cm, the mass of dustfall was measured by gravimetric method. The glycol water was collected every 30±2 d. After evaporation, drying at 105°C, cooling at room temperature, the dust was weighted by analytical balance. The experimental site and equipment for dustfall measurement is showed in Fig. 2.

a. experimental site b. glass collection tank c. crucible d. Drying oven f. analytical balance

Fig.2: Experimental site and equipment of dustfall experiment

3.2.2. Cover transmittance measurement

Glass pieces were used as the sample of collector cover during the experiment. The glass pieces' size is 50 mm × 50 mm × 3 mm. The glass pieces were placed at three tilted angles of 0°, 40° and 90°. Monthly transmittance changes of glass pieces were measured every month, and the cumulative transmittance changes from the 1st month were also measured. As shown in Fig. 3, the transmittance was measured by a spectrophotometer, the transmittance of each glass pieces was tested twice to reduce the test error.

a. spectrophotometer b. glass pieces

Fig.3: Spectrophotometer and glass pieces

3.3. Uncertainty analysis

Measuring instruments used in the experiment included analytical balance, Vernier caliper, spectrophotometer. Main parameters of these instruments are showed in Tab. 1.

Tab. 1: Test instrument list

Item	Instrument	Model	Range	Resolution	Accuracy
Dust weight	analytical balance	JJ224BC	0~220g	0.1mg	±0.2mg
Inner diameter of glass collection tank	Vernier caliper		0~150mm	0.02mm	-
Transmittance	spectrophotometer	Cary-5000	300~2500nm	0.0001	0.0008

3.3.1. Uncertainty of dustfall

The relative synthetic uncertainty of dustfall was calculated by eq.7:

$$U(\mathrm{d}) = \sqrt{U(\mathrm{S})^2 + U(\mathrm{w})^2} \quad \text{(eq. 7)}$$

Where, U(d) was the synthetic uncertainty of dustfall; U(S) was the uncertainty of opening area of glass collection tank; U(w) was the uncertainty of dust weight.

The resolution of the Vernier caliper used to measure the inner diameter was 0.02 mm. Considering the average distribution, the confidence probability p= 95% was taken, and the corresponding inclusion factor k = 1.65. For the inner diameter of glass collection tank, the standard uncertainty u(L) of measurement results was 0.006 mm. Inner diameter of glass collection tank was 139 mm. After calculation, the uncertainty of opening area of glass collection tank was 0.0062%.

The accuracy of the analytical balance used to measure the dust weight was 0.2 mg. Considering the normal distribution, the probability of confidence is 95.45% and the corresponding inclusion factor k = 2. The standard uncertainty of the measurement results u(w) was 0.1 mg. The relative uncertainty U(w) was 0.25% when the measured dust was about 40 mg.

Therefore, the relative synthetic uncertainty of dustfall U(d) = 0.25%.

3.3.2. Uncertainty of transmittance

According the uncertainty analysis method, the relative uncertainty of transmittance $U(\tau)$ = 0.0667 %.

4. Experiment results

According to the experimental results shown in Fig. 4, total amount of dustfall at the experimental site was 58.653 t/km^2. And the maximum monthly dustfall was 9.718 t/(km^2·30d) in April, the minimum monthly dustfall was 2.254 t/(km^2·30d) in September. Seasonal changes of rainfall was obvious. There was rare rainfall in winter (December ~ March), while there was rich rainfall in summer (July ~ September). The maximum monthly rainfall is in July.

The transmittance of glass piece was affected by dustfall and rainfall. Monthly transmittance changes were different in different season. During December to March, there was rich dustfall and rare rainfall. The transmittance decreased obviously according to the increase in dustfall (Except February). From July to September, there was little dustfall and rich rainfall. The transmittance decreased a little and the glass kept clean. Relative change of transmittance was only 1.9%. In the first transition season (from October to November), there was little dustfall and rainfall. The transmittance decreased slowly. In the second transition season (from April to June), there was lot dustfall and rainfall. The transmittance fluctuated greatly.

Based on the annual experimental data, the cumulative transmittance in June and February increased significantly comparing with previous month, but the rainfall did not change significantly. Therefore the effect of rainfall needed further analysis.

Fig. 5 shows the maximum 24h rainfall in each month. It could be seen that the maximum 24h rainfall in June

and February was 12.1 mm and 7.3 mm respectively. During February, the maximum 12h rainfall was 7.3 mm. And the maximum 24h rainfall in May and January was 3 mm and 0 mm, respectively. In meteorology, if 12 hours rainfall ($r12$) was more than 5mm and less than 15 mm, 24 hours rainfall ($r24$) was more than 10mm and less than 25 mm, the rain was called moderate rain. If 12 hours rainfall ($r12$) was more than 15 mm and less than 30 mm, 24 hours rainfall ($r24$) was more than 25 mm and less than 50 mm, the rain was called heavy rain. According the analysis above, the increase of transmitters in June and February could be attributed to the occurrence of moderate rain or heavy rain in that month. As the monthly rainfall didn't reflect the rainfall intensity, it was more reasonable to use 24h maximum rainfall ($r24$) in eq. 2 when analyzing the impact of dustfall and rainfall on the cover transmittance.

During the experiment, the monthly and cumulative transmittance changes of the 0°, 40° and 90° glass pieces are shown in Fig. 6 and Fig. 7. The transmittance of clean glass piece (τ_m) was 0.8497. The decrease in the transmittance of the glass piece decreased with the increase of the tilted angle θ, and the change trend was non-linear. Transmittance of 40° glass piece was more like that of 0° glass piece.

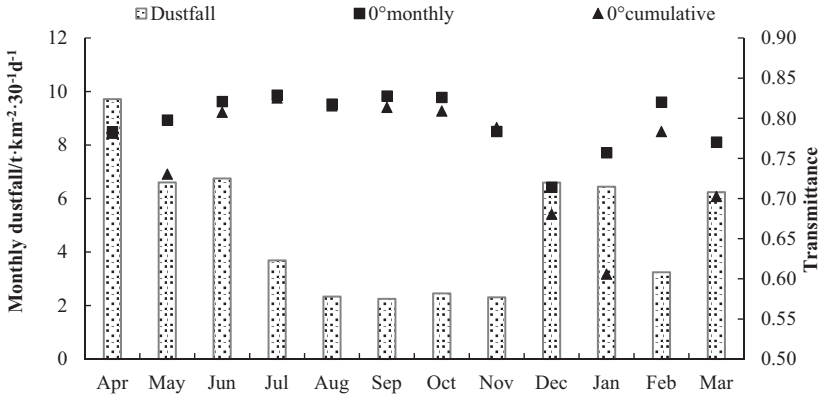

Fig.4: Results of monthly dustfall and transmittance on horizontal surface

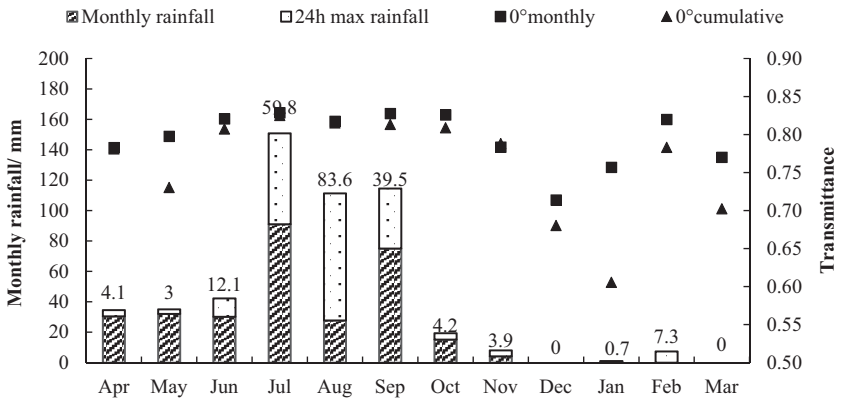

Fig.5 Results of monthly rainfall and transmittance on horizontal surface

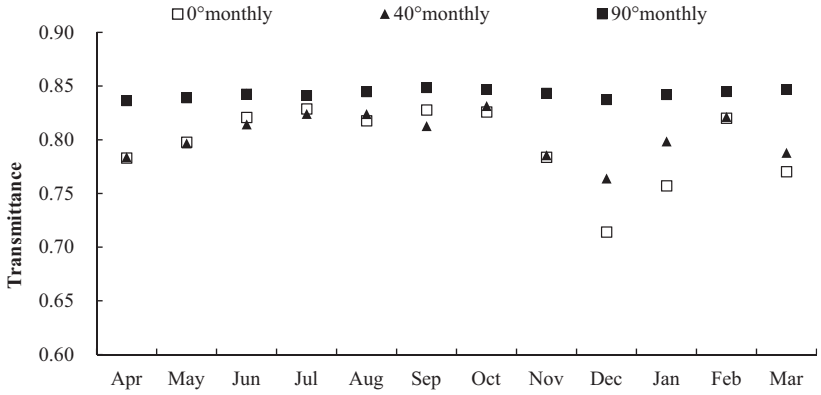

Fig.6: Results of monthly transmittance on different tilted surface

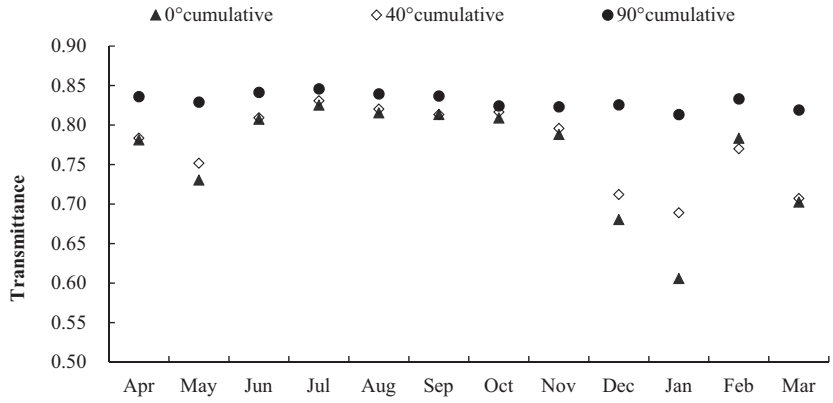

Fig.7: Results of cumulative transmittance on different tilted surface

5. Discussion

5.1. Dust deposition

The dust deposition could be calculated by eq. 1. In the equation, daily gravity settling dust mass could be achieved from experiment results.

Assuming that PM_{10} is composed of 4 kinds of particulate matter with diameter of 10μm, 5μm, 2.5μm and 1μm, the volume ratio of the 4 kinds of particulate matter are 72.2%, 15.3%, 8.3% and 4.2%, according to the results of Wu G. et al. (2005) and Wu C. et al. (2006). As a result, the amount of daily dust deposition can be calculated by eq. 8.

$$\tau_j = \tau_c \cdot \exp\left[K_d \sum_{j=1}^{n} R_j \left(D_{r,j-1} + \frac{d_d \cos\theta}{d_{p40}} + v_{dR,\theta,\mathrm{pm10}} C_{PM10,j} T \times 10^{-3}\right)\right] \quad \text{(eq. 8)}$$

$$v_{dR,\theta,pm10} = \frac{0.722 v_{d,\theta,\mathrm{dp10}}}{d_{p10}} + \frac{0.153 v_{d,\theta,\mathrm{dp5}}}{d_{p5}} + \frac{0.083 v_{d,\theta,\mathrm{dp2.5}}}{d_{p2.5}} + \frac{0.042 v_{d,\theta,\mathrm{dp1}}}{d_{p1}} \quad \text{(eq. 9)}$$

Where, j is days in a month;C_{PM10} is outdoor daily PM_{10} concentration, mg/m^3; $v_{dR,\theta,\mathrm{pm10}}$ is ratio of settling velocity to diameter of particulate matter; $v_{dR,\theta,\mathrm{dp}}$ is settling velocity of particulate matter with diameter of 10μm, could be calculated by equation proposed by Zhao (2006), You (2012) and Chen (2011); d_p is the diameter of particulate matter, m.

5.2. Regress of R and K_d

With the data of dustfall, rainfall, daily PM_{10} concentration and measured transmittance by above experiment in Beijing, the Rainfall Factor R and extinction coefficient K_d could be regressed, and the following equations are

obtained:

$$\tau_j = \tau_c \cdot \exp\left[-5.146\times10^{-7} \sum_{j=1}^{n} R_j \left(D_{r,j-1} + \frac{d_{d,\mathrm{d}} \cos\theta}{d_{p40}} + v_{dR,\theta,\mathrm{pm10}} C_{PM10,j} T \times 10^{-3} \right) \right] \quad \text{(eq. 10)}$$

$$\text{Where, } R = \begin{cases} 1 & r_{24} \le 2 \\ 0.13 & r_{24} \ge 6 \\ 1 - 0.218\times(r_{24} - 2) & 2 < r_{24} < 6 \end{cases} \quad \text{(eq. 11)}$$

It can be seen from eq. 11 that the rainfall factor R is divided into three stages. And b_1= 2, b_2= b_3= 6, $r'$and r is 1 and 0.13, respectively in eq. 2. The function is graphically shown in Fig. 8.

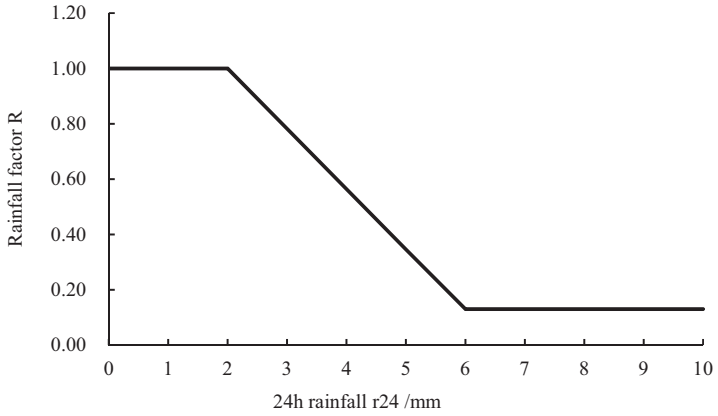

Fig. 8: Regressed rainfall factor *R*

With eq. 9, eq. 10 and eq. 11, the cover transmittance on titled surface can be calculated. The calculated and measured transmittance are compared in Fig. 9. It can be seen that the maximum relative deviation between calculated and experiment transmittance is 6.42%. Therefore, the correlation can fit the influence of environmental factors such as dustfall and rainfall on the transmittance of the collector cover. The fitting result is accurate enough and can be used for further analysis such as maintenance strategy of solar thermal system operating in Beijing or other areas with similar climate.

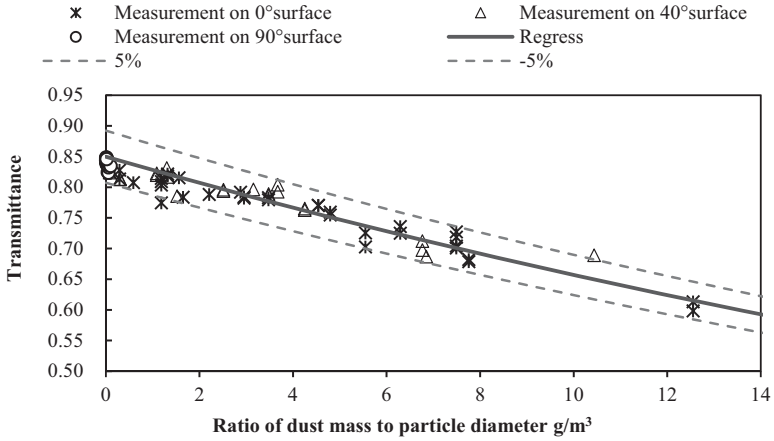

Fig. 9: Comparison of regress data and experimental data

6. Conclusion

A dust deposition model, as well as the correlation of environmental factors, such as dustfall and rainfall, on cover transmittance have been proposed in this paper. With a 12-month experiment of atmospheric dust and cover transmittance in Beijing, an empirical formula has been established to evaluate the effect of dustfall and

rainfall on the cover transmittance of solar flat-plate under natural environment. The detailed results are summarized as follows:

1) The dust deposition on the surface of collector cover is affected by the dustfall and rainfall. The correlation of dustfall and rainfall on cover transmittance has also been established as the following equation:

$$\tau_j = \tau_c \cdot \exp\left[K_d \sum_{j=1}^{n} R_j \left(D_{r,j-1} + \frac{d_d \cos\theta}{d_{p40}} + v_{dR,\theta,\mathrm{pm10}} C_{PM10,j} T \times 10^{-3} \right) \right]$$

2) A 12-month experiment in Beijing has been conducted. During December to March, there was rich dustfall and rare rainfall. The transmittance decreased obviously according to the increase in dustfall. From July to September, there was little dustfall and rich rainfall. The transmittance decreased a little and the glass kept clean.

3) The K_d and R were got by regress of experimental result as: $K_d = -5.146\times10^{-7}$ and

$$R = \begin{cases} 1 & r_{24} \le 2 \\ 0.13 & r_{24} \ge 6 \\ 1 - 0.218 \times (r_{24} - 2) & 2 < r_{24} < 6 \end{cases}$$

4) The maximum relative deviation between calculated and experiment transmittance is 6.42%.Therefore, the correlation is accurate enough and can be used for further analysis such as maintenance strategy of solar thermal system operating in Beijing or other areas with similar climate.

7. Acknowledgment

All authors are also grateful for the financial support provided by the *National Key R&D Program of China* (Grant No. 2016YFC0700402) and the *Applied Technology Research Fund of CABR* (Project No. 20170109330730026)

8. References

Chen C., 2011. Effect of outdoor inhalable particles on indoor air quality and its control. Tsinghua University, Beijing.

El-Nashar A.M., 2009. Seasonal effect of dust deposition on a field of evacuated tube collectors on the performance of a solar desalination plant. Desalination. 239(1), 66-81.

Elminir H. K., Ghitas A. E., Hamid R. H., 2006. Effect of dust on the transparent cover of solar collectors. Energy Conversion and Management. 47, 3192-3203.

Hou Y., Li A., 2015. Influence of dust accumulation on performance of flat-plate solar collector. Building Science. 31(4), 68-71.

Katzan C. M., Edwards J. L., 1991. Lunar dust transport and potential interactions with power system components. NASA report.

Liu J., 2014. A research for the thermal performance of solar collector. Lanzhou University of Technology, Lanzhou.

Wu C., Wu G., Li Z., 2006. Study of the Adhesion Behavior of Dust on the Surface of the Glass. Industrial Safety and Environmental Protection. 2006(9), 1-3.

Wu G., Wu C., Peng X., 2005. Mechanism of adhesion and cleaning between the surface of structural glass and dust. Journal of Safety Science and Technology. 2005(5), 28-32.

You R., Zhao B., Chen C., 2012. Developing an Empirical Equation for Modeling Particle Deposition Velocity onto Inclined Surfaces in Indoor Environments. Aerosol Science and Technology. 40(10), 1090-1099.

Zhao B., Wu J., 2006. Modeling particle deposition from fully developed turbulent flow in ventilation duct. Atmospheric Environment. 40, 457-466.

Compound Parabolic Concentrator for Pentagon Shape Absorber

Bennett Widyolar[1,2], Lun Jiang[1,2], Ali Hassanzadeh[1,2], and Roland Winston[1,2]

[1] University of California, Merced (USA)

[2] Advanced Solar Research Institute (UC Solar), Merced (USA)

Abstract

The design and development of new medium-temperature solar thermal external compound parabolic concentrator (XCPC) is presented. A nonimaging reflector is paired with an evacuated tube absorber for efficient heat collection between 100-300 °C. Several absorber geometries are simulated, with the final selection of a modified pentagon absorber shape chosen for manufacturability. The modified absorber shape, gap loss, and truncated reflector result in a geometric efficiency of 93% compared to an ideal CPC. Several selective coatings are compared for down-selection, and a Mylar reflective film with ~89% reflectance is chosen for its low cost and durability. The final prototype has a 4.56 m^2 aperture. Simulations predict an optical efficiency of 71% and thermal efficiency of 50% at 200 °C and experimental test results have confirmed an optical efficiency of 62% and a thermal efficiency near 50% at 200 °C. The stagnation temperature was measured at 333 °C. World-wide installations are presented.

Keywords: External compound parabolic concentrator, XCPC, medium temperature, nonimaging, solar thermal

1. Introduction

Low temperature collectors (<100 °C) for residential and commercial hot water typically take the form of flat plate or evacuated tube collectors, the latter of which dominates the market space due to its widespread adoption in China. Parabolic trough collectors (PTC) have historically been the most commonly used high temperature collectors (>300 °C) for industrial process heating (IPH) and concentrating solar power (CSP), but have shared the space with compact linear Fresnel (cLFR), dish, and recently with centralized solar tower installations. The space in between these two classes of collectors (100 °C < medium temperature < 300 °C) has historically been served by high temperature collectors at lower-than-design operating temperatures. Today there exist several newer options including stationary evacuated flat plates (Buonomano et al. 2016), compound parabolic concentrators (Duff et al. 2004, Kim et al. 2013), semi-tracking micro linear fresnel reflector systems (Sultana et al. 2015), semi-passive tracking combined systems (Li et al. 2017), and tracking miniature trough (Fernandez et al. 2010) and dish (Cohen and Grossman 2016) systems. The best performance of these systems typically approaches 50% conversion efficiency at 200 °C under global irradiance.

In this paper we report on the most recent round of developments to the XCPC collector, a non-tracking solar thermal collector, and the experimental performance results of the prototype tested at the University of California, Merced (UCM).

2. Collector Design

The external compound parabolic concentrator (XCPC) consists of an evacuated tube receiver paired with a nonimaging reflector and is depicted in Figure 1. Inside the evacuated tube is a selectively coated metal fin which acts as the absorbing surface of the collector. The nonimaging reflector concentrates incoming radiation over a wide range of angles onto the absorber surface. This eliminates the need for any mechanical tracking mechanism as the optics provide passive sun-tracking. The combination of concentration and an evacuated receiver allows the XCPC to reach temperatures between 100 - 300 °C.

doi:10.18086/swc.2017.31.18 Available at http://proceedings.ises.org

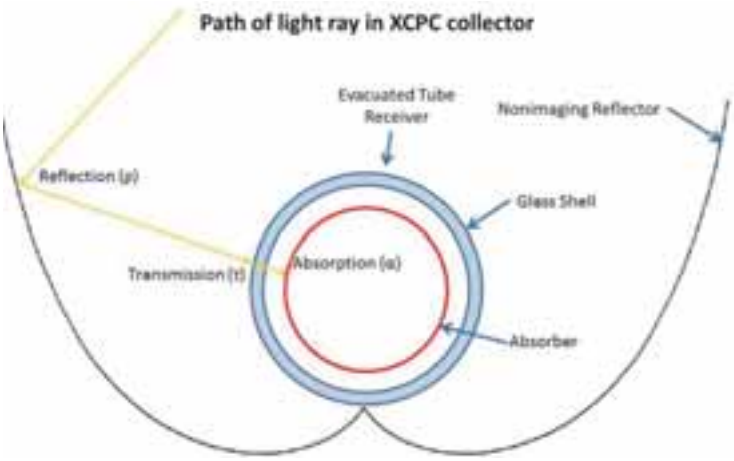

Figure 1 – Path of light ray in an XCPC collector.

The CPC profile was designed for a cylindrical absorber, but due to manufacturing limitations (specifically the geometric requirements of the ultrasonic welding machine at the prototyping facility) a new absorber geometry needed to be found. Optical simulations were performed in LightTools for the reflector profile with different absorber shapes shown in Figure 2 to determine the geometric efficiency of each case. The results of these simulations are summarized in Table 1.

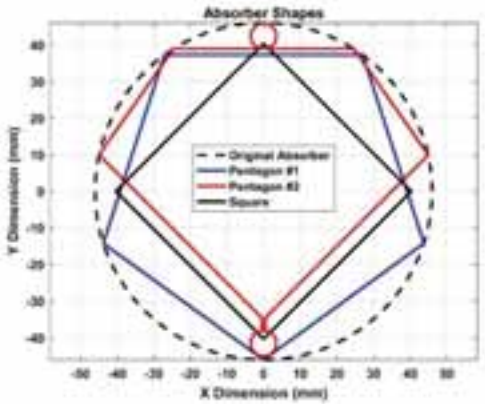

Figure 2 – Simulated absorber geometries: original circular absorber (dashed black), pentagon #1 (blue), pentagon #2 (red), and rotated square (black).

Table 1 – Geometric efficiency of CPC with different absorber shapes

Shape	Geometric Efficiency
Original Circle	1.00
Pentagon #1	0.97
Pentagon #2	0.94
Upper Tube Exposed	0.90
Lower Tube Exposed	0.84
Square	0.89

Pentagon #2 was selected after the geometry of Pentagon #1 prevented it from being welded shut by the ultrasonic welding machine. As is customary for practical reasons, the reflector was truncated to 95% of the original aperture width yielding a final design concentration ratio of 1.4X. Encasing the absorber in a glass tube results in a gap between the bottom of the absorber and the tip of the reflector. This should be minimized to reduce associated optical losses. For this design the gap was reduced to 3 mm to allow a 0.8 mm space between the absorber and the glass.

The incidence angle modifier (IAM) profile shown in Figure 4 was generated for the collector (truncated, with gap loss, and new absorber shape) by sweeping the incoming incidence angle from 0-60°.

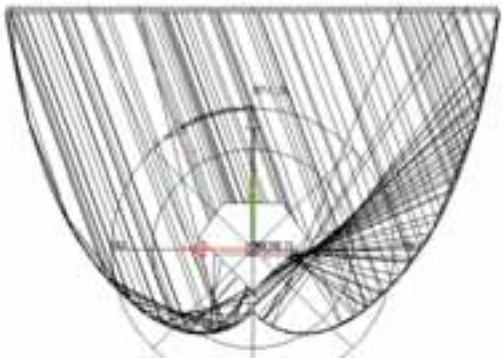

Figure 3 – Ray Trace Analysis of 40° E/W Collector with pentagon shaped absorber

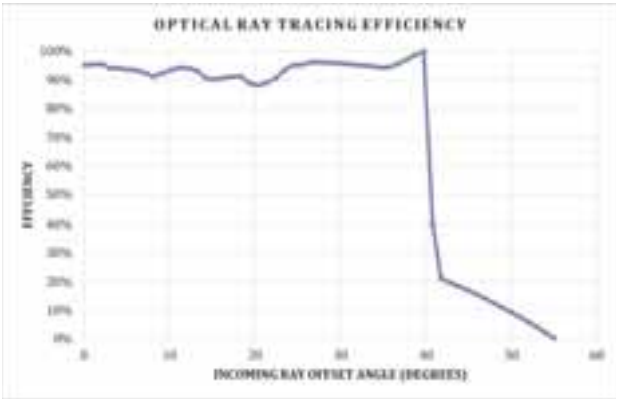

Figure 4 – Incidence Angle Modifier for 40° E/W Collector

The energy-weighted geometric efficiency η_g is calculated from Equation 1, where $\eta_{g,\theta}$ is the geometric efficiency as a function of incidence angle reported in Figure 5.

$$\eta_g = \frac{\int_0^\theta \eta_{g,\theta} \cos\theta d\theta}{\int_0^\theta \cos\theta d\theta} \qquad \text{(Eq. 1)}$$

As a result of the modified absorber shape and the 3 mm gap between the absorber and the bottom of the CPC, the total geometric efficiency is reduced to 93% compared to an ideal CPC. The optical design parameters of the final down-selected CPC design are listed in Table 2.

Table 2 – E/W XCPC Optical Design Parameters

Parameter	Value
Configuration	East-West
Acceptance Angle θ	±40°
Truncation Ratio (% of width)	0.95
Final Aperture Width	406 mm
Absorber Shape	Pentagon
Absorber Perimeter	285 mm
Concentration Ratio	1.4X

3. Materials Selection and Prototype Development

A selective coating is designed to absorb as much of the solar spectrum as possible while emitting as little as possible during operation. Several commercial flat-absorber vacuum tubes with different coatings were placed side by side outdoors, with thermocouples inserted to measure temperature. They were all uncovered at the same time and the temperature rise was recorded. The results showed a difference in performance between suppliers. Most coatings exhibited performance differences between batches, however, the Sunselect and TiNoX coatings showed stable quality and performance and were down-selected for a second round of testing. The second round of testing was performed again with the two commercially available flat absorber vacuum tubes, and for two coating manufacturers who were able to supply material for the prototype XCPC absorber. An image of the test setup is shown in Figure 5 and the results of the second test are presented in Figure 6.

As a result of these tests, SunSelect applied over a copper substrate was down-selected as the selective coating for the E/W XCPC prototype. The coating has a solar-weighted absorptance of 95% and an emissivity of 5% at 100 °C.

Borosilicate glass is typically used in solar applications because of its high solar transmittance. A borosilicate glass sample from the glass tube supplier was tested at NREL in 2007 and the transmission profile is presented in Figure 7. A total solar-weighted transmission of 91.7% is obtained which is consistent with the two Fresnel losses

going in and out of the glass.

Figure 5 – Side-By-Side Stagnation Test Setup

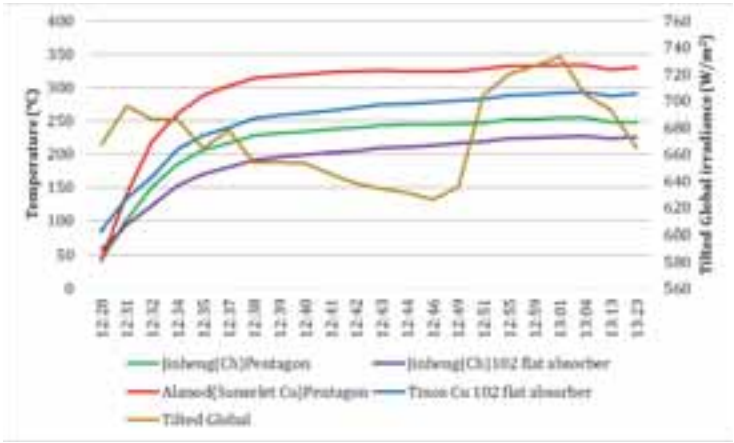

Figure 6 - Stagnation test results.

Several commercial reflector materials exist with high reflectance (>90%) and good outdoor stability. At the time of prototyping a reflective Mylar film was found for roughly $1/m^2. The hemispherical reflectance of the film was measured at 89%, which was maintained after 2 years of outdoor exposure (see Figure 8). As a result the film was selected for the E/W XCPC prototype reflector.

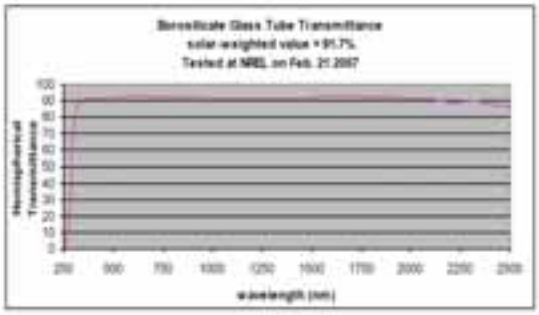

Figure 7 – Borosilicate glass transmission profile tested at NREL in 2007. The solar-weighted transmission is 91.7%.

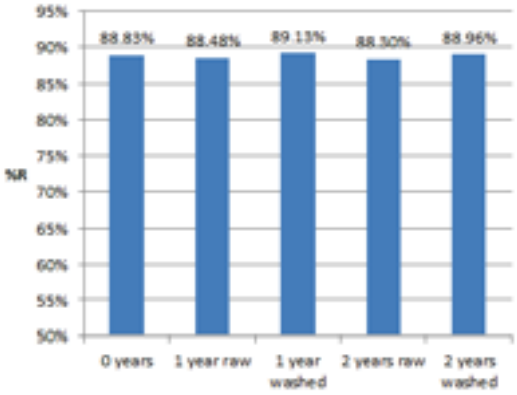

Figure 8 – Aluminized polymer film reflectance over time

A rendering of the final prototype design is shown in Figure 9 with a close up of the plumbing connections in Figure 10. Final specifications for the prototype are listed in Table 3.

Figure 9 – Final E/W XCPC collector prototype. 6 CPCs are plumbed off a centralized manifold box.

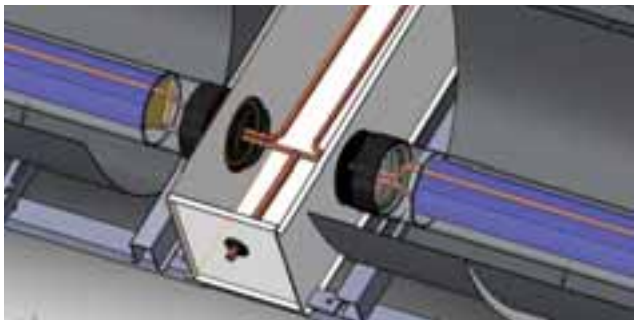

Figure 10 – Manifold Connections – Each side of the collector has 3 CPCs plumbed in series and both sides are plumbed in parallel.

Inside the evacuated glass tube is the selectively coated copper fin formed into the shape of a pentagon. A copper pipe is ultrasonically welded to the top and bottom of the pentagon with a 180° U-bend at the end. The copper pipe transitions into the glass tube via a glass to metal seal and the entire tube is evacuated and sealed below 10^{-4} mbar. A gas getter maintains the vacuum integrity and provides visual indication of vacuum quality.

The reflectors are formed of aluminum and overlaid with a reflective Mylar film. Their shape is supported by 4 ribs along the length of each reflector. The entire collector is formed by combining three XCPCs on either side of a central manifold box. Inside the manifold box, the tubes are piped together using copper flare connections and surrounded with fiberglass insulation. The two sides of the manifold box are piped in parallel, each with three CPCs piped in series.

Table 3 – E/W XCPC Collector Prototype Specifications

Parameter	Value
Selective Coating	SunSelect
Solar Weighted Absorptance (α)	0.95
Emissivity ($\varepsilon_{100\,°C}$)	0.05
Copper Pipe OD	8 mm
Copper Pipe Thickness	0.75 mm
Absorber Tube Length	1.9 m
Glass Material	Borosilicate
Solar Weighted Transmission (τ)	0.92
Glass Tube OD	102 mm
Glass Tube Thickness	2.2 mm
Reflector Material	Mylar
Total Hemispherical Reflectance (ρ)	0.89
CPCs per Collector	6
Aperture Area	4.5 m^2
Gross Area	5.4 m^2

4. Optical and Thermal Performance Models

Simulation of the completed design was performed in LightTools for 1 million rays using optical parameters of the materials used in the XCPC prototype. Ray trace diagrams are presented in Figure 11. At normal irradiance, an optical efficiency η_0 of 71% is obtained.

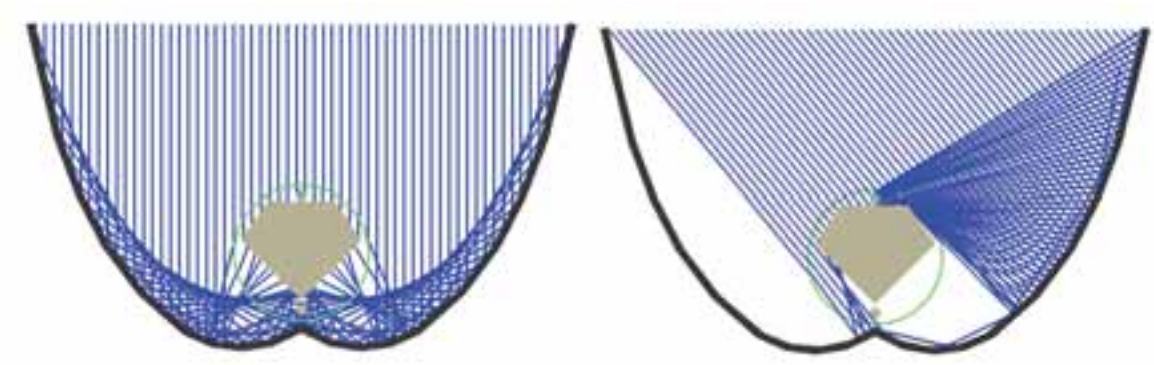

Figure 11 – Ray tracing of E/W XCPC collector for normal incidence and off-angle incidence.

A two-dimensional finite element model was created for the absorber where the polygonal fin shape was approximated by a generic 20-sided polygon (shown for n = 6 in Figure 12) and the tube length was divided into 40 nodes.

Uniform solar irradiance is assumed to be incident on all fins, which also radiate outward and conduct with their radial and axial neighbors. The fins at the top and bottom of the absorber are assumed to be at thermal equilibrium with the copper pipe, providing a conduction pathway to the interior surface of the pipe where heat is transferred to the fluid via convection. Since the absorber tubes are evacuated, no other convection is modelled. The heat

transfer coefficient between the inner pipe wall and the fluid is calculated based on the Nusselt number for laminar flow and using the Gnielinski and Dittus-Boelter correlations for turbulent flow.

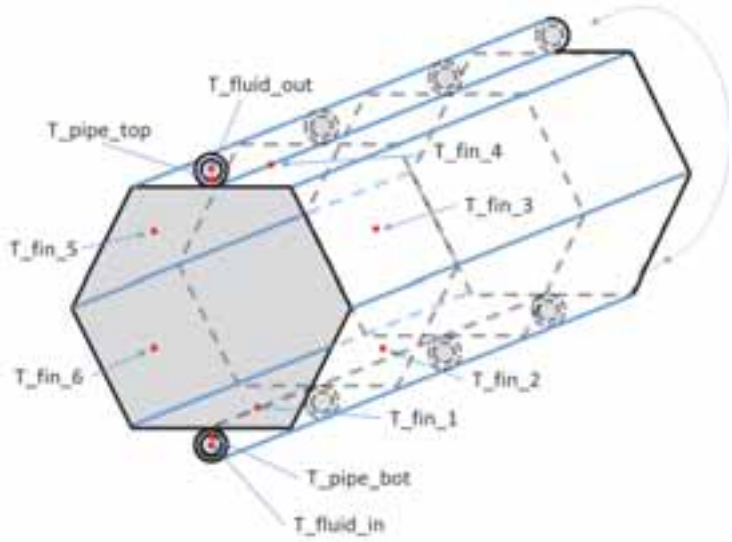

Figure 12 – Finite Element Analysis Mesh. The pentagon absorber is approximated by an n-sided polygon (shown for 6 sides here). The actual model used a 20-sided polygon and the length of the absorber was divided into 40 nodes.

Table 4 – Heat transfer model parameters

Parameter	Value
L_abs	1.8 m
n	40 nodes
L_fin	272 mm
n_fins	20 nodes
Fin_thickness	0.125 mm
Fin and Pipe material	Copper (Cu)
Piper inner diameter	6.5 mm
Pipe outer diameter	8 mm
G	1000 W/m^2
$\dot{m}$	75 g/s
k_{Cu}	400 W/m-K
ε	0.05 @ 100 °C, 0.08 assumed @ 200 °C

The parameters used in the model are listed in Table 4, assuming fluid properties for the mineral oil Duratherm 600. The emissivity of the selective coating is known to be 0.05 at 100 °C and was interpolated linearly to an emissivity of 0.08 at 200 °C. Matrix inversion was used to solve for the temperature at each node and the process was repeated until the temperature change between iterations was less than 0.01 °C.

The input solar irradiance to the model is calculated according to equation 2 and the solar irradiance absorbed by each fin from equation 3.

$$Q_{in} = A_{absorber} C_x G \quad \text{(Eq. 2)}$$

$$Q_{fin,absorbed} = \frac{Q_{in}\eta_0}{n_{fins} n} \quad \text{(Eq. 3)}$$

The net thermal generation of the collector ($Q_{thermal}$) is calculated based on the inlet and outlet temperatures from the model. This simulation was performed for temperatures between 25 °C to 400 °C and the efficiency calculated according to equation 5 is plotted versus temperature in Figure 13.

$$Q_{thermal} = \dot{m} c_p \Delta T_{col} \quad \text{(Eq. 4)}$$

$$\eta = \frac{Q_{thermal}}{Q_{in}} \quad \text{(Eq. 5)}$$

The efficiency jump between 125/150 °C is due to the transition from laminar to turbulent flow at which point the calculation of the heat transfer coefficient between the pipe wall and the fluid changes. Average temperatures along the length of the tube are presented in Figure 14 for an inlet temperature of 200 °C, showing a maximum temperature rise along the fin length of 40 °C.

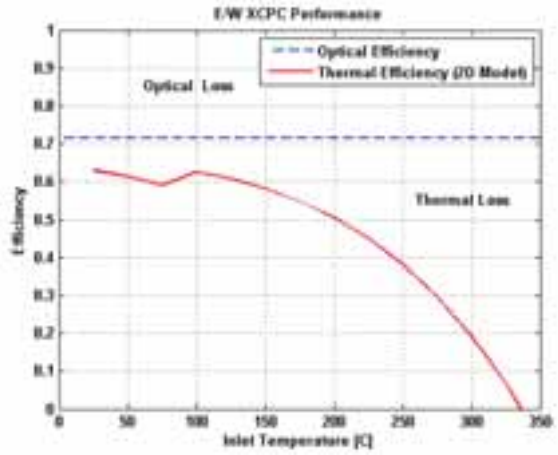

Figure 13 – Simulated performance results for an input irradiance of 1000 W/m².

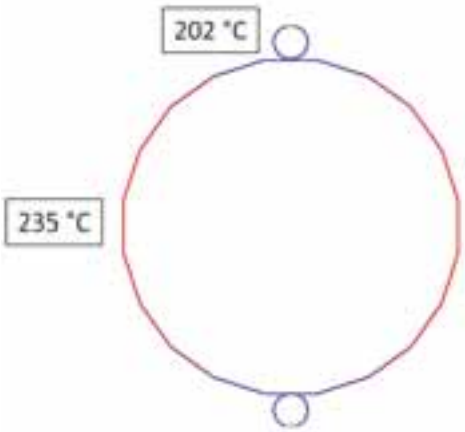

Figure 14 – Temperature profile of fins for an inlet temperature of 200 °C.

5. Experimental Test Results

Performance of the prototype XCPC collector was tested at the University of California Merced Castle Research Facility. In this section is a description of the test platform, testing methods, and experimental performance results.

The half-collector prototype (3 tubes) was mounted on a dual axis tracker to measure on and off-axis performance for characterization. A precision spectral pyranometer (PSP) and normal incidence pyrheliometer (NIP) mounted on the tracker measure the solar resource. The main test platform is a medium temperature oil loop (Figure 15) which contains a circulation pump, primary heating element, coriolis flow meter, thermocouple clusters, and an in-line calorimeter. A total of 33 sensors are installed in the system, including: 1 Coriolis flow meter (± 0.1 %); 25 K-type thermocouples, 4 pressure gauges, 1 current clamp sensor, 1 Precision Spectral Pyranometer (PSP), and 1 Normal Incidence Pyrheliometer (NIP). Data is collected using an Agilent 34970A data acquisition unit, which scans and records all sensor readings every 5 seconds. The instrument and measurement error are listed in Table 5.

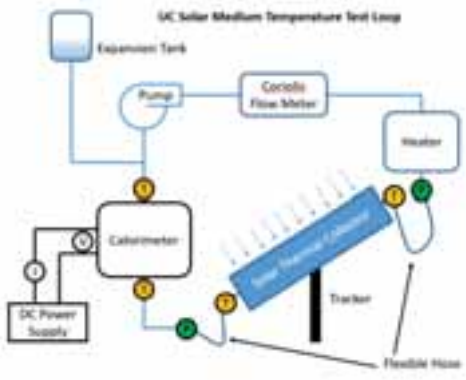

Figure 15 – UC Solar Medium Temperature Test Loop Schematic

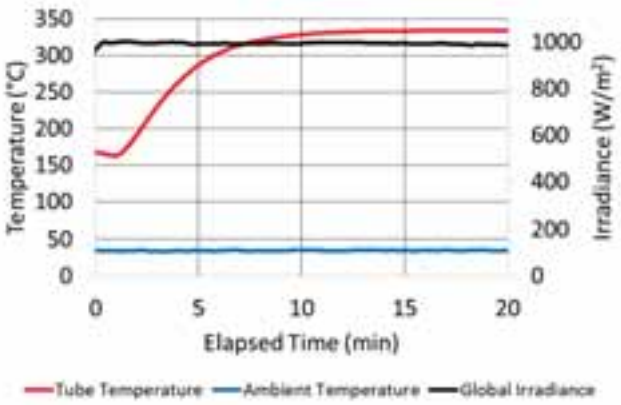

Figure 16 – Stagnation test results

Table 5 – Instrument and measurement error

Device	Instrument Error	Keysight Measurement Error	Temperature Coeff. [/°C ambient above 28°C]
k-Type thermocouple	±1.1°C or 0.4% (whichever is greater)	±1.0°C	+0.03%
Coriolis Mass Flow Meter	±0.1% of reading	±0.01% of reading	+0.001% of reading
UNI-T UT210 current clamp meter	±2.0% of reading	NA	NA
DC Voltage Measurement	NA	±0.0045% of reading + 0.003% of range	±0.0005% of reading + 0.0003% of range
Precision Spectral Pyranometer (PSP)	±2.5% of reading	±0.0050% of reading + 0.0040 of range	±0.0005% of reading + 0.0005% of range
Normal Incidence Pyrheliometer (NIP)	±2.5% of reading	±0.0050% of reading + 0.0040 of range	±0.0005% of reading + 0.0005% of range

A stagnation test was performed on August 11, 2017. Three thermocouples inserted at various lengths inside the upper fluid channel of a single evacuated tube on the XCPC collector measure the temperature over time. The results of this test are shown in Figure 16. The inside of the evacuated tube reached a final stagnation temperature of 333 °C.

Optical testing was performed between August 20th and September 6th using the setup shown in Figure 17. The efficiency is calculated according to equation 6, where $\dot{m}$ is the mass flow rate of the HTF in kg/s, c_p is the heat capacity of the fluid in kJ/kg-K, ΔT_{col} is the temperature difference across the collector in °C, A_{col} is the aperture area of the collector in m^2, and G is the global solar irradiance in kW/m^2.

$$\eta_{thermal,flow} = \frac{Q_{thermal,flowrate}}{Q_{solar}} = \frac{\dot{m}c_p\Delta T_{col}}{A_{col}G} \qquad \text{(Eqn. 6)}$$

These tests were performed using city water as the heat transfer fluid. Thermocouple clusters measured the average inlet and outlet temperature and the flow rate was measured manually by recording the time it took to fill up a 5 gallon bucket (which actually contains 5.6 gallons). The heat capacity of water was assumed to be a constant 4.18 kJ/kg-K. Results are presented in Figure 18 from which an average optical efficiency of 62% was obtained.

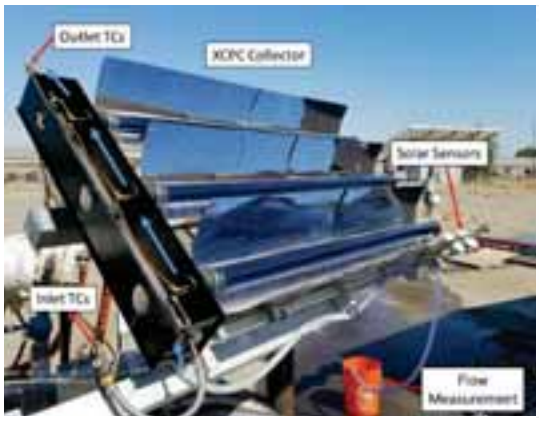

Figure 17 – Optical Testing

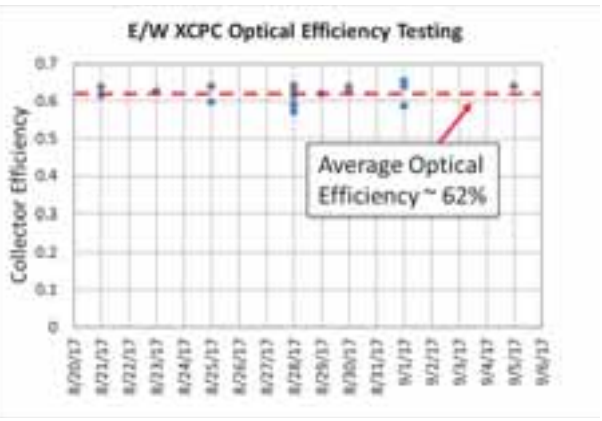

Figure 18 – Optical Test Results

The XCPC collector (Figure 19) was tested at elevated temperatures using the oil test loop. The instantaneous thermal efficiency of the collector was calculated using the standard flow rate method (equation 7) and also using

a calorimetric technique discussed below.

A calorimeter installed in-line with the solar collector generates heat using two 1 kW resistive heating elements placed inside two counter-flow tubes. The heat transfer oil enters the outer annulus of the counter-flow tube and exits through the inner annulus where it is in direct contact with the heating element (Figure 20). The two heating elements and oil flow path are constructed in parallel and the entire calorimeter is wrapped in aerogel insulation with the heated portions encased in all glass vacuum tubes to limit heat loss to the environment. Two k-type thermocouple clusters containing six thermocouples each measure the inlet and outlet temperatures of the calorimeter.

Figure 19 – Oil Testing

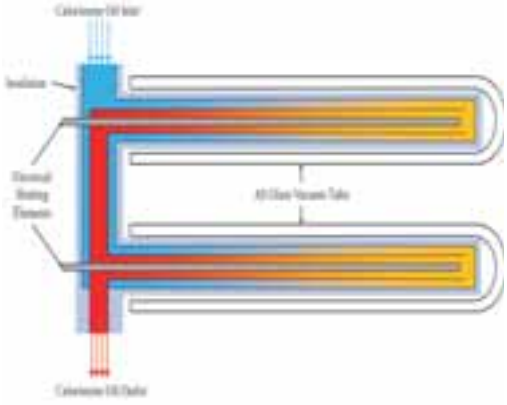

Figure 20 – Calorimeter Schematic

Since the calorimeter is plumbed in-line with the collector it sees the same heat transfer fluid (C_p) and flow rate as the collector. A known amount of power input generates a repeatable temperature rise across the calorimeter. By comparing the temperature rise across the calorimeter to the temperature rise across the collector, the power output of the collector can be determined. For example if the collector raises the temperature 10 °C and the calorimeter also raises the temperature 10 °C from 2 kW of power, we know the collector is generating 2 kW of thermal power.

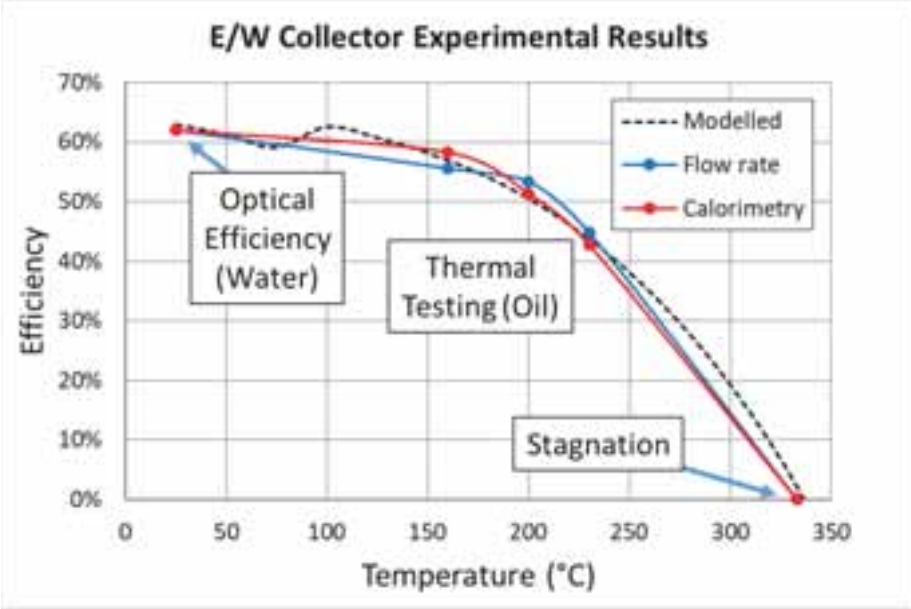

Figure 21 – Experimental Results

The use of a calorimeter provides a redundant measurement which eliminates the flow rate measurement and dependence on heat capacity which is prone to change from the manufacturers specifications over time. Instead they are replaced by more reliable temperature, current, and voltage measurements. The thermal efficiency

determined by the calorimeter is calculated according to equation 7, where ΔT_{cal} is the temperature rise across the calorimeter, V_{cal} is the DC supply voltage, and I_{cal} is the DC current. Results are presented in Figure 21.

$$\eta_{thermal,cal} = \frac{\mathrm{Q_{thermal,cal}}}{\mathrm{Q_{solar}}} = \frac{\frac{\Delta T_{col}}{\Delta T_{cal}} \cdot V_{cal} \cdot I_{cal}}{A_{col} G} \qquad \text{(Eq. 7)}$$

6. Installations

Figure 22 – Merced, CA Installation

The Merced installation shown in Figure 22 is a 20 kW array of the E/W collectors described in this paper installed alongside an earlier generation 20 kW N/S array. These arrays are used to provide thermal power for various projects including solar cooling (Widyolar et al. 2014), solar drum drying (Ferry et al. 2016), and is currently being commissioned for solar wastewater evaporation.

Some representative data is presented below in Figures A, and B for September 8th, 2016. The total solar energy incident on plane of the collector array between 11:45 pm and 5:00 pm was 175.5 kWh, resulting in a thermal generation of 76.9 kWh and 70.6 kWh of cooling from the chiller.

Experimental testing on a single E/W collector showed an efficiency of 55% at an operating temperature of 160 °C while the efficiency of the array tested in this experiment at the same temperature was around 44%. The decrease is attributed to heat losses through the insulated pipes which interconnect the collectors in the array. A rough calculation shows this is on the order of 2-3 kW from the 150 m of ¾" pipe insulated with 2" of fiberglass. Accounting for this heat loss makes the data from this experiment consistent with the previously reported test results. The E/W array took approximately 2 hours to warm up to an outlet temperature of 180 °C and provided 15-20 kW of direct solar powered cooling for an additional 6 hours. A solar COP of 0.44 demonstrated by the E/W array is comparable with other documented double effect solar thermal cooling systems.

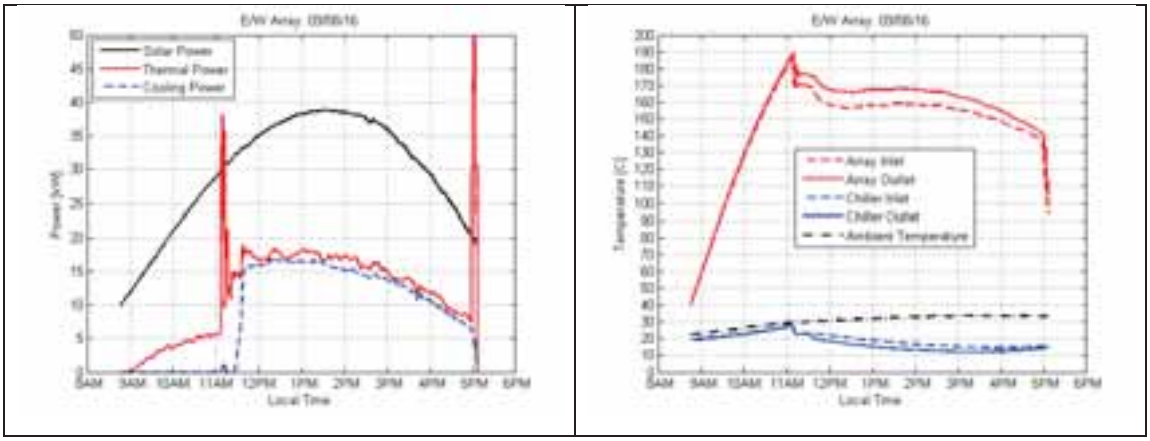

Figure 23 – Sept 8th, 2016 – E/W Array Performance	Figure 24 – Sept 8th, 2016 – E/W Array Temperatures

Table 7 – East-West Array – September 8th, 2016

		Range (instantaneous)	Operational Average*
Collector efficiency	Thermal power captured at 160 °C per available solar power.	0.350 – 0.565	0.438
Thermal COP	Cooling power per captured thermal power	0.721 – 1.101	0.919
Solar COP	Cooling power per available solar power	0.288 – 0.488	0.402

*Operational average taken between 11:45 am and 5:00 pm.

Figure 25 – UlaanBaatar, Mongolia Installation

The Mongolia installation shown in Figure 25 is a 5 kW E/W array installed to provide space heating (Winston et al. 2014). The collector system is installed completely off-grid, using a small PV panel to power a 24 VDC circulation pump which circulates antifreeze through the collector array. The heat is transferred into the ger by a heat exchanger, which is stored in 55 gallon insulated drums of hot water.

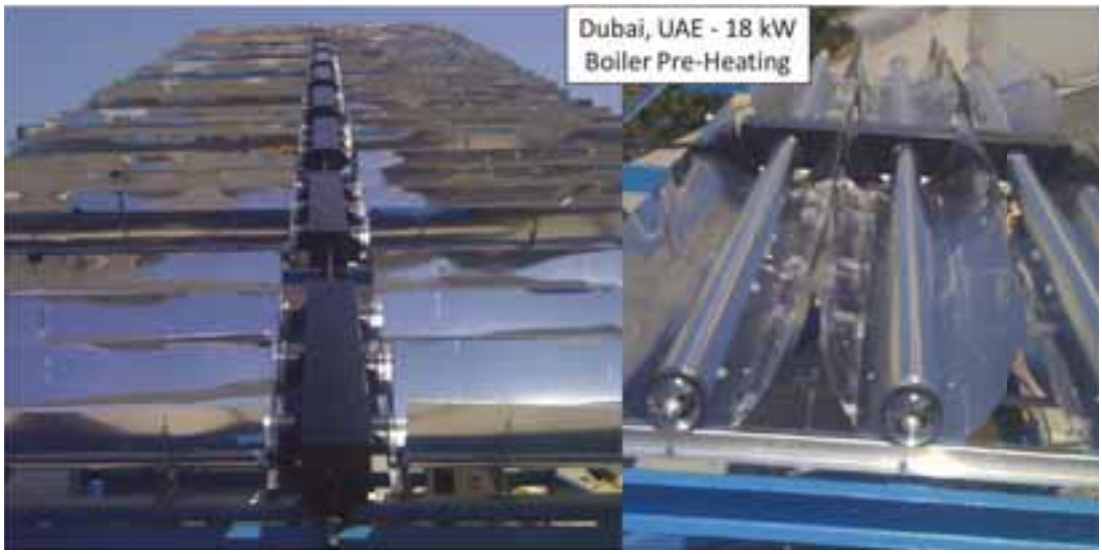

Figure 26 – Dubai, UA Installation

The Dubai installation shown in Figure 26 is the most recent installation and is currently being used to provide boiler pre-heating for sugar refining.

7. Conclusion

In this paper we present the most recent round of developments on the external compound parabolic concentrator (XCPC). The XCPC is a wide-angle concentrator which allows it to (1) collect sunlight year-round from a stationary position, (2) accommodate installation misalignment, and (3) collect a significant fraction of the diffuse solar resource while still providing 1.4X concentration on the absorber. The evacuated tube absorber allows efficient operation regardless of external climate conditions (hot or cold). Optical and thermal simulations have match the experimental data very closely. The collector has an optical efficiency of 62% and a thermal efficiency of 59% at 100 °C and 50% at 200 °C. Current installations are located in California, Mongolia, and the United Arab Emirates and the technology is being commercialized in the USA and India.

8. References

Buonomano, A., Calise, F., d'Accadia, M.D., Ferruzzi, G., Frascogna, S., Palombo, A., Russo, R. and Scarpellino, M., 2016. Experimental analysis and dynamic simulation of a novel high-temperature solar cooling system. Energy Conversion and Management, 109, pp.19-39.

Cohen, S., Grossman, G., 2016. Development of a solar collector with a stationary spherical reflector/tracking absorber for industrial process heat. Solar Energy. 128, 31-40.

Duff, W., Winston, R., O'Gallagher, J., and Bergquam, J., 2004. Performance of the Sacramento demonstration ICPC collector and double effect chiller. Solar Energy. 76, 175-180.

Fernández-García, A., Zarza, E., Valenzuela, L., Pérez, M., 2010. Parabolic-trough solar collectors and their applications. Renewable and Sustainable Energy Reviews. 14, 1695-1721.

Ferry, J., Alleyne, F., Milczarek, R., Winston, R. and Olson, D., 2016. Efficiency and Design Analysis of a Solar Thermal Powered Flat Plate Dryer. In ASABE Annual International Meeting (p. 1). American Society of Agricultural and Biological Engineers.

Kim, YS., Balkoski, K., Jiang, L. and Winston, R., 2013. Efficient stationary solar thermal collector systems operating at a medium-temperature range. Applied Energy. 111, 1071-1079.

Li, Q., Zheng, C., Shirazi, A., Mousa, O., Moscia, F., Scott, J., 2017 Design and analysis of a medium-temperature, concentrated solar thermal collector for air-conditioning applications. Applied Energy. 190, 1159-1173.

Sultana, T., Morrison, G., Taylor, R., Rosengarten, G., 2015. TRNSYS modeling of a linear fresnel concentrating collector for solar cooling and hot water applications. Journal of Solar Energy Engineering. 137.

Widyolar, B., Winston, R., Jiang, L. and Poiry, H., 2014. Performance of the Merced Demonstration XCPC Collector and Double Effect Chiller. Journal of Solar Energy Engineering, 136.

Winston, R., Widyolar, B. and Jiang, L., 2014. Nonimaging Optics Heating up Mongolia's Harsh Winter. In SPIE Optical Engineering+ Applications (pp. 91910D-91910D). International Society for Optics and Photonics.

Development of Solar Thermal During 2011 to 2015 and Developing Anticipation for the Technology During 2016 to 2020 in China

Ruicheng Zheng[1], Tao He[1], Xinyu Zhang[2], Min Wang[2] and Bojia Li[1]

[1] China Academy of Building Research, Beijing (China)

[2] Committee of Solar Thermal Conversion, China Renewable Energy Society, Beijing (China)

Abstract

In this paper it is introduced the development of solar thermal including solar hot water, solar heating combisystem, solar cooling, solar drying, solar cooker, solar desalination and solar thermal power etc during 2011 to 2015 and looking forward to these technologies developing including anticipation for technique progress and projects spreading during 2016 to 2020 in China.

Keywords: solar hot water, solar heating combisystem, solar cooling, solar drying, solar cooker, solar desalination, solar thermal power

1. Introduction

There are two influence factors for development of solar thermal during 2011 to 2015 in China. The favorable factor is policy supporting from governments, such as "the Demonstration Items for Renewable Energy Application in Buildings" supported by the Ministry of Finance and Ministry of Housing and Urban-Rural Development of PRC and demonstration projects of "Green Small Towns" and "New Energy Cities" supported by National Energy Administration, the Ministry of Finance and Ministry of Agriculture of PRC etc. The unfavorable factor is market environment. As national economy developing speed changing slowly especially gliding of real estate which has a close relation with solar thermal, developing of solar thermal also meet some difficulties. So it is necessary taking positive and useful measures to overcome them on the base to sum up the past experience for China's whole profession of solar thermal.

China's fast developing of solar thermal mainly depended on application of solar hot water in the past and now this market becomes saturated. Therefore an important countermeasure is extending application fields, such as from solar water heating system extending to solar heating combisystem, from solar heat for buildings extending to solar heat for industrial and agricultural processes and we will have a rather favorable circumstances in the next years. For decreasing serious air pollution, in the 13th Five-year plan (from 2016 to 2020) China government has decided a higher goal for renewable energy application and especially has made a guiding principle on cleaning space heating in countrysides of northern China. So under this background we can anticipate hopefully that solar thermal in China will have a better development in the future, and we should pay more attention to technical progress which includes raising product quality and improving system optimum design etc. At the same time we should also promote the international cooperation with developed countries having advanced technology of solar thermal and raise our ensemble capacity.

2. Development of Solar Thermal During 2011 to 2015

2.1. Industry of solar thermal

China has the largest solar thermal industry and market in the world. But it is different with many developed countries where the flat-plate solar collectors are the main products; manufactures for evacuated tube solar collector are still the most, although some manufactures have started to produce flat-plate solar collectors during these years in China. Figure 1 is shown year-quality of sale for collectors and the figure 2 is capacity in operation of solar thermal systems from 2005 to 2015 in China. We can know from these two figures that 2013

doi:10.18086/swc.2017.31.19 Available at http://proceedings.ises.org

is a changing year, the year-quantity of sale for collectors decreased after this year, but the capacity in operation of solar thermal systems has still a little increasing.

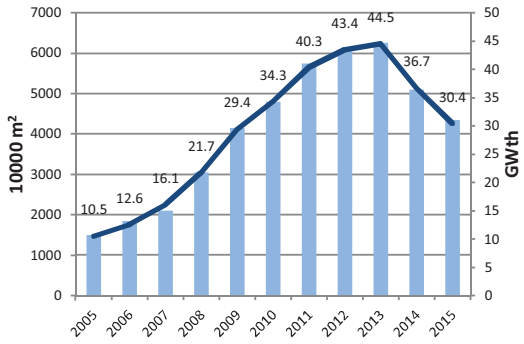

Fig. 1: Year-quantity of sale for collectors

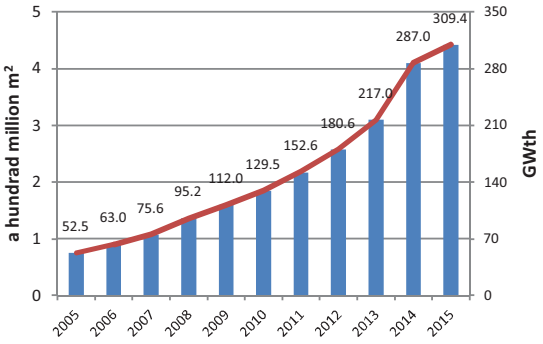

Fig. 2: Capacity in operation of solar thermal systems

2.2. Developing for new products

During 2011 to 2015 China enterprises of solar thermal developed following two key new products:

- Evacuated tube solar collector reaching 150 ℃ working temperature, when reduced temperature difference T_m* is 0.13 (m^2℃) / W, the collector instantaneous efficiency is 53%, its efficiency curve is shown in fig.3. The scale of year output can get three hundred thousand evacuated tubes and one hundred thousand collectors.
- Selective coating for flat-plate solar collector, absorptance is 0.94～0.95, emissivity is 0.05～0.07 and having better anti-aging performance. Automatic production lines for absorber plate with selective coating have been built in Sichuan, Shandong and Fujian provinces etc. The whole production capacity is 11 million m^2 and having own intellectual property.

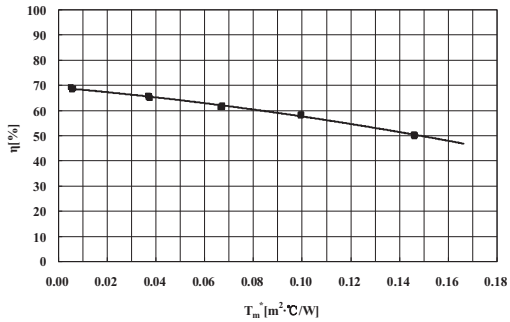

Fig. 3: Efficiency curve of collector

Fig. 4: Collector instead of balcony railing for a solar hot water system

The other important new product is solar air collectors having different structure types and some solar air collectors have realized industrialization.

2.3 Solar water heating system

During 2011 to 2015 application for solar water heating systems had some bigger progress and mainly reflected following three aspects:

- National standard 《Minimum allowable values of energy efficiency and energy efficiency grades for domestic solar water heating systems》 GB 26969-2011 was published and practiced in 2011. The standard gives the energy efficiency grades according to the coefficient of thermal performance for domestic solar water heating systems. There are three levels of energy efficiency grades, the highest is first level and the threshold enter to market is to reach the third level. So some worse quality domestic solar water heating systems are limited to sell in the market.

- As high-rise residential buildings in the cities are main users of solar hot water in China, so some suitable system types are developed to meet this special situation, such as collective-individual system (collective installation of solar collectors, individual installation of water tanks in each apartments) for easy hot water metering. At the same time to develop some new models for solar collectors integrated in buildings, such as collector instead of balcony railing (shown in Fig.4) etc and suitable installation measures to raise the safety and reliability for meeting the requirement of compulsory installation polices.

- Some new system auto-control measures are developed and got practical application, such as household heat exchange control to reach well-distributed heat supply for a collective-individual system. Heat metering was widely used; performance testing for a solar water system on site has became usual business of national or local testing agencies in China. Some projects have realized long term performance monitor and testing data can be delivered by internet.

2.4 Solar heating combisystem

Developing of solar heating combisystem is since 2000 in China and it is an important transition from demonstration projects changing to scale application duration 2011 to 2015. National standard 《Technical code for solar heating system》 and complement《Technical Handbook for Solar Heating》published and in practice in 2009 and in 2012 respectively, so give a stronger technical support to application of solar heating combisystem in China. Most projects of solar heating combisystem used short-term heat storage and application for solar heating combisystems with seasonal heat storage is still at the staring stage in China, but following two projects established a better foundation to developing of solar heating combisystem in the future.

- More than 0.4 million m^2 building area of peasant residences using solar heating combisystems with short-term heat storage have been built in suburbs of Beijing (Fig.5). From monitoring to the solar heating effects in a typical residence during whole winter, solar fraction is 100% in the case of room average temperature 12℃ and the highest room temperature 16℃. The solar cost of the system is 0.44 RMB / kWh, when the working life of the system is 15 years.

- For solar heating combisystems with seasonal heat storage, the technical level and application scale of China have a bigger difference compare with developed countries such as Denmark, Germany and Canada etc. Therefore the international cooperation project “Sino-Danish Renewable Energy Development Programme: Testing, Research & Demonstration for Large Scale Solar District Heating Systems” which was finished in 2015 gave a lot of best experience to China’s technicians and will promote its better application in China in the future.

Fig. 5: Peasant residence of solar heating in suburb of Beijing

Fig.6: Parabolic-trough collectors for solar cooling

2.5 Solar cooling

Technology of solar cooling is developed since 1970’s in China but its application is still at the demonstration stage. Following is some achievements in this field during 2011 to 2015.

- To develop heat-operated refrigerating machine be suitable to solar application, such as 50 kW adsorption refrigerating machine and 1.N-effect absorption refrigerating machine etc.

- National standard 《Technical code for solar air conditioning system of civil buildings 》 GB 50787-2012 was published and practiced in 2012.

- A solar adsorption air conditioning system (the total area of the solar collectors is 49.4m^2) was successfully used to a national grain depot and got better effects. At the condition of daily solar irradiation 16-21 MJ / (m^2 day), the average daily refrigerating power is 3.3-4.4 kW and operation time of the refrigerating machine in the system is 6.5-8.5h during each day.
- A solar lithium bromide absorption air conditioning system (323m^2 solar collectors and 35kW refrigeration unit) was completed in 2013 and has being stably worked till now. Average solar fraction during whole summer can reach 83% in the case of average environment temperature 32℃ and room average temperature 26℃ and average efficiency of the solar collector system is 50%.
- To develop a lower cost parabolic-trough collector for solar cooling and build some demonstration projects of solar air conditioning (Fig.6). According to the on-site testing for a demonstration project in 4 days having different solar radiation, average efficiency of the solar collector system is 55% and the average solar fraction is 68% in the case of 30℃ average environment temperature and 25.6℃ average room temperature.

2.6 Solar drying

Before 1980's there are only 4 solar drying devices of 183 m^2 total collector areas, but it developed faster after 2000 in China. At the present more than 200 solar drying systems were built and total solar collector areas are more than 4 million m^2, but the most is small system with collector areas lower than 200 m^2. There are two main types of solar drying device, using greenhouse or solar collector. The main drying materials are agricultural products including grain fruit and tobacco etc, and industry products including wood (Fig.7) and building materials etc.

Fig. 7: Solar wood drying

Fig.8 Concentrating solar cooker of sheet steel

Professional standard 《General specification for solar drying system》 NB / T 34022-2015 was published and practiced in 2015. It is a first standard for solar drying in China and gives a very important guidance to optimum design and normal installation of the solar drying devices. As solar air collector is a key component of the solar drying device, national standards 《Specification for solar air collectors》 GB / T 26977-2011and 《Test methods for the thermal performance of solar air collectors》 GB / T 26976-2011 which were practiced in 2011 promoted the quality improving of solar air collector greatly.

2.7 Solar cooker

Solar cooker was developed since 1950's in China. As solar cooker has important action for the peasants in the areas where lack of fuel but having better solar radiation, its developing is always stable and the capacity in operation for solar cookers is more than 4 million nowadays in China. In normal using condition one solar cooker can save about 1000kg firewood every year and is about 2 years of paying back time for cost.

There are main two types of solar cookers, box solar cooker and concentrating solar cooker. As Chinese cooking habit, the most of type is concentrating solar cooker in China (Fig.8), box solar cookers are fewer. China's agriculture professional standard 《Focusing solar cooker》 NY / T 219-2003 is the first concentrating solar cooker product standard of this field in the world.

2.8 Solar desalination

China is one of the 13 poor water countries listed by UN and water resource per person is only 1/4 of the world average level. So solar desalination is a continual interest technology for long time in China, but it is still at the research and experiment stage, although to get some better results such as patent of invention "solar air injection desalination device" etc in recent years, there is not demonstration project of practical application up to now.

2.9 Solar thermal power

During 2011 to 2015 solar thermal power including four types of tower, parabolic-trough, dish and Fresnel was all developed at different level in China. Some enterprises have already the capacity to produce heliostat, Stryn generator and evacuated collector tube be used at parabolic-trough collectors etc. There are more than 14 enterprises who can produce evacuated collector tube be used at parabolic-trough collectors and more than 7 enterprises of producing heliostat in China. Part of products passed the testing of foreign professional agency and performance can reach international level. Several solar thermal power systems have been built in China, such as China's first 1MW tower solar thermal power station (Fig.9) located in Badaling of Beijing, generated in August, 2012 and 1MW dish Stryn solar thermal power system (Fig.10) located in Tongchuan of Shanxi Province, completed in 2016 and Stryn generators are developed and produced by Xian Aero-Engine Plc.

Fig. 9: Tower solar thermal power station in Badaling of Beijing

Fig. 10: Dish Stryn solar thermal power system in Tongchuan

3. Technique prospect for solar thermal during 2016-2020

In 2020 the renewable energy will be 15% of total final energy use in China and among them contribution of solar thermal is 13.7% share. Therefore solar thermal is a key technique for completing this object and we should make more efforts during 2016-2020.

3.1 Industry of solar thermal

The industry of solar thermal in China will enter a key transitional stage, only those enterprises which have technical innovative capacity can be developed faster and change stronger. Therefore some enterprises have started cooperation with concerned department in advanced countries for improving own technical capacity. The industry developing will focus to new products and technologies suitable to middle and high temperature application of solar thermal, such as evacuated collector tube with working temperature higher than 250 ℃.

3.2 Solar water heating system

As solar water heating systems integrated in buildings are main types of solar hot water application nowadays in China, the most important tasks are further raising the system's energy saving effects and quality improving of hot water supply. It is necessary focus to system optimum design, automatic-control, heat metering and to step up efforts recommending different types of fine solar water heating systems integrated in buildings by publishing atlas of excellent projects and holding various training etc. At the same time supervision to compulsory installation for solar water heating systems will be strengthened, so that the market can get further normalization.

3.3 Solar heating combisystem

Solar heating combisystem will realize scale application gradually as two favorable policy decisions from government in the future. One is winter space heating by clean energy in northern part of areas; another is to

supply space heating for buildings in Tibet.

Coal is the main energy for space heating in northern part of China and it is an important influence factor to cause air pollution in winter. Therefore the government makes a policy decision to change this situation by using clean energy for space heating instead of coal for decreasing air pollution. In this year a demonstration item for space heating using clean energy in northern part of areas has been initiated by 4 ministries together, the Ministry of Finance, the Ministry of Housing and Urban-Rural Development, the Ministry of Environmental Protection and National Energy Administration. The item can get different level's financial support from the Ministry of Finance according to city's size. As one of clean energies, solar heating combisystem can be practiced in the item and get a chance to develop faster in the future.

Although the weather is very cold in Tibet, but there is no space heating measures in buildings in the past. Therefore to supply space heating is a very important decision for improving living condition of Tibet people. Tibet has the best solar energy sources but lacks of common energies, so to build scale demonstration projects of solar heating combisystems in Tibet can solve space heating problem and avoiding environment pollution at once. Several projects of solar heating combisystems have been carried out in practical implement items for space heating of Tibet, at the same time in the national research plan of the 13th Five-year Development Plan, some research and application items of solar heating combisystem for space heating in Tibet have been also listed. It can be expected that China's technique level of solar heating combisystem will be raised substantially after these items completing.

3.4 Solar cooling

As PV cost decreased continuously in recent years, solar PV electric refrigerating comes into a fine developing chance and a discussion of comparison for solar PV electric refrigerating and solar thermal power refrigerating is resulted. But to China's condition most of areas need space heating in winter and air conditioning in summer, so solar thermal power refrigerating can get better effects and cost performance compare with PV electric refrigerating. Therefore solar cooling using thermal power refrigerating should still have more application and we should pay more attention to two aspects. One is to expand the application scale of solar cooling in suitable areas such as in Turpan of Xinjiang Uygur Autonomous Region where it is dry, hot daytime but cool at night in summer and solar radiation is very nice. Another is to raise technical level for new product research such as to develop small unit of refrigerating capacity lower than 50kW etc. Fortunately, a large demonstration project of solar cooling has been practiced in Turpan, and it will promote the technology progress of solar cooling in China through experience summarization of this project's design, construction and operation etc.

3.5 Engineering construction national standards

In the past there are two types of engineering construction national standard in China. One is mandatory standard which includes some (at least having one) compulsory provisions. The compulsory provisions are only concerning safety, personal healthy etc requirements and must be executed strictly. Another is voluntary standard which has not compulsory provisions. But this system will be reformed in the future, only mandatory standard is still national standard, whole texts are compulsory provisions in it and the provisions will include the requirements to capacity, performance and technical measures, except safety etc. Voluntary standard will be changed to professional or association standard and not be controlled by government. For getting better reforming results some items have been started to research the compiling principle and text contents included in each mandatory standard etc. As the importance of energy efficiency and renewable energy to economy developing, one of the items is "compiling research to code for energy efficiency and renewable energy application in buildings" which includes the contents of solar thermal application in buildings. After the item completing the next task is to compile "Code for energy efficiency and renewable energy application in buildings" according to the item's research results and this code will produce an advantage to standardize application of solar thermal in buildings as well as to improve its energy saving effects in China.

3.6 Solar drying

Most of solar thermal application including solar hot water, heating combisystem and cooling is in buildings in the past, but in the future more will be changed to the fields of industry and agriculture in China. Solar drying is a main technique type used in the fields of industry and agriculture, so it can be expected that solar drying will meet an excellent developing chance and have larger scale of application. In the aspect of technology progress,

we should focus attention on to develop solar air collectors which have high efficiency and can be suitable to solar drying systems for different materials, low cost heat storage devices and build more demonstration projects.

3.7 Solar cooker

Tourism industry developed very faster in recent years in China. So an important developing direction of solar cooker is to research and produce new box solar cookers which are easy carry, having low cost and used to field cooking such as barbecue etc for tour. Some enterprises have produced several model machines, the next step is to improving performance further and to form a certain manufacture scale.

3.8 Solar desalination

During 2016-2020 solar desalination should be changed from theory and experiment research to demonstration application in China. The main focuses are integrating technique for solar thermal system with common sea water desalinization, system optimum design, to raise economical efficiency and to build demonstration projects for solar desalination in the islands where lack of fresh water etc.

3.9 Solar thermal power

During 13th Five-year plan more demonstration projects for solar thermal power will be started in China and several projects of solar thermal power have been approved by the National Energy Administration. After these projects finishing and generating, they can get financial subsidies by 1.15 CNY/kWh of sales price to power network. Compared with PV solar thermal power can be combined heat and power production, so research for technology of heat and power cogeneration suitable to solar thermal power is one of the important tasks in the field of solar thermal power, especially against the background of space heating using clean energy.

4. References

[1] China Association of Building Energy Efficiency. Report on the status and development of China building energy efficiency. China Architecture & Building Press, 2012, 3: 321-364.

[2] China Solar Thermal Energy Industry Federation, Special Committee of Solar Thermal Use of China Rural Energy Industry Association, Special Committee of Solar Thermal Use of China Rural Energy Conservation Association. Report on the development of solar thermal industry of China （2013～2014）. 2015:7-32.

[3] Zheng Ruicheng. Han Aixing. Developing situation for solar heating in China. Construction Science and Technology, 2013:12-16.

[4] Yi Songlin, Zhang Biguang. Solar energy and heat pump drying. China Chemistry Industry Press, 2011,9:12-20.

[5] China Renewable Energy Society, Energy Research Institute, National Development and Reform Commission, Center for Renewable Energy Development, 2050 Road map for solar energy development in China, 2014,12: 30-49

Solar Thermal Desalination Technology

Investigation of optimal design of direct contact humidification-dehumidification desalination cycle

Saeed Dehghani, Farzaneh Mahmoudi, Abhijit Date and Aliakbar Akbarzadeh

Energy Conversion and Renewable Energy Group, School of Aerospace, Manufacturing and Mechanical Engineering, RMIT University, Melbourne 3083, VIC, Australia

Abstract

Ongoing water scarcity around the world caused researchers to investigate renewable based desalination systems for providing fresh water. Direct contact humidification-dehumidification desalination is one of the recently introduced technologies for decentralized small-scale water supply. Major energy source of the cycle is heat that can be provided from any available low-grade heat sources such as waste heat or solar thermal collectors. In this paper, a thermodynamic based analysis implemented to the cycle. And through a theoretically investigation, effect of various operational variables such as bottom and top temperature, flow rates and components effectiveness on the cycle performance parameters has been studied in order to evaluate the cycle performance and address optimal working condition. Understanding optimum working condition of the system can provide outstanding technical information for fabrication and sizing of experimental test rig as well as actual module in advance.

Keywords: humidification dehumidification, HDH, Desalination, Solar energy, GOR

1. Introduction

Providing fresh water is a vital need of human being for living all around the world. Desalination methods are the main technological solution for producing fresh water from saline or impure water. Therefore, various type of desalination methods were proposed and developed that can be categorized in membrane and thermal type.

The first and widely commercialized desalination processes based on evaporation technique are multi-stage flash distillation, multiple effect distillation and vapor compression. The second category of desalination processes uses membrane technologies including reverse osmosis, electro-dialysis and membrane distillation.[1] Humidification-dehumidification (HDH) desalination distillation is a one of recently well-studied technologies among the researchers.

The main features of the HDH cycle including remote area water supply, small scale application makes it a competitive alternative application among other desalination technologies. Availability of solar irradiation and any type of impure water such as seawater or brine can make it a sustainable solution for producing pure water. Therefore, all regions of the world like small islands close to the equator with availability of daily solar irradiance as well as saline water the HDH technology is a considerable option. Moreover, the components of the HDH technology is using available and affordable materials that can be find in market as well as maintenance of the system in not demanding in the terms of skilled labor [2, 3].

Basically, the direct contact (DC) HDH desalination system utilizes two main components for producing distilled water. These are humidifier and dehumidifier. As it shown in Fig. 1 in humidifier saline water after heating up through heat source sprayed over air in order to moisturizing it by increasing the air temperature. Then, the hot moisturized air transferred to dehumidifier in which cold fresh water spraying over it and condensed the vapor content of the humid air by decreasing the temperature of it. The distilled water with fresh cooling water will be collected together at the bottom of the dehumidifier and fresh water will be cooled down through a heat exchanger and sprayed again. It should be note that; humidifier and dehumidifier are heat and mass exchange (HME) devices in which there is simultaneous heat and mass transfer occurrence for these devices. Heated fresh water after dehumidifying process can be cooled down with saline water before it enters to heater. Therefore, the fresh water can be cool down as well as the saline water can be preheated in practical approaches for system designing. However, as matter of simplicity this possibility is not incorporated in this study.

There are different configurations of HDH cycles based on which stream is heated up as well as which stream is open or close. In close air/water cycles, air/water is circulated in a closed loop between humidifier and

doi:10.18086/swc.2017.32.01 Available at http://proceedings.ises.org

dehumidifier while water/air is open loop. The air in these systems can be circulated by either natural convection or fan forced by adding a blower. For instance, closed-air open-water (CAOW) water-heated cycle is demonstrated in Fig. 1. Therefore, different types of the HDH cycle can be considered such as close-air open-water(CAOW) air-heated cycle, close-water open-air (CWOA) water-heated and close-water open-air cycle (CWOA) air-heated. [2, 4, 5]

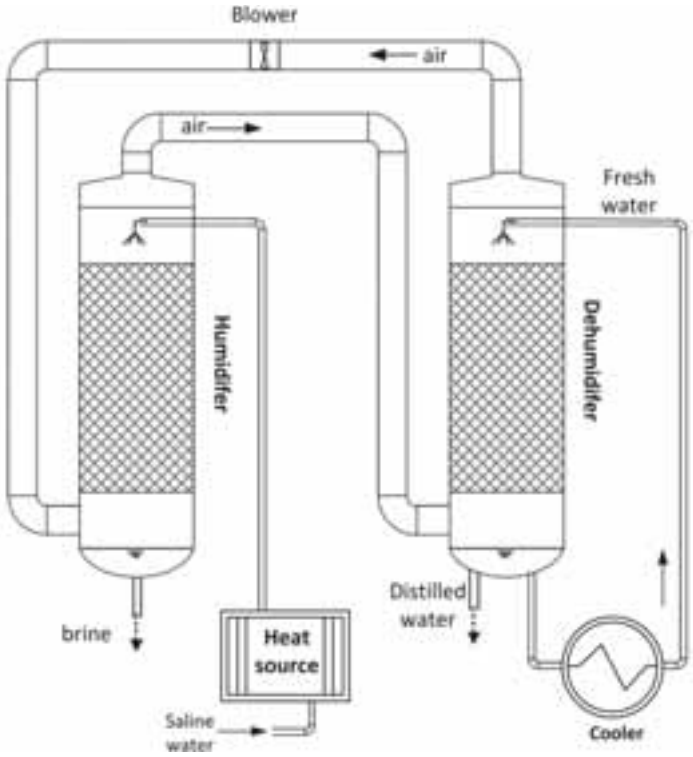

Fig. 1: Overview of the humidification-dehumidification with direct contact dehumidifier

There have been numerous works on non-direct condensers for dehumidification in the HDH cycle.[5-10] Moreover, in this area, several studies have been performed to replace the thermal energy sources of the process from fossil fuel with renewable ones and especially solar energy.[11-13] Also, in other studies, an alternative low-grade heat source such as industrial waste heat or geothermal [14-17]were considered for supplying thermal energy demand of the cycle. These sources of heat can be applied to the HDH cycle with direct contact as well. To make the dehumidifying process in non-direct HDH cycle cost effective, an efficient low cost dehumidification method can be alternated to condense water vapor out of the air stream. With a large fraction of the air/vapor mixture being non-condensable, direct contact condensation is considerably more effective than film condensation. In addition, direct contact condensation within a packed bed is more effective than droplet direct contact condensation.

Bharathan et al. [18] initially introduced a direct contact condenser approach to enhance the heat transfer rate in presence of non-condensable gas. James et al. [19] fabricated a laboratory scale direct contact condenser to study the variation of temperature, humidity, and condensation rate through the condenser system. They evaluated their result by considering a finite volume method for analyzing the packing condenser.

Eslamimanesh and Hatamipour[20, 21] conduct a theoretical analysis for the open-air open-water HDH cycle to study effect of working parameters on water production rate as well as an economic study of the system. Mehrgoo and Amidpour investigated the optimum water production rate utilizing constructal design theory for a fixed-size HDH system.[22] Ettouney [19] introduced different types of the dehumidifier including vapor compression, desiccant air drying, and membrane air drying.

A lack of study for the CAOW water-heated cycle can be observed from the literature review. Therefore, in this study a comprehensive theoretical analysis of a HDH cycle with direct contact dehumidifier performed in order to understand the optimum working condition of the system.

2. Mathematical modeling

In order to study cycle's behavior with variation of operational variables a theoretical study of the HDH cycle from thermodynamic standpoint a theoretical modeling is implemented. As it shown in Fig. 2 the cycle components are considered "black-box" that do not consider transport properties inside the components.

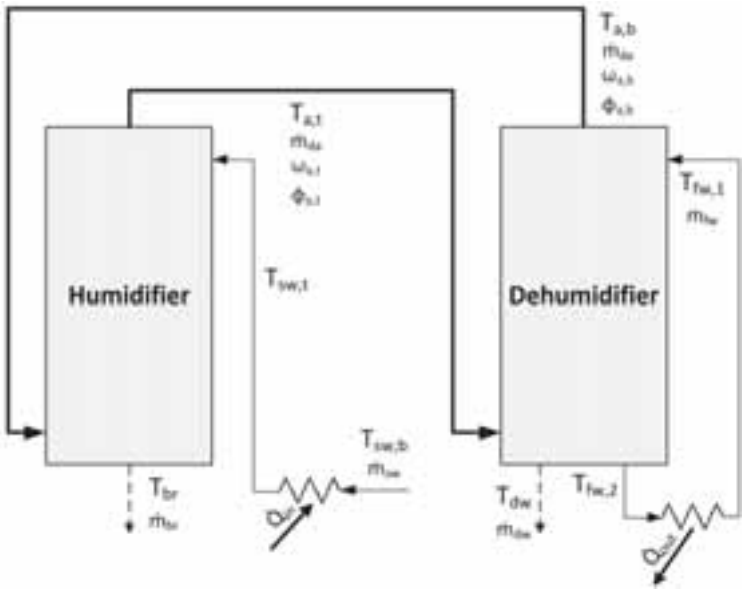

Fig. 2: Schematic diagram of the humidification-dehumidification with direct contact dehumidifier

Following assumptions are considered in theoretical modeling of the direct contact HDH cycle.

- Cycles operate at steady state and steady flow conditions.
- Humidifier and dehumidifier are adiabatic and there is no heat loss from any of the cycle pipelines to their surroundings.
- Pumping and fan powers are negligible in comparison to total thermal energy input of the system.[5, 23]
- Kinetic and potential energy terms are excluded in the energy balance.
- The water condensed in the dehumidifier is assumed to leave at a temperature which is the average of the humid air temperatures at inlet and outlet of the dehumidifier.[5]

The presented model in this study is based on the energy and mass balance implementation on each system components including humidifier, dehumidifier, heater and cooler, so they can be find in thermodynamic text books.[24] However, to solve the governing equation some cycle variables should be known. These parameters are saline water temperature of humidifier inlet, fresh water temperature of the dehumidifier inlet, effectiveness of humidifier and dehumidifier as well as relative humidity of air entering humidifier and dehumidifier. Therefore, for a range of variation of these variables the analysis is performed.

The governing equations can be summarized as following:

Humidifier energy and mass balance:

$$\dot{m}_{sw} + \dot{m}_{da}\omega_{a,b} = \dot{m}_{br} + \dot{m}_{da}\omega_{a,\mathrm{t}} \tag{1}$$

$$\dot{m}_{sw}h_{sw,t} + \dot{m}_{da}h_{a,b} = \dot{m}_{br}h_{br} + \dot{m}_{da}h_{a,\mathrm{t}} \tag{2}$$

Dehumidifier energy and mass balance:

$$\dot{m}_{da}\omega_{a,t} = \dot{m}_{dw} + \dot{m}_{da}\omega_{a,b} \tag{3}$$

$$\dot{m}_{fw}h_{fw,1} + \dot{m}_{da}h_{a,t} = \dot{m}_{fw}h_{fw,2} + \dot{m}_{da}h_{a,b} + \dot{m}_{dw}h_{dw} \tag{4}$$

It should be noted that, the dry mass flow of air is constant through the humidifier. Also, enthalpy of humid air is considered as a binary mixture of dry air and water vapour, in other words: $h_a = h_{da} + \omega h_v$

Heater and cooler:

$$\dot{Q}_{in} = \dot{m}_{sw}\left(h_{sw,t} - h_{sw,b}\right) \tag{5}$$

$$\dot{Q}_{out} = \dot{m}_{fw}\left(h_{\mathrm{fw},2} - h_{fw,1}\right) \tag{6}$$

In order to discover outlet streams conditions in the humidifier and dehumidifier, effectiveness equation needs to be defined and considered for mathematical solution. Principally, effectiveness compares the actual thermal energy versus ideal thermal energy transferred from each stream and is defined as actual enthalpy rate variation to the maximum possible enthalpy rate variation, in other words $\varepsilon = \Delta\dot{H}/\Delta\dot{H}_{\max}$ [25]. Therefore, effectiveness of humidifier and dehumidifier would be extracted as following:

$$\varepsilon_h = \max\left(\frac{\dot{H}_{a,t} - \dot{H}_{a,b}}{\dot{H}_{a,t}^{ideal} - \dot{H}_{a,b}}, \frac{\dot{H}_{sw,t} - \dot{H}_{br}}{\dot{H}_{sw,t} - \dot{H}_{br}^{ideal}}\right) \tag{7}$$

$$\varepsilon_d = \max\left(\frac{\dot{H}_{a,t} - \dot{H}_{a,b} + \dot{H}_{dw}}{\dot{H}_{a,t} - \dot{H}_{a,b}^{ideal} + \dot{H}_{dw}}, \frac{\dot{H}_{fw,2} - \dot{H}_{fw,1}}{\dot{H}_{fw,2}^{ideal} - \dot{H}_{fw,1}}\right) \tag{8}$$

In both humidifier and dehumidifier, the ideal outlet air enthalpy happens when the outlet air is fully saturated at the water inlet temperature, and the ideal outlet seawater enthalpy is when its temperature is equivalent to the inlet air temperature.

In addition to considering effectiveness equations, relative humidity of air at bottom and top air streams should be known. Nawayseh et al. [11] assumed that exit air from humidification column was saturated according to the experimental. Moreover, distilled water temperature is assumed as average of the humid air temperatures at inlet and outlet of the dehumidifier, in other words $T_{dw} = (\mathrm{T}_{a,t} + \mathrm{T}_{a,b})/2$ as is required that the number of equations and unknowns should be same. [5] Therefore, by solving the system of nonlinear equations, unknown variables can be obtained.

For incorporating accurate and reliable thermodynamic properties of the moist air and water and seawater, ASHRAE handbook[26] as well as Engineering Equation Solver (EES) software[27] are applied. EES software has completer library of thermophysical properties for a wide range of substances including moist air properties with the formulation presented by Hyland and Wexler[28] as well as water properties using the formulation of IAPWS (International Association for Properties of Water and Steam) [29].

The obtained system of nonlinear equations was solved utilizing the EES software, which calculates moist air and water properties using built-in functions. These functions have been previously defined in software and evaluate the thermophysical properties of various substances based on a set database in the software. EES is a numerical solver, using an iterative procedure for solving the system of equations. The EES automatically identifies and groups equations that are solved simultaneously. The convergence of the numerical solution is verified by using two methods: (i) 'Relative equation residual' which is the difference between left-hand and right-hand sides of an equation divided by the magnitude of the left-hand side of the equation; and (ii) 'Change in variables changing in each iteration. The calculations are converged if the relative equation residuals are less than certain value for example 10^{-6} or if variable change is less than 10^{-9}. Both relative equation residuals and change in variables are adjustable for desirable precision. Besides, there are two stopping criteria consisting of (i) 'number of iteration' and (ii) 'elapsed time' that can be set for obtaining variables with higher accuracy. EES software is widely used by the scientific community for thermodynamic system evaluations for thermodynamic analysis.[30, 31]

3. Cycle metrics

In order to evaluate the HDH cycle performance in the terms of thermal energy recovery, energy efficiency and water production rate, performance parameters of the cycle are defined.[2] they are basically non-dimensional parameters.

Gain output ratio (GOR): GOR is the ratio of the latent heat of evaporation of the distillate water produced to the total heat input to the cycle from the heat source. It represents the amount of heat recovered in the cycle.

$$GOR = \frac{\dot{m}_{dw} h_{fg}}{\dot{Q}_{in}} \tag{9}$$

Recovery ratio (RR): recovery ratio is the amount of distilled water over inlet saline water to the cycle, which is a criterion for water production efficiency of the cycle. It should be noticed that for low recovery ratios, brine disposal treatment is not necessary.

$$RR = \frac{\dot{m}_{dw}}{\dot{m}_{sw}} \times 100 \tag{10}$$

4. Result and discussion

In order to study the effect of cycle's variables on the performance a range of variation is considered. The fresh water temperature in the cycle at the entrance to dehumidifier may range between 15–30 °C due to the seasonal temperature changes. The top brine temperature in the cycle at the humidifier inlet is assumed to be in the range of 65–80 °C which is basically a low-grade heat source temperature. The effectiveness of both the humidifier and dehumidifier are assumed to be within the range of 65–95%. As there is direct contact humidification and dehumidification process, it is expected that air is fully saturated. However, to study the effect of air humidity a relative humidity range of 70–100% is considered. Therefore, under the basic working condition including, fresh water temperature of 20 ºC and top brine temperature of 70 ºC as well as humidifier and dehumidifier effectiveness of 85% and top and bottom relative humidity of 90% simulation are performed.

In order to find effect of mass flow rate of saline water, fresh water and air on the system efficiency, mass flow rate ratio of humidifier is defined. ($mr_h = \dot{m}_{sw} / \dot{m}_{da}$). In Fig. 3 effect of these mass flow rates on GOR is illustrated. As it shown, by increasing both the flow rate of fresh water and flow rate of dry air at a constant saline water flow rate, the GOR of the cycle would be enhanced. In practical approaches the minimum values of mass flow rate ratio of saline water to fresh water based on available heat source and heat sink capacity can be determined. Therefore, here in a case of flow rate of saline water to fresh water equal to 0.5, higher value of GOR can be obtained.

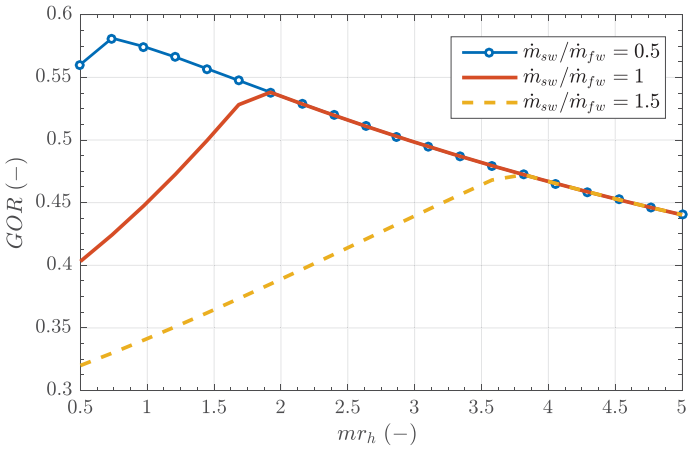

Fig. 3: Effect of mass flow rates saline water, fresh water and air on the cycle GOR

By determining the ratio of the saline water to fresh water, the effect of operational parameters on cycle performance can be studied in detail. Therefore, for flow rate ratio of saline water to fresh water equal to 0.5, impact of operational parameter on cycle performance are investigated in following section.

Fig. 4a demonstrates the GOR against mass rate ratio at fresh water inlet temperatures. As it shown by increasing the humidifier inlet fresh water temperature, both gain output ratio and recovery ratio are decreasing. The maximum value of GOR and RR happening at the same mass flow rate ratio of saline water to dry air. However, for lower temperature of fresh water the optimum happening at smaller mass flow rate ratios. A maximum of 0.62 for GOR can be obtained.

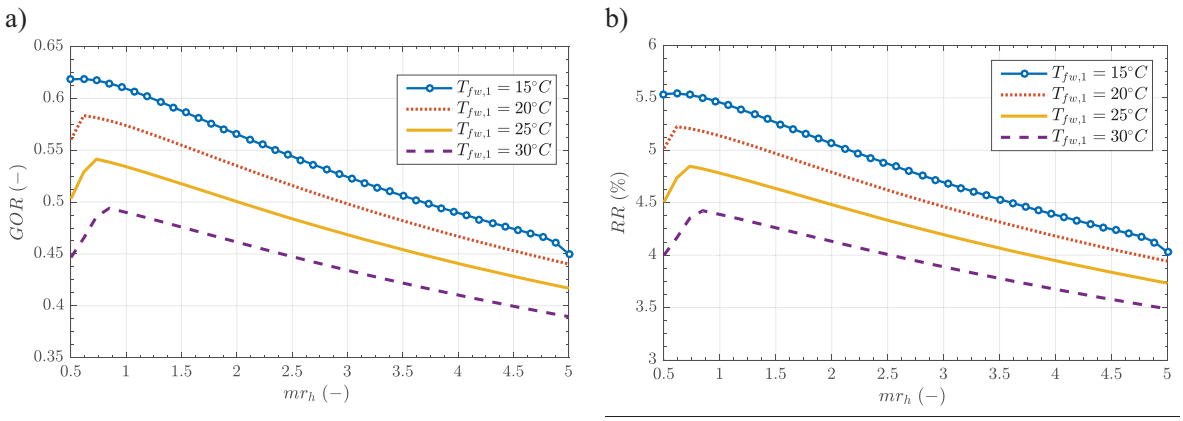

Fig. 4: Effect of inlet fresh water temperatures on gain-output-ratio (a), recovery ratio (b) at different mass flow rate ratios of humidifier

In Fig. 5 the effect of top brine temperature on GOR and RR in depicted. Generally, higher temperature of top brine temperature results is higher GOR and recovery ratio, however; the recovery ratio shows higher values of improvement for higher temperature in comparison to lower temperatures of top brine temperature. Moreover, the optimum value of mass flow rate ratio is slightly rising for higher temperatures of top brine temperature.

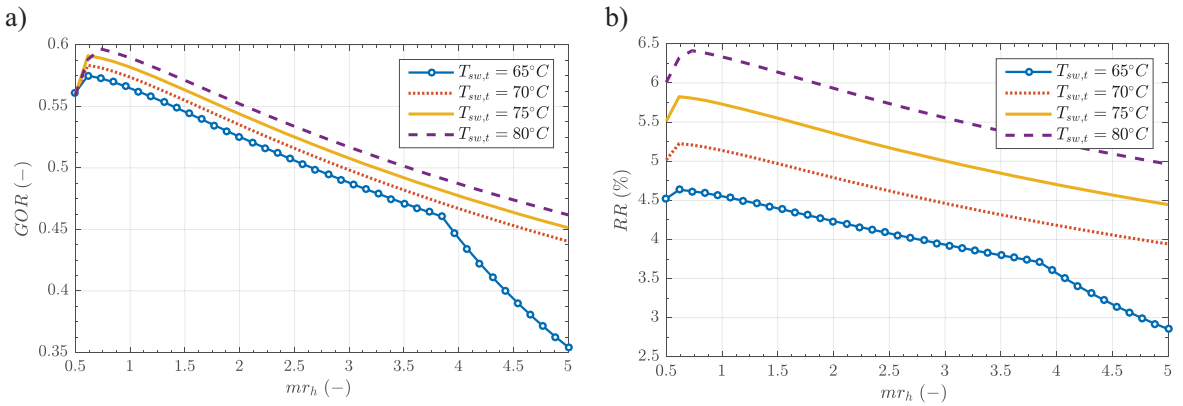

Fig. 5: Effect of top brine temperature on gain-output-ratio (a), recovery ratio (b) at different mass flow rate ratios of humidifier

Relation between the humidifier effectiveness with GOR as well as recovery ratio is shown in Fig. 6. As it displayed, improving the humidifier effectiveness affects the enhancement of both recovery ratio and GOR. Also, optimum point of mass flow rate ratio is almost same for all of the humidifier effectiveness values.

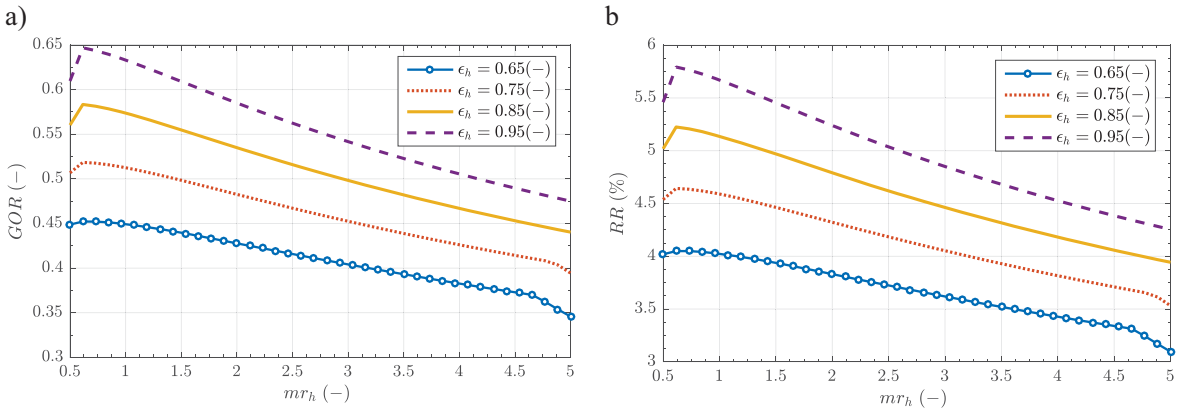

Fig. 6: Relation between the gain-output-ratio (a), recovery ratio (b) and humidifier effectiveness against mass flow rate ratios of saline water to dry air (mr_h)

In Fig. 7, relation of dehumidifier effectiveness with GOR and RR are presented. In general, by increasing the dehumidifier effectiveness both gain-output-ratio and recovery ratio would be enhanced. However, a high effectiveness dehumidifier value would keep wider spectrum of the mass flow rate ratios rather than a low effectiveness values.

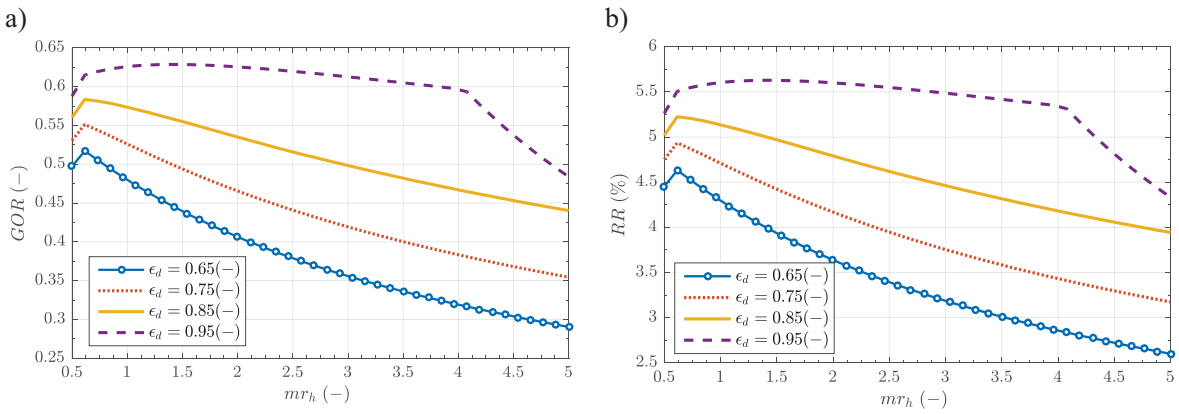

Fig. 7: Relation between the gain-output-ratio (a), recovery ratio (b) and dehumidifier effectiveness against mass flow rate ratios of saline water to dry air (mr_h)

Variation of the GOR and recovery ratio at different mass flow rate ratios is displayed in Fig. 8. As it shown, by intensifying the relative humidity of the air after humidifier outlet, both GOR and RR slightly would be grown. Further, the optimum mass flow rate ratio value shows a slight raise for higher mass flow rate ratios. It should ne mentions that in the experimental study [11] outlet air from humidification column indicated as fully saturated. However, to investigate the effect of air humidity on cycle performance this variable is studied as well.

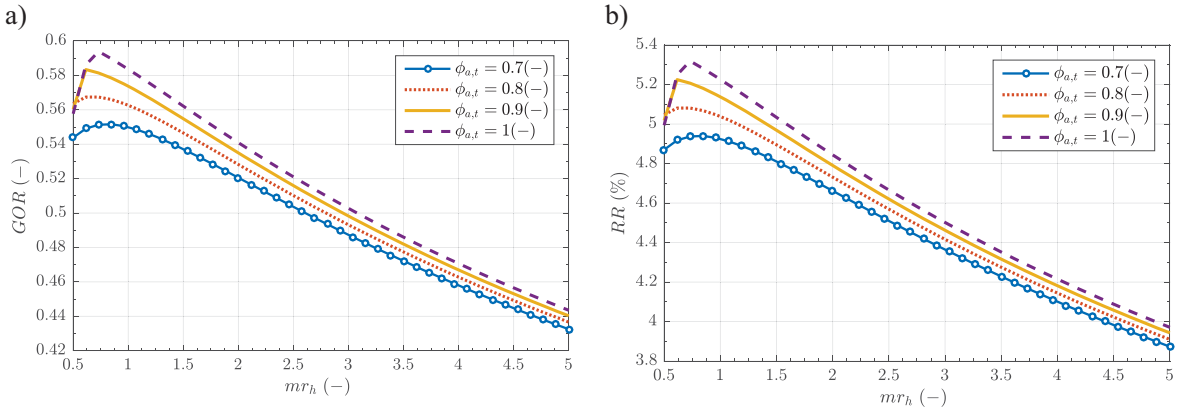

Fig. 8: variation of gain-output-ratio (a), recovery ratio (b) and air humidity after humidifying process against mass flow rate ratios of humidifier

In Fig. 9, variation of gain output ratio and recovery ratio for different values of air humidity are presented. Both GOR and recovery ratio are enhancing by growing the relative humidity. The effect relative humidity after dehumidifying process is pretty similar to the effect of relative humidity after humidification. The reason is that both processes are naturally similar to each other except the working temperature is different.

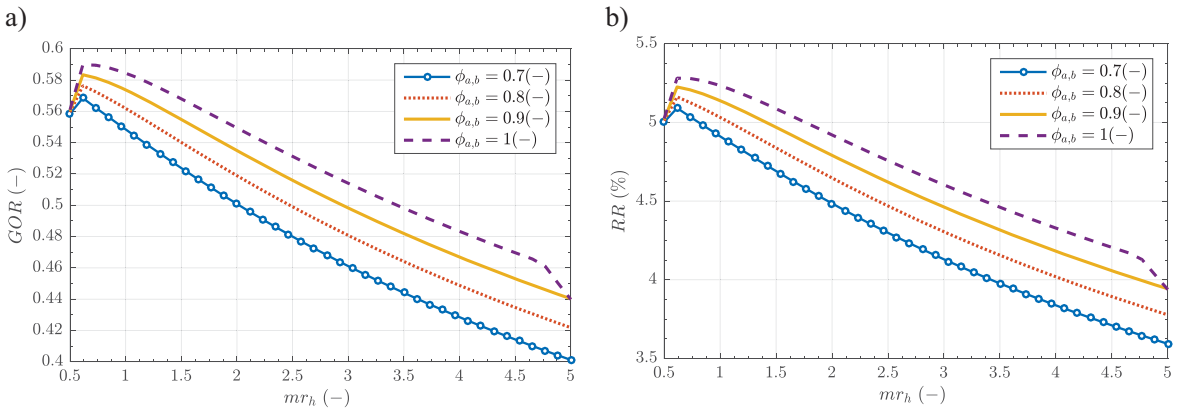

Fig. 9: variation of gain-output-ratio (a), recovery ratio (b), and air humidity after dehumidifying process against mass flow rate ratios of humidifier

5. Conclusion

A parametric study of close-air open-water water-heated HDH cycle with direct contact dehumidifier are performed in order to investigate the optimum working condition of system. To investigate the optimal working condition firstly the mass flow rate of fresh water to saline water is determined. It shown that, by increasing both the flow rate of fresh water and flow rate of dry air at a constant saline water flow rate, the GOR of the cycle would be enhanced. Notice that, in practical design approaches the values of mass flow rate ratio of saline water to fresh water can be determined based on available heating and cooling capacities. Then, at different working condition the optimum mass flow rate ratio of saline water to dry air are discovered. Air flow rate can be adjusted at constant saline water flow rate to reach desirable mass flow rate ratio.

Effect of the top brine temperature on recovery ratio in comparison to its effect on GOR is more considerable as it shows higher values of enhancement. Also, higher top brine temperature is the main variable than can help to improve the recovery ratio of the cycle.

Dehumidifier effectiveness is more important that humidifier effectiveness at high values of effectiveness. Also, the cycle can work on a wider spectrum of mass flow rate ratios with highly effective dehumidifier. As the effect of relative humidity on cycle metrics are small, therefore considering a fully saturated air can be assumed too.

Quantity	Symbol	Unit
Temperature	T	°C
flow rate	$\dot{m}$	kg s^{-1}
heat rate	$\dot{Q}$	kW
enthalpy rate (kW)	$\dot{H}$	kW
Water to air mass flow rate ratio (–)	mr	–
specific enthalpy (kJ/kg)	h	kJ kg^{-1}
Recovery ratio (%)	RR	%
gain output ratio (–)	GOR	–
specific heat capacity at constant pressure	cp	$Jkg^{-1}K^{-1}$
	Greek letters	
absolute humidity of dry air or humidity ratio	ω	$kg_{water}\, kg_{air}^{-1}$
relative humidity	φ	–
effectiveness	ε	–
difference or change	Δ	
	Subscripts	
air	a	
dry air	da	
distilled water	dw	
bottom	b	
top	t	
Seawater, saline water	sw	
maximum	max	
middle	m	
brine	br	
humidifier	h	
dehumidifier	d	
fw	*fresh water*	
1,2	*states of condition*	
	Acronyms	
closed-air open-water system	CAOW	
Direct contact	DC	
Cold-water open-air	CWOA	
Humidification-dehumidification	HDH	
heat and mass exchanger	HME	

6. References

[1] García-Rodríguez L. Seawater desalination driven by renewable energies: a review. Desalination. 2002;143(2):103-13.
[2] Narayan GP, Sharqawy MH, Summers EK, Lienhard JH, Zubair SM, Antar MA. The potential of solar-driven humidification–dehumidification desalination for small-scale decentralized water production. Renewable and Sustainable Energy Reviews. 2010;14(4):1187-201.
[3] Kabeel AE, Elmaaty TA, El-Said EMS. Economic analysis of a small-scale hybrid air HDH–SSF (humidification and dehumidification–water flashing evaporation) desalination plant. Energy. 2013;53:306-11.
[4] Prakash Narayan G, St. John MG, Zubair SM, Lienhard V JH. Thermal design of the humidification dehumidification desalination system: An experimental investigation. International Journal of Heat and Mass Transfer. 2013;58(1–2):740-8.
[5] Narayan GP, Sharqawy MH, Lienhard V JH, Zubair SM. Thermodynamic analysis of humidification dehumidification desalination cycles. Desalination and Water Treatment. 2010;16(1-3):339-53.
[6] Farid M, Al-Hajaj AW. Solar desalination with a humidification-dehumidification cycle. Desalination. 1996;106(1):427-9.
[7] MÜLLER-HOLST H. SOLAR THERMAL DESALINATION USING THE MULTIPLE EFFECT HUMIDIFICATION (MEH)-METHOD. In: Rizzuti L, Ettouney HM, Cipollina A, editors. Solar Desalination for the 21st Century: A Review of Modern Technologies and Researches on Desalination Coupled to Renewable Energies. Dordrecht: Springer Netherlands; 2007. p. 215-25.
[8] Yuan G, Wang Z, Li H, Li X. Experimental study of a solar desalination system based on humidification–dehumidification process. Desalination. 2011;277(1):92-8.
[9] Kabeel AE, Hamed MH, Omara ZM, Sharshir SW. Experimental study of a humidification-dehumidification solar technique by natural and forced air circulation. Energy. 2014;68:218-28.
[10] He WF, Xu LN, Han D. Parametric analysis of an air-heated humidification-dehumidification (HDH) desalination system with waste heat recovery. Desalination. 2016;398:30-8.
[11] Farid MM, Parekh S, Selman JR, Al-Hallaj S. Solar desalination with a humidification-dehumidification cycle: mathematical modeling of the unit. Desalination. 2003;151(2):153-64.
[12] Müller-Holst H, Engelhardt M, Herve M, Schölkopf W. Solarthermal seawater desalination systems for decentralised use. Renewable Energy. 1998;14(1):311-8.
[13] Yamalı C, Solmus İ. A solar desalination system using humidification–dehumidification process: experimental study and comparison with the theoretical results. Desalination. 2008;220(1):538-51.
[14] Kabeel AE, El-Said EMS. A hybrid solar desalination system of air humidification–dehumidification and water flashing evaporation: Part I. A numerical investigation. Desalination. 2013;320:56-72.
[15] Elminshawy NAS, Siddiqui FR, Addas MF. Development of an active solar humidification-dehumidification (HDH) desalination system integrated with geothermal energy. Energy Conversion and Management. 2016;126:608-21.
[16] El-Dessouky HTA. Humidification-dehumidification desalination process using waste heat from a gas turbine. Desalination. 1989;71(1):19-33.
[17] He WF, Zhang XK, Han D, Gao L. Performance analysis of a water-power combined system with air-heated humidification dehumidification process. Energy. 2017;130:218-27.
[18] Bharathan D, Parsons BK, Althof JA, Institute SER. Direct-contact Condensers for Open-cycle OTEC Applications: Model Validation with Fresh Water Experiments for Structured Packings: Solar Energy Research Institute, 1988.
[19] Klausner JF, Li Y, Mei R. Evaporative heat and mass transfer for the diffusion driven desalination process. Heat and Mass Transfer. 2005;42(6):528.
[20] Eslamimanesh A, Hatamipour MS. Mathematical modeling of a direct contact humidification–dehumidification desalination process. Desalination. 2009;237(1):296-304.
[21] Eslamimanesh A, Hatamipour MS. Economical study of a small-scale direct contact humidification–dehumidification desalination plant. Desalination. 2010;250(1):203-7.
[22] Mehrgoo M, Amidpour M. Constructal design and optimization of a direct contact humidification–dehumidification desalination unit. Desalination. 2012;293:69-77.
[23] Sharqawy MH, Antar MA, Zubair SM, Elbashir AM. Optimum thermal design of humidification dehumidification desalination systems. Desalination. 2014;349:10-21.
[24] Bejan A. Advanced Engineering Thermodynamics: Wiley, 2016.
[25] Narayan GP, Mistry KH, Sharqawy MH, Zubair SM, Lienhard JH. Energy Effectiveness of Simultaneous Heat and Mass Exchange Devices. Frontiers in Heat and Mass Transfer. 2010;1(2).
[26] N/A. ASHRAE Handbook - Fundamentals (SI Edition). American Society of Heating, Refrigerating and Air-Conditioning Engineers, Inc.; 2009
[27] Klein SA, Alvarado FL. Engineering Equation Solver Version 8.400 http://www.fchart.com/ees/.
[28] Hyland RW, Wexler A. Formulations for the thermodynamic properties of the saturated phases of H2O from 173.15 K to 473.15 K. ASHRAE Transactions(Part 2A). 1983.
[29] Pruss A, Wagner W. The IAPWS formulation 1995 for the thermodynamic properties of ordinary water substance for general and scientific use. Journal of Physical and Chemical Reference Data. 2002;31(2):387-535.

[30] Prakash Narayan G, Lienhard V JH, Zubair SM. Entropy generation minimization of combined heat and mass transfer devices. International Journal of Thermal Sciences. 2010;49(10):2057-66.
[31] Zmeureanu R, Yu Wu X. Energy and exergy performance of residential heating systems with separate mechanical ventilation. Energy. 2007;32(3):187-95.

Sustainable Seawater Desalination by Permeate Gap Membrane Distillation Technology

Farzaneh Mahmoudi[1], Mohammad E. Pishbin, Saeed Dehghani[1], Abhijit Date[1], Aliakbar Akbarzadeh[1]

[1]Energy CARE Group, School of Aerospace, Manufacturing and Mechanical Engineering, RMIT University, Melbourne (Australia)

Abstract

Membrane distillation (MD) as a thermally driven process with moderate operating temperatures is a known effective technology for salt-water desalination. In this research, the permeate gap membrane distillation configuration (PGMD), as a novel sustainable MD design having internal heat recovery characteristics, is introduced, designed and the system performance investigated in terms of permeate water flux rate and specific thermal energy consumption (STEC). The experimental results show that, increasing the feed flow rate from 0.1 to 1.1 L/min for the feed salinity in a range of (0−30) ppt, led to increasing the fresh water flux from 2 to 12 kg/m^{2}h, however STEC of the system also showed an increase and varied in a range of 1000 and 2500 kWh/m^3.

Furthermore, a single node theoretical model is developed and the modeling results validated with experimental values. It is concluded, optimization of the MD module performance to improve internal heat recovery and produce higher fresh water rate would be achievable by adjusting the effective membrane surface area and feed flow rate.

Keywords: Sustainable desalination, permeate gap membrane distillation, specific thermal energy consumption, permeate flux rate

1. Introduction

According to the World Water Council, 17% of the world population will be living in short of the fresh water supply by 2020 (Charcosset, 2009). Therefore, the demand for alternative sustainable water sources including ground water, desalinated water and recycled water increased in recent years and thus, the implementation of desalination plants is growing on a large scale. Fresh water can be derived from sea water by evaporation processes e.g., multi-stage flash (MSF), multi- effect distillation (MED) or by membrane based processes, including reverse osmosis (RO), electro dialysis (ED) and membrane distillation (MD).

Membrane distillation is a separation process which involves phase change (liquid-vapour equilibrium) across a hydrophobic, highly porous membrane. In contrast to most membrane separation processes, which are isothermal and have driving forces as trans membrane hydrostatic pressures, concentrations, electrical or chemical potentials, MD is a non-isothermal process.

The commercially developed RO technology consumes high electrical energy normally ranging from 6 to 12 kwh/m^3 that is presently being generated from non-renewable and polluting fossil fuels (Bai et al.). In contrast, MD is a thermal desalination process using lower top temperature (80 °C or less) with respect to the traditional thermal desalination processes.

However, the MD process is still under study and the lack of experimental data has indicated that there is a need for more comprehensive research in this field. The central issues are the external energy source for MD units, lack of MD membranes and fabrication of modules for each MD configuration. Overall, optimization of MD plants is required in order to reach higher MD performance and to decrease energy consumption (Meindersma et al., 2006), an appropriate redesign of the MD module is demanded in order to achieve mass transfer improvement and to increase the membrane surface area per module volume. Moreover, the energy source of the MD process is an

doi:10.18086/swc.2017.32.02 Available at http://proceedings.ises.org

important issue for commercialization of this technology as a sustainable process. Membrane distillation associated with renewable energy is considered to be a highly promising process, especially for situations where low-temperature solar, waste or other heat is available. The STEC of MD systems varies based on the module configuration, setup scale and operating condition. A wide dispersion of reported values is observed in literatures for STEC, which the ranges from 1 to 9000 kWh/m^3 (Khayet, 2013).

Generally direct contact membrane distillation (DCMD) as depicted in Fig. 1-left is the most studied MD configuration (Alkhudhiri et al., 2012). In DCMD the membrane is in direct contact with the feed solution on one side and the permeate on the other side with the temperature difference across the two sides of the membrane as the process driving force. A novel introduced configuration of MD, is called PGMD which by creating a third channel for produced fresh water via an impermeable film on the permeate side, the cold fluid in the condenser side separates from the permeate and therefore it could be any other liquid like saline feed water. The permeate is extracted from the highest module position, so that the gap between the membrane and the impermeable film fills with permeate during the operation (Fig. 1- right).

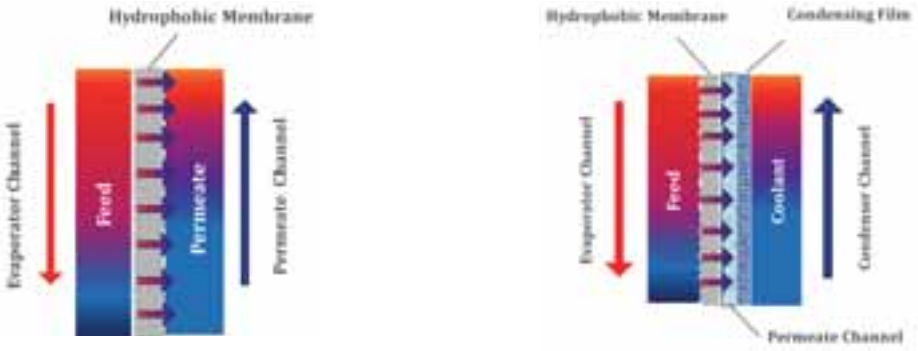

Fig. 1. Left: DCMD configuration; Right: PGMD module arrangement with internal heat recovery

In recent years, some commercial MD modules in different configurations have been developed. (Zaragoza et al., 2014) made a comparison among the most advanced commercial MD prototype technologies with different configurations (air gap, permeate gap and vacuum) and different structures including plate-and-frame and spiral wound. Concerning comparing different MD configuration, Cipollina et al.(Cipollina et al., 2012) also developed a lab scale plate-and-frame membrane distillation module for solar energy seawater desalination and investigated three different channel configurations during this research, including free air gap, permeate-gap and partial vacuum air gap. Winter et al. also developed and optimized MD setup with lowest STEC to reduce the external energy demand of the system, with a 10 m^2 spiral wound PGMD configuration (Winter et al., 2012).

In this paper, by considering the result of comprehensive literature review regarding recent projects in MD field, an experimental approach by designing and developing a lab scale PGMD system configuration is followed to provide a good estimation of the most important characteristic value of a MD setup, including permeate flux, STEC, GOR and its dependency to the modular design and particularly operating conditions. Furthermore the numerical modeling of the heat and mass transfer phenomena in this configuration is studied and a single node theoretical model is developed using some simplifying assumption and the modeling results validated with comparing to the experimental data

2. Laboratory scale PGMD system experimental rig

A novel optimized experimental approach was based on a lab scale plate-and-frame PGMD module with 0.12 m^2 effective membrane area. The hydrophobic PTFE membrane, with 0.22 µm nominal pore size and (140 - 200) µm thickness, with an effective surface area (760 * 160) mm^2, was applied. This plastic PP film had a thermal conductivity similar to that of the PTFE membrane. The permeate channel was separated from the condenser

channel by an impermeable 100 µm clear polypropylene film, which filled with plastic net spacers both as mechanical support between membrane and condensing polymeric films and also as turbulence promoters. The gap width in condenser and evaporator channels was adjusted to 1.5 mm and the gap width in the permeate channel was 3 mm and rubber gasket frames were used for sealing purpose.

A schematic diagram of the lab scale experimental setup is shown in Fig. 2-left. The feed water was pumped from a 100 L storage tank using a small 12 V DC water pump, the feed flow rate to the module controlled either by adjusting the DC pump voltage or by an in-line control valve. A 100 µm pore size mechanical filter was installed before the pump to protect the module and pump from unwanted solids. To adjust the inlet feed temperature to the condenser channel, the lab cooling circuit was used.

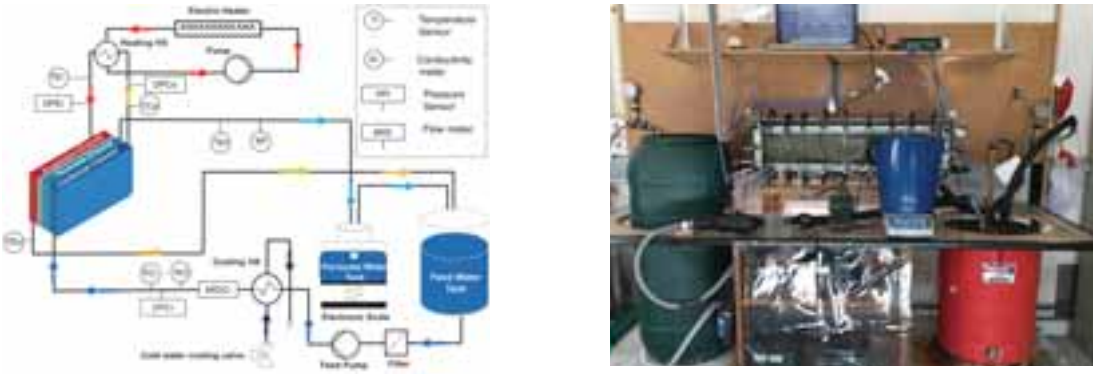

Fig. 2. Left: Schematic diagram of the MD experimental setup; Right: Actual indoor lab scale PGMD experimental setup

The feed water gradually preheats whilst flowing through the condenser channel and using the latent heat of condensation and conduction via the PP condensing film. The condenser outlet temperature was increased by using an external electrical heat source immersed in an insulated electric water tank (2.4 KW), to provide the required evaporator channel inlet temperature for the PGMD module. In the evaporator channel the hot water vaporizes at the membrane surface, diffuses through the hydrophobic PTFE membrane pores and condenses on the permeate channel film. The evaporator channel outlet feed, with higher salinity than the inlet feed to the condenser channel, returns to the feed tank. In order to maintain the feed tank salinity at a constant level, the fresh water pumped from permeate tank by applying a floating ball valve and electronic scale. The produced fresh water exited from the top manifold of the permeate gap. Each experiment ran for at least 90 min to reach a steady state condition and the average values of the recorded data in the steady state condition were used for analysis. Fig. 2-right, shows the indoor lab scale MD setup.

3. Mathematical Model Development in PGMD

To predict the PGMD module performance, a single node theoretical model is developed using some simplifying assumption. The following assumptions are considered:

Steady state condition; stagnant air inside the membrane pores; permeate channels fully filled with pure water; no total pressure difference across the membrane, so no mass transfer by viscous flow; no heat loss by conduction to the environment; stagnant permeate in the permeate channel and so no heat transfer by convection in the permeate gap.

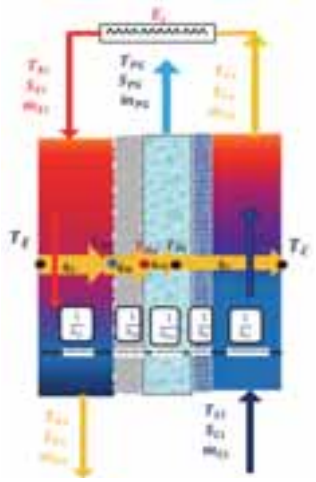

Fig. 3. Single node approach for mathematical modeling of PGMD module

To model the PGMD system, the above assumptions, heat and mass conservation laws in all channels and the five main thermal resistances between evaporator and condenser channels, as shown in Fig. 3 are considered. In addition, by defining the known variables including: T_{Ci}, T_{Ei}, $\dot{m}_{Ci}$, $\dot{m}_{Ei}$, S_{Ci} and S_{Ei} which are respectively temperature (°C), mass flow rate (kg/s) and salinity (g/kg) at the condenser and evaporator channels inlets, governing equations are developed. It is also required to specify the membrane properties, bulk conditions and module geometry in order to carry out numerical modeling.

The convective heat flux from the evaporator channel to the membrane surface is expressed in Eq. 1:

$$\dot{q}_E = h_E\left(\frac{T_{Ei}+T_{Eo}}{2} - T_{Me}\right) \tag{1}$$

Where, $\dot{q}_E$ is the evaporator channel heat flux (W/m^2), h_E is the heat transfer coefficient at the evaporator channel (W/m^2K). T_{Ei} and T_{Eo} are respectively the temperatures at the evaporator channel inlet and outlet and T_{Me} is the temperature at the evaporator side of the membrane surface.

The heat transfer rate from the membrane surface $\dot{q}_M$ arises from the latent heat of the produced vapour flux and the heat transferred by conduction across both the membrane matrix and the gas-filled membrane pores (Khayet, 2011).

Also

$$\dot{q}_M = \frac{K_m}{\delta_m}\left(T_{Me} - T_{Mp}\right) + J_p h_{fg} \tag{2}$$

In this equation T_{MP} is the membrane surface temperature at the permeate gap side, h_{fg} is the water vaporization enthalpy (kJ/kg), K_m and δ_m are the membrane thermal conductivity (W/mK) and thickness (m) respectively. J_p (Kg /m^2s) (based on Eq. 3) is defined as a function of partial vapour pressure on the two sides of the membrane and of the membrane mass transfer coefficient (C_m).

$$J_p = C_m \left(P_{v,swe} - P_{v,swp} \right) \tag{3}$$

For the applied membrane samples with specified structure and under the system operating condition, the dominant mass transfer mechanism is defined as a combination of Knudsen and molecular diffusion (0.01 < Kn <1) (Schofield et al., 1987, Alklaibi and Lior, 2006, Alkhudhiri et al., 2012, Nakoa et al., 2014) . Figures for membrane mass transfer coefficient (C_m) also was in a range of $3\times10^{-7} < C_m < 5\times10^{-7}$ kg/Pa m^{2}s for (30 - 80) °C temperature range and assuming atmospheric pressure in the membrane pores, which was in close agreement with some reported values(Winter, 2014, Swaminathan et al., 2016, Dow et al., 2016, Kullab, 2011).

Based on the assumptions made, the produced permeate is considered stagnant in the permeate channel, so that the heat transfer from the gap takes place only in the form of conduction calculable by Eq. 5.

$$\dot{q}_{PG} = \frac{1}{\frac{\delta_{PG}}{2K_{PG}}} (T_{Mp} - T_{PG}) \tag{4}$$

In this equation, T_{PG} is the permeate temperature at the permeate gap, K_{PG} (W/mK) and δ_{PG} (m) are the permeate gap thermal conductivity and thickness, respectively.

Moreover, the heat is transferred from the permeate gap to condenser channel by a series combination of thermal resistances including permeate channel and impermeable polymeric film and condenser side thermal resistances. Therefore, the condenser channel heat flux ($\dot{q}_C$) is defined as below:

$$\dot{q}_C = \frac{1}{\frac{\delta_{PG}}{2K_{PG}} + \frac{\delta_F}{K_F} + \frac{1}{h_C}} (T_{PG} - \frac{T_{Ci} + T_{Co}}{2}) \tag{5}$$

Similarly, in this equation h_C (W/m^{2}K) is the heat transfer coefficients at the impermeable polymeric film and condenser channel, K_F (W/mK) and δ_F (m) are the impermeable polymeric film thermal conductivity and thickness, respectively, T_{Ci} and T_{Co} are the temperatures at the condenser channel inlet and outlet, respectively.

Considering the energy balance correlations for both evaporator and condenser channels and the total membrane surface area (A_m), Eq. 6 and 7 could be assumed respectively for the evaporator channel and condenser channel heat fluxes ($\dot{q}_{hot}$ and $\dot{q}_{cold}$).

$$\dot{q}_{cold} = \frac{\dot{m}_{Ci}\ C_{pC} \left(T_{Co} - T_{Ci} \right)}{A_m} \tag{6}$$

$$\dot{q}_{hot} = \frac{\dot{m}_{Ei} C_{pE} \left(T_{Eo} - T_{Ei} \right)}{A_m} \tag{7}$$

Given the assumption of a steady state condition, it may be concluded that:

$$\dot{q}_E = \dot{q}_M = \dot{q}_{PG} = \dot{q}_C = \dot{q}_{cold} = \dot{q}_{hot} \tag{8}$$

Solving the 7 main equations (1 to 7) using the Matlab Equation solver, the 7 unknown variables (T_{Me}, T_{MP}, T_{PG}, T_{Co}, T_{Eo}, J_P, $\dot{q}$), as depicted in the mathematical modelling schematic, may be calculated. Furthermore, to be able describe the performance of a MD system, permeate flux (J_P), STEC and GOR parameters are investigated as the most important characteristic values which are defined as:

The permeate flux J_P could be defined by dividing the permeate output rate $\dot{m}_{PG}$ (kg/s) to the total membrane area (Am):

$$J_p = \frac{\dot{m}_{PG}}{A_m} \tag{9}$$

The quantity q_{STEC} is the amount of total energy input (E_i) to produce 1 m^3 of fresh water (Sanmartino et al., 2016). In this equation $\dot{V}_P$ is the produced distillate rate (m^3/s).

$$q_{STEC} = \frac{E_i}{\dot{V}_p} = \frac{\dot{m}_{Ei} C_p (T_{Ei} - T_{Co})}{\dot{V}_p} \tag{10}$$

The GOR is an indication of how well the total energy input to the system is utilized to produce fresh water:

$$GOR = \frac{\dot{m}_{PG} h_{fg}}{E_i} \tag{11}$$

4. Results and discussion

In this section, the effect of different feed water flow rates and salinities on internal heat recovery through the system, besides the most important characteristic values including permeate flux, STEC, and GOR are presented.

The effect of feed water salinity on internal heat recovery is depicted in Fig. 4-left. As seen in this figure, the amount of internal heat recovery inside the cold flow channel, decreased by increasing the feed flow rate within the system operating condition. Increasing of feed flow rate, lead to the lower feed residence time in the flow channels, so there was less time for heat transfer between hot and cold channels, so the temperature rises in condenser channel was less significant (Xu et al., 2016, Khayet, 2011, Guillén-Burrieza et al., 2015). In addition, as seen in this figure, by increasing the feed water salinity from fresh water feed (nearly 0% salinity) to seawater salinity (around 30 ppt) and then up to a higher value to 130 ppt, the temperature rise in the condenser channel (internal heat recovery rate) decreased. This pattern could be explained by the negative effect of salinity on permeate flux rate, which leads to a lower amount of released latent heat of condensation at the higher salinity.

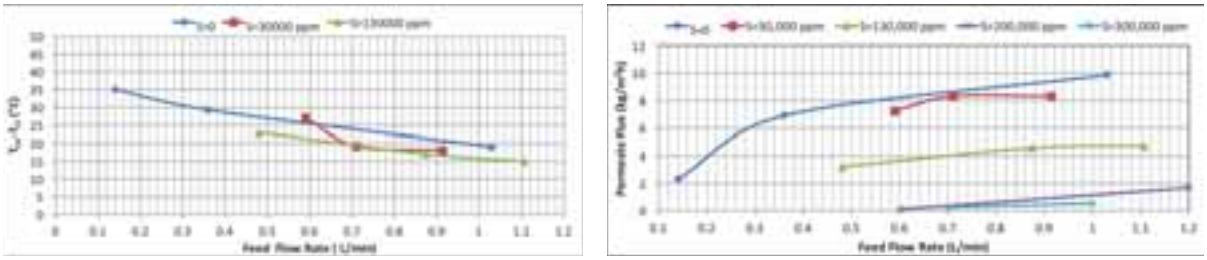

Fig.4. Left: Fresh water temperature rise (T_{Co}-T_{Ci}) by internal heat recovery through the membrane, Right; Permeate flux at different feed flow rates and salinities, test condition: TCi=15ºC, TEi=82ºC

The effect of the feed flow rate on permeate flux is also shown in Fig. 4-right. As it is seen in this graph by increasing the feed flow rate, the permeate flux increases. For fresh water feed (assuming zero percent salinity), increasing feed flow rate from 0.14 to 1.03 L/min, led to approximately 400 per cent increase in the permeate flux. For a feed sample with 130 ppt (nearly four times seawater salinity), doubling the feed flow rate led to a similar upward trend on produced distillate rate. That is the, J_p increases from approximately 3 to 5 kg/m^{2}h (nearly 70 per cent increase). This effects may be explained by the higher turbulence in the flow channel at the higher feed flow rate, associated with higher value for the Reynolds number, which improved the heat transfer rate in flow channels and reduced the temperature polarization effect on the two sides of the membrane surface. As a result, the temperature difference across the membrane surface increased, leading to higher permeate flux.

Fig. 4-left also presents the effect of salinity on permeate flux, which shows a decrease in permeate water flux for saline water compared to the fresh water feed case. The produced distillate rate decreased significantly for high salt concentration (200-300) ppt, which is near the saturated state of saline feed water. As seen in this graph, for a feed sample with 20 ppt salinity and at nearly 1 L/min flow rate, the distillate flux decreased to less than 2 kg/m^{2}h.

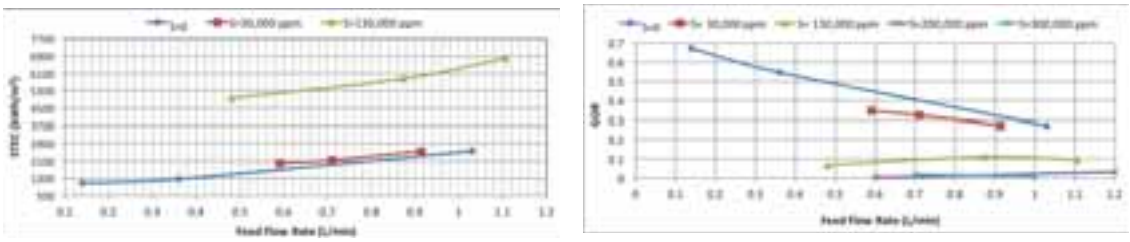

Fig.5. Left: STEC Right; GOR at different feed flow rates and salinities, test condition: TCi=15ºC, TEi=82ºC

The effect of feed flow rates on STEC of the system is shown in Fig. 5-left. The results show that by increasing the feed flow rate, the required amount of thermal energy will increase. High feed flow rate leads to shorter feed residence time in the flow channel, therefore a less efficient sensible heat recovery in condenser channel is possible. As a result, for a similar operating condition, T_{Co} decreases and the amount of external heat demand (STEC) to reach the designed value for T_{Ei}, increases. On the other hand, as seen in Fig. 4, right by increasing the feed flow rate, the permeate flux rate increases (higher value of $\dot{V}_P$ in Eq. 10). However, the overall the effect of higher energy demand is not completely compensated by higher permeate flux, so the STEC values increase at the higher feed flow rate. As is seen from this figure, at higher feed salinities, the STEC is also increases because of the lower permeate output at higher salinities which is also confirmed by previous studies (Winter et al., 2011, Cipollina et al., 2012).

Gained output ratio is an alternative representation of the STEC and for analyzing the thermal efficiency of the desalination systems may be used to quantify the module's capability for internal heat recovery. As is explained by Winter et al. (Winter et al., 2012), in MD desalination systems because of heat loss by conduction through the MD module, all the thermal energy input can not be applied to the evaporation process and the GOR must be less than 1. However, in ideal MD systems with optimum internal heat recovery with high surface area for heat transfer

between hot and cold fluids, a higher value of GOR would be possible.

As investigated in this study and illustrated in Fig. 5-right, by increasing feed flow rate and feed water salinity, GOR values show a downward trend. The maximum value achieved for GOR was approximately one, which confirmed the high heat loss rate through the lab scale module and insufficient internal heat recovery by the developed PGMD module with the geometry described. A longer module flow channel with higher membrane surface area will provide more efficient sensible heat recovery leading to a higher GOR value and so develop a more thermally efficient MD system (Winter et al., 2012).

Based on the developed theoretical model described in section 3, the influences of feed flow rate and salinity on two important desalination system characteristic of permeate flux (J_p) and internal heat recovery rate (T_{Co}-T_{Ci}) are plotted and the results are compared with the measured values. Figs. 6 shows a good comparison between experimental results and theoretical values for produced fresh water rate and for internal heat parameters. Comparison is made for feed flow rate in the range 0.1 to 1.1 L/min and with three inlet feed salinities of approximately (0, 30 and 130) ppt. As is evident from these graphs, values obtained from numerical modeling using heat and mass balance equations and using the Matlab Equation solver for a single node model, as explained in the mathematical model development section, are in good agreement with experimental measured values. The developed theoretical model could be applied as a reliable tool, to design the geometrical configuration of an optimized PGMD system based on simulation of the system performance.

The theoretical study also provides a basis for developing a more efficient PGMD module by estimating the effect of system parameters including module length, feed flow rate and temperature on the main output parameters including permeate flux rate and STEC .

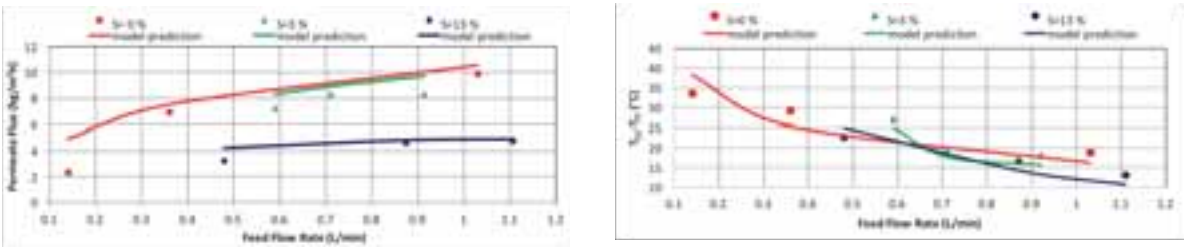

Fig. 6 Theoretical and experimental value comparison for influence of feed flow rate and salinity on: Left: permeate flux; Right: internal heat recovery at condenser channel(Bai et al.)

5. Conclusion

A lab scale plate-and- frame PGMD module with 0.12 m^2 effective membrane area has been developed and tested. A set of experimental test has been performed to investigate the designed MD module's main characteristics in different operating condition including feed flow rate and salinity. Under the designed system conditions, T_{Ci}=15 ºC, T_{Ei}=82 ºC, feed flow rate in range of 0.1 to 1.1 L/min and feed salinity in a range of (0 - 30) ppt the permeate flux varied from (2-12) kg/m^2h, specific thermal energy consumption was between 1000 and 2500 kWh/m^3 and GOR was below 1.

The experimental results show that lower feed flow rate provides higher residence time and lower STEC (higher GOR). Operation at lower STEC is also achievable by increasing flow channel length and providing more contact time between feed stream and membrane surface leading to higher heat recovery and lower external energy demand of the system. However, working at low feed flow rate and high membrane surface area results in lower permeate flux and higher investment cost respectively. Therefore, to develop a sustainable PGMD configuration design, from the design point of view, the module length and effective membrane surface area need to be optimized in order to improve internal heat recovery rate in the system and so reduce the external energy demand, especially in the situation where the external energy source derives from non-renewable fossil fuels. In conclusion, the research results provides an reliable technical data for a scaled up PGMD module characterization to design a more

efficient and sustainable desalination system via minimizing the thermal energy demand of the system and also producing higher distillate rate.

6. References

ALKHUDHIRI, A., DARWISH, N. & HILAL, N. 2012. Membrane distillation: A comprehensive review. *Desalination,* 287**,** 2-18.

ALKLAIBI, A. & LIOR, N. 2006. Heat and mass transfer resistance analysis of membrane distillation. *Journal of Membrane Science,* 282**,** 362-369.

BAI, F., AKBARZADEH, A. & SINGH, R. *A Novel System Of Combined Power Generation And Water Desalination Using Solar Energy*, Solar09, the 47th ANZSES Annual Conference.

CHARCOSSET, C. 2009. A review of membrane processes and renewable energies for desalination. *Desalination,* 245**,** 214-231.

CIPOLLINA, A., DI SPARTI, M. G., TAMBURINI, A. & MICALE, G. 2012. Development of a Membrane Distillation module for solar energy seawater desalination. *Chemical Engineering Research and Design,* 90**,** 2101-2121.

DOW, N., GRAY, S., LI, J.-D., ZHANG, J., OSTARCEVIC, E., LIUBINAS, A., ATHERTON, P., ROESZLER, G., GIBBS, A. & DUKE, M. 2016. Pilot trial of membrane distillation driven by low grade waste heat: Membrane fouling and energy assessment. *Desalination,* 391**,** 30-42.

GUILLÉN-BURRIEZA, E., ALARCÓN-PADILLA, D.-C., PALENZUELA, P. & ZARAGOZA, G. 2015. Techno-economic assessment of a pilot-scale plant for solar desalination based on existing plate and frame MD technology. *Desalination,* 374**,** 70-80.

KHAYET, M. 2011. Membranes and theoretical modeling of membrane distillation: a review. *Adv Colloid Interface Sci,* 164**,** 56-88.

KHAYET, M. 2013. Solar desalination by membrane distillation: Dispersion in energy consumption analysis and water production costs (a review). *Desalination,* 308**,** 89-101.

KULLAB, A. 2011. Desalination Using Membrane Distillation Experimental and Numerical Study Doctoral Thesis

.

MEINDERSMA, G. W., GUIJT, C. M. & DE HAAN, A. B. 2006. Desalination and water recycling by air gap membrane distillation. *Desalination,* 187**,** 291-301.

NAKOA, K., DATE, A. & AKBARZADEH, A. 2014. A research on water desalination using membrane distillation. *Desalination and Water Treatment,* 56**,** 2618-2630.

SANMARTINO, J. A., KHAYET, M. & GARCÍA-PAYO, M. C. 2016. Chapter 4 - Desalination by Membrane Distillation A2 - Hankins, Nicholas P. *In:* SINGH, R. (ed.) *Emerging Membrane Technology for Sustainable Water Treatment.* Boston: Elsevier.

SCHOFIELD, R. W., FANE, A. G. & FELL, C. J. D. 1987. Heat and mass transfer in membrane distillation. *Journal of Membrane Science,* 33**,** 299-313.

SWAMINATHAN, J., CHUNG, H. W., WARSINGER, D. M., ALMARZOOQI, F. A., ARAFAT, H. A. & LIENHARD V, J. H. 2016. Energy efficiency of permeate gap and novel conductive gap membrane distillation. *Journal of Membrane Science,* 502**,** 171-178.

WINTER, D. 2014. Membrane Distillation A Thermodynamic, Technological and Economic Analysis.

WINTER, D., KOSCHIKOWSKI, J. & RIPPERGER, S. 2012. Desalination using membrane distillation: Flux enhancement by feed water deaeration on spiral-wound modules. *Journal of Membrane Science,* 423-424**,** 215-224.

WINTER, D., KOSCHIKOWSKI, J. & WIEGHAUS, M. 2011. Desalination using membrane distillation: Experimental studies on full scale spiral wound modules. *Journal of Membrane Science,* 375**,** 104-112.

XU, J., SINGH, Y. B., AMY, G. L. & GHAFFOUR, N. 2016. Effect of operating parameters and membrane characteristics on air gap membrane distillation performance for the treatment of highly saline water. *Journal of Membrane Science,* 512**,** 73-82.

ZARAGOZA, G., RUIZ-AGUIRRE, A. & GUILLÉN-BURRIEZA, E. 2014. Efficiency in the use of solar thermal energy of small membrane desalination systems for decentralized water production. *Applied Energy,* 130**,** 491-499.

7. Appendix: Nomenclature

Quantity	Symbol	Unit
Membrane surface area	A_m	m^2
Membrane mass transfer coefficient	C_m	
Condenser channel specific heat capacity	C_{pC}	$J\ kg^{-1}\ K^{-1}$
Evaporator channel specific heat capacity	C_{pE}	$J\ kg^{-1}\ K^{-1}$
Hydraulic diameter	D_h	m
Total energy input	E_i	W
Gained output ratio	GOR	
Specific heat of vaporization	h_{fg}	$J\ kg^{-1}$
Heat transfer coefficient at the condenser channel	h_C	$Wm^{-2}\ K^{-1}$
Heat transfer coefficient at the evaporator channel	h_E	$Wm^{-2}\ K^{-1}$
Heat transfer coefficient at the impermeable polymeric film	h_F	$Wm^{-2}\ K^{-1}$
Heat transfer coefficient at the permeate gap	h_{PG}	$Wm^{-2}\ K^{-1}$
Heat transfer coefficient at the membrane	h_M	$Wm^{-2}\ K^{-1}$
Permeate flux	J_p	$Kg\ m^{-2}\ s$
Evaporator channel thermal conductivity	K_E	$W\ m^{-1}\ K^{-1}$
Membrane thermal conductivity	K_m	$W\ m^{-1}\ K^{-1}$
Permeate gap thermal conductivity	K_{pg}	$W\ m^{-1}\ K^{-1}$
Module length	L	m
Feed flow rate	$\dot{m}_f$	$kg\ s^{-1}$
Inlet mass flow rate at the condenser channels	$\dot{m}_{Ci}$	$kg\ s^{-1}$
Inlet mass flow rate at the evaporator channels	$\dot{m}_{Ei}$	$kg\ s^{-1}$
Outlet mass flow rate at the evaporator channels	$\dot{m}_{Eo}$	$kg\ s^{-1}$
Permeate output rate	$\dot{m}_{PG}$	$kg\ s^{-1}$
Pure water vapour pressure	$P_{v,w}$	Pa
Saltwater vapour pressure	$P_{v,sw}$	Pa
Specific thermal energy consumption	q_{STEC}	$kWh\ m^{-3}$
Convective heat flux from the condenser channel	q_C	Wm^{-2}
Condenser channel heat flux	$\dot{q}_{cold}$	Wm^{-2}
Convective heat flux from the evaporator channel	q_E	Wm^{-2}
Evaporator channel heat flux	$\dot{q}_{hot}$	Wm^{-2}
Heat transfer rate from the membrane surface	q_M	Wm^{-2}
Specific conductive heat flux	$\dot{q}_{M.C}$	Wm^{-2}
Specific latent heat flux	$\dot{q}_{M\,L}$	Wm^{-2}
Salinity	S	$g\ kg^{-1}$
Feed water salinity in the input of the condenser channel	S_{Ci}	$g\ kg^{-1}$

Feed water salinity in the input of the evaporator channel	S_{Ei}	$g\ kg^{-1}$
Feed water salinity in the output of the evaporator channel	S_{Eo}	$g\ kg^{-1}$
Temperature at condenser inlet	T_{Ci}	ºC
Temperature at condenser outlet	T_{Co}	ºC
Temperature at evaporator inlet	T_{Ei}	ºC
Temperature at evaporator outlet	T_{Eo}	ºC
Temperature at the membrane surface on the evaporator side	T_{Me}	ºC
Temperature at the membrane surface on the permeate gap side	T_{Mp}	ºC
Temperature in permeate gap channel	T_{PG}	ºC
Permeate flow rate	V_p	$m^3\ s^{-1}$
Impermeable film thickness	δF	m
Membrane thickness	δ_m	m
Permeate gap thickness	δ_{PG}	m

Solar and Heat Pump Systems

Field tests of a novel solar-assisted dual source multifunctional heat pump

Giorgio Besagni[1], Lorenzo Croci[1], Riccardo Nesa[1,2], Luca Molinaroli[2] and Pietro Quaglia[1,2]

[1] RSE S.p.A., Power System Development Department, via Rubattino 54, 20134 Milano (Italy)

[2] Politecnico di Milano, Department of Energy, via Lambruschini 4a, 20156, Milano (Italy)

Abstract

In this paper, we present the results of field study concerning a novel solar-assisted dual-source multifunctional heat pump, installed in a detached house in Milan. The system couples hybrid photovoltaic/thermal (*PVT*) panels with multifunctional and reversible heat pump. The proposed system is equipped with an "*air source*" evaporator and a "*water source"* evaporator, connected in series and operated alternatively, based on the ambient conditions and system parameters. The "*air source*" evaporator is an external unit; conversely, the "*water source"* evaporator is connected with a storage tank, fed by the *PVT* system. The *PVT* system is connected with the heat pump by two storage tanks to be used to produce domestic hot water and to be used in "*water source"* evaporator. Based on the operating conditions, the hot water is sent to one of the storage tank. The proposed system has been tested experimentally; the results show that the system was able to maintain high efficiency in the different seasons and was able to produce domestic hot water. It was found that the use of the "*water source"* evaporator was able to compensate the performance degradation of the "*air source"* source evaporator caused by the low ambient temperature.

Keywords: Solar assisted heat pump, Hybrid photovoltaic/thermal panels, Dual Source, Domestic hot water, PVT, SAHP

1. Introduction

Multifunctional heat pumps are widely used for heating and cooling applications, as well as for the production of domestic hot water (*DHW*), by exploiting different heat sources (i.e., ground source, air source or water source). In particular, the coefficient of performance (*COP*) of air-source heat pumps depends on the ambient temperature, T_{amb} (viz. T_{amb} is related to the evaporating temperature, T_{eva}). As a consequence, in the winter season, when heating is needed and T_{amb} is lower, the system performance decreases, owing to the lower evaporating temperature. Conversely, considering a reversible heat pump in the summer season, when cooling is needed and T_{amb} is higher, the system performance decreases, owing to the higher condensing temperature. In this respect, the coupling between solar technologies and heat pumps—"*solar-assisted heat pumps*" (*SAHPs*)—is a promising technology to overcome the above-mentioned limitations, to reduce the consumption of energy resources and to meet the targets set by the recent regulations (i.e., European Union targets). Generally speaking, heat pumps can be coupled with photovoltaic (*PV*) panels, thermal collectors or hybrid photovoltaic/thermal (*PVT*) panels, as outlined in the literature surveys proposed by Kamel et al. (Kamel, Fung e Dash 2015) and by Mohantaj et al. (Mohanraj, et al. 2017). In practical applications, heat pumps are coupled with thermal or *PVT* panels, in direct or indirect expansion configurations. In direct expansion *SAHP*, the solar panel corresponds to the evaporator of heat pump; conversely, in indirect expansion *SAHP*, an intermediate heat exchanger is used to couple the solar system and the heat pump. In addition, *SAHP* systems can be classified into three sub-categories: (a) parallel systems, (b) series systems and (c) dual-source systems. In parallel systems, the heat pump receives energy from the ambient, and the solar energy is supplied directly for either space heating or for *DHW* production. In series systems, solar energy is supplied to the evaporator of the heat pump, thus raising the evaporating temperature (thus, increasing the *COP*) and cooling the solar collectors (thus, increasing the efficiency of the solar panels). In the dual-source systems, the evaporator can receive energy from either the atmosphere or from the solar energy, depending on the ambient conditions and system operation .

doi:10.18086/swc.2017.33.01 Available at http://proceedings.ises.org

This paper contributes to the existing discussion concerning multifunctional *SAHP* for heating and cooling applications, as well as for the production of *DHW*. In the last decades, different systems have been proposed and, in the following, a brief literature survey is proposed to better outline the framework of this research. Wang et al. (Wang, et al. 2011) experimentally investigated, in a laboratory-scale experimental setup, an indirect dual-source ("*air-source*" and "*water-source*" evaporators) *SAHP* for space heating and cooling and water heating. A storage tank, connected to thermal panels, was used to supply heat to the "*water-source*" evaporator or to produce *DHW*. They reported *COP* = 4, in the heating mode. Bridgeman and Harrison (Bridgeman e Harrison 2008) experimentally investigated, in a laboratory-scale experimental setup, the performance of an indirect series *SAHP* for water heating. They observed *COP* = 2.8 – 3.3, depending on the evaporator and condenser temperatures. Loose et al. (Loose, et al. 2011) performed field tests of various combined *SAHP* systems with different heat sources, for space heating and water heating. The system employed solar thermal collectors and geothermal heat pump with borehole heat exchangers. The collectors fed the storage tank directly when the sufficient solar radiation was available. Otherwise, low grade energy from the collectors would be used in the heat pump for space heating. Bakirci et al. (Bakirci e Yuksel 2011) investigated the performance of an indirect SAHP system for space heating. The solar collectors directly charged a storage tank which was linked to an evaporator to provide a heat source for the heat pump. They observed *COP* in the range of 3.3 – 3.8. Bai et al. (Bai, et al. 2012) theoretically studied, by using a TRNSYS model, an indirect combined hybrid *PVT SAHP* system for *DHW* production. Year round performance results were simulated under the different climatic conditions (Hong Kong and different locations in France) and an average *COP* = 4.9 has been observed.

From the above-mentioned literature survey, as well as from the literature surveys proposed by different authors (Hepbasli e Kalinci 2009, Ozgener e Hepbasli 2007, Parida, Iniyan e Goic 2011, Tian e Zhao 2013), it is observed that there is a lack of field studies concerning practical demonstration and fields studies concerning multifunctional dual source ("*air-source*" and "*water-source*" evaporators) *SAHP*. To this end, this paper presents the field tests of a novel solar-assisted dual-source multifunctional heat pump, installed in a detached house in Milan. The system couples hybrid *PVT* panels with a multifunctional and reversible heat pump. The paper is organized as follows. First, the experimental setup and methods are presented and described; second, the experimental results are commented and discussed; finally, main conclusions are drawn

2. Experimental setup and methods

In this section, the experimental setup and the experimental methods are presented and described. First, the multifunctional heat pump system and main characteristic of the components are presented and discussed (Section 2.1). Second, the details concerning the operation procedures are outlined (Section 2.2). Finally, the experimental techniques (Section 2.3) and performance parameters (Section 2.4) are described and commented.

2.1 Experimental setup

The multifunctional heat pump system (Fig. 1) has been designed and installed in a detached house (Fig. 2) located in Milan, at RSE Spa headquarter. The detached house has an heating/cooling area equal to 64 m^2, with a nominal load equal to 4 kW_{th} (indoor temperature equal to 20 °C and outdoor temperature equal to -5 °C). Fig. 1 displays the layout of the multifunctional heat pump, which is composed by five parts: (a) a solar system, (b) a *DHW* storage tank and an "*intermediate-temperature*" storage tank, (c) a reversible heat pump, (d) terminal heating and cooling systems (viz. fan coils) and (e) circulating pumps (Tab. 1). Further details concerning the different components of the system are provided in the following.

Solar system. The solar system consists in seven *PVT* panels and a *PV* panel (Fig. 2). The *PV* panel has the same size and cells characteristic of the *PVT* panels, to compare the performance of the two technologies. The seven *PVT* panels (south-oriented, 45° titled angle) have 1.75 kW_{el} nominal power and are of the roll-bond technology (Fig. 3a). They are composed by polycrystalline silicon cells, a steel heat-exchanger and a 0.002 m insulation. In the heat exchanger part of the *PVT*, water/ethylene glycol mixture has been used as working fluid, to prevent icing-related issues, with a nominal flow rate equal to 0.630 m^3/h. It is worth noting that the comparison between *PV* and *PVT* panels is not presented here and is a matter of ongoing research activities.

Storage tanks. The *DHW* storage tank (0.186 m^3 in volume) has been used to produce hot water; conversely, the "*intermediate-temperature*" storage tank (0.300 m^3 in volume, Fig. 3b) has been used as "*water-source*" from the heat pump, instead of the "*air-source*" one, to improve the performance in cold days and avoid defrosts and

reduce temperature fluctuations. Inside the "*intermediate-temperature*" storage tank water/ethylene glycol mixture has been used as working fluid, to prevent icing-related issues. The "*intermediate-temperature*" is connected to the heat pump, by a plate heat exchanger (Fig. 3c) and the maximum flow rate "*intermediate-temperature*" towards the "*water-source*" heat exchanger is 1.45 m^3/h.

Heat pump unit. The heat pump is a R410A reversible heat pump, 7 kW_{th} nominal heating capacity and 3.47 nominal COP (water leaving temperature equal to 35 °C and air temperature equal to 7 °C), equipped with an electronic expansion valve and a variable speed compressor.

Circulating pumps. As shown in Fig. 1, the experimental system includes circulating loops: (a) solar collector loops; (b) "*intermediate-temperature*" storage tank to heat pump; (c) indoor terminal fan-coil side loop and (d) *DHW* circulating loops. Details on pumps used are provided in Table 1.

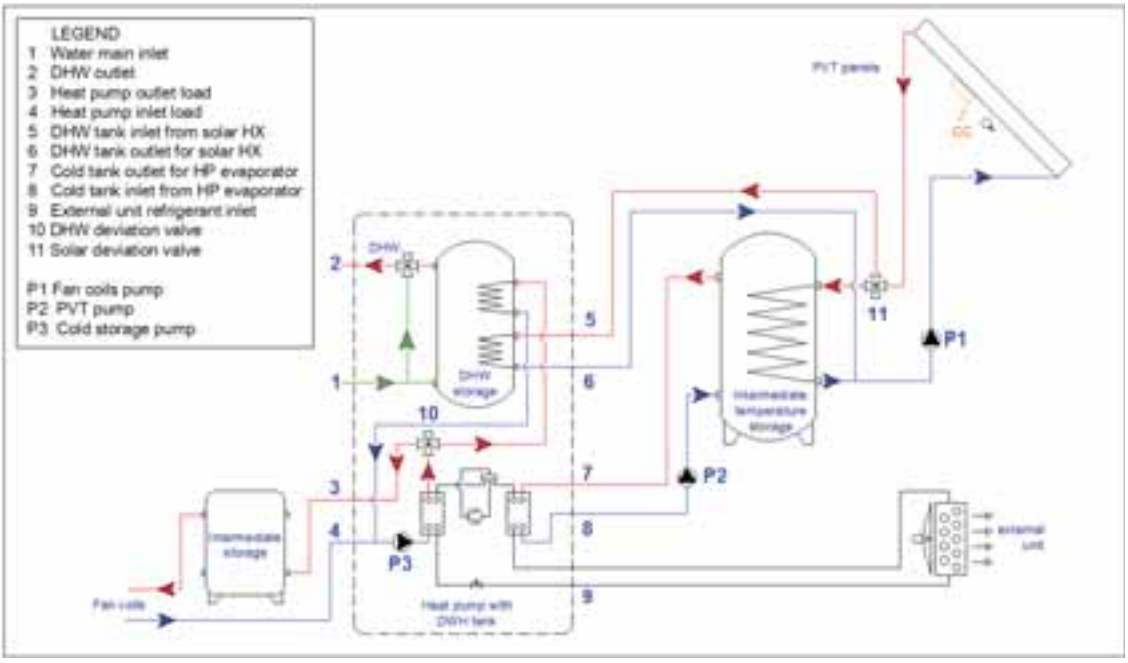

Fig. 1: Experimental layout

Fig. 2: Photo of the detached house at RSE Spa

(a) PVT roll-bond panels

(b) "*intermediate-temperature*" tank

(c) Plate heat exchanger between the heat ump and the "intermediate-temperature" tank

Fig. 3: Details of the experimental setup

Tab. 1: Details on circulating pumps used (see Fig. 1 for further details)

Code (Fig.1)	Location	Technical details	Power [W]
P1	Solar circulating pump	DEB Evolplus Small 60/180 M PWM	5 - 100
P2	"*intermediate temperature*" circulating pump	WILO Stratos Para 25/1-7 PWM	5 - 70
P3	Fan-coil circulating pump	WILO Stratos TEC RS 25/7 PWM	3 - 70
P4	*DHW* circulating pump	WILO ZRS 12/7	86 (fixed speed)

2.2 Operation modes and control

The multifunctional heat pump has been tested starting from 17th January 2017 and the monitoring is still ongoing. The system has been tested in three operation modes in order to study the influence of the different operation parameters; each mode was controlled aiming to (a) minimize the electricity consumption by the heat pump, using solar thermal energy, and (b) maximizing the production of electricity of *PVT* panels keeping their operating temperature as low as possible. The operating principles for each mode are provided in the following.

- **Mode#1. Heating mode without *DHW* production (from 17/01/2017 to 13/03/2017).** The internal set-point temperature was set at $T_{set\text{-}point}$ = 22 °C, with night attenuation of 4 °C (from 22.00 to 7.30). In this operation mode, the temperature of the water produced by the heat pump and sent to the fan-coils was set by using a climatic curve: T_3 = 43 °C with T_{amb} = 0 °C and T_3 = 35 °C with T_{amb} = 15 °C. In this

operation mode, valve *V1* was set to deviate all thermal energy produced by the *PVT* panels to the "*intermediate-temperature*" storage tank. The "*intermediate-temperature*" storage tank, is used as the "*water-source*" for the heat pump when T_{amb}, is low and the resulting *COP* would decrease. Changes from "*air-source*" evaporator to "*water-source*" evaporator are obtained by switching on/off the pump *P2* and switching on/off the external "*air-source*" unit.

- **Mode#2. Heating mode with *DHW* production (from 13/03/2017 to 24/05/2017).** The operation mode *mode#1* has been modified as follows: (a) a daily profile of *DHW* production was set to produce 1*50 l* (corresponding to, approximately, 4 KWh); (b) valve *V1* was set to deviate the glycol-water mixture, at the outlet of the *PVT* panels, depending on the temperature of the storage tanks (a) towards the "*intermediate-temperature*" *DHW* storage ($T_{intermediate\text{-}temperature}$ < 38 °C), (b) towards the *DHW* tank ($T_{intermediate\text{-}temperature} \geq$ 38 °C) or towards the "*intermediate-temperature*" storage tank ($T_{DHW,tank} \geq$ 58 °C); (c) the *DHW* storage tank set-point temperature was set to $T_{DHW,set\text{-}point}$ = 48°C and its lower temperature has been set $T_{DHW,mantenance}$ = 42°C. In the case, the temperature of the *DHW* storage tank would fall below $T_{DHW,mantenance}$, the heat pump would be used been used to increase the *DHW* tank temperature.
- **Mode#3. Cooling mode with *DHW* production (from 24/05/2017, ongoing).** The internal set-point temperature was set at $T_{set\text{-}point}$ = 24 °C. In addition, the operation mode *mode#2* was modified as follows: (a) a daily profile of *DHW* production has been set to produce 1*50 l* (corresponding to approximately, 3 KWh; the DHW corresponding power is lower compared with the previous operation mode, owing to the higher inlet water temperature, T_1); (b) valve *V1* was set to deviate the glycol-water mixture, at the outlet of the *PVT* panels, depending on the temperature of the storage tanks towards the *DHW* storage tank ($T_{intermediate\text{-}temperature} \geq$ 36 °C) or towards the "*intermediate-temperature*" storage tank ($T_{DHW,tank} \geq$ 57 °C);).

2.3 Measurement system and procedure

All the main variables, to describe mass and energy balances, have been measured. The flow rate in each circuit has been measured by an electromagnetic flowmeter meter (E&H Promag P50, ±0.2% read value). All the inlet and outlet temperatures of the main equipments, the supply and return water temperatures of the different locations, were measured by RTD Pt100 4wire 1/5DIN, inserted inside the pipes. The indoor and outdoor (near the *PVT* panels) temperature and humidity were measured by an Pt100 4wire hygrometer (Siap+Micros). The solar radiation intensity has been measured by a thermopile pyranometers (pyranometer Kipp&Zonen CMP11), mounted at a 45° inclined angle near the *PVT* panels. The power consumption of the heat pump and the circulating pumps (solar pumps, intermediate-storage tank, fan-coil pump) were measured by multifunction electric meters (Shark 100, ±0.1%, and FRER MonoNano, ±0.5%). Evaporating and condenser pressures were measured by pressure transducers (Keller series 21Y). All the temperature probes were verified with a calibration procedure by using thermostatic batch, at RSE Spa. All data were recorded automatically at every 6 seconds interval in a data logger (Advantech ADAM 5000 and 4000 data logging devices) to be further post-processed.

2.4 Performance evaluation

The performance of the system has been evaluated based on the mass and energy balances, based on the recorded data (flow rates and temperatures). In particular, the energy fluxes across every component has been computed as follows:

$$Q = \dot{m} c_p (T_{inlet} - T_{outlet}) \quad \text{(Eq. 1)}$$

In Eq. (1), T_{inlet} and T_{outlet} refer to the inlet and outlet temperatures, m is the mass flow rate, c_p is the specific heat of water. Based on the heat fluxes and the electric power measured, the *COP* (during heating mode; *mode#1* and *mode#2*, Eq. (2)) and the *EER* (during the cooling mode; *mode#3*, Eq. (3)) have been computed as follows:

$$COP = \frac{Q_{HP \rightarrow fan-coil} + Q_{HP \rightarrow DHW-tank}}{P_{el}} \quad \text{(Eq. 2)}$$

$$EER = \frac{Q_{HP \leftarrow fan-coil} + Q_{HP \rightarrow DHW-tank}}{P_{el}} \quad \text{(Eq. 3)}$$

In Eqs. (2-3), P_{el} is the electric power provided to the systems; $Q_{HP \rightarrow fan\text{-}coil}$ and $Q_{HP \leftarrow fan\text{-}coil}$ is computed based on T_3 and T_4 and $m_3 = m_4$ (please refer to Fig. 1 for the location of the subscripts) and refer to the heat transfer from the heat pump towards the fan-coils and vice-versa; conversely, $Q_{HP \rightarrow DHW\text{-}tank}$ refers to the het flux provided from the heat pump to the *DHW* tank and is computed as follows:

$$Q_{HP \rightarrow DHW-tank} = \sum_{t=0}^{n=N} \rho V_{DHW,tank} c_p (T_{t=n} - T_{t=n-1}) \quad \text{(Eq. 4)}$$

In Eq. (4), $V_{DHW,tank}$ is the volume of the *DHW* tank, ρ is the density of water, and t is the time variable. Please note that Eq. (4) is computed under the following constrains: (a) the temperature of the *DHW* storage is below $T_{DHW,maintenance}$, (b) the temperature of the *DHW* storage tank is increasing with time; (c) heat pump status is ON.

To study the influence of the "*water source*" evaporator and the "*air-source*" evaporator, Eq. (2) has been modified as follows, based on the status of the storage tank circulating pump (pump *P2*, Fig. 1):

$$COP_{"water\text{-}source"} = \frac{Q_{HP \rightarrow fan-coil} + Q_{HP \rightarrow DHW-tank}}{P_{el}} \quad if\ pump\ P2 = ON \quad \text{(Eq. 5)}$$

$$COP_{"air\text{-}source"} = \frac{Q_{HP \rightarrow fan-coil} + Q_{HP \rightarrow DHW-tank}}{P_{el}} \quad if\ pump\ P2 = OFF \quad \text{(Eq. 6)}$$

3. Experimental results

In this section, the experimental results are presented and discussed. First, the ambient conditions in the monitored period are presented. Second, the performance of the heat pump are presented and commented with reference to the three different operating modes. Finally, the influence of the "*water-source*" and the "*air-source*" evaporators on the performance are commented.

3.1 Ambient conditions

In order to provide an overview of the heat pump working conditions, Fig. 4 displays the value of ambient conditions in the monitored period. In particular, Fig. 4 displays the daily averaged values of the ambient temperature and relative humidity. It is worth noting that the heat pump was operated in a quite broad range of operating conditions (i.e., daily averaged T_{amb} ranged between 0 and 33 °C; conversely, the instantaneous values of T_{amb} ranged between -5°C and 40 °C).

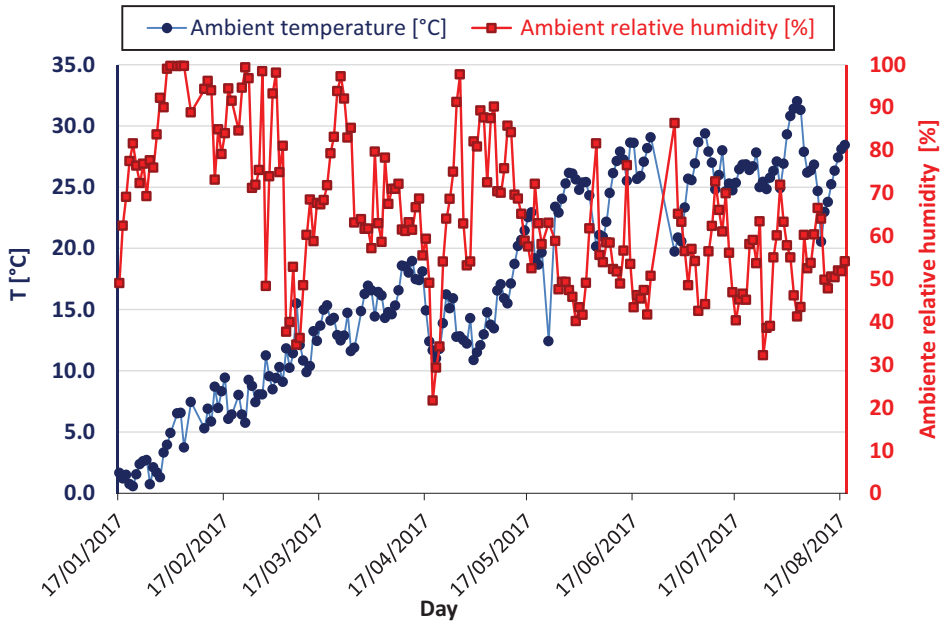

Fig. 4: Daily-averaged ambient conditions: ambient temperature and relative humidity

3.2 Seasonal performance

Fig. 5 displays the daily-averaged performance of the multifunctional heat pump in the three operating modes described in Section 2.2. In addition, in Fig. 5, T_{amb} is displayed for the sake of clarity. The performance of the multifunctional heat pump are computed by using Eq. (2)—the *COP*—and Eq. (3)—the *EER*. In the operation *mode#1*, the useful effect of the heat pump is $Q_{HP \rightarrow fan\text{-}coil}$ (there is no *DHW* production; $Q_{HP \rightarrow DWH\text{-}tank} = 0$); conversely, in the other operation modes (viz. *mode#2* and *mode#3*) the useful effect of the heat pump consists in both $Q_{HP \rightarrow fan\text{-}coil}$ and $Q_{HP \rightarrow DWH\text{-}tank}$. Please note that the electric consumption, P_{el}, considered in the evaluation of *COP* and *EER* does not account for the contribution of the auxiliaries (i.e., circulation pumps, stand-by consumption, etc…): (a) the solar circulating pump (its consumption was approximately 4.1 % of the total energy consumption); (b) the "*intermediate-temperature*" circulating pump (its consumption was approximately 1.2 % of the total energy consumption); (c) the Fan-coil circulating pump (its consumption was approximately 3.7 % of the total energy consumption), (d) the DHW circulating pump and all other auxiliaries (their consumptions were approximately 14.2 % of the total energy consumption).

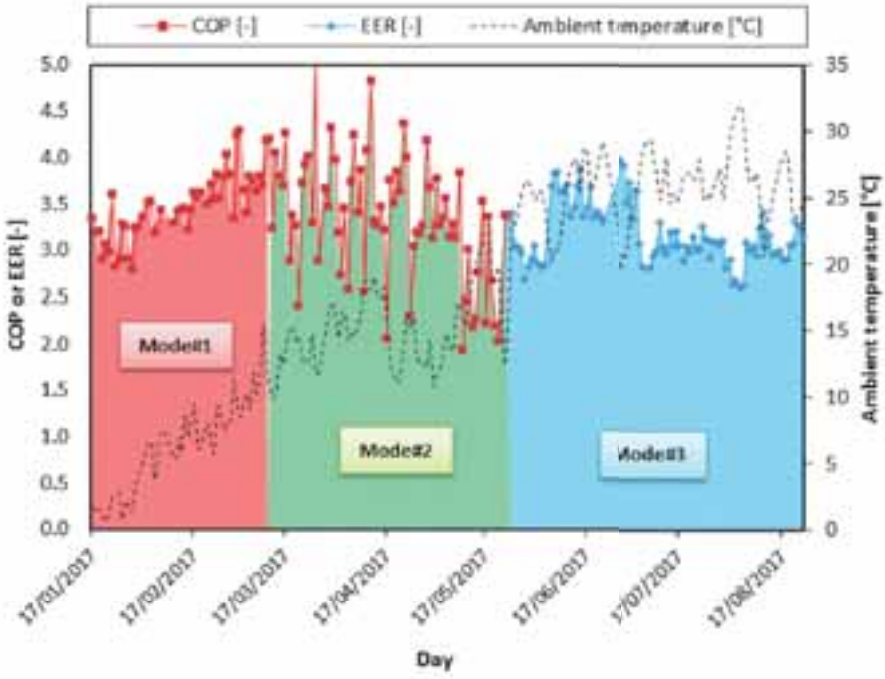

Fig. 5: Daily-averaged performance of the multifunctional heat pump depending on the operation mode and ambient temperature

In the operation mode *mode#1*, the daily-averaged *COP* is in the range of 3 and 4.5; as expected, *COP* increases with time, owing to the increasing daily-averaged T_{amb}. The relationship between T_{amb} and the heat pump performance can be further understood, by considering the layout of the system. Indeed, the performance of an heat pump may be related (for fixed component design), to the evaporating and condensing temperatures/pressures. In the present case: (a) the condensing pressure is related to the internal conditions, that, for a fixed set-point are periodical with time; (b) evaporating temperature T_{eva} is related to T_{amb}, owing to the variable speed compressor and the electronic expansion valve. Therefore, a variation in the ambient temperature, mainly affects T_{eva} and, thus, affect the performance of the system. To better discuss this concept, Fig. 6 displays the relationship between the variables of the heat pump (i.e., evaporator pressure and condensing pressure), T_{eva} and *COP*. The reader may refer to the studies proposed by Kuang and Wang (Kuang e Wang 2006) and Ma and Zhao (Ma e Zhao 2008) for a more detailed discussion on the role of variable speed compressors in heat pumps. In addition, in Fig. 6 is also displayed the influence of the "*water-source*" evaporator. This point is further discussed in Section 3.3. In the operation mode *mode#2*, the performance of the system, compared with *mode#1*, shows a larger variability and are slightly lower. This behavior can be explained based on the system operations as well as on the ambient conditions. First, in this period, beside DHW production, $Q_{HP \rightarrow fan\text{-}coil}$ is very low and, in some days, $Q_{HP \rightarrow fan\text{-}coil} \approx 0$, owing to the high T_{amb} (the internal set-point temperature can be achieved also with very low heat pump load). Therefore, *COP* is mostly related to $Q_{DHW\text{-}tank}$. Second, it should be noted that

$Q_{HP \rightarrow DHW\text{-}tank}$, is produced at higher temperature compared with $Q_{HP \rightarrow fan\text{-}coil}$; therefore the expected performance of the heat pump is reduced. In this respect it is well known that Eq. (2) does not take into account the grade of heat produced, as it is related to energy balances and neglect the entropy/exergy concept. In the operation mode *mode#3*, in the cooling mode with DHW production, the daily-averaged *EER* is in the range of 3 and 4.5. The discussion concerning the relationship between the ambient conditions and the system performance is similar to the above-discussion for the operation mode *mode#1*. It is worth noting that, owing to the high ambient temperature, in the summer season, the *PVT* panels are able to contribute to the maintenance temperature of the *DHW* storage tank, thus reducing $Q_{HP \rightarrow DHW\text{-}tank}$ and, thus, the energy consumption of the heat pump.

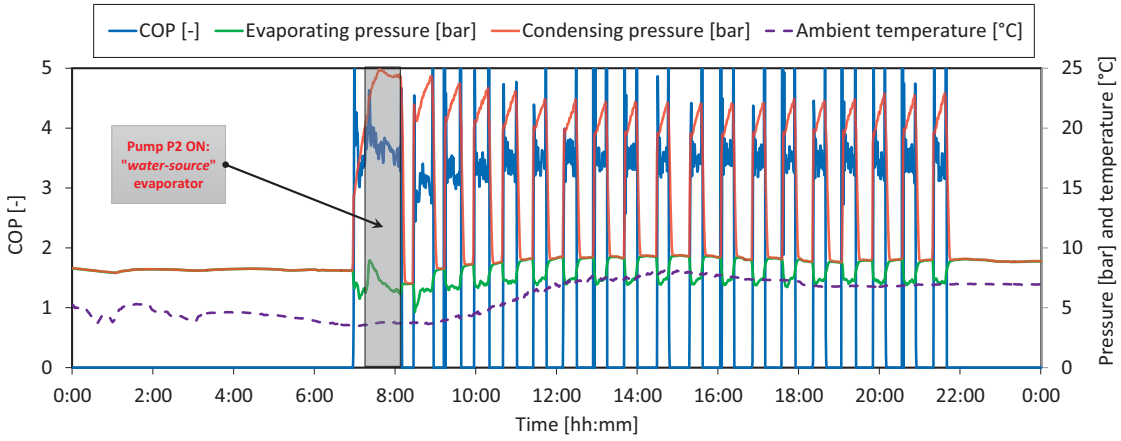

Fig. 6: Daily performance of the multifunctional heat pump: performance parameters (data obtained at 13/02/2017, *mode#1*)

3.3 Comparison between water source and air source

In this section, an insight in the performance of the system is proposed, by analyzing the contribution of the "*water-source*" evaporator and the "*air-source*" evaporator to achieve the averaged performance described in Section 3.2. To this end, by applying Eqs. (5-6) in the in the operation mode *mode#1*, the corresponding "*water-source*" the "*air-source*" performances have been obtained; the results of this analysis have been summarized in Fig. 7, in terms of daily-averaged values. Please note that in some days (viz. the data not displayed in Fig. 7), the "*water-source*" evaporator was not used. Applying the whole dataset, (in the operation mode#1) and applying Eqs. (5-6), an average *COP* increase approximately 35.5% from the "*air-source*" mode to the "*water-source*" mode has been observed. In order to better understand the relationship between "*water-source*"/"*air-source*" evaporators and the COP, Fig. 8 proposes three daily profiles of the heat pump operation.

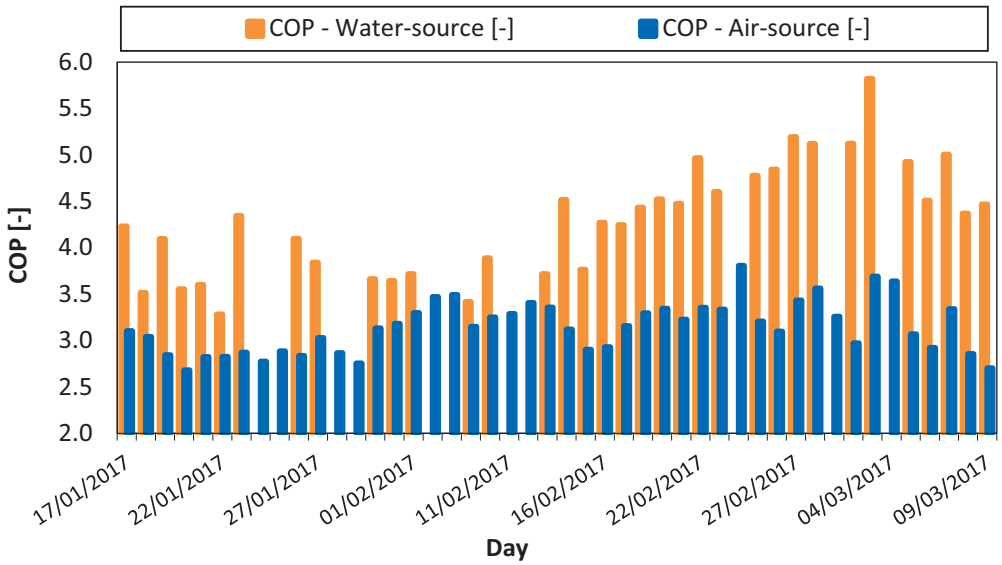

Fig. 7: Daily-averaged performance of the multifunctional heat pump: influence of "*water-source*" and "*air-source*" evaporators (data obtained during operation mode *mode#1*)

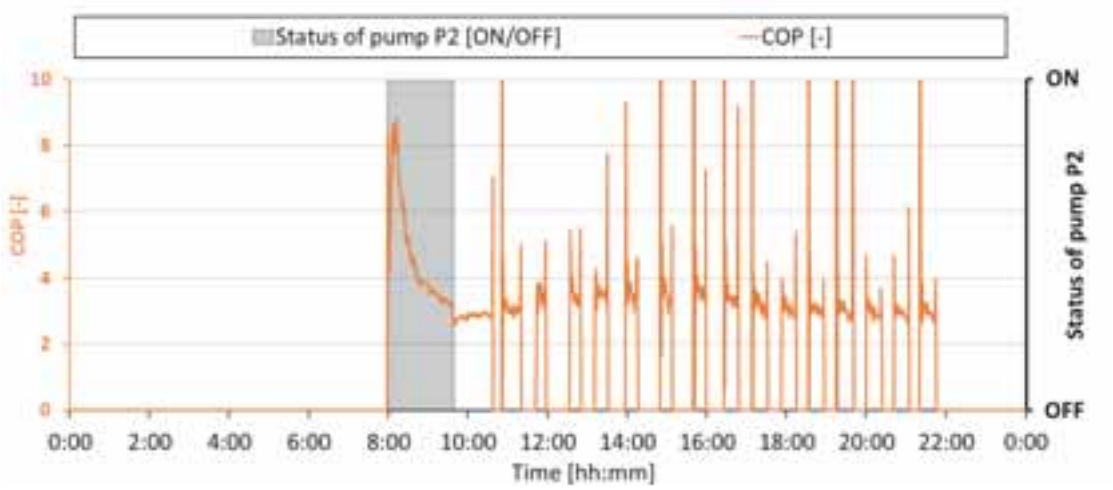

(a) data obtained at 17/01/2017, operation mode *mode#1*

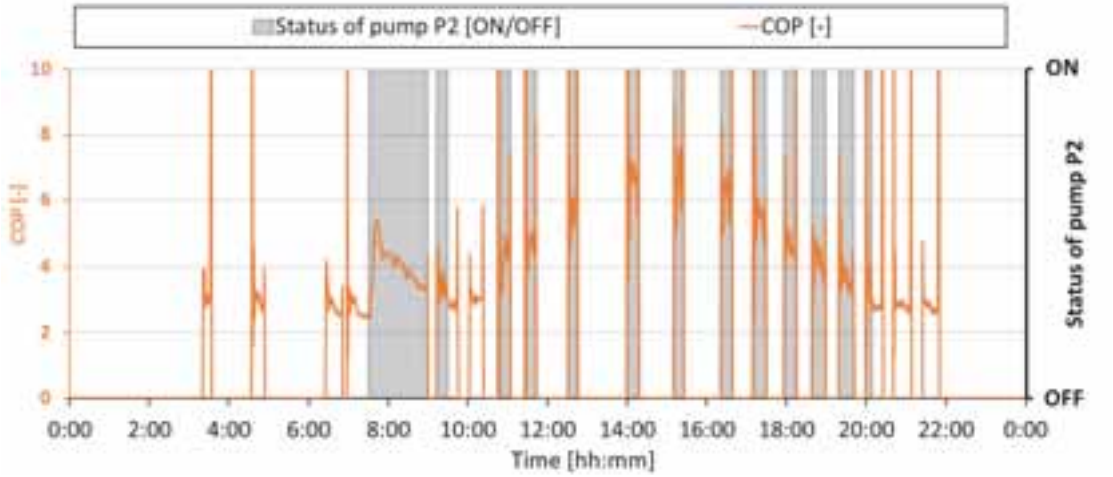

(b) data obtained at 23/01/2017, operation mode *mode#1*

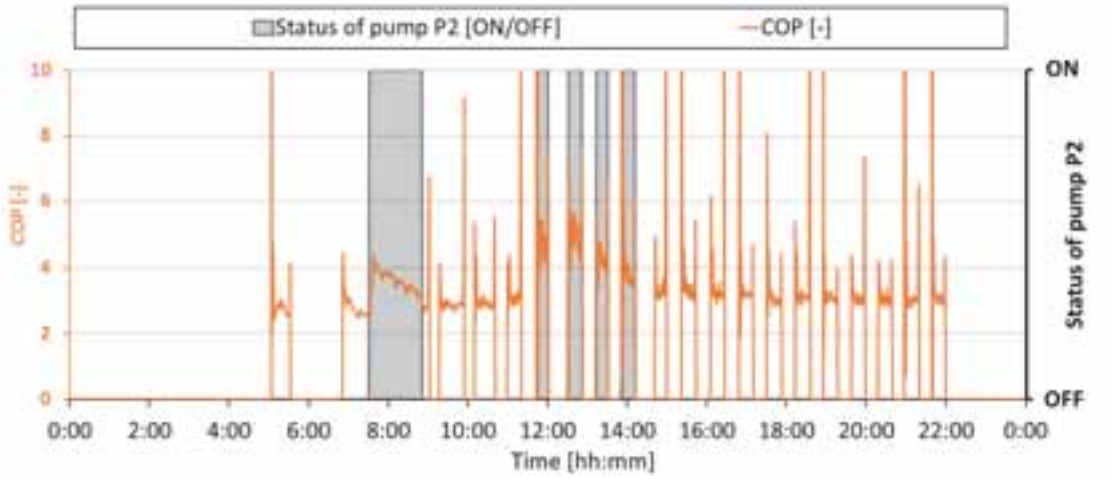

(c) data obtained at 27/01/2017, operation mode *mode#1*

Fig. 8: Daily performance of the multifunctional heat pump: influence of "*water-source*" and "*air-source*" evaporators

Fig. 8 clearly displays the significant increase of *COP*, owing to the use of the "*water-source*" evaporator. For example, it can be observed that, in Fig. 8a, by activating the pump *P2* at 8.00 AM the *COP* increases from 2.7 to 8 (instantaneous values). Similar considerations can be drawn for the other days displayed in Fig. 8b and Fig. 8c. It is important to emphasize that the "*water-source*" evaporator avoided the defrost cycles of the aerothermal heat pumps and the subsequent decrease in the performances. In this respect, the reader may refer to the defrost-related issues described by Zhang et al. (Zhang, et al. 2017). It should be noted that the *COP* obtained using water as source has been obtained in the most unfavorable conditions: the morning, when maximum building load and with the highest delivery water temperature. Unfortunately, the use of the water source is limited in time and depends on the thermal energy available in the "*intermediate-temperature*" storage tank. Future studies should be focused on alternative technical solutions for storage tanks (i.e., phase change material, *PCM*, storage tanks), to improve the availability of the "*water-source"*.

4. Conclusions, outcomes and outlooks

This paper presented the very first results of field study concerning a novel solar-assisted dual-source multifunctional heat, installed in a detached house in Milan. The system couples *PVT* panels with a dual-source ("*air source*" and "*water source"* evaporators) multifunctional and reversible heat pump. The multifunctional heat pump has been tested starting from 17th January 2017 (the monitoring is still ongoing) in three operation modes: (a) heating mode without *DHW* production; (b) heating mode with *DHW* (150 l) production; (c) cooling mode with *DHW* (150 l) production.

4.1 Conclusions and outcomes

The main results of the filed study are as follows:

- the averaged performance (*COP* and *EER*) of the multifunctional heat pump is approximately 3, in the three different operation modes;
- the thermal energy produced by the *PVT* panels have been successfully used to support the "water-source" evaporator in the winter/spring seasons;
- the thermal energy produced by the *PVT* panels have been successfully used to support the production of *DHW* in the summer period;
- the use of "*water-source*" evaporator allows to significantly increase the performance of the plant;
- the use of "*water-source*" evaporator allows to avoid defrost cycles;

4.2 Outlooks

Ongoing research as well as future studies may concern both experimental and numerical researches. On the experimental part, outlooks are as follows:

- extent the field study to the autumn ambient conditions, to provide a complete seasonal overview of the system operation;
- relate the daily and the seasonal operations, to provide a multi-scale evaluation of the heat pump performance;
- propose a comprehensive thermodynamic evaluation (energy and exergy evaluation) of the whole system;
- compare the performance of PV and PVT systems and provide insights in the relationships between operating conditions (i.e., temperatures, flow rates, ambient conditions) and the panels performances (i.e., thermal and electrical energy production);
- study alternative technical solutions for storage tanks (i.e., phase change material, *PCM*, storage tanks), to improve the availability of the "*water-source*".

On the numerical part, future studies would concern the testing and validation of a TRNSYS approach, to extend the results of the present experimental study to different climatic conditions and, finally, to assess the economic feasibility of the proposed system.

5. Nomenclature and abbreviation list

5.1 Acronyms

COP	Coefficient of performance
DHW	Domestic hot water
EER	Energy Efficiency Ratio
HP	Heat Pump
PV	Photovoltaic
PCM	Phase Change Material
PVT	Hybrid thermal-photovoltaic
SAHP	Solar-assisted-heat pump

5.2 Symbols

c_p	Specific heat of water	[kJ/kg K]
m	Mass flow rate	[kg/s]
N	Time discretization in Eq. (4)	[-]
$Q_{HP \rightarrow DWH\text{-}tank}$	Heat transfer from the heat pump to the *DHW* tank	[kW]
$Q_{HP \leftarrow fan\text{-}coil}$	Heat transfer from the heat pump to the fan-coils	[kW]
T	Temperature	[°C]
t	Time in Eq. (4)	[min]
$V_{DHW,tank}$	Volume of the *DHW* storage tank	[m^3]
$V_{DHW,tank}$	Volume of the *"intermediate-temperature"* storage tank	[m^3]
ρ	Density of water	[m^3/kg]

5.3 Subscripts

amb	Ambient conditions
el	Electrical energy
eva	Evaporator
inlet	Inlet condition
outlet	Outlet condition
th	Thermal energy

6. Acknowledgements

This work has been financed by the Research Fund for the Italian Electrical System under the Contract Agreement between RSE S.p.A. and the Ministry of Economic Development - General Directorate for Nuclear Energy, Renewable Energy and Energy Efficiency stipulated on July 29, 2009 in compliance with the Decree of March 19, 2009. The authors are also grateful to CLIVET Spa for elaborating and providing the heat pump employed in the research activities.

7. References

Bai, Y., T. T. Chow, C. Ménézo, and P. Dupeyrat. "Analysis of a Hybrid PV/Thermal Solar-Assisted Heat Pump System for Sports Center Water Heating Application." *International Journal of Photoenergy* 2012 (2012).

Bakirci, Kadir, and Bedri Yuksel. "Experimental thermal performance of a solar source heat-pump system for residential heating in cold climate region." *Applied Thermal Engineering* 31 (2011): 1508-1518.

Bridgeman, Andrew, and S. Harrison. "Preliminary experimental evaluations of indirect solar assisted heat pump systems." *Proceedings of the 3rd Canadian solar building conference. Fredericton.* 2008.

Hepbasli, Arif, and Yildiz Kalinci. "A review of heat pump water heating systems." *Renewable and Sustainable Energy Reviews* 13 (2009): 1211-1229.

Kamel, Raghad S., Alan S. Fung, and Peter R. H. Dash. "Solar systems and their integration with heat pumps: A review." 87 (2015): 395-412.

Kuang, Y. H., and R. Z. Wang. "Performance of a multi-functional direct-expansion solar assisted heat pump system." *Solar Energy* 80 (2006): 795-803.

Loose, Anja, Harald Drück, Nadine Hanke, and Frank Thole. "Field Test and Performance Monitoring of Combined Solar Thermal and Heat Pump Systems." *ISES Solar World Congress, At Kassel, Germany.* 2011.

Ma, Guo-Yuan, and Hui-Xia Zhao. "Experimental study of a heat pump system with flash-tank coupled with scroll compressor." *Energy and Buildings* 40 (2008): 697-701.

Mohanraj, M., Ye. Belyayev, S. Jayaraj, and A. Kaltayev. "Research and developments on solar assisted compression heat pump systems – A comprehensive review (Part A: Modeling and modifications) ." *Renewable and Sustainable Energy Reviews* , 2017: In Press

Ozgener, Onder, and Arif Hepbasli. "A review on the energy and exergy analysis of solar assisted heat pump systems." *Renewable and Sustainable Energy Reviews* 11 (2007): 482-496.

Parida, Bhubaneswari, S. Iniyan, and Ranko Goic. "A review of solar photovoltaic technologies." *Renewable and Sustainable Energy Reviews* 15 (2011): 1625-1636.

Tian, Y., and C. Y. Zhao. "A review of solar collectors and thermal energy storage in solar thermal applications." *Applied Energy* 104 (2013): 538-553.

Wang, Qin, Yu-qian Liu, Guo-feng Liang, Jia-rong Li, Shu-fei Sun, and Guang-ming Chen. "Development and experimental validation of a novel indirect-expansion solar-assisted multifunctional heat pump." 43 (2011): 300-304.

Zhang, Yaning, Qin Ma, Bingxi Li, Xinmeng Fan, and Zhongbin Fu. "Application of an air source heat pump (ASHP) for heating in Harbin, the coldest provincial capital of China." *Energy and Buildings* 138 (2017): 96-103.

Cost energetic analyses of ice storage heat exchangers in solar-ice systems.

Daniel Carbonell , Daniel Philippen, Mattia Battaglia and Michel Y. Haller.

SPF, Institut für Solartechnik, HSR, Hochschule für Technik,
CH-8640 Rapperswil, Switzerland

Abstract

The aim of the present paper is to analyze flat plates (FP) and capillary mats (CM) heat exchangers for solar-ice systems. The optimum heat exchanger area needed in the ice storage is based on energetic transient system simulations and on cost indicators. Solar-ice systems using ice storage volumes from 2 to 5 m^3 and selective uncovered collectors with 15 to 25 m^2 in the city of Zurich were able to achieve system performance factors SPF_{SHP+} ranging from 3.5 to 6 with both CM and FP in a single family house with 10 MWh yearly heating demand. Considering the cost of the system, only simulations with CM were able to achieve lower heat generation cost than that of a ground source heat pump (GSHP) with even higher SPF_{SHP+} (an SPF_{SHP+} of 4 was assumed for GSHP). For example a system with a collector area of 15 m^2 and 5 m^3 of ice storage volume can reach heat generation cost of 29 Rp./kWh, 0.5 Rp./kWh below the GSHP average reference cost, with an increase of SPF_{SHP+} of 20 % respect to the GSHP system. However, the targets can only be achieved using an appropriate heat exchanger area. The optimal heat exchanger area was found to be around 4 to 5 m^2 per m^3 of ice storage for CM and around 10 to 14 m^2/m^3 for FP. These heat exchanger ratios correspond to a distance between heat exchangers of around 12 - 17 cm for both CM and FP. These results were obtained assuming a conservative maximum ice fraction of 80 %.

Keywords: ice storage, heat exchangers, solar-ice.

1. Introduction

One of the main priorities of the European Commision is to decrease the annual greenhouse gas (GHG) emissions in 2050 by 80% compared to the status of 1990 (Europen Commision, 2012). In order to reach this ambitious goal, the energy supply system needs to be decarbonised. The heating and cooling demands in Europe are responsible of 40 % of the total energy demand. Therefore, the increase of system efficiency as well as raising the share of renewable energy in the heating and cooling sector is necessary to mitigate the climate change by reducing the GHG emmissions. A promising example for a heating system with a high share of renewable energy is the combination of solar thermal and heat pump systems with ice storages, the so-called solar-ice systems. The interest in solar-ice systems is growing in central Europe, where climatic conditions are appropriate for this technology. One of the reasons for the market push of solar-ice systems is due to the regulations established for drilling boreholes. For this reason, solar-ice systems have been established as an alternative to ground source heat pump (GSHP) systems.

Some of the advantages of solar-ice systems respect to GSHP (Carbonell et al., 2016b, 2015) are: i) usually not restricted to regulations of water and soil ii) no need to regenerate the ground as in regions densely populated with boreholes iii) the ice storage is accessible, allowing for solving leakages or replace heat exchangers, iv) the ice storage can be installed in the cellar when no ground space is available v) it is a flexible system able to adapt to building size restrictions, i.e. the same system performance can be reached with different combinations of collector area and ice storage volume and vi) higher performance compared to GSHP can be achieved while being cost competitive if direct solar heat is used extensively. However, solar-ice systems have some disadvantages respect to GSHP such as: i) higher number of hydraulic components, ii) added complexity

doi:10.18086/swc.2017.33.02 Available at http://proceedings.ises.org

of the control, iii) higher installation cost if the same performance is desired, iv) degradation of performance when ice grows, v) need of a back-up system to cover peak demands after long cloudy and cold periods.

Some of the frequently asked questions and answers concerning solar-ice systems are (Carbonell et al., 2017a):

- *"How can a solar-ice system, which is based on a 0 °C temperature source for the heat pump, perform better than a GSHP system which has usually a higher temperature source?"* The main reason is that a solar-ice system can also use solar heat directly without the need of the heat pump. During times when solar heat is used directly, the system performance in terms of heat provided divided by electricity consumed can be up to fifty times higher compared to a GSHP system (only pumps consume energy). Moreover, since solar collectors are also used directly as a source for the heat pump, the source temperatures in solar-ice systems when the sun is shining can be considerably higher than in a GSHP.
- *"Whats is the use of the ice? Can it be spared?"* The key aspect of the solar-ice system concept relies on reducing the need of the storage volume by making use of the high latent heat of fusion released when ice is formed. Icing a specific quantity of water releases the same energy as cooling the same amount of water from 80 °C to 0 °C. Thus, although remaining always above the solidification temperature of water would lead to higher system performance, the required storage volume would be prohibitively large for this concept.

The principal idea of a solar-ice system is shown schematically in Fig. 1.

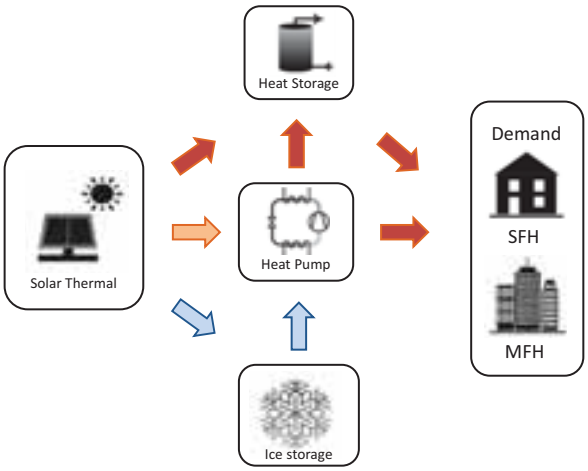

Fig. 1: Principle concept of solar-ice systems. The arrows show the heat fluxes that are on different temperature levels, i.e. red, orange and blue for high (>30 °C), medium (>10 °C) and cold (<10 °C) respectively.

Most of ice storages installed in Europe are based on ice-on-coil heat exchangers, and although other heat exchanger concepts exist on the market, their specific advantages and disadvantages remain unclear.

Several heat exchanger concepts for extracting the latent heat from water can be used. Each concept has to ensure that the ice layer on the specific heat exchanger reaches thicknesses that do not result in too high heat transfer resistance, and thus, in too low source temperatures for the heat pump. When ice grows on the surface of the heat exchanger the overall heat transfer coefficient of the heat exchanger decreases. If ice is not actively removed, the heat exchanger design has to ensure that the heat transfer capacity will be high enough at the maximum design mass ice fraction (ratio between mass of ice and total mass of water and ice) or ice thickness on the surface of the heat exchangers. For example, let's assume that flat heat exchanger plates covering all the height of the ice storage are installed with a distance of 10 cm between each heat exchanger plate. If the heat transfer capacity with 3 cm of ice on the surface is not high enough, the temperature of the heat transfer

fluid will drop until the minimum temperature accepted by the heat pump is reached and the heat pump will be stopped for security reasons. If this occurs, the ice thickness can not exceed 3 cm and part of the latent storage capacity will be lost as 2 cm out of the theoretical maximum of 5 cm will not be used. Thus, the maximum ice fraction will never grow above 60% and the desired maximum accepted ice fraction may not be reached.

In principle, two main strategies exist for the design of heat exchangers for ice storages (Philippen et al., 2015) i) ice-on-hx and ii) free-of-ice-hx. In ice-on-hx, large heat exchanger areas, homogeneously distributed throughout the whole storage volume, are necessary. Heat exchangers such as coils, plates or capillary mats can be used. In free-of-ice-hx, several concepts such as ice slurries (Kauffeld et al., 2005) or de-icing, e.g by hot gas in ice harvesting system (ASHRAE, 2007) or by solar thermal collectors (Philippen et al., 2012) can be used. From all these concepts, only the ice-on-hx concepts are established in the solar and heat pump heating market. In this paper, the ice-on-coil and ice-on-plate concepts will be analyzed from an energetic and economic point of view.

2. Methodology

Dynamic system simulations are used in order to assess the heat exchanger area and heat exchanger type on a system level. The simulations have been conducted with the simulation environment TRNSYS-17 (Klein et al., 2010). The basic components to model a solar-ice system are: collectors, heat pump, ice storage, sensible thermal storage, building, climate and control. The ice storage model has been developed and validated in Carbonell et al. (2017b), the remaining component models were provided in Carbonell et al. (2016b), where a complete solar-ice system based on a de-icing concept was validated with monitored data of a pilot plant.

The time step of yearly simulations is set to 120 seconds. As a verification process several systematic checks are done for all simulations. Heat balances are checked in all individual components, hydraulic loops and also from the system perspective. The convergence criteria from TRNSYS is set to 5e-4, which allows to achieve heat imbalances always below 1.% with respect to the total heat demand. Iteration problems are also checked for all simulations and are always below 10 time steps per year simulated. In most cases iteration problems are in the order of 1 - 5 per year.

2.1. Hydraulic scheme of the simulated system

The hydraulic scheme of the complete solar-ice heating system is shown in Fig. 2. The main components of the heating system are the collector field, the combi-storage, the heat pump and the ice storage.

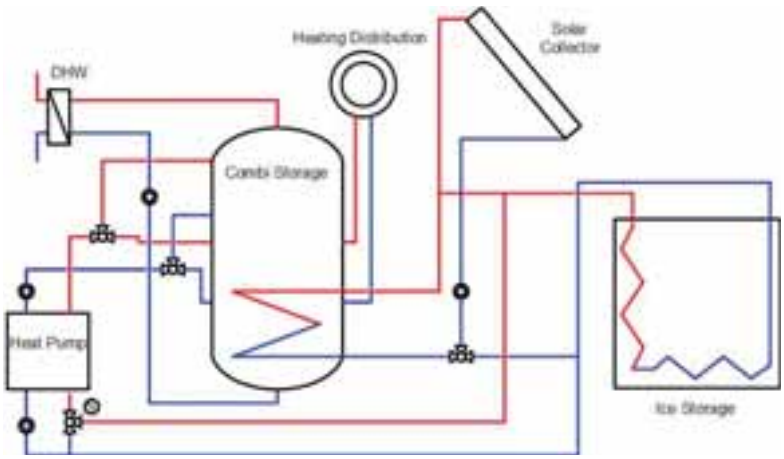

Fig. 2: Simplified hydraulic scheme of the analysed heating system.

The main energy source of the system is the solar irradiation. Some additional energy is extracted from the air, especially when uncovered collectors are used [1]. Part of the total solar irradiation is transformed by the collectors to useful heat for the system. This energy is transferred, either to the heat pump, to the ice storage, or to the combi-storage. When the heat pump is running, two operation modes are possible, depending on whether the collectors are able to provide energy or not: i) the heat pump uses the solar energy directly in a series operation mode, meaning that collectors are used as heat sources or ii) the heat pump uses only the ice storage as its source. With the hydraulic set-up proposed here, when the heat pump is running with solar energy as a source, the mass flow from the solar collector field is divided: one part goes to the heat pump and the other part goes to the ice storage. The split of the mass flow is basically controlled by each circulation pump, i.e. solar pump and heat pump evaporator pump. If these mass flows are not equal, its difference will flow to the ice storage. On these conditions, if more energy is available from the collector field than is needed by the heat pump, the ice storage is also loaded while the heat pump is running. On the contrary, if the collector output is lower than the heat pump needs, both, the ice storage and the collector field are used to provide heat to the evaporator of the heat pump. If none of these heat sources are available, which means that the ice storage is full of ice and the solar radiation and the ambient temperature are very low, the temperature of the heat pump evaporator drops below the minimum allowed value and the heat pump stops. In this case, a direct electric back-up is used. A method to reduce the need of back-up in winter times is to send the whole mas flow from the collector to the heat pump. The idea is to use the collectors even if the temperature is lower than 0 ^{o}C[2]. This can be achieved with the proposed hydraulic scheme by setting the mass flow from the collector equal to the one demanded by the heat pump. This tends to reduce the working temperature of the circuit and as a consequence decrease the heat pump COP. However, it reduces the times where the ice storage is used and thus the times where the direct electric back-up is used. Usually, reduction of the time use of the direct electric back-up is compensated by the loss of heat pump performance.

2.2. System control

The system part on the secondary side of the heat pump, i.e. the heating distribution and the DHW-preparation, and the heat pump itself are controlled in a standard way. The brine cycle on the primary side, on the other hand, needs some special operation modes to decide how to use the solar heat. The backup needs to be controlled too, such that it runs when there is a heating demand in the building and the ice storage is fully iced (no source available for the heat pump). Further, season-based priorities regarding the use of the solar heat are implemented. The solar-ice system has a global control with three main priorities in the following hierarchy:

1. Use of direct solar heat to provide the space heat to the building without switching on the heat pump.
2. Switching on the heat pump when not enough energy is available in the combi-storage in order to provide space heat. When heat pump is on, solar energy is prioritized as energy source.
3. Use solar heat to load the combi-storage and ice storage when the heat pump is off. Loading the combi-store is usually referred as direct solar heat. Direct solar heat is usually prioritized in spring, summer and autumn, but in winter the loading of the ice storage is prioritized.

The control has to cope with the fact that the ice storage is a cold sink for a long time during the year. Unless a logic is implemented, that switches to loading of the combi-storage when appropriate, the ice storage would be loaded predominantly. The control mode that actively stops the loading of the cold storage and tries to divert the solar heat on a higher temperature level to the combi-storage is called warm storage priority. If the warm storage priority is not active, the control mode cold storage priority is on, which loads the ice storage. For small sized systems regarding collector field and ice storage it is usually a better option to use a cold storage

[1] All results shown in this paper are obtained with selective uncovered collectors.
[2] In this case the ice storage would provide a higher temperature, i.e. around 0 ^{o}C.

priority in winter in order to avoid the time when the direct electric back-up is needed. As soon as there is no risk to fully ice the storage, then warm storage priority should be used.

2.3. Performance indicators

The main performance indicator for the systems is the System Performance Factor calculated as described in Malenkovic et al. (2012):

$$SPF_{SHP+} = \frac{Q_{DHW} + Q_{SH}}{P_{el,T}} = \frac{Q_D}{P_{el,T}} \quad (1)$$

Q is the yearly heat energy demand and $P_{el,T}$ the total yearly electric energy consumption. The subscripts SHP, DHW, SH and D stand for solar and heat pump, domestic hot water, space heating, and total demand respectively.

The total electricity consumption is calculated as:

$$P_{el,T} = P_{el,pu} + P_{el,hp} + P_{el,cu} + P_{el,back-up} + P_{el,pen} \quad (2)$$

where the subscripts pu, hp, cu, aux and pen refer to circulation pumps, heat pump, control unit, back-up and penalties respectively. The symbol "+" in the $SHP+$ from Eq. 1 refers to the consideration of the heat distribution circulating pump in the electricity consumption. Therefore, the system performance indicator used in this work includes all circulation pumps of the system and also all thermal losses/gains from storages and piping. Penalties for not providing the heating demand at the desired comfort temperature are calculated according to Haller et al. (2012). $P_{el,aux}$ is the energy used from the direct electric back-up system.

3. System energetic performance with varying heat exchanger type and area

Dynamic yearly system simulations have been carried out for different heat exchanger areas and for two types of heat exchangers, capillary mats (CM) and flat plates with stainless steel (FP-SS). Simulations have been performed for ice storage volumes of 3 m^3, 4 m^3 and 5 m^3 and collector areas of 15 m^2, 20 m^2 and 25 m^2. All simulations are carried out using a single family house building located in Zurich with approximately 9.5 MWh of total heating demand for SH and DWH.

Results for the SPF_{SHP+} are shown in Fig. 3 as a function of the ratio between the heat exchanger area and the ice storage volume and as a function of the distance between heat exchangers. The same distances between heat exchangers are used both for CM and FP-SS. However, since FP-SS have almost twice the area[3] compared to CM, results for FP-SS are shifted towards higher A_{hx}/V_{ice} axis. Both heat exchanger types are able to provide very high SPF_{SHP+}, up to 6 for the sizes used in these simulations. System performances above 4[4] are always achieved if the collector area is $\geq$ 20 m^2. For collector areas in the order of 15 m^2, an SPF_{SHP+} above 4 can be achieved with CM and $V_{ice} = 4$ m^3 and with FP-SS if $V_{ice} = 5$ m^3. Using a collector area of 15 m^2 and an ice storage volume of 5 m^3 both heat exchangers are able to provide an SPF_{SHP+} above 4.

Very high system performances, in the order of 5 to 6, can be achieved with different component sizes. These results confirm the flexibility of the system concept, i.e. the same SPF_{SHP+} can be obtained using different configurations of ice storage volume and collector area. This allows to achieve a specific SPF_{SHP+} even if there are restrictions such as small cellar capacity or available roof area. However, there is a limit on the lowest size of the collector field since the solar-ice system is based purely on solar energy as heat source. The system flexibility of solar-ice systems was discussed in Carbonell et al. (2014). Of particular interest are results with 4 m^3, since this storage volume could fit in many cellars of single family homes using two separated storages of 2 m^3 allowing to achieve an $SPF_{SHP+} \geq 5$ with collector areas of 20 m^2.

[3] The two faces of the flat plate heat exchanger are considered as heat exchanger area.
[4] As a reference GSHP is used with an SPF_{SHP+} of 4.

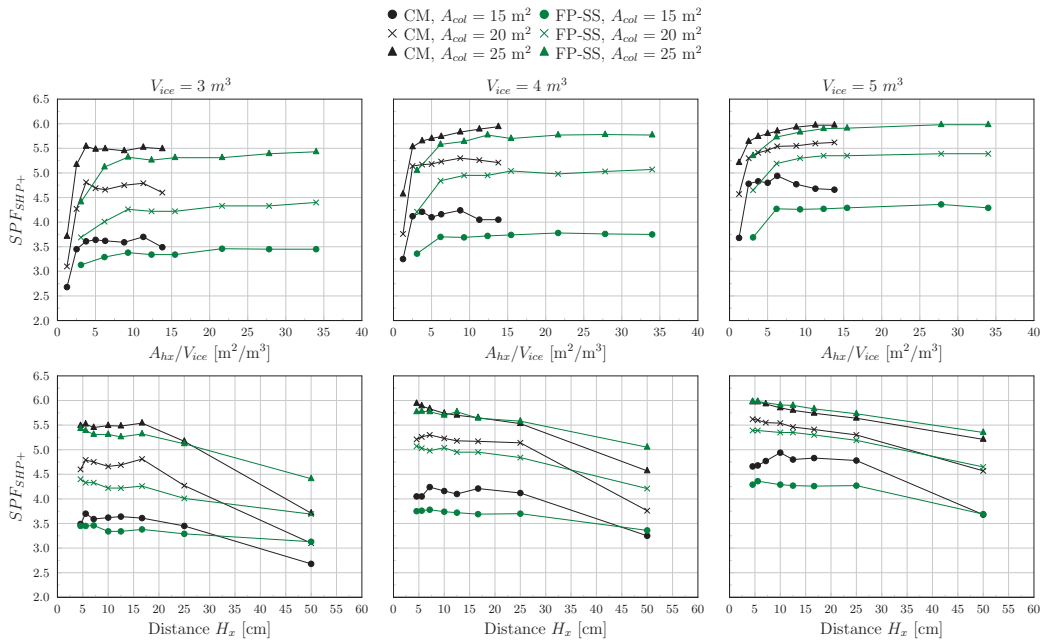

Fig. 3: Yearly system performance as function of (top) heat exchanger area divided by ice storage volume and (bottom) distance between heat exchangers for three ice storage volumes of (left) 2 m^3, (mid) 4 m^3 and (right) 5 m^3.

Regarding the heat exchanger type, the SPF_{SHP+} is usually higher for CM compared to FP-SS except for large distance between heat exchangers, e.g. $>$ 25 cm for V_{ice} =3 m^3. System performances for CM when distances between heat exchangers are small are higher because of the better heat transfer coefficient when icing at high ice fractions. The SPF_{SHP+} of CM is worse than that of FP-SS for cases where the distance between heat exchangers is way higher than that between the tubes in one CM. One can imagine a CM like a FP with empty spaces between tubes. Let's imagine the limit case where all tubes in one CM are in contact to each other. Under those circumstance CM would be worse than FP because of the higher resistance of polypropylene compared to stainless steel. When ice fills all the gaps between tubes, there is the added limitation that not all area is used due to the spaces between tubes.

Differences between FP-SS and CM are more prominent for low collector areas and low ice storage volumes. Results for 25 m^2 and 5 m^3 tend to an asymptotic solution where differences between CM and FP-SS are negligible. In those situations the direct electric back-up is not used because the system components are sized largely enough such that not all the latent heat capacity of the storage is necessary. The direct electric back-up is shown in Fig. 4 as a function of the ratio between A_{hx} and V_{ice}. Clearly, the increase of collector area and storage volume decrease the use of the direct electric back-up. The direct electric back-up is used exclusively in winter, when the ice storage if full (maximum ice fraction of 80 % has been assumed) and there is not enough solar energy to provide the heat for the evaporator of the heat pump. The use of the electric back-up is the dominant factor that influences the SPF_{SHP+}. In larger systems where the electric back-up is avoided, the system performance is quite independent of the heat exchanger area and less dependent on the collector area or ice storage volume. A SPF_{SHP+} value below 5.5 usually indicates the need of direct electric back-up.

In order to establish the optimum heat exchanger area in terms of SPF_{SHP+} it is of importance to investigate the maximum ice fraction achieved, as shown in Fig. 5. If the heat exchanger area is too low for the specific system design, some latent heat may not be used because the heat transfer coefficient will be too low at the maximum ice thickness achieved. This would lead to a situation where the heat pump would not be able to extract enough power from the ice storage while there is still liquid water present. For CM the maximum ice fraction of 80 % is reached approximately for ratios of A_{hx}/V_{ice} of 5-10 m^2/m^3. For FP the maximum ice fraction is reached at

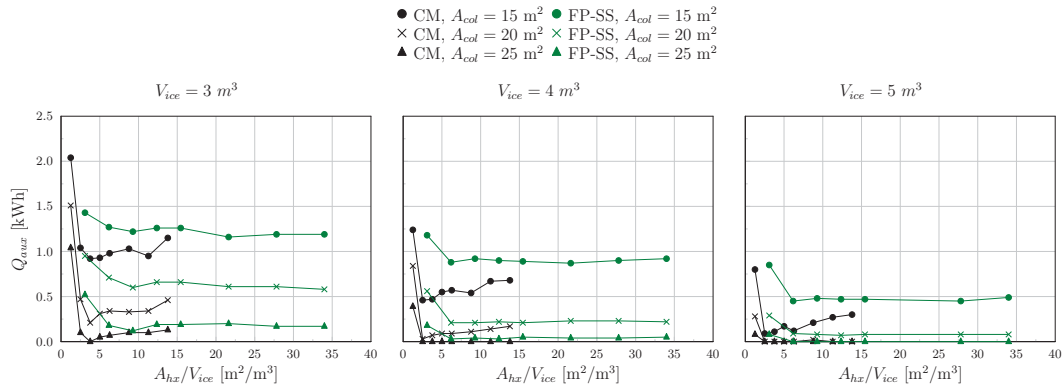

Fig. 4: Direct electric back-up as a function of heat exchanger area divided by ice storage volume for three ice storage volumes of (left) 2 m^3, (mid) 4 m^3 and (right) 5 m^3.

higher ratios of 10-15 m^2/m^3. For both cases these ratios correspond to a distance of around 7-12 cm between heat exchangers.

For some configurations, it is not possible to use all latent heat of the storage. For example for $V_{ice} = 5$ m^3 and $A_{col} = 25$ m^2, non of the heat exchangers setup can achieve an ice fraction of 80 %. This indicates that the system is oversized and either the ice storage or the collector area could be decreased and the system performance would not be penalized much. For example in Fig. 3 the $\text{SPF}_{\text{SHP+}}$ of $A_{col} = 25$ m^2 is almost the same if the storage volume is 4 m^3 or 5 m^3. Another way to make use of the latent heat and also to increase the $\text{SPF}_{\text{SHP+}}$ would be to give more priority to the warm storage loading.

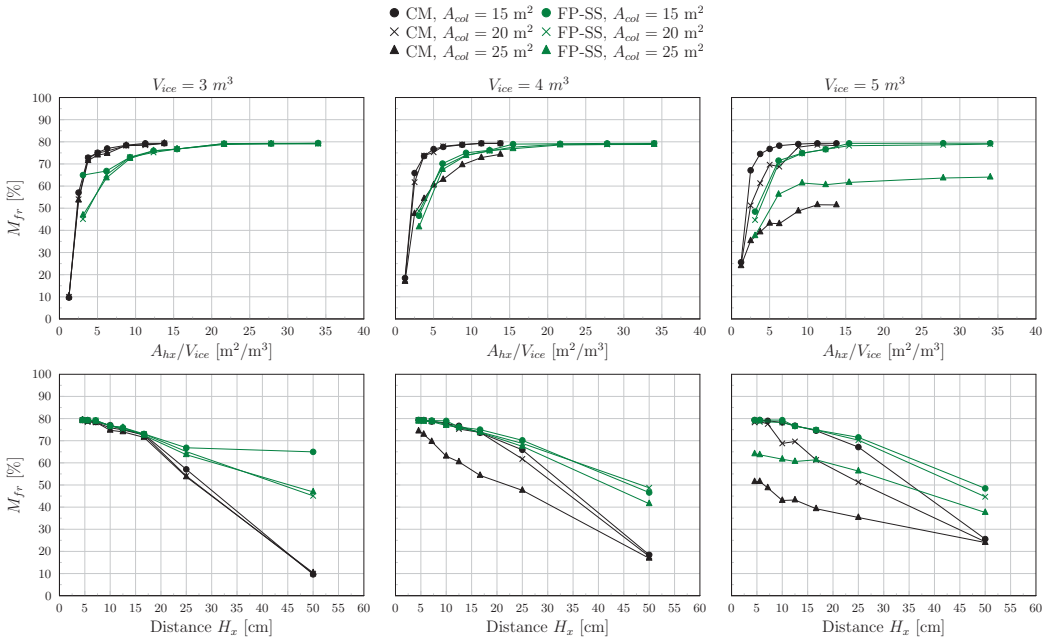

Fig. 5: Maximum yearly mass ice fraction as a function of (top) heat exchanger area divided by ice storage volume and (bottom) distance between heat exchangers for three ice storage volumes of (left) 2 m^3, (mid) 4 m^3 and (right) 5 m^3.

4. Cost analyses of solar-ice systems

In the section above the system performance in terms of energy has been provided. In this section, costs are taken into consideration in order to further evaluate different system designs. For all analyzed heating systems, investment costs and heat generation costs for prices of the Swiss energy market in 2016/2017 are calculated. The comparison of costs is used to find the optimum heat exchanger area considering both energetic system performance and a good value for the money.

The investment costs of the solar-ice systems are based on real costs that were gathered from several sources. Some data was obtained from the realization of two demonstration projects of solar-ice systems in Rapperswil-Jona, Switzerland. The data from the solar part was obtained from the SFOE project ReSoTech (Philippen et al., 2016). This data was used to derive cost functions per component. The cost functions are then used to calculate investment costs per specific system size simulated. All received cost functions were verified by a Swiss seller of heating systems in terms that they represent actual average market prices.

A ground source heat pump system is used as a reference to compare the system performance in terms of energetic efficiency and cost. Using a borehole length of 130 m for a single family house in the region of Zurich an SPF_{SHP+} around 4 is expected. Investment costs for GSHP are based on two offers of Swiss sellers for a GSHP system that supplies heat to a single family house (Causi, 2010). The cost functions were derived from average costs of the two offers. These two offers were used to estimate an uncertainty range on the heat generation cost. The average heat generation cost of a GSHP system based on the annuity is calculated as 39.6 $\pm$ 3.3 Rp./kWh.

For each system the present value of costs and the annuity are calculated following the methodology of VDI (2012) and Bangerter (1985) with some simplifications. Heat generation cost are calculated using the annuity factor. Main assumptions for the economic analysis are given in Table 1 and details for the calculation method were provided in Philippen et al. (2015). The electricity prices are taken from the price list of a regional Swiss utility and represent typical prices for small customers. The increase of electricity cost is based on the assessment of this utility. An interest rate of 2% is assumed, which represents an average interest used in credits for buying a house or for refurbishing it in Switzerland. An increase of the interest rate would shift all heat cost predictions to higher values, but differences between systems on the range of interest would be similar.

Tab. 1: Assumptions for calculation of heat generation costs.

Rate of interest	2.0 % p.a.
Analysis period	25 years
Yearly Maintenance	0.25 % of investment costs
Lifetime	25 years
Electricity costs (incl. VAT)	Fixed costs: 171 Fr. per year Variable costs: 0.13 Fr. per kWh
Increase of electricity costs	1 % p.a.

The system performance (top) and the heat generation cost (bottom) are shown in Fig. 6 as a function of the distance between heat exchangers for CM and FP-SS for $A_c = 15$ m^2 and all storage volumes analyzed in the section above. The SPF_{SHP+} is repeated here in order to compare directly graphs of SPF_{SHP+} and cost. The reference values for the GSHP system are included in all graphs. The objective is to achieve a solar-ice system with same or higher performance than GSHP and with similar heat generation costs. Therefore, the focus is on solar-ice systems with an $SPF_{SHP+} \geq 4$. It should be noted that cost calculations are based on offers for installations in single family houses that vary significantly among each other. Therefore, heat generation cost should be seen as orders of magnitude. To consider the large variation a 10% error band in the installation cost

has been assumed for all cases. The uncertainty range of the heat generation cost of the GSHP is estimated as 39.6 ± 3.3 Rp./kWh which can be visualized in Fig. 6 and 7 as a gray shadow area.

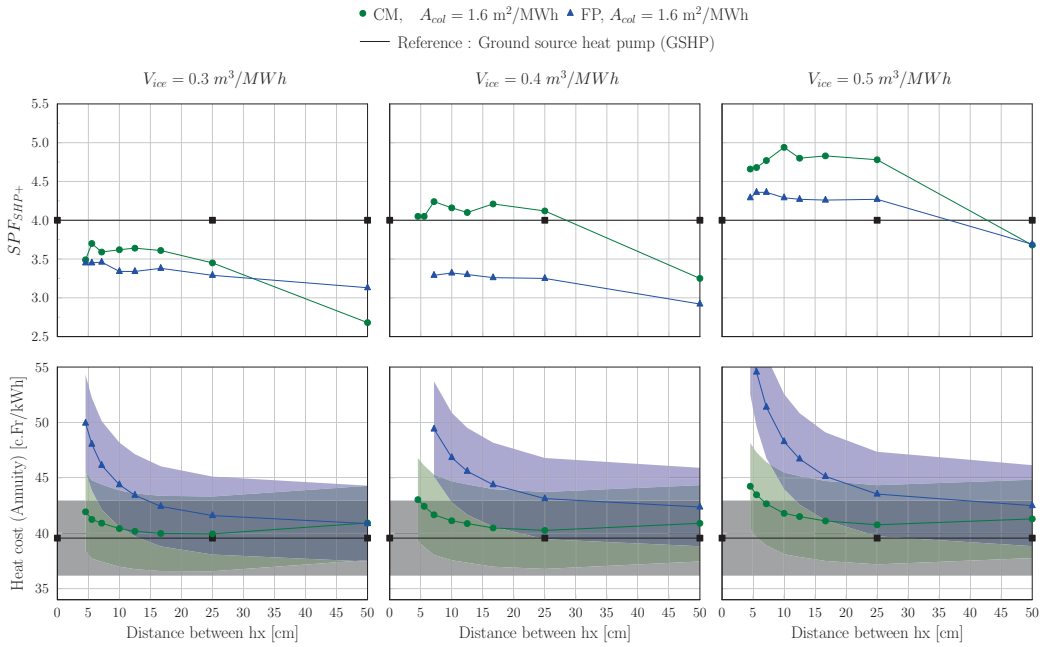

Fig. 6: System performance (up) and heat generation cost (bottom) as function of the distance between heat exchangers. Three ice storage volumes are used: (left) 3 m^3, (mid) 4 m^3 and (right) 5 m^3.

The heat generation cost calculated using the annuity factor are shown in bottom part of Fig. 6. There are two configurations where the $SPF_{SHP+} \geq 4$ and the heat generation cost are within the uncertainty range of the GSHP. Both configurations are using 15 m^2 of collectors, and 4 (CM) and 5 (CM and FP) m^3 storage volumes. These two system set-ups are of particular interest due to the cost comparable to GSHP and high efficiency. All systems using FP-SS show higher heat generation cost compared to CM. However, FP-SS are oxygen tight, and thus black steel can be used in the collector loop. In the other hand, CM made of polypropylene are usually installed with stainless steel pipes in the collector loop increasing its cost. Unfortunately, this cost difference has not been considered in the present calculation.

Using the cost function alone is not a good approach to decide on the heat exchanger area. For example, the lowest area seems to provide the cheapest system even when the energetic performance is relatively low. Thus, besides the cost function, the SPF_{SHP+} and also the maximum ice fraction achieved as shown in Fig. 5 should be used. Considering all these values it seems that the optimum heat exchanger area is in the order of 4-5 m^2/m^3 for CM and around 10-14 m^2/m^3 for FP-SS. Those ratios correspond to distances between heat exchangers of 12 - 17 cm for both heat exchanger types.

The heat generation cost along with the system performance are shown in Fig. 7 as a function of the collector area using a distance between heat exchangers of 16.6 cm. The heat generation costs increase linearly with collector area. The minimum of the cost function can not be observed with the simulated collector area.

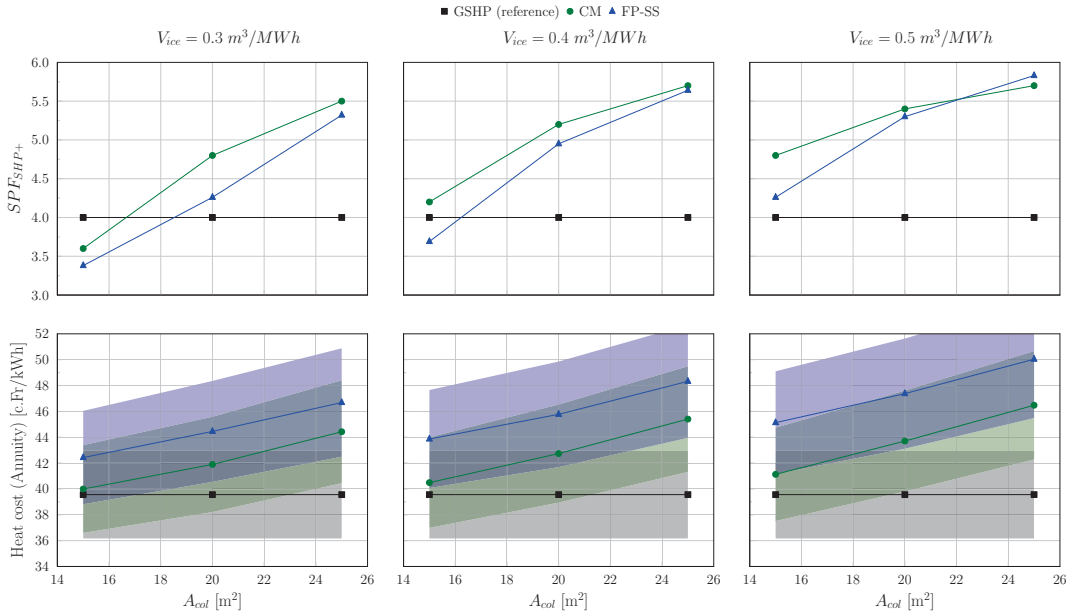

Fig. 7: System performance (up) and heat generation cost (bottom) as function of the collector area and ice storage volume for a distance of 16.6 cm between heat exchangers.

5. Conclusions

In this paper, the complete solar-ice system has been simulated with a well validated ice storage model from Carbonell et al. (2016a). From the system simulations the following conclusions can be drawn:

- A solar-ice system with ice storages volumes between 0.3 and 0.5 m^3/MWh (of total heating demand), and collector areas between 1.6 to 2.1 m^2/MWh can reach an SPF_{SHP+} in the range of 3.5 to 6 in Zurich for a single family home with 9.5 MWh total (SH + DHW) heating demand.
- Besides the sizes of the ice storage and collector field areas, the most relevant factor affecting the SPF_{SHP+} is the electric back-up necessary to run the system in winter periods. Control strategies should be focus on reducing it as a first target. When the electric back-up is minimized, control strategies should focus on the maximization of direct solar heat.
- Solar-ice systems can reach very high SPF_{SHP+} regardless of the heat exchanger type, but when the heat generation cost are included, capillary mats seem to be the most economic option. However, the heat exchanger area needs to be well design to reach these targets. An ice storage volume of 4 m^3 with capillary mats and 15 m^2 of collector area can reach an SPF_{SHP+} of 4.2, which represents an increase of SPF_{SHP+} of 5 % respect to GHSP with a similar heat generation cost.
- Considering both energetic and economic indicators, capillary mats are found to be the most promising solutions for solar-ice applications when compared to the other heat exchangers analysed along the project. Nevertheless, other factors could be used to choose other heat exchangers. For example, one may choose flat plates made of stainless steel instead of capillary mats due to the robustness of the heat exchanger, with a life time guarantee in the range of 25 years. Another reason to select stainless steel heat exchangers can be that they are oxygen tight and therefore an expensive stainless steel piping system in the collector loop can be avoided. The cost of the stainless steel piping system needed when plastic capillary mats are used could overcome the more expensive heat exchangers. However, this has not been considered in the cost calculations, where the piping system was the same for all heat exchangers.

- A strategy to reduce the direct electric back-up in small systems, e.g. using ice storages in the range of 0.3 - 0.4 m^3 per MWh of total heating demand and collectors areas in the range of 1.6 - 2.1 m^2/MWh, is to reduce the working temperature of the primary brine loop connecting the solar collectors, ice storage and heat pump. For those systems, priority should be set to use the collectors as primary source for the heat pump in winter, even that the working temperature decreases well below 0 ^oC. In those circumstances, the use of the ice storage would increase the instantaneous COP of the heat pump. However, it would increase the operating times of the direct electric back-up. The better instantaneous heat pump COP can hardly compensate the higher use of the electric back-up at a COP of 1. For larger systems, where the back-up is seldom used in winter, the control should give priority to the combi-storage. Those systems will have roughly an SPF_{SHP+} in the order of 5.5 or above. However, results form this paper suggest that only "small" sized systems with an SPF_{SHP+} around 4 - 4.5 could be cost competitive.

Acknowledgments

The authors would like to thank the Swiss Federal Office of Energy (SFOE) for the financing support received under the project Ice-Ex.

References

ASHRAE (2007). *Handbook : HVAC Applications*. American Society of Heating, Refrigerating and Air-Conditioning Engineers, Inc.

Bangerter, H. (1985). *Baukostendaten 1985, Rentenbarwert- und wahre Mittelwertfaktoren*. Band 1.

Carbonell, D., Battaglia, M., Daniel, D. P., and Haller, M. Y. (2017a). *Ice-Ex - Heat Exchanger Analyses for Ice Storages in Solar and Heat Pump Applications*. Institut für Solartechnik SPF for Swiss Federal Office of Energy (SFOE), Research Programme Solar Heat and Heat Storage, CH-3003 Bern.

Carbonell, D., Battaglia, M., Philippen, D., and Haller, M. Y. (2017b). Numerical and experimental evaluation of ice storages with ice on capillary mat heat exchangers for solar-ice systems. *International Journal of Refrigeration (submitted)*, -:–.

Carbonell, D., Granzotto, M., Battaglia, M., Philippen, D., and Haller, M. Y. (2016a). Experimental investigations of heat exchangers in ice storages for combined solar and heat pump systems. In *11^{th} ISES EuroSun Conference*, Palma (Mallorca), Spain. International Solar Energy Society (ISES).

Carbonell, D., Philippen, D., Granzotto, M., Haller, M. Y., and Frank, E. (2014). Simulation of combined solar thermal, heat pump, ice storage and waste water heat recovery systems. Design criteria and parametric studies. In *Proceedings of EuroSun*, Aix les Bains, France. International Solar Energy Society (ISES).

Carbonell, D., Philippen, D., and Haller, M. Y. (2016b). Modeling of an ice storage buried in the ground for solar heating applications. Validations with one year of monitored data from a pilot plant. *Solar Energy*, 125:398–414.

Carbonell, D., Philippen, D., Haller, M. Y., and Frank, E. (2015). Modeling of an ice storage based on a de-icing concept for solar heating applications. *Solar Energy*, 121:2–16.

Causi, A. (2010). *Simulation und Vergleich von Wärmepumpen-Heizungen welche Erdsonden respektive Eisspeicher und Solarkollektoren als Wärmequellenutzen*. Bachelor Thesis, Hochschule für Technik Rapperswil,Institut für Solartechnik SPF, Switzerland.

Europen Commision (2012). Energy roadmap 2050. Technical report, European Commision.

Haller, M. Y., Dott, R., Ruschenburg, J., Ochs, F., and Bony, J. (2012). The reference framework for system simulation of the IEA SHC Task44/HPP Annex 38: Part A : General simulation boundary conditions. Technical Report IEA-SHC Task44 Subtask C.

Kauffeld, M., Kawaji, M., and Egolf, P. W. (2005). *Handbook on Ice Slurries - Fundamentals and Engineering*. International Institute of Refrigeration (IIR), 1st edition.

Klein et al. (2010). Trnsys 17: A transient system simulation program, solar energy laboratory. Technical report, University of Wisconsin, Madison, USA, http://sel.me.wisc.edu/trnsys.

Malenkovic, I., Eicher, S., and Bony, J. (2012). *Definition of main system boundaries and performance figures for reporting on SHP systems*. IEA-SHC Task44 Subtask B.

Philippen, D., Caflish, M., Brunold, S., and Haller, M. Y. (2016). *ReSoTech - Reduction of Market Prices of Solar Thermal Systems due to New Technological Approaches – Phase 1: Analysis of Potentials and Possible*. Institut für Solartechnik SPF for Swiss Federal Office of Energy (SFOE), Research Programme Solar Heat and Heat Storage, CH-3003 Bern.

Philippen, D., Carbonell, D., Granzotto, M., Zenhäusern, D., Haller, M. Y., and Brunold, S. (2015). *High-Ice - System development for high solar thermal gains with ice storage and heat pump*. Institut für Solartechnik SPF for Swiss Federal Office of Energy (SFOE), Research Programme Solar Heat and Heat Storage, CH-3003 Bern.

Philippen, D., Haller, M. Y., Logie, W., Thalmann, M., Brunold, S., and Frank, E. (2012). Development of a heat exchanger that can be de-iced for the use in ice stores in solar thermal heat pump systems. In *Proceedings of EuroSun*, Rijeka and Opatija, Croatia. International Solar Energy Society (ISES).

VDI (2012). *VDI-Richtlinie, Economic efficiency of building installations, Fundamentals and economic calculation, Part 1*.

Combined solar thermal and heat pump systems within the funding program of large-scale solar thermal systems in Austria – Status investigation and progress report

Franz Helminger[1], Bernd Windholz[1], Christian Fink[2] and Samuel Knabl[2]

[1] Center for Energy/AIT – Austrian Institute of Technology GmbH, Vienna (Austria)

[2] AEE Intec, Gleisdorf (Austria)

Abstract

The Austrian "Klima- und Energiefonds" started 2010 a funding program for the development and further market penetration of large-scale solar thermal systems. The most interesting projects in terms of innovation were selected for a system monitoring, analysis and optimization of about 12 months by a scientific partner. Since 2010 about 25 combined solar thermal and compression heat pump systems (STHP systems) were selected within this framework and for eleven of these systems monitoring data is available. In this paper the selected systems are categorized and findings from the monitored systems are presented. Therefore, the performance of the systems is assessed with technical, economic and ecological parameters. In principle, the compression heat pump suits well to the solar thermal system to generate low temperature heat for space heating purposes and hot water preparation. The compression heat pump acts flexible and generates heat whenever the solar energy is not available. STHP systems show also a very positive effect for reductions of environmental impacts. But lack of standards for planning and realization leads to higher effort, higher risk and costs. Up to now the knowledge transfer by the scientific partners to the market players is essential for the further development of this technology.

Keywords: large-scale solar thermal system, compression heat pump, monitoring

1. Introduction

The Austrian "Klima- und Energiefonds" introduced a funding program for large-scale solar thermal systems in 2010 for innovative solar thermal concepts of between 100 and 2000 m² collector area. In this funding program the implementation of following concepts is addressed:

- Solar process heat applications
- Solar district heating systems
- Solar cooling applications (until 2015)
- Solar combisystems with high solar fractions of above 20 %
- Novel technologies and innovative concepts (since 2013)

A scientific consultancy in the application phase for the funding program ensures the high quality of the addressed systems. For the most interesting projects a system monitoring is done for a period of about 12 months. Therefore operating data is continuously recorded and analyzed. Based on this analysis the heat generation systems (solar thermal, heat pump, biomass, oil, etc.) and their controls as well as the heat distribution systems are optimized. Any existing cold supply is analyzed, as well. Conclusions of the system monitoring and optimizations are published.

Since 2010 about 25 combined solar thermal and compression heat pump systems (STHP systems) have been funded and selected for the monitoring. For eleven of these systems monitoring data of the entire period is available. In this paper the selected STHP systems are categorized and findings from the monitored STHP systems are presented. In chapter 2 an overview and categorization is given. In chapter 3 an assessment of the STHP systems by means of following parameters is shown:

- Specific solar gains
- Mean collector temperature

doi:10.18086/swc.2017.33.03 Available at http://proceedings.ises.org

- Seasonal performance factor (SPF) of the heat pump system
- Operation time and number of operating cycles of the compression heat pump
- Greenhouse gas impact measured by CO_2 equivalents and primary energy consumption

In chapter 4 the results are summarized and a conclusion is given.

2. Overview and categorization

Solar thermal systems and compression heat pumps can be combined in many ways. The possibilities how to combine these systems were analyzed and described within the IEA SHC Task 44 documented by (Paula 2014) and (Ruschenburg and Herkel 2013). The main categories are "parallel", "serial", "regenerative" and "complex" concepts. A short description of these four concepts is given in Tab. 1, Fig. 1 shows the energy flow schemes of the four concepts.

Tab. 1: Short description of different STHP concepts and their functionality

Concept	Short description
Parallel	Heat from the solar system and the heat pump is fed in one heat storage. The solar system and the heat pump work independent from each other, only coupled via the storage.
Serial	The solar system and the heat pump are hydraulically connected in a way, that the solar system delivers heat to the evaporator of the heat pump. This concept allows low temperatures in the solar system and the collectors act as air heat exchangers (ST+PV hybrid collectors and unglazed collectors).
Regenerative	The solar system delivers heat into ground heat exchangers to regenerate the ground. In that way heat from sunny periods is used in cold periods and the ground acts as seasonal storage.
Complex	Combination of parallel, serial and/or regenerative concepts.

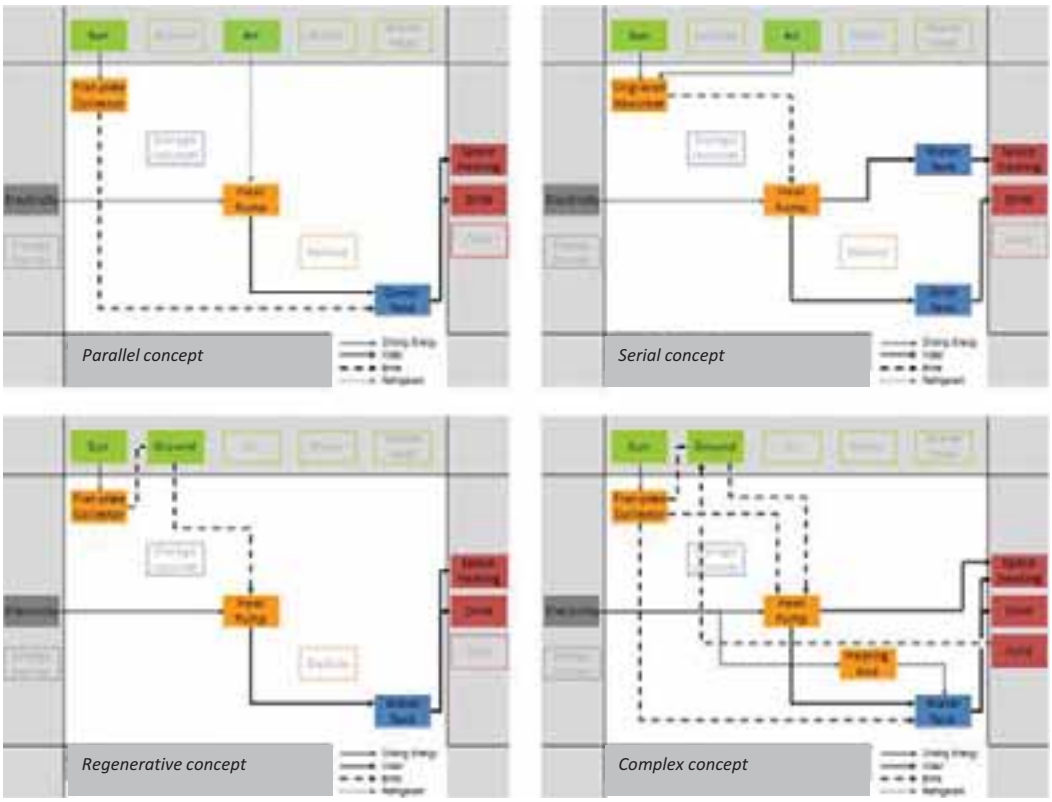

Fig. 1: Energy flow schemes of four STHP concepts by IEA SHC Task 44 (Paula 2014)

Of the 25 selected systems (sum of dark and light blue bars in Fig. 1), 19 (76%) STHP systems can be assigned as complex systems and six (24%) STHP systems as parallel systems. For eleven of the 25 selected STHP systems the monitoring is already finished and monitoring data of the entire period of 12 months is available (dark blue bars in Fig. 1). Ten of the monitored systems are complex systems and one system is a parallel system.

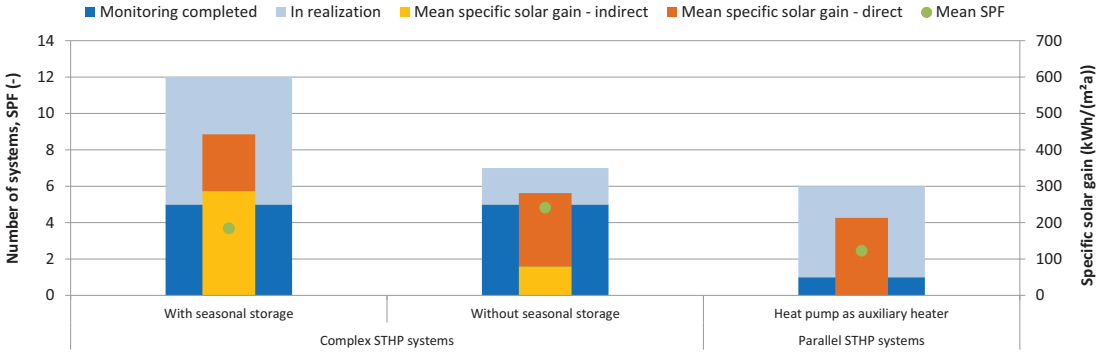

Fig. 2: Classification of selected STHP systems and overall results

For further distinction and better overview including the functionality following subcategories are established (see Fig. 1):

Complex STHP systems:

- Systems with seasonal storage
- Systems without seasonal storage

Parallel STHP systems:

- Systems with heat pump as auxiliary heater

The subcategory „systems with seasonal storage“ covers systems with horizontal ground collectors and depth probes. Heat from the solar system can be delivered to the ground and used by the heat pump. In “systems without a seasonal storage” systems are summarized where the combination of solar thermal and compression heat pump enables solar heat at the evaporator of the compression heat pump without a seasonal storage. Within the category “parallel systems” a (brine-to-water or air-to-water) heat pump acts as auxiliary heater to the solar system. 14 systems are in implementation (light blue bars in Fig. 1), seven of these systems are covered by the category “systems with seasonal storage”, two belong to “systems without seasonal storage” and five systems are “systems with heat pumps as auxiliary heater”. In three of five “systems with seasonal storage” with finished monitoring, the heat pump is used for heating and cooling and the seasonal storage is partly regenerated by the heat pump. The following assessment covers only heating mode of the systems.

3. Assessment

For the assessment of the specific solar gains and the mean collector temperature two different operating modes of the solar system are distinguished. The operating mode “direct” considers the solar gains and collector temperatures in periods where the heat is directly delivered to the respective use (e. g. space heating or hot water preparation) or to a short-term storage (i.e. buffer tank). The operating mode “indirect” includes solar gains and collector temperatures in periods where the heat is given to the evaporator of the compression heat pump or to a seasonal storage. The solar gains in the two operating modes are shown in Fig. 2, which also shows the mean seasonal performance factor (SPF) of the heat pump. The SPF is the ratio of the useful heat taken from the condenser of the compression heat pump divided by the electrical energy consumption of the compression heat pump. It is typically analyzed to assess the efficiency of a heat pump and gives also a value for the assessment of the economical operation. It was analyzed only for heating mode and not taking into account auxiliary devices like circulation pumps due to the fact that auxiliary devices need not to be measured regarding the funding scheme.

All STHP systems with completed monitoring are analyzed and the results are given at Fig. 3 to Fig. 5 for each subcategory. This graphs show the specific solar gains (direct and indirect operating mode), the mean collector temperature (direct and indirect operating mode) and the SPF as most significant parameter of the heat pump.

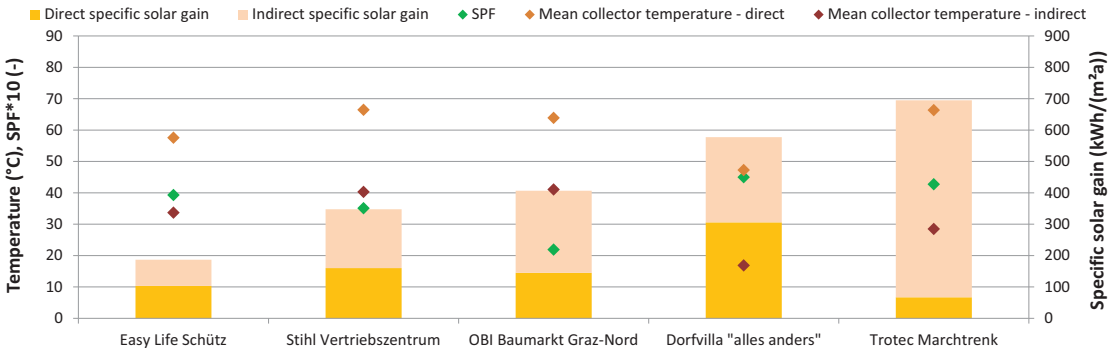

Fig. 3: Results of complex systems with seasonal storage

By means of the specific solar gains in ”direct” and ”indirect” operating mode different behavior of each STHP system is presented. In all STHP systems heat from the solar system in ”direct” operating mode is generated at a higher temperature level than in ”indirect” operating mode. The average of the mean collector temperature in ”indirect” operating mode is about 25 K lower than in ”direct” operating mode. With lower collector temperatures the efficiency of the solar collector and the solar gain increases. In many cases heat at lower temperature cannot be used directly and needs to be lifted by the compression heat pump. This operating mode causes an electrical energy demand. The higher the difference of the temperature of the heat source to the heat sink of the heat pump, the higher the electrical energy demand and lower the SPF.

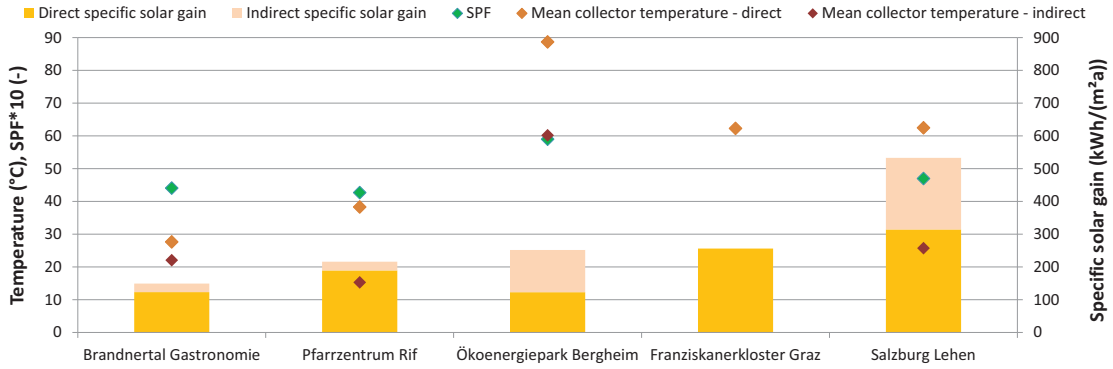

Fig. 4: Results of complex systems without seasonal storage

An optimization of the respective STHP system in consideration of diametrical optimization criteria (minimum electrical energy costs, maximum reduction of CO_2 emissions, etc.) is a sophisticated task and done by the operators with different optimization targets and different framework conditions (e.g. storage sizes, collector area, energy prices, etc.).

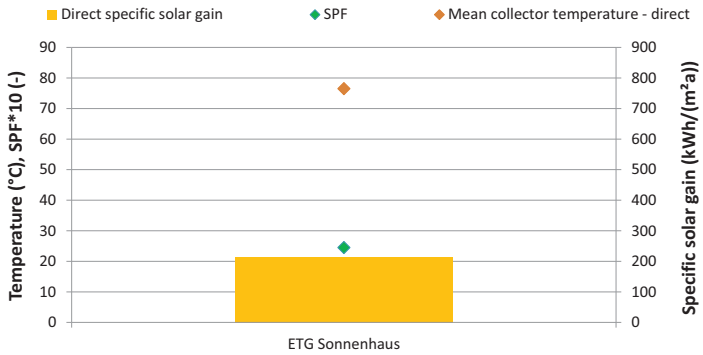

Fig. 5: Results of parallel systems with heat pump as auxiliary heater. In this specific case an air-to-water heat pump is used.

The specific solar gain differs significantly within each category. Even if the configuration of the STHP systems is similar within one category, each STHP system is planned, realized and operated individually (collector area, storage size, orientation of solar collectors, heat demand, temperature level of consumers, etc.). Therefore, it is not possible to give clear conclusions and generally applicable recommendations.

The monitoring results of the compression heat pumps are very good for almost all STHP systems, only at „OBI Baumarkt Graz-Nord“ and „ETG Sonnenhaus“ the SPF is low. At these two STHP systems, the operating conditions for the compression heat pumps are very unfavorable and therefore, a higher SPF cannot be reached. At the STHP system „OBI Baumarkt Graz-Nord“ the ground collectors are placed below a parking area and are not sufficiently insulated against outside air. The operating temperature of these ground collectors is very close to the outside temperature and especially in winter lower than expected. At the STHP system „ETG Sonnenhaus“ the air-to-water heat pump is operated only in December and January with a very high temperature lift from outside temperature to the heat delivery system.

The compression heat pump at the STHP system „Franziskanerkloster Graz“ was not operated during the monitoring period and therefore, the SPF can not be calculated.

A continuous operation of the heat pump is generally an advantage for an economical use. To assess the continuity of the heat pump operation of the STHP systems the yearly operation period, the mean operation period per activation in the monitoring year, the mean operation period per activation in the month with longest operation period and the number of activations per year are compared in Tab. 2. The mean operation period per activation in the monitoring year is between ten minutes and about ten hours. Very short operation periods per activation have negative consequences for the lifetime of the compressor(s) of the heat pump (lubrication gap has to be built up), and for the SPF, because on start up (takes at least one minute) the efficiency is lower than in steady state operation. Mean operation periods below 30 minutes are disadvantageous, but can not be avoided due to varying energy demands.

Tab. 2: Analysis of activation periods and number of activations of the compression heat pump

		Yearly operation period (h)	Mean operation period per activation in the monitoring year (min)	Mean operation period per activation in the month with longest operation period (min)	Number of activations per year
Systems with seasonal storage	Easy Life Schütz	2790	90	62	1868
	Stihl Vertriebszentrum	790	44	63	1074
	OBI Baumarkt Graz-Nord	313	14	21	1349
	Dorfvilla "alles anders"	1887	176	206	644
	Trotec Marchtrenk	1113	43	69	1536
Systems without seasonal storage	Brandnertal Gastronomie	570	10	10	3552
	Pfarrzentrum Rif	1067	24	32	2721
	Ökoenergiepark Bergheim	3055	114	371	1609
	Franziskanerkloster Graz	No heat pump operation during monitoring period			
	Salzburg Lehen	3744	567	781	396
Heat pump as auxiliary heater	ETG Sonnenhaus	146	194	182	45

Fig. 6 shows the results given in Tab. 2 and emphasises that due to different applications of the STHP systems and different share of energy from the solar system and the compression heat pump, a wide range of operation periods occured in the monitored systems. An example with continuous operation of the heat pump is given in

”Salzburg Lehen”, where the yearly operation period is long (3750 hours, about 5 month). The main reason for this behavior is that the capacity of the STHP system is very low compared to the energy demand. The STHP system covers a part of the base load, therefore, it is activated continuously.

During monitoring periods numerous improvement measures were implemented in the considered STHP systems. In some cases, due to planning mistakes (e.g. dimensioning of storage), just small improvements were possible. High effort would be necessary to correct such planning mistakes. In some STHP systems the heating capacity of the compression heat pump is too high compared to the energy demand or the storage size. This leads to short activation periods of the compression heat pump, because the compression heat pump is deactivated when the storage is loaded and no heat is needed. The dimensioning of the compression heat pump has to be done according to standards and is calculated to cover the energy demand at the coldest day of the year. To compare STHP systems the mean operation period per activation is assessed, on the one hand for the monitoring year and on the other hand for the month with the longest operation period. The mean operation period of the month with the longest operation period is normally longer than the mean operation period of the monitoring year. Only for the STHP systems „Easy Life Schütz“ and „ETG Sonnenhaus“ the mean operation period of the monitoring year is longer than the mean operation period of the month with the longest operation period. At both STHP systems the reason is the specific use of the buildings. The mean operation period should be longer than about 45 to 60 minutes. Otherwise, a compression heat pump with less capacity would be sufficient to cover the energy demand. Looking at the past years, the lowest outside temperature of each year was rising. Therefore, the nominal capacity of the overall heating system is rarely needed, the heating system is operated in partial load, and operating periods are shorter. A bigger but more expensive energy storage could improve the situation and lead to lower electrical energy demand of the heat pump.

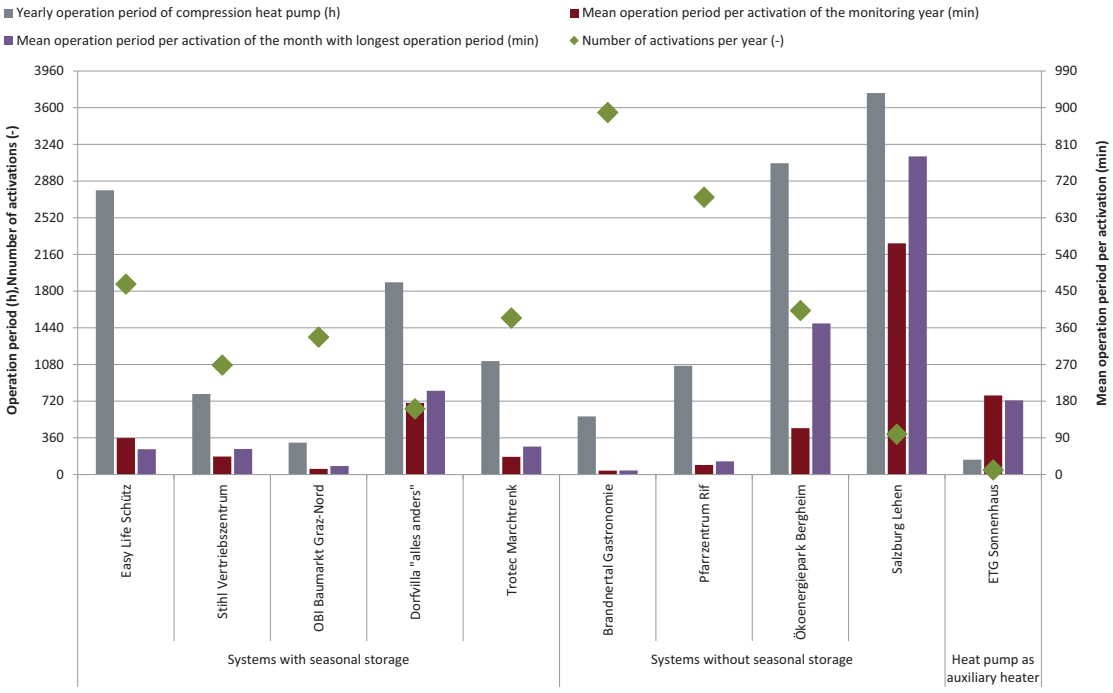

Fig. 6: Operation periods and activations of compression heat pump

STHP systems enable a reduction of negative environmental impacts (CO_2 emissions, primary energy consumption, etc.) compared to heating systems operated with fossil fuels. An ecological assessment of the yearly reduction of CO_2 equivalents and primary energy consumption was done by comparing the monitoring results to a reference scenario. Therefore, following assumptions were made:

- As reference scenario a gas boiler with 96 % efficiency was chosen.
- At STHP systems without any additional heating system (listed below) it was assumed that the gas boiler delivers the overall energy demand without storage losses.

Easy Life Schütz	Stihl Vertriebszentrum	OBI Baumarkt Graz-Nord
Dorfvilla "alles anders"	Trotec Marchtrenk	Pfarrzentrum Rif
ETG Sonnenhaus		

- At STHP systems with additional heating systems (listed below) it was assumed that just the energy delivered from the solar system and the heat pump is compared to the reference.

Brandnertal Gastronomie	Ökoenergiepark Bergheim	Salzburg Lehen

  This assumption neglects that the behavior of the additional heating systems is affected by the operation of the STHP system and the reference. At these STHP systems the heat pump operates as a booster and lifts low temperature heat to heat at temperature levels used by the heat consumers. It is neglected that the additional heating systems have an influence to the ecological emissions. As this paper wants to present the effect of the STHP systems, all these neglections cause a simplification of the analysis.
- The electrical energy consumption of auxiliary devices of the STHP systems was estimated out of the monitoring results as it was not measured. The electrical energy consumption of the auxiliary devices was assumed to be 3.5 % of the electrical energy consumption of the compression heat pump of each STHP system.
- At the STHP system “Franziskanerkloster Graz” the heat pump was not activated during the monitoring period. As there is an additional heating system, just the solar heat delivered to the entire system is compared to the reference. The electrical energy consumption of the auxiliary devices was assumed to be 3.5 % of the solar heat delivered to the entire system.

The CO_2 equivalents and primary energy consumptions for Austria and EU-25 (abbreviated EU) were determined for the reference scenario and the monitored STHP systems (see Tab. 3 and Tab. 4). Following factors from (Öko-Institut Freiburg) were used:

- Greenhouse gas emissions to air – CO_2 equivalent for natural gas in Austria
- Greenhouse gas emissions to air – CO_2 equivalent for natural gas in EU
- Greenhouse gas emissions to air – CO_2 equivalent for electrical energy in Austria
- Greenhouse gas emissions to air – CO_2 equivalent for electrical energy in EU
- Resource requirements – primary energy consumption ratio for natural gas in Austria
- Resource requirements – primary energy consumption ratio for natural gas in EU
- Resource requirements – primary energy consumption ratio for electrical energy in Austria
- Resource requirements – primary energy consumption ratio for electrical energy in EU

Tab. 3: Yearly reduction of CO_2 equivalents using emission factors for Austria and EU, respectively

		Yearly reduction of CO_2 equivalents (t)	
		Austrian energy mix	EU energy mix
Systems with seasonal storage	Easy Life Schütz	7.58	6.59
	Stihl Vertriebszentrum	44.05	38.34
	OBI Baumarkt Graz-Nord	91.01	73.94
	Dorfvilla "alles anders"	14.30	14.55
	Trotec Marchtrenk	38.14	40.47
Systems without seasonal storage	Brandnertal Gastronomie	4.07	3.65
	Pfarrzentrum Rif	9.71	9.83
	Ökoenergiepark Bergheim	312.18	311.55
	Franziskanerkloster Graz	20.10	21.27
	Salzburg Lehen	239.60	242.02
Heat pump as auxiliary heater	ETG Sonnenhaus	3.93	4.05

Tab. 4: Yearly reduction of primary energy consumption using consumption factors for Austria and EU, respectively

		Yearly reduction of primary energy consumption (MWh)	
		Austrian energy mix	EU energy mix
Systems with seasonal storage	Easy Life Schütz	29.82	19.46
	Stihl Vertriebszentrum	173.35	113.07
	OBI Baumarkt Graz-Nord	336.16	165.41
	Dorfvilla "alles anders"	65.06	63.91
	Trotec Marchtrenk	180.44	191.94
Systems without seasonal storage	Brandnertal Gastronomie	16.47	11.81
	Pfarrzentrum Rif	43.95	42.70
	Ökoenergiepark Bergheim	1394.78	1316.76
	Franziskanerkloster Graz	94.84	100.40
	Salzburg Lehen	1082.62	1048.22
Heat pump as auxiliary heater	ETG Sonnenhaus	18.09	18.22

The results of the assessment shown in Tab. 3 and Tab. 4 vary in a wide range due to the fact that the heat demands of the STHP systems are very different. The ecological improvement was additionally analysed by a comparison of relative improvements of each STHP system. Therefore, the ratio of the yearly reduction of emissions and primary energy consumption of the monitored STHP systems to the CO_2 emissions and primary energy consumption of the reference scenario was determined and is shown in Fig. 7 for CO_2 equivalents and in Fig. 8 for primary energy consumption. In both graphs the grey bars represent the reduction, if the STHP system was powered by the EU energy mix and the dark red bars represent the reduction, if the STHP system was powered by the Austrian energy mix. The reduction of CO_2 equivalents is between 40 % and 96 % for the EU energy mix, and between 53 % and 97 % for the Austrian energy mix. The reduction of primary energy consumption is between 19 % and 95 % for the EU energy mix, and 41 % and 96 % for the Austrian energy mix.

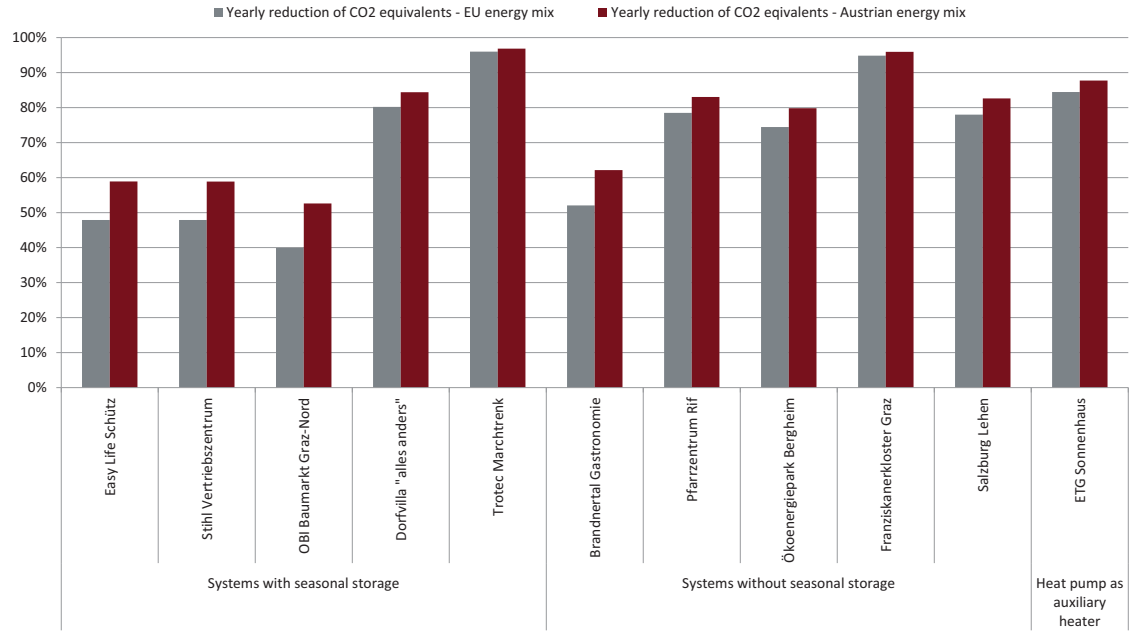

Fig. 7: Yearly reduction of CO_2 equivalents (Austrian and EU energy mix, respectively) by use of STHP systems compared to a gas boiler

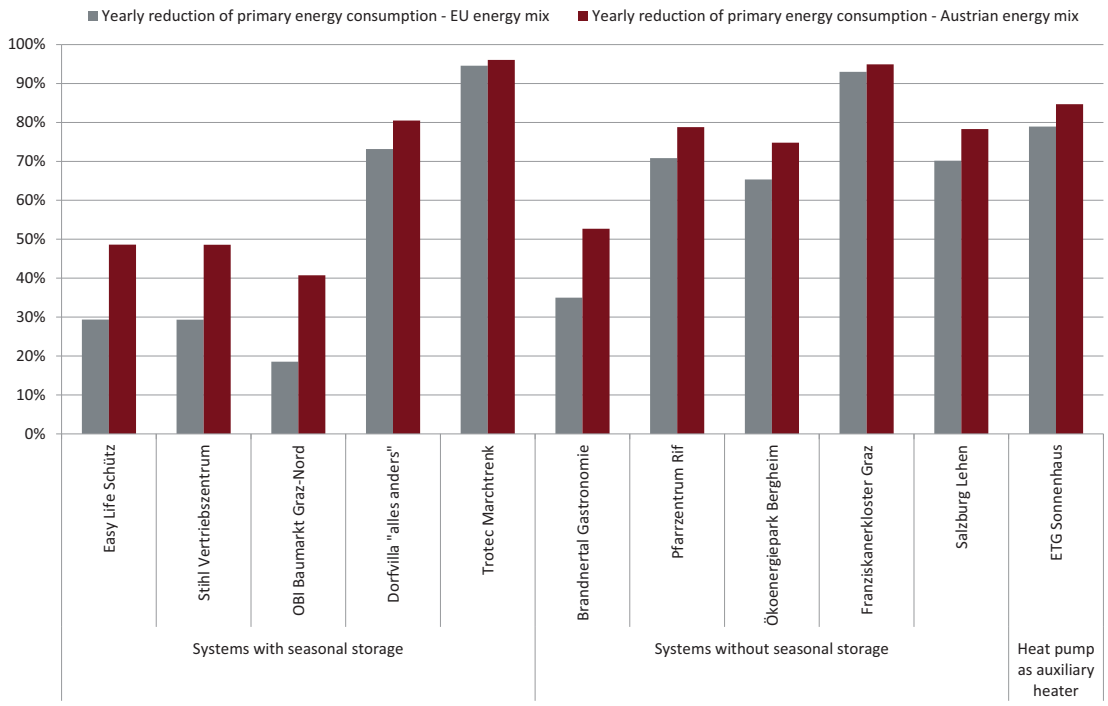

Fig. 8: Yearly reduction of primary energy consumption (Austrian and EU energy mix, respectively) by use of STHP systems compared to a gas boiler

4. Conclusion

The number of STHP systems within the framework of the funding program for large-scale solar thermal systems was increasing in recent years. Eleven systems are realized and monitoring results are available, additional 14 systems are selected and should be realized within coming years.

In principle, the compression heat pump suits well to the solar thermal system to generate low temperature heat for space heating purposes and hot water preparation. The compression heat pump acts flexible and generates heat whenever the solar energy is not available. STHP systems show also a very positive impact for reductions of environmental impacts.

Although experience in STHP systems is available for planers, installers, operators, and owners, the lack of standards for planning and realization leads to higher effort, higher risk and costs. Up to now the knowledge transfer from the scientific partners to the market players is essential for the further development of this technology. Within the framework of the funding program some planers with long-time experience apply for funding, but also planers with no or nearly no experience take part. For both groups tools, standards and guidelines for STHP systems would lower costs and risks. As the STHP systems are mainly composed for the individual situation, a detailed simulation is advantageous. Some of the planers do not take care of this and therefore the risk for mistakes and dissatisfaction occurs.

5. References

Öko-Institut Freiburg. *GEMIS: Globales Emissions-Modell integrierter Systeme*. Accessed September 22, 2017. http://www.umweltbundesamt.at/gemis.

Paula, M., 2014. IEA Solares Heizen und Kühlen Task 44: Solar und Wärmepumpensysteme. Bundesministerium für Verkehr, Innovation und Technologie, Vienna.

Ruschenburg, J., Herkel, S., 2013. A Review of Market-Available Solar Thermal Heat Pump Systems. A technical report of IEA SHC Task 44/subtask A, Fraunhofer ISE, Freiburg.

STEAMING PROCESS FOR SILICON ENRICHMENT IN ZEOLITES FOR HEAT PUMP APPLICATIONS AND SOLAR DRIVEN THERMAL ADSORPTION STORAGE

Thomas H. Herzog[1], Dr. Wolfgang Lutz[2] and Eric Weisheit[3]

[1] Technical University of Applied Science, Berlin / Wildau (Germany)

[2] Brandenburg University of Technology (BTU) Cottbus – Senftenberg, Berlin / Cottbus (Germany)

[3] InvenSor GmbH, Berlin (Germany)

Abstract

Silicon enriched zeolites of type DAY (dealuminated Y) have been investigated by BET-Isotherm measurements, infrared spectroscopy, thermogravimetric and water sorption measurements with respect to their characterization of crystal state and water uptake properties. Variation of the adsorption behavior of samples is a result of a steaming process at different temperatures in dependence of time. It was found that different Si/Al ratios affects the typical characteristic of the silicon enriched zeolites, relating to their ad- and desorption temperatures. In comparison with other usual DAY zeolites it was found a different microporous and mesoporous hierarchy of the pore system. As a result of the steaming process, the silicon enriched zeolites enable more possibilities of low temperature application under specific conditions.

Keywords: dealumination; water adsorption; zeolites; adsorption heat pump; thermal adsorption storage

1. Introduction

In recent years more and more new materials have been developed which are specifically adapted for applications in solar driven heat pumps or thermal adsorption storage processes. But actually low-temperature heat pumps gain in importance, due to the increasing necessity to provide cold in industrial processes. It is well known that thermally driven heat pumps are ecological much more efficient in comparison with electrically operated heat pumps. In conjunction with the use of renewable energies it is even possible to develop such a system as carbon-neutral alternative. Quite expensive materials such as silicoaluminophosphates (SAPO) find application in adsorption heat pumps which depend upon low-temperature heat for regeneration aluminiumphosphates (ALPO) have proven their operational capability in low-temperature heat pump applications, too. But silica gel is still most commonly used in those applications due to its low price. On basis of previous results, which have shown that dealuminated Y zeolites [1, 2] are possible substitutes for SAPO's and ALPO's, we redesigned the adsorption affinity of DAY zeolite to a bigger operating range for water vapor pressures level and capacity that it is actually needed in the process. This way offers the possibility to substitute materials of nearby all types.

From catalysis it is well known that a post-synthesis modification of zeolites by hydrothermal treatment [3] reduces the lattice aluminum concentration and improves the thermal stability and catalytic performance. A partial dealumination of the parent zeolite Y by steaming reduces the hydrophilic character of the zeolite as well as leads to a lower energy for water desorption. The observed healing process of the aluminium framework defects by silicon building units reduces the loss of microporous sorption volume.

The aim of this contribution is therefore to describe more in detail the steaming process and its influence on the water adsorption properties of DAY with respect to optimized adsorption/desorption heats and the influence on the secondary pore system hierarchy.

doi:10.18086/swc.2017.33.04 Available at http://proceedings.ises.org

2. Methods and materials

The adsorption properties of the potential heat pump application materials have been studied by different thermogravimetric methods (TG/DTA), the TG-programs for the H_2O desorption measurements started at 298 K and then followed by a heating range with 3 K/min up to temperature of 723 K, in permanent N_2 current of 1l/h. The samples where preconditioned for 48 h, at temperature of 298 K in a p/p_s=0,33 water atmosphere.

The investigated samples were also studied by gravimetric isotherm measurements using a McBain-Bakr quartz spring balance (tempered at 303 K). The high vacuum glass apparatus works in a pressure range between 10^{-5} up to 1013 mbar and in a temperature range between - 253K up to + 368K (± 0.1K). The apparatus has a measuring sensitivity of 4 mg / mm, with a amplitude of 0.01 mm measured with a Cathetometer. The minimum sample value is between 150 and 100 mg.

The BET nitrogen isotherms of the different DAY and parental NaY samples were measured with a Quantachrome NOVAe 2000e after outgassing the samples at a temperature of 623 K for minimum 2h.

The DAY samples were obtained by a steam treatment at 1 bar water pressure and temperatures of 673 K up to 973 K in dependence on time (1-5 h). The parent NaY zeolite with a framework Si/Al ratio of 2.6 was introduced into the active NH_4Y modification by ion-exchange. The resulting framework Si/Al ratios were characterized by infrared spectroscopic measurements using the specific double-ring vibration band at 278 cm^{-1} for the parent NaY sample for calculation.

3. Results and discussions

In Table 1 the chemical composition and adsorption capacity of the DAY samples are presented. For better overview and understanding the results of the parent zeolites NaY (Grace), SAPO-34 and Silica gel are included are presented, too. A moderate dealumination up to Si/Al=3.4 doesn't have a strong influence on the adsorption capacity, which is still comparable the reference materials that are used for heat pump applications actually. At higher Si/Al-ratios the water sorption capacity is reduced, for desorption temperatures up to 523 K. In contrast, the influence on the BET surface is quite strong. It depends on the operating temperature and healing time that is given during the synthesis. For the optimized synthesis condition process it is necessary to find a perfect combination of the three conditions temperature, healing time and Si/Al ratio.

Tab. 1: Si/Al-ratio and adsorption capacity of 48h in RH=33% (p/ps=0.33; 20.45 mbar partial water vapor pressure) conditioned samples, desorbed up to a temperature of 723 K, BET Surface.

Sample	Dealumination conditions	Si/Al	Adsorpt. capacity in g/g	BET Surface in m²/g
DAY1	673K; 1h	2.8	0.32	
DAY2	673K; 3h	3.1	0.31	
DAY3	773K; 1h	3.4	0.30	623
DAY4	773K; 3h	3.8	0.29	578
NaY		2.6	0.32	684
SAPO-34		-	0.30	630 - 650
Silica gel		-	0.20	600 - 700

From Fig.1 (see below) it is easy to find out, that the steaming process has a positive influence on the desorption capability of the modified Y-type zeolites. In spite of the difference of the desorption level that is reachable at 120°C by DAY2 and SAPO-34, the desorption kinetics of DAY2 seems to be better, due to the steeper slope of the TG-curve at the beginning.

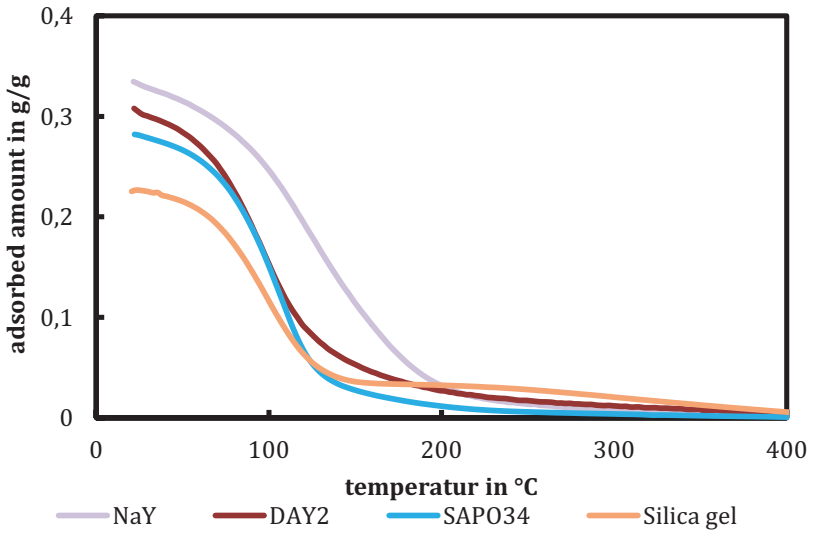

Fig. 1: Thermogravimetric profiles of the parent Y-zeolite, the dealuminated forms of Y-zeolite (DAY2) , SAPO34 and silica gel.

The low angel of the presented thermogravimetric profiles at a temperature above 200 °C is without interest for the relevant regeneration temperatures of those materials. But the clear shift from the light purple parental NaY to the dark red DAY2 curve shows that the dealuminating steaming process gives the opportunity to lower the regeneration temperature level and related to that the desorption time and performance of such a material.

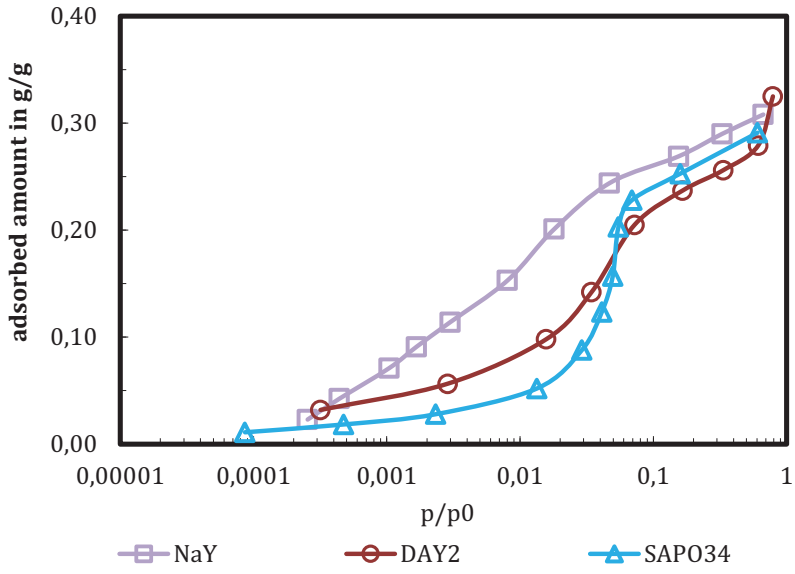

Fig. 2: Water isotherms of zeolite NaY, the dealuminated form of a Y-type zeolite and the zeotype SAPO-34 at 298 K.

The adsorption isotherms shown in Figure 2 of DAY2 and SAPO-34 show a similar beneficial steep rise in the usual working range for low temperature heat pimp applications. This results through the dealumination of the parental Y type zeolite (NaY). The Figure 2 gives also information about the position of the water isotherms of the dealuminated zeolite and the SAPO-34 compared with the parent NaY. As it can be seen, the DAY2

isotherm is shifted towards the SAPO-34 isotherm into the pressure interval between 0.01-0.3 mbar as the heat pump needs for low temperature applications.

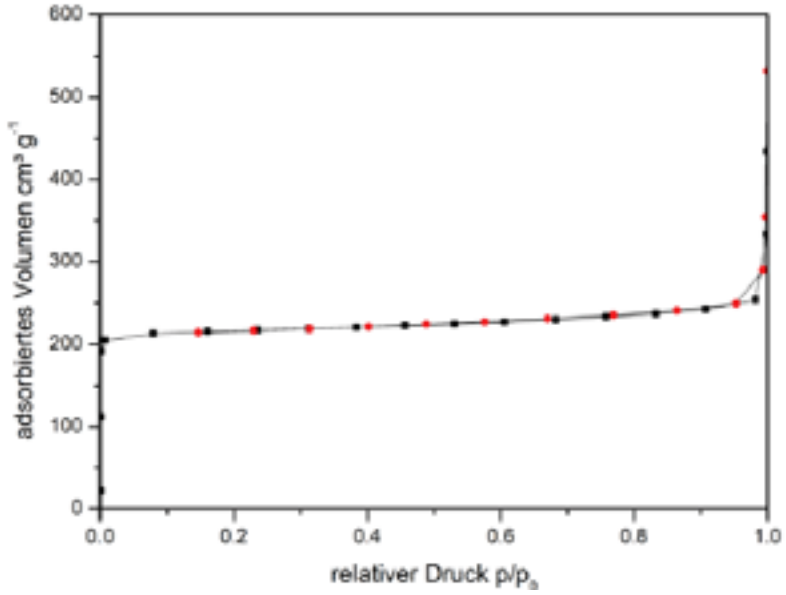

Fig. 3: Nitrogen isotherm of the parental NaY zeolite measured with a Quantachrome NOVAe 2000e after outgassing the samples at a temperature of 623 K for minimum 2h.

The influence of the dealuminting steaming process on the inner pore system of the Y-type zeolite is proven with the measurements given in Fig. 3 and 4 and the results illustrated in Table 2.The microporous inner pore structure is dissolving partly, through the influence of free H_3O^+ molecules, provided by the steaming process. Those molecules are able to remove the alumina part of the faujasite structure, in result the adsorption capacity is degrades slightly (see Tab. 1), the transformation of secondary pore system at the surface to a larger average diameter, has a positive influence on the mass transfer in and out of the material itself. Which explains the observed shift of the desorption temperature to the lower temperatures in Fig. 1. and a previous observation that the dealumination process improves the adsorption kinetic (not shown).

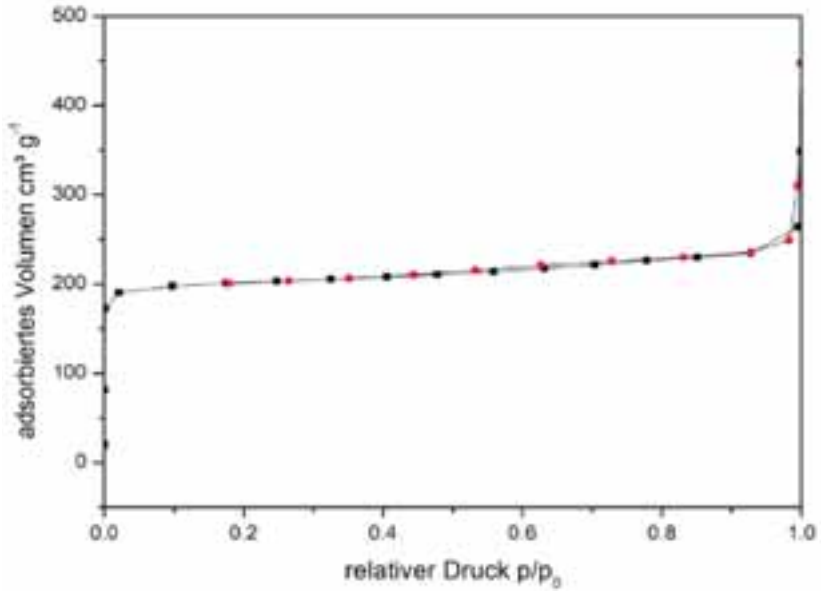

Fig. 4: Nitrogen isotherms of DAY3 zeolite measured with a Quantachrome NOVAe 2000e after outgassing the samples at a temperature of 623 K for minimum 2h.

Tab. 2: BET surface, pore diameter (BJH), pore volume (BJH), pore volume (p/p_0 = 0.97), micropore volume (t-Plot) micropore surface (t-Plot)

parameter	NAY	DAY3	DAY4	unit
BET surface	684 ± 20	623 ± 20	578 ± 20	$m^2\ g^{-1}$
pore diameter (BJH)	3,6	4,0	3,8	nm
pore volume (BJH)	0,49	0,40	0,48	$cm^3\ g^{-1}$
pore volume (p/p_0 0,97)	0,39	0,41	0,38	$cm^3\ g^{-1}$
micropore volume (t-Plot)	0,31	0,28	0,23	$cm^3\ g^{-1}$
micropore surface (t-Plot)	629	539	463	$m^2\ g^{-1}$

As it is shown in Table 2 the influence of the streaming process on the BET surface is quite strong. It depends on the operating temperature and the so called healing time (time for regenerating the disturbed inner lattice structure) that is given during the dealumination. For the optimized synthesis condition process it is necessary to find a perfect combination of the three conditions temperature, healing, time and Si/Al ratio (see Table 1).

4. Conclusions

The optimized post synthesis steaming process seems to be a powerful tool to tailor the hydrophilic character and the inner structure of Y-type zeolites and to reach the special needs of nearby all kind of heat pumps and storages.

Acknowledgements

We thank Dirk Enke (University of Leipzig) for the N2-isotherm measurements and the financial support by the German Federal Ministry of Education and Research, grant number 01LY1609B, is acknowledged.

References

[1] Kakiuchi H., Takewaki T. et al. (2002). Adsorption heat pump, and use of adsorption material as adsorption material for adsorption heat pump. 2002. European Patent Application, EP 1 363 085 A1.

[2] Jänchen J, Ackermann D, Stach H.. Adsorption properties of aluminophosphate molecular sieves – potential applications for low temperature heat utilization. In: Wang, R.Z., Editor, SHPC 2002, Int. Sorp. Heat Pump Con., Shanghai, 2002; 635-638.

[3] McDaniel, C.W., Maher, P.K. New ultrastable form of faujasite. In: Molecular Sieves, Soc. Chem. Ind., London, 1968; 186-194.

[4] Thomas H. Herzog, Jochen Jänchen, Eythymius M. Kontogeorgopoulos, Wolfgang Lutz. Steamed Zeolites for Heat Pump Applications and Solar Driven Thermal Adsorption Storage., Energy Procedia, Volume 48, 2014, Pages 380–383, SHC 2013

Model-based Analysis of Solar Thermal and Heat Pump Systems using TRNSYS

Danny Jonas[1], Danjana Theis[2], Josef Meiers[1] and Georg Frey[1]

[1] Saarland University, Chair of Automation and Energy Systems, Saarbrücken (Germany)

[2] htw saar, University of Applied Sciences, Saarbrücken (Germany)

Abstract

The combination of solar thermal and heat pump (STHP) systems is a promising hybrid concept for the efficient and sustainable energy supply of buildings. In general, the modeling and simulation of such complex energy systems is a challenging task as it requires expert knowledge in modeling as well as in the behavior of the real systems. As an alternative to the complex and lengthy general modeling process, a TRNSYS-based stand-alone tool is presented which enables users to analyze different predefined SHP concepts with hardly any knowledge in modeling and simulation itself. The predefined STHP concepts are explained in detail and the simulation results for a comparison of the performance of different system concepts are presented. The predefined systems are ground or air source heat pump systems with or without parallel integration of solar thermal collectors. In addition to earlier work, these system concepts are extended by solar thermal and ice storage heat pump systems. On the one hand, the simulation results show that in case of moderate climate and new as well as renovated buildings, solar thermal and air source heat pump systems can compete with ground source heat pump systems without solar integration and can achieve the same or even higher values of seasonal performance factors. On the other hand, the results show that solar thermal and ice storage systems are efficient solar thermal heat pump systems, which can achieve higher SPFs than air source heat pump systems and for new buildings even SPFs in the range of ground source heat pump systems. Furthermore, this contribution shows the advantages and the possible performance improvements by parallel integration of solar collectors in different system concepts.

Keywords: modeling, simulation, solar thermal, heat pumps, combined systems, performance, TRNSYS

1. Introduction

The combination of solar systems and heat pumps (HP) is a promising hybrid concept for the efficient energy supply of buildings. The notion combined solar and heat pump (SHP) system comprises basically all combinations of these systems, including photovoltaic (PV) and solar thermal (ST) systems. Combined solar thermal and heat pump (STHP) systems only comprise combinations with ST integration. Depending on the heat source of the HP, STHP systems can be divided in systems with ground source (SGSHP), air source (SASHP), ice storage (SISHP) and others, like combined solar and water source or waste heat source HP systems. Independently of the heat source of the HP, the systems can be classified in parallel, serial and regenerative system concepts by the interaction between ST system and HP (Frank et al., 2010). Parallel systems (fig. 1a) are systems with independent supply of useful energy for space heating (SH) and/or domestic hot water (DHW) preparation by the ST system and the HP. Serial systems (fig. 1b) are systems in which the ST system is used as heat source of the HP. Regenerative system concepts (fig. 1c) are systems in which the ST system is used for the regeneration of the main source of the HP, usually the ground. Furthermore, there is the possibility to combine these system concepts, as individual concepts do not exclude each other (Frank et al., 2010; Ruschenburg and Herkel, 2015). The classification in parallel, serial and regenerative system concepts (or combinations) can be indicated with -P, -S and -R at the end of the abbreviation of the general STHP concept, e.g., SGSHP-P means parallel combined solar thermal and ground source heat pump systems.

doi:10.18086/swc.2017.33.05 Available at http://proceedings.ises.org

During the past decade, a wide range of combinations of these systems entered the market. A statistical analysis on market-available STHP systems can be found in Ruschenburg et al. (2013) and Ruschenburg and Herkel (2013, 2015). As a main result, parallel systems were identified as the market-dominating system concepts with a proportion of 61% of the surveyed systems (Ruschenburg et al., 2013). Hence, the following investigations will focus mainly on parallel STHP systems with ground or air source HP and on HP systems without ST collectors. As addition, (serial and serial plus parallel) concepts with ice storage systems will be considered as solar only concept without additional heat source.

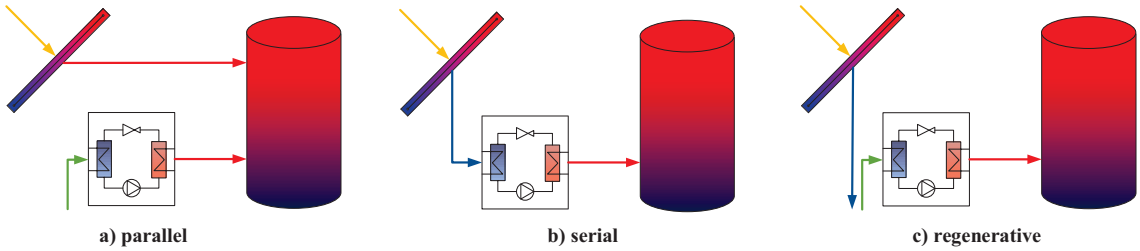

Fig. 1: Classification of solar thermal and heat pump systems in parallel, serial and regenerative system concepts

The variety of possible investigations on SHP systems requires well-validated simulation tools. One possibility to simulate these systems is the use of the simulation environment TRNSYS. Model design in TRNSYS is a complex task, which requires expert knowledge in different fields. The objective of this work, based on the former contributions published in Jonas et al. (2017a, 2017b, 2017c), is the development of a user-friendly TRNSYS-based simulation tool (SHP-SIMFRAME) which can be used for the simulation and the model-based analysis of different SHP concepts. In Dott et al. (2013) and Haller et al. (2013a), the International Energy Agency (IEA) Solar Heating and Cooling Programme (SHC) Task 44 / Heat Pump Programme (HPP) Annex 38 defined boundary conditions for a better comparability of results of STHP system simulations, which are also implemented in the simulation tool of this contribution (see section 3). At present, the tool contains four predefined STHP systems (GSHP, ASHP, SGSHP-P, SASHP-P). However, it will be expanded by SISHP systems and PV systems to analyze SHP concepts for heat and electricity supply of buildings. Overviews of simulation results of STHP systems within the IEA SHC Task 44 / HPP Annex 38 were provided by Haller et al. (2014, 2015). The authors presented summaries of simulations which were performed by different authors and different simulation platforms using the boundary conditions of IEA SHC Task 44 / HPP Annex 38. Investigations focused on SGSHP-P and SASHP-P systems can be found in Carbonell et al. (2014a, 2014b), Jonas et al. (2017a) and Poppi et al. (2016).

In the following sections, the system concepts (section 2) and the model design in TRNSYS as well as the developed TRNSED application (section 3) will be explained in detail. This is followed by a simulation study of the considered STHP concepts (section 4). Finally, section 5 provides the main conclusions and an outlook on further work.

2. System concepts

Fig. 2 shows the considered system concepts without ST collector integration (fig. 2a) and with parallel ST collector integration (fig. 2b) regardless of the heat source of the HP. The GSHP system consists essentially of a brine/water HP with borehole heat exchanger as heat source and a buffer storage tank as heat sink of the HP. The buffer storage tank is used for the energy supply of the SH system and the heat exchanger for DHW preparation. The HP charges the buffer storage tank in two different zones. The lower and middle zones of the storage are used for the SH circuit, the upper zone supplies the DHW circuit on a higher temperature level. Depending on the current demands, the heating by the HP is switching to the different zones with priority on DHW preparation. The SGSHP-P system corresponds to the GSHP system with additional solar loop. The solar collectors supply the buffer storage with solar energy via two internal heat exchangers depending on the current solar collector outlet temperature. If the temperature of the solar collectors is high enough, the upper heat exchanger is charged and the return of the upper heat exchanger is used as input for the lower heat exchanger. Otherwise, the solar collectors supply only the lower heat exchanger with solar energy. The advantage of this solution is to supply the upper

DHW zone of the storage with solar energy on a high temperature level, if possible, and thus avoid storage mixing and exergy losses and achieve better storage stratification. The ASHP system and the SASHP-P system correspond to the GSHP and SGSHP-P systems with a replacement of the GSHP by an ASHP. The SISHP-S systems correspond to the GSHP system with a replacement of the borehole heat exchanger by an ice storage, which is charged by solar absorbers, as heat source of the HP. The SISHP-S+P concept corresponds to the SISHP-S system with additional solar loop using solar collectors for the direct supply of the buffer storage tank (indicated by "-S+P" instead of "-S,P" which could be used for concepts with switching of solar absorbers from heat source to direct buffer storage (heat sink) charging).

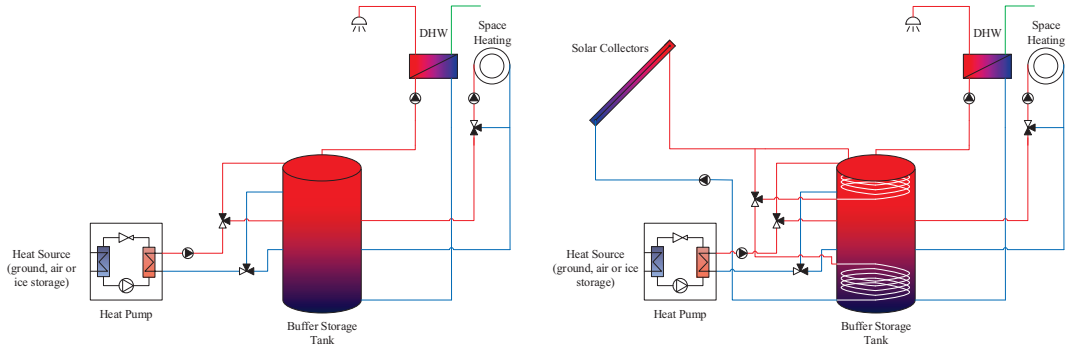

a) GSHP, ASHP and SISHP-S **b) SGSHP-P, SASHP-P and SISHP-S+P**

Fig. 2: STHP system concepts

According to the approaches in Frank et al. (2010) and Ruschenburg and Herkel (2015), visualizations of the energy flows of the considered STHP system concepts are shown in fig. 3. At this, flows of final energies, which are obtained externally (like electricity as driving energy for the HP), are shown on the left boundaries of the flow charts. The environmental energy sources (like sun, ground or ambient air) of the HP and the ST systems are shown on the upper boundaries. The useable energy output of the system (e.g. for SH or DHW preparation) is placed on the right boundaries. The system components (like HP, ST collectors or absorbers, thermal storages on the source or sink side of the HP and backup heating systems) have fixed positions and are highlighted if existing in the respective concepts. In case of the considered system concepts, the ST collectors (flat-plate collectors), the solar absorbers (uncovered collectors), the source side storage (ice storage), the HP and the sink side storage (buffer storage) are highlighted as well as the used environmental energy sources (sun and ambient air or ground). In addition, the electricity used as driving energy for the HP is highlighted as well. The energy flows between the components are shown as connections in the flow chart. The distinction between various carrier media is indicated by different types of lines.

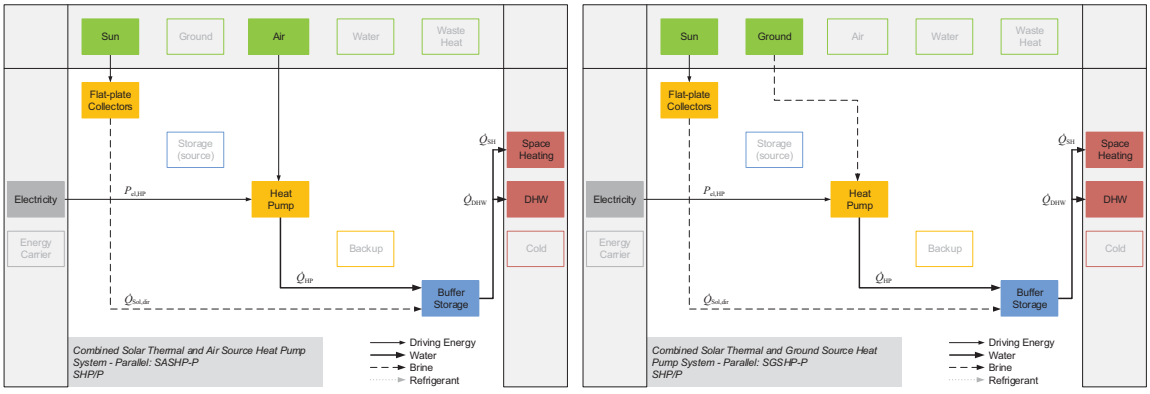

a) SASHP-P **b) SGSHP-P**

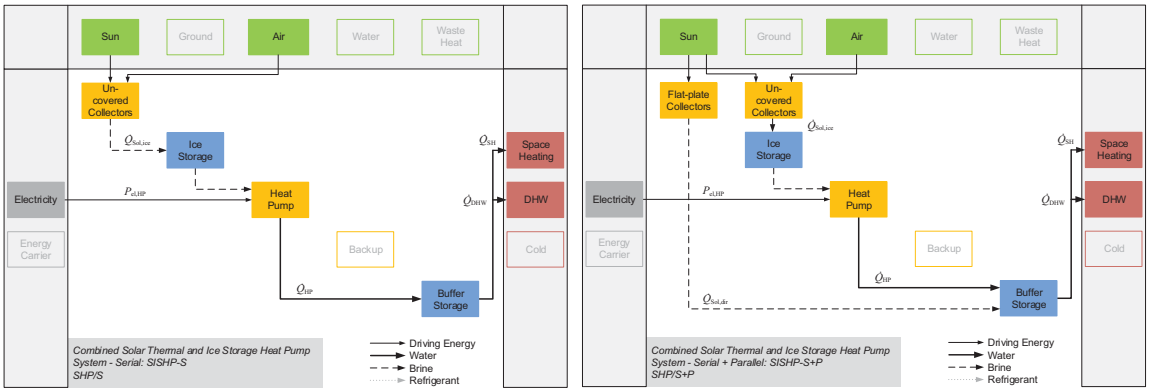

c) SISHP-S d) SISHP-S+P

Fig. 3: Visualization of energy flows in the considered solar thermal and heat pump system concepts

3. Model design and simulation framework

3.1 Background

The aim during the development of the TRNSED application SHP-SIMFRAME was to create a tool, which can be used for the simulation of SHP systems with hardly any knowledge in modeling or programming. The tool should be a user-friendly framework which can be used to perform parameter studies and analyses of SHP systems (e.g. for different locations and/or buildings) or test individual components (e.g. ST collectors or HPs) for the use in SHP systems by editing the component specific parameters and data sets. In its latest version, SHP-SIMFRAME contains GSHP, ASHP, SGSHP-P and SASHP-P system models. In future work, the tool will be expanded by SISHP systems including the TRNSYS models used for the simulation study of this contribution. Furthermore, as the name "SHP"-SIMFRAME implies, it will be extended by electrical solar energy (PV and PV thermal) systems to analyze SHP concepts for the heat and the electricity supply of buildings.

3.2 TRNSYS models

The simulation models of the main system components, especially the SHP system components, in TRNSYS are summarized in tab. 1. For a better structure and a higher level of modularity and flexibility, the TRNSYS model is divided in the subsystems *Reference System and Storage*, *SHP* and *SHP Control*. The subsystems include TRNSYS equation blocks, which are used as inputs and outputs of the subsystems for their connection via variables (see Kuethe et al., 2008). The subsystem *Reference System and Storage* include the reference system of the IEA SHC Task 44 / HPP Annex 38 (including boundary conditions and building model) and the Multiport-Store Model Type 340. General boundary conditions contain weather data for three different locations which represent warm (Athens), moderate (Strasbourg) and cold (Helsinki) climates (Meteonorm, 2009)[1] and ground properties for the simulation of ground coupling losses of the building and ground heat exchangers (Haller et al., 2013a). Within the reference framework, three different buildings are defined. The different buildings represent single-family houses (SFH) with heat loads for SH of 15 kWh/m²a (SFH15), 45 kWh/m²a (SFH45) and 100 kWh/m²a (SFH100) for the climate of Strasbourg. SFH15 represents a new building with very high energetic quality, SFH45 a renovated building with good thermal quality of the building envelope and SFH100 a non-renovated existing building. The boundary conditions also include the design supply and return temperatures of the heat distribution system for SH for the different locations and buildings (Dott et al., 2013) as well as the DHW draw off profiles. The DHW draw off profiles correspond to an average draw off of 140 l per day with a draw off temperature of 45 °C and are equivalent to an energy consumption for DHW preparation of 5.845 kWh/d with a cold water temperature of 10 °C. According to the boundary conditions of IEA SHC Task 44 / HPP Annex 38, the borehole heat exchangers are simulated as double-U pipes. The main properties of the borehole heat exchangers

[1] The permission of Meteotest for using Meteonorm climate data for simulations within the IEA SHC Task 44 / HPP Annex 38 is gratefully acknowledged.

are also defined within the framework (Haller et al., 2013a). The annual heat loads for SH (Q_{SH}) and DHW preparation (Q_{DHW}) for the climate of Strasbourg and the different buildings are summarized in tab. 2. Further information on the reference system, boundary conditions and building models can be found in Dott et al. (2013) and Haller et al. (2013a, 2015).

Tab. 1: TRNSYS models of the main system components

Component	TRNSYS Model
Building	Type 56 (TRNSYS, 2014)
Solar collector / absorber	Type 832 (Haller et al., 2013b)
Compressor HP	Type 401 (Wetter and Afjei, 1997)
Borehole heat exchanger	Type 557a (TESS, 2014)
Buried ice storage tank	Type 343 (Hornberger, 2006)
Multiport storage tank	Type 340 (Drück, 2006)
Single speed pump	Type 3d (TRNSYS, 2014)
Variable speed pump	Type 803 (Heimrath and Haller, 2007)
Pipe	Type 31 (TRNSYS, 2014)
Bi-directional noded pipe	Type 604a (TESS, 2014)
Buried noded pipe	Type 952 (TESS, 2014)
Flow diverter	Type 11f (TRNSYS, 2014)
Tee-piece	Type 11h (TRNSYS, 2014)

Tab. 2: Annual heat loads for SH and DHW preparation

Location	Building	Q_{SH} [kWh/a]	Q_{DHW} [kWh/a]
Strasbourg	SFH15	2474	2076
	SFH45	6476	2076
	SFH100	14031	2076

In general, the *SHP* subsystem includes the HP and the heat source models. In case of *GSHP* systems, the subsystem contains the components for the heat source circuit, the brine/water HP, the pump for buffer storage charging and the pipes from the HP to the storage. The heat source circuit consists of the vertical borehole heat exchanger, the heat source pump, buried pipes and an additional circuit with adiabatic pre-pipe in front of the input of the borehole heat exchanger. The adiabatic pre-pipe is used for a better representation of the short-term behavior of the borehole heat exchanger in the simulation due to missing short-term heat capacity effects of Type 557. More information on the pre-pipe concept, the model validation and parameterization rules can be found in Bertram (2015) and Pärisch et al. (2015). In case of *ASHP* systems, the subsystem includes the air/water HP, the pump for buffer storage charging and the pipes from the HP to the storage. In case of *SISHP-S* systems, the subsystem contains the components for the heat source circuit, the brine/water HP, the pump for buffer storage charging and the pipes from the HP to the storage. The heat source circuit consists of the buried ice storage tank model, the heat source pump to the HP, buried pipes and an additional solar absorber circuit with solar absorber circuit pump and pipes from the solar absorber to the ice storage tank for ice storage charging. Furthermore, in case of systems with parallel ST (flat-plate collectors) integration (*SGSHP-P*, *SASHP-P* and *SISHP-S+P*), the subsystems contain an additional solar loop with ST collectors, solar circuit pump and pipes from the solar collectors to the buffer storage. Using the example of a SGSHP-P (fig. 4a) and a SISHP-S (fig. 4b) system, the subsystem SHP is shown graphically in fig. 4. The subsystem *SHP control* includes the control of the HP and ST system and consists of a combination of differential controllers (Type 2b) and equation blocks. Due to their simplicity, the subsystems of SHP control are not shown graphically. The used control strategies and parametrization possibilities are described in section 3.3.

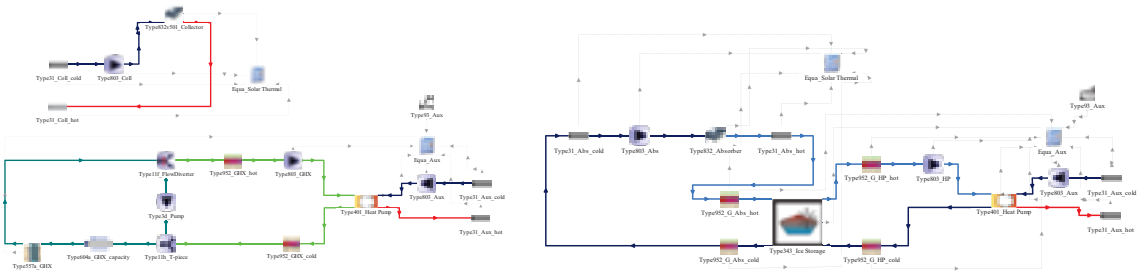

a) SGSHP-P **b) SISHP-S**

Fig. 4: TRNSYS Subsystem SHP

3.3 TRNSED application

The developed TRNSED application for the simulation of SHP systems are based on the TRNSYS models illustrated in section 3.2. In addition to a navigation page (see fig. 5a) as initial interface, the tool consists of the submodules *Simulation Parameters*, *Climate and Building*, *Solar Collectors* (in case of ST integration), *Heat Pump* (*and Ground Source* in case of GSHP, SGSHP-P), *Storage Tank*, *Controllers* and *Outputs* for the parameterization of the simulation models. The submodules of the tool and the assignments to the TRNSYS subsystems mentioned before are illustrated in fig. 5b. In future work, an Ice Storage submodule will be added for the simulation of SISHP-S and SISHP-S+P systems.

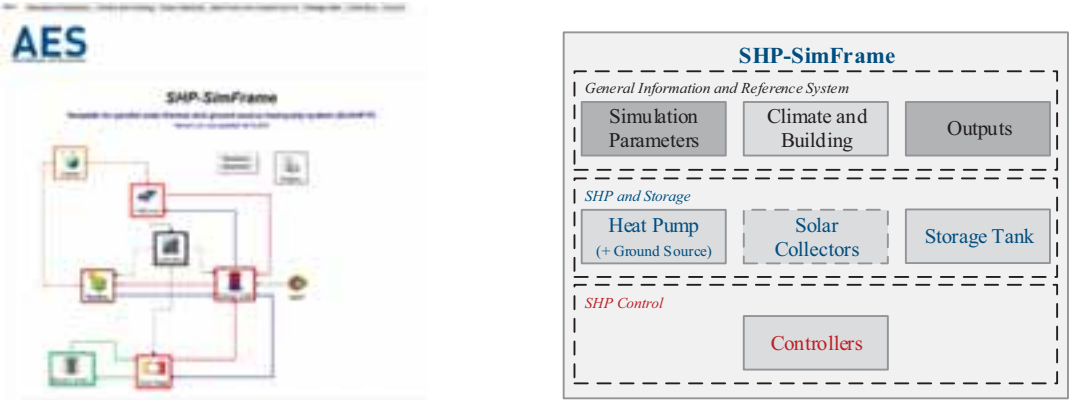

a) Navigation page, example: SGSHP-P **b) Submodules**

Fig. 5: TRNSED application as stand-alone tool

The submodule *Simulation Parameters* can be used to set general simulation parameters like the simulation time step and length depending on the simulation requirements. The submodule *Climate and Building* allows the user to choose the pre-defined climate data (Helsinki, Strasbourg and Athens) and the building type (SFH15, SFH45, SFH100) from a pull-down menu. The *Outputs* submodule contains a selection of predefined outputs, which can be selected for the graphical (plotter) and data file (printer) based evaluation of the simulation results. The *Storage Tank* submodule is used to set the general thermal storage parameters (volume, initial tank temperature, insulation thickness and additional loss factors) and the relative heights of the temperature sensors for the control of the SHP system. This includes temperature sensors for storage protection, for collector loop control as well as for charging of the DHW zone and the SH zone. In addition, within this submodule, the user can specify the relative heights of the storage tank connections. This includes in general the relative heights of the HP connections (for reheating the SH zone and DHW zone) and the SH and the DHW supply connections. In case of ST integration, the submodule also includes the relative heights of the connections to the solar loop. In general, the *Heat Pump* submodule contains a pull-down menu to select data sets, which are used in Type 401 for the HP modeling, and the definition of HP parameters like power, heat exchanger temperature differences of the HP, mass flow rates, set points of low-pressure and high-pressure thermostat or heat-up and cool-down constants. In addition, within this submodule, the user can specify the piping between the HP and the storage tank. In case of ASHP systems, the user has the possibility to define additional parameters for a better consideration of icing and defrosting effects. Furthermore, in case of GSHP systems, this submodule allows the user to define ground properties and borehole properties like number and depth of the boreholes, space between boreholes or the length of buried pipes between ground heat exchanger and HP. In case of STHP systems, SHP-SIMFRAME includes the submodule *Solar Collectors*. This module allows the user to define the solar collector field (area, tilt, azimuth and specific mass flow) and the collector loop pipes properties as well as the solar collector efficiency parameters. The submodule *Controllers* can be used to set the control parameters for the solar loop and the reheating of the storage tank for SH and DHW preparation by the HP. The set point calculation of the supply temperature $T_{Set,SH}$ for SH depends on different factors (e.g. the ambient temperature or the design heat load of the specific building and location) and is described in Dott et al. (2013). The HP buffer storage charging for SH is turned on if the difference between the storage temperature sensor for SH ($T_{S,SH,up}$) and the set point for the supply temperature $T_{Set,SH}$ for SH falls below $\Delta T_{SH,on}$

(predefined: 0 K) until the temperature difference is higher than $\Delta T_{SH,off}$ (predefined: 3 K). The buffer storage charging for DHW depends on the value of the storage temperature sensor for DHW preparation ($T_{S,DHW}$) and is turned on if the temperature falls below $T_{DHW,on}$ (predefined: 53 °C) until it reaches $T_{DHW,off}$ (predefined: 55 °C). In SGSHP-P and SASHP-P systems, the solar loop is switched on if the difference between the supply temperature of the ST collectors (T_{Sol}) and the storage temperature sensor ($T_{S,c}$) is higher than $\Delta T_{Sol,on}$ (predefined: 5 K) and will remain on until the temperature difference falls below $\Delta T_{Sol,off}$ (predefined: 2 K). If the difference between T_{Sol} and $T_{S,DHW}$ is higher than $\Delta T_{Sol,DHW,on}$ (predefined: 5 K), the upper heat exchanger is additionally charged by the solar loop and the return of the upper heat exchanger is used for the supply of the lower heat exchanger (DHW mode) until the temperature difference falls below $\Delta T_{Sol,DHW,off}$ (predefined: 2 K). Otherwise, the ST collectors supply only the lower heat exchanger with solar energy (SH mode). In addition, for storage protection, a maximum storage temperature ($T_{Set,S,max}$, predefined: 80 °C) of the storage temperature sensor for storage protection ($T_{S,sp}$) is defined (storage protection mode). Furthermore, a high limit cut-out for the ST collector temperature is defined in the controller to avoid damage of the components in the solar circuit if the supply temperature of the ST collectors (T_{Sol}) reaches $T_{Set,Sol,max}$ (predefined: 130 °C). In this case (ST protection mode), the solar loop is turned off until T_{Sol} falls below a defined temperature $T_{Set,Sol,max,off}$ (predefined: 120 °C).

4. Simulation study

4.1 Parameter

An exemplary application of the model-based analysis of STHP systems is the investigation of the influence of system concepts on the seasonal performance factor (SPF, see section 4.2). The performed TRNSYS simulations consider GSHP, ASHP, SGSHP-P and SASHP-P (using SHP-SIMFRAME) as well as SISHP-S and SISHP-S+P systems. The simulations were performed for SFH15, SFH45 and SFH100 and the climate of Strasbourg with variations of the solar collector area (or absorber area in case of SISHP systems) with a maximum available roof area of 25 m². The main model parameters for the simulation of the HP, the solar collectors and the solar absorbers are summarized in tab. 3-6. In case of SFH100, characteristics of market available air/water HPs and brine/water HPs were used as data basis for the parameterization of the HP models. In case of SFH15 and SFH45, the power data was down-scaled to a nominal heating power of 6 kW due to a better fitting of the design heat loads.

Tab. 3: Key values of brine/water heat pump models, performance data based on data sheets of Viessmann BW301.B10 (Viessmann, 2017)

Parameter	Value
COP at B0/W35 [-]	5.01
condenser power at B0/W35 [kW]	
- nominal heating power for Strasbourg SFH100	10.36
- scaled heating power for Strasbourg SFH15 and SFH45	6.01

Tab. 4: Key values of solar collector models, flat-plate selective (Heimrath and Haller, 2007)

Parameter	Value
collector optical efficiency η_0 [-]	0.80
heat loss coefficient c_1 [W/m²K]	3.50
temperature dependence of heat loss coefficient c_2 [W/m²K²]	0.015
effective thermal capacity of the collector c_5 [J/m²K]	7000
first order IAM b_0 [-]	0.18
IAM for diffuse radiation K_d [-]	0.90

Tab. 5: Key values of air/water heat pump models, performance data based on data sheets of Viessmann Vitocal 350-A AWHI 351.A10 (Viessmann, 2013)

Parameter	Value
COP at A2/W35 [-]	3.66
condenser power at A2/W35 [kW]	
- nominal heating power for Strasbourg SFH100	10.60
- scaled heating power for Strasbourg SFH15 and SFH45	6.36

Tab. 6: Key values of solar absorber models, based on measured data and parameter identification of the TRNSYS model with GenOpt

Parameter	Value
collector optical efficiency η_0 [-]	0.699
heat loss coefficient c_1 [W/m²K]	32.79
wind speed dependence of the heat loss coefficient c_3 [J/m³K]	4.64
sky temperature dependence of the heat loss coefficient c_4 [-]	0.9338
effective thermal capacity of the absorber c_5 [J/m²K]	20000
wind speed dependence of the zero loss efficiency c_6 [s/m]	0.034
first order IAM b_0 [-]	0.0327
IAM for diffuse radiation K_d [-]	1.00

For the control of the systems, the predefined control parameters from section 3.3 were used. In case of SISHP systems, an additional controller for the charging of the ice storage is needed. In these system concepts, the solar absorber loop is switched on if the difference between the supply temperature of the solar absorbers ($T_{Sol,abs}$) and the ice storage temperature sensor ($T_{S,ice,c}$) is higher than $\Delta T_{Sol,abs,on}$ (predefined: 3 K). The solar absorbers loop will remain on until the temperature difference falls below $\Delta T_{Sol,abs,off}$ (predefined: 1 K). In addition, a maximum ice storage temperature ($T_{Set,S,ice,max}$, predefined: 15 °C) of the ice storage temperature sensor ($T_{S,ice,c}$) is defined. If the ice storage temperature reaches this value, the solar absorber loop is turned off until $T_{S,ice,c}$ falls below a defined temperature $T_{Set,S,ice,max,off}$ (predefined: 14 °C). In case of SISHP-S+P systems, the predefined control concept from section 3.3 was used for the control of the ST collector loop.

4.2 Performance figures

The SPF quantifies the final energy efficiency of a whole SHP system and is defined as the overall useful energy output to the overall driving final energy input for an adopted system boundary over a period of one year (Malenković et al., 2013). In some cases, the systems may not permanently provide the DHW tapping temperatures or the room temperature of the building. For a better comparison between simulation results, penalty functions are defined as direct electric heating for times in which the system does not reach the required comfort criteria (Heimrath and Haller, 2007; Jordan et al., 2003). The SPF of the overall SHP system with penalties ($SPF_{SHP+,pen}$) is defined as the amount of useful energy for SH (Q_{SH}) and DHW preparation (Q_{DHW}) divided by the amount of electric energy consumption ($W_{el,SHP+,pen}$) of the overall SHP system (including all electrical consumptions of the SHP system and penalties) (Haller, 2013):

$$SPF_{SHP+,pen} = (Q_{SH}+Q_{DHW}) / W_{el,SHP+,pen} \quad \text{(eq. 1)}$$

For the comparison of simulation results of SHP systems with a defined reference system (e.g. without ST collectors) the relative increase $\Delta SPF_{SHP+,pen}$ is defined as:

$$\Delta SPF_{SHP+,pen} = (SPF_{SHP+,pen} - SPF_{SHP+,pen,ref}) / SPF_{SHP+,pen,ref} \quad \text{(eq. 2)}$$

where $SPF_{SHP+,pen}$ is the SPF of the considered system and $SPF_{SHP+,pen,ref}$ is the SPF of the corresponding reference system. Another figure for the comparison of system concepts to a reference system are the absolute electricity savings $W_{save,el}$, defined as difference between the electric energy consumption of the defined reference system $W_{el,SHP+,pen,ref}$ and the considered system configuration $W_{el,SHP+,pen}$:

$$W_{save,el} = W_{el,SHP+,pen,ref} - W_{el,SHP+,pen} \quad \text{(eq. 3)}$$

4.3 Results and discussion

The results of the evaluation of SPFs for the different STHP systems concepts and buildings are shown in fig. 6 and are summarized, with respect to the used collector / absorber areas and storage sizes, in tab. 7. In general, SGSHP-P systems achieve the highest SPFs for all types of building, which are in the range of 4.3 to 6.2 (SFH15), 4.9 to 6.7 (SFH45) and 4.5 to 5.4 (SFH100). For GSHP systems without ST integration, the SPFs are 3.1 (SFH15), 4.0 (SFH45) and 4.1 (SFH100). ASHP systems without ST collectors achieve the smallest SPFs, which are 2.6 (SFH15), 3.1 (SFH45) and 2.9 (SFH100). SISHP-S systems achieve higher values of SPF than ASHP systems for all types of building and in case of SFH15 even the same values as GSHP systems, which are in the range of 3.0 to 3.1 (SFH15), 3.6 to 3.7 (SFH45) and 3.4 (SFH100). The smaller values of SPF in case of SFH15 buildings with high fraction of DHW demand (46 %) show the impact of demand on high temperature level for DHW and as a result a lower performance of the HP in all system combinations without ST collectors. Additionally, the SH demand occurs predominantly in winter season with low ambient / source temperatures, especially in case of ASHP systems, and the HP runs with a lower performance. The simulation results show that the SPF can be

increased for all system concepts by adding a parallel ST collector system. Due to the direct use of solar thermal energy, SASHP-P systems can even reach higher SPFs than GSHP systems without ST integration. In case of SFH15 with a minimum collector area of 5 m² (SPF: 3.4) and in case of SFH45 with a minimum collector area of 10 m² (SPF: 4.2). However, in case of SFH100 the simulated SASHP-P systems cannot reach the performance of GSHP systems.

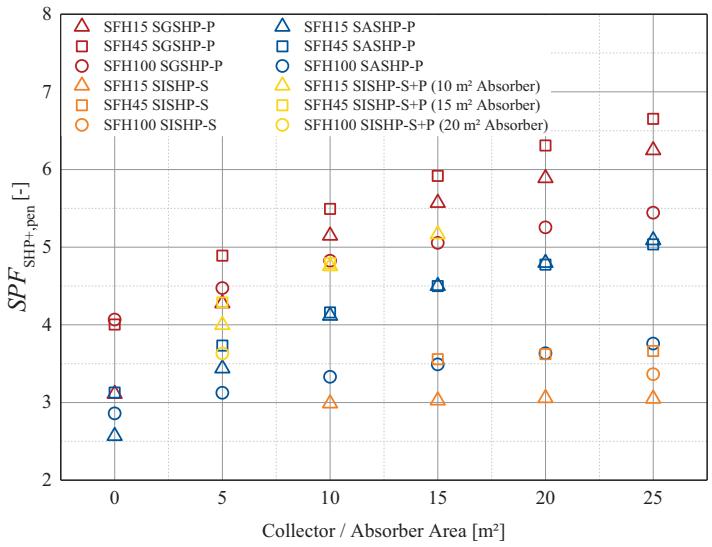

Fig. 6: SPF for Strasbourg depending on ST collector area (SGSHP-P, SASHP-P and SISHP-S+P) or absorber area (SISHP-S). SGSHP-P includes GSHP systems and SASHP-P includes ASHP systems (collector area = 0 m²).

The SPFs of SISHP-S systems can also be increased by adding small areas of ST collectors and can reach higher SPFs than GSHP systems without ST integration with a minimum collector area of 5 m² for SFH15 (SPF: 4.0) and SFH45 (SPF: 4.3). In case of SFH100, the simulated SISHP-S+P systems cannot reach the performance of GSHP systems. In case of SISHP systems, the benefit of adding flat-plate collectors to a SISHP-S system with design absorber area is higher than adding additional solar absorbers. If the roof area is limited to 25 m², this is shown by an increase of the SPF in the range of 33.8 % to 72.9 % in case of SFH15 and 20.5 % to 34.7 % in case of SFH45. In comparison, the maximum increase of SPF by adding additional solar absorbers is 2.0 % for SFH15 and 3.0 % for SFH45.

Tab. 7: Simulation parameter and results for the climate of Strasbourg

Building	System	A_C [m²]	A_{Abs} [m²]	V_{Buffer} [l]	V_{Ice} [m³]	SPF [-]	ΔSPF [%]	$W_{save,el}$ [kWh]
SFH15	GSHP	-	-	1000	-	3.1	*Reference for SGSHP-P*	
	SGSHP-P	5	-	1000	-	4.3	37.5	397
		10	-	1000	-	5.1	65.5	576
		15	-	1500	-	5.6	79.0	643
		20	-	2000	-	5.9	89.3	686
		25	-	2000	-	6.2	100.8	731
	ASHP	-	-	1000	-	2.6	*Reference for SASHP-P*	
	SASHP-P	5	-	1000	-	3.4	33.9	446
		10	-	1000	-	4.1	60.2	663
		15	-	1500	-	4.5	75.2	757
		20	-	2000	-	4.8	86.7	819
		25	-	2000	-	5.1	98.1	873
	SISHP-S	-	10	1000	10	3.0	*Reference for SISHP*	
		-	15	1000	10	3.0	1.3	20
		-	20	1000	10	3.1	2.3	34
		-	25	1000	10	3.0	2.0	31

Building	System	A_C [m²]	A_{Abs} [m²]	V_{Buffer} [l]	V_{Ice} [m³]	*SPF* [-]	Δ*SPF* [%]	$W_{save,el}$ [kWh]
SFH15	SISHP-S+P	5	10	1000	10	4.0	33.8	383
		10	10	1000	10	4.8	59.2	563
		15	10	1500	10	5.2	72.9	639
SFH45	GSHP	-	-	1000	-	4.0	*Reference for SGSHP-P*	
	SGSHP-P	5	-	1000	-	4.9	22.2	386
		10	-	1000	-	5.5	37.2	577
		15	-	1500	-	5.9	47.8	689
		20	-	2000	-	6.3	57.6	778
		25	-	2000	-	6.7	66.1	847
	ASHP	-	-	1000	-	3.1	*Reference for SASHP-P*	
	SASHP-P	5	-	1000	-	3.7	19.3	441
		10	-	1000	-	4.2	33.0	675
		15	-	1500	-	4.5	43.8	830
		20	-	2000	-	4.8	52.7	940
		25	-	2000	-	5.0	61.0	1032
	SISHP-S	-	15	1000	10	3.6	*Reference for SISHP*	
		-	20	1000	10	3.6	1.9	43
		-	25	1000	10	3.7	3.0	69
	SISHP-S+P	5	15	1000	10	4.3	20.5	407
		10	15	1000	10	4.8	34.7	617
SFH100	GSHP	-	-	1000	-	4.1	*Reference for SGSHP-P*	
	SGSHP-P	5	-	1000	-	4.5	10.0	357
		10	-	1000	-	4.8	18.6	617
		15	-	1500	-	5.1	24.2	767
		20	-	2000	-	5.3	29.2	888
		25	-	2000	-	5.4	33.8	994
	ASHP	-	-	1000	-	2.9	*Reference for SASHP-P*	
	SASHP-P	5	-	1000	-	3.1	9.3	476
		10	-	1000	-	3.3	16.4	792
		15	-	1500	-	3.5	22.0	1012
		20	-	2000	-	3.6	27.1	1195
		25	-	2000	-	3.8	31.5	1341
	SISHP-S	-	25	1000	20	3.4	*Reference for SISHP*	
	SISHP-S+P	5	20	1000	20	3.6	7.9	349

5. Conclusions and outlook

This contribution presented the TRNSYS-based stand-alone tool SHP-SIMFRAME for the simulation of STHP systems and a performance evaluation of different STHP system concepts. The main advantages of the tool for the end-users are the possibility to analyze different predefined SHP concepts without any knowledge in modeling and simulation itself as well as the related time saving and error prevention for model-based system design or system analysis by simulation. On the one hand, the performance evaluation shows that in case of moderate climate and new as well as renovated buildings, SASHP-P systems can compete with GSHP systems without solar integration and can achieve the same or even higher values of SPF. On the other hand, the results show that SISHP-S systems are efficient STHP systems, which can achieve higher SPFs than ASHP systems and for new buildings even SPFs in the range of GSHP systems. Furthermore, SISHP-S+P systems with parallel integration of solar collectors can achieve higher values of SPF for new as well as for renovated buildings than GSHP systems and even than SASHP-P systems with same ST collector area. However, the highest performance in the simulations can be reached by SGSHP-P systems for all type of buildings and in case of the considered non-renovated building, the SPFs of GSHP systems cannot be reached by the considered SASHP-P and SISHP-S+P systems with a limited available roof area of 25 m². In addition, the results illustrate the need of simulation tools to design SHP systems depending on the boundary conditions of the specific application and the comparison of

different system concepts. In future work, SHP systems with electrical solar energy (PV and PV thermal) systems will be investigated and integrated in the simulation framework.

Acknowledgements

This work was partially funded by the Saarland State Chancellery (Department WT/2). The authors are grateful for this support and thank the project partners, Viessmann Heizsysteme GmbH and SEG Kioto GmbH, for their support and cooperation. The authors would also like to express their gratitude to the participants of the IEA SHC Task 44 / HPP Annex 38 for the provision of the reference framework for system simulations.

References

Bertram, E., 2015. Heat Pump Systems with Vertical Ground Heat Exchanger and Uncovered Solar Thermal Collectors. Ph.D. dissertation, Leibniz University of Hannover, Hannover, Germany.

Carbonell, D., Haller, M., Frank, E., 2014a. Potential benefit of combining heat pumps with solar thermal for heating and domestic hot water preparation. Energy Procedia 57, 2656-2665. DOI:10.1016/j.egypro.2014.10.277

Carbonell, D., Haller, M., Philippen, D., Frank, E., 2014b. Simulations of combined solar thermal and heat pump systems for domestic hot water and space heating. Energy Procedia 48, 524-534. DOI:10.1016/j.egypro.2014.02.062

Dott, R., Haller, M. Y., Ruschenburg, J., Ochs, F., Bony, J., 2013. The reference framework for system simulations of the IEA SHC Task 44 / HPP Annex 38, Report C1 Part B: Building and space heat load, final revised Edition, IEA SHC Task 44 / HPP Annex 38.

Drück, H., 2006. TRNSYS Type 340 MULTIPORT Store-Model. Institut für Thermodynamik und Wärmetechnik, Universität Stuttgart, Stuttgart, Germany.

Frank, E., Haller, M. Y., Herkel, S., Ruschenburg, J., 2010. Systematic classification of combined solar thermal and heat pump systems. In: Proceedings of the EuroSun 2010 Conference, Graz, Austria. DOI:10.13140/2.1.3838.6883

Haller, M. Y., 2013. Simulation Reports for the IEA SHC Task 44 / HPP Annex 38, Report C3, final Edition, IEA SHC Task 44 / HPP Annex 38.

Haller, M. Y., Dott, R., Ruschenburg, J., Ochs, F., Bony, J., 2013a. The reference framework for system simulations of the IEA SHC Task 44 / HPP Annex 38, Report C1 Part A: General boundary conditions, final revised Edition, IEA SHC Task 44 / HPP Annex 38.

Haller, M. Y., Perers, B., Bales, C., Paavilainen, J., Dalibard, A., Fischer, S., Bertram, E., 2013b. TRNSYS Type 832 v5.01 Dynamic Collector Model by Bengt Perers. SPF Institut für Solartechnik, Hochschule für Technik HSR, Rapperswil, Switzerland.

Haller, M., Carbonell, D., Mojic, I., Winteler, C., Bertram, E., Bunea, M., Lerch, W., Ochs, F., 2014. Solar and heat pump systems - Summary of simulation results of the IEA SHC Task 44 / HPP Annex 38. In: Proceedings of the 11th IEA Heat Pump Conference, Montreal, Canada.

Haller, M.Y., Carbonell, D., Bertram, E., Heinz, A., Bales, C., Ochs, F., 2015. System simulations, in: Hadorn, J.-C. (Ed.), Solar and heat pump systems for residential buildings. Wilhelm Ernst & Sohn, Berlin, Germany, 159-207.

Heimrath, R., Haller, M. Y., 2007. The Reference Heating System, the Template Solar System of Task 32, Report A2 of Subtask A, IEA SHC Task 32.

Hornberger, M., 2006. „ICEPIT" Simulation program for vertically stratified storage bed for heat and cold storage. Documentation of Type 343, Transsolar, Stuttgart, Germany.

Jonas, D., Frey, G., Theis, D., 2017a. Simulation and Performance Analysis of Combined Parallel Solar Thermal

and Ground or Air Source Heat Pump Systems. Solar Energy 150, 500-511. DOI:10.1016/j.solener.2017.04.070

Jonas, D., Theis, D., Felgner, F., Frey, G., 2017b. A TRNSYS-based Simulation Framework for the Analysis of Solar Thermal and Heat Pump Systems. Applied Solar Energy 53(2), 126-137. DOI:10.3103/S0003701X17020074

Jonas, D., Theis, D., Felgner, F., Frey, G., 2017c. A User-friendly Simulation Framework for the Analysis of Solar Thermal and Heat Pump Systems using TRNSYS. In: Proceedings of the 8th IEEE International Renewable Energy Congress (IREC2017), Amman, Jordan. DOI: 10.1109/IREC.2017.7926052

Jordan, U., Vajen, V., Streicher, W., Letz, T., 2003. Performance of solar combisystems, in: Weiss, W. (Ed.), Solar Heating Systems for Houses. Routledge, Abingdon, Oxon, United Kingdom, 125-162.

Kuethe, S., Wilhelms, C., Zass, K., Heinzen, R., Vajen, K., Jordan, U., 2008. Modelling complex systems with TRNSYS SIMULATION STUDIO. Proceedings of the EuroSun 2008 Conference, Lisbon, Portugal.

Malenković, I., Pärisch, P., Eicher, S., Bony, J., Hartl, M., 2013. Definition of Main System Boundaries and Performance Figures for Reporting on SHP Systems, Deliverable B1, final Edition, IEA SHC Task 44 / HPP Annex 38.

Meteonorm, 2009. Meteonorm 6.1.0.9, Global Meteorological Database for Engineers, Planners and Education. Meteotest, Bern, Switzerland.

Pärisch, P., Mercker, O., Oberdorfer, P., Bertram, E., Tepe, R., Rockendorf, G., 2015. Short-term experiments with borehole heat exchangers and model validation in TRNSYS. Renewable Energy 74, 471-477. DOI:10.1016/j.renene.2014.07.052

Poppi, S., Bales, C., Haller, M., Heinz, A., 2016. Influence of boundary conditions and component size on electricity demand in solar thermal and heat pump combisystems. Applied Energy 162, 1062-1073. DOI:10.1016/j.apenergy.2015.10.190

Ruschenburg, J., Herkel, S., 2013. A review of market-available solar thermal heat pump systems, A technical report of subtask A, IEA SHC Task 44 / HPP Annex 38.

Ruschenburg, J., Herkel, S., 2015. System description, categorization, and comparison, in: Hadorn, J.-C. (Ed.), Solar and heat pump systems for residential buildings. Wilhelm Ernst & Sohn, Berlin, Germany, 7-22.

Ruschenburg, J., Herkel, S., Henning, H.-M., 2013. A statistical analysis on market-available solar thermal heat pump systems. Solar Energy 95, 79-89. DOI:10.1016/j.solener.2013.06.005

TESS, 2014. TESS Component Library, version 17. Thermal Energy System Specialists, LLC, Madison, Wisconsin, United States of America.

TRNSYS, 2014. TRNSYS - a Transient System Simulation Program, version 17.2. Solar Energy Laboratory, University of Wisconsin, Madison, Wisconsin, United States of America.

Viessmann, 2013. Planungsanleitung VITOCAL, Luft/Wasser-Wärmepumpen, Viessmann Werke GmbH & Co KG, Allendorf, Germany.

Viessmann, 2017. Planungsanleitung VITOCAL, Sole/Wasser- und Wasser/Wasser-Wärmepumpe, Viessmann Werke GmbH & Co KG, Allendorf, Germany.

Wetter, M., Afjei, T., 1997. TRNSYS Type 401 Compressor heat pump including frost and cycle losses. Zentralschweizerisches Technikum, Luzern, Horw, Switzerland.

SolarHybrid Heating And Cooling – An Environmental Friendly And Economic HVAC Solution

Daniel Neyer[1, 2], Manuel Ostheimer[2], Florian Gritzer[2]

[1] daniel neyer brainworks, 6700 Bludenz (Austria)

[2] University of Innsbruck, 6020 Innsbruck (Austria)

Abstract

Due to increasing living comfort and climate change, an increase in building air-conditioning demand can be expected. Solar air-conditioning is intuitively a good solution, because of the coincidence of solar irradiation and cooling demand. The Austrian research project SolarHybrid deals with the systematic processing and optimization of solar thermal and photovoltaic driven cooling technologies, especially in order to design promising (solar-) hybrid solutions. The project includes the construction and measurements of functional models of a single/half effect NH_3/H_2O absorption chiller and a NH_3 vapour compression chiller. The system design and optimization is carried out by means of annual dynamic system simulations for three load profiles.

The combination of the absorption chiller and the vapour compression chiller represent an interesting initial position for effective and economic attractive solar driven HVAC solutions. Under the considered boundary conditions the solar thermal configurations appear to be more efficient and more cost competitive than the PV or PVT variations. Solar heating and cooling can become cost competitive when systems are designed clever with simplified HVAC layouts, advanced control strategies and high efficient components.

Keywords: ammonia vapour compression chiller, absorption chiller, hybrid system, solar cooling

1. Introduction

The supply of heat and cold in the building and industrial processes has a large potential for non-renewable primary energy savings. However, the substitution of non-renewable energy sources should always follow the basic premise of firstly reducing energy demands before applying renewable systems. High solar fraction and thus high non-renewable primary energy saving can be achieved with solar thermal (ST) or solar electric (PV) supported systems. However, there is a controversial discussion about these two technologies and their technical and economic aspects ongoing. Both solar technologies can offer energetic and/or economic advantages depending on the boundary conditions and the ratio of heating to hot water demand.

Within the project SolarHybrid different hybrid concepts for solar heating and cooling (SHC) are investigated. The major challenge for introduction of SHC systems to the market are the initial investment costs. Therefore, one focus of this project is the radical reduction of system components (e.g. no storage, etc.). The approach to achieve this goal is (i) to define possible system configurations, (ii) to examine them in software simulations, (iii) to test the real components in Hardware-in-the-Loop (HiL) tests, (iv) to validate the simulations with the measured data and run annually simulation studies and (v) to evaluate the results in terms of technical and economic performance.

Both technologies (ST, PV) but also the combined one (PVT) are investigated, their applications in HVAC system are optimized and new solar hybrid systems are developed. The aim is to improve the efficiency of individual components and the overall HVAC systems. The systems are optimized in order to increase primary energy efficiency and economic feasibility in respect to entire load profiles. The optimized components are integrated into system solutions resulting in innovative, radically minimized solar hybrid solutions.

doi:10.18086/swc.2017.33.06 Available at http://proceedings.ises.org

The economic and energetic optimization of the solar thermal concepts is achieved by means of adapted hydraulic layouts, radically minimized number of components and improved, more efficient control strategies. The technical as well as the economic potential is assessed by means of the T53E4 Tool (Neyer 2016). Extensive sensitivity analyses are used to determine the impact of changing technical and economic boundary conditions on key performance indicators (KPIs).

In the course of the project two components were built and optimized for the hybrid operation; (i) a vapour compression chiller (VCC) and (ii) an absorption chiller (ACM). The ammonia/water ACM, developed in the research project DAKTris (2013), has been further optimized in SolarHybrid, and was driven in hybrid operation with the ammonia VCC in Hardware-in-the-Loop laboratory measurements.

The project is based on detailed research of the components and systems, their modelling and the different load profiles. The systematic analysis of the simulation approaches and the individual models with their part load behaviour and application limits are an essential base for modelling. Through the appropriate choice of the models, dynamic system simulation models are created. Further investigations are carried out with suitable dynamic simulation models, which were adapted according to the laboratory measurements. Three profiles are investigated; an office building, a hotel and a potential study. The hybrid systems are optimized regarding non-renewable primary energy savings and economics. Figure 1 is showing the overall methodological approach of the project.

Fig. 1: Methodological approach and workflow of SolarHybrid

This paper is focusing on the simulation results of the hotel profile and the potential study of the hybrid ACM and VCC operation.

2. Methodology

Three main methods are described here. The assessment and its key performance indicators, the steady state and dynamic laboratory measurements and the simulation study for the hotel and the potential study. Table 1 summarizes the main nomenclature and subscripts.

Table 1: Nomenclature and Subscripts

ACM SE	Absorption chiller, Single effect	f_{sav}	Savings	PV	Photovoltaic
C	Cooling	in	Input	Q	Energy [kWh]
CR	Cost ratio (-)	η	Efficiency	ref	Reference system
DHW	Domestic hot water	HB	Hot Backup	SH	Space heating
ε	Primary Energy Factor (kWh/kWh_{PE})	loss	Losses	SPF	Seasonal Performance Factor (-)
EC	Energy Carrier	NRE	Non-renewable	sys	System
el	Electrical	out	Output	VCC	Vapour compression chiller
equ	Equivalent	PER	Primary Energy Ratio	WD	Water Distribution

2.1 Assessment – T53E^4-Tool

The performance assessment of SHC systems can be complex. Performance indicators can be determined in numerous ways by taking different system boundaries into account or using different energy quantities. Performance evaluation of integrated SHC systems distinguish in the distribution of collected solar heat and backup energy sources to space heating (SH), domestic hot water (DHW) and cooling (C) applications.

The assessment is performed with the techno-economic evaluation tool of IEA SHC Task 53. The T53E^4-Tool offers a database of primary energy factors (ε), efficiencies and economic data for all main SHC components. The evaluation is based on non-renewable primary energy for electricity and all energy carriers. Electricity exported towards the grid does not reduce the primary energy effort of the system, but the economic benefits is considered. The most important key figures are briefly discussed, the according equations are shown in Table 2. The key figures are fully discussed and defined in the IEA SHC Task 53 (Neyer et al. 2016).

- Non-renewable Primary Energy Ratio (PER_{NRE})

The evaluation is carried out based on non-renewable primary energy (NRE). The PER_{NRE} quantifies the non-renewable primary energy efficiency of the system (eq. 1). The primary energy factors (ε) required for the conversion are depending on type of energy, the location of the plant and the season.

- Non-renewable primary energy savings ($f_{sav.NRE}$)

The primary energy of the entire SHC system is compared with a reference system. The standardized Task 53 reference system is an air-cooled compression chiller (VCC) and a natural gas boiler and its primary energy ratio $PER_{NRE.ref}$ is calculated according equation 2. Applying both PERs (SHC and ref) the savings can be calculated according to equation 3.

- Equivalent Seasonal Performance Factor (SPF_{equ})

The SPF_{equ} is the ratio of useful energy (supplied to satisfy the needs of the building) to consumed energy from external sources (eq. 4). The energy inputs are converted into electrical equivalents units according to the primary energy factor of electricity (ε_{el}).

- Cost Ratio (CR)

The cost ratio is determined with the levelized costs of energy for the SHC system ($C_{use.SHC}$) and the levelized costs of energy for the reference system ($C_{use.REF}$). These costs include investment, replacement, maintenance, electricity, energy, water as well as feed-in tariffs. The costs are discounted according to the annuity method and are summed up on a yearly basis. If the CR equals one cost equity is reached for the SHC system compared to the reference system.

Table 1: Overview technical and economic key performance figures defined in IEA SHC Task 53

Non-renewable Primary Energy Ratio	$PER_{NRE} = \frac{\sum Q_{out}}{\sum\left(\frac{Q_{el,in}}{\varepsilon_{el}} + \frac{Q_{in}}{\varepsilon_{in}}\right)}$	(eq. 1)
	$\mathrm{PER_{NRE.ref}} = \frac{\sum \mathrm{Q_{out}}}{\sum\left(\frac{\mathrm{Q_{out.heat}+Q_{loss.ref}}}{\varepsilon_{\mathrm{in}}*\eta_{\mathrm{HB.ref}}} + \frac{\mathrm{Q_{out.cold}}}{\mathrm{SPF_{C.ref}}*\varepsilon_{\mathrm{el}}} + \frac{\mathrm{Q_{el,ref}}}{\varepsilon_{\mathrm{el}}}\right)}$	(eq. 2)
Non-renewable primary energy savings	$f_{sav.NRE} = 1 - \frac{PER_{NRE.ref}}{PER_{NRE.sys}}$	(eq. 3)
Equivalent Seasonal Performance Factor	$SPF_{equ.sys} = \frac{PER_{NRE.sys}}{\varepsilon_{el}}$	(eq. 4)
Levelized Costs of energy	$C_{use} = \frac{C_{an}}{\sum Q_{out}}$	(eq. 5)
Cost Ratio	$CR = \frac{C_{use,SHC}}{C_{use,REF}}$	(eq. 6)

2.2 Measurements & Hardware-in-the-Loop

Two chiller prototypes were tested in the laboratories; (i) an ammonia/water (NH_3/H_2O) absorption chiller (ACM)

and (ii) a vapour compression chiller (VCC). The ACM was developed in the research project DAKTris (2013), it has a nominal cooling capacity of 20 kW and enables the possibility to switch from single- to half-effect (SE/HE). This permits the possibility of high heat rejection temperatures (up to 45°C), the use of a dry cooling tower and the possibility of high useful temperatures in heat pump mode. Within this project, the ACM is adapted and optimized concerning the findings in DAKTris and the requirements of SolarHybrid (e.g. automation of the solvent compensation, etc.). In consideration of the hybrid operation of both chillers the cooling capacity of the VCC is also 20 kW (at evaporation temperature 4°C, condensing temperature 50°C) and the chosen refrigerant is ammonia (R717). The main components of the vapour compression chiller are a frequency controlled piston compressor, a flooded evaporator and a hot gas bypass.

In a first step steady state performance of both chillers are measured and characteristic curve diagrams are generated. Further dynamic Hardware-in-the-loop (HiL) tests of the components integrated in the simulated overall systems and the evaluation of the results are carried out.

- Laboratory infrastructure

The Unit for Energy Efficient Buildings at the University of Innsbruck provides the lab infrastructure for various tests of HVAC components. The infrastructure contains a heat-sink and -source facility. The sink is cooled by a vapour compression chiller (50 kW cooling power) and offers, depending on climatic conditions, the possibility of free-cooling. Three immersion heaters supply the heat for the source, each with a capacity of 15 kW. The temperature ranges up to 95°C for the source and down to -10°C for the sink. Four test benches with a capacity of 10 kW and 30 kW respectively are affiliated.

A multifunctional software is developed with the software platform LabView (National Instruments – NI) to provide the control of the laboratory. It is working on compactRIO (NI) real time devices and enables flexible and easy configurable tests. The communication is based on a dynamic link library, which offers the possibility to connect arbitrary software (TRNSYS, Matlab, Excel, BCVTB, etc.) to the lab.

- Steady state measurements

Steady state measurements are used to identify the performance at several conditions. The settings are adjusted accordingly considering the settling time and the measurement period to calculate a representative mean value and the corresponding deviation.

The measurements of the ACM and the VCC are executed at a wide range of operating conditions. The absorption chiller is tested in SE and HE mode, various volume flows (LT: 1.5–3, MT: 4.25–6, HT: 3–4.5 m³/h) and inlet temperatures (LT: 6–22, HT: 80–90, MT: SE 20–35, HE 20–45°C). The compression chiller capacity is varied through the compressor speed and with the hot gas bypass as well as variable volume flow rates (LT: 2–3.5, MT: 3.5–6 m³/h) and inlet temperatures (LT: 12–22, MT: 25–45°C).

- Dynamic measurements

Overall system performance and components interaction can be evaluated by dynamic measurements. Building up complex systems is time and cost intensive, therefore Hardware-in-the-Loop (HiL) tests are a promising alternative. HiL tests combine system simulations and real component testing. The overall system is designed in an adequate accuracy with a software (here TRNSYS) and the investigated components are connected to the lab. This coupling of simulation and lab in real time enables the determination of the overall system performance.

Based on the steady state results (limiting boundary conditions) and defined system configurations (see next paragraph) a simulation model is set up in TRNSYS. Each configuration is measured under the boundary conditions of two significant days (one sunny, one cloudy) at the chosen location in different variations (different temperatures, mass flows, control strategies, machine modes, etc.).

Following description is one variation of the combined chiller and heat pump mode of ACM and VCC (configuration c). The main purpose of this system is the supply of heat and simultaneously the optional allocation of cooling energy. The defined temperature levels are 12/6°C for LT circuit, 14/40°C for MT circuit and variable HT input (60~95°C). HT (4.5 m³/h) and LT (3.5 m³/h) volume flows are fixed, MT (min. 0.5 m³/h) volume flow is controlled to reach set outlet temperature (40°C). The ACM delivers as much as possible (depends on solar irradiation) and the VCC is complementing to deliver the set LT outlet temperature.

Subsequent to the measurements the evaluated data and energy balances are used to fit the simulation model of the ACM and VCC. Annual simulation studies are carried out accordingly.

- System configurations for Hil tests

As a consequence to the idea of minimized and reduces number of components the measured configurations are defined accordingly as direct solar thermal driven systems. The climatic conditions are simulated for different locations (Innsbruck, Sevilla, etc.). The solar collector field, the cooling tower and the other components are designed accordingly. The grid provides the required electrical energy.

a) Chiller-mode ACM and VCC: The generator (HT) circuit of the ACM is directly connected to a solar collector field (ST), re-cooling (MT) circuits of both machines are connected in parallel with a dry cooling tower and the chilled water (LT) outlet of the ACM is connected in serial to the inlet of the VCC.

b) Heat pump-mode ACM (SE and HE): HT circuit of ACM is directly connected to the collector, MT mass flow is controlled to reach the desired temperature at the MT outlet of the ACM and the chilled water could be used optionally.

c) Combined chiller- and heat pump-mode ACM and VCC: HT circuit of ACM is directly connected to the ST, MT and LT circuits of the ACM are connected in serial to the VCC, MT mass flow is controlled to deliver the defined temperature and VCC capacity is controlled to reach set LT temperature.

2.3 Simulation studies

The simulations are set up in TRNSYS and base on a load file approach. This concept enables the separation of building- and HVAC-simulation.

- HVAC simulation models

The individual models (ACM, VCC, cooling tower, etc.) have been investigated and improved on their partial load behaviour. The ACM and VCC are built up as characteristic curve models and are adjusted to the measured steady state and dynamic data.

The ACM model (Type 1005, Neyer et al., (2015b)) is based on semi-physical models of a single-effect (SE) ACM (Hannl et al., 2012) and a half-effect (HE) ACM (Zotter et al., 2015). The model can switch between the two operating modes (SE/HE) and its nominal capacity is scalable. A new characteristic curve model has been developed for the VCC. It's also based on a semi-physical simulation model (Luger 2017) that was fitted to the according measurements. The deviation between the simulation model and the daily dynamic measurements is smaller than 3% of the total energy balance.

- Load profile

The building simulation of a four-star hotel was set up in TRNSYS. This hotel has a capacity of 240 beds and an area of 10'080 m². Internal loads and geometry are based on different standards (e.g. SIA, etc.). The south oriented building has a high quality thermal envelope. Shading is achieved by construction and active shading elements. The hotel includes the following zones: accommodation, reception, lobby, bar/restaurant, kitchen and spa area with a pool. Geometry, design and control strategies determine the load profiles and energy demand for space heating, pool heating, domestic hot water and cooling accordingly. The ventilation includes heat recovery in winter and the air change rates and specified temperatures correlate with each usage.

In table 3 the annual energy demands and maximum loads for the locations Innsbruck and Sevilla are summed up.

Table 3: Energy demand and loads for the hotel profile in Innsbruck and Sevilla

	Innsbruck		Sevilla	
Application	Demand [MWh]	Load [kW]	Demand [MWh]	Load [kW]
Space heating (SH)	271.2	190	7.1	38
Pool heating (pool)	274.8	208	227.8	205

Domestic hot water (DHW)	562.5	260	562.5	260
Air–conditioning (C)	85.7	80	315.5	135

The load profiles are used individual and in several combinations: DHW only, DHW+C, DHW+C+SH+pool.

- HVAC layouts for the hotel

Six HVAC layouts are compared in detail for the hotel profile and are briefly described here.

REF: The standard Task 53 reference system consists of a modulating natural gas boiler and an air-cooled vapour compression chiller.

ST: The solar thermal collector field (ST) feeds a hot water storage tank, which is used to ensure the heat supply and operation of the ACM. A natural gas backup boiler is used for DHW and SH only. The ACM is used to cover the base load (19 kW) and the conventional VCC (70 kW) covers the remaining demand using grid electricity. Both chillers operate with a dry cooling tower.

HP: A heat pump operates reversible and feeds the hot water storage tank for domestic hot water usage and a cold water storage. Groundwater is used as the source for the heat pump.

HP+PV: A PV area, which is dimensioned for the operation of the reversible heat pump, complements the system. The HP is not controlled specifically, thus the coincidence of HP operation and PV electricity results from the simultaneousness from load and irradiation. The demand of electricity from the grid and the excess of PV electricity result correspondingly.

PVT: The system consists of a solar thermal collector field for domestic hot water purpose with a natural gas backup. The PVT collector is used to preheat the fresh water for the pool heating and to cool the PV accordingly. The cooling is supplied by a water-cooled conventional VCC (dry cooler).

PVT(P2H): in this variation the surplus PV electricity is used to heat up the hot water storage (power to heat).

PV(P2H): The reference system is equipped with PV. The PV is only used to heat up the hot water storage (power to heat).

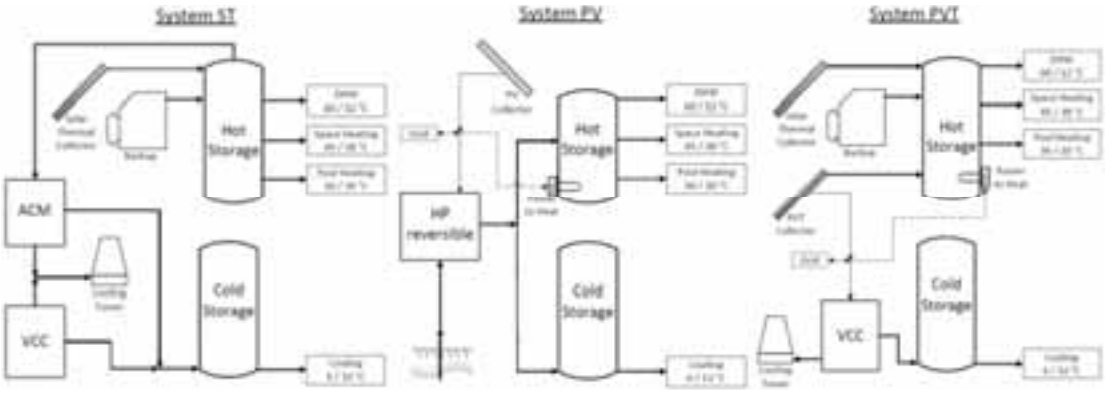

Fig. 2: Principle schemes of three solar hybrid HVAC solutions

The collector area for the entire system was varied during the simulation study: solar thermal (ST: 220, 420, 720, 820, 920, 1'120 m²) and photovoltaic (PV: 26, 49.5, 73, 84.5, 94, 130 kWp), PVT (420m² ST + 5, 12.5, 25, 50, 75, 100 kWp) and PV(P2H) (25, 46, 100, 150, 100, 200, 300 kWp).

- Potential study

The same configurations that are measured in the dynamic Hardware-in-the-Loop test are investigated in annual simulations. The system configurations are described above (cf. configurations a, b, c for HiL tests). The absorption chiller (in different modes) is directly solar driven, no hot water storage is included. Due to the design of the system the collector can deliver sufficient generator power to run the ACM if the solar irradiation is greater than 200 W/m². The maximum potential is investigated by means of constant return temperatures of LT- and MT-circuit and the operation through the entire year as soon as there is sufficient radiation available.

Selected boundaries for configuration (c) are presented in table 4. Three operation modes are analysed in order to reach different solar fractions: the ACM in single operation (without LT outlet temperature set point), the ACM with controlled VCC support (to reach the set LT temperature) and the ACM with maximum capacity VCC. The MT inlet temperature (returned to the chiller) is kept constant at 14°C and controlled to reach 40°C outlet (useful) temperature. The LT inlet is kept constant at 12°C or at ambient temperature plus 3 K to simulate an air source heat pump. The measurements are executed for the location of Innsbruck and Sevilla and are distinguished between the use of MT only and the simultaneous MT and LT usage.

Table 4: matrix of boundary conditions of the annual simulation for configuration (c)

Use	Location	LT return	MT temp	LT set temp.	Operation mode
MT MT+LT	Innsbruck	Amb. +3 K	14/40°C	Free floating	ACM only
	Innsbruck Sevilla	12°C		6°C	ACM + VCC controlled
				Free floating	ACM + max VCC

3. Results

This paper only shows a short selected survey of measured and simulated results. More details can be found in the final report of the project SolarHybrid (Neyer 2017).

3.1 Measurements & Hardware-in-the-Loop

- Characteristic curves vapour compression & absorption chiller

The steady state measurements of ACM and VCC are executed according to the defined measurement matrix. Figure 3 shows the performance maps of ACM (left) and VCC (right).

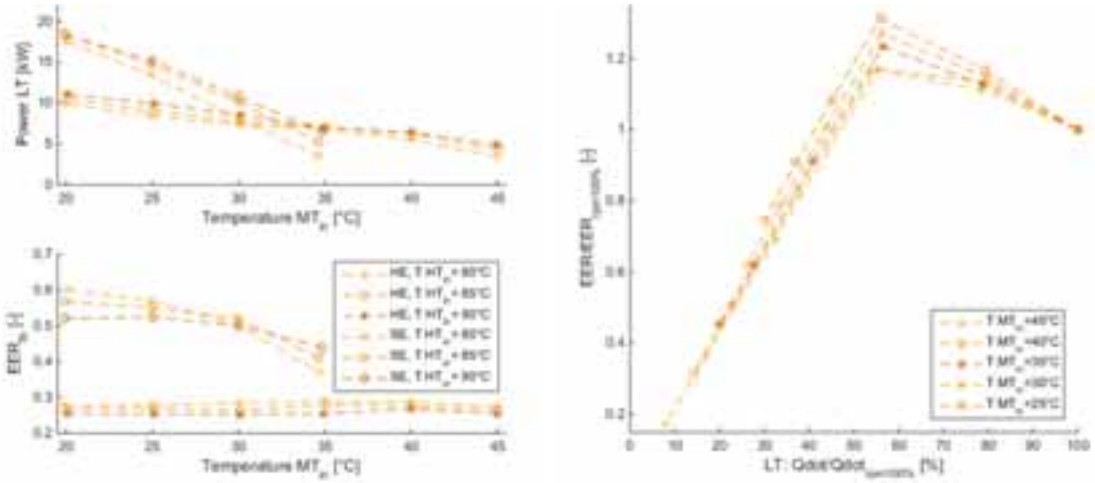

Fig. 3: Performance maps of ACM (left) and VCC (right), LT_{out}=12°C, $\dot{v}_{MT}$=6.5m³/h, $\dot{v}_{LT.ACM}$=3m³/h and $\dot{v}_{LT.VCC}$=3.5m³/h

The LT inlet temperature is kept at 12°C for both cases (left ACM, right VCC). The MT volume flow is 6.5 m³/h, LT volume flow is 3 m³/h for the ACM and 3.5 m³/h for the VCC measurements. The upper diagram of the ACM map shows the LT capacity and the lower diagram the Energy Efficiency Ratio (EER_{th}) in dependence on the MT_{in} inlet temperature. The different lines represent different modes (SE/HE) and different HT inlet temperatures. In SE mode recooling temperatures up to 35°C are possible; HE modes enables recooling temperatures up to 45°C, but at nearly half EER (caused by double generator power). In terms of energy production, switching from SE to HE could be reasonable at a MT inlet temperature higher 32°C (cf. upper diagram).

The VCC map shows values in relation to the nominal capacity, x-axis indicates the relative LT capacity and y-axis the relative EER. The lines represent different MT inlet temperatures, the capacity is first reduced by controlling rpm (100, 75, 50% – right three points of each line) and second on the basis of opening hot gas bypass (left three points of each line). The EER of the VCC is maximized at minimal rpm with closed hot gas bypass,

caused by better heat transfer in condenser and evaporator.

Both machines show a good performance, especially under consideration of the prototype status. The adaptations of the ACM show the expected impact and improve the performance significant. The VCC show EERs far above average small-scaled chillers and enables a capacity control for a large range.

- Dynamic measurements

Following the results of the described configuration (c) – combined chiller and heat pump mode of ACM and VCC – are discussed. The measurements are analysed visually, energies are summed up and characteristic numbers (e.g. electrical/thermal seasonal performance factor – SPF) are calculated.

Figure 4 shows the course of the cloudy day (Innsbruck); the upper diagram shows the capacities (HT, MT, LT, electrical) of ACM and VCC and the irradiation (multiplied with factor 10) on the collector field; the lower diagram shows the corresponding temperature (MT, LT in- and outlet; HT inlet temperatures multiplied with factor 0.1; ambient temperature)

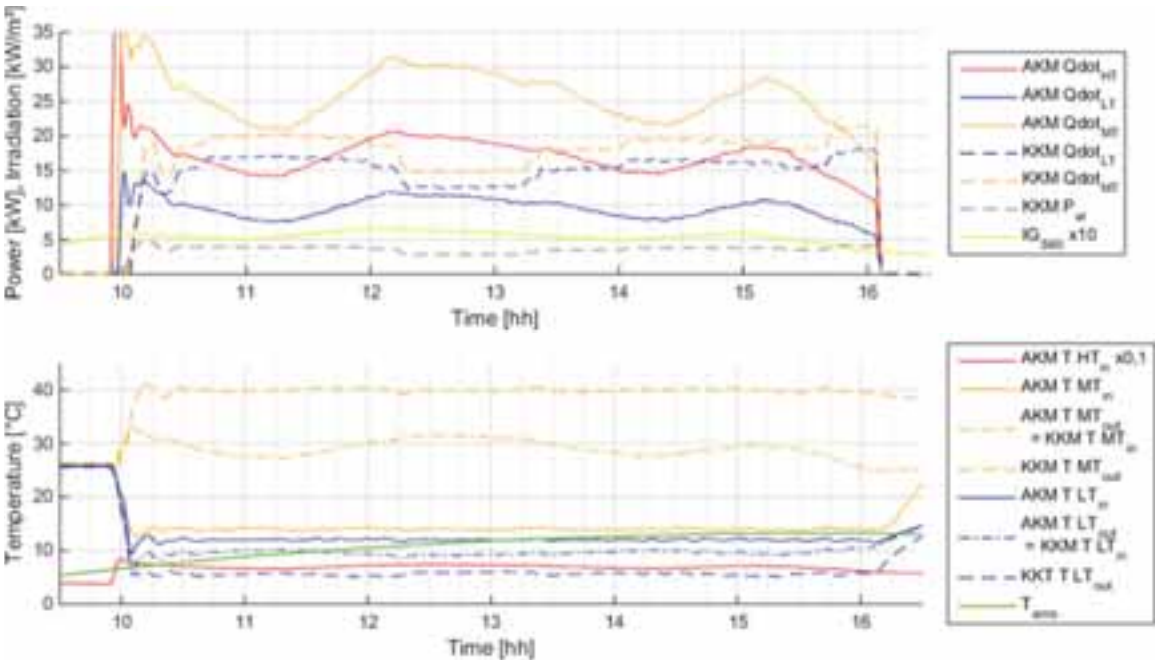

Fig. 4: Combined chiller and heat pump mode of ACM and VCC – trend over the cloudy day (upper diagram: powers and irradiation; lower diagram: temperatures)

The power devolution shows the correlation between ACM and VCC, as soon as the ACM delivers less power the VCC increases the capacity to reach the set point. This results in a constant LT outlet temperature (cf. Figure 4 lower diagram), constant MT outlet temperature is reached by means of controlled MT mass flow.

Table 5 shows the energy balances and system SPFs over the daily courses (sunny and cloudy day). The SPFs are distinguished in used energy (MT or MT+LT); the thermal SPF (SPF_{th}) represents the ratio of delivered energy (MT, MT+LT) to provided thermal energy (HT); SPF_{el} (electrical) shows the ratio of delivered energy to electrical energy (all circuit pumps, ACM solvent pump, VCC compressor).

Table 5: Energy Balances and SPFs of combined chiller and heat pump mode of ACM and VCC

	Energy ACM [kWh]			**Energy VCC** [kWh]			**ACM+VCC** [kWh]		**System SPF [-]**			
									MT+LT		**MT**	
	Q_{HT}	Q_{LT}	Q_{MT}	Q_{MT}	Q_{LT}	Q_{el}	Q_{MT}	Q_{LT}	SPF_{th}	SPF_{el}	SPF_{th}	SPF_{el}
Sunny day	233	125	349	96	80	21	445	205	2,03	20,19	1,50	13,82
Cloudy day	102	57	152	102	86	21	254	143	2,04	12,33	1,49	7,89

The configuration with the ACM and VCC used as heat pump reaches in all cases electrical efficiencies of >8. The difference between sunny and cloudy day get obvious but still provide optimization potential as the pumps are all calculated with constant power, including further speed-controlled auxiliaries enables systems with electrical performance of > 10.

3.2 Simulation studies results

- Hotel profile

Table 6 shows the most important results of all six simulated HVAC systems for the entire building load (DHW+C+SH) and the location of Innsbruck.

The solar yield is highest for ST (423 MWh), the PVT variation consist of ST+PVT_{th} (220+46 MWh) and PVT_{el} (61 MWh). The PV variation yield is 112 MWh. The demand for backup (natural gas) and/or grid electricity is reduced according to the yield. The surplus PV electricity is fed into the grid for the PV/PVT variations. A corresponding non-renewable primary energy input (PE_{NRE}) is resulting and expressed as savings ($f_{sav.NRE}$) in relation to the reference system.

Table 6: Comparison energy balances, costs and savings for maximum building load (DHW+C+SH/562+82+542 MWh/a) for each system

	Unit	REF	ST	HP	HP+PV	PVT	PV(P2H)
Collector area	m²	-	720	-	720	420 (ST)+ 326 (PVT)	652
Solar yield	MWh/a	-	423	-	112	ST:220, PVT_{th}:46, $_{el}$:61	113
Gas	MWh/a	1210	795	-	-	880	1071
Electricity supply	MWh/a	48	32	518	408	33	30
Electricity feed in	MWh/a	-	-	-	2	39	-
Sum Primary Energy	MWh/a	1498	963	1295	1020	1060	1265
Spec. Investment	€/kW	330	1200	500	890	1397	890
Investment ratio SHC/REF	-	-	3.6	1.5	2.7	4.2	2.7
$f_{sav.NRE}$	-	-	0.35	0.12	0.30	0.295	0.16
Cost Ratio (CR)	-	-	0.36	1.04	1.05	1.05	1.04

To analyse the costs, the specific investment costs are listed in Table 6. These were calculated with the standardized values of the T53E[4]-tool. The ratio of the investment costs of the entire system compared to the reference ranges from 1.5 for the heat pump up to 4 for the PVT variation. In addition to the investment costs, the costs for replacement, consumption-related costs (electricity, gas, water), maintenance costs and feed-in tariffs are reported. Figure 5 shows a comparison of the distribution of these cost categories in relation to the reference costs.

In case of the reference system, the energy costs for natural gas (73%) are dominant, while the proportion of investment is increasing significantly in the case of all renewable variations. In case of the solar thermal systems, the costs for natural gas; for the heat pump systems, the cost of electricity are the largest cost drivers.

All results of the techno-economic analysis are summarized in Figure 6 (left: Innsbruck, right: Sevilla). The cost ratio (CR) and the non-renewable primary energy savings ($f_{sav.NRE}$) are mapped. The markers represent the simulated variations, which are distinguished by collector size, by application (DHW only, DHW+C, DHW+C+SH) and by the system configuration (ST/PV/PVT). In general, it is obvious that the larger the collector size the larger the non-renewable primary energy savings can get but simultaneously rising cost ratios (CR) are observed.

Figure 6 shows the difference between the individual profiles as well as the system variations and the two locations. With the pure DHW systems, the highest savings ($f_{sav.NRE}$) are achieved (lowest energy quantity, highest solar coverage for the same area). The profile DHW+C+SH leads to the flattest curves (maximum energy quantity).

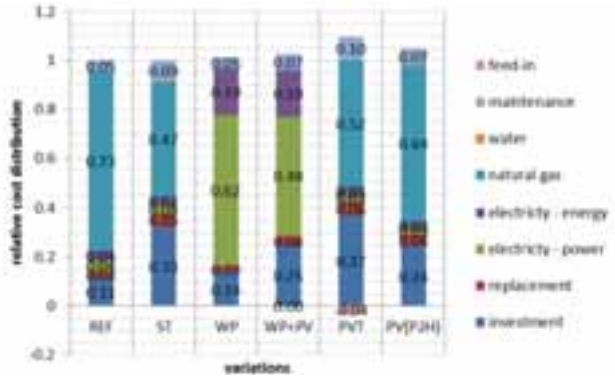

Figure 5: Relative cost allocation for the total building load (DHW+C+SH/562+82+542 MWh/a) relative to the reference (REF) for each system

With increasing collector size, the PVT quickly reaches a maximum of savings ($f_{sav.NRE}$) despite further rising of costs. This is due to the fact that, from a certain size, the user's self-consumption is no longer increased as the electricity consumption and the coincidence is low. On the other hand, increased PVT areas lead to larger ratios to preheat the DHW and thus the average collector temperature increases. Since uncovered PVT collectors usually have comparatively low stagnation temperatures, rising temperature can lead to a further reduced thermal yield.

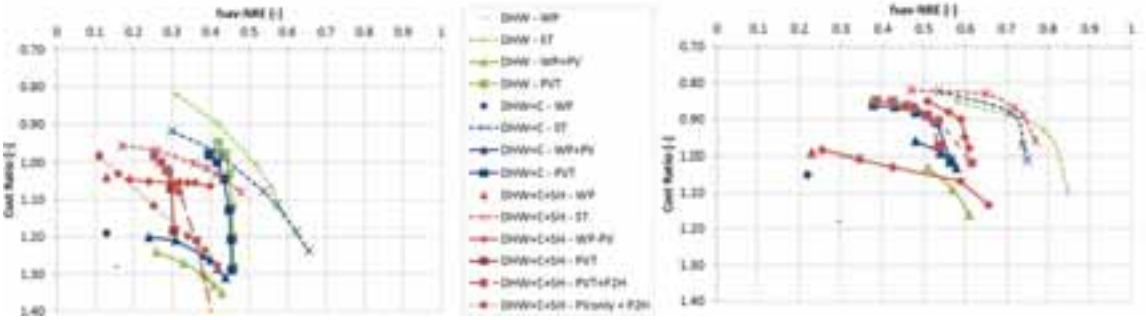

Figure 6: Technical and economical comparison of plant configurations: ST, HP, HP+PV, PVT, PV (P2H) for Innsbruck (left) and Sevilla (right)

Compared to the reference, the heat pump achieves $f_{sav.NRE}$ up to 15% (20% for SEV) with additional costs up to 28% (only DHW, IBK). The higher the energy demand the more favourable the HP. A CR of 1.04 (1 for SEV) can be achieved with the complete profile. The ratio of the investment costs to the energy costs, which account for 80% (IBK, cf. Fig.5) of the total profile, is decisive here. The cost can be reduced with high efficient solution accordingly.

If the heat pump is expanded by the PV, small increases in the CR will result for Innsbruck, but pays off in case of SEV immediately. If the PV area is increased, the costs increase accordingly. This result can essentially be attributed to the uncontrolled self-consumption and the trend of the profile.

The ST variations show the largest differences between the profiles as well as the different collector sizes. In the case of small areas, the savings in non-renewable primary energy are lower than in PV and PVT variations, but at lower costs (IBK). In Sevilla all variations of the ST show higher savings than the other solutions. The results (CR, $f_{sav.NRE}$) coincide with analyses of other measured and simulated plants in SHC Task 53 (Neyer 2016).

In sum, depending on the design and boundary conditions, ST, PV or even PVT could be preferred. Under the chosen boundary conditions, the ST systems can achieve the best results regarding costs and non-renewable primary energy savings due to the existing buffer storage and the time resolution and evolution of the profile.

- Potential study

The results of all five case studies of the potential study are shown in Figure 7. Each curve represents the three possibilities in operation mode (c.f. table 4). The ACM only operation mode can thus be found on the right hand side showing the highest savings. They are almost 100%, only a small electricity demand is lowering the $f_{sav.NRE}$ accordingly. The more the VCC is supporting the lower the solar fraction und consequently the lower the savings. At the same time the CostRatio drops rapidly as more energy can be delivered and the domination of investment is reduces. Worst performance is presented by the air-heat pump mode (AMB-14-40, only calculated for IBK). The lower the source temperature (especially in winter) the lower the efficiency and thus lower the savings and the CostRatio. If both LT and MT can be used the performance increases accordingly. Due to the higher solar yield the results for Sevilla are improved compared to Innsbruck.

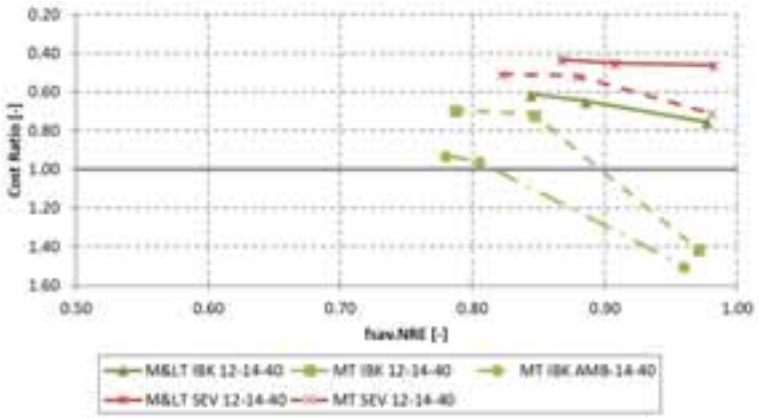

Figure 7: Comparison of the simulation results for Seville and Innsbruck for the heat pump cases with 12/6°C cold water (evaporator) and 14/40°C hot water (condenser) temperature; nomenclature: use(MT, MT+LT) Location LT return, MT in/out

Summing up the potential study illustrates that non-renewable primary energy savings >80% and CostRatio's mostly below 0.8 and as far as 0.4 can be reached. As the economic performance is still investment cost dominated a sensitivity analysis on different parameters was performed.

- Sensitivity analysis

The effect of the sensitivity analysis is shown by means of the shift of the trend lines. The parameters that are varied are the total investment costs, the electricity price, the electrical and thermal efficiency of the systems, as well as the reference performance.

Figure 8 is showing the summary of the sensitivity analysis (left; MT IBK 12-14-40, ACM+VCC) and for one curve of Figure 7 (MT IBK 12-14-40). The investment costs show the largest gradient and thus present the highest influence on the cost performance followed by the performance of the reference system and the entire electrical efficiency.

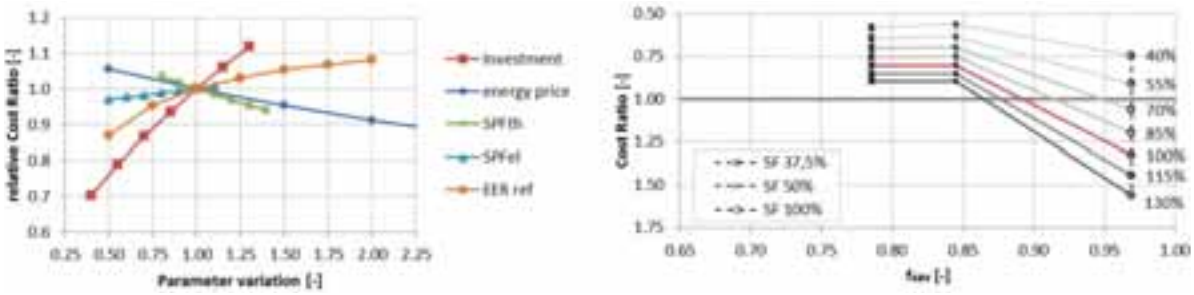

Figure 8: Sensitivity analysis for the heat pump case (MT IBK 12-14-40) as overview (left) and on investment costs variation from 40% to 130% of the Task 53 standard values (right); SF: solar fraction

Figure 8 (right) shows that if the invest costs could be reduced by roughly 35% the 100% solar driven ACM would reach a CostRatio below one and thus represent a highly primary energy savings solution that is cost competitive.

4. Summary & outlook

In SolarHybrid solar heating and cooling systems were investigated intensively by means of simulations, measurements of prototypes and the assessment & benchmarking against conventional system and other solar solutions.

- The combination of the single/half-effect ammonia/water absorption chiller and the ammonia vapour compression chiller represent an interesting initial position for effective and attractive solar driven HVAC solution
- Under the considered boundary conditions, the solar thermal configurations appear to be more efficient and more cost competitive than the PV or PVT variations.
- Solar heating and cooling can become cost competitive when systems are designed clever with simple HVAC layouts, advanced control strategies and high efficient components.

5. Acknowledgment

The presented work refers to the project SolarHybrid, which is carried out in collaborative work by the University of Innsbruck, FH OÖ Forschungs und Entwicklungs GmbH and the companies Engie Kältetechnik GmbH and Pink GmbH. The project is funded by the Austrian Climate and Energy Fund and is carried out within the framework of the Energy Research Program 2013.

6. References

DAKTris: Dynamisches Betriebsverhalten von AKM im gebäudeübergreifenden TRI-Generation Betrieb (FFG Projekt Nr. 840650). Wien: Österreichische Förschungsförderungsgesellschaft - FFG.

Hannl, D., Rieberer, R., 2012. Analyse einer Ammoniak/Wasser Absorptionskaelteanlage – Betriebserfahrungen und Simulationsmodellbildung, DKV-Tagung 2012, Wuerzburg

Luger, Stefan: Giovanni, Aldo: (2017) Analyse einer Kompressionskältemaschine zur Kaltwassererzeugung mit kleiner Leistung im überfluteten Thermosiphonbetrieb mit Drehzahl- und Heißgasbypass- Leistungsregulierung mit dem natürlichen Kältemittel Ammoniak, Bachelorarbeit am MCI Innsbruck, Juli 2017

Neyer, Daniel; Neyer, Jacqueline; Thür, Alexander; Fedrizzi, Roberto; Vittoriosi, Alice (2015a): Final Deliverable: Collection of criteria to quantify the quality and cost. International Energy Agency.

Neyer, D.; Thür, A.; Neyer, J.; Zotter, G.; Rieberer, R.; Pink, W.; Halmdienst, C., (2015b) Operating Conditions of a NH3/H2O Chiller for Tri-Generation Systems – Chiller Adaption and First Results. SAC 2015, Rom

Neyer D., Neyer J., Stadler K., Thür A., (2016). Deliverable C3-1: TASK 53 - Energy-Economy-Ecology-Evaluation Tool T53E4-Tool, Tool Description and introductory Manual, SHC Task 53

Neyer, D.; Neyer, J.; Thür, A.; Nocke, B.; Vicente, P.; Mugnier, D. (2016a): Assessment of Solar Heating and Cooling – Comparison of Best Practice Thermal and PV Driven Systems, 11th ISES EuroSun 2016.

Neyer, D.; Ostheimer, M.; et al. (2017): publizierbarer Endbericht - SolarHybrid, Klima und Energiefond, https://www.energieforschung.at/assets/project/final-report/SolarHybrid-final.pdf, last accessed May 16th 2018

SolarHybrid, 2014. Solare Hybridsysteme zum Heizen und Kühlen - Mit Optimierungen zu minimierten und kostengünstigen Systemkonzepten, Energy Mission Austra, e!Mission 2013, FFG Nr. 843855, Vienna, Austria

Stadler, Katharina; Neyer Daniel, (2015): Technische und ökonomische Bewertung von Kraft-Wärme-Kälte-Kopplungen. Masterarbeit. FH Oberösterreich, Wels.

Zotter, G. et al.(2015) Optimierung einer Ammoniak/Wasser-Absorptionskältemaschine für Kraft-Wärme-Kältekopplungen auf Basis von BHKWs kleiner Leistung, Dresden, Deutscher Kaelte- und Klimatechischer Verein (DKV)

Smart control strategy for PV and heat pump system utilizing thermal and electrical storage and forecast services

Emmanouil Psimopoulos[1,2], Elena Bee[3], Rasmus Luthander[2], Chris Bales[1]

1 Energy Technology, Dalarna University, Borlänge, Sweden

2 Department of Engineering Sciences, Uppsala University, Uppsala, Sweden

3 Department of Civil, Environmental and Mechanical Engineering - University of Trento, Trento, Italy

Abstract

In this study, a detailed model of a single-family house with exhaust air heat pump, PV system and energy hub developed in the simulation software TRNSYS 17 is used to evaluate energy management algorithms that utilize weather and electricity price forecasts. A system with independent PV and heat pump is used as a base case. The three smart and predictive control algorithms were developed with the scope to minimize annual cost of bought electricity by the use of the thermal storage of the building, the hot water tank and electrical storage. The results show reduction of the final energy of 26.4%, increase of the self-consumption to 60% and decrease of the net annual cost for electricity of 15% when using the forecast services in combination with thermal and electrical storage compared to the base case.

Keywords: photovoltaics, heat pump, forecast services, thermal storage, electrical storage

Nomenclature

DHW	Domestic hot water
FE	Final energy
HP	Heat pump
PV	Photovoltaics
NCOE	Annual cost of electricity
SC	Self-consumption [%]
SH	Space heating

1. Introduction

Sophisticated control of HPs can provide the flexibility to match the onsite PV electricity production with the household load for space heating (SH) and domestic hot water (DHW). Batteries have the advantage of being able to store electricity for later use and are a suitable option for short term storage of PV electricity in buildings (Luthander et al., 2015), while thermal storage has also been studied in combination with heat pumps. For example, according to Fischer and Madani (2017), rule based approaches lead to cost reduction by 2 to 4%. Salpakari and Lund (2016) studied the optimal cost control for PV systems with thermal and electrical energy storage based on the electricity price and Thygesen and Karlsson (2016) proposed a control strategy based on a perfect short-term weather forecast for a PV system with a heat pump and thermal and energy storage that showed low profitability. Strategies for improving PV self-consumption in residential buildings with energy storage and

doi:10.18086/swc.2017.33.07 Available at http://proceedings.ises.org

the various control approaches, including rule based and predictive control have been reviewed thoroughly by Luthander et al., (2015) and Fischer and Madani (2016) respectively. The majority of the studies that focus on PV are in combination with battery storage but heat pumps plus hot water storage have shown increasing interest in recent years (Binder et al., 2012; Hesaraki and Holmberg, 2013; Thygesen and Karlsson, 2014; Luthander et al., 2015; Hirvonen et al., 2016; Fischer et al. 2017). This study evaluates predictive control measures for systems with PV and heat pumps for a single-family house in Sweden. For the base case, a detailed model of a new single-family house with a grid-connected PV system, exhaust air heat pump and hot water storage is used. In this base case scenario, the heat pump is not controlled to increase the internal use of the PV electricity. The model is further developed to include electrical storage.

1.1 Aim of study

The objective of this study is to develop and evaluate algorithms that use forecasts of weather and electricity price on hourly basis in order to reduce the annual final energy and net cost of electricity. In a previous study, Psimopoulos et al. (2016) developed control algorithms to utilize more effectively the excess PV electricity production. The previous results have focused on energetic improvement such as to increase the self-consumption (SC) and to reduce the bought electricity from the grid, namely final energy (FE). In the follow-up study presented here, a simplified economical evaluation of the running cost and revenue is used as for generating the net cost of electricity that is used for the optimization. In Sweden, it is already possible for house owners and PV micro producers to have an electricity tariff coupled with the Nord Pool spot market price, with tariffs on hourly basis (Sommerfeldt and Madani, 2015). What is new in this work is the proposed operational control strategies in addition to the short time-step weather data and load profiles for both domestic hot water (DHW) and electricity demand. Another difference to other studies is that the exhaust air heat pump, very common in Sweden, cannot supply the full heating rate required and thus control of the electrical auxiliary heater is important and also modelled in detailed in this study.

The scope of the study is for a modern single family house with exhaust air heat pump located in Sweden. The stochastical load patterns are based on monitoring data for single family houses described in Widén et al., (2012, 2009). All these are implemented in the simulation software TRNSYS 17, where the components in the model are parameterized to match the specifications of existing products on the market. Net cost of energy is considered in the analysis based on spot market price and no feed-in subsidies. A full economic evaluation including investment cost is out of scope of this paper, rather the focus is on impact of advanced control algorithms assuming the system already exists.

2. Methodology

2.1 Boundary conditions for the system

The system with heat pump supplies a typical Swedish single family house (SFH) with a gabled roof of one floor that has an overall U-value of 0.2 W m^{-2} K^{-1} and 143 m^2 heated floor area. A detailed model of the house with six zones, developed in the simulation software TRNSYS, is described in detail and validated by Persson and Heier (2010). TRNSYS' type 56 is used for the house model. Three zones (rooms) have a set temperature of 20°C, while two zones have 21°C and one zone has 22°C as set temperatures (Persson and Heier, 2010). The location of the house is Norrköping, Sweden (58.6°N, 16°2E). Measured high-resolution (one minute) meteorological data by the Swedish Meteorological and Hydrological Institute (SMHI) from the year 2011 in Norrköping is used in the simulations. The weather data is used both for calculation of the PV electricity production and for calculations of energy gains and losses in the house. Fresh water temperature, which affects the heating demand, is dependent on the time of the year and modelled using a function described by Heimrath and Haller (2007). Two adults and two children are living in the house, and the internal heat energy gain, assumed to be the same as the electricity demand for appliances, is calculated using a Markov-chain model for occupancy and energy use as described in Widén et al. (2009). The DHW demand is derived from the MacSheep project and adjusted for this study (Bales et al., 2015), see Table 1. Domestic electricity and DHW loads have a 2 minute resolution over the period of one year.

Tab. 1: SH, DHW and appliance data

2979	**Discharge energy [kWh year^{-1}]**
70.9	Discharge DHW volume [m^3 year^{-1}]
45	Discharge DHW temperature [°C]
194.2	Daily Average DHW draw-off [kg]
2.44 – 972.2	DHW flow [kg h^{-1}]
3437	Electricity for appliances [kWh year^{-1}]
14046	Space heating load [kWh year^{-1}]
5650	Max load for appliances [W]

2.2. Hot water storage tank, heat pump and auxiliary heater

A variable speed, exhaust air HP delivers heat both for SH and DHW but cannot supply them both at the same time. The HP model is based on the performance map of the HP, with heat capacity and power input as dependent variables together with inlet air temperature, inlet air flow rate and compressor speed as independent variables. A hot water storage tank of 180 litres is used for DHW whereas the SH is supplied by the HP through a buffer store of 25 litres. The HP is activated according to a heating curve and compensatory control algorithm dependent on the SH supply temperature. An electric auxiliary heater is activated when the thermal power provided by the heat pump is insufficient to meet thermal power need. The auxiliary heater is turned off during the predefined summer period. Table 2 shows the values used in this study for the DHW storage, heat pump and auxiliary heater. The models for the HP, DHW storage and internal control algorithms are based on common commercial products on the market. The performance characteristics as well as detailed control algorithm are based on those for a commercial integrated product with heat pump and DHW store as one 60x60 cm appliance unit.

Tab. 2 : Specifications of hot water storage tank, exhaust air heat pump and auxiliary heater

Preference	Quantity
DHW storage tank capacity [litre]	180
Electric compressor power [kW]	0.27-2.05
Thermal power of HP [kW]	1.14 – 4.99
Heat pump COP	2.4 – 4.7
Electric auxiliary heater [kW]	0.5 – 6.5

2.3. Battery storage and PV system

Three PV system sizes and three battery storage sizes are used to study the impact on the energetic and economic performance in terms of self-consumption, and final energy, with details described in Table 3. The tilt angle is defined by the roof of the building whereas the azimuth angle is chosen to optimize the yearly PV electricity production. The PV panels, inverter and lithium-ion batteries are modelled according to the specification of products available on the market.

Tab. 3: Specifications of the PV system and battery storage

Preference	Quantity/name
Capacity PV [kW]	3.12, 5.7, 9.36
Inverter efficiency [%]	97.7
PV tilt [°]	27
PV azimuth [°]	0
Capacity battery [kWh]	3.6, 7.2, 10.8
Round-trip battery losses [%]	10%

2.4. Electricity tariff

Figure 1 shows the annual variation of the Nord Pool spot market price for year 2011 in central Sweden. The purchased electricity price that is used for this study includes the following: the spot market price, the grid fee, the electricity certificate and the value added tax. For the case of the feed-in electricity to the grid, only the spot market price and the electricity certificate without the current tax reduction subsidy available in Sweden are considered. For the end user, this results in a mean value of 0.08 €/kWh of various fees is added to the hourly spot market price for the purchased electricity and 0.015 €/kWh is added to the hourly spot market price for the excess electricity fed to the grid. The added values are derived from 2011 market data (Nord Pool, 2016).

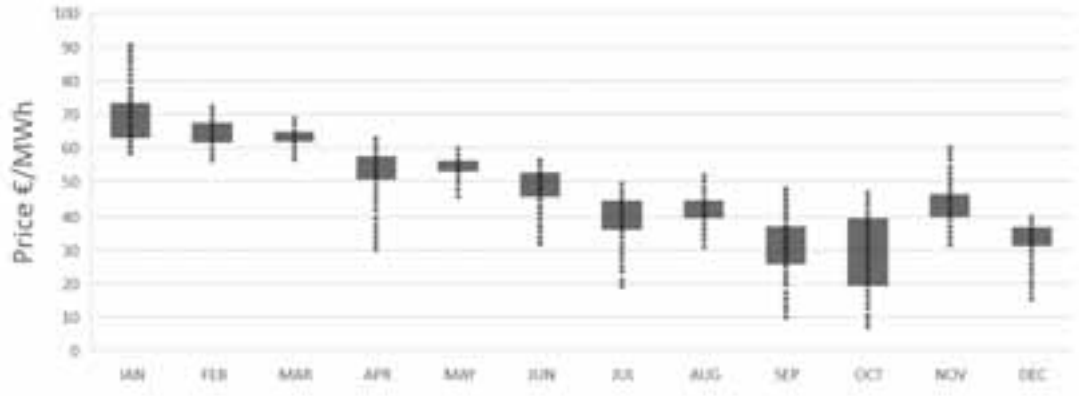

Fig. 1: Spot market electricity prices for Sweden in year 2011. Boxes include 50% of the values for each month

2.5 Sensitivity analysis of electricity tariff

Since the dynamic (spot) price is a small fraction of the end user price, this study also evaluates the potential of the amplified electricity price deviation that is shown in Figure 2, by investigating to what extent the applied algorithm based on the price forecast is sensitive to the hourly and daily price oscillation. To do that, data from 2011 were amplified by applying a factor of 2 to the deviation from the twenty four hours running average.

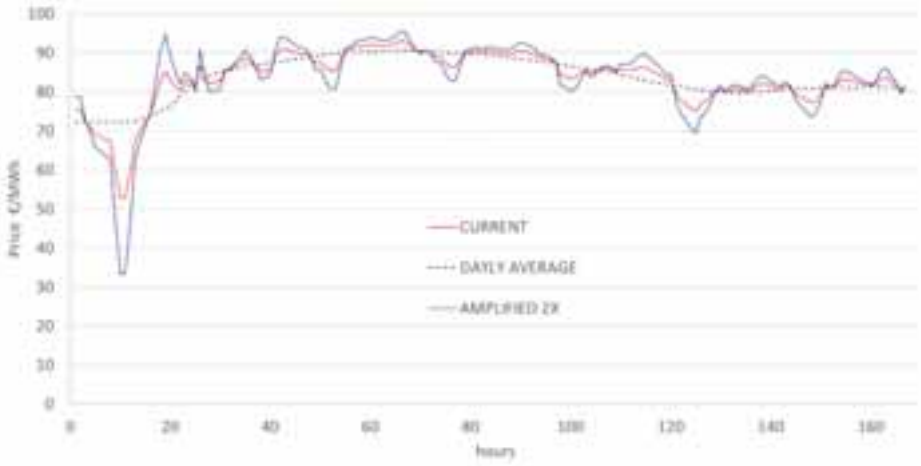

Fig. 2: Amplified electricity price deviation from the 24h running average (example of the first week in January 2011)

2.6 Performance indicators

The key figures for this study that are used to evaluate the energy and economic performance of the residential PV system are: final energy and self-consumption, annual electricity demand and annual net cost of electricity for the heating system and appliances. A mathematical description of self-consumption can be found in Luthander et al. (2015). If $L(t)$ denotes the instantaneous electric load including appliances, heat pump and auxiliary heater, and $P(t)$ is the instantaneous power from the PV system, the directly consumed PV power $M(t)$ can be defined as:

$$M(t) = \min\{L(t), P(t)\} \quad \text{(eq. 1)}$$

if no electric storage is used. When adding battery storage to the system, this can be extended to

$$M(t) = \min\{L(t), P(t) + S(t)\} \quad \text{(eq. 2)}$$

where $S(t) < 0$ denotes power to storage (charging) and $S(t) > 0$ denotes power from storage (discharging). The final energy for the simulation period (FE) is equal to the electric load that cannot be supplied by PV electricity:

$$FE = \int_{t_1}^{t_2} L(t)\, dt - \int_{t_1}^{t_2} M(t)\, dt \quad \text{(eq. 3)}$$

Self-consumption can then be defined as:

$$SC = \frac{\int_{t_1}^{t_2} M(t)\, dt}{\int_{t_1}^{t_2} P(t)\, dt} \quad \text{(eq. 4)}$$

The annual net cost of electricity (NCOE) can be defined as in equation 5. The cost of the purchased electricity is equal to the added values denoted as fixed fees C_{fixed} per kWh and the spot market price C_{sp}. The revenue consist of the spot price C_{sp} and the electricity certificates C_C:

$$NCOE = Cost - Income \quad \text{(eq. 5)}$$

$$Cost = \int (C_{sp} + C_{fixed}) P_{from\ grid}\, dt \quad \text{(eq. 6)}$$

$$Revenue = \int (C_{sp} + C_C)\, P_{to\ grid}\ dt \quad \text{(eq. 7)}$$

$P_{from\ grid}$ and $P_{to\ grid}$ are the power that the system requires from the grid or feed in to the grid, respectively.

3. Control strategies with forecast services

Smart control strategy is beneficial to demand response of the HP system and the optimal utilization of the thermal and electrical storage by the PV electricity production. One control action on the heating system based on electricity prices is to limit the need to purchase of energy when it is expensive. In those periods, if PV production is not sufficient to cover the total energy need, the storage system has a crucial role. In this study the price is defined as high or low by comparing the current price with the average price in a near-future interval of time. That means that the price is considered low or high relatively to what occurs in the hours ahead, and is not related to the average cost over the year. Figure 3 explains the logic that determines whether the current price is low or high.

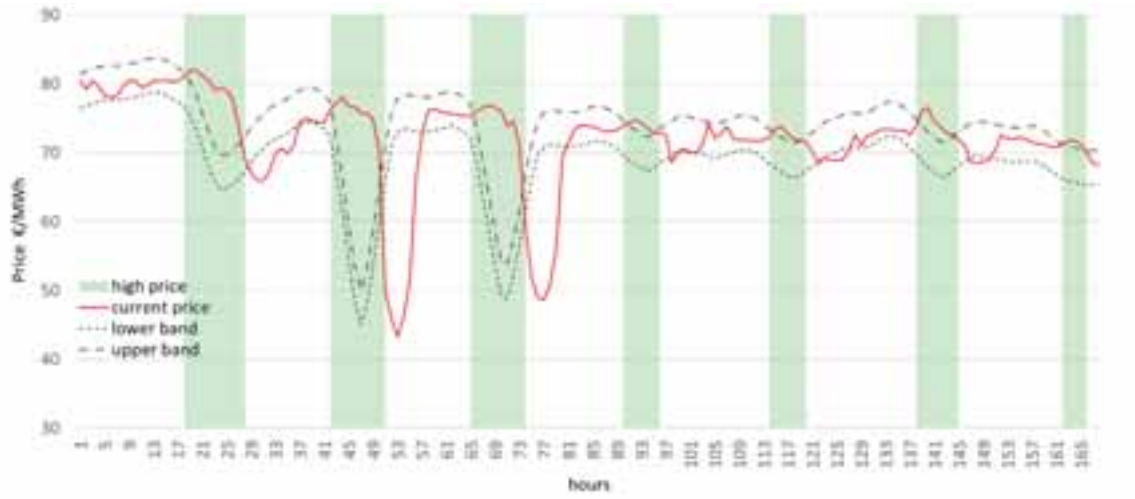

Fig. 3: Example of high price periods (data from a week in January 2011)

In Figure 3, the highlighted intervals are the hours when the price is high, i.e. when the current price is higher than the upper limit. The next day spot market data are obtained by using a perfect forecast, which is derived from the same electricity price data input file shifted one day ahead. The upper and lower limits are obtained by calculating the running average of the near future. The band width is therefore another parameter of this algorithm.

The weather forecast can be used for various applications. In this study the day-ahead global irradiance and the beam component are used as input to the PV model. A perfect forecast is used by shifting the original weather data file one day ahead in order to forecast the PV electricity production. A forecast of space heat demand is not generated or used.

Three algorithms were developed, utilizing either thermal storage by means of the thermal mass of the house (Algorithm 1) or the DHW tank storage, with the electrical storage (Algorithm 2) as well as a combination of using thermal mass storage and the electrical storage (Algorithm 3). The main objective is to control the temperature set points in the room regulators for the space heating using the variable spot market price and the set point in the DHW tank by the day-ahead of PV electricity forecast based on irradiance forecast and a night saving mode. The thermal comfort of the living space (room air temperature) and the availability of DHW were maintained between strict limits. A penalty function for both the SH and the DHW was implemented and monitored for deviations from the base case standards. For the room temperatures a minimum limit was defined as 19.5°C in the largest zone of the house and a minimum of 45°C in the tap. The penalty functions are based on the guidelines of the IEA SHC Task 32 and based on IEA Task 26 handbook (Weiss 2003). Both strategies are combined with overheating the zones of the house and the DHW tank when excess PV electricity is available. Constraints are also implemented to prevent increasing the cost and to prevent discomfort when the heating demand is high. Constraints of the control decisions that are not listed in the Table 4 are:

- The auxiliary heater is not allowed to be activated when overheating occurs.
- To prevent discomfort and probably use of auxiliary heater for reheating, it is not allowed to lower the zones' temperature set point when ambient temperature drops below 0 °C and high price occurs.
- It is not allowed to overheat the zones when the ambient temperature exceeds 10°C and low price occurs.

The developed control strategies are described as follows:

- The base case includes the house equipped with a PV system and a heat pump for DHW storage and SH. The HP is controlled solely by the need of SH and the temperature in the DHW storage tank. There is no active use of storage to optimize self-consumption/costs. For a more detailed comparison for the cases with the algorithms that combine both electrical and thermal storage the base case is also simulated with batteries and expressed as ALGb.
- In the first control algorithm (ALG1), the aim is to control the heat pump providing the SH load by the low and high dynamic price and to utilize the excess PV production to reduce net cost and to increase self-consumption. The control is implemented as follows: when high price occurs the room regulators lower the temperature by 0.5 K whereas the set point temperatures in all the zones are increased by 0.5 K during periods with low price. ALG1 is implemented with two variations ALG1 and ALG1a.The ALG1a difference includes the amplified dynamic price explained in section 2.5 but with the same control strategy.
- The second control algorithm (ALG2) is applied to the base case system with an additional electrical storage in batteries. The temperature set point of the DHW tank is triggered by the day-ahead weather forecast. The task of the saving function is to limit the cost for charging the DHW tank to the reference value which is compensated later by PV electricity. The time period during which this control is active if from hours 00:00 until hour 06:00. A precondition is that the PV power production between 07:00 and 08:00 exceeds a minimum threshold. Charging of the batteries is controlled by excess PV production to increase self-consumption whereas the HP is controlled solely by the need of SH and temperature in the DHW storage tank.
- The aim of the third control algorithm (ALG3) is to combine the energy storage in the thermal mass of the house, in the DHW tank and in the batteries together with a combination of price forecast and a forecast of the PV power production. The task is to use the batteries to reduce the final energy and to increase self-consumption. The HP is switched on when there is excess PV power production, otherwise it is controlled by the low and high dynamic price signals. The priority is to supply first the electrical loads and then the charging of the battery if there is additional excess PV power.

It should be noted that the battery charging is only allowed during times with excess PV power production after the desired set points in the DHW storage tank have been reached (algorithm 2) or if the SH overheating set point is reached (ALG3). The priority is given to the thermal storage in the course of any day. Table 4 lists the control schemes for on-off control of the HP for the three cases. For ALGb, the main control is that the battery charging is allowed only when excess PV power occurs.

Tab. 4: Control schemes for on-off control of the HP for the three algorithms

		ALG1	ALG2	ALG3
Spot price forecast	High price	Lower set point 0.5 K for SH	None	Lower set point 0.5 K for SH
	Low price	Increase set point 0.5 K for SH	None	Increase set point 0.5 K for SH
PV forecast	Threshold 500 Wh	-	$E_{PV} > 500$ Wh	-
Night saving	00:00-06:00	-	Lower set point 5K for DHW	-
PV excess $P_{PVe} > 320W$	Threshold 320W	Increase set point 1 K for SH	Increase set point 6 K for DHW	Increase setpoint 1 K for SH
PV excess $P_{PVe} > 0W$	Threshold 0W	-	Battery charging	Battery charging
Upper limits		$T_{zones} < 23$ °C	$T_{DHW\ tank} < 54$ °C	$T_{zones} < 23$ °C
		T_{set} DHW reference 48 °C ± 2 K hysteresis		

4. Results

In this section the results for the key performance indicators, i.e. FE, SC and NCOE, are presented. The developed control strategies are evaluated and compared to the base case with and without batteries. The system was simulated for the base case and each of the algorithms with the three different PV sizes, each with its own battery storage size chosen according to the PV capacity (3.1 kW PV and 3.6 kWh battery, 5.7 kW PV and 7.2 kWh battery, 9.3 kW PV and 10.8 kWh battery). Table 5 shows a summary of the key figures for the base case of 5.7 kW PV system without any smart control and with the implementation of the three control strategies. ALG1 is implemented with two variations, ALG1 and ALG1a. ALG1a uses the amplified dynamic price and is compared to the base case with the amplified dynamic price. Moreover ALGb refers to the base case with electrical storage and respectively ALG2 and ALG3 are also compared to ALGb.

Tab. 5: Key figures for the 5.7 kW PV and the three algorithms plus ALG1a (for all cases appliances use 3437 kWh year^{-1} and the PV array produces 6285 kWh year^{-1})

	Base case	ALG1	ALG1a	ALGb	ALG2	ALG3
Space heat [kWh year^{-1}]	14046	14385	14373	14050	14152	14382
DHW [kWh year^{-1}]	3657	3653	3652	3658	3711	3653
Heat pump electricity [kWh year^{-1}]	5932	6242	6695	5937	6375	6620
Aux heater electricity [kWh year^{-1}]	1568	1267	990	1595	1546	1101
PV self-consumption [%]	31	35	42	47	57	60
Final energy [kWh year^{-1}]	8994	8710	8467	8080	7728	7364
NCOE [Euros]	958	947	934	909	920	883

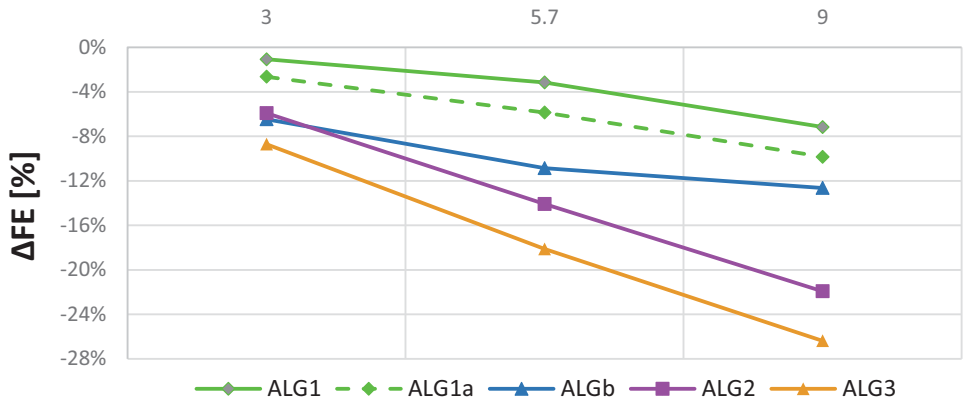

Fig. 4: Comparison of the change in final energy between the base case and the control algorithms ALG1, 2 and 3. ALG1a is shown with the dashed line and refers to the case with the amplified dynamic spot market price and ALG1b refers to the base case with batteries.

Figures 4, 5 and 6 compare the changes between base case and the three algorithms for the three key figures of final energy (ΔFE), net cost of energy (ΔNCOE) and self-consumption (ΔSC) respectively. All algorithms give greater cost and final energy savings the greater the PV system that is installed. ALGb, 2 and 3 including the electrical storage give higher savings in final energy as well as net costs than ALG1, which only uses thermal storage. ALG3 gives the highest reduction in final energy, saving 828, 1630 and 2278 kWh compared to the base case for the 3.1, 5.7 and 9.3 kW PV sizes respectively. Compared to ALGb the savings are 213, 654 and 1186 kWh respectively.

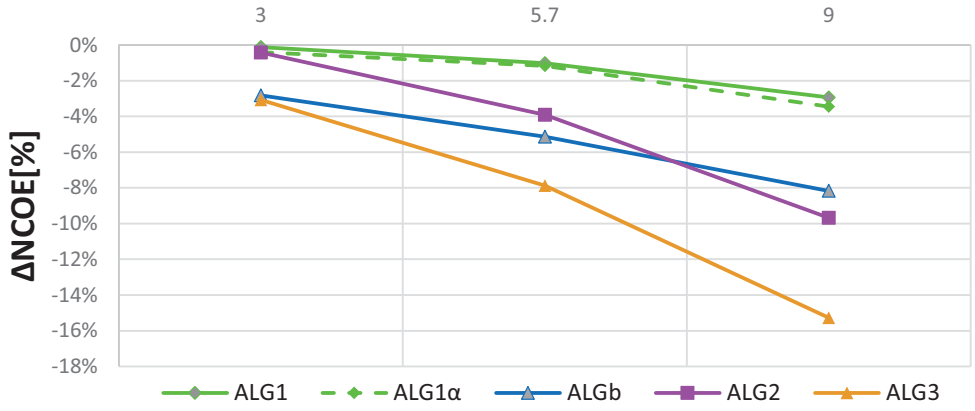

Fig. 5: Comparison of the Annual cost of electricity of the household between the base case and the control algorithms ALG1, 2 and 3. The electrical load for the household appliances is considered constant. ALG1a refers to the case with the amplified dynamic spot market price and ALG1b refers to the base case with batteries.

ALG1 gives gives small net cost savings even with the amplified dynamic price variation (ALG1a), while savings in final energy are larger as are the differences between ALG1 and ALG1a. The net cost savings for ALG3 is 36, 75 and 108 Euros for the small, medium and large PV systems respectively. The NCOE for the two variations of the ALG1 shows no difference even if the SC and final energy show benefits. It is also shown in Figure 5 that ALG2 gives higher cost savings than the base case with batteries, ALGb, only for the largest PV size whereas ALG3 has highest cost savings for all sizes.

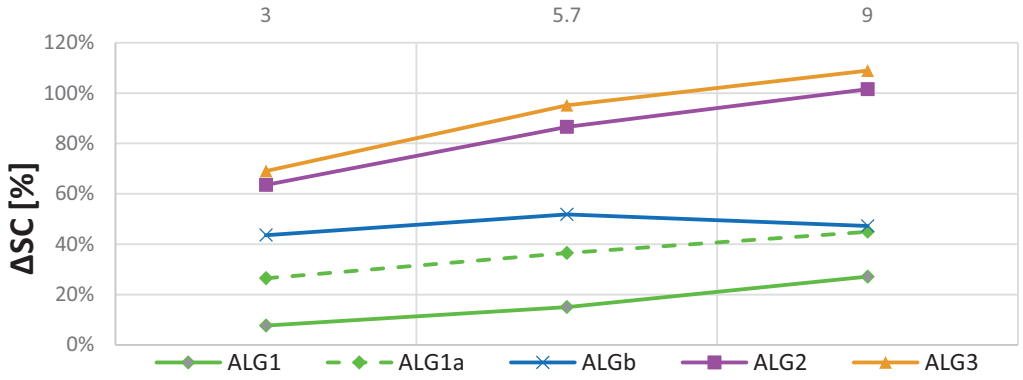

Fig. 6: Comparison of the increase of self-consumed electricity between the base case and the control algorithms ALG1, 2 and 3. Alg1a refers to the case with the amplified dynamic price and ALG1b refers to the base case with batteries.

ALG2 and 3 give twice as large an increase in self- consumption for the system with 9.3 kW PV compared to the base case. It should be pointed also that for the case of the ALG1a the increase in self-consumption is also more than twice as large between the ALG1 and ALG1a. In terms of absolute values the self-consumption for the medium system is 35.6% up to 60.4%, while the highest occur for the smallest size system and is 74.7%. Analyzing the results of the two scenarios of the electricity tariff for the base case, the comparison between the base case with the amplified dynamic price and ALG1a, it is found that the net cost is not affected by the amplified dynamic prices. Even if the cost is decreasing the revenue's decrease in this case results in a near zero change in the net cost. Table 6 lists the costs and revenues of the comparison of the base case and ALG1 and ALG1a while Table 7 lists the costs and revenue using ALG2 and ALG3 compared to ALGb. Both tables also give the average annual tariffs for buying and selling electricity. The tariff for buying is nearly double that for selling and does not vary with the algorithm, while that for selling varies slightly due to the different times of selling resulting from different algorithms.

Tab. 6: Cost and revenue and average tariffsfor base case and ALG1 and ALG1a

	Base case	**ALG1**
Cost (tariff)	1225 € (0.136 €/kWh)	1184 € (0.136 €/kWh)
Revenue (feed-in tariff)	267 € (0.065 €/kWh)	237 € (0.064 €/kWh)
	Base case Amplified	**ALG1a**
Cost (tariff)	1223 € (0.136 €/kWh)	1154 € (0.136 €/kWh)
Revenue (feed-in tariff)	259 € (0.068 €/kWh)	220 € (0.067 €/kWh)

Tab. 7: Cost and revenue and average tariffs for the base case with batteries ALG1b compared to ALG2 and ALG3

	ALGb	**ALG2**	**ALG3**
Cost (tariff)	1098 € (0.137 €/kWh)	1058 € (0.137 €/kWh)	1007 € (0.137 €/kWh)
Revenue (feed-in tariff)	188 € (0.066 €/kWh)	137 € (0.066 €/kWh)	124 € (0.065 €/kWh)

5. Discussion

The inclusion of forecast services in the control decisions increases the complexity of the rule-based decision.

In the current scenario in Sweden, there is a subsidy for feeding in excess electricity to the grid in order to motivate households to become micro producers and prosumers. With the feed-in subsidy, the revenue of selling electricity is very close to the savings from self-consuming the electricity. Increasing the self-consumption would, therefore, have a minor effect on the total costs. It is, however, not decided how long this subsidy will last, which makes it important to study ways to increase the revenue when the subsidy does not exist anymore. The chosen scenario of this study is therefore one where there is not feed-in subsidy and thus a large difference in tariffs for buying and selling, nearly a factor two. From the evaluation of the economic performance, it can be seen that the revenues of the excess electricity fed into the grid have an impact on the annual cost. Especially when cost saving decisions are implemented, there the cost reduction is partly cancelled out by the the reduction of the revenues, which limits the reduction in net annual costs. The limitation of rule-based algorithms for solving the multi-objective control tasks derives from the need to adjust the control decision seasonally and to develop logical solutions with constraints and priorities that are predefined and not updated throughout the course of the year.

One other point to be considered in the evaluation of the results is the use of a perfect forecast both for the weather forecast and also for the dynamic price. Using a real weather forecast, which includes uncertainties, the actual savings and benefits will be even lower than the ones from this study. In Sweden, the price for the coming 24 hours is decided at noon, and a perfect forecast is thus available.

6. Conclusion

This study shows the benefits of smart control using weather and electricity forecast services for decreasing annual net cost of electricity and final energy with the developed algorithms and for increasing the self-consumption. The improvements tend to increase with the larger system sizes. With the largest PV system the annual net cost is decreasing faster for all the algorithms than for the smaller PV systems, with highest cost savings forALG3 (thermal and electrical storage as well as predictive control). For ALG3 and largest PV array the following improvements compared to the base case system (without battery) with same PV array size are achieved: 26% reduction in final energy; self-consumption is nearly doubled to 60% ; and 15% decrease in net annual cost of electricity. For the same PV size and algorithm, the improvements compared to the base case system with battery are lower, namely: 16% reduction in final energy; 42% increase in self-consumption; and 8% decrease in net annual cost.

Using a battery (ALGb) gives greater savings than using thermal energy storage only (ALG1), for the battery and hot water store sizes used in the study. With the medium-sized PV system of 5.7 kW ALG1 gives only a small reduction in netannual cost but with electrical storage the reduction in net costs for electricity are 4 to 8% depending on algorithm used. The final energy can be decreased by 283 kWh (ALG1) up to 1630 kWh (ALG3). With the chosen scenario in this study, the proposed algorithms result in small improvements for cost savings up to 3 % for the smallest system of 3.1 kW when thermal and electrical storage are combined. Final energy is also reduced for this system by 101 kWh (ALG1) up to 828 kWh (ALG3).

7. References

Baetens, R., De Coninck, R., Van Roy, J., Verbruggen, B., Driesen, J., Helsen, L., Saelens, D., 2012. Assessing electrical bottlenecks at feeder level for residential net zero-energy buildings by integrated system simulation. Appl. Energy 96, 74–83. doi:10.1016/j.apenergy.2011.12.098

Bales, C., Betak, J., Broum, M., Chèze, D., Cuvillier, G., Haberl, R., Hafner, B., Haller, M., Hamp, Q., Heinz, A., Hengel, F., Kruck, A., Matuska, T., Mojic, I., Petrak, J., Poppi, S., Sedlar, J., Sourek, B., Thissen, B., Weidinger, A., 2015. Optimized solar and heat pump systems, components and dimensioning: MacSheep - New Materials and Control for a next generation of compact combined Solar and heat pump systems with boosted energetic and exergetic performance .

Binder, J., Williams, C.O., Kelm, T., 2012. Increasing PV Self-Consumption, Domestic Energy Autonomy and Grid Compatibility of PV Systems Using Heat-Pumps, Thermal Storage and Battery Storage. 27th Eur. Photovolt. Sol. Energy Conf. Exhib. 4030–4034. doi:10.4229/27THEUPVSEC2012-5AV.1.55

Fischer, D., et al. 2016. "Impact of PV and variable prices on optimal system sizing for heat pumps and thermal storage." Energy Build. 128: 723-733. doi:10.1016/j.enbuild.2016.07.008

Fischer, D., Madani, H., 2017. "On heat pumps in smart grids: A review." Renew. Sustain. Energy Rev. 70: 342-357. doi: 10.1016/j.rser.2016.11.182

Heier, J., Bales, C., Martin, V., 2015. Combining thermal energy storage with buildings – a review. Renew. Sustain. Energy Rev. 42, 1305–1325. doi:10.1016/j.rser.2014.11.031

Heimrath, R., Haller, M., 2007. The Reference Heating System, the Template Solar System of Task 32 [WWW Document]. URL http://archive.iea-shc.org/publications/downloads/task32-Reference_Heating_System.pdf (accessed 3.30.16).

Hesaraki, A., Holmberg, S., 2013. An investigation of energy efficient and sustainable heating systems for buildings: Combining photovoltaics with heat pump, in: Smart Innovation, Systems and Technologies. pp. 189–197. doi:10.1007/978-3-642-36645-1_18

Hirvonen, J., Kayo, G., Hasan, A., Sirén, K., 2016. Zero energy level and economic potential of small-scale building-integrated PV with different heating systems in Nordic conditions. Appl. Energy 167, 255–269. doi:10.1016/j.apenergy.2015.12.037

Luthander, R., Widén, J., Nilsson, D., Palm, J., 2015. Photovoltaic self-consumption in buildings: A review. Appl. Energy 142, 80–94. doi:10.1016/j.apenergy.2014.12.028

Nord Pool, 2016. Historical Market Data [WWW Document]. URL http://nordpoolspot.com/historical-market-data/ (accessed 3.15.16).

Pérez-Lombard, L., Ortiz, J., Pout, C., 2008. A review on buildings energy consumption information. Energy Build. 40, 394–398. doi:10.1016/j.enbuild.2007.03.007

Persson, T., Heier, J., 2010. Småhusens framtida utformning : Hur påverkar Boverkets nya byggregler? [How do the new Swedish building codes affect detached houses of the future?]. Region Gävleborg, Sweden.

Psimopoulos, E., Bales, C., Leppin, L., Luthander, R. (2016) Control Algorithms for PV and Heat Pump System Utilizing Thermal and Electrical Storage, 11th ISES EuroSun 2016

Salpakari, J., Lund, P., 2016. "Optimal and rule-based control strategies for energy flexibility in buildings with PV." Appl. Energy 161: 425-436. doi: 10.1016/j.apenergy.2015.10.036

Thygesen, R., Karlsson, B., 2014. Simulation and analysis of a solar assisted heat pump system with two different storage types for high levels of PV electricity self-consumption. Sol. Energy 103, 19–27. doi:10.1016/j.solener.2014.02.013

Thygesen, R. and B. Karlsson 2016. "Simulation of a proposed novel weather forecast control for ground source heat pumps as a mean to evaluate the feasibility of forecast controls' influence on the photovoltaic electricity self-consumption." Appl. Energy 164: 579-589 Thygesen, R., Karlsson, B., 2016

Weiss W., Solar Heating Systems for Houses – A Design Handbook for SolarCombisystems, Solar Heating and Cooling Executive Committee of theInternational Energy Agency (IEA), James & James, London, 2003

Widén, J., 2014. Improved photovoltaic self-consumption with appliance scheduling in 200 single-family buildings. Appl. Energy 126, 199–212. doi:10.1016/j.apenergy.2014.04.008

Widén, J., Lundh, M., Vassileva, I., Dahlquist, E., Ellegård, K., Wäckelgård, E., 2009. Constructing load profiles for household electricity and hot water from time-use data - Modelling approach and validation. Energy Build. 41, 753-768. doi: 10.1016/j.enbuild.2009.02.013

Widén, J., Molin, A., Ellegård, K., 2012. Models of domestic occupancy, activities and energy use based on time-use data : deterministic and stochastic approaches with application to various building-related simulations. J. Build. Perform. Simulation, Taylor Fr. 5, 27–44.

MODELING OF SOLAR ASSISTED HEAT PUMPS COMBINED WITH PHOTOVOLTAIC THERMAL MODULES

Riccardo Simonetti, Luca Molinaroli and Giampaolo Manzolini
Department of Energy, Politecnico di Milano, Via Lambruschini 4, 20156 Milano, (Italy)

Abstract

This work summarizes the performance of a Solar Assisted Heat Pump integrating Photovoltaic thermal (PV/T) modules. This configuration reduces the disadvantage of low temperature heat recovery typical of PV/T modules as the fluid temperature is used to drive the heat pump evaporator instead of an end-user and, consequently, can be close to the ambient one. A detailed model featuring real components is developed in MATLAB® to correctly predict the SAHP performance as function of the design parameters (number of PV/T modules) and ambient conditions (solar irradiance and ambient temperature). In addition, an optimization tool was combined with the model to maximize the COP (Coefficient of Performance) by varying the water flow rate circulating in the PV/T panels. Results outline the benefits of this concept with respect to conventional air/water heat pumps in particular when the ambient temperature is below zero as the frost formation issue is not present. COP reaches high values, between 2.5 and 4.9 in the case with 12 PV/T panels and between 2.2 and 6.2 with 24. Advantages in terms of electricity production are outlined as well, with an increasing of 8-9% of the power produced.

Keywords: Solar Assisted Heat Pumps, Photovoltaic Thermal modules.

1. Introduction

Photovoltaic thermal (PV/T) modules combine thermal and electricity production. The main drawback of this technology is the low thermal efficiency and stagnation temperature because of the high thermal losses (Aste, et al., 2014; Zondag, et al., 2003). Insulation systems like vacuum chamber or the adoption of concentrators can be considered but require the installation of auxiliary rejection systems to control the PV cell temperature when the heat demand is absent (Kumar, et al., 2015). Another option to exploit the PV/T potentiality without increasing the module complexity consists of their integration with a heat pump (HP) leading to the so-called solar-assisted heat pump (SAHP) concept: the heat recovered by the PV/T modules supplies the heat duty of the HP evaporator (Ji, et al., 2008). A detailed study over this system was conducted by (Nuntaphan, et al., 2009) that has experimental analyzed the performance of an indirect SAHP coupled with solar flat collectors including a hot water storage of 300 dm^3. Results demonstrate higher system efficiency with respect to traditional configurations (air/water HP or thermal panels), with a gain that reaches 40%. (Li, et al., 2014) has analyzed an indirect SAHP with flat solar collectors for residential heating. The study was done with a model developed in TRNSYS and results demonstrated that 68.1% of the heating and domestic hot water demand was covered by the SAHP. Moreover, the performance is increased by 140% respect of a standard HP and the energy saving is close to 52%. (Liu, et al., 2014) has investigated a system with a SAHP and vacuum solar collectors for residential use. An experimental set-up is used to validate a model built in TRNSYS. The study shows that, considering a system designed for a solar fraction of 20%, about 66% of the thermal load can be covered in the worst month and it is possible to reduce the energy consumption by 55% with respect to a traditional layout with a boiler . (Calise, et al., 2016) has studied the performance of a three-generation system composed by an indirect SAHP integrating PV/T solar panels for heating/cooling loads in a residential application. The model, developed in TRNSYS, shows that the system can cover the entire thermal load and the average performance is 30% higher than a standard HP. The SAHP configuration fixes the PV/T low stagnation temperature issue as the PV/T operating temperature can be close to the ambient one. In addition, the PV power output increases with respect to conventional PV module because of the PV cell cooling effect (Migliorini, et al., 2017). In this work, a detailed modeling of the SAHP concept is carried out to assess the system performance and power output as function of the ambient conditions (irradiance and ambient temperature) and the design specification (number of PV/T modules and thermal efficiency). Physical behavior of all the components of the system are completely characterized, heat transfer coefficients and pressure drops are determined using typical correlation referenced in literature and a solver for a

doi:10.18086/swc.2017.33.08 Available at http://proceedings.ises.org

system with non-linear equations is used. An optimization tool is also implemented to maximize the performance in each different ambient condition, varying the volumetric flow rate that flows in the PV/T panels. With this comprehensive tool, developed in MATLAB®, it is possible to automatically obtain optimized performance maps for a variable number of PV/T modules.

The paper is structured as follows. Section 2 describes the concept and the layout of the system studied. In Section 3 models of the components are explained. Section 4 presents the methodology proposed to define design condition and the optimization method used. In Section 5 main results of the paper are presented and discussed. Finally, in Section 6 conclusions are drawn.

2. The Concept

A schematic of the concept modelled in this work is reported in Fig. 1.

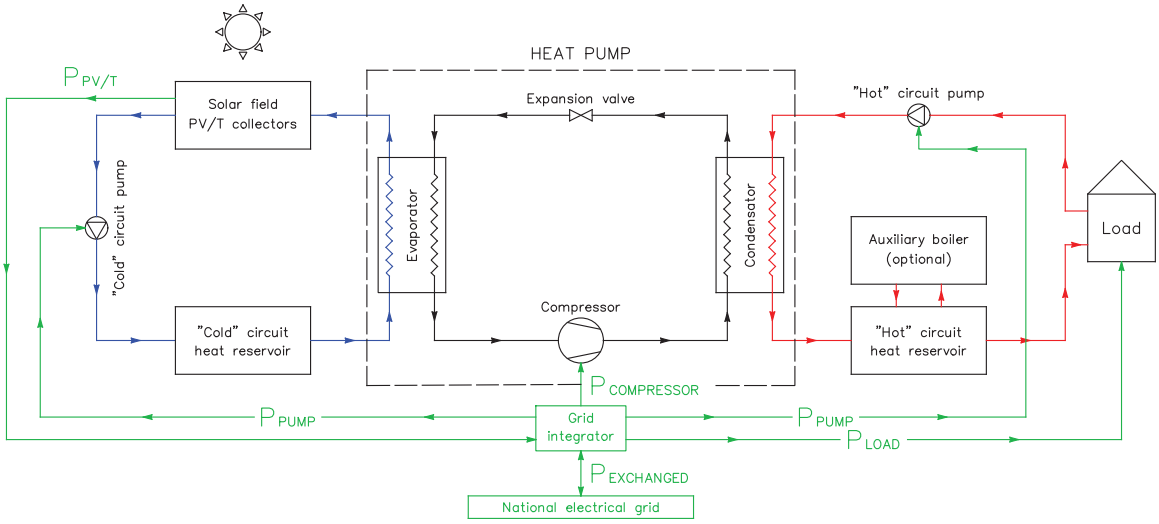

Fig. 1: Schematic of the system modelled in this work

The system consists of a water-to-water HP, PV/T modules and a thermal storage, being the latter component mandatory to decouple the solar energy availability with the thermal load. PV/T modules convert solar energy in thermal and electric ones: the first of them is used in the evaporator of the HP; the electric energy can be used to reduce/cover the HP electric energy demand together with the house ones. PV/T connection to the national grid is considered to account for the electricity excess/deficit with respect to the HP and house loads. The SAHP system considered in this work is designed to cover both Domestic Heat Water (DHW) and Space Heating (SH) consumptions of a single-family house. The heat pump nominal heating capacity and COP are equal to 8.52 kW and 3.19 respectively, whereas PV/T module performance feature commercially available ones (SoLink, 2017). The HP is modelled in MATLAB® considering the governing equations of each component as detailed in the next section, whereas the PV/T are modelled combining datasheet information and experimental measurements carried out at SolarTech^{Lab} of Politecnico di Milano (Bombarda, et al., 2016).

3. Mathematical Model

The SAHP model solves heat and mass balances assuming stationary conditions, neglecting the transient effect of solar radiation (G) variation and the thermal energy storage balance heat load variations. All the components of the HP (compressor, condenser, evaporator and expansion valve) and PV/T modules are considered as black-boxes, with governing equations to describe their physical behavior. The aim is to have a complete model that correctly describes the considered system within limited computational time to perform a detailed analysis in different ambient conditions and with a different number as well as typology of PV/T modules. Fig. 2 shows the refrigerant loop, the domestic water loop (as called primary circuit) and the water-glycol loop (as called secondary circuit). Glycol is used to prevent water freezing in winter time. HP operating points are numbered starting from the inlet of the compressor following the refrigerant fluid.

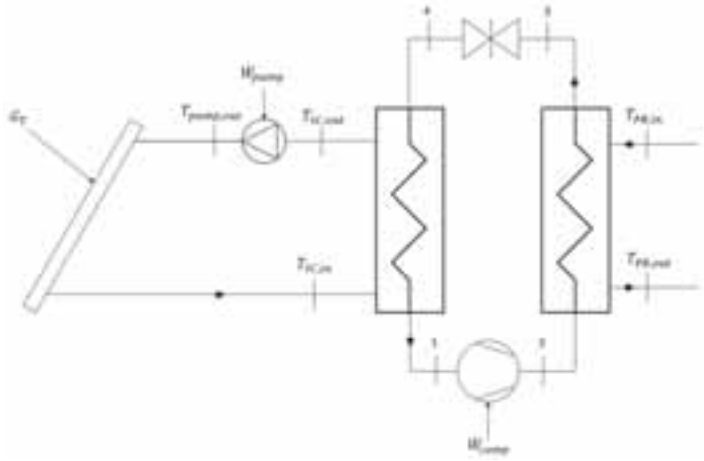

Fig. 2: Schematic of mathematical model

3.1. Compressor

The behavior of the compressor is described with polynomial equations to determine the refrigerant flow rate $\dot{m}_{refr}$ and the electric power consumption $\dot{W}_{comp}$ as functions of condensation and evaporation temperatures T_{cond} and T_{evap}. The 10 coefficients of the polynomial equations are provided by manufacturers (eq. 1 and eq. 2).

$$\dot{m}_{refr} = a_0 + a_1 T_E + a_2 T_C + a_3 T_E^2 + a_4 T_E T_C + a_5 T_C^2 + a_6 T_E^3 + a_7 T_E^2 T_C + a_8 T_E T_C^2 + a_9 T_C^3 \qquad \textit{(eq. 1)}$$

$$\dot{W}_{comp} = b_0 + b_1 T_E + b_2 T_C + b_3 T_E^2 + b_4 T_E T_C + b_5 T_C^2 + b_6 T_E^3 + b_7 T_E^2 T_C + b_8 T_E T_C^2 + b_9 T_C^3 \qquad \textit{(eq. 2)}$$

Coefficients a_i and b_i are evaluated by manufacturers at defined conditions. The compressor used in this work (**Emerson ZH30K4E-TFD**) (Emerson, 2017) has superheating temperature set to 5K, eq. 3 and eq. 4 determine the refrigerant flow rate and the electric power consumption with a different superheating:

$$\dot{m}_{refr}\big|_{\Delta T_{sh}} = \dot{m}_{refr}\big|_{\Delta T_{sh}=5K} \cdot \frac{\rho(p_{evap}, T_{evap}+\Delta T_{sh})}{\rho(p_{evap}, T_{evap}+5K)} \qquad \textit{(eq. 3)}$$

$$\dot{W}_{comp}\big|_{\Delta T_{sh}} = \dot{W}_{comp}\big|_{\Delta T_{sh}=5K} \cdot \frac{\rho(p_{evap}, T_{evap}+\Delta T_{sh})}{\rho(p_{evap}, T_{evap}+5K)} \qquad \textit{(eq. 4)}$$

However, part of the electric power absorbed by the compressor is dissipated as heat to the environment. This heat is assumed to be 10% of the total power, and this assumption is taken into account by means of eq. 5:

$$h_2 = h_1 + 0.9 \cdot \frac{\dot{W}_{comp}}{\dot{m}_{refr}} \qquad \textit{(eq. 5)}$$

The refrigerant at point 2 is superheated vapor and enters the condenser. The set of the compressor operating conditions is defined by the envelope, as shown in Fig. 3.

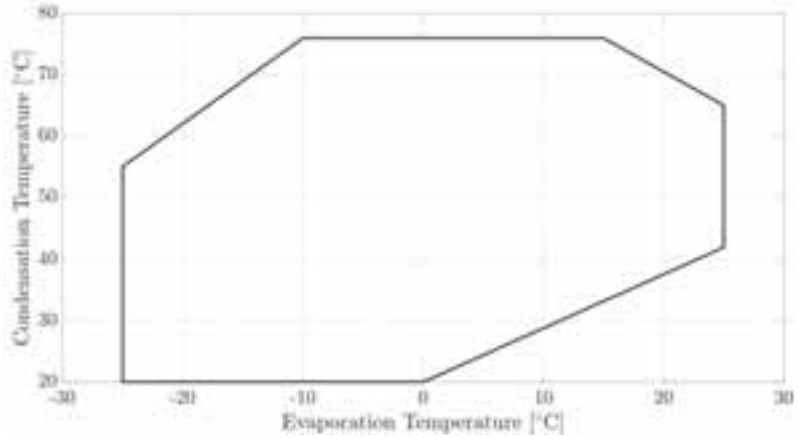

Fig. 3: Operating field of the compressor

3.2. Condenser

The condenser is a plate heat exchanger that transfers heat from the working fluid of the heat pump to the domestic water. This component is modelled by means of the eq. 6:

$$\dot{Q}_{condenser} = \sum_{i=0}^{zones} U_i \cdot A_i \cdot LMTD_i \qquad \textit{(eq. 6)}$$

Where$LMTD_i$ is the logarithmic mean temperature difference of each zone. The condenser is divided into two parts: the de-superheating zone and the condensation zone. Subcooling zone is neglected because of its negligible impact on the condenser's energy balance. For the two modelled sections, thermal transmittance (U) is calculated as the sum of the heat transfer contributions related to the refrigerant fluid, the domestic water and the thickness of the plate between them, as shown in eq. 7.

$$U = \left(\frac{1}{h_{conv,refr}} + \frac{s_{PLATE}}{k_{PLATE}} + \frac{1}{h_{conv,water}}\right)^{-1} \qquad \textit{(eq. 7)}$$

The conductive heat transfer coefficient h_{conv} is determined using the correlation of Kim (Kim, 1999) for single-phase fluids (superheated refrigerant vapor and liquid water) and the modified correlation of Shah (Shah, 1979) for the two-phase refrigerant fluid, as shown in eq. 8 and eq. 9 respectively:

$$Nu = 0.295 \cdot Re^{0.64} \cdot Pr^{0.32} \cdot (\pi/2 - \beta)^{0.09} \qquad \textit{(eq. 8)}$$

$$h_{conv} = \int_0^1 0.2092 \cdot Re_{LS}^{0.78} \cdot Pr_{LS}^{0.33} \cdot \frac{k_{LS}}{D_H} \cdot \left[(1-x)^{0.8} + \frac{3.8 \cdot x^{0.76} \cdot (1-x)^{0.04}}{\left(\frac{p_{SAT}}{p_{CRIT}}\right)^{0.38}}\right] dx \qquad \textit{(eq. 9)}$$

where $Nu = \frac{h_{conv} \cdot D_H}{k}$ is the Nusselt number, $Re = \frac{G \cdot D_H}{\mu}$ is the Reynolds number, $Pr = \frac{\mu \cdot C_p}{k}$ is the Prandtl number, $G = \frac{\dot{m}_{refr}}{N \cdot B \cdot t}$ is the specific flow rate of a single channel, $D_H = 2 \cdot t$ is the hydraulic diameter, $\beta = 65° \cdot \frac{\pi}{180°}$ is the Chevron angle and $N = \frac{N_{condenser}-1}{2}$ is the number of channels for the refrigerant flow. B and t are set as 0.08 m and 0.00205 m. Thermophysical properties are evaluated at mean temperature of the zone for the mono-phase fluids. The two areas of the heat transfer result from the model solution while the overall condenser surface defined at design condition, will be assumed constant in any other operating point, as discussed in next section.

With the aim of enhancing model accuracy, pressure drops are considered. Longo correlation (Longo & Zilio, 2013) is used to represent the physic behavior of the condensation, as shown in eq. 10.

$$\Delta p = \frac{15}{8} \cdot KEV \qquad with\ KEV = \frac{G^2}{2 \cdot \bar{\rho}} \qquad \textit{(eq. 10)}$$

For the de-superheating part, Martin correlation (Martin, 1996) is implemented in eq. 11 and eq. 12.

$$f = \left[\frac{\cos\beta}{\left(0.18 \cdot \tan\beta + 0.36 \cdot \sin\beta + \frac{f_0}{\cos\beta}\right)^{0.5}} + \frac{1-\cos\beta}{(3.8 \cdot f_1)^{0.5}}\right]^{-2} \quad with \begin{cases} \begin{cases} f_0 = \frac{64}{Re} \\ f_1 = \frac{597}{Re} + 3.85 \end{cases} & Re < 2000 \\ \begin{cases} f_0 = (1.8 \cdot log_{10}\, Re - 1.5)^{-2} \\ f_1 = \frac{39}{Re^{0.289}} \end{cases} & Re \geq 2000 \end{cases} \qquad \textit{(eq. 11)}$$

$$\Delta p = f \cdot \frac{L}{D_H} \cdot KEV \qquad \textit{(eq. 12)}$$

3.3. Expansion Valve

The working principle of the expansion valve is described by an isenthalpic transformation, where the refrigerant undergoes a pressure drop with no enthalpy variation. Eq. 13 expresses this behavior:

$$h_4 = h_3 \qquad \textit{(eq. 13)}$$

The task of this component is to maintain a defined superheating of refrigerant vapor at the evaporator outlet to avoid liquid droplets transport inside the compressor. In this paper, a constant superheating of 5K is used.

3.4. Evaporator

This component, similarly to the condenser, is a plate heat exchanger, so it is modelled in a similar way. Evaporation and superheating zones are identified. Tough the superheating section is small in terms of heat transfer rate, it has to be included in order to have an accurate model. The governing equation is:

$$\dot{Q}_{evaporator} = \sum_{i=0}^{zones} U_i \cdot A_i \cdot LMTD_i \qquad \textit{(eq. 14)}$$

Thermal transmittance U is calculated using eq. 7 and the convective heat transfer coefficient h_{conv} is obtained from eq. 8 for single-phase fluids and from Han, Lee and Kim correlation (Han, et al., 2003) for the evaporating refrigerant fluid, as shown in eq. 15.

$$Nu = Ge_1 \cdot Re_{LS}^{Ge_2} \cdot Bo_{eq}^{0.3} \cdot Pr_{LS}^{0.4} \qquad \textit{(eq. 15)}$$

Ge_1 and Ge_2 are functions of the heat exchanger geometry and Bo_{eq} is the boiling number. They can be evaluated as follow:

$$Ge_1 = 2.81 \cdot \left(\frac{P_{COR}}{D_H}\right)^{-0.041} \cdot (\pi/2 - \beta)^{-2.83} \qquad \textit{(eq. 16)}$$

$$Ge_2 = 0.746 \cdot \left(\frac{P_{COR}}{D_H}\right)^{-0.082} \cdot (\pi/2 - \beta)^{0.61} \qquad \textit{(eq. 17)}$$

$$Bo_{eq} = \frac{q_{wall}}{G_{eq} \cdot \Delta h_{L-V}} \qquad \textit{(eq. 18)}$$

where P_{COR} is the corrugation pitch, $q_{wall} = G \cdot (h_{VS} - h_4)$ is the specific thermal power at the wall and $G_{eq} = G \cdot \left[1 - x_4 + x_4 \cdot \left(\frac{\rho_{LS}}{\rho_{VS}}\right)^{0.5}\right]$ is the equivalent specific flow rate of a single channel and x_4 is the fraction of vapor in the refrigerant flow rate at the inlet of the evaporator. In analogy with the condenser, also the evaporation and superheating areas are obtained by solving the analytical model and the total surface of the evaporator is determined at design condition.

To model pressure drop, as condenser the correlation of Martin is used for the superheated vapor. In the evaporation zone, the following correlation is chosen (Longo, et al., 2016).

$$\Delta p = \frac{5}{3} \cdot KEV \qquad \textit{(eq. 19)}$$

3.5. Refrigerant Fluid

The fluid used in the heat pump is R134a and is modelled using lookup tables created starting from the software REFPROP 9.1 (NIST, 2017), which implements equations of state of different compounds. The selected discretization step (1 °C for the temperature, 25 kPa for the pressure and 500 J/kg for the enthalpy) of the tables was selected to guarantee high accuracy while keeping a fast model convergence.

3.6. PV/T Modules

For solar panels, both thermal and electric modeling is needed. Thermal behavior is described by eq. 20, which takes into account optical losses of the glass and of the PV array and convective losses to the environment. Here, radiative losses are linearized with first order temperature differences which is a reasonable assumption considering the low operating temperature.

$$\eta_{th} = \eta_{opt} - a_1 \cdot \frac{(T_{pump,out} + T_{SC,in})/2 - T_{amb}}{G_T} = \frac{\dot{V}_{SC} \cdot \rho_{sc} \cdot c_{SC} \cdot (T_{pump,out} - T_{SC,in})}{G_T \cdot A_{panel} \cdot N_{panels}} \qquad \textit{(eq. 20)}$$

Coefficients η_{opt} and a_1 are obtained from an experimental campaign carried out at SolarTech^{Lab} at Politecnico di Milano between spring and summer of 2017. PV/T modules are roll-bond type, with poly-crystalline solar cells. Tab. 1 summarized the main characteristics of panels used.

Tab. 1: Characteristic of PV/T panels

A_{panel} [m²]	η_{opt}	a_1 [(W/m²)/K]	$\eta_{el,REF}$	$\dot{W}_{REF}$ [W$_p$]	γ [%/K]	$T_{cell,REF}$ [°C]
1.63	0.528	13.658	0.153	250	0.42	56

Electric behavior of PV cells is modelled using the power coefficient approach. The generated power is function of the solar irradiance G and the temperature of the cells (both considered uniform on the panel surface), as shown in eq. 21.

$$\eta_{el} = \eta_{el,REF} \cdot \left[1 + \gamma \cdot \left(T_{cell} - T_{cell,REF}\right)\right] = \frac{\dot{W}_{el}}{G_T \cdot A_{panel} \cdot N_{panels}} \quad \textit{(eq. 21)}$$

where $\eta_{el,REF}$ and $T_{cell,REF}$ are taken from the datasheet of the panel and T_{cell} is evaluated as the mean fluid temperature of the fluid circulating on the panel $\bar{T}_{fluid}$ plus a constant value, which is here assumed equal to 10K.

Pressure drops of PV/T panels are modelled using a polynomial curve of grade two extrapolated from a test done by the manufacturer, as shown in eq. 22.

$$\Delta p_{panel} = 980.9 \cdot \dot{V}_{SC}^2 + 4475 \cdot \dot{V}_{SC} \quad \textit{(eq. 22)}$$

where the volumetric flow rate is expressed in [l/min].

3.7. Hydraulic Loop

Secondary hydraulic loop is considered in the model including a volumetric pump, whose power consumption is modelled as follow:

$$\dot{W}_{pump} = \dot{V}_{SC} \cdot \frac{\Delta p_{sc}}{\eta_{pump}} \quad \textit{(eq. 23)}$$

Pump efficiency is assumed to be constant equal to 15%, a typical value for centrifugal pumps, and the pressure drop is calculated considering the hydraulic circuit, the evaporator and PV/T modules. Tab. 2 summarizes the characteristic of the hydraulic circuit, while eq. 24 shows the modelization of exchanger pressure drops.

Tab. 2: Characteristic of secondary hydraulic circuit

Tubes Length [m]	Losses [Pa/m*(l/min)²]	Volumetric Glycol Fraction (X_{SC})
7	9	0.3

$$\Delta p_{evaporator} = 51570 \cdot \dot{V}_{SC}^2 + 3.229 \cdot \dot{V}_{sc} - 0.2362 \quad \textit{(eq. 24)}$$

where the volumetric flow rate is expressed in [l/min]. However, a fraction of the pump power is dissipated as heat, which produces an increase of temperature of the fluid. This increase is considered by means of the eq. 25.

$$\dot{Q}_{diss,pump} = \dot{V}_{SC} \cdot \Delta p_{SC} \cdot \frac{1-\eta_{pump}}{\eta_{pump}} = \dot{V}_{SC} \cdot \rho_{SC} \cdot c_{SC} \cdot \left(T_{pump.out} - T_{SC,out}\right) \quad \textit{(eq. 25)}$$

4. Model Resolution and Optimization

Equations described in Section 3 are implemented in a MATLAB® code. To resolve the SAHP system, other equations are needed and a design condition must be defined. Firstly, energy balances of each zone of condenser and evaporator and surface balances of heat exchangers are introduced, as shown in the following equations.

$$\dot{m}_{refr} \cdot \left(h_{SV}(T_{cond}) - h_3\right) = U_{cond} \cdot A_{cond} \cdot \frac{\left(T_{cond} - T_{PR,in}\right) - \left(T_{cond} - T_x\right)}{log\frac{T_{cond} - T_{PR,in}}{T_{cond} - T_x}} = \dot{V}_{PR} \cdot \rho_{PR} \cdot c_{PR} \cdot \left(T_x - T_{PR,in}\right) \quad \textit{(eq. 26)}$$

$$\dot{m}_{refr} \cdot \left(h_2 - h_{SV}(T_{cond})\right) = U_{de-sh} \cdot A_{de-sh} \cdot \frac{\left(T_{cond} - T_x\right) - \left(T_2 - T_{PR,out}\right)}{log\frac{T_{cond} - T_x}{T_2 - T_{PR,out}}} = \dot{V}_{PR} \cdot \rho_{PR} \cdot c_{PR} \cdot \left(T_{PR,out} - T_x\right) \quad \textit{(eq. 27)}$$

$$\dot{m}_{refr} \cdot \left(h_{SV}\left(T_{evap}\right) - h_4\right) = U_{evap} \cdot A_{evap} \cdot \frac{\left(T_{SC,out} - T_{evap}\right) - \left(T_y - T_{evap}\right)}{log\frac{T_{SC,out} - T_{evap}}{T_y - T_{evap}}} = \dot{V}_{SC} \cdot \rho_{sc} \cdot c_{SC} \cdot \left(T_{SC,out} - T_y\right) \quad \textit{(eq. 28)}$$

$$\dot{m}_{refr} \cdot \left(h_1 - h_{SV}\left(T_{evap}\right)\right) = U_{sh} \cdot A_{sh} \cdot \frac{\left(T_y - T_{evap}\right) - \left(T_{SC,in} - T_1\right)}{log\frac{T_y - T_{evap}}{T_{SC,in} - T_1}} = \dot{V}_{SC} \cdot \rho_{sc} \cdot c_{SC} \cdot \left(T_y - T_{SC,in}\right) \quad \textit{(eq. 29)}$$

$$A_{condenser} = A_{cond} + A_{de-sh} \quad \textit{(eq. 30)}$$

$$A_{evaporator} = A_{evap} + A_{sh} \quad \textit{(eq. 31)}$$

T_x and T_y are the temperatures of the primary and secondary circuits at which the condensation and evaporation of the refrigerant fluid starts and stops respectively. The design condition determines the total area of the condenser and the evaporator together with the correct number of plates of the two heat exchangers which are determined with an empirical correlation (eq. 32):

$$N_{plates} = 2 \cdot \left\lceil \frac{\left(\frac{\dot{Q}_{HX}}{\dot{Q}_{plate}} + 2\right)}{2} \right\rceil \qquad \textit{(eq. 32)}$$

$\dot{Q}_{plate}$ is the heat exchanged by a single plate, set at 200 W/plate, after a preliminary analysis on different commercial softwares. Finally, $A_{condenser}$, $A_{evaporator}$, and the two $\dot{Q}_{HX}$ are obtained solving the complete model in a standard working condition that is common used to build the datasheet of a water-to-water heat pump. Tab. 3 shows the temperatures of this condition.

Tab. 3: Temperatures at the design condition

T_{evap} [°C]	ΔT_{sh} [K]	$T_{SC,in}$ [°C]	$T_{SC,out}$ [°C]	T_{cond} [°C]	ΔT_{sub} [K]	$T_{PR,in}$ [°C]	$T_{PR,out}$ [°C]
2	5	10	7	50	0	40	45

The model developed is a system of non-linear equations, that can be solved with the function *fsolve* available in the MATLAB® library. Fig. 4 describes the logical steps followed for all the simulations:

- In the first step, geometrical parameters of the evaporator and the condenser are calculated from the design condition. In this situation, T_{evap} and T_{cond} are set, as well as temperatures at the inlet and at the outlet of the heat exchangers and superheating in point 1 and subcooling in point 3 of the refrigerant cycle. All the unknown variables can be explicated and the solver is not required. Solar irradiance and ambient temperature for a fixed number of PV/T modules are a result in this case and their values can be used to do a preliminary evaluation of the energetic feasibility of the system;
- Secondly, *fsolve* function solves the system of equations (that with some passages can be reduced to a system of 5 non-linear equations in 5 variables, which are T_{evap}, T_{cond}, $T_{SC,out}$, A_{evap} and A_{cond}), using as input parameters the solar irradiance and the ambient temperature, which are exogenous variables, and the number of PV/T panels;
- If a solution is found by the solver, a series of physical boundaries are introduced to check the working point feasibility. The following equations explain this approach.

  $$img(solution) \neq 0 \quad \forall\, solution \qquad \textit{(eq. 33)}$$

  $$A_{evap}, A_{cond} > 0 \qquad \textit{(eq. 34)}$$

  $$envelope\left(T_{evap}, T_{cond}\right) = true \qquad \textit{(eq. 35)}$$

  $$T_{SC,out} > T_{freezing}(X_{SC}) \qquad \textit{(eq. 36)}$$

  Constrains are applied after the resolution of the system to avoid solver function failure when an intermediate unfeasible solution is found but the final solution is feasible.

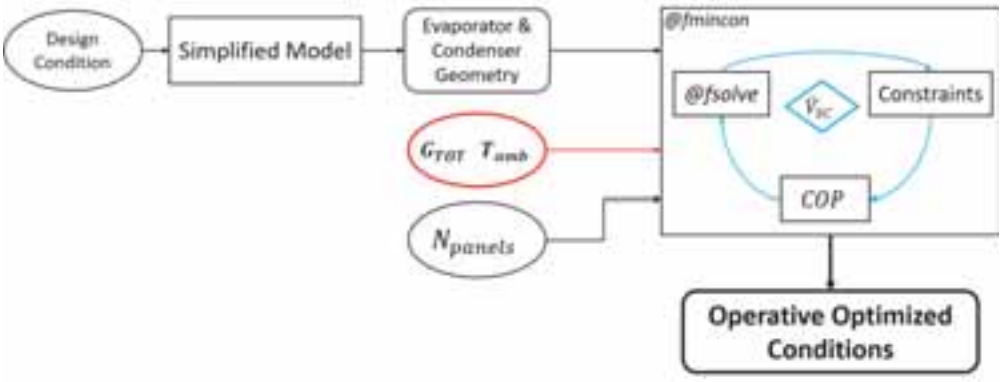

Fig. 4: Explanation of the logical steps followed for a simulation

In addition to the physical model of the SAHP, an optimization tool is used to maximize the performance parameter COP (Coefficient of Performance), which is expressed by eq. 37.

$$COP = \frac{\dot{Q}_{cond}}{\dot{W}_{comp}+\dot{W}_{pump}} \qquad (eq.\ 37)$$

The optimization is done with the function *fmincon* varying the volumetric flow rate $\dot{V}_{SC}$. Another constraint is introduced to implement the behavior of the PV/T panels: the flow rate must be between $0.008\overline{3}$ l/s (0.5 l/min) and $0.0\overline{3}$ l/s (2 l/min) for each line of PV/T panels in parallel to avoid low heat transfer coefficient and too high pressure drops. Fig. 5 is an example that shows the presence of a maximum of the COP in the range previously defined: thermal power at the condenser presents a limited grown, following the grown of the secondary loop flow rate, the electric consumption of the compressor is approximatively constant but the pump consumption increases strongly with a quadratic behavior. The opposite trends result in a maximum of the COP.

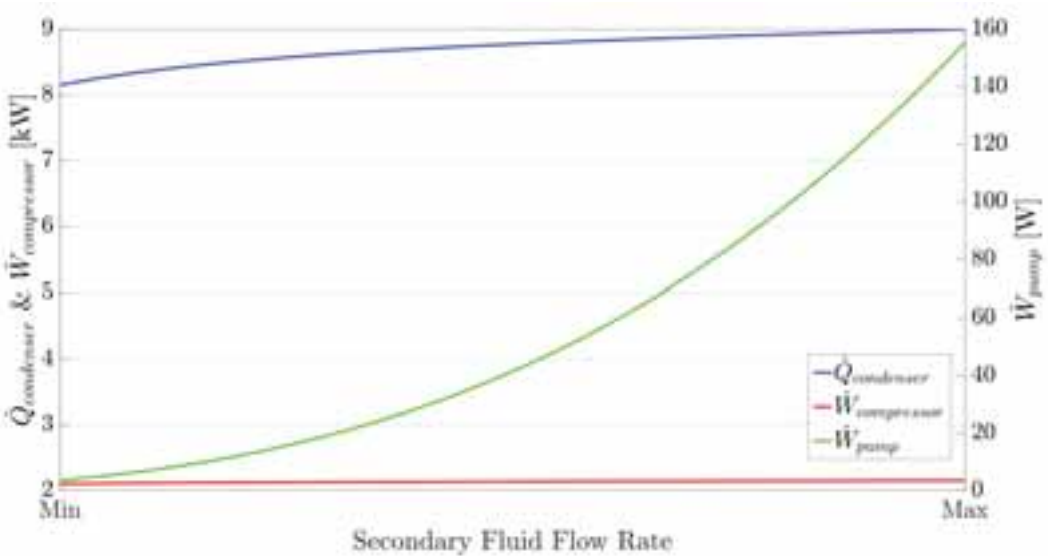

Fig. 5: Explanation of the presence of a maximum of COP as function of secondary fluid flow rate

In the end, Tab. 4 shows the results of the mathematical model obtained in the design condition, which are the same independently of the number of PV/T modules. Tab. 5 shows the solar irradiance needed to produce heat required in the evaporator in the design condition for 12, 16, 20 and 24 PV/T panels respectively.

Tab. 4: Results of the model in the design condition

COP	$\dot{Q}_{condenser}$ [kW]	$A_{PLATE,condenser}$ [m²]	$A_{PLATE,evaporator}$ [m²]	$N_{PLATE,condenser}$	$N_{PLATE,evaporator}$	T_{amb} [°C]
3.19	8.52	0.0258	0.0197	46	36	7

Tab. 5: Solar irradiance required in the design condition with different number of PV/T modules

	12 PV/T	**16 PV/T**	**20 PV/T**	**24 PV/T**
G_T [W/m²]	642.95	494.34	404.55	344.47

5. Results

Starting from the design conditions, the model is used to assess the performance of a SAHP system at different ambient conditions. In particular, solar irradiance was varied between 0 W/m² to 1000 W/m² with steps of 100 W/m², ambient temperature from -20°C to 20°C with steps of 5 °C.

Fig. 6 shows the behavior of the COP as a function of solar irradiance and ambient temperature for a layout with 12 and 24 panels, corresponding to a peak power of the installation of 3 kW_{el} and 6 kW_{el} respectively. As expected, COP increases with the ambient temperature and solar irradiance. The dependency is linear and the influence of solar irradiance is more pronounced than the one the ambient temperature. The case with more PV/T modules has better performance, even though differences are quite limited. In both cases, a non-operating zone is present (blue zone) representing the freezing conditions of the water plus glycol mixture points.

It is important to notice that the system can work also during the night with an acceptable COP (greater than 2). This is possible because of the high a_1 of the PV/T panels that permits to absorb enough energy from the environment (evaporation temperature is lower than the ambient one in these cases) and provide the heat required by the heat pump. This possibility increases the flexibility of the system extending the achievable working conditions to the all day.

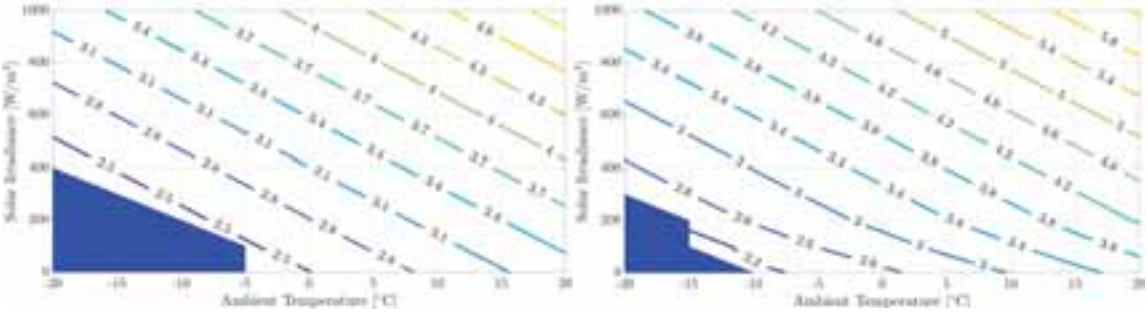

Fig. 6: Representation of COP for an indirect SAHP with 12 (left) and 24 (right) PV/T panels as a function of ambient temperature and solar irradiance

In Fig. 7, the ratio between the electric power produced by the PV/T modules and the power consumption of the HP and circulating pump for 12 (left) and 24 (right) PV/T is reported. When the ratio is greater than 1, the system is energetic self-sufficient, reducing the impact of heat pump consumption on the energetic costs and also the impact of the renewable power production on the national grid: the simultaneous production and consumption by the HP reduces the electricity import/export with respect to a more conventional solution with only PV modules and conventional heating system. In the case with 12 PV/T panels, the energetic self-sufficient condition is reached only with a high solar irradiance (between 600 and 800 W/m²), instead of the case with 24 panels that a lower value is needed, around 200-300 W/m².

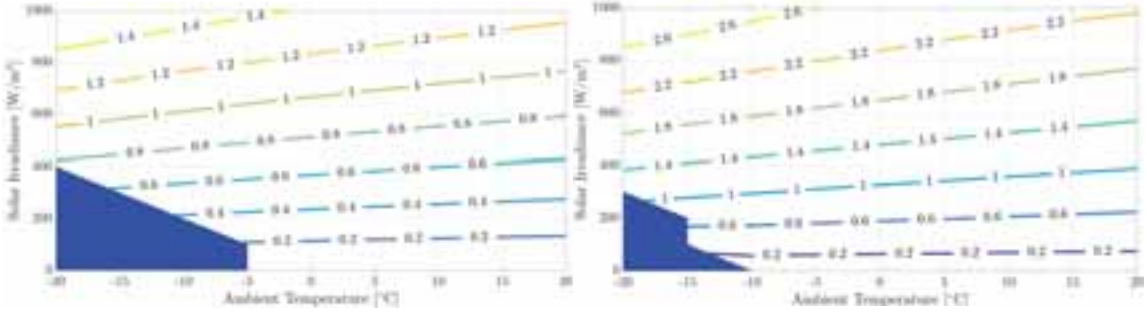

Fig. 7: Representation of the ratio between the electric power produced by PV/T modules and electric consumption of the SAHP with 12 (left) and 24 (right) PV/T panels as a function of ambient temperature and solar irradiance

Fig. 8 presents the advantages of this system with 12 PV/T panels respect of traditional technologies (air heat pump and PV modules). In the left graph, the difference between the inlet temperature of the evaporator and the ambient temperature is shown. It is possible to see that in most cases the temperature of the SAHP heat source is higher than the air temperature, which is the source of the standard air-to-water technology. Therefore, the proposed system improves the HP COP at constant thermal power produced, reducing the operational costs of the

machine. In addition, the typical performance decay of air-to-water heat pumps at ambient temperature below zero as consequence of the frost formation is not present here further increasing the SAHP performance gain.

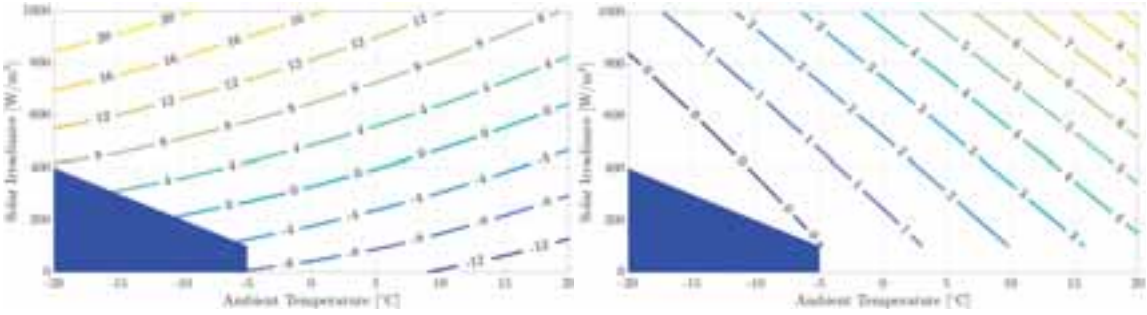

Fig. 8: Representation of the difference between the secondary fluid inlet temperature and the ambient temperature (left) and the increase of electric production of the PV/T modules (right) as functions of ambient temperature and solar irradiance

On the right of Fig. 8 the advantages in terms of electric power production are also reported, outlining the benefits of cooled cells with respect to conventional modules. As it is described in eq. 21, decreasing the temperature of the cell enhances the electric power production at the same solar irradiance. This effect is mainly visible with favorable ambient conditions and the increase reaches 8-9%. The standard PV module used for the comparison has the same peak power of the PV/T module and the power production is evaluated from the NOCT method.

6. Conclusions

In this paper, an analytical model of a solar-assisted heat pump combined with Photovoltaic Thermal modules is developed using the software MATLAB®. Governing equations for the heat pump and characteristic curve of the PV/T modules are identified. The compressor is modelled with polynomial expressions provided by manufacturer as function of the condensation and evaporation temperatures. Condenser and evaporator are discretized in two zones each (de-superheating and condensation the former, evaporation and superheating the latter) and physical behaviors are described by mean of the thermal transmittance U, evaluated using correlations from literature for mono-phase and two-phase heat transfer. The modeling considers also an isenthalpic expansion valve and R134a refrigerant fluid is used. Regarding PV/T modules, thermal and electric power are determined using the characteristic curve and the power method typical of PV technology. Two hydraulic circuits are considered to transfer the heat from the PV/T panels to the evaporator and from the condenser to the thermal load. A mixture of water and glycol is considered in the PV/T loop to prevent freezing phenomena.

MATLAB® *fsolve* function is used to resolve the system of equations related to the SAHP. The sizing of the heat exchangers is performed at design condition that is the same of a standard water-to-water heat pump. An optimization tool is also used to find the optimum operating condition of the whole system accounting for the circulating flow in the PV/T modules. This tool is the *fmincon* function of MATLAB® library. Solar irradiance and ambient temperature are varied to obtain the performance map of the system assuming different number of PV/T panels.

Results show that the COP of the SAHP varies between 2.5 and 4.9 in the case with 12 PV/T panels, and between 2.2 and 6.2 with 24 PV/T modules. The advantage of having more PV/T modules is quite limited in terms of thermal performance, but enlarges the operating conditions of the system (i.e. minimum ambient temperature) and increases the electric production. The study shows that the heat recovered by the PV/T modules is enough to permit the functioning of the heat pump also during the night with an acceptable COP (greater than 2), increasing the flexibility of the system. Other advantages are found regarding the temperature of the cold source respect of an air-to-water heat pump and the electric power production compared to a standard PV panel. For the first case, a higher temperature than the ambient temperature at the inlet of the evaporator is reached in most of the considered conditions. Advantages are even higher when the ambient temperature goes below zero, where a standard air source heat pump suffers of frost formation. Related to the electric production, the present paper shows that a cooled PV/T panel produces more power respect of a non-cooled PV panel, reaching values of 8-9% over referred to the standard production.

Future works will investigate all the advantages pointed out in this paper with experimental campaigns to confirm the results of the model.

References

Aste, N., Del Pero, C. & Leonforte, F., 2014. Water flat plate PV-thermal collectors. A review. *Solar Energy,* Volume 102, pp. 98-115, DOI: https://doi.org/10.1016/j.solener.2014.01.025.

Bombarda, P. et al., 2016. Thermal and electric performances of roll-bond flat plate applied to conventional PV modules for heat recovery. *Applied Thermal Energy,* Volume 105, pp. 304-313, DOI: https://doi.org/10.1016/j.applthermaleng.2016.05.172.

Calise, F., Dentice d'Accadia, M., Figaj, R. & Vanoli, L., 2016. A novel solar-assisted heat pump driven by photovoltaic/thermal collectors: Dynamic simulation and thermoeconomic optimization. *Energy,* Volume 95, pp. 346-366, DOI: https://doi.org/10.1016/j.energy.2015.11.071.

Emerson, 2017. *Emerson.* [Online] Available at: http://www.emersonclimate.com/europe/en-eu/products/compressors/scroll_compressors/comfort/heating/copeland_scroll_heating_compressors/pages/copeland_scroll_heating_technical_details.aspx?what=list&prodid=30867&bra=1&fam=17&prod=c&Ar=HP&prod_pic=1&ref=8&p [Accessed 1 October 2017].

Han, D., Lee, K. & Kim, Y., 2003. Experiments on the characteristics of evaporation of R410A in brazed plate heat exchangers with different geometric configurations. *Applied Thermal Engineering,* 23(10), pp. 1209-1225, DOI: https://doi.org/10.1016/S1359-4311(03)00061-9.

Ji, J. et al., 2008. Experimental study of photovoltaic solar assisted heat pump system. *Solar Energy,* Volume 82, pp. 43-52, DOI: https://doi.org/10.1016/j.solener.2007.04.006.

Kim, Y., 1999. An Experimental Study on Evaporation Heat Transfer Characteristics and Pressure Drop in Plate Heat Exchanger. *M.S. thesis, Yonsei University.*

Kumar, A., Baredar, P. & Qureshi, U., 2015. Historical and recent development of photovoltaic thermal (PVT) technologies. *Renewable and Sustainable Energy Reviews,* Volume 42, pp. 1428-1436, DOI: https://doi.org/10.1016/j.rser.2014.11.044.

Li, H., Sun, L. & Zhang, Y., 2014. Performance investigation of a combined solar thermal heat pump heating system. *Applied Thermal Engineering,* 71(1), pp. 460-468, DOI: https://doi.org/10.1016/j.applthermaleng.2014.07.012.

Liu, H., Jiang, Y. & Yao, Y., 2014. The field test and optimization of a solar assisted heat pump system for space heating in extremely cold area. *Sustainable Cities and Society,* Volume 13, pp. 97-104, DOI: https://doi.org/10.1016/j.scs.2014.05.002.

Longo, G., Mancin, S., Righetti, G. & Zilio, C., 2016. HFO1234ze(E) vaporisation inside a Brazed Plate Heat Exchanger (BPHE): Comparison with HFC134a and HFO1234yf. *International Journal of Refrigeration,* Volume 67, pp. 125-133, DOI: https://doi.org/10.1016/j.ijrefrig.2016.04.002.

Longo, G. & Zilio, C., 2013. Condensation of the low GWP refrigerant HFC1234yf inside a brazed plate heat exchanger. *International Journal of Refrigeration,* 36(2), pp. 612-621, DOI: https://doi.org/10.1016/j.ijrefrig.2012.12.018.

Martin, H., 1996. A theoretical approach to predict the performance of chevron-type plate heat exchangers. *Chemical Engineering and Processing: Process Intensification,* 35(4), pp. 301-310, DOI: https://doi.org/10.1016/0255-2701(95)04129-X.

Migliorini, L., Molinaroli, L., Simonetti, R. & Manzolini, G., 2017. Development and experimental validation of a comprehensive thermoelectric dynamic model of photovoltaic modules. *Solar Energy,* Volume 144, pp. 489-501, DOI: https://doi.org/10.1016/j.solener.2017.01.045.

NIST, 2017. *REFPROP.* [Online] Available at: https://www.nist.gov/srd/refprop [Accessed 1 October 2017].

Nuntaphan, A., Chansena, C. & Kiatsiriroat, T., 2009. Performance analysis of solar water heater combined with heat pump using refrigerant mixture. *Applied Energy,* 86(5), pp. 748-756, DOI: https://doi.org/10.1016/j.apenergy.2008.05.014.

Shah, M., 1979. A general correlation for heat transfer during film condensation inside pipes. *International Journal of Heat and Mass Transfer,* 22(4), pp. 547-556, DOI: https://doi.org/10.1016/0017-9310(79)90058-9.

SoLink, 2017. *SoLink PVT.* [Online] Available at: http://www.solink.it [Accessed 1 October 2017].

Zondag, H., De Vries, D., Van Helden, W. & Van Zolingen, R., 2003. The yield of different combined PV-thermal collector designs. *Solar Energy,* Volume 74, pp. 253-269, DOI: https://doi.org/10.1016/S0038-092X(03)00121-X.

Strategies, Policies, and Case Studies for Renewable Heat and Electricity

Huyro Smart Ecological Farm in Peru, an Approach to Sustainability

Miguel Hadzich[1], Sandra Vergara[1] and Juan Pablo Pérez[1]

[1] Pontificia Universidad Católica del Perú, Lima (Perú)

Abstract

The present work shows the results of the Huyro Ecological Farm project during its first 6 years of operation in Cusco, Peru. In an attempt to make it 100% sustainable and self-sufficient, many efforts were made to supply energy, water, communications and even food security within the 3 hectares of tropical wetland land.

This paper presents the evaluation of the sustainability of the project that includes the operation of renewable energy equipment and its validation in the field, in order to create a policy that allows the transfer and commercialization of the technologies used on farm to the community. With the use of the Star of Sustainability method we are able to see, visually and efficiently, the process of sustainability of technological projects.

Keywords: Sustainability, ecological farm, smart farm, evaluation, qualitative methods, solar energy

1. Introduction

The Rural Sector Support Group GRUPO PUCP is an operating unit of the Department of Engineering at the Pontificia Universidad Católica del Perú (PUCP) and has developed several designs and implemented equipment in various areas of Peru. This study considers the results of Huyro Ecological Farm conducted by GRUPO PUCP in Peruvian territory during the last six years.

The Huyro Ecological Farm is a training center dedicated to the development and diffusion of research and application of the appropriate eco technologies or appropriate technologies, complemented by rural tourism focused mainly on agro tourism that generates ecological awareness, change of habits and that drive the self-sufficiency of the population, as well as the preservation of the natural resources of the area. See Fig.1

The ecological farm offers the following benefits to the Peruvian community: It is an educational place to teach students of universities, institutes, schools and general public; a place for research in science and engineering; a reserve of Peruvian biodiversity as guardians of seeds; an example of a self-sufficient and sustainable project with ecological agro industry; Peru's first smart farm with state-of-the-art technology; a model for gastronomy, hotel and tourism projects and finally a model of Scientific Park of Appropriate Technologies that makes it the leader among Innovation Centers in provinces in Peru.

Fig. 1. Photos of the main house and hostel in Huyro Ecological Farm in Cusco.

doi:10.18086/swc.2017.34.01 Available at http://proceedings.ises.org

2. Methodology

Hypothesis

There is a place in the tropical zone of Cusco where you can live using only the kindness of nature, obtaining energy, water, communications with equipment that use renewable energy as a source of energy. Food security is obtained from the processing of fruits and products of the area based on solar energy, achieving a technological, economic, political, social and environmental sustainability of its operation.

Methodology used

The proposed method, Sustainability Star (Hadzich 2014, Ref 1), allows us to analyze the sustainability process of the technology projects that were implemented on the farm during the last 6 years of operation and provides us with a clear view to either decide the continuity of the projects or their cancelation. The Star has 5 tips that analyze the Technological (T), Economic (E), Political (P), Social (S) and Environmental (A) factors which from now own we will refer to as TEPSA (in Spanish). See Fig. 2

Each of these factors includes several aspects within themselves. In TECHNOLOGY we consider aspects such as utility, sustainability, operation, reliability and maintenance; in ECONOMY we consider the income, employment, savings, affordability and innovation; in POLITICS we consider the political interest, the acceptance, legal aspects, promotion and distribution; in SOCIAL we consider the compatibility, motivation, life improvement, participation and capacity; and in ENVIRONMENT we consider the friendliness, climate, pollution, awareness, and health.

We believe it is a good tool to be used in all projects with a technological and political base in their development processes. This method could also be used in other situations where projects have been completed technological base and gives us a good insight to decide the continuation or closure thereof.

SUSTAINABILITY DEVELOPMENT: TEPSA oR 5 E´s

T	Tecnología - Technology	**E**	Engineering
E	Economía - Economics	**E**	Economics
P	Politica - Political	**E**	Ethical
S	Social - Social	**E**	Equity
A	Ambiental - Environmental	**E**	Environment

Fig. 2: Factors of sustainable development in the Sustainability Star

To analyze the index that corresponds to each tip of the Star, a 25 question survey is made, defining the break percentage of the shape. These surveys refer to TECHNOLOGY (utility, sustainability, operation, reliability, maintenance), ECONOMY (income, employment, savings, affordability, innovation), POLITICS (political interest, acceptance, legal, promotion, and distribution), SOCIAL (compatibility, motivation, life improvement, participation and capacity) and ENVIRONMENTAL (friendly, climate, pollution, awareness, and health).

If all surveys questions have positive answers then the star will be perfect without any break, as shown in Fig. 2 and the project will be considered as 100% SUSTAINABLE .

In order to decide the percentage corresponding to each point of the star we use a survey of 25 questions which defines the percentage of the Star Broken. See Fig. 3. Negative responses from the survey will fall inside the star percentage values that indicate the failure of the project in each of TEPSA factors.

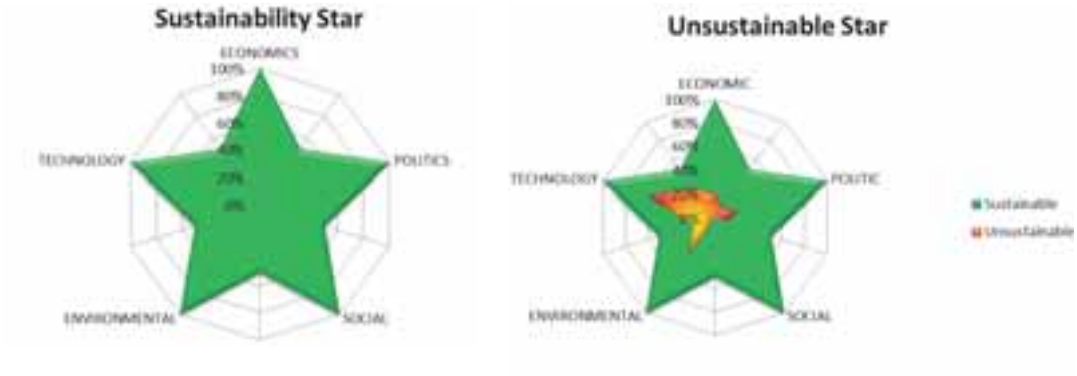

Fig 3: Example of Sustainability Stars – Perfect (left) and Broken (right).

3. Case Studied

The Huyro Ecological Farm is a training center dedicated to the development and diffusion of research and application of appropriate technologies or technologies that use renewable energies, complemented by rural scientific tourism focused mainly on agro tourism.The goal is to generate ecological awareness and change of habits that promote self-sufficiency and self-development of the population of the region, as well as the well care of natural resources.

This centre is a place that has the adequate infrastructure and equipment to be self-sufficient, provides its own electricity and the mechanical forces are obtained from the water, wind and sun sources. It provides its own food with eco farms. To avoid environmental pollution, water and solid waste are recycled and treated in treatment plants. It is a privileged place for demonstrating the operation of GRUPO PUCP technologies and to spread the achievements of the projects that have been developed.

The Huyro Ecological Farm has as its mission: To educate, train and promote awareness and to carry out actions that contribute to the development of sustainable communities. It provides on-site and distance classes, courses, workshops, internships and seminars on the subject of appropriate technologies, renewable energies and organic crops and provides national and international students with an opportunity to study and work voluntarily and learn about techniques for sustainable development.

It has an adequate infrastructure to provide the services required with architecture adapted and respectful to its surroundings; the design includes planned areas, flexible and dynamic spaces to meet educational needs, tourism and recreation in order to assure positive interaction with the environment and effective prevention of the ecological deterioration of the site.

Huyro Ecological Farm is located in Huayopata district, province of La Convención, department of Cusco, Perú, and 3 hours away from the historic Sanctuary of Machu Picchu. See Figs. 4 and 5.

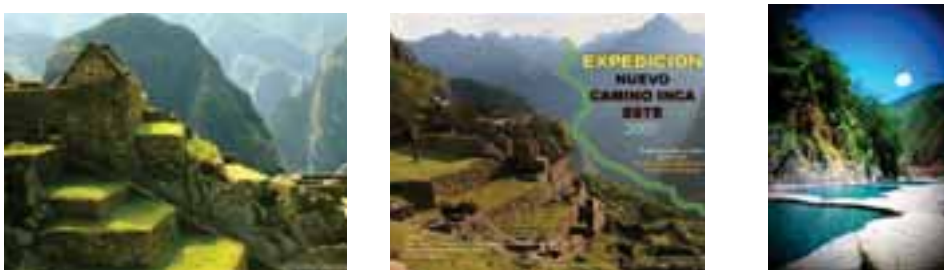

Fig. 4: Photos of Machu Picchu and Thermal Baths in Santa Teresa.

Fig.5: Satellite location of the project regarding Aguas Calientes - Machu Picchu. Google Map or Google Earth.

The technologies used on the farm are being disseminated to the community and the academic world of schools, technological institutes and universities that visit it continuously. See Fig. 6. This interaction of the farm with the visitors enables the products and technologies shown to reach the real world of the communities in need through their free distribution and marketing. GRUPO PUCP carries out the sale and demonstration of the technologies to visitors of the farm making it, both, an educational and commercial place.

Fig. 6: Catalog and Spanish Project of the Huyro Ecological Farm

See Catalog and Complete Project in Spanish in http://miguelhadzich.com/granja-ecologica-huyro/

4. Analysis of the farm's sustainability

The Huyro Ecological Farm obtains profits through training, research, development and transfer of appropriate technologies, volunteering and sustainable tourism. These activities generate economic benefits that can be reinvested to seek maximum profitability and generate the least negative impact. See Fig. 7

		T	E	P	S	A
		Technology	Economy	Politic	Social	Environmental
Energy	ELECTRICITY	Photovoltaic panels		Advice to settlers	Training	Solar energy
		Hydraulic Wheels		Advice to settlers	Educational site	Hydraulic energy
		Interconnected network	Services pay	PUCP Subsidy		Hydraulic energy
	HEAT	Solar thermal		Advice to settlers	Educational site	Solar energy
		Solar Dryers		Advice to settlers	Educational site	Solar energy
		Solar concentrators		Advice to settlers	Educational site	Solar energy
		Wood fired ovens		Advice to settlers	Educational site	Reforested biomass
		Improved kitchens		Advice to settlers	Educational site	Reforested biomass
	TRANSPORT	Van	Fuel purchase	PUCP Subsidy		Contamination
		Tractor		PUCP Subsidy		Contamination
	COMMUNICATIONS	Phone		PUCP Subsidy		
		Internet		PUCP Subsidy	Free Wifi for schools	
Water	Potable	Interconnected network	Monthly payment	PUCP Subsidy		Hydraulic energy
		Rainwater harvesting		Advice to settlers	Educational site	Hydraulic energy
	Irrigation	Sprinkler irrigation		Association of irrigat	Educational site	Hydraulic energy
		Flood irrigation				Hydraulic energy
Food	Orchard Crops		Consumption of Vegetables		Educational site	Biomass
			Consumption of corn, beans		Educational site	Biomass
	Fruits	Drying citrus, banana, mango			Gift coffee seedlings, fruits	Biomass
	Agroindustry	Solar Chocolate Factory	Sale of products	Advice to settlers	Educational site	Biomass
		Solar Coffee Factory	Sale of products	Advice to settlers	Educational site	Biomass
		Solar Tea Factory	Sale of products	Advice to settlers	Educational site	Biomass
	Miscellaneous supplies		Purchase of oil, rice, noodles	PUCP Subsidy		
	Trash	Recycling System			Educational site	
		Biodigesters			Educational site	Biomass
	Foresta and Flowers	Nursery	Sale of seedlings and seeds	Advice to settlers	Educational site	Biodiversity
	Lodging	Chainsaws	Sale of firewood			Biomass
		Rooms for 16 people	Sale of food and lodging rental			

Fig. 7: General scheme of the Sustainability and Self-sufficiency of the Huyro Ecological Farm

4.1 TECHNOLOGICAL SUSTAINABILITY

The Farm generates its own energy thanks to the natural resources of the area; it provides its own electricity and its own mechanical forces of the sources of water, wind, sun and biomass using technologies already developed by the GRUPO PUCP in its 25 years of life. All agro-industrial technologies are operating within the farm as a model for visitors and finished products are available for sale.
Each technology is available to interested people through workshop courses that are taught throughout the year. See survey on Technology Sustainability in Fig. 8.

			TECHNOLOGY SUSTAINABILITY	
			Survey about machines or project operation	
	YES	NO		
1.-	x		**Do you tkink that the machine is going to be useful?**	
2.-		x	**Technology (or machine) is constantly being used during the last year?**	
3.-	x		**Do you think the machine can easily operate?**	
4.-		x	**Do you think is a reliable technology?**	
5.-	x		**Do you think that local technicians can repair, copy or modify -all or part- of this machine?**	

Fig. 8: Survey on the Technological Sustainability of the Huyro Ecological Farm

The supply of electric energy is through a hybrid system of photovoltaic panels, hydraulic wheel and connection to the grid. There are 6 photovoltaic panels of 300 Wp each, as well as a hydraulic wheel of 4m in diameter. Water consumption is supplied by 5 different sources: drinking water from the nearby town, water for technical irrigation, water from the springs or rainwater collection and water pumping from the Lucumayo River. Mobile and internet services were installed through a private company. All the waste is recycled and the organic matter is converted into compost and processed in biodigesters.

To generate electricity there are 6 photovoltaic panels of 300 Wp each, with atotal 1.8 kWp, which generate electrical energy with an average solar irradiation of 5.54 kWh / m2 day. There is also a (1) 2.4 m diameter hydraulic wheel that provides 2 kW of electric power at 12 V with an inverter at 220 V AC. In addition, there is (1) Pelton hydraulic turbine of 500 W to 220 V AC. For emergencies, there is an interconnected electrical grid which unfortunately has many fluctuations in voltage (180-230) and causes the machines to fail continuously.

To produce HEAT we have installed: Solar heat pipes and traditional hot water heaters. Hot boxes also provide hot water from firewood improved stoves. The wood used comes from controlled forest and only the surpluses of the largest trees are burned. There are two (2) Scheffler concentrators used for roasting products and cooking food. There are solar dryers both tunnel type (1) and domes (2) for the drying of products.

There are 5 WATER sources: Freshwater that comes from the city located 5 km away through the public network. This service costs US$ 3.00 a month to the board of irrigators. Technical irrigation supplies the farm with water through a 4-inch pipe from Huyro River specifically for sprinkler irrigation. In a future project, water from the Lucumayo River will be pumped to the house located 300 m away from it and at an altitude of 10 meters.. The farm can access water from the springs for flood irrigation. Finally, there is a traditional rainwater harvesting system using filters. For health reasons all water for human consumption has to be boiled.

Due to the good location of the land in relation to the transmission towers, there is a good telephone line service for cell phones and internet connection for which you pay $ 80 per month.

4.2 ECONOMICAL SUSTAINABILITY

Food security is achieved with the products of fruit trees and first need products to supply a family of 5 members. On the farm the following first need products produced are: Corn, sweet potato, cassava, beans, uncucha, potato, etc. Fruits such as oranges, mandarins, lemons, pineapples, avocados, bananas, medlars, raspberries, lucuma, cherimoya, passion fruit, cocoa and wild plants are produced. For controlled firewood trees we have pacae, walnut, tóroc, among others. There are medicinal and aromatic plants such as fennel, lavender, matic, chamomile, coca, tea, coffee, anise, etc. See Fig. 9 annual agricultural calendar of the farm.

The heat for cookers and ovens is obtained from wood from ecologically managed forest. To dry and roast products, solar thermal energy is used through Scheffler concentrators and linear parabolic plants that process coffee and cocoa in an agro-industrial and ecological way to produce solar coffee and chocolate.

Farm products are sold to villagers, such as tea, coffee, chocolate, sugar cane, jams, honey, etc .; souvenirs, books and videos regarding each of the technologies shown are also sold. The sale process is similar to that of the "Tiendecita Verde" of the GRUPO PUCP in Lima.

Internship programs are carried out for students from other countries; this project is carried out through the Field School program of PUCP. Refer to http://fieldschool.pucp.edu.pe/courses/engineering-ecological-technologies-cusco/general-information/#.U441K_l5OSp

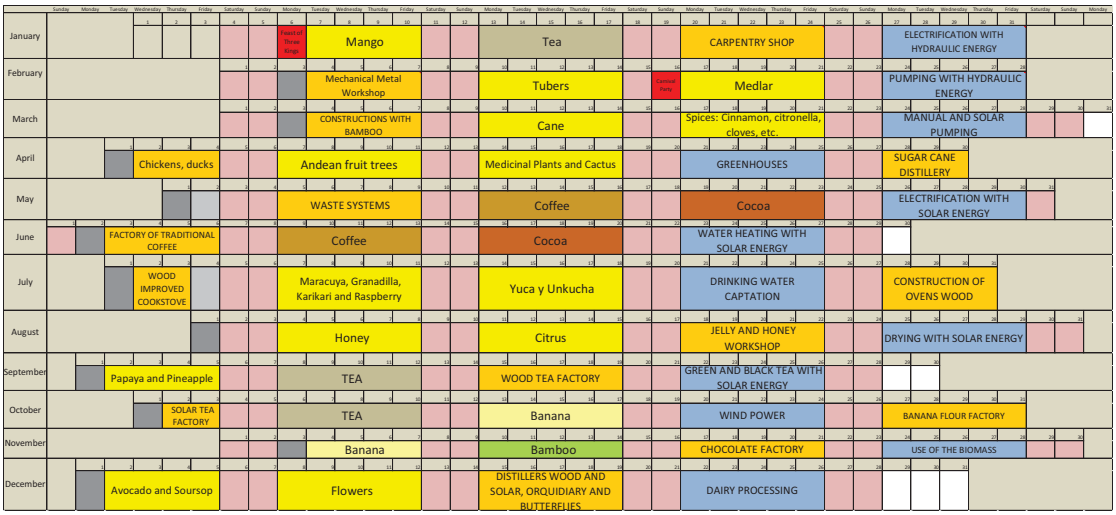

Fig. 9: Annual agricultural calendar of the Huyro Ecological Farm

Ecotourism and educational tourism are promoted for colleges, institutes and universities where GRUPO PUCP technologies installed on the farm are displayed and explained as well as the balanced coexistence between the natural environment and the dwellers. See Fig. 10. Rural ecotourism is promoted through guided tours, birdwatching activities and research projects designed for this type of climatic zones.

Fig. 10: Ecotourism and Training in the Huyro Ecological Farm

				ECONOMIC SUSTAINABILITY	
				Survey about machines and project cost	
	YES		NO		
6.-	x				**Do you see an economic improvement in your life or business when using this technology?**
7.-	x				**It has generated work for someone with the use of this technology in the community?**
8.-	x				**You think that you have saved on fuel or electricity when using this renewable technology?**
9.-			x		**Do you (or your neighbors) purchase or install a similar machine?**
10.-	x				**Do you think that this technology can be produced and sold in your community in the future?**

Fig. 11: Survey on the Economic Sustainability of Huyro Ecological Farm

In order for the farm to start generating more economic incomes that will make it profitable it is necessary to implement a tea factory that complements the existing coffee and chocolate factories. It is also necessary to increase the production of dried local fruits, especially citrus fruits such as orange, lime, grapefruit, mandarin as well as pineapple, mango and banana. See survey on Economical Sustainability in Fig. 11.

In addition, it is necessary to finish the preliminary research on the wild and native plants and implement the current nursery in a more modern and ecological way, using solar energy for thermal effects and laminar flow germinators for in vitro propagation of some endangered species.

For AGROINDUSTRY, there is a solar and coffee chocolate processing plant operating with 1.8 kWp photovoltaic panels that supply roasting machines (0.5 kW motor), a small 300 W refrigerator, (3) small electric motors for grinding - 0.25 kW each- as well as an electric motor of 0.5 kW for the de-pulping of coffee during production times. See Fig.12.

Fig. 12: Photo of the solar coffee and chocolate processing plant

The following figure 13 shows the financial evaluation of the farm project. The recovery time of the investment is calculated in around 9 years, but the farm can start generating incomes since its third year of operation.

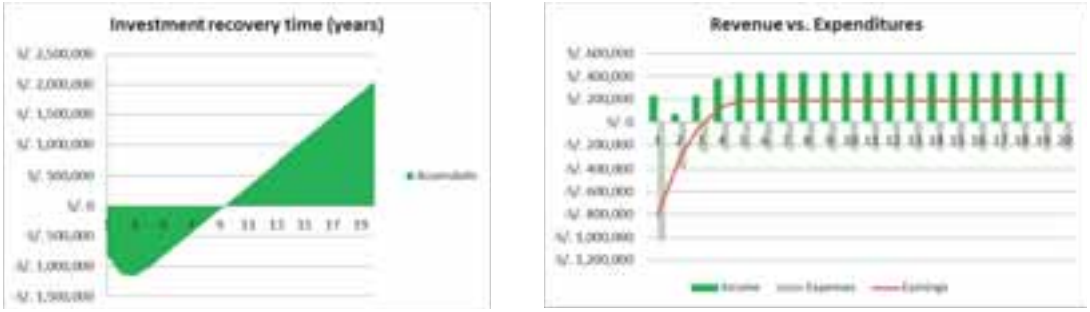

Fig. 13: Financial evaluation of the project

4.3 POLITICAL SUSTAINABILITY

We have a good social relationship with neighbours, as well as with the local and regional authorities. It has the recognition of the Huyro District Municipality and the Huayopata Governorship. See survey on Political Sustainability in Fig. 14.
It fosters an environment of solidary work amongst community residents and project staff.
Work is being carried out with the NGO “Projects Abroad” and with the “Colibrí Association” which also have offices in Huyro to encourage volunteering activities.

			SUSTAINABILITY POLICY	
			Survey on political and organizational project management	
	YES	NO		
11.-		x		**There has been interest in the project or the machine by any political authority?**
12.-	x			**The authorities of the community accept the project? There are requests from the community to some authority?**
13.-	x			**The project complies with the laws and regulations of the community and technical institutions ?**
14.-	x			**Do you believe that the government, person, or institution should promote this technology to other Peruvians?**
15.-	x			**The people of the town know the project?**

Fig. 14: Survey on the Political Sustainability of Huyro Ecological Farm

4.4 SOCIAL SUSTAINABILITY

The technologies developed are easily inserted into the sociocultural environment of the community, promoting development and revaluing local creativity. See survey on Social Sustainability in Fig. 15.

Community participation is sought through projects and activities that are carried out, especially with local schools and colleges. See Fig. 16. We have several projects with students from our own university supported by the Social Responsibility Direction focused on the construction of improved stoves in schools in the area.
We work with local people especially with builders, carpenters and metal mechanics.

			SOCIAL SUSTAINABILITY	
			Survey on the perception of the community about the project	
	YES	NO		
16.-	x			**The project is accepted "normal way" for the community?**
17.-	x			**There is interest in the community or their neighbors for the proposed technology?**
18.-		x		**The project has improved the standard of living of someone in the community ?.**
19.-	x			**The people have participated in some part of the project or activity?**
20.-	x			**There are people in your community with the necessary capabilities for operation and maintenance?**

Fig. 15: Survey on the Social Sustainability of Huyro Ecological Farm

Fig. 16: Visit of universities and colleges of the sector.

4.5 ENVIRONMENTAL SUSTAINABILITY

All systems, whether they are machines or processes, operate with technologies designed to maintain the ecological balance of the place. The use of renewable energy sources is mandatory and essential in all projects. Primarily local resources are responsibly used preserving the flora and fauna of the place making sure it is kept as a pleasant place where you can interact with nature.

All facilities have an environmentally friendly architecture to avoid negative influence in the management of its natural resources. See survey on Environmental Sustainability in Fig. 17.

				ENVIRONMENTAL SUSTAINABILITY	
				Survey on the impact of the project or the machine on the environment	
	YES		NO		
21.-	x				**The project is seen as a friendly environment technology ?**
22.-	x				**You do you think this machine is good for our Earth planet?**
23.-			x		**The project has created some kind of contamination in the environment?**
24.-	x				**Mind that this technology is clean rather than other similar package?**
25.-			x		**The use of this technology affects your health?**

Fig. 17: Survey on the Environmental Sustainability of the Huyro Ecological Farm

5. Conclusions

The Farm Sustainability Assessment shows us a great development in the fields of social, political and environmental components and the weaknesses in the economic and technological factors in which we are in the continuous process of improvement. In the case of the Huyro Ecological Farm, we are on the way to achieve 100% sustainability, but we still need to put a lot more effort to achieve this, especially in the field of food security.

We are aiming at attracting more tourists and environmental researchers so that their stay on the farm is pleasant and instructive. Thus, we plan to install more technologies such as a solar pool, a solar Jacuzzi, a solar tea factory, among others, that will become a model for the introduction of these technologies in the ecological hotels and rural communities of the surrounding areas and eventually be able to spread them throughout the world.

The Huyro Ecological Farm will be fully sustainable from the 9th year of operation. All constructions and technologies installed on the farm will be built by training/teaching local people, volunteers and participating students. We are trying to achieve sustainability through hard work and constancy.

Finally, the following Fig. 18 shows the evolution of sustainability in the Huyro Ecological Farm in the 5 years of existence and the positive advances in the different TEPSA aspects to try to achieve the necessary self-sufficiency and sustainability can be noticed.

Fig. 18: Evolution of the Sustainability of the Huyro Ecological Farm from 2012 to 2017

The proposed methodology for the evaluation of technological projects has proven to be a good tool for decision making, since it allows us to evaluate the results of a project by analyzing it's sustainability.

The evaluation of the sustainability of projects depends not only on technological and economic conditions of the equipment that works with renewable energy but also depends heavily on the social and political situations of the places where these projects are to be implemented.

6. References

Hadzich M., Ortiz I., Muñoz J.J., Bautista E. (2014). Metodología para la evaluación de la sostenibilidad de innovaciones tecnológicas en ambientes rurales. *Tesis doctoral Escuela Técnica Superior de Ingenieros Industriales, Universidad Politécnica de Madrid.*

Rogers E. Teoría de la Difusión de la Innovación (2003)
http://redc.revistas.csic.es/index.php/redc/article/viewFile/155/209

Palaniappan, V. S. (1998). Economics of solar air pre-heating in south Indian tea factories: a case study. *Solar Energy, 31-37.*

Creus, A., (2010). Energía Termosolar. Cataluña: Ceys

Zanabria Pacheco P., (2012). Radiación Solar en el Cusco. Lima: Guzlop.

SUSTAINABILITY ASSESSMENT OF SOLAR THERMAL COLLECTOR SYSTEMS FOR HOT WATER PREPARATION

Harald Kicker[1], Gernot M. Wallner[1] and Reinhold W. Lang[1]

[1] Institute of Polymeric Materials and Testing / Johannes Kepler University, Linz (Austria)

Abstract

Solar thermal collector systems are of high relevance and interest for the supply of low temperature heat for different purposes. Especially, hot water systems are dominating the solar-thermal market with non-pumped systems gaining more and more importance. The main objective of this paper is to assess various small and medium sized solar-thermal collector systems as to their sustainable development metrics. For the assessment a 5-step methodology developed by Ashby et al. (2016) was used. In ecological terms solar thermal hot water preparation significantly contributes to sustainability with energetic amortization times around 1 year. From an economic point of view systems in temperate climate zones for multi-family houses based on conventional metal/glass-collectors exhibit outstanding levelized costs of heat values. In hot climate zones small domestic hot water systems for single family houses fulfill both economic and ecological criteria. For such systems polymeric materials offer a better overall performance and mass production and ease of installation capability. The societal acceptance is high in less industrialized countries, but needs some improvement in industrialized countries, especially for most promising installations in multi-family houses.

Keywords: solar thermal collector; sustainable development; assessment

1. Introduction

Solar thermal collector systems are of high relevance and interest for the supply of low temperature heat for different purposes. Especially, hot water systems are dominating the solar-thermal market with non-pumped systems gaining more and more importance (Mauthner et al., 2016). Alternatives to the small hot water systems are medium-sized combi-systems allowing also for space heating or large systems for district heating and cooling or process heat. The main objective of this paper is to assess various solar-thermal collector systems as to their sustainable development metrics. Special focus is given to solar thermal collector systems for domestic hot water preparation.

2. Methodology and approach

The much-quoted definition of sustainable development by the Brundtland Commission tells: *'Sustainable development is development that meets the needs of the present without compromising the ability of future generations to meet their own needs'* (The Brundtland Report of the World Council on Economic Development, WCED 1987). But how is sustainable development to be achieved? The definition lacks of concrete guidance how to reach the goals.

Ashby et al. (2016) developed a 5-step analysis methodology for assessing sustainability of complex systems and multi-dimensional problems. The approach is to split the problem into layers and to follow a five-step strategy for assessing. The 5-step analysis includes:

- the definition of the prime objective as well as the size and time scale,
- the identification of the stakeholders,
- the fact-finding step to research both the factual background of the articulations and the validity of the concern expressed by the stakeholder,
- the synthesis of the facts for examination of how the facts influence human, natural and manufactured capital, and

doi:10.18086/swc.2017.34.02 Available at http://proceedings.ises.org

- the reflection step assessing the picture that has emerged and considering priority changes.

For the assessment of solar thermal collector systems for hot water preparation this 5-step methodology was used in this work.

3. Main results and conclusions

The layered approach to assess solar thermal collector systems as to their sustainable development metrics and the key findings are elucidated in the following. Due to the variety of solar thermal systems a special focus is on domestic hot water preparation, which is still the most important field of application. Further solar thermal technologies are currently evaluated.

Step 1: Background information, prime objective and scale

To meet carbon-reduction targets heat generation from renewable sources is of utmost importance. Direct conversion of sunlight via solar thermal collectors has many attractions. Mean solar irradiance varies between 150 and 250 W/m^2 dependent on the world region. In the use phase, solar thermal systems emit negligible CO_2 and they reduce dependence on imported energy. Historically solar thermal has grown at 15% per year for the last 15 years. Worldwide a capacity of 410 GW_{th} was installed corresponding to a total of 586 million m^2 of collector area. The annual collector yield of water-based systems in operation by end of 2014 was about 1.2 exajouls saving about 0.1 gigatonnes of CO_2 (Mauthner et al., 2016). While 2014 about 94% of the energy provided by solar thermal systems was used for domestic hot water, currently a trend to larger solar thermal systems coupled to district heating networks is discernible. Solar thermal at present contributes about 1% to total heat consumption. The potential contribution is much larger. Many national governments seek to realize this potential by offering subsidies and feed-in-tariffs.

In Europe targets for a 20% reduction in carbon emissions by 2020 and an 80% reduction by 2050 were defined. To which extent are these targets achievable by solar thermal? Is it a sustainable development?

Solar heat is intermittent. Most of the solar heat is generated in summer. However, the heating demand is significantly higher in winter. Hence, seasonal storage of heat is required. Economic storage is work-in-progress, yet just rather limited available. Large-scale investment is required. Furthermore, a significant drop in the growth rates of solar thermal are discernible, especially in Europe. Hence, efforts are put on significant cost reductions of solar thermal systems to regain market growth. In this study the focus is on systems for domestic hot water preparation.

Step 2: Stakeholders and their concerns

Contemporary news headlines suggest a range of stakeholders. Many current newslines are dealing with large systems. Only less can be found on the currently most important field of application which is domestic hot water preparation.

- “Drake Landing: A ray of sunshine for solar thermal energy”. Monty Kruger from CBC News posted that 2 or 3 sunny summer days are enough to heat homes throughout cold seasons in Alberta town`s solar community. (CBC News, February 14, 2016).
- “Gigantic Danish Solar Heating System Completed”. The world’s biggest solar heating system, completed in less than a year after signing the contract, consists of 156,694 m^2 of collectors and will provide 20% of the total heat consumption in Silkeborg. (Energy Supply, January 17, 2017).
- “Italy: new subsidy scheme for solar thermal up to 1000 m^2”. Large solar thermal plants will receive an incentive of 55 €/m^2 per year, over a period of 5 years. (solar district heating, February 6, 2013).
- “First Solar Civic Participation Project”. Crowdfunding participation model for solar thermal plants has reached €1.5 Mio. (EuroHeat&Power Industry News, November 2014).
- “Weltgrößter Solarspeicher soll Grazern einheizen”. Günter Pilch and Markus Zotter note that 20% of the district heating demand in Graz could be covered by solar thermal in 2019. (Kleine Zeitung, February 27, 2016).
- “ECREE begins move to exploit solar thermal energy potential in Ghana” The ECOWAS Center for Renewable Energy and Energy Efficiency (ECREE), has began processes to help Ghana exploit the

abundant solar thermal energy potential for domestic and industrial use. (ghanaweb.com, September 26, 2017).

- "The sleeping giant is waking up" Bhoo Thirumalai, the Chief Executive Officer of Aspiration Energy and a solar aficionado, is a busy man these days. For years, the man who co-founded the successful IT company had been trying to rev it up with limited success. But suddenly things seem to be falling in place. (thehindubusinessline.com, August 29, 2017)
- "Clean Energy Isn't Just the Future—It's the Present" Solar power geysers to heat hot water sit on the roofs of a residential shack in the Alexandra township outside Johannesburg, South Africa (Bloomberg, April 19, 2017)

Based on these quotes and the value creation chain of the solar thermal industry the following key stakeholders are suggested:

- Government: Solar thermal could provide a contribution to meeting renewable energy commitments. Government has the power to make it happen through subsidies and feed-in tariffs.
- Heat providers: Solar thermal and large-scale storages allow for the substitution of economically inefficient fossil fuel co-generation plants with the by-product electricity, which is hard to sell economically due to the low electricity market prices.
- Heat system industry: Solar thermal is an interesting alternative in their product portfolio. Some of them already invested in collector manufacturing facilities.
- Collector makers: Many small- or medium-sized collector makers are on the market. Their profit margins are diminishing due to large enterprises established in China offering cheap products mainly for hot water preparation.
- Installers: Current system technologies for hot water preparation or space heating are not easy-to-install. More reliable system designs are needed for small-sized installers. Large-scale systems offer interesting market opportunities for more specialized companies.
- Property owners: They are attracted by subsidies. In some regions solar thermal systems allow for independent hot water supply and improvement in comfort (especially in less industrialized countries).
- NGOs: are campaigning for decentralized, renewable energy to halt climate change.
- R&D: Solar thermal is an attractive research field with open issues (e.g., thermal energy storage; function-oriented design and simulation of systems). Funding for research on solar thermal systems is stimulating.
- Investors: Crowdfunding initiatives are attracting general public. Large-scale systems are of interest for investors. To meet carbon-reduction targets heat generation from renewable sources is of utmost importance.

The relationship between the stakeholders is displayed in Figure 1 reflecting also their specific influence / power and their interests.

Significant concerns for solar thermal heat is that this technology is in many cases to expensive. In contrast to photovoltaic power, there is still a lack of transparency and continuity regarding subsidies for solar thermal collector systems. Furthermore the intermittency of heat generation and the problem that heat storage is seen challenging, especially for domestic hot water systems with high performance collectors and poor performance storages. PV for hot water preparation (supplemented by heat pumps) is supposed by some as the smarter and cheaper solution.

Step 3: Fact-finding

To research the factual background of the articulations and the validity of the concerns expressed by stakeholders a comprehensive approach considering materials, environment, society, economics, legislation and energy issues was used.

In terms of sustainable development the overall question is, if solar collector systems can make a substantial contribution to carbon reduction targets in the next decades. Figure 2 summarizes the issues needing research.

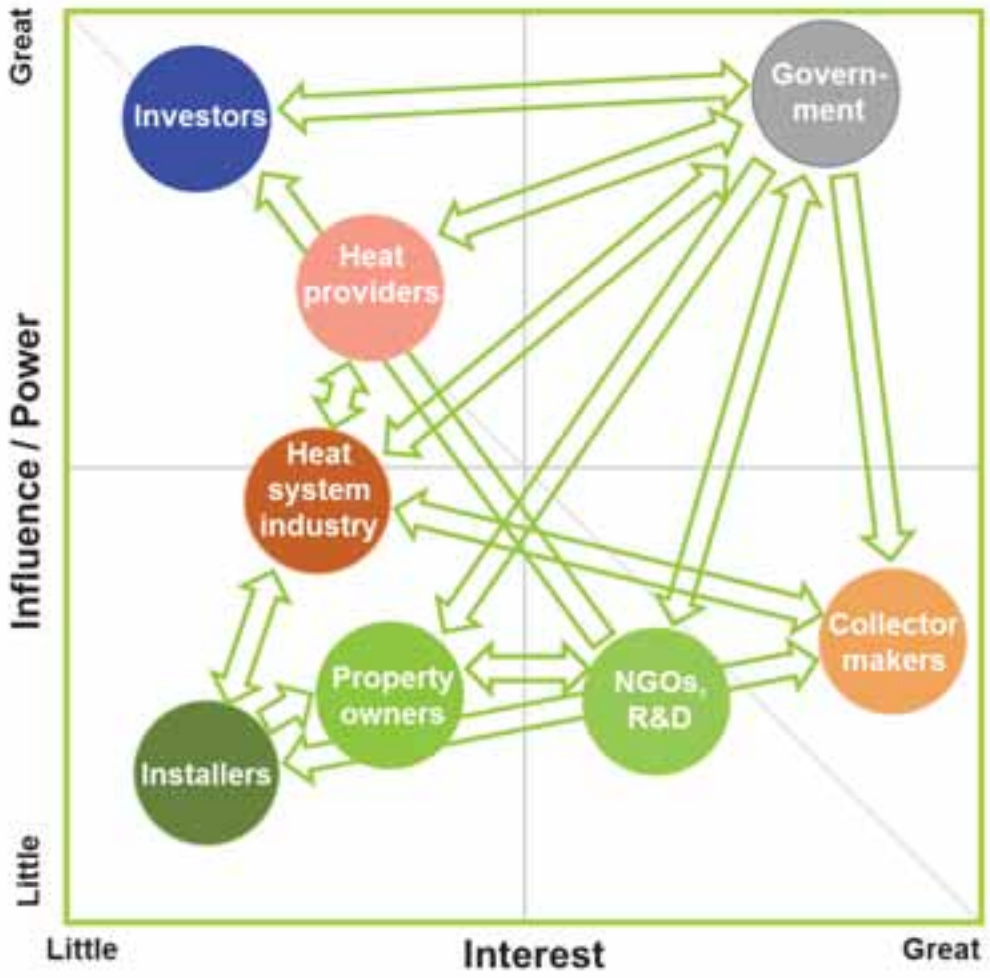

Fig. 1: Stakeholder matrix reflecting their influence and interest.

(a) Materials. State of the art solar thermal collector systems are mainly based on metals like copper, aluminum or steel and silicate glass for the collector, piping and storage. As evident in many other fields of application, a transformation to mass technologies and full market penetration is often associated with a material substitution towards polymeric materials. Interestingly, also for solar thermal systems major research efforts are put on the development of all polymeric collectors, piping and storages. Here, two different approaches are discernible. On the one hand, high performance plastics and related processing technologies are developed for space heating systems. On the other hand, affordable, overheating protected solar thermal collector systems made from commodity polymeric materials are developed. Research work focuses on failsafe overheating protection measures and novel material formulations with improved long term performance in the temperature range between 80 and 95 °C. For both issues adequate solutions have been developed, so that the main issue is now the industrial implementation and transformation (Bradler et al., 2017; Fischer et al., 2016; Grabmann et al., 2016a, 2016b; Geretschläger and Wallner, 2016; Kahlen et al., 2010a, 2010b, 2010c, 2010d; Köhl et al., 2012; Kurzböck et al., 2012; Olivares et al., 2010a, 2010b; Povacz et al., 2014, 2016; Wallner et al., 2016). Therefore, investors and venture capital is needed to successfully implement polymer based alternatives, especially for often poor.

(b) Energy. Mauthner et al. (2016) have shown that the annual collector yield of all water-based solar thermal systems in operation by the end of 2014 worldwide was 335 TWh (= 1,208 PJ) corresponding to a final energy savings equivalent of 36.1million tons of oil and 116.4 million tons of CO_2. 94% of the provided energy by solar thermal collector systems was used for domestic hot water heating. This is dominated by small-scale systems in single-family houses (68%) and larger applications (27%) for multi-family houses, schools, hotels etc. Swimming pool heating adds 4% and 2% of the energy supply and CO_2 reduction is contributed by solar combi systems for

hot water preparation and heating. Regarding hot water preparation the most important issue is to replace electric hot water power systems in less-industrialized countries in sub-tropical and tropical climate zones. So far, no comprehensive investigation has been carried out to which extent this measure could contribute to fossil-based energy savings.

(c) The Environment. It is a well-known fact, that the use of metals, especially aluminum, for solar thermal collector systems has a significantly higher environmental impact than the use of polymeric materials (Arnaoutakis et al., 2017; Battisti and Corrado, 2005; Carlsson et al., 2014; Kicker, 2009; Koroneos and Nanaki, 2012; Singh et al., 2016; Weiss et al., 2015; Zambrana-Vasquez et al., 2015). In case of polymers a worse environmental effect was deduced for high performance polymers compared to commodity plastics such as polyolefins. Nevertheless, solar thermal systems reveal energetic and environmental amortization times ranging from 0.5 to 1.5 years depending on the system type and the location (Buchinger, 2017; Carlsson et al., 2014; Kicker, 2009; Weiß et al., 2015).

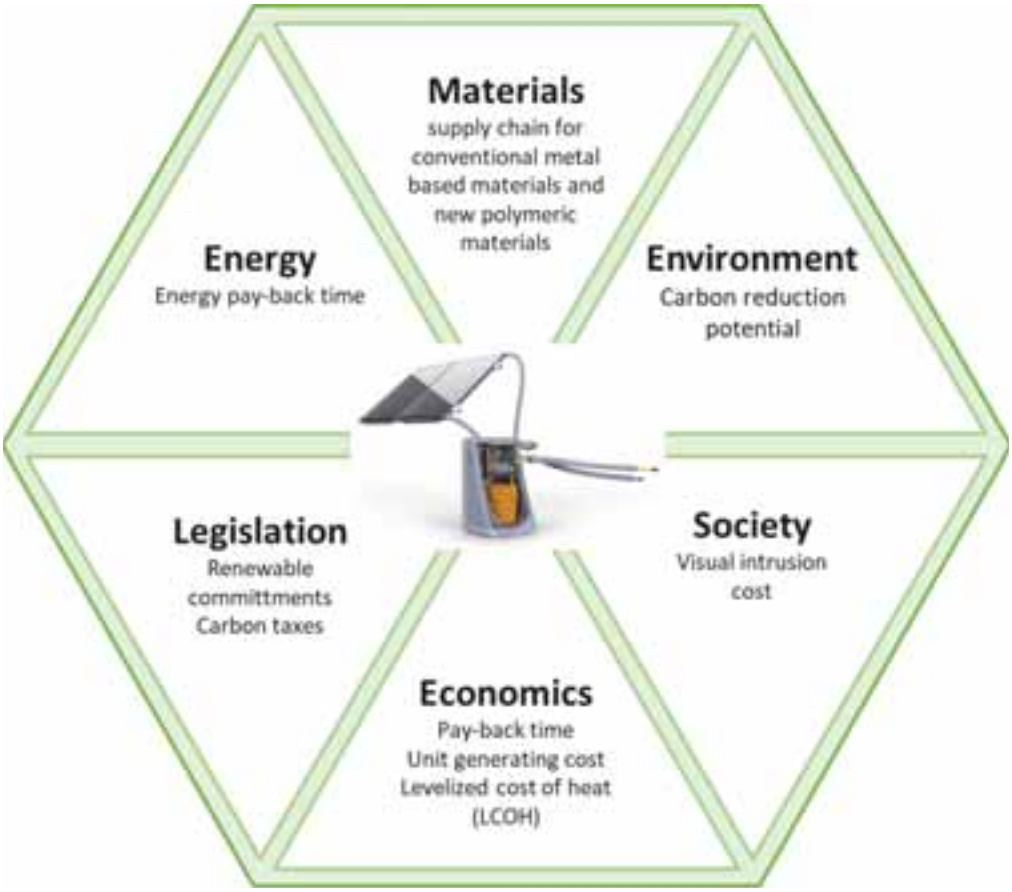

Fig. 2: Fact-finding summary.

(d) Legislation. The production of heat accounts for more than 50% of global final energy consumption. At present 75% of global energy use for heat (129 exajouls) is met with fossil fuels. About 1/3 of global energy-related carbon dioxide emissions (10 gigatonnes of CO_2) is related to the production of heat (Eisentraut and Brown, 2014). In 2015 many nations have agreed to hold global temperatures well below 2°C above pre-industrial levels and to pursue efforts to limit the temperature increase to 1.5°C. This implies that global CO_2 emissions have to peak as soon as possible and that rapid emission reductions must follow (Streck, 2015). This agreement is a clear commitment to a sustainable development. However, this commitment still lacks a regulatory framework and is often not subject to public law. Moreover, current standardization procedures for solar thermal systems are dominated by individual countries and by the copper and glass industry.

(e) Economics. To assess the costs of the heat generated by solar thermal collector systems recently the levelized cost of heat (LCOH) evaluation procedure has been implemented. Important parameters affecting the LCOH are depicted in equation 1. Of significant importance are investment costs, the saved final energy and the lifetime (Fischer, 2017; Louvet et.al, 2017; Mauthner et al., 2016).

$$LCOH = \frac{I_0 - S_0 + \sum_{t=1}^{T} \frac{C_t(1-TR) - DEP_t * TR}{(1+r)^t} - \frac{RV}{(1+r)^T}}{\sum_{t=1}^{T} \frac{E_t}{(1+r)^t}} \qquad \text{(eq. 1)}$$

Where:

$LCOH$: levelized cost of heat in €/kWh
I_0: initial investment in €
S_0: subsidies and incentives in €
C_t: operation and maintenance costs (year t)
TR: corporate tax rate in %
DEP_t: asset depreciation (year t) in €
RV: residual value in €
E_t: saved final energy (year t) in kWh
r: discount rate in %
T: period of analysis in year

Fischer (2017) has shown that the LCOH for conventional, fossil oil based hot water preparation for a single family house (SFH) in Austria amounts to 10 €ct/kWh$_{th}$. The LCOH for conventional, metal based, pumped flat plate collector systems for a single family house are ranging from 12 to 15 €ct/kWh$_{th}$. It is a clear fact that the costs for solar hot water preparation with conventional flat plate collectors in SFH is too high and needs significant reduction. On the other hand, Buchinger (2017) shows that LCOH for an all polymeric pumped flat plate collector system can go down to 2 €ct/kWh$_{th}$, if the performance and the degree of utilization is high, which is especially achieved for small systems in hot climate regions. For thermosiphon systems with evacuated tubes no LCOH figures are currently available. Data are evaluated and established in IEA SHC Task 54.

(f) Society. The news-quotes show that present solar thermal collector systems are widely seen as large-scale installations for district heating. Although the market is dominated by systems for hot water preparation the stakeholders do not recognize this fact. Presumably, the situation is different for China.

For domestic hot water preparation in Europe solar thermal collector systems for single family houses are widely accepted by the public, but seen as much too expensive for an auxiliary source of heat for summer season. In this region solar thermal collectors are commonly replaced by photovoltaic modules and electric heaters. Interestingly, solar thermal hot water preparation for multi-family houses, which is already more economic than fossil based technologies or much more efficient than PV based systems, is of limited acceptance in society. Most likely, the outstanding advantages of this system type have not been communicated to the people, the building developers and the investors.

Due to limited data availability, the fact-finding procedure cannot be concluded at this stage. More comprehensive data sets have to be established especially regarding the overall energy needs for hot water preparation and the fossil fuel and non-renewable electricity substitution potential as well as the levelized costs of heat for the different solarthermal system types and technologies. Hence, the steps 4 and 5 of the sustainability assessment dealing with the “Synthesis of the facts” and the “Reflection step” are carried out and described in a follow-up paper. Further research work is focused on these steps and will also consider other solar thermal system types such as the integration of large collector fields in district heating systems with seasonal storage tanks.

4. Acknowledgements

This research work was performed in the platform project IEA SHC Task 54 “Cost Reduction of Solar Thermal Systems” (www.iea-shc.org). The Austrian participation in the project is funded by the Austrian ministry of traffic, innovation and technology (bmvit).

5. References

Arnaoutakis, N., Souliotis M., Papaefthimiou, S., 2017. Comparative experimental Life Cycle Assessment of two commercial solar thermal devices for domestic applications, Renewable Engergy, 111, 187-200.

Ashby, M. F., Ferrer- Balas, D., Coral, J. S., 2016. Materials and Sustainable Development, Oxford.

Battisti, R., Corrado, A., 2005. Environmental assessment of solar thermal collectors with integrated water storage, Journal of Cleaner Production, 13/2005, 1295-1300.

Buchinger, R., 2017. One World Solar System. Presentation at IEA SHC Task 54 Meeting 10/4/17, Linz, AT

Bradler, P. R., Fischer, J., Pohn, B., Wallner, G. M., Lang, R. W., 2017. Effect of stabilizers on the failure behavior of glass fiber reinforced polyamides for mounting and framing of solar energy applications, Energy Procedia, 119, 828-834.

Carlsson, B., Persson, H., Meir, M., Rekstad, J., 2014. A total cost perspective on use of polymeric materials in solar collectors - Importance of environmental performance on suitability, Applied Energy, 125, 10-20.

Eisentraut, A., Brown, A., 2014. Heating without global warming – Market Developments and Policy Considerations for Renewable Heat, International Energy Agency, Paris.

Fischer, J., Bradler, P. R., Schlaeger, M., Wallner, G. M., Lang, R. W. 2016. Novel Solar Thermal Collector Systems in Polymer Design – Part 5: Fatigue Characterization of Engineering PA Grades for Pressurized Integrated Storage Collectors, Energy Procedia, 91, 27-34.

Fischer, S., 2017. Die LCOH-Methode zur Berechnung von Wärmegestehungskosten, Presentation at IEA SHC Task 54 Meeting 10/4/17, Linz, AT

Geretschläger, K. J., Wallner, G. M., 2016. Aging characteristics of glass fiber-reinforced polyamide in hot water and air, Polymer Composites, 9 pages (doi:10.1002/pc.23945).

Grabmann, M. K., Wallner, G. M., Ramschak, T., Buchinger, R., Lang R. W., 2016. Global Aging and Lifetime Prediction of Polymeric Materials for Solar Thermal Systems – Part 1: Polypropylene Absorbers for pumped Systems, Proceedings EuroSun 2016, International Solar Energy Society, 6 pages.

Grabmann, M. K., Wallner, G. M., Ramschak, T., Ziegler, G., Lang R. W., 2016. Global Aging and Lifetime Prediction of Polymeric Materials for Solar Thermal Systems – Part 2: Polyamid 66 Glass-fiber Reinforced Absorbers for Integrated Storage Collectors, Proceedings EuroSun 2016, International Solar Energy Society, 6 pages.

Kahlen, S., Wallner, G. M., Lang, R. W., Meir, M., Rekstad, J., 2010. Aging behavior of polymeric solar absorber materials: Aging on the component level, Solar Energy, 84, 3, 459-465.

Kahlen, S., Wallner, G. M., Lang, R. W., 2010. Aging behavior and lifetime modeling for polycarbonate, In Solar Energy, 84, 5, 755-762.

Kahlen, S., Wallner, G. M., Lang, R. W., 2010. Aging behavior of polymeric solar absorber materials–Part 1: Commodity plastics, Solar Energy, 84, 9, 1567-1576.

Kahlen, S., Wallner, G. M., Lang, R. W., 2010. Aging behavior of polymeric solar absorber materials–Part 2: Engineering plastics, Solar Energy, 84, 9, 1577-1586.

Kicker, H., 2009. Vergleichende Ökobilanzierung von solarthermischen Kollektoren, Bachelor Thesis, University of Leoben, A

Köhl, M., Meir, M. G., Pappilon, P., Wallner, G. M., Saile, S., 2012. Polymeric materials for solar thermal applications, Wiley-VCH, Weinheim

Koroneos, C. J., Nanaki, E. A., 2012. Life cycle environmental impact assessment of a solar water heater, Journal of Cleaner Production, 37, 154-161.

Kurzböck, M., Wallner, G. M., Lang, R. W., 2012. Black pigmented polypropylene materials for solar absorbers, Energy Procedia, 30, 438-445.

Louvet, Y., Fischer, S., Furbo, S., Giovanetti, F., Mauthner, F., Mugnier, D., Philippen, D., 2017. LCOH for Solar Thermal Applications, IEA SHT Task 54 INFO Sheet A.2

Mauthner, F., Weiss, W., Spörk-Dür, M., 2016. Solar Heat Worldwide – Markets and Contribution to the Energy Supply 2014 – 2016 Edition, IEA-SHC, bmvit, Gleisdorf.

Olivares, A., Rekstad, J., Meir, M., Kahlen, S., Wallner, G. M., 2010. A test procedure for extruded polymeric solar thermal absorbers, Solar Energy Materials and Solar Cells, 91, 4, 445-452.

Olivares, A., Rekstad, J., Meir, M., Kahlen, S., Wallner, G. M., 2010. Degradation model for an extruded polymeric solar thermal absorber, Solar Energy Materials and Solar Cells, 94, 6, 1031-1037.

Streck, C., 2015. The Paris Agreement – Briefing Note, ClimateFocus, Amsterdam.

Povacz, M., Wallner, G. M., Lang, R. W., 2014. Black-pigmented polypropylene materials for solar thermal absorbers–Effect of carbon black concentration on morphology and performance properties, Solar Energy, 110, 420-426.

Povacz, M., Wallner, G. M., Grabmann, M. K., Beißmann, S., Grabmayer, K., Buchberger, W., Lang, R. W., 2016. Novel solar thermal collector systems in polymer design–Part 3: aging behavior of PP absorber materials, Energy Procedia, 91, 392-402.

Singh, R., Lazarus,I. J., Souliotis, M., 2016. Recent developments in integrated collector storage (ICS) solar water heaters: A review, Renewable and Sustainable Energy Reviews, 54, 270-298.

United Nations, 1987. Our Common Future - Brundtland Report. Oxford University Press, Page 41.

Wallner, G. M., Povacz, M., Hausner, R., Lang, R. W., 2016. Lifetime modeling of polypropylene absorber materials for overheating protected hot water collectors, Solar Energy, 125, 324-331.

Weiß, R., Piekarczyk, A., Ramschak, T., Preiß, D., Lutschounig, K., Kicker, H., Wallner, G. M., Meir, M., Weiss, K-A., Köhl, M. 2015. Ökobilanz von polymerbasierten solarthermischen Kollektoren im Vergleich zu konventionellen Kollektoren, Proceedings 25. Symposium Termische Solarenergie, 9 pages.

Zambrana-Vasquez, D., Aranda-Uson, A., Zabalza-Bribian, I., Janez, A., Llera-Sastresa, E., Hernandez, P., Arrizabalaga, E., 2015. Environmental assessment of domestic solar hot water systems: a case study in residential and hotel buildings, Journal of Cleaner Production, 88, 29-42.

SOLAR HEATING AND COOLING IN AUSTRALIA'S BUILT ENVIRONMENT – AN INDUSTRY ROADMAP

Marc R. Sheldon[1] and Dr. Subbu Sethuvenkatramam[2]

[1] Coolgaia Pty Ltd, Brisbane, QLD (Australia)

[2] CSIRO Energy Centre, Newcastle, NSW (Australia)

Abstract

The Australian market is simultaneously small and large – 24 million residents live in a country the size of the USA. It has the highest average solar radiation per square metre of any continent in the world. Despite this, solar energy use in 2014-15 represented 0.6 per cent of Australia's total primary energy consumption and 2.4% of electricity production. The energy used by buildings represents about 20% of total energy consumption in Australia, contributing about 26% of national (anthropogenic) greenhouse emissions. Of that energy, on average 40% are used for space conditioning and domestic hot water. This paper will discuss Australia's market for heating and cooling, and how solar heating and cooling (SHC) can be used in Australia's built environment to augment, replace or improve existing heating and cooling technology solutions. Specific opportunities for improving the market uptake of SHC technologies have been identified in the context of declining political appetite for subsidies.

Keywords: solar heating, solar cooling, regulatory, roadmap

1. Introduction

Australia is in a globally unique position. Most of its landmass boasts an annual average solar radiation of more than 19 MJ/m2 per day, overall 58 million petajoules (PJ) per year, nearly 10,000 times the national annual energy consumption. High energy prices, low PV module and inverter costs over recent years in conjunction with a highly competitive market resulted in the highest penetration of household scale distributed solar PV in the world (Australian Energy Council, 2016) with 23.2% of all households owning home solar electric panels (Roy Morgan, 2017). This contrasts with the weakening growth of rooftop solar thermal domestic hot water systems, installed in 10.29% of Australian households (Australian Bureau of Statistics, 2017; Clean Energy Council, 2017).

Despite local R&D and commercialisation of solar thermal hot water systems dating back to 1950s, installations of larger-scale solar thermal systems, both for heating and cooling, continue to be elusive. Unique national market conditions, a changed legislative situation as well as an uncertain political climate has stunted possible market growth in the recent past. This situation is further exacerbated by Australia's range of local conditions - climate zones ranging from temperate to equatorial and arid to tropically humid provide for special challenges. No single solution fits all requirements.

Rising gas and electricity prices have caused stress on the operating budget of various built environment sectors. Solar generated thermal energy is well suited to replace a large extent of fossil fuel based thermal energy used in various built environment applications. Technically mature solar energy solutions are available for delivering thermal energy in the built environment These solutions provide a viable path forward to minimise both energy use and related cost in the built environment.

In this context, we analyse the current SHC market situation in Australia, discuss market barriers for growth and provide suggestions for market-suitable SHC installation types in the built environment. We then advance recommendations for regulatory support measures, financial market stimulation, research and development activities, pilot projects, skills training for trade and consultants and market education. The motivation for this work is to outline a roadmap for the SHC industry to grow and deliver on positive energy and greenhouse gas emissions outcomes for Australia.

2. The Australian Market

The built environment is one of the largest consumers of energy in Australia. While energy use per household has been steadily decreasing since the early 2000s (Coleman, 2017), the overall residential sector energy consumption increased from 402 PJ in 2008 to 441.1 PJ in 2017 (DEWHA, 2008). A key driver is the growth of occupied

doi:10.18086/swc.2017.34.03 Available at http://proceedings.ises.org

residential households and the increasing size of these households. Household numbers increased 6.06 million in 1990 to 9.4 million in 2017, an increase of 55% (DEWHA, 2008). Over the same period, total residential floor area rose from 685 million square metres to 1,564 million square metres, an increase of 128% (DEWHA, 2008).

In comparison, total commercial building energy consumption in Australia grew from 134.6 PJ in 2009 to 159.4 PJ in 2017, a growth of 18.4% principally due to 16% growth in commercial building stock from 135,726,000 m^2 in 2009 to 157,376,000 m^2 in 2020 (Pitt&Sherry, 2012).

In Australia, space conditioning represents the single largest energy user in both the residential and commercial building environment, closely followed by domestic hot water generation (Lecamwasam et al, 2012). In some building types, thermal end use of energy can be even more significant. For example, in hospitals natural gas usage is nearly 50% of total annual energy use, predominantly used for space heating and water heating requirements (Pitt&Sherry, 2012).

Still, the trend of energy use in Australia was more differentiated in the recent past. While overall energy consumption rose, per building energy use in the residential sector declined. Nevertheless, for all buildings the cost of energy increased disproportionally to its use. In the residential sector, per-household consumption of gas grew by only 5.7% from 2008 to 2013, but its expenditure grew by 64% (Coleman, 2017). Similarly, per-household electricity consumption declined by 4.7% and its expenditure grew by 69.3% from 2008 to 2013 (Coleman, 2017). The cost development in the commercial building sector was comparable (Pitt&Sherry, 2012).

From the generation perspective, solar thermal and PV installers have been adding capacities targeting applications in the built environment. The solar PV market grew by 7% in 2016, with small-scale (< 10 kWe) solar PV rooftop systems making up more than 90% of the national installed solar PV generation capacity (Clean Energy Regulator, 2017; Australian PV Institute, 2017). In 2016 the average size of new installed small-scale solar PV rooftop generation surpassed 6 kWe (Australian Energy Council, 2017). Overall, there is more than 5 GW installed Solar PV capacity under the 10 kWe range and 800 MW in the 10 to 100 kWe range.

The domestic Australian solar thermal market also predominantly consists of rooftop solar hot water systems. Spurred by federal and some state subsidies for the installation of solar hot water systems and the national phase-out of electric resistance hot water systems, growth in the solar thermal market was strong through 2010. Despite the marginal growth in installed base, new installations for the domestic solar thermal market declined by more than 60% and continue to shrink (Clean Energy Council, 2017). With an average installed market price of A$4,500, the Australian 2016 rooftop solar hot water market was just under A$223 million p.a. (Table 1 provides annual market figures from Clean Energy Council, 2017).

Table 1: Annual Installations of Solar Hot Water Heaters (Clean Energy Council, 2017)

Year	ACT	NSW	NT	QLD	SA	TAS	VIC	WA	Nat'l	Installed Base
2006										**161,446**
2007	453	8,765	1,414	16,830	2,869	350	9,157	11,139	50,977	**212,423**
2008	1,001	20,203	1,236	23,330	5,103	906	21,208	12,398	85,385	**297,808**
2009	1,974	85,456	1,731	36,659	8,794	2,269	42,120	15,692	194,695	**492,503**
2010	960	38,525	1,303	34,262	6,812	1,433	27,733	16,065	127,093	**619,596**
2011	1,038	25,331	1,267	30,937	5,444	1,725	26,446	12,862	105,050	**724,646**
2012	734	10,810	1,171	18,973	3,473	899	21,594	11,812	69,466	**794,112**
2013	453	9,145	884	13,410	2,983	827	19,608	10,989	58,299	**852,411**
2014	451	9,641	1,026	13,433	1,930	962	20,613	10,672	58,728	**911,139**
2015	572	8,609	1,063	11,799	2,557	803	23,019	10,205	58,627	**969,766**
2016	497	6,963	660	9,793	1,914	822	20,514	8,390	49,553	**1,019,319**

Commercial scale solar hot water systems data (available through clean energy regulator) presents a grim picture. Studies commissioned by the Clean Energy Regulator (CER) indicate the number of Small Scale Technology certificates (STC) created for commercial hot water systems is expected to drop from 131,000 in 2016 to 34,000 in 2019 (Parisot, 2017).

Solar thermal cooling is still a niche in Australian built environment, counting less than 20 active installations. With very few exceptions, these installations are demonstration plants, research and development systems or proof-of-concept installations. Despite the more common use of solar thermal air heating in colder climatic conditions (e.g. North America), space heating with solar thermal collectors has not taken off in Australia, likely due to moderate day time temperature in many parts of the country and lack of market awareness of its benefits.

Large-scale solar thermal systems servicing hot water, heating and cooling needs of a commercial built environment application are very few. Discounting the demonstration projects in this space, Table 2 shows typical examples of operational solar assisted heating, cooling and hot water delivery systems operational in Australia.

Table 2: Representative Solar Heating and Cooling projects

Type of installation	Location	Typical system details	Operational since
Hot water / space heating	University building, Australian National University, Canberra, ACT	392 m2 collector area (140 evacuated tube collectors)	2012
Hot water / space heating / boiler preheat	Monash University, Clayton, VIC	1 MWth collector area (evacuated tube collectors)	2017
Space cooling / hot water	Hospital building – Echuca Regional Hospital, VIC	406 m2 collector area (evacuated tube collectors), 500 kWth single stage absorption chiller	2011
Space heating & cooling / hot water	Educational building – Hamilton, NSW	400 m2 collector area (flat plate collectors)	2013

Use of solar electricity for partially meeting the heating, cooling and hot water needs of residential and commercial buildings is achieved through grid connected solar PV installations. However, these systems are not directly coupled to thermal energy use in the buildings. Theoretical studies of using PV integrated air conditioning systems for Australian climates have been explored, but there are no known demonstration systems that are designed specifically to meet the thermal energy needs of a building.

Market Development

The key drivers for continued heating and cooling demand in Australia are overall population and economic growth. Since 2000, Australia's population grew between 1% and 2% annually (Australian Bureau of Statistics, 2017a). Similarly, national GDP growth was always positive and mostly above 2% p.a. in the same timeframe (Reserve Bank of Australia, 2017). With positive economic outlook, this growth is expected to continue. As a result, the overall residential sector energy consumption is forecast to increase to 467 PJ in 2020, the number of occupied households is expected to increase to almost 10 million and aggregate residential floor space to rise to 1,682 million square metres by 2020 (DEWHA 2008). Total commercial building energy consumption is forecast to grow to 169.6 PJ, a growth principally due to an increase in commercial building stock to 165,970,000 square metres in 2020 (Pitt&Sherry, 2012). In both residential and commercial sectors, energy cost is expected to continue to rise disproportionally, outpacing energy use growth significantly (Letts, 2017; Potter and Tillett, 2017; Mountain and Gassem, 2017).

Escalating energy costs will likely continue to be the main driver for end users adopting onsite energy generation options. Declining solar PV system costs will further drive growth in the solar rooftop PV market in Australia. Solar thermal rooftop hot water will face growing competition from alternative technologies.

Heating and Cooling Requirements

Heating and Cooling requirements are substantially different based on building use and the local climate zone of the building. In general, Australian building occupants have a high tolerance for cool buildings in winter and little tolerance for warm buildings in summer. Historically, Australian residential buildings have little insulation and building envelopes that are not air-tight. Minimum energy efficiency standards have been part of the NCC since 2006 and are mandatory for new buildings. Nevertheless, a large proportion of residential and mid-tier commercial building stock uses significant energy for active heating and cooling to reach appropriate occupancy comfort levels. Even new buildings on average have only minimum legally required energy efficiency features, making a functional active heating and cooling system essential for some level of thermal comfort.

The Australian Standard AS5389-2016 *Solar heating and cooling systems— Calculation of energy consumption* nominates 6 climate zones with locations of similar climatic characteristics for the purposes of evaluating the annual energy performance of solar water heaters. Using the modelling from DEWHA, 2008, we derived a representative heating and cooling load range for each zone; the definitions are shown in Table 3.

Table 3: Australian Climate Zones, comfort space conditioning requirements and representative annual residential heating/cooling loads (for NatHERS 3 to 5 star buildings estimated per DEWHA, 2008)

Climate Zone	Space Conditioning Requirements	Representative Heating Load (MJ/m2)	Representative Cooling Load (MJ/m2)
SC1: Warm humid summer, mild winter	Little heating requirements, cooling requirements for 3 to 6 months per year.	20 - 40	150 - 300
SC2: Hot dry summer, warm winter	Heating requirements for 1 to 2 months, cooling requirements for 3 to 6 months per year.	50 - 150	150 - 300

SC3:	**Warm temperate**	Heating requirements for 1 to 2 months, cooling requirements for 1 to 2 months per year.	50 - 180	45 - 150
SC4:	**Mild temperate**	Heating requirements for 3 to 5 months, cooling requirements for 1 to 2 months per year.	280 - 360	30 - 50
SC5:	**Cool temperate to Alpine climate**	Predominant heating requirements, with heating needs for 8+ months per year.	450 - 570	15 - 40
SC6:	**High humidity summer, warm winter**	Predominant cooling requirements for most of the year.	0	400 - 570

Note that climate zone SC6 and SC1 have monsoonal weather patterns, with notable overcast and precipitation during the summer months. For climate zones SC1, SC3 and SC6 the average annual latent load is significantly higher than in the other climate zones. Figure 1 depicts the distribution of the climate zones in Australia.

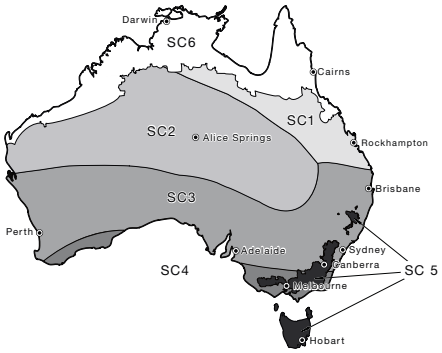

Figure 1: Climate Zones in Australia as per AS5389-2016

Regulatory and other support measures

In line with other countries, Australia introduced several measures to make renewable energy use more affordable. These include state-by-state feed-in tariffs with a subsidised fixed rate for all small-scale renewable energy producers based on the energy fed back to the grid from sources such as solar or wind. All attractive state feed-in tariffs for new installations have been discontinued between 2011 and 2015. There is no current nationalised feed-in tariff, prompting consumers to self-consume onsite generated power.

The federal government also introduced a solar rebate scheme to encourage installation of these systems. The **Renewable Energy Target (RET)** is national government scheme designed to reduce emissions of greenhouse gases in the electricity sector and encourage additional generation of electricity from sustainable and renewable sources. It provides both large-scale generation certificates (LGC) for large-scale power stations and **small-scale technology certificates (STC)** for owners of small-scale systems. Certificates are then purchased by electricity retailers and submitted to the CER to meet the retailers' legal obligations under the Renewable Energy Target. Small-scale technology certificates are created based on the estimated amount of electricity a system produces or replaces (that is, electricity from non-renewable sources) over the life of the renewable energy system.

The **Clean Energy Finance Corporation (CEFC)** is a statutory authority established by the Australian Government under the Clean Energy Finance Corporation Act 2012. It acts as a specialist clean energy financier, investing with commercial rigour to increase the flow of finance into renewable energy, energy efficiency and low emissions technologies. Its investment portfolio ranges from large-scale solar and wind farms to technology-specific research and development activities.

Additionally, there are several national and state programs that encourage energy efficiency in buildings. None of them explicitly nominate the use of renewable energy solutions, but onsite renewable energy generation is an accepted tool to help in improving energy efficiency as per these programs.

On a federal level, the **National Construction Code (NCC) Volume 1, Section J** defines energy efficiency requirements for commercial buildings (class 3 to 9). While it is a national code, it is individually modified and enforced by state law. Section J and the remainder of the NCC mention solar and other renewable energy generation systems only in passing and do not mandate their use. The **National House Energy Ratings Scheme (NatHERS)** is aimed at promoting energy efficiency in residential buildings. A software tool uses defined building characteristics (i.e. climate zone, orientation, building materials etc.) to estimate its annual energy use. Under NCC energy efficiency provisions, every new home or renovation needs to have at least a 6-star NatHERS rating.

The **National Australian Built Environment Rating System (NABERS)** is a national rating system that

measures the environmental performance of Australian commercial buildings and tenancies. It rates buildings according to their measured operational performance over the preceding year pertaining to energy and water use, waste handling and indoor environment. Research suggests that offices with high NABERS Energy ratings tend to offer higher investment returns, whilst offices with low NABERS Energy ratings tend to offer lower investment returns (Slow, 2013).

Relying very much on NABERS is the 2010 **Building Energy Efficiency Disclosure (BEED)** Act, which requires anyone selling or leasing office buildings or space greater than 1,000 m2 to obtain a Building Energy Efficiency Certificate (BEEC). BEECs are only valid for 12 months and include a NABERS Energy for offices star rating. The program, called **Commercial Building Disclosure (CBD)**, aims to improve the energy efficiency of Australia's large office buildings and to ensure prospective buyers and tenants are informed. Since inception, more than 72% of the Australian national office market has received an energy rating (McMahon, 2016). Buildings with at least two consecutive NABERS Energy ratings, demonstrated an average reduction in energy use of 8.7% and a reduction in greenhouse gas emissions of 11.5% (Ernst & Young, 2015). A similar program for the federal government is the **Energy Efficiency in Government Operations (EEGO)** Policy, which aims to reduce the energy consumption of government operations with emphasis on building energy efficiency. EEGO mandates the use of Green Lease Schedules (GLS) to form part of lease documentation (or MOUs where the Government owns the building). GLS are designed to ensure that buildings are operated at the required level of energy efficiency, including a required minimum 4.5 stars NABERS Energy for Based Building rating. Contractual language in the GLS is usually coached in “best effort” terms, with little recourse for the tenant in case of a breach of the energy efficiency terms. All state governments in Australia except for Tasmania have similar requirements, at minimum 4.5 stars NABERS Energy for offices rating for all new buildings and fitouts and at minimum 3.5 stars for existing buildings and fitouts.

In addition, some states and municipal governments provide local incentives and funding schemes to drive building energy efficiency and the use of renewable energies. Amongst these are Environmental Upgrade Agreements (EUAs) in New South Wales and in Melbourne – called 1,200 Buildings in Victoria, the Energy Savings Scheme in New South Wales, Victorian Energy Upgrade, ACTSmart Business Energy and Water Program in Canberra, Energy Savers in Queensland and the South Australian Energy Productivity Program. Furthermore, most state electricity utilities have programs with funding for provable peak demand reduction projects, demand management projects and renewable energy buyback schemes. The extent and funding depth varies with each project; Energex offers up to $185 per kW peak demand savings in select supply areas (Energex, 2017).

Outside of government measures, the Green Building Council of Australia (GBCA) manages the **Green Star** rating system, a voluntary sustainability rating system for buildings in Australia. It assesses the sustainability of building projects at all stages of the life cycle. Ratings can be achieved in the planning phase for communities, during design, construction or fit out of buildings, or during the ongoing operational phase and range from one star (minimum practice) to three star (good practice) and six star (world leadership). Energy-efficiency outcomes for Green Star rated buildings are good with 66% less electricity use and 62% fewer greenhouse gas emissions than average Australian buildings (Green Building Council of Australia, 2013), the rated buildings tend to be Premium and Grade A buildings (Ernst & Young, 2015), with limited investment going to the mid-tier market. This market makes up more 50% of the Australian commercial office stock (Ernst & Young, 2015) and is typically comprised predominantly of smaller buildings, often better suited for solar energy use due to a larger proportion of roof space to lettable floor space.

AS5389-2016 (draft) is another initiative to encourage adoption of solar heating and cooling systems in buildings. This draft standard provides an approach for estimating energy consumption of solar heating and cooling systems for receiving government support such as STCs.

Australia ratified the Paris climate agreement committing to achieve 26–28% reduction in greenhouse gas emissions below 2005 levels by 2030. CSIRO’s low emissions technology roadmap advocates fuel switching as one of the options to achieve deep cuts in emissions from the built environment that can help in achieving the 2030 emission reduction targets. In the context of the RET being phased out by 2030, an alternate policy landscape to specifically encourage renewable energy use in the built environment is unclear.

3. Market Barriers / Challenges

The authors of this paper interviewed various stakeholders related to the use of solar heating and cooling technologies in the built environment. This included representatives from the building industry, solar equipment

manufacturers, HVAC contractors, consultants and entities dealing with regulatory bodies. A summary of findings from these discussions are provided below.

Initial Cost

Due to Australia's small market size, local production of complex solar heating and cooling components is limited. Importing such equipment results in a relatively large logistics costs due to the distance from the manufacturing countries. This is further exacerbated by limited experience of consulting engineers, contractors and installers with new, custom designed SHC installations. To mitigate potential risks, these projects are often quoted with high risk margins that make them financially nonviable.

A necessary optimisation or retrofit of a heating or cooling delivery system is often fruitful ground for the introduction of renewable energy systems. While a suitable SHC application with attractive payback periods might be a good fit, consultants and system designers often lack the required knowledge and resources (e.g. a design and optimisation tool) to help them identify such introduction opportunities.

Stakeholders are often not aware of appropriate local, regional or federal energy efficiency programs as outlined above. Bureaucratic hurdles to participate in these programs can also be too onerous for the program to be useful, resulting in unused funds which could offset some of the high initial costs.

Lack of awareness of benefits & unrealistic expectations

While there is strong general interest in renewable energy technologies, most of the stakeholders including architects, engineers and building owners do not have sufficient information on capabilities and benefits of solar generated thermal energy and its use in the built environment. Consequently, SHC solutions are either not considered for a project, or poorly planned and designed. These badly designed and commissioned systems bring a negative reputation to the technology, further limiting market growth.

Unrealistic expectations also bring negative reputation to the technology. These expectations range from an expected payback of less than two years, delivery of complete comfort during all periods of the day to maintenance free operation and more. Oftentimes the end-users would not have had similar expectations on the incumbent technology and may be more forgiving for any performance deficiencies of the incumbent technology.

Inexperienced and untrained consultants and trade

SHC systems are not covered in the standard training repertoire of architects, engineers and installers. As a result, a commercial building may be designed such that any inclusion of SHC technologies may result in expensive variations or site preparation costs. This is compounded by the limited number of component suppliers and installers.

Consultant fee models are often predicated on providing standard systems design with only small variations. The business model does not allow for providing a bespoke solution capable of leveraging SHC technology for the best outcome. In addition, most engineers and installers are unsure of the correct use of the technology and inflate the costing of the project to tackle "unknown" risks.

Technical and financial risks

Project owners are often worried about the risks associated with SHC technology installations. These risks can be related to performance, maintenance or the commercial benefits. Negative risk perception is fueled by the lack of suitable local reference installations and access to historical data. Badly designed and underperforming SHC deployments add to this perception. Finally, specialized international SHC vendors often approach the Australian market with insufficient focus and funds, partnering with small, local companies for commercial representation. These small companies do not have the reliability of major vendors, resulting in real execution risk with the associated risk of losing warranty and maintenance options if such a small company were to change direction or enter liquidation.

Split Incentives

Not unique to solar generated thermal energy systems, split incentives are a barrier to the high initial deployment cost of any energy efficiency measures in buildings. So far, the additional capital cost of an SHC installation is not always offset by a commensurate increase in sales or lease price. The tenant or final building operator would reap the rewards of the efficiency measure and the entity making the capital investment would have foregone possible higher profits. Given the higher initial cost of SHC systems, split incentives result in landlords often not not motivated to install such systems in their buildings.

Alternative Technology advancements

New technology innovations disrupt the current technology development and diminish the unique benefits provided by solar thermal heating and cooling solutions. An example is the slowdown in the rooftop solar thermal market due to the decline of PV prices. In residential applications, home owners often prefer a single solar energy collection technology meeting their energy needs rather than dealing with two sets of system installers and technologies. The potentially higher installation cost (labour) of a solar thermal system could be the further differentiator between the installed cost of a solar PV system and a solar thermal system. More disruption potential can be expected from the maturing of electrical storage (so that it becomes competitive with thermal storage) and a potential reduction in price of high efficiency heat pump systems.

4. Opportunities

Solar thermal generated energy for active use in the built environment is available in several forms:

- Solar Thermal driven Absorption/Adsorption Chillers – using heat from solar thermal collectors (flat plate, evacuated tube, concentrating) to drive absorption chillers (LiBr/Water, NH_3/Water, Zeolite/Water, Silica Gel/Water etc.)
- Solar Thermal driven Desiccant Chillers – using heat from solar thermal collectors (flat plate, evacuated tube, concentrating) to drive desiccant chillers (solid or liquid)
- Solar Thermal Heating Hot Water and/or Domestic Hot Water – using heat from solar thermal collectors (flat plate, evacuated tube, concentrating) to generate hot water, either for heating hot water (HHW) or for domestic hot water (DHW)
- Solar PV assisted high-efficiency chillers – using electricity generated from solar PV to drive high-efficiency chillers
- Solar PV assisted high-efficiency heat pump – using electricity generated from solar PV to drive high-efficiency heat pumps to generate HHW or DHW

Ongoing research has been conducted into the cost comparison of solar thermal, solar PV assisted thermal energy generation and conventional heating and cooling. The more rapid change in PV pricing as compared to the components of solar thermal cooling systems make PV-assisted cooling systems increasingly viable alternatives to solar thermal cooling and substantially improve the financials of a deployed system (Otanicar et al, 2012; Kohlenbach and Dennis, 2010; Greenaway and Kohlenbach, 2016). As current representative residential electricity prices continue increasing, the financial performance and ROI of both solar thermal and solar PV-assisted cooling systems will also become more attractive.

Small-scale solar thermal HHW and DHW systems compare well financially to gas or standard heat-pump systems. Solar PV-assisted high-efficiency heat pumps (Mayekawa, 2017; Sanden, 2017) provide a very competitive alternative for HHW and DHW systems, even for medium-sized HHW and DHW requirements. In medium-sized and larger deployments, solar thermal HHW and DHW systems are also financially attractive (Witts, 2017).

Not all situations provide a good fit for solar thermal generated energy. Smaller-scale deployments result in a disproportionately expensive solar thermal driven cooling system. For cooling needs of 20 kWth or less and standard residential or commercial office requirements, there are few criteria to make such a system cost-competitive with a small-scale split system air conditioner or a solar PV-assisted split system air conditioner.

Beyond the need for sufficient annual solar radiation, the essential criteria for the fit of solar generated thermal energy to a buildings heating and cooling needs are:

- Appropriately located available roof space
- Diurnal load match (more than 50% of thermal energy used should be during average daytime hours)
- Annual combined thermal needs (heating in winter, cooling in summer) or significant all-year heating or cooling needs, overall more than 200 $MJ/m^2/a$
- Combined domestic hot water and heating/cooling loads to maximise utilisation

For the purposes of this analysis, we used building classifications following those of the Australian National Construction Code (NCC).

Table 4 summarises the findings, highlighting cost-efficient suitability for solar thermal energy use for providing heating, cooling and domestic hot water by colour; comfort tolerance was classified as the willingness of the building occupants to tolerate building temperatures marginally outside the generally accepted temperature set points of 21°C to 24°C. Green symbolises a good fit, orange an average fit and red highlights a likely bad fit.

Table 4: Australian Built Environment, space conditioning, hot water requirements and market information (estimated as per DEWHA, 2008; Pitt&Sherry, 2012; Goldsworthy and Sethuvenkatraman, 2016)

Application	Residential	School	Universities & VET	Office	Public buildings	Hotel	Restaurant	Retail			Hospital
								Super-market	Retail strip	Shopping centres, excl. super-market	
Typical operating hours	3pm-12pm	9am-3pm	8am-9pm	8am-5pm	9am – 5pm	24 hours	8am-10pm 24 hours (chain)	7am-10pm	8:30am-6pm	8:30am-6pm	24 hours
Operating days	50 - 100	200	240	240	240	365	310-360	360	310	360	365
Comfort tolerance	Low	High	Medium	Low	Low	Low	Medium	Medium	Medium	Medium	Low
Indicative capacity range	2 to 15kW	5 to 50kW	50 to 500kW	5 to 500kW	30 to 500kW	100kW to 1MW	10 to 50kW	50 to 200kW	10 to 30kW	100kW to 1MW	100kW to 1MW
Relative hot water use	High	Low	Low	Low	Low	High	High	Medium	Low	Low	High
Fresh air requirement	Low	High	High	Low	Medium	Low	High	Low	Low	Low	High
Latent load	Average	Above average	Average	Average	Average	Average	Above average	Average	Average	Average	Above average
National HVAC energy use (PJ/a)	192	0.8	5.5	27.6	1.1	8.3	NA	NA	NA	NA	9.9
HVAC energy intensity (MJ/m²/a)	115	<18	180, 440	380	300-550	690	NA	NA	NA	NA	680
Current stock size (number / '000 m2)	8,452,743 / 1,564,000	9,414 / 44,023	4,585 / 18,571	NA / 43,403	3010	4,445 / 11,787	13,987 / NA	1,891 / NA	346,704 / 22,599		1,322 / 13,984
Incumbent technology	AC, Split	AC, Split	AC, Ducted / Package, Central plant	AC, Ducted / Package, Central plant	AC, Ducted / Package, Central plant	AC, Ducted / Package, Central plant	AC, Split, Ducted / Package	AC, Ducted / Package	AC, Split, Ducted / Package		AC, Ducted / Central plant
Complexity of incumbent technology	Low	Low	Medium	Medium	Medium	Medium	Low to Medium	Medium	Low	Medium to High	High

In a country the size of Australia, climate Zones are a vital decision criteria to deploy a system using solar generated thermal energy, i.e. monsoonal high cloud cover during summer months in SC1 (and parts of SC6) is likely to result in low solar yield. Similarly, solar heat driven desiccant chillers will have limited value in SC2 because of predominantly arid summers.

Every project is different and requires specific adjustment. Nevertheless, in addition to the above essential criteria for deploying solar generated thermal energy systems in Australia we believe sizeable opportunities exist with deployments outlined in Table 5[1].

Table 5: Opportunities for deployment of solar generated thermal energy systems in the built environment in Australia

Climate Zone		Residential	School	Universities & VET	Office	Public buildings	Hotel	Restaurant	Retail	Hospital
SC1	Heat	◆◆ / ■■/ ▲▲	◆ / ▲				▲▲▲ / ◆◆◆	(▲ / ◆)[2]		◆◆◆ / ▲▲▲
	Cool	△△	△ / (◇)[3]	◇◇◇ / (△△)[4]	□□ / (△△)[4]	□□ / ◇◇ / (△△)[4]	□ / ◇ / (△△)[4]	(△)[2]	□□ / (△△)[4]	◇◇◇
SC2	Heat	◆◆ / ■■/ ▲▲	◆ / ■/ ▲	■■	■■	■■	▲▲▲ / ◆◆◆	(▲ / ◆)[2]		◆◆◆ / ▲▲▲
	Cool	△△	△	(△△)[4]	□□ / (△△)[4]	□□ / ◇◇ / (△△)[4]	□ / ◇ / (△△)[4]	(△)[2]		

[1] Solar generated thermal energy use in SC6 will need to be evaluated on a case-by-case basis and will likely represent marginal cases
[2] Not a good diurnal load match; for worthwhile deployments, requires daytime usage.
[3] Dependent on fresh air requirements and latent load
[4] For smaller deployments

SC3	Heat	◆◆ / ■■/ ▲▲	◆ / ■/ ▲	(■■)	(■■)	(■■)	▲▲▲ / ◆◆◆ / (■■)[1]	(▲ / ◆ / ■)[2]	(■■)[1]	◆◆◆ / ▲▲▲ / (■■■)[1]
	Cool	△△	△ / (◇)[3]	(◇◇◇)[1] / (△△)[4]	□□ / (△△)[4]	□□ / ◇◇ / (△△)[4]	□ / ◇ / (△△)[4]	(△)[2]	(□□) / (△△)[4]	(◇◇◇)[1]
SC4	Heat	◆◆ / ■■/ ▲▲	◆ / ■/ ▲	■■■	(■■■)	■■■	▲▲▲ / ◆◆◆ / ■■■	(▲ / ◆ / ■)[2]	■■	◆◆◆ / ▲▲▲ / ■■■
	Cool	△△	△	(△△)[4]	(△△)[4]	(△△)[4]	(△△)[4]	(△)[2, 4]		
SC5	Heat	◆◆ / ■■	◆ / ■■	■■	(■■)	■■	◆◆ / ■■	(◆ / ■)[2]	■■	◆◆ / ■■
	Cool			□ / △						□
SC6	Heat	◆◆ / ■■/ ▲▲	◆ / ■/ ▲				▲▲▲ / ◆◆◆	(▲ / ◆)[2]		◆◆◆ / ▲▲▲
	Cool	△△	△ / (◇)[3]	◇◇◇ / (△△)[4]	(△△)[4]	(△△)[4]	(△△)[4]	(△)[2,4]	□□ / (△△)[4]	◇◇

▲: Solar Domestic Hot Water - solar PV, high efficiency heat pump, tank, optionally with reverse cycle air conditioner for space heating

◆: Solar Domestic Hot Water - solar thermal collectors, tank

■: Solar Heating and Domestic Hot Water - solar thermal collectors, tank

□: Solar Thermal Cooling AB - solar thermal collectors, tank, thermal (absorption, adsorption) chiller

◇: Solar Thermal Cooling DES - solar thermal collectors, tank, desiccant systems

△: Solar PV Cooling - solar PV, high efficiency vapour compression chiller

As solar energy is an intermittent energy source, backup and possibly storage will be needed to guarantee the intended service during all periods of the day in a year.

5. Recommendations

To address the market barriers and enable local and international heating and cooling industry to better address the Australian market, we recommend a three-pronged approach:

Regulate	Support	Inform
Standardisation / Best Practice design – extend AS5389	Environment Upgrade Agreements (EUA)	Training/Knowledge dissemination
	On-Bill Finance	Pilot projects
	Energy Performance Contracts (EPCs) / Energy Services Companies (ESCOs)	

Regulate - Standardisation / Best Practice design

We recommend a project for documenting global best practice for a modular design of a solar thermal heating/cooling system for use in Australia. It needs to provide for options for different collector technologies (flat plate, evacuated tube, concentrating), optional different chiller technologies (absorption / adsorption / desiccant / none), optional HHW and optional DHW systems. Integration into existing systems also needs to be addressed (i.e. utilising existing air handling units, providing boiler pre-heat etc.). Standardisation of solar thermal system design for a given application has the potential to address many of the barriers discussed above:

- Has the potential to lower the initial cost of the system by reducing the design and installation time.
- Increases confidence of various stakeholders in the value chain to move ahead with implementing solar thermal projects.
- Supports the development of components and equipment associated with the technology and helps in improving the availability of local components rather than importing.

This activity must be firmly supported by regulatory means that help in estimation of energy savings from the standardized designs. Extension of AS5389 to incorporate various solar heating and cooling technologies is one typical example. Additionally, efforts should be directed towards developing best practice design documents that can be used by installers (e.g. Master Plumbers' and Mechanical Services Association of Australia and Sustainability Victoria, 2009)

Support

We believe there are various renewable energy support mechanisms already available for large scale utilisation. However, some of the following approaches have been largely overlooked or not yet deployed consistently across Australia. We suggest a reinvigorated approach towards these policies.

[1] For parts of climate zone as per requirements

Environmental Upgrade Agreement (EUA)

An Environmental Upgrade Agreements (EUA) is a contractual agreement between a building owner, a finance provider and a local council. The building owner agrees to undertake environmental upgrades to their building and the finance provider agrees to advance capital to the building owner to fund the works. The money is repaid to the lender through council rates. This environmental upgrade charge is collected quarterly as a line item on top of the normal council rates. Once payments are completed, the building owner owns all capital equipment covered by the agreement, i.e. it is a balance sheet item.

As such it allows a building owner to access capital at a better rate over a longer term than a conventional bank loan. EUAs also allow some of the costs of the upgrade to be shared with tenants, where the tenant also benefits from the cost saving delivered by the upgrade. Furthermore, it minimizes financial risk to the lender, as the loan is attached to the land/property.

EUAs are currently only available in Victoria (Department of Energy, Land, Water and Planning, 2015) and New South Wales (Office of Environment & Heritage, 2016). Extending these agreements and consolidating their contractual structure, commercial and technical prerequisites based on the above best practice design would remove financial risk and at least partially address the problem of split incentives for retrofits of buildings.

Support - On-Bill Finance

On-bill financing is an alternative way of obtaining access to capital to fund building energy efficiency upgrades, where repayments are made through an electricity utility as part of the energy bill. The energy utility will typically aim to make the monthly payments equal to or less than the energy savings achieved through the upgrade works. Here as well, building owners can access capital at a better rate over a longer term than a conventional bank loan and costs can be shared with tenants, lowering financial risk and mitigating split incentives. In Australia, On-bill financing is currently offered by AGL and Origin Energy for medium to large customers only (Office of Environment & Heritage, 2016a). On completion of payments, the building owner owns all capital equipment covered by the contract, i.e. it is a balance sheet item. We recommend extending standard demand-management practices of all electricity utilities to include on-bill financing for solar generated thermal energy projects, adhering to the above standards and leveraging the best practice design to mitigate technical risk.

Support - Energy Performance Contracts (EPCs) / Energy Services Companies (ESCOs)

Already established in Australia, Energy Performance Contracting (EPC) is when an Energy Service Company (ESCO) is engaged to improve the energy efficiency of a facility, with the guaranteed energy savings paying for the capital investment required to implement improvements. Under a performance contract for energy saving, the ESCO implements and operates the project and guarantees cost savings over an agreed term, lowering financial and technical risk. We recommend working with reputable national and international ESCOs to extend their offering to include solar generated thermal energy projects in Australia, leveraging EUAs, On-bill Financing and the best practice design. Quick wins could be had by integrating an ESCO-operated solar thermal component into a district cooling system such as the CitySmart Brisbane project.

Inform - Training/Knowledge dissemination

Solar generated thermal heating and cooling technology and the relevant design and installation criteria need to be integrated into the standard University and Vocational Education and Training (VET) curriculum for architects, engineers and trades. To this end, the best practice design document needs to become part of the respective curricula and a continued professional development training program needs to be instituted in close cooperation with the relevant industry bodies (Australian Institute of Architects, Australian Institute of Refrigeration, Air Conditioning and Heating). Once implemented, it will reduce technical risk and facilitate that solar generated thermal heating and cooling systems can be designed, built, commissioned and operated by anyone in the industry.

Inform – Pilot Projects

Australia is not home to any commercial large-scale solar thermal cooling projects. We recommend using the outlined Regulate, Support and Inform recommendations to initiate showcase commercial solar generated thermal energy projects with the CEFC acting as a cornerstone investor working with proven national or international industry operators with appropriate and demonstrated experience. This includes adding solar thermal generated thermal energy options to district level heating/cooling infrastructure in early or late planning stages, such as the district cooling system to service downtown Brisbane (Citysmart, 2016).

We believe that if acted upon soon, these recommendations will enable Australia to build a thriving local market

for solar generated thermal energy systems, saving energy, greenhouse gases and money for all stakeholders in its built environment.

6. Acknowledgments

The authors wish to acknowledge the Australian Renewable Energy Agency (ARENA) for funds received through the Promoting Use of Solar Cooling and Heating in Australia (PUSCH) project.

7. References

Australian Bureau of Statistics, 2017. 2016 Census Quick Stats, Retrieved from http://www.censusdata.abs.gov.au/census_services/getproduct/census/2016/quickstat/036

Australian Bureau of Statistics, 2017a. 3101.0 - Australian Demographic Statistics, Mar 2017, Retrieved from http://www.abs.gov.au/ausstats/abs@.nsf/Latestproducts/3101.0Main%20Features15Mar%202017?opendocument&tabname=Summary&prodno=3101.0&issue=Mar%202017&num=&view=

Australian Energy Council, 2016. Factsheet Renewable Energy in Australia, Retrieved from https://www.energycouncil.com.au/media/1318/2016-06-23_aec-renewables-fact-sheet.pdf

Australian Energy Council, 2017. Solar Report, March 2017, Retrieved from https://www.energycouncil.com.au/media/7687/australian-energy-council-solar-report_march-2017.pdf

Australian PV Institute, 2017. Large-Scale PV Systems, Retrieved from http://pv-map.apvi.org.au/power-stations.csv

Clean Energy Council, 2017. Clean Energy Australia Report 2016, Retrieved from https://www.cleanenergycouncil.org.au/dam/cec/policy-and-advocacy/reports/2017/clean-energy-australia-report-2016/CEC_AR_2016_FA_WEB_RES.pdf

Clean Energy Regulator, 2017. Postcode Data for small-scale installations - Small Generation Units (S.G.U.) – solar (deemed), Retrieved from http://www.cleanenergyregulator.gov.au/RET/Forms-and-resources/Postcode-data-for-small-scale-installations#SGU--Solar-Deemed

CitySmart, 2016. District Cooling System, Retrieved from https://www.citysmart.com.au/portfolio/district-cooling/

Coleman S (2017). Australia state of the environment 2016: built environment, independent report to the Australian Government Minister for the Environment and Energy, Australian Government Department of the Environment and Energy, Canberra.

DEWHA – Department of the Environment, Water, Heritage and the Arts, 2008. Energy Use in the Australian Residential Sector 1986 – 2020, retrieved from https://industry.gov.au/Energy/EnergyEfficiency/Documents/04_2013/energy-use-australian-residential-sector-1986-2020-part1.pdf and https://industry.gov.au/Energy/EnergyEfficiency/Documents/04_2013/energy-use-australian-residential-sector-1986-2020-part2.pdf

Department of Energy, Land, Water and Planning, 2015. Environmental Upgrade Finance, Retrieved from https://www.energy.vic.gov.au/energy-efficiency/environmental-upgrade-agreements

Energex, 2017. Positive Payback for Business, Retrieved from https://www.energex.com.au/home/control-your-energy/positive-payback-program/positive-payback-for-business/eligible-areas

Ernst & Young, 2015. Mid-tier commercial office buildings in Australia - Research into improving energy productivity, Retrieved from https://www.gbca.org.au/uploads/97/36449/Mid-tier%20Commercial%20Office%20Buildings%20Sector%20Report_FINAL.pdf

Goldsworthy, M., Sethuvenkatraman, S., 2016. CSIRO internal report.

Green Building Council of Australia, 2013. The Value of Green Star - A Decade of Environmental Benefits, Retrieved from https://www.gbca.org.au/resources/gbca-publications/the-value-of-green-star/

Greenaway, T., Kohlenbach, P., 2016. Assessment of potential energy and greenhouse gas savings in the commercial building sector by using solar energy for air-conditioning purposes. International High- Performance Built Environment Conference 2016.

Kohlenbach, P., Dennis, M., 2010. Solar Cooling in Australia: The future of air-conditioning? 9th IIR Gustav Lorentzen Conference 2010.

Lecamwasam, L., Wilson, J., Chokolich, D., 2012. Guide to Best Practice Maintenance & Operation of HVAC Systems for Energy Efficiency, Retrieved from http://www.environment.gov.au/system/files/energy/files/hvacbestpracticeguide-complete.pdf

Letts, S., 2017. Gas prices: Deal done but the days of cheap gas are long gone, in: ABC News, 29.9.2017, Retrieved from http://www.abc.net.au/news/2017-09-28/gas-prices-deal-done-but-the-days-of-cheap-gas-are-long-gone/8998570

Master Plumbers' and Mechanical Services Association of Australia, Sustainability Victoria, 2009. Large Scale Solar Thermal Systems Design Handbook, Retrieved from http://www.sustainability.vic.gov.au/-/media/resources/documents/publications-and-research/knowledge-archive/small-scale-renewable-technology/commercial-and-industrial-solar-water-heaters/large-scale-solar-thermal-design-handbook-dec-2009.pdf?la=en

Mayekawa, 2017. Mayekawa unimoAW – Air Source CO_2 Heat Pump (Hot Water Supply), Retrieved from http://www.mayekawa.com.au/products/heat-pumps/heatcom-co2-transcritical-heat-pump/

McMahon, E., 2016. Sustainable offices are the future, The Sydney Morning Herald, 13.5.2016, Retrieved from http://www.smh.com.au/business/property/sustainable-offices-are-the-future-20160512-gotn0k.html

Mountain, B., Gassem, A., 2017. The MarkIntell Major Retailer Residential Electricity Price Series, Retrieved from https://www.markintell.com.au/pdfs/indices_10_2017.pdf

Office of Environment & Heritage, 2016. Upgrade your building, Retrieved from http://www.environment.nsw.gov.au/business/upgrade-agreements.htm

Office of Environment & Heritage, 2016a. Stage 1: Financial Options, Retrieved from http://www.environment.nsw.gov.au/business/financing-options.htm#options

Otanicar, T., Taylor, R., Phelan, P., 2012. Prospects for solar cooling – An economic and environmental assessment. Solar Energy 86, 1287–1299

Parisot, L., 2017. Small-scalle technology certificates data modelling for 2017 to 2019, Retrieved from http://www.cleanenergyregulator.gov.au/DocumentAssets/Documents/Modelling%20report%20by%20Jacobs%20-%20January%202017.pdf

Pitt&Sherry, 2012. Baseline Energy Consumption and Greenhouse Gas Emissions in Commercial Buildings in Australia, Retrieved from http://www.environment.gov.au/energy/publications/commercial-buildings-baseline-study

Potter, B., Tillett, A., 2017. Australian households pay highest power prices in world, in: Australian Financial Review, 4.08.2017, Retrieved from http://www.afr.com/news/australian-households-pay-highest-power-prices-in-world-20170804-gxp58a

Reserve Bank of Australia, 2017. The Australian Economy and Financial Markets Chart Pack, 4 October 2017, Retrieved from http://www.rba.gov.au/chart-pack/pdf/chart-pack.pdf?v=2017-10-15-22-07-27

Roy Morgan, 2017. Solar Electric Panels hot items in Queensland & South Australia, Retrieved from http://www.roymorgan.com/findings/7262-solar-energy-electric-panels-march-2017-201707061419

Sanden, 2017. Sanden Eco Plus, Retrieved from https://www.sanden-hot-water.com.au

Sheldon, M. 2011. Small- to medium-scale solar cooling in Australia – Data and Lessons from an operating installation in the Outback, conference presentation at AuSES Solar 2011 conference, Sydney.

Slow, K., 2013. IPD / Department of Industry NABERS Energy Analysis - Selected Charts, Quarter Ending June 2013, Retrieved from http://cbd.gov.au/sites/prod.cbd/files/NABERS-energy-office-market-analysis-june-2013.pdf

Witts, S., 2017. Monash Uni's solar thermal solution, Retrieved from http://www.ecogeneration.com.au/monash-unis-solar-thermal-project-hits-its-target/

On the Economics of Solar Chemical Processes – Case Study for Solar-Co-Production of Methanol and Power

Henrik von Storch[1], Martin Roeb[2], Hannes Stadler[1], Christian Sattler[2], Bernhard Hoffschmidt[2]

[1] German Aerospace Center (DLR), Jülich (Germany)

[2] German Aerospace Center (DLR), Cologne (Germany)

Abstract

In several studies, the efficiency of solarized industrial processes was assessed and showed promising results. However, the economic competitiveness of such processes is a mainly unanswered question. In this work, the economic performance of a solar aided methanol production process is determined. The assessment yields promising results for the considered co-production process. The presented results also show that for a penetration of renewable energies beyond electricity production, the common support model of fixed feed-in-tariffs is not suitable. A reasonable cost for CO_2 emissions or reward for their reduction will allow finding the most economic application for renewable energies independent of the end product of the process. When reasonable rewards of 75 $/t_{CO2}$ for the reduction of CO_2 emissions compared to fossil reference processes are considered, the process can produce methanol and electricity at competitive prices.

Keywords: Solar thermochemistry, CSP, solar fuels, reforming, economics

1. Introduction

The necessity to reduce greenhouse gas emissions by substituting fossil energy carriers by renewable energy sources such as solar- and wind energy is widely accepted and ongoing today. Regarding the production of electricity, this process has already well advanced in several countries. For instance, in Germany more than 30 % of the electricity was produced from renewable energies in 2015 [1]. However, as also increasingly discussed, the implementation of renewable energies has to advance towards industrial processes to achieve a complete energy transition. von Storch et al. [2] as well as Bai et al. [3] proposed processes for production of methanol with the aid of solar energy that also include further energy streams into and out of the process. In both publications, solar energy is concentrated (i.e. concentrated solar power (CSP)) to provide high temperature heat. Furthermore, both give promising results for the processes regarding the efficiency of solar energy utilization. However, for new renewable energy applications to be commercialized, favorable economics are necessary. Bai et al. [3] give an estimation on economic performance and show methanol prices between 440 and 516 $/t, but they are not put into context with market prices and common costs for renewable energy utilization. In von Storch et al. [2], economic aspects of the proposed process are not assessed at all. On the one hand, it is necessary to determine product costs for such processes to assess their potential to become commercially viable. On the other hand it is also necessary to carry out an economic assessment in order to carry out process optimization. For instance, as stated by von Storch et al. [2], the possibility of implementing thermal energy storage to increase operating hours of the investigated process is a central advantage of the considered technology. However, implementation of thermal energy storage can only enhance the economic performance, and not the efficiency. Hence, the suitable storage size can only be determined through economic optimization of a process. The same applies for the solar multiple, which represents the energy provided by the solar part at nominal operation in relation to the nominal energy input into the reforming process. The larger the solar multiple, the higher the capacity factor for the reforming process, but the larger and more expensive the solar receiver and heliostat field. Therefore, the optimal solar multiple can only be found through economic considerations.

In order to close the gap regarding information on the performance of these processes, the process presented by von Storch et al. [2], which is based on solar aided reforming of natural gas for methanol production (SOLME process), is assessed regarding its economic performance in this work.

2. The SOLME Process

The SOLME process presented by von Storch et al. [2] is a process that produces methanol and electric power form

doi:10.18086/swc.2017.34.04 Available at http://proceedings.ises.org

concentrated solar radiation and natural gas. A simplified flowchart of the process is presented in Figure 1. To provide the concentrated solar irradiation, a solar power tower is used: A heliostat field concentrates solar irradiation onto a central receiver where the irradiation is absorbed and converted into heat. As central receiver, an open volumetric receiver, as thermal storage a ceramic brick storage, both similar to the system installed at the solar tower Jülich (cf. Alexopoulos and Hoffschmidt [4]) are considered. Air is used as heat transfer fluid and transports the heat from the receiver or thermal storage to the reforming reactor. In the reforming reactor natural gas is converted into syngas via the reforming reaction. The syngas is cooled, compressed and given into a methanol synthesis reactor, where it is converted into methanol. Due to a large recycle stream in the methanol synthesis, it is necessary to purge an off-gas. This off-gas consists of inert species as well as unreacted methane, hydrogen and carbon monoxide. Hence it has a significant heating value. It can be combusted to provide heat to the reforming reactor or co-combusted in a power plant, for instance a combined cycle gas turbine power plant (CCGT). The off heat that is available from syngas cooling and as heat of reaction from methanol synthesis cannot be completely integrated into the process. It is considered, that the heat is used in a water-steam cycle to generate additional electricity. A more detailed description of the SOLME process can be found in refs [2, 5].

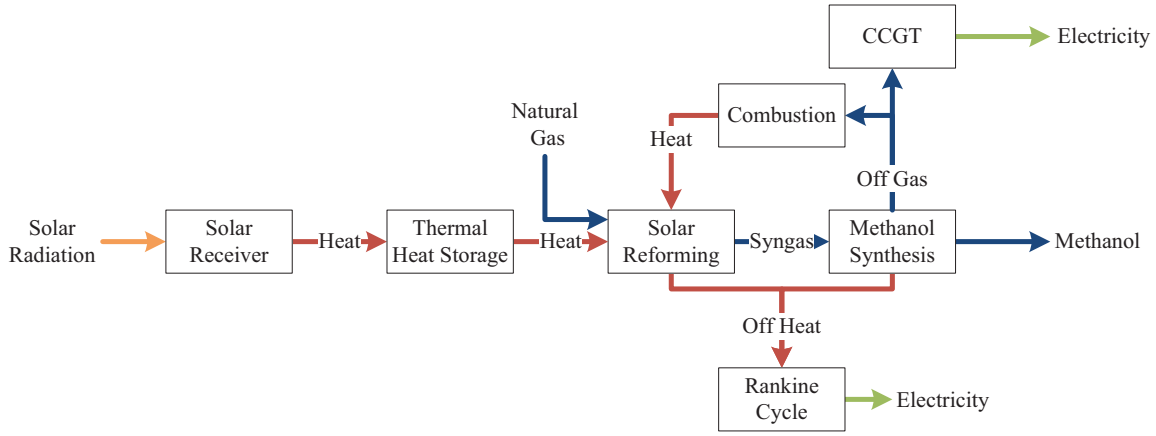

Figure 1 – Schematic of the SOLME process

As can be seen in Figure 1, the process consumes solar energy, natural gas and water to produce electricity and methanol. The production of two products from a renewable and a fossil energy resource complicates the economic assessment. Usually the utilization of renewable energies makes the product more expensive. In the case of facilities for the production of electricity, this is taken care of by increased feed-in-tariffs; which act as subsidy. For methanol production facilities, this procedure is not known.

Regarding the energetic performance of the process, von Storch et al. [2] report that the SOLME process can produce a given amount of electricity and methanol from the same amount of solar energy but approx. 5 % less natural gas than a system of conventional methanol synthesis and solar power plant. This indicates that the hybrid process for methanol and power production is more efficient regarding natural gas consumption than a separate production of solar power and conventional methanol would be. They state that the SOLME plant, that is scaled by the solar receiver with a capacity of 50 MW produces 127.5 GWh of Methanol and 21.41 GWh of electricity per year from 176.1 GWh of solar energy (onto heliostat field) and 148.4 GWh natural gas. The same size SOLME plant is assessed in this work. However due to the parameter variations, which are mentioned in the following chapter, the amounts of methanol and electricity produced will vary.

3. Methodology and procedure

Several options exist for the economic assessment of a process such as the SOLME that produces two products. Firstly, realistic market price for the products can be retrieved from a suitable source and the achievable profit can be determined based on capital cost and operational cost. However, as this would lead to negative profits for most processes that use renewable energy resources, for processes using renewable energy resources the concept of *levelised cost of electricity* (LCOE) is commonly used [6]. In this concept, the capital cost and operational cost (C_{OPEX}) of the process are determined. The capital cost is usually taken into account as the annuity of the initial investment ($C_{Annuity}$), considering a certain weighted average cost for capital (WACC). By division of the total cost with the amount of produced electricity, the LCOE is determined, as shown in equation (1). The resulting value indicates the minimum electricity price, to achieve the required interest rate/profit. This concept can also be applied

to other products than electricity, for instance to methanol. However, it cannot be applied in the same way to processes, which produces two products such as the SOLME process. Therefore, for this process, a realistic price for methanol (c_{Methanol}) is considered and the revenues subtracted from the annual costs in determining the LCOE. The resulting equation is shown in (2), where $m_{\mathrm{Methanol,SOLME}}$ is the annual amount of methanol produced in the process. The LCOE determined through this procedure can subsequently be compared with other processes. Then the LCOE is also the objective criterion to be minimized.

$$LCOE = \frac{C_{Annuity} + C_{OPEX}}{E_{El}} \tag{1}$$

$$LCOE_{\mathrm{SOLME}} = \frac{C_{\mathrm{Annuity,SOLME}} + C_{\mathrm{OPEX,SOLME}} - m_{\mathrm{Methanol,SOLME}} \cdot c_{\mathrm{Methanol}}}{E_{\mathrm{El,SOLME}}} \tag{2}$$

It is aimed to minimize the LCOE by variation of two central parameters: Solar multiple and thermal storage size. The solar multiple is defined as the nominal thermal capacity of a receiver in relation to the nominal thermal input of the reforming process. The heliostat field is size is fixed to provide sufficient concentrated solar irradiation to the receiver for nominal operation at noon of the 21st of March, which is a flux of 50 MW. The procedure is presented in detail by von Storch et al. [2]. The resulting heliostat field has a size 62,854 m² at the location in In Amenas in Algeria. The solar multiple is varied by scaling the non-solar part of the SOLME process. This means that the solar energy collected by the heliostat field and transformed into thermal energy in the solar receiver is fixed, the time period over which the process consumes and the amount that has to be dumped because the storage is full are varied. Energy consumption for operation of the heliostat field are taken into account as parasitic losses based on data published in the ECOSTAR report [7], where 6.5 W_{el} per square meter of heliostat field are stated. This results in a total consumption of 408.6 kW during solar operation. Based on heliostat field layout, the solar operating time is 4383 hours per year. Other major parasitic losses, such as blower for the air system are taken into account in the process model directly.

Despite a rapid reduction in costs for renewable energy technologies, processes that use renewable energy resources usually still have a higher cost of product than processes that use fossil fuels. This can be well observed at recent solar power projects, such as the recently inaugurated solar power plant *crescent dunes.* Besides subsidized loans, this kind of solar power plant is mainly supported through an increased feed-in-tariff, in this case 135 $/MWh [8] (the market price of electricity in that region is approx. 80 $/MWh [9]). The total subsidy for the project through increased feed-in-tariff can be estimated by multiplication of the difference in electricity price (in this case approximately 55 $/MWh) with the total amount of electricity produced. In the case of the SOLME plant, compared to a conventional solar power plant of identical scale, less electricity is produced because a fraction of the solar energy input is used in the methanol production. However, as the methanol is sold at a conventional market price (cf. paragraph above), the additional cost due to the solar field, receiver, etc. is spread over a lower amount of electricity. Hence, the resulting LCOE will be higher than for a conventional solar power plant even if the economic performance of the SOLME plant may be better. Therefore, comparison of the LCOE of the SOLME plant with published LOCEs of real solar power plants will lead deceptive conclusions.

To compare the economic performance of the SOLME process and conventional solar plants realistically, the total necessary subsidy to achieve marketable product prices should be determined. This can be done in several ways, for instance by considering a fixed annual sum or by considering a *reward* for the reduction of CO_2-emissions compared to the state of the art. In this work, both is done. Considering rewards for the reduction of CO_2-emissions is especially interesting, as it could be an effective measure to help achieving the superordinate goal in renewable energies utilization: The reduction of greenhouse gas emissions. Through this procedure, the more economic route for reduction of greenhouse gas emissions through solar energy utilization can be determined; in this case between a conventional solar power plant and the SOLME plant. Therefore in a parameter variation, the results for LCOE are determined in dependence of reward for reduction of carbon dioxide emission. The reward is varied between 0 and 200 $/$t_{CO2.}$ This reward can be considered as a potential income from excess CO_2 certificates as they exist in the EU. Currently the prices of the certificates are below 10 €/t (cf. https://www.eex.com/de/). However, they are expected to rise in the future and achieve values up to 76 €/t (100 $/t) according to Schlesinger et al. [10].

In order to obtain a comparable and realistic price for methanol, the price is determined based on own simulations rather than obtaining data from literature or real market prices. This ensures that comparable assumptions and boundary conditions are used for the SOLME process and the reference methanol price. The determination of reference methanol price is based on the process used as reference methanol process for energetic performance

assessment by von Storch et al. [2]. The resulting value is 180\$/$t_{Methanol}$. However, the value is varied to determine if it will affect the optimum values for storage size and solar multiple. In the case of the reference solar power plant, the receiver and storage size as well as solar multiple are set to the same values as in the SOLME process to ensure comparability of the results. This is done to obtain a comparable plant regarding the duration of which it can provide electricity to the grid throughout the year.

Determining the capital cost of SOLME process

The capital cost of the processes can roughly be categorized as conventional process units and CSP components. The cost of conventional process units is determined according to data by Ulrich and Vasudevan [11] and the prices converted from 2004 to prices of 2014 with the chemical engineering cost index (CEPCI) [12, 13]. The calculation is done in US-\$. If prices are retrieved in other currency, it is converted to US-\$ with the average exchange rate applicable for the year of publication from [14]. In accordance with Ulrich and Vasudevan [11], the bare module component costs (C_{BM}) are multiplied by a factor of 1,534 to yield the grass roots cost (C_{GR}), which includes fees and contingencies as well as auxiliary facilities, i.e. represents the total investment.

The prices for CSP-related components are retrieved from the ECOSTAR Report [7] and Vogel and Kalb [15]. The values used for the components are given in Table 1. Some of the data used to determine the prices of CSP components is several years old already. It is well known that significant cost reductions were achieved in the meantime. However, no reliable, detailed data is publicly available. Therefore, based on the predictions by Trieb [16], a reduction in CSP-Component cost by 30 % are assumed to take into account current developments.

Table 1 – Cost data for CSP components

Component	Source	Value and basis in source	In 2014-\$	30 % reduced value
Tower	ECOSTAR Report [7]	2 mio. €$_{2003}$	3.55 Mio. \$	2.73 mio. \$
Heliostat Field	Vogel and Kalb [15]	100 \$$_{2002}$/m²	146.64 \$/m²	102.65 \$/m²
			9.22 Mio. \$ (total)	6.45 mio. \$
Receiver	ECOSTAR Report [7]	115 €$_{2003}$/kW$_{th}$	204 \$/kW$_{th}$	142.8 \$/kW$_{th}$
Storage	ECOSTAR Report [7]	60 €$_{2003}$/kWh$_{th}$	106 \$/kWh$_{th}$	74.2 \$/kWh$_{th}$

The price of the Rankine cycle (RC) of the reference solar power plant is based on information from the ECOSTAR Report [7] according to equation (1) in dependence of the of its nominal electric output, assuming a value of 0.6 as scaling factor as recommended by Ulrich and Vasudevan [11].

$$C_{\mathrm{BM,PB}} = 1{,}064{,}400\,\frac{\$}{\mathrm{kW}} \cdot \left(\frac{P_{\mathrm{RC,el,nom}}}{10\ \mathrm{MW}}\right)^{0.6} \qquad \text{(eq. 1)}$$

For the combustion of the off-gas in a CCGT, it is assumed that it is co-combusted in an industrial scale CCGT rather than building a small scale CCGT for this purpose only. Therefore, the specific cost for a 200 MW CCGT plant are determined based on information from Ulrich and Vasudevan [11] and the fraction of capacity that can be attributed to the SOLME plant is considered in the investment cost. The specific cost (grass roots) is 3250 \$/kW$_{el}$.

Further relevant parameters for calculation of annuity and operating costs of the plant are given in Table 2. The WACC and expected lifetime are based on values proposed by Dieckmann et al. [17] for the near term future. The operation and maintenance cost (O&M) of CSP related components are set to 2% of the investment per year in accordance with Hernández-Moro and Martínez-Duart [18]. The O&M cost factor is set to 0.5% for all other components. The cost for demineralized water is determined with information provided by Ulrich and Vasudevan [11]. As cost for natural gas, based on the average values published for Henry Hub spot price between 2010 and 2016 [19], a value 0.012\$/kWh (3.5 \$/MBtu) is assumed.

Table 2 – Annuity input data for SOLME plant

Parameter	Value
WACC	6.5%
Payback time	25 years
O&M	
CSP – related components	2 % of investment/year
Other components	0.5 % of investment/year
Cost for demineralized water	0.35 Mio. $/year
Natural gas price	0.012 $/kWh

Determining CO_2-emissions reduction

The CO_2-emissions reduction is estimated by the difference in natural gas consumption compared to a benchmark value. In the case of methanol production, benchmark is based on a conventional methanol production plant based on the information by von Storch et al. [2]. In the case of electricity production, the benchmark is based on a CCGT plant. Indirect CO_2-emissions are not taken into account in this case, as it is assumed that they are similar for all processes.

Based on the composition of the natural gas and the molar weight of CO_2, 42.6 $t_{CO2}/Mmol_{Natural\ Gas}$ are considered. This leads to specific emissions of 1.865 $t_{CO2}/t_{Methanol}$ as benchmark value. For electricity production, a CCGT with 60 % efficiency is assumed for the benchmark. Based on the same natural gas composition, this leads to specific emissions of 416 t_{CO2}/GWh_{el}. The reference solar power plant does not consume natural gas. Therefore, no CO_2-emissions are considered.

4. Results & Discussion

LCOE of SOLME process

At first, it was assessed, if the assumed methanol price has an influence on the optimum values for solar multiple and storage size. The results for LCOE of the SOLME process for different methanol prices are shown in Figure 2 in dependence of solar multiple and Figure 3 in dependence of storage size. In both figures, it can be seen that the assumed methanol price has a relevant influence on the LCOE, which was to be expected because the methanol revenues are higher when methanol prices are higher. Thus the remaining costs on which the LCOE is based are lower. Furthermore, it can be seen, that an optimum evolves for both solar multiple (approx. 3.4) and storage size (approx. 150), which is not dependent on methanol price in the considered range.

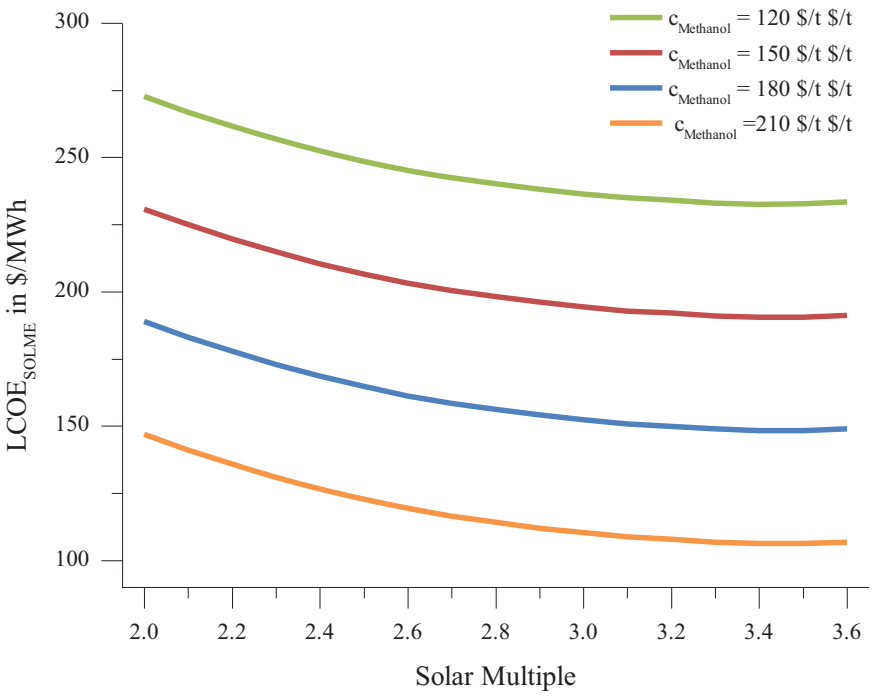

Figure 2 – LCOE for SOLME in dependence of Solar Multiple for different assumed methanol prices, assuming a storage size of 150 MWh

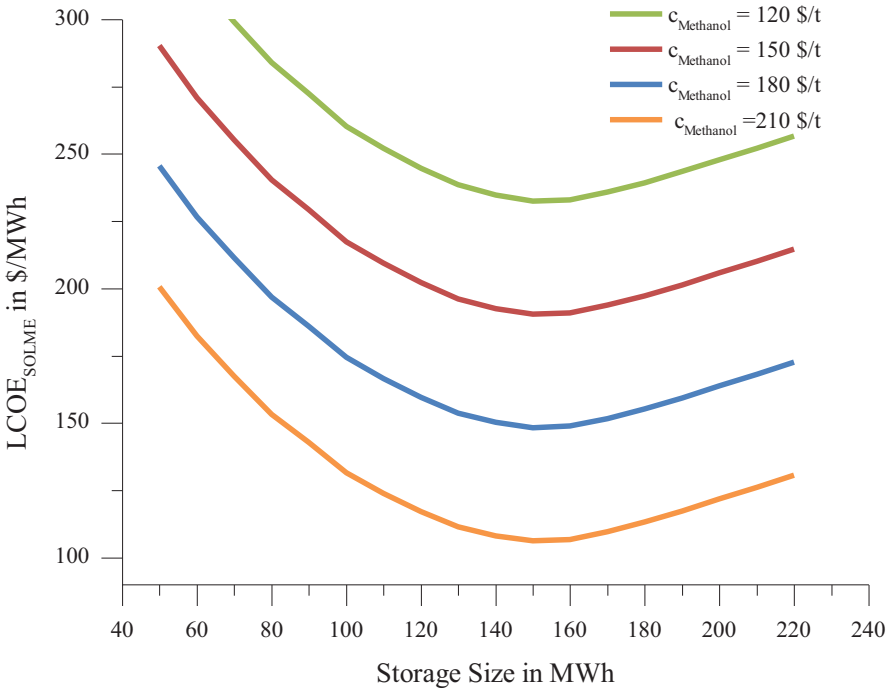

Figure 3 – LCOE for SOLME in dependence of thermal storage size for different assumed methanol prices, assuming a SM of 3.4

The results shown in Figure 2 and Figure 3 show that the optimum for the two considered optimization parameters can be found independently of the assumed methanol price. Hence it is justified to set the methanol price to a realistic value, which is 180 $/t in this work.

In Figure 4, the results of the optimization of the LCOE by variation of solar multiple and storage size is shown. It can be seen that the lowest value for LCOE is achieved at a solar multiple of 3.4 and storage size of 150 MWh. The resulting value of LCOE is 148.3 $/MWh. For the same storage size and solar multiple, the LCOE of the reference solar power plant is 124.4 $/MWh.

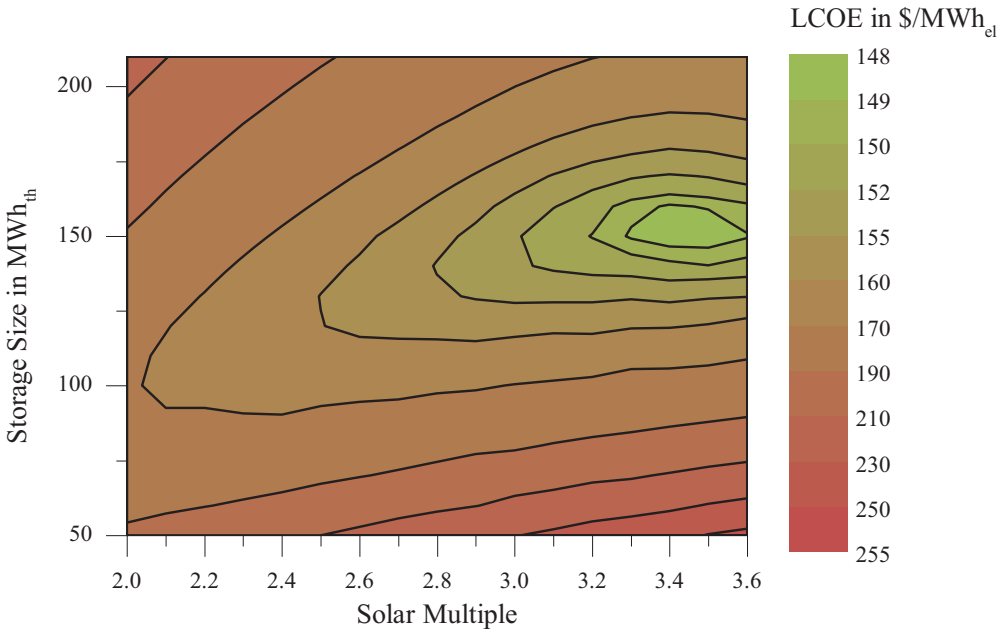

Figure 4 – Optimization of LCOE by variation of storage size and solar multiple

In the optimum configuration, the process achieves 7395 operating hours per year, which corresponds to a capacity factor of 86 %. This means that nearly continuous operation is possible, except for periods of continuously low solar irradiance during winter. Some further key results on the operation of the process at this configuration are given in Table 3. It can be seen that the nominal thermal input into the process is 10.74 MW. Consequently, with a 150 MWh thermal storage, a storage-only operation of 14 hours is possible. The results on process costs are summarized in Table 4.

Table 3 – Key parameters on the operation of SOLME with solar multiple of 3.4 and 150 MWh storage size

Parameter	Result
Nominal thermal input	10.74 MW
Dumped energy	3.61 %
Produced methanol	22,361 t/year
Produced electricity (net)	15.9 GWh/year

Table 4 – Key results on economic aspects of SOLME process for solar multiple of 3.4 and 150 MWh storage size

Parameter		Result
Total investment cost (grass roots price)		45.7 Mio. $
	Heliostat Field	6.5 Mio. $
	Solar Receiver	5.2 Mio. $
	Thermal Energy Storage	11.1 Mio $
	Non-Solar part	20.5 Mio. $
	Power block (1.40 MW)	5.93 Mio. $
	CCGT (2.27 MW)	4.63 Mio. $
	Air heated reforming reactor	2.36 Mio. $
Annual costs		6.39 Mio $
Annuity of investment		3.75 Mio. $
Operation & Maintenance (annually)		0.6 Mio. $
Natural gas consumption(annually)		1.68 Mio. $
Cost for demineralized water		0.35 Mio. $
Revenue methanol		4.03 Mio. $
LCOE		148.3 $/MWh

The reference solar power plant has an annual net production of electricity of 31.0 GWh with the same heliostat field as the SOLME plant at total investment costs of 37.9 Mio. $. The resulting annuity is 3.1 Mio. $, the operation and maintenance costs are 0.76 Mio. $, resulting in an LCOE of 124.4 $/MWh.

The necessary subsidy for each of the plants can be determined by multiplying the produced electricity with the difference between the LCOE and the market price. As proposed above, 80 $/MWh can be assumed as market price. For the SOLME plant, this yields a required annual funding of 1.086 Mio. $. For the reference solar power plant the required annual funding is 1.379 Mio. $. Hence, the SOLME process can be commercially viable with a lower funding than the conventional solar power plant.

Influence of reward for CO_2 emissions reduction on LCOE

The key results that are relevant to determine the influence of a reward for the reduction in CO_2-emissions are summarized in Table 5. The CO_2-emissions of the SOLME plant are compared with the previously defined benchmark values. No CO_2-emissions are considered for reference solar power plant. Therefore, it achieves a reduction in CO_2-emissions compared to the benchmark by 100 %. As can be seen in Table 5, the SOLME plant achieves a yearly reduction in CO_2-emissions by 13,197 t, the reference solar power plant by 12,909 t

Table 5 – Data on CO_2 Emissions of SOLME process, reference solar power tower and reference methanol plant and CCGT

Parameter	Result
Natural gas consumption (SOLME)	824 Mmol
CO_2-emissions	
SOLME	35,132 t
Benchmark Methanol (22.361 $t_{Methanol}$)	41,703 t
Benchmark electricity SOLME (15.9 GWh_{el})	6,614 t
Benchmark electricity SPT (31.0 GWh_{el})	12,909 t
Reduction of CO_2 Emissions by SOLME plant	13,197 t
Reduction by reference solar power plant (31.0 GWh)	12,909 t

The influence of a reward for the reduction of CO_2 emissions on the LCOE of the SOLME process as well as the reference solar power plant is shown in Figure 5. It can be seen that the LCOE is reduced with increasing reward. It can also be seen that the reduction is faster for the LCOE of the SOLME plant than for the reference solar power plant. This is caused by the higher reduction in CO_2-emissions of the SOLME process as indicated in Table 5. Without, or with low rewards, the LCOE of the SOLME plant is higher than the LCOE of the reference solar power plant. However, for a reward of 50 $/t$_{CO2}$ or higher, the LCOE of the SOLME is lower than for the reference solar power plant. The SOLME plant achieves a competitive LCOE of 80 $/MWh at a reward of 80 $/t$_{CO2}$, while the conventional solar power plant only achieves this value at 110 $/t$_{CO2}$. This shows that even without further CSP-component cost reduction, the SOLME process has the capacity to achieve competitiveness, if suitable funding mechanism, such as reasonably priced CO_2-emissions certificates exist.

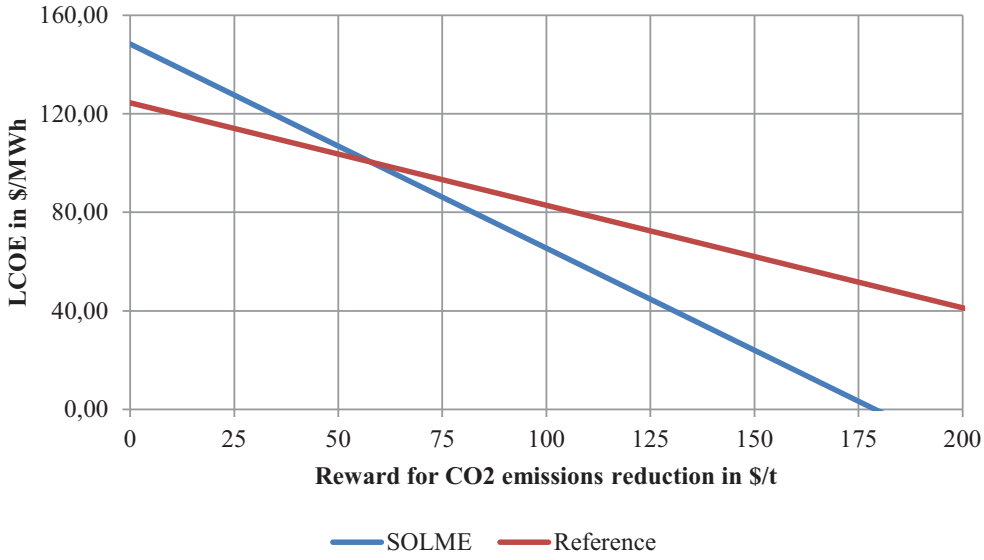

Figure 5 – Influence of reward for reduction of CO_2-emissions on LCOE

5. Summary and Conclusions

The economic performance of a process for hybrid solar-fossil co-production of methanol and electric power (SOLME process) is assessed. A reasonable price for methanol is fixed and the resulting levelized cost of electricity (LCOE) is determined. The solar multiple and thermal storage size are varied to optimize the economic performance and find the minimum LCOE. A value of 148.3 $/MWh is achieved for a solar multiple of 3.4 and a thermal storage size of 150 MWh, which allows up to 14 hours of off-sun / storage-only operation.

The resulting LCOE is higher than for a comparable solar power plant that produces only electricity, which would achieve 124.4 $/MWh. This is the case, because the additional cost of the CSP-components is spread over a lower amount of electricity, when the methanol is sold at market price. By determining the required subsidy to achieve competitive operation independent of product, it is shown that the SOLME process is closer to commercial viability. For electricity from renewable resources, power purchase agreements are commonly concluded with electricity prices higher than the market price. This is caused by the requirement of many utility services to reduce their overall CO_2 emissions. This practice does not exist for commodities such as methanol. A suitable mechanism to support the utilization of renewable energies in commodities production could be reasonably priced certificates for CO_2-emissions. When considering a possible reward for the reduction of CO_2-emissions, favorable results for the SOLME process are obtained. Because it causes a higher reduction in CO_2-emissions than a conventional solar power plant, it achieves a competitive LCOE of 80$/MWh$_{el}$ at a reward of 80 $/t$_{CO2}$. The conventional solar power plant would require a reward of 110 $/t$_{CO2}$ to achieve the same LCOE. This also shows that the SOLME process requires lower subsidy to become commercially competitive than a conventional solar power plant.

In conclusion it can be stated that the SOLME process achieves a very promising economic performance, even at current CSP component prices. However, currently no effective funding mechanisms exist to support the production of less carbon intensive commodities.

References

1. Renewable Energies in Numbers (in German:Erneuerbare Energien in Zahlen), 2016, Umweltbundesamt (Federal Environmental Agency), URL: www.umweltbundesamt.de/themen/klima-energie/erneuerbare-energien/erneuerbare-energien-in-zahlen, Accessed: 28.03.2017
2. von Storch, H., Roeb, M., Stadler, H., Sattler, C., Bardow, A., Hoffschmidt, B., On the assessment of renewable industrial processes: Case study for solar co-production of methanol and power, Applied Energy, 183 (2016), 121-132, http://dx.doi.org/10.1016/j.apenergy.2016.08.141
3. Bai, Z., Liu, Q., Lei, J., Li, H., Jin, H., A polygeneration system for the methanol production and the power generation with the solar–biomass thermal gasification, Energy Conversion and Management, (2015), DOI: 10.1016/j.enconman.2015.02.031
4. Alexopoulos, S., Hoffschmidt, B., Solar tower power plant in Germany and future perspectives of the development of the technology in Greece and Cyprus, Renewable Energy, 35 (2010), 1352-1356, DOI: 10.1016/j.renene.2009.11.003
5. von Storch, H., *Methanol Production via Solar Reforming of Methane*, RWTH Aachen, Fakultät für Maschinenwesen, 2016, Dissertation, URL: http://publications.rwth-aachen.de/record/661077/files/661077.pdf
6. Projected Costs of Generating Electricity 2010, International Energy Agency, Nuclear Energy Agency, Organisation for Economic Co-operation and Development, Washington, Palo Alto, 2010, ISBN: 9789264084308.
7. Ferriere, A., Romero, M., Tellez, F., Zarza, E., Steinfeld, A., Langnickel, U., Shpilrain, E., Popel, O., Epstein, M., Karni, J., Road Map Deliverable (WP 3 Deliverable No7), R. Pitz-Paal, J. Dersch, B. Milow (Eds.), European Concentrated Solar Thermal Road Mapping (ECOSTAR), SES-CT-2003-502578, 2005, URL: http://www.promes.cnrs.fr/uploads/pdfs/ecostar/ECOSTAR.Roadmap.pdf, Date Accessed: 01 October 2015
8. Parkinson, G., World's biggest solar tower + storage plant to begin generation this month, 14 May 2015, RE new economy, URL: http://reneweconomy.com.au/2015/worlds-biggest-solar-tower-storage-plant-to-begin-generation-this-month-22860, Accessed: 14 September 2015
9. Electric Power Monthly - Table 5.6.A. Average Price of Electricity to Ultimate Customers by End-Use Sector, 26 August 2015, U.S. Energy Information and Administration (eia), URL: http://www.eia.gov/electricity/monthly/epm_table_grapher.cfm?t=epmt_5_6_a, Accessed: 14 September 2015
10. Schlesinger, M., Hofer, P., Kemmler, A., Kirchner, A., Koziel, S., Ley, A., Piegas, A., Seefeldt, F., Straßburg, S., Weinert, K., Lindenberger, D., Knaut, A., Malischek, R., Nick, S., Panke, T., Paulus, S., Tode, C., Wagner, J., Lutz, C., Lehr, U., Philip, U., Entwicklung der Energiemärkte - Energiereferenzprognose - Kurzfassung zum Endbericht, Bundesministerium für Wirtschaft und Technologie, Berlin/Köln/Osnabrück, 2014, URL: http://www.bmwi.de/BMWi/Redaktion/PDF/Publikationen/entwicklung-der-energiemaerkte-energiereferenzprognose-kurzfassung,property=pdf,bereich=bmwi2012,sprache=de,rwb=true.pdf, Date Accessed: 12. August 2015
11. Ulrich, G.D., Vasudevan, P.T., Chemical engineering process design and economics : a practical guide, 2nd ed., Process Pub., Durham, N.H., 2004, ISBN: 0970876823.
12. CEPCI - Economic Indicators, Jan. 2015, Chemical Engineering, URL: http://www.isr.umd.edu/~adomaiti/chbe446/literature/ChECostIndexJan2015.pdf, Accessed: 29. April 2015
13. CEPCI - Economic Indicators, Jan. 2008, Chemical Engineering, URL: http://www.engr.uconn.edu/~ewanders/Design/Chemical%20Engineering%20Cost%20Indices%20Jan%202008.pdf, Accessed: 07. May 2015
14. Historical Exchange Rates, Oanda, URL: http://www.oanda.com/lang/de/currency/historical-rates/, Accessed: 07. May 2015
15. Vogel, W., Kalb, H., Large-Scale Solar Thermal Power: Technologies, Costs and Development, Wiley, 2010, ISBN: 9783527630004.
16. Trieb, F., Global potential of concentrating solar power, in Proceedings of the SolarPACES 2009, Berlin, Germany, 15.-18. September 2009.
17. Dieckmann, S., Dersch, J., Giuliano, S., Puppe, M., Lüpfert, E., Hennecke, K., Pitz-Paal, R., Taylor, M., Ralon, P., LCOE reduction potential of parabolic trough and solar tower CSP technology until 2025, in Proceedings of the AIP Conference Proceedings, 2017, pp. 160004, AIP Publishing.
18. Hernández-Moro, J., Martínez-Duart, J.M., CSP electricity cost evolution and grid parities based on the IEA roadmaps, Energy Policy, 41 (2012), 184-192, http://dx.doi.org/10.1016/j.enpol.2011.10.032
19. Henry Hub Natural Gas Spot Price, U.S. Energy Information Administration, URL: https://www.eia.gov/dnav/ng/hist/rngwhhda.htm, Accessed: 10.10.2017

Sustainable Building Materials and Components

Thermoelectric Modules Testing for Sustainable Buildings Applications

Mohamed Al Musleh[1], Evangelia Topriska[1] and David Jenkins[2]

[1] Heriot Watt university, Dubai (United Arab Emirates)

[2] Heriot Watt University, Edinburgh (United Kingdom)

Abstract

In order for buildings to be sustainable from an operational point of view, the basics are to save energy and maximize efficiency. This is only possible with the availability and around the clock collection of real-time data for energy use. These data can be collected via sensors installed all around the building which then feed back to the building management system or to the occupants. Transmitting data and powering those sensors remains a challenge. With today's wireless technologies and microcontrollers, transmitting is well developed, however, sensor power sources are still in the developing stage. This work describes the testing of Thermoelectric Generators (TEG) at the ultra-low temperature difference level (5ºC and below). TEGs are used as energy harvesters that make use of the temperature difference within the building energy systems, to power wireless sensors, thus eliminating the need of a battery and the maintenance/operation costs that come with it.

Keywords: Smart Buildings, Sustainable Buildings, Thermoelectric, Wireless Sensing, Energy-Harvesting.

1. Introduction

Thermoelectricity is the direct conversion of a temperature gradient to electricity and vice versa. TEG modules are made of multiple Thermoelectric (TE) blocks connected electrically in series and thermally in parallel, to maximize power generation. This effect is known as Seebeck effect, where the generated electricity depends on the temperature difference between the two sides of the TEG module. The Seebeck coefficient of the blocks is used, as shown in the relationship of Equation 1:

$$E_{emf} = S\,\Delta T \qquad \text{(eq. 1)}$$

Where E_{emf} represents the generated electromotive force, S is the Seebeck coefficient which is material dependent, and ΔT is the temperature gradient difference (Ahıska and Mamur 2014). Figure 1 shows a schematic diagram of a typical TEG.

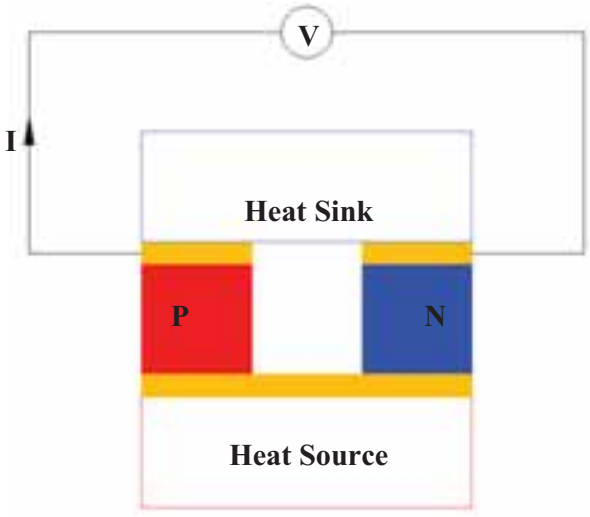

Figure 1 schematic diagram of a typical TEG.

doi:10.18086/swc.2017.35.01 Available at http://proceedings.ises.org

To run building resources and energy systems at a more sustainable level, systems feedback is required. This feedback is achieved using a network of sensors distributed around the building. Such sensors can measure building temperature, indoor light intensity, air quality, etc. and are either wired or wireless. Wireless sensors are often referred to as wireless sensor network (WSN). WSN could use batteries as a power source but the maintenance stays as a challenge from an operational point of view. Using ambient energy harvesters to power such sensors is a feasible option and TEGs are one of the techniques used for energy harvesting to power sensors. However, most of the commercially available TEG based energy harvesters require high-temperature difference, which is targeting industrial applications. Within the built environment low-temperature difference applications are common, if heating and hot-water systems are excluded. Typical examples of built environment applications are the temperature difference of an exterior wall surface, of a cold air duct with respect to the surroundings temperature, the heat emitted from a light fixture, the heat emitted from information technology (IT) equipment such as wireless routers, or security equipment such as surveillance cameras. Figure 2a shows a thermal image highlighting the heat emission from lighting fixture, where measured temperature difference is about 10°C. Figure 2b shows a thermal image of two different IT and security equipment, a wireless communication router and surveillance camera. The wireless router temperature is measured to be about 5°C above surroundings, while the surveillance camera measured at 9.6°C above surroundings. TEG used as power source for WSN has an increasing research interest but researchers in the field often face difficulties of the availability of TEG performance test data at very low-temperature difference. Therefore, the aim of this study is to provide such performance data and ultimately develop a universal test setup for TEG at this temperature range. (Salerno 2010) (Snyder 2008) (Moczygemba 2015) (Huang et al. 2011) (He et al. 2015) (Wang et al. 2013) (Wellington City Council 2017).

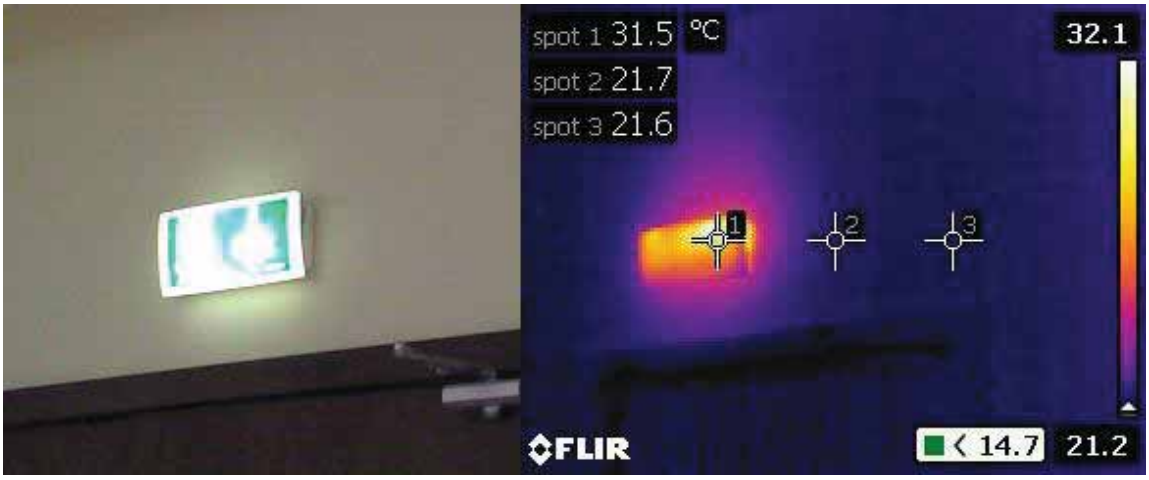

(a)

(b)

Figure 2 Thermal Image of (a) a lighting fixture and (b) IT equipment

2. Experimental Setup

A TG12-4 TEG module was acquired for this test, which is a Marlow Industries Inc. product. This is designed as a universal TEG, rated at 4 watts at a temperature difference of 180°C (Marlow Industries). The experimental setup consisted of a high precision temperature controlled hotplate, which acted as a heat source. The hot side of the TEG was placed on top of the hot plate using thermal paste to maximize heat transfer and a K-type thermocouple was placed between the TEG and the hotplate to measure the hot side temperature. On the other side of the TEG a heat sink was used to dissipate the heat and an electric fan was attached to the heat sink to ensure cooling via forced convection. Another K-type thermocouple was placed between the TEG and the heat sink to measure the cold side temperature. Schematic diagram of the test setup is shown in Figure 3. Both thermocouples were connected to a temperature data logger shown at the left of the test setup photo in Figure 4. A digital multimeter was used to measure the generated open-circuit voltage (V_{OC}) and short-circuit current (I_{SC}) of the TEG. The complete experimental setup is shown in Figure 3 below.

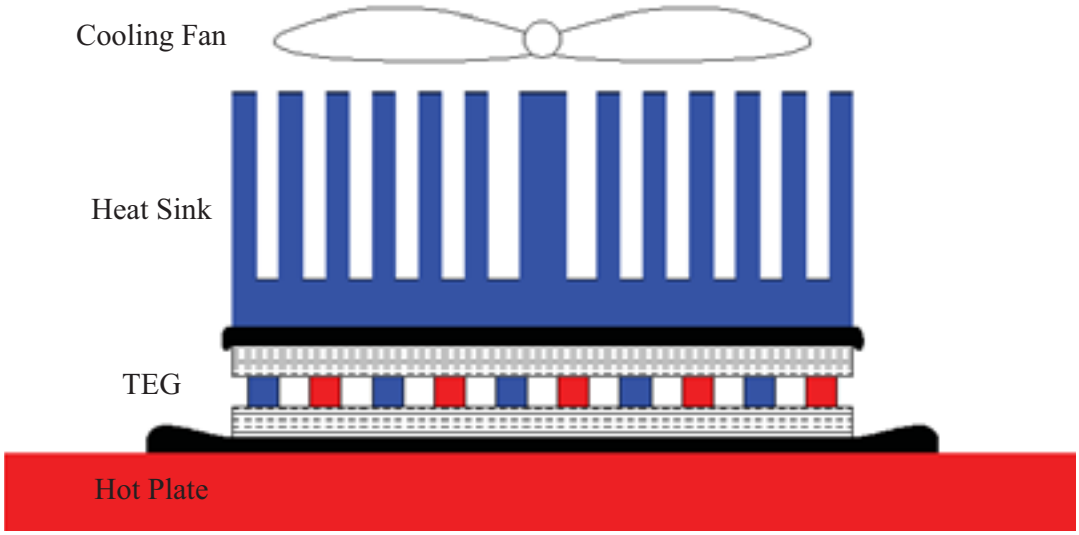

Figure 3 schematic diagram of the experimental setup.

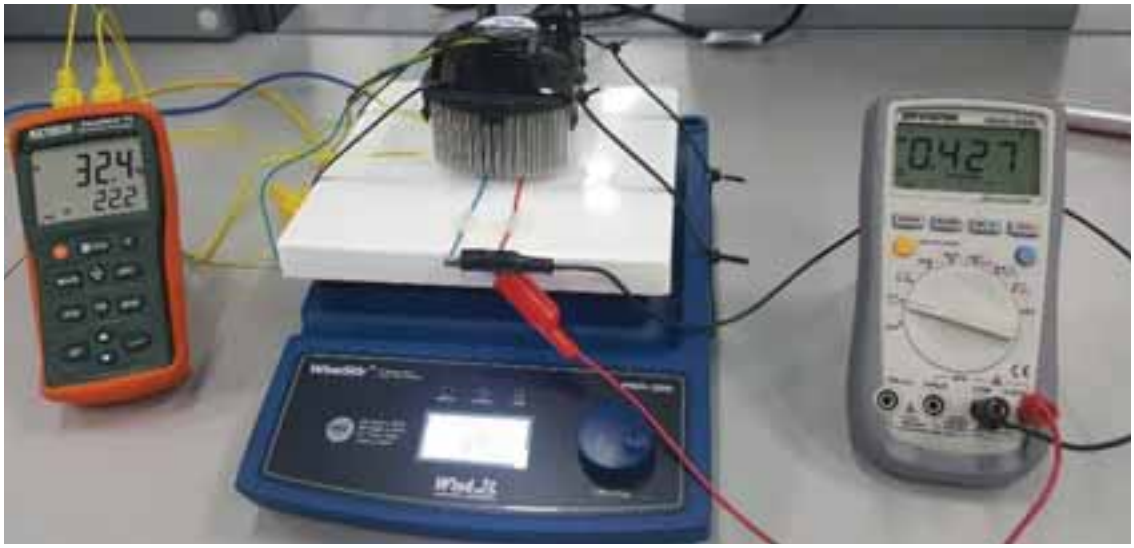

Figure 4 The complete setup of the experiment showing the temperature data logger at left, the hotplate with the TEG mounted on it below the heat sink, and the multimeter at the right.

As cooling was performed using an air-cooled heat sink, it was rather complicated to estimate the heat dissipation from the TEG. To further investigate the heat flux through the TEG and device efficiency it was found appropriate

to use water blocks on both sides of the TEG. The all copper water block is shown in Figure 5 were sourced out for this test.

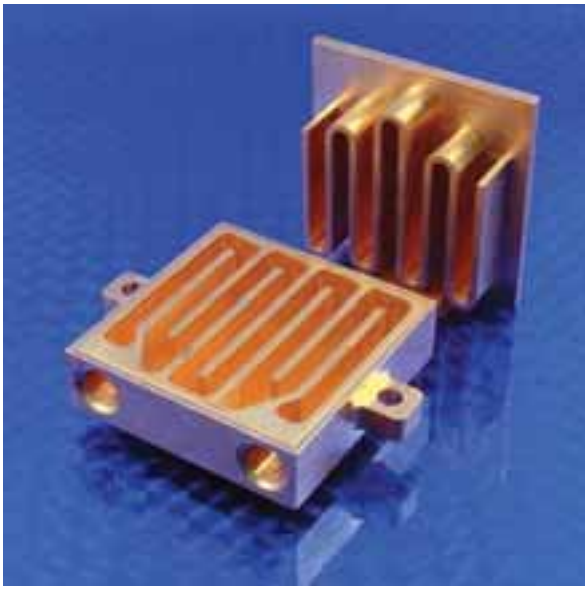

Figure 5 The all copper water block which was sourced out for the test.
(Image source: customthermoelectric.com)

One block for the hot water cycle attached to the TEG hot side and the other for the cooling water cycle on the cold side. 3D designed and printed holders were used for holding the water block in place and to make sure that TEG is always in the center. The complete setup of the TEG installed on the water block is shown in Figure 6.

Figure 6 the TEG installed on one side of the water blocks.

The test setup is planned to be attached to a heat exchanger supply unit. The unit will supply to two separate water cycles, one is hot and the other is cold. Both cycles have inlet and outlet temperature recorders along with recording the water flow rate.

3. Experimental Results

The temperature of the hotplate was increased in steps of 0.5°C above the room temperature, allowing enough time for both sides of the TEG to reach a steady state temperature. Both V_{OC} and I_{SC} were measured at each step and the recorded values are shown in Figure 7 below.

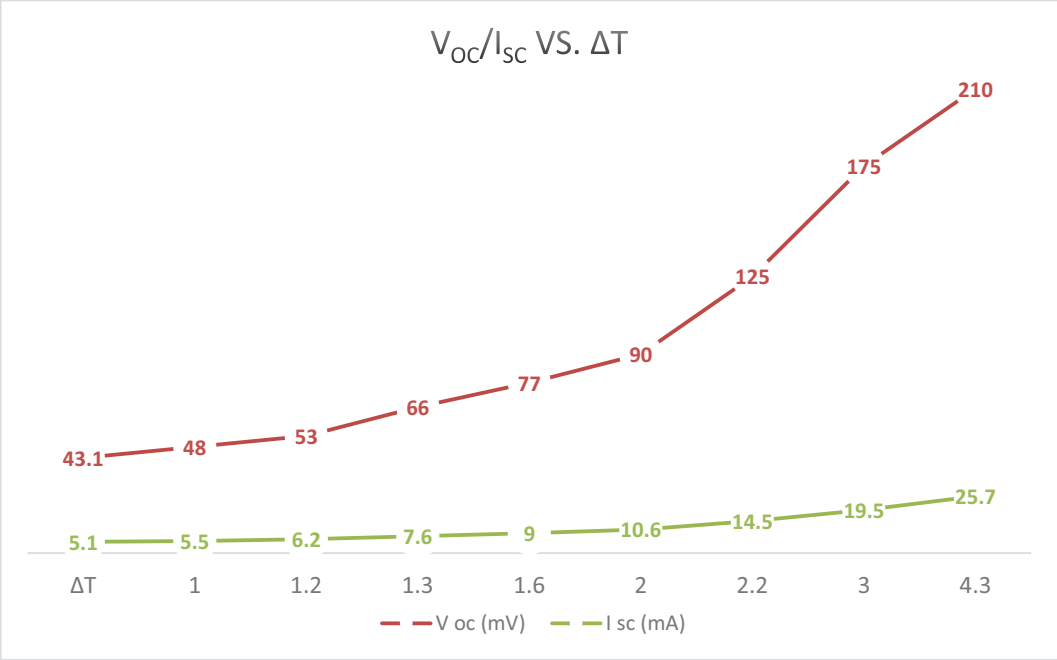

Figure 7 Open-circuit voltage (V_{OC}) and short-circuit current (I_{SC}) vs. temperature difference (ΔT) Using hot plate and air cooled heat sink.

The temperature deference covered a small range of 1-5 C°, which is considered as very low-temperature difference in TEG applications. This range was investigated being the most commonly available range within buildings. The open-circuit voltage and short-circuit current were observed to be directly proportional to the temperature difference, and closely following the increase in the TEG hot side temperature as shown in Figure 7. Using the measured values and using Equation 1, the Seebeck coefficient was calculated, to an average of 40.72 mV/C° over the test range.

A similar test was performed using the heat exchanger unit and the water blocks. Both cycles were set to a water flow of 2 liters per minute. An important observation using this setup is that precise control can be applied to the temperature difference (ΔT). ΔT across the TEG was increased from 0°C up to 7°C. V_{OC} and I_{SC} were measured at various temperature differences as shown in Figure 8.

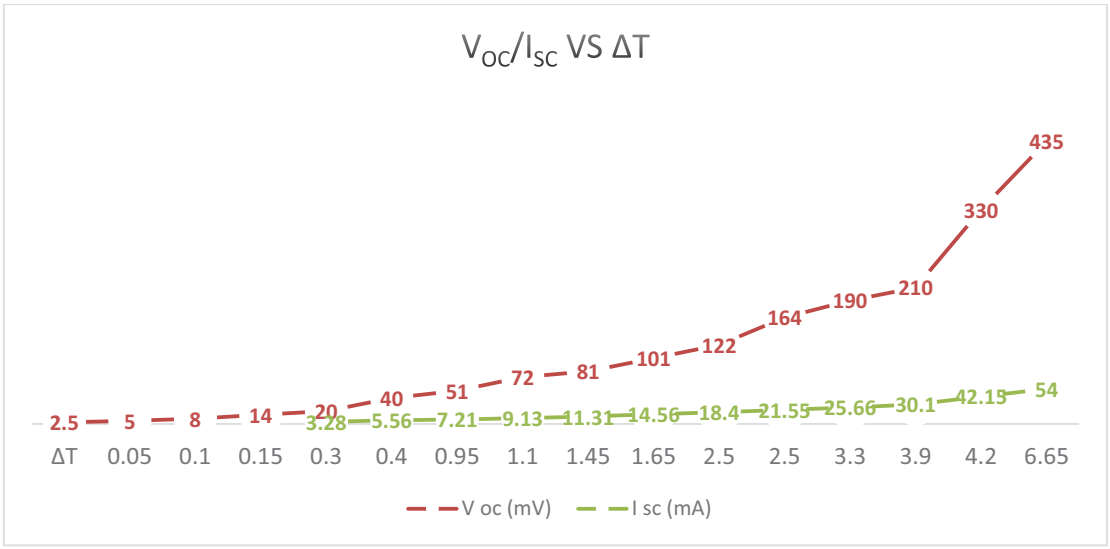

Figure 8 Open-circuit voltage (V_{OC}) and short-circuit current (I_{SC}) vs. temperature difference (ΔT) Using heat exchanger unit and water blocks.

Comparing the two sets of results highlighted much higher power generation with the water blocks setup at similar

ΔT. This variation requires further investigation, but could be due to one or more of the following:

- Nonuniform cooling of the heat sink in the air-cooled experiment.
- Nonuniform heating by the hot plate.
- The better thermal conductivity of the all copper water blocks.
- Improved heat dissipation from the TEG cold side with water blocks.
- The elimination of thermocouples between the TEG and hot/cool sides in the water blocks experiment.

4. Conclusions and Future Recommendations

The experimental results highlight a good indication of the TEG energy harvesting capabilities at the very low-temperature difference. It was difficult to estimate the overall device efficiency due to the fact that the first setup used an air cooled heat sink. Closed water cycle setup to cool the TEG was developed and tested. The continuous monitoring of the inlet temperature, the outlet temperature, and the flow rate will allow more accurate estimation of the heat dissipation and overall efficiency. The V_{OC} and I_{SC} are used as an indication for power output data. For more accurate electrical generation characterization connecting a load or I-V tracer is essential. Testing of TEG electrical output using I-V tracer is planned for future research and publication. I-V tracer will provide under load test for accurate load current and voltage. In addition to that programable I-V tracer simulate dynamic load setup which continuously adjust the virtual load impedance to match TEG internal impedance. Impedance matching is essential to track the maximum power point of generated power. It was clearly noted that the TEG performance was much better using the water blocks setup. Further investigation is required to identify the reasons. Possible reasons are that the pure copper water blocks offer enhanced uniform heat transfer on both sides and the continuous water flow continuously removing large amounts of heat from the cold side compared to the air-cooled heat sink of the first test. Current tests were run using 30mmx30mm TEG, while the second test used 40mmx40mm water block, a future test is planned using a purpose made 40mmx40mm TEG designed for extra low temperature applications. The matching size of 40mmx40mm will minimize error sources when it comes to accurately measure thermal energy or input power to the TEG for accurate efficiency evaluation. A computer model is under development using COMSOL Multiphysics, the model will use the experimental data as a basis of calibration in order to develop accurate model to be used for virtual testing if TEGs.

5. References

David Salerno, “ultralow voltage energy harvester uses thermoelectric generator for battery-free wireless sensors”, LT Journal of analog innovation, Vol. 20, No. 3, 2010.

G. Jeffrey Snyder,” Small Thermoelectric Generators”, The Electrochemical Society Interface, 2008.

Joshua Moczygemba, 'Energy harvesting TEG power strap for industrial, chemical, oil and gas applications product overview and performance', Marlow Industries, Inc.,2015.

Product technical datasheet, ‘TG12-4 Thermoelectric Generator’, Marlow Industries, Inc.

Qian Huang, Chao Lu, Mark Shaurette, and Robert F. Cox, “Environmental thermal energy scavenging powered wireless sensor network for building monitoring”, Proceedings of the 28th international association for automation and robotics in construction (ISARC), PP 1376-1380, 2011.

Raşit Ahıska, Hayati Mamur, “A review: thermoelectric generators in renewable”, International journal of renewable energy research, Vol.4, No.1, 2014.

Wei He, Gan Zhang, Xingxing Zhang, Jie Ji, Guiqiang Li, Xudong Zhao, “Recent development and application of thermoelectric generator and cooler”, Journal of Applied Energy 143, PP1–25, 2015.

Wensi Wang, Victor Cionca, Ningning Wang, Mike Hayes, Brendan O’Flynn, and Cian O’Mathuna, “Thermoelectric energy harvesting for building energy management wireless sensor networks”, International journal of distributed sensor networks, Volume 2013.

Wellington City Council Website "Make a commercial building more sustainable" Last Accessed 21st Mar 2017.

TOWARDS NOVEL GLAZING WITH SEASONAL DYNAMICS BASED ON MICRO COMPOUND PARABOLIC CONCENTRATORS

Jing Gong[1], André Kostro[2], Andreas Schüler[1]

1 Solar Energy and Building Physics Laboratory, Ecole Polytechnique Fédérale de Lausanne (EPFL), CH-1015 Lausanne, Switzerland

2 BASF Schweiz AG, Klybeckstrasse 141, CH-4057 Basel, Switzerland

Abstract

Thermal loss and overheating caused by glazing is a key issue in reducing CO2 emission and energy consumption of buildings. A novel glazing based on micro compound parabolic concentrators (CPCs) is proposed. The glazing consists of a polymer layer with embedded micro CPCs, which is attached to a glass pane of glazing. Thanks to the geometry and the micrometric size of the embedded CPCs, the proposed novel glazing can reduce energy consumption in cooling, improve visual comfort and maintain clear view through glazing. In the present work, the potential benefits of such glazing are preliminary estimated for Dubai. The seasonal dynamics are investigated by analyzing the direct solar transmittance for the working hours on the spring equinox and the winter solstice. The improvement of visual comfort is studied based on the assessment of glare. First samples with micro CPCs are fabricated, and the high transparency is achieved. The optical characterization using goniophotometer confirms the seasonal dynamics of the novel glazing.

Keywords: Advanced glazing, Microstructures, Compound parabolic concentrators, Seasonal dynamics, Visual comfort.

1. Introduction

The design of highly glazed building has become a worldwide trend in modern architecture. However, glazing may induce large thermal loss in winter while increase cooling load in summer, and it may also cause glare [1, 2, 3]. In the past decades, various glazing systems and daylighting systems have been developed to provide thermal and visual comfort. The "smart windows" coated with electrochromic or thermochromics materials are able to regulate the thermal radiation leading to lower solar gains in summer and higher solar gains in winter [4]. However, different color rendering from the normal spectrum of those windows can reduce the interest to users. A venetian blind should be combined with the electrochromic windows to block direct sunlight in order to avoid glare [5]. Anidolic systems consist of light-redirecting device can be alternatives. However, the installation of an anidolic system which varies in size going from 0.5 to 1 m long can be an architectural challenge [6]. The usage of blinds by occupants is not always made according to the solar availability, and therefore large performance gaps may appear between theoretical prediction and reality. With the use of blinds, the view through glazing will be obstructed.

In order to solve the problems, a multifunctional glazing based on micro compound parabolic concentrators (CPCs) is proposed. An important property of CPCs [7] is acceptance angle. Light arriving within the acceptance angle is concentrated and leaves the concentrator through the exit aperture of the structure, while the light out of acceptance angle will be reflected back to exterior through the input aperture. The glazing consists of a polymer layer with embedded micro CPCs, which is attached to a glass pane of glazing. Thanks to the geometry and the micrometric size of the CPCs, the proposed novel glazing can have the potential advantages with respect to three aspects: reducing energy consumption in cooling, improving visual comfort and clear view through glazing.

In the present work, we focus on the preliminary investigation of the potential advantages of the proposed glazing. The glazing is modelled for ray-tracing simulation, and the angular-dependent transmittance at the azimuth angle of 0˚ is calculated. The potential benefits of such glazing for Dubai are estimated by simlations. Seasonal thermal dynamics is investigated by calculating the direct solar transmittance for the working hours on the winter solstice

doi:10.18086/swc.2017.35.02 Available at http://proceedings.ises.org

and on the spring equinox. The improvement of visual comfort is studied based on the assessment of glare. First samples with micro CPCs are fabricated. Structural characterization by optical microscope is carried out. The redirection performance and the light-blocking ability are qualitatively demonstrated. The optical characterization by goniophotometer is conducted.

2. Methods

The CPC [8] was initially the essential component of a solar concentrator, and generally consist of two symmetric parabolas (named parabola L and parabola R respectively in our case), as shown in Figure 1 (a). The focal point for parabola L (F_L) lies on parabola R, likewise the focal point of parabola R (F_R) lies on parabola L. By definition, the axis of parabola L passes through the focal point of parabola L and the axis of parabola R likewise passes through the focal point of parabola R. The angle that the axes of the parabola L and R make with axis of the CPC defines the acceptance angle of the CPC [9]. All radiations arriving within the acceptance angle is concentrated and leaves the concentrator via the lower exit of the structure, while the radiations out of acceptance angle will be reflected back out through the input aperture.

The program CFSPro [10] which is developed especially for the study of complex fenestration system, is used to obtain the angular-dependent transmittance by ray-tracing simulation. The design of the geometry of the CPC is based on the calculation developed by Rabl [11]. In order to understand the potential benefit of the angular-selective transmittance for the reduction of energy consumption in heating and cooling, simulation referring to the double glazings with CPC30-30 and with CPC40-40 on south-facing facades is conducted for Dubai. In the case study, the transmittance of direct solar light in the visible range is calculated for the working hours (from 8:00 to 17:00) on the winter solstice and on the spring equinox. Monthly average high temperature and average low temperatures are show in Figure 1[12].

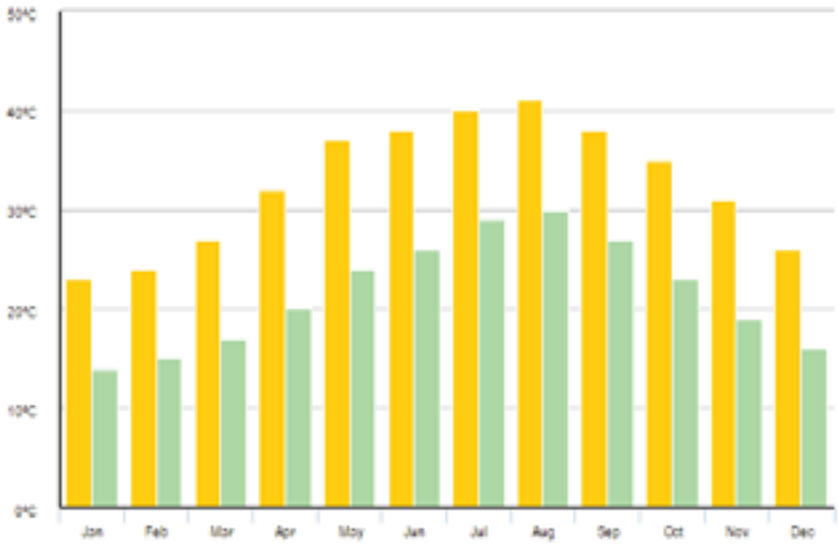

Figure 1 monthly average high and average low temperatures in Dubai.

Comfortable daylight environment in schools and offices can improve the occupants' productivity and tend to reduce the absenteeism [13, 14]. The improvement of daylight environment is investigated with the assessement of the risk of glare by Daylight Glare Index (DGI). A DGI is calculated by

$$DGI = 10log0.478\sum_{i=1}^{n}\frac{L_{s,i}^{1.6}\cdot\Omega_{s,i}^{0.8}}{L_b + 0.07\omega_{s,i}^{0.5}L_{s.i}}$$

where $L_{s,i}$ (cd/m^2) is the luminance of a glare source (i) in the field of view, $\Omega_{s,i}$ (sr) is the solid angle subtended by the source, modified for the effect of the position of the observer in relation to the source, L_b (cd/m^2) is the average luminance of the visual field excluding the glare sources, and $\omega_{s,i}$ (sr) is the solid angle subtended by the glare source.In the present paper, a viewpoints were chosen in the standard Reinhart-defined room [15] with the

dimension of 8.2-m long × 3.6-m wide × 2.8-m high. The view point was set at 1-m distance from the window, with a height of 1.25 m and the line of sight points towards the wall, in order to simulate a working position in a realistic state, referred to as employee position. This viewpoint is in the area where direct sunlight was generally received during most of the year with a conventional glazing, and is considered as an uncomfortable position.

The preparation of embedded micro CPCs requires the fabrication and the replication of microstructures, as well as the coating with reflective materials on the selective surfaces of microstructures [16, 17]. The master mold with the desired microstructures for the sample in the present manuscript is produced by laser ablation. In the present work, a PDMS stamp of the negative microstructure with respect to the master mold is prepared. Then another PDMS stamp with the positive microstructure is replicated from the first PDMS stamp. After that, the negative microstructures are replicated from the PDMS positive template by UV-cured acrylated hyperbranched polymer (HBP) on a glass substrate. The selected surfaces of the HBP microstructures on the glass substrate are coated with aluminum by physical vapor deposition. Then the grooves of microstructures are filled with the identical HBP to encapsulate the micro-CPCs, and a sample with clear view is achieved.

3. Results and Discussions

Double glazing with the embedded micro CPCs in a polymer layer, which is attached to the inner side of the outer glass pane, is modeled, as shown in Fig. 1 (a). The refractive indexes of glass and the used polymer are the same (refractive index n = 1.5). The thickness of the glass panes and the thickness of the polymer layer for modelling are bigger by factors of 10-100 than that of reality, for the convenience of viewing. In winter where solar elevation angles are low, the solar radiation is partially redirected by the reflective parabolic surface and then enters in the interior space. In contrast, in summer where the elevation angle is high, the direct solar radiation is reflected outside after two or more reflections. The transmittance of the visible light as the function of elevation angles at the azimuth angle of 0˚ is calculated, for the conventional double glazing and the double glazing integrated with two different geometries of CPCs (Fig. 1 (b)). Symmetric CPC of a half acceptance angle of 30˚ is labelled as CPC30-30 and with a half acceptance angle of 40˚ it is labelled as CPC40-40. Due to the refractive index of 1.5 of the polymer, the incident angles corresponding to the acceptance angles for the two CPCs embedded in the polymer layer are 48.6˚ (CPC30-30) and 74.6˚ (CPC40-40). For CPC30-30, the transmittance is at about 0.64 which is approximately the same as that of the low-e double glazing in the angular range between 0˚ and 25˚. Beyond 25˚, a fraction incident light is redirected by two or more times and then leave the system through the input aperture. Therefore the transmittance significantly reduces beyond 25˚ and reach 0 at about 50˚. Likewise, for CPC40-40, the transmittance stay at 0.72 in the angular range between 0˚ and 12˚. After 12˚ the transmittance gradually reduce, and this trend is unlike that of CPC30˚, as the curvature of the parabolic mirrors is smoother than that of CPC30-30. The transmittance stays at 0 beyond 80˚.

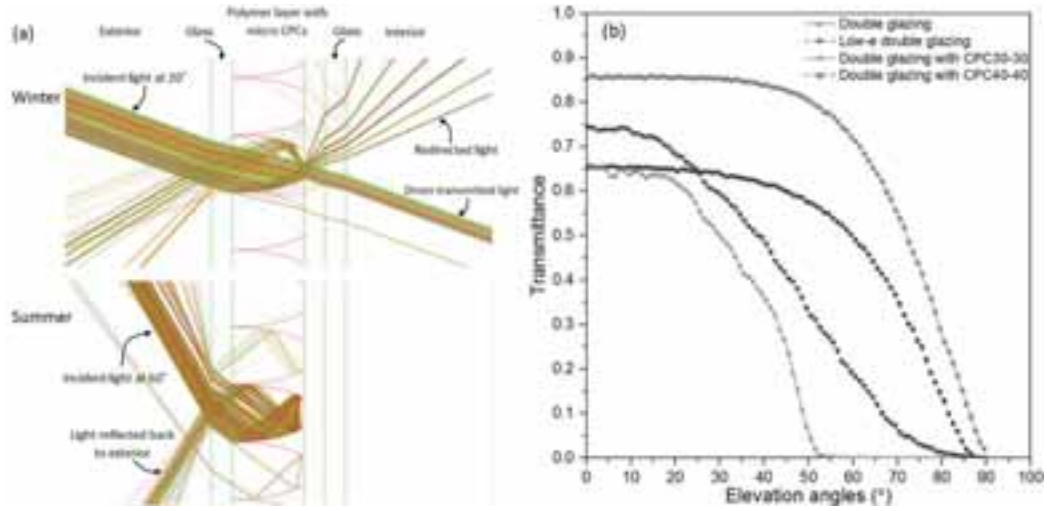

Figure 2: (a) Model of embedded micro CPCs in a polymer layer attached to the inner surface of the outer glass pane of a double glazing for ray-tracing simulation; (b) simulated transmittance as the function of elevation angles of the sun at the azimuth angle of 0˚

In order to understand the potential benefit of the angular-selected transmittance for the reduction of energy

consumption in cooling, calculation of direct solar transmittance of visible light is conducted for the working hours (8:00-17:00) on the spring equinox and (b) on the winter solstice for the CPCs applied to a vertical double glazing in Dubai.

For CPC30-30 on the spring equinox, the direct solar transmittance remains at 0 between 10:00 to 15:00, suggesting the potential strong reduction in cooling. The transmittance between 8:00 to 10:00 and 15:00 to 17 is also reduced to the average transmittance of 0.09. On winter solstice, the transmittance from 8:00 to 9:00 and from 16:00-17:00 is similar to that of low-e double glazing. A reduction with the average amplitude of 0.2 is observed between 9:00 and 16:00, and at noon the direct transmittance is reduced from 0.61 to 0.35. Compared with the case on spring equinox, the reduction of the transmittance on winter solstice is moderate. However, a moderate reduction may be preferred, as the average high temperature in Dubai is above 20℃ but not as harsh as that in spring and summer.

For CPC40-40 on the spring equinox, the transmittance from 8:00 to 17:00 remains rather constant at about 0.15. On the winter solstice, the transmittance is modestly reduced. The transmittance is reduced from 0.61 to 0.47 at noon on the winter solstice. Interestingly, the transmittance from 8:00 to 9:00 and from 16:00 to 17:00 is about 0.1 higher than that of low-e double glazing. The increase might contribute to the improvement of thermal comfort in the early morning and in the late afternoon, considering that the average low temperature in December in Dubai is in the order of 15℃.

The conventional double glazing with micro CPCs might not be the best configuration for the application in Dubai. Nonetheless, it shows the working principle of glazing with micro CPCs to achieve the seasonal dynamics. Moreover, the polymer film with embedded micro-CPCs can be attached to large variety of glass panes. In the future, optimization of the configurations will be conducted.

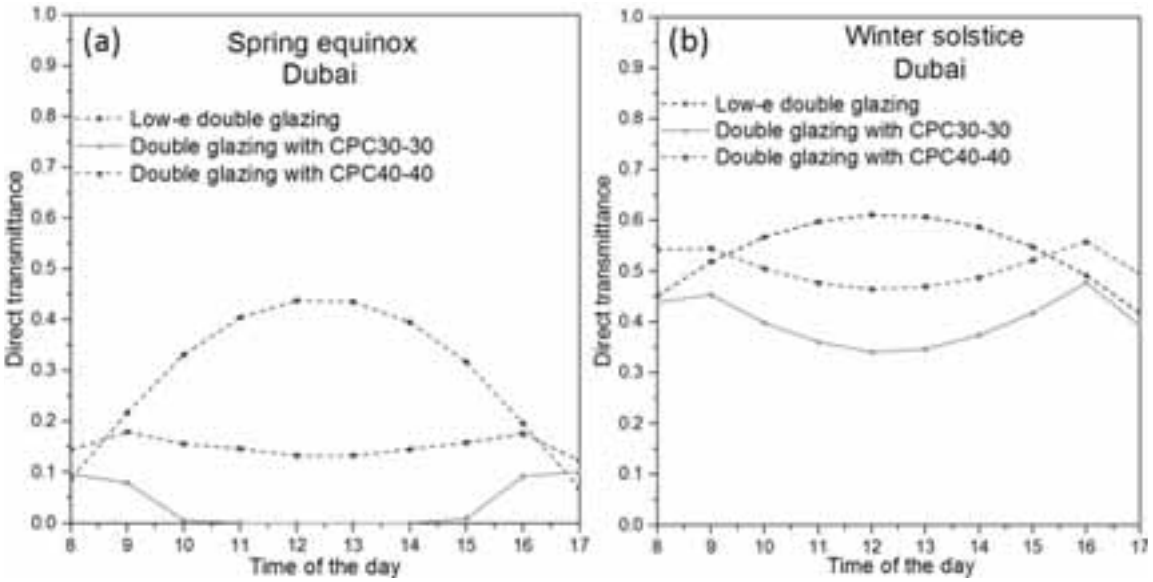

Figure 3: Plots of direct visible solar transmittance of visible light during working hours (8:00-17:00) (a) on the winter Solstice and (b) on the spring equinox for the CPCs applied to a vertical double glazing in Dubai.

Figure 4: The plots of hourly Daylight Glare Index (DGI) values: a) on the spring equinox, and b) on the winter solstice at the employee's position. Intuitively speaking, glare is likely to happen when the direct light source in the field of view. For the case with low-edouble glazing, the direct sunlight of incident angle larger than 53.5˚ will not reach the eye of the employee. Therefore, on the spring equinox, the DGI falls in the acceptable level for the three types of glazings during the working hours (from 8:00 to 17:00). On the winter solstice, the improvement of thermal comfort is evident using micro CPCs. The case with low-e double glazing suffers from glare for 60% of the daytime on the spring equinox. The glazing with CPC30-30 and CPC40-40 suppress the risk of glare to only 20% and 30% of the daytime.

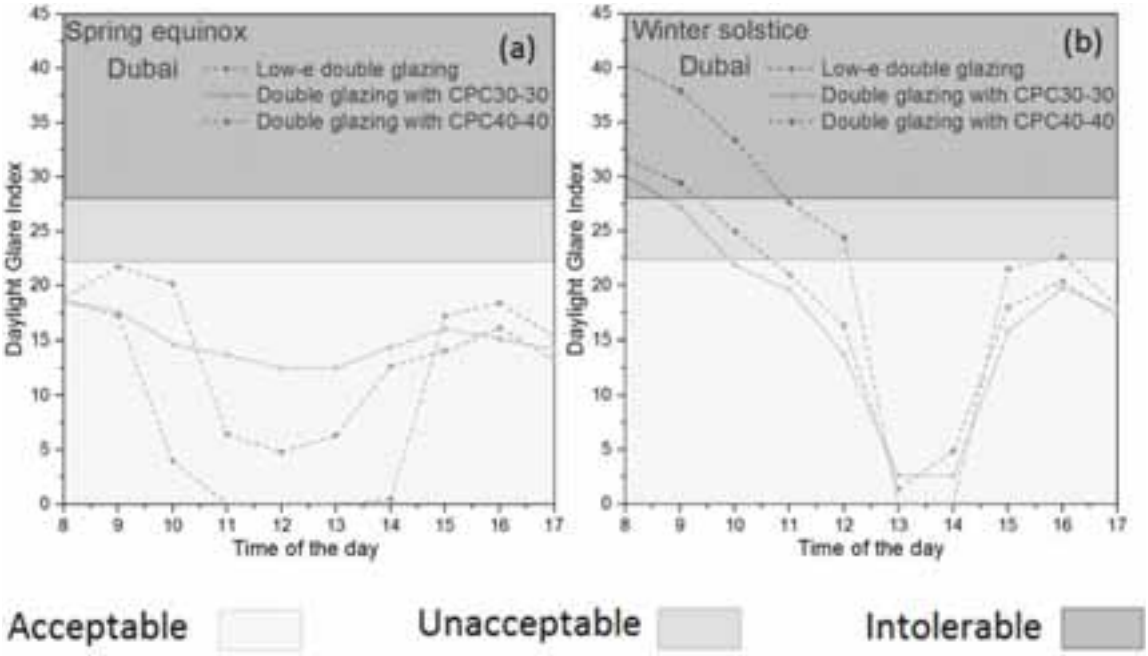

Figure 4: The plots of hourly Daylight Glare Index (DGI) values: a) on the spring equinox, and b) on the winter solstice at the employee's position.

The preparation of embedded micro CPCs requires the fabrication and the replication of microstructures, as well as the deposition with reflective materials on the microstructures [18,19]. An example of the HBP microstructures based on the theoretical design of micro CPC30-30 is shown in Figure 5 (a). The width of the outgoing aperture is 34 μm, and the height of the microstructure is around 80 μm. The dash arrow shows the surface where the highly reflective materials are deposited. In the present work, the thickness of the deposited materials is in the order of 50 nm. Due to the micrometric size of the microstructures, a clear view seen through the glazing with embedded micro-mirrors is achieved, as indicated in Fig. 2 (b). The present sample consists of a single glass pane with an attached polymer layer in which micro CPC30-30 are embedded. The area with micro CPC30-30 is 5 cm x 4 cm. The redirection performance and the blocking ability of the sample are studied with a collimated beam, as indicated in Figure 6 (a). At a low incident angle, the incident light splits into redirected part and direct-transmitted part after going through the CPCs. At a high incident angle, the majority of light is reflected outside after two or more reflections, that explains why the sample looks bright when it is observed from the side of the light source, as shown in Figure 6 (b).

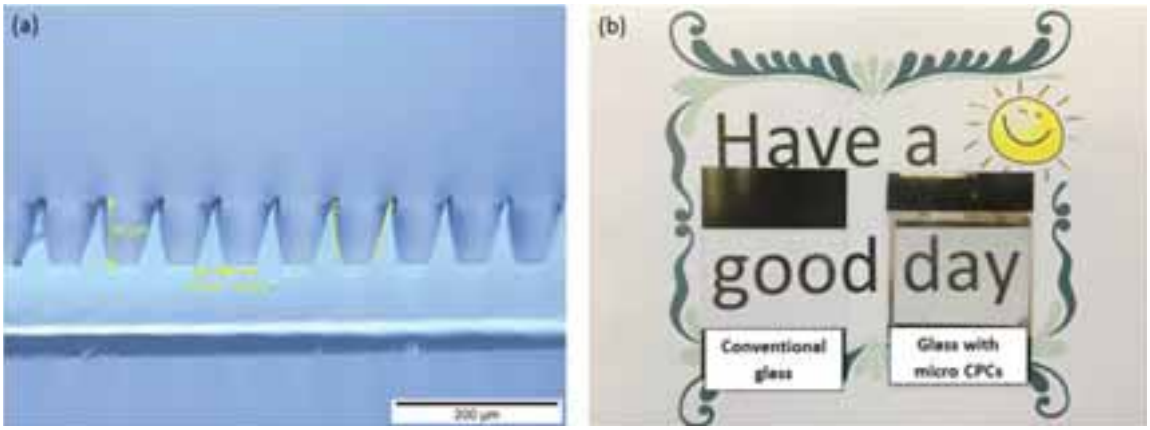

Figure 5: (a) An example of HBP microstructure; (b) the views seen through the conventional glass and the glass with the polymer layer which consists of embedded micro CPCs. The viewing direction is perpendicular to the surface.

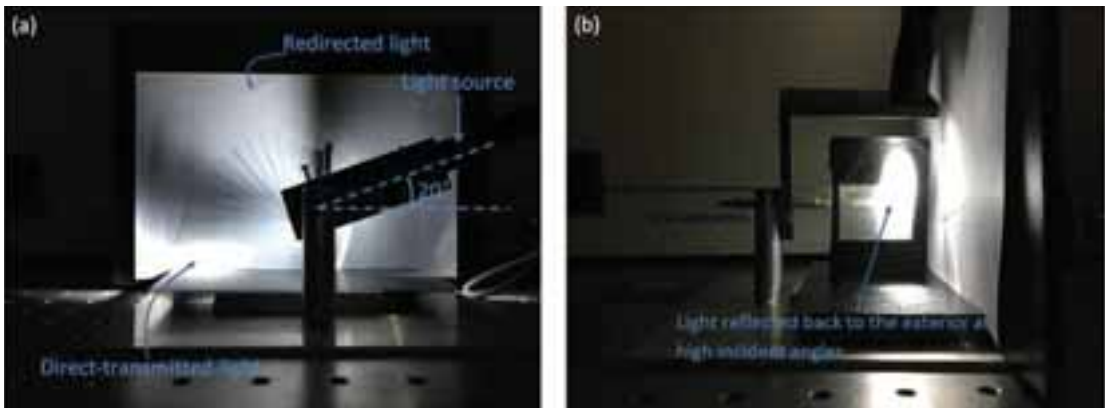

Figure 6: The redirection performance and the blocking ability of the sample are studied with a collimated beam at the incident angle of (a) 20˚ from the front side and (b) 60˚ viewing from the side of the light source.

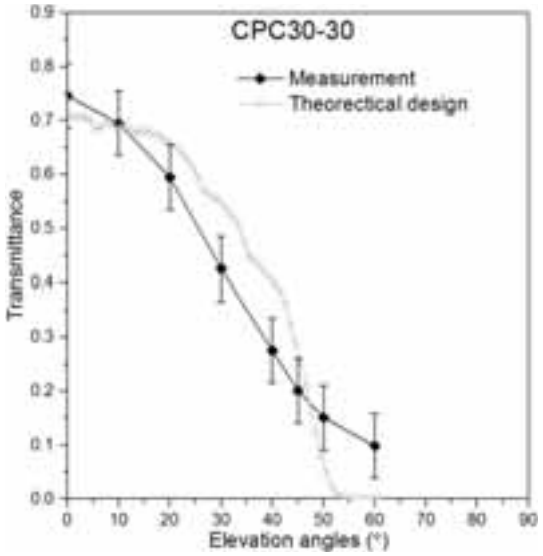

Figure 7: Comparison between the measurement result from goniophotometer and the simulated transmittance.

The angular dependent transmittance is further observed Measurement of transmittance as the function of elevation angles at the azimuth angle of 0˚ is carried out using goniophotometer. As shown in Figure 7, the transmittance reduces with the increase of elevation angle. The transmittance at the elevation angle of 0˚ is about 0.75 while at the elevation angle of 60˚ it is only about 0.1. The optical properties of the sample suggest that the seasonal thermal regulation may be realized. The microstructure is fabricated following the geometry of the CPC 30-30. The deviation of the measurement from the simulation can be due to the three reasons: i) the height of the fabricated microstructure is about 80 μm while the theoretical design is about 90 μm; ii) shrinkages change the shape of the microstructure during polymerization for replication; and iii) the thickness of the deposited reflective material is insufficient and the light may directly transmitted through the reflective parabolic surface. In the future, rigorous parameters concerning the fabrication of microstructures, replication and deposition will be carried out, in order to minimize the deviation.

4. Conclusions

A novel glazing with embedded micro CPCs in a polymer layer which is attached to a glass pane is developped. A case study by simulation referring to seasonal thermal regulation due to the transmittance of direct solar light for Dubai shows that the novel glazing may reduce energy consumption in cooling and improve thermal comfort. The assessment of glare indicates that the novel glazing can reduce the risk of glare from 60% to only 20%. First samples with micro CPCs are fabricated, and the high transparency is achieved. The optical characterization using goniophotometer shows that the desired angular-dependent transmittance is obtained.

5. Acknowledgement

The authors would like to thank the Swiss Competence Center for Energy Research (SCCER) for funding of this project. The authors would like to show our gratitude to BASF Switzerland regarding the assistance for the preparation of samples.

6. References

1 Radhi, H. (2009). Evaluating the potential impact of global warming on the UAE residential buildings–a contribution to reduce the CO 2 emissions. Building and Environment, 44(12), 2451-2462.
2 Xing, Y., Hewitt, N., & Griffiths, P. (2011). Zero carbon buildings refurbishment—A Hierarchical pathway. Renewable and sustainable energy reviews, 15(6), 3229-3236.
3 Li, D. H., Yang, L., & Lam, J. C. (2013). Zero energy buildings and sustainable development implications–A review. Energy, 54, 1-10.
4 Bahaj, A. S., James, P. A., & Jentsch, M. F. (2008). Potential of emerging glazing technologies for highly glazed buildings in hot arid climates. Energy and Buildings, 40(5), 720-731.
5 Lee, E. S., DiBartolomeo, D. L., Klems, J., Yazdanian, M., & Selkowitz, S. E. (2005). Monitored energy performance of electrochromic windows controlled for daylight and visual comfort. Lawrence Berkeley National Laboratory.
6 Scartezzini, J. L., & Courret, G. (2002). Anidolic daylighting systems. Solar Energy, 73(2), 123-135.
7 Rabl, A. (1976). Comparison of solar concentrators. Solar Energy, 18(2), 93-111.
8 Welford, W.T., & Winston, R. (1978). Optics of nonimaging concentrators. Light and solar energy. United States: Academic Press Incorporated,New York, NY.
9 Stine, W. B., & Geyer, M. (2001). Power from the Sun (2015, August 16): http://www.powerfromthesun.net/book.html
10 Kostro, A., Geiger, M., Scartezzini, J. L., & Schüler, A. (2016). CFSpro: ray tracing for design and optimization of complex fenestration systems using mixed dimensionality approach. Applied optics, 55(19), 5127-5134.
11 Rabl, A. (1976). Comparison of solar concentrators. Solar Energy, 18(2), 93-111.
12 Dubai: Annual Weather Averages (2017) http://www.holiday-weather.com/dubai/averages/
13 Demir, A., & Konan, A. P. D. N. (2013). Impact of Daylighting on Student and Teacher Performance. Journal of Educational and Instructional Students in the World, 1.
14 Sop Shin, W. (2007). The influence of forest view through a window on job satisfaction and job stress. Scandinavian Journal of Forest Research, 22(3), 248-253.
15 Reinhart, Christoph F., J. Alstan Jakubiec, and Diego Ibarra. "DEFINITION OF A REFERENCE OFFICE FOR STANDARDIZED EVALUATIONS OF DYNAMIC FAÇADE AND LIGHTING TECHNOLOGIES 2." Proceedings of Building Simulation 2013, IBPSA Conference, Chambery, France. 2013.
16 Kostro, A., & Schüler, A. (2017). U.S. Patent No. 9,695,629. Washington, DC: U.S. Patent and Trademark Office.
17 Kostro, A., Gonzalez Lazo, M. A., Leterrier, Y., Siringil, E., Hoffmann, P., & Schüler, A. M. (2015). Laser ablation and nanoimprint lithography for the fabrication of embedded light redirecting micromirrors. In Proceedings of International Conference CISBAT 2015 Future Buildings and Districts Sustainability from Nano to Urban Scale (No. EPFL-CONF-213287, pp. 15-20). LESO-PB, EPFL.
18 Kostro, A., & Schüler, A. (2017). U.S. Patent No. 9,695,629. Washington, DC: U.S. Patent and Trademark Office.
19 Kostro, A., Gonzalez Lazo, M. A., Leterrier, Y., Siringil, E., Hoffmann, P., & Schüler, A. M. (2015). Laser ablation and nanoimprint lithography for the fabrication of embedded light redirecting micromirrors. In Proceedings of International Conference CISBAT 2015 Future Buildings and Districts Sustainability from Nano to Urban Scale (No. EPFL-CONF-213287, pp. 15-20). LESO-PB, EPFL.

Optimization of Coupled Building Roof Solar Reflectance and Thermal Insulation Level for Annual Energy Saving Under Different Climate Zones

Cristina Piselli [1], Anna Laura Pisello[1,2], Alvaro de Gracia[3], Mohammad Saffari[4], Franco Cotana[1,2] and Luisa F. Cabeza[4]

[1] CIRIAF – Interuniversity Research Center, University of Perugia, Perugia (Italy)

[2] Department of Engineering, University of Perugia, Perugia (Italy)

[3] Departament d'Enginyeria Mecanica, Universitat Rovira i Virgili, Tarragona (Spain)

[4] GREiA Innovació Concurrent, INSPIRES Research Centre, University of Lleida, Lleida (Spain)

Abstract

The aim of this work is to assess building energy performance optimization potential of cool roof solutions in different climate conditions worldwide through dynamic thermal-energy simulation and optimization analysis. Moreover, given the dependence of roof performance on insulation level, the influence of roof insulation variation on optimum roof solar reflectance is evaluated. Therefore, the multi-dimensional optimization of combined building roof solar reflectance capability and thermal insulation level is carried out to minimize annual energy consumption for air-conditioning of standard ASHRAE building model for small offices, in each considered climate zone. Findings of this research highlight how the classic approach of super-insulated buildings for energy saving needs to be reframed for the office case, by integrating other passive solutions for truly environmentally friendly and comfortable buildings.

Keywords: Cool Roof, Solar Reflectance, Thermal Insulation, Building energy saving, Optimization

1. Introduction

Cool roofs are a widely acknowledged strategy for building thermal-energy performance improvement, by acting mainly on energy requirement for cooling (Levinson and Akbari, 2010; Pisello, 2017) and Urban Heat Island (UHI) phenomenon mitigation (Akbari and Kolokotsa, 2016; Santamouris et al., 2017). In fact, given their high solar reflectance and thermal emissivity properties, compared to conventional construction materials, cool materials are able to decrease heat release to the outdoor urban environment and to the indoor ambient air Santamouris, 2015).

However, the effectiveness of cool roofs along the whole year is affected by building boundary conditions, including envelope characteristics, building end-use, and climate conditions. For instance, the use of such materials in heating-dominated regions may generate penalties in terms of heating energy use in winter (Hosseini and Akbari, 2014; Kolokotroni et al., 2013). With the aim of estimating the impact of using cool roofs under different climatic conditions, Synnefa et al. (2007) simulated the heating and cooling load of residential building in 27 cities around the world. For the case study locations, the heating penalty was shown to be lower than the cooling load reduction. Hosseini and Akbari (2016), instead, focused on cold climates and demonstrated that cool roofs provided annual energy savings in all considered climates for the simulated prototype office and retail buildings. Considering researches focused cool roofs performance in Italian climate context, Costanzo et al. (2013) showed the suitability of cool roofs for the reduction of building annual energy consumption in three Italian cities and with different insulation levels. They stated that the use of such materials in heating-dominated regions should be preliminarily evaluated in association with high insulation levels and very efficient heating systems. Instead, Zinzi et al. (2014) defined an energy-rating scheme for cool roofs application in residential buildings in different Italian climate zones based on numerical calculation results.

doi:10.18086/swc.2017.35.03 Available at http://proceedings.ises.org

As regards building envelope characteristics, a key parameter influencing benefits achievable through cool roofs is the level of roof insulation (Daouas, 2016). The effect of cool roofs in improving building indoor thermal comfort conditions was found less important with low thermal transmittance roofing systems (Synnefa et al., 2007; Di Giuseppe and D'Orazio, 2015). On the other hand, Smith et al. (2012) stressed that in temperate climates standard energy saving approaches, e.g. lowering thermal transmittance, while useful may be unnecessary, unless other parameters are poorly designed. A further study carried out in a hot-arid climate (Radhi et al., 2017), demonstrated that the difference in heat gains through the roof with and without thermal insulation is lower when a cool roof is implemented that with other roof systems.

Given the significant interaction between roof coating optical properties and sub-roof insulation level in affecting building energy efficiency, different optimization studies involving these two envelope characteristics were carried out. For instance, Gentle et al. (2011) performed a systematic analysis of the combined effect of three roof parameters, i.e. solar albedo, thermal emittance, and sub-roof R-value. Cool roofs were shown to optimize cost and environmental benefits when the sub-roof R-value is tailored to the spectral properties of the roof. Moreover, the impact on energy saving of an additional PCMs layer in the roof was assessed (Aguilar et al., 2013). Farhan et al. (2016), instead, developed a BIM-based approach to decide the most effective technology to be implemented to reduce CO_2 emission and improve the thermal comfort level of residential buildings. Through a two-step experimental and numerical analysis, Ramamurthy et al. (2015a, 2015b) studied the joint influence of roof albedo and insulation on its energy performance. They highlighted that both albedo and insulation thickness play a significant role in reducing the combined heating and cooling load attributable to the roof, and that wintertime penalties of cool roofs are negligible compared to summertime benefits. Similarly, Arumugam et al. (2015) optimized the interaction of this two roof characteristics in different Indian climate zones via energy simulation and parametric analysis. The insulation thickness increase was demonstrated to provide incremental benefits in energy savings which were reduced after a limit.

2. Motivation

Building upon the previous literature, the purpose of this work is to contribute in defining a method for assessing the effectiveness of implementing cool roofs in different climate zones in terms of annual energy saving of the HVAC system, with varying different boundary conditions. Given the consolidated research about cool roofs performance as passive cooling technique and the awareness of the influence of roof R-value on their effectiveness, acknowledged by a variety of scientific contributions worldwide, this study proposes a replicable method for enhancing building thermal-energy performance by optimizing roof configuration. In particular, roof solar reflectance capability and thermal insulation level are considered as key drivers influencing roof performance. Therefore, the optimum combination of solar reflectance value and insulation layer thickness for minimizing building annual energy consumption for air-conditioning is evaluated in different international climate zones. The procedure consists of an integrated and timesaving approach based on the coupling of dynamic simulation and optimization analysis.

Finally, this work is aimed at filling the gap between theory and practice by providing indications for the effective use of roof coatings in buildings, by taking into account mainly their energy efficiency. Therefore, findings on cool roofs effectiveness, which are usually referred to case specific experimental campaigns, can be generalized with varying boundary conditions. In fact, the general proposed procedure can be replicated in a variety of climate contexts in the world. Therefore, guidelines for the efficient implementation of cool roofs in different climate conditions can be developed based on findings of this work.

3. Methodology

The methodology presented in this work is based on numerical analysis via dynamic energy simulation and optimization. In particular, the optimum roof configuration is investigated with the aim of minimizing building annual energy consumption for heating and cooling with varying climate zone conditions. The two roof characteristics selected as variables affecting building energy performance are the coating solar reflectance and the thermal insulation layer thickness. The range of considered roof solar reflectance (ρ_{solar}) values for the study varies from 0.1, i.e. dark roof, to 0.8, i.e. cool roof. Regarding roof thermal insulation, standard expanded polystyrene (EPS), i.e. characterized by thermal conductivity equal to 0.04 W/m K, is used considering a

thickness range ($I_{thermal}$) from 0.01 m to 0.25 m. The minimum thickness value is not 0, but very close to, because this value is not allowed by the simulation software.

For the purpose of this study, different climate zones worldwide are considered as case study weather conditions and the ASHRAE standard building model for small office building (ASHRAE,2016) is used as case study building, when modifying only the envelope components thermal transmittance (U-value) with varying the climate zone. Firstly, one-dimensional optimization analysis is carried out when varying the sole roof solar reflectance or thermal insulation thickness. When varying the thermal insulation level, two different roof solar reflectance scenarios are defined: "standard roof", where ρ_{solar} value is left equal the value of the ASHRAE prototype model (ASHRAE,2016) , i.e. 0.3, and "cool roof", where ρ_{solar} value is set equal to 0.8. Therefore, the sensitivity of building annual energy consumption to each parameter variation is evaluated to assess their separate contribution in different climate zones. One-dimensional optimization analysis is carried out only for six cities that representative of six defined heating degree days (HDD) ranges. Such ranges are reported in detail in the following section 4 (Fig. 2). Secondly, multi-dimensional optimization analysis is performed to define the optimum roof configuration by coupling solar reflectance capability and thermal insulation level in each considered climate condition. The methodology procedure is summarized in Fig. 1.

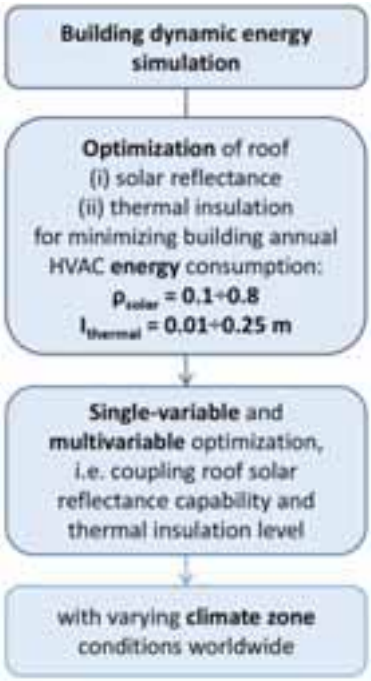

Fig. 1: Methodology implemented in the work

3.1. Numerical modeling

To perform the numerical analysis, the acknowledged simulation engine EnergyPlus v8.4 (Crawley et al., 2000) is used to develop the dynamic energy simulations. EnergyPlus is a whole-building thermal-energy simulation program (Crawley et al., 2001), based on previous validated BLAST and DOE-2 programs. EnergyPlus includes many advanced modeling tools, such as heat balance load calculations, integrated loads, user-configurable HVAC system description, system and plant calculations in same time step, simple input and output data formats, simulation of materials with variable thermal properties, etc. Further capabilities that give power to this calculation engine are advanced fenestration analysis as well as general envelope calculations (outside and inside surface convection algorithms), advanced infiltration, ventilation, room air and multi-zone airflow calculations, environmental emissions and developed economic evaluation including energy costs, and life cycle costs. Additionally, it includes several developed human thermal comfort algorithms for analyzing occupants' thermal well-being and indoor air quality.

In this study, the conduction transfer function (CTF) algorithm is selected among the available calculation algorithms to calculate transient heat conduction transfer (U.S. DOE, 2016).

3.2. Optimization

For the additional optimization analysis, the generic optimization program GenOpt v3.1.1 (Wetter, 2000) is selected. This tool is capable of solving building energy performance related optimization problems developed with dynamic simulation software. It can be coupled with several simulation engines, including EnergyPlus. GenOpt performs optimization of a user-defined objective function, such as, for instance, annual energy consumption, which depends on selected independent variables. The objective function is expressed as a target quantity or a relation that has to be minimized or maximized. Generally, GenOpt optimization problems are described as shown in eq. 1:

$$min_{x \in X} f(x) \qquad \text{(eq. 1)}$$

where $f: X \rightarrow \mathbf{R}$ is the user-specified objective function that measures the system performance and $x_1, x_2 \in X \subset \boldsymbol{R}^n$ is the set of user-specified design parameters set for the independent variables. In this study, the optimization design parameters are roof solar reflectance and thermal insulation thickness, which are considered as independent continuous variables. Therefore, any value on the real line between lower and upper bounds can be used, as shown in eq. 2:

$$X = \left\{ x \in \boldsymbol{R}^n \middle| l^i \leq x^i \leq u^i, i \in \{1, \dots, n\} \right\} \qquad \text{(eq. 2)}$$

where $l \in \mathbf{R}^n$ and $u \in \mathbf{R}^n$ are the lower and upper bound, respectively, for design options and $-\infty \leq l^i < u^i \leq \infty$ for $i \in \{1, \dots, n\}$.

The objective function is defined to minimize building annual energy consumption for air-conditioning by finding out the optimum values for roof solar reflectance or thermal insulation level, in one-dimensional optimization analysis, and the optimum combination of roof solar reflectance capability and thermal insulation, in multi-dimensional optimization procedure (eq. 3).

$$f(x) = E_{total}(x_1, x_2) \qquad \text{(eq. 3)}$$

Various integrated mathematical optimization algorithms are available to be chosen in GenOpt. In the present work, the Generalized Pattern Search (GPS) implementation of the Hooke-Jeeves algorithm is used for both one- and multi-dimensional optimization analysis. Multiple starting points are selected to avoid falling in local optima (Evins, 2013).

4. Case study

4.1. Climate zones

To perform the study for a variety of climate conditions worldwide, 28 cities representing different climate zones according to the international Köppen-Geiger classification (Kottek et al., 2006), including temperate, tropical, continental, and arid conditions, are simulated. The cities, selected based on (Synnefa et al., 2007), are listed in Tab. 1, which indicates the climate zone and the heating degree days (HDD) for each city.

4.2. Case study building

For the purpose of the application of the above-defined methodology, the ASHRAE validated standard building model for small office building (ASHRAE, 2016), characterized by high internal heat gains, is selected. The standard case study office building model presents a single-floor rectangular prism shape. A single-floor building model is selected because of the major influence of roof properties on the floor just below it. Moreover, office buildings are suitable for the installation of cool roofs (Hosseini and Akbari, 2016).The external walls are wood-framed with intermediate insulating layer, while the roof presents wood joints, EPS insulation, added to achieve acceptable roof U-value in the different climates, and coating asphalt shingles. The main building envelope features (Winiarski et al., 2007) are summarized in Fig. 2. The building is equipped with air-source heat pump and gas furnace as back up. The air distribution is constant air volume, with one unit per occupied thermal zone (Winiarski et al., 2006). Heating and cooling set-point temperatures are set equal to 20°C and 26°C, respectively, according to EN 15251:2007 (2007). Internal heat gains, due to lighting and equipment, are equal to about 15.6 W/m^2 in the whole building (ASHRAE, 2016).

The main envelope components, i.e. external wall, roof, and window, of the standard ASHRAE model are

modified in terms of their thermal properties, to achieve suitable thermal transmittances in each climate zone. Values are set in each climate zone according to the indications of the Italian current building regulation (Repubblica Italiana, 2015). The Italian regulation defines the maximum acceptable U-values for the external envelope components in a zone with varying the HDD. According to these general indications, U-values are set based on the HDD of each selected city. The thermal transmittance values of the different envelope components are adjusted by modifying the thickness of the thermal insulation in the opaque components and the window layers of the standard models (when necessary), in order to be as close as possible to the limit value. The final U-values defined in each climate zone are summarized in Fig. 2. Furthermore, the specific model inputs in terms of site location and design days for each climate scenario are implemented according to the EnergyPlus weather files (U.S. DOE's BTO, 2016).

Tab. 1: Selected cities and corresponding climate zones (Kottek et al., 2006) and HDD

Zone (Köppen-Geiger)	City	HDD
Aw: Tropical wet and dry	Rio de Janeiro, Brazil	5
	Miami, USA	128
BWh: Hot desert climate	Abu Dhabi, UEA	31
	Cairo, Egypt	393
BSh: Hot semi-arid climate	New Delhi, India	271
BSk: Cold semi-arid climate	Tehran, Iran	1495
	Thessaloniki, Greece	1057
Cfa: Humid subtropical climate	Sydney, Australia	717
	Tokyo, Japan	2388
	Buenos Aires, Argentina	1212
Cfb: Temperate oceanic climate	Johannesburg, South Africa	1099
	Paris, France	2643
Cwb: Subtropical highland climate	Mexico City, Mexico	954
	Nairobi, Kenya	155
Csa: Hot-summer Mediterranean climate	Athens, Greece	477
	Barcelona, Spain	1388
	Palermo, Italy	751
	Rome, Italy	1415
	Casablanca, Morocco	845
	Ankara, Turkey	3299
Csb: Warm-summer Mediterranean climate	Porto, Portugal	1496
	San Francisco, USA	2653
Dfa: Hot-summer humid continental climate	Beijing, China	2866
	New York, USA	4750
Dfb: Warm-summer humid continental climate	Moscow, Russia	4748
	Montreal, Quebec, Canada	4861
Dfc: Subarctic climate	Tarvisio, Italy	3959
	Tampere, Finland	4068

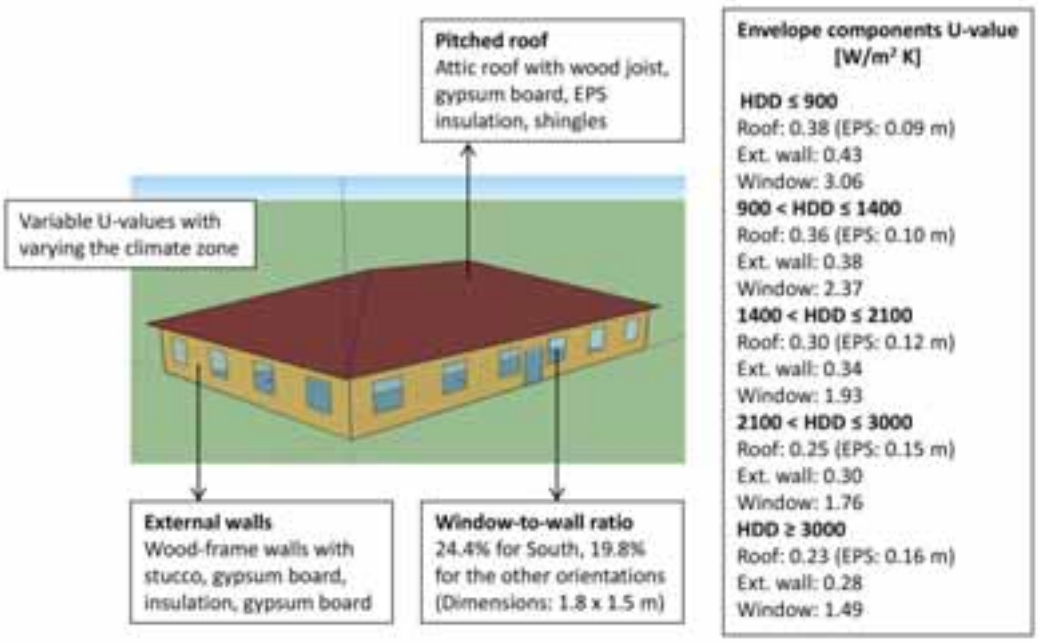

Fig. 2: Case study small office building model and envelope characteristics

5. Results

5.1. Sensitivity to roof solar reflectance variation

Firstly, the one-dimensional optimization of roof solar reflectance in the climate conditions of six selected cities representative of the HDD ranges defined in Fig. 2, i.e. Abu Dhabi, Palermo, Buenos Aires, Rome, Paris, and Tampere, is carried out. Results show that in a standard small office building the optimum roof solar reflectance corresponds to the maximum available cool capability, namely 0.8, in almost all climates except that in the almost totally heating dominated subarctic zone of Tampere (Finland). Accordingly, the configuration characterized by the lowest performance is the dark roof, i.e. ρ_{solar} equal to 0.1, in all climate zones except Tampere, where the situation is inverted and $\rho_{solar} = 0.1$ results to be the optimum value.

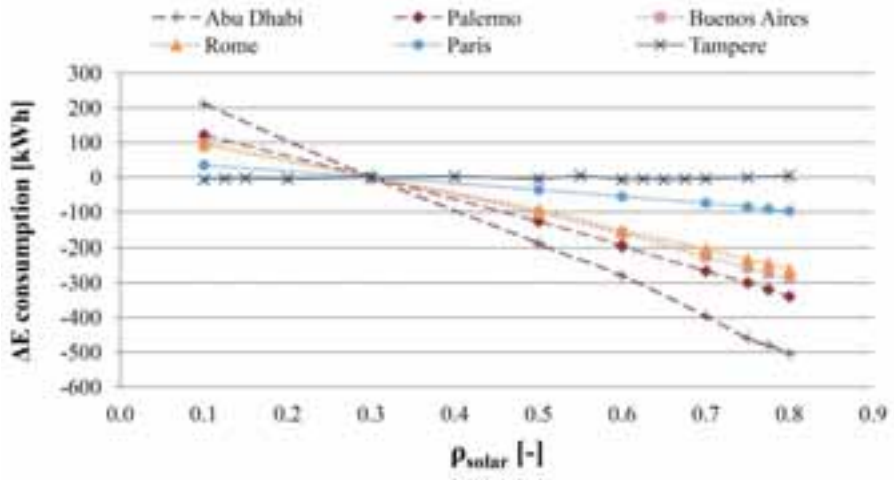

Fig. 3: Total building HVAC energy consumption difference variation with varying only roof solar reflectance in the selected climate zones

Moreover, the sensitivity of annual building energy performance to roof solar reflectance variation in the different climate zones is assessed. Fig. 3 depicts the trend of total HVAC energy consumption difference (ΔE) between roof ρ_{solar} scenarios in the considered range (0.1 ÷ 0.8) and the "standard roof" ($\rho_{solar} = 0.3$) for each selected case study city. Trend lines demonstrate how the influence of roof solar reflectance is mostly perceived

in hot and warm climate conditions, which are totally or mainly cooling dominated. The difference in terms of annual HVAC energy need of the office building is equal to 3.7%, corresponding to about 716 kWh, 5.2% (461 kWh), 5.9% (384 kWh), and 4.3% (357 kWh) in Abu Dhabi, Palermo, Buenos Aires, and Rome, respectively, between ρ_{solar} equal to 0.8 (optimum) and 0.1 (worst). Whereas, in Paris and Tampere, the building annual HVAC ΔE consumption variation trend is flatter (in particular in the subarctic city) with energy savings equal to about 132 kWh (3.7%) and 12 kWh (0.1%), respectively, between the optimum and worst ρ_{solar}.

5.2. Sensitivity to roof thermal insulation level variation

To analyze the impact of roof thermal insulation on the energy performance of the office building, the same one-dimensional optimization method is applied in the six selected representative cities by varying only the roof thermal insulation level. As previously mentioned, two different scenarios are considered for the roof solar reflectance, i.e. (i) "standard roof" and (ii) "cool roof".

As regards models with "standard roof", i.e. ρ_{solar} equal to 0.3, the maximum available roof thermal insulation thickness of 0.25 m is found to be the optimum value in all considered climates. However, the thermal insulation level variation is mainly perceived in extreme climate conditions, namely in Abu Dhabi and Tampere, as depicted in Fig. 4, which reports the trend of total HVAC ΔE consumption between roof $I_{thermal}$ scenarios in the considered range (0.01 ÷ 0.25) and the "standard roof" ($I_{thermal}$ according to HDD) for each case study city. In Abu Dhabi and Tampere the annual HVAC energy savings in the case study building are equal to 3.2% (about 615 kWh) and 5.6% (526 kWh), respectively, between $I_{thermal}$ equal to 0.25 (optimum) and 0.01 (worst). On the contrary, in temperate and milder climates, especially in those cooling dominated, the building annual HVAC energy need is only reduced by 2.7% (about 242 kWh), 3.0% (195 kWh), 1.7% (142 kWh), and 5.3% (194 kWh) in zone Palermo, Buenos Aires, Rome, and Paris, respectively, with the optimum and worst $I_{thermal}$.

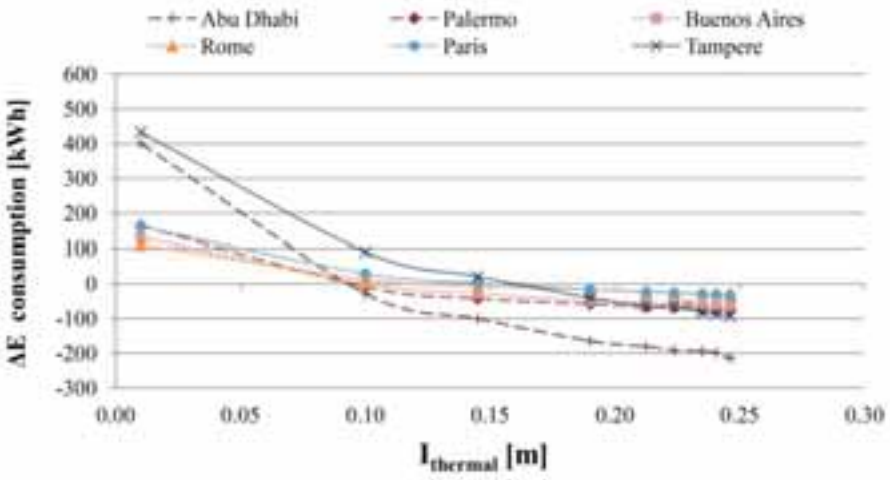

Fig. 4: Total building HVAC energy consumption difference variation with varying only roof thermal insulation thickness in the selected climate zones with "standard roof"

On the contrary, in the models with "cool roof", i.e. ρ_{solar} equal to 0.8, the annual HVAC energy consumption is minimized by applying the thinnest thermal insulation (0.01 m) as roof layer in milder climates, i.e. Palermo, Buenos Aires, Rome. Instead, in extremely hot conditions, i.e. Abu Dhabi, the optimum is increased up to 0.04 m. Finally, in heating dominated climates, namely Paris and Tampere, the optimum corresponds to the maximum available value, i.e. 0.25 m. Nevertheless, the trend of annual HVAC energy need variation is flatter (Fig. 5) and the roof thermal insulation optimization is less significant, except that in extreme cold conditions, i.e. Tampere. In fact, the cooling load is predominant in all other case study climate contexts. Accordingly, in Palermo, Buenos Aires, Rome, and Paris about 2% benefit (138 kWh, 118 kWh, 171 kWh, and 62 kWh, respectively) is observed in terms of total energy saving, while in Abu Dhabi only 0.2% (42 kWh), between the optimum and worst $I_{thermal}$. Conversely, in Tampere the HVAC energy consumption reduction increases up to 5.9%, corresponding to about 556 kWh, between $I_{thermal}$ equal to 0.25 (optimum) and 0.01 (worst).

It has to be noticed that the annual HVAC energy consumption of the case study building is more affected by roof solar reflectance variation than thermal insulation level variation, in the considered cities, except that in the

coldest climate conditions.

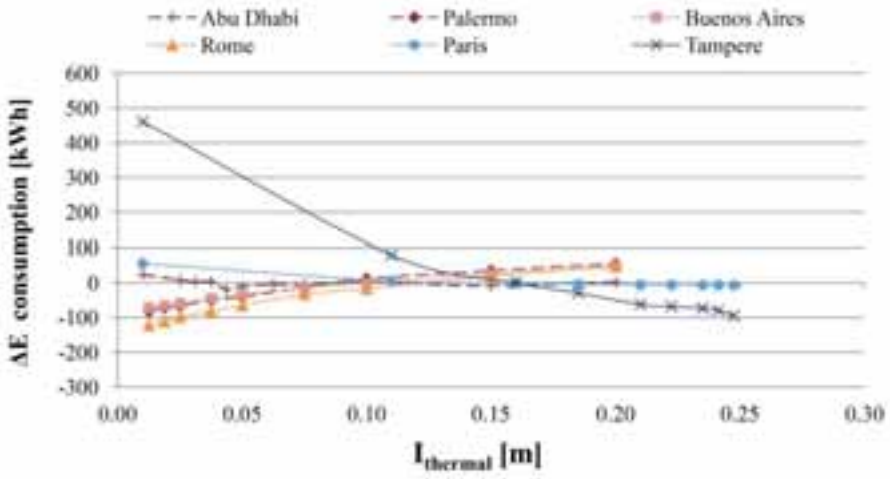

Fig. 5: Total building HVAC energy consumption difference variation with varying only roof thermal insulation thickness in the selected climate zones with "cool roof"

5.3. Optimum roof configuration with varying climate zone

Results of the multi-dimensional optimization analysis are reported in Fig. 6 and Tab. 2 for all the simulated case study climate conditions. In particular, Tab. 2 shows the optimum roof configuration (i.e. combination of ρ_{solar} and $I_{thermal}$) in each city and the corresponding total, heating, and cooling energy consumption. The roof configuration which minimizes building annual HVAC energy consumption is mostly characterized by high solar reflectance (ρ_{solar} equal to 0.8), except in the three coldest cities, while the optimum insulation level is more variable with varying the climate context. In temperate and Mediterranean zones, $I_{thermal}$ is almost negligible, since values between 0.01 and 0.04 m are found to optimize the roof energy performance (Tab. 2). On the contrary, in the extremely hot zones a suitable thermal insulation level is required to minimize heat gains. On the other hand, in the colder zones, the maximum available $I_{thermal}$ equal to 0.25 m is required to reduce heating energy losses through the roof. Therefore, Tab. 2 shows how in the majority of considered climate zones, i.e. milder, the optimum roof configuration in order to minimize annual HVAC energy consumption involves the combination of high solar reflectance capability and low insulation level (blue rectangle).

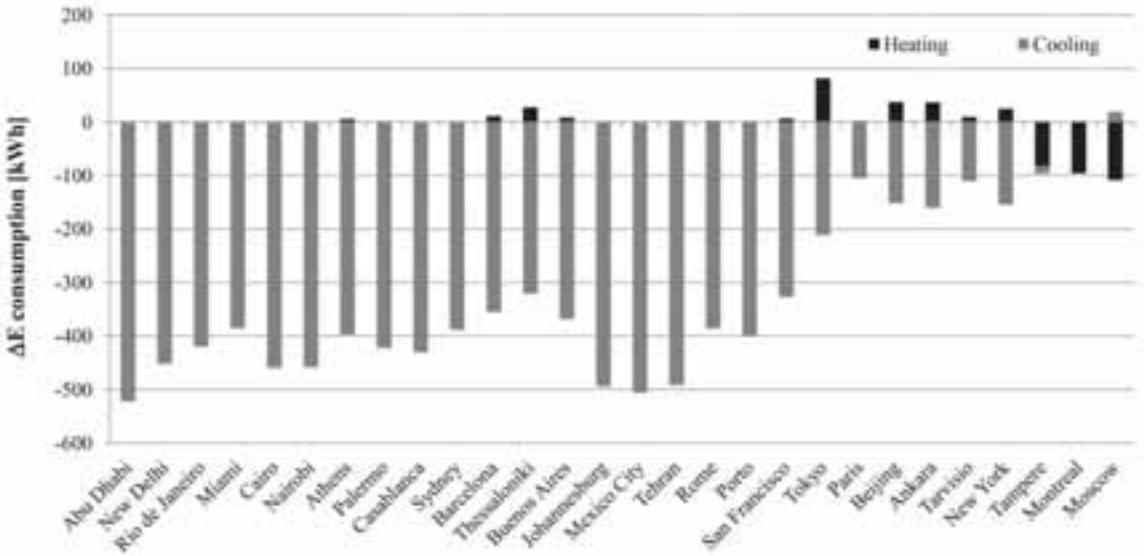

Fig. 6: Building HVAC energy consumption difference between the optimum and the "standard roof" configuration in each climate zone, reporting the separate contributions for heating and cooling

Moreover, Fig. 6 depicts the ΔE in terms of heating and cooling energy need between the "standard", i.e.

characterized by ρ_{solar} = 0.3 and $I_{thermal}$ according to the regulation (Repubblica Italiana, 2015) depending on HDD, and the optimum roof configuration in each climate. The comparison of annual HVAC energy saving with the optimum roof configuration, with respect to the "standard", demonstrates how the optimization of combination of roof solar reflectance and thermal insulation generates non-negligible annual energy saving in all considered climate conditions. However, benefits are mainly perceived in cooling dominated climates. Office building annual energy consumption for air-conditioning is reduced by about 1% to 11%. The maximum achievable actual energy saving is equal to 522 kWh, 507 kWh, 493 kWh, and 490 kWh, in Abu Dhabi, Mexico City, Johannesburg, and Tehran, respectively, always in terms of cooling energy consumption. On the contrary, the energy need reduction decreases up to 90 kWh, 95 kWh, and 97 kWh in the coldest Moscow, Montreal, and Tampere, respectively, in terms of heating energy saving. In general, the cooling load is predominant in almost all considered climate conditions, due to building end-use and associated high internal gains too.

Tab. 2: Optimum roof configuration and corresponding heating, cooling, and total HVAC energy consumption for the case study building in each climate

City	Optimum ρ_{solar} [-]	Optimum $I_{thermal}$ [m]	Heating [kWh]	Cooling [kWh]	Total HVAC [kWh]
Abu Dhabi, UEA	0.8	0.11	0	18513	18513
New Delhi, India	0.8	0.09	0	15685	15685
Rio de Janeiro, Brazil	0.8	0.03	0	13815	13815
Miami, USA	0.8	0.01	1	14077	14078
Cairo, Egypt	0.8	0.01	0	10897	10897
Nairobi, Kenya	0.8	0.01	0	8028	8028
Athens, Greece	0.8	0.01	35	7397	7432
Palermo, Italy	0.8	0.01	0	8345	8345
Casablanca, Morocco	0.8	0.01	18	7591	7609
Sydney, Australia	0.8	0.01	5	6902	6907
Barcelona, Spain	0.8	0.01	80	5523	5603
Thessaloniki, Greece	0.8	0.01	225	5504	5729
Buenos Aires, Argentina	0.8	0.01	106	5977	6083
Johannesburg, South Africa	0.8	0.01	56	6154	6210
Mexico City, Mexico	0.8	0.01	5	6253	6258
Tehran, Iran	0.8	0.01	312	10934	11246
Rome, Italy	0.8	0.01	106	7707	7813
Porto, Portugal	0.8	0.01	44	6292	6336
San Francisco, USA	0.8	0.01	39	2571	2610
Tokyo, Japan	0.8	0.04	786	4308	5094
Paris, France	0.8	0.25	1050	2350	3400
Beijing, China	0.8	0.25	2143	4864	7007
Ankara, Turkey	0.8	0.25	1871	3007	4878
Tarvisio, Italy	0.8	0.25	3094	2187	5280
New York, USA	0.8	0.24	1539	4440	5979
Tampere, Finland	0.4	0.25	7437	1416	8853
Montreal, Quebec, Canada	0.2	0.24	8406	2816	11222
Moscow, Russia	0.1	0.25	7610	2192	9802

6. Discussion

Findings of the above mentioned analyses show that, in order to minimize the annual energy consumption for air-conditioning in a standard small office building worldwide, roof solar reflectance plays a significant role.

Roof thermal insulation level is also important, yet mainly in heating dominated climates or extreme climate conditions. However, in accordance with existing works in literature (Radhi et al., 2017), when coupling cool roof and thermal insulation capability, the role of roof insulation in improving building energy performance becomes negligible, for the case study building in the majority of considered climate zones. In fact, office buildings are characterized by high internal gains, and, therefore, heating load is dampened down by such heat gains, while cooling load becomes predominant also in heating dominated climate contexts. However, in the coldest zones, a consistent insulating layer is required to limit the significant heating energy need.

Thermal insulation level increase provides benefits mainly in terms of heating load reduction. Therefore, when implementing a "standard roof", characterized by higher external heat gains with respect to the "cool roof", high thermal insulation provides significant benefits in terms of both cooling and heating energy saving. On the other hand, in the "cool roof" scenario, the cooling load is already minimized by the positive passive cooling effect due to the low roof coating solar absorptance. In this scenario, although high thermal insulation level provides positive effect in the cold season (heating load reduction), the cooling load is even increased when thick insulating layers are implemented. Since, in the case study building typology, i.e. office building, the cooling load is predominant, the annual HVAC energy consumption is generally minimized with low thermal insulation thickness, with the exception of the coldest climates. Accordingly, building annual HVAC energy consumption is more sensitive to roof solar reflectance variation, with respect to roof thermal insulation variation. Moreover, when "cool roof" is applied over the building, the effect of thermal insulation variation is less significant, except that in extremely cold conditions, because in the case study building the heating need is generally a small percentage of the annual HVAC energy requirement.

In milder climate contexts, characterized by hot summer and mild/cold winter, the expected optimum roof configuration, i.e. combination of roof solar reflectance and thermal insulation, would be with high solar reflectance, which minimizes the cooling energy consumption, and maximum available thermal insulating layer thickness, which minimizes the heating energy consumption. Nevertheless, due to the predominance of cooling load in the case study building typology (characterized by high internal gains) and to the penalties in terms of cooling need associated to high insulation levels, the optimum configuration is characterized by maximum solar reflectance and minimum thermal insulation.

7. Conclusions and future developments

In this work, a replicable method for optimizing the combination of cool roof and roof thermal insulation as passive strategies for building energy efficiency in different climate contexts is proposed. To this aim, optimization analysis based on dynamic thermal-energy simulation is carried out with the final purpose of minimizing annual energy requirement for air-conditioning by optimizing the roof configuration of a small office building in different climate contexts worldwide. In particular the combination of two key parameters affecting roof energy performance is taken into account, i.e. solar reflectance and thermal insulation thickness.

Results show that between the two considered roof characteristics, solar reflectance capability mostly affects building energy performance. Moreover, "cool roof" optimizes the annual HVAC energy consumption of the case study building in the majority of climate conditions. On the other hand, building energy performance is more sensitive to roof thermal insulation variation when a low reflectance "standard roof" is implemented. Nevertheless, when considering the combination of roof solar reflectance capability and thermal insulation level, the optimum configuration is characterized by high cool capability, i.e. R_{solar} equal to 0.8, and low insulating layer thickness, i.e. $I_{thermal}$ between 0.01 and 0.04 m, in the majority of climate zones (milder zones). The exception is represented by the extremely hot and the coldest considered climate zones, where an insulating layer up to 0.11 m and 0.25 m is required, in the hottest and the coldest zones, respectively, to limit the significant thermal energy gains or losses through the roof. All in all, the optimum combination of roof solar reflectance capability and thermal insulation level provides the maximum annual energy saving.

Although the present study refers to selected climate zones, reliable indications are provided also for other regions in the world with similar climate classifications. Moreover, the same analysis procedure is reproducible for other climate conditions. In addition, findings of this work highlight how both climate conditions and further boundary conditions affecting building energy performance, namely end-use and envelope characteristics, e.g. coating optic-energy properties, have to be taken into account simultaneously when targeting building envelope

thermal requirements. Given the promising multivariable optimization results of this paper, future developments of this work can be the investigation of economic and life-cycle benefits associated to coupling cool roof and thermal insulation design of building envelopes. Furthermore, this optimization methodology can be implemented to study the influence of further building boundary conditions in the optimum roof configuration, e.g. end-use, type of HVAC system, occupancy, internal gains. The final goal is to develop guidelines for the efficient implementation of cool roofs in different climate conditions.

8. Acknowledgements

The research leading to these results has received funding from the European Union's Horizon 2020 research and innovation programme under grant agreement N°657466 (INPATH-TES). The work is partially funded by the Spanish government (ENE2015-64117-C5-1-R (MINECO/FEDER) and ENE2015-64117-C5-3-R (MINECO/FEDER)). The authors from the University of Lleida would like to thank the Catalan Government for the quality accreditation given to their research group (2014 SGR 123). Anna Laura Pisello's acknowledgments are due to the UNESCO Chair "Water Resources Management and Culture", for supporting her research. Alvaro de Gracia would like to thank Ministerio de Economia y Competitividad de España for Grant Juan de la Cierva, FJCI-2014-19940.

9. References

Aguilar, J.L.C., Smith, G.B., Gentle, A.R., Chen, D., 2013. Optimum integration of albedo, sub-roof R-value, and phase change material for cool roofs. Proceedings of BS 2013: 13th Conference of the International Building Performance Simulation Association, Le Bourget Du Lac, France, 25-30 August 2013, 1315–1321.

Akbari, H., Kolokotsa, D., 2016. Three decades of urban heat islands and mitigation technologies research. Energy Build. 133, 834–842.

Arumugam, R.S., Garg, V., Ram, V.V., Bhatia, A., 2015. Optimizing roof insulation for roofs with high albedo coating and radiant barriers in India. J. Build. Eng. 2, 52–58.

ASHRAE, 2016. ASHRAE Standard 90.1-2016 - Energy Standard for Buildings Except Low-Rise Residential Buildings.

Costanzo, V., Evola, G., Marletta, L., 2013. Cool roofs for passive cooling: performance in different climates and for different insulation levels in Italy. Adv. Build. Energy Res. 7, 155–169.

Crawley, D.B., Pedersen, C.O., Lawrie, L.K., Winkelmann, F.C., 2000. Energy plus: Energy simulation program. ASHRAE J. 42, 49–56.

Crawley, D.B., Lawrie, L.K., Winkelmann, F.C., Buhl, W.F., Huang, Y.J., Pedersen, C.O., Strand, R.K., Liesen, R.J., Fisher, D.E., Witte, M.J., Glazer, J., 2001. EnergyPlus: Creating a new-generation building energy simulation program. Energy Build. 33, 319–331.

Daouas, N., 2016. Impact of external longwave radiation on optimum insulation thickness in Tunisian building roofs based on a dynamic analytical model. Appl. Energy. 177, 136–148.

Di Giuseppe, E., D'Orazio, M., 2015. Assessment of the effectiveness of cool and green roofs for the mitigation of the Heat Island effect and for the improvement of thermal comfort in Nearly Zero Energy Building. Archit. Sci. Rev. 58, 134–143.

EN 15251:2007 - Indoor Environmental Input Parameters for Design and Assessment of Energy Performance of Buildings Addressing Indoor Air Quality, Thermal Environment, Lighting and Acoustics, 2007.

Evins, R., 2013. A review of computational optimisation methods applied to sustainable building design. Renew. Sustain. Energy Rev. 22, 230–245.

Farhan, S.A., Shafiq, N., Azizli, K.A.M., Soon, F.K., Jie, L.C., 2016. Optimization of residential roof design using system dynamics and building information modeling. In Engineering Challenges for Sustainable Future, Proceedings of the 3rd International Conference on Civil, offshore and Environmental Engineering, ICCOEE 2016, Kuala Lumpure, 15-17 August 2016, 193–198.

Gentle, A.R., Aguilar, J.L.C., Smith, G.B., 2011. Optimized cool roofs: Integrating albedo and thermal emittance with R-value. Sol. Energy Mater. Sol. Cells. 95 (12), 3207–3215.

Hosseini, M., Akbari, H., 2014. Heating energy penalties of cool roofs: the effect of snow accumulation on roofs. Adv. Build. Energy Res. 8, 1–13.

Hosseini, M., Akbari, H., 2016. Effect of cool roofs on commercial buildings energy use in cold climates. Energy Build. 114, 143–155.

Kolokotroni, M., Gowreesunker, B.L., Giridharan, R., 2013. Cool roof technology in London: An experimental and modelling study. Energy Build. 67, 658–667.

Kottek, M., Grieser, J., Beck, C., Rudolf, B., Rubel, F., 2006. World map of the Köppen-Geiger climate classification updated. Meteorol. Zeitschrift 15, 259–263.

Levinson, R., Akbari, H., 2010. Potential benefits of cool roofs on commercial buildings: Conserving energy, saving money, and reducing emission of greenhouse gases and air pollutants. Energy Effic. 3 (1), 53–109.

Pisello, A.L., 2017. State of the art on the development of cool coatings for buildings and cities. Sol. Energy. 144, 660–680.

Radhi, H., Sharples, S., Taleb, H., Fahmy, M., 2017. Will cool roofs improve the thermal performance of our built environment? A study assessing roof systems in Bahrain. Energy Build. 135, 324–337.

Ramamurthy, P., Sun, T., Rule, K., Bou-Zeid, E., 2015. The joint influence of albedo and insulation on roof performance: An observational study. Energy Build. 93, 249–258.

Ramamurthy, P., Sun, T., Rule, K., Bou-Zeid, E., 2015. The joint influence of albedo and insulation on roof performance: A modeling study. Energy Build. 102, 317–327.

Repubblica Italiana - Ministero dello Sviluppo Economico, 2015. Decreto interministeriale 26 giugno 2015 - Applicazione delle metodologie di calcolo delle prestazioni energetiche e definizione delle prescrizioni e dei requisiti minimi degli edifici (in Italian). http://www.sviluppoeconomico.gov.it/index.php/it/normativa/decreti-interministeriali/2032966-decreto-interministeriale-26-giugno-2015-applicazione-delle-metodologie-di-calcolo-delle-prestazioni-energetiche-e-definizione-delle-prescrizioni-e-dei-requisiti- (accessed on March 6th, 2017).

Santamouris, M., 2015. Regulating the damaged thermostat of the cities - Status, impacts and mitigation challenges. Energy Build. 91, 43–56.

Santamouris, M., Ding, L., Fiorito, F., Oldfield, P., Osmond, P., Paolini, R., Prasad, D., Synnefa, A., 2017. Passive and active cooling for the outdoor built environment - Analysis and assessment of the cooling potential of mitigation technologies using performance data from 220 large scale projects. Sol. Energy 154, 14–33.

Smith, G.B., Aguilar, J.L.C., Gentle, A.R., Chen, D., 2012. Multi-parameter sensitivity analysis: A design methodology applied to energy efficiency in temperate climate houses. Energy Build. 55, 668–673.

Synnefa, A., Santamouris, M., Akbari, H., 2007. Estimating the effect of using cool coatings on energy loads and thermal comfort in residential buildings in various climatic conditions. Energy Build. 39, 1167–1174.

U.S. Department of Energy (DOE), 2016. EnergyPlus Engineering Reference: The Reference to EnergyPlus Calculations, 1444.

U.S. Department of Energy's (DOE) Building Technologies Office (BTO), 2016. EnergyPlus - Weather Data. https://energyplus.net/weather (accessed on March 1st, 2017).

Wetter, M., 2000. Design Optimization with GenOpt. Build. Energy Simul. User News 21, 19–28.

Winiarski, D., Jiang, W., Halverson, M., 2006. PNNL's CBECS Study. Review of Pre- and Post-1980 Buildings in CBECS – HVAC Equipment. Pacific Northwest National Laboratory, Richland, WA.

Winiarski, D., Halverson, M., Jiang, W., 2007. PNNL's CBECS Study. Analysis of Building Envelope Construction in 2003 CBECS Buildings. Pacific Northwest National Laboratory, Richland, WA.

Zinzi, M., Carnielo, E., Federici, A., 2014. Preliminary studies of a cool roofs' energy-rating system in Italy. Adv. Build. Energy Res. 8, 84–96.

Testing, Standards, and Certification for Solar Thermal Technologies

ACCELERATED AGING TESTS OF ABSORBER COATINGS FOR UNGLAZED METALLIC SOLAR COLLECTORS

Summary

During the expected minimum life-span of 20 years, the absorber coating of unglazed thermal solar collectors is directly exposed to different stresses like heat, rain and ice. With increasing application possibilities for this type of collectors (e.g. for borehole regeneration), there is a need for the quality certification of absorber coatings. However, there is no standard procedure available to assess the durability of spectrally selective coatings for unglazed collectors. Existing aging tests (ISO 22975-3) are designed for absorber coatings used in glazed solar collectors, where the degradation loads (e.g. for humidity and condensation) are very different. Preliminary steps for developing an accelerated lifetime testing procedure are presented. First results showing the optical performance after aging of two spectrally selective absorber coatings on stainless steel are reported.

Keywords: unglazed solar thermal collectors, spectrally selective absorber coatings, time of wetness, accelerated aging, optical performance.

1. Introduction

For certifying new absorber coatings, the expected service life must be predicted. Accelerated aging tests considering the relevant degradation factors are required. The in-service conditions and environmental stresses must be measured. High temperature, high humidity and moisture, and airborne pollutants were identified by the IEA Working Group MSTC (Materials in Solar Thermal Collectors) as the most relevant degradation factors for glazed flat plate collectors, used for domestic hot water production (Brunold et al., 2000). However, the loads in terms of humidity, condensation, snow/icing and hail largely differ in the case of unglazed collectors, because their absorber coating is directly exposed to the environmental stresses (Dudita et al., 2016).

Several degradation mechanisms are influencing the performance and lifetime of absorber coatings, including metal oxidation, elements diffusion and modification of the antireflective layer (Carlsson et al., 2000; Dudita et al., 2015a). This might influence the optical performance expressed by the solar absorptance (α_s) and thermal emittance (ε_t), and the long term durability of the absorber coating. High temperature increases the metal oxidation rate leading to a decrease in α_s and an increase of ε_t. Humid air and condensation occurring on the absorber surface can lead to hydration reactions of inorganic oxides and electrochemical corrosion. The corrosion can be accelerated by airborne pollutants.

Accelerated lifetime testing of materials is thus highly important for the service life estimation, especially for certification of new products prior to their market introduction. However, there is currently no standard procedure to assess the durability of unglazed metallic absorbers. Existing tests (ISO 22975-3) are specially designed for glazed solar collectors (Brunold et al., 2000).

For developing an accelerated lifetime testing (ALT) procedure, realistic loads for the absorber surface are needed. For unglazed solar thermal collectors, the degradation due to temperature and high humidity and condensation might be predominant. We have performed, as a first step, simulations to determine the temperature frequency distribution (TFD) and time of wetness (TOW) frequency distribution for the absorber surface. A representative TOW diagram which is needed to quantify the humidity induced stress, is presented in this paper. Wetting due to rain or due to environmental humidity condensing on the absorber surface was considered. Moreover, we have performed preliminary tests to assess the durability of new selective coatings on stainless steel substrate that can potentially be used in unglazed collectors. Our tests are based on the procedure mentioned in ISO 22975-3, nonetheless higher testing temperature were also included. Two samples from under development selective coatings were exposed to high humidity and condensation, at

doi:10.18086/swc.2017.36.01 Available at http://proceedings.ises.org

constant temperature (sample temperature between 40 °C and 70 °C) and constant humidity (95% RH). The optical degradation of the coatings was monitored with the help of a Bruker IFS 66/S spectrometer with a custom made configuration. A detailed description of the experimental procedure is described elsewhere (Dudita et al., 2015b).

2. Durability assessment of spectrally selective absorber coatings for unglazed solar thermal collectors

The temperature frequency distribution and the time of wetness (TOW) expected for absorber plates of unglazed collectors in different system configurations were determined by means of transient system simulations (TRNSYS v.17). In particular, a heat pump heating system with a small ice storage tank, where the collectors are operated in very harsh conditions, was selected (Mojic et al., 2015). The simulation model of the collector (TRNSYS Type 832 v5.10) includes condensation, frost and rain heat gains. As boundary conditions for the simulations, weather data for different climatic regions were considered.

An example of a yearly time of wetness (TOW) frequency distribution (humidity or condensation) for an unglazed collector is represented in Fig. 1 together with the one specific for the glazed collectors from IEA SHC Task X. The climate data represent a typical year for Zürich (Switzerland), with a time resolution of 6 minutes. Since unglazed collectors are operated at lower temperatures and in the simulated system frequently below dew point, their TOW distribution shows much larger frequencies at low temperatures. Ultimately, the established load profiles, together with the experimentally determined activation energies for the different degradation modes, will be used to define the parameters of the accelerated aging tests.

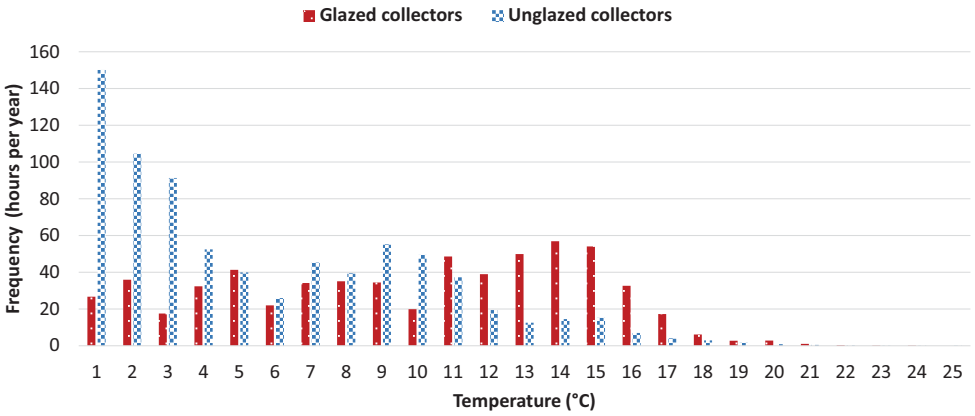

Fig. 1 Yearly time of wetness frequency distributions for absorber surfaces of glazed and unglazed collectors (criteria for the TOW were a relative humidity at the absorber surface of RH ≥ 99 % or a rain rate >= 3mm/h)

The resistance of absorber coatings to high humidity and condensation conditions was investigated for two different absorber coatings. An adapted procedure based on ISO 22975-3 for the qualification of solar absorber coatings used in glazed collectors was followed. Different testing sample temperatures (40°C to 70°C), high humidity and condensation conditions were applied for the two spectrally selective coatings (Type A and Type B) deposited via physical vapor deposition on stainless steel substrate. The optical performance expressed as the variation of solar absorptance and thermal emittance remained constant in the 40°C test (see Fig. 2 and Fig. 3). Higher testing temperatures (60°C and 70°C) were used to estimate the activation energy and the coatings lifetime.

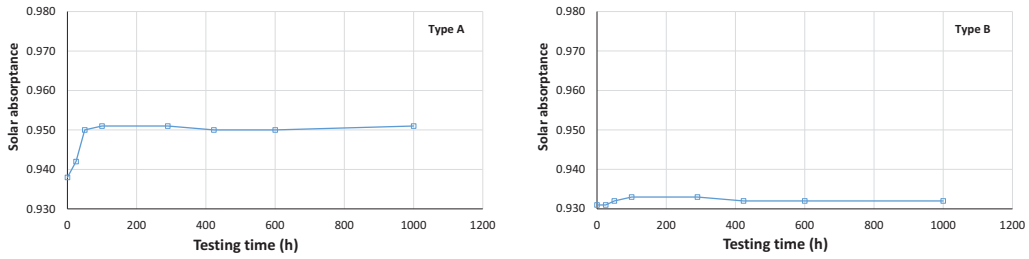

a) b)

Fig. 2 Solar absorptance after different testing duration in high humidity (95%) and condensation at 40°C for two spectrally selective absorber coatings: Type A (a) and Type B (b)

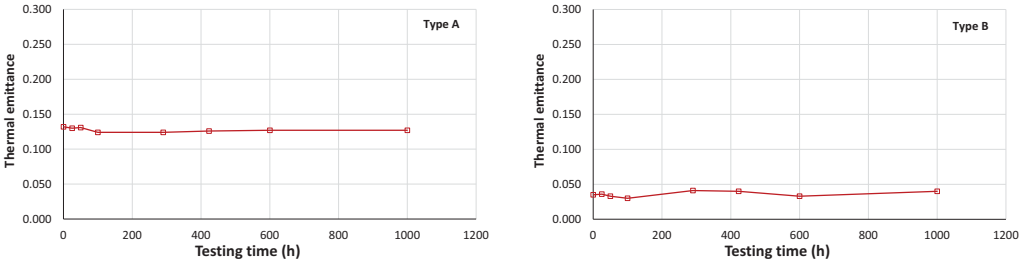

a) b)

Fig. 3 Thermal emittance after different testing duration in high humidity (95%) and condensation at 40°C for two spectrally selective absorber coatings: Type A (a) and Type B (b)

3. Concluding remarks

The market of unglazed solar thermal collectors with spectrally selective coatings on metal substrate is continuously increasing as new applications like boreholes regeneration or combination with ice storages are emerging. There is currently no standard procedure to assess the durability of unglazed metal-based absorbers used for unglazed solar thermal collectors. However, accelerated lifetime testing of materials is highly important for the development and certification of (new) products prior to their market introduction. Introduction of new materials for the absorber coating is hindered by insecurities regarding lifetime.

First results of a project aiming at the development of an accelerated aging procedure for spectrally selective coatings on metal substrate for unglazed collectors are presented. Realistic load profiles, e.g. the yearly time of wetness (TOW) frequency distribution due to humidity or condensation generated by simulations are shown.

In order to propose an accelerating aging procedure, further studies are necessary. In particular, an appropriate Performance Criterion (PC) must be established to set limits on the acceptable change of the optical properties of the absorber coating, corresponding to an acceptable decrease of the performance of a typical energy system with uncovered solar collectors.

4. References

Brunold, S., Frei, U., Carlsson, B., Möller, K., and Köhl, M., 2000. Accelerated life testing of solar absorber coatings:: Testing procedure and results. Solar Energy *68*, 313–323.

Carlsson, B., Möller, K., Köhl, M., Frei, U., and Brunold, S., 2000. Qualification test procedure for solar absorber surface durability. Solar Energy Materials and Solar Cells *61*, 255–275.

Dudita, M., Omlin, L., Ruesch, F., Gantenbein, P., Brunold, S., and Duta, A., 2015a. Durability of aluminium based solar selective absorbers under condensed water. In Proceedings of International Conference CISBAT 2015 Future Buildings and Districts Sustainability from Nano to Urban Scale

(LESO-PB, EPFL), pp. 45–50.

Dudita, M., Brunold, S., Ruesch, F., Omlin, L., Gantenbein, P., Marot, L., and Kaufmann, A., 2015b. Durability of solar selective absorbers under condensation test. In 25. OTTI Symposium Thermische Solarenergie (Kloster Banz, Bad Staffelstein, Germany: OTTI e.V., Regensburg).

Dudita, M., Zenhäusern, D., Mojic, I., Thissen, B., and Brunold, S., 2016. Durability of Spectrally Selective Absorber Coatings Used for Unglazed Solar Thermal Collectors. In 11th ISES EuroSun Conference - International Conference on Solar Energy for Buildings and Industry, Palma (Mallorca).

Mojic, I., Haller, M.Y., Heinz, A., Hengel, F., and Thissen, B., 2015. New Generation of a Highly Compact Solar Heat Pump System with boosted Energetic Efficiency. In Proceedings of International Conference CISBAT 2015 Future Buildings and Districts Sustainability from Nano to Urban Scale (LESO-PB, EPFL), pp. 723-728.

Analysis of Test Methods for Durability and Performance of Heat-pipes for Solar Thermal Application

HE Zinian

Beijing Solar Energy Research Institute Group Co., Ltd, Beijing (China)

Abstract

After introducing the configuration of a heat-pipe for solar thermal application, this paper analyses test methods for two main aspects which affect the durability of heat-pipes, i.e. high temperature resistance and freeze resistance, and also analyses test methods for three important parameters which indicate the performance of heat-pipes, i.e. starting temperature, temperature uniformity and heat transfer power. For each durability test and performance test of heat-pipes, their significance and necessity, as well as their test objective, test principle, test conditions, test apparatus, test procedure, test results, etc. are respectively introduced in this paper. These test methods have been newly developed as the International Standard ISO 22975-2: 2016, which will play an important role in enhancing product quality and reducing test cost of heat-pipes.

Keywords: Heat-pipe, test methods, durability test, performance test, International Standard

1. Introduction

Heat-pipe is a highly efficient heat transfer element and has been widely used for solar thermal application. For this reason, ISO/TC 180 has recently developed the International Standard ISO 22975-2: 2016 titled as Solar Energy – Collector components and materials, Part 2: Heat-pipe for solar thermal application – Durability and performance.

ISO 22975-2: 2016 specifies test methods for durability and performance of heat-pipes, and is applicable to all heat-pipes for use with evacuated tubes, including glass-metal sealed evacuated tubes and double-glass evacuated tubes, as well as for use with flat-plate collectors.

For each durability test and performance test of heat-pipes, their significance as well as test objective, test principle, test condition, test apparatus, test procedure, test results, etc. will be introduced in the paper.

2. Configuration of the heat-pipe

Heat-pipes operate only by utilizing latent heat of phase-change of the working fluid for heat transfer. Heat-pipes can be basically classified into two categories according to backflow manner of the working fluid. One is the heat-pipe with a capillary wick, and the other one is the heat-pipe without a capillary wick. For the former, backflow of the liquefied working fluid relies on the capillary action; whereas for the later, backflow of the liquefied working fluid relies on its gravity. Therefore, the later is also called as the gravity heat-pipe.

Since this international standard is only applicable to gravity heat-pipes, so the gravity heat-pipe essentially consists of evaporator, condenser, adiabatic section and working fluid, as shown in Fig. 1, and there is a highly evacuated space inside the heat-pipe. For the gravity heat-pipe, the liquefied working fluid returns from the condenser to the evaporator due to its own weight.

doi:10.18086/swc.2017.36.02 Available at http://proceedings.ises.org

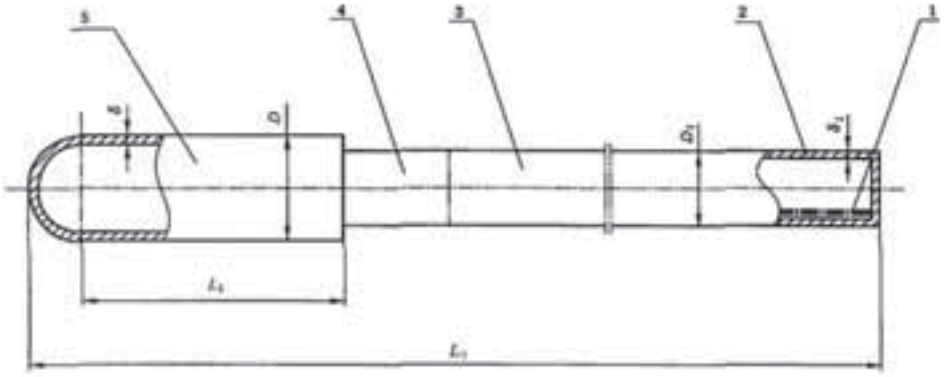

1) Working fluid
2) **Shell (container)**
3) **Evaporator**
4) Adiabatic section
5) **Condenser**

Fig. 1: Typical configuration of a heat-pipe for solar thermal application

3. Durability of heat-pipes

3.1. High temperature resistance test

As heat-pipes used for solar thermal application may probably undergo an exposure state under the sun to reach a quite high temperature, for example, in the range of 180 °C to 280 °C for different applications, so it is necessary to perform a high temperature resistance test.

This test is intended to assess the capability of the heat-pipe to withstand quite high temperature without failure.

The test needs indoor environment. The test shall be carried out using a set of test apparatus which consists of a heating chamber and a thermometric system, of which the test temperature shall be at 180 °C ± 5 °C or 230 °C ± 5 °C or 280 °C ± 5 °C, depending on specific application and manufacturer's declaration.

In the test, place all sample heat-pipes with a tilt angle 90° ± 1° into the heating chamber; increase the temperature slowly (maximum 20 K/min) up to the selected test temperature; maintain the test temperature for 30 h; then let heat-pipes naturally cool down; after the heat-pipes have cooled to room temperature, visually inspect for damage such as leakage, breakage, distortion or deformation.

The heat-pipes will be qualified if there is no visual evidence of damage.

3.2. Freeze resistance test

As heat-pipes used for solar thermal application may undergo a freeze weather condition in winter season in many areas to reach a rather low temperature, such as below 0 °C, so it is very important to perform a freeze resistance test.

This test is intended to assess the extent to which the heat-pipe which is claimed to be freeze resistant, can withstand freezing without failure.

The test needs indoor environment. The test shall be carried out using a set of test apparatus which consists of an appropriate freezing device and a thawing device. The freezing temperature shall be at −20 °C ± 1 °C and the thawing temperature shall be at 20 °C ± 1 °C.

In the test, place all sample heat-pipes with a tilt angle 90° ± 1° into the freezing device for 60 min; remove the heat-pipes from the freezing device and insert them into the thawing device, keeping the evaporator in lower position; measure the temperature on the condenser surface; wait for 5 min after the temperature

difference between the thawing device and the condenser surface is less than 9 K, which indicates that heat-pipes have started to operate again; repeat above-mentioned steps 20 times; then visually inspect for damage such as leakage, breakage, distortion or deformation.

The heat-pipes will be qualified if there is no visual evidence of damage.

4. Performance of heat-pipes

4.1. Starting temperature of heat-pipes

Heat-pipes used for solar thermal application always face such a problem, whether and when the heat-pipe can start operating. From the evaporation point of view, as there is a negative pressure inside the heat-pipe, the evaporation temperature of the liquefied working fluid should be lower than that at atmospheric temperature, so as to easily start operating of the heat-pipe, and undoubtedly the lower starting temperature the better for solar thermal application. Therefore, starting temperature is one of the important parameters of heat-pipes.

This test is intended to determine the minimum temperature required for a heat-pipe to start operating.

The test needs indoor environment. The test shall be carried out using a set of test apparatus which consists of a cold water bath at 10 °C ± 0.5 °C and a hot water bath at 25 °C ± 0.5 °C or 30 °C ± 0.5 °C or 40 °C ± 0.5 °C, depending on specific application for different working temperature of the heat-pipe; however, 40 °C ± 0.5 °C shall be the maximum test temperature.

In the test, fit a surface temperature sensor to the condenser; immerse the lower end of the heat-pipe in the cold water bath with a tilt angle 90° ± 1°; wait for at least 3 min after stable conditions are reached; remove the heat-pipe from the cold water bath and immerse its lower end in the hot water bath; measure and record the temperature on the condenser surface every 10 s until at least 120 s after stable conditions are reached; record the condenser surface temperature together with the hot water bath temperature.

The measurement results shall be reported together with ambient temperature, cold water bath temperature, hot water bath temperature, insertion depth of the heat-pipe, distance of measuring point from top of the condenser and variation of the condenser surface temperature.

4.2. Temperature uniformity of heat-pipes

Under normal operating conditions, steam of the working fluid inside the heat-pipe is in a saturated state, and pressure of the saturated steam determines temperature of the saturated steam. As the pressure drop produced when saturated steam moves from the evaporator to the condenser is very small, so the temperature drop is also very small. That is why the heat-pipe possesses excellent isothermal. If there is an obvious temperature difference between the evaporator and the condenser, i.e. the heat-pipe loses the temperature uniformity; it means that non-condensable gas produced during the manufacturing stays in the condenser. Undoubtedly the smaller temperature differences the better for solar thermal application. Therefore, temperature uniformity is also one of the important parameters of heat-pipes.

This test is intended to measure the temperature difference between the evaporator and the condenser when the heat-pipe operates under normal conditions.

The test needs indoor environment. The test shall be carried out using a thermostatic hot water bath at 90 °C ± 0.5 °C.

In the test, fit a surface temperature sensor to the condenser at a point between 18 mm and 22 mm from top of the condenser; insert the heat-pipe into the thermostatic hot water bath to a depth of 3/5 - 2/3 of the total length of the heat-pipe at a tilt angle 90° ± 1°; measure and record the temperature on the condenser surface every 10 s until at least 60 s after stable conditions are reached; record the temperature difference between the hot water bath temperature and the stable condenser surface temperature.

The measurement results shall be reported together with ambient temperature, test temperature in water bath,

insertion depth of the heat-pipe, measuring point from top of the condenser, and condenser temperature variation.

4.3. Heat transfer power of heat-pipes

As a highly efficient heat transfer element for solar thermal application, it is concerned that how much power can be transferred. Therefore, heat transfer power is certainly one of the important parameters of heat-pipes.

As heat transfer power depends on operating temperatures and tilt angles of the heat-pipe, so this test is intended to determine the heat transfer power of the heat-pipe at different operating temperatures and different tilt angles.

The test needs indoor environment. The test apparatus includes tilt-angle adjustable mounting support, evaporator electric heating barrel, condenser cooling liquid jacket, thermostatic liquid bath, flow meter, etc. shown in Fig. 2.

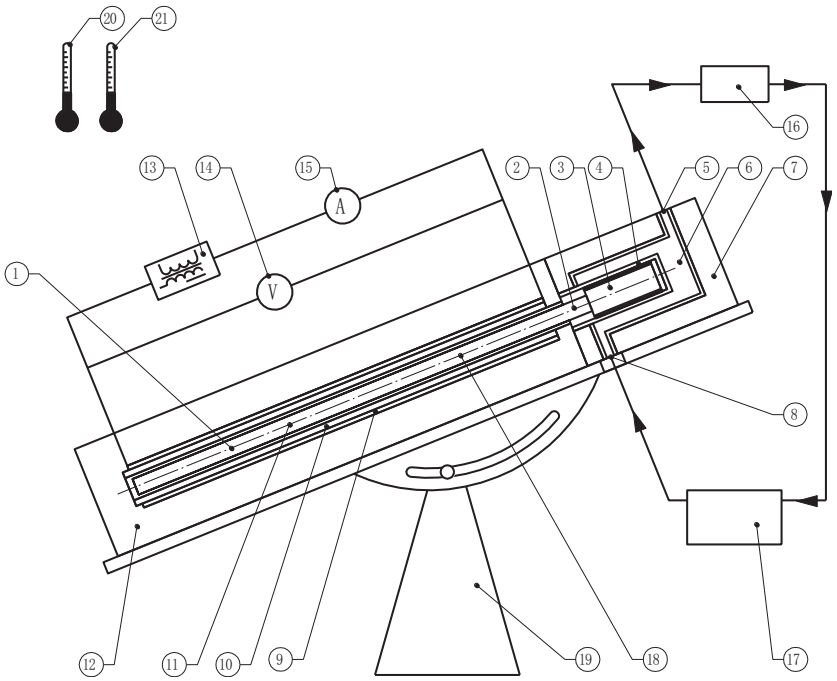

1) heat-pipe evaporator
2) heat-pipe adiabatic section
3) heat-pipe condenser
4) heat transfer paste
5) temperature difference sensor
6) cooling liquid jacket
7) thermal insulation
8) inlet temperature sensor
9) electric heating barrel
10) heat-uniform tube
11) evaporator temperature sensor
12) thermal insulation
13) voltage regulator
14) volt meter
15) ampere meter
16) flow meter
17) thermostatic liquid bath
18) evaporator temperature sensor
19) tilt-angle adjustable support
20) thermometer
21) humidity meter

Fig. 2: Typical test apparatus for measuring the heat transfer power of a heat-pipe

In accordance with the energy conservation law, the heat transfer power of the heat-pipe shall be calculated according to Equation (1).

$$\dot{Q} = \dot{Q}_1 - \dot{Q}_2 \qquad \text{(eq. 1)}$$

where

$\dot{Q}$ = heat transfer power of heat-pipe, W
$\dot{Q}_1$ = thermal power transferred to cooling liquid from heat-pipe, W
$\dot{Q}_2$ = thermal power transferred to cooling liquid from environment or apparatus, W; normally $\dot{Q}_2$ is negligible if the cooling liquid jacket is well insulated

The thermal power received by cooling liquid shall be calculated according to Equation (2).

$$\dot{Q}_1 = \dot{m} C_p (\vartheta_2 - \vartheta_1) \qquad \text{(eq. 2)}$$

where

$\dot{m}$ = mass flow rate of cooling liquid, kg/s
C_p = specific heat capacity of cooling liquid, J/(kg • K)
ϑ_2 = inlet temperature of cooling liquid, °C
ϑ_1 = outlet temperature of cooling liquid, °C

In the test, the evaporator of the heat-pipe is inserted into the sleeve of the electric heating barrel; a copper tube shall be placed between the evaporator and the electric heating elements to ensure uniform heating power distribution; the outer surface of the electric heating barrel shall be thermally insulated; meanwhile, the condenser of the heat-pipe is inserted into the sleeve of the cooling liquid jacket and surrounded with heat transfer paste which has not been used previously; the outer surface of the cooling liquid jacket shall be thermally insulated.

After measuring all necessary parameters, such as mass flow rate $\dot{m}$, inlet temperature ϑ_2 and outlet temperature ϑ_1 of the cooling liquid, then determine the heat transfer power $\dot{Q}_1$ at different operating temperatures and different tilt angles, according to Equation (2).

The test operating temperatures shall be respectively at 60 °C ± 0.5 °C, 90 °C ± 1 °C and 120 °C ± 2 °C (when the heat-pipe is claimed to be able to operate at above 100 °C).

The tilt angle of the heat-pipe shall be from the lowest recommended angle to 90°, i.e. respectively the lowest recommended angle, 20° ± 1°, 30° ± 1°, 45° ± 1°, 60° ± 1°, 75° ± 1°, 90° ± 1°.

In this test, the maximum heat transfer power $\dot{Q}_{max}$ also could be determined. This test shall be conducted directly after carrying out the test of heat transfer power at the test operating temperature 120 °C ± 2 °C and test tilt angle 90° ± 1°.

For determining the maximum heat transfer power $\dot{Q}_{max}$, the procedure shall be as follows:

Slowly increase the power input to the evaporator electric heating barrel, i.e. at a rate of less than 5 W/min; observe the test operating temperature of the heat pipe; once there is an obvious sudden temperature increase, or the temperature shows obvious oscillation and instability, it means that the heat-pipe has reached its heat transfer limit; then quickly reduce the power input to the evaporator electric heating barrel to a point just before the heat transfer limit; when steady state conditions have been achieved, begin to record the values of mass flow rate $\dot{m}$ of the cooling liquid, and inlet/outlet temperature difference $(\vartheta_2 - \vartheta_1)$ of the cooling liquid, at intervals of 30 s for a period of 10 min; finally calculate the maximum heat transfer power $\dot{Q}_{max}$ of the heat-pipe according to Equations (2), using the averages of the recorded values for mass flow rate and inlet/outlet temperature difference of the cooling liquid.

5. Conclusion

Heat-pipe is one of the important components in solar thermal application. Through a lot of experiments and accumulated practical experience, this paper analyses two main aspects which affect the durability of heat-pipes, including high temperature resistance and freeze resistance,

In addition, this paper also analyses three important parameters which indicate the performance of heat-pipes,

including starting temperature, temperature uniformity and heat transfer power.

Based on these achievements, under the joint efforts of WG 3 members, ISO/TC 180 has recently developed International Standard ISO 22975-2: 2016. The newly developed International Standard will play an important role in enhancing product quality and reducing test cost of heat-pipes.

6. References

Chinese National Standard, GB/T 14812 – 2008, Testing method for heat transfer performance of heat-pipes.
Chinese National Standard, GB/T 24767 – 2009, The gravity heat-pipe for solar application.
QAiST, Topic report for WP2 Solar thermal collectors, Performance testing of evacuated tubular collectors, 2012.

In-situ Testing of Large Collector Arrays – Challenges and Methodological Framework

Daniel Tschopp[1], Philip Ohnewein[1], Robert Hausner[1], Christoph Rohringer[1]

[1] AEE – Institute for Sustainable Technologies, A-8200 Gleisdorf

Abstract

In this paper, the major challenges of in-situ collector array testing are analyzed and a framework to address them is developed. The study of the challenges is based on theoretical investigations as well as on data evaluations of a solar district heating (SDH) plant which was equipped with high-precision measurement equipment.

Keywords: in-situ testing, collector array, in-situ measurement, large solar thermal plants, solar district heating

1. Introduction

1.1 The need for in-situ testing of large scale solar thermal plants

Large scale solar thermal plants (>500 m² collector area, >350 kW_{th} nominal thermal power) are a cost-effective way to provide renewable heat (ESTIF, 2015). The market has experienced considerable growth recently, with close to 500,000 m^2 of solar collectors (350 MW_{th}) installed in large scale systems in Europe in 2016. The driving force has been solar district heating applications in Denmark, where the world's largest plant in Silkeborg (156,694 m² flat plate collectors; 110 MW_{th}) started operating in December 2016 (Weiss, Spörk-Dür and Mauthner 2017).

Key factors to increase the market penetration of large solar thermal plants are the reduction of investment risks and the realization of cost saving potentials during the plant operation by means of performance guarantees (for the thermal power output and/or solar yield), efficient monitoring and ongoing optimization.

These measures rely on an accurate and reliable assessment and characterization of the collector array performance for the observed operational behavior. To this aim, an in-situ test procedure to evaluate the thermal power output of large collector arrays under transient conditions is developed. Hereafter we refer to this procedure as the in-situ collector array test.

1.2 In-situ collector array test

The cornerstones of the test procedure are the following:

- focusing on large scale collector arrays with flat plate collectors (flat plate collectors are the most common collector technology deployed in large scale applications)
- the outcome of the test is a characterization of the thermal power output with a set of characteristic parameters which are estimated from measurement data, using a parametrized model of the collector array
- the test considers 'real operation conditions' like soiling, shading, etc. which affect the collector array performance (for single collectors under laboratory conditions, these 'disturbances' can be controlled or are not relevant)
- applicability of the procedure to the most common plant configurations and measurement setups
- the system boundaries of the collector array model are the return and supply lines on the primary side of the heat exchanger (or the equivalent position if there is no heat exchanger)
- the modeling of the collector array puts emphasis on the most important influencing factors on the thermal performance, but restrains from a detailed representation to facilitate the application of the procedure

doi:10.18086/swc.2017.36.03 Available at http://proceedings.ises.org

- a major requirement is a short test period and the reliance on data from the normal plant operation whenever possible
- provision of a standardized and traceable framework for data acquisition, data processing and parameter estimation

The in-situ test procedure will have some similarities with the ISO 9806 standard for single collector tests, but focuses on large collector arrays instead of single collectors and moves from laboratory to 'real-world' conditions. The aim is not to test single collectors in the field, but rather to examine the behavior of an 'average collector' within the array arrangement. In-situ testing of collector arrays is also useful when single collector tests are very difficult to implement, e.g. for large collectors assembled directly at the construction site.

Work on using in-situ data to determine collector (array) parameters date back more than twenty years and include Perers (1993), Bosanac and Nielsen (1997) and Spirkl et al. (1997). These approaches are based on the modeling and data evaluation techniques of single collectors in the spirit of EN 12975. In later work, approaches to identify the collector (array) parameters based on dynamic system simulations were also used (see e.g. Almeida et al. (2014)). In the literature, there is no methodologically sound procedure for testing large collector arrays available.

1.3 Content and structure of this work

In this paper, the major challenges of in-situ collector array testing are analyzed and a framework to address them is developed. The study of the challenges is based on theoretical investigations as well as on data evaluations of a solar district heating (SDH) plant which was equipped with high-precision measurement equipment. To develop an in-situ collector array test, reliable data of large scale installations are essential.

The structure of the paper is as follows. In chapter 2, the main steps of the in-situ collector array test are outlined with the help of a flowchart. In chapter 3, the measurement setup of the SDH plant which was used to gain measurement data for the development of the methodology is shown. In chapter 4, the challenges of the test procedure are analyzed in detail. In chapter 5, a framework to address these challenges is presented. Chapter 6 summarizes the results and gives an outlook on future work.

2. Flowchart of the in-situ collector array test

Fig. 1 shows a simplified flowchart of the collector array test. The first steps are to create a model of the solar thermal plant and to collect, pre-process, select and assess the measurement data. Based on these preliminary tasks, the model input data, i.e. the time series with the explanatory variables and the dependent variable which enter the parameter estimation procedure, are created. The parameters are then estimated and a test report is issued.

[A] Plant representation

The representation of the solar thermal plant is done by adapting a general modeling approach which is suitable for the most common configurations. The representation encompasses the (i) typical collector array parameters (gross collector area, total fluid content, etc.), (ii) collector array geometry (row spacing, azimuth and tilt angle of the collectors, etc.) which is necessary for the irradiance modeling, (iii) hydraulic arrangement and (iv) information on the measurement setup (type of sensors, sensor positions, sensor precisions, installation conditions, sampling rate, …) and available data.

[B.1] Measurement data acquisition and data pre-processing

For commercial installations, the quality of the measurement data is almost always an issue. The measurement data needs to be checked for missing values, sensor readings outside physically plausible ranges, synchronization problems of the data logger, etc. Redundancies of the measurement setup (e.g. both beam irradiance, diffuse irradiance and total irradiance are measured) can be used for additional inspections. An often used check for in-situ collector array testing is to compare the daily sum of the global irradiance and the daily collector yield and verify if the relationship is approximately linear (Perers 1993).

[B.2] Measurement data selection

After pre-processing we have validated data. The next step is to select specific intervals to be used in the subsequent parameter estimation procedure. For example, data when there is no volume flow in the collector array might be excluded. If there is a lot of data available, it can be necessary to cluster the data and reduce it to

'characteristic days' with typical operational and ambient conditions to obtain a representative sample.

[B.3] Test data assessment

The test data needs to meet certain criteria, and these have to be checked before applying the parameter estimation procedure. Crucial is a sufficient variation, especially of the irradiance and the return temperature, as well as a limited correlation of the explanatory variables (e.g. test data with low irradiance values and low and high temperatures as well as high irradiance values and low and high temperatures).

[C] Model input data

The test data is then transformed to the explanatory variables and the dependent variable of a general collector array model, which yields the same core parameters for all arrays. The explanatory variables include for example (i) the beam irradiance on the tilted collectors calculated from the DNI measurement, the position of the sun and the collector orientations and (ii) the primary volume flow, derived from the return and flow temperatures and fluid properties of the primary side and the power output measurement of the secondary side. This allows some flexibility regarding the measurement setup. Oftentimes, the model input data are exactly the same as the test data. As long as the transformation from the test data to the model input data does not depend on the estimated parameters itself, the transformed variables can be treated like measured values, but with additional modeling and measurement uncertainties.

[D] Parameter identification

The next step is the parameter identification which yields the collector array parameters (heat losses coefficients, incidence angle modifier, etc.). As the collector array model is based on differential equations, a dynamic parameter estimation procedure is needed. For each set of parameters, a time series for the predicted output values is calculated and the parameters are chosen in such a way, that the mean prediction error (predicted output values minus measured output values) is minimized.

[E] Test report

The final step is the documentation of the results in a test report. The documentation contains the obtained parameters, their significance, uncertainties, etc. and descriptions of the plant representation, measurement data, data selection, etc.

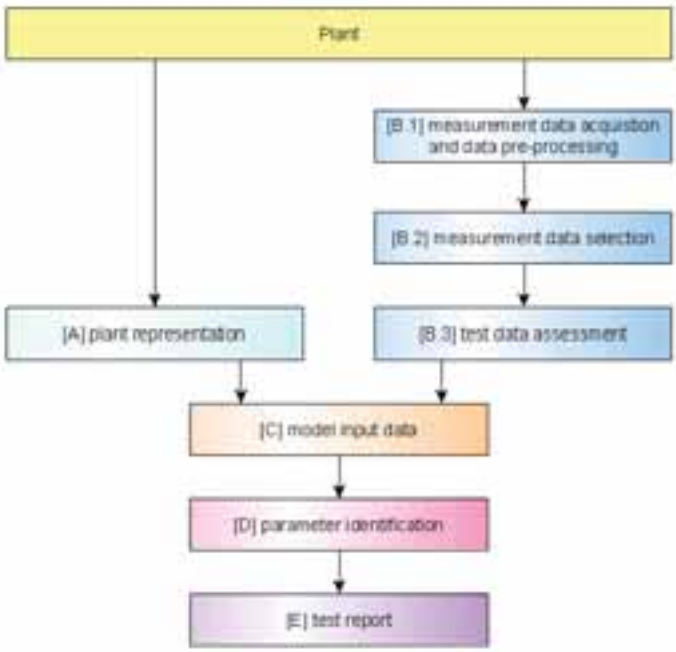

Fig. 1: Flowchart of the in-situ collector array test

3. High-precision measurement of a SDH plant

A cornerstone to develop the in-situ collector array test is the availability of high-precision measurement data of large solar thermal plants. To this aim, a large solar thermal plant in Graz (Austria), depicted in Fig. 2, was equipped with high-precision measurement equipment (i.e. high-precision irradiance, temperature and volume sensors as specified below). In this plant, six collector arrays with high-efficiency flat plate collectors of five different producers are measured (total gross collector area: 2,150 m^2). Fig. 3 shows the positions of the volume flow and temperature measurements. Each array has a separate volume flow sensor (electromagnetic flow sensor *KROHNE OPTIFLUX 4000*). The inlet and outlet temperature of each array and the flow temperatures for each row are measured. For one specific row, additional measurements of the inlet and outlet temperatures of single collectors are put in place. All temperatures are measured directly in the fluid with PT100 sensors of tolerance class DIN EN 60751, F 0.1. Total irradiance in the collector plane is captured by a pyranometer (*Kipp & Zonen SMP 21*). For the measurement of beam irradiance, a pyrheliometer with an active solar tracking system device is used (*Kipp & Zonen SHP 1*). Wind speed and ambient temperatures are measured in three different spots. The sampling rate is one second. The aim of the measurement instrumentation is to achieve precisions comparable to outdoor measurements of accredited collector test laboratories. The setup allows a direct side-by-side comparison of the different collector types. Data are available since August 2016.

Fig. 2: High-precision measurement of a large solar thermal plant in Graz (Austria)

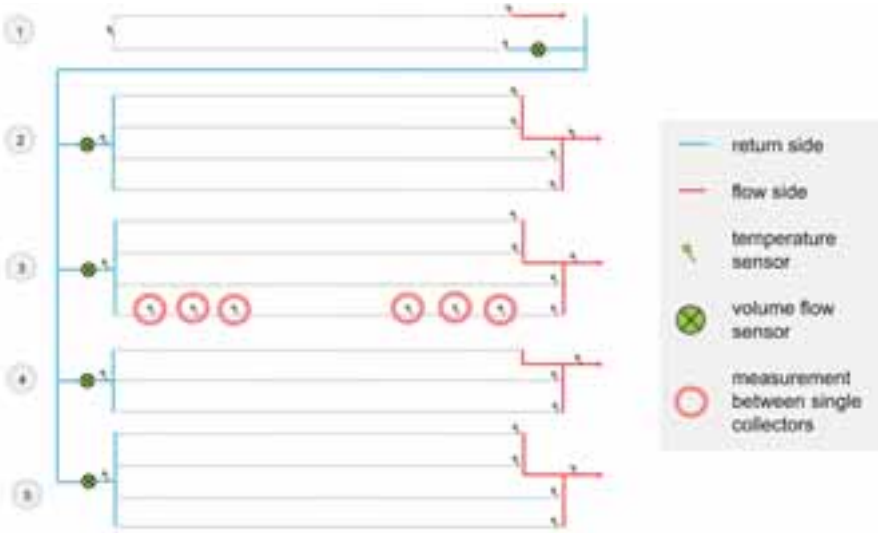

Fig. 3: Measurement setup of the volume flow and temperature sensors

4. Major challenges of in-situ collector array testing

General requirements of technical test procedures are the validity, reliability and accuracy of the procedure. The main challenges to achieve this are listed below.

4.1 Correct determination of the beam and diffuse irradiance on the collector plane

Problem description

The beam and diffuse irradiance on the collector plane are the most important influencing factors of the thermal power output of the collector array. Three main issues are relevant here:

- **Internal shading** due to collectors placed in front
- **External shading** due to surrounding objects (buildings, trees, etc.)
- **Unequal distribution of beam and diffuse irradiance and non-representative sensor readings.** Typically, not all parts the collector array receive the same amount of beam and diffuse irradiance. The front row is not exposed to internal shading and external shading depends on the position in the array relative to the sun and the surrounding objects. Different sky view factors between the collectors and along the collector height of single collectors, different albedo values of the ground, etc. lead to a varying diffuse irradiance. This makes a representative measurement of the irradiance on a single 'reference position' difficult. The irradiance recorded by the radiation sensors and the irradiance the collectors are exposed to might diverge to a point where the sensors are shaded and the rest of the field is not or vice versa.

These issues have been analyzed using data of the SDH test plant described in chapter 3. Fig. 4 shows two images of the 3D model of the plant, taken in the morning and afternoon for a sample day. At 8.43h (left), external shading can be spotted, at 16.30h (right) internal shading can be seen. Furthermore, the pyranometer positioned in the middle of the array, is shaded by an external object, whereas most collectors are not.

Fig. 4: Irradiance analysis of the test plant (2017-09-27)

Implications for in-situ collector array testing

When internal and external shading is not accounted for and the sensor readings differ from the irradiance the collectors are exposed to, the assessment of the collector array performance is not adequate because the energy input to the system is not calculated correctly. Usually the irradiance is overestimated, as the pyranometer which measures the total tilted irradiance is placed above the collectors where it is less exposed to shading and has a larger sky view factor than the lower parts of the collector. If a collector has an optical efficiency of $\eta_0 = 0.8$ and the irradiance on the collector at normal incidence is overestimated by 10% (e.g. 880 W/m^2 instead of 800 W/m^2), then the calculated optical efficiency is mistakenly assumed to be $\eta_0 = 0.73$, which makes a huge difference.

4.2 Collector array dynamics

Problem description

Large collector arrays show a highly dynamic behavior due to abrupt changes of the irradiance, return temperature and volume flow (variable speed pumps are the standard in large scale applications). For in-situ testing, there is only a limited possibility to impose stationary conditions due to technical and economic constraints. The dynamic behavior places an import role in the overall collector array assessment.

For large collector arrays, the dwelling time of the fluid in the collector array (i.e. the time that elapses between the entrance of a fluid element volume in the collector array and its exit) is determined by the volume flow rate. It is often in the range of 2 to 3 minutes and can reach up to 10 minutes. The dwelling time influences the dynamic behavior to a large extend, the time constant and the heat capacity will vary accordingly.

In Fig. 5, the issues regarding the dynamics are exemplified by analyzing the response of the outlet temperature when swift changes of the irradiance, return temperature and volume flow rate occur. Depicted are five arrays of the test plant. After the volume flow rate decreases (1), the outlet temperature rises steadily over the course of ten minutes (2) and starts decreasing again after the volume flow rate is put back to the initial level (3). A swift increase of the return temperature (4) leads to lower outlet temperatures. The two effects interfere (5).

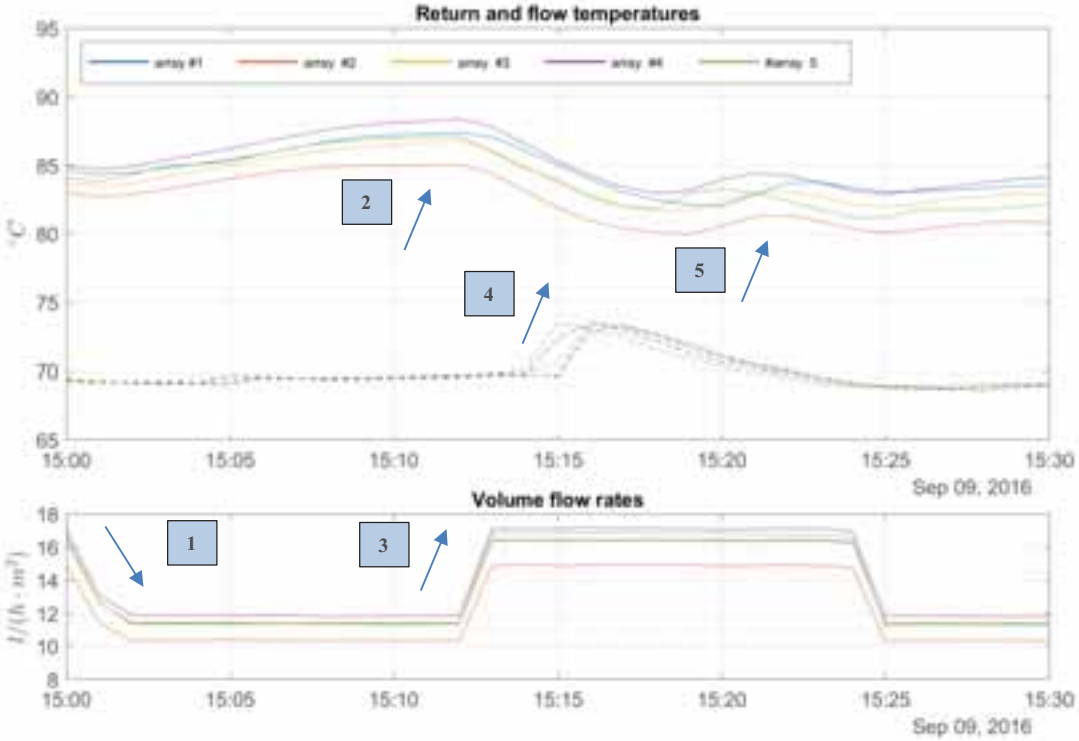

Fig. 5: Delayed response of the collector array outlet temperature (2, 5), when swift changes of the volume flow rate (1, 3) and return temperature (4) occur. Depicted are five arrays of the test plant.

Implications for in-situ collector array testing

If the modeling of the collector array outlet temperature does not take the delay that the dwelling time causes into account, then changes of the irradiance, return temperature and volume flow rate are mistakenly assumed to have an immediate effect. This leads to an inaccurate prediction of the short-term thermal power output and wrong estimates for the time constant and heat capacity values.

4.3 Availability of measurement data

Problem description

The challenges regarding the available measurement data are the following:

- **Limited operating range**. Most large scale installations feed into a district heating network. The most common connection is Return/Supply (R/S), which implies that the return and flow temperatures of the solar loop will usually be close to the (stable) grid return and flow temperatures. Data with a low temperature rise between the return and flow side (these conditions are needed to determine the zero loss coefficient) are usually not available.
- **High correlation of total tilted irradiance and the mean collector array minus ambient temperature**, as low irradiance levels lead to lower outlet temperatures and higher irradiance levels lead to higher outlet temperatures.
- **Sensor readings are not representative**. This problem is most prominent for the irradiance measurement as was pointed out before. But the issue also applies to the wind speed or ambient temperature measurements. The wind speed in the collector plane varies a lot across the array and cannot be measured adequately for collector arrays (for single collector testing, ISO 9806 requires to measure the wind speed on four edges of the collector).
- **Accuracy and precision of commercial measurement equipment.** Commercial installations often use low-cost sensors (especially for the irradiance measurements) and sensors might not be installed correctly (e.g. temperature sensors with too low penetration depth).
- **Missing measurement points.** Some inputs might not be directly measured, it can be needed to calculate them (e.g. the primary volume flow, derived from the return temperature, flow temperature and fluid properties of the primary side and the thermal power measurement of the secondary side). This can lead to additional uncertainties.

In Fig. 6, a bi-variate histogram of the total irradiance on the collector plane and the collector array mean minus ambient temperature of one-year data of one subfield of the test plant is shown. This distribution is typical for SDH plants. Most of the data lies in a close range and the irradiance and temperature are positively correlated.

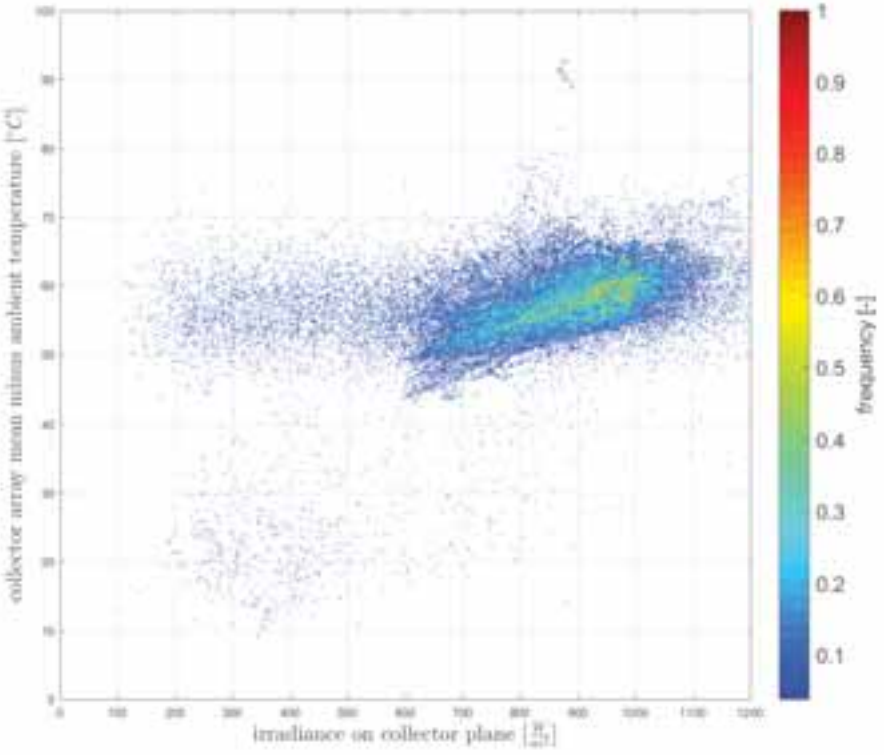

Fig. 6: Bi-variate histogram of the total irradiance on the collector plane and the collector array mean minus ambient temperature

Implications for in-situ collector array testing

A limited operating range and a high correlation of the irradiance and the collector array temperatures can lead to unstable parameters and overfitting. Optical parameters (zero loss efficiency, incidence angle modifier) and heat loss coefficients cannot be distinguished properly. Sensor readings that are not representative and low measurement data quality can lead to a bias.

4.4 Conflict of interest regarding the goals of the procedure

Problem description

For in-situ collector array testing, the following trade-offs need to be addressed:

- **Precision vs. easy applicability**. A detailed modeling of the collector array and strong restrictions regarding measurement data (sensor precisions, data range, data variation, etc.) lead to a more precise characterization of the collector array, but hinder an easy applicability. For example, a detailed modeling of the temperature and flow distribution increases the exactness, but requires a big effort and detailed analysis.
- **Comparability vs. broad applicability**. Different flat plate collector types, collector tilts and orientations, hydraulic layouts, flow conditions in the absorber pipes, varying levels of soiling, etc. might compromise the comparability. At the same time, the test procedure needs to be flexible regarding different plant configurations.
- **Choice of system boundaries**. The choice of system boundaries depends foremost on the available measurement points, but also encompasses choices regarding the attribution of losses. For example, if the heat exchanger losses are not attributed to the collector array, systems with no heat exchanger and active anti-freezing protection might have a disadvantage.

Implications for in-situ collector array testing

The advantages and disadvantages need to be balanced. The general approach of the developed in-situ collector array test is to lean towards easy and broad applicability rather than exactness.

5. Framework for in-situ collector array testing

A framework to address these challenges is covered in this chapter. The major building blocks are:

- **Collector rows as basic modeling blocks**. The core entity when modeling the primary side of large collector arrays is one collector row. A collector row has a well-defined volume flow and inlet and outlet temperature. These variables can be measured at the system boundaries or inferred if they are not given directly. The temperature rise between the cold and hot side of a collector row is usually sufficiently large, such that the thermal power output can be determined with reasonable accuracy. A collector row has also a well-defined (mean) dwelling time. Furthermore, a collector row can in most cases be treated as homogenous regarding tilt, azimuth and irradiance (the internal shading of the collectors is usually similar for all collectors of one row). Irradiance measurements in the collector plane in one spot of the row have in most cases the same (potential) bias for all collectors. A collector row behaves similar to a large collector and can (for the most part) be described with collector parameters. However, changes in the flow regime (laminar/turbulent) need to be carefully evaluated.
- **Finite volume collector array model**. A reasonable simplification to model a single collector row is a finite volume model which treats the collector row as a pipe with one-dimensional heat transfer in the flow direction. The predicted variable of the model is the collector row outlet temperature. By applying an energy input/output balance to a fluid element volume one obtains a hyperbolic differential equation for the fluid temperature. The fluid temperature $T_f(z,t)$ at position z and time t can be modeled as follows

$$\frac{\partial T_f(z,t)}{\partial t} = -\frac{V(t)}{A_f} \cdot \frac{V_{col}}{A_{col}} \cdot \rho_f \cdot c_f \cdot \frac{1}{(mc)_{sp}} \cdot \frac{\partial T_f(z,t)}{\partial z} + \frac{1}{(mc)_{sp}} \cdot \alpha(R(t)) - \frac{1}{(mc)_{sp}} \cdot \gamma(T_f(z,t) - T_a(t))$$

where $V(t)$ is the volume flow, A_f is the pipe cross section area, V_{col} is the total fluid content of the row, A_{col} is the total collector area, $(mc)_{sp}$ is the specific heat capacity, $\alpha(t)$ is an absorption function for the beam

and diffuse irradiance $R(t)$, γ is a heat loss function (usually a second order polynomial) and $T_a(t)$ is the ambient temperature. This modeling approach is widely used (see e.g. Lemos, Neves-Silva, and Igreja (2014))

If there is no significant maldistribution of the volume flow across the array, then the effect on the thermal performance will be marginal, and a whole collector array can be modeled as a single row (and a single row as a pipe). Modeling the collector array as a single pipe or multiple pipes with one-dimensional heat transfer in the flow direction is a reasonable balance between precision and easy applicability as well as comparability and broad applicability.

- **Irradiance modeling**. For a correct determination of the beam and diffuse irradiance on the collector plane an irradiance model of the plant is necessary, which is able to calculate the irradiance distribution on the collector array (beam and diffuse) based on the sensor readings (total tilted irradiance and beam DNI irradiance). Many tools and algorithms were developed, they date back to the 1970s (see e.g. Appelbaum and Bany (1979)). However, they need to be adapted to large collector arrays. The simplest approach is to check if there is any internal or external shading and exclude these conditions from the parameter estimation procedure.
- **Design of experiments**. Whenever possible, data of the normal plant operation should suffice for in-situ testing. If the operating range or the variation in the data are so little, that the test procedure cannot be applied, a carefully designed test to obtain more data can be conducted. For most plants, the return temperature can be lifted (diminishing the load or mixing return and flow side). This variation has to be done for different irradiance levels to gain uncorrelated measurements of the irradiance and collector array temperatures. Additionally, periods with low temperatures at the heating up or cooling down operation phase of the plant can be used.
- **Reducing modeling complexity**. To reduce the modeling complexity, basic checks can be performed to make sure that minor influencing factor on the thermal performance remain within acceptable ranges. For example, instead of modeling the volume flow distribution, one can check if the flow distribution is roughly balanced by evaluating the outlet temperatures of the collector rows.
- **Statistical data evaluation, modeling of uncertainty**. To deal with commercial measurement equipment and missing measurement points, the explanatory variables and the dependent variable need to be modeled stochastically and the measurement and modeling uncertainties need to be taken into account.

6. Conclusion and Outlook

The major challenges for in-situ testing of large collector arrays were identified and a framework to address them was developed. The next step is to elaborate the in-situ test procedure based on this framework, implement it in a software environment, apply it to the test plant and validate it.

References

Almeida, P., M.J. Carvalho, R. Amorim, J.F. Mendes, and V. Lopes. 2014. “Dynamic Testing of Systems – Use of TRNSYS as an Approach for Parameter Identification.” *Solar Energy* 104 (6): 60–70

Appelbaum, J., and J. Bany. 1979. “Shadow Effect of Adjacent Solar Collectors in Large Scale Systems.” *Solar Energy* 23 (6): 497–507

Bosanac, M., and J. E. Nielsen. 1997. “In Situ Check of Collector Array Performance.” *Solar Energy* 59 (4–6): 135–42

ESTIF. 2015. “Solar Thermal Markets in Europe. Trends and Market Statistics 2014.” ESTIF, Brussels

Lemos, Joao M., Rui Neves-Silva, and Jose M. Igreja. 2014. *Adaptive Control of Solar Energy Collector Systems*. Advances in Industrial Control. Cham: Springer International Publishing

Perers, B. 1993. “Dynamic Method for Solar Collector Array Testing and Evaluation with Standard Database and Simulation Programs.” *Solar Energy* 50 (6): 517–26

Spirkl, Wolfgang, Julius Muschaweck, Peter Kronthaler, Wolfgang Schölkopf, and Justus Spehr. 1997. “In Situ Characterization of Solar Flat Plate Collectors under Intermittent Operation.” *Solar Energy* 61 (3): 147–52

Werner Weiss, Monika Spörk-Dür, and Franz Mauthner. 2017. “Solar Heat Worldwide - Global Market Development and Trends in 2016, Detailed Market Figures 2015 - 2017.” Gleisdorf: AEE - Institute for Sustainable Technologies

Acknowledgement

The research project “MeQuSo” is supported by the Austrian Climate and Energy Fund and carried out as part of the Energy Research Programe (FFG 848 766). The results will be contributed to IEA SHC Task 55 ‘Towards the Integration of Large SHC Systems into District Heating and Cooling (DHC) Networks’.

Urban and Regional Planning to Maximize Renewable Energy

Innovative and sustainable Energy Supply Concepts for a new quarter in Mannheim, Germany

Dominik Bestenlehner, Harald Drück

Research and Testing Centre for Thermal Solar Systems (TZS)
Institute for Thermodynamics and Thermal Engineering (ITW)
University of Stuttgart, Pfaffenwaldring 6, 70550 Stuttgart, Germany

Abstract

The former military area "Benjamin Franklin" in Mannheim, Germany, is converted in a completely new urban area with the aim of providing a high living standard and an innovative energy supply. The actual proposed energy supply concept for the sub quarter "Sullivan" was assessed. Two alternative concepts focusing on renewable energy sources have been developed. For this, some approaches from [1], [2], [3] have been applied and further extended. The developed concepts have been compared to the actual one, related to primary energy demand and economics.

Keywords: energy concepts, quarters, urban area, district heating, solar thermal, photovoltaic, heat pump

1. Introduction

Mannheim is a city in the Rhine-valley in Germany approx. 100 km South from Frankfurt with around 300,000 inhabitants. After the withdrawal of the American Army, the military area "Benjamin Franklin Village" was handed over to the city of Mannheim. Such a large area with around 1.4 million square meters almost in the city centre offers wide possibilities for further urban development. Strategic, future-oriented urban development implies not only architecture but also innovative energy supply. A similar realized and detailed evaluated project can be found in [3]

Not only due to the European and German goals of CO_2-emission reduction, the city of Mannheim decided to request a sustainable and renewable energy supply concept for the "Benjamin Franklin Village". Further drivers for this innovative supply concept are the aim of creating attractive living areas and not least economic reasons. Besides several architectonical requirements the city of Mannheim demands a primary energy factor of fp = 0.55 for the heat supply for the buildings.

The area "Benjamin Franklin Village" is subdivided into five smaller urban areas with different focal activities such as living (Franklin center, Sullivan, area of Officers cantonment), services sector (Funari Barracks), and trade and commerce (Columbus area). Additionally the current development status varies depending on the remaining tasks to prepare the land for building. Since the pre-preparation of parts of the area is finished but the planning phase is not yet finalized, the authors decided to investigate several energy supply concepts for the living sub quarter "Sullivan" in detail, Fig 1.

As a result of an ideas competition, the city of Mannheim decided to award the local energy provider's concept for supply energy to the sub quarter "Sullivan". The core components of the concept are the already available district heating grid of Mannheim with a primary energy factor $f_p = 0.65$, which is able to provide additionally the heat for Sullivan, and a combination of an air to water heat pump and a photovoltaic (PV) system to reduce the primary energy factor. In this present concept, neither an adaptive control, nor a prognoses tool related to demand and weather is implemented. Therefore, the authors decided to assess the proposed energy concept in detail and to develop alternative concepts with the focus on a higher level of sustainability and innovation combined with an improved economic feasibility.

doi:10.18086/swc.2017.37.01 Available at http://proceedings.ises.org

Fig. 1: Bird's view of the Benjamin franklin Village in Mannheim, Germany, incl. the subdivision into the five quarters, source: www.mz.de, modified by the author

In the following, the awarded concept is presented and further used as the reference concept for the three developed alternative concepts. The comparison between the in total four concepts comprises as key aspects the primary energy demand, CO_2 emissions and the economics.

2. Reference concept

The awarded concept of the local energy supplier uses as basis heat source the already existing district heating grid (primary district heating grid). This heating grid is located directly outside of the quarter "Sullivan" and can be extended by a secondary heating grid for providing heat into "Sullivan". Additionally, an air-to-water heat pump feeds heat into the grid. Since the temperature level of the heating grid is 70 °C, a special, double stage, high temperature heat pump will be installed. To reach the required primary energy factor for the heat supply in the urban sub quarter Sullivan, ca. 1 500 m² PV modules (250 kW_p) shall be installed. The provided electricity is used to operate the compressor of the heat pump. Fig 2 shows the scheme for this concept.

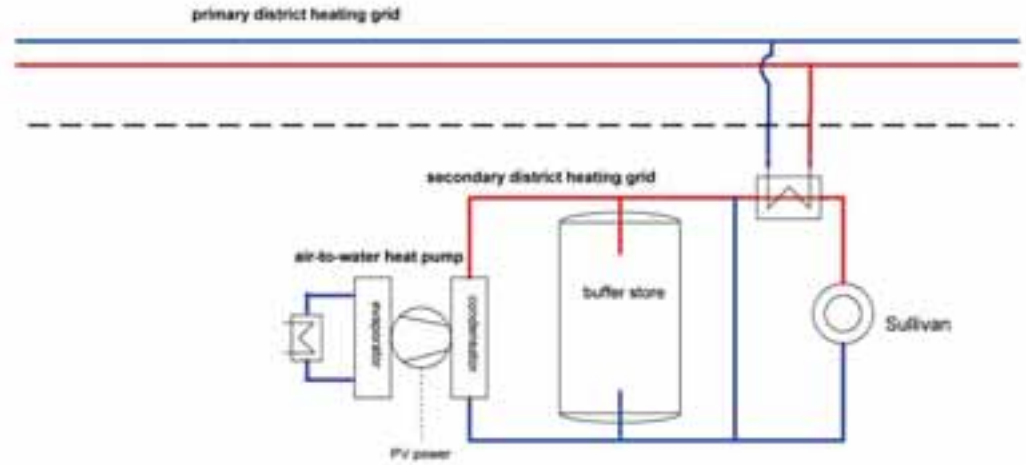

Fig. 2: Scheme of the reference concept comprising heating grid, air-to-water heat pump and PV

Detailed simulation studies show that the primary district heating grid feeds the entire year heat into the secondary

heating grid. The air-to-water heat pump provides only a small share of the energy. During summer, the available PV power and the ambient air temperatures are much higher than in winter when the maximum heat load occurs. Therefore, the energy share delivered by the heat pump is significant higher than during winter times. The total energy delivered by the heat pump is 980 MWh/a with a seasonal performance factor of 3.0. This represents 15 % of the total energy demand of the urban area. Even during the summer months, the heat pump covers less than 50 % of the heat demand. The amount of energy provided by the heat pump balances exactly with the amount of energy required to reduce the primary energy factor of the entire system from 0.65 (primary district heating grid) to 0.55. Since all further developed concepts compete with this conventional concept, it is defined as "reference concept".

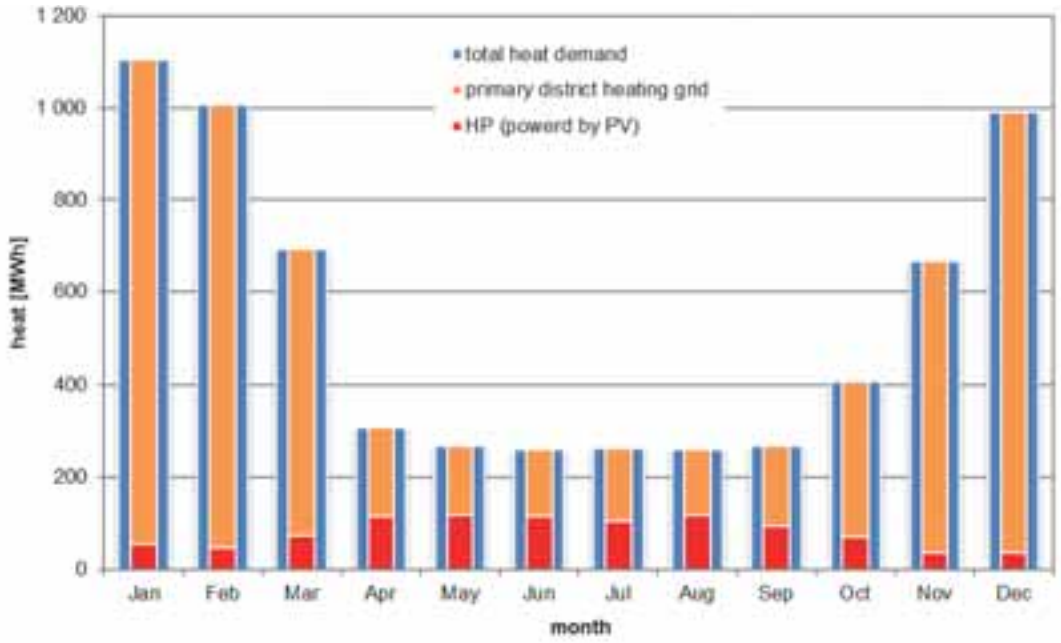

Fig. 3: Energy balance of the reference concept

3. Alternative concepts

For additionally reducing the primary energy factor of the heat supply of the quartier Sullivan, alternative innovative concepts are required. Since the energy provided by the sun has a primary energy factor of 0.0 by definition, the concepts shall aim for a high solar thermal fraction. A seasonal thermal energy store (STES) offers the possibility to increase further the solar thermal fraction. An integration of PV into the further investigated alternative concepts was not taken into account due to the missing concurrency between generated PV-power and heat demand. Only on a yearly bases, the energy balance of such combinations might be balanced. Furthermore also under exergetic aspects it is considered as much more appropriate rather to use PV-power directly to substitute conventional produced electricity than converting it into heat.

The following chapters present three alternative concepts with different characteristics. These concepts have been compared to the reference concept related to economics, CO_2 emissions, primary factor and solar fraction.

Concept 1: Solar district heating grid with short term thermal energy store

The first alternative concept for providing the required heat to "Sullivan" is also based on a district heating grid. But in contrast to the reference concept it is partly fed by solar thermal energy. The primary district heating grid of the city of Mannheim provides only the energy demand, which solar thermal cannot cover. The concept comprises 5,000 m² solar thermal flat plate collectors, and a 400 m³ hot water buffer store. To avoid stagnation during times without sufficient heat demand, the solar thermal collector field feeds into the return flow of the primary district heating grid. Fig. 4 shows the scheme with the separation between primary and secondary district heating grid and the hydraulics.

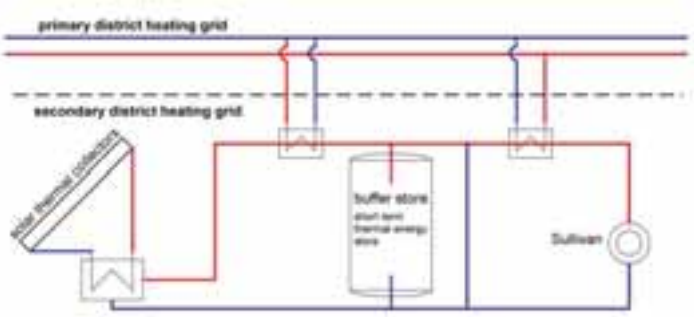

Fig. 4: Scheme of the first concept based on solar district heating grid and a short term thermal energy store

Fig. 5 shows the energy balance on a monthly basis. During summer time, the energy gains from the solar collector field covers entirely the heat demand of the quarter. The heat provide into the return flow of the primary district heating grid to avoid stagnation is not diagrammed. Due to the relatively high inclination angle of 45° of the solar thermal collector field, this heat can be neglected. No seasonal thermal energy storage is included. This approach leads to a relatively high annual solar fraction of 34 % with lowest system and investment effort.

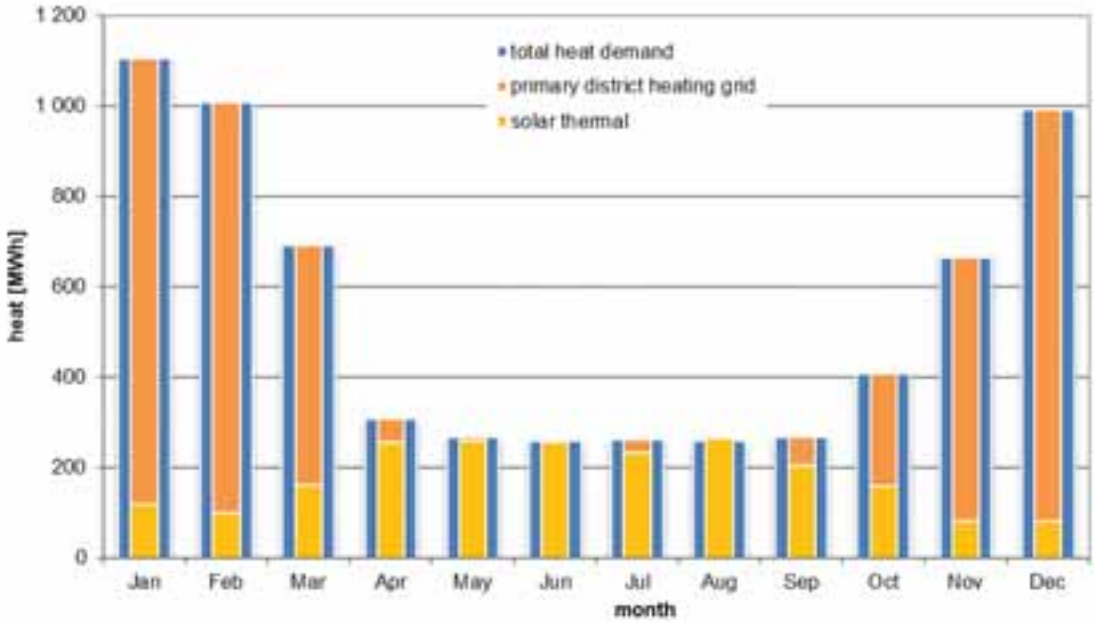

Fig. 5: Monthly energy balance of concept 1, comprising solar district heating grid and a short term thermal energy store

Concept 2: Solar district heating grid with seasonal thermal energy store and compression heat pump

The second concept aims for a solar fraction of 50 % and a separated district heating grid. No heat exchange between the primary and the secondary heating grid takes place. To reach a solar fraction of 50 %, a solar thermal collector field of 7 600 m² is required, which is about 50 % larger than in concept 1. A seasonal thermal energy store with a volume of 7 200 m³ stores the additional heat from the solar collector field, Due to this large store, the volume of the short term buffer store is reduced by half, compared to concept 1, to 200 m³. A heat pump (HP) decreases the temperature in the seasonal thermal energy store and therefore increases the effective usable storage capacity. Additionally, the efficiency of the solar thermal collectors increase with decreasing operation temperature. The heat pump only operates in winter times and decreases the temperature in the seasonal thermal energy store down to 18 °C. A further temperature decrease in the seasonal thermal energy store is not efficient any more. Due to available groundwater at a temperature level of 18 °C, the heat source of the heat pump is changed at 18 °C from the seasonal thermal energy store to the groundwater. The heat pump has a nominal electrical power of 400 kW, the highest monthly thermal power occurs in February with 1.27 MW. The buffer

store covers the peak power demands that rises up to 2.8 MW_{th}. Therefore, no auxiliary heating system additionally to the heat pump is required. Fig. 6 shows the hydraulics of this concept.

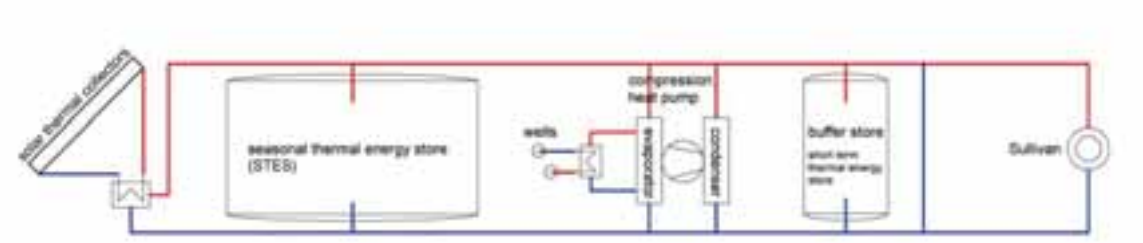

Fig. 6: Scheme of the second concept based on a solar district heating grid, a seasonal thermal energy store and compression heat pump

Fig. 7 shows the monthly energy balance of concept 2. The solar thermal collector charges during the months April to September the seasonal thermal energy store. During October and November, this heat is discharged and supplied directly into the district heating grid (light blue). Eventually in November, the temperature level of the heat discharged from the seasonal thermal energy store is not sufficient any more. With the help of the heat pump, the seasonal thermal energy store is discharged further and delivers into the grid (green). After reaching a temperature level of 18 °C in the seasonal thermal energy store, the heat pump uses the available groundwater as heat source and provides the energy demand for the district heating grid (violet) Although, the seasonal thermal energy store feeds only in total 560 MWh/a heat into the grid, its implementation increases the efficiency of the heat pump and the solar thermal collector significantly, [8].

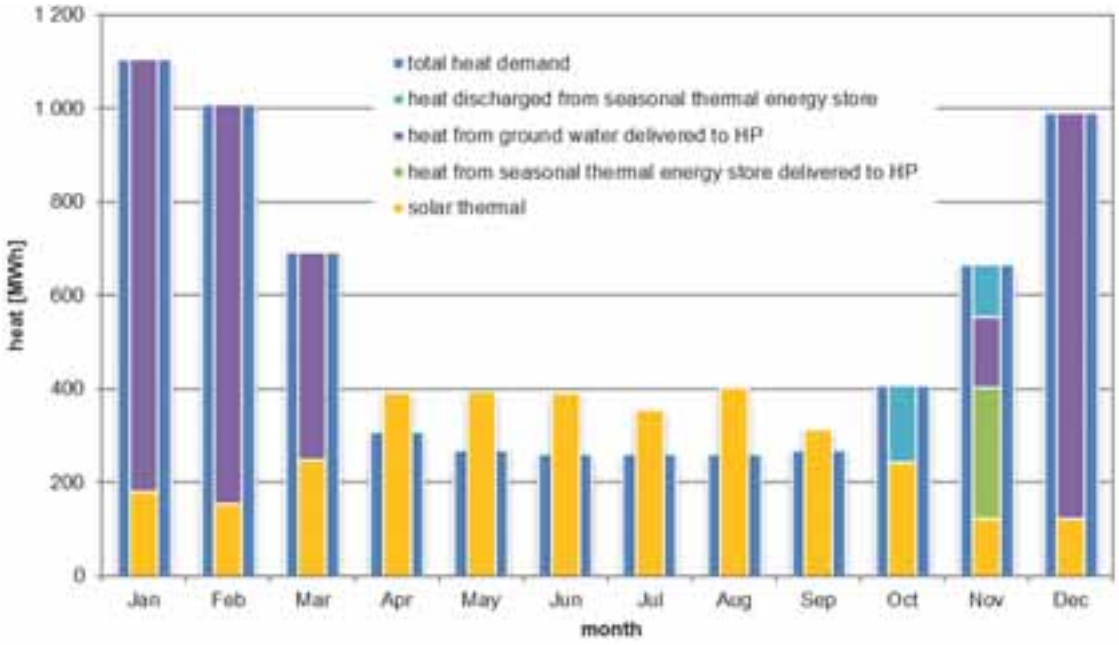

Fig. 7: Monthly energy balance of concept 2, based on a solar district heating grid, a seasonal thermal energy store and a compression heat pump

Concept 3: Solar district heating grid with seasonal thermal energy store and absorption heat pump

The third concept bases on the second concept, but an absorption heat pump replaces the compression heat pump. The collector area with 7,600 m², the size of the seasonal thermal energy store with 7,200 m³ and of the buffer store with 200 m³ stay the same. The difference is the integration of the heat provided by the primary district

heating grid. The primary grid feeds on the on hand directly into the secondary grid and on the other hand indirectly via the generator of the absorption heat pump. The implementation of an absorption heat pump allows for an efficient use of the heat of the primary district heating grid. Simultaneously, the solar thermal collectors and the seasonal thermal energy store operate more efficiently compared to a system without heat pump. The absorption heat pump has a nominal output power of 700 kW. The primary district heating grid covers the additional heat demand directly.

This concept is similar to a solar district heating grid realized in the project "Ackermannbogen" in the city of Munich, Germany. Only the size of the concept here exceeds the system in Munich by a factor of three. Fig. 8 shows the scheme of the concept three.

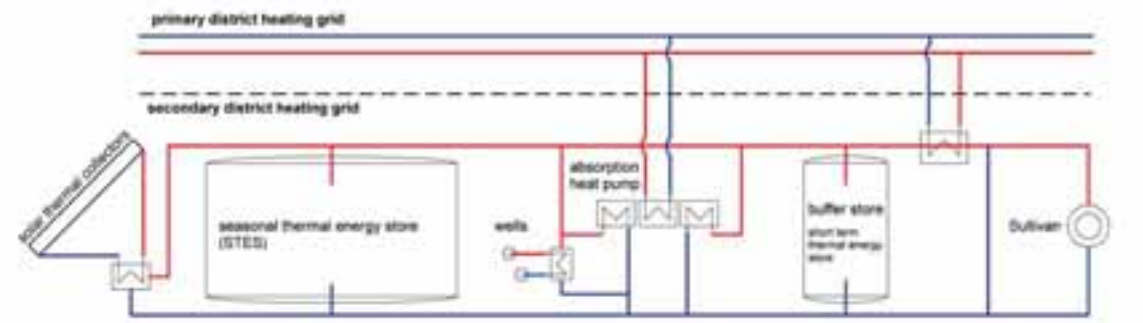

Fig. 8: Scheme of the third concept based on a solar district heating grid and the already available district heating grid, a seasonal thermal energy store and an absorption heat pump

The solar collector field charges the seasonal thermal energy store during summer. The absorption heat pump uses the seasonal thermal energy store and the groundwater as heat source. Additionally in the core winter months December, January, February the primary district heating grid provides the remaining heat demand, as the absorption heat pump cannot cover the total demand due to its limited size.

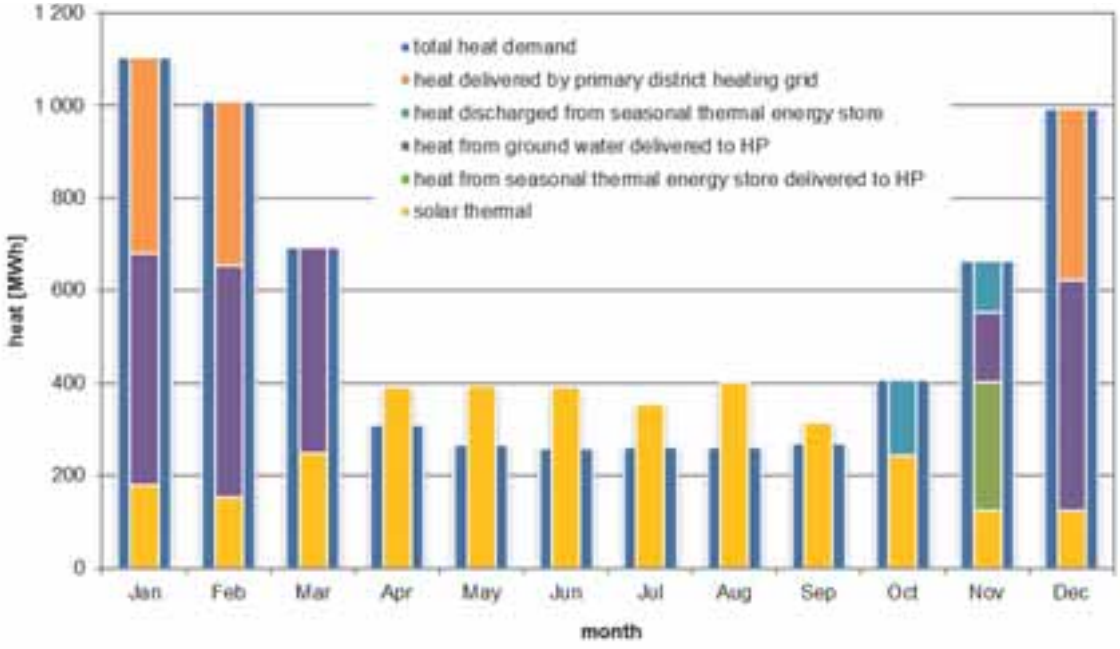

Fig. 9: Monthly energy balance concept 3, based on a solar district heating grid and the already available district heating grid, a seasonal thermal energy store and a absorption heat pump

4. Evaluation of concepts

The evaluation of the reference concepts and the three developed alternative concepts bases on four performance figures:

- Primary energy factor
- CO_2 emission in kg per MWh heat
- Solar fraction
- Specific costs in € per MWh heat

The primary energy factor fp [-] serves in several standards and directives in the building sector as performance figure. The primary energy factor puts all efforts and losses, occurring during generating, treatment, storage, transportation and distribution, into relation to the delivered usable energy. In contrast to the cumulative energy demand, the primary energy factor only takes into account the energy carrier. Hence it omits the required raw materials, semi-finished products and services, such as a power plant. Table 1 shows the primary energy factor used for the evaluations.

Tab 1: Primary energy factor for different energy carriers

Energy carrier	Primary energy factor	source
Solar thermal	0	EnEV [11]
Photovoltaic	0	EnEV [11]
District heating, Mannheim	0.65	certificate power plant, city of Mannheim
Electricity mix, Germany	1.8	EnEV [11]

Since the primary energy factor only indicates one aspect of the environmental stress, the **CO_2 emissions** are introduced as a further evaluation criteria. The CO_2 emissions [kg/MWh] represents the amount of climate-damaging CO_2 equivalents emitted per MWh final energy. The used data represent not only the energy carrier, but also the production, use and disposal of the energy conversion systems. Bases of the calculation is the database GEMIS, Version 4.93, see table 2 [12]

Tab 2: CO_2 emissions of different energy carrier

Energy carrier	equivalent CO_2 emissions [kg/MWh]
Solar thermal, flat plate collector	13
Photovoltaic, multi crystalline	62
District heating mix, Mannheim	295
Electricity mix, Germany	617

The **solar fraction** [-] is the ratio between the useful, solar generated heat supplied to the system and the total heat demand. The solar fraction is a common and wide spread performance figure to classify and compare solar thermal systems.

The **specific heat costs** [€/MWh] is the ratio between the annual total costs and the generated heat based on VDI 2067 [13]. The solar heat costs enable an economic comparison between different concepts and technologies.

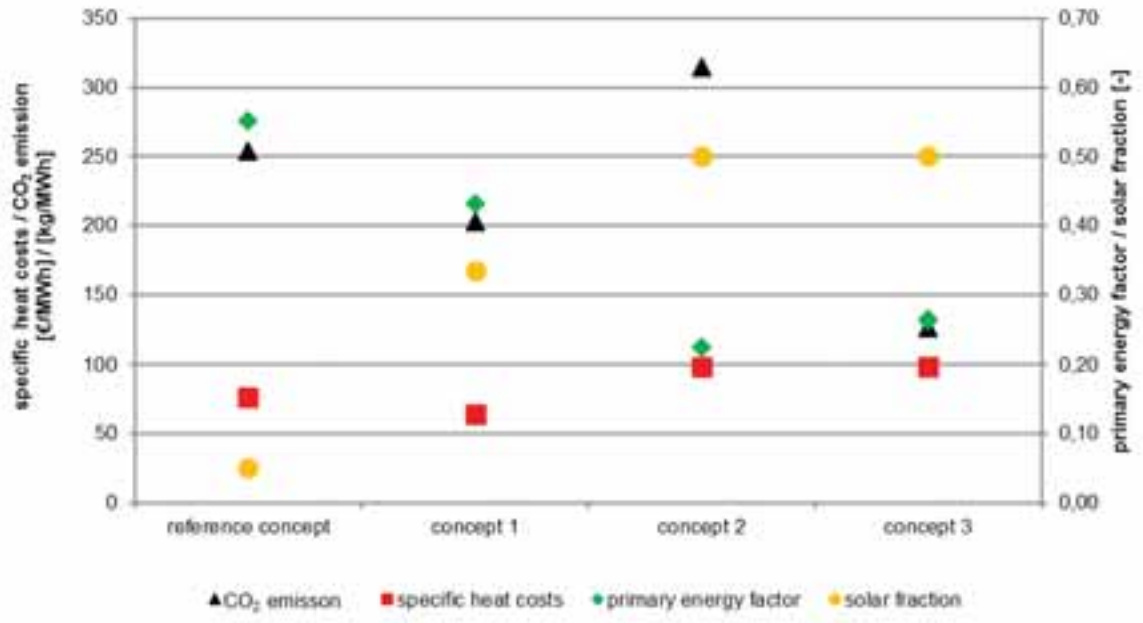

Fig 10: Comparison of the performance figures of the different concepts

Fig. 10 shows the comparison between the reference concept and the three alternative concepts. Concept one has the lowest specific cost, even lower than the reference concept. The primary energy factor of all three alternative concepts are lower than the one of the reference concept. Related to the CO_2 emissions concept one and three have lower emissions than the reference concepts, although concept two has the highest CO_2 emissions. This is due to the high share of heat generated by the compression heat pump and therefore the high electricity demand. If an additional installation of a PV system is considered (as it is within the reference system), the CO_2 emissions would be reduced significantly.

5. Conclusions

The evaluations of the three alternative concepts show a significant potential for improvements related to the primary energy demand and the solar fraction. Further, concept one and three have reduced CO_2 emissions compared to the reference concept. Only concept two has higher CO_2 emissions due to the implementation of a compression heat pump. Even for systems with 50 % solar fraction the specific heat costs are in the same range of the reference concept.

6. Acknowledgement

The activities described in this publication are funded by the Ministry of Science, Research and Arts of the federal State of Baden-Wuerttemberg and the European Regional Development Fund (EFRE). Support code: FEIH_ZAFH_562822 within the project ENsource. The authors gratefully acknowledge this support and carry the full responsibility for the content of this publication.

7. References

[1] Stübler, A., Bestenlehner, D., Drück, H., Demonstrationsvorhaben Stadtquartier Jenfelder Au – Kopplung von regenerativer Energiegewinnung mit innovativer Stadtentwässerung, Forschungsbericht zum BMBF-Vorhaben 033L047D (November 2011 bis Februar 2015), Stuttgart, 2015.

[2] Andrea Stübler, Dominik Bestenlehner, Harald Drück, Energy saving potentials of cold district heating networks, Proceedings of 17th EWA International Symposium, WATEnergyResources – Water, Energy and Resources: Innovative Options and Sustainable Solutions" held during IFAT 2014, Munich, Germany, 5-9 May 2014, Published and distributed by: European Water Associations (EWA), 53773 Hennef, Germany, info@ewa-online.eu, www.EWA-online.eu

[3] Jan Sievers, Jörg Londong, Andrea Stübler, Dominik Bestenlehner, Harald Drück, Wenke Schönfelder, Heat recovery potential of domestic grey water in the pilot project Jenfelder Au in Hamburg, Proceedings of 17th EWA International Symposium, WATEnergyResources – Water, Energy and Resources: Innovative Options and Sustainable Solutions" IFAT 2014, Munich, Germany, 5-9 May 2014, Published and distributed by: European Water Associations (EWA), 53773 Hennef, Germany, info@ewa-online.eu, www.EWA-online.eu

[4] Gohl, N., Bestenlehner, D., Drück, H.: Extension of Germany's Largest Solar District Heating System with Seasonal Thermal Energy Storage, Proceedings to the ISES Solar World Congress 2017/ International Conference on Solar Heating and Cooling for Buildings and Industry, October 29th to November 2nd, Abu Dhabi, UAE

[5] Bundesministerium der Justiz und für Verbraucherschutz: Verordnung über energiesparenden Wärmeschutz und energiesparende Anlagentechnik bei Gebäuden (Energieeinsparverordnung - EnEV)

[6] Stadt Mannheim: Rahmenplan, Benjamin Franklin Village, Stadt Mannheim, Fachberiech Stadtplanung, Projektgruppe Konversion, Mannheim, 2014

[7] Bauer, D.; Drück, H.; Lang, S.; Marx, R.; Plaz, T.: Weiterentwicklung innovativer Technologien zur solaren Nahwärme und saisonale Wärmespeicherung, Forschungsbericht zum BMWi-Vorhaben 0325998A (Januar 20013 bis September 2015), Stuttgart, 2016.

[8] Marx, R., Bauer, D., Drück, H.: Medium Scale Seasonal Thermal Energy Stores for Solar Thermal Applications within the European Project EINSTEIN, Proceedings of 13th International Conference on Energy Storage, Greenstock, 19.-21.05.2015, Beijing, China

[9] Weiss, W.: Solar Heating Systems for Houses: A Design Handbook for Solar Combisystems. Verlag: Earthscan, Auflage: illustrated edition, ISBN-13: 978-1902916460, 2003.

[10] I.f.E.-u.U.H. GmbH: Klimaschutzkonzeption Mannheim 2020, ifeu-Institut für Energie-und Umweltforschung Heidelberg GmbH, Heidelberg, 2009

[11] Energieeinsparverordnung, ENEV, 2016, German directive, http://www.bmub.bund.de/fileadmin/Daten_BMU/Download_PDF/Energieeffizient_Bauen/energiesparverordnung_lesefassung_bf.pdf, accessed 12/10/2017

[12] Institut Wohnen und Umwelt GmbH (IWU) - institute for housing and environment, „Kummulierter Energieaufwand und CO2 Emissions-faktoren verschiedener Energieträger und -versorgungen", Darmstadt, 2014

[13] VDI 2067-1, Economic efficiency of building installations, VDI Düsseldorf, 2012

Analysis of the match of heating load and wind turbine production – a case study for the Faroe Islands

Hans Georg Beyer, Barður A. Niclasen

Department of Science and Technology, University of the Faroe Islands, Tórshavn (Faroe Islands)

Abstract

In search for options to replace the fossil based heat supply of the housing stock of the Faroe Islands, the application of electrical heating in combination with an increase of wind power penetration in the electricity grid is analyzed. This option is favored by the – as compared to other geographical regions - good seasonal match of the wind generation and the temperature driven heating load at this location. For this case the requirements for oversizing of the wind generation capacity, inclusion of storage and/or use of back-up energy for a save load supply are analyzed.

Keywords: heat supply. wind power, Faroe Islands

1. Introduction

The Faroe Islands - located remotely at 62° North, 7.5° West in the North Atlantic - have a population of ~55 thousand people. Due to the Gulf Stream, the climate is comparatively mild showing an annual mean temperature of about 10°C with only limited deviations in summer and winter. This results in an overall moderate heating load for the housing stock but calls for heating in all month. Currently the heat supply is almost completely based on oil. According to the aim of reducing the dependence on fossil fuels and limiting CO_2 emissions, replacements are needed here. With the - due to the high latitude - limited solar resources in winter but an elevated wind power potential, the use of electrical heat (with the option of using heat pumps) powered by a grid with a high wind power penetration can be considered as option for an alternative heat supply. Additional benefits of linking wind power to heat supply systems are discussed e.g. by Østergaard 2013, Xydis 2015 and Zhang et al. 2015. This paper will give a more detailed assessment of this option by inspecting first the seasonal match of monthly heat demand and monthly energy gain of wind turbines. For the Faroe Islands – showing a favorable seasonal match – details on system performance are analyzed by simulations based on on-site wind and temperature data with 10min time resolution.

As bases for these studies the next section will show a simple approach for modelling the heat requirements of buildings based on temperature information used here for the assessment of the characteristics of both the monthly and short term energy demand. With a similar simplified approach, the characteristics of the monthly energy gain and short term power output of a wind turbine installation are assessed. Heat demand and wind generation are set in relation by scaling the heat demand according to turbine generation, i.e. a selection of an appropriate number of houses to be heated (or heated space area) by a wind installation.

2. Characteristics of the heat demand

For the assessment of the characteristics of the heating load, a simple linear dependence of required heating power to ambient temperature is assumed. Heating is assumed to be necessary when ambient temperature is lower than 18°C, the required power rises linear with the with temperature difference to 18°C. Rated heating power is set to refer to an ambient temperature of -18°C (see. eqn.1). The required monthly or annual energy can be evaluated based on time series information on the ambient temperature and the rated heating power as given by eq. 1. The temperature information can be compressed into the parameter heating degree days (HDD) – basically the (monthly or annual) time integral of the difference of 18°C and the ambient temperature taken for situations with ambient temperatures < 18°C.

doi:10.18086/swc.2017.37.02 Available at http://proceedings.ises.org

$$E = \sum_i \delta * (\ (18°C - T_a(t)) * \frac{1}{36°}\ P_{(-18C)}$$

$$\delta = \begin{cases} 0\ if\ T_a \geq\ 18℃_{\circ\circ} \\ 1\ if\ T_a <\ 18℃ \end{cases} \qquad \text{(eq. 1)}$$

$$E = HDD * \frac{1}{36°} * P_{(-18C)}\ ,$$

HDD: heating degree days [°C days]

A first impression of the temperature conditions can be gained from the monthly mean temperatures. Fig.1 gives these numbers for the site Tórshavn, Faroe Islands. Monthly mean temperatures vary but in the rage of 6-12℃. These data are all taken from the RETScreen data base (Anonymous, 2014).

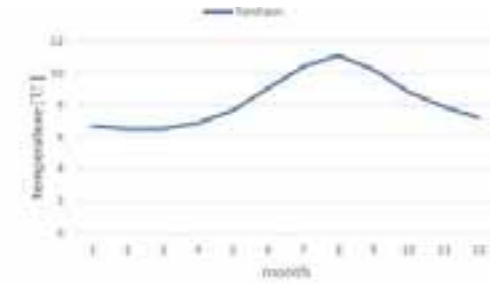

Fig. 1: Mean monthly temperatures for the Town of Tórshavn, Faroe Islands. Data taken from the RETScreen data base].

The respective values of the HDD - as indicator for the heating load as sketched above – for Tórshavn are shown in Fig.2, They are also supplied by the RETscreen data base. For comparison, data for a site in Norway (Ålesund) are given. As compared to Torshavn, that site shows an overall higher heating demand with a well pronounced reduction of needs in summer. For Torshavn there is less variability in the monthly heating requirements. The heating load in summer remains at about half of the heating load in winter.

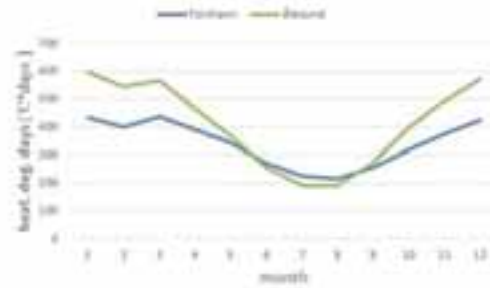

Fig. 2: Monthly heating degree days (HDD for Tórshavn and Ålesund (Norway). Overall, there is less need for heating in Torshavn, but a remaining requirement in summer.

3. Characteristics of wind turbine generation

For the calculation of the monthly turbine generation, based on information of monthly average wind speeds at 10m above ground level (information offered by the RETScreen data base) speeds are scaled up to 50m agl. (a conservative assumption for larger wind turbines) assuming a logarithmic profile for a roughness length of 0.15m. A monthly energy gain is calculated with the assumption of Rayleigh distributed wind speeds, using a power curve for a typical $1MW_{rated}$ turbine.

A first view on the wind resource on the Faroe Islands is given by Fig.3. Shown are the monthly mean wind speeds at 10m agl. as supplied by RETScreen. This indicates good wind conditions with an annual mean wind speed of ~6.5m/s at 10m above ground level in an industrial/harbor environment. The good wind conditions on the Faroe Islands are confirmed by data on the annual performance of a commercial wind farm close to Torshavn (Annonymous 2017).

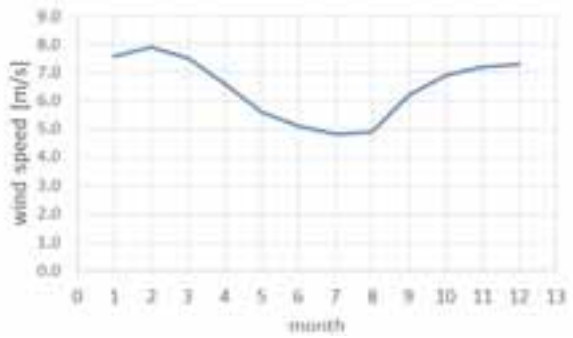

Fig. 3: Monthly means of the wind speed in Tórshavn at 10m above ground level. Data are taken from the RETSrceen data base.

Based on the monthly mean wind speeds scaled up to a hub height of 50m as described above, and assuming a Rayleigh distribution of the of wind speed, the monthly mean power output of a typical 1MW turbine is estimated (see Fig. 4). With the assumption of 0.15m roughness length used for this site, the results are conservative estimates of the energy gain.

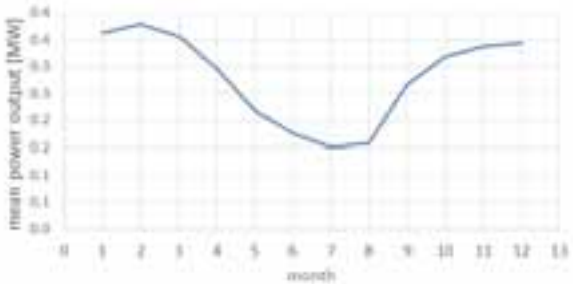

Fig. 4: Estimated monthly mean power output of a 1MWrated turbine at Tórshavn.

4. Linking wind resource and heating load

Comparing the pattern of the monthly heating load as determined the pattern of HDD values and the monthly power generation for Tórshavn, the good match of these sets is obvious (see Fig.5, correlation coefficient of the two sets is 0.87). However, not for all month a wind turbine sized to cover the annual demand would be able to cover each monthly load).

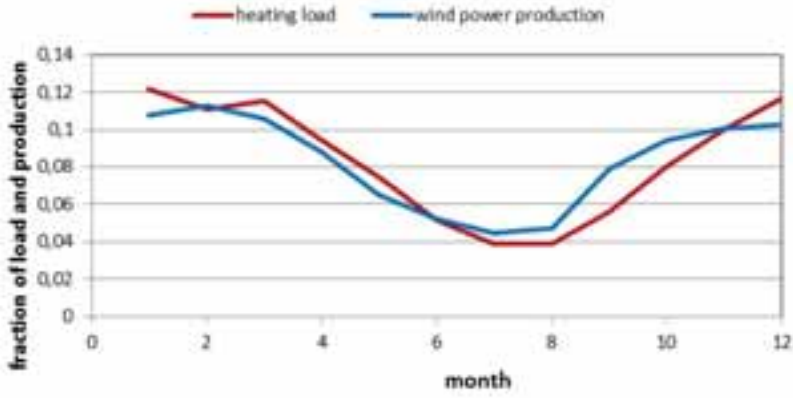

Fig. 5: Estimated normalized monthly energy gain from a wind turbine together with the normalized monthly heating load calculated on basis of the heating degree days (site: Tórshavn). Both production and demand are given as monthly fraction of the annual sum.

This pattern can now be compared to that of other locations. With the scaling of the heating load applied, it should be remarked that the results for each location refer to different relations of heated space to turbine size (the $1MW_{rated}$ system used as standard here), resulting from the specific wind and temperature (HDD) conditions.

The sites scanned here comprise of different locations in Northern and North-Western Europe including the Atlantic isles. Fig 6 gives with the comparison of the load and generation patterns for two locations on the Faroe

Islands, besides Torshavn the site of Akraberg on the southernmost of the Islands. Fig.7 gives the data for the sites Lerwick, Shetlands and Ålesund, Western Norway, Fig 8 for Bremen, Germany and Cardiff, Wales.

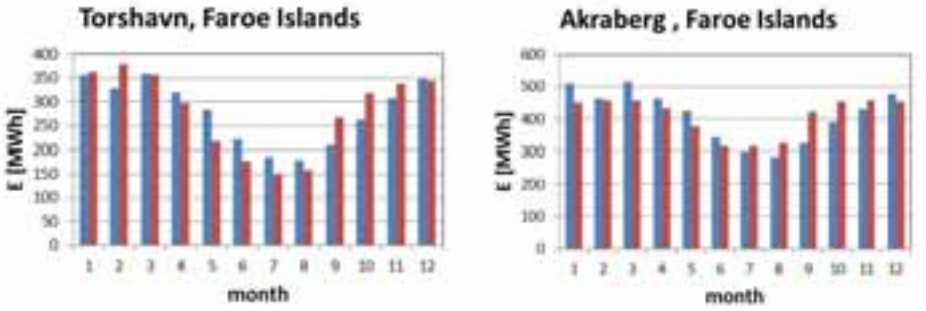

Fig. 6: Estimated normalized monthly energy gain from a wind turbine together with the normalized monthly heating load calculated on basis of the heating degree days. Both production and demand are given as monthly fraction of the annual sum.

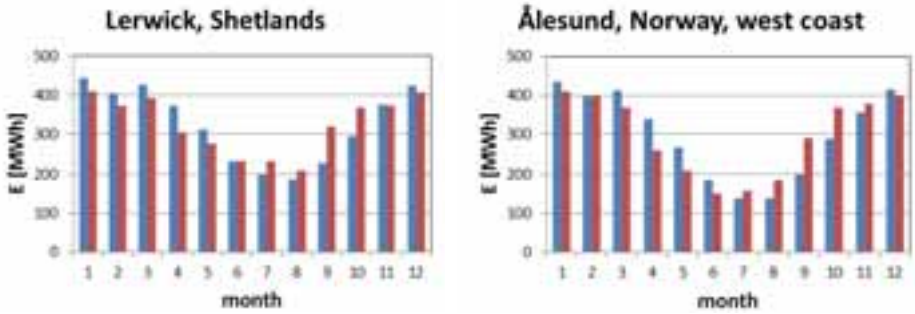

Fig. 7: Same as Fig.5, but for the Sites Lerwick and Ålesund, showing similar pattern as the Faroe Islands sites

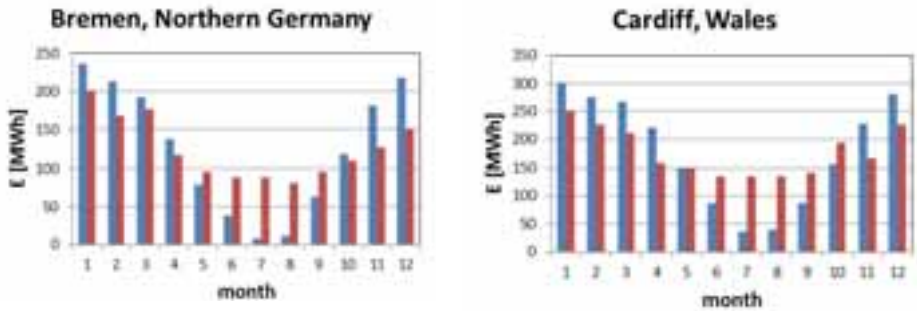

Fig. 8: Same as Fig.5, but for the sites Bremen and Cardiff. For these sites, except for magnitude, the pattern remains similar to those of the more northerly sites. Difference is in the heating load (blue) in summer being reduced to almost zero, causing a larger spread of the pattern of the monthly heating loads.

For Akraberg – with wind speeds superior to those at Torshavn, the monthly pattern in wind generation is even less pronounced than for Torshavn. For both sites monthly wind generation and load are closely correlated with a similar spread. This pattern is repeated for Lerwick and Ålesund, with Ålesund showing a higher parallel sprread in both monthly load and generation. For Bremen and Cardiff, with less favorable wind conditions and thus lower wind generation. With the load scaling according to annual production a remarkable surplus in generation occurs in the summer month. This is due to the heating load approaching zero in summer. In contrast production deficits occur in winter. With still a good correlation of production and load, the mismatch is a consequence of the different spreads of the two series – variability of the monthly heating load much bigger than variability of the monthly production.

The quality of the match of these series of monthly energy data can be related to basic characteristics of the meteorological series. To show this kind of dependency, the Root mean square of the differences in monthly generation and load, both normalized by the respective annual sums is extracted for an extended set of stations (all represented in the RETScreen set) in North-Western Europe (see Tab.1).

Tab. 1: Maximum difference of monthly normalized HDD and normalized wind speed and root mean square of the monthly difference of normalized load and production

site	RMS mon. en. miss.	max. mon. met. missmatch
Akraberg, Faroe Islands	0.116	0.209
Torshavn, Faroe Islands	0.139	0.143
Lerwick, Shetlands	0.139	0.206
Aberdeen, Scotland	0.168	0.424
Ålesund, Norway Westcoast	0.170	0.246
Røros, Norway Interior	0.200	0.366
Brest, France, Bretagne	0.217	0.499
Plymouth, England Chanal Coast	0.271	0.456
Cardiff, Wales	0.341	0.524
Bremen, Northern Germany	0.377	0.688
Lille, Northern France	0.380	0.780
Dresden, Eastern Germany	0.435	0.876
Bo ulonge Seine, Northern France	0.466	0.746
Karlsruhe, Suth-Western Gernaby	0.494	0.929

In addition, as a measure for the similarity in the monthly sets of wind speed and ambient temperature is set up. It is given as the maximum difference of the normalized monthly HDD and the normalized monthly wind speed, both normalized by the average of the respective set. The values for the sites selected are also given in table 1. Fig. 9 shows the relation of the energetic mismatch to the meteorological mismatch, presenting a good correlation of the two sets. Thus, the feasibility of wind heating systems at a site can be pre-assessed by inspecting the sets of monthly HDD's and wind speeds.

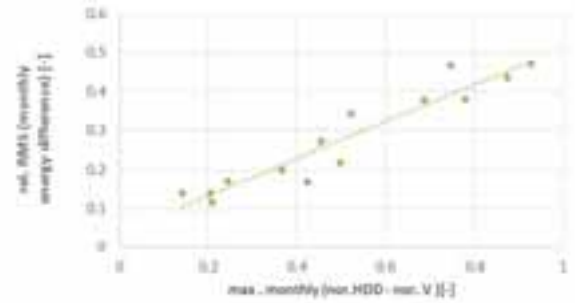

Fig. 9: Relation of the root mean square of the monthly difference of normalized load and production -as measured of the energetic mismatch – to the maximum difference of monthly normalized HDD and normalized wind speed as measure of 'meteorological mismatch' (data see tab.1).

5. Analyses of system performance at a well matched site with higher time resolution

For more insight in expected system performance, a more detailed study is done based on annual 10min time series of wind speed and ambient temperature measured at one of the smaller Faroe Islands, Nólsoy. These sets, showing a time resolution of 10min had been measured by the Danish Meteorological Institute. The annual set for 2008 is used here, showing a mean wind speed of 9.4m/s. These data are used directly as input to calculate the power output series of a 1MW wind turbine. The heating load is calculated according to the linear dependence that forms the basis of eqn.1. Thermal inertia of the building is neglected here, which, for the prevailing wood-based construction type on the Faroe Islands - and as the heating system of the houses contain but the storage capacity of conventional oil-fired systems – should be not too far from reality here.

Fig. 10 gives a first impression of the system performance based on the 10 min. data. Given are the evolution of the accumulated heating load and the accumulated turbine generation over the year. As for the monthly resolved data for Torshavn discussed above, there is a lack in generation in the late spring/early summer months. From an in-depth analysis of the series of the accumulated deficit (see e.g. Haas 1995), a storage dimensioned to host 30 times the average daily load is identified to be necessary for a continuous supply of the load.

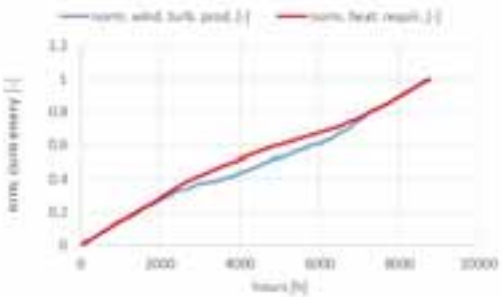

Fig. 10: Annual evolution of normalized cumulated heating load (red) and normalized cumulated wind turbine production for temperature and wind conditions at the site Nólsoy and matched annual load and production.

This requirement for storage could be reduced by an oversizing of the wind turbine. Combinations of oversizing of the wind generation and required storage size resulting from this type of calculation are given in Fig. 11. It has to be remarked that these calculations to not take into account storage losses that would provoke an increase in turbine size.

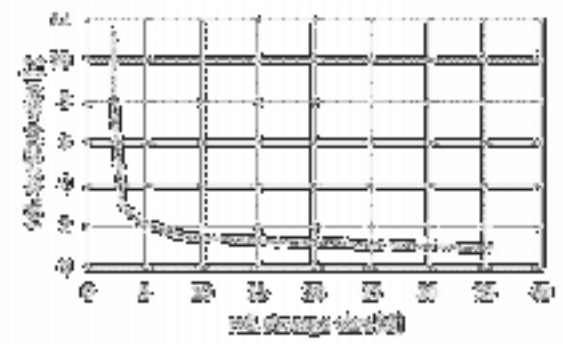

Fig. 11: Combinations of relative turbine and storage size for systems assuring the continuous supply of the load based on the data set for the site Nólsoy, Faroe Islands. Turbine size is normalized by the size of the turbine assuring the annual match of production and load, the storage size is normalized to the average annual load.

For a storage with the indicated almost monthly capacity pumped hydro may be considered as the only practical option – a solution currently discussed for the Faroe Islands to stabilize the isolated grid on the isle of Suðuroy (see Ludescher-Huber, 2017). On a smaller scale, thermal storage, buffering the heat on a daily scale may be applied, as demonstrated be a dedicated wind/heating micro grid in operation for some year on Nolsøy (Thomsen et al, 2015).

The requirement for storage may be reduced by an oversizing of the wind generation. Fig. 12 gives the combinations of storage size and turbine size representing the limit sizes for autonomous systems, i.e. systems not allowing for a loss of load.

As example a wind generation doubled as compared to the matching size would reduce the required storage size to about 5 days – a magnitude not totally out of reach for battery based electricity storage or thermal storage, depending on the absolute system size.

Another option for avoiding the need for large storage sizes is to either allow for a loss of load or the use of backup energy, i.e. the use of a backup power source. Fig. 9 gives the fraction of unserved power for systems with various turbine sizes and a 1-day storage. For a system with the turbine sized to match the annual load the annual unserved load – or need for backup energy - amounts to ~60 days of consumption.

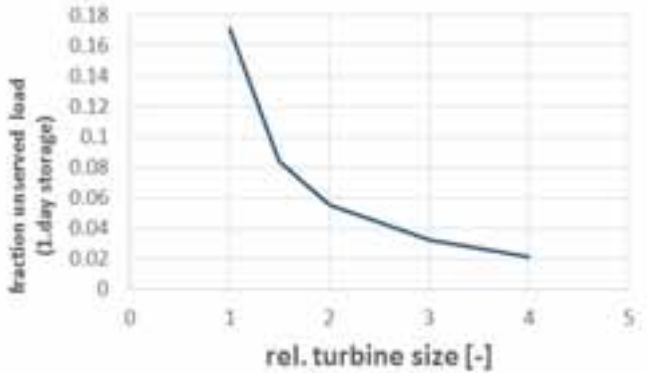

Fig. 12: Fraction of unserved power (normalized by the annual load) in systems using a storage to cover one day of load and various turbine sizes (data base and normalization as for fig. 11).

Thus, even in a region with a favorable seasonal match of heating load and wind turbine generation the effort for a complete coverage of the load by wind generation remains substantial and asks for dedicated studies on optimal system design,

6. Conclusion and outlook

As given here, the monthly pattern of power generation of wind turbines matches quite well to the heating load of houses for the inspected Atlantic and North-Sea climates. For the case of turbines scaled to match the annual load, however, some deficit will occur in the April to June period. As counter measures, either an over dimensioning of the wind capacity and/or the inclusion of storage or the limited use of backup energy has to be considered.

7. References

Anonymous, 2014. RETScreen Clean Energy Project Analyzer, www.nrcan.gc.ca/energy/softwarw-tools/7465, as of 02-10-2014

Anonymous, 2017. 20l5, a year of records for SEV, http://www.sev.fo/Default.aspx?ID=8&PID=6&NewsID=2836, as of 24.03.2017

Haas A., 1995. Zur Bestimmung des Speicherbedarfs in solarelektrischen Energieversorgungasystemen aus Charakteristiken der Einstrahlung, PhD Thesis, University of Oldenburg, Germany

Ludescher-Huber E., 2017. Wind power based pumped storage on Suðuroy, http://www.nordicenergy.org/wp-/uploads/2013/11/Wind-power-based-pumped-storage_Norconsult.pdf as of 12.08.201

Østergaard P.A., 2013. Wind power integration in Aalborg Municipality using compression heat pumps and geothermal absorption heat pumps, Energy, 49, pp.502-508

Thomsen B., J.M. Guerrero, P.B. Thøgersen, 2015. Faroe Islands Wind-Powered Space Heating Microgrid Using Self-Excited 220-kW Induction Generator, Transactions on Sustainable Energy, 5,pp. 1361-1366

Xydis G., 2015. Wind Energy Integration through District Heating. A Wind Resource Based Approach, Resources, 4, pp. 110-127

Zhang N., X. Lu, M. B. McElroy, C. P. Nielsen, X. Chen, Y. Deng, C. Kang, 2016. Reducing curtailment of wind electricity in China by employing electric boilers for heat and pumped hydro for energy storage, Applied Energy, 184, 987-994

Renewable Energy Assessment in Italy and Brazil: An economic and Political Comparison

Vincenzo Franzitta[1], Domenico Curto[1] and Alessia Viola[1]

[1] University of Palermo, Palermo (Italy)

Abstract

The aim of this study is a comparison among Italian and Brazilian electrical energy system with a particular focus on renewable energy sources. The energy sector has a key role in the sustainable development of a country, so it influences economic and political choices. The work would underline differences, common point among two country, specially, in this particular socio-economic period and it should emphasize that green economy could be a possible answer to financial crisis. The main purpose of this study is a presentation of Italian and Brazilian energy system with a particular focus on renewable sources. The energy sector has a key role in the sustainable development of these countries and it could influence economic and political choices or their economic climb. The work will be divided into four sections: Section I will introduce all details of the question; Section II will explain the renewable assessments or the countries, Section III will talk how renewable energy investment could be for economic crisis and the last section will show final conclusions.

.

Keywords: energy policy, renewable energy, solar, economic, sustainable.

1. Introduction

The idea of economic growth has dominated politics and policies since 1945. Environmental concerns and sustainable development were introduced at a later time. Expectations of win–win, sustainable growth through technological(Schneider et al. 2010) and efficiency improvements, have not been fulfilled. The present economic crisis opens up a social opportunity to ask fundamental questions.

The energy assumed a central role in human life since the ancient time because the economic progress developed thanks to an idea of deranged use of available resources like water, energy or land (Mathiesen et al. 2011).

An immediate consequence of the financial crisis that shook the large majority of countries is the reduction of economic activity and increased unemployment. Since economic activity is closely linked to energy consumption, it is expected that the quantity of energy consumed will also decrease. At first glance this seems to be good news: with lower demand, prices should fall, as occurs when stores offer sales.

The Paris Agreement on climate change, which entered into force in November 2016, is at its most recent heart an agreement about energy (IEA - International Energy Agency 2011). Anyway, political and economic crisis influenced the global energy markets, so the aim of this paper is a presentation how their knowledge is essential to define a future energy programs. The description is based on the study of two different Country: Italy and Brazil, as far for their geographical but so close for many common points.

As regards climate change and environmental-energy programs, Italy as a member of the European Union was a signatory to the United Nations Framework Convention on Climate Change (International Energy Agency 2010) (UNFCCC) and to the Kyoto Protocol and on October of 2016 Italy ratified the Paris Agreement. In fact, already in the past, Italy has implemented a number of sectoral and cross-sectoral policies to have a direct or indirect effect on the reduction of greenhouse gas emissions. Legislation introduced to improve the energy performance of buildings, strengthening their thermal demand requirements. These include compulsory standards for new buildings and renovation of older buildings.

After less than a year since its signing, Brazil has officially validated the Paris Agreement at the national level. This was

doi:10.18086/swc.2017.37.03 Available at http://proceedings.ises.org

an essential step because Brazil, one of the world's biggest greenhouse gas emissions (GHG) emitters, has a fundamental role in this scenario. The INDCs (Intended Nationally Determined Contributions) submitted by the country set an absolute emission reduction of 37% until 2025 and 43% until 2030, having as base 2005 levels. Figure 1 shows a comparison between Italian and Brazilian CO_2 emissions' trend.

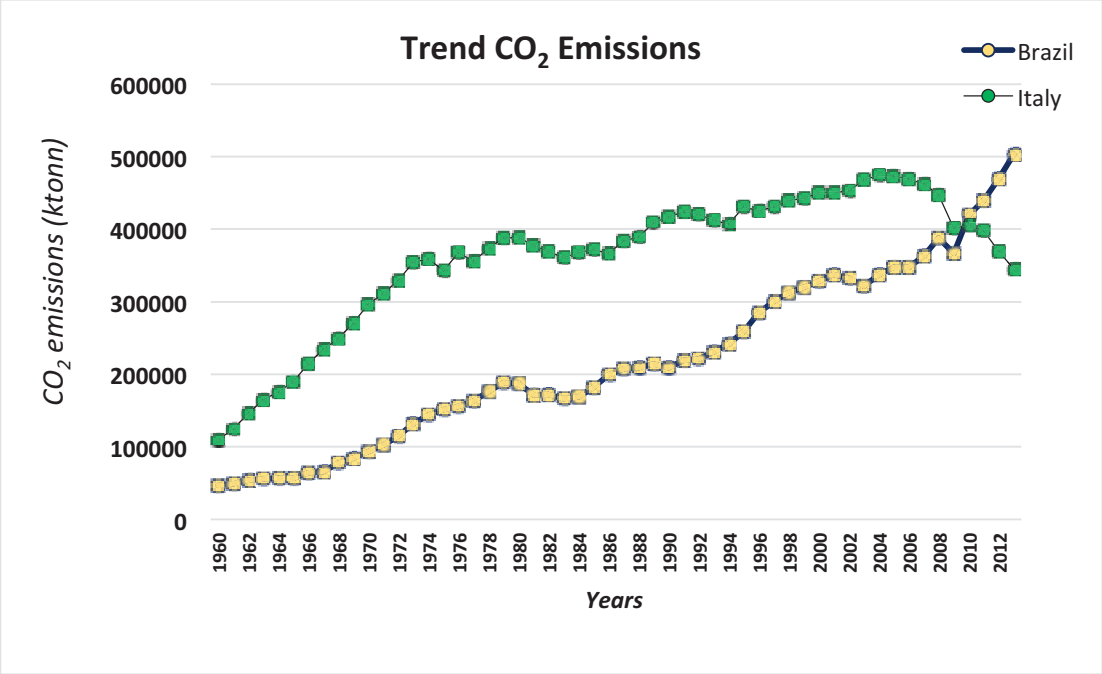

Fig. 1: Comparison of CO_2 emissions (period 1960-2012) (Data from http://resourceirena.irena.org)

Remark that figure 1 represents data until 2011, year that signs economic slowdown for Italy but growth for Brazil.. Connected to CO_2 emissions and political actions to fight global warming, it is interesting to evaluate climate variation in the time, considering actual and past data.

The monthly mean historical rainfall and temperature data show the baseline climate and seasonality by month, for specific years, and for rainfall and temperature.

Figures 1a and 2b display mean historical monthly temperature and rainfall for Brazil and Italy during the period 1900-2012. The dataset was produced by the Climatic Research Unit (CRU) of University of East Anglia (UEA).

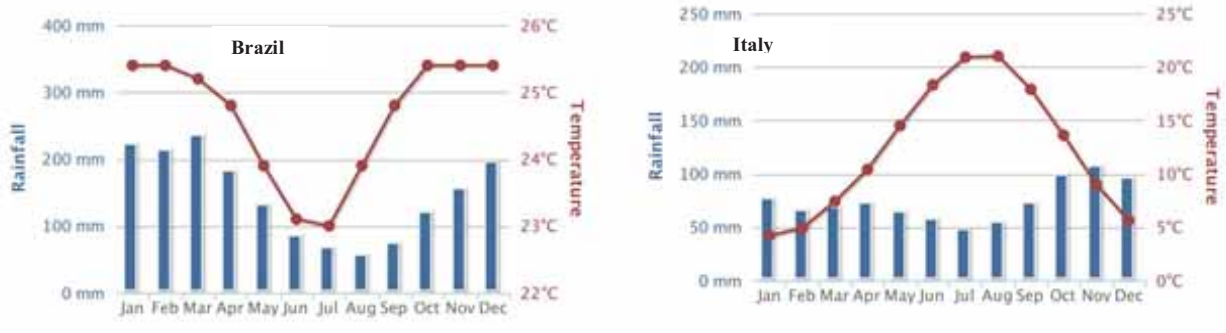

Fig. 1:Mean historical monthly temperature and rainfall (1900-2012) a) Brazil and b) Italy (Data from http://sdwebx.worldbank.org/climateportal/)

According these data, a significant amount of rainfall characterized Brazilian climate and influenced hydropower generation in Country. The next sections will explain all renewable energy sources available in the two countries and the financial effects that turned out.

2. Renewable energy study in Italy

Italy is a large mountainous country and runs from Alps to Mediterranean Sea. Its surface is 300.000 km^2 and we find some islands like Sicily, Sardinia and other small islands. Italy has almost 59 million inhabitants of whom 22 million are in active employment. The country is divide into 20 independent regions and all of which are part of the constitutional structure of State. Italy was a founding member of the European Union and is part of the G8 group of countries. It enjoys a GDP per capita just above the European average. It has developed a framework to implement an energy market policy that is consistent with European requirements. The Table 1.1 recaps all principal information(GSE 2016.).

Tab. 1: Italian General Information

General Data	
Inhabitants	60.6 [million]
Surface	301.340 [km^2]
Density	200 [ab/km^2]
Gross Domestic Product	30.527,27 mln $US

Italian energy sector is strong dependent on foreign energy markets and electricity generated from thermal generation. Specifically, Italy produces small volumes of natural gas and oil but most fossil fuels are imported and augmented by local production of energy from renewable sources.

European Government imposed that by 2020, the renewable energy should account for 20% of the EU's final energy consumption so to meet this shared target, each member state needs to increase its production and use of renewable energy in electricity, heating and cooling, and transport. In 2015 renewable energy production (only electrical) was been of 106.686 GWh thanks to a large contribution of hydropower and solar plant. Figure 3 shows an evolution of electricity generation from 2000-2014 years.

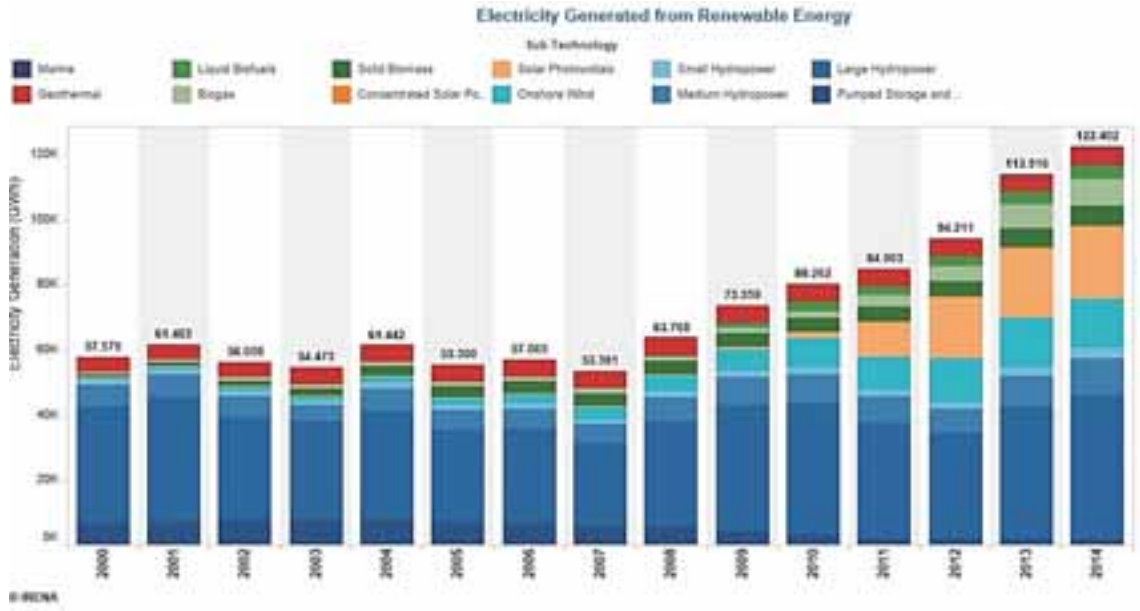

Fig. 3: Italian Electricity Generation from RES (renewable energy system) (Data from http://resourceirena.irena.org) (Data from http://resourceirena.irena.org)

The installed power at the end of 2015 is 51,475 MW and represents a little increase respect to the previous year thanks to the installation of new wind farms and photovoltaic plants. Between 2002 and 2015, the gross efficient power installed in Italy changed from 19,221 MW to 51,475 MW, an increase of 32,254 MW and an annual average growth rate of 7.9% overall power; The years 2011 and 2012 are characterized by higher power. Figure 4 shows RES plant installed between 2002-2015 (GSE 2016).

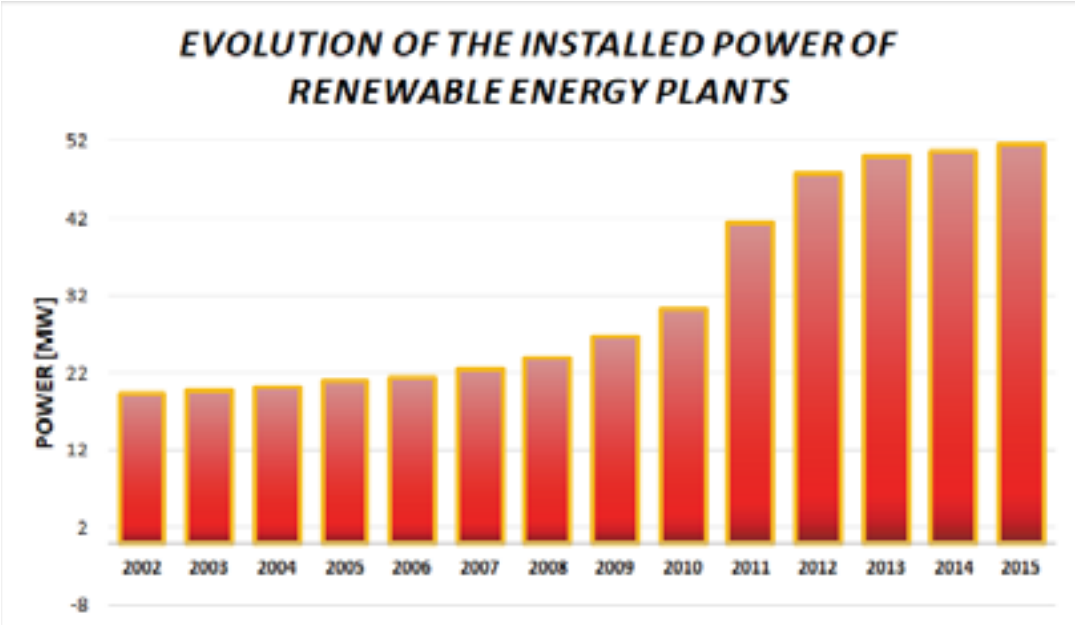

Fig. 4: Trend of the installed power of renewable energy plants.

Electricity demand 2016, equal to 314.3TWh (-0.8% by 2015), was met for 88.2% by national production (277.2TWh: + 2.5% by 2015) and for the remaining quota from net imports from abroad (37.0 TWh: -20.2% by 2015). National production recorded a substantial increase in the thermoelectric component and a substantial reduction in hydroelectric power. Renewable production is down due to the reduction in renewable hydroelectric production and, for the first time, of photovoltaic. Three counterproductive sources: wind, bioenergy and geothermal power generation.

Consumption is down 0.6% compared with 2015 and is 295.5TWh. The distribution by industry shows an increase in industry, a substantial stability of the attested service and a decline in both the domestic and the agricultural sectors. In terms of power installed, at December 31, 2016, the gross efficient generation power was 117.081MW, down 2,960MW (-2.5%) compared to 2015. This phenomenon is due to discharges in the thermoelectric park, increasing the capacity of renewable sources such as photovoltaics, wind and hydroelectric power (GSE 2016).

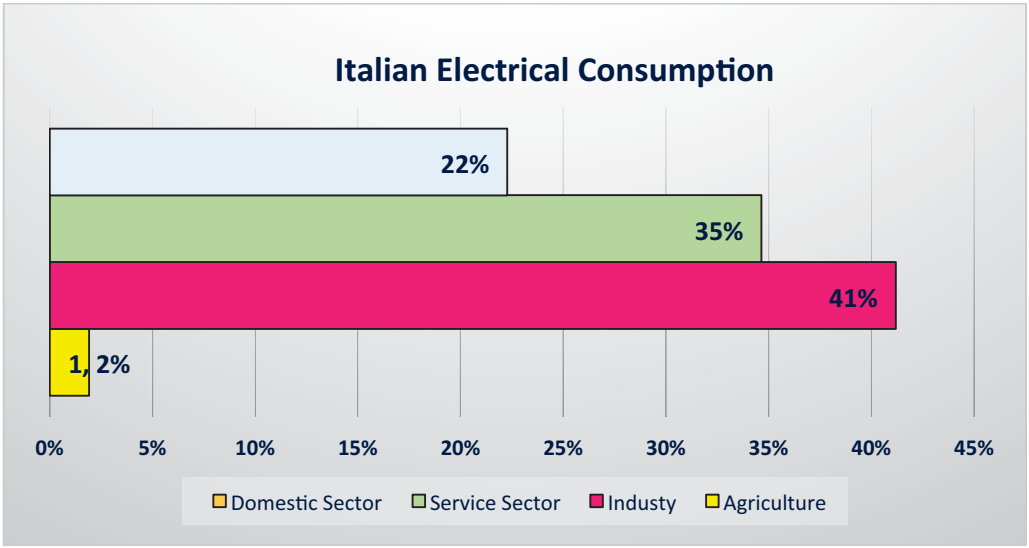

Fig. 5: Electrical consumption for year 2015.

3. Investigation on Brazilian energy sources

Brazil, officially the Federative Republic of Brazil, is the largest country in both South America and Latin America. As the world's fifth-largest country by area and sixth by population, it is the largest country to have Portuguese as an official language and the only one in the Americas. Brazil is one of the states with the best performance of economic development. It is part of the so-called BRICS (Brazil, Russia, India, China and South Africa) namely Countries that in recent years, and probably in the near future, recorded the highest rates of economic growth. The government plays a substantial role in the Brazilian electricity sector. Until the 1990s, the government controlled the electricity sector almost completely(Hira & de Oliveira 2009; Da Silva et al. 2005).

Tab. 2: Brazilian General Information

General Data	
Inhabitants	207.8 [million]
Surface	8 514 877 [km^2]
Density	23 [ab/km^2]

Fig. 6: Brazil GDP (2008-2016)

In 2004, the Brazilian government implemented a new model for the electricity sector. This hybrid approach to government involvement splits the sector into regulated and unregulated markets for different producers and consumers. This approach allows for both public and private investment in new generation and distribution projects.

As for conventional source, the thermoelectric generation, above all, coming from natural gas, and for oil reserve, EIA estimates that Brazil had 13.2 billion barrels of proved reserves, the second-largest level in South America after Venezuela. More than 94% of Brazil's reserves are located offshore, and 80% of all reserves are found offshore near the state of Rio de Janeiro.

Regarding renewable sources, Brazil is one of the countries with the highest contribution of renewable energy; in fact the main considerable are: water resources and biomass. The percentage of renewables in the energy mix has been increasing over time and is expected to increase further to rise from 42.4% to 47% of the domestic total Brazilian in 2030, as required by the National Energy Plan (PNE). The hydroelectric potential in Brazil is among the top five in the world: the country has nearly 20% of the planet and has approximately 11% of global hydropower production. The use

of hydraulic source comes from1883.

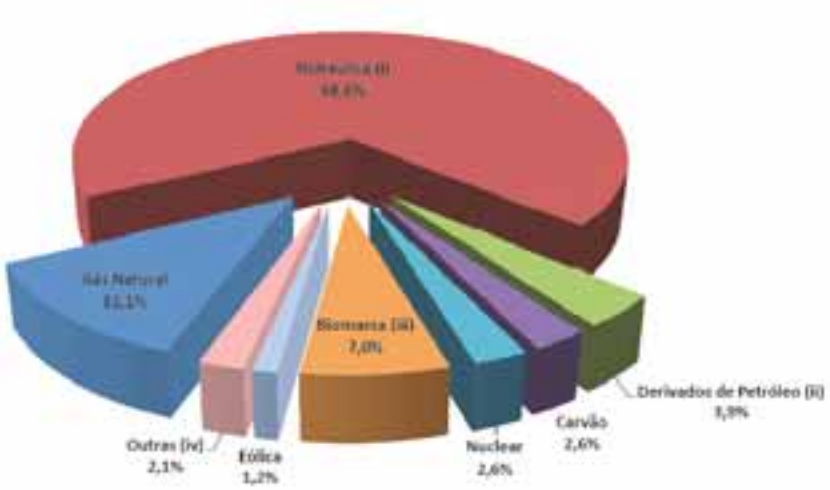

Fig. 7: Renewable and conventional sources

The exploitable hydropower potential is still estimated about 250 GW of installed power. Most of this potential is localized in the Amazon basin, while the north areas aren't still used. Hydroelectric plants are about 70% of the total electrical capacity installed in Brazil, amounting to 84 GW. Of these, approximately 14 GW are produced by Itaipù, built in Parana River on the border between Brazil and Paraguay; production values are split 50% between the two countries. Currently Itaipù hydroelectric plant produces about 90 to 100 TWh per year; the unused part of the production from Paraguay to Brazil is counted as the import of electricity. The Brazilian wind potential is estimated at about 350 GW14, concentrated mainly in northeast areas of country that is characterized by a high wind. There are 986 square kilometers of sand dunes with strong winds in the coast of Rio Grande do Sul. Another promising region is Minuano. A for solar energy, Brazil is a privileged country regarding solar irradiation.

However, exploitation of this resource is still insignificant because there are installed only 26 MW. The average energy conversion from photovoltaic systems is very interesting: the annual solar radiation is at its maximum value (approximately 2,300 kWh / m2) in the semi-arid northeast regions while the minimum (about 1,100 kWh / m2) in the northwest and southeast area. Figure 8 describes power installed in the period 2005-2016.

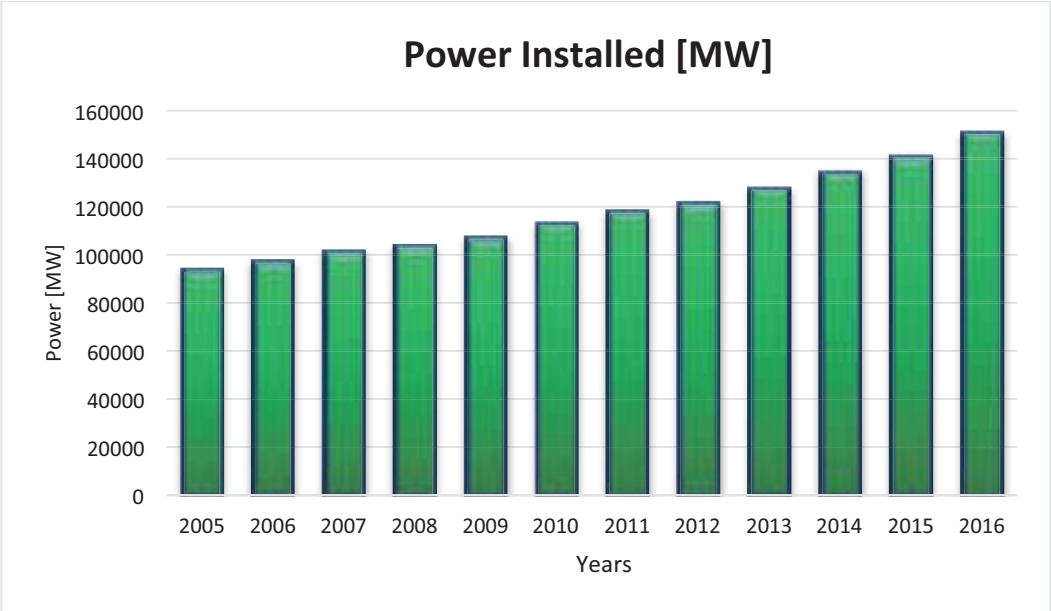

Fig. 8: Renewable energy plant installed in Brazil.

4. Economic impacts of renewable energy industry

In developing countries, where per capita consumption is relatively small, energy efficiency alone will not resolve the problem, because in many cases the final energy services (lighting, heating, cooking etc.) are still insufficiently available. Thus, global production and consumption of energy must increase to fulfill this repressed demand(IRENA 2017).

In this field, the renewable energies (such as wind, solar, biomass and small scale hydropower) will have a major role to play. Not only are these energy sources less polluting, but by their nature, are produced in small units. The decentralization of energy production leads to increased supply security and the creation of jobs. For example, this occurs in the production of ethanol from sugar cane in Brazil. The production of ethanol generates 4 – 21 times as many jobs as those needed to the produce the equivalent amount of energy from oil. For the same quantity of electricity, the number of jobs generated with wind energy is nearly 100 times greater than that generated by nuclear. The 120 GW of installed capacity in wind turbines throughout the world produce 260 TWh of electricity and avoid the emission of 158 million tons per year of CO2, which would occur if this energy was produced from fossil fuels. This is a market of about US $ 48 billion, which creates some 400,000 jobs (as shown in figure 8).

As for Europe, the wind industry remains one of the mainstays of the renewable energy sector in Europe. Employment declined slightly to 329,700 in 2015 (EurObserv'ER, 2017). Germany was the leader in wind jobs with 43% of the total in the European Union, followed by the United Kingdom, Denmark, Italy and France. The European solar PV industry continued to see a fall in employment in 2015. At 114,450, it has lost two thirds of jobs since 2011. Germany, the United Kingdom, France, and Italy are the leaders, with 67% of the European PV jobs in 2015. If we consider the huge potential of renewable energy sources for Brazil and Italy, more investments may cause an increase of the jobs in this sector.

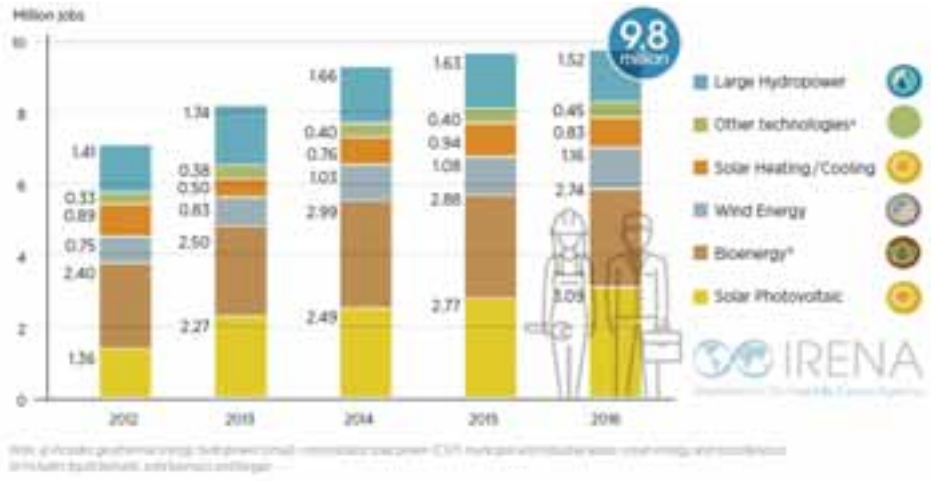

Fig.9: Global renewable energy employment

5. Conclusion

In conclusion, this paper gives information about energy supply in Italy and Brazil, focusing on the renewable energy sector.

The first part of the work describes a brief energy summary for Brazil and Italy in terms of capacity installed and electrical consumption. Furthermore, many international researches underline that the market for renewable sources grows and the financial crisis may be an opportunity. The presence of a stable, favourable policy framework continued to be a key factor for renewable energy job creation. New wind power installations in the United States, Germany, India and Brazil, meanwhile, contributed to the increase in global wind employment by 7%, to reach 1.2 million jobs.

Liquid biofuels (1.7 million jobs), solid biomass (0.7 million) and biogas (0.3 million) were also major employers, with jobs concentrated in feedstock supply. Brazil, China, the United States and India were key bioenergy job markets.

Jobs in solar heating and cooling declined 12% to 0.8 million amid an installation slowdown in major markets such as China, Brazil and the European Union. Large hydropower employed 1.5 million people (direct jobs), with around 60% of those in operation and maintenance. Key job markets were China, India, Brazil, the Russian Federation and Vietnam.

Differently for Italy, according to EurObserver data, employment in renewables in Italy has even declined from 121,850 occupied in 2011 to 97,100 in 2015, a less than 20%. A plausible explanation is that Italy's growth in renewables sector is reduced to minimum because in the electricity sector invested a significant share of incentives.

In conclusion, the investment in sustainable energy sector can be a correct politic choice to improve programs thus it may be an attractive opportunity and challenge for the future.

6. References

GSE, Energie rinnovabili al 2020 Scenari tendenziali.

GSE, 2016. La valutazione delle ricadute economiche e occupazionali dello sviluppo delle fonti energetiche rinnovabili in Italia. Gestore Servizi Elettrici - Unità Studi, Statistiche e Sostenibilità. , p.39.

Hira, A. & de Oliveira, L.G., 2009. No substitute for oil? How Brazil developed its ethanol industry. *Energy Policy*, 37(6), pp.2450–2456.

IEA - International Energy Agency, 2011. *Solar Energy Perspectives*, Paris: OECD Publishing.

IRENA, 2017. Renewable Energy and Jobs: Annual Review 2017. , p.16. +

Mathiesen, B.V., Lund, H. & Karlsson, K., 2011. 100% Renewable energy systems, climate mitigation and economic growth. *Applied Energy*, 88(2), pp.488–501.

Schneider, F., Kallis, G. & Martinez-Alier, J., 2010. Crisis or opportunity? Economic degrowth for social equity and ecological sustainability. Introduction to this special issue. *Journal of Cleaner Production*, 18(6), pp.511–518.

Da Silva, E.P. et al., 2005. Analysis of hydrogen production from combined photovoltaics, wind energy and secondary hydroelectricity supply in Brazil. *Solar Energy*, 78(5), pp.670–677.

Development and Experimental Validation of a Multi-Functional Façade Model within an Object Oriented Platform

Deniz Kizildag, Joaquim Rigola and Assensi Oliva
Heat and Mass Transfer Technological Center (CTTC)
Universitat Politècnica de Catalunya-BarcelonaTech (UPC)
ETSEIAT Colom 11 08222 Terrassa, Barcelona, Spain
cttc@cttc.upc.edu, http://www.cttc.upc.edu

Abstract

The present work is on the experimental validation of a multi-functional façade model developed within an object-oriented simulation platform. An existing building façade is retrofitted by means of PV and vacuum insulation panels, which form a ventilation channel. For the optimum performance of the PV panel element, the channel thickness is chosen by means of the numerical tool so as to maximize the heat evacuated from the ventilation channel throughout the year, thus enhancing the efficiency of the whole system. The multi-functional façade is properly instrumentalized and is exposed to real meteorological conditions in order to assess its long term reliability, durability, and energy performance. Moreover, with the gathered experimental data, the developed numerical model will be validated.

Keywords: PV panel, ventilated façade, numerical simulation, object-oriented numerical platform, experimental validation.

1. Introduction

Energy efficient buildings have a large potential due to the necessity of reducing energy consumption and carbon emissions in line with European climate and energy targets for the year 2020. In order to improve the overall impact of the buildings, different strategies and architectonic solutions are being implemented, stimulating the development of accurate tools and methodologies in order to analyze their performance properly (Clarke and Hensen (2015)). The employment of multi-functional façades with double skins seems attractive due to their high potential to provide structural and energetic advantages, as well as aesthetic and comfort perception. Moreover, they can provide space for integrated PV panels (Agathokleous and Kalogirou, 2016). The channel formed within two skins can generate a microclimate around the building. The temperature gradients can facilitate natural and hybrid ventilation (Gratia and De Herde, 2007) and it can be used for heat recovery purposes, reducing the heating and cooling loads of the building (Ioannidis et al., 2017).

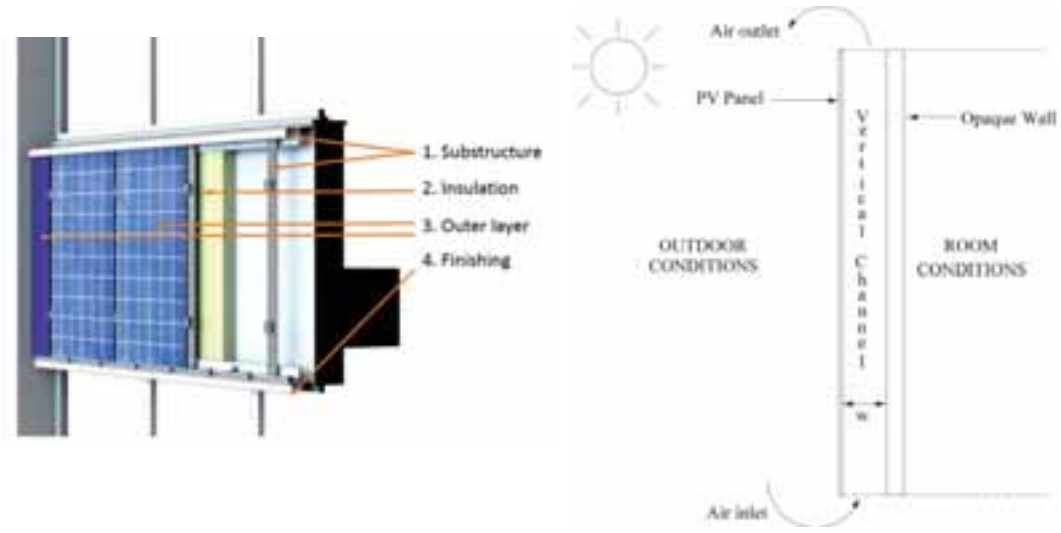

Fig. 1 Schematic view of the PV Ventilated Façade design (left), sketch of the functioning PV Ventilated Façade (right).

doi:10.18086/swc.2017.37.04 Available at http://proceedings.ises.org

The present work aims at taking to a further step a previous investigation on the implementation of a numerical model capable of predicting the thermal and fluid dynamic behavior of a multi-functional ventilated façade (Kizildag et al., 2015) within the existing parallel and object-oriented platform NEST (Damle et al., 2011). This methodology was recently employed within the framework of an innovative project (Retrofitting Solutions and Services for the enhancement of Energy Efficiency in Public Edification, RESSEEPE Project) in the task of envelope retrofitting. In the framework of this task, numerical simulations taking into account different configurations formed by a PV panel, a natural convection ventilation channel, and vacuum insulation panels were performed. The numerical study yielded a design which optimizes the PV panel efficiency under the weather conditions of Coventry, where one of the demo sites of the mentioned research project is located. In Figure 1, the schematic view of the final design for the retrofitting of the existing building is depicted. Note that this final design is the outcome of the synthesis of both thermal and structural analyses carried out in the design stage.

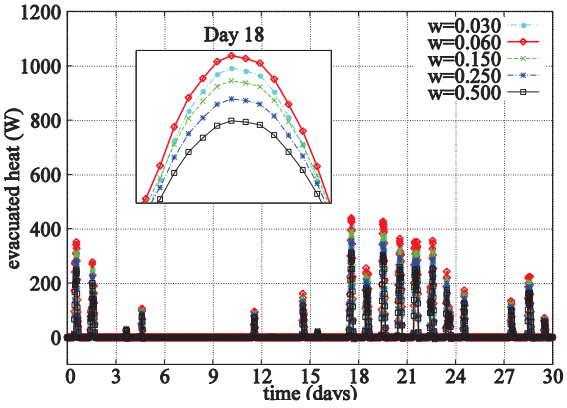

Fig. 2 Numerical analysis of the evacuated heat for different channel widths in the pre-design stage.

In Figure 2, an example of the influence of the possible ventilation channel widths on the evacuated heat is depicted for a typical month, based on the meteorological data obtained from Meteonorm ® software for the closest location to the John Laing Building in Coventry. Note, however, that the chosen channel thickness (see Figure 1) considers the overall effect of the results obtained for the whole year, which does not necessarily correspond to the optimum solution for a given period.

2. Mathematical and numerical modeling

In the NEST numerical platform, the system is a collection of some basic elements that can individually be solved for given boundary conditions, which are obtained from neighbor elements. By means of efficient coupling strategies, different levels of modelling can be put together in problems of complex heat transfer and fluid flow phenomena, for which multi-functional façades represent a good example. For instance, the critical elements of the façade or the building can be simulated by means of CFD models based on large-eddy or direct numerical simulations (Lehmkuhl et al., 2007), providing high precision results where necessary. The coupling of these results with lower order of modelling is powerful in allowing for carrying out simulations corresponding to extended domains in space and time.

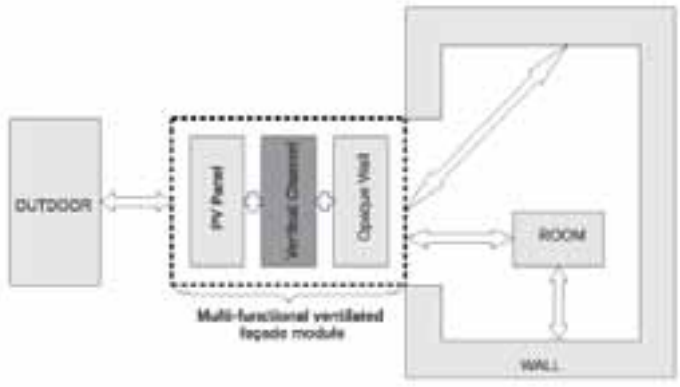

Fig. 3 Scheme of the NEST system as a collection of elements to model the Coventry demo site ventilated PV façade.

The NEST numerical platform is especially powerful in that it also allows parallel computation, which can redistribute the available computational resources according to the demands of the employed elements. The implemented module of the numerical tool aims at modelling an existing building envelope retrofitted by means of PV panel that is installed in the façade to form a vertical channel. The scheme of the resulting multi-functional ventilated façade module is shown in Figure 3.

Details of the mathematical and numerical model for the employed elements to form the PV Ventilated Façade is given by Kizildag et al. (2015). Note that *PV Panel* is modelled as an opaque one-dimensional conduction element with internal heat generation, assuming that the portion of the incident solar energy which is not used in the electricity generation is absorbed by the panel. This study basically addresses the thermal performance of the element.

Regarding the *Vertical Channel* element, it is worth noting that Bernoulli equation is applied in the inlet of the channel, assuming acceleration from an unperturbed point at the bottom of the channel. As for the thermal boundary conditions, improving the mathematical model employed in the previous work (Kizildag et al., 2015), the inlet temperature is no longer set constant at the mean outdoor temperature value of the simulated period, but it is dynamically adapted from the available meteorological data. The governing continuity, momentum, and energy equations regarding the *Vertical Channel* element are discretized by means of appropriate numerical schemes as explained in (Patankar, 1980) and using SIMPLEC algorithm.

Opaque Wall element is modeled in the same fashion as the PV Panel element, except for the existence of the inner heat generation terms. This element, which models the insulation layer, uses the thermophysical properties corresponding to the aerogel-based superinsulating mortar or vacuum insulation panels (VIP) provided by the manufacturers of these architectonic solutions, applied in the retrofitting of the demo building.

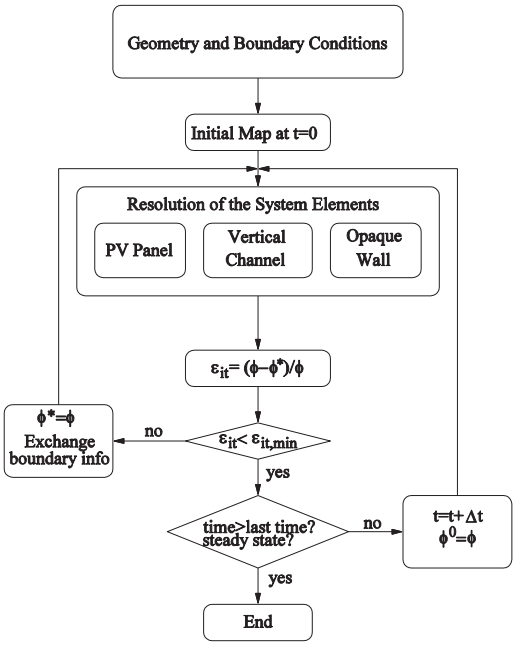

Fig. 4 Global resolution algorithm of the numerical tool.

The global resolution algorithm of the numerical model is shown in Figure 4. At each iteration, once the inputs (e.g. temperature, heat flux etc.) are obtained from the neighbors, the governing equations for each element are solved and the final outputs are supplied again to the neighboring elements as boundary conditions. Iterations continue until convergence is reached at a given time step and next time step calculation starts as the variables are updated. Details of the numerical platform are provided in (Damle et al., 2011).

3. Experimental validation of the numerical model in demo site

The validation of the numerical model was performed separately for each element constituting the PV façade using subsystems for which an analytical solution exists (see Kizildag et al., 2015 for details). As for the PV Panel and Opaque Wall, an analytical solution exists. Regarding the Vertical Channel, the analytical solution presented in (Bar-Cohen and Rohsenow, 1984) was used. Detailed results of the code validation were given in (Kizildag et al., 2014).

The present work, however, is aimed at completing this initial analytical validation by a proper experimental

validation. Thus, in order to validate the implemented numerical model, the whole PV façade module of the retrofitted façade of the John Laing building (see Figure 5), composed of a PV panel, a ventilation channel, VIP panels and brick layers, was instrumentalized.

Fig. 5 Retrofitted façade of the John Laing Building in Coventry University.

The façade is equipped with a pyranometer measuring the global solar radiation in the plane of the façade, and a temperature sensor registering the outdoor ambient temperature in the vicinity of the prototype. Within the ventilation channel, two anemometers are placed, one in the midheight, the other in the 90% of the PV panel height locations. Two temperature sensors are also located in these locations. Another temperature sensor is also placed in the inner surface of the VIP panel which confines the ventilation channel. See Figure 6 for the images corresponding the instrumentalization of the PV façade.

Fig. 6 Pyranometer and outdoor temperature sensor (left), anemometer and inner tempearure sensors (right).

The experimental data from the sensors installed in this facility is gathered by a data acquisition system during prolonged periods of time. In Figure 7, the measured meteorological data for the PV façade for the winter and spring periods are depicted. Note that, during the winter period, the available solar energy on the plane of the façade is significantly lower with respect to spring conditions, which makes the months of March and April periods more suitable for the analysis of the façade. For the validation of the numerical model, the gathered meteorological data is feeded in the numerical model as the boundary conditions of the studied case, and the numerical outcomes of the model is than compared with the experimental data obtained from the temperature and air velocity sensors located within the cavity of the ventilation channel. To that end, three representative variables are selected:

- average air velocity within the ventilation channel
- temperature at the outlet of the channel

- temperature at the VIP surface, adjacent to the ventilation channel

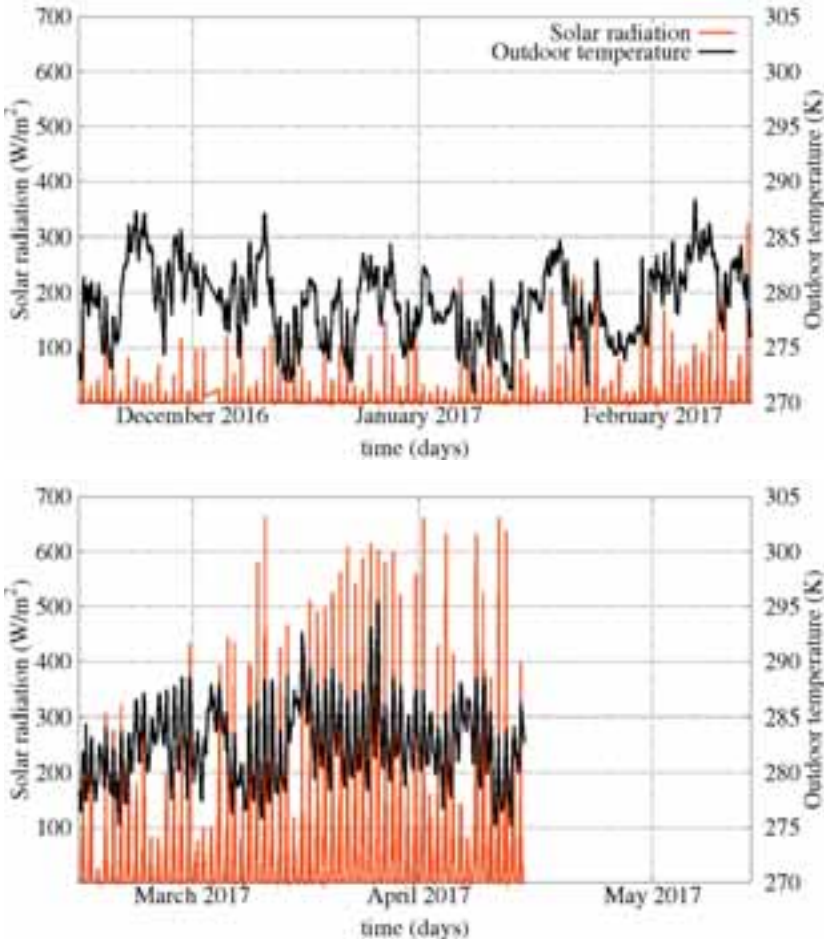

Fig. 7 Solar radiation and ambient temperature in demo site during winter (top) and spring (bottom).

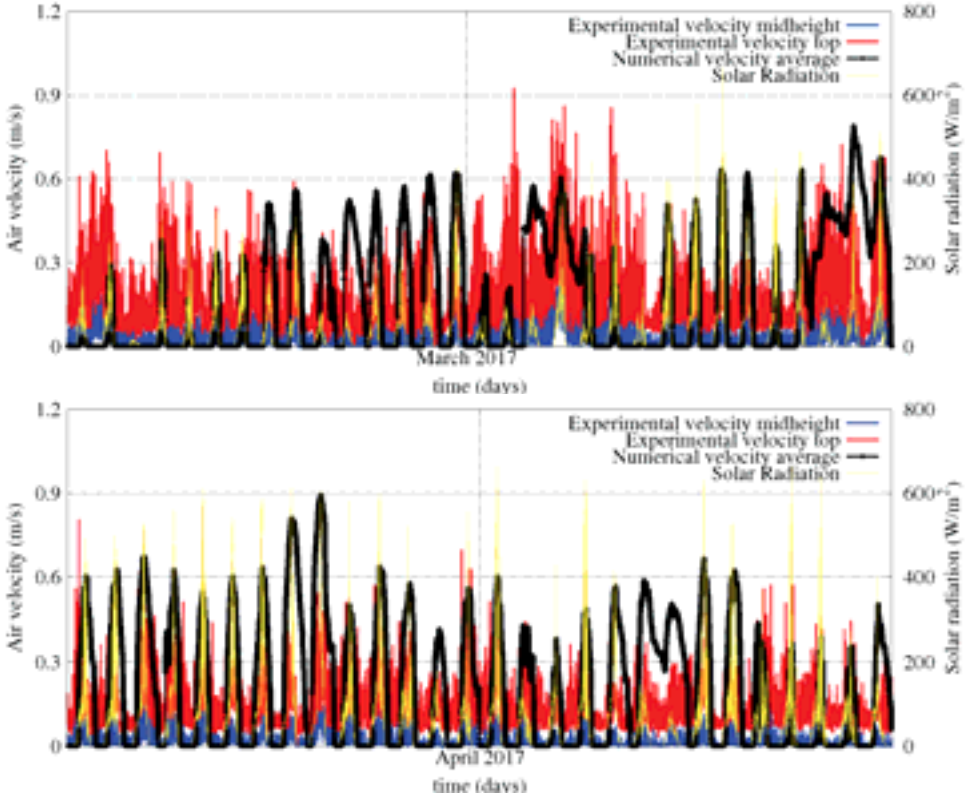

Fig. 8 Comparison of the numerical model's average velocity field with the experimental readings for March 2017 (top) and April 2017.

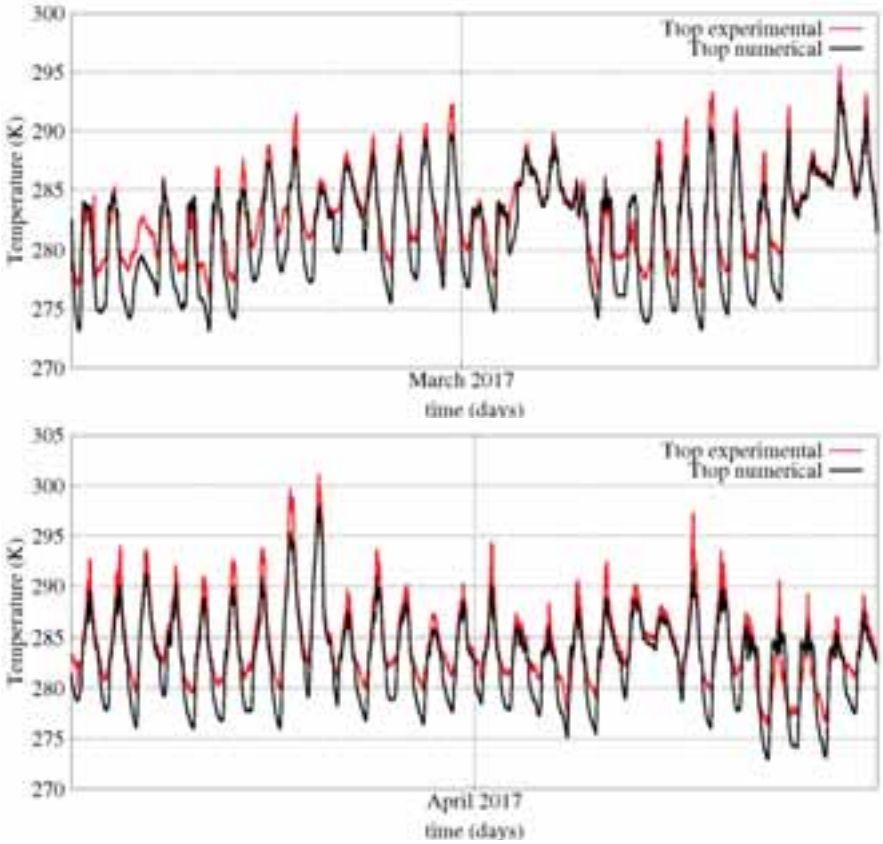

Fig. 9 Comparison of PV Façade air outlet temperatures obtained numerically and experimentally for March 2017 (top) and April 2017 (bottom).

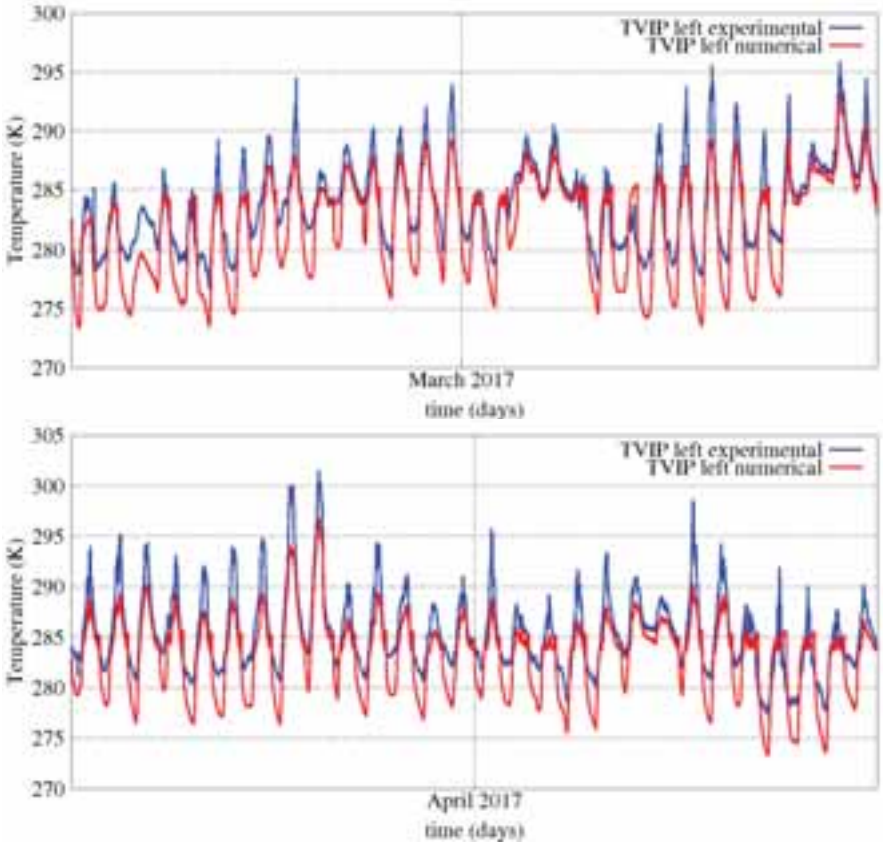

Fig. 10 Comparison of VIP surface temperature, confining the channel, obtained numerically and experimentally for March 2017 (top) and April 2017 (bottom).

The data corresponding to these selected variables are comparatively presented in Figures 8-10. The numerical data here presented for these considerably large periods of time –of the order of months- is in significantly good agreement with the gathered experimental data, thus providing a reasonable confidence in the potential of the numerical model in anticipating the thermal and fluid dynamics performance of the studied PV façade.

It has to be noted that, the model outcome is consistent with the complex physical phenomena taking place in the PV ventilated façade, as the temperature evolution data can fully follow the trend of the experimental temperature evolutions registered in two depicted key locations (see Figures 9 and 10). As for the air velocity within the ventilation channel, the numerical outcomes correlate very well with the availability of solar radiation, however they somewhat overestimate the velocities registered by the anemometer located at the top location of the channel (see Figure 8). Similarly, the estimated temperatures, while reproducing the phenomena correctly, are a few degrees lower than the experimental readings. These discrepancies can be attributed to many circumstances, such as:

- 1D numerical model vs 3D physical phenomenon: The employed numerical model is necessarily a 1D model, due to the impossibility of the detailed numerical resolution of the complex phenomena within the air channel for prolonged periods of time, typically one year. Any higher order model, such as CFD models, is not feasible for the present study.
- 1D model necessarily employs empirical data, such as friction factor or heat transfer coefficient which are derived for general situations which may not be in line with the actual studied case.
- The empirical data employed is derived for steady-state conditions, while the present study involves a transient behavior.
- The placement of the physical sensors, cables and other connection devices within the air velocity affects the overall behavior of the flow in the ventilation channel. These details are not considered in these simulations.
- The inlet and outlet geometry of the channel deviates from the initially studied case, which can justify important discrepancies with respect to the flow configuration.
- The employed anemometers have associated errors which can lead to discrepancies.
- Shadows are reported to be partially present on the studied façade, which can cause virtually higher or lower available radiation data on the façade.
- Temperature indoors is considered as a given constant value throughout the simulations.

To have a closer look at the model performance, data corresponding to the 1st week of April 2017 is depicted in Figure 11. The data is in line with the main conclusions mentioned above regarding the agreement of the numerical and experimental data, considering the assumptions that are included in this numerical study.

Thus it can be said that, the numerical tool, after being validated using the experimental data gathered in the John Laing Building, certifies the proper functioning of the ventilation channel placed behind the PV panel. The channel is shown to effectively dissipate the heat accumulated in the PV panel element, thus avoiding it to reach temperatures in which the correct functioning and overall efficiency of the PV element would be negatively affected.

Overall, the present numerical methodology for the long term thermal and fluid dynamics behavior analysis of a PV Ventilated Façade is shown to be an effective tool to design and optimize similar configurations. It is especially interesting to note that, due to the modular design of the validated software, new and more efficient materials or different innovative architectural solutions which are daily emerging in the market can be readily implemented in this validated numerical tool to address each time a wider range of situations regarding the retrofitting of the buildings.

4. Analysis of PV Ventilated Façade technology extrapolated to whole building

As an additional step of the present work, the numerical tool is employed to analyze the heat dissipation behavior of the channel, in the event that the PV ventilated façade technology is applied to the total available opaque surfaces present in the western façade of the demo building. In line with the objectives of the RESSEEPE project, it is of importance to extrapolate the results of the demo site module to the whole façade, thus highlighting the overall savings that could be provided by this retrofitting technology.

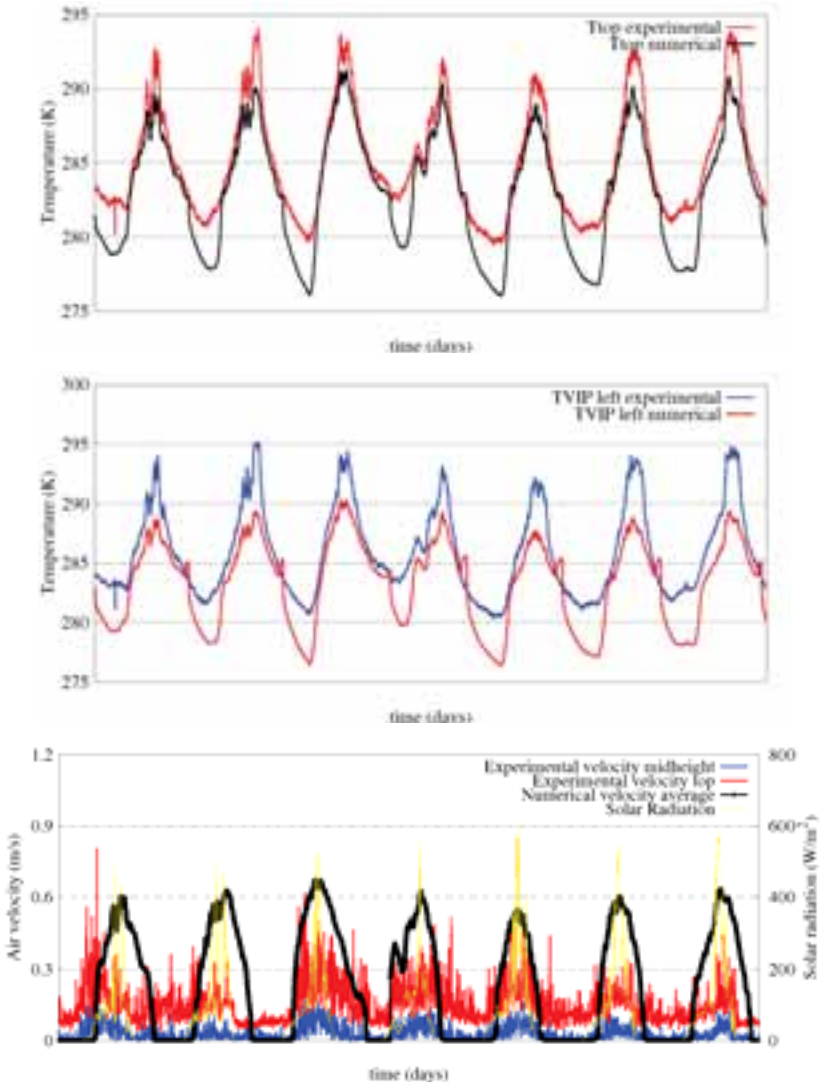

Fig. 11 Numerical vs experimental data for the 1st week of April. Temperature at the outlet of the channel (top), temperature at VIP surface (middle), average channel air velocity (bottom).

In Figure 12, the instantaneous total heat which would be evacuated by means of the ventilation channels is compactly depicted during the periods of winter and spring. This calculation is carried out by means of the already presented and validated numerical tool, using as boundary conditions the meteorological data gathered in the demo site, for the hypothetical case of installing the identical PV Ventilated Façade to all the available opaque spaces, excluding the already existing windows. Note that the evacuated heat, represented by the blue lines, have higher influence at higher levels of incident solar energy. During the winter months, the available solar energy is reduced and the outdoor ambient temperatures are relatively lower, thus the effect of the ventilation channel is not expected to be critical during these months, as confirmed by the outcomes of the numerical tool. However, from the detailed results depicted in Figure 13, it can be observed that the façade would effectively remove important portions of heat during the times of high solar availability, such as in May, by means of the ventilation channel.

Table 1 Total incident solar energy and the dissipated portion by the ventilation channel during 6 months.

Month	Incident Heat (kWh)	Dissipated Heat (kWh)	Percentage (%)
December	1375	203	14.8
January	1369	146	10.7
February	2578	760	29.5
March	6636	2371	35.7
April	11395	4784	42.0
May	11606	4788	41.3

In Table 1, the monthly total incident solar energy is given together with the dissipated portion by means of the PV Ventilated Façade. The tabulated data shows that, in the hypothetical case of installing this technology to the whole western façade of the John Laing building, over 40% of the absorbed heat by the PV panel would be effectively dissipated, leading to the optimum and efficient functioning of the PV panel.

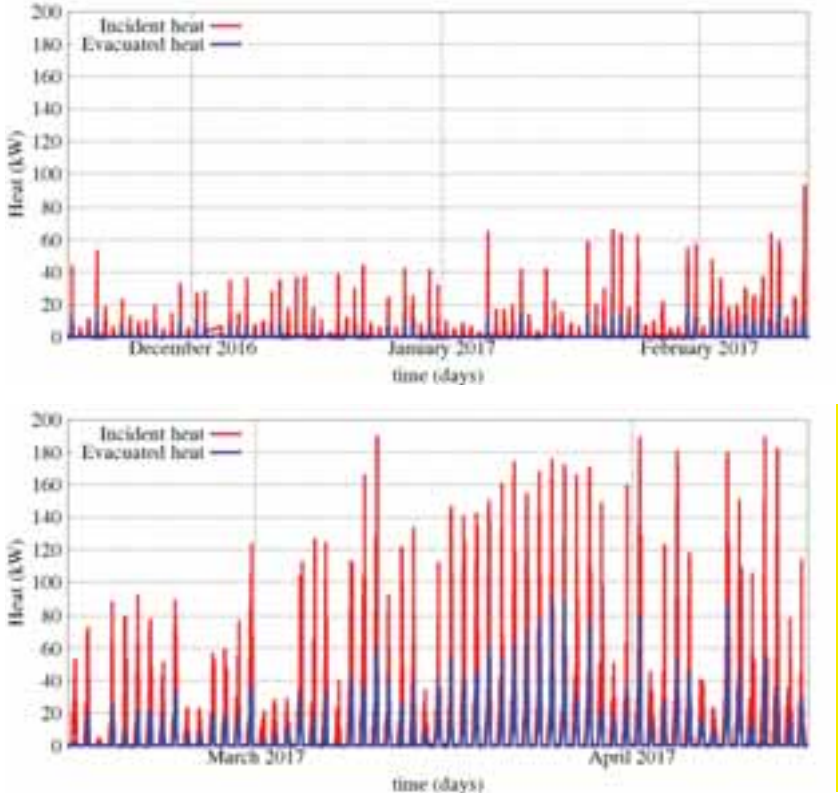

Fig. 12 Incident vs evacuated heat calculated for the hypothetic implementation of the technology to the whole façade.

In order to complement the data presented in **¡Error! No se encuentra el origen de la referencia.**, and to study the improvement experimented by the system thanks to the presence of the ventilation channel, the validated tool has been employed to comparatively study the influence of the ventilation channel on the PV panel temperatures. Note that, according to the technical specifications of the implemented panels in Coventry demo site, the efficiency of the electricity production of the panels reduce approximately by 0.451 % for each ºC of temperature rise experimented in the mean temperature of the cells. To that end, an additional simulation has been performed, simulating the thermal behavior of the façade for an identical system, but without the channel, i.e. the PV Panel is modelled to be attached directly to the VIP element. Considering the projection of this technology to the whole western façade of the John Laing building, the additional electrical energy delivered to the system is depicted in Table 2. Note that, the daily average PV panel temperatures are evaluated for the periods where there is solar availability within a day, i.e. during sunshine hours. The data reveal the key function of the ventilated façade, which make the PV panel function close to the ideal temperature conditions, and thus contributing it to deliver a considerably higher amount of electrical energy when compared with a hypothetical solution without ventilation channel.

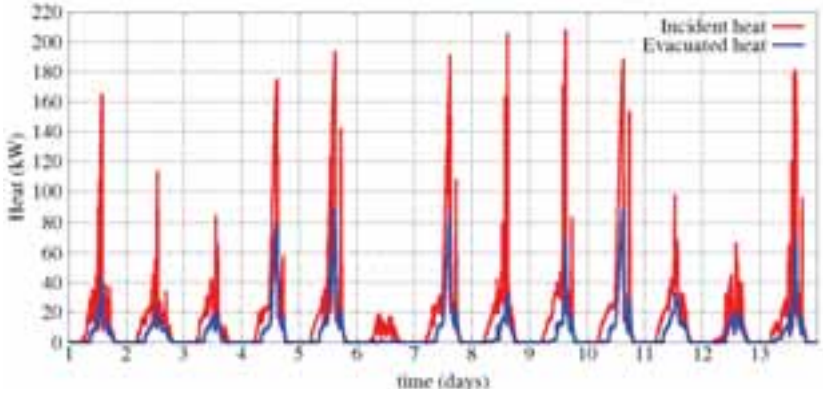

Fig. 13 Hypothetical instantaneous evacuated heat during the first two weeks of May 2017.

Table 2 Projection of the improvement of the electrical energy generation due to the presence of the ventilation channel for the meteorological data gathered in May 2017.

Day	Daily average PV panel temperature without channel (º C)	Daily average PV panel temperature with channel (º C)	Additional electrical energy delivered to the system (kWh)
1	27.975	21.089	9.38
2	24.622	19.056	6.53
3	24.205	19.216	5.63
4	36.878	25.405	28.23
5	36.527	25.009	31.09
6	14.354	13.966	0.19
7	38.207	26.269	30.87
8	26.303	21.255	7.73
9	29.523	23.260	12.78
10	36.562	25.237	32.09
11	30.433	22.162	13.81
12	28.305	21.219	8.08
13	31.207	22.351	17.35

In summary, the analysis extrapolated to the whole building by means of the validated numerical model shows that PV Ventilated Façade can be an interesting solution, evacuating the excess of heat through the ventilation channel by means of natural convection, thus contributing to the corresponding ventilation of the PV Panel, enhancing its efficiency. The analysis is carried out, not only for the particular module instrumentalized, but also for the whole western façade of the demo building, on the hypothesis of applying the mentioned technology to the entire façade.

5. Conclusions

It has been shown in the demo site located in John Laing Building in Coventry University by means of instrumentation that the designed and installed module of PV Ventilated Façade is functioning properly, as the ventilation channel effectively serves to evacuate the excess of the heat to enhance the overall performance.

The numerical methodology, employed in the design stage of the PV Ventilated Façade, is properly validated by means of experimentation. It has been shown that, besides the limitations of the assumptions, which are necessary so as to provide feasible numerical simulations for complex phenomena in physically large domains such as buildings and for typically extended periods of time, the numerical tool is capable of reproducing the general behavior of the retrofitted PV Façade studied in the present study.

Although the tested period does not cover a representatively long time span, however the initial outcomes in terms of both energy efficiency and the reliability of the system are promising.

The final outcome of this study is the experimental validation of an existing numerical tool which is capable of design, optimization, and long term performance prediction of PV Ventilated Façades or similar retrofitting or newly-built architectonical solutions. Additionally, due to its modular structure, the present tool can be extended to a wider range of retrofitting solutions, with the straightforward implementation of the numerical models of the newly emerging innovative materials and devices.

6. Acknowledgments

This work has been financially supported by the European Community FP7 Programme, EeB.NMP.2013-3 No 609377 “RESSEEPE Project”. The authors thankfully acknowledge this support.

The authors gratefully thank all RESSEEPE partners who participated in the tasks related with the PV Ventilated Façade experimentation, specially EURECAT, TECNALIA, and LEITAT, together with Coventry University for their support and contributions in the facility implementation.

7. References

Agathokleous R.A., Kalogirou S.A., 2016. Double skin facades (DSF) and building integrated photovoltaics (BIPV): a review of configurations and heat transfer characteristics, Renewable Energy 89, 743–756.

Bar-Cohen A., Rohsenow W.M., 1984. Thermally optimum spacing of vertical, natural convection cooled, parallel plates. Journal of Heat Transfer, 126(1), pp. 116-12.

Clarke J.A., Hensen J.L.M., 2015. Integrated building performance simulation: Progress, prospects and requirements. Building and Environment.

Damle R., Lehmkuhl O., Golomer G., Rodríguez I., 2011. Energy Simulation of Buildings with an Object-Oriented Tool. In Proceedings of the ISES Solar World Congress, Kassel, Germany.

Gratia E., De Herde A., 2007. Are energy consumptions decreased with the addition of a double-skin? Energy and Buildings 39, 605–619.

Ioannidis Z., Buonomano A., Athienitis A.K., Stathopoulos T., 2017. Modeling of double skin façades integrating photovoltaic panels and automated roller shades: Analysis of the thermal and electrical performance. Energy and Buildings 154, 618-632.

Kizildag D., Lehmkuhl O., Rigola J., Oliva A., 2014. A Multi-Functional Ventilated Façade model within a parallel and object-oriented numerical platform for the prediction of the thermal performance of buildings. In Proceedings of the Eurosun 2014 Conference, pp. 1-10.

Kizildag D., Lehmkuhl O., Rigola J., Capdevila R., Oliva A., 2015. Thermal optimization of multi-functional façades as energy efficient solution in retroffiting public buildings, IPBSA, Hyderabad, India.

Lehmkuhl O., Pérez-Segarra C.D., Borrell R., Soria M., Oliva A., 2007.TERMOFLUIDS: A new Parallel unstructured CFD code for the simulation of turbulent industrial problems on low cost PC cluster. In Proceedings of the Parallel CFD 2007 Conference, pp. 1–8.

Patankar, S.V., 1980. Numerical Heat Transfer and Fluid Flow, Hemisphere Publishing Corporation.

Sustainable Strategic Urban Planning: Methodology for Urban Renovation at district level

Estefanía Vallejo[1], Cristina Criado[2], Eneko Arrizabalaga[3] and Ali Vasallo[1]

[1] CARTIF Foundation, Boecillo (Spain)

[2] ACCIONA Construction, Madrid (Spain)

[3] TECNALIA Research and Innovation, Bilbao (Spain)

Abstract

Sustainable urban renovation is characterized by multiple factors (e.g. technical, socio-economic, environmental and ethical perspectives), different spatial scales and a number of administrative structures that should address the evaluation of alternative scenarios or solutions. This defines a complex decision problem that includes different stakeholders where several aspects need to be considered simultaneously. In spite of the knowledge and experiences during the recent years, there is a need of methods that lead the decision-making processes.

In response, a methodology based on the global idea and implications of working towards a more sustainable and energy efficient cities as a holistic procedure for urban renovation at district level is proposed in the European Smart City project CITyFiED. The methodology has the energy efficiency as main pillar and the local authorities as client. It is composed of seven phases that ensures an effective dialogue among all the stakeholders, aiming to understand the objectives and needs of the city to define a set of Strategies for Sustainable Urban Renovation and their integration within the Strategic Urban Planning of the cities.

Keywords: Sustainability, Decision making, Urban Renovation, Indicators, Energy planning

1. Introduction

Urban planning and regeneration process are concepts that involve a number of dimensions, e.g. technical, socio-economic, environmental and ethical perspectives. Sustainable urban regeneration is characterized by multiple factors, different spatial scales and a number of administrative structures that should address the evaluation of alternative scenarios or solutions. This defines a complex decision problem that includes a number of different stakeholders where several aspects need to be considered simultaneously. It is usually based on series of qualitative and quantitative data related to empirical observations, physical conditions and trends. In the decision-making process, cities need to invest a great deal of resources and time in the collection of information to deliver such assessments and decisions. However, very little is known about how decisions are made and the processes that lead to them.

There is a need to better identify, analyse, model and map resources and the current situation of urban settlements and solutions to achieve a more efficient built environment and match its demands with efficient sustainable energy sources at the least cost. Such energy planning is already mandated in the Energy Efficiency Directive (Directive 2012/27/EU). This needs to be done at local, regional and national levels to help develop energy strategies and ensure their consistency at national level and with EU policies; in fact, promoting sustainable urban development is a key element of the European Cohesion Policy and a continuous process.

During the last years, a great deal of research have been develop on one hand, by Technical Committees and Working Groups, which have been working in the field of Smart Cities, such us ISO TC/268, developing requirements, frameworks, guidance and supporting techniques and tools related to the achievement of sustainable development. On the other hand, there are many EU projects working to create models on energy efficient and sustainable city planning, such as PLEEC, or financial entities, such us The Word Bank, who has developed the Urban Regeneration Decision Tool.

Despite the vast amount of knowledge and tangible experiences that have being generated, there is still a need of deployment of holistic methodologies which comprise a global approach at city level and embrace the concept of sustainability. This implies the development of procedures, tools, key performance indicators and guidelines to

doi:10.18086/swc.2017.37.05 Available at http://proceedings.ises.org

cover the large scale and complexity of this approach. In this context, under the umbrella of Sustainable Strategic Urban Planning, a novel methodology for urban renovation at district level is proposed and validated by the European Smart City project CITyFiED (Grant Agreement Nº 609129).

2. CITyFiED Methodology for city renovation at district level

According to the United Nations, in 2014 more than half of the world's population was living in urban areas and two third of the world's population will be living in an urban area by 2050 (United Nations, 2014) being Europe the most urbanized continent (URBACT, 2015). The forecast for 2050 in this case is to increase the percentage up to 75 percent (Eurostat, 2016). Besides, urban areas are engines of regional and national growth as they generate 53 percent of gross national product (GNP) in low-income countries, 73 percent in middle-income countries, and 85 percent in high-income countries (World Bank, 1999).

These features bring about many desirable advantages for citizens. Although the concentration in cities usually supposes an increase of density and less consumption of resources, cities use two-thirds of the world's energy and generate three-fourths of the world's CO_2 emissions (Smart Cities Council, 2013). In addition, urban areas have important drawbacks, being waste production, carbon emissions, pollution, lack of preservation of heritage and environment, traffic congestion, etc. (Broere, 2012). It is analysed that the exposure of citizens to these problems is more than two times higher than in the case of people living in rural areas (Eurostat, 2016).

It seems that residential sector of small and medium sizes cities are the strategic lines of action to solve these problems due to their potential. The total number of dwellings in Europe in 2014 was 249,652.26 thousands and from those, around 45% were built before 1969, 32% between 1970 and 1989 and only 9.3% in the 90's. Moreover, the energy consumption of the residential sector was 263.22 Mtoe what supposes 158.76 kWh/m^2, still far from the H2020 set objectives (BPIE database). This data shows an elevated average age of the building stock in Europe with low energy performance and therefore, susceptible of being renovated. On the other hand, an 83% of cities in Europe are small and medium cities in terms of population (50.000-250.000 inhabitants) (Dijkstra and Poelman, 2012).

Above all, urban lifestyle needs to be sustainable, and sustainability should be understood from three points of view: *environmental, socio-economic and institutional*. Citizens' current way of life must be reconsidered and cities need to find a way to regenerate themselves in order to ensure long-term sustainability and overcome the current challenges they are facing.

In CITyFiED Methodology, the sustainable city renovation is understood as regeneration of actions, policies, and processes within a city, which address interrelated technical, spatial, and socio-economic problems in order to reduce environmental impact, mitigate environmental risk, and improve environmental quality of urban systems, lifestyles and assets. It aims to enable the replicability and mass-market deployment of energy-efficient retrofit of districts, considering as a reference the large CITyFiED demonstration cases in the cities of Lund (Sweden), Laguna de Duero (Spain) and Soma (Turkey), decision-making processes and business models.

Fig. 1: Phases of CITyFiED Methodology and the twofold scale

The Methodology is a procedure composed of 7 phases and a decision making process that aims to understand the city (objectives and needs) in order to deliver a set of customized Strategies for the Sustainable Urban Renovation at district level with the energy efficiency as the main pillar and local authorities as clients.

Each phase ensures an effective dialogue among all stakeholders and considers ways to strengthen confidence in decision-making processes. The present approach has been validated through the active participation of the CITyFiED network of cities.

The methodological approach foresees the creation of an External Consultancy Group (ECG) to closely cooperate with the local authorities when understanding the city and setting up the most suitable set of strategies for the

urban renovation at district level. The process is supported by different tools and levels of indicators that would enable the assessment of the suggested actions (Strategies for Sustainable Urban Renovation) as compared to the original situation and objectives.

Three levels of indicators have been defined: City Level Indicators (Level 1) at city & district level, Project Level Indicators KPIs (Level 2), and Impact Assessment Indicators at city level (Level 3).

2.1. Involvement of Stakeholders

The Methodology addresses the roles and responsibilities of the stakeholders involved along the application phases. In the first place, the *Municipalities*, representing the interest of citizens. They also promote the renovations at city or district levels to increase the sustainable performance of cities. Therefore, the experts representing the Municipality are conceived as collaborative clients in the methodology approach, divided into several committees as they are usually organized.

Public Participation understood as citizens, NGOs, neighbors associations, etc. are other group of stakeholders involved in sustainable renovations through different participation techniques cause "*all members of society have a key role in addressing the energy climate challenge with their local authorities*" (CoM, 2010).

Besides, *External Stakeholders* are required to carry out the renovation as constructors, financial entities, energy companies, investors, etc. As one key innovative aspect of the methodology, it proposes the foresight of an *External Consultancy Group (ECG)* to offer their services and closely cooperate with the Municipality. This is a multidisciplinary consultancy that supports the local authorities when understanding the city and setting up the most suitable set of Strategies for Sustainable Urban Renovation (SSUR), facilitating consequently the decision-making process.

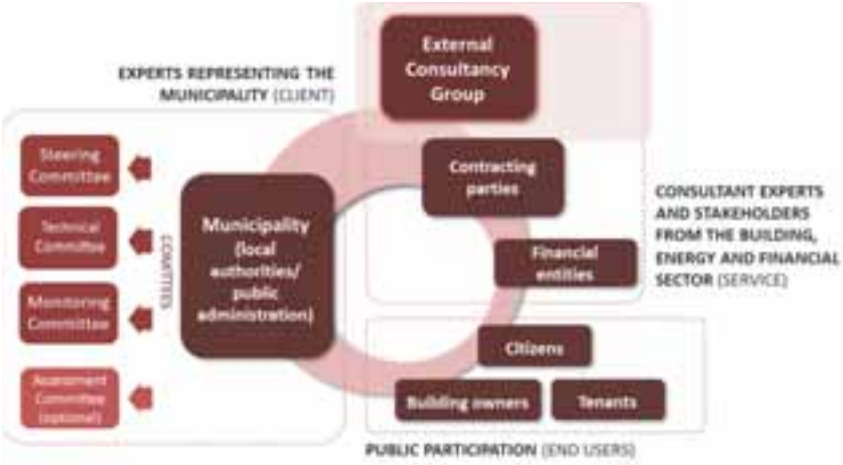

Fig. 2: Stakeholders defined in the Methodology

These stakeholders are sorted in different groups as shown in Fig. 2**:**

Experts representing the Municipality (Client)

- *Steering committee.* This committee includes those capable actors to make decisions in the local authorities' bodies, providing "(…) strategic direction and political support during the process" (CoM, 2010). Their mission is focused on the first stages of the process, i.e., understanding the city and diagnosis, selection of scenarios, etc.
- *Technical committee*. It is recommended to create this commission from a multi-criteria perspective, including urban planners, technicians, engineers, architects, designers, environmental consultants, etc.
- *Monitoring committee*. This committee is in charge of the monitoring strategy definition and implementation during the execution and for the final evaluation.
- *Advisory committee*. Other politicians or technicians from higher levels of the Public Administration could form an additional group of stakeholders to advice the Steering committee, i.e., regional and state technicians.

Consultant experts and stakeholders from the building, energy and financial sector (Service)

- *External Consultancy Group (ECG).* This group is conceived as a multi-perspective consultancy. It consists of technical consultants, technological institutes, research institutions, academia, energy experts, engineers, etc. that assess the Municipality during first phases of the methodology to define the initial situation, evaluate measures and scenarios and define the Strategies for the Sustainable Urban Renovation (SSUR). The addition of this group reduces risks by guaranteeing the achievement of the final objectives
- *Contracting parties.* These are independent companies and entities involved in the execution of the works that normally should be selected through tender/bidding process (e.g. architecture firms, building and energy companies, etc.). They should establish a fluent dialogue with the technical committee.
- *Financial institutions.*

Public participation (End users)

This group is formed by citizens, neighbourhood associations, housing associations, NGOs, etc. Their feedback is collected during all the process, but especially during diagnosis, decision-making and final evaluation. Building owners and tenants are deeply involved in the strategies definition.

3. Phases of the Methodology

The Methodology is deployed in seven phases as can be seen in Fig. 3. Each phase ensures an effective dialogue among all the stakeholders previously defined in order to ease the decision-making processes. It combines both district and city scales, starting with the city and district analysis, proposing initiatives at district level and pursuing the impact of the renovation and the accomplishment with the initial objectives at both scales.

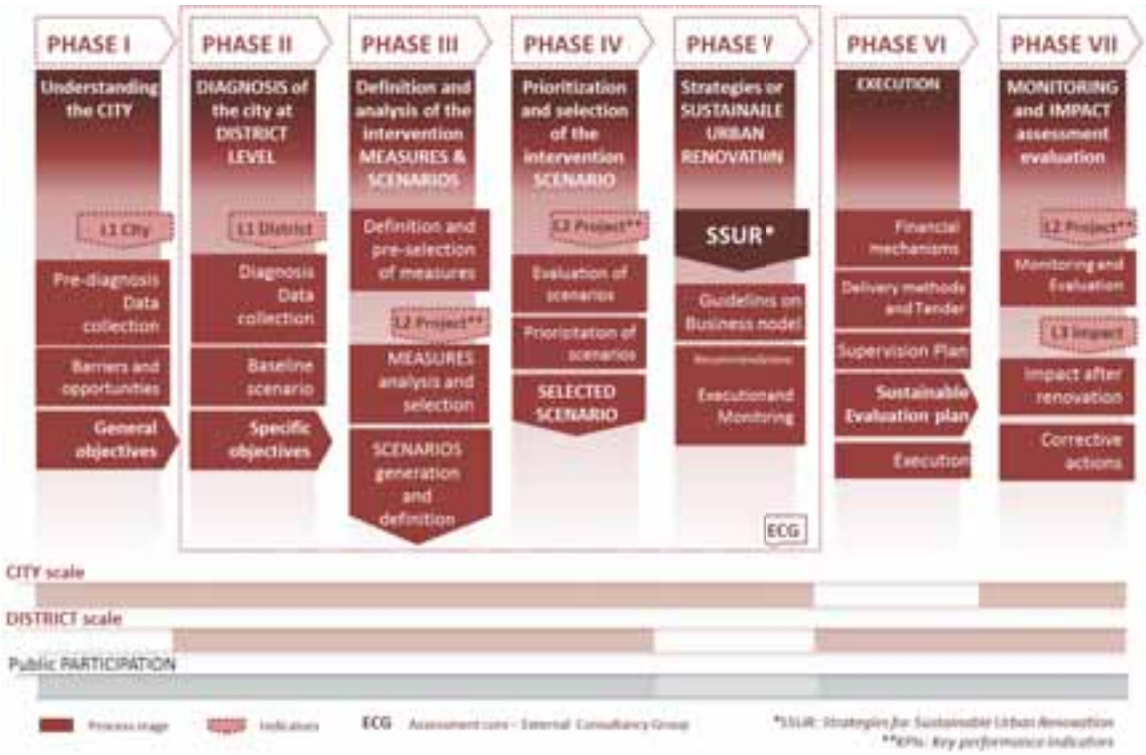

Fig. 3: Methodological approach for urban renovation and planning

Phase I: Understanding the city

This phase aims to make a first approach to the city understanding, evaluating its context and needs with a set of **City Level Indicators** as a supporting tool and taking into account public participation. This analysis, combined with the definition of the long-term city vision, enables the identification of the city sustainable pathway within

its Strategic Urban Planning and the definition of the general objectives that guide this transition.

The **pre-diagnosis and data collection** of the city is precisely the first step of this phase. Here, the most relevant factors at city level from different perspectives are evaluated in order to contextualize the current situation of the city. The complexity of urban areas, together with the ambitious scope of the methodology and the guidelines for sustainable development from the EC, makes necessary to consider a multi-criteria or holistic perspective during this analysis. However, in order to facilitate the application of the methodology it was necessary to limit the scope of the evaluation. Therefore, considering that the purpose of the CITyFiED project, the matrix of Fig. 4 was defined to gather all the relevant areas to be analyzed. The columns of this matrix are defined as "city strategic areas" which represent the main ambits that will be treated by the implementation of specific improvement interventions at district and city scale. On the other hand, the rows of the matrix are defined as "application areas" and represent the different sectors of the city in which the different interventions can be implemented.

Fig. 4: CITyFiED Application Areas and City Strategic Areas

Following this perspective, the pre-diagnosis will cover aspects of the city such as culture, economy, urban morphology or the main constraints and opportunities for the implementation of measures (legal framework, financial opportunities, etc.). This analysis will contribute to the required initial city context knowledge for the definition of the general objectives of the Strategic Urban Planning.

However, the quantification of specific City Level Indicators (Level 1) that can be compared to other city values provides a better understanding of the improvement potential and needs of different areas of the city evaluated. This is covered by the second step, in which a set of indexes related to the city level analysis "Level 1 City indicators" serve to **evaluate the sustainability standards**, identify city's strengths and weaknesses, and help setting general and specific objectives for the city.

Although many cities are implementing various low-carbon practices, it is still unclear how this sustainability or low carbon level can be certified. In this context, the methodology developed defines its own set of indicators considering the many efforts that have been previously made at developing indicators-based frameworks capable of evaluating cities' sustainability. The final selection of indicators that at this point includes 17 mobility related indicators, 14 building related indicators and 14 energy related indicators, was carried out following a rigorous internal and external validation process. The internal validation involved CITyFiED project partners (technicians, experts, etc.) and participants involved in the demo sites. The external validation on the other hand, involved the cities of the City Cluster and the Community of Interest, and took part during the Workshop about the CITyFiED Methodology performed in Laguna de Duero (Spain) in March 2017, with approximately 60 attendees.

Besides, each of the defined Level 1 City indicator has its specific reference value defined, considering the average values for the European cities. This allows understanding the distance between the initial situation of the city and the reference value in a way that cities can identify easily the area in which are performing worse than it is supposed to. The complementation of this indicator based analysis with different techniques such as the **SWOT analysis and Workshops** that include the main stakeholders involved in the planning process will facilitate both the definition of the **long-term city vision** and their **general objectives**.

Phase II: Diagnosis of the city at district level

In this second phase of the methodology the city is understood as an aggregation of districts. Taking into account the results in Phase I and following a bottom-up approach, the city is analyzed at district level to define the specific objectives for the districts object of the intervention. These specific objectives will serve to outline the different

set of measures that can be implemented in Phase III.

In a first step, a decision needs to be made by the Municipality regarding the district that will be selected for the transformation. This selection will be made taking into account the main characteristics of the district evaluated in terms of the potential to contribute to the transformation of the city, as well as the urgency of the specific needs of each district. The second step on the other hand, corresponds to the **diagnosis of the district** that will be evaluated for the city. The diagnosis will cover the following aspects; socio-economic analysis (age distribution of the inhabitants, the average household disposable income, the unemployment rate, etc.), morphological aspects (spatial distribution of the buildings, age and use of buildings, etc.), social analysis including aspects such as building owners and public participation, or environmental factors such as the potential for integrating renewable energy sources. Special attention should be paid in the analysis to aspects such as public participation activities developed by the Municipality with regard to the measures that are susceptible to be implemented, since these aspects are critical to identify non-technological barriers and to avoid difficulties during their implementation.

Level 1 indicators are also calculated at district level, when appropriate. This will contribute to the definition of the **baseline of the district** and will establish a direct link between the changes in the district and the impacts in the entire city, both will be evaluated in Phase VII. The values of these indexes will allow understanding better the context information at district scale with the quantitative values of indicators that are in line with the analysis carried out at city scale in the Phase I of the methodology. Besides, having the specific values of these indicators at district scale will aid to define **specific objectives** and measures and to stablish the prioritization criteria.

Taking into account all the information gathered at district scale, the energy demand and consumption of the base case scenario needs to be modelled for the district to allow the comparison with the forecast scenarios in the next phases. In this regard, energy planners usually need to combine various tools with different scales, and approaches, which makes difficult to develop a baseline analysis. Over the last 20 to 30 years, many different tools for building energy modelling have been developed. Several reviews, such as (Swan & Ugursal, 2009) and (Bourdic & Salat, 2012), describe different modelling approaches that can be used for evaluating the energy consumption of buildings at the district level. In the case of the tools that are designed for building energy modelling, the availability varies depending on the scale of the project. As mentioned by (Martos, Pacheco-Torres, Ordóñez, & Jadraque-Gago, 2016), the development of tools for evaluating and predicting the future energy consumption of cities and districts will be one of the biggest challenges in the field. However, the situation is much better in terms of the availability and reliability of tools for analysis of single buildings or a reduced building group. There are several tools, such as EnergyPlus and TRNSYS, that are broadly accepted and that allow for a very detailed and dynamic building energy simulation. Other modelling approaches such as BIM models, as well as the life cycle approach, are also identified as useful for this baseline definition stage. All these type of models and approaches need to be combined at this phase to achieve an appropriate analysis of the district.

This baseline analysis combined with the context information and the district scale Level 1 indicators will be used for the definition of the specific objectives of the district. These objectives are the conclusion from Phases I and II. They consist on targets related to improve the environmental, economic and social profile of the district and the city, and can be related to specific measures that are susceptible to be implemented in the district in order to contribute to the compliance of the targets of the city.

Phase III: Definition and analysis of the intervention and scenarios

The main target of this phase is to define the possible retrofitting scenarios to be considered for being implemented in the selected district according to the city (general objectives) and district needs (specific objectives). These scenarios consist of groups of measures that aid to forecast the impact on the sustainability performance. Before defining the scenarios, it is necessary to decide which measures should be discarded and for that purpose, the potential of each measure with respect to the objectives achievement is analyzed individually.

The ECG is the responsible of these activities. As a multidisciplinary group, it assists the Municipality to facilitate the analysis and the decision-making process. The ECG performs this supported on different recommendations, simulation tools and Indicators. In addition, the Technical and Steering committees from the Municipality can follow and control the process with them.

The measures to be considered are named as **Energy Conservation Measures** (ECMs). They are defined as "*measures that are applied to a building or group of buildings to improve energy efficiency and are life cycle cost*

effective and also they involve energy conservation, cogeneration facilities, renewable energy sources, improvements in operations and maintenance, or retrofit activities" (CITyFiED, D4.18). The catalogue of ECMs proposed in the methodology collects the CITyFiED "Basket of technologies" (CITyFiED, D1.7); a reduced list with the most efficient measures identified within CITyFiED Project approach. They are grouped into different categories: the first two focus on decreasing the energy consumption and the third one promotes the use of renewable energy sources, saving CO_2 and Primary Energy.

The steps to achieve by the ECG during Phase III are mainly two. The first one is the **measures preselection**, which consists of a preliminary choice of measures applying a filter, the specific objectives set in Phases I and II. The methodology establishes the relationships between ECMs and objectives, so it is possible to discard some of them at this early stage. In addition, the results of the Level 1 indicators, the feedback from the citizens (public participation activities) and Municipality, and other aspects identified during the analysis at both scales i.e., non-technological barriers, financial opportunities, etc., should be considered for this preliminary step.

The second step consist of a **feasibility analysis** of the preselected measures and the **final selection** of those that will be part of the retrofitting scenarios. For this analysis, it is necessary to evaluate the environmental, economic, technical and social aspects. In order to guide this study qualitatively, estimations from research on energy and CO_2 emissions levels of savings, payback periods, social issues, etc. are included in the catalogue of measures, as well as general recommendations for district retrofitting that affect the measures selection based on CITyFiED experiences (CITyFiED, D2.1 and D6.4) or other sources (STBA).

On the other hand, "Level 2 indicators" defined in the CITyFiED project could be calculated to assess Environmental, Technical, Economic and Social aspects along the application areas, and compare the results obtained for each ECM. The ECG could consider calculating at this stage only the most relevant indicators with respect to the objectives. Finally, previous recommendations and L2 indicators make possible to select a list of the most cost-effective measures ECMs to reach the sustainable objectives that the city desires.

Scenarios are tools to predict the results that could be obtained in case of their implementation. There is a high number of possible ECMs combinations, so it is necessary to generate the scenarios with the information already obtained, considering also experts' intuition and experience. The procedure proposed starts defining those measures considered as indispensable to proceed with the intervention as the starting point. Then, the rest of scenarios are defined increasing the performance from that set point. They are sorted in three groups depending on the €/Kg CO_2 savings ratio estimation – basic, efficient and advanced.

When each scenario is specified, it is necessary to recapitulate the information to analyze the retrofitting scenarios as units in next Phase IV, due to the result of the combination of some ECMs could be different from the addition of the individual results.

Phase IV: Prioritization and selection of the intervention scenario

The objective of this phase is to identify the most convenient solution from the potential scenarios. The ECG expertise, Level 2 indicators applied to the alternative scenarios and multi-criteria analysis, are the basis for the decision-making process. Finally, the discussion is expected to be carried out between technicians, citizens and local authorities.

The first step is focused on the **evaluation of alternative scenarios**. Here, the results of the different scenarios defined in the Phase III are evaluated considering the economic, social, technical and environmental dimensions. With this aim the defined Level 2 indicators at project level are evaluated for each scenario following different approaches, such as energy simulation tools for district renovation, building information modelling (BIM), geographic information systems (GIS) tools and the Life Cycle Analysis (LCA).

The results obtained from this analysis are used in the **scenario prioritization** step. It is necessary to take into account that the prioritization of strategies and scenarios needs to be based on the evaluation of a number of criteria that cannot be optimized simultaneously. Therefore, in the context of urban energy planning it can be said that there is no a unique optimum scenario within the set of alternative options for achieving a specific goal for the city.

Different methodologies are needed to support the decision-making once the evaluation studies have been carried out. With this aim, Multi-criteria Decision Analysis (MCDA) offers a wide range of methodologies and tools to

support decision-makers, allowing the combination of their own preferences with the data available (from modelling or not) to reach their own conclusions in a structured and consistent way. In the last few decades, the number of MCDA methods has substantially increased and nowadays, there are hundreds of methods available (Hobbs & Horn, 1997). Many studies and different classifications of these methods can be found in the literature. In the review carried out by (Pohekar & Ramachandran, 2004), an assessment of more than 60 studies regarding the application of multi-criteria decision making to sustainable energy planning is presented. In the same way, the study by Diaz-Balteiro *et al.* (Diaz-Balteiro, González-Pachón, & Romero, 2016) offers an extensive review of 271 papers using MCDA methods for measuring systems sustainability. The study shows that the use of methodologies such as the AHP developed by Saaty (Saaty, 1980) is in general, increasing in recent years. From the literature review, it can be concluded that using multi-criteria analysis in the context of urban renovation has attracted the attention of decision makers for a long time and that although there is not a specific method that can be prioritized, some of them seem to be more appropriate if we consider the development of the last few years. For CITyFiED methodology, the method proposed for the prioritization, in order to combine both the quantitative results of the scenarios and the qualitative relevance of each criterion, is the AHP.

In the first step of the application of the AHP method, a **disaggregation of the problem** has to be done defining a hierarchy of the interrelated elements, identifying the general objective, the specific objectives or criteria and the potential alternatives or scenarios.

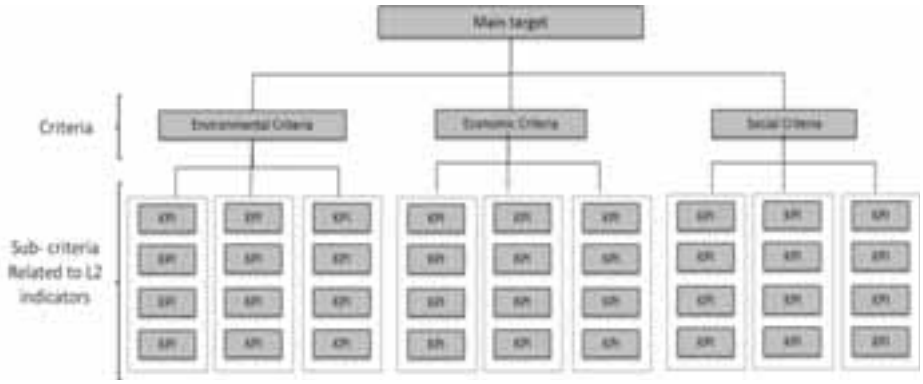

Fig. 5: Hierarchical problem structuring example

The specific objectives defined at district scale in the Phase II can be used as the basis to define the main criteria for the prioritization. In the same way, the sub-criteria that contribute to the consecution of the specific criteria can be related to the Level 2 indicators evaluated for each scenario. Therefore, for the identification and selection of the prioritization criteria, a clear connection can be made at this stage with the Level 2 indicators. This decision will be taken by an open dialog and consensus between technicians and local authorities. Including public participation at this stage of the process and taking it into account in the decision making is really relevant for engaging citizens in climate challenge.

In a second step, the **weighting of each criterion** needs to be also defined following the same procedure. Finally, through the complete application of the AHP method, the evaluation of the performance of each scenario for each prioritization criteria is carried out. The scenario with the highest result is identified as the most suitable one.

Phase V: Strategies for Sustainable Urban Renovation (SSUR)

The main target of this phase is to define the set of Strategies for Sustainable Urban Renovation (SSUR) where the ECMs of the selected scenario are further developed. In addition, these strategies should be integrated within the Strategic Urban Plan of the city, as a long-term vision plan for the city.

Local authorities, especially the Technical committee - and the ECG if it is desired by the Municipality – are in charge on the development of the SSUR, which is understood as a highly participatory management tool, that is to say this document is a process, not a project. It contents all the development of the previous phases.

First of all, the documents presents the causes for developing a Strategy for Sustainable Urban Renovation, the past of the city is explained as well as current situation. This means to give the answers to the questions *where do we come from?* And *where are we?* The vision of the city from Phase I is defined, by explaining the local authorities' motivations for implement sustainable strategies; *Where do we want to go?*

Secondly, the document exposures the work done by the ECG together with the Technical committee regarding the city analysis and diagnosis, the scope definition, to be specific, the district selected. Moreover, it is also presented the scenarios evaluation and the final selection.

Finally, it presents the Strategy which compromises *"a co-ordinated set of participatory and continuously improving processes of analysis, debate, capacity-strengthening, planning and investment, which integrates the economic, social and environmental objectives of society, seeking trade-offs where this is not possible"* (OECD 2001).

The Strategy does not end with the exposure of the selected scenario in Phase IV, but also it will guide and coordinates the process during its implementation through a **Strategy Implementation Plan (SIP)**, which will detail the intervention actions to be applied in the district, the schedule which includes a temporary planning for each actuation line during the period of SIP´s life, and finally the budget of the implementation plan.

On the other hand, one of the most important aspects during the definition of the strategies is the need to guarantee its success through not only ensuring an **effective participation of the citizens** (CoM, 2010), but also the identification of the **non-technological barriers** and the **potential business models** that will enable the realization of specific strategies.

Non-technological aspects, such as financial, organizational, legal, cultural and social, have be explored during the process (from phases I to IV). For that, a participatory methodology was designed in CITyFiED project to involve key stakeholders, this procedure is based on interviews that should be adapted according to the specific of the cities to identify the barriers and potential for energy efficient retrofitting.

CITyFiED Methodology will proposed also a mechanism to analyse possible business models and investment schemes for the cities to identify the most convenient, in order to minimize gaps and risks of the suggested strategies.

Last but not least, the document Strategies for Sustainable Urban City Renovation should detail recommendations to ensure that the skip from Planning to Implementation phases will be done properly. In that sense, the Strategy should define the **Method of Procurement (MOP),** detailing the factors that influence it, such us project characteristics, cost issues, timing, external factors, client resources, etc.

In addition, recommendations for the Monitoring and Impact Assessment Evaluation Phase (Phase VII) are also given, regarding the need to develop a **Sustainable Evaluation Plan (SEP)**, which coordinates the activities and guarantee the city goals achievement. The SEP, understood as a protocol to evaluate the sustainability and quality of the interventions at district level after their implementation (Phase VI). It should be based on the evaluation of the energy performance and energy savings through well-known Measurement & Verification (M&V) protocols (e.g. IPMVP, FEMP or ASHRAE), the economic issues, such as return of investment (ROI) and cost effectiveness of the solutions, the Quality control of the interventions, the Social acceptance and a Life Cycle Analysis (LCA), to evaluate the CO_2 emission reduction.

Phase VI: Execution plan

The strategies from the SSUR document are implemented in this phase, according to the recommendations from planning to implementation and the SEP guidelines pre-defined in Phase V. The detail definition of these activities depend in other aspects, i.e., technical definition, that could not be defined before the SSUR. Therefore, these issues and specific guidelines to put into practice the strategies – delivery method, procurement process, risk allocation, etc. - are further developed in Phase VI, acting as an overall Execution Plan.

The Municipality, the ECG and financial institutions are involved in these activities, as well as building owners and citizens. Contracting parties group are the principal figure for the execution of works, including designers, ESCOs, energy suppliers, technology providers, etc. Their participation starts at this stage because in public procurements they usually have to be selected through a tender/bidding process.

Part of the execution procedure is to clarify the **financial resources** to put into practice the SSUR according to the Business model identified and the ownership of the properties to be renovated. In the case of public ownership of the buildings the Municipality usually acts as financier; while in private ownership the ESCO business model is highly recommended. The most relevant public financing mechanisms are grants, interest subsidies, revolving funds and financial instruments (Núñez *et al.*, 2013).

A **Project Delivery Method** has to be identified by the Municipality to define the contracting formats between the stakeholders to achieve the delivery (CMAA, 2012). There are different methods but the most recommended is the Integrated Project Delivery (IPD), defined as "*a collaborative alliance (...) that harnesses the talents and insights of all participants to optimize project results, increase value to the owner, reduce waste, and maximize efficiency (...)*" (AIA, 2007) . Its principles focus on the collaboration since the beginning of the project to avoid future problems and the share of risks and responsibilities between the stakeholders.

The Procurement starts after, to define the process of services or works acquisition for the implementation of the strategies. In public procurement is usually mandatory to select the entities through a tender/bidding process. Attending to the scope the Municipality could contract just the implementation (Build), if it wills to develop the technical definition of the strategies. By contrary, it could offer the design and the execution to different entities (Design / Build) or the same one (Design + Build). The winners of the tender will be part of the Contracting parties group. The tender documents can be prescriptive if the requirements are technically specified or performance based, and in the second case also related to reduce the environmental impact what is known as sustainable procurement (Pless *et al*., 2012).

In parallel to the two previous activities, the district and strategies need to be further developed into detail from the technical and economical perspectives. It is recommended to support the technical definition on BIM approach that allows to address responsibilities, layouts, schedule, risks, etc. in a collaborative framework, and it is identified as the most adequate to maximize the benefits of IPD principles (AIA, 2007). Depending on the procurement selected the technical definition of the strategies is performed before or after tender/bidding processes.

Another relevant aspect is to include a **Risk Management Plan** in the context of IPD, to eliminate or reduce the risk that could be avoided, establish mitigation actions to reduce the probability of occurrence, or develop contingency strategies for those risks that could be predicted or avoided (Association of Project Managers, 2000).

The follow-up strategy during the execution of works (Phase VI) and evaluation phase (Phase VII) is the SEP already pre-defined in SSUR document and that is completed by the Monitoring and Technical Committees during this phase once the technical definition of the strategies is achieved. The follow-up of the intervention should be reported monthly or bimonthly, and gathered in annual reports in the SSUR. In parallel, regular meetings should be established between the actors involved to control and make decisions and changes approval.

Phase VII: Monitoring and impact assessment evaluation

The main objective of this last phase is to evaluate and monitor the strategies implemented during the previous phase, because at this stage, actions and construction works are completed, so it is necessary to **assess the impact in the sustainability at district and city level**, and finally to deploy **corrective actions** if the impact obtained it is not the expected. So that, the objective of the monitoring plan is twofold, evaluate the performance and impact of the strategies at district level (Level 2 indicators) and city level (Level 3 indicators).

Within CITyFiED project a Sustainable Evaluation Plan (SEP) has been defined (CITyFiED, D4.10) in order to assess the impact in the sustainability at district/project level. The objective of the plan developed was to reduce the complexity of some existing standards such as BREEAM and/or LEED and integrate new pillars in the evaluation according to the new trends, i.e. ICTs and LCA. Thus, Fig. 6 illustrates the protocol proposed, including its pillars: Energy, ICTs, Quality control of interventions, Economic evaluation, Social acceptance and LCA.

As it can be seen in Fig. 6, the left hand side represents the analysis before the implementation (Baseline calculated during Phase II), meanwhile the right hand side denotes the assessment after intervention; at the top, Level 2 indicators (KPIs) give an objective the framework for calculating the evidences of assessment, and at the bottom, LCA covers the project from the beginning to the end of the works. In the middle, the ECMs appear, which refer to the interventions themselves.

Starting from the left hand side, it is shown that the energy concerns begin with social awareness, both at citizens' level and at organizational level (public authorities, sustainability plans, etc.). Collecting all these aspects through metering determines the retrofitting strategy as well as the best ECM for the specific building or district.

On the right hand side, the status after the execution phase is evaluated. The main aspect is the energy performance in terms of energy savings, which is partially achieved by the investment in new ICT technologies (digital homes),

and the ECMs. To ensure the expected energy savings, the ECM has to be implemented in the correct way following Quality Control of interventions rules during Phase VI. These energy savings drive to cost savings at consumption. And thanks to the energy efficiency, less invoice costs and new technologies, together with the involvement of citizens, the social acceptance of these solutions is increased.

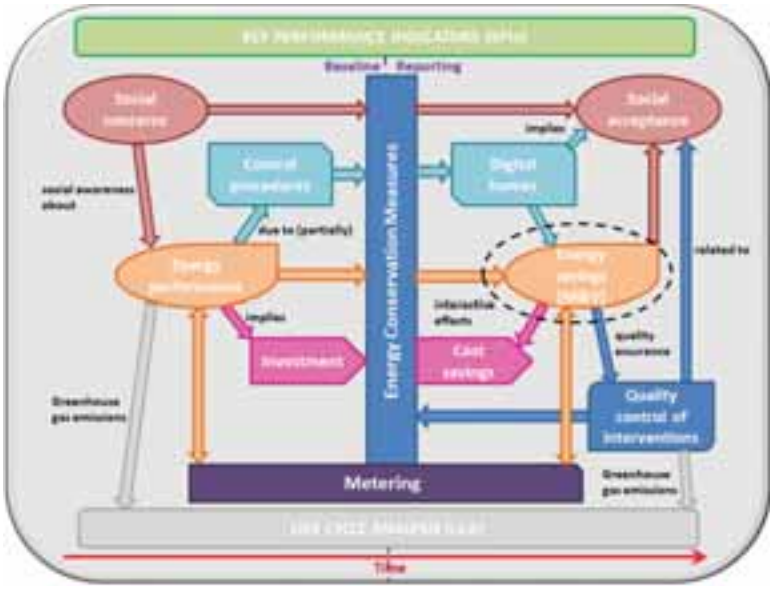

Fig. 6: CITyFiED Sustainability Evaluation Plan (SEP) at district level

The CITyFiED Methodology, as a systematic process, considers that if the results obtained after the deployment of the SEP not achieve the expected results at district level, corrective actions should be applied, starting from the analysis of SSUR if necessary. The deviation between the expected results and the obtained ones, is part of the evaluation and means that the General and Specific objectives defined during Phase I and II are only partially achieved. This experience is part of the correction actions for future city renovations that all the stakeholders from the Municipality should consider, too.

In the same way, the impact of the interventions at city level will be evaluated. For that purpose, there was defined a set of indicators (Level 3: Impact Assessment Indicators at city level) in order to evaluate the following categories of impacts after the strategy implementation: *Energy impact:* Energy savings obtained; *Environment impact:* CO_2 emissions avoided with the intervention; *Economic impact:* investment mobilized and its return to the users, companies and municipalities as well as benefits of retrofitting to the users associated to the cost savings; and *Benefits for SMEs.*

4. Conclusions

This Methodology is a holistic procedure for the city renovation at district level that considers a multi-criteria perspective. The integration of the three levels of indicators supports the diagnosis, selection as well as final evaluation of measures and retrofitting scenarios during the project, serving as a control and decision-making tool. The CITyFiED project aims to enable the replicability and mass-market deployment of energy-efficient retrofit of districts. The approach and the indicators were conceived and are being refined considering as a reference the large CITyFiED demonstration cases in the cities of Lund (Sweden), Laguna de Duero (Spain) and Soma (Turkey), including decision-making processes and business models. The approach is also being validated through the active participation of the CITyFiED network of cities, assuring its flexibility and adaptability to different European cities. Then, the future work is to complete its development, continue its external validation activities with the CITyFiED network of cities and extract conclusions.

Acknowledgments: This project has received funding from the European Union's Seventh Programme for research, technological development and demonstration under grant agreement N° 609129. The authors would like to thank the rest of the partners of the CITyFiED project for their help and support.

References

American Institute of Architects California Council, 2007. *Integrated Project Delivery – A Working Definition*.

ASHRAE Guideline 14-2002, June 2002. *Measurement of Energy and Demand Savings*, ASHRAE Standards Committee,

Bourdic, L., & Salat, S., 2012. Building energy models and assessment systems at the district and city scales: a review. *Building Research & Information*, *40*(4), 518–526.

Broere, W., 2015. Urban underground space: Solving the problems of today's cities. Tunnelling and Underground Space Technology.

CITyFiED Consortium, 2017. *CITyFiED Project, Grant Agreement no. 609129*.

Covenant of Mayors, 2010. *How to develop a Sustainable Energy Action Plan (SEAP) - Guidebook*. Belgium: Publication Office of the European Union.

Diaz-Balteiro, L., González-Pachón, J., & Romero, C. (2016). *Measuring systems sustainability with multi-criteria methods: A critical review.* European Journal of Operational Research, 258(2), 607–616.

Dijkstra, L., Poelman, H., 2012. *Cities in Europe. The new OECD-EC definition.*

Efficiency Valuation Organization. (September 2010). *International Performance Measurement and Verification Protocol, Concepts and Options for Determining Energy and Water Savings*, Volume 1, EVO 10000 – 1:2010.

Dodd, N., Garbarino, E., Gama, M., 2016. *Green Public procurement Criteria for Office Building Design, Construction and Management. Joint Research Centre.* EC.

Eurostat. (2016). *Urban Europe. Statistics on cities, towns and suburbs.*

FEMP M&V Guidelines, *The M&V Guidelines: Measurement and Verification for Federal Energy Management Projects*, U.S. Department of Energy, Version 3.0.

Hernández, J.L., García, J., Zubia, C., Pablos, L., Cueva, F., Vasallo, A. *Novel sustainability assessment procedure proposal for Smart Cities*, Central Europe towards Sustainable Building 2016 (CESB 2016), Prague, Czech Republic, 22-24 June 2016.

Hobbs, B. F., & Horn, G. T. F. (1997). *Building public confidence in energy planning: a multimethod MCDM approach to demand-side planning at BC gas.* Energ. Pol., 25(3), 357–375.

Martos, a., Pacheco-Torres, R., Ordóñez, J., & Jadraque-Gago, E. (2016). *Towards successful environmental performance of sustainable cities: Intervening sectors. A review. Renewable and Sustainable Energy Reviews, 57*, 479–495.

Núñex, F., Olivero, S., Medarova-Bergstorm, K., Rizos, V., 2013. *Financing models for smart cities. Guidance document. Financing Working Group. Smart Cities Stakeholder Platform.*

OECD. (2001). *Strategies for Sustainable Development*. The DAC guidelines. France. pp. 16.

Petts, J., Leach, B.. 2000. *Evaluating Methods for Public participation: Literature Review. R&D Technical Report E135.* Bristol: Environment Agency. pp. 26-33.

Pohekar, S. D., & Ramachandran, M. (2004). *Application of multi-criteria decision making to sustainable energy planning - A review. Renewable and Sustainable Energy Reviews, 8*(4), 365–381.

Saaty, T. (1980). *The analytic hierarchy process.* New York: McGraw-Hill.

Smart Cities Council, 2013. *Smart Cities' readiness guide. The planning manual for building tomorrow's cities today.*

Swan, L. G., & Ugursal, V. I. (2009). *Modeling of end-use energy consumption in the residential sector: A review of modeling techniques. Renewable and Sustainable Energy Reviews, 13*(8), 1819–1835.

The Association of Project Managers, 2000. *Project risk analysis and management.* Great Britain.

The Construction Management Association of America (CMAA), 2012. *An owner's guide to project delivery methods.*

United Nations. (2014). *World Urbanisation Prospects.*

URBACT II. (2015). *Sustainable regeneration in urban areas*

World Bank, 1999. *World Development Report 1999/2000: Entering the 21st Century*. Ch. 6.

Web References:

BPIE EU Buildings database <http://ec.europa.eu/energy/en/eu-buildings-database> September 2017

Energy eficiency directive <https://ec.europa.eu/energy/en/topics/energy-efficiency/energy-efficiency-directive> March 2017

EnergyPlus. Building Energy Simulation Software. Retrieved from <http://apps1.eere.energy.gov/buildings/energyplus/> September 2017

Technical Committee ISO TC/268 <http://www.iso.org/iso/home/standards_development/list_of_iso_technical_committees/iso_technical_committee.htm?commid=656906>, March 2017

PLEEC Project <http://model.pleecproject.eu> March 2017

Urban Regeneration Decision Tool by World Bank <http://urban-regeneration.worldbank.org/about>, March 2017

Responsible Retrofit Guidance Wheel of the Sustainable Traditional Buildings Alliance (STBA) <http://responsible-retrofit.org/wheel/> September 2017

Urban Planning for Solar Energy – IEA SHC TASK 51

Maria Wall[1], Mark Snow[2], Johan Dahlberg[3], Marja Lundgren[3], Carmel Lindkvist[4], Gabriele Lobaccaro[5], Tanja Siems[6], Katharina Simon[6] and Maria Cristina Munari Probst[7]

[1] Energy and Building Design/Lund University, Lund (Sweden)

[2] Faculty of the Built Environment (FBE)/UNSW, Sydney (Australia)

[3] White Arkitekter AB, Stockholm (Sweden)

[4] Department of Architecture and Planning/NTNU, Trondheim (Norway)

[5] Department of Architecture and Technology/NTNU, Trondheim (Norway)

[6] Institute for Urban Design and Urban Research/University of Wuppertal, Wuppertal (Germany)

[7] Laboratory for Solar Energy and Building Physics (LESO-PB)/EPFL, Lausanne (Switzerland)

Abstract

An increased use of solar energy is a key ingredient for forging resilient cities. This recognises the importance of the urban fabric being able to use renewable energy sources to become increasingly self-sustainable. In that regard, the integration of active solar energy systems in the built environment will allow cities to reach a high level of sustainability. In this framework, the main objective of the IEA SHC Task 51 Solar Energy in Urban Planning, was to provide support to urban planners, authorities and architects to develop urban areas with architecturally integrated solar energy solutions. The scope includes solar energy issues related to new and existing urban development areas and sensitive solar landscapes. This paper presents an overview of the Task's results from 11 countries including reviews on legal framework, barriers and opportunities, on planning processes and on educational issues. Approaches, methods and tools are presented as well as a collection of case stories with lessons learnt and a web-based learning platform.

Keywords: solar energy, urban planning, solar landscapes, methods, tools, education, case stories, IEA

1. Introduction

A large portion of the potential for energy efficiency in existing buildings and potential to utilize solar energy still remains unused. Globally, goals and specific targets are set up to reduce our environmental impact on climate and secure future supply of energy. The built environment accounts for over 40% of the world's total primary energy use and 24% of greenhouse gas emissions (Hegger et al, 2008). A combination of making buildings more energy-efficient and using a larger fraction of renewable energy is therefore a key issue. Political statements and directives are already moving towards zero-energy buildings and communities (Sartori et al, 2010; Voss and Musall, 2011). An increased use of solar energy, enabling renewable energy supply, is firmly acknowledged as a key ingredient for forging resilience and future proofing of our cities on the one hand. On the other hand, it is an important part of the development ahead, where the urban fabric strives to utilize passive solar gains and daylight to reduce the energy use in buildings and for lighting outdoor environments, as well as to improve the inhabitants' comfort (Compagnon, 2004).

The main objective of the IEA Solar Heating & Cooling Programme, Task 51 Solar Energy in Urban Planning, is to provide support to urban planners, authorities and architects to achieve urban areas, and eventually whole cities, with architecturally integrated solar energy solutions (active and passive). The objective contributes to urban planning by providing guidance for urban planners and policy makers on a large fraction of renewable energy supply. This includes approaches, methods and tools capable of assisting cities in developing a long term urban solar energy strategy. Heritage and aesthetic issues are carefully considered. Also, the goal is to prepare for and strengthen education at universities on solar energy in urban planning, by testing and developing teaching material for programmes in architecture, architectural engineering and urban planning. The material will serve a dual

doi:10.18086/swc.2017.37.06 Available at http://proceedings.ises.org

purpose by being inclusive for postgraduate courses and continuing professional development (CPD).

The scope of the Task includes solar energy issues related to 1) new urban area development, 2) existing urban area development and 3) sensitive and protected landscapes (solar fields). Both solar thermal and photovoltaics are taken into account. In addition, passive solar - as passive solar heating, daylight access and outdoor thermal comfort - is considered in the urban environment. Solar energy integration in existing and in new city districts are two different contexts with different opportunities and constraints. Furthermore, ground based active solar applications are interfacing with urban environments, creating solar landscapes that juxtaposition with the existing urban form with varying levels of aesthetic acceptance. In open landscapes, solar fields need to harmonize with the rural landscape and nature. Understanding the existing parameters under which planners operate and the challenges this presents is a key consideration of this Task.

2. Objectives, materials and methods

The Task's work started in 2013 and ends in 2017: it involved a consolidated scientific collaboration between researchers and practitioners from Australia, Austria, Canada, China, Denmark, France, Germany, Italy, Luxembourg (observer), Norway, Sweden and Switzerland. The Task was structured in four Subtasks:

Subtask A: Legal framework, barriers and opportunities. Lead: Australia.

Subtask B: Processes, methods and tools. Lead: Sweden.

Subtask C: Case studies and action research. Lead: Norway.

Subtask D: Education and dissemination. Lead: Germany.

Subtask A sets the current boundary conditions for solar integration, deals with the assessment of available potential and elucidates opportunities. Subtask B deals with processes, methods and tools and developments for the applied phase related to specific situations (new development areas, existing urban areas, landscapes). Subtask C focuses on implementation issues e.g. tests of processes, methods and tools, through case stories and showing relevant examples as case studies. Finally, Subtask D covers the dissemination focused on tertiary education and continuing professional development (CPD). The whole Task was led by Sweden.

Although Task 51 is organized in different subtasks, most of the work has been collaborative across subtasks. A central part of the work was carried out as action research. Action research is a reflective process of progressive problem solving led by individuals working with others in teams or as part of a "community of practice" to improve the way they address issues and solve problems (Stringer, 2014). Action research involves the process of actively participating in an organization change situation whilst conducting research. In Task 51, this was reflected in the participants' collaboration with urban planners and other key actors within local urban planning developments in each participating country. In this way information about important issues to address was identified. The goal has then been to develop knowledge that is useful for practicing urban planners and for education of architects and planners.

For Subtask A, a historical reflection was completed in parallel with sourcing country information regarding the legislative frameworks and voluntary initiatives that impact on the uptake of solar energy in urban areas. This included a review of legal cases that define the treatment and judgement of decisions where solar energy implementation was claimed to have created conflict or where urban development threatened solar access of existing systems. Whilst the treatment of passive solar protection is well defined, the research looked to review how active solar technologies are applied to urban environments and the planning controls that might promote or constrain their use. It also investigated the cultural and aesthetic sensitivities and parameters directly affecting technological choice and the acceptable application of urban solar systems.

The main topic in Subtask B was the planning process descriptions. Through collecting and sharing knowledge among experts in Task 51, the local planning prerequisites, including legislation and praxis, have been analysed in order to find commonalities to describe a generic planning process valid across countries in Subtask B. This work was carried out first on a national level by the experts collecting and describing the formal and informal planning processes through the steps of 1) short interviews during the Task definition phase, 2) analyzing legislation and 3) expert participation in urban planning projects in the form of action research. The aim was to explore when and how knowledge on solar energy (passive and active strategies) could enter planning processes.

The work on collecting local legislation and praxis has been reported in a common report between Subtask A on Legislation and Subtask B on Processes, Methods and Tools. In Task meetings, workshops were held where the experts analyzed national planning process similarities between different countries. The experts then agreed upon a common generic planning process described at different spatial scales, showing what actually is taking place in urban planning in all these cases. The scales found in all countries were 1) comprehensive/strategical planning scale 1:2000-1:100 000, 2) urban and landscape design scale 1:1000-1:5000, 3) detailed development plans 1:500-1:2000 and 4) architectural design stage 1:10-1:500.

Another objective in Subtask B was to identify supportive instruments that can assist planners during the planning process. These supportive instruments were defined as *Approaches*, i.e. means of incorporating solar methods and tools, *Methods*, i.e. planned procedures to assess and evaluate solar in relation to other aspects in urban planning (including landscape planning) and *Tools,* i.e. a rule of thumb, a calculation or a modelling software giving geometrical or numerical results; e.g. solar maps, solar potential software, GIS software, etc. This definition also implies a hierarchy where approaches include methods that incorporate tools in a planned procedure. The identification of existing as well as the development of new approaches, methods and tools was carried out during the action research work within national planning contexts and is presented in a report on *Approaches, methods and tools for enhancing solar energy* targeting urban planners. The approaches, methods and tools within the scope are instruments to support decision-making and to combine qualitative and quantitative aspects of relevance for spatial concerns in urban planning.

Bringing the generic planning process and the existing and new approaches, methods and tools on active and passive (daylight, solar gains and micro climate) solar measures together creates the base for the guidelines, developed as a homepage. The aims are to inform and support decision-making, orienting on existing and new approaches, methods and tools to inspire planners to find new ways of developing the planning process to enhance solar energy in the urban and landscape context.

The main objective of Subtask C was to stimulate successful practice and facilitate its replicability, by documenting experiences, helping cities avoid pitfalls already encountered by others, and creating arenas for mutual interaction between researchers and city managers. In that regard, the work was focused on case stories of new, existing urban areas and landscape planning related to active solar systems (both photovoltaics and solar thermal) and interrelated technical (i.e. solar potential, cost investment, product technology, energy production, daylight, quality of visibility etc.) and non-technical aspects (i.e. planning process, right of light, policy and legislation, etc.). More than 30 case stories from 11 countries have been analysed and compared in extensive reports (Lobaccaro et al., 2017). Lessons learnt for different targets groups have been condensed into guidelines for solar energy in urban planning (Fig. 1). Finally, a webpage of case studies linked to a world-map has been established. This serves as a user-friendly consultation and dissemination instrument: it is a sort of case stories' platform from which the users can download dedicated brochures where detailed information related to both single case stories and/or the case study comparisons have been collected.

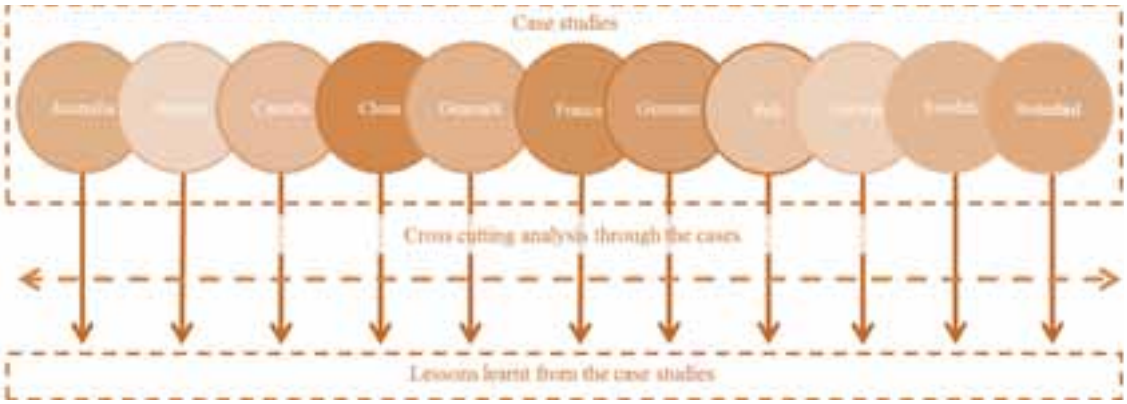

Fig. 1: A scheme of the methodology used for the case studies analysis

The work on education and dissemination in Subtask D started with a review of the present situation (Fig. 2). As a first step, existing courses and software tools in nine countries were surveyed and evaluated. The applied methodologies were based on a developed questionnaire handed out to a broad range of international institutes of

urban planning and direct interviews with researchers and academics were undertaken.

An overview of existing software tools within solar energy was generated. These tools where tested and evaluated by students through an urban design task. Various criteria were applied such as usability, integration into other popular 3D modelling software and readability of results. Based on the results, it became evident that there was a lack of existing courses on solar energy in the urban context for students. This formed the basis for the development of an e-learning platform including a software package. This platform was then tested and evaluated during a series of symposia with experts and practitioners.

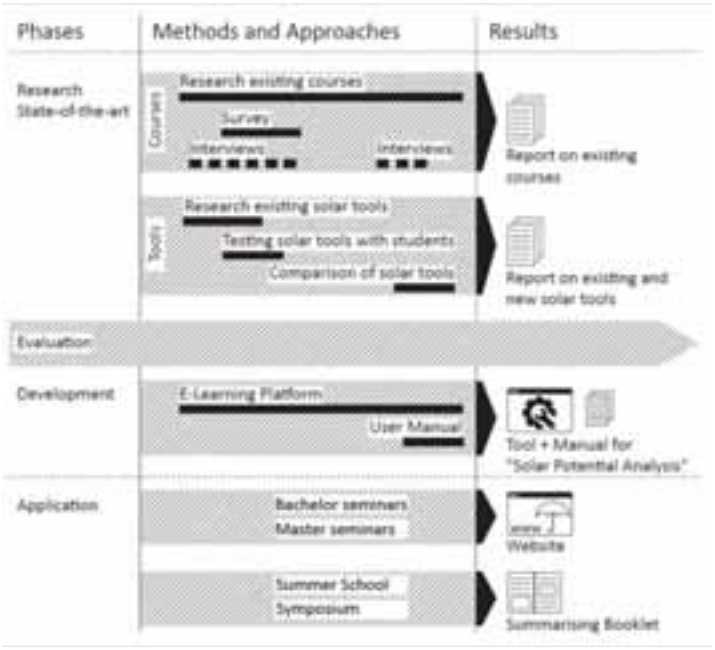

Figure 2: Overview of the methodology and approach concerning education and dissemination (Source: Subtask D, K. Simon)

3. Results

The Task is now in its final stage with some results already published. All results will be available as soon as they go through the review process within the IEA SHC programme. Main results are presented and discussed below.

3.1 Legislation and voluntary initiatives

The current status of solar energy in urban planning regarding legislation and voluntary initiatives were documented from 11 countries. As a starting point, recognition was given that many ancient civilizations have purposefully harnessed the sun's energy to add comfort to living spaces (Butti and Perlin, 1980) and incorporated into the rule of law safeguards to protect its practical inclusion as evidenced by ancient lights proclamations and Greek philosopher Hippocrates's air light treatise enshrining the sensible use of sunlight along with clear air and water. These well-founded learnings have witnessed significant upheaval through the technological innovation of electricity and urban densification pressures and consequently changing planning values and priorities. Urban plans and building widths, building heights, story heights, façade design and window heights did, until the early 20th century, comply with the physics of daylight distribution and natural ventilation (Lechner, 2008). This meant a certain limitation in widths and heights already on an urban level. When electricity and mechanical ventilation started to support the indoor climate as a standard, these limitations were broken and significant knowledge was lost during the second half of the 20th century.

The increased population growth in combination with the environmental gains of walkable and public transport cities, as well as higher real estate prices in the city centre work towards increased density. Increased density will at certain points at different latitudes be counterproductive for energy use, since both electricity demand will rise due to low winter daylight levels and summer cooling loads increase when natural cooling is diminished. The contrasting relationships between building energy use and transport energy use after certain levels of density and urban form have been eloquently presented by Steemers (2003). Research has shown that the relation between

density and lower daylight is not linear, but relates to urban and building design. This pinpoints the important role of urban planning in harnessing daylight as a natural source instead of using electricity and also utilising building integrated solar structures for onsite energy generation and thermal shading that does not prohibit natural light entering buildings.

As the deployment of active solar energy systems has grown in cities, the challenge of protecting sufficient solar access into the future becomes more prominent as urban consolidation and densification intensifies (Snow and Prasad, 2011). Within this context is also the critical pursuit of energy-efficient buildings as well as achieving comfortable urban environments (Samimi and Nasrollahi, 2014). Whilst the provision of solar access rights has historically focused on daylight (Lechner, 2014), there is an emerging need to revisit the legal framework and the extent to which it enhances or hinders deployment of sustainable energy technologies. Despite the need to establish a satisfactory legal regime for solar access protection was recognised many ago, the analysis from national perspectives is that the law on this issue is still unsatisfactory. There is considerable scope for legal reform in many countries and the typical subjective judgement of considering solar access under the characterisation of 'nuisance' creates significant investment uncertainty and barriers to uptake that could be remedied by more informed decision-making processes.

3.2 Solar energy in urban planning processes

Urban planning is a political process that exists to balance society's common interests against individual interest mainly when it comes to land use. The political process as well as the planning process differs between national, regional and local contexts (Newman and Thornley, 1996). The smallest common denominator is that all urban planning deals with land use regulation in some way.

The focus of urban planning and the power of land allocation differs somewhat between countries. This implies that the possibility to affect urban planning to implement solar energy to a higher extent differs as well. In some countries, the largest potential may be to influence local planners on the municipal level who have a large influence on the built environment while in other countries the potential may lie with influencing decision makers on a regional or national scale who can more directly influence policy and legal instruments on a wider scale.

A comparison between studied local processes has been carried out by experts which has shown that a generic planning process can be described using a spatial scale. Other aspects that relate to administrative and legal frameworks in planning, i.e. laws and regulations, policies, ambitions, voluntary initiatives etc. are too dependent on local contexts to generalize.

The generic planning process developed in Task 51 involves four stages; 1) comprehensive/strategical planning, 2) urban and landscape design, 3) detailed development plans and 4) architectural design (Fig. 3). Also, approaches, methods and tools (AMTs) have been collected, summarised and related to which specific stage of the urban planning process they are relevant. The AMTs can be divided into four types; 1) regulatory, policy and governance approaches, 2) integrated design and planning support, 3) assessment methods and tools and 4) awareness and consultation methods. Each type is exemplified with existing or newly developed AMTs and relate to the four stages of the urban planning process.

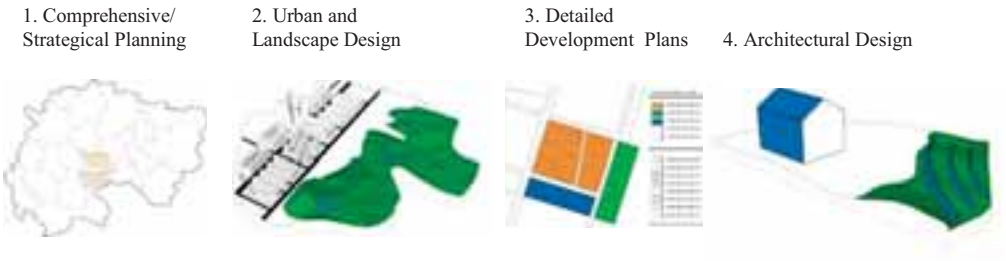

Fig. 3: Illustration of four stages of urban planning

Guidelines for comprehensive/strategical planning

Within comprehensive/strategical planning, visions and strategies to reach certain goals are developed and connected to land use and zoning. Plans can be regional and/or at municipal/city scale. Examples of key

considerations and decisions taken at this stage are; visions for cities/municipalities, general land use, larger infrastructure etc.

Comprehensive and strategic planning are often visionary plans stretching 20-30 years, which gives a general direction for a city, municipality or region. They are used to identify potential development areas and the need for larger infrastructure but should also include a clear idea of how to provide the city, municipality and/or region with clean energy. Solar maps are one of the most common and efficient methods of integrating solar energy at this scale, which acts as an inventory of the solar potential in existing urban structures (Kanters et al., 2014). Solar maps can also be used to overlay solar potential with other aspects such as heritage concerns, energy infrastructure, future renewable energy goals and the impact of new urban developments on existing urban fabric. As active solar and daylight will become more and more present in urban planning, there is a need for targets, goals and assessments in early comprehensive and strategic planning stages.

Guidelines for urban and landscape design

In the urban and landscape design stages, the urban fabric and morphology is decided for a city district and for a landscape area. Examples of key considerations and decisions taken in this stage are street widths, volumes, typologies, spatial patterns and orientation.

New urban environments

Planning of new urban environments in the 21st century requires focus on the need for energy efficient design and an energy generating built environment. Urban planning is complex, and there is a need to bring in the relevant aspects at stake at the right stages of the planning process. This is in order to support spatial planning and energy, both relating to free energy such as daylight and to active solar, such as solar thermal and photovoltaics, for future urban development and renewal projects. In situations where new urban areas lack existing energy infrastructure, the possibilities for including solar energy are at their most favourable and the design scheme will be crucial.

The role of the urban planner is to design areas that can be built to last. For different reasons, solar energy installations may not be feasible when the area is designed, but buildings change over time while typologies and the urban fabric tend not to. An urban design that does not include solar energy considerations today may effectively hinder it in the future.

Major aspects that have a large impact on solar energy potential are density, street widths, building heights, roof angles i.e. the typology of an area (Kanters, 2015). Today the solar energy potential can easily be estimated through rough simulations from early drawings to more detailed models. A rule of thumb is that the more complex the model, the more complex the simulation.

In urban areas, solar energy also needs to be considered from a load matching perspective. Load matching implies that the solar energy generation is compared to the energy use of buildings and neighbourhoods (Voss and Musall, 2011). This is meaningful because solar energy in urban areas is most relevant when the generated energy is used locally rather than exported to the electrical grid or a district heating system. Criteria for load matching evaluation annually can easily be estimated through a comparison between local energy performance standards and a solar potential study although it is also important to consider seasonal and daily variations in energy use and potential energy generation. In e.g. northern latitude countries this is imperative as energy use peaks at night and in winter while solar energy generation peaks during the daytime and in summer.

Urban typologies also have a huge impact on daylight access both inside buildings but also on streets and public spaces. Studies and research show that different urban design proposals for the same density give very different daylight conditions and that the daylight design aspect on urban and building design scales are crucial for daytime, sunlit areas in dense areas (Baek Pedersen, 2009; Sattrup, 2012).

Existing Urban Areas

The existing building stock will have the biggest impact regarding climate emissions from operational energy use for the foreseeable future due to the high energy use compared to new buildings. Currently, most of the attention is devoted to the reduction of energy needs, but the transition towards a more comprehensive renovation including localized renewable energy generation is imperative. Prices for solar technologies are dropping and regulations are encouraging local energy generation. More than half of the global PV capacity from now to 2050 will be installed on buildings (IEA, 2014), producing a little less than half the total PV electricity needed. There is a risk that such a massive deployment will sometimes lead to prioritising only the return of investment for private owners

through a solar refurbishment, which is often riskier and less lucrative than early-design implementation for a new settlement.

This deep intervention on the urban morphology requires a rational method to properly organize the arrangement of installations according to site characteristics and a compromise between heritage protection, energy and spatial planning. A match between building energy needs, solar energy generation potential and site identity has to be aimed to tailor coherent strategies of solar refurbishment and define homogeneous zones with particular architectural integration quality requirements.

In order to deal with the local energy production, new methods and tools have been introduced into urban planning, such as assessment methods supporting urban planners and real estate owners in estimating the solar potentials of existing built surfaces. One major outcome of this Task is the LESO-QSV Method (Fig. 4), which is based on the above (Munari Probst and Roecker, 2015).

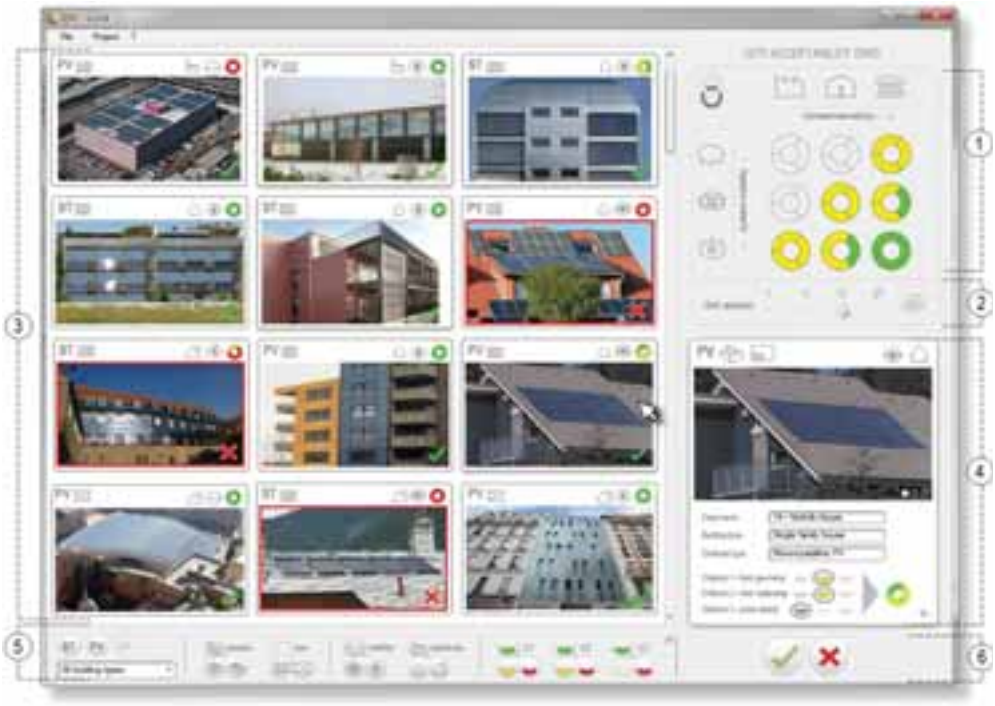

Fig. 4: Main screen of the LESO-QSV GRID program: 1 - Acceptability grid of the specific city: i.e. required integration quality for each criticity level (system visibility; context sensitivity). These are the criteria to be met for the installation to be accepted; 2 - Acceptability grid setting bar (for municipality use only): integration requirements can be selected by using pre-established grids (more or less severe), or built to measure; 3 - Integration examples showcase: a database of more than 100 cases is shown according to the selected filters setting (5). This showcase is meant to: help municipalities to set a convenient acceptability grid by showing the impact in acceptancy of pre-defined sets of quality requirements; work as a model for authorities for how to objectively evaluate integration quality; inspire architects, installers, building owners; 4 - Case details window: The window appears while clicking on a specific case. The detailed evaluation of quality becomes visible, together with other more precise information and additional pictures of the case; 5 - Filter bar: The case studies can be filtered according to solar system type, position, dimension, context sensitivity, system visibility, integration quality; 6 - Accepted / not accepted cases button filter. (Source: Maria Cristina Munari Probst and Christian Roecker)

Guidelines for detailed development plans

Detailed development plans set the implementation conditions for the urban design, and the land use is regulated into legally binding documents. Examples of key considerations and decisions taken in this stage are maximum building height, limitations on material choices and type of building (residential, office, school etc.).

Detailed development plans are legally binding documents that set the prerequisites for the building design in contrast to the more visionary process in the urban design stage. An important factor here is a meaningful dialogue between urban planners, the local authorities (both planning and building permit offices) and developers and real estate owners. Academic institutions and research institutes have proven to be front runners in driving and facilitating stakeholder dialogue and incorporating new solutions into urban planning. Since planning traditions vary and this is bound by local planning traditions and legal frameworks (Newman and Thornley, 1996), it is

difficult to give general advice.

Experiences have shown that specific requirements often attached to land procurement deals have in some cases proven an efficient approach to introducing solar energy in urban areas. Also, since the interest for solar energy is growing rapidly the concept of "solar rights" or "right to light" will probably need to be considered by many urban planners in the near future. Solar rights work differently in different contexts but involves cases where an existing building becomes shaded by a new building which can affect either daylight and sunlight access or energy output from a solar energy installation.

Guidelines for architectural design

At the architectural design stage, new and existing buildings or landscape integrated systems are designed, new or altered. Examples of key considerations and decisions taken in this stage are architectural composition and pattern/surface/facade design.

New buildings

The integration of solar energy in buildings has been studied extensively through the completed IEA SHC Task 41 – Solar Energy and Architecture. More information about this can be found here http://task41.iea-shc.org/. Also, a webpage on innovative solar products is available showing examples for building integration as continuation from the project IEA SHC Task 41 (Munari Probst et al, 2012; Wall et al, 2012).

Existing buildings

The reduction of building energy use and the replacement of fossil energy by renewables have become priorities for authorities and planners. As active solar is entering, architectural alteration, materiality, geometry and detailing in buildings can be affected, resulting in new forms of architectural expression which are slowly modifying our existing city landscapes. The increased use of active solar systems in buildings is necessary, but clearly poses major challenges for existing environments. The large size of solar systems at the building scale asks for thoughtful design, as these systems otherwise may end up compromising the aesthetics of the buildings, and may affect the identity and the quality of entire contexts. Luckily, good architectural integrations are possible also in the most critical situations, but they clearly need appropriate design and economic investments. A good knowledge of basic solar physics, of simple dimensioning tools for early design phases and currently available products designed for building integration can be very helpful for this purpose.

Before aesthetic standards can be established, objective criteria need to be developed. While it is often thought that aesthetics is a matter of taste, recent studies confirm the existence of clear criteria against which the suitability of solar power installations can be evaluated. Solar installations can be made qualitatively, evaluated through three simple and objective criteria: the project's geometry, materiality and modular pattern. These criteria provide a framework for assessing how harmoniously an installation fits into the surrounding urban environment. In several cities in Scandinavia, guidelines for stakeholders seeking building permits have been published with advice from IEA SHC Task 41 and in relation to the architectural guidelines regarding respect of existing qualities in the built environment. With additional support from the LESO-QSV method, several reference examples can be consulted. The method can also be used to create a "criticity" grid identifying different situations for which the municipal authorities will set quality standards in view of local considerations.

Approaches, methods and tools for solar energy

Urban planners are typically generalists who have to consider many different aspects. It is important that methods, tools and approaches are designed to aid urban planners in their work rather than increasing their workload. There exists a large amount of software tools today where solar insolation of an urban area can be calculated and visualised, but there is a lack of approaches and methods of how to integrate the results from such tools into traditional urban planning processes. The software tools available also vary in complexity, user friendliness and quality of end result. Extensive work has been carried out in developing approaches, methods and tools that aid in understanding solar potential in an urban planning context as well as defining which level of detail potential studies need to be at in different phases of urban planning. Generally, in early phases, such as comprehensive and strategical planning as well as urban design on a city district scale, the potential studies can be quite rough as many parameters can change later on while in latter phases such as building design, the potential studies need to be more detailed.

3.3 Lessons learnt from the case stories

Case stories provide an international overview of different types of examples where solar energy in urban planning is applied in new, existing and landscape areas. The case stories reflect the objective of Task 51 with cases placing different emphasis on legislation, education and approaches, methods and tools. In addition, case stories indicate other influencing aspects for solar energy in urban planning such as economy and the role of stakeholders. Table 1 below outlines which cases emphasize the aforementioned aspects featured in Task 51.

Solar energy does not necessarily feature in legislation, but is often one of the options to help meet national energy reduction targets. Legislation played a key influential role in many of the case stories but also there were indications that legislation could go further to incentivize solar energy in urban planning. For example, solar landscape case stories offered creative opportunities to overcome restrictive legislation by exploiting the dual use of agricultural land as a cheap alternative for a common use of food production and to generate energy from large scale solar energy systems.

The use of public institutions to aid the take-up of solar energy other than legislative governing bodies is through educational institution. Education was important for case stories as a mechanism to ensure professionals of urban planning have the knowledge and skill to consider solar as an option for renewable energy solutions for a district. However, there is still some ground to cover in education in terms of raising awareness of how to implement solar energy into an urban area. There were indications in responding to the 'how' questions in the case stories. One approach are holistic approaches of involving all relevant stakeholders of urban planning. This involvement extends to citizen engagement, which is crucial in building agreements, understanding and achieving solutions. This approach ensures wide representation of stakeholders and increases the chances of reaching ambitious goals by overcoming barriers in developing solar energy in urban planning through an open communication forum.

Approaches, methods and tools are key instruments from which design and energy strategies can be formulated to achieve the optimum solutions for implementing solar energy in both new and existing urban environments. All case stories used both technical and non-technical approaches, methods and tools, thus highlighting the need for a multidisciplinary attitude to contemplate appropriate solutions of solar energy in the complex environment of urban planning. Indeed, case stories highlighted that the planning process for solar energy is complex with consideration on how solar energy can contribute to the development of the area as well as work within the confines of an allocated area where options for design may be limited. Examining the potential and use of design expertise are essential steps in the planning process and should include local conditions and context, in particular, the scale of the area, options for design layouts as well as technical knowledge.

Finally, economy is influential in developing different solar energy solutions, as there are diverse economic factors. These economic factors include affordability of urban areas; the energy market; available financial incentives; financial benefits of introducing solar as a single solution or an integrated solution. There are also solar group purchase initiatives which motivate small property owners to realize solar installations while reducing investment costs. Above all, the case stories exemplify the scope and possibilities for implementing solar energy in urban planning on a global scale, which is beneficial both for the environment and for the societies living in urban areas.

Tab. 1: Type of lessons learnt found in the case stories

Lessons learnt	Case stories
Legislation	Freiham Munich Nord, **Germany**; Lund Brunnshög and Malmö Hyllie, Uppsala Frodeparken, **Sweden**; Le Albere, Agrovoltaico, **Italy**; The Eco Neighborhood of Ravine Blanche, The sustainable city of Beauséjour, Agrinergie 5, Lyon Confluence, **France**; VerGe project - Lugano-Paradiso, **Switzerland**; Sarnia Photovoltaic Power Plant, **Canada,** Zero Emission Office Building, **Norway**.
Education	Øvre Rotvoll, **Norway;** Lyon Confluence, **France**
Stakeholder and researcher involvement	aspern+ Die Seestadt Wiens, Stadtwerk Lehen, Graz Reininghaus, **Austria**; FredericiaC and Gehry City Harbour, **Denmark;** Residential Plot B45, **China**; The Eco Neighborhood of Ravine Blanche, **France**; Dale, **Norway**; VerGe project - Lugano-Paradiso, **Switzerland**.

Economy	Energy Innovation Solar Purchase Group, **Switzerland**; Freiham Nord Munich, **Germany**; aspern+ Die Seestadt Wiens, **Austria**; Violino District in Brescia, **Italy**; Solar in Halifax Regional Municipality, **Canada**; Dale, **Norway**; Sarnia, **Canada**; Solar District Heating Brædstrup, **Denmark**; Agrovoltaico, **Italy** and Agrinergie 5, **Reunion Island, France.**
Planning process	Solar District Heating Brædstrup, FredericiaC, Gehry City Harbor in Sønderborg, **Denmark**; Lund Brunnshög, Malmö Hyllie **Sweden**; Photovoltaic Village in Alessandria, **Italy**.

3.4 From research to education

A state-of-the-art of education on solar energy in urban planning in nine countries was carried out and summarised in two different parts. Part 1 on approaches and methods in education showed through a survey that solar energy as it relates to urban planning was rarely part of the curriculum at universities. The identified courses are instead mostly offered in other disciplines. Technical aspects, especially on the architectural level, are taught in most of the courses, particularly in the undergraduate level. The main reason for these shortcomings is the short duration of the relevant courses during the studies. Due to relevant aspects in the planning of sustainable settlements, usually the subject of solar integration is only addressed on the periphery during urban development design assignments (Siems et al., 2017a). The identified continuing professional development (CPD) programmes generally dealt with key aspects, such as climate change, and not specifically with solar energy in urban planning. In Part 2 of the review, solar tools in education are discussed and experiences in using the selected software tools in university are compared. The differences among the analysed software tools are large, both in functional scope and operation. Only the software plug-in DIVA for Rhino3D achieved high marks of usability and precise calculation results. Its short initiation period for new users, its high computing power, and its visual results in the form of false-colour imaging makes this tool eminently suitable for use in training and continuing education. However, number-based output of the calculation results for further use in other software tools and a version for the Mac OS would be welcome.

The identified gaps and barriers in existing courses and pedagogy provide knowledge that can be implemented in relevant seminars, lectures and tools for educating the next generation of architects, urban planners and specialist planners by developing a web-based platform. Therefore, a tool, called Solar Potential Analysis for both students and life-long learning was created. The software tool itself is accompanied by a detailed user manual. The entire software package is free to use without limitations. The goal of this web-based platform is to help students to integrate solar energy in their design projects by providing relevant materials such as explanations, tutorials, illustrations etc. One part of this is the open source tool “Solar Potential Analysis” which allows for analysis of solar potentials and visualisation of the results as false-colour images. In parallel with the digital software tool, a set of manual tools such as "register cards" were designed for bachelor and master courses to aid exercises and seminars in relation to solar energy. The set will be freely available online to download.

The University of Wuppertal organised an interdisciplinary summer school to educate students from various disciplinary backgrounds. Such summer schools and courses provide valuable input to improve teaching methods and assessment tools for solar energy planning such as the tool “Solar Potential Analysis” and the developed manual set of tools. Teaching methodologies and results from the summer schools were documented in a booklet (Siems and Simon, 2017b).

4. Conclusions and outlook

There is considerable scope for legal reform in many countries as to solar access protection. Planners are increasingly calling for more sophisticated decision support tools to assess active solar energy potential and measures to determine the impacts of future development, the range of technological options that may more readily accommodate shade impacts as well as aesthetic solutions. This is becoming more important as solar energy targets are being pursued in an aim to transition to low carbon cities to build resilience. It also allows building owners utilise their solar access assets to harvest energy and reduce their exposure to external energy price variability and supply constraints. Ultimately, the research found that active solar systems have a critical role to play and their deployment will conflict with future development heights if there is not a more cohesive relationship between planning approval processes and building innovation.

There is more work needed that aims to help urban planners and designers in understanding the complexity in

dealing with daylight, active solar and energy performance in cities that are rapidly densifying. The role of the urban planner is to design areas that can be built to last. Urban design that addresses the need for daylight and sunlight will not only contribute to a healthier urban environment, it will also enable photovoltaics and solar thermal technologies to be implemented if not now, in the future.

The case stories illustrate that while technical and non-technical aspects of solar energy are important, they are still often considered as separate entities. However, within the complexity of urban planning, these entities are part of a holistic picture. The development of urban areas takes into account social contexts, economic frames, legislative constraints/enablers and stakeholders' expertise and/or access to expertise. The integration of solar energy in urban planning requires taking into account complexity and the need for holistic approaches.

The research also illustrated the importance of introducing solar with systematic respect to the urban context to preserve heritage and avoid unnecessary aesthetic conflicts. There is a risk if these aspects are not taken seriously that the social acceptance of solar technologies may decrease and in the long run slow down the pace of solar utilisation.

With increasing global population growth, cities will require more resources while at the same time renewable energy sources are expected to expand rapidly and the needed land to support cities can be expected to increase. Renewable energy systems are set to be a major land use in the near future and more research is needed to understand the environmental and social impacts of these systems and how rapidly growing cities affect the land use in the immediate surroundings.

Teaching at universities and colleges cannot be considered separate from research or practice. Creating a connection between the areas of "research and teaching", as well as between "research and practice" is an essential integral objective for research projects. Therefore, research is used as a connective link between teaching and practice and/or the public with far-reaching impacts. Researching new insights is not the only important factor here, but also information exchange and dissemination. Education and dissemination need to be strengthened to rapidly ensure that knowledge and support are offered for present and future professionals and educators. The research results should be disseminated through a public and easily accessible platform. The work of Task 51 will hopefully support such developments and knowledge transfer.

5. Acknowledgements

The authors wish to thank all the experts within the research project IEA SHC Task 51, who worked with great ambitions and with good team spirit to collaborate and willingly contribute their expertise.

The authors also wish to express their gratitude to the IEA SHC Executive Committee for supporting the Task 51 and in this way strengthen the international collaboration among researchers and practitioners. We are especially grateful for the financial support from the Swedish Energy Agency; ARQ; Australian PV Institute (APVI) / Australian Renewable Energy Agency (ARENA); The Research Council of Norway (NFR); Norwegian University of Science and Technology (NTNU); German Ministry for Economic Affairs and Energy; Swiss Federal Office for Energy. Funding from these organizations enabled the leaderships of Task 51.

6. References

Baek Pedersen, P., 2009. Sustainable Compact City. Arkitektens Forlag, ISBN: 9788790979232.

Butti, K., Perlin, J., 1980. A Golden Thread: 2500 years of solar architecture and technology. Cheshire Books. ISBN 978-0-442-24005-9.

Compagnon, R., 2004. Solar and daylight availability in the urban fabric. Energy and Buildings, 36, 321–328.

Hegger M, Fuchs M., Stark T., Zeumer M., 2008. Energy Manual. Sustainable architecture. Birkhäuser – Edition Detail, Basel.

IEA, 2014. Technology Roadmap Solar Photovoltaic Energy. OECD/IEA, Accessed 2017-09-10 at http://www.iea.org/publications/freepublications/publication/technology-roadmap-solar-photovoltaic-energy---2014-edition.html.

Kanters, J., Wall, M., Kjellsson, E., 2014. The Solar Map as a Knowledge Base for Solar Energy Use. Energy Procedia, 48(0), 1597-1606. doi: http://dx.doi. org/10.1016/j.egypro.2014.02.180

Kanters, J., 2015. Planning for solar buildings in urban environments. An analysis of the design process, methods and tools. PhD thesis. Report EBD-T--15/19, Div. of Energy and Building Design, Lund University.

Lechner, N., 2014. Heating, Cooling, Lighting: Sustainable Design Methods for Architects. Wiley Publication, 4th Edition. ISBN: 978-1-118-58242-8.

Lobaccaro, G., Lindkvist, C., Wall, M., Wyckmans, A. (eds.), 2017. Illustrative Prospective of Solar Energy in Urban Planning. Collection of International Case Studies. IEA SHC Task 51/Report C1. DOI: 10.18777/ieashc-task51-2017-0002. http://task51.iea-shc.org/data/sites/1/publications/2017-06-Task51-Report-C1.pdf. Accessed 07.10.2017.

Munari Probst MC., Roecker C., Deschamps, L. Website: Innovative solar products for architectural integration. IEA SHC Task 41 and Task 51. Created in 2012. http://solarintegrationsolutions.org/. Accessed 07.10.2017.

Munari Probst, M. C., Roecker, C., 2015. Solar energy promotion & urban context protection: LESO-QSV (Quality-Site-Visibility) method, 2015 PLEA Architecture in (R)evolution, Bologna, IT.

Newman, P., Thornley, A., 1996. URBAN PLANNING IN EUROPE - International competition, national systems and planning projects, Routledge, London. ISBN 0-203-73618-4 (adobe reader format).

Samimi, M., Nasrollahi, F., 2014. Intelligent Design using Solar-Climatic Vision; Energy and Comfort Improvement in Architecture and Urban Planning using SOLARCHVISION. Technische Universität Berlin. ISBN 978-3-7983-2676-7

Sartori I, Napolitano A., Marszal A.J., Pless S., Torcellini P., Voss K., 2010. Criteria for Definition of Net Zero Energy Buildings. In Proceedings of Eurosun 2010, Graz.

Sattrup, P.A., 2012. Sustainability – Energy Optimization – Daylight and Solar Gains. Diss, Royal Danish Academy of Fine Arts. Accessed 2017-10-12 at http://orbit.dtu.dk/fedora/objects/orbit:120303/datastreams/file_6dd05f64-05b1-419d-81c8-e0ef92f3e892/content

Siems, T., Simon, K., Wall, M. (eds.), 2017a. State-of-the-Art of Education on Solar Energy in Urban Planning. Part I: Approaches and Methods in Education. IEA SHC Task 51/Report D1 Part 1. DOI: 10.18777/ieashc-task51-2017-0001. http://task51.iea-shc.org/data/sites/1/publications/170601_Task51_ReportD1_Part1.pdf. Accessed 07.10.2017.

Siems, T., Simon, K., 2017b. Summer Schools on Solar Energy in Urban Planning. Teaching Methodologies and Results. IEA SHC Task 51/Report D2. DOI: 10.18777/ieashc-task51-2017-0003. http://task51.iea-shc.org/data/sites/1/publications/2017-06-Task51-Report-D2-English.pdf. Accessed 07.10.2017.

Snow, M., Prasad, D., 2011. Building-integrated Photovoltaics (BIPV). EDG 68 MS. Australian Institute of Architects (AIA) Environmental Design Guide. July 2011. ISSN 1442-5017.

Steemers, K., 2003. Energy and the city: density, buildings and transport. Energy and Buildings 35 pp3-14.

Stringer, E.T., 2014. Action Research. Fourth Edition, SAGE Publications Inc, London.

Voss K., Musall E., 2011. Net zero energy buildings. International projects of carbon neutrality in buildings. Institut für Internationale Architektur-Dokumentation, Munich.

Wall, M., Munari Probst, MC., Roecker, C., Dubois, MC., Horvat, M., Bruun Jørgensen, O., Kappel, K., 2012. In Energy Procedia Volume 30, 2012, pp 1250-1260. 1st International Conference on Solar Heating and Cooling for Buildings and Industry (SHC 2012). http://dx.doi.org/10.1016/j.egypro.2012.11.138

Wind Energy, Ocean Energy, Hydro and Other Direct Conversion Renewables

Research of Natural Renewable Energy Resources of Coast and Seas of the Far East

Valeriy V. Knyazhev and Vladimir V. Loshchenkov
Institute of Marine Technology Problems FEB RAS, Vladivostok (Russia)

Abstract

In article renewed energy sources on Far East of Russia are considered: thermal energy, energy of salinity gradients, tide, waves, currents, a wind and solar power. Estimations of power resources of these energy sources are given. Places in which they are offered can are effectively used.

A system of autonomous power supply for a coastal facility for the cultivation of hydrobionts from renewable sources on the island of Popov is proposed. A device for growing hydrobionts on artificial automated plantations in the water column without diving with an autonomous power supply from renewable sources has been developed..

Keywords: source of energy, thermal, salinity, tide, wave, current, wind, solar, hydrobionts

1. Introduction

The Far East of Russia is the region of Russia where the primary start of development and use of ocean energy sources is possible, this is facilitated by the fact that the Far East has a long coastline and most of the territory of the Far East is not connected to the unified energy system. And as the population density in these territories is small, it is economically justified to use autonomous energy sources, and, first of all, renewable energy sources of the ocean. The territory of the Far East stretching from the south to the north of 4500 km, more than 70% of the length of its borders falls on the shorelines of the seas of the Arctic and Pacific Oceans, covers different natural areas, and almost everywhere the potential of renewable energy sources is very high. The Far East has the longest coastal line among the regions - 17,700 km. (with islands).

The population of the Earth grows; requirements for marine foodstuff accordingly increase. The aquatic organisms grown in pollution-free natural settings of seas of the Far East of Russia are especially appreciated. Aquaculture development in this region is complicated small population, remoteness, absence of the production engineering, allowing to develop continuous process in the conditions of a frigid climate and high ecological requirements. This paper is devoted researches in power supply from renewed sources and working out of a perspective complex of a marine aquaculture.

2. Source of energy

2.1. Thermal energy of the ocean

In ocean thermal energy conversion (OTEC) the difference in temperatures of warm surface water and cold deep water is used to generate energy. The resources of this type of energy in the oceans are huge. But basically they can be used in the tropical zone of the ocean. In the Russian Far East, only in the southern regions and only part of the year is it advisable to transform the thermal energy of the ocean by traditional methods. It is still possible to increase temperature differences using warm water from shallow natural and artificial, sun-warmed water bodies or warm drains of some enterprises.

Therefore in the laboratory of the energy of the ocean it was proposed to use the temperature difference between the outdoor air and sea water in the cold seasons of the year. For the northern regions of the Far

doi:10.18086/swc.2017.38.01 Available at http://proceedings.ises.org

East, these seasons are long and the potential of the thermal energy of the northern seas is extremely high. In addition, energy can be obtained from this source precisely when energy requirements are high. Transformers of thermal energy of the ocean with low-boiling heat-carriers were proposed.

2.2. Salinity gradient energy

Places where there are differences in salinity (concentration) of natural waters and solutions can be used as energy sources, which are called salinity gradient energy (SGE) sources. As sources of energy, salinity gradients are considered, first of all, the mouths of rivers flowing into the sea. The energy density of these sources is high. So, it can be imagined that in the mouths of rivers flowing into the seas, so much energy is lost, as if they ended in waterfalls with a height of 240 meters, since the osmotic pressure of the sea water exceeds 2.4 x 10^6 Pa (24 atm).

Amur the river most abounding in water in considered region. The average discharge of water in its mouth 12.8-11.4 m^3/s. Resources of energy of this river are huge. But so the river Amur runs into shallow Amur liman between island Sakhalin and continent at building there to power station of a point of a water fence of fresh water and not diluted sea water would be carried on the big distance.

Estimations of potentials of energy of gradients of salinity of some large rivers flowing into Okhotsk Sea are resulted in the Table 1.

Tab. 1: Energy potential SGE in the mouths of the rivers flowing into Okhotsk Sea

The river	Area of the river basin, km^2	Rate of the flow, m^3/s	Average power, MW
Penzhina	73500	680	1514
Uda	61300	510	1135
Okhota	19100	200	445.2
Poronay	7990	120	267.1

For the largest rivers of the Primorsky krai (Primorye) flowing into the Sea of Japan, the energy potential was assessed (Fig. 1) (Knyazhev, 2010). The total energy potential in the estuaries of the rivers will be 1.5 x 10^3 MW, while theoretically possible annual energy production will amount to 4.25 x 10^7 MJ. Resources SGE in other areas of the Far East is much higher. The total runoff of the rivers of the Pacific Ocean basin is 1212 km^3 / year, which corresponds to the theoretical resources of the SGE about 2.7 x 10^9 MJ.

Several methods have been proposed for the conversion of EGS. This is primarily membrane methods of energy conversion using semipermeable osmotic membranes and ion-selective membranes (reverse electrodialysis), as well as energy conversion methods, in which the transfer of water molecules occurs through surfaces that separate the different phase states of solutions, etc.

The development of osmotic power plants, the testing of semipermeable membranes and small experimental power blocks was carried out in the USA, Israel, Italy, and Japan. And in November 2009 in Norway in Tofte, south of Oslo, the state-owned energy company Statkraft launched the world's first osmotic power plant, which generates energy by mixing sea and fresh water.

Reverse electrodialysis plants allow direct conversion of energy from salinity gradients to electrical energy. Research on the development and testing of reverse electrodialysis plants was conducted in the USA, Sweden and Israel.

In the Netherlands, on the dam Afsluitdijk separating the man-made lake IJsselmeer from the sea, a pilot RED-Stack installation operates. And in Trapani (Sicily), a prototype of the pilot installation of the REAPower (Reverse Electrodialysis Alternative Power) plant, which uses brines from evaporative ponds and seawater is tested.

The main element of the reverse electrodialysis installation is an electrodialysis battery, which is a stack of alternating anion and cation-exchange membranes placed between the electrodes. Solutions with different concentrations are fed into chambers formed by pairs of membranes and working frames, so that chambers with solutions of high and low concentrations alternate. The directional movement of ions from the chambers from a high concentration to the chambers with a low concentration leads to the accumulation of an electrical

potential on the electrodes.

Fig. 1: SGE resourses rivers of Prymorye, Russia

In the laboratory of non-traditional energetics of IMTP FEB RAS, studies of the energy conversion of salinity gradients by the method of reverse electrodialysis were carried out. This method has a number of advantages and is most suitable for converting energy in the mouths of rivers flowing into the sea [2]. An experimental reverse electrodialysis installation was developed and created. Tests of the experimental installation in full-scale conditions on sea water from Alekseev Bay on the island of. Popov and fresh water from an artesian well confirmed that this method can be used to directly convert SGE into electricity.

2.3. Energy of the tides

In the Far East, the highest tides in the Penzhina Bay in the north of the Sea of Okhotsk, they reach 12.9 m there. In the Sea of Okhotsk, tides of a mixed type predominantly prevail, predominantly of the irregular diurnal one. Employees of the Ocean Energy Laboratory together with specialists from Moscow and Leningrad, together with the creator of the first in the country Kislogubskaya TPS (Tidal Power Station) L.B. Bernshtein from the Institute "Hydroproject" carried out work on the investigation of tidal regimes in the Penzhina Bay and in the Tugur Bay, proposed preliminary TPS projects. Expeditions were made to the Tugur Bay and the Penzhinskaya Bay to measure tidal sea level fluctuations (Fig. 2-Fig. 4).

According to the results of these studies, the energy resources of the tides in the Okhotsk Sea are the following potential integral values: the energy production of a tidal power plant in the Tugur Bay is estimated at about 6.8 x 10^{10} MJ / year, which corresponds to a power of more than 2000 MW; the energy production of a tidal power plant in the Penzhina Bay is estimated at about 6.8 x 10^{11} MJ / year, which corresponds to a capacity of more than 20 000 MW. Since such an amount of energy could not be used by the nearest consumers, it was proposed to export electricity to neighboring countries - Japan and China.

Fig. 2: Penzhina Bay, Cape Sredniy, loading the expedition on the vessel at low tide

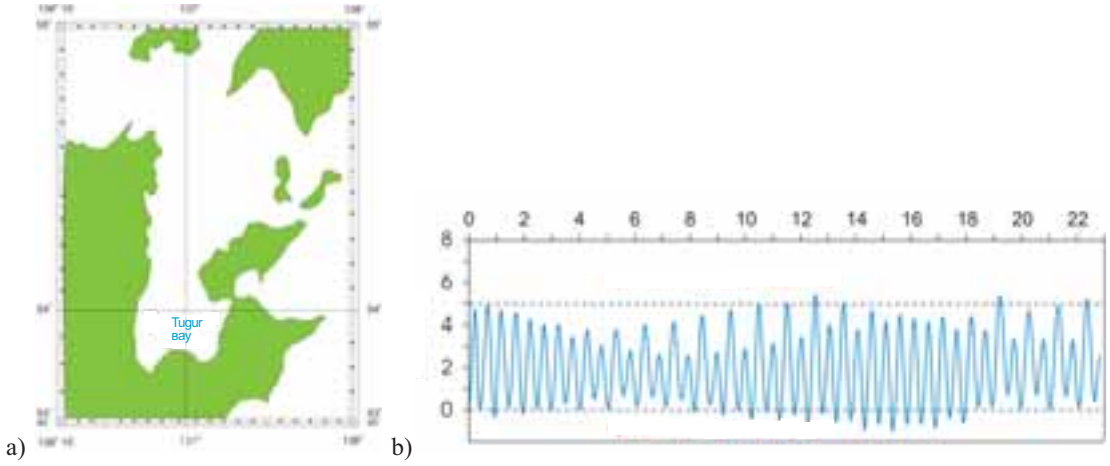

Fig. 3: a) Map of the Tugur Bay, b) Tidal level fluctuations. Tugur Bay. 5 - 28 August 1981 y.

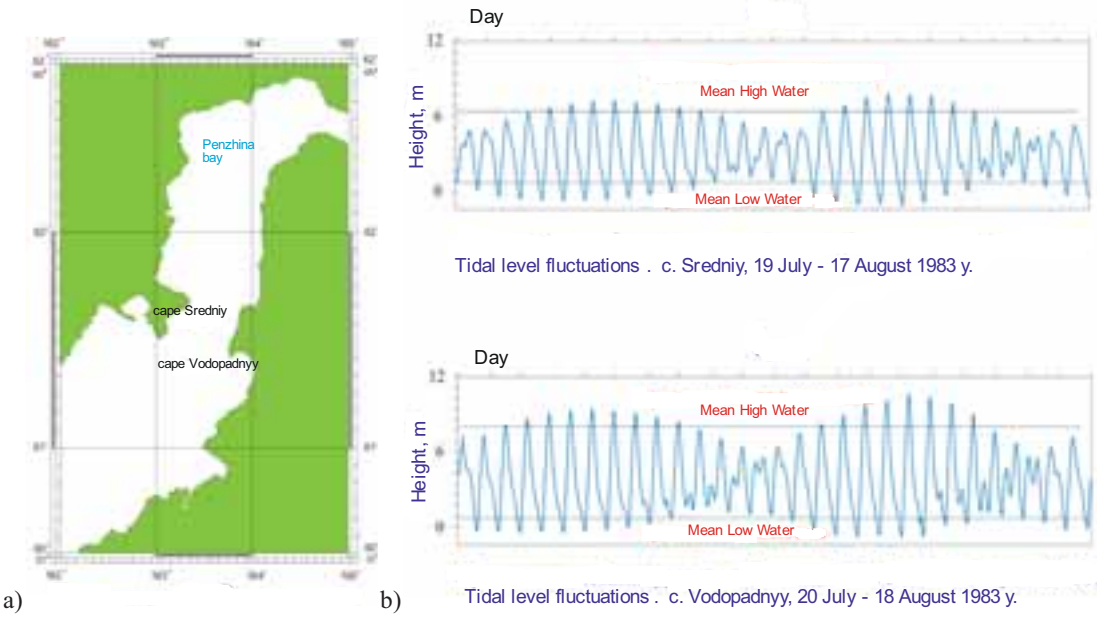

Fig. 4: a) Map of the Penzhina Bay, b) Tidal level fluctuations. Penzhina Bay

2.4. Current energy

Near the Far Eastern coast of Russia, tidal currents in narrow areas have speeds sufficient to effectively use them. In the Kurile Straits and in the Shantar Islands, the speed of tidal currents is up to 3.5 m / sec. It is there that it is possible to install hydroturbines in the water column to convert the energy of tidal currents. The power of such stations can increase gradually, adding as necessary new turbines. In this they have an advantage over the dams of TPS, when creating, which require huge initial capital costs for the construction of dams.

2.5. Energy waves

In the laboratory of the energy of the ocean, the problems of conversion of wave energy, wave energy resources in the World Ocean were studied. Several designs of wave energy stations have been proposed and patented, which have greater efficiency and lower material intensity.

The energy resources of waves in the Far Eastern Seas are high (Sichkarev, Akulichev, 1989) in Tab. 2 and 3 show the values of the wave energy fluxes, renewable power and annual energy in these seas.

Tab. 2: Flows of wave energy of the Far East seas (kW/m)

The sea	Winter	Spring	Summer	Autumn	Average annual
Bering	58/411	43/351	26/411	54/465	45/465
Okhotsk	34/351	31/294	18/351	32/189	29/351
Japan	49/351	40/351	17/189	37/351	36/351

Tab. 3: Renewed capacity and annual energy of water area of the Far East seas

The sea	The area, m^2, $\cdot 10^{12}$	Flows of wave energy (kW/m)	Renewed power, W, 10^{11}	Annual energy, J, $\cdot 10^{18}$
Bering	2.30	45	1,9	6,00
Okhotsk	1,59	29	1,01	3,19
Japan	0,98	36	0,71	2,24

2.6. Wind energy

Wind energy can be used not only on the sea, but also on land. And it was on land this source of energy was originally started to be exploited for technological purposes. As a result, significant progress has been made in the world in wind energy. In developed and developing countries, many wind turbines have been installed. As a result, in densely populated Europe there are almost no places to install large-capacity wind turbines. Therefore, and also because the resources of wind energy above the ocean surface considerably exceed them above the land, more and larger wind farms are installed on the sea shelf.

The coastal areas of the Far East have huge resources of wind energy; most of them belong to areas with winds of strong and medium intensity. According to experts in Russia, about 30% of the economic potential of wind energy is concentrated in the Far East. The advantage of using wind energy in these areas is that the maximum average speed here falls on autumn and winter - the periods of the greatest need for electricity and heat. The resources of wind energy over the water areas of the Far Eastern seas are much higher.

2.7. Solar energy

Primorsky Krai belongs to the regions of the Russian Far East and the whole of Russia, where it is advisable to use solar energy for energy supply purposes. The average number of sunny days per year for the Primorsky Kray is 310, with a sunshine duration of more than 2000 hours. Moreover, there are areas where the number of days without the sun is only 26 per year; the duration of sunshine is 2,494 hours. On the northern coast, the duration of sunshine is 1900 ... 2100 hours, on the southern coast the duration of sunshine is 2000 ... 2200 hours.

In general, the power input of solar energy to the territory of Primorsky Krai is about 30 billion kW. The practical resources of solar energy, taking into account environmental and other limitations, achieve: when receiving only thermal energy - 16 million kW; when receiving only electric energy - 4.9 million kW (Fig.5).

Fig. 5: Solar energy resources of Primosky kray

3. The system of energy supply of promising aquaculture complexes

The system of autonomous power supply of the long-shore factory of an aquaculture from renewed sources on an island of Popov is offered (Fig.6). The design of an experimental power system is fulfilled taking into account local natural settings and long-term meteorological and hydrological measurements for all-the-year-round providing of flow processes. Heat, cold and electricity ensure department of cultivation and

department of deep rehash of aquatic organisms.

An autonomous automatic plantation (Fig.7) on the deep-water shelf with remote dispatching control and control, a wave electro-pneumatic installation and a system of buoyancy, aeration and lifting devices that provide long-term processes are developed. Remote dispatch control over the biological and technological parameters of plantations and depth change control excludes diving operations.

The technical project of a specialized semisubmersible vessel-dock of service of marine plantations develops. The vessel will effect installation and removal of sectors of plantations and will handle a crop.

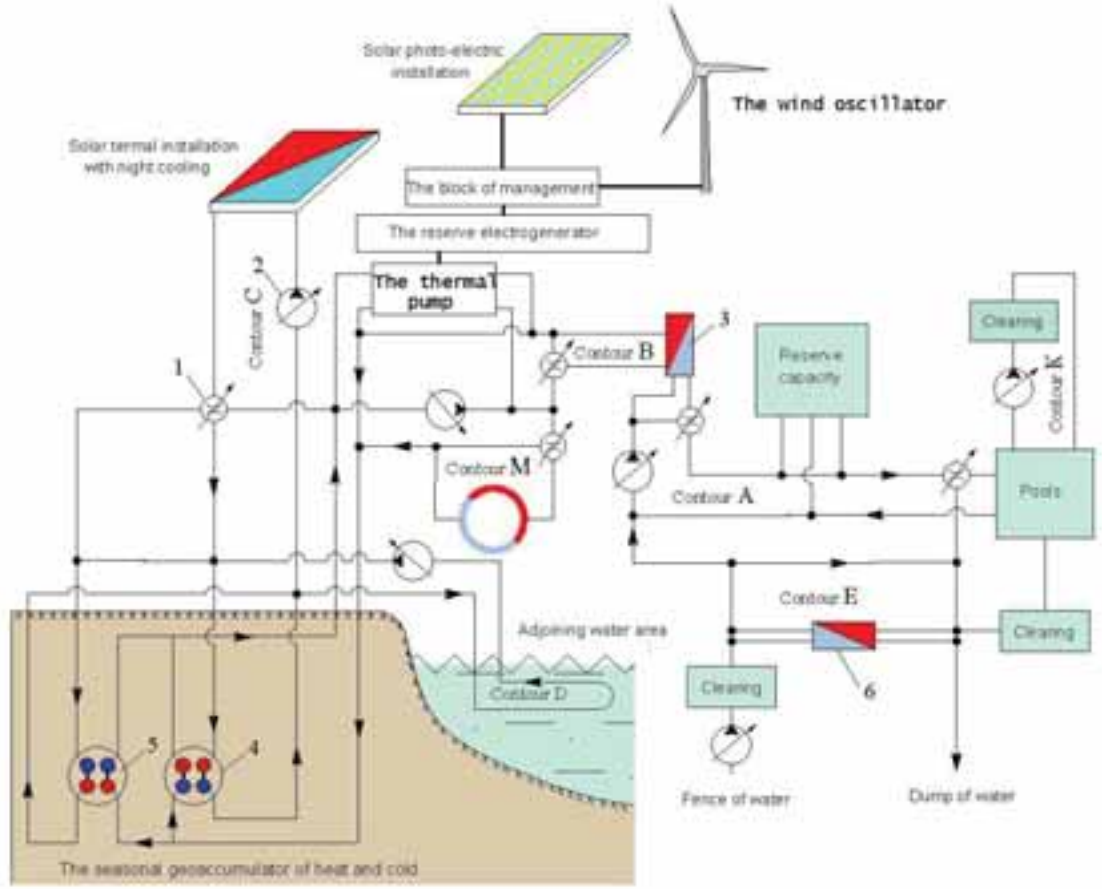

Fig. 6: The system of autonomous power supply of the long-shore factory of an aquaculture from renewed sources on an island of Popov. 1 - the managing valve; 2 - the pump circulating; 3 - the exchanger; 4 - probes of sector of heating; 5- probes of sector of refrigeration.

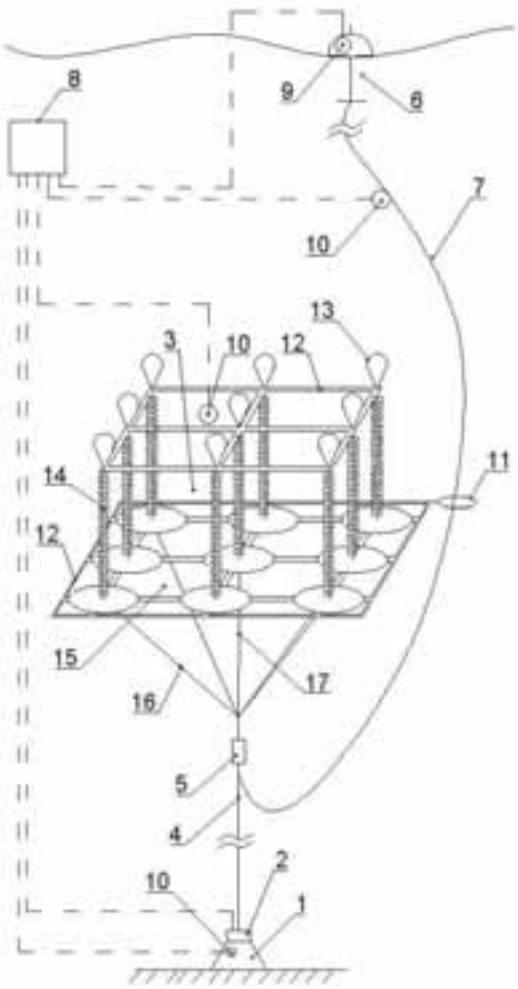

Fig. 7: Plantation Schemes on the Deep-water Shelf

1-bottom anchor; 2 - electric cable winch; 3 - platform; 4 - anchor cable-rope; 5 - automatic mechanical spring-loaded rod air valve; 6 - wave energy device; 7 - a cable-cable with the air pipeline; 8 - automatic program control and control unit with dispatching satellite communication; 9 - a set of sensors: battery charge, air pressure in the pontoon and the height of surface waves; 10 - set of depth, light, temperature, salinity, oxygen content and water flow rate; 11 - rigid loop; 12 - rigid grating; 13 - flexible floats; 14 - collector cables with hydrobionts; 15 - rigid lattice of hollow tubes; 16 - flexible braces; 17 - a cable-cable with the air pipeline; 18 - air lift pick-up; 19 - cable rope with air line and air-lift pipe.

4. References

Knyazhev, V.V., 2010. A Study on Energy from Salinity Gradient in Primorye, Russia, Proc. 9st Pacific/Asia Offshore Mech. Symp., (ISOPE PACOMS-2010), Busan, Korea, pp. 179-181.

Sichkarev, V.I., Akulichev, V.A., 1989. Wave Power Station in the Ocean, ed. Nauka, Moscow.

OFFSHORE WIND ENERGY POTENTIAL AROUND THE EAST COAST OF THE RED SEA, KSA

Mostafa Mahdy [1*], AbuBakr S. Bahaj [1] and Abdulsalam S Alghamdi [2]

[1] Sustainable Energy Research Group, Energy & Climate Change Division (www.energy.soton.ac.uk), Faculty of Engineering and the Environment, University of Southampton SO17 1BJ, Southampton (United Kingdom)

[2] Electrical Engineering Department, King Abdulaziz University, Jeddah (Saudi Arabia)

[*] Corresponding author, E-mail: m.mahdy@soton.ac.uk

Abstract

Under its Vision 2030, the Kingdom of Saudi Arabia (KSA) announced an ambitious strategy to diversify their economy from oil dependency. One of the goals of the vision is an initial target to produce 9.5 GW of electricity from renewable energy sources. Offshore wind energy conversion is considered to be mature technology with more than 12 GW of installed capacity globally. Offshore wind has advantages when compared with onshore wind, such as, higher wind speed, reduced turbulence, minimal visual and noise impacts. KSA has two shorelines, one is laying on the Arabian Gulf and the other is on the Red Sea. The work presented here evaluates offshore wind potentials in in the East Coast of the Red Sea in KSA which was chosen due minimum restrictions and has no close oil extraction facilities. The evaluation was based on a Boolean Mask model linked coupled analysis undertaken in Geographical Information System developed for the Red Sea area.

Using the UK's London Array wind farm as a minimum required area for offshore wind farms, the work identifies ten different locations as possible areas for the first offshore wind farms in KSA. The analysis considered the deployment of two types of turbine of capacities 3.6MW and 5MW. The results for the higher capacity turbine indicate that over 12.3 GW of offshore wind power can be generated from the identified sites. These results and the produced location maps could be used to help stakeholders in KSA in planning for the exploitation of offshore wind energy in KSA. Thus providing a pathway to contribute to achieving the 9.5 GW national target.

Keywords: Wind energy, offshore wind, GIS, Boolean Mask, Red Sea, KSA

1. Introduction

Offshore wind energy is considered mature technology with over 12 GW of installed capacity globally. The recent contract for difference (CfD) announcement in the UK showed halving the cost per MWh to £57.5 compared to the previous round (CB, 2017). Onshore wind on the other hand is further ahead in terms of economics, however, it has some disadvantages, such as the value of the land areas, noise, high vibrations, visual impacts, bird paths hazards, and shadow flicker effect. Shadow flicker effect that is an infrequent event, which could happen, when the sun's light is at horizon. Shadow flicker could be responsible for photo-induced seizures or photosensitive epilepsy and other disturbance to humans near the turbines (Knopper & Ollson, 2011). Offshore wind on the whole does not suffer from these disadvantages, and has two extra advantages: the average wind speed is larger than over onshore areas and the turbulence wind effect is minimized when compared to installation over land. The latter is important as fatigue stress encountered is smaller enhancing offshore wind turbines life.

The Kingdom of Saudi Arabia (KSA) has a total area of 2.2 million km^2, and a population of more than 30 million. KSA lies between latitude of 17.5 °N and 31 °N and longitude of 36.6 °E and 50 °E (Bahakeem, 2015). The west coastline of KSA is more than 1800 km in length and is situated around the Red Sea and the Gulf of Aqaba with a boundary between Haql to the north and Jazan to the south (Fig.1).

The energy consumption of KSA has been on rapid rise to cope with the growing demand of the industrial, water

doi:10.18086/swc.2017.38.02 Available at http://proceedings.ises.org

and building sectors. Most of this energy is derived from fossil fuels leading to high carbon emissions. This dependence is as a result of the vast oil resources in KSA estimated to be more than 250 billion barrels of oil reserves or one-fifth of total known global reserves (Bahakeem, 2015). Hence there is an urgent need for KSA to move towards low carbon renewable energy production.

In order to decrease its reliance on fossil fuels and balance its economy, KSA has developed the Vision 2030 programme under which it plans to generate 9.5 gigawatts of electricity from renewable energy sources (Gazette, 2016). This is more likely to be derived from solar energy and wind energy. Hence, this work is directed towards the latter, but concentrated on offshore wind around the Sea Area of KSA where we will identify suitable locations for offshore wind farms (OWF) and evaluate their potential. To our knowledge, only one article was found that considers the offshore wind resources in KSA but the study was focused on the east coast of the country (Rehman, 2005).

In summary, the aims of this work is to identify the suitable areas in KSA for offshore wind focusing on the the Red Sea regions, estimate the electrical power potential form the identified sites and provide suitability maps for these locations.

Fig.1: Study area map, KSA is shaded with light green, the Red Sea east shoreline is the red line, adopted from (esri, 2012).

2. Methodology

In this work the required outcome is a spatial siting of the wind farms. Such a problem comprises a large number of suitable alternatives and multiple constraints to choose the alternative with zero constraint. Both the constraints and alternatives can be determined or evaluated and weighted by stockholders, or scholars based on their knowledge and experience (Estoque, 2011).

The map of the study region is divided to grid as an equal size, the smallest part of such grid is called a cell, which corresponds to one of the feasible alternative. For instant, to decide the suitable cell for offshore wind energy in the Red sea, wind speed, water depth, distance to shore, distance to the electricity grid, shipping routes, military areas, cables paths, and reserved natural parks, are the constraints to be considered in the analysis and before taking a final decision. Fig.2 provides a flow chart summarising the whole assessment process, under the Boolean Mask technique utilised in this study to solve the problem.

Boolean Mask (overlay), is used to locate sites with no restrictions (constrains). Boolean relations [and, or, and not] are used, from which the name has been derived.The created map layer has two colours (boundaries), one represents areas that has a value of 1 (the unrestricted areas) and the other represents areas of value 0 value (restricted areas). Boolean mask is a powerful tool for simple and quick spatial decisions (Jiang & Eastman, 2000).

In this work, we need to create a primary map for suitable offshore wind farms in the Red Sea, around the KSA coast, and evaluate the potential electrcila power from these farms. The **Constraints** can be explained as a tool to eliminate alternatives (cells). The limitations or restrictions of the constraints are defined as a (true/false) relationship. For example, if the commercial wind power development becomes feasible around wind speed greater than 3 m/s, so all areas with wind speed less than this threshold (3 m/s) will be given 0 value, while other areas will take the value of 1.

The equation used to calculate the Boolean Map is adopted from (Eastman, Jiang, & Toledano, 1998), and is given by:

$$Boolean\ Mask = \left(\prod_{j=1}^{l} C_j\right) \qquad \text{(eq. 1)}$$

Where:

C_j is the constraint j (Boolean Mask j),

Π is the product of constraints, and

ℓ is the number of constraints.

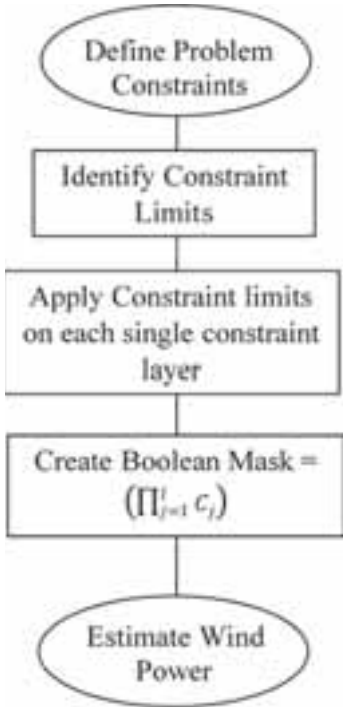

Fig.2: Flow chart summarising the whole assessment process, under the Boolean Mask technique utilised in this work.

3. Analysis

To satisfy the conditions of the sites around the Red Seas in KSA coasts, nine constraints were considered, and are summarised in Table 1. In addition, the table also provides the two limits for each constraint, where only two values are identified; zero value, which is the undesirable areas (cells) according to the constraint definitions, while the value of one is assigned the other areas (cell).

3.1 Relevant Data

A map layer in ArcGIS was created for each constraint, using the available and relevant spatial data. The bathymetry data for the Red Sea around the shores of KSA was adopted from (The British Oceanographic Data Centre, 2014), the source file of water depth data was in raster form, with a sell size of 800 x 800 m, and the file "GCS_WGS_1984" is the Geographic Coordinate System used. Due to the source file cell size and the coordinating system type, all constraints layers were confined to same cell size and GCS_WGS_1984 coordinate system. Fig.3, shows the water depth map for the Red Sea, which has a range from 0 to -3000 m. The areas with the required depth for offshore wind farm are concentrated in the South West part of the KSA. Wind speed data was adopted from the "Wind Atlas for Egypt" (Mortensen et al., 2006) and from the Global Atlas for Renewable Energy (Kieffer & Couture, 2015). The map layer in Fig.4 shows the average wind speed in [m/s] at a height of 10 m over a flat and uniform sea, which has a range between 3 and 7 m/s. Locations with desirable wind speed are centred in the North West part of the KSA.

Fig.5 shows all constraints in the study area, KSA has only two maritime reserved parks in the Red Sea named "Umm al-Qamari Islands" and "Farasan Islands". Locations and shape dimensions of these parks were taken from the official web site of the Saudi Wildlife Authority (SWA, 2017). Shipping Routes in the Red Sea adjacent to the KSA coast line were identified using the data available from ship density maps of Marine Traffic website (The MarineTraffic, 2015). Submerged undersea cable locations and paths were extracted from the submarine cable map of (TeleGeography Company, 2015). Marine military restricted areas was assessed from Royal Saudi Navy Forces official website (RSNF, 2017). According to Saudi Aramco (Aramco, 2017), all petrol oil extraction areas are located on the Arabian Gulf, so the oil extraction constraint was excluded.

Table 1: Constraints 0, and 1 definitions and data source data.

Constraint	Symbol	0 description and data source	1
Wind Speed (m/s)	W_B	Areas with wind speed less than 3.0 m/s **or** more than 25.0 m/s at a height of 10 m over a flat and uniform sea (Archer & Jacobson, 2005), wind speed data were adopted from (Mortensen, Said, & Badger, 2006) and (Kieffer & Couture, 2015).	Else
Water Depth (m)	D_B	Depths less than 5.0 m **or** more than 60.0 m, the bathymetry data was adopted from British Oceanographic Data Centre (BODC) (The British Oceanographic Data Centre, 2014).	Else
Distance to the shore (km)	S_B	Distance less than 1.5 km or more than 200.0 km, the distances data was adopted and processed using ArcGIS Program (esri, 2012).	Else
Distance to the Grid (km)	G_B	Distance more than 250.0 km, the distances data was adopted and processed using ArcGIS Program (esri, 2012).	
Military Practice & Exercise Areas	M_B	Locations were adopted from (RSNF, 2017)..	Else
Shipping Routes	R_B	Shipping areas adopted from (The MarineTraffic, 2015)	Else
Maritime Boundaries	B_B	Boundaries were adopted and processed using ArcGIS Program (esri, 2012)..	Else
Nature Reserves	N_B	Places in the sea area protected by the power of law to reserve the endangered marine ecosystem species, marine parks were adopted from (SWA, 2017).	Else
Under Sea Cables	U_B	Locations of the submerged sea cables (TeleGeography Company, 2015).	Else

Fig.6 shows the map layer of the National Electricity Transmission Grid of KSA (the grid is drawn as a line network in a black colour), which was adopted from the Global Energy Network Institute (GENI, 2017). The Euclidean Distance Tool was deployed to calculate the distance between nearest electricity line to each cell, (Fig.6). Fig.7 shows the coastline of the Red Sea of KSA in km and was drawn using data from (esri, 2012). Euclidean Distance Tool within the ArcGIS programme was applied to create a map shown in Fig.7, which illustrates the distance from each cell to the coastline of KSA.

3.2 Boolean Mask

A Boolean mask was created to eliminate restricted cells, constraint cell value = 0, and unrestricted cell value = 1, see Fig.5. The Raster Calculator tool was used to produce the final Boolean Mask, and is shown in Fig.8. The below equation was used:

$$\text{Boolean Mask} = W_B \times D_B \times S_B \times G_B \times M_B \times R_B \times B_B \times N_B \times U_B \quad \text{(eq. 2)}$$

Where: W_B, D_B, S_B, G_B, M_B, R_B, B_B, N_B, and U_B are defined in Table 1 above.

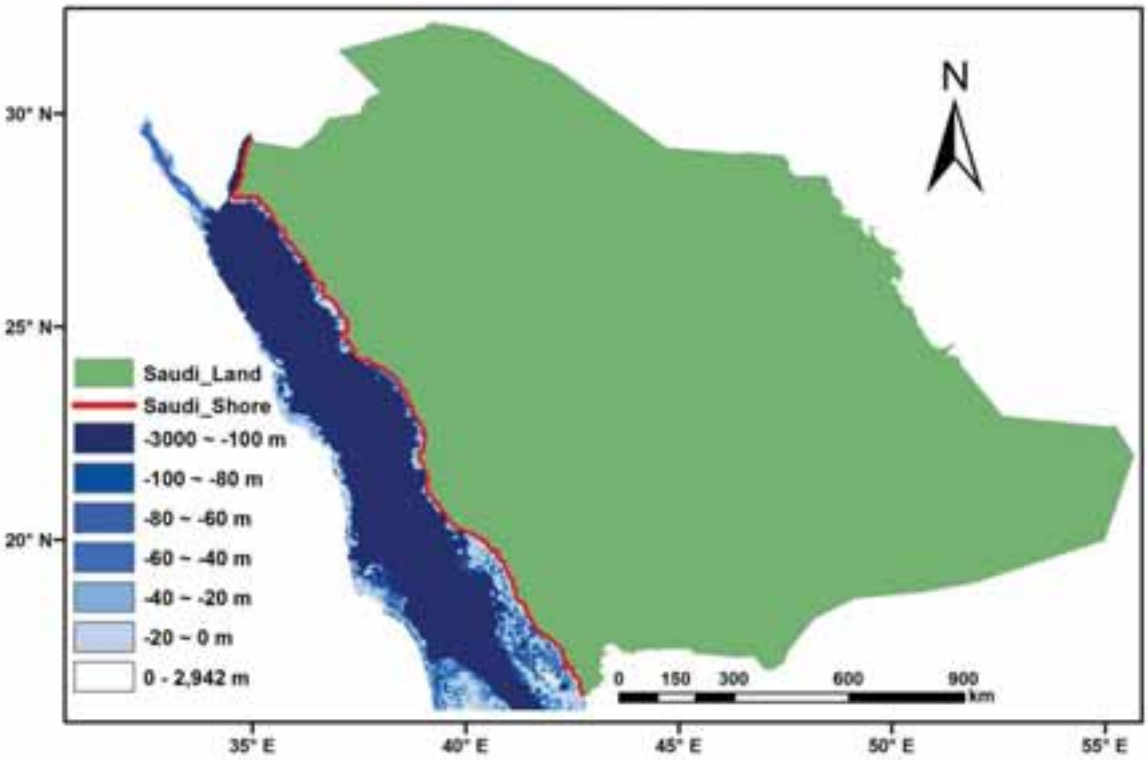

Fig.3: Bathometry map of the Red Sea.

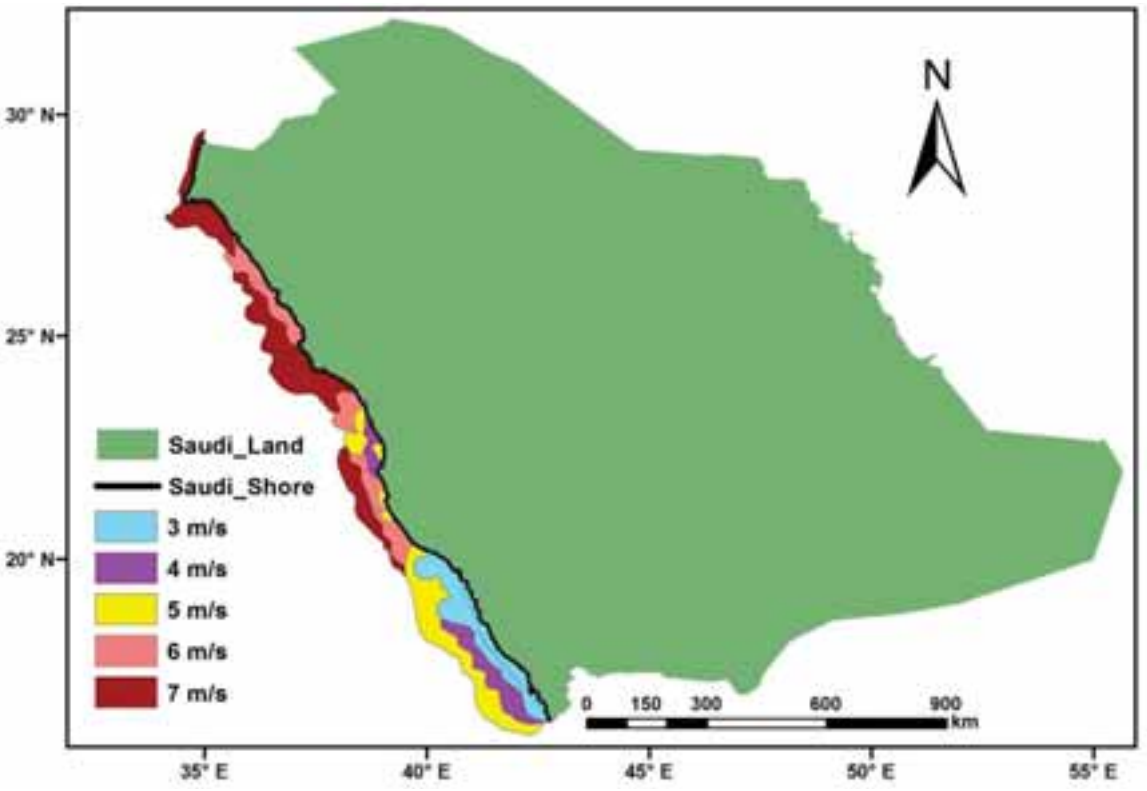

Fig. 4: Wind Speed [m/s] map around the Red Sea coastline of KSA.

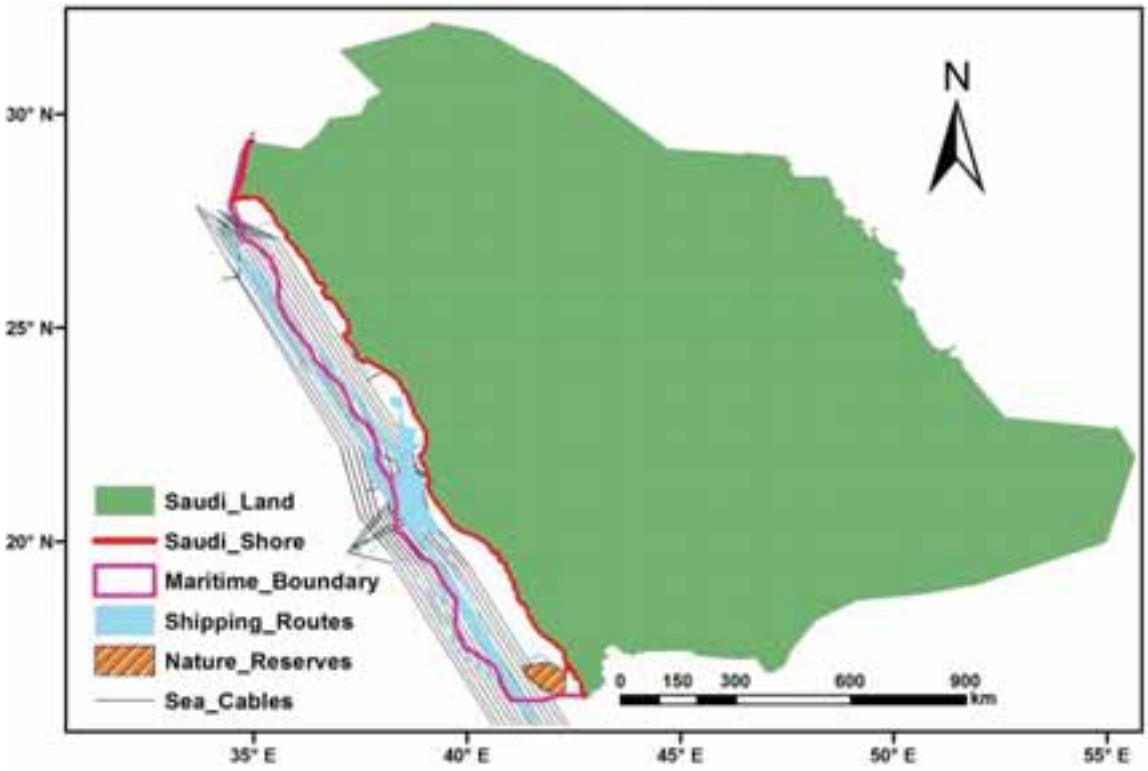

Fig. 5: Raster layer for the all restricted areas around the Red Sea region of KSA.

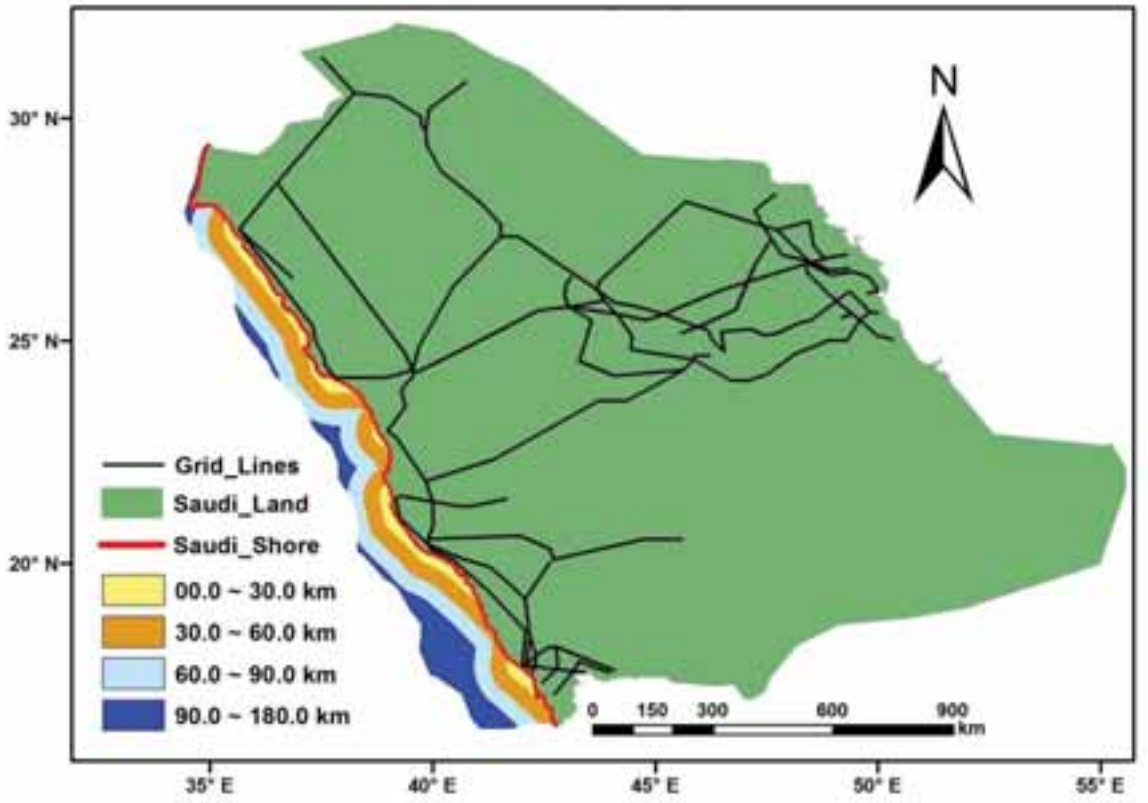

Fig. 6: KSA electricity grid lines for and the distance between cells and the grid near the Red Sea region of KSA.

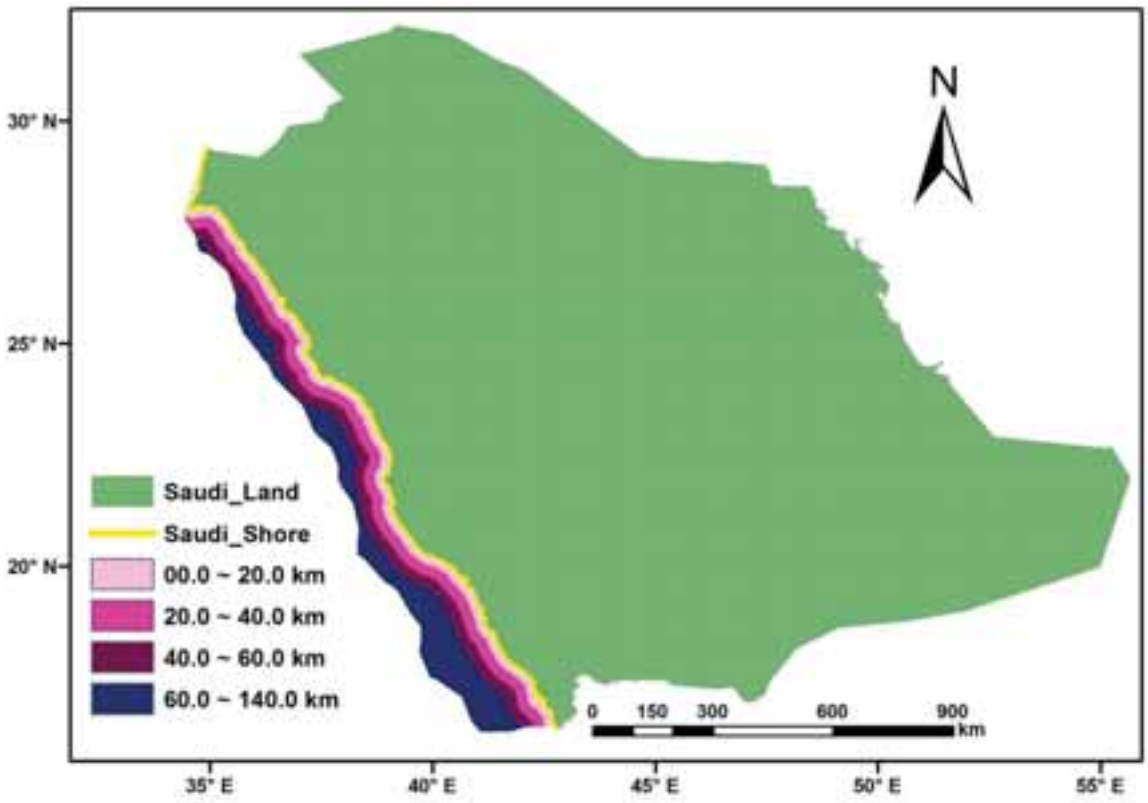

Fig. 7: Layer map of the distance between cells and shoreline around the Red Sea region of KSA.

4. Results, Discussion and Conclusions

The results shown here were based on analysis undertaken for the wind energy potential for the offshore Red Sea region of KSA. The analysis is based on a the development of a Geographical Information System (GIS) encompassing Boolean Mask technique through which a model was developed to create a map for offshore wind farm locations in the Red Sea, KSA. The developed model to solve the spatial sitting for offshore wind farms is efficient and was successful to deal with the conflicting constraints.

Using the UK's London Array wind farm which has an area of 122 km^2 (The Crown Estate, 2012) as a minimum required area (threshold) for offshore wind farms, the analysis was set to identify different locations as possible areas for offshore wind farms in KSA. Ten different locations which conform to the London array threshold were identified using the Boolean Mask map as shown in Fig.8.As can be seen from the figure, the largest locations can be found in the middle part of the coastline stretch, which is due to the main two constraints (wind speed and water depth), which are centred in two different directions of the map, see Fig.3, 4, and also the results in Fig.9.

To estimate the offshore wind power potential for the identified sites, we use the analysis to estimate the array spacing between offshore wind turbines developed by (Sheridan, Baker, Pearre, Firestone, & Kempton, 2012) given by Equation 3 below.

$$S = R_d^2 \times L_d \times L_c \qquad \text{(eq. 3)}$$

Where:

S is the array spacing between offshore wind turbines

R_d is rotor diameter

L_d is the downwind spacing factor

L_c is the crosswind spacing factor

Furthermore, and according to E.ON data (E.ON, 2012), to reduce turbulence interaction between turbines, the ideal turbine spacing is 5 to 8 times rotor diameter. In our analysis we confine the turbine capacities to a 5 MW and 3.6MW turbines to estimate offshore wind power for the identified sites. The 5 MW turbine has a 126m rotor diameter and the characteristics of the turbine were adapted from (Jonkman, Butterfield, Musial, & Scott, 2009). The 3.6 MW turbine has a 107m rotor diameter and the characteristics of the turbine were adapted from (Ajayi, Fagbenle, & Katende, 2011).

Table 2 shows the area for each possible location for offshore wind farm. The two dimensions a, and b are length and width of the rectangular of the locations measured in ArcGIS. The power in GW represent the full power captured by the turbines and was calculated for both 5MW, and 3.6MW using Equation 3. While the last two columns of the table show the estimated actual power assuming a capacity factor, C_f, of equal 0.4 and 0.5. The Capacity Factor which also known as the Load Factor ranges from 0.32 to 0.43 for 80m – 107m rotor diameter, and from 0.40 to 0.50 for turbines with rotor diameter more than 120m (Estate, 2017).

Table 2: Estimate offshore wind power for the chosen sites, where a, and b are the length and width of the rectangles of the location shown in Fig.9.

Location, see Fig. 10	a [km]	b [km]	Area [km^2]	Power (GW)		Estimated Power for	
						$C_f = 0.40$	$C_f = 0.50$
				3.6MW turbine	5.0MW turbine	3.6MW turbine	5.0MW turbine
Location 1	11.8	27.8	328.0	1.7	2.6	0.7	1.3
Location 2	7.2	33.0	237.6	1.2	1.9	0.5	0.9
Location 3	7.2	24.6	177.1	0.9	1.4	0.4	0.7
Location 4	9.2	18.5	170.2	0.9	1.3	0.4	0.7
Location 5	5.3	26.9	142.6	0.7	1.1	0.3	0.6
Location 6	14.3	24.1	334.6	1.8	2.7	0.7	1.4
Location 7	11.8	33.2	391.8	2.0	3.1	0.8	1.5
Location 8	18.6	47.6	885.4	4.6	7.0	1.8	3.5
Location 9	7.3	38.0	277.4	1.4	2.2	0.6	1.1
Location 10	7.7	21.8	167.9	0.9	1.3	0.3	0.7
Total			3122.5	16.1	24.6	6.4	12.3

As can be seen form Table 2, the total estimated wind power for the identified sites is around 6.4 GW and 12.3 GW for the 3.6MW and 5MW turbines, respectively. These results confirm that offshore wind energy conversion can play a major role in the short and long term plan for the renewable energy expansion in KSA. For instant, utilising the 5MW turbine route would more than satisfy the 9.5 GW target stipulated in the KSA Vision 2030. Hence this work can be used to plan for offshore wind expansion in KSA and provide a knowledge platform for stakeholders interested in wind energy deployment.

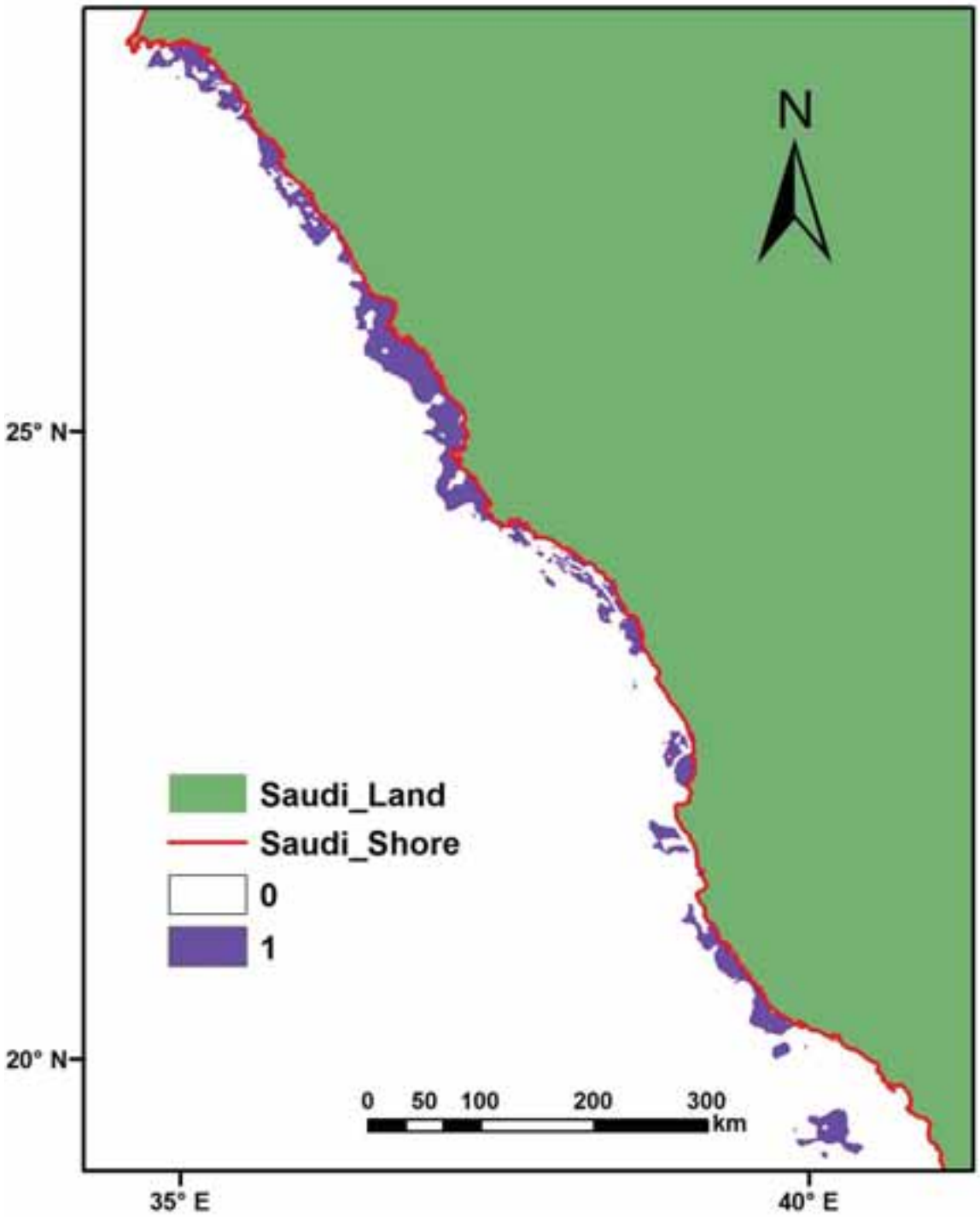

Fig. 8: Final Boolean Mask for offshore wind areas around the Red Sea, KSA.

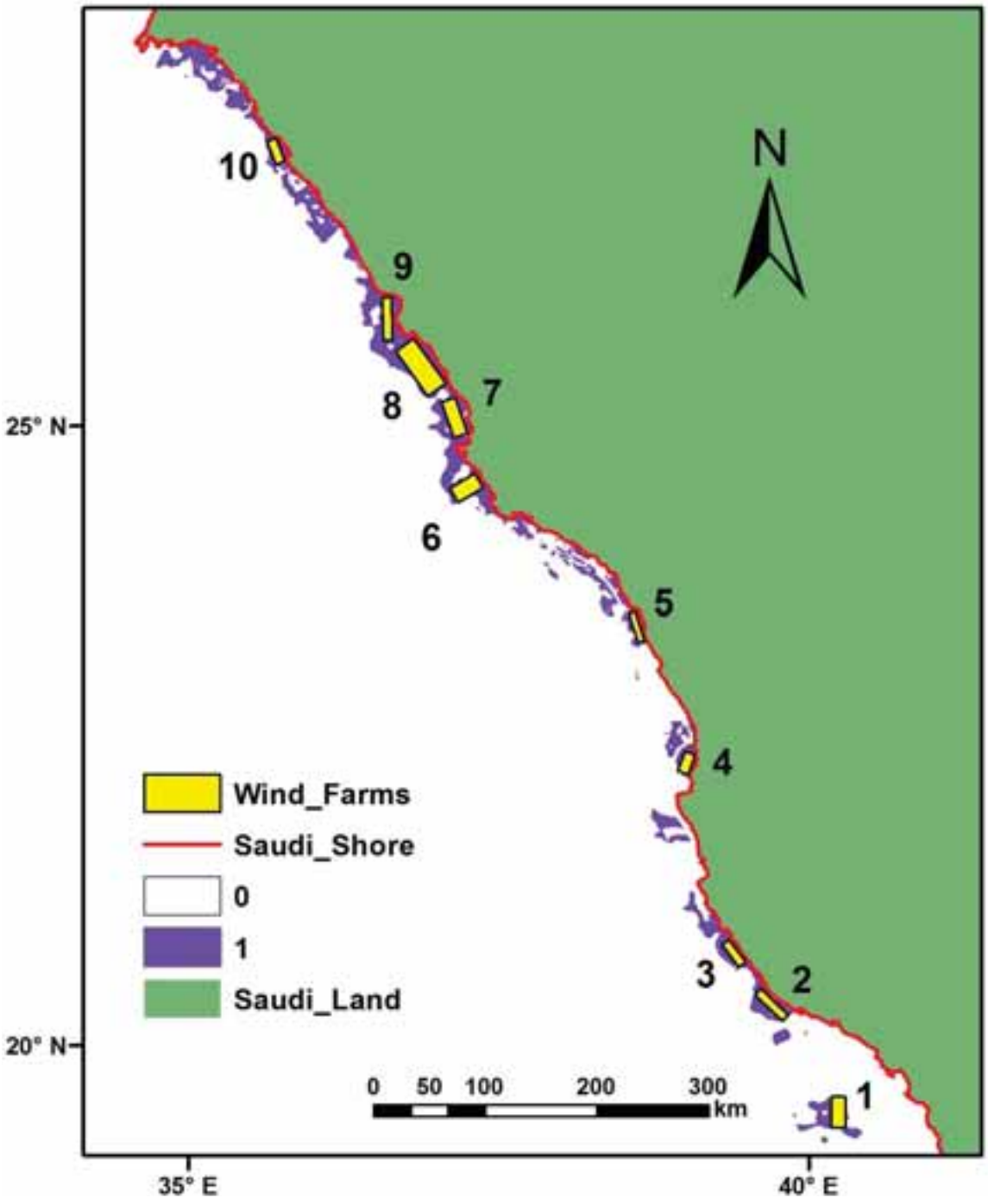

Fig. 9: Locations of the proposed offshore wind farms around the Red Sea region of KSA.

5. Acknowledgment

This work within the activities of the Energy and Climate Change Division and the Sustainable Energy Research Group at the University of Southampton (www.energy.soton.ac.uk) and that of King Salman bin Abdulaziz Chair for Energy Research at King Abdulaziz University (KAU), KSA. The research is part of a PhD programme sponsored by the Faculty of Engineering, Port Said University, Egypt.

6. References

Ajayi, O., Fagbenle, O. R., & Katende, J., 2011. Wind profile characteristics and econometrics analysis of wind power generation of a site in Sokoto State, Nigeria. Energy science and technology, 1(2), 54-66.
Aramco. (2017). Petrol oil extraction map, KSA. Retrieved from http://www.saudiaramco.com/en/home.html
Archer, C. L., & Jacobson, M. Z., 2005. Evaluation of global wind power. Journal of Geophysical Research: Atmospheres, 110(D12).
Bahakeem, A. S., 2015. A Hybrid Renewable Energy Model For Medina City of Saudi Arabia Using Integer Linear Programming. Journal of Electrical and Electronics Engineering (IOSR-JEEE), 9,(5).
CB, S. V., 2017. CfD allocation round two. Retrieved from https://home.kpmg.com/content/dam/kpmg/uk/pdf/2017/09/cfd-allocation-round-two-energy-update.pdf
E.ON., 2012. Offshore Wind Energy Factbook. E. ON Climate & Renewables GmbH.
Eastman, J. R., Jiang, H., & Toledano, J., 1998. Multi-criteria and multi-objective decision making for land allocation using GIS Multicriteria analysis for land-use management (pp. 227-251): Springer.
esri., 2012. The ArcGIS Help Library. Retrieved from http://help.arcgis.com/en/arcgisdesktop/10.0/help/
Estate, T. C., 2017. Offshore wind operational report January – December 2016. Retrieved from https://www.thecrownestate.co.uk/media/1050888/operationalwindreport2017_final.pdf
Estoque, C., 2011. GIS-based multi-criteria decision analysis,(in natural resource management). Ronald, D1– Division of spatial information science, University of tsukuba.
Gazette, S., 2016. Full Text of Saudi Arabia's Vision 2030. Saudi Gazette, 26.
GENI., 2017. National Electricity Transmission Grid of Saudi-Arabia. Retrieved from http://www.geni.org/globalenergy/library/national_energy_grid/saudi-arabia/index.shtml
Jiang, H., & Eastman, J. R., 2000. Application of fuzzy measures in multi-criteria evaluation in GIS. International Journal of Geographical Information Science, 14(2), 173-184.
Jonkman, J., Butterfield, S., Musial, W., & Scott, G. (2009). Definition of a 5-MW reference wind turbine for offshore system development. National Renewable Energy Laboratory, Golden, CO, Technical Report No. NREL/TP-500-38060.
Kieffer, G., & Couture, T., 2015. Renewable energy target setting. IRENA, Masdar.
Knopper, L. D., & Ollson, C. A., 2011. Health effects and wind turbines: A review of the literature. Environmental Health, 10(1), 78.
Mortensen, N. G., Said, U. S., & Badger, J., 2006. Wind Atlas of Egypt: RISO National Laboratory, New and Renewable Energy Authority, Egyptian Meteorological Authority.
Rehman, S., 2005. Offshore wind power assessment on the east coast of Saudi Arabia. Wind Engineering, 29(5), 409-419.
RSNF., 2017. Marine military restricted areas for the Royal Saudi Navy Forces Retrieved from https://www.rsnf.gov.sa/RoyalNavy/Pages/home.aspx
Sheridan, B., Baker, S. D., Pearre, N. S., Firestone, J., & Kempton, W., 2012. Calculating the offshore wind power resource: Robust assessment methods applied to the US Atlantic Coast. Renewable Energy, 43, 224-233.
SWA., 2017. Protected areas map. Retrieved from https://www.swa.gov.sa/en/protected-areas/protected-areas-map
TeleGeography Company., 2015. Submarine Cable Map. Retrieved from http://www.submarinecablemap.com/
The British Oceanographic Data Centre., 2014. The GEBCO_2014 Grid Retrieved from www.gebco.net
The Crown Estate., 2012. Round 3 Offshore Wind Site Selection at National and Project Levels. Retrieved from
The MarineTraffic., 2015. Ship Density Maps. Retrieved from https://www.marinetraffic.com/

A

B

C

D

E

F

G

H

I

J

K

L

M

N

O

P

Q

R

S

T

U

V

W

Y

Z

Contact details

Email swc@ises.org
shc2017@iea-shc.org
swc2017@pse.de

Conference of

ISES International Solar Energy Society

SHC SOLAR HEATING & COOLING PROGRAMME INTERNATIONAL ENERGY AGENCY

Hosted by

Masdar INSTITUTE
A Part of Khalifa University of Science and Technology

Online management

projects in solar energy

PSE